JOURNAL
OF THE
PHYSICAL SOCIETY
OF JAPAN

Volume 14
1959

Published by the
PHYSICAL SOCIETY OF JAPAN

Digitized by the Internet Archive
in 2024

https://archive.org/details/physical-society-of-japan-journal_january-december-1959_14_1-12

JOURNAL OF THE PHYSICAL SOCIETY OF JAPAN Vol. 14, No. 1, JANUARY, 1959

16″ Variable Energy Cyclotron

Hiroo KUMAGAI,* Kazuo ÔNO, Hisao SHÔNO,* Izuo HAYASHI,*
Keiichi KURODA and Minoru IMAIZUMI

Institute for Solid State Physics, University of Tokyo

(Received October 3, 1958)

A variable energy 16″ Cyclotron was constructed to produce 1∼2 Mev deuterons and 2∼4 Mev α-particles by new designs in its magnet and oscillator system.

As far, deuterons in the energy range from 1.3 to 2 Mev and α-particles in the range from 3 to 4 Mev are used for (d, p), (α, p) reactions, coulomb excitations etc.

Although the variation of accelerating energy for a cyclotron is a considerably difficult problem, we found that it is possible, by some adjustments of the acceleration parameters of the cyclotron, to produce deuterons and α-particles over the sufficiently wide range of energy within a minute.

The cyclotron will be used for producing 2∼4 Mev protons by changing a part of the resonator.

§ 1. Introduction

The 16″ cyclotron of the Institute for the Solid State Physics, University of Tokyo, was designed to produce 1∼2 Mev deuterons and 2∼4 Mev α-particles, and to produce 2∼4 Mev protons by changing a part of the resonator.

The construction was begun in 1953 as a project of the Comittee for Nuclear Research of the Institute of Science and Technology, and the initial testing was done in June 1955. In summer 1956, when the construction of all the beam handling system was finished, analysed deuterons were obtained at the reaction chamber.

Since September 1956, deuterons in the energy range from 1.3 to 2 Mev and α-particles in the range from 3 to 4 Mev have been accelerated and used for (d, p)[1] (α, p) reactions, Coulomb excitations etc. 2∼3 Mev protons were detected with an inner probe, but not yet used for any nuclear research.

The key point of a variable energy cyclotron is in the designs of its magnet and variable frequency oscillator. The magnet of this cyclotron is so constructed that the magnetic field distribution does not change significantly by increasing the magnetic field strength.

The B-constant type of a magnet[2] was adopted to minimize the change of the magnetic field distribution, the cause of the change being believed to be in the local saturations of iron in the core.

The oscillator has a specially designed variable frequency resonator having a branch near the dee, to which a variable capacitor of coaxial type is connected in deuteron operation, and a coaxial tube with an adjustable shorting bar is connected in proton operation in order to change the frequency continuously.

The main part of the cyclotron is shown in Fig. 1.

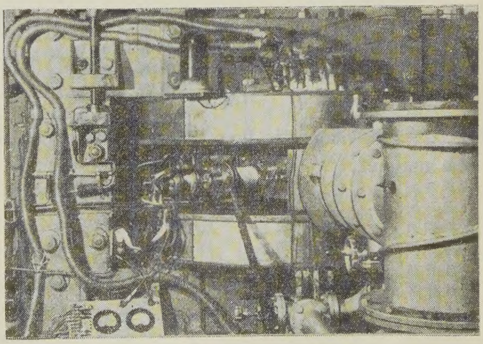

Fig. 1. Main part of the Cyclotron.

§ 2. Components of the Cyclotron

A. *Magnet*

For a variable energy cyclotron, the magnet should be designed to maintain the required field distributions for a wide range of the magnetic field strength. It is believed that the change of field distribution with the exciting current comes from local saturations of

---

* Now at Institute for Nuclear Study, University of Tokyo.

M 55'' 63/20 new

iron in the iron core, especially in the pole pieces. To maintain the constancy of the field distribution, it is desirable to minimize the local saturations. Ideally, if a magnet were so constructed that the density of magnetic flux is constant in all the core, the local saturation should not have any place until the magnetic field strength at the gap reaches to the saturation value of iron.

The magnet of this cyclotron is constructed of 7 tons of iron. The radius of the pole faces are 18.25 cm and the gap distance is 5 cm. Fig. 2 shows that, from the pole to the yoke, the cross section increases from 1 to 2.4 times of that of the pole face and the magnetic flux density is almost constant in all sections. The excitation curve of the magnetic field is shown in Fig. 3.

The radial and azimuthal variations of the magnetic field were measured by means of a coil mounted on an arm pivoted at the center of the magnet. The integrated electromotive force generated by the coil was plotted by a recording fluxmeter[3]. The radial magnetic field distributions at the excitation from 12,180 gauss to 20,050 gauss are shown in Fig. 4. Below 14,000 gauss, the effect of a Rose shim at the edge of the pole pieces becomes too large, then a lower limitation of acceleration energy with the present Rose shim will

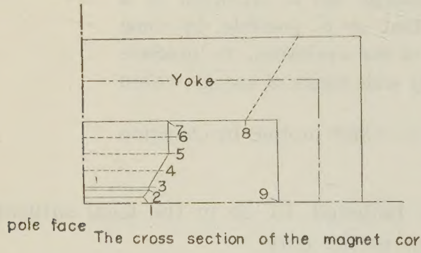

The cross section of the magnet core

(a)

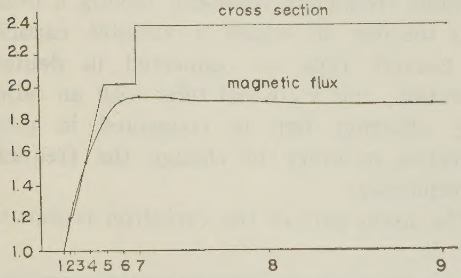

The magnetic flux density in the core of the magnet

(b)

Fig. 2. The magnetic flux density in the core of the magnet.

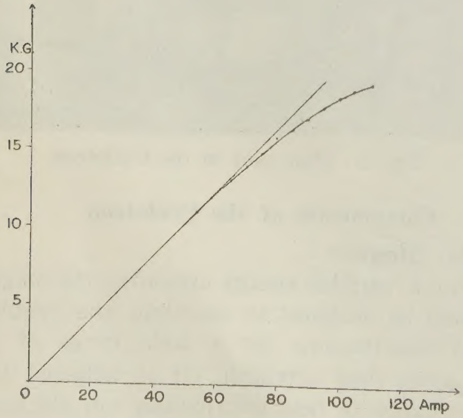

Fig. 3. Excitation curve of the magnet.

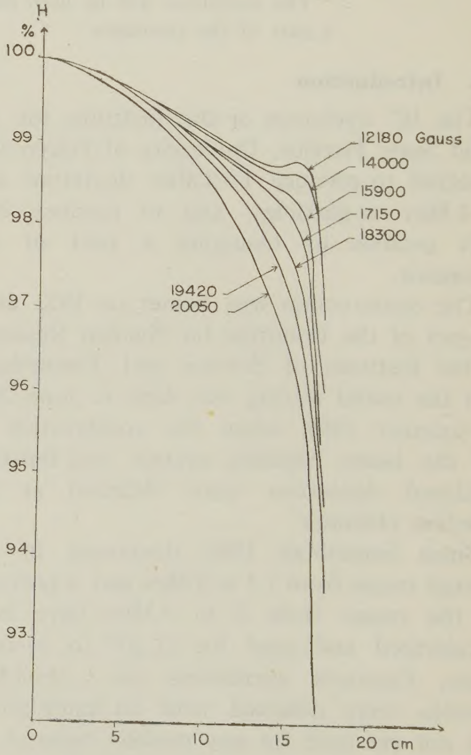

Fig. 4. Radial distributions of the magnetic field.

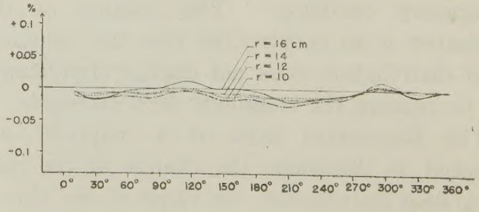

Fig. 5. Azimuthal distributions of the magnetic field.

be set at this point.

The azimuthal variations at the 18,000 gauss excitation are shown in Fig. 5. for some radii. The slight variation comes from the effect of six bolts connecting the pole pieces to the yoke. The amplitude of the variation is less than 0.02%.

The magnet current is controlled by a DC amplifier and an amplidyne generator, which supplies the exciting current of the main motor generator set. The current is stabilized within one part in 1,000.

B. *Oscillator*

This cyclotron has a remarkable design in the frequency variable resonator. The new design of the oscillator must allow for adjustment of the frequency continuously over the range from 10 to 14 Mc for the acceleration of 1～2 Mev deuterons, and from 20 to 28 Mc for 2～4 Mev protons. As illustrated in Fig. 6, this resonator has a branch near the dee, on which either a variable capacitor of coaxial type (See Fig. 7) or a coaxial tube with an adjustable shorting bar is connected according to the kind of accelerated particles.

The main part of the resonator consists of 4″ and 10″ copper tubes and the capacitor consists of five coaxially connected copper tubes, the maximum diameter of which is 8″. The coaxial tube with an adjustable

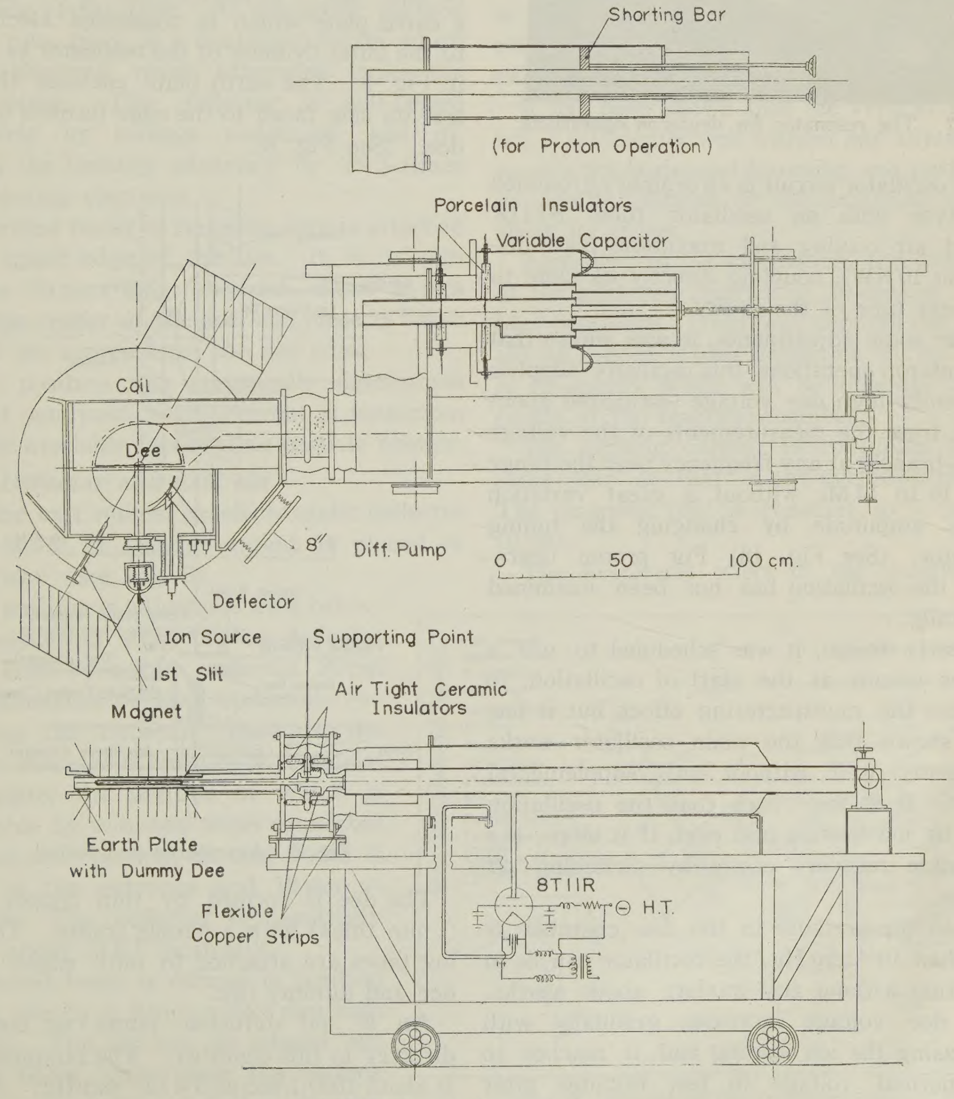

Fig. 6. Oscillator System

shorting bar consists of also 4″ and 10″ copper tubes.

Airtight ceramic insulators are used for supporting dee stem and for placing the main part of the resonator out of vacuum, hence adjustments of frequency and exchanges of resonator are very easily performed. Dee position is freely adjustable by moving the inner tube at the shorting point.

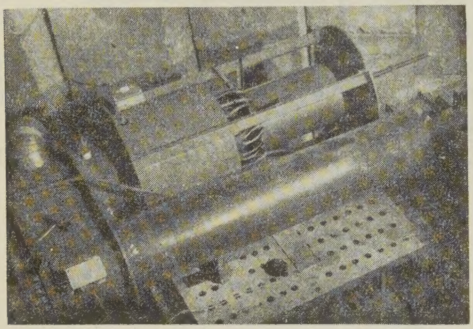

Fig. 7. The resonator for deuteron operations.

The oscillator circuit is an ordinary grounded grid type with an oscillator tube, 8T11R (forced air cooling and maximum plate dissipation 10 KW), coupling directly its plate to the inner tube of the cavity.

After some adjustments, it was shown that for deuteron operations, this oscillator supplies sufficiently high dee voltage (estimated about 20 KV from the measurements of the voltage at the branch) at any frequency over the range from 10 to 14 Mc without a great variation in its amplitude by changing the tuning capacitor. (See Fig. 18) For proton operations, the oscillation has not been examined in details.

In early design, it was scheduled to use a booster circuit at the start of oscillation, to suppress the multipactering effect but it has been shown that the main oscillator works sufficiently well without any supplemental circuit. It is very rare that the oscillation stops by ion loading and even if it stops, the oscillation recovers easily by switching off and on.

When the pressure in the dee chamber is less than 10^{-4} mm Hg, the oscillator can be in operation without any anxiety about sparks. The dee voltage increases gradually with decreasing the ion loading and it reaches to the normal voltage in few minutes after switching on.

Some troubles were encountered, in which a break down of the airtight ceramic insulator by over heating due to $R-F$ loss. A forced air cooling of the airtight ceramic insulators is adopted.

The input power of the oscillator is less than 10 KW at the maximum operation. And the oscillator plate voltage is supplied with a forced air cooled 3 phase selenium rectifiers delivering 10,000 volts at 1 ampere.

C. *Dee chamber and vacuum system*

The dee chamber is made of non magnetic stainless steel of 1.2 cm thick. The pole tips of the magnet take a role of a part of the chamber, and vacuum is held by ring gaskets between the pole pieces and the chamber. A half space of the chamber is occupied by a earth plate which is connected electrically to the outer cylinder of the resonator as shown in Fig. 6. The earth plate encloses the dee and its side faced to the edge forms a dummy dee. (See Fig. 8).

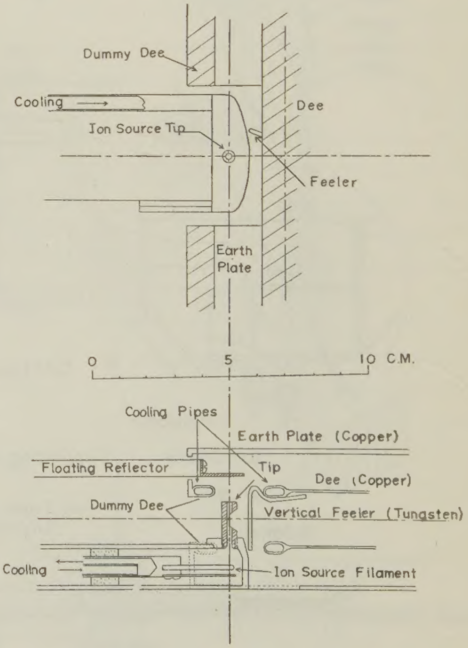

Fig. 8. Ion source and feeler.

The dee is formed by thin copper plates (1 mm thick) with a simple frame. The cooling pipes are attached to only edges of the dee and dummy dee.

An 8″ oil diffusion pump is connected directry to this chamber. The pumping speed is about 1000 l/sec at 5×10^{-6} mmHg. Another diffusion pump of 6″ is also connected at the beam duct as shown in Fig. 9. Because the vacuum system has a sufficiently large capacity in speed, it is possible to start the operation within an hour after switching on of the diffusion pumps, and about 20 minutes after repair of the ion source filament, for this procedure the air is let into the whole chamber.

D. *Ion source and feeler*

As illustrated in Fig. 8, the ion source is a standard type with a d.c. filament (1.5 mm dia. hair pin type)[4].

A conventional low voltage arc discharge takes place in a 5 mm outer dia., 2.2 mm inner dia. and 16 mm long tungsten-copper tube.

Ions are extracted through a 4 mm long cut open side of the tube. At the upper position of the tube there is a floating reflector which reflect electrons which otherwise strike the earth plate. This reflector is self-biased negatively by leakage resistance, and increases the ionising efficiency by 2∼3 times by reflecting electrons.

A vertical feeler of tungsten wire is attached to the upper edge of the dee. It is 1.5 mm dia. by 20 mm long, deviates about 10 mm from the center of the dee, and projects 5 mm toward ion source from the dee edge.

This position was empirically determined so that analysed beam current is maximum over the available accelerating particle energy.

E. *Deflector and exit slit*

At the exit radius, an electrostatic deflector which is 70° in angular extent is placed in clockwise. (See Fig. 5).

The position is adjustable by a below. The supporting stem of the deflector is insulated by a 7 cm outer dia. 20 cm long cylindrical ceramic insulator.

Facing the deflector, there is the septum made of 0.3 mm thick molybdenum plate, the position of which is adjustable by two steel wires connected with belows. Normal channel width is 3 mm at the entrance and 12 mm at the exit. The deflector is negatively biased about 30 KV normally.

Deflected beam is defined in position and in size by a 2 mm wide 3 mm high exit slit. The slit can be placed out of the beam path when the isotope productions or the radiation damage experiments are performed.

§ 3. Beam handling System

A. *Beam analyser*

The extracted beam from a cyclotron has, in general, an energy width of few percent. This width is too large to use the beam for nuclear research, and an energy selecting system should be added as a part of cyclotron.

The geometrical arrangement of the system is shown in Fig. 9. The analysing magnet is a double focussing type[5].

The particles extracted through the exit slit are deflected 45° by the analysing magnet placed at a distance of 1.5 m from the exit slit, and focussed at the center of the reaction chamber through a 5 mmϕ second slit which is placed at the entrance of the reaction chamber, at a distance of about 3 m from the exit of the analysing magnet.

It has been shown that the vertical focussing is sufficiently well without any adjustment, so only the horizontal focussing was performed by small rotations of the analysing magnet about its center.

According to the calculation, the dispersion of the analysing magnet is 20 kev/cm. for 2 Mev deuterons. Therefore through the second slit of 5 mmϕ, 2 Mev deuterons having 10 kev in its energy width will be obtained at the center of the reaction chamber.

The exciting current is controlled by the same way as that of the cyclotron magnet. The magnetic field is constant to 1 part in 10,000.

The hysteresis effect of the magnet was

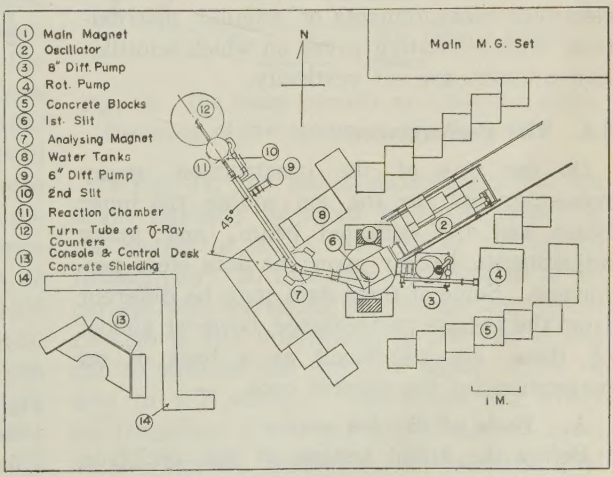

Fig. 9. Layout of the cyclotron room.

200 gauss when it was excited from 0 to 9,000 gauss, and decreased to 7,500 gauss, the normal field for 2 Mev deuterons. It corresponds to about 100 kev in energy. When the exciting currents are used for the estimation of the beam energy it must be cared about the hysteresis effect.

B. *Reaction chamber*

The reaction chamber was designed as simple and functional as possible.

The inner dia. of the chamber is 41 cm and it enables to contain a nuclear camera for measuring angular distribution with nuclear plates.

The windows at 0° and 90° are used to set scintillation counters which can be used for excitation measurements, or one of which as a monitor. When γ-rays are measured, the chamber has a role as only a part of the beam duct. (See Fig. 10) Slit system is attached at the entrance window, and can be changed its dia. from 20 mm to 3 mm.

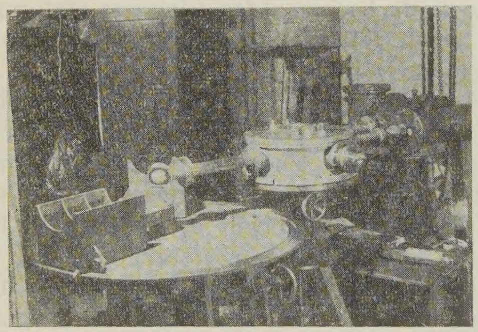

Fig. 10. The reaction chamber and the apparatus for measuring angular distribution of γ-rays.

The reaction chamber can be also used for electronic measurements of angular distributions with a rotating cover on which scintillation counters are set vertically.

§ 4. The Performance

On the way of the construction, many measurements for the ion source, the inner beam and the deflected beam, and many adjustments basing upon the data were performed. Some of these data may be different from the present performance, however almost of them are significant as a base of an estimation for the present ones.

A. *Tests of the ion source*

Before the initial testing of the cyclotron as a whole, the characteristics of the ion source have been measured.

At first, the most effective condition of discharge for deuteron is determined. The normal condition is at the arc voltage of 50∼100 volt and the gas flow of 0.7 cc/min. The ratios of the compositions D_1^+, D_2^+, and D_3^+ were roughly 50:40:10.

It was found that for obtaining high efficiency for D_1^+, it is desirable to decrease the filament current as far as discharge is maintained.

For α-particles, the normal condition is determined so as to adjust the arc voltage higher than 200 V, and the gas flow of 1.8 cc/min.

Both a horizontal feeler and a vertical one were tested to compare the extraction efficiency, and the vertical feeler was adopted because of its rather higher efficiency.

In the case of D_2 ions in excess of 50 mA are extracted from the ion source, at the normal condition.

The beam intensity depends remarkably on the shape of the tip of the ion source, especially on its inner diameter, and the shape was empirically determined as mentioned in § 3. D. (See Fig. 8)

B. *Measurements of the inner beam*

Since the initial testing in June 1955, many

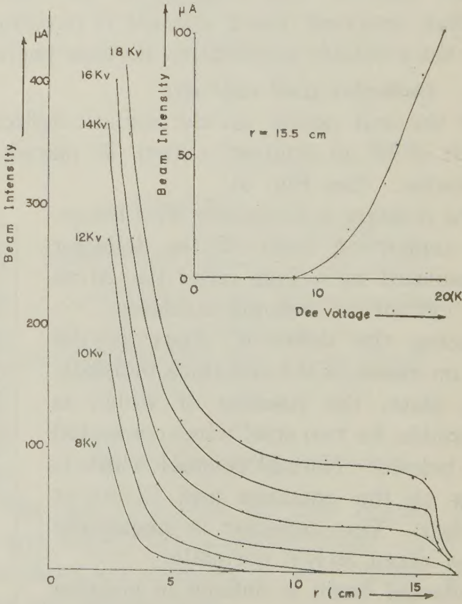

Fig. 11. Radial intensity distributions of inner beam for different dee voltages. The magnetic field is so adjusted that the intensity is maximum at r=15.5 cm.

adjustments had been performed, and after a month, the intensity of the inner beam increased up to 150μA of deuterons at the exit radius. To obtain the informations for the accelerating performance of the cyclotron, the measurements for the inner beam were performed from the various standpoints.

Using an inner probe, the radial distributions of the beam intensity were measured for the different dee voltages, where the magnetic field was so adjusted that the intensity is maximum at $r=15.5$ cm (See Fig. 11).

The beam intensity at the exit radius increases with increasing the dee voltage, and the dee voltage higher than 10 kV is necessary for ions to reach to the exit.

Out of the radius of about 10 cm, all the curves are almost constant showing that the magnetic focussing is sufficiently well. We observed also the radial distributions of the beam height using a piece of tungsten meshes, and found that the height is about 5 mm and almost constant out of the radius of 5 cm. It indicates that magnetic focussing effect is also sufficient out of the radius of 5 cm. The effectiveness of magnetic focussing action at the small radius is attributed to the constant magnetic field gradient (0.1 percent per centimeter) from the centre along the radius. Thus, it may be considered that the smooth decrease of intensity in the region from $r=$ 5 cm to 10 cm is due to the phase shifts with respect to the electric voltage[6)7)].

According to the calculation of Cohen[8)], the smooth decrease of intensity as mentioned above should not be observed under such a sufficient magnetic focusing action, because of the sharp bunching during initial few accelerations. However, in our cyclotron, the conditions for the initial few accelerations may be different with that of Cohen's calculation. That is; on account of relatively small geometry with respect to the dee voltage (dee gap, 2 cm, dee height, 1.6 cm, distance between ion source and Dee, about 1 cm, distance between ion source and feeler, about 1 cm as shown in Fig. 8, and dee voltage about 20 kV for 18,000 gauss) and of the effect of vertical feeler which forms weak field region between dee and itself along the ion path, ions get rather early into the field free region at the initial half rotation as illustrated in Fig. 12 and a sharp bunching may not occur. As will be seen by the following measurements, it is more plausible in our case to assume that ions have rather broad bunching in the initial few accelerations than to assume a sharp bunching.

Measuring the beam intensity as a function of the frequency of dee voltage, one can obtain the resonance curves of the cyclotron acceleration, where the magnetic field strength is constant. Fig. 13 shows the curves measured at $r=11,15$ and 16 cm. The difference of the frequencies of the peaks is due to the magnetic field decreasing toward the outside. It should be noted that the curve have asymmetric forms.

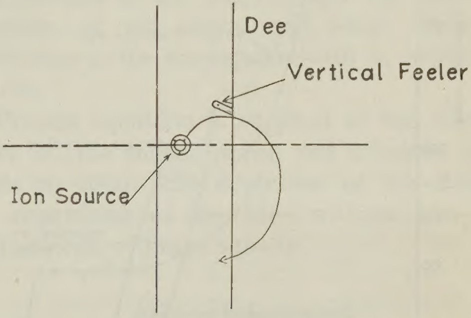

Fig. 12. Path of ion which is accelerated by the peak R.F. voltage, 20 kV. at $H=18,00^\circ$ gauss.

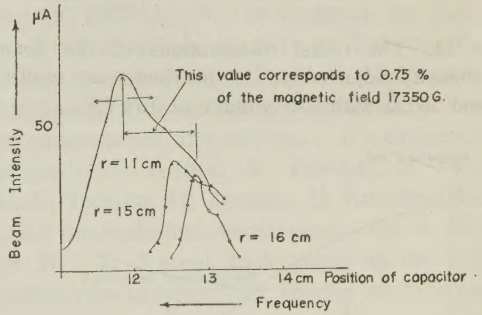

Fig. 13. The beam intensity as a function of the frequency of dee voltage at different radii.

In Fig. 14, the radial distributions of the beam intensity adjusted to be maximum at the radius of 8, 11, and 16 cm are shown respectively. In this case the decrease of ion current with increasing the radius from about $r=5$ cm is also interpreted by the loss of ions due to positive and negative phase shifts of ions to R-F voltage. The radius R_{res} where the frequency of the particle rotation is equal to the applied frequency, can be determiend as the radius where the curve becomes flat, because the loss due to the positive phase shifts ceases at the radius.

From Fig. 14, it can be seen that the radii, R_{res}, for curves I and II are those at $r \doteqdot 12$ cm and $r \doteqdot 7.5$ cm. The difference between the applied magnetic fields at $r \doteqdot 12$ cm and 7.5 cm is 0.75% as shown in Fig. 15 and this is consistent with the frequency difference between the peaks of resonance curves for $r=11$ cm and $r=16$ cm in Fig. 13.

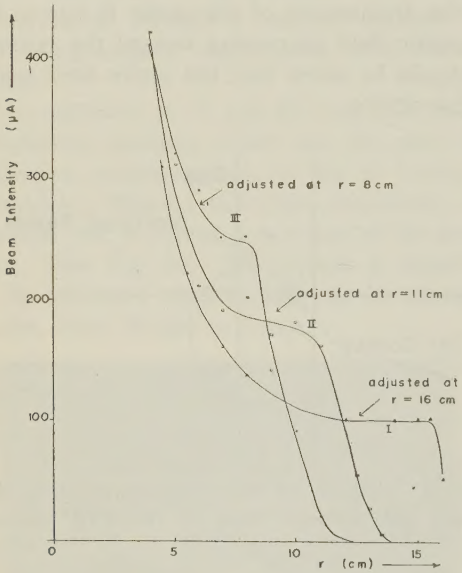

Fig. 14. The radial distributions of the beam intensity adjusted to be maximum at $r=8,11$ and 16 cm with R-F voltage of 15 kV.

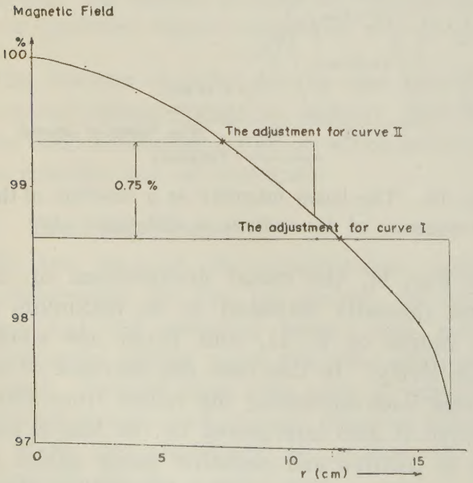

Fig. 15. The radial distribution of the applied magnetic field. The cross points represent the magnetic fields at the resonant radii: $R_{res}=7.5$ cm and $R_{res}=12$ cm.

Using Fig. 15, both the maximum phase shifts (positive and negative) are roughly estimated as about 80° for favorable ions for the adjustment at $r=16$ cm and at the dee voltage of 15 kV.

The curves II and III in Fig. 14 have considerably long tails. This shows that ions have not any sharp bunching actually.

We measured also the dependence of the beam intensity on vacuum. For H_2^+ molecular ions, the intensity decreases significantly with increasing the pressure, because of the dissociations of the molecules by the residual gases as shown in Fig. 16.

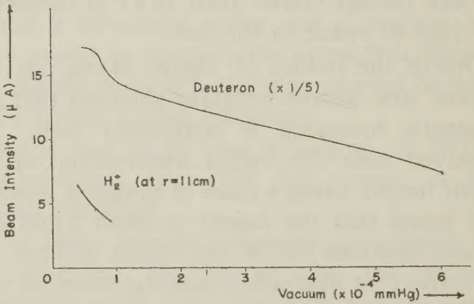

Fig. 16. The dependence of the beam intensity on vacuum.

C. *Performance of the deflector and the analysing system*

The ions extracted by the deflector amount to 30~50μA and its horizontal width is about 2 cm at the position of first slit.

Through the first slit, the beam of few μA is obtained at the entrance of the analysing magnet and its horizontal width is about 6 cm.

At the first setting, only the one-third of the entrance aperture of the analysing magnet allowed to pass the ions.

Moving the analysing magnet toward inside of the deflection, it has become possible that the ions can reach to the second slit passing through the almost whole aperture.

Deuteron beam obtained at the center of the reaction chamber is about 0.3μA, when the 5 mmφ slit is set at the entrance.

For determining the absolute energies corresponding to the current of the analysing magnet, a resonance of F^{19} $(p\,p'\gamma)$ at $E_p=$ 935 kev (resonance width 8 kev) was observed using H_2^+ ions.

The result is shown in Fig. 17 where a thin LiF target of few kev thick was used and the slit was 4 mm wide.

From the half width of the resonance peak, it can be estimated that the energy width of the beam is less than 14 kev for 935 kev protons.

This value is slightly large with compared to the calculation, and the small deviation is believed in the aberration of the analysing magnet.

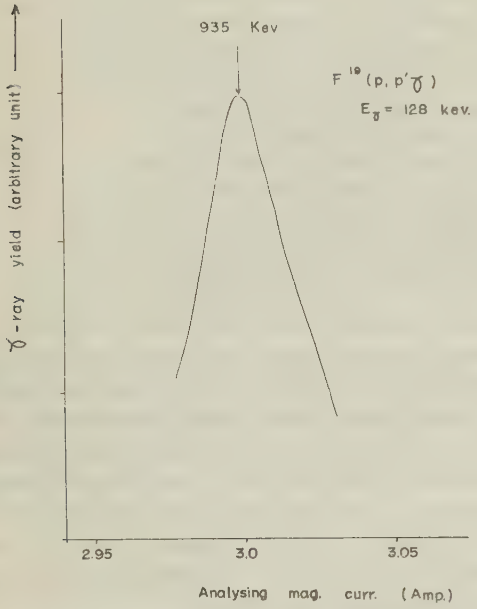

Fig. 17. Absolute measurement of the beam energy.

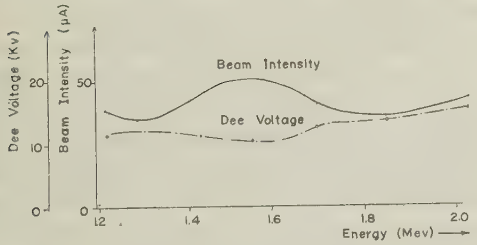

Fig. 18. Variation of the dee voltage and the beam intensity with the beam energy.

D. *Variation of energy*

At the early measurements, it has been shown that the inner beam intensity does not change significantly with variations of the beam energy, as shown in Fig. 18, and that the intensity of analysed beam does change since, for extracting the particles in good direction toward the analysing magnet, the path of the acceleration in cyclotron should be concerned.

For example, when the cyclotron is only adjusted at the higher energy so as to obtain a maximum intensity at the reaction chamber, the beam intensity of lower energy (1.3~1.4 Mev) decreases by one tenth of that of the higher.

Since the magnetic field distribution is not strictly constant, it is impossible to maintain the accelerating path always constant even if the Dee voltage is adjusted to be proportional to the acceleration energy.

It seems to us that the dee voltage higher than that proportional to E favours the acceleration at lower energy.

Readjustments of the direction of deflector, the position of ion source, and the relative position of ion source and feeler, become necessary as the accelerating path in cyclotron varies.

Present condition is adjusted at the higher part of the energy region and it makes possible to obtain the deuterons of 1.5~2 Mev or α-particles of 3~4 Mev without any readjustment within a minute.

Acknowledgements

The construction of the cyclotron was initially started as a project of the Comittee for Nuclear Research in the Institute for Science and Technology, University of Tokyo, whose leading members were Prof. T. Mutô and K. Murakawa. We are deeply grateful to their encouragements and advices. We express our thanks to H. Yoshiki, R. Yamada, S. Takeuchi, S. Tanaka, O. Tanaka, H. Kamitsubo and A. Itô for technical assistances. Dr. S. Suwa and Dr. T. Kamei took parts in the initial construction to whom our thanks are sincerely expressed.

References

1) K. Ôno et al: J. Phys. Soc. Japan **14** (1959) No. 2.
2) H. Kumagai: Reports of Inst. Sci. & Tech. Uni. of Tokyo. **6** (1952) 63.
3) H. Yoshiki and H. Kumagai: Reports of Inst. Sci. & Tech. Univ. of Tokyo. **8** (1954) 243.
4) R. S. Livingston and R. J. Jones: R.S.I. **25** (1954) 552.
5) W. G. Cross: Rev. Sci. Inst. **22** (1951) 717.
6) M. E. Rose: Phys. Rev. **53** (1938) 715.
7) M. S. Livingston: J. Appl. Phys. **15** (1944) 2.
8) B. L. Cohen: Rev. Sci. Inst. **24** (1953) 589.

JOURNAL OF THE PHYSICAL SOCIETY OF JAPAN Vol. 14, No. 1, JANUARY, 1959

Note on the Cluster Expansion Theory of Classical Fluids. Watermelon Approximation

By Ryuzo ABE

Department of Physics, Tokyo Institute of Technology, Oh-okayama, Meguro, Tokyo

(Received August 25, 1958)

The irreducible clusters appearing in the cluster expansion theory of fluids are classified according to the number of the branch points, to which three or more bonds are connected. All the terms arising from the irreducible clusters with two and only two branch points are summed up and the contribution of these terms to the free energy is obtained exactly in a simple closed form. This enables us to improve the results of calculation of the thermodynamic functions based on Montroll and Mayer's method, in which only clusters without branch point are taken into consideration. This kind of summation procedure seems to be necessary to avoid the divergence difficulty in the case of Coulomb interaction between particles in quantum mechanical systems as well as in classical systems.

§ 1. Introduction

Several attempts have been presented to deal with large clusters in the cluster expansion of the formulae for the free energy and the radial distribution function of dense gas and liquids. Montroll and Mayer[1] have proposed the ring approximation in which only the ring type of irreducible clusters is taken into account. Rushbrooke and Scoins[2] presented the netted chain approximation for the radial distribution function and Hiroike[3] applied it to the evaluation of the free energy. The nature of these approximations seems to be somewhat obscure, though the ring approximation is derived from an alternative view-point[4] which is physically more intuitive. Moreover summation procedure over infinite terms seems to be necessary to avoid divergence difficulty in a certain kind of problems of physical interest. For instance, for a system of particles with Coulomb forces, the usual cluster integrals are known to diverge to infinity owing to the long-range character of the interaction, except when the infinite terms of the clusters of ring type are all summed up. The situation is similar also in the case of quantum theory[5].

On the other hand, the calculation of the free energy without recourse to the cluster expansion has been discussed by different authors[6] with the aid of the collective coordinate description. In particular, Yukhnovsky[7] has investigated the special type of interactions between elementary excitations and obtained the expressions which can be applied to the system with weak interaction. Although this method provides a systematic way of calculating the free energy, the application to the singular potential such as the hard-sphere one is impossible since the existence of the Fourier component of potential is required in this method.

The purpose of this paper is to obtain an expression applicable to the singular potential and analogous to Yukhnovsky's one, from the standpoint of cluster expansion theory. In § 2 the irreducible cluster integrals are classified according to the number of junctions, where junctions are defined to be the points to which three or more bonds are connected. The summation over 0-junction clusters (simple rings) has been performed by Montroll and Mayer. It will be shown that the contributions of 2-junction clusters can be summed up into a closed form by means of the theory of Fourier transforms. The 2-junction cluster has the form of watermelon and therefore our approximation will be called *watermelon approximation*. In § 3 some discussions concerning the correlation energy of an electron gas will be given.

§ 2. Watermelon Approximation

Let us consider a uniform fluid of N identical particles in the volume V and at the temperature T. The potential energy is assumed to be the sum of potentials $\phi(r)$ due to pairs of particles.

The Helmholtz free energy A of the system is expanded in the virial series as[8)]

$$\frac{A}{NkT}=\ln\left(\frac{h^2}{2\pi mkT}\right)^{3/2}\frac{\rho}{e}-\sum_{n=1}^{\infty}\frac{1}{n+1}\beta_n\rho^n \qquad (1)$$

where $\rho=N/V$ is the number density and β_n is the irreducible integral defined by

$$\beta_n=\frac{1}{n!\,V}\iint\cdots\times\int dx_1dx_2\cdots dx_{n+1}\sum_{\substack{n+1\geq i>j\geq 1\\ \text{All products which are more}\\ \text{than singly connected.}}}\prod f_{ij}\,. \qquad (2)$$

Here f_{ij} is given by

$$f_{ij}=\exp\left[-\phi(r_{ij})/kT\right]-1\,. \qquad (3)$$

It is convenient here to express each term in the sum of integrand of (2) by a graph consisting of the numbered points, $1, 2, \cdots, n+1$, and of bonds connecting points i and j, representing the factor f_{ij} in the summand. Then the graphs drawn in this way will have the junctions, the points to which three or more bonds are connected. For example, in Fig. 1 the points 3, 4 and 6 are junctions.

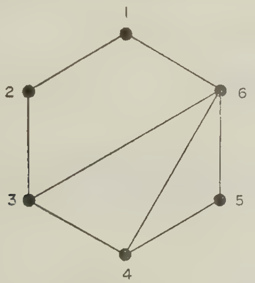

Fig. 1.

Then it is obvious that the various graphs contributing to β_n can be classified according to the number of junctions and β_n may be written as

$$\beta_n=\beta_n^{(0)}+\beta_n^{(2)}+\cdots+\beta_n^{(n+1)}\,, \qquad (4)$$

where $\beta_n^{(0)}$ means the contribution of 0-junction clusters, $\beta_n^{(2)}$ that of 2-junction clusters, etc., (the 1-junction cluster does not appear in the irreducible integral). If one retains only the first term in Eq. (4), one is led to Montroll and Mayer's approximation, i.e., the ring approximation corresponds to 0-junction approximation. If one further takes $\beta_n^{(2)}$, one is led to 2-junction approximation. This 2-junction cluster has the form represented in Fig. 2 which resembles the shape of a watermelon, and therefore we will call 2-junction approximation-watermelon approximation. It will be shown below that the cluster expansion for the free energy, Eq. (1), can be written in a closed form even if we consider 2-junction clusters besides 0-junction clusters.

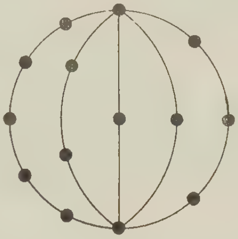

Fig. 2.

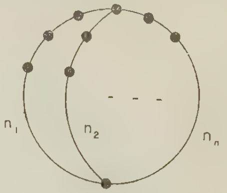

Fig. 3.

Let us consider $\beta_n^{(2)}$ for a given n ($\geqslant 3$) and assume that there are m lines between two junctions. We assume further that $n_1, n_2, \cdots, n_m$ particles lie on these lines respectively (see Fig. 3). Since only one of n_i's can be zero, the largest number of m is n, corresponding to the case where there are $n-1$ lines with only one particle and one line without particle. Furthermore it is evident that $m\geqslant 3$, since the case $m=2$ is not allowed for the 2-junction clusters. Therefore we have a relation

$$n\geqslant m\geqslant 3. \qquad (5)$$

We observe here the integral characterized by the set of numbers $(n_1, n_2, \cdots, n_m)$:

$$I(n_1, n_2, \cdots, n_m)=\frac{1}{V}\int^{(n_i)}\prod f_{ij}\,dx_1dx_2\cdots dx_{n+1}\,, \qquad (6)$$

where $\overset{(n_i)}{\prod} f_{ij}$ represents the product of f_{ij}'s corresponding to Fig. 3. In order to calculate this, it is convenient to introduce the Fourier transform of f_{ij} defined by

$$f_{ij}=\frac{1}{V}\sum_{k}F(k)e^{ik\cdot(x_i-x_j)}\,. \qquad (7)$$

If we substitute this into Eq. (6) (we set the coordinates of junctions to be x_1 and x_2) and integrate over the coordinates of particles on the connecting lines, we have

$$I=\frac{1}{V^{m+1}}\sum_{k_1,\cdots,k_m}\int F^{n_1+1}(k_1)e^{ik_1\cdot(x_1-x_2)}F^{n_2+1}(k_2)e^{ik_2\cdot(x_1-x_2)}\cdots\times F^{n_m+1}(k_m)e^{ik_m\cdot(x_1-x_2)}\,dx_1dx_2\,. \qquad (8)$$

If we further integrate over $\boldsymbol{x}_1$ and $\boldsymbol{x}_2$, we have

$$I=\frac{1}{V^{m-1}}\sum_{\boldsymbol{k}_1,\cdots,\boldsymbol{k}_{m-1}} F^{n_1+1}(\boldsymbol{k}_1)F^{n_2+1}(\boldsymbol{k}_2)\cdots F^{n_m+1}(-\boldsymbol{k}_1-\boldsymbol{k}_2-\cdots-\boldsymbol{k}_{m-1}) \,. \tag{9}$$

Therefore $I(n_1, n_2, \cdots, n_m)$ is written as

$$I(n_1, n_2, \cdots, n_m)=\int u_{n_1}(\boldsymbol{x})u_{n_2}(\boldsymbol{x})\cdots u_{n_m}(\boldsymbol{x})\,d\boldsymbol{x} \,, \tag{10}$$

where $u_n(\boldsymbol{x})$ is defined by

$$u_n(\boldsymbol{x})=\frac{1}{V}\sum_{\boldsymbol{k}} F^{n+1}(\boldsymbol{k})e^{i\boldsymbol{k}\cdot\boldsymbol{x}} \,. \tag{11}$$

We shall proceed to calculate the number of different ways in which the clusters characterized by the set $(n_1, n_2, \cdots, n_m)$ are constructed from the particles $1, 2, \cdots, n+1$. If we denote this by $C(n_1, n_2, \cdots, n_m)$, $\beta_n^{(2)}$ is evaluated by summing the product CI over possible set of n_i's and deviding by $n!$.

We may calculate $C(n_1, n_2, \cdots, n_m)$ in the following manner. First we select two particles as the junctions out of $n+1$ particles; the number of ways is $\binom{n+1}{2}$. Secondly n_1 particles are selected out of $n-1$ particles and arranged on the line; the number of ways is $\binom{n-1}{n_1}n_1!$. Thirdly n_2 particles are selected out of $n-n_1-1$ particles and arranged on the line; the number of ways is $\binom{n-1-n_1}{n_2}n_2!$, and so on. Using the equation $\sum_{i=1}^{m} n_i=n-1$, we may write the product of these numbers as

$$\binom{n+1}{2}\binom{n-1}{n_1}\binom{n-1-n_1}{n_2}\cdots\binom{n-1-n_1-n_2\cdots-n_{m-2}}{n_{m-1}}n_1!\,n_2!\cdots n_m!=(n+1)!/2 \,.$$

In calculating C we must note that if there are lines with the same number of particles, the interchange of these lines never leads to different clusters and therefore if we denote the number of lines with one particle by ε_1, that with two particles by ε_2, etc., we have

$$C(n_1, n_2, \cdots, n_m)=\frac{(n+1)!}{2}\,\frac{1}{\varepsilon_1!\,\varepsilon_2!\cdots} \,. \tag{12}$$

From Eqs. (10) and (12), we obtain the expression for the contribution of the clusters with a given value of m to the irreducible integral β_n in the following form:

$$\beta_{nm}^{(2)}=\frac{n+1}{2}\left[\sum_{\substack{(n_1,\cdots n_m)\\ n_i\geq 1}}\frac{1}{\Pi\varepsilon_i!}\int\prod_{i=1}^{m}u_{n_i}(\boldsymbol{x})\,d\boldsymbol{x}+\sum_{\substack{(n_1,\cdots n_{m-1})\\ n_i\geq 1}}\frac{1}{\Pi\varepsilon_i!}\int\prod_{i=1}^{m-1}u_{n_i}(\boldsymbol{x})f(\boldsymbol{x})\,d\boldsymbol{x}\right], \tag{13a}$$

where each term in the second sum stands for the contribution of a graph with single line on which no point lies. Furthermore $(n_1, n_2, \cdots, n_m)$ means the summation over the set of these n_i's. This summation is, however, easily transformed into multiple summations over n_i's as follows,

$$\beta_{nm}^{(2)}=\frac{n+1}{2}\left[\frac{1}{m!}\sum_{\substack{n_1,n_2,\cdots,n_m\\ n_i\geq 1}}\int\Pi\,u_{n_i}(\boldsymbol{x})\,d\boldsymbol{x}+\frac{1}{(m-1)!}\sum_{\substack{n_1,n_2,\cdots n_{m-1}\\ n_i\geq 1}}\int\Pi\,u_{n_i}(\boldsymbol{x})f(\boldsymbol{x})\,d\boldsymbol{x}\right]. \tag{13b}$$

For the number of ways in which the set $(n_1, n_2, \cdots, n_m)$ appears in the first sum of Eq. (13b) is $m!/\Pi\,\varepsilon_i!$ and therefore this is equal to the first sum of Eq. (13a). The situation is the same of the second sum.

Let us now consider the free energy arising from the clusters of watermelon type and define $(-A'/NkT)_W$ as

$$\left(-\frac{A'}{NkT}\right)_W=\sum_{n\geq 3}\frac{\beta_n^{(2)}}{n+1}\rho^n\,. \tag{14}$$

Then we obtain, from Eq. (13b),

$$\left(-\frac{A'}{NkT}\right)_W=\frac{1}{2}\sum_{\substack{n\geq 3\\ m\geq 3}}\left[\frac{1}{m!}\sum_{\substack{n_i\geq 1\\ \Sigma n_i=n-1}}\rho^n\int\Pi\, u_{n_i}(\boldsymbol{x})\,d\boldsymbol{x}+\frac{1}{(m-1)!}\sum_{\substack{n_1\geq 1,\cdots,n_{m-1}\geq 1\\ \Sigma n_i=n-1}}\rho^n\int\Pi\, u_{n_i}(\boldsymbol{x})f(\boldsymbol{x})\,d\boldsymbol{x}\right].$$

If we use the relation $n=1+\sum_i n_i$ and carry out the summations over n_i's, we have

$$\left(-\frac{A'}{NkT}\right)_W=\frac{\rho}{2}\int\sum_{m=3}^{\infty}\frac{h^m(\boldsymbol{x})}{m!}\,d\boldsymbol{x}+\frac{\rho}{2}\int\sum_{m=2}^{\infty}\frac{h^m(\boldsymbol{x})}{m!}f(\boldsymbol{x})\,d\boldsymbol{x}\,, \tag{15}$$

where $h(\boldsymbol{x})$ is given by

$$h(\boldsymbol{x})=\sum_{i=1}^{\infty}\rho^i u_i(\boldsymbol{x})\,. \tag{16}$$

If we perform the summation over m, we have

$$\left(-\frac{A'}{NkT}\right)_W=\frac{\rho}{2}\int\left\{e^{h(\boldsymbol{x})}-1-h(\boldsymbol{x})-\frac{h^2(\boldsymbol{x})}{2}\right\}d\boldsymbol{x}+\frac{\rho}{2}\int\left\{e^{h(\boldsymbol{x})}-1-h(\boldsymbol{x})\right\}f(\boldsymbol{x})\,d\boldsymbol{x}\,, \tag{17}$$

and, from Eqs. (11) and (16), it follows that

$$\begin{aligned}h(\boldsymbol{x})&=\frac{1}{V}\sum_{\boldsymbol{k}}\left[\rho F^2(\boldsymbol{k})+\rho^2F^3(\boldsymbol{k})+\cdots\right]e^{i\boldsymbol{k}\cdot\boldsymbol{x}}\\&=\frac{1}{V}\sum_{\boldsymbol{k}}\frac{\rho F^2(\boldsymbol{k})}{1-\rho F(\boldsymbol{k})}e^{i\boldsymbol{k}\cdot\boldsymbol{x}}\,.\end{aligned} \tag{18}$$

On the other hand, the free energy term arising from 0-junction clusters has been calculated by Montroll and Mayer[1] and takes the form:

$$\left(-\frac{A'}{NkT}\right)_R=\frac{\rho}{2}F(0)-\frac{1}{2V\rho}\sum_{\boldsymbol{k}}\left[\ln\{1-\rho F(\boldsymbol{k})\}+\rho F(\boldsymbol{k})+\frac{\rho^2F^2(\boldsymbol{k})}{2}\right]. \tag{19}$$

In this way the summation over 2-junction clusters together with 0-junction clusters has been reduced to a simple quadrature. By means of Eqs. (1), (17), (18) and (19) the free energy under the ring and watermelon approximations is evaluated. It should be noted here that the first term of Eq. (17) has a form similar to that obtained by Yukhnovsky[7]. The essential difference is, however, that his expression cannot be applied to the singular potentials while ours can be applied to such cases.

§ 3. Discussions

In this paper it is shown that the summation over 2-junction clusters is reduced to a single integral in the coordinate space. In general the summation over n-junction clusters may be reduced to $(n-1)$-fold integral after the integration over the coordinates of particles on the lines connecting various junctions. This suggests that the cluster expansion may be summed up in a series of which each term represents the contribution of clusters characterized by the number of junctions. In fact the theory of classical fluids along this line will be developed by Morita[9] in his forthcoming papers.

An interesting problem which can be treated by the present method is an evaluation of the free energy of the system with Coulomb forces. In this case the function $h(\boldsymbol{x})$ defined by Eq. (18) is the screened potential such as $A\exp(-\kappa r)/r$. If one retains here only the clusters with $m=3$ as shown in Fig. 4, the free energy term contains an integral:

$$\frac{\rho}{2}\int_0^\infty \frac{1}{3!}\frac{A^3 \exp(-3\kappa r)}{r^3} r^2\, dr\,, \qquad (20)$$

if the term $m=3$ is retained in Eq. (15). This integral is of logarithmic divergence at $r=0$. However if one sums the terms with $m \geqslant 3$, the result is no longer divergent as is seen in Eq. (17).

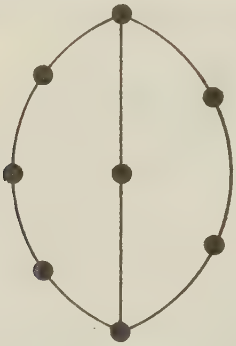

Fig. 4.

The same situation may exist in quantum theory, since at high temperatures the quantum statistics reduces to classical one. In fact Montroll and Ward[5] have shown that the correlation energy of an electron gas[10] can be obtained by summing the graphs which are of ring type (by replacing the particles in classical theory by torons). The corresponding summation in turn leads to the Debye-Hückel equation in classical theory. Therefore it may follow that the summation of the clusters shown in Fig. 4 will lead to the divergence in quantum theory as well as in classical one. However this difficulty will be avoided if the clusters $m \geqslant 3$ are summed up. It seems that the summation of this type will be important if one wishes to improve on the approximation employed in calculating the correlation energy of an electron gas at high densities.

In conclusion the author wishes to express his sincere thanks to Prof. H. Ichimura and Mr. K. Hiroike for helpful discussions and also to Mr. T. Morita for giving him a number of kind suggestions and informing the result about the generalization of the present method before publication.

References

1) E. W. Montroll and J. E. Mayer: J. Chem. Phys. **9** (1941) 626.
2) G. S. Rushbrooke and H. I. Scoins: Proc. Roy. Soc. **A 216** (1953) 203.
3) K. Hiroike: J. Phys. Soc. Japan **13** (1958) 1497.
4) H. S. Green: Proc. Roy. Soc. **A 189** (1947) 103.
5) E. W. Montroll and J. C. Ward: Phys. Fluids **1** (1958) 55.
6) D. Zubarev: Dok. Akad. Sci. U.S.S.R. **95** (1954) 757.
J. K. Percus and G. J. Yevick: Phys. Rev. **110** (1958) 1.
7) I. Yukhnovsky: J. Exp. Theor. Phys. **34** (1958) 379.
8) J. E. Mayer and M. G. Mayer: "Statistical Mechanics" (Wiley, New York, 1940) p. 291.
9) T. Morita: to be published.
10) M. Gell-Mann and K. A. Brueckner: Phys. Rev. **106** (1957) 364.

Journal of the Physical Society of Japan Vol. 14, No. 1, January, 1959

High Electric Field Effects in Germanium *p*−*n* Junction

By Jiro Yamaguchi and Yoshihiro Hamakawa
Faculty of Engineering, Osaka University, Osaka

(Received November 25, 1957)

When the squarewave pulses of 5∼160 μs duration with the repetition rate of 1,000 pulses per sec. are impressed across the germanium $p-n$ junction of grown type in the reverse direction, the critical voltage of the avalanche beginning rises up with the temperature of the specimen.

On the other hand, the onset voltage of negative resistance decreases with the increasing ambient temperature of specimens and duration of pulse impressed across the $p-n$ junction. Furthermore, even if the ambient temperature of specimens is widely changed, the barrier temperature, which is estimated from the saturation current in reverse direction, is almost constant. Therefore, the temperature rise in barrier layer is also necessary for the onset of negative resistance, though the avalanche ionization is essential.

At the negative resistance region, the property of jumping or oscillation occurs. Which of the two prevails, depends on the circuit resistance and other experimental conditions. These properties seems to have relation with the barrier temperature.

§ 1. Introduction

When a pulse voltage is applied to the germanium $p-n$ junction in reverse direction, the volt-ampere characteristics of the junction may be divided into the following regions, i.e., saturation current, excess current, avalanche, negative resistance and ohmic property. They appear successively with the increasing voltage of pulse source. These regions are shown as OA, AB, BC, CDE in Fig. 1 and FG in Fig. 9.

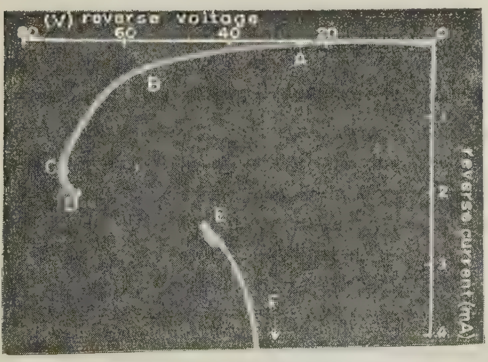

Fig. 1. Volt-ampere characteristic of reverse direction.

On the problem of the high electric field effects in germanium $p-n$ junction, many experimental and theoretical studies have been made in recent years. McKay[1)] has discussed the avalanche process in silicon step junction and Miller[2)] has reported that the charge multiplication takes place in the step junction of germanium at prebreakdown voltage. The negative resistance properties have been experimentally studied for point contact diodes[3-5)] and the critical temperature of pulse breakdown, which has been measured at different ambient temperatures of specimens and calculated by postulating a simple model with considerations of the power dissipation at the contact, is estimated at the barrier to (95∼147)°C[4)] or 90°C[5)]. At the same time the jumping or oscillation characteristics have been shown also with germanium point contact diodes. Recently, the experimental results of negative resistance property have been shown in grown or alloyed junctions of germanium[6)] and silicon[7-8)]. Gunn has theoretically demonstrated the negative resistance property by the concept of avalanche injection and obtained the relation of $V_a \propto J^{-1/2}$, where V_a and J are the voltage across the avalanche and current density, respectively. However, their experimental results show that the above relation can not be observed, but only a sudden decrease of voltage as the current is increased.

In this report, we discuss the relative distinction between the avalanche multiplication and the onset of negative resistance and that between jumping and oscillation property in the negative resistance region, taking into consideration the open-circuit voltage of the $p-n$ junction and the barrier temperature, which is estimated from the saturation current of the junction as described below.

The applied voltage used in this investigation is the squarewave pulses, which enables the electric behavior of junction to be clear. The $p-n$ junction in this study is of the base and collector of $n-p-n$ grown type transistors, which are made in our country and hermetically sealed in capsules. The resistivities of p-region and n-regions are 0.1 and 1 Ω cm respectively, therefore the impurity concentrations are estimated to be 2.4×10^{16} and 2.0×10^{15} cm^{-3}. The distribution of net impurity concentration in the junction is of linear gradient.

§ 2. Experimental Procedures

Fig. 2 shows the electric circuit for measuring the property of $p-n$ junction. As a power source we used squarewave pulses having a duration of 5∼160 μs with the repetition rate of 1,000 pulses per sec.. C.R.O-1 and 2 are respectively used for showing the volt-ampere characteristic as in Fig. 1, the wave form of the voltage and that of the current in the junction.

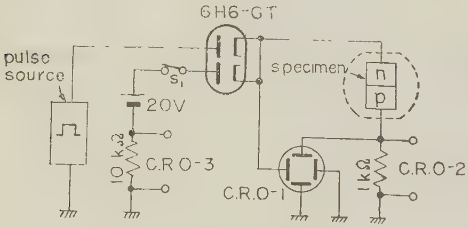

Fig. 2. Connection diagram for measurement.

Fig. 3 (a), shows the characteristic of the saturation current at different temperatures of the specimen, expressing that the current is nearly constant for a wide range of applied voltage as well known and Fig. 3 (b) indicates a plot of saturation current (i_s) measured at 20 V versus ambient temperature of (−23∼87)°C of the specimen. By this relation, we can estimate the barrier temperature. The relation of these two quantities can be expressed by

$$i_s \simeq i_0 \exp\left(-\frac{0.62\,\text{eV}}{kT}\right),$$

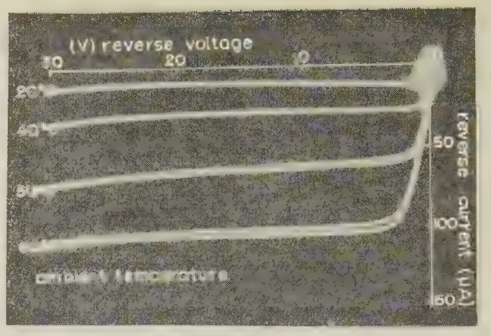

Fig. 3 (a). Saturation current at different temperatures.

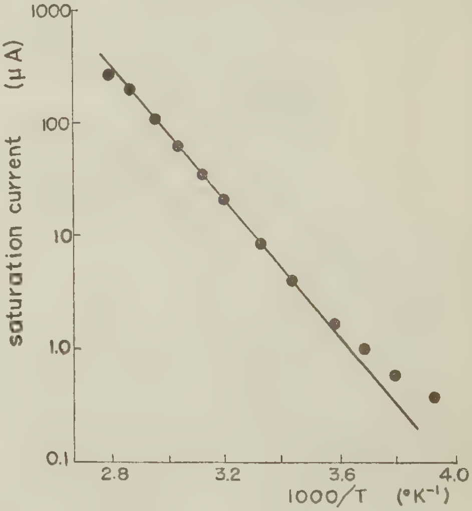

Fig. 3 (b). Relation between saturation current and temperature of specimen.

where k, T and i_0 are Boltzmann's constant, absolute temperature and a certain constant respectively.

§ 3. Experimental Results and Discussions

(a) *Avalanche multiplication*

When the applied voltage is raised over the value represented at the point B in Fig. 1, the di/dv increases rapidly with the voltage. From the experimental results, the critical voltage of the current increase, i.e., the voltage indicated at the point B does not depend on the duration of pulses (5∼160)μs, but grows with the ambient temperature of specimen as shown in Fig. 4. The relative temperature coefficient of critical voltage at room temperature can be obtained from Fig. 4 and is estimated to be 8×10^{-4} (°C^{-1}), which is of the same order as the temperature coefficient for multiplication characteristics of silicon step junction[1]. Furthermore, approximate calculations show that, as the width constant of the specimens used is 8.6×10^{-5} cm²⁾, the maximum field intensity in the junction at the critical voltage is 265 kVcm⁻¹. Miller reported that the maximum field in the junction at the prebreakdown is 237 kV cm⁻¹ for germanium step junctions. Consequently, the critical voltage described above would correspond to the onset voltage of avalanche multiplication.

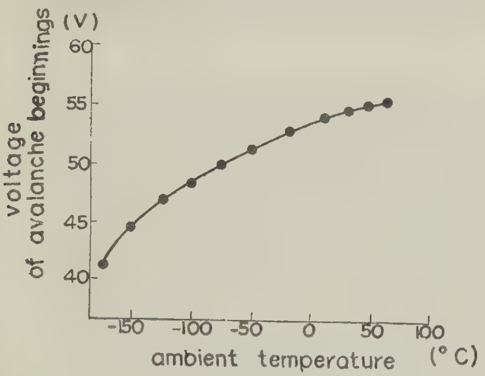

Fig. 4. Critical voltage of avalanche beginning versus ambient temperature.

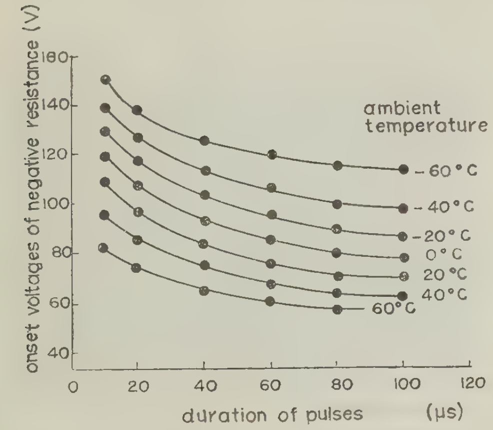

Fig. 5. Onset voltage of negative resistance versus pulse duration at different ambient temperatures.

(b) *Onset of negative resistance*

When the impressed voltage is raised from the avalanche region and attains the value corresponding to the point C in Fig. 1, the current increases extremely rapid, di/dv becomes infinite and the negative resistance property occurs. Fig. 5 shows the relation of the onset voltage of negative resistance versus pulse duration, ambient temperature being taken as a parameter. From this result, the onset voltage of negative resistance seem to depend on the temperature of the junction.

(c) *Barrier temperature*

The barrier temperature in the avalanche and breakdown regions is estimated by the relation of Fig. 3 (b).

When the squarewave pulses, their duration being 10 μs with the repetition rate of 1,000 p/s, are applied to the specimen, the wave form of saturation current can be observed at the pulse interval by C.R.O-3 in Fig. 6. We can observe from Fig. 6 (a) that the saturation current of the reverse direction is comparatively small in the regions of saturation current and excess current but increases slightly in the avalanche region. When the junction operates at the negative resistance region, the saturation current rapidly increases and has simultaneously a decay component (i_e), on which we will discuss below. It is noticeable that the i_e component does not appear at the onset of negative re-

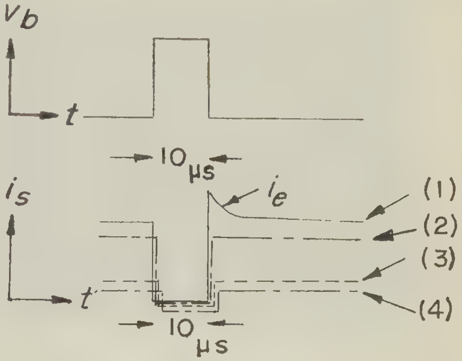

(a)

(1) Negative resistance region (in which electrical jumping or oscillation occurs).
(2) At the onset point of negative resistance.
(3) Avalanche region.
(4) Excess and saturation current region.

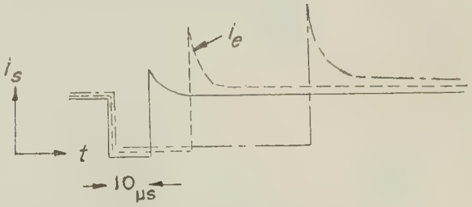

(b)

Negative resistance region at different duration of impressed pulses.

Fig. 6. Wave forms of current in reverse direction.

sistance region, i.e. the point C, but predominates at DE in Fig. 1.

From these experimental results, the temperature rise in the junction barrier, which can be estimated from i_s, is negligibly small in the saturation current region and large in the negative resistance region.

Table I. Barrier temperature (°C).

Region / Ambient temperature	Avalanche ionization	Negative resistance	Ohmic property
−70	−10∼28	40*∼ 52	52∼ 70
−30	18∼38	42*∼ 58	58∼ 80
0	30∼43	46*∼ 65	65∼ 90
30	40∼58	62*∼ 87	87∼ 95
60	84∼90	90*∼100	100∼110

(Duration of pulses is 20 μs, and numerical values marked with * are obtained at the onset of negative resistance region.)

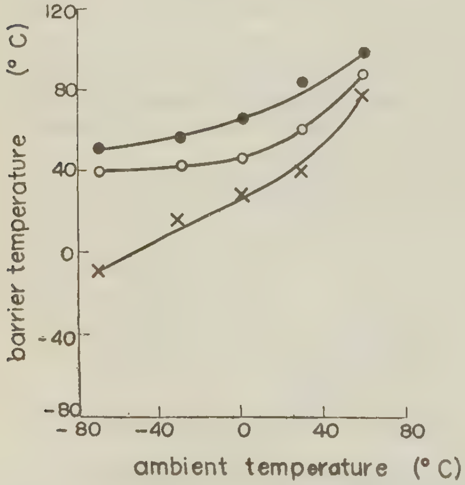

Fig. 7. Barrier temperature versus ambient temperature, the dots express ohmic property, the circles onset of negative resistance and the crosses onset of avalanche multiplication.

Table I and Fig. 7 show the relation between the barrier temperature at different operating regions and the ambient temperature of specimen. From Fig. 7, it is concluded that even if the ambient temperature of the specimen is (−70∼20)°C, the barrier temperature at the onset point of negative resistance is approximately constant at (40∼54)°C. It is remarkable that the onset of negative resistance property in $p-n$ junction neccesiates not only the avalanche ionization but the temperature rise in the barrier. On the other hand, the barrier temperature at the critical voltage of avalanche multiplication increases with the ambient temperature.

As shown in Fig. 6 (a) and (b) the decay component (i_e) of the saturation current does not appear in the saturation and avalanche regions, but appears in the negative resistance region of jumping or oscillation and grows with the increasing pulse duration.

Microplasmas have been observed at the breakdown in silicon $p-n$ junction8),9), hence, if similar phenomenon is applied to our case of germanium $p-n$ junction, it may be suggested that in the negative resistance region the barrier is electrically punched through in some spots by the pulse voltage, microplasmas may arise and i_e may be the current through hot patches in junction which would be caused by plasmas. Just after the pulse termination, the junction recovers with the time constant of several μs, which corresponds to the decay time of i_e. On the contrary, the barrier still exists in the avalanche region, because i_e could not be observed.

(d) *Negative resistance and ohmic property*

When the voltage of pulse source is raised still more, the volt-ampere characteristic indicated at the point D in Fig. 1 jumps to that of the point E, or the electrical oscillation occurs at the frequency of 200 kc∼1 Mc between the point D and E. The wave forms of voltage and current are shown in Fig. 8. It is significant that the line $\overline{CDE}$ in Fig. 1 is considered to be the resistance line of the external circuit. As the pulse voltage of electric source is further raised, the volt-ampere relation is expressed as a straight line as shown in Fig. 9. In this range the $p-n$ junction has merely the ohmic property. As explained above, the characteristic of $p-n$ junction may be in brief expressed as the lines OC and EF in Fig. 10, which correspond to the property before and after the breakdown. Hence, when the voltage of pulse source and the resistance line of external circuit are assumed to be OG and GH, the operating point of the junction will be given at the point C or E. Therefore, it is expected that whether the electric jumping

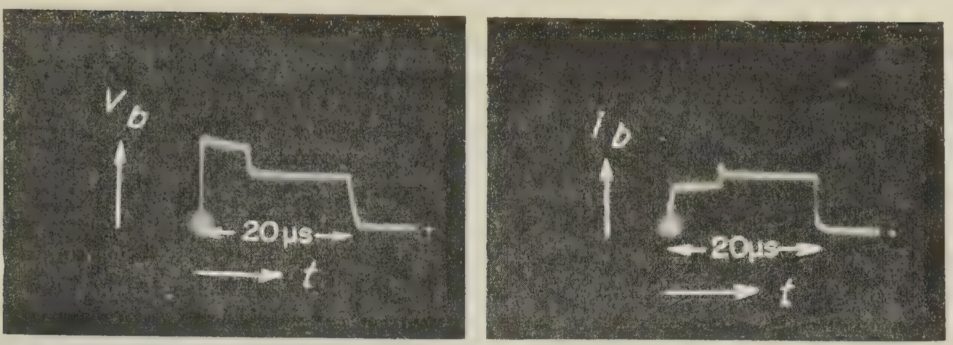

(a) Jumping property

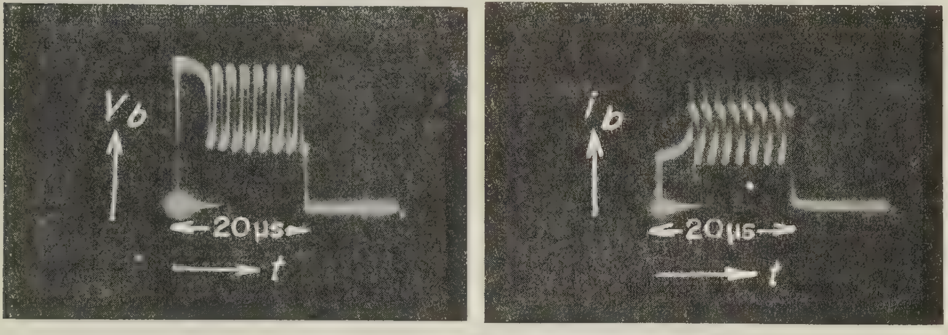

(b) Oscillating property

Fig. 8. Wave forms of voltage and current in negative resistance region.

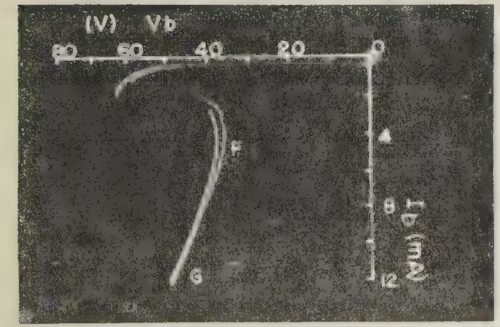

Fig. 9. Volt-ampere characteristic at ohmic region. (Taken with half-wave rectified voltage of single phase 60 c/s instead of pulse source in Fig. 2).

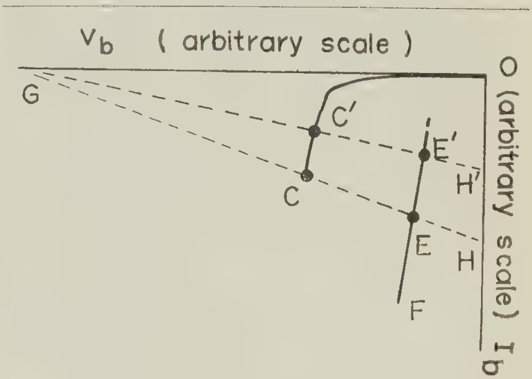

Fig. 10. Simplified characteristics of *p-n* junction, before and after the breakdown.

or oscillation prevails in negative resistance region, depends on the difference of the barrier temperature at the point E and that of C. Namely, the electrical oscillation occurs when the barrier temperature at the point C is higher than the one at E and the electrical jumping occurs in the opposite case.

This argument is ascertained by the experiment, in which several resistances are inserted in the external circuit and the operating point of $p-n$ junction is changed in the volt-ampere characteristic as shown in the points (C, E) or (C′, E′) of Fig. 10. The experimental results are indicated in Fig. 11. In this figure, the hyperbolas express the equi-power line, and (D_1, E_1)(D_2, E_2)(D_3, E_3) (D_4, E_4) and D_5 represent respectively the operating point of $p-n$ junction with the external resistances shown in Table II. The five D_s' and the four E_s' correspond to D and E in Fig. 1 in their property. Hence we can observed that the $p-n$ junction operates in the jumping, oscillation or avalanche region with the change of external resistance. In the above discussion, the points C and D in the volt-ampere characteristic are considered to be in the same position, because the region of CD is short in Fig. 1 and the temperature dependence of the bulk resistance of specimen is not taken into consideration.

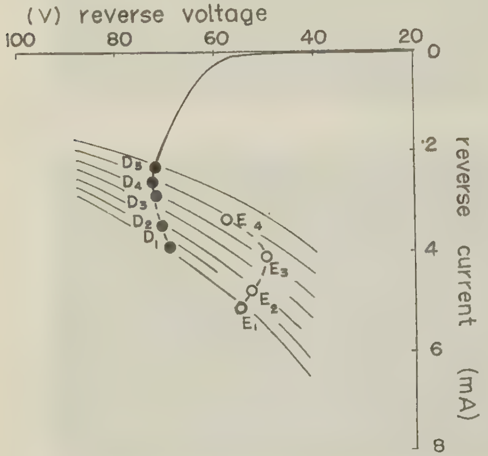

Fig. 11. Volt-ampere characteristics in negative resistance region.

Table II. Explanation of Fig. 11.

Externally inserted resistance ($k\Omega$)	Operating point	Electrical property
4	D_1, E_1	jumping
about 4.5	D_2, E_2	Boundary of jumping and oscillation
7~8	D_3, E_3	oscillation
about 8.5	D_4, E_4	Boundary of oscillation and avalanche
9	D_5	Avalanche ionization

Fig. 12 shows the domains of avalanche, oscillation and jumping property at different external resistances and pulse durations.

Gunn has suggested from the concept of avalanche injection that the relation of $V_a J^{1/2} \simeq$ constant holds in the negative resistance region, but $V_a J$ is constant in the equi-power dissipation. Hence it would be impossible to observe stably the negative resistance region on the volt-ampere characteristic. Moreover, Rose has discussed the fluctuating frequency in the negative resistance region and his conclusion is that the oscillation of current is explained by statistical problems of chance fluctuation of microplasmas.

In our standpoint of view, the oscillation frequency would depend on

i. The time required from the onset of negative resistance to the growth of microplasmas.

ii. The time of extinguish of the current through punched spots in junction.

iii. The time required from the state of avalanche ionization, which is partly determined by the voltage of electric source and external resistance, to the onset of negative resistance.

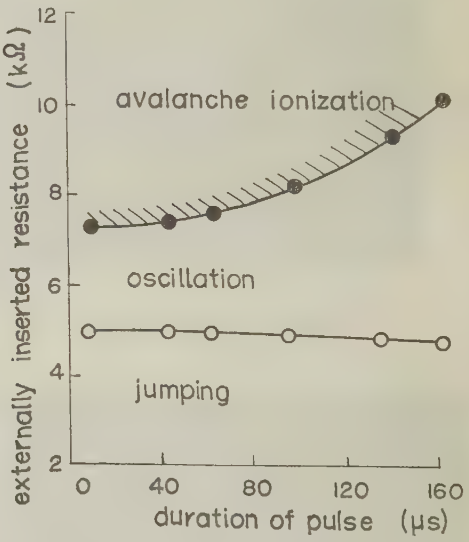

Fig. 12. Domains of negative resistance and avalanche region.

(e) *Open-circuit voltage*

The wave forms of the terminal voltage across the $p-n$ junction, which are observed in C.R.O-1 of Fig. 1, are shown in Fig. 13. The pulse duration in this case is 20 μs. As shown in Fig. 13 (a) and (b) the terminal voltage in the saturation current and avalanche regions has the decay component with the time constant of about 20 μs at the interception of pulses. As is well known, the decay component is caused by the diffusion of stored charge carriers in the $p-n$ junction. On the other hand, in the negative resistance region, the decay component can not be observed as shown in Fig. 13 (c). Therefore in the former, the barrier still exsists, but in the latter, the barrier is extinguished and the $p-n$ junction becomes only a resistance. Besides, v_1 in Fig. 13 (b) is the

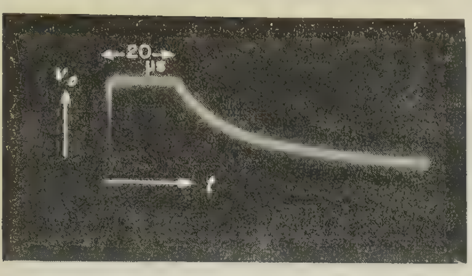

(a)
Saturation and excess current region.

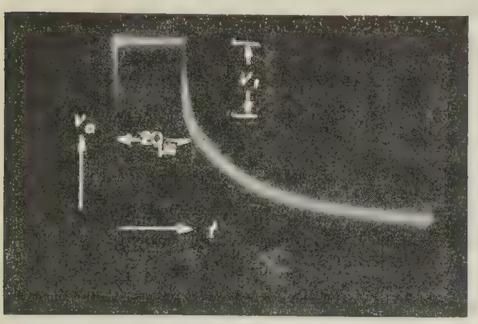

(b)
Avalanche region.

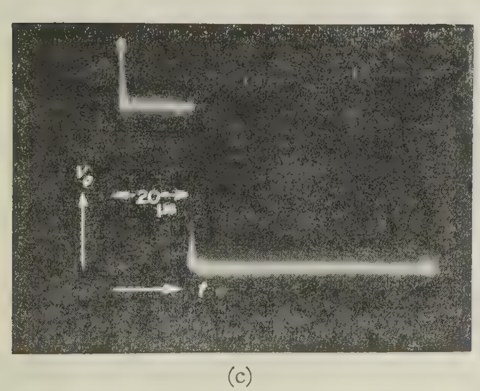

(c)
Negative resistance region.

Fig. 13. Wave forms of open-circuit voltage.

voltage drop in the bulk resistance of the specimen.

§ 4. Conclusion

In the avalanche region, the critical voltage of avalanche beginning rises with the ambient temperature of specimen which is somewhat lower than the barrier temperature.

In the onset of negative resistance region, the barrier temperature is (40∼54)°C at the ambient temperature of (−70∼20)°C, i.e., the former is nearly constant while the latter changes widely.

In the negative resistance region, the characteristic of the $p-n$ junction shows the electrical jumping or oscillation. Which of the two prevails, is caused by the temperature rise in the barrier and can be controlled by the resistance inserted in the external circuit.

Acknowledgments

The authors are indebted to Sony Corp. and Kobe Kogyo Corp., for the supply of the $p-n$ junctions. They are also grateful to the staff members of 2nd lectureship of our school for valuable discussions and to Mr. H. Matsushiro, Mr. S. Horiuchi and Mr. K. Sugimoto for the experimental helps.

References

1) K. G. McKay: Phys. Rev. **94**, (1954) 877.
2) S. L. Miller: Phys. Rev. **99**, (1955) 1234.
3) S. Benzer: J. A. Phys. **20**, (1949) 804.
A. I. Bennett and L. P. Hunter: Phys. Rev. **81** (1951) 152.
J. R. Tillman and J. C. Henderson: Phil. Mag. **44** (1953) 677.
R. E. Burgess: P. Phys. Soc. **68** B, (1955) 908.
4) A. Lempicki and C. Wood: P. Phys. Soc., **67**, B, (1954) 328.
5) M. Kikuchi and Y. Tarui: J. Phys. Soc. Japan **10** (1955) 722.
6) J. B. Gunn: *Progress in semiconductors* **2** (John Wiley and sons. Inc.) (1957) 213.
7) H. S. Veloric and M. B. Prince: B. S. T. J. July, (1957) 975.
8) D. J. Rose: Phys. Rev. **105**, (1957) 413.
9) A. G. Chynoweth and K. G. McKay: Phys. Rev. **102**, (1956) 369.

JOURNAL OF THE PHYSICAL SOCIETY OF JAPAN Vol. 14, No. 1, JANUARY, 1959

Interaction of Conduction Electrons with Acoustic Phonons

By Nobuo MIKOSHIBA

Electrotechnical Laboratory, Nagatacho, Tokyo

(Received July 26, 1958)

The interaction of conduction electrons with acoustic phonons is studied from the general point of view. Parmenter's theory of acousto-electric effect in the high frequency range is criticized for several reasons. It is shown that Weinreich's relation between acousto-electric effect and the absorption coefficient of acoustic waves holds only in the high frequency range, and the limitation to its application is also discussed. New magneto-acoustic resonance suggested by the present author is examined qualitatively.

§ 1. Introduction

As is well-known[1)], there are three different types of the interaction of conduction electrons with acoustic waves corresponding to three frequency ranges of waves:

(1) the low frequency range ($\omega\tau \ll 1$, $ql < 1$),

(2) the intermediate frequency range ($\omega\tau < 1$, $ql > 1$) and

(3) the high frequency range ($\omega\tau > 1$, $ql \gg 1$).

Here ω and q are the angular frequency and the wave number of acoustic waves, τ and l are the relaxation time and the mean free path of conduction electrons. The presence of the intermediate frequency range results from the difference between the average velocity (or Fermi velocity) of conduction electrons v_0 and the sound velocity s. From the relations $\omega = sq$ and $l = \tau v_0$, we get

$$\omega\tau = \left(\frac{s}{v_0}\right) ql \,. \qquad (1.1)$$

Then if $s/v_0 < 1$, the intermediate frequency range occurs.

In the low frequency range we may treat acoustic waves *classically as potential waves* for conduction electrons. On the other hand, in the high frequency range we treat them *as an acoustic phonon beam* which scatters conduction electrons. There are two approaches in treating acoustic waves in the intermediate frequency range. One is the approach from the low frequency range as treated in Pippard's theories of the absorption of acoustic waves[1)] and of magneto-acoustic resonance[2)]. The other is the approach from the high frequency range as in Paranjape's[3)] and Kittel's[4)] theories of the absorption of waves. There are three phenomena relating to the interaction of conduction electrons with acoustic waves:

(1) acousto-electric effect,

(2) the absorption of acoustic waves and

(3) magneto-acoustic resonance.

In this paper we restrict ourselves to discuss only the phenomena in the high (and the intermediate) frequency range and to treat the interaction of conduction electrons with *acoustic phonon beam* (*longitudinal waves*). First we examine the critical frequencies between three frequency ranges at liquid helium temperature, taking Cu as an example for metals and n-Ge for semiconductors. The results are listed in Table I.

Table I. The critical frequency between three frequency ranges.

	Cu	n-Ge
τ (sec)	10^{-10}*	10^{-10}
l (cm)	1.6×10^{-2}	4×10^{-4}**
v_0 (cm/sec)	1.6×10^{8}	4×10^{6}
s (cm/sec)	4.5×10^{5}	5×10^{5}
ω_1 (rad/sec)***	2.8×10^{7}	1.3×10^{9}
ν_1 (cyc/sec)	4.5×10^{6}	2.1×10^{8}
ω_2 (rad/sec)****	10^{10}	10^{10}
ν_2 (cyc/sec)	1.6×10^{9}	1.6×10^{9}

* We take the specimen of the highest purity.

** $v_0 = (8\kappa T/\pi m^*)^{1/2}$, $m^*/m = 0.1$, where m^* is the effective mass of conduction electrons.

*** $\omega_1 = (1/\tau)(s/v_0)$ and $\nu_1 = \omega_1/2\pi$

**** $\omega_2 = 1/\tau$ and $\nu_2 = \omega_2/2\pi$

Since the maximum available frequency of acoustic waves at the present time may be $\nu \sim 5\times10^{8}$ cyc/sec, it is difficult to realize the condition for the high frequency range. However, it may be possible in future, to realize such conditions by developments in techniques of producing high frequency acoustic waves together with that of purification of materials which reduces the critical frequency ν_2. As mentioned above, the approach of treating acoustic waves as phonon beams is approximately applicable to the intermediate frequency range, so that the theoretical results presented in § 2 and § 3 can be applied to Cu for $\nu > 4.5$ Mc/sec and to n-Ge for $\nu > 210$ Mc/sec.

In § 2 we calculate acousto-electric effect by the low temperature approximation according to Van Den Beukel's method[5] who has used the high temperature approximation inadequate for the physical situations. In this connection Parmenter's theory[6] of electron-trapping by acoustic waves is criticized. In § 3 the absorption coefficient of acoustic waves by conduction electrons is calculated for metals and semiconductors. For metals Paranjape and Kittle have already calculated the coefficient which agreed very well with experiments[7]. Weinreich's relation[8] between the acousto-electric effect and the absorption coefficient is satisfied in our case, too. A limit of applicability of his relation is also discussed. In the last section § 4, new magneto-acoustic resonance phenomenon in the high frequency range is discussed in detail, which has been suggested by the present author in the previous paper[1].

§ 2. Acousto-Electric Effect in the High Frequency Range

We assume acoustic waves travelling in x-direction. Conduction electrons are scattered on the average to x-direction by acoustic phonons which constitute acoustic waves. On the other hand, thermal phonons or impurities scatter on the average conduction electrons to the opposite direction. Then the stationary current flows along x-direction. Under the open circuit condition, the stationary current is cancelled by the electromotive force which is called acousto-electromotive force. In general, we call this phenomena acousto-electric effect. Now we shall calculate the order of magnitude of acousto-electric effect at liquid helium temperature.

For simplicity we take the following four assumptions[5].

(I) *Free electron model.* The energy of an electron is given by

$$\mathrm{E}(\boldsymbol{k})=\frac{\hbar^2k^2}{2m^*}\,, \tag{2.1}$$

where $\boldsymbol{k}$ is the wave number vector of a conduction electron and m^* is its effective mass.

(II) *The presence of the relaxation time* τ. The distribution function of conduction electrons is expressed as

$$f(\boldsymbol{k})=f_0(\boldsymbol{k})-\frac{\partial f_0(\boldsymbol{k})}{\partial \mathrm{E}}\boldsymbol{k}_x\mathrm{C}(\mathrm{E})\,. \tag{2.2}$$

Here $f_0(\boldsymbol{k})$ is Fermi function. The change of the distribution function per unit time due to thermal phonons or impurities is written as follows:

$$\left(\frac{\partial f}{\partial t}\right)_{ti}=-\frac{f-f_0}{\tau}=\frac{1}{\tau}\frac{\partial f_0}{\partial \mathrm{E}}\boldsymbol{k}_x\mathrm{C}(\mathrm{E})\,. \tag{2.3}$$

We assume for simplicity

$$\frac{1}{\tau}=\mathrm{QE}^{\alpha}\,, \tag{2.4}$$

where Q is the numerical factor depending on the scattering processes of conduction electrons. In the case of the scattering by thermal phonons at low temperatures, the expression (2.3) is not valid. But for the other scattering processes the assumption (2.3) may be valid in general. The values of α are as follows:

For metals,

(a) $\alpha=-3/2$ for $\mathrm{T}>\Theta$ and

(b) $\alpha=1/2$ for $\mathrm{T}\ll\Theta$ (impurity scattering),

where Θ is Debye temperature.

For semiconductors,

(a) $\alpha=1/2$ for lattice scattering,

(b) $\alpha\cong-3/2$ for ionized impurity scattering and

(c) $\alpha=0$ for neutral impurity scattering.

(III) *The expansion of the distribution function.* We shall expand the distribution function as

$$f(\boldsymbol{k}\pm\boldsymbol{q})\cong f(\boldsymbol{k})\pm\frac{\partial f(\boldsymbol{k})}{\partial k_x}q\,. \tag{2.5}$$

To make this assumption, it is necessary to compare k_0 with q. If we take as $\nu=5\times10^8$ cyc/sec, $q=7\times10^3\,\mathrm{cm}^{-1}$ for Cu or $q=6.5\times10^3\,\mathrm{cm}^{-1}$ for n-Ge. On the other hand $k_0=m^*v_0/\hbar=1.4\times10^8\,\mathrm{cm}^{-1}$ for Cu or $k_0=3.5\times10^5\,\mathrm{cm}^{-1}$ for n-Ge. Then we can assume $|\boldsymbol{k}|\gg|\boldsymbol{q}|$ and (2.5) for metals and semiconductors at liquid helium temperature.

(IV) *The occupation number of acoustic* *phonons is larger than 1.* Then we can put

$$\mathrm{N}(\boldsymbol{q})\pm 1 \simeq \mathrm{N}(\boldsymbol{q}) \equiv \mathrm{N}\,. \tag{2.6}$$

With the use of above assumptions we shall calculate the change of the distribution function of conduction electrons due to acoustic phonons. Taking the volume of the system as unity,

$$\left(\frac{\partial f}{\partial t}\right)_{ac} = \frac{\mathrm{C}^2 q^2 \mathrm{N}}{\rho h \nu}\{[f_{\boldsymbol{k}+\boldsymbol{q}}(1-f_{\boldsymbol{k}})-f_{\boldsymbol{k}}(1-f_{\boldsymbol{k}+\boldsymbol{q}})]\Omega^{+} + [f_{\boldsymbol{k}-\boldsymbol{q}}(1-f_{\boldsymbol{k}})-f_{\boldsymbol{k}}(1-f_{\boldsymbol{k}-\boldsymbol{q}})]\Omega^{-}\}\,, \tag{2.7}$$

where C is the well-known coupling constant of conduction electrons with phonons and ρ the density of materials.
And

$$\left.\begin{aligned} &\Omega^{\pm} = \Omega(\mathrm{E}_{\boldsymbol{k}} - \mathrm{E}_{\boldsymbol{k}\pm\boldsymbol{q}} \pm h\nu) \\ &\Omega(x) = \frac{\sin(xt/\hbar)}{x/\hbar}\,. \end{aligned}\right\} \tag{2.8}$$

Using (2.5), (2.7) becomes

$$\left(\frac{\partial f}{\partial t}\right)_{ac} \cong \frac{\mathrm{C}^2 h q^3 \mathrm{N}}{4\pi^2 \rho m^* \nu} k_x \frac{\partial f_0}{\partial \mathrm{E}} (\Omega^{+} - \Omega^{-})\,. \tag{2.9}$$

Next, the change of the distribution function due to acousto-electromotive force F is given by

$$\left(\frac{\partial f}{\partial t}\right)_{el} = \frac{e\mathrm{F}}{\hbar}\cdot\frac{\partial f_0}{\partial k_x} = \frac{e\mathrm{F}\hbar}{m^*}k_x\frac{\partial f_0}{\partial \mathrm{E}}\,, \tag{2.10}$$

where e is the charge of a conduction electron.

Now we can derive the expression for C(E) with the use of Boltzmann equation

$$\left(\frac{\partial f}{\partial t}\right)_{ac} + \left(\frac{\partial f}{\partial t}\right)_{el} + \left(\frac{\partial f}{\partial t}\right)_{ti} = 0\,; \tag{2.11}$$

i.e.

$$\mathrm{C(E)} = -\frac{he}{2\pi \mathrm{Q}\mathrm{E}^{\alpha} m^*}\left[\mathrm{F} + \frac{\mathrm{C}^2 q^3 \mathrm{N}}{2\pi\rho\nu e}(\Omega^{+} - \Omega^{-})\right]. \tag{2.12}$$

From the condition that there is no electric current,

$$\int f_{\boldsymbol{k}} k_x d\boldsymbol{k} = 0\,. \tag{2.13}$$

Substituting (2.2) and (2.12) into (2.13) and solving it for F,

$$\mathrm{F} = \frac{\mathrm{C}^2 q^3 \mathrm{N}}{2\pi\rho\nu e}\cdot\frac{(\mathrm{K}^{-} - \mathrm{K}^{+})}{\mathrm{K}^0}\,, \tag{2.14}$$

where

$$\mathrm{K}^0 = \int \mathrm{E}^{-\alpha}\frac{\partial f_0}{\partial \mathrm{E}}\cdot k_x^2 d\boldsymbol{k} \quad \text{and} \quad \mathrm{K}^{\pm} = \int \mathrm{E}^{-\alpha}\frac{\partial f_0}{\partial \mathrm{E}}\cdot \boldsymbol{k}_x^2 \Omega^{\pm} d\boldsymbol{k}\,. \tag{2.15}$$

Now, we shall calculate K⁰, K± for metals and semiconductors. The calculation of K⁰ is carried out very easily and gives

$$\mathrm{K}^0 = \begin{cases} -\dfrac{2\pi(2m^*)^{5/2}}{3\hbar^5}\cdot \mathrm{E}_0^{(3/2)-\alpha} & \text{for metals and} \\ -\dfrac{2\pi(2m^*)^{5/2}}{3\hbar^5}\cdot \Gamma\left(\dfrac{5}{2}-\alpha\right)\cdot(\kappa T)^{(3/2)-\alpha}\cdot \exp(\mathrm{E}_0/\kappa T) & \text{for semiconductors}\,, \end{cases} \tag{2.16}$$

where E_0 is Fermi energy and $\Gamma(n)$ is gamma function of the n-th order:

$$\Gamma(n) = \int_0^{\infty} x^{n-1} e^{-x} dx\,. \tag{2.17}$$

The calculation of K± is as follows: let us introduce the polar coordinate (k, θ, φ) in $\boldsymbol{k}$-space and take the polar axis parallel to $\boldsymbol{q}$ (i.e. $\boldsymbol{k}_x$). Then

$$\mathrm{K}^{\pm} = \int \mathrm{E}^{-\alpha}\frac{\partial f_0}{\partial \mathrm{E}} k^4 \cos^2\theta\cdot\Omega^{\pm}\left(\mp\frac{\hbar^2 kq}{m^*}\cos\theta - \frac{\hbar^2 q^2}{2m^*} \pm h\nu\right) dk \sin\theta d\theta d\varphi\,. \tag{2.18}$$

Since $\Omega^{\pm}$ has the properties similar to δ-function, it will be allowed to put

$$\cos^2\theta = \left[\frac{4\pi m^*\nu \mp \hbar q^2}{2\hbar kq}\right]^2, \tag{2.19}$$

When the relations[9),

$$\frac{ks}{\pi} > \nu \qquad \text{or} \qquad \frac{2m^*s^2}{h}\,, \tag{2.20}$$

are satisfied,

$$\int_0^\pi \Omega^\pm \sin\theta d\theta = \frac{\pi m^*}{\hbar kq}\,. \tag{2.21}$$

With the use of (2.19) and (2.21) we get

$$\mathrm{K}^\pm = -\frac{\pi^2 m^{*2}(4\pi m^*\nu \mp \hbar q^2)^2}{2\hbar^5 q^3}\mathrm{E}_0^{-\alpha} \tag{2.22}$$

for metals and

$$\mathrm{K}^\pm = -\frac{\pi^2 m^{*2}(4\pi m^*\nu \mp \hbar q^2)^2 \Gamma(1-\alpha)}{2\hbar^5 q^3}(\kappa T)^{-\alpha}\cdot \exp\left(E_0/\kappa T\right) \tag{2.23}$$

for semiconductors. That the relations (2.20) can be satisfied is shown by the following estimations:

$$\begin{cases} \dfrac{k_0 s}{\pi} = 2\times 10^{13} \quad \text{for Cu}\,, \quad 5.6\times 10^{10} \quad \text{for } n\text{-Ge}\,, \\ \nu = 5\times 10^8 \quad \text{and} \\ \dfrac{2m^*s^2}{h} = 5\times 10^{10} \quad \text{for Cu}\,, \quad 6\times 10^9 \quad \text{for } n\text{-Ge}\,. \end{cases}$$

After all, from (2.14), (2.16), (2.22) and (2.23)

$$\mathrm{F} = \begin{cases} \dfrac{3\pi^2 \mathrm{C}^2 m^{*1/2}\nu}{\sqrt{2}\,\rho e s^3 \mathrm{E}_0^{3/2}}\gamma & \text{for metals} \\ \dfrac{3\pi^2 \mathrm{C}^2 m^{*1/2}\nu}{\sqrt{2}\,\rho e s^3 (\kappa T)^{3/2}} \cdot \dfrac{\Gamma(1-\alpha)}{\Gamma(\frac{5}{2}-\alpha)}\cdot\gamma & \text{for semiconductors}\,, \end{cases} \tag{2.24}$$

where

$$\gamma = \mathrm{N}h\nu s \tag{2.25}$$

is the acoustic flow intensity. It is interesting to note that for metals F is temperature-independent and agrees with the values obtained by the high temperature approximation. For semiconductors F differs from Van Den Beukel's value[5)] only by the factor of $\Gamma(1-\alpha)/\Gamma(\frac{5}{2}-\alpha)$ (See Table II).

Table II. The numerical values of $\Gamma(1-\alpha)/\Gamma(\frac{5}{2}-\alpha)$.

	α	$\Gamma(1-\alpha)/\Gamma(\frac{5}{2}-\alpha)$
lattice scattering	1/2	$\sqrt{\pi}$
ionized impurity scattering	−3/2	$\sqrt{\pi}/8$
neutral impurity scattering	0	$4/3\sqrt{\pi}$

Now let us estimate the order of magnitude of acousto-electromotive force, taking the unit of F and γ as volts/cm and watts/cm² respectively. When $\nu = 5\times 10^8$ cyc/sec,

$$\mathrm{F} = \begin{cases} 6.5\times 10^{-9}\gamma & \text{for Cu} \\ 1.1\times 10^{-4}\gamma & \text{for } n\text{-Ge} \end{cases} \tag{2.26}$$

where it was assumed that C=6.2 ev for Cu and C=1.7 ev, $\alpha = -3/2$ for n-Ge. Even at the present time, it may be possible to detect the effect for n-Ge.

Finally we criticize Parmenter's theory[6] of electrons trapped by acoustic waves in the high frequency range. His theory leads to

$$F=10^{-6}\gamma^{3/4} \qquad \text{for Cu} \tag{2.27}$$

under the same conditions with (2.26). But we may conclude that Parmenter's theory cannot be applied to real systems for two reasons.

(1) Parmenter neglected *the scattering processes of trapped electrons by thermal phonons or impurities* which are present even at very low temperatures.

(2) Parmenter's mechanism producing the relatively larger value of F, (2.27), may contribute to the absorption of acoustic waves. On the contrary, the experimental value[7] of the absorption coefficient is in agreement with the theoretical value due to the electron-phonon interaction and has *no contribution from his mechanism.* Our results (2.24) or (2.26) satisfies Weinreich's phenomenological relation between acousto-electric effect and the absorption coefficient (see the next section), and so (2.24) is verified *indirectly* by the experiment of the absorption.

§ 3. Absorption of Acoustic Phonon Beam by Conduction Electrons

With the use of the approximations of § 2, we shall calculate the change of the occupation number N of acoustic phonons by conduction electrons. Similar arguments leading to (2.7) give

$$\left(\frac{\partial N}{\partial t}\right)_{el}=\frac{C^2q^2N}{\rho h\nu}\sum_k\{[f_{k+q}(1-f_k)-f_k(1-f_{k+q})]\Omega^+ + [f_k(1-f_{k-q})-f_{k-q}(1-f_k)]\Omega^-\}\ . \tag{3.1}$$

From (2.5) and $\sum_k \to 2\int dk \Big/ (2\pi)^3$,

$$\left(\frac{\partial N}{\partial t}\right)_{el}=\frac{\hbar C^2q^3N}{8\pi^4m^*\rho\nu}(K^+ + K^-) \tag{3.2}$$

where

$$K^{\pm}=\int\frac{\partial f}{\partial E}k_x\Omega^{\pm}dk\ . \tag{3.3}$$

In the same method as § 2, we get

$$K^{\pm}=\begin{cases} -\dfrac{\pi^2m^{*2}(4\pi m^*\nu\mp\hbar q^2)}{\hbar^4q^2} & \text{for metals ,} \\ -\dfrac{\pi^2m^{*2}(4\pi m^*\nu\mp\hbar q^2)}{\hbar^4q^2}\exp(E_0/\kappa T) & \text{for semiconductors .}\end{cases} \tag{3.4}$$

Substituting (3.4) into (3.2)

$$\left(\frac{\partial N}{\partial t}\right)_{el}=-\frac{2m^{*2}C^2\nu}{\rho\hbar^3s}N \quad \text{and} \quad -\frac{2m^{*2}C^2\nu}{\rho\hbar^3s}N\exp(E_0/\kappa T)\ . \tag{3.5}$$

As is well known the absorption coefficient of acoustic waves Λ is defined by

$$\frac{\partial U}{\partial t}=-\Lambda\gamma\ , \tag{3.6}$$

where

$$U=Nh\nu \tag{3.7}$$

is the acoustic energy density. Making the comparison of (3.5) with (3.6) we get the absorption coefficient by conduction electrons,

$$\Lambda=\begin{cases}\dfrac{2m^{*2}C^2\nu}{\rho\hbar^3s^2} & \text{for metals ,}\\[2ex] \dfrac{2m^{*2}C^2\nu}{\rho\hbar^3s^2}\exp(E_0/\kappa T) & \text{for semiconductors .}\end{cases}\tag{3.8}$$

The estimation of (3.8) under the same conditions as (2.26) gives

$$\Lambda=\begin{cases}20\ \text{nepers/cm} & \text{for Cu}\\ 0.02\times\exp(E_0/\kappa T)\ \text{nepers/cm} & \text{for } n\text{-Ge .}\end{cases}\tag{3.9}$$

It has been shown that the theoretical value of Λ in metals is in good agreement with the experiments at low temperatures in the intermediate frequency range. However, it will be difficult in semiconductors to detect the absorption by conduction electrons owing to the small factor of $\exp(E_0/\kappa T)$.

Recently, Weinreich[8)] has proposed a general relationship between the absorption coefficient of acoustic waves and acousto-electromotive force:

$$\Lambda=\delta\frac{nes}{\gamma}F\tag{3.10}$$

where n is the number density of conduction electrons and δ is the numerical factor depending on the scattering processes of conduction electrons. The relation (3.10) can be obtained easily by the following considerations. The momentum transfers of acoustic waves to conduction electrons occur with the energy losses. Then

$$\frac{dU}{dt}=s\frac{dp_{ac}}{dt}=-ns\frac{dp_{el}}{dt}\ .\tag{3.11}$$

where p_{ac} and p_{el} are the momentum of waves and an electron respectively and the momentum conservation was assumed.

From the acceleration equation, $dp_{el}/dt=eF$,

$$\frac{dU}{dt}=-nesF\ .\tag{3.12}$$

Comparing (3.12) with (3.6) we can get Weinreich's relation.

It is proved in our case that Weinreich's relation is satisfied if we put[11)]

$$n=\begin{cases}\dfrac{2^{3/2}}{3\pi^2}\left(\dfrac{m^*E_0}{\hbar^2}\right)^{3/2} & \text{for metals ,}\\[2ex] \dfrac{1}{2^{1/2}\pi^{3/2}}\left(\dfrac{m^*kT}{\hbar^2}\right)^{3/2}\exp(E_0/\kappa T) & \text{for semiconductors}\end{cases}\tag{3.13}$$

and choose δ as

$$\delta=\begin{cases}1 & \text{for metals ,}\\[1ex] \dfrac{4}{3\sqrt{\pi}}\cdot\dfrac{\Gamma(\frac{5}{2}-\alpha)}{\Gamma(1-\alpha)} & \text{for semiconductors .}\end{cases}\tag{3·14}$$

On the other hand, the other relationship may be present which connect Λ with F. This relationship combines with the process of Ohmic losses of the energy of conduction electrons by thermal phonons or impurities. Then instead of (3.12) we obtain

$$\frac{dU}{dt}=-\sigma F^2\ .\tag{3.15}$$

Here we denote σ as the electrical conductivity. Again making the comparison of (3.15) with (3.6), the relation

$$\Lambda=\delta\frac{\sigma}{\gamma}F^2=\delta\frac{nev_d}{\gamma}F\tag{3.16}$$

is obtained where v_d is the drift velocity of conduction electrons given rise by acoustic waves. Ohmic relation (3.16) was used essentially by Pippard in his theory[1)] of the absorption of acoustic waves in the low frequency range; however, F is *the oscillating field* contrary to the d.c. field in the high frequency range.

Why Weinreich's and Ohmic relations are separately satisfied in the high and the low frequency ranges can be understood as follows. First, it is necessary to point out the following facts. Since in the low frequency range the mean-free path of conduction electrons l

is smaller than the wave length of acoustic waves λ, conduction electrons suffer *the oscillating forces*. Then the electronic current relative to the ionic motion or acousto-electric field cancelling the current oscillate like acoustic waves, i.e.

$$\mathrm{F}=\mathrm{F}_{0s}+\mathrm{F}_{DC}\,,\quad \mathrm{F}_{0s}\gg\mathrm{F}_{DC}\,. \tag{3.17}$$

In the other case, since $l\gg\lambda$ and *the width of the wave packets of monochromatic waves must be larger than* λ[6], conduction electrons suffer the *d.c. forces*: i.e.

$$\mathrm{F}=\mathrm{F}_{0s}+\mathrm{F}_{DC}\,,\quad \mathrm{F}_{0s}\ll\mathrm{F}_{DC}\,. \tag{3.18}$$

In fact, the treatment of acoustic waves as acoustic phonon beam is the approximation neglecting F_{0s}.

From the above discussions, the absorption coefficient Λ connect mainly with F_{0s} and F_{DC} in the low and high frequency ranges respectively. In general, the losses of energy (or momentum) of acoustic waves take place in two processes shown in Fig. 1.

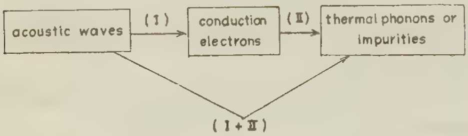

Fig. 1. The processes of the energy loss of acoustic waves.

Undoubtedly Weinreich's relation concerns only with process (I) and Ohmic relation with process (I+II). In the high frequency range Λ is determined by process (I) because $\mathrm{F}\cong\mathrm{F}_{DC}$. In fact, since $\mathrm{F}\ll 1$ volt/cm, $v_d\ll s$. Then for the same F (3.16) gives smaller value of Λ than (3.10). The temperature of the system of conduction electrons may rise during acoustic waves are passing through materials.

The circumstances are very different in the low frequency range. Since F is oscillating like acoustic waves, in process (I) the energy is *going and coming* between acoustic waves and conduction electrons. Then the net losses of energy is determined by process (I+II) i.e. Ohmic relation.

§ 4. Magneto-Acoustic Resonance in the High Frequency Range

Recently Pippard[2] has proposed a concept of magneto-acoustic resonance to interpret the experiments of Bömmel[11] who detected the resonance-like behavior of the absorption coefficient in a magnetic field. Morse *et. al.*[12], however, analyzed their experiments with some different concepts. But as was pointed out by the present author[1], Pippard's and Morse *et. al.*'s concepts are applicable only to the intermediate frequency range and new magneto-acoustic resonance may be expected in the high frequency range. In this section we shall discuss qualitatively new magneto-acoustic resonance of the latter type.

When a magnetic field is applied in z-direction, the wave function and the energy eigenvalue of a conduction electron are given by[13]

$$\psi(n,\ x_0,\ k_z)=\varphi_n(x-x_0)\exp\left(-\frac{m\omega_c}{\hbar}x_0y\right)\exp(-ik_z\cdot z) \tag{4.1}$$

$$\mathrm{E}(n,\ x_0,\ k_z)=\hbar\omega_c\left(n+\frac{1}{2}\right)+\frac{\hbar^2k_z^2}{2m}\,, \tag{4.2}$$

if we choose the vector potential as $\mathrm{A}_x=\mathrm{A}_z=0$, $\mathrm{A}_y=\mathrm{H}x$. Here

$$x_0=-\frac{\hbar k_y}{m\omega_c}\,,\qquad \omega_c=\frac{e\mathrm{H}}{mc} \tag{4.3}$$

and $\varphi_n(x-x_0)$ represents the n-th order wave function of a harmonic oscillator centered at x_0. The change of the occupation number of acoustic phonons by conduction electrons is given, similar to (3.1), by

$$\begin{aligned}\left(\frac{\partial\mathrm{N}}{\partial t}\right)_{el}=&\frac{\mathrm{C}^2q^2\mathrm{N}}{\rho h\nu}\sum_{n,x_0,k_z}W_{n,n'}\\&\times\left\{\left[f\left(n',\,x_0-\frac{\hbar q_y}{m\omega_c},\,k_z+q_z\right)(1-f(n,\,x_0,\,k_z))-f(n,\,x_0,\,k_z)\left(1-f\left(n',\,x_0-\frac{\hbar q_y}{m\omega_c},\,k_z+q_z\right)\right)\right]\Omega^+\right.\\&\left.+\left[f(n,\,x_0,\,k_z)\left(1-f\left(n',\,x_0+\frac{\hbar q_y}{m\omega_c},\,k_z-q_z\right)\right)-f\left(n',\,x_0+\frac{\hbar q_y}{m\omega_c},\,k_z-q_z\right)(1-f(n,\,x_0,\,k_z))\right]\Omega^-\right\}\end{aligned} \tag{4.4}$$

where

$$\left.\begin{aligned} \Omega^{+}&=\Omega\left\{\mathrm{E}(n,\ x_0,\ k_z)-\mathrm{E}\left(n',\ x_0-\frac{\hbar q_y}{m\omega_c},\ k_z+q_z\right)+h\nu\right\}, \\ \Omega^{-}&=\Omega\left\{\mathrm{E}(n,\ x_0,\ k_z)-\mathrm{E}\left(n',\ x_0+\frac{\hbar q_y}{m\omega_c},\ k_z-q_z\right)-h\nu\right\} \end{aligned}\right\} \tag{4.5}$$

and

$$\left.\begin{aligned} W_{nn'}&=|J_{nn'}|^2, \\ J_{nn'}&=\int_{-\infty}^{\infty}\exp(iq_x x)\cdot\varphi_n(x-x_0)\cdot\varphi_{n'}\left(x-x_0\pm\frac{\hbar q_y}{m\omega_c}\right)dx \end{aligned}\right\} \tag{4.6}$$

Though it is very difficult to compute (4.4) exactly, the following qualitative conclusions can be obtained. When acoustic phonon beam is travelling in the direction perpendicular to the magnetic field, $q_z \doteqdot 0$, y-component of phonon beam changes the center x_0 of conduction electrons and x-component produce the transition between oscillator states of electrons. Asymmetry of the role of x- and y-component of phonon beam results from the asymmetrical choice of the vector potential. Therefore, in general, the transverse component of phonon beam gives rise the change in both x_0 and n. From (4.5) the integral must be finite only when

$$\mathrm{E}(n,\ x_0,\ k_z)-\mathrm{E}\left(n',\ x_0\mp\frac{\hbar q_y}{m\omega_c},\ k_z\right)\pm h\nu=0\ . \tag{4.7}$$

Substituting (4.2) into (4.7), we get the condition of magneto-acoustic resonance in the high frequency range:

$$|n-n'|\hbar\omega_c=\hbar\omega\ , \tag{4.8}$$

which is different from the resonance in the intermediate frequency range by a factor[1] of $(\pi/2)(s/v_0)$. It is interesting to note that cyclotron resonance[14] in semiconductors corresponds rather to magneto-acoustic resonance in the high frequency range.

When acoustic phonon beam is travelling in z-direction, the transition between oscillator states does not occur. The resonance-like behavior cannot be expected in this case.

It will be important to point out that magneto-acoustic resonance occurs not only in the absorption of waves but in acousto-electric effect. Physical considerations give a picture that under the resonance condition the component of electronic momentum parallel to $\boldsymbol{q}$ will rapidly increase receiving the acoustic momentum, then the current or acousto-electromotive force will have *the resonance-like behaviors.*

§ 5. Concluding Remarks

As was mentioned in § 1, the high frequency range has not been achieved up to the present. It is, however, expected to make the experimental proof of our theory in future.

From the experimental point of view, it is easier for metals to detect (1) the absorption coefficient by conduction electrons, (2) magneto-acoustic resonance in the absorption of waves. On the contrary, however, it is easier

Table III. The main results obtained in this paper.

	metals	semiconductors
acousto-electric effect	$\mathrm{F}=\dfrac{3\pi^2C^2m^{*1/2}\nu}{\sqrt{2}\,\rho e s^3 E_0{}^{3/2}}\gamma$	$\mathrm{F}=\dfrac{3\pi^2C^2m^{*1/2}\nu}{\sqrt{2}\,\rho e s^3(\kappa T)^{3/2}}\dfrac{\Gamma(1-\alpha)}{\Gamma(\frac{5}{2}-\alpha)}\gamma$
absorption coefficient	$\Lambda=\dfrac{2m^{*2}C^2\nu}{\rho\hbar^3s^2}$	$\Lambda=\dfrac{2m^{*2}C^2\nu}{\rho\hbar^3s^2}\exp(E_0/\kappa T)$
coefficient of Weinreich's relation	$\delta=1$	$\delta=\dfrac{4}{3\sqrt{\pi}}\dfrac{\Gamma(\frac{5}{2}-\alpha)}{\Gamma(1-\alpha)}$
magneto-acoustic resonance to be easily detected	M.A.R. of Λ	M.A.R. of F

for semiconductors to detect (1) acousto-electric effect, (2) magneto-acoustic resonance in acousto-electromotive force. In conclusion, we tabulated the main results obtained in this paper in Table III.

The author should express his thanks to Drs. G. M. Hatoyama, M. Shibuya and W. Sasaki for their encouragements and valuable discussions.

References

1) A. B. Pippard: Phil. Mag. **46** (1955) 1104. N. Mikoshiba: J. Phys. Soc. Japan **13** (1958) 759.
2) A. B. Pippard: Phil. Mag. **2** (1957) 1147.
3) B. V. Paranjape: Proc. Phys. Soc. **A66** (1953) 572.
4) C. Kittel: Acta Metallurgica **3** (1955) 295.
5) Van Den Beukel: Appl. Sci. Research **B5** (1956) 459.
6) R. H. Parmenter: Phys. Rev. **89** (1953) 990. In the recent paper (to be published), he has concluded that his theory was applicable only to the high frequency range.
7) W. P. Mason and H. E. Bömmel: J. Acoust. Soc. America **28** (1955) 930. R. W. Morse and H. V. Bohm: Phys. Rev. **108** (1957) 1094.
8) G. Weinreich: Phys. Rev. **107** (1957) 317.
9) A. H. Wilson: "The Theory of Metals" (Cambridge) (1953) 256.
10) C. Kittel: "Introduction to Solid State Physics" (John. Wiley and Sons) (1956) 249, 349.
11) H. E. Bömmel: Phys. Rev. **100** (1955) 758.
12) R. W. Morse, H. V. Bohm and J. D. Gavenda: Phys. Rev. **109** (1958) 1394.
13) S. Titeica: Ann. Phys. **22** (1935) 129.
14) G. Dresselhaus, A. F. Kip and C. Kittel: Phys. Rev. **100** (1955) 618.

JOURNAL OF THE PHYSICAL SOCIETY OF JAPAN Vol. 14, No. 1, JANUARY, 1959

On the Dielectric Losses in Impure Ionic Crystals

By Tosiyuki NINOMIYA*

Department of Applied Physics, Faculty of Engineering, University of Tokyo, Tokyo

(Received August 28, 1958)

Mechanisms of the dielectric loss due to vacancy-impurity complexes are re-examined by considering effects of polarization of both impurity- and lattice ions. We find that these effects cause some amounts of dielectric loss and a loss curve is well represented by a Debye type one. We point out that these effects may remove the quantitative discrepancy between the previous theory and experiments.

§ 1. Introduction

Ionic crystals containing divalent impurity cations show dielectric loss peaks at low temperature in low frequency range. These loss peaks are nearly of Debye type and considered to be those due to impurity-vacancy complexes.

The relation between the number of complexes and the magnitude of a loss peak has been given as[1)]

$$\tan\delta=\frac{8\pi e^2a^2}{3\varepsilon kT}N_c\frac{\omega\tau}{1+\omega^2\tau^2}\,, \tag{1.1}$$

where a is the anion-cation distance in the solvent crystal, N_c the number of complexes per unit volume, ε the dielectric constant and τ the relaxation time.

Teltow and Wilke[2)] used this equation to analyse their result of measurements on the dielectric loss in silver bromide crystals containing small amounts of cadmium bromide and found that the calculated number of complexes is about two and a half times smaller than the total number of impurity ions, although their experimental result suggested that practically all of the impurity ions were associated with the vacancies. Similar results have been obtained in sodium chloride crystals by Haven[3].

---

* Present Address: the Institute for Solid State Physics, University of Tokyo, Tokyo, Japan.

This discrepancy is considered to be partly due to the over-simplification of the model used in deriving Eq. (1.1). Lidiard has explored the possibility of explanation of this, but the reason still remains uncertain. The purpose of this paper is to present another possibility.

§ 2. Polarization of Complexes

When a pure crystal is polarized, we may imagine that the positive ions remain in their original positions, while the negatives are displaced. The displacement of the ions may be considered to have the effect of introducing a point dipole at each negative lattice point. In a crystal containing foreign cations a displacement of an impurity ion relative to the negative ions is different from that of the cations of the host crystal because of its different amount of charge or ionic radius. This different displacement introduces a dipole m at the site of impurity ion. In this section this effect will be taken into account. In Fig. 1 a part of the twelve nearest neighbouring positions of an impurity ion in a lattice of NaCl type is shown. The potential energies at various points due to the dipole, the moment of which is parallel to the external field, are as follows:

$$\left.\begin{aligned} &\varphi(101)=0.354m/a^2\,, \\ &\varphi\left(\frac{1}{2}\,\frac{1}{2}\,\frac{3}{2}\right)=0.110m/a^2\,, \\ &\varphi(011)=0\,, \qquad \text{etc.}\,. \end{aligned}\right\} \tag{2.1}$$

Therefore, this dipole restricts a change of orientation of the complex, part of which the impurity ion is.

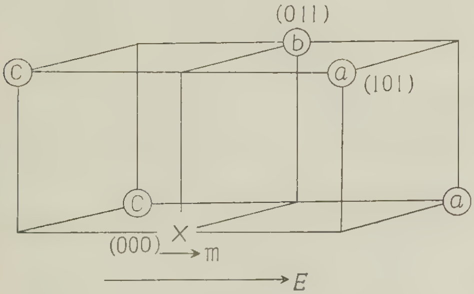

× : impurity ion
C : nearest neighbour

Fig. 1. A part of the twelve nearest cation neighbours to an impurity ion in a lattice of NaCl type. If the impurity ion is part of a complex, one of these twelve sites will be vacant.

Secondly the effect is considered which arises from a change of dipole moment of the complexes. An impurity ion which is associated with a cation vacancy is attracted towards the vacancy electrostatically. The polarization of the impurity ion due to the vacancy differs from that of a nearest neighbour cation to the vacancy and this also introduces a dipole $-\sqrt{2}\,\beta ea$, the moment of which is parallel to that of the complex, at the impurity ion site.

When a cation moves from the (101) site to the (011) via the $\left(\frac{1}{2}\,\frac{1}{2}\,\frac{3}{2}\right)^*$, it must surmount a potential barrier, the height of which is

$$U+\frac{1}{2}eaE-(0.354-0.110)em/a^2 -\frac{1}{2}\left(E+\frac{4\pi}{3}P\right)\beta ea\,, \tag{2.2}$$

where U is the height of the barrier in the absence of an external field and P is the polarization of the crystal. The third term of the formula (2.2) is that which results from the presence of the potential of constraint given by Eq. (2.1) and the fourth term is the work done by the external field when the dipole $\sqrt{2}\,\beta ea$ follows the motion of the vacancy to change its orientation.** Approximately

$$E+\frac{4\pi}{3}P=\frac{\varepsilon+2}{3}E\,, \tag{2.3}$$

where ε is the dielectric constant of the pure solvent crystal. m is proportional to the strength of the external field,

$$m=\alpha E\,. \tag{2.4}$$

---

* Haven suggested that a positive ion passes near the tetrahedral hole on its way from one site to another. Even if an ion migrates via any other point, the equation (2.15) which gives the polarization of the complexes does not change.

** Note that the Lorentz internal field acts on an ion to make polarize but does no work when an ion jumps from one lattice site to another[4]. Strictly speaking E is replaced by $E+\frac{4\pi}{3}(P_i+P_c)$ in the second term of the formula (2.2). But, in the case of usual concentration of impurity, $\frac{4\pi}{3}(P_i+P_c)$ is far smaller than E and can be neglected.

Inserting this into the formula (2.2), we have

$$U+\frac{1}{2}(1+p)eaE \tag{2.5}$$

as the height of barrier, where

$$p=-0.488\alpha/a^3-\frac{\varepsilon+2}{3}\beta\ .$$

The height of the potential barrier to surmount on the way to the (101) site from the (011) is

$$U=\frac{1}{2}(1+q)eaE\ , \tag{2.6}$$

where

$$q=-0.220\alpha/a^3-\frac{\varepsilon+2}{3}\beta\ .$$

Those for other processes of vacancy migration are treated similarly.

Next the exchange of positions between the impurity ion and its attached vacancy is considered. When the vacancy is at the (101) site, the electrostatic interaction energy of the dipole m with the vacancy is $-0.354me/a^2$, since the cation vacancy has the charge $-e$ effectively. The height of the barrier which the impurity ion must surmount in the exchange process is

$$\begin{aligned} U'-eaE+\varphi+0.354me/a^2+\frac{\varepsilon+2}{3}\beta eaE \\ =U'-(1+p')eaE\ , \end{aligned} \tag{2.7}$$

where

$$p'=-\left(0.354\alpha/a^3+\varphi/eaE+\frac{\varepsilon+2}{3}\beta\right)$$

and φ is the potential energy of the dipole m at the peak of the barrier. The activation energy for the inverse process is

$$\begin{aligned} U'+eaE+\varphi-0.354me/a^2-\frac{\varepsilon+2}{3}\beta eaE \\ =U'+(1+q')eaE\ , \end{aligned} \tag{2.8}$$

where

$$q'=-\left(0.354\alpha/a^3-\varphi/eaE+\frac{\varepsilon+2}{3}\beta\right).$$

Because φ is proportional to m and, therefore, to E, p' and q' are independent of E.

The equations giving the numbers n_a, n_b, n_c of dipoles with (a), (b), (c) orientations are

$$\begin{aligned} \frac{dn_a}{dt}=&-2n_aw_1\left\{1+\frac{ea}{2kT}(1+q)E\right\}+2n_bw_1\left\{1-\frac{ea}{2kT}(1+p)E\right\} \\ &-n_aw_2\left\{1+\frac{ea}{kT}(1+p')E\right\}+n_cw_2\left\{1-\frac{ea}{kT}(1+q')E\right\}, \end{aligned} \tag{2.9}$$

$$\frac{dn_b}{dt}=2n_aw_1\left\{1+\frac{ea}{2kT}(1+q)E\right\}-4n_bw_1+2n_cw_1\left\{1-\frac{ea}{2kT}(1+q)E\right\}, \tag{2.10}$$

$$\begin{aligned} \frac{dn_c}{dt}=&2n_bw_1\left\{1+\frac{ea}{2kT}(1+p)E\right\}-2n_cw_1\left\{1-\frac{ea}{2kT}(1+q)E\right\} \\ &+n_aw_2\left\{1+\frac{ea}{kT}(1+p')E\right\}-n_cw_2\left\{1-\frac{ea}{kT}(1+q')E\right\}, \end{aligned} \tag{2.11}$$

where w_1 is the jump frequency with which a vacancy will jump from one attached position to another particular attached position in the absence of the external field and w_2 is that with which an impurity ion and its attached vacancy will exchange their positions. When E varies harmonically with time,

$$E=E_0\exp(i\omega t)\ ,$$

the steady state solutions of (2.9) to (2.11) to the first order in E are

$$n_a=\frac{1}{3}N_c-E_0\exp(i\omega t)\frac{2eaN_c}{3kT}\left\{\left(1+\frac{p+q}{2}\right)w_1+\left(1+\frac{p'+q'}{2}\right)w_2\right\}\Big/2(w_1+w_2)+i\omega\ , \tag{2.12}$$

$$n_b=\frac{1}{3}N_c\ , \tag{2.13}$$

$$n_c=\frac{1}{3}N_c+E_0\exp(i\omega t)\frac{2eaN_c}{3kT}\left\{\left(1+\frac{p+q}{2}\right)w_1+\left(1+\frac{p'+q'}{2}\right)w_2\right\}\Big/2(w_1+w_2)+i\omega\ , \tag{2.14}$$

where N_c is the total number of the complexes per unit volume and

$$p+q=p'+q'=-\left[0.708\alpha/a^3+\frac{2(\varepsilon+2)}{3}\beta\right].$$

The polarization of the complexes is then

$$\begin{aligned}P_c&=ea(n_c-n_a)\\&=\frac{2e^2a^2N_c}{3kT}E_0\exp(i\omega t)\left(1+\frac{p+q}{2}\right)\Big/1+\frac{i\omega}{2(w_1+w_2)}\,.\end{aligned}\tag{2.15}$$

§ 3. Polarization of the Lattice Ions of the Host Crystal and of Impurity Ions

The total polarization of a crystal is the sum of three parts; the polarization of the complexes, of the lattice ions of the host crystal and of the impurity ions. The first has been obtained in Sec. 2. In this section the last two are considered.

The field which acts on the lattice ions to make polarize is

$$F_l=E+\frac{4\pi}{3}(P_l+P_i)\,,\tag{3.1}$$

where P_l is the polarization of the host crystal lattice ions and P_i is that of the impurity ions. Then we obtain

$$P_l=\frac{\varepsilon-1}{4\pi}E+\frac{\varepsilon-1}{3}P_i\,.\tag{3.2}$$

When we let α_i be the polarizability of an impurity ion,

$$\begin{aligned}P_i&=N_i\alpha_i\left[E+\frac{4\pi}{3}(P_l+P_i+P_c)\right]-\beta P_c\\&\approx N_i\alpha_i\left(E+\frac{4\pi}{3}P_l\right)-\beta P_c\,,\end{aligned}\tag{3.3}$$

where N_i is the number of the impurity ions per unit volume.

The total polarization is

$$\begin{aligned}P&=P_c+P_l+P_i\\&=\frac{\varepsilon-1}{4\pi}E+\frac{\varepsilon+2}{3}N_i\alpha_i\left(E+\frac{4\pi}{3}P_l\right)\\&\quad+\left(1-\frac{\varepsilon+2}{3}\right)P_c\end{aligned}\tag{3.4}$$

and the dielectric loss due to the complexes is given as

$$\begin{aligned}&\tan\delta\\&=\left(1-\frac{\varepsilon+2}{3}\beta\right)\left(1+\frac{p+q}{2}\right)\frac{8\pi e^2a^2}{3\varepsilon kT}N_c\frac{\tau\omega}{1+\tau^2\omega^2}\,,\end{aligned}\tag{3.5}$$

where $\tau=1/2(w_1+w_2)$. This expression gives the value which is $\left(1-\frac{\varepsilon+2}{3}\beta\right)\left(1+\frac{p+q}{2}\right)$ times larger than that used usually.

§ 4. Discussions

It is difficult to make an accurate evaluation of $\left(1-\frac{\varepsilon+2}{3}\beta\right)\left(1+\frac{p+q}{2}\right)$, unless the calculation is made on the basis of the Born-Mayer model. In this situation we shall make a rather rough estimation of it for silver bromide and compare it with the results of measurements of Teltow and Wilke. It is obtained from the continuum model that a nearest cation neighbour to a vacancy is displaced by $\frac{1}{8\pi}\left(1-\frac{\varepsilon_0}{\varepsilon}\right)$ towards the vacancy. If a displacement of an impurity ion, which is part of a complex, is same to this, β is obtained to be about 0.02. However, the displacement of the ion can be expected to be a little larger, when we calculate it on the basis of the discrete model, and the impurity ion is attracted more strongly to the vacancy than the silver ion because of its double charge. Therefore, it seems reasonable to estimate that β becomes about 0.03.

On the other hand, when an external field is applied, the displacement of the positive ions relative to the negatives is given as $\frac{a^3}{2\pi e}(\varepsilon-\varepsilon_0)E$. Since the electrostatic force which acts on an impurity ion to make polarize is twice times that for a silver ion, the displacement of an impurity cadmium ion may be larger than that of silver ions. But the six nearest anion neighbours to the impurity ion are displaced inwards, and there may exist a larger repulsive interaction between the anions and the foreign ion. Therefore, the displacement of the impurity ion due to an external field may not be able to be twice times that of a silver ion. When the ratio of a displacement of an impurity ion to that of a silver ion is 1.5 and 1.25, $0.708\alpha/2a^3$ has the value of about 0.48 and 0.24 respectively. Using that $\beta\sim 0.03$, the value of

$$\left(1-\frac{\varepsilon+2}{3}\beta\right)\cdot\left(1+\frac{p+q}{2}\right)$$

is shown in Table I. In the above estimation of m and β, the contribution from the differring electronic polarizability is neglected, since this is considered to be small.

Table I. Values of the correction factor.

The ratio of amount of displacement	$\left(1-\frac{\varepsilon+2}{3}\beta\right)\left(1+\frac{p+q}{2}\right)$
1.5	0.31
1.25	0.52

The correction factor is required to be about 0.4 from the result of measurements of Teltow and Wilke, if all the vacancies are associated with the impurity ions under the conditions of their experiments. Therefore, if the amount of displacement of a cadmium ion is 1.25 to 1.5 times larger than that of a silver ion under an external field, the experimental result can be explained, and this amount seems not unreasonable.

If the observed loss curve is wider than a simple Debye curve as in the case of alkali halide crystals[5)], although this is not sure in the data of Teltow and Wilke, the number calculated from the peak height is ought to be smaller than the number of complexes actually present. Then the correction factor required is larger than 0.4 and a smaller displacement of an impurity ion is enough to explain the discrepancy.

§5. Conclusion

In the calculation of the magnitude of dielectric loss due to impurity-vacancy complexes, the effect of polarization of both impurity and lattice ions is investigated. This leads to a change of the magnitude of the loss, without shift of its peak frequency in the isothermals of loss plotted against the frequency. It may be possible to explain Teltow and Wilke's work by considering the effects mentioned above, although an accurate value of the correction factor can not be obtained, unless we perform a detailed computation on the basis of Born-Mayer model. The result of such a calculation on alkali halide crystals will be published later.

Acknowledgement

I would like to express my sincere thanks to Professor Y. Suge and Professor T. Inui for their guidance and encouragement. I am also much indebted to Dr. A. B. Lidiard and Dr. S. Sonoike for many valuable discussions.

References

1) A. B. Lidiard: Defects in Crystalline Solids (London: Physical Society) (1955) p. 283.
2) J. Teltow and G. Wilke: Naturwiss. **41** (1954) 423.
3) Y. Haven: Defects in Crystalline Solids (London: Physical Society) (1955) p. 261.
4) A. B. Lidiard: Handbuch der Physik XX (Berlin: Springer-Verlag) (1957) p. 325.
5) Y. Haven: J. Chem Phys. **21** (1953) 171.

JOURNAL OF THE PHYSICAL SOCIETY OF JAPAN Vol. 14, No. 1, JANUARY, 1959

On the Theory of the Thermoelectricity in Two-Band Semiconductors

By Eijirō HAGA

Department of Physics, Faculty of Science, Niigata University, Niigata

(Received September 3, 1958)

In many literatures the thermoelectromotive force of a circuit composed of two different conductors is expressed by an integral of the field $\oint\vec{E}\cdot\vec{dl}$ along the circuit with two junctions of different temperature. This definition is not free from ambiguity when we deal with the thermoelectricity of two-band semiconductors. In the present paper a theory of the thermoelectricity of two-band semiconductors is developed with consideration of temperature dependence of the gap energy. The Thomson relations are proved to be satisfied.

§ 1. Introduction

Let us imagine a circuit which is composed of two kinds of conductors *I* and *II*. They are connected with two junctions (x_1 and x_2, respectively), whose temperature is kept constant (T_1 and T_2, respectively; $T_2>T_1$). In many literatures on the theory of thermoelectricity the thermoelectromotive force of such a circuit is identified with the electric field integrated along the circuit

$$\Theta_{I,II}(T_1,\ T_2)=-\int_{x_0}^{x_3}E_x\,dx \qquad (1)$$

under the subsidiary condition that the current is zero.

First we consider n-type semiconductors or single-band metals with an assumption that the position of the band edge of the conduction band does not vary with temperature. Then, the electric field is given by

$$-eE_x=T\frac{d}{dx}\frac{\mu}{T}+\frac{K_2}{TK_1}\frac{dT}{dx}\,, \qquad (2)$$

where μ is the Fermi level *measured from the bottom of the conduction band* and

$$K_n=-\frac{1}{4\pi^3}\int\tau v_x{}^2\mathcal{E}^{n-1}\frac{\partial f_0}{\partial\mathcal{E}}\,d\Omega\,. \qquad (3)$$

Here f_0 is the Fermi distribution function, $d\Omega$ the volume element in the reduced wave vector space and other notations are as ordinary. Integrating Eq. (2) along the circuit, we have by partial integration

$$-e\int_{x_0}^{x_3}E_x dx=[\mu]_{x_0}^{x_3}+\int_{x_0}^{x_3}\frac{1}{T}\left(\frac{K_2}{K_1}-\mu\right)\frac{dT}{dx}dx\,. \qquad (4)$$

In many literatures the first term in the above is tacitly assumed to be zero. This, however, is not true as far as the integration is carried out along the interior of the conductors excluding junctions. Instead we have

$$[\mu]_{x_0}^{x_3}=\{\mu_{II}(x_2)-\mu_I(x_2)\}-\{\mu_{II}(x_1)-\mu_I(x_1)\} \qquad (5)$$

which does not vanish in general. To find the thermoelectromotive force of the circuit we must add to the right-hand side of Eq. (4) the integration *across* the junctions. The latter is seen to be equal to the algebraic sum of the jumps of the bottom level, $\mathcal{E}_c$, of the conduction band at the junction:

$$-\{\mathcal{E}_{cII}(x_1)-\mathcal{E}_{cI}(x_1)\}+\{\mathcal{E}_{cII}(x_2)-\mathcal{E}_{cI}(x_2)\}, \qquad (6)$$

since eE is nothing other than gradient of the bottom level of the conduction band:

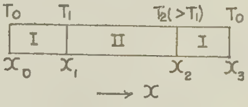

Fig. 1.

$$eE_x=\frac{d\mathcal{E}_c}{dx}\,. \qquad (7)$$

And we see that expressions (5) and (6) cancel each other as the Fermi level

$$\zeta=\mathcal{E}_c+\mu \qquad (8)$$

(not μ) is continuous at the junctions. Hence we are allowed to identify the second term of Eq. (4) with the thermoelectromotive force of the circuit multiplied by elementary charge as usually done in literatures.

The above situation will more easily be

seen if we trace throughout the circuit the Fermi level instead of the bottom level of the conduction band. In this respect Eq. (2) may be rewritten as (see Eq. (7) and (8))

$$-\frac{d\zeta}{dx}=\frac{1}{T}\left(\frac{K_2}{K_1}-\mu\right)\frac{dT}{dx}\,. \tag{9}$$

Now, the experimentally measurable thermoelectromotive force is the difference of the Fermi levels at x_0 and x_3, $\zeta(x_0)-\zeta(x_3)$, the temperatures at x_0 and x_3 being assumed to be equal to each other (say, equal to T_0°K). Hence, after integrating Eq. (9) along the circuit we have

$$e\Theta_{I,II}(T_1,\ T_2)\equiv\zeta(x_0)-\zeta(x_3)$$
$$=\int_{T_1}^{T_2}\frac{1}{T}\left(\frac{K_2}{K_1}-\mu\right)_{II}dT-\int_{T_1}^{T_2}\frac{1}{T}\left(\frac{K_2}{K_1}-\mu\right)_{I}dT\,. \tag{10}$$

It will be reasonable to define the absolute thermoelectromotive force, Θ, of a conductor to be the height of the Fermi level at the hot end relative to that at the cold end:

$$\Theta(T_1,\ T_2)=\frac{1}{e}\{\zeta(T_2)-\zeta(T_1)\} \tag{11}$$

which is equal to

$$\Theta(T_1,\ T_2)=-\frac{1}{e}\int_{T_1}^{T_2}\frac{1}{T}\left(\frac{K_2}{K_1}-\mu\right)dT \tag{12}$$

according to Eq. (9). Then the thermoelectromotive force of the circuit is given as

$$\Theta_{I,II}=\Theta_I-\Theta_{II}\,. \tag{13}$$

Differentiating Eq. (12) with respect to T and putting $T_2=T$, we have for the absolute thermoelectric power $Q=d\Theta/dT$

$$Q(T)=-\frac{1}{eT}\left(\frac{K_2}{K_1}-\mu\right). \tag{14}$$

Hitherto we have assumed that bottom level of the conduction band does not vary with temperature. As is well known this is not true in general. Nevertheless we can assert that the above consideration is valid even when the bottom level depends on temperature, because the force acting on an electron is equal to $-d\mathcal{E}_c/dx$, irrespective of whether the bottom level varies with temperature or not.

The situation is more complicated if we deal with two-band semiconductors. The gap energy between the bottom level, $\mathcal{E}_c$, of the conduction band and the top level, $\mathcal{E}_v$, of the valence band

$$\mathcal{E}_g=\mathcal{E}_c-\mathcal{E}_v \tag{15}$$

depends on temperature ($d\mathcal{E}_g/dT\sim10^{-4}$ ev/degree, being of the same order of magnitude as the very thermoelectric power of semiconductors), so that the "electric field" acting on electrons and that on holes, which should be identified with $e^{-1}d\mathcal{E}_c/dx$ and $e^{-1}d\mathcal{E}_v/dx$, respectively, are in general different to each other at the presence of temperature gradient. Therefore the integrated "electric field" (the left hand of Eq. (4)) loses the definite meaning in thermally inhomogeneous two-band semiconductors, and hence it will be more convenient to work with the gradient of the Fermi level from the outset.

§ 2. Thermoelectricity in Two-Band Semiconductors

In two-band semiconductors, the electric current density at the presence of temperature gradient is given by

$$j_x=j_x^{(1)}+j_x^{(2)} \tag{16}$$

with

$$\frac{j_x^{(1)}}{e}=\left(eE_x^{(1)}+T\frac{d}{dx}\frac{\mu}{T}\right)K_1^{(1)}+\frac{1}{T}K_2^{(1)}\frac{dT}{dx}\,,$$
$$\frac{j_x^{(2)}}{e}=\left(eE_x^{(2)}+T\frac{d}{dx}\frac{\mathcal{E}_g+\mu}{T}\right)K_1^{(2)}-\frac{1}{T}K_2^{(2)}\frac{dT}{dx}\,, \tag{17}$$

where affices (1) and (2) refer to electrons and holes, respectively. In Eq. (17) $E_x^{(1)}$ and $E_x^{(2)}$ denote the "electric fields" acting on electrons and holes, respectively:

$$eE_x^{(1)}=\frac{d\mathcal{E}_c}{dx}\,,\quad eE_x^{(2)}=\frac{d\mathcal{E}_v}{dx}\,. \tag{18}$$

These are not equal to each other at the presence of temperature gradient as mentioned in the previous section. Instead, we have, from Eqs. (15) and (18),

$$eE_x^{(2)}+\frac{d\mathcal{E}_g}{dx}=eE_x^{(1)}\,. \tag{19}$$

Taking this into consideration we have from Eqs. (16) and (17)

$$\frac{d\zeta}{dx}=eE_x^{(1)}+\frac{d\mu}{dx}=\frac{1}{K_1^{(1)}+K_1^{(2)}}\frac{j_x}{e}-\frac{1}{K_1^{(1)}+K_1^{(2)}}[(K_2^{(1)}-\mu K_1^{(1)})-(K_2^{(2)}+(\mathcal{E}_g+\mu)K_1^{(2)})]\frac{1}{T}\frac{dT}{dx}\,. \tag{20}$$

The expression for the absolute thermoelectric power in two-band semiconductors may easily be formed from Eq. (20) with $j_x=0$ (see § 1). We have

$$Q=\frac{1}{eT}\frac{1}{K_1^{(1)}+K_1^{(2)}}[(K_2^{(2)}+(\mathcal{E}_g+\mu)K_1^{(2)})-(K_2^{(1)}-\mu K_1^{(1)})] \,. \tag{21}$$

This may be written in the form

$$Q=\frac{1}{\sigma^{(1)}+\sigma^{(2)}}(\sigma^{(1)}Q^{(1)}+\sigma^{(2)}Q^{(2)}) \tag{22}$$

with

$$\sigma^{(1)}=e^2K_1^{(1)} \,, \qquad \sigma^{(2)}=e^2K_1^{(2)} \tag{23}$$

and

$$Q_1=-\frac{1}{eT}\left(\frac{K_2^{(1)}}{K_1^{(1)}}-\mu\right), \qquad Q_2=\frac{1}{eT}\left(\frac{K_2^{(2)}}{K_1^{(2)}}+\mathcal{E}_g+\mu\right). \tag{24}$$

In the above $\sigma^{(1)}(\sigma^{(2)})$ is the electronic (hole) conductivity and $Q^{(1)}(Q^{(2)})$ is the absolute thermoelectric power when only electrons (holes) would contribute to the conduction in the absence of holes (electrons). Eq. (20) may be rewritten in terms of Q as

$$\frac{d\zeta}{dx}=\frac{e}{\sigma}j_x+eQ\frac{dT}{dx} \,, \tag{25}$$

where $\sigma=\sigma^{(1)}+\sigma^{(2)}$ is the total conductivity. The physical meaning of this equation is obvious. The first term is the ohmic potential drop and the second is of thermoelectric origin.

The *energy flow* carried by charge carriers is given by

$$C_x=-(K_2^{(1)}-K_2^{(2)})\frac{d\zeta}{dx}-\frac{1}{T}[K_3^{(1)}-\mu K_2^{(1)}+K_3^{(2)}+(\mathcal{E}_g+\mu)K_2^{(2)}]\frac{dT}{dx}-\mathcal{E}_c\frac{j_x}{e}+\mathcal{E}_g\frac{j_x^{(2)}}{e} \,. \tag{26}$$

Here also we have used the relation Eq. (19). Inserting Eq. (17) for $j_x^{(2)}$ and substituting Eq. (20) for $d\zeta/dx$, we may express the energy flow in terms of j_x and dT/dx. We have

$$C_x=(eTQ-\zeta)\frac{j_x}{e}-\kappa_e\frac{dT}{dx} \,. \tag{27}$$

Here

$$\kappa_e=\frac{1}{T}\left[\left(K_3^{(1)}-\frac{K_2^{(1)2}}{K_1^{(1)}}\right)+\left(K_3^{(2)}-\frac{K_2^{(2)2}}{K_1^{(2)}}\right)\right]+\frac{1}{T}\frac{(K_1^{(1)}K_2^{(2)}+K_2^{(1)}K_1^{(2)}+\mathcal{E}_gK_1^{(1)}K_1^{(2)})^2}{(K_1^{(1)}+K_1^{(2)})K_1^{(1)}K_1^{(2)}} \tag{28}$$

is the electronic thermal conductivity. The first term of Eq. (27) means the energy flow accompanied by the current and states that the energy carried by unit current is equal to

$$TQ-\frac{\zeta}{e} \,. \tag{29}$$

Hence we see that the absolute Peltier heat, π, defined as the energy relative to the Fermi level carried by unit current is

$$\pi=TQ \,. \tag{30}$$

The rate of heat production in unit volume, H, is given as

$$H=-\frac{dC_x}{dx} \,. \tag{31}$$

Inserting Eq. (27) into Eq. (31) and using Eq. (25) (note that $d\mathcal{E}_c/dx=eE_x^{(1)}$) we have

$$H=\frac{j_x^2}{\sigma}-T\frac{dQ}{dT}j_x\frac{dT}{dx}+\frac{d}{dx}\left(\kappa_e\frac{dT}{dx}\right). \tag{32}$$

The second term of Eq. (32) is the Thomson heat and we have for the Thomson coefficient

$$\sigma_T=T\frac{dQ}{dT} \,. \tag{33}$$

Eqs. (30) and (33) are the so called Thomson relations,

§ 3. Discussion

The transport theory of the thermoelectricity for two-band semiconductors was first developed by Johnson and Lark-Horovitz⁽¹⁾. They first derived the expression for Thomson coefficient by calculating the rate of heat production and then integrated the Thomson relation (Eq. (33)) to find the expression for thermoelectric power. In calculating the rate of heat production they overlooked the heat released (or absorbed) by recombinations (or creations) of electron-hole pairs. If the variation of the gap energy with temperature is neglected as done by them the recombination heat may be expressed in our notations as

$$\varepsilon_g \frac{1}{e} \frac{dj_x^{(1)}}{dx} = -\varepsilon_g \frac{1}{e} \frac{dj_x^{(2)}}{dx} \tag{34}$$

which does not vanish in general at the presence of temperature gradient. We can easily ascertain that the recombination heat is automatically included in our calculation (see Eq. (26) for the rate of energy flow).

Tauc²⁾ followed the traditional way of identifying electric field integrated along whole circuit with its thermoelectromotive force tacitly assuming the gap energy to be independent of temperature. His results are legitimate as far as the assumptions made are granted. As pointed out in § 1, however, the temperature derivative of the gap energy is of the same order of magnitude as the thermoelectromotive force itself, so that we must emphasize that the temperature dependence of the gap energy must be taken into consideration in the transport theory of thermoelectricity of two-band semiconductors.

The writer wishes to express his cordial thanks to Mr. I. Yokota and Mr. S. Miyatani for their useful discussions and kind advices, and also to Professor A. Okazaki for his interests and encouragements for this work.

The present work was supported by the Scientific Research Fund of the Ministry of Educations.

References

1) V. A. Johnson and K. Lark-Horovitz: Phys. Rev. **92** (1953) 226.
2) J. Tauc: Phys. Rev. **95** (1954) 1394.

JOURNAL OF THE PHYSICAL SOCIETY OF JAPAN Vol. 14, No. 1, JANUARY, 1959

Photo-voltaic Effect in Se-photocells having Artificial Intermediate Layers of CdSe, CdTe, ZnSe and ZnTe

By Hirosi TUBOTA and Hiromichi SUZUKI

General Education Department, Kyusyu University

(Received September 15, 1958)

Measurements of the photovoltages generated in the Se-photocells which have each an artificial intermediate layer such as CdSe, CdTe, ZnSe and ZnTe have been made. From the results obtained, the double barrier effect on both side contacts of selenide or telluride layer was concluded.

§ 1. Introduction

It is believed that in selenium rectifiers the rectifying barrier lies at the contact between Se (*p*-type) and CdSe (*n*-type) formed by the reaction of Se and a counter electrode alloy¹⁾. There should be also a rectifying barrier at the contact between the counter electrode metal and CdSe layer. But it is generally admitted that the effect of the former barrier should be predominant to the latter and that, in practice, the effect at the contact between CdSe and the counter electrode metal may be negligible in the rectification.

We considered more closely the problem whether any individual information about the effects at both side contacts of CdSe layer could be obtained. In connection with this problem, we studied photo-voltaic effects in selenium photocells having artificial intermediate layers of selenides and tellurides of Cd and Zn. To interpret the results obtained, it seems to be useful to consider the effects at both side contacts of selenide or telluride layers.

§ 2. Experiments

Selenium barrier layer photocells used in this study were prepared in our laboratory, depositing thin films of CdSe (n-type), CdTe (p-type), ZnSe (p-type) and ZnTe (p-type) respectively by vacuum evaporation on an ordinary commercial selenium rectifier disk which has not any counter electrode. Then, on these films, metals such as Au, Cd, Zn and In were, respectively, evaporated as a transparent counter electrode. The thickness of an evaporated film was estimated by the weighing method.

Measurements of open circuit photovoltages (V_p) generated in these photocells were made by a conventional method at room temperature. At first we obtained V_p also from the voltage current characteristics under illumination[2]. But, as we ascertained that the agreement of the values obtained by the above two methods was fairly good, we used the open circuit method for simplicity thereafter. The sample was set so as to receive only the direct beams from a light source. The light source (100 watt tungsten lamp) was placed at a fixed distance (25 cm) from the sample throughout this study. As a filter to cut off the infrared radiation effective for the temperature rise of samples, we used a copper sulfate saturated solution. All measurements were made at the stationary state reached after the exposure to light.

In the first series, we measured the photovoltages (V_p) for the samples with CdSe layers of various thicknesses. As the counter electrodes, evaporated Au-layers with the same thickness were used in this series. The actual preparations of these samples were as follows: on a Se rectifier disk, four CdSe layers (diameter: 1 cm) with different thickness were separately deposited, and then Au-layers with the same thickness were deposited on each CdSe layer. Table I shows the typical values of V_p obtained at the three periods after the preparation of the samples. It is seen from the table that as the thickness of CdSe layer varies from 0.4μ to 1.5μ, there is a maximum value of V_p, and each value of V_p for different thickness of CdSe layer is nearly constant, at least, during two weeks after the preparation of the sample.

Table I. V_p of photocells with CdSe layers (Counter electrode: Au, about 0.1μ thickness).

Thickness of CdSe layer (in μ)	V_p (in Volt)		
	Immediately	After 1 day	After 14 days
0.4	0.036	0.038	0.037
0.7	0.044	0.044	0.045
1.0	0.080	0.081	0.081
1.5	0.043	0.045	0.044

In the second series, the measurements for the counter electrodes of different kinds of metals mentioned above in the case of CdSe layer of the same thickness were made. The samples were prepared such as in the first series of experiments, namely, a set of samples with CdSe layers of the same thickness and the counter electrodes of different kinds was formed on one Se rectifier disk. The results for two kinds of thickness of CdSe layer are shown in Table II.

Table II. V_p of photocells with CdSe layer for the electrodes of different kinds of metals (in volt).
(Thickness of counter electrodes: about 0.1μ).

Thickness of CdSe layer (in μ)	Electrode metal			
	Au	Cd	Zn	In
0.7	0.09	0.11	0.16	0.05
1.0	0.10	0.14	0.18	0.07

In the third series, we observed the dependence of the magnitude of V_p upon the thickness of metal electrodes in the case of CdSe layer of a fixed thickness. The results showed that V_p merely decreases as the thickness of the electrode increases from about 0.1μ to 1μ in the case of Au electrode.

In all measurements for the case of CdSe layer, we observed that the sense of V_p agrees with that of commercial selenium photocells, that is, it is negative at the counter electrode. In comparison with our samples, we measured V_p of the commercial selenium photocells and

Table III. V_p of photocells with CdTe, ZnSe and ZnTe layers for the electrodes of different kinds of metals (in volt).
(Thickness of counter electrodes: about 0.1μ).

Electrode metal		Au	Cd	Zn	In
Material	Thickness				
ZnSe	0.3μ	0.0001	0.0007	−0.003	−0.003
ZnTe	1.0μ	0.0001	0.0001	0.0001	−0.0001
CdTe	0.5μ	0.0000	0.05	0.001	0.0003

obtained the value of about 0.1 volt in our experimental procedure. But in the cases of CdTe, ZnSe and ZnTe, we found that the values of V_p for nearly all samples were small compared with that of the case of CdSe and also there was the reverse sign of V_p for Zn and In electrodes, as seen in Table III.

§ 3. Discussion

To explain the behaviors observed in the study mentioned above, it seems to be reasonable to consider the double barrier layers appeared on contacts of counter electrode metal-intermediate layer (*n* or *p*)-selenium (*p*) such as shown in Figs. 1 and 2. It may be considered that V_p should be attributed to two effects at the two barriers, one from the metal-intermediate layer contact and the other from the intermediate layer-selenium contact. In the dependence of V_p upon the thickness of an intermediate layer, there is the maximum value of V_p as shown in Table I. This may be explained as follows: As the thickness of the layer increases, the barrier is gradually formed, therefore V_p increases with the thickness at first due to electron-hole generation by light. As the thickness increases further, the light is more absorbed in the bulk of the intermediate layer and can hardly reach the intermediate layer-selenium contact. Then there should be a maximum value of V_p.

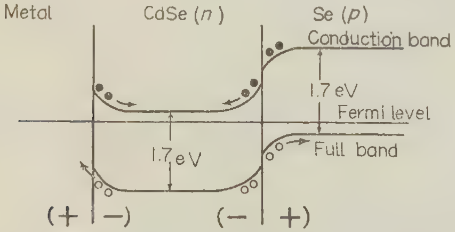

Fig. 1. Energy level scheme in the case of CdSe intermediate layer.

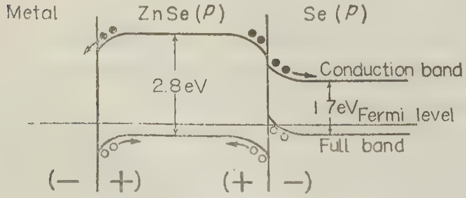

Fig. 2. Energy level scheme in the case of ZnSe intermediate layer.

In the case of CdSe, the fact that the sense of V_p is in agreement with that of commercial selenium photocells suggests that the effect at the contact of CdSe-Se is predominant to that at the contact of metal-CdSe. On the other hand, in the cases of ZnSe and ZnTe, the appearance of the reverse sign of V_p suggests that, for example, the contact of ZnSe-Se is more effective than that of In-ZnSe. At the contact of ZnSe-Se, there may be some other types of energy level schemes different from that shown in Fig. 2. But, considering the predominant effect at this contact, we assume the type as shown in the figure. It is difficult to make further discussions without a sufficient knowledge of band structure and optical properties of these materials.

The authors wish to express their sincere thanks to Prof. A. Okazaki for his continual advice and encouragement, and also to Shindengen-Kōgyō Company for offer of selenium rectifier disks. The present investigation was supported partly by the Scientific Research Expenditure of the Ministry of Education.

References

1) S. Poganski: Zeits. f. Phys. **134** (1953) 469.
A. Hoffman and F. Rose: ibid. **136** (1953) 152.
J. Yamaguchi: J. Phys. Soc. Japan **10** (1955) 234.
H. Tubota and H. Suzuki: Memoirs of Faculty of Sci. Kyusyu Univ. Ser. B, **2** (1957) 95.
2) Y. Matukura and A. Okazaki: ibid. **1** (1953). 89.

JOURNAL OF THE PHYSICAL SOCIETY OF JAPAN Vol. 14, No. 1, JANUARY, 1959

Lattice Scattering Mobility of Electrons in Cadmium Sulphide

By Hisao MIYAZAWA, Hajime MAEDA and Hiroshi TOMISHIMA

Matsuda Research Laboratory,
Tokyo-Shibaura Electric Co., Kawasaki

(Received October 1, 1958)

The Hall mobility of electrons has been measured between 90~400°K with many dark-conducting CdS/Ga, CdS/Cl and CdS/Cd single crystals. Among these results several typical data taken with crystals having non-degenerate carrier concentrations were chosen for analysing temperature dependence of the mobility. Assuming the observed mobility at lower temperatures is slightly influenced by the impurity scattering and Conwell Weisskopf formula is available here, it has been found that the plausible lattice scattering mobility after correction is well given by the following polar scattering form

$$\mu_L = A\{\exp(\Theta/T) - 1\}$$

with $A = 92.5 \pm 15$ cm²/volt sec and $\Theta = 370 \pm 30$°K.

In order to reach this result it is necessary to suppose there are about $10^{17} \sim 10^{18}$ uncontrollable deep-lying centers per unit volume in the present crystals, which permanently capture the conduction electrons and act as scatterers. The value of the characteristic temperature seems to be reasonable as compared with the one ($\Theta = 250 \sim 300$°K) previously obtained by Philips group in view of the infrared absorption band ($\Theta' = 335$°K) and the fine structure data in the edge emission ($\Theta = 460$°K).

§ 1. Introduction

After the development of Frerich's vapor method for growing artificial crystals, there exists an extensive literature on both electrical and optical properties of cadmium sulphide single crystals because of their striking photoconductive nature. Two dominant factors which determine the photoconductive sensitivity are the mean lifetime and the mobility of excited carriers, though they are usually inseparable in the observation of photocurrent. It has been said that the large photoconductivity of cadmium sulphide is mainly attributed to long mean lifetime of photoelectrons¹⁾, while electron mobility which is rather small is relatively ineffective. However, the lifetime is extremely structure-sensitive and depends upon capture cross section of many kinds of crystal imperfections or impurity centers of which atomic picture is not yet disclosed. On the other hand, the electron mobility is not so structure-sensitive that it is comparatively easy to get the intrinsic value. In any case, it is always desirable to know each individual parameter by all means.

As for the electron mobility of cadmium sulphide, the most detailed and precise study up to the present may be the one carried out by Kröger et al at Philips Laboratories²⁾. They observed the Hall effect and the resistivity on many single crystal specimens in the wide temperature ranges and obtained the Hall mobility of electrons. Their final results conclude that the temperature variation of Hall mobility as limited by lattice scattering between 200 and 700°K is accounted for with a characteristic temperature of longitudinal optical modes $\Theta = 250 \sim 300$°K, and a scattering at acoustical modes $aT^{-3/2}$ with $a = 3 \sim 8 \times 10^6$ cm² deg$^{3/2}$/volt sec, using the reasonable effective electron mass $0.2m_0 \sim 0.3m_0$ deduced from thermoelectric power data together with Hall coefficient.

However, their conclusion is based on the data that, between 75 and 300°K, Hall mobility of photoconducting specimens containing fairly large amount of ionized centers under illumination and, above 300°K, Hall mobility of the heavily doped dark-conducting specimens, respectively, may be regarded as lattice scattering mobility without any correction, since there appears no appreciable effect of impurity scattering. There will be little problem at higher temperatures where lattice scattering predominates, but at lower temperatures it will be questionable whether the observed mobility is influenced only by lattice scattering. Apparently, there is considerable discrepancy below 200°K between their calculated curve and observed one, which they also have thought of but have given up how to deal with. Therefore, in order to increase our understanding it will be worthwhile to reconsider the temperature dependence of Hall mobility by subtracting the impurity scattering effect.

As in our laboratories similar experimental work was carried out on cadmium sulphide single crystals having non-degenerate and suitable dark-conducting carriers still at lower temperatures, an attempt was made to estimate plausible lattice scattering mobility, assuming the observed data are combination of lattice and impurity effects. Though our correction method will be inaccurate to a certain extent because of the controversial assumptions, the procedures and the results which lead to a little higher characteristic temperature than that obtained by Philips group will be described in this paper.

§ 2. Experimental Results

Fairly dark-conducting single crystals, containing Cl or Ga respectively, were prepared by the ordinary vapor method, letting HCl or Ga vapor in the silica reaction tube during the growing of crystals. Crystals containing excess Cd, which were conductive too, were obtained by the heat treatment of pure crystals in H_2 atmosphere. Among these single crystals a number of favorable flakes, whose dimensions were about $10 \times 2 \times 0.1\,\mathrm{mm}^3$, were picked up for the present purpose. The specimens were electroded with indium metal and furnished with tungsten whisker probes.

The resistivity and the isothermal Hall coefficient have been measured for a number of these specimens between 90 and 400°K, from which several typical data have been chosen and are shown in Fig. 1 and Fig. 2. It is noticed that the carrier concentrations of these specimens are non-degenerate and in accordance with difference of the resistivity from one specimen to another there comes out a systematic correlation in the Hall coefficients.

The observed value of Hall mobility μ is given by the relation

$$\mu = R/\rho \,, \tag{1}$$

where R is the Hall coefficient and ρ is the resistivity. The values of μ are plotted in Fig. 3 as a function of temperature. A

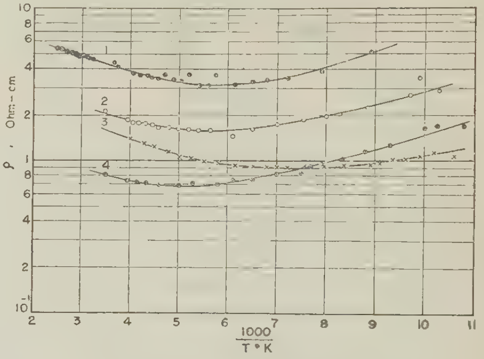

Fig. 1. Resistivity as a function of temperature.
1. CdS/Ga #1–17 2. CdS/Ga #1–5
3. CdS/Cd #3–5 4. CdS/Ga #1–15

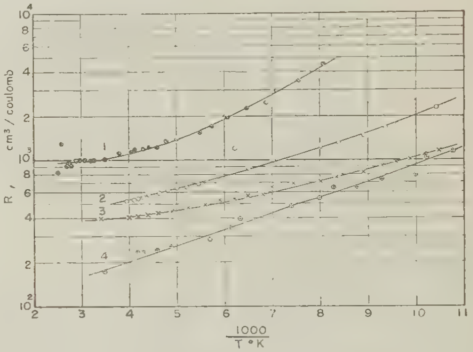

Fig. 2. Hall coefficient as a function of temperature.
1. CdS/Ga #1–17 2. CdS/Ga #1–5
3. CdS/Cd #3–5 4. CdS/Ga #1–15

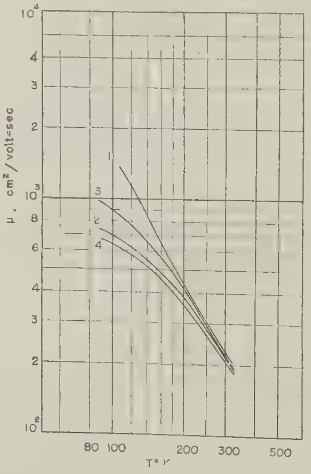

Fig. 3. Hall mobility vs temperature characteristics calculated from the data of Fig. 1 and Fig. 2.
1. CdS/Ga #1–17 2. CdS/Ga #1–5
3. CdS/Cd #3–5 4. CdS/Ga #1–15

general tendency is again noticed that the slope of the mobility curve at lower temperatures is steeper in the specimen of higher resistivity or higher Hall coefficient.

There are many other data in which the Hall coefficients are too small or too large. The former group, indicating small Hall coefficients, is unfavorable for the present purpose, because the carrier concentrations are degenerate and the Hall mobilities at lower temperatures are too flat to be correctly analysed. For the latter group of low carrier concentrations, on the other hand, it is difficult to observe isothermal Hall voltage accurately at lower temperatures because of high resistance between probes. Hence, all these data are omitted here.

§ 3. Assumptions

To obtain the lattice scattering mobility from the observed Hall mobility, several assumptions were made for the convenience of subsequent calculations as follows:

(1) The mechanisms of the lattice scattering and the impurity scattering are independent of each other, and the total scattering probability $1/\tau$, where τ is the relaxation time, can be written as

$$1/\tau=1/\tau_L+1/\tau_I \, . \qquad (2)$$

Here τ_L and τ_I are the relaxation times as determined by lattice scattering and impurity scattering respectively.

(2) As for the impurity scattering mobility, it is assumed that the modified Conwell-Weisskopf's formula is valid for these crystals, since the carrier concentrations are non degenerate and the scattering center concentrations are expected not so high in the present case.

(3) It is also assumed that whole scattering centers are singly charged, since their is no explicit evidence that the centers have double or more charges. Here, as shown in Fig. 4, the concentration of monovalent scattering centers N_I can be expressed as

$$N_I(T)=N_0+n(T) \, , \qquad (3)$$

where $n(T)$ is the conduction electron density slightly depending upon temperature and N_0 is the temperature-independent term which unfortunately is a priori unknown and should be properly adjusted. It is considered N_0 equals twice the density of deep-lying acceptor centers which may permanently trap some of the conduction electrons.

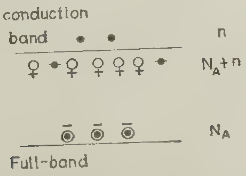

Fig. 4. Model for impurity scattering centers. The total density $N_I=N_O+n$, where $N_O=2N_A$.

(4) The mobility ratio μ/μ_d, where μ_d is the drift mobility, is taken as unity, i.e.

$$\mu=\mu_d \, . \qquad (4)$$

The carrier density is computed without significant reason from the relation

$$n=(3\pi/8)(1/Re) \, . \qquad (5)$$

Strictly speaking, these are incorrect because the relations are influenced by scattering mechanisms, but the effect on the final results may not be so serious that the computation can be carried out along this line.

§ 4. Analysis

According to the preceding assumptions the lattice mobility *vs* the temperature characteristics will be obtained in the following way.

In the first place, in order to eliminate the impurity mobility from the observed mobility, combination law between the lattice mobility and the impurity mobility must be investigated. Let us consider there are two scattering mechanisms A and B independent of each other, of which relaxation times are τ_A and τ_B respectively, and then τ_A and τ_B are power functions of the kinetic energy E of conduction carriers expressed as

$$\left.\begin{aligned}\tau_A&=a(T)E^{p/2} \, ,\\ \tau_B&=b(T)E^{q/2} \, ,\end{aligned}\right\} \qquad (6)$$

where $a(T)$ and $b(T)$ are temperature-dependent coefficients, p and q are the scattering indices of the two mechanisms respectively. Then the total scattering probability $1/\tau$ is given as $1/\tau=1/\tau_A+1/\tau_B$, and the drift mobility μ can be obtained, performing the average over the Boltzmann distribution at a temperature T:

$$\begin{aligned}\mu&=\frac{e}{m^*}\cdot\frac{4}{3\sqrt{\pi}}(kT)^{-5/2}\\ &\quad\times\int_0^\infty E^{3/2}\tau\exp(-E/kT)\cdot dE\\ &=\frac{e}{m^*}\cdot\frac{4}{3\sqrt{\pi}}a(T)\cdot(kT)^{p/2}\\ &\quad\times\int_0^\infty\frac{x^{(q+3)/2}\exp(-x)}{(a/b)(kT)^{(p-q)/2}+x^{(q-p)/2}}\,dx \, , \qquad (7)\end{aligned}$$

where m^* is effective mass of the electrons, k is Boltzmann's constant and x is defined as E/kT. Transformation of (7) into a convenient form gives

$$\frac{\mu}{\mu_A}=\frac{1}{\Gamma\left(\frac{5+p}{2}\right)}\times\int_0^\infty\frac{x^{(q+3)/2}\exp(-x)}{\left\{\Gamma\left(\frac{5+q}{2}\right)\Big/\Gamma\left(\frac{5+p}{2}\right)\right\}\cdot\left[\frac{\mu_A}{\mu_B}\right]+x^{(q-p)/2}}\,dx\,, \tag{8}$$

where $\Gamma(x)$'s are gamma functions. Here, μ_i is the mobility when the mechanism i is predominant. The (μ/μ_A) *vs* (μ/μ_B) curves are shown in Fig. 5 by numerical calculation for several cases. For the case $p=1$, $q=3$ and $p=-1$, $q=3$, one can use the numerical table calculated by Dingle et al in "Semiconductor Integrals".[3)]

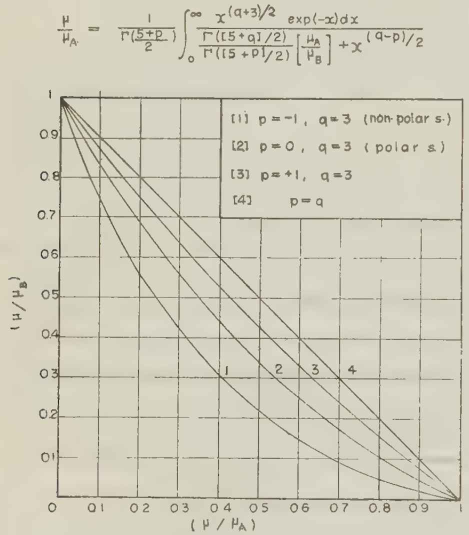

Fig. 5. Combination law between mobilities μ_L, μ_I and μ.

For the present case, the scattering index of impurity scattering, say q, is 3. On the other hand, the scattering index of the lattice scattering p has to be determined suitably. When the non-polar scattering by acoustical modes is dominant, $p=-1$. If this is the case, logarithmic plot of the corrected lattice mobility against the temperature T should form a straight line probably with the slope of $-3/2$. At first, such an analysis was tried on several data, which resulted in $\mu_L \propto T^{-2.1}$, indicating steeper slope than the expected one. In addition, there are a few specimens, whose mobility curves plotted against the temperature in logarithmic scales possess upwards concave part with reasonable accuracy, even if no correction is made. Two examples are curve 1 and curve 2 in Fig. 3. In the meantime, it was reported by Yoshinaga et al[4)] that there was a sharp and strong optical absorption band at 43μ owing to the lattice vibration in the hexagonal cadmium sulphide.

Taking into account these facts, the analysis with $p=-1$ was abolished and the predominance of the polar scattering by optical modes was presumed. The relaxation time of the polar scattering by optical modes τ_L is calculated by Callen and others[5)]. In this case, the result is somewhat complicated and the scattering index p can not be uniquely determined. However, the approximate results may be given by

$$\left.\begin{aligned}\tau_L &\propto E^0 \qquad 0<E<\hbar\omega_0=k\Theta\,,\\ &\propto E^{1/2} \quad \hbar\omega_0<E<10\hbar\omega_0\,,\end{aligned}\right\} \tag{9}$$

where ω_0 is the angular frequency of the longitudinal optical modes, and Θ is its characteristic temperature. For cadmium sulphide $\Theta\sim 400°\text{K}$ as discussed later, while τ and τ_L should be averaged over the Boltzmann distribution. Since the present aim is principally to correct the data below 200°K, no serious error is expected even though it is supposed $\tau \propto E^0$

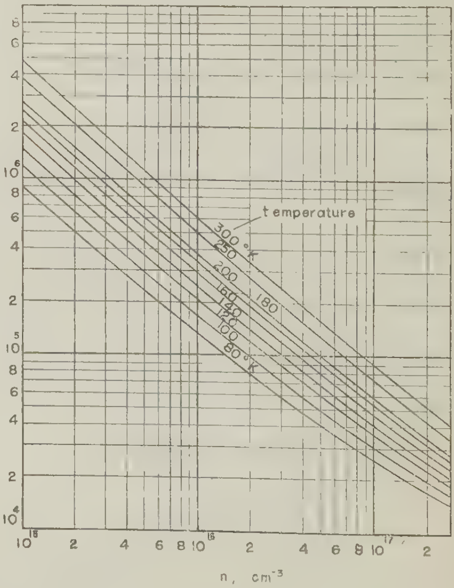

Fig. 6. Impurity scattering mobility μ_I *vs* carrier density n characteristics for several temperatures, calculated from modified Conwell-Weisskopf's formula with $m^*=0.3\,m$ and $\kappa=12$.

or $p=0$ for all electrons. If p were unity, on the other hand, slightly smaller μ_L would result. This is easily understandable in Fig. 5, where the combination law curve 3 instead of curve 2 has to be used in the latter case.

In the second place, it is necessary to evaluate the impurity mobility μ_I. According to the modified Conwell-Weisskopf's formula[6)]

$$\left.\begin{aligned} \mu_I &= \frac{2^{7/2}}{\pi^{3/2}}\cdot\frac{\kappa^2 k^{3/2}}{m^{*1/2}e^3}\cdot\frac{T^{3/2}}{N_I}\left[\ln(1+b)-\frac{b}{1+b}\right]^{-1}, \\ b &= \frac{6}{\pi}\cdot\frac{\kappa m^* k^2}{\hbar^2 e^2}\cdot\frac{T^2}{n}, \end{aligned}\right\} \tag{10}$$

where κ is the static dielectric constant. n and N_I have been defined in Eq. (3). Substitution of the numerical values of the constants with $m^*=0.3\,m_0$ and $\kappa=12$ measured by Kröger et al gives

$$\left.\begin{aligned} \mu_I &= \left(\frac{n}{N_I}\right)\times 8.7\times10^{18} \\ &\quad\times\left(\frac{T^{3/2}}{n}\right)\left[\ln(1+b)-\frac{b}{1+b}\right]^{-1}, \\ b &= 4.7\times10^{14}\times\left(\frac{T^2}{n}\right). \end{aligned}\right\} \tag{11}$$

Fig. 6 shows $(N_I/n)\mu_I$ *vs* n for several temperatures. Since $n=(3\pi/8)(1/Re)$ and $N_I=N_0+n$, the impurity mobility $\mu_I(T, N_0)$ can be evaluated from (11) or Fig. 6, if the value of N_0 is expediently given for each specimen. With thus evaluated $\mu_I(T, N_0)$ and the observed $\mu(T)$, the lattice mobility $\mu_L(T)$ can be straightway settled by means of the combination law curve 2 in Fig. 5.

In the last place, therefore, it must be mentioned how to determine the value of N_0. The determination of N_0 for each specimen was performed in the following way.

(1) Let the upper limit of N_0 be $N_0^{\max}$, then $N_0^{\max}$ is defined now by putting $\mu=\mu_I$ at the lowest temperature of the present observation, say 90°K. Since always $\mu\leqq\mu_I$, this gives $N_0^{\max}$ from (11), where the substitution of the observed n(90°K) and μ(90°K) gives $N_I^{\max}$, in turn $N_0^{\max}$.

(2) Let the lower limit of N_0 be $N_0^{\min}$. The method obtaining $N_0^{\min}$ is based upon the hypothesis that the resultant $\mu_L(T)$ *vs* T curve must not be upwards convex but be at least a straight line, provided the plot is made in both logarithmic scales. This was performed by the trial and error method which, in practice, was rather easy.

These values are listed in Table I together with other observed quantities.

From $N_0^{\max}$ and $N_0^{\min}$ a set of $\mu_L^{\max}(T, N_0^{\max})$ and $\mu_L^{\min}(T, N_0^{\min})$ will follow for each specimen, whose results are shown in Fig. 7. As for the most plausible lattice scattering mo-

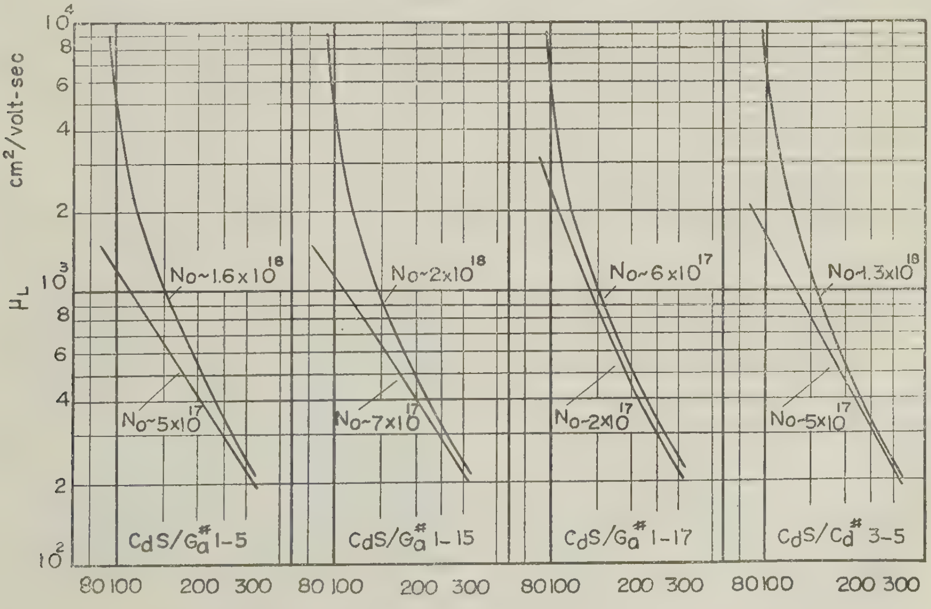

Fig. 7. Upper and lower limits of $\mu_L(T)$ for each specimen.

Table I.

Sample	μ_{RT} (cm^2/volt sec)	n_{RT} (cm^{-3})	$N_0^{\max}$ (cm^{-3})	$N_0^{\min}$ (cm^{-3})
CdS/Ga #1–17	220	0.7×10^{16}	0.6×10^{18}	0.2×10^{18}
CdS/Cd #3– 5	218	1.8	1.3	0.5
CdS/Ga #1– 5	210	1.6	1.6	0.5
CdS/Ga #1–15	205	4.3	2.0	0.7

bility $\mu_L(T)$ it would be appropriate to extract the common part of the regions limited by these curves. Solid bars at each temperature in Fig. 8 indicate the final regions obtained in this way.

In the present case, μ_L will be given by

$$\mu_L(T)=A\{\exp(\Theta/T)-1\}\ . \tag{12}$$

Then, to fit (12) with the above results two constants A and Θ must lie between the two sets of values listed in Table II. The $\mu_L(T)$ *vs* T curves calculated by substituting these values into (12) are given in Fig. 8.

In conclusion, the final and the best empirical formula for $\mu_L(T)$ is given by

$$\mu_L(T)=(92.5\pm15)\{\exp(370\pm30/T)-1\}\ \text{cm}^2/\text{volt sec}\ , \tag{13}$$

which passes through the mid region limited by the two curves in Fig. 8.

Table II.

	A (cm^2/volt sec)	Θ (°K)
Upper limit	80.6	400
Lower limit	107	340

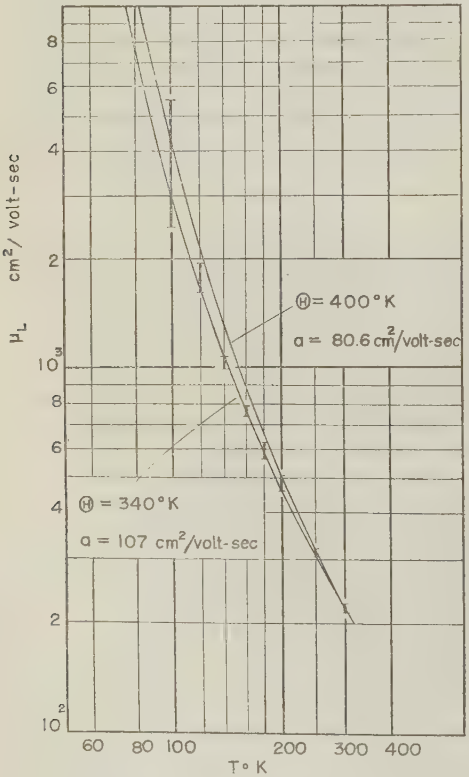

Fig. 8. Regions of the most plausible $\mu_L(T)$ (solid bars and theoretical curves calculated from $\mu_L=A\{\exp(\Theta/T)-1\}$ with the values given in the figure.

§ 5. Discussion

Despite a number of controversial assumptions, it is believed the resultant characteristic temperature Θ, say 370°K, is a reasonable one in view of the infrared absorption band observed by Yoshinaga et al. Since the absorption band has its peak at 43μ, it follows that the characteristic frequency ν_t of the transverse wave and the corresponding temperature $\Theta'(=h\nu_t/k)$ equal 6.98×10^{12} sec^{-1} and 335°K respectively. Meanwhile, the characteristic frequency ν_l of the longitudinal wave, which is responsible for the scattering of electrons in NaCl type polar lattices, is given by

$$\nu_l=\nu_t\left(\frac{\kappa}{\kappa_0}\right)^{1/2} \tag{14}$$

where κ_0 is the optical dielectric constant[7]. Since κ_0 is about 6 in the present materials, (14) gives $\nu_l \doteqdot 1.4\nu_t$. Though the structure of cadmium sulphide single crystal is not cubic but hexagonal, the corresponding characteristic temperature Θ of the longitudinal wave should be nearly equal to or slightly higher than 335°K of Θ'. Another evidence of Θ is a characteristic vibrational fine structure of the edge emission at low temperature[8]. The results obtained by Kröger and Meyer suggest $\Theta=460$°K. At least it cannot be emphasized that the values of Θ lower than 300°K are preferable.

It is also plausible that the concentrations $N_0/2$ of deep-lying centers for the present specimens are of the order 10^{17} cm^{-3}, because carrier compensations in some degree are inevitable at the present stage of crude crystal growing techniques. Probably these centers may be responsible for the trapping of positive holes and always make them immobile when photoconduction is induced in insulating crystals under illumination.

All of these results are suggestive that the intrinsic electron mobility of cadmium sulphide possesses remarkable polar nature and rather larger value at lower temperatures, but there exists a considerable effect of the impurity scattering which is depressing the mobility and cannot be neglected.

The authors are indebted to professor Y. Uemura and Mr. K. Maeda for many helpful discussions.

References

1) R. W. Smith: RCA Rev., **12** (1951) 350.
2) F. A. Kröger, H. J. Vink and J. Volger: Philips Res. Rep. **10** (1955) 39.
3) R. B. Dingle, Doreen Arndt and S. K. Roy: App. Sci. Research **B 6** (1956) 144, 155.
4) H. Yoshinaga et al: Oral presentation at the annual meeting of Phys. Soc. Japan Oct. 1957.
5) H. B. Callen: Phys. Rev. **76** (1949) 1394.
6) P. P. Debye and E. M. Conwell: Phys. Rev. **93** (1954) 693.
7) H. Fröhlich and N. F. Mott: Proc. Roy. Soc. **A 171** (1939) 496.
Their results have been modified by R. Kubo in "Electron Emission and Semiconductors." (Sangyo Tosho, Tokyo: (1950) p. 421, in Japanese).
8) F. A. Kröger and H. J. G. Meyer: Physica **20** (1954) 1149.

JOURNAL OF THE PHYSICAL SOCIETY OF JAPAN Vol. 14, No. 1, JANUARY 1959

Relaxation Time Anisotropy in Cadmium Sulphide Studied with Electrical Resistivity and Magneto-Resistance Effect

By Taizō MASUMI

Department of Applied Physics, University of Tokyo, Tokyo, Japan

(Received October 3, 1958)

Anisotropic temperature dependences of electrical resistivity and magneto-resistance effect in hexagonal cadmium sulphide single crystal have been observed in several impurity-doped conducting and photoconducting crystals. The experimental results indicate some unusual anisotropic behaviours. They seem to suggest that the relaxation time anisotropy plays some important roles in transport phenomena of cadmium sulphide single crystals having hexagonal crystal structure.

§ 1. Introduction

A great many of theoretical and experimental investigations about the electronic energy band structure of semiconductors and metals[1),2)] have been made in recent years. Extensive investigations of electrical, magnetic and optical properties on a crystal provide some useful knowledges about the electronic band structures in the crystal. In particular, experiments on the cyclotron resonance, infrared absorption, magneto-absorption, de Haas-van Alphen effect, and the galvanomagnetic effect play significant roles in the study of usual semiconductors such as germanium, silicon and indium antimonide[2)].

The author has studied the magneto-resistance effect in hexagonal cadmium sulphide[3),4)], the electronic band structure of which has not been investigated yet[5)] though we have a large number of investigations about the photoconductive properties in the crystal[6)]. The experimental results on the magneto-resistance effect in cadmium sulphide give some useful knowledges about the energy band structures of conduction band and scattering mechanisms for free electrons, whereas the experiments on galvanomagnetic effect in semiconductors generally do not supply the individual informations about the anisotropies of energy surfaces and scattering mechanisms. Nevertheless, temperature dependences of the transverse magneto-resistance effect in cadmium sulphide show an unusual anisotropic behaviour as shown later, that is considered to be one of the most remarkable features of galvanomagnetic effect in this crystal. These situations seem to warn that we should pay our attentions to the existence of the anisotropic scattering mechanisms for conduction electrons in hexagonal cadmium sulphide, even though the energy surfaces of conduction band in the crystal are not sufficiently clarified.

We shall show the experimental results on the anisotropic temperature dependences of electrical resistivity and magneto-resistance effect in cadmium sulphide and discuss the probability of existence of the relaxation time anisotropy in cadmium sulphide based on these experimental results.

§ 2. Experimental Procedures

The samples used for the experiments are conducting thin flakes and blocks doped with Ga or Cl or with excess-Cd and also photoconducting flakes of cadmium sulphide single crystals that have hexagonal crystal structure, being of Wurtzite lattice type. In flaky crystals, the *c*-axis of the crystal lies in the flaky surface and the surface is perpendicular to one of the three *a*-axes. From a large flake, we have cut out the two specimens each direction of which is the $[01\bar{1}0]$ or [0001] direction as shown in Fig. 1 (a) and (b). We have used some rods made from block crystals merely as subsidiary specimen for the measurement of magneto-resistance effect that were ground by carborundum to have specified direction with help of X-rays. The conduction of the crystal is n-type and the resistivity of samples ranges from $\rho=0.05\sim5$ ohm cm with Hall coefficient $R=10\sim10^3$ cm^3/coulomb at room temperature for impurity doped crystals to $\rho=10^6\sim10^{10}$ ohm cm for photoconducting crystals in dark at room temperature. Sizes of specimens are of the order of $3\sim5\,\text{mm}\times1\sim2\,\text{mm}\times0.02\sim0.2\,\text{mm}$ with the longitudinal direction $[01\bar{1}0]$ or [0001], along which the directions of current $\boldsymbol{I}$ are fixed. The electrodes are indium-soldered ones forming good ohmic contacts whose contact resistance may be sufficiently negligible. The two specimens cut out from the same parent flake the one of which has the $\boldsymbol{I}$-direction of $[01\bar{1}0]$ and the another the $\boldsymbol{I}$-direction of [0001] were soldered in the same block of of indium metal at one end of each sample so that they have a common electrode and keep almost a common temperature at the same time as possible.

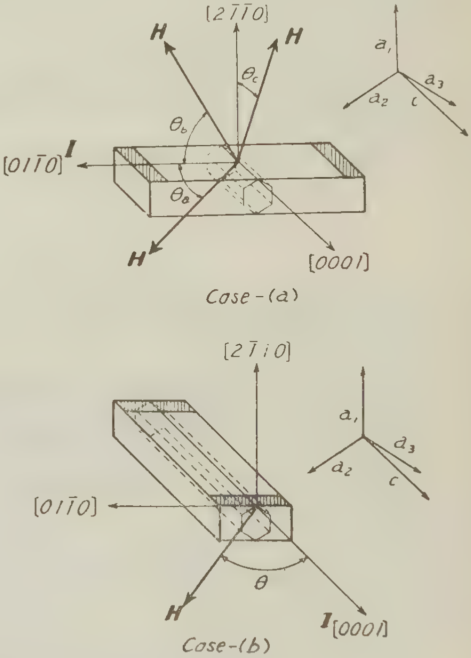

Fig. 1. Schematic Arrangements of the $\boldsymbol{I}$- and $\boldsymbol{H}$-directions for the orientations of hexagonal cadmium sulphide single crystals.

Another electrode of each specimen was attached independently separated with each other. The electrodes are used for both current and potential leads. A source of errors in magneto-resistance measurement[7),8),9)] due to such an arrangement has been checked not to be serious in the experiments as discussed in the previous paper[4)].

Measurements of electrical resistivity and magneto-resistance effect have been made by measuring the potential differences between two ends of the sample and their changes with application of magnetic field passing a fixed current less than 10 mA at most. The voltages and their changes across the sample were measured by potentiometer with help of DC-bridge adjusted suitably and the resistivity measurements for high resistive photoconducting crystals were done by high sensitive DC amplifier. For the measurements of magneto-resistance effect in impurity-doped crystals, magnetic fields ***H*** up to 12 kilogauss are produced by an electromagnet, and the misalignment of ***H*** and ***I*** was decreased as possible. As the elimination of photoeffect in these intrinsic photoconductors is very important even in this case, sufficient cares must be taken. Samples were contained in a enclosed cryostat avoiding the temperature drifts strictly. The observed temperature dependences of electrical resistivity and magneto-resistance effect in the experiment range from 100°K to 300°K.

§ 3. Experimental Results

Experimental results have been expressed in the form of temperature dependences of "relative resistivities" both for the current direction of ***I***-[01$\bar{1}$0] and ***I***-[0001] or their ratios normalized at room temperature for electrical resistivity. For magneto-resistance effect, results have been shown in the form of "their relative changes due to magnetic field ***H***", $(\rho-\rho_0)/\rho_0=(\Delta\rho)_H/\rho$, as a function of magnetic field strength H and the angle θ between the current ***I*** (or the direction of the fixed axis in some cases) and ***H***, and also of temperature T.

An example of anisotropic temperature dependences of electrical resistivities for the two current directions [01$\bar{1}$0] and [0001] is shown in Fig. 2 in logarithmic scale. It is natural that each temperature dependence shows the common appearances in its qualitative sense, however, it should be noticed that there is the quantitative difference between them. This difference may be primarily considered to be due to the anisotropic temperature dependences of mobility of electrons in these crystals, for the concentration of free electrons should have the same temperature dependence in the two crystals cut out from the same parent crystal. If we define the anisotropy parameter $K_\rho(T)$ by the relation,

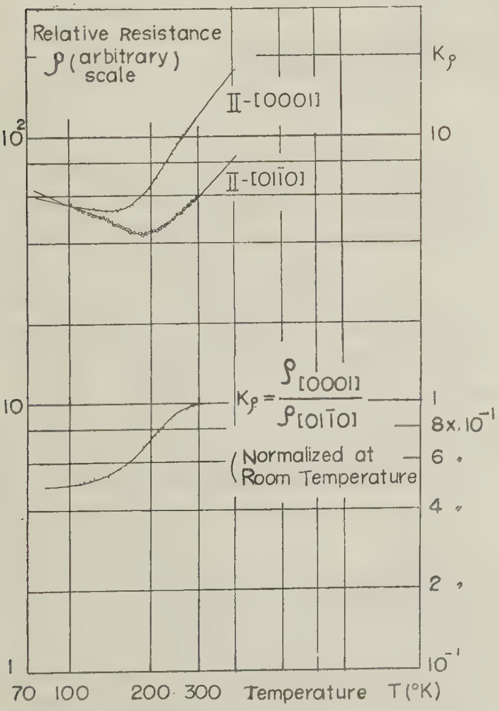

Fig. 2. Anisotropic temperature dependences of electrical resistivity for CdS-Cl specified with $\rho_{[0001]}\simeq1.0$ ohm-cm at room temperature.

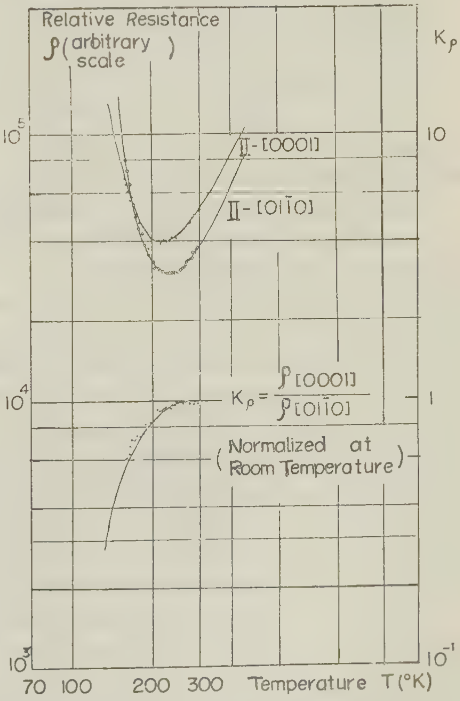

Fig. 3. Anisotropic temperature dependences of electrical reistivity for photoconductive CdS (inverse of photoconductivity). specified with dark resistivity $\rho_{[0001]}=10^6\sim10^{10}$ ohm-cm at room temperature.

$$K_\rho(T)=\frac{R_{[0001]}(T)}{R_{[01\bar{1}0]}(T)}\Big/\frac{R_{[0001]}(300^\circ\mathrm{K})}{R_{[01\bar{1}0]}(300^\circ\mathrm{K})} \qquad (3.1)$$

where $R_{[0001]}(T)$, $R_{[01\bar{1}0]}(T)$ are the observed resistances for the current directions of I-[0001] and I-[01$\bar{1}$0], $K_\rho(T)$ indicates the anisotropic behaviours of two mobilities $\mu_{[0001]}(T)$ and $\mu_{[01\bar{1}0]}(T)$ for temperature, because

$$K_\rho(T)=\frac{\rho_{[0001]}(T)}{\rho_{[01\bar{1}0]}(T)}\Big/\frac{\rho_{[0001]}(300^\circ\mathrm{K})}{\rho_{[01\bar{1}0]}(300^\circ\mathrm{K})}$$

$$=\frac{\mu_{[01\bar{1}0]}(T)}{\mu_{[0001]}(T)}\Big/\frac{\mu_{[01\bar{1}0]}(300^\circ\mathrm{K})}{\mu_{[0001]}(300^\circ\mathrm{K})} \qquad (3.1')$$

Fig. 2 shows the temperature dependence of $K_\rho(T)$ in the logarithmic scale. Remarkable features in the curve are the deviation of K_ρ from the unity in low temperature region (160∼200°K) and its restoring appearance in lower temperature region (100∼160°K). In order to interpret these behaviours, the following observation would be useful.

Similar experiments on high resistive photoconducting CdS crystals had been made and the results of the measurements of resistivity under the illumination of light with the fixed

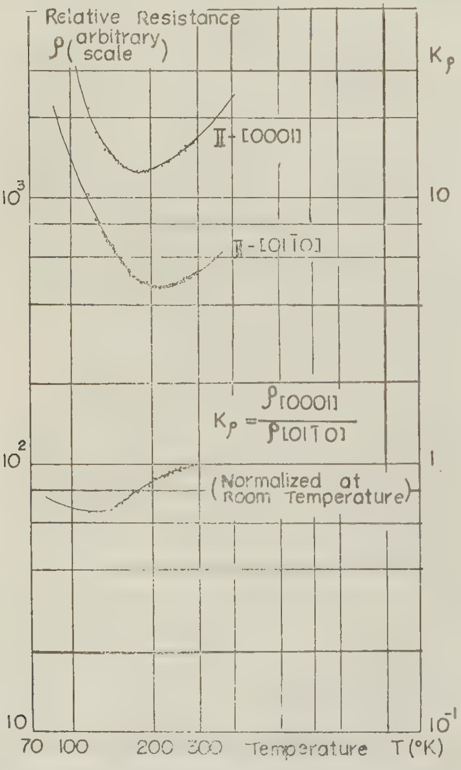

Fig. 4. Anisotropic temperature dependences of electrical resistivity for CdS-Cl specified with $\rho_{[0001]}\simeq0{\cdot}75$ ohm-cm at room temperature.

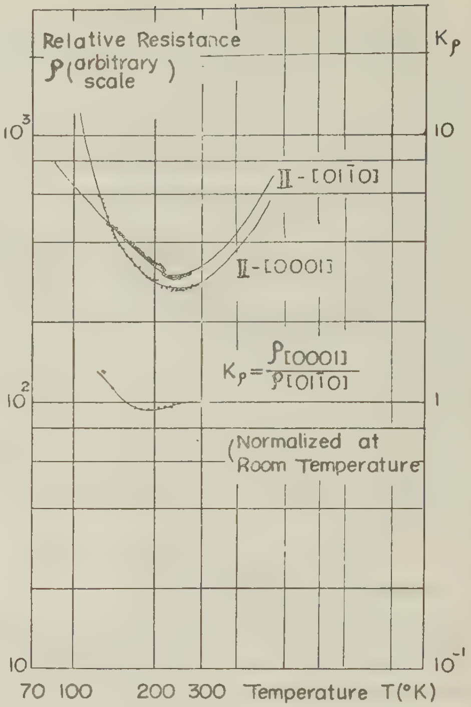

Fig. 5. Anisotropic temperature dependences of electrical resistivity for CdS-Ga specified with $\rho_{[0001]}=0.15$ ohm-cm at room temperature.

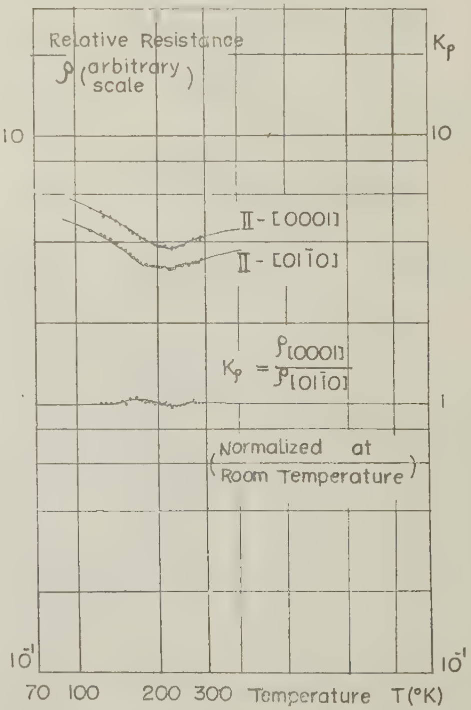

Fig. 6. Amisotropic temperature dependences of electrical resistivity for CdS-Cl spedified with $\rho_{[0001]}\simeq0.05$ hom-cm at room temperature.

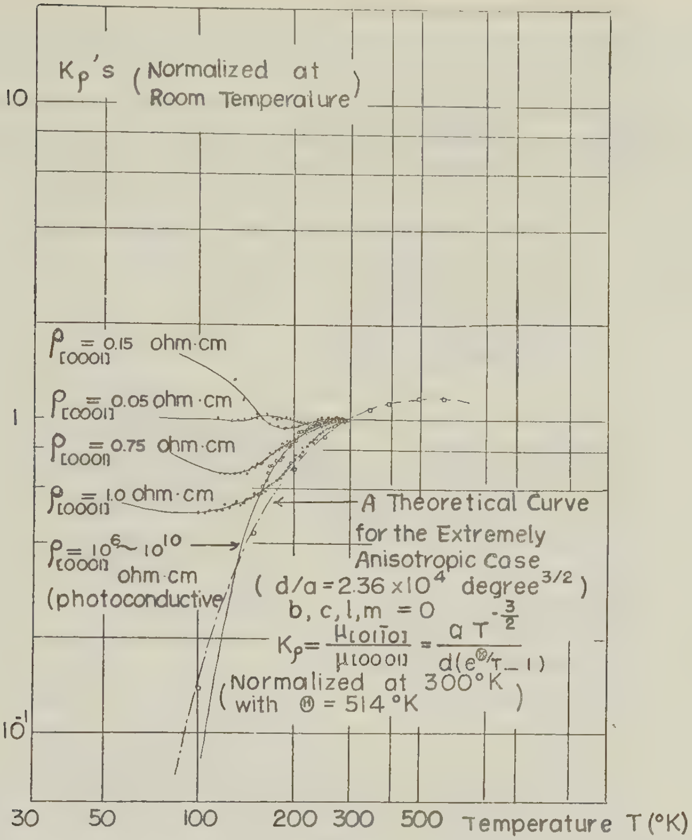

Fig. 7 (a). Summarized temperature dependence of Kρ's, for the CdS crystals with various grades of resistivity and comparison with the calculated curve.

intensity (i.e. inverse of photoconductivity) is shown in Fig. 3. Inferring from the general feature in this case, it may be unlikely that the restoring behaviours of K_ρ would appear in the lower temperature region.

Furthermore, the experimental results of similar observations on lower resistive CdS–Cl or CdS–Ga crystals shown in Fig. 4, 5 and 6, give some additive informations about the abnormal behaviours of K_ρ. The restoring characteristic of K_ρ in impurity doped crystals seem to become more appreciable as the decrease of resistivity though the situation is semi-quantitative.

The summarized results of temperature dependences of K_ρ's normalized at room temperature for the crystals with various values of relative resistivity are illustrated in Fig. 7(a) and these situations show some interesting features about the anisotropic temperature dependence of electrical resistivity in hexagonal cadmium sulphide single crystal.

These results suggest us that the similar anisotropic temperature dependences of mobility will be found also in the experiment of the magneto-resistance effect. Some examples of the angular dependences of magneto-resistance effect, $(\Delta\rho)_H/\rho H^2$, upon θ with a fixed strength of magnetic field at the fixed temperatures are illustrated in Fig. 8 and 9 for the ***I***-direction [01$\bar{1}$0] and [0001] in CdS–Ga crystals. Experimental details of the results and their general features are to be published in the another paper,4) and then, here, we would merely add some temperature dependences for various combination of ***H*** and ***I*** and a few corrections.

Temperature dependences of magneto-resistance effects for the ***I***-direction [01$\bar{1}$0] and ***H*** having the angle θ from 0 to 90 degrees between the directions [01$\bar{1}$0] and and [2$\bar{1}\bar{1}$0] are shown in Fig. 10 and similar dependences for the ***I***-direction [0001] and ***H***

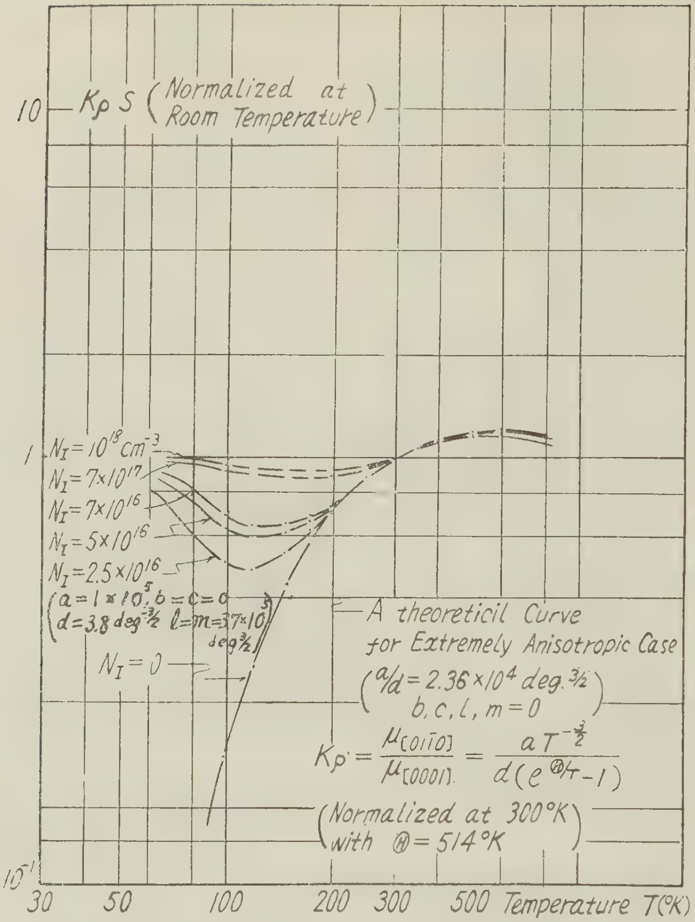

Fig. 7 (b). Calculated temperature dependences of Kρ'S for CdS crystals with several grades of impurity concentration N_I.
($N_I=2.5\times10^{16}$ cm^{-3} corresponds to $\rho_{[0001]}=1.0$ ohm-cm at room temperature with the value of mobility $\mu_n=200$ cm^2/volt. sec).

having the angle θ between the directions [0001] and [$2\bar{1}\bar{1}0$] in Fig. 11*. Generally, the transverse magneto-resistance effects for the both current directions with common **H**-[$2\bar{1}\bar{1}0$] show the similar temperature dependences with slopes whose values are clearly larger than −3 and also the longitudinal effect for the **I**-direction [0001], while the longitudinal effect for the **I**-direction [$01\bar{1}0$] has scarecely observed at each temperature.

But one of the more characteristic features of the magneto-resistance effects in cadmium

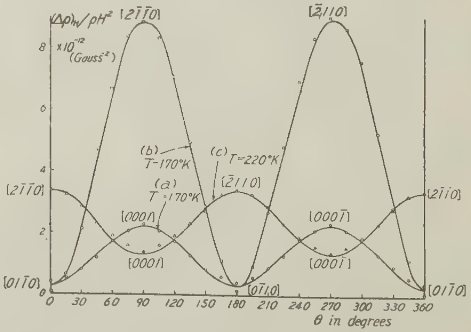

Fig. 8. $(\Delta\rho)_H\rho H^2$ versus θ in CdS-Ga at low temperatures for the fixed direction of **I**-[$01\bar{1}0$] with H=8900 Gauss.

---

* Relative values of transverse magneto-resistance effect for the I-direction [$01\bar{1}0$] seem to be corrected to be rather smaller than that for the I-direction [0001], at a fixed temperature, though the semi-quantitative result is reported in the previous paper[4)], where we described the former to be slightly larger than the latter.

sulphide is the anisotropic temperature dependences of the transverse effects for the $\boldsymbol{I}$-direction $[01\bar{1}0]$ illustrated in Fig. 12. It is most remarkable that there is a clear difference between the temperature dependences of the transverse effect with $\boldsymbol{H}$-[0001] and that with $\boldsymbol{H}$-$[2\bar{1}\bar{1}0]$. Although the former varies nearly as T^{-3} as observed in germanium by Pearson and Suhl[10], the latter presents a slightly different appearance. If we define the another parameter $K_{(\Delta\rho)_H/\rho H^2}$ analogous to K_ρ by the relation,

$$K_{(\Delta\rho)_H/\rho H^2}=\frac{(\Delta\rho_{[01\bar{1}0]})_H/\rho_{[01\bar{1}0]}\,H^2{}_{[0001]}}{(\Delta\rho_{[01\bar{1}0]})_H/\rho_{[01\bar{1}0]}\,H^2{}_{[2\bar{1}\bar{1}0]}}\,, \qquad (3.2)$$

we obtain the temperature dependence curve of $K_{(\Delta\rho)_H/\rho H^2}$ similar with the curve of K_ρ versus T, although the measurements of $(\Delta\rho)_H/\rho H^2$ and therefore $K_{(\Delta\rho)_H/\rho H^2}$'s involve more amounts of experimental errors than that of ρ and K_ρ. The general tendency of $K_{(\Delta\rho)_H/\rho H^2}-T$ curve shows a plausible agreement with that of the $K_\rho-T$ curve in its qualitative sense.

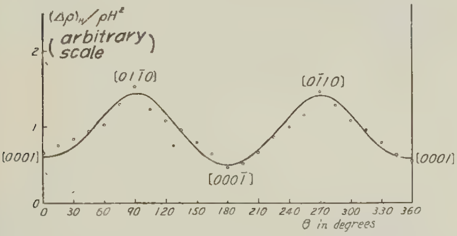

Fig. 9. $(\Delta\rho)_H/\rho H^2$ versus θ in CdS-Ga at 180°K for the fixed direction of I-[0001] with H=9350 Gauss.

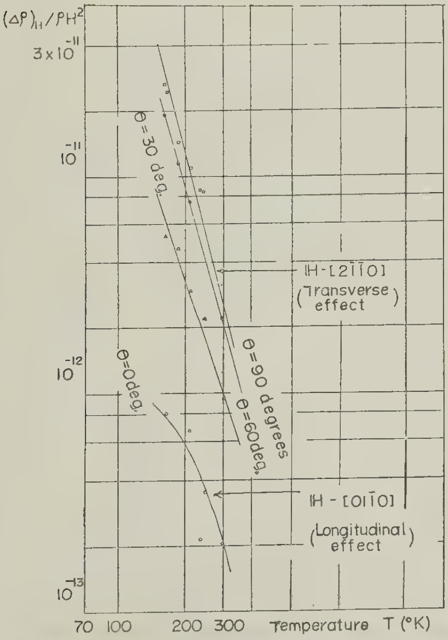

Fig. 10. Temperature dependence of magneto-Resistance effects in CdS-Cl for the fixed direction of II-$[01\bar{1}0]$.

Therefore, it may be considered that these experimental results suggest the special features of galvanomagnetic effect in hexagonal cadmium sulphide.

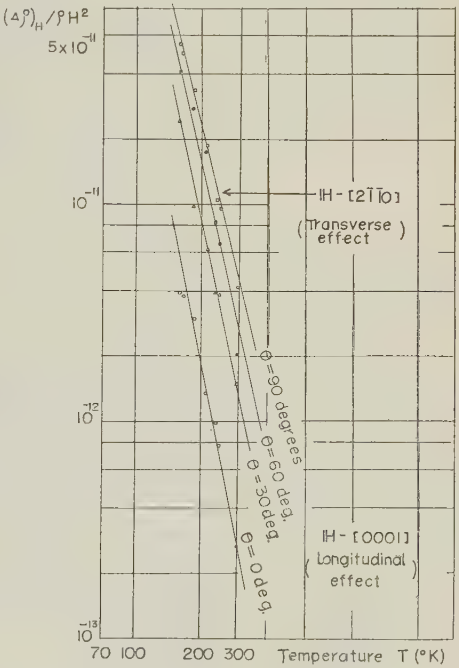

Fig. 11. Temperature dependence of magneto-resistance effects in CdS-Cl for the fixed direction of II-[0001].

§ 4. Discussions

It has been shown that there are unusual anisotropic temperature dependences of the galvanomagnetic effects in hexagonal cadmium sulphide single crystal and these behaviours have been studied through the anisotropy parameters K_ρ and $K_{(\Delta\rho)_H/\rho H^2}$ for several photoconducting and impurity-doped conducting crystals.

K_ρ or $K_{(\Delta\rho)_H/\rho H^2}$ defined by the preceeding relations is able to be written as follow, for example,

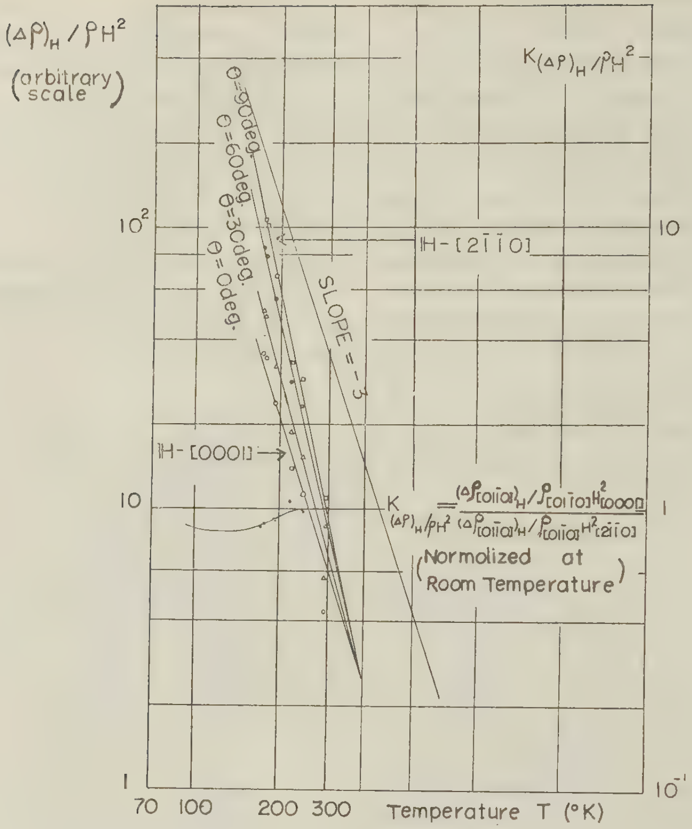

Fig. 12. Anisotropic temperature rependences of transverse magneto-resistance effects in CdS-Ga for the fixed direction of II-[01$\bar{1}$0].

$$K_\rho(T)=\frac{\mu_{[01\bar{1}0]}(T)}{\mu_{[0001]}(T)}\Big/\frac{\mu_{[01\bar{1}0]}(300^\circ\mathrm{K})}{\mu_{[0001]}(300^\circ\mathrm{K})}=\frac{K_m(T)}{K_\tau(T)}$$
$$=\left[\frac{m^*_{[0001]}(T)}{m^*_{[01\bar{1}0]}(T)}\Big/\frac{m^*_{[0001]}(300^\circ\mathrm{K})}{m^*_{[01\bar{1}0]}(300^\circ\mathrm{K})}\right]$$
$$\times\left[\frac{\tau_{[01\bar{1}0]}(T)}{\tau_{[0001]}(T)}\Big/\frac{\tau_{[01\bar{1}0]}(300^\circ\mathrm{K})}{\tau_{[0001]}(300^\circ\mathrm{K})}\right] \tag{4.1}$$

where m^*'s are the effective masses, τ's the relaxation times, $K_m(T)$ and $K_\tau(T)$ the effective mass ratio and the relaxation time anisotropy parameter normalized at 300°K, the suffixes specify the crystal orientations, and we have used a single simple valley model because of the lack of clear informations for the energy surfaces. Then, it may be expected that K_ρ and $K_{(\Delta\rho)_H/\rho H^2}$ are independent of temperature in usual isotropic media, because the effective masses and their ratio are independent of temperature for the crystal having usual carrier concentration and canceled out apparently, and the relaxation times τ's also have the similar temperature dependences for the different directions. Glicksman[11] discussed about the probability of existence of different "type" scattering entering with an anisotropic temperature dependence or the anisotropic impurity scattering in order to explain the deviation of relaxation time anisotropy K_τ from the unity in germanium which is strongly concentration dependent and/or temperature dependent. But he considered these situations to be unlikely and Goldberg[12],[13] also determined the relaxation time anisotropy $K_\tau \fallingdotseq 1.0$ for lattice scattering and $K_\tau > 1$ for moderate amounts of impurity scattering from the magnetoconductance measurements and the cyclotron resonance value for the mass ratio K_m. In hexagonal cadmium sulphide, however, it may be considered that the relaxation time anisotropy is still an important factor for the interpretation of the experimental result of galvanomagnetic effect.

These situations suggest that a possible phenomenological interpretation for the anisotropic temperature dependences of electrical resistivity and magneto-resistance effects in cadmium sulphide rises from the anisotropic weighting for the both types of scattering at the acoustical vibrational modes and the longitudinal optical modes of the lattice in their competitive process, and the impurity scattering also plays subsidiary roles in some cases. Some trial drawings of K_ρ involving the anisotropic relaxation time

$$K_\rho = k\cdot\frac{\rho_{[0001]}}{\rho_{[01\bar{1}0]}} = k\cdot\frac{\mu_{[01\bar{1}0]}}{\mu_{[0001]}} = k\cdot\frac{\left[\dfrac{a}{\mu_{op[0001]}}+\dfrac{c}{\mu_{ac[0001]}}+\dfrac{l}{\mu_{imp[0001]}}\right]}{\left[\dfrac{b}{\mu_{op[01\bar{1}0]}}+\dfrac{d}{\mu_{ac[01\bar{1}0]}}+\dfrac{m}{\mu_{imp[0'\bar{1}0]}}\right]} \tag{4.2}$$

and

$$\mu_{op} = \alpha\cdot\{\exp(\Theta/T)-1\}$$

$$\mu_{ac} = \beta T^{-3/2}$$

$$\mu_{imp} = \gamma\cdot T^{3/2}$$

is plotted in Fig. 7 (a) and (b), where the constants are properly chosen taking accounts of the anisotropic weighting that is considered to be probable from magneto-resistance data and normalizing K_ρ at room temperature, and Debye temperature Θ has the value obtained from the infrared absorption data by Yoshinaga et al.[14]. General behaviour of calculated K_ρ shows a fairly good agreement with that of observed K_ρ for the medium resistive and photoconductive crystals in the temperature region from 160~300°K in qualitative sense. The restoring behaviours of K_ρ in lower temperature region for impurity-doped crystals seem to be partly due to the apparent restoring of lattice and partly due to the impurity scattering, as shown in Fig. 7 (b).

But these situations are not completely justified because other factors such as detailed structure of energy band and so on also may play some roles in the present phenomena. For example, the non-vanishing longitudinal magneto-resistance effects for the I-direction [0001] and vanishing longitudinal effects for the I-direction [01$\bar{1}$0] can not be explained generally by the Herring's so-called "simple many valley energy band" model[15] usually considered in germanium and in silicon, and more complicated model may be necessary. Besides the situation, the crystals may contain some crystal imperfections such as point imperfections, dislocations, stacking faults and possibly boundary planes which give rise to some extra temperature dependences. But it would be unlikely that these extra dependences play an important role in the present experiment. Therefore, the foregoing interpretation seems to be one of the plausible proposals even though it is not completely definite. Further investigations to confirm these situations are now in progress.[16]

In any case, our experimental results about the anisotropic temperature dependences of electrical resistivity and transverse magneto-resistance effects in Fig. 7 and Fig. 12 reveal us the existence of anisotropic scattering mechanisms in hexagonal cadmium sulphide being of Wurtzite lattice type.

§ 5. Acknowledgements

The author would like to express his sincere gratitudes to Professor Y. Suge, Professor T. Inui and Professor S. Tanaka of Tokyo University for their continual encouragements, and, Professor Y. Uemura of Tokyo University, Dr. H. Miyazawa of Matsuda Research Laboratories of Tokyo-Shibaura Electric Company and Dr. F. A. Kroeger of Philips Research Laboratories for their kind discussions. He is also indebted to Dr. Miyazawa and, independently, Dr. S. Ibuki of Mitsubishi Electric Manufacturing Company for their supplying the cadmium sulphide single crystals. Sincere thanks are also, especially, due Dr. H. Mimura, Dr. T. Tanaka and Dr. M. Kobayashi for their most helpful discussions.

References

1) F. Herman: Rev. Mod. Phys., **30** (1958) 102.
2) B. Lax: Rev. Mod. Phys., **30** (1958) 122.
3) S. Tanaka and T. Masumi: Journ. Phys. Soc. Japan, **13** (1958) 314.
4) Y. Suge, S. Tanaka and T. Masumi: To be published in the Proceedings of the International Conferences on Solid State Physics in Electronics and Telecommunications at Brussels in June 1958.
5) F. A. Kroeger, H. J. Vink and J. Volger: Physica, **20** (1954) 1095.
F. A. Kroeger, H. J. Vink and J. Volger: Philips Research Reports, **10** (1955) 39.
6) See for example, R. H. Bube: Proc. I.R.E., Dec. (1955) 1836.

7) R. F. Broom: Proc. Phys. Soc., **71** (1958) 500.
8) R. F. Wick: Journ. Appl. Phys., **25** (1954) 741.
9) J. R. Drabble and R. Wolfe: Journ. Electronics and Control, **3** (1957) 259.
10) G. L. Pearson and H. Suhl: Phys. Rev., **83** (1951) 768.
11) M. Glicksman: Phys. Rev., **108** (1957) 264.
12) C. Goldberg: Phys. Rev., **109** (1958) 331.
13) C. Goldberg and W. E. Howard: Phys. Rev., **110** (1958) 1035.
14) H. Yoshinaga et al.: The Preprints for the Session of Meetings of the Phys. Soc. Japan, in March 1958, **1** (1958) 187 (in Japanese). Recently, slightly different values are reported by the same workers. But they have no remarkable effects on all our numerical results; A. Mitsuishi, H. Yoshinaga and S. Fujita: Journ. Phys. Soc. Japan, **13** (1958) 1235.
15) C. Herring: Bell Sys. Tech. Journ., **34** (1955) 237.
16) T. Masumi: To be published.

JOURNAL OF THE PHYSICAL SOCIETY OF JAPAN Vol. 14, No. 1, JANUARY, 1959

Quantum Theory of Galvanomagnetic Effect. I. Basic Considerations

Ryogo KUBO, Hiroshi HASEGAWA
Department of Physics, University of Tokyo
and Natsuki HASHITSUME
Ochanomizu University

(Received October 4, 1958)

A quantummechanical theory of galvanomagnetic effect is developed on the basis of the general theory of irreversible processes previously reported by Kubo (J. Phys. Soc. Japan **12** (1957) 570). The present theory applies to arbitrary shape of Fermi surface, as far as it makes a closed surface in the momentum space. Complications due to the interband effect and Harper's broadening effect are neglected here. On these assumptions it is proved that the static conductivity can be expressed generally in terms of the migration process of the center coordinate of the cyclotron motion. This is based on the assumption that the relative coordinates to describe the cyclotron motion are essentially bounded quantities in classical and also in quantummechanical sense. Without referring to any dubious use of transport theory, a very satisfactory logical basis is thus obtained for treating galvanomagnetic effect. This method is particularly useful for strong field. Applications will be reported in a subsequent paper.

§ 1. Introduction

The elementary theory of galvanomagnetic effect as one finds in standard textbooks[1] usually starts from the transport equation of electrons which describes the time change of the velocity distribution function by the drift due to the external electric force and the Lorentz force and by the collision term due to the scattering of electrons by phonons or lattice defects. Although the scattering is usually treated by quantum-mechanical perturbation theory, this transport equation is essentially classical or semi-classical, because it does not take into account the quantization of electron orbits by the presence of magnetic field. This is an approximation which is legitimate only in weak field, and so the elementary theory does not account for some peculiar effects which appear when the magnetic field becomes strong.

It is now well known that the quantization of electron orbits in magnetic field gives rise to some interesting and important phenomena. Such quantum effect is most clearly exhibited in the de Haas-van Alphen effect²⁾ in diamagnetic susceptibility and in the diamagnetic or cyclotron resonance phenomena³⁾. De Haas-van Alphen like oscillations are observed in transport phenomena such as magneto-resistance⁴⁾, Hall effect⁵⁾, thermoelectric power⁶⁾ and thermal conduction⁷⁾. Similar oscillation is seen also in optical absorption spectra of semiconductors⁸⁾. Besides such oscillations the quantization effect will completely change the transport properties of metals and semiconductors at very high magnetic field from the prediction of the elementary theory. The magneto-resistance, for instance, will show saturation according to the elementary theory when the magnetic field becomes so strong that the condition

$$\omega_0 \tau_r \gg 1 \tag{1.1}$$

is satisfied. Here ω_0 is a measure of the cyclotron frequencies determined by the magnetic field H and τ_r is that of the relaxation time. The condition (1.1) is that the electrons will complete many cycles of cyclotron motion before they get scattered. This classical saturation will be violated at very high magnetic field where the energy spacing of Landau levels becomes comparable to the Fermi potential. This was pointed out by Titeica⁹⁾ many years ago who made the first attempt for a quantum-mechanical theory of magneto-resistance. By Titeica's calculation, the magneto-resistance should increase linearly with the magnetic field at extremely high magnetic field. This conclusion should not, however, be taken as an explanation of the linear increase of magneto-resistance often observed by experiments at moderately strong magnetic fields¹⁰⁾.

The oscillatory effect of magneto-resistance was first discussed theoretically by Davydov and Pomeranchuk¹¹⁾. They treated the case of impurity scattering and applied the theory to the case of bismuth. More recently Lifshitz and his coworkers¹²⁾ treated the conduction problem by extending the kinetic equation to include the non-diagonal elements of the density matrix but without much examination of the collision term. Their conclusion is that the oscillation of magneto-resistance is essentially due to the oscillatory change of state density so that it is parallel to the de Haas-van Alphen effect oscillation. Similar theories have been also developed by Adams and Argyres¹³⁾. They treated the longitudinal magnetoresistance. Argyres further examined the transverse magnetoresistance¹⁴⁾.

The present authors started this work three years ago. Some of the results have been already reported on several occasions¹⁵⁾, although a full report has not been made yet. We have found that the quantum theory of galvanomagnetic effect can be constructed quite consistently on a very sound basis. The logical basis is more satisfactory than that of usual theory of conduction. This point has not been made clear in any of the previous work. This is the main reason why we now publish our work.

Our work is based upon the general theory of conductivity as developed by one of the present authors¹⁶⁾. The conductivity tensor can be rigorously expressed as a time integral of a sort of correlation function (response function, to be rigorous) which describes the spontaneous fluctuation of the current in the system under consideration in the absence of electric field. We now apply this formula by analyzing the dynamical motion of an electron in a magnetic field. It is seen that the cyclotron motion of crystal electrons with rather arbitrary energy function can be most conveniently described by a new set of canonical variables which consists of the center coordinates (X, Y), the relative coordinates (ξ, η) and the coordinate and momentum in the direction of the magnetic field (z, p_z). Thus the electric current in the x–y plane may be split into two parts, the current due to the displacement of the center and the current due to the relative motion. It will be shown that the symmetric part of conductivity tensor is completely expressed in terms of the center migration. On the other hand, the relative current contributes to the antisymmetric part a finite value which corresponds to its ideal value for vanishing scattering. The present theory thus gives a very clearcut formulation for the calculation of the galvanomagnetic coefficients, which can be applied to various cases, to metals or to semiconductors, with phonon scattering or with impurity scattering. When applied to metals with phonon scattering, the result will be the same as given by

Titeica[9] long time ago. If the scattering is due to impurities, it will be much the same as that discussed by Davydov and Pomeranchuk[11]. These authors, however, assumed rather intuitively that the conduction is interpreted by the center migration process. Our present theory will give a proof for their assumption and a more rigorous formulation.

§ 2. Dynamics of a Crystal Electron in Magnetic Field

Let us begin with a discussion of dynamics of a crystal electron in magnetic field. We consider crystal electrons which are described by the Bloch states $E_0(\boldsymbol{p})$ where $\boldsymbol{p}$ is crystal momentum $\hbar\boldsymbol{k}$, $\boldsymbol{k}$ being the Bloch wave vector. In a magnetic field $\boldsymbol{H}$, which is generaetd from the vector potential $\boldsymbol{A}$,

$$\mathrm{rot}\,\boldsymbol{A}=\boldsymbol{H}$$

and in the presence of a perturbation potential U, the crystal electrons may be approximately described by the effective Hamiltonian,

$$\mathcal{H}=E_0(\boldsymbol{\pi})+U(\boldsymbol{r})\,, \tag{2.1}$$

where $\boldsymbol{\pi}$ is the quasi-momentum defined by

$$\boldsymbol{\pi}=\boldsymbol{p}+\frac{e}{c}\boldsymbol{A}$$

satisfying the commutation rule,

$$\pi\times\pi=\frac{\hbar e}{ic}\boldsymbol{H}\,.$$

Or, if the direction of $\boldsymbol{H}$ is chosen as the z-axis, the definitions are

$$\left.\begin{aligned}\pi_x&=p_x+\frac{e}{c}A_x\,,\\ \pi_y&=p_y+\frac{e}{c}A_y\,,\\ \pi_z&=p_z\end{aligned}\right\} \tag{2.2}$$

and the commutation relations are

$$\left.\begin{aligned}&[\pi_x,\ \pi_y]=\frac{\hbar e}{ic}H\,,\\ &[\pi_x,\ x]=[\pi_y,\ y]=\hbar/i\end{aligned}\right\} \tag{2.3}$$

and other obvious ones.

Eq. (2.1) is based on the work of Peierls and Luttinger[17]. We shall use this Hamiltonian throughout the present work, so that we may briefly summarize the assumptions involved.

1) Since $E_0(\boldsymbol{p})$ represents a particular band, we have tacitly assumed that the interband effect (due to the change of wave functions in magnetic field) may be neglected. Some time ago, Adams pointed out that the interband effect is important for the large diamagnetism of bismuth[18]. It has not, however, been made clear how important the same effect would be for the galvanomagnetic effect particularly for those semimetals or semiconductors which have rather small energy gaps between bands. We here leave this question open for a future study.

2) We treat the coordinate $\boldsymbol{r}$ in (2.1) as a continuous variable although it is in fact discrete labeling the expansion coefficients in terms of the Wannier functions. This is perfectly correct as far as no approximation is introduced for the function $E_0(\boldsymbol{p})$ and so $E_0(\hbar\nabla/i)$ is a differential operator with infinite order. But here we may allow approximations such as the effective mass approximation under circumstances. We thus neglect such a broadening effect of the Landau levels as discussed by Harper and Zilberman[19].

Now let us introduce a new set of variables instead of the cartesian coordinates and their conjugate momenta. We define namely the variables,

$$\xi=\frac{c}{eH}\pi_y\,,\quad \eta=-\frac{c}{eH}\pi_x\,, \tag{2.4}$$

and

$$X=x-\xi\,,\quad Y=y-\eta\,, \tag{2.5}$$

From Eq. (2.3) we see at once that

$$[\xi,\ \eta]=\frac{\hbar}{i}\frac{c}{eH}\equiv\frac{l^2}{i}\,, \tag{2.6a}$$

$$[X,\ Y]=-\frac{\hbar}{i}\frac{c}{eH}\equiv-\frac{l^2}{i}\,, \tag{2.6b}$$

$$[\xi,\ X]=[\eta,\ X]=[\xi,\ Y]=[\eta,\ Y]=0\,. \tag{2.6c}$$

By these commutation rules the variables

$$(\xi,\ \eta)\,,\quad (X,\ Y)\quad \text{and}\quad (p_z,\ z) \tag{2.7}$$

make a complete set of canonical variables. There are of course other choice of canonical variables, for instance

$$(x,\ \eta)\,,\quad (X,\ y)\quad \text{and}\quad (p_z,\ z)\,.$$

This set is obtained from (2.7) by the canonical transformation

$$e^{-i\eta X/l^2}\xi e^{i\eta X/l^2}=\xi+X=x\,,$$

$$e^{-i\eta X/l^2}Ye^{i\eta X/l^2}=Y+\eta=y\,.$$

This can be regarded also as a gauge transformation.

The physical meaning of the variables (2.7) can easily be seen from the equation of motion. Consider the motion of an electron in the absence of the perturbation U. Since the Hamiltonian $E_0(\boldsymbol{\pi})$ does not involve X and Y, these variables do not change in time. Therefore the coordinates (X, Y) specify the position of the cyclotron motion in the x–y plane perpendicular to the magnetic field. We shall call X and Y the *center coordinates*. By Eq. (2.5) ξ and η are then the *relative coordinates* to specify the cyclotron motion relative to the center (X, Y). The center coordinates, X and Y, have, according to (2.6b), the quantum-mechanical uncertainty

$$\Delta X \Delta Y = 2\pi l^2 \equiv hc/eH$$

from which follows the well known fact that each eigen-state of $E_0(\pi_x, \pi_y, p_z)$ has the degeneracy of $1/2\pi l^2$ per unit area of the x–y plane. Here l corresponds to the classical radius of the lowest Landau level for an electron with a spherical mass. A similar uncertainty relation holds for the relative coordinates, ξ and η, for they are the canonical variables for one-dimensional periodic motion.

More generally, even in the presence of the perturbation potential U, we may use the center and relative coordinates. The equation of motion, either classical or quantum-mechanical, is easily obtained from the assumed Hamiltonian (2.1). (The function $E_0(\boldsymbol{\pi})$ must be well ordered in the noncommutable variables π_x and π_y). Namely,

$$\left.\begin{aligned} \dot{\xi} &= \frac{\partial E_0}{\partial \pi_x} - \frac{c}{eH}\frac{\partial U}{\partial y}, \\ \dot{\eta} &= \frac{\partial E_0}{\partial \pi_y} + \frac{c}{eH}\frac{\partial U}{\partial x}, \end{aligned}\right\} \tag{2.8a}$$

$$\left.\begin{aligned} \dot{X} &= \frac{c}{eH}\frac{\partial U}{\partial y}, \\ \dot{Y} &= -\frac{c}{eH}\frac{\partial U}{\partial x}, \end{aligned}\right\} \tag{2.8b}$$

$$\dot{p}_z = -\frac{\partial U}{\partial z}, \quad \dot{z} = \frac{\partial E_0}{\partial p_z}. \tag{2.8c}$$

Eq. (2.8a) may alternatively be written as

$$\left.\begin{aligned} \dot{\pi}_x &= -\frac{eH}{c}\frac{\partial E_0}{\partial \pi_y} - \frac{\partial U}{\partial x}, \\ \dot{\pi}_y &= \frac{eH}{c}\frac{\partial E_0}{\partial \pi_x} - \frac{\partial U}{\partial y}. \end{aligned}\right\} \tag{2.9}$$

It should be further noticed that the velocity $\boldsymbol{v} = (v_x, v_y, v_z)$ is written as

$$\left.\begin{aligned} v_x &\equiv \dot{x} = \dot{\xi} + \dot{X} = \frac{\partial E_0}{\partial \pi_x}, \\ v_y &\equiv \dot{y} = \dot{\eta} + \dot{Y} = \frac{\partial E_0}{\partial \pi_y}, \\ v_z &\equiv \dot{z} = \frac{\partial E_0}{\partial p_z}. \end{aligned}\right\} \tag{2.10}$$

As one sees by Eq. (2.8b), the motion of the center coordinates is induced by the perturbation potential U. When U induces scattering, the center will make jumps as shown schematically in Fig. 1. It is also easily verified that the equation (2.8) is equivalent to the familiar equation of motion written in terms of the Lorentz force.

For the sake of illustration and also for a later reference, we treat the simplest case where the potential U gives a constant force field, namely

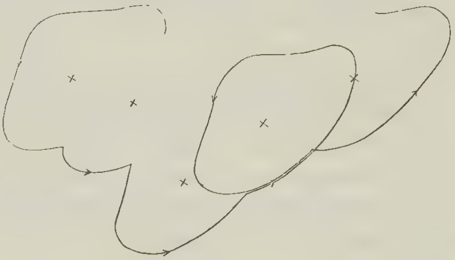

Fig. 1. Migration of centre.

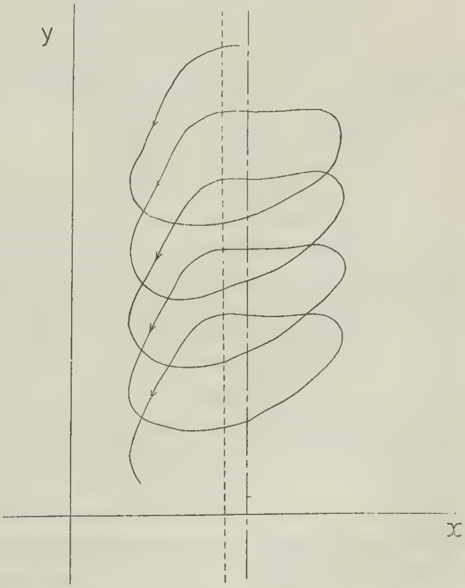

Fig. 2. Drift of centre in crossed uniform magnetic and electric fields. —·—·— is the locus of the centre coordinate, while -------- represents the locus if there wave no drift motion.

$$\frac{\partial U}{\partial x} = -eE\,, \quad \frac{\partial U}{\partial y} = 0\,. \tag{2.11}$$

Then Eq. (2.8b) shows that

$$\dot{Y} = cE/H\,. \tag{2.12}$$

The center makes a drift with the velocity (2.12) perpendicularly to the direction of the magnetic field and the force field (see Fig. 2). This holds quite generally irrespective of the form of the energy function $E_0(\boldsymbol{p})$. This drift motion is generally accompanied by a shift of the relative coordinates. This shift is determined by the condition that

$$\overline{\frac{\partial E_0}{\partial \pi_x}} = 0\,, \quad \overline{\frac{\partial E_0}{\partial \pi_y}} = \dot{Y} = \frac{cE}{H} \tag{2.13}$$

where the bar denotes the time average or the quantum-mechanical average with respect to a stationary state. This follows from the assumption that the variables ξ and η are bounded. We shall later come back to this point (§ 5).

§ 3. General Formula of the Conductivity Tensor

In a previous paper[16] (referred as K), one of the present authors showed that the conductivity tensor can be generally expressed by the formula (K. (5.11))

$$\sigma_{\mu\nu}(\omega) = \int_0^\infty dt e^{-i\omega t} \int_0^\beta d\lambda \langle \mathfrak{j}_\nu(-i\hbar\lambda) \mathfrak{j}_\mu(t) \rangle \qquad (\mu,\ \nu = x,\ y,\ z) \tag{3.1}$$

which gives, in particular for the static conductivity,

$$\sigma_{\mu\nu} = \int_0^\infty dt \int_0^\beta d\lambda \langle \mathfrak{j}_\nu(-i\hbar\lambda) \mathfrak{j}_\mu(t) \rangle\,. \tag{3.2}$$

In these expressions, β is $1/kT$ and $\mathfrak{j}_\nu$ is the current density operator in ν-direction. We shall use for the sake of convenience the second quantization formalism and write

$$\mathfrak{j}_\nu = \int_{\text{unit volume}} \psi^\dagger j_\nu \psi d\boldsymbol{r} \tag{3.3}$$

where j_ν is the current operator for one electron,

$$j_\nu = -ev_\nu \tag{3.4}$$

and $\psi^\dagger$ and ψ are quantized wave functions normalized per unit volume. In the following, density operators like (3.3) will be denoted by gothic letters.

In Eqs. (3.1) and (3.2), the time dependence of the current density means its motion induced by the *natural motion* of the system in the *absence* of the electric field. The average denoted by the bracket is taken over the equilibrium ensemble. Namely it means as usual the operation

$$\langle A \rangle = \mathrm{Tr}\,\rho A$$

where ρ is the equilibrium density matrix.

In the classical limit Eq. (3.1) goes into

$$\sigma_{\mu\nu}(\omega) = \int_0^\infty dt e^{-i\omega t} \langle \mathfrak{j}_\nu(0) \mathfrak{j}_\mu(t) \rangle \tag{3.5}$$

so that the conductivity is essentially the time integral of the correlation function of the current density which fluctuates in thermal equilibrium. Eq. (3.1) takes care of all possible quantum-mechanical complications by the integration over the imaginary parameter $i\hbar\lambda$ involved in $\mathfrak{j}_\nu(-i\hbar\lambda)$. The integrand

$$\int_0^\beta d\lambda \langle \mathfrak{j}_\nu(-i\hbar\lambda) \mathfrak{j}_\mu(t) \rangle = \phi_{\mu\nu}(t) \tag{3.6}$$

is not itself the correlation function, but it represents the response of the system revealed in the current component $\mathfrak{j}_\mu$ to the pulse of electric field applied in ν-direction so that it is the *response function* (which is essentially reduced to the correlation function in the classical limit).

It is possible, however, to write the conductivity in terms of the correlation function of the current fluctuation, for the symmetric part of the tensor, but not for the antisymmetric part, in the following expression,

$$\sigma_{\mu\nu}{}^s(\omega) = \frac{1}{2E_\beta(\omega)} \int_{-\infty}^\infty \frac{1}{2} \langle \{\mathfrak{j}_\nu(0) \mathfrak{j}_\mu(t)\} + \{\mathfrak{j}_\mu(0) \mathfrak{j}_\nu(t)\} \rangle e^{-i\omega t} dt \tag{3.7}$$

where the curly bracket means the symmetrized product of the two operators inside and $E_\beta(\omega)$ is

$$E_\beta(\omega) = \frac{\hbar\omega}{2} \coth \frac{\beta\hbar\omega}{2}\,.$$

This equation reduces to

$$\sigma_{\mu\nu}{}^s = \frac{1}{2kT} \int_{-\infty}^\infty \frac{1}{2} \langle \{\mathfrak{j}_\nu(0) \mathfrak{j}_\mu(t)\} + \{\mathfrak{j}_\mu(0) \mathfrak{j}_\nu(t)\} \rangle dt \tag{3.8}$$

for the static conductivity (K (7.14), (7.17)).

The above would be enough for the present purpose. A more detailed discussion of the general theory is referred to K. It should be emphasized, however, that these basic formulae are quite rigorous so that they provide us the safest ground from where we may proceed to actual calculation for any specific model even when the traditional method of using the Boltzmann-Bloch type transport equation can not be trusted.

We add here a brief remark for illustration that the simplest case of classical formula of the galvanomagnetic effect is easily obtained from Eq. (3.1) if the response functions (3.6) are assumed to be

$$\left.\begin{aligned} \phi_{xx}=\phi_{yy}&=\frac{e^2n}{m}e^{-t/\tau}\cos\omega_0 t\,,\\ \phi_{xy}=-\phi_{yx}&=-\frac{e^2n}{m}e^{-t/\tau}\sin\omega_0 t\,,\\ \phi_{zz}&=\frac{e^2n}{m}e^{-t/\tau}\,, \end{aligned}\right\}\tag{3.10}$$

where n is the electron density, m the electron mass, ω_0 the cyclotron frequency eH/mc, and τ the ordinary relaxation time. τ may be regarded also the correlation time for the electron velocity. The initial values of these response functions, $\phi_{xx}(0)$, $\phi_{xy}(0)$, etc. are in accordance with the same rules (K, Eqs. (8.5), (8.15) and (8.18)). By inserting (3.10) into (3.2) we get

$$\sigma=\frac{e^2n}{m}\begin{pmatrix} \dfrac{\tau}{1+\omega_0{}^2\tau^2} & -\dfrac{\omega_0\tau^2}{1+\omega_0{}^2\tau^2} & 0\\ \dfrac{\omega_0\tau^2}{1+\omega_0{}^2\tau^2} & \dfrac{\tau}{1+\omega_0{}^2\tau^2} & 0\\ 0 & 0 & \tau \end{pmatrix}\tag{3.11}$$

which is a well-known formula of the conductivity tensor of electrons with spherical mass and isotropic relaxation time.

§ 4. The v-representation and the ξ–X Representation of the Conductivity Tensor. Illustration by a Simple Model

We have seen in § 2 that the velocity of an electron in the x–y plane, which is normal to the direction of the magnetic field, can be split into two components, the center velocity and the relative velocity. Therefore the current density in Eq. (3.1) may be written as

$$\begin{pmatrix}\mathfrak{j}_x\\ \mathfrak{j}_y\end{pmatrix}\equiv -e\begin{pmatrix}\mathfrak{v}_x\\ \mathfrak{v}_y\end{pmatrix}=-e\begin{pmatrix}\dot{\mathfrak{X}}\\ \dot{\mathfrak{Y}}\end{pmatrix}-e\begin{pmatrix}\dot{\xi}\\ \dot{\eta}\end{pmatrix},\tag{4.1}$$

where the gothic letters are expressions like Eq. (3.3) with various velocity components. If the holes are considered the sign of e should be reversed. The conductivity tensor may be thus expressed in two ways. One representation is to write it in terms of (v_x, v_y) operators. We call this the *v-representation*. The other way is to split the whole expression into the center velocity and the relative velocity components. This will be called the *ξ–X representation.*

These two representations are of course correct and give the same answer if they are treated correctly. But they may be applied with advantage in different conditions. The v-representation is useful for weak field and also in moderately strong field. The ξ–X representation is particularly convenient for strong field.

It is very instructive to consider the following simple example in order to see how these two representations are related to each other.

Let us consider classical electrons. Each electron is supposed to be making cyclotron motion in the x–y plane with the cyclotron frequency ω_0, the mass being assumed to be spherical. The radius of the orbit is also assumed to be constant for the sake of simplicity. These simplifications will not spoil the essential things in our consideration. The scattering is supposed to occur with the mean free time τ_0 and the scattering angle α, which varies statistically. Our model is thus illustrated by Fig. 3, where the circular arcs represent the orbit of an electron, which suffers scattering at the points P_1, P_2, P_3 and so on at the time t_1, t_2, $t_3\cdots$. The center makes then a zig-zag motion $C_0C_1C_2\cdots$.

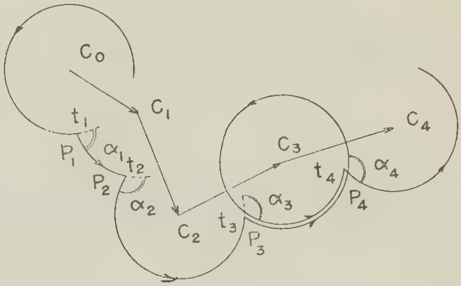

Fig. 3.

It is convenient to introduce the complex representation,

$$\left.\begin{aligned} u&=v_x+iv_y\,,\\ R&=X+iY\,,\\ \gamma&=\xi+i\eta\,, \end{aligned}\right\}\tag{4.2}$$

in which we may write

$$\left.\begin{aligned} u(t)&=u_0e^{i\omega_0t}\exp\{i\textstyle\sum\alpha_jF(t-t_j)\}\ ,\\ \dot{R}(t)&=\textstyle\sum\varDelta_jR\delta(t-t_j)\ ,\\ \dot{r}(t)&=u(t)+\textstyle\sum\varDelta_jr\delta(t-t_j)\ ,\end{aligned}\right\}\qquad(4.3)$$

where

$$F(t)=\begin{cases}1\ , & t>0\\ 0\ , & t<0\end{cases}$$

and

$$\varDelta_jR=-\varDelta_jr=e\exp\{i(\omega_0t_j+\sum^{j-1}\alpha_k)\}(1-e^{i\alpha_j})u_0/i\omega_0\qquad(4.4)$$

is the jump of the center by the j-th scattering. Eq. (4.3) describes the stochastic change of our variables. By assumptions we have

$$\langle e^{-i\nu(t_j-t_{j-1})}\rangle=\int_0^\infty e^{-i\nu t}e^{-t/\tau_0}dt/\tau_0=\frac{1}{1+i\nu\tau_0}\qquad(4.5)$$

for any ν and also

$$\langle e^{i\alpha}\rangle=\langle\cos\alpha\rangle=c\qquad(4.6)$$

for the scattering angle.

From Eqs. (4.3) and (4.4) with the help of (4.5) and (4.6) we may easily calculate the correlation functions and their Fourier transforms. Giving the details of the calculation in the Appendix, we summarize here only the results.

$$\int_0^\infty\langle v_x(0)v_x(t)\rangle e^{-i\omega t}dt=\int_0^\infty\langle v_y(0)v_y(t)\rangle e^{-i\omega t}dt=\frac{\tau}{2}\overline{v_x^2}\left\{\frac{1}{1+i(\omega-\omega_0)\tau}+\frac{1}{1+i(\omega+\omega_0)\tau}\right\}\ ,\qquad(4.7a)$$

$$\int_0^\infty\langle v_x(0)v_y(t)\rangle e^{-i\omega t}dt=-\int_0^\infty\langle v_y(0)v_x(t)\rangle e^{-i\omega t}dt=\frac{\tau}{2i}\overline{v_x^2}\left\{\frac{1}{1+i(\omega-\omega_0)\tau}-\frac{1}{1+i(\omega+\omega_0)\tau}\right\}\ ,\qquad(4.7b)$$

$$\int_0^\infty\langle\dot{X}(0)\dot{X}(t)\rangle e^{-i\omega t}dt=\int_0^\infty\langle\dot{Y}(0)\dot{Y}(t)\rangle e^{-i\omega t}dt=\frac{i\overline{v_x^2}}{2\omega_0}\left\{\frac{\omega-\omega_0}{1+i(\omega-\omega_0)\tau}+\frac{\omega+\omega_0}{1+i(\omega+\omega_0)\tau}\right\}\ ,\qquad(4.8a)$$

$$\int_0^\infty\langle\dot{X}(0)\dot{Y}(t)\rangle e^{-i\omega t}dt=-\int_0^\infty\langle\dot{Y}(0)\dot{X}(t)\rangle e^{-i\omega t}dt=\frac{\overline{v_x^2}}{2\omega_0^2}\left\{\frac{\omega-\omega_0}{1+i(\omega-\omega_0)\tau}-\frac{\omega+\omega_0}{1+i(\omega+\omega_0)\tau}\right\}\ ,\qquad(4.8b)$$

$$\int_0^\infty\langle\dot{\xi}(0)\dot{\xi}(t)\rangle e^{-i\omega t}dt=\int_0^\infty\langle\dot{\eta}(0)\dot{\eta}(t)\rangle e^{-i\omega t}dt=\frac{i\omega}{2}\frac{\overline{v_x^2}}{\omega_0^2}\left\{\frac{1-i\omega_0\tau}{1+i(\omega-\omega_0)\tau}+\frac{1+i\omega_0\tau}{1+i(\omega+\omega_0)\tau}\right\}\ ,\qquad(4.9a)$$

$$\int_0^\infty\langle\dot{\xi}(0)\dot{\eta}(t)\rangle e^{-i\omega t}dt=-\int_0^\infty\langle\dot{\eta}(0)\dot{\xi}(t)\rangle e^{-i\omega t}dt=\frac{\overline{v_x^2}}{2\omega_0^2}\left\{2\omega_0+\frac{\omega(1-i\omega_0\tau)}{1+i(\omega-\omega_0)\tau}-\frac{\omega(1+i\omega_0\tau)}{1+i(\omega+\omega_0)\tau}\right\}\ ,\qquad(4.9b)$$

$$\int_0^\infty\langle\dot{\xi}(0)\dot{X}(t)\rangle e^{-i\omega t}dt=\int_0^\infty\langle\dot{X}(0)\dot{\xi}(t)\rangle e^{-i\omega t}dt=-\frac{i\omega}{2}\frac{\overline{v_x^2}}{\omega_0^2}\left\{\frac{1}{1+i(\omega-\omega_0)\tau}+\frac{1}{1+i(\omega+\omega_0)\tau}\right\}\ ,\qquad(4.10a)$$

$$\int_0^\infty\langle\dot{\xi}(0)\dot{Y}(t)\rangle e^{-i\omega t}dt=\int_0^\infty\langle\dot{X}(0)\dot{\eta}(t)\rangle e^{-i\omega t}dt=-\frac{\omega}{2}\frac{\overline{v_x^2}}{\omega_0^2}\left\{\frac{1}{1+i(\omega-\omega_0)\tau}-\frac{1}{1+i(\omega+\omega_0)\tau}\right\}\ ,\qquad(4.10b)$$

where

$$\tau=\tau_0/(1-c)$$

is the ordinary relaxation time for the electrons.

The conductivity tensor and its components in the center and the relative velocities can be easily obtained from these equations since they are essentially these Fourier integrals of the corresponding correlation functions multiplied by ne^2/kT, where n is the electron density. By the equipartition law, we may put

$$\overline{v_x^2}/kT=1/m$$

so that we have, for instance,

$$\left.\begin{aligned}\sigma_{xx}(\omega)&=\frac{ne^2}{m}\frac{\tau}{2}\left\{\frac{1}{1+i(\omega-\omega_0)\tau}+\frac{1}{1+i(\omega+\omega_0)\tau}\right\}\ ,\\ \sigma_{yx}(\omega)&=\frac{ne^2}{m}\frac{\tau}{2i}\left\{\frac{1}{1+i(\omega-\omega_0)\tau}-\frac{1}{1+i(\omega+\omega_0)\tau}\right\}\ .\end{aligned}\right\}\qquad(4.11)$$

This is the classical formula obtained by inserting (3.10) into (3.5). The quantization effect is not taken into account in the present model, but we can see from the above results several things which help very much the understanding of the real situation.

The real part of the conductivity $\sigma_{xx}(\omega)$ is written as (K, (7.18))

$$\mathrm{Re}\,\sigma_{xx}(\omega)=\frac{ne^2}{kT}\,\mathrm{Re}\int_0^\infty\langle v_x(0)v_x(t)\rangle e^{-i\omega t}dt=\pi\frac{ne^2}{kT}\langle|v_x(\omega)|^2\rangle\,, \tag{4.12}$$

where $v_x(\omega)$ is the Fourier component of the fluctuating velocity v_x and so $\langle|v_x(\omega)|^2\rangle$ is its spectral density. This is shown in Fig. 4 by the bold curve. Similar spectral densities are also shown in the figure. They of course satisfy the relation

$$\langle|\dot{X}(\omega)|^2\rangle+\langle|\dot{\xi}(\omega)|^2\rangle+2\,\mathrm{Re}\,\langle\dot{X}(\omega)\dot{\xi}(\omega)\rangle=\langle|v_x(\omega)|^2\rangle\,. \tag{4.13}$$

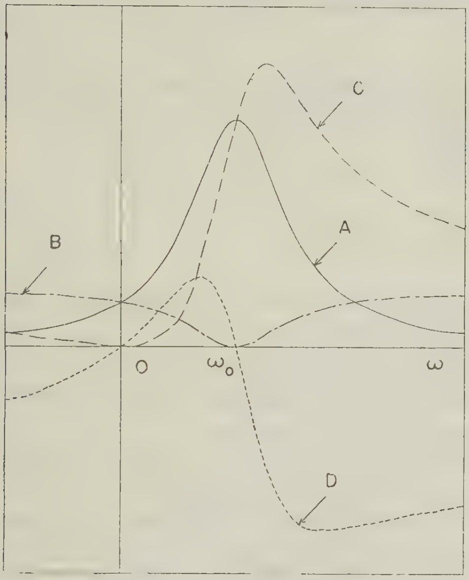

Fig. 4. Fourier components of the symmetric part of correlation functions. Curve A shows the real part of the first term of Eq. (4.7a). In the same way B corresponds to Eq. (4.8a), C. to Eq. (4.9a), and D to Eq. (4.10a).

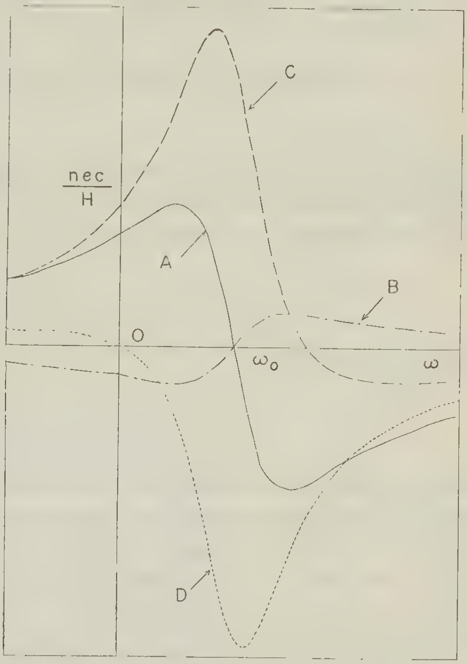

Fig. 5. Fourier components of the antisymmetric part of correlation functions. Curve A shows the real part of the first term of Eq. (4.7b). In the same way B corresponds to Eq. (4.8b), and C to Eq. (4.9b). Curve B is twice the real part of the first term of Eq. (4.10b).

Now the spectral density $\langle|v_x(\omega)|^2\rangle$ in this model has a resonance peak at the cyclotron frequency ω_0. This is the cyclotron resonance, which is broadened by the scattering processes. If we want to find the static conductivity, it means that we must then know the exact form of the broadened line in the tail at the frequency zero. The Lorentzian form in the present model is merely due to our great simplifications. The general problem of calculating the static conductivity in the v-representation is thus reduced to the line shape problem of the cyclotron resonance. The traditional method of using the transport equation involves an implicit assumption with regard to the type of the line shape, which is hard to prove in general and is in fact valid only in a certain limited condition.

In Fig. 4, we see that

$$\langle|\dot{X}(\omega)|^2\rangle_{\omega=0}=\langle|v_x(\omega)|^2\rangle_{\omega=0} \tag{4.14}$$

and other spectral densities vanish at $\omega=0$, i.e.,

$$\langle|\dot{\xi}(\omega)|^2\rangle_{\omega=0}=\langle\dot{\xi}(\omega)\dot{X}(\omega)\rangle_{\omega=0}=0 \tag{4.15}$$

(see Eqs. (4.7a–4.10a)).

This means that the static conductivity can be expressed as

$$\sigma_{xx}=\frac{ne^2}{kT}\int_0^\infty\langle\dot{X}(0)\dot{X}(t)\rangle dt\ . \tag{4.16}$$

It should be noticed that this expresses the Einstein relation,

$$\sigma_{xx}=\frac{ne^2}{kT}D \tag{4.17}$$

where D is the diffusion constant of the center. This is seen easily by rewriting Eq. (4.16) as

$$\sigma_{xx}=\frac{ne^2}{kT}\lim_{t\to\infty}\frac{1}{2t}\int_0^t\int_0^t\langle\dot{X}(t')\dot{X}(t'')\rangle dt'dt''=\frac{ne^2}{kT}\lim_{t\to\infty}\frac{1}{2t}\langle(X(t)-X(0))^2\rangle\equiv\frac{ne^2}{kT}D$$

(see K, Eq. (9.2))

Fig. 5 shows similarly the frequency dependence of Re $\sigma_{yx}(\omega)$ and its various components in the ξ–X representation. From Eqs. (4.7b)–(4.10b) we see that the cross terms involving the center and relative velocities vanish at $\omega=0$, and that

$$\int_0^\infty\langle\dot{\xi}(0)\dot{\eta}(t)\rangle dt=\overline{v_x^2}/\omega_0\ . \tag{4.19}$$

Therefore we have

$$\sigma_{yx}=\int_0^\infty\langle v_x(0)v_y(t)\rangle dt=\frac{nec}{H}+\frac{ne^2}{kT}\int_0^\infty\langle\dot{X}(0)\dot{Y}(t)\rangle dt \tag{4.20}$$

where the first term coming from Eq. (4.19) coincides with the ideal value which should be attained when the relaxation time τ becomes infinite (vanishing scattering).

Eqs. (4.16) and (4.20) suggest that the ξ–X representation can be used conveniently only for the calculation of the static conductivity. The vanishing of various terms mentioned above occurs only in the static limit. But it has certainly a great advantage over the v-representation as far as the static conductivity is concerned, particularly when the cyclotron frequency is large (strong magnetic field), because it is not the cyclotron resonance picture but is essentially the migration picture of the center coordinate. This limitation and the advantage of the ξ–X representation must be borne in mind. In the following section we shall prove (4.16) and (4.20) in a general way.

Another important point to be seen by our model is that the correlation of the successive jump of the center is strong when $\omega_0\tau$ is small and decreases with the increase of $\omega_0\tau$. This is easily seen because the center positions C_0, C_1, $C_2\cdots$ will be on a circle if $\omega_0\tau\sim0$, which means that the jumps C_0C_1, C_1C_2, $\cdots$ are correlated. An explicit calculation can be made by using Eq. (4.4) to obtain

$$\left.\begin{aligned}&\langle(\Delta_1X)^2\rangle=\langle(\Delta_1Y)^2\rangle=\frac{2\overline{v_x^2}}{\omega_0^2}(1-c)\ ,\\&\langle\Delta_1X\Delta_jX)\rangle=\langle\Delta_1Y\Delta_jY\rangle=-\frac{\overline{v_x^2}}{\omega_0^2}(1-c)^2c^{j-2}\,\mathrm{Re}\,(1-i\omega_0\tau)^{-(j-1)}\ ,\qquad(j\geqq2)\end{aligned}\right\} \tag{4.21}$$

$$\left.\begin{aligned}&\langle\Delta_1X\Delta_1Y\rangle=0\ ,\\&\langle\Delta_1X\Delta_jY\rangle=\langle\Delta_1Y\Delta_jX\rangle=-\frac{\overline{v_x^2}}{\omega_0^2}(1-c)^2c^{j-2}\,\mathrm{Im}\,(1-i\omega_0\tau)^{-(j-1)}\ ,\qquad(j\geqq2)\end{aligned}\right\} \tag{4.22}$$

From this we see that the correlation between the jumps $\overrightarrow{C_0C_1}$ and $\overrightarrow{C_{j-1}C_j}$ is of the order of

$(\omega_0\tau)^{-(j-1)}$ when the magnetic field is strong ($\omega_0\tau \gg 1$).

The expressions (4.16) and (4.20) are calculated with the use of the formula (see Appendix)

$$\int_0^\infty \langle \dot{R}^*(0)\dot{R}(t)\rangle dt = \frac{1}{\tau_0}\left\{\frac{1}{2}\langle \Delta_1 R^* \Delta_1 R\rangle + \sum_{j=2}^{\infty}\langle \Delta_1 R^* \Delta_j R\rangle\right\} = \frac{\overline{v_x^2}+\overline{v_y^2}}{i\omega_0}\frac{1}{1-i\omega_0\tau} . \tag{4.23}$$

The result, of course, coincides with (3.11).

The above consideration shows the important fact that the calculation of conductivity can be simplified very much under the condition of strong field, because then the correlation of the successive jumps may be neglected.

§ 5. Conductivity Expressed in Terms of the Center Migration

We shall now show that the basic equation (3.1) may be simplified by certain assumptions, to equations similar to (4.16) and (4.20). Namely the static conductivity components can be expressed in terms of the center velocity.

It is convenient to use the complex variables u, R and γ defined by (4.2) and also the corresponding current densities

$$\left.\begin{aligned} \boldsymbol{u} &= \int \psi^\dagger u \psi d\boldsymbol{r} = \int \psi^\dagger (v_x + i v_y)\psi d\boldsymbol{r} , \\ \dot{\boldsymbol{R}} &= \int \psi^\dagger \dot{R}\psi d\boldsymbol{r} = \int \psi^\dagger (\dot{X}+i\dot{Y})\psi d\boldsymbol{r} , \\ \dot{\boldsymbol{\gamma}} &= \int \psi^\dagger \dot{\gamma}\psi d\boldsymbol{r} = \int \psi^\dagger (\dot{\xi}+i\dot{\eta})\psi d\boldsymbol{r} . \qquad (\boldsymbol{u}=\dot{\boldsymbol{R}}+\dot{\boldsymbol{\gamma}}) \end{aligned}\right\} \tag{5.1}$$

Then the conductivity tensor components may be written as

$$\left.\begin{aligned} \sigma_{xx}+\sigma_{yy} &= \frac{e^2}{2}\int_0^\infty dt \int_0^\beta d\lambda \{\langle \boldsymbol{u}^*(-i\hbar\lambda)\boldsymbol{u}(t)\rangle + \langle \boldsymbol{u}(-i\hbar\lambda)\boldsymbol{u}^*(t)\rangle\} , \\ \sigma_{xx}-\sigma_{yy} &= \frac{e^2}{2}\int_0^\infty dt \int_0^\beta d\lambda \{\langle \boldsymbol{u}(-i\hbar\lambda)\boldsymbol{u}(t)\rangle + \langle \boldsymbol{u}^*(-i\hbar\lambda)\boldsymbol{u}^*(t)\rangle\} , \\ \sigma_{yx}-\sigma_{xy} &= \frac{e^2}{2i}\int_0^\infty dt \int_0^\beta d\lambda \{\langle \boldsymbol{u}^*(-i\hbar\lambda)\boldsymbol{u}(t)\rangle - \langle \boldsymbol{u}(-i\hbar\lambda)\boldsymbol{u}^*(t)\rangle\} , \\ \sigma_{yx}+\sigma_{xy} &= \frac{e^2}{2i}\int_0^\infty dt \int_0^\beta d\lambda \{\langle \boldsymbol{u}(-i\hbar\lambda)\boldsymbol{u}(t)\rangle - \langle \boldsymbol{u}^*(-i\hbar\lambda)\boldsymbol{u}^*(t)\rangle\} , \end{aligned}\right\} \tag{5.2}$$

$$\sigma_{xz}+i\sigma_{yz} = e^2\int_0^\infty dt \int_0^\beta d\lambda \langle \boldsymbol{v}_z(-i\hbar\lambda)\boldsymbol{u}(t)\rangle . \tag{5.3}$$

Each of the terms on the right-hand side of Eq. (5.2) is expressed in the ξ-X representation, in which it consists of four terms.

Let us first consider the term which involves the relative velocities $\dot{\gamma}$ and $\dot{\gamma}^*$, which will be transformed as follows.

$$\begin{aligned} \int_0^\infty dt \int_0^\beta d\lambda \langle \dot{\boldsymbol{\gamma}}^*(-i\hbar\lambda)\dot{\boldsymbol{\gamma}}(t)\rangle &= -\int_0^\beta d\lambda \langle \dot{\boldsymbol{\gamma}}^*(-i\hbar\lambda)\boldsymbol{\gamma}(0)\rangle \\ &= -\frac{1}{i\hbar}\,\mathrm{Tr}\,[\rho\boldsymbol{\gamma}^*]\boldsymbol{\gamma} = -\frac{1}{i\hbar}\,\mathrm{Tr}\,\rho[\boldsymbol{\gamma}^*, \boldsymbol{\gamma}] = -2\frac{nc}{eHi} , \end{aligned} \tag{5.4}$$

where n is the electron density. The last expression is obtained from the commutation law

$$[\boldsymbol{\gamma}^*, \boldsymbol{\gamma}] = \int \psi^\dagger [\gamma^*, \gamma]\psi d\boldsymbol{r} = 2l^2 \int \psi^\dagger \psi d\boldsymbol{r} = 2l^2 n \tag{5.5}$$

(see (2.6a)). To rewrite the second line of (5.4) we used the identity,

$$\frac{1}{i\hbar}[\rho,\ A]=\int_0^\beta \rho\dot{A}(-i\hbar\lambda)d\lambda \tag{5.6}$$

which holds for a canonical density matrix $\rho=C\exp(-\beta\mathcal{H})$ (K, Eq. (3.9)). The second line is obtained from the first by simple integration with the assumption that

$$\lim_{t\to\infty}\int_0^\beta d\lambda\langle\dot{\gamma}^*(-i\hbar\lambda)\gamma(t)\rangle=\lim_{t\to\infty}\frac{1}{i\hbar}\langle[\gamma^*(0),\ \gamma(t)]\rangle=0\ . \tag{5.7a}$$

Here again Eq. (5.6) is used.

Similarly, if we assume

$$\lim_{t\to\infty}\int_0^\beta d\lambda\langle\dot{\gamma}(-i\hbar\lambda)\gamma(t)\rangle=\lim_{t\to\infty}\frac{1}{i\hbar}\langle[\gamma(0),\ \gamma(t)]\rangle=0 \tag{5.7b}$$

and the conjugates of (5.7a, b), we get

$$\left.\begin{aligned}&\int_0^\infty dt\int_0^\beta d\lambda\langle\dot{\gamma}(-i\hbar\lambda)\dot{\gamma}^*(t)\rangle=\frac{2cn}{eHi}\ ,\\&\int_0^\infty dt\int_0^\beta d\lambda\langle\dot{\gamma}(-i\hbar\lambda)\dot{\gamma}(t)\rangle=0\ ,\\&\int_0^\infty dt\int_0^\beta d\lambda\langle\dot{\gamma}^*(-i\hbar\lambda)\dot{\gamma}^*(t)\rangle=0\ .\end{aligned}\right\} \tag{5.8}$$

Eqs. (5.4) and (5.8) show that

$$(\sigma_{xx})_{\dot{\gamma}\dot{\gamma}}=(\sigma_{yy})_{\dot{\gamma}\dot{\gamma}}=0\ ,\qquad(\sigma_{yx})_{\dot{\gamma}\dot{\gamma}}=-(\sigma_{xy})_{\dot{\gamma}\dot{\gamma}}=\frac{nec}{H}\ , \tag{5.9}$$

where the suffix means the contribution from the relative velocity. Therefore, if the conditions (5.7) are fulfilled the relative velocity gives only the ideal value $(-enc/H)$ to the antisymmetric conductivity. This is in accordance with what we saw by Eq. (4.19) for our simple model.

The conditions (5.7) will be satisfied if the variables ξ and η are *bounded*. Then it is admissible to put

$$\lim_{t\to\infty}\int_0^\beta d\lambda\langle\dot{\gamma}^*(-i\hbar\lambda)\gamma(t)\rangle=\int_0^\beta d\lambda\langle\dot{\gamma}^*(-i\hbar\lambda)\rangle\langle\gamma\rangle\ , \tag{5.10}$$

where we assumed essentially an ergodic property of the variable γ (see K, § 3). Or simply this means that the correlation between the variables $\dot{\gamma}^*(-i\hbar\lambda)$ and $\gamma(t)$ will be lost as the time t grows infinite. In the last expression we have

$$\langle\dot{\gamma}(-i\hbar\lambda)\rangle=\langle\dot{\gamma}\rangle=0 \tag{5.11}$$

because of the bounded nature of γ. This gives (5.7a). Other conditions, (5.7b) and the conjugates, are understood in the same way.

Next we consider the cross terms involving the relative and the center velocities. Like Eq. (5.4) they may be transformed as

$$\begin{aligned}\int_0^\infty dt\int_0^\beta d\lambda\langle\dot{\boldsymbol{R}}(-i\hbar\lambda)\dot{\gamma}(t)\rangle&=-\int_0^\beta d\lambda\langle\dot{\boldsymbol{R}}(-i\hbar\lambda)\gamma(0)\rangle\\&=-\frac{1}{i\hbar}\mathrm{Tr}\,[\rho,\ \boldsymbol{R}]\gamma=-\frac{1}{i\hbar}\mathrm{Tr}\,\rho[\boldsymbol{R},\ \gamma]=0\ ,\end{aligned} \tag{5.12}$$

$$\begin{aligned}\int_0^\infty dt\int_0^\beta d\lambda\langle\dot{\gamma}(-i\hbar\lambda)\dot{\boldsymbol{R}}(t)\rangle&=\int_0^\infty dt\int_0^\beta d\lambda\langle\dot{\gamma}(-t)\dot{\boldsymbol{R}}(i\hbar\lambda)\rangle=\int_{-\infty}^0 dt\int_0^\beta d\lambda\langle\dot{\gamma}(t)\dot{\boldsymbol{R}}(i\hbar\lambda)\rangle\\&=\int_0^\beta d\lambda\langle\gamma(0)\dot{\boldsymbol{R}}(i\hbar\lambda)\rangle=\int_0^\beta d\lambda\langle\dot{\boldsymbol{R}}(-i\hbar\lambda)\gamma(0)\rangle=0\ ,\end{aligned} \tag{5.13}$$

where we made the assumptions

$$\lim_{t\to\infty}\int_0^\beta d\lambda\langle\dot{\boldsymbol{R}}(-i\hbar\lambda)\boldsymbol{\gamma}(t)\rangle=0\ ,\qquad \lim_{t\to\infty}\int_0^\beta d\lambda\langle\boldsymbol{\gamma}(-t)\dot{\boldsymbol{R}}(i\hbar\lambda)\rangle=0\ . \tag{5.14}$$

If Eqs. (5.12) and (5.13) (and their conjugates) are right, we see from (5.2) that

$$(\sigma_{xx})_{\dot{R}\dot{\gamma}}=(\sigma_{yy})_{\dot{R}\dot{\gamma}}=(\sigma_{yx})_{\dot{R}\dot{\gamma}}=(\sigma_{xy})_{\dot{R}\dot{\gamma}}=0\ . \tag{5.15}$$

Namely the cross terms involving the relative and the center velocities do not contribute anything to the static conductivity. This is again in accord with our former consideration.

The assumptions (5.14) are similar to (5.7) and are understood in a similar manner. Namely they are based on the assumptions that γ is *bounded* and that

$$\langle\dot{\boldsymbol{R}}\rangle=0\ . \tag{5.16}$$

The last assumption should be true, because otherwise there would be a constant current flowing in the absence of the applied electric field.

Another point to be remarked in the transformation (5.12) is the last step which interchanges the order of the operators in the trace operation. The classical correspondence of this is the partial integration of the type

$$\iiiint dXdYd\xi d\eta\left\{\frac{\partial}{\partial X}\exp(-\beta\mathscr{H})\right\}\cdot\xi$$
$$=\iiint dYd\xi d\eta[\{\exp(-\beta\mathscr{H})\}_{X=X_2}-\{\exp(-\beta\mathscr{H})\}_{X=X_1}]\cdot\xi-\iiiint dXdYd\xi d\eta\exp(-\beta\mathscr{H})\frac{\partial\xi}{\partial X}\ ,$$

where X_1 and X_2 are the boundaries of the domain under consideration. This surface contribution will vanish since the electron density is constant on the average even when there the perturbation potential U.

Thus, we have seen that the static conductivity is rather simply expressed in the ξ–X re-exists presentation as

$$\sigma_{xx}=e^2\int_0^\infty dt\int_0^\beta d\lambda\langle\dot{\boldsymbol{X}}(-i\hbar\lambda)\dot{\boldsymbol{X}}(t)\rangle\ ,\qquad \sigma_{yy}=e^2\int_0^\infty dt\int_0^\beta d\lambda\langle\dot{\boldsymbol{Y}}(-i\hbar\lambda)\dot{\boldsymbol{Y}}(t)\rangle\ , \tag{5.17a}$$

$$\sigma_{yx}=\frac{nec}{H}+e^2\int_0^\infty dt\int_0^\beta d\lambda\langle\dot{\boldsymbol{X}}(-i\hbar\lambda)\dot{\boldsymbol{Y}}(t)\rangle\ ,\qquad \sigma_{xy}=-\frac{nec}{H}+e^2\int_0^\infty dt\int_0^\beta d\lambda\langle\dot{\boldsymbol{Y}}(-i\hbar\lambda)\dot{\boldsymbol{X}}(t)\rangle \tag{5.17b}$$

if the condition is satisfied that the variables ξ and η are *bounded*.

This is satisfied when the electrons are free with a constant mass or when the effective mass theory is valid. It will be so more generally when the cyclotron orbits (in semiclassical sense) are closed in the momentum space. In these cases, the probability amplitudes in the momentum space will be limited in a certain neighborhood of the classical paths. Since the general canonical distribution, or the Fermi distribution in the case of independent electrons, will cut off the larger orbits with higher energies, the quasimomenta and therefore the relative coordinates can be regarded as bounded even in a quantummechanical sense. This consideration shows also that we should treat holes rather than electrons if the band in consideration is almost full as we do usually. This of course will change the sign of the first term of (5.17b).

Therefore, by neglecting the interband effect and Harper's broadening effect (§ 2) and by excluding the existence of the extended orbits[12] we may expect the bounded character of the relative coordinates and so use Eq. (5.17), which expresses the conductivity in terms of the migration of the center coordinate.

It should be remarked also that Eq. (5.17) may be written in another form as far as the symmetric part is concerned.

As was indicated by (3.8), the symmetric part can be written in terms of the correlation function (see K, § 3). So we have

$$\left.\begin{aligned}\sigma_{xx}&=\frac{e^2}{2kT}\int_{-\infty}^{\infty}dt\langle\{\dot{X}(0)\dot{X}(t)\}\rangle dt\,,\\ \sigma_{yy}&=\frac{e^2}{2kT}\int_{-\infty}^{\infty}dt\langle\{\dot{Y}(0)\dot{Y}(t)\}\rangle dt\,,\\ \sigma_{yx}+\sigma_{xy}&=\frac{e^2}{2kT}\int_{-\infty}^{\infty}dt\langle\{\dot{X}(0)\dot{Y}(t)+\dot{Y}(0)\dot{X}(t)\}\rangle\,,\end{aligned}\right\}\tag{5.18}$$

where the right hand sides are the correlation functions of the center current densities. These equations are the generalization of Eq. (4.16) and the Einstein relation to correlate the conductivity and the diffusion constant of the center coordinate.

It may be added that the components σ_{xz} and σ_{yz} are expressed as

$$\sigma_{xz}=e^2\int_0^\infty dt\int_0^\beta d\lambda\langle v_z(-i\hbar\lambda)\dot{X}(t)\rangle\,,\qquad \sigma_{yz}=e^2\int_0^\infty dt\int_0^\beta d\lambda\langle v_z(-i\hbar\lambda)\dot{Y}(t)\rangle\,.\tag{5.19}$$

This is seen from (5.3) by writing it in the ξ-X representation and by transforming it like (5.12) with the use of an assumption similar to (5.14).

Before concluding this section, the nature of the above derived equations, (5.17), (5.18) and (5.19), should be briefly discussed. It is noticed that all of these expressions will vanish if there exists no scattering potential U, except $\sigma_{yx}=-\sigma_{xy}$ which goes into enc/H. This is obvious, since the electrons will then simply drift with the velocity cE/H at right angles to the directions of the magnetic field and the electric field (Eq. (2.12)).

The important point here, however, is that the integrals in Eqs. (5.17)~(5.19) vanish with the perturbation potential. In other words, these are very convenient expressions to start from the limit of strong field. The potential U may then be treated by some sort of perturbation calculation. By complete calculation of such perturbation series, these equations will of course give the correct answer for all values of the magnetic field. But the strong field case could be treated by some lower order calculation of the perturbation.

§ 6. Approximations for Strong Field

Let us now apply the results of the previous section to the case where the magnetic field is so strong that the condition (1.1) is satisfied.

In the classical theory, this is the condition that the expansion

$$\frac{\tau}{1+\omega_0^2\tau^2}=\frac{1}{\omega_0^2\tau}\left\{1-\frac{1}{\omega_0^2\tau^2}+\cdots\right\}\tag{6.1}$$

can be used. This series is a sort of perturbation expansion since $1/\tau$ is essentially the second order quantity in the perturbation potential U. We also remark that the first term of (6.1) may as well be regarded as the first term of the expansion (4.23) in the correlation of successive jumps of the center displacement.

Guided by this classical consideration, two different standpoints can be conceived for the calculation of the strong field properties.

a) The first standpoint is to regard the peaturbation U as weak and use the direct perturbation calculation or its modification if necessary.

b) The second standpoint is that the perturbation potential is considered as local. This means that the electrons are free most of the time and collide the scattering center (the perturbation may be strong in its direct neighborhood) with short duration of collision. Then the correlation of the successive jumps is neglected so that the problem is reduced to the calculation of the scattering in the presence of the magnetic field.

6.1) *Perturbational Calculation.*

By the equation of motion (2.8b), the integrand of Eq. (5.18) is already second order in U. Therefore, from the standpoint (a), the lowest perturbation calculation will give

$$\sigma_{xx} \sim \frac{e^2}{2kT}\int_{-\infty}^{\infty} dt \langle \dot{\boldsymbol{X}}(0)\dot{\boldsymbol{X}}^0(t)\rangle_0 \,, \tag{6.2}$$

where

$$\dot{\boldsymbol{X}} = \int \psi^\dagger \dot{X}\psi d\boldsymbol{r} = \int \psi^\dagger \frac{1}{i\hbar}[X,\ U]\psi d\boldsymbol{r} = \frac{c}{eH}\int \psi^\dagger \frac{\partial U}{\partial y}\psi d\boldsymbol{r} \tag{6.3}$$

and $\dot{\boldsymbol{X}}^0(t)$ means the motion of $\dot{\boldsymbol{X}}$ induced by the unperturbed Hamiltonian

$$\mathcal{H}_0 = \int \psi^\dagger E_0(\pi)\psi d\boldsymbol{r} + \mathcal{H}_s \tag{6.4}$$

(see Eq. (2.1)), whereas the total Hamiltonian is

$$\mathcal{H} = \mathcal{H}_0 + \boldsymbol{U} = \mathcal{H}_0 + \int \psi^\dagger U \psi d\boldsymbol{r} \,. \tag{6.5}$$

In Eq. (6.4) $\mathcal{H}_s$ is the Hamiltonian for the scatters and is assumed to be commutable with the first term. The suffix 0 in (6.2) after the bracket means that the average is taken over the grand canonical distribution

$$\rho_0 = C_0 \exp(-\beta\mathcal{H}_0 + \beta\zeta N) \,, \qquad N = \int \psi^\dagger \psi d\boldsymbol{r}$$

instead of the true distribution $\rho = C\exp(-\beta\mathcal{H} + \beta\zeta N)$.

As one sees by (6.3), the expression (6.2) is proportional to U^2/H^2, disregarding the H-dependence of other factors.

In one-electron operators, Eq. (6.2) may be written as

$$\sigma_{xx} \sim 2\frac{e^2}{2kT}\int_{-\infty}^{\infty} dt \langle \mathrm{Tr}\, f(E_0)\dot{X}(1-f(E_0))\dot{X}^0(t)\rangle_s \tag{6.6}$$

where f is the Fermi distribution

$$f(E_0) = \{\exp[\beta(E_0(\pi) - \zeta)] + 1\}^{-1} \,,$$

ζ being the Fermi potential, and $\langle\ \ \rangle_s$ means the average over the distribution of scatterers. The factor 2 in front takes care of the spin weight. $\dot{X}^0(t)$ represents the unperturbed motion of $\dot{X}$,

$$\begin{aligned} \dot{X}^0(t) &= \exp\{i(E_0 + \mathcal{H}_s)t/\hbar\}\dot{X}\exp\{-i(E_0 + \mathcal{H}_s)t/\hbar\} \\ &= \frac{1}{i\hbar}[X,\ \exp\{i(E_0 + \mathcal{H}_s)t/\hbar\}U\exp\{-i(E_0 + \mathcal{H}_s)t/\hbar\}] \\ &= \frac{1}{i\hbar}[X,\ \exp(iE_0t/\hbar)U^0(t)\exp(-iE_0t/\hbar)] \,, \end{aligned} \tag{6.7}$$

where $U^0(t)$ is the time change of the perturbation caused by the natural motion of the scatterers. If U is due to lattice defects such as impurities it will be static.

The eigenvalues of

$$E_0(\pi) = E_0(\pi_x,\ \pi_y,\ p_z) \tag{6.8}$$

will be denoted by $E_{\nu' p_z'}$, and the eigenstates and eigenvalues of the scatterers are denoted by α' and $E_{\alpha'}$. By the commutation law (2.6b) each of $E_{\nu' p_z'}$ is degenerate with the multiplicity $L^2/2\pi l^2$ if we take the domain with the volume L^3 in order to see the dimensional relation clearly. These degenerate states may be labeled by X' or Y' depending on the choice of the representation. Summations over p_z' and X' should be replaced by the integrals as follows:

$$\sum_{p_z'} \to \frac{L}{h}\int_{-\infty}^{\infty} dp_z' , \qquad \sum_{X'} \to \frac{L}{2\pi l^2}\int_0^L dX' .$$

By these considerations, Eq. (6.6) can be written as

$$\begin{aligned}\sigma_{xx} \sim 2\frac{e^2}{2kT}\sum_{\nu'}\frac{1}{h}\int dp_z' \, \frac{1}{2\pi l^2}\int \frac{dX'}{L} f(E_{\nu' p_z'}) \\ \times \sum_{\nu''}\frac{L}{h}\int dp_z'' \cdot \frac{L}{2\pi l^2}\int_L dX''(X'-X'')^2 \cdot (1-f(E_{\nu'' p_z''}))W(\nu' p_z' X', \nu'' p_z'' X'')\end{aligned} \tag{6.9}$$

when W represents the transition probability for an electron to be scattered from the state $\nu' p_z' X'$ to $\nu'' p_z'' X''$. Here W is explicitly calculated to be

$$W(\nu' p_z' X', \nu'' p_z'' X'')$$

$$= \frac{1}{\hbar^2}\int_{-\infty}^{\infty} dt \langle (\nu' p_z' X' | U | \nu'' p_z'' X'')(\nu'' p_z'' X'' | U^0(t) | \nu' p_z' X')\rangle_s \exp\{i(E_{\nu'' p_z''} - E_{\nu' p_z'})t/\hbar\} \tag{6.10a}$$

$$= \frac{2\pi}{\hbar}\sum_{\alpha'}\sum_{\alpha''} P_{\alpha'} |(\nu' p_z' X' \alpha' | U | \nu'' p_z'' X'' \alpha'')|^2 \delta(E_{\nu' p_z'} + E_{\alpha'} - E_{\nu'' p_z''} - E_{\alpha''}) \tag{6.10b}$$

by Eq. (6.7), where $P_{\alpha'}$ is the probability distribution of the scatterer states.

The potential U is a sum of single scatterer potential

$$U = \sum_{\text{scatterers}} U_j , \tag{6.11}$$

which are randomly distributed in the whole space. The product of the matrix elements

$$(\nu' p_z' X' | U_j | \nu'' p_z'' X'')(\nu'' p_z'' X'' | U_l | \nu' p_z' X') \tag{6.12}$$

will vanish if the scatterers j and l are far apart in space. Therefore (6.10) is essentially proportional to the total number N_s of scatterers in space. The expression (6.9) itself depends, however, only on the number density of scatterers N_s/L^3 as it should be.

Eq. (6.9) is similar to the Einstein relation,

$$\sigma_{xx} = \frac{e^2}{2kT} n_{\text{eff}} \cdot D . \tag{6.13}$$

If we consider the present problem in a semiclassical way we would expect that this equation will be written as

$$\begin{aligned}\sigma_{xx} = 2\frac{e^2}{2kT}\sum_{\nu'}\frac{1}{h}\iint dp_z' dz' \, \frac{1}{2\pi l^2}\iint dX' dY' f(E_{\nu' p_z'}) \\ \times \int dp_z'' \iint dX'' dY'' \cdot (X'-X'')^2 (1-f(E_{\nu'' p_z''}))\Phi(\nu' p_z' X' Y', \nu'' p_z'' X'' Y'') ,\end{aligned} \tag{6.14}$$

where Φ is the transition probability by scattering in which an electron jumps from $(\nu' p_z')$ to $(\nu'' p_z'')$ with the center displacement from $(X'Y')$ to $(X''Y'')$. Eq. (6.9) takes account of the fact that the center coordinates X and Y have the uncertainty of $2\pi l^2$. The relation of (6.14) and (6.9) may easily be seen.

Eq. (6.2) or (6.9) can be applied to calculation of the case of phonon scattering. In fact, the example of metals with isotropic mass has been calculated. The result agrees with that obtained by Titeica[9)]. It is important to note that, this simplest perturbational calculation does not give convergent answers if the scattering potential is static, for instance, caused by lattice imperfections like impurities. Therefore, in order to get any reasonable answer, we must go at least one step further than this simplest Born approximation.

The reason for this bad divergence may be seen from the following consideration. For simplicity we take the mass as spherical. An electron passing through a scattering potential along the z-direction will spend the time of the order of

$$\tau_d \sim a/v_z = ma/p_z$$

in the potential. By the equation of motion (2.8b), the center displacement will be then of the order of

$$\Delta X \sim \frac{c}{eH}\frac{\overline{\partial U}}{\partial y}\cdot\tau_d\,,$$

where $\overline{\partial U/\partial y}$ is a time average of $\partial U/\partial y$. This rough estimation corresponds to the Born approximation. Then we would have

$$n_s\sigma_s\int v_z dp_z\cdot(\Delta X)^2 \propto \int\frac{dp_z}{p_z} \tag{6.15}$$

for the calculation of conductivity. Here n_s is the scatterer density, σ_s the cross section, so that $n_s\sigma_s v_z$ is the mean free time. The divergence of the type (6.15) is exactly that appears in (6.9) when applied to impurity scattering. This could be interpreted also in another way. An electron with p_z equal to zero will hit a scatterer again and again, if the scattering occurs really at a point scatterer. This infinite repetition is the source of the divergence.

6.2) *Higher Approximations*

For a better calculation, we go back to (5.18a) or its equivalent,

$$\sigma_{xx} = 2\frac{e^2}{2kT}\int_{-\infty}^{\infty} dt\,\mathrm{Tr}\,\{f(\mathcal{H})\dot{X}(1-f(\mathcal{H}))\dot{X}(t)\}\,, \tag{6.18}$$

where $\mathcal{H}$ is the one-electron Hamiltonian

$$\mathcal{H} = E_0 + U\,.$$

Since the potential U is assumed to be static (6.18) can be transformed into

$$\sigma_{xx} = 2\int_{-\infty}^{\infty} dE\left(-\frac{\partial f}{\partial E}\right)G_{xx}(E)\,, \tag{6.19}$$

where

$$G_{xx}(E) = \pi\hbar e^2\,\mathrm{Tr}\,\{\delta(E-\mathcal{H})\dot{X}\delta(E-\mathcal{H})\dot{X}\} = e^2\rho(E)\frac{1}{2}\int_{-\infty}^{\infty} dt\langle\dot{X}\dot{X}(t)\rangle_E\,. \tag{6.20}$$

Here $\rho(E)$ is the state density

$$\rho(E) = \mathrm{Tr}\,\delta(E-\mathcal{H})$$

and $\langle\ \rangle_E$ means the microcanonical average for a given E.

Now the resolvent for $\mathcal{H}$ is defined by

$$R(\gamma) = \frac{1}{\mathcal{H}-\gamma}\,. \tag{6.21}$$

With the use of this, $\delta(E-\mathcal{H})$ is expressed as[20)]

$$\delta(E-\mathcal{H}) = \lim_{\eta\to+0}\frac{1}{2\pi i}(R(E+i\eta)-R(E-i\eta)) = \lim_{\eta\to+0}\frac{1}{2\pi}\frac{\eta}{(\mathcal{H}-E)^2+\eta^2}\,, \tag{6.22}$$

so (6.20) may be calculated by any useful approximation for $R(\gamma)$. A damping-theoretical expansion of $R(\gamma)$ is given by[20)]

$$R(\gamma) = D(\gamma) - D(\gamma)UD(\gamma) + \cdots \tag{6.23}$$

where

$$D(\gamma)=\frac{1}{E_0+G(\gamma)-\gamma} \tag{6.24}$$

is the diagonal part of $R(\gamma)$ with respect to E_0. $G(\gamma)$ here determines the shift and broadening in the limit $\gamma\rightarrow E\pm i0$ and is obtained by solving the integral equation of the form

$$G(\gamma)=-\{UD(\gamma)U\}_{\text{diagonal}}+\cdots . \tag{6.25}$$

The diagonal part of $\delta(E-\mathcal{H})$, Eq. (6.22), thus calculated will be denoted by $S(E)$,

$$S(E)=\{\delta(E-\mathcal{H})\}_{\text{diag.}} \tag{6.26}$$

Eq. (6.20) is then replaced by

$$G_{xx}(E)\sim\pi\hbar e^2\,\mathrm{Tr}\,\{S(E)\dot{X}S(E)\dot{X}\}=\frac{\pi e^2}{\hbar}\,\mathrm{Tr}\,\{S(E)[X,\ U]S(E)[U,\ X]\}\,. \tag{6.27}$$

This is a higher approximation by which the broadening of the quantum levels is taken into account and the divergence above mentioned is avoided. Davydov and Pomeranchuk[11] in fact tacitly used this approximation. More detailed discussion of this will be given in the next paper.

A brief remark may be added about the standpoint (b) mentioned at the beginning of this section. Eq. (6.20) may be approximated by

$$G_{xx}(E)=e^2\rho(E)\sum_j\frac{1}{2\hbar^2}\int_{-\infty}^{\infty}dt\langle[X,\ U_j][U_j,\ X]_t\rangle_E \tag{6.28}$$

where the sum is taken over the scatterers in a unit volume. The cross terms which involve different scatterers are omitted here. Furthermore the time change $[U_j,\ X]_t$ is considered only in the neighborhood of the particular scatterer j. Namely the electron is supposed to move there only under the influence of U_j. Therefore, this approximation starts from solving the scattering problem in which an electron is scattered from $\nu' p_z' X'$ to $\nu'' p_z'' X''$. If the exact solution of this is obtained, Eq. (6.19) and (6.28) may be used to calculate σ_{xx}. The divergence of the type (6.15) will not occur in this method so that one should get finite answer even if the broadening is neglected in the state density. The broadening is however, important particularly for the amplitude of de Haas-van Alphen like oscillations, so that it may be necessary to take account of it.

§ 7. Conclusion

We have seen in the present paper that the description by the migration of the center of cyclotron motion is particularly useful for the understanding and for practical calculations of conductivity at high magnetic field. A general treatment is developed here on the basis of the new theory of transport phenomena given by one of the present authors. A great advantage of this method is that it avoids any dubious use of transport equations so that the logical structure of the theory is even more satisfactory than the ordinary conduction theory. After the proof of general formulae for the conductivity expressed in terms of the center velocities, approximation methods have been discussed. Detailed applications to metals and semiconductors will be reported soon in a forthcoming paper which makes the second part of the series.

Appendix

By Eqs. (4.3), (4.5) and (4.6), we have

$$\left\langle u^*(0)\int_0^\infty u(t)e^{-i\omega t}dt\right\rangle = \left\langle u_0^*\sum_{k=0}^{\infty}\int_{t_k}^{t_{k+1}} e^{i\overset{k}{\Sigma}\alpha_j}\, e^{-i(\omega-\omega_0)t}dt\cdot u_0\right\rangle$$

$$=\frac{\overline{u_0^*u_0}}{i(\omega-\omega_0)}\left\langle\sum_{k=0}^{\infty} e^{i\overset{k}{\Sigma}\alpha_j}(e^{-ij(\omega-\omega_0)t_k}-e^{-i(\omega-\omega_0)t_{k+1}})\right\rangle$$

$$=\frac{\overline{u_0^*u_0}}{i(\omega-\omega_0)}\sum_{k=0}^{\infty}c^k[\{1+i(\omega-\omega_0)\tau_0\}^{-k}-\{1+i(\omega-\omega_0)\tau_0\}^{-k-1}]$$

$$=\overline{u_0^*u_0}\frac{\tau_0}{1-c+i(\omega-\omega_0)\tau_0}=\overline{u_0^*u_0}\frac{\tau}{1+i(\omega-\omega_0)\tau}\,. \tag{A.1}$$

Similarly

$$\int_0^\infty\langle u(0)u^*(t)\rangle e^{-i\omega t}dt=\overline{u_0^*u_0}\frac{\tau}{1+i(\omega+\omega_0)\tau} \tag{A.2}$$

which may be obtained from (A.1) by replacing ω by $-\omega$ and i by $-i$. Also by the assumption that

$$\overline{v_xv_y}=0\,,\qquad \overline{v_x^2}=\overline{v_y^2}$$

we have

$$\int_0^\infty\langle u(0)u(t)\rangle e^{-i\omega t}dt=\int_0^\infty\langle u^*(0)u^*(t)\rangle e^{-i\omega t}dt=0\,. \tag{A.3}$$

Eqs. (4.7a) and (4.7b) in the text follow from (A.1), (A.2) and (A.3).

The correlations of center velocities are calculated as follows:

$$\int_0^\infty\langle\dot{R}^*(0)\dot{R}(t)\rangle e^{-i\omega t}dt=\lim_{T\to\infty}\frac{1}{T}\int_0^T dt'\int_0^\infty\langle\dot{R}^*(t')\dot{R}(t'+t)\rangle e^{-i\omega t}dt$$

$$=\frac{1}{\tau_0}\left[\frac{1}{2}\langle\Delta_1R^*\Delta_1R\rangle+\sum_{k=2}^{\infty}\langle\Delta_1R^*\Delta_kRe^{-i\omega(t_k-t_1)}\rangle\right]. \tag{A.4}$$

By Eq. (4.4) we get

$$\left.\begin{aligned}&\langle\Delta_1R^*\Delta_1R\rangle=\frac{\overline{u_0^*u_0}}{\omega_0^2}\langle(1-e^{-i\alpha_1})(1-e^{i\alpha_1})\rangle=\frac{2\overline{u_0^*u_0}}{\omega_0^2}(1-c)\,,\\&\langle\Delta_1R^*\Delta_kRe^{-i\omega(t_k-t_1)}\rangle\\&\quad=\frac{\overline{u_0^*u_0}}{\omega_0^2}\langle(1-e^{-i\alpha_1})(e^{i\overset{k-1}{\Sigma}\alpha_j}-e^{i\overset{k}{\Sigma}\alpha_j})e^{i(\omega_0-\omega)(t_k-t_1)}\rangle=-\frac{\overline{u_0^*u_0}}{\omega_0^2}c^{k-2}(1-c)^2\left\{\frac{1}{1+i(\omega-\omega_0)\tau_0}\right\}^{k-1}.\end{aligned}\right\} \tag{A.5}$$

These formulas give (4.21) and (4.22) for $\omega=0$. When (A.5) is inserted into (A.4), Eq. (A.4) is reduced to

$$\int_0^\infty\langle\dot{R}^*(0)\dot{R}(t)\rangle e^{-i\omega t}dt=\frac{1-c}{\tau_0}\left[1-\frac{1-c}{1-c+i(\omega-\omega_0)\tau_0}\right]\frac{\overline{u_0^*u_0}}{\omega_0^2}=\frac{\overline{u_0^*u_0}}{\omega_0^2}\frac{i(\omega-\omega_0)}{1+i(\omega-\omega_0)\tau}\,. \tag{A.6}$$

Similarly

$$\int_0^\infty\langle\dot{R}(0)\dot{R}^*(t)\rangle e^{-i\omega t}dt=\frac{\overline{u_0^*u_0}}{\omega_0^2}\frac{i(\omega+\omega_0)}{1+i(\omega+\omega_0)\tau}\,. \tag{A.7}$$

Eqs. (A.6) and (A.7) give Eqs. (4.8a) and (4.8b). Eqs. (4.10a) and (4.10b) are obtained from

$$\int_0^\infty \langle \dot{R}^*(0)u(t)\rangle e^{-i\omega t}dt = -\frac{i\overline{u_0^*u_0}}{\omega_0^2}\,\frac{1}{1+i(\omega-\omega_0)\tau}$$

and

$$\int_0^\infty \langle u^*(0)\dot{R}(t)\rangle e^{-i\omega t}dt = \frac{i\overline{u_0^*u_0}}{\omega_0^2}\,\frac{1}{1+i(\omega+\omega_0)\tau}$$

which are derived by similar calculation. The correlation of $\langle\dot{\gamma}^*(0)\dot{\gamma}(t)\rangle$ can be calculated in the same way, so these calculations are omitted here.

References

1) A. H. Wilson: *The Theory of Metals*, Camb. Univ. Press. (1953).
2) D. Shoenberg: *Progress in Low Temperature Physics*, **2** (1957) 226.
R. G. Chambers: Canadian J. Phys. **34** (1956) 1395.
3) G. Dresselhaus, A. F. Kip and C. Kittel: Phys. Rev. **98** (1955) 368.
R. N. Dexter, H. J. Zeiger and B. Lax: Phys. Rev. **104** (1956) 637.
4) P. B. Alers and R. T. Webber: Phys. Rev. **91** (1953) 1060.
T. G. Berlincourt and J. K. Logan: Phys. Rev. **93** (1954) 348.
M. C. Steele: Phys. Rev. **99** (1956) 1951.
5) J. M. Reynolds, et al.: Phys. Rev. **96** (1954) 1203.
L. C. Brodie: Phys. Rev. **93** (1954) 935.
T. G. Berlincourt and M. C. Steele: Phys. Rev. **98** (1955) 956.
M. C. Steele: Phys. Rev. **99** (1956) 1751.
6) M. C. Steele and J. Babiskin: Phys. Rev. **94** (1954) 1394; **98** (1955) 359.
7) J. L. Olsen and H. M. Rosenberg: Advances in Physics **2** (1953) 28.
P. B. Alers: Phys. Rev. **101** (1956) 41.
8) B. Lax: Rev. Mod. Phys. **30** (1958) 122.
E. Burstein and G. S. Picus: Phys. Rev. **105** (1957) 1123.
S. Zwerdling, B. Lax and L. M. Roth: Phys. Rev. **108** (1957) 1402; **109** (1958) 2207.
9) S. Titeica: Ann. d. Physik [5] **22** (1935) 129.
10) R. G. Chambers: Proc. Roy. Soc. **A238** (1956) 344.
11) B. Davydov and T. Pomeranchuk: Jour. Phys. USSR, **2** (1940) 147.
12) E. M. Lifshitz: J. Phys. and Chem. Solids **4** (1958) 11.
E. M. Lifshitz and A. M. Kosevich: J. Phys. and Chem. Solids **4** (1958) 1.
I. M. Litshitz, M. Ia. Azbel and M. I. Kaganov: J. Exp. Th. Phys. U.S.S.R. **31** (1956) 63.
13) P. N. Argyres and E. N. Adams: Phys. Rev. **104** (1956) 900.
P. N. Argyres: J. Phys. and Chem. Solids, **4** (1958) 19.
14) P. N. Argyres: Phys. Rev. **109** (1958) 115.
15) Reported by R. Kubo in the Conference on Physics of Magnetic Phenomena, Moskow USSR, May 1956, the International Conference on the Electronic Properties of Metals at Low Temperatures, Geneva N. Y., August 1958, and also in Theoretical Physics Institute, University of Colorado, July and August 1958. Phys. Rev. Letters, **1** (1958) 279.
16) R. Kubo: J. Phys. Soc. Japan **12** (1957) 570.
17) R. E. Peierls: Z. Physik **80** (1933) 763.
J. M. Luttinger, Phys. Rev. **84** (1951) 814.
18) E. N. Adams: Phys. Rev. **85** (1952) 41; **89** (1953) 633.
19) P. G. Harper: Proc. Phys. Soc. **A68** (1955) 874, 879.
G. E. Zilberman: Soviet Phys. JETP **3** (1956) 835; J. Exp. Theor. Phys. USSR **30** (1956) 1092.
20) L. van Hove: Physica, **21** (1955) 901; **22** (1956) 343.
N. M. Hugenholtz: Physica, **23** (1957) 481.

JOURNAL OF THE PHYSICAL SOCIETY OF JAPAN Vol. 14, No. 1, JANUARY, 1959

Excitation of the Molecular Vibration by Collision

By Kazuo TAKAYANAGI

Department of Physics, Saitama University, Urawa

(Received September 18, 1958)

Excitation of the molecular vibration in H_2+H_2 collision is studied using the so-called modified wave number method. The same problem has been investigated quite recently by Salkoff and Bauer who applied the distorted wave method thoroughly without making the modified wave number approximation. Thus the present work serves as a test of the accuracy of the modified wave number method which has been used by many authors to study this sort of problem. The result obtained here is in good agreement with the result by Salkoff and Bauer.

§ 1. Introduction

It has been believed that the method of distorted waves[1] is suitable for calculating the probability of the collisional transition of the molecular vibrations.* When we apply this method to a particular case, there are two problems we have to work out—the determination of the potential function and the three-dimensional treatment of the collision problem. The intermolecular potential function, especially its dependence on the internal coordinates of the colliding molecules, is very hard to obtain either theoretically or experimentally. Theoretical calculation of the potential involves the usual difficulty of the many-body problem. Therefore, we have to content ourselves with assuming a function inferred from an insufficient amount of the experimental data. On the other hand, the three-dimensional treatment of a collision process forces us to solve a great number of the radial equations. It is not usual that a hundred or more equations have to be solved for the thermal collision. Although the numerical integration makes it always possible to get the answer, it is too laborious and not worth doing for an ambiguous potential.

The modified wave number method (MWN method) was then introduced to save the labour. The outline of the method will be given in § 2. This method has been applied by many authors[2)~9)] to the various cases. The results are in more or less reasonable agreement with the observed data. However, because of the ambiguity in the potential used, we could not definitely say something about the accuracy of the MWN method.

The recent development of the electronic computing technic has improved the situation and encourages us to treat the three-dimensional collision problem thoroughly for various potential functions. Salkoff and Bauer[10] were the first to carry out this sort of calculation. They studied the vibrational transition in the hydrogen molecule using the Morse type intermolecular potential. They applied the distorted wave method without making the MWN approximation. This gives us a good chance to test the accuracy of the MWN method. What we have to do is to calculate the transition probability using the MWN method for the same potential function as used by Salkoff and Bauer. Fortunately, the one-dimensional problem for the Morse type potential has been solved analytically[11], so that the whole calculations can be done within a few days by using a hand-operated calculating machine. This has been done and will be reported in § 3, which will be followed by some discussions in § 4.

§ 2. Modified Wave Number Approximation

In the distorted wave method, the effective cross section for the inelastic transition $n\rightarrow m$ is given by

$$Q_{n\rightarrow m}$$
$$=4\pi\frac{k_m}{k_n}\sum_j(2j+1)\left|\int_0^\infty 2\mu F_m{}^jF_n{}^jV_{mn}\,dR\right|^2, \quad (1)$$

where k_n, k_m are the initial and the final wave numbers, μ the reduced mass, and V_{mn} is the matrix element of the intermolecular potential V with respect to the internal states

---

* Rotational transitions have generally large probabilities, except for the hydrogen molecule, so that the distorted wave method which is essentially the first order perturbation method can not be applied adequately to the rotational transitions.

m, n. We have assumed here that the scattering potential V_{nn} and V_{mm} are spherically symmetric, so that the radial parts F_n, F_m of the distorted waves are obtained by solving the radial equations of the form†

$$\{d^2/dR^2 - j(j+1)/R^2 + k_l^2 - 2\mu V_{ll}(R)\}F_l^j(R) = 0\,. \tag{2}$$

These radial functions are normalized asymptotically as

$$F_l^j(R) \xrightarrow[R\to\infty]{} \sin(k_l R - \tfrac{1}{2}\pi j + \eta_{lj})/k_l\,;$$

$Q_{n\to m}$ can be written as

$$Q_{n\to m} = (\pi/k_n^2)\sum_j (2j+1)\,p^j_{n\to m}(k_n)\,, \tag{3}$$

where

$$p^j_{n\to m}(k_n) = 4k_n k_m \left|\int_0^\infty 2\mu F_m^j F_n^j V_{mn}\, dR\right|^2 \tag{4}$$

is the transition probability for the partial wave with given j.

The basic assumption in the MWN approximation is to regard the centrifugal potential $j(j+1)/R^2$ as a slowly varying function when compared with the scattering potential $2\mu V_{ll}$, at least in the limited region of R where the main contribution to the integral in (4) comes from. Then we may replace $k_l^2 - j(j+1)/R^2$ by an effective wave number $\tilde{k}_l^2 \equiv k_l^2 - j(j+1)/R_0^2$, where R_0 is a constant distance chosen in the most important region. This means that we replace $p^j_{n\to m}(k_n)$ in (3) by $p^0_{n\to m}(\tilde{k}_n)$. Thus the three-dimensional problem is reduced to the one-dimensional problem. The objection to this procedure will be that the centrifugal potential is not a gentle function for large j. Furthermore, $\tilde{k}_l^2$ becomes negative for very large j. However, a large value of j means that the collision is a distant one, so that the contribution to the transition from such partial waves will be unimportant. Thus we may safely omit the contribution from the higher j for which $\tilde{k}_n^2$ or $\tilde{k}_m^2$ becomes negative.

§ 3. Vibrational Transition in the Hydrogen Molecule

If the scattering potentials V_{nn}, V_{mm} and the transition matrix element V_{mn} are assumed as

$$V_{nn}(R) = V_{mm}(R) = \mathcal{E}\cdot[\exp\{-\alpha(R-R')\} - 2\exp\{-\alpha(R-R')/2\}] \tag{5a}$$

$$V_{mn}(R) = U\cdot[\exp\{-\alpha(R-R'-\zeta)\} - 2\exp\{-\alpha(R-R'-\zeta)/2\}]\,, \tag{5b}$$

the transition probability per collision in the one-dimensional problem (or S-wave collision) is given by[11]

$$p^0_{n\to m}(k_n) = \frac{\pi^2}{4}\left|\frac{U}{\mathcal{E}}\right|^2 \frac{\sinh 2\pi q_n \sinh 2\pi q_m}{(\cosh 2\pi q_n - \cosh 2\pi q_m)^2}(q_n^2 - q_m^2)^2$$
$$\times e^{4\beta}[\{1-(2e^{-\beta}-1)\delta\}\phi + \{1+(2e^{-\beta}-1)\delta\}\phi^{-1}]^2\,, \tag{6}$$

where

$$q_l = 2k_l/\alpha\,,\qquad \delta = 2d/(q_n^2 - q_m^2)\,,\qquad d = 2\sqrt{2\mu\mathcal{E}}/\alpha\,,\qquad \beta = \alpha\zeta/2\,,$$

and

$$\phi = |\Gamma(\tfrac{1}{2} - iq_m - d)|/|\Gamma(\tfrac{1}{2} - iq_n - d)|\,.$$

Salkoff and Bauer[10] studied the inelastic collision:

$$\begin{array}{ccc} H_2 + H_2 & \longrightarrow & H_2^* + H_2\,, \\ \text{(state 0)} & & \text{(state 1)} \end{array}$$

where H_2^* means a hydrogen molecule in the first excited state of the vibration. They assumed the potential functions which can be rewritten in the form (5a, b) where $\mathcal{E} = 1.045 \times 10^{-4}$, $\alpha = 1.832$, $R' = 6.427$, $U = 1.465 \times 10^{-6}$, and $\zeta = 1.200$. Thus we can apply the formula (6) to obtain the one-dimensional probability $p_{0\to 1}$ for the transition from the state 0 to the state 1. We have taken the following values for the other parameters needed: $2\mu = 3675.$, the vibrational energy change $\Delta E = 2.004 \times 10^{-2}$. The resulting probability is shown in Fig. 1.

---

† Atomic units are used in this paper, unless otherwise stated.

The contribution from the partial wave with given j to the effective cross section for the inelastic process is

$$\sigma_j=(\pi/k_0^2)(2j+1)p^0_{0\to1}(\tilde{k}_0)\ , \quad \tilde{k}_0^2\simeq k_0^2-j^2/R_0^2\ . \tag{7}$$

For the potential function used here, the effective scattering potential $V_{\mathrm{eff}}(R)=V_{00}(R)+j(j+1)/2\mu R^2$ is shown in Fig. 2 for several values of j. In the energy region we are going to consider, the classical turning points (abbreviated as ctp. hereafter) for the initial and the final kinetic energies are in the range $3\lesssim R\lesssim 5$. Therefore, we shall first take $R_0=4.0$ in the following calculations. As an example, σ_j for $q_0=22.0$ (the corresponding incident energy is 3.01 ev) is plotted in Fig. 3. This curve is very similar to the curve obtained by Salkoff and Bauer for 3 ev.

By replacing the summation (3) with an integration over $\tilde{k}_0$, the effective cross section

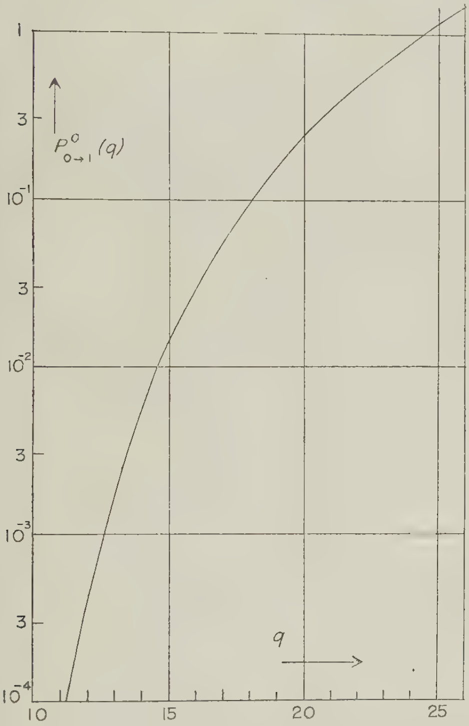

Fig. 1. One-dimensional transition probability $p^0_{0\to1}$ as a function of $q=2k/\alpha$.

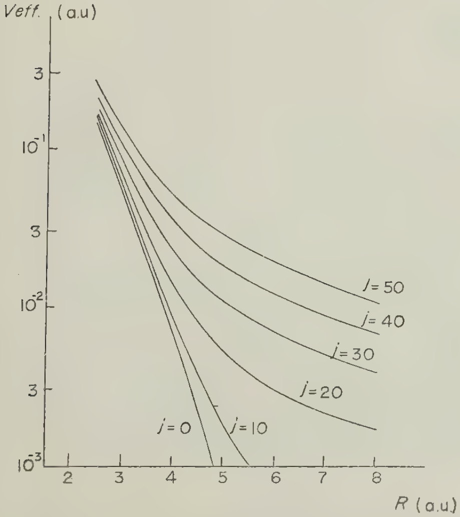

Fig. 2. $V_{\mathrm{eff}}=V_{00}(R)+j(j+1)2\mu R^2$.

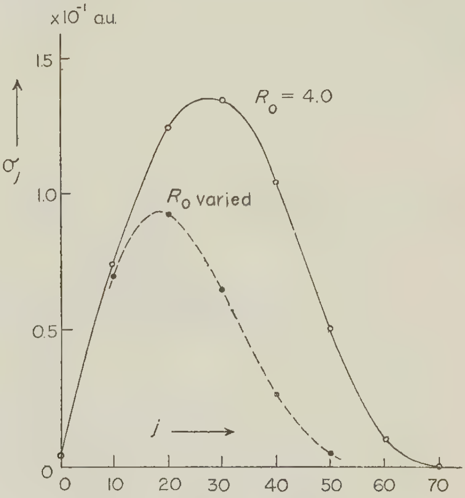

Fig. 3. Partial cross section σ_j for $q_0=22.0$.

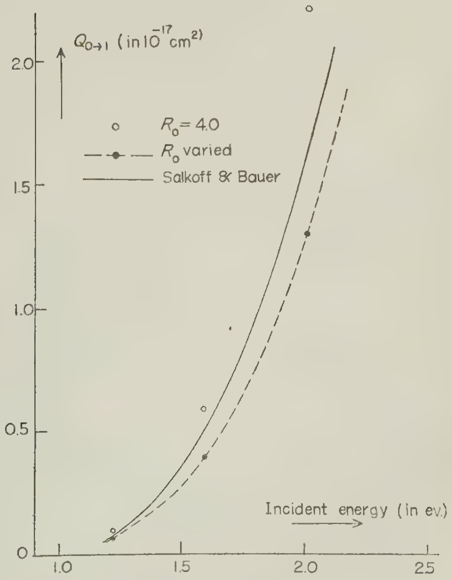

Fig. 4. Effective cross section $Q_{0\to1}$.

for the transition 0→1 is given by

$$Q_{0\to1}=(2\pi R_0^2/k_0^2)\int_0^{k_0} p_{0\to1}^0(\tilde{k})\tilde{k}\,d\tilde{k}\,. \qquad (8)$$

The integrations have been carried out numerically. The effective cross section thus obtained is shown in Fig. 4 and Fig. 5, where the corresponding curves by Salkoff and Bauer and also by Bauer (semi-classical calculation)[12] are shown for comparison.

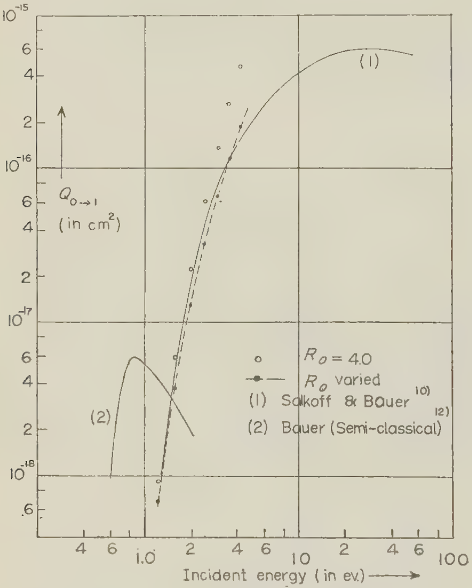

Fig. 5. Effective cross section $Q_{0\to1}$.

It is seen in these figures that the agreement of our result with the result by Salkoff and Bauer is fairly good. However, the discrepancy becomes appreciable in the high energy region. To explain this, it must be noted that in our expression (7) of σ_j, $p^0(\tilde{k})$ is generally a monotonously increasing, steep function of $\tilde{k}$ (see Fig. 1). Since $\tilde{k}$ is an increasing function of R_0 for given k and j, a larger value of R_0 will give a larger σ_j. The choice of R_0 in our calculation is rather arbitrary. A reasonable choice may, however, be made by taking the ctp. for the mean wave number $\bar{k}=\frac{1}{2}(k_0+k_1)$. Since the ctp. for $\bar{k}$ for the high energy collision is much smaller than 4.0 (see Fig. 2), it is expected that the reasonable choice of R_0 will reduce the discrepancy we are considering. The broken lines in Figs. 3, 4, 5 show the result after making this improvement. In Fig. 3 the ctp. for each value of j and $\bar{k}$ (=19.19 in this case) has been chosen as R_0, while in Figs. 4 and 5 the ctp. for k_0 and $j=30$ has been adopted.* The discrepancy between our values and those obtained by Salkoff and Bauer now lies within a factor 1.5 for the whole energy region investigated. Thus we may have some confidence in the validity of the MWN method in this sort of problem.

§ 4. Discussions

We shall now examine the small discrepancy between our result (after the improvement at the end of § 3) and the result obtained by Salkoff and Bauer. For the most part of the energy region we have studied, our cross section is slightly smaller than theirs. This will be explained as follows: Generally speaking, the steeper the repulsive part of the potential is, the larger the transition probability will be.[4),13)] In MWN method, the function $j(j+1)/R^2$ is replaced by a constant. This makes the effective potential V_{eff} less steep and so the probability becomes smaller than the true value. This will probably be the major reason for the discrepancy.

In the high energy region, our cross section goes up quickly and becomes larger than their value. The reason for this will be found in the formula (6). This formula was obtained under the condition that the wave functions should vanish at $R\to-\infty$. However, in the three-dimensional problems, we have to impose the condition that the radial wave functions vanish at $R=0$. This difference in the boundary condition may become important for the high energy collision in which the wave functions can penetrate deeply into the repulsive potential. When we use the formula (6), the wave functions penetrate more deeply, because the boundary condition is less strict. This will explain the discrepancy in the high energy region.

The one-dimensional probability $p_{0\to1}^0$ becomes larger than unity for $q_0>24$ as is seen in Fig. 1. Corresponding to this, the result obtained for $q_0>24$ (the incident energy > 3.58 ev) is unreliable. The distorted wave approximation have to be given up then.

Since the hydrogen is an extreme case with the very high vibrational frequency, it is desirable that the other examples with lower frequencies are also investigated with and without the MWN approximation.

---

* The ctp. for k_0 is very near the ctp. for $\bar{k}$, except for the low energy collisions.

References

1) N. F. Mott and H. S. W. Massey: *The Theory of Atomic Collisions*. Oxford Univ. Press (1949) Chapter VIII.
2) K. Takayanagi: Progr. Theor. Phys. **8** (1952) 497.
K. Takayanagi and T. Kishimoto: ibid **9** (1953) 578; **10** (1953) 369 (errata).
3) R. N. Schwartz and K. F. Herzfeld: J. Chem. Phys. **22** (1954) 767.
4) K. Takayanagi and S. Kaneko: Sci. Repts. Saitama Univ. **A 1**, No. 3 (1954) 111.
5) T. Inoue and T. Takahashi: J. Phys. Soc. Japan **10** (1955) 208.
6) F. I. Tanczos: J. Chem. Phys. **25** (1956) 439.
7) K. Takayanagi: Proc. Phys. Soc. London **A 70** (1957) 348.
8) P. G. Dickens and J. W. Linnett: Proc. Roy. Soc. **A 243** (1957) 84.
9) K. Takayanagi: Sci. Repts. Saitama Univ. **A 3**, No. 1 (1958) 1.
10) M. Salkoff and E. Bauer: J. Chem. Phys. **29** (1958) 26.
11) J. Lennard-Jones and A. F. Devonshire: Proc. Roy. Soc. **A 158** (1937) 253.
A. F. Devonshire: ibid 269.
12) E. Bauer: J. Chem. Phys. **23** (1955) 1087.
13) K. Takayanagi: Progr. Theor. Phys. **8** (1952) 111.

JOURNAL OF THE PHYSICAL SOCIETY OF JAPAN Vol. 14, No. 1, JANUARY, 1959

On the Viscosity of Irradiated Polymers I.

By Mitio INOKUTI

Department of Applied Physics, Faculty of Engineering,
University of Tokyo, Tokyo, Japan

(Received September 18, 1958)

The change of the intrinsic viscosity of a polymeric substance due to irradiation with high-energy radiations is discussed for various types of initial molecular size distributions. It is shown that the intrinsic viscosity can at first decrease in certain cases by irradiation, even if it reaches infinity finally at the gel point. It is further concluded that such a behavior of the intrinsic viscosity is possible, only if the initial molecular size distribution is sufficiently broad.

§ 1. Introduction

A polymeric substance undergoes crosslinking and/or degradation under irradiation with high-energy radiations. Crosslinking or degradation naturally causes changes of molecular size distribution and then of physical and chemical properties of the polymeric substance. Among them the intrinsic viscosity of the polymer in an appropriate solvent is not only one of the most important quantities that reveal molecular size distribution, but has also been experimentally studied by many workers.

Theories of molecular size distribution in crosslinked and/or degraded polymers, proposed by Flory, Stockmayer and Charlesby are unfortunately inconvenient for calculation of the intrinsic viscosity. Recently Saito[1)-3)] developed a theory that can be used to calculate it. He also noted that in the course of irradiation the intrinsic viscosity can in certain cases decrease at first and then increase to reach infinity finally.[3)] Such a sort of phenomenon has really been observed in some experiments[4),5)]. However, he carried out explicit calculation only for the case where the initial molecular size distribution is Poisson-like,[3)] although his formulation is in practice applicable to an arbitrary initial distribution.

In the present paper we discuss the intrinsic viscosity of irradiated polymers according to Saito's theory for various types of initial distributions so as to clarify relationship between the initial distribution and the radiation-induced change of intrinsic viscosity.

§ 2. General Formulation

Let N be the total number of monomers in a polymeric substance, and $N\ m(p,\ R)\ dp$ be the number of polymers whose degree of polymerization lies between p and $p+dp$ when the substance is irradiated up to radiation dose R. The molecular size distribution function $m(p,\ R)$ satisfies a normalization condition because of the constancy of N, namely,

$$\int_0^\infty pm(p,\ R)dp=1\ . \tag{1}$$

If high-energy radiations introduce cross-linking with probability $\dot{c}$ per monomer unit per unit radiation dose and degradation with probability $\dot{r}$ per monomer unit per unit radiation dose, $m(p,\ R)$ will be given by the following procedure according to Saito's theory. It is convenient to define two variables

$$t=\dot{c}R \tag{2}$$

$$\tau=\dot{r}R \tag{3}$$

and to regard the distribution function $m(p,\ R)$ as a function of p, t and τ, i.e., $m(p,\ t,\ \tau)$. Then $m(p,\ t,\ \tau)$ is the solution of an integro-differential equation

$$\frac{\partial m(p,\ t,\ \tau)}{\partial t}+2pm(p,\ t,\ \tau)=\int_0^p l(p-l)m(l,\ t,\ \tau)m(p-l,\ t,\ \tau)dl \tag{4}$$

under the initial condition

$$m(p,\ 0,\ \tau)=\left\{m(p,0)+2\tau F(p)+\tau^2\int_p^\infty F(p')\,dp'\right\}e^{-p\tau}\ , \tag{5}$$

where $m(p,\ 0)$ is the initial distribution function and

$$F(p)=\int_p^\infty m(p',\ 0)\,dp'\ . \tag{6}$$

Further we define the following notations for $\beta\geqq 0$:

$$f_\beta(t,\ \tau)=\int_0^\infty m(p,\ t,\ \tau)p^\beta dp\ , \tag{8}$$

$$f_\beta(0)=\int_0^\infty m(p,\ 0)p^\beta dp\ . \tag{9}$$

According to Staudinger's law the intrinsic viscosity $\eta(R)$ at radiation dose R is proportional to $f_{\alpha+1}(t,\ \tau)$, where α is characteristic of the polymer species and $1/2\leqq\alpha<1$; namely,

$$\frac{\eta(R)}{\eta(0)}=\frac{f_{\alpha+1}(t,\ \tau)}{f_{\alpha+1}(0)}\ . \tag{10}$$

The formal solution that can be obtained by making use of Laplace transform is generally inconvenient for explicit calculation of $m(p,\ t,\ \tau)$ and $f_{\alpha+1}(t,\ \tau)$ for an arbitrary initial distribution. For the present we take interest in the initial derivative of the intrinsic viscosity with respect to radiation dose, or the coefficient $A_1(\lambda,\ \alpha)$ in the expansion

$$\eta(R)/\eta(0)=1+A_1(\lambda,\ \alpha)R+A_2(\lambda,\ \alpha)R^2+\cdots, \tag{11}$$

where

$$\lambda=\dot{r}/\dot{c}\ . \tag{12}$$

To obtain $A_1(\lambda,\ \alpha)$ we first establish a power-series expansion with respect to R.

If we put

$$m(p,\ t,\ \tau)=e^{-2\nu t}\sum_{k=0}^{\infty}\varphi_k(p,\ \tau)t^k \tag{13}$$

in (4), we have the recurrence formula for $\varphi_k(p,\ \tau)$

$$(k+1)\varphi_{k+1}(p,\ \tau)=\sum_{j=0}^{k}\int_0^p l(p-l)\varphi_j(l,\ \tau)\varphi_{k-j}(p-l,\ \tau)dl\ . \tag{13}$$

It is evident by (13) that

$$\varphi_0(p,\ \tau)=m(p,\ 0,\ \tau)\ . \tag{14}$$

Then we have by (13) and (14)

$$\varphi_1(p,\ \tau)=e^{-p\tau}\left[\int_0^p l(p-l)m(l,\ 0)m(p-l,\ 0)dl+4\tau\int_0^p l(p-l)m(l,\ 0)F(p-l)dl+O(\tau^2)\right]. \tag{15}$$

Taking note of the relation

$$\tau=\lambda t \tag{16}$$

obtained by (2), (3) and (12), and substituting (14) and (15) into (13), we have

$$m(p,\ t,\ \tau)=m(p,\ 0)+\{\psi(p)-(\lambda+2)pm(p,\ 0)\}t+O(t^2)\ , \tag{17}$$

where $\psi(p)$ is defined by

$$\psi(p)=2\lambda F(p)+\int_0^p l(p-l)m(l,\ 0)m(p-l,\ 0)dl\ . \tag{18}$$

Therefore

$$f_{\alpha+1}(t,\ \tau)=f_{\alpha+1}(0)+t\int_0^{\infty}\{\psi(p)-(\lambda+2)pm(p,\ 0)\}p^{\alpha+1}dp+O(t^2)\ . \tag{19}$$

Comparing (19) with (9) and (10), we arrive at the expression for $A_1(\lambda,\ \alpha)$, namely,

$$A_1(\lambda,\ \alpha)=\frac{\dot{c}}{f_{\alpha+1}(0)}\left\{\int_0^{\infty}\psi(p)p^{\alpha+1}dp-(\lambda+2)f_{\alpha+2}(0)\right\}. \tag{20}$$

Taking note of (18) and the relation

$$\int_0^{\infty}F(p)p^{\alpha+1}dp=\frac{1}{\alpha+2}f_{\alpha+2}(0)\ , \tag{21}$$

we can reduce (20) to the final result

$$A_1(\lambda,\ \alpha)=-\left(\frac{\dot{c}\alpha}{\alpha+2}\right)\left\{\frac{f_{\alpha+2}(0)}{f_{\alpha+1}(0)}\right\}\{\lambda-\lambda_0(\alpha)\}\ , \tag{22}$$

where $\lambda_0(\alpha)$ is the zero point of $A_1(\lambda,\ \alpha)$, namely,

$$\lambda_0(\alpha)=\left(\frac{\alpha+2}{\alpha}\right)\left\{\frac{I(\alpha)}{f_{\alpha+2}(0)}-2\right\}, \tag{23}$$

and $I(\alpha)$ stands for the following repeated integral:

$$I(\alpha)=\int_0^{\infty}dp\ p^{\alpha+1}\int_0^p dl\ l(p-l)m(l,\ 0)m(p-l,\ 0) \tag{24–1}$$

$$=\int_0^{\infty}dl\ lm(l,\ 0)\int_0^{\infty}dp(p+l)^{\alpha+1}pm(p,\ 0)\ . \tag{24–2}$$

Now we note a theorem given by Saito[1], which states the condition for formation of a gel, or such a macroscopically large molecular network as can be regarded as a polymer with an infinitely large degree of polymerization.

Theorem. Gel formation occurs as a result of crosslinking and degradation, if and only if $\lambda < 4$, whatever the initial molecular size distribution may be.

In connection with the theorem, Saito[3] pointed out that $\lambda_0(\alpha) < 4$ when the initial distribution is Poisson-like. This fact is physically interesting, because it implies that, for $\lambda_0(\alpha) < \lambda < 4$, the value $\eta(R)/\eta(0)$ decreases in the beginning, even if it reaches infinity at the gel point. (See Fig. 1.)

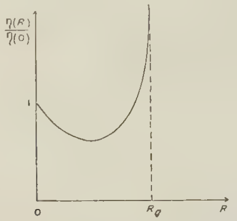

Fig. 1. Schematic representation of the behavior of $\eta(R)/\eta(0)$ for such a value of λ that $\lambda_0(\alpha) < \lambda < 4$, where R_g means the gel point.

Now we examine the relationship between the initial distribution $m(p, 0)$ and $A_1(\lambda, \alpha)$, so as to clarify for what kind of initial distribution such a behavior of the intrinsic viscosity $\eta(R)/\eta(0)$ is possible. A general discussion of the problem mathematically requires a theory of functionals. For the present we will content ourselves with the examination of some particular types of initial distributions.

§ 3. Applications to Some Types of Initial Molecular Size Distributions

1) *Poisson distribution*

When the initial distribution is Poisson-like, namely,

$$m(p, 0) = u^{-2} e^{-p/u}, \tag{25}$$

where u stands for the initial number average degree of polymerization, we have

$$f_\beta(0) = u^{\beta-1} \Gamma(\beta+1), \tag{26}$$

$$I(\alpha) = u^{\alpha+1} \Gamma(\alpha+5)/6. \tag{27}$$

By (22), (23), (26) and (27) we obtain the following result already given by Saito[3]:

$$A_1(\lambda, \alpha) = -\dot{c}\alpha u\{\lambda - \lambda_0(\alpha)\}, \tag{28}$$

where

$$\lambda_0(\alpha) = (\alpha+2)(\alpha+7)/6. \tag{29}$$

Clearly $\lambda_0(\alpha) < 4$ for $1/2 \leqq \alpha < 1$ and therefore $\eta(R)/\eta(0)$ can behave as represented in Fig. 1.

2) *Uniform distribution*

When the initial distribution is uniform, namely,

$$m(p, 0) = \frac{1}{u^2} \delta\left(\frac{p}{u} - 1\right), \tag{30}$$

where u stands for the initial degree of polymerization, we have

$$f_\beta(0) = u^{\beta-1}, \tag{31}$$

$$I(\alpha) = 2^{\alpha+1} u^{\alpha+1}. \tag{32}$$

Substituting (31) and (32) into (22) and (23), we obtain

$$A_1(\lambda, \alpha) = -\left(\frac{\dot{c}u\alpha}{\alpha+2}\right)\{\lambda - \lambda_0(\alpha)\}, \tag{33}$$

$$\lambda_0(\alpha) = \frac{2(\alpha+2)}{\alpha}(2^\alpha - 1). \tag{34}$$

Since $\lambda_0(\alpha) < 4$ for $1/2 \leqq \alpha < 1$ in this case, $\eta(R)/\eta(0)$ never behaves as represented in Fig. 1. In other words, the intrinsic viscosity begins to increase definitely so far as gel formation is possible or $\lambda < 4$. The situation is quite different from that of the case where the initial distribution is Poisson-like.

3) *Rectangular distribution*

We define the rectangular distribution as

$$m(p, 0) = \begin{cases} (2\xi u^2)^{-1} & (1-\xi \leqq p/u \leqq 1+\xi) \\ 0 & \text{(otherwise)}, \end{cases} \tag{35}$$

where u is the number average degree of polymerization and ξ is to be called as dimensionless width parameter. The function is normalized as (1). For the present we regard ξ as a small quantity. Then, for this initial distribution,

$$f_\beta(0)=\frac{u^{\beta-1}}{2(\beta+1)\xi}\{(1+\xi)^{\beta+1}-(1-\xi)^{\beta+1}\}=u^{\beta-1}\left\{1+\frac{\beta(\beta-1)}{3!}\xi^2+\frac{\beta(\beta-1)(\beta-2)(\beta-3)}{5!}\xi^4+\cdots\right\}, \quad (36)$$

$$I(\alpha)=2^{\alpha+1}u^{\alpha+1}\left[\frac{2}{(\alpha+2)(\alpha+3)}+\frac{(\alpha+1)\xi^{-2}}{(\alpha+2)(\alpha+3)(\alpha+5)}\{(1+\xi)^{\alpha+5}+(1-\xi)^{\alpha+5}-2\}\right]$$
$$=2^{\alpha+1}u^{\alpha+1}\left\{1+\frac{(\alpha+1)(\alpha+4)}{12}\xi^2+\frac{\alpha(\alpha+1)^2(\alpha+4)}{360}\xi^4+\cdots\right\}. \quad (37)$$

Substituting (36) and (37) into (22) and (23), we have

$$A_1(\lambda,\ \alpha)=-\left(\frac{\dot{c}u\alpha}{\alpha+2}\right)\left\{1+\frac{(\alpha+1)}{3}\xi^2-\frac{\alpha(\alpha+1)(\alpha+4)}{45}\xi^4+\cdots\right\}\{\lambda-\lambda_0(\alpha)\}, \quad (38)$$

$$\lambda_0(\alpha)=\left(\frac{\alpha+2}{\alpha}\right)\left\{2(2^\alpha-1)-\frac{2^\alpha\alpha(\alpha+1)}{6}\xi^2+\frac{2^\alpha\alpha(\alpha+1)(\alpha+4)(3\alpha+5)}{180}\xi^4+\cdots\right\}. \quad (39)$$

Evidently (38) and (39) agree with (33) and (34) respectively in the limit $\xi\to0$.

According to (38), $\lambda_0(\alpha)<4$ if ξ is sufficiently large. (e.g. $\xi\gtrsim0.42$ for $\alpha=1/2$.) Thus we see that the intrinsic viscosity can behave as represented in Fig. 1, if the initial distribution is sufficiently broad.

4) *Superposition of two uniform distributions*

Let us consider a superposition of two uniform distributions

$$m(p,\ 0)=\frac{1}{2u^2}\left\{\delta\left(\frac{p}{u}-1-\zeta\right)+\delta\left(\frac{p}{u}-1+\zeta\right)\right\}, \quad (40)$$

where u is the number average degree of polymerization and ζ is to be called as dimensionless width parameter. The function is also normalized as (1). Further we regard again ζ as a small quantity. Then, for this initial distribution,

$$f_\beta(0)=\frac{u^{\beta-1}}{2}\{(1+\zeta)^\beta+(1-\zeta)^\beta\}=u^{\beta-1}\left\{1+\frac{\beta(\beta-1)}{2!}\zeta^2+\frac{\beta(\beta-1)(\beta-2)(\beta-3)}{4!}\zeta^4+\cdots\right\}, \quad (41)$$

$$I(\alpha)=2^{\alpha-1}u^{\alpha+1}\{(1+\zeta)^{\alpha+3}+(1-\zeta)^{\alpha+3}+2(1-\zeta^2)\}$$
$$=2^{\alpha+1}u^{\alpha+1}\left\{1+\frac{(\alpha+1)(\alpha+4)}{4}\zeta^2+\frac{\alpha(\alpha+1)(\alpha+2)(\alpha+3)}{12}\zeta^4+\cdots\right\}. \quad (42)$$

Substituting (41) and (42) into (22) and (23), we have

$$A_1(\lambda,\ \alpha)=-\frac{\dot{c}u\alpha}{\alpha+2}\left\{1+(\alpha+1)\zeta^2-\frac{\alpha(\alpha+1)(\alpha+2)}{3}\zeta^4+\cdots\right\}\{\lambda-\lambda_0(\alpha)\}, \quad (43)$$

$$\lambda_0(\alpha)=\frac{\alpha+2}{\alpha}\left\{2(2^\alpha-1)-\frac{2^\alpha\alpha(\alpha+1)}{2}\zeta^2+\frac{2^\alpha\alpha(\alpha+1)(\alpha+2)(2\alpha+5)}{6}\zeta^4+\cdots\right\}. \quad (44)$$

The expressions (43) and (44) again reduce to (33) and (34) respectively in the limit $\zeta\to0$ as expected.

According to (44), $\lambda_0(\alpha)<4$ if ζ is sufficiently large. (e.g. $\zeta\gtrsim0.23$ for $\alpha=1/2$.) The situation is qualitatively similar to the case where the initial distribution is rectangular.

5) *Poisson distribution with cut-off*

Let us consider the Poisson distribution with cut-off

$$m(p,\ 0)=\begin{cases}C\ e^{-p/v} & (p\geqq q)\\ 0 & (q>p\geqq0),\end{cases} \quad (45)$$

where C is the normalization factor, q is the degree of polymerization at the cut-off, and v is the number average degree of polymerization prior to cutting off. This distribution may be approximately realized by fractionation techniques. The normalization condition (1) determines C as follows:

$$C=v^{-2}e^{\sigma}(1+\sigma)^{-1}\,, \tag{46}$$

where

$$\sigma=q/v \tag{47}$$

is a parameter specifying cut-off and will be regarded as small. The number average degree of polymerization u turns out to be

$$u=v+q=v(1+\sigma)\,. \tag{48}$$

Then, for this initial distribution,

$$f_\beta(0)=Cq^{\beta+1}A_\beta(\sigma)\,, \tag{49}$$

$$I(\alpha)=C^2\int_{2q}^{\infty}dp\,p^{\alpha+1}\,e^{-p/v}\int_{q}^{p-q}dl\cdot l(p-l)=\frac{2^{\alpha+3}q^{\alpha+5}C^2}{3}\{2A_{\alpha+4}(2\sigma)-3A_{\alpha+2}(2\sigma)+A_{\alpha+1}(2\sigma)\}\,, \tag{50}$$

where the integral $A_\beta(\sigma)$ is defined as follows:

$$A_\beta(\sigma)=\int_{1}^{\infty}x^\beta e^{-\sigma x}\,dx\,. \tag{51}$$

For small σ, it may be expanded into power series, namely,

$$A_\beta(\sigma)=\int_{0}^{\infty}x^\beta e^{-\sigma x}\,dx-\int_{0}^{1}x^\beta\,e^{-\sigma x}\,dx=\frac{\Gamma(\beta+1)}{\sigma^{\beta+1}}-\sum_{j=0}^{\infty}\frac{(-1)^j\sigma^j}{j!(\beta+1+j)}\,. \tag{52}$$

By employing (22), (23) and (46)–(52), we arrive at the following result:

$$\begin{aligned}A_1(\lambda,\ \alpha)&=-\dot{c}u\alpha(1+\sigma)^{-1}\left\{1+\frac{\sigma^{\alpha+2}}{\Gamma(\alpha+3)}+O(\sigma^{\alpha+3})\right\}\{\lambda-\lambda_0(\alpha)\}\\&=-\dot{c}v\alpha\left\{1+\frac{\sigma^{\alpha+2}}{\Gamma(\alpha+3)}+O(\sigma^{\alpha+3})\right\}\{\lambda-\lambda_0(\alpha)\}\,.\end{aligned} \tag{53}$$

$$\lambda_0(\alpha)=\frac{(\alpha+2)(\alpha+7)}{6}\left\{1+\frac{\sigma^2}{2}+O(\sigma^3)\right\}\,. \tag{54}$$

The expressions (53) and (54) naturally reduce to (28) and (29) respectively in the limit $\sigma\to 0$.

Thus the cut-off introduces the tendency that $A_1(\lambda,\ \alpha)$ increases if λ is kept constant. And the region of λ such that $\lambda_0(\alpha)<\lambda<4$ becomes narrower with the increase of σ. The situation that a sufficient width is necessary for the behavior of the intrinsic viscosity as given in Fig. 1 is quite the same as in other cases discussed in the foregoing paragraphs.

§ 4. Discussions

So far we have examined the relationship between the initial molecular size distribution and the radiation-induced change of intrinsic viscosity. The result can be summarized in the statement that the intrinsic viscosity shows in certain cases a minimum when it is plotted against radiation dose, only if the initial distribution is sufficiently broad. Mathematically this fact may be a consequence of the situation that $I(\alpha)$ involves a type of convolution integral. (See (24–1)).

Our present conclusion must be of significance in connection with analysis of experimental data, since the quantity $A_1(\lambda,\ \alpha)$ is rather easily observed experimentally and the initial distribution can be controlled to some extent. Consequently, by observed values of

$A_1(\lambda, \alpha)$ we can estimate the value of λ, if the initial distribution is given; on the other hand, we can obtain informations about the latter, if the former is determined through other data, for example, gel point, gel fraction etc.

In view of our conclusion, especially interesting is Y. Hirano's observation$^{6)}$ that $A_1(\lambda, \alpha)$ in aqueous solution of polyvinyl alcohol decreases through a treatment which presumably modifies the initial distribution so as to realize approximately the Poisson distribution with the cut-off. Detailed discussion about this experiment as well as its analysis will be reported elsewhere.

It is also remarkable that there exists such λ that $\lambda_0(\alpha) > \lambda > 4$ according to (34), (39) or (44), if the initial distribution is nearly uniform. For such a value of λ, the intrinsic viscosity increases initially, even if degradation dominates over crosslinking so that gel formation is impossible or $\lambda > 4$. This sort of situation seems to have not yet been observed experimentally, perhaps because of difficulty in realizing a sufficiently narrow initial distribution.

Acknowledgements

The author should like to express his sincere thanks to Prof. A. Amemiya of the University of Tokyo and Prof. O. Saito of the Tyûô University for their helpful discussions as well as continuous encouragements. He especially appreciates Prof. Saito's kindness of giving him informations about his own work prior to publication. Further he is grateful to Mr. Y. Hirano, Mr. T. Watanabe and other members of the Group for the Study of Irradiated Polymers of Tokyo for their interest and valuable comments. He is also indebted to the Ministry of Education for the Scientific Research Fund.

References

1) O. Saito: J. Phys. Soc. Japan **13** (1958) 198.
2) O. Saito: J. Phys. Soc. Japan **13** (1958) 1451.
3) O. Saito: J. Phys. Soc. Japan **13** (1958) 1465.
4) R. M. Black and B. J. Lyons: Nature **180** (1957) 1346.
5) A. Danno: J. Phys. Soc. Japan **13** (1958) 722.
6) Y. Hirano: private communication; to be reported at the Meeting of the Union of Societies of Chemistry and Related Sciences, Tokyo, November 1958.

JOURNAL OF THE PHYSICAL SOCIETY OF JAPAN Vol. 14, No. 1, JANUARY, 1959

Zerosplitting Cone of Nuclear Quadrupole Resonance Spectrum for Spin 5/2

By Kenji SHIMOMURA

Minami Bunkô, Hiroshima University, Hiroshima

and Noriyoshi INOUE

Shinonome Bunkô, Hiroshima University, Hiroshima

(Received September 30, 1958)

Zerosplitting loci of nuclear quadrupole resonance spectrum of iodine nucleus of iodic acid were studied. The directions of axes of zerosplitting cones of $\nu_1(\pm 1/2 \leftrightarrow \pm 3/2)$ and $\nu_2(\pm 3/2 \leftrightarrow \pm 5/2)$ lines have been found to be appreciably different from each other. The situation was interpreted by use of Cohen's theory of Zeeman splitting and zerosplitting condition was presented. The directions of axes of zerosplitting cones of ν_1 and ν_2 lines were shown to be coincident with the y- and z-axes of the principal axes of field gradient tensor at the resonant nucleus, respectively. Cohen's theory was verified by the comparison of the experimental values of zerosplitting angles with the theoretical ones.

§ 1. Introduction

The zerosplitting cone[1] which specifies the direction of zerosplitting of Zeeman line of nuclear quadrupole resonance spectrum is a pair of elliptical or circular cones having D_{2h} symmetry, about one of the principal axes of field gradient tensor at the resonant nucleus. Its form depends only on the nuclear spin and the value of the asymmetry parameter η of field gradient tensor. So a study of zerosplitting cone can reveal the nature of crystalline electric field, i.e., asymmetry parameter and orientations of principal axes of field gradient tensor, and can yield a check on the assignment of transition in the zero-field. And this purpose is also attained by the study of Zeeman splitting, which depends on the nuclear species. However, the zerosplitting method is superior to the Zeeman splitting method in some respects; (1) the relation between zerosplitting angle and asymmetry parameter does hold good to any nucleus of the same spin, (2) the sample may be rotated about any arbitrary axis of the sample[1], (3) measurements of strength of magnetic field and spacings of Zeeman components are not needed. So we can deal simply and immediately with more complex substance by studying the zerosplitting cone.

We have studied the zerosplitting cones for the two transitions $\pm 1/2 \leftrightarrow \pm 3/2$ and $\pm 3/2 \leftrightarrow \pm 5/2$ of pure quadrupole spectrum of iodine nucleus of iodic acid. Livingston et al[2] have presented the extensive study of Zeeman splittings on this substance and observed extra Zeeman component resulting from a proton interaction.

We have found the directions of the axes of the zerosplitting cones for the two transitions are quite different from each other. The situation has been interpreted by use of Cohen's numerical table[3] for the Zeeman-splitting parameter, and the experimental values for zerosplitting angles have been compared with Cohen's theoretical calculations.

§ 2. Experimental Results

A single crystal of iodic acid has been prepared by crystalizing from aqueous solution of iodine pentoxide with small quantity of nitric acid. The crystal was set on the Zeeman analyser[1], which was operated at about 100~320 gauss. The spectrometer was a frequency-modulated superregenerative detector of 6J6 ×2 push-pull Lecher-wire tuned type[4] and the absorption lines were observed on a persistent-screen cathode-ray oscilloscope, and the loci of zerosplitting directions were studied at about 25°C~30°C.

At the first step, $\nu_1(\pm 1/2 \leftrightarrow \pm 3/2)$ line, and at the second step, $\nu_2(\pm 3/2 \leftrightarrow \pm 5/2)$ line were studied with proper hf coils for these resonance frequencies but without changing the setting of the crystal.

The experimental results are shown in Fig. 1 and 2, where y_1, y_2, y_3, y_4; z_1, z_2, z_3, z_4 denote the nonequivalent directions¹⁾ of the axes of zerosplitting cones of ν_1 and ν_2 lines, respectively. As shown in Fig. 1 and 2, the directions of axes of zerosplitting cones associating to ν_1 and ν_2 lines are appreciably different from each other. Additional splitting of zerosplitting component of Zeeman lines due to neighbouring proton has not been observed.

§ 3. Discussions

By taking into consideration of large asymmetry parameter $\eta=0.451^{2),5)}$ at room temperature, we should rather use an exact formula which is applicable to the case of arbitrary η than the approximate one⁶⁾.

For arbitrary η, Cohen³⁾ has given the following formula for the Zeeman splitting of nuclear quadrupole resonance spectrum

$$E_{\pm m}=E_{\pm m}^{0}\mp g\beta H \times[A\cos^2\theta+\tfrac{1}{4}\sin^2\theta(B+2C\cos 2\phi)]^{1/2} \qquad (1)$$

where H denotes a magnetic field, g represents the g-factor of the resonant nucleus, β

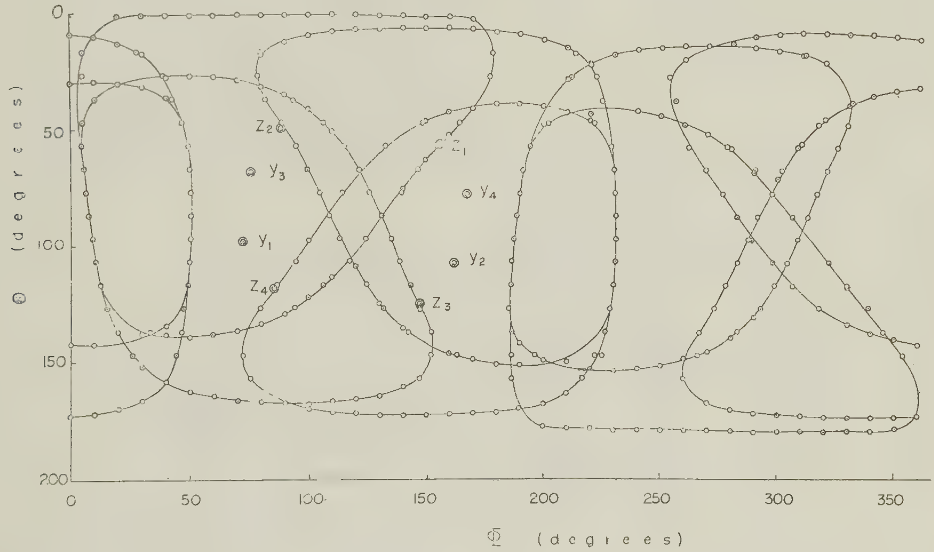

Fig. 1. Zerosplitting-direction pattern of ν_1 line. Θ and Φ are polar angles specifying zerosplitting-direction with respect to an orthogonal coordinate axes fixed to the sample.

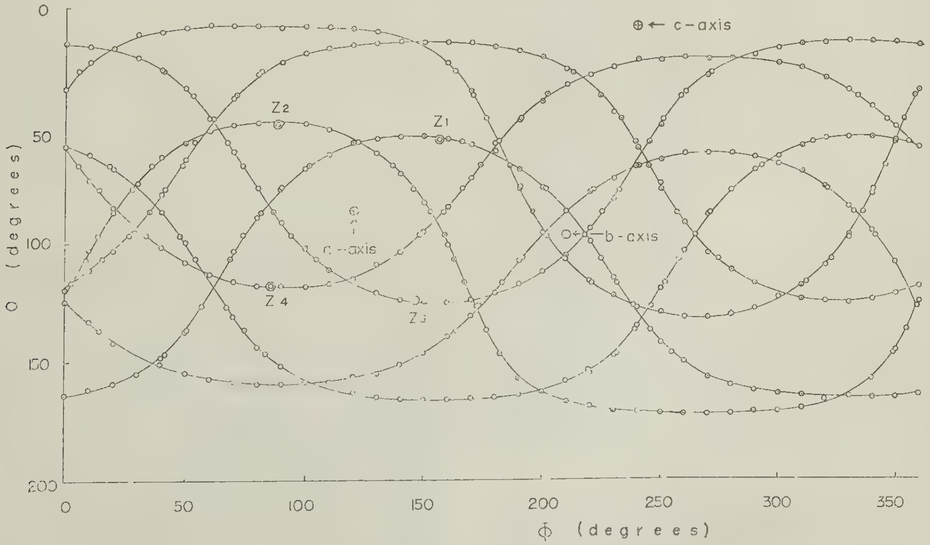

Fig. 2. Zerosplitting-direction pattern of ν_2 line.

is the Bohr magneton, θ and ϕ are the polar angles of H with respect to the principal axes x, y, z, and A, B and C are Zeeman-splitting parameters which have been given in a numerical table by Cohen.

The zerosplitting should be expected when the Zeeman splitting of one level becomes equal to that of the other one, so the zerosplitting condition may be written as

$$\sin^2\theta=\frac{\gamma}{\alpha+\beta\cos 2\phi}, \qquad (2)$$

where α, β and γ are zerosplitting parameters and are given in Table I.

Table I. Zerosplitting parameters α, β and γ for spin 5/2.

±1/2↔±3/2 η	α	β	γ
0.1	16.8578	− 2.3706	7.9188
0.2	16.4600	− 4.5748	7.6900
0.3	15.8790	− 6.4924	7.3512
0.4	15.2002	− 8.0664	6.9464
0.451	14.8411[a]	− 8.7350[a]	6.7274[a]
0.5	14.4975	− 9.2956	6.5140
0.6	13.8204	−10.2114	6.0792
0.7	13.1967	−10.8584	5.6568
0.8	12.6380	−11.2818	5.2532
0.9	12.1440	−11.5234	4.8684
1.0	11.7090	−11.6172	4.5000

±3/2↔±5/2 η	α	β	γ
0.1	16.2617	0.0052	16.1052
0.2	16.9820	0.0364	16.3952
0.3	18.0000	0.1020	16.8052
0.4	19.1324	0.1880	17.2608
0.451	19.7042[a]	0.2317[a]	17.4903[a]
0.5	20.2317	0.2692	17.7016
0.6	21.2041	0.3204	18.0880
0.7	22.0037	0.3226	18.3996
0.8	22.6136	0.2648	18.6268
0.9	23.0360	0.1420	18.7684
1.0	23.2799	− 0.0458	18.8260

[a] As the Zeeman-splitting parameters for $\eta=0.451$ are not given in Cohen's table, these values were obtained from our calculations of Zeeman-splitting parameters*.

In the case of $\eta=0.4$, it is easily shown from Eq. (2) with proper zerosplitting parameters that θ satisfying the zerosplitting condition may exist for any value of ϕ. While, in the case of $\eta=0.5$ it may be shown that not all values of ϕ can exist; as Fig. 3 shows, θ will increase from the minimum value $\theta_{\min}$ to the maximum value $\pi/2$ with decreasing (or increasing) ϕ from $\pi/2$ to the minimum (or maximum) value $\phi_{\min}$ (or $\pi-\phi_{\min}$). Since a zerosplitting cone always possesses an opposite partner[1)], they make a pair of cones which is parallel to the y-axis** (Fig. 3). Therefore, the direction of axis of zerosplitting cone of ν_1 line should be the y-axis of field gradient tensor. On the contrary, for $\eta=0.4$ a cone which has an axis parallel to the z-axis should be observed. The abrupt

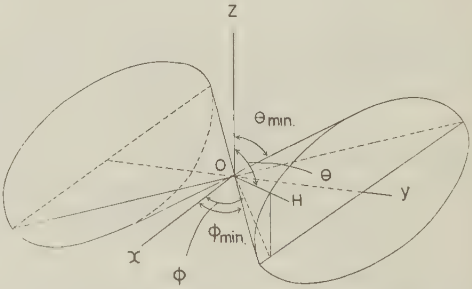

Fig. 3. Zerosplitting cone which is parallel to the y-axis. OH denotes the direction of magnetic field which causes zerosplitting of Zeeman line.

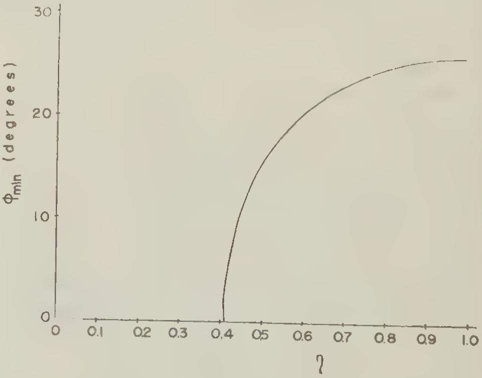

Fig. 4. The variation of $\phi_{\min}$ as a function of η, where $\phi_{\min}$ are derived from Eq. (2) by putting $\theta=\pi/2$. The value of η where $\phi_{\min}$ vanishes indicates the critical value of η.

---

* The Zeeman-splitting and zerosplitting parameters for η varying from 0.01 to 1.0 in intervals of 0.01 will be published later in other papers.

** It has been mentioned that the loci of zerosplitting directions of ν_1 and ν_2 lines form elliptic cones around the z-axis (see reference 6). But it is not correct.

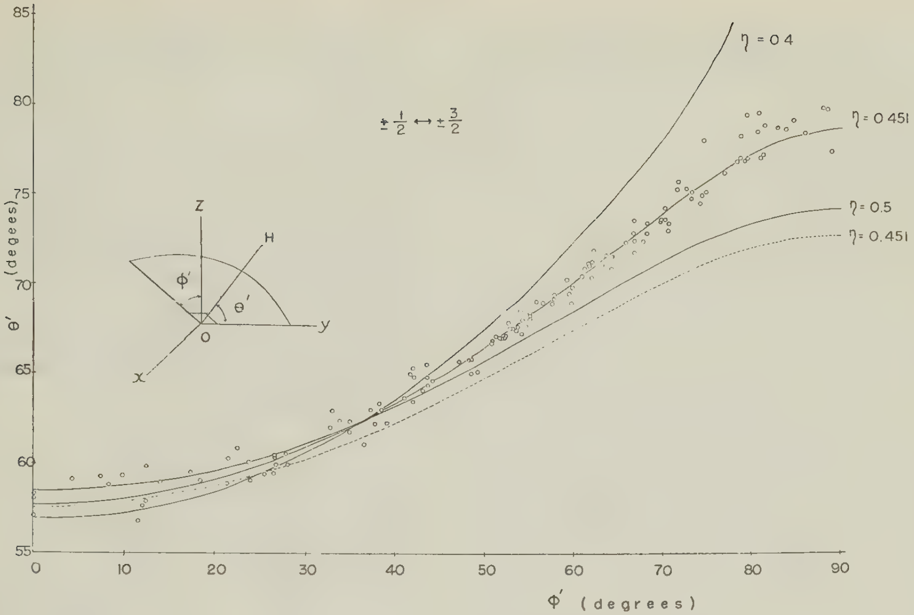

Fig. 5. Zerosplitting angle θ' as a function of ϕ'.
solid line: calculated values from Eq. (3) and Table I
dotted line: calculated values from

$$\sin^2\theta=\frac{8}{8+\left(I+\frac{1}{2}\right)^2-\frac{\eta}{3}\left(I+\frac{1}{2}\right)^2\left(I-\frac{1}{2}\right)\left(I+\frac{3}{2}\right)\cos 2\phi}$$

(see reference 6)
circle: experimental points.
xyz are the principal axes of field gradient tensor, and OH represents the direction of magnetic field which causes zerosplitting of Zeeman line.

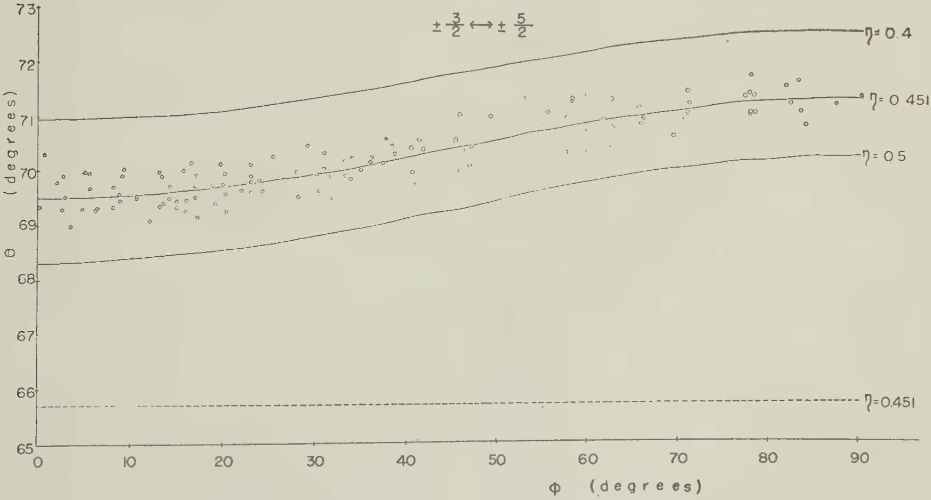

Fig. 6. Zerosplitting angle θ as a function of ϕ.
solid line: calculated values from Eq. (2) and Table I
dotted line: calculated values from

$$\sin^2\theta=\frac{16}{16+\frac{\eta^2}{36}\left[\left(I-\frac{1}{2}\right)\left(I+\frac{1}{2}\right)\left(I+\frac{3}{2}\right)\right]^2}$$

(see reference 6)
circle: experimental points.

change* of the direction of the cone from the z-axis to the y-axis should occur at a critical value of η where $\phi_{\min}$ vanishes. From Fig. 4, we may obtain $\eta=0.41$ as the critical point. On the other hand, for the case of ν_2 even when $\eta=1.0$ the axis of cone should be expected to be coincident with the z-axis from the same treatment.

Since $\eta=0.451$ for I^{127} of HIO_3 at room temperature, we may obtain the y-axis and z-axis from the Zeeman analysis$^{1)}$ of ν_1 and ν_2 lines, respectively. In fact y_1, y_2, y_3, y_4 have been found to be perpendicular to z_1, z_2, z_3, z_4, respectively. After we have determined the y- and z-axes, we may obtain the x-axis. Therefore the experimental relation between θ and ϕ satisfying the zerosplitting condition is obtained from the calculations of the angles between the zerosplitting direction and the principal axes xyz of field gradient tensor, and is compared with the theoretical one which is derived from Cohen's table. The comparisons are shown in Fig. 5 and 6. In Fig. 5 instead of θ and ϕ, θ' and ϕ' which are the polar angles defined in Fig. 5 are used. In terms of θ', ϕ' the zerosplitting condition may be written as

$$\sin^2\theta'=\frac{\alpha-\beta-\gamma}{\alpha-\beta-(\alpha+\beta)\sin^2\phi'}\,. \qquad (3)$$

Our experimental data are in good agreement with the theoretical curves for $\eta=0.451$ in Fig. 5 and 6. They show that the value of $\eta=0.451$ is consistent with our experiments and that Cohen's calculations of Zeeman splitting of pure quadrupole spectrum are borne out by our experiments.

A part of this work was supported by the Scientific Research Expenditure of the Ministry of Education.

References

1) K. Shimomura: J. Phys. Soc. Japan **12** (1957) 657.
2) R. Livingston and H. Zeldes: J. Chem. Phys. **26** (1957) 351.
3) M. H. Cohen: Phys. Rev. **96** (1954) 1278.
4) H. G. Dehmelt: Z. Physik **130** (1951) 356.
K. Shimomura: J. Sci. Hiroshima Univ. Ser. A**17** (1954) 383.
5) G. W. Ludwig: J. Chem. Phys. **25** (1956) 159.
6) T. P. Das and E. L. Hahn: "*Nuclear Quadrupole Resonance Spectroscopy*" Acad. Press Inc., Pub., New York, 1958, Chap. 1.

---

* Such abrupt change of the direction of zerosplitting cone from the z-axis to the y-axis can also be seen in the cases of spin 7/2 and 9/2, but cannot be seen in the case of spin 3/2.

JOURNAL OF THE PHYSICAL SOCIETY OF JAPAN, Vol. 14, No. 1, JANUARY, 1959

Non-Similarity Theory of Decaying Turbulence

By Yutaka SHIGEMITSU

Transportation Technical Research Institute, Tokyo

(Received September 20, 1958)

As a development of our statistical theory of turbulence, extension of the initial-period similarity-law of decaying turbulence (isotropic turbulence, wake, jet) is attempted so that non-similarity characters may be included. Based upon the cascade conception that large vortices produce small ones successively, we introduce a Poisson process of the mixture of these vortices and derive non-stationary expressions of Reynolds stress and Euler correlation. By evaluating them approximately we obtain decaying law deviating gradually from the linear-decay-law. For the case of isotropic turbulence, double correlation functions are determined by substituting Kármán-Howarth's self-preserving solution into the above formula, and further a triple correlation h is derived by solving Kármán-Howarth's equation with our evaluated u^2 and f. These theoretical results are checked by many previously proposed experimental data.

§ 1. Introduction

In our previous papers, Statistical Theory of Turbulence, I[1], II[2], III[3], turbulence is considered as a chaotic state of flow of vortices. Based upon this physical conception, all the turbulent quantities are expressed in terms of mean values taken over the areas of these vortices in order to make the Reynolds equations conclusive. These area integrals, whose domains are denoted by D, are mathematical foundations of our theory (cf. § 4∼6, I). Then, discussions proceed by dividing turbulent flow essentially into two groups; one has a decaying character in turbulent energy in the direction of the main flow such as turbulent wake behind a body or grid and free jet, and the other has a non-decaying character like pipe flow and boundary layer.

As for the structure of decaying turbulence we proposed the following physical interpretations[1),2)]: Just behind the obstacle vortex motions are formed by taking energy from the main flow. First they are carried away retaining a regular flow pattern, for instance in the form of Kármán vortex street whose stability is proved when the effect of viscosity is neglected, and then their arrangements become gradually irregular. In this chaotic state of vortices, they affect each other chiefly by their viscous force, and many chances happen where new small vortices are produced in discontinuous flow between adjacent vortices by taking their energy. These second vortices produce further the third ones under the same circumstances. Namely, the conception of a vortex chaos motion is accompanied by that of cascade process from large to small vortices. It is the essential feature of decaying turbulence that the turbulent energy is originally supplied by the primary vortices produced just behind the body and then transmitted successively into small vortices of descending order through the cascade process, being partly dissipated into heat. Viewed from the Eulerian point turbulent intensities are decaying along the flow. In the non-decaying turbulence, on the other hand, the turbulent energy does not necessarily decay owing to the strong primary vortices produced everywhere outside the laminar sub-layer.

In the decaying turbulence, statistical studies have been made on an ideal vortex chaos motion consisting of only one type of vortices produced at one position in the field of flow. According to the results[2)] similarity characters in mean velocity, Reynolds stress, Euler correlations, etc. can be all attributed to the two similarity characters, hydrodynamical and statistical; the three-dimensional expressions for them are

$$\overline{V}_*=F_\alpha(r/\sqrt{4\nu t}\,,\theta,\phi)t^{(1/2)-\alpha}\,, \tag{1.1}$$

$$P_*=P_{*\alpha}(r/\sqrt{4\nu t}\,,\theta,\phi;y,z)\,. \tag{1.2}$$

$\overline{V}_*$ is the mean velocity distribution, transmitted to the D-domain, in every vortex nearest to a fixed point x, y, z in the field. t is a time interval since the production of a vortex motion and is connected with x by the mean velocity of flow, α is a parameter relating to the initial condition of a vortex motion, and r, θ, ϕ are the coordinates in the D-domain. P_* is the probability distribution function that a relative location r, θ, ϕ of the nearest vortex filament at an instant to the referring x, y, z-point is moving in the D-domain* with time. The expression (1.1) is due to the exact solution $V_*=F_\alpha'(r/\sqrt{4\nu t})t^{(1/2)-\alpha}$ of Navier-Stokes equations for a single viscous vortex motion (cf. § 9, I). When α is chosen as unity, this similarity law can give the relations $u^2, \overline{uv}, \cdots \backsim t^{-1}$ besides their similarity-preservation characters. These characters are widely found out in decaying turbulence behind the transition region just behind a body. Thus, $\alpha=1$ could be adapted to the primary vortices mentioned above, and this similarity law has been defined as that in the initial period.

It is obvious that the initial-period similarity-law is concerned only with the primary vortices, the cascade phenomena being neglected; the deviation from observed results for the far downstream region is seen clearly in turbulent flow behind a grid, although not so conspicuous in decaying shear turbulence. On the other hand, many investigations have been made since Kolmogoroff on the cascade process in wave number of the spectrum of isotropic turbulence. Even in this case of flow, however, it is not possible to determine completely the energy decay and the spectrum curve as a whole. In these circumstances, it becomes necessary to extend our initial-period similarity-law to include the non-similarity character of cascade process in the general decaying turbulence; that is the objective of the present paper. In the following three sections fundamental descriptions will be given, and then some results will be drawn chiefly in the case of isotropic turbulence so that they may be surveyed in the light of many experimental data.

§ 2. Poisson Process in Vortex Chaos Motions

In such a complicated cascade phenomena as mentioned above, it is impossible to develop a purely hydrodynamical study based upon Navier-Stokes equations only, so that we shall make use of the P_*-function to express the non-similarity nature statistically. At a fixed point in the field, many vortices with different generations produced upstream are being carried away. When the generation is denoted by m, it has an important character to be counted with a round number beginning with $m=1$ of the primary vortices, and this is a function of α at the same time. As the x-ordinate t referring to $m=1$ vortices is taken, with the origin $t=0$ chosen as the time when they come in chaotic states and cascade phenomena begin. The position of outbreak of $m=1$ vortices is fixed just behind a body, but other vortices are being produced from the preceding ones in the whole time interval $0\sim t$. Let us consider the behaviour at t of a group of $m(t_0)$-vortices which were born as the m-generation in the time interval t_0, t_0+dt_0 $(t>t_0)$. In order to formulate the cascade phenomena statistically, we idealize the situations so that some parts of the number of $m(t_0)$-vortices are changing with time into those of the following generations without a loss in total number. Let the probability with which $m(t_0)$-vortices are mixed in the whole generations at t be denoted by $\overline{P}_*'(m(t_0), t)\,dt_0$, and their distribution function in the $D_{m(t_0)}$-domain by $P'_{*m(t_0)}$ as mentioned in § 1, then the P_*-function can take the following general expression (cf. § 7, I),

$$P_*(m(t_0), t)\,dt_0=\overline{P}_*'(m(t_0);\, x(t), y, z) \times P'_{*m(t_0)}(r/\sqrt{4\nu t}, \theta, \phi;\, x(t), y, z)\,dt_0\,. \qquad (2.1)$$

As for the rate of mixture of all the m-vortices produced in $0\sim t$, the following $\overline{P}_*$-function is given

$$\overline{P}_*(m, t)=\int_0^t \overline{P}_*'(m(t_0), t)\,dt_0\,, \qquad (2.2)$$

and by the definition we must have

$$\sum_{m=1}^{\infty} \overline{P}_*(m, t)=1\,, \qquad (2.3)$$

where the variables y, z are omitted for simplicity of expression. In the statistical study of cascade process, it is important to determine the function $\overline{P}_*'(m(t_0), t)\,dt_0$ at first. In the similarity theory, since the P_*-function is concerned only with one type of vortices produced at an instant the above deliberations are not necessary.

---

* Strict definitions of these functions and the similarity conditions were given in § 4, 9, I and § 4, 5, 9, II in an idealized two-dimensional vortex chaos motion.

As mentioned in §1, one vortex, except that of $m=1$, is born from two vortices. In order to determine the $\overline{P}_*'$-function, we introduce the following probability that $m(t_0)$- and $m'(t_0')$-vortices produce new small ones in a unit time interval at t;

$$p_*(m(t_0), m'(t_0'), t)\,. \tag{2.4}$$

Apparently p_* is the rate of total sum of newly born vortices in a unit time interval to that of their parent vortices at the beginning, and this is a transition probability having the dimensions of inverse of time. In the actual state (2.4) may take a complicated functional form, but if p_* is expanded into a power series in the independent variables, the first term remains finite because the cascade phenomena began at $t=0$. Therefore, as a first approximation, we may take

$$p_*(m(t_0), m'(t_0'), t)=p_* \qquad \text{(constant)}\,, \tag{2.5}$$

taking only the first term. This is one of the fundamental hypotheses in our non-similarity theory viewed from the statistical point.

Mathematical derivation of $\overline{P}_*'$- or $\overline{P}_*$-function from (2.5) is well known in statistical mathematics as follows: for the convenience of explanation, let us consider first a discontinuous cascade process, by dividing t into N equal short intervals, so that the transition probability at one step becomes p_*t/N. In such circumstances that the $m=1$ vortices given at $N=0$ and of $m\geqq 2$ vortices are transmitted into their respective next generations at every step of t/N, the probability of the mixture of m-vortices is known as the binomial distribution;

$$\{N!\,(p_*t/N)^{m-1}(1-p_*t)^{N-m+1}\}/\{(m-1)!\,(N-m+1)!\}\,.$$

With a relation $\lim\limits_{N\to\infty}(1-p_*t/N)^N=\exp(-p_*t)$ utilized, this is proved to tend to

$$(p_*t)^{m-1}\exp(-p_*t)/(m-1)!$$

as $N\to\infty$. Also, the probability that $m(t_0)$-vortices exist at t can be proved to be

$$\{(p_*t_0)^{m-2}\exp(-p_*t)/(m-2)!\}\,p_*dt_0\,.$$

Namely, based upon the first approximative character (2.5), $\overline{P}_*'$- or $\overline{P}_*$-function is proved to take the following expression;

$$\left.\begin{aligned}&\overline{P}_*(m,t)=(\tau^{m-1}e^{-\tau})/(m-1)!\,,\quad \tau=p_*t\,,\\&\overline{P}_*'(m(t_0),t)\,dt_0=\{(\tau_0{}^{m-2}e^{-\tau})/(m-2)!\}\,d\tau_0\,,\\&\hspace{14em}(m\geqq 2)\,.\end{aligned}\right\} \tag{2.6}$$

This is well known as the Poisson distribution. (2.6) has the behaviour as shown in Fig. 1, and the conditions (2.2) and (2.3) are clearly fulfilled. It is significant that the variable t and the parameter p_* combine into a new independent variable τ, which facilitates the subsequent analysis. Further, owing to our cascade process of the vortex chaos motion, mean values of turbulent quantities should be expressed in terms of the non-dimensional time τ instead of t, while in the similarity law it is sufficient to take the latter.

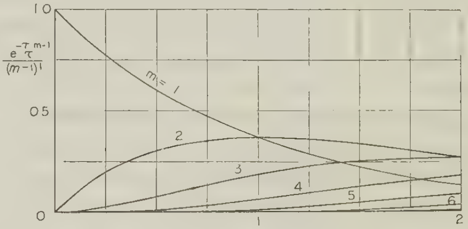

Fig. 1. General view of Poisson process of $\bar{P}_*$-function.

§3. Expressions for Turbulent Intensity and Scale

As mentioned in §1 referring to the similarity law, our statistical theory requires another hydrodynamical hypothesis besides (2.5). As written as (1.1), the $\overline{V}_*$-function for $m(t_0)$-vortices is considered to take the following form,

$$\overline{V}_{*m(t_0)} = F_{\alpha(m)}(r/\sqrt{4\nu(t-t_0)}\,,\,\theta,\,\phi;\,t-t_0)(t-t_0)^{(1/2)-\alpha(m)}, \tag{3.1}$$

but here F_α is a non-similar velocity distribution function of $m(t_0)$-vortices in the $D_{m(t_0)}$-domain and $(t-t_0)^{(1/2)-\alpha}$ is a decaying term. In the study of cascade process it is necessary to relate the generation of vortices m to their classification α. It is deduced from the exact solution of the Navier-Stokes equations for a two-dimensional viscous vortex motion, that the suffix α, being able to take any value larger than 1, is determined by the initial condition of these vortices and every F_α-function has an arbitrary constant in it corresponding to this condition (cf. § 9, I). Moreover the kinetic energy of a vortex motion $\iint_D \rho \overline{V}_*^2 dS$ is proved to be proportional to $t^{2(1-\alpha)}$ in this case (cf. § 6, II). On the other hand, it is widely found out, especially in isotropic turbulence, that the rate of dissipation of fluctuating energy is increasing with the wave number, and so in our cascade conception mentioned in § 1 it is necessary to give large values of α to small scale $m \geqq 2$ vortices. Then, considering our condition $\alpha=1$ for $m=1$, we shall introduce the following simple hydrodynamical assumption;*

$$\alpha(m)=m\ . \tag{3.2}$$

(2.5) and (3.2) are the two fundamental hypotheses in our non-similarity theory.

With the determination of the classification of vortices, it becomes necessary to presume time variation of the mean state of every group of $m(t_0)$-vortices. In the cascade phenomena, $m(t_0)$-vortices are carried away with the flow, being affected by many other vortices. These disturbing effects are not similar in time as suggested by the non-similarity characters of (2.6) and (3.2), and unlike the case of similarity law $\overline{V}_{*m(t_0)}$-function in (3.1) and $P'_{*m(t_0)}$-function in (2.1) are not considered to fulfill the similarity conditions. However, if F- and P_*'-functions are expanded in $t-t_0$, the first terms retain similar forms, so that as a first approximation we can take such similar formulae, using (3.2),

$$\left.\begin{aligned} \overline{V}_{*m(t_0)} &= F_m(r/\sqrt{4\nu(t-t_0)}\,,\theta,\phi)(t-t_0)^{(1/2)-m}\ ,\\ P'_{*m(t_0)} &= P_m'(r/\sqrt{4\nu(t-t_0)}\,,\theta,\phi;y,z)\ . \end{aligned}\right\} \tag{3.3}$$

This character will be called local similarity. In short, we have idealized the situations as follows; every group of $m(t_0)$-vortices holds the respective similarity conditions independently from each other, and non-similarity is characterized only through (2.5). The statements are our basic attitudes required to extend, at the first step, the previous similarity theory into non-similarity one. The above extension can be reduced to the fundamental hypotheses (1.1) and (1.2) of the initial-period similarity-law ($\alpha=1$), when the transition probability p_* is made to vanish in (2.6).

Our previous statistical theory has given fundamental expressions for turbulent quantities in the general case (cf. § 7, I). In vortex chaos motions consisting of all the generations produced in $0 \sim t$, the u-intensity at the $x(t)$, y, z-point is obtained in the form,

$$\boldsymbol{u}^2=\sum_{m=0}^{\infty}\int_0^t\left\{\iiint_{D_{m(t_0)}} P_*(m(t_0),t)\overline{V}^2_{*m(t_0)}\sin^2\theta\sin^2\phi\, dS\right\}dt_0\ ,\qquad dS=r^2\,dr\,d\theta\,d\phi\ , \tag{3.4}$$

by neglecting the fluctuational part V_*' of the V_*-function in view of the independency character mentioned above (cf. § 7, I). Introducing (2.1) and (2.6), we have

$$\left.\begin{aligned} \boldsymbol{u}^2 &= \boldsymbol{u}_1'^2 e^{-\tau}+\sum_{m=2}^{\infty}\int_0^t \boldsymbol{u}'^2_{m(\tau_0)}\{\tau_0{}^{m-2}e^{-\tau}/(m-2)!\}\,d\tau_0\ ,\\ \boldsymbol{u}'^2_{m(\tau_0)} &= \iiint_{D_{m(\tau_0)}} P'_{*m(\tau_0)}\overline{V}^2_{*m(\tau_0)}\sin^2\theta\sin^2\phi\, dS\ , \end{aligned}\right\} \tag{3.5}$$

therefore, by (3.3) we obtain

$$\left.\begin{aligned} \left(\frac{\boldsymbol{u}}{\overline{U}}\right)^2 &= \frac{A_1}{\tau}e^{-\tau}+\sum_{m=2}^{\infty}\int_0^\tau \frac{A_{m(\tau_0)}}{(\tau-\tau_0)^{2m-1}}\,\frac{\tau_0{}^{m-2}e^{-\tau}}{(m-2)!}\,d\tau_0\ ,\\ A_{m(\tau_0)} &= \overline{U}^{-2}\iiint_{D_{m(\tau_0)}} P_m'(r/\sqrt{4\nu(\tau-\tau_0)/p_*},\theta,\phi;y,z)\\ &\quad\times F_m{}^2(r/\sqrt{4\nu(\tau-\tau_0)/p_*},\theta,\phi)\,p_*{}^{2m-1}\sin^2\theta\sin^2\phi\, dS\ . \end{aligned}\right\} \tag{3.6}$$

As an example of turbulent scale, the u-correlation function $f(k,\tau)$ $(=\overline{u(x)u(x+k)}/\boldsymbol{u}^2(x))$ at the x, y, z- and $x+k, y, z$-points will be taken. It is seen by the local similarity (3.3) that a group of $m(\tau_0)$-vortices preserve the respective similar correlation function $f_{m(\tau_0)}(\xi_{m(\tau_0)})$. In the same manner as the above transformation, $f(k, \tau)$ can be formulated, with every f_m-function combined independently into the Poisson process;

---

* By the definition of turbulent dissipation it is seen that u_k-intensity tends to be inversely proportional to wave number k, but an assumption is required to explain that the rate of dissipation $\nu(\partial u_k/\partial x)^2$ is increasing with k.

$$\left(\frac{u}{U}\right)^2 f(k, \tau)=\frac{f_1(\xi_1)A_1}{\tau}e^{-\tau}+\sum_{m=2}^{\infty}\int_0^{\tau}\frac{f_{m(\tau_0)}(\xi_{m(\tau_0)})A_{m(\tau_0)}}{(\tau-\tau_0)^{2m-1}}\frac{\tau_0^{m-2}e^{-\tau}}{(m-2)!}d\tau_0\,, \tag{3.7}$$

where A_m is the same as (3.6) and ξ_m is adjusted to a certain distance k. Of course (3.6) is included in (3.7) as $k=0$. It is easily proved by our fundamental formula, that (3.7) or (3.6) holds for other components of turbulent scale or intensity with different circular functions of θ, ϕ in the coefficient $A_{m(\tau_0)}$ (cf. § 6, I).

In decaying turbulence, $A_{m(\tau_0)}$ depends generally upon y, z as seen in (3.6). If some y_0, z_0-points can be plotted where $P_m' F_m'$ takes a similar functional form in the $D_{m(\tau_0)}$-domain irrespective of $x(\tau)$, $A_{m(\tau_0)}$ is independent of $x(\tau)$. Such a character may be assumed approximately to hold in the actual state of flow. These points in similar relation mean the respective similarity preservation of every $m(\tau_0)$-vortices there, and the dependency of the $\overline{P}_*$-function in (2.1) on y, z can be attributed only to the variation of parametric constant p_*. Thus, (3.7) or (3.6) is regarded as the general formula of transient phenomena along the main flow of the double correlation function or the intensity of decaying turbulence.

§ 4. Initial Condition of a Vortex Motion

For the purpose of evaluating (3.7) or (3.6), it becomes necessary to survey the term A_m precisely. When p_* is made zero in (3.6), it becomes $(u/\overline{U})^2=(A_1/p_*)t^{-1}$, corresponding to the initial period. In isotropic turbulence, it was proved by the conception of the completely irregular arrangement of vortices that P_1' become $1/S_1$ independently of x, y, z by denoting the volume of the spherical D_1-domain of radius R by S_1, and F_1 became $F_1'(r/\sqrt{4\nu t})$ of the exact solution of the Navier-Stokes equations (cf. § 4, II). Therefore, as the coefficient A_1/p_*, we get

$$A_1/p_*=\{3\pi/(16\overline{U}^2\sqrt{s_0}^{\,3})\}\int_0^{s_0}F_1'^2(\sqrt{s})\sqrt{s}\,ds\,,$$

$$R/\sqrt{4\nu t}=s_0\,, \tag{4.1}$$

with t counted since the outbreak of this $m=1$ vortex. In the similarity law, s_0 was taken to be independent of t and A_1/p_* was assumed to be constant for $0\sim t$ along the flow. At $t=0$, A_1/p_* becomes indefinite, and $(u/\overline{U})^2$ diverges if it retains still this constant value. In the initial-period similarity-law, however, this singularity can be excluded from the theory with the origin $t=0$ shifted from the instant of the outbreak to the time when the chaotic states of vortices begin to appear behind the transition region, as has been done in the paper. This treatment of the initial-period similarity-law in isotropic turbulence does not loose the generality in other types of decaying turbulence. In the study of cascade process, however, this problem must be considered directly, as $m\geqq 2$ vortices are produced incessantly in whole the time interval $0\sim t$. In the above-mentioned Navier-Stokes equations which imply molecular diffusion of vorticity concentrated at first at one point, the real state of outbreak of vortex motion is not described. The production and growth seem to depend upon different mechanism, and the above equations concern only with the latter. We suppose that at the beginning of growing period the vortex motion has a finite extent and also has a constant value of (4.1). In the study of turbulence based upon the conception of vortex chaos motion, vortices must be taken into account only in this period. In the production period (4.1) is supposed to become zero at $t=0$. Otherwise, the integration in (3.7) or (3.6) would become divergent at $\tau=\tau_0$, the outbreak instant of $m\geqq 2$ vortices.

The essential problem about the coefficient A_m lies in the determination of the integration constant contained in the F_m-function, rather than in the discussion on this functional form near $\tau=\tau_0$. As mentioned in the last section, this arbitrary constant and the suffix $\alpha(m)$ are determined by the initial condition of the vortex motion of m. For an $\alpha=1$ vortex this constant is known to be related with the circulation which existed at $t=0$,[4] while for others there is no theoretical or experimental ground to suppose this character. If this production mechanism were clarified, the relation of α versus m could be given as a theoretical result as well as this arbitrary constant in F_m. In this section, we shall give rather phenomenological discussions to A_m based on an energy conception in the cascade process, without conjecturing the fine structure, P'_{*m}- and $F_m{}^2$-functions in the D_m-domain. For simplicity, A_m is assumed to be constant with respect to $\tau-\tau_0$ and to avoid the singularity the term $(\tau-\tau_0)^{1-2m}$ in (3.7) is replaced roughly with $(1+\tau-\tau_0)^{1-2m}$. As mentioned in § 1, m-vortices are born with their energy supplied from the preceding m-1-vortices. Then, taking a constant coefficient a we assume approximately

$$(\boldsymbol{u}_1/\overline{U})^2=A_1\tau^{-1}e^{-\tau}\ , \quad A_1=A \quad (\text{constant})\ ,$$

$$(\boldsymbol{u}_2/\overline{U})^2$$
$$=\int_0^\tau a\{(\boldsymbol{u}_1/\overline{U})^2/e^{-\tau}\}(1+\tau-\tau_0)^{-3}e^{-\tau}\,d\tau_0\ ,$$

$$(\boldsymbol{u}_3/\overline{U})^2$$
$$=\int_0^\tau a\{(\boldsymbol{u}_2/\overline{U})^2/(\tau e^{-\tau})\}(1+\tau-\tau_0)^{-5}\tau_0 e^{-\tau}\,d\tau_0\ ,$$

etc.

On the other hand, it was proved that for $\alpha=1$ vortices energy dissipation due to molecular viscosity is zero (cf. § 6, II). Thus, if we derive such a decaying formula as (3.6) in an ideal cascade process of $\alpha(m)=1$ this formula agrees with $\boldsymbol{u}^{-2}\propto\tau$ of the initial period. For this reason a is given as 1.5, and the ratio A_m/A is determined. Namely, we get the following relations,

$$A_m/A=1.5^{m-1}[(\tau-\tau_0)^{2m-1}/\{(1+\tau-\tau_0)^{2m-1}\tau^{m-1}\}]\ ,$$
$$(m\geqq 2)\ , \quad (3.2)'$$

where A is a parametric constant relating to the supplied energy from the main flow to the primary vortices just behind the body. Then, (3.7) becomes

$$\frac{1}{A}\left(\frac{\boldsymbol{u}}{\overline{U}}\right)^2 f(k,\tau)=\frac{f_1(\xi_1)}{\tau}e^{-\tau}$$
$$+\sum_{m=2}^{\infty}\int_0^\tau \frac{1.5^{m-1}f_m(\xi_m)}{(1+\tau-\tau_0)^{2m-1}\tau^{m-1}}\,\frac{\tau_0{}^{m-2}e^{-\tau}}{(m-2)!}d\tau_0\ .$$
$$(3.7)'$$

In spite of such an approximative estimation, probably (3.7)′ may not loose the essentiality of our foregoing discussions.

§ 5. Decaying Law

Substitution of (3.2)′ into (3.6) gives a relative expression of the u-intensity against $x(\tau)$, y_0, z_0-points. As for other components of turbulent intensity, the same functional form is derived with a different coefficient A. Thus, we have obtained the general expression of decaying law in the decaying turbulence. Fig. 2 shows the relation of $(\boldsymbol{u}/\overline{U})^{-2}A$ versus τ. In this figure a computed curve in an ideal case of $\alpha(m)=1$ as mentioned in § 4 is indicated, whose departure from the dotted straight line $(\boldsymbol{u}/\overline{U})^{-2}A=\tau$ is not large until about $\tau=1.7$. In another ideal case of $\alpha(1)=1$ and $\alpha(m\geqq 2)=\infty$ where the effect of viscous dissipation by $m\geqq 2$ vortices is extremely large, the relation $(u/\overline{U})^{-2}A=\tau e^\tau$ is derived with all the integrals in (3.6) vanishing. The relation (3.6) must be located between these two curves, as shown with a thick line. It is not easy to expand (3.6) into a series of τ, but this curve suggests that it is not preferable to express the cascading energy decay

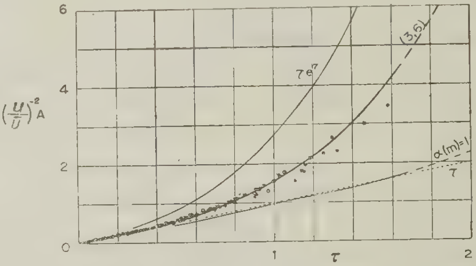

Fig. 2. Decaying law of decaying turbulence. +, Y are our previous data of u-intensity along the $\boldsymbol{u}^2$-maximum- and centre-line behind a circular cylinder of $d=1.5$ cm under $\overline{U}_0=3.74$ m/sec. Others correspond to the observed values behind a grid under the following conditions:

	$\overline{U}_0$(m/sec)	M(cm)	d(cm)	
○	9.06	0.16	0.03	Batchelor-Townsend[5]
⊖	12.96	〃	〃	
⦶	6.20	〃	〃	
⊙	12.86	0.64		Batchelor Townsend[6]
▽	11.30	1.68		Liepmann-Laufer-Liepmann[7]
▼				Dryden[8]
⧨	19.68	0.14	0.02	Hama[9]
⧩	15.00	〃	〃	
⛛	9.61	〃	〃	
△	10.00	1.00	0.20	Tsuji[10]
◬	〃	5.00	1.00	

$\overline{U}_0$ is undisturbed velocity, M is mesh-length and d is diameter of rod of grid or the clinder.

with a simple form t^{-n} that is characteristic of the similarity theory.

It is widely observed in isotropic turbulence, that most of the data of energy decay obey the linear-decay-law $u^{-2} \backsim t$ in narrow range of t and then the decaying becomes more rapid. In order to check the above result experimentally, we gathered the recent data whose deviation from the linear-decay-law was clearly recognized. Since A and p_* cannot be determined experimentally, each experimental result is adjusted to this curve with proportional factors multiplied to $(u/\overline{U})^{-2}$ and t. In turbulent wake with a uniform undisturbed velocity, the relation between x and τ is approximately linear except very near the body. Then, our previous data of u-intensity measured until far downstream behind a circular cylinder along the centre- and u^2-maximum-line are replotted in this figure, since these lines seem to consist of $x(\tau), y_0, z_0$-points (cf. § 14, II). Even in the case of non-uniform flow like a circular jet, etc., this criterion becomes possible if the relation of $x \sim \tau$ is determined. It is an important conclusion of Fig. 2 that the previous experimental measurements have attained only considerably narrow range of τ of about 1.6 in the Poisson process. Variation of the mixture of different vortices in this range can be seen in Fig. 1. Although the above criterion is concerned only with the functional form of (3.6), it can cover almost all the data with a single curve including the relation $u^{-2} \backsim t$ near $\tau=0$. If this curve is shown versus t as in the case of similarity law, it requires a family of many curves corresponding to different values of p_*.

§ 6. Double Correlation in Isotropic Turbulence

As an example of double correlation, the f-function of (3.7) will be considered. For the purpose of evaluation in the general case of decaying turbulence, we must know every locally similar function f_m of $m(\tau_0)$-vortices, whose determination should be based upon our previously proposed similarity theory (cf. § 10, II). Since such a quantitative derivation is difficult in the general case, discussions in this section will be limited to the simple case of isotropic turbulence.

In the previous papers it was pointed out that the isotropic turbulence is the completely irregular vortex chaos motion in a uniform flow (cf. § 3, II). Further, in this chaotic motion consisting of a single type of α-vortices double correlation function f' was obtained as a similar form, as evaluated in an ideal two-dimensional vortex chaos motion (cf. § 4, II). Extension from two- to three-dimensional description is not difficult. As for the triple correlation function h', it is easily proved to vanish by the character of spherical symmetry in a single D-domain. Moreover, we had the power-decay-law $u^{-2} \backsim t^{2\alpha-1}$ in this case. These results on f', h' and u^{-2} in isotropic turbulence are the same as the basic assumptions of Kármán-Howarth's self-preserving solution of their equation[11]. Namely, when the independent variable is written as $\xi'=k'/\lambda'$, their equation is reduced to

$$\left.\begin{aligned} &\frac{d^2 f'}{d\xi'^2}+\left(\frac{4}{\xi'}+\frac{5\xi'}{2(2\alpha-1)}\right)\frac{df'}{d\xi'}+5f'=0\,, \\ &\frac{du^2}{dt}=-10\nu\left(\frac{u}{\lambda'}\right)^2, \end{aligned}\right\} \qquad (6.1)$$

and f' in the above ideal case is obtained by solving (6.1).*

In the cascade process of isotropic turbulence, the above statement holds for every locally similar f_m-function in (3.7), where $\alpha=m$ and t is replaced by τ for $m=1$ and by $\tau-\tau_0$ for $m \geqq 2$. Hence, for f_m-function at two points with ascertain distance k, the Kármán-Howarth solution of (6.1) becomes[11]

$$\left.\begin{aligned} &f_m(\xi_m)=(2m-1)^{5/4}\xi_m^{-5/2}\exp\left(-\xi_m^2/(4m-2)\right)M\{(2m-9/4),\,3/4(\xi_m^2/(2m-1))\}\,, \\ &\xi_1=\sqrt{5/4}\,\sqrt{p_*/10}\,(k/\sqrt{\nu\tau}) \quad (=\xi)\,, \qquad \xi_m=\sqrt{(2m-1)\tau/(\tau-\tau_0)}\,\xi \quad (m \geqq 2)\,, \end{aligned}\right\} \qquad (6.2)$$

where

---

* Functional forms of similar double correlation can be integrated by another analysis with $\overline{V}_*$-function used in the D-domain, as has been done in the two-dimensional case (of § 4, II). It can be shown, however, that they agree with the Kármán-Howarth solution without a contradiction in every value of α.

$$M\{a, b(c)\}=c^{(1/2)+b}e^{-(1/2)c}\left\{1+\sum_{i=1}^{\infty}\frac{(b-a+\frac{1}{2})(b-a+\frac{3}{2})\cdots(b-a+(2i-1)/2)}{i!(2b+1)(2b+2)\cdots(2b+i)}c^{i}\right\}.$$

Namely, (3.7)′ and (6.2) determine completely the non-similar double correlation f as a function of ξ and τ.

Concerning with general properties of f, (3.7) indicates $f(0,\tau)=1$, $f(\xi,\tau)<1$ and $f(\xi,0)=f_1(\xi)$. When (6.2) is introduced, it has a character $f_m(\sqrt{(2m-1)\tau/(\tau-\tau_0)}\,\xi)<f_1(\xi)$ and so $f(\xi,\tau)<f_1(\xi)$ holds generally in (3.7). Further, as every $df_m/d\xi_m$ becomes zero of the first order at the origin, $\partial f(0,\tau)/\partial\xi=0$ is easily derived. But, in (6.2) $\partial^2 f_m(0)/\partial\xi_m{}^2=-1$ and so by (3.7)′ we get

$$\frac{1}{A}\left(\frac{u}{U}\right)\frac{\partial^2 f(0,\tau)}{\partial\xi^2}=\frac{-c^{-\tau}}{\tau}\left\{1+\sum_{m=2}^{\infty}\frac{1.5^{m-1}(2m-1)}{(m-2)!}\int_0^{\tau}\frac{\tau}{\tau'}\frac{(1-\tau'/\tau)^{m-2}}{(1+\tau')^{2m-1}}d\tau'\right\},$$

$$\tau'=\tau-\tau_0\,,$$

where all the integrals $\int_0^{\tau}d\tau'$ diverge because the term $(1-\tau'/\tau)^{m-2}/(1+\tau')^{2m-1}$ becomes unity at $\tau'=0$. By the above discussions it is concluded that $f(\xi,\tau)$ has the following characters;

$$\left.\begin{array}{lll} f(0,\tau)=1\,, & f(\xi,0)=f_1(\xi)\,, & f(\xi,\tau)<f_1(\xi)<1\,, \\ \partial f(0,\tau)/\partial\xi=0\,, & \partial^2 f(0,\tau)/\partial\xi^2=-\infty\,. & \end{array}\right\} \tag{6.3}$$

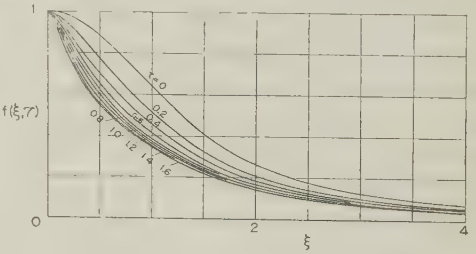

Fig. 3. Theoretical curves of f-correlation function.

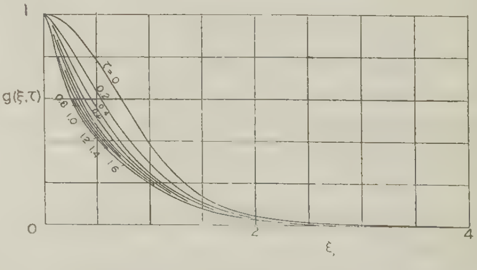

Fig. 4. Theoretical curves of g-correlation function.

In the self-preserving solutions, f'-function can be expanded into a power series of ξ at the origin and λ' in (6.1) is the same[11] as $\sqrt{-2/(d^2f'(0)/dk'^2)}$ which gives the physical meaning of micro-scale to λ'. Physical reason of its non-zero value can be comprehended by remembering that (6.1) is consisting only of one type of vortices with a finite extent except at the instant of production. In the cascade process, however, the last singularity character in (6.3) implies that the micro-scale is zero even if $\sqrt{-10\nu u^2/(du^2/dt)}$ remains finite not being written as $\sqrt{-2/(d^2f'(0)/dk'^2)}$ as shall be mentioned precisely in § 7. This is caused by the condition (3.2)′ where the extents of $m\geqq 2$ vortices have been assumed to grow from zero in the time interval $\tau_0=0\sim\tau$. As mentioned in § 4, in the study of vortex chaos motion vortices should be taken into account only in their growing period with non-zero extents. If some strict discussions are made on the problem of production of a vortex motion, this singularity could be excluded from the analysis.

Fig. 3 shows functional forms of f versus ξ with parametric values of τ, integrated numerically by (3.7)′ and (6.2). As for g-correlation, it can be evaluated in the same manner with a locally similar g_m-function used instead of f_m. The results are shown in Fig. 4. They are also given in Tables I and II. Obviously the continuity condition $g=f+(k/2)(\partial f/\partial k)$ holds between them, as every g_m is connected with f_m by this relation in (3.7). Figs. 3 and 4 suggest that (6.3) may be adaptable widely to double correlation functions of decaying turbulence. Although the mathematical expression of $\partial f/\partial\tau$ is difficult to derive, it is seen in these figures that f or g begins to deviate rapidly from f_1

Table I. Computed results of f-correlation function.

$\xi \backslash \tau$	0.0	0.2	0.4	0.6	0.8	1.0	1.2	1.4	1.6
0.0	1.0000	1.0000	1.0000	1.0000	1.0000	1.0000	1.0000	1.0000	1.0000
0.1	0.9952	0.9763	0.9605	0.9482	0.9335	0.9221	0.9122	0.9054	0.8982
0.2	0.9803	0.9335	0.9000	0.8654	0.8421	0.8219	0.8045	0.7962	0.7821
0.4	0.9244	0.8281	0.7531	0.7192	0.6853	0.6589	0.6377	0.6201	0.6054
0.6	0.8392	0.7171	0.6450	0.5980	0.5653	0.5409	0.5223	0.5076	0.4958
0.8	0.7386	0.6107	0.5407	0.4978	0.4672	0.4487	0.4336	0.4219	0.4129
1.0	0.6417	0.5197	0.4562	0.4186	0.3908	0.3767	0.3650	0.3557	0.3486
1.2	0.5422	0.4342	0.3796	0.3479	0.3274	0.3137	0.3038	0.2964	0.2907
1.6	0.3763	0.2992	0.2604	0.2390	0.2252	0.2158	0.2091	0.2042	0.2004
2.0	0.2652	0.2109	0.1837	0.1685	0.1587	0.1521	0.1474	0.1439	0.1413
2.4	0.1912	0.1522	0.1328	0.1216	0.1146	0.1098	0.1064	0.1039	0.1019
3.0	0.1282	0.1020	0.0890	0.0815	0.0768	0.0736	0.0713	0.0696	0.0683
4.0	0.0718	0.0571	0.0499	0.0457	0.0430	0.0412	0.0400	0.0390	0.0383
5.0	0.0470	0.0374	0.0326	0.0299	0.0282	0.0270	0.0262	0.0255	0.0251

Table II. Computed results of g-correlation function.

$\xi \backslash \tau$	0.0	0.2	0.4	0.6	0.8	1.0	1.2	0.4	1.6
0.0	1.0000	1.0000	1.0000	1.0000	1.0000	1.0000	1.0000	1.0000	1.0000
0.1	0.9902	0.9592	0.9330	0.9103	0.8910	0.8737	0.8582	0.8445	0.8224
0.2	0.9608	0.8863	0.8215	0.7899	0.7569	0.7269	0.7072	0.6877	0.6724
0.4	0.8529	0.7180	0.6378	0.5856	0.5495	0.5232	0.5034	0.4876	0.4736
0.6	0.7008	0.5550	0.4793	0.4351	0.4069	0.3879	0.3745	0.3640	0.3590
0.8	0.5321	0.4077	0.3483	0.3157	0.2959	0.2832	0.2746	0.2685	0.2656
1.0	0.3821	0.2894	0.2470	0.2244	0.2110	0.2025	0.1969	0.1929	0.1902
1.2	0.2606	0.1978	0.1694	0.1544	0.1455	0.1399	0.1360	0.1331	0.1314
1.6	0.1051	0.0820	0.0711	0.0651	0.0613	0.0589	0.0572	0.0559	0.0550
2.0	0.0409	0.0325	0.0284	0.0260	0.0245	0.0235	0.0228	0.0222	0.0218
2.4	0.0152	0.0121	0.0106	0.0097	0.0091	0.0087	0.0085	0.0083	0.0081
3.0	0.0062	0.0049	0.0043	0.0039	0.0037	0.0036	0.0034	0.0034	0.0033

or g_1 of the self-preserving form and tends to the so-called cascade type with a sharp peak at the origin. This is an important result of our study, together with a character of gradual deviation of the decaying law from that of the initial period as shown in Fig. 2. Thus, the above results suggest that, in general decaying turbulence, the initial-period similarity-law may be useful particularly in the problems of force relation which are all attributed to the distribution of turbulent intensity, such as evaluation of mean-velocity profile, of momentum loss and so forth. On the other hand, in correlation function or spectrum distribution in a total intensity, preferable results cannot be expected without considering the cascade process.

Because of experimental convenience measurements are made chiefly on g-correlation. In Fig. 5, three curves of g at $\tau=0.4$, 1.0, 1.6 are drawn with the abscissa k/L_g, L_g being the integral scale $\int_0^\infty g\,dk$, and the previously observed values are plotted respectively taking a suitable abscissa, as an exact experimental determination of L_g is rather difficult. In these experimental data values of τ are unknown except for few cases, and furthermore the above-mentioned rapidly changing character makes it difficult to check the systematic deviation experimentally. It can be said, however, that experimental data fall almost in the narrow range of these curves and, at the same time, decaying data agree favourably with the theoretical curve in the same range of τ as seen in Fig. 2.

It may be necessary to note on the conception of the final period proposed by Batchelor and Townsend⁵⁾. At the last stage of decay, they derived self-preserving formula by neglecting inertia terms in Kármán-Howarth equation. In our study, this neglect means that the transition probability function $p_*(m(t_0), m'(t_0'), t)$ tends to zero at $t\to\infty$. We suppose this may be true, but since only the first term is taken in p_*-function as indicated by (2.5) our Poisson process should not be extended to the final period in the above meaning. Batchelor and Townsend[5] further obtained self-preserving solution $f=\exp(-\xi^2/2)$ and $\boldsymbol{u}^{-2}\propto t^{5/2}$ by assuming Loitziansky's invariant, which corresponds to our vortex chaos motion consisting only of $\alpha=7/4$ vortices produced at an instant. As seen in Fig. 2, our decaying law includes $\boldsymbol{u}^{-2}\propto t^{5/2}$ in about $\tau=1\sim1.5$, but the correlation function remains in cascade type as shown in Figs. 3 and 4, being different from the above self-preserving type. Batchelor and Townsend[5] observed auto-correlation function instead of f, but if many measurements are made on g- or f-correlation itself at large values of τ, the situations may be more clarified.

As is well known in the study of isotropic turbulence, double correlation and one- or three-dimensional spectrum are related to each other by a simple mathematical formula, based on Taylor's hypothesis. In numerical calculation, however, it is very difficult to transform f into a spectrum function exactly up to such a high wave number as attained by modern hot-wire technique. Then, as the character of spectrum function we shall refer only to the well known $-5/3$-power law, that is equivalent[12] to $1-f\propto k^{2/3}$. It is shown in Fig. 6 that the range being approximated by this relation increases rapidly when the cascade process opens.

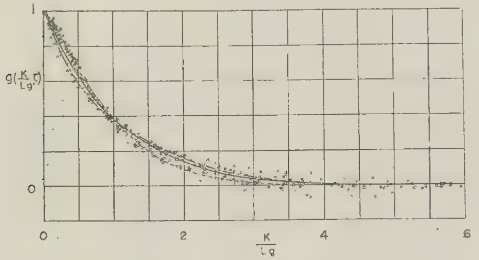

Fig. 5. Comparison of g-correlation with experimental results.

Dotted-, full-, chain-line indicate the curves of $\tau=0.4$, 1.0, 1.6 in Fig. 4. Several marks correspond to the observed values behind a grid by several authors under the following conditions:

	$\overline{U}_0$ (m/sec)	M (cm)	d (cm)	x/M	$R_M\times 10^{-5}$	
○	10.00	1.00	0.2	20		Tsuji[10]
⊙	〃	〃	〃	60		
⊖	〃	〃	〃	120		
⦶	〃	〃	〃	200		
⊘	〃	〃	〃	350		
⦸	〃	〃	〃	550		
△	〃	10.16			3.0	Liepmann-Laufer-Liepmann[7]
◬		〃			1.0	
▽		〃			0.4	
⛛	20.00	14.00	0.2	10		Hama[9]
▷	〃	〃	〃	30		
⊳	〃	〃	〃	50		
⊲	〃	〃	〃	70		
□				37		Corrsin[13]
⊡				231		
⧄		15.24			1.3	Townsend[14]
⧅				50	3.2	
◫	parallel	2.54		60		Stewart-Townsend[15]
⊟	cylinder	〃		〃		
⊞	square	5.08		30		
⊕	mesh	2.54		35		
⊠	slots	1.90		47		
⊗		〃		〃		

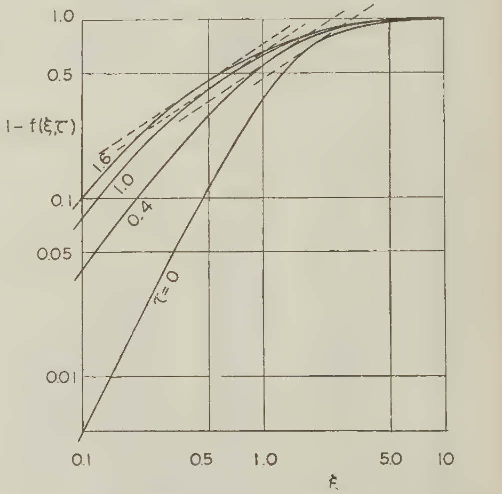

Fig. 6. Comparison of the 2/3-power law (dotted lines) with our curves of $1-f$ (full lines).

§7. Triple Correlation in Isotropic Turbulence

In isotropic turbulence Kármán and Howarth have derived the fundamental equation of motion[11],

$$\frac{\partial(\boldsymbol{u}^2 f)}{\partial t}-2\nu\boldsymbol{u}^2\left(\frac{\partial^2 f}{\partial k^2}+\frac{4}{k}\frac{\partial f}{\partial k}\right)=-2\boldsymbol{u}^3\left(\frac{\partial h}{\partial k}+\frac{4}{k}h\right), \qquad (7.1)$$

where h is the triple correlation function. In principle, (7.1) is a mathematically transformed expression from the Reynolds equations, and it is not closed in itself, since it has three unknown dependent variable $\boldsymbol{u}^2$, f and h. However, since $\boldsymbol{u}^2$ and f were given as functions of τ and ξ in the preceding sections, our original purpose to complete the Reynolds equations has been achieved at least in the case of isotropic turbulence. As interpreted so far, $\boldsymbol{u}^2$ and f have been derived through many simplification of situations, and if this approximative analysis shall be made on h

too such a result $h=0$ will be obtained because every locally similar h_m is zero. Thus, even if our non-similarity characters are well supported experimentally in the forms of $\boldsymbol{u}^2$ and f, it is still interesting to survey them in the form of h-correlation by solving (7.1).

When $\boldsymbol{u}^2$ and f are expressed in terms of functions of τ and ξ, (7.1) takes the following form,

$$\frac{-\partial((\boldsymbol{u}/\overline{U})^2 f)}{\partial\tau}+\frac{(\boldsymbol{u}/\overline{U})^2}{4\xi\tau}\frac{\partial(f+2g)}{\partial\xi}=\frac{1}{\sqrt{2}}\left(\frac{\boldsymbol{u}}{\overline{U}}\right)^3\frac{1}{\sqrt{\tau}}\left(\frac{dh'}{d\xi}+\frac{4}{\xi}h'\right),$$

where

$$h=(\sqrt{p_*}\sqrt{\nu}/\overline{U})h'(\xi,\tau),$$

with the continuity equation used. This is regarded as an ordinary linear differential equation of the first order for h, with a parametric constant τ. Therefore, on integrating under the boundary condition $h=0$ at $\xi=0$, we get

$$\left.\begin{aligned}h(\xi,\tau)&=\left(\sqrt{\frac{2}{A}}\frac{\sqrt{p_*}\sqrt{\nu}}{\overline{U}}\right)\frac{\int_0^\xi H(\xi,\tau)\xi^4\,d\xi}{\xi^4},\\ H(\xi,\tau)&=\left\{-I\tau\frac{\partial(f/I)}{\partial\tau}+\frac{1}{4\xi}\frac{\partial(f+2g)}{\partial\xi}\right\}\sqrt{\frac{I}{\tau}},\\ I&=A(\boldsymbol{u}/U)^{-2}.\end{aligned}\right\}\tag{7.2}$$

In the phenomenological studies, triple correlation h which is caused by the inertia terms in the original Navier-Stokes equations is considered to play a role to transfer fluctuating energy from low- to high-frequency range and to break similarity preservation in double correlation. While, in our statistical study of cascade process the cause of non-similarity has been given through the transition probability p_* as mentioned repeatedly. It is very instructive that based upon the simplified relation $p_*=constant$, h is proved to be connected directly with $\sqrt{p_*}$ as indicated in (7.2).

At the origin $k=0$, (7.1) tends to

$$\left.\begin{aligned}\frac{d\boldsymbol{u}^2}{dt}&=-10\nu\frac{\boldsymbol{u}^2}{\lambda^2},\\ \lambda^{-2}&=\frac{1}{5}\lim_{k\to0}\left\{\frac{\boldsymbol{u}}{\nu}\left(\frac{\partial h}{\partial k}+\frac{4}{k}h\right)-\left(\frac{\partial^2 f}{\partial k^2}+\frac{4}{k}\frac{\partial f}{\partial k}\right)\right\}.\end{aligned}\right\}\tag{7.3}$$

By (6.3) and (7.2) every term in λ^{-2} is proved to be divergent, while λ^{-2} is clearly finite owing to our decaying law shown in Fig. 2, and so it is interpreted that every singularity cancels each other in λ^{-2}. Anyway, it may be necessary to notice that the relation $-10\nu\boldsymbol{u}^2/(d\boldsymbol{u}^2/dt)=-2/(d^2f(0)/dk^2)$ does not hold unless f can be expanded into a power series of k at the origin.

Values of h were determined by computing (7.2) numerically. Near the origin reliable results could not be expected owing to the singular character. Also since numerical differentiations contained in H cannot give sufficiently accurate values, these results in Fig. 7 should be regarded as showing only the general characters of h-function. However, such a tendency can be ascertained that with a given value of p_* the function h is gradually growing with τ, unlike the case of double correlation in Fig. 3 or 4.

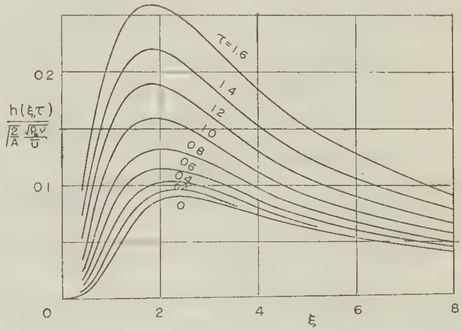

Fig. 7. Computed curves of h-correlation function.

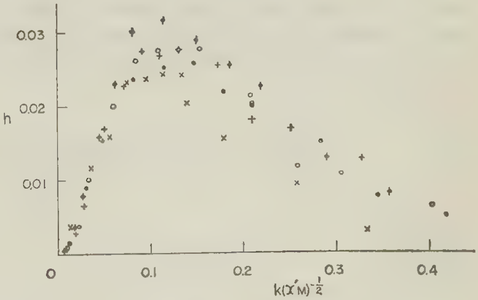

Fig. 8. Time dependency of h-correlation observed behind a grid by R. W. Stewart[16], where × $x/M=20$, ● $x/M=30$, ○ $x/M=60$, + $x/M=90$, ⧫ $x/M=120$ and $R_M=5300$.

We have not so much observation on h-correlation even in isotropic turbulence. Further, as the value of τ is uncertain in the observed results, variation of h versus τ cannot be checked definitely. But, referring to Stewart's data16) inserted in Fig. 8 which have been observed along the x-direction in one case of flow behind a grid, the above-mentioned growing character can be ascertained at least qualitatively. Fortunately, h-correlation was measured together with f-correlation case15) 16)17) by case. Then, in the same manner as in Fig. 5, our computed results of f in the preceding section can be compared with these experimental data, and as for the relative forms of h they also can be checked experimentally at the same time with the same abscissa as in f. Fig. 9 shows the results.

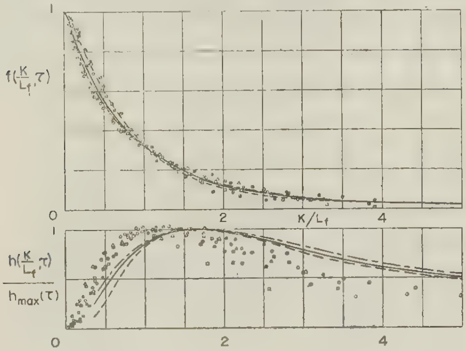

Fig. 9. Comparison of f- and h-correlation with experimental results, plotted against the same abscissa k/L_f. Dotted-, full-, chain-line show the curves respectively of $\tau=0.4$, 1.0, 1.6 in Figs. 3 and 7. Several marks correspond to the observed values of f and h at the same time behind a grid under the following conditions:

	x/M	$R_M\times10^{-5}$	
○	30	0.53	Stewart-Townsend15)
⊙	〃	2.12	
⦶	〃	4.24	
⊖	〃	11.50	
□	20	0.53	Stewart16)
▲	30	〃	
◫	60	〃	
⊟	90	〃	
⧄	120	〃	
△		$R_\lambda=56.2$	Stewart17)

For f-correlation, the theory and experiment agree very well as for g-correlation, but in h-correlation disagreements are found to some extent. It seems that our too simplified picture of cascade process is responsible for the disagreement in h-correlation, although undetectable in the decaying law and double correlations. However, it may need many other experimental results on triple correlation to make this point clearer. Furthermore, the comparison in the form of transfer function in the Fourier-transformed equation of (7.1), may probably give useful results.

Here we should like to say some concluding remarks: (i) The fundamental hypotheses of our non-similarity theory are (2.5) and (3.2), the latter of which is concerned with the production of vortex motion together with (3.2)′, strict discussions being hopeless at present. However, unless such a relation as (3.2) is taken, it becomes difficult to interpret the experimental evidence that turbulent dissipation increases with wave number, and a rough estimation of (3.2)′ seems to have given not very bad result. (ii) It is not so old when the interrelation between (2.5) and (2.6) has come to be clarified, but (2.6) has been used successfully in many other statistical studies of cascade phenomena, such as cascade shower of the cosmic ray18) and so forth. We think, an appropriateness of Poisson process in the decaying turbulence is due to mechanism of this flow that even at the beginning of vortex chaos motion it is accompanied inevitably by the cascade phenomenon from large to small vortices—non-zero transition probability. It seems also to give an apparently favourable effect on our theory that the present experimental technique attains only narrow range of τ. Otherwise, inadequateness of the simple assumption (2.5) could be found out more clearly through experimental observations. (iii) It is a characteristic point of this paper that the theory holds independently of the magnitude of the parametric constant p_*. As mentioned in § 1, p_* is due to disturbing effects of vortices in their chaotic states, and when the irregularity of their states increases, i.e. the functional form of P_* tends to be constant in the D-domain (cf. § 8, I), the value of p_* becomes large. It is due to this character that the deviation from the initial-period similarity-law is found clearly in turbulent wake behind a grid, rather than in decaying shear turbulent flows. Even in shear turbulence, however, this theory may be useful particularly for the purpose of evaluating correlation or spectrum function.

In conclusion the author wishes to express his gratitude to Professor I. Tani and members of the Turbulence Research Group in Japan for their valuable advice and discussions. Thanks are also due to Dr. K. Maeda for

helpful suggestion in mathematical aspect.

References

1) Y. Shigemitsu: J. Phys. Soc. Japan **10** (1955) 472.
2) Y. Shigemitsu: J. Phys. Soc. Japan **10** (1955) 890.
3) Y. Shigemitsu: J. Phys. Soc. Japan **10** (1955) 1077.
4) W. Müller: *Einführung in die Theorie der zähen Flüssigkeiten* (1932) § 31.
5) G. K. Batchelor and A. A. Townsend: Proc. Roy. Soc. London **A 194** (1948) 527.
6) G. K. Batchelor and A. A. Townsend: Proc. Roy. Soc. London **A 193** (1948) 539.
7) H. W. Liepmann, J. Laufer and K. Liepmann: NACA TN 2473 (1951).
8) H. L. Dryden: Quart. Appl. Math. **1** (1943) 7.
9) R. Hama: Rep. Inst. Sci. Tech., Univ. Tokyo **7** (1953) 145.
10) H. Tsuji: J. Phys. Soc. Japan **10** (1955) 578.
11) T. v. Kármán and L. Howarth: Proc. Roy. Soc. London **A 164** (1938) 192.
12) L. Agostini et J. Bass: *Les Théories de la Turbulence* (1950) § 25.
13) F. N. Frenkiel: J. Appl. Mech. **15** (1948) 311.
14) A. A. Townsend: Proc. Camb. Phil. Soc. **44** (1948) 560.
15) R. W. Stewart and A. A. Townsend: Phil. Trans. Roy. Soc. London **A 867** (1951) 359.
16) R. W. Stewart: Proc. Camb. Phil. Soc. **47** (1951) 146.
17) I. Proudman: Proc. Camb. Phil. Soc. **47** (1951) 158.
18) H. J. Bhabha and W. Heitler: Proc. Roy. Soc. London **A 159** (1937) 432.

Short Notes

This section is intended to secure prompt publication of important discoveries in physics. The reports should not exceed 800 words in length. A figure of size 7 cm×7 cm will be counted as 150 words.

J. PHYS. SOC. JAPAN **14** (1959) 104

Anisotropic Conductivity of CdS Single Crystals

By Shōji TANAKA, Mineo KOBAYASHI
and Taizō MASUMI
Department of Applied Physics,
University of Tokyo, Tokyo, Japan

(Received October 4, 1958)

The conductivity, Hall effect and magneto-resistance effect of CdS single crystal have been investigated by many workers (1)–(7). But the structure of electronic energy band of this material has not been clarified enough up to now. As CdS crystal has the Wurtzite type crystal lattice and not the cubic symmetry, it might have the anisotropic conductivity if the energy band or the relaxation time is anisotropic along the directions of the crystal axis. In this report the conductivity of CdS single crystal has been measured by microwave method in 9500 MC region at room temperature.

The microwave method is very useful for the measurements of the anisotropic natures of crystals, since the free selection of the polarization of electromagnetic waves to the crystal axis is possible and especially in the conductivity measurements no electrical contacts with metal electrodes are required.

Samples used in this experiment are thin flakes of Cl-doped *N*-type CdS single crystals, dimensions of which are about 3∼4 mm in diameter. The *c*-axis of these crystals lies in the face of flat crystals and one of the *a*-axis is perpendicular to this face. The samples are held by the polystyrene bar in the center of H_{011}-mode cavity and the crystal face is parallel to the electric field of the microwave, and these samples can rotate around the bar holder. The microwave power entering into the cavity is absorbed by the conducting crystal and so the *Q*-value greatly decreases. The conductivity of the sample is deduced from the measurement of this *Q*-value.

The typical result is shown in Fig. 1 and it indicates that the conductivity parallel to the *c*-axis is almost twice of that perpendicular to the *c*-axis, and the angular dependence of the conductivity is expressed by elliptic equation (1)

$$\frac{\sigma_\theta}{\sigma_{\parallel}}=1-\frac{\sigma_{\parallel}-\sigma_{\perp}}{\sigma_{\parallel}}\sin^2\theta, \qquad (1)$$

where $\sigma_{\parallel}$ and $\sigma_{\perp}$ are the conductivity of the sample parallel and perpendicular to the *c*-axis respectively, and θ is the angle between the *c*-axis and the electric field. The value of $\sigma_{\perp}/\sigma_{\parallel}$ fluctuates about 20% from sample to sample, and this may be caused by the measurement error.

The conductivity of semiconductor is determined by the effective mass of charge carriers and the scattering mechanism of them with the crystal lattice or impurity centers. As CdS has the hexagonal crystal lattice, it might be considered that the role of the anisotropic scattering could not be neglected. To investigate these problems, the measurements of the anisotropy and temperature dependencies of the magneto-resistance, Hall effect and conductivity are now in progress (7).

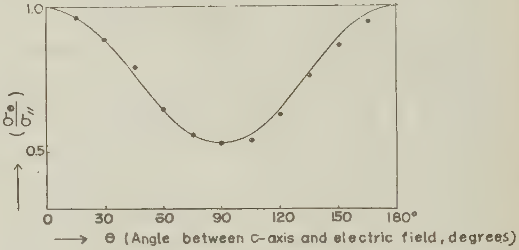

Fig. 1. Hysteresis loop (50C/sec) for a fused sample at 121°C.

References

1) R. W. Smith: RCA Review **12** (1951) 350.
2) R. H. Bube: Jour. of Chem. Phys. **23** (1955) 18.
3) F. A. Kröger, H. J. Vink and J. Volger: Physica **20** (1954) 1095.
4) F. A. Kröger, H. J. Vink and J. Volger: Philips Research Reports **10** (1955) 39.
5) I. Broser and R. Warminsky: Ann. der. Physik **7** (1950) 289.
6) S. Tanaka and T. Masumi: Jour. Phys. Soc. Japan **13** (1958) 314.
7) Y. Suge, S. Tanaka and T. Masumi: to be published.

J. PHYS. SOC. JAPAN **14** (1959) 105

Piezoelectric Properties of Triglycine Sulphate Crystal

By Kazuo HUSIMI and Keisuke KATAOKA
Electrical Communication Laboratories, Tokyo

(Received October 4, 1958)

During the study of switching processes by the ultrasonic method, a large piezoelectric voltage was observed in triglycine sulphate[1]. The crystal of triglycine sulphate belongs to C_2 (monoclinic) and has eight independent piezoelectric constants, but here we report only on their tensile components that have been measured by the dynamic method.

The crystal axes of the samples are determined with the aid of X-ray analysis. Table I shows the dimensions of the samples and the measured piezoelectric constants. Measurements were done at 30°C. From the results, it is proved that the piezoelectric constant d_{23} is very large. The resonant characteristic of a typical sample is shown in Fig. 1 which shows a very large coupling factor of 0.44. The values of d_{21} and d_{22} are also shown in the table.

Table I

Sample	l (mm)	f_r (kc/s)	k	d (stat-Cl/dyne)	S^E (cm²/dyne)
c axis No. 1	12.8	102.15	0.44	$d_{23}=2.51\times10^{-6}$	$S_{23}=8{\cdot}71\times10^{-12}$
〃 No. 2	20.5	64.31	0.44	$d_{23}=2.52\times10^{-6}$	$S_{23}=8.57\times10^{-12}$
a axis No. 11	13.0	152.85	0.19	$d_{21}=7.06\times10^{-7}$	$S_{21}=3.77\times10^{-12}$
〃 No. 12	17.8	111.72	0.17	$d_{21}=6.60\times10^{-7}$	$S_{21}=3.76\times10^{-12}$
Thickness No. 21	1.23	1581.0	0.18	$d_{22}=6.60\times10^{-7}$	$S_{22}=3.93\times10^{-12}$

In Fig. 2 is shown the temperature dependence of the piezoelectric output measured by ultrasonic method. In this procedure, a constant ultrasonic excitation is applied to the sample so the output voltage is proportional to the piezoelectric constant. A small error arising from the thermal coefficient of the quartz crystal is involved. In the figure, the characteristic of d_{23} is shown with an arbitrary unit in the ordinate, which has a large peak value with increasing temperature, and a large thermal hysteresis. No piezoelectric output appears above the Curie point, but polarization of the same polarity reappears when the crystal is cooled below the Curie point. This fact seems to indicate that a certain ferroelectric effect remains above the Curie point. The decrease of the piezoelectric output near the Curie point is steep, but is not discontinuous, unlike the case of BaTiO$_3$ single crystal. This shows that the transition is of the second order.

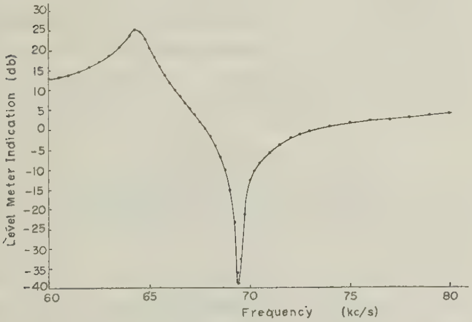

Fig. 1. The resonance characteristic of the typical sample.

The samples used here has been offered by Prof. G. Ōhara of Tōhoku University for which we express our thanks. We also thank to Mr. Y. Niizeki for the X-ray analysis.

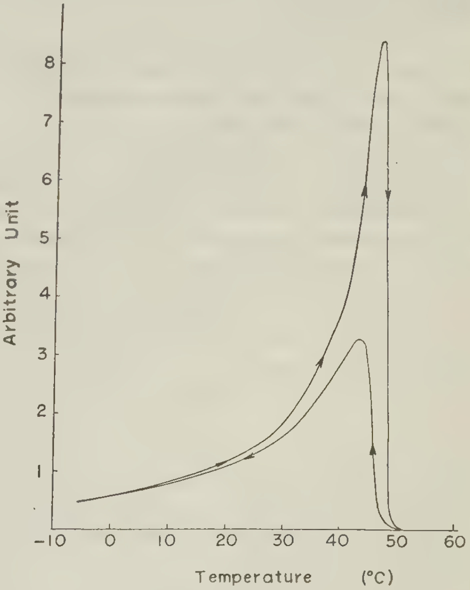

Fig. 2. The temperature characteristic of the piezoelectric output.

Reference

1) K. Husimi and K. Kataoka: J Phys. Soc. Japan **13** (1958) 661.

J. Phys. Soc. Japan **14** (1959) 106

On the Transition Temperature of Copper Ferrite

By Haruyuki OHNISHI, Teruo TERANISHI
and Syohei MIYAHARA
Department of Physics, Faculty of Science,
Hokkaido University, Sapporo, Japan

(Received October 30, 1958)

It is well known that slowly cooled copper ferrite has tetragonally deformed spinel structure at room temperature. Snoek[1] and Bertaut[2] examined its tetragonality with quenched specimens and found those quenched above 760°C to have cubic structure. Ohnishi and Miyahara[3] found, however, the temperature of transition from tetragonal to cubic structure is 360°C by means of a high temperature X-ray camera. Recently, Inoue and Iida[7] reported an anomaly of specific heat near the above temperature. In order to clarify the physical meaning of these two temperatures we made further experiments concerning the crystal structure of $CuFe_{2-t}Cr_tO_4$.

All specimens are made from CuO, Fe_2O_3 and Cr_2O_3. Mixtures of these oxides are heated at about 900°C for two weeks and cooled to room temperature at the rate of 0.5°C/min. This treatment prevents eventual reduction of the cupric ion. Lattice parameters and the distributions of cupric ions on 8a (tetrahedral) and 16d (octahedral) sites of spinel structure are determined by a "Norelco" X-ray diffractometer.

Tetragonality $\sigma=(c-a)/a$ at room temperature and the fraction x of cupric ions at 8a site are plotted against the content t of chromium. From these two curves tetragonality σ is given as a function of x as shown in Fig. 1, and the critical value of x beyond which tetragonality vanishes is about 0.25. This value is equal to that of Bertaut's pure copper ferrite specimens quenched from 760°C.

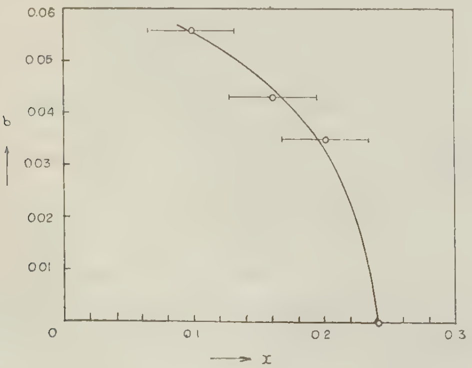

Fig. 1. Variation of tetragonality with copper ion distribution.

Tetragonalities σ of slowly cooled copper ferrite-chromites at various temperatures T are shown in Fig. 2.

Beside the above experiment $CuFe_2O_4$ is quenched from 790°C and annealed at 390°C (A) and 320°C (B), respectively. Specimen A deforms into tetragonal spinel after 15 minutes, while specimen B remains in cubic structure even after 24 hours. From this fact it can be said that the curves in Fig. 2 represent the lattice deformation as functions of temperature where copper ions migrate scarcely. Under this condition $CuFe_2O_4$ transforms from cubic to tetragonal structure at 360°C.

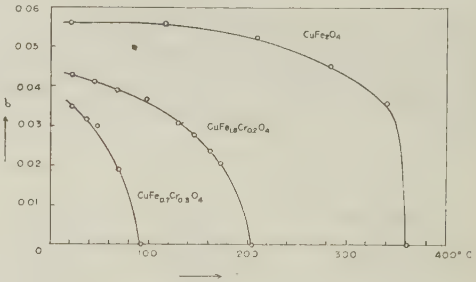

Fig. 2. Variation of tetragonality with temperature.

The origin of tetragonal deformation of $CuFe_2O_4$ is thought to be either the Jahn-Teller effect[5] or covalent force[6] of cupric ions. For $CuFe_2O_4$ the bulk tetragonality decreases as temperature is raised and it vanishes at the critical temperature 360°C. The tetragonality also decreases by mixing chromium or by quenching, both of which causes the increase of the fraction of cupric ions in 8a site to the critical value $x=0.25$.

Here it can be concluded that for $CuFe_2O_4$ 760°C is not any specific temperature but the one at which the ionic distribution $x=0.25$ (which is the critical value of tetragonal deformation) is realized.

References

1) J. L. Snoek: Rev. Techn. Philips **8** (1946) 359.
2) E. F. Bertaut: J. Phys. et radium **12** (1951) 252.
3) H. Ohnishi and S. Miyahara: read at the meeting of the Japan Physical Society in November 1956.
4) G. I. Finch, A. P. B. Sinha and K. P. Sinha: Proc. Roy. Soc. **242** (1957) 28.
5) J. D. Dunitz and L. E. Orgel: J. Phys. Chem. Solids **3** (1957) 20.
6) J. B. Goodenough and A. L. Loeb: Phys. Rev. **98** (1955) 391.
7) T. Inoue and S. Iida: J. Phys. Soc. Japan **13** (1958) 656.

J. PHYS. SOC. JAPAN **14** (1959) 107~108

Grain Boundary Migration and Dimensional Change of Low Carbon Steel

By Minoru OKADA
Department of Welding Engineering, Osaka University
and Toichi WATANABE
Department of Mechanical Engineering, Osaka City University

(Received November 14, 1958)

It has been reported by previous investigators[1),2)] that a dimensional change occurs in the same direction to that of cold-working, provided that a low carbon steel is subjected to the low-temperature annealing after the cold-working. The purpose of this note is to propose a mechanism of this phenomenon.

Steel rods containing 0.2%C, 32 mm in diameter, were prepared for the experiment and they were extended or compressed by about 14%. After the deformation, each specimen was annealed for a half hour at different temperatures and the measurements of the change in length or diameter were made, as illustrated in Figs. 1 and 2.

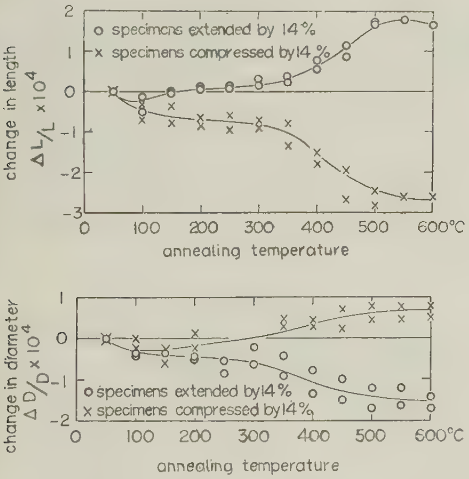

Figs. 1 and 2. The dimensional change of steel rods due to the annealing subsequent to the cold-working.

The main points are as follows:

(1) At anneals below 100°C, the volume contraction was observed in both extended and compressed specimens.

(2) At anneals above 100°C, an increase and a decrease in the length of specimen and vice versa in the diameter were observed, respectively for extended and compressed specimens. Such dimensional changes occurred distinctly in the range of annealing temperatures 350 to 500°C, while the volume of the specimen remained nearly constant during the anneals, as understood from Figs. 1 and 2.

The dimensional changes observed for anneals above 100°C may be related to the grain boundary migration owing to piled-up dislocations[3)]; dislocations piled-up against a grain boundary would tend to migrate in such a direction that their stress concentration may be released. If the affinity between a dislocation and its atmosphere is sufficiently strong enough to impede the backward motion of piled-up dislocations in a slip plane, the grain boundary would migrate at elevated temperatures in such a way of releasing the high stress concentrations. This is the case for low carbon steel where dislocations are strongly anchored by the Cottrell atmosphere; some evidences for the migration of grain boundary were obtained, as clearly shown in Fig. 3. As can be seen in the figures, grain A has grown into grain B and the slip lines exist in the grain A (remarkable in (a)).

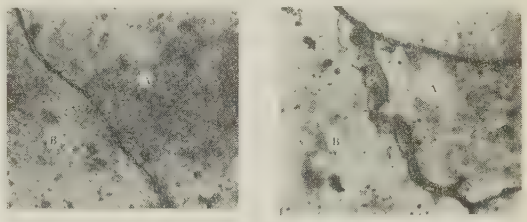

(a) (b)

Fig. 3. The migration of grain boundary. The steel specimen containing 0.045%C and 0.005%N was compressed by about 5% at room temperature after etching with 1.5% Nital subsequent to polishing and annealed in vacuum at 500°C for a half hour, and then slightly etched with 1.5% Nital. ×370.

As the results, cold-worked mild steels would change their length in the same direction to that of cold-working without any noticeable volume change.

On the other hand, the volume contraction found at anneals below 100°C is considered to be mainly attributable to the disappearance of excess point defects[4)] introduced by cold-working.

The authors wish to express their hearty thanks to Professor J. Takamura of Kyoto University for his valuable discussions.

References

1) H. Sekiguchi and M. Inagaki: The Japan Institute of Metals. **19** (1955) 24, 28, 220, 286 (in Japanese).
2) M. Okada and T. Watanabe: The Japan Institute of Metals. **22** (1958) 440 (in Japanese).

3) W. T. Read and W. Shockley: Phys. Rev. **78** (1950) 275.
4) For example; J. Takamura: Nippon Buturi Gakkaishi **13** (1958) 542.

J. Phys. Soc. Japan **14** (1959) 108

Electron Spin Resonance of Mn-activated Phosphors

By On Matumura

Department of Physics, Faculty of Science, Kyusyu University

(Received October 29, 1958)

The electron spin resonance of Mn^{++} in various powder salts has been measured at 3 cm wave length at room temperature. The crystal structure of these salts are rutil, fluorite, rock salt, zinc blende, and wurtzite type respectively, and Mn^{++} are believed to be in cubic or nearly cubic crystalline field surrounded by 4, 6, or 8 negative ions in these phosphors.

Table I.

Phosphors	g	A $10^{-4}\,cm^{-1}$	Number of surrounding negative ions
MgF_2	2.001	90.6	8
CdF_2	2.001	90.6	8
CaF_2	2.003	92	
SrF_2	2.002	93	
BaF_2	2.004	91	
MgO	2.001	81.2	6
CdO	2.001	87.3	
CaO	1.999	87.7	
MgS	2.001	71.9	
CaS	2.001	75.7	
SrS	2.000	75.0	
MgSe	2.004	71.2	
CaSe	2.004	72.9	
CaTe	2.003	67.2	
ZnO		79	4
CdS	2.002	64.8	
CdSe	2.003	61.5	
MgTe	2.013	58.1	
ZnS	2.001	63.8	4
ZnSe	2.01	60	
CdTe		56.9	
ZnTe		56	

The results are interpreted in terms of the following spin Hamiltonian, with $S=5/2$ and $I=5/2$;

$$\mathscr{H}=g\beta \boldsymbol{H}\cdot\boldsymbol{S}+A\boldsymbol{I}\cdot\boldsymbol{S}+\text{higher order terms.}$$

The obtained values of g and A are summarized in the Table I.

From the electro-negativity of Mn^{++} and negative ions and the numbers of the surrounding negative ions, the amount of the ionic character can be calculated after Pauling[1]. As seen in Fig. 1, an almost linear relation exists between the coupling constant A of h. f. splitting and the ionicity[2].

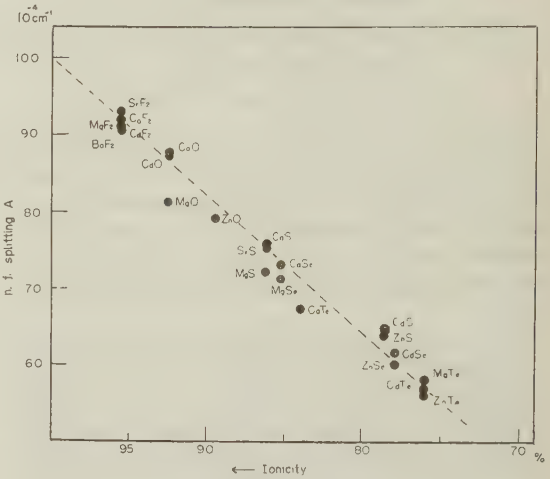

Fig. 1.

Further discussions on the g-values[3], the luminescence wave length, and other properties will be given in the near future. The author is indebted to Prof. Z. Miduno for his discussions and to Mr. K. Hôrai for many details of the experiments. This research is partially supported by the Grant for Promotion of Science from the Ministry of Education.

References

1) L. Pauling: *Nature of the Chemical Bond.* Cornell Univ. Press, (1940) p. 69.
2) J. S. van Wieringen: Dis. Faraday Soc. **19** (1955) 118.
3) H. Watanabe: Prog. Theor. Phys. **18** (1957) 405.

J. PHYS. SOC. JAPAN **14** (1959) 109~110

Some Ferroelectrical Properties of Triglycine Sulfate

By Hiroo TOYODA, Shigeru WAKU,
Hiroyuki SHIBATA and Yoichi TANAKA
*Electrical Communication Laboratory,
Nippon Telegraph and
Telephone Public Corporation, Tokyo*

(Received November 14, 1958)

We have measured some ferroelectrical properties of triglycine sulfate single crystals at room temperature, 0°C, and −73°C. The crystals were prepared by cooling or evaporation methods[1]. They were cut perpendicularly to the b-axis, and polished by fine sand paper or etched in water, their thickness ranging from 0.015 to 0.11 cm. The electrical contacts were made by silver conducting paste or by platinum wire spring, in both cases gold electrodes being evaporated directly on the crystal.

Coercive fields, obtained from the hysteresis loops at 50 c/s, remarkably increase with the amplitude of applied field. A relation $E_c=aE_{\max}{}^b$ holds in a good approximation, where $b=0.5$ for 20°C ($E_{\max}=0.35\sim15$ kv/cm corresponds to $E_c=0.2\sim1.35$ kv/cm), and $b=0.4$ for −73°C ($E_{\max}=5.5\sim22$ kv/cm corresponds to $E_c=4.0\sim6.8$ kv/cm) ($d=0.039$ cm). The results also suggested that the coercive field would increase with frequency of applied field, as Domansky[2] has reported, but a preliminary measurement failed owing to disturbance by hysteresis loss. The spontaneous polarization remains constant in this field region, but we have obtained the values, 3.1~3.3 coul/cm² at 20°C and 4.5~4.8μ coul/cm² at −73°C, which were considerably larger than those ever reported[3], except the one by Husimi[4]. The coercive field has a tendency to decrease with increasing thickness.

Temperature °C	α kv/cm		Mobility calculated from the high field linearity; cm²/volt·sec.
	Low field	High field	
23	1.8~2.2	6	4~5
0	5.5	9.4	1.1~1.5
−73	—	—	1.5~2.0×10⁻²

Polarization reversal was measured by applying repeated pulses, duration of which was 1 to 100μ sec. Figs. 1 and 2 give the typical results for 100μ sec and various pulse heights ($d=0.02$ cm). Stadler and Meitzler[5] have reported that the piezoelectric output of barium titanate was not proportional to the average polarization, but that the relation between these two properties had a hysteresis loop. We have used the ultrasonic method, developed by Husimi[6], and ascertained that in the case of T.G.S. the relation was almost linear.

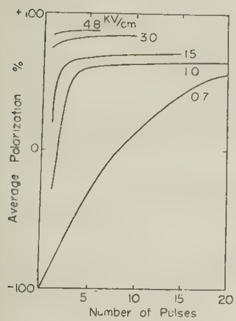

Fig. 1. Polarization reversal under successive Pulses of 100μ sec. at 30°C.

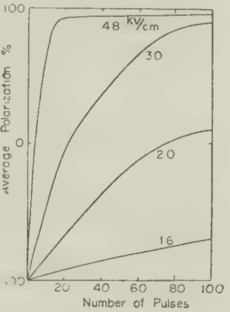

Fig. 2. Polarization reversal under successive pulses of 100μ sec. at −73°C.

We have also measured the switching current. Fig. 3 shows the maximum current density per unit crystal area at three different temperatures ($d=0.023$ cm). All curves look quite alike and can be divided into two parts, namely the high field region and the low field region[7]. It is known that the former is nearly proportional to the field strength, while the latter changes with field strength as $\exp(-\alpha/E)$. The higher field region, however, may be rather better represented in the same exponential form, though the constant α differs from the one for lower field.

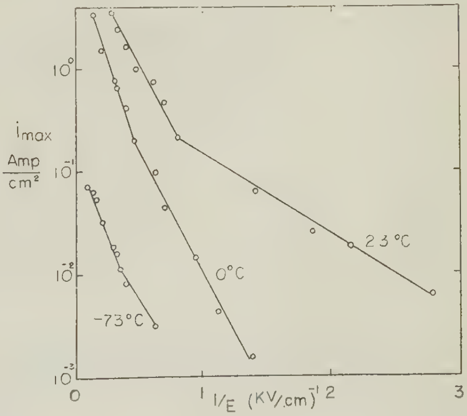

Fig. 3. Maximum of switching current at three different temperatures.

References

1) Y. Tanaka and S. Waku: J. App. Phys. Japan **27** (1958) 561.
2) S. Domansky: Proc. Phys. Soc. **72 B** (1958) 306.
3) L. Taurel et al.: Compt. rend. **246** (1958) 70.
4) K. Husimi et al.: J. Phys. Soc. Japan **13** (1958) 661.
5) A. H. Meitzler and H. L. Stadler: Bell Sys. Tech. J. **37** (1958) 719.
6) K. Husimi and K. Kataoka: J. App. Phys. **29** (1958) 1247.
7) E. Fatuzzo: Helv. Phys. Acta. **31** (1958) 309.

J. PHYS. SOC. JAPAN **14** (1959) 110

The Far Infrared Reflectivity of NaCl, KCl and KBr Crystals

By Akiyoshi MITSUISHI, Hiroshi YOSHINAGA and Shigeru FUJITA

Department of Applied Physics, Faculty of Engineering, Osaka University, Osaka, Japan

(Received November 19, 1958)

The far infrared reflectivity of NaCl, KCl and KBr crystals was remeasured with the vacuum grating spectrograph[1] of much high resolving power as compared with the measurements in 1930's. The measurements were made in the spectral region from 30 to 200μ at two incident angles, 12° and 52°, assuming the reflectivity of an Al coated mirror as 100%.

Fig. 1 shows the reflection curves obtained in the vicinity of reflection peaks. Very strong and broad peaks centered at 53μ (NaCl), 63μ (KCl) and 79μ (KBr) respectively have been well known as the Reststrahlen peaks. The sub-maxima placed at 38μ (NaCl), 46μ (KCl) and 58μ (KBr) respectively (at 12° incidence) were first found by Czerny in 1930[2].

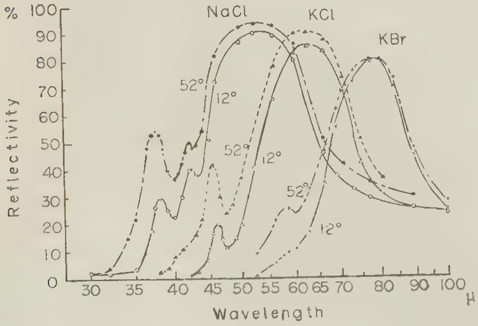

Fig. 1. The far infrared reflection curves of NaCl, KCl and KBr at two incident angles, 12° and 52°.

For NaCl a new weak but definite sub-maximum was found at 42.5μ (at 12° incidence) in the present investigation. No reflection peak was observed beyond 100μ.

In the transmission measurements of NaCl Barnes and Czerny found two weak minima at 40.5μ and 51μ besides the main band at 61.1μ[3]. The three reflection peaks in the present investigation may correspond to these three absorption bands.

Recently Rosenstock studied the problem of infrared absorption by rocksalt lattice[4]. According to his calculation there are five infrared active modes of lattice vibration. Among these one produces the strongest absorption, the other two the next strongest and the remaining two the next strongest. This agrees qualitatively with the experimental results which showed one strong band and two weak bands in both the reflection and transmission measurements, but the calculated wavelengths do not agree.

The reflectivity increases and reflection peaks shifts slightly to the shorter wavelength side as the incident angle increases. From the reflectivities at 12° and 52° incidence the optical constants could be derived graphycally as was done by Simon in the prism infrared region[5], but as the polarization of radiation in the spectrograph has not yet been measured no such attempt was made at present.

At the temperature of liquid air the two sub-maxima of NaCl are clearly observed and the reflectivity increases and reflection curve shifts as a whole slightly to the shorter wavelength side. These results will be reported later.

References

1) H. Yoshinaga et al: J. Opt. Soc. Am. **48** (1958) 315.
2) M. Czerny: Z. Phys. **65** (1930) 600.
3) R. B. Barnes and M. Czerny: Z. Phys. **72** (1931) 447.
4) H. B. Rosenstock: J. Phys. Chem. Solids: **4** (1958) 201.
5) I. Simon: J. Opt. Soc. Am. **41** (1951) 336.

J. PHYS. SOC. JAPAN **14** (1959) 111~112

Diffusion of Manganese in Single Crystals of Copper

By Akira IKUSHIMA
Department of Physics, University of Tokyo

(Received November 6, 1958)

The experimental study on the diffusion of transition elements in noble metals seems to be one of the procedures to elucidate the anomalous behaviors of the transition impurities dissolved dilutely in noble metals. Moreover, there is a merit in the case of the tracer experiment of diffusion that the state of transition impurities in extremely small concentration is investigated.

The diffusion experiments of iron[1),3)], cobalt[2),3)] and nickel[3)] in copper have been carried out by the present author and other investigators. And, here the diffusion experiment of Mn^{54} in single crystals of 99.99% copper is reported.

The experimental procedures were the same as previously reported[1)]. It is, however, to be noted that the following plating bath seemed to be practical: $Mn^{54}Cl_2$ in aqueous solution (Mn^{54} was obtained in this form from the Radiochemical Centre in England); NH_4Cl, 30 gramme per one litre of water; with a carbon anode.

The penetration curves are shown in Fig. 1, and the diffusion coefficients calculated from these plots are given in Table I. Fig. 2 shows the data plotted as log D versus the inverse of the absolute temperature. The straight line fitted by the least square calculation is expressed as $D=D_0 \exp(-Q/RT)$ cm²/sec. with

$$\log_{10} D_0 = 7.00 \pm 0.32 \ (D_0 \text{ in cm}^2/\text{sec.}),$$

$$Q = 91400 \pm 1600 \text{ cal/mole.}$$

The last figures in these equations are the probable errors. Mackliet[3)] measured the diffusion coefficient of this system at 1069°C and his data is consistent with the present work. But, the values of D_0 and Q estimated by Mackliet differ radically from the present results. Mackliet's data is shown in Fig. 2.

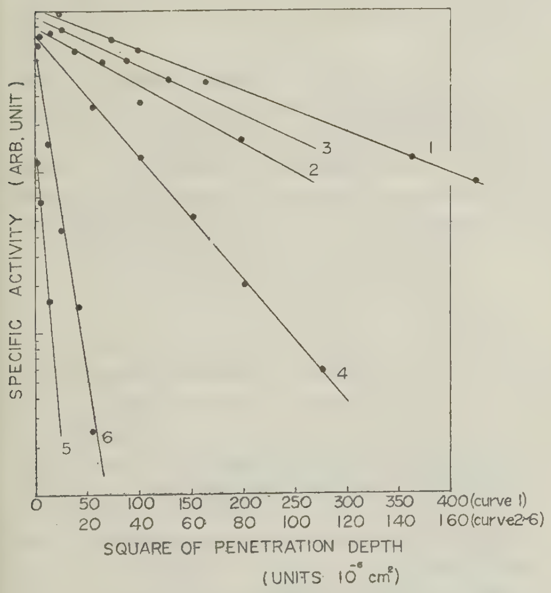

Fig. 1. Penetration curves.

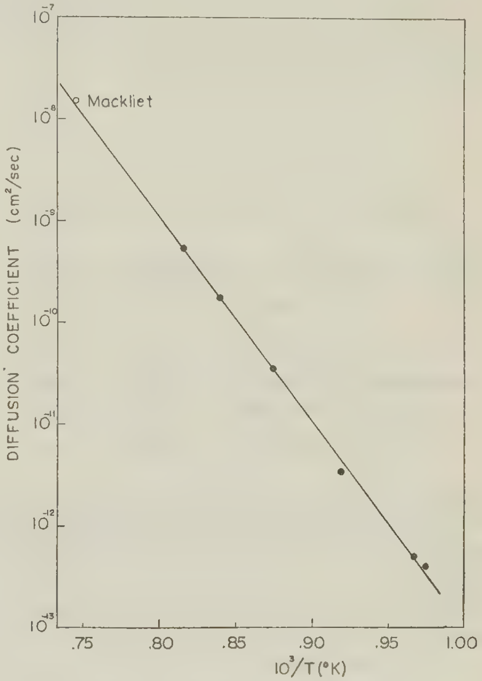

Fig. 2. Plot of log D *vs* 1/T.

Table I. Diffusion coefficients of Mn^{54} in Cu.

No.	Temperature (°C)	Time (sec.)	D (cm²/sec.)
1	950±1	6.85×10^4	4.82×10^{-10}
2	918±1	5.29×10^4	1.79×10^{-10}
3	871±1	3.97×10^5	3.59×10^{-11}
4	817±1	1.75×10^6	3.32×10^{-12}
5	761±1	1.34×10^6	5.07×10^{-13}
6	754±2	2.67×10^6	4.09×10^{-13}

D_0 and Q of the present results are fairly larger than those of Cu^{64} in Cu[4)], Co^{60} in Cu[2),3)] and Ni^{63} in Cu[3)]. The existing theories of diffusion cannot easily account for the large value of Q and especially that of D_0. The latter may be attributed to the deformation of incomplete d-shell of the manganese atom at the saddle point of diffusion, from which the reduction of vibrational frequency results.

The author wishes to thank Professor Y. Tomono for many valuable advices and continuous encour-

agement. This work is partly supported by the Scientific Research Expenditure from the Ministry of Education.

References

1) Y. Tomono and A. Ikushima: J. Phys. Soc. Japan **13** (1958) 762.
2) M. Sakamoto: J. Phys. Soc. Japan **13** (1958) 845.
3) C. A. Mackliet: Phys. Rev. **109** (1958) 1964.
4) A. Kuper, H. Letaw, J. L. Slifkin, E. Sonder and C. T. Tomizuka: Phys. Rev. **96** (1954), 1224; Phys. Rev. **98** (1955) 1870.

J. PHYS. SOC. JAPAN **14** (1959) 112~113

The Variation of Superstructure in Iron Selenide Fe_7Se_8

By Atsushi OKAZAKI

Department of Physics, Faculty of Science, Kyusyu University, Fukuoka Japan

(Received Nov. 17, 1958)

X-ray diffraction studies of single crystal specimens of iron selenide (Fe_7Se_8) have shown that this compound can exist in structural forms distinct from the hexagonal superstructure reported by Okazaki and Hirakawa[1]. The second structure (the triclinic superstructure) is obtained by slow cooling after annealing the hexagonal superstructure at 290°C. The fundamental lattice of this superstructure is of a pseudo NiAs type.

The structure analysis of this superstructure has been made at room temperature by single crystal X-ray work with oscillation, rotation and Weissenberg photographies, the preliminary results of which are as follows:

Laue symmetry: triclinic,

Lattice constants: $A=\sqrt{3}B=12.53$, $B=2a=7.23_6$ and $C=4c=23.5_4$ Å, $\alpha=89.8°$, $\beta=89.4°$ and $\gamma=90.0°$,

where the capital and small letters designate the unit cell dimensions of the super and fundamental lattices, respectively.

The observed extinction rule indicates that the arrangement of iron vacancies is as shown in Fig. 1 (a). This is identical with that in Fe_7S_8, reported by Bertaut[2], although the sulphide is monoclinic. In Fig. 1 (b) the unit cell of the hexagonal superstructure is shown for comparison. In both superstructures the arrangements of the iron vacancies in the AB planes are identical. Only the stacking sequence of these planes along the C axis and hence the C axis length are characteristic to each structure.

The transition between the triclinic superstructure ($C=4c$) and the hexagonal one ($C=3c$) has been observed with oscillation and rotation photographs obtained by using a single crystal high-temperature camera having a cylindrical Ni-foil heater (Dent and Taylor[3]). The accuracy of temperature measurement is within ±2°C and the stability during the exposure time (about 30 min.) is ±0.5°C over the whole temperature range of this experiment.

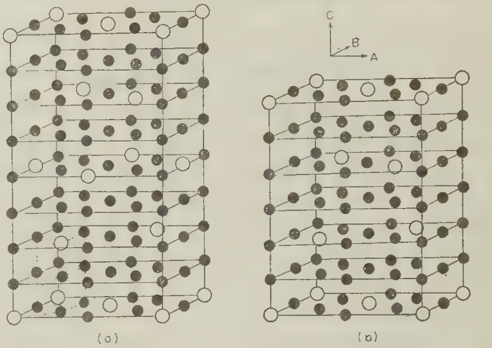

Fig. 1. Unit cells of Fe_7Se_8 superstructures. (a): triclinic ($C=4c$), (b): hexagonal ($C=3c$). Open and solid circles represent vacancies and Fe atoms, respectively. Se atoms are omitted for clarity. Broken lines indicate the fundamental unit cell.

The transition begins at about 240°C and proceeds gradually and is complete at 298°C. During this transition the diffraction pattern of the '$4c$ structure' in the oscillation photograph is replaced gradually by that of the '$3c$ structure' as shown schematically in Fig. 2. That the triclinic deformation of the unit cell decreases gradually is also seen in the complete rotation photographs.

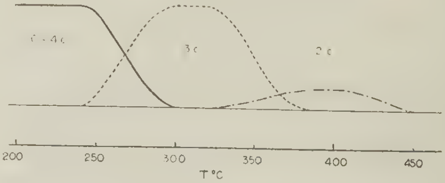

Fig. 2. The diffraction intensity of each type lattice as a function of temperature (schematic).

The third superstructure ($C=2c$) appears at 320°C. The transition from the hexagonal structure is similar to that between the triclinic and hexagonal one and is complete at 388°C. The diffraction intensities of this crystallographic phase are of the order of 1/5 compared with those of the others (also shown in Fig. 2) and the observed extinction rule cannot be explained from the arrangement of the iron vacancies alone. It seems that the arrangement of these vacancies are somewhat disorder. This superstructure disappears at about 450°C, but the remaining (0001) and (0003) reflexions referred to the fundamental NiAs type lattice suggest the partial ordered state in which the iron vacancies remain within the alternative *AB* planes but distributed at random in these planes. Such a situation has been reported by Jellinek on $Cr_7S_8$⁴⁾. At about 460°C the distribution of vacancies becomes completely random.

A slight deviation of chemical composition from Fe_7Se_8 may cause not only the change of the transition temperatures but also the transition process. With specimens prepared earlier the third structure was not observed. The transition process and temperature reported here are those with specimens having reliable stoichiometric composition. The full paper will be published in the near future.

References

1) A. Okazaki and K. Hirakawa: J. Phys. Soc. Japan **11** (1956) 930.
2) E. F. Bertaut: Acta Cryst. **6** (1953) 557.
3) L. S. Dent and H. F. W. Taylor: J. Sci. Inst. **33** (1956) 89.
4) F. Jellinek: Acta Cryst. **10** (1957) 620.

J. PHYS. SOC. JAPAN **14** (1959) 113~114

Effects of Deuteron Bombardment on CdS Single Crystals

By Shoji TANAKA and Toshio TANAKA
Department of Applied Physics, University of Tokyo, Tokyo, Japan

(Received November 15, 1958)

Concerning the lattice defects in CdS crystals many investigations have been carried out. The identity of those defects, however, is not yet clarified completely.

We have studied the effects resulting from bombardment of CdS single crystals with deuterons to clarify the nature of defects in this material. The present article describes some results obtained up to now.

The samples used in this experiment are flake-shaped pure CdS single crystal having high dark resistivity, grown by the Frerichs' technique. Deuteron bombardments are performed in air at room temperature by the cyclotron at the Institute of Physical and Chemical Research and the total number of deuterons is about 10^{16} per cm² and their energies about 2 Mev.

The resistivity of the crystals is reduced by these bombardments from about 10^{10} ohm-cm to about 10^4 ohm-cm. Plotting the resistivity logarithmically as a function of reciprocal temperature, one obtains straight lines with slope about 0.4 ev (Fig. 1). It may be considered that the deuteron bombardments produce probably not only donors but also acceptors (compensation defects). Therefore, the donor levels seem to lie about 0.4 ev below the conduction band.

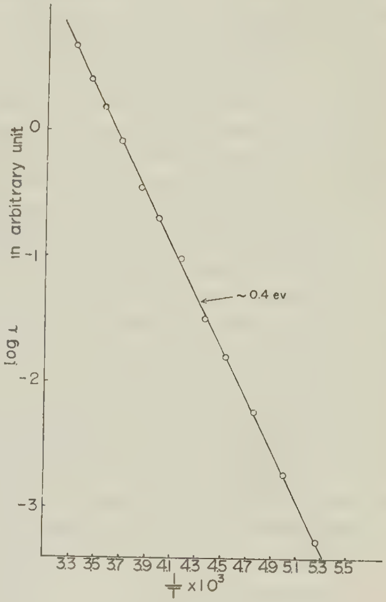

Fig. 1. Temperature-dependency of dark-current for a crystal after deuteron-bombardment.

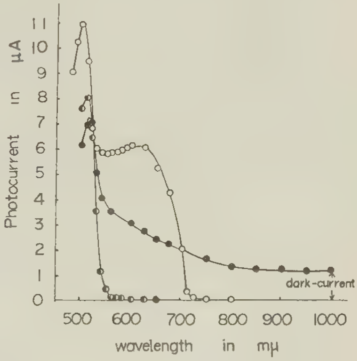

Fig. 2. Spectral distribution of photocurrent.

Before bombardment
(measured at room temperature) ...... ◐
After bombardment
(measured at room temperature) ...... ●
(measured at low temperature) ...... ○

Lambe, Klick¹⁾, Bube²⁾, Broser, Broser-Warminsky³⁾ and other investigators have observed trapping levels lying as deep as the donor levels in the bombarded samples. So it might be resonable that the donor levels are attributed to sulfur vacancies or interstitial cadmium ions. Recently, Melamed[4) also proposed from luminesence experiments that sulfur vacancies are the origin of the donor centers.

Beside, such deuteron bombardment causes the considerable increase of photosensitivity of the crystals and its spectral distribution becomes to show new response to the long wavelength side of the fundamental absorption edge (Fig. 2). This long wavelength response is obscure at room temperature but becomes more predominant at low temperatures, and it increases with bombardment. It may be interpreted as giving the energy corresponding to transition* from lattice defect levels to the conduction band. The defect levels are therefore considered to be about 2.0 ev below the conduction band. These centers exist also in some unbombarded crystals and moreover seem to be produced by some heat treatments.**

The other effects than those above mentioned are also produced. That is, the rise and decay of photocurrent become slow after the bombardment, where the decay consists of a fast component and a slow component which increases with bombardment. The decay time of the slow component is sensitive to temperature, that is to say, it amounts to even more than an hour at low temperatures but decreases abruptly above approximately $-100°$C. Furthermore, the thermally stimulated current and the steady-state photocurrent also show sharp falls at the same temperature. These results might be due to the formation of hole traps by the deuteron bombardment.

References

1) J. Lambe and C. C. Klick: Phys. Rev. **98** (1955) 909.
2) R. Bube: Phys. Rev. **99** (1955); Phys. Rev. **101** (1956) 1668.
3) I. Brose and R. Broser-Warminsky: Brit. J. Appl. Phys. Suppl. **4** (1954) 90.
4) N. T. Melamed: Phys. Rev. **107** (1957) 1727.

---

* More accurately speaking it seems that this transition is made through the shallow excited state of the defect, as considered from the shape of spectral distribution curve of photocurrent.

** Further investigations on the heat treatments are in progress.

Errata

Diffraction of Electromagnetic Waves by Circular Plate and Hole*

By Yûkichi NOMURA and Shigetoshi KATSURA

J. Phys. Soc. Japan **10** (1955) 285

Page	Column	Line	Equation		should be read
286	right	(Fig. 1)		hale	hole
287	right	21		electric	magnetic
287	right	23		magnetic	electric
288		9	(13)	$\frac{\partial U}{\partial r}\sin m\varphi$	$\frac{\partial U}{\partial r}\sin\varphi$
288		14	(15)	$U_{m+1}^{(z)}\mp U_{m-1}^{(2)}$	$U_{m+1}^{(2)}\mp U_{m-1}^{(2)}$
288		18	(17)	$\frac{\partial S_n{}^m}{\partial z}(r,0)$	$a\frac{\partial S_n{}^m}{\partial z}(r,0)$
289		18	(25)	$=\sum_{n=0}^{\infty}\frac{a_n{}^m}{b_n{}^m}u_n{}^m(x)$	$=x^{m/2}\sum_{n=0}^{\infty}\frac{a_n{}^m}{b_n{}^m}u_n{}^m(x)$
289		20	(26)	$G_{\nu u}{}^m\frac{A_\nu{}^m}{B_\nu{}^m}=$	$G_{\nu n}{}^m\frac{A_\nu{}^m}{B_\nu{}^m}=$
290		15		at $s=-\mu$ is	at $s=\mu$ is
290		24	$X_{10}{}^0$	$\left(\frac{16}{21}-\frac{32}{9\pi^2}\right)\beta^4$	$\left(\frac{8}{21}-\frac{32}{9\pi^2}\right)\beta^4$
290		25	$X_{20}{}^0$	$+0.0022519\beta^6$	$+0.0438120\beta^6$
290		25	$X_{20}{}^0$	$+i0.0046310\beta^7$	$-i0.0130070\beta^7$
290		26	$X_{30}{}^0$	$-0.010785\beta^6$	$-0.00038480\beta^6$
290		26	$X_{30}{}^0$	$-i0.012892\beta^7\cdots$	$+i0.00064393\beta^7\cdots$
291		8	$X_{32}{}^0$	$-\frac{4}{148}\beta^3+\cdots$	$-\frac{2}{99}\beta^2+\cdots$
291		9	$X_{03}{}^0$	$-0.010785\beta^6$	$-0.00002960\beta^6$
291		9	$X_{03}{}^0$	$-i0.012892\beta^7$	$+i0.00004953\beta^7$
291		12		$X_{20}{}^0$	$X_{20}{}^2$
293		10	(37)	$\frac{A_n{}^{m-1}\mp A_n{}^{m+1}}{B_n{}^{m-1}-B_n{}^{m+1}}$	$\frac{\sum_{n=0}^{\infty}(-)^n(A_n{}^{m-1}\mp A_n{}^{m+1})}{\sum_{n=0}^{\infty}(-)^n(B_n{}^{m-1}-B_n{}^{m+1})}$
293		11	(37)	$\frac{2A_n{}^0-A_n{}^2}{B_n{}^0-B_n{}^2}$	$\frac{\sum_{n=0}^{\infty}(-)^n(2A_n{}^0-A_n{}^2)}{\sum_{n=0}^{\infty}(-)^n(B_n{}^0-B_n{}^2)}$
293		11	(37)	$\frac{E_2A_n{}^1}{k^3\cos\alpha B_n{}^1}$	$\frac{E_2\sum_{n=0}^{\infty}(-)^nA_n{}^1}{k^3\cos\alpha\sum_{n=0}^{\infty}(-)^nB_n{}^1}$
296		11		orient	orients
296		12		circhlar	circular
296		14		orient	orients
297		5		half	twice
297		7	(54)	$2\sigma=t=$	$\sigma/2=t=$
297	left	20	(55)	$H_z=-E_1\sin\alpha\exp(\cdots)$	$H_z=-\frac{k}{\mu\omega}E_1\sin\alpha\exp(\cdots)$
297		21		are equal	are not equal

---

* Tables of values of $G_{n\nu}{}^m$, $X_{n\nu}{}^m$, $A_n{}^m$, $a(x)$, $b(x)$, $c(x)$, $d(x)$, and $F_0(ka,\theta)\pm F_2(ka,\theta)$, where $F_m(ka,\theta)=\sum_{n=0}^{\infty}A_n{}^m j_{2n+m}(ka\sin\theta)$, are published in Rep. Res. Inst. (B-Elect. Comm.) Tohoku Univ. **10** (1958) 1, with the aids of which various physical quantities can be calculated.

Page	Column	Line	Equation		should be read
297		28		$J_{0y}=\mp\frac{k}{\mu\omega}E_1\exp\cdots$	$J_{0y}=\mp\frac{k}{\mu\omega}E_1\cos\alpha\exp\cdots$
299		(Figs. 6, 7, 8, 9)	abscissa	$\rightarrow\frac{r}{a}$	$\rightarrow\left(\frac{r}{a}\right)^2$
300		5		energy flow on	energy flow in the case of $E_2=0$ on
300		8		$\frac{\partial\Pi_y}{\partial z}$	$\frac{\partial\tilde{\Pi}_y}{\partial z}$
300		11, 12	(62)	E_1^2	E_1
300		11, 12	(62)	D_n^s	$\tilde{D}_n^s$
300		12	(62)	$\sum_{s=0}^{\infty}(-i)^2$	$\sum_{s=0}^{\infty}(-i)^s$
300		(Fig. 10)	abscissa	0	0.25
300		14	(63)	D_n^s	$\tilde{D}_n^s$
301		2	(64)	D_0^0	$\tilde{D}_0^0$
301		2	(64)	A_0^0	$\tilde{A}_0^0$
302		8		$\frac{J_{m+2s}'(\rho\gamma)}{(\rho\gamma)^m}I_1$	$\frac{J_{m+2s}'(\rho\gamma)}{(\rho\gamma)^m\rho^m}I_1$
302		20		x and z	x and z_1
302		21		$\rho+(z_1+i)^2=$	$\rho^2+(z_1+i)^2=$

Errata

Diffusion Processes in Polymers under Irradiation; Polyvinyl Alcohol and CCl$_4$ System

By Tsutomu WATANABE

J. Phys. Soc. Japan **13** (1958) 1316

Page	Column	Line	Wrong	Corrected
1316	left	5	does	dose
1317	right	3 from the bottom	···shown Fig. 1.	···shown in Fig. 1.
1318	right	eq. (9)	$v=\sqrt{\frac{\partial I\bar{u}}{\beta}}$	$v=\sqrt{\frac{\delta I\bar{u}}{\beta}}$
1318	right	eq. (10)	$\frac{\partial r}{\partial t}=kv$	$\frac{\partial\gamma}{\partial t}=kv$
1318	right	eq. (11)	$\gamma''=\frac{r}{1+P_0\varepsilon r}$	$\gamma''=\frac{\gamma}{1+p_0\varepsilon r}$
1319	left	1	P_0	p_0
1319	left	10	P_0	p_0
1320	left	2 from the bottom	$\log\gamma$	$\log r$
1323	left	14	···degradation, or the sexuences···	···degradation, nor the sexuences···
1323	right	eq. (A.7)	$v_1=\frac{\delta Iu_1}{4\beta}r^2$	$v_1=\frac{\delta u_1}{2}r^2$
1324	left	eq. (A.8)	$v(1)=\frac{\delta Iu(1)}{4\beta}\cdot\varDelta r$	$v(1)=\frac{\delta u(1)}{2}\cdot\varDelta r$
1324	right	References 4)	A. Dhapiro	A. Chapiro
1324	right	References 5)	E. E. Shneider	E. E. Schneider

JOURNAL OF THE PHYSICAL SOCIETY OF JAPAN Vol 14, No. 2, FEBRUARY, 1959

Yields and Angular Distributions of Protons from $F^{19}(d, p)F^{20}$ and $F^{19}(d, p)F^{20*}$

By Kazuo ÔNO, Junji SHIMADA, Keiichi KURODA,
Osamu TANAKA, Hiromichi KAMITSUBO, Atsuko ITO,
Shigeya TANAKA and Minoru IMAIZUMI

Institute for the Solid State Physics, University of Tokyo

(Received October 3, 1958)

The reactions $F^{19}(d, p)F^{20}$ and $F^{19}(d, p)^{20*}$ have been studied with deuteron bombarding energy of 1.3 Mev to 2.0 Mev. Angular distributions of protons leaving F^{20} in 0.65 Mev excited state show a pronounced peak at about 60° over the entire deuteron energy range. On the other hand, those leaving F^{20} in the ground state vary with the deuteron bombarding energy and most of them show no peak in the forward direction and a large peak in the backward direction. The absolute yields of the reactions have been measured at $\theta_{cm}=54°$ and $\theta_{cm}=104°$ as functions of the bombarding energy. A marked difference in the energy dependence of the yields for the two reactions is noted. The yield for the reaction $F^{19}(d, p)F^{20}$ at $\theta_{cm}=104°$ shows a broad maximum centered at about 1.70 Mev deuteron energy, on the other hand that from the $F^{19}(d, p)F^{20*}$ reaction at $\theta_{cm}=54°$ shows a slow increase with increasing deuteron energy. These results at our bombarding energies show that the reaction $F^{19}(d, p)F^{20}$ seems to proceed mostly by compound nucleus formation and the reaction $F^{19}(d, p)F^{20*}$ (0.65 Mev) seems to be caused by the stripping process of *d* neutrons.

§ 1. Introduction

The angular distributions of the proton groups from the reactions $F^{19}(d, p)F^{20}$ and $F^{19}(d, p)F^{20*}$ (0.65 Mev level) have been investigated by many authors. The $F^{19}(d, p)F^{20}$ reaction is of particular interest because of the possibility of determining the spin of the ground state of F^{20}. Bromley et al[1] at Rochester University measured the angular distributions of the protons from the reactions using 3.6 Mev deuterons. From the results they concluded that the proton group leaving F^{20} in the ground state could be interpreted as a mixture of $l_n=0$ and $l_n=2$ stripping. The results fix the spin of F^{20} definitely as 1 which would be in disagreement with data from β decay.[2],[3] However, their statistical error was rather large and angular distributions in the backward direction ($\theta_{cm}>100°$) were not measured. After that, the same reaction was also investigated by Takemoto et al[4] with 0.75–1.45 Mev deuterons and by Black[5] with 14.3 Mev deuterons. These two results can not determine whether F^{20} in the ground state is formed by capturing *s*-neutron or not, because in Takemoto's experiment the proton angular distributions are nearly isotropic, and in the other the angular distribution has been measured from 20 to 100 degrees, which indicates only the existence of captured *d* neutrons. Subsequently, El Bedewi[6] observed the angular distributions from 21 excited states of F^{20} using 8.9 Mev deuterons but could not observe that of the ground state because of low intensity.

Recently, two experiments have been made by Ôno et al[7] with 2.03 and 1.92 Mev deuterons and Seward et al[8] with 4.52, 3.82 and 3.52 Mev deuterons, in order to probe the angular distribution characterized by two l_n values, which were obtained by Bromley et al. These results showed no peak near 0° and a large peak in the backward direction. According to their results, the reaction may proceed by compound-nucleus formation and the interpretation of the results of the earlier experiments in terms of Butler-type simple stripping reaction may be unjustified.

The present investigation extends our previous measurements to the lower deuteron energy of 1.3 Mev. Six angular distributions were obtained in the range of deuteron bombarding energy from 1.3 Mev to 2.1 Mev. In order to confirm the compound nucleus formation in the reaction, excitation curves at $\theta_{cm}=54^\circ$ and $\theta_{cm}=104^\circ$ were also obtained in this deuteron energy range.

The angular distributions of protons from the reaction $F^{19}(d,p)F^{20}$ (0.65 Mev) have also been reported by many authors.[1),4),5),6),8)] These results were in good agreement with each other and showed the typical Butler-type stripping peak corresponding to the capture of *d* neutrons. Our present results both from the angular distributions and the excitation curves in $F^{19}(d,p)F^{20*}$ confirm also that the stripping process is dominant in the reaction at our bombarding energies.

§ 2. Appratus

The deuteron beam of the present work was supplied from the 16 inches variable energy cyclotron reported elsewhere[9)]. Analyzed beam currents in excess of 0.1 microamperes are focused at the center of the reaction chamber through a 3 mm second slit, at a distance of about four meters from the cyclotron. The focused beam has an energy spread of about 0.4% (calculated but not yet measured). The absolute errors in the deuteron energies are considered to be ±50 kev and the relative ones are estimated to be within ±10 kev.

The target was prepared by evaporation of PbF_2 onto a thin gold foil. The thickness of the target is 30 kev for 5.3 Mev P_0 alpha particles. Ag absorbers of 15 mg/cm² thickness were employed to prevent any deuterons from reaching to the detector. The current collected in the absorber was measured by a direct current amplifier and recorder which has an accuracy better than 5%. The protons emitted, after passing through the absorbers of Ag, were detected in 50 micron Sakura nuclear plate.

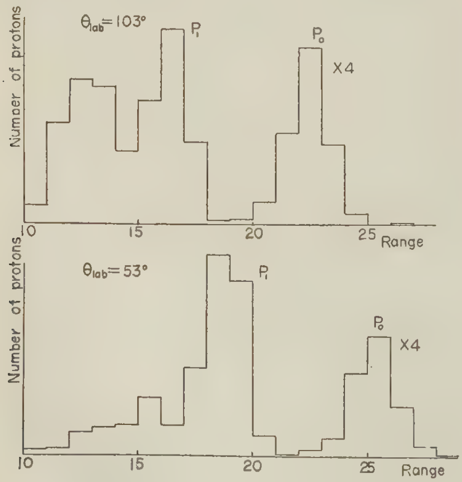

Fig. 1. The spectra of proton emergence at $\theta_{lab}=53^\circ$ and $\theta_{lab}=103^\circ$ for deuteron energy of 1.85 Mev. P_0 and P_1 correspond to protons leaving F^{20} in the ground state and in 0.65 Mev excited state respectively.

§ 3. Results and Discussions

Data on the angular distributions were ob-

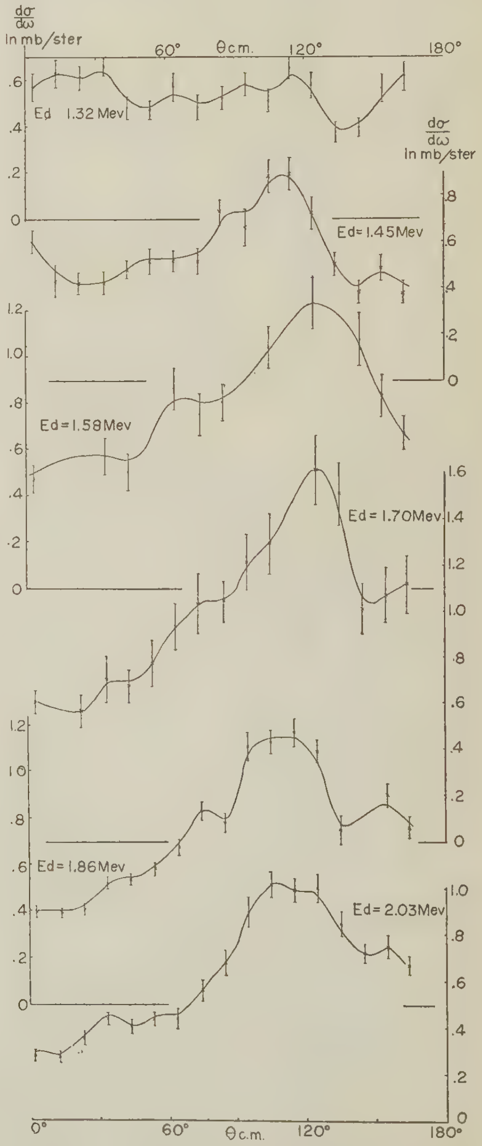

Fig. 2. Angular distributions of the proton from $F^{19}(d,p)F^{20}$ for various bombarding energies in the C.M. system.

tained in 10-degree intervals from −10 to 160 degrees. The spectra of proton emerging at $\theta_{lab}=53°$ and $\theta_{lab}=103°$ for deuteron energy of 1.85 Mev are shown in Fig. 1. Proton groups of P_0 corresponding to the first excited state were fairly well resolved.

$F^{19}(d, p)F^{20}$—The angular distributions of P_0 at laboratory deuteron energies of 1.32, 1.45, 1.58, 1.70, 1.86 and 2.03 Mev are shown in Fig. 2.

The expected stripping maximum at zero degree is not observed. A small peak at about 60 degrees for deuteron energies of 1.45, 1.58, 1.70 and 1.86 Mev may perphaps bear significance of the stripping process of *d* neutrons, which have been observed by Black at $E_d=14.3$ Mev. Here, the most striking aspect of the curves is a large and broad peak in the backward direction and a strong energy dependency of their shapes. Although the low energy angular distributions measured by Takemoto et al at bombarding energies of 1.45, 1.20, 1.00 and 0.65 Mev show rather flat curves and do not show a backward maximum, their results continue smoothly to our curve obtained at $E_d=1.36$ Mev. A broad backward peak and a strong energy dependency of the shape in the angular distributions have also been found at the bombarding energies of 4.13, 3.82 and 3.53 Mev by Seward et al.[8)]

The absolute yields at $\theta_{cm}=54°$ and $\theta_{cm}=104°$ are shown in Fig. 3. The yield at $\theta_{cm}=104°$ shown a broad maximum centered at about 1.7 Mev. It should be noted that protons emitted have maximum intensity near 100°.

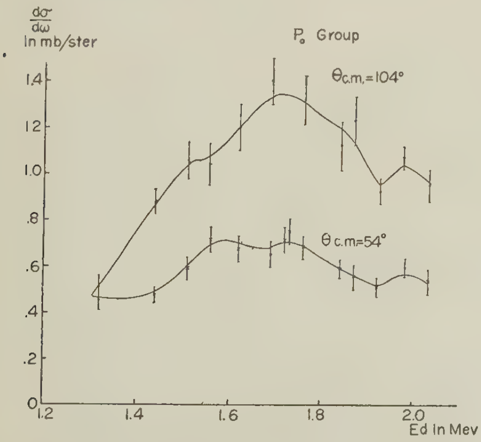

Fig. 3. Absolute yields for $F^{19}(d, p)F^{20}$ for protons emitted at 54° and 104° with respect to the incident deuteron direction.

These results show that the stripping process can not account for these distributions and yields, but compound nucleus formation plays a strong role. This may be due to a small overlapping between the states of F^{19} and F^{20}.

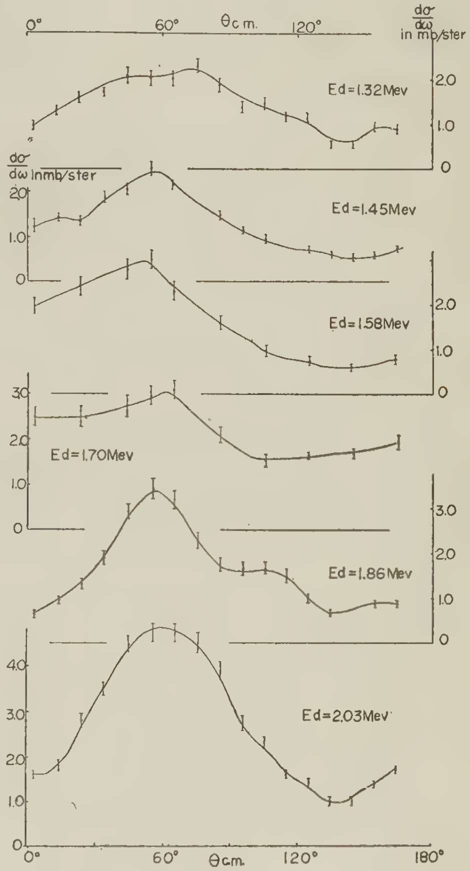

Fig. 4. Angular distributions of proton from $F^{19}(d, p)F^{20*}$ (0.65 Mev) for various bombarding energies in the C.M. system.

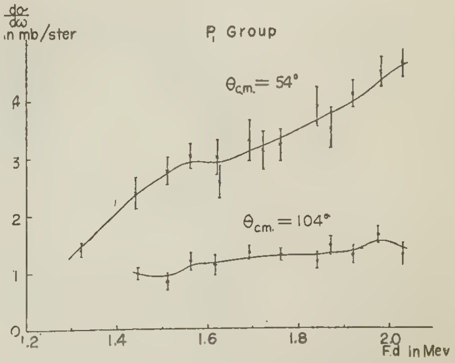

Fig. 5. Absolute yields for $F^{19}(d, p)F^{20*}$ (0.65 Mev) for protons emitted at 54° and 104° to the incident deuteron direction.

From the results obtained by us and by Seward et al, the spin of the ground state F^{20} is not necessarily 1 and the earlier interpretation in terms of stripping is unjustified.

$F^{19}(d, p)F^{20*}$ (0.65 Mev)—The angular distributions and the absolute yields of the reaction are shown in Fig. 4 and Fig. 5 respectively. All of the distributions show similarly a large peak at about 60° and the forward peak becomes more remarkable with increasing deuteron energy. This indicates that most of the cross section is due to stripping, in agreement with the results obtained hitherto by many authors.1),4) The yield at $\theta_{cm}=54°$, corresponding to the stripping peak, shows a slow increase with increasing the bombarding energy. This circumstances can be also interpreted that the reaction proceeds mostly by stripping process. Small peaks in the yield curve and some difference in shape between the six angular distributions may be due to some contribution from compound nucleus formation.

Acknowledgements

The authors are indepted to Professor T. Muto and Professor H. Kumagai for valuable discussions. We also thank to Mr. Y. Wakabayashi of Konishiroku Photo Manufacturing Co. for supplying nuclear plates for us.

References

1) D. A. Bromley, J. A. Bruner and H. W. Fulbright: Phys. Rev. **89** (1953) 396.
2) D. E. Alburger: Phys. Rev. **88** (1952) 1257.
3) C. Wong: Phys. Rev. **95** (1954) 761.
4) S. Takemoto, T. Dazai, R. Chiba, S. Suganomatsu and S. Ito: Phys. Rev. **101** (1956) 772.
5) C. F. Black: Phys. Rev. **90** (1953) 381. Ph. D. Thesis, Massachusetts Institute of Technology 1953 (unpublished).
6) E. A. El Bedewi: Proc. Phys. Soc. (London) **A 69** (1956) 221.
7) K. Ôno, J. Shimada, K. Kuroda and S. Tanaka: J. Phys. Soc. Japan **12** (1957) 745.
8) F. D. Seward, I. Slaus, H. W. Fulbright: Phys. Rev. **107** (1957) 159.
9) H. Kumagai, K. Ôno, S. Shono, I. Hayashi, K. Kuroda and M. Imaizumi: J. Phys. Soc. Japan **14** (1958) 1.

JOURNAL OF THE PHYSICAL SOCIETY OF JAPAN Vol. 14, No. 2, FEBRUARY, 1959

Elastic and Inelastic Scattering of 14.1-MeV Protons by Medium Weight Nuclei

By Ken KIKUCHI*, Shinsaku KOBAYASHI and Kazuhisa MATSUDA

Institute for Nuclear Study, University of Tokyo,
Tanashi-Machi, Tokyo

(Received November 1, 1958)

The absolute differential cross sections for the elastic scattering and the inelastic scattering (proceeding to the 1st excited state) of 14.1 Mev protons have been measured for Ni, Fe, Cr and Ti with a five-degree (or less) interval ranging from 20 to 165 degrees. The scattered protons were detected by NaI (Tl) scintillation counter whose energy resolution was about 2.3%. Even at small angles the protons inelastically scattered could be discriminated from those elastically scattered. The angular distributions of inelastic protons agree to that expressed by $|j_2(qR)|^2$ which one would expect from the theoretical prediction based upon the Born approximation.

§ 1. Introduction

Recently theoretical investigations on the inelastic scattering of nucleons by complex nuclei have been made by many authors on the basis of the direct interaction between the incident nucleon and the target nucleus. It is generally considered that the contribution of the direct interaction is most remarkable when the residual nucleus is left at low-lying excited states. In fact a number of measurements[1,2,3] on the angular distribution of protons inelastically scattered by light nuclei have resulted in giving marked forward peaks in contrary to that proposed by the statistical assumption of nuclear reaction. However, most of these experimental results are not in agreement with the simple calculation of the direct process on the assumption of the Born approximation. Moreover, some of these in the low energy region[5] show strong resonance behaviour depending on a small change of the incident energy. Therefore it may be suggested that the theoretical prediction based on the Born approximation has better validity when the incident energy becomes so large that any explicit resonance phenomena does not take place. It is the case when medium weight nuclei are bombarded by nucleons of moderate energy, for which few measurements have been made. One of these works is that made with 17 Mev porton beam at Princeton,[4] in which the angular distribution of proton group corresponding to the 1st excited state of iron nucleus is observed. From this measurement, however, one may not obtain the conclusion on the validity of the Born approximation, because large errors are contained in the measurements at extreme forward angles where the yield from the Rutherford scattering dominates over the inelastic protons concerned. There large errors come mainly from the rather small magnitude of the Q-value for the process, which makes it very difficult to discriminate the protons inelastically scattered from those elastically scattered. Therefore it seems to be worth while to investigate this point employing other target nuclei such as titanium, cromium or nickel, which have larger negative Q-values and have the ground and the excited states of the some nuclear spin 0^+ and

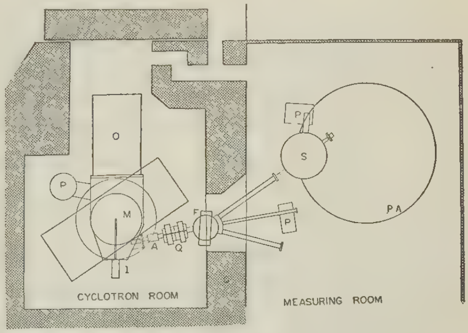

Fig. 1. Cyclotron and Scattering system.
M: magnet, O: oscillator, I: ion source,
P: vacuum pump, A: small vacuum can,
Q: quadrupole magnets, F: sector magnet,
C: concrete shielding, S: scattering chamber,
P.A: Pit for analyzer magnet.

---

* Now at University of Minnesota.

2^+ respectively as those of Fe^{56}. On the other hand, we have tried to make the resolution of the detecting system so high as to discriminate the inelastic protons in the forward angles.

§ 2. Apparatus and Design of the Experiment

The general feature of the experimental arrangement is shown schematically in Fig. 1. Fig. 2 shows the scattering chamber, together with the collimation system, and the detecting system.

1. *Production of the proton beam*

The proton beam is deflected by an A. C. deflector from I. N. S. cyclotron* and, passing through the magnetic shielding channel leaves the cyclotron chamber. Then it is focused by a pair of quadrupole magnets and is deflected by a sector magnet. The combined lens action of the quadrupole magnets and the sector magnet produces a beam spot about 5 mm wide and 10 mm high, whose intensity can be changed stably from 1 μ A to 0.01 μ A or less, before the collimator slits. The beam then passes through the collimator which has two defining apertures of graphite, 5 mm diameter and spaced 80 cm apart. To removed slit scattered protons from the beam, five graphite baffles each 7.5 mm in diameter are arranged as shown in Fig. 1. This collimator limits the beam size within 9 mm in diameter at the target position.

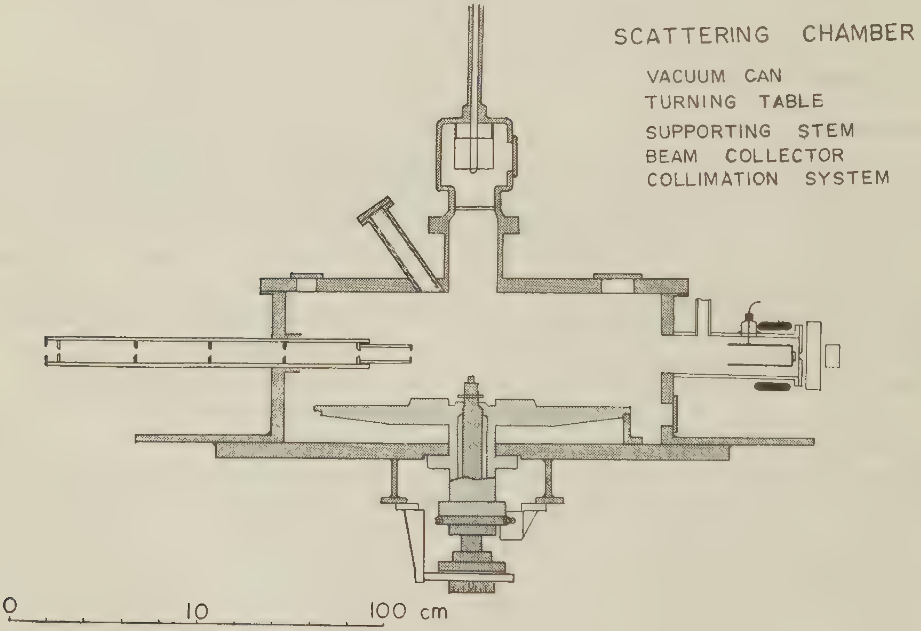

Fig. 2. Scattering chamber.

2. *Scattering chamber*

Details of the scattering chamber will be described elsewhere, so will mention here only the outline of it. It consists of a turning table on which the main detector is mounted, the target assembly and a vacuum can containing them. The turning table can be easily rotated around a fixed centre shaft which also supports the target assembly. The accuracy of the mechanical construction of the table system is such that the precision of the scattering angle is about 0.01 degree. The target can be supplied through an air lock from the center of the lid without breaking the chamber vacuum. The vacuum can has an inner diameter of nearly 100 cm and a height of 40 cm, whose side wall has 32 windows and entrance and exit holes. These windows allow us each 5 degree observations, but we used two of them for the monitor counters. The degrees of misalignment might be less than 0.3 mm per 100 cm.

---

* The construction report of this I.N.S. cyclotron will be published in this Journal in near future.

3. *Beam collector*

The unscattered beam is collected in the Faraday cup. In order to reduce the effects of secondary electrons, the collector cup is equipped with a couple of magnets which produce magnetic fields of about 300 gausses in vertical and horizontal directions. At the bottom of the cup an aperture, 3 mm in diameter, is equipped through which a part of the unscattered beam can be extracted from the vaccum and supplied into an ionization-chamber for the beam energy measurement which placed behind the cup. This aperture is closed with a small piece of permanent magnet during the cross-section measurement and can be opened by changing the polarity of the Faraday cup magnet.

4. *Energy of the incident beam*

The energy of cyclotron beam was maintained at 14.1 MeV, though our cyclotron, with its wide range magnet and variable frequency oscillator system, can offer proton beams of energies from 7.5 MeV up to 15 MeV to the scattering chamber without much intensity change.

The energy of the incident beam was determined by the measurement of, range in aluminium. The unscattered proton beam enters into an argon-filled shallow parallel-plate ionization chamber, after passing through the small aperture prepared at the bottom of the Faraday cup mentioned above. By changing the thickness of aluminium-absorbers placed in front of the ionization-chamber, one can measure the Bragg[6] curve, which determines the mean range of the incident beam.

The energy spread of the incident proton is estimated to be 0.5% or less from the spatial spread of the beam spot in front of the collimator after the deflecting magnet. The time variation of the energy is very difficult to be estimated but it may be less than 0.5% because the stability of the magnet is very high and the resonance condition of the cyclotron for the Faraday cup current is very sharp,—half width of the resonance is about 1.5 kilo cycles per sec. in part of 10 mega cycles per sec.

5. *Detector and electronics*

The scattered protons were detected by a NaI (Tl) crystal of dimension of about 18×18×1.4 mm, which was slightly thickner than the range of the protons. With this size of the crystal, the γ-ray back ground was generally negligible for protons of this energy range. But, when the detector was set at large scattering angles, a rather intense γ-ray back ground was observed because of the proximity to the beam collimator. However this back-ground was not so serions as to disturb the detection of protons concerned because γ-rays yield only small[7] pulses in such thin crystal. The detector slit was 5 mm in diameter, had a 7.5 mm baffle slit before it and was about 20 cm apart from the target.

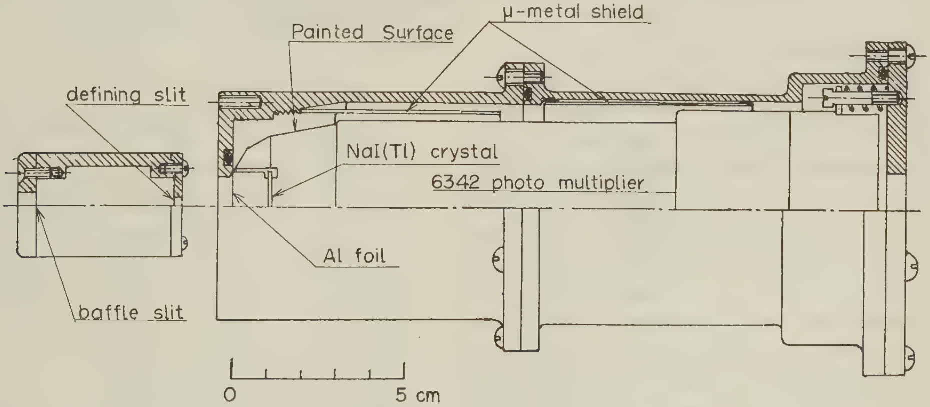

Fig. 3. Detector.

As can be seen from Fig. 3*, the crystal was supported by wires and placed inside an air-tight housing having a thin aluminium window for penetration of the protons. This housing, containing the photo-multiplier together, was filled with dry air at atmospheric pressure. The inner surface of the housing facing to the crystal was painted with titanium oxide paint for reflection of light.

---

* We owe this design to Professor A. Isoya.

The signal pulses, after passing through a cathod follower attached to the turning table in the scattering chamber, were sent to the counting room about 50 m apart from the measuring room. And after amplified by a linear amplifier the pulses were fed to a Jhonston type 10 channel pulse height analyser. All the electronic equipments were constructed in the electronics devision of our laboratory.

6. *Target*

With the exception of Cr foils, the target foils were obtained from commercial sources. Rolled foils of iron and titanium—about 5 μ thick—were considered to be quite uniform. The Cr foils were prepared by electroplating following the method of P. Kafalas et al.[6] The Cr foils had a contamination of oxygen but the others were fairly clear. The thickness of the nickel foil was about 1 mg/cm² and that of the cromium foil was about 0.5 mg/cm².

The areas of the foils used were measured to less than 1 per cent by direct measurement with a comparator. The weights were determined to 1 percent with a microbalance.

7. *Experimental procedure*

At each scattering angle where cross section was measured, the followings were recorded: the pulse height spectrum in the desired proton group, the number of elastically scattered protons observed in the 90° monitor counter and the charge collected in the Faraday cup during the time required for the spectral measurement. The counting time for each measurement was adjusted so that the statistical errors in the number of counts should be much less than the errors originating in the subtraction of back-ground. The counting rate was adjusted by controlling the beam intensity so that the counting loss may be much less than 1%. The target foils were fixed at 45° to the incident beam and the forward and the backward cross sections were measured without changing their inclinations. All the relative differential cross sections were determined with regard to the counts of the monitor counter and the absolute values were determined from the reading of the integrator.

Probable errors of the differential cross sections of elastic scattering were not more than 5%, which was mainly due to the inaccuracy of the integrator, the non-uniformity of target foils and some effects of the slit edge scattering.

Most errors of the inelastic cross section come from the back-ground subtraction especially in forward angles. Our procedure was as follows: we extended the rather constant back-ground at the lower energy side of the inelastic peak and, on the other hand, we also extended the lower energy tail of the elastic peak. Joining smoothly of these two curves, we obtained the back-ground spectrum to the inelastic peak when the yield and shape of the elastic peak played as some guide to the procedure. Then we estimated the possible upper and lower limit of these back ground and determined the probable errors of the inelastic cross sections.

§ 3. Results and Disscussions

1. *Elastic scattering*

To exhibit some of the regularities in the data, smooth curves fitted to the experimental points have been plotted in Figs. 4 through 7.

For elastic scattering in this energy region there are some data[7,8] by other investigators, one of which is also shown in Fig. 4 in comparison with ours. The behavior of both

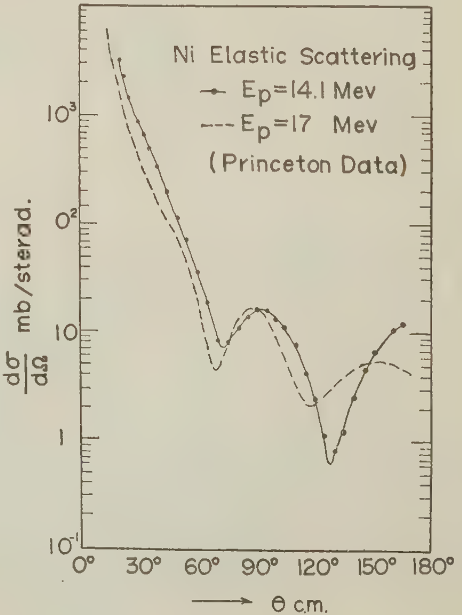

Fig. 4. The angular distribution of protons elastically scattered from Ni measured at E_p= 14.1 Mev.

curves is very similar and seems to agree with what one would expect from the picture of a incident wave scattered by a optical potential. Since the calculation based upon the five-parameters optical potential is very tedious and, as the matter of fact, can not be accomplished without using an electronic computer, has not been done. For iron, the angular distribution of 7.4 MeV protons was also observed in order to see the energy dependence of the elastic scattering phenomena. As can be easily seen from Fig. 5,

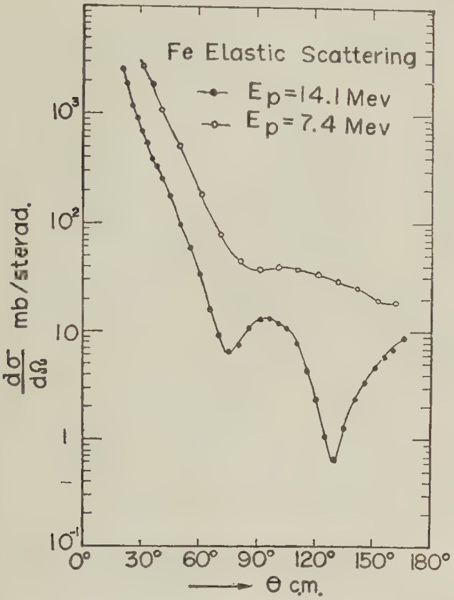

Fig. 5. The angular distributions of protons elastically scattered from Fe measured at $E_p=$ 14.1 Mev and 7.4 Mev.

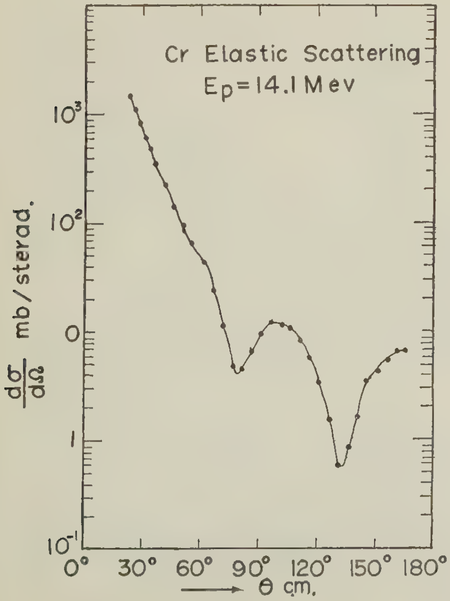

Fig. 6. The angular distribution of protons elastically scattered from Cr measured at $E_p=$ 14.1 Mev.

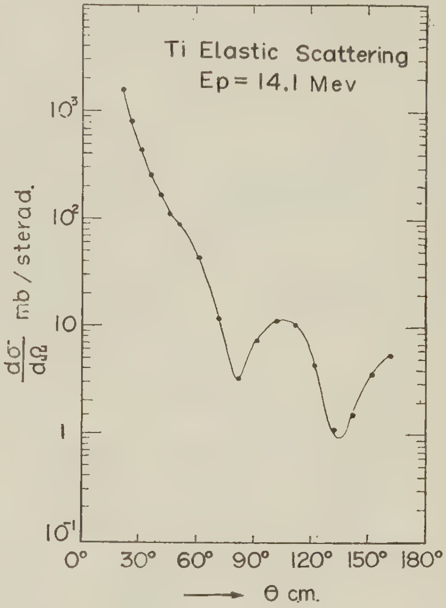

Fig. 7. The angular distribution of protons elastically scattered from Ti measured at $E_p=$ 14.1 Mev.

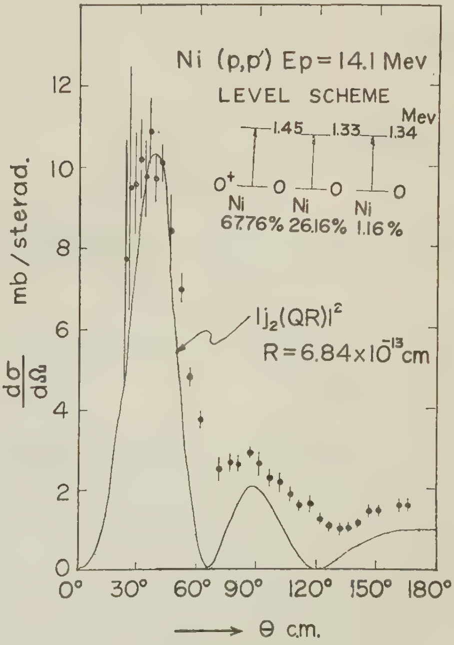

Fig. 8. The angular distribution of protons inelastically scattered from Ni ($Q \sim -1.4$ Mev) at $E_p=14.1$ Mev.

the energy dependence is remarkable but is a reasonable from the point of view that the incident beam is scattered by an optical potential with a Coulomb force. For energies between 7.4 MeV and 14 MeV further measurements are to be made.

2. *Inelastic scattering proceeding to the 1st excited state*

Because natural elements were used as targets, in some cases the observed proton groups included those corresponding to the 1st excited states of different isotopes. However, almost all of these levels have the same spin and parity 2^+, so the protons due to these levels are considered to give not very different angular distributions. In fact one can see from Figs. 8, 10 and 11 that the observed angular distributions are in fair agreement with those expected from the simple calculation based upon the Born approximation. If one adopts the Born approximation and assumes surface interaction as the base of the theoretical calculation, the angular distribution of protons in the $0^+ \rightarrow 2^+$ excitation can be fitted by the expression $|j_2(QR)|^2$ independent of the type of interaction.[9] Kajikawa, Sasakawa and Watari[10] calculated the angular distribution at 17 MeV for iron with distorted wave. Their results show no dip in forward direction, but our results can be fitted with the more simple approximation. Our procedure of back-ground substraction have some ambiguity and the experimental results do not

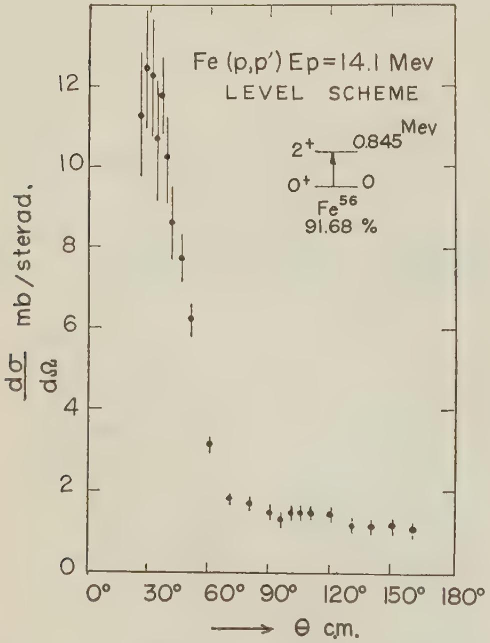

Fig. 9. The angular distribution of protons inelastically scattered from Fe ($Q = -0.845$ Mev) at $E_p = 14.1$ Mev.

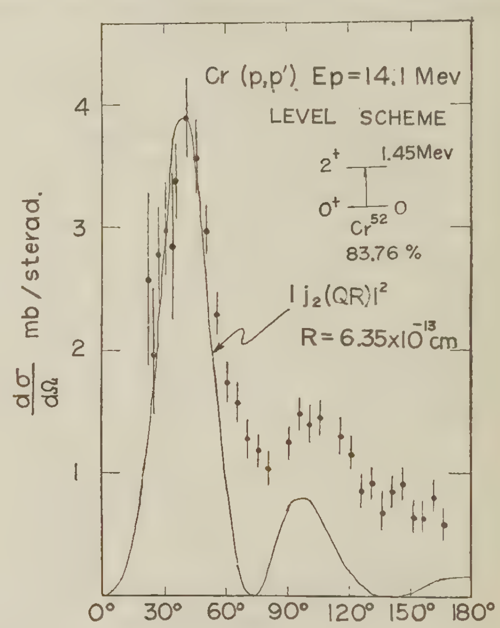

Fig. 10. The angular distribution of protons inelastically scattered from Cr ($Q = -1.45$ Mev) at $E_p = 14.1$ Mev.

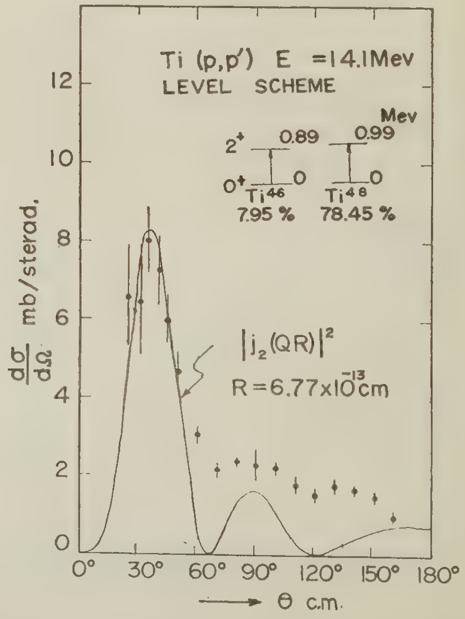

Fig. 11. The angular distribution of protons inelastically scattered from Ti ($Q \sim -1$ Mev) at $E_p = 14.1$ Mev.

completely exclude the possibility of monotonic increase of differential cross section as decreasing angle. But such case is considered to have very small probability to occur throughout these mass range and at this incident energy as can be seen from the figures. In order to obtain more accurate data at forward directions, we must look forward to the magnetic reaction-particle analyser which we are now preparing.

Moreover, we must mention the rather large differences of forward cross section between these nuclei. The peak cross section of cromium is less than half of the that of iron or nickel in spite of rather same elastic cross section at these small angle. We do not want however to deduce, a premature conclusion from this experimental results, but the neutron shell of Cr^{52} may play some part in this point. Backward structures of angular distributions are specific to each element. But, this may not be attributed to the effects of target contamination by light nuclei, because the positions are different from those calculated by kinematics.

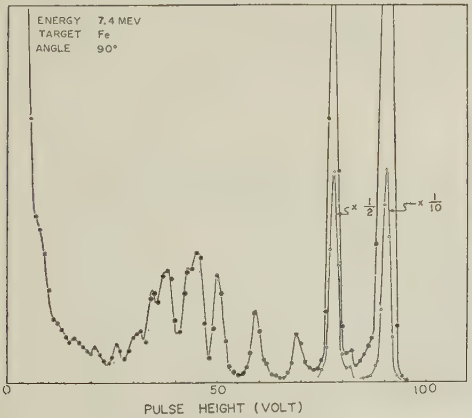

Fig. 12. Pulse-height distribution from scattering from Fe at the laboratory angle of 90° (E_p= 7.4 Mev).

3. *Other results*

We measured the emitted spectra of inelastic protons from iron at E_p=14.1 MeV and 7.4 MeV. The results are shown Figs. 12 and 13. We measured the spectrum of emitted protons at several angles when the incident energy was 14.1 MeV. There were no remarkable differences between the spectra at 60°, 90°, 120° and 150° except at low excitation energy and at γ-ray back-ground. We searched an anomalous inelastic scattering peak suggested by B. L. Cohen.$^{10)}$ We did not find any peak corresponding to the excitation of about 3 MeV region, but at about $Q=-4.5$ MeV we found rather large yield of inelastic scattering throughout all angular range. From the peak shape it seems to correspond to a few single levels. The differential cross section for this

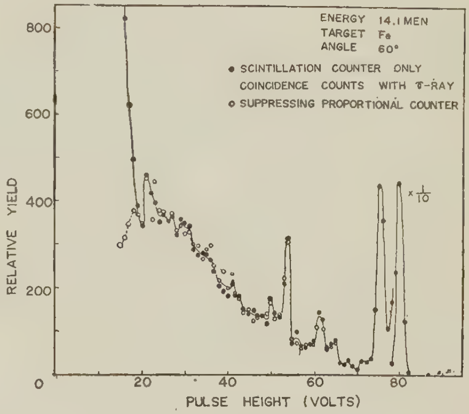

Fig. 13. Pulse-height distribution from scattering from Fe at the laboratory angle 60° (E_p=14.1 Mev).

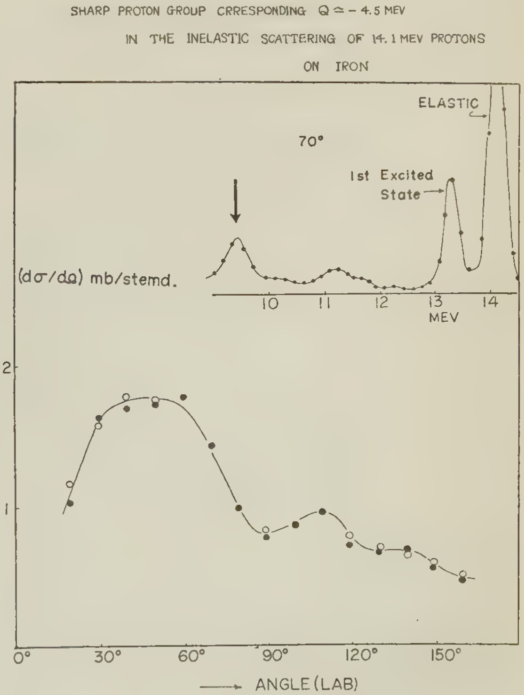

Fig. 14. Sharp proton group corresponding Q≃ −4.5 Mev in the inelastic scattering of 14.1 Mev protons on iron.

peak was measured and is shown in Fig. 14. Its angular distribution shows remarkable forwardness as the semi-classical calculation suggests.[11]

Acknowledgment

This work was performed as one of the test experiments of I.N.S. cyclotron and parts of the work were done by the temporal visiting physicists from other universities; Drs. K. Hisatake (Tokyo Institute of Technology) J. Muto (Kyoto University) I. Kumabe (Kyoto University) N. Ryu (Hiroshima University) and S. Yamabe (Osaka University) and Mrs. K. Takeshita (Kyushu University) Ito (Kyoto University) and Okano (Kyoto University). The authors wish to thank Professors S. Kikuchi and I. Nonaka for their constant encouragements; to Mr. S. Tanaka for advice on Cr foil Preparation.

They are also ought to say thanks to Mrs. T. Karasawa, A. Suzuki and H. Ogawa and other operating crew of the cyclotron.

References

1) R. W. Peelle: Phys. Rev. **105** (1957) 1311.
2) P. C. Gugelot and R. P. Phillips: Phys. Rev. **101** (1956) 1614.
3) R. G. Freemantle, D. J. Prowse, A. Hossain and J. Rotblat: Phys. Rev. **96** (1954) 1270.
R. M. Eisberg and N. M. Hintz: Phys. Rev. **103** 645 (1956).
4) G. Schrank, P. C. Gugelot and I. E. Dayton: Phys. Rev. **96** (1954) 1156.
5) M. Kondo and T. Yamazaki: J. Phys. Soc. Japan **13** (1958) 771.
S. Yamabe, M. Kondo, T. Yamazaki and A. Toi: ibid 777.
6) P. Kafalas and J. W. Irving Jr.: Phys. Rev. **104** (1956) 703.
7) I. E. Dayton and G. Schrank: Phys. Rev. **101** (1956) 1358.
8) B. B. Kinsey and T. Stone: Phys. Rev. **103** (1956) 975.
9) N. Autern, S. T. Butler and H. McManus: Phys. Rev. **92** (1953) 350.
S. Hayakawa and S. Yoshida: Progr. Theoret. Phys. (Japan) **14** (1955) 1.
10) R. Kajikawa, T. Sasakawa and W. Watari: Progr. Theoret. Phys. Japan **16** (1956) 152.
11) B. L. Cohen: Phys. Rev. **105** (1957) 1549.
B. L. Cohen and S. W. Mosko: Phys. Rev. **106** (1957) 995.
12) S. Hayakawa, M. Kawai and K. Kikuchi: Prog. Theor. Phys. **13** (1955) 415.

Journal of the Physical Society of Japan Vol. 12 No. 2, February, 1959

Thermodynamic Foundation of the Theory of Plasma

By Taro Kihara

Department of Physics, Faculty of Science, University of Tokyo

(Received October 30, 1958)

Thermodynamics of irreversible processes is applied to dense plasmas in a weak magnetic field. Basic equations of "magneto-thermo-hydrodynamics" are derived together with relations between transport coefficients. Extremely dilute plasmas and plasmas at the Debye-Hückel limit are discussed as particular cases.

§ 1. Introduction

In a previous article[1] entitled "Macroscopic Foundation of Plasma Dynamics" the author assumed, at the beginning, the Euler equation of motion for each plasma component. In this equation a role was played by the partial pressure whose existence was tacitly supposed. The treatment was also restricted to the case where the plasma temperature was uniform. Under these assumption and restriction the aim of that article was to consolidate, in an elementary way, the foundation for the plasma dynamics.

The present article is a thermodynamic approach to foundation of plasma theory or basis of so to speak magneto-thermo-hydrodynamics;

it will supplement the previous one.

The thermodynamics of irreversible processes, which has been developed since Onsager's reciprocity theorem, will be applied in the following to the phenomenological theory of plasma. Such a treatment does not seem to have existed up till now.

In the present article neither the existence of partial pressures nor the uniformity of the temperature is supposed. But we assume instead the following: (i) the plasma is nearly in thermal equilibrium; (ii) the magnetic field in the plasma is weak. Just as in the preceding article we consider a plasma composed of several species of charged and neutral particles in which neither ionization nor recombination occurs and no temperature difference exists between plasma components. For simplicity we assume this time that the viscosity is negligible.

§ 2. Equation of Motion for Plasma

Let n_j and $\boldsymbol{v}_j$ be, respectively, the number density and the flow velocity of jth component. Then the equation of continuity for the component is

$$\partial n_j/\partial t+\operatorname{div}(n_j\boldsymbol{v}_j)=0\,. \qquad (2.1)$$

Denoting by n_jm_j and n_je_j the mass and the charge densities of the jth component, respectively, we adopt the equation of motion

$$\sum n_jm_j\left(\frac{\partial}{\partial t}+\boldsymbol{v}\cdot\operatorname{grad}\right)\boldsymbol{v}$$
$$=\sum n_j[e_j(\boldsymbol{E}+c^{-1}\boldsymbol{v}_j\times\boldsymbol{B})+m_j\boldsymbol{g}]-\operatorname{grad}P$$

for the plasma as a whole. Here $\boldsymbol{v}$ is the average flow

$$\boldsymbol{v}=\sum n_jm_j\boldsymbol{v}_j/\sum n_jm_j \quad (\sum\equiv\sum_j \text{ throughout})\,,$$

$\boldsymbol{E}$ is the electric field, $\boldsymbol{B}$ is the magnetic flux density, $\boldsymbol{g}$ is the gravitaional acceleration, and P is the pressure. (The Gauss system of units is used, $c=3\times10^{10}$ cm/sec.)

By virtue of the assumptions (i) and (ii) in the preceding section, both $|\boldsymbol{v}_j-\boldsymbol{v}|^2$ and $(\boldsymbol{v}_j-\boldsymbol{v})\times\boldsymbol{B}$ are negligible. Hence the equation of motion can be rewritten in the form

$$\sum n_j\boldsymbol{F}_j-\operatorname{grad}P=0\,, \qquad (2.2)$$

where

$$\boldsymbol{F}_j\equiv e_j(\boldsymbol{E}+c^{-1}\boldsymbol{v}\times\boldsymbol{B})+m_j\left[\boldsymbol{g}-\left(\frac{\partial}{\partial t}+\boldsymbol{v}\cdot\operatorname{grad}\right)\boldsymbol{v}\right], \qquad (2.3)$$

and $\boldsymbol{E}+c^{-1}\boldsymbol{v}\times\boldsymbol{B}$ is the electric field in the coordinate system moving with the velocity $\boldsymbol{v}$.

One of our objectives is to "decompose" (2.2) and derive the equation of motion for each component. For this purpose we first transform, following Prigogine[3)], the term of grad P.

Let us start from two thermodynamic relations for the Gibbs function G for a system composed of N_j particles of jth species at the temperature T and the pressure P:

$$dG=-SdT+VdP+\sum\mu_jdN_j\,,$$
$$G=\sum N_j\mu_j\,.$$

Here V and S are, respectively, the volume and the entropy of the system; μ_j is the chemical potential per particle for jth species. From these two relations follows

$$\sum N_jd\mu_j=-SdT+VdP$$

or, per unit volume ($n_j=N_j/V$),

$$\sum n_j(d\mu_j+s_jdT)=dP\,. \qquad (2.4)$$

Here s_j is the entropy per particle,

$$s_j=-\left(\frac{\partial\mu_j}{\partial T}\right)_{P,\,\text{composition}}, \qquad (2.5)$$

the subscript "composition" indicating the derivative at constant relative concentrations, i.e. at constant $(\sum n_j)^{-1}n_i$'s. Hence,

$$\sum n_j\left[d\mu_j-\left(\frac{\partial\mu_j}{\partial T}\right)_{P,\,\text{composition}}dT\right]=dP\,. \qquad (2.6)$$

When the plasma is nearly in thermal equilibrium, we have therefore

$$\sum n_j(\operatorname{grad}\mu_j)_T=\operatorname{grad}P\,, \qquad (2.7)$$

where, in general,

$$(\operatorname{grad}\psi)_T=\operatorname{grad}\psi-\left(\frac{\partial\psi}{\partial T}\right)_{P,\,\text{composition}}\operatorname{gard}T\,. \qquad (2.8)$$

The equation of motion (2.2) has thus been transformed into

$$\sum n_j[\boldsymbol{F}_j-(\operatorname{grad}\mu_j)_T]=0\,. \qquad (2.9)$$

Its decomposition is equivalent to finding $\boldsymbol{R}_j$ $(\sum\boldsymbol{R}_j=0)$ in

$$n_j[\boldsymbol{F}_j-(\operatorname{grad}\mu_j)_T]+\boldsymbol{R}_j=0\,. \qquad (2.10)$$

§ 3. Entropy Production

The thermodynamics of irreversible processes is based on the Gibbs relation

$$TdS=dU+PdV-\sum\mu_jdN_j$$

for each small region of a system. Here dS, dU, dV and dN_j are, respectively, increments of the entropy, internal energy, volume, and number of particles of jth species in the small region. By use of the local time derivatives of the entropy density, s, and the density of the internal energy, u, the Gibbs relation can be transformed into a simple form

$$T\frac{\partial s}{\partial t}=\frac{\partial u}{\partial t}-\sum\mu_j\frac{\partial n_j}{\partial t}\,.$$

Now, $\partial u/\partial t$ is equal to the inflow of heat plus work done by electromagnetic, gravitational and inertia forces. Hence the time rate of increase of the entropy density s is given by

$$T\frac{\partial s}{\partial t}=-\mathrm{div}\,\boldsymbol{q}^*+\sum n_j\boldsymbol{v}_j\cdot\boldsymbol{F}_j-\sum\mu_j\frac{\partial n_j}{\partial t} \tag{3.1}$$

with the (absolute) heat flow $\boldsymbol{q}^*$, $\boldsymbol{F}_j$ being given by (2.3).

By virtue of (2.1) we get

$$\begin{aligned}&T^{-1}(-\mathrm{div}\,\boldsymbol{q}^*-\sum\mu_j\partial n_j/\partial t)\\&=T^{-1}[-\mathrm{div}\,\boldsymbol{q}^*+\sum\mu_j\,\mathrm{div}\,(n_j\boldsymbol{v}_j)]\\&=-\mathrm{div}\,T^{-1}(\boldsymbol{q}^*-\sum\mu_jn_j\boldsymbol{v}_j)-T^{-1}\boldsymbol{q}^*\cdot\mathrm{grad}\ln T\\&\quad-\sum n_j\boldsymbol{v}_j\cdot\mathrm{grad}\,(\mu_j/T)\,.\end{aligned}$$

Introducing the heat function per particle

$$h_j=\mu_j+Ts_j\,,$$

we have

$$T\,\mathrm{grad}\,(\mu_j/T)=(\mathrm{grad}\,\mu_j)_T-h_j\,\mathrm{grad}\ln T\,.$$

Thus (3.1) is transformed into

$$\frac{\partial s}{\partial t}=-\mathrm{div}\left(\frac{\boldsymbol{q}}{T}+\sum s_jn_j\boldsymbol{v}_j\right)+\left(\frac{\partial s}{\partial t}\right)_{\mathrm{irr}}, \tag{3.2}$$

$$\begin{aligned}T\left(\frac{\partial s}{\partial t}\right)_{\mathrm{irr}}&=-\boldsymbol{q}\cdot\mathrm{grad}\ln T\\&\quad+\sum n_j\boldsymbol{v}_j\cdot[\boldsymbol{F}_j-(\mathrm{grad}\,\mu_j)_T]\,,\end{aligned} \tag{3.3}$$

where

$$\boldsymbol{q}=\boldsymbol{q}^*-\sum h_jn_j\boldsymbol{v}_j$$

is the "reduced heat flow" due to conduction. Since $\boldsymbol{q}/T+\sum s_jn_j\boldsymbol{v}_j$ in (3.2) is the entropy flow, $(\partial s/\partial t)_{\mathrm{irr}}$ indicates the rate of entropy production due to irreversible processes. Eq. (3.3) holds when both factors of each summand are small in absolute values.

§ 4. Linear Relations

(a) *Equations of motion for components*

The linear relation between forces

$$-\mathrm{grad}\ln T\,,\quad n_j[\boldsymbol{F}_j-(\mathrm{grad}\,\mu_j)_T]$$

and fluxes

$$\boldsymbol{q}\,,\quad \boldsymbol{v}_j$$

can be expressed in the "mixed" form

$$\left.\begin{aligned}\boldsymbol{q}&=-K_{00}\,\mathrm{grad}\ln T+\sum_i K_{0i}\boldsymbol{v}_i\,,\\ n_j[\boldsymbol{F}_j-(\mathrm{grad}\,\mu_j)_T]&=-K_{j0}\,\mathrm{grad}\ln T+\sum_i K_{ji}\boldsymbol{v}_i\,.\end{aligned}\right\} \tag{4.1}$$

Here the phenomenological coefficients are scalars independent of forces or fluxes. It is to be noted that the magnetic field is included through $\boldsymbol{F}_j$, although it does not contribute to the work in (3.1) or (3.3). If it had not been included, the phenomenological coefficients would be tensors depending on the magnetic field.

Since the entropy production is always positive, the quadratic form for the coefficients is positive definite, in particular

$$K_{00}>0 \text{ and } K_{jj}>0 \text{ for any } j\,, \tag{4.2}$$

the thermal conductivity $\lambda\equiv K_{00}/T$ being positive. Onsager's reciprocity is, in the present case[4)],

$$K_{0j}=-K_{j0}\,,\quad K_{ji}=K_{ij}\,. \tag{4.3}$$

Taking the equation of motion (2.9) into account we know that

$$\sum K_{0i}=\sum K_{i0}=0\,,\quad \sum_i K_{ji}=\sum_i K_{ij}=0\,. \tag{4.4}$$

The second set of equations (4.1) gives the equation of motion of each component. The term $\boldsymbol{R}_j$ in (2.10) has thus been determined to be

$$\boldsymbol{R}_j=K_{j0}\,\mathrm{grad}\ln T-\sum_i K_{ji}\boldsymbol{v}_i\,,$$

or, by vertue of (4.4),

$$\boldsymbol{R}_j=K_{j0}\,\mathrm{grad}\ln T+\sum_i(-K_{ji})(\boldsymbol{v}_i-\boldsymbol{v}_j)\,. \tag{4.5}$$

This is an inner force composed of thermal diffusion and friction due to relative motion. The symmetry $K_{ji}=K_{ij}$ indicates Newton's law of reaction. For two-component plasmas the coefficient of friction $-K_{12}$ is always positive; but for many-component plasmas it is possible for some friction coefficients to be negative.

(b) *Electric and thermal conductivities*

When

$$\boldsymbol{g}-\left(\frac{\partial}{\partial t}+\boldsymbol{v}\cdot\mathrm{grad}\right)\boldsymbol{v}=0\,,$$

and

$$(\mathrm{grad}\,\mu_j)_T=0 \text{ for all } j\,,$$

(3.3) reduces to

$$T\left(\frac{\partial s}{\partial t}\right)_{\mathrm{irr}}=-\boldsymbol{q}\cdot\mathrm{grad}\ln T+\boldsymbol{J}\cdot\left(\boldsymbol{E}+\frac{\boldsymbol{v}}{c}\times\boldsymbol{B}\right)$$

with the electric current density $\boldsymbol{J}=\sum n_je_j\boldsymbol{v}_j$. The linear relation between forces ($-\mathrm{grad}\ln T$, $\boldsymbol{E}+c^{-1}\boldsymbol{v}\times\boldsymbol{B}$) and fluxes ($\boldsymbol{q}$, $\boldsymbol{J}$) can be expressed in the form

$$\left.\begin{aligned} \boldsymbol{q}&=-T\lambda\,\mathrm{grad}\ln T+\alpha\boldsymbol{J}\,,\\ \boldsymbol{E}+c^{-1}\boldsymbol{v}\times\boldsymbol{B}&=\alpha\,\mathrm{grad}\ln T+\sigma^{-1}\boldsymbol{J}\,.\end{aligned}\right\}\quad(4.6)$$

Here the phenomenological coefficients are scalars; and Onsager's reciprocity has been taken into account. The λ is the thermal conductivity, σ the electric conductivity; they are both positive. (When the plasma is a gas composed of electrons and positive ions, the sign of α is negative.)

In case T is uniform, the second equation of (4.6) reduces to the Ohm's law

$$\boldsymbol{E}+c^{-1}\boldsymbol{v}\times\boldsymbol{B}=\sigma^{-1}\boldsymbol{J}\,,\qquad(4.7)$$

which is one of the basic equations assumed in the *conventional* magnetohydrodynamics[5]. Essential contents of the magnetohydrodynamics, however, do not explicitly depend on the Ohm's law, but rather

$$\mathrm{rot}\,(\boldsymbol{E}+c^{-1}\boldsymbol{v}\times\boldsymbol{B}-\sigma^{-1}\boldsymbol{J})=0\,,\qquad(4.8)$$

which follows from (4.6) under much weaker restriction, namely if

$$\mathrm{rot}\,(\alpha\,\mathrm{grad}\ln T)\equiv\mathrm{grad}\,\alpha\times\mathrm{grad}\ln T=0$$

(cf. the following).

(c) *Induction equation in the magnetohydrodynamics*

When a neutral plasma is composed of electrons and several heavier species and all the heavier species have equal mean velocities (which are therefore close to $\boldsymbol{v}$), then (3.3) reduces to

$$T\left(\frac{\partial s}{\partial t}\right)_{\mathrm{irr}}=-\boldsymbol{q}\cdot\mathrm{grad}\ln T+n_e(\boldsymbol{v}_e-\boldsymbol{v})\cdot[\boldsymbol{F}_e-(\mathrm{grad}\,\mu_e)_T]\,,$$

where the subscript e refers to electrons and (2.9) has been used. The electric current is expressed by $\boldsymbol{J}=-en_e(\boldsymbol{v}_e-\boldsymbol{v})$ in which $-e$ is the electron charge. Neglecting the gravitational and inertia forces for electrons we obtain therefore

$$T\left(\frac{\partial s}{\partial t}\right)_{\mathrm{irr}}=-\boldsymbol{q}\cdot\mathrm{grad}\ln T+\boldsymbol{J}\cdot\left[\boldsymbol{E}+\frac{\boldsymbol{v}}{c}\times\boldsymbol{B}+\frac{1}{e}(\mathrm{grad}\,\mu_e)_T\right].$$

The corresponding linear relation is

$$\left.\begin{aligned}&\boldsymbol{q}=-T\lambda\,\mathrm{grad}\ln T+\alpha\boldsymbol{J}\,,\\ &\boldsymbol{E}+c^{-1}\boldsymbol{v}\times\boldsymbol{B}+e^{-1}(\mathrm{grad}\,\mu_e)_T\\ &\quad=\alpha\,\mathrm{grad}\ln T+\sigma^{-1}\boldsymbol{J}\,.\end{aligned}\right\}\quad(4.9)$$

Since the displacement current is negligible near the thermal equilibrium, the current density $\boldsymbol{J}$ is equal to $(c/4\pi)\,\mathrm{rot}\,\boldsymbol{H}$, $\boldsymbol{H}$ being the magnetic field. Then, the induction equation

$$\frac{\partial\boldsymbol{B}}{\partial t}=-c\,\mathrm{rot}\,\boldsymbol{E}$$

becomes

$$\frac{\partial\boldsymbol{B}}{\partial t}=\mathrm{rot}\,(\boldsymbol{v}\times\boldsymbol{B})-\frac{c^2}{4\pi}\,\mathrm{rot}\,(\sigma^{-1}\,\mathrm{rot}\,\boldsymbol{H})+\boldsymbol{a}\,,\qquad(4.10)$$

in which

$$\begin{aligned}\boldsymbol{a}&=\mathrm{rot}\,[e^{-1}(\mathrm{grad}\,\mu_e)_T-\alpha\,\mathrm{grad}\ln T]\\ &=\mathrm{rot}\,[(e^{-1}Ts_e-\alpha)\,\mathrm{grad}\ln T]\\ &=\mathrm{grad}\,(e^{-1}Ts_e-\alpha)\times\mathrm{grad}\ln T\,.\end{aligned}$$

Here s_e is the entropy per electron defined by (2.5); and (2.8) has been used. When and only when $\boldsymbol{a}$ vanishes, (4.10) takes the usual form of induction equation which plays an essential role in the magnetohydrodynamics. It is important to note that here no use has been made of the too-restrictive Ohm's law (4.7).

(d) *Ordinary and thermal diffusions*

When a neutral two-component plasma is under uniform pressure, and if

$$\frac{\boldsymbol{v}}{c}\times\boldsymbol{B}=0,\quad \boldsymbol{g}-\left(\frac{\partial}{\partial t}+\boldsymbol{v}\cdot\mathrm{grad}\right)\boldsymbol{v}=0\,,$$

then (3.3) reduces to

$$\begin{aligned}T(\partial s/\partial t)_{\mathrm{irr}}&=-\boldsymbol{q}\cdot\mathrm{grad}\ln T+\sum_{j=1,2}n_j\boldsymbol{v}_j\cdot[e_j\boldsymbol{E}-(\mathrm{grad}\,\mu_j)_T]\\ &=-\boldsymbol{q}\cdot\mathrm{grad}\ln T+\boldsymbol{J}\cdot[\boldsymbol{E}-e_1^{-1}(\mathrm{grad}\,\mu_1)_T]\,.\end{aligned}$$

The corresponding linear relation is again

$$\left.\begin{aligned}&\boldsymbol{q}=-T\lambda\,\mathrm{grad}\ln T+\alpha\boldsymbol{J}\,,\\ &\boldsymbol{E}-e_1^{-1}(\mathrm{grad}\,\mu_1)_T=\alpha\,\mathrm{grad}\ln T+\sigma^{-1}\boldsymbol{J}\,.\end{aligned}\right\}\quad(4.11)$$

The term $e_1^{-1}(\mathrm{grad}\,\mu_1)_T$ can be transformed into a symmetric form. From our assumptions

$$n_1e_1+n_2e_2=0\,,$$

$$n_1(\mathrm{grad}\,\mu_1)_T+n_2(\mathrm{grad}\,\mu_2)_T=0\,,$$

(the latter being the Gibbs-Duhem relation), follows

$$e_2(\mathrm{grad}\,\mu_1)_T=e_1(\mathrm{grad}\,\mu_2)_T\,,$$

and we obtain in fact

$$e_1^{-1}(\mathrm{grad}\,\mu_1)_T=(e_1-e_2)^{-1}[(\mathrm{grad}\,\mu_1)_T-(\mathrm{grad}\,\mu_2)_T]\,.$$

For $\boldsymbol{E}=0$, we have the equation of diffusion

$$\begin{aligned}\boldsymbol{v}_1-\boldsymbol{v}_2&=\boldsymbol{J}/n_1e_1\\ &=-\frac{\sigma}{n_1e_1^2+n_2e_2^2}[(\mathrm{grad}\,\mu_1)_T-(\mathrm{grad}\,\mu_2)_T]\\ &\quad-\frac{\alpha\sigma}{n_1e_1}\,\mathrm{grad}\ln T\,.\end{aligned}$$

Introducing the "modified" diffusion coefficient D^* and the thermal diffusion ratio k_T by

$$v_1-v_2=-D^*\left[\frac{1}{kT}\{(\mathrm{grad}\,\mu_1)_T-(\mathrm{grad}\,\mu_2)_T\}+\frac{(n_1+n_2)^2}{n_1n_2}k_T\,\mathrm{grad}\ln T\right], \qquad (4.12)$$

with the Boltzmann constant k, we obtain finally

$$D^*/kT=\sigma/(n_1e_1^2+n_2e_2^2), \qquad (4.13)$$

$$\frac{(n_1+n_2)^2}{n_1n_2}k_T=\frac{n_1e_1^2+n_2e_2^2}{n_1e_1}\frac{\alpha}{kT}. \qquad (4.14)$$

The former is a relation between the electric conductivity and the diffusion coefficient; such a relation is called the Einstein relation in general.

§ 5. Ideal-Gas Plasma

It is sometimes convenient to introduce the fugacity p_j^* which is related to the chemical potential μ_j by

$$\mu_j=\mu_j^+(T)+kT\ln p_j^*,$$

where $\mu_j^+(T)$ is a function of the temperature only. Then, by use of the definition (2.8), we have

$$n_j(\mathrm{grad}\,\mu_j)_T=(n_jkT/p_j^*)(\mathrm{grad}\,p_j^*)_T. \qquad (5.1)$$

For an extremely dilute plasma approximated by an ideal gas, the ratio p_j^*/n_jkT, which is called activity coefficient, is unity, and hence

$$(n_jkT/p_j^*)(\mathrm{grad}\,p_j^*)_T=(\mathrm{grad}\,P_j)_T=\mathrm{grad}\,P_j, \qquad (5.2)$$

where $P_j\equiv n_jkT$ is the partial pressure for jth component ($\sum P_j=P$). The term $\boldsymbol{a}$ in (4.10) is then calculated to be

$$\boldsymbol{a}=\mathrm{grad}\ln T\times\mathrm{grad}\,(e^{-1}kT\ln n_e+\alpha).$$

For ideal-gas plasmas holds a similarity law as stated in the previous article.

The modified diffusion coefficient D^* coincides, in the present case, with the conventional diffusion coefficient D defined by

$$v_1-v_2=-D(n_1^{-1}\,\mathrm{grad}\,n_1-n_2^{-1}\,\mathrm{grad}\,n_2), \qquad (5.3)$$

and (4.13) becomes

$$D/kT=\sigma/(n_1e_1^2+n_2e_2^2). \qquad (5.4)$$

An ideal-gas plasma at uniform temperature can be treated, as in the previous article, without assumptions (i) and (ii) made in § 1. Even the assumption that no temperature difference exists between plasma components can partially be removed. When the relaxation between temperatures of components is sufficiently slow, the partial pressure P_j, which is equal to the fugacity p_j^*, is given by n_jkT_j, T_j being the component temperature. If we define, instead of the diffusion coefficient D in (5.3), the coefficient δ by

$$v_1-v_2=-\delta[(kT_1/n_1)\,\mathrm{grad}\,n_1-(kT_2/n_2)\,\mathrm{grad}\,n_2],$$

then δ is related to the electric conductivity σ as

$$\sigma=(n_1e_1^2+n_2e_2^2)\delta,$$

which, in case $T_1=T_2=T$, reduces to (5.4) since $kT\delta=D$.

§ 6. Debye-Hückel Plasma

When a plasma is not far from an ideal gas, it can be treated in a similar way as in the Debye-Hückel[6)] theory of electrolytic solutions. Under the assumption that the constituent particles have no internal structure, the pressure P and the internal energy u per unit volume are given by the Debye-Hückel limiting law

$$P=kT\left(\sum n_j-\frac{1}{6}\frac{\kappa^3}{4\pi}\right),$$

$$u=kT\left(\frac{3}{2}\sum n_j-\frac{1}{2}\frac{\kappa^3}{4\pi}\right),$$

where κ is Debye characteristic constant defined by

$$\kappa^2=4\pi\sum n_je_j^2/kT. \qquad (6.1)$$

The condition for these relations to hold is that the Debye shielding length κ^{-1} is much larger than the mean distance $(\sum n_j)^{-1/3}$ between constituent particles. The fugacity p_j^* is calculated to be

$$p_j^*=n_jkT-\frac{1}{2}n_je_j^2\kappa, \qquad (6.2)$$

the activity coefficient for the jth component being $1-e_j^2\kappa/2kT$.

Debye-Hückel's elementary but ingenious theory on electrolytic solutions has been confirmed by Kramers[7)], Kirkwood[8)], and Mayer[9)] so far as the Debye-Hückel limiting law is concerned. One might however doubt the validity of the Debye-Hückel theory in the case of gaseous plasmas, because the plasma oscillation with the thermal energy is not explicitly considered. For treatment of thermodynamic properties, however, it is not necessary to separate a particular type of collective modes of motion. It is true, as Pines and Bohm[10)] have shown, that the motion of electrons can be divided, by use of the so-called random phase approximation, into collective motion known as plasma oscillation on one hand and individual particle motion with a type of shielded interparticle potential on the other. This shielding, however, is different from the Debye-Hückel shielding. It is also to be noted that the Debye-Hückel limiting law will not be derived from the random phase approximation, which may hold only for random motion of electrons.

The partial pressure P_j satisfying (5.2) does not exist in general for the Debye-Hückel plasma. In fact

$$\frac{n_j kT}{p_j^*}(\mathrm{grad}\, p_j^*)_T = \mathrm{grad}\,(n_j kT) - \frac{n_j e_j^2}{2T}\,\mathrm{grad}\,(\kappa T) + \frac{1}{3}\frac{n_j}{\sum n_j}\sum n_j e_j^2 \frac{\kappa}{T}\,\mathrm{gard}\, T\,.$$

No similarity law exists in general, too.

Let us finally consider a neutral two-component Debye-Hückel plasma at uniform temperature and pressure in order to find a relation between the modified diffusion coefficient D^* defined by

$$\boldsymbol{v}_1 - \boldsymbol{v}_2 = -(D^*/kT)[(\mathrm{grad}\,\mu_1)_T - (\mathrm{grad}\,\mu_2)_T]\,, \tag{6.3}$$

and the conventional D defined by (5.3). The chemical potential μ_1 is then a function of n_1 only, and

$$\left(\frac{\partial\mu_1}{\partial n_1}\right)_{T,P} = \frac{\partial\mu_1(n_1, n_2)}{\partial n_1} - \frac{\partial\mu_1(n_1, n_2)}{\partial n_2}\frac{\partial P(n_1, n_2)}{\partial n_1}\bigg/\frac{\partial P(n_1, n_2)}{\partial n_2}\,,$$

$\mu_1(n_1, n_2)$, $\mu_2(n_1, n_2)$ and $P(n_1, n_2)$ being the chemical potentials and the pressure, respectively, at that temperature. Since

$$\frac{\partial\mu_1(n_1, n_2)}{\partial n_1} = \frac{kT}{n_1} - \frac{\pi e_1^4}{\kappa kT}\,,$$

$$\frac{\partial\mu_1(n_1, n_2)}{\partial n_2} = -\frac{\pi e_1^2 e_2^2}{\kappa kT}\,, \quad \text{etc.,}$$

we have, neglecting the square of a small quantity,

$$\left(\frac{\partial\mu_1}{\partial n_1}\right)_{T,P} = \frac{1}{n_1}\left[kT - \frac{\pi n_1 e_1^2(e_1^2 - e_2^2)}{\kappa kT}\right]$$

or

$$\left(\frac{\partial\mu_1}{\partial n_1}\right)_{T,P} = \frac{1}{n_1}\left[kT - \frac{\kappa}{4}\,\frac{n_1 e_1^2(e_1^2 - e_2^2)}{n_1 e_1^2 + n_2 e_2^2}\right].$$

Taking $n_1 e_1 \approx -n_2 e_2$ into account we obtain

$$\left(\frac{\partial\mu_1}{\partial n_1}\right)_{T,P} = \frac{1}{n_1}\left[kT - \frac{\kappa}{4}e_1(e_1 + e_2)\right],$$

from which follows, at a constant pressure,

$$(\mathrm{grad}\,\mu_1)_T = [kT - \kappa e_1(e_1 + e_2)/4]n_1^{-1}\,\mathrm{grad}\, n_1\,.$$

Similarly

$$(\mathrm{grad}\,\mu_2)_T = [kT - \kappa e_2(e_1 + e_2)/4]n_2^{-1}\,\mathrm{grad}\, n_2\,.$$

From these expressions we obtain

$$(\mathrm{grad}\,\mu_1)_T - (\mathrm{grad}\,\mu_2)_T = [kT - \kappa(e_1 + e_2)^2/4](n_1^{-1}\,\mathrm{grad}\, n_1 - n_2^{-1}\,\mathrm{grad}\, n_2)\,, \tag{6.4}$$

Hence the relation

$$D = D^*[1 - \kappa(e_1 + e_2)^2/4kT] \tag{6.5}$$

holds between two definitions of the diffusion coefficient. These two coincide for $e_1 = -e_2$ i.e. fully ionized gas composed of electrons and one-valued ions.

In terms of the conventional diffusion coefficient D, (4.13) becomes

$$\frac{D}{\sigma} = \frac{kT - \kappa(e_1 + e_2)^2/4}{n_1 e_1^2 + n_2 e_2^2}\,. \tag{6.6}$$

It is interesting to note that the relation

$$(\mathrm{grad}\,\mu_1)_T - (\mathrm{grad}\,\mu_2)_T = kT(n_2^{-1}\,\mathrm{grad}\, n_1 - n_1^{-1}\,\mathrm{grad}\, n_2)$$

holds for the Debye-Hückel plasma, although the right-hand side does not depend on the Debye constant explicitly.

The author wishes to thank Dr. N. Hashitzume for many helpful comments.

References

1) T. Kihara: J. Phys. Soc. Japan **13** (1958) 473.

2) L. Onsager: Phys. Rev. **37** (1931) 405, **38** (1931) 2265.
See S. R. de Groot: *Thermodynamics of Irreversible Processes* (North-Holland, 1952).

3) I. Prigogine: *Etude Thermodynamique des Phénomènes irréversibles* (1947), p. 101.

4) H. B. G. Casimir: Revs. Modern Phys. **17** (1945) 343.
See S. R. de Groot: loc. cit. § 79.

5) For example, T. G. Cowling: *Magnetohydrodynamics* (Interscience, 1957).

6) P. Debye and E. Hückel: Phys. Z. **24** (1923) 185.

7) H. A. Kramers: *Collected Scientific Papers*, p. 361.

8) J. G. Kirkwood: J. Chem. Phys. **2** (1934) 767.
J. G. Kirkwood and J. C. Poirier: J. Phys. Chem. **58** (1954) 591.

9) J. E. Mayer: J. Chem. Phys. **18** (1950) 1426.

10) D. Pines and D. Bohm: Phys. Rev. **85** (1952) 338.

Journal of the Physical Society of Japan Vol. 14, No. 2, February, 1959

Hall Effect in Oxide Cathodes

By Tadaichi Yabumoto

Institute of Electronic Engineering, Shizuoka University, Hamamatsu, Japan

(Received September 6, 1958)

The measurement of Hall effect in oxide cathodes has been carried out in various methods of preparing samples.

The apparent electron mobility in a temperature range, 700°K∼1200°K, was about $10^3 \sim 10^4$ cm²/v. sec.

These values are very high as compared with that for a single crystal. The effect of porosity upon the mobility seems to exist to some extent, the porosity being changed by means of the different preparations and treatments of the cathodes.

From the viewpoint of pore conduction the mean free path of an electron is about $10^{-5} \sim 10^{-3}$ cm which seems to be of the same order with the size of pores existing in the actual oxide cathodes.

§ 1. Introduction

According to the hypothesis of pore conduction which was originally proposed by Loosjes and Vink the electric current in an oxide cathode at high temperatures is predominantly carried by the electron gas emitted into pores of the cathode.

Theories and experiments based on this model have been reported by several authors[1-4].

From this hypothesis the electron mobility is expected to be remarkably larger than that of an electron through the crystal because the mean free path of an electron will be of the same order of magnitude with the mean size of a pore.

As for the Hall effect in oxide cathodes, there have been several reports discussing both on the basis of semiconductor model and on this model[5-7].

In this paper, the Hall effect and conductivity were measured with samples of various porosity prepared by five methods* and some discussions were made.

§ 2. Experimental Procedure

Samples of different porosities were prepared by the following five methods.

(1) Oxide cathodes were treated with H_2O vapour. Oxide cathodes were heated at about 800°K for one hour in water vapour of about 10^{-2} mm Hg which was excluded by flashing the getter after the treatment and the oxide cathodes were then reactivated[8].

(2) Oxide cathodes were heated under low pressures of the air. After activation was accomplished, the oxide cathodes were exposed in the air and heated in its atmosphere of several mm Hg.

(3) Oxide cathodes were prepared by changing the ratio of BaO and SrO. The degree of sintering seems to vary with the composition of BaO and SrO. It has been known that sintering is most remarkable at 100% BaO. Samples with three kinds of composition were tested at molecular ratio of 50 : 50, 90 : 10, and 100 : 0 of BaO and SrO.

(4) $Ba\cdot Sr(CO_3)_2$ or $BaCO_3$ layers were pressed with high pressures in a mould and heated in vaccuum.

(5) Pressed $Ba\cdot Sr(CO_3)_2$ or $BaCO_3$ layers in in case (4) were heated at about 1200°C in the air.

By these processes we could get the oxide cathodes of different degrees of sintering.

The compositions and treatments of the samples are given in Table I.

The porosity of these samples could not be given quantitatively but appears to be larger in the order W 10–3, H 10–4, H 10–5, H 10–7, P 0–1, N 0–1. In the sample No–1 it was sintered visibly to a high degree.

These samples with the size of 2×1×2 mm were mounted between two platinum sleeves and two platinum probes for Hall voltage measurements were also inserted into these $Ba\cdot Sr(CO_3)_2$ coatings.

The structure of a experimental tube is

---

* These results were reported at the spring and the annual meetings of the Physical Society of Japan in 1953.

Table I. Sample's treatments and compositions

No. of samples	Treatments	Compositions
W 10–3	treated with H_2O vapour	$(Ba \cdot Sr)O_2$
H 10–4	exposed in the air and treated at its atmosphere of several mm Hg	$(Ba \cdot Sr)O_2$
H 10–5	treated with the same method as H 10–4	BaO 90% SrO 10%
H 10–7	normally processed	100% BaO contained 2∼3% $Ba(NO_3)_2$
P 0–1	pressed at high pressures at $BaCO_3$	100% BaO
N 0–1	treated in the air at about 1200°C	100% BaO

shown in Fig. 1.

Platinum sleeves and platinum probes were used to aboid the interface effect in the conductivity and Hall voltage meausements.

$Ba \cdot Sr(CO_3)_2$ was pressed by springs not to make cracks in the coating at the processing of oxide cathodes.

The cathode was heated by tungsten heaters inserted into the platinum sleeves.

High input impedance tube was necessary to measure the Hall voltage because the resistance between probes is above several megohms. For this purpose, tube 954 was used at a low plate voltage and the input voltage was applied to the third grid of that tube. The measuring circuit is shown in Fig. 2.

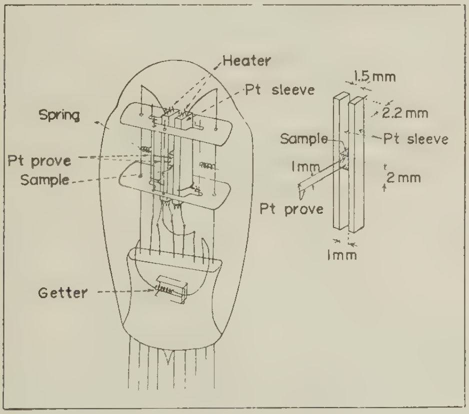

Fig. 1. The structure of experimental tube.

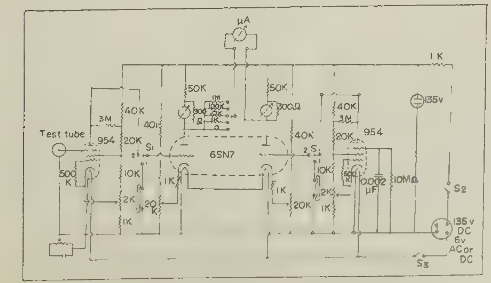

Fig. 2. Measuring circuit for Hall voltage.

In this circuit the input impedance was above 10 megohms. Hall voltage was amplified and measured by balancing method as shown in this figure.

The voltage across a sample was applied within a range where Ohm's law is valid.

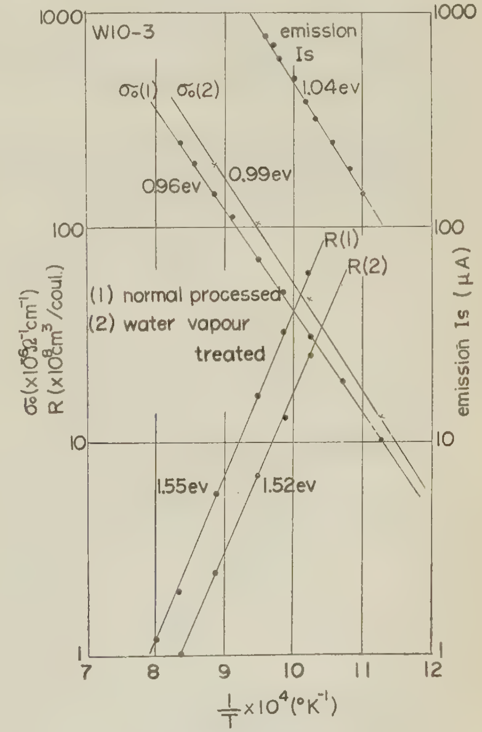

Fig. 3a. Temperature dependency of electrical conductivity σ_0 and Hall coefficient R.

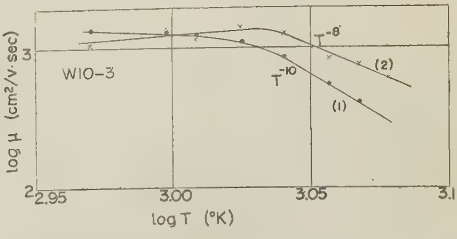

Fig. 3b. Temperature dependency of electron mobility.

The magnetic field up to 400 gauss was supplied by a solenoid and the higher field was by an electromagnet with iron core. Maximum field used was 1500 gauss.

Hall voltage and conductivity were measured in a temperature range of 700°K~1250°K. At the lower temperatures we could not measure the Hall voltage by this instrument because of the high resistance and noise from samples.

§ 3. Experimental Results

1. *Conductivity and Hall coefficient*

Hall coefficient was calculated by the equation

$$V_H = R\left(\frac{H\cdot I}{d}\right),$$

where V_H denotes the Hall voltage, H the applied magnetic field strength, I the electric current and d the thickness of the sample respectively.

The value of the Hall coefficient was obtained from the linear region of V_H/I vs. H curves. In these measurements the sign of Hall coefficient was always negative and mobility was obtained from $\mu = R\sigma_0$, where μ is the apparent mobility and σ_0 is the conductivity without magnetic field.

As an example σ_0, R and μ for W 10-3 were illustrated in Fig. 3. In this figure, (1)

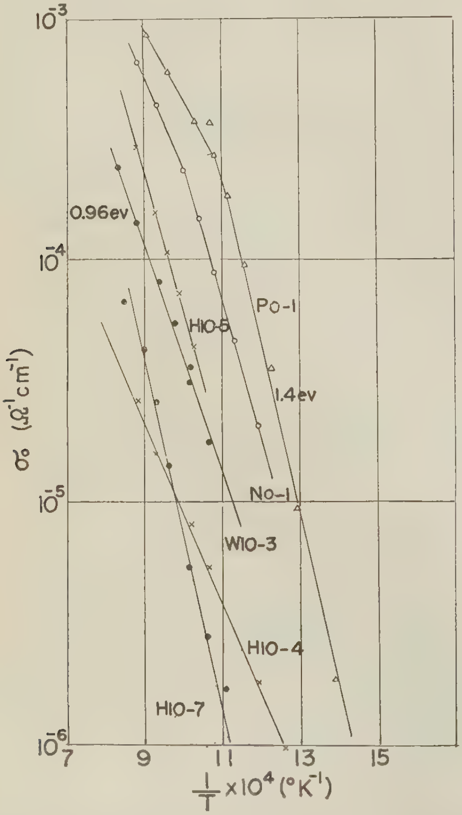

Fig. 4. Temperature dependency of conductivity for various samples.

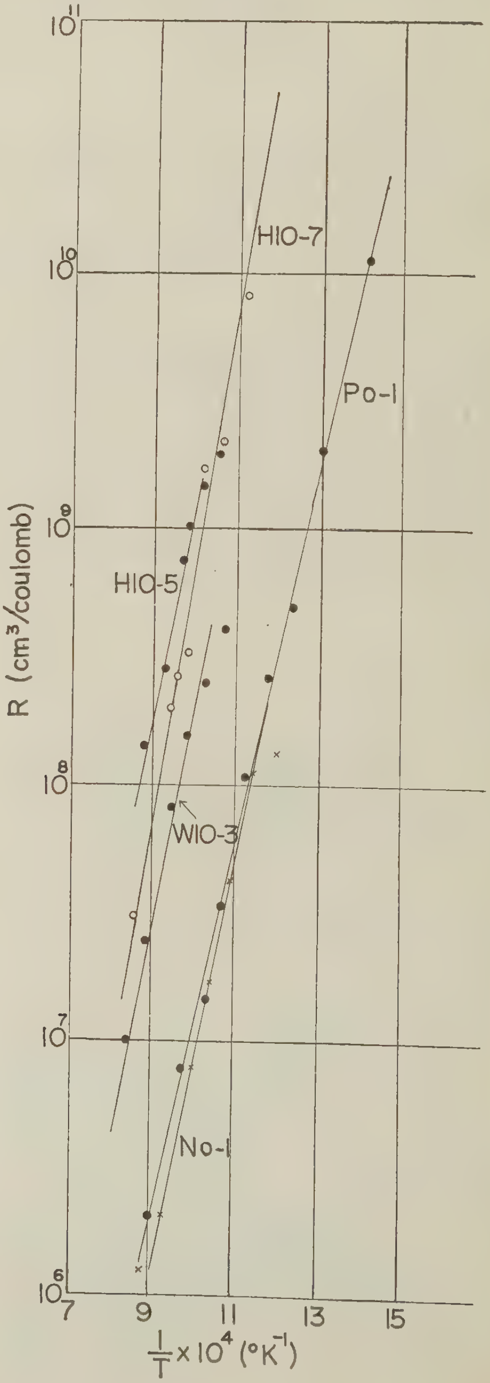

Fig. 5. Temperature dependency of Hall coefficinet for various samples.

is for the oxide cathode prepared by the normal method, (2) is for the one treated with water vapour by above mentioned method after measurement for case (1).

σ_0, R and μ vs. temperature curves for various samples are shown in Fig 4, 5 and 6 respectively.

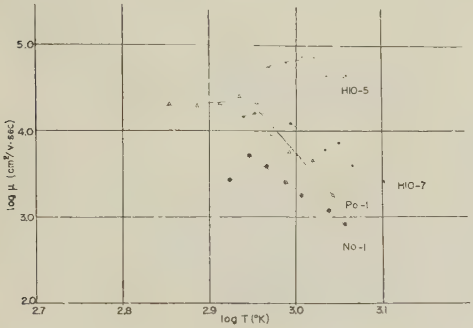

Fig. 6. Temperature dependency of electron mobility for various samples.

The maximum of the Hall coefficient vs. $1/T$ curve as seen by Forman[7)] did not appear as shown in Fig. 5.

The apparent value of μ is $10^3 \sim 10^4$ cm²/V. sec for various samples, which is higher by about three or four decades than that of a single crystal which is $3 \sim 9$ cm²/V. sec[9)].

The value of μ at various temperatures for different samples are given in Table II.

Table II. The apparent value of μ (cm²/V sec for some samples

Temperature (°K)	N 0–1	P 0–1	H 10–7	H 10–5
1123	8.55×10^2	1.77×10^3	4.30×10^3	4.27×10^4
1067	1.07×10^3	4.60×10^3	4.12×10^3	7.02×10^4
972	5.30×10^3	5.48×10^3	$8.8\ \times10^3$	6.13×10^4
932	3.89×10^3	9.12×10^3	6.37×10^3	5.67×10^4
890	5.32×10^3	1.97×10^4	$9.7\ \times10^3$	
824	2.76×10^3	1.83×10^4		

From this table the apparent mobility seems to have some correlations with the method of peparing samples and accordingly to the porosity of samples. For the samples like N 0–1 which is supposed to have a high degree of sintering, the mobility is relatively small. The Hall voltage has linear relations with magnetic field and current, but in some cases, for instance the porous specimen of equimolecular mixture of barium and strontium without treatment, showed an oscillatory behavior as shown in Fig. 7. Its sign is negative at low magnetic field and with increasing field varies alternately from negative to positive and from positive to negative. This fact will be understood on the aspect that electrons in a pore have long mean free paths corresponding to the mean size of pores and make a cyclic motion in the transverse magnetic field.

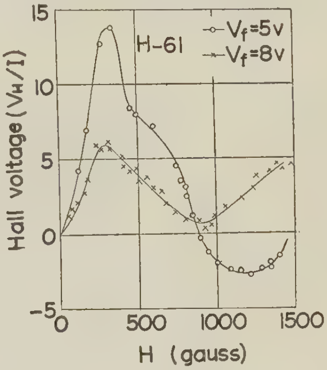

Fig. 7. An extraordinary change of Hall voltage with magnetic field.

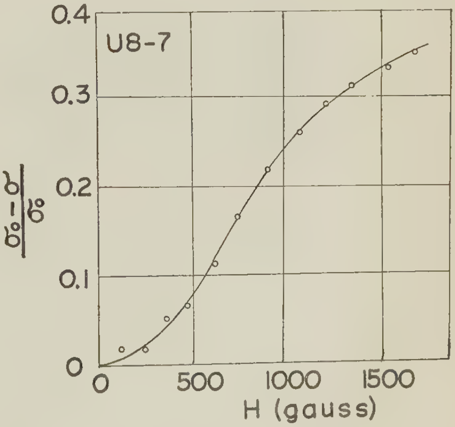

Fig. 8. The curve of magneto-resistive effect.

2. *Magneto-resistive effect*

The change of conductivity with transverse magnetic field is also very large as shown in Fig. 8. This fact has also been observed by other investigators[6–7)].

The relation of $\sqrt{\Delta\sigma/\sigma_0}$ vs. H is shown in Fig. 9 with the heater voltage as a parameter, where $\Delta\sigma=\sigma_H-\sigma_0$, σ_H being the conductivity with magnetic field and σ_0 the conductivity without magnetic field. This effect is more remarkable at high temperatures as shown in the figure.

This phenomenon is also explained by the pore conduction model for which the mean free path of an electron is large compared with that of an electron through the crystal and the temperature effect is explained by an idea that if the temperature was raised, the ratio of the conduction in a pore to the conduction in a bulk crystal will be increased and electrons will be more influenced by magnetic field.

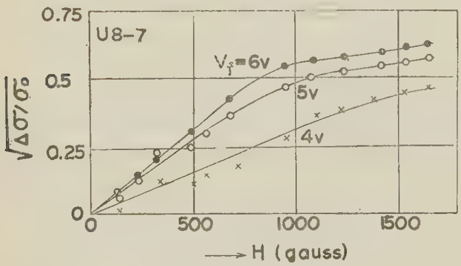

Fig. 9. The curve of $\sqrt{\Delta\sigma/\sigma_0}$ *vs. H.*

§ 4. Discussion

This remarkably large value of apparent mobility in oxide cathods compared with that of a single crystal can be considered reasonably from the pore conduction hypothesis. Instead, such a large mobility cannot be interpreted as the behavior of the electron in bulk of the polycrystalline. The effect of crystal boundary will be expected to lower the value of electron mobility through the crystal.

If we take the oxide grain to be a giant molecule which scatter isotropically the free thermal electrons in the pore, the conductivity, Hall coefficient and mobility are given by,

$$R=(3\pi/8)\cdot(1/ne)\ ,$$

$$\sigma=ne\mu,\ \ \mu=4el/3\sqrt{2\pi mkT}$$

where n is the number of electrons/cm³, and l is the meam free path which is of the order of the mean size of the pore. The number of electrons calculated from the Hall coefficient by this relation at various temperatures are given in Table III.

The number of electrons per cm³ are about $10^{11}\sim10^{12}$ at 1100°K and these values are similar to that of Ishikawa et al.[6]. The calculated values of the mean free path are given in Table IV.

These values of l are $10^{-5}\sim10^{-3}$ cm at 1000°K, varying with samples and estimated to be about the same as the size of a pore existing in the actual oxide cathodes.

In the sample N 0-1 it is especially small corresponding to the high degree of sintering.

Table III. The mean number of electrons per cm³ in the pores for some samples

Temperature (°K)	N 0-1	P 0-1	H 10-7	H 10-5
1125	5.1×10^{12}	3.09×10^{12}	6.24×10^{10}	4.4×10^{10}
1065	3.04×10^{12}	8.29×10^{11}	3.84×10^{10}	2.24×10^{10}
972	3.68×10^{11}	4.33×10^{11}	3.81×10^{9}	4.36×10^{9}
890	5.63×10^{10}	5.83×10^{10}	7.51×10^{9}	
824	4.68×10^{10}	1.23×10^{10}		

Table IV. The calculated value of mean free path l (cm)

Temperature (°K)	N 0-1	P 0-1	H 10-7	H 10-5
1125	5.93×10^{-6}	1.21×10^{-5}	3.27×10^{-5}	2.93×10^{-4}
1065	7.5×10^{-6}	3.07×10^{-5}	3.81×10^{-5}	3.02×10^{-4}
972	1.19×10^{-5}	3.51×10^{-4}	6.31×10^{-5}	3.95×10^{-4}
890	1.62×10^{-5}	1.27×10^{-3}	6.66×10^{-5}	
824	1.64×10^{-5}	1.12×10^{-3}		

§ 5. Conclusion and Acknowledgements

From the measurements of Hall coefficient and conductivity in a temperature range, 700K~1200°K, the apparent electron mobility in an oxide cathode is very large compared with that of a single crystal and the magnetoresistive effect is also large.

The difference of the preparation of samples, accordingly the difference of porosity seems to show some effects on the mobility. These facts can be reasonably explained by the pore conduction hypothesis and make this model more valid.

This work has been carried out at the Electrical Communication Laboratory, Nippon Telegraph and Telephone Public Corporation during his tenature of office.

The author wishes his sincere thanks to Mr. Yukio Kamiya for technical assistance and also his thanks to the members of electron physics of the E. C. L. for the corporation.

References

1) R. Loojes and H. J. Vink: Philips Res. Rep. **4** (1949) 449
2) E. B. Hensley: J. Appl. Phys. **23** (1952) 1122
3) J. R. Young: J. Appl. Phys. **23** (1952) 1129
4) R. C. Hughes and P. P. Coppola: Phys. Rev. **88** (1952) 364
5) D. A. Wright: Brit. J. Appl. Phys. **1** (1950) 150
6) Ishikawa, Sato, Okumura and Sasaki: Phys. Rev. **84** (1951) 371
7) R. Forman: Phys. Rev. **96** (1954) 1479
8) T. Yabumoto and Y. Kamiya: J. Appl. Phys. Japan **25** (1956) 374
9) .E. M. Pell: Phys. Rev. **87** (1952) 457

JOURNAL OF THE PHYSICAL SOCIETY OF JAPAN Vol. 14, No. 2, FEBRUARY, 1959

Transformation des Reseaux Metalliques sous l'Influence des Elements d'Insertion: Transformation du Nickel sous l'Influence de l'Azote

par Nobuzo TERAO et Aurel BERGHEZAN

European Research Associates, 95, rue Gatti de Gamond,
Uccle-Bruxelles/Belgium

(Received October 8, 1958)

A detailed study has been undertaken on the transformation of nickel lattices under the influence of nitrogen as an "insertion" impurity. For this study, thin polycrystalline and monocrystalline layers of evaporated nickel have been heated in an atmosphere of ammonia. This nitriding process has been followed kinetically by electron diffraction. Using these techniques, it has been shown that the "insertion" of nitrogen atoms takes place in successive steps. First, a considerable expansion of the initial f.c.c. lattice of nickel (from $a=3{,}52$ to $a=3{,}72$ Å) is observed with the formation of Ni_4N. Then, if the nitriding is continued, this f.c.c. lattice of expanded nickel (Ni_4N) is transformed into a hexagonal lattice of Ni_3N.

The exact structure of these nitrides has been determined and a mechanism of the transformation from the expanded cubic nickel lattice (Ni_4N) to the hexagonal nickel lattice (Ni_3N) has been proposed. This mechanism consists, in part, of a series of microslips on the (111) plane and in the $[11\bar{2}]$ direction of nickel atoms, similar to those produced in the martensitic transformation of cobalt, which transforms the stacking order of the {111} planes of the f.c.c. lattice into the stacking order of the {0001} planes of the hexagonal lattice. In addition, the diffusion of nitrogen results in another stacking transformation from the cubic $\{1\bar{1}0\}$ planes into the $\{1\bar{2}10\}$ planes of the hexagonal variety.

§ 1. Introduction

Il a été rapporté dans la littérature que, comme certains autres métaux, le nickel et le chrome, présentent également des transformations allotropiques. Ces nouvelles formes allotropiques sont actuellement de plus en plus considérées comme correspondant à de fausses transformations. C'est pourquoi, notre attention s'est portée sur cette question et c'est le nickel qui sera traité ici.

Normalement ce métal se présente sous la forme cubique à faces centrées, mais certains auteurs ont signalé une variété hexagonale compacte qui n'est plus ferromagnétique[1)~4)]. A l'intérêt théorique de cette transformation, un intérêt pratique a été associé, à savoir des propriétés catalytiques très différentes des deux variétés. Cependant, ces dernières années, la variété hexagonale a été de plus en plus mise en doute et il semble maintenant qu'elle soit en réalité une fausse transformation due à l'insertion dans le réseau du nickel d'atomes de carbone, d'azote et même d'hydrogène5)~12).

Ainsi, Le Clerc et Michel8) et Jacobson et Westgren7) ont montré par rayons X que l'insertion des atomes de carbone dans le réseau du nickel conduit à l'obtention d'une variété hexagonale, qui n'est autre que le carbure: Ni_3C. De son côte Nagakura14) a examiné plus en détail la formation et la décomposition du carbure de nickel et proposé un mécanisme pour cette transformation.

De même, K. H. Jack11) a montré par rayons X que l'insertion des atomes d'azote dans la maille du nickel conduit á une forme hexagonale compacte. Il a trouvé, en outre, quelques réflexions de sur-structure et conclu que la structure de Ni_3N est isomorphe avec celle de ε-Fe_3N et ε-$Fe_3(C, N)$, confirmant ainsi une conclusion antérieure de Sachsze et Juza9) basée sur l'observation d'une seule raie de sur-structure. Plus récemment, J. J. Trillat et ses collaborateurs13),16) ont étudié par diffraction électronique l'action de l'azote sur le nickel en utilisant deux méthodes, á savoir d'une part l'action directe de l'azote et d'autre part l'action d'ions provenant de l'air et produits par un canon à ions. Leurs résultats montrent que les atomes d'azote s'insèrent d'abord dans le réseau cubique à faces centrées du nickel et le dilatent considérablement, puis le transforment en un réseau hexagonal correspondant au nitrure: Ni_3N. En chauffant ce nitrure Ni_3N dans le vide, il redonne le nickel ordinaire de départ.

Dans le but d'apporter une contribution plus importante à ce problème de la transformation du nickel sous l'influence d'atomes d'azote, nous avons essayé dans ce travail de déterminer la structure exacte de la forme hexagonale finale: Ni_3N, celle de la forme intermédiaire dilatée signalée par Trillat et enfin, le mécanisme de cette fausse transformation allotropique sous l'influence d'atomes d'insertion.

§ 2. Méthode Expérimentale

L'action de l'azote sur le nickel a été effectuée en adoptant le procédé utilisé antérieurement par J. J. Trillat et l'un de nous13), par passage de gaz ammoniac séché sur des couches minces de nickel, polycristallines ou monocristallines, chauffées à des temperatures variables (150–300°C). Les couches minces de nickel ont été préparées par vaporisation sous vide sur support de sel gemme et leur épaisseur était d'environ 200–400 Å. La durée de la nitruration était comprise entre une et sept heures. Après refroidissement complet en atmosphère de NH_3, les préparations sont retirées du four et examinées par diffraction électronique par transmission.

§ 3. Résultats

I. Nitruration des couches minces de nickel polycristallin

1°) *Structure de la forme finale de nitruration*: Ni_3N

Comme dans les travaux précédents13),16) il a été trouvé que le nickel cubique se transforme par nitruration en une variété hexagonale qui n'est autre que le nitrure de nickel: Ni_3N. La cinétique de cette transformation a été suivie par de nombreux essais, qui ont montré que le degré de nitruration est assez variable avec les conditions expérimentales.

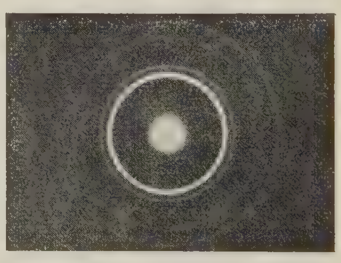

Fig. 1. Diagramme de diffraction électronique du nickel polycristallin.

Avant la nitruration, la couche mince de nickel est formée en général de très petits cristaux donnant des diagrammes de diffraction électronique aux anneaux continus assez élargis. La Fig. 1 montre un exemple de ces diagrammes. Ce nickel, c.f.c. de maille $a=3{,}52$ Å, se dilate fortement par nitruration jusqu'à atteindre la maille $a=3{,}72$ Å. Ensuite, en continuant la nitruration cette forme cubique dilatée se transforme en une variété hexagonale. Simultanément à cette dernière transformation, les anneaux de diffraction électronique deviennent fins et ponctués indiquant un grossissement important des cristaux. Les deux ou trois variétés peuvent coexister, mais, au fur et à mesure que la nitruration se

Tableau I. Résultats des mesures sur le Ni_3N.

N°	Diffraction électronique					Diffraction de rayons X*		
	Classification	Indice h k i l	Intensité	d_{obs} (Å)	d_{cal} (Å)	Indice hex. comp. h k l	Intensité	d_{obs} (Å)
1	i	(0001)	tf	4.311	4.305	(001)		
2	S	$10\bar{1}0$	f	3.992	3.990			
3	S	$10\bar{1}1$	m	2.925	2.928			
4	P	$11\bar{2}0$	M	2.310	2.304	100	m	2.32
5	P	0002	M	2.151	2.152	002	m	2.14
6	P	$11\bar{2}1$	F	2.031	2.032	101	tF	2.044
7	S	$20\bar{2}0$	f	1.995	1.996			
8	S	$10\bar{1}2$	m	1.892	1.897			
9	S	$20\bar{2}1$	m	1.810	1.808			
10	P	$11\bar{2}2$	F	1.572	1.573	102	F	1.569
11	S	$21\bar{3}0$	tf	1.509	1.507			
12	S	$20\bar{2}2$	tf	1.463	1.462			
13	i	(0003)	—	—	1.435	(003)		
14	S	$21\bar{3}1$	m	1.423	1.423			
15	S	$10\bar{1}3$	f	1.347	1.351			
16	P	$30\bar{3}0$	F	1.329	1.328	110	m	1.332
17	i	$(30\bar{3}1)$	f	1.270	1.270	(111)		
18	S	$21\bar{3}2$	tf	1.235	1.235			
19	P	$11\bar{2}3$	F	1.216	1.218	103	m	1.218
20	S	$20\bar{2}3$	tf	1.164	1.164			
21	P	$22\bar{4}0$	f	1.152	1.152	200	f	1.157
22	P	$30\bar{3}2$	M	1.131	1.132	112	m	1.132
23	P	$22\bar{4}1$	M	1.112	1.113	201	m	1.114
24	P	0004	m	1.073	1.071	004	f	1.074
25	S	$21\bar{3}3$, $10\bar{1}4$	f	1.037	1.040			
26	P	$22\bar{4}2$	f	1.014	1.017	202	f	1.017
27	S	$31\bar{4}2$	tf	0.982	0.982			
28	P	$11\bar{2}4$	m	0.972	0.975	104	f	0.9736
29	S	$20\bar{2}4$	tf	0.944	0.946			
30	S	$32\bar{5}0$	tf	0.913	0.915			
31	S	$40\bar{4}2$	tf	0.903	0.905			
32	P	$22\bar{4}3$	m	0.895	0.898	203	m	0.9005
33	P	$41\bar{5}0$	tf	0.869	0.869	210	tf	0.8738
34	P	$41\bar{5}1$	m	0.852	0.853	211	m	0.8560
35	P	$30\bar{3}4$	m	0.834	0.836	114	m	0.8382
36	P	$11\bar{2}5$	m	0.804	0.806	105		

* Données par R. Bernier (1951)—Réf. (10).

poursuit, les variétés cubiques disparaissent pour ne laisser apparaître en fin de compte que la variété hexagonale comme on peut le voir sur la Fig. 2 reproduisant le diagramme de diffraction du nickel après une heure de nitruration à 230°C. L'interprétation de ce diagramme sera notre premier objectif. Le Tableau I résume les mesures des 32 premiéres raies classées en trois groupes de réflexions. P=raies principales, *s*=raies de sur-structure et *i*=raies interdites. Au delà de ces 32 raies on ne mentionne dans le tableau que les raies principales. Les raies principales, toujours assez fortes, sont attribuées à la structure hexagonale compacte de paramètres:

$$a = 2.66_0 \text{ Å} ; \qquad c = 4.30_4 \text{ Å}$$

$$c/a = 1.618 .$$

Les réflexions "*i*" sont attribuées à la même maille bien qu'elles soient interdites pour la maille hexagonale compacte. Par contre, les raies "*s*" très faibles ne peuvent être attribuées à cette maille, mais à une maille supérieure toujours hexagonale de paramètres:

$$a_s = \sqrt{3}\, a = 4.60_7 \text{ Å} , \qquad c_s = c = 4.30_4 \text{ Å} .$$

Cette maille supérieure semble bien être une maille de sur-structure, dans laquelle les atomes de nickel et d'azote sont arrangés, comme indiqué dans la Fig. 3. Les grands cercles montrent l'arrangement des atomes de nickel qui forment la maille hexagonale compacte et les petits cercles la position des atomes d'azote. Les traits de lignes représentent la maille hexagonale compacte supposée dans certains travaux anterieurs[10),15)]. Cet arrangement en sur-structure des atomes de nickel et d'azote dans la maille du Ni_3N est en accord avec les travaux par rayons X de Jack[11)], mais diffère de la structure proposée par Nagakura[14)] pour le carbure de nickel: Ni_3C.

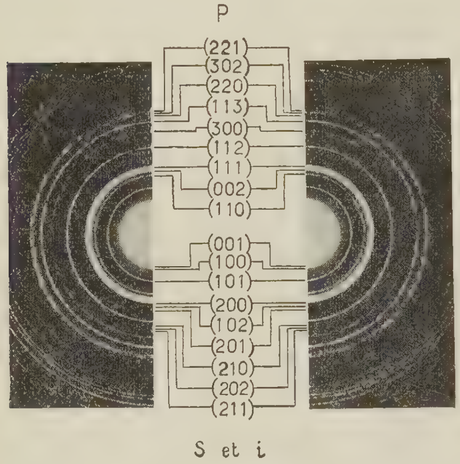

Fig. 2. Diagramme de diffraction électronique du Ni_3N.

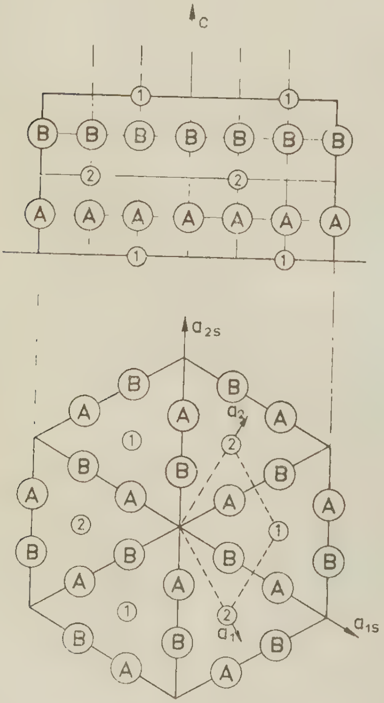

Fig. 3. Structure de Ni_3N.

2°) *Structure de la forme intermédiaire dilatée*

Comme montré précédemment, la transformation du nickel sous l'influence des atomes d'azote a lieu suivant le schéma:

$$Ni_{c.f.c.} \rightarrow Ni_{c.f.c.} \text{ dilaté} \rightarrow Ni_3N$$
(hexagonal compacte).

Les diagrammes de diffraction électronique du nickel dilaté montrent que la forme cubique à faces centrées se conserve, bien qu'on observe, en outre, certains anneaux supplémen-

Tableau II. Mesures faites sur les diagrammes du Ni dilaté.

Ni d(Å)	Indice h k l	Ni dilaté		
		Intensité	d_{obs}(Å)	d_{cal}(Å); $a=3.72$ Å
	100	tf	3.72	3.72
	$(1\frac{1}{2}0)$	(ttf	3.3)	3.33
	110	tf	2.62	2.63
2.03	111	F	2.15	2.15
1.76	200	M	1.86	1.86
	210	tf	1.65	1.66
	211	tf	1.52	1.52
1.25	220	M	1.31	1.32
	221, 300	tf	1.24	1.24
	310	ttf	1.18	1.18
1.06	311	M	1.11	1.12
1.02	222	m	1.07	1.08
0.88	400	f	0.92	0.93
0.81	331	M	0.85	0.85
0.79	420	M	0.83	0.84
0.72	422	M	0.75	0.76
0.68	511, 333	m	0.71	0.72

taires, toujours faibles et très diffus. Les mesures faites sur plusieurs diagrammes et sur des échantillons différents sont résumées dans le Tableau II. On y remarque que la raie de diffraction 3,3 Å est très faible et diffuse. C'est probablement pourquoi elle n'est que rarement visible.

La Fig. 4 montre le diagramme de diffraction du nickel dilaté coexistant avec le nickel ordinaire initial et la Fig. 5 montre le diagramme du nickel dilaté seul. Comme les raies (100), (110), (210), (211)··· sont interdites pour le cristal cubique à faces centrées formé d'une seule sorte d'atomes, nous avons attribué ces réflexions à un réseau de sur-structure, toujours cubique à faces centrées contenant en plus des atomes de nickel un atome d'azote.

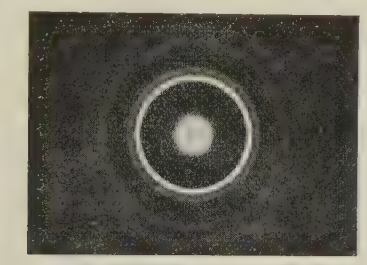

Fig. 4. Diagramme de diffraction électronique de (Ni+Ni dilaté).

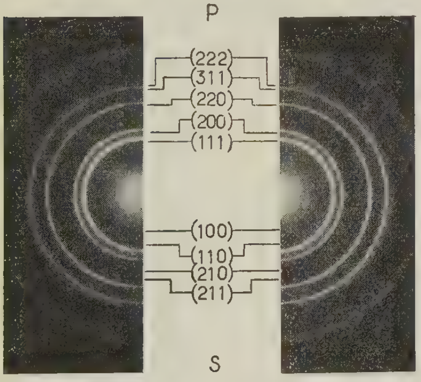

Fig. 5. Diagramme de diffraction électronique du nickel dilaté.

La position la plus probable de cet atome d'azote dans la maille de sur-structure est: (1/2, 1/2, 1/2) car l'autre position probable (1/4, 1/4, 1/4) est exclue par les dimensions respectives des atomes de nickel et d'azote. Cela conduit à admettre l'existence d'une nouvelle forme de nitrure de nickel: Ni_4N dont les positions exactes des deux sortes d'atomes sont:

$$\text{Ni}\begin{cases}(0,\ 0,\ 0);\quad (1/2,\ 1/2,\ 0)\\(0,\ 1/2,\ 1/2);\quad (1/2,\ 0,\ 1/2)\end{cases}$$

$$\text{N}\quad (1/2,\ 1/2,\ 1/2)\,.$$

II. Nitruration des couches minces de nickel monocristallin

Lorsque l'évaporation du nickel se fait sur une face (001) de NaCl chauffé à 400–450°C, la couche mince de nickel est monocristalline à l'exception de quelques macles qui donnent lieu à des taches de diffraction satellites. Les diagrammes de diffraction électronique indiquent que la couche a l'orientation suivante:

$$(001)_{\text{Ni}}//(001)_{\text{NaCl}}$$

$$[100]_{\text{Ni}}//[100]_{\text{NaCl}}$$

La nitruration a été conduite de la même façon que sur le nickel polycristallin. Les couches monocristallines ont l'avantage de mieux montrer certaines réflexions qui sont trop faibles et trop diffuses et de permettre de déterminer la relation d'orientation entre le nickel initial et le nickel nitruré.

Au cours de la nitruration la maille cubique à faces centrées du nickel monocristallin se dilate d'abord comme dans le cas du nickel polycristallin de $a=3.52$ Å à 3,72 Å. Les diagrammes de diffraction électronique sont formés de taches individuelles tout comme le nickel de départ, montrant ainsi que l'orientation monocristalline est conservée. Toutefois, les taches du nickel dilaté sont toujours diffuses. Par contre, dès l'apparition de la forme hexagonale (Ni_3N), on observe sur les diagrammes de diffraction l'apparition d'anneaux fins et ponctués. Cela permet de distinguer facilement les diffractions de la forme cubique (Ni+Ni dilaté) de celles de la forme hexagonale (Ni_3N) surtout lorsque ces formes coexistent dans le même échantillon.

La Fig. 6 montre le diagramme du nickel monocristallin de départ dont la face (001) est perpendiculaire au faisceau d'électrons. Après

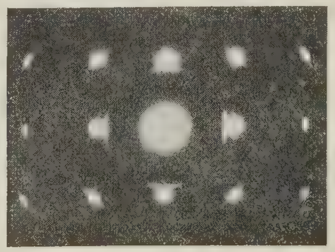

Fig. 6. Diagramme de diffraction électronique du nickel monocristallin.

nitruration d'une heure à 230°C on obtient le diagramme représenté dans la Fig. 7(a) où on observe encore les taches du nickel initial à côté des taches correspondant au nickel dilaté, toujours c.f.c. de maille $a = 3.72$ Å. On remarque en outre sur ce diagramme, qu'il contient en plus des taches normales du cristal c.f.c., des taches de sur-structure (100), (110), (210)··· comme on le voit schématisé sur la Fig. 7(b).

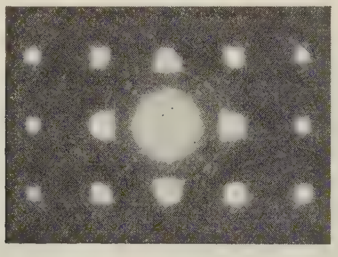

Fig. 7 (a). Diagramme de diffraction électronique de ($Ni+Ni_4N$).

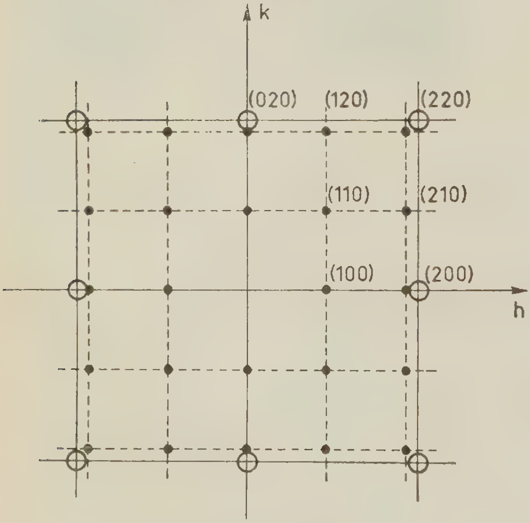

Fig. 7 (b). Schéma correspondant à la fig. 7 (a).
○ Ni
• Ni_4N

La Fig. 8(a) montre le diagramme de diffraction d'une nitruration plus poussée, sur lequel on voit la coexistence des trois formes: nickel initial, nickel dilaté (Ni_4N) et les anneaux du nickel hexagonal (Ni_3N) renforcés sélectivement par endroits à cause de l'orientation privilégiée d'ensemble du nickel initial.

Le Tableau III résume les résultats des mesures faites sur plusieurs diagrammes analogues à celui de la Fig. 8(a) où les trois formes coexistent dans le même échantillon. On a toutefois éliminé de ce tableau les données de la forme hexagonale (Ni_3N) car elles sont exactement les mêmes que celles obtenues par la nitruration du nickel polycristallin et

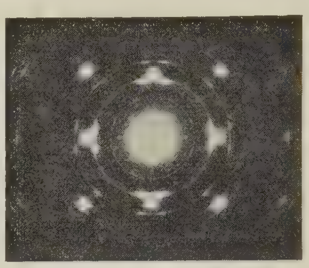

Fig. 8 (a). Diagramme de diffraction électronique de ($Ni+Ni_4N+Ni_3N$).

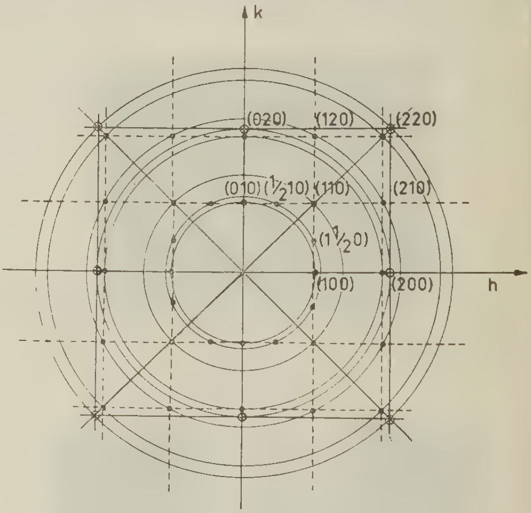

Fig. 8 (b). Diagramme schématique de diffraction électronique du Ni et Ni dilaté.
○ réflection de Ni
● réflection de Ni dilaté

Tableau III. Mesures faites sur les diagrammes du type Fig. 8(a) (couches monocristallines).

Ni d(Å)	Indice h k l	Ni dilaté		
		Intensité	d_{obs}(Å)	d_{cal}(Å); $a=3.72$Å
	100	F	3.63	3.72
	1½0	M	3.33	3.33
	110	tf	2.64	2.63
1.76	200	F	1.87	1.86
	210	f	1.66	1.66
1.25	220	M	1.31	1.32
0.88	400	M	0.93	0.93
0.79	420	M	0.83	0.84
0.62	440	M	0.65	0.66

rapportées dans le Tableau I. Sur le Tableau III on remarque que la valeur 3,63 Å de la tache (100) est beaucoup plus petite que la valeur 3,72 Å mesurée sur le diagramme de la Fig. 7(a) et sur le nickel polycristallin: cette différence dépasse largement l'erreur expérimentale.

La Fig. 8(b) montre le diagramme schématique de la partie centrale de la Fig. 8(a) où les diffractions de la forme cubique (100), (1, 1/2, 0), (110) et (210) sont nettement visibles. On n'a pas trouvé de traces de diffraction telles que (1/2, 1/2, 0), (1/2, 0, 0) etc.; toutes les raies précédentes ont été dessinées dans la Fig. 8(b). On ne sait pas encore à quoi attribuer ce diagramme, mais nous supposons qu'il correspond à un stade intermédiaire entre le nickel dilaté (Ni_4N) et le nickel hexagonal (Ni_3N). Pour le préciser il nous faudrait plus de mesures sur plusieurs diagrammes pris sur échantillons différents, mais en pratique il est très difficile d'arrêter la nitruration exactement à ce stade assez fugace.

En continuant la nitruration, toutes les taches du nickel ordinaire de départ et du nickel dilaté (Ni_4N) disparaissent et on n'obtient en fin de compte (3 heures à 230°C) que la forme hexagonale. En poursuivant encore la nitruration, il se produit une coalescence de petits cristaux issus de la transformation $Ni_4N \rightarrow Ni_3N$, ayant comme conséquence l'augmentation de leur désorientation relative et la disparition de l'orientation initiale privilégiée.

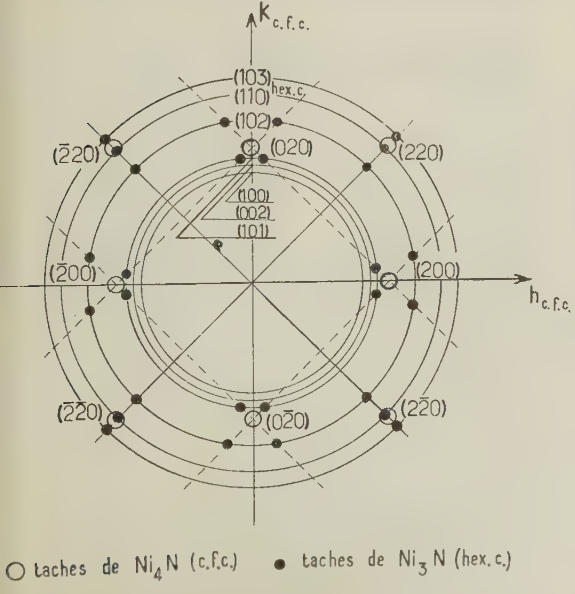

Fig. 9. Relation d'orientation entre Ni_4N et Ni_3N.

Les diagrammes de diffraction électronique des couches monocristallines permettent en outre, de déterminer la relation d'orientation entre le nickel dilaté (Ni_4N) et le Ni_3N. Celle-ci est montrée dans la Fig. 9* et elle peut s'écrire:

$$\left.\begin{array}{l}(111)_{Ni_4N}//(0001)_{Ni_3N}\\ [10\bar{1}]_{Ni_4N}//[2\bar{1}\bar{1}0]_{Ni_3N}\end{array}\right\} Ni_3N\ ;$$

indice d'hexagonal compacte.

III. Mécanisme de la transformation de la forme cubique dilatée (Ni_4N) en la forme hexagonale (Ni_3N)

La relation d'orientation établie au chapitre précédent montre que les rangées les plus compactes d'atomes des deux systèmes cristallins (cubique et hexagonale) sont parallèles. Cette donnée expérimentale est importante car elle indique que le mécanisme de la transformation du nickel dilaté (Ni_4N) cubique en nickel hexagonal (Ni_3N) se fait par des microglissements sur les plans {111}, semblables à

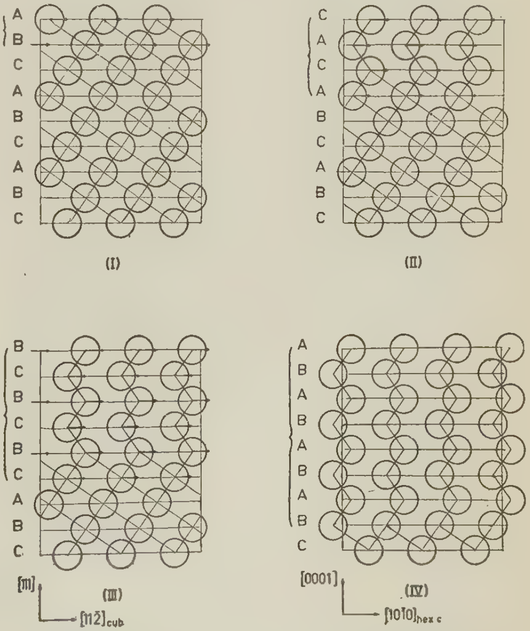

Fig. 10. Transformation du réseau c.f.c en hexagonal par microglissements dans le plan (111) direction [112].

---

* Dans la Fig. 9, on n'a indiqué que les diffractions les plus importantes et les indices des anneaux du Ni_3N ont été donnés d'après la maille hexagonale compacte.

ceux qui provoquent la transformation martensitique du cobalt. C'est-à-dire que chaque glissement est produit par le déplacement d'une dislocation partielle dans la direction $[11\bar{2}]$[17].

Si ce mécanisme ressemble au mécanisme de la transformation martensitique du cobalt, les phénomènes qui le régissent sont différents; alors que dans le cas du cobalt, le glissement est provoqué par les changements de volume dus aux chocs thermiques; dans le cas de la transformation du nickel dilaté (Ni_4N) en (Ni_3N) le glissement semble être provoqué par les tensions internes résultant de la diffusion des atomes d'azote dans le réseau cristallin du nickel. Ces microglissements qui affectent les atomes de nickel ont comme conséquence le changement de l'ordre d'empilement des plans $\{111\}_{\text{cubique}}$, en un empilement des plans $\{0001\}_{\text{hexagonal}}$ (Fig. 10). En plus, la diffusion d'atomes d'azote supplémentaires dans le réseau du Ni_4N (cubique) provoque un autre changement d'empilement: Lesplans $\{1\bar{1}0\}_{\text{cubique}}$ deviennent après la transformation les plans $\{1\bar{2}10\}$ de la variété hexagonale.

Voyons ce mécanisme plus en détail:

Considérons d'abord l'arrangement des atomes dans les mailles, initiale du (Ni_4N) et finale du (Ni_3N). La maille cubique à faces centrées du Ni_4N a en plus de l'ordre d'empilement ABCABC··· des plans $\{111\}$, l'ordre d'empilement $\alpha\beta\alpha\beta'\alpha\beta\alpha\beta'\cdots$ des plans $\{1\bar{1}0\}$ comme on le voit sur la Fig. 11(a). En ne considérant que les atomes de nickel, les plans β et β' sont les mêmes; ils ne se distinguent que par la position des atomes d'azote. D'autre part, la maille du Ni_3N est hexagonale compacte et elle a donc l'ordre d'empilement ABAB··· des plans $\{0001\}$. Cependant, pour bien définir cette maille, il est nécessaire en outre de considérer l'empilement des atomes dans le plan $(1\bar{2}10)$. L'ordre est comme suit: $123, 1'2'3', 123, 1'2'3'\cdots$ et il est indiqué dans la Fig. 11(b) en projection plane. Si on considère dans cet ordre d'empilement la distribution relative des atomes, les planes: 1–1′, 2–2, et 3–3′ sont équivalents; ils se distinguent par la position exacte de chaque atome qui se déplace parallèlement de la distance $(\sqrt{3}/2)a$ $[10\bar{1}0]$ hexagonal compacte.

Le mécanisme de la transformation du Ni_4N (cubique) en Ni_3N (hexagonal) peut être séparé

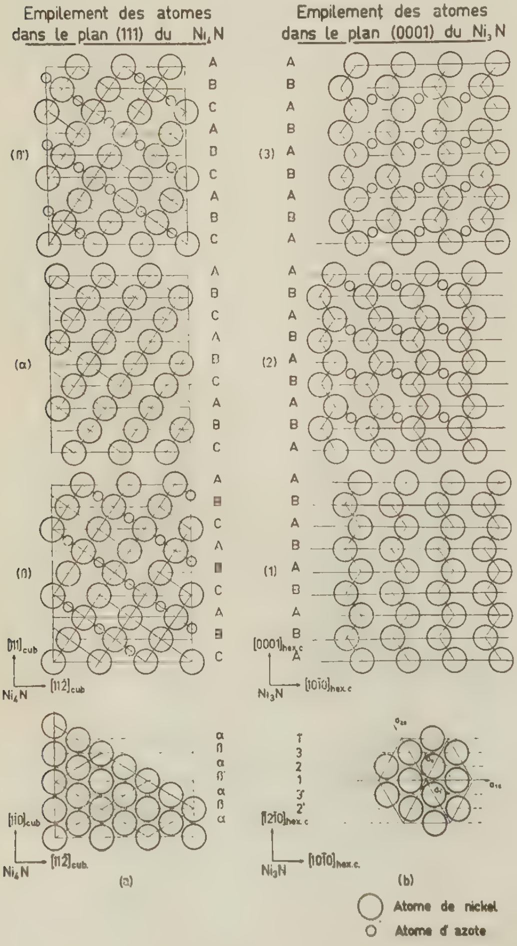

Fig. 11.

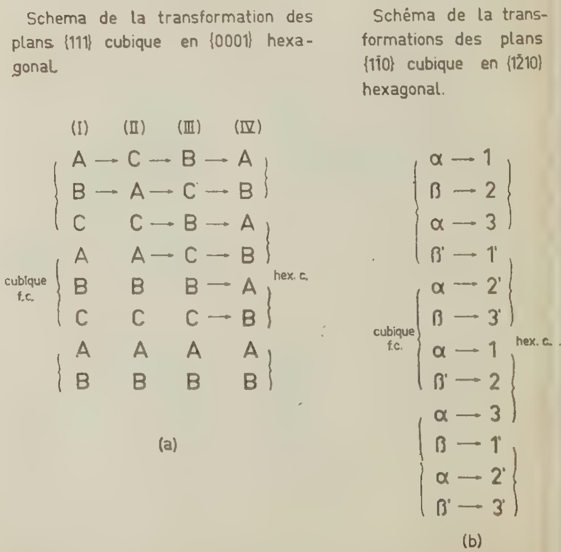

Fig. 12.

en deux transformations élémentaires bien qu'interdépendantes: microglissements dans les plans {111} provoquant la transformation du réseau cubique faces centrées en hexagonal et ceci en 4 mouvements visibles dans le schéma de la Fig. 12(a), et diffusion d'atomes d'azote provoquant le changement dans l'ordre d'empilement des plans $\{1\bar{1}0\}_{\text{cubique}}$ en $\{1\bar{2}10\}_{\text{hexagonal}}$ visible dans le schéma de la Fig. 12(b).

Pour certains détails il est encore nécessaire de considérer les dimensions respectives des atomes de nickel et d'azote dans les réseaux des deux nitrures. On voit alors qu'un des mécanismes probables de la transformation $\alpha \rightarrow 1$ et $\beta \rightarrow 2$ serait comme indiqué respectivement dans les Figs. 10 et 13. En outre, les transfsrmations $\beta \rightarrow 3'$, $\beta' \rightarrow 2$ et $\beta' \rightarrow 3'$ doivent être identiques à la transformation $\beta \rightarrow 2$.

Suivant ces mécanismes "types" indiqués plus haut, les atomes d'azote diffusent seulement dans le plan $(1\bar{1}0)$, mais la diffusion peut se produire dans un plan perpendiculaire et elle est nécessaire pour réaliser les transformations $\alpha \rightarrow 3$, $\beta' \rightarrow 1'$, $\alpha \rightarrow 2'$ et $\beta \rightarrow 1'$. Par exemple, prenons trois plans voisins superposés:

$$\begin{cases} \alpha \longrightarrow 3 \\ \beta' \longrightarrow 1' \\ \alpha \longrightarrow 2' . \end{cases}$$

La transformation $\beta' \rightarrow 1'$ s'effectue si les atomes d'azote du plan β' diffusent vers les deux plans α voisins. Si des atomes d'azote supplémentaires sont fournis de l'extérieur aux plans α, les transformations $\alpha \rightarrow 3$ et $\alpha \rightarrow 2'$ se produisent à leur tour. Un mécanisme pareil à celui-ci est possible dans le cas d'autres plans voisins superposés:

$$\begin{cases} \alpha \longrightarrow 3 \\ \beta \longrightarrow 1' \\ \alpha \longrightarrow 2' . \end{cases}$$

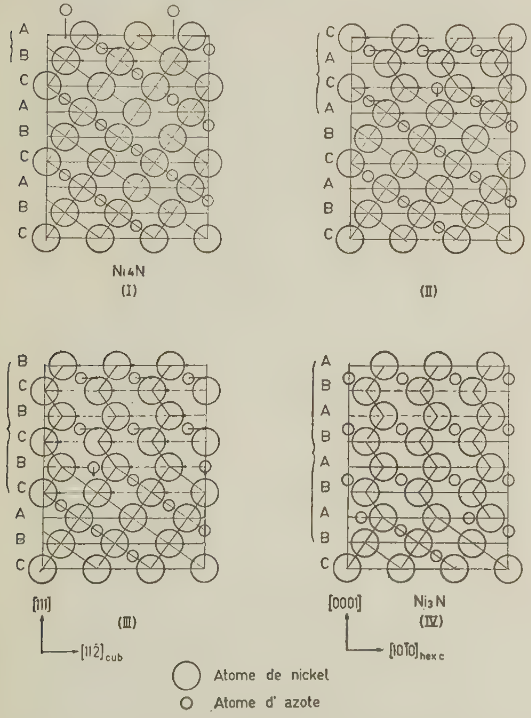

Fig. 13. Mécanisme de transformation du Ni_4N (c.f.c) en Ni_3N (hexagonal) par des microglissements successifs dans le plan (111) et diffusion simultanée d' azote dans le réseau.

Il semble cependant que le mouvement réel de l'atome d'azote est encore plus compliqué et plus irrégulier que le modèle idéalisé décrit plus haut. Ceci est indiqué par le fait que si l'on fait subir la nitruration à un monocristal de nickel, il conserve son orientation monocristalline seulement jusqu'au stade du Ni_4N, mais au fur et à mesure que la nitruration avance vers le Ni_3N, l'orientation monocristalline se détruit au profit d'un agrégat polycristallin. Si le mécanisme idéal que nous avons schématisé était le vrai, le monocristal devrait se conserver jusqu'au stade final du Ni_3N. Comme l'expérience montre l'inverse, cela indique que le mécanisme est plus compliqué encore; surtout la diffusion d'atomes d'azote dans les plans perpendiculaires aux plans $\{1\bar{1}0\}$ doit se faire le long des imperfections de structure à l'échelle atomique. A travers ces voies des imperfections de structure, les atomes d'azote peuvent pénétrer de l'extérieur dans la maille directement dans les plans de type β et β', et non seulement dans les plans de type α comme indiqué dans le schéma.

En conclusion, le processus de nitruration des couches minces de nickel, polycristallines et monocristallines, étudié par diffraction électronique, montre que la diffusion de l'azote dans le nickel conduit, suivant le degré de nitruration, à la formation de différents nitrures. D'abord, l'insertion des atomes d'azote provoque une dilatation considérable de la maille du nickel initial (de $a=3.52$ Å à 3.72 Å) par la formation du Ni_4N. Ensuite, si la nitruration est poursuivie, cette maille c.f.c.

dilatée se transforme en une maille hexagonale compacte correspondant au Ni_3N. Les structures exactes de ces nitrures ont été déterminées et un mécanisme détaillé de la transformation de la forme cubique dilatée (Ni_4N) en la forme hexagonale (Ni_3N) a été proposé.

Ce mécanisme comprend d'une part, le changement de l'ordre d'empilement des plans $\{111\}_{\text{cubique}}$ en un empilement des planes $\{0001\}_{\text{hexagonal}}$: ce changement se produit par des microglissements sur les plans $\{111\}$ qui affectent seulement les atomes de nickel. D'autre part, la diffusion d'atomes d'azote dans le réseau du Ni_4N (cubique) provoquent un autre changement d'empilement: les $\{1\bar{1}0\}_{\text{cubique}}$ deviennent après la transformation les plans $\{1\bar{2}10\}$ de la variété hexagonale. Il est très difficile de savoir lequel de ces deux changements se produit le premier, la diffusion d'atomes d'azote provoquant le glissement qui affecte les atomes de nickel ou le glissement des atomes de nickel qui permet ensuite la diffusion de l'azote, car expérimentalement les deux apparaissent simultanement.

Ce mécanisme un peu idéalisé ne correspond pas tout à fait au mécanisme réel plus compliqué. De ce fait on doit admettre que la diffusion à l'intérieur d'un cristal des atomes de petits diamètres, comme celui d'azote qui est un atome essentiellement d'insertion, ne se fait pas exclusivement par des voies de cheminement interstitielles.

Remerciements

Ce travail fait partie d'un projet plus ample supporté matériellement par l'Union Carbide Corporation, New York et il nous est très agréable de la remercier ici et de lui exprimer notre reconnaissance pour ce soutien. Nous sommes également reconnaissants au Dr. R. H. Gillette pour son encouragement constant et l'intérêt qu'il a mis dans ce travail.

Bibliographie

1) L. R. Ingersoll et S. S. de Vinney: Phys. Rev. **26** (1925) 86.
2) G. P. Thomson: Nature **123** (1929) 912.
3) G. Bredig et E. S. v. Bergkampf: Z. phys. Chem. Bodenstein Festband (1931) 172.
4) A. Colombani et J. Wyart: C. R. Acad. Sci. **215** (1942) 129.
A. Colombani: C. R. Acad. Sci. **215** (1942) 17.
5) H. A. Bahr et Th. Bahr: Ber. Deut. Chem. Gesell. **61 B** (1928) 2177.
6) L. R. Ingersoll: Nature **126** (1930) 204; J. Am. Chem. Soc. **53** (1931) 2008.
7) B. Jacobson et A. Westgren: Z. phys. Chem. **B 20** (1933) 361.
8) G. Leclerc et A. Michel: C. R. Acad. Sci. **208** (1939) 1583.
9) R. Juza et W. Sachsze: Z. anorg. Chem. **251** (1943) 201.
10) R. Bernier et A. Michel: Bull. soc. chim. France **16** (1949) 119, 365.
R. Bernier: Ann. chim. **6** (1951) 104.
A. Michel: C. R. Acad. Sci. **243** (1956) 373.
11) K. H. Jack: Acta. Cryst. **3** (1950) 392; **5** (1952) 404.
12) K. H. Jack: Proc. Roy. Soc. **A 195** (1948) 34.
13) J. J. Trillat, L. Tertian, N. Terao et C. Lecomte: Bull. soc. chim. France (1957) 804.
14) S. Nagakura: J. Phys. Soc. Japan **12** (1957) 482; Acta. Cryst. **10** (1957) 601.
15) J. J. Trillat, L. Tertian et N. Terao: C. R. Acad. Sci. **243** (1956) 666.
J. J. Trillat, L. Tertian et C. Lecomte: C. R. Acad. Sci. **244** (1957) 596.
16) S. B. Hendricks et P. B. Kosting: Z. Krist. **74** (1930) 511.
17) T. R. Anantharanan et J. Christian: Phil. Mag. **43** (1952) 1338.

JOURNAL OF THE PHYSICAL SOCIETY OF JAPAN Vol. 14, No. 2, FEBRUARY, 1959

Stress-Ordering Effect on Thermal Expansion of CuAu Single Crystals

By Makoto HIRABAYASHI

The Research Institute for Iron, Steel and Other Metals,
Tohoku University, Sendai

(Received October 14, 1958)

Linear thermal expansion of CuAu single crystals was measured. When a bar-formed specimen was slowly cooled from above the transition temperature under compressive stress along its longitudinal direction, it was confirmed that the *c*-axes of the ordered phase were predominantly lined up in one of the cubic axes nearest to the stress direction. Furthermore a linear relationship was established to hold between the compressive stress previously applied and the amount of the dilatometric change due to the order-disorder transition. However, even when some of the crystals were initially annealed free from external stress, the tetragonal *c*-axes were not distributed statistically along the three original cubic axes.

§ 1. Introduction

As well known, the copper-gold alloy with the equi-atomic composition forms a face-centered tetragonal ordered phase CuAu I below 380°C, whereas above this temperature an orthorhombic ordered phase CuAu II is formed up to 410°C[1]. The lattice constants of CuAu I and CuAu II are considerably different from those of the disordered cubic phase existing stably above 410°C, as given in Table I. Namely, compared with the disordered cell, the *a*-direction of CuAu I expands by about 2.3%, while the *c*-direction contracts by about 5.3%. Therefore, if the ordering treatment for single crystal is performed under compressive stress along one of the cubic axes, the tetragonal *c*-axis of the ordered phase may preferentially be lined up in this direction. In order to confirm this expectation, we measured linear thermal expansion of single crystals of CuAu, and found the stress-ordering effect on the dilatometric change.

Table I. Lattice constants of CuAu in kX unit[1].

	Ordered phase		Disordered phase
	CuAu I	CuAu II*	
a	3.952	3.954	3.865
b	—	39.66	—
c	3.662	3.652	—

* CuAu II is thought of as formed from CuAu I by step shifts which occur at every fifth unit cell along its *b*-direction.

§ 2. Experimental

Three single crystals were grown by the Tammann-Bridgman method in vacuum. They had rod shape of 15~30 mm in length and 2~4 mm in diameter. Chemical analysis of the alloy showed the composition to be 49.8 atomic per cent gold. Crystallographical directions of the rods, along which linear expansion was measured, were determined by

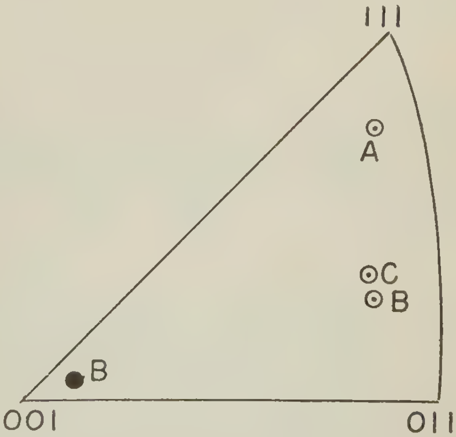

Fig. 1. Stereographic representation of the crystallographical directions of three single crystals of CuAu. Open circles correspond to the longitudinal directions. The closed circle represents the lateral direction of crystal B, along which thermal expansion was measured.

X-ray back reflection Laue method in the disordered state. The result is shown in Fig. 1. Thermal expansion was measured by a simple vertical dilatometer, which had also been used in the study of the polycrystalline specimens of CuAu[2].

Figs. 2 and 3 show thermal expansion curves in the longitudinal direction of the crystal A. Rates of heating and cooling are about 2 deg/min. Before the measurements for each curve in Fig. 2, the crystal was heat-treated as follows: for curve *a* the crystal was annealed for 8 hr at about 350°C, for 5 hr at about 300°C and then slowly cooled to room temperature, and for curve *c* it was quenched from 500°C into water. Curve *b* shows a cooling run from 500°C. These treatments were carried out without any external stress. It should be noted in this figure that the transition from order to disorder accompanies the linear contraction of about 1.4%.

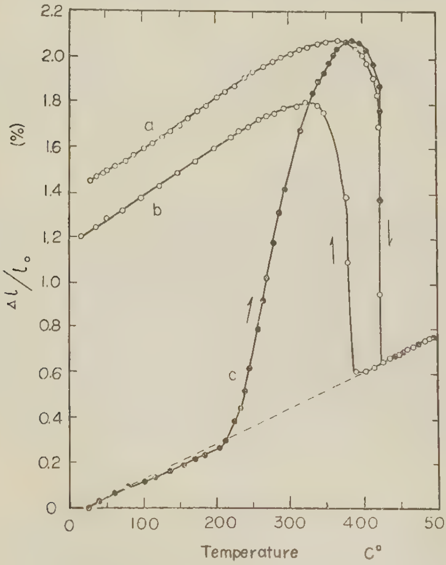

Fig. 2. Thermal linear expansion along the longitudinal direction of the crystal A. Curves *a* and *c* correspond to heating of ordered and disordered states, respectively. Curve *b* is a cooling one.

On the other hand, when the same initial ordering treatment as described above was carried out under compression along the longitudinal direction of this crystal, the disordering by reheating accompanied the expansion instead of the contraction along this direction, as shown in Fig. 3. This figure shows that the expansion increases with the compressive stress, and, hence, that the *c*-axis of the ordered phase tends to be parallel with the cubic axis, which is nearest to the stress direction. Similar behaviour was also observed on dilatometric measurements of the longitudinal direction of the crystal B. Thus, the expectation described before was confirmed.

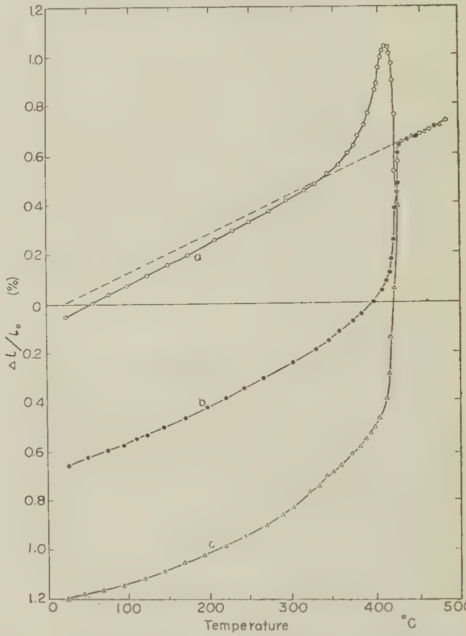

Fig. 3. Thermal linear expansion curves of the crystal A on reheating from the states cooled slowly under compression. Curves *a*, *b* and *c* correspond to the compressive stresses 273, 417 and 522 gr/mm², respectively.

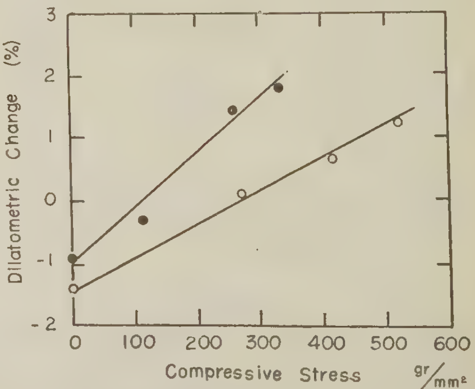

Fig. 4. Longitudinal dilatometric changes due to disordering as a function of compressive stress applied previously. Open and closed circles correspond to the crystals A and B, respectively. Positive sign of the ordinate means expansion on dis-ordering.

Moreover, the linear relationship was found to hold between the change in thermal expansion due to disordering by reheating and the compressive stress applied during the previous ordering process. Fig. 4 gives the results for the crystals A and B.

The linear thermal expansion coefficient shows clearly two-step changes at about 400° and 420°C corresponding to the transitions from CuAu I to CuAu II and from CuAu II to disorder, respectively. Fig. 5 gives some examples for the crystal A. These curves show similar temperature dependence to the expansion coefficient curves of the polycrystalline specimens[2].

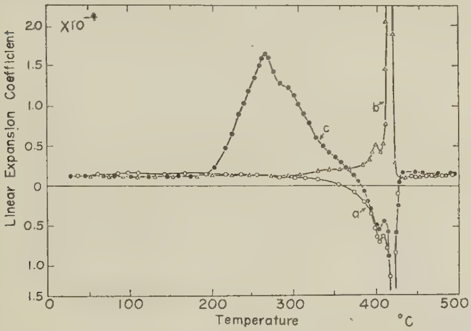

Fig. 5. Linear expansion coefficient in the longitudinal direction of the crystal A. Curves *a* and *c* correspond to curves *a* and *c* in Fig. 2 respectively, and curve *b* corresponds to curve *b* in Fig. 3.

§ 3. Discussion

It must be remarked that even when the crystals A and B are initially annealed without external stress, the tetragonal *c*-axes are not distributed statistically along the three original cubic axes. Because, if the *c*-axes were equally distributed along the three cubic axes, these specimens would have to expand on disordering by reheating along the directions measured. However, the contraction actually took place as seen in Fig. 2, so the tetragonal *c*-axes of the ordered crystal A should mostly be located along a cubic axis near the lateral direction. Also this was confirmed in the case of the crystal B as follows. As shown in Fig. 6, the crystal expands along the longitudinal direction, while it contracts along the lateral direction on ordering under no external stress. The latter direction is located closely to the cubic axis as given in Fig. 1. Therefore it can be concluded that, for the crystal B as well as the crystal A, the tetragonal *c*-axes line up predominantly along the original cubic axis nearly perpendicular to the grown axis. However, such circumstances do not generally hold for all crystals prepared. In fact, the crystal C annealed under no external stress expands along the longitudinal direction, which is located near that of the crystal B as given in Fig. 1, by about 0.86% on the transition from order to disorder, just as expected from the statistical distribution of the tetragonal axis.

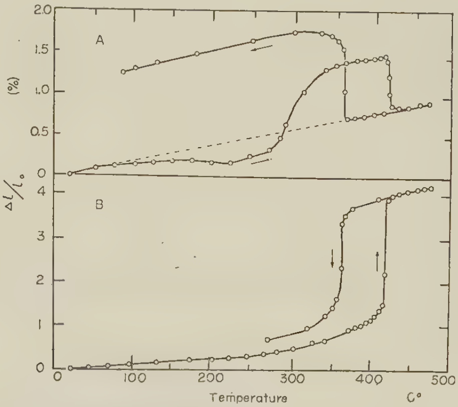

Fig. 6. Thermal expansion curves of the crystal B on heating and cooling at the rate of about 2 deg/min. Upper curves (A) correspond to the measurement along the longitudinal direction of the crystal initially disordered. Lower curves (B) correspond to the lateral direction of the ordered crystal.

In the early stage of ordering in the CuAu crystal, it is reasonably expected that the ordered nuclei have their axes nearly, not precisely, parallel to those of the disordered phase, because they form coherently on {110} planes of the disordered structure[3]. The later stage of ordering is accompanied by the formation of twins with the {110} habit planes[4]. Such a twin formation can easily be understood on the basis of the minimum strain energy, but it makes difficult to interpret quantitatively the present results. If it is simply assumed, however, that the tetragonal *c*-axis directs parallel with the three original cubic axes, the fraction of *c*-axis distributed along each of them may be estimated from the measurements of dilatometric changes along two different directions of the crystal. From Fig. 6 for the crystal B, it was roughly estimated that the fraction of the ordered region, whose c-axis was assumed to direct along the cubic axis closest to the longitudinal direction, was only about two per cent of the total volume. The reason for such highly unequal distribution of the c-axis* is not yet clear, but the twin formation and such an internal stress as induced in the process of crystal growth from the melt may play an important role. This is probably supported by the present result that the external stress applied during the superlattice formation forces to change the c-axis distribution in the ordered crystal.

The author wishes to express his sincere thanks to Professor S. Ogawa for his kind advices and discussions. This work was supported in part by the fund of the Ministry of Education in Aid of Scientific Researches.

References

1) C. H. Johansson and J. O. Linde: Ann. Physik **28** (1936) 1.
2) M. Hirabayashi: J. Japan Inst. Met. **B15** (1951) 565.
3) M. Hirabayashi and S. Ogawa: J. Phys. Soc. Japan **11** (1956) 907.
4) G. C. Kuczynski, R. F. Hochman and M. Doyama: J. Appl. Phys. **26** (1955) 871.

---

[*] Evidence for an unequal distribution of the tetragonal axes has been found by the X-ray diffraction study of the ordered alloy Cu_3Pd [M. Hirabayashi and S. Ogawa: J. Phys. Soc. Japan **12** (1957) 259].

JOURNAL OF THE PHYSICAL SOCIETY OF JAPAN Vol. 14, No. 2, FEBRUARY, 1959

Selenium Rectifiers with Artificial Layers of Selenides of Cadmium, Tin, Bismuth and Lead*

By Yoshiro MORIGUCHI

Nippon Electric Co., Ltd., Kawasaki-shi, Japan

(Received October 30, 1958)

Artificial layers of selenides of Cd, Sn, Bi and Pb are made between the bulk Se and the counter electrode of selenium rectifiers with the method of vacuum evaporation. The d.c. and a.c. characteristics of these rectifiers are observed in order to get some informations about the actions of the barrier layer in usual selenium rectifiers. The results suggest that the roles of SnSe layer should never be neglected in the rectifying action in selenium rectifiers as well as those of CdSe layer, and the selenides of Bi and Pb seem to be undesirable materials.

§ 1. Introduction

In selenium rectifiers, it has been well known that the selenides of the counter-electrode metals exist between the bulk selenium layer and the counter electrode¹⁾, and that among the selenides, CdSe layer, which has the largest resistivity, should play the most important role as the barrier material in selenium rectifiers²⁾. The direct experimental substantiations for the role of CdSe in the rectifying action are, however, not so many at present, and it seems to be desirable to investigate directly the roles of the selenides of cadmium as well as the other counter-electrode metals in selenium rectifiers.

In the present experiment, the selenides of some kinds of metals were prepared by the method of vacuum fusion, and they were evaporated in vacuum to make thin layers between the bulk selenium and the counter electrode. The d.c. and a.c. characteristics of these rectifiers were observed and some informations about the rectifying characteristics of the selenide layers were obtained.

---

[*] This work was performed at Kurume University.

Table I. Bulk properties of the selenides.

Material	Density	Crystal structure	Type of semiconductor	Forbidden gap E_g (eV)	Activation energy ΔE (eV)	Resistivity (Ω cm)	Density of impurity centers (cm^{-3})
CdSe	5.8[a]	Zincblende or Wurtzite	n	1.73[d]	0.55[e]	$\sim 10^{6}$[e]	$\sim 10^{13}$[e]
SnSe	6.18[a]	Distorted rock salt	p	0.8[f]		$\sim 10^{-2}$[f]	10^{17}[f]
Bi_2Se_3	6.82[a] 7.70[b]	Hexagonal	n	0.2[g]	0.003[g]	$\sim 10^{-2}$[g]	10^{18}[g]
BiSe	7.98[c]	Hexagonal	n	0.4[g]		$\sim 10^{-3}$[g]	10^{20}[g]
PbSe	8.10[a]	Rock salt	p	0.48[h] 0.34[i]	0.014[h]	$\sim 10^{-2}$[h]	
Se	4.81[j]	Hexagonal	p	1.7∼2.0[k]	0.3[l]	$10^{5}\sim 10^{7}$[m]	10^{15}[m]

a) N. A. Lange: *Handbook of Chemistry*, Handbook Publishers, Ohio, (1939).
b) E. Dönges: Z. f. anorg. u. allg. Chem. **265** (1951) 56.
c) J. D. H. Donnay and W. Nowacki: *Crystal Data*, The Geological Soc. America, (1954).
d) R. H. Bube: Phys. Rev. **98** (1955) 431.
e) H. Tubota, H. Suzuki and K. Hirakawa: Reported at the branch meeting of the Phys. Soc. of Japan Oct. 30, (1956).
f) Y. Matukura, T. Yamamoto and A. Okazaki: Mem. Fac. Sci. Kyusyu Univ. Ser. **B**, Vol. **1**, No. 3 (1953) 98.
g) K. Hashimoto: Mem. Fac. Sci. Kyusyu Univ. Ser. **B**, Vol. **2**, No. 4 (1958) 141.
h) E. Hirahara and M. Murakami: J. Phys. Soc. Japan **9** (1954) 671.
i) A. F. Gibson: Proc. Phys. Soc. London **B 65** (1952) 378.
j) L. M. Nijland: Philips Res. Rep. **9** (1954) 259.
k) E. Billig: Proc. Phys. Soc. **B 65** (1952) 216.
l) H. W. Henkels: J. Appl. Phys. **21** (1950) 725.
m) H. W. Henkels: J. Appl. Phys. **22** (1951) 1265.

§ 2. Experimental Results

The selenides used in the present experiment were made by heating the stoichiometric amounts of selenium and each metal in an evacuated silica tube. Their bulk properties are listed in Table I. These selenides were evaporated on the surface of selenium of a commercial selenium rectifier (40×40 mm) which had no counter electrode, and then upon the surface of the selenide, counter electrodes of 1 cm² area were sprayed or evaporated as shown in Fig. 1. As counter electrodes, sprayed ternary alloy of Cd, Sn and Bi (melting point 140°C) was mainly used, and the evaporated pure metals were sometimes used. The thickness of the evaporated selenide was estimated from the weight of selenide evaporated on a glass plate which was placed close to the sample during the evaporation, assuming the density of the film as that of the bulk material which is given in Table I, but there may be errors of about 10% in thickness according to the inaccuracy of both weighing and the value of density.

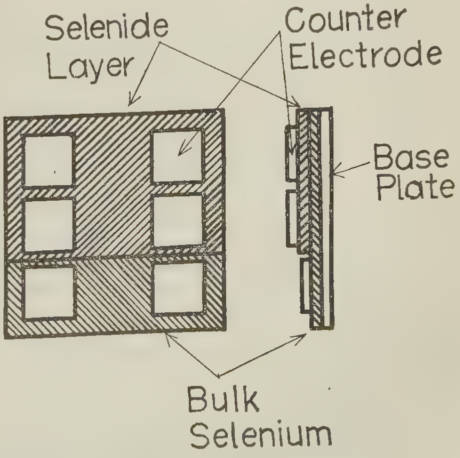

Fig. 1. The construction of the samples.

On the selenium rectifiers prepared in the above-mentioned manner, the d.c. and a.c. measurements were carried out mainly at room temperature, and for a few samples at liquid air temperature. The a.c. characteristics for frequency 1000 c/sec were measured by a substitution method using a usual a.c. bridge, and the impedance of rectifiers were analyzed assuming a parallel circuit of resistance and capacitance. The typical examples of d.c. and a.c. characteristics obtained in the experiment are shown in Figs. 2∼9.

(1) *Rectifiers with CdSe layer*

Some examples of the d.c. characteristics of the rectifiers which have the CdSe layers of different thickness are shown in Fig. 2. As shown in the figure, the resistance of the rectifiers in the forward direction, the threshold voltage which is given by the forward characteristics, and the reverse breakdown voltage seem to increase with increasing thickness of CdSe layer. The threshold voltage V_D and the bulk resistance R_S obtained from the linear part in the forward characteristics are listed in Table II which includes the resistivity of CdSe calculated from the values of R_S and the thickness of the CdSe layer d using the following equation:

$$\rho=\frac{S}{d}(R_S-R_{Se}), \tag{1}$$

where S is the area of the counter electrode, and R_{Se} the resistance of the bulk Se layer. It is difficult to estimate the value of R_{Se} correctly; here the value of the bulk resistance in the forward direction of a rectifier, which was made on a part of the same rectifier disk without any artificial layer and had not been electrically formed at all, were used as the value of R_{Se}. The value obtained here was about 20 Ω/cm². (The bulk resistance was determined below the current density of 3 mA/cm² in this experiment. The value of the bulk resistance of usual selenium rectifiers which is determined for the higher current density is far smaller than the value obtained here, but the value of the resistance obtained at the higher current density seems to be uncorrect on account of the temperature rise in the barrier.)

The characteristics of the sample (3-3) at liquid air temperature is also shown in Fig. 2. As seen in the figure and in Table VII, the values of V_D and R_S increase extremely at low temperature, but the peak back voltage scarcely changes.

The a.c. characteristics obtained for the same samples are shown in Fig. 6. It is obvious from the figure that as the thickness of CdSe layer increases, the barrier capacitance becomes smaller and the bias voltage dependency of the capacitance also decrease; the behaviours seem to be in favour of the Mott barrier. It is also shown in the figure that the capacitance and its bias voltage dependency at low temperature are far smaller than at room temperature. In addition it is seen that in some samples which have the comparatively large impedance in the forward direction, the capacitance decreases as the forward bias voltage increases, as has already been reported by Strosche[3]. It was not able to confirm whether the effect might be observed for all samples, because the exact measurement of the capacitance in the forward direction was difficult on account of the low resistance, especially in low impedance samples. The effect was already observed for usual selenium rectifiers, too[4].

(2) *Rectifiers with SnSe layer*

The d.c. characteristics of a few selenium rectifiers which have SnSe layers of different thickness are shown in Fig. 3. The threshold voltage V_D and the spreading resistance R_S are far smaller in these rectifiers than in the rectifiers with CdSe layers at room temperature, and consequently, these rectifiers have a fairly good rectifying property, although the current in the reverse direction is not so small. The threshold voltage V_D and the spreading resistance R_S at room temperature for all samples are listed in Table III. This table shows that the values of V_D and R_S are scarcely dependent upon the thickness of SnSe layer, and the values of R_S are nearly equal to the resistance of the bulk selenium layer itself, suggesting that the resistance of SnSe layer is negligibly small. It is shown in Fig. 3 and in Table VII, however, that at low temperature the values of both V_D and R_S become remarkably large.

The capacitance-bias voltage relations for the same samples are shown in Fig. 7, denoting that at room temperature, both the capacitance and its bias voltage dependency are not only nearly independent of the thickness of

SnSe layer, but also far larger than in the case of CdSe layer. At low temperature, however, the capacitance as well as its bias voltage dependency becomes so small that the features resemble those for CdSe layer. In addition, the decrease of the capacitance in the forward direction appears at low temperature, although the effect could not be observed at room temperature on account of the very low impedance.

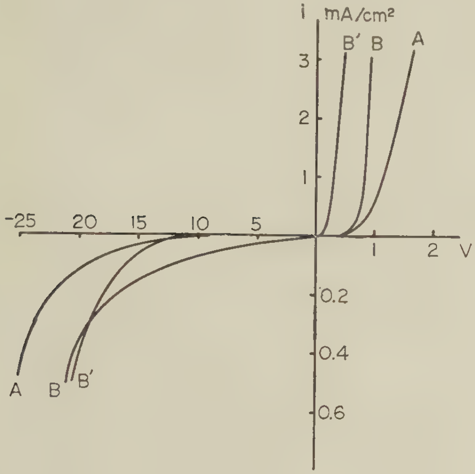

Fig. 2. The d.c. characteristics of typical Se rectifiers with CdSe layer. Curves A and B are for the samples 3–1 and 3–3, respectively, at room temperature, and curve B′ is for the sample 3–3 at liquid air temperature. The abscissa for curve B′ in the forward direction should be read ×10 (Thicknesses of CdSe=0.73μ and 0.50μ for samples 3–1 and 3–3, respectively.)

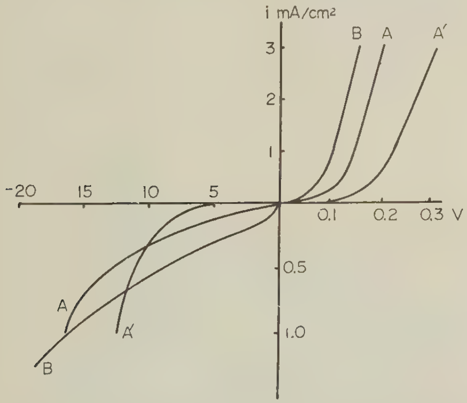

Fig. 3. The d.c. characteristics of the typical Se rectifiers with SnSe layer. Curves A and B are for the samples 10–6 and 14–3, respectively, at room temperature, and curve A′ is for the sample 10–6 at liquid air temperature. The abscissa for the curve A′ in the forward direction should be read ×10. (Thicknesses of SnSe=0.8μ and 1.2μ for samples 10–6 and 14–3, respectively.)

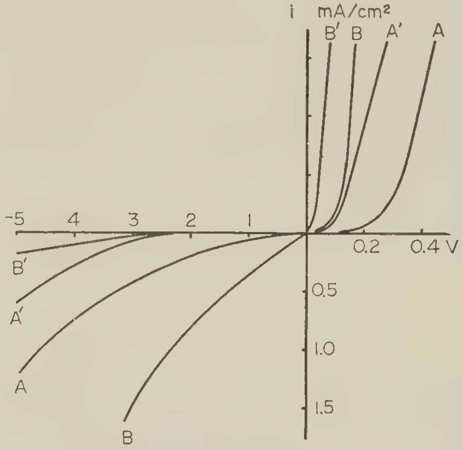

Fig. 4. The d.c. characteristics of the typical Se rectifiers with Bi_2Se_3 and BiSe layers. Curves A and A′ are for the sample 13–5 (Bi_2Se_3) at room temperature and at liquid air temperature respectively, and curves B and B′ for the sample 5–1 (BiSe) at room and liquid air temperatures, respectively. The abscissa for the curves A′ and B′ in the forward direction should be read ×10. (Thicknesses of the selenides=0.45μ and 0.50μ for samples 13–5 and 5–1, respectively.)

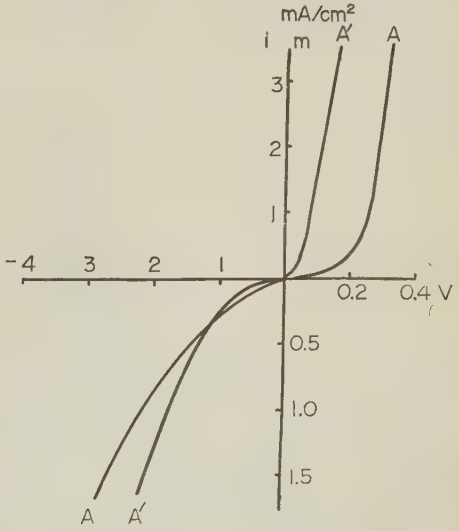

Fig. 5. The d.c. characteristics of the typical Se rectifier with PbSe layer. Curves A and A′ are for the sample 13–1 at room and liquid air temperatures, respectively. The abscissa for the curve A′ in the forward direction should be read ×10. (Thickness of PbSe=1.4μ.)

The selenide of tin, SnSe is also known to exist, but the effects of this material could not be measured, because it decomposed when evaporated in vacuum.

(3) *Rectifiers with Bi_2Se_3 and BiSe layers*

Both Bi_2Se_3 and BiSe are known as the selenides of bismuth. The crystal structures of these two selenides are very similar to each other, and it seems to be difficult to know which is really existing in usual selenium rectifiers.

The d.c. characteristics of some rectifiers with both Bi_2Se_3 and BiSe layers are shown in Fig. 4. As seen in the figure, both threshold voltage V_D and spreading resistance R_S in this case are smaller than in the case of CdSe, but larger than in the case of SnSe, and the breakdown voltage in this case is far smaller than in the cases of both CdSe and SnSe. In this case also, both V_D and R_S increase with decreasing temperature as seen

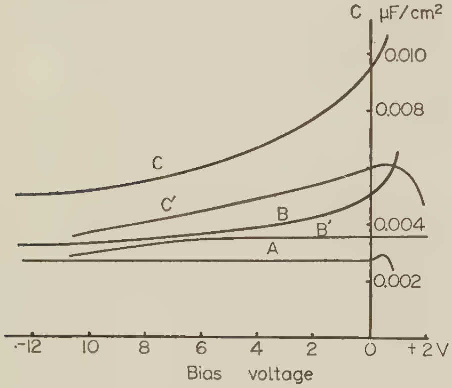

Fig. 6. The capacitance-voltage characteristics of the Se rectifiers with CdSe layer. Curves A, B and C are for the samples 11–6, 3–1 and 3–3, respectively, at room temperature, and curves B′ and C′ are for 3–1 and 3–3, respectively, at liquid air temperature. (Thicknesses of CdSe=1.6μ, 0.73μ and 0.50μ for samples 11–6, 3–1 and 3–3, respectively.)

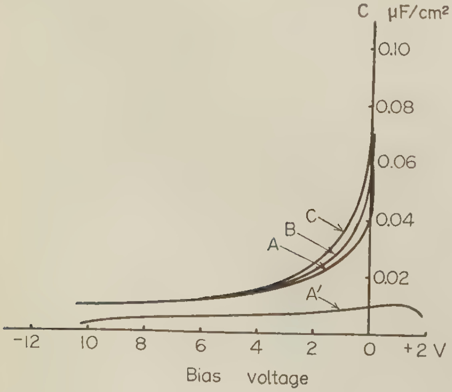

Fig. 7. The capacitance-voltage characteristics of the Se rectifiers with SnSe layer. Curves A, B and C are for the sample 10–6, 14–3 and 14–5, respectively, at room temperature, and curve A′ is for the sample 10–6 at liquid air temperature. (Thicknesses of SnSe=0.8μ, 1.2μ and 0.1μ for samples 10–6, 14–3 and 14–5 respectively.)

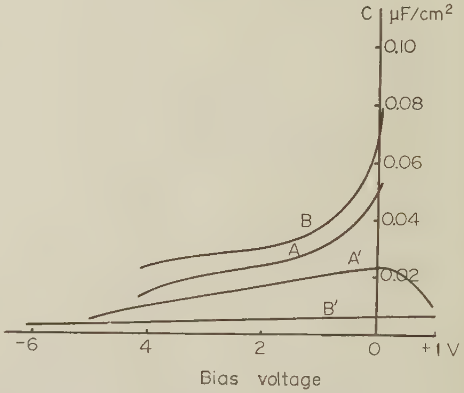

Fig. 8. The capacitance-voltage characteristics of the Se rectifiers with Bi_2Se_3 and BiSe layers. Curves A and A′ are for the sample 13–5 (Bi_2Se_3) at room and liquid air temperatures, respectively, and curves B and B′ are for the sample 5–1 (BiSe) at room and liquid air temperatures, respectively. (Thicknesses of the selenides=0.45μ and 0.50μ for samples 13–5 and 5–1, respectively.)

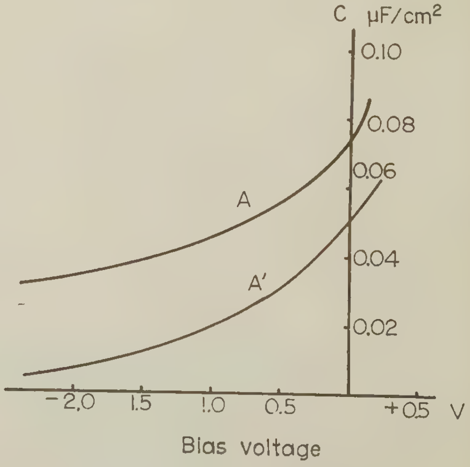

Fig. 9. The capacitance-voltage characteristics of the Se rectifiers with PbSe layer. Curves A and A′ are for the sample 13–1 at room and liquid air temperatures, respectively. (Thickness of PbSe=1.4μ for sample 13–1.)

in the figure and in Table VII.

The a.c. characteristics for these samples are shown in Fig. 8. Both capacitance and its bias voltage dependency of these samples are fairly large at room temperature and become considerably small at low temperature.

It should be noted that there is no essential difference between Bi_2Se_3 and BiSe. There was a noticiable fact, however, that when the thin Cd or Sn layer as the counter electrode is evaporated upon Bi_2Se_3 or BiSe layer, the colour of Bi_2Se_3 or BiSe layer near the Cd or Sn electrode changes into that of CdSe or SnSe, respectively, in a few days. From this fact, it might be doubtful that Bi_2Se_3 or BiSe layer could keep its purity between the selenium layer and the counter electrode metal even in the rectifiers with artificial Bi_2Se_3 or BiSe layer.

(4) *Rectifiers with PbSe layar*

Though the alloy which was used as the counter electrode of the selenium rectifier did not contain Pb, the characteristics of the rectifiers with PbSe layer were also measured in order to compare the results with those mentioned above. The results are shown in Fig. 5, Fig. 9, Table VI and VII. At room temperature, the value of threshold voltage V_D is smaller than in the case of CdSe, and larger than in the case of SnSe, and the spreading resistance R_S, capacitance and its bias voltage dependency are nearly the same as in the case of SnSe. The breakdown voltage is very small and these samples have very poor rectifying characteristics, especially at low temperature.

§ 3. Discussion

(1) *Case of CdSe layer*

Being an *n*-type semiconductor, CdSe seems to make a barrier layer between selenium and CdSe, and another one between CdSe and counter electrode metal. As seen in Table I, the donor density in CdSe is about the order of $10^{13}/cm^3$ and far smaller than the acceptor density in selenium which is about the order of $10^{16}/cm^3$ in usual rectifiers, and the following two cases, therefore, should be considered, as pointed out by Strosche[3].

(a) When the donors in CdSe layer are sufficiently abundant to make the space charge layer near the contact to selenium layer, both space charge layers, i.e., a *p–n* junction between CdSe and selenium, and a Schottky or Mott barrier between CdSe and counter electrode, should effectively act as the rectifying layers, and the characteristics of the rectifier should be analyzed by the double barrier layer theory[5]. The two barrier layers between CdSe and selenium, and between CdSe and counter electrode are named respectively the 1st and 2nd barrier layers for simplicity, and their diffusion potentials are respectively denoted as V_{D1} and V_{D2}. Considering the rectifying direction of this rectifier, the 1st barrier layer is the main barrier and the 2nd the sub-barrier and accordingly,

$$V_{D1} > V_{D2} . \qquad (2)$$

The equivalent circuit for this case is expressed as in Fig. 10 (c) or 10 (d), and when the bias voltage is applied in the forward direction, the sub-barrier layer is subjected to a large voltage in the reverse direction as in Fig. 10 (b). Consequently, if the bias voltage in the forward direction becomes sufficiently large, the sub-barrier layer dies away by breakdown, and the main barrier layer also disappears on account of the large forward bias, and the rectifier shows an ohmic characteristics for the forward voltage greater than a fixed value. This voltage is the so-called threshold voltage V_D, and then the threshold voltage V_D is given by the following equation:

$$V_D = V_{D1} + V_{C2} , \qquad (3)$$

where V_{C2} is the breakdown voltage of the sub-barrier layer. Considering the values of the forbidden gap E_G and the impurity level ΔE for selenium and CdSe, the value of V_{D1} seems to be about 1 volt at room temperature, and then the value of V_D must be greater than 1 volt, even if the value of V_{D2}, and accordingly the value of V_{C2} are sufficiently small. The observed values of V_D listed in Table II are plotted against the thickness of CdSe layers in Fig. 11. In the figure, the value of V_D increases as the thickness of the layer increases, and approaches a constant value (about 1.2 volt) as the thickness of the layer becomes greater than about 1 micron.

Although equation (3) implies that the value of V_D must be independent of the thickness of the layer, the fact that the observed value decreases with the decreasing thickness may be explained by the following reason: (i) the nonuniformity of the thickness of the CdSe layer is relatively great when the layer is thin, and the weak point in the barrier layer are comperatively numerous, (ii) the ions or atoms of tin or bismuth in the counter electrode metal may diffuse to make the selenides of tin or bismuth in the layer of CdSe during the forming process of the rectifier and there may be some bridge across the barrier layer. The explanations seems to be supported by the tendency that the apparent resistivity ρ is smaller in samples with thin layers than in those with thick layers as seen in Table II. If these assumptions may be accepted, the value of V_D for the samples with sufficiently thick layer, about 1.2 volt, may correspond to the value of V_D given by equation (3). Using this value and assuming the value of V_{D1} to be about 1.0 volt as mentioned above, the value of V_{C2} is estimated to be about 0.2 volt. According to the relation between breakdown voltage and diffusion potential given by Billig[6], $V_{C2}\approx 0.2$ volt corresponds to $V_{C2}\approx 0.01$ volt. This relation can also explain qualitatively the great change of the apparent threshold voltage V_D with temperature.

In order to consider the a.c. characteristics of these samples, the equivalent circuit as shown in Fig. 10 (d) may be used, and the impedances of the 1st and 2nd barrier layers, the resistance of CdSe layer between both barrier layers, and the capacitance between the selenium and the counter electrode are denoted as A_1-jB_1, A_2-jB_2, R_L and C_L respectively. When this circuit is substituted by a usual parallel circuit of resistance R and capacitance C, the following relations hold:

$$R=(A_1+A_2+R_L)+\frac{(B_1+B_2)^2}{(A_1+A_2+R_L)}, \qquad (4)$$

$$\omega C=\omega C_L+\frac{B_1+B_2}{(A_1+A_2+R_L)^2+(B_1+B_2)^2} \qquad (5)$$

and

$$\left.\begin{aligned} R_L&=\frac{d}{S}\rho \\ C_L&=\frac{\kappa S}{4\pi d}\,. \end{aligned}\right\} \qquad (6)$$

Here, ω is the angular frequency of the applied ripple voltage, d the thickness of CdSe layer, S the area of the electrode, and ρ and κ are the resistivity and the dielectric constant of CdSe, respectively.

Assuming that

$$A_1+A_2+R_L \gg B_1+B_2\,, \qquad (7)$$

the relation

$$C\approx C_L=\frac{\kappa S}{4\pi d} \qquad (8)$$

is obtained from equation (5) and it suggests that C is apparently independent of the bias voltage and is inversely proportional to the thickness of CdSe layer. The observed capacitance for the sample with thick CdSe layer scarcely depends upon the bias voltage as seen in Fig. 6. The zero bias capacitance C_0 of all samples are plotted against the thickness of CdSe layer in Fig. 12, which shows that the relation (8) is approximately satisfied. From this figure the dielectric constant κ is obtained to be about 6 according to equation (6), and this value does not seem to be an unreasonable one, though it is about twice the value estimated by applying Landsberg's theory[7] for some of these samples[8].

The above discussion is based upon the assumption of the condition (7) which holds for $A_i \gg B_i$, or $R_L \gg B_i$, where the suffix i ($i=1$ or 2) refers to the 1st and 2nd barrier layers respectively. Taking the equivalent circuits of the 1st and 2nd barrier layers to be the parallel circuits of the resistance and capacitance as shown in Fig. 10 (d), the impedance of each barrier is given as follows:

$$A_i=\frac{R_i}{1+R_i^2\omega^2C_i^2}\,, \qquad B_i=\frac{R_i^2\omega C_i}{1+R_i^2\omega^2C_i^2}\,. \qquad (9)$$

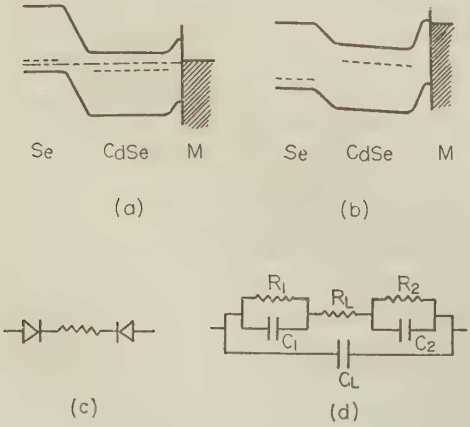

Fig. 10. Barrier model of Se rectifiers with CdSe layer.
(a) Equilibrium state. (b) Bias voltage is applied in the forward direction. (c) and (d) are the equivalent circuits of this rectifier.

(i) For $A_i \gg B_i$, equation (9) gives

$$R_i \omega C_i \ll 1 \,. \tag{10}$$

Though it is impossible to estimate correctly the values of the parameters in equation (10) from the present experiment, R_i must be smaller than $10^4\,\Omega\text{cm}^2$ in order to satisfy the condition (10), assuming the value $C_i \approx 0.1\mu\text{F}/\text{cm}^2$ which does not seem to be unreasonable. If the above values for R_i and C_i are adopted, $B_i \ll A_i \ll 10^4\,\Omega\text{cm}^2$, and from equation (4), R must be smaller than $10^4\,\Omega\text{cm}^2$, while the observed values of R are about $10^4 \sim 10^6\,\Omega\text{cm}^2$.

(ii) For $R_L \gg B_i$, it is required from equation (4) and (7) that $R_L \approx R \approx 10^4 \sim 10^6\,\Omega\text{cm}^2$, and using this value and equation (6), the resistivity of the CdSe, ρ, is obtained to be about $10^{10} \sim 10^{11}\,\Omega\text{cm}$, which is far greater than either the resistivity of bulk CdSe (in Table I), or the one which is obtained from spreading resistance R_S for the same sample (in Table II). But it may be possible that the resistance of CdSe layer, which exists in such a position as shown in Fig. 10 (a), is not necessarily equal to that of bulk CdSe on account of possible recombination and injection of carriers at the boundary between CdSe and selenium.

(b) When the donors in the CdSe layer are not sufficiently abundant to compensate the space charge in the selenium side, the donors in the CdSe layer are all ionized and then the layer acts as a Mott barrier. In this case, the barrier layer is single and, as is well known, the threshold voltage V_D is the difference between the work functions of selenium and counter electrode metal, and does not depend upon the thickness of the layer as in the assumption (a). The experimental dependency of V_D on the thickness of the CdSe layer which is seen in Fig. 11 may be explained as in the assumption (a). However, the observed value of V_D, if it should be the contact potential difference, seems to be rather too large, especially at low temperature.

The equivalent circuit for the barrier layer of this type is given by simple parallel circuit of a resistance and a capacitance, and consequently, the apparent capacitance does not depend upon the bias voltage and is always inversely proportional to the thickness of the CdSe layer. This situation seems to be well satisfied by the experimental results as shown in Figs. 6 and 12.

Further, the appropriateness of the assumption (a) and (b) should be considered in other ways. When a single barrier exists in a metal rectifier, the forward current is expressed as follows.

$$i_f \propto \exp\left[e(V - i_f R_S)/kT\right] \,, \tag{11}$$

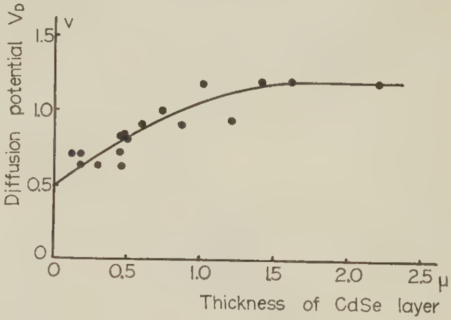

Fig. 11. The variation of the diffusion potential of Se rectifiers with thickness of CdSe layer at room temperature.

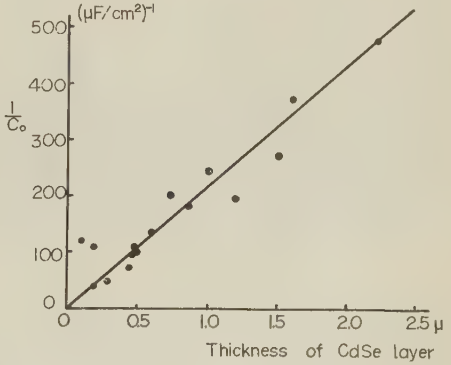

Fig. 12. The variation of zero-bias capacitance of Se rectifiers with thickness of CdSe layer at room temperature.

where, e is the electron charge, V the applied voltage, k the Boltzmann constant, T the absolute temperature. Accordingly, the plot of $\ln i_f$ vs. $V - i_f R_S$ should produce a straight line, and its slope should give a value corresponding to e/kT which is theoretically about $37\,\text{V}^{-1}$ at room temperature. Such a plot is given in Fig. 13 which shows that, though the linearity is nearly satisfied, the slope α is about a half of the theoretical value as seen in Table II. For the explanation for the fact that the experimental slope α is smaller than the theoretical one, the double barrier theory seems possible to be applied as pointed out by Numata[5]. Further, for the experimental fact that the capacitance of the rectifier decreases in the forward direction, the bouble barrier theory seems also applicable, because the reversely biased sub-barrier layer should affect the total capacitance.

Considering the facts mentioned above in addition to the fact that the apparent threshold voltage has a large value at low temperatures, the assumption (a) seems more reasonable than (b), though (a) has some difficulty concerning the value of the resistance of the CdSe layer, R_L.

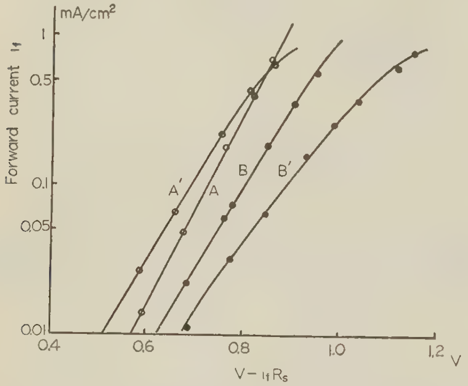

Fig. 13. The relation between the forward current and applied voltage in Se rectifiers with CdSe layer. Curves A and B are respectively for samples 3–1 and 11–6 before electrical forming, and curves A′ and B′ are respectively for samples 3–1 and 11–6 after electrical forming at room temperature.

(2) *Case of SnSe layer*

According to Grimm and Nasledov[9], a rectifying layer may exist between selenium and SnSe when they contact together. This layer and the barrier layer which seems to exist between SnSe and the counter electrode metal should construct a double barrier layer as in the case of the CdSe layer. In this case, however, the SnSe layer should not form a Mott barrier on account of its low resistivity.

The value of the threshold voltage V_D in the case of SnSe seems to be independent of the thickness of the layer, and is far smaller than that in the case of CdSe as seen in Table III. The value of the spreading resistance R_S is also independent of the thickness of the layer and nearly equal to the value of the resistance of the selenium layer itself.

The zero bias capacitance C_0 is plotted against the thickness of the layer in Fig. 14, and the figure shows that the capacitance seems to be also independent of the thickness of the layer neglecting the scattering among the samples, and the value of C_0 is far larger than in the case of the CdSe. These results show that the term ωC_L in equation (5) is sufficiently small compared with the second term and the term R_L is also negligible compared with the term A_l, being compatible with the low resistivity of SnSe.

The experimental relation between the forward current and the voltage across the barrier layer ($V - i_f R_S$) is shown in Fig. 15 which shows that the linearity between $\ln i_f$ and $V - i_f R_S$ is very good and the slope of the straight line is almost equal to the theoretical value 37 V^{-1} for a single barrier layer as seen in Table III. This fact seems to mean that the rectifier of this construction is typical one which is applicable for the usual theory of the rectification assuming a single barrier layer.

The experimental relation between the capacitance C and the bias voltage V is illustrated in Fig. 16, showing that there is the linear relation between $1/C^2$ and the bias voltage, that is, the Schottky capacitance relation[10]. It is reasonable to assume that the barrier layer is single and the Schottky type. Then the density of the impurity centers in the barrier layer and the diffusion potential are given from the straight line in Fig. 16. The density of the impurity centers N and the diffusion potential V_D' obtained thereby are also given in Table III. The value of the density of the impurity centers is in very good agreement with that in Table I which was obtained for bulk SnSe by the measurement of the Hall coefficient. However, the value of V_D' is somewhat larger than that of V_D.

From the above-mentioned facts, in the rectifier with SnSe layer, SnSe seems to build up a single and fairly stable barrier layer with either the selenium or the counter electrode metal at least at room temperature.* At low temperature, however, both V_D and R_S are greater, and both capacitance and its bias voltage dependency are smaller than those at room temperature, respectively, as in the case of CdSe layer. These facts seem to show not only that the bulk resistance of the SnSe layer increases with decreasing temperature, but also that the sub-barrier may come out to play a role in the rectification on account of the movement of the Fermi level resulting from the temperature decrease.

---

* Grimm and Nasledov[9] seem to assume that the rectifying contact is the contact between selenium and SnSe layer.

(3) *Case of Bi_2Se_3 and BiSe layer*

As both Bi_2Se_3 and BiSe are *n*-type, the barrier model and the equivalent circuit of a rectifier with the Bi_2Se_3 or BiSe layer may be illustrated in a manner similar to Fig. 10 for the case of the CdSe layer. As these materials have, however, far smaller resistivity than CdSe, the bulk resistance of the Bi_2Se_3 or the BiSe layer, R_L, as well as the layer capacitance ωC_L may be neglected in equations (4) and (5) as in the case of the SnSe layer. Consequently, the capacitance of the rectifier, C, is supposed to be independent of the thickness of the layer, and it is experimentally shown in Fig. 17.

The relation between $\ln i_f$ and $V-i_fR_S$ is linear as seen in Fig. 19, but the slope α is smaller than the theoretical value. This seems to suggest the existence of a double barrier layer. But in the region of large reverse bias voltage, the sub-barrier layer should disappear and Schottky barrier should be built up, so that $1/C^2$ becomes linearly proportional to the reverse bias voltage as seen in Fig. 18. The density of the impurity center N and the diffusion potential V_D' obtained from this figure are listed in Table IV and V. However, the densities of the impurity centers obtained here are smaller than those of the bulk materials listed in Table I.

At low temperatures, the impedances of both the barrier layer and the Bi_2Se_3 or BiSe layer become large, and the second term in equation (5) becomes smaller than the first term ωC_L. Consequently, the capacitance decreases and tends to be independent of the applied voltage so that the characteristic approaches that of a Mott barrier, as shown in Fig. 8.

As mentioned in § 2 (3), CdSe and SnSe may be produced in the layer of the bismuth selenide when the counter electrode metal is sprayed on the layer, and the selenides of cadmium and tin may play an important part in the rectifying characteristics of the recti-

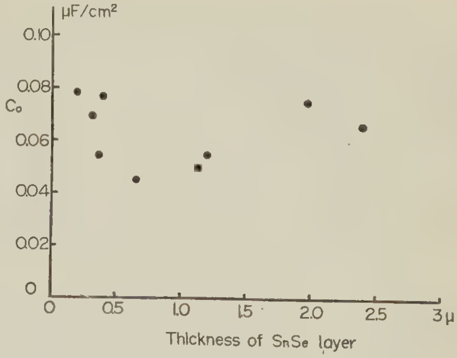

Fig. 14. The variation of zero-bias capacitance of Se rectifiers with thickness of SnSe layer at room temperature.

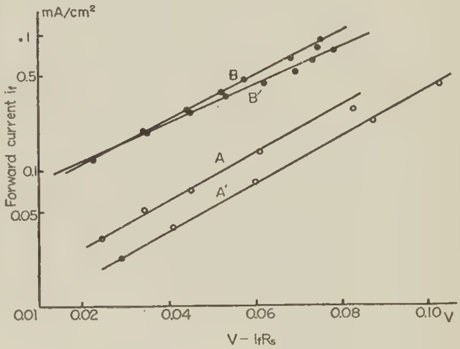

Fig. 15. The relation between the forward current and applied voltage in Se rectifiers with SnSe layer. Curves A and B are respectively for the sample 10-5 and 14-5 before electrical forming, and curves A′ and B′ are for the same samples after electrical forming at room temperature.

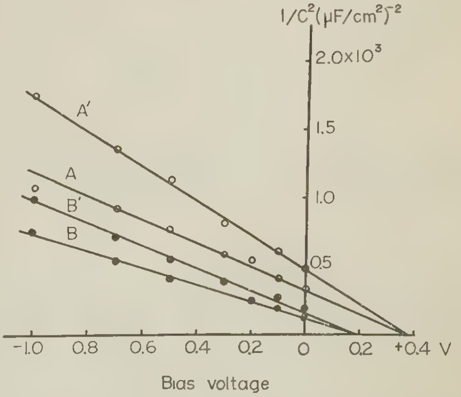

Fig. 16. $1/C^2$-voltage relation of Se rectifiers with SnSe layer. Curves A and B are respectively for the sample 10–6 and 14–1 before electrical forming, and curves A′ and B′ are for the same sample after forming at room temperature.

fier. The facts that there is no essential difference between the characteristics of the rectifiers with the Bi_2Se_3 and with the BiSe layers, and that the density of the impurity centers in the barrier layer does not agree with that of bulk materials, may suggest the above possibility, but it was impossible to ascertain this point in the present experiment.

(4) *Case of PbSe*

PbSe is a *p*-type semiconductor and its resistivity is of the same order with SnSe, so the behaviors of the rectifier with the PbSe layer may be expected to be similar to those with the SnSe layer. This expection seems to be well satiefied in the capacitance measurement as shown in Figs. 17 and 18. But the slope α obtained from the plot of $\ln i_f$ vs. $V-i_fR_S$ (Fig. 19) is fairly smaller than the theoretical value as shown in Table VI, and this may be attributed to the existence of the sub-barrier layer. The poor rectification shown in Fig. 5 seems to suggest that the main barrier layer is not so predominant. This fact shows that Pb is an undersirable component for the counter electrode alloy in the usual selenium rectifier.

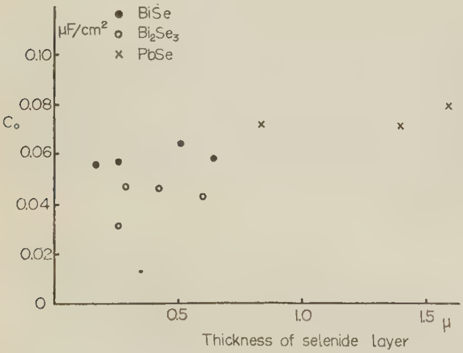

Fig. 17. The variation of zero-bias capacitance of Se rectifiers with thickness of Bi_2Se_3, BiSe and PbSe layers at room temperature.

(5) *Case of usual selenium rectifiers*

If a usual selenium rectifier has the selenides of cadnium, tin and bismuth between the bulk selenium and the counter electrode alloy, as mentioned in § 1, the characteristics of the rectifier must be considered from a point of view of "multi-contacts" of these selenides and the selenium or the counter electrode. Especially, the SnSe layer seems to play an important role in the rectification as well as the CdSe layer, and the following characteristics in the usual selenium rectifier may be explained from the above view-point:

(i) The value of apparent "diffusion potential" is not always constant but scatters in the range from about 0.3 to 0.6 volt. This is perhaps because of the fact that the SnSe layer ($V_D \approx 0.1$ volt), Bi_2Se_3 or BiSe layer ($V_D \approx 0.2$ volt) and CdSe layer ($V_D \approx 1.2$ volt) exist together and the fractions of the effective area of these selenides are different from sample to sample.

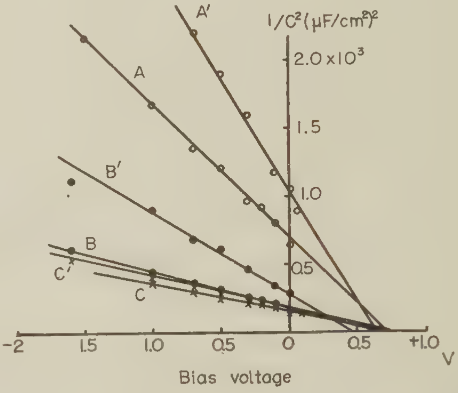

Fig. 18. $1/C^2$-bias voltage relation of Se rectifiers with Bi_2Se_3 (A, A'), BiSe (B, B') and PbSe (C, C') layers. Lines A, B and C are respectively for samples 4–1, 4–2 and 5–3 before electrical forming, and A', B' and C' are for the same samples after forming at room temperature.

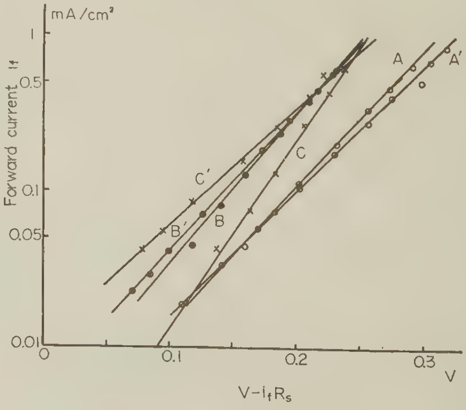

Fig. 19. The relation between the forward current and applied voltage in Se rectifiers with Bi_2Se_3 (A, A'), BiSe (B, B') and PbSe (C, C') layers. Lines A, B and C are respectively for the sample 13–6, 13–4 and 13–1 before electrical forming, and A', B' and C' are for the same samples after electrical forming at room temperature.

(ii) The slope of the line of $\ln i_f$ vs. $V-i_fR_S$ is smaller than that expected from the single barrier theory and the slope decreases as the bias voltage increases. Besides the double barrier theory, the "multi-contact" theory[11] has also been represented to explain this fact.

(iii) The "diffusion potential" increases[12] and the capacitance decreases[13] remarkably at low temperature. These may be explained by the considerations of the double barrier layer as mentioned in (1) and (2) of this section.

The above considerations suggest that though, of course, the *p–n* junction between the CdSe and selenium plays an important role in the rectifying characteristics of usual selenium rectifiers, the roles of the sub-barrier layer which exists between the selenides and the counter electrode, and of the other selenides layers besides CdSe should never be neglected.

Besides, it is expected that the CdSe in usual selenium rectifiers has a far smaller resistivity than the pure CdSe, some halogen being added in the bulk selenium; the difference in the resistivity between CdSe and the other selenides in usual rectifiers might not be so large as in the present experiments.

Some experiments have already been done to increase the breakdown voltage of the selenium rectifier by means of making an artificial layer between the bulk selenium and the counter electrode[14]. As the used materials have high resistances, the high resistance layer in the rectifier increases the forward resistance and decreases the rectification ratio. It is important to discuss what conditions are necessary to get a useful artificial layer.

(i) The material should not react with the selenium or the counter electrode metal to make other compound. This is necessary to avoid an aging effect in the rectifier.

(ii) The material is desirable to make a stable and single barrier layer with the selenium or the counter electrode, without making the sub-barrier layer. The effect of the sub-barrier layer is to increase the apparent threshold voltage and make the forword characteristics worse as is discussed relating to the action of the CdSe layer in (1) of this section.

(iii) The material should not have high resistivity if it makes a stable barrier layer. The layer of an insulator or high resistivity material is effective to increase the breakdown voltage in the insulator breakdown phenomena. The breakdown phenomena in rectifiers are, however, essentially different from those in the insulator, and it is well known that it is the weak points in the barrier layer, patches, which have the important meaning in the selenium rectifier breakdown phenomena[15]. Considering the above fact, it is rather more necessary to make a perfect, patchless barrier layer than to make a insulating layer in order to increase the breakdown voltage in the selenium rectifier. When an insulator or high resistivity material is used to make a layer thick enough to be patchless, the forward resistance of the rectifier increases and the rectification ratio becomes worse.

On the contrary, some material of low resistivity may make a stable barrier layer with the selenium or the counter electrode, and the layer may be thick enough to prevent patches and to increase the breakdown voltage without increasing the forward resistance of the rectifier. The SnSe used in the present experiment seems to be an example of such a material, though its diffusion potential is not so large that the breakdown voltage is not satisfactorily large.

Fig. 11 seems to show that the artificial CdSe layer should be thicker than 1 micron to make a stable and patchless barrier layer. The material which is desirable for making the artificial layer should have, therefore, the resistivity of smaller than $10^4\,\Omega$cm in order that one could neglect the resistance of the layer of 1 micron thickness compared with that of the bulk selenium.

In addition to the three conditions mentioned above, it is of course necessary that the material should make a high main barrier layer with the selenium or the counter electrode to give a high breakdown voltage, and from this view point SnSe is not very good. If there are some materials which satisfy the above conditions and have diffusion potentials of greater than a few tenth volt, they should be much available for artificial barrier layers in selenium rectifiers.

§ 4. Conclusion

The characteristics of selenium rectifiers,

Table II. Results for selenium rectifiers with CdSe layer at room temperature.

Sample	Electrode	Thickness of layer $d(\mu)$	Before electric forming*					After electric forming*				
			Threshold voltage V_D (V)	Spreading resistance R_S (Ω/cm^{-2})	Resistivity of CdSe ρ (Ω cm)	Logarithmic slope α (V^{-1})	Zero bias capacitance C_0 (μF/cm^2)	Threshold voltage V_D (V)	Spreading resistance R_S (Ω/cm^2)	Resistivity of CdSe ρ (Ω cm)	Logarithmic slope α (V^{-1})	Zero bias capacitance C_0 (μF/cm^2)
3–1	Wood Metal	0.73	0.92	94	0.96×10^6	14	.0039	1.00	170	2.0×10^6	12	.0050
3–2	〃	0.60	0.81	80	0.93 〃	12	.0083	0.90	110	1.3 〃	12	.0073
3–3	〃	0.50	0.72	54	0.54 〃	16	.0102	0.80	54	0.54 〃	12	.0094
3–4	〃	0.19	0.66	37	0.52 〃	14	.0090	0.70	29	0.11 〃	15	.0085
3–5	〃	0.12	0.66	37	0.83 〃	17	.0085	0.70	35	0.67 〃	14	.0083
4–5	〃	0.46	0.54	34	0.22 〃	15	.0159	0.61	42	0.39 〃	12	.0149
6–1	〃	0.45	0.68	34	0.38 〃	11	.0160	0.71	44	0.60 〃	14	.0139
6–2	〃	0.20	0.58	31	0.70 〃	17	.0276	0.62	24	0.35 〃	15	.0243
11–1	〃	0.45	0.74	37	0.33 〃	15	.0086	0.82	54	0.71 〃	14	.0083
11–2	〃	0.30	0.63	30	0.27 〃	17	.0178	0.62	37	0.83 〃	18	.0177
11–4	〃	1.2						0.93	140	0.98 〃	12	.0052
11–5	〃	1.5	0.39	104	0.61 〃	13	.0041	1.20	290	1.79 〃	7.6	.0037
11–6	〃	1.6	0.99	154	0.89 〃	12	.0031	1.20	330	1.99 〃	7.4	.0027
15	〃	0.48						0.83	21	0.05 〃		.0090
16	〃	0.86						0.91	32	0.14 〃		.0055
17	〃	1.0						1.18	88	0.68 〃		.0041
18	〃	2.2						1.20	260	1.1 〃		.0021

* The electrical forming was always done with the constant power, 300 mW/cm, for 2 hours for all samples.

Table III. Results for selenium rectifiers with SnSe layer at room temperature.

Sample	Electrode	Thickness of layer d (μ)	Before electric forming*						After electric forming*					
			Threshold voltage V_D (V)	Spreading resistance R_S (Ω/cm²)	Logarithmic slope α (V^{-1})	Zero bias capacitance C_0 (μF/cm²)	Diffusion potential V_D' (V)	Density of impurity centers N (cm^{-3})	Threshold voltage V_D (V)	Spreading resistance R_S (Ω/cm²)	Logarithmic slope α (V^{-1})	Zero bias capacitance C_0 (μF/cm²)	Diffusion potential V_D' (V)	Density of impurity centers N (cm^{-3})
4–3	Wood Metal	1.2	0.10	16	38	.092	0.50	2.2×10^{17}	0.10	24	40	.051	0.40	1.2×10^{17}
5–6	〃	0.3	0.10	20	42	.087	0.38	1.6 〃	0.12	31	34	.069	0.34	1.3 〃
10–5	〃	0.3	0.11	25	41	.060	0.35	1.8 〃	0.12	31	41	.053	0.32	1.3 〃
10–6	〃	0.8	0.10	25	41	.055	0.38	1.6 〃	0.12	27	41	.045	0.38	1.1 〃
14–1	〃	2.5	0.06	22	36	.085	0.14	2.2 〃	0.06	20	35	.066	0.16	1.6 〃
14–2	〃	2.2	0.06	22	38	.110	0.12	2.2 〃	0.055	20	48	.075	0.20	1.7 〃
14–3	〃	1.2	0.075	22	34	.075	0.23	2.2 〃	0.08	24	33	.055	0.25	1.5 〃
14–4	〃	0.4	0.065	20	36	.086	0.20	2.6 〃	0.065	22	35	.076	0.24	2.1 〃
14–5	〃	0.1	0.07	23	38	.115	0.19	2.1 〃	0.075	23	33	.077	0.24	2.1 〃
8–1	Cd	0.6	0.085	19	41	.068			0.13	35	41	.044		
10–1	〃	0.8	0.09	19	39	.065			0.11	16	42	.053		
10–2	〃	0.3	0.10	23	37	.072			0.12	21	38	.066		

Table IV. Results for selenium rectifiers with Bi_2Se_3 layer at room temperature.

Sample	Electrode	Thickness of layer d (μ)	Before electric forming*						After electric forming*					
			Threshold voltage V_D (V)	Spreading resistance R_S (Ω/cm²)	Logarithmic slope α (V^{-1})	Zero bias capacitance C_0 (μF/cm²)	Diffusion potential V_D' (V)	Density of impurity centers N (cm^{-3})	Threshold voltage V_D (V)	Spreading resistance R_S (Ω/cm²)	Logarithmic slope α (V^{-1})	Zero bias capacitance C_0 (μF/cm²)	Diffusion potential V_D' (V)	Density of impurity centers N (cm^{-3})
4–1	Wood Metal	0.26	0.23	36	24	.0399	0.70	1.4×10^{17}	0.25	15	25	.0304	0.61	0.84×10^{17}
5–2	〃	0.62	0.27	39	22	.0569	0.92	4.5 〃	0.26	28	22	.0439	0.79	2.3 〃
13–5	〃	0.45	0.28	26	24	.0459	0.61	2.0 〃	0.30	50	20	.0475	0.61	2.0 〃
13–6	〃	0.27	0.30	36	21	.0457	0.66	2.1 〃	0.31	49	19	.0487	0.61	2.1 〃

Table V. Results for selenium rectifiers with BiSe layer at room temperature.

Sample	Electrode	Thickness of layer d (μ)	Before electric forming*						After electric forming*					
			Threshold voltage V_D (V)	Spreading resistance R_S (Ω/cm^2)	Logarithmic slope α (V^{-1})	Zero bias capacitance C_0 (μF/cm^2)	Diffusion potential V_D' (V)	Density of impurity centers N (cm^{-3})	Threshold voltage V_D (V)	Spreading resistance R_S (Ω/cm^2)	Logarithmic slope α (V^{-1})	Zero bias capacitance C_0 (μF/cm^2)	Diffusion potential V_D' (V)	Density of impurity centers N (cm^{-3})
4–2	Wood Metal	0.62	0.14	28	34	.085	0.58	5.0×10^{17}	0.14	26	30	.0590	0.45	2.3×10^{17}
5–1	〃	0.50	0.14	14	30	.088	0.63	5.0 〃	0.12	21	36	.0839	0.46	3.1 〃
13–3	〃	0.26	0.24	38	23	.056	0.49	1.5 〃	0.25	44	23	.0567	0.46	2.2 〃
13–4	〃	0.15	0.24	30	23	.053	0.47	1.8 〃	0.24	34	21	.0557	0.46	1.9 〃

Table VI. Results for selenium rectifiers with PbSe layer at room temperature.

Sample	Electrode	Thickness of layer d (μ)	Before electric forming*						After electric forming*					
			Threshold voltage V_D (V)	Spreading resistance R_S (Ω/cm^2)	Logarithmic slope α (V^{-1})	Zero bias capacitance C_0 (μF/cm^2)	Diffusion potential V_D' (V)	Density of impurity centers N (cm^{-3})	Threshold voltage V_D (V)	Spreading resistance R_S (Ω/cm^2)	Logarithmic slope α (V^{-1})	Zero bias capacitance C_0 (μF/cm^2)	Diffusion potential V_D' (V)	Density of impurity centers N (cm^{-3})
5–3	Wood Metal	1.6	0.21	18	19	.077	0.76	6.9×10^{17}	0.20	21	17	.0805	0.65	5.5×10^{17}
13–1	〃	1.4	0.24	18	27	.077	0.70	5.7 〃	0.23	24	17	.0727	0.58	4.5 〃
13–2	〃	0.83	0.25	13	26	.078	0.74	6.4 〃	0.24	16	16	.0717	0.58	4.5 〃

Table VII. Comparison of results between room and liquid air temperatures. (After electric forming)

Sample	Selenide	Thickness of layer d (μ)	Electrode	Values at room temperature			Values at liquid air temperature		
				Threshold voltage V_D (V)	Spreading resistance R_S (Ω/cm^2)	Zero bias capacitance C_0 (μF/cm^2)	Threshold voltage V_D (V)	Spreading resistance R_S (Ω/cm^2)	Zero bias capacitance C_0 (μF/cm^2)
3–1	CdSe	0.73	Wood Metal	1.00	170	.0050	4.6	1900	.0035
3–3	〃	0.50	〃	0.80	54	.0094	2.2	700	.0060
10–6	SnSe	0.75	〃	0.10	25	.055	1.8	400	.0101
13–5	BiSe	0.45	〃	0.30	50	.0475	1.00	560	.0234
5–1	〃	0.51	〃	0.12	21	.0839	2.85	1500	.0064
13–3	〃	0.27	〃	0.25	44	.0567	1.00	580	.0292
5–3	PbSe	1.6	〃	0.20	21	.0805	0.68	700	.0069
13–1	〃	1.4	〃	0.23	24	.0727	0.42	350	.0500

which have an artificial layer of some selenides, were measured to give the following results:

(1) The CdSe layer plays an important role in a rectifying characteristics of selenium rectifiers, but it seems to make a double barrier layer with the bulk selenium and the counter electrode metal. The resistivity of pure CdSe is too large to give a good rectification ratio, though the CdSe in the usual selenium rectifier is expected to have a smaller resistance than the pure one, because some halogens are usually added in the bulk selenium of rectifiers.

(2) The SnSe layer also seems to play an important role in usual selenium rectifier, and it is of particular interest that the forward current voltage characteristic of the rectifier with the SnSe layer is in good agreement with the single barrier theory.

(3) The selenides of bismuth and lead should be unsuitable as an artificial layer because of the low main barrier and the comperatively high sub-barrier.

(4) Materials with resistivity smaller than about $10^4\ \Omega$cm seems to be preferable to materials with high resistivity as artificial layers in selenium rectifiers.

The author should like to express his sincere thanks to Prof. A. Okazaki for his kind guidance. The author is greatly indebted also to Prof. H. Tubota, Mr. H. Suzuki, Mr. K. Hashimoto, Mr. S. Asanabe and Shindengen Kogyo K. K. for the offer of the samples used in the present experiment.

References

1) J. Yamaguchi and S. Katayama: J. Phys. Soc. Japan **5** (1950) 386.
J. Yamaguchi and T. Miyauchi: Electrotech. Pap. I. E. E. Japan **3** (1951) 5.
2) A. Hoffman and E. Rose: Z. f. Phys. **136** (1953) 152.
J. Yamaguchi: J. Phys. Soc. Japan **10** (1955) 234.
3) H. Strosche: Z. f. Phys. **145** (1956) 597.
4) M. Ono: Reported at the Branch Meeting of the Phys. Soc. Japan, April, 1957.
5) T. Numata: Mem. Fac. Sci. Kyusyu Univ. Ser. **B**, No. **3** (1953) 79.
6) E. Billig: Proc. Roy. Soc. London **A 207** (1951) 156.
7) P. T. Landsberg: Proc. Roy. Soc. **A 206** (1951) 463 and 477; Proc. Phys. Soc. **B 65** (1952) 397.
8) Y. Moriguchi and A. Okazaki: Proc. Phys. Soc. London **B 70** (1957) 991.
9) V. R. Grimm and D. N. Nasledov: Soviet Physics-Technical Physics **1** (1956) 687.
10) H. K. Henisch: "*Rectifying Semiconductor Contacts*," Oxford University Press (1957) p. 214.
11) H. J. Yearian: J. Appl. Phys. **21** (1950) 214.
V. A. Johnson, R. N. Smith and H. J. Yearian: ibid. **21** (1950) 283.
12) R. Cooper: Proc. Phys. Soc. **B 65** (1952) 409.
Y. Matukura and A. Okazaki: Mem. Fac. Sci. Kyusyu Univ. Ser. **B**, No. **4** (1954) 119.
13) Y. Moriguchi: Kurume Univ. Jour. **6** (1955) 10 (in Japanese).
14) J. Yamaguchi, T. Kanazawa and T. Matozaki: Electrotech. Pap. I. E. E. Japan **74** (1954) 1382 (in Japanese).
W. Hartmann: Phys. Z. **37** (1936) 862.
15) W. Schottky: Z. f. Phys. **118** (1942) 539.

JOURNAL OF THE PHYSICAL SOCIETY OF JAPAN Vol. 14, No. 2, FEBRUARY, 1959

Studies on (Ba-Pb)(Ti-Zr)O_3 System

By Takuro IKEDA

Kobayashi Institute of Physical Research, Kokubunji, Tokyo

(Received November 6, 1958)

Structural studies on (Ba-Pb)(Ti-Zr)O_3 system were performed, and the phase diagram of the whole system was determined. In the vicinity of $BaTiO_3$, low temperature phases are brought to room temperature by adding Pb and Zr. Substituting some amount of Pb by Ba in Pb(Ti-Zr)O_3, Curie point becomes lower, but the morphotropic boundary between F_α and F_β phase shifts only gradually to the Ti side, and may lie nearly at the same composition with varying temperature. The axial ratio in F_β phase decreases with decreasing Ti concentration, while $90° - \alpha$ in F_α decreases with increasing Ba and hardly depends on Ti-Zr ratio,

Some solid solution ceramics along the morphotropic bundary with Ba 5–20% and Ti 40–50% are excellent for piezoelectric materials, and those containing Ba *ca.* 30% and Ti 5–25% have large dielectric constants and low temperature coefficients.

§ 1. Introduction

Many structural studies on the perovskite type crystals of $A^{2+}B^{4+}O_3$ have been published; *e.g.* $BaTiO_3$, $PbZrO_3$ etc. The properties of the binary and ternary systems of them have been also investigated. Above all, the solid solutions consisting of Ba^{++}, Pb^{++} and Ti^{4+}, Zr^{4+} are interesting from both physical and technical aspects. The structures of (Ba-Pb)TiO_3 system have been studied by Shirane et al[1], Pb(Ti-Zr)O_3 by Shirane[2] and Sawaguchi[3], and (Pb-Ba)ZrO_3 by Shirane *et al*[4]. Ferroelectricity of $BaTiO_3$ is strengthened by adding $PbTiO_3$. $PbTiO_3$ is ferroelectric at room temperature and transforms into the paraelectric phase at 490°C. $PbZrO_3$, on the other hand, is antiferroelectric and of orthorhombic structure at room temperature and transforms to cubic structure at 230°C. The solid solution system of $PbTiO_3$ and $PbZrO_3$ has been studied in detail by Sawaguchi[3]. The phase diagram and the crystal deformation of that system determined by him are shown in Fig. 1(a) and (b). A_α indicates the same antiferroelectric phase as that of $PbZrO_3$, and F_β the tetragonal and ferroelectric one. F_α is also a ferroelectric phase, but its crystal structure belongs to rhombohedral class. The phase boundary between F_α and F_β is nearly parallel to the temperature axis and is called "morphotropic". The phase relation of Ba(Ti-Zr)O_3 system has been given by a few authors. Fig. 2 is the one reported by Kell and Hellicar[5], which was determined by dielectric and elastic measurements.

From industrial aspects, improvements of the electromechanical properties of $BaTiO_3$ have been desired. The addition of $PbTiO_3$ to $BaTiO_3$ produces a better piezoelectric ceramics. For instance, Mason[6] has shown that an addition of several mole percent of

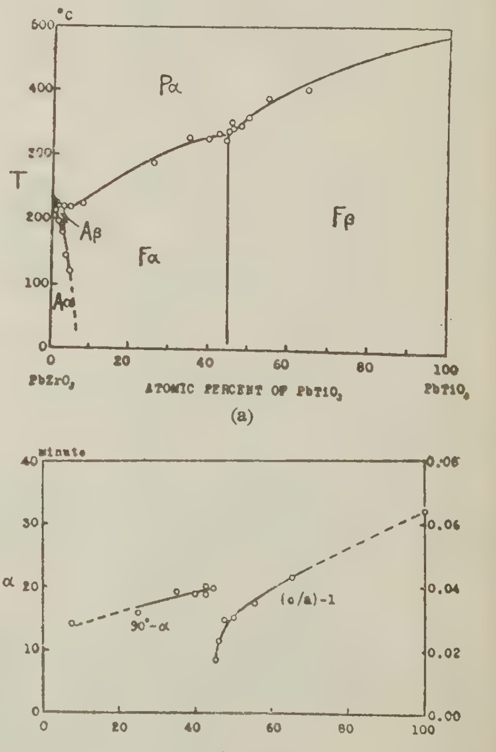

(a)

(b)

Fig. 1. Phase diagram and crystal deformation of Pb(Ti-Zr)O_3. (Sawaguchi)

Pb increases the coercive field and flattens the temperature variation of constants. The ceramics of Ba(Ti-Zr)O_3 with proper amount of Zr have large value of g, the piezoelectric output voltage coefficient, which is shown by Kell *et al*[5]. The ceramics of Pb(Ti-Zr)O_3 have been shown to be very useful by Jaffe and others[7]. The ceramics with composition near the morphotropic transformation show large piezoelectricity. (They are named PZT in short.) Fig. 3 shows one of their results, where k_r is the radial electromechanical coupling coefficient and ε the dielectric constant at room temperature. Varying composition, values of k_r and ε have sharp maxima at that boundary. Moreover, the solid solutions in the vicinity of the boundary have high Curie points ($>300°C$) and so their frequency constants, dielectric constants and coupling coefficients have relatively low temperature coefficients. Inspite of these good qualities, the sintering technique is difficult on account of the volatility of PbO.

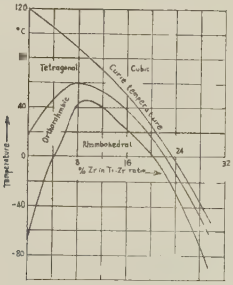

Fig. 2. Phase diagram of Ba(Ti-Zr)O_3. (Kell and Hellicar)

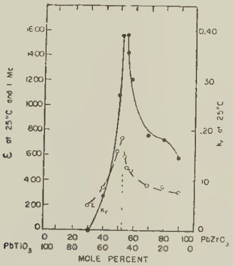

Fig. 3. Dielectric constant and radial coupling coefficient in Pb(Ti-Zr)O_3. (Jaffe *et al*)

The present author has mainly studied following respects: a determination of the phase diagram of (Ba-Pb)(Ti-Zr)O_3 system, measurements of anomalous properties of the solid solutions with composition near the morphotropic transformation, an examination of the phase relation in the vicinity of $BaTiO_3$ with small amount of Pb and Zr, and an improvement of piezoelectric ceramics PZT, etc.

Smolenskiĭ and others[8] have investigated the solid solution $BaTiO_3$-$PbZrO_3$, only a part of the present system, but have not reported a structural study. In the present paper, various properties of the whole system of (Ba-Pb)(Ti-Zr)O_3 are examined.

§ 2. Preparation of Samples

Proper mole percent of $BaCO_3$, PbO, TiO_2 and ZrO_2 were mixed and calcined at 1050°–1250°C. They were then crushed, pressed and sintered at 1250°–1500°C. (Samples containing larger amount of PbO were fired at lower temperatures.) $BaCO_3$ and ZrO_2 were of reagent grade, and PbO was of c.p. grade. TiO_2 was specially prepared by fractional distillation of $TiCl_4$, and was fairly pure (99.57%); impurities contained were Na_2O: 0.07, K_2O: 0.07, Fe: 0.003, $Zr < 0.01$, $SiO_2 < 0.01$. The evaporation of PbO during a firing process could not be ignored. Accordingly, a proper amount of PbO was laid around the sample in the crucible, and only inner parts of the piled-up discs of the sample were used for measurements. The samples fired were not chemically analyzed, but their compositions were specified by their mixing concentrations and were indicated by the amount of Ba and Ti in most cases.

§ 3. Solid Solutions with Small Concentration of Pb and Zr in the Vicinity of $BaTiO_3$

The polymorphic transitions show anomalies, as peaks or humps, on the curve of dielectric constant *vs.* temperature. The resonant frequency *vs.* temperature curve has clear minima or dents at the transition points. In the case of $BaTiO_3$, the temperatures at which any anomalies appear in the dielectric measurements are identical with those in the elastic one. The ceramics which have been pre-poled under the high electric field in the ferroelectric range show piezoelectricity and can be used for elastic measurement in the self-resonance. The phase diagram of Ba(Ti-Zr)O_3 system has been determined by Kell and Hellicar by such dielectric and elastic measurements, as shown in Fig. 2. With increasing Pb concentration, Curie point is raised, while two lower transition points are lowered. On the other hand, increasing Zr concentration, the two lower transition points are raised; the humps on the dielectric constant curve become less clear but the indentation on the elastic one are still distinguishable. With varying composition, these points determined by both dielectric and elastic means are plotted in Fig. 4 (a). The phase diagram at room temperature is given, as shown in Fig. 4 (b). F shows a ferroelectric phase, and P a paraelectric one (belonging to the cubic class). Suffix β indicates the tetragonal phase (after Sawaguchi's notation), and 1 and 2 correspond to the lower phases of $BaTiO_3$, *i.e.* the rhombohedral phase and the orthorhombic one, respectively. The boundaries which are not determined clearly are shown by dotted lines.

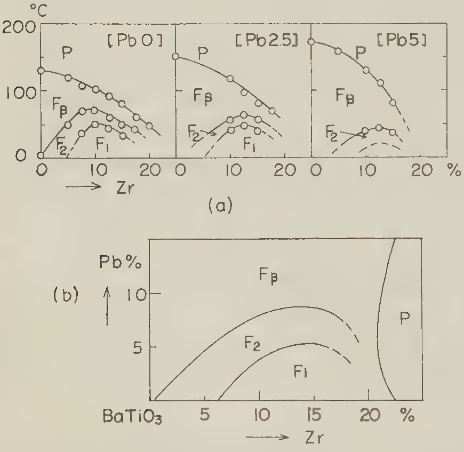

Fig. 4 (a). Shift of transition points. (b) Phase diagram in the vicinity of $BaTiO_3$.

The solid solution ceramics with proper amount of Pb and Zr have large dielectric constant and piezoelectric coefficient, owing to the shift of transition points. Various constants vary remarkably with temperature, and they seemed to be unpreferable for industrial purposes.

§ 4. Structural Studies of the Solid Solutions with Less than 50 Percent of Ba

(a) *Dielectric measurement*

In the solid solutions with small Ba concentration, the dielectric constant *vs.* temperature curve shows a sharp peak at Curie point. Increasing Ba concentration, Curie point becomes lower and the peak of the dielectric constant curve changes to a broad maximum, as shown in Fig. (a). The temperature corresponding to the maximum of the dielectric constant is considered to be Curie point, and these points of several solid solutions are plotted by dotts in Fig. (b). Some samples with small concentration of Ba and Ti near $PbZrO_3$ show other humps on the dielectric constant curve, which correspond to the transition from antiferroelectric state to ferroelectric one, according to Shirane[1] and Sawaguchi[3]. The solid solutions Pb(Ti-Zr)O_3 containing small amount of $PbTiO_3$ have been investigated in detail by Sawaguchi.

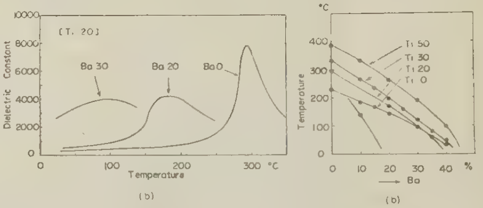

Fig. 5 (a). Dielectric constant of (Ba-Pb) (Ti20-Zr80)O_3. (b) Transition point for various composition.

(b) *X-ray measurement and phase diagram at room temperature*

In obtaining the phase diagram, the boundary between A_α and F_α was determened by above means; A_α is the antiferroelectric phase similar to $PbZrO_3$, and F_α is the ferroelectric one of rhombohedral structure appearing in Pb(Ti-Zr)O_3 and (Pb-Ba)ZrO_3 systems.

In the Pb(Ti-Zr)O_3 system, the boundary between F_α and F_β has been shown to be nearly parallel to the temperature axis and to be at the composition of Pb(Ti45-Zr55)O_3 by Sawaguchi[3]. In the present case, that boundary could not be determined by the dielectric means on account of absence of a hump. The powder photographs of several samples were taken at room temperature with a camera of 57.3 mm in diameter, using CuKα radiation. The lattice constants are shown in Fig. 6. The solid solutions on the left side with larger Ti concentration belong to F_β phase, and their tetragonalities become smaller with increasing Zr concentration, as shown in Fig. 7. These on the right side belong to F_α phase. Their rhombohedral angles α's were determined by using a diffractmeter of the Rigakudenki Co.; where the back reflection side ($h^2+k^2+l^2=20$, 22, 24 and 26) was examined (*cf.* the paper of Shirane and Hoshino[4]).

In the case of Ba 0, namely Pb(Ti-Zr)O_3, the boundary is located at the composition of Ti 42.5–45. With increasing Ba, the boundary shifts gradually to the larger Ti side at room temperature. The phase diagram at room temperature is thus determined and shown in Fig. 8. How the boundary between F_α and F_β changes with varying temperature is considered in the next paragraph.

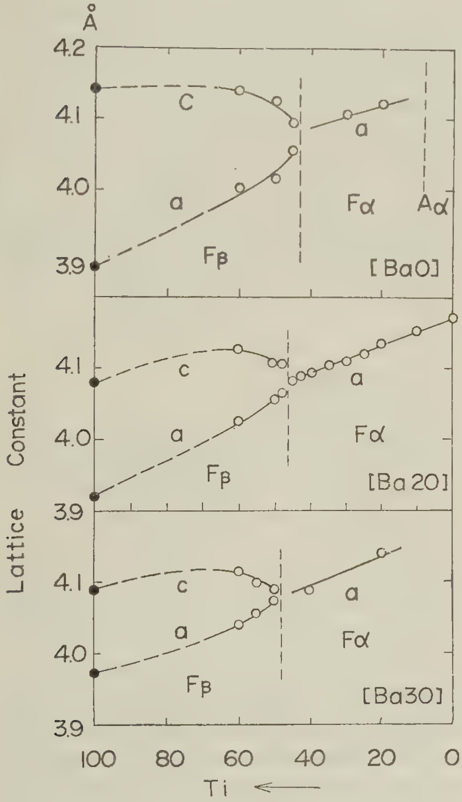

Fig. 6. Lattice constants (●—after Shirane)

(c) *Elastic measurement and examination of the boundary between* F_α *and* F_β

As the solid solution above the Curie point is not piezoelectric, a self-resonance method cannot be used for elastic measurement. The elastic property of a non-piezoelectric sample is determined by observing the resonance of the so-called composite-bar consisting of the quartz rod (X-cut and Y-long) and the specimen cemented endwise with each other.

In the case of the composition near $BaTiO_3$, a minimum or a dent appears at the temperature corresponding to a maximum or a hump of dielectric constant *vs.* temperature curve. In the solid solutions with less than 40% of Ba and 20–55% of Ti, peculiar phenomena are observed. A few examples of the temperature variations of the resonant-frequencies of the composite-bar are shown

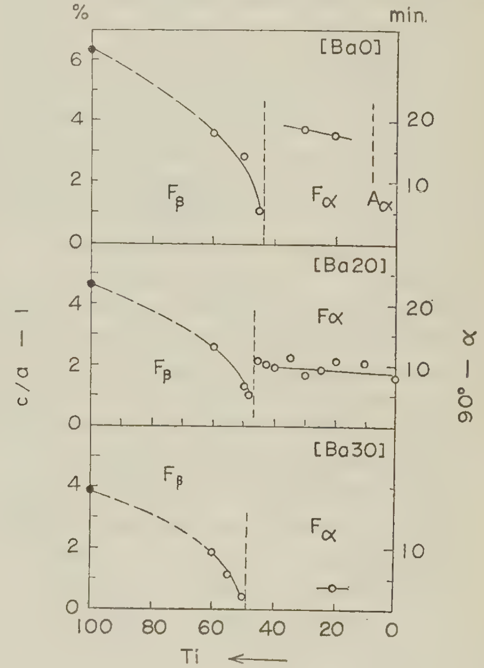

Fig. 7. Tetragonality in F_β and rhombohedrality in F_α.

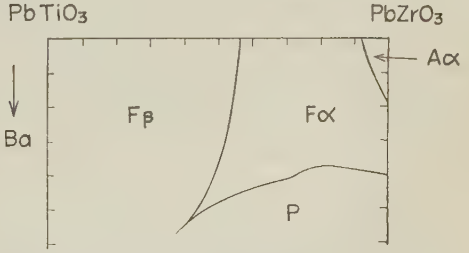

Fig. 8. Phase diagram (less than 60 Ba).

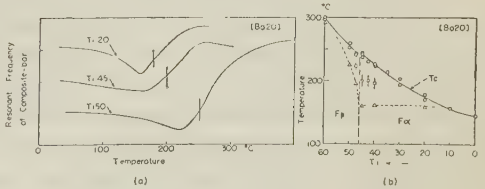

Fig. 9 (a). Resonant freqency of composite-bar (Vertical short line indicates Curie point). (b) Phase change in (Ba20-Pb80) (Ti-Zr)O_3.

○ Maximum of dielectric constant.

△ Minimum of resonant-frequency.

☐ X-ray measurement.

in Fig. 9 (a), where loose minima appear at the temperatures other than Curie points. In Fig. 9 (b), a solid curve shows the shift of Curie point with composition, and the variation of the temperature corresponding to the minimum of the resonant-frequency is shown by a dotted line.

An identification of phase of the region closed by both curves was performed by the powder photographs at temperatures indicated by square marks, using a camera with 70 mm diameter. Their patterns approach to pseudo-cubic ones, and the structures cannot be distinctly decided, but any deviation from each phase at room temperature is not observed. So the boundary between F_α and F_β phases may be almost parallel to the temperature axis (perpendicular to the composition axis), and is shown by the broken line in the figure. Then, that boundary may be called "morphotropic" also, by the same reasoning as in the case of $Pb(Ti\text{-}Zr)O_3$ system.

Such loose minima observed in the elastic measurements do not seem to be related with the phase transition, and often appear near the morphotropic boundary in the solid solutions with more than several percent of Ba. They may occur as a result of, for instance, a gradual temperature variation of elastic constant or a coexistence of the decreasing factor and increasing one. Thermal expansions of these specimens are extraordinarilly small below T_C and show only a bend at T_C, but any relation between these facts and above elastic data is not understood yet.

§ 5. Dielectric and Electromechanical Properties

(a) *Dielectric properties*

The dielectric constants of the solid solutions at room temperature changes systematically with composition. Even by using poorly sintered samples with 13–24% of porosity, the outline of the distribution is seen. Fig. 10 (a) shows the sections with various Ba concentration. Two maxima are found in each section; one of them (on the left side) is accompanied with the morphotropic transformation, and with increasing Ba, another large peak appears and shifts to the right side. The cause of an appearance of the latter maximum is not understood. Generally speaking, with increasing concentration of Ba, the value of the dielectric constant becomes larger and the peak at Curie point goes on to a broader one. The dense ceramics with composition of Ba 30–35 and Ti 5–25 have considerably large dielectric constant, *e.g.* 3000–6000. Fig. 10 (b) shows a few samples of their behavior *vs.* temperature (their porosity: 3–5%).

The dielectric hysteresis of the solid solution with larger amount of Ti and smaller of Ba does not reach a saturation yet by a field of 40 KV/cm (50 c/s) and so the coercive field is not determined quantitatively. Nonetheless, the tendency of the change of the coercive field with composition can be seen; the coercive field of the solid solution on the upper left side of the phase diagram (Fig. 8) is higher than that on the lower right side. The dielectric hysteresis of the one with larger than 20% of Ba and smaller than 50% of Ti seems to show a saturation by 40 KV/cm.

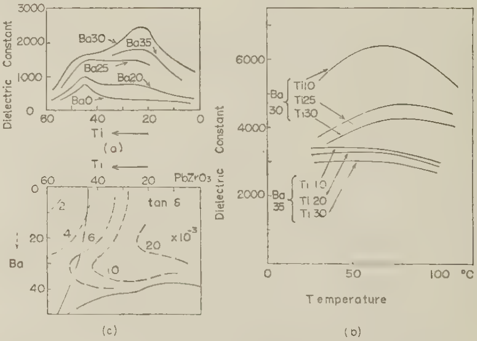

Fig. 10 (a). Dielectric constant at room temperature. (b) Temperature variation of dielectric constant (dense specimen). (c) Distribution of dielectric loss.

The dielectric loss factor (than δ) of the ceramics at room temperature was also examined. Fig. 10 (c) shows the distribution by several contour-lines. The values of the samples containing about 30% of Ba are larger than those on the upper left side, but they remain as small as 1–2%.

(b) *Electromechanical properties*

As described above, the electromechanical coupling of the solid solution ceramics becomes stronger with the composition near the morphotropic transformation of $Pb(Ti\text{-}Zr)O_3$, as reported by Jaffe *et al.* But, the poling field necessary to give a sufficient coupling is very high, and the ceramics with large Ti concentration have the coupling coefficients increasing with the poling field.

Substituting Pb by Ba, the situation can be improved. Namely, the poling field of even 30 KV/cm brings a sufficient coupling to the ceramics. The dense ceramics carefully sintered can have 40% of k_r, the radial electromechanical coupling coefficient. Fig. 11 (a) shows a tendency of the distribution of k_r; where the porosities of the samples are 12–20%.

The temperature variations of the frequency constant $f_r \cdot 2r$ (f_r: resonant frequency, $2r$: diameter) and the coupling k_r of an example are shown in Fig. 11 (b). The variations are smaller than those of other piezoelectric ceramics.

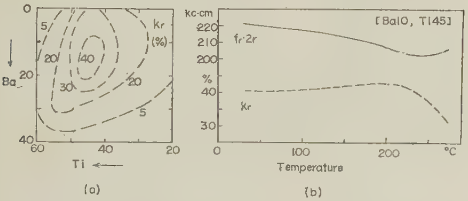

Fig. 11 (a). Distribution of radial electromechanical coupling coefficient (k_r) (prepoled by 30 KV/cm). (b) Temperature variation of frequency constant and k_r.

The internal frictions of these samples are of the order of $(1.5\text{–}3) \times 10^{-3}$, but the values for those with smaller loss depend more or less on their porosities, and so the distribution is hard to understand. Although the value of the internal friction is thus less reliable, a certain tendency is seen in its ratio to the dielectric loss; approximately speaking, the ratio becomes smaller in going on to the lower right side apart from $PbTiO_3$ side. This ratio may be considered to give a measure of the electromechanical coupling in the single crystal[9].

§ 6. Discussion and Conclusion

Roth[10] tended to classify perovskite crystals of ABO_3 including the solid solutions by the ionic radii of A^{++} and B^{4+} ions and the polarizability of A^{++} ion. His anticipation concerning the present system may be a success to some extent, but, for a detailed discussion, further knowledges on other solid solution systems (especially those containing Sn^{4+} ion) are necessary. Using the present datum and others to be studied in future, an experimental classification will be possible and advance Roth's consideration.

In the case of $Pb(Ti\text{-}Zr)O_3$ system, the axial ratio in F_β phase decreases with increasing Zr concentration, and on the contrary, the deviation from 90° in F_α is nearly constant with varying composition. Sawaguchi interpreted this fact by the latent meta-stability of F_α state in $PbTiO_3$ side. With increasing Ba content, both $c/a-1$ and $90°-\alpha$ become smaller, but above situation is the same in the section of constant Ba, and the morphotropic boundary does not shift so much to the Ti side, as shown in Figs. 7 and 8. Namely, the effect of Ba addition is a diminution of space for rattering of B^{4+} ion, which causes a lowering of Curie point and a weakening of ferroelectricity, and, on the other hand, the stabilities of F_α and F_β are decided mainly by the concentration ratio of Ti and Zr.

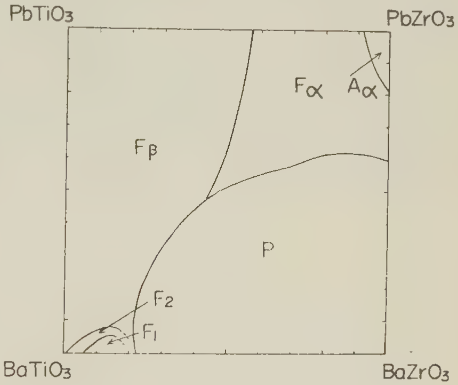

Fig. 12. Phase diagram of (Ba-Pb)(Ti-Zr)O_3 system.

Next, the elastic properties will be considered. s^P, the elastic compliance coefficient for constant polarization, changes by an amount at the phase transition and shows an ordinary temperature variation in one phase, and s^E, that for constant field, varies in correspondence with a change of electromechanical coupling; then, the elastic constant of the ceramics shows a minimum or a dent at the transition point. In the case of the solid solution near the morphotropic transformation, however, a loose minimum is seen in the curve of the resonant-frequency *vs.* temperature, and notwithstanding, any change of phase cannot be clearly found at that temperature. This may be considered as described in § 4 (c), but further study will be necessary to elucidate these phenomena.

In the present system, some useful materials were found for industrial applications. As shown in Fig. 11 (a), those possessing the radial coupling 40% by prepoling under the field of 30 KV/cm are obtained in certain compositions. These are considered to have better qualities than those investigated by Jaffe *et al* in a few respects; lower poling field, easier sintering, etc. The solid solutions containing about 30% of Ba have higher dielectric constants and relatively low dielectric losses. The ceramics of (Pb-Ba)ZrO_3 are often used for dielectric materials, but temperature coefficients of their dielectric constants are larger. The present dielectric ceramics may show some remarkable improvements.

Acknowledgement

The author wishes to express his sincere thanks to Dr. O. Nomoto, Mr. M. Marutake and Mr. A. Takeda in our institute for their useful discussions. He is also grateful to Dr. H. Hagihara and Mr. H. Yamashita in our institute for the X-ray photographing, to Mr. S. Nagasaki and Mr. K. Teranishi of the Rigakudenki Co. for the X-ray analysis by a diffractometer, and to Mr. K. Uchino and Mr. Y. Yasui of our institute and Mr. Y. Sasaki of the Waseda University for their help to the experiment.

The present study was supported by the Scientific Expenditure of the Ministry of Education.

References

1) G. Shirane and K. Suzuki: J. Phys. Soc. Japan **6** (1951) 274.
2) G. Shirane, K. Suzuki and A. Takeda: J. Phys. Soc. Japan **7** (1952) 12.
3) E. Sawaguchi: J. Phys. Soc. Japan **8** (1953) 615.
4) G. Shirane and S. Hoshino: Acta Cryst **7** (1954) 203.
5) R. C. Kell and N. J. Hellicar: Acustica **6** (1956) 235.
6) W. P. Mason: "*Piezoelectric Crystals and Their Application to Ultrasonics*".
7) B. Jaffe, R. S. Roth and S. Marzullo: J. Res. NBS **55** (1955) 239.
8) G. A. Smolenskiĭ, A. I. Agranovskaya and N. N. Krainik: Doklady Nauk SSSR **91** (1953) 55.
9) T. Ikeda: J. Phys. Soc. Japan **13** (1958) 809.
10) R. S. Roth: J. Res. NBS **58** (1957) 75.

JOURNAL OF THE PHYSICAL SOCIETY OF JAPAN Vol. 14, No. 2, FEBRUARY, 1959

The Electronic Structure of the M Center

By Hiroshi MIMURA and Teturo INUI
Department of Applied Physics, Faculty of Engineering,
University of Tokyo

(Received November 15, 1958)

The electronic structure of the *M* center for LiF has been investigated by L.C.A.O. approximation, assuming *L*-shape model by Seitz. In this treatment, we have orthogonalized the wave function of the *M* electron to the core state of Li ion, and evaluated the three center integrals more accurately than the former paper[1]. The calculated value for the M band absorption is 0.078 compared with the experimental value 0.103 in atomic unit. Some discussions concerning to the approximation and symmetry problem are given.

§1. Introduction

In a former paper[1], one of us (T.I.) in collaboration with Y. Uemura and Y. Toyozawa has investigated the electronic structure of the *M* center in L.C.A.O. approximation. A number of criticisms with respect to that paper and, in more general sense, to L.C.A.O. method applied to the color center problem have been given.

1) The A.O. belonging to the atom A has its charge density considerably in the region of a neighbouring atom B and therefore is not orthogonal to the core function of B[2),3)].

2) To reproduce the real charge distribution of a trapped electron faithfully, we should take many A.O.s so that there appear so many three center integrals[3)].

3) The energy is obtained as the difference of the several large quantities each of which is computed only approximately[4)].

In the following we will try some improvements to answer the criticisms (1) and (3). We choose the case of LiF because of its simplicity. As before, we assume *L*-shaped model for the *M* center which consists of the complex of two adjacent negative ion vacancies and a positive vacancy. We take the rectangular axes x, y and z shown in Fig. 1.

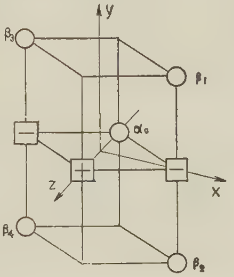

⊞ (⊟) means the lattice vacancy of the positive (negative) ion.

○ represents the Li ion, the A.O. of which is taken into account on L.C.A.O. treatment.

Fig. 1. Seitz's model for the M center.

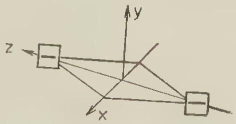

⊟ means the lattice vacancy of the negative ion.

Fig. 2. D_{2h} model for the M center.

§2. Calculation of Energy Levels

The one electron Hamiltonian assumed here for the *M* center electron is, neglecting the polarization of the ions,

$$H=-\tfrac{1}{2}\Delta+\sum_{(\mathrm{Li})} V(\boldsymbol{r}-\boldsymbol{R}_p)+\sum_{(\mathrm{F})} U(\boldsymbol{r}-\boldsymbol{R}_q)\,, \qquad (1)$$

where $V(\boldsymbol{r}-\boldsymbol{R}_p)$ (or $U(\boldsymbol{r}-\boldsymbol{R}_q)$) is the potential due to the p-th Li (or the q-th F) ion. We assign $p=0$ for the α ion, $p=1, 2, 3$ and 4 for the β ions, and $\sum_{(\mathrm{Li})}$ (or $\sum_{(\mathrm{F})}$) denotes the sum over Li ions (or F ions).

As F ions are more distant from the *M* center, $\sum_{(\mathrm{F})} U(\boldsymbol{r}-\boldsymbol{R}_q)$ is approximated by $\sum_{(\mathrm{F})}(1/|\boldsymbol{r}-\boldsymbol{R}_q|)$, hence it has no localized state. We approximate $V(\boldsymbol{r}-\boldsymbol{R}_p)$ by the Hartree potential for $2s$ orbital of free Li atom which

---

[*] Last year Dr. B. S. Gourary informed us kindly that the results of our 1st calculations[1)] are doubtful because the internuclear distances we used were wrong. Really we have made a foolish mistake in writing the numerical values of lattice constant of Lithium and Sodium Chlorides though the actual calculations were done using correct values. We made an independent calculation and confirmed every numerical values were correct within the accuracy of calculation. (Appendix III)

We express our thanks to Dr. B. S. Gourary for his valuable remarks.

has the following form[7]

$$V(\boldsymbol{r}-\boldsymbol{R}_p)=-\frac{1}{r_p}\{1+(2+5.4r_p)e^{-5.4r_p}\}\ ,$$
$$\text{where } \boldsymbol{r}_p=\boldsymbol{r}-\boldsymbol{R}_p\ . \quad (2)$$

We minimize the expectation value of the Hamiltonian H with the restriction that the corresponding wave function is orthogonal to the core (1*s*) functions which are the eigen functions of the *same* Hamiltonian. The (1*s*) function we have chosen has the analytic form $\phi_{1s}=Ne^{-\mu_0 r}$ where μ_0 is determined to minimize the expectation value of H. The actual procedure is as follows.

We neglect the overlap between the (1*s*) states and within the region where the charge distribution of the (1*s*) electron is remarkable we regard the potential as constant except $V(\boldsymbol{r}-\boldsymbol{R}_p)$, i.e.

$$\begin{aligned} H\phi_{1s,k}&=\left(E(\mu_0)+\frac{\alpha_M}{d}-\sum_m^{(\text{vac})}\frac{\pm 1}{|\boldsymbol{R}_k-\boldsymbol{R}_m|}\right)\phi_{1s,k}\\ &=E_{1s,k}\phi_{1s,k} \end{aligned} \quad (3)$$

α_M/d represents the Madelung potential, d is the lattice constant and $\sum_m^{(\text{vac})}$ denotes the sum of the Coulomb terms taken over the absent ions.

Determine μ_0 and $E(\mu_0)$ from the following equation

$$\left(\frac{\partial E(\mu)}{\partial \mu}\right)_{\mu_0}=0\ ,$$
$$\text{where } E(\mu)=\left(\phi_{1s}\left|-\frac{\varDelta}{2}+V(\boldsymbol{r}-\boldsymbol{R}_p)\right|\phi_{1s}\right) \quad (4)$$

then we obtain $\mu_0=2.2$, and $E(\mu_0)=-1.156$ (a.u.).

Let us now take our attention to the (localizing) site i, and denote the corresponding A.O. by ψ_i understanding that i represents the site as well as its quantum state.

We define the O.A.O. φ_i from the A.O. ψ_i by

$$\varphi_i=\psi_i-\sum_{(k\neq i)}S(\phi_{1s,k}|\psi_i)\phi_{1s,k}\ , \quad (5)$$

where $\phi_{1s,k}$ represents the (1*s*) state localized at the k-th ion, $\sum_{(k\neq i)}$ means the sum taken over all Li ions except the i-th ion. $S(\phi_{1s,k}|\psi_i)$ represents the overlap integral between $\phi_{1s,k}$ and ψ_i.

The matrix element of H with respect to φ_i and φ_j is given by

$$\begin{aligned} &(\varphi_i|H|\varphi_j)\\ &=(\psi_i|H|\psi_j)-\sum_{(k\neq i,j)}S(\phi_{1s,k}|\psi_i)S(\phi_{1s,k}|\psi_j)E_{1s,k}, \end{aligned} \quad (6)$$

where $E_{1s,k}$ is the eigenvalue of $\phi_{1s,k}$. The last term of the equation (6) represents the orthogonalization correction. We decompose $(\psi_i|H|\psi_j)$ into $(\psi_i|H_0|\psi_j)$ and $(\psi_i|H_1|\psi_j)$, where

$$\left.\begin{aligned} H_0&=-\frac{1}{2}\varDelta+V(\boldsymbol{r}-\boldsymbol{R}_i)+\sum_{(k\neq i)}\frac{\pm 1}{|\boldsymbol{r}-\boldsymbol{R}_k|}\\ H_1&=\sum_{\text{Li}(k\neq i)}\left(V(\boldsymbol{r}-\boldsymbol{R}_k)-\frac{-1}{|\boldsymbol{r}-\boldsymbol{R}_k|}\right). \end{aligned}\right\} \quad (7)$$

All the matrix elements which have been given in reference 1) are these matrix elements with respect to H_0 here, H_1 is the correction for it.

The wave functions are written as follows:

$$\left.\begin{aligned} &(A_1\text{ state})\quad \varPsi_{A_1}=\alpha_1\varPhi_1+\alpha_2\varPhi_2+\alpha_3\varPhi_3\\ &\qquad\begin{cases}\varPhi_1=\varphi_{s,0}\\ \varPhi_2=\varphi_{z,0}\\ \varPhi_3=\varphi_{s,1}+\varphi_{s,2}+\varphi_{s,3}+\varphi_{s,4}\ ,\end{cases}\\ &(B_1\text{ state})\quad \varPsi_{B_1}=\beta_1\varPhi_1+\beta_2\varPhi_2\\ &\qquad\begin{cases}\varPhi_1=\varphi_{x,0}\\ \varPhi_2=\varphi_{s,1}+\varphi_{s,2}-\varphi_{s,3}-\varphi_{s,4}\ ,\end{cases}\\ &(B_2\text{ state})\quad \varPsi_{B_2}=\gamma_1\varPhi_1+\gamma_2\varPhi_2\\ &\qquad\begin{cases}\varPhi_1=\varphi_{y,0}\\ \varPhi_2=\varphi_{s,1}-\varphi_{s,2}+\varphi_{s,3}-\varphi_{s,4}\ ,\end{cases} \end{aligned}\right\} \quad (8)$$

where φ_s, φ_z are 2*s*- and 2p_z-orbitals, the suffices 0, 1, 2, 3 and 4 indicate the position of ion to which the given O.A.O. belongs. We have only to solve the secular equations

$$\text{Det}|(\varPhi_m|H|\varPhi_n)-E(\varPhi_m|\varPhi_n)|=0 \quad (9)$$

for the above states.

The approximations to evaluate the three center integrals are as follows. In reference (1) we put

$$\int\psi_i\sum_{(k)}\frac{\pm 1}{|\boldsymbol{r}-\boldsymbol{R}_k|}\psi_j d\tau=\sum_k\frac{\pm 1}{|\boldsymbol{R}_m-\boldsymbol{R}_k|}\int\psi_i\psi_j d\tau\ , \quad (10)$$

where R_m is the maximum overlapping point of ψ_i and ψ_j. In this paper, we decompose $\int\psi_i\sum_{(k)}(\pm 1/|\boldsymbol{r}-\boldsymbol{R}_k|)\psi_j d\tau$ into two parts, i.e., the main part and the remainder. The former part consists of Coulomb terms due to a few neighbouring ions and is evaluated by Coulson-Barnett method[5]. As for the calculation of the remainder, we take sum $\sum_{k'}{}'(\pm 1/|\boldsymbol{R}_m-\boldsymbol{R}_{k'}|)$ over the remainder ions k's. For most combinations of ψ_i and ψ_j, the sums $\sum_{k'}{}' (\pm 1/|\boldsymbol{R}_m - \boldsymbol{R}_{k'}|)$ become zero and in these cases we put $\int \psi_i \sum_{k'}{}' (\pm 1/|\boldsymbol{r} - \boldsymbol{R}_{k'}|)\psi_j d\tau$ as zero. For $\int \psi_{s1} \sum_{k'}{}' (\pm 1/|\boldsymbol{r} - \boldsymbol{R}_{k'}|)\psi_{s2} d\tau$ the sum $\sum_{k'}{}' (\pm 1/|\boldsymbol{R}_m - \boldsymbol{R}_{k'}|)$ does not vanish, we apply Coulson-Barnett method for the ions for which $|\boldsymbol{R}_m - \boldsymbol{R}_k| \leq \sqrt{3}\, d$, and for the exterior ions we use the same approximation as (10), i.e.,

$$\int \psi_i \sum_{k'}{}' \frac{\pm 1}{|\boldsymbol{r} - \boldsymbol{R}_{k'}|} \psi_j d\tau = \sum_{k'}{}' \frac{\pm 1}{|\boldsymbol{R}_m - \boldsymbol{R}_{k'}|} \int \psi_i \psi_j d\tau \,.$$

For $\int \psi_{s1} \sum_{k} (\pm 1/|\boldsymbol{r} - \boldsymbol{R}_k|)\psi_{p\pi 0} d\tau$, where $\psi_{p\pi 0}$ is the component of p-type function perpendicular to the direction joining α and β ions, we have to take sum only over the absent ions and then to reverse sign.

§ 3. Results of Calculation and Remarks

The results are given in the Table I. As seen from the table, the difference of $E(A_1) - E(B_1)$ which corresponds to the M absorption band, does not depend critically on the

Table I.

a) Energy levels (in atomic unit)

	$E(A_1)$	$E(B_1)$	$E(B_2)$	$E(A_1)-E(B_1)$
approximation I*	-0.443	-0.386_5	-0.043	0.056_5
II**	-0.191	-0.125_5	-0.050	0.065_5
III***	-0.150	-0.072	0.003_5	0.078
(Results by Gourary and Luke⁴⁾)				
C. I. expansion	-0.197	-0.153	-0.099	0.044
C. S. expansion	-0.267	-0.174	-0.097	0.093
observed				0.103

b) Coefficient of L.C.A.O.

	α_1	α_2	α_3	β_1	β_2	γ_1	γ_2
approximation I	1	0.53	-0.33	1	-0.82	1	0.04
II	1	0.60	0.02	1	0.12_5	1	0.20
III	1	0.67_5	0.03	1	0.17	1	0.35
(Results by Gourary and Luke)							
**** C. I. expansion	1	0.532		1		1	
	(0.56)	(0.56)		(0.44)		(0.35)	

* approximation according to reference (1).

** approximation according to the present paper for evaluation of three center integrals, but neglecting the orthogonalization correction and the H_1 term (7).

*** approximation according to the present paper with orthogonalization including the H_1 term.

**** The values in the parentheses denote the decay constant. The corresponding value for our A.O. is 0.65.

Table II.

	experimental⁸⁾	theoretical
oscillator strength (f_M)	0.08	0.19
width of spin resonance $\langle \sigma_M{}^2 \rangle^{1/2}$	102 (gauss)	119

where $f_M = \frac{1}{3} \frac{2}{|E(A_1) - E(B_1)|} \left| \left(\Phi_{A_1} \middle| \frac{\partial}{\partial x} \middle| \Phi_{B_1} \right) \right|^2$, for $E(A_1) - E(B_1)$, we take the value of M band absorption wave length. $\langle \sigma_M{}^2 \rangle^{1/2}$ means the root mean square of the spin resonance line. f value calculated by the wave function in approximation (I) is 0.01.

approximations. Presumably this is caused by cancellation of errors common for upper and lower states. However, for the calculation of the oscillator strength, the approximation (I) gives a poor result inconsequence of the lack of the above-mentioned reason. To compare our results with experimental facts[8], we calculate oscillator strength f and hyperfine coupling constant a, using the wave function in approximation II. The results are plausible as shown in Table II.

The hyperfine interaction with α ion predominates over that with β ion, so that we should expect theoretically the resolved quartet which contradicts the experimental fact. For this point we would remark that we have neglected the interaction with F ion which has a possibility of broadening each component of the quartet to a broad line.

Lately, Gourary and Luke[4] have applied their "point ion lattice" method to the M center. Our results of approximation II resemble those of their "C.I. expansion" orthogonalized to the central ion core state, and it is not unreasonable because of their parallelism between both treatments. Although their C.S. expansion with strict point ion lattice model gives the good results for the absorption wave length, their results seem to be somewhat fortuitous because there remains some arbitrariness for the artificial selection of the wave function to avoid the rapid change near the nucleus.

Our treatment for the orthogonalization is, of course, not satisfactory, for we have used the one electron Hamiltonian in Hartree's sence, hence, neglected the exchange energy, (we are rather to use here the effective potential which reproduces the free atom spectrum which arises from the transition of the valence electron alone), and we have neglected the core state of the F ion. In spite of these facts, we believe that the estimation and check of the effect of the orthogonalization for L.C.A.O. approximation as done here is worthdoing.

Acknowledgement

The authors wish to express their hearty thanks to Professors B. S. Gourary, Y. Uemura and Y. Toyozawa for their valuable discussions and helpful advices. This work was supported by a grant in Aid for Fundamental Scientific Research from the Ministry of Education.

Appendix I. The Model of *M* Center

Recently, Kuwabara and Misu[9] have suggested that the symmetry of the M center is D_{2h} instead of C_{2v} based on the assumption that the second and the third excited states are nearly degenerate. However, as the following estimation shows such degeneracy can not be expected if we consider the effect of crystalline field. A possible model which has D_{2h} symmetry is a pair of two negative vacancies trapping an electron which is responsible for E.S.R. The one electron Hamiltonian of the M electron for this model is given by $H=-\frac{1}{2}\Delta-\sum_{\substack{i=1,2\\ \text{(vacancy)}}} V_{\text{ion}}(i)+V_{\text{pol}}+V_{\text{crys}}$. If we assume the polarization field (V_{pol}) to be equal for the second and third excited states, and neglect V_{crys} (field from perfect crystal), both states are degenerate. Then we can estimate the splitting of levels taking the difference of the expectation values of V_{crys} with respect to ψ_{B_2} and ψ_{B_3}. Using the point ion lattice approximation and the simple p-type wave functions ($\psi_{px}=Nxe^{-\mu r/\bar{a}}$ and $\psi_{py}=Nye^{-\mu r/\bar{a}}$) set at the origin, we obtain $(\psi_{py}|V_{\text{crys}}|\psi_{py})=0$ and $(\psi_{px}|V_{\text{crys}}|\psi_{px})=\overline{V}_{\text{crys}}$. The order of magnitude for $\overline{V}_{\text{crys}}$ is estimated as about 1 eV. We subtract the expectation value of the term $-(\Delta/2)-\sum_{\substack{i=1,2,3\\ \text{(vacancy)}}} V_{\text{ion}}(i)$ from the total energy values for B_1 state of L-shape model which have been calculated by Gourary[4]. Such values are $-\overline{V}_{\text{crys}}=0.8$ eV ($\mu=1.25$) and 1.5 eV ($\mu=1.5$) for LiF. The corresponding value for KCl is $-\overline{V}_{\text{crys}}=1.1$ eV ($\mu=1.5$). Therefore it seems rather difficult to conclude from Kuwabara and Misu's experiment that the M center has D_{2h} symmetry. Does there remain any possibility that M center has C_{2v} symmetry from the same experiment ? To answer this question, we calculate the energy of the second A_1 state by approximation III which gives $E_{A_1}{}^{(2)}=0.022$ (a.u.) while $E_{B_2}=0.003_5$(a.u.). The difference is rather small. Thus the possibility of the accidental degeneracy of these state is not completely excluded.

D_{2h}		
A_1	S	ground
B_1	P_z	1st excited
B_2	P_x	2nd 〃
B_3	P_y	3rd 〃

Appendix II. The Ionic Potential

As mentioned in § 3 we are rather to use the effective potential which reproduces the spectrum of the free atom. Such a potential for Li is given nummerically in a paper by Kohn and Rostoker[6] and we approximate this by the following analytic form:

$$V(r)=-\frac{1}{r}(1+(2+3.4r)e^{-3.4r}) \qquad (11)$$

Using this $V(r)$ and carrying out similar procedure as mentioned above we obtain the value of $(\varphi_{s0}|H|\varphi_{s0})/(\varphi_{s0}|\varphi_{s0})$ which are summarized in the following table.

$(\psi_{s0}\|H\|\psi_{s0})/(\psi_{s0}\|\psi_{s0})$ $=-0.148$ (a.u.)	using approximation II
$(\varphi_{s0}\|H\|\varphi_{s0})/(\varphi_{s0}\|\varphi_{s0})$ $=-0.094$ (a.u.)	approximation III with Hartree potential (2)
$(\varphi_{s0}\|H\|\varphi_{s0})/(\varphi_{s0}\|\varphi_{s0})$ $=-0.099_5$ (a.u.)	approximation III with effective potential (11)

As seen from the table the dependence of the results on V_{ion} is rather insensitive.

Appendix III. Results of Calculation Using the Approximation I

Energy Levels (in approximation I) (in eV).

	Lif	LiCl	NaF	NaCl
A_1	-12.05	-4.84	-15.29	-5.57
B_1	-10.51	-2.76	-12.98	-3.84
B_2	-1.17	-1.45	-1.35	-1.44
A_1-B_1	1.54	2.08	2.31	1.73
Experiment	2.79	1.90	2.43	1.72

References

1) T. Inui, Y. Uemura and Y. Toyozawa: Prog. Theor. Phys. **8** (1952) 355.
2) C. Herring: Photoconductivity Conference (1954) 81.
3) T. Kojima: Phys. Soc. Japan **12** (1957) 908.
4) B. S. Gourary and P. J. Luke: Phys. Rev. **107** (1957) 960.
5) C. A. Coulson and M. P. Barnett: Quantum Mechanical methods in valence theory (1951) 238.
6) W. Kohn and N. Rostoker: Phys. Rev. **94** (1954) 1111.
7) T. Inui and Y. Uemura: Prog. Theor. Phys. **5** (1950) 252.
8) N. Lord: Phys. Rev. **106** (1957) 1100.
9) G. Kuwabara and A. Misu: J. Phys. Soc. Japan **13** (1958) 1038.

Journal of the Physical Society of Japan Vol. 14, No. 2, Feburary, 1959

Oxide-Cored Cathode

By Keiichi Ando*, Osami Kamigaito, Yoshihiro Kamiya, Shigetoshi Takahashi and Ryozi Uyeda

Physical Institute, Nagoya University, Nagoya, Japan

(Received September 3, 1958)

We invented the *oxide-cored cathode*. It is a fine platinum wire having an oxide-core. A thin platinum rod is bored along the axis, the empty core made by boring is filled with oxide powder and then the rod is drawn through a series of dies, forming a wire. For example, the diameter of the wire is 0.3 mm and that of the core 0.03 mm. The wire is cut into short pieces and when heated, the cross-section of the piece becomes an electron source.

The oxide-cored cathode was tested in conventional electron microscopes and was found to emit electrons from the cross-section of the core only and that generally, it is more durable than pure tungsten cathode.

§ 1. Introduction

Since Yamaguti[1)] used oxide-coated cathode in his electron diffraction experiment, the use of oxide-cathode has become a common technique of electron diffraction in Japan. After 1950, it was also used in electron microscopy and was adopted for commercial electron microscopes[2)].

The oxide-coated platinum cathode never burns out because of its low running temperature and yet it gives an electron source as bright as that of pure tungsten. Moreover, when a small area is activated, the electron source can be made small. By using such an electron source, Honjo[3)] obtained high resolution electron diffraction patterns with an old style diffraction camera and Sakaki and Möllenstedt[4)] increased the resolving power of the velocity analyzer. The defect of oxide-cathode is its instability, particulartly when the activated area is small. The electron emission gradually decays after a coating, following which a recoating is required every two hours, more or less, according to running conditions.

A few years ago, one of the authors (R.U.)[5)] invented a new type of oxide-cathode, the *oxide-cored cathode*, in which the above mentioned defect is almost entirely eliminated. The aim of the present paper is to describe the method used to prepare the new type cathode and to give some experimental results obtained from its use.

§ 2. Method of Preparation

The oxide-cored cathode is prepared as follows: A thin rod of platinum is bored along the axis not quite through, resulting in a center core with one end open and one end closed. The core is filled with strontium-barium carbonate which is especially prepared for oxide-cathode**. The carbonate is decomposed to oxide by heating in a vacuum at about 950°C for approximately one hour. Then the platinum rod is drawn through a series of dies, forming a wire. To prevent contamination of the oxide, the open end of the core must be closed when the rod is taken out of the vacuum.

The oxide-cored wire is cut into short lengths. Both ends are closed with knippers. If the ends are left open, the oxide absorbs water vapor, increases in volume and is extruded from the core. On that event, the oxide spreads over the tip, making the electron source large. One piece of oxide-cored wire is spot-welded to a heater-wire, as illustrated in Fig. 1, and the tip is cut off before it is used as an electron emitter. After the tip is cut, it is desirable to have it kept in vacuum. However, the tip is not affected within about one hour except when the atmosphere is unusually humid.

The thickness of the core is from $20\mu\phi$ to $100\mu\phi$. For example, the original platinum rod is $2\,\mathrm{mm}\phi$ with a core of $0.6\,\mathrm{mm}\phi$. When the rod is drawn finally through a die of 0.3 mmϕ, a core of 90μϕ is obtained. For a core thinner than 60μϕ, it is convenient to carry out the drawing in two stages. For example, the first rod is 1.8 mmϕ with a core of 0.7 mmϕ. When it is drawn through a die of 0.5 mmϕ, the core becomes 0.2 mmϕ. A core a little thicker than 0.5 mmϕ is bored in the second rod the outer diameter of which is also 1.8 mmϕ. The wire drawn from the first rod is inserted into the core of the second rod. Then the second rod is drawn through a die of 0.3 mmϕ. Thus a core of 35μϕ is obtained.

---

* now at Sony Co. Ltd.

** Material furnished by Prof. S. Sasaki of the Kyoto University.

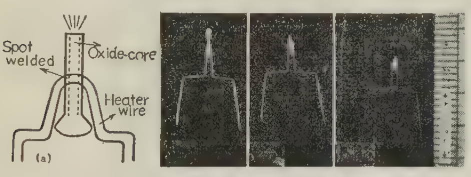

(b) (c) (d)

Fig. 1. Oxide-cored cathode.
(a) Schematic illustration.
(b) Both ends of the cored piece closed.
(c) One end cut.
(d) Pasted with alumina.

The oxide-cored wire can also be made of nickel. Since, however, the drawing is much easier for platinum than for nickel, we used platinum in most cases. According to our experience, a core of about 60μϕ is most suitable for usual purposes of electron microscopy and electron diffraction. The outer diameter of the cored wire was, in most cases, 0.3 mmϕ. For the heater-wire, we tried platinum and tungsten. The former was used in most cases. To improve the heating effect, cored piece and the heater-wire were often covered with alumina paste (Fig. 1 d). We found that the effect of the paste was not remarkable.

§ 3. Experiment I

The arrangement used in the first experiment is schematically illustrated in Fig. 2. This is a Müller type electron microscope of very low magnification. The image of the emitting tip is observed on the fluorescent screen.

Electron emission. Early in the experiment complicated patterns appeared on the screen. They were caused by oxide contamination of the cathode tip through careless cutting. When the cathode tip was carefully cut, a single spot appeared on the screen. Searching for the meaning of the spot, the following experiment was tried. After confirming the presence of a single spot, the cathode was taken out of the vacuum. Using a binocular microscope, we put a tiny spot of oxide beside the cross-section of the core (Fig. 2b). This caused the appearance of a second spot beside the first one. Judging by the size of the two spots and the distance between, we proceeded on the inference that the first spot corresponds to the cross-section of the core. If the oxide were spread over the tip and formed an electron source much larger than the cross-section, the second spot would be superposed on the first. Even when the oxide is spread on the tip,[6] the oxide layer is

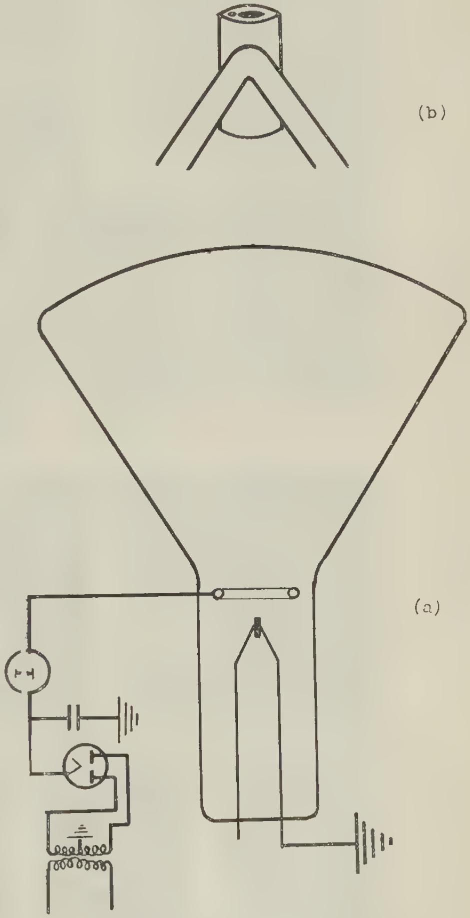

Fig. 2. Illustrating the arrangement of experiment I.

quickly removed in vacua which, in the present experiment, are 10^{-3}–10^{-4} mmHg.

Work function When the temperature of cathode was raised the spot on the screen grew brighter; but the size of the spot did not increase markedly. This indicates that the electron emitting area is almost the same independent of the temperature.

The temperature of the cathode was measured by an optical pyrometer and was varied between 1,100–1,600°K. Then the work function of the oxide-core was determined and it usually turned out to be between 1.5–2.5eV. Sometimes, however, it was as low as 1.2eV, the value in high vacuum[7], and sometimes more than 3.0eV. Results were not reproducible probably because partial pressures of gases and vapors in vacua could not be controlled. The current density was calculated by dividing total current I by the area of cross-section of the core. At 1,300°K it was usually between 0.1–1.0 A/cm². This is the same as the current density for pure tungsten between 2,400–2,600°K. Usually the work function increases gradually and accordingly the current density decreases with time. In the present experiment we often found a thin yellowish layer deposited over the cross-section of the core. This layer is one of the causes of cathode deterioration. The origin of the layer may be the oil vapor coming from the diffusion pump or other residual vapors in the vacuum.

§ 4. Experiment II

The arrangement of the second experiment is illustrated in Fig. 3. This is an old style electron microscope, the electron lenses of which were not used. The electron gun is of a telefocal type[8]. The oxide-cored cathode was set in the gun. To study the electron beam from a large electron emitter, sometimes the whole tip of the cored cathode was coated with oxide, referred to in this section as oxide-coated cathode. For comparison, the usual tungsten hair-pin cathode was also used.

Electron beam from the electron gun To study the electron beam from the gun, the aperture discs at the anode and at the specimen position were taken out (Fig. 3). Thus the whole electron beam fell on the screen. Since the usual fluorescent screen was too bright, we used a glass plate coated with gold. Patterns observed on the screen were remarkably different for different electron emitters, each varying with Wehnelt voltage V_w. Therefore, for each electron emitter we took a series of photographs with varying Wehnelt voltage. Series for oxide-cored, oxide-coated and tungsten hair-pin cathode are reproduced in Figs. 4, 5 and 6, respectively. To make the exposure time adequate, these photographs were taken at cathode temperatures much lower than those for practice in electron microscopy. The pattern on the screen changed slightly with the variation of the temperature. We confirmed, however, that there is no qualitative change such as the apparence and disapparence of the ring pattern (Fig. 5).

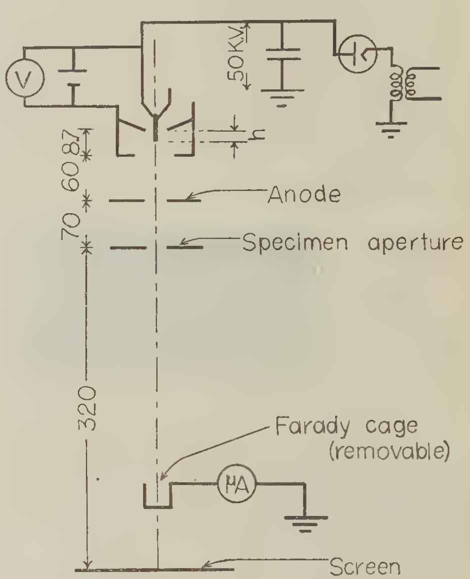

Fig. 3. Illustrating the arrangement of experiment II.

For the tungsten hair-pin cathode, there are the ring pattern indicating a hollow electron beam[9] and the cross-section of a caustic surface[8]. This series is essentially the same as that observed by Steigerwald[8]*. Also for oxide-coated cathode, the ring pattern is observed. The complexity of the pattern may be due to the heterogeneous electron emission at the tip. For the oxide-cored

---

* In "Abb. 6" of Steigerwald's paper, the ring and the caustic both contract to a spot at the same Wehnelt voltage. This is a merit of his electron gun.

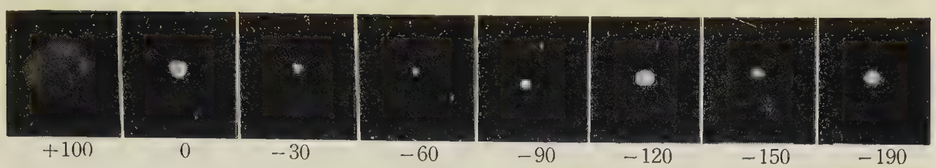

Fig. 4. Oxide-cored cathode. cut-off = −230 volt.

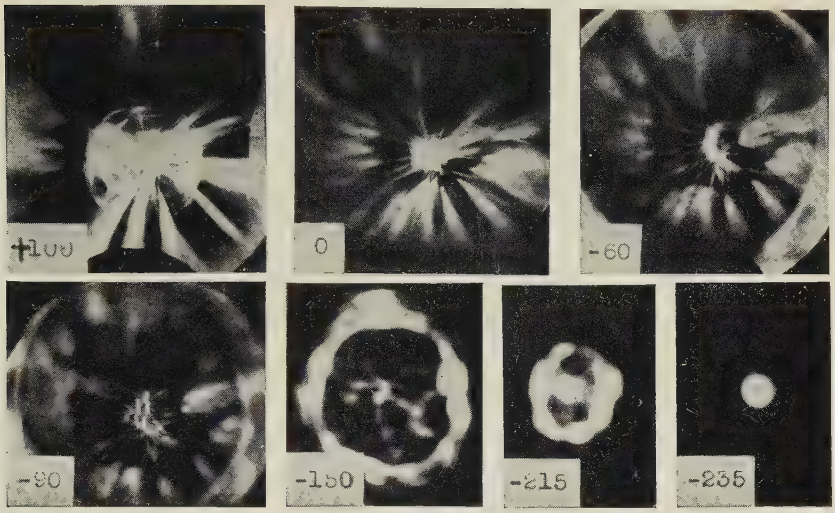

Fig. 5. Oxide-coated cathode. cut-off = −245 volt.

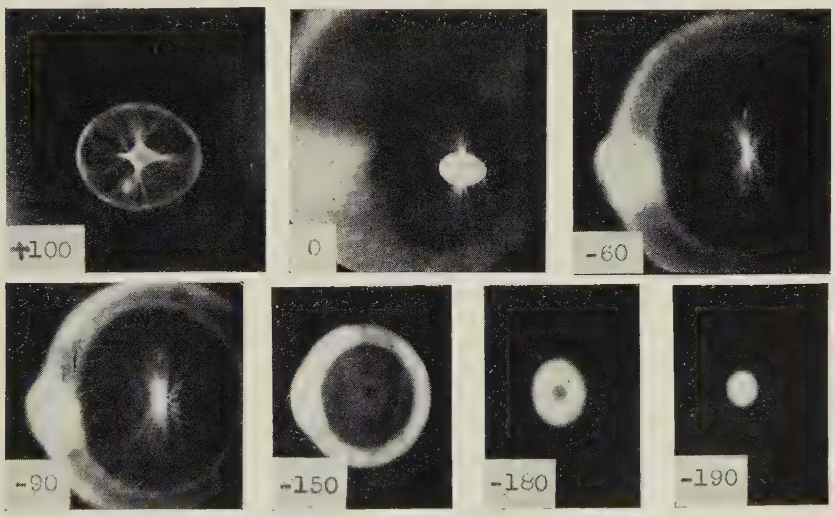

Fig. 6. Tungsten hair-pin cathode. cut-off = −200 volt.

cathode, it is remarkable that the electron beam is always thin showing no ring pattern. At Wehnelt voltage $V_w = -60$ volt, the spot is the smallest and it is the image of the cross-section of the oxide-core. This was confirmed by directly observing the shape of the cross-section by a light microscope. It was also confirmed as follows.

Using a razor blade, a thin line was marked on the face of a cored piece and then the oxide was placed on the line. With this cathode, the image of the core and the line appeared distinctly at a certain Wehnelt voltage (Fig. 7). The image of the very tip of the cathode may be formed in the same way for the tungsten hair-pin and the oxide-coated cathode. However, the image is not recognizable because electrons emitted from the area surrounding the very tip are not focussed simultaneously.

By this experiment we were able to reconfirm one of the results of the previous experiment, i.e. electrons are emitted only from the cross-section of the core. It is also noteworthy that this experiment is useful in a study of the focussing action of Wehnelt cylinder, although this problem is not treated in this paper.

Current density and total current In order to study the current density on the specimen plane as well as the total electron current from the gun, a small aperture of about 0.1 mmϕ was placed on the specimen table of the electron microscope and the current i through the aperture was measured through a Farady cylinder (Fig. 3). Current density j is given by i/s, where s is the area of the aperture. The position of the aperture was always adjusted by the specimen shifting mechanism of the electron microscope, so that i took the maximum value. In the following description, i and j both refer to the maximum values. For each electron emitter, measured values of I and j were plotted against V_w. Figs. 8, 9 and 10 give the plots for the oxide-cored, exide-coated and tungsten hair-pin cathode, respectively. It is remarkable that the result depends very much on the kind of electron emitter even when the same Wehnelt cylinder is used.

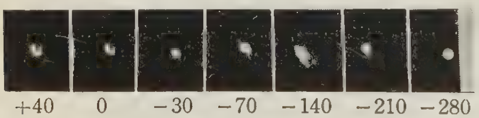

Fig. 7. Oxide-cored cathode with a knife mark.

For oxide-cored cathode, a sharp maximum of j appears at a certain value of V_w. This maximum corresponds to the focussed image of the cross-section of the core. Total current I is almost constant except near the cut-off voltage. This implies that almost all electrons emitted from the cross-section of the core depart from the electron gun.

For oxide-coated cathode, no distinct maximum of j appears because no distinct image is formed. Total current I increases rapidly with the decreases of $(-V_w)$. This implies that the electron emitting area is limited by the action of the Wehnelt cylinder. Total current I is increased when the area is enlarged with the decrease of $(-V_w)$. It is event that $j-V_w$ and $I-V_w$ diagrams depend not only on the design of Wehnelt cylinder but also on the size and shape of the electron emitter. We can say that Fig. 8 and Fig. 9 are an example of a small area and that of a large area electron emitter, respectively. The small area electron emitter gives a high current density with a small total current.

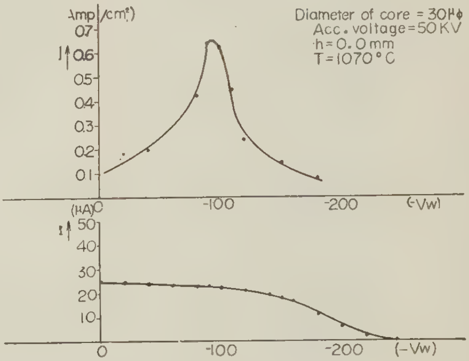

Fig. 8. Oxide-cored cathode.

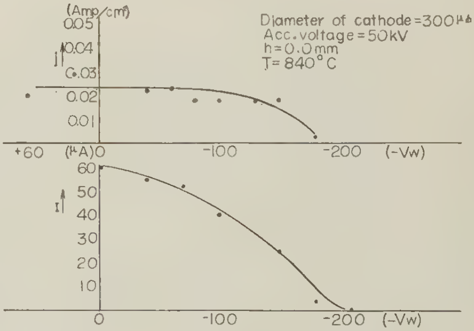

Fig. 9. Oxide-coated cathode.

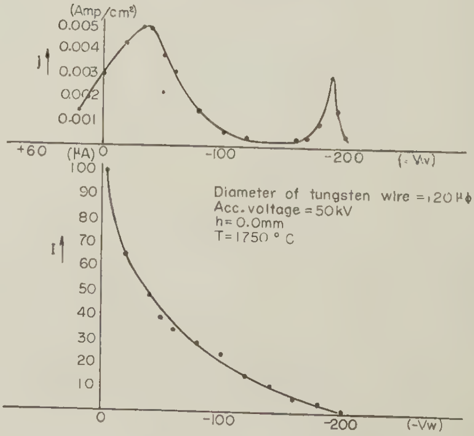

Fig. 10. Tungsten hair-pin cathode*.

For tungsten hair-pin cathode, two maxima of j appear.* The maximum near the *cut-off* appears when the ring of the hollow beam contracts to a spot and that at a lower value of $(-V_w)$ corresponds to the focussed image of the very tip of the hair-pin. Total current I increases rapidly with the decrease of $(-V_w)$.

Durability of oxide-cored cathode In the course of the experiment, we often took the cathode out of the vacuum and inspected the tip under a light microscope. Usually, the thin yellow layer, as described in Sec. 3, was found when the emission had decreased. Sometimes, however, the oxide evaporated gradually from the surface, resulting in a shallow hollow. Even under such a condition electrons were emitted not only from the boundary but from the whole cross-section of the hollow. In a few cases, we found that the core about 3 mm in length was perfectly hollow when the emission stopped.

It is most difficult to compare the durability of cathodes, because any comparison must be carried out under the same vacuum condition and at the same emission current density on the surface of emitters. In as much as we could not make a comparison under fixed conditions, we must infer the durability from our experience. We carried out a series of experiments with five tungsten hair-pin cathodes of 0.12 mmϕ and more than ten oxide-cored cathodes of core diameter 30–60 $\mu\phi$. During the experiments, the vacuum condition and the current density on the specimen surface (not on the emitter surface) were nearly the same. Tungsten cathode usually burned out after 10 hours while oxide-cored cathodes were still usable even after 30 hours. Thus we may say that the oxide-cored cathode is more durable than the tungsten cathode.

§ 5. Discussions

There are known to have been only a few trials for making electron sources smaller than 100$\mu\phi$. One is Hibi's "pointed filament".[10] He used a very sharp tungsten needle with a tip having the radius of curvature less than 5 microns. When the needle is heated, electrons are emitted not only from the conical side as well. Therefore, Wehnelt cylinder must have the area limiting action to make the effective electron source small. If the Wehnelt cylinder be appropriate, the "pointed filament" would give the smallest electron source.

Another trial was made by von Ardenne[6]. He covered a small crystal of lantern boride with a molybdenum sheet having a small hole in it. The crystal emits electrons through the hole. Although recent developments of his work are unknown, it would seem difficult to make electron sources smaller than 30$\mu\phi$ by his method.

Cored cathode is not only possible for oxide but also for any good electron emitter. We have already tried tantal-cored tungsten cathode and are going to try lantern boride-cored molybdenum cathode which, when completed, may give small electron emitter more stable and more durable than oxide-cored cathode.

Acknowledgement

The authors wish to express their thanks to Prof. N. Sasaki and Dr. R. Ueda of Kyoto University for furnishing the cathode material and valuable discussions.

References

1) T. Yamaguti: Proc. Phys. Math. Soc. Japan **16** (1934) 95.
2) T. Masuda: Specification pamphlet "Tron-scope Model Tras-50D" Akashi Mfg. Co. Ltd. (1956).
3) G. Honjo: J. Phys. Soc. Japan **8** (1953) 776.
4) Y. Sakaki & G. Möllenstedt: Optik **13** (1956) 193.
5) R. Uyeda: Proceedings of the First Regional Conference on Electron-Microscopy in Asia and Oceania (1956) 146.
6) M. v. Ardenne: Tabellen der Elektronen Physik (I). (1956) 81.
7) D. Kamke: Handbuch der Physik **33** (1956) 1.
8) K. H. Steigerwald: Optik **5** (1949) 469.
9) C. E. Hall: Introduction to Electron Microscopy (1953) Chap. 7.
10) T. Hibi: J. Electronmicroscopy **4** (1956) 10.

---

* Data were taken at a temperature far lower than for the practice in electron microscopy. Otherwise, total current I becomes too large at low values of $(-V_w)$.

JOURNAL OF THE PHYSICAL SOCIETY OF JAPAN Vol. 14, No. 2, FEBURARY, 1959

Study of Metallic Carbides by Electron Diffraction
Part III. Iron Carbides

By Sigemaro NAGAKURA

Tokyo Institute of Technology, Oh-okayama, Meguro-ku, Tokyo

(Received October 2, 1958)

Thin iron films formed by evaporation were carburized in CO gas stream. The carbides ε, χ and θ were found to be formed in the temperature ranges (i) below 250°C, (ii) from 250° to 350°C and (iii) above 350°C, respectively. The ε-carbide is hexagonal with lattice constants $a=4.767$ Å and $c=4.354$ Å, and its structure belongs to the space group $P6_322$, iron atoms occupying $6g$ positions with the parameter $x=1/3$ and carbon atoms $2d$ positions. Irreversible phase transitions from ε to χ and from χ to θ take place at 380°~400°C and at about 550°C, respectively. By the transitions changes in the chemical compositions may be very small. Observation on the crystal growth suggests that a mechanism of the ε-carbide formation is different from that of the χ- and θ-carbide formations.

§ 1. Introduction

It has been reported that there exist four kinds of iron carbides: the ε-, χ-, θ- and cubic carbides. The θ-carbide (cementite) is the best known iron carbide of the chemical composition Fe_3C and of the orthorhombic structure.[1-3] The χ-carbide (Hägg carbide or percarbide) was found by Hägg[4], Jack[5], and Hofer, Cohn and Peebles[6]. It gives a complex X-ray powder pattern resembling that of the θ-carbide and according to Jack the structure is probably either orthorhombic or hexagonal. The ε-carbide was found by Hofer, Cohn and Peebles[6] and gives a X-ray powder pattern due to a c.p.h. structure. From the electron diffraction study, Pinsker[7] proposed the existence of a cubic carbide of lattice constant $a_0=3.875$ Å. Its chemical composition was considered to be Fe_4C. Different chemical compositions have been given to the ε- and χ-carbides: according to Cohn and Hofer[8], the chemical compositions of the ε- and χ-carbides are equal to each other and correspond to $Fe_{2.4}C$, while, according to Jack, the chemical composition of the χ-carbide is $Fe_{20}C_9$ ($Fe_{2.2}C$)[5] and that of the ε-carbide varies in a range from Fe_2C to Fe_3C[9].

Trillat and Oketani[10] studied by the electron diffraction thin evaporated iron films carburized by CO and $CO+H_2$ gases and produced the χ- and θ-carbides but failed in producing the ε-carbide. The present author studied the iron carbides by the same method and some of the results have been reported[11]. The present paper describes the results of their formation, crystal structure, decomposition and phase transition in detail.

§ 2. Experimental Method

The method of preparation of the iron carbides was similar to that of the nickel carbide reported in the previous paper (Part I of this series)[12]. Evaporated iron films of thickness 200~300 Å were carburized in CO gas stream. Two kinds of iron films were used, namely, polycrystalline films without preferred orientation (P.C. films) and films with single crystalline orientation (S.C. films). The P.C films were prepared by evaporating iron on cleavage faces of single crystal of rock-salt kept at room temperature and the S.C. films by evaporating on the faces kept at about 500°C. Photo. 1 (a) reproduces an electron diffraction pattern of a P.C. film, showing the Debye rings due to the α-iron (b.c.c.). The half-breadth of the rings corresponds to a mean particle size of 50 Å. The temperature of the cementation ranged from 140°C to 500°C and the time of the treatment, from 1 to 6 hrs.. When the temperature was lower than about 350°C, the iron films were not carburized but oxidized to Fe_3O_4, as reported by Trillat and Oketani.[10] It was found, however, that when the specimen films were covered by fine iron powder, prepared by reduction of iron oxide powder in hydrogen stream at about 400°C for several hours, they were carburized without oxidation even below 350°C. At temperatures above 400°C this procedure was rather unfavourable because it accelerated the deposition of amorphous carbon on the specimen film.

The phase transition and decomposition of the iron carbides in vacuum were studied in two ways: (i) the carbide films were heated in a vacuum furnace for 2 min.～16 hrs., and (ii) they were heated in an electron diffraction camera at the rate of temperature rise 2°～4°C per min. and changes of the diffraction pattern were continuously observed. The temperature of the specimen film was measured by a thermo-couple placed as near as possible to the film. The accuracy of the thermo-couple indication is considered to be several degrees[12]. In both the treatments no oxidation of the carbide films took place.

§ 3. Formation of Iron Carbides

The P.C. films were carburized comparatively easily: the cementation for several hours converted the iron films completely to the carbide ones. The carburized products which gave electron diffraction patterns as reproduced in Photo. 1 (b), (c) and (d) were obtained in the temperature ranges shown in Fig. 1 (a), i.e. (i) below 250°C, (ii) 250°～350°C and (iii) above 350°C, respectively. As shown later these products were identified with the ε-, χ- and θ-carbides. When the iron films were carburized at temperatures above 350°C, a pattern due to amorphous carbon superposed on the carbide pattern. Above 400°C the diffraction patterns were sometimes composed only of the amorphous carbon. No product which can be identified with the cubic carbide was found throughout this work.

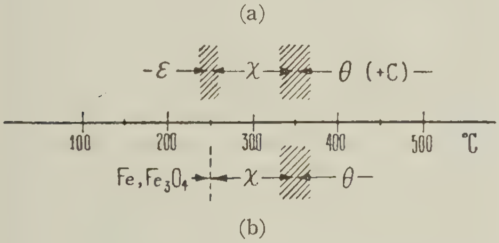

Fig. 1. Temperature range of the carbide formation (a) from P. C. films and (b) from S. C. films. The hatch indicates the region where two kinds of the carbides were produced.

Formation of the carbides from the S.C. films was more difficult than from the P.C. films. Fig. 1 (b) shows the temperature ranges of the carbide formation from the S.C. films. The ε-carbide could not be produced even after a prolonged treatment for 20 hrs., the heat treatment below 250°C only resulting in oxidation of the iron films. Above 250°C, however, the χ- and θ-carbides with certain epitaxial relations to the α-iron could be formed. The diffraction patterns of the χ-carbide were accompanied often by reflections due to Fe_3O_4 (Photo. 2).

Surface of the iron powder which was used to prevent the specimen films from being oxidized during the cementation was also examined. It was found that below 350°C the surface of the powder was oxidized to Fe_3O_4 and above 400°C it was covered by the amorphous carbon.

1. ε-carbide

Photo. 1 (b) is an electron diffraction pattern of the carbide produced by the cementation at 230°C for 6 hrs.. In Table I its spacings and intensities are tabulated. The reflections are classified in two groups: *M*- and *s*-reflections. The *M*-reflections are strong and can be indexed by a c.p.h. structure having lattice constants

$$a_h=2.752\text{Å},\quad c_h=4.353\text{Å}$$

and

$$c_h/a_h=1.576,$$

which are different only slightly from the X-ray data of the ε-carbide due to Hofer *et al.* ($a_h=2.749$ kX, $c_h=4.340$ kX, $c_h/a_h=1.579$)[6]. The mean particle size was estimated to be 55Å from the half-breadth of the Debye rings. It is worth-while to mention the fact that this particle size is not appreciably different from that of the original α-iron. The *s*-reflections are very weak and broad. All the reflections can be indexed by a new hexagonal lattice of constants

$$a=\sqrt{3}\,a_h=4.767\text{Å},\quad c=c_h=4.354\text{Å}$$

and

$$c/a=0.913_4.$$

The axial ratio c_h/a_h was measured in electron diffraction patterns at various temperatures and the result was plotted in Fig. 2. The plots

Table I. Diffraction data of ε-carbide

No.	Electron Diffraction						X-ray Diffraction*		
	Classification	*hkil*	d_{obs}(Å)	d_{cal}(Å)	I_{obs}	I_{cal}	*hk·l*	d_{obs}(Å)	Int.
1	*s*	$10\bar{1}0$	4.0~4.4	4.129	*vw, br*	4	—	—	—
2	*s*	$10\bar{1}1$	2.8~3.2	2.996	*vw, br*	6	—	—	—
3	*M*	$11\bar{2}0$	2.388	2.384	15	14	10.0	2.38	*w*
4	*M*	0002	2.172	2.177	18	17	00.2	2.16	*m*
5	*M*	$11\bar{2}1$	2.084	2.091	87	79	10.0	2.08	*vs*
6	*s*	$20\bar{2}0$	—	2.064	—	2	—	—	—
7	*s*	$10\bar{1}2$	—	1.926	—	2	—	—	—
8	*s*	$20\bar{2}1$	—	1.864	—	4	—	—	—
9	*M*	$11\bar{2}2$	1.607	1.607	13	10	10.2	1.60	*m*
10	*s*	$21\bar{3}0$	—	1.560	—	0.6	—	—	—
11	*s*	$20\bar{2}2$	—	1.498	—	0.3	—	—	—
12	*s*	$21\bar{3}1$	—	1.491	—	3	—	—	—
13	*M*	$30\bar{3}0$	1.378	1.376	10	10	11.0	1.37	*m*
14	*s*	$10\bar{1}3$	—	1.369	—	0.7	—	—	—
15	*s*	$21\bar{3}2$	—	1.268	—	0.3	—	—	—
16	*M*	$11\bar{2}3$	1.234	1.240	9	6	10.3	1.24	*m*
17	*M*	$22\bar{4}0$	—	1.192	—	0.6	20.0	—	—
18	*s*	$20\bar{2}3$	—	1.187	—	0.3	—	—	—
19	*M*	$30\bar{3}2$	1.161	1.163	18	8	11.2	1.16	*m*
20	*M*	$22\bar{4}1$		1.149		4	20.1		
21	*s*	$31\bar{4}0$	—	1.145	—	0.1	—	—	—
22	*s*	$31\bar{4}1$	—	1.107	—	0.3	—	—	—
23	*M*	0004	—	1.089	—	0.4	00.4	—	—

* See Reference No. 6.

against the temperature t can be fitted by a straight line

$$c_h/a_h=1.575(1+17\times10^{-6}t).$$

The temperature coefficient is remarkably larger than that of Ni_3C ($=6\times10^{-6}$). Details of the structure of the ε-carbide will be discussed in § 4.

2. *χ-carbide*

Photo. 1 (c) reproduces an electron diffraction pattern of the carbide produced by carburizing a P.C. film at 300°C for 3 hrs. and Photo. 2, that of the carbide produced by carburizing a S.C. film at 260°C for 6 hrs.. In Table II observed spacings and visual intensities of the Debye rings are tabulated. Most of them agree very well with the X-ray data of the χ-carbide due to Jack. However, many additional reflections which could not be observed in his pattern were found. From the X-ray powder pattern Jack mentioned that the unit-cell of the χ-carbide was probably either orthorhombic with lattice constants $a=9.04_3$ kX, $b=\sqrt{3}a=15.66_3$ kX and $c=7.92_1$ kX or hexagonal with lattice constants $a'=2a=18.08_6$ kX and $c'=c=7.92_1$ kX,[5] but these reflections could not be indexed by his unit-cell, suggesting that his unit-cell is not correct.

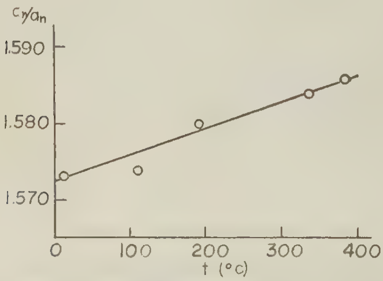

Fig. 2. Thermal change of the axial ratio c_h/a_h of ε-carbide.

3. *θ-carbide*

Photo. 1 (d) reproduces an electron diffraction pattern of the carbide formed by carburizing a P.C. film at 350°C for 3 hrs.. In Table III observed spacings and visual intensities are tabulated and compared with the X-ray data of the θ-carbide[13]. They agree very well. The structure is orthorhombic

Table II. Diffraction data of χ-carbide.

	Electron Diffraction		X-ray Diffraction			Electron Diffraction		X-ray Diffraction	
No.	d(Å)	Int.	d(Å)	Int.	No.	d(Å)	Int.	d(Å)	Int.
1	5.37	*w*	—	—	44	—	—	1.340	*vw*
2	5.05	*w*+	—	—	45	1.322	*w*	1.320	*w*
3	4.25	*w*	—	—	46	—	—	1.280	*vw*
4	3.98	*vw*	—	—	47	1.275	*vw*	1.272	*vw*
5	3.34	*w, br*	3.305	*vvw*	48	1.234	*w*	1.250	*s*
6	3.25	*w*	—	—	49			1.241	*w*
7	2.90	*vw, br*	2.917	*vvw*	50	—	—	1.224	*vw*
8			2.857	*vvw*	51	1.216	*s, br*	1.215	*vs*
9	2.63	*vw*	2.637	*w*	52	1.204	*vw*	1.206	*m*
10	2.499	*m*	2.494	*m*	53	—	—	1.195	*vvw*
11	2.413	*m*	2.411	*m*	54	—	—	1.188	*vvw*
12	2.38	*vw*	—	—	55	—	—	1.183	*vvw*
13	2.275	*w*+	2.276	*m*	56	—	—	1.174	*m*
14	2.205	*s, br*	2.199	*s*	57	1.162	*vw*	1.169	*m*
15			2.182	*m*	58	1.158	*w*+	1.160	*s*
16	2.100	*m*	2.114	*w*	59	—	—	1.148	*w*
17			2.095	*w*	60	1.139	*w*	1.143	*m*
18	2.071	*vs*	2.072	*vvs*	61	1.126	*w*	1.128	*vs*
19	2.033	*s*	2.041	*vvs*	62	1.111	*w*+	1.116	*m*
20	2.016	*s*	2.019	*w*	63			1.112	*m*
21			2.003	*m*	64	—	—	1.105	*vvw*
22	—	—	1.985	*w*	65	1.086	*w*	—	—
23	1.976	*s*	1.976	*m*	66	1.063	*vw*	—	—
24	1.918	*m*	1.915	*m*	67	1.042	*w, br*	—	—
25	—	—	1.904	*vvw*	68	1.022	*vw*	—	—
26	1.815	*s*	1.816	*m*	69	1.003	*vw*	—	—
27			1.810	*s*	70	0.982	*w*	—	—
28	—	—	1.781	*vvw*	71	0.971	*w*	—	—
29	1.765	*w*	1.767	*m*	72	0.938	*vw*	—	—
30	1.725	*w*	1.725	*w*	73	0.926	*vw*	—	—
31	1.674	*w*+	1.682	*w*	74	0.912	*w*	—	—
32	1.658	*w*	1.656	*vw*	75	0.904	*vw*	—	—
33	—	—	1.636	*vvw*	76	0.887	*vw, br*	—	—
34	1.626	*w*	1.624	*w*	77	0.868	*w, br*	—	—
35	1.571	*s*	1.578	*vs*	78	0.840	*w*	—	—
36	1.529	*m*	1.525	*vvw*	79	0.823	*vw*	—	—
37	1.514		1.514	*vw*	80	0.805	*vw*	—	—
38	1.450	*vw*	1.498	*vvw*	81	0.785	*vw*	—	—
39	—		1.437	*vvw*	82	0.774	*vw*	—	—
40	1.430		1.429	*vvw*	83	0.759	*vw*	—	—
41	—	—	1.397	*vvw*					
42	1.375	*w*+	1.377	*m*					
43	1.336		1.342	*m*					

Table III. Diffraction data of θ-carbide.

No.	hkl[1)]	d_{obs}(Å)	d_{cal}(Å)[2)]	I_{obs}	I_{cal}[3)]
1	(001)	6.948	6.925	*s*	—
2	(010)	5.086	5.077	*w*	—
3	(100)	4.543	4.518	*vw*	—
4	(011)	4.055	4.052	*vw*	—
5	101	3.771	3.750	*w*	60
6	110	3.386	3.374	*m*	40
7	002		3.364		68
8	111	3.015	3.017	*w*	68
9	(012)	2.810	3.803	*w*	—
10	(102)	2.685	2.697	*w*	—
11	020	2.543	2.538	*w*	110
12	112	2.384	2.382	*vs*	1800
13	021		2.375		1900
14	200	2.258	2.258	*s*	1600
15	(003)	—	2.242	*vw*	—
16	120	2.212	2.213	*m*	1400
17	(201)	2.144	2.140	*vw*	—
18	121	2.106	2.105	*m*	3800
19	210	2.063	2.063	*s*	3800
20	(013)	—	2.051	—	—
21	022	2.031	2.026	*m*	3500
22	103	2.015	2.008	*vs*	6300
23	211	1.977	1.972	*s*	3700
24	202	1.871	1.873	*vs*	86
25	113		1.867		2400
26	122	1.851	1.849	*s*	4200
27	212	1.758	1.758	*m*	1500
28	(030)	—	1.693	—	—
29	220	1.685	1.687	*m*	16
30	004		1.682		430
31	023		1.680		1100
32	(031)	1.641	1.641	*vw*	—
33	221	1.639	1.636	*m*	670
34	(014)	1.599	1.596	*vw*	—
35	(203)		1.591		—
36	130	1.583	1.585	*w*	1600
37	(104)	1.576	1.576	*vvw*	—
38	123		1.575		58
39	131	1.544	1.542	*w*	350
40	213	1.514	1.518	*vw*	37
41	(032)		1.512		—
42	222	1.508	1.508	*m*	950
43	(300)		1.505		—
44	114		1.505		240
45	301	1.463	1.469	*vvw*	12
46	310	1.447	1.443	*vvw*	6
47	132	1.437	1.433	*vvw*	48
48	311	1.410	1.412	*w*	
49	024	1.400	1.402	*w*	510
50	(302)	—	1.375	—	—

Table III. (Continued)

No.	*hkl*1)	d_{obs}(Å)	d_{cal}(Å)2)	I_{obs}	I_{cal}3)
51	230	—	1.354	*vvw*	28
52	(033)	—	1.351	*vvw*	—
53	204	1.348	1.349	*w*	70
54	223		1.348		200
55	(005)		1.345		—
56	124	1.339	1.339	*w*	350
57	231	1.331	1.327	*m*	11
58	312		1.326		6200
59	214	1.303	1.303	*w*	0
60	320		1.301		11
61	(015)	—	1.300	—	—
62	133	1.290	1.294	*w*	11
63	105	1.283	1.289	*vvw*	300
64	321	1.271	1.271	*vvw*	0
65	040		1.269		15
66	232	1.256	1.256	*vw*	550
67	303	1.249	1.250	*w*	12
68	115		1.250		390
69	041		1.247		6
70	140	1.221	1.222	*w*	3200
71	313	1.212	1.213	*m*	4000
72	322		1.208		22
73	141	1.201	1.203	*vvw*	580
74	(034)	1.189	1.193	*m*	—
75	224		1.191		280
76	025		1.189		1900
77	042		1.188		
78	215	1.167	1.164	*vw*	3500
79	233	1.157	1.159	*m*	4800
80	(205)	—	1.156	—	—
81	134	1.150	1.153	*m*	190
82	125		1.150		540
83	142		1.149		170
84	400	1.127	1.129	*s*	750
85	330		1.125		4600
86	(304)	1.121	1.121	*m*	—
87	323		1.121		0
88	006		1.121		2800
89	(401)	—	1.113	—	—
90	331	1.109	1.109	*w*	840
91	240		1.106		0
92	043	1.102	1.105	*vw*	4800
93	410		1.102		20
94	314	1.095	1.095	*vw*	2000
95	(016)		1.095		0
96	241		1.092		—
97	(106)	1.087	1.088	*vw*	0
98	411	1.082	1.087	*vvw*	1800
99	143	1.072	1.073	*vvw*	64
100	402		1.070		16

---

1) (*hkl*) is the forbidden reflection. 2) Calculated from the lattice constants $a=4.5155$Å, $b=5.0773$Å, $c=6.7265$Å (25°C) due to W. Hume-Rothery *et al.*13). 3) See reference No. 2 (X-ray data).

with lattice constants

$a=4.516$ Å, $b=5.077$Å and $c=6.727$Å.

In the pattern many forbidden reflections are observed, but they may be considered to be due to the multiple reflection of electrons.

Photo. 3 reproduces an electron diffraction pattern of the θ-carbide formed from a S.C. film after the cementation at 500°C for 1 hr.. The carbide grows on the film of α-iron with a definite epitaxial relation: it is either

$$(1\bar{2}1)_\theta//(110)_\alpha,\quad [111]_\theta//[001]_\alpha,$$

or

$$(111)_\theta//(001)_\alpha,\quad [\bar{2}11]_\theta//[0\bar{1}0]_\alpha.$$

Trillat and Oketani represented the epitaxial relation by relations $(111)_\theta//(001)_\alpha$ and $(1\bar{2}1)_\theta//(110)_\alpha$[14]. But this representation is not consistent, because an angle between $(111)_\theta$ plane and $(1\bar{2}1)_\theta$ is 87°39′, while $(001)_\alpha$ and $(110)_\alpha$ are perpendicular.

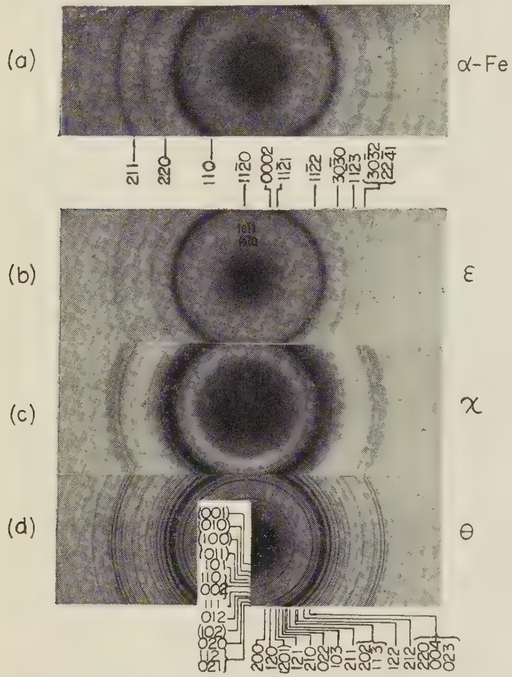

Photo. 1. Electron diffraction patterns of
(a) α-iron film evaporated in vacuum,
(b) ε-carbide film produced by the cementation at 230°C for 6 hrs,
(c) χ-carbide film produced by the cementation at 260°C for 6 hrs, and
(d) θ-carbide film produced by the cementation at 350°C for 3 hrs. Indices in brackets correspond to the forbidden reflections.

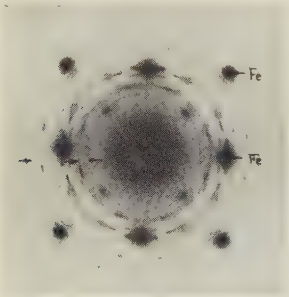

Photo. 2. Electron diffraction pattern of a S.C. film carburized at 260°C for 6 hrs., showing an epitaxial growth of χ-carbide with respect to α-iron. Spots and rings due to Fe_3O_4 (indicated by arrows) are also observed.

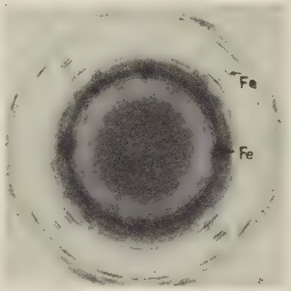

Photo. 3. Electron diffraction pattern of a S.C. film carburized at 500°C for 1 hr, showing an epitaxial growth of θ-carbide with respect to α-iron.

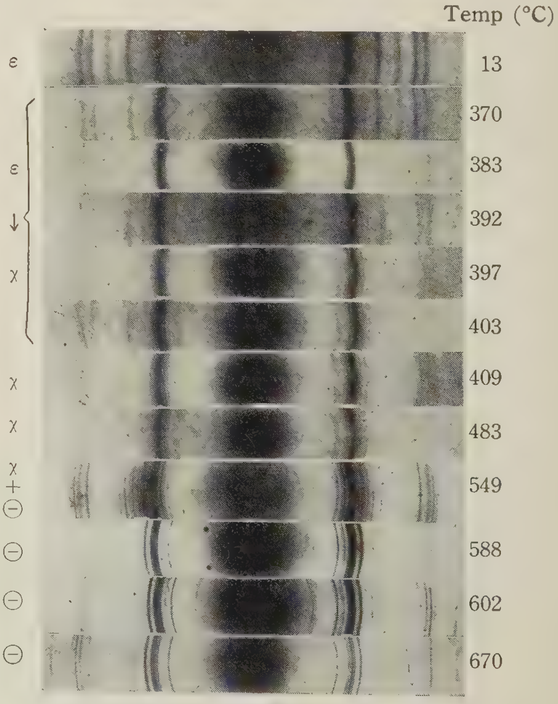

Photo. 4. A series of electron diffraction patterns showing the phase transition from ε-carbide to χ-carbide and from χ-carbide to θ-carbide.

§ 4. Crystal Structure of ε-carbide

The feature of the electron diffraction pattern of the ε-carbide mentioned in § 3.1 resembles that of the nickel carbide described in the previous paper (Part I[12] & II[15]). The strong M-reflections, which can be indexed by the c.p.h. lattice, suggest a c.p.h. arrangement of iron atoms similar to the case of the nickel carbide. The s-reflections are considered to be due to a regular arrangement of carbon atoms among the octahedral interstices of iron atoms. The systematic absence of the s-reflections of ε-carbide, however, is different from that of nickel carbide, resulting in the ' hexagonal lattice ' instead of the ' rhombohedral lattice ' of the nickel carbide. The most appropriate interpretation of the observed pattern of the ε-carbide is given by assuming the space group $P6_322$ and the atomic positions:

Fe atoms: $6g$, $x, 0, 0;\ 0, x, 0;\ \bar{x}, \bar{x}, 0;$
$\bar{x}, 0, 1/2;\ 0, \bar{x}, 1/2;\ x, x, 1/2,$
with $x=1/3$,

C atoms: $2d$, $1/3, 2/3, 3/4;\ 2/3, 1/3, 1/4,$
(or $2c$, $2/3, 1/3, 3/4;\ 1/3, 2/3, 1/4$).

In Table I calculated intensities are compared with the observed intensities. The observed intensities were obtained by photometry using Karle and Karle's method. Both values are normalized at the $(30\bar{3}0)$ ring. They coincide fairly well*. The basal plane projection of the structure is illustrated in Fig. 3. Here, iron atoms (A, B) take the c.p.h. arrangement and carbon atoms (C_2, C_3) occupy one-third of the octahedral interstices of the iron atoms. In the lattice the carbon atoms also form a c.p.h. stacking order. The stacking order of atomic planes along c-axis can be represented by a formula, $(C_2)A(C_3)B(C_2)\cdots$. The structure is different from that of the nickel carbide, $(C_1)A(C_2)B(C_3)A(C_1)B(C_2)A(C_3)B(C_1)\cdots$, only in respect of the stacking order of the carbon layers.

The half-breadth of M-reflections, β_M, was 1.1×10^{-3} for all the observed rings and that of s-reflections, β_s, was about 3×10^{-3}: β_s is about three times as large as β_M. This fact suggests that there exists a kind of disorder in the carbon lattice. In case of the nickel carbide the s-reflections elongated only along c^*-axis in the reciprocal lattice and this was considered to be due to a kind of one-dimensional stacking disorder of the carbon layers.[15]

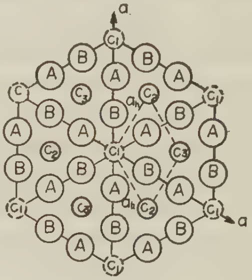

Fig. 3. Basal plane projection of the structure of ε-carbide. Iron atoms are indicated by A and B, and carbon atoms by C_2 and C_3. The position C_1 are unoccupied. The dashed lines indicate the unit-cell due to Hofer *et al.*. Height of atoms: A: 0, B: 1/2, C_2: 3/4, C_3: 1/4, (C_1: 1/4 or 3/4).

In case of the ε-carbide, however, no appreciable difference was found between the half-breadths of $(10\bar{1}1)$ and $(10\bar{1}0)$ rings, suggesting that the disorder takes place not only in the stacking order of the carbon layers but also in the carbon layers themselves. Thus, a domain of an ε-carbide crystal with respect to the arrangement of iron atoms is considered to be composed of a number of secondary domains with respect to the arrangement of carbon atoms. The domain sizes estimated from the half-breadths β_M and β_s are about 55Å and 20Å, respectively.

In the above we have discussed the structure by assuming that the chemical composition of the ε-carbide is Fe_3C. According to Jack, however, the composition varies in the range from Fe_3C to Fe_2C without any considerable structural difference. If so, ' extra ' carbon atoms should occupy the positions (C_1) in Fig. 2.

The epitaxial relation between the ε-carbide and α-iron could not be determined, since the ε-carbide was not formed from the S.C. films. But it is very likely that the epitaxial relation found in case of the transformation from b.c.c. into c.p.h. of Ti, Zr, Li etc. holds also in the present case: that is

---

* For the particle size of 55Å and the wavelength of 0.06Å (40 keV) the primary extinction coefficient $f\ (=I/|F|^2$, where I is the intensity and F the structure amplitude)[15] is calculated to be 0.97 for the (0002) reflection which has the largest structure amplitude. Therefore, the effect need not be taken into consideration.

$$(00.1)_{\varepsilon}//(\bar{1}01)_{\alpha},\quad [11.0]_{\varepsilon}//[111]_{\alpha},$$

were the c.p.h. index is used for the ε-carbide.

§ 5. Phase Transition of Iron Carbides

All kinds of iron carbide films kept in a desiccator more than a year showed no appreciable change of their electron diffraction patterns, indicating that they are very stable at room temperature. The diffraction pattern of ε-carbide films kept at 350°C in vacuum for 30 min. showed no appreciable change but it changed to the pattern of the χ-carbide when kept at 400°C for several min.. The pattern of the χ-carbide did not show any change by heating at 450°C for 30 min. but it changed to the pattern of the θ-carbide when kept at 550°C for 2 min.. When a θ-carbide film was heated at 600°C, iron rings appeared in the electron diffraction pattern after 10 min.. After heating for 16 hrs. at temperatures above 600°C the diffraction pattern was composed of rings due to the θ-carbide, the α-iron and the graphitic carbon. The pattern of the θ-carbide became very spotty by the heating, showing that a considerable crystal growth had taken place.

The changes in the electron diffraction pattern of the ε-carbide by heating were observed continuously using the high temperature electron diffraction camera. A series of the diffraction patterns is reproduced in Photo. 4. No appreciable change was observed up to 370°C but at 383°C new rings began to appear, their intensities increasing with temperature at the cost of those of the ε-carbide rings. Finally, the pattern changed to that of the χ-carbide at 403°C. The pattern of the χ-carbide changed at 549°C to become that of the θ-carbide. Thus, we can see that the ε-carbide transforms to the χ-carbide at 380°∼400°C and the χ-carbide transforms to the θ-carbide at about 550°C. The transformations are irreversible. It is worth mentioning that the ε-carbide did not show any appreciable crystal growth by the heating, while the χ- and θ-carbides showed crystal growth.

By the above phase transitions we could never find in our electron diffraction patterns any indication of precipitation of carbon, which should appear if the chemical compositions of the ε-, χ- and θ-carbides are as much different from each other as have been reported. This suggests that the change in the composition by the transitions is, if any, very small. A possible amount of the change can be estimated as follows. Let us put the chemical composition of the ε- or χ-carbide to $Fe_{3-x}C$ and that of the θ-carbide to Fe_3C, and compare the intensity of the $(0002)_C$ ring of the graphite with that of the $(101)_\theta$ ring of the θ-carbide on the assumption that the decomposition $Fe_{3-x}C \rightarrow Fe_3C + C$ took place by the phase transitions. The scattering angle of the $(0002)_C$ ring is near to that of the $(101)_\theta$ ring and the former ring is strongest among the graphite rings, while the latter ring is weakest among the lower order rings of the θ-carbide, though this could be clearly observed in our electron diffraction patterns (see Photo. 1 (d)). In general, the integrated intensity per unit length of a Debye ring is given by

$$P = p\beta = I_0 \frac{\lambda}{8\pi L} \frac{j}{s^2} \left| \frac{F}{v} \right|^2 \Delta V,$$

where p is the peak intensity, β the half-breadth, I_0 the intensity of incident electron, λ the wave-length, L the camera length, j the multiplicity factor, $s = 2\sin\theta/\lambda$ (θ: Bragg angle), F the structure amplitude, v the unit-cell volume and ΔV total volume of the sample irradiated by the electron beam. Calculation shows that

$$P_C = p_C\beta_C = I_0 \frac{\lambda}{8\pi L} \cdot 2.8\times10^{-1} \Delta V_C$$

for the $(0002)_C$ ring of graphite and

$$P_\theta = P_\theta\beta_\theta = I_0 \frac{\lambda}{8\pi L} \cdot 4.8\times10^{-3} \Delta V_\theta$$

for the (101) ring of the θ-carbide. The particle size of the precipitated carbon is usually so small that the half-breadth of its Debye ring may amount to ten times as broad as that of the θ-carbide (cf. Part I, Photo 7 & 8 of Ni_3C). In our electron diffraction pattern of the θ-carbide a ring, its peak height being one-tenth of p_θ, was observed clearly. Thus, if some amount of graphite was precipitated by the phase transitions to produce the $(0002)_C$ ring of the peak intensity $p_C = (1/10)p_\theta$, the above equations lead to

$$\frac{\Delta V_C}{\Delta V_\theta}=1.7\times10^{-2}.$$

Since ΔV=(number of molecules×molecular mass)/density, this gives

$$\frac{\text{number of molecules of carbon}}{\text{number of melecules of Fe}_3\text{C}}=\frac{1}{13}\,.$$

Then, the chemical composition of the initial carbide, $Fe_{3-x}C$, must be $13Fe_3C+C=Fe_{39}C_{14}$, or $Fe_{2.8}C$. Therefore, the amount of change in the composition x must be smaller than 0.2 by the phase transitions.

§ 6. Discussion

The ε-carbide could not be produced from the iron films prepared on the substrates kept at elevated temperatures though it could be produced easily from the P.C. films. This is considered to be due to that, for the ε-carbide formation, imperfections in α-iron crystals, such as lattice vacancies, dislocations and grain boundaries, play an important role to accelerate the diffusion of carbon atoms and to form nuclei of the carbide crystals as it was the case with the formation of the nickel carbide (Part I). As mentioned above (§ 3.1) the particle size of the ε-carbide is nearly equal to that of the original α-iron. This suggest that one crystal of α-iron converts to one ε-carbide crystal and no recrystallization takes place in the process of the ε-carbide formation. It was found that in the carbide lattice carbon atoms are distributed regularly among the octahedral interstices of iron atoms, though the regularity does not spread over the matrix crystal.

The χ- and θ-carbides could be produced always from both P.C. and S.C. films. Their crystal structures are very complex and bear no simple crystallographic relations to the α-iron. They are produced at higher temperatures than that of the ε-carbide formation and their particle size becomes much larger than that of the α-iron. Therefore, the mechanism of their formation is considered to be different from that of the ε-carbide: nuclei of the χ- and θ-carbide crystals are formed on the crystal surface of the α-iron and grow up gradually. The imperfections in the α-iron crystals are not considered to play an essential role in these cases.

It was revealed that the phase transition of iron carbides, $\varepsilon\to\chi\to\theta$, takes place irreversibly without any appreciable change in the composition. Hofer *et al.*[6] reported that the magnetic Curie point of the ε-carbide is 380°C, but according to the present result this temperature should not be the Curie point but the structural transition point from ε to χ. It was also found that the χ-carbide transforms to the θ-carbide at about 550°C. Cohn and Hofer[16] proposed a method of preparation of pure θ-carbide sample by heating a mixture of the χ-carbide and the α-iron, but admixing of the α-iron is unnecessary.

Acknowledgement

The author should like to express his hearty thanks to Professor S. Oketani for his guidance throughout the present work, and also to Professor G. Honjo for his valuable discussion and helpful advice. This work was supported by a Grant in Aid for Fundamental Scientific Research from the Ministry of Education.

References

1) S. B. Hendricks: ZS. f. Krist., **74** (1930) 534.
2) A. Westgren: Artrick ur Jernkontrets Annaler för Ar 1932, 458.
3) H. Lipson and N. J. Petch: J. Iron Steel Inst., (1940) 95.
4) G. Hägg: ZS. f. Krist., **89** (1934) 92.
5) K. H. Jack: Proc. Roy. Soc., **A 195** (1948) 34; 41; 56.
6) L. J. E. Hofer, E. M. Cohn and W. C. Peebles: J. Am. Chem. Soc., **71** (1949) 189.
7) E. M. Cohn and L. J. E. Hofer: J. Chem. Phys., **21** (1953) 554.
8) Z. G. Pinsker: Trudy Inst. Krist. Akad. Nauk SSSR, **10** (1952) 104.
9) K. H. Jack: Paper MG/C/50 of the Metal Physics Comittee. The British Iron & Steel Research Association, 53.
10) J. J. Trillat et S. Oketani: C. R. **230** (1950), 2203; Metaux et Corr., **302** (1950); **308** (1951).
11) S. Oketani and S. Nagakura: J. Japan Inst. Metals **20** (1956) 460. S. Nagakura: *ibid.*, **20** (1956) 465 (in Japanese).
12) S. Nagakura: J. Phys. Soc. Japan **12** (1957) 482.
13) W. Hume-Rothery, G. N. Raynor & A. T. Little: J. Iron & Steel Inst. (1941) 143.
14) J. J. Trillat et S. Oketani: C. R. **233** (1951) 51
15) S. Nagakura: J. Phys. Soc. Japan **13** (1958) 1005.
16) L. J. E. Hofer and E. M. Cohn: J. Chem. Phys., **18** (1950) 766.

JOURNAL OF THE PHYSICAL SOCIETY OF JAPAN Vol. 14, No. 2, FEBRUARY, 1959

On the Magnetic Properties of Vanadium Sulfide and Selenide*

By Ichiro TSUBOKAWA

The Research Institute for Iron, Steel and Other Metals,
Tohoku University, Sendai, Japan

(Received November 4, 1958)

Magnetic, thermal and crystallographic properties of sulfide as well as selenide of vanadium with nickel arsenide structure were investigated experimentally. The antiferromagnetic Néel points for these compounds were found to be about 1040° and 163°K respectively. A correction for the atom core diamagnetism was applied to the observed susceptibilities; the inverse susceptibility decreased linearly with the fall of temperature. Based on this result, the Curie constant, C_M, the spin quantum number, S and the asymptotic Curie temperature, θ, were obtained as 1.63, 2.9/2 $-3000°$ for sulfide and 2.15, 3.2/2 and $-2570°$ for selenide respectively. Anomalous heat absorptions at the magnetic transition in both compounds were 615 and 50 cal/mol respectively. Experimental results obtained are discussed briefly.

§ 1. Introduction

It is well known that many of the compounds between the first transition elements and those of the fifth or the sixth group in the periodic table of elements have nickel arsenide structure. Investigations of the magnetic properties for these compounds were mostly concerned with those which contain cations with more than half filled 3d-shells. Anderson[1)] suggested that the superexchange interaction due to Kramers' model is ferromagnetic or antiferromagnetic according as the 3d-shells of cation are filled less than or more than half, respectively. Ferromagnetic chromium telluride[2)] as well as antiferromagnetic manganese telluride[3)] were thought to be a suitable example of his theory. Contrary to this consideration, however, chromium sulfide[4)], selenide[5)] and antimonide[6)] are known to be antiferromagnetic. From such a point of view, it is interesting to investigate whether the vanadium compounds, VS and VSe, are antiferromagnetic or ferromagnetic, since it is clear that the 3d-shell of these compounds is considered to be of less than half filled type.

§ 2. Specimens and Experimental Results

According to Bilts and Kocher[7)] as well as Hoschok and Klemm[8)], vanadium sulfide forms a eutectic with vanadium and was reported to have nickel arsenide structure with the parameters a=3.34Å, c=5.78Å and c/a=1.73. It was also reported that there is a nickel arsenide structure phase in V-Se system ranging from 55.5 to 61.5 atomic percentage of selenium with parameters a=3.587Å, c=5.989Å and c/a=1.670.

The specimens of these compounds used in the present experiment were prepared as follows: Powders of vanadium (99.8%) and sulfur or selenium (99.99%) were mixed in stoichiometric proportion (fifty atomic percent), sealed in evacuated silica tubes and preheated at 1000°C for a week. To promote the reaction, the products were pulverized, mixed again and reheated in the same way. All specimens thus obtained were examined by X-ray technique; the diffraction lines of vanadium sulfide and selenide shown in Table I could be indexed as the nickel arsenide structure, and their lattice constants were calculated to be a=3.33Å, c=5.82Å and a=3.66Å, c=5.95Å respectively. These values coincide well with the results of the former investigations mentioned above.

The temperature dependence of magnetic susceptibility was obtained by the magnetic balance of an automatically recording type[9)]. The values of susceptibility were corrected by taking into consideration the diamagnetism of inner atomic cores[10)]. Such corrections for each compound are shown in Table II.

The corrected values of susceptibility are

---

* This investigation was supported in part by the Grant-in-Aid of Fundamental Scientific Research of Ministry of Education.

Table I. X-ray analyses of VS and VSe. (Cu-K_α)

VS			VSe		
I	hkl	$\sin^2\theta$	I	hkl	$\sin^2\theta$
s	100, 002	0.072	vvw	002	0.067
vs	101	0.090	vs	101	0.076
vvs	102	0.140	vvs	102	0.126
m	110	0.214	vs	110	0.177
w	103	0.230	m	103	0.209
w	004	0.280	vw	112	0.244
w	104, 202	0.361	m	201	0.253
s	114	0.494	w	004	0.267
vw	121	0.516	m	202	0.303
vw	122	0.568	w	203	0.386
vvw	123	0.657	m	121	0.430
			s	114	0.444
			m	122	0.479
			w	300	0.530
			m	123	0.562
			vvw	205	0.651

Table II. Diamagnetic susceptibility of atom core.

Compounds	χ_d
$V^{2+}S^{2-}$	-0.593×10^{-6}
$V^{2+}Se^{2-}$	-0.61×10^{-6}

plotted aginst temperature in Fig. 1, which shows a maximum at 1040° and 163°K for vanadium sulfide and selenide respectively. The inverse of susceptibility is also traced in the same figure. These curves show that the Curie-Weiss law holds very well for the temperature range higher than the maximum of susceptibility.

The specific heats as a function of temperature for vanadium sulfide and also selenide were obtained by an automatically recording calorimeter of the adiabatic type[11]. In both compounds, Λ-shaped anomaly is found at about the same temperature corresponding to the maximum in χ-T curves. The results are shown in Fig. 2. Anomalous heat absorption considered to be due to the magnetic transformation for vanadium sulfide and selenide were estimated from the above C_p-T curves as 615 and 50 cal/mol respectively.

§ 3. Discussion of the Results

As shown in Fig. 1, each compound has a maximum in the susceptibility-temperature curve, and the temperature corresponding to this maximum of susceptibility may be considered as the antiferromagnetic Néel point, T_N. The values of T_N are listed in the last column of Table III. Such supposition was confirmed by the experimental results of specific heat, in which anomaly occurred at about the same temperature as that T_N. It should be noted here that in the case of vanadium sulfide, the temperature corresponding to the maximum of susceptibility is seen to be about 100° higher than that of the well-defined peak of the specific heat, however, it is also to be noticed that the hump in susceptibility shown in the figure is so broad that the point of maximum is not so well defined as in the case of specific heat. On the other

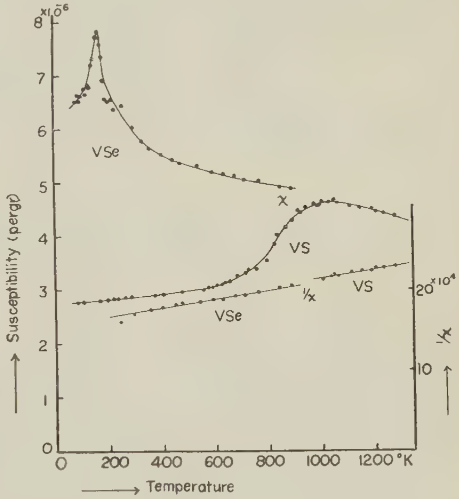

Fig. 1. Susceptibility versus temperature curves of vanadium sulfide and selenide. (Inverse susceptibility was also plotted.) These curves were corrected for the diamagnetism of inner atom core.

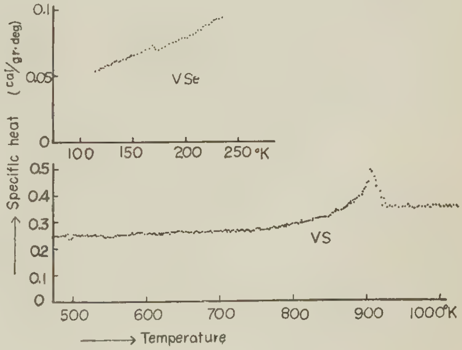

Fig. 2. Specific heat versus temperature curves of vanadium sulfide and selenide.

hand, Suzuoka et al[12] found the anomlous change of electrical resistivity and of dilatation due to temperature at about the same point as that corresponding to the maximum of susceptibility. From the inverse susceptibility above the Néel point, we can determine the Curie constant C_M, the magnetic spin quantum number S by assuming that the Landé factor is two and the asymptotic Curie temperature θ. The results are shown in Table III.

Table III. Curie constant C_M, spin quantum number S and asymptotic Curie point θf or vanadium compounds.

Compounds	C_M	θ	S	T_N
VS	1.68	−3000°	2.9/2	1040°K
VSe	2.15	−2570°	3.2/2	163°K

From the observed values of θ and T_N, the ratio θ/T_N were obtained to be −3 and −16 for vanadium sulfide and selenide respectively. In the case of the crystal lattice with nickel arsenide structure, each cation in the crystal has three kinds of cation neighbor with nearly equal inter-atomic distance. In the molecular field approximation, the ratio θ/T_N for such a case can be expressed as a function of ratios among the exchange integrals for each kind of neighbor, and it was found that the minimum value of θ/T_N is −5[13]. Hence the present result for sulfide is acceptable, while that for selenide lies beyond the theoretical expectation.

As the divalent ion of vanadium is in a state of ^{4}F, the spin quantum number of ca 3/2 obtained above seems to correspond to it. Thus the 3d shell of vanadium ion in the above mentioned compounds is considered to be less than half-filled; based on the simple Kramers and Anderson superexchange mechanism[1], it is to be expected that the sulfide and selenide of vanadium will be ferromagnetic, while the experimental results show that they are antiferromagnetic. However, a recent development of the theory by Slater[14], Anderson-Hasegawa[15] and Kanamori[16] shows that an other influence on the behavior of superexchange interaction arises from the different ionic states of cations in the crystal lattice. On this point of view, the superexchange mechanism of the present compounds should be discussed more in detail.

Acknowlegements

The author wishes to express his hearty thanks to Prof. T. Hirone for his kind encouragement throughout the course of the present study. He also wishes to express his sincere thanks to S. Maeda and N. Tsuya for their useful discussions.

References

1) P. W. Anderson: Phys. Rev. **79** (1950) 705.
2) H. Haraldsen and E. Kowalski: Z. anorg. u. allge. Chem. **224** (1935) 329.
C. Cuillaud: Compt. Rend. **222** (1946) 1225.
I. Tsubokawa: J. Phys. Soc. Japan **11** (1956) 662.
3) C. F. Squire: Phys. Rev. **56** (1939) 922.
A. Serres: de Phys. Rad. **8** (1947) 146.
E. Uchida, H. Kondoh and N. Fukuoka: J. Phys. Soc. Japan **11** (1956) 27.
4) H. Haraldsen and A. Neuber: Z. anorg. u. allge. Chem. **234** (1937) 337.
H. Haraldsen: Z. anorg. u. allge. Chem. **234** (1937) 372.
M. Yuzuri, T. Hirone, H. Watanabe, S. Nagasaki and S. Maeda: J. Phys. Soc. Japan **12** (1957) 385.
5) H. Haraldsen and E. Kawalski: Z. allge. u. allge. Chem. **224** (1935) 329.
I. Tsubokawa: J. Phys. Soc. Japan **11** (1956) 662.
6) H. Haraldsen, T. Ronsenquist and F. Gronvold: Aach. Math. Naturvidensk **50** (1949) 95.
T. Hirone, S. Maeda, I. Tsubokawa and N. Tsuya: J. Phys. Soc. Japan **11** (1956) 1083.
7) W. Biltz and A. Kocher: Z. anorg. u. allge. Chem. **241** (1939) 324.
E. Hoschek and W. Klemm: Z. anorg. u. allge. Chem. **242** (1939) 60.
8) H. Hoschek and W. Klemm: Z. anorg. u. allge. Chem. **242** (1939) 49.
9) T. Hirone, S. Maeda and N. Tsuya: Rev. Sci. Instr. **25** (1954) 516.
10) I. Tsubokawa: J. Phys. Soc. Japan. **13** (1958) 1432.
11) T. Hirone, S. Maeda, I. Tsubokawa and N. Tsuya: Sci. Rep. RITU. **A-5** (1953) 513.
12) T. Suzuoka et al: *unpublished.*
13) T. Hirone and K. Adachi: J. Phys. Soc. Japan. 12 (1957) 156.
14) J. C. Slater: Quarterly Progress Report, M. I. T. July 15, 1 (1953).
15) P. W. Anderson and H. Hasegawa: Phys. Rev. **100** (1955) 675.
16) J. Kanamori: Busseiron Kenkyu **105** (1957) 80 (in Japanese).

JOURNAL OF THE PHYSICAL SOCIETY OF JAPAN Vol. 14, No. 2, FEBRUARY, 1959

Spectro-Polarization Characteristics of the Sodium Nitrate Polarizer

By Tasaburô YAMAGUTI
College of Arts and Sciences, Chiba University
Isao MAKINO, Shingo SHINODA and Ippei KUROHA
Taga works, Hitachi Ltd

(Read April 3, 1957; Received October 20, 1958)

The polarization characteristics of the sodium nitrate polarization prism are measured. Polarization effect is complete from 350 to 1,000 mμ; and transmission of light uncorrected for reflection at the surfaces is about 90% at above 400 mμ and 37% at 350 mμ. Possibility of making a polarization prism for a wide wavelength range from 250 to 1,000 mμ is discussed.

§ 1. Introduction

A method making the sodium nitrate polarization prism is already reported by one of the authors[1]. The present work is concerned with the polarization characteristics of the prism for monochromatic rays of several wavelengths from 350 to 1,000 mμ.

§ 2. Experimental

The polarization prism used for the measurement has a structure shown in Fig. 1, the length and aperture are 27 mm and 11×11 mm respectively; an angle between the prism axis and the thin single crystal plate of sodium nitrate is 23°. The optical axis of the crystal is perpendicular to the prism axis and makes an angle of 23° with the normal of the crystal plate.

In order to measure variations of transmission of polarized light through the prism with those of both wavelengths and angular positions of the prism, the prisms are set in Hitachi photo-electric spectrophotometer as are shown in Fig. 2.

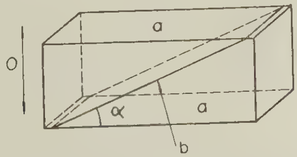

Fig. 1. A sodium nitrate polarization prism. a: SK5 glass, b: single crystal of sodium nitrate, o: the optical axis, and α: the angle 23° of the glass prism.

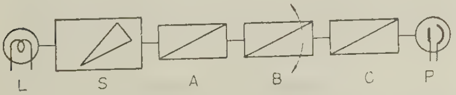

Fig. 2. Experimental apparatus. L: tungsten lamp, S: spectrometer, A, B and C: the polarization prisms and P: photocell.

In the early measurement with no use of the prism C in the figure, intensities of light passed through two prisms, A fixed in a definite angular position and B in positions rotated successively by 10°, were measured by the photocell P. The photocell, however, has sensitivities slightly varying with angles between the plane of polarization of the incident light and a definite plane of the photocell including the direction of the incident light. To eliminate these sensitivity differences and the effect of partially polarized light produced by the optical system, the polarization prism C is set in parallel to A. Keeping A and C in the fixed positions, the prism B is rotated to positions at which transmission measurements are to be done.

The experimental procedure is as follows. At first, the prism B is removed from the apparatus and intensity of the incident beam of each wavelength is adjusted so as the reading of the photocurrent indicates 100 for the light passed through the two prisms A and C. Then the prism B is set in the apparatus and is rotated successively by 10°, and at each position the photocurrent of the beam passed through the three prisms, i.e. transmission, is read. Curves in Fig. 3 show transmission thus measured for each wavelength versus rotation angles of B. These curves, however, are shown separately by displacing them towards the right hand side in distances nearly proportional to the wavelength differences of the incident light to see clearly the angular dependence of transmission

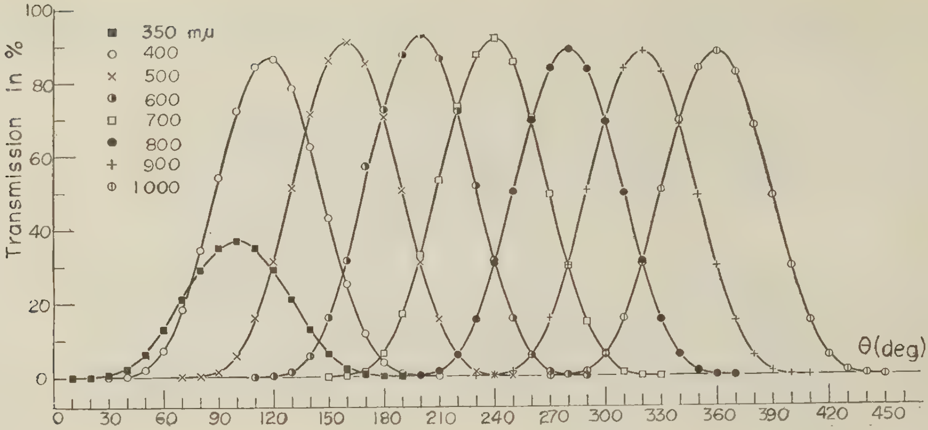

Fig. 3. Transmission of polarized monochromatic light versus rotation angles of the sodium nitrate analyser B. The curves for the different wavelengths are shown by shifting them each other to avoid confusion. Transmission values have not been corrected for reflection at the surfaces.

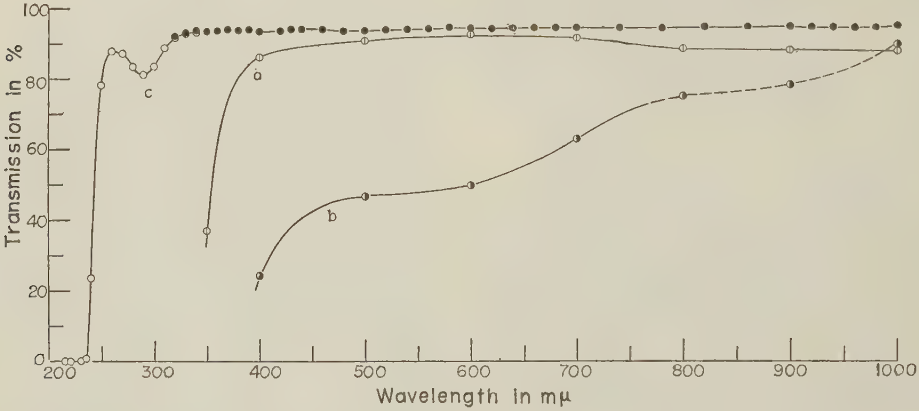

Fig. 4. Maximum transmission versus wavelengths. a: the sodium nitrate polarizer, b: H Polaroid, and c: two fused silica plates 1.5 mm thickness combined by the thin single crystal of sodium nitrate about 0.1 mm thickness.

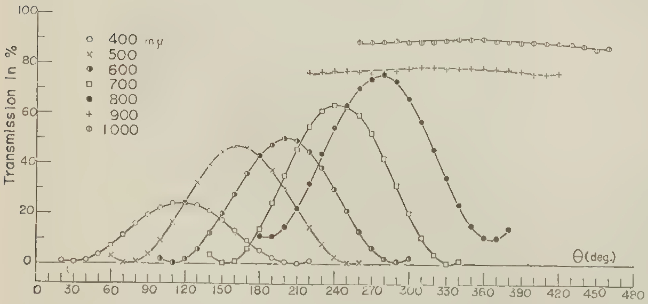

Fig. 5. Transmission versus rotation angles of H Polaroid. Light of 800 mμ being partially polarized, infra-red of more longer wavelengths completely unpolarized.

for all the wavelengths. Denoting the angle of B rotated from the position parallel to A by θ, the transmission can be expressed by $\cos^4\theta$ in the present arrangement of the three prisms. Actually, transmission observed to each wavelength is in a good agreement with $\cos^4\theta$.

In Fig. 4 the curve a represents the maximum transmission of polarized light passed through B plotted against the wavelengths. We can see from the figure that the transmission for infra-red and visible light is about 90% and is still large 37% at a short wavelength 350 mμ. To compare these polarization characteristics with those of H type Polaroid, two plates of Polaroid are set in place of the prisms A, B and C. Holding the plate placed near to the light source in a fixed position, another is rotated as in the above case to measure the photoelectric current of the photocell P. The results are given in Fig. 5. If Polaroid used in the present experiment is complete one as a polarization plate, the intensity must be expressed by $\cos^2\theta$. From the curves in the figure it can be said that the polarization effect is complete for visible light, whereas is remarkably incomplete at 800 mμ and is lost completely at longer wavelengths. Transmisson observed at parallel positions of the two plates versus wavelength is gived by the curve b in Fig. 4. It is remarkably small at 400 mμ and increases to the value of the order of 50% at visible light region. Large values at infra-red, however, are due to the unpolarized light passed through Polaroids which lost the polarization properties over these wavelength ranges.

§ 3. Discussions

Remarkable decrease of transmission of the present polarization prism for ultra-violet below 350 mμ can be ascribed to the absorption of SK5 glass. To make a polarization prism for ultra-violet it will be adequate to use prisms of fused silica, between which a sodium nitrate single crystal is to be grown. The limit of short wavelength of light to be polarized by such a polarization prism is experimentally determined, putting as an absorber two fused silica plates of 1.5 mm thickness combined by the thin single crystal of sodium nitrate of about 0.1 mm thickness in the photo-electric spectrophotometer. The light source is a tungsten lamp for above 320 mμ and a hydrogen discharge tube below 340 mμ. The results are shown by the curve c in Fig. 4, transmission values are not corrected for reflections at the plate surfaces. The plate transmits light above 250 mμ nearly perfectly. Since usual fused silica has absorption band at 240 mμ, the absorption below 250 mμ may be due to fused silica and the small adsorption at 290 mμ observed is considered as being due to absorption by sodium nitrate. Hence it can be expected that a sodium nitrate polarization prism made of fused silica prism will have a superior properties enabling to polarize light from 250 to 1,000 mμ or even longer. Several polarization prisms of this type were abready made and the characteristics of them will be reported in another paper.

In conclusion one of the authors (T. Y.) thanks to the Educational Department for financial suport.

Reference

1) T. Yamaguti: J. Phys. Soc. Japan **10** (1955) 219.

JOURNAL OF THE PHYSICAL SOCIETY OF JAPAN Vol. 14, No. 2, FEBRUARY, 1959

The Steady Flow of Viscous Fluid at Low Reynolds Numbers passing obliquely through a Plane Grid made of Equal Parallel Circular Cylinders

By Kō TAMADA

Department of Aeronautical Engineering, Faculty of Engineering, Kyoto University

and Hiroomi FUJIKAWA

Junior College of Engineering, University of Osaka Prefecture

(Received September 30, 1958)

The flow of a viscous fluid at low Reynolds numbers passing obliquely through a plane grid made of equal, parallel, circular cylinders regularly spaced is discussed on the basis of Oseen's equations of motion. Explicit expressions for the force experienced by a cylinder in the grid, for the direction of the flow at infinity downstream, and for the pressure drop caused by the grid are obtained correct to the first order in the Reynolds number and in the diameter-distance ratio of the grid.

Among these the following results may be worth mentioning. The flow is deflected by the grid more or less to the direction of the normal to the grid surface and is always slowed down at infinity downstream. At very small Reynolds numbers, the flow becomes almost perpendicular to the grid even at far upstream and, hence, the component of force tangential to the grid surface vanishes, while the normal component of force to the grid surface becomes equal, in its magnitude, to the drag when the grid is set at right angles to the uniform stream whose velocity is equal to the normal component of the original velocity.

§ 1. Introduction

In a previous paper[1], the present writers have investigated on the basis of Oseen's equations the flow of a viscous incompressible fluid passing perpendicularly through a plane grid made of equal, parallel, regularly spaced, circular cylinders. The type of drag force obtained there suggests that the solution of Stokes's equations may also exist for this problem. (As is well known, there is no solution of Stokes's equations for the case of a single cylinder.) This was really verified recently by Miyagi[2]. The Oseen solution tends to the Stokes's for vanishingly small Reynolds numbers. However, the situation is somewhat different when the flow impinges on the grid obliquely. Namely, Stokes's equations do not permit an oblique flow to the grid surface. Thus, we are obliged to appeal, at least, to the Oseen approximation to treat the oblique case. In this respect, it may be interesting to investigate the behaviour of the Oseen solution at very small Reynolds numbers. Also, the new case may have some interesting characteristics. Especially, each cylinder experiences additional components of force parallel to the grid surface owing to the presence of the corresponding components of the flow, and, as a result, the direction of the flow at far downstream will be deflected. It is the purpose of the present paper to study theoretically the problem just mentioned. The whole analysis is based on the Oseen approximation as in the previous paper. The flow in question is quasi-two-dimensional in the sense that the state of flow is quite the same in all planes perpendicular to the axes of the cylinders. As a consequence, the two components of fluid velocity lying in these planes are independent of the remaining component which is parallel to the axes of the cylinders. This fact takes an important role in the analysis and produces considerable simplification. However, the analysis is yet fairly complicated, and the writers content themselves this time with the derivation of the first order solution for small Reynolds numbers. Explicit expressions for the force acting on a cylinder, for the velocity at infinity downstream and for the angle of deflection of the flow are derived to this approximation. Transition from the Oseen to the Stokes approximation is also discussed. Detailed numerical calculations are made concerning the force and flow deflection for various Reynolds numbers and for three values of the diameter-distance ratio of the grid, assuming a fixed initial flow direction.

§ 2. Fundamental Equations and Solutions

We take the rectangular coordinates x, y, z in such a way that the fluid velocity has the components U, 0, W at infinity upstream, that the z-axis coincides with the axis of one cylinder of the grid and that the grid surface makes an angle ω with the x-direction (Fig. 1). Also, let a be the radius of each cylinder, h the distance between the axes of two neighbouring cylinders, p the pressure, and u, v, w the x, y, z components of the velocity at any point. Since all quantities such as u, v, w and p are obviously independent of the z-coordinate in the present problem, Oseen's equations of motion and the equation of continuity may be written in the forms

$$\left.\begin{aligned} &U\frac{\partial u}{\partial x}=-\frac{1}{\rho}\frac{\partial p}{\partial x}+\nu\Delta u\,,\\ &U\frac{\partial v}{\partial x}=-\frac{1}{\rho}\frac{\partial p}{\partial y}+\nu\Delta v\,,\\ &U\frac{\partial w}{\partial x}=\nu\Delta w\,,\\ &\text{and}\\ &\frac{\partial u}{\partial x}+\frac{\partial v}{\partial y}=0\,, \end{aligned}\right\} \tag{1}$$

where ρ is the density of the fluid, ν the kinematic coefficient of viscosity and Δ stands for $(\partial^2/\partial x^2)+(\partial^2/\partial y^2)$. Three components u, v, w of the velocity should all vanish on the surface of each cylinder.

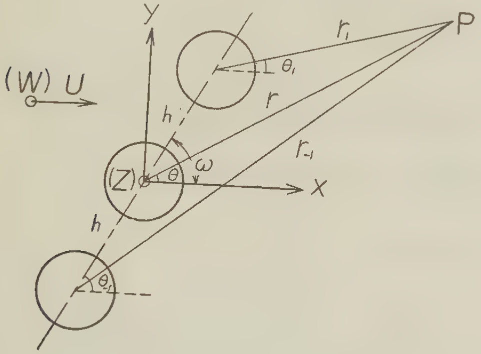

Fig. 1.

Elimination of p from (1) yields

$$\left(\Delta-2k\frac{\partial}{\partial x}\right)\left(\frac{\partial}{\partial\bar{\zeta}}\right)(u-iv)=0\,,\qquad \left(\Delta-2k\frac{\partial}{\partial x}\right)w=0\,,\qquad \Re\frac{\partial}{\partial\bar{\zeta}}(u-iv)=0\,, \tag{1.a}$$

with

$$\zeta=x+iy\,,\qquad \bar{\zeta}=x-iy\,,\qquad k=U/2\nu\,. \tag{2}$$

Eqs. (1) and the boundary conditions clearly show that the flow component in the z-direction does not affect at all the components of flow in the x, y plane. That is to say, u, v and p are identical with those for the purely two-dimensional case in which $w=0$. Thus, (u, v)-field and w-field may be treated separately. In the following discussions, however, we shall treat both fields in parallel for convenience sake. Now, when there is only one cylinder in the otherwise uniform stream, appropriate solutions of (1.a) take on the forms

$$u-iv=U+f(\zeta)+g(r,\theta)\,,\qquad w=W+g^*(r,\theta)\,, \tag{3}$$

where

$$\left.\begin{aligned} &f(\zeta)=\sum_{m=1}^{\infty}A_m(a/\zeta)^m\,,\qquad \zeta=re^{i\theta}\,,\\ &g(r,\theta)=e^{kr\cos\theta}\sum_{m=-\infty}^{\infty}a_mK_m(kr)e^{im\theta}\,,\\ &a_{-j}=\bar{a}_{j-1}\,,\qquad (j=1,2,\cdots)\\ &g^*(r,\theta)=e^{kr\cos\theta}\sum_{m=-\infty}^{\infty}C_mK_m(kr)e^{im\theta}\,,\\ &C_{-j}=\bar{C}_j\,,\qquad (j=0,1,2,\cdots) \end{aligned}\right\} \tag{4}$$

A_m's ,a_m's, C_m's being arbitrary constants and K_m denotes the modified Bessel function*. Therefore, introducing auxiliary coordinates

$$\zeta_s = r_s e^{i\theta_s} = \zeta - she^{i\omega} , \qquad (s=0, \pm 1, \cdots) \tag{5}$$

we may generalize for the present problem the said solutions in the forms

$$u - iv = U + \mathcal{E} + \sum_{s=-\infty}^{\infty} \{f(\zeta_s) + g(r_s, \theta_s)\} , \qquad w = W + \sum_{s=-\infty}^{\infty} g^*(r_s, \theta_s) , \tag{6}$$

where the functional forms of f, g and g^* are the same as in (4). Insertion of one more constant $\mathcal{E}$ will be understood in the following.

§ 3. Boundary Conditions

Let us first consider the boundary condition at infinity. Since g and g^* in (6) vanish exponentially at infinity upstream, we obtain the results: (cf. Appendix, (A.2))

$$u - iv \rightarrow U + \mathcal{E} - i\pi a h^{-1} e^{-i\omega} A_1 , \qquad w \rightarrow W , \qquad \text{for} \quad x \rightarrow -\infty .$$

Since $u - iv$ must be equal to U there, we get

$$\mathcal{E} = i\pi a h^{-1} e^{-i\omega} A_1 . \tag{7}$$

On the other hand, at infinity downstream, it can be shown (Appendix, 1) that

$$\left.\begin{aligned} &u - iv \rightarrow U + 2i\frac{\pi a}{he^{i\omega}} A_1 + \frac{2\pi}{kh \sin\omega} \Re \sum_{m=0}^{\infty} a_m , \\ &w \rightarrow W + \frac{\pi}{kh \sin\omega} \sum_{m=-\infty}^{\infty} C_m , \qquad \text{for} \quad x \rightarrow +\infty . \end{aligned}\right\} \tag{8}$$

Thus, it may be seen that the velocity at infinity downstream is different from that of the undisturbed stream, i.e. the flow is deflected by the grid, and, as is shown later, the flow is always slowed down. Owing to continuity, however, the component of velocity normal to the grid surface should obviously be recovered at infinity downstream, and this requires the relation

$$\Re\left(A_1 + \frac{1}{ka} \sum_{m=0}^{\infty} a_m \right) = 0 . \tag{9}$$

In view of the change in velocity at infinity downstream, there may be some doubt in applying the Oseen approximation in a manner as above where the x-component U of the undisturbed flow is taken as the representative velocity. However, this point is not serious as far as the induced flow in the y-direction remains small. Moreover, as will be seen later, a large part of the flow field reduces to the Stokes field at sufficiently small Reynolds numbers, and the Oseen field survives only at far upstream.

We now proceed to the fulfilment of the boundary conditions on the cylinders. As the solutions (6) satisfy already the periodicity of the flow field, it is sufficients to consider the boundary conditions $u = v = w = 0$ on the cylinder $r = a$ only. In order to apply the conditions, we expand the solutions (6) in Fourier series in θ on the surface $r = a$ (Appendix, 2). Then, by equating each coefficient of $e^{in\theta}$ $(n = 0, \pm 1, \cdots)$ to zero, we obtain the following sets of simultaneous algebraic equations for determining A_m's, a_m's and C_m's:

$$\left.\begin{aligned} &A_n + \sum_{m=-\infty}^{\infty} \{g_{m(-n)} + G_{m(-n)}\} a_m = 0 , \qquad (n=1, 2, \cdots) \\ &\sum_{s=1}^{\infty} F_{sn} A_s + \sum_{m=-\infty}^{\infty} \{g_{mn} + G_{mn}\} a_m = \begin{cases} -U , & (n=0) \\ 0 , & (n=1, 2, \cdots) \end{cases} \\ &\sum_{m=-\infty}^{\infty} (g_{mn} + G_{mn}) C_m = \begin{cases} -W , & (n=0) \\ 0 . & (n=\pm 1, \pm 2, \cdots) \end{cases} \end{aligned}\right\} \tag{10}$$

---

* The relation $a_{-j} = \bar{a}_{j-1}$ follows from the equation of continuity, the third Eq. in (1.a).

The expressions for g_{mn}, G_{mn} and F_{sn} are given in (11.a) below. By means of these equations and the two relations in (4):

$$a_{-m}=\bar{a}_{m-1}\,,\quad (m=1,2,\cdots)\qquad C_{-m}=\bar{C}_m\,,\quad (m=0,1,2,\cdots)$$

we can solve the unknowns A_m's, a_m's and C_m's. Thus, elimination of A_n's from (10) gives

$$\left.\begin{aligned} &\sum_{m=-\infty}^{\infty}\chi_{mn}a_m=\begin{cases}-U\,, & (n=0)\\ 0\,, & (n=1,2,\cdots)\end{cases}\\ &\text{with}\\ &\chi_{mn}=g_{mn}+G_{mn}-H_{mn}\,,\end{aligned}\right\}\tag{11}$$

where

$$\left.\begin{aligned} &g_{mn}=K_m(ka)I_{m-n}(ka)\,,\\ &G_{mn}=2\sum_{l=-\infty}^{\infty}(-1)^l e^{i(l+m)\omega}T_{l+m}I_l(ka)I_{l+n}(ka)\,,\\ &T_{l+m}=\sum_{s=1}^{\infty}K_{l+m}(skh)\begin{matrix}\cosh\\ \sinh\end{matrix}(skh\cos\omega)\,,\qquad \begin{matrix}(l+m=\text{even})\\ (l+m=\text{odd})\end{matrix}\\ &H_{mn}=\sum_{s=1}^{\infty}F_{sn}\{g_{m(-s)}+G_{m(-s)}\}\,,\\ &F_{sn}=\begin{cases}\dfrac{(-1)^s}{s!\,n!}\dfrac{s}{s+n}B_{(s+n)/2}\left(\dfrac{2\pi a}{he^{i\omega}}\right)^{s+n}, & (s+n=\text{even})\\ 0\,, & (s+n=\text{odd}\geqq 3)\end{cases}\\ &F_{1,0}=i\pi ah^{-1}e^{-i\omega}\,,\end{aligned}\right\}\tag{11.a}$$

$I_m(ka)$ and $K_m(ka)$ in these expressions denote the modified Bessel functions and B_m's are the Bernoulli numbers. It may be remarked here that the first equation in (10) proves the relation (9) expected previously. (Detailed proof is given in the Appendix, 3.)

§ 4. Approximate Solutions for $ka \ll 1$ and $(kh)^{-1}=O(1)$

There are two parameters ka and kh besides ω in the present problem. Since $k=U/2\nu$, $4ka$ and $2kh$ are the Reynolds numbers of the flow referred respectively to the diameter of the cylinder and the central distance between the neighbouring cylinders. We shall first treat the case in which ka is very small but kh is not. Close examination of the coefficients of the equations (10) and (11) for this case suggests a method of successive approximation. In the present paper, however, the first step only will be carried out for brevity. Namely, we retain only first three constants A_1, a_0 and C_0. (These three are sufficient to represent relevant characteristics of the flow at low Reynolds numbers.) Thus, Eqs. (10) and (11) may be replaced by

$$\left.\begin{aligned} &\chi_{00}a_0+\chi_{(-1)0}\bar{a}_0=-U\,,\\ &A_1+\{g_{0(-1)}+G_{0(-1)}\}a_0-\{g_{(-1)(-1)}+G_{(-1)(-1)}\}\bar{a}_0=0\,,\\ &(g_{00}+G_{00})C_0=-W\,.\end{aligned}\right\}\tag{12}$$

Making use of the expansions of $I_m(ka)$ and $K_m(ka)$ for small ka, we obtain (Appendix, 4)

$$\chi_{00}=S+2T_0+O\{(ka)^2\}\,,\qquad \chi_{(-1)0}=\frac{1}{2}+2T_1e^{-i\omega}-\frac{i\pi}{kh}e^{-i\omega}+O\{(ka)^2\}\,,$$

where

$$\left.\begin{aligned} &S=\log\frac{2}{ka}-\gamma\ ,\\ &T_0=\sum_{s=1}^{\infty}K_0(skh)\cosh\,(skh\ \cos\omega)\ ,\\ &T_1=\sum_{s=1}^{\infty}K_1(skh)\sinh\,(skh\cos\omega)\ ,\end{aligned}\right\}\tag{13}$$

γ being Euler's constant. With these expansions the first equation in (12) and its conjugate give at once

$$a_0=-\frac{U}{\Delta}\left\{S-\frac{1}{2}+2T_0-\left(2T_1-\frac{i\pi}{kh}\right)e^{-i\omega}\right\}+O\{(ka)^2\}\ ,\tag{14}$$

with

$$\Delta=(S+2T_0)^2-\left(2T_1+\frac{1}{2}\cos\omega\right)^2-\left(\frac{\pi}{kh}-\frac{1}{2}\sin\omega\right)^2+O\{(ka)^2\}\ .\tag{14.a}$$

Then, from the second equation in (12) combined with the expansions (cf. Appendix, 4)

$$\begin{aligned} &g_{0(-1)}=O(ka)\ ,\qquad g_{(-1)(-1)}=(ka)^{-1}+O(ka)\ ,\\ &G_{0(-1)}=-\overline{G}_{(-1)(-1)}=O(ka)\ ,\end{aligned}$$

we find

$$A_1=-(ka)^{-1}\bar{a}_0+O(ka)\ .\tag{15}$$

Further, it can be shown (Appendix, 4) that

$$g_{00}=S+O\{(ka)^2\}\ ,\qquad G_{00}=2T_0+O\{(ka)^2\}\ ,$$

and hence the last equation in (12) gives

$$C_0=-W(S+2T_0)^{-1}+O\{(ka)^2\}\ .\tag{16}$$

§ 5. Force and Velocity

By summing up the stress acting on the surface of a cylinder (Appendix, 5) or by applying the theorem of momentum to the fluid between two control surfaces taken parallel to the grid surface at $x=\pm\infty$, we can deduce formulae for calculating the force acting on the cylinder. These may be written as

$$X+iY=2\pi\rho UaA_1\ ,\qquad Z=-2\pi\mu\sum_{m=-\infty}^{\infty}C_m\ ,\tag{17}$$

where X, Y, Z are respectively the x, y, z-components of force per unit length of the cylinder and μ is the viscosity coefficient of the fluid. Inserting (15) and (16) into (17) and making some calculations, we get the results:

$$\left.\begin{aligned} &\frac{F_n}{\mu U}=\frac{4\pi}{\Delta}\left\{\left(S+2T_0-\frac{1}{2}\right)\sin\omega+\frac{\pi}{kh}\right\}\ ,\\ &\frac{F_t}{\mu U}=\frac{4\pi}{\Delta}\left\{\left(S+2T_0-\frac{1}{2}\right)\cos\omega-2T_1\right\}\ ,\\ &Z/(\mu W)=2\pi(S+2T_0)^{-1}\ ,\end{aligned}\right\}\tag{18}$$

where F_n and F_t denote respectively the force components normal and tangential (in the x, y-plane) to the grid surface, namely

$$F_n = X\sin\omega - Y\cos\omega\,, \qquad F_t = X\cos\omega + Y\sin\omega\,, \tag{19}$$

and the expressions for S, T_0, T_1 and Δ were given in (13) and (14.a) before. If we take, as a special case, $\omega=\pi/2$ and $W=0$ in (18), the result is seen to agree with that given in the previous paper[1]. Again, if we make $h\to\infty$ in (18), we reproduce the result derived by Tomotika, Aoi and Yosinobu[3] for the case of a single cylinder.

On the other hand, we may evaluate the velocity at infinity downstream ($x\to+\infty$) by the preceding equations (8) and (9) combined with (15) and (16). After some calculations, we may obtain

$$(q_n)_\infty = Q_n\,, \qquad (q_t)_\infty = Q_t - F_t/(\rho h Q_n)\,, \qquad (w)_\infty = W - Z/(\rho h Q_n)\,, \tag{20}$$

where we have put as in (19)

$$\left.\begin{aligned} q_n &= u\sin\omega - v\cos\omega\,, & q_t &= u\cos\omega + v\sin\omega\,,\\ Q_n &= U\sin\omega\,, & Q_t &= U\cos\omega\,. \end{aligned}\right\} \tag{21}$$

It will be seen that the second and the third equations in (20) represent the momentum balance in the t and z-directions respectively, while the first equation indicates continuity as mentioned earlier. Further, momentum consideration in the n-direction leads to the equation

$$h(p_{-\infty} - p_\infty) = F_n \tag{22}$$

which gives the pressure drop at far downstream.

The deflection of the flow at infinity downstream may also be estimated by (20). In particular, when the flow is two-dimensional, i.e. $W=0$, the angle of deflection δ is given by the equation

$$\tan\delta = \frac{v_\infty}{u_\infty} = -\frac{F_t}{\rho U^2 h - F_t\cot\omega}\,. \tag{23}$$

§ 6. Approximate Solutions for $ka \ll 1$ and $kh \ll 1$

We next proceed to consider the case where the parameters ka and kh are both small. Though the preceding analysis is based on the assumption that kh is not small, the main result (18) does never diverge when $kh\to 0$. In fact, if we reconsider the course of the preceding analysis, for the case ka and kh are both small, we shall find at each stage of reductions that the neglected terms happen to be higher order than the retained with respect to ka or kh or both. Thus, it may be seen that the final result (18) are also valid for the case under consideration. However, the series (13) defining the functions T_0 and T_1 in (18) are shown to converge quite slowly when kh is very small. Therefore, it is necessary first to find out some suitable expressions of these functions for small kh. This is done in the Appendix, 6. According to the analysis given there, T_0 and T_1 can be expanded asymptotically as

$$\left.\begin{aligned} &2T_0 \sim \frac{\pi}{\sin\omega}\,\frac{1}{\lambda} + \log\frac{\lambda}{4\pi} + \gamma + O(\lambda)\,,\\ &2T_1 \sim (\pi\cot\omega)\lambda^{-1} - \cos\omega + O(\lambda)\,, \qquad \lambda = kh\,, \end{aligned}\right\} \tag{24}$$

Inserting these in (18) and making some reductions, we get

$$\left.\begin{aligned} &\frac{F_n}{\mu Q_n} = \frac{4\pi}{\Delta} + O\{(kh)^2\}\,, & &\Delta = \log\frac{h}{2\pi a} + \frac{1}{2}\,,\\ &F_t = \rho h Q_n Q_t\,, & &Z = \rho h Q_n W\,, \end{aligned}\right\} \tag{25}$$

where F_n, F_t, Z and Q_n, Q_t, W are respectively the n, t, z-components of force and of velocity as before. Comparing the first equation with the result obtained in the previous paper[1], it is found that the force component F_n normal to the grid surface becomes equal to the drag when the grid is placed at right angles to the direction of the uniform stream of velocity $Q_n = U \sin \omega$. Also, it is seen that the expressions for F_t and Z are both quadratic in velocity and do not depend upon μ explicitly. Further, substituting (25) in (20), we find that the direction of the flow at infinity downstream becomes normal to the plane of the grid.

§ 7. Numerical Discussion

In Figs. 2~4 are shown the results of numerical calculations concerning the components of force acting on a cylinder, per unit length, of the grid. In these figures, the full-line and the chain-line curves represent the results for the case $\omega = 60°$ computed by the formulae (18) and (25) respectively, while the broken-line curves are for the case $\omega = 90°$. From Fig. 2 it will be seen that $F_n/\mu Q_n$ $(Q_n = U \sin \omega)$ is little influenced by the stagger angle ω and its dependence on the Reynolds number is much the same as in the case $\omega = 90°$ (cf. reference 1).

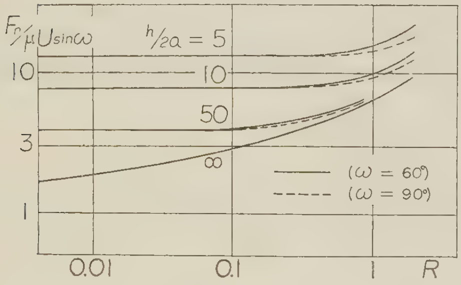

Fig. 2.

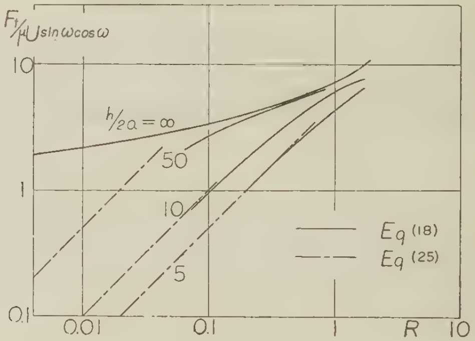

Fig. 3. (ω=60°)

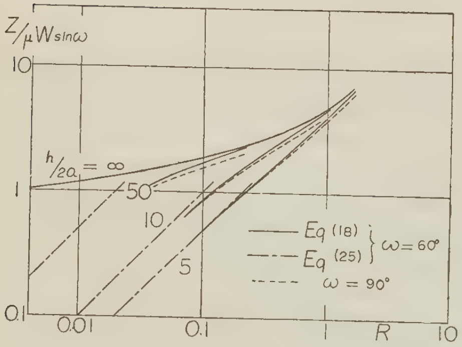

Fig. 4.

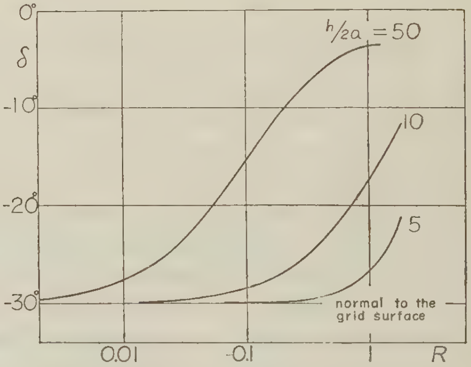

Fig. 5. (ω=60°)

Table I. Values of $F_n/(\mu U \sin \omega)$.

R \ ω, h/2a	60°			90°			
	5	10	50	5	10	50	∞
0	13.03	7.580	3.846	13.03	7.580	3.846	0
0.08	13.03	7.592	3.956	13.04	7.593	3.915	2.775
0.2	13.13	7.709	4.316	13.08	7.648	4.202	3.479
0.4	13.38	8.041	4.961	13.24	7.854	4.825	4.306
0.8	14.50	9.118	6.228	13.85	8.589	6.076	5.647
1.6	18.78	12.32	8.922	16.32	11.02	8.644	8.201
3.2	72.5			28.13	19.55	15.71	14.98

On the other hand, we see in Fig. 3 and Fig. 4 that F_t and Z decrease rapidly with decreasing Reynolds number. This indicates that the mean direction of the flow in the vicinity of the grid becomes more and more perpendicular to the grid surface as the Reynolds number is reduced. The tendency is evidently more marked for closer spaced grid (smaller $h/2a$).

Fig. 5 shows the angle of deflection of the flow for the two-dimensional motion in the x, y-plane, as calculated by Eq. (23) for $\omega=60°$. From this figure we see clearly how nearly the flow becomes normal to the grid surface at low values of the Reynolds number. Further, since δ is always negative and since the normal component of the flow is continuous, we may conclude that the flow is necessarily slowed down at infinity downstream.

Some of the numerical data for drawing Figs. 2~5 are also listed in Tables I~III. We may compute, if necessary, the components of force X, Y, the velocity and pressure drop at infinity downstream, from these data together with Eqs. (19), (20) and (22).

The writers wish to express their thanks to the Ministry of Education for a grant-in-aid for fundamental scientific research.

Table II. Values of $F_t/(\mu U \sin\omega\cos\omega)$ ($\omega=60°$).

R \ $h/2a$	5	10	50	∞
0.08	0.400	0.769	2.423	3.205
0.2	0.995	1.811	3.763	4.018
0.4	1.961	3.254	4.803	4.972
0.8	3.729	5.362	6.264	6.520
1.6	6.240	7.480	8.802	9.470

Table III. Values of $Z/(\mu W \sin\omega)$.

ω	60°				90°		
R \ $h/2a$	5	10	50	∞	5	10	50
0.08	0.3899	0.7096	1.611	1.801	0.3885	0.6974	1.468
0.2	0.9405	1.523	2.296	2.332	0.9316	1.467	2.014
0.4	1.783	2.508	2.996	3.000	1.750	2.352	2.598
0.8	3.298	3.990	4.205	4.205	3.176	3.594	3.642
1.6	6.449	6.974	7.029	7.029	5.955	6.085	6.087
3.2	20.90	21.39	21.40	21.40	18.51	18.53	18.53

Appendices

1. Velocity at infinity

According to (4), (5), (6) in the main text, the complex velocity $u-iv$ in the x, y-plane is given by

$$\left.\begin{array}{l} u-iv=U+\mathcal{E}+\sum\limits_{s=-\infty}^{\infty} f(\zeta_s)+\sum\limits_{s=-\infty}^{\infty} g(r_s,\theta_s)\,, \\ \text{where} \\ \zeta_s=r_s e^{i\theta_s}=\zeta-she^{i\omega}\,, \qquad \zeta=re^{i\theta}\,, \\ f(\zeta_s)=\sum\limits_{m=1}^{\infty} A_m(a/\zeta_s)^m\,, \\ g(r_s,\theta_s)=e^{kr_s\cos\theta_s}\sum\limits_{m=-\infty}^{\infty} a_m K_m(kr_s)e^{im\theta_s}\,, \\ \qquad a_{-m}=\bar{a}_{m-1}\,. \qquad (m=1,2,\cdots) \end{array}\right\} \qquad (A.1)$$

For $|\zeta|\gg a$, $f(\zeta_s)\cong A_1a/\zeta_s$ and we get

$$\sum_{s=-\infty}^{\infty} f(\zeta_s)=A_1a\left\{\frac{1}{\zeta}+\sum_{s=1}^{\infty}\frac{2\zeta}{\zeta^2-(she^{i\omega})^2}\right\}=-i\frac{\pi a}{he^{i\omega}}A_1\coth\left\{\frac{\pi r}{h}e^{i(\theta-\omega-(\pi/2))}\right\}.$$

Therefore, when $r\to\infty$

$$\sum_{s=-\infty}^{\infty} f(\zeta_s) \to \mp i \frac{\pi a}{h e^{i\omega}} A_1 \,, \qquad \begin{array}{l} \pi+\omega > \theta > \omega \ \text{(upstream)} \\ \omega > \theta > \omega-\pi \ \text{(downstream)} \end{array} \tag{A.2}$$

On the other hand, viscous term $\sum g(r_s, \theta_s)$ is seen to vanish exponentially at infinity upstream, but it may have finite contribution at far downstream. To show this, we use the well-known formula

$$\left. \begin{array}{l} K_m(R) e^{im\Theta} = \dfrac{1}{2} \displaystyle\int_0^\infty (\pm it)^m \exp\left\{ \mp \frac{i}{2}\left(Zt - \frac{\bar{Z}}{t} \right) \right\} \frac{dt}{t} \,, \\ Z = Re^{i\Theta} \,, \qquad \Im(Z) \lesseqgtr 0 \,. \end{array} \right\} \tag{A.3}$$

By means of this, we may rewrite $g(r_s, \theta_s)$ for $h/2 > \Im(\zeta) > -h/2$ in integral forms

$$\begin{aligned} g(r_s, \theta_s) = \frac{1}{2} e^{kx} \int_0^\infty \exp\Big[& \mp \frac{ik}{2}\left(\zeta t - \frac{\bar{\zeta}}{t} \right) \\ & - skh \left\{ \cos\omega \mp \frac{i}{2}\left(e^{i\omega} t - \frac{e^{-i\omega}}{t} \right) \right\} \Big] \alpha(\pm it) \frac{dt}{t} \,, \qquad \begin{array}{l} (s \geqq 1) \\ (s \leqq -1) \end{array} \end{aligned} \tag{A.4}$$

with

$$\alpha(\xi) = \sum_{m=-\infty}^{\infty} a_m \xi^m \,.$$

Then, summing up the results with respect to s, we obtain

$$\begin{aligned} \sum_{s=s_1}^{s_2} g(r_s, \theta_s) = \mp \frac{1}{2} e^{kx} \int_0^\infty & \exp\left\{ \mp \frac{ik}{2}\left(\zeta t - \frac{\bar{\zeta}}{t} \right) \right\} \\ & \times \left[1 - \exp kh \left\{ \cos\omega \mp \frac{i}{2}\left(e^{i\omega} t - \frac{e^{-i\omega}}{t} \right) \right\} \right]^{-1} \alpha(\pm it) \frac{dt}{t} \,, \end{aligned} \tag{A.5}$$

where $s_1 = 1$, $s_2 = \infty$ with upper signs, and $s_1 = -\infty$, $s_2 = 0$ with lower signs. Now, for the estimation of the velocity at far downstream, it will be sufficient to take a special limit $\zeta = x \to +\infty$. Changing the variable of integration in (A.5) by

$$u = i + \frac{1}{2}\left(t - \frac{1}{t} \right) ,$$

we get

$$\begin{aligned} \sum_{s=1}^{\infty} g(r_s, \theta_s) = \frac{1}{2} \int_{i-\infty}^{i+\infty} & e^{-ikxu} [\exp kh \{ \sqrt{(-iu)(2+iu)} \sin\omega - iu \cos\omega \} - 1]^{-1} \\ & \times \tilde{\alpha}(u) \{ (-iu)(2+iu) \}^{-1/2} du \,, \end{aligned}$$

with $\tilde{\alpha}(u) = \alpha(\pm it)$.

To evaluate this integral, we consider a contour integral as shown in Fig. 6. Since there is no singular point inside the contour, and the integral along the upper branch gives just the integral in question, we find

$$\sum_{s=1}^{\infty} g(r_s, \theta_s) = \frac{1}{2} \left\{ -i\pi R + \int_{-X}^{-\varepsilon} + \int_{\varepsilon}^{X} \right\} .$$

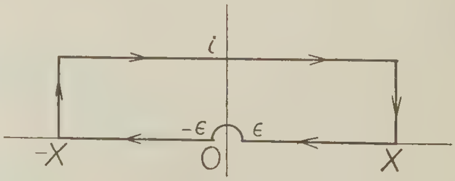

Fig. 6.

Here, the residue R at $u=0$ $(t=-i)$ is easily calculated to be*

$$R = \frac{i\alpha(1)}{2kh \sin\omega} \,, \qquad \alpha(1) = 2\Re \sum_{m=0}^{\infty} a_m \,.$$

---

* The relation $a_{-m} = \bar{a}_{m-1}$ has been used.

Further, for its highly oscillatory character for $kx \gg 1$, the integrand of the remaining integrals may be replaced by its approximate form near $u=0$. Thus we obtain

$$\lim_{x \to +\infty} \sum_{s=1}^{\infty} g(r_s, \theta_s) = \frac{i\alpha(1)}{4kh \sin \omega} \left\{ -i\pi + \left(\int_{-X}^{-\varepsilon} + \int_{\varepsilon}^{X} \right) \frac{e^{-ikxu}}{u} du \right\} . \tag{A.6}$$

Now, as (A.5) shows, the corresponding expression for the sum taken from $s=-\infty$ to $s=0$ can be obtained from the above by replacing i by $-i$, ω by $-\omega$ and changing the sign of the resulting expression. Then, adding this to (A.6), we arrive at the result

$$\lim_{x \to +\infty} \sum_{s=-\infty}^{\infty} g(r_s, \theta_s) = \frac{\alpha(1)}{2kh \sin \omega} \left\{ \pi + \int_{-\infty}^{\infty} \frac{\sin kxu}{u} du \right\} = \frac{\pi \alpha(1)}{kh \sin \omega} = \frac{2\pi}{kh \sin \omega} \Re \sum_{m=0}^{\infty} a_m . \tag{A.7}$$

This, in conjunction with (A.2), proves the first equation in (8) in the main text. Quite similarly the second equation in (8) may be verified, since, as is seen from (4), g^* has a common form with g except for the constants C_m's.

2. Fourier expansion of the velocity on a cylinder

On the cylinder $|\zeta| = a$, we have

$$f(\zeta) = \sum_{n=1}^{\infty} A_n e^{-in\theta} , \tag{A.8}$$

and for $|s| \geqq 1$

$$f(\zeta_s) = \sum_{m=1}^{\infty} A_m a^m (\zeta - she^{i\omega})^{-m} = \sum_{n=0}^{\infty} \left\{ \sum_{m=1}^{\infty} (-1)^m \frac{(m+n-1)!}{n!(m-1)!} \left(\frac{a}{she^{i\omega}} \right)^{m+n} A_m \right\} e^{in\theta} .$$

Also, making use of the formula

$$e^{ka \cos \theta} = \sum_{l=-\infty}^{\infty} I_l(ka) e^{il\theta} ,$$

we get at once the expansion

$$g(r, \theta) = \sum_{n=-\infty}^{\infty} \left\{ \sum_{m=-\infty}^{\infty} g_{mn} a_m \right\} e^{in\theta} , \qquad g_{mn} = K_m(ka) I_{m-n}(ka) . \tag{A.9}$$

On the other hand,

$$g(r_s, \theta_s) = e^{-skh \cos \omega} e^{ka \cos \theta} \sum_{m=-\infty}^{\infty} a_m K_m(kr_s) e^{im\theta_s} ,$$

and $K_m(kr_s)e^{im\theta_s}$ can be expanded by the addition theorem for the modified Bessel function (Ref. 4), i.e. for $s \geqq 1$

$$K_m(kr_s) e^{im\theta_s} = (-1)^m \sum_{l=-\infty}^{\infty} K_{m+l}(skh) I_l(ka) e^{i(l+m)\omega} e^{-il\theta} .$$

Inserting this and rearranging, we get

$$g(r_s, \theta_s) = \sum_{n=-\infty}^{\infty} \left\{ \sum_{m=-\infty}^{\infty} (-1)^m a_m \sum_{l=-\infty}^{\infty} e^{-skh \cos \omega} K_{m+l}(skh) I_l(ka) I_{n+l}(ka) e^{i(m+l)\omega} \right\} e^{in\theta} , \qquad (s \geqq 1)$$

and replacing ω by $\omega + \pi$, a corresponding result for $s \leqq -1$. Then, summation with respect to s yields

$$\mathcal{E} + \sum_{s=-\infty}^{\infty}{}' f(\zeta_s) = \sum_{n=0}^{\infty} \left(\sum_{m=1}^{\infty} F_{mn} A_m \right) e^{in\theta} , \tag{A.10}$$

and

$$\sum_{s=-\infty}^{\infty}{}' g(r_s, \theta_s) = \sum_{n=-\infty}^{\infty} \left(\sum_{m=-\infty}^{\infty} G_{mn} a_m \right) e^{in\theta} , \tag{A.11}$$

where $\sum'$ means a sum excluding the term for $s=0$, and F_{mn} as well as G_{mn} are given in (11.a) in the main text*. Thus, substituting (A.8)∼(A.11) in (A.1), we finally obtain

$$\begin{aligned}(u-iv)_{r=a} = U + \sum_{n=1}^{\infty} A_n e^{-in\theta} + \sum_{n=-\infty}^{\infty} \left\{ \sum_{m=-\infty}^{\infty} g_{mn} a_m \right\} e^{in\theta} \\ + \sum_{n=0}^{\infty} \left\{ \sum_{m=1}^{\infty} F_{mn} A_m \right\} e^{in\theta} + \sum_{n=-\infty}^{\infty} \left\{ \sum_{m=-\infty}^{\infty} G_{mn} a_m \right\} e^{in\theta} .\end{aligned} \tag{A.12}$$

In a similar manner, we may obtain

$$(w)_{r=a} = W + \sum_{n=-\infty}^{\infty} \left\{ \sum_{m=-\infty}^{\infty} (g_{mn} + G_{mn}) C_m \right\} e^{in\theta} . \tag{A.13}$$

Equating to zero the coefficients of $e^{in\theta}$ in (A.12) and (A.13), we arrive at the results (10) in the main text.

3. Verification of Eq. (9)

The first equation of (10) in the main text reads

$$\left.\begin{aligned} A_1 + \sum_{m=-\infty}^{\infty} \{ g_{m(-1)} + G_{m(-1)} \} a_m = 0 , \\ g_{mn} = K_m I_{m-n} , \qquad G_{mn} = 2 \sum_{l=-\infty}^{\infty} (-1)^l e^{i(l+m)\omega} T_{l+m} I_l I_{l+n} . \end{aligned}\right\} \tag{A.14}$$

The argument ka of the functions K_m and I_m will be omitted for brevity. Now, since $a_{-m} = \bar{a}_{m-1}$ $(m=1, 2, \cdots)$,

$$\Re \sum_{m=-\infty}^{\infty} g_{m(-1)} a_m = \Re \sum_{m=0}^{\infty} (K_m I_{m+1} a_m + K_{m+1} I_m \bar{a}_m) = \frac{1}{ka} \Re \sum_{m=0}^{\infty} a_m , \tag{A.15}$$

where the well-known relation $I_m K_{m+1} + I_{m+1} K_m = 1/ka$ has been used. On the other hand, taking the relation $a_{-m} = \bar{a}_{m-1}$ into account,

$$\sum_{m=-\infty}^{\infty} G_{m(-1)} a_m = 2 \sum_{m=0}^{\infty} \left[\sum_{l=-\infty}^{\infty} (-1)^l T_{l+m} I_l I_{l-1} e^{i(l+m)\omega} a_m + \sum_{l=-\infty}^{\infty} (-1)^l T_{l-m-1} I_l I_{l-1} e^{i(l-m-1)\omega} \bar{a}_m \right] .$$

Rewriting l as $-l+1$ in the second sum and noting $T_{-l-m} = T_{l+m}$ which is obvious from (11.a) in the main text, it is easily seen that

$$\Re \sum_{m=-\infty}^{\infty} G_{m(-1)} a_m = 0 . \tag{A.16}$$

Insertion of (A.15) and (A.16) into (A.14) proves the relation (9) in the main text.

4. Expansions for small *ka*

Here we concern the expansion of χ_{mn} given in (11) and (11.a) for small ka. First, we assume that $ka \ll 1$ but $kh = O(1)$, so that $a/h = O(ka)$. Making use of the expansions for $I_m(ka)$ and $K_m(ka)$, we obtain

$$g_{00} = K_0 I_0 = S + O\{(ka)^2\} , \qquad S = \log(2/ka) - \gamma ,$$

where γ denotes as before Euler's constant. Also, $T_l(kh) = O(1)$ and $I_{\pm l}(ka) = O\{(ka)^l\}$, and we have

---

* The relation (7) in the text has also been taken into account.

$$G_{00}=2\sum_{l=-\infty}^{\infty}(-1)^l T_l I_l^2 e^{il\omega}=2T_0+O\{(ka)^2\}\ .$$

Further, since

$$\begin{aligned}
&g_{0(-s)}=K_0 I_s=O\{(ka)^s\}\ ,\\
&F_{s0}=O\{(a/h)^s\}=O\{(ka)^s\}\ , \qquad \text{or} \qquad 0\ ,\\
&G_{0(-s)}=2\sum_{l=-\infty}^{\infty}(-1)^l T_l I_l I_{l-s}\, e^{il\omega}=O\{(ka)^s\}^{*}\ ,
\end{aligned}$$

it will be seen that

$$H_{00}=\sum_{s=1}^{\infty}F_{s0}\{g_{0(-s)}+G_{0(-s)}\}=O\{(ka)^2\}\ .$$

From these, we attain

$$\chi_{00}=g_{00}+G_{00}-H_{00}=S+2T_0+O\{(ka)^2\}\ . \tag{A.17}$$

In the next place, we get likewise the results

$$g_{(-1)0}=K_1 I_1=\frac{1}{2}+O\{(ka)^2\}\ ,$$

$$G_{(-1)0}=2\sum_{l=-\infty}^{\infty}(-1)^l T_{l-1} I_l^2 e^{i(l-1)\omega}=2T_1 e^{-i\omega}+O\{(ka)^2\}\ .$$

Also, we have

$$H_{(-1)0}=\sum_{s=1}^{\infty}F_{s0}\{g_{(-1)(-s)}+G_{(-1)(-s)}\}=\frac{i\pi}{kh}e^{-i\omega}+O\{(ka)^2\}\ ,$$

because

$$\begin{aligned}
&F_{s0}=\begin{cases} i\pi a/(he^{i\omega})\ , & \qquad\qquad\qquad\qquad (s=1)\\ O\{(ka)^s\}\ , \qquad\qquad \text{or} \quad 0\ , & (s=2,\ 3,\ \cdots)\end{cases}\\
&g_{(-1)(-s)}=K_1 I_{s-1}=K_1 I_0\ , \quad (s=1) \quad \text{or} \quad O\{(ka)^{s-2}\}\ , \quad (s=2,\ 3,\ \cdots)\\
&G_{(-1)(-s)}=2\sum_{l=-\infty}^{\infty}(-1)^l T_{l-1} I_l I_{l-s}\, e^{i(l-1)\omega}=O\{(ka)^s\}\ .
\end{aligned}$$

These results lead to

$$\chi_{(-1)0}=g_{(-1)0}+G_{(-1)0}-H_{(-1)0}=\frac{1}{2}+2T_1 e^{-i\omega}-i\pi/(khe^{i\omega})+O\{(ka)^2\}\ . \tag{A.18}$$

5. Formulae for the force components

By summing up the stress acting on the surface of a cylinder and taking into account the boundary conditions $u=v=0$ there, we can verify without difficulty a general formula

$$X+iY=\oint(ip+\mu\Omega)d\zeta\ , \qquad \Omega=(\partial v/\partial x)-(\partial u/\partial y)\ , \tag{A.19}$$

where p, μ, X, Y are respectively the pressure, the viscosity coefficient and x, y-components of force experienced by the cylinder, and integration should be carried out along the surface of the cylinder. Again, we have for the z-component of force the formula

---

[*] $I_l I_{l-s}=O\{(ka)^{|l|+|l-s|}\}$ and $|l|+|l-s|\geqq s$.

$$Z=a\mu\int_0^{2\pi}(\partial w/\partial r)_{r=a}d\theta\ , \tag{A.20}$$

where r, θ are the polar coordinates having the origin at the centre of the cylinder. Now, it can be shown after some reduction that to the Oseen approximation

$$p=-\rho U u_h\ , \qquad \mu\Omega=\rho U v_u\ , \tag{A.21}$$

where the suffices h and u mean the harmonic and unharmonic parts respectively. Introducing these results in (A.19) and remembering the condition $v_h+v_u=0$ on the cylinder, we reach the formula

$$X+iY=-i\rho U\oint(u-iv)_h\,d\zeta\ . \qquad \text{(A.22}$$

Substitution in this the expression

$$(u-iv)_h=U+\mathcal{E}+\sum_{s=-\infty}^{\infty}\sum_{m=1}^{\infty}A_m\left(\frac{a}{\zeta_s}\right)^m$$

proves the first formula of (17) in the main text. We next treat Z. First, we may obtain Fourier expansion in θ of w at an arbitrary point simply by replacing ka by kr in (A.13). Then, differentiating this, putting $r=a$ and inserting the result into (A.20), we have

$$Z=2\pi a\mu\sum_{m=-\infty}^{\infty}C_m(g'_{m0}+G'_{m0})\ .$$

But, by means of the recurrence formulae for I_m and K_m, we get

$$g'_{m0}=k(g_{m,1}-g_{m+1,1})\ , \qquad G'_{m0}=k(G_{m,1}+G_{m(-1)})\ .$$

Substituting these and using the third set of equations (for $n=\pm1$) of (10) in the main text, we have

$$Z=-2\pi\mu(ka)\sum_{m=-\infty}^{\infty}C_m(g_{m+1,1}+g_{m,-1})\ .$$

From the definition of g_{mn} together with the well-known relation $I_mK_{m+1}+I_{m+1}K_m=(ka)^{-1}$, we finally obtain the second formula of (17) in the main text.

6. Expansions for small *kh*

The asymptotic expansions (24) used in the main text will now be derived. To this end, we consider a function $T_j^*(\lambda, \omega)$ defined as

$$T_j^*(\lambda, \omega)=\sum_{s=1}^{\infty}e^{s\lambda\cos\omega}K_j(s\lambda)\ . \tag{A.23}$$

By means of the formula

$$K_j(\rho)=\frac{1}{2}\int_{-\infty}^{\infty}e^{-\rho\cosh\tau-j\tau}d\tau\ ,$$

this function may be written in the form

$$T_j^*=\frac{1}{2}\int_{-\infty}^{\infty}\frac{e^{-\lambda x}}{1-e^{-\lambda x}}e^{-j\tau}d\tau\ , \qquad x=\cosh\tau-\cos\omega\ . \tag{A.24}$$

Then, inserting the expansion

$$\frac{1}{1-e^{-\lambda x}}=\frac{1}{\lambda x}+\frac{1}{2}+\sum_{n=1}^{\infty}(-1)^{n+1}\frac{B_n}{(2n)!}\lambda^{2n-1}x^{2n-1}\ , \qquad (B_n\text{: Bernoulli number})$$

and performing term-wise integration formally, we get

$$2T_j{}^*=J_{-1}^{(j)}\frac{1}{\lambda}+\frac{1}{2}J_0^{(j)}+\sum_{n=1}^{\infty}(-1)^{n+1}\frac{B_n}{(2n)!}J_{2n-1}^{(j)}\lambda^{2n-1}\,, \tag{A.25}$$

where

$$J_{-1}^{(j)}=-\int^{\lambda}J_0^{(j)}d\lambda\,,\qquad J_0^{(j)}=2e^{\lambda\cos\omega}K_j(\lambda)\,,\qquad J_{2n-1}^{(j)}=(-1)^{2n-1}\frac{d^{2n-1}}{d\lambda^{2n-1}}J_0^{(j)}\,. \tag{A.26}$$

In particular, for $j=0$, it can be shown that

$$J_{-1}^{(0)}=\frac{2(\pi-\omega)}{\sin\omega}+2\left(\gamma-1+\log\frac{\lambda}{2}\right)\lambda+O(\lambda^2)\,,$$

$$J_0^{(0)}=-2\left(\gamma+\log\frac{\lambda}{2}\right)+O(\lambda)\,,$$

$$J_{2n+1}^{(0)}=2\{(2n)!\}\lambda^{-(2n+1)}+O(\lambda^{-2n})\,.$$

Substitution of these in (A.25) yields

$$2T_0{}^*=\frac{2(\pi-\omega)}{\sin\omega}\frac{1}{\lambda}+\log\frac{\lambda}{2}+\gamma-2+\sum_{n=0}^{\infty}\frac{(-1)^nB_{n+1}}{(n+1)(2n+1)}+O(\lambda)$$

However, since

$$\sum_{n=0}^{\infty}\frac{(-1)^nB_{n+1}}{(n+1)(2n+1)}=4\int_0^{\infty}\frac{\tan^{-1}\tau}{e^{2\pi\tau}-1}d\tau=2-\log(2\pi)\,,$$

we have

$$2T_0{}^*=\frac{2(\pi-\omega)}{\sin\omega}\frac{1}{\lambda}+\log\frac{\lambda}{4\pi}+\gamma+O(\lambda)\,. \tag{A.27}$$

In a similar manner, for $j=1$, we get

$$J_{-1}^{(1)}=-2\{\log(\lambda/2)+\gamma\}+2(\pi-\omega)\cot\omega-(2\cos\omega)\lambda+O(\lambda^2)\,,$$

$$J_0^{(1)}=2\lambda^{-1}+2\cos\omega+O(\lambda)\,,$$

$$J_{2n+1}^{(1)}\cong 2\{(2n+1)!\}\lambda^{-(2n+2)}\,.$$

These results combined with (A.25) give

$$2T_1{}^*=\left[-2\{\log(\lambda/2)+\gamma\}+2(\pi-\omega)\cot\omega+1+\sum_{n=0}^{\infty}\frac{(-1)^nB_{n+1}}{n+1}\right]\frac{1}{\lambda}-\cos\omega+O(\lambda)\,.$$

Further we note that

$$\sum_{n=0}^{\infty}\frac{(-1)^nB_{n+1}}{n+1}=4\int_0^{\infty}\frac{1}{e^{2\pi t}-1}\frac{t}{1+t^2}dt=2\gamma-1$$

which can be derived by putting $z=0$ after differentiating Binet's formula:

$$\log\Gamma(z)=\{z-(1/2)\}\log z-z+(1/2)\log(2\pi)+2\int_0^{\infty}\frac{\tan^{-1}(t/z)}{e^{2\pi t}-1}dt\,.\qquad(\Re(z)>0)$$

Thus, we arrive at

$$T_1{}^*=\{-\log(\lambda/2)+(\pi-\omega)\cot\omega\}\lambda^{-1}-(1/2)\cos\omega+O(\lambda)\,. \tag{A.28}$$

Finally, (A.27), (A.28) and the relation

$$T_j(\lambda, \omega)=(1/2)\{T_j^*(\lambda, \omega)+(-1)^j T_j^*(\lambda, \pi-\omega)\}$$

yield the required expansions (24) in the main text.

References

1) K. Tamada and H. Fujikawa: Quart. J. Mech. and Applied Math. **10** (1957) 425.
2) T. Miyagi: J. Phys. Soc. Japan **13** (1958) 493.
3) S. Tomotika, T. Aoi and H. Yosinobu: Proc. Roy. Soc. **A**, **219** (1953) 233.
4) G. N. Watson: *Theory of Bessel Functions.* Cambridge Univ. Press (1922) p. 361.

JAOURNL OF THE PHYSICAL SOCIETY OF JAPAN Vol. 14, No. 2, FEBRUARY, 1959

Some Problems on Heat Conduction in Stratiform Bodies

By Václav VODIČKA
Plzeň Czechoslovakia

(Received October 8, 1958)

Problems on heat conduction in multilayer bodies lead usually to complicated calculations[1-5]. The present paper gives an idea of specific difficulties arising in the case of infinite composite solides. General deductions are applied to a special class of questions.

I. GENERAL THEORY

This first main part of our paper gives mathematical formulation of the basic problem. We also indicate a formal solution by means of the Laplace transformation method combined with a systematic use of matrix analysis.

§1. Statement of the Problem

Let

$$x_0 < x_1 < x_2 < \cdots < x_{n-2} < x_{n-1} \qquad (n \geq 1)\,,$$

a_k^2, λ_k, u_{k0} $(k=1, 2, \cdots, n)$, u_0 and ω be given constants. We have to determine the solution $u_k=u_k(x, t)$ of the equations

$$\frac{\partial u_k}{\partial t}=a_k^2\frac{\partial^2 u_k}{\partial x^2}\,, \quad x_{k-1}<x<x_k \qquad (k=1, 2, \cdots, n-1)\,, \quad t>0 \tag{1.1}$$

$$\frac{\partial u_n}{\partial t}=a_n^2\frac{\partial^2 u_n}{\partial x^2}\,, \quad x>x_{n-1}\,, \qquad t>0 \tag{1.2}$$

with the initial data

$$u_k(x, 0)=u_{k0}\,, \quad x_{k-1}<x<x_k \qquad (k=1, 2, \cdots, n-1) \tag{2.1}$$

$$u_n(x, 0)=u_{n0}\,, \quad x>x_{n-1} \tag{2.2}$$

and with the local conditions

$$u_1(x_0, t)=u_0 \cos \omega t\,, \quad t>0 \tag{3.1}$$

$$u_k(x_k, t)=u_{k+1}(x_k, t) \qquad (k=1, 2, \cdots, n-1)\,, \quad t>0 \tag{3.2}$$

$$\lambda_k\frac{\partial u_k}{\partial x}=\lambda_{k+1}\frac{\partial u_{k+1}}{\partial x}\,, \quad x=x_k \qquad (k=1, 2, \cdots, n-1)\,, \quad t>0\,. \tag{3.3}$$

In addition to this, $u_n(x, t)$ must be finite for $x \to +\infty$.

The physical interpretation of the relations (1.1)–(3.3) in the sense of one-dimensional heat conduction in solids is obvious.

§ 2. The Laplace Transforms of (1.1)–(3.3)

Putting generally

$$L[f(t)]=F(p)=p\int_0^\infty e^{-pt}f(t)dt\ , \qquad f(t)=L^{-1}[F(p)]=\frac{1}{2\pi i}\int_{\gamma-i\infty}^{\gamma+i\infty}\frac{E(p)}{p}e^{pt}dp \tag{4}$$

the above problem reduces to finding the solution $U_k=U_k(x, p)$ of

$$U_k''=\frac{p}{a_k^2}U_k=-\frac{p}{a_k^2}u_{k0}\ , \quad x_{k-1}<x<x_k \qquad (1\le k\le n-1) \tag{5.1}$$

$$U_n''-\frac{p}{a_n^2}U_n=-\frac{p}{a_n^2}u_{n0}\ , \quad x>x_{n-1} \tag{5.2}$$

$$U_1(x_0, p)=u_0\frac{p^2}{p^2+\omega^2} \tag{6.1}$$

$$U_k(x_k, p)=U_{k+1}(x_k, p) \qquad (1\le k\le n-1) \tag{6.2}$$

$$\lambda_k U_k'(x_k, p)=\lambda_{k+1}U'_{k+1}(x_k, p) \qquad (1\le k\le n-1) \tag{6.3}$$

with the finite value of $\lim\limits_{x\to+\infty} U_n(x, p)$, primes denote the x-derivatives.

From (5.1) and (5.2) we have generally

$$U_k(x, p)=A_k\,\mathrm{ch}\,\frac{(x-x_{k-1})\sqrt{p}}{a_k}+B_k\,\mathrm{sh}\,\frac{(x-x_{k-1})\sqrt{p}}{a_k}+u_{k0}\ , \quad x_{k-1}<x<x_k \qquad (1\le k\le n-1) \tag{7.1}$$

$$U_n(x, p)=A_n\exp\left[-\frac{(x-x_{n-1})\sqrt{p}}{a_n}\right]+u_{n0}\ , \quad x>x_{n-1} \tag{7.2}$$

and the conditions (6.1)–(6.3) lead to the system

$$A_1=u_0\frac{p^2}{p^2+\omega^2}-u_{10} \tag{8.1}$$

$$\left.\begin{aligned}A_{k+1}&=A_k\,\mathrm{ch}\,\frac{l_k\sqrt{p}}{a_k}+B_k\,\mathrm{sh}\,\frac{l_k\sqrt{p}}{a_k}+u_{k0}-u_{k+1,0}\\ B_{k+1}&=\frac{a_{k+1}\lambda_k}{a_k\lambda_{k+1}}\left(A_k\,\mathrm{sh}\,\frac{l_k\sqrt{p}}{a_k}+B_k\,\mathrm{ch}\,\frac{l_k\sqrt{p}}{a_k}\right) \qquad (1\le k\le n-2)\end{aligned}\right\} \tag{8.2}$$

$$\left.\begin{aligned}A_n&=A_{n-1}\,\mathrm{ch}\,\frac{l_{n-1}\sqrt{p}}{a_{n-1}}+B_{n-1}\,\mathrm{sh}\,\frac{l_{n-1}\sqrt{p}}{a_{n-1}}+u_{n-1,0}-u_{n0}\\ B_n&=-\frac{a_n\lambda_{n-1}}{a_{n-1}\lambda_n}\left(A_{n-1}\,\mathrm{sh}\,\frac{l_{n-1}\sqrt{p}}{a_{n-1}}+B_{n-1}\,\mathrm{ch}\,\frac{l_{n-1}\sqrt{p}}{a_{n-1}}\right)\ ;\end{aligned}\right\} \tag{8.3}$$

$$l_k=x_k-x_{k-1} \qquad (1\le k\le n-1_0) \tag{8.4}$$

of equations for the unknowns $A_k\ B_k$.

§ 3. Solution of the System (8.1)–(8.3)

Introducing the matrices

$$\left.\begin{aligned} &K_k=\left\|\begin{matrix}A_k\\ B_k\end{matrix}\right\| \quad (1\le k\le n-1)\,, \qquad P_k=\left\|\begin{matrix}u_{k0}-u_{k+1,0}\\ 0\end{matrix}\right\| \quad (1\le k\le n-2) \\ &M_k(p)=\left\|\begin{matrix} \operatorname{ch}\dfrac{l_k\sqrt{p}}{a_k}\,, & \operatorname{sh}\dfrac{l_k\sqrt{p}}{a_k} \\ \beta_k \operatorname{sh}\dfrac{l_k\sqrt{p}}{a_k}\,, & \beta_k\operatorname{ch}\dfrac{l_k\sqrt{p}}{a_k}\end{matrix}\right\|, \quad \beta_k=\frac{a_{k+1}\lambda_k}{a_k\lambda_{k+1}} \qquad (1\le k\le n-2)\end{aligned}\right\} \tag{9}$$

enables us to write the equations (8.2) in the form

$$K_{k+1}=M_k(p)K_k+P_k \qquad (1\le k\le n-2)\,. \tag{9.1}$$

Putting

$$N^{(k,\kappa)}=N^{(k,\kappa)}(p)=M_k(p)M_{k-1}(p)M_{k-2}(p)\cdots M_\kappa(p) \qquad (\kappa=1,2,\cdots,k;\ k=1,2,\cdots,n-2) \tag{10}$$

we obtain from (9.1)

$$K_{k+1}=N^{(k,1)}K_1+Q^{(k)} \qquad (1\le k\le n-2) \tag{11}$$

$$Q^{(1)}=P_1\,,\quad Q^{(k)}=\sum_{\kappa=1}^{k-1}N^{(k,\kappa+1)}P_\kappa+P_k \qquad (2\le k\le n-2)\,. \tag{11.1}$$

If we define β_{n-1} by the analogous relation

$$\beta_{n-1}=\frac{a_n\lambda_{n-1}}{a_{n-1}\lambda_n} \tag{12}$$

to the other β_k —see (9)—, then we conclude from (8.3)

$$\left(\operatorname{ch}\frac{l_{n-1}\sqrt{p}}{a_{n-1}}+\beta_{n-1}\operatorname{sh}\frac{l_{n-1}\sqrt{p}}{a_{n-1}}\right)A_{n-1}+\left(\operatorname{sh}\frac{l_{n-1}\sqrt{p}}{a_{n-1}}+\beta_{n-1}\operatorname{ch}\frac{l_{n-1}\sqrt{p}}{a_{n-1}}\right)B_{n-1}=u_{n0}-u_{n-1,0}\,.$$

Substituting into this equation for A_{n-1}, B_{n-1} from the last relation (11) yields

$$\begin{aligned}&\left[n_{11}^{(n-2,1)}\left(\operatorname{ch}\frac{l_{n-1}\sqrt{p}}{a_{n-1}}+\beta_{n-1}\operatorname{sh}\frac{l_{n-1}\sqrt{p}}{a_{n-1}}\right)+n_{21}^{(n-2,1)}\left(\operatorname{sh}\frac{l_{n-1}\sqrt{p}}{a_{n-1}}+\beta_{n-1}\operatorname{ch}\frac{l_{n-1}\sqrt{p}}{a_{n-1}}\right)\right]A_1\\ &\quad+\left[n_{12}^{(n-2,1)}\left(\operatorname{ch}\frac{l_{n-1}\sqrt{p}}{a_{n-1}}+\beta_{n-1}\operatorname{sh}\frac{l_{n-1}\sqrt{p}}{a_{n-1}}\right)+n_{22}^{(n-2,1)}\left(\operatorname{sh}\frac{l_{n-1}\sqrt{p}}{a_{n-1}}+\beta_{n-1}\operatorname{ch}\frac{l_{n-1}\sqrt{p}}{a_{n-1}}\right)\right]B_1\\ &\quad=-q_{11}^{(n-2)}\left(\operatorname{ch}\frac{l_{n-1}\sqrt{p}}{a_{n-1}}+\beta_{n-1}\operatorname{sh}\frac{l_{n-1}\sqrt{p}}{a_{n-1}}\right)-q_{21}^{(n-2)}\left(\operatorname{sh}\frac{l_{n-1}\sqrt{p}}{a_{n-1}}+\beta_{n-1}\operatorname{ch}\frac{l_{n-1}\sqrt{p}}{a_{n-1}}\right)\\ &\quad+u_{n0}-u_{n-1,0}\,;\end{aligned} \tag{13}$$

$n_{rs}^{(n-2,1)}$ and $q_{rs}^{(n-2)}$ are the elements of the matrices $N^{(n-2,1)}$ and $Q^{(n-2)}$, as defined in (10) and (11.1).

Recapitulating, the values A_k, B_k $(1\le k\le n-1)$, A_n are determined as follows: A_1 by (8.1), B_1 by (13), A_k, B_k $(2\le k\le n-1)$ are expressible in terms of A_1 and B_1 by means of (11) and the same can be done for A_n by means of the second relation (8.3).

§ 4. Theoretical Solution of the Problem (1.1)–(3.3)

Inserting the values A_k, B_k into (7.1) and (7.2) gives the Laplace transforms $U_k(x, p)$ and from this we obtain by (4) the wanted functions $u_k(x, t)$.

Practically, the unusual difficulty of our problem is evident from the impossibility of giving, in the general case, explicit forms of the matrices (10) which have a substantial role in the above deductions. Nevertheless, even in those exceptional cases where it is possible to calculate the matrices (10) one obtains complicated transforms $U_k(x, p)$ and the integration needed in the second formula (4) is not easy.

Now, we shall treat briefly an interesting class of cases where the above mathematical complications become smaller or disappear on the whole.

II. A SPECIAL SUBCLASS OF PROBLEMS

This second main part is devoted to the problems characterised by $\beta_k=1$ $(1 \leq k \leq n-2)$. Having deduced general formulas we shall treat some special questions of this group.

§ 5. The Case $\beta_k=1$ $(1 \leq k \leq n-2)$

Here we have by (9)

$$M_{\nu+1}(p)\cdot M_\nu(p)=\begin{Vmatrix} \operatorname{ch}\left(\frac{l_\nu}{a_\nu}+\frac{l_{\nu+1}}{a_{\nu+1}}\right)\sqrt{p}\,, & \operatorname{sh}\left(\frac{l_\nu}{a_\nu}+\frac{l_{\nu+1}}{a_{\nu+1}}\right)\sqrt{p} \\ \operatorname{sh}\left(\frac{l_\nu}{a_\nu}+\frac{l_{\nu+1}}{a_{\nu+1}}\right)\sqrt{p}\,, & \operatorname{ch}\left(\frac{l_\nu}{a_\nu}+\frac{l_{\nu+1}}{a_{\nu+1}}\right)\sqrt{p} \end{Vmatrix}; \qquad \nu=1, 2, \cdots, n-3$$

and from this, according to (10),

$$N^{(k,\kappa)}=\begin{Vmatrix} \operatorname{ch}\sigma_{k\kappa}\sqrt{p}\,, & \operatorname{sh}\sigma_{k\kappa}\sqrt{p} \\ \operatorname{sh}\sigma_{k\kappa}\sqrt{p}\,, & \operatorname{ch}\sigma_{k\kappa}\sqrt{p} \end{Vmatrix}, \quad \sigma_{k\kappa}=\sum_{\nu=\kappa}^{k}\frac{l_\nu}{a_\nu} \qquad (1 \leq \kappa \leq k,\ 1 \leq k \leq n-2)\,. \tag{14}$$

Using this, along with (9), formulae (11.1) give without difficulty

$$Q^{(1)}=\begin{Vmatrix} u_{10}-u_{20} \\ 0 \end{Vmatrix}, \quad Q^{(k)}=\begin{Vmatrix} u_{k0}-u_{k+1,0}+\sum\limits_{\kappa=1}^{k-1}(u_{\kappa 0}-u_{\kappa+1,0})\operatorname{ch}\sigma_{k,\kappa+1}\sqrt{p} \\ \sum\limits_{\kappa=1}^{k-1}(u_{\kappa 0}-u_{\kappa+1,0})\operatorname{sh}\sigma_{k,\kappa+1}\sqrt{p} \end{Vmatrix} \qquad (2 \leq k \leq n-2) \tag{15}$$

and the relation (13) appears in the form

$$\left.\begin{aligned} &A_1(\operatorname{ch}\sigma_{n-1,1}\sqrt{p}+\beta_{n-1}\operatorname{sh}\sigma_{n-1,1}\sqrt{p})+B_1(\operatorname{sh}\sigma_{n-1,1}\sqrt{p}+\beta_{n-1}\operatorname{ch}\sigma_{n-1,1}\sqrt{p}) \\ &\quad =u_{n0}-u_{n-1,0}+\sum_{\kappa=1}^{n-2}(u_{\kappa+1,0}-u_{\kappa 0})(\operatorname{ch}\sigma_{n-1,\kappa+1}\sqrt{p}+\beta_{n-1}\operatorname{sh}\sigma_{n-1,\kappa+1}\sqrt{p})\,, \\ &\sigma_{n-1,1}=\sum_{\nu=1}^{n-1}\frac{l_\nu}{a_\nu}\,, \quad \sigma_{n-1,\kappa+1}=\sum_{\nu=\kappa+1}^{n-1}\frac{l_\nu}{a_\nu} \qquad (1 \leq \kappa \leq n-2)\,. \end{aligned}\right\} \tag{16}$$

Calculating, by means of (8.1), (16), (11), (14), (15) and (8.3), the expressions A_k, B_k and substituting into (7.1), (7.2) leads to the following complicated transforms $U_k(x, p)$ of the wanted functions $u_k(x, t)$:

$$\left.\begin{aligned} U_1(x, p)&=\frac{1}{\operatorname{sh}\sigma_{n-1,1}\sqrt{p}+\beta_{n-1}\operatorname{ch}\sigma_{n-1,1}\sqrt{p}}\left\{\left(u_0\frac{p^2}{p^2+\omega^2}-u_{10}\right)\right. \\ &\times\left[\operatorname{sh}\left(\sigma_{n-1,1}-\frac{x-x_0}{a_1}\right)\sqrt{p}+\beta_{n-1}\operatorname{ch}\left(\sigma_{n-1,1}-\frac{x-x_0}{a_1}\right)\sqrt{p}\right]+\operatorname{sh}\frac{(x-x_0)\sqrt{p}}{a_1} \\ &\times\left.\left[u_{n0}-u_{n-1,0}+\sum_{\kappa=1}^{n-2}(u_{\kappa+1,0}-u_{\kappa 0})(\operatorname{ch}\sigma_{n-1,\kappa+1}\sqrt{p}+\beta_{n-1}\operatorname{sh}\sigma_{n-1,\kappa+1}\sqrt{p})\right]\right\}+u_{10} \\ U_{k+1}(x, p)&=\frac{1}{\operatorname{sh}\sigma_{n-1,1}\sqrt{p}+\beta_{n-1}\operatorname{ch}\sigma_{n-1,1}\sqrt{p}}\left\{\left(u_0\frac{p^2}{p^2+\omega^2}-u_{10}\right)\right. \\ &\times\left[\operatorname{sh}\left(\sigma_{n-1,k+1}-\frac{x-x_k}{a_{k+1}}\right)\sqrt{p}+\beta_{n-1}\operatorname{ch}\left(\sigma_{n-1,k+1}-\frac{x-x_k}{a_{k+1}}\right)\sqrt{p}\right]+\operatorname{sh}\left(\frac{x-x_k}{a_{k+1}}+\sigma_{k1}\right) \\ &\times\left.\sqrt{p}\left[u_{n0}-u_{n-1,0}+\sum_{\kappa=1}^{n-2}(u_{\kappa+1,0}-u_{\kappa 0})(\operatorname{ch}\sigma_{n-1,\kappa+1}\sqrt{p}+\beta_{n-1}\operatorname{sh}\sigma_{n-1,\kappa+1}\sqrt{p})\right]\right\} \\ &+(u_{k0}-u_{k+1,0})\operatorname{ch}\frac{(x-x_k)\sqrt{p}}{a_{k+1}}+\sum_{\kappa=1}^{k-1}(u_{\kappa 0}-u_{\kappa+1,0})\operatorname{ch}\left(\frac{x-x_k}{a_{k+1}}+\sigma_{k,\kappa+1}\right)\sqrt{p}+u_{k+1,0} \\ &\qquad\qquad\left(1 \leq k \leq n-2;\ \sum_{\kappa=1}^{0}=0\right) \end{aligned}\right\} \tag{17}$$

$$U_n(x,p)=u_{n0}+\frac{\beta_{n-1}}{\operatorname{sh}\sigma_{n-1,1}\sqrt{p}+\beta_{n-1}\operatorname{ch}\sigma_{n-1,1}\sqrt{p}}\exp\left(-\frac{x-x_{n-1}}{a_n}\sqrt{p}\right)$$
$$\times\left[u_0\frac{p^2}{p^2+\omega^2}-u_{10}+\sum_{\kappa=1}^{n-1}(u_{\kappa0}-u_{\kappa+1,0})\operatorname{ch}\sigma_{\kappa1}\sqrt{p}\right].$$

The wanted functions $u_k(x, t)$ are to be found from their Laplace transforms (17) by contour integration, according to the second formula (4). Of course, the results are in general formidably complicated and so we confine ourselves merely to some simpler special cases which are also of considerable physical interest.

§ 6. A Homogeneous Semiinfinite Solid

In this simplest case we have to put $a_k=a$, $\lambda_k=\lambda$ $(1\le k\le n)$ and it follows

$$\beta_{n-1}=1\,,\qquad \sigma_{k\kappa}=\frac{1}{a}(x_k-x_{\kappa-1})\,.$$

The Laplace transforms (17) appear in the form

$$\left.\begin{aligned}
U_1(x,p)&=u_{10}+\left(u_0\frac{p^2}{p^2+\omega^2}-u_{10}\right)\exp\left(-\frac{x-x_0}{a}\sqrt{p}\right)\\
&\quad+\operatorname{sh}\frac{(x-x_0)\sqrt{p}}{a}\sum_{\kappa=1}^{n-1}(u_{\kappa+1,0}-u_{\kappa0})\exp\left(-\frac{x_\kappa-x_0}{a}\sqrt{p}\right)\\
U_{k+1}(x,p)&=u_{k+1,0}+\left(u_0\frac{p^2}{p^2+\omega^2}-u_{10}\right)\exp\left(-\frac{x-x_0}{a}\sqrt{p}\right)\\
&\quad+\operatorname{sh}\frac{(x-x_0)\sqrt{p}}{a}\sum_{\kappa=1}^{n-1}(u_{\kappa+1,0}-u_{\kappa0})\exp\left(-\frac{x_\kappa-x_0}{a}\sqrt{p}\right)+\sum_{\kappa=1}^{k}(u_{\kappa0}-u_{\kappa+1,0})\operatorname{ch}\frac{(x-x_\kappa)\sqrt{p}}{a}\\
&\qquad\qquad(1\le k\le n-2)\\
U_n(x,p)&=u_{n0}+\exp\left(-\frac{x-x_0}{a}\sqrt{p}\right)\left[u_0\frac{p^2}{p^2+\omega^2}-u_{10}+\sum_{\kappa=1}^{n-1}(u_{\kappa0}-u_{\kappa+1,0})\operatorname{ch}\frac{(x_\kappa-x_0)\sqrt{p}}{a}\right]
\end{aligned}\right\}\tag{18}$$

or, with a single formula valid in the whole range $x>x_0$,

$$U(x,p)=u_{10}\left\{1-\exp\left(-\frac{x-x_0}{a}\sqrt{p}\right)\right\}+\frac{1}{2}\sum_{\kappa=1}^{n-1}(u_{\kappa+1,0}-u_{\kappa0})\left[1-\exp\left(-\frac{x+x_\kappa-2x_0}{a}\sqrt{p}\right)\right.$$
$$\left.+\operatorname{sgn}(x-x_\kappa)\left\{1-\exp\left(-\frac{|x-x_\kappa|}{a}\sqrt{p}\right)\right\}\right]+u_0\frac{p^2}{p^2+\omega^2}\exp\left(-\frac{x-x_0}{a}\sqrt{p}\right).\tag{18.1}$$

Regarding the well-known operational relations

$$\left.\begin{aligned}
&L^{-1}[1-e^{-|\kappa|\sqrt{p}}]=\operatorname{sgn}\kappa\,\Phi\left(\frac{\kappa}{2\sqrt{t}}\right),\quad \Phi(x)=\frac{2}{\sqrt{\pi}}\int_0^x e^{-\xi^2}d\xi\\
&L^{-1}\left[\frac{p^2}{p^2+\omega^2}e^{-\kappa\sqrt{p}}\right]=e^{-\kappa\sqrt{\omega/2}}\cos(\omega t-\kappa\sqrt{\omega/2})-\frac{1}{\pi}\int_0^\infty\frac{\rho e^{-\rho t}}{\rho^2+\omega^2}\sin\kappa\sqrt{\rho}\,d\rho\\
&\quad=\frac{2}{\sqrt{\pi}}\int_{\kappa/(2\sqrt{t})}^\infty e^{-\xi^2}\cos\omega\left(t-\frac{\kappa^2}{4\xi^2}\right)d\xi\,,\qquad \kappa>0
\end{aligned}\right\}\tag{19}$$

we obtain from (18.1) the following solution of our special case:

$$u(x,t)=u_{10}\Phi\left(\frac{x-x_0}{2a\sqrt{t}}\right)+\frac{1}{2}\sum_{\kappa=2}^{n-1}(u_{\kappa+1,0}-u_{\kappa0})\left[\Phi\left(\frac{x+x_\kappa-2x_0}{2a\sqrt{t}}\right)+\Phi\left(\frac{x-x_\kappa}{2a\sqrt{t}}\right)\right]$$
$$+u_0\left[\exp\left(-\frac{x-x_0}{a}\sqrt{\frac{\omega}{2}}\right)\cos\left(\omega t-\frac{x-x_0}{a}\sqrt{\frac{\omega}{2}}\right)-\frac{1}{\pi}\int_0^\infty\frac{\rho e^{-\rho t}}{\rho^2+\omega^2}\sin\frac{(x-x_0)\sqrt{\rho}}{a}d\rho\right]$$

$$
\begin{aligned}
&= u_{10}\Phi\left(\frac{x-x_0}{2a\sqrt{t}}\right)+\frac{1}{2}\sum_{\kappa=1}^{n-1}(u_{\kappa+1,0}-u_{\kappa 0})\left[\Phi\left(\frac{x+x_\kappa-2x_0}{2a\sqrt{t}}\right)+\Phi\left(\frac{x-x_\kappa}{2a\sqrt{t}}\right)\right] \\
&\quad+\frac{2u_0}{\sqrt{\pi}}\int_{x-x_0/(2a\sqrt{t})}^{\infty} e^{-\xi^2}\cos\omega\left[t-\frac{(x-x_0)^2}{4a^2\xi^2}\right]d\xi\,,
\end{aligned}
\tag{20}
$$

§ 7. A Semiinfinite Solid Composite of Two Homogeneous Parts

Let the first part be $x_0 \leq x \leq x_{n-1}$, the second $x > x_{n-1}$; let the corresponding thermal constants be a, λ in the first and A, Λ in the second part of the solid.

Hence, we have to put, in (17),

$$
a_k = a\,,\quad \lambda_k=\lambda \qquad (1\leq k\leq n-1)\,,\qquad a_n=A\,,\quad \lambda_n=\Lambda\,.
$$

It follows

$$
\beta_{n-1}=\frac{A\lambda}{a\Lambda}\,,\quad \sigma_{k\kappa}=\frac{1}{a}(x_k-x_{\kappa-1})\,,\qquad 1\leq k\leq n-1,\ 1\leq\kappa\leq k
$$

and the Laplace transforms (17) appear in the form

$$
\begin{aligned}
U_{k+1}(x,p) &= u_{k+1,0}+\frac{1}{\operatorname{sh}\dfrac{x_{n-1}-x_0}{a}\sqrt{p}+\beta_{n-1}\operatorname{ch}\dfrac{x_{n-1}-x_0}{a}\sqrt{p}} \\
&\times\left\{\left(u_0\frac{p^2}{p^2+\omega^2}-u_{10}\right)\left(\operatorname{sh}\frac{x_{n-1}-x}{a}\sqrt{p}+\beta_{n-1}\operatorname{ch}\frac{x_{n-1}-x}{a}\sqrt{p}\right)\right. \\
&\left.+\operatorname{sh}\frac{x-x_0}{a}\sqrt{p}\sum_{\kappa=1}^{n-1}(u_{\kappa+1,0}-u_{\kappa 0})\left(\frac{x_{n-1}-x_\kappa}{a}\sqrt{p}+\beta_{n-1}\operatorname{sh}\frac{x_{n-1}-x_\kappa}{a}\sqrt{p}\right)\right\} \\
&+\sum_{\kappa=1}^{k}(u_{\kappa 0}-u_{\kappa+1,0})\operatorname{ch}\frac{x-x_\kappa}{a}\sqrt{p}\qquad\left(0\leq k\leq n-2,\ \sum_{\kappa=1}^{0}=0\right)
\end{aligned}
\tag{21.1}
$$

$$
\begin{aligned}
U_n(x,p) &= u_{n0}+\frac{\beta_{n-1}}{\operatorname{sh}\dfrac{x_{n-1}-x_0}{a}\sqrt{p}+\beta_{n-1}\operatorname{ch}\dfrac{x_{n-1}-x_0}{a}\sqrt{p}}\exp\left(-\frac{x-x_{n-1}}{A}\sqrt{p}\right) \\
&\times\left[u_0\frac{p^2}{p^2+\omega^2}-u_{10}+\sum_{\kappa=1}^{n-1}(u_{\kappa 0}-u_{\kappa+1,0})\operatorname{ch}\frac{x_\kappa-x_0}{a}\sqrt{p}\right].
\end{aligned}
\tag{21.2}
$$

Of course, it is obvious, by technical sense of our problem, that there must exist a single expression of all $U_k(x, p)$, $1\leq k\leq n-1$, valid in the whole region $x_0 < x < x_{n-1}$. And in fact, difficult transformations lead to the following formula replacing all the relations (21.1):

$$
\begin{aligned}
U(x,p) &= u_0\frac{p^2}{p^2+\omega^2}\cdot\frac{N(x)}{N(x_0)}+\frac{1}{2}(u_{n0}-u_{10})+u_{10}\left[1-\frac{N(x)}{N(x_0)}\right] \\
&+\frac{1}{4}\sum_{\kappa=1}^{n-1}(u_{\kappa+1,0}-u_{\kappa 0})\left\{2\operatorname{sgn}(x-x_\kappa)\left\{1-\exp\left(-\frac{|x-x_\kappa|}{a}\sqrt{p}\right)\right\}\right. \\
&-\frac{1}{N(x_0)}\left[(\beta+1)\exp\left(\frac{-x+x_0-x_\kappa+x_{n-1}}{a}\sqrt{p}\right)+(\beta-1)\left(\exp\left(\frac{x+x_0-x_\kappa-x_{n-1}}{a}\sqrt{p}\right)\right.\right. \\
&\left.\left.\left.+2\exp\left(-\frac{x_{n-1}-x_\kappa}{a}\sqrt{p}\right)\operatorname{sh}\frac{x-x_0}{a}\sqrt{p}\right)\right]\right\}\,,\qquad x_0\leq x\leq x_{n-1}\,;
\end{aligned}
\tag{22}
$$

$$
N(x)=\operatorname{sh}\frac{x_{n-1}-x}{a}\sqrt{p}+\beta\operatorname{ch}\frac{x_{n-1}-x}{a}\sqrt{p}\,,\qquad \beta=\frac{A\lambda}{a\Lambda}\,,
\tag{22.1}
$$

The problem is then reduced to finding the original functions $u(x, t)$ and $u_n(x, t)$ from their Laplace transforms (22) and —see (21.2)—

$$\begin{aligned}U_n(x,p)&=\beta u_0\frac{p^2}{p^2+\omega^2}\cdot\frac{\exp\left(-\frac{x-x_{n-1}}{A}\sqrt{p}\right)}{N(x_0)}+u_{n0}-\beta u_{10}\frac{\exp\left(-\frac{x-x_{n-1}}{A}\sqrt{p}\right)}{N(x_0)}\\&+\beta\frac{\exp\left(-\frac{x-x_{n-1}}{A}\sqrt{p}\right)}{N(x_0)}\sum_{\kappa=1}^{n-1}(u_{\kappa 0}-u_{\kappa+1,0})\,\mathrm{ch}\,\frac{x_\kappa-x_0}{a}\sqrt{p}\,,\qquad x>x_{n-1}\,.\end{aligned}\tag{23}$$

To obtain the solution $u(x,t)$, $u_n(x,t)$ of our problem we make use of the very general operational relation

$$\begin{aligned}&L^{-1}\left[\frac{p^2}{p^2+\omega^2}\cdot\frac{\mathrm{sh}\,\kappa\sqrt{p}+\alpha\,\mathrm{ch}\,\kappa\sqrt{p}}{\mathrm{sh}\,\lambda\sqrt{p}+\gamma\,\mathrm{ch}\,\lambda\sqrt{p}}\right]\\&=\frac{2}{(\gamma^2+1)\,\mathrm{ch}\,2\lambda\sqrt{\frac{\omega}{2}}+2\gamma\,\mathrm{sh}\,2\lambda\sqrt{\frac{\omega}{2}}+(\gamma^2-1)\cos 2\lambda\sqrt{\frac{\omega}{2}}}\Bigg\{\cos\omega t\Bigg[\left(\mathrm{sh}\,\kappa\sqrt{\frac{\omega}{2}}+\alpha\,\mathrm{ch}\,\kappa\sqrt{\frac{\omega}{2}}\right)\\&\times\left(\mathrm{sh}\,\lambda\sqrt{\frac{\omega}{2}}+\gamma\,\mathrm{ch}\,\lambda\sqrt{\frac{\omega}{2}}\right)\cos\kappa\sqrt{\frac{\omega}{2}}\cos\lambda\sqrt{\frac{\omega}{2}}+\left(\mathrm{ch}\,\kappa\sqrt{\frac{\omega}{2}}+\alpha\,\mathrm{sh}\,\kappa\sqrt{\frac{\omega}{2}}\right)\\&\times\left(\mathrm{ch}\,\lambda\sqrt{\frac{\omega}{2}}+\gamma\,\mathrm{sh}\,\lambda\sqrt{\frac{\omega}{2}}\right)\sin\kappa\sqrt{\frac{\omega}{2}}\sin\lambda\sqrt{\frac{\omega}{2}}\Bigg]+\sin\omega t\Bigg[\left(\mathrm{sh}\,\kappa\sqrt{\frac{\omega}{2}}+\alpha\,\mathrm{ch}\,\kappa\sqrt{\frac{\omega}{2}}\right)\\&\times\left(\mathrm{ch}\,\lambda\sqrt{\frac{\omega}{2}}+\gamma\,\mathrm{sh}\,\lambda\sqrt{\frac{\omega}{2}}\right)\cos\kappa\sqrt{\frac{\omega}{2}}\sin\lambda\sqrt{\frac{\omega}{2}}-\left(\mathrm{ch}\,\kappa\sqrt{\frac{\omega}{2}}+\alpha\,\mathrm{sh}\,\kappa\sqrt{\frac{\omega}{2}}\right)\\&\times\left(\mathrm{sh}\,\lambda\sqrt{\frac{\omega}{2}}+\gamma\,\mathrm{ch}\,\lambda\sqrt{\frac{\omega}{2}}\right)\sin\kappa\sqrt{\frac{\omega}{2}}\cos\lambda\sqrt{\frac{\omega}{2}}\Bigg]\Bigg\}\\&-\frac{2}{\pi}\int_0^\infty\frac{\xi^3e^{-\xi^2t}}{\xi^4+\omega^2}\cdot\frac{\alpha\cos\kappa\xi\sin\lambda\xi-\gamma\sin\kappa\xi\cos\lambda\xi}{\sin^2\lambda\xi+\gamma^2\cos^2\lambda\xi}d\xi\,,\qquad\kappa>\lambda\,.\end{aligned}\tag{24}$$

This complicated formula follows from the second relation (4) and its derivation presupposes an adequate experience in calculating contour integrals of multivalued functions in their Riemann surfaces.

Specialising in suitable way the parameters α, γ, κ, λ, ω, the formula (24) yields all the original functions needed in (22), (23) and the complete solution of the problem appears with toilsome calculations in the form

$$\begin{aligned}u(x,t)&=\frac{u_0}{\Delta}\Bigg\{(\beta+1)^2\exp\left(\frac{-x-x_0+2x_{n-1}}{a}\sqrt{\frac{\omega}{2}}\right)\cos\left(\omega t-\frac{x-x_0}{a}\sqrt{\frac{\omega}{2}}\right)\\&+(\beta-1)^2\exp\left(\frac{x+x_0-2x_{n-1}}{a}\sqrt{\frac{\omega}{2}}\right)\cos\left(\omega t+\frac{x-x_0}{a}\sqrt{\frac{\omega}{2}}\right)+(\beta^2-1)\Bigg[\exp\left(\frac{x-x_0}{a}\sqrt{\frac{\omega}{2}}\right)\\&\times\cos\left(\omega t+\frac{x+x_0-2x_{n-1}}{a}\sqrt{\frac{\omega}{2}}\right)+\exp\left(-\frac{x-x_0}{a}\sqrt{\frac{\omega}{2}}\right)\cos\left(\omega t-\frac{x+x_0-2x_{n-1}}{a}\sqrt{\frac{\omega}{2}}\right)\Bigg]\Bigg\}\\&-\frac{2\beta u_0}{\pi}\int_0^\infty\frac{\xi^3e^{-\xi^2t}}{(\xi^4+\omega^2)D(\xi)}\sin\frac{(x-x_0)\xi}{a}d\xi+\frac{2\beta u_{10}}{\pi}\int_0^\infty\frac{e^{-\xi^2t}}{\xi D(\xi)}\sin\frac{(x-x_0)\xi}{a}d\xi\\&+\frac{1}{2}\sum_{\kappa=1}^{n-1}(u_{\kappa+1,0}-u_{\kappa 0})\Bigg\{\Phi\left(\frac{x-x_\kappa}{2a\sqrt{t}}\right)+\frac{2}{\pi}\int_0^\infty\frac{e^{-\xi^2t}}{\xi D(\xi)}\Bigg[\beta\sin\frac{x-2x_0+x_\kappa}{a}\xi\\&+(\beta-1)\sin\frac{x-x_\kappa}{a}\xi\left(\sin^2\frac{x_{n-1}-x_0}{a}\xi-\beta\cos^2\frac{x_{n-1}-x_0}{a}\xi\right)\Bigg]d\xi\Bigg\}\,,\\&\qquad x_0\le x\le x_{n-1}\end{aligned}\tag{25.1}$$

$$
\begin{aligned}
u_n(x,t)=\frac{2\beta u_0}{\Delta}\Bigg\{&(\beta+1)\exp\left[\left(\frac{x_{n-1}-x_0}{a}-\frac{x-x_{n-1}}{A}\right)\sqrt{\frac{\omega}{2}}\right]\cos\left[\omega t-\left(\frac{x_{n-1}-x_0}{a}+\frac{x-x_{n-1}}{A}\right)\sqrt{\frac{\omega}{2}}\right]\\
&+(\beta-1)\exp\left[-\left(\frac{x_{n-1}-x_0}{a}+\frac{x-x_{n-1}}{A}\right)\sqrt{\frac{\omega}{2}}\right]\cos\left[\omega t-\left(\frac{x_{n-1}-x_0}{a}-\frac{x-x_{n-1}}{A}\right)\sqrt{\frac{\omega}{2}}\right]\Bigg\}\\
&-\frac{2\beta u_0}{\pi}\int_0^\infty\frac{\xi^3e^{-\xi^2t}}{(\xi^4+\omega^2)D(\xi)}\left(\sin\frac{x_{n-1}-x_0}{a}\xi\cos\frac{x-x_{n-1}}{A}\xi+\beta\cos\frac{x_{n-1}-x_0}{a}\xi\sin\frac{x-x_{n-1}}{A}\xi\right)d\xi\\
&+\frac{2\beta u_{10}}{\pi}\int_0^\infty\frac{e^{-\xi^2t}}{\xi D(\xi)}\left(\sin\frac{x_{n-1}-x_0}{a}\xi\cos\frac{x-x_{n-1}}{A}\xi+\beta\cos\frac{x_{n-1}-x_0}{a}\xi\sin\frac{x-x_{n-1}}{A}\xi\right)d\xi\\
&+\frac{2\beta}{\pi}\sum_{\kappa=1}^{n-1}(u_{\kappa+1,0}-u_{\kappa 0})\int_0^\infty\frac{e^{-\xi^2t}}{\xi D(\xi)}\cos\frac{x_\kappa-x_0}{a}\xi\left(\sin\frac{x_{n-1}-x_0}{a}\xi\cos\frac{x-x_{n-1}}{A}\xi\right.\\
&\left.+\beta\cos\frac{x_{n-1}-x_0}{a}\xi\sin\frac{x-x_{n-1}}{A}\xi\right)d\xi\,,\qquad x>x_{n-1}
\end{aligned}
\tag{25.2}
$$

$$
\left.
\begin{aligned}
\Delta=(\beta+1)^2\exp\left[\frac{2(x_{n-1}-x_0)}{a}\sqrt{\frac{\omega}{2}}\right]&+(\beta-1)^2\exp\left[-\frac{2(x_{n-1}-x_0)}{a}\sqrt{\frac{\omega}{2}}\right]\\
&+2(\beta^2-1)\cos\frac{2(x_{n-1}-x_0)}{a}\sqrt{\frac{\omega}{2}}\\
D(\xi)=\sin^2\frac{x_{n-1}-x_0}{a}\xi+\beta^2\cos^2\frac{x_{n-1}-x_0}{a}\xi\,,&\qquad\beta=\frac{A\lambda}{a\Lambda}\,.
\end{aligned}
\right\}
\tag{25.3}
$$

Apart from many new questions on the heat conduction in semiinfinite solids our formulae (25.1)–(25.3) include as simple special cases numerous current problems as known from elementary textbooks on the subject[6,7]. We expressly remind of two simple examples.

7.1. The case $A=a$, $\Lambda=\lambda$. Here we have a homogeneous semiinfinite solid as treated in § 6. And in fact, our formulae (25.1)–(25.3) change in the present conditions into the former result (20). Especially fargoing simplifications occur if $u_{10}=u_{20}=\cdots=u_{n0}$ or if $\omega=0$.

7.2. The case $\beta\neq 1$. This corresponds to a semiinfinite solid consisting of two homogeneous parts. Special attention is to be paid to the case $u_{10}=u_{20}=\cdots=u_{n-1,0}$ and to the class of problems characterised by $\omega=0$.

§ 8. A Nonhomogeneous Solid of n Parts

It is possible to find the original functions to the Laplace transforms (17), but the result is formidably complicated. In order to have reasonable formulae we make here, in addition to the above basic assumption $\beta_1=\beta_2=\cdots=\beta_{n-2}=1$, another simplifying presupposition $u_{10}=u_{20}=\cdots=u_{n0}=u^{(0)}$. In this case our general relations (17) give

$$
\left.
\begin{aligned}
U_{k+1}(x,p)&=u^{(0)}+\frac{1}{Q}\left(u_0\frac{p^2}{p^2+\omega^2}-u^{(0)}\right)\\
&\times\left[\operatorname{sh}\left(\sigma_{n-1,k+1}-\frac{x-x_k}{a_{k+1}}\right)\sqrt{p}+\beta\operatorname{ch}\left(\sigma_{n-1,k+1}-\frac{x-x_k}{a_{k+1}}\right)\sqrt{p}\right]\qquad(0\leq k\leq n-2)\\
U_n(x,p)&=u^{(0)}+\frac{\beta}{Q}\left(u_0\frac{p^2}{p^2+\omega^2}-u^{(0)}\right)\exp\left(-\frac{x-x_{n-1}}{a_n}\sqrt{p}\right)
\end{aligned}
\right\}
\tag{26}
$$

$$
Q=\operatorname{sh}\sigma_{n-1,1}\sqrt{p}+\beta\operatorname{ch}\sigma_{n-1,1}\sqrt{p}\,,\qquad\beta=\frac{a_n\lambda_{n-1}}{a_{n-1}\lambda_n}\;;
\tag{26.1}
$$

the values $\sigma_{k\kappa}$ are defined in (14) and (16).

Making appropriate use of the operational formula (24) one obtains from (26) the following solution of our present case:

$$\left.\begin{aligned}
u_{k+1}(x,t)=\frac{u_0}{\varDelta}\Big\{&(\beta+1)^2\exp\left[\left(\sigma_{k1}+2\sigma_{n-1,k+1}-\frac{x-x_k}{a_{k+1}}\right)\sqrt{\frac{\omega}{2}}\right]\cos\left[\omega t-\left(\sigma_{k1}+\frac{x-x_k}{a_{k+1}}\right)\sqrt{\frac{\omega}{2}}\right]\\
&+(\beta-1)^2\exp\left[-\left(\sigma_{k1}+2\sigma_{n-1,k+1}-\frac{x-x_k}{a_{k+1}}\right)\sqrt{\frac{\omega}{2}}\right]\cos\left[\omega t+\left(\sigma_{k1}+\frac{x-x_k}{a_{k+1}}\right)\sqrt{\frac{\omega}{2}}\right]\\
&+(\beta^2-1)\exp\left[\left(\sigma_{k1}+\frac{x-x_k}{a_{k+1}}\right)\sqrt{\frac{\omega}{2}}\right]\cos\left[\omega t-\left(\sigma_{k1}+2\sigma_{n-1,k+1}-\frac{x-x_k}{a_{k+1}}\right)\sqrt{\frac{\omega}{2}}\right]\\
&+(\beta^2-1)\exp\left[-\left(\sigma_{k1}+\frac{x-x_k}{a_{k+1}}\right)\sqrt{\frac{\omega}{2}}\right]\cos\left[\omega t+\left(\sigma_{k1}+2\sigma_{n-1,k+1}-\frac{x-x_k}{a_{k+1}}\right)\sqrt{\frac{\omega}{2}}\right]\Big\}\\
&-\frac{2\beta u_0}{\pi}\int_0^\infty\frac{\xi^3e^{-\xi^2t}}{\xi^4+\omega^2}\cdot\frac{\sin\left(\sigma_{k1}+\frac{x-x_k}{a_{k+1}}\right)\xi}{\sin^2\sigma_{n-1,1}\xi+\beta^2\cos^2\sigma_{n-1,1}\xi}\,d\xi\\
&+\frac{2\beta u^{(0)}}{\pi}\int_0^\infty\frac{e^{-\xi^2t}}{\xi}\cdot\frac{\sin\left(\sigma_{k1}+\frac{x-x_k}{a_{k+1}}\right)\xi}{\sin^2\sigma_{n-1,1}\xi+\beta^2\cos^2\sigma_{n-1,1}\xi}\,d\xi\,,\qquad x_k\le x\le x_{k+1}\qquad(0\le k\le n-2)\\
u_n(x,t)=\frac{2\beta u_0}{\varDelta}\Big\{&(\beta+1)\exp\left[\left(\sigma_{n-1,1}-\frac{x-x_{n-1}}{a_n}\right)\sqrt{\frac{\omega}{2}}\right]\cos\left[\omega t-\left(\sigma_{n-1,1}+\frac{x-x_{n-1}}{a_n}\right)\sqrt{\frac{\omega}{2}}\right]\\
&+(\beta-1)\exp\left[-\left(\sigma_{n-1,1}+\frac{x-x_{n-1}}{a_n}\right)\sqrt{\frac{\omega}{2}}\right]\cos\left[\omega t+\left(\sigma_{n-1,1}-\frac{x-x_{n-1}}{a_n}\right)\sqrt{\frac{\omega}{2}}\right]\Big\}\\
&-\frac{2\beta u_0}{\pi}\int_0^\infty\frac{\xi^3e^{-\xi^2t}}{\xi^4+\omega^2}\cdot\frac{\sin\sigma_{n-1,1}\xi\cos\frac{x-x_{n-1}}{a_n}\xi+\beta\cos\sigma_{n-1,1}\xi\sin\frac{x-x_{n-1}}{a_n}\xi}{\sin^2\sigma_{n-1,1}\xi+\beta^2\cos^2\sigma_{n-1,1}\xi}\,d\xi\\
&+\frac{2\beta u^{(0)}}{\pi}\int_0^\infty\frac{e^{-\xi^2t}}{\xi}\cdot\frac{\sin\sigma_{n-1,1}\xi\cos\frac{x-x_{n-1}}{a_n}\xi+\beta\cos\sigma_{n-1,1}\xi\sin\frac{x-x_{n-1}}{a_n}\xi}{\sin^2\sigma_{n-1,1}\xi+\beta^2\cos^2\sigma_{n-1,1}\xi}\,d\xi\,,\\
&\qquad\qquad\qquad\qquad\qquad\qquad\qquad\qquad\qquad\qquad x>x_{n-1}\,;
\end{aligned}\right\}\qquad(27)$$

$$\varDelta=(\beta+1)^2\exp\left(2\sigma_{n-1,1}\sqrt{\frac{\omega}{2}}\right)+(\beta-1)^2\exp\left(-2\sigma_{n-1,1}\sqrt{\frac{\omega}{2}}\right)+2(\beta^2-1)\cos2\sigma_{n-1,1}\sqrt{\frac{\omega}{2}}\,,$$
$$\beta=\frac{A\lambda}{aA}\,,\quad\sigma_{01}=0\,.\qquad(27.1)$$

§ 9. Final Remark

Evidently, our preceding results can be immediately applied to the solution of the well-known advanced problems of theoretical electricity. The author of this paper hopes shortly to treat belonging questions is another paper.

References

1) V. Vodička: Appl. Sci. Res. **A5** (1955) 108.
2) V. Vodička: Appl. Sci. Res. **A5** (1955) 115.
3) V. Vodička: Math. Nachr. **14** (1955) 47.
4) V. Vodička: ZAMP **7** (1956) 422.
5) V. Vodička: Arch. Bud. Masz. **4** (1957) 63.
6) H. S. Carslaw and J. C. Jaeger: *Conduction of Heat in Solids*, Oxford, 1947.
7) H. S. Carslaw and J. C. Jaeger: *Operational Methods in Applied Mathematics*, Oxford, 1947.

Short Notes

This section is intended to secure prompt publication of important discoveries in physics. The reports should not exceed 800 words in length. A figure of size 7 cm×7 cm will be counted as 150 words.

J. PHYS. SOC. JAPAN **14** (1959) 225

Nuclear Magnetic Resonance of RbBr

By Junkichi ITOH and Yukio YAMAGATA

Department of Physics, Osaka University, Osaka

(Received November 28, 1958)

We have made nuclear magnetic resonance studies of alkali halides having alkali and halogen ions of similar electronic configurations. In these alkali halides, comparison with the theories[1,2] can be made with less ambiguity, because the masses of the ions are nearly equal. We measured spin-lattice relaxation time T_1 as well as paramagnetic chemical shift σ (referred to the resonance in dilute aqueous solution of the same salt*) for RbBr and KCl. In this note, we shall describe the results for RbBr.

The measured values of T_1 and σ at room temperature were as follows: T_1 (Rb^{87})=0.27 sec, T_1 (Br^{81})=0.16 sec, σ(Rb)$=1.6\times10^{-4}$, and σ(Br)$=1.05\times10^{-4}$.

First we shall compare the experimental results with the theory given by Yosida and Moriya[2], in which some small degree of covalency was assumed in the bond between alkali and halogen ions. According to their theory, the ratios of σ and $1/T_1$ for Rb and Br are simply given by the ratios of $\langle r^{-3}\rangle$ (average of r^{-3} over covalent p-orbital), s-p hybridization degree and nuclear quadrupole moments. On forming small covalent bond, one valence electron ($4p$-electron) of Br ion will transfer to the outer orbital of Rb ion. This orbital may be $5s$-$5p$ hybridized orbital, the weight of s-orbital being probably predominant. So, the calculated ratios of σ and $1/T_1$ for Rb and Br are very much smaller than the experimental one, though σ and T_1 for Br alone may be well interpreted by taking appropriate degree of covalency. Even if we assume a configurational interaction in Rb ion by which $4p$-orbital is partially mixed with $5p$-orbital, the experimental ratios may not be interpreted appropriately.

Next, we shall compare the experimental results with Kranendonk's theory[1], in which only the electrostatic effect of charges outside of the ion core is taken into account. The calculated ratio of $1/T_1$ for Rb and Br, with appropriate values of Sternheimer's antishielding factors,[3,4] gives much better approach to the experimental ratio than the covalency theory, but it is still smaller by a factor of 10 or so. However, ion core deformation by charges outside of it may not produce σ of the order which we have measured, in the framework of the original Sternheimer's theory.[3]

Also, we measured the relative intensities of Rb^{85} and Br^{81} resonances, from which it was concluded that $1/2\leftrightarrow-1/2$ transitions alone contribute to the observed resonance in these cases, while the width of the resonance lines was equal to the dipolar width. This indicates that imperfections of the crystal may produce static quadrupole energies of the same order of magnitude in Rb and Br.

These experimental results show that there seems no substantial difference in the nuclear magnetic resonance of Rb and Br in RbBr crystal, and that σ, T_1, and the quadrupole effects due to crystal imperfections may be determined, at least in their orders of magnitude, by the electronic configuration of the ion, regardless of the sign of ionic charge. To interpret the nuclear magnetic resonance of alkali halides, a more elaborate theory should be used, in which the overlapping of ion cores, the deformation of ion core by outside charges, possible covalent nature in the bond, etc. are taken into consideration.

We have made similar experiments on K and Cl nuclei in KCl. The details of the experiments will be published elsewhere.

---

* Concentration dependence of the shift in nuclear magnetic resonance of Rb or Br was found in aqueous solution of alkali halides containing Rb or Br ion, as in iodide ion in aqueous solution of alkali iodides.[5] So, the chemical shift σ of solid RbBr referred to dilute aqueous solution of RbBr might not be true shift σ_0 from corresponding free ion. σ_0 is necessary for the comparison with the theories. But, in the cases of Rb and Br, this concentration dependence was much less than that in I. Therefore, σ may be considered to be close to σ_0 and, since the values of σ_0 cannot be decided accurately, we used σ for the discussions of the experimental results.

References

1) J. van Kranendonk: Physica **20** (1954) 781.
2) K. Yosida and T. Moriya: J. Phys. Soc. Japan **11** (1956) 33.
3) H. M. Foley, R. M. Sternheimer and D. H. Tycko: Phys. Rev. **93** (1954) 734.
T. P. Das and R. Bersohn: Phys. Rev. **102** (1956) 733.
4) R. M. Sternheimer and H. M. Foley: Phys. Rev. **102** (1956) 731.
E. G. Wikner and T. P. Das: Phys. Rev. **109** (1958) 360.
5) J. Itoh and Y. Yamagata: J. Phys. Soc. Japan **13** (1958) 1182.

J. Phys. Soc. Japan **14** (1959) 226~227

Anisotropy of Ordinary Hall Effect in Silicon Iron

By Eiji TATSUMOTO and Tetsuhiko OKAMOTO
Department of Physics, Faculty of Science, Hiroshima University, Hiroshima

(Received December 12, 1958)

The observation of the Hall effect of ferromagnetic single crystals has not been made except on iron by Webster¹⁾ In his measurements the ordinary effect was not observed because of the insufficient intensity of the applied magnetic fields. In the present experiment, by using the single crystal strips of 1.23% silicon iron, and by applying the magnetic fields on them up to 30,500 gauss, not only the extraordinary but also the ordinary Hall effect was observed at room temperature. The single crystals were made by Fujiwara's method,²⁾ the size being about 0.5 mm × 9.5 mm × 35 mm and crystallographic orientations (001)−[100], (001)−[110] and $(\bar{1}\bar{1}0)$−[111].* The polycrystals were also measured. Some of the results of the preliminary measurements are presented here.

The Hall effects observed are satisfactorily represented by the empirical formula,³⁾ $E_H=(R_0H+R_1M)I/t$, where E_H is the Hall voltage measured directly, R_0 and R_1 the ordinary and the extraordinary Hall coefficient respectively, H the intensity of magnetizing field, M the mean intensity of magnetization, I the primary current and t the thickness of specimen. The extraordinary Hall coefficient observed in comparatively low fields is not anisotropic just as in the case of Webster,¹⁾ and the magnitude is 49.2 volt. cm/gauss. amp. The ordinary effect observed in the applied fields higher than about 26,000 gauss, however, is distinctly anisotropic, and moreover is affected by the tensions within the elastic range applied in the direction of the primary current; that is, the ordinary Hall coefficients sensitively vary according to the tensions, but their signs do not change in any case, as shown in Fig. 1. In the extraordinary Hall effect, the effect of tension was scarcely observed. Dependence of the ordinary Hall coefficients on the tensions is different among three kinds of the single crystals. Accordingly, the difference depends on the shapes of crystal lattice distorted by the tensions and seems to have some definite relation with the rate of the deformation of the crystal lattices. On the polycrystals, however, no effect of the tension has been observed. In the ferromagnetic cystals free from external tension, the crystal lattice has already been deformed by the spontaneous magnetostriction to the tetragonal lattice, the c axis of which is one of the easy axes <100>. Consequently, it should be considered that the ordinary Hall coefficients observed without tension have already been modified comparatively by the spontaneous deformation of the crystal lattice. There remains a question, however, whether they should still have anisotropy even if the crystal lattice were cubic. Because of the positive sign of the ordinary Hall coefficient in every cause, almost all or all the charge carriers are positive holes, so that the anisotropy and the effect of the tensions might be attributed to the nonspherical forms of the Fermi energy surface of the conduction band, which probably touches the boundary of Brillouin zone. It may be of interest to observe the Hall effect on the single crystals, such as nickel, the charge carriers of which are presumed to be electrons, in contradistinction from the case of hole conduction. In conclusion, one may expect that a complete investigation concerning these problems will give an essential information for understanding the structure of the conduction band in ferromagnetics.

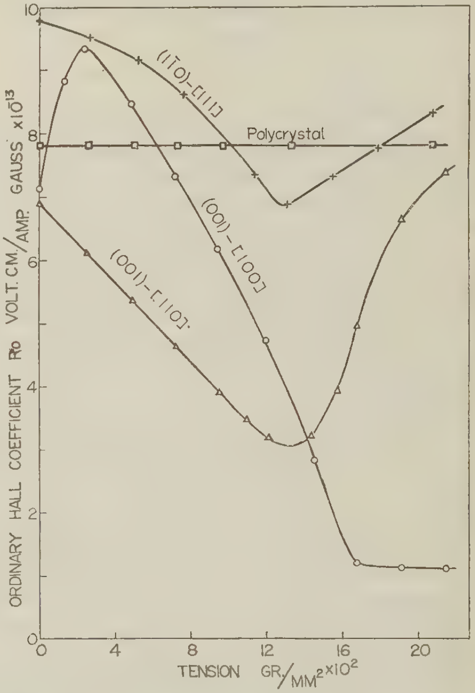

Fig. 1. Dependence of ordinary Hall coefficient on the tensions applied in the direction of primary current.

---

* For example, the notation (001)−[100] signifies that (001) and [100] coincide respectively with the surface plane and the longitudinal direction of a single crystal strip.

References

1) W. L. Webster: Proc. Cambr. Phil. Soc. **23** (1927) 800.

2) T. Fujiwara and E. Tatsumoto: J. Sci. Hiroshima Univ. Ser. **A**, **16** (1940) 235.
3) E. M. Pugh and N. Rostoker: Rev. Mod. Phys. **25** (1953) 151.

J. Phys. Soc. Japan **14** (1959) 227

Electrostatic Transformer Type Particle Accelerator using Ceramic $BaTiO_3$ —Ferrostac—

By Toshikazu SHIBATA, Atsutomo TOI, Tokuo SUITA

Department of Nuclear Engineering, College of Engineering, Osaka University, Osaka

and

Shunkichi KISAKA

Matsushita Electric Industrial Corp. Ltd., Osaka

(Received December 15, 1958)

A particle accelerator for engineering use which utilizes the electrostatic transformer principle[1] has been constructed with ferroelectric materials such as ceramic $BaTiO_3$. The accelerator consists of a high voltage generator and an accelerating tube with an ion source and suitable accessories.[2] The essential feature of this accelerator is that the high voltage generator has rotating ferroelectric ceramic discs or capacitors which carry electric charges.

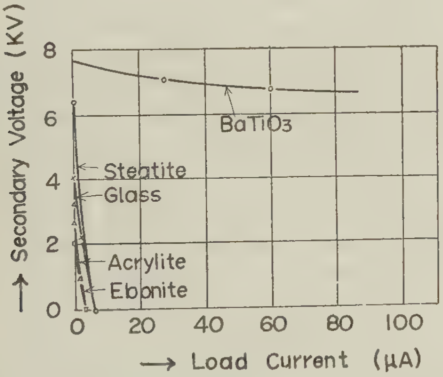

Fig. 1. Relations between the secondary voltages and the load currents at the constant primary voltage (8 kV) for various materials.

Various dielectric materials have been tried as the rotating discs and the results shown in Fig. 1 were obtained. In Fig. 1 some relations between the secondary currents and the secondary voltages for the 1:1 electrostatic transformers at a constant primary voltage of 8 kv are shown. It is clearly seen that much more secondary current or beam current can be obtained without marked voltage drop in the case of $BaTiO_3$ which is desirable for high beam current accelerator for engineering use like radiation source and nuclear fusion injector.

The constructed Ferrostac of 150 kv for neutron production is shown in Fig. 2. The ion source is of the rf type using 20 megacycles per second and kept at earth potential. The zirconium-tritium or titanium-tritium target is connected to the negative high potential terminal of the high voltage generator. Any potentials for the intermediate electrodes and focussing electrode may easily be obtainable through proper brushes of the generator. The deuteron beam current obtained so far is about 100 microamperes and the neutron intensity is about $10^9\, n$/sec. The beam current, however, will be increased by improving the ion source.

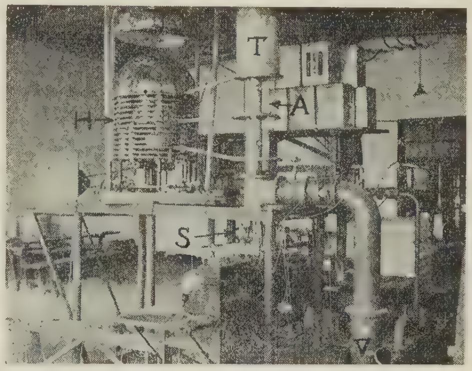

Fig. 2. 150 kV Ferrostac

H: High voltage generator (electrostatic transformer)
A: Accelerating tube
T: Target
S: Ion source
V: Vacuum pump

The accelerator of this type seems to combine several advantages of Van de Graaff and Cockcroft-Walton type accelerators in having (a) simple construction, (b) high beam current and (c) low cost per beam current. At the present stage, however, it has some problems such as mechanical vibration, secondary voltage fluctuation, surface discharge and brush contact. To improve these points, some fundamental researches are being done. And 400 kv Ferrostac, 1 mV Ferrostac and also an electrostatic accelerator which utilizes the electrostatic generator principle are being constructed.

References

1) J. M. Malpica: R.S.I. **22**, 364 (1951).
2) Shibata, Toi, Hayakawa and Suita: Second Symposium on Peaceful Uses of Atomic Energy, Japan (1958), No. D–51.
3) Suita, Kisaka, Kaname and Iwata: Annual Meeting of E. E. Japan, No. 257 (May, 1953), No. 225 (Oct., 1954), No. 262 (May, 1954), No. 329 (May, 1956).

J. PHYS. SOC. JAPAN, **14** (1959) 228~229

Optical Properties of SiC in Infrared Region

By Masaharu NAMBA
Fuji Denki Seizo K.K., Research Dept., Kawasaki

(Received October 20, 1958)

It is well known that silicon carbide is the valence crystal and p- or n-type semiconductor. Unfortunately, unlike silicon, germanium and other semiconducting materials, it is impossible to get SiC single crystals thicker than about 0.5 mm for the present and is very difficult to polish the ones thinner than about 0.05 mm. Therefore the optical absorption of SiC in infra-red region described here may not be accurate quantitatively.

i) Transmission measurements

The transmission studies were carried out on a Perkin-Elmer double pass monochrometer in the range from 2.5μ to 16μ at room temperature.

As shown in Fig. 1 silicon carbides are found to have high transparency for infra-red radiation up to 5μ, although for p-type black SiC ($=10^{-1}\,\Omega$ cm) transparency is practically zero because of their high impurity contents ($5\times10^{19}\sim10^{20}$ cm^{-3}) and large free carrier concentrations ($n\sim5\times10^{18}$ cm^{-3}).

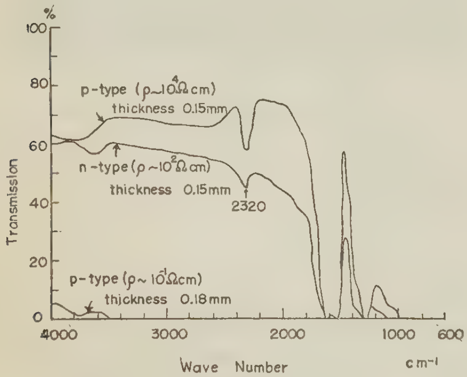

Fig. 1. Transmission of SiC.

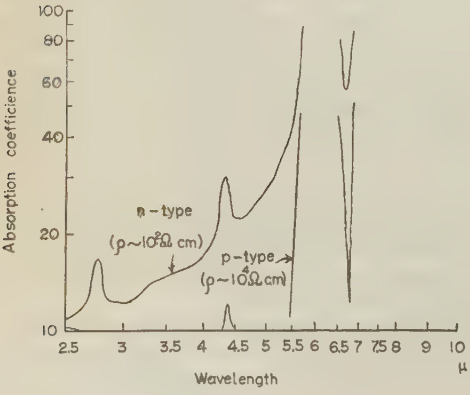

Fig. 2. Absorption coefficient of SiC.

ii) Absorption coefficient

Absorption coefficient at room temperature were determined by transmission measurements. From this method, owing to the thickness of our specimens used, it was impossible to measure absorption coefficients more than about 100 cm^{-1} and less than 10^{-1} cm. The experimental curve for n-type sample given in Fig. 2 roughly has the same slope as required by the Drude theory of free carrier absorption.

Besides this absorption there are absorption bands due to impurity and lattice vibration. The available thermal-ionization energy data for SiC indicate that the 1s state of the impurity level is explained in terms of a hydrogen-like model for the unionized impurity and is given by 0.275 e.v.[1]. Then, the corresponding optical absorption appears at $\nu=2320$ cm^{-1} ($h c\nu=0.288$ e.v.) for p- and n-type specimens. Now, since the tetrahedral bond length of sillicon carbide lies between those of sillicon and diamond, the lattice absorption frequency may be expected to exist between the ones of sillicon and diamond. Then, our measurement shows the existence of a principal transmission minimum ($\nu=1600$ cm^{-1}) and secondary minimum in the long wave side of the former. Although we can not discuss on this aspect in detail, the observed absorption is very strong compared with sillicon and diamond,[2] and resembles to the cases of some ionic crystals.

iii) Reflective power

The Coblentz's data on reflection[3], shown in Fig. 3, remind us of selective reflection of ionic crystals. If it is so, this experimental result will be understood in the same manner as the infra-red dispersion by ionic crystals.

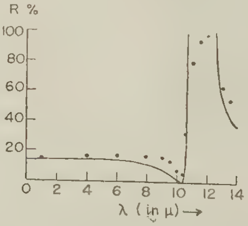

Fig. 3. Reflection of SiC.

Solid line=theoretical curve
Dotted line=Coblentz's experimental curve

Fig. 3 indicates that the wavelength at which the maximum reflection occurs is 12μ and ε_∞, the high frequency dielectric constant, 5.124, and then the dispersion frequency or wavelength λ_0 computed by Havelock's theorem is given by 12.415μ (assuming ε_0, static dielectric constant, $=7$).

If we write the dispersion formula as follows[4]:

$$\varepsilon=\varepsilon_\infty+\frac{\varepsilon_0-\varepsilon_\infty}{1-(\lambda_0/\lambda)^2}, \qquad (1)$$

then the reflective power R is given by the well-known formula

$$R=\left|\frac{n-1}{n+1}\right|^2, \qquad (2)$$

where n is the refractive index ($=\sqrt{\varepsilon}$). The theoretical curve based on Eqs. (1) and (2) is shown by solid line in Fig. 3. There is good agreement between theory and experiment, from which we have to conclude that the sillicon carbide may be classified between the valence and ionic type.

References

1) J. T. Kendall: J. Chem. Phys. **21** (1953) 821.
2) R. J. Collins and H. Y. Fan: Phys. Rev. **39** (1954) 674.
3) Coblenz: International critical tables, 5, (1929) 258.
4) Born and Huang: Dynamic theory of crystal lattice, (1954) 83.

J. PHYS. SOC. JAPAN **14** (1959) 229

Note on the Spin of Excited States of Cadmium 110

By Mitsuo SAKAI*, Haruko OHMURA and Teruo MOMOTA**

Department of Physics, Faculty of Science, University of Tokyo

(Received November 28, 1958)

The spin of long-lived Ag^{110m} (253 day) was very recently determined as 6 by the atomic beam magnetic resonance method.[1] Since our analysis published in the last year[2] which concerned the angular correlation measurement of gamma rays from this nucleus was based upon the assumption of 5–or 4+ for the spin and parity of this level, it was considered worth while to examine our results once again.

The decay scheme is presented in Fig. 1. As the spin and parity of short-lived Ag^{110} is known to be 1+ by the information from beta disintegrations, the 116–KeV electromagnetic transition now should be of E5 or M5 character. Hence the K/L ratio of this gamma ray might be expected to be 0.185 or 1.05[3]. According to the experimental value of 1.3[4], the electromagnetic character can be concluded as M5. Consequently the parity of this isomeric level should be +. The low energy beta component decaying from this level to the 2.93 MeV level of the daughter nucleus of Cd^{110} has the log ft value of 4.2[5], which indicates the spin and parity of this level might be 7+, 6+ or 5+. These possibilities could not exist in our previous analysis in which the spin and parity of the third 1.541–MeV level was assumed to be either 2+ or 3+. Therefore the third alternative of 4+ should now be considered. In our preceding paper this possibility was rejected by reason of the rather big difference between the angular correlation patterns $\langle\gamma_3\gamma_4\rangle$ and $\langle\gamma_3\gamma_6\rangle$ even though we have got $\langle\gamma_4\gamma_6\rangle$ consistent with that of spin sequence of $0-2-4$. The similarity between $\langle\gamma_3\gamma_4\rangle$ and $\langle\gamma_3\gamma_6\rangle$ is a requisite for this spin sequence. But, to our regret, the accuracy of the experiment was not high enough to exclude this posibility complet-ly. Analyzing the data under the assumption of the third alternative for the spin of the 1.54–Mev level, we found that the spin 5 for the 2.930–Mev level with γ_2 of almost M1 character is the unique solution and that the spin 4 or 5 (less probably 6) of the 2.476–Mev level is only possible in case of γ_3 having the mixing ratio of about -0.2. The revised spin assignment is shown in Fig. 1.

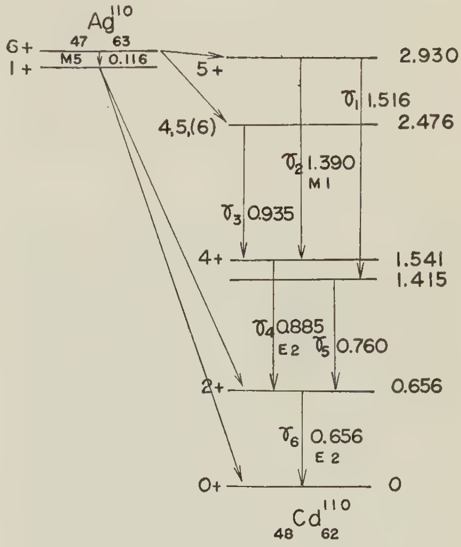

Fig. 1.

References

1) Ewbank, Nierenberg, Shugart and Silsbee: Phys. Rev. **110** (1958) 595 (L).
2) Sakai, Ohmura and Momota: J. Phys. Soc. Japan **12** (1957) 985.
3) M. E. Rose: Beta and Gamma Ray Spectroscopy (Ed. K. Siegbahn) Appendix IV Amsterdam: North Holland Publishing Co. 1955.
4) K. Siegbahn: Phys. Rev. **77** (1950) 233.
5) T. Azuma: J. Phys. Soc. Japan **10** (1955) 161.

---

* Now at the Institute for Nuclear Study, University of Tokyo.

** Now at the Japan Atomic Energy Research Institute. Tokai-mura, Ibaraki-ken, Japan.

J. PHYS. SOC. JAPAN **14** (1959) 230~231

Electronmicroscopic Observations on the KI Single Crystal

By Tetsuhiko TOMIKI*

The Research Institute for Steel, Iron
and other Metals,
Tohoku University, Sendai, Japan

(Received November 27, 1958)

During electronmicroscopic studies on alkali halides, it was found that KI single crystal has properties different from those observed hitherto on KCl, NaCl and KBr single crystals[1]. The experimental results obtained are summarized as follows:

(i) Fresh (100) cleavage surfaces of KI have a group of steps each of which is parallel to each other and is generally less than 0.1 microns in height (Fig. 1*a*). This step splits usually into two branches of cleavage steps, or vice versa (Fig. 1*b*). These properties have never been observed on the KCl, KBr and NaCl crystals.

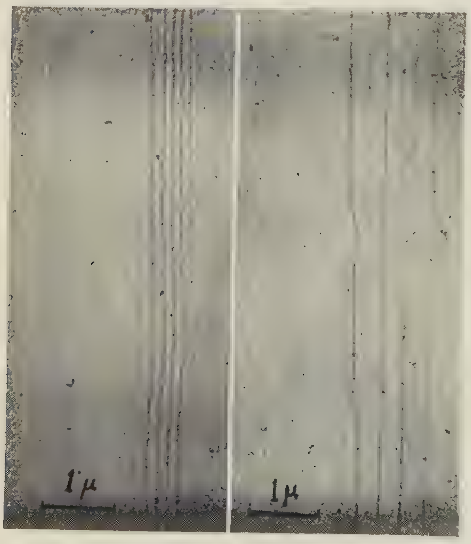

(a) (b)

Fig. 1.

(ii) After evacuating the evaporation apparatus in which the freshly cleaved KI specimen was placed, this apparatus was filled with air to make the crystal expose to it. The crystallites came out on the (100) surface of this specimen, when the evaporation apparatus was evacuated again (Fig. 2). The similar phenomenon has already been reported on the KCl single crystal.[2]

(iii) When the KI single crystal was irradiated with x-ray (Cu target; applied potential=30 kv) on the (100) at the distance of 50 *cm* from the target for 60 minutes, the crystallites grew in a irregular shape as shown in Fig. 3. However, the crystallites did not grow on the KCl specimen x-rayed under the same conditions.

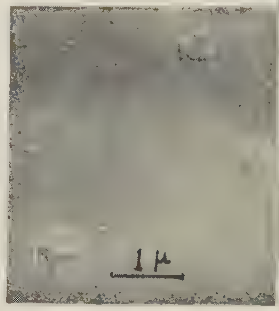

Fig. 2.

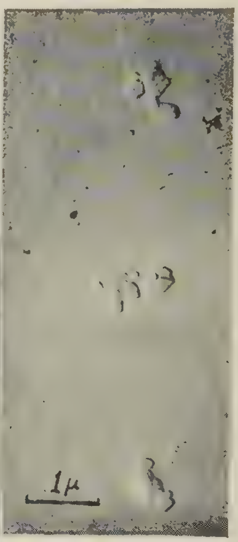

Fig. 3.

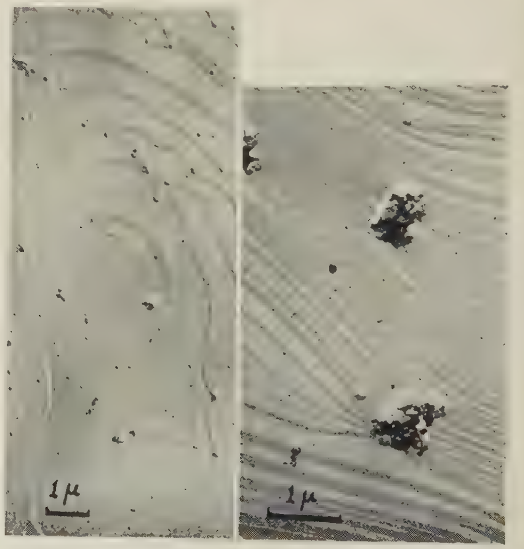

(a) (b)

Fig. 4.

(iv) When the KI single crystal was bombarded with electron beam of an electron microscope (Current=30μA; applied potential=50 kV) on its (100) surface, KI molecules evaporated from the surface and crystallites grew there at the same time. The surface area, where pits are produced by evaporation caused by bombardment with electrons for 15 minutes, is shown in Fig. 4a. The surface structures similar to contour lines in a map represent lamellae by which pits are formed. The grains on the (100) represent the grown-up crystallites. Fig. 4*b* shows another part of the surface where crystallites have grown at the convergent points of the stratified structures produced by evaporation. The shape of these crystallites resembles to those of crystallites on the x-rayed surface (*cf*. Fig. 3). Therefore, the crystallites will probably be composed of KI. The alkali halide single crystals bombarded with high speed electrons have been investigated only little.[3] Many problems are left unsolved.

---

* The present address: Department of Physics, The Faculty of Science, Tohoku University, Sendai, Japan.

It is planned to extend to electronmicroscopic observations on the KI single crystal.

The author would like to express his thanks to Prof. S. Ogawa who provided him an opportunity to achieve this experiment. His gratitudes are also due to Dr. M. Hirabayashi for his kind operations of x-ray apparatus.

References

1) T. Hibi and K. Ishikawa: J. Phys. Soc. Japan **13** (1958) 717.
T. Hibi and K. Yada: to be published.
T. Hibi and T. Tomiki: to be published.
T. Tomiki and M. Ueta: to be published.
2) D. Sönken: Zs. Naturforschg. **11a** (1956) 646.
3) S. Yoshida and T. Ikeda: Repts. Res. Inst. Sci. Measurements **7** (1958) 1.
F. W. Geck: Zs. Naturforschg. **12a** (1957) 562.
A. D. Whapham: Phil. Mag. **3** (8) (1958) 103.

J. PHYS. SOC. JAPAN **14** (1959) 231

Ferrimagnetic Resonance of Polycrystalline Nickel Ferrite-Chromites

By Hiroo YONEMITSU

Matsuda Research Laboratory,
Tokyo Shibaura Electric Co.,
Kawasaki-City, Japan

(Received December 5, 1958)

A series of dense mixed polycrystals $NiFe_{2-x}Cr_xO_4$ were prepared with $x=0$, 0.10, 0.20, 0.30, 0.40, 0.60, 0.80 and 1.20 by the usual ceramic techniques. The X-ray diffraction patterns obtained on a Norelco type diffractometer using FeK_α radiation, showed only spinel phase for all samples. Ferrimagnetic resonance absorption spectra showed no changes about the full half-width ΔH for all compositions below $x=0.60$, as shown in Fig. 1. Their absorption powers, however, were weakened with the increase of chromium contents x. Saturation magnetization at room temperature for the annealed samples are shown in Fig. 2.

This behavior resembles to the one for the nickel ferrite-aluminate series reported by Maxwell and Pickart[1)], except for the fact that in the latter case ΔH is increased with Al contents. Further investigations on the cation distribution of these mixed crystals and the constant ΔH characteristics are now in progress and the results will be published in this Journal.

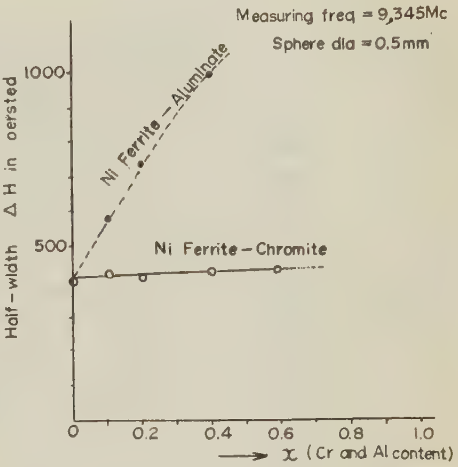

Fig. 1. Ferrimagnetic resonance half-width ΔH *vs*. x.

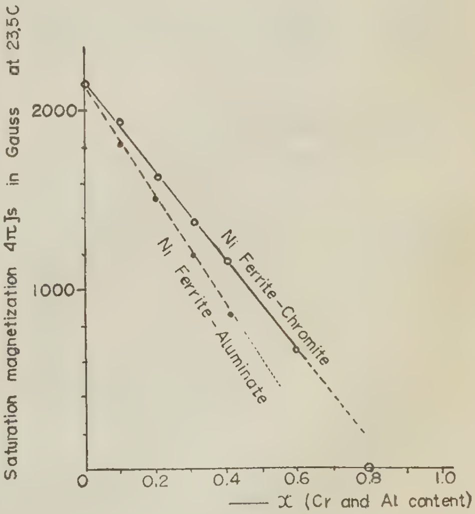

Fig. 2. Saturation magnetization $4\pi J_s$ *vs*. x at room temperature.

Reference

1) L. R. Maxwell and S. J. Pickart: Phys. Rev. **92** (1953) 1120; ibid. **93** (1954) 682.

J. Phys. Soc. Japan **14** (1959) 232~233

Barrier Temperature at Turnover in Germanium *p-n* Junction

By Jiro YAMAGUCHI and Yoshihiro HAMAKAWA
Faculty of Engineering, Osaka University, Osaka

(Received December 5, 1958)

In this note, the additional considerations are given for the barrier temperature at turnover in the reverse direction of germanium grown *p-n* junction, which has been previouly reported.[1]

The experimental procedures are the same as our previous publication.[1] Fig. 1(a) shows the experimental results of the barrier temperature of grown type junction at turnover, which is estimated from the saturation current in reverse direction. In this figure and the following ones, circles, crosses and dots express the results measured by the pulse of 160, 80 and 40 μs duration, respectively, in repetition frequency of 1000 c/s. It is found that the barrier temperature at turnover is nearly constant for a given specimen in the range of ambient temperature of (−180~20)°C.

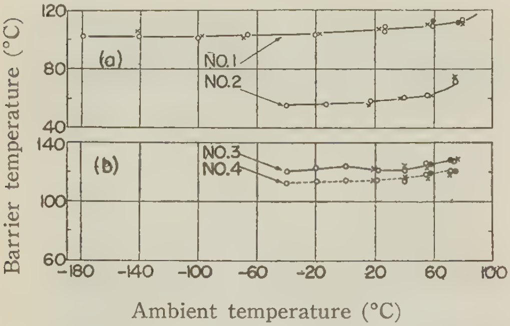

Fig. 1. Turnover barrier temperature estimated from saturation current at different ambient temperatures.

(a): grown junction, (b): point contact

On the other hand, the barrier temperature can be estimated by another means[2] which has been adopted to the point contact diode. Following this method, we can obtain the relation between turnover power and ambient temperature as Fig. 2 for specimens of No. 1 and No. 2 and the turnover barrier temperature can be indicated by the intersection of linear part of these plots to the abscissa. These results and physical properties of specimens are summarized in 1st and 2nd row of Table I and there is a discrepancy between the barrier temperatures obtained by the above two methods.

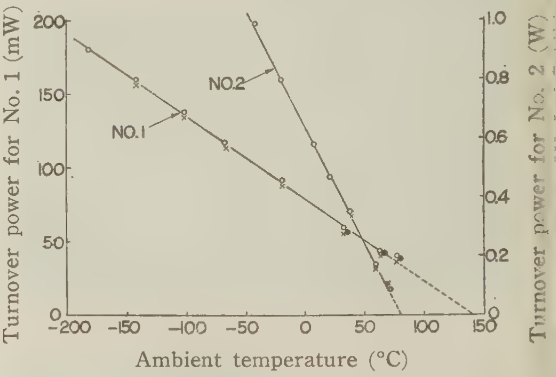

Fig. 2. Powers dissipated at turnovr versus ambient temperature in case of grown junctions.

Furtheremore, we take the same considerations for the specimens of point contact type. These results are shown in Fig. 1 (b) and also in the 3rd and 4th row of Table I. From these results, the difference of barrier temperature measured by above methods is rather small. Comparing the results of point contact type with those of junction type, we can confirm that there may be the non-uniformity or patch in the germanium junction,

Table I. Experimental results and physical properties of the specimens.

specimen No.	barrier temperature at turnover (°C)		type and size of specimen	property of high resistivity side	
	measured from saturation current	measured from turnover power		specific resistivity (Ω-cm)	intrinsic temperature (°C)
1	105~112	143± 5	grown junction (collector-base of 2T52)	1	148
2	56~ 62	82± 3	grown junction (3×3×10 mm)	6	83
3	120~130	118± 8	point contact (IN34)	3~5	90~115
4	114~123	119±11	point contact (INA4)	3~6	83~115

like as in the sillicon p-n junction,[3-4] and the turnover occurs, when the barrier temperature reaches the intrinsic temperature at any spot in junction.

The authors are indebted to Sony, Corp., Kobe Kogyo, Corp. and Nippon Electric Company Ltd. for the supply of the specimens.

References

1) J. Yamaguchi and Y. Hamakawa: J. Phys. Soc. Japan **14** (1959) 15.
2) S. Benzer: J. Attl. Phys. **20** (1949) 804.
A. Lempicki and C. Wood: Proc. Phys. Soc. B, **67** (1954) 328.
R. E. Burgess: Proc. Phys. Soc. B, **68** (1955) 908.
3) A. G. Chynoweth: J. Attl. Phys. **29** (1958) 1103.
4) J. L. Moll and B. Senitzky: Phys. Rev. **110** (1958) 612.

J. PHYS. SOC. JAPAN **14** (1959) 233~234

Interaction of Water Vapour with Germanium Real Surface

By Koji KAWASAKI, Kyoichi KANOU and Yoshiyasu SEKITA

Electrotechnical Laboratory, Nagatacho, Chiyodaku, Tokyo, Japan

(Received December 6, 1958)

The adsorption isotherm of water vapour and the surface conduction current in the atmospheres of various relative humidities were measured for germanium treated by CP4 etching solution.

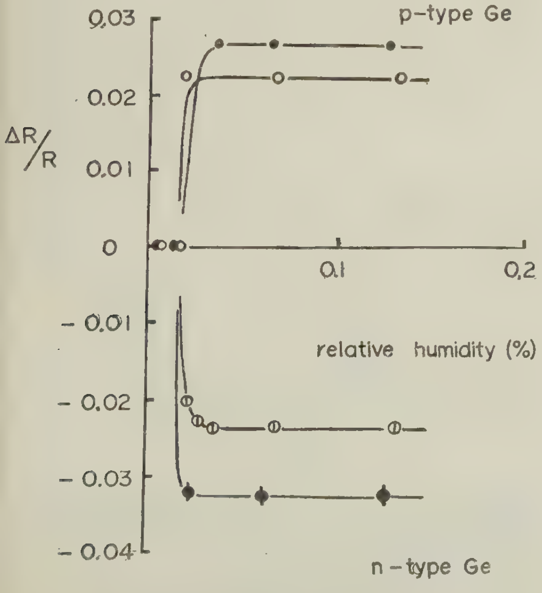

Fig. 1. Relative variation of resistance, $\Delta R/R$, as a function of relative humidity.

It was found that in general, the resistance R of n-type germanium decreases with the adsorption of water vapour, while that of p type sample increases with the adsorption.

The relative variation of resistance, $\Delta R/R$, of

Table I.

Samples	Specific Resistivity ($\Omega\cdot$cm)	$\Delta R/R$	ΔN_R (no./cm^2)
p-type			
1	6.0	0.0038	1.6×10^{11}
2	1.2	0.0080	4.9×10^{11}
3	0.6	0.028	4.1×10^{12}
4	0.8	0.009	6.2×10^{11}
5	6.0	0.0026	1.1×10^{11}
6	1.2	0.0058	5.9×10^{11}
7	6.0	0.028	5.6×10^{11}
8	0.9	0.041	1.6×10^{12}
N-type			
1	9.1	-0.0014	1.5×10^{10}
2	0.9	-0.012	8.4×10^{11}
3	2.5	-0.0195	6.5×10^{11}
4	8.3	-0.023	1.3×10^{11}
5	47	-0.0089	1.2×10^{10}
6	0.9	-0.014	9.5×10^{11}
7	3.1	-0.043	7.2×10^{11}

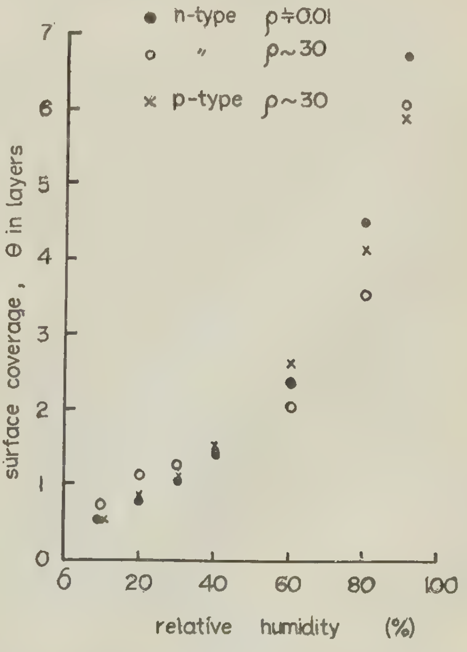

Fig. 2. Adsorption isotherms of water vapour on germanium at 25°C.

n- and *p*-type germanium in the atmospheres of very low relative humidities are shown in Fig. 1. $\Delta R/R$ seems to be saturated at such low humidities. Saturation values of $\Delta R/R$ and the number ΔN_R of charge carriers per unit area which must be introduced into the samples to produce the observed change in resistance with the adsorption of water vapour are shown in Table I for several samples. In the table, the values of ΔN_R range between 10^{11} and 10^{12} for both *n*- and *p*-type. These values are larger than those obtained by S. R. Morrison.1)

Next, the adsorption isotherms of water vapour on germanium surfaces were obtained by the gravimetric method using powdered specimens, i.e., by suspending the sample on the end of a sensitive quartz spring in a glass vacuum vessel and measuring the spring elongation with a cathetometer. Typical adsorption isotherms on the samples outgassed at 25°C are shown in Fig. 2, where θ is the surface coverage as determined by the B.T.E. method. These isotherms are nearly in accordance with Law's data.2)

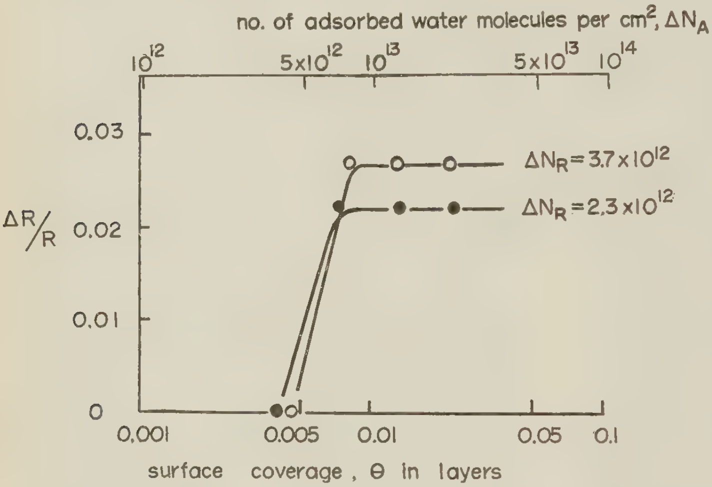

Fig. 3. $\Delta R/R$ with number of the adsorbed water molecules or surface coverage.

From Fig. 1 and the logarithmic expression of adsorption isotherm given in Fig. 2, $\Delta R/R$ for *p*-type germanium is plotted in Fig. 3 versus the surface coverage θ. It can be seen that $\Delta R/R$ increases with θ and is saturated at a certain critical value of θ. This critical value of the surface coverage θ lies between 5×10^{-3} and 8×10^{-3}. The number ΔN_A of the adsorbed water molecules per unit area at this critical values of θ is about $(5\sim8)\times10^{12}$.

References

1) S. R. Morrison: J. Phys. Chem. **57** (1953) 860.
2) J. T. Law: J. Phys. Chem. **59** (1955) 67.

J. Phys. Soc. Japan **14** (1959) 234~235

Size Distribution of Radioactivity of the Natural Radioactive Dust

By Koji Kawasaki and Keiji Kato
Electrotechnical Laboratory, Nagatacho Chiyodaku, Tokyo, Japan

(Received October 7, 1958)

In order to provide further information on the particle size distribution of the radioactivity of the natural radioactive dust in the atmosphere near ground, an apparatus has been designed and the distribution of radioactivity has been measured.

A copper wire was set as shown in Fig. 1 and the radioactivity captured by the wire was measured by a G.M. counter. According to this measurement, the radioactivity of the dusts captured by the wire was almost zero when the wire was maintained at a high positive potential, but was measurable when the wire was at a negative potential. These results indicate that the polarity of radioactive dust particles captured is positive, although there may exist in the atmosphere neutral particles that have not been detected by this experiment. Furthermore, the radioactive substances were identified as RaB, RaC and ThB by the decay rate curve, as already reported.1),2)

Based on these facts, an apparatus for the determination of the size distribution of the natural radioactive dust was designed as shown in Fig. 2. The air that is taken in by the blower flows into the cylindrical ion separator. The separator captures the charged particles or the "ions", as they are called in the atmospheric electricity, that have mobilities higher than the cut off mobility determined by the equation

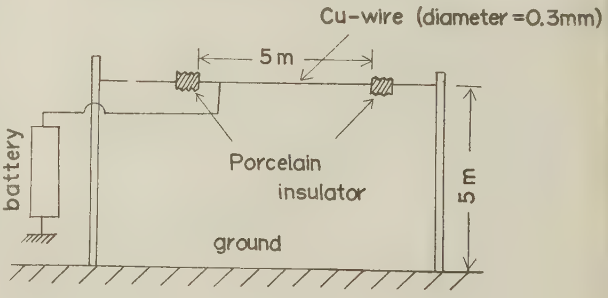

Fig. 1.

$$k=Q\ln\frac{D}{d}\Big/2\pi lV. \qquad (1)$$

where k is the cut off mobility, D and d are the diameters of the outer and the inner cylinder respectively, l is the length of the cylinder, Q is the airflow, and V is the applied voltage. The charged particles having the mobilities lower than the cut off mobility pass through the ion separator, flow into the electric precipitator and are captured by the precipitator effectively.[2] After the ions have been collected, the chamber of the electric precipitator is closed by the glass valves A_1 and A_2, and the d.c. high voltage applied on the tungsten wire of the precipitator is removed. This chamber is then used as a G.M. counter, commercial methane being introduced into the chamber through the glass valve B_1 and exhausted through B_2, at slightly above atmospheric pressure. From this measurement, the fraction of total radioactivity can be plotted versus the cut off mobility. Particle size is related to mobility by

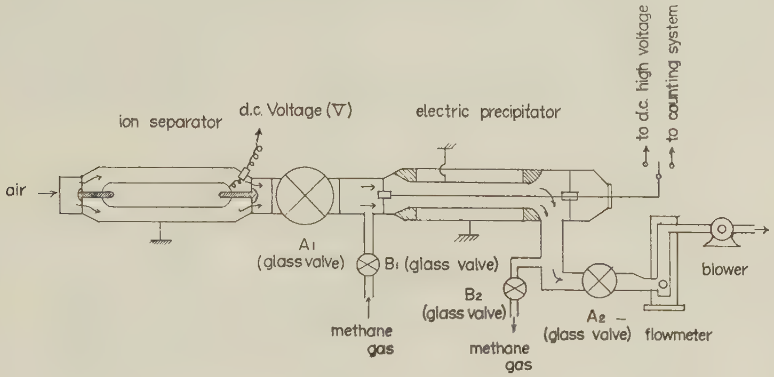

Fig. 2.

$$k=e\{1+(b/pr)\}/6\pi\eta r \qquad (2)$$

where e is the charge of particle, η the viscosity of the air, r the radius of dust particle, p the pressure and b a constant.

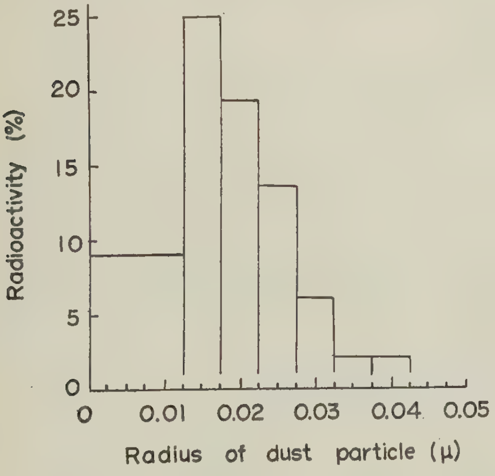

Fig. 3.

A typical result of the particle size distribution of radioactivity is shown in Fig. 3. It is found out that most of the natural radioactivity in the atmosphere attaches itself to particles having radii in the range 0.01 to 0.04 micron and predominance of the activity is in the vicinity of 0.0175 micron. These results are nearly in accordance with the data given by Wilkening.[3]

References

1) M. Kawano: J. Meteorological Soc. Japan, 35, 343, 1957.
2) N. Yano and H. Naruse: Papers in Meteorology and Geophysics, 7, 34, 1956.
3) M. H. Wilkening: Rev. Sci. Instr. 23, 13, 1952.

J. Phys. Soc. Japan **14** (1959) 235~236

Zeeman Study of Nuclear Quadrupole Resonance Spectrum in *p*-Dibromobenzene

By Kenji Shimomura

Minami Bunkô, Hiroshima University, Hiroshima

(Received November 27, 1958)

The Zeeman analysis[1] of bromine quadrupole resonance spectrum in p-dibromobenzene was performed employing the Zeeman analyzer which has been described previously.[1] The single crystal was obtained by descending slowly a cylindrical glass container with a bottom tapered to a point, through a vertical furnace having a large temperature gradient.

The experimental results of the Zeeman analysis are shown in Fig. 1, which shows two nonequivalent directions[2] of z-axes of field gradient tensor. The angle between them was found to be $71°59'\pm12'$, which is in fairly good agreement with the angle between the two Br–Br directions $71°11'$

which has been obtained from the X-ray analysis.[3]

The points representing the zerosplitting angles are plotted in Fig. 1 together with the zerosplitting loci. The point D is plotted on the line AC connecting the point C which specifies the zerosplitting direction with the center A of the zerosplitting locus so that AD represents the angle $\theta-53°$, where θ is the zerosplitting angle at C, and 53° is arbitrarily chosen in order to clearly locate the maximum and minimum directions of the zerosplitting angles about A. From the maximum or minimum value of zerosplitting angle one obtains[1] $\eta=0.05\pm0.01$ for the asymmetry parameter of field gradient tensor at the bromine nucleus. On the other hand, from the study of Zeeman splitting Kojima et al[4] have obtained $\eta=0.12\pm0.01$, which is larger than our value. Our value seems to be more reasonable since it is nearly the same as those of p-diiodobenzene $4.77\pm0.40\%$, $3.65\pm0.50\%$[5] which have been definitely obtained from the frequency measurements of iodine resonances.

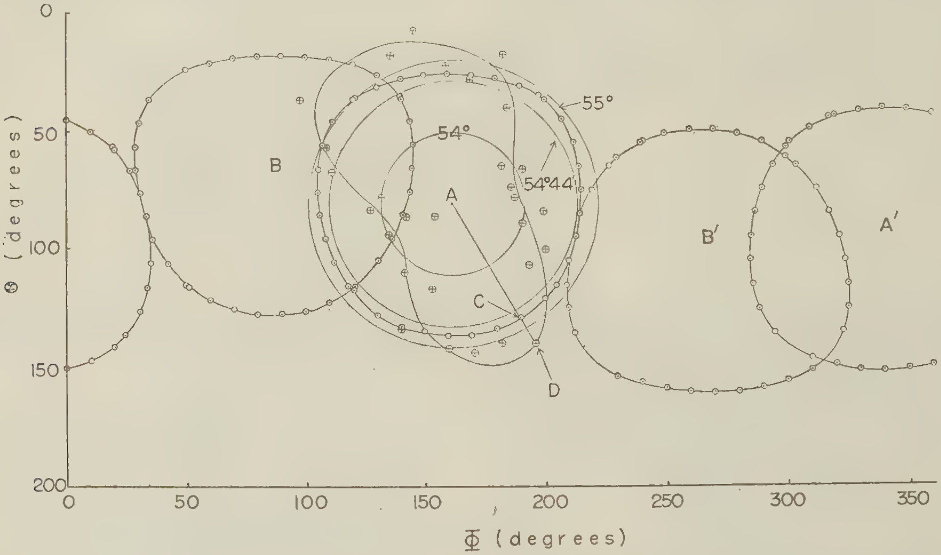

Fig. 1. Zerosplitting-direction patterns of Zeeman lines of bromine in p-dibromobenzene. Θ, Φ are polar angles specifying zerosplitting-direction with respect to the axes fixed to the sample.

○ represents the direction of zerosplitting.

⊕ represents the zerosplitting angle.

Three circles around A designate the 54°, 54°44′, and 55° zerosplitting angles. A′ and B′ are the equivalent directions of A and B, respectively.

From the value of η and the resonance frequency[6] of pure quadrupole resonance spectrum of bromine we may obtain[7] 80.9%, 2.0%, and 17.1% for the amount of single, double, and ionic character for C–Br bond, respectively.

References

1) K. Shimomura: J. Phys. Soc. Japan **12** (1957) 657.

2) K. Shimomura: J. Phys. Soc. Japan **12** (1957) 652.

3) R. W. G. Wyckoff: *Crystal Structures*, Interscience Publishers, Inc., New York (1953) Vol. III.

4) S. Kojima, K. Tsukada, and Y. Hinaga: J. Phys. Soc. Japan **10** (1955) 498.

5) G. W. Ludwig: J. Chem. Phys. **25** (1956) 159.

6) E. Manring, C. Brown, and D. Williams: Phys. Rev. **90** (1953) 348.
A. L. Schawlow: J. Chem. Phys. **22** (1954) 1211.

7) K. Shimomura: J. Phys. Soc. Japan **12** (1957) 1356.

Errata

On the Ferromagnetic Phase in Manganese-Aluminum System

By Hiroshi Kōno

J. Phys. Soc. Japan **13** (1958) 1444

Page	Column	Line		(should be read)
1445	right	Fig. 2.	⊙ for 49, 49.5, 50 and 50.5% Mn	○
			◬ for 57 and 58% Mn	△
1446	left	13	evolved	absorbed
		15	bracking	breaking
	right	38	50%	55%
		42	was	way
		foot note	$54.93x+26.98\{(100-x)/100\}$	$\{54.93x+26.98(100-x)\}/100$,
1447	left	Table II	$c=4.38$Å	$c=4.36$Å
	right	3	$c/a=1.63$, $c=4.38$Å	$c/a=1.62$, $c=4.36$Å
1448	right	Table III	102 105	105 105
1449	left	2	910°C	610°C
	right	3	evolution	heat evolution
		Fig. 7(b).	The value of ρ at the level of abscissa is $1\times10^{-4}\ \Omega\,\mathrm{cm}$	
		bottom	◬	▽
1450	left	28	(011)	(001)

PROGRESS OF THEORETICAL PHYSICS

CONTENTS

Progress of Theoretical Physics Vol. 20, No. 1, July 1958

Relativistic Magnetohydrodynamics .... Ken-iti Goto .. 1
On the Orbital Approach to the Many-Electron Problem in Molecule .... Sigeru Huzinaga .. 15
On the Representations of Field Quantities .... Hitoshi Wakita .. 35
Theory of Line-Shapes of the Exciton Absorption Bands .... Yutaka Toyozawa .. 53
Low Energy Electron-Hydrogen Scattering .... T. Ohmura, Y. Hara and T. Yamanouchi .. 82
An Attempt at Reformulating Pion-Nucleon Interaction, II —*Scattering of Antiproton by Nucleon*— .... O. Hara and Y. Fujii .. 89

Letters to the Editor:

Rigidity for Octupole Type Surface Deformation and Shell Structure .... S. Suekane and W. Watari .. 108
Steller Syntheses of the α-Particle Nuclei heavier than Ne^{20} .... C. Hayashi, M. Nishida, N. Ohyama and H. Tsuda .. 110
The Global Symmetry of Pion-Baryon Interactions and Bound States of Hyperon-Nucleon System .... Y. Yamaguchi .. 112
A Note on the Specification of Nuclear Potentials .... T. Hamada .. 114
Contents of Journ. Phys. Soc. of Japan, Vol. 13, No. 6 116

Progress of Theoretical Physics Vol. 20, No. 2, August 1959

Global Symmetry and the Branching Ratios for the K^- Capture by the Nucleon .... Ken KAWARABAYASHI..117
Phenomenological Model on the Interactions of Elementary Particles, II .... K. FUJII and K. IWATA..126
Charge-Transfer Forces in Molecular Compounds .... Shigeyuki AONO..133
Isotopic Spin Selection Rule in Σ-Decays .... T. EGUCHI and S. NAGATA..144
Electromagnetic Properties of Nucleons .... A. KANAZAWA, S. FURUI and T. SAKUMA..149
On the Exchange Magnetic Moments .... E. KUROBOSHI and Y. HARA..163
Proton-Proton Scattering and Pion Theory of Nuclear Forces..Shoichiro OTSUKI..171
Neutron-Proton Scattering and Pion Theory of Nuclear Forces .... Wataro WATARI..181
Cluster Sums and Related Coefficients of the Ising Model...Shigetoshi KATSURA..192
Effects of Virtual Nucleon Pairs to the Electromagnetic Structure of the Nucleon .... S. GOTO and S. MACHIDA..216

Letters to the Editors:

On a Non-Adiabatic Approximation Method in the Non-Linear Interaction Theory .... S. OZAKI..239
An Example of One-Dimensional Oscillatory Motion in Magnetohydrodynamics .... N. MUGIBAYASHI..241
Absorption Effects in Antinucleon Phenomena .... Y. KAKUDO, T. KAMMURI and R. NAKASIMA..243
Equivalent Hamiltonian of an Electron Gas at High Density .... T. NISHIYAMA..245
Coupling Constant of Kaon-Baryon Interaction, I .... A. KOMATSUZAWA, R. SUGANO and Y. NOGAMI..246
Coupling Constant of Kaon-Baryon Interaction, II .... A. KOMATSUZAWA, R. SUGANO and Y. NOGAMI..249
A Note on the Magnetic Relaxation in a Low Field .... M. TANAKA..251
A Remark on the Anomalous Magnetic Moment in the Static Model .... Y. HARA and K. KAWARABAYASHI..252
Contents of Journ. Phys. Soc. of Japan, Vol. 13, No. 7 255

Price $ 1.25 per copy
$ 15.00 per year (postage inclusive)
Annual dues for foreign members (individual subscribers)
$ 12.00 (postage inclusive)
〃 for foreign members of the Physical Society of Japan
$ 10.00 (postage inclusive)

Application for members, subscriptions and orders for back numbers should be sent, directly or through book-dealers, to

The Publication Office
in
Yukawa Hall, Kyoto University, Kyoto, Japan

. . . .

ANNOUNCEMENT

REVISED Price List of Back Numbers (for subscribers abroad)

*Vols. 1–4	$ 6.40 each
*Vols. 5 & 6	$13.00 each (single copy: $2.50)
*Vols. 7 and succeeding ones	$ 8.00 each (single copy: $1.50)

Back number prices are effective for volumes other than last four (4) volumes (the current volume inclusive).

Thus, volumes 1 through 16 will be regarded as back numbers while volume 20 is being published.

The revised prices will be effective on and after August 1, 1958.

. . . .

JOURNAL OF THE PHYSICAL SOCIETY OF JAPAN Vol. 14, No. 3, MARCH, 1959

Gamma Rays from the Proton Bombardment of ^{24}Mg, ^{25}Mg and ^{26}Mg

By Iwao MIURA, Tetsuo WAKATSUKI, Yasuo HIRAO
and Eiji OKADA

Department of Physics, Faculty of Science,
Osaka University, Osaka

(Received November 24, 1958)

The gamma-rays following the inelastic scattering of protons by ^{24}Mg, ^{25}Mg and ^{26}Mg were investigated at proton energies up to 5.7 MeV.

The energy spectra of the gamma-rays at several proton energies have been obtained for each isotopes.

2^+ was assigned to the second, third and fourth excited level of ^{26}Mg considering the gamma-ray branching ratios for those levels.

The yields of gamma-rays from the first excited levels were found to have peaks at proton energies of 4.0, 4.6 and 5.05 MeV for ^{24}Mg$(p, p'\gamma)$ reaction, 4.9 and 5.4 MeV for ^{26}Mg$(p, p'\gamma)$ reaction respectively. These resonances correspond to the levels at 6.1, 6.7 and 7.14 MeV for ^{25}Al, and 13.0 and 13.5 MeV for ^{27}Al.

To determine the spins for those levels, angular distributions were measured at resonance energies. Spin values of 3/2 and 5/2 are probable for 7.14 MeV level in ^{25}Al and 13.0 MeV level in ^{27}Al respectively.

For the 13.5 MeV level in ^{27}Al, the spin of 3/2 is also probable, but 5/2 can not be excluded because of the presence of the cascade gamma-rays from higher levels.

The total cross sections for the gamma-ray emission are estimated to be about 700 mb at 5.05 MeV resonance for ^{24}Mg and a few hundreds mb for the 4.9 and 5.4 MeV resonances for ^{26}Mg.

§ 1. Introduction

Inelastically scattered protons by magnesium have been observed by numerous workers at proton energies between 2.4 and 15.3 MeV[1].

The 1st excited state of ^{24}Mg was determined as 1.371±0.002 MeV by electro-static analysis[2]. The 2nd and 3rd excited state of ^{24}Mg proved to be a doublet of 4.13±0.02 and 4.24±0.02 MeV using magnetic analysis[3].

On the other hand in the study of beta-decay of ^{24}Na, the energies of gamma-rays from the excited levels of ^{24}Mg were determined by magnetic spectrometer as 2.7535±0.0010 (2nd → 1st) and 1.3680±0.0010 MeV (1st → gnd)[4], and the spins and parities of the gnd, 1st and 2nd state were assigned 0^+, 2^+ and 4^+ respectively.

Recently a large amount of informations has become available on ^{23}Na+P reactions, and the 3rd excited state of ^{24}Mg was assigned $J=2^+$, and the level at 5.26 MeV was observed with $J=3$ and probably negative parity[5].

The angular distribution measurements of inelastically scattered alpha particles to 1.37 and 4.2 MeV level also agree with direct surface interaction for $(0^+) \to (2^+)$ transition and the level at 4.12 MeV (4^+ state) is not excited[6]. These results are consistent with the above spin assignments.

As the excited states of ^{25}Mg, the magnetic analysis of inelastic scattering of 8-MeV protons by natural magnesium have revealed levels at 0.61, 1.62, 1.98, 2.56, 2.76, 3.41 and 3.91 MeV, all ±0.02 MeV[3]. In the study of gamma-rays in ^{25}Mg$(p, p'\gamma)$ reaction, the branching ratios of the levels at 0.98, 1.61 and 1.96 MeV were obtained[7]. From these results, the spins and parities of lower levels can be assigned as shown in Fig. 7. These assignments are also consistent with those from (d, p) angular distributions, log ft value in decay of ^{25}Na and ^{25}Al, shell model predictions and classifications of corresponding levels in the mirror nucleus ^{25}Al. The energy levels in ^{25}Mg were determined more accurately from ^{24}Mg$(d, p)^{25}$Mg reaction at deutron energy 1.8 MeV[8] and ^{27}Al$(d, \alpha)^{25}$Mg at 2.1 MeV[8] as also shown in Fig. 7.

The level energies of ^{26}Mg were found very accurately from the ^{25}Mg(d, p)^{26}Mg reaction⁹⁾ using enriched targets as shown in Fig. 9. The magnetic analysis of inelastically scattered protons in ^{26}Mg(p, p')^{26}Mg* reaction at proton energy 8 MeV gives levels at 1.83±0.02 and 2.96±0.02 MeV³⁾.

The shape of the β^+ spectrum determined the spin of the 1st level of ^{26}Mg as 2^{+}¹⁰⁾. The angular distribution study in ^{25}Mg(d, p)^{26}Mg reaction indicates for the 2nd, 3rd and 4th excited states to have $J=2^+$ or 3^+¹¹⁾, but 2^+ assignments are more probable for the 2nd and 4th excited states from the analogy to the levels of ^{26}Al¹²⁾.

In this paper we report the study of the gamma-rays produced in ^{24}Mg(p, $p'\gamma$), ^{25}Mg(p, $p'\gamma$) and ^{26}Mg(p, $p'\gamma$) reactions, and discuss the properties of these levels. From the angular distributions of these gamma-rays the properties of the levels of the compound nuclei are also discussed.

§ 2. Experimental Methods

Experimental arrangement was the same as previously described¹³⁾. The 5.7 MeV proton beam from 44 inch cyclotron was used and the energy was degarded at 0.1 MeV intervals down to 2.5 MeV by aluminum absorbers. The proton beam current was a few hundredths of a microampere.

The targets used were magnetically separated isotopes of a few tenths of a mg/cm² in thickness on gold backings. In the present experiment we intended principally to investigate ^{26}Mg(p, $p'\gamma$) reaction. The mass separator was arranged to get the ^{26}Mg target as purely as possible. There was, therefore, some impurity of ^{24}Mg in the target of ^{25}Mg.

The detector was a scintillation spectrometer consisting of a NaI(Tl) crystal 3″ in diameter and in length, viewed by a Dumont 6364 photomultiplier. For the pulse height analysis 20 channel analyser was used.

§ 3. Results and Discussions

1. ^{24}Mg

The level scheme is shown in Fig. 1. The yield of the 1.37 MeV radiation by the deexcitation of the 1st excited state of ^{24}Mg was measured at right angles to the beam as a function of the incident proton bombarding energy. The results is shown in Fig. 2 and in Table I.

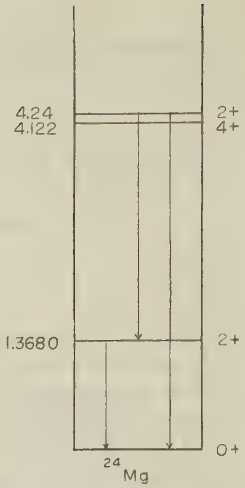

Fig. 1. The level scheme of ^{24}Mg, and the gamma-rays observed in our work.

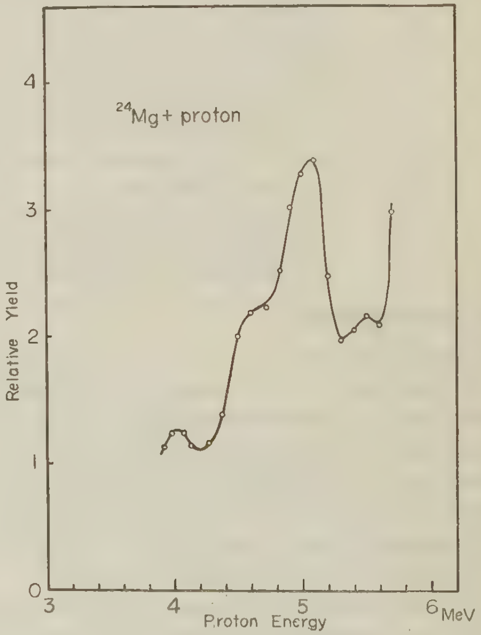

Fig. 2. The yield of the 1.37 MeV radiation by deexcitation of the 1st excited state of ^{24}Mg measured at right angles to the beam as a function of the proton energy.

Table I. Resonances in ^{24}Mg(p, $p'\gamma$).

Resonance energy (MeV)	Corresponding level energy in ^{25}Al (MeV)
4.0	6.1
4.6	6.7
5.05	7.14
~5.4	~7.5

The peak at 4.0 MeV agrees with the previous experimental data[19)], and peak at 4.6 MeV is newly found resonance. The large resonance peak at 5.05 MeV agrees with the experiment by Greenless[14)], and the uncertain small resonance is observed at 5.4 MeV. The total cross section for the excitation of the 1st excited state at 5.05 MeV proton energy is about 700 mb.

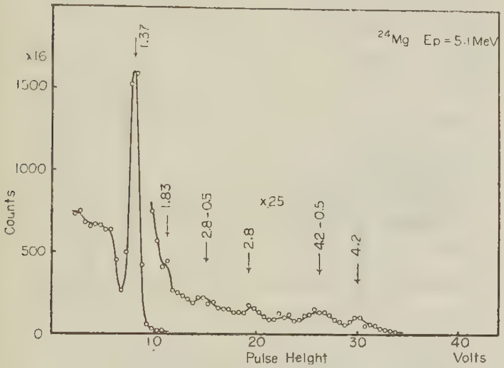

Fig. 3. The gamma-ray spectrum: ^{24}Mg+proton at 5.1 MeV and 90° with respect to the proton beam.

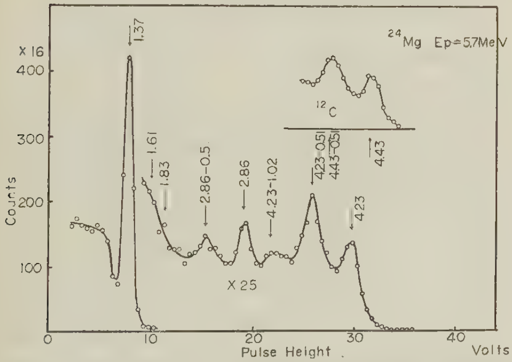

Fig. 4. The gamma-ray spectrum: ^{24}Mg+proton at 5.7 MeV and 90° with respect to the proton beam.

Table II. Gamma-rays in ^{24}Mg$(p, p'\gamma)$ reaction at proton energy 5.7 MeV.

Gamma-ray energy (MeV)	Relative intensity	Origin of the gamma-ray
4.23	7.0	3rd-gnd in ^{24}Mg
2.86	2.5	3rd-1st in ^{24}Mg
(2.75)		(2nd-1st in ^{24}Mg)
1.83	0.5	1st-gnd in ^{26}Mg
1.61	0.5	3rd-gnd in ^{25}Mg
1.37	100	1st-gnd in ^{24}Mg

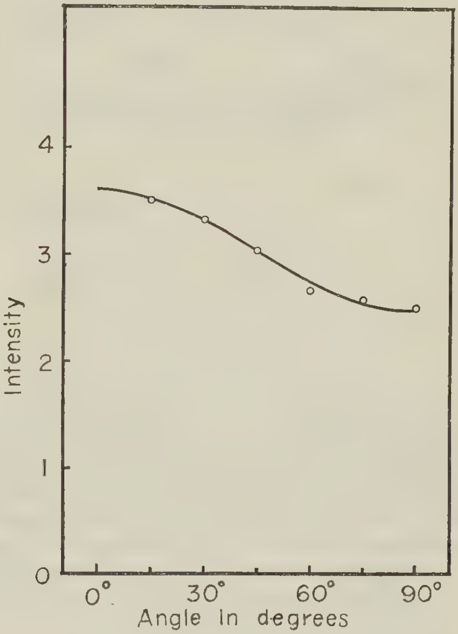

Fig. 5. Angular distribution of the 1.37 MeV gamma-ray in ^{24}Mg$(p, p'\gamma)$ reaction at proton energy 5.1 MeV.

The gamma-ray spectra are shown in Fig. 3 and 4. The arrows indicate the positions of the peaks and the numbers show the corresponding gamma-ray energies calibrated by the 4.43 MeV gamma-ray in ^{12}C$(p, p'\gamma)$ and 1.33 and 1.17 MeV gamma-ray of ^{60}Co.

The relative intensities of those gamma-rays are calculated using the shapes of the 4.43 MeV gamma-ray of ^{12}C$(p, p'\gamma)$, 2.75 and 1.37 MeV gamma-ray of ^{24}Na, and 1.33 and 1.17 MeV gamma-ray of ^{60}Co, and the known efficiences for those energies. The origins of the gamma-rays and their relative intensities at proton energy of 5.7 MeV are shown in Table II.

The branching ratio of those gamma-rays agrees with the previous experiment[16)].

Next, to determine the spin of the resonance level at proton energy of 5.05 MeV, the angular distribution of the 1.37 MeV gamma-ray was measured. The result of this measurement is shown in Fig. 5. The solid line in this figure represents are least squares fit to the data, using even Legendre polynomials up to P_4, and is given by

$$W(\theta)=1+(0.259\pm0.013)P_2+(0.012\pm0.023)P_4$$

Fig. 6 shows the results of the calculation using the theory by Biedenharn et al[16],[17]. The results of the present experiment is also shown in this figure. This result shows that the angular distribution can be represented by P_0 and P_2 only, and therefore the spin of the compound state at 7.1 MeV of ^{26}Al is probably 3/2.

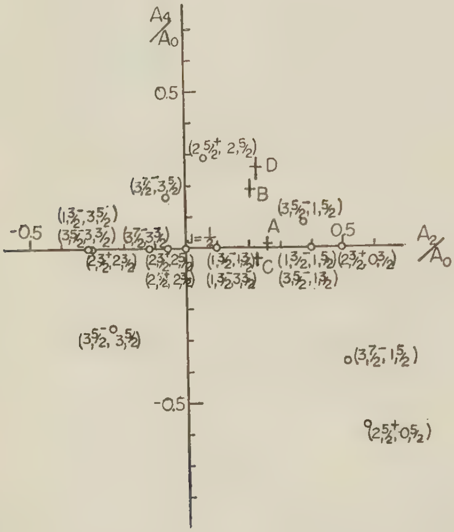

Fig. 6. The results of the calculation using the theory by Bienharn et al. Open points indicate A_2/A_0 and A_4/A_0 for various $(1, J^{\pi}, 1', s')$, where $W(\theta)=A_0+A_2P_2(\cos\theta)+A_4P_4(\cos\theta)$ is the angular distribution of the gamma-ray of the $(2^+)\rightarrow(0^+)$ and state transition in $(p, p'\gamma)$ reaction, 1 and 1′ are the orbital angular momenta of incoming and outgoing proton respectively, J^{π} is the spin and parity of the compound state, and s' is the channel spin of the outgoing channel.

Cross A, B, C and D indicate the experimental results of the 1.37 MeV gamma-ray angular distribution in ^{24}Mg$(p, p'\gamma)$ reaction at proton energy 5.1 MeV and the 1.83 MeV gamma-ray angular distributions in ^{26}Mg$(p, p'\gamma)$ reaction at proton energy 4.9, 5.4, and 5.7 MeV respectively.

The angular distribution measurement of the inelastically scattered protons by magnesium[18] shows that the corresponding compound state seems to have the spin 3/2. From the energy dependence of this angular distribution it is probable that the reaction proceeds mainly through the compound nucleus. These results are consistent with the present experiment.

2. ^{25}Mg

The low lying levels of ^{25}Mg are studied by many workers, as is shown in Fig. 7. The present results are also consistent with these informations. The gamma-ray spectrum at proton energy 5.7 MeV is shown in Fig. 8.

The arrows indicate the positions of the peaks and the numbers show the corresponding gamma-ray energies. The results are tabulated in Table III.

The yield curve of the most intense gamma-ray of 1.37 MeV was measured as a function

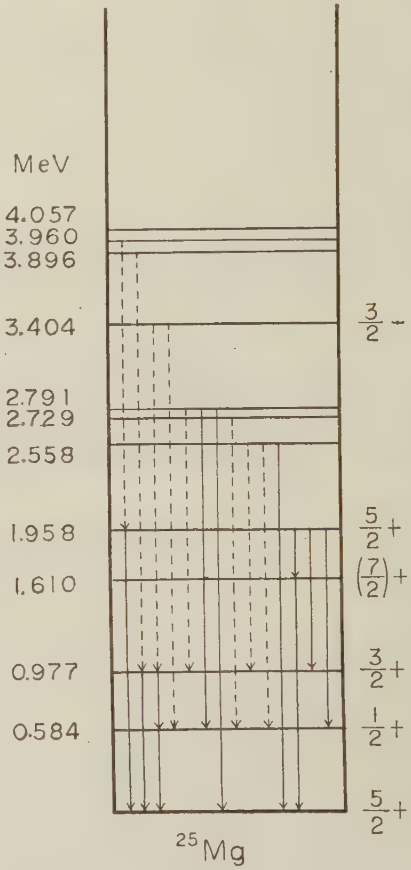

Fig. 7. The level scheme of ^{25}Mg. and the gamma-rays observed in our work.

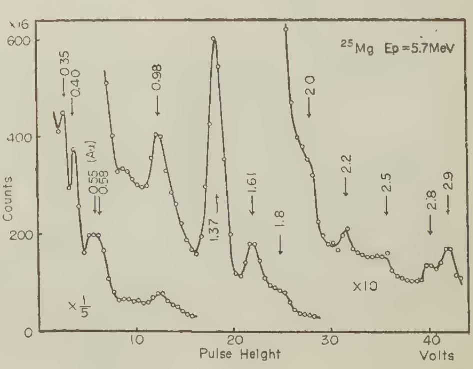

Fig. 8. The gamma-ray spectrum: ^{25}Mg+proton at 5.7 MeV and 90° with respect to proton ceam.

Table III. Gamma-rays in ^{25}Mg(p, $p'\gamma$) reaction at proton energy 5.7 MeV.

Gamma-ray energy (MeV)	Relative intensity	Origin of the gamma-ray
2.9	1	3rd–1st in ^{24}Mg (9th–2nd in ^{25}Mg)
2.8	0.3	7th–gnd in ^{25}Mg (2nd–1st in ^{24}Mg) (8th–1st in ^{25}Mg)
2.5	0.3	5th–gnd in ^{25}Mg (8th–2nd in ^{25}Mg)
2.2	0.5	7th–1st in ^{25}Mg (6th–1st in ^{25}Mg)
2.0	1	4th–gnd in ^{25}Mg (5th–1st in ^{25}Mg) (10th–4th in ^{25}Mg)
1.8	4	1st–gnd in ^{26}Mg (7th–2nd in ^{25}Mg)
1.61	10	3rd–gnd in ^{25}Mg (5th–2nd in ^{25}Mg)
1.37	30	1st–gnd in ^{24}Mg (4th–1st in ^{25}Mg)
0.98	7	2nd–gnd in ^{25}Mg (4th–2nd in ^{25}Mg)
0.58		1st–gnd in ^{25}Mg
0.55		Au
0.40		2nd–1st in ^{25}Mg
0.35		4th–3rd in ^{25}Mg

of incident proton energy and proved to have the same shape as that of the 1.37 MeV gamma-ray from ^{24}Mg(p, $p'\gamma$) reaction described above, while the yield curve of 1.61 MeV gamma-ray, which is certainly due to the deexcitation from the 3rd to the ground state, shows the quite different form from it. It is, therefore, concluded that the most part of this intense gamma-ray is due to the impurity of ^{24}Mg in the target of ^{25}Mg. The other results in Table III agree with the data of the other experiments$^{7)}$.

3. ^{26}Mg

The yield of the 1.83 MeV radiation by the deexcitation of the 1st excited state ef ^{26}Mg was measured at right angles to the beam as a function of the proton bombarding energy. The result is shown in Fig. 10 and Table IV.

The total cross section for the excitation of the 1st excited state at 4.9 and 5.4 MeV proton energy are estimated to be a few tenths of a barn.

The gamma-ray spectra at these resonances are shown in Fig. 11–14, and tabulated in Table V. The gamma-ray energies and their relative intensities were calculated using the same method as above described.

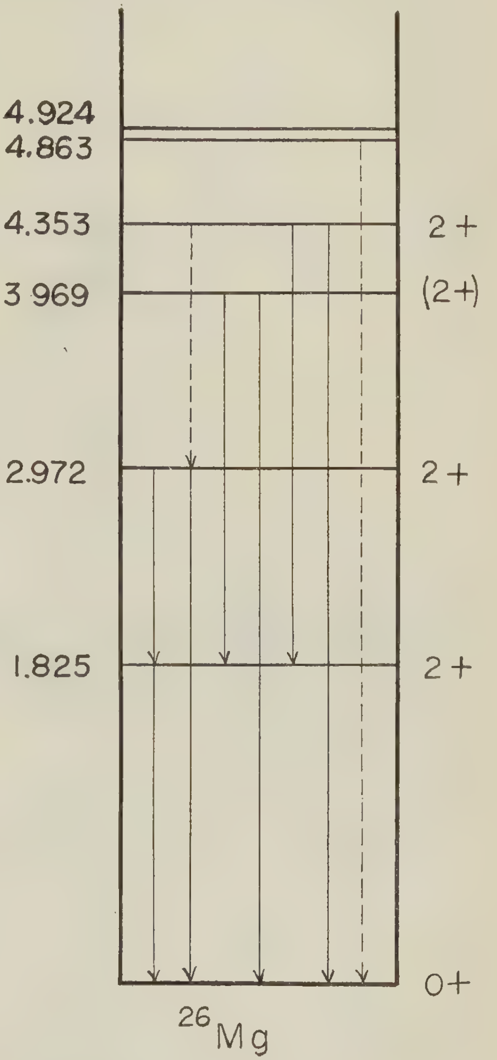

Fig. 9. The level scheme of ^{26}Mg, and the gamma-rays observed in our work.

As previously described, the 1st state has been assigned 2$^+$ from ^{26}Al(β^+), and the 2nd, 3rd and 4th state are assigned 2$^+$ or 3$^+$ from ^{25}Mg(d, p)^{26}Mg. In the present experiment, from the gamma-ray intensity ratios in Table V we may discussed the spins and parities for these states by the use of the Moszkowski's formula based on the single particle model.

Considering the results of ^{25}Mg(d, p)^{26}Mg reaction, we may consider only 2$^+$ or 3$^+$ for these states, If the spin and parity of the 2nd state at 2.97 MeV is 2^+, the transition to the gnd state is $E2$, and the transition probability is, therefore, $2.8\times10^{12}\,\mathrm{sec}^{-1}$.

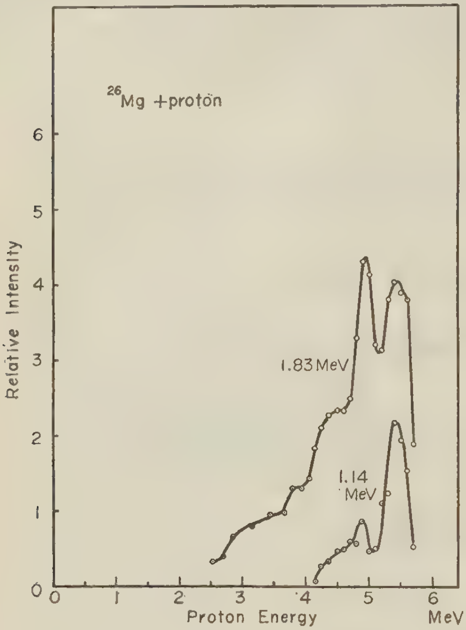

Fig. 10. The yield of the 1.83 MeV radiation by the deexcitation of the 1st excited state of ^{26}Mg and the yield of the 1.14 MeV radiation by the transition to the 1st state from the 2nd state, measured at right angles to the beam as a function of the proton energy.

Table IV. Resonances in ^{26}Mg$(p, p'\gamma)$ reaction.

Resonances energy (Mev)	Corresponding level energy (MeV) in ^{27}Al
2.9	11.0
3.8	11.9
4.4	12.5
4.95	13.02
5.45	13.50

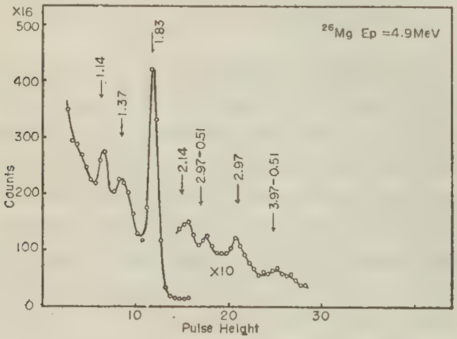

Fig. 11. The gamma-ray spectrum: ^{26}Mg+proton at 4.9 MeV and 90° with respect the beam.

If that is 3^+, the transition is $M3$, and the transition probability is, therefore, 2.8×10^{7} sec^{-1}.

For both cases, the cascade transition to the 1st state is $M1$, and the transition probability is $4.2\times10^{13}\,\mathrm{sec}^{-1}$.

From the experimental data in Table V, the intensity ratios of these gamma-rays, $I(2.97\,\mathrm{MeV})/I(1.14\,\mathrm{MeV})$, are both 0.12 at 5.7 and 5.4 MeV of proton energy. Then it is conculded that the spin and parity of the 2nd state at 2.97 MeV is 2^+.

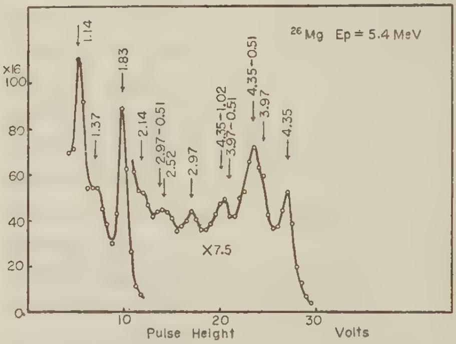

Fig. 12. The gamma-ray spectrum: ^{26}Mg+proton at 5.4 MeV and 90° with respect to the beam.

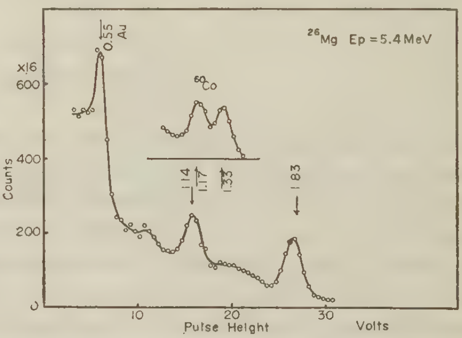

Fig. 13. The gamma-ray spectrum: ^{26}Mg+proton at 5.4 MeV and 90° with respect to the beam.

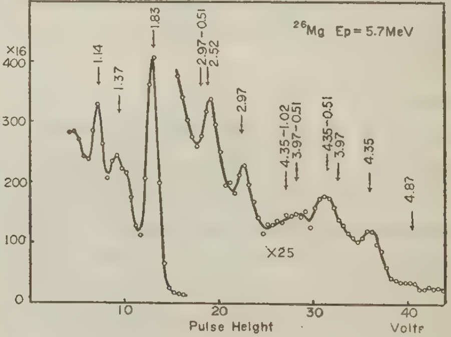

Fig. 14. The gamma-ray spectrum: ^{26}Mg+proton at 5.7 MeV and 90° with respect to the beam.

Next we consider the 3rd state at 3.97 MeV. In this case also the state has the spin of 2^+ or 3^+ only, and then the transition to the gnd state is $E2$ or $M3$, respectively, and the transion probability is, therefore, 1.2×10^{14} sec^{-1} or 2.2×10^{8} sec^{-1}, respectively.

The two cascade transitions to the 1st and 2nd state are both $M1$, and these transition probabilities are 2.8×10^{14} sec^{-1} and 2.8×10^{13} sec^{-1}, respectively.

Trble V. Gamma-rays in ^{26}Mg(p, $p'\gamma$) reaction.

Gamma-ray energy (MeV)	Relative intensity Ep=5.7	5.4	4.9 (MeV)	Origin of the gamma-ray
4.87	0.7			5th-gnd in ^{26}Mg
4.35	4	40		4th-gnd in ^{26}Mg
3.97	1	3		3rd-gnd in ^{26}Mg
2.97	2	6	4	2nd-gnd in ^{26}Mg
(3.06)				(5th-1st in ^{26}Mg)
2.52	1.5	2.5		4th-1st in ^{26}Mg
2.14		1.5		3rd-1st in ^{26}Mg
1.83	100	100	100	1st-gnd in ^{26}Mg
1.37	14	13		1st-gnd in ^{24}Mg
(1.38)				(4th-2nd in ^{26}Mg)
1.14	20	45	16	2nd-1st in ^{26}Mg
0.5		8		An
				(5th-4th in ^{24}Mg)

From the experimental data, these gamma-ray intensities are found to be of the same order. Then, it is concluded that the 3rd state at 3.97 MeV has probably the spin of 2^+.

The 4th state at 4.35 MeV has also 2^+ or 3^+, and the transition to the gnd state is $E2$ or $M3$, respectively, and then the transition probability is 2.0×10^{13} sec^{-1} or 3.7×10^{8} sec^{-1}, respectively.

The cascade transitions to the 1st, 2nd and 3rd state are all $M1$ and these transition probabilities are 4.5×10^{14} sec^{-1}, 7.3×10^{13} sec^{-1}, and 1.5×10^{12} sec^{-1}, respectively.

From the experimental data, the intensity ratios, I(4.35 MeV)/I(2.52 MeV) etc., are found to be 2 or 3, or larger. In this case, as the energy of gamma-ray 4.35 MeV is very close to 4.43 MeV gamma-ray from ^{12}C(p, $p'\gamma$) reaction, we must take precaution against carbon which may deposit on the target during preparation or bombardment. But we took good care of the target preparations and the energy calibrations of the gamma-ray spectra, and then the intensity of the 4.43 MeV gamma-ray was found to be negligible compared to that of the 4.35 MeV gamma-ray. It is, therefore, concluded that the spin and parity of the 4th

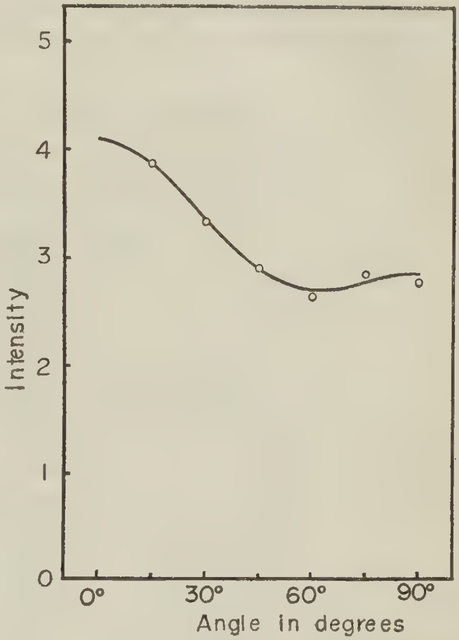

Fig. 15. Angular distribution of the 1.83 MeV gamma-ray in ^{26}Mg(p, $p'\gamma$) reaction at proton energy 4.9 MeV.

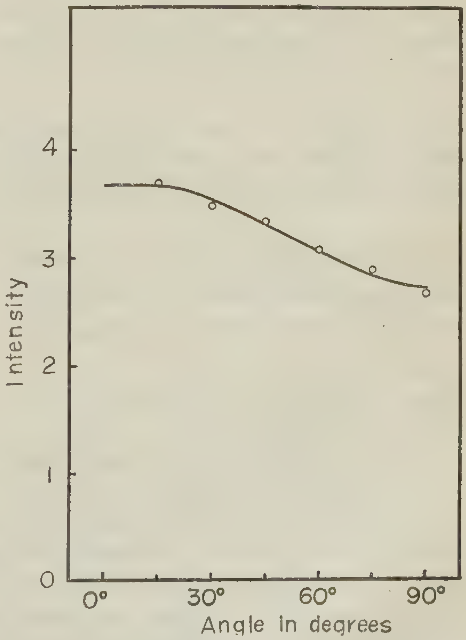

Fig. 16. Angular distribution of the 1.83 MeV gamma-ray in ^{26}Mg(p, $p'\gamma$) reaction at proton energy 5.4 MeV.

state at 4.35 MeV is also probably 2^+. These results show good agreement with the spins and parities of $T=1$ isotopic spin triplet levels in ^{26}Al[12].

The angular distributions of 1.83 MeV gamma-ray at proton energy 4.9 MeV, 5.4 MeV and 5.7 MeV are shown in Fig. 15, 16 and 17 respectively.

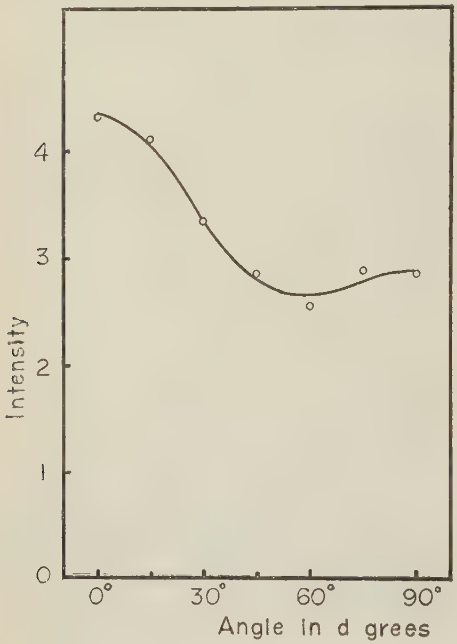

Fig. 17. Angular distribution of the 1.83 MeV gamma-ray in $^{26}Mg(p, p'\gamma)$ reaction at proton energy 5.7 MeV.

The solid lines in these figures represent the least squares fit to the data using even Legendre polynominals up to P_4 and are given by

$$W(\theta)=1+(0.206\pm0.015)P_2+(0.187\pm0.028)P_4$$

$$W(\theta)=1+(0.229\pm0.013)P_2-(0.036\pm0.023)P_4$$

$$W(\theta)=1+(0.227\pm0.018)P_2+(0.255\pm0.034)P_4$$

respectively.

These results and the calculations from the theory are shown in Fig. 6.

At proton energy 4.9 MeV, about 20% of the intensity of the 1.83 MeV gamma-rays is due to the cascade transitions from the 2.97 MeV and higher levels. At proton energy 5.4 and 5.7 MeV, these amount to about 50% and 20% respectively. Therefore, the expansion coefficients of the angular distributions of the 1.83 MeV gamma-ray by the direct excitation of this level by proton may be somewhat larger than these experimental results. At proton enengy 4.9 MeV, in spite of these circumstances, the coefficient of P_4 is too large to be neglected. Therefore, the level at 13.0 MeV in ^{27}Al have probably the spin of 5/2, considering the barrier penetrabilily. At proton energy 5.4 MeV, the angular dirtribution can be fairly represented by P_0 and P_2, and the spin of the level at 13.5 MeV in ^{27}Al is probably 3/2, but the possibility of 5/2 can not be excluded on account of the presence of the cascade gamma-rays as described above.

Both the angular distributions at proton energy 4.9 and 5.7 MeV can be represented by P_0, P_2 and P_4. This fact indicates that the spin of the 1st state of ^{26}Mg is 2 or larger, and is consistent with the result of β^+ decay.

Acknowledgment

The authors wish to thank Prof. K. Ogata and Mr. J. Okano for the preparation of the targets.

This work was supported by the Grant for Scientific Research of the Ministry of Education.

References

1) P. M. Endt and C. M. Braams: Rev. Mod. Phys. **29** (1957) 683.
2) Donahue, Jones, McEllistrem and Richards: Phys. Rev. **89** (1953) 824.
3) Hansman, Allen, Arthur, Bender and McDole: Phys. Rev. **88** (1952) 1296.
4) A. Hedgran and Lind: Ark. Fys. **5** (1952) 177.
5) Grand, Rutherglen, Flack and Hutchinson: Proc. Phys. Soc. London **A**, **68** (1955) 369.
6) H. J. Watters: Phys. Rev. **103** (1956) 1763.
7) Gove, Bartholomew, Paul and Litherland: Nucl. Phys. **2** (1956) 132.
8) Endt, Enge, Haffner and Buechner: Phys. Rev. **87** (1952) 27.
9) Endt, Haffner and Van Patter: Phys. Rev. **86** (1952) 518.
10) M. J. Laubitz: Proc. Phys. Soc. London **A**, **68** (1955) 1033.
11) J. R. Holt and T. N. Marsham: Proc. Phys. Soc. London **A**, **66** (1953) 258.
12) Green, Singh and Willmott: Proc. Phys. Soc. London **A**, **68** (1956) 335.
13) Okada, Miura, Wakatsuki and Hirao: J. Phys. Soc. Japan **13** (1958) 541.
14) G. W. Greenlees: Proc. Phys. Soc. London **A**, **68** (1955) 97.

15) J. O. Newton: Phys. Rev. **96** (1954) 241.
16) Kraus, Schiffer, Prosser and Biedenharn: Phys. Rev. **104** (1957) 1667.
17) Hirao, Okada, Miura and Wakatsuki: J. Phys. Soc. Japan **13** (1958) 233.
18) Yamabe, Kondo, Yamazaki and Toi: J. Phys. Soc. Japan **13** (1958) 777.
19) L. J. Koester: Phys. Rev. **85** (1952) 643.

JOURNAL OF THE PHYSICAL SOCIETY OF JAPAN Vol. 14, No. 3, March, 1959

Convex-Core Model of Molecules in Crystalline State

By Taro KIHARA and Saburo KOBA

Department of Physics, Faculty of Science, University of Tokyo

(Received December 4, 1958)

The convex-core model of nonspherical molecules, introduced for the sake of treating the second virial coefficients of nonpolar gases (T. Kihara: Revs. Modern Phys. **25** (1953) 831), is applied to crystals of methane, carbon dioxide, and nitrogen. By use of model parameters determined from the second virial coefficients, lattice constants and cohesive energies are calculated. For methane, results of the calculations agree with observed values when the zero-point energy and the effect of potential non-additivity are taken into account. The crystal structure, the lattice constant and the cohesive energy of carbon dioxide are explained by use of a convex-core model with an embedded electric quadrupole.

§ 1. Introduction

The structure, the lattice constant, and the cohesive energy of a molecular crystal at absolute zero temperature can, in principle, be explained in terms of the potential energy between the constituent molecules. In the case of spherical molecules (i.e. inert-gas atoms) we can use, to a good approximation, the intermolecular potential

$$U(r)=U_0\left[\left(\frac{r_0}{r}\right)^{12}-2\left(\frac{r_0}{r}\right)^{6}\right] \qquad (1.1)$$

depending only on the distance r between centers of molecules. Here r_0 and U_0 are two parameters, which can be determined from the second virial coefficients of the corresponding gas. There are several theoretical investigations on inert-gas crystals$^{1)-7)}$.

Few investigations have been made, however, for crystals of polyatomic molecules. The present article is an application of a nonspherical molecular model, which has been introduced by one of the authors$^{8)}$ in order to treat the second virial coefficients of nonpolar gases. The model will be explained in the next section.

Table I.

$(r_i/a)^2$	n_i	$(r_i/a)^2$	n_i	$(r_i/a)^2$	n_i
1	12	22	24	43	120
2	6	23	48	44	24
3	24	24	8	45	120
4	12	25	84	47	96
5	24	26	24	48	24
6	8	27	96	49	108
7	48	28	48	50	30
8	6	29	24	51	48
9	36	31	96	52	72
10	24	32	6	53	72
11	24	33	96	54	32
12	24	34	48	55	144
13	72	35	48	57	96
15	48	36	36	58	72
16	12	37	120	59	72
17	48	38	24	60	48
18	30	39	48	61	120
19	72	40	24	63	144
20	24	41	48	64	12
21	48	42	48	65	48

In this article crystals of methane, carbon dioxide, and nitrogen are treated. These molecules are nonpolar and almost convex in shape; hence they can be approximated by our model. The crystal structures of these three are all cubic; moreover they are modifications of the face-centered cubic structure of spherical molecules. For the face-centered cubic lattice, the number n_i of ith neighbors of a lattice point and the distance r_i to the ith neighbors (divided by the nearest neighbor distance a) have been calculated in detail[4)]; the results are given in Table I, a part of which will be used in the following.

§ 2. The Convex-Core Model of Molecules

We assume an appropriate convex body called core inside each molecule. The core of a (free) carbon dioxide molecule CO_2 is defined by a thin rod connecting the two O's, the length l of the core being $l=2.30$ A. The core of a nitrogen molecule N_2 is also a thin rod connecting the two N's, the length of the core being $l=1.094$ A. Let us define the core of a methane molecule CH_4 by a regular tetrahedron connecting the midmost points of C–H bonds. The distance of a vertex from the centered carbon atom will be denoted by l; then $2l=1.093$ A, the C–H bond length. (There is no definite reason for this particular choice of the core of a methane molecule. However, for other hydrocarbon molecules in gaseous states, the choice of midpoints of C–H bonds as vertexes of a core is known to be adequate[8)].)

The shortest distance between two cores will be called "intercore distance" and denoted by ρ. The potential energy U between two molecules is assumed to be a function of ρ only, and moreover

$$U(\rho)=U_0\left[\left(\frac{\rho_0}{\rho}\right)^{12}-2\left(\frac{\rho_0}{\rho}\right)^{6}\right], \qquad (2.1)$$

which is a generalization of (1.1). Here ρ_0 and U_0 are model constants determined from the second virial coefficients of the corresponding gas. Thus,

$\rho_0=3.15$ A, $U_0/k=226$°K for methane,
$\rho_0=3.36$ A, $U_0/k=309$°K for carbon dioxide,
$\rho_0=3.47$ A, $U_0/k=124$°K for nitrogen,

k being the Boltzmann constant. The cores and their parallel bodies at distance $\rho_0/2$ are shown in Fig. 1.

The model can be applied only to nonpolar molecules which are nearly convex in shape. In gaseous state the model is also applicable to molecules with electric quadrupole moment, because the quadrupole interaction is mostly cancelled there[9),10)]. In crystalline state, however, this interaction must be taken into account, for CO_2 in particular.

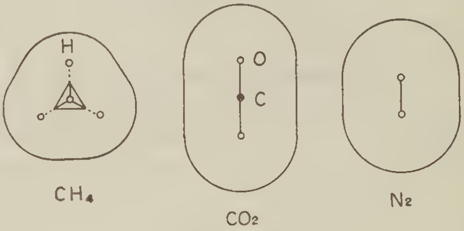

Fig. 1.

§ 3. Methane CH_4

(a) *Core-model interaction*

The carbon atoms in a methane crystal occupy the lattice points of a face-centered cubic structure. At temperatures below 20.4° K, the molecules do not freely rotate and seem to be parallel to each other with all the C–H bonds directed towards the body diagonals[11)]. The distance between nearest neighboring carbon atoms will be called "nearest neighbor distance" and denoted by a (so that the lattice constant by $\sqrt{2}\,a$).

A methane molecule has 12 nearest neighbor molecules at the intercore distance $a-2\sqrt{2/3}\,l$. In general, the square of the intercore distance ρ_i^2 to ith neighbors is given in Table II, where n_i is the number of ith neighbors.

Now, if the potential additivity is assumed and the zero-point energy is neglected, the cohesive energy per molecule is given by the minimum of

$$\frac{1}{2}U_0\sum_{i=1}^{\infty}n_i\left[\left(\frac{\rho_0}{\rho_i}\right)^{12}-2\left(\frac{\rho_0}{\rho_i}\right)^{6}\right] \qquad (3.1)$$

as a function of the nearest neighbor distance a. The expression (3.1) can be evaluated by use of Table II and, for farther molecules, Table I. It takes its minimum

$$-3.29 \text{ kcal/mol} \quad \text{at} \quad a=4.00 \text{ A}.$$

Observed values of the cohesive energy and the nearest neighbor distance are, respectively[12)],

$$-2.51 \text{ kcal/mol} \quad \text{and} \quad a=4.16 \text{ A}.$$

The discrepancy may be partly due to the zero-point energy and partly due to non-additivity of the intermolecular potential. In fact, according to our calculations to be mentioned in (b), the zero-point energy is about 0.48 kcal/mol and the effect of potential non-additivity is about 0.23 kcal/mol. These two effects slightly increase the nearest neighbor distance a.

Table II.

i	ρ_i^2	n_i
1	$\left(a-2\sqrt{\frac{2}{3}}l\right)^2$	12
2	$\left(\sqrt{2}a-\frac{2}{\sqrt{3}}l\right)^2$	6
3	$(\sqrt{3}a-\sqrt{2}l)^2$	24
4	$\left(2a-2\sqrt{\frac{2}{3}}l\right)^2$	12
5	$5a^2-8\sqrt{\frac{2}{3}}al+\frac{8}{3}l^2$	24

(b) *Zero-point energy and non-additive van der Waals interaction*

For methane crystal, the zero-point energy of rotational vibration must be taken into account besides that of the translational vibration. We assume for the rotational vibration the Einstein theory of specific heat, according to which the specific heat of the rotational vibration is

$$C_{V,\mathrm{rot}}=3k\left(\frac{\Theta_E}{T}\right)^2\exp\frac{\Theta_E}{T}\left[\exp\frac{\Theta_E}{T}-1\right]^{-2}$$

per molecule. Here $\Theta_E=h\nu_E/k$; and $h\nu_E$ is the frequency of the rotational vibration times Planck's constant. Then the zero-point energy of the rotational vibration is given by $(3/2)k\Theta_E$ per molecule; that of the translational vibration is given by $(9/8)k\Theta_D$ as usual, Θ_D being the Debye characteristic temperature. By use of observed values of the specific heat due to Clusius[13], Θ_D and Θ_E for methane are determined as

$$\Theta_D=78°\mathrm{K} \quad \text{and} \quad \Theta_E=102°\mathrm{K}\,.$$

Hence the total zero-point energy is calculated to be 0.48 kcal/mol.

The potential energy of the van der Waals attraction between three spherically symmetric atoms at large separation is of the form

$$-\mu(r_{12}^{-6}+r_{23}^{-6}+r_{31}^{-6})$$
$$+\nu(r_{12}r_{23}r_{31})^{-3}(3\cos\theta_1\cos\theta_2\cos\theta_3+1)\,.$$

Here r_{ij} is the distance between ith and jth atoms; θ_i's are inner angles of a triangle formed by the three atoms. Between μ and ν holds the approximate relation[14]

$$4\nu=3\alpha\mu$$

with the polarizability α. The μ is given by

$$\mu=3m_ec^2\alpha|\chi_{\mathrm{mol}}|/L\,,$$

in which m_e is the electron mass, c the light velocity, $L=6.025\times10^{23}$, and χ_{mol} is the molar diamagnetic susceptibility. The relations hold also for molecules with isotropic polarizability and susceptibility. Using[15]

$$\alpha=2.60\ \mathrm{A}^3\,,\qquad \chi_{\mathrm{mol}}=-12.2\times10^{-6}\ \mathrm{cm}^3$$

we have

$$\mu=12.9\times10^{-11}\ \mathrm{erg\ A}^6 \quad \text{for methane.}$$

According to Axilrod[16] contribution of the non-additive ν-term to the cohesive energy is $18.9\nu a^{-9}$ per molecule, which is 0.23 kcal/mol.

§ 4. Carbon Dioxide CO_2

(a) *Core-model interaction*

The carbon atoms in a carbon dioxide crystal form a face-centered cubic lattice, which is composed of four simple cubic lattices. On each simple cubic lattice the CO_2 molecules are in the same direction towards the body diagonals, the direction being different on different simple lattices[17] (Fig. 2). The distance between nearest neighboring carbon atoms will again be denoted by a.

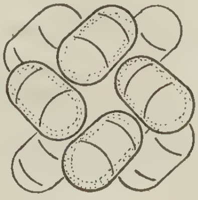

Fig. 2.

A carbon atom has 12 nearest neighboring carbon atoms at the distance a; the intercore distance to any of the 12 nearest neighbors is

$$\left(a^2-\sqrt{\frac{2}{3}}al+\frac{2}{9}l^2\right)^{1/2} \quad \text{if} \quad l\leqq\frac{3}{2}\sqrt{\frac{3}{2}}a\,.$$

A carbon atom has 6 second neighboring carbon atoms at the distance $\sqrt{2}a$; the intercore distance to any of the 6 second neighbors is

Table III.

i	j	ρ_{ij}^2	n_{ij}
1	1	$a^2-\sqrt{\frac{2}{3}}al+\frac{2}{9}l^2$	12
2	1	$2a^2-2\sqrt{\frac{2}{3}}al+l^2$	6
3	1	$3a^2-\sqrt{6}\,al+\frac{2}{3}l^2$	12
3	2	$3a^2-\sqrt{\frac{2}{3}}al+\frac{2}{9}l^2$	12
4	1	$4a^2-4\sqrt{\frac{2}{3}}al+l^2$	6
4	2	$4a^2$	6
5	1	$5a^2-\sqrt{6}\,al+\frac{1}{3}l^2$	12
5	2	$5a^2-\sqrt{6}\,al+\frac{2}{3}l^2$	12
6	1	$6a^2-2\sqrt{6}\,al+l^2$	2
6	2	$6a^2-\sqrt{6}\,al+\frac{3}{4}l^2$	6
7	1	$7a^2-5\sqrt{\frac{2}{3}}al+\frac{2}{3}l^2$	12
7	2	$7a^2-\sqrt{6}\,al+\frac{2}{9}l^2$	12
7	3	$7a^2-\sqrt{6}\,al+\frac{1}{3}l^2$	12
7	4	$7a^2-\sqrt{\frac{2}{3}}al+\frac{2}{9}l^2$	12
8	1	$8a^2-4\sqrt{\frac{2}{3}}al+l^2$	6
9	1	$9a^2-5\sqrt{\frac{2}{3}}al+\frac{2}{3}l^2$	12
9	2	$9a^2-\sqrt{6}\,al+\frac{2}{9}l^2$	12
9	3	$9a^2-\sqrt{6}\,al+\frac{2}{3}l^2$	12
10	1	$10a^2-2\sqrt{6}\,al+l^2$	12
10	2	$10a^2-2\sqrt{\frac{2}{3}}al+l^2$	12
11	1	$11a^2-5\sqrt{\frac{2}{3}}al+\frac{2}{3}l^2$	12
11	2	$11a^2-\sqrt{6}\,al+\frac{1}{3}l^2$	12
12	1	$12a^2-8\sqrt{\frac{2}{3}}al+l^2$	6
12	2	$12a^2-4\sqrt{\frac{2}{3}}al+l^2$	12
12	3	$12a^2$	6
13	1	$13a^2-7\sqrt{\frac{2}{3}}al+\frac{2}{3}l^2$	12
13	2	$13a^2-5\sqrt{\frac{2}{3}}al+\frac{1}{3}l^2$	12
13	3	$13a^2-5\sqrt{\frac{2}{3}}al+\frac{2}{3}l^2$	24
13	4	$13a^2-\sqrt{6}\,al+\frac{2}{9}l^2$	12
13	5	$13a^2-\sqrt{\frac{2}{3}}al+\frac{2}{9}l^2$	12
14	1	$15a^2-7\sqrt{\frac{2}{3}}al+\frac{2}{3}l^2$	12
14	2	$15a^2-5\sqrt{\frac{2}{3}}al+\frac{1}{3}l^2$	24
14	3	$15a^2-\sqrt{6}\,al+\frac{2}{3}l^2$	12
15	1	$16a^2-8\sqrt{\frac{2}{3}}al+l^2$	6
15	2	$16a^2$	6
16	1	$17a^2-7\sqrt{\frac{2}{3}}al+\frac{2}{3}l^2$	12
16	2	$17a^2-5\sqrt{\frac{2}{3}}al+\frac{1}{3}l^2$	12
16	3	$17a^2-5\sqrt{\frac{2}{3}}al+\frac{2}{3}l^2$	12
16	4	$17a^2-\sqrt{6}\,al+\frac{1}{3}l^2$	12
17	1	$18a^2-10\sqrt{\frac{2}{3}}al+l^2$	6
17	2	$18a^2-2\sqrt{6}\,al+l^2$	12
17	3	$18a^2-2\sqrt{\frac{2}{3}}al+l^2$	12

$$\left(2a^2-2\sqrt{\frac{2}{3}}\,al+l^2\right)^{1/2} \quad \text{if} \quad l\leqq\sqrt{\frac{2}{3}}\,a\,.$$

A carbon atom has 24 third neighboring carbon atoms at the distance $\sqrt{3}\,a$; the intercore distance to a half of the third neighbors are

$$\left(3a^2-\sqrt{6}\,al+\frac{2}{3}l^2\right)^{1/2} \quad \text{if} \quad l\leqq\sqrt{\frac{3}{2}}\,a\,,$$

and those to the others are

$$\left(3a^2-\sqrt{\frac{2}{3}}\,al+\frac{2}{9}l^2\right)^{1/2} \quad \text{if} \quad l\leqq\frac{3}{2}\sqrt{\frac{3}{2}}\,a\,.$$

In general, when $l\leqq\sqrt{2/3}\,a$, we denote by ρ_{ij} the intercore distance to n_{ij} cores of ith neighbors, $\sum_j n_{ij}$ being the total number n_i of the ith neighbors. Values of ρ_{ij}^2 and n_{ij} are given in Table III.

If the potential additivity is assumed and the zero-point energy is neglected, the cohesive energy per molecule is given by the minimum of

$$\frac{1}{2}U_0\sum_{i,j}n_{ij}\left[\left(\frac{\rho_0}{\rho_{ij}}\right)^{12}-2\left(\frac{\rho_0}{\rho_{ij}}\right)^{6}\right] \tag{4.1}$$

as a function of the nearest neighbor distance a. The expression (4.1) can be evaluated by use of Table III and, for farther molecules, Table I. It takes its minimum

$$-4.72\ \text{kcal/mol} \quad \text{at} \quad a=4.19\ \text{A}\,.$$

Observed values of the cohesive energy and the nearest neighbor distance are, respectively[9],[18],

$$-6.44\ \text{kcal/mol} \quad \text{and} \quad a=3.94\ \text{A}\,.$$

The discrepancy cannot be explained by the zero-point energy or by the potential non-additivity. In fact, electrostatic interactions are dominant, as shown in the following.

(b) *Electric quadrupole interaction*

The CO_2 molecule has an electric quadrupole[19]

$$Q\equiv\sum_i e_i(z_i^2-x_i^2)=3.12\times10^{-26}\ \text{e.s.u.}\,,$$

where (x_i, y_i, z_i) are coordinates of an electric charge e_i, z_i being in the direction of the molecular axis.

The potential energy between the two quadrupoles at the distance r is given by

$$\frac{3}{4}\frac{Q^2}{r^5}f(\theta_1,\varphi_1;\theta_2,\varphi_2)$$

in which

$$\begin{aligned}&f(\theta_1,\varphi_1;\theta_2,\varphi_2)\\&\quad=1-5\cos^2\theta_1-5\cos^2\theta_2-15\cos^2\theta_1\cos^2\theta_2\\&\quad+2[4\cos\theta_1\cos\theta_2-\sin\theta_1\sin\theta_2\cos(\varphi_1-\varphi_2)]^2\,.\end{aligned}$$

Here θ_1, φ_1 are polar angles of the axis of one quadrupole with respect to the line connecting the both, and θ_2, φ_2 are those of the other. For the CO_2 crystal, the function f is given in Table IV, which is due to Jansen, Michels, and Lupton[20]. It is important to note that the sign of f is negative for first and second neighbors.

Table IV.

Shell No. i	Shell No. j	Distance from center	Number of molecules	$f(\theta_1,\varphi_1;\theta_2,\varphi_2)$
1	1	a	12	$-\frac{19}{9}$
2	1	$\sqrt{2}\,a$	6	$-\frac{28}{9}$
3	1	$\sqrt{3}\,a$	12	$-\frac{31}{81}$
3	2	$\sqrt{3}\,a$	12	$+\frac{1}{9}$
4	1	$2a$	6	$+3$
4	2	$2a$	6	$-\frac{13}{9}$

Contribution of the quadrupole interaction to the cohesive energy is

$$-\frac{1}{2}\times21.4\,Q^2/a^5 \tag{4.2}$$

per molecule. The sum of (4.1) and (4.2) takes its minimum

$$-5.90\ \text{kcal/mol} \quad \text{at} \quad a=4.16\ \text{A}\,.$$

These values are close to the corresponding observed values written in the foregoing.

(c) *Crystal stability*

The crystal which we have treated is not a structure of closest packing. For the core-model of CO_2 there are two closest packing structures in which the molecules are parallel; they correspond to cubic and hexagonal closest packings of spheres. The cohesive energies of these two are almost the same.

In fact, if we consider the core-model interaction only and do not take account of the quadrupole interaction, then the closest packing structures become more stable, the cohesive energy being −5.26 kcal/mol in comparison with −4.72 kcal/mol for the face-centered cubic structure treated in (a).

However, the electric quadrupole interaction decreases the stability of the closest packing structures; they are less stable than the cubic structure when the quadrupole moment is larger than 1.2×10^{-26} e.s.u.

Thus we draw our conclusion. The core-model of molecules with an embedded quadrupole can be applied to the CO_2 crystal and explains its cohesive energy, lattice constant, and crystal stability.

§ 5. Nitrogen N_2

Below 35°K nitrogen crystallizes into a cubic structure which is somewhat similar to the structure of carbon dioxide. In detail, however, the midmost point of the N–N bond is not on the face-centered cubic lattice. It is somewhat shifted along the molecular axis; and the point dividing the bond in the ratio 4 to 7 is on the lattice[17]. This shift cannot be explained by our convex-core model of molecules.

If we neglect the shift, we obtain, for our core-model of molecules, the cohesive energy

$$-1.99\ \text{kcal/mol}\,, \qquad a \text{ being } 3.83\ \text{A}\,.$$

Here the potential additivity has been assumed, and the zero-point energy has been neglected. These results agree rather well with observed values[12),20)]

$$-1.65\ \text{kcal/mol} \quad \text{and} \quad a=4.00\ \text{A}\,.$$

(A nitrogen molecules has an electric quadrupole $Q=1.29\times10^{-26}$ e.s.u.[19], whose interaction energy is -0.30 kcal/mol. Sum of the zero-point energy and the effect of potential non-additivity is about 0.6 kcal/mol.)

References

1) J. E. Lennard-Jones and A. E. Ingham: Proc. Roy. Soc. A, **107** (1925) 636.
2) R. H. Fowler: *Statistical Mechanics*, 2nd Ed. (Cambridge, 1936) Chap. 10.
3) J. A. Prins, J. M. Dumoré and L. T. Tjoan: Physica **18** (1952) 307.
4) T. Kihara and S. Koba: J. Phys. Soc. Japan **7** (1952) 348.
5) T. H. K. Barron and C. Domb: Proc. Roy. Soc. A, **227** (1955) 447.
6) L. Jansen and J. M. Dawson: J. Chem. Phys. **23** (1955) 482.
7) E. R. Dobbs and G. O. Jones: Rep. Progr. Phys. **20** (1957) 516.
8) T. Kihara: Rev. Mod. Phys. **25** (1953) 831. See also,
T. Kihara: J. Phys. Soc. Japan **12** (1957) 564.
T. Kihara and A. Ôuchi: ibid. **12** (1957) 1052.
9) J. A. Pople: Proc. Roy. Soc. A, **221** (1954) 508.
10) B. J. Castle, L. Jansen and J. M. Dawson: J. Chem. Phys. **24** (1956) 1078.
11) T. Nagamiya: Progr. Theor. Phys. **6** (1951) 702.
12) K. K. Kelley: U. S. Bur. Mines Bull. **383** (1935). See also, ref. 20 and
H. W. Schamp, Jr., E. A. Mason, A. C. B. Richardson and A. Altman: Phys. Fluids. **1** (1958) 329.
13) K. Clusius: Z. phys. Chem. **B**, **3** (1929) 41.
14) Y. Midzuno and T. Kihara: J. Phys. Soc. Japan **11** (1956) 1045.
15) Landolt-Börnstein: *Zahlenwerte und Funktionen*, 6-Aufl. (Springer, 1951) I Band, 3 Teil, S. 511 und S. 534.
16) B. M. Axilrod: J. Chem. Phys. **19** (1951) 724.
17) R. W. G. Wyckoff: *Crystal Structures* (Interscience, New York, 1948) Chap. IV text p. 38 and illus. p. 21, Figs. IV 32a, 32b.
18) W. E. Giauque and C. J. Egan: J. Chem. Phys. **5** (1937) 45.
19) W. V. Smith and R. Howard: Phys. Rev. **79** (1950) 132.
20) L. Jansen, A. Michels and J. M. Lupton: Physica **20** (1954) 1235.

JOURNAL OF THE PHYSICAL SOCIETY OF JAPAN Vol. 14, No. 3, MARCH, 1959

Interaction of Exciton with Electron Trapping Centers in Alkali Halide Crystals

1. *F* and *U* Centers in KCl and KBr Crystals

By Masayasu UETA, Masamitsu HIRAI
and Hiroyuki WATANABE

*Department of Physics, The Faculty of Science,
University of Tohoku, Sendai*

(Received September 24, 1958)

The quantum efficiency for the bleaching of *F* centers in the KCl crystal with incident ultra violet lights in the region of the fundamental absorption band was obtained to have five times larger value than that with the visible light in *F*-absorption region. With the estimation of the absorption coefficient of the crystal at the fundamental absorption tail, it is infered that one exciton can bleach at least six *F* centers. From the similar experiments to measure the quantum efficiency for the process of $U \rightarrow F$ transformation using monochromatic lights, it is concluded that one exciton is able to transform about three *U* centers. Dependence of the quantum efficiency on the wavelength of exciting light was determined in the KBr crystal.

§I. Introduction

It is well known that exciton is formed in alkali halide crystal with the irradiation of ultra violet light in the region of characteristic absorption band. The investigation of exciton has been developed by many authors¹⁾ from both theoretical and experimental view point, and much knowledges of its fine structure, fluorescence and photoemission have been accumulated.

On the interaction of excitons with electron-trapping centers, there are two important experiments of the external photoelectric effect by Apker and Taft²⁾ and photoconductivity measurements by Inchauspé³⁾. Both experiments suggest that the exciton can migrate through crystal and is captured by *F* center which is an electron trapped by a negative ion vacancy and transfer its large energy to *F* center and ionize it effectively. From the photoconductivity measurements of KBr containing *F* centers, Inchauspé has obtained the curve giving $\eta\omega_0$ versus wavelength of the irradiation light as shown in Fig. 1. Here η is the number of photoelectrons produced per *incident* quantum on the crystal surface and ω_0 is the displacement of a photoelectron in the field direction by unit electric field. Therefore, η is not the true quantum yield giving the number of photoelectrons per quantum *absorbed* in crystal.

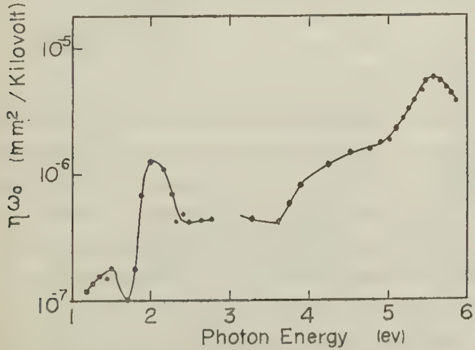

Fig. 1. The Photoconductivity measurement in KBr crystal containing *F* centers at −80°C (by Inchauspé).

We found that ultra violet lights from the high intensity hydrogen discharge tube through LiF window can bleach *F* centers very easily in KCl crystals. A KCl crystal containing *F* centers of density of 5×10^{17}/cc was set in front of the window of hydrogen lamp to be irradiated by light. One half of irradiated surface was covered with potassium iodide or glass plate to cut off the ultra violet light in the fundamental absorption band—we call it for brevity as extiton light—because, the exciton absorption band of KCl crystal starts at the wavelength shorter than 200 mμ and the ultra violet cutoffs are 250 mμ and 290 mμ for the KI and glass plates, respectively. After a short irradiation period of 30 seconds or so, the portion of the crystal which was irradiated by unfiltered light changes its red purple coloration due to F center to bluish color with more rapid rate compared to the another filtered portion, in spite of larger photon numbers in F-absorption region than ultra violet region.

Absorption spectra show that F band was bleached in part and M band enhanced, however, after a continued irradiation, the relative height of M-bands was reversed. This fact shows that M centers are more easily bleached than F centers by the exciton light.

These observation suggested the possibilities of quantum yield determinations for the ionization process of F centers and $U\rightarrow F$ transformation by the exciton, from both measurements of light quanta absorbed by the crystal and the number of F centers destroyed (in the case of $F\rightarrow M$) or increased (in the case of $U\rightarrow F$). These principles are the main logic of experiments described in the present report.

Through this report, all experiments and measurements were carried out at room temperature and KCl and KBr crystals obtained from Harshaw Chemical Company were used.

§ 2. Bleaching of F Centers by the Exciton in KCl Crystal

F centers were prepared additively by the conventional method with heating crystals with potassium metal at 560°C for 12 hours in a pyrex glass tube. The potassium metal was carefully distilled to take off the trace of hydrogen gas. Crystals thus treated contain only F centers and there is no trace of U centers due to the hydrogen atom in ultra violet region.

Concentrations of F centers n_0 were determined optically as 5×10^{17} per cubic centimeters using Smakula's formula[4].

$$n_0 f=1.31\times10^{17}\frac{n}{(n^2+2)^2}\cdot\alpha_m\cdot H\,,$$

where n is the index of refraction of the crystal at the wavelength of F-absorption peak; α_m is the absorption coefficient in cm^{-1} at the maximum of the F-band; H is the half width of the F-band in electron volts; f is the oscillator strength. Putting $n=1.49$, $H=0.38$, $f=0.81$ for the KCl crystal, we get the simplified equation: $n_0=1.19\times10^{16}(-\log_{10} I/I_0)$, I/I_0: transmission at F-band peak.

The number of light quanta from hydrogen discharge tube in exciton region (shorter wavelength region than 200 mμ) was determined by the proper set of filters as follows.

Very crose to the window of the hydrogen discharge tube a pure uncolored KCl crystal of 0.5 mm thickness and a KCl+F crystal of 3 mm thickness were set at position of 1 and 2 as shown schematically in Fig. 2 and the

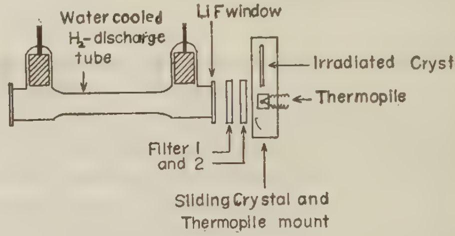

Fig. 2. Schematic arrangement of filters and thermopile to measure the light quanta.

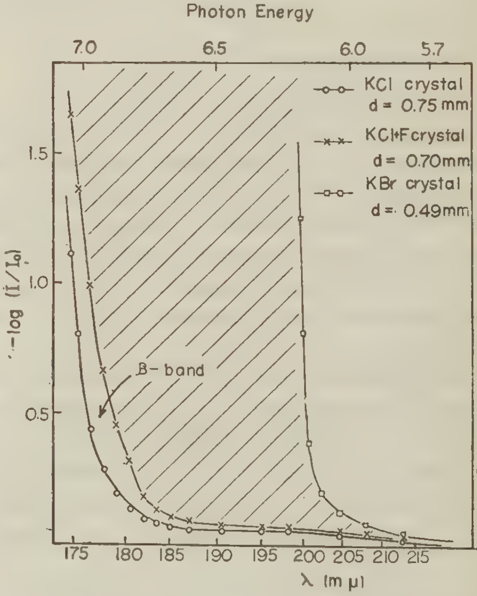

Fig. 3. Absorption curves of KCl, KBr and KCl +F crystals.

photon energy transmitted through these filters was measured with the thermopile made by Kipp. KCl+F crystal means the KCl crystal containing only F centers. Sensitivity* of our thermopile is 115 mV/W/cm². Thermopile was set always at a constant place of 14 mm distance from the window of hydrogen discharge tube. Next, only filter 1 was replaced by a cleaved pure KBr crystal of 0.5 mm thickness and measured the photon energy. The difference of these two quantities gives the energy of ultra violet light contained between wavelengths of the characteristic absorption edges of KCl and KBr crystals i.e. from 200 mμ to 180 mμ as shown by the shadowed area in Fig. 3. The number of photon was thus measured as $9.3\times10^{13}/\mathrm{cm}^2\,\mathrm{sec}$ averaged to the light of 190 mμ when the hydrogen lamp was discharging with 2 KW powers. Fig. 3 are the absorption curves of KCl, KBr filter and KCl+*F* crystal. These absorption curves were measured with the vacuum monochromator constructed in this Laboratory, having a concave grating of which diameter of Rowland circle is 998 mm.

---

* The writers are deeply indebted to Dr. H. Sadone, Electro-technical Laboratory, Osaka, who has determined the absolute sensititivity of the thermopile.

Samples of KCl+*F* ($d\sim$ 0.3 mm) crystals were alternatively placed at the position of thermopile and irradiated with the lights filtered by the KCl+*F* crystal of 3 mm thickness. As visible *F*-lights from the hydrogen lamp are filtered by the *F* centers in this crystal, samples are irradiated mainly with ultra violet light in the region of 205 mμ–180 mμ, because the tail of the exciton band extends to 210 mμ as shown in Fig. 3. At several stages of irradiation period, decreases of absorption maximum of *F* band were measured. The number of decreased *F* centers is calculated simply according to the equation:

$$\Delta n = 1.19\times10^{16}\cdot\Delta(\log_{10} I_0/I)$$

Here $\Delta(\log_{10} I_0/I)$ is the decrease of the absorption coefficient at absorption peak of the *F*-band. A constant factor p greater than 1 must be multiplied to the equation to obtain the real decrease, because the bleaching of *F* centers enhances the *M*-band simultaneously and the second *M*-absorption band superposes to the *F*-band[5]. However the quantum efficiency for the case of exciton-light irradiation is discussed with comparison to the case for visible light irradiation, and in both case the constant is common. Therefore, the factor can be omitted. Another factor *S* which gives the illuminated area of the crystal surface must be multiplied to the equation too, but for the uniform irradiation it is canceled out in the expression of quantum efficiency.

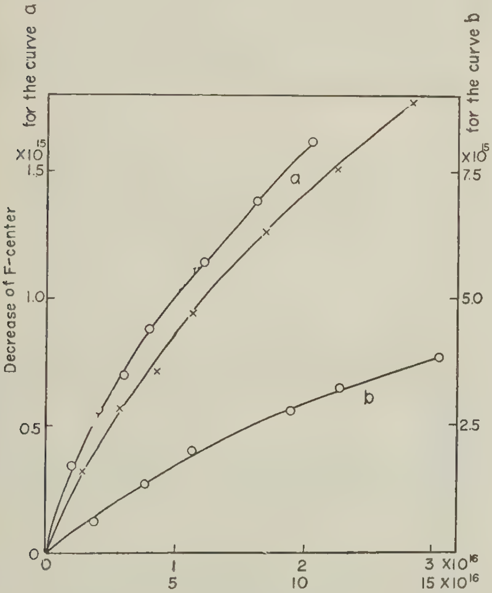

Total incident or absorbed quanta
Upper scale is for curve a
Lower scale is for curve b

Fig. 4. The relations between light quanta and bleached *F* centers in KCl+*F* crystals when they are irradiated by the ultraviolet light (curve a) and *F* light (curve b).

Fig. 4a shows the relations between the number of decreased *F* centers and the total *incident* light-quanta in the tail of exciton bands for two samples.

§ 3. Quantum Efficiency for the Bleaching of *F* Centers by *F*-light in KCl Crystal

The difference of energies measured with the thermopile in two cases, where one case has a glass plate and a pure KCl crystal of 0.3 mm thickness interposed respectively at positions 1 and 2 in Fig. 2 and another case has a glass and a KCl+*F* crystal of 0.3 mm thickness as filter 1 and 2 respectively, gives the energy of lights absorbed in *F*-band. When the hydrogen lamp was operated with the same condition as before, the number of photon (averaged to the wavelength of *F*-band peak) was calculated to $6.3\times10^{14}/\mathrm{cm}^2\,\mathrm{sec}$.

KCl+*F* crystals of about 0.3 mm thickness were placed at the position of filter 2 and they were irradiated by the light from the hydrogen lamp through the same glass filter. The number of decreased *F* centers are obtained as before and are plotted as a function of *absorbed* total quanta in Fig. 4b. The concentration of *F* center is very large, therefore, through the course of bleaching experiment, the absorbed light quanta remained to the constant value.

From Fig. 4a and 4b it is shown that the quantum efficiency for the destruction of F centers by the *incident* exciton-light is 0.15 and it is five times greater than that due to the *absorbed* F-light, compared the tangents of slopes at zero irradiation.

§ 4. Quantum Efficiency for the $U \rightarrow F$ Transformation by U-light and Exciton-light in KCl Crystal

The U center is considered a negatively charged hydrogen ion H-occupying substitutionally halogen ion site. U centers display a bell shaped absorption band in ultra violet region and its absorption maximum situates at 216 mμ and 228 mμ in KCl and KBr crystal, respectively. When the crystal containing U centers is irradiated by the U-light, $U \rightarrow F$ transformation occurs. There is no enhanced centers other than F center in this conversion process.

Hilsch[6)] has measured the quantum efficiency for the $U \rightarrow F$ transformation in KBr crystal and obtained 0.30 at room temperature. However, the effect of exciton lights on U centers has not been investigated so far as we know.

High concentration of U centers is prepared as follows. KCl crystal containing high density of F centers colored additively was heated with hydrogen gas of 100 atomospheric pressure in Ni–Cr bomb at 540°C for several hours. All F centers initially existed are converted to U centers without any loss.

A. *Quantum efficiency with the light including both exciton and U-light*

The photon energy absorbed by KCl+U crystals in the region of U-absorption band and exciton absorption tail was measured as follows. Two pure KCl crystal plates were set at positions of filter 1 and 2 in Fig. 2 and transmitted photon energy from the hydrogen discharge tube was measured with thermopile. Next, filter 2 was replaced by the KCl+U crystal and transmitted photon energy was measured. The difference of these two energies gives the photon energy which is absorbed in the KCl+U crystal at the region of U band and exciton tail, corrected the reflection loss on the surface.

KCl+U crystals were irradiated at the position of filter 2 and the increase of F centers were measured. The number of enhanced F centers is plotted in Fig. 5a versus total absorbed photon numbers averaged at 200 mμ.

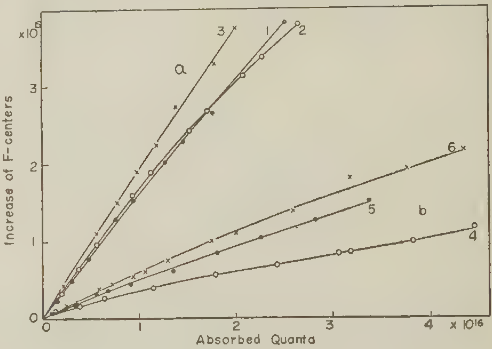

Fig. 5. The relations between total absorbed light quanta and numbers of enhanced F centers in KCl+U crystals when they are irradiated with U+exciton light (curve a) and U light only (curve b).

The thickness of pure KCl filters and irradiated KCl+U crystals and absorbed light quanta are shown in Table I for three samples.

From the slope of Fig. 5a the number of enhanced F centers per sec at zero irradiation time was obtained as given in the fifth column. The quantum efficiency was then calculated and is given in the sixth column of Table I.

B. *Quantum efficiency with the U-light only*

The energy difference between the photon energies transmitted two sets of filters, one set has a pure KBr and a pure KCl crystal as the filter 1 and 2 and the another set has the same KBr and a KCl+U crystal at the

Table I. Quantum efficiency for the $U \rightarrow F$ transformation with U-light including exciton light.

KCl+U crystal No.	Crystal thickness (mm)	KCl crystal-filter thickness (mm)	Absorbed quanta/cm² sec	Increase of F-centers per sec	Quantum efficiency
1	0.59	0.89	7.9×10^{14}	1.27×10^{14}	16%
2	0.56	0.56	4.7×10^{14}	8.1×10^{13}	17%
3	0.88	0.80	5.4×10^{14}	9.9×10^{13}	18%

position of filter 1 and 2, gives the photon energy absorbed in U-band only, as shown in the shadowed area in Fig. 6. Fig. 6 is a group of absorption curves of the pure KCl, KBr and KCl+U crystals of about 0.7 mm thickness.

KCl+U crystals were set at position of filter 2 and irradiated with the light filtered by the KBr crystal.

Fig. 5b shows the relation between the absorbed total light quanta and the number of F centers formed from U centers. Description of samples, filter thickness, number of absorbed quanta, enhanced F centers and quantum efficiency are given in Table II.

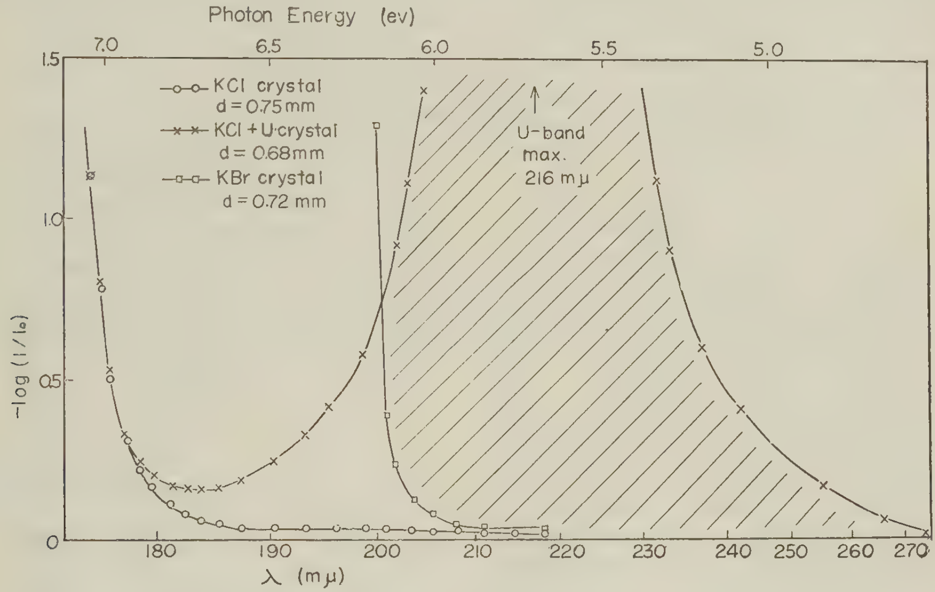

Fig. 6. Absorption curves of KCl, KBr and KCl+U crystals.

Table II. Quantum efficiency for the $U\rightarrow F$ transformation with U-light only.

KCl+U crystal No.	Crystal thickness (mm)	KBr crystal-filter thickness (mm)	Absorbed quanta/cm² sec	Increase of F-centers per sec	Quantum efficiency
4	0.88	0.80	3.2×10^{14}	1.8×10^{13}	5.6%
5	0.59	0.62	5.6×10^{14}	3.0×10^{13}	5.4%
6	0.58	0.60	2.9×10^{14}	1.8×10^{13}	6.2%

From Table I and II it is shown that the quantum efficiency of the $U\rightarrow F$ transformation with U-light including the exciton tail is three times larger than that with U-light only. From these facts, we can conclude that the ultra violet light in the exciton absorption tail has a large quantum efficiency for the transformation of U centers to F centers, because of the very small absorption coefficient in the tail.

From the preliminary experiment it was observed that when the KCl+U crystal of 3.75 mm thickness was irradiated with the monochromatic light of 190 mμ, the quantum efficiency has a large value as much as four.

§ 5. Quantum Efficiency of the $U\rightarrow F$ Transformation and its Dependence on Photon Energy in KBr Crystal

U centers were prepared in the KBr crystal as described before. The Concentration of U centers $[U]$ are calculated with the following equation given by Hilsch[7].

$$[U]=5.1\times10^{16}\cdot f_\lambda\cdot K_\lambda: \quad \text{at room temperature.}$$

Where K_λ is the absorption coefficient measured in mm^{-1} and f_λ's are constants depending on the wavelength of light with which the absorption coefficient is measured, and have the following values.

$\lambda(m\mu)$	absorp. peak 228	Hg 245	Hg 254	Cd 257	Hg 265
f_λ	1	8	21.2	43.2	235

The value of 7.3×10^{17}/cc was determined to the concentration of U centers in our crystals.

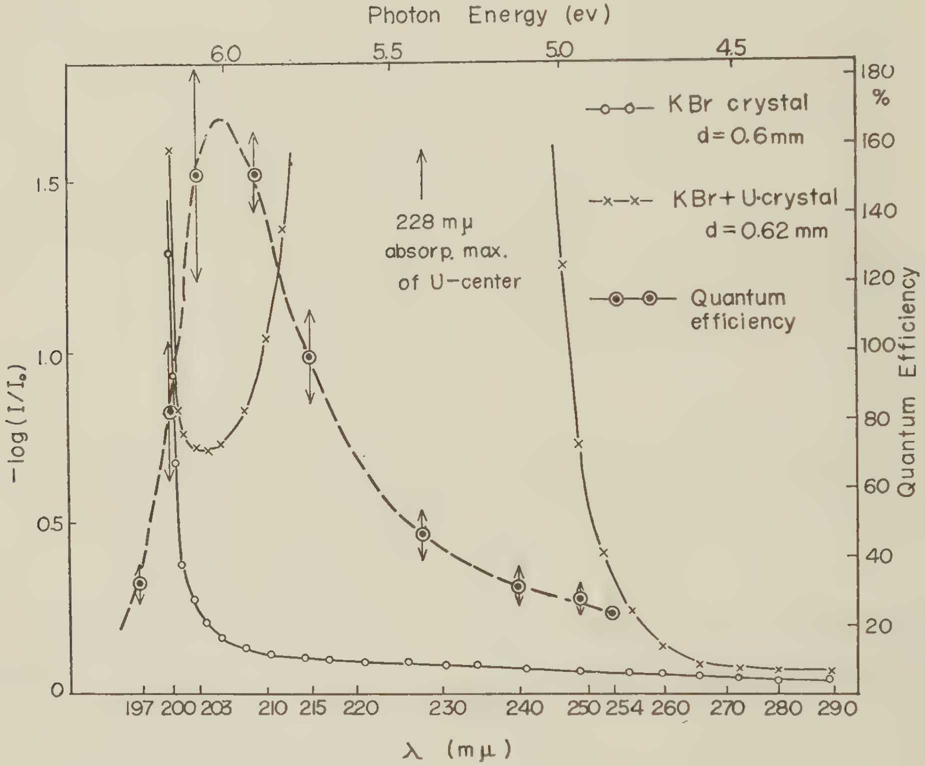

Fig. 7. Absorption curves of KBr, KBr+U crystals and the dependence of the quantum efficiency for the process of $U\rightarrow F$ transformation on the wavelength of the exciting light.

In KBr+U crystals U-absorption and the exciton bands situate closer with each other compared to the KCl crystal as shown in Fig. 7 and there are no proper filters to separate two absorption bands, therefore, the similar method performed in the case of KCl crystal can not be applied to KBr crystal. However the monochromatic lights in the region of 250 mμ–190 mμ are obtained with high intensity using a vacuum monochromator constructed for the irradiation purpose. Optical system of the vacuum monochromator is shown in Fig. 8. M_1 and M_2 are off axial parabolic mirror[*] of 130×130 mm dimension, 360 mm focal length, and G is a plane replica grating which was purchased from Bausch and Lomb Optical Company having a dimension of 102 ×102 mm as a ruled area. The blaze wavelength of the grating is 200 mμ. When the hydrogen lamp are discharging with 2 KW power the photon intensity from the monochromator are 1×10^{13}, 4×10^{12}, 2×10^{12} and 1.8×10^{12} quanta per cm² per sec at 249 mμ, 230 mμ, 200 mμ and 190 mμ respectively. Each monochromatic light has a band pass of 6 mμ.

Quantum efficiency of the $U\rightarrow F$ transformation with the monochromatic light of Hg 253.7 mμ was measured as 18%. This value are determined with relatively high accuracy, because, the monochromatic light of 253.7 mμ from a mercury lamp is very intense and the response of the thermopile to this light is large. We have chosen this value of 18% as a standard, and obtained the absolute quantum efficiency for the monochromatic light with measuring the relative photon intensity and the relative numbers of enhanced F centers by the monochromatic light against for the standard 253.7 mμ light.

---

[*] By the courtesy of Professor T. Sakurai, Institute of Scientific measurements, Tohoku University, these parabolic mirrors were polished in his Laboratory.

KBr+U crystals of about 3 mm thickness was irradiated at first with a monochromatic light, say 203 mμ, for ten minutes and measured the number of enhanced F centers using the Smakula's equation, putting $n=1.53$, $H=0.36$ (ev) and $f=0.85$. For the successive ten minutes the crystal in turn was irradiated with light of 253.7 mμ and the increment of F centers was measured. Thus, alternative ten mitutes' irradiation with 203 mμ and 253.7 mμ lights are repeated three times on the same crystal, and the numbe of F centers created independently with two monochromatic lights were averaged respectively.

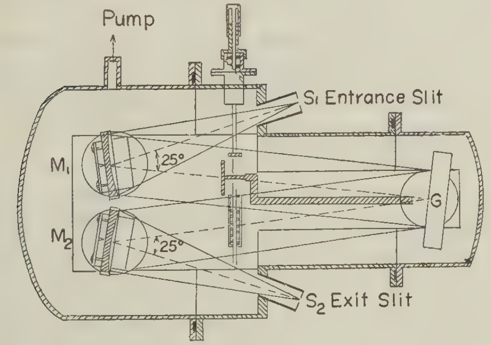

Fig. 8. The optical system of the vacuum monochromator.

The relative intensity of the two monochromatic lights at the surface of crystal was obtained with measuring the fluorescence impressed on the sensitive flourescent film placed at the position of the crystal. A pump oil and sodium salicylate film were used for the fluorescent film. Both films are confirmed to have the same quantum efficiency to the monochromatic ultra violet lights from 300 mμ down to 100 mμ[8]. The relative intensities of monochromatic lights measured using two films coincided with each other within 10%.

The absorption spectra of KBr+U and pure KBr crystal of 0.6 mm thickness are shown in Fig. 7. It is clear that the exciton tail is not affected by the existence of U centers, i.e. there is no band corresponding to β-band in the existence of F centers. The same conclusion can be said to the KCl crystals (c.f. Fig. 6).

Quantum efficiencies of the $U\rightarrow F$ transformation thus obtained in KBr crystal with monochromatic lights are shown in Fig. 7. Crystals used have the thickness of more than 3 mm and transmissions of crystals at all monochromatic lights were lower than 5%. Therefore, the correction for the differences of absorption coefficients was unnecessary.

At 203 mμ and 209 mμ, the quantum efficiency has the maximum value and drops rapidly towards the exciton band which has a large absorption coefficient.

§ 6. Discussions

A. *Bleaching of F centers by the exciton*

The quantum efficiency for the bleaching of F centers with the incident light in the exciton band was determined as 0.20 from Fig. 4a. To obtain the real quantum efficiency η_0 which gives the number of F centers bleached per absorbed quantum, we have to estimate the fraction of the energy absorbed in the crystal.

KCl+F crystals were irradiated by the ultra violet light from the hydrogen lamp through the thick crystal containg F centers of high density and so, ultra violet lights in shorter wavelength region than the β-band are filtered. On the other hand, the exciton band extends to the 210 mμ as shown in Fig. 3. Therefore, the effective ultra violet light for the bleaching of F centers is limited mainly in the region between 180 mμ to 205 mμ of which total light quanta were determined as 9.3×10^{13} per cm^2 per sec. In these wavelength region, the spectral intensity distribution[9] of light from the hydrogen lamp is measured to have nearly the uniform intensity.

Absorption curve of the exciton band in the tail shows that the light quanta which are absorbed in the crystal will be at most 3% of the total incident quanta. From these facts, it may be concluded that the quantum efficiency η_0 for the bleaching of F centers per one exciton is at least six.

It is unknown whether or not the mechanism of the bleaching of F centers by the exciton is the same to the process of F-light illumination, though the absorption spectra of the crystal after a short irradiation show the enhancement of M band and with continued irradiations, R band become to appear. Now let us assume the same mechanism for both cases.

When the F center absorbs F-light, it should be ionized in the first step with quantum efficiency 1 at room temperature, because Pick[10] has obtained it at even low temperature in his observation of the photochemical reaction of $F \rightarrow F'$. At room temperature F' center is unstable and the back reaction of $F' \rightarrow F$ occurs. This back reaction explains the apparent small quantum efficiency for the bleaching of F centers by the F-light that we obtained as 0.04.

The efficiency of the F center bleaching by the incident ultra violet light is obtained to have 0.20 as shown in Fig. 4 and it is five times larger than that with the F-light. Therefore, if the assumption is correct that the effect of excitons on F centers is the same as in the case of F-light irradiation, we have to conclude that one incident photon of ultra violet light ionizes five F centers. If we calculate the real quantum efficiency η_0: the number of ionized F centers per one absorbed quantum or exciton: it will reach a quite large value. On the other hand, the thermal dissociation energy of F center was calculated as 1.95 ev for the KCl crystal by Mott and Gurney[11] and the energy of an exciton is about 6 ev, and so, even in the case that all energy of the exciton is used to ionize the F centers, the maximum value of F centers destroyed should be at most three. Therefore, the action of excitons on F centers which we observed can not be explained from the ionization process only and the thermal effect which produce the reaction of such as $F \rightarrow$ colloid must be considered to happen simultaneously.

Theisen and Scott[12] has discovered the easy thermal bleaching of F centers in KCl crystal when the crystal containing F centers was kept in dark at above 150°C. They plotted the number of F centers bleached thermally as a function of time and obtained the activation energy of 10.5 ± 1.5 kg cal/mol for the process of $F \rightarrow$ colloid. Though the mechanism by which the F centers coagulate is unclear at the present time, if the exciton energy is given in full to the thermal process for the formation of colloid, one exciton can bleach more than ten F centers. Therefore, the observed quantum efficiency of six for the bleaching of F centers by an exciton will be reasonable value.

As mentioned before, at the initial state of the irradiation with the exciton light, the crystal shows the enhancement of M band as in the case of F-light irradiation. From this fact it may be concluded that the energy of an exciton is shared to both processes for the ionization of an F center and for the thermal bleaching of F centers to the formation of colloids.

B. *Excitation of U center*

In KBr crystrl, η_0 for the process of $U \rightarrow F$ transformation with U-light was determined as 0.46 at the U-band peak, which nearly coincides with the result measured by Hilsch.

On the conversion of $U \rightarrow F$, Mott and Gurney[13] concluded that the excited state of the U center is metastable as a result of crossing of the crystalline Franck-Condon curves and that a hydrogen atom escapes from the center in the metastable state. By this mechanism the increases of efficiencies we obtained when the crystal are irradiated with lights of higher photon energies will be explained.

With the photon energies of 209 mμ and 203 mμ, η_0 has the value larger than 1. Here the absorption coefficients of the crystal are the superposition of the absorptions due to the U-band and exciton band. Therefore, the total light quanta is shared to both absorption bands in proportion to the absorption coefficients. From Fig. 7 it is estimated that the light quanta absorbed in the exciton tail are 1/7 and 1/2.5 of the total quanta, respectively. From these facts η_0 for the ionization of U centers are calculated to have the values of five and three with the exciton lights of 209 mμ and 203 mμ, respectively.

With the lights of shorter wavelength than 203 mμ decreased rapidly. This fact might be explained as due to the destruction of excitons by the mutual interaction, because at these wavelength region the absorption coefficient of the crystal is large and almost of all incident exciton lights are absorbed in a thin layer of the crystal and the density of excitons is large.

This drop of the quantum efficiency is also observed at shorter wavelength than $h\nu = 5.5$ ev by Inchauspé in his photoconductivity measurements shown in Fig. 1.

§ 7. Conclusion

The large quantum efficiency for the bleaching of color centers with the ultra violet light in the region of the fundamental absorption tail was observed. It has to be considered that the effect of the exciton is mainly the thermal action, and that the color centers *F* and *U* are not uniformly distributed even in the case of the additive coloration but exist locally as the aggregations of atomic centers and receive the exciton energy with a good efficiency.

To obtain the definite conclusion, more detailed experiments have being carried out at the lower temperatures.

The authors wish to express our cordial thanks to Professor T. Muto for his kind interests. This work was aided by the Scientific Research Fund of the Ministry of Education.

References

1) J. Frenkel: Phys. Rev. **37** (1931) 17; 1276.
J. Frenkel: Phys. Z. **8** (1936) 185.
J. C. Slater and W. Shockley: Phys. Rev. **50** (1936) 705.
F. Seitz: Rev. Mod. Phys. **26** (1954) 27.
Y. Takeuchi: Progr. Theor. Phys. **18** (1957) 421.
T. Muto and H. Okuno: J. Phys. Soc. Japan **11** (1956) 633; **12** (1957) 108.
T. Muto and S. Oyama: J. Phys. Soc. Japan **12** (1957) 101.
D. L. Dexter: Phys. Rev. **83** (1951) 435; **108** (1957) 707.
W. Martienssen: J. Phys. Chem. Solids **2** (1957) 256.
E. G. Schneider and H. M. O'Bryan: Phys. Rev. **51** (1937) 293.
P. L. Hartman, J. R. Nelson and J. G. Siegfried: Phys. Rev. **105** (1957) 123.
A. W. Overhauser: Phys. Rev. **101** (1956) 1702.
Y. Toyozawa: Progr. Theor. Phys. **20** (1958) 53.
K. J. Teegarden: Phys. Rev. **105** (1957) 1222.
C. J. Delbecq. P. Pringsheim and P. Yuster: J. Chem. Phys. **19** (1951) 574; **20** (1952) 746.
J. N. Ferguson: Phys. Rev. **60** (1944) 220.
2) L. Apker and E. Taft: Phys. Rev. **79** (1950) 914; **81** (1951) 698; **82** (1951) 814.
L. Apker and E. Taft: J. Chem. Phys. **20** (1952) 1648.
H. R. Philipp and E. A. Taft: J. Phys. Chem. Solids **1** (1956) 159.
H. R. Philipp and E. A. Taft: Phys. Rev. **106** (1957) 671.
3) N. Inchauspé: Phys. Rev. **106** (1957) 898.
4) A. Smakula: Z. Phys. **59** (1930) 603.
5) C. D. Van Doorn and Y. Haven: Phys. Rev. **100** (1955) 753.
6) See the Review by R. W. Pohl: Phys. Z. **39** (1938) 36.
7) R. Hilsch: Ann. physique **29** (1937) 407.
8) F. S. Johnson, K. Watanabe and R. Tousey: J. Opt. Soc. Amer. **41** (1951) 702.
9) D. M. Packer and C. Lock: J. Opt. Soc. Amer. **41** (1951) 699.
10) H. Pick: Ann. Physik **31** (1938) 365.
11) N. F. Mott and R. W. Gurney: *Electronic Processes in Ionic Crystals* 2nd Ed. (Oxford, 1948) Chap. 4.
12) F. E. Theisen and A. B. Scott: J. Chem. Phys. **20** (1952) 529.
13) See ref. 11.

JOURNAL OF THE PHYSICAL SOCIETY OF JAPAN, Vol. 14, No. 3, MARCH, 1959

Electrical Resistivity and Superstructure of $CuAu_3$

By Makoto HIRABAYASHI

The Research Institute for Iron, Steel and Other Metals,
Tohoku University, Sendai

(Received October 14, 1958)

The superlattice formation in the alloy $CuAu_3$ containing 75.0_6 atomic per cent gold was studied by measurements of electrical resistivity and by means of X-ray diffraction with a single crystal. After the alloy was quenched from 450°C, the isothermal change in resistivity was measured at various temperatures between 100° and 220°C. In most of the isothermal measurements, the resistivity increased monotonously with the time of annealing, possessing an activation energy of 25 ± 2 Kcal/mol. It was found, however, that after prolonged annealing at 162 and 175°C sluggish decrease in resistivity took place following initial increase. The transition point of this alloy was determined as 200 ± 5°C.

Corresponding to the resistivity measurement, X-ray diffraction patterns were taken at various states of ordering at 100°, 150° and 180°C as well as at the states quenched from 210° and 450°C. It was confirmed that nucleation and growth of small anti-phase domains in the disordered lattice take place in accordance with the rise in resistivity, and that the development of order within the domains plays an important role in the reduction of resistivity. Then even after three months annealing at 180° and 100°C, the ordered alloy $CuAu_3$ has a two-dimensional, rather than one-dimensional, anti-phase domain superstructure with the linear dimension of nearly 11 times the fundamental face-centered cubic cells. In every stage examined, the main lattice reflections were surrounded by fairly strong diffuse scatterings, which is considered to be caused by the thermal motion of atoms, not by the lattice distortion due to ordering. Finally, comparing with the alloy Cu_3Au, the change in resistivity due to ordering was discussed in connection with the result of X-ray study.

§ 1. Introduction

According to the statistical theories of order-disorder phenomena in binary alloys, one can expect three superlattices at the compositions of the atomic ratios 3:1, 1:1 and 1:3 for alloys of a face-centered cubic structure forming an isomorphous series in the disordered solid solutions. The copper-gold alloy is a representative of such alloys. In addition to the superlattices Cu_3Au and CuAu, which have been investigated in detail since the earliest works on the order-disorder transition in alloys, the superlattice at the composition 1 Cu and 3 Au was confirmed by X-ray diffraction and measurements of several physical properties1) as well as by electron diffraction2). For the alloy $CuAu_3$, it was previously reported that the electrical resistivity increases as the ordering proceeds below the transition point1), but the residual resistance of the highly ordered state is slightly lower than that of the disordered one3),4). On the other hand, for the alloy Cu_3Au, as well known, the ordered state possesses a remarkably lower resistivity than that of the disordered state. It was recently found5), however, that the resistivity of Cu_3Au increases during the initial process of ordering immediately below the transition point, and suggested that such increase may be due to the formation of small ordered nuclei. Since there seems an analogy with regard to the electrical resistivity between $CuAu_3$ and Cu_3Au, we attempted to clarify the correlation between the resistometric and structural change due to ordering of $CuAu_3$.

In the course of the present work, two papers concerning with $CuAu_3$ were published by Wright and Goddard6) and by Batterman7). Wright and Goddard found that the resistivity of $CuAu_3$ increases initially and then decreases slowly during isothermal annealing at 167°C, and supposed that the presence of small ordered domains may be attributed to the resistivity increase. Batterman made an X-ray work in order to determine the degree of order as well as the transition point of this alloy, and found the presence of anti-phase domains of size about 50 A in the well annealed state. These works are closely related to the present paper, so that they will be often refered later. In this paper, we will show the results of isothermal measurement of resistivity and X-ray diffraction study using a single crystal of $CuAu_3$, and then show the presence of anti-phase ordered domains as well as its contribution to the anomalous resistivity.

§ 2. Experimental Procedures

The $CuAu_3$ alloy was prepared by melting together weighed amounts of electrolytic copper (99.9%) and gold (99.99%). Chemical analysis showed the composition to be 75.0_6 atomic per cent gold, which agreed well with the result obtained by X-ray measurement of the lattice parameter in the disordered state, as will be given later. The ingot, about 4 gr in weight, was homogenized for several hours at 850°C in vacuum, and then in part swaged and drawn into wire of about 0.4 mm in diameter. A single crystal was grown from the residual ingot in a thin ceramic tube by means of the Tammann-Bridgman method in vacuum. Both the wire and the single crystal were again annealed at 750°C for several hours. In all cases, to attain the disordered state, the specimens sealed in evacuated glass tubes were heated at 450°C for two hours, and then quenched into ice water. The isothermal annealing was done in either vacuum or an oil bath.

The electrical resistivity was measured by the potentiometric method. The leads were spot-welded to the wire of about 8 cm in length. This specimen had been used to measure the resistivity at low temperatures[4].

All X-ray diffraction patterns were taken by Cu $K\alpha$ radiation. The diameter of the single crystal was reduced to about 0.2 mm by etching in aqua regia. At each stage of ordering the crystal was mounted on an X-ray goniometer with either the [001] or the [$\bar{1}$10] direction set accurately along the axis of rotation. Then stationary and oscillation photographs were taken, using cylindrical film cassettes of 10 and 7 cm in diameter. A 114.6 mm Debye-Scherrer camera was also used to determine the lattice parameters in both the annealed and the quenched states.

§ 3. Experimental Results

(A) *Electrical resistivity*

The electrical resistivity of the alloy quenched from 450°C was measured during isothermal annealing at various temperatures from 100° to 220°C. Typical results are shown in Fig. 1, where the change of the specific resistivity is plotted for the initial period of annealing. A monotonous increase in resistivity takes place at each temperature. However, by successive measurements at 162° and

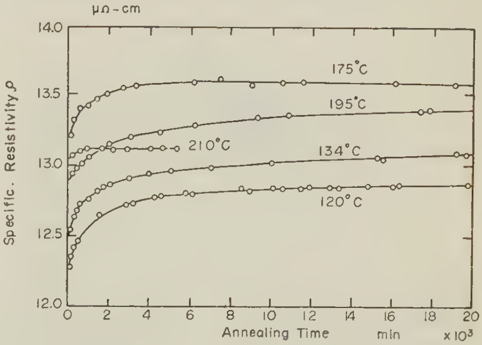

Fig. 1. Specific resistivity as a function of annealing time at various temperatures.

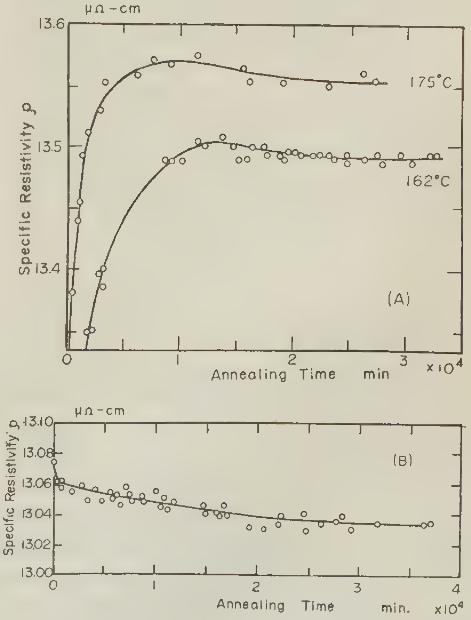

Fig. 2. Specific resistivity plotted against annealing time at 162° and 175°C (A), and at 100°C (B). In the latter, the specimen was previously annealed at 162°C for 3.5×10^4 min.

175°C, it was found that the resistivity decreased gradually over the maximum near 1×10^4 min, as shown in Fig. 2 (A). Furthermore, at 100°C annealing following 162°C annealing of 3.5×10^4 min, the resistivity decreased with increasing time of annealing as shown in Fig. 2 (B), though even after 3.5×10^4 min at 100°C the decrement was only about 0.2% of the initial value. Accordingly it is reasonably suggested that the ordering reaction of this alloy proceeds through a multistage rather than a single-stage process.

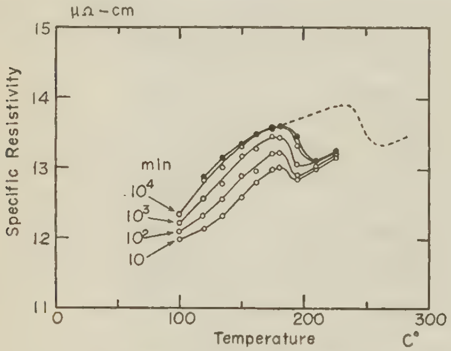

Fig. 3. Isochronous curves of resistivity against temperature. Each closed circle shows the resistivity finally reached at each temperature, and a dotted line shows a curve obtained when the specimen was reheated from 180°C at a rate of about 2 deg/min.

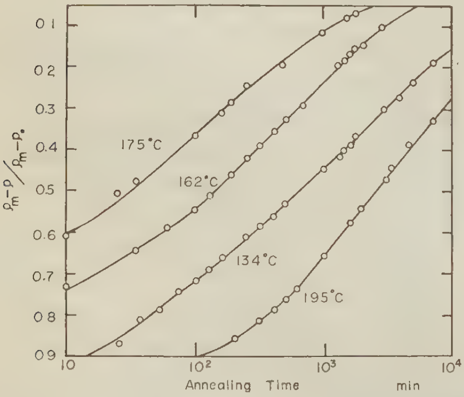

Fig. 4. $\rho_m-\rho/\rho_m-\rho_0$ plotted against annealing time.

Fig. 3 shows the specific resistivity at the annealing times 10, 10^2, 10^3 and 10^4 minutes, in addition to terminal value finally reached at each temperature. The transition temperature is determined as 200±5°C from the maximum negative temperature coefficient of the resistivity corresponding to the finally reached states, which may approximately be thought as thermal equilibrium. The increase in resistivity at 210° and 220°C is probably due to the formation of the short range order. If the alloy is heated at the rate of about 2 deg/min, after the resistivity has reached the maximum at 180°C, the transition from order to disorder occurs near 240°C, as depicted by the dotted line in Fig. 3. This fact agrees well with our previous report[1)], and the heating curve is entirely different from thermal equilibrium since the heating rate is too large to maintain the equilibrium state.

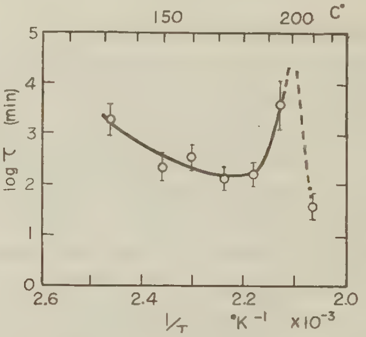

Fig. 5. Relaxation time $\log\tau$ *versus* reciprocal temperature $1/T$.

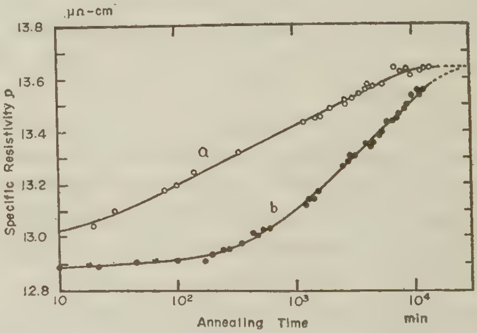

Fig. 6. Resistivity change at 180°C annealing. The meaning of curves (a) and (b) is stated in the text.

Next, in order to obtain an activation energy in the first stage of ordering process, the function $\rho_m-\rho/\rho_m-\rho_0$ was plotted against $\log t$. Here ρ_m and ρ_0 are the maximum and initial resistivity respectively, and t is the annealing time. Typical curves of this function are given in Fig. 4, from which one may obtain the relaxation time τ at each temperature. In Fig. 5 the values of $\log\tau$ are plotted as a function of the reciprocal of the absolute temperatures. The value τ corresponding to the first stage of ordering is appreciably longer than that of Cu_3Au[8], and one may expect much longer value of τ for the second stage of ordering, which corresponds to the decreasing resistivity. If the ordering of atoms is a diffusion process, the relaxation time should approximately satisfy the equation, $\tau=\tau_0\exp(-W/kT)$, where τ_0 is a constant, W the activation energy necessary for ordering and T the absolute temperature. Thus the activation energy 25±2 Kcal/mol is evaluated from the slope of the curve in the temperature range below 165°C. It appears from Fig. 5 that the transition rate is highest around 180°C and is rather lower near the critical temperature. Such a behavior was already reported for other ordered alloys, such as Cu_3Au[8] and CuAu[9], and coincides with the theoretical predictions[10].

Fig. 6 shows the change in specific resistivity at 180°C plotted against annealing time. Curves (a) and (b), marked with open and closed circles, correspond to ordering processes immediately after quenching from 450°C to ice water and immediately after annealing at 210°C for 30 hr, respectively. Here it is noted that the initial ordering rate of the alloy quenched from the higher temperature is higher than that of the alloy having fairly high degree of short range order.

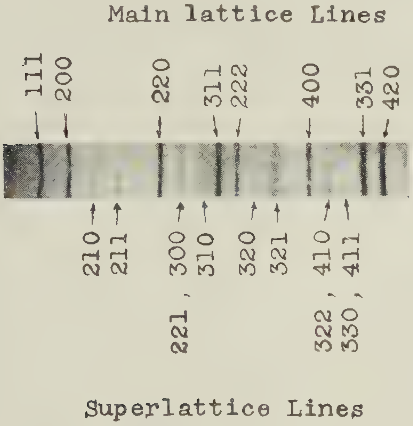

Photo. 1. Debye-Scherrer photograph of $CuAu_3$ annealed for about four months at 150°C. Monochromatic Cu $K\alpha$ radiation is used, and the exposure time is about 24 hours.

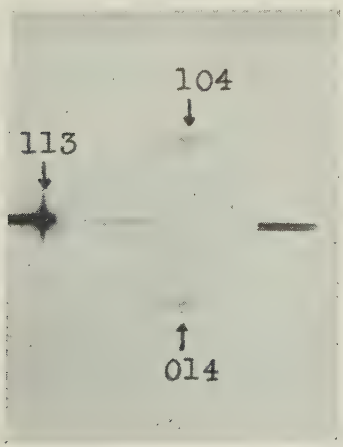

Photo. 2. Oscillation photograph of $CuAu_3$ annealed for 5 hr at 180°C. [$\bar{1}$10] is vertical, and the crystal is oscillated by 25～30° from [001] direction. Diffuse superlattice reflections 104 and 014 are shown.

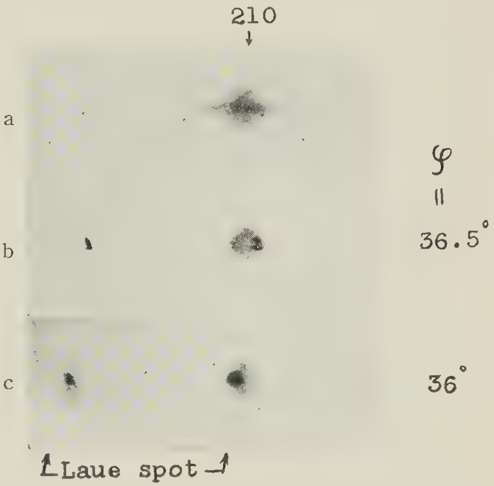

Photo. 3. Cross-like superlattice spot 210 of $CuAu_3$ annealed for 10 hr at 180°C. [001] is vertical. φ is the angle between the incident beam and [100] direction. a: oscillation photograph, b and c: stationary photographs.

(B) *X-ray diffraction study*

(1) Polycrystalline specimen

The polycrystalline specimen was used to determine the lattice parameteres in both the ordered and disordered states and also to detect the superstructure lines. The lattice constants of the alloy quenched from 450°C and annealed at about 150°C for four months were 3.9764 and 3.9730 kX respectively, which were determined by means of the Nelson-Riley graphical-extrapolation method using Cu $K\alpha$ radiation*. Accordingly the linear contraction due to ordering is about 0.085%, which agrees well with the dilatometric study[1]. Many superlattice lines were clearly observed on the powder pattern of the highly ordered alloy, as shown in Photo. 1. Here it should be pointed out that the line breadths of the superlattice reflections vary with their indices. This photograph was taken by using a LiF monochromator and a 90 mm-camera of Burger-type, in which the film was tightly held against the inner cylindrical surface.

---

* Wavelengths used: Cu $K\alpha_1$=1.5374 kX, Cu $K\alpha_2$=1.5412 kX.

(2) Single crystal specimen

After the single crystal was quenched from 450°C into ice water and was annealed at 100°, 150°, 180° and 210°C for various durations, X-ray diffraction photographs were taken of the superlattice reflections and of the diffuse scattering around the main lattice reflections. At first the series of 180°C annealing after quenching from 450°C will be described. In this course the diffraction patterns were taken at each stage of annealing for 30 min, 100 min, 5 hr, 10 hr, 37 hr, 108 hr, 219 hr and one month. After keeping for 30 min at this temperature, any superlattice reflections could not yet be observed. They became faintly visible from the stage of 100 min annealing and grew intense with time of annealing. Photos. 2 and 3 show examples of superlattice reflections at the annealing states for 5 and 10 hr, respectively. In Photo. 2 two superlattice reflections appear very faintly and broad, while in Photo. 3 one can clearly see the cross-like spot of the 210 reflection. After 37 hr annealing at this temperature, such cross-like superlattice reflections became more definite, as shown in Photo. 4 (A) and (B). The former corresponds to the sections passing through such superlattice spots as 100, 110 and 221 in reciprocal space, and the latter corresponds to a series of the successive sections passing through 001, 012, 123 and 223. The diffuse scatterings around the main lattice spots 113 and 133 are observed in these photographs. Similar diffraction patterns were obtained in both the states of 108 and 219 hr annealing.

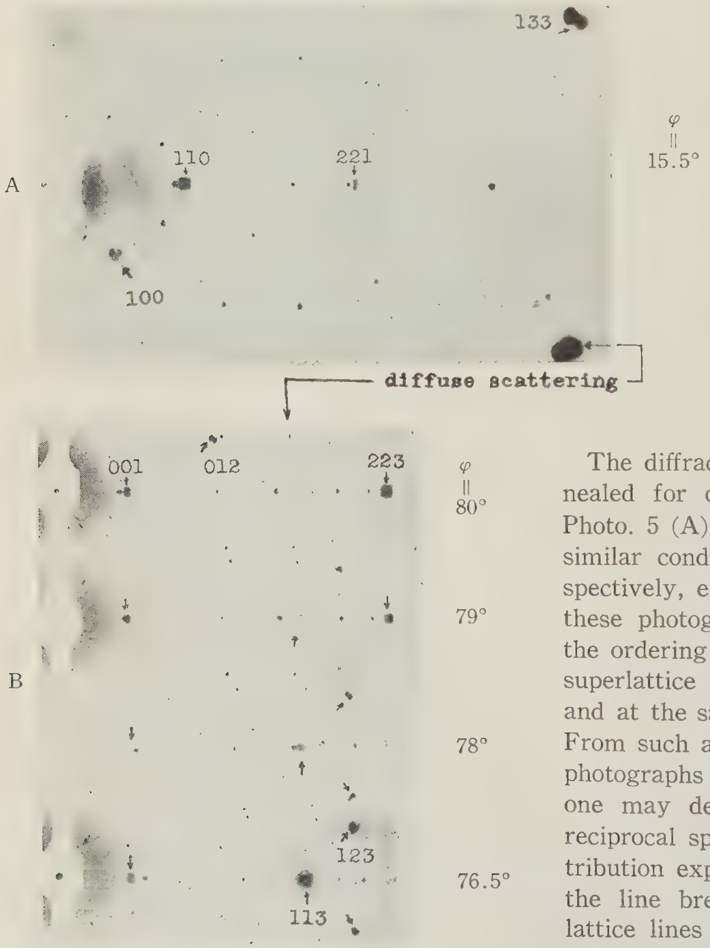

Photo. 4 (A) and (B). Stationary crystal photographs of CuAu$_3$ annealed for 37 hr at 180°C. [$\bar{1}$10] is vertical. In addition to many superlattice reflections, main lattice reflections surrounded by diffuse scattering are observed.

The diffraction patterns of the crystal annealed for one month at 180°C are given in Photo. 5 (A) and (B), which are taken under similar conditions to Photos. 4 (A) and 3 respectively, except annealing durations. From these photographs, it will be noticed that, as the ordering advances, the splitting points of superlattice reflections approach each other and at the same time their intensity increases. From such a number of successive stationary photographs for many superlattice reflections, one may deduce the intensity distribution in reciprocal space as given in Fig. 7. This distribution explains reasonably the variation of the line breadth with indices of the superlattice lines seen in Photo. 1. From Fig. 7 it is suggested that the highly ordered alloy CuAu$_3$ has such an anti-phase domain structure as observed in the partially ordered state of Cu$_3$Au[11,12], or in the ordered alloy Ag$_3$Mg[13,14], Cu$_3$Pd[13,15] and others. The size of anti-phase domain, which can be determined from the separation of splitting superlattice reflections, increases with time of annealing. The result is given in Fig. 8. After one month annealing at 180°C, the domain size reaches about 11 times the lattice constant. Comparing Fig. 8 with the curve (a) in Fig. 6, one can find fairly good correspondence between the increase in the domain size and that in the electrical resistivity.

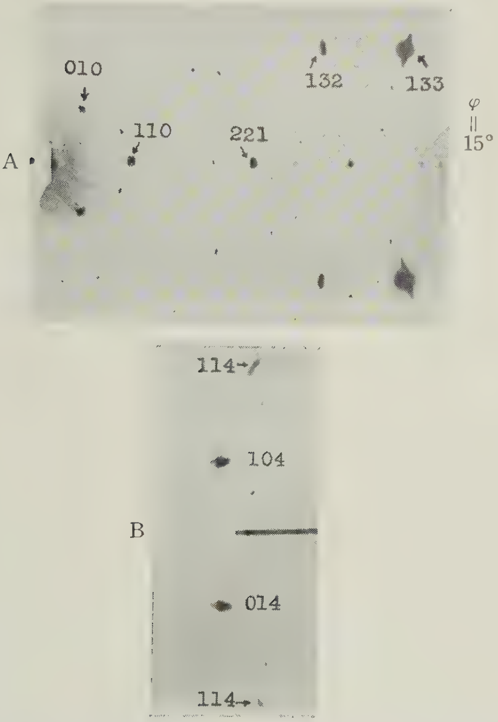

Photo. 5 (A) and (B). Stationary and oscillation photographs of $CuAu_3$ annealed for one month at 180°C. $[\bar{1}10]$ is vertical.

X-ray photographs were also taken at various annealing states between 2 hr and 45 days at 150°C after being quenched from 450°C. In the diffraction patterns the general appearance seems almost similar to that at 180°C annealing mentioned above. The superlattice reflections begin to appear from about 5 hr annealing, and the diffuse scattering surrounding the main lattice reflections is observed from the initial period of annealing. Even after 45 days annealing, however, the splitting superlattice spots are comparatively broad, and on the average the size of anti-phase domains is nearly 10 times the fundamental cell.

After the alloy was annealed for one month at 180°C, it was subsequently heated at 100°C, in order to examine how far this heating affected the ordered structure, because the resistivity decreases continuously during a similar heat treatment as shown in Fig. 2 (B). Photo. 6 gives the diffraction patterns of the alloy annealed for two months at 100°C. The

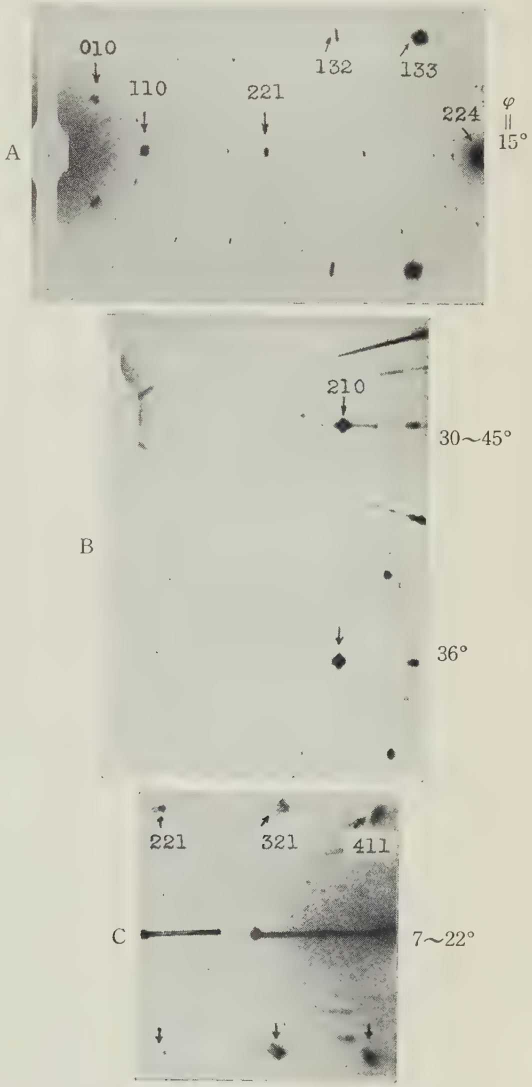

Photo. 6. Diffraction photographs of $CuAu_3$ annealed for one month at 180°C and subsequently for two months at 100°C.

(A): $[\bar{1}10]$ is vertical. Stationary photograph $\varphi=15°$.
(B): [001] is vertical. Oscillation and stationary photographs showing superlattice reflection 210.
(C): [001] is vertical. Oscillation photograph showing splitting superlattice reflections 221, 321 and 411.

separation of splitting superlattice reflections does not change from the stage reached after one month annealing at 180°C, but the intensity of them becomes stronger. It means that in this course the domain growth takes little place but the degree of order within the domains increases. Here it is noticeable that the diffuse scattering around the main lattice points such as 133 and 224 remains with considerably large intensity, and, especially that, the anomaly of intensity is seen in 221 as well as in 321 in Photo. 6 (C). The former reflection seems to consist of a pair of splits, and the component in the side of lower diffraction angle is fairly weaker than that in the side of higher angle. The latter consists of two pairs of splits, and the components in the side of lower angle are also weaker than those in the side of higher angle. From the microphotometry of 321 reflection in this photograph, it was found that each component of lower angle side had only almost half the intensity of that of higher angle side. Such an asymmetry in intensity is also seen in Photo. 5 (B). But it appears to increase with the advance of ordering at 100°C. The discussion on this fact will be given in the following section.

The diffuse scattering around the main lattice reflections was examined in detail in the short-range ordered state quenched from 210°C after keeping for 30 hr. In this stage the main lattice reflections were certainly surrounded by the diffuse scattering, while very diffuse super-

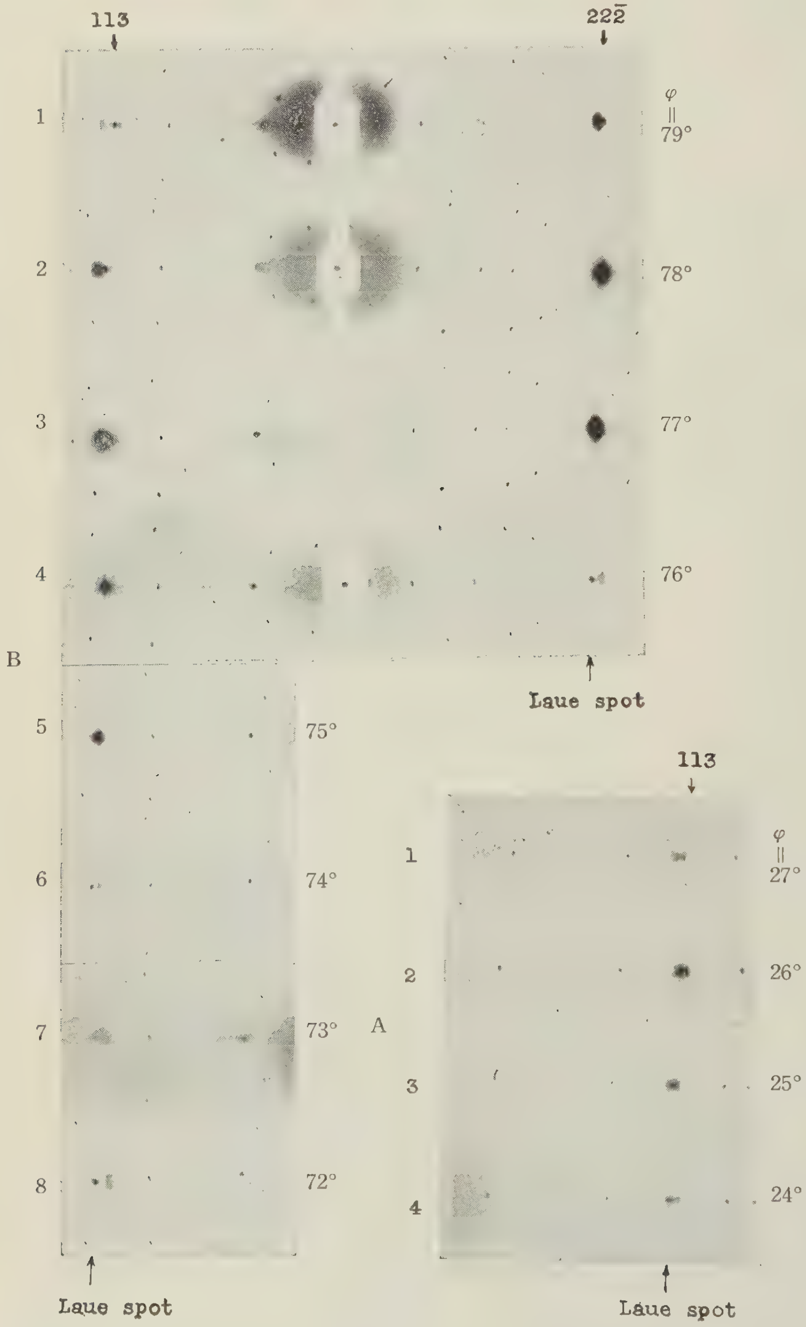

Photo. 7.

(A): Series of stationary photographs showing diffuse scattering around the main lattice spot 113. $[\bar{1}10]$ is vertical.

(B): Series of stationary photographs showing diffuse scattering around the main lattice spots 113 and $22\bar{2}$. $[\bar{1}10]$ is vertical.

ing kinetics[18]. In terms of this effect it is reasonably interpreted that the ordering rate varies appreciably, even at the same temperature of annealing, by the initial condition with or without local order as shown in Fig. 6.

The present X-ray diffraction study in the course of annealing at 150° and 180°C shows that the development of order is made not through homogeneous increase in short-range order throughout the crystal, but essentially through a nucleation and growth of small ordered domains in the disordered lattice. From Figs. 6 and 8, it is conclusively said that the growth of the anti-phase domains takes place in the first stage of ordering, where the resistivity increases. At the early period of this stage only a few domains exist in the lattice, while prolonged annealing causes a large number of domains with a fairly definite size of about 44 A to occur. In the second stage of ordering, corresponding to the decrease in resistivity, the domain growth takes little place but the degree of order within domains increases progressively.

Now we shall consider the increase in resistivity at the initial stage of the ordering process in the light of the present X-ray diffraction study. Such inverse change of resistivity is not so unusual but is already found in such ordered alloys as Cu_3Au[5], Cu_3Pd[19] and Ag_3Mg[14], all of which form anti-phase domain structures. Rise in resistivity of these alloys has been qualitatively explained by the presence of anti-phase ordered nuclei, of which the linear dimension is smaller than the mean free path of conduction electrons. The latter is given in monovalent metals by the formula $\lambda = h/\rho e^2(3/\pi N^2)^{1/3}$, where ρ is the specific resistivity, e the electronic charge and N the number of conduction electrons per unit volume[20]. Assuming that there is one conduction electron per atom for $CuAu_3$, the value of λ is about 100 A for the annealing state at 180°C. This value is larger than the size of the anti-phase domain, 44 A, existing at 180°C, so that such domains may act as scattering centers for electrons. Therefore, as the ordering proceeds, the inhomogeneity enhanced by the formation of small anti-phase domains induces the increase in resistivity, but the growth of domains intends to decrease the resistivity. Thus the rise of resistivity in the initial stage of ordering is probably caused by the fact that the effect of formation of domain boundaries overcomes that of domain growth. Formation and growth of domains is stopped when the lattice is closely filled with domains, and then the subsequent reduction of resistivity is reasonably thought to be produced with the development of order in the domains. Successive coalescence of the anti-phase domains, which may likewise induce the decrease of resistivity, is not observed in the present X-ray study of the isothermal ordering.

Next we shall discuss the superstructure of the ordered alloy $CuAu_3$. Even at the final state of annealing above 100°C, $CuAu_3$ possesses the anti-phase domain structure with about 44 A in length, which accords well with the value estimated by Batterman[7]. At the present time, as described above, we know a number of the ordered alloys of A_3B type with various anti-phase domain structures, i.e. as the one-dimensional anti-phase domain Ag_3Mg[13),14], Au_3Cd[13], Au_3Zn[21] and so on, and as the two-dimensional one Cu_3Pd[15], Au_4Zn[21] and Au_3Mn[22]. From the intensity distribution of superlattice reflections in reciprocal space given in Fig. 7, it is probable that the highly ordered state of $CuAu_3$ has the two-dimensional anti-phase domain structure rather than the one-dimensional one. The reason is given in the following. If the latter would be the case, every original superlattice spot should be flanked by four satellites in reciprocal space. On the other hand, if the former would be the case, the central spot at every superlattice reflection position should vanish leaving only satellites, because the central spot would also be split, as previously reported in our paper[15]. In the highly ordered state of $CuAu_3$, the central spot of every superlattice reflection position is hardly observable or much weaker than the satellite splits as shown in many photographs*. It is not clear from the diffraction patterns to which satellites the central spot is split and what kind of two-dimensional domain is realized, but any other origin than described above can hardly be conceivable for the vanishment of the central spot. It remains unsolved whether such an anti-phase domain structure exists in the stable state as in several ordered alloys mentioned above or in the intermediate one as in Cu_3Au[11),12)], because it takes extremely long duration to attain the ordered state in an equilibrium below the transition point as low as 200°C. In order to answer this question, however, it seems necessary to obtain a more highly ordered state of the alloy by any other means than a prolonged heating, e.g. by irradiation of high energy particles. It is of some interest to note, here, that the anti-phase domain in $CuAu_3$ has, roughly speaking, similar size to that in Cu_3Au. The latter sizes are 7, 10~11 and 18~19 times the fundamental face-centered cubic cell at 300°, 320° and 330°C, respectively[12)].

---

* The superlattice reflections of Cu_3Au reported in the references 11) and 12) also seem to show the disappearance of the central spot of superlattice reflection similarly to the present patterns of $CuAu_3$.

The remarkably asymmetrical intensity of splitting superlattice reflections seems somewhat complicated but is interesting*. Some possible explanations may be considered. One of them is the effect of diffuse intensity due to difference in size of the component atoms in alloys proposed by Warren, Averbach and Roberts[23)]. This effect has actually been observed in the short-range ordered state of $CuAu_3$[7)] as well as of Cu_3Au[23)] and CuAu[24)]. It is hardly expected, however, that the contribution of the size effect gives rise to highly asymmetrical intensities of splits in superlattice reflections, as these splits are very close to each other. An alternative explanation of this phenomenon is probable on the analogy of X-ray pattern observed in precipitation process of an Al-Cu alloy[25)]. X-ray diffraction photographs of the alloy containing 4 weight per cent copper showed diffuse streaks emerging from diffraction spot on one side only. It was qualitatively explained[26)] by a combination of varying lattice parameter and varying structure amplitude owing to the segregation of solute copper atoms on to particular atmic planes in the matrix. The asymmetrical splittings shown in the present X-ray photographs of $CuAu_3$ may be interpreted in the same way. It may reasonably be supposed in the anti-phase domain structure of this alloy that out-of-step boundaries differ in the lattice spacing as well as in the structure amplitude from the inside of domains. Therefore the spacing and the structure amplitude vary periodically with the same period as that of out-of-step. If both of the modulations synchronize in such a way that the maximum spacing coincides with the minimum structure amplitude, the split spot of the superlattice reflection on the lower diffraction angle side becomes weaker than that on the opposite side. Of course, this is only a qualitative explanation, and the knowledge on amplitudes of both of the modulations is necessary to explain this phenomenon quantitatively.

Finally the diffuse scattering will be discussed. The characteristic diffuse streaks, which are directed along ⟨110⟩ directions, have also been observed in early stages of ordering in CoPt[27)] and CuAu[28)], and in these cases qualitatively explained by the lattice distortion associated with the ordering process. The fact that the unit cells of both the ordered and disordered structures of these alloys differ considerably from each other in the crystal symmetry as well as in the lattice spacing has been considered to be a main cause of such a lattice distortion. In $CuAu_3$, however, the circumstances are not the same, i.e. no change in the crystal symmetry takes place and the change in the lattice spacing is far less than in these alloys. Therefore, the diffuse diffraction due to a lattice distortion could not be expected in the present case. In fact, it was concluded from the low temperature diffraction patterns that the diffuse diffraction observed in $CuAu_3$ is caused by the thermal scattering. This conclusion is also supported by the considerably low Debye temperature[29)] and the diffuse intensity distribution in reciprocal space shown in Fig. 9. The diffuse diffractions in this figure have the same sectional shapes of equal diffusion surfaces caused by thermal vibration of certain cubic crystals with the elastic anisotropic factor $2c_{44}/c_{11}-c_{12}$ of more than unity.

In conclusion the author wishes to express his sincere thanks to Professor S. Ogawa for his kind guidance throughout the work. His thanks are also due to Mr. D. Watanabe for his valuable discussions, and to Mr. K. Fujiwara for his helpful assistance in measurement of the resistivity. This work was supported in part by the fund of the Ministry of Education in Aid of Scientific Researches.

---

* Such a phenomenon has been pointed out in Cu_3Pd by Wilkens and Schubert[21)].

References

1) M. Hirabayashi: J. Phys. Soc. Japan **6** (1951) 129.
M. Hirabayashi: J. Japan Inst. Metals **16** (1952) 67.

2) S. Ogawa and D. Watanabe: J. Phys. Soc. Japan **7** (1952) 36.

8) H. Sato: Phys. Rev. **106** (1957) 674.

4) M. Hirabayasi and Y. Muto: J. Phys. Soc. Japan **12** (1957) 830.

5) F. P. Burns and S. L. Quimby: Phys. Rev. **97** (1955) 1567.

6) P. Wright and K. F. Goddard: Proc. Phys. Soc. **71** (1958) 506.

7) B. W. Batterman: J. Appl. Phys. **28** (1957) 556.

8) S. Siegel: J. Chem. Phys. **8** (1940) 860.
N. W. Load: J. Chem. Phys. **21** (1953) 692.

9) G. Borelius: J. Inst. Metals **74** (1947) 17.
M. Hirabayashi: J. Japan Inst. Metals **15** (1951) 565.

10) Y. Takagi and T. Oguchi: Bull. Tokyo Inst. Tech. **B3** (1950) 211.
G. J. Dienes: Acta Met. **3** (1955) 549.

11) A. Guinier and R. Griffoul: Rev. mét. **45** (1948) 387.

12) H. Reather: Z. angew. Phys. **4** (1952) 53.

13) K. Schubert, B. Kiefer, M. Wilkens and R. Haufler: Z. Metallk. **46** (1955) 692.

14) K. Fujiwara, M. Hirabayashi, D. Watanabe and S. Ogawa: J. Phys. Soc. Japan **13** (1958) 167.

15) D. Watanabe and S. Ogawa: J. Phys. Soc. Japan **11** (1956) 226.
M. Hirabayashi and S. Ogawa: J. Phys. Soc. Japan **12** (1957) 259.

16) J. M. Cowley: Phys. Rev. **77** (1950) 669.

17) M. Shimoji: J. Phys. Soc. Japan **11** (1951) 91.

18) S. Iida: J. Phys. Soc. Japan **10** (1955) 769.

19) F. E. Jaumot and A. Sawatzky: Acta Met. **4** (1956) 118.

20) N. F. Mott and H. Jones: *Theory of the Properties of Metals and Alloys* (Oxford Univ. Press, 1936).

21) M. Wilkens and K. Schubert: Z. Metallk. **48** (1957) 550.

22) D. Watanabe: J. Phys. Soc. Japan **13** (1958) 535.

23) B. E. Warren, B. L. Averbach and B. W. Roberts: J. Appl. Phys. **22** (1951) 1493.

24) B. W. Roberts: Acta Met. **2** (1954) 597.

25) G. D. Preston: Proc. Roy. Soc. **A, 167** (1938) 526.

26) A. J. C. Wilson: *X-ray Optics* (Methuen & Co. Ltd. 1949).

27) J. B. Newkirk, R. Smoluchowski, A. H. Geisler and D. L. Martin: Acta Cryst. **4** (1951) 507.

28) M. Hirabayashi and S. Ogawa: J. Phys. Soc. Japan **11** (1956) 907.

29) Y. Muto and M. Hirabayashi: to be published.

JOURNAL OF THE PHYSICAL SOCIETY OF JAPAN Vol. 14, No. 3, MARCH, 1959

Electrical Resistivity of Arc-evaporated Carbon Film

By Hiroo TOYODA,

Electrical Communication Laboratory, Nippon Telegraph and Telephone Public Corporation,

and Masahisa NAGASHIMA

Faculty of Technology, Waseda University

(Received November 14, 1958)

The electrical resistivities of arc-evaporated carbon films were studied. The resistance has a large negative temperature coefficient. The annealing diminishes remarkably both the resistance and its temperature dependency. The specific resistivity depends on the film thickness and increases rapidly below 500Å. It seems that the lattice imperfections play the most important role, and then from the annealing curve, their distributions are discussed. The aging effect on the resistance were also measured.

§1. Introduction

Several years ago, Bradley has invented an useful method of preparing the relica for electron microscope by arc-evaporated carbon film1). The evaporated film has a very amorphous structure and therefore can reproduce a faithful replica of the specimen. Since his invention, this technique became one of the most important and usual methods for electron microscopy2), but the various properties of the carbon film were not fully studied. Blue and Danielson3) have measured its electrical resistivities, while Agar4) and Cosslett5) have studied the relation between the optical densities and the film thickness. Kakinoki et al.6) have studied the structure by electron diffraction and discussed its singularity.

Carbon films are produced under several conditions, for example, thermal decomposition of organic compounds (pyrolytic carbon)7)–10), painting with colloidal carbon11), decomposition from carbon brush12), and so on. But, in most cases, these products lack the uniformity or contain some volatile matters, whose driving-off requires the heat-treatment at higher temperature. On the contrary, the arc-evaporated carbon film has a uniform thickness and homogeneous composition over the whole area, and furthermore, the evaporation can be made on substrates maintained at desired temperature, hence making possible to study the annealing of lattice imperfections in carbon.

As consequences of measuring the properties of the film, believed as the most amorphous carbonaceous solids, we have obtained some interesting results about the aging effects of electrical resistances, the relation between the conductivities or their temperature coefficients and the film thickness, and the annealing effects on them.

§2. Experimental Methods

Carbon rod for carbon replica, 0.5 cm in diameter, of Tokai Electrode Co. was used as the evaporating material. The sharpening contact was heated by alternating current. The substrates were photographic glass plate or transparent fused quartz, 0.5 cm × 1.5 cm in sizes. These substrates were arranged in a bell-jar, about 12 cm apart from the carbon source. The vacuum was maintained below 10^{-4} mmHg and the evaporating are was about 50Å/sec.

The film thickness was measured by a multiple-beam-interferometer13) using the light of 5461Å of Hg lamp. We measured also the optical density against the incandescent tungsten light by a microphotometer.

Gold film electrodes were evaporated on the carbon film at the two ends, leaving the naked carbon film 0.5 cm in breadth and 1 cm in length. The electrical resistance was measured potentiometrically or by micro-micro-ammeter under vacuum or in argon or air. In the case of glass substrates, the annealing was achieved under 400°C, while the quratz substrates were heated to 900°C in various atmospheres.

§ 3. Results

Optical densities were defined as $D = \log_{10}(I_0/I)$, where I is the light intensity transmitted through the film, while I_0 the one without film. If the films have the same absorption coefficient and the reflection at the surface is neglected, following relation should hold.

$$I = I_0 e^{-\alpha\tau},$$

where α is absorption coefficient and τ is thickness. I and I_0 were measured by a microphotometer.

There holds an approximately linear relation between the film thickness determined by multiple-beam-interferometer and the optical densities (Fig. 1). Cosslett has pointed out that the proportional constant has depended on the process of evaporation and that for thinner films than 200Å, the relation has deviated from the linearity. Thorn and Winslow[14)] have found two straight lines with different gradients according to the temperature of heated carbon source. Also in our cases, there exist some random variances from the straight line, but the relation is useful to deduce the thickness of thinner samples from its optical density, as it cannot be determined by the interferometry.

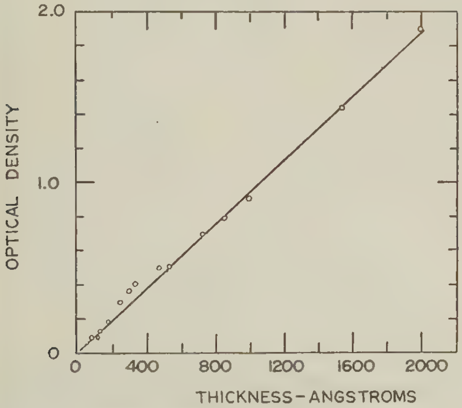

Fig. 1. Optical density versus film thickness.

Heat treatment of films always brings the optical density to increase. About 30 per cent increase was observed by 400°C annealing. The increase, however, is very small compared with the rise of electrical conductivities.

Though the coefficients of thermal expansion differ between glass and fused quartz about ten times, there is no difference between the temperature coefficients of electrical resistances of carbon films evaporated on both substrates. But when the thinner films were heated above 250°C, the carbon evaporated on glass was more easily annealed than the one on fused quartz. The annealing of carbon, 200Å thick, at 380°C brought 20 per cent difference of resistance between two substrates, though for the film thicker than 400Å this was not the case. The following results are concerned with quartz substrates.

Annealing was performed in atmospheres of argon or air of atmospheric pressure below 400°C, there being found no differences between them, and above it, the heat treatment in vacuum of 10^{-5} mmHg was used.

Fig. 2 shows an example of resistance change with temperature and annealing effects on it. The annealing begins at once above the evaporated temperature and brings a rapid decrease of resistance. Below the annealing temperature, the resistance changes with temperature reversibly. The curves of $\log R$ versus $1/T$ are concave downwards for all specimens and for all temperature ranges. As it is, however, known that the expression $R = R_\infty \exp(\Delta E/2kT)$ holds for carbonace-

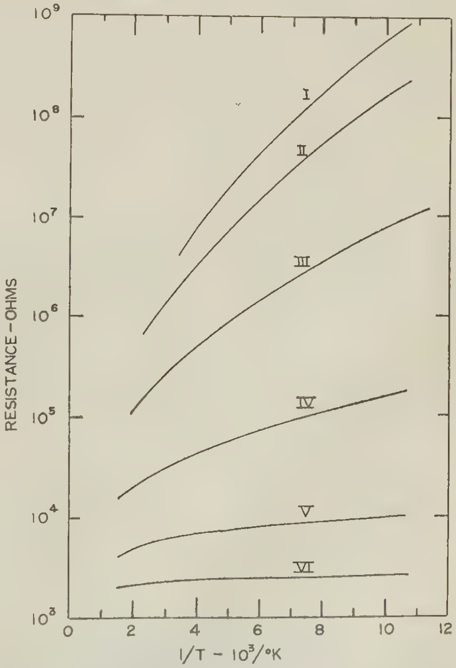

Fig. 2. Temperature dependence and annealing effect of resistance. Thickness is 380 Å. Annealing temperature: I, Unannealed; II, 140°C; III, 245°C; IV, 380°C; V, 500°C; VI, 900°C.

ous solids having the conjugate double bond[15)-17)], we will adopt this representation frequently. Fig. 2 suggests that ΔE for each film is not a constant, but it may have a continuous distribution over a certain region.

Blue pointed out that the curve of $\log R$ versus $\log T$ was linear and we also found it true, namely, $R=aT^{-b}$. b decreases with the film thickness and the annealing temperaperature. We have found $b=9$ for the 100Å film without annealing.

The thicker becomes the film, the less rapidly the resistance changes with temperature in the reversible region, while the more easily the annealing takes place. In Fig. 3, one can see the dependence of annealing effect on the film thickness. It shows the specific resistivity changes at 0°C accompanied with annealing.

The electrical resistivities at 0°C of the unannealed films change with film thickness. Below 500Å, the specific resistivity increases rapidly with the decrease in thickness. Above 500Å, it is almost constant and equals to 0.5 to 1 ohm-cm (Fig. 4).

Though the relation $R=R_\infty \exp(\Delta E/2kT)$ does not strictly hold, we have calculated the energy gap ΔE as an indicator of temperature coefficient, combining the value at

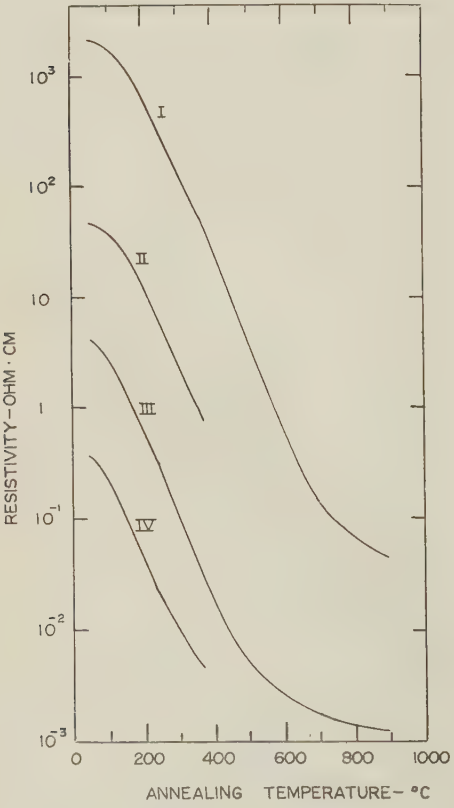

Fig. 3. Annealing effects on the specific resistivity at 0°C, for four films. Thickness: I, 110 Å; II, 200 Å; III, 380 Å; IV, 2000 Å.

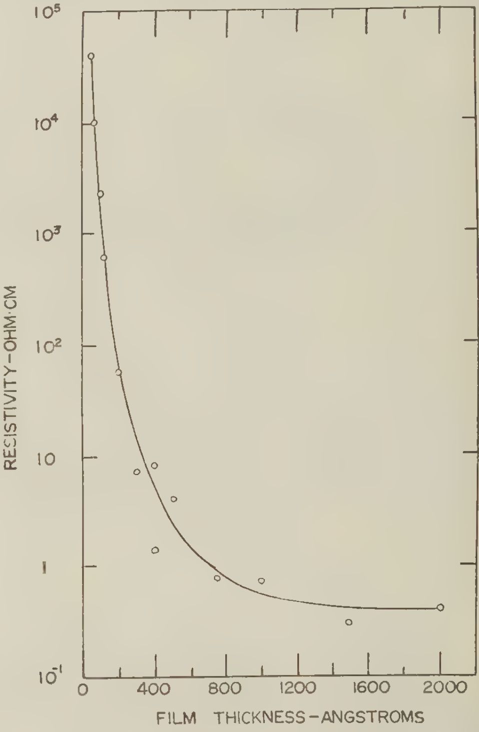

Fig. 4. Specific resistivity at 0°C versus film thickness.

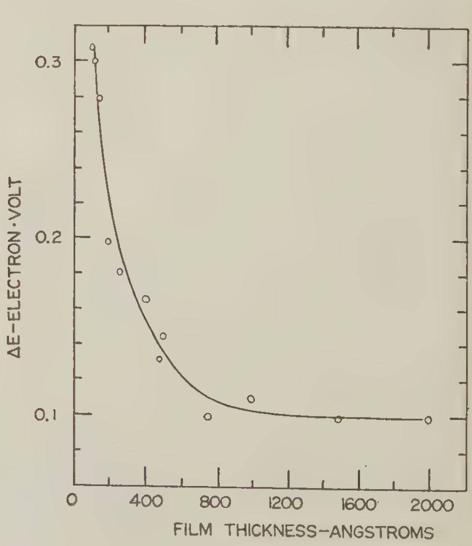

Fig. 5. ΔE versus film thickness. ΔE is calculated from the straight line combining the values at 0° and −73°C in Fig. 2.

−73°C with the value at 0°C by a straight line. ΔE depends also on the film thickness and is larger for thinner film. (Fig. 5) With the rise of annealing temperature, ΔE falls as well as resistivity (Fig. 6)

Fig. 7 shows the relation between the specific resistivity at 0°C and ΔE. It includes the values of ten films of different thickness ranging from 100 to 2000Å, unannealed and annealed at various temperatures under 900°C. There is a clear dependency, and in spite of different thickness or of annealing temperature, the carbon films of definite specific resistivity have the same temperature coefficient of resistivity. The result suggests the following fact; the carbon films with different thickness have different structures before annealing and the annealing rates for them are also different, but even though there are these varieties, when the specific resistivities become the same order, the carbon film have the resembling microscopic structure. It is, however, expected that this simple relation might not hold, when the thickness is extremely small.

In all experiments described above, the films were taken off after evaporation from the vacuum into the air and replaced in the resistance measuring vessel. The time exposed to the air was so long that the gas adsorption, if occurred, would reach the saturated state. Then, we intended to measure

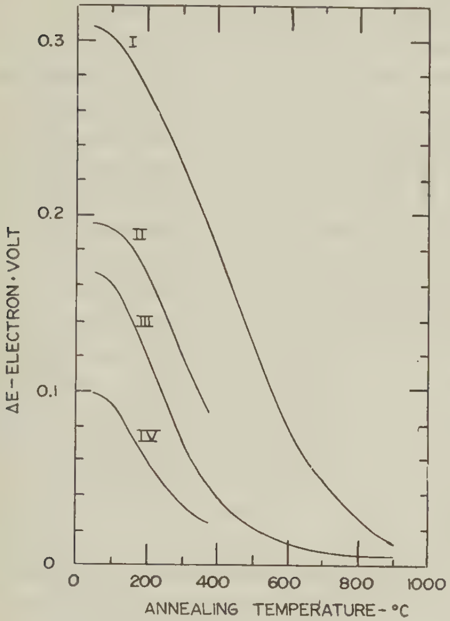

Fig. 6. Annealing effects on ΔE of four films. Thickness: I, 110 Å; II, 200 Å; III, 380 Å; IV, 2000 Å.

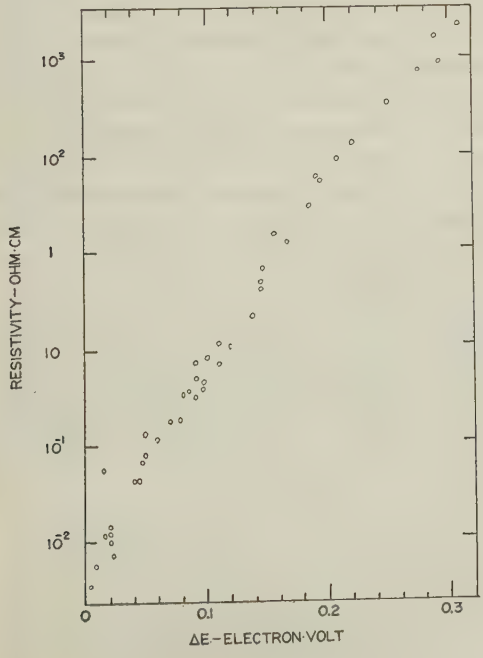

Fig. 7. Specific resistivity at 0°C versus ΔE.

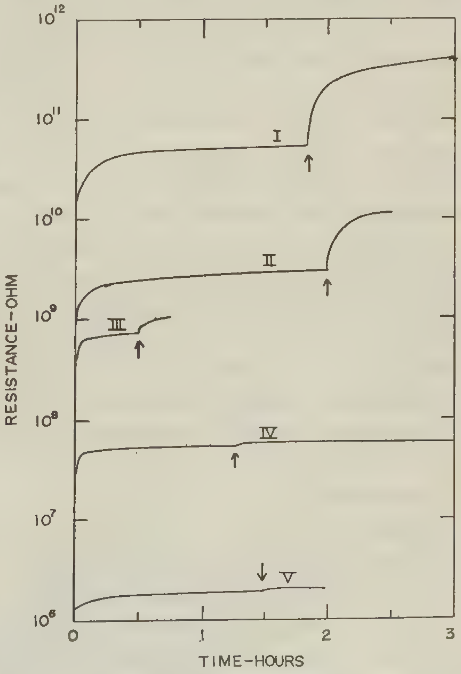

Fig. 8. Aging effects on resistance in vacuum and in air. Thickness: I, 40 Å; II, 50 Å; III, 80 Å; IV, 290 Å; V, 450 Å. Arrow shows the introduction of air of atomospheric pressure. Note; for I, full time scale is six hours.

the aging effect of resistance just after the evaporation.

Quartz substrates were preliminarily gold-evaporated at both ends, leaving bare space of $0.5\times0.5\,\mathrm{cm}^2$. D.C. 100 volt was given between the electrodes during and after the evaporation, and we observed the changes of electric resistances by micro-micro-ammeter. During the evaporation, the current indication could not be defined, presumably by disturbance of A.C. induction or ion current.

Fig. 8 shows the resistance variation after the deposition for several specimens of different thickness. Electric resistances for all films increased with time, and the smaller the thickness, the more remarkable the change. Though there seemed to be some differences according to the evaporation rate, they could not be made clear. Introduction of air brought further irreversible resistance increase for some thinner films.

The aging of silver or other metal film strongly depends on the evaporating condition and the thickness[18)-20)]. Aggregation makes the resistance higher, while the diffusion of Frenkel type doublet imperfections to the regular sites makes the resistance lower. For carbon film, however, the resistance always increases, more or less, whatever the thickness is. It is known that the evaporated carbon rather hardly aggregates in island, and our vacuum is not so good that it is inevitably influenced by oxygen. Furthermore, the irreversible increase after the air introduction suggests the possibility of oxidation. However, if the gas adsorption is a principal cause, it is questionable why the time constants of resistance increase are comparable for all thickness. There may be some effects of cooling of substrate after the evaporation and we are now clarifing them.

§ 4. Discussion

Carbonaceous solid is a general name for the extensive materials spreading over the range of aromatic compounds to graphite as two limiting cases. It is specified as having the π-electron network[21)-23)], and one can find a continuous characteristic change in the sequence, though the magnitude varies over some tens order. On the other hand, carbon atoms construct the tetravalent large crystal, namely, diamond. This has also some varieties in electric conduction and optical absorption or other properties[24,25], but these depend principally on the impurities or mosaic structure, in other words, on extrinsic causes[26)]. Kakinoki et al. have discussed the probable existence of diamond structure in carbon film, and if so, it might play some important roles in electric conduction. From the fact that the carbon film is black and subjected to the continuous annealing effect, we will, here exclude the contribution of diamond structure.

In organic compounds, when thermally decomposed, there develops progressively the π-electron network and carbonized materials become more and more conductive with the treatment temperature. The effective size of π-electron network determines the conduction electron density and the forbidden energy gap[27)]. It is not equal to the crystallite size, but depends on lattice imperfections, volatile impurities, and the electronic configuration on the periphery carbon atoms. The last one serves as surface acceptor level in some cases[28)]. The carbon film has as large number of lattice imperfections as other evaporated metals. These imperfections not only play the role of scattering for conduction, but also destroy the π-electron network and so diminish the effective size.

Vand has given a good analyzing method to investigate the decay of scattering centers[29)], and it is effective for studing the resistance annealing of neutron-irradiated polycrystalline graphite[30)]. For the carbon film which has very small crystallites, one can not, however, apply Vand's method in its original form. Vand's thought are as following; lattice defects decay in mutually independent process and the rate of decay is expressed by a relation,

$$dN/N=-c\cdot\exp(-\mathcal{E}/kT)\cdot dt,$$

where N is number of defects, c is a frequency factor, and $\mathcal{E}$ is a decay activation energy. Using an appropriate approximation, he has found a distribution of defects as function of $\mathcal{E}$. For materials with larger crystallites, one can put

$$R_i=R-TdR_T/dT=\int_{-\infty}^{\infty} r(\mathcal{E})\cdot N(\mathcal{E})\cdot d\mathcal{E},$$

where R: total resistance,

R_T: resistance caused by thermal oscillation of lattice,

R_i: resistance caused by lattice imperfections.

From the annealing curve, one can not obtain $r(\mathcal{E})$ and $N(\mathcal{E})$ separately, but their product.

For the carbon film, it is obvious that R_i is not proportional to the number of imperfections, but we have assumed that ΔE might be proportional to N. The assumption is not strictly well-founded. It is, however, well known that the forbidden band energy gap become progressively small in the sequence from aromatic compound to graphite with the increase of crystallite size. If ΔE is proportional to N, it turns into the assumption, from the relation seen in Fig. 7, that N would be proportional to $\log R$. Several years ago, we have studied the oxidation effect on the carbon contact resistance. Oxidation increases the resistance considerably and also augments the adsorption power of alkali$^{31),32)}$. adsorption gives the activity of carbon, which is considered as singularity of electronic configuration on the peryphery carbon atom. As a result, we have found that the adsorption was proportional to the logarithm of contact resistance. Though the two cases are not always parallel, linear dependency of ΔE on N is one of the simplest and probable thoughts.

Blue has found that there happened no development of long-range-order in the film by the annealing below 900°C. And furthermore, from a correlation, as seen in Fig. 7, among all the thickness which we have measured, it is not unreasonable to apply a common model of same crystallite size to all the films.

According to these assumptions and using Vand's tempering method, we have calculated the function, $F_0(\mathcal{E})=\Delta e(\mathcal{E})\cdot N(\mathcal{E})$, which belongs to the imperfection distribution before annealing. Δe is the contribution to ΔE of one imperfection. Fig. 9 shows $F_0(\mathcal{E})$ for three thickness. The ordinate is in arbitrary unit, but the curves are normalized under the condition that

$$\int_{\mathcal{E}_0}^{\infty} \Delta e(\mathcal{E}) N(\mathcal{E}) d\mathcal{E}$$

is proportional to ΔE. $\mathcal{E}_0$ corresponds to the evaporated temperature and the appropriate forms are assumed for the curves above the highest annealing temperature. It is clear that when the film thickness becomes smaller the peak rises and the distribution spreads over the wider region of activation energy. The distributions are not so different from the one for displaced atoms in neutron-irradiated polycrystalline graphite, but somewhat shift to higher energy.

When annealed at 900°C, the specific resistivities of films reach the same order as the carbonized organic compounds. Accordingly, the evaporated carbon has enormous number of lattice imperfections and the annealing brings them into regular sites without much larger crystallite growth. Extinction of imperfections increases the effective size of π-electron system and diminishes ΔE and the resistivity.

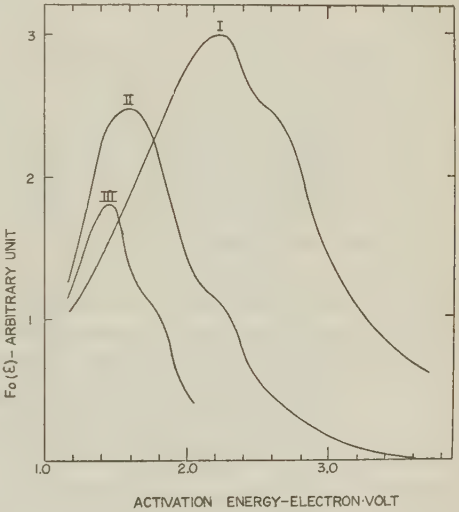

Fig. 9. $F_0(\varepsilon)=\Delta e(\varepsilon)\ N(\varepsilon)$ for three films. Thickness: I, 110 Å; II, 380 Å; III, 2000 Å. Though the ordinate is in arbitrary unit, the curves, drawn as $\int_{\varepsilon_0}^{\infty} F_0(\varepsilon)d\varepsilon \propto \Delta E$, are mutually comparable. If Δe (contribution of one imperfection) is independent of ε, the curves show the distribution of the number of imperfections, except unknown proportional constant.

It is not clear why the resistance increases irreversibly at room temperature after the evaporation. In the research of carbon contact resistance, which is sensitive to the surface gas adsorption, author* has found that in some cases there happened a reversible adsorption effect of oxygen on resistance$^{32)}$. Uebersfeld and Erb^{32} have observed the reversible effect of oxygen on paramagnetic resonance absorption. These may be explained as an interaction between the free radical on the peryphery carbon atom and oxygen. For polycrystalline graphite, it was reported that an irreversible oxidation at elevated temperatures becomes fast, when neutron-irradiated, the effect being caused by displaced atoms$^{34)}$. One can expect that the evaporated carbon, containing many imperfections, is apt to be influenced by gas adsorption, but it is a problem left hereafter to clarify the whole mechanism.

§ 5. Summary

The results are summarized as following.

1) Arc-evaporated carbon films have much higher resistivities than the orther carbon materials, in spite of their large carbon contents.

2) Resistivity depends on film thickness. It is equal to a nearly constant value as thickness exceeds 500Å, but it increases rapidly with decreasing film thickness below 500Å.

3) Themperature coefficient of resistivity is negative and depends on film thickness in a similar way as resistivity.

4) Annealing reduces the resistivity and its temperature dependency. Annealing rate becomes slow as the film thickness decreases.

5) For the films with various thickness from 100 to 2000Å and annealed at different temperatures up to 900°C, there holds an approximately linear correlation between ΔE and logarithm of resistivity. The relation seems to justify the application of a common structure model to all the films.

6) These special characteristics are considered to be attributed to the imperfections existing in the evaporated carbon. Lattice imperfections destroy π-electron network in carbon, and even if the films have the same crystallite size, the contents of imperfections bring about remarkable varietis of electric resistivity or its temperature coefficient.

7) Annealing displaces the imperfections into regular sites, and results in resistance and temperature dependency decrease. From the change of ΔE accompanied by annealing, distribution of imperfections as a function of decay activation energy is calculated. The distributions have maxima about at 1.5 to 2.1 eV, depending on film thickness.

8) As film thickness becomes extremely small, e.g., below 100Å, an effect of irreversible oxidation on resistance is observed.

We wish to thank Mr. H. Hirabayashi for his kindful advices and are grateful to Mr. H. Shibata and Miss T. Ayakawa for their co-operations.

References

1. D. E. Bradley: Brit. J. Appl. Phys. **5** (1954) 65.
J. Appl. Phys. **27** (1956) 1399.
2) E. Smith and J. Nutting: Brit. J. Appl. Phys. **7** (1956) 214.
3) M. D. Blue and G. C. Danielson: J. Appl. Phys. **28** (1957) 583.
4) A. W. Agar: Brit. J. Appl. Phys. **8** (1957) 35.
5) A. Cosslett and V. E. Cosslett: Brit. J. Appl. Phys. **8** (1957) 374.
6) J. Kakinoki et al.: Acta Cryst. **10** (1957) 829.
7) Blanc-Lapiere et al.: Compt. rend. **233** (1951) 141; 241.
8) A. R. G. Brown et al.: Nature **172** (1953) 1145.
9) H. Scmellenmeyer: Z. phys. Chem. **205** (1956) 349.
10) G. Becherer: Z. Phys. **205** (1956) 208.
11) W. J. Smith and N. J. Hoeflich: Bull. Amer. Meteorol. Soc. **35** (1954) 602.
12. R. H. Savage: J. Appl. Phys. **18** (1948) 1.
13) S. Tolansky: *Multiple Beam Interferometry* (Oxford Univ. Press, 1948).
14) R. J. Thorn and G. H. Winslow: J. Chem. Phys. **23** (1955) 1729.
15) H. Hirabayashi and H. Toyoda: J. Phys. Soc. Japan **7** (1952) 337.
16) S. Mrozowaki: Phys. Rev. **85** (1952) 609.
17) E. E. Loebner: Phys. Rev. **102** (1956) 46.
18) R. A. Aziz and G. D. Scott: Canad. J. Phys. **35** (1957) 785.
19) R. B. Belsler: J. Appl. Phys. **28** (1957) 109.
20) T. Sakurai: J. phys. radium **17** (1956) 274.
21) H. Akamatsu and H. Inokuchi: J. Chem. Phys. **20** (1952) 1481.
22) N. Riehl: Ann. Physik **20** (1957) 93.
23) J. C. Slonczewski and P. R. Weiss: Phys. Rev. **109** (1958) 272.
24) E. W. Mitchell: Proc. Phys. Soc. **B, 70** (1957) 527.
25) P. W. Wedepohl: Proc. Phys. Soc. **B, 70** (1957) 177.
26) F. C. Champion: Advances in Physics **5** (1956) 383.
27) H. Toyoda: Tanso **2** (1952) 4.
28) T. Gabor: Aust. J. Chem. **10** (1957) 135.
29) V. Vand: Proc. Phys. Soc. **55** (1943) 222.
30) M. Burton and T. J. Neubert: J. Appl. Phys. **27** (1956) 557.

31) H. Hirabayashi and H. Toyoda: Tanso **4** (1954) 2.
32) H. Hirabayashi: Elec. Comm. Lab. Tech. J. (To be published).
33) J. Uebersfeld et E. Erb: Compt. rend. **243** (1956) 363.
34) W. L. Koshiba and G. L. Dienes: Bull. Amer. Phys. Soc. Ser. II, **1** (1956) 137.

JOURNAL OF THE PHYSICAL SOCIETY OF JAPAN Vol. 14, No. 3, MARCH, 1959

Electrical Properties of Stannous Selenide

By Sizuo ASANABE*

Department of Physics, Faculty of Science,
Kyusyu University

(Received November, 22, 1958)

The electrical resistivity, Hall coefficient and thermoelectric power were investigated over the temperature range from 100°K to 800°K on pure and impurity-doped SnSe crystals. An anomalous hump of the Hall coefficient was found to occur at about 200°C in most of the as-grown crystals and this seems to make the conventional analysis based on a simple semiconductor model impossible. Anisotropies in the resistivity and Hall coefficient were also studied on single crystals and the observed anisotropy in the resistivity seems to be ascribed to an anisotropy in the effective mass of holes. Hole mobility varies as $T^{-2.0}$ at high temperatures and its discrepancy from $T^{-1.5}$ law is explained on the assumption of both optical and acoustical mode scatterings. Further investigation was made of the anomalous Hall coefficient on heating the specimen at various temperatures in vacuum. This anomalous phenomenon was found to depend on the heat-treatment history of the crystal and the experimental results were analysed on such a simple model that acceptors are introduced into SnSe by impurity diffusion above 200°C and caused to disappear on heating at lower temperatures. General features observed seem to be in fair agreement with the proposed model.

§ 1. Introduction

The systematic investigations have recently been made of IV–VI intermetallic compounds in our laboratory with respect to the electrical properties and crystal structures. The crystal structure of SnSe included in the same group has already been reported to be orthorhombic[1] and the preliminary experiments on electrical properties have shown that SnSe behaves as an ordinary *p*-type semiconductor[2]. The original aim of the present investigation was to obtain such physical quantities as the energy gap between the conduction band and valence band, its temperature dependence, the effective mass of electrons or holes, the ionization energy of impurity levels, etc. by performance of the further investigation on electrical properties of very pure SnSe single crystals. In the course of the experiment, we have encountered an anomalous phenomenon which might make the performance of our original aim impossible: the Hall coefficient exhibits an anomalous hump at about 200°C for most of the as-grown crystals as will be described later. According to a simple semiconductor model the Hall coefficient of a *p*-type semiconductor decreases with increasing temperature corresponding to the ionization of acceptors. After full ionization of the acceptors the Hall coefficient takes a constant value and then begins to decrease rapidly with the onset of intrinsic conduction. There should be no temperature range in which the Hall coefficient takes a positive temperature coefficient.

---

* Now at Research Laboratory, Nippon Electric Company Ltd., Kawasaki-shi, Japan.

The positive temperature coefficient of Hall coefficient found in Ge has been explained by impurity band conduction[3] or two hole model[4]. The Hall coefficients of p-type SnTe[5] and p-type GeTe[6] have also been found to take positive temperature coefficients and those of p-type GeSe[7], n-type InAs[8] and n-type GaAs[9] to show an anomalous behaviour. The mechanism is not yet fully understood, but in the case of n-type GaAs it is suggested that at 650°C a number of vacancies exist, possibly occupied by impurities, which trap electrons from the conduction band and give rise to a larger value of the Hall coefficient[10]. Our interests have transfered to the problem of studying some mechanism for the explanation of the observed anomalous behaviour for SnSe.

§ 2. Preparation of Specimens

In the earlier experiment[2] SnSe crystals were prepared in air from a melt containing larger amount of Se than in stoichiometric proportions which was covered with rock salt powder to protect from oxidization. This method is undesirable from such points of view that the obtained crystal might be affected considerably by oxygen, rock salt and excess selenium. All specimens used in the present investigation were prepared in vacuum as follows: the stoichiometric amounts of tin (J. M. 99.998% pure) and selenium (S. K. 99.999% pure) were sealed into an evacuated quartz tube. The inside of some quartz tubes was previously coated with thin carbon film in order to reduce oxygen diffusion, if any, from the wall of the tube into the SnSe melt. When the mixture of tin and selenium contained in the tube is heated to melt and then cooled to solidify, the tube is always forced to be broken and this results in the oxidization of SnSe by air. The unfavourable circumstance, however, may be avoided by a double-sealing technique: in spite of the break-up of the inner tube, the crystal is free from oxidization for the benefit of the outer tube. Putting the tube vertically into a furnace, where there is monotonously longitudinal and no transverse temperature gradient, it was kept at 1000°C for two days to expect the complete reaction. It was then cooled rapidly to 900°C and then with the cooling rate of 10°C per hour to 700°C (the melting point of SnSe=860°C). The melt begins to solidify from the bottom of the tube. In order to reduce such crystal imperfections as dislocations which might be present on solidification, the tube was annealed at 700°C for one day and cooled to 400°C with the speed of about 20°C per hour. The final stage of cooling process to room temperature was done by natural cooling after switching off the heater current. On cutting the obtained SnSe single crystal there must be paid a great care because of easy cleavage along the plane normal to c-axis. Specimens were cut in the shape of a rectangular parallelepiped of about $2\times 3\times 10\,\mathrm{mm}^3$ whose surfaces were polished by emery-paper. Some of the specimens used for anisotropy measurements were cut nearly in the shape of a cube whose edges were parallel to the three crystal axes.

§ 3. Experimental Procedures

An ordinary d.c. method was used on measuring the resistivity and Hall coefficient. Metallic electrodes were applied by means of vacuum evaporation of gold. Four constantan probes, the three on one surface and the rest on the opposite one, were welded by a condenser discharge method on a specimen set on a porcelain sample holder. The sample container was evacuated for low temperature measurements and was filled with nitrogen gas for high temperature measurements. In the course of low temperature measurement the sample container was immersed into a liquid air Dewar vessel between pole pieces of an electromagnet. High temperatures were realized by exchanging the Dewar vessel for a silica tube surrounded by a heating coil. The potential drop between a pair of resistivity probes was found to be linear with applied d.c. current up to 120 mA at both room and liquid air temperatures. Hall voltages at both temperatures were also shown to be a linear function of magnetic field strength up to 5 kilogauss which was measured using a search coil calibrated by a proton resonance technique. The d.c. current of 10 mA and magnetic field of 4 kilogauss were chosen for the most of the measurements. On measuring the potential difference between resistivity probes or Hall probes, we tried to eliminate the effect of the thermo-electromotive force which might be present, by reversing the direction of the current or the magnetic field.

So long as the resistivity and Hall coefficient are independent of magnetic field intensity, the galvano-magnetic effect can be expressed by the following equation[11]:

$$E_i=\rho_{ij}I_j+\varepsilon_{ijk}R_{km}I_jH_m\,, \tag{1}$$

where E_i, I_j and H_m represent, respectively, the rectangular components of the electric field, current density and magnetic field applied to a crystal. ρ_{ij} and R_{km} are the tensor quantities corresponding to the resistivity and Hall coefficient. In the case of SnSe which belongs to the space group D_{2h}, the above tensor components may be written in the form[12]

$$\rho_{ij}=\begin{bmatrix}\rho_{11} & 0 & 0\\ 0 & \rho_{22} & 0\\ 0 & 0 & \rho_{33}\end{bmatrix}, \quad R_{km}=\begin{bmatrix}R_{11} & 0 & 0\\ 0 & R_{22} & 0\\ 0 & 0 & R_{33}\end{bmatrix}. \tag{2}$$

ε_{ijk} in equation (1) is a tensor of the third rank which is equal to zero when $i=j$ or k, or $j=k$, but equal to 1 when $ijk=123$, 231 or 312 and equal to -1 when $ijk=213$, 321 or 132. Taking a, b or c-axis of the crystal as x_1, x_2 or x_3-axis, respectively, and I or H in an adequate direction, we can measure six tensor components in consideration of equations (1) and (2). This situation is shown in Table I.

Table I. Description of directions of both electric current I_j and magnetic field H_m to determine ρ_{ij} and R_{km}.

$E_i=\rho_{ij}I_j+\varepsilon_{ijk}R_{km}I_jH_m$					Measurable quantities
I_j	H_m	E_1	E_2	E_3	
I_1	H_2	$\rho_{11}I_1$	0	$R_{22}I_1H_2$	ρ_{11}, R_{22}
I_2	H_3	$R_{33}I_2H_3$	$\rho_{22}I_2$	0	ρ_{22}, R_{33}
I_3	H_1	0	$R_{11}I_3H_1$	$\rho_{33}I_3$	ρ_{33}, R_{11}

On measuring the thermoelectric power a pair of copper-constantan thermo-couples were inserted between brass current electrodes and the specimen. In order to obtain the temperature gradient two copper blocks with heating coils were in good thermal contact to the brass electrodes, but insulated electrically by thin mica films.

§ 4. Experimental Results

(i) *Resistivity and Hall coefficient*

The resistivity ρ and Hall coefficient R have been measured over the temperature range from 100°K to 800°K. The d.c. current and magnetic field were applied parallel and perpendicular, respectively, to the plane perpendicular to c-axis of the single crystal. In Fig. 1 (a), (b) and (c) are, respectively, shown the values of ρ, R and Hall mobility defined as $(8/3\pi)R\sigma$ for pure SnSe crystals. Fig. 2 shows the similar experimental results on impurity-doped and annealed SnSe crystals. The specimens used in these investigations

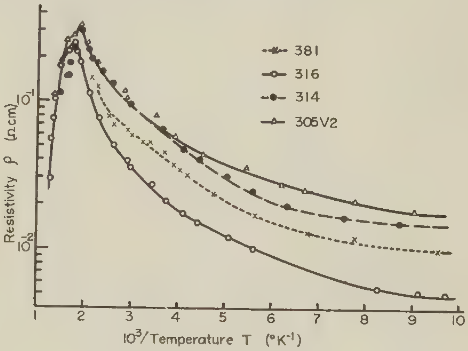

(a) Resistivity

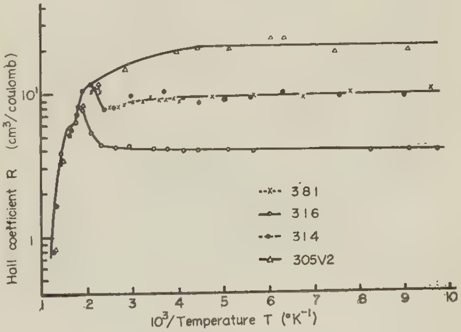

(b) Hall coefficient

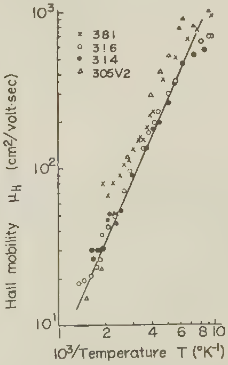

(c) Hall mobility

Fig. 1. Resistivity (a), Hall coefficient (b) and Hall mobility (c) versus inverse absolute temperature for pure SnSe crystals (p-type).

are listed in Table II. Specimens 381O$_2$ and 3NC11 were prepared for the purpose of detecting the effect of oxygen or rock salt on electrical properties by comparing the data with those of the specimen (S5) used in the earlier experiment[2].

(ii) *Anisotropy*

In Fig. 3 (a) and (b) ρ_{ij} and R_{km} defined in § 3 are plotted, respectively, against inverse absolute temperature for single crystal 311 prepared in a carbon-coated quartz tube. Measurements of ρ_{ij} and R_{km} were made first in the low temperature range and then in high temperatures according to the description given in Table I. All curves are on heating and numbers on the high temperature curves represent the order of the measurements. Once the specimen was heated up to high temperatures, then ρ_{ij} and R_{km} took smaller values than the initial ones at room temperature as seen in Fig. 3. Further investigation will be described later with respect to these irreversible phenomena. R_{km} shown in Fig. 3 (b) is the value after a correction due to sample dimension[13]. R_{km} after a correction seems to take a definite value independent of km in the low temperature measurements. Figs. 4 and 5 show ρ_{ij} in temperatures near room temperature for other SnSe crystals 305V1 and 305V3.

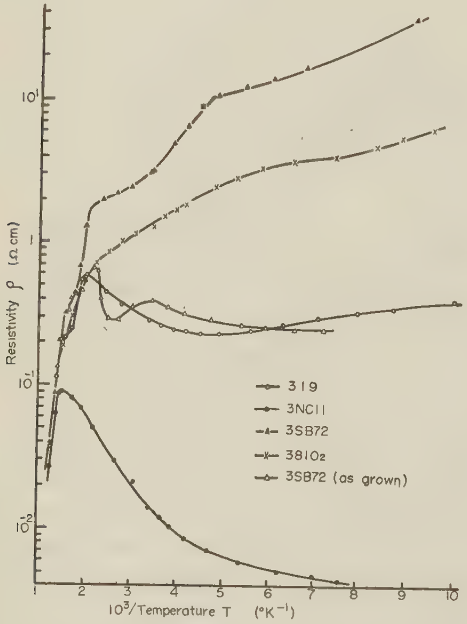

(a) Resistivity

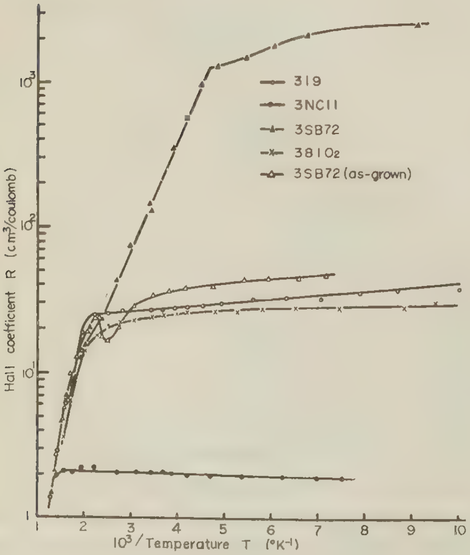

(b) Hall coefficient

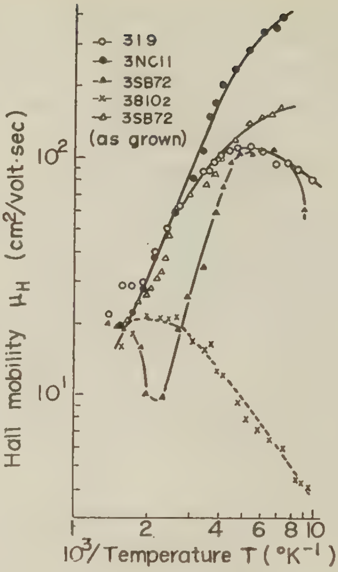

(c) Hall mobility

Fig. 2. Resistivity (a), Hall coefficient (b) and Hall mobility (c) versus inverse absolute temperature for impurity-doped and annealed SnSe crystals. For comparison, the data for as-grown sample 3SB72 are also included.

(iii) *Thermoelectric power*

The potential difference between both ends of the specimen due to the temperature gradient was measured, the temperature difference being within 10°C. Fig. 6 shows the thermoelectric power determined from the slope of the curve of the thermo-electromotive force plotted against the temperature difference.

Table II. Description of specimens.

Specimens	Origins of component materials Sn	 Se	Original composition	Heat-treatment	Crystal type
381	J.M.	S.K.	SnSe		single
316	J.M.	A.S.	SnSe		poly
314	J.M.	A.S.	SnSe		single
305V2	C.P.	C.P.	SnSe		single
3NC11	J.M.	S.K.	SnSe+10%NaCl	having any history of heat-treatment	poly
3I9	J.M.	S.K.	SnSe+a little I	200°C, 91.5 hr. in vac.	poly
3SB72	J.M.	S.K.	SnSe+0.1% Sb	200°C, 91.5 hr. in vac.	single
$381O_2$	381		SnSe	200°C, 12 hr. after 600°C, 70 hr. in air	single
311	J.M.	S.K.	SnSe*		single
305V1	C.P.	C.P.	SnSe		single
305V3	C.P.	C.P.	SnSe		single

Symbols:

J.M.	Johnson-Massey & Co.
S.K.	Shindengen Kogyo K. K.
A.S.	American Smelting and Refining Co.
C.P.	Commercial pure.

* Prepared in a carbon-coated quartz tube.

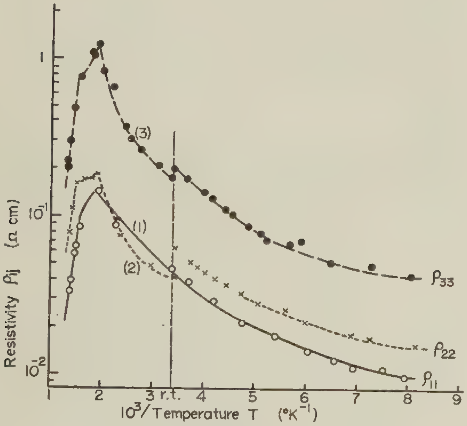

(a) Resistivity

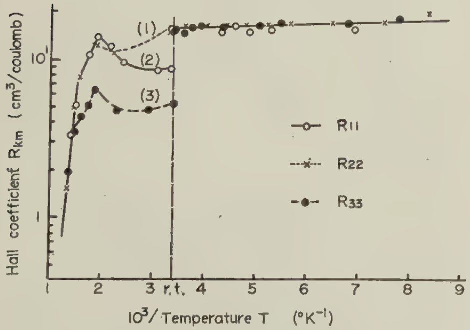

(b) Hall coefficients

Fig. 3. Tensor components corresponding to resistivity (a) and Hall coefficient (b) versus inverse absolute temperature for SnSe single crystal 311. Numbers on high temperature curves represent the order of measurements.

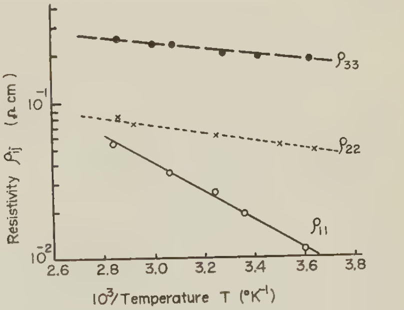

Fig. 4. Resistivity tensor components versus inverse absolute temperature for SnSe single crystal 305V1.

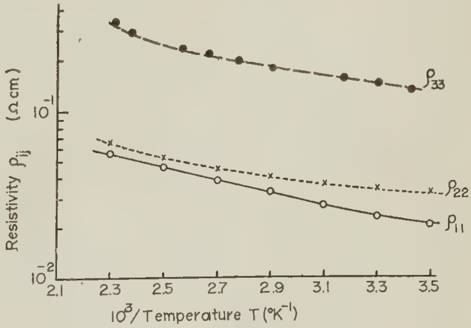

Fig. 5. Resistivity tensor components versus inverse absolute temperature for SnSe single crystal 305V3.

Specimens used in the measurements are also listed in Table II. The thermoelectric force of the single crystal 314 was measured in a direction perpendicular to *c*-axis.

(iv) *Irreversible phenomena*

In connection with the anomalous hump of R shown in Fig. 1 (b) or with the discontinuities of ρ_{ij} and R_{km} in Fig. 3, the detailed investigation is considered to be essential. We, here, attempted to make further experiments in order to clear up whether the anomalous hump of R should be reversible with the temperature, and how the discontinuities of ρ_{ij} and R_{km} should be dependent on the temperature and time of the heat-treatment.

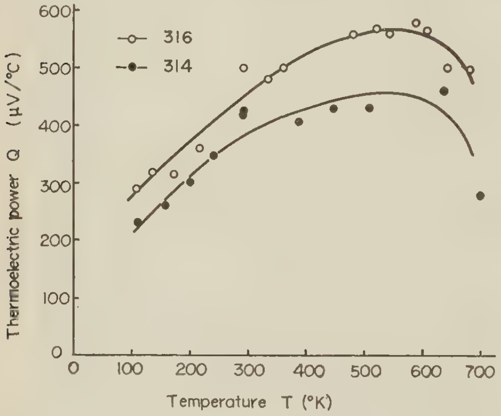

Fig. 6. Thermoelectric power versus absolute temperature for SnSe crystals.

(*a*) *Irreversible change*

When ρ and R of an as-grown crystal were measured with increasing temperature they exhibited maxima at about 200°C as shown by the O-curve in Fig. 7. When the temperature was decreased from the temperature corresponding to these maxima, ρ and R did not vary in accordance with the original curves but took higher values at room temperature: these increased gradually as the specimen was repeatedly subjected to heating cycles between 200°C and room temperature. This aspect is shown in Table III: each column of the table shows, from the left, respectively, the order of a heating cycle, the maximum temperature, the time for which the specimen was maintained at the maximum temperature, the cooling speed to room temperature. The values of ρ and R measured at room temperature after each heat-treatment are also shown in the last two columns. "*Low*" cooling speed means that of about 50°C per hour and "*high*" means such a speed that the time required for the decrease of temperature to a half value of the maximum temperature is of the order of ten minutes. The anomalous hump of R is no longer seen on the B-curve in Fig. 7 (b), which corresponds to the measurement after the 16th heat-treatment in Table III. The anomalous hump was observed to be appreciable again when the specimen

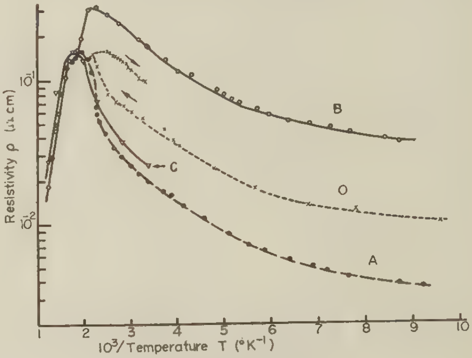

(a) Resistivity

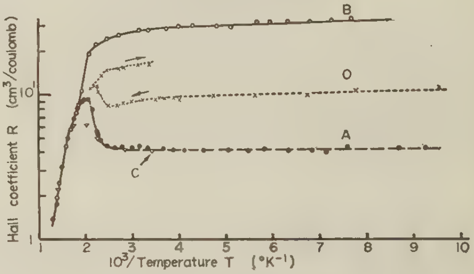

(b) Hall coefficient

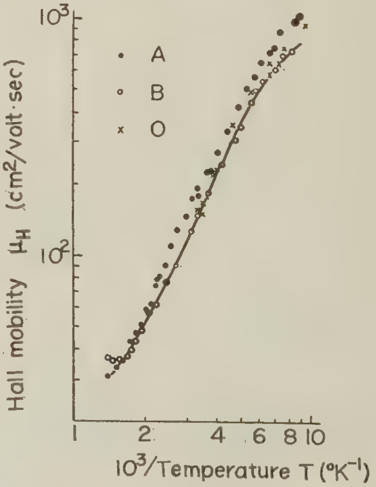

(c) Hall mobility

The curve is calculated from equation (4).

Fig. 7. Resistivity (a), Hall coefficient (b) and Hall mobility (c) versus inverse absolute temperature for SnSe single crystal 381. Curves O, B, A and C are obtained on as-grown, annealed, quenched, and again quenched crystal, respectively.

Table III. Changes in resistivity $\rho_{r.t.}$ and Hall coefficient $R_{r.t.}$ at room temperature with a series of heat-treatment for SnSe single crystal 381.

Order	$T_{\max}$ (°C)	Time (hr.)	Cooling speed	$\rho_{r.t.}\times 10^2$ (Ω cm)	$R_{r.t.}$ (cm^3/coulomb)
0	as-grown	——	——	5.33	9.8
1	199	3.0	low	9.24	15.9
2	206	0.5	low	11.8	21.2
3	243?	0.5	low	9.91	15.0
4	154	0.5	low	12.8	19.3
5	300	8.0	high	2.93	7.91
6	275	0.5	low	4.08	13.7
7	531	0.5	high	1.95	4.55
8	496	0.5	low	1.43	4.25
9	193	0.5	low	2.89	7.83
10	206	0.5	low	5.53*	14.2
11	215	0.5	low	3.31	20.9
12	222	0.5	low	4.06	20.6
13	212	0.5	low	4.03	25.0
14	199	0.5	low	3.59	27.9
15	204	0.5	low	3.78	30.6
16	184	0.5	low	16.3	28.2
17	519	0.5	high	2.03	4.32
18	490	0.5	low	1.87	4.47
19	431	0.5	low	——	——
20	200	12.0	low	13.4	19.4
21	346	0.5	low	5.51	9.88
22	494	0.5	low	3.05	7.41
23	437	0.5	high	2.53	4.09

* This series of low resistivity may be ascribed to a systematic error caused by a crack found parallel to the plane perpendicular to *c*-axis.

was gradually heated to 200°C after quenching to room temperature from 519°C after the 17th heat-treatment in Table III. This is shown by the A-curve in Fig. 7 (b). Repeating the similar measurement after quenching to room temperature from 490°C, ρ or R varied as shown by the C-curve which is nearly identical with the A-curve in Fig. 7. Fig. 7 (c) shows the Hall mobility, $R\sigma$, corresponding to the three measurements, O, A and B. The principal results obtained in the present experiment are summarized as follows:

(1) R at room temperature increases after the heat-treatment below 200°C and is independent of cooling speed, but by the heat-treatment above 200°C R at room temperature becomes smaller with higher cooling speed or higher temperature of the heat-treatment.

(2) The anomalous hump, being found to be irreversible, appears when R is small at room temperature, but disappears after R becomes larger by the heat-treatment below 200°C.

(3) The irreversible change in ρ or R seems to be ascribed to that in hole concentrations, because the Hall mobility undergoes no change in spite of the remarkable changes observed in ρ and R as seen in Fig. 7.

(*b*) *Correlation between R at room temperature and the heat-treatment temperature*

It is easily seen from the above experiment (*a*) that R at room temperature undergoes a remarkable change after the specimen is subjected to a heat-treatment at high temperatures. And from the fact (3) in (*a*) it seems that the heat-treatment at high temperatures should cause some new acceptor level to occur close to the valence band. It is worth while studying how R at room temperature depends on the temperature of the heat-treatment. The specimen sealed into an evacuated Pyrex tube is suddenly put into a furnace whose temperature was kept at 100°C. The specimen was kept at 100°C for 100 minutes and then quenched to room temperature by putting it out of the furnace. Then ρ and R were measured at room temperature. Next, the similar heat-treatment was made at 160°C for 100 minutes again. Repeating the measurement after increasing the temperature of the heat-treatment, R at room temperature varied as the B′-curve in Fig. 8 (a). The A′-curve shows the result obtained by repeating again the similar experiment after that of the B′-curve. Hall mobility does not change through the series of the heat-treatment as shown in

Fig. 8(b). Though the A′- and B′-curves in Fig. 8(a) are, respectively, in close resemblance to the A- and B-curves in Fig. 7(b), it is noted that the abscissa of Fig. 8(a) is not the temperature of the measurement but that of the heat-treatment and measurements of Fig. 8(a) are always made at room temperature.

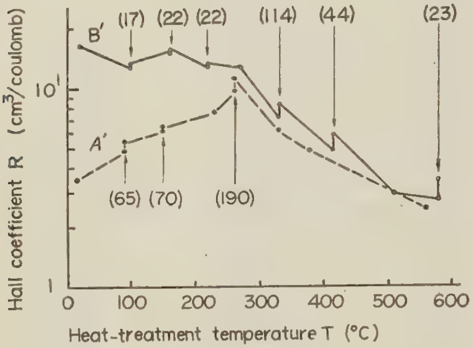

(a) Hall coefficient

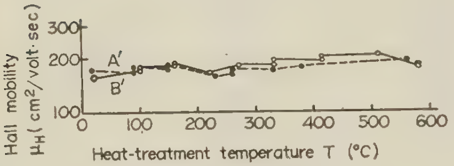

(b) Hall mobility

Fig. 8. Hall coefficient (a) and Hall mobility (b) at room temperature versus temperature of subsequent heat-treatment for SnSe single crystal 382. The heat-treatment period at each temperature is 100 min. Curves B′ and A′ are obtained on the first and second cycles of the heat-treatment, respectively. Numbers in parentheses show the times (in hours), for which the sample is being kept at room temperature not completely in dark, and which correspond to the period between two measurements indicated by the arrows from the numbers.

(c) *Correlation between R at room temperature and the heat-treatment time*

As seen in Fig. 8(a), R with a small value is inclined to become gradually larger, while a specimen is being kept at room temperature not completely in dark. And it is seen from the experiment (*a*) that R takes a larger value by a series of heating cycles below 200°C. In order to understand the anomalous behaviour of R it seems useful to investigate how R at room temperature depends on the time of heat-treatment for a fixed temperature of heat-treatment. The results of annealing effect at various temperatures are shown in Fig. 9. Here the left part of the curves shows a decrease in R which occurs when the temperature of heat-treatment is above 200°C and the right part corresponds to the heat-treatment below 200°C. In both cases the heat-treatment was made in an evacuated Pyrex tube. In Fig. 9 it is evident that for annealing at high temperatures R falls to a constant value in a few minutes, while R increases slowly with time for annealing at low temperatures. The value of R for long annealing time at low temperatures is also shown on each curve in the right part. A similar aspect by heat-treatment is seen in ρ and there is no remarkable change in the Hall

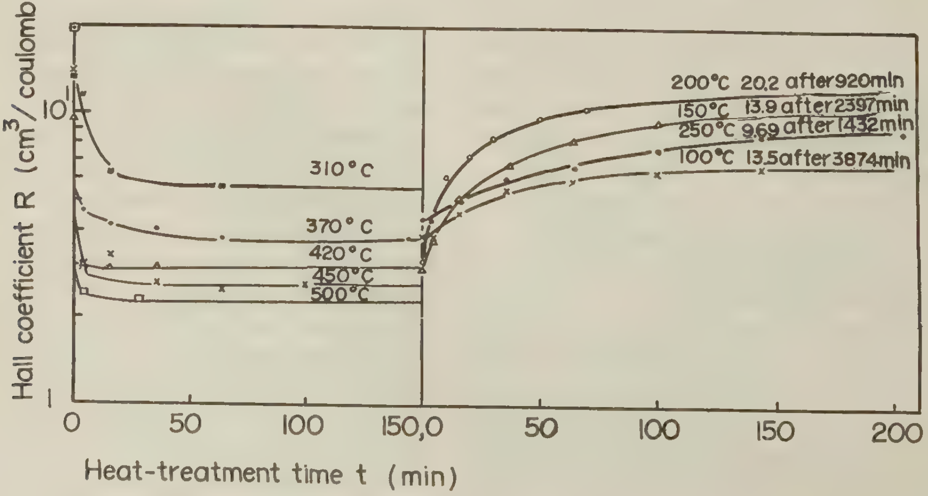

Fig. 9. Hall coefficient at room temperature versus time for various annealing temperatures for SnSe single crystal 382.

mobility. It may be concluded that R approaches in a long time a definite value independent of temperature in the case of heat treatment below 200°C, while R reaches in a few minutes a constant value characteristic to the annealing temperature in the case of heat-treatment above 200°C. In Fig. 10 the above constant saturation value of R is plotted against the annealing temperature above 200°C for a number of specimens listed in Table IV (as for 3SB72 and 3NC11, see Table II).

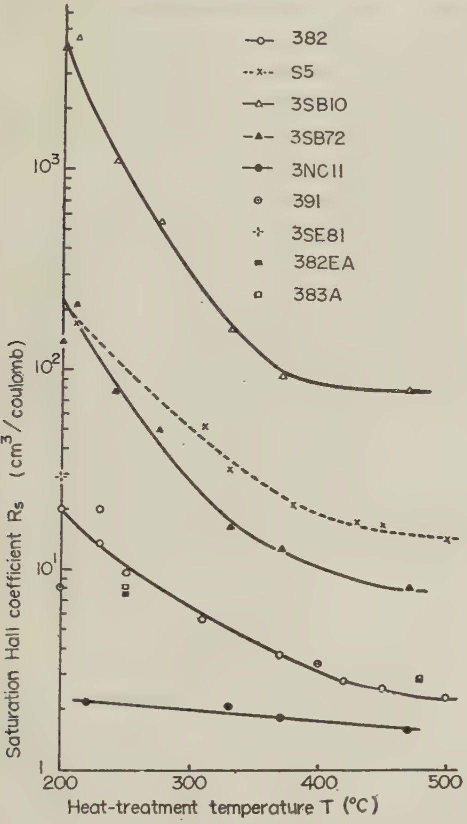

Fig. 10. Saturation Hall coefficient versus temperature of heat-treatment for various pure, impurity-doped and annealed SnSe crystals.

§ 5. Discussion

(i) *Resistivity and Hall coefficient*

It is seen in Fig. 1 that for pure as-grown specimens (314, 316 and 381) which have no heat-treatment history, the resistivity increases monotonously with increasing temperature up to 200°C and then falls via a weak step at about 350°C, and the Hall coefficient, being constant in the temperature range from liquid-air to room temperature, shows an anomalous hump at 200°C and then falls abruptly via a step at about 350°C similar to that in the resistivity. As seen in Fig. 2, among impurity-doped specimens the annealed antimony-doped one 3SB72 especially has large values of the resistivity and Hall coefficient in low temperatures, but the Hall coefficient decreases abruptly from −70°C and approaches a common curve for pure SnSe specimens. This behaviour suggests that antimony atoms in SnSe act as donors at low temperatures and as acceptors at high temperatures. Here, such a model may be proposed that donor levels lie above the valence band by 0.15 eV estimated from the slope of the curve of the Hall coefficient in the low temperature range. If there is any covalent character in SnSe and antimony atoms enter into the lattice by substitution

Table IV. Description of specimens.

Specimens	Origins of component materials Sn	Se	Original composition	Heat-treatment	Crystal type
382	J.M.	S.K.	SnSe		single
S5*	C.P.	C.P.	SnSe		single
3SB10	J.M.	S.K.	$Sn_{0.995}Sb_{0.005}Se$	200°C, 91.5 hr. in vac.	single
391	J.M.	S.K.	$SnSe_{1.002}$		single
8SE81	381		SnSe**	200°C, 150 hr. in Se-gas	single
382EA	382		SnSe***	750°C, 3 hr. in 10 cmHg-A-gas	single
383A	J.M.	S.K.	SnSe	750°C, 3 hr. in 10 cmHg-A-gas	single

Symbols: J.M. Johnson-Massey & Co.
S.K. Shindengen Kogyo K. K.
C.P. Commercial pure.

* used in the earlier experiment[2].

** Se-film evaporated on the surface before heat-treatment.

*** the surface cleaned by HNO_3 before heat-treatment.

for tin atoms, it is reasonable for antimony atoms to act as donors in low temperatures. While no remarkable change is observed in the Hall coefficient for iodine-doped (3I9) or heat-treated ($381O_2$) SnSe, the impurity scattering is observed to be predominant in low temperatures as seen in Fig. 2 (c). The reason is not yet understood why the temperature dependence of the Hall mobility of the annealed antimony-doped specimen is remarkably different from that of the as-grown one as shown in the figure. As there is almost no difference between pure and impurity-doped SnSe as to high temperature curves of the resistivity and Hall coefficient, it may be considered that a certain conduction mechanism is dominant at high temperatures which is independent of impurity concentrations. We shall discuss with respect to this point in a later section.

As seen in Fig. 1 (c) the Hall mobility of holes in SnSe varies with temperature as $T^{-2.0}$. If we take into account an optical mode scattering in addition to an acoustical mode scattering and an impurity scattering, the mobility is given approximately as [14]

$$1/\mu=bT^{3/2}+c\{\exp(\Theta/T)-1\}^{-1}+aT^{-3/2}\,. \tag{3}$$

The first term of the equation corresponds to the acoustical scattering and the second the optical one with the Debye temperature Θ and the last the impurity one. In the case of the specimen 381 the experimental points are well represented by the following equation:

$$\begin{aligned}1/\mu=&5.6\times10^{-7}T^{3/2}\\&+3.6\times10^{-2}\{\exp(580/T)-1\}^{-1}\\&+7.0\times10^{-1}T^{-3/2}\,,\end{aligned} \tag{4}$$

as shown in Fig. 7 (c). In the earlier experiment[2] the reversal of the Hall coefficient was observed at high temperatures and the results were analysed to show $b=3.2$ as the ratio of electron to hole mobility and $E_g=0.8$ eV as the energy gap between conduction band and valence band, but we cannot perform the analysis of the present results on a simple semiconductor model. The reason will be presented later. The specimens used in the present experiment have smaller Hall coefficients but larger hole mobility than in the earlier specimen[2]. This means that there took place much compensation between donors and acceptors due to more impurities in the latter. It is of interest that the difference in electrical properties between the earlier specimen and the present ones seems to be attributed to the deviation from stoichiometric compositions in the former, because the effect of oxygen or rock salt which might be considered to exist in the specimen there has been proved to be less important for electrical properties in the high temperature range as shown by 3NC11 in Fig. 2.

(ii) *Anisotropy*

As the shape of specimens used in the study of anisotropy is nearly cubic a uniform current flow is difficult to be realized and Hall voltage must be corrected owing to the geometry of a specimen. From these points of view a cubic specimen seems to be undesirable, but it may be worse to make measurements and discussions on three specimens of different orientations elongated along the direction of the current flow: an anisotropy may be covered with some differences of electrical properties from sample to sample. We, here, adopted a cubic specimen, the relative values being more important than the absolute ones in an anisotropy experiment.

The first of characteristics which are seen in Fig. 3 is that once a specimen is heated up to high temperatures, the Hall coefficient does not go back to its initial value but takes a smaller value. As this will be discussed later in detail, we shall here restrict the discussion to the low temperature range. The fact that there is no anisotropy observed in R after correction seems reasonable in consideration of the proportionality of the Hall coefficient to inverse carrier concentrations. From Figs. 3 (a), 4 and 5, it is found that there holds the relation,

$$\rho_{33}>\rho_{22}\gtrsim\rho_{11} \tag{5}$$

and the ratio, $\rho_{33}:\rho_{22}:\rho_{11}$, seems to be independent of the temperature except for the specimen 305V1. The electrical resistivity ρ is written in the form

$$\rho=(pe\mu_h)^{-1}\,, \tag{6}$$

where p and μ_h are the hole concentration and mobility, respectively. The mobility is expressed by

$$\mu_h=\frac{e}{m_h}\tau_h \tag{7}$$

in terms of effective mass m_h and life time

τ_h of holes. Then we attempt to attribute the anisotropy observed in the resistivity to that of mobility or effective mass of holes, assuming an isotropy of τ_h. From equations (5), (6) and (7) the following relation holds between m_{11}, m_{22} and m_{33}:

$$m_{33} > m_{22} \gtrsim m_{11} \qquad (8)$$

where each suffix corresponds to that of the resistivity. If a constant energy surface is nearly of the shape of the ellipsoid of the revolution which is elongated in the direction of x_3-axis in momentum space, the relation (8) may be understood. This seems to be compatible with the fact that the lattice spacing along x_3-axis is great compared with other spacings. On account of the incompleteness of the experiment, we cannot make further discussion in connection with the electronic structure[15].

(iii) *Thermoelectric power*

The thermoelectric power Q in the impurity range of non-degenerated semiconductors is expressed by Johnson and Lark-Horovitz[16] as follows:

$$\begin{aligned} Q=(k/e)[\ln(|R|T^{3/2})-\ln r-7.16 \\ +q+(3/2)\ln(m_h/m_0)]\,, \qquad (9) \end{aligned}$$

where R is the Hall coefficient, m_0 the free electron mass, r and q are numerical factors which depend upon relative proportions of lattice and impurity scatterings, the lattice scattering being assumed to be due to the acoustical mode only. As seen in Fig. 1 (c) lattice scattering is predominant in low temperatures and we may approximately assume $q=2$ and $r=1.18$, respectively. Then the effective mass of holes may be estimated by substituting R in Fig. 1 (b) and Q in Fig. 6 into equation (9):

$m_{314}=0.5m_0$ for single crystal 314,

and

$m_{316}=1.4m_0$ for polycrystal 316.

As to the difference between the above two estimated values of m we cannot discuss in detail with confidence, but may explain as follows: effective mass which contributes to hole flow to build up the thermo-electromotive force may be probably regarded as the mean of m_{11} and m_{22} for the single crystal sample 314 or of m_{11}, m_{22} and m_{33} for the polycrystalline one 316, respectively. The relations,

$$\left.\begin{aligned} & m_{11} < m_{314} < m_{22} \\ \text{and} \\ (m_{11} \lesssim)\ \ & m_{22} < m_{316} < m_{33}\,, \end{aligned}\right\} \qquad (10)$$

and then

$$m_{314} < m_{316} \qquad (11)$$

will be expected from the relation (8). The relation (11) is in a qualitative agreement with the experimental results.

(iv) *Irreversible phenomena*

The irreversible change observed in the resistivity or Hall coefficient may be ascribed to the change in hole concentrations because the value of hole mobility is independent of the heat-treatment. In order to make the matters in question clear we will summarize the principal results given in § 4 (iv):

(1) Hole concentration at room temperature increases by the heat-treatment above 200°C and approaches a constant value in a few minutes.

(2) The increased hole concentration decreases slowly by the heat-treatment below 200°C.

(3) For the heat-treatment above 200°C hole concentration at room temperature takes a saturation value which is characteristic to the temperature of heat-treatment, and for the heat-treatment below 200°C it approaches in a long time a definite value which is independent of the temperature of heat-treatment.

(4) The saturation values of hole concentrations which are characteristic to the temperature of heat-treatment differ from sample to sample depending upon the impurity concentrations.

(5) The above saturation values seem to approach a definite value with increasing temperature of the heat-treatment.

Recognizing the above five facts we can explain straightforwardly an anomalous hump at 200°C and a step at 350°C on the A-curve in Fig. 7 (b). The increase in the Hall coefficient with increasing temperature may be attributed to a decrease in hole concentration corresponding to the low temperature heat-treatment by (2). With further increasing temperature the Hall coefficient decreases due to increase in hole concentration by (1). The observed step at 350°C seems to show that the intrinsic conduction begins to take place, being superposed on the increase in hole concentration by (1) and (5).

At first we assumed a "*trap model*" to explain the anomalous phenomena. This states that there are electron trap levels below the conduction band and a number of electrons are trapped at high temperatures. On quenching a specimen from high temperatures trapped electrons are not afforded to escape from the trap levels. If the direct recombination of trapped electrons with holes in the valence band is forbidden, trapped electrons must jump in the conduction band to recombine with holes in the valence band by getting sufficient thermal energy. This occurs with increasing temperature and will result in an anomalous hump on the A-curve in Fig. 7(b). But we should abandon the above trap model, because it seems unable to explain a decrease in hole concentrations which occured in the intrinsic range in the specimen S5 showing the reversal of the Hall coefficient at high temperatures.

Then an alternative model—an "*impurity-diffusion model*"—is proposed. When SnSe is heated at above 200°C a certain number of acceptors are generated under thermal equilibrium. On quenching, these acceptors are left generated. This causes to increase hole concentrations even at room temperature because an ionization energy (not a formation energy) of the acceptors is considered to be very small as suggested from the A-curve in Fig. 7(b) in which the Hall coefficient is shown to be constant down to liquid air temperature. We should distinguish these acceptors from the original ones whose density is never changed by the heat-treatment. Acceptors generated on quenching disappear gradually to re-establish a new condition of thermal equilibrium at room temperature as shown in Fig. 8(a). The time required for this recovery is very long on account of the small thermal energy at room temperature. An increase in the Hall coefficient with increasing temperature to 200°C may be then expected reasonable. It is considered probable that acceptors are formed by diffusion of a certain kind of impurity atoms into certain sites in SnSe at high temperatures just as in the case of Cu in Ge[17]. The impurity atoms do not seem to come from the surface but seem to exist originally in the bulk, because the acceptor formation does not depend upon thickness of the specimen or cleanness of the surface (382EA). Another possible mechanism for the acceptor formation is expected to be lattice imperfections which might be present at high temperatures. If the acceptors were originated only from the Frenkel-type imperfections[18], the acceptor density should increase exponentially with increasing temperature of heat-treatment as $\exp(-E/kT)$ and never approach a definite value at high temperatures as seen in all of the specimens. And then the acceptor density generated at high temperatures should be a function of the temperature of heat-treatment only and should not depend upon impurity concentrations as seen in Fig. 10. It is likely that a considerable number of Se vacancies exist in SnSe crystals and impurity atoms diffuse into these vacancies to act as acceptors. Precautions were taken to reduce Se vacancies while preparing the specimen 391 or 3SE81, but it was not clarified whether Se vacancies might not be reduced or the reduction of Se vacancies might be ineffective on acceptor formation. And also in order to reduce the imperfections, e.g. dislocations, which are likely occupied by impurity atoms, care was taken in preparing the specimen 382EA or 383A, but no useful results were obtained. In the present investigation we have nothing to refer to the kind of impurity atoms or the location of acceptor sites.

We shall here discuss the experimental results on a simple model described above, assuming that impurity X-atoms (w_0/cm^3) in certain sites (w_0/cm^3) act as acceptors when they diffuse into certain sites (v_0/cm^3) of vacancies. To distinguish the above impurity atoms from the original impurity atoms which are never affected by the heat-treatment the term X-atom is adopted. If the vacancies are occupied by p(cm^{-3}) of X-atoms at the temperature T, the variation of p with time may be written in the form

$$\frac{dp}{dt}=C_1(v_0-p)(w_0-p)-C_2p^2, \qquad (12)$$

where C_1 and C_2 are functions of T. The first term on the right side of equation (12) represents the acceptor formation and the second term the acceptor disappearance, respectively. Under thermal equilibrium equation (12) is equal to zero and this leads to

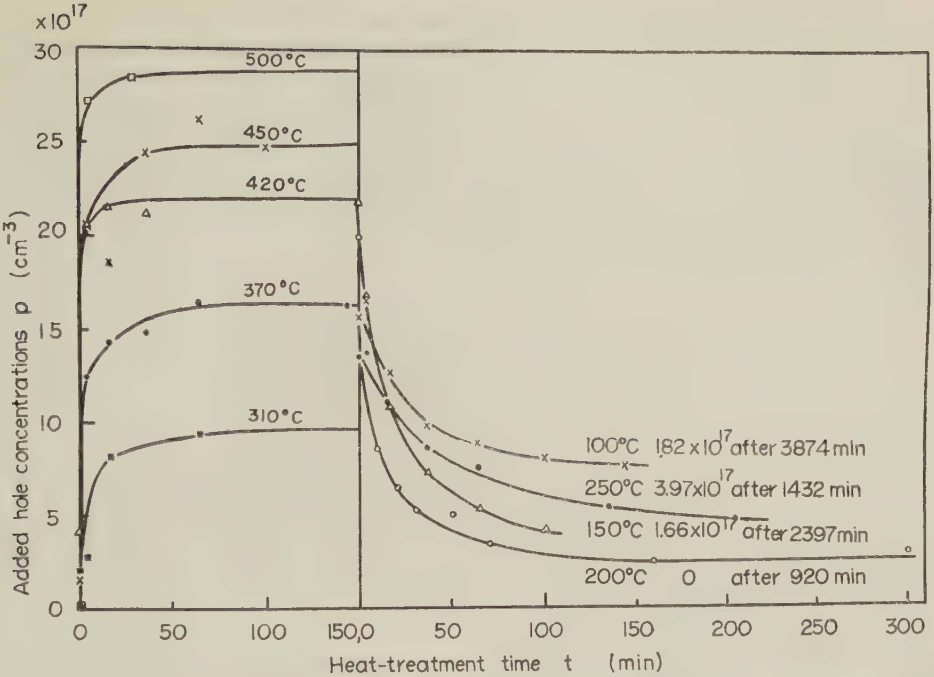

Fig. 11. Variation of added hole concentrations with time for various annealing temperatures for SnSe single crystal 382. The added hole concentrations are derived from the Hall coefficients given in Fig. 9.

$$p=\begin{Bmatrix}\alpha\\ \beta\end{Bmatrix}$$

$$=\{(v_0+w_0)\pm\sqrt{(v_0-w_0)^2+4\gamma v_0w_0}\}/2(1-\gamma) \qquad \text{for} \quad \gamma \neq 1\,, \qquad (13)$$

where

$$\gamma=C_2/C_1\,. \qquad (14)$$

Introducing equation (13) into equation (12) we obtain

$$\frac{dp}{dt}=C_1(1-\gamma)(p-\alpha)(p-\beta)\,. \qquad (15)$$

Thus, under the initial condition of $p=p_0$ at $t=0$ the solution of equation (15) is expressed as follows:

$$p=\frac{\alpha-\beta A\exp\left[C_1(1-\gamma)(\alpha-\beta)t\right]}{1-A\exp\left[C_1(1-\gamma)(\alpha-\beta)t\right]}\,, \qquad (16)$$

where

$$A=\frac{p_0-\alpha}{p_0-\beta}\,. \qquad (17)$$

Under thermal equilibrium p is easily proved to be represented by β (not by α). And it is also seen that the general feature of the curve of p versus t in equation (16) corresponds to the left part for $p_0<\beta$ or to the right part for $p_0>\beta$ of Fig. 11 in which the numbers of added holes calculated from the Hall coefficient in Fig. 9 are plotted against the time of heat-treatment.

First, in the case of the heat-treatment below 200°C the hole disappearance exceeds the hole formation as observed in the experiment. Thus, the first term of equation (12)

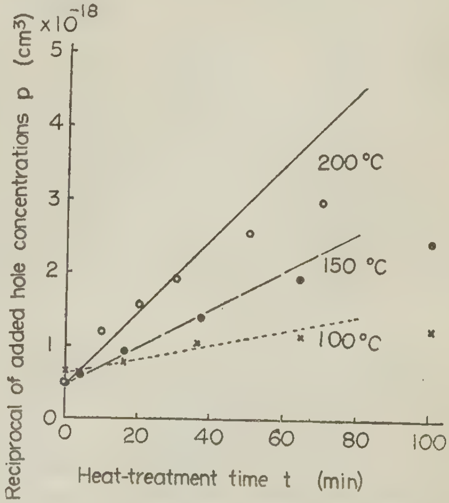

Fig. 12. Reciprocal of added hole concentrations versus time for three annealing temperatures for SnSe single crystal 382.

may be neglected approximately, obtaining

$$\frac{1}{p}=\frac{1}{p_0}+C_2 t\,. \qquad (18)$$

Fig. 12 shows the plots of $1/p$ versus t at three different temperatures. We can obtain C_2 at each temperature by drawing a rough straight line. The linear relationship in the plot of $\log C_2$ versus $1/T$ is shown in Fig. 13, obtaining

$$C_2=1.8\times10^{-16}\exp(-0.25/kT)\,,\quad (kT \text{ in eV})\,. \qquad (19)$$

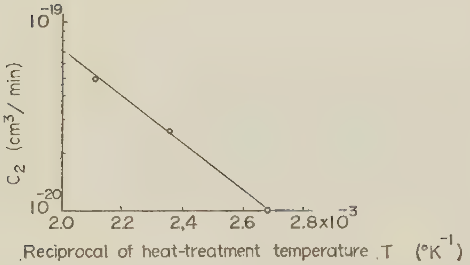

Fig. 13. Plot of C_2 versus reciprocal of heat-treatment temperature for SnSe single crystal 382.

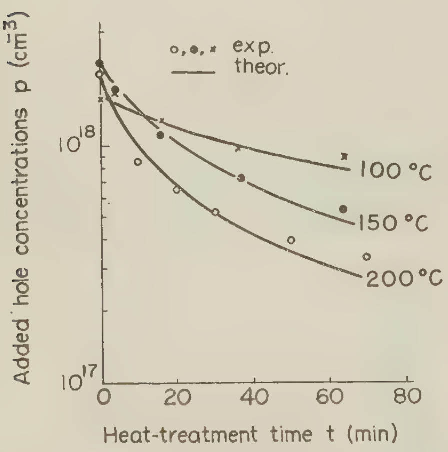

Fig. 14. Comparison between theoretical and experimental values with respect to added hole concentrations versus time for three annealing temperatures for SnSe single crystal 382.

A comparison of the theoretical curve with the experimental points for p is shown in Fig. 14. The experimental values tend to deviate from the theoretical curve with increasing time and increasing temperature. This deviation seems to be ascribed to the above neglect of the first term in equation (12).

Next, we shall discuss with respect to the heat-treatment above 200°C. Under thermal equilibrium condition, p is equal to β as mentioned above, and under the assumption $v_0=w_0$ which means that all of Se vacancies are occupied by the same number of X-atoms when the crystal is grown from the melt, equation (13) is reduced to the simple form,

$$\beta=\frac{v_0}{1+\sqrt{\gamma}}\,. \qquad (20)$$

On the other hand, C_1 and C_2 may be, respectively, written in the forms

$$\left.\begin{aligned} &C_1=C_{10}\exp(-E_1/kT) \\ \text{and}\quad & \\ &C_2=C_{20}\exp(-E_2/kT)\,, \end{aligned}\right\} \qquad (21)$$

where C_{10} (or C_{20}) is independent of T, and E_1 (or E_2) corresponds to the formation (or disappearance) energy of acceptors. We thus obtain

$$\beta=\frac{v_0}{1+\sqrt{C_{20}/C_{10}}\exp\{-(E_2-E_1)/2kT\}} \qquad (22)$$

by substituting equations (14) and (21) into equation (20). Experimental values of β obtained from the curves in Fig. 10 are shown

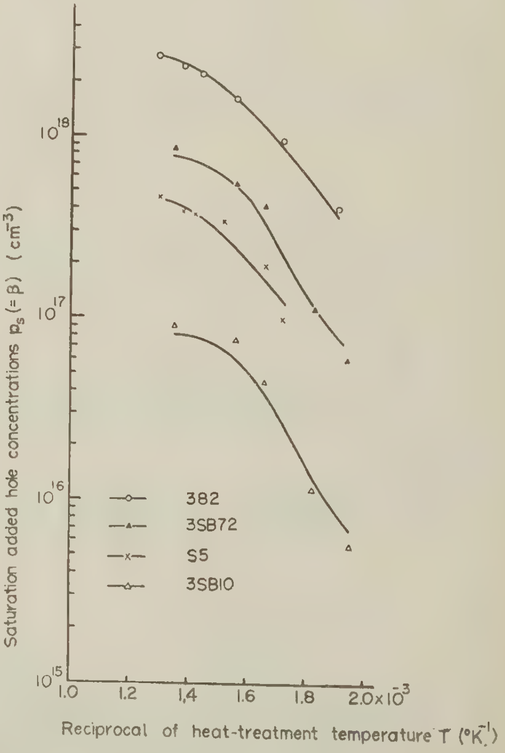

Fig. 15. Comparison between theoretical and experimental values with respect to saturation added hole concentrations versus reciprocal of heat-treatment temperature.

in Fig. 15. It is easily seen that these experimental points may be represented by equation (22), which is expected to show nearly a straight part at the low temperature range. From the average slope of their straight parts for samples 382, S5, 3SB10 and 3SB72, the value $E_2-E_1=1.18$ eV is obtained. Using this value we may estimate the value of v_0 and $\sqrt{C_{20}/C_{10}}$ so that the theoretical curves can fit the experimental points. The theoretical curves with the common value of $\sqrt{C_{20}/C_{10}}=2\times10^{-5}$ and the different values of $v_0\times10^{-17}=34$, 5.3, 1.1 and 9.6, respectively, for samples 382, S5, 3SB10 and 3SB72 are shown in Fig. 15. Thus C_1 may be expressed as follows:

$$C_1=4.5\times10^{-7}\exp(-1.43/kT)\,. \tag{23}$$

Calculated curves of C_1 and C_2 are shown in Fig. 16 and that of γ in Fig. 17.

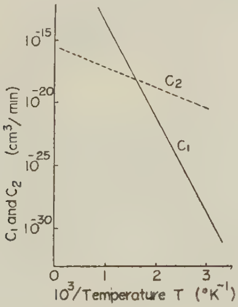

Fig. 16. Plots of C_1 and C_2 versus inverse absolute temperature.

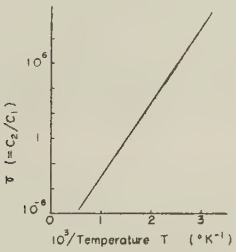

Fig. 17. Plot of $\gamma(=C_2/C_1)$ versus inverse absolute temperature.

At last, we shall show that the steep increase in p as seen in Fig. 11 may be explained on the proposed model. At elevated temperatures, we obtain from equation (16)

$$p\approx v_0-\frac{v_0-p_0}{1+(v_0-p_0)C_1t} \tag{24}$$

because $\gamma\ll1$ from Fig. 17. The time required for attainment of p to a half of (v_0-p_0) is of the order of 10^{-4} min. at 1000°K. When $\gamma=1$ which corresponds to 670°K, p is represented from equation (12) as follows:

$$p\approx\frac{v_0}{2}+\left(p_0-\frac{v_0}{2}\right)\exp(-2C_1v_0t)\,. \tag{25}$$

The value of p reaches approximately the half maximum after $t\approx1/2C_1v_0\approx10^{-1}$ min. The values of these times agree qualitatively with the experimental results shown in Fig. 11.

§ 6. Conclusion

The electrical resistivity, Hall coefficient and thermoelectric power of SnSe crystals were investigated, but we could not analyse fully on a simple semiconductor model. The reason is that a conventional assumption that the hole density in the valence band is equal to the sum of electron density in the conduction band and acceptor density does not hold on account of acceptor formation at high temperatures. Experimental results could be interpreted qualitatively on a simple model of acceptor formation. Impurity band conduction model or two holes model does not seem to be applicable for the present case of SnSe, because either model is expected to imply only the reversible phenomena with temperature, while there take place the irreversible phenomena in SnSe. And also the positive temperature coefficient observed in the Hall coefficient of SnTe or GeTe is reported to be reversible with temperature. In these points of view the anomalous Hall coefficient for SnSe may be concluded to be essentially different from the positive temperature coefficient observed in some materials described above. The irreversible phenomena observed in SnSe seem to resemble the case of GaAs or GeSe. Such a change in carrier concentrations with the heat-treatment as observed in SnSe is also observed in pulled Si[19] crystals though in the case of Si the donors are found to be introduced at about 500°C after a long time of the heat-treatment and caused by the presence of oxygen[20] probably. Appearance of donors at lower temperatures and their disappearance at higher temperatures seem to be equivalent to saying that acceptors disappear at lower temperatures and appear at higher temperatures.

We attempted to ascribe the mechanism of acceptor formation to the impurity diffusion rather than lattice imperfection and resulted in a qualitative agreement with the experimental results. The value of 0.59 eV of $(E_2-E_1)/2$ is of comparable order with 0.55 eV or 0.80 eV as the corresponding formation energy of donors found in PbS or PbSe and PbTe at high temperatures[21], in which the mechanism is not yet known. But some arbitrary assumptions were adopted in the present discussion to simplify the calculations: the numbers of X-atoms are equal to X-atom sites or vacancies in their numbers. In reality, we can say nothing as to the kinds of X-atoms or the mechanism by which the acceptor is formed. It is probable that the number of Se vacancies will vary with temperature and at high temperatures lattice imperfections of other kinds may take place. But the fact that experimental results can be explained on a simple impurity diffusion model seems to suggest that the model described above is a main factor in the mechanism of acceptor formation. A further investigation especially on optical absorption is desired to obtain the energy gap and the trap level, if any.

In conclusion, the author should express his sincere thanks to Prof. A. Okazaki for his kind guidance and encouragement. He is also indebted to Dr. T. Okada, Dr. K. Hirakawa, Messrs. Y. Matsukura and K. Hashimoto for their interests in the present investigation.

References

1) A. Okazaki and I. Ueda: J. Phys. Soc. Japan **11** (1956) 470.
2) Y. Matsukura, T. Yamamoto and A. Okazaki: Mem. Fac. Sci. Kyusyu Univ. Ser. **B, 1** (1953) 98.
3) C. S. Hung: Phys. Rev. **79** (1950) 727.
4) T. Fukuroi and K. Hanzawa: reported at the Meeting of the Physical Society of Japan, Oct. 31, 1956.
5) K. Hashimoto and K. Hirakawa: J. Phys. Soc. Japan **11** (1956) 716.
6) Y. Moriguchi and K. Koga: J. Phys. Soc. Japan **12** (1957) 100.
S. Asanabe and A. Okazaki: Mem. Fac. Sci. Kyusyu Univ. Ser. **B, 2** (1958) 136.
7) A. Okazaki and S. Asanabe: reported at the Meeting of the Physical Society of Japan, Apr. 9, 1957.
8) O. G. Folberth und H. Weiss: Z. Naturforsch. **11 a** (1956) 510.
9) O. G. Folberth und H. Weiss: Z. Naturforsch. **10 a** (1955) 615.
10) J. T. Edmond, R. F. Broom and F. A. Cunnell: "*Report of the Meeting on Semiconductors*" held by the Physical Society, London (1956) p. 109.
11) W. P. Mason, W. H. Hewitt and R. F. Wick: J. Appl. Phys. **24** (1953) 166.
12) T. Okada: Mem. Fac. Sci. Kyusyu Univ. Ser. **B, 1** (1955) 157.
13) I. Isenberg, B. R. Russel and R. F. Green: Rev. Sci. Instr. **19** (1948) 685.
14) E. Hirahara and M. Murakami: J. Phys. Soc. Japan **9** (1954) 671.
15) T. Okada: Mem. Fac. Sci. Kyusyu Univ. Ser. **B, 1** (1955) 168.
16) V. A. Johnson and K. Lark-Horovitz: Phys. Rev. **92** (1953) 226.
17) R. A. Logan: Phys. Rev. **95** (1955) 615.
18) S. Mayburg: Phys. Rev. **95** (1955) 38.
19) C. S. Fuller, J. A. Ditzenburger, N. B. Hannay and E. Buehler: Acta Met. **3** (1955) 97.
20) For example, C. S. Fuller and R. A. Logan: J. Appl. Phys. **28** (1957) 1427.
21) R. A. Smith: Physica **20** (1954) 910.

JOURNAL OF THE PHYSICAL SOCIETY OF JAPAN Vol. 14, No. 3, March, 1959

A Note on the Theories Underlying the Polarimetric Study of Very Thin Dielectric Surface Layers

By Sadao NOMURA and Koreo KINOSITA

Department of Physics and Chemistry,
Gakushuin University, Mejiro, Tokyo

(Received December 6, 1958)

Polarimetric study of very thin dielectric surface layers on dielectric substrates has been most frequently based on Drude's theory, or on Sissingh and Groosmuller's theory obtained by improving the approximation of Drude's calculation. These theories are derived by modifying the boundary conditions for Maxwell's equations. A quite different approach to this problem is possible, however, which is based on discussions concerning the interference of light inside the surface layer.

It has been proved by several workers that Drude's theory is consistent with the interference theory. It is proved in this paper that Sissingh and Groosmuller's theory is also consistent with the interference theory. Some formulae derived in the process of proof are believed to be useful for further discussions in this field.

§ 1. Introduction

The usual method of polarimetric study of a thin dielectric surface layer, be it the so-called *transition layer* or an alien film, on a homogeneous dielectric substrate consists in allowing a parallel beam of linearly polarized light fall on the surface and observing some of the parameters of the elliptical vibration orbit of the reflected light. It is at least in principle possible to express any parameter P of this vibration ellipse like

$$P=P(d, \varepsilon; \varepsilon_1, \varepsilon_2, \varphi_1, \alpha_0, \lambda)\,, \qquad (1)$$

where the symbols in the right-hand side stand for the following quantities respectively (see Fig. 1):

d : thickness of the surface layer.
ε, ε_1 and ε_2: dielectric constants of the surface layer, the ambient medium and the substrate respectively.
φ_1: angle of incidence.
α_0: azimuth of the incident linearly polarized light.
λ : wavelength of light.

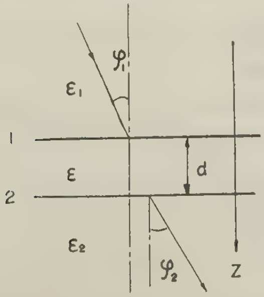

Fig. 1. Illustration for Eq. (1).

The refractive indices of the surface layer, the ambient medium and the substrate are given by $n=\sqrt{\varepsilon}$, $n_1=\sqrt{\varepsilon_1}$ and $n_2=\sqrt{\varepsilon_2}$ respectively.

Parameters included in Eq. (1) other than d and ε may be regarded as known quantities. Hence, if we know the functional form of P, and if ε is homogeneous throughout the surface layer or if it denotes the mean dielectric constant of the layer, we can evaluate some simple combination of d and ε, say nd, by the measurement of P. It will be possible to evaluate d and ε separately if two mutually independent P's can be measured. Equations of the type of Eq. (1) shall be called the *equations of polarimetry* in this paper.

The equation of polarimetry which has been most frequently used in this kind of study is that of Alkemade1) and Drude2) (Eq. (8)). Some workers3),4) preferred to Sissingh and Groosmuller's3) two equations (Eqs. (13) and (15)) derived by improving the approximation of Drude's calculation. The above mentioned authors start from a model illustrated in Fig. 2 (a), in which it is assumed that

1° ε is a continuous function of z (z is the coordinate parallel to the inward normal of the surface): $\varepsilon(z)$. $\varepsilon(z)$ is equal to ε_1 at the boundary 1 and is equal to ε_2 at the boundary 2.

2° $d \ll \lambda$.

They derive the boundary conditions for Maxwell's equations valid for the *composite surface* 1–2 by integrating Maxwell's equations under the assumption 2°, and obtain the amplitude reflectives, so to say the modified Fresnel coefficients, valid for this composite surface. In this calculation Drude neglects the second and the higher powers in d/λ and arrives at Eq. (8), whereas Sissingh and Groosmuller take the second powers in d/λ into consideration and arrive at Eqs. (13) and (15). It would be noteworthy that, although these theories assume a continuous variation of ε in the surface layer, what is actually evaluted is nothing but $\bar{\varepsilon}$, a kind of mean value of $\varepsilon(z)$ (see below). For the convenience of later reference, we shall call these theories *the boundary condition theories.*

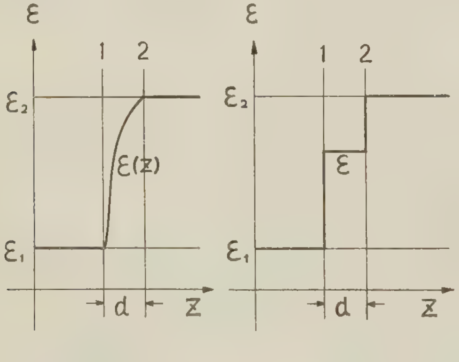

(a) (b)

Fig. 2. Models adopted in (a) *boundary condition theory* and (b) *interference theory.*

A quite different approach to this problem is possible, in which one starts assuming that the dielectric constant is homogeneous and is equal to ε throughout the surface layer (Fig. 2(b)). In this case, any parameter of the elliptical orbit of the reflected light can be calculated by considering the interference of light in the surface layer, or rather *film.* Theories of this kind shall be cited as the *interference theories.*

Now, a question arises: Do the boundary condition theory and the interference theory yield the same equation(s) of polarimetry if $\bar{\varepsilon}$ in the former theory is equated with ε in the latter theory? As for the first order theories in which only the first powers of d/λ are taken into account, it has been proved by several workers[5] that Drude's result is consistent with that of the interference theory. But no proof has yet been given of the agreement of the results of Sissingh and Groosmuller's theory with those of the interference theory where terms up to the second powers in d/λ are taken into account.

The immediate purpose of this paper is to present an elegant proof of this consistency. Some formulae derived in the process of proof are believed to be useful for further discussions in this field.

§ 2. Preparatory Notes

For the convenience of later reference, a brief description of the equations of polarimetry referred to above will be given in this section. To avoid unnecessary complications, it will be assumed in this and the following sections that

$$\varepsilon_1 = 1 \quad \text{and} \quad \alpha_0 = \pi/4\,. \tag{2}$$

From the second assumption it follows that the ratio in amplitude reflectivity of the p- and the s-components of the electric vector, $\boldsymbol{r}_p/\boldsymbol{r}_s$, is equal to the ratio in (complex) amplitude of the p- and the s-components of the reflected beam, $\boldsymbol{R}_p/\boldsymbol{R}_s$.

a) *Drude's theory (D-theory)*

In this theory in which only the first powers in d/λ are taken into account, it can be shown[2] that

$$\frac{\boldsymbol{R}_p}{\boldsymbol{R}_s} = \frac{\boldsymbol{r}_p}{\boldsymbol{r}_s} = -\frac{\cos(\varphi_1+\varphi_2)}{\cos(\varphi_1-\varphi_2)} \times \left\{1 + i\frac{4\pi}{\lambda}\,\frac{\varepsilon_2}{1-\varepsilon_2}\,\frac{\cos\varphi_1 \sin^2\varphi_1}{\sin^2\varphi_1 - \varepsilon_2\cos^2\varphi_1}\,\eta\right\}. \tag{3}$$

Here φ_2 denotes the angle of refraction of the substrate for the angle of incidence φ_1, and

$$\eta = \int_1^2 \frac{(\varepsilon-1)(\varepsilon-\varepsilon_2)}{\varepsilon}\,dz\,. \tag{4}$$

If φ_1 is equal to φ_B, the *Brewsterian angle* of the substrate, i.e. if

$$\varphi_1 = \varphi_B = \tan^{-1}\sqrt{\varepsilon_2}\,, \qquad \varphi_1+\varphi_2 = \pi/2\,, \tag{5}$$

Eq. (3) is reduced to

$$\left[\frac{\boldsymbol{R}_p}{\boldsymbol{R}_s}\right]_B = i\,\frac{\pi}{\lambda}\,\frac{\sqrt{1+\varepsilon_2}}{1-\varepsilon_2}\,\eta\,. \tag{6}$$

The suffix B indicates that this is the value for $\varphi_1 = \varphi_B$. If we represent the ratio in real amplitude R_p/R_s and the phase difference of the p- and the s-components by ρ and Δ respectively,

$$\frac{\boldsymbol{R}_p}{\boldsymbol{R}_s} = \frac{R_p}{R_s} e^{i\Delta} = \rho e^{i\Delta} . \tag{7}$$

From Eq. (6) and Eq. (7) we get*

$$\rho_{\mathrm{B}} = \pm \frac{\pi}{\lambda} \frac{\sqrt{1+\varepsilon_2}}{1-\varepsilon_2} \eta , \tag{8}$$

$$\Delta_{\mathrm{B}} = \pm \pi/2 . \tag{9}$$

Eq. (9) means that if $\varphi_1 = \varphi_{\mathrm{B}}$ one of the principal axes of the elliptical orbit of the reflected beam lies in the plane of incidence, or that the Brewsterian angle φ_{B} is equal to the *principal angle of incidence* φ_p.

Thus measurement of ρ, the ellipticity of the orbit at the Brewsterian angle incidence, will give η. If we apply the mean value theorem to Eq. (4) and define the *mean dielectric constant* of the surface layer $\bar{\varepsilon}$ by

$$\eta = \frac{(\bar{\varepsilon}-1)(\bar{\varepsilon}-\varepsilon_2)}{\bar{\varepsilon}} d , \tag{10}$$

a combination of d and $\bar{\varepsilon}$ as given by Eq. (10) can be determined experimentally. If we could assign an appropriate value to $\bar{\varepsilon}$ by some other reasoning, we would be able to evaluate d itself.

b) *Sissingh and Groosmuller's theory* (*SG-theory*)

These authors[3)] took the second powers in d/λ into account and arrived at the following equation under the same assumptions as those underlying the derivation of Eq. (6).

$$\left[\frac{\boldsymbol{R}_p}{\boldsymbol{R}_s}\right]_{\mathrm{B}} = i \frac{\pi}{\lambda} \frac{\sqrt{1+\varepsilon_2}}{1-\varepsilon_2} \eta + \frac{4\pi^2}{\lambda^2} \frac{1}{4(1-\varepsilon_2)^2(1+\varepsilon_2)} \eta \Theta . \tag{11}$$

Here η is given by Eq. (4) and

$$\Theta = -(1+\varepsilon_2) \int_1^2 \frac{\varepsilon^2(3+\varepsilon_2) - \varepsilon(1+4\varepsilon_2-\varepsilon_2^2) + \varepsilon_2(1-\varepsilon_2)}{\varepsilon} dz . \tag{12}$$

From Eq. (11) are derived the following equations which correspond to Eqs. (8) and (9).

$$\left\{ \begin{aligned} \rho_{\mathrm{B}} &= \pm \frac{\pi}{\lambda} \frac{\sqrt{1+\varepsilon_2}}{1-\varepsilon_2} \eta , && (13) \\ \cot \Delta_{\mathrm{B}} &= \frac{\pi \Theta}{\lambda(1-\varepsilon_2^2)\sqrt{1+\varepsilon_2}} . && (14) \end{aligned} \right.$$

The difference between D-theory and SG-theory lies in that the latter clears up the inequality between φ_p and φ_{B} ($\Delta_{\mathrm{B}} \neq \pm\pi/2$). The difference is very small, however, and can be shown to be

$$\varphi' = \varphi_p - \varphi_{\mathrm{B}} = -\frac{2\pi^2}{\lambda^2} \frac{\varepsilon_2 \sqrt{\varepsilon_2}}{(1+\varepsilon_2)(1-\varepsilon_2^2)^2} \eta \Theta . \tag{15}$$

Now, if we make measurements of φ' and ρ_{B}, we can make a separate evaluation of the thickness and the dielectric constant of the surface layer from the simultaneous equations of polarimetry, Eqs. (13) and (15). For this, however, again we have to apply the mean value theorem to Eqs. (4) and (12) and equate the mean value of the dielectric constant $\bar{\varepsilon}$ defined by Eq. (10) and that defined by the following equation:

$$\Theta = \frac{-(1+\varepsilon_2)\{\bar{\varepsilon}^2(3+\varepsilon_2) - \bar{\varepsilon}(1+4\varepsilon_2-\varepsilon_2^2) + \varepsilon_2(1-\varepsilon_2)\}}{\bar{\varepsilon}} d . \tag{16}$$

c) *The interference theory*

If we adopt the model illustrated in Fig. 2 (b) and calculate $\boldsymbol{r}_p$ and $\boldsymbol{r}_s$ considering the interference due to multiple reflections inside the surface layer, we can easily obtain

$$\frac{\boldsymbol{R}_p}{\boldsymbol{R}_s} = \frac{\boldsymbol{r}_p}{\boldsymbol{r}_s} = \rho e^{i\Delta} = \frac{r_{1p}+r_{2p}\exp(-iax)}{1+r_{1p}r_{2p}\exp(-iax)} \Bigg/ \frac{r_{1s}+r_{2s}\exp(-iax)}{1+r_{1s}r_{2s}\exp(-iax)} , \tag{17}$$

---

* The sign of the right side of Eq. (8) is to be chosen so as to make d included in η positive.

where r_{1p}, r_{1s} and r_{2p}, r_{2s} represent the Fresnel coefficients of the p- and s-components of the electric vector at the boundaries 1 and 2 respectively, and

$$x = d/\lambda\,, \tag{18}$$

$$a = 4\pi n \cos\varphi\,. \tag{19}$$

φ in Eq. (19) stands for the angle of refraction of the film corresponding to the angle of incidence φ_1 (Fig. 3).

Eq. (17) is too complicated for practical application to the polarimetric study of a film, but approximate equations can be derived by expanding it in powers of x $(=d/\lambda)$. It is expected that the first and the second approximations agree with D-theory and SG-theory respectively. This will be shown to be the case in the following sections.

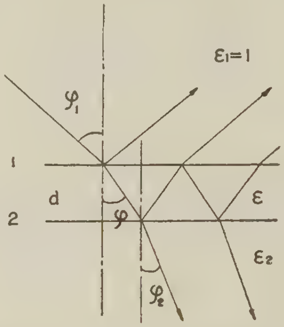

Fig. 3. Interference theory.

§ 3. Expansion of Eq. (17)

a) *Fresnel coefficients for* $\varphi_1 = \varphi_B$

r_{1p} in the right side of Eq. (17) is given by

$$r_{1p} = \frac{\tan(\varphi_1-\varphi)}{\tan(\varphi_1+\varphi)} = \frac{\begin{vmatrix} \tan\varphi_1 & \sin\varphi_1 \\ 1 & \sqrt{n^2-\sin^2\varphi_1} \end{vmatrix}}{\begin{vmatrix} 1 & -\sin\varphi_1 \\ \tan\varphi_1 & \sqrt{n^2-\sin^2\varphi} \end{vmatrix}} \cdot \frac{\begin{vmatrix} 1 & \sin\varphi_1 \\ \tan\varphi_1 & \sqrt{n^2-\sin^2\varphi_1} \end{vmatrix}}{\begin{vmatrix} \tan\varphi_1 & -\sin\varphi_1 \\ 1 & \sqrt{n^2-\sin^2\varphi_1} \end{vmatrix}}\,. \tag{20}$$

When $\varphi_1 = \varphi_B = \tan^{-1}\sqrt{\varepsilon_2}$, i.e. when the angle of incidence is equal to the Brewsterian angle of the substrate, Eq. (20) is reduced to

$$[r_{1p}]_B = \frac{\varepsilon-k}{\varepsilon+k}\,, \tag{21}$$

where

$$k = \sqrt{\varepsilon\varepsilon_2+\varepsilon-\varepsilon_2}\,. \tag{22}$$

It can be shown in the same way that

$$[r_{2p}]_B = -\frac{\varepsilon-k}{\varepsilon+k}\,, \tag{23}$$

$$[r_{1s}]_B = -\frac{k-1}{k+1}\,, \tag{24}$$

$$[r_{2s}]_B = -\frac{\varepsilon_2-k}{\varepsilon_2+k}\,. \tag{25}$$

b) *Expansion of Eq. (17)*

If we put

$$L(x) = r_{1p} + r_{2p}\exp(-iax)\,, \tag{26}$$

$$N(x) = \frac{1+r_{1s}r_{2s}\exp(-iax)}{(1+r_{1p}r_{2p}\exp(-iax))(r_{1s}+r_{2s}\exp(-iax))}\,, \tag{27}$$

Eq. (17) can be written as

$$\boldsymbol{R}_p/\boldsymbol{R}_s = \boldsymbol{L}(x)\boldsymbol{N}(x)\,. \tag{28}$$

Expanding the right side in power series in $x=d/\lambda$, we get

$$\frac{R_p}{R_s}=\rho e^{i\Delta}=L(0)N(0)+\begin{vmatrix} L'(0) & L(0) \\ -N'(0) & N(0) \end{vmatrix}x$$

$$+\frac{1}{2}\left\{\begin{vmatrix} L''(0) & L(0) \\ -N''(0) & N(0) \end{vmatrix}+\begin{vmatrix} L'(0) & N'(0) \\ -L'(0) & N'(0) \end{vmatrix}\right\}x^2+O(x^3)\,. \tag{29}$$

$L(x), L'(x), \cdots$ and $N(x), N'(x), \cdots$ are, in general, complex numbers. But it is obvious from Eqs. (26) and (27) that

$L^{(n)}(0)$ and $N^{(n)}(0)$ are real* for even values (including zero) of n,

and

$L^{(n)}(0)$ and $N^{(n)}(0)$ are imaginary for odd values of n.

Hence, if we put

$$L'(0)=iL_R'(0)\,,\qquad N'(0)=iN_R'(0) \tag{30}$$

and substitute into Eq. (29), an expression for R_p/R_s is obtained *in which all the parameters are real*:

$$\frac{R_p}{R_s}=\rho e^{i\Delta}=L(0)N(0)+i\begin{vmatrix} L_R'(0) & L(0) \\ -N_R'(0) & N(0) \end{vmatrix}x$$

$$+\frac{1}{2}\left\{\begin{vmatrix} L''(0) & L(0) \\ -N''(0) & N(0) \end{vmatrix}-\begin{vmatrix} L_R'(0) & N_R'(0) \\ -L_R'(0) & N_R'(0) \end{vmatrix}\right\}x^2+O(x^3)\,. \tag{31}$$

Now we shall calculate $[R_p/R_s]_\mathrm{B}$ and $[R_p/R_s]_\mathrm{p}$, i.e. the ratio in complex amplitude of the p- and the s-components for $\varphi_1=\varphi_\mathrm{B}$ and $\varphi_1=\varphi_\mathrm{p}$ respectively.

1° $[R_p/R_s]_\mathrm{B}$

From Eqs. (21) and (23) it follows that

$$[L(0)]_\mathrm{B}=0\,. \tag{32}$$

Hence

$$[R_p/R_s]_\mathrm{B}=i[L_R'(0)N(0)]_\mathrm{B}x+\frac{1}{2}[L''(0)N(0)-2L_R'(0)N_R'(0)]_\mathrm{B}x^2+O(x^3)\,. \tag{33}$$

2° $[R_p/R_s]_\mathrm{p}$

This has to be a pure imaginary number because $\Delta=\pi/2$ for $\varphi_1=\varphi_p$. Hence the first and the third terms in the right side of Eq. (31) drop, and we obtain

$$[R_p/R_s]_\mathrm{p}=i[L_R'(0)N(0)+L(0)N_R'(0)]_\mathrm{p}x+O(x^3)\,. \tag{34}$$

§ 4. The First Order Theory

If we neglect the second and the higher power terms in $x=d/\lambda$ in Eq. (33), we get

$$[R_p/R_s]_\mathrm{B}=[\rho\exp i\Delta]_\mathrm{B}=i[L_R'(0)N(0)]_\mathrm{B}\,x\,. \tag{35}$$

As $[L_R'(0)N(0)]_\mathrm{B}$ is real, this means that $\Delta_\mathrm{B}=\pi/2$, or that the Brewsterian angle φ_B agrees with the principal angle of incidence φ_p in this approximation. Accordingly,**

$$\rho_\mathrm{B}=\pm[L_R'(0)N(0)]_\mathrm{B}=\rho_\mathrm{p}\,. \tag{36}$$

$[L_R'(0)]_\mathrm{B}$ and $[N(0)]_\mathrm{B}$ are immediately obtained from Eqs. (26) and (27) respectively:

$$[L_R'(0)]_\mathrm{B}=-[ar_{2p}]_\mathrm{B}\,, \tag{37}$$

$$[N(0)]_\mathrm{B}=\left[\frac{1+r_{1s}r_{2s}}{(1+r_{1p}r_{2p})(r_{1s}+r_{2s})}\right]_\mathrm{B}\,. \tag{38}$$

---

[*] $L^{(n)}(x)$ and $N^{(n)}(x)$ represent the n-th derivatives of $L(x)$ and $N(x)$ respectively.

[**] The right sides of Eqs. (35) and (34) are identical. See Eq. (32).

$[r_{1p}]_{\mathrm{B}}$, $[r_{2p}]_{\mathrm{B}}$, $[r_{1s}]_{\mathrm{B}}$ and $[r_{2s}]_{\mathrm{B}}$ have been given in Eqs. (21)–(25). Substituting these equations into Eq. (36), we get

$$\rho_{\mathrm{B}}=\rho_{\mathrm{p}}=\pm\frac{\pi}{\lambda}\frac{\sqrt{1+\varepsilon_2}}{\sqrt{1-\varepsilon_2}}\eta\,, \tag{39}$$

where

$$\eta=\frac{(\varepsilon-1)(\varepsilon-\varepsilon_2)}{\varepsilon}d\,. \tag{40}$$

In deriving Eq. (39) we need a_{B}, the value of a for $\varphi_1=\varphi_{\mathrm{B}}$. This can be calculated by writing $\cos\varphi$ in Eq. (19) as a function of φ_1, ε_1 and ε and computing its value for $\varphi_1=\varphi_{\mathrm{B}}$.

$$a_{\mathrm{B}}=4\pi k/\sqrt{1+\varepsilon_2}\,. \tag{41}$$

Thus it has been proved that the interference theory in which the second powers in d/λ are neglected agrees with D-theory.

§ 5. The Second Order Theory

Now let us proceed to the approximation in which the terms up to the second powers in $x=d/\lambda$ are taken into account.

As is clear from its derivation, Eq. (34) holds in the second order theory as well. The parameters included in this equation can be expanded about $\varphi_1=\varphi_{\mathrm{B}}$ as follows:

$$\left.\begin{aligned}
[\boldsymbol{L}(0)]_{\mathrm{p}}&=[\boldsymbol{L}(0)]_{\mathrm{B}}+\boldsymbol{C}_1\varphi'+\cdots\,,\\
[\boldsymbol{L}_R'(0)]_{\mathrm{p}}&=[\boldsymbol{L}_R'(0)]_{\mathrm{B}}+\boldsymbol{C}_2\varphi'+\cdots\,,\\
[\boldsymbol{N}(0)]_{\mathrm{p}}&=[\boldsymbol{N}(0)]_{\mathrm{B}}+\boldsymbol{C}_3\varphi'+\cdots\,,\\
[\boldsymbol{N}_R'(0)]_{\mathrm{p}}&=[\boldsymbol{N}_R'(0)]_{\mathrm{B}}+\boldsymbol{C}_4\varphi'+\cdots\,.
\end{aligned}\right\} \tag{42}$$

Here

$$\varphi'=\varphi_{\mathrm{p}}-\varphi_{\mathrm{B}}\,. \tag{43}$$

$\boldsymbol{C}_1$, $\boldsymbol{C}_2$, $\boldsymbol{C}_3$ and $\boldsymbol{C}_4$ are functions of ε_1, ε and ε_2 which can be shown to be of the order of 1～10 for the cases usually met with. The difference between the principal angle of incidence and the Brewsterian angle, φ', must be a small quantity of the second order, because this was equal to zero in the first order theory. Hence

$$\boldsymbol{C}_i\varphi'x=O(x^3)\qquad i=1,2,3,4 \tag{44}$$

and may be neglected in the present approximation. Accordingly,

$$\begin{aligned}
[\boldsymbol{R}_p/\boldsymbol{R}_s]_{\mathrm{p}}&=i[\boldsymbol{L}_R'(0)\boldsymbol{N}(0)+\boldsymbol{L}(0)\boldsymbol{N}_R'(0)]_{\mathrm{p}}\,x\\
&=i[\boldsymbol{L}_R'(0)\boldsymbol{N}(0)+\boldsymbol{L}(0)\boldsymbol{N}_R'(0)]_{\mathrm{B}}\,x\\
&=i[\boldsymbol{L}_R'(0)\boldsymbol{N}(0)]_{\mathrm{B}}\,x\,.
\end{aligned} \tag{45}$$

The last transformation is due to Eq. (32).

Since

$$[\boldsymbol{R}_p/\boldsymbol{R}_s]_{\mathrm{p}}\equiv\pm i\rho_{\mathrm{p}}\,,$$

Eq. (45) means that ρ_{p} is again given by Eq. (36). Thus it has been proved that the interference theory in which the terms up to the second powers in d/λ are taken into account gives the same ρ for $\varphi_1=\varphi_p$ as that calculated by SG-theory if ε in the former theory is assumed to be equal to $\bar{\varepsilon}$ in the latter theory (See Eq. (13)).

$[\boldsymbol{R}_p/\boldsymbol{R}_s]_{\mathrm{B}}$ in the second order theory is given by Eq. (33) in which $O(x^3)$ is neglected. This is not equal to $[\boldsymbol{R}_p/\boldsymbol{R}_s]_{\mathrm{p}}$ given by Eq. (45). But ρ_{B}, which is calculated from Eq. (33) as

$$\rho_{\mathrm{B}}^2=[\boldsymbol{R}_p/\boldsymbol{R}_s]_{\mathrm{B}}^*[\boldsymbol{R}_p/\boldsymbol{R}_s]_{\mathrm{B}}\,,$$

can be shown to be equal to ρ_{p} in so far as $O(x^3)$ is neglected. Hence

$$\rho_{\mathrm{p}}=\rho_{\mathrm{B}} \tag{46}$$

in the second order theory as well as in the first order theory. (This relation is only implicitely suggested in Sissingh and Groosmuller's paper[3)].)

Next we shall show that Eq. (14) is consistent with the second order interference theory. Making use of the relation

$$\boldsymbol{R}_p/\boldsymbol{R}_s\equiv\rho\cos\varDelta+i\rho\sin\varDelta$$

we can compute $\varDelta_{\mathrm{B}}$, the difference in phase between the p- and the s-components at $\varphi_1=\varphi_{\mathrm{B}}$, from Eq. (33):

$$\cot\varDelta_{\mathrm{B}}=\frac{1}{2}\left[\frac{\boldsymbol{L}''(0)}{\boldsymbol{L}_R'(0)}-\frac{2\boldsymbol{N}_R'(0)}{\boldsymbol{N}(0)}\right]_{\mathrm{B}}x\,. \tag{47}$$

In this expression, $[\boldsymbol{L}_R'(0)]_{\mathrm{B}}$ and $[\boldsymbol{N}(0)]_{\mathrm{B}}$ have been calculated in Eqs. (37) and (38), and $[\boldsymbol{L}''(0)]_{\mathrm{B}}$ and $[\boldsymbol{N}_R'(0)]_{\mathrm{B}}$ can be immediately obtained from Eqs. (26) and (27). Substituting these values into Eq. (47), and further substituting Eqs. (21)–(25) for r_{1p}, r_{2p}, r_{1s} and r_{2s}, we obtain

$$\cot\varDelta_{\mathrm{B}}=\frac{a_{\mathrm{B}}}{4k}\frac{\varTheta_1}{1-\varepsilon_2{}^2}x\,, \tag{48}$$

where

$$\varTheta_1=\frac{-(1+\varepsilon_2)\{\varepsilon^2(3+\varepsilon_2)-\varepsilon(1+4\varepsilon_2-\varepsilon_2{}^2)+\varepsilon_2(1-\varepsilon_2)\}}{\varepsilon}\,. \tag{49}$$

Substituting for a_{B} from Eq. (41), and for x from Eq. (18), we finally obtain

$$\cot \Delta_B = \frac{\pi \Theta_1 d}{\lambda(1-\varepsilon_2^2)\sqrt{1+\varepsilon_2}} . \tag{50}$$

Thus it has been proved that $\cot \Delta_B$ calculated by the second order interference theory agrees with that given by SG-theory (Eq. 14) if ε in the former theory is assumed to be equal to $\bar{\varepsilon}$ in the latter theory*.

Now that the expressions for ρ_p and Δ_B in both theories agree with each other, it is almost self-evident that the same holds good of $\varphi' = \varphi_p - \varphi_B$. To make sure, we shall prove this below.

As was pointed out in the derivation of Eq. (34), the sum of the real terms in Eq. (31) must vanish for $\varphi_1 = \varphi_p$:

$$[\boldsymbol{L}(0)\boldsymbol{N}(0)]_p + \frac{1}{2}\left[\begin{vmatrix} \boldsymbol{L}''(0) & \boldsymbol{L}(0) \\ -\boldsymbol{N}''(0) & \boldsymbol{N}(0) \end{vmatrix} - \begin{vmatrix} \boldsymbol{L}_R'(0) & \boldsymbol{N}_R'(0) \\ -\boldsymbol{L}_R'(0) & \boldsymbol{N}_R'(0) \end{vmatrix}\right]_p x^2 = 0 . \tag{51}$$

Substituting from Eq. (42) and neglecting the third order terms in $x = d/\lambda$ (see Eq. (44)), we get

$$\varphi' = -\frac{1}{2\boldsymbol{C}_1[\boldsymbol{N}(0)]_B}\left[\begin{vmatrix} \boldsymbol{L}''(0) & \boldsymbol{N}_R'(0) \\ 2\boldsymbol{L}_R'(0) & \boldsymbol{N}(0) \end{vmatrix}\right]_B x^2 .$$

Here

$$\boldsymbol{C}_1 = \left[\frac{\partial \boldsymbol{L}(0)}{\partial \varphi}\right]_B , \tag{53}$$

as is clear from the derivation of Eq. (42).

All the parameters included in Eq. (51) can be written in terms of $[r_{1p}]_B$, $[r_{2p}]_B$, $[r_{1s}]_B$ and $[r_{2s}]_B$. If we further substitute for these Fresnel coefficients from Eqs. (21)–(25), we obtain

$$\varphi' = \varphi_p - \varphi_B = -\frac{2\pi^2}{\lambda^2}\frac{\varepsilon_2\sqrt{\varepsilon_2}}{(1+\varepsilon_2)(1-\varepsilon_2^2)^2}\eta\Theta \tag{54}$$

in agreement with Sissngh and Groosmuller's theory. (Here η is defined by Eq. (41), and Θ is defined as $\Theta_1 d$ using Θ_1 given by Eq. (48)).

This work was partly supported by the Scientific Research Expenditure of the Ministry of Education.

References

1) A. C. Alkemade: Wied. Ann. **20** (1883) 22.
2) P. Drude: *Lehrbuch der Optik* (Leipzig, 1912).
3) R. Sissingh und J. Th. Groosmuller: Phys. Z. **27** (1926) 518.
4) K. Kinosita: J. Opt. Soc. Amer. **43** (1953) 924.
5) C. E. Leberknight and B. J. Lustman: J. Opt. Soc. Amer. **29** (1939) 59.
C. Strachan: Proc. Cambr. Phil. Soc. **29** (1933) 116.
A. B. Winterbottom: Trans. Faraday. Soc. **42** (1946) 487; J. Opt. Soc. Amer. **38** (1948) 1074.
A. Vašíček: Phys. Rev. **57** (1940) 925.

---

* Θ given by Eq. (16) is equal to $\Theta_1 d$ if we put $\bar{\varepsilon} = \varepsilon$.

JOURNAL OF THE PHYSICAL SOCIETY OF JAPAN Vol. 14, No. 3, MARCH, 1959

Electronmicroscopic Observations of Alkali Halide Crystals

By Tetsuhiko TOMIKI*

The Research Institute for Iron, Steel and other Metals,
Tohoku University, Sendai, Japan

(Received November 21, 1958)

A technique making a sheet of replica which casts two surfaces simultaneously is described. This was successfully applied to the alkali halide crystals which were rubbed gently with velvet or which were irradiated either with x-ray or with ultra-violet light. With using such a replica, it was possible to obtain the informations regarding to the effects which were induced by these treatments inside the crystal just beneath the outer surface, and it was also possible to measure with precision the depth in which region these treatments influenced. The results obtained were also described.

§ 1. Introduction

Except for the specimen in a form of thin film, it is usual to use the replica of a specimen as an object of the electron microscope. Though the various methods have been found for making replicas¹⁾, there remains several points to be improved. One of them will be successive electronmicroscopic observations on the same spot of the surface²⁾.

During the course of electronmicroscopic studies of the alkali halide crystals³⁾,⁴⁾ which were coloured additively or with X-ray etc., it was necessary to observe the interior of the crystal. In order to achieve this experiment, the specimen was cleaved along the {100} surface normal to the outer surface, and the fresh cleavage plane obtained was examined electronmicroscopically by means of replica techniques. Although this method offers a greater amount of informations regarding to the effects induced in the inner part of the crystal by the applied treatments, it was inconvenient to measure the distance of the observed spot from the outer surface. Moreover, according to this procedure, it was impossible to observe the interior directly beneath the outer surface.

The present paper describes the technique improved on these points.

§ 2. Method

The description is given to the case of alkali halide crystals whose replica is usually made by obliquely deposited Cr film reinforced subsequently with C film in a high vacuum (see, Fig. 1(a)). The deposited film is removed from the crystal by solving it into the water. This film is used as an object of the electron microscope.

If the proper amounts of chromium and carbon are deposited on the specimen, the deposited film both on the (010) and on the (001) planes can be removed from the surfaces as a sheet of replica, avoiding that it

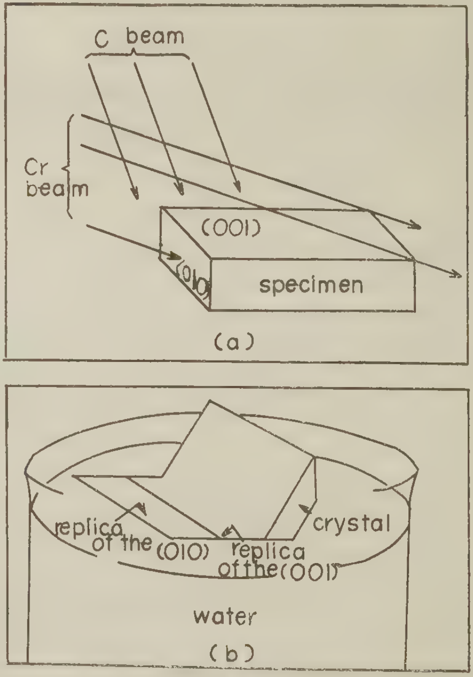

Fig. 1

---

* The present address: Department of Physics, The Faculty of Science, Tohoku University, Sendai, Japan.

was destroyed along the intersection of these two planes by the force of surface tension of the solvent water (see, Fig. 1 (b)). This procedure was especially favourable to the case of alkali halide crystals, because these crystals have flat cleavage surfaces and hence a linear intersection of the two cleavage planes.

Though this method is a slight modification of the one stage replica technique, this will presumably be applicable to metal which is observed by two stage replica, if the proper precautions are taken.

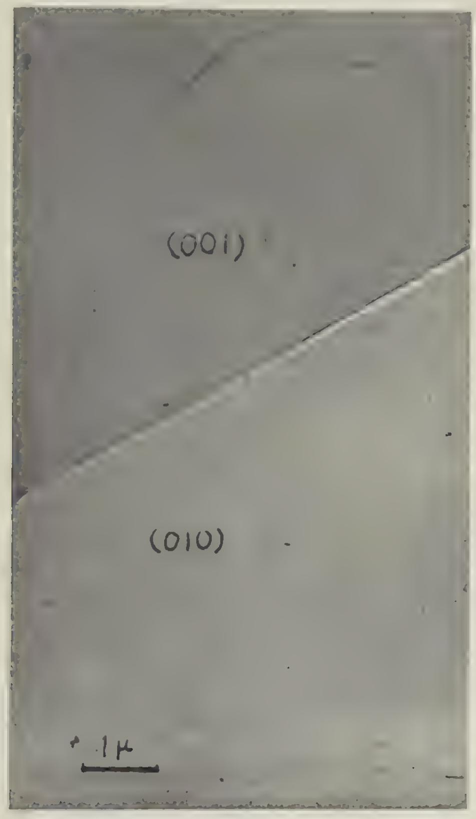

Fig. 2.

§ 3. Experimental Results

(a) After the plate of the KCl single crystal was cleaved from the block crystal, it was cut along the (010) plane normal to the outer (001) surface, and the replica was made both for the fresh (010) cleavage plane and for the outer (001) plane according to the procedure described above. Fig. 2 is the electron micrograph taken with such a replica. It can be observed that a few straight cleavage steps on the (010) plane run quite parallel to the intersection of the two planes.

(b) When the (001) surface of the KCl single crystal was rubbed gently with velvet, this surfaces turns into quite complicated one: Crystallites appear on the one part of the surface as a result of the thermal effects induced by the mechanical friction between the velvet and the surface of the crystal, and shallow grooves are formed on the other part. The latter phenomenon is probably induced both by the adhesion of the contact surfaces and by the mechanical corrosion according to the present status of the experiment of friction⁵⁾. Fig. 3 is the electron image of such a surface and the fresh (010) surface which was obtained by cutting the specimen normal to the (001) surface after the rubbing. The broken line in the figure corresponds to the intersection of the two planes. The parallelopiped crystal, whose edges are parallel to the ⟨110⟩ of the basal plane, appeared aligning along the [101] and $[\bar{1}01]$ directions on the fresh (010) plane down to the depth of 5 microns below the intersection of the two planes.

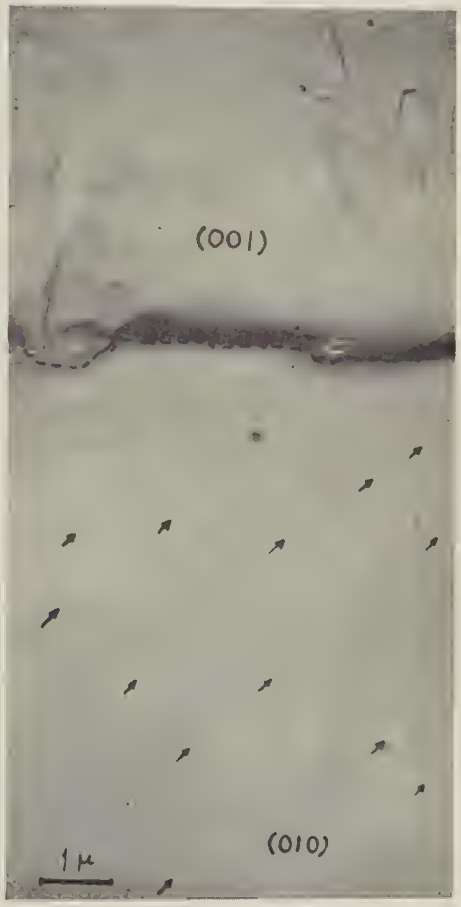

Fig. 3.

(c) Fig. 4 shows both the (001) surface of the KCl crystal which was irradiated with X-ray (Cu target; the applied potential=30 kv) and the fresh (010) plane which was obtained by cutting this crystal after the irradiation. In this case, the distance between the specimen and the X-ray source was 50 *cm*, and the irradiating time was 60 minutes. The cleavage steps on the fresh (010) plane can be seen as white lines nearly parallel to the intersection of the two planes. However, they are not straight as in the case of Fig. 2, but become to be slightly wavy. It must be noted that the crystallites did not grow on the irradiated (001) surface of this crystal (see, Fig. 4) and of the crystal which was irradiated with X-ray for 60 minutes at the distance of 5 *cm* from the target, even though the latter crystal was deeply coloured. (This fact does not contradict to the phenomena reported earlier by Hibi and Yada[2], because the crystallites of the KCl specimen come out on the X-rayed surface with the irradiation time of several hours. In the case of the KI single crystal which was irradiated with X-ray at the distance of 50 *cm* from the target for 60

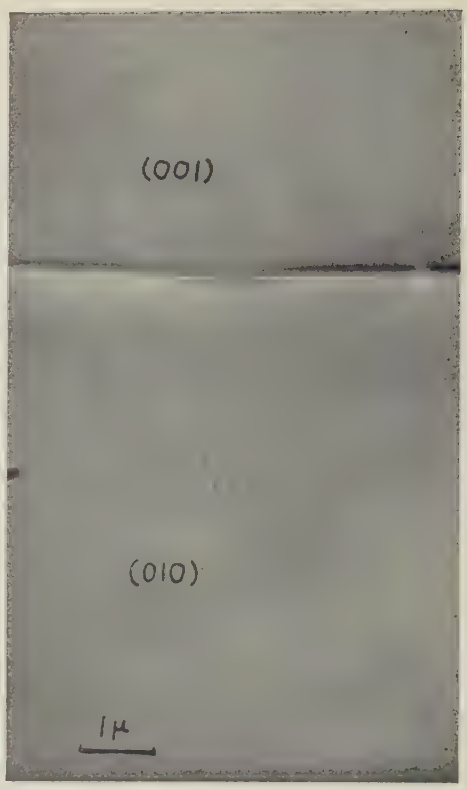

Fig. 4.

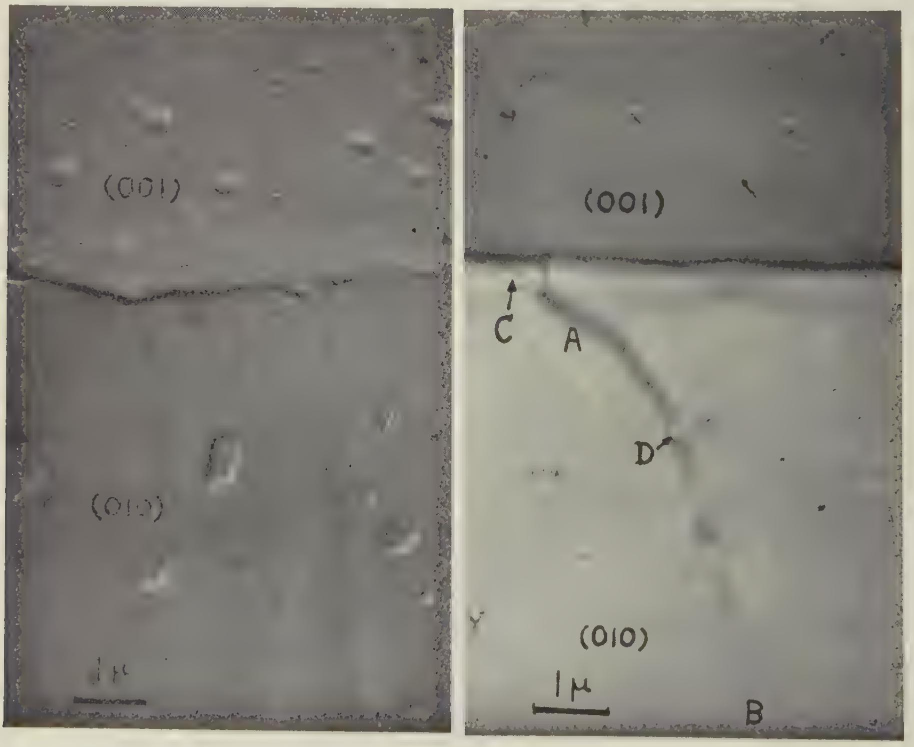

(a) (b)

Fig. 5.

minutes, the crystallites grew on the irradiated surface⁶⁾.)

(d) On the contrary, if the KCl crystal is illuminated with light lying in the tail of the first fundamental absorption band, growth of crystallites occurs both on the irradiated (001) surface and the side planes parallel to the incident beam, although the colour of the crystal was hardly observable. This is illustrated with Fig. 5 (*a*) which is the electron image both of the (001) irradiated surface and of the (010) side surface of the KCl crystal which was illuminated with ultra-violet light for 30 minutes at the distance of 1 *mm* from the light source. Here, the light source was a hydrogen dischage tube with LiF window. We can see that the crystallites grew on these surfaces. The intersection of these two planes is not a straight line, but is a zigzag which will probably represent the crystal imperfections such as the mosaic structure or the grain composed with a low angle boundary in the single crystal.

Fig. 5 (*b*) shows the (001) front surface as well as the fresh (010) cleavage plane which was produced after the illumination with ultra-violet light for 15 minutes at the distance of 1 *mm* from the light source. The wavy steps appeared on the (010) cleavage plane down to the depth of 7 to 5 microns beneath the front surface as the result of the illumination. The step **AB** corresponds to the crystal imperfection such as internal surface or the grain boundary, because this step is perpendicular to the direction of the cleavage steps. Perhaps this is the first time that such a imperfection is observed electonmicroscopically on the single crystal without the process such as etching or decoration.

The wavy steps have been confirmed electronmicroscopically that they always appear whenever the crystal growth occurs³⁾,⁴⁾. The nature of these steps have not yet been clarified, but it is probably that they are produced by the thermal spikes of excitons when they were annihilated at the crystal imperfections. The important results obtained from Fig. 5 (*b*) are as follows:—

(*i*) The crystallites on the (001) front surface grew as a result of the ionic motions inside the crystal and this fact confirms also the experimental results obtained by Hibi and Yada²⁾ (see, for example, the crystallite **C** in Fig. 5 (*b*)).

(*ii*) The step **AB** changed its shape into the zigzag one as the growth of the crystallites proceeded and this fact is also quite in agreement with the suggestions made on the previous experiments³⁾,⁴⁾.

The physical considerations regarding to these phenomena induced by irradiation with ultra-violet light will be described in detail in relation to the action of exciton in another place⁷⁾.

§ 4. Conclusions

A method for making a replica which casts simultaneously both the (001) and the (010) surfaces of alkali halide crystal was described, and some results using with such a replica proved that this method is very effective to observe the inner part of the crystal just beneath the surface on which the various treatments were applied.

Acknowledgements

The author would like to express his sincere thanks to Prof. S. Ogawa, Prof. T. Hibi and to Prof. M. Ueta who gave him valuable guidances and kind helps. His gratitudes are also due to Dr. M. Hirabayashi, Ogawa Laboratory, for his kind operations of the X-ray apparatus.

References

1) See, for example, D. E. Bradley: J. Appl. Phys. **27** (1956) 1399.
T. Hibi: J. Appl. Phys. **23** (1952) 957.
R. W. G. Wyckoff and R. C. Williams: J. Appl. Phys. **15** (1944) 712.
2) E. D. Hyam and J. Nutting: Brit. J. Appl. Phys. **7** (1956) 1399.
J. F. Kankivell: Brit. J. Appl. Phys. **4** (1953) 141.
G. R. Booker: Brit. J. Appl. Phys. **5** (1954) 349.
D. E. Bradley: Brit. J. Appl. Phys. **6** (1955) 430.
J. T. Fouri: J. Appl. Phys. **29** (1958) 608.
T. Hibi and K. Yada: J. Phys. Soc. Japan (to be published).
3) T. Hibi and K. Ishikawa: J. Phys. Soc. Japan **13** (1958) 709.
4) T. Hibi and T. Tomiki: J. Phys. Soc. Japan (to be published); Sci. Rep. Res. Inst. Tohoku Univ. (to be published).
5) A discussion on friction: Proc. Roy. Soc. A, **212** (1952) 439.
F.B. Bowden and D. Tabor: *Friction and Lubrication of Solids* (Oxford Clarendon Press, 1950).
6) T. Tomiki: J. Phys. Soc. Japan **14** (1959) 230.
7) T. Tomiki and M. Ueta: to be published.

Journal of the Physical Society of Japan Vol. 14, No. 3, March, 1959

Nuclear Magnetic Resonance Studies of Water Sorbed on Fibrous Materials

By Akira Odajima

Research Institute of Applied Electricity,
Hokkaido University, Sapporo

(Received August 6, 1958)

Nuclear magnetic resonance of the water molecules sorbed on the native cellulose, " mulbery paper " was studied.

The measurements of the line width were made under the condition of water content ranging from 10 to 180% at 20°C, by using Varian high resolution type spectrometer.

Within the range of 10 to 20%, the line widths rapidly decreased with increasing water content, and gradually decreased beyond the region. Although this tendency was similar to that of dielectric relaxation, the experimental value of τ_N obtained from Kubo-Tomita equation was much greater in the order of magnitude than that of the dielectric relaxation time τ_D. Accordingly, τ_N and τ_D do not satisfy the BPP's relation of $\tau_N=1/3\cdot\tau_D$. This result suggested to us that the water molecules in the sorbed state do not rotate with spherical symmetry like in the liquid state.

§1. Introduction

Several authors have recently measured the motion of water molecules in the sorbed state, using a nuclear magnetic resonance (NMR) method.[1)-3)]

When the molecular motion becomes rapid and the correlation time small, a high homogeneity of the magnetic field is necessary to measure the line width of absorption line narrowed by the motional-narrowing. Accordingly, no experiment has not yet been made except in the case of low water content, namely except in the case of rather restricted motion.

We tried to extend the measurement in the region of high water content, by using a high resolution magnet of Varian Association Spectromete.r[*)]

According to either BPP theory[4)] or Kubo-Tomita's one[5)], spin-lattice relaxation time T_1 and spin-spin relaxation time T_2 are related with the correlation time τ_N of Brownian motion of nuclear spins. Thus, we can get τ_N through the observation of either T_1 to T_2.

On the other hand, the relaxation time τ_D for the reorientation of the electric dipole of sorbed water molecules has been obtained through the measurements of the dielectric relaxation.[6)-8)] Both τ_N and τ_D are the parameters indicating molecular motion and are expected not to be independent of each other. If we assume the spherical symmetric rotation of a molecule, the theory of Brownian motion gives us the following relation between τ_N and τ_D

$$\tau_N=1/3\cdot\tau_D=4\pi\eta a^3/3k_0T\ , \qquad (1)$$

where η is the viscosity coefficient, and a the radius of molecule. It is well known by experiments that Eq. (1) holds approximately in the case of liquid.[4)] However, our experiments showed that Eq. (1) does not hold for water molecules sorbed on fibrous materials.

At the last section it is discussed that it may be appropriate to consider the unspherical symmetric rotation for the motion of sorbed water insteated of the spherical symmetric ones.

§2. Measurements and Results

Employing a Varian high resolution type NMR spectrometer, we have measured the line widths of water sorbed on the native cellulose, " mulberry paper ", in the range of the water contents from 10 to 180% (weight of sorbed water/weight of dry cellulose) at 20°C. Samples were placed in 6 mm O.D. glass

---

[*)] NMR measurements were carried out at the Chemical Research Institute of Non-Aqueous Solutions, Tohoku University.

tube. The portion of the magnetic field occupied by the samples was found to be uniform within 0.9 milligauss. For samples whose water content was less than 10%, the line widths were too broad to be detectable. This means that the absorption line due to protons in the cellulose is undetectable. The examples of the line width are shown in Fig. 1.

At first it seemed probable to presume that the motion of the OH groups in the cellulose, which are free from hydrogen bonds, becomes more active, as the water content increases. However, in the measurement on the cellulose diacetate-acetone solution within 10% (weight of cellulose/weight of solvent), the absorption line due to the CH_3 group is the only observable and no other absorption lines coming from OH and CH are observable as shown in Fig. (1d). These facts tell us that the freedom of the motion of each radical in the cellulose is hindered considerably even in the case of a liquid solution. Thus, we can reasonably assume that the protons in the water molecules absorbed on the cellulose are the only observable.

Half width *vs.* water content is shown in

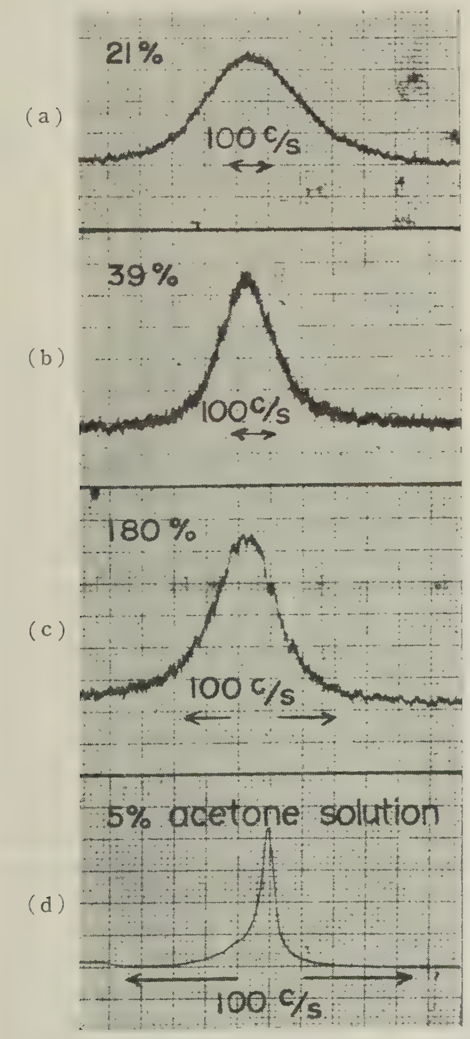

Fig. 1. Absorption lines of sorbed water on the native cellulose (a, b, c) and that of diacetate-acetone solution. (a) 21% (b) 39% (c) 180% (d) 5% acetone solution

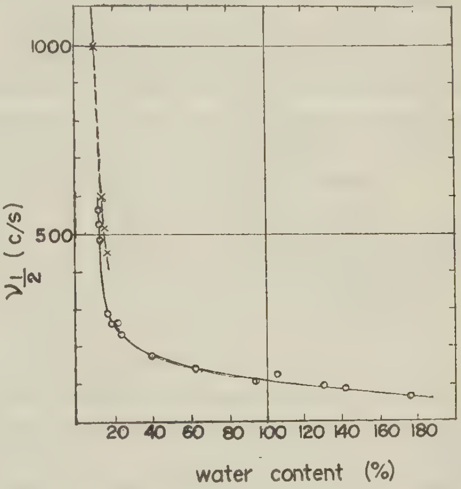

Fig. 2. Variations of half width of absorption lines vs. water content. (—○—○—) Our data, (—×—×—) Shaw's data.

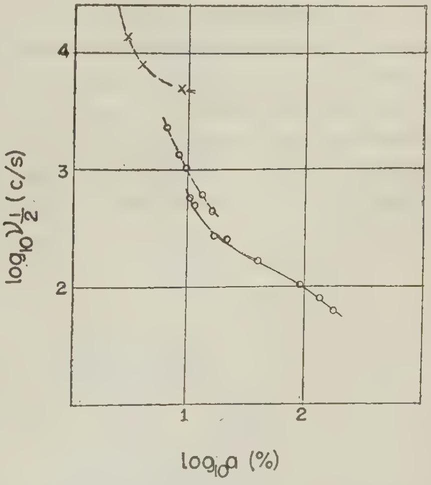

Fig. 3. Variation of half width of lines as a function of water content A (%) in the logarithmic scale. Solid line represents our data. One of the broken line (- - × - - × - -) represents Tanaka's data and the other (- -○- -○- -) Shaw's data.

Fig. 2. In Fig. 3 the data obtained by other researchers,[1)–2)] are shown for comparison with our data. There is a fairly good agreement between the gradients of each curve in the same range of concentration. As is shown in Fig. 2 and Fig. 3, the line widths rapidly decrease with increase with increasing water content within the range of the water content of 10 to 20%, and gradually decrease beyond the region.

§ 3. Apparent Correlation Time of NMR

The theories of Kubo-Tomita[5)] and Solomon[9)] show that the line width may be expressed in terms of the correlation time, τ_N. If the correlation function of the local magnetic dipolar field is given by the following equation, in the condition of $\tau_N < \omega^{-1}$,

$$K(t) = \exp(-|t|/\tau_N) , \tag{2}$$

the spin-spin relaxation time T_1 of two spin system is expressed by

$$T_2^{-1} = \frac{3}{20} \frac{\hbar\gamma^4}{b^6} \left[3\tau_N + \frac{5\tau_N}{1+\omega^2\tau_N^2} + \frac{2\tau_N}{1+4\omega^2\tau_N^2} \right] , \tag{3}$$

where γ is the nuclear gyromagnetic ratio and b is the inter-proton distance in a water molecule.

In the derivation of Eq. (3), the inter-molecular interaction is neglected, but this approximation is supposed to be unreasonable in case of a considerable amount of sorbed water. The contribution from inter-molecular protons to T_2 is estimated to be the same order with that from intra-molecular protons, in the case of free water.[4)] Consequently, it shoud be considered that the spin-spin interaction between protons in another molecules contributes to T_2 of sorbed water in addition to between protons in a water molecule.

If we assume the correlation time as the type of Eq. (2), however, it is shown by Kubo-Tomita[5)] that Eq. (3) consists too in many spin system, substituting for b^{-6} to $\sum_j b_j^{-6}$ where $\sum_j$ means the summation over inter-molecular protons.

T_2 is also given by another form of

$$T_2^{-1} = \frac{\langle \sigma_0^2 \rangle}{3} \left\{ 3\tau_N + \frac{5\tau_N}{1+\omega^2\tau_N^2} + \frac{2\tau_N}{1+4\omega^2\tau_N^2} \right\} , \tag{4}$$

where $\langle \sigma_0^2 \rangle$ is the second moment of rigid case. It is shown that the spin-spin relaxation time $(T_2)_0$ in the rigid case is given by

$$(T_2^{-1})_0 = \sqrt{\langle \sigma_0^2 \rangle} . \tag{5}$$

As the $(T_2)_0$ of sorbed water, we will use the value measured for ice at −40°C,

$$(T_2)_0 = 5 \times 10^{-6} \text{ sec.} \tag{6}$$

In the case that an absorption line is sharpened in the type of the Lorentian curve, a half width is related to T_2 by the following equation

$$\Delta\nu_{1/2} = T_2^{-1}/\pi + \Delta\nu' , \tag{7}$$

where $\Delta\nu'$ is a broadening due to an inhomogeneity of a magnetic field.

Using above equations, from Eq. (4) to Eq. (7), we have a relation between τ_N and the water content, which is shown in Fig. 4. In the same figure, we have plotted a similar relation between dielectric relaxation time τ_D and the water content in case of wood[6)], paper,[7)] and starch.[8)] It is worth noted that τ_N is much larger than τ_D in the same concentration.

§ 4. Comparison with the Dielectric Measurement

According to the dielectric measurements on sorbed water[7)], sorbed water is classified into two classes, that is, localized sorbed water and mobil sorbed water, the latter having two states moreover. Also, through the dielectric measurements the states of sorbed water are grouped by water content into three categories, viz. 0–5%, 5–20% and over 20%.[6)] Comparing the molecular polarizability of each state of sorbed water, Windle and Shaw[10)] concluded that localized water was bound so that it had little freedom of rotation.

In the NMR measurement of sorbed water, the observation of the line width due to localized water is beyond the range of the observation of our apparatus. Therefore, the observed variation of the line widths, which are plotted in Figs. 2 and 3, are reasonably expected to come from mobile water. It is quite apparent that mobile water is not unique but divided into two states having different dependence on water content, that is, the state with a sharp gradient and that with a gradual gradient. The boundary of these states is at the water content of 20%. According to the conventional idea of a mobile state of sorbed water, such a water molecule is expected to be similar to water in the liquid phase[10]. However, these authors[10] found that the molecular polarizability of mobile water was smaller than that of free water, and also explained this fact by assuming that mobile water consists of the truly mobile water molecule, which is quite similar to free water, and intermediate water, which is in a intermediate state between localized and truly mobile ones. This interpretation seems to be qualitatively applicable to the explanation of the existence of the two states of mobile water in the NMR observation.

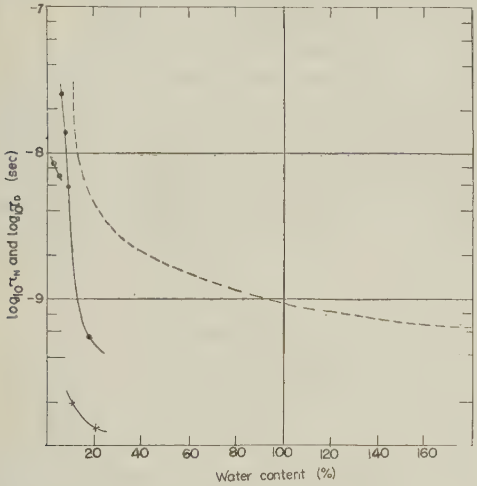

Fig. 4. Comparison of the correlation times τ_N of NMR calculated from Eq. (2) with the dielectric relaxation times τ_D at 20°C, respectively. Broken curve represents τ_N. Solid curves represent τ_D obtained from Takeda's data (--×--×--), Seidman's data (--○--○--) and and Ono's data (—●—●—). Ono's curve is plotted bxtrapolating from the values at −15°C to those at at 20°C.

§ 5. Discussion and Conclusion

Although there is a qualitative similarity between two correlation times τ_N and τ_D, there is a quantitative discrepancy between the experimental result shown in Fig. 4 and the relation expected from Eq. (1), as mentioned in the preceding section.

In the free water molecule, τ_N and τ_D are found to be about 10^{-11} sec. Then, the experimental value of τ_N of sorbed water is seemed to be anomalously greater in the order of magnitude than that of free water.

Concerning the reason why the order of magnitude of τ_N differs from τ_D, we were inclined to presume that the water molecules in the sorbed state do not rotate with spherical symmetry even in mobile water, because τ_N must be in the same order of magnitude with that of τ_D is the spherical symmetric rotation as is shown in Eq. (1). In the liquid phase the water molecules rotate breaking the hydrogen bond among molecules, and the rate of this breaking is expected to proceed isotropically. Thus it is possible to treat such a rotation as a spherical symmetric.

In the sorbed state, however, some of the water molecules are bound so strongly with hydrophilic group of the adsorbent that these molecules are considered to be localized. The remainder of the sorbed water molecules is expected to deposit on the monolayer of such localized water molecules. The farther from the adsorbent the water molecules deposit, the more freely the water molecules can move. Thus, as the water content increases, the fraction of free water molecules increase. On the other hand, the fibre is swollen by the water molecules which are sorbed among the non-crystallized state of the fibre. Hence, the interaction between water and the cellulose molecules which are sorbed at the non-crystallized parts of fibre may be expected to rotate as freely in the plane of adsorbed layer as free water does, but such molecules are also expected to be strongly bound in the vertical direction of the sorbing surface.

It is easily shown that Eq. (3) is not satisfied in the simplest 2-dimensional case in the unspherical symmetric rotation. Namely, the term of finite value caused by the stationary part of the magnetic dipolar field fluctuating randomly still remains in the line width, though the correlation time τ_N becomes very small. The term was given by Gutowsky and Pake[11] as follows:

$$(T_2^{-2})_{rot}=\frac{1}{4}(3\cos^2\alpha-1)(T_2^{-2})_{rig}\,, \qquad (8)$$

where α is the angle between a direction of a nucleus paier and an axis of rotation.

Therefore, if we apply Eq. (3) to the case of the restricted motion of molecules, the correlation time obtained from Eq. (3) will be no more than an apparent one. We should consider a modification of Kubo-Tomita's equation[5] to apply to the general case of unspherical symmetric rotations of molecules.

However, it seems to us that the mechanisms, by which the anomaly in the apparent correlation time is caused in the sorbed state of water, are very complicated. One of them may be supposed to be the fact that the potential barrier hindering the rotation of water molecules is existent in the sorbed state of water. We have already given the theory on the restricted rotation in the field of the potential barrier and the application to T_1 and T_2 of NMR.[12)] But, it may be doubtful that the hindering potential is kept in constant within the correlation time of the Brownian motion of water molecules without being disturbed from thermal fluctuations.

If it is considered that the time variation of the potential barrier occurs rapidly, we had better consider that the rotational motion of water molecules is anisotropic. It is thus considered that values of mobilities are not equal in the vertical and the horizontal direction to the absorbent plane. The anisotropic Brownian motion of molecules has been also reported by us in another paper.[13)]

Both of these mechanisms give the modification of Eq. (3) to T_2 and correct meaning to the correlation time not being the apparent correlation one.

If we take into account effects of the unspherical symmetry rotations, we may come to a conclusion that there is a possibility to give agreement between the NMR results and dielectric result of sorbed water. It is not yet decided, however which mechanisms mentioned above should be correct in the sorbed state of water, because we have to have more accurate information of motions in sorbed water.

In conclusion it may be desirable to measure the spin-lattice relaxation time T_1 in addition to T_2 and especially to obtain the activation energy of motions from data of T_1 and T_2 *vs.* temperature relation. The discussion of these problems will be given in the near future.

Although the effects of multiple phase were treated for T_1 and T_2 of sorbed water,[3),14)] the present paper neglected the non-uniformity of the sorbed state, since the water molecules sorbed on fibrous materials are considered to be distributed uniformly.

However, it seems to us unquestionable that the BPP relation of $\tau_N=1/3\cdot\tau_D$ would not hold for many other cases of the molecular motions, for instance, in case of the molecular motion of polymeric materials in the region of temperature above "glassy transition temperature". Further considerations toward these lines are being undertaken.

Acknowledgement

The author would like to express his hearty thanks to Professor S. Watanabe, Faculty of Engineering, Hokkaido University for his helpful suggestions and co-operations.

Thanks are also due to Professor G. Hazato and his co-workers at Tohoku University for their kind co-operations to carry out measurements, and Assistant Professors A. Miyake, Shizuoka University and J. Sohma, Hokkaido Gakugei University for invaluable discussions and helps.

References

1) K. M. Shaw and R. H. Elskin: J. Chem. Phys. **21** (1953) 565.
2) K. Tanaka and K. Yamagata: Bull. Chem. Soc. Japan **28** (1955) 90.
3) J. G. Zimmerman et al: J. Phys. Chem. **60** (1956) 1157; **61** (1957) 1328.
4) N. Bloembergen, E. M. Purcell and R. V. Pound: Phys. Rev. **75** (1958) 629.
5) R. Kubo and K. Tomita: J. Phys. Soc. Japan **9** (1954) 888.
6) M. Takeda: Bull. Chem. Soc. Japan **24** (1951) 169.
7) R. Seidman and S. G. Mason: Canad. J. Chem. **32** (1954) 744.
8) S. Ono, T. Kuge and N. Koizumi: Bull. Chem. Soc. Japan **31** (1958) 34; 40.
9) I. Solomon: Phys. Rev. **99** (1955) 559.
10) J. J. Windle and T. M. Shaw: J. Chem. Phys. **22** (1954) 1752; **25** (1956) 435.
11) H. S. Gutowsky and G. E. Pake: J. Chem. Phys. **18** (1950) 97.
12) A. Odajima: Busseiron-Kenkyu **2-4** (1958) 111 (in Japanese).
13) A. Odajima: Busseiron-Kenkyu **2-3** (1958) 532 (in Japanese).
14) A. Miyake: J. Chem. Phys. **27** (1954) 1425.

JOURNAL OF THE PHYSICAL SOCIETY OF JAPAN Vol. 14, No. 3, MARCH, 1959

Phenomenological Theory of Visco-elasticity of Three Dimensional Bodies

Misazo YAMAMOTO
*Department of Chemistry, Faculty of Science,
Kyoto University*

(Received October 29, 1958)

A phenomenological theory of the non-linear visco-elasticity of three dimensional bodies is presented. We start from the two elementary models of the classical linear theory of visco-elasticity, that is, the so-called Maxwell and Voigt models. These models are extended to three dimensional non-linear case by adopting the energy consideration. The three dimensional Maxwell model is defined by "series connection" of a "non-Hookeian spring", i.e. the internal elastic mechanism and a "non-Newtonian dashpot", the energy dissipation mechanism, and the three dimensional Voigt model is represented by the "parallel connection" of these mechanisms. Making use of the Maxwell model, we discuss the tensile viscosity for the stationary simple elongation of elastico-viscous liquids. Our models are shown to be successful in analyzing the so-called normal stress effects, i.e., the Weissenberg effect for elastico-viscous liquids and the Poynting effect for visco-elastic solids. The non-linearity in visco-elastic properties is classified into three cases: elastic, viscous or relaxational, and geometric non-linearities. An essential feature of the three dimensional bodies is the geometric non-linearity. The typical examples of this are the said normal stress effects and the velocity gradient dependence of the tensile viscosity coefficient.

§ 1. Introduction

Elegant phenomenological theories[1] on linear visco-elasticity have been developed since the foremost works of Maxwell,[2] Voigt,[3] Kelvin[4] and others. In these theories two fundamental models and the so-called superposition principle play important roles. One of the two models is the Maxwell model corresponding to viscous liquids having instantaneous rigidity (elastico-viscous liquids), and the other is the Voigt model corresponding to elastic solids possessing retarded elasticity (visco-elastic solids). These are schematically represented by series and parallel connections of a spring and a dashpot, respectively. The mechanical properties of each model can be described in terms of strain and stress by a suitable first order linear differential equation with respect to time. Making use of the superposition principle the theories have been extended to cases of more general visco-elastic properties which are described by suitable higher order differential equations. This generalization corresponds to considering the generalized Maxwell model which is a parallel connection of a number of Maxwell models, or to considering the generalized Voigt model which is a series connection of several Voigt models. Furthermore the relaxation time spectrum and/or the retardation time spectrum have been introduced to characterize these generalized models, in terms of which various mechanical properties of these materials can be consistently described. From the mathematical point of view they have the same structure as in the cases of electric circuits, dielectrics, etc. In fact these theories have been unified in the form of the so-called excitation-response theory.[5]

Recently, several observations have been made on a number of mechanical behaviors including large deformations of the samples, stimulated by the progress made in chemical physics of highpolymeric substances. Examples of these phenomena are the so-called structural viscosity (non-Newtonian flow),[6] the Weissenberg effect,[7] etc. Many of these phenomena cannot be described by the said classical linear theories. The structural viscosity is a typical example which results from the non-linearity in stress-strain relations. As to the Weissenberg effect, we observe not the shearing stress but the normal stress components for simple shearing flow, as has been pointed out in the preceding paper.[8)] These normal components are, moreover, essentially non-linear with respect to the rate of shearing (the velocity gradient). Thus, it is not only the non-linearity in stress-strain relations but also the three dimensional character of bodies that should be considered in the study of such mechanical properties. Here we can see the essential difference from linear cases such as electric circuits, etc.

In the case of purely elastic materials, three dimensional phenomenological theories of elasticity involving non-linear properties have been successfully developed by several authors. Their details are given, for example, in Novozhilov's text, Truesdell's review articles, etc.[9)–12)] The tension vs. elongation curve of vulcanized rubber is upword convex in the range of relatively small elongation. Mooney[13)] showed that this behavior is due to the shrinkage of free sides of the sample which corresponds to the incompressible character of this material. When a cylindrical piece of certain elastic materials such as steel, lead or vulcanized rubber is subjected to a torsional couple, the cylinder shows a change in its length (usually it elongates).[14)] We call this interesting phenomenon the Poynting effect. Mooney[11)] and Rivlin[12)] pointed out that, in order to constrain the simple shearing deformation to these elastic materials, it is necessary to apply an additional tension in the deformation-direction the magnitude of which is proportional to the square of the displacement gradient. They also suggested that the Poynting effect is essentially due to this additional normal tension. Accordingly in the recent terminology, both this effect and the Weissenberg effect which is considered to be the visco-elastic analogue of that effect, are called the normal stress effects.

In the meantime, the theory of elasticity has been established so general that the stress tensor is given its expression for *any* finite deformation of three dimensional bodies, with the help of differential geometry, and that many elastic behaviors are successfully analyzable by this general theory. As regards visco-elasticity, on the other hand, the phenomenological theory mentioned at the beginning of this section just corresponds to the classical *linear* theory of elasticity. And it has been hoped to extend the theory to include the said non-linear three dimensional visco-elastic effects. Indeed several attempts have been made for this purpose up to the present,[15)–18)] but there is no satisfactory theory yet, we believe. Many of these were carried out by applying the simple mechanical models (the Maxwell model and/or the Voigt model) independently to every component of the stress and strain tensors. It is needless to say that these theories cannot describe the cross effect such as the Weissenberg effect.

In this paper, we shall try to formulate phenomenologically a general theory of visco-elasticity in due consideration of the non-linear as well as three dimentional characters. To this end, we start from the Maxwell and the Voigt model which are essentially one dimensional, and extend them to corresponding three dimensional ones. Then it will be shown that the three dimentional Maxwell model has the mechanical properties of elastico-viscous liquids, whereas the three dimensional Voigt model corresponds to visco-elastic solids. Furthermore, non-linearity of the stress-strain relations will be classified into three categories: elastic, viscous (relaxational) and geometric non-linearities. It will be suggested that the structural viscosity is mostly due to the relaxational non-linearity. The Weissenberg effect is essentially the geometric effect, thereby the elastic and relaxational non-linearities being of minor importance.

In Part A of this paper we review the one dimensional models and then give the general consideration for their three dimensional extension. The three dimensional Maxwell model is treated in Part B, and the Voigt model in Part C. Simple elongations (compressions) and simple shearings are also studied in those parts for each of the two models. We treat the so-called tensile viscosity for steady simple elongation of the elastico-viscous liquids and the Poynting effect of the *visco-elastic solids*. In Part D we discuss about the classification of non-linearity and about the generalization of the models.

A. General Consideration

§ 2. Maxwell Model and Voigt Model

In this section, we shall review the classical, one dimensional mechanical models. The so-called Maxwell model and Voigt model are represented by series and parallel connection of a spring and a dashpot, respectively. The spring obeys the Hooke's law

$$\sigma_E=\kappa\alpha_E \tag{1}$$

and the dashpot contains the Newtonian liquid

$$\sigma_\eta=\eta\alpha_\eta\ . \tag{2}$$

σ and α are stress and strain, respectively. The suffixes E and η denote the elastic and the viscous part of them, κ the elastic modulus, and η the viscosity coefficient. Then, these two models are characterized by the conditions

$$\sigma=\sigma_E=\sigma_\eta \qquad \text{(Maxwell)} \tag{3}$$

and

$$a=\alpha_E=\alpha_\eta\ , \qquad \text{(Voigt)} \tag{4}$$

respectively, with apparent stress σ and apparent strain a.

Denote the work done by external force per unit time by dW/dt, the rate of change of the elastic energy in the system by dw/dt, and the rate of energy dissipation by $\delta\mathcal{E}/dt$, in the unit volume of material. Now we have

$$\frac{dW}{dt}=\sigma\dot{a}\ , \tag{5}$$

$$\frac{dw}{dt}=\sigma_E\dot{\alpha}_E \tag{6}$$

and

$$\frac{\delta\mathcal{E}}{dt}=\sigma_\eta\dot{\alpha}_\eta\ . \tag{7}$$

The law of energy-conservation

$$\frac{dW}{dt}=\frac{dw}{dt}+\frac{\delta\mathcal{E}}{dt} \tag{8}$$

can be written as follows:

$$\sigma\dot{a}=\sigma_E\dot{\alpha}_E+\sigma_\eta\dot{\alpha}_\eta\ . \tag{9}$$

Eqs. (1)–(4) and (9) lead the well-known stress-strain relations

$$\dot{a}=\frac{\dot{\sigma}}{\kappa}+\frac{\sigma}{\eta} \qquad \text{(Maxwell)} \tag{10}$$

and

$$\sigma=\kappa a+\eta\dot{a}\ . \qquad \text{(Voigt)} \tag{11}$$

In the extension of those models to three dimensional non-linear case, we may adopt Eqs. (3), (4) and (8) as the fundamental equations of the theory.

§ 3. Deformation and Internal Deformation

Let us consider a deformation of visco-elastic material, owing to which two points A_0 and B_0 initially at a close distance $\overrightarrow{A_0B_0}=\varDelta\boldsymbol{r}_0$ in the material are shifted during a time interval t to A and B at distance $\overrightarrow{AB}=\varDelta\boldsymbol{r}$, respectively. The deformation tensor $\boldsymbol{a}(t)$ may be defined as

$$\varDelta\boldsymbol{r}=\boldsymbol{a}(t)\cdot\varDelta\boldsymbol{r}_0\ , \tag{12}$$

refering to a spatially fixed coordinate system. $\boldsymbol{a}(t)$ is either a symmetric or an asymmetric tensor depending on the nature of deformation.

Consider the change of deformation in the time interval $(t,\ t+\delta t)$. Eq. (12) leads to

$$\varDelta\boldsymbol{r}+\delta(\varDelta\boldsymbol{r})=(\boldsymbol{a}+\delta\boldsymbol{a})\cdot\varDelta\boldsymbol{r}_0=(\boldsymbol{1}+\delta\boldsymbol{a}\cdot\boldsymbol{a}^{-1})\cdot\varDelta\boldsymbol{r}\ , \tag{13}$$

which means that the deformation produced in δt is represented by $(\boldsymbol{1}+\delta\boldsymbol{a}\cdot\boldsymbol{a}^{-1})$. The time rate of change in the relative coordinate of two points $\varDelta\boldsymbol{r}$ is, then, given by

$$\frac{d(\varDelta\boldsymbol{r})}{dt}=\frac{d\boldsymbol{a}}{dt}\cdot\boldsymbol{a}^{-1}\cdot\varDelta\boldsymbol{r}\ . \tag{14}$$

Besides the above deformation tensor, we will soon introduce two "internal" deformation tensors $\boldsymbol{a}_E$ and $\boldsymbol{a}_\eta$ which are responsible for elastic and dissipative mechanisms, respectively. Whereas $\boldsymbol{a}$ is directly observable quantity in the measurement of deformation, $\boldsymbol{a}_E$ and $\boldsymbol{a}_\eta$ are virtual quantities corresponding to change in lengths of spring and dashpot, respectively, in the classical visco-elastic models. The equations analogous to Eqs. (12) and (14) may be supposed to hold for these internal deformation tensors, if suitable definitions are given to displacements in internal mechanisms.

§ 4. Energy Relation

The rate of displacement of points on the surface of a unit cube of material is represented by deformation-rate tensor $(d\boldsymbol{a}/dt)\cdot\boldsymbol{a}^{-1}$. Hence, denoting the stress tensor as $\boldsymbol{\sigma}$, the time-rate of work done by external force per unit volume of the material is written in the form

$$\frac{dW}{dt}=\Sigma_{ij}\sigma_{ij}\left(\frac{d\boldsymbol{a}}{dt}\cdot\boldsymbol{a}^{-1}\right)_{ij}$$

$$=\mathrm{Sp}\left[\boldsymbol{\sigma}\cdot\frac{d\boldsymbol{a}}{dt}\cdot\boldsymbol{a}^{-1}\right], \tag{15}$$

with the well-known stability condition $\boldsymbol{\sigma}=\boldsymbol{\sigma}^{+}$, where $+$ denotes the transposed tensor.

The analogous expressions may be written down for two internal mechanisms. Let us introduce the effective internal stress tensors $\boldsymbol{\sigma}_E$ and $\boldsymbol{\sigma}_\eta$ which correspond to forces acting on the spring and the dashpot, respectively, in the classical sense. The rate of change of the elastic energy per unit volume of material may be read

$$\frac{dw}{dt}=\mathrm{Sp}\left[\boldsymbol{\sigma}_E\cdot\frac{d\boldsymbol{\alpha}_E}{dt}\cdot\boldsymbol{\alpha}_E{}^{-1}\right], \tag{16}$$

and the rate of energy dissipation will be given

$$\frac{\delta\mathcal{E}}{dt}=\mathrm{Sp}\left[\boldsymbol{\sigma}_\eta\cdot\frac{d\boldsymbol{\alpha}_\eta}{dt}\cdot\boldsymbol{\alpha}_\eta{}^{-1}\right]. \tag{17}$$

The law of energy-conservation

$$\frac{dW}{dt}=\frac{dw}{dt}+\frac{\delta\mathcal{E}}{dt} \tag{8}$$

must be satisfied by these rates of energy change. The second law of thermodynamics requires non-negative dissipation of energy, that is,

$$\frac{\delta\mathcal{E}}{dt}\geq 0\,. \tag{18}$$

B. Maxwell Model

§ 5. Internal Deformation in Maxwell Model

The three dimensional Maxwell model may be characterized by the condition

$$\boldsymbol{\sigma}=\boldsymbol{\sigma}_E=\boldsymbol{\sigma}_\eta\,, \tag{19}$$

which is the analogue of Eq. (3). From Eqs. (15)-(17) and (19) we find a particular solution of Eq. (8):

$$\frac{d\boldsymbol{\alpha}}{dt}=\frac{d\boldsymbol{a}}{dt}\cdot\boldsymbol{a}^{-1}\cdot\boldsymbol{\alpha}+\left(\frac{d\boldsymbol{\alpha}}{dt}\right)^{*}, \tag{20}$$

where we have made use of the abbreviations

$$\boldsymbol{\alpha}\equiv\boldsymbol{\alpha}_E \tag{21}$$

and

$$\left(\frac{d\boldsymbol{\alpha}}{dt}\right)^{*}\equiv-\frac{d\boldsymbol{\alpha}_\eta}{dt}\cdot\boldsymbol{\alpha}_\eta{}^{-1}\cdot\boldsymbol{\alpha}_E\,. \tag{22}$$

Eq. (20) may be interpreted as follows: For the case of visco-elastic material, the deformation tensor $\boldsymbol{a}(t)$ which can be observed does not directly give the situation of the internal elastic mechanism or the stress state. For instance, actually the state of internal elastic mechanism may relax even when the observed deformation is fixed.

Define the internal deformation tensor $\boldsymbol{\alpha}$ as the deformation tensor of equivalent elastic material exhibiting the same stress state as in our visco-elastic material. If the dissipative mechanism were absent, the real and internal deformations produced in the time interval δt

$$(\mathbf{1}+\delta\boldsymbol{a}\cdot\boldsymbol{a}^{-1})\text{ and }(\mathbf{1}+\delta\boldsymbol{\alpha}\cdot\boldsymbol{\alpha}^{-1}) \tag{23}$$

should be identical. In the actual case, however, there occurs a difference between them due to dissipation mechanism. This is the meaning of Eq. (20).

The dissipative term in Eq. (20), $(d\boldsymbol{\alpha}/dt)^*$ must satisfy the following restrictions:

i) $$(d\boldsymbol{\alpha}/dt)^*\to\mathbf{0}\quad\text{with}\quad\boldsymbol{\alpha}\to\mathbf{1}\,. \tag{24}$$

ii) The energy of dissipation must be non-negative:

$$\frac{\delta\mathcal{E}}{dt}=\mathrm{Sp}\left[\boldsymbol{\sigma}\cdot\left(\frac{d\boldsymbol{\alpha}}{dt}\right)^{*}\cdot\boldsymbol{\alpha}^{-1}\right]\geq 0\,. \tag{25}$$

In what follows, except in § 12, we shall adopt a simplest form of the dissipative term

$$\left(\frac{d\boldsymbol{\alpha}}{dt}\right)^{*}=-\beta(\boldsymbol{\alpha}-\mathbf{1})\,, \tag{26}$$

where β is a positive scalar function depending on the invariants associated with the internal deformation tensor $\boldsymbol{\alpha}$. Eq. (26) satisfies the above restrictions. β represents a measure of the rate of dissipation, and $\tau=1/\beta$ is the so-called relaxation time. When β is constant, we may call Eq. (20) to be linear.

Eq. (20) with Eq. (26) determines the internal deformation tensor $\boldsymbol{\alpha}(t)$ with the knowledge of the apparent deformation $\boldsymbol{a}(t)$ as a function of time.

§ 6. Internal Strain Tensor and Strain Energy

The internal deformation tensor $\boldsymbol{\alpha}(t)$ is in general a real asymmetric tensor. However, there are an orthogonal tensor $\boldsymbol{R}$ and two *real positive* symmetric tensors $\boldsymbol{\alpha}_s$ and $\boldsymbol{\alpha}_s'$ such that

$$\boldsymbol{\alpha}=\boldsymbol{R}\cdot\boldsymbol{\alpha}_s=\boldsymbol{\alpha}_s'\cdot\boldsymbol{R} \tag{27}$$

where

$$\boldsymbol{R}^{+}\cdot\boldsymbol{R}=\boldsymbol{R}\cdot\boldsymbol{R}^{+}=\boldsymbol{1}\,, \tag{28}$$

$$\boldsymbol{\alpha}_s\cdot\boldsymbol{\alpha}_s=\boldsymbol{\alpha}^{+}\cdot\boldsymbol{\alpha}\,,\quad \boldsymbol{\alpha}_s'\cdot\boldsymbol{\alpha}_s'=\boldsymbol{\alpha}\cdot\boldsymbol{\alpha}^{+}\,, \tag{29}$$

and $\boldsymbol{\alpha}_s$ and $\boldsymbol{\alpha}_s'$ have the same eigenvalues. Geometrically $\boldsymbol{R}$ corresponds to a rotation, and $\boldsymbol{\alpha}_s$ and $\boldsymbol{\alpha}_s'$ to pure extension or compression along each of three principal directions. Eq. (29) implies that arbitrary deformation $\boldsymbol{\alpha}$ is given by a "pure deformation" $\boldsymbol{\alpha}_s$ preceding to a rotation $\boldsymbol{R}$, or $\boldsymbol{\alpha}_s'$, following to $\boldsymbol{R}$. We shall call $\boldsymbol{\alpha}_s$ and $\boldsymbol{\alpha}_s'$ right and left internal strain tensors, respectively. The left internal strain tensor $\boldsymbol{\alpha}_s'$ defines the internal strain ellipsoid in the deformation state. On the other hand, three principal axes of the right internal strain tensor $\boldsymbol{\alpha}_s$ give the initial directions of the principal axes of internal strain ellipsoid. $\boldsymbol{R}$ represents the mutual rotation of the material during the deformation.

A internal deformation tensor will physically be characterized by a set of three invariants associated with its internal strain tensor, because the internal state of the material may not be affected by pure rotation. While the factors I_1, I_2 and I_3 of λ^2, λ^1 and λ^0, respectively, of the eigenvalue equation,

$$|\boldsymbol{\alpha}_s-\lambda\boldsymbol{1}|=0 \tag{30}$$

give an example of such a set, it will be convenient to take instead the following three expressions:*)

$$I\equiv I_1=\mathrm{Sp}\,\boldsymbol{\alpha}_s=\mathrm{Sp}\,\boldsymbol{\alpha}_s'\,, \tag{31}$$

$$\begin{aligned} J&\equiv I_1^2-2I_2\\ &=\mathrm{Sp}\,\boldsymbol{\alpha}_s\cdot\boldsymbol{\alpha}_s=\mathrm{Sp}\,\boldsymbol{\alpha}_s'\cdot\boldsymbol{\alpha}_s'\\ &=\mathrm{Sp}\,\boldsymbol{\alpha}\cdot\boldsymbol{\alpha}^{+}=\mathrm{Sp}\,\boldsymbol{\alpha}^{+}\cdot\boldsymbol{\alpha}\end{aligned} \tag{32}$$

and

$$K\equiv I_3=|\boldsymbol{\alpha}_s|=|\boldsymbol{\alpha}_s'|=|\boldsymbol{\alpha}|\,. \tag{33}$$

Any scalar function of deformation will have to be considered to depend solely on these three invariants. The increment of free energy density in the material due to internal elastic deformation is a typical example of such scalar functions:

$$w=w(I,\ J,\ K)\,. \tag{34}$$

We shall call this quantity the internal strain energy density.

§ 7. Stress Tensor

Consider a unit cube of the material whose edges are parallel to the coordinate axes at time t when the internal deformation is $\boldsymbol{\alpha}(t)$. Let the sample be subjected to an additional virtual small internal deformation $\boldsymbol{1}+\boldsymbol{\varepsilon}$, $(\boldsymbol{\varepsilon}\ll\boldsymbol{1})$. Thereby the internal deformation changes to $(\boldsymbol{1}+\boldsymbol{\varepsilon})\cdot\boldsymbol{\alpha}$. By $w(\boldsymbol{\alpha};\ \boldsymbol{\varepsilon})$ we denote the internal strain energy density of this sample. The virtual displacement of points on the surfaces of our unit cube is given by the components of $\boldsymbol{\varepsilon}$. Then, it is obvious from the consideration on the work done by surroundings to our unit cube that the stress $\boldsymbol{\sigma}$ is obtained by differentiation

$$\sigma_{ij}(\boldsymbol{\alpha})=\left(\frac{\partial w(\boldsymbol{\alpha};\ \boldsymbol{\varepsilon})}{\partial\varepsilon_{ij}}\right)_{\boldsymbol{\varepsilon}\to 0}. \tag{35}$$

As will be seen in the Appendix A, the internal strain tensor, Eq. (29), and, therefore, $w(\boldsymbol{\alpha};\ \boldsymbol{\varepsilon})$ contain symmetrically the nondiagonal elements of the virtual deformation tensor, $\boldsymbol{\varepsilon}$. Hence, the stress tensor, Eq. (35), is symmetrical:

$$\boldsymbol{\sigma}(\boldsymbol{\alpha})=\boldsymbol{\sigma}^{+}(\boldsymbol{\alpha})\,, \tag{36}$$

which is a condition of stability of the deformation.

$w(\boldsymbol{\alpha};\ \boldsymbol{\varepsilon})$ is considered to be a function of the three invariants associated with the internal deformation $(\boldsymbol{1}+\boldsymbol{\varepsilon})\cdot\boldsymbol{\alpha}$. Then, as a result, Eqs. (31)–(35) lead the stress tensor into the expression

$$\boldsymbol{\sigma}=R_M\boldsymbol{\alpha}_s'+2Q_M\boldsymbol{\alpha}\cdot\boldsymbol{\alpha}^{+}+P_M\boldsymbol{1} \tag{37}$$

where the scalar coefficients R_M, Q_M and P_M are the functions of I, J and K given by

$$\left.\begin{aligned} &R_M=\partial w/\partial I\,,\\ &Q_M=\partial w/\partial J\\ \text{and}\quad &\\ &P_M=[\partial w/\partial K]K\,.\end{aligned}\right\} \tag{38}$$

Detail of the calculation is given in the Appendix A.

We adopt Eqs. (20) and (37) as the fundamental equations describing the stress-deformation relation of the three dimensional nonlinear Maxwell model.

§ 8. Flow Tensor

Now, we define a new tensor $\boldsymbol{J}$

---

*) Rivlin et al. define the strain tensor by $\boldsymbol{\alpha}^{+}\cdot\boldsymbol{\alpha}=\boldsymbol{\alpha}_s\cdot\boldsymbol{\alpha}_s$ instead of $\boldsymbol{\alpha}_s$ or $\boldsymbol{\alpha}_s'$, in terms of which three invariants are given by

$$J=\mathrm{Sp}\,\boldsymbol{\alpha}^{+}\cdot\boldsymbol{\alpha}\,, \tag{31$'$}$$

$$L=\mathrm{Sp}\,\boldsymbol{\alpha}^{+}\cdot\boldsymbol{\alpha}\cdot\boldsymbol{\alpha}^{+}\cdot\boldsymbol{\alpha} \tag{32$'$}$$

and

$$K^2=|\boldsymbol{\alpha}^{+}\cdot\boldsymbol{\alpha}| \tag{33$'$}$$

instead of Eqs. (31), (32) and (33).

$$\boldsymbol{J}=\boldsymbol{a}^{-1}\cdot\boldsymbol{a}\ . \tag{39}$$

$\boldsymbol{J}$ represents the residual deformation of the material just after the internal strain (and, also stress) is suddenly removed, i.e., the deformation impressed upon the dissipative mechanism during the time interval in which the stress is constrained. We may call $\boldsymbol{J}$ the flow tensor. This is the three dimensional analogue of the length of dashpot in the classical Maxwell model.

From Eq. (20) the equation of motion of $\boldsymbol{J}$ is written in the form

$$(d\boldsymbol{J}/dt)\cdot\boldsymbol{J}^{-1}=-\boldsymbol{a}^{-1}\cdot(d\boldsymbol{a}/dt)^{*} \tag{40}$$

or

$$d\boldsymbol{J}^{-1}/dt=\boldsymbol{a}^{-1}\cdot(d\boldsymbol{a}/dt)^{*}\ . \tag{41}$$

The energy dissipation density, Eq. (17), may be read

$$\frac{\delta\mathcal{E}}{dt}=\mathrm{Sp}\left[\boldsymbol{\sigma}\cdot\boldsymbol{a}\cdot\left(\frac{d\boldsymbol{J}}{dt}\cdot\boldsymbol{J}^{-1}\right)\cdot\boldsymbol{a}^{-1}\right]. \tag{42}$$

If $(d\boldsymbol{a}/dt)^{*}$ is a tensor function of $\boldsymbol{a}$ (and $\boldsymbol{a}^{-1}$) only, we can exchange the order of product of the last two factors in the square bracket of Eq. (42), and Eq. (42) reduces to

$$\frac{\delta\mathcal{E}}{dt}=\mathrm{Sp}\left[\boldsymbol{\sigma}\cdot\frac{d\boldsymbol{J}}{dt}\cdot\boldsymbol{J}^{-1}\right]. \tag{43}$$

Eq. (43) suggests that the energy dissipation is, as has been expected, produced by the "flow" of the material.

§ 9. Steady State

Steady states may be characterized by time-independence of internal deformation $\boldsymbol{a}$ because of the direct connection of $\boldsymbol{a}$ with stress $\boldsymbol{\sigma}$ which should be constant in such states. Then, the right-hand side of Eq. (20) must be equal to zero, that is,

$$\frac{d\boldsymbol{a}}{dt}\cdot\boldsymbol{a}^{-1}\cdot\boldsymbol{a}+\left(\frac{d\boldsymbol{a}}{dt}\right)^{*}=\boldsymbol{0}\ . \tag{44}$$

The dissipation term of Eq. (44), $(d\boldsymbol{a}/dt)^{*}$ is considered to be a function of $\boldsymbol{a}$ only, and its time-derivative should vanish in steady states. Hence we have the necessary condition of steady state such that

$$\frac{d}{dt}\left(\frac{d\boldsymbol{a}}{dt}\cdot\boldsymbol{a}^{-1}\right)=\boldsymbol{0}\ . \tag{45}$$

With the deformation satisfying this condition the steady internal deformation tensor $\boldsymbol{a}$ is obtained from Eq. (44).

§ 10. Steady Simple Elongation (Compression)

In this and the next section, we shall treat two typical examples of steady deformations, i.e., the steady simple elongation (or compression) and the steady simple shearing flow.

The deformation tensor for simple elongation in the x-direction is written in the form

$$\boldsymbol{a}(t)=\begin{bmatrix} a(t) & 0 & 0 \\ 0 & a'(t) & 0 \\ 0 & 0 & a'(t) \end{bmatrix}. \tag{46}$$

The so-called Poisson ratio s may be defined by

$$s=-\log a'(t)/\log a(t)\ . \tag{47}$$

This seems to be a reasonable extension of that in the case of small deformation

$$s=-(a'-1)/(a-1),\qquad |a-1|,\ |a'-1|\ll 1\ . \tag{48}$$

The volume of the material in the deformation state is given by

$$v(t)=a(t)^{(1-2s)}v_0\ , \tag{49}$$

where v_0 is the initial volume. $s=1/2$ corresponds to incompressibility of the material.

The condition of steady state, Eq. (45) results in the exponentially varying components of the steady deformation tensor:

$$a(t)=e^{\lambda' t} \tag{50}$$

and

$$a'(t)=e^{-s\lambda' t}\ . \tag{51}$$

In these expressions we have adopted the initial condition, $\boldsymbol{a}(0)=\boldsymbol{1}$. λ' is the parameter characterizing the rate of deformation.

Substituting of Eqs. (46), (50) and (51) into Eq. (44), and making use of Eq. (26) for the dissipation term, we obtain the steady internal deformation tensor

$$\boldsymbol{\alpha}=\begin{bmatrix} \alpha & 0 & 0 \\ 0 & \alpha' & 0 \\ 0 & 0 & \alpha' \end{bmatrix}=\begin{bmatrix} \beta/(\beta-\lambda') & 0 & 0 \\ 0 & \beta/(\beta+s\lambda') & 0 \\ 0 & 0 & \beta/(\beta+s\lambda') \end{bmatrix}. \tag{52}$$

The Poisson ratio s^{*} of the internal deformation may be defined similarly to Eq. (47):

$$s^{*}=-\frac{\log\alpha'}{\log\alpha}=-\frac{\log\left[1+s(\lambda'/\beta)\right]}{\log\left[1-(\lambda'/\beta)\right]}. \tag{53}$$

When the rate of deformation λ' is sufficiently smaller than β, we have simply

$$s^*=s, \quad (\lambda'/\beta)\ll 1\,. \tag{54}$$

In our case $\boldsymbol{\alpha}$ is symmetric, and

$$\boldsymbol{\alpha}_s=\boldsymbol{\alpha}_s'=\boldsymbol{\alpha}, \quad \boldsymbol{R}=\mathbf{1}\,. \tag{55}$$

Substitution of Eq. (53) into Eq. (37) gives the following expression of stress tensor

$$\sigma_{11}=\frac{R_M}{[1-(\lambda'/\beta)]}+\frac{2Q_M}{[1-(\lambda'/\beta)]^2}+\frac{P_M}{[1-(\lambda'/\beta)][1+s(\lambda'/\beta)]^2}\,, \tag{57}$$

$$\sigma_{22}=\sigma_{33}=\frac{R_M}{[1+s(\lambda'/\beta)]}+\frac{2Q_M}{[1+s(\lambda'/\beta)]^2}+\frac{P_M}{[1-(\lambda'/\beta)][1+s(\lambda'/\beta)]^2}\,, \tag{58}$$

$$\sigma_{ij}=0\,, \qquad (i\neq j=1,\ 2,\ 3)\,. \tag{59}$$

The rate of dissipation of energy density, Eq. (25), is written in this case as

$$\frac{\delta\mathcal{E}}{dt}=\beta\,\mathrm{Sp}\,[\boldsymbol{\sigma}\cdot(\mathbf{1}-\boldsymbol{\alpha}^{-1})] \tag{60}$$

$$=\lambda\Big[R_M\Big\{\frac{1}{[1-(\lambda'/\beta)]}-2s\frac{1}{[1+s(\lambda'/\beta)]}\Big\}+2Q_M\Big\{\frac{1}{[1-(\lambda'/\beta)]^2}-2s\frac{1}{[1+s(\lambda'/\beta)]^2}\Big\}$$
$$+P_M(1-2s)\frac{1}{[1-(\lambda'/\beta)][1+s(\lambda'/\beta)]^2}\Big]\,. \tag{61}$$

The so-called tensile viscosity coefficient $\eta^*(\lambda')$ is defined by

$$\eta^*(\lambda')=(1/\lambda'^2)(\delta\mathcal{E}/dt)\,. \tag{62}$$

From Eqs. (61) and (62) we can easily obtain the explicit expression of $\eta^*(\lambda')$. In particular, in the case of incompressible materials, we obtain

$$\eta^*(\lambda')=\frac{3}{2\beta}\Big[\frac{R_M}{[1-(\lambda'/\beta)][1+\frac{1}{2}(\lambda'/\beta)]}+\frac{Q_M[4-(\lambda'/\beta)]}{[1-(\lambda'/\beta)]^2[1+\frac{1}{2}(\lambda'/\beta)]^2}\Big]\,. \tag{63}$$

If λ' is sufficiently smaller than β, $\eta^*(\lambda')$ can be expanded in a power series with respect to λ'/β such that

$$\eta^*(\lambda')=\frac{3}{\beta}\Big[\Big(\frac{R_M}{2}+2Q_M\Big)+\Big(\frac{R_M}{4}+\frac{3}{2}Q_M\Big)\Big(\frac{\lambda'}{\beta}\Big)+\cdots\Big]\,. \tag{64}$$

If the side surfaces of the sample are free from any external forces, we have

$$\sigma_{22}=\sigma_{33}=0\,. \tag{65}$$

In this case, Eq. (58) determines the value of the Poisson ratio s^* when the functional form of the internal strain energy w, i.e., those of the coefficients R_M, Q_M and P_M are known. However, it would be difficult to obtain molecular-theoretically the complete form of w as a function of strain invariants. In many cases the treatment of dilatation-dependence of w is more difficult than that of its shape-dependence, because of the liquid-like molecular distribution in many visco-elastic materials. In such cases we can obtain theoretically the expressions of R_M and Q_M but P_M, and Eq. (58) with Eq. (65) determines the value of hydrostatic pressure P_M with the experimental value of the Poisson ratio. The tensile stress $\sigma=\sigma_{11}$ becomes

$$\sigma=(s+1)\Big(\frac{\lambda'}{\beta}\Big)\Big[R_M\frac{1}{[1-(\lambda'/\beta)][1+s(\lambda'/\beta)]}$$
$$+2Q_M\frac{[2-(1-s)(\lambda'/\beta)]}{[1-(\lambda'/\beta)]^2[1+s(\lambda'/\beta)]^2}\Big]\,. \tag{66}$$

In Fig. 1 are shown the curves of α, α', s^*, σ and η^* versus (λ'/β) for the incompressible material $(s=1/2)$ having the free side surfaces. If R_M, Q_M and β are constant, α,

σ and η^* diverge at $\lambda'=\beta$. Then sample cannot be elongated with larger rate of deformation λ' than the reciprocal of the relaxation time $\beta=1/\tau$, even if any large tensile force acts on both ends of the sample. In actual cases, however, R_M, Q_M and β should not be constants but functions of λ', and any value of deformation-rate may be observed.

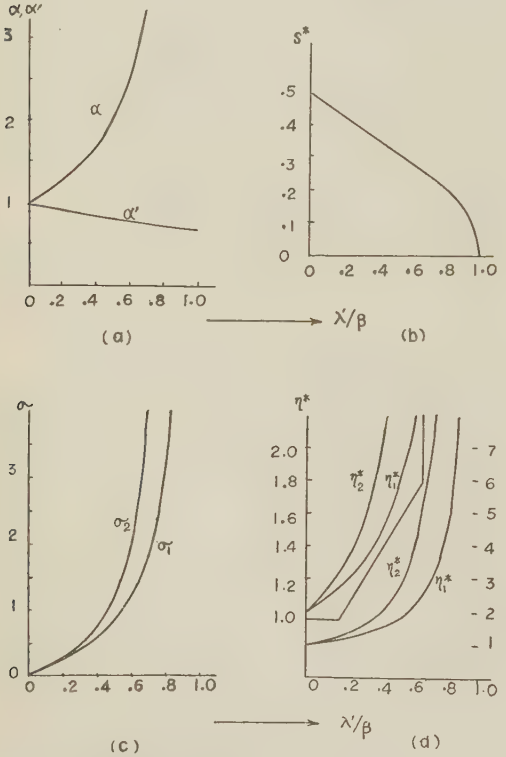

Fig. 1. Internal strain, internal Poisson ratio, tensile stress and tensile viscosity coefficient for the simple elongation of an incompressible Maxwell material.

$$\sigma_{11}=\frac{3}{2}[R_M\sigma_1+4Q_M\sigma_2]\ ,$$

$$\sigma_{22}=\sigma_{33}=0\ ,$$

$$\eta^*=\frac{3}{2\beta}[R_M\eta_1{}^*+4Q_M\eta_2{}^*]\ .$$

The curve of η^* vs. λ' intersects the η^*-axis with a finite, positive slope; the "tensile flow" has essentially the property of so-called non-Newtonian "anti-structural" viscosity. This behavior is experimentally observed by Nitschmann and Schrade for concentrated diphenyl chloride solutions of nitrocellulose.[19]

§ 11. Steady Simple Shearing Flow

Consider the steady simple shearing flow in the x-direction with a constant velocity gradient λ in the y-direction. The deformation tensor

$$\boldsymbol{a}(t)=\begin{bmatrix}1 & \lambda t & 0\\ 0 & 1 & 0\\ 0 & 0 & 1\end{bmatrix} \tag{67}$$

of course satisfies the condition of steady state, Eq. (45). Assuming the dissipation term, Eq. (26), Eq. (44) gives the following steady internal deformation tensor:

$$\boldsymbol{a}=\begin{bmatrix}1 & \lambda/\beta & 0\\ 0 & 1 & 0\\ 0 & 0 & 1\end{bmatrix}. \tag{68}$$

This is a typical asymmetric tensor, and the symmetrization is necessary. $\boldsymbol{a}_s$, $\boldsymbol{a}_s'$ and $\boldsymbol{R}$ in Eq. (27) may be written in the form

$$\boldsymbol{a}_s=\begin{bmatrix}\cos\theta & \sin\theta & 0\\ \sin\theta & \cos\theta+2\dfrac{\sin^2\theta}{\cos\theta} & 0\\ 0 & 0 & 1\end{bmatrix}, \tag{69}$$

$$\boldsymbol{a}_s'=\begin{bmatrix}\cos\theta+2\dfrac{\sin^2\theta}{\cos\theta} & \sin\theta & 0\\ \sin\theta & \cos\theta & 0\\ 0 & 0 & 1\end{bmatrix} \tag{70}$$

and

$$\boldsymbol{R}=\begin{bmatrix}\cos\theta & \sin\theta & 0\\ -\sin\theta & \cos\theta & 0\\ 0 & 0 & 1\end{bmatrix}, \tag{71}$$

where

$$\theta=\mathrm{Tan}^{-1}(\lambda/2\beta) \tag{72}$$

gives the angle of "rotation" of the effective internal elastic mechanism around the z-axis.[*]

Eqs. (37), (68) and (70) cast the stress tensor into such a form that

$$\sigma_{11}=R_M\cos\theta[1+2(\lambda/\beta)^2]+2Q_M[1+(\lambda/\beta)^2]+P_M, \tag{73}$$

$$\sigma_{22}=R_M\cos\theta+2Q_M+P_M, \tag{74}$$

$$\sigma_{33}=R_M+2Q_M+P_M, \tag{75}$$

$$\sigma_{12}=\sigma_{21}=R_M\sin\theta+2Q_M(\lambda/\beta) \tag{76}$$

and

$$\sigma_{13}=\sigma_{31}=\sigma_{32}=\sigma_{23}=0\ . \tag{77}$$

The rate of the dissipation of energy density, Eq. (60), is reduced to

---

[*] θ is related to the extinction angle χ of the flow birefringence in the form

$$(\pi/4)-(\theta/2)=\chi\ . \tag{A}$$

$$\frac{\delta\mathcal{E}}{dt}=\lambda[R_M\sin\theta+2Q_M(\lambda/\beta)]=\lambda\sigma_{12}. \tag{78}$$

The viscosity coefficient $\eta(\lambda)$ is given by

$$\eta(\lambda)=(1/\lambda^2)(\delta\mathcal{E}/dt)=\sigma_{12}/\lambda \tag{79}$$

$$=R_M\sin\theta/\lambda+2Q_M/\beta\,. \tag{80}$$

For sufficiently small values of λ, we have the following expanded form of $\eta(\lambda)$:

$$\eta(\lambda)=\frac{1}{\beta}\left[\left(\frac{R_M}{2}+2Q_M\right)-\frac{R_M}{8}\left(\frac{\lambda}{\beta}\right)^2+\cdots\right]. \tag{81}$$

Comparison of Eq. (81) with Eq. (64) gives the so-called Trouton's relation

$$\eta^*(\lambda'=0)=3\eta(\lambda=0) \tag{82}$$

at the limit of zero rate of the deformations.

For such a special case that

$$R_M=0\,,\quad Q_M=\sigma_0/2=\text{const.} \tag{83}$$

and

$$\beta=\text{const.}\,,$$

the stress tensor is reduced to the simple form

$$\boldsymbol{\sigma}=\sigma_0\begin{bmatrix}1+(\lambda/\beta)^2 & \lambda/\beta & 0\\ \lambda/\beta & 1 & 0\\ 0 & 0 & 1\end{bmatrix}+P_M\mathbf{1}\,. \tag{84}$$

This is identical with that obtained in the previous paper[8] on the Weissenberg effect for the Gaussian network structure. This system shows the typical Newtonian flow. The non-linear additional tension in the flow-direction $\sigma_0(\lambda/\beta)^2$ plays an important rôle in the Weissenberg effect. Since the detailed analysis of this effect has been given in the previous paper, we omit it here. In more general cases, the viscosity coefficient is no longer constant, and the Weissenberg effect also has more complicated velocity gradient-dependence.

§ 12. Visco-elasticity of Gaussian Network

In this section, we shall consider an application of the present theory to visco-elasticity of the weak rubber-like network model constructed by Gaussian chains, which has been treated in detail in the preceding papers.[20),8)] It has been shown that the internal strain energy function w of such system is written in the form

$$w=\frac{3\kappa T}{2a^2}\Sigma_N\frac{1}{N}\iiint\mathrm{Sp}[\boldsymbol{\alpha}^+\cdot(\boldsymbol{\xi}\boldsymbol{\xi})\cdot\boldsymbol{\alpha}]\times F_0(\boldsymbol{\xi},N)d\boldsymbol{\xi}+E(|\boldsymbol{\alpha}|)\,, \tag{85}$$

where $F_0(\boldsymbol{\xi},N)d\boldsymbol{\xi}$ gives the number of chains in the natural state which consist of N-free rotating segments of the fixed length a and which have the end-to-end distance between $\boldsymbol{\xi}$ and $\boldsymbol{\xi}+d\boldsymbol{\xi}$. If the distribution of chains in the natural state is spherically symmetric, Eq. (85) is reduced to

$$w=Q\,\mathrm{Sp}\,(\boldsymbol{\alpha}^+\cdot\boldsymbol{\alpha})+E(|\boldsymbol{\alpha}|)\,, \tag{86}$$

where

$$Q=\frac{3kT}{2a^2}\frac{1}{3}\Sigma_N\frac{1}{N}\iiint\xi^2F_0(\boldsymbol{\xi},N)d\boldsymbol{\xi} \tag{87}$$

is a constant scalar coefficient characterizing the network structure. $E(|\boldsymbol{\alpha}|)$ is a part of the inner energy due to the liquid-like segmental distribution and depends only on the dilatation of the material.

From Eqs. (37) and (38) we have the following expression of the stress tensor:

$$\boldsymbol{\sigma}=\boldsymbol{\sigma}_n+P\mathbf{1}\,, \tag{88}$$

$$\boldsymbol{\sigma}_n=2Q\boldsymbol{\alpha}\cdot\boldsymbol{\alpha}^+. \tag{89}$$

In order to obtain directly the stress-deformation relation, Eq. (20) is substituted into the time derivative of Eq. (89) with the result

$$\frac{d\boldsymbol{\sigma}_n}{dt}=\frac{d\boldsymbol{\alpha}}{dt}\cdot\boldsymbol{\alpha}^{-1}\cdot\boldsymbol{\sigma}_n+\boldsymbol{\sigma}_n\cdot\boldsymbol{\alpha}^{+-1}\cdot\frac{d\boldsymbol{\alpha}^+}{dt}+\left(\frac{d\boldsymbol{\sigma}_n}{dt}\right)^*, \tag{90}$$

where

$$\left(\frac{d\boldsymbol{\sigma}_n}{dt}\right)^*=2Q\left[\left(\frac{d\boldsymbol{\alpha}}{dt}\right)^*\cdot\boldsymbol{\alpha}^++\boldsymbol{\alpha}\cdot\left(\frac{d\boldsymbol{\alpha}^+}{dt}\right)^*\right] \tag{91}$$

gives the stress production due to the dissipative mechanism. The expression of $(d\boldsymbol{\sigma}_n/dt)^*$ in the network theory is given by

$$\left(\frac{d\boldsymbol{\sigma}_n}{dt}\right)^*=\frac{3kT}{a^2}\Sigma_N\frac{1}{N}\iiint(\boldsymbol{\xi}\boldsymbol{\xi})[G(\boldsymbol{\xi},N,t)-\beta(\boldsymbol{\xi},N)F(\boldsymbol{\xi},N,t)]d\boldsymbol{\xi}\,. \tag{92}$$

In this equation $F(\boldsymbol{\xi},N,t)$ is the distribution function of chains in the deformation state, $\beta(\boldsymbol{\xi},N)$, the probability of the breakage of chains, and $G(\boldsymbol{\xi},N,t)$, the instantaneous distribution function of deformed chains. If $G(\boldsymbol{\xi},N)$ is spherically symmetric and $\beta(\boldsymbol{\xi},N)$ is a constant β_n, Eq. (92) is reduced to

$$\left(\frac{d\boldsymbol{\sigma}_n}{dt}\right)^*=\kappa\mathbf{1}-\beta_n\boldsymbol{\sigma}_n\,. \tag{93}$$

On the other hand, the simple expression of $(d\boldsymbol{\alpha}/dt)^*$ in our phenomenological theory, Eq. (26), leads to the following stress production:

$$\left(\frac{d\boldsymbol{\sigma}_n}{dt}\right)^* = 2\beta Q_M(\boldsymbol{a}+\boldsymbol{a}^+) - 2\beta\boldsymbol{\sigma}_n\,. \tag{94}$$

This expression is essentially different from that of the network theory, Eq. (93). Let us consider instead of Eq. (26) the internal deformation production

$$\left(\frac{d\boldsymbol{a}}{dt}\right)^* = -\beta(\boldsymbol{a}-\boldsymbol{a}^{+-1}) + (\boldsymbol{x}-\boldsymbol{x}^+)\boldsymbol{a}^{-1} \tag{95}$$

with the antisymmetric tensor $(\boldsymbol{x}-\boldsymbol{x}^+)$ satisfying the equation

$$2Q(\boldsymbol{x}-\boldsymbol{x}^+) = \frac{d\boldsymbol{a}}{dt}\cdot\boldsymbol{a}^{-1}\cdot\boldsymbol{a}\cdot\boldsymbol{a}^+ - \boldsymbol{a}\cdot\boldsymbol{a}^+\cdot\boldsymbol{a}^{+-1}\frac{d\boldsymbol{a}^+}{dt}\,. \tag{96}$$

This also satisfies Eqs. (24) and (25). In this case Eq. (91) is reduced to the essentially similar expression to that of the network model, Eq. (93). Then, the Gaussian weak network model is characterized by Eqs. (86), (95) and (96) in our phenomenological theory.

Eqs. (26) and (95) are both qualified for the internal deformation production due to the dissipative mechanism. Eq. (26) leads to the simple equation for internal deformation and the complicated stress equation. On the other hand, Eq. (95) makes the stress simple and the internal deformation equation complex. Which expression would better be used can not be determined from our treatment of this paper, but comparison with experimental results.

For the system in which Eqs. (85) and (95) are satisfied, the essentially similar results as those of the last two sections may be obtained for the steady simple elongation (compression) and for the steady simple shearing flow, although the detailed calculations are ignored here.

C. Voigt Model

§ 13. Stress Tensor in the Three Dimensional Voigt Model

Corresponding to Eq. (4), we can characterize the three dimensional Voigt model with such a condition that

$$\boldsymbol{a} = \boldsymbol{a}_E = \boldsymbol{a}_\eta\,. \tag{97}$$

The law of energy conservation, Eq. (8), is written in this case with Eqs. (15)–(17) that

$$\mathrm{Sp}\left[\{\boldsymbol{\sigma}-\boldsymbol{\sigma}_E-\boldsymbol{\sigma}_\eta\}\cdot\frac{d\boldsymbol{a}}{dt}\cdot\boldsymbol{a}^{-1}\right] = 0\,. \tag{98}$$

Then, we have a tensor relation

$$\boldsymbol{\sigma} = \boldsymbol{\sigma}_E + \boldsymbol{\sigma}_\eta\,. \tag{99}$$

This relation should be considered as the fundamental stress equation for the three dimensional Voigt model.

The stress-strain relation is obtained by expressing $\boldsymbol{\sigma}_E$ and $\boldsymbol{\sigma}_\eta$ in terms of $\boldsymbol{a}$ and $\dot{\boldsymbol{a}}$.

§ 14. Elastic Stress Tensor

The elastic stress-strain relation can be obtained by the similar procedure to the case of the stress tensor for the three dimensional Maxwell model in § 7. Define the symmetric tensors $\boldsymbol{a}_s$ and $\boldsymbol{a}_s'$ by

$$\boldsymbol{a} = \boldsymbol{a}_s'\cdot\boldsymbol{R} = \boldsymbol{R}\cdot\boldsymbol{a}_s \tag{100}$$

with the relations

$$\boldsymbol{a}_s^+ = \boldsymbol{a}_s\,, \quad \boldsymbol{a}_s'^+ = \boldsymbol{a}_s' \tag{101}$$

and

$$\boldsymbol{R}^+\cdot\boldsymbol{R} = \boldsymbol{R}\cdot\boldsymbol{R}^+ = \mathbf{1}\,. \tag{102}$$

We choose the following three invariants associated with $\boldsymbol{a}$

$$I' = \mathrm{Sp}\,\boldsymbol{a}_s = \mathrm{Sp}\,\boldsymbol{a}_s'\,, \tag{103}$$

$$J' = \mathrm{Sp}\,\boldsymbol{a}^+\cdot\boldsymbol{a} = \mathrm{Sp}\,\boldsymbol{a}\cdot\boldsymbol{a}^+ \tag{104}$$

and

$$K' = |\boldsymbol{a}|\,. \tag{105}$$

The elastic strain energy density w may be a function of these three invariants:

$$w = w(I',\ J',\ K')\,. \tag{106}$$

Then, the elastic stress tensor $\boldsymbol{\sigma}_E$ is written in the form

$$\boldsymbol{\sigma}_E = R_V\boldsymbol{a}_s + 2Q_V\boldsymbol{a}\cdot\boldsymbol{a}^+ + P_V\mathbf{1}\,, \tag{107}$$

where the coefficients R_V, Q_V and P_V are given by

$$R_V = \partial w/\partial I'\,,$$

$$Q_V = \partial w/\partial J' \tag{108}$$

and

$$P_V = [\partial w/\partial K']K'$$

analogous to Eqs. (37) and (38).

§ 15. Viscous Stress Tensor

At a glance it might seem that a similar relation to that of $\boldsymbol{\sigma}_E$ hold for $\boldsymbol{\sigma}_\eta$ with replacement of $\boldsymbol{a}$ by $\mathring{\boldsymbol{a}} = (d\boldsymbol{a}/dt)\cdot\boldsymbol{a}^{-1}$. However, it is not the case. For example, let us consider the simple shearing deformation,

$$\boldsymbol{a} = \begin{bmatrix} 1 & \lambda(t) & 0 \\ 0 & 1 & 0 \\ 0 & 0 & 1 \end{bmatrix}. \tag{109}$$

In this case,

$$\boldsymbol{\mathring{a}}=\begin{bmatrix} 0 & \dot{\lambda} & 0 \\ 0 & 0 & 0 \\ 0 & 0 & 0 \end{bmatrix} \tag{110}$$

and

$$\boldsymbol{\mathring{a}}\cdot\boldsymbol{\mathring{a}}^{+}=\begin{bmatrix} \dot{\lambda}^2 & 0 & 0 \\ 0 & 0 & 0 \\ 0 & 0 & 0 \end{bmatrix}. \tag{111}$$

Hence we have

$$\boldsymbol{\mathring{a}}_s=\begin{bmatrix} \dot{\lambda} & 0 & 0 \\ 0 & 0 & 0 \\ 0 & 0 & 0 \end{bmatrix}. \tag{112}$$

Then all non-diagonal elements of the viscous stress tensor corresponding to Eq. (109) should vanish; the relaxation terms do not exist in the shearing stress components $\sigma_{12}=\sigma_{21}$. This results contradicts to our common observations. It is expected that the dissipation mechanism depends not only on the rate of deformation but also on the deformation state. Then we must start from the general tensor relations.

Let us consider a symmetric tensor $\boldsymbol{A}$. Any symmetric tensor, say, $\boldsymbol{B}$, of which principal axes coincide with those of $\boldsymbol{A}$, is represented in such a form that

$$\boldsymbol{B}=s\boldsymbol{1}+t\boldsymbol{A}+u\boldsymbol{A}^2\ , \tag{113}$$

where the scalar coefficients s, t and u are functions of the invariants of $\boldsymbol{A}$ and $\boldsymbol{B}$[10]. On the other hand, for any symmetric tensor, say, $\boldsymbol{C}$, consider three symmetric arbitrary tensors $\boldsymbol{A}_1$, $\boldsymbol{A}_2$ and $\boldsymbol{A}_3$ of which the sets of the principal directions do not coincide with each other. It can be shown that there is a symmetric tensor $\boldsymbol{C}'$ which is a linear combination of these three tensors and of the square of one of these, say, $\boldsymbol{A}_1$, with suitable scalar coefficients a_i:

$$\boldsymbol{C}'=a_1\boldsymbol{A}_1+a_2\boldsymbol{A}_2+a_3\boldsymbol{A}_3+a_4\boldsymbol{A}_1^2, \tag{114}$$

and of which the set of the principal directions is the same as that of the tensor $\boldsymbol{C}$. (Appendix B.)

Eqs. (113) and (114) suggest that any symmetric tensor may be expressed by a suitable linear conbination of three reference symmetric tensors with different sets of principal directions, their squares and the unit tensor.

In our case, $\boldsymbol{\sigma}_\eta$ is a symmetric tensor depending on $\boldsymbol{\mathring{a}}$. If $\boldsymbol{\mathring{a}}$ has any kind of symmetry property, for example, rotational symmetry around a axis or reflection symmetry with a plane, etc., $\boldsymbol{\sigma}_\eta$ should have the same symmetry property. Hence, as the reference tensors we can choose the following three symmetric tensors

$$(1/2)(\boldsymbol{\mathring{a}}+\boldsymbol{\mathring{a}}^{+}),\quad \boldsymbol{\mathring{a}}_s \text{ and } \boldsymbol{\mathring{a}}_s', \tag{115}$$

where

$$\boldsymbol{\mathring{a}}_s^2=\boldsymbol{\mathring{a}}^{+}\cdot\boldsymbol{\mathring{a}} \text{ and } \boldsymbol{\mathring{a}}_s'^2=\boldsymbol{\mathring{a}}\cdot\boldsymbol{\mathring{a}}^{+}. \tag{116}$$

The viscous stress tensor $\boldsymbol{\sigma}_\eta$ may be written in such a form

$$\begin{aligned}\boldsymbol{\sigma}_\eta=&\,p\boldsymbol{1}+q_1(\boldsymbol{\mathring{a}}+\boldsymbol{\mathring{a}}^{+})^2+r_1(\boldsymbol{\mathring{a}}+\boldsymbol{\mathring{a}}^{+})\\ &+q_2\boldsymbol{\mathring{a}}^{+}\cdot\boldsymbol{\mathring{a}}+r_2\boldsymbol{\mathring{a}}_s+q_3\boldsymbol{\mathring{a}}\cdot\boldsymbol{\mathring{a}}^{+}+r_3\boldsymbol{\mathring{a}}_s'.\end{aligned} \tag{117}$$

The scalar coefficients p, q's and r's are functions of invariants of the reference tensors (115) and, in general, of those associated with the deformation tensor. The condition of positiveness of the energy dissipation,

$$\frac{\delta\mathcal{E}}{dt}=\mathrm{Sp}\,[\boldsymbol{\sigma}_\eta\cdot\boldsymbol{\mathring{a}}]\geq 0 \tag{118}$$

makes a restriction to those scalar coefficients.

Among others the most important are Eqs. (99), (107) and (117), and these are the fundamental stress-strain equations for the three dimensional Voigt model.

§ 16. Simple Elongation (Compression)

As an example of deformation, let us consider a simple elongation (compression) along the coordinate axes. The deformation tensor is diagonal:

$$\boldsymbol{a}=\begin{bmatrix} a_1(t) & 0 & 0 \\ 0 & a_2(t) & 0 \\ 0 & 0 & a_3(t) \end{bmatrix} \tag{119}$$

and, hence, is equal to the strain tensors $\boldsymbol{a}_s$ and $\boldsymbol{a}_s'$. Then, Eq. (107) gives the diagonal elastic stress tensor of which the normal components have the form

$$(\boldsymbol{\sigma}_E)_{ii}=R_V a_i+2Q_V a_i^2+P_V\ . \tag{120}$$

Furthermore, $\boldsymbol{\mathring{a}}=(d\boldsymbol{a}/dt)\cdot\boldsymbol{a}^{-1}$ is also diagonal, and the three reference tensors coincide with each other:

$$\begin{aligned}&(1/2)(\boldsymbol{\mathring{a}}+\boldsymbol{\mathring{a}}^{+})=\boldsymbol{\mathring{a}}_s=\boldsymbol{\mathring{a}}_s'\\ &=\begin{bmatrix} \dot{a}_1(t)/a_1(t) & 0 & 0 \\ 0 & \dot{a}_2(t)/a_2(t) & 0 \\ 0 & 0 & \dot{a}_3(t)/a_3(t) \end{bmatrix}.\end{aligned} \tag{121}$$

The viscous stress tensor $\boldsymbol{\sigma}_\eta$ is also diagonal, and from Eq. (117) its normal components are written in the form

$$(\boldsymbol{\sigma}_\eta)_{ii}=r(\dot{a}_i/a_i)+q(\dot{a}_i/a_i)^2+p\ . \tag{122}$$

r, q and p are the functions of invariants associated with $\boldsymbol{a}(t)$ and $\mathring{\boldsymbol{a}}(t)$. They must satisfy the condition (118) which is reduced to

$$r\sum_i (\dot{a}_i/a_i)^2+q\sum_i (\dot{a}_i/a_i)^3+p\sum_i (\dot{a}_i/a_i)\geq 0\,. \tag{123}$$

From Eqs. (120) and (122) we have the total stress tensor of which diagonal elements are

$$\begin{aligned}\sigma_{ii}(t)=P_V'+2Q_Va_i^2(t)+R_Va_i(t)\\ +q(\dot{a}_i/a_i)^2+r(\dot{a}_i/a_i)\,.\end{aligned} \tag{124}$$

Let us consider a special case in which an incompressible material is stretched in the x-direction by a simple tensile force. The diagonal components of deformation and of stress tensor should have the following forms, respectively:

$$\begin{aligned}a_1(t)=a(t)\,,\\ a_2(t)=a_3(t)=1/\sqrt{a(t)}\,,\end{aligned} \tag{125}$$

and

$$\begin{aligned}\sigma_{11}(t)=\sigma(t)\,,\\ \sigma_{22}=\sigma_{33}(t)=0\,.\end{aligned} \tag{126}$$

Eq. (124) and both the second members of Eqs. (125) and (126) determine the hydrostatic pressure P_V', and tensile stress component $\sigma(t)$ is reduced to the form

$$\begin{aligned}\sigma(t)=2Q_V\left(a^2(t)-\frac{1}{a(t)}\right)+R_V\left(a(t)-\frac{1}{\sqrt{a(t)}}\right)\\ +\frac{5}{4}q\left(\frac{\dot{a}(t)}{a(t)}\right)^2+\frac{3}{2}r\frac{\dot{a}(t)}{a(t)}\,.\end{aligned} \tag{127}$$

The restrictive condition Eq. (123) for r, q and p becomes

$$q(\dot{a}(t)/a(t))+2r\geq 0\,. \tag{128}$$

§ 17. Simple Shearing Deformation

Making use of the arguments of § 11, we can easily write down the exression of stress tensor for the simple shearing deformation, Eq. (109), using the similar procedure to that of the last section, such as

$$\sigma_{11}=E\lambda^2+r'\dot{\lambda}+q'\dot{\lambda}^2+P\,, \tag{129}$$

$$\sigma_{22}=r''\dot{\lambda}+q''\dot{\lambda}^2+P\,, \tag{130}$$

$$\sigma_{33}=R_V(1-2/\sqrt{4+\lambda^2})+P\,, \tag{131}$$

$$\sigma_s\equiv\sigma_{12}=\sigma_{21}=E\lambda+\eta\dot{\lambda}\,, \tag{132}$$

$$\sigma_{23}=\sigma_{32}=\sigma_{31}=\sigma_{13}=0\,. \tag{133}$$

In these expressions we have adopted the abbreviations

$$E=(R_V/\sqrt{4+\lambda^2})+2Q_V\,, \tag{134}$$

$$\eta=r_1\,, \tag{135}$$

$$r'=r_3\,,\quad r''=r_2\,, \tag{136}$$

$$q'=q_1+q_3\,,\quad q''=q_1+q_2\,, \tag{137}$$

and

$$P=(2R_V/\sqrt{4+\lambda^2})+2Q_V+P_V+p\,. \tag{138}$$

The condition of positive dissipation of energy, Eq. (118), requires the positiveness of "viscosity coefficient",

$$\eta\geq 0\,. \tag{139}$$

The other coefficients may take arbitrary signs and magnitudes.

Eq. (132) shows that the shearing stress σ_s satisfies formally the classical Voigt equation. However, in our case, the coefficients E and η are in general not constants but functions of λ and $\dot{\lambda}$, that is, Eq. (132) does not exclude non-linearity in the shearing stress-deformation relation.

The term $E\lambda^2$ in σ_{11} is an additional tension analogous to that arises in the three dimensional Maxwell model which gives rise to a normal stress effect (Weissenberg effect). In the present model, a visco-elastic normal stress effect exists as will be discussed in the next section. This is called the Poynting effect. $r'\dot{\lambda}$ and $q'\dot{\lambda}^2$ in σ_{11} and similar terms in σ_{22} can be interpreted as (nonlinear) relaxation cross effects. These are due to the terms associated with $\mathring{\boldsymbol{a}}_s$ and $\mathring{\boldsymbol{a}}'_s$ in Eq. (117).

§ 18. Poynting Effect

Let the circular cyclindrical Voigt material, of which the radius is R and the length is h, be twisted by a torsional couple acted on its ends. Denote the twisting angle $\Delta\Phi(t)$. The simple shearing deformation is produced in the φ-direction with the displacement gradient

$$\lambda(t)=(\Delta\Phi(t)/h)r=sr \tag{140}$$

in the z-direction.

Denote by M the moment of force which is applied on the ends of cylinder. This is obtained by integration of the shearing stress, Eq. (132), over the cross sectional area, that is,

$$M=\kappa s+\mu\dot{s}\,, \tag{141}$$

where

$$\kappa=\int_0^R 2\pi\rho^2E(s\rho)d\rho \tag{142}$$

and

$$\mu=\int_0^R 2\pi\rho^2\eta(s\sigma)d\rho\,. \tag{143}$$

Then, the moment of force and the twisting angle obey the classical Voigt type stress-deformation relation.

Non-isotropic terms in the normal stress components give rise to the additional pressure, as has been seen in the treatment of the Weissenberg effect in the previous paper[8]. Distribution of pressure $\Pi(r)$ is obtained by solving the Euler equation with the stress tensor Eqs. (129)–(133). In the simple case of $R=0$, $\Pi(r)$ becomes

$$\Pi(r)=P_0+\tfrac{1}{2}\overline{E}s^2r^2+(\overline{r'}-r'')\dot{s}r+(\tfrac{1}{2}\overline{q'}-q'')\dot{s}^2r^2\,, \tag{144}$$

where

$$\overline{E}=\left\{2\int_r^R E(s\,\rho)\rho\,d\rho\right\}\Big/r^2\,, \tag{145}$$

$$\overline{r'}=\left\{\int_r^R r'(s\rho)d\rho\right\}\Big/r\,, \tag{146}$$

$$\overline{q'}=\left\{2\int_r^R q'(s\rho)\rho\,d\rho\right\}\Big/r^2\,, \tag{147}$$

and P_0 is the pressure acting on the side surface of the cylinder. In order to keep the length of the cylinder constant, it is necessary to apply the total pressure Π_t on the ends, of which magnitude is given by

$$\Pi_t=SP_0+Ks^2+\psi\dot{s}+\chi\dot{s}^2\,; \tag{148}$$

where $S=\pi R^2$ is the area of the cross section and we have made use of the following notations:

$$K=\pi\int_0^R\overline{E}(\rho)\rho^3d\rho\,, \tag{149}$$

$$\psi=2\pi\int_0^R(\overline{r'}-r'')\rho^2d\rho \tag{150}$$

and

$$\chi=\pi\int_0^R(\overline{q'}-2q'')\rho^3d\rho\,. \tag{151}$$

If the ends of the cylinder are free from the normal stress, its length may elongate or shorten depending on the signs and magnitudes of K, ψ and χ.

Although experimental investigation of this effect has been scarcely made, it should play an important rôle in the analysis of visco-elastic properties of the sample, as that of the Weissenberg effect in the case of the Maxwell model. Especially, responses of the sample to sinusoidal twisting experiment will give valuable informations about its mechanical behaviors. Non-linear visco-elastic properties may be detected by the treatments of overtones in the responded stress and/or strain components. Those in the shearing stress or strain give a measure of the "structural viscosity" of such material, and those of the normal stress and/or strain correspond to the Poynting effect. Analysis of phase and magnitude relations between such excitations and responses will give the estimation of conformity of our three dimensional Voigt model with actual visco-elastic materials.

D. General Discussions

§ 19. Non-linear Behaviors

In the classical theory of visco-elasticity, the considerations are restricted within the framework of linear relations between stress and strain; the elastic modulus and the viscosity coefficient are independent of the stress and the strain state. These systems are characterized by the internal elastic energy density which is proportional to the square of the internal elastic strain or of the elastic stress, and by the constant relaxation or retardation time.

Our three dimensional visco-elastic theory permits us to treat non-linear visco-elastic properties such as non-Newtonian flow, normal stress effect, etc. Non-linearity of visco-elasticity can be classified in three types: elastic, viscous or relaxational, and geometric non-linearities.

Define the elastic linearity by the (internal) strain energy density which is proportional to the sum of squares of three eigenvalues associated with the (internal) deformation tensor, apart from the additional term depending only on the dilatation. Such additional strain energy corresponds to the additional isotropic hydrostatic pressure in the stress tensor. This definition may be a natural extension of that of the classical theory. A typical example of such elastically linear system is the Gaussian network of which strain energy density is given by Eq. (86), and it corresponds to the linear tension-elongation relation of a Gaussian chain. The stress tensor of our elastically linear system is written in such a form as Eqs. (88) and (89) with a constant elastic modulus Q and the hydrostatic pressure P which depends only on the dilatation. We can attribute the dependence of Q on the stress state and the existence of R-term to the elastic non-linearity of our theory of visco-elasticity.

Relaxational linearity for the Maxwell model is defined by the constant "relaxation coefficient" β in Eq. (26). To be more general, β should be replaced by a fourth order "relaxation tensor" $\boldsymbol{\beta}=(\beta_{ij,kl})$, and creation of the internal deformation is written in the form

$$\left(\frac{d\boldsymbol{\alpha}}{dt}\right)^*_{ij}=-\beta_{ij,kl}(\alpha_{kl}-\delta_{kl})\ . \tag{152}$$

When $\boldsymbol{\beta}$ is constant, the system may be called relaxationally linear. In this case, Eq. (20), which determines the internal deformation tensor, is essentially linear with respect to every components of the internal deformation tensor.

Although the resultant stress tensor is essentially the same as that corresponding to Eq. (26) for stational simple shearing flow, the system with different type of creation of the internal deformation, Eq. (95), should be classified in the relaxationally non-linear system. The relaxation tensor is given in this case by

$$\beta_{ij,kl}=[\{\beta(\boldsymbol{\alpha}-\boldsymbol{\alpha}^{+-1})+(\boldsymbol{x}-\boldsymbol{x}^+)\boldsymbol{\alpha}^{-1}\}\cdot \\ \cdot(\boldsymbol{\alpha}-\mathbf{1})^{-1}]_{ik}\delta_{jl}\ . \tag{153}$$

In the case of the Voigt model, the definition of viscous linearity becomes very arbitrary. One of its possible definitions will be given by the following stress tensor

$$\boldsymbol{\sigma}_\eta=\eta(\mathring{\boldsymbol{\alpha}}+\mathring{\boldsymbol{\alpha}}^+) \tag{154}$$

with a constant viscosity coefficient η. This viscous stress tensor gives the shearing stress-deformation relation of simple Voigt type, Eq. (11), for simple shearing deformation, if the system is elastically linear, too. Furthermore, this viscous stress leads to no cross effects in viscous stress-deformation relation, excepting the symmetrization in each pair of complemental non-diagonal elements. The other terms in Eq. (117), apart from the hydrostatic pressure $p\mathbf{1}$, give non-linear stress-strain relations in the usual sence, and/or cross effects at least for asymmetric deformations. Then, the said definition of the viscous linearity, Eq. (154), is reasonable in our system. Deformation-rate dependence of η and/or existence of the other terms in Eq. (117) give causes of viscous non-linearity.

Even if the system is elastically and viscously linear in the above sense, some non-linear behaviors and cross effects may happen to occur between stress and deformation components. One of the typical examples is the normal stress effect. The square terms $\sigma_0(\lambda/\beta)^2$ in Eq. (84) and $E\lambda^2$ in Eq. (129) are such non-linear cross terms, which are essentially due to the three dimensional nature of materials. We shall call these the geometric non-linearities. It is easily shown that the upward convex tension-elongation curve of rubber-like elasticity in the range of relatively small elongation is another example of the geometric non-linearity.

The experimental separation of non-linearity into these three parts can be carried out by independent observations of two or more different stress-strain relations. A typical set of such observations is those of the shearing viscosity and of the Weissenberg effect for elastico-viscous liquids. The details of this analysis have already reported in the previous paper[8].

§ 20. Generalized Model

Visco-elastic properties of the Maxwell and Voigt models in the classical theory are mathematically expressed by the first order linear differential equations of stress, strain and their time derivatives, Eq. (10) and (11). More general linear visco-elastic properties correspond to linear differential equations which contain higher time derivatives of stress and strain. It is well known that suitable parallel and/or series connections of the simple Maxwell and/or Voigt models represent these general linear visco-elastic properties. This generalization has led to the considerations of the so-called relaxation and retardation times, or, in other words, to the considerations of the relaxation and retardation spectra. This is closely connected with the principle of superposition, which has meanings only for the linear systems.

The stress-strain relations of our three dimensional theory are in general non-linear in the usual sense. Then, such generalization procedure may strictly be impossible. However, we can consider formally the parallel and/or series connections of three dimensional Maxwell and Voigt models. Parallel connection is characterized by the condition

$$\boldsymbol{\alpha}=\boldsymbol{\alpha}_1=\boldsymbol{\alpha}_2=\cdots \tag{155}$$

and

$$\boldsymbol{\sigma}=\boldsymbol{\sigma}_1+\boldsymbol{\sigma}_2+\cdots\ , \tag{156}$$

and series connection, by

$$\boldsymbol{\alpha}=\boldsymbol{\alpha}_1+\boldsymbol{\alpha}_2+\cdots \tag{157}$$

and

$$\boldsymbol{\sigma}=\boldsymbol{\sigma}_1=\boldsymbol{\sigma}_2=\cdots . \tag{158}$$

The concept of the relaxation and retardation time spectra may not be kept in these system in which the principle of superposition is no longer estimated. When we restrict our consideration in the special deformation, however, it is possible to define the relaxation and retardation times and their spectra. Let us consider the case of simple shearing. Define the relaxation time for a Maxwell model of which creation of the internal deformation is given by Eq. (26), by

$$\tau(\lambda)=1/\beta(\lambda) . \tag{159}$$

This is in general a function of the velocity gradient. For the generalized Maxwell model, relaxation time spectrum may be given by the quantity

$$F(\tau)=(1/\tau)[R(\lambda\tau)(\sin\theta/\lambda\tau)+Q(\lambda\tau)] \tag{160}$$

with

$$\tan\theta=\lambda\tau/2 . \tag{161}$$

Then, the spectrum depends in general on the velocity gradient λ. On the other hand, the retardation time for a Voigt model may be defined by

$$\tau^*(\lambda,\ \dot{\lambda})=\eta(\dot{\lambda})/E(\lambda) , \tag{162}$$

Retardation time spectrum of the generalized Voigt model takes the form

$$G(\tau^*)=E(\tau^*)/\tau^* \tag{163}$$

as usual. This depends on the magnitudes of the deformation and its time derivative, too. It is easily seen that these definitions of the spectra are natural extensions of those in the classical theory.

§ 21. Summary

A phenomenological theory was presented on the non-linear visco-elastisity of three dimensional bodies. The Maxwell and the Voigt model which were essentially one dimensional were extended to corresponding three dimensional ones. We started from the energy consideration, and defined the "series and parallel connections" of mechanical elements, i.e., the spring and the dashpot. In the case of the three dimensional Maxwell model, we introduced the internal deformation as the deformation of equivalent elastic body which possesses the same stress state as that of our visco-elastic body at each instant. The stress tensor was obtained by application of the three dimensional theory of elasticity to the above internal deformation. In the Voigt case, the stress is divided into two parts; the elastic part and the viscous part. It was assumed that the elastic stress tensor obeys the same stress-strain relation as that of the theory of elasticity, while the viscous stress tensor may have the more complex strain dependence. For examples of applications of our theory, we treated the simple elongation and the simple shearing for both models. Non-linearities in the stress-strain relations were classified into three categories: elastic, viscous (relaxational) and geometric non-linearities. It was shown that deformation-rate dependence of the so-called tensile viscosity and the normal stress effects (the Weissenberg effect and the Poynting effect) are essentially geometric non-linear behaviors due to the three dimensional character of the materials. A typical example of the elastic non-linearity is the upward concave tension-elongation relation of the rubber elasticity for large extension of the sample. The structural viscosity, or, in the other terminology, the non-Newtonian flow is mainly due to the viscous (relaxational) non-linearity.[8)]

If the deformation is not uniform, the treatment of the problem becomes in general complex, and the exact solution may hardly be obtained. In such cases the so-called variation-principle of the stress-strain relation should play an important rôle for the derivation of an approximate solution. This problem is now being considered by the author.

Acknowledgement

The author wishes to express his appreciation to Professor T. Yamamoto for the continuous encouragement and the suggestive discussions, and also for his kind inspection of the manuscript. He is very much indebted to Professor J. Furukawa who has suggested the concept of the internal deformation. His sincere thanks are also due to Professor M. Kurata and the members of our laboratory (Quantum Chemistry Laboratory, Kyoto University) and of Research Group of High Polymer in Kyoto for their fruitful discussions.

The present investigation has been partly supported by the Scientific Research Grant of the Ministry of Education.

Appendix A

Let us consider two closely occupied points A and B of the internal effective elastic mechanism. The distance between them is changed by the internal deformation from $\delta \boldsymbol{r}_0$ to $\delta \boldsymbol{r}$. The square distance is written in the form

$$(\delta s)^2=(\delta \boldsymbol{r})^+\cdot(\delta \boldsymbol{r})=(\delta \boldsymbol{r}_0)\cdot(\boldsymbol{\alpha}^+\cdot\boldsymbol{\alpha})\cdot(\delta \boldsymbol{r}_0)$$
$$=\sum_{ij}(\boldsymbol{\alpha}^+\cdot\boldsymbol{\alpha})_{ij}\delta r_{0i}\delta r_{0j}\,, \tag{A.1}$$

which must be positive for any δr_0. This implies that the symmetric tensor $\boldsymbol{\alpha}^+\cdot\boldsymbol{\alpha}$ is real positive, i.e., its three eigenvalues λ_1^2, λ_2^2 and λ_3^2 are all real positive. We define the new real positive symmetric tensor $\boldsymbol{\alpha}_s$ which has three positive eigenvalues λ_1, λ_2 and λ_3 and the same principal directions as those of $\boldsymbol{\alpha}^+\cdot\boldsymbol{\alpha}$. Obviously, we have

$$\boldsymbol{\alpha}_s\cdot\boldsymbol{\alpha}_s=\boldsymbol{\alpha}^+\cdot\boldsymbol{\alpha}\,. \tag{A.2}$$

The tensor $\boldsymbol{R}$ defined by

$$\boldsymbol{R}=\boldsymbol{\alpha}\cdot\boldsymbol{\alpha}_s^{-1} \tag{A.3}$$

is orthogonal:

$$\boldsymbol{R}\cdot\boldsymbol{R}^+=\boldsymbol{R}^+\cdot\boldsymbol{R}=\boldsymbol{1}\,. \tag{A.4}$$

Define the real positive symmetric tensor

$$\boldsymbol{\alpha}_s'=\boldsymbol{R}\cdot\boldsymbol{\alpha}_s\cdot\boldsymbol{R}^{-1}\,, \tag{A.5}$$

which has the same eigenvalues as those of $\boldsymbol{\alpha}_s$ but different principal axes. Eqs. (A.3) and (A.5) give the expected separations of internal deformation tensor $\boldsymbol{\alpha}$ such that

$$\boldsymbol{\alpha}=\boldsymbol{R}\cdot\boldsymbol{\alpha}_s=\boldsymbol{\alpha}_s'\cdot\boldsymbol{R}\,. \tag{27}$$

Let us prove that when a small deformations, say, $(\boldsymbol{1}+\boldsymbol{\varepsilon})$, $(\boldsymbol{\varepsilon}\ll\boldsymbol{1})$ is superposed on $\boldsymbol{\alpha}$, $\boldsymbol{\alpha}_s(\boldsymbol{\varepsilon})$ contains the components of $\boldsymbol{\varepsilon}$ symmetrically. Actually, the equation giving $\boldsymbol{\alpha}_s(\boldsymbol{\varepsilon})$,

$$\boldsymbol{\alpha}_s(\boldsymbol{\varepsilon})\cdot\boldsymbol{\alpha}_s(\boldsymbol{\varepsilon})=\boldsymbol{\alpha}^+\cdot(\boldsymbol{1}+\boldsymbol{\varepsilon}^+)\cdot(\boldsymbol{1}+\boldsymbol{\varepsilon})\cdot\boldsymbol{\alpha}$$
$$\simeq\boldsymbol{\alpha}^+\cdot\boldsymbol{\alpha}+\boldsymbol{\alpha}^+\cdot(\boldsymbol{\varepsilon}+\boldsymbol{\varepsilon}^+)\cdot\boldsymbol{\alpha} \tag{A.6}$$

is symmetric with respect to the components of $\boldsymbol{\varepsilon}$, and the above statement is proved. Then, any invariant of the tensor $\boldsymbol{\alpha}_s(\boldsymbol{\varepsilon})$ symmetrically contains the components of $\boldsymbol{\varepsilon}$.

The stress tensor $\boldsymbol{\sigma}$ is given by differentiating the internal elastic strain energy density with respect to each component of $\boldsymbol{\varepsilon}$, and by taking the limiting process, $\boldsymbol{\varepsilon}\to\boldsymbol{0}$. The internal elastic strain energy is a function of the invariants of $\boldsymbol{\alpha}_s(\boldsymbol{\varepsilon})$. Symmetrical property of the stress tensor, which is a stability condition of the deformation, is maintained because of the above circumstance. Usually, the following three invariants of $\boldsymbol{\alpha}_s$ are used:

$$I_1=\sum_i\lambda_i=\mathrm{Sp}\,\boldsymbol{\alpha}_s\,, \tag{A.7}$$
$$I_2=\sum_{i<j}\lambda_i\lambda_j\,, \tag{A.8}$$
$$I_3=\lambda_1\lambda_2\lambda_3=|\boldsymbol{\alpha}_s|\,. \tag{A.9}$$

However, in what follows, we shall choose the different sets of invariants (I, J, K) or (J, L, K),

$$I\equiv I_1=\sum_i\lambda_i=\mathrm{Sp}\,\boldsymbol{\alpha}_s\,, \tag{A.10}$$
$$J\equiv I_1^2-2I_2=\sum_i\lambda_i^2=\mathrm{Sp}\,\boldsymbol{\alpha}_s\cdot\boldsymbol{\alpha}_s=\mathrm{Sp}\,\boldsymbol{\alpha}^+\cdot\boldsymbol{\alpha}\,, \tag{A.11}$$
$$K\equiv I_3=\lambda_1\lambda_2\lambda_3=|\boldsymbol{\alpha}_s|=|\boldsymbol{\alpha}| \tag{A.12}$$

and

$$L\equiv I_1^4+2I_2^2+2I_1I_3-4I_1^2I_2$$
$$=\sum_i\lambda_i^4=\mathrm{Sp}\,(\boldsymbol{\alpha}_s)^4=\mathrm{Sp}\,\boldsymbol{\alpha}^+\cdot\boldsymbol{\alpha}\cdot\boldsymbol{\alpha}^+\cdot\boldsymbol{\alpha}\,. \tag{A.13}$$

In the text, we have used the set (I, J, K). Making use of another set (J, L, K) we obtain another expression of the stress tensor, although this difference may be only apparent. Rivlin et. al.[14] have adopted the different set of invariants,

$$I_1'\equiv J=\mathrm{Sp}\,\boldsymbol{\alpha}^+\cdot\boldsymbol{\alpha}\,, \tag{A.14}$$
$$I_2'\equiv\tfrac{1}{2}(J^2-L)=\sum_{i<j}\lambda_i^2\lambda_j^2\,, \tag{A.15}$$
$$I_{3'}\equiv K^2=|\boldsymbol{\alpha}^+\cdot\boldsymbol{\alpha}|\,, \tag{A.16}$$

which corresponds to their definition of strain tensor, $\boldsymbol{\alpha}^+\cdot\boldsymbol{\alpha}$.

In obtaining the expressions of stress tensor necessary are the differentials of the invariants associating with the internal deformation $(\boldsymbol{1}+\boldsymbol{\varepsilon})\cdot\boldsymbol{\alpha}$ with respect to each components of $\boldsymbol{\varepsilon}$ for the limiting case of $\boldsymbol{\varepsilon}\to\boldsymbol{0}$. That is,

i) $I(\boldsymbol{\varepsilon})$

In Eq. (A.6), put $\boldsymbol{\alpha}_s(\boldsymbol{\varepsilon})=\boldsymbol{\alpha}_s+\Delta\boldsymbol{\alpha}_s$. We have at once

$$\boldsymbol{\alpha}_s\cdot\Delta\boldsymbol{\alpha}_s+\Delta\boldsymbol{\alpha}_s\cdot\boldsymbol{\alpha}_s=\boldsymbol{\alpha}^+\cdot(\boldsymbol{\varepsilon}+\boldsymbol{\varepsilon}^+)\cdot\boldsymbol{\alpha}\,. \tag{A.17}$$

Then, Eqs. (27) and (A.5) result in

$$\Delta\boldsymbol{\alpha}_s+\boldsymbol{\alpha}_s^{-1}\cdot\Delta\boldsymbol{\alpha}_s\cdot\boldsymbol{\alpha}_s=\boldsymbol{\alpha}_s^{-1}\cdot\boldsymbol{\alpha}^+\cdot(\boldsymbol{\varepsilon}+\boldsymbol{\varepsilon}^+)\cdot\boldsymbol{\alpha}$$
$$=(\boldsymbol{R}^+\cdot\boldsymbol{\alpha}_s'^{-1}\cdot\boldsymbol{R})\cdot(\boldsymbol{R}^+\cdot\boldsymbol{\alpha}_s')\cdot(\boldsymbol{\varepsilon}+\boldsymbol{\varepsilon}^+)\cdot\boldsymbol{\alpha}_s'\cdot\boldsymbol{R}$$
$$=\boldsymbol{R}^+\cdot(\boldsymbol{\varepsilon}+\boldsymbol{\varepsilon}^+)\cdot\boldsymbol{\alpha}_s'\cdot\boldsymbol{R}\,. \tag{A.18}$$

Therefore we get

$$2\,\mathrm{Sp}\,\Delta\boldsymbol{\alpha}_s=\mathrm{Sp}\,(\boldsymbol{\varepsilon}+\boldsymbol{\varepsilon}^+)\cdot\boldsymbol{\alpha}_s' \tag{A.19}$$

or,

$$I(\varepsilon)=\mathrm{Sp}\,\boldsymbol{\alpha}_s+\tfrac{1}{2}\textstyle\sum_{ik}(\varepsilon_{ik}+\varepsilon_{ki})(\boldsymbol{\alpha}_s')_{ki}\,. \qquad (A.20)$$

Making use of the symmetrical property of $\boldsymbol{\alpha}_s$ we obtain

$$\left(\frac{\partial I(\varepsilon)}{\partial \mathcal{E}_{ik}}\right)_{\varepsilon\to 0}=(\boldsymbol{\alpha}_s')_{ik}\,. \qquad (A.21)$$

ii) $J(\varepsilon)$

From Eq. (A.6), we have

$$\begin{aligned}J(\mathcal{E})&=\mathrm{Sp}\,\boldsymbol{\alpha}_s(\varepsilon)\cdot\boldsymbol{\alpha}_s(\varepsilon)\\&=\mathrm{Sp}\,\boldsymbol{\alpha}^+\cdot\boldsymbol{\alpha}+\mathrm{Sp}\,\boldsymbol{\alpha}^+\cdot(\varepsilon+\varepsilon^+)\cdot\boldsymbol{\alpha}\\&=\mathrm{Sp}\,\boldsymbol{\alpha}^+\cdot\boldsymbol{\alpha}+\textstyle\sum_{ik}(\mathcal{E}_{ik}+\mathcal{E}_{ki})\cdot(\boldsymbol{\alpha}\cdot\boldsymbol{\alpha}^+)_{ki}. \qquad (A.22)\end{aligned}$$

Then,

$$\left(\frac{\partial J(\varepsilon)}{\partial \mathcal{E}_{ik}}\right)_{\varepsilon\to 0}=2(\boldsymbol{\alpha}\cdot\boldsymbol{\alpha}^+)_{ik}\,. \qquad (A.23)$$

iii) $K(\varepsilon)$

In this case,

$$K(\varepsilon)=|(\mathbf{1}+\varepsilon)||\alpha|\simeq(1+\textstyle\sum_i\mathcal{E}_{ii})|\boldsymbol{\alpha}|\,, \qquad (A.24)$$

and we have

$$\left(\frac{\partial K(\varepsilon)}{\partial \mathcal{E}_{ik}}\right)_{\varepsilon\to 0}=|\boldsymbol{\alpha}|\delta_{ik}\,. \qquad (A.25)$$

iv) $L(\varepsilon)$

The expressions

$$\begin{aligned}L(\mathcal{E})&=\mathrm{Sp}\,[(\boldsymbol{\alpha}_s)^4]\\&=\mathrm{Sp}\,[\boldsymbol{\alpha}^+\cdot(\mathbf{1}+\varepsilon^+)\cdot(\mathbf{1}+\varepsilon)\cdot\boldsymbol{\alpha}\cdot\boldsymbol{\alpha}^+\cdot(\mathbf{1}+\varepsilon^+)\\&\quad\cdot(\mathbf{1}+\varepsilon)\cdot\boldsymbol{\alpha}]\\&=\mathrm{Sp}\,\boldsymbol{\alpha}^+\cdot\boldsymbol{\alpha}+2\,\mathrm{Sp}\,[(\varepsilon+\varepsilon^+)\cdot\boldsymbol{\alpha}\cdot\boldsymbol{\alpha}^+\cdot\boldsymbol{\alpha}\cdot\boldsymbol{\alpha}^+]\\&=\mathrm{Sp}\,\boldsymbol{\alpha}^+\cdot\boldsymbol{\alpha}+2\textstyle\sum_{ik}(\mathcal{E}_{ik}+\mathcal{E}_{ki})(\boldsymbol{\alpha}\cdot\boldsymbol{\alpha}^+\cdot\boldsymbol{\alpha}\cdot\boldsymbol{\alpha}^+)_{ki}\end{aligned} \qquad (A.26)$$

give the differentials

$$\left(\frac{\partial L(\varepsilon)}{\partial \mathcal{E}_{ik}}\right)_{\varepsilon\to 0}=(\boldsymbol{\alpha}\cdot\boldsymbol{\alpha}^+\cdot\boldsymbol{\alpha}\cdot\boldsymbol{\alpha}^+)_{ik}\,. \qquad (A.27)$$

Eqs. (A.21), (A.23), (A.25) and (A.27) give the expressions of stress tensor for the two sets of invariants (I, J, K) and (J, L, K) such that

i) For the set (I, J, K):

$$\boldsymbol{\sigma}=R\boldsymbol{\alpha}_s'+2Q(\boldsymbol{\alpha}\cdot\boldsymbol{\alpha}^+)+P\mathbf{1}\,, \qquad (A.28)$$

where

$$R=\partial w(I,\ J,\ K)/\partial I\,, \qquad (A.29)$$

$$Q=\partial w(I,\ J,\ K)/\partial J \qquad (A.30)$$

and

$$P=[\partial w(I,\ J,\ K)/\partial K]K\,. \qquad (A.31)$$

ii) For the set (J, L, K):

$$\boldsymbol{\sigma}=2Q'(\boldsymbol{\alpha}\cdot\boldsymbol{\alpha}^+)+4S'(\boldsymbol{\alpha}\cdot\boldsymbol{\alpha}^+\cdot\boldsymbol{\alpha}\cdot\boldsymbol{\alpha}^+)+P'\mathbf{1}\,, \qquad (A.32)$$

where

$$Q'=\partial w(J,\ L,\ K)/\partial J\,, \qquad (A.33)$$

$$S'=\partial w(J,\ L,\ K)/\partial L \qquad (A.34)$$

and

$$P'=[\partial w(J,\ L,\ K)/\partial K]K\,. \qquad (A.35)$$

Appendix B

Take the three linearly independent symmetric tensor $\boldsymbol{A}_1$, $\boldsymbol{A}_2$ and $\boldsymbol{A}_3$ which have different sets of principal axes from each other. Let us prove that for any symmetric tensor $\boldsymbol{A}$, we can find a suitable linear combination of above three tensors and the square of any-one of them, say $\boldsymbol{A}_1$, such that the linear combination has the same set of principal axes as that of $\boldsymbol{A}$. Through the transformation of coordinate which diagonalizes $\boldsymbol{A}$, above three reference tensors and, thus, their squares cannot be brought into diagonal forms simultaneously. If one of our reference tensors happens to become diagonal, our statement is trivial. Then, we assume that our reference tensors are all non-diagonal in the new coordinate system. We can define the three dimensional "vectors" of which elements are the non-diagonal elements of reference tensors and of their squares, that is,

$$\boldsymbol{l}_i=(\boldsymbol{A}_{i,23},\ \boldsymbol{A}_{i,31},\ \boldsymbol{A}_{i,12})\,,$$

$$\boldsymbol{l}_{i+3}=((\boldsymbol{A}_i^2)_{23},\ (\boldsymbol{A}_i^2)_{31},\ (\boldsymbol{A}_i^2)_{12})\,. \qquad (B.1)$$

Because of linear independence of the vectors, we have the relation

$$a_1\boldsymbol{l}_1+a_2\boldsymbol{l}_2+a_3\boldsymbol{l}_3+a_4\boldsymbol{l}_4=\mathbf{0} \qquad (B.2)$$

with suitable coefficients a_i. Hence, with these coefficients, our linear combination of tensors may be brought into a diagonal form together with tensor $\boldsymbol{A}$.

References

1) For example, B. Gross: *Mathematical structure of the Theory of Viscoelasticity* (Hermann & Cie., Paris, 1953).

2) J. C. Maxwell: Phil. Mag. (4) **35** (1868) 129; 185.

3) W. Voigt: Abh. Kön. Gesell. Wiss. Göttingen **36** (1890).

4) Lord Kelvin (Sir W. Thomson): *Elasticity*, Encyclopaedia Britannica, 9th Ed. (1875); Papers **3** (London, 1890).

5) H. Takahasi: J. Phys. Soc. Japan **7** (1952) 439.

6) L. J. Sharman, R. H. Sones and L. H. Cragg: J. Appl. Phys. **24** (1953) 703.
E. Wada: J. Sci. Res. Inst. **47** (1953) 149;

159; 168; J. Polymer Sci. **14** (1954) 305.
J. D. Ferry, M. L. Williams and D. M. Stern: J. Phys. Chem. **58** (1954) 987.
F. J. Padden and T. W. DeWitt: J. Appl. Phys. **25** (1954) 1086.
T. W. DeWitt, H. Markovitz, F. J. Padden and L. J. Zappas: J. Colloid Sci. **10** (1955) 174.
7) K. Weissenberg: Nature **159** (1947) 310; Proc. 1st Intern. Congr. Rheology, Holland, 1948 (North-Holland Publ. Co., Amsterdam, 1949) 29.
H. Markovitz and R. B. Williamson: Trans. Soc. Rheology **1** (1957) 25.
W. Philippoff et al.: J. Appl. Phys. **27** (1956) 984; **28** (1957) 1118; Trans. Soc. Rheology **1** (1957) 109.
M. Kurata, T. Kotaka and M. Tamura: J. Appl. Phys. (to be published).
8) M. Yamamoto: J. Phys. Soc. Japan **13** (1958) 1200.
9) V. V. Novozhilov: *Foundation of the Nonlinear Theory of Elasticity* (Graylock Press, 1953).
10) C. Truesdell: J. Rat. Mech. Anal. **1** (1952) 125.
11) M. Mooney: J. Colloid Sci. **6** (1951) 96.
12) R. S. Rivlin: J. Rat. Mech. Anal. **4** (1955) 323; *Large Elastic Deformations*, Rheology vol. 1, ed. by F. R. Eirich (Academic Press, New York, 1956) Chap. 10.
13) M. Mooney: J. Appl. Phys. **11** (1940) 582.
14) J. H. Poynting: Proc. Roy. Soc. **A, 82** (1909) 546; **A, 86** (1912) 534; Note in India-Rubber J. (Oct. 4, 1913) 6.
15) T. Alfrey: *Mechanical Behavior of High Polymers* (Interscience Publ., New York, 1948) 205.
T. Alfrey and E. F. Gurnee: *Dynamics of Visco-elastic Behavior*, Rheology vol. 1, ed. by F. R. Eirich (Academic Press, New York, 1956) Chap. 11.
16) R. S. Rivlin: J. Rat. Mech. Anal. **5** (1956) 179.
17) Yoh-Han Pao: J. Appl. Phys. **28** (1957) 591.
18) W. Segawa: J. Phys. Soc. Japan **12** (1957) 996; Busseiron-Kenkyu **2–4** (1958) 13 (in Japanese).
19) Hs. Nitschmann and J. Schrade: Helv. Chem. Acta. **31** (1948) 297.
20) M. Yamamoto: J. Phys. Soc. Japan **11** (1956) 413; **12** (1957) 1148.

JOURNAL OF THE PHYSICAL SOCIETY OF JAPAN Vol. 14, No. 3, MARCH, 1959

Quantum Theoretical Study on Single, Double and Triple Bonds between Carbon Atoms

By Sigeru NAGAHARA

Department of Physics, Faculty of Literature and Science,
Toyama University

(Received October 30, 1958)

We study the characteristic features of single, double and triple bonds between carbon atoms by idealizing the problem to the electronic structure of fictitious diatomic molecules $\equiv C-C\equiv$, $=C=C=$ and $-C\equiv C-$, where the "open" bonds of carbon atoms are represented by a suitably hybridized orbitals, associated with free spins. Thus, adiabatic potentials are non-empirically and numerically computed and bond energies and equilibrium internuclear distances are evaluated. We obtain 3.1 e.v., 1.25 e.v. and 0.20 Å, 0.10 Å for the values of relative bond energy differences and bond distance differences of single and triple, double and triple bonding. The corresponding experimental values are 2.9 e.v., 1.0 e.v., and 0.34 Å, 0.12 Å respectively.

§ 1. Introduction

The nature of the single bond was quantum-mechanically disclosed by many authors by working out quantitative theories of the *ss*- and *sp*-bonds. However the quantum-mechanical nature of the double and triple bonds has not yet been fully known. The double bond was first discussed by Hückel[1] on the basis of quantum mechanics. The theory was later improved to some extent by Pauling[2], Penney[3] and Mulliken[4]. It was known that the double or triple bond was due to two or three *p*-electrons partly associated with *s*-electrons.

Although the relation between bond order and bond length is of great importance in the theory of carbon compounds, the quantum theoretical study for these has not yet been fully carried out. Systematical and quantum theoretical investigation of the true nature of single, double and triple bonds is of great importance, especially from a chemical point of view. Among the bonds between simpler atoms (for example, oxygen, nitrogen and carbon atoms), those formed between two carbon atoms are of special interest in organic chemistry. The typical cases of these bonds occur in C_2H_6, C_2H_4 and C_2H_2, so that the problem is a study of the electronic structure of polyatomic molecules. In this paper, we intend to study the characteristics of single, double and triple bonding between carbon atoms.

It has been suggested that each bond in a polyatomic molecule possesses an energy which is independent of the other bonds in the molecule and that the dissociation energy of the molecule will be equal to the sum of the energies of various bonds occurring in the molecule (semi-empirical "rule of bond additivity")[5]. For example, the energy of formation of methane is equal to fourtimes of the energy of a C—H bond; that of ethane to the sum of the bond energies of one C—C bond and six C—H bonds, etc.

In general, for the molecule C_nH_{2n+2}, we may write

$$E=(n-1)E_{C-C}+(2n+1)E_{C-H} \tag{1}$$

where E_{C-C} and E_{C-H} represent respectively the bond energies of the C—C and C—H bonds. We may therefore use the data for the molecules from C_5H_{12} to $C_{12}H_{26}$ for the calculation of the energies of the C—C and C—H bonds and using the method of least squares, obtain[6],

$$E_{C-C}=62.77\text{ kcals}\ ,\quad E_{C-H}=85.56\text{ kcals}\ . \tag{2}$$

In a similar manner, the double bond energy $E_{C=C}$, the triple bond energy $E_{C\equiv C}$ are deter mined from the dissociation energies of ethylene molecular system, and of acetylene molecular system, and we obtain

$$E_{C=C}=101.16\text{ kcals}\ , \tag{3}$$

$$E_{C\equiv C}=128,15\text{ kcals}\ . \tag{4}$$

§ 2. Quantum Theoretical Treatment of Single, Double and Triple Bonds between Carbon Atoms

According to chemical experiences mentioned above, each "bond" seems to retain its individuality fairly well irrespective of the condition of neighbouring bonds, and the bond distances of single, double and triple bonds between carbon atoms are

$R_{C-C}=1.54$ Å, $R_{C=C}=1.32$ Å, $R_{C\equiv C}=1.20$ Å

respectively (see Fig. 1 and Table I).

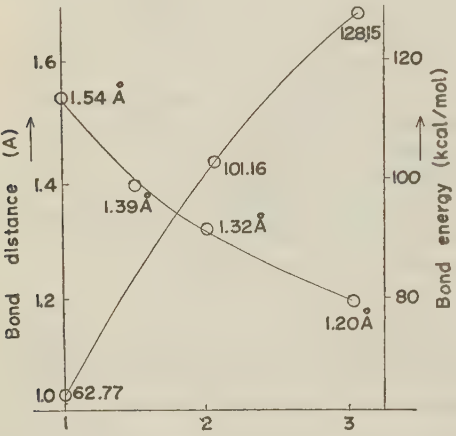

Fig. 1. Bond energies and bond distances between carbon atoms.

Table I. Dissociation energy D of C_nH_{2n+2}.

C_nH_{2n+2}	D Expt.	D Calc. (kcal/mol)
CH_4	348.6	342.2
C_2H_6	579	576.1
C_3H_8	811.6	810.0
C_4H_{10}	1044.8	1043.2
C_5H_{12}	1277.8	1277.8
C_6H_{14}	1511.9	1511.7
C_7H_{16}	1745.8	1745.6
C_8H_{18}	1979.5	1979.5
C_9H_{20}	2213.5	2213.4
$C_{10}H_{22}$	2447.1	2447.2
$C_{11}H_{24}$	2681.3	2681.1
$C_{12}H_{26}$	2914.2	2915.0

We may therefore hope to be able to study the characteristic features of these carbon-carbon bonds by idealizing the problem to fictitious diatomic molecules $\equiv C-C\equiv$, $=C=C=$ and $-C\equiv C-$, where the "open" bonds of the carbon atoms are represented by suitably hybridized orbitals, associated with free spins, which mean all possible structures having α or β spin in each "open" bond.

In other wards, we do not explicitly take account of the presence of hydrogen atoms (or other atoms forming bonds with the carbon atoms) but only consider their effects by keeping the carbon atoms in their appropriate valence states, and 1*s* electrons are not treated quantum-mechanically but we take account of the effect of the shielding of the nuclear field by them.

Thus we have merely to deal with only an eight electron system, with the Hamiltonian

$$\mathscr{H}=\sum(H_i+\varDelta H_i)+\sum G_{ij}+\frac{16}{R} \qquad (5)$$

where

$$H_i=-\frac{1}{2}\varDelta_i-\frac{4}{r_{ci}}-\frac{4}{r_{c'i}} \qquad (6)$$

H_i is the hamiltonian operator for the *i*th electron in the field of the nuclei alone, and

$$\varDelta H_i=2\left\{\int\frac{1}{r_{cj}}c^2(j)\,d\tau_j+\int\frac{1}{r_{c'j}}c'^2(j)\,d\tau_j\right\}-\frac{2}{r_{ci}}-\frac{2}{r_{c'i}} \qquad (7)$$

$$G_{ij}=1/r_{ij} \qquad (8)$$

R is the carbon-carbon internuclear distance.

$\varDelta H_i$ is a correction term which takes account of the finite extention of 1*s* electron orbitals in the carbon atoms. $c(j)$ and $c'(j)$ are the wave functions of 1*s* electrons in the carbon atoms C and C' respectively.

All quantities are measured in atomic units: lengths in units of the Bohr radius $a_H=0.529$ Å; energies in units of 27.204 e.v. (This is twice the ionization energy of the hydrogen atom.) In these units, the kinetic energy operator for an electron is $-\frac{1}{2}\varDelta$, the potential energy of an electron at a distance r from a nucleus of charge Z is $-Z/r$, and the repulsion energy of two electrons i and j at a distance r_{ij} apart is $1/r_{ij}$.

A. H-L-S-P *Method*

There are two fairly distinct and fundamental methods of investigating the electronic structure of polyatomic molecules. One is associated principally with the names Hund7), Mulliken8), Lennard-Jones9) and others10), (namely the molecular orbital method), while the other owes its development chiefly to Heitler, London11), Slater12) and Pauling13) (namely the valence bond method). The H-L-S-P method on based on the idea of electron pairs. The spin of an electron on one nucleus is coupled with that of another electron on another nucleus to give a resultant spin zero, and the pair then forms a saturated bond. Pairing occurs between the spins in such a way as to give a maximum bonding energy, and the number of free spins capable of being paired with electrons on other atoms constitutes the valency of the atom.

It is a well-known fact[14] that the valence bond method including ionized states and the molecular orbital method including interaction between configurations eventually give identical results. The H–L–S–P method is the one most closely associated with the chemical treatment of molecular structure. In this paper, we consider the localized fictitious molecular system and therefore calculate by the H–L–S–P method.

B. *Models*

We take the following models for these diatomic molecular system. (see Fig. 2–6). Model I and Model II represent the tetrahedrally hybridized bonding[15] in ethane and acetylene molecule. Model III shows the trigonally hybridized bonding in an ethylene molecule as superposition of a σ bond formed by overlaps of two trigonal hybrids and a π-bond formed by overlaps of two unhybridized p-type orbitals (trigonal sp^2 hybridization model). Model IV[16] shows the tetrahedrally hybridized bonding in ethylene and Model V is the π-model in an acetylene molecule which is composed of one σ and two π bonds and here also the π-bonds are formed between electrons in non-hybridized p status. The σ electrons, two to each carbon atom, are located in sp hybrid orbitals, formed by the linear combination of one s and one p wave function and the molecule is therefore linear.

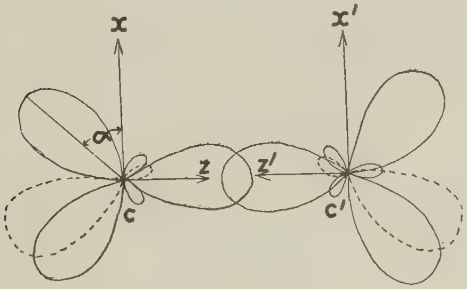

Fig. 2. Model I. The tetrahedrally hybridized bonding in ethane molecule.

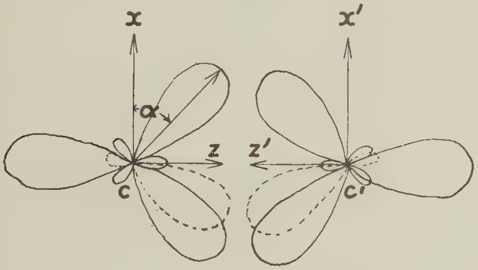

Fig. 3. Model II. The tetrahedrally hybridized bonding in acetylene molecule.

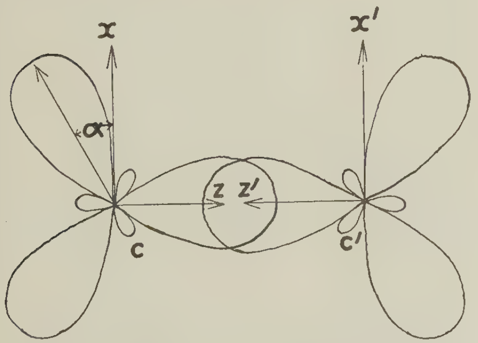

The π orbitals on C and C' are not shown to avoid confusion. They are directed perpendicularly to the plane of the paper.

Fig. 4. Model III. The trigonally hybridized bonding in ethylene molecule (trigonal sp^2 hybridization model).

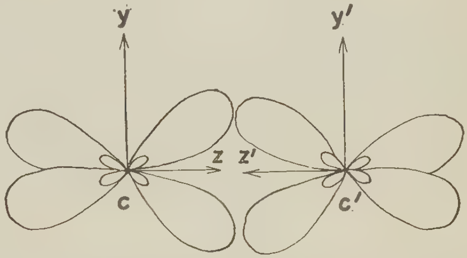

Fig. 5. Model IV. The tetrahedrally hybridized bonding in ethylene molecule.

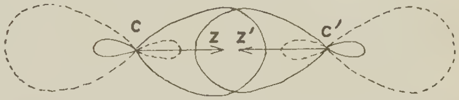

The four π-orbitals of the two atoms C and C' are not shown. They are in perpendicular pairs at right angles to the line CC'.

Fig. 6. Model V. The π-model in acetylene molecule.

C. *Atomic orbitals*

Of the free atom AO's, the self-consistent field AO's of Hartree and Fock are the most accurate for atomic calculations, but it is not guaranteed that they are the best for molecular calculations as well. For the latter, the simple atomic orbitals of Zener[17] and Slater[18] are most often used.

The following set of Slater atomic orbitals is therefore adopted:

$$\left.\begin{aligned}
(1s)&=(\delta'^3/\pi)^{1/2}\exp(-\delta' r)\\
(2s)&=(\delta^5/3\pi)^{1/2}r\exp(-\delta r)\\
(2p_x)&=(\delta^5/\pi)^{1/2}r\sin\theta\sin\phi\exp(-\delta r)\\
(2p_y)&=(\delta^5/\pi)^{1/2}r\sin\theta\cos\phi\exp(-\delta r)\\
(2p_z)&=(\delta^5/\pi)^{1/2}r\cos\theta\exp(-\delta r)
\end{aligned}\right\}\qquad (9)$$

where

$$\delta'=5.70\,,\qquad \delta=1.625 \qquad (10)$$

The atomic orbitals on one atom are normalized and mutually orthogonal, except that the nodeless Slater $2s$ is not orthogonal to the $1s$. Orthogonal $2s$ functions are formed from the original $2s$ and $1s$ in the following way[19]:

$$\begin{aligned}
s&=\frac{(2s)-0.2205(1s)}{0.9754}\\
&=(2s)+a(2s)-b(1s)
\end{aligned}\qquad (11)$$

where

$$a=0.024\,,\qquad b=0.2205\,. \qquad (12)$$

The normalized orbitals are then orthogonal to all the other orbitals of the same atom. The notations c, s, x, y, z will be adopted for the carbon $1s$, $2s$, $2p_x$, $2p_y$ and $2p_z$ orbitals respectively, with c', s', x', y', z' for the corresponding orbitals of the second carbon atom. The $2p_z$ orbitals are directed along the inter-

Table II. Interatomically orthogonal $2s$, $2p$-hybrid orbitals.

$$\varphi_i^N=a_{i1}^N s+a_{i2}^N x+a_{i3}^N y+a_{i4}^N z$$

Model I and Model II.

$$a_{ij}^I,\ a_{ij}^{II}\quad\begin{bmatrix}
v\,, & \sqrt{\frac{2}{3}}\,, & 0\,, & \mp\sqrt{\frac{2}{3}}\tan\alpha\\
v\,, & -\frac{1}{\sqrt{6}}\,, & -\frac{1}{\sqrt{2}}\,, & \mp\sqrt{\frac{2}{3}}\tan\alpha\\
v\,, & -\frac{1}{\sqrt{6}}\,, & +\frac{1}{\sqrt{2}}\,, & \mp\sqrt{\frac{2}{3}}\tan\alpha\\
\sqrt{2}\tan\alpha, & 0\,, & 0\,, & \pm\sqrt{3}\,v
\end{bmatrix}$$

Model III.

$$a_{ij}^{III}\quad\begin{bmatrix}
\frac{1}{\sqrt{2}}w\,, & \frac{1}{\sqrt{2}}\,, & 0\,, & -\frac{1}{\sqrt{2}}\tan\alpha\\
\frac{1}{\sqrt{2}}w\,, & -\frac{1}{\sqrt{2}}\,, & 0\,, & -\frac{1}{\sqrt{2}}\tan\alpha\\
0\,, & 0\,, & 1\,, & 0\\
\tan\alpha\,, & 0\,, & 0\,, & w
\end{bmatrix}$$

Model IV.

$$a_{ij}^{IV}\quad\begin{bmatrix}
\frac{1}{\sqrt{2}}w\,, & \frac{1}{\sqrt{2}}\,, & 0\,, & -\frac{1}{\sqrt{2}}\tan\alpha\\
\frac{1}{\sqrt{2}}w\,, & -\frac{1}{\sqrt{2}}\,, & 0\,, & -\frac{1}{\sqrt{2}}\tan\alpha\\
\frac{1}{\sqrt{2}}w'\,, & 0, & \frac{1}{\sqrt{2}}\,, & \frac{1}{\sqrt{2}}\tan\beta\\
\frac{1}{\sqrt{2}}w'\,, & 0, & -\frac{1}{\sqrt{2}}\,, & \frac{1}{\sqrt{2}}\tan\beta
\end{bmatrix}$$

Model V.

$$a_{ij}^{V}\quad\begin{bmatrix}
0\,, & 1\,, & 0\,, & 0\\
0\,, & 0\,, & 1\,, & 0\\
\sin\alpha'\,, & 0\,, & 0\,, & -\cos\alpha'\\
\cos\alpha'\,, & 0\,, & 0\,, & \sin\alpha'
\end{bmatrix}$$

where

$$v=\left(\cos^2\alpha-\frac{2}{3}\right)^{1/2}\Big/\cos\alpha\,,\qquad w=(\cos 2\alpha)^{1/2}/\cos\alpha\,,$$

$$w'=(\cos 2\beta)^{1/2}/\cos\beta\,,\qquad (\tan^2\alpha+\tan^2\beta=1).$$

nuclear axis, and the positive direction of both $2p_z$ orbitals is taken in the positive z direction.

D. *Interatomically orthogonal* 2*s*, 2*p*-*hybrid in homopolar bonds*

In general, we construct the interatomically orthogonal $2s$, $2p$ hybrid AO's in homopolar bonds corresponding to each model. The results are shown in Table II.

These include the most frequently used orthogonal sets[20] as follows:

$$\left.\begin{array}{l} \text{For } 90^\circ \text{ bond angle: } s,\ \sigma,\ \sigma',\ \sigma'' . \\ \text{For tetrahedral bond angle:} \\ \qquad\qquad te,\ te',\ te'',\ te''' . \\ \text{For } 120^\circ \text{ (trigonal) bond angles:} \\ \qquad\qquad tr,\ tr',\ tr'',\ \sigma . \\ \text{For } 180^\circ \text{ (diagonal) bond angles:} \\ \quad s,\ \sigma,\ \pi,\ \pi', \text{ or } di,\ di',\ \pi,\ \pi' . \end{array}\right\} \qquad (13)$$

Symbols differing by the use of one or more primes in (13) denote mutually orthogonal and geometrically equivalent but differently oriented AO's.

E. *Structures associated with free spins*

We discuss the case of Model I. We consider the possible structures associated with free spins in the "open" bonds of carbon atoms. Since the bonding orbinals φ_4 and $\varphi_{4'}$, which are supposed to point to z and z' directions respectively, are occupied by electrons with anti-parallel spin, the possible spin orientations are (α, β) and (β, α). For each of these two, there are $2^6=64$ possible structures corresponding to the spin orientation of the remaining six electrons housed in φ_1, φ_2, φ_3, $\varphi_{1'}$, $\varphi_{2'}$ and $\varphi_{3'}$. We shall divide these orbitals into two groups $(\varphi_1, \varphi_2, \varphi_3)$ and $(\varphi_{3'}, \varphi_{2'}, \varphi_{1'})$, and, according to their spin orientation $(\alpha\alpha\alpha)$, $(\alpha\alpha\beta)$, $(\beta\alpha\alpha)$, $(\alpha\beta\alpha)$, $(\alpha\beta\beta)$, $(\beta\alpha\beta)$, $(\beta\beta\alpha)$ and $(\beta\beta\beta)$, denote the structures of these two groups by A, B, C, $\cdots$ and H and a, b, c, $\cdots$ and h respectively. Then the structures of the total eight electron system can be specified by the combination as Pq, where P and q stand for any one of A, B, $\cdots$, H and of a, b, $\cdots$, h respectively, and by the spin orientation of the bonding electrons. For the structures with (α, β) spin of $(\varphi_4, \varphi_{4'})$ we shall use the symbol Pq, and for those with (β, α) spin of $(\varphi_4, \varphi_{4'})$ the symbol $\overline{Pq}$ will be employed.

Then, the unnormalized wave function for any one of the structures Pq, say Aa, is given by

$$\phi_{Aa}=(|\varphi_1\varphi_2\varphi_3\varphi_4\bar{\varphi}_{4'}\varphi_{3'}\varphi_{2'}\varphi_{1'}|)\ , \qquad (14)$$

and the function for $\overline{Aa}$ is

$$\phi_{\overline{Aa}}=(|\varphi_1\varphi_2\varphi_3\bar{\varphi}_4\varphi_{4'}\varphi_{3'}\varphi_{2'}\varphi_{1'}|)\ . \qquad (15)$$

The notation $(|\cdots|)$ represents the usual Slater determinant (multiplied by $1\sqrt{8!}$), the orbitals without bar including α-spin and with bar β-spin functions of electrons in them.

The wave function of the structure corresponding to the electron pair bond between φ_4 orbital and $\varphi_{4'}$ orbital is

$$\Phi_{Pq}=\frac{1}{\sqrt{2}}(\phi_{Pq}-\phi_{\overline{Pq}})\ . \qquad (16)$$

F. *General formulas for electronic energy*

We have to derive the general formulas for the adiabatic potential which characterizes the nature of binding of the molecular system. We shall illustrate it in the case of Model I.

According to the chemical experiences as mentioned in § 1, we may hope that the bond energy can be calculated by the wave function of the electrons which are housed in carbon-carbon atoms, and therefore if we remove the surrounding atoms in the real saturated compound to infinite distance, the energy of this system is the sum of the energy E of the fictitious molecular system defined in § 2 and the proper energy of the surrounding atoms. Thus when we consider the nature of bond between carbon atoms in this case, we may calculate the energy E of the fictitious molecular system.

Based on this idea, the total energy E of the fictitious molecular system with open bonds $\equiv$C$-$C$\equiv$ is found to be given by

$$E=\frac{\Sigma\int\Phi_{Pq}{}^*\mathscr{H}\Phi_{Pq}\,d\tau}{\Sigma\int\Phi_{Pq}{}^*\Phi_{Pq}\,d\tau}=\frac{\left\langle\int\Phi_{Pq}{}^*\mathscr{H}\Phi_{Pq}\,d\tau\right\rangle}{\left\langle\int\Phi_{Pq}{}^*\Phi_{Pq}\,d\tau\right\rangle} \qquad (17)$$

where $\langle Q\rangle$ means the average value of the quantity Q taken over all 2^6 possible structures Pq mentioned in § E. For the proof of this formula, the reader is refered to Appendix I.

In our calculation, as the overlap integrals $S_{ij'}$ between the non-bonding orbitals are small, we expand E in powers of $S_{ij'}$ and we neglect all terms of third and higher powers in $S_{ij'}$. Thus in our approximation, we take into calculation terms up to the second power in non-orthogonality between non-bonded orbital·.

When we substitute (16) in (17), we obtain

$$\begin{aligned}E=&\left\langle\left[\frac{1}{2}\int(\phi_{Pq}-\phi_{\overline{Pq}})^*\mathscr{H}(\phi_{Pq}-\phi_{\overline{Pq}})\,d\tau\right]\right\rangle\\ &\div\left\langle\left[\frac{1}{2}\int(\phi_{Pq}-\phi_{\overline{Pq}})^*(\phi_{Pq}-\phi_{\overline{Pq}})\,d\tau\right]\right\rangle\\ =&\left\langle\left[\frac{1}{2}\left(\int\phi_{Pq}{}^*\mathscr{H}\phi_{Pq}\,d\tau\right)+\frac{1}{2}\left(\int\phi_{Pq}{}^*\mathscr{H}\phi_{\overline{Pq}}\,d\tau\right)-\left(\int\phi_{\overline{Pq}}{}^*\mathscr{H}\phi_{Pq}\,d\tau\right)\right]\right\rangle\\ &\div\left\langle\left[\frac{1}{2}\left(\int\phi_{Pq}{}^*\phi_{Pq}\,d\tau\right)+\frac{1}{2}\left(\int\phi_{\overline{Pq}}{}^*\phi_{\overline{Pq}}\,d\tau\right)-\left(\int\phi_{\overline{Pq}}{}^*\phi_{Pq}\,d\tau\right)\right]\right\rangle.\end{aligned}\tag{18}$$

If we calculate the integration $\int\phi_{Aa}{}^*\mathscr{H}\phi_{Aa}\,d\tau$ substituting (14) in ϕ_{Aa}, we obtain

$$\begin{aligned}\int\phi_{Aa}{}^*\mathscr{H}\phi_{Aa}\,d\tau=&(\phi_{Aa}|\mathscr{H}|\phi_{Aa})\\ =&\sum(-1)^P\int\varphi_1{}^*(1)\alpha(1)\varphi_2{}^*(2)\alpha(2)\varphi_3{}^*(3)\alpha(3)\varphi_4(4)\alpha(4)\\ &\times\varphi_{4'}{}^*(5)\beta(5)\varphi_{3'}{}^*(6)\alpha(6)\varphi_{2'}{}^*(7)\alpha(7)\varphi_{1'}{}^*(8)\alpha(8)\\ &\times\mathscr{H}P\varphi_1(1)\alpha(1)\varphi_2(2)\alpha(2)\varphi_3(3)\alpha(3)\varphi_4(4)\alpha(4)\\ &\times\varphi_{4'}(5)\beta(5)\varphi_{3'}(6)\alpha(6)\varphi_{2'}(7)\alpha(7)\varphi_{1'}(8)\alpha(8)\\ &\times d\tau_1\,d\tau_2\,d\tau_3\,d\tau_4\,d\tau_5\,d\tau_6\,d\tau_7\,d\tau_8\\ =&\int\phi_{Aa}^{(0)*}\mathscr{H}\phi_{Aa}^{(0)}\,d\tau-\int\phi_{Aa}^{(0)*}\mathscr{H}\phi_{Aa}^{(1)}\,d\tau+\cdots\\ =&E_0-C_0-\sum_{Aa}^{(1)}\{(ij':ij')+S_{ij'}(H_{ij'}+H_{j'i})\\ &+S_{ij'}^2(\sum_{k\neq i,j'}H_{kk})+2S_{ij'}\sum_{k\neq i,j'}(ij':kk)+S_{ij'}^2\sum_{k,l\neq j,j'}(kk:ll)\}+\cdots\\ =&E_0-C_0-\sum_{Aa}^{(1)}\{(ij':ij')-S_{ij'}^2(ii:j'j')+S_{ij'}^2(ii:j'j')\\ &+2_{ij'}H_{ij'}-S_{ij'}^2(H_{ii}+H_{j'j'})+S_{ij'}^2(\sum H_{kk})\\ &+2S_{ij'}\sum_{k\neq i,j'}(ij':kk)-S_{ij'}^2\sum_{k\neq i,j'}\{(ii:kk)+(j'j':kk)\}\\ &+S_{ij'}^2\sum_{k\neq i,j'}\{(ii:kk)+(j'j':kk)\}+\cdots\\ =&E_0-C_0-\sum_{Aa}^{(1)}S_{ij'}^2\{\sum H_{kk}+\sum_{i>j}(ii:jj)\}\\ &-\sum_{Aa}^{(1)}\{(ii':ij')-S_{ij'}^2(ii:j'j')+2S_{ij'}H_{ij'}\\ &-S_{ij'}^2(H_{ii}+H_{j'j'})+2_{ij'}\sum_{k\neq i,j'}(ij':kk)\\ &-S_{ij'}^2\sum((ii:kk)+(j'j':kk))\}+\cdots\\ =&E_i-C_0-E_0(\sum_{Aa}^{(1)}S_{ij'}^2)-C_{Aa}^{(1)}+\cdots\end{aligned}\tag{19}$$

where

$$E_0=\int\phi_{Aa}^{(0)*}\mathscr{H}\phi_{Aa}^{(0)}\,d\tau=\sum H_{ji}+\sum_{(i>j)}(ii:jj)\tag{20}$$

(Coulomb integral term)

$$C_{Aa}^{(1)}=\sum_{Aa}^{(1)}G_{ij}\,,\tag{21}$$

(Interatomic exchange integral)

$$C_0=\sum\nolimits_{Aa}^{(1)} G_{ij} \,. \tag{22}$$

(Interatomic exchange integral)

$$\begin{aligned}G_{ij'}&=(ij':ij')-S_{ij'}^2(ii:j'j')+2S_{ij'}H_{ij'}-(H_{ii}+H_{j'j'})S_{ij'}^2\\&\quad+2S_{ij'}\sum_{k\neq i,j'}(ij':kk)-S_{ij'}^2\sum_{k\neq i,j'}\{(cii:kk)+(j'j':kk)\}\end{aligned} \tag{23}$$

$$H_{ij'}=\int\varphi_i{}^*(1)H(1)\varphi_{j'}(1)\,d\tau_1 \tag{24}$$

(One-electron potential and kinetic energy integral)

$$(ij':ij')=\int\varphi_i{}^*(2)\varphi_{j'}{}^*(2)\frac{1}{r_{12}}\varphi_i(1)\varphi_j{}'(1)\,d\tau_1\,d\tau_2 \tag{25}$$

(Exchange integral)

$$\begin{aligned}\phi_{Aa}^{(1)}&=\sum\nolimits_{Aa}^{(1)}(-1)^P P\varphi_1(1)\alpha(1)\varphi_2(2)\alpha(2)\varphi_3(3)\alpha(3)\varphi_4(4)\alpha(4)\\&\quad\times\varphi_{4'}(5)\beta(5)\varphi_{3'}(6)\alpha(6)\varphi_{2'}(7)\alpha(7)\varphi_{1'}(8)\alpha(8)\,.\end{aligned} \tag{26}$$

The notation $\sum_{Aa}^{(1)}$ means the summation over all possible single exchanges in the structure *Aa*.

In a similar manner, we obtain

$$\begin{aligned}\int\phi_{\overline{Aa}}{}^*\mathscr{H}\,\phi_{\overline{Aa}}\,d\tau&=(\phi_{\overline{Aa}}|\mathscr{H}\,|\phi_{\overline{Aa}})\\&=E_0-C_0-E_0\sum\nolimits_{\overline{Aa}}^{(1)}S_{ij'}^2-C_{\overline{Aa}}^{(1)}+\cdots\end{aligned} \tag{27}$$

$$\begin{aligned}-\int\phi_{\overline{Aa}}{}^*\mathscr{H}\,\phi_{Aa}\,d\tau&=-(\phi_{A\bar{a}}|\mathscr{H}\,|\phi_{Aa})\\&=E_0S_{44'}^2-C_0S_{44'}^2-E_0(\sum\nolimits_{Aa}^{(1)}S_{ij'}^2)S_{44'}^2+C_{44'}^{(1)}+\cdots\end{aligned} \tag{28}$$

where

$$C_{44'}^{(1)}=G_{44'}\,. \tag{29}$$

Thus, substituting (19)–(29) in (18), we obtain:

$$\begin{aligned}E&=\{E_0(1+k-ks^2)-C_0(1+k-ks^2)-C_s{}^{(1)}(1+k)+C_b{}^{(1)}\}\div(1+k-ks^2)\\&\fallingdotseq E_0-C_0+\frac{C_b{}^{(1)}}{1+k}-C_s{}^{(1)}+\frac{ks^2}{1+k}(C_b{}^{(1)}-C_s{}^{(1)})\end{aligned} \tag{30}$$

where

$$E_0=\sum H_{ii}+\sum{}'(ii:jj) \tag{31}$$

$$C_0=3(12:12)+3(14:14) \tag{32}$$

$$C_s{}^{(1)}=\frac{3}{2}G_{11'}+3G_{12'}+3G_{14'} \tag{33}$$

$$C_b{}^{(1)}=G_{44'} \tag{34}$$

$C_s{}^{(1)}$ and $C_b{}^{(1)}$ are defined in such a way that the former contains only $G_{ij'}$, associated with non-bonding electron orbitals φ_i and $\varphi_{j'}$, while the latter contains only $G_{ij'}$, associated with bonding electron orbitals.

$$k=S_{44'}^2 \tag{35}$$

$$s^2=\langle\sum\sum\nolimits_{Pq}^{(1)}S_{ij'}^2\rangle \tag{36}$$

In a similar manner, the general formulas for electronic energy in the cases of Model II, Model III, Model IV and Model V are obtained. The results are given in Table III.

G. *Numerical calculation*

The adiabatic potential between two atoms in the molecule is the eigenvalue of electronic energy as a function of the distance between the nuclei. In order to know explicitly this dependence on the distance we have to evaluate the eigenvalue for various distances. For this purpose we have to carry out the numerical calculations of molecular integrals $S_{ij'}$, $H_{ij'}$, $(pq:rs)$ etc., which may be rather tedious and laborious, but they can be carried out in

Table III. The general formulas for electronic energy in each model.

Model I and Model II:

$$\begin{aligned}E_0=&2H_{ss}+4H_{xx}+2H_{zz}+\left(\frac{16}{3}\tan^4\alpha-\frac{4}{3}\tan^2\alpha+\frac{16}{3}\right)(ss:ss)-\frac{8}{3}(1-2\tan^2\alpha)(1+\tan^2\alpha)(sz:sz)\\&+\left(-\frac{16}{3}\tan^4\alpha+4\tan^2\alpha+\frac{2}{3}\right)(zz:zz)+\frac{4}{3}(3-2\tan^2\alpha)(xx:zz)-\frac{16}{3}\tan^2\alpha(xz:xz)\\&+2(xx:yy)+(ss:s's')+2(ss:z'z')+(zz:z'z')+4(xx:s's')\\&+4(xx:z'z')+2(xx:x'x')+2(xx:y'y)+\frac{16}{R}\end{aligned}$$

Model III:

$$\begin{aligned}E_0=&2H_{ss}+4H_{xx}+2H_{zz}+\left(\frac{11}{2}+\frac{3}{2}\tan^4\alpha-\tan^2\alpha\right)(zz:ss)-2(1+3\tan^2\alpha)(1-\tan^2\alpha)(sz:sz)\\&+\left(-\frac{3}{2}\tan^4\alpha+2\tan^2\alpha\right)(zz:zz)+(6-\tan^2\alpha)(xx:zz)-2\tan^2\alpha(xz:xz)+\frac{1}{2}(xx:xx)+(ss:s's')\\&+2(ss:z'z')+(zz:z'z')+4(xx:s's')+4(xx:z'z')+2(xx:x'x')+2(xx:y'y')+\frac{16}{R}\end{aligned}$$

Model IV:

$$\begin{aligned}E_0=&2H_{ss}+4H_{xx}+2H_{zz}+\left(\frac{1}{2}+\tan^2\alpha\tan^2\beta\right)\{(ss:ss)+2(ss:zz)+(zz:zz)\}\\&-4\tan^2\alpha\tan^2\beta\,(sz:sz)+3(ss:xx)+3(xx:zz)+(xx:xx)+2(xx:yy)-2(sx:sx)-2(zx:zx)+(ss:s's')\\&+2(ss:z'z')+(zz:z'z')+4(xx:s's')+4(xx:z'z')+2(xx:x'x')+2(xx:y'y')+\frac{16}{R}\end{aligned}$$

Model V:

$$\begin{aligned}E_0=&2H_{ss}+4H_{xx}+2H_{zz}+2\sin^2\alpha'\cos^2\alpha'\{(ss:ss)-2(ss:zz)+(zz:zz)-4(sz:sz)\}\\&+2(ss:zz)+2(xx:yy)+4(xx:ss)+4(xx:zz)+(ss:s's')+2(ss:z'z')+(zz:z'z')+4(xx:s's')\\&+4(xx:z'z')+2(xx:x'x')+2(xx:y'y')+2(1-\sin^2 2\alpha')(ss:z'z')+\frac{16}{R}\end{aligned}$$

Model I and Model II:

$$\begin{aligned}C_0=&3(12:12)+3(14:14)=\left(\frac{8}{3}\tan^4\alpha-\frac{2}{3}\tan^2\alpha-\frac{1}{3}\right)(ss:ss)+\left(\frac{1}{3}+2\tan^2\alpha-\frac{8}{3}\tan^4\alpha\right)(xx:xx)\\&+\left(\frac{5}{3}-\frac{8}{3}\tan^2\alpha+\frac{32}{3}\tan^4\alpha\right)(sz:sz)+\left(2-\frac{8}{3}\tan^2\alpha\right)(zx:zx)-\frac{4}{3}\tan^2\alpha(xx:zz)+(xy:xy)\end{aligned}$$

Model III:

$$\begin{aligned}C_0=&(12:12)+2(13:13)+2(14:14)+(34:34)=\left(-\frac{1}{4}-\frac{1}{2}\tan^2\alpha+\frac{3}{4}\tan^4\alpha\right)(ss:ss)\\&+\left(\frac{1}{4}+\tan^2\alpha-\frac{3}{4}\tan^4\alpha\right)(zz:zz)+(2-2\tan^2\alpha+3\tan^4\alpha)(sz:sz)+3(zx:zx)\\&-\frac{1}{2}\tan^2\alpha(xx:zz)-\tan^2\alpha(zx:zx)\end{aligned}$$

Model IV:

$$\begin{aligned}C_0=&(12:12)+2(13:13)+2(14:14)+(34:34)=-\left(\frac{1}{4}+\frac{1}{2}\tan^2\alpha\tan^2\beta\right)(ss:ss)\\&+\left(\frac{3}{4}+\frac{1}{2}\tan^2\alpha\tan^2\beta\right)(zz:zz)-\frac{1}{2}(zz:xx)+(2-2\tan^2\alpha\tan^2\beta)(sz:sz)+2(zx:zx)\end{aligned}$$

Model V:

$$\begin{aligned}C_0=&(12:12)+2(13:13)+2(14:14)+(34:34)\\=&\sin^2\alpha'\cos^2\alpha'\{(zz:zz)-(ss:zz)-2(sz:sz)\}+2(sz:sz)+3(zx:zx)\end{aligned}$$

Model I:

$$\begin{aligned}C_s^{(1)}=&\frac{1}{2}(ss':ss')+(xx':xx')+2(sx':sx')+2(zx':zx')+(sz':sz')+(xy':xy')\\&-[2\tan^4\alpha\{(ss':ss')+(zz':zz')-2(ss':zz')-2(sz':sz')-2(sz':s'z)\}\\&+2\tan^2\alpha\{(ss':zz')+(sz':sz')+(sz':s'z)-(zz':zz')\}+4\sqrt{6}\,v\tan^3\alpha\{(ss':sz')-(zz':sz')\}\\&+2\sqrt{6}\,v\tan\alpha(zz':sz')]+3[\{(S_{11'}H_{11'}-S^2_{11'}H_{11})\}+\{(2S_{12'}H_{12'}-S^2_{12'}(H_{11}+H_{22})\}\\&+\{2S_{14'}H_{14'}-S^2_{14'}(H_{11}+H_{4'4'})\}]\end{aligned}$$

where

$$v=\left(\cos^2\alpha-\frac{2}{3}\right)^{1/2}\Big/\cos\alpha$$

Model II:

$$\begin{aligned}C_s^{(1)}=&\frac{1}{2}G_{44'}+3G_{12'}+3G_{14'}=\frac{1}{3}(ss':ss')+\frac{1}{2}(zz':zz')+\frac{1}{3}(xx':xx')-\frac{2}{3}\{(ss':xx')\\&+(sx':sx')+(sx':s'x)\}+2(sx':sx')+2(zx':zx')+(sz':sz')+(xy':xy')\\&-\frac{2}{3}[\tan^4\alpha\{(ss':ss')+(zz':zz')-2(ss':zz')-2(sz':sz')-2(sz':s's)\}+\tan^2\alpha\{(ss':zz')\\&+(sz':sz')+(sz':s'z)-(ss':ss')+2(xx':zz')+2(zx':zx')+2(zx':z'x)-2(ss':xx')-2(sx':sx')\\&-2(sx':s'x)\}+2\sqrt{6}\,v\tan^3\alpha\{(zz':sz')-(ss':sz')\}+\sqrt{6}\,v\tan\alpha\\&\times\{(ss':sz')+2(xx':sz')+2(sx':z'x)+2(sx':zx')\}\\&+[(S_{44'}H_{44'}-S_{44'}^{2}H_{44})+3\{2S_{12'}H_{12'}-S_{12'}^{2}(H_{11}+H_{2'2'})\}+3\{2S_{14'}H_{14'}-S_{14'}^{2}(H_{11}+H_{4'4'})\}]\end{aligned}$$

where

$$v=\left(\cos^2\alpha-\frac{2}{3}\right)^{1/2}\Big/\cos\alpha$$

Model III:

$$\begin{aligned}C_s^{(1)}=&G_{11'}+G_{12'}+2G_{13'}+2G_{14'}+G_{34'}=\frac{1}{2}(ss':ss')+\frac{1}{2}(xx':xx')+2(sx':sx')+2(zx':xx')+(sz':sz')\\&+(xy':xy')-\frac{1}{2}[\tan^4\alpha\{(ss':ss')+(zz':zz')-2(ss':zz')-2(sz':sz')-2(sz':s'z)\}\\&+2\tan^2\alpha\{(ss':zz')+(sz':sz')+(sz':s'z)-(zz':zz')\}+4w\tan^3\alpha\{(ss':sz')-(zz':sz')\}\\&+4w\tan\alpha(zz':sz')]+[2\{S_{11'}H_{11'}-S_{11'}^{2}H_{11}\}+\{2S_{12'}H_{12'}-S_{12'}^{2}(H_{11}+H_{2'2'})\\&+2\{2S_{14'}H_{14'}-S_{14'}^{2}(H_{11}+H_{4'4'})\}]\end{aligned}$$

where

$$w=(\cos 2\alpha)^{1/2}/\cos\alpha$$

Model IV:

$$\begin{aligned}C_s^{(1)}=&G_{11'}+G_{12'}+2G_{13'}+2G_{14'}+G_{34'}=\frac{3}{4}(ss':ss')+\frac{3}{4}(xx':xx')+\frac{1}{2}(zz':zz')+2(sx':sx')\\&+2(zx':zx')+(sz':sz')+(xy':xy')+3(sz':s'z)-\frac{1}{2}\{(ss':zz')+(sz':sz')+(sz':s'z)+(xx':zz')\\&+(zx':zx')+(zx':z'x)\}-\Big[\frac{1}{4}\tan^4\beta\{(ss':ss')+(zz':zz')-2(ss':zz')-2(sz':sz')-2(sz':s'z)\}\\&+\frac{1}{2}\tan^2\alpha\{ss':ss')+(ss':xx')+(sx':sx')+(sx':s'x)-(ss':zz')-(sz':sz')-(sz':s'z)\\&-(zz':xx')-(zx':zx')-(zx':z'x)\}+\tan\alpha\tan^3\beta\{(zz':sz')-(ss':sz')\}+\tan\alpha\tan\beta\{(ss':sz')\\&+(xx':sz')+(sx':zx')+(sx':z'x)+2(sx':z'x)-2(sx':zx')\}\Big]+[2(S_{11'}H_{11'}-S_{11'}^{2}H_{11})\\&+\{2S_{12'}H_{12'}-S_{12'}^{2}(H_{11}+H_{2'2'})\}+2\{2S_{13'}H_{13'}-S_{13'}^{2}(H_{11}+H_{3'3'})\}\\&+2\{2S_{14'}H_{14'}-S_{14'}^{2}(H_{11}+H_{4'4'})\}+\{2S_{34'}H_{34'}-S_{34'}^{2}(H_{33}+H_{4'4'})\}]\end{aligned}$$

Model V:

$$\begin{aligned}C_s^{(1)}=&\frac{1}{2}G_{33'}+G_{12'}+2G_{13'}+2G_{14'}+G_{34'}=\frac{1}{2}(ss':ss')+\frac{1}{2}(zz':zz')+2(sx':sx')+2(zx':zx')\\&+(sz':sz')+(xy':xy')+[(S_{33'}H_{33'}-S_{33'}^{2}H_{33})+\{2S_{34'}H_{34'}-S_{34'}^{2}(H_{33}+H_{4'4'})\}]\end{aligned}$$

Model I:

$$\begin{aligned}C_b^{(1)}=&(zz':zz')+[4\tan^4\alpha\{(ss':ss')+(zz':zz')-2(ss':zz')-2(sz':sz')-2(sz':s'z)\}+4\tan^2\alpha\{(ss':zz')\\&+(sz':sz')+(sz':s'z)-(zz':zz')\}+8\sqrt{6}\,v\tan^3\alpha\{(ss':sz')-(zz':sz')\}+4\sqrt{6}\,v\tan\alpha(zz':sz')]\\&-S_{44'}^{2}(44:4'4')+2(S_{44'}H_{44'}-S_{44'}^{2}H_{44})+[2S_{44'}\sum_{k\neq 4,4'}(44':kk)-S_{44'}^{2}\sum_{k\neq 4,4'}\{(44:kk)+(4'4':kk)\}]\end{aligned}$$

where

$$v=\left(\cos^2\alpha-\frac{2}{3}\right)^{1/2}\Big/\cos\alpha$$

Model II:

$$\begin{aligned}C_b^{(1)}=3G_{11'}=&\frac{1}{3}(ss':ss')+\frac{4}{3}(xx':xx')+\frac{4}{3}\{(ss':xx')+(sx':sx')+(sx':s'x)\}\\&+\frac{4}{3}[\tan^4\alpha\{(ss':ss')+(zz':zz')-2(ss':zz')-2(sz':sz')-2(sz':s'z)\}+\tan^2\alpha\{(ss':zz')+(sz':sz')\\&+(sz':s'z)-(ss':ss')+2(xx':zz')+2(zx':zx')+2(zx':z'x)-2(ss':xx')-2(sx':sx')-2(sx':s'x)\}\\&+2\sqrt{6}\,v\tan^3\alpha\{(zz':sz')-(ss':sz')\}+\sqrt{6}\,v\tan\alpha\{(ss':sz')+2(xx':sz')+2(sx':z'x)+2(sx':zx')\}]\\&-3S_{33'}^2(11:1'1')+6(S_{11'}H_{11'}-S_{11'}^2H_{11})+3[S_{11'}\sum_{k\neq1,1'}(11':kk)-S_{11'}^2\sum_{k\neq1,1'}\{(1'1':kk)+(11:kk)\}]\end{aligned}$$

where

$$v=\left(\cos^2\alpha-\frac{2}{3}\right)^{1/2}\Big/\cos\alpha$$

Model III:

$$\begin{aligned}C_b^{(1)}=G_{33'}+G_{44'}=&(zz':zz')+(xx':xx')+[\tan^4\alpha\{(ss':ss')+(zz':zz')-2(ss':zz')-2(sz':sz')-2(sz':s'z)\}\\&+2\tan^2\alpha\{(ss':zz')+(sz':sz')+(sz':s'z)-(zz':zz')\}+4w\tan^3\alpha\{(ss':sz')-(zz':sz')\}\\&+4w\tan\alpha(zz':sz')]-S_{33'}^2(33:3'3')-S_{44'}^2(44:4'4')+2(S_{33'}H_{33'}-S_{33'}^2H_{33})\\&+2(S_{44'}H_{44'}-S_{44'}^2H_{44})+2S_{33'}\sum_{k\neq3,3'}(33':kk)-S_{33'}^2\sum_{k\neq3,3'}\{(33:kk)+(3'3':kk)\}\\&+2S_{44'}\sum_{k\neq4,4'}(44':kk)-S_{44'}^2\sum_{k\neq4,4'}\{(44:kk)+(4'4':kk)\}\end{aligned}$$

where

$$w=(\cos 2\alpha)^{1/2}/\cos\alpha$$

Model IV:

$$\begin{aligned}C_b^{(1)}=G_{33'}+G_{44'}=&-\frac{1}{2}(ss':ss')+\frac{1}{2}(xx':xx')+\{(ss':zz')+(sz'+sz')+(sz':s'z)+(xx':zz')\\&+(zx':zx')+(zx':z'x)\}+\Big[\frac{1}{2}\tan^4\beta\{ss':ss')+(zz':zz')-2(ss':zz')-2(sz':sz')-2(sz':s'z)\}\\&+\tan^2\alpha\{(ss':ss')+(ss':xx')+(sx':sx')+(sx':s'x)-(ss':zz')-(sz':sz')-(sz':s'z)-(zz':zz')\\&-(zx':zx')-(zx':z'x)\}+2\tan\alpha\tan^2\beta\{(zz':sz')-(ss':sz')\}+2\tan\alpha\tan\beta\{(ss':zz')+(xx':sz')\\&+(sx':zx')+(sx':z'x)\}\Big]-S_{33'}^2(33:3'3')-S_{44'}^2(44:4'4')+2(S_{33'}H_{33'}-S_{33'}^2H_{33})\\&+2(S_{44'}H_{44'}-S_{44'}^2H_{44})+2S_{33'}\sum_{k\neq3,3'}(33':kk)-S_{33'}^2\sum_{k\neq3,3'}\{(33:kk)+(3'3':kk)\}\\&+2S_{44'}\sum_{k\neq4,4'}(44':kk)-S_{44'}^2\sum_{k\neq4,4'}\{(44:kk)+(4'4':kk)\}\end{aligned}$$

where

$$\tan^3\alpha+\tan^2\beta=1$$

Model V:

$$\begin{aligned}C_b^{(1)}=G_{11'}+G_{22'}+G_{44'}=&\frac{3}{2}(zz':zz')+2(xx':xx')+\Big[\frac{3}{2}\cos^4\alpha'\{(ss':ss')+(zz':zz')-2(ss':zz')\\&-2(sz':sz')-2(sz':s'z)\}+3\cos^2\alpha'\{ss':zz')+(sz':sz')+(sz':s'z)-(zz':zz')\}\\&+6\cos^3\alpha'\sin\alpha'\{(ss':sz')-(zz':sz')\}+6\cos\alpha'\sin\alpha'(zz':sz')\Big]-2S_{xx'}^2(xx:x'x')\\&-S_{44'}^2(44:4'4')+4(S_{xx'}H_{xx'}-S_{xx'}^2H_{xx})+2(S_{44'}H_{44'}-S_{44'}^2H_{x4})\\&+2[2S_{xx'}\sum_{k\neq x,x'}(xx':kk)-S_{xx'}^2\sum_{k\neq x,x'}\{(xx:kk)+(x'x:kk)\}]\\&+2S_{44'}\sum_{k\neq4,4'}(44':kk)-S_{44'}^2\sum_{k\neq4,4'}\{(44:kk)+(4'4':kk)\}\end{aligned}$$

where

$$a=\tan\alpha'$$

a straight forward way by making use of table of Kotani et al.[21], and other tables[22].

In order to make use of the tables for our calculation we have to prepare some supplementary formulas and tables for the integrals, (see Appendix II). Actually we have used only ordinary desk machine of the type "Tiger".

§ 3. Result and Discussion

The numerical calculations of the adiabatic potential are carried out in cases as follws:

For Model I and Model II

$\alpha=\tan^{-1}(1/\sqrt{8})$

For Model III $\alpha=30°$

For Model IV $\alpha=\beta=\tan^{-1}(1/\sqrt{2})$

For Model V $\alpha'=45°$

The results of evaluating the adiabatic potential according to the general formulas given in Table III are shown in Table IV. The potential curve $E(R)-E(\infty)$ are plotted in Fig. 7. The binding energies of the molecular system and corresponding equilibrium distances between two nuclei are evaluated from these curves. It should, however, be noted that, when the molecular system dissociates into each atom, it may give rise to valence atoms, not normal atoms. Relative values of $E(\infty)$ in each model are shown in Table V.

Table IV. Relative bond distances and bond energies.

	Bond distance	Bond energy
Relative value of C−C and C≡C	Calc. 0.20Å	Calc. 3.1 ev.
	Expt. 0.34Å	Expt. 2.9 ev.
C=C and C≡C	Calc. 0.10Å	Calc. 1.25 ev.
	Expt. 0.12Å	Expt. 1.0 ev.

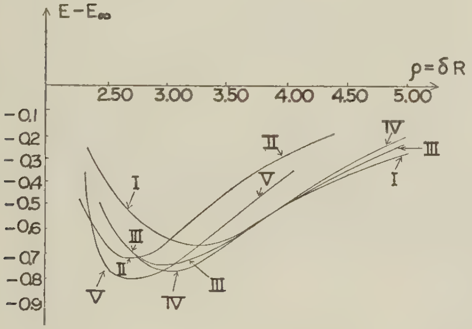

Fig. 7. Adiabatic energy potnntial $E(R)-E(\infty)$ in each model neglecting the inner shells. (in the atomic unit: the unit of energy=27.204 e.v.)

Table V. The relative values of $E(\infty)$ in each model.

Beardsley: Phys. Rev. **39** (1932) 913.
Ufford: Phys. Rev. **53** (1938) 568.
Van Vleck: J. Chem. Phys. **2** (1934) 297.
J. Chem. Phys. **3** (1935) 20.
M. Kotani: "*Quantum Chemistry*" (*The valence theory*) (1939) 145.
C. A. Coulson: "*valence*" (1951) 196.
Voge: J. Chem. Phys. **4** (1936) 581.

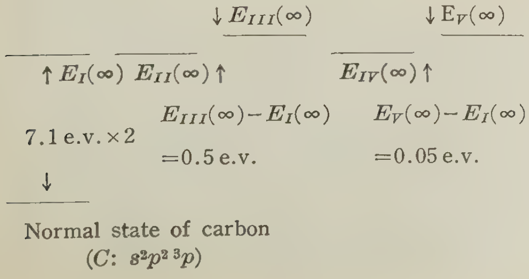
↓$E_{III}(\infty)$
↓$E_{V}(\infty)$
↑$E_{I}(\infty)$ $E_{II}(\infty)$↑
$E_{IV}(\infty)$↑
$E_{III}(\infty)-E_{I}(\infty)$ =0.5 e.v.
$E_{V}(\infty)-E_{I}(\infty)$ =0.05 e.v.
7.1 e.v.×2
↓
Normal state of carbon
(C: $s^2p^2\,{}^3p$)

Thus we obtain 3.1 e.v., 1.25 e.v., and 0.20 Å, 0.10 Å for the values of relative bond energy differences and bond distance differences of single and triple, double and triple bonding. The experimental values of these quantities are 2.9 e.v., 1.0 e.v., and 0.34 Å, 0.12 Å, respectively.

These results of our numerical computation are in good agreement with the experimental values, in spite of all possible sources of error in molecular calculation by H–L–S–P method, in addition to the approximations adopted here.

There are several possible sources of error in the numerical values carried out by our calculation as follows:

Best energies should really be determined by a method which includes inner shell electrons explicitly. Of this question, we shall discuss later in detail.

The forms of the AO's which are used in constructing the atomic bond orbital should themselves be determined by a variational procedure. Even in atoms, Slater functions cannot be made to fit the true self-consistent field²³⁾. The use of Slater functions reduces the electronic interaction between non-neighbors too much, since Slater functions die down more rapidly than Hartree-Fock SCF orbitals at large distances²⁴⁾. The Slater $2p$ AO's with $2\delta=3.25$ which we have used might thus need to be strongly modified. This question of the form of the atomic orbitals to be used in molecular calculations appears to be one of the most serious and difficult problems²⁵⁾.

There are other sources of error caused by neglecting the ionized states and higher permutation terms in H–L–S–P method. But among higher permutation terms, some of double permutation terms, for example, in the case of Model III, ((44′)(33′)), ((43′)(4′3)), ((14′)(12)), ((44′)(12)) etc., are taken in our calculation.

Approximation of expansion in powers of

overlap integrals $S_{ij'}$, between non-bonding orbitals is made for obtaining the general formulas of adiabatic energy potential in each model and further approximations are made for the evaluation of hybrid Coulomb-exchange molecular integrals (for the latter, see Appendix II).

Table VI.

Bond distance	Calc.		Expt.
	a case	b case	
R_{C-C} Model I	1.06 Å	1.50 Å	1.54 Å
$R_{C=C}$ Model III	0.98 Å	1.30 Å	1.32 Å
Model IV	0.98 Å	1.30 Å	
$R_{C\equiv C}$ Model II	0.85 Å	*	1.20 Å
Model V	0.90 Å	1.09 Å	

* For Model II, the adiabatic energy potential does not show minimum.

Absolute values of the equilibrium distances between two nuclei in each model are shown in Table VI, compared with the experimental values. These values shift uniformly toward smaller values than the corresponding experimental values. We can account for this discrepancy by taking account of the effect of inner shells. If we estimate the contribution to the energy by taking account of 1s electrons, we obtain the following expression.

$$\varDelta E=\varDelta_1-\mathcal{E} \tag{37}$$

where

$$\varDelta_1=\frac{20}{R}-24(C:c'c')+4(cc:c'c') \tag{38}$$

(Coulomb interaction energy between 1*s* electrons and 1*s* electrons in each carbon atom)

$$\mathcal{E}=\varDelta_2+\varDelta_3+\varDelta_4 \tag{39}$$

(Exchange interaction energy term between 1*s* electrons and *s*, *x*, *y*, *z* electrons)

$$\varDelta_2=2(cs':cs')+2(cz':cz')+4(cx':cx') \tag{40}$$

$$\left.\begin{array}{ll} \varDelta_3=6A_{c1'}+2A_{c4'} & \text{for Model I and Model II} \\ \varDelta_3=4A_{c1'}+2A_{c4'} & \text{for Model III} \\ \varDelta_3=4A_{c1'}+4A_{c3'} & \text{for Model IV} \\ \varDelta_3=2A_{c3'}+2A_{c4'} & \text{for Model V} \end{array}\right\} \tag{41}$$

$$\left.\begin{array}{ll} \varDelta_4=6B_{c1'}+2B_{c4'} & \text{for Model I and Model II} \\ \varDelta_4=4B_{c1'}+2B_{c4'} & \text{for Model III} \\ \varDelta_4=4B_{c1'}+4B_{c3'} & \text{for Model IV} \\ \varDelta_4=2B_{c3'}+2B_{c4'} & \text{for Model V} \end{array}\right\} \tag{42}$$

$$A_{ci'}=2S_{ci'}H_{ci'}-S_{ci'}^2(H_{cc}+H_{i'i'}) \tag{43}$$

$$B_{ci'}=2S_{ci'}\sum_{j=c,i'}(ic':jj)-S_{ci'}^2\sum_{j\neq c,i'}((i'i':jj)+(cc:jj)) \tag{44}$$

$$S_{ci'}=\int c(1)\varphi_{i'}(1)\,d\tau_1\,. \tag{45}$$

Carrying out the numerical evaluation of $\varDelta E$, we obtain the total energy which takes into account of the 1*s* electrons and these results are shown in Fig. 8.

Evaluating from these potential curves, we obtain the equilibrium distances between two nuclei in each model and the results are shown in Table VII. These results are in very good agreement with experimental values. It has been pointed out by James[26] that the inner shells of the atoms may have an important effect on the value of molecular binding and may either increase or decrease it and since their effect is associated with electron exchange, it appears that they cannot be replaced by an equivalent potential field without serious error. The effect of the inner shells (chiefly Δ_3 effect) seems to give rise to a repulsive potential in our calculation, varying much more rapidly with distance than the other terms in the adiabatic potential. For sufficiently large separations of the atoms, this effect would presumably sink to negligible value, but for internuclear distances of the order of the equilibrium distance, it is by no means unimportant.

We consider the absolute values of bond energy, (for example, in the case of Model I). When the molecule dissociates into each atom, it may give rise to atoms in valence states. We have to study the valence state of carbon atom. Van Vleck[27] pointed out that the valence state which is characteristic of tetravalent carbon compounds involving four electron pair bonds, is shown to involve an increase of about 7.1 e.v. in the internal energy of the carbon atom over that in the ground state. Thus, we assume that each bond in the tetravalent carbon valence atom has one-fourth of 7.1 e.v. The absolute value of bond energy between carbon-carbon atoms is calculated by the following formula.

$$E_{C-C}=|E(R_e)-E(\infty)|-2\times\tfrac{1}{4}\times 7.1\text{ e.v.}$$
$$=|E(R_e)-E(\infty)|-3.55\text{ e.v.} \qquad (46)$$

where $E(R_e)$ represents the adiabatic potential

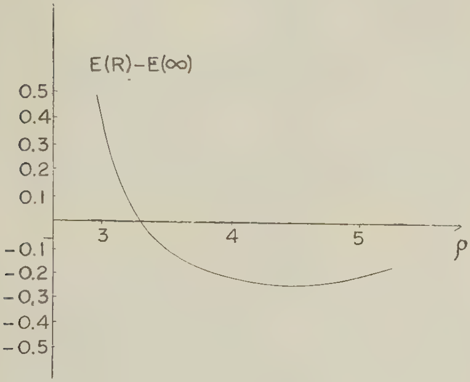

Fig. 8. Adiabatic energy potential $E(R)-E(\infty)$ in the case of Model I taking into account the inner shells, (in the atomic units; the units of energy and length being 27.204 e.v. and 0.529 Å respectively).

Table VII.

Bond energy	Calc.		Expt.
	a case	b case	
E_{C-C} Model I	15.0 e.v.	3.04 e.v.	2.9 e.v.

a case: case of neglecting the inner shells.
b case: case of taking into account the inner shells.

Table VIII.

		Binding energy (e.v.)		Equilibrium separation (A)	
		Calc.	Expt.	Calc.	Expt.
Li.	H–L a.b.*	1.09	1.14	2.4	2.67
.	H–L a.†	0.33		3.07	
.	H–L †	0.28		3.18	
.	Variational†	0.62			
LiH.	H–L a.b.△	2.30	2.56	1.44	1.6
Na.	H–L††	0.81	0.76	2.83	3.08
K.	H–L††	0.55	0.51	4.18	3.91
.	Semi-empirical with H–L°	0.19		4.0	
KH.	Semi-empirical and Ionic terms.°	0.8	2.06	2.0	

a: signifies use of interaction operator±
b: denotes neglectz of inner shells
* J. E. Bartlett and W. E. Furry: Phy. Rev. **38** (1931) 1615.
† H. M. James: J. C. P. 2 (1934) 794. Phy. Rev. **43** (1933) 589.
△ E. Hutchisson and M. Muskat: Phys. Rev. **40** (1932) 340.
†† N. Rosen and S. Ikehara: Phys. Rev. **43** (1933) 5.
†† N. Rosen: Phys. Rev. **38** (1931) 255.
○ H. Hellmann: J.C.P. **3** (1933) 61. Acta physicochimica U.R.S.S. (1935) 913.
± H. M. James: J.C.P. **2** (1934) 794.

energy in equilibrium internuclear distance.

We obtain 3.04 e.v. in the case of taking account of the inner shells and 1.50 e.v. in the case of neglecting these inner shells for bond energy E_{C-C}. Compared with the experimental value $E_{C-C}=2.9$ e.v., the satisfactory agreement is obtained in the case of taking account of the inner shells and the latter shows good agreement also in equilibrium internuclear distances.

But in the calculation of the heats of dissociation of Li_2 molecule, James shows, for instance, that the nice agreement which Bartlett and Furry[28)] found between their calculated value 1.09 e.v. of the heat of dissociation of Li_2 by the Heitler-London method and the observed value 1.14 e.v. is completely destroyed when one includes the effect of the 1*s* electrons, the calculated value is then 0.3 e.v. Consequently better wave functions are needed than those in the Heitler-London method. James finds that by using a variational method he can increase the calculated value to 0.7 e.v. (see Table VIII). Omission of the inner shells in the calculation of Li_2 molecule tends to correct for a serious underestimate of the binding energy associated with the external electrons and also shifts the computed equilibrium nuclear distance strongly toward smaller values.

The general formula (30) corresponds to the equation (2) or (4) in the paper of Serber[29)] who calculated the energies of a number of hydrocarbon molecules by the H–L–S–P method. Our general formulas involve no semi-empirical parameters but are calculated non-empirically. Results obtained here show that the non-empirical calculation can give useful quantitative knowledge in the problems. Therefore, these formulas have more advanced contents for the evaluation of bond energies and bond distances between carbon atoms. Our results seem to encourage further work along similar lines about various chemical bonds between atoms other than carbon.

Acknowledgement

The author wishes to express his sincere thanks to Prof. M. Kotani, who suggested the problem for his much helpful advice and continuous encouragement throughout this work. This work has been supported in part by the scientific Research Expenditure of the Ministry of Education.

Appendix I

Proof of

$$E=\left(\Sigma\int\Phi_{Pq}^{*}\mathscr{H}\Phi_{Pq}\,d\tau\Big/\Sigma\int\Phi_{Pq}^{*}\Phi_{Pq}d\tau\right)=\left(\left\langle\int\Phi_{Pq}^{*}\mathscr{H}\Phi_{Pq}\,d\tau\right\rangle\Big/\left\langle\int\Phi_{Pq}^{*}\Phi_{Pq}d\tau\right\rangle\right)$$

As an example, we discuss the case of model I. The wave function of the complete ethane molecule is

$$\Psi=\Sigma^{\dagger}\{(|\varphi_1\varphi_2\varphi_3\varphi_4\bar{\varphi}_{4'}\varphi_{3'}\varphi_{2'}\varphi_{1'}\hbar_1\hbar_2\hbar_3\hbar_{3'}\hbar_{2'}\hbar_{1'}|)-(|\varphi_1\varphi_2\varphi_3\bar{\varphi}_4\varphi_{4'}\varphi_{3'}\varphi_{2'}\varphi_{1'}\hbar_1\hbar_2\hbar_3\hbar_{3'}\hbar_{2'}\hbar_{1'}|)\} \qquad (A.1)$$

where h_i etc. are the wave functions of the bonding electrons in the surrounding atoms.

According to the determinant theory, the determinant

$$(|\varphi_1\varphi_2\varphi_3\varphi_4\bar{\varphi}_{4'}\varphi_{3'}\varphi_{2'}\varphi_{1'}\hbar_1\hbar_2\hbar_3\hbar_{3'}\hbar_{2'}\hbar_{1'}|)$$

is expanded in the sum of the products of the minor eight-by-eight determinants having only the wave functions φ_i and the minor six-by-six determinants having only the wave functions h_i as follows:

$$(|\varphi_1\varphi_2\varphi_3\varphi_4\bar{\varphi}_{4'}\varphi_{3'}\varphi_{2'}\varphi_{1'}\hbar_1\hbar_2\hbar_3\hbar_{3'}\hbar_{2'}\hbar_{1'}|)=\Sigma^{\dagger\dagger}M_{A\alpha}(\varphi:\ i_1,i_2,\cdots,i_8)N_{A\alpha}(h:\ j_1,j_2,\cdots j_6) \qquad (A.2)$$

---

† Where Σ means the summation over all possible spin configurations corresponding to the 8×8 structures P_q.

†† Where Σ means the summations over all possible combination $(i_1, i_2, \cdots, i_8)$ and $(j_1, j_2, \cdots, j_6)$ of the coordinates of the electrons which are put in the $M_{A\alpha}(\varphi: i_1, i_2, \cdots, i_8)$ and $N_{A\alpha}(h: j_1, j_2, \cdots, j_6)$.

where

$$M_{Aa}(\varphi:\ i_1,\ i_2,\cdots,\ i_8)=(|\varphi_1\varphi_2\varphi_3\varphi_4\bar{\varphi}_{4'}\varphi_{3'}\varphi_{2'}\varphi_{1'}|) \tag{A.3}$$

$$N_{Aa}(h:\ j_1,\ j_2,\cdots,\ j_6)=(|\hbar_1\hbar_2\hbar_3\hbar_{3'}\hbar_{2'}\hbar_{1'}|) \tag{A.4}$$

In a similiar way, we obtain

$$(|\varphi_1\varphi_2\varphi_3\bar{\varphi}_4\varphi_{4'}\varphi_{3'}\varphi_{2'}\varphi_{1'}\hbar_1\hbar_2\hbar_3\hbar_{3'}\hbar_{2'}\hbar_{1'}|)=\Sigma M_{\overline{Aa}}(\varphi:\ i_1,\ i_2,\cdots,\ i_8)N_{\overline{Aa}}(h:\ j_1,\ j_2,\cdots,\ j_6) \tag{A.5}$$

where

$$\left.\begin{aligned}M_{\overline{Aa}}(\varphi:\ i_2,\ i_2,\cdots,\ i_8)&=(|\varphi_1\varphi_2\varphi_3\bar{\varphi}_4\varphi_{4'}\varphi_{3'}\varphi_{2'}\varphi_{1'}|)\\ N_{\overline{Aa}}(h:\ j_1,\ j_2,\cdots,\ j_6)&=N_{Aa}(h:\ j_1,\ j_2,\cdots,\ j_6)\end{aligned}\right. \tag{A.6}$$

If we integrate the $\int\Psi^*\mathscr{H}\Psi d\tau$, substituting (A.2) and (A.5) in Ψ, we obtain:

$$\begin{aligned}\int\Psi^*\mathscr{H}\Psi d\tau=\Sigma\Sigma\Sigma\int&(M_{Rs}{}^*(\varphi:\ i_1',\ i_2',\cdots,\ i_8')-M_{\overline{Rs}}{}^*(\varphi:\ i_1',\ i_2',\cdots,\ i_8')\\ &\times N_{Rs}(h:\ j_1',\ j_2',\cdots,\ j_6')\mathscr{H}(M_{Pq}-M_{\overline{Pq}})(\varphi:\ i_1,\ i_2,\cdots,\ i_8)\\ &\times N_{Pq}(h:\ j_1,\ j_2,\cdots,\ j_6)d\tau_1,\ d\tau_2,\cdots,\ d\tau_{14}\ .\end{aligned} \tag{A.7}$$

When there is at least one pair of the different co-ordinates (for example, we assume this pair as j_1 and j_1') in the combinations $(j_1,\ j_2,\ \cdots,\ j_6)$ and $(j_1',\ j_2',\cdots,\ j_6')$ of the coordinates of the electrons which are horsed in the minor determinants $N_{Pq}(h:\ j_1,\cdots,\ j_6)$ and $N_{Rs}(h:\ j_1',\cdots,\ j_6')$, we integrate the $\int(M_{Rs}-M_{\overline{Rs}})^*N_{Rs}\mathscr{H}(M_{Pq}-M_{\overline{Pq}})N_{Pq}d\tau_{j_1}d\tau_{j_1'}$ for these coordinates j_1 and j_1' and we remove the surrounding atoms to infinite distance and then the integral $\int(M_{Rs}-M_{\overline{Rs}})^*N_{Rs}{}^*\mathscr{H}(M_{Pq}-M_{\overline{Pq}})N_{Pq}d\tau_{j_1}d\tau_{j_1'}$ vanishes. Therefore, we may consider only the case of the same combinations $(j_1,\cdots,\ j_6)$ and $(j_1,\cdots,\ j_6)$ of the coordinates of the electrons which are put in the $N_{Pq}(h:\ j_1,\ j_2,\cdots,\ j_6)$ and $N_{Rs}(h:\ j_1,\ j_2,\cdots,\ j_6)$.

As the hamiltonian $\mathscr{H}$ is invariant for all permutations over 1, 2, ⋯, 14, the following equality is obtained:

$$\begin{aligned}\int\Psi^*\mathscr{H}\Psi d\tau=\Sigma\int&(M_{Rs}{}^*(\varphi:\ 1,\ 2,\cdots,\ 8)-M_{\overline{Rs}}{}^*(\varphi:\ 1,\ 2,\cdots,\ 8))N_{Rs}{}^*(h:\ 9,\ 10,\cdots,\ 14)\\ &\times\mathscr{H}(M_{Pq}-M_{\overline{Pq}})(\varphi:\ 1,\ 2,\cdots,\ 8)N_{Pq}(h:\ 9,\ 10,\cdots,\ 14)d\tau\end{aligned} \tag{A.8}$$

The spin configurations of the electrons which are put in the wave functions φ_i, correspond to the spin configurations of the electrons which are put in the wave functions h_i respectively and so if we integrate for the spin coordinates of the electrons which are put in the wave functions h_i, the interaction energy between the structure Pq and Rs does not vanish only in the case that the structures Pq and Rs have the same configuration of spin.

Thus, we obtain

$$\begin{aligned}\int\Psi^*\mathscr{H}\Psi d\tau=\Sigma\int&(M_{Pq}{}^*(\varphi:\ 1,\ 2,\ \cdots,\ 8)-M_{\overline{Pq}}{}^*(\varphi:\ 1,\ 2,\cdots,\ 8))\\ &\times\mathscr{H}(M_{Pq}(\varphi:\ 1,\ 2,\cdots,\ 8)-M_{\overline{Pq}}(\varphi:\ 1,\ 2,\cdots,\ 8))d\tau_1,\ d\tau_2,\cdots,\ d\tau_8\end{aligned} \tag{A.9}$$

In a similar way, we obtain

$$\begin{aligned}\int\Psi^*\Psi d\tau=\Sigma\int&(M_{Pq}{}^*(\varphi:\ 1,\ 2,\cdots,\ 8)-M_{\overline{Pq}}{}^*(\varphi:\ 1,\ 2,\cdots,\ 8))\\ &\times(M_{Pq}(\varphi:\ 1,\ 2,\cdots,\ 8)-M_{\overline{Pq}}(\varphi:\ 1,\ 2,\cdots,\ 8))d\tau_1,\ d\tau_2,\cdots,\ d\tau_8\end{aligned} \tag{A.10}$$

Taking account of the equality of $(M_{Pq}-M_{\overline{Pq}})\propto(\phi_{Pq}-\phi_{\overline{Pq}})\propto\Phi_{Pq}$, we obtain

$$E'=\int\Psi^*\mathscr{H}\Psi d\tau_1\cdots d\tau_{14}\Big/\int\Psi^*\Psi d\tau_1\cdots d\tau_{14}$$

$$=\left(\Sigma\int\Phi_{Pq}{}^*\mathscr{H}\Phi_{Pq}d\tau_1\cdots d\tau_8\right)\Big/\left(\Sigma\int\Phi_{Pq}{}^*\Phi_{Pq}d\tau_1\cdots d\tau_8\right)+\mathcal{E}_0=E+\mathcal{E}_0 \qquad \text{(A.11)}$$

where $\mathcal{E}_0$ is the proper energy of the surrounding atoms.

Appendix II. Evaluation of Molecular Integrals

In this appendix II, the evaluation of the molecular integrals occuring in our calculation is explained.

A. The overlap integral S_{ij}', one-electron potential and kinetic energy integrals, exchange integrals for interatomically orthogonal $2s$, $2p$- hybrid orbitals are expressed in convienent form and are easily evaluated using the Table of Kotani, et. al..

B. In computing the hybrid Coulomb-exchange integrals, we use the following approximation.[30]

$$ij':kk)=S_{ij}'(\bar{i}\,\bar{j}':kk) \qquad \text{(A.12)}$$

Where $\bar{i}$ and $\bar{j}'$ are the atomic orbitals associated with the center of gravity, which has to be chosen in a suitable way.

These exchange integral term associated hybrid Coulomb-exchange integrals are not negligible.

C. The molecular integrals involving $1s$ orbitals are calculated as follow:

One-electron potential and kinetic energy integrals and Coulomb integrals are calculated by using Roothaan's formulas.[31]

Exchange integrals and hybrid Coulomb-exchange integrals are calculated by the following approximation formulas[32]

$$(cj':cj')=S_{cj'}{}^2(\bar{c}\,\bar{j}':\bar{c}\,\bar{j}') \qquad \text{(A.17)}$$

$$(cj':kk)=S_{cj'}(\bar{c}\,\bar{j}':kk) \qquad \text{(A.18)}$$

References

1) E. Hückel: Z. Physik **60** (1930) 423.
2) L. Pauling: J. Amer. Chem. Soc. **53** (1931) 1367.
3) W. G. Penney: Proc. Roy. Soc. A, **144** (1933) 166.
4) R. S. Mulliken: Phys. Rev. **41** (1932) 751; **43** (1933) 279; **56** (1939) 778.
5) J. H. Van Vleck and A. Sherman: Rev. Mod. Phys. **7** (1935) 167.
Y. K. Syrkin and M. E. Dyatkina: *Structure of Molecules and the Chemical Bond* (Butterworth, 1946) 237; Proc. Roy. Soc. A, **207** (1951) 1; J. Phys. Chem. **56** (1952) 287.
M. Kotani: *Quantum Chemistry* (*Valence Theory*) (Kyoritsu-sha, Tokyo, 1939) 70. (in Japanese)
6) Y. K. Syrkin and M. E. Dyatkina: *Structure of Molecules and the Chemical Bond* (Butterworth, 1946) 239.
7) F. Hund: Z. Physik **42** (1927) 93; **52** (1928) 601; 759; **63** (1930) 719.
8) R. S. Mulliken: Rev. Mod. Phys. **4** (1932) 19; Phys. Rev. **40** (1932) 55; **41** (1932) 49; **43** (1933) 279.
9) Lennard-Jones: Trans. Faraday Soc. **25** (1929) 668.
10) C. C. J. Roothaan: Rev. Mod. Phys. **23** (1951) 69.
11) W. Heitler and F. London: Z. Physik **44** (1927) 455.
12) J. C. Slater: Phys. Rev. **37** (1931) 481; **38** (1931) 1109; 1931.
13) L. Pauling: J. Amer. Chem. Soc. **53** (1931) 1367.
L. Pauling and J. Sherman: J. Amer. Chem. Soc. **59** (1937) 1450.
14) J. H. Van Vleck: J. Chem. Phys. **3** (1935) 803.
15) C. A. Coulson: *Valence* (Oxford Univ. Press., 1951) 187.

16) W. G. Penney: Proc. Roy. Soc. **A, 144** (1934) 166.
C. A. Coulson and W. E. Moffitt: Phil. Mag. **40** (1949) 1.
W. G. Penney: *The Quantum Theory of Valence* (London, 1935) 72.
J. C. Slater: Phys. Rev. **38** (1931) 1109.
L. C. Pauling: J. Amer. Chem. Soc. **53** (1931) 1367.
C. W. Ufford: Phys. Rev. **54** (1938) 568.
H. A. Levy and L. O. Brockway: J. Amer. Chem. Soc. **59** (1937) 2085.
17) C. Zener: Phys. Rev. **36** (1930) 51.
18) J. C. Slater: Phys. Rev. **36** (1930) 57.
19) R. S. Mulliken, Rieke, Orloff and Orloff: J. Chem. Phys. **17** (1949) 1248.
20) R. S. Mulliken: J. Chem. Phys. **19** (1951) 900.
R. S. Mulliken: J. chim. phys. **46** (1949) 497.
21) M. Kotani et al: Proc. Phys.-Math. Soc. Japan **20** (1938) Extra No. 1.
M. Kotani et al: Proc. Phys.-Math. Soc. Japan **22** (1940) Extra No. 2.
M. Kotani et al: *Table of Molecular Integrals* (Maruzen, Japan, 1955).
22) C. J. Roothaan: J. Chem. Phys. **19** (1951) 1445.
R. Rüdenberg: J. Chem. Phys. **19** (1951) 1459.
23) D. R. Hartree and M. M. Black: Proc. Roy. Soc. **A, 139** (1933) 311.
24) Mulliken, Rieke, Orloff and Orloff: J. Chem. Phys. **17** (1949) 1248.
25) W. Moffitt: Proc. Roy. Soc. **A, 196** (1949) 510; 524; **A, 210** (1951) 224; 245.
W. Moffitt and J. Scanlan: Proc. Roy. Soc. **A, 218** (1953) 464; **A, 220** (1953) 530.
W. Moffitt: Proc. Roy. Soc. **A, 218** (1953) 486; Rep. Proc. Phys. XVII (1954) 173.
C. W. Sherr: J. Chem. Phys. **22** (1954) 194.
A. C. Hurley: Proc. Phys. Soc. **A, 68** (1955) 149; **69** (1956) 49.
26) H. M. James: J. Chem. Phys. **2** (1934) 794.
27) J. H. Van Vleck: J. Chem. Phys. **3** (1935) 20.
28) J. H. Bartlett and W. H. Furry: Phys. Rev. **38** (1931) 1615.
29) R. Serber: J. Chem. Phys. **3** (1935) 81.
30) Per-Olov Löwdin: J. Chem. Phys. **21** (1953) 374.
A. L. Sklar: J. Chem. Phys. **7** (1939) 984.
A. London: J. Chem. Phys. **13** (1945) 396.
31) C. J. Roothaan: J. Chem. Phys. **19** (1951) 1445.
32) See ref. 30.

JOURNAL OF THE PHYSICAL SOCIETY OF JAPAN Vol. 14, No. 3, MARCH, 1959

On the Non-Orthogonality Difficulty in Ferromagnetism

By Fumihiko TAKANO

Department of Physics, Tokyo University of Education

(Received October 31, 1958)

In a many-electron system, one is faced to some difficulties when one-electron wave functions are not orthogonal to each other. For example, the inner product (Φ, Φ) (Φ is a Slater determinant made from these non-orthogonal wave functions) loses its meaning as the number of electrons becomes large. We avoid this difficulty by using the expansion coefficients instead of the inner products, in order to define the matrix elements of operators. Applying this method to a magnetic problem, in which there are some doubts about the validity of the Heisenberg model $\mathscr{H}=-2\sum_{i>j} J_{i,j}\boldsymbol{S}_i\cdot\boldsymbol{S}_j$, we can derive the energy of the ground state and the energy spectrum of spin waves. The results are written as

$$W_0=\sum_{i=1}^{N} f_{i,j}+\tfrac{1}{2}\sum_i\sum_j(g_{ij,ij}-g_{ij,ji}) ,$$

and

$$\varepsilon(K)=\sum_{j=1}^{N}\alpha_K(j)\beta_K(j) .$$

Some mathematical difficulties which occur in the case of the state in which more than two spins are reversed are discussed.

§ 1. Introduction

The Heisenberg model, usually used in magnetic problems, has a difficulty arising from non-orthogonality of atomic functions. This is the following: Let us consider an electronic configuration in which each atomic orbital φ_i (i denotes the number specifying an atom) is occupied by one electron, and solve the spin degeneracy in this configuration. If the orbitals are orthogonal to each other, the Hamiltonian for a spin system can be rigorously written in a usual form[1]

$$\mathscr{H}=-2\sum_{i>j} J_{i,j}\boldsymbol{S}_i\cdot\boldsymbol{S}_j , \tag{1.1}$$

where $J_{i,j}$ is the exchange energy between the orbitals φ_i and φ_j, and $\boldsymbol{S}_i$ is the spin operator of the orbital i. In this case, however, $J_{i,j}$ has always a positive value, and all materials should be ferromagnetic. This is contrary to the original idea of the Heisenberg model in which we can distinguish ferro- and antiferro-magnetism according to the sign of $J_{i,j}$.

To keep the advantage of the original Heisenberg model we must use the non-orthogonal atomic orbitals. In this case, however, the Hamiltonian cannot be written in such a simple form as Eq. (1.1). Therefore, an attempt to investigate the situation in detail will be important and desirable. We suppose that the form of Eq. (1.1) is probably valid as a first approximation, but it is difficult to show this mathematically because of the following situation. As Slater[2] has pointed out, the inner product (Φ, Φ) of the Slater determinant made from the non-orthogonal orbitals tends to infinity as the number N of electrons becomes large. This is physically meaningless. Of course, this divergence should cancel out in the expression $(\Phi, A\Phi)/(\Phi, \Phi)$. However, it is very difficult to prove this for general cases.

In this paper we shall avoid this difficulty using the expansion coefficients instead of the inner products to define the matrix elements of operators. This method is very useful in the problems in which non-orthogonal functions appear. Previously, the author applied this method to liquid He⁴, and succeeded to obtain the smooth connection between the Bose condensation theory and the phonon-roton model[3].

We consider the idealized case only, in which each atom has only one electron. Moreover, the orbital configuration of electrons is limited to non-ionized one. Thus, there is just the same number of orbitals as electrons, and there is neither empty nor doubly occupied orbital. The extension to more realistic case in which each atom has more than two electrons can be done easily. Moreover, we shall treat the ferromagnetic case only, although the antiferro-magnetic one can be treated similarly.

For the ground state of a ferromagnet, in which all electrons have parallel spins, there is no spin degeneracy, and the energy eigenvalue can be easily calculated by calculating the value of $(\Phi, H\Phi)/(\Phi, \Phi)$[4]. For an excited state, in which a certain number of spins are reversed, the situation is not so simple as for the ground state, and it is difficult to get the energy eigenvalue by calculating the value of $(\Phi, H\Phi)/(\Phi, \Phi)$. In this paper, we use the above-mentioned method and obtained the rigorous expression for the energy spectrum of spin waves. The solution, in which more than two spins are reversed, would be obtained in a similar way, but we could not do it due to some mathematical difficulties.

In § 2, we shall show the outline of the method used. In § 3, this method will be applied to the case of hydrogen molecule in order to illustrate the features of this method. In § 4 and § 5, we shall treat the N-electron system and derive the energy spectrum of spin waves. Some difficulties in the problem of the scattering between spin waves will be discussed in § 6.

§ 2. Outline of the Method

As mentioned above, the difficulty of the non-orthogonality arises when one wants to calculate a matrix element in a form $(\Phi_i, A\Phi_j)$, where Φ_i, Φ_j are many-electron wave functions. Here, we do not use such an inner product at all, but use the following procedure. Let us consider a set of functions $|i)$, which is complete in the Hilbert space considered, but not orthonormal. We represent an operator A in terms of the following $a_{j,i}$,

$$A|i)=\sum |j)a_{j,i} . \qquad (2.1)$$

Using this matrix representation, the eigenvalues α of A is determined from

$$|a_{j,i}-\alpha\delta_{j,i}|=0 . \qquad (2.2)$$

Compare this equation with that appears in the usual method, i.e., with

$$|A_{j,i}-\alpha(j|i)|=0 , \qquad (2.2')$$

where $A_{j,i}=(j|A|i)$ is the inner product of $A|i)$ with $(j|$. The relation between $a_{j,i}$ and $A_{j,i}$ is

$$A_{j,i}=\sum_k (j|k)a_{k,i} . \qquad (2.3)$$

The basic concept of the present paper is to use Eq. (2.2) instead of Eq. (2.2′).

In the present problem, there are two different ways of choosing $|i)$. We shall illustrate these two methods in the following.

(I) The direct application of the above method leads to the following results. As was done by Dirac[1], we write $\psi_0=\varphi_1(1)\varphi_2(2)\cdots\varphi_N(N)$ where φ_j's are atomic orbitals, and limit the space considered to that which is made from $N!$ functions $P\psi_0$, where P denotes the permutation operator of electron coordinates. According to Eq. (2.2), we can define the matrix elements $h_{P',P}$ of the Hamiltonian H by

$$HP\psi_0=\sum_{P'} P'\psi_0 h_{P',P} . \qquad (2.4)$$

Then, the effective Hamiltonian $\mathscr{H}$ for spin variables can be written as

$$\mathscr{H}=\sum_{P_\sigma}(-1)^{P_\sigma}h_{1,P}P_\sigma , \qquad (2.5)$$

where P_σ is the permutation operator of electron spins, and the relation $h_{P',P}=h_{1,P'^{-1}P}$ is used. The derivation of Eq. (2.5) is completely similar to that due to Dirac[1].

This method appears to be quite simple, but the difficulty arises when we want to calculate the value of $h_{1,P}$. As is seen from Eq. (2.3), it is necessary to calculate the inverse of the overlap matrix $(P'\psi_0|P\psi_0)$. The dimension of this overlap matrix, however, is $N!$ and it is as difficult as to use the inner product to calculate the inverse matrix when atomic orbitals are not orthogonal. Moreover, in order to derive the form such as Eq. (1.1) from Eq. (2.5), it is necessary to write P_σ in the form of the product of the interchange $P_{(i,j)}$, and to express $P_{(i,j)}$ in terms of $(S_i\cdot S_j)$, $P_{i,j}=\frac{1}{2}(1+4(S_i\cdot S_j))$. And then we must pick up the terms proportional to $(S_i\cdot S_j)$. Since the number of such terms is very large, we have the same difficulty and in the usual method.

(II) Next, we use the one electron wave functions φ_i (atomic orbitals) as $|i)$ in Eq. (2.1). Hamiltonian of our system consists from the sum of one-electron functions and of two-electron functions,

$$H=\sum_{i=1}^{N} f(r_i)+\sum_{i>j}\sum g(r_{ij}) . \qquad (2.6)$$

we define the matrix elements of f and g in accordance with Eq. (2.1),

$$\left.\begin{aligned} f(1)\varphi_i(1)&=\sum_{j=1}^{N}\varphi_j(1)f_{j,i}\,,\\ g(1,2)\varphi_i(1)\varphi_j(2)&=\sum_{k=1}^{N}\sum_{l=1}^{N}\varphi_k(1)\varphi_l(2)g_{kl,ij}\,. \end{aligned}\right\} \tag{2.7}$$

Using these $f_{j,i}$ and $g_{kl,ij}$, we can define the matrix elements of H. The relations between these $f_{j,i}$ and $g_{kl,ij}$ and the usual matrix elements $F_{j,i}\equiv(j|f|i)$, $G_{kl,ij}\equiv(kl|g|ij)$ can be written as

$$\left.\begin{aligned} f_{j,i}&=\sum_{k}t_{j,k}F_{k,i}\,,\\ g_{kl,ij}&=\sum_{m}\sum_{n}t_{k,m}t_{l,n}G_{mn,ij}\,, \end{aligned}\right\} \tag{2.8}$$

where t is the inverse of the overlap matrix S ($S_{i,j}=(\varphi_i|\varphi_j)$). In this case, the dimension of the overlap matrix S is only N, compared with $N!$ of $(P'\psi_0|P\psi_0)$ used in method (I). Thus, the inverse matrix t can be calculated very easily. For example, let us assume that the overlap integral $(\varphi_i|\varphi_j)$ has a value 1 when $i=j$ and a value α when i and j are nearest neighbours to each other and vanishes otherwise. The formal expansion of the inverse matrix of $(P'\psi_0|P\psi_0)$ by power series of α converges only when $N\alpha^2<1$, which means that α must vanish in practice. When one uses t instead, however, the expansion parameter is $z\alpha^2$ (z=the number of nearest neighbours) and the expansion converges if $z\alpha^2<1$.

If $z\alpha^2>1$, we must use another method to calculate the matrix t, and this is in fact possible. However, when α is too large, the approximation of Heitler-London, in which atomic functions are used, becomes inferior to the band approximation, in which the functions of Bloch type are used. Slater[4] discussed about this point by using Wannier functions and Bloch functions in each case. We can do so quite similarly by using atomic functions φ_j instead of Wannier functions and the tightly bound approximation $(1/\sqrt{N})\times\sum_j e^{ikR_j}\varphi_j(r)$ of Bloch functions. Since the essential point does not differ from that of Slater, we shall discuss no more about this point, and employ the viewpoint of Heitler-London, only.

It is to be noted here that the method (II) is not equivalent to (I), while the latter is equivalent to the usual method. In the method (I) we consider $N!$ functions $P\psi_0$, where each function $P_i\psi_0$ has the same energy as ψ_0. In the method (II), however, we must consider functions involving ionic states, although some of these are inhibited by Pauli principle. It is not permissible in the method (II) to neglect the ionic states from the begining, because then it is not equivalent to the method (I) or the usual method. In other words, when and only when the spaces to be considered are the same, the method using the expansion coefficients is equivalent to the usual method using the inner products. In the method (II), $H\psi_0=H\varphi_1(1)\varphi_2(2)\cdots\varphi_N(N)$ does not involve $P\psi_0$ except $P=1$ and $P=P_{(ij)}$ (interchange), but necessarily involve many ionized states such as $\varphi_1(1)\varphi_1(2)\cdots\varphi_N(N)$. Thus, the space to be considered is not same to that of the usual method in which we neglect the ionized states. In the method (I), however, we restrict the space to $N!$ states $P\psi_0$ from the begining, that is same as the usual method. In this case, $H\psi_0$ involves all $P\psi_0$ generally, so that the calculation becomes very complicate. Here, we employ the method (II). In this case we must find an approximation equivalent to the usual method in which we neglect the ionized states. Before going into the general discussion, we shall treat the hydrogen molecule by three methods, the usual method, method (I) and (II), in order to illustrate the features of each method and to find the approximation in the method (II) equivalent to that in the usual method in which the ionized states are neglected.

§ 3. A Simple Example; Hydrogen Molecule

In order to show the equivalence or the difference among three methods mentioned in § 2, and to find the above-mentioned approximation for the method (II), first we treat a simple example, that is, a hydrogen molecule.

(a) *Usual method*

Let two protons of the hydrogen molecule be a and b, ane the s-functions of each atom be $a(r)$, $b(r)$, respectively. In the approximation neglecting the ionized states, we may consider only two orbital configurations, $|1)=a(1)b(2)$ and $|2)=b(1)a(2)$. Thus the secular equation can be written as

$$\begin{vmatrix} H_{11}-W & H_{12}-W(1|2) \\ H_{21}-W(2|1) & H_{22}-W \end{vmatrix}=0\,, \tag{3.1}$$

where $H_{i,j}=(i|H|j)$. If we set $\int a(r)b(r)d^3r=\alpha$

then $(1|2)=(2|1)=\alpha^2$. From the symmetry consideration, we can set $H_{11}=H_{22}\equiv A$, $H_{12}=H_{21}\equiv B$. Using these notations, the solution of Eq. (3.1) can be written as

$$W_t=\frac{A-B}{1-\alpha^2}\,,\quad W_s=\frac{A+B}{1+\alpha^2}\,. \tag{3.2}$$

Corresponding orbital wave functions are

$$\Psi_t=\frac{1}{\sqrt{2}}(|1)-|2))\,,\quad \Psi_s=\frac{1}{\sqrt{2}}(|1)+|2))\,. \tag{3.3}$$

These are well-known results.

(b) *Method* (I)

In this method, we define the matrix elements of H as follows,

$$H|1)=|1)h_{11}+|2)h_{21}\,,$$
$$H|2)=|1)h_{12}+|2)h_{22}\,.$$

From the symmetry considerations, we can set $h_{11}=h_{22}\equiv a$, $h_{12}=h_{22}\equiv b$. The secular equation can be written as

$$\begin{vmatrix} a-W & b \\ b & a-W \end{vmatrix}=0\,.$$

The roots of this equation are

$$W_s=a-b\,,\quad W_t=a+b\,. \tag{3.2$'$}$$

The corresponding wave functions are same as Eq. (3.3). The overlap matrix $(i|j)$ has a form as

$$\begin{pmatrix} 1 & \alpha^2 \\ \alpha^2 & 1 \end{pmatrix},$$

so that the inverse of this matrix becomes

$$\frac{1}{1-\alpha^4}\begin{pmatrix} 1 & -\alpha^2 \\ -\alpha^2 & 1 \end{pmatrix}.$$

Thus, a and b can be written in terms of A and B, using Eq. (2.3)

$$a=\frac{1}{1-\alpha^4}(A-\alpha^2B)\,,\quad b=\frac{1}{1-\alpha^4}(-\alpha^2A+B)\,. \tag{3.3}$$

Substituting Eq. (3.4) into Eq. (3.2′), it is easily seen that Eq. (3.2′) coincides with Eq. (3.2).

(c) *Method* (II)

The Hamiltonian of this system can be written as

$$H=f(1)+f(2)+g(12)\,.$$

We can define the matrix elements of f and g in accordance with Eq. (2.7),

$$f(1)a(1)=a(1)f_0+b(1)f_1\,,\qquad f(1)b(1)=a(1)f_1+b(1)f_0\,,$$
$$g(12)a(1)b(2)=a(1)b(2)k_0+b(1)a(2)j_0+(a(1)a(2)+b(1)b(2))l\,,$$
$$g(12)b(1)a(2)=a(1)b(2)j_0+b(1)a(2)k_0+(a(1)a(2)+b(1)b(2))l\,,$$
$$g(12)a(1)a(2)=(a(1)b(2)+b(1)a(2))l'+a(1)a(2)k_1+b(1)b(2)j_1\,,$$
$$g(12)b(1)b(2)=(a(1)b(2)+b(1)a(2))l'+a(1)a(2)j_1+b(1)b(2)k_1\,.$$

As was previously stated, we can not neglect the ionized states $a(1)a(2)$ and $b(1)b(2)$ from the begining. It is to be noted that the above matrix representation of g is not hermitian because $l\neq l'$. Using these matrix elements, the secular equation can be written as

$$\begin{vmatrix} 2f_0+k_0-W & j_0 & f_1+l & f_1+l \\ j_0 & 2f_0+k_0-W & f_1+l & f_1+l \\ f_1+l' & f_1+l' & 2f_0+k_1-W & j_1 \\ f_1+l' & f_1+l' & j_1 & 2f_0+k_1-W \end{vmatrix}=0\,. \tag{3.5}$$

Now, we set $\varphi_{1,2}=1/\sqrt{2}\,(a(1)b(2)\pm b(1)a(2))$, $\psi_{1,2}=1/\sqrt{2}\,(a(1)a(2)\pm b(1)b(2))$, and use φ_2, φ_1, ψ_1, ψ_2 as a new base of the representation. Then, Eq. (3.5) becomes

$$\begin{vmatrix} 2f_0+k_0-j_0-W & 0 & 0 & 0 \\ 0 & 2f_0+k_0+j_0-W & 2(f_1+l) & 0 \\ 0 & 2(f_1+l) & 2f_0+k_1+j_1-W & 0 \\ 0 & 0 & 0 & 2f_0+k_1-j_1-W \end{vmatrix}=0. \tag{3.6}$$

Thus, the triplet state φ_2 is separated out and the energy of this state is given

$$W_t=2f_0+k_0-j_0\,. \tag{3.7}$$

(The state ψ_t is separated out also, but this is an ionized state which we are not interested in.) This arises from the fact that the state in which all spins are parallel does not interact with the ionized states in which at least one spin must be reversed, and it is due to this fact that the energy of the ferromagnetic ground state can be easily calculated.

It is also easy to calculate the energy W_s of the singlet state from Eq. (3.6), but the problem is how to get the solution which coincides with Eq. (3.2). As mentioned in § 2, to neglect the third and fourth lines in Eqs. (3.5) and (3.6) leads to a result quite different from (*a*) and (*b*).

To neglect the ionized states in the usual method, corresponds to the approximation that $(aa|H|aa)$ is set to be very large compared with $(aa|H|ab)$ etc., and that the ratios $(aa|H|ab)/(aa|H|aa)$ etc. are set equal to zero. The essential difference between $(aa|H|aa)$ and $(aa|H|ab)$ etc. is that the former involves the term $G_0\equiv(aa|g|aa)$ while the latters do not. Thus, we may also make an approximation setting $G_0\rightarrow\infty$ in the method (II). G_0 corresponds to the ionization energy in the treatment in which the atomic orbitals are not changed even when the atom is ionized.

According to Eq. (2.8), the matrix elements involving G_0 are k_1, j_1 and l'. Thus, we may set

$$\left.\begin{aligned} k_1&=g_{aa,aa}\sim t_{a,a}^2G_0\ ,\\ j_1&=g_{bb,aa}\sim t_{b,a}^2G_0\ ,\\ l'&=g_{ab,aa}\sim t_{a,a}t_{b,a}G_0\ .\end{aligned}\right\}\tag{3.8}$$

That is to say, $g_{kl,ij}$ involves the term proportional to G_0 when and only when $i=j$, and we can set

$$g_{kl.ij}\sim t_{k,i}t_{l,j}G_0\ .\tag{3.8'}$$

The relation will be used in the general case considered in § 4.

Thus, in the limit of $G_0\rightarrow\infty$, the equation, determining the single energy W_s, can be written as

$$\begin{vmatrix} 2f_0+k_0+j_0-W_s & 2(f_1+l)\\ 2t_{a,a}t_{b,a}G_0 & (t_{a,a}^2+t_{b,a}^2)G_0\end{vmatrix}=0\ ,$$

where we have used the fact that W_s does not involve G_0. Solving this equation, we get

$$W_s=2f_0+k_0+j_0-\frac{4(f_1+l)t_{aa,}t_{b,a}}{(t_{a,a}^2+t_{b,a}^2)}\ .\tag{3.9}$$

of course, we also get this solution by solving Eq. (3.6) exactly and then setting $G_0\rightarrow\infty$.

Now, t is the inverse matrix of $\begin{pmatrix}1 & \alpha\\ \alpha & 1\end{pmatrix}$, so that

$$t=\frac{1}{1-\alpha^2}\begin{pmatrix}1 & -\alpha\\ -\alpha & 1\end{pmatrix}\ .\tag{3.10}$$

Substitution of Eq. (3.10) into Eq. (3.9) gives

$$W_s=2f_0+k_0+j_0+\frac{4\alpha(f_1+l)}{1+\alpha^2}\ .\tag{3.9'}$$

We can easily see that Eqs. (3.7) and (3.9′) coincide with Eq. (3.2) using the following relation;

$$f_0=\frac{1}{1-\alpha^2}(F_0-\alpha F_1)\ ,\quad f_1=\frac{1}{1-\alpha^2}(-\alpha F_0+F_1)\ ,$$

where

$$F_0\equiv(a|f|a)\ ,\quad F_1\equiv(b|f|a)$$

and

$$k_0=\frac{1}{(1-\alpha^2)^2}(K+\alpha^2J-2\alpha L)\ ,$$

$$j_0=\frac{1}{(1-\alpha^2)^2}(J+\alpha^2K-2\alpha L)\ ,$$

$$l=\frac{1}{(1-\alpha^2)^2}((1+\alpha^2)L-\alpha(K+J))\ ,$$

where

$$K=(ab|g|ab)\ ,$$

$$J\equiv(ab|g|ba)\ ,$$

$$L\equiv(aa|g|ab)\ .$$

The wave function for the singlet state has a form $\varphi_1+c\psi_1$ where φ_1 is nothing but Ψ_s of Eq. (3.6). $c\psi_1$ expresses the mixing of the ionized states, but c is of the order of L/G_0 and we can set $c=0$ in our approximation. For the ionized state, the wave function is of the form as $\psi_1+c'\varphi_1$, where c' is of the order of 1 compared with L/G_0. That is, the ionized state is largely affected, but the non-ionized state is hardly affected.

From the above discussion, we can find the approximation in the method (II), which is equivalent to neglect ionized states in the usual method: We must include the ionized states at first, but, in solving the secular equation, we may set $G_0\rightarrow\infty$. G_0 is involved in the terms such as $g_{kl,ii}$ which is set $t_{k,i}t_{l,i}\ G_0$ in this approximation.

At first sight, it might appear that the method (I) is much simpler than the method (II). The above example, however, is a two-electron system, so that the dimension of the overlap matrix is $2!=2$ in the method (I), which is same as in the method (II). In a N-electron system, the dimension of the overlap matrix is much less in the method (II) than in the method (I), and the former is much simpler than the latter.

§ 4. *N*-electron System

In this section, the method (II) is applied to N-electron system. As mentioned in § 1, we treat the idealized case, in which each of N atoms has one electron. Thus, there are N atomic orbitals, which is denoted as φ_1, $\varphi_2, \cdots, \varphi_N$. The Hamiltonian of the system has a form, Eq. (2.6),

$$H=\sum_{i=1}^{N} f(r_i)+\sum_{i>j}\sum g(r_{ij}) . \tag{4.1}$$

Since there are many orbital configurations, it is convenient to write the Hamiltonian in the form of second quantization. In our case, the basic one-electron wave functions are not orthogonal to each other, but we can follow the Fock's method[6] to quantize the Hamiltonian as follows: The functions

$$\varphi_{i_1}(1)\varphi_{i_2}(2)\cdots\varphi_{i_N} . \quad (i_n=1,\, 2,\, \cdots,\, N) \tag{4.2}$$

are linearly independent with each other, though not orthogonal. We confine the space considered to that consists from these functions and expand the projection of any function to this space in terms of these functions. For the sake of simplicity we consider the orbital parts of the wave functions only, and shall attach the spin parts after a while. Thus, we can write

$$\psi=\sum_{\{i_n\}} c(\{i_n\})\varphi_{i_1}(1)\varphi_{i_2}(2)\cdots\varphi_{i_N}(N) .$$

Now, we must solve the equation

$$i\hbar\frac{\partial\psi}{\partial t}=H\psi .$$

Using the matrix elements defined in Eq. (2.7), we obtain the following relation,

$$\sum_{n=1}^{N} f(n)\varphi_{i_1}(1)\cdots\varphi_{i_N}(N)=\sum_{j}\sum_{n=1}^{N} f_{j,i_n}\varphi_{i_1}(1)\cdots\varphi_{i_{n-1}}(n-1)\varphi_j(n)\varphi_{i_{n+1}}(n+1)\cdots\varphi_{i_N}(N) ;$$

$$\tfrac{1}{2}\sum_{m\neq n}\sum g(m,\, n)\varphi_{i_1}(1)\cdots\varphi_{i_N}(N)=\tfrac{1}{2}\sum_{k}\sum_{l}\sum_{m\neq n}^{N}\sum^{N} g_{kl,i_m i_n}\varphi_{i_1}(1)\cdots\varphi_{i_{m-1}}(m-1)\varphi_k(m)\varphi_{i_{m+1}}(m+1)$$
$$\cdots\varphi_{i_{n-1}}(n-1)\varphi_l(n)\varphi_{i_{n+1}}(n+1)\cdots\varphi_{i_N}(N) .$$

Thus, the equation for the coefficients c's is obtained by equating the coefficients of $\varphi_{i_1}(1)\varphi_{i_2}(2)\cdots\varphi_{i_N}(N)$ in both sider of $i\hbar(\partial\psi/\partial t)=H\psi$,

$$i\hbar\frac{\partial c(\{i_n\})}{\partial t}=\sum_{n=1}^{N}\sum_{j} f_{i_n,j}\, c(i_1,\, \cdots,\, i_{n-1},\, j,\, i_{n+1},\, \cdots,\, i_N)$$
$$+\tfrac{1}{2}\sum_{n\neq m}^{N}\sum^{N}\sum_{k}\sum_{l} g_{i_m i_n,kl}\, c(i_1,\, \cdots,\, i_{m-1},\, k,\, i_{m+1},\, \cdots,\, i_{n-1},\, l,\, i_{n+1},\, \cdots,\, i_N) .$$

Here, we attach the spin function to each orbital, and express c's in terms of the occupation numbers of each orbital. Taking into account of Fermi statistics, we introduce the annihilation and creation operators a_{is}, a_{is}^*. Then the above equation becomes

$$i\hbar\frac{\partial c(\{n_{i,s}\})}{\partial t}=\mathscr{H}\, c(\{n_{i,s}\}) ,$$

where

$$\mathscr{H}=\sum_{i,j}\sum_{s} f_{j,i}a_{js}^*a_{is}+\tfrac{1}{2}\sum_{k,l}\sum_{i,j}\sum_{s,s'} g_{kl,ij}a_{ks}^*a_{is'}^*a_{js'}a_{is} , \tag{4.3}$$

and

$$[a_{is}^*a_{j,s'}]_+=\delta_{i,j}\delta_{s,s'} , \qquad [a_{i,s},\, a_{j,s'}]_+=0 \qquad \text{etc.} \tag{4.4}$$

Eqs. (4.3) and (4.4) are completely same in form as in the case of orthogonal orbitals. In our case, the orbitals are not orthogonal. So that, if we use the inner products to define the matrix elements, the Hamiltonian involves much higher powers of a, a^* and is much complicated than Eq. (4.3). As was proved above, if we use the expansion coefficients instead of the inner products, we obtain the same form of Hamiltonian as in the case of orthogonal orbits. The only difference between orthogonal and non-orthogonal orbitals is the coefficients $f_{j,i}$ and $g_{kl,ij}$ which become $(j|f|i)$ and $(kl|g|ij)$ in the case of orthogonal orbitals. As mentioned in § 3, the special care must be taken if the configurations considered are limited.

In the following, we shall calculate the energy eigenvalues of $\mathscr{H}$, Eq. (4.3), in the case of ferromagnet. The approximation used must be equivalent to that in the usual method in which we neglect the ionized states.

(a) *Ground State*

The energy of the state Φ_0 in which all spins are parallel can be calculated very easily. In this state, each orbital is occupied by one electron and there are neither empty nor doubly occupied orbitals. Let the spins of all electrons are oriented to z direction, which is denoted by $s=+$. Then

$$a_{i+}^*\Phi_0=0\,, \qquad a_{i-}\Phi_0=0 \qquad \text{for all } i\,.$$

Using these properties, we obtain immediately

$$\mathscr{H}\Phi_0=\left\{\sum_{i=1}^{N} f_{i,i}+\tfrac{1}{2}\sum_{i=1}^{N}\sum_{j=1}^{N}(g_{ij,ij}-g_{ij,ji})\right\}\Phi_0=W_0\Phi_0\,. \tag{4.5}$$

If we express W_0 in terms of $(j|f|i)$'s and $(kl|g|ij)$'s we get

$$W_0=\sum_{i,j} t_{i,j}(j|f|i)+\tfrac{1}{2}\sum_{ij}\sum_{kl}(t_{i,k}t_{j,l}-t_{i,l}t_{j,k})(kl|g|ij)\,, \tag{4.6}$$

which completely coincides with the result which Löwdin$^{4)}$ obtained by the usual method.

(b) *Excited States* (*Energy Spectrum of Spin Waves*)

In order to consider the excited states, we define the operator which transfers an electron at j site to l site reversing its spin,

$$B_{l,j}^*=a_{l-}^*a_{j+}\,. \tag{4.7}$$

$B_{l,j}^*\Phi_0=\Phi_{l,j}$ is the state in which there are two electrons with $+$ and $-$ spins at l site and a hole at j when $l\neq j$. $\Phi_{l,l}$ is the state in which each atom has one electron but the spin at l site is reversed.

First, we calculate $\mathscr{H}\Phi_{l,j}$

$$\mathscr{H}\Phi_{l,j}=W_0\Phi_{l,j}+[\mathscr{H},\,B_{l,j}^*]\Phi_0 \tag{4.8}$$

The second term of this equation becomes

$$\begin{aligned}[\mathscr{H},\,B_{l,j}^*]\Phi_0=\{&\sum_m(f_{m,l}+\sum_n g_{mn,ln})B_{m,j}^*\\ &-\sum_i(f_{j,i}+\sum_n(g_{nj,ni}-g_{nj,in}))B_{l,i}^*-\sum_m\sum_i g_{mj,li}B_{l,i}^*\}\Phi_0\,.\end{aligned} \tag{4.9}$$

The physical meaning of each term on the right hand side is obvious as follows; The first term represents the transition of negative spin at l site to m, the second of positive spin at i to j, that is, of the hole at j to i. While the negative spin moves in the first term, the positive spin moves in the second, so that there is the exchange term with other spins $\sum g_{nj,in}$. The last term represents the transitions of negative spin at l to m and positive spin at i to j.

It is very difficult to solve Eq. (4.9) exactly. However, we need not solve it exactly. As mentioned in § 3, we adopt the approximation which is equivalent to neglect the ionized states in the usual method. This approximation is to set $(jj|g|jj)\equiv G_0\to\infty$. Now, we pick up the term proportional to G_0 in Eq. (4.9),

$$(\mathscr{H}-W_0)\Phi_{l,j}=[\mathscr{H},\,B_{l,j}^*]\Phi_0\sim G_0\sum_m\{t_{m,l}t_{l,l}B_{m,j}^*-t_{m,l}t_{j,l}B_{m,l}^*\}\Phi_0\,. \tag{4.10}$$

For the ionized state, $l \neq j$, the right hand side of this equation does not vanish, so that the other terms which was not written in Eq. (4.10) may be neglected. For the non-ionized state, $l=j$, Eq. (4.10) vanishes and the rigorous expression of $[\mathscr{H}, B_{l,j}^*]\Phi_0$ must be used.

Taking the Fourier transform for the motion of the center of gravity, we define

$$B_{K,j}^* \equiv \frac{1}{\sqrt{N}} \sum_l e^{iKl} B_{l,l-j}^* , \qquad \Phi_{K,j} = B_{K,j}^* \Phi_0 , \tag{4.11}$$

where the states $j \neq 0$ correspond to ionized states. The inverse transformation of Eq. (4.11) is

$$B_{l,j}^* = \frac{1}{\sqrt{N}} \sum_K e^{-iKl} B_{K,l-j}^* , \qquad \Phi_{l,j} = \frac{1}{\sqrt{N}} \sum_K e^{-iKl} \Phi_{K,l-j} . \tag{4.11'}$$

Using Eqs. (4.11) and (4.11′), we obtain from Eqs. (4.9) and (4.10),

$$\begin{aligned}(\mathscr{H}-W_0)\Phi_{K,0} &= \sum_n g_{0n,n0}(1-e^{iKn})\Phi_{K,0} \\ &\quad + \sum_{j\neq 0} \{f_{j,0}(e^{-iKj}-1) - \sum_n (g_{jn,0n}-g_{jn,n0}) + e^{-iKj} \sum_n (g_{jn,0n}-g_{nj,0n}e^{-iKn})\}\Phi_{K,j} \\ &\equiv \mathcal{E}'(K)\Phi_{K,j} + \sum_{j\neq 0} \beta_K(j)\Phi_{K,j}\end{aligned} \tag{4.12}$$

$$(\mathscr{H}-W_0)\Phi_{K,j} = G_0\{t_0 t_j(e^{iKj}-1)\Phi_{K,0} + \sum_{j'\neq 0}(t_0 t_{j-j'}e^{iK(j-j')} - t_j t_{-j'}e^{-iKj'})\Phi_{K,j'}\} , \qquad (j \neq 0) , \tag{4.13}$$

where we have used the property of the translational symmetry, that is,

$$t_{m,m+j} = t_{0,j} \equiv t_j , \qquad f_{m,m+j} = f_{0,j} , \qquad g_{m+k,m+l,m+i,m+j} = g_{kl,ij} .$$

We need the energy eigenvalue of the non-ionized state $\Phi_{K,0}$. If we neglect the state $\Phi_{K,j}$ $(j \neq 0)$ in Eqs. (4.12) and (4.13), the result is quite different from the usual approximation, as was mentioned in § 3. Since $(\mathscr{H}-W_0)\Phi_{K,j}$ $(j \neq 0)$ involves $\Phi_{K,0}$ in the order of G_0, we cannot neglect $\Phi_{K,j}$ in the right hand side of Eq. (4.12). This is the only complicated feature of this method.

Now, we consider the transformation which eliminates $\Phi_{K,0}$ from Eq. (4.13). To do this, we may set

$$\Psi_{K,j} = \Phi_{K,j} - \alpha_K(j)\Phi_{K,0} , \qquad (j \neq 0) . \tag{4.14}$$

The transformation is not unitary. We need not use, however, the unitary transformation, because our Hamiltonian, Eq. (4.3), is not hermitic. Since, $(\mathscr{H}+W_0)\Phi_{K,0}$ is lower order compared with $(\mathscr{H}-W_0)\Phi_{K,j}$, we get

$$(\mathscr{H}-W_0)\Psi_{K,j} \simeq (\mathscr{H}-W_0)\Phi_{K,j} .$$

We use Eq. (4.14) to express the right hand side of Eq. (4.13) in terms of $\Psi_{K,j}$ instead of $\Phi_{K,j}$ and determine $\alpha_K(j)$ in such a way that the coefficient of $\Phi_{K,0}$ may vanish. Then, the equation for $\alpha_K(j)$ becomes

$$t_0 t_j(e^{iKj}-1) + \sum_{j'\neq 0} \alpha_K(j')[t_0 t_{j-j'}e^{iK(j-j')} - t_j t_{-j'}e^{-iKj'}] = 0 . \tag{4.15}$$

This can be solved easily,

$$\alpha_K(j) = c_K \sum_{j_1} s_{j_1} e^{iKj_1} t_{j_1,j} , \tag{4.16}$$

where c_K is determined from the condition $\alpha_K(0)=1$, which gives

$$(c_K)^{-1} = \sum_{j_1} s_{j_1} e^{iKj_1} t_{-j_1} . \tag{4.17}$$

s_j is the overlap integral $s_j \equiv s_{0,j} = (\varphi_0, \varphi_j)$. Eqs. (4.16) and (4.17) can be written in another form,

$$\alpha_K(j) = \frac{c_K}{N} \sum_{K_i} e^{-iK_i j} \frac{t(K_i)}{t(K+K_i)} = \frac{c_K}{N} \sum_{K_i} e^{-iK_i j} \frac{s(K+K_i)}{s(K_i)} , \tag{4.16'}$$

$$(c_K)^{-1} = \frac{1}{N} \sum_{K_i} \frac{t(K_i)}{t(K+K_i)} = \frac{1}{N} \sum_{i} \frac{s(K+K_i)}{s(K_i)} , \tag{4.17'}$$

where $s(K)$ and $t(K)$ are the Fourier transforms of s_j and t_j, respectively,

$$s(K) = \sum_j s_j e^{iKj} , \qquad t(K) = \sum_j t_j e^{iKj} . \tag{4.18}$$

These $s(K)$ and $t(K)$ are eigenvalues of the matrices $(s_{i,j})$ and $(t_{i,j})$ respectively, and we have the relation

$$s(K)t(K) = 1 . \tag{4.19}$$

It is clear from Eq. (4.16) that when $K=0$, we have

$$\alpha_0(j) = \delta_{j,0} . \tag{4.20}$$

Now, substituting Eq. (4.14) into Eq. (4.12), we obtain

$$(\mathscr{H} - W_0)\Phi_{K,0} = [\mathcal{E}'(K) + \sum_{j \neq 0} \alpha_K(j)\beta_K(j)]\Phi_{K,0} + \sum_{j \neq 0} \beta_K(j)\Psi_{K,j} . \tag{4.21}$$

Since $(\mathscr{H} - W_0)\Psi_{K,j}$ does not contain $\Phi_{K,0}$ in the order of G_0, we can neglect $\Psi_{K,j}$ on the right hand side of Eq. (4.21), and we have the energy of the state $\Phi_{K,0}$, given by

$$\mathcal{E}(K) = \mathcal{E}'(K) + \sum_{j \neq 0} \alpha_K(j)\beta_K(j) , \tag{4.22}$$

or using the relation $\alpha_K(0)=1$, $\beta_K(0)=\mathcal{E}'(K)$

$$\mathcal{E}(K) = \sum_j \alpha_K(j)\beta_K(j) . \tag{4.22'}$$

Thus, the energy eigenvalue of the state in which one spin is reversed is obtained in the approximation neglecting the ionized states. This is just the energy spectrum of spin waves. The above expression is valid irrespective of the value of the overlap integral. The only approximation made is to set $G_0 \to \infty$, that is, to neglect the ionized states in usual method.

The calculation of the energy of the state, in which more than two spins are reversed, is necessary in order to discuss the interaction between spin waves, but there is a mathematical difficulty, as will be discussed later. Before doing this, we shall discuss a little more about the energy spectrum in the next section.

§ 5. Concrete Expression for Energy Spectrum of Spin Waves

The expression for energy spectrum of spin waves, given above has the form

$$\mathcal{E}(K) = \sum_j \alpha_K(j)\beta_K(j) , \tag{5.1}$$

where $\alpha_K(j)$ and $\beta_K(j)$ are given by Eqs. (4.16) and (4.12), respectively,

$$\alpha_K(j) = c_K \sum_{j_1} s_{j_1} e^{iKj_1} t_{j_1,j} = \frac{c_K}{N} \sum_{K_i} e^{-iK_i j} \frac{s(K+K_i)}{s(K_i)} \tag{5.2}$$

$$\beta_K(j) = f_{j,0}(e^{-iKj} - 1) - \sum_n (g_{jn,0n} - g_{nj,0n}) + e^{-iKj} \sum_n (g_{jn,0n} - g_{nj,0n} e^{-iKn}) . \tag{5.3}$$

First, we can see, immediately,

$$\mathcal{E}(0)=0\,, \tag{5.4}$$

since $\alpha_0(j)=\delta_{j,0}$ and $\beta_0(j)=0$. This is an expected result, because for $K=0$ the wave function has the same symmetry as the ground state.

The above expression is rigorous, as mentioned in § 4, how large the overlap integral may be, but contains unfamiliar quantities such as $f_{j,0}$, $g_{jn,0n}$, etc. These quantities can be expressed in terms of familiar quantities such as $(j|f|0)$, $(jn|g|0n)$, etc. using Eq. (2.8). In so doing, however, we obtain very complicated expression, so we make further assumptions not unreasonable in order to get a simple expression.

The first assumption is that the atomic orbitals overlap only between nearest neighbours. Then, we can set

$$\left.\begin{aligned}(\varphi_i,\,\varphi_j)\equiv s_{i,j}&=1\,, &&\text{for }\ i=j\,,\\ &=\alpha\,, &&\text{for }\ i=j+\delta\ (i\text{ and }j\text{ are nearest neighbours of each other})\,,\\ &=0\,, &&\text{otherwise}\,,\end{aligned}\right\} \tag{5.5}$$

and

$$\left.\begin{aligned}(\varphi_i,\,f\varphi_j)&=F_0\,, &&\text{for }\ i=j\,,\\ &=F_1\,, &&\text{for }\ i=j+\delta\,,\\ &=0\,, &&\text{otherwise}\,,\end{aligned}\right\} \tag{5.6}$$

and, finally, $(kl|g|ij)$ vanishes except the following elements,

$$(0\delta|g|0\delta)=K\,,\qquad (0\delta|g|\delta 0)=J\,,\qquad (00|g|0\delta)=L\,,\qquad (00|g|00)=G_0\,. \tag{5.7}$$

Here, we have assumed that the overlap integral between nearest neighbours has no directional dependence.

Secondly, we assume that $z\alpha^2<1$, where z is the number of nearest neighbours.

Under these assumptions, we expand $\mathcal{E}(K)$ in power series of α and keep the terms up to α^2. This can be calculated very easily, but the calculation of the next term of α^3 becomes very complicated. This expansion converges if the second assumption is valid. If α is so large that $z\alpha^2>1$, the expansion loses its meaning. In such a case, however, our basic assumption that the ionized states can be neglected becomes invalid, and the band approximation becomes better than the Heitler-London approximation, as was mentioned in § 2. Since we have implicity assumed that the Heitler-London approximation is good, the second assumption can be permitted.

Under these assumptions, we obtain the eigenvalue $s(K)$, Eq. (4.18) of the matrix $(s_{i,j})$,

$$s(K)=1+\alpha\gamma(K)\,,\qquad \gamma(K)\equiv\sum_{\delta}e^{iK\delta}\,, \tag{5.8}$$

where the summation in $\gamma(K)$ is extended over the lattice points of nearest neighbours.

After a long but straightfoward calculation, we obtain for the energy spectrum of spin waves,

$$\mathcal{E}(K)=(\gamma(0)-\gamma(K))\{J-2\alpha F_1-2\alpha^2F_0+\alpha^2(1-2\gamma(0))K-\alpha^2[2-\gamma(0)-2\gamma(K)]J\}+0(\alpha^3)\,, \tag{5.9}$$

where $\gamma(0)=\sum 1$ is equal to the number z of nearest neighbours.

In the case of orthogonal orbitals, we obtain

$$\mathcal{E}(K)=J(\gamma(0)-\gamma(K))$$

setting $\alpha=0$. This is a results expected from the Hamiltonian

$$\mathscr{H}=-2J\sum_{<i,j>}S_i\cdot S_j\,,$$

where the summation is extended over all pairs of nearest neighbours.

§ 6. Interactions Among Spin Waves

Let us consider the states, in which more than two spins are reversed. An example of such states can be written as

$$\Phi_{l_1 l_2 \cdots l_n ; j_1 j_2 \cdots j_n} = a^*_{l_1 -} a^*_{l_2 -} \cdots a^*_{l_n -} a_{j_n +} \cdots a_{j_2 +} a_{j_1 +} \Phi_0 \, . \tag{6.1}$$

This is a state in which the up spins at j_1, j_2, $\cdots$, j_n are reversed and moved to l_1, l_2, $\cdots$, l_n. This can be expressed by using the operator $B^*_{l,j}$ defined in Eq. (4.7),

$$\Phi_{l_1 l_2 \cdots l_n ; j_1 j_2 \cdots j_n} = B^*_{l_1, j_1} B^*_{l_2, j_2} \cdots B^*_{l_n, j_n} \Phi_0 \, , \tag{6.1$'$}$$

although this division into the product of $B^*_{l,j}$ is not unique.

When operating $\mathscr{H}$ on this state, we obtain

$$(\mathscr{H} - W_0) \Phi_{l_1 l_2 \cdots l_n ; j_1 j_2 \cdots j_n} = \sum_{p=1}^{n} \prod_{i \neq p} B^*_{l_i, j_i} [\mathscr{H}, B^*_{l_p, j_p}] \Phi_0 + \sum_{p>q=1}^{n} \sum^{n} \prod_{i \neq p,q} B^*_{l_i, j_i} [[\mathscr{H}, B^*_{l_p, j_p}] B^*_{l_q, j_q}] \Phi_0 \, , \tag{6.2}$$

because $[[[\mathscr{H}, B^*] B^*] B^*] = 0$. This expression, of course, is independent of the method of division Eq. (6.1$'$). Now, the single commutator in the first term of Eq. (6.2) was calculated in § 4, Eq. (4.9), and the double commutator in the second term can be calculated as

$$\begin{aligned} [[\mathscr{H}, B^*_{l,j}] B^*_{l',j'}] = \sum_{mn} \{ & g_{mn, ll'} a^*_{m-} a^*_{n-} a_{j'+} a_{j+} \\ & + g_{jj', mn} a^*_{l-} a^*_{l'-} a_{n+} a_{m+} - g_{mj', ln} a^*_{m-} a^*_{l'-} a_{n+} a_{j+} - g_{mj, l'n} a^*_{m-} a^*_{l-} a_{n+} a_{j'+} \} \, . \end{aligned} \tag{6.3}$$

The terms which are proportional to G_0 in Eq. (6.3) is

$$-G_0 \sum (t_{m,l} t_{j',l} a^*_{m-} a^*_{l'-} a_{l+} a_{j+} + t_{m,l'} t_{j,l'} a^*_{m-} a^*_{l-} a_{l'+} a_{j'+}) \, . \tag{6.4}$$

Since Eqs. (6.3) and (6.4) are of 4-th power of a^*_- and a_+, we can write these as quadratic forms of $B^*_{l',j}$. The way of expressing these in such forms, however, is not unique, as mentioned above. For example, we can write

$$a^*_{l-} a^*_{l'-} a_{j'+} a_{j+} = B^*_{l\,j} B^*_{l',j'}$$

or

$$= -B^*_{l,j'} B^*_{l',j} \, .$$

Now proceding the discussion as in § 4, we first calculate $[[\mathscr{H}, B^*_{K,j}] B^*_{K',j'}]$ and properly express the terms corresponding to Eq. (6.4) in terms of $B^*_{K_1,j_1}$. Then, we make the transformation given by Eq. (4.14), i.e.,

$$B^*_{K,j} = C^*_{K,j} + \alpha_K(j) B^*_{K,0} \, . \tag{6.5}$$

If the expression for the ionized states does not contain the non-ionized states at all, we can carry out the similar calculation as in § 4, and we get the interaction terms between non-ionized spin waves. These express the scatterings between two spin waves and the direct interactions among more than three spin waves do not appear.

Unfortunately, this is not the case. The transformation (6.5) can not eliminate the effect of the ionized states on non-ionized states, when more than two spins are reversed. This transformation can be used only in the case of one spin reversed. So that, we must find another method than that of § 4.

This, however, is very difficult. For example, consider the state in which two spins are reversed. From Eqs. (4.9) and (6.4), we obtain

$$\begin{aligned} (\mathscr{H} - W_0) \Phi_{ll', jj'} & \\ = G_0 \sum_{m} \{ & t_0 t_{m,l'} \Phi_{lm, jj'} + t_0 t_{m,l} \Phi_{ml, jj'} \\ & - t_{m,l'} t_{j',l'} \Phi_{lm, jl'} - t_{m,l} t_{j,l} \Phi_{l'm, j'l} \\ & - t_{m,l'} t_{j,l'} \Phi_{lm, l'j'} - t_{m,l} t_{j',l} \Phi_{l'm, jl} \} \, . \end{aligned} \tag{6.6}$$

For the non-ionized states, that is, when $(l, l') = (j, j')$ (this means that $l = j$, $l' = j'$ or $l = j'$, $l' = j$), the right hand side of this equation vanishes, so that the rigorous expression must be used. In other cases, we may pick up the non-ionized states from the right hand side, and must find the method to eliminate these states from Eq. (6.6). Obviously, when $l, l' \neq j, j'$ (this means that $l \neq j, j'$ and $l' \neq j, j'$), Eq. (6.6) does not contain the non-ionized state. When one of the pairs is equal, for example $l=j,\ l'\neq j'$, the non-ionized states appear in a following form

$$G_0 t_0 t_{j',l}(\Phi_{lj',lj'}-\Phi_{ll',ll'})$$

This term can be eliminated by the transformation (6.5) or Eq. (4.14). However, when this transformation is applied to the case $l,\ l'\neq j,\ j'$, $(\mathscr{H}-W_0)\Phi_{ll',jj'}$ becomes to involve non-ionized states. These states appear from the term $\Phi_{ll',lj'}$ involved in $(\mathscr{H}-W_0)\Phi_{ll',jj'}$. So, we must proceed in a following way: First, we mix the one hole states ($l=j,\ l'\neq j'$, for example) in the two-hole states, $l,\ l'\neq j,\ j'$ to eliminate the former from the equation for the latter. Next, we mix the non-ionized states $(l,\ l')=(j,\ j')$ in the one-hole states to eliminate the former from the equation for the latter. Finally, we express $(\mathscr{H}-W_0)\Phi_{ll',ll'}$ in terms of these new ionized states and pick up the non-ionized states.

This procedure, however, can not be applied in practice, because Eq. (6.6) involves four indices in the right hand side and we must solve about N^4 equations. Of course, the motion of the center of gravity can be separated out, so that the number of the effective states is reduced to about N^3, which is still very large and the rigorous calculation is nearly hopeless. The more the number of the reversed spins is, the more this difficulty increased. We can not find the approximate treatment, so that the discussion about this point is deferred to another occasion.

§ 7. Conclusions and Discussions

We have developed a general method to treat the non-orthogonal wave functions and applied this to Heisenberg model in magnetic problems. This method was previously applied to liquid Helium by the author, who obtained the modified phonon-roton model which showed the phase transition of second order due to Bose condensation. In the magnetic case treated in this paper, we calculated the energy eigenvalues of the ferromagnetic ground state and of the excited state in which one spin is reversed. This latter represents the energy spectrum of spin waves. These results are rigorous for any values of the overlap integrals. Only approximation made is that we have neglected the ionized states. This is a reasonable approximation if the treatment of Heitler-London type is valid.

The energy spectrum of spin waves has a very simple form but it contains unfamiliar quantities, such as $f_{j,i}$ or $g_{kl,ij}$. If these quantities are expressed by familiar ones $(j|f|i)$ or $(kl|g|ij)$ the expression becomes very complicated, so that we have calculated it under the two assumptions mentioned in § 5.

We have treated an idealized case only, that is, each atom is assumed to have only one electron. The extension to more realistic case is possible, but the result will be much more complicated. Although the problem treated in this paper is considered to be rather academic, so that it is questionable whether such an extension to realistic cases has any physical meaning, and the results obtained here can be considered to give a qualitatively correct conclusions even in the realistic cases. These are the reasons why we do not attempt to extend the discussion to more realistic cases.

We have wished to calculate the interactions among spin waves, but the mathematical complexity has prevented it. It is certain, however, that, in order to describe the scatterings between spin waves, the Hamiltonian such as Eq. (1.1) is not sufficient. The terms which involve more than three spin variables are necessary. Thus, when the atomic orbitals are not orthogonal to each other, it is still questionable whether the interactions between spin waves deduced from Eq. (1.1) have any physical meaning. The energy spectrum of spin waves, deduced from Eq. (1.1), has a physical meaning, however, if the values of the exchange integrals $J_{i,j}$ are taken properly. For example, we can use the coefficient of $(\gamma(0)-\gamma(K))$ in Eq. (5.6) as J_δ in Eq. (1.1).

The higher order terms, which are necessary to discuss the interactions among spin waves, may be of higher order of α. Therefore, if the overlap integral α is so small that the higher terms of α can be neglected, the Hamiltonian, Eq. (1.1), may be used as a first approximation.

As was mentioned in § 1, the method used in this paper is very powerful in the case in which a set of non-orthogonal functions plays an important role. In the case treated here, it is possible to calculate the energy spectrum of spin waves by the usual method under certain assumptions[7], so that it might appear somewhat troublesome, to use this method in order to obtain the results mentioned above. The Hamiltonian, Eq. (4.3), in our method, however, has a very simple form and we can say that our method is much easier than the usual method. For example, the superexchange interactions which are discussed by several authors[8] may also be discussed by using our Hamiltonian.

The author wishes to express his sincere thanks to Prof. R. Kubo in Tokyo University and Prof. M. Toda in this university for their valuable discussions.

References

1) P. A. M. Dirac: *The Principles of Quantum Mechanics*, 3rd ed. (Oxford, 1947) 211.
2) J. C. Slater: Rev. Mod. Phys. **23** (1953) 199.
3) F. Takano: J. Phys. Soc. **12** (1957) 1185.
4) For example, F. O. Löwdin: J. Chem. Phys. **18** (1950) 367.
5) J. C. Slater: Phys. Rev. **52** (1937) 198.
6) V. Fock: Z. Physik **75** (1932) 622.
7) R. Kubo and T. Yokota: unpublished.
H. Hasegawa: unpublished.
8) J. Yamashita and J. Kondo: Phys. Rev. **109** (1958) 730.
J. Carr: Phys. Rev. **92** (1953) 28.

JOURNAL OF THE PHYSICAL SOCIETY OF JAPAN Vol. 14, No. 3, MARCH, 1959

On Quantitative Measurement of Turbulence by Means of a Constant Resistance Hot-wire Anemometer

By Nisiki HAYASI

Transportation Technical Research Institute, Mitaka, Tokyo

(Received November 14, 1958)

Constant resistance hot-wire anemometry has been improved to measure velocity fluctuation quantitatively. For this purpose, the effects of the resistance of the galvanometer circuit and current variation due to resistance variation of hot-wire are calculated for general case. The values of the turbulent energy reached by the older method would be several part of correct ones in our experiment. A direct calibration method using alternating current has been devised. This method is easy to apply. Experiments show that the results obtained by the two methods completely agree with each other. Owing to the possibility of the calibration in the actual circuit, the constant resistance method would be superior to the constant current method.

§ 1. Introduction

Since H. L. Dryden[1] carried out his pioneer work for the hot-wire anemometer technique, many authors have developed and refined this powerful equipment for the studying of turbulence. Most investigators, however, have dealt with the constant current method, while few authors[2),6),7] have used the constant resistance method. In either method, the effect of the variations of electric current and heat transfer due to the variation of hot-wire resistance and other effects scattered the experimental results when the temperature of hot-wire was varied, thus permitting in general only qualitative measurements to be done.

Simmons and Salter[7] showed the effect of current variation due to resistance variation in a special version of constant resistance method. Kovásznay[4] pointed out this effect in the constant current method. Shigemitsu[6] neglected this effect in the simplest one of constant resistance method. Ruetenik[5] showed the main effect of the heat transfer variation due to resistance variation.

In this paper, the first effect is evaluated for the general case of the constant resistance method. Moreover it is pointed out that, in general, the effect of the finite resistance of the galvanometer circuit cannot be ignored. When these effects are taken into account, the results are independent of the wire temperature.

Further, the direct calibration method for the dynamic characteristics using alternating current is developed to save calculation. This calibration is easy to apply. The experimental results obtained by the use of the calculation method and the direct calibration method completely agree with each other. Owing to the possibility of the calibration in the actual circuit, the constant resistance hot-wire anemometer would be superior to the constant current hot-wire anemometer.

§ 2. Measurement of Turbulent Intensity by Calculation Method

The equation of cooling of the hot-wire is

$$\frac{dH}{dt}=i^2r-f(u,\ r)(T-\Theta)\ , \qquad (1)$$

where H and T are the heat energy and the absolute temperature of the wire, u and Θ are the velocity and the absolute temperature of air, i is the electric current, r is the resistance of the wire, and

$$\left.\begin{aligned} &f(u,\ r)=K(r)+D(r)u^m\ ,\\ &K(r)=akL\ ,\\ &D(r)=bkL(d/\nu)^m\ , \end{aligned}\right\} \qquad (2)$$

where a and b are constants, k and ν are the thermal conductivity and the kinematic viscosity of air, and L and d are the length and the diameter of the wire.

On the other hand

$$\frac{dH}{dt}=ms\frac{dT}{dt}\ , \qquad (3)$$

where m and s are the mass and the specific heat of the wire, respectively. If we use the temperature coefficient of resistance α, we have

$$\left.\begin{aligned} &T-\Theta=\frac{r-r_0}{\alpha r_0}\ ,\\ &\frac{dT}{dt}=\frac{1}{\alpha r_0}\frac{dr}{dt}\ , \end{aligned}\right\} \qquad (4)$$

where r_0 is the resistance of the wire at air temperature. From (1), (3) and (4),

$$\frac{ms}{\alpha r_0}\frac{dr}{dt}=i^2r-f(u,r)\frac{r-r_0}{\alpha r_0}\ . \qquad (5)$$

In the case of stationary state with constant wind velocity U, we have

$$i_e{}^2\bar{r}=f(U,\ \bar{r})\frac{\bar{r}-r_0}{\alpha r_0}\ , \qquad (6)$$

where $\bar{r}$ is the resistance of the wire and i_e is the electric current through it. To keep the wire resistance constant, it is convenient to use a Wheatstone bridge.

When the air speed fluctuates,

$$u=U+u'\ ,\quad r=\bar{r}+r'\ . \qquad (7)$$

If we can neglect small quantities of $O(u'/U)^2$, $O(u'r'/U\bar{r})$ and $O(r'/\bar{r})^2$, we have from (5) and (7)

$$\begin{aligned} \frac{ms}{\alpha r_0}\frac{dr'}{dt}=i^2(\bar{r}+r')&\\ -\{f(U,\ \bar{r})+f_u(U,\ \bar{r})u'+f_r(U,\ \bar{r})r'\}&\\ \times\frac{\bar{r}-r_0}{\alpha r_0}-\frac{f(U,\ \bar{r})}{\alpha r_0}r'\ ,& \qquad (8) \end{aligned}$$

where suffices u and r represent partial differentiation. If the circuit constants are such as shown in Fig. 1,

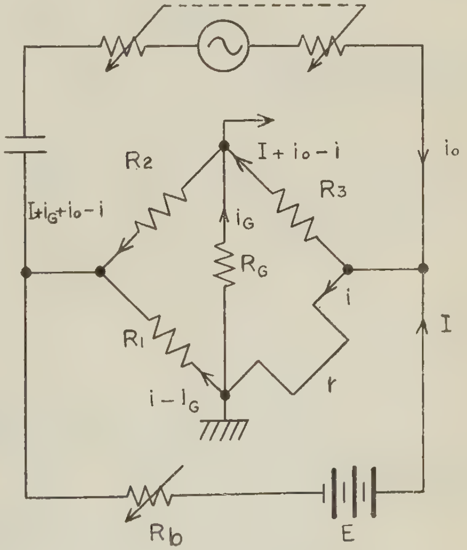

Fig. 1. Bridge circuit.

$$\begin{aligned} &\bar{r}R_2=R_1R_3\ ,\\ &i=(E+i_0R_b)R_3G/(\bar{r}\Delta)\ ,\\ &i_e=ER_3/B\ ,\\ &I=[\{E(\bar{r}+R_3)-i_0R_3(\bar{r}+R_1)\}G\\ &\qquad+E(G-R_1R_G)r']/(\bar{r}\Delta)\ , \end{aligned}$$

where small quantities of $O(i_0r'/E)$ are neglected and

$$\Delta=\Delta_1+\Delta_2r'\ ,$$

$$\Delta_1 = BG/\bar{r}\ ,$$
$$\Delta_2 = \{G(R_b+R_3)+R_1(R_1R_3-R_bR_G)\}/\bar{r},$$
$$B = R_b(\bar{r}+R_3)+R_3(\bar{r}+R_1)\ ,$$
$$G = R_G(\bar{r}+R_1)+R_1(\bar{r}+R_3)\ .$$

If we choose $i_e \gg |i_0|$, then we have, neglecting small quantities,

$$\left.\begin{aligned} &\bar{i} = i_e\ ,\\ &\bar{I} = i_e(1+\bar{r}/R_3)\ ,\\ &i^2(\bar{r}+r') = i_e^2\{\bar{r}+2i_0\bar{r}R_b/E+(1-\rho)r'\}\ , \end{aligned}\right\} \quad (9)$$

where bar denotes the time average and

$$\rho = 2\bar{r}\Delta_2/\Delta_1\ .$$

Hence from (6), (8) and (9), we have

$$M\frac{dr'}{dt}+r' = c_1u'+c_2i_0\ , \qquad (10)$$

where M is the time constant of the wire defined as

$$\left.\begin{aligned} &M = ms/(i_e^2r_0\alpha A)\ ,\\ &c_1 = -(\bar{r}-r_0)f_u/(i_e^2r_0\alpha A)\ ,\\ &c_2 = 2R_b\bar{r}/(EA)\ ,\\ &A = \frac{r_0}{\bar{r}-r_0}+\rho+\frac{\bar{r}-r_0}{i_e^2\alpha r_0}f_r\ . \end{aligned}\right\} \quad (11)$$

From (6) and (9), we have

$$f_u(U,\ \bar{r}) = \frac{\alpha r_0\bar{r}}{2\sqrt{U}(\bar{r}-r_0)}\left(\frac{R_3}{\bar{r}+R_3}\right)^2\frac{\partial\overline{I^2}}{\partial\sqrt{U}}\ . \qquad (12)$$

Also (2) gives

$$f_r = K'+D'u^m\ .$$

In this equation,

$$K = ak_1L_1\left(\frac{\theta}{\theta_1}\right)^\omega\left\{1+\frac{\beta}{\alpha}\left(\frac{r}{r_1}-1\right)\right\}\ ,$$

where θ is the effective temperature of air, suffix 1 represents the standard state,

$$\theta = \frac{1}{2}(T+\Theta),\quad \theta_1 = \frac{1}{2}(T_1+\Theta)\ ,$$

and β is the coefficient of linear expansion of the wire. Thus

$$K = ak_1L_1\left\{\frac{T_1+\Theta+(r-r_1)/\alpha r_1}{T_1+\Theta}\right\}^\omega\left\{1+B\left(\frac{r}{r_1}-1\right)\right\}\ ,$$

where $B = \beta/\alpha$. Hence

$$K' = K\left\{\frac{\omega}{\alpha r_1(T_1+\Theta)+r-r_1}+\frac{1}{r-r_1+r_1/B}\right\}\ ,$$

On the other hand,

$$D = bk_1L_1\left(\frac{d_1}{\nu_1}\right)^m\{1+\beta(T-T_1)\}^{m+1}\left(\frac{\theta}{\theta_1}\right)^{\omega-5m/2}\left(\frac{\theta+C}{\theta_1+C}\right)^m,$$

where $C = 107$°C. Then

$$D' = D\left\{\frac{m+1}{r-r_1+r_1/B}+\frac{\omega-5m/2}{\alpha r_1(T_1+\Theta)+r-r_1}+\frac{m}{\alpha r_1(T_1+\Theta+2C)+r-r_1}\right\}\ .$$

If we choose $r = r_1 = \bar{r}$, $T_1 = \bar{T}$,

$$f_r(U,\ \bar{r}) = \frac{f}{\bar{r}}\left\{\frac{\omega}{\alpha(\bar{T}+\Theta)}+B\right\}+\frac{mDU^m}{\bar{r}}\left\{B-\frac{5}{2}\,\frac{1}{\alpha(\bar{T}+\Theta)}+\frac{1}{\alpha(\bar{T}+\Theta+2C)}\right\}\ .$$

But from (2), we have

$$mDU^m = Uf_u\ .$$

Therefore, considering that B is negligible (0.0023 for platinum, 0.00083 for tungsten), we obtain, from (6) and (12),

$$f_r = \frac{\overline{I^2}r_0R_3^2}{(\bar{r}-r_0)(\bar{T}+\Theta)(R_3+\bar{r})^2}\left[\omega-\frac{3\sqrt{U}\,\partial\overline{I^2}}{4I^2\,\partial\sqrt{U}}\left\{1+\frac{4}{3}\,\frac{C}{\bar{T}+\Theta+2C}\right\}\right]\ . \qquad (13)$$

Usually, ω can be taken as 3/4.

On the other hand, the output voltage of the bridge is

$$e=\sigma r' , \tag{14}$$

where

$$\sigma=-i_e R_1 R_G/G ,$$

When we use the hot-wire in fluctuating air flow, $i_0=0$. Then

$$M\frac{dr'}{dt}+r'=c_1 u' . \tag{15}$$

To find the relation between r' and u', these are expressed as time-dependent Fourier series

$$u'=\sum_n (A_n \cos \omega_n t+B_n \sin \omega_n t) ,$$

$$r'=\sum_n (C_n \cos \omega_n t+D_n \sin \omega_n t) .$$

If we put these formulas in (15), we get

$$r'=\sum_n \frac{c_1}{\sqrt{1+M^2\omega_n^2}}\left\{A_n \cos(\omega_n t-\phi_n)+B_n \sin(\omega_n t-\phi_n)\right\} ,$$

$$\phi_n=\tan^{-1}(M\omega_n) .$$

That is, the fluctuation of the wire resistance is reduced in the ratio of $|c_1|/\sqrt{1+M^2\omega^2}$ in amplitude, and retarded by an amount of $\tan^{-1}(M\omega)$ in phase. When this effect is eliminated by use of a compensating amplifier, the equivalent bridge output becomes

$$e=\sigma c_1 u'. \tag{16}$$

σc_1 is the sensitivity of the hot-wire anemometer.

As c_1 can be calculated by (11), (12) and (13), the turbulent intensity $\sqrt{\overline{u'^2}}$ can be found by means of (16) by measuring $\sqrt{\overline{e^2}}$.

From (9), it is clear that ρ represents the effect of current variation due to resistance variation. By definition ρ is always positive, and hence, by (11), A is increased, so that M, c_1 and c_2 are decreased. Thus the time constant of the wire decreases with the sacrifice of the sensitivity.

§ 3. Measurement of Turbulent Intensity by Calibration Method

For the calibration of the hot-wire, we place it in the wind at constant speed without fluctuation, and superpose an alternating current on the direct current through the wire:

$$i_0=a\cos\omega t . \tag{17}$$

Then

$$M\frac{dr'}{dt}+r'=c_2 i_0,$$

$$r'=\frac{c_2}{\sqrt{1+M^2\omega^2}}a\cos(\omega t-\phi) ,$$

$\phi=\tan^{-1}(M\omega)$. If we use such ω as $M\omega\ll 1$, $r'=c_2 i_0$, so that the bridge output becomes

$$e_c=\sigma c_2 i_0 . \tag{18}$$

When the dynamic calibration has been performed, c_2 can be obtained by (18). Now, from (11) and (12), we have

$$c_1=-\frac{1}{4I\sqrt{U}}\frac{\partial\overline{I}^2}{\partial\sqrt{U}}c_2 .$$

Thus

$$e=-\frac{e_c}{4Ii_0\sqrt{U}}\frac{\partial\overline{I}^2}{\partial\sqrt{U}}u' . \tag{19}$$

From this equation, measurement of turbulent intensity can be immediately carried out without complicated calculation.

§ 4. Comparison with Experiment

To investigate the effectiveness of the above-mentioned methods, a series of measurements of the same turbulence with various hot-wires were performed. For this purpose, the decay of turbulence behind a square mesh grid at air speed of 4 m/s was investigated. The grid was $2.8\times2.5\,\mathrm{mm}^2$, made with circular rods of 0.75 mm diameter. This grid was placed in an N.P.L. type wind tunnel with $20\times30\,\mathrm{cm}^2$ rectangular test section. Turbulent intensity was measured at the center line of the test section. The hot-wire was Wollaston processed platinum wire whose diameter was 2.5 micron. We used an equal arm Wheatstone bridge in the same manner as Shigemitsu[6] had done. In this case, R_b can be far greater than $\bar{r}$, and the output voltage over the hot-wire is approximately $1.5+\bar{r}/R_G$ times that over the galvanometer without superposed alternating current[3]. This point is important for the measurement of small velocity fluctuation, although, in this case, the calibration method cannot be used.

The output of the bridge was led to a compensating amplifier and mean-square unit[3].

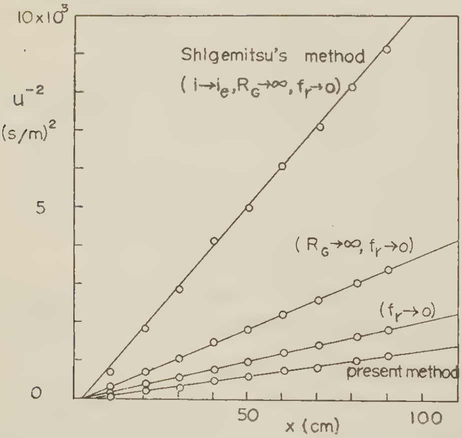

Fig. 2. Error due to various simplified assumptions.

The temperature of the wire was varied from 175°C to 413°C. In Fig. 2, the result at 413°C is plotted using the calculation method—(16)—and the calibration method—(19). In this figure, the result obtained by the use of Shigemitsu's method[6] is also shown for comparison. The latter is about ten times as large as other two results.

Shigemitsu assumes that the current and heat transfer variations due to the resistance variation are infinitesimal and the resistance of the galvanometer circuit infinite. So the above-mentioned difference may be deemed due to the effects of these variations and of the finite resistance of the galvanometer circuit. In order to clarify this, the result calculated by the assumption of infinitesimal heat transfer variation and the result calculated by further assumption of infinite resistance of the galvanometer circuit are also plotted in this figure. From this figure, it is clear that the main cause of the difference is the current variation due to the resistance variation, nevertheless the effects of the finite resistance of the galvanometer circuit and heat transfer variation cannot be ignored.

In Fig. 3 is shown the effect of temperature variation for Shigemitsu's method. The scatter of the results is due to the temperature variation of this effect.

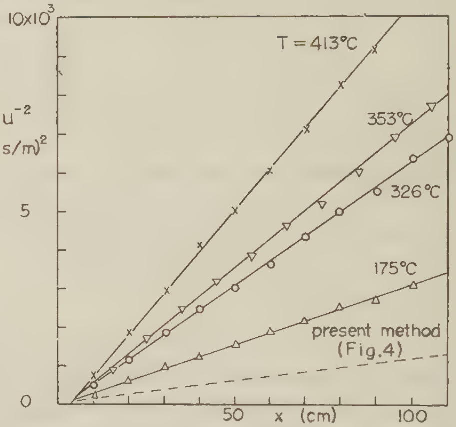

Fig. 3. Temperature dependence of the result obtained by the old method.

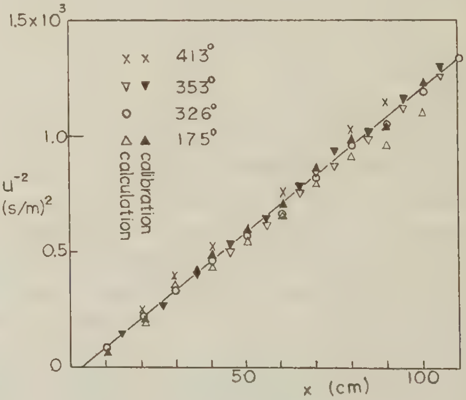

Fig. 4. Temperature independence of the result obtained by the present method.

In Fig. 4, the results obtained by using our two methods are presented. It will be seen that the temperature effect is completely eliminated, and further, all the experimental points lie on a single line. Thus we may safely state that the present results are quantitatively correct.

§ 5. Summary

Two experimental methods for quantitative measurement of turbulence are described. These two methods have been applied to investigate the decay of the turbulent energy behind a grid. In spite of the variation of the temperature of the hot-wire, results obtained were in complete agreement with each other. It is remarked that the older method which neglects the effects of the finite resistance of the galvanometer circuit and the current variation due to resistance variation of hot-wire would lead to values about ten times as large as correct ones at the highest wire temperature in our experiment.

In conclusion, the author wishes to express his hearty gratitude to Dr. Masando Hanajima and Mr. Yutaka Shigemitsu for their kind support. His cordial thanks are also due to Professor Itiro Tani, Professor Isao Imai and Mr. Junji Iwayanagi for the interest shown to this work.

References

1) H. L. Dryden and A. M. Kuethe: N. A. C. A. Tech. Rep. No. 320 (1929).
2) R. Hama: Rep. Inst. Sci. Technol., Univ. Tokyo **7** (1953) 145.
3) N. Hayasi: to be published as Rep. Transp. Tech. Res. Inst.
4) L. Kovásznay: N. A. C. A. Tech. Memo. No. 1130 (1947).
5) J. R. Ruetenik: J. Aero. Sci. **22** (1955) 502.
6) Y. Shigemitsu: J. Phys. Soc. Japan **5** (1950) 157; 207.
7) L. F. G. Simmons and C. Salter: Proc. Roy. Soc. London **A**, **145** (1934) 212.

JOURNAL OF THE PHYSICAL SOCIETY OF JAPAN Vol. 14, No. 3, MARCH, 1959

The Effect of the Room Shape on the Sound Field in Rooms (Studies on the Measurement of Absorption Coefficient by the Reverberation Chamber Method I)

By Kozi SATO and Masaru KOYASU

Kobayasi Institute of Physical Research, Kokubunji,
Tokyo, Japan

(Received August 18, 1958)

In order to carry out accurate measurements of absorption coefficient by Sabine formula, the assumption of diffuse distribution of sound energy in the reverberation chamber must be fulfilled. Thus, this work was started from the basic researches of the sound field in the two and three dimensional model rooms.

The standing wave pattern of each normal mode was investigated using the dust figures and other methods.

At low frequencies, normal mode of vibration existed even when the room shape was made adequately irregular, and for each normal mode, spatial variation of sound pressure did not depend on room shape.

However, as the room shape becomes irregular, the nodal lines of successive normal modes distribute at random in space. Also, in the properly irregular room, the variation of decay rate for each normal mode was much smaller than that of a rectangular room.

§ 1. Introduction

The acoustics of the theatres, concert halls, auditoria, etc. and the noise reduction in factories, offices, houses have recently become a significant problem. One of the important problems in these cases lies in measuring an accurate absorption coefficient of acoustic materials and furnitures by the reverberation chamber method.

A large number of literatures have been published as to the measurement of absorption coefficient by the reverberation chamber method[1]. And it is believed that the sound field in the chamber forms the most important problem. Namely, the reverberation chamber formulae presuppose the following two conditions as premises:

1. To obtain the uniform distribution of sound energy throughout the reverberation chamber.
2. To secure the equal transfer of sound energy in all directions throughout the reverberation chamber.

Thus it is essential that the assumption of uniform distribution of sound energy should hold in the reverberation chamber.

Generally it is accepted that, as the frequency of sound becomes lower and the wavelength of sound draws closer to the size of the reverberation chamber, the sound field goes against the assumption mentioned above. Such being the case, many attempts have been made to approach to the premised conditions by considering the room shapes, use of microphones and loudspeakers, the position of a sample material and so on. Since most of the typical reverberation chambers had been set up before the aforementioned condition of uniform sound field was apprehended from the viewpoint of the present wave theory of acoustics[2], these counterplans have mostly been taken up empirically.

As far as the rectangular reverberation chamber is concerned, the relation between the room size and the sound field has been thoroughly investigated by Hunt *et al*[3]. However, full investigations on general room shape have not yet been made in relation to the characteristics of the reverberation chamber. Although Venzke recently submitted a report on the relation between the shape of the reverberation chamber and the measured decay curve[4], the results alone are believed not necessarily to bear witness to the irregular chamber with plane walls being the same with the rectangular one. Also, Nimura and Shibayama are conducting analyses and experiments on the subject of the relation between room shape and steady-state characteristics[5]. However, consideration from another angle is now urged for the reverberation chamber.

In a sense as mentioned above, we thought it most desirable to start off with the basic studies on the sound field within the room. Since the number of normal modes decreases particularly at low frequencies, it would be necessary to consider the characteristics of individual normal modes which participate with the sound field at those frequencies. Even when the room shape is extremely irregular, there exist distinct normal modes determined by room shape. This fact is well-known at least from theoretical considerations. In this case, we believe that the spatial distribution of nodal lines of successive normal modes and the direction of propagation of the wave front would play an important role.

This paper intends to report the results of model room experiments relating the effect of the shape and size of the room on the steady-state and transient characteristics of sound waves in it, within the range of comparatively low frequencies. As a result of these experiments, it was made sure that, in a properly irregular room, nodal lines of successive normal modes distributed at random throughout the room. It was also confirmed that the fluctuation in decay rate of all the normal modes became smaller in this case than in the case of rectangular room.

§ 2. Two-Dimensional Model Room Experiments

The shape and size of two-dimensional model rooms are shown in Fig. 1. Side walls were 5 cm in height. The bottom and side walls were made of wood with a thickness

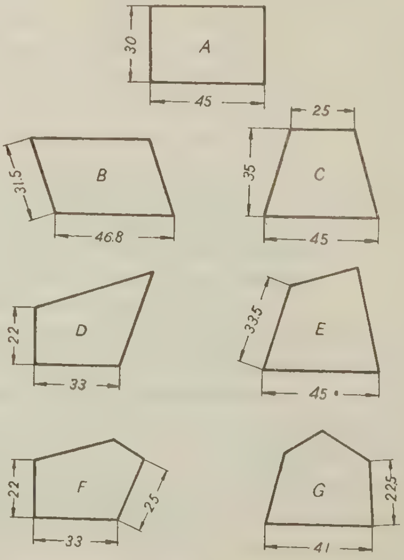

Fig. 1. Plan of two dimensional models. Size in centimeter.

of 3 cm, and a glass plate with a thickness 1 cm was used for the upper surface so that we can look into dust figures to be mentioned later. Although every considerations were taken to make each area of model equal, it was impossible to attain the perfect equality of all areas under the various conditions including the experimental apparatus. However, since the comparison among the same mode of vibration was the main purpose of these experiments, the difference of areas in some measure was believed to be allowable after all.

2.1. Spectrum of normal modes

With a view to obtaining a spectrum of normal mode of vibration, sound from the loudspeaker was sent into the model room through the hole made in the side walls, changing continually the frequencies of the oscillator. Sound pressure received by the microphone which was fixed on the other point was amplified and registered by the level recorder.

Attaching a tube with a length of 30 cm (in which aluminum wires were heavily stuffed) to the driver unit, and letting sound go into the model room through the orifices made at the end, we had the loudspeaker suffer from reaction as little as possible. Loudspeaker and microphone were placed in the different corners of the model room. Exchanging their positions from the one to the other, spectrum of several combinations was measured for each model room.

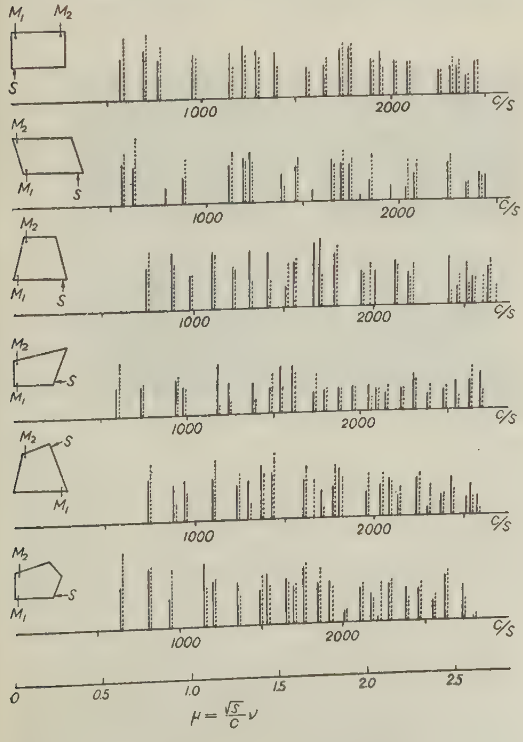

Fig. 2. Spectrum of normal mode of vibration. microphone position: —— M_1, - - - M_2

Spectrum of normal modes for each model room is shown in Fig. 2 as an example. The scale seen at the bottom of the illustration for the purpose of correcting the area difference is the non-dimensional frequency μ whose relation with frequency ν is as follows:

$$\mu=\frac{\sqrt{S}}{c}\nu\,. \tag{1}$$

Here S is the area of the model and c is the velocity of sound[6]. For the convenience of comparison, the abscissa of spectrum in each model room was made to match on μ.

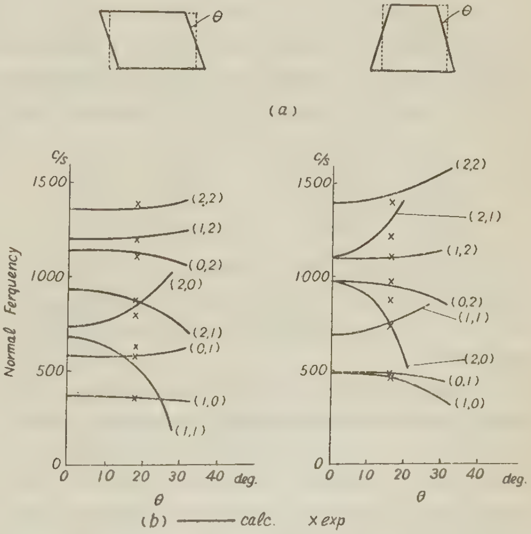

Fig. 3. Normal frequencies of parallelogram and trapezoid.

(i) *The normal frequency in parallelogram and trapezoid*

Since parallelogram and trapezoid are the simplest transformation from rectangle, the change in the normal frequency is considered to form the basis of general transformations. Furthermore, the calculation in this case was comparatively easy by Feshbach's perturbation method, and so the comparison with that was also made.

When the transformation as shown in Fig. 3 (a) takes place, frequency ν_N of normal mode of vibration $N\ (n_x, n_y)$ is given in the following formula[7].

$$\nu_N^2=\nu_{N0}^2-\frac{c^4}{16\pi^4}\sum{}'\frac{A_{KN}^2}{\nu_{K0}^2-\nu_{N0}^2} \tag{2}$$

ν_{N0} and ν_{K0} are the normal frequencies in $N(n_x, n_y)$, $K(k_x, k_y)$ mode of the original rectangle and the sum of the second term equals the answer with $K=N$ excluded. Bolt and others calculated on the trapezoid room[8]. Here we further calculate the A_{KN} of parallelogram room, which is carried out as follows:

$$A_{KN}=(-1)^{(k_x+k_y+n_x+n_y-2)/2}\cdot 4\alpha M_K M_N \times\left\{\left(\frac{b}{a}\right)^2\frac{n_x^2(k_y^2+n_y^2)}{(k_y^2-n_y^2)^2}-\frac{n_y^2}{k_y^2-n_y^2}\right\}. \tag{3}$$

In this case

$$M_N=\left\{\frac{(2-\delta_{0n_x})(2-\delta_{0n_y})}{4ab}\right\}^{1/2},$$

$$\delta_{0n}=\begin{cases}1 & n=0\\ 0 & n\neq 0\end{cases}$$

$\alpha=\tan\theta$, $2a$ and $2b$ are lengths of the sides of the original rectangular room. And in this case k_x and k_y obey different combination rules for n_x, n_y from those of trapezoid room.

n_x	k_x	n_y	k_y
even	odd	even	odd
odd	even	odd	even

Fig. 3 (b) shows the change of normal frequencies with θ as calculated from Eqs. (2) and (3), and compared with the result of experiments.

In some of the normal modes, the calculation and experiments show so large a disagreement that the approximation by the perturbation method does not seem to hold good, as shown in the figure. However, the figure will serve to tell the tendency of variation.

Some modes in the illustration show the same normal frequency with that in the rectangular room, while others are considerably different. For the case of parallegram and trapezoid shown in Fig. 3 (a), the distance between one pair of opposite sides is the same with that of the original rectangular room. The shift of normal frequency is very small for those modes which form nodal lines parallel to these sides.

The mode of vibration with nodal lines extending in only one direction in the rectangle results from plane waves going back and forth in the direction perpendicular to nodal lines. It follows from this that when the distance between the opposite sides does not change by transformation, the frequency comes under little influence.

(ii) *The distribution of adjacent normal frequencies*

Next, for the convenience of comparison of differences in the distribution of normal frequencies which occur to each room shape, the differences were arranged into Fig. 4 which is based upon Bolt's *frequency spacing index* Ψ[6]. Using the aforementioned non-dimensional frequency μ, Ψ is given by the following formula.

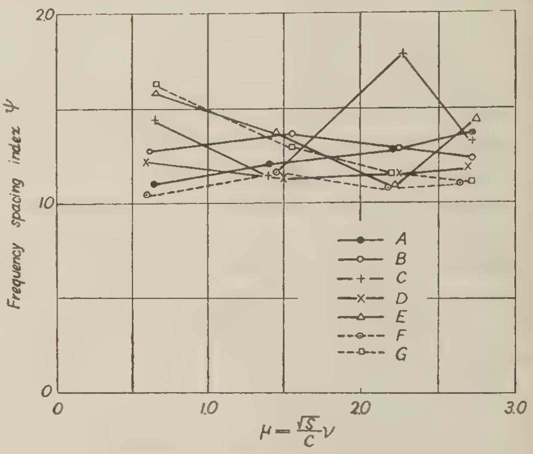

Fig. 4. Frequency distribution of normal mode (expressed by frequency spacing index).

$$\Psi=N\sum_{\mu_a}^{\mu_b}\delta_N^2/(\mu_b-\mu_a)^2 \tag{4}$$

In this case, N is the number of spaces in the normal modes between μ_a and μ_b, and $\delta_N=\mu_{N+1}-\mu_N$. If the distribution of normal modes is at equal intervals, the formula becomes $\Psi=1$. It follows from this that the modes D, F, etc. in Fig. 1 are the nearest to the formula $\Psi=1$ throughout the range. Also, in the case of non-symmetrical polygons, when the longitudinal and latitudinal lengths are almost in the same order as in the models, E, G, etc., there is a tendency that normal modes get together into several groups. This is, of course, one of the examples. For instance, if the ratio of the longitudinal length to the latitudinal one is changed, the distribution varies even in the case of rectangle.

2.2. Mode of normal vibrations (Position of nodal lines)

The position of nodal lines of normal modes has hitherto been checked up by moving the microphone and has been figured out from the sound pressure distribution or from the phase-reversal[9]. This method becomes extremely troublesome when the nodal lines get complicated due to the irregularity of the room shape. And it takes a lot of time just to examine one mode. Under the circumstances, we took up the dust figures for the investigation of normal modes. Since experimental methods and the details of results will be given in another report, we mention here in this report only the results used in these model room experiments.

Cork dust was scattered on the floor of model room, and a horn speaker unit was fixed at the hole made in the side wall through which sound was let in. When the frequency of sound is brought in line with that of the normal vibrations of the room, the dust starts to move and forms a stripe pattern. This pattern is formed around the position of maximum particle velocity, in the same manner as in one dimensional Kundt tube experiment. Therefore, it is possible to locate the rough position of nodal lines.

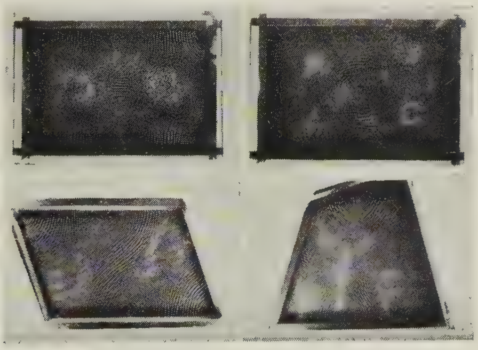

Fig. 5. Dust figures of normal mode of vibration.

Photos in Fig. 5 show examples of the dust figures of normal modes obtained by this method, while Fig. 6 shows schematically the variation of nodal lines with room shape, based upon these dust figures.

When there are parallel walls or symmetry as in the case of parallelogram or trapezoid, the variation of nodal lines has a certain regularity. On the other hand, the more the room shape becomes irregular, the more complicated the nodal lines become. This seems to be an important factor for obtaining the uniformity of sound field. Sound field after sound source is off is obtained by the superposition of the decaying normal modes excited at the time of cut off[10]. The nodal lines in the rectangular room are so regular that nodal lines of different modes overlap one another to some extent. In such a case the normal modes taking part in decay become extremely different in nature (axial, tangential or oblique modes) in different parts of the room. On the other hand, when the room shape and so the position of nodal lines are irregular, the superposition of decaying normal modes would show nearly the same nature throughout any part of the room.

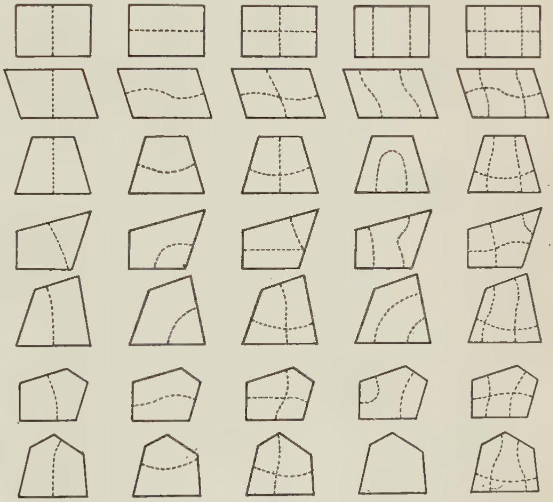

Fig. 6. Schematic representation of nodal lines obtained from dust figures.

2.3. Sound pressure distribution of normal modes

Letting sound into the model room in the same way as in the spectrum measurements, we measured the sound pressure distribution by probe tube microphone.

Fig. 7 shows sound pressure distribution of some normal modes for each model room in the range of low frequencies. The direction of the microphone movement and the position of nodal lines found from dust figures are shown in the illustration.

Sound pressure level is different in different corners except in those of rectangular model. This was rather an expected result, since nodal lines found by dust figures become asymmetric and approach the corners in some cases.

Next, the ratios between maximum and minimum values of sound pressure level in the room showed no apparent difference for different room shapes. The results thus attained accord also with those of Bolt's experiments which was done for a slightly deformed rectangular room[9].

§ 3. Three-Dimensional Model Room Experiments

A three dimensional model room was constructed with nonparallel walls and the sound field of this model was compared with that of three-dimensional rectangular models. The shape of the bottom of the irregular room is a non-symmetrical pentagon based upon the model F in Fig. 1. Its shape and size are shown in Fig. 8. On the other hand, the rectangular models used for comparison comprised two kinds; the model I had the same base area and volume with irregular model (48 cm × 37 cm × 35 cm), while the model II was relatively large in size and volume (125 cm × 75 cm × 50 cm).

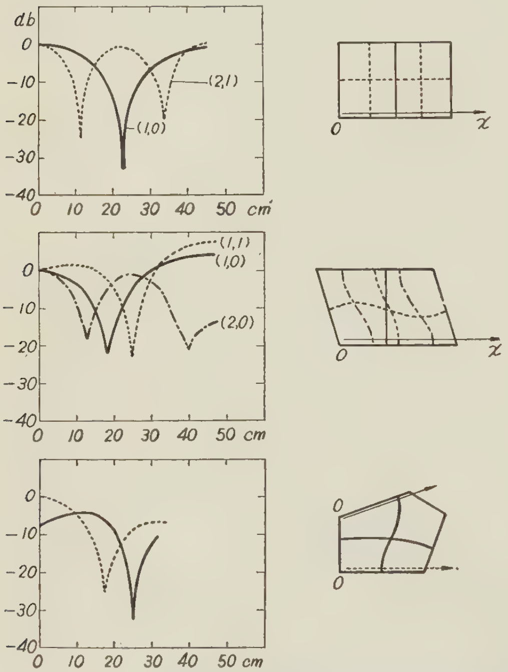

Fig. 7. Sound pressure distribution along a line parallel to the wall.

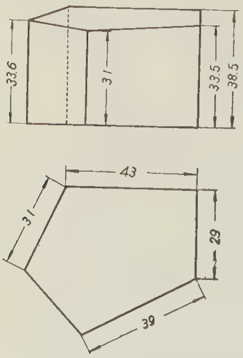

Fig. 8. Three-dimensional model with non-parallel walls. Size in centimeter

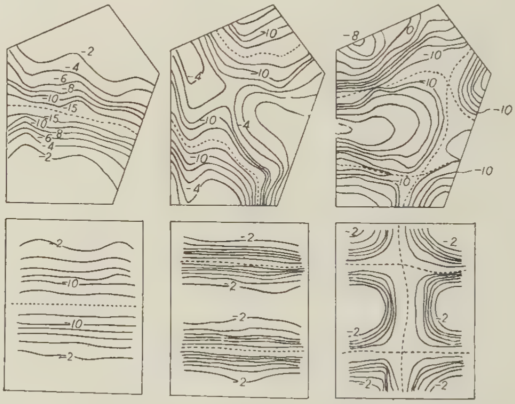

Fig. 9. Sound pressure distribution of normal modes. Figures show relative level in decibel and dotted line shows the nodal line.

3.1. Sound pressure distribution

(i) *Sound pressure distribution by pure tone*

Fig. 9 shows an example of the sound pressure distribution of normal modes for the irregular model and the rectangular model I on the plane parallel to the floor. The sound pressure distribution is shown with contour lines drawn at the intervals of 2 decibels from the position of maximum sound pressure. The dotted lines in the illustration indicate the minimum sound pressure (nodal lines). Since sound pressure contour lines get close together around the nodal lines, only the lines of −15 and −20 decibels and the nodal lines are shown for pressure levels lower than −10 decibels. The ratios between maximum and minimum values of sound pressure level were 30 to 40 decibels in either case of model rooms.

(ii) *Sound pressure distribution by warble tone*

Next, we investigated sound pressure distribution when various normal modes were excited at the same time. Since the size of the actual reverberation chamber that was to be designed would be 10 to 20 times as large as the model in linear dimensions (chamber volume: 250∼500 m^3), we adopted 1000∼2000 cycles per second for the center frequency of warble tone. As an example Fig. 10 shows the comparison of sound pressure distribution between the irregular room and rectangular model I, with 1260 cycles per second as its center. While the sound pressure of irregular room changes intricately in different parts, that of rectangular one is distributed almost symmetrically and becomes minimum in the center of the room. But the range of variations of sound pressure level was almost the same in each room shape. This value is extremely small as compared with the difference of the sound pressure levels for each normal mode by pure tone, which tells the fact that the warble tone has the effect of uniformizing the sound field.

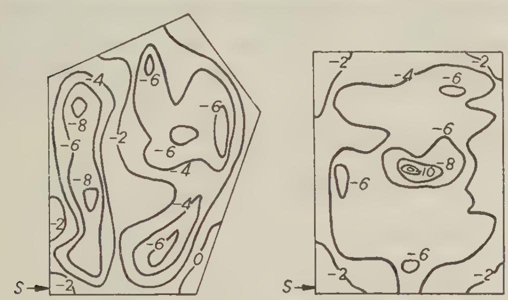

Fig. 10. Sound pressure distribution by warble tone. $\nu_0 = 1260$ c/s, $\Delta\nu = 250$ c/s

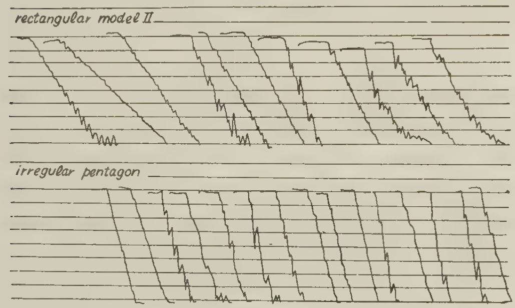

Fig. 11. Decay curves for each normal mode.

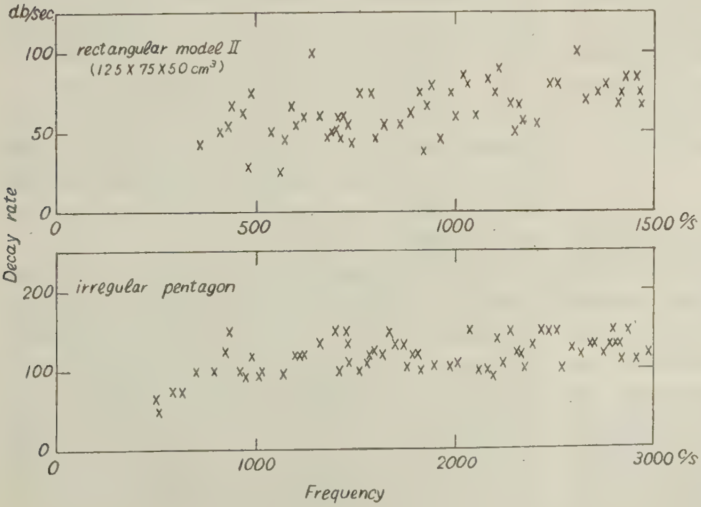

Fig. 12. Decay rate for each normal mode.

3.2. The effect of room shape on the decay of sound

(i) *Decay curve for each normal mode*

We further investigated the decay of each normal mode in the irregular model and rectangular model room II by pure tone. Fig. 11 shows one of the example of decay curves recorded in order from low to high frequencies.

Since the rectangular model had eight times as large volume as the irregular one, it would be safe to suppose that the normal mode of the irregular model that corresponds to a certain normal mode of the rectangular model has about twice the frequency as that of the rectangular room. Therefore, when the comparison on decay was made as in the case of Fig. 11, we made the frequencies in case of rectangular room correspond to twofold frequencies in case of irregular room.

Next, we determined from this record the decay rate of each decay curve, which is shown in Fig. 12. In this case, due to the large volume of the rectangular room, the reverberation time becomes about twofold in the average (one-half in decay rate). So the ordinate was doubled for the rectangular model for the convenience of comparison. What is evident from the results of the two model rooms is that the fluctuations in the decay rate of irregular room are much smaller than those in the rectangular model. This applies to all the normal modes except to some normal modes with low frequencies. Namely, at frequencies higher than 700 cycles per second in the irregular room, the ratio of the fastest to the slowest of the decay rate is only one and a half. On the other hand, in the case of rectangular room, normal modes which are extremely slow in decay rate are found below about 1000 cycles per second (which corresponds to 2000 cycles per second in the irregular room.)

In the case of rectangular room, all the normal modes whose decay is extremely slow correspond to the normal modes caused by sound waves reflecting back and forth between a pair of walls which stand opposite each other (*axial mode*) or to similar ones, while in the case of non-symmetrical rooms as this irregular room which has no parallel walls, the average difference of reflection distance between the walls becomes small for all the normal modes. For this reason, it is quite natural to think that the fluctuations of the reverberation time become small for irregular rooms.

(ii) *Decay curve by warble tone*

Next, using the warble tones with center frequencies of 1260 and 2650 cycles per second (620 and 1260 cycles per second in rectangular model II), we measured the decay curves from which we obtained the decay rate as shown in Table I. It is clear, when compared with the aforementioned measurements by pure tone (Fig. 12), that the decay rate in this case would be obtained by averaging the decay rates of each normal mode within the variation range of warble tone. With 1260 cycles per second for center frequency in the irregular room, the decay curve is perfectly logarithmic, while in case of 620 cycles per second for rectangular model, that corresponds to 1260 cycles per second for irregular room, the decay curve is bent and the decay rate at the beginning part of the decay curve is steeper than that at the tail. This is because the normal modes whose decay is extremely slow are included within the range.

Table I. Decay rate when warble tone is used for sound source.

Irregular model		Rectangular model II	
frequency	decay rate	frequency	decay rate
2650±300 c/s	120 db/sec	1260±150 c/s	67 db/sec
1260±250	109	620±120	50 (0∼−15 db)* 27 (from −15 db)

* This shows that the range from steady-state (0 db) to −15 db is different from the range less than the above in decay rate.

§ 4. Conclusion

One of the most important problems in measuring the absorption coefficient of acoustic materials by the reverberation chamber method depends upon the realization of uniform sound field. For this reason, we conducted the model room experiments to investigate the effects of the room shape and size upon the sound field in the room. The object we set for the basic consideration is how the normal modes depend on the room shape and size. The following is the summary of the experimental results.

(1) As was expected from theoretical consideration, there exist normal modes determined by the room shape, and the sharpness of pressure distribution for each normal mode is not affected by the room shape. But, when the room shape becomes properly irregular, the nodal lines of normal modes get distributed in a complicated manner, and so the number of normal modes taking part in decay become almost uniform in any part of the room.

(2) In this case, the fluctuation in the decay rates of each normal mode begin to decrease from the comparatively low frequencies. This fact would indicate that the distinct axial mode becomes difficult to exist in such an irregular room.

From the experimental results mentioned above, we believe that, in order to obtain a desirable sound field for a reverberation chamber, one of the advantageous way is to make the room shape properly irregular, and that this would prove far more advantageous at least than a rectangular chamber with the same volume. Moreover, in this way we can anticipate fully satisfactory results.

We express a deep gratitude to Mr. K. Kubo who participated and cooperated with us in the experiments of dust figures which formed one of the basis of our study.

References

1) For example, P. E. Sabine: J. Acoust. Soc. Amer. **11** (1939) 41.
H. J. Sabine: J. Acoust. Soc. Amer. **22** (1950) 387.
E. Meyer: J. Acoust. Soc. Amer. **8** (1937) 155.
2) P. M. Morse and R. H. Bolt: Rev. Mod. Phys. **16** (1944) 69.
3) F. V. Hunt, L. L. Beranek and D. Y. Maa: J. Acoust. Soc. Amer. **11** (1939) 80.
4) G. Venzke: Acustica **6** (1956) 2.
5) T. Nimura and K. Shibayama: J. Acoust. Soc. Japan **10** (1954) 245; 250.
6) For three dimensional case, R. H. Bolt: J. Acoust. Soc. Amer. **19** (1947) 79.
7) H. Feshbach and A. M. Clogston: Phys. Rev. **59** (1941) 189.
8) R. H. Bolt, H. Feshbach and A. M. Clogston: J. Acoust. Soc. Amer. **14** (1942) 65.
9) R. H. Bolt: J. Acoust. Soc. Amer. **11** (1939) 184.
10) V. O. Knudsen: J. Acoust. Soc. Amer. **4** (1932) 20.

Short Notes

This section is intended to secure prompt publication of important discoveries in physics. The reports should not exceed 800 words in length. A figure of size 7 cm × 7 cm will be counted as 150 words.

J. PHYS. SOC. JAPAN **14** (1959) 374

Germanium-Silicon Alloy Junctions

By Yasuo MATUKURA

Electrotechnical Laboratory, Tokyo, Japan

(Received December 9, 1958)

When a germanium dot is heated on a silicon wafer, a molten alloy of the equilibrium compositions of Ge and Si is formed on the silicon wafer. As cooled with a temperature gradient, Si-enriched Ge–Si alloy is recrystallized on the adjacent pure Si, and the succeeding recrystallization produces gradually Ge-enriched Ge–Si alloy, which energy gap[1)] is abruptly modified from Si value to Ge–Si alloy's one and then gradually to Ge one. If alloy is made from Ge and Si doped with opposite type impurity of the segregation constants, k_1 and k_2, respectively, these impurities will be segregated during the successive solidification. Difference ΔC between n- and p-type impurities at any point g, where g is a fraction which has solidified, is given by the following formula[2)].

$$\Delta C = k_1 C_{01}(1-g)^{k_1-1}\left[\frac{k_1 C_{01}}{k_2 C_{02}}(1-g)^{k_2-k_1}-1\right], \quad (1)$$

where, C_{01} and C_{02} are the impurity concentrations in the initial molten phase. If C_{01}, C_{02}, k_1, k_2, and alloy temperature are suitably chosen so as to make ΔC zero at some g, then a pn junction will grow. Fig. 1 shows relations between g and ΔC calculated by Eq. (1). This estimation was made for alloying of arsenic doped n–Si and gallium doped p–Ge at 1150°C so as to produce pn junctions at $g=0$, $g=0.5$ and $g=0.8$. Donor concentrations in Si is 7.3×10^{14} cm^{-3}, and acceptor concentrations in Ge are shown in Fig. 1. The segregation constants for the alloy were assumed the same as the ones for Si at 1420°C[3)].* In the figure, the variations of the composition and of the energy gap E_g of recrystallized alloy are shown together.

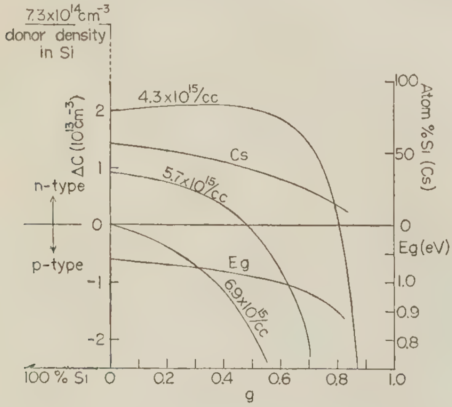

Fig. 1. The variations of ΔC, band gap, and alloy composition with the fraction of solidification. Parameter is the acceptor density in *Ga* doped *p–Ge*.

Preliminary experiments were performed by using arsenic doped 2.5 Ωcm n–Si and gallium doped 0.05 Ωcm p–Ge so as to produce a pn junction at $g=0$. A small dot of Ge was put on a Si wafer of thickness of 0.3 mm and heated at 1150°C for 30 minutes in H_2 gas, and then cooled at the rate of 2°C/min. The measurements by hot probe method and a result of etching on the section of Ge–Si alloy showed that a pn junction was formed at $g=0.1$. This result shows that the assumptions for the segregation constants is almost reasonable. The influence of impurity diffusion on ΔC was estimated to be very small.

As the total thickness of recrystallized Ge–Si alloy was about 1 mm, the gradient of ΔC, a, in Fig. 1 can be estimated at the pn junctions. If $L_a = n_i/a$ is compared with L_d[4)] by using the values of the intrinsic resistivity[5)], it is seen that these pn junctions are nearly of abrupt type rather than graded one.** In Ge–Si alloy recrystallized at high temperatures, the variation of E_g is so small that E_g at both sides of the pn junction grown at $g\neq0$ will be nearly equal, and the pn junction is localized in nonuniform semiconductor[6)]. On the other hand, the variation of E_g will be increased by low temperature alloying. In this case, it is seen that E_g at both sides of a pn junction is not equal. At $g=0$, it is considered that one side of the pn junction has E_g of Si and the other side smaller E_g. This tendency will be increased by decreasing alloy temperature. Further investigations on the characteristics of these particular pn junction will be reported later.

The author is indebted to Mr. M. Kikuchi for helpful discussions.

References

1) E. R. Johnson and S. M. Christian: Phys. Rev. **95** (1954) 560.
2) W. G. Pfann: J. Metals **4** (1952) 861.
3) D. Navon: J. Appl. Phys. **29** (1958) 579.
4) W. Shockley: Bell. Syst. Tech. J. **28** (1939) 435.
5) Alfred Levitas: Phys. Rev. **99** (1955) 1810.
6) H. Kroemer: R.C.A. Rev. **18** (1957) 332.

---

* Segregation constants for Si–Ag are a little smaller than the ones for Si. Those for Ge–Si should be measured.

** If $|k_2-k_1|$ is small, it seems that pn junctions are of graded type.

J. Phys. Soc. Japan **14** (1959) 375~376

Electronmicroscopic Observation of the KCl Crystal Containing Potassium Colloid Particles

By Tadatosi Hibi
Research Institute of Scientific Measurements
and Tetsuhiko Tomiki*
The Research Institute of Iron, Steel and Other Metals, Tohoku University, Sendai, Japan

(Received January 20, 1959)

As reported previously[1], electronmicroscopic observations on the additively coloured KCl crystals illuminated with green light showed that the small hemispherical humps having a spongy structure appeared on the illuminated surface. It was suggested there that these structures might be caused by the coagulation of potassium metal. This experiment was started to observe colloidal particles in KCl crystal electronmicroscopically. When KCl single crystal was heated in the atmosphere of potassium vapour for 4 hours at 550°C, followed by the furnace cooling to room temperature in about 12 hours, the crystal was decorated with potassium particles along the dislocation lines. Fig. 1 is the *optical* microscopic photograph of such a crystal. Since the crystal in this case was *not* deformed mechanically beforehand, the decorated networks of dislocation are not so regular as those reported by many authors[2], but it is sure that the colloidal particles are imbedded in the crystal. When the fresh (001) cleavage plane of this crystal is observed electronmicroscopically using one stage replica technique, hemispherical pits surrounded by tiny droplets can be seen on the flat (001) plane as shown in Fig. 2. These pit structures have not been observed on the freshly cleaved (001) surface of the KCl single crystal either grown from the melt or coloured additively with excess metal. Moreover, the diameter of these pits have a mean value of 0.5 microns and, on the other hand, the colloid particles of Fig. 1 are estimated as larger than 0.4 microns in diameter. Judging from these facts, it will be reasonable to consider that these pits have a relation to the colloid particles, though Scott and his coworkers[3] had failed to observe colloid *centres* in the alkali halide crystal with an electron microscope.

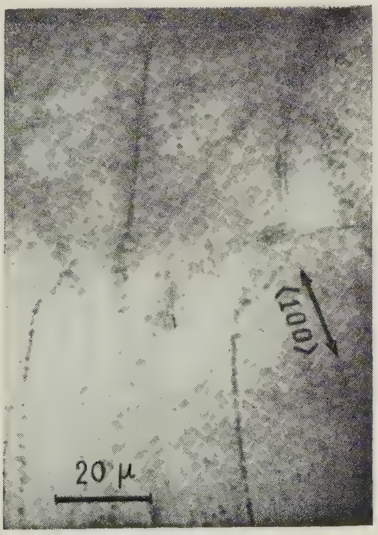

Fig. 1.

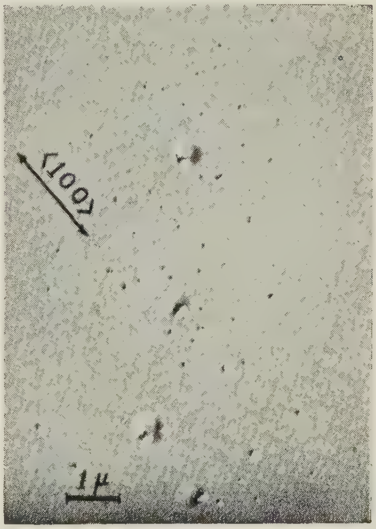

Fig. 2.

If the above explanation is valid, the pit will probably be produced by the scattering of the colloidal metal, under the actions of cleaving process, etc., arround the position at which it was located, thus leading to the formation of tiny droplets of colloid as satellites of the pit. Usually, etching techniques[4] provide the "etch" pits on the surface where dislocations exist, but the surface layer of several microns in thickness is removed from the crystal at the same time. This is one of the disadvantages in achieving the electronmicroscopic observation on the relation between the pattern of cleavage steps and dislocations. It has generally been accepted that the points where colloid particles exist have a close relationship to the crystal imperfections. Then the pit reported here may also offer one of the useful means for the electronmicroscopic studies of the crystal imperfections as the chemical or thermal etch pit did for optical microscopy. The experiments are now in progress with the deformed crystal which was decorated with excess metals.

---

* Present Address: Department of Physics, The Faculty of Science, Tohoku University, Sendai, Japan.

One of the authors (T. Tomiki) would like to express his thanks to Prof. S. Ogawa who provided him kindly an opportunity to achieve this experiment.

References

1) T. Hibi and T. Tomiki: Rept. Res. Inst. Tohoku Univ. (to be published).
2) See, for example, J. C. Fischer and Other Ed.: "*Dislocations and Mechanical Properties of Crystals* (John Wiley and Sons, Inc. New York, 1956) Chap. I.
3) A. B. Scott, W. A. Smith and M. A. Thompson: J. Phys. Chem. **57** (1953) 757.
4) See the reference 2) and also M. Sakamoto and S. Kobayashi: J. Phys. Soc. Japan **13** (1958) 800.

J. PHYS. SOC. JAPAN **14** (1959) 376

Etch Patterns on Ferroelectric Triglycine Sulfate

By Hiroo TOYODA

Electrical Communication Laboratory,
Nippon Telegraph and Telephone
Public Corporation, Tokyo

(Received January 16, 1959)

Etch patterns are useful to investigate the domain structure of ferroelectric crystals and to study their polarization reversal, as has been demonstrated by the special etch pits exhibited by barium titanate etched in various acids[1)-4)]. Researches on the etch pits of GASH have been also reported[5),6)], though the correspondence to domain structure was not clear. The author has examined the effect of various etchants on triglycine sulfate and found out obvious correlation between the etch pits and the polarization of ferroelectric domains.

Etchants examined are methyl alcohol, ethyl alcohol, n-butyl alcohol, ethylene glycol, ethylene glycol mono-methyl ether, water, acetone, ether, carboxyl acids, and some alcohols containing potassium hydroxide, etc...

Mono-valent alcohols examined gave similar etch pits, though the etching rate decreased with the increase of molecular weight. Methanol gives clear patterns in a relatively short time. By applying an electric field to a thin crystal, cut perpendicularly to b-axis, it was confirmed that negative pole surface has a compapatively flat appearance, while positive end becomes very uneven. Fig. 1 shows a pattern on a crystal etched in methanol at 27°C for four hours, after removing the evaporated gold electrodes. Natural cleavage surfaces exhibit various etch patterns with either rectilinear or irregular boundaries. Most of the rectilinear patterns penetrate throughout the crystal parallelly to b-axis, while this is not the case for irregular ones. When re-etched in methanol after applying an electric field above Curie temperature, complete disappearance of all kinds of boundaries proves that the crystal has turned into a single domain.

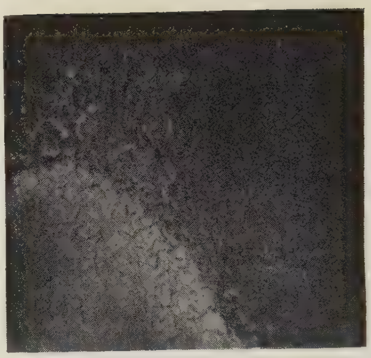
Fig. 1. Etch pits produced by methyl alcohol. (Darker area in the flat part is the silhouette of the electrode on the back surface). (×53).

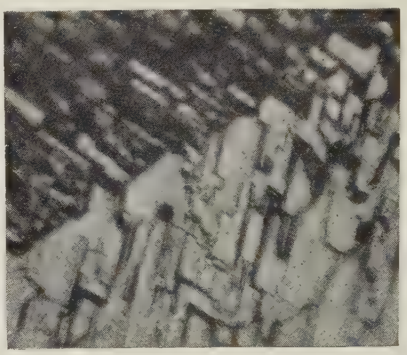
Fig. 2. Etch pattern produced by methyl cellosolve. (×180)

Alcohols containing KOH give sharp striped patterns. Ethylene glycol gives different rectilinear markings. Ethylene glycol mono-methyl ether, the so-called methyl cellosolve, etches the surfaces in a somewhat characteristic manner. Fig. 2 shows an example of a natural b-plane of the crystal immersed in this etchant for two weeks at room temperature. The figure again shows a twin boundary, which was ascertained to correspond to a domain boundary.

More comprehensive description will be published elsewhere.

References

1) J. A. Hooton and W. J. Merz: Phys. Rev. **98** (1955) 409.
2) D. S. Campbell and D. J. Stirland: Brit. J. Appl. Phys. **7** (1956) 62.
3) R. C. DeVries and J. E. Burke: J. Amer. Ceram. Soc. **40** (1957) 200.
4) V. J. Tennery and F. R. Anderson: J. Appl. Phys. **29** (1958) 755.
5) A. N. Holden et al: Phys. Rev. **98** (1955) 546.
6) A. Nishioka and K. Sekikawa: ECL Res. Rep 57-278, Oct. 1957.

J. Phys. Soc. Japan **14** (1959) 377

The Proton Magnetic Resonance Absorption of the Trichloroacetic Acid in Solid Phase

By Masashi Yagi and Masayasu Ueta

Department of Physics, The Faculty of Science, University of Tohoku

(Received December 20, 1958)

Simple chain monocarbonic acids RCOOH has been confirmed by the several experimental results[1–4] and by the proton magnetic absorption[5] to take the coagulation state of dimers which are formed through the bridge with two hydrogen bonds in the liquid phase. But in the solid state, the crystal structures are not well known except for the formic acid which has been observed to have the chain structure[6].

One of the present authors[7] has studied the acetic acid CH_3COOH with the proton magnetic resonance method at the temperatures ranging from the room temperature to about −180°C. In this material, however, R contains three hydrogen atoms and the resonance due to these hydrogen atoms in the COOH radical, therefore, it was difficult to talk definitely about the situation of the hydrogen bonding between two radicals. This ambiguity is avoided by the investigation using the trichloro-acetic acid: CCl_3COOH. The melting point of this material is 57°C.

Samples of the commercial guaranteed reagent (purity of 99%) were redistilled and solidified in the thin glass tube. Experiments were carried out in the magnetic field of 2500 gauss with using the conventional regenerative oscillator method. The derivative curve of the resonance absorption obtained at the room temperature has a fine structure as shown in Fig. 1. The absorption curve obtained by integrating the derivative curve given in Fig. 2 indicates the symmetrical pattern consists of the main and side pairs of peaks which separated with 2.9 and 5 gauss respectively. The line shape is considered as the two proton system of the small interbroadening.

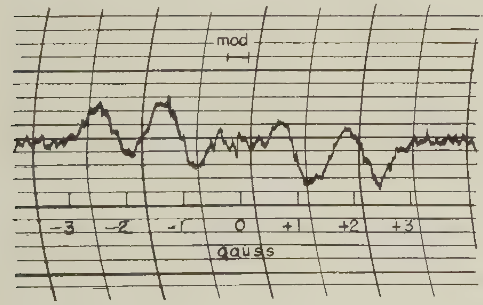

Fig. 1. The derivative of the proton magnetic resonance absorption of the trichloro-acetic acid at 16°C.

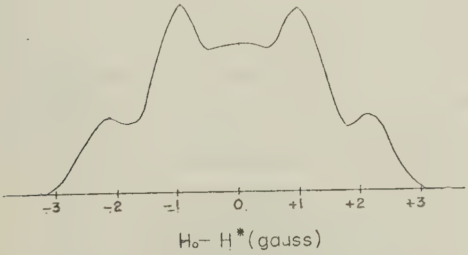

Fig. 2. The resonance absorption line obtained by integrating the derivative curve of Fig. 1.

The separation of the main peaks of the absorption line in two proton system is given as $\alpha=3\mu r^{-3}$ if the crystal lattice is assumed to be rigid and the interaction between two neighbouring two proton systems is neglected as small. When α is equated to the value of 2.9 gauss which was obtained from the derivative curve, the distance r between two protons in the solid of the trichloro-acetic acid is calculated to have the value of 2.4_7 Å. The second moment corrected against the field modulation was obtained from the derivative curve as 2.6_7 gauss^2. From this value of the second moment, the distance r of H–H was also calculated and was given the value of 2.4_5 Å, by neglecting the interaction with other neighbours. From these values the distance of two protons was determined as 2.46±0.03Å.

On the other hand, from the data in liquid and vapor phase of chain mono-carbonic acids and the formic acid, the value of the distance of H–H in dimers is estimated to have the value of 2.2∼2.5 Å. From these facts it is concluded that the trichloro-acetic acid takes the form of dimer in the solid state. Nearly the same rosonance absorption curves were kindly taken at the Laboratory of Professor Kakiuchi, The Institute for the Solid State Physics, Tokyo University.

The full report of this work will be published with the results of other chain mono-carbonic acids.

The present authors are deeply indebted to Profesor Y. Kakiuchi for his interest to this investigation.

References

1) R. E. Lundin, F. E. Harris and L. K. Nash: J. Amer. Chem. Soc. (1952) 4654.
2) L. Pauling and L. O. Brockway: Proc. Nat. Acad. Sci. **20** (1934) 336.
3) P. J. Corish and W. H. T. Davison: J. Chem. Soc. (1955) 2431.
4) E. Freedman: J. Chem. Phys. **21** (1953) 1784.
5) B. N. Bhar, W. Forsting and G. Lindstrom: Ark. Fys. **10** (1956) 59.
6) F. Holtzberg, B. Post and I. Fankuchen: Acta Cryst. **6** (1953) 127.
7) M. Yagi: to be published in Sci. Rep. Tohoku Univ.

J. PHYS. SOC. JAPAN, **14** (1959) 378

On the Dielectric Loss of Oxidized High-Density Polyethylene

By Shigeharu OKAMOTO
Department of Applied Physics, Waseda University, Tokyo
and Keisaku TAKEUCHI
Kijima Communication Wire Co., Ltd., Tokyo

(Received January 21, 1959)

In recent papers by a number of authors, it has been reported that for branched low-density polyethylene three peaks are observed in the mechanical loss data measured as a function of temperature, while for unbranched high-density polyethylene only two loss peaks can be observed and the so-called β peak is missing.

In connection with the mechanical losses, it is of interest to observe dielectric losses as a function of temperature. But reports in this field are very few. In a recent note[1], Oakes and Robinson have reported that for one type of oxidized polyethylene (probably a low-density one) there exist three dielectric loss peaks. On the other hand, Nakajima and Saito[2] mentioned, that for oxidized high-density polyethylene two dielectric loss peaks (β and γ) could be observed, but not the so-called α peak in the temperature range below 105°C.

In view of these situations, careful observations were carried out on the temperature dependency of the dielectric loss using high-density polyethylene.

The high-density polyethylene used was Hi-zex 3500, supplied as pellets by Mitsui Chemical Industry Co., Ltd. The photo-oxidation of the polyethylene specimen has been carried out by exposure to the ultraviolet radiation from a mercury quartz lamp for 60 hrs. Dielectric measurements were made over a temperature range of −75 to +100°C and a frequency range of 30 to 10^6 c/s.

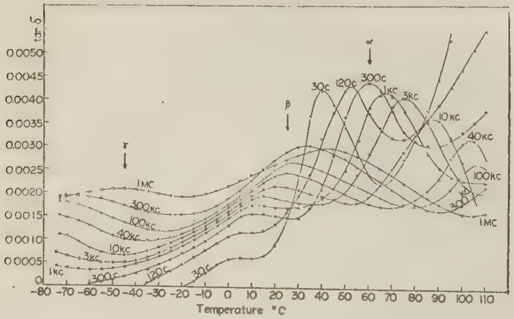

Fig. 1. The change of tan δ as a function of temperature at various frequencies for high-density polyethylene.

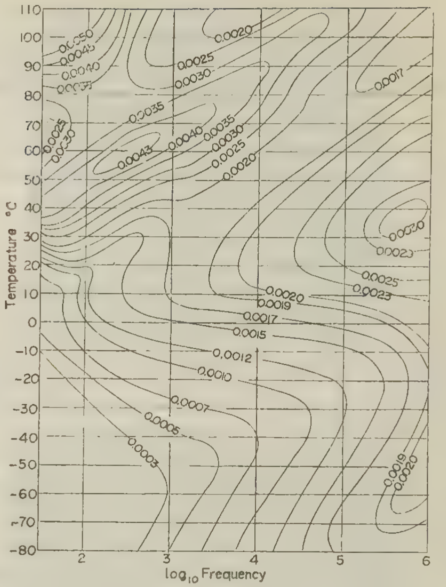

Fig. 2. Tan δ contour map for high-density polyethylene.

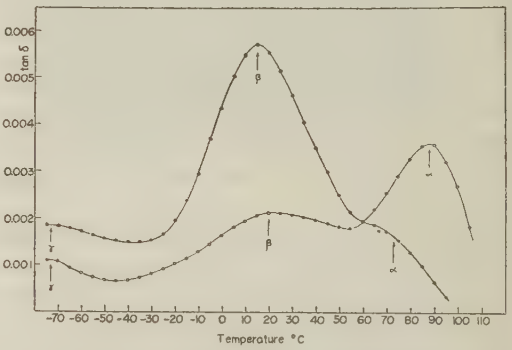

Fig. 3. Variation of tan δ of the high-density (○) and the low-density polyethylene (●) at 10 kc/s. Both samples were exposed to ultraviolet radiation for 60 hrs.

The results of dielectric loss tangent (tan δ) on the high-density polyethylene are shown in Fig. 1, 2 and 3.

As shown by Fig. 1, three loss peaks could be clearly observed also for the high-density polyethylene. Furthermore, as can be seen in Fig. 3, for the high-density polyethylene sample the α peak rises at a temperature higher by about 15°C than for the low-density sample. The shift of the α peak for high-density sample towards higher temperatures may be attributed to its high degree of crystallinity. The activation energies obtained from the results of our experiments were 25, 20 and 6 kcal/mol for the peaks α, β and γ respectively.

References

1) W. G. Oakes and D. W. Robinson: J. Polymer Sci. **14** (1954) 505.
2) T. Nakajima and S. Saito: J. Polymer Sci. (in press).

J. PHYS. SOC. JAPAN **14** (1959) 379~380

Nuclear Quadrupole Resonance Spectra of N^{14} in Urea Crystal

By Takehiko CHIBA, Masaharu TOYAMA
and Yonezo MORINO

*Department of Chemistry, Faculty of
Science, University of Tokyo*

(Received January 27, 1959)

There have been reported only a few papers1)–5) on the pure nuclear quadrupole resonance of N^{14}. We have observed N^{14} resonance in urea crystal. The apparatus used was a Pound-Knight-Watkins type spectrometer6) with Zeeman modulation of 230 cps. The signal was displayed on a recorder through a lock-in detector. Particular care was taken so as to apply a modulation field strong enough to cause a sufficient Zeeman shift of the resonance line even when the atom under study had a fairly large asymmetry parameter η. (The field strength of the Zeeman field in the usual run was about 60 Gauss.)

It has been established from the study of NMR7), x-ray8), neutron diffraction9), and infrared spectra10),11) that all the atoms in urea molecule are located in a plane. A transition was observed with proton resonance by Kromhout and Moulton12) in the range from about 0°C to 100°C. This transition was considered to be due to rapid reorientation of NH_2 groups around the C–N axes. If this is actually the case, it may be difficult to observe a nuclear quadrupole resonance at higher temperatures. Thus the measurement was first made at dry-ice temperature and a fairly strong absorption was found at 2.87 Mc. The asymmetrical shape of the line indicated the presence of large η. It is also examined by measuring the resonance at different field strength of modulation. At a certain weak field of modulation the absorption became very weak in urea, though still strong in hexamethylene tetramine which has $\eta=0$. The change of the shape with the change in the sweep velocity or in the sweep direction (from higher frequency to lower one or vice versa) showed an appreciable saturation effect similar to the case mentioned by Bray4). From the shape of the absorption and the change of signal strength with the modulation field it was concluded that the observed line was the higher frequency component of the doublet due to η. The other component is expected to lie somewhere around 2.6 Mc, but no attempt to find the line has been successful heretofore.

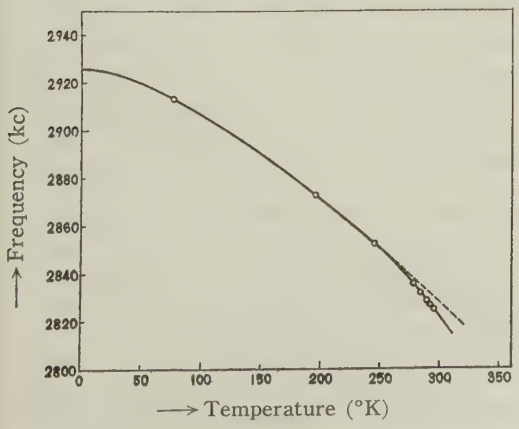

Fig. 1. Temperature dependence of N^{14}-resonance frequency in urea crystal.

The temperature dependence of the resonance line was also measured. The line became weaker with increasing temperature and was barely observable at 22°C. At this temperature the frequency of the line was definitely smaller than those at the lower temperatures, as shown in Fig. 1. The frequency change is normal at lower temperature range, the fractional change being much larger than those in the usual cases such as Cl resonance. This may be due to large amplitudes of oscillation of NH_2 groups about the C–N axes. Near 0°C the curve of the temperature dependence makes a distinct bend downward. This anomaly can be considered to be due to the setting-in of rapid reorientation of NH_2 groups, in good accord with the corresponding change in the line width of the proton resonance12).

Table I. N^{14}-resonance frequency in urea crystal.

Temperature (°K)	Frequency (kc)
177	2913.2
196	2872.8
245.5	2852.3
278.0	2835.7
284.0	2832.0
289	2828.7
292	2827
295	2825

References

1) G. D. Watkins and R. V. Pound: Phys. Rev. **85** (1952) 1062.
2) C. T. O'Konski and T. J. Flautt: J. Chem. Phys. **27** (1957) 815.
3) F. W. Terman and T. A. Scott: Bull. Amer. Phys. Soc. Ser. II, **3** (1958) 23.
4) P. A. Casabella and P. J. Bray: J. Chem. Phys. **28** (1958) 1182.
5) P. A. Casabella and P. J. Bray: J. Chem. Phys. **29** (1958) 1105.
6) G. D. Watkins and R. V. Pound: Phys. Rev. **82** (1951) 343.

7) E. R. Andrew and D. Hyndman: Discuss. Faraday Soc. **19** (1955) 195.
8) P. Vaughan and J. Donohue: Acta Cryst. **5** (1952) 530.
9) J. E. Worsham: Acta Cryst. **10** (1957) 319.
10) W. E. Keller: J. Chem. Phys. **16** (1948) 1003.
11) R. D. Waldron and R. M. Badger: J. Chem. Phys. **18** (1950) 566.
12) R. A. Kromhout and W. G. Moulton: J. Chem. Phys. **23** (1955) 1673.

J. PHYS. SOC. JAPAN **14** (1959) 380∼381

Electrical Properties of Dilute Alloys of Zinc with Manganese at Low Temperatures

By Yoshio MUTO, Yoshio TAWARA, Yoshio SHIBUYA and Tadao FUKUROI

The Research Institute for Iron, Steel and Other Metals, Tohoku University, Sendai

(Received January 21, 1959)

It seems that anomalous electrical properties of dilute alloys at low temperatures are classified into two groups. The alloys of the first group such as Cu–Sn alloys have a minimum in the resistance-temperature curves in zero magnetic field and their magnetoresistance behaves similarly as the narmal alloys. The alloys of the second group such as Cu–Mn alloys have a maximum and subsequently a minimum in the resistance-temperature curves and show the decrease of the resistance in the magnetic field below the temperature corresponding to the resistance-maximum. Although no plausible explanation of the resistance-minimum has yet been given, K. Yoshida1) showed that in the case of Cu–Mn alloys the decrease of resistance below the temperature presumably corresponding to the resistance-maximum might be related to the *s–d* interaction between the conduction electrons and the *d*-electrons of Mn ions. The solvent metals of dilute alloys which exhibit the resistance-anomaly at low temperatures are confined as yet to the monovalent noble metals such as Au, Ag and Cu except for Mg, the only divalent metal in which the resistance-anomaly has been found so far. We believe that it is quite interesting to examine whether Zn is really the normal solvent metal without any resistance-anomaly as has been believed and whether dilute alloys of Zn containing a small amount of Mn does not show a spin dependent characteristic in their electrical properties.

Three specimens including pure Zn (99.96 percent) were used for the preliminary experiments. All specimens were melted under an atmosphere of argon in a high-frequency induction furnace in crucibles described below. The alloy containing 0.099 atomic percent Mn melted in an alumina crucible was contaminated with Fe included in the crucible, the quantity of Fe, however, being less than that of Mn. By using the crucibles made of S. B. glass in place of alumina, pure Zn and its alloy of 0.43 atomic percent Mn were melted. It was then confirmed that the amount of Fe contained in the above just mentioned specimens was sufficiently small.

The electrical resistance of pure Zn is constant below 5°K and the resistance increases with the intensity of magnetic field. For the alloy containing 0.099 atomic percent Mn, the resistance-minimum appears at about 14°K and its maximum does not appear down to 1.5°K as depicted in Fig. 1. The inset, however, shows more clearly that the rate of resistance-increase diminishes as the temperature becomes lower. Fig. 2 shows that, in the range of liquid hydrogen temperatures the resistance increases with the intensity of magnetic field in the same way as for pure Zn, while in the range of liquid helium temperatures the resistance decreases with the intensity of magnetic field and the rate of decrease is more enhanced with lowering temperature. For the alloy of 0.43 atmic percent Mn, a

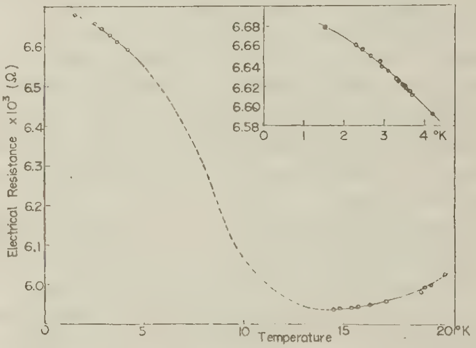

Fig. 1. Electrical resistance versus temperature of Zn alloy with 0.099 atomic percent Mn. The inset is the enlarged figure below 5°K.

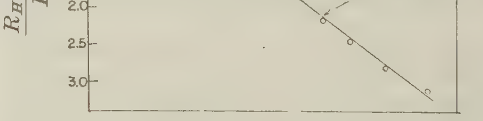

Fig. 2. $(R_H-R_0)/R_0$ versus magnetic field strength for Zn alloy with 0.099 atomic percent Mn at 20.4°K, 4.2°K and 1.54°K, respectively.

similar behaviour is also found.

Since the electrical properties of these alloys are quite similar to each other and the behaviour in magnetic field resembles to those of Cu-Mn alloys[2),3)], we are led to presume that these phenomena are closely related to the magnetic states of Mn ions. More detailed reports including electrical properties of Zn-Sn alloys will shortly be published elsewhere.

The authors wish to express their sincere thanks to Assist. Prof. S. Tanuma for his helpful suggestions and discussions. The present work was supported partly by the Grant in Aid for Fundamental Scientific Research from the Ministry of Education.

References

1) K. Yoshida: Phys. Rev. **107** (1957) 396.
2) A. N. Gerritsen: Physica **19** (1953) 6.
3) R. W. Schmitt and I. S. Jacobs: J. Phys. Chem. Solids **3** (1957) 324.

J. PHYS. SOC. JAPAN **14** (1959) 381~382

On the Growth Conditions of Germanium

By Takeo SASAKI

Research Laboratory, Nippon Electric Co., Ltd.
Kawasaki, Japan

(Received December 17, 1958)

The effect of the growth conditions of pulled, single crystal germanium on the structural and physical properties has been investigated.

The n-type germanium single crystals containing a very small amount of arsenic, are pulled in the (111) direction, and four kinds of crystals with different growth conditions shown in Table I are chosen. These conditions comply with the suggestion by F. D. Rosi and E. Billing[1)] giving the thermal stress for the pulled crystal.

The CP-4 etch pit density in the cross section perpendicular to the growth direction is found to depend on the growth condition which is represented by the growth rate for convenience, as shown in Fig. 1. But it is not apparent which factor is the most effective.

Next, it is easy to find the spiral pits among the many concentric pits by the Rhodes' etching technique[2)] as shown in Fig. 2. These spiral pits, however, are not caused from the thermal stress as shown in Fig. 1. The terrace width of the spiral

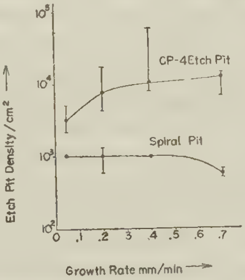

Fig. 1. The dependency of CP-4 etch pit and spiral pit density on the growth rate.

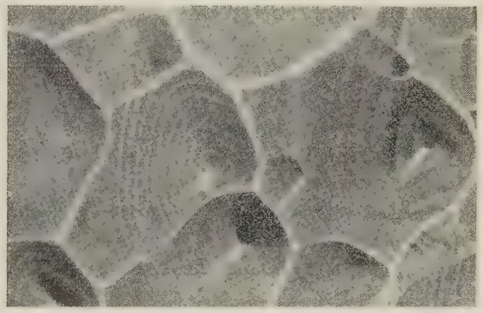

Fig. 2. The spiral etch pits in (111) surface (×960).

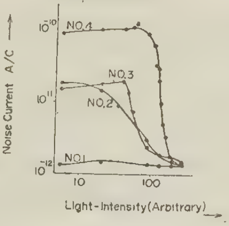

Fig. 3. The relationship between noise and light-intensity.

Table I

	sample No.	1	2	3	4
	growth rate	50	200	400	700μ/min
growth condition	temperature gradient in the liquid-solid interface*	35	35	130	130°C/cm
	temperature variation during the crystal growth**	0.5	1.0	3.0	5.0°C/min

* The temperature gradient was varied by using the crucibles which had different wall heights.

** The temperature variation was represented by the rate of the temperature decrease for maintaining the constant diameter of the pulled crystal in the initial stage of the growth.

pit is relatively large, being of the order of 0.8 μ, and has no dependency on the growth condition. The terrace width of the concentric pit, on the other hand, depends on the growth rate and from this fact the platelet growth is considered to occur in germanium[3].

To measure the noise characteristics germanium bars, each measuring $0.3\times0.3\times3$ mm are cut from these samples, and after the surfaces have been carefully treated each of them is hermetically sealed in a case having a glass window. The amount of noise has turned out to be inversely proportional to frequency within the range of from 100 c/s to 10 kc/s and it increases with increasing growth rate or dislocation density[4]. The variation of the noise when the samples are illuminated is shown in Fig. 3. The value of the noise remains constant when the light intensity is low, but it decreases suddenly when the intensity exceeds a certain value. This critical point is closely related to the growth condition. The number of photo-excited carriers at these points are calculated to be of the order of 10^{14} or 10^{15}/cm^3, which is comparable to the number of the original conduction electrons. Thus the existence of the qualitative relationship between the dislocation density and the noise has been verified. But the reason why the noise decreases abruptly is not yet explained and further experiments are now being made to clarify this phenomenon.

Finally the author would like to express his appreciation to Dr. Y. Ishikawa for his encouragement during the course of these experiments.

References

1) E. Billing: Proc. Roy. Soc. London **A**, **235** (1956) 37.
F. D. Rosi: R. C. A. Rev. **19** (1958) 349.
2) R. G. Rhodes et al: J. Electronics & Control **3** (1957) 403.
3) W. A. Tiller: J. Appl. Phys. **29** (1958) 611.
4) L. Bess: Phys. Rev. **103** (1956) 72.

J. PHYS. SOC. JAPAN **14** (1959) 382

Non-Existence of Bound States with Positive Energy

By Tosio KATO

Department of Physics,
University of Tokyo

(Received February 3, 1959)

Consider the wave-mechanical system described by the schrödinger equation

$$\Delta\varphi+[\lambda-V(x,y,z)]\varphi=0\,. \qquad (1)$$

It has been believed that such a system has *no bound state with positive energy* if the potential V tends to zero at infinity with a certain order of rapidity. Mathematically speaking, this amounts to saying that (1) has no positive eigenvalue λ with a square-integrable eigenfunction φ.

Strangely enough, however, it seems that this fact has never been proved, except in the special case in which V is spherically symmetric and therefore permits the separation of variables. It is true that some sufficient conditions[1] have been proposed for the non-existence of positive eigenvalues in the general case, but these conditions are rather strong and restrict the behavior of V in the *whole space*. To the best of the author's knowledge, no sufficient condition has been given which restricts only the *asymptotic behavior* of V at infinity. It is to be remarked that the underlying mathematical problem is far from trivial once V is allowed to deviate from spherical symmetry even slightly.

Recently we have been able to prove the following theorem, which gives a satisfactory answer to the above question.

Theorem. *If* $V(x,y,z)$ *is continuous for* $r>0$ *and* $V=o(r^{-1})$ *for* $r\to\infty$, *then* (1) *has no positive eigenvalue with a square-integrable eigenfunction* $\varphi\not\equiv0$.

The assumption that $V=o(r^{-1})$ does not admit of any essential improvement. As is well known[2], there is an example of a potential V with the asymptotic form

$$V=-\frac{4k\sin 2kr}{r}+O\left(\frac{1}{r^2}\right), \qquad r\to\infty\,, \qquad (2)$$

for which there is a positive eigenvalue $\lambda=k^2$ with a square-integrable eigenfunction φ.

The above theorem can be extended to the differential equation of the form (1) in the n-dimensional space. The proof will be published elsewhere[3].

References

1) W. L. Miranker: Comm. Pure Appl. Math. **10** (1957) 491.
E. Wienholtz: Math. Ann. **135** (1958) 50.
2) J. v. Neumann und E. P. Wigner: Phys. Z. **50** (1929) 465. It should be remarked that the V of this paper apparently differs from (2), but this is due to a mistake of calculation.
3) T. Kato: Comm. Pure Appl. Math. **12** (1959), to appear.

J. PHYS. SOC. JAPAN **14** (1959) 383

The Crystal Structure of $CoCl_2 \cdot 6H_2O$

By Jōji MIZUNO, Kazutoshi UKEI
and Tadashi SUGAWARA

*The Research Institute for Iron, Steel and
Other Metals, Tohoku University,
Sendai, Japan*

(Received January 28, 1959)

It was reported by Haseda and Kanda1) that the susceptibilities of powered samples of $CoCl_2 \cdot 6H_2O$ show an antiferromagnetic behavior below about 3°K. The magnetic measurement on a single crystal of this salt is in progress, and it has been found up to now that the antiferromagnetic order of spins occurs along c axis of the monoclinic lattice2). The complete structure determination of the salt has not yet been done, while it is indispensable to the elucidation of the magnetic behavior. The present work was thus undertaken.

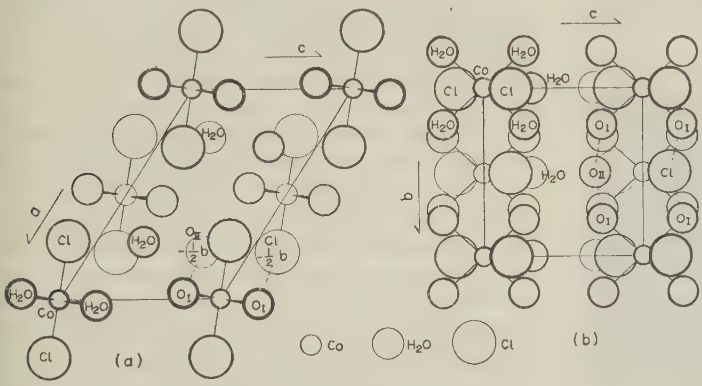

Fig. 1. The arrangement of atoms projected (*a*) on (010) and (*b*) on (100). Broken lines represent the hydrogen bond.

The single crystal used was the same (monoclinic prismatic) in its habit as Groth described3). X-ray rotation and oscillation photographs were taken about a and b axes, using Mn-filtered FeK_α and Zr-filtered MoK_α. Unit cell dimensions were given as $a=10.34$ Å, $b=7.06$ Å, $c=6.67$ Å. For the angle β and the density values found in literatures, 122°19′ and 1.924 gr/cm³, were used. These data gave two formula units per unit cell. Space group was determined as C_{2h}^3-C2/m. Atomic positions were obtained from (*hol*) Patterson map and from (*hol*) and (*okl*) Fourier maps, as given in Table I.

Table I. Atomic positions in $CoCl_2 \cdot 6H_2O$.

Kind of atom	Position	x	y	z
Co	origin	0	0	0
Cl	4(*i*)	0.278	0	0.175
O_I	8(*j*)	0.0288	±0.221	0.255
O_{II}	4(*i*)	0.275	0	0.700

The arrangement of atoms projected on (010) and (100) is shown in Fig. 1 (a) and (b), respectively. As seen from Fig. 1, two Cl^- ions and four water molecules are octahedrally coordinated to Co^{2+} ion to form the group $[CoCl_2 \cdot 4H_2O]$, and the other two water molecules of the formula unit are relatively free. The groups seem to be joined with one another by hydrogen bonds, O_I---H—O_{II}—H---O_I and O_I—H---Cl, in the plane parallel to (001). This structure leads to the perfect cleavage parallel to (001) by Groth3).

In a powdered sample of $NiCl_2 \cdot 6H_2O$ isomorphous to $CoCl_2 \cdot 6H_2O$ an anomalous magnetic behavior has been observed below 6~8°K4). According to a preliminary study on the structure analysis of this salt by one of the authors5) the arrangement of atoms seems to be similar to that in $CoCl_2 \cdot 6H_2O$. Full reports on the crystal structure of these two salts will be published later.

The authors wish to express their sincere thanks to Prof. E. Kanda and Prof. S. Ogawa for their continued encouragements throughout this work.

References

1) T. Haseda and E. Kanda: J. Phys. Soc. Japan **12** (1957) 1051.
2) T. Haseda: Private communication.
3) P. Groth: *Chemische Kristallographie*, 1 Teil (Wilhelm Engelmann, Leipzig, 1906) 248.
4) T. Haseda and M. Date: J. Phys. Soc. Japan **13** (1958) 175.
5) J. Mizuno: Read at the Annual Meeting of the Phys. Soc. Japan held in Oct. 1958.

J. PHYS. SOC. JAPAN **14** (1959) 383~384

Change of Surface Recombination Velocity of Germanium by γ ray Irradiation, Using P-N-P Alloy Transistor

By Kiich KOMATSUBARA

Semiconductor dep. Kobe Kogyo Cop. Kobe

(Received September 6, 1958)

In this note, the change of surface recombination velocity, S, as a function of γ ray dosage is discussed. Values of S are derived from the change of α_{eb} vs. emitter current, Ie, curves of transistor.

The equation for α_{eb} as a function of Ie for p-n-p alloy junction transistor has been presented by Webster1) as follows,

$$\frac{1}{\alpha_{eb}} \approx \frac{SWA_s}{D_p A_e}\left(\frac{1+z}{1+2z}\right)+\left[\frac{\sigma_b W}{\sigma_e L_e}+\frac{W}{D_p \tau}\right](1+z)\,, \tag{1}$$

where

$$z=\frac{W\mu_e I_e}{D_p A_e \sigma_b}\,, \tag{2}$$

σ_b is conductivity, τ is the hole life time in base Germanium, D_p, μ_e, σ_e, and L_e are well known constants, W and A_e are constructional constants, and A_s is effective area for surface recombination.

This equation reduces to the asymptotic expression for large value of Z as

$$\left.\frac{1}{\alpha_{eb}}\right)_{z\to\text{large}}=\frac{SWA_s}{2D_p A_e}+\left[\frac{\sigma_b W}{\sigma_e L_e}+\frac{W}{D_p \tau}\right](1+z)\,, \tag{3}$$

and the difference between the original equation and this asymptote is

$$\left.\frac{1}{\alpha_{eb}}\right)_{\text{diff}} \approx \frac{SWA_s}{2D_p A_e}\left(\frac{1}{1+2z}\right)\equiv f(s)\,. \tag{4}$$

If the value of Ie is extrapolated to the zero value, then this equation becomes

$$f(s)\approx\frac{SWA_s}{2D_p A_e}\,.$$

This difference is the function of S only, if it is assumed that, for small carrier injection, A_s is constant independent of γ irradiation.

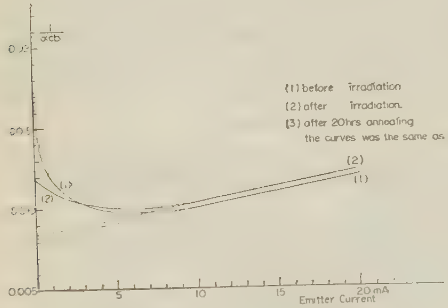

Fig. 1. The changes of $\alpha_{eb}-I_e$ curves by 2.9×10^7 röntgen γ ray dose.

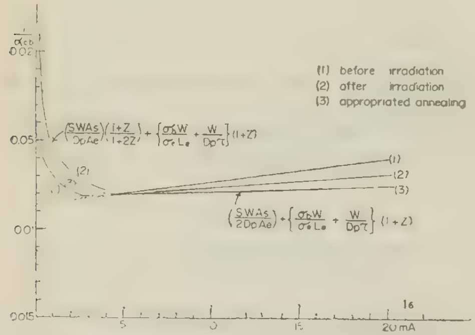

Fig. 2. The changes of $\alpha_{eb}-I_e$ curves by 5×10^7 röntgen γ ray dose.

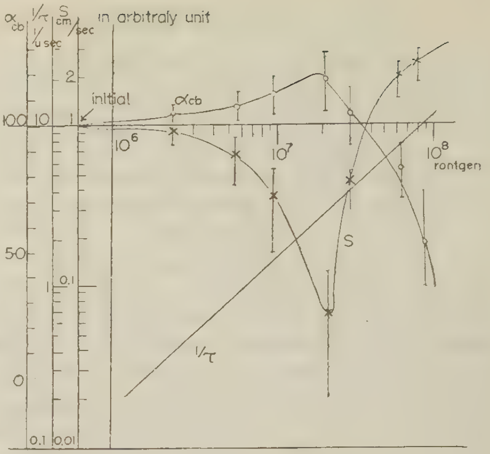

Fig. 3. The changes of S α_{cb} and $1/\tau$ by γ ray dose in p–n–p G_e alloy transistor.

The curves of α_{eb} as a function of Ie are shown in Figs. 1 and 2 as examples. Fig. 1 shows the case of 2.25 röntgen dose, and Fig. 2 shows 5.7 röntgen dose. In Fig. 3 the change of S and of α_{eb} and hole life time as a function of dose are shown. At this measurement, seven groups of several transistors each were used, and each groups were exposed to γ ray field of afout 3×10^5 röntgen per hour for different time intervals. So it was not the measurement of successive changes of same transistor, and the measurements had some troubles because of very prompt annealing effect, especially in the case of small dosages of γ ray where the changes of S were small and negative, the annealing speed of S was very large. For examples, at 2.2×10^7 röntgen dose, the value of S recovered perfectly after twenty hours from removing the γ field at about 30°C atmospheric temperature. And in the case on heavy dosage of γ rays, where the change in values of S was positive, the annealing speed was relatively small. The reason for the changes of the value of S by γ ray dosages is not yet clarified at the present stage of research. But the decrease of the conductivity in the interior of germanium should have caused the decrease of S2). The changes of S may be explained if we assume that the surface conductivity becomes gradually low and changes to P type (P type channel on N type germanium) and increases again successively by the dosage of γ rays.

This analogy to the view point of chemical impurity may have to be regarded as rough approximation, however, as the surface state density would become large by γ irradiation and deep lying vacancy level may act as recombination centers.

References

1) W. M. Webster: Proc. Inst. Radio Eng. **42** (1954) 914.
2) B. H. Schuly: Physica **20** (1954) 1031.

J. PHYS. SOC. JAPAN **14** (1959) 385～386

Preparation of Anodic Oscillator Tube using Glow Discharge

By Kazuyuki OGAWA

Matsuda Research Laboratory, Tokyo Shibaura Electric Co., Kawasaki

(Received January 8, 1959)

Generally, oscillatory phenomena in gas discharge have very complex features on the variation of its frequency, wave form, coherency, amplitude etc. Hence, there are poor reproducibilities among each experiments. Author reports some notes on the preparation of fairly stable anodic oscillator tube, with which the quantitative treatment of its characteristics is acceptable. This tube may be called "oscillatron" for convenience.

Fig. 1 illustrates the typical structure of oscillatron. A is a needle anode (about 1 mm diameter), *K* is a circular disc cathode (about 20 mm diameter) and *A*–*K* spacing is a little thicker than the Faraday dark space which is determined by the nature and pressure of gas. Both electrodes are made of pure molybdenum and are simply pinched upon the nickel poles of the glass seal. The glass envelope should be made sufficiently large so that the wall effect is negligibly small.

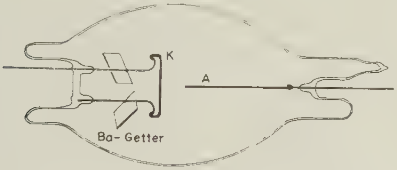

Fig. 1. Construction of oscillatron.

The evacuation and the filling processes of gas must be carried out very carefully, for the anodic oscillation is greatly affected by gaseous impurity, especially by molecular gases such as air, H_2, H_2O vapour. For example, in our laboratory, the procedures of the preparation are as follows. The electrodes were electrolytically polished, and after mounting the whole assemblage was washed up ethyl alcohol and boiling distilled water alternately. The glass tube was also cleaned beforehand and the glass work was done in an atmosphere of dry nitrogen gas in order to prevent oxidation of the metal parts. After baking out the tube at high temperature and after heating the electrodes with high frequency current, the pressure of residual gas reached to 4.5×10^{-8} mmHg. When all usual processes of evacuation were finished, the internal pressure of the tube was kept as low as 2.5×10^{-7} mmHg for 30 minutes even after the pumping was cut off. Then, the pure Ne or Ar gas, which was spectroscopically inspected, was introduced and the tube was operated by d. c. current under abnormal glow untill the glass wall was covered

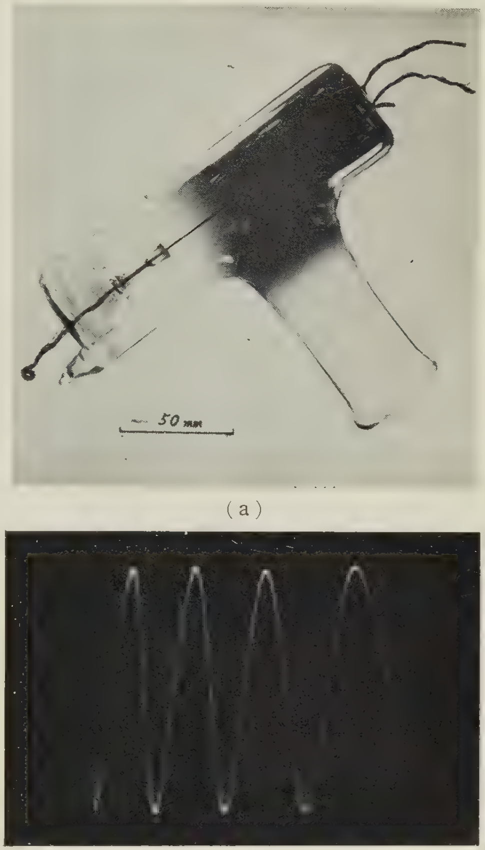

(a)

(b)

Fig. 2.

(a) Oscillatron for spectroscopic analysis of anodic phenomena.

(b) Wave form of the voltage oscillation at 20 mA (Ne 50 mmHg, A–K spacing 10 mm).

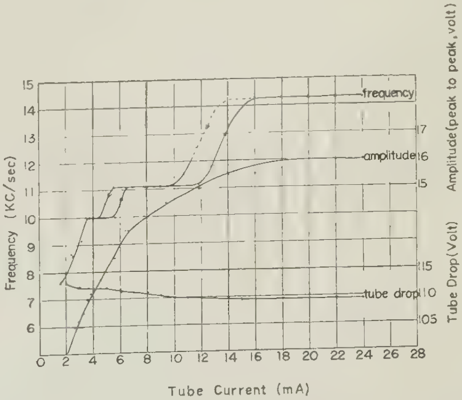

Fig. 3. Variation of the frequency, amplitude, tube drop *vs* the tube current of oscillatron (Ne 50 mmHg, A–K spacing 10 mm).

with a sufficiently thick layer of sputtered molybdenum, the polarity of d.c. source was reversed now and then in order that the both electrodes equally sputtered. The essential part of this process had been proposed by T. Jurriaanse et al.[1] with regard to production of reproducible and stable cathode drop. When it is necessary to use the tube of knotty shape or the very large one for requirement of individual experiment, conventional barium getter must be also used to absorb the gas resulting from naked parts of the glass wall. Lastly, the gas was renewed and the tube was sealed off.

Fig. 2 (a) shows a type of oscillatron which was used for spectroscopic analysis of the anodic phenomena, and (b) shows the oscillogram of its voltage oscillation between the electrodes. Fig. 3 shows the variation of frequency, average tube drop, and amplitude of the oscillation over whole range of the tube current. The oscillation includes the anodic mode only, and above 16 mA the oscillation is very stable and reproducible within a fluctuation by a few per cent. The tendency of these characteristics is almost the same for any type of oscillatron as long as the tube is prepared with great care.

Studies on the anodic oscillation using oscillatron will be reported on other papers.

Reference

1) T. Jurriaanse, F. M. Penning and J. H. A. Moubis: Philips Res. Rep. **1** (1945/46) 225.

J. PHYS. SOC. JAPAN **14** (1959) 386

Terminal Zone Cropping and Ultimate Zone Purification

By Louis GOLD

Edgerton, Germeshausen and Grier, Inc.
160 Brookline Avenue, Boston
15, Massachusetts

(Received January 8, 1959)

An aspect of zone melting which apparently has not been reported on as yet[1] concerns the explicit degree of purification achieved after any number of passes. A rather fundamental parameter, termed the purification factor, was introduced several years ago to identify the potential state of purity achieved in an ingot at any stage of the zone refinement process[2].

To apply this concept in paractice, the technique of terminal zone cropping may be employed; the initial zone serves as a sink for impurities having a distribution coefficient $k>1$, whereas the final zone accretes impurities having $k<1$. Such a procedure was found helpful in the preparation of single crystals of beryllium[3].

It is well known that as the number of passes $n\rightarrow\infty$, an equilibrium distribution of impurity in the ingot is approached. Further purification may be accomplished by removal of the terminal zone. If the back reflection of impurity from the terminal zone into the bulk of the ingot is ignored, a rather straightforward analysis of the purification becomes possible. This simplification allows ready calculation of the upper bound on the degree purification-- the actual state of purity that can be attained cannot exceed the values computed by the reduced formalism. For certain situations approximating the semi-infinite ingot, the idealized purification factor to be offered here may suffice.

Thus the cumulative total fraction of impurity potentially removable in the terminal zone can be expressed as follows:

$$P_T=1-\frac{1}{c_0L}\int_0^{L-l}c_n(x)dx \qquad (1)$$

where c_0 is the initial impurity concentration, L is the ingot length and l the zone width. $C_n(x)$ is the positional impurity concentration after the nth pass for which a number of formulae has been worked out[4)-6)]; these are of varying degrees of complexity. Still another manner of describing $c_n(x)$ has been formulated which appears particularly suited for explicit numerical computation[2]. Thus in the relation

$$c_n(x)/c_0=1-Q_n(1-k)e^{-(k/l)x} \qquad (2)$$

the quantity Q_n involves the summation

$$Q_n=\sum_{p=n}^{1}A_p\frac{((k/l)x)^{n-p}}{(n-p)\,!} \qquad (3)$$

where the A_p obtain from a certain, iterative generating function.

Purification factor data of likely practical value are to be made available at a later time when a full account of the findings will be offered.

References

1) W. G. Pfann: *Zone Melting* (John Wiley and Sons, New York, 1958).
2) L. Gold and V. Johnson (Unpublished work at Lincoln Laboratory).
3) L. Gold: Thesis MIT Metallurgy Dept. 1947; see Nucl. Sci. Abst. **3** (1949) 27.
4) N. W. Lord: J. Metals **5** (1953) 1531.
5) J. L. Birman: J. Appl. Phys. **26** (1955) 1195.
6) W. G. Pfann: J. Metals **5** (1953) 1441.

JOURNAL OF THE PHYSICAL SOCIETY OF JAPAN, Vol. 14, No. 4, APRIL, 1959

Measurement of Bremsstrahlung Spectra with Sodium Iodide Scintillation Crystal

By Motoharu KIMURA, Naosi MUTSURO, Yuji OHNUKI, Katsufusa SHODA,
Masumi SUGAWARA, Tsutomu TOHEI and Haruo YUTA

Department of Physics, Faculty of Science,
Tohoku University

(Received August 21, 1958)

The bremsstrahlung spectra of the 8.5 MeV electrons for the forward direction were measured with a scintillation spectrometer of a sodium iodide crystal 4 in. in diameter and 4 in. in length. Be, Ni and Pt of several thickness were used as the targets. The measured spectra were compared with our semi-empirical calculation. The calculation was based upon the response function for NaI crystal which was constructed referring to the method developed by NBS group and also to the actual response curve for the monochromatic gammas of 1.12 and 6.14 MeV, instead of using Monte Carlo method which had generally been used in the former researches. The agreement is rather good if we assume Schiff's formula for the intrinsic bremsstrahlung spectra.

§ 1. Introduction

It is of importance to measure the bremsstrahlung spectrum as accurate as possible because of its extensive use in the investigation of photonuclear reactions and of the experimental check of the theory of bremsstrahlung. Many experiments have been made using a pair spectrometer and other detectors.(1)–(4) Recently, Starfelt and Koch(5) measured the bremsstrahlung spectra for the electron energies of 2.72, 4.54 and 9.66 MeV using the scintillation spectrometer of a sodium iodide crystal 5 in. in diameter and 9 in. in length. These results show that the spectral shapes obtained with the beryllium and aluminun targets agree with theories of Schiff, Sauter, and Gluckstern and Hull, for the electron energies of 2.72 and 4.54 MeV. However, the 9.66 MeV-experiment gives 20% higher value as compared with the theory at the low energy regions of photon. For gold target, the experimental cross sections at the higher photon energies were larger than the theory, the discrepancies increasing with decreasing primary electron energy.

In the present experiment, the forward bremsstrahlung spectra produced by 8.5 MeV electrons were measured by scintillation spectrometer using a sodium iodide crystal of 4 in. in diameter and 4 in. in length. Targets of beryllium ($Z=4$), nickel ($Z=28$) and platinum ($Z=78$) were used. The results show that the measurements for Z-dependence agree with the theory(6) if we neglect the effect of the target thickness. In order to obtain the target-thickness dependence of bremsstrahlung spectra, three platinum targets of 0.2, 0.08 and 0.025 mm thickness were used. These results were compared with the theory taking into account the multiple scattering of electron in the target. Complete agreement was not obtained. The discrepancy is believed to be the edge effect of the target, that is, the target in the donut presented an effective thickness less than the geometrical one because an important fraction of the radiation would originate at the target edge during the shrinkage of the betatron orbit.

For the comparison of the theory with the present experiments, the bremsstrahlung theory of Schiff(6) was used. Assuming an exponential screening law of atomic potential $Ze/r\cdot\exp(-r/a)$, Shiff integrated the Bethe-Heitler differential cross section(7) over all the outgoing electron angles and obtained the analytical expression of the intrinsic differential cross section $d^2\sigma/d\Omega\, dE$. Because of the Born approximation, his expression is restricted to energies that are large compared with m_0c^2. Taking into account the multiple scattering of electrons in the target, Hisdal(8) calculated the corrected bremsstrahlung spectra in the forward direction using Schiff's(6) and Morliere's(9) theory. His calculation was used for the comparison with our measurement of 0.2, 0.08 and 0.025 mm Pt target.

§ 2. Experimental Procedures and Results

8.5 MeV electrons were produced by the betatron acceleration of 40 MeV Synchrotron of Tohoku University. The shrinking electrons by the saturation of flux bars bombarded the target in the donut, and produced the continuous X-ray which passed through two collimators and led to the head of a scintillation spectrometer which was situated 4 meters from the target. The experimental arrangement is shown in Fig. 1.

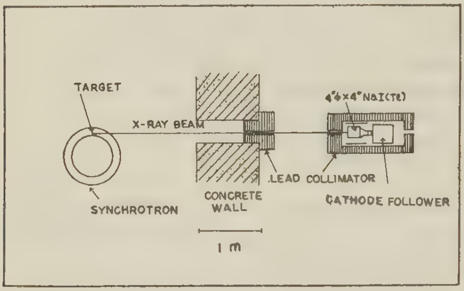

Fig. 1. Experimental arrangement for the measurement of bremsstrahlung spectra.

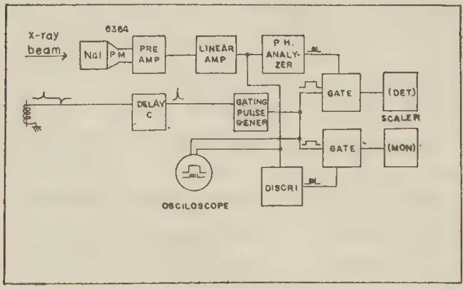

Fig. 2. Block diagram.

The block diagram of the scintillation spectrometer is given in Fig. 2. The photomultiplier DuMont 6364 and the sodium iodide crystal of 4 in. in diameter and 4 in. in length which was polished and mounted in our laboratory were used. In order to avoid the high back ground counting rate, the gate circuits were used which were open during the burst of X-ray beam. Using these gate circuits, the background countings were suppressed to about 1/30 of those when the gating was not applied. The background counts were measured under the same condition with that when the bremsstrahlung spectra was measured but with shielding the X-ray beam by a lead brick in front of the last collimator. The measured background counting rate is shown in Fig. 3. Fortunately, the background counting rate was independent of the beam intensity and was equal to the natural background, thus

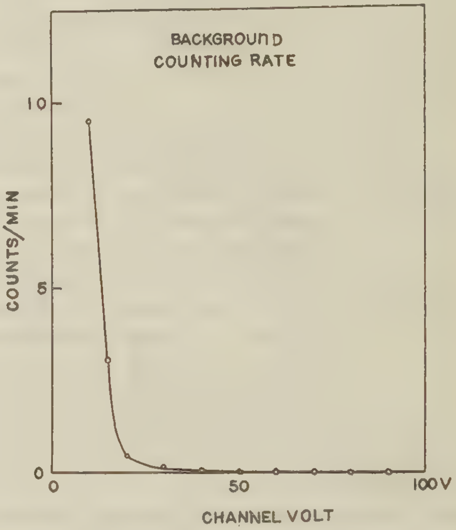

Fig. 3. Measured back-ground counting rate.

the measured spectra of the bremsstrahlung, $S(E_0, E)$ is represented by the normalized ratio, Γ as follows;

$$S(E_0, E)=\text{const}\cdot\Gamma\,, \tag{2.1}$$

where E and E_0 are the photon and the total electron energy respectively and Γ is given by

$$\Gamma=\frac{N_D-n_D t}{N_M-n_M t}\,, \tag{2.2}$$

where N_D and N_M are the measured counts of the detector and the monitor respectively and n_D and n_M their background counting rates and t the time requied for the measurement of N_D and N_M.

In order to measure the counts of the monitor, N_M, "Self monitoring" method was applied for almost all of the measurement. Using the same detector crystal for the measurement of N_D, the integral counts of pulses higher than a certain level were used as the normalization of the channel counts. As shown in Fig. 2, the monitor counts were led from the A–1 amplifier through a discriminator.

Because of the short duration of the beam, the pile up effect of the detector was expected to be important, making the normalized ratio dependent on the beam intensity. In order to avoid this effect, moderately low intensity of the beam was used for the measurements. The energy of bremsstrahlung photons was frequently checked by comparison with the 1.12 MeV gamma-ray line from Zn^{65}. The pulse height of Zn^{65} line was always measured before and after each run. The linearlity of the amplifier was checked by several gamma-ray sources of different energies. The drift of the spectrometer was within 1∼0.5% during the course of several hours' run.

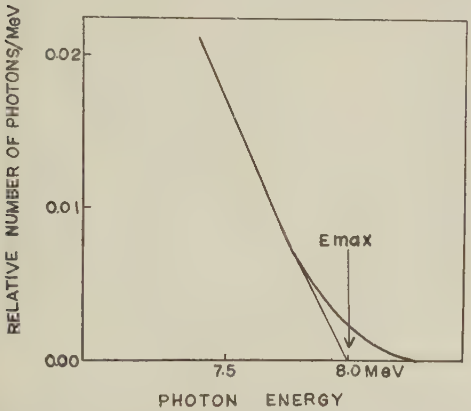

Fig. 4 (a). Calculated shape near the high energy end of the bremsstrahlung spectrum. The cross point of the tangent along the linear part of the curve with the energy axis indicates the maximum energy of photons, Emax.

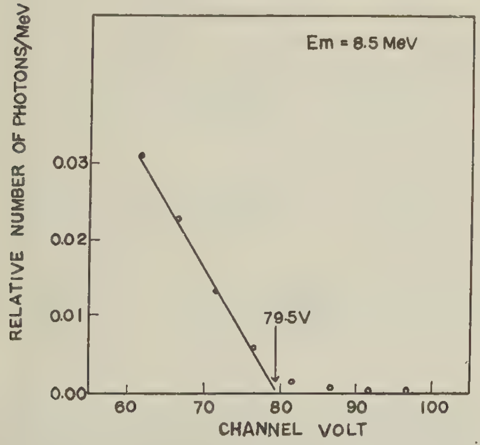

Fig. 4 (b). Measured shape near the high energy end of the bremsstrahlung spectrum.

The maximum energy of photons was determined as shown in Fig. 4. If the cross section of the bremsstrahlung are approximately given near the high energy end of the spectrum by

$$\begin{aligned} \frac{d^2\sigma}{d\Omega\, dE} &= a(E_m - E) \qquad && E_m \geq E \\ &= 0 && E_m < E\,, \end{aligned} \tag{2.3}$$

where E_m is the maximum energy of photons and a is a constant to be determined experimentally, then the curve corresponding to the measured spectrum near the high energy end of the spectrum will easily be calculated with the following assumption. We assumed that the energy spread of electrons has 4% half width with Gaussian distribution and the response function of the gamma ray as shown in section 3. The resulting curve is shown in Fig. 4 (a). Drawing a tangent along the linear part of the curve, the cross point with the photon-energy axis will indicate the maximum energy of bremsstrahlung photons, E_m. An actual example is shown in Fig. 4 (b).

Beryllium, nickel and platinum were used as the targets. The thickness was determined by micrometer as shown in Table I.

Table I.

Target material	Z	Thickness in mm	Thickness in radiation length
Be	4	0.5	0.0012
Ni	28	0.2	0.0136
Pt	78	0.2	0.0695
Pt	78	0.08	0.0278
Pt	78	0.025	0.0087

The measured bremsstrahlung spectra for various targets are shown in Figs. 5, 6, 7, 8, 9 and 10, comparing with the theory. These will be discussed in more detail in section 4.

§ 3. Calculation of Bremsstrahlung Spectra from the Response Function

1) *Differential cross section of the bremsstrahlung,* $d^2\sigma/d\Omega\, dE$

The differential cross section of the bremsstrahlung was calculated by Schiff[6] from integrated Bethe-Heitler[7] differential cross section, considering the screening effect. From his expression, differential cross section $d^2\sigma/d\Omega\, dE$ for the forward direction is given as follows;

$$\frac{d^2\sigma}{d\Omega\, dE} = \frac{4Z^2}{137} \cdot \left(\frac{e}{m_0c^2}\right)^2 \left(\frac{E_0}{m_0c^2}\right)^2 \cdot \frac{dE}{2\pi E} \cdot \left\{ -\frac{(2E_0-E)^2}{E_0^2} + \frac{E_0^2+(E_0-E)^2}{E_0^2} \ln M(0) \right\}$$

$$(E \leq E_0 - m_0c^2)\,. \tag{3.1}$$

where E_0 in the total energy of electrons and E is the photon energy, and $M(0)$ and the constant C are given by

$$\left.\begin{aligned}\frac{1}{M(0)}&=\left(\frac{m_0c^2E}{2E_0(E_0-E)}\right)^2+\frac{Z^{2/3}}{C^2}\,,\\ C&=111\,.\end{aligned}\right\}\tag{3.2}$$

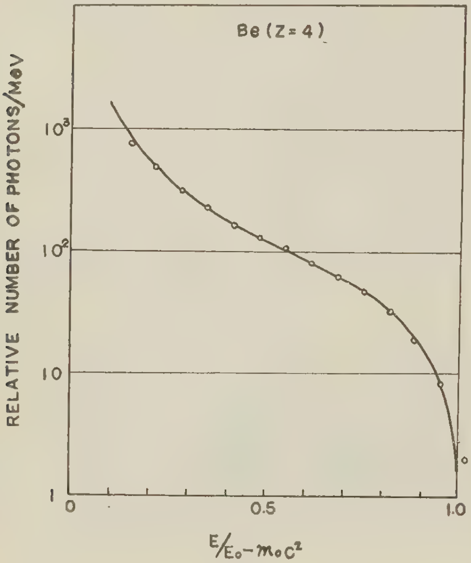

Fig. 5. Measured spectrum for Be(Z=4) of 0.5 mm thickness (open circle) and calculated curve from Schiff's formula. (solid line)
Emax=8.1 MeV

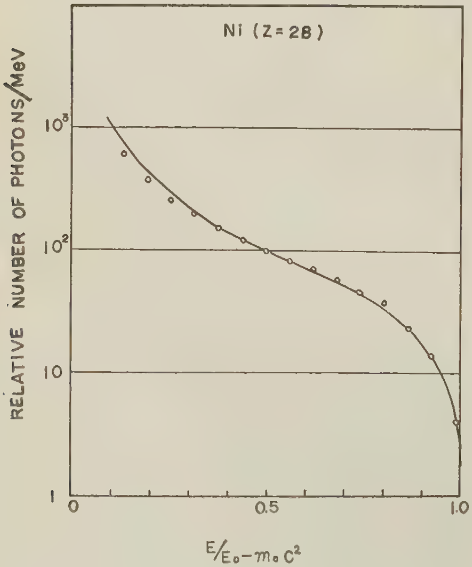

Fig. 6. Measured spectrum for Ni(Z=28) of 0.2 mm thickness (open circle) and calculated curve from Schiff's formula. (solid line)
Emax=8.6 MeV

For the convenience of remaining calculations, a following notation is used,

$$n(E_0,E)=\frac{1}{E}\left\{-\frac{(2E_0-E)^2}{E_0^2}+\frac{E_0^2+(E_0-E)^2}{E_0^2}\ln M(0)\right\}\,.\tag{3.3}$$

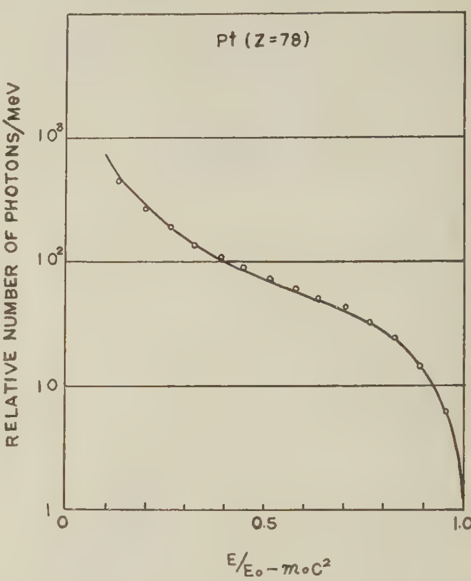

Fig. 7. Measured spectrum for Pt(Z=78) of 0.2 mm thickness (open circle) and calculated curve from Schiff's formula. (solid line)
Emax=8.5 MeV

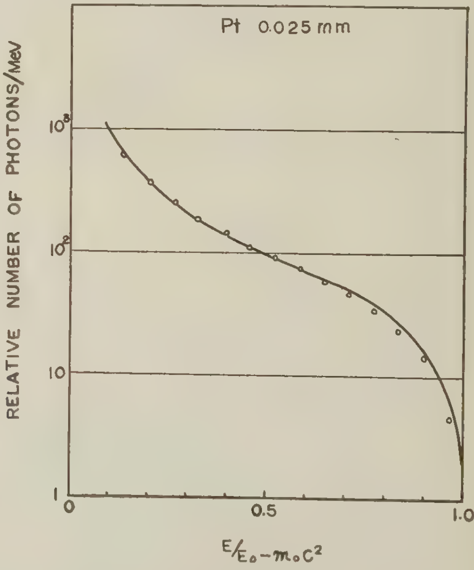

Fig. 8. Measured spectrum for Pt of 0.025 mm thickness (open circle) and calculated curve correcting the target thickness. (solid line)
Emax=8.5 MeV

Since this expression is valid in an infinitely thin target, corrections must be applied for the case of finite thickness. For a target of less than 0.1 radiation length, the effect of energy loss and absorption in the target and the double radiation process should be negligible10). Another correction comes from the multiple elastic scattering which the electrons undergo in the target before radiating. Hisdal8) evaluated the bremsstrahlung spectra in the forward direction corrected for the multiple scattering in the target of platinum. He tabulated the factors by which the intrinsic differential spectrum must be multiplied in order to obtain the relative corrected spectrum in Pt. For our calculation of the spectra of Pt target, extra and interpolated values from his table were used.

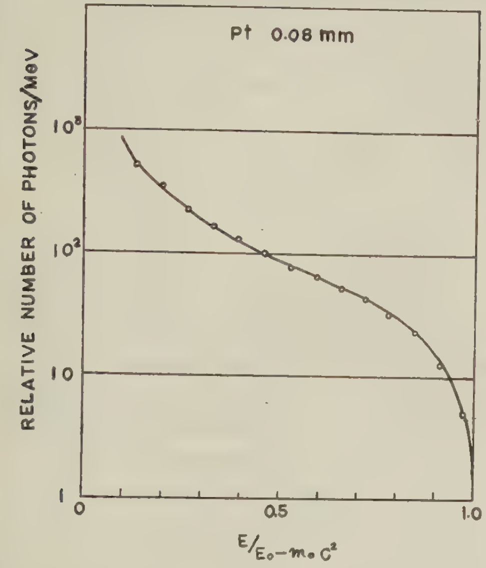

Fig. 9. Measured spectrum for Pt of 0.08 mm thickness (open circle) and calculated curve correcting the target thickness. (solid line) Emax=8.4 MeV

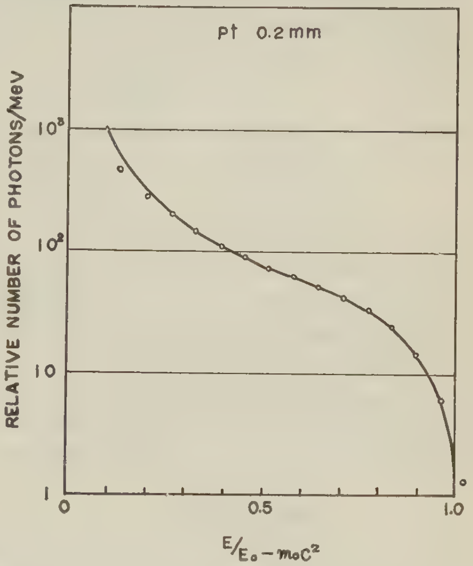

Fig. 10. Measured spectrum for Pt of 0.2 mm thickness (open circle) and calculated curve correcting the target thickness. (solid line) Emax=8.5 MeV

---

2) *Response function of sodium-iodide scintillator*

Response function $R(E, E'')$ is expressed by Berger and Doggett11) as follows;

$$R(E, E'')=Y(E)\left\{\int_0^E \frac{K(E, E')}{\sqrt{2\pi\alpha E'}} \exp\left[-\frac{(E''-E')^2}{2\alpha E'}\right] dE' + \frac{p(E)}{\sqrt{2\pi\alpha E}} \exp\left[-\frac{(E''-E)^2}{2\alpha E}\right]\right\}, \tag{3.4}$$

where E is the energy of impinging photon and E'' is the output pulse height expressed in energy scale. $Y(E)$ is the efficiency of the crystal for the photon of energy E, and 1st and 2nd term in the large blacked represent the compton tail and photo peak. The exponential factor means the Gaussian distribution of the secondary electron energy. Since the integration of $R(E, E'')$ over E'' is the efficiency of the crystal,

$$\begin{aligned}\int_0^\infty R(E, E'')\, dE'' &= Y(E)\left[\int_0^E K(E, E')\, dE + p(E)\right] \\ &= Y(E)\,,\end{aligned} \tag{3.5}$$

following normalization will be obtained;

$$\int_0^E K(E, E')\, dE' + p(E) = 1\,. \tag{3.6}$$

This means that $\int_0^E K(E, E')\,dE'$ is the fraction of Compton tail and $P(E)$ is the fraction of photo peak.

Since there are one and two quanta escapes in the response curve of 6.14 MeV photons as shown in Fig. 12, one and two quanta escape fractions, p_{π_1} and p_{π_2} must be added in our response function as follows;

$$
\begin{aligned}
R(E, E'') = Y(E)\Bigg\{ & \int_0^E \frac{K(E, E')}{\sqrt{2\pi\alpha E'}} \exp\left[-\frac{(E''-E')^2}{2\alpha E'}\right] dE' \\
& + \frac{p_{\pi_2}(E)}{\sqrt{2\pi\alpha(E-2m_0c^2)}} \exp\left[-\frac{(E''+2m_0c^2-E)^2}{2\alpha(E-2m_0c^2)}\right] \\
& + \frac{p_{\pi_1}(E)}{\sqrt{2\pi\alpha(E-m_0c^2)}} \exp\left[-\frac{(E''+m_0c^2-E)^2}{2\alpha(E-m_0c^2)}\right] + \frac{p(E)}{\sqrt{2\pi\alpha E}} \exp\left[-\frac{(E''-E)^2}{2\alpha E}\right]\Bigg\}, \qquad (3.7)
\end{aligned}
$$

where α is a constant and gives the width of Gaussian distribution and is chosen to be 0.00146.

The functions K, p_{π_2}, p_{π_1} and p can be evaluated using the Monte Carlo method. However, in the present calculation, these function were determined referring to the synthesis procedure of Koch and Wyckoff[12] which based on the experimental data obtained by monoenergetic electrons. From their synthesis procedure, these functions are expressed in terms of the photoelectric (τ), pair (π), Compton (σ) and total (μ) absorption cross sections.

$$
\left.
\begin{array}{ll}
\text{photo fraction:} & p(E) = \dfrac{\tau + a\pi + b\sigma}{\mu} \\[2ex]
\text{fraction of one quantum escape:} & p_{\pi_1}(E) = \dfrac{A_1\pi}{\mu} \\[2ex]
\text{fraction of two quanta escapes:} & p_{\pi_2}(E) = \dfrac{A_2\pi}{\mu}\,,
\end{array}
\right\} \qquad (3.8)
$$

where the constant a is the fraction of the total pair production events for which both annihilation quanta are absorbed in the crystal and the constants A_1 and A_2 are the fraction of the total pair production events for which one quantum and two quanta escape from the crystal respectively. The relation between A_1, A_2 and a is

$$A_1 + A_2 + a = 1\,. \qquad (3.9)$$

The constant b is the fraction of the Compton scattered photons that are multiply scattered and totally absorbed in the crystal. Koch and Wyckoff[12] showed that the strinking similarity exists between the Compton electron distributions for a single- and multiple-interactions for the same photon energies. Thus, the function K of the Compton tail was chosen as the Compton electron distributions for a single interaction,

$$
\begin{aligned}
K(E, E') = 0.135\,\frac{1-b}{\mu}\left(\frac{m_0c^2}{E}\right)^2 \Bigg[& \frac{E}{E-E'} - \frac{E'}{E} \\
& + \frac{1}{E^2}\,\frac{\{E^2 - E'(m_0c^2+E)\}^2}{(E-E')^2}\Bigg] \\
& \left(E' \leq \frac{E}{1+m_0c^2/2E}\right) \qquad (3.10)
\end{aligned}
$$

where the numerical coefficient 0.135 was determined to fit the total cross section of Compton scattering electrons in a sodium iodide. Instead of (3.6), the normalization of the response function, (3.7), is given in terms of p, p_{π_1}, p_{π_2} and $K(E, E')$ as follows,

$$\int_0^E K(E, E')\,dE' + p(E) + p_{\pi_1}(E) + p_{\pi_2}(E) = 1\,. \qquad (3.11)$$

The energy resoluion of the response function expressed by (3.7) is obtained as follows:

$$\frac{2\Delta E}{E} = 2\sqrt{\frac{\ln 2 . 2\alpha}{E}}\,. \qquad (3.12)$$

From the measured spectrum of 1.12 MeV gamma ray line, which gives the energy resolution 8.5%, the constant α is determined 0.00146 as stated before. The measured spectrum and the response function using the constant $\alpha = 0.00146$ give the energy resolutions 4.7% and 3.6% at 6.14 MeV respectively. This deviation comes from the difference of the distributions of the response function and the actual spectrum; the response function contains the Gaussian distribution only which comes from the statistical fluctuation as given in (3.7), whereas, the actual spectrum contains the non Gaussian part which comes from the energy loss from the crystal.

The fractions of photo-peak, one quantum, escape, two quanta escapes and Compton tail are determined from the areas of these parts in the measured spectra of 1.12 MeV and 6.14 MeV gamma-ray lines using the normalization relation (3.11). Since the constants A_1, A_2 and a are independent of the photon energies and only depend on particular geometry of the scintillator, these constants are determined from the measured fractions at 6.14 MeV using the relations (3.8) and (3.9) as follows:

$$A_1=0.500$$

$$A_2=0.083$$

$$a=0.417\,.$$

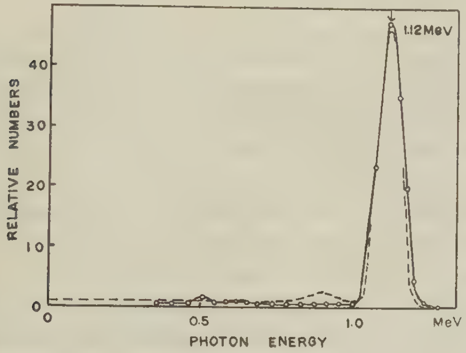

Fig. 11. Pulse height distribution produced by the 1.12 MeV gamma rays from Zn^{65} (solid) and the response function used for the calculation (dashed). The dashed curve is drawn from (3,7) using the constants as shown in the text.

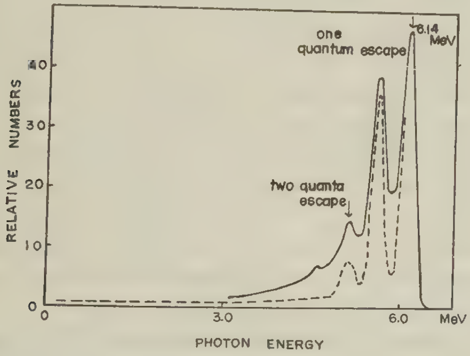

Fig. 12. Pulse height distribution produced by the 6.14 MeV gamma rays from the reaction of $F^{19}(p, \alpha)O^{16}$ (solid) and the response function used for the calculation (dashed). The dashed curve is drawn from (3,7) using the constants as shown in the text.

At the same time, the parameter b in (3.8) is determined from measured fractions. To determine p and b as the function of the gamma ray energy, the inter- and extrapolation procedure are performed along the data of Koch and Wyckoff, using p and b at 1.12 MeV and 6.14 MeV. The curves of p and b given in Fig. 13.

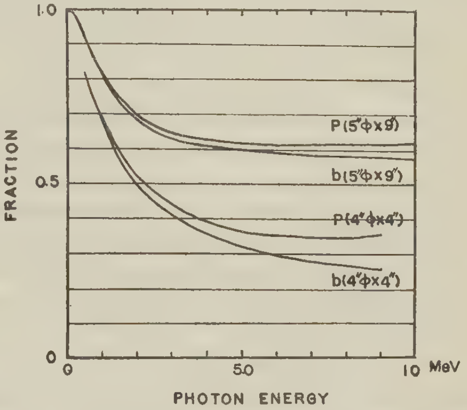

Fig. 13. Fractions of photopeak p and Compton tail b. The values of $p(5''\phi\times 9'')$ and $b(5''\phi\times 9)$ are taken from Koch and Wyckoff (reference (12)). The values of $p(4''\phi\times 4')$ and $b(4''\phi\times 4'')$ are determined experimentally and used for the present calculation.

The efficiency of the sodium iodide crystal of 4 in. in diameter and 4 in. in length was taken from the data of the sodium iodide crystal 5 in. in diameter 4 in. in length$^{11)}$. Because of long distance (4 m) between the target and the last collimator and of smallness (0.8 cmϕ) of its slit aperture, the efficiency of the crystal is given as the following;

$$Y(E)=1-\exp\left[-\mu(E)L\right] \qquad (3.13)$$

where L is the length of the crystal. This efficiency almost agrees with that of $5''\phi\times 4''$, which was used for the present calculations.

3) *Bremsstrahlung spectrum*

The bremsstrahlung spectrum converted into the measured spectrum, $S(E_0, E'')$ is given from (3.3) and (3.7), without constant factor, by

$$S(E_0, E'')=\int_0^{E_0} n(E_0, E)\cdot R(E, E'')\,dE\,. \quad (3.41)$$

This can be decomposed into four terms, that is, the integrals containning Compton tail (S_c), one quantum escape (S_{π_1}), two quanta escapes (S_{π_2}) and photo peak (S_p)

$$S(E_0, E'')=S_p(E_0, E'')+S_{\pi_1}(E_0, E'')+S_{\pi_2}(E_0, E)+S_c(E_0, E'') , \tag{3.15}$$

where

$$\left.\begin{aligned}
S_p(E_0, E'')&=\int_0^{E_0} dE\, Y(E)\frac{p(E)}{\sqrt{2\pi\alpha E}} \exp\left[-\frac{(E''-E)^2}{2\alpha E}\right] n(E_0, E)\\
S_{\pi_1}(E_0, E'')&=\int_0^{E_0} dE\, Y(E)\frac{p_{\pi_1}(E)}{\sqrt{2\pi\alpha(E-m_0c^2)}} \exp\left[-\frac{(E''-E+m_0c^2)^2}{2\alpha(E-m_0c^2)}\right] n(E_0, E)\\
S_{\pi_2}(E_0, E'')&=\int_0^{E_0} dE\, Y(E)\frac{p_{\pi_2}(E)}{\sqrt{2\pi\alpha(E-2m_0c^2)}} \exp\left[-\frac{(E''-E+2m_0c^2)^2}{2\alpha(E-2m_0c^2)}\right] n(E_0, E)\\
S_c(E_0, E'')&=\int_0^{E_0} dE\int_0^{E} dE'\, Y(E)\frac{K(E, E')}{\sqrt{2\pi\alpha E'}} \exp\left[-\frac{(E''-E')^2}{2\alpha E'}\right] n(E_0, E) .
\end{aligned}\right\} \tag{3.16}$$

These four terms were calculated to the 2nd order of approximation, the error being less than 0.5%.

The most important correction came from the absorption of photons in the glass of the donut. In this case, the corrected spectrum should be expressed by

$$S(E_0, E'')=\int_0^{E_0} \alpha(E)\cdot n(E_0, E) R(E, E'')\, dE , \tag{3.17}$$

where $\alpha(E)$ is the correction for absorption to the photon energy E. Furthermore, if the target thickness were taken into account, $S(E_0, E'')$ should be expressed in the term of the correction factor $\pi(t, E)$ for the multiple scattering in the target,

$$S(E_0, E'') =\int_0^{E_0} \alpha(E)\, \pi(t, E)\, n(E_0, E)\, R(E, E'')\, dE , \tag{3.18}$$

where t is the thickness of the target. The theoretical curves of beryllium and nickel were calculated from (3.17). The target thickness was only taken into account in the theoretical curves of platinum targets. These curves are shown in Figs. 5, 6, 7, 8, 9 and 10, together with the measured spectra.

§ 4. Discussion

The absorption of photons between the target and the head of scintillation spectrometer, the effects of the finite thickness of the targets and the effects of penetration of collimator edge and the scattering by the wall surface in the collimator must be taken into account for the theoretical curve. The absorption of photons was negligible in aluminium of the sodium iodide crystal housing and the air between the target and the head, and was the most important in the glass of the donut. This correction factor was around 10%, and was applied to the spectra. The collimator effect mainly came from the last lead collimator with the aperture of 8 mmϕ. An approximate calculation of this effect showed that both contributions of transmitted photons through the wall of the collimator and of scattered photons were about 1% in together at all energy. Because of the uncertainly of the calculation and the smallness of the magnitude, these effects were neglected. Normalizing point of theory with experiment was chosen at the point of $E/(E_0-m_0c^2)=0.5$. Near the high energy end of bremsstrahlung, statistical error became high because of low counting rate, and some deviations of the theory from experiment occurred. However, little may be said about the high energy end of bremsstrahlung. Recently, Fuller et al[13] measured the shape of the high-energy end of the bremsstrahlung spectrum, using the resonance scattering of photons by the 15.11 MeV level in C^{12}. The data indicate an excess number of photons in the tip of spectrum, when compared with Bethe-Heitler spectra corrected for target thickness.

In order to see the Z-dependence of Bremsstrahlung, the ratio Ni/Pt and Be/Pt are given Fig. 14 together with the theoretical ratios. These ratios are normalized to 1 at $E/(E_0-m_0c^2)=0.5$. If the differential cross section of bremsstrahlung with atomic number Z were given in the form of $n_Z(E_0, E)$, then the theoretical ratio $\Gamma(Z_1/Z_0)$ will be given as follows; neglecting the thickness of targets;

$$\Gamma(Z_1/Z_0)=\frac{\int_0^{E_0} \alpha(E) R(E, E'') n_{Z_1}(E_0, E)\, dE}{\int_0^{E0} \alpha(E) R(E, E'') n_{Z_0}(E_0, E)\, dE} . \tag{4.1}$$

The main contribution of $R(E, E'')$ to the integrals is photo- and one quantum escape-peak at the energy of E and $E-0.511$ (MeV). Thus the ratio $\Gamma(Z_1/Z_0)$ depends only slightly on the shapes of the response functions in the region of slow change of $n_{Zi}(E_0, E)$ with E. Therefore $\Gamma(Z_1/Z_0)$ gives us the direct knowledges for the bremsstrahlung spectra independent of the ambiguity of the shape of the response function. As shown in Fig. 14, the measured ratios agree with the theoretical ratios within the statistical error, neglecting the thickness of targets.

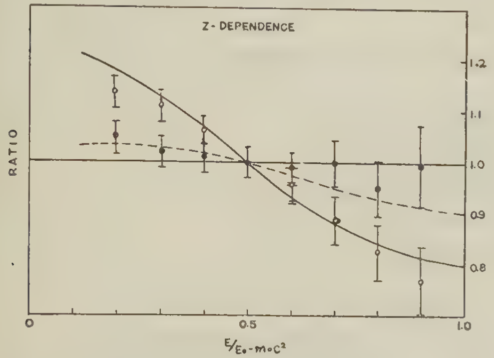

Fig. 14. *Z*-dependence of the experimental and the theoretical ratio

● : experimental point of Ni/Pt
○ : experimental point of Be/Pt
- - - -: theoretical curve of Ni/Pt
———: theoretical curve of Be/Pt

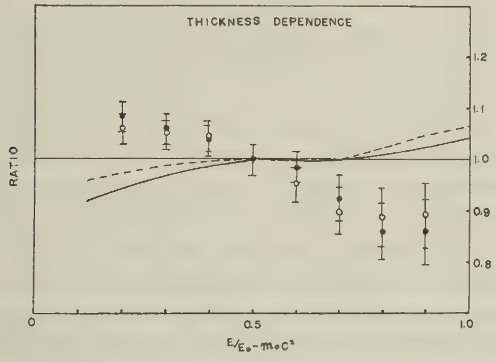

Fig. 15. Thickness dependence of the experimental and the theoretical ratio

● : experimental point of 0.025 mm/0.2 mm
○ : experimental point of 0.08 mm/0.2 mm
- - - -: theoretical curve of 0.025 mm/0.2 mm
———: experimental curve of 0.08 mm/0.2 mm

The measured spectra for the platinum targets of 0.2, 0.08 and 0.025 mm thickness are shown in Figs. 8, 9 and 10. The ratios 0.08 mm/0.2 mm and 0.025 mm/0.2 mm are shown in Fig. 15, which also shows the theoretical curve corrected for the target thickness. These ratios are normalized to 1 at $E/(E_0-m_0c^2)=0.5$. Not so good agreement was obtained. The shrinking velocity of the betatron orbit is the order of $10^{-4}\sim10^{-5}$ cm per one revolution, and the effective thickness of target will be less than the geometrical value. The effects of target thickness will be very difficult to be discussed quantitatively.

In the calculation of *Z*-dependence, the thickness of targets was neglected, that is the case of the infinitely thin target was used. There exists, however, fairly large deviations of the spectra of both experiments and calculations from standard one of 0.2 mm thickness of Pt target. Thus, we can not say much about the *Z*-dependence of the results, where the accurate estimation of the effect of target thickness is very difficult. In conclusion, though we found it rather difficult to check the theory of Schiff in full, it was a fairly useful method to calculate the shape of bremsstrahlung using the response function determined experimentally.

Acknowledgement

The authors are indebted to the Van de Graaf group in Tokyo University for their help in measuring the response of the 6.14 MeV gamma ray from $F^{19}(p, \alpha\gamma)O^{16}$ reaction. They wish to thank Mr. C. Ishii for his suggestion to the response function. The calculational help of Miss N. Komatsu will be greatly appreciated. The also should like to acknowledge The Ministry of Education for the financial support to the construction of accelerator and the measuring installations.

References

1) H. W. Koch and R. E. Corter: Phys. Rev. **77** (1950) 165.
2) D. J. Lees and L. H. Matcaffe: Proc. Phys. Soc. A, **63** (1950) 661.
3) D. J. Allen-Williams and R. R. Appleyard: Brit. J. Radiol. **22** (1949) 106.
4) R. M. Warner, Jr. and E. F. Sharder: Rev. Sci. Instr. **25** (1954) 663.
5) N. Starfelt and H. W. Koch: Phys. Rev. **102** (1956) 1598.
6) L. I. Schiff: Phys. Rev. **83** (1951) 253.
7) H. A. Bethe and W. Heitler: Proc. Roy. Soc. London A, **146** (1934) 83.
8) E. Hisdal: Phys. Rev. **105** (1957) 1821.
9) G. Moliere: Z. Naturforsch. **3a** (1948) 78.

10) J. D. Lawson: Nucleonics **10** (1952) No. 11, 61.

11) M. J. Berger and J. Doggett: J. Res. Nat. Bur. Stand. **56** (1956) 355.

12) H. W. Koch and J. M. Wyckoff: J. Res. Nat. Bur. Stand. **56** (1956) 319.

13) E. G. Fuller, E. Hayward and H. W. Koch: Phys. Rev. **109** (1958) 630.

JOURNAL OF THE PHYSICAL SOCIETY OF JAPAN, Vol. 14, No. 4, APRIL, 1959

Scattering of Protons by Ne^{20} and Ne^{22}

By Yukiyasu ODA, Minoru TAKEDA,
Chuin HU and Shohei KATO

Department of Physics, Faculty of Science,
Osaka University, Osaka, Japan

(Received December 8, 1958)

The angular distributions of protons scattered elastically and inelastically by Ne^{20} and Ne^{22} have been observed at six energies from 4.95 to 5.50 Mev. The shape of angular distribution of inelastically scattered protons varies rapidly with incident energy in boths cases of Ne^{20} and Ne^{22}. An anomaly is found at 5.25 Mev in the reaction Ne$^{20}(p, p')$Ne^{20} ($Q=-1.63$ Mev). The elastic scatterings also exhibit the corresponding features. These results suggest that the reaction proceeds mainly through the compound nucleus formation process. The spin and parity of the compound state seem likely to be 5/2(+).

§ 1. Introduction

The present work is a study of the variation with incident energy of the differential cross sections for elastic and inelastic scattering of protons by neon nuclei. Protons of energies up to 5.5 Mev were produced by the Osaka University 44 inches cyclotron[1].

Natural neon contains three isotopes. The most abundant isotope Ne^{20} has the first excited state at 1.63 Mev above the ground state. The angular distributions of protons scattered inelastically from Ne^{20}, exciting the 1.63 Mev level, were measured by Heitler et al[2] and Freemantle, et al[3] at the proton energies of 4.2 and 9.5 Mev respectively. At present there are two types of theories that attempt to explain and predict angular distributions of product particles in nuclear reactions. The first is based on the formation and subsequent decay of a compound nucleus[4]. General theories applicable to this types of reactions are able to give information on the angular distribution[5]. If the reaction proceeds through a single level of the compound nucleus, the angular distribution is symmetric about the scattering angle $\theta=90°$ in centre-of-mass system. If some levels with different natures are involved in the reaction, the distribution may become more complex and be asymmetric about the 90° angle when the interference between outgoing waves of different parities is present. Finally if the reaction proceeds through a large number of levels of the compound nucleus which are contained within the energy spread of the incident beam in the so-called continuum region of the primary energy, the distribution is again symmetric about $\theta=90°$. In these cases interferences between the many overlapping levels are thought to be cancelled out by each other on the statistical average.

The second type of theories considers that the reaction proceeds either through a direct interaction between the incident proton and a nucleon in the target nucleus or through excitation of the nuclear rotational state[6].

It has been shown by McManus and Butler[7] that the angular distribution of inelastically scattered protons studied at 9.5 Mev by Freemantle et al is well interpreted by the direct interaction process mentioned above. On the other hand, the theoretical calculation for this experimental result based on the excitation of the rotational state has been carried out by Yoshida[8].

The experimental works described here were undertaken in order to get further information of the problem mentioned above. The results obtained at six points of incident energy from 4.95 Mev to 5.5 Mev will be shown.

§ 2. Apparatus

The Osaka University 44″ Cyclotron produced the proton beam used for the experiment. Fairly standard techniques of scattering experiment were used, some details of which are stated below. The whole layout is shown elsewhere[9] and the experimental arrangement in Fig. 1. The movable scintillation counter could be set within 0.1 degree of any angle between −70° and 164°. The protons scattered by the gas target passed through the slit system composed of two rectangular slits before counter.

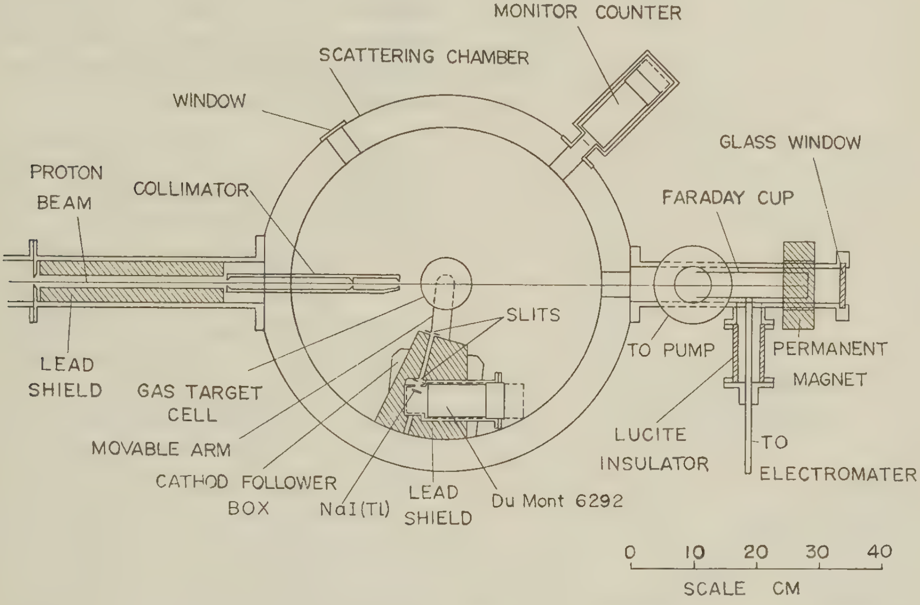

Fig. 1. The experimental arrangement.

NaI(Tl) scintillation crystals cut to the dimension of about $0.8 \times 12 \times 20$ mm³ were used as detectors with Du Mont 6291 or 6292 photomultiplier tubes. When the latter type tube was used, somewhat special arrangement as shown in Fig. 1 was adopted. Although the pulse heights of the gamma ray backgrounds in this detector were not so high, it affected fairly the accurate counting of the inelastically scattered proton groups at large scattering angles. Various efforts such as to interpose the lead gamma-ray absorbers into the beam ducts, covering the beam-exposured faces of various slits with gold foils, and the shielding of the detector with lead plate reduced these background by about a factor of thirty. The pulses generated in the scintillation detector system were amplified and analysed by an Atomic Model 510 20-channel analyzer. Some typical pulse height spectra obtained are shown later in Fig. 3 (a), (b) and (c). The energy resolution of these detectors were about 4.5%.

§ 3. Procedures of Experiment

A. *Measurements of energies of the incident proton beams*

The thickness of the aluminium absorption foils interposed to the beam in front of the scattering chamber were chosen so that the beam energies would be reduced successively by nearly 0.1 Mev. The absolute values of the beam energies corresponding to each thickness of these foils were determined as follows by referring to the excitation function for the $C^{12}(p, p)C^{12}$ reaction published by the Rice Institute group[10]. Changing the foil thickness successively, we observed the variation of the yields of the protons elastically scattered at the scattering angle $\theta=160°$ from propan target. A typical comparison is shown in Fig. 2. The values of the beam energies determined in this way were always compared reasonably with that obtained by other methods. The uncertainty of the values thus obtained seems to be within 30 Kev. The energy spread of the primary beam, on the other hand, seemed to be about 50 Kev, which would be increased gradually with reduction of the beam energy by inserting of absorption foils.

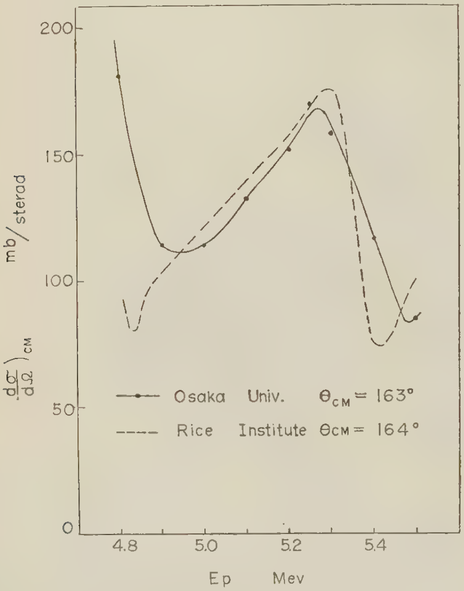

Fig. 2. Determination of the energies of the incident protons.

B. *Pulse-height spectrometry*

Fig. 3 (a) shows a typical pulse-height spectrum obtained from the detector at the scattering angle $\theta=90°$. We observed three proton groups, elastic scattering group from neon nuclei, inelastic ($Q=-1.63$ Mev) group from Ne^{20} and the inelastic scattering ($Q=-1.27$ Mev) group from Ne^{22}.

Beside these groups from neon, the elastic scattering group from helium, contamination in the target, was found a little in the region of scattering angles $\theta<100°$. It overlapped with the inelastic scattering from Ne^{22} at the angle $\theta\sim75°$ and with that from Ne^{20} at the angle $\theta\sim90°$. The corrections were about 4% for the inelastic scattering group from Ne^{20} at $\theta=90°$ and almost negligible for the elastic scattering groups at the forward angles.

The inelastic scattering groups from both neon isotopes were affected by the background at the forward angles $\theta<30°$ as is shown in Fig. 3 (b). This background seems to be produced by the slit-edge and multiple scattering of the incident and scattered beam. The intensities of this background decreased rapidly with increasing scattering angle and its effects were sufficiently small at $\theta=30°$.

At the backward scattering angles the inelastic groups from Ne^{20} suffered further from the background of gamma-rays which seemed to be produced at the collimator slits for the incident beam, (Fig. 3 (c)). In the region of medium scattering angle $40°<\theta<140°$, the amounts of background which affected the inelastic scattering groups from Ne^{20} were at most 5% in total number.

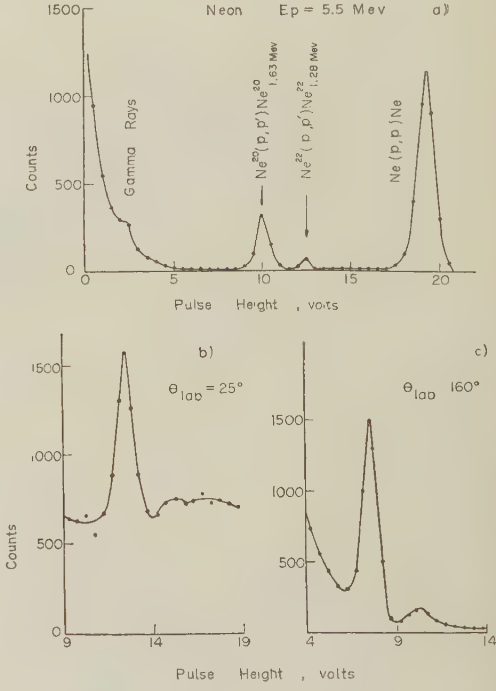

Fig. 3. The pulse-height spectra of the protons scattered from neon.

C. *Deduction of the differential cross section*

The differential cross section in laboratory system $\sigma(\theta)$ at a scattering angle θ is given in usual way. The correction owing to the finite size of the target and the beam were less than 1% even at small scattering angles. The zero of the scattering angle was checked experimentally by the comparisons of the yields at two corresponding scattering angles with respect to the incident beam ($\theta=\pm60°$, and $\pm70°$). The gas pressures were of the order of 150 mm Hg. As the intensities of protons at small angles are very large due to the elastic scattering, the counting rates were always adjusted so that the counting loss corrections would not exceed 1%.

Besides the errors for those factors stated above, there were further sources of errors. As will be shown in section 4, the measured cross sections showed remarkable variations with the change of proton energy. A change of energy by 0.1 Mev made in some extreme cases the cross sections varies by amounts of factor. Therefore we paid our attentions to the error resulting from the drift of the energy of incident beam which the small variations of the operating conditions of cyclotron might produce. However, the effects were found to be fairly small.

Considering all the factors mentioned in this section, the accuracies of our cross section measurement would be about 6% in relative values and about 10% in absolute values.

D. *Measurements*

The cyclotron were usually operated continuously for some ten hours. At every operation, the energies of the incident beam were measured as has been stated in section A. Six sets of measurements of the angular distributions for both scatterings were then performed at 5.50, 5.40, 5.30, 5.20, 5.05 and 4.95 Mev of incident proton energies. The inelastic scatterings from Ne^{22} were studied simultaneously. The angles of scattering in these measurements ranged from 20° to 164.5° in laboratory system with steps of 5° or 10°.

§ 4. Experimental Results

Fig. 4 shows the results for the elastic scattering from neon. At the smallest angle of scattering $\theta=21°$, the observed values are within 10% deviation from the calculated values based on pure Rutherford scattering.

Fig. 5 represents the results for the inelastic scattering from Ne^{20}. An anomaly is found at the energy of 5.25 Mev. Kondo, et al in our laboratory have measured also the scatterings of protons from neon by emulsion technique[11]. Both results are compatible in the position of the anomaly, the shapes of the angular distributions at corresponding energies and the feature of variations of cross sections with energy, except the relatively small differences in absolute values of cross sections especially in the region of reasonance peak.

§ 5. Discussion

As we can see in Figs. 4 and 5, the angular distributions of both elastic scattering groups from neon and inelastic scattering groups from Ne^{20} change their shapes rapidly with proton energy. At the energy of 5.25 Mev, we observe also an anomaly in the elastic scattering.

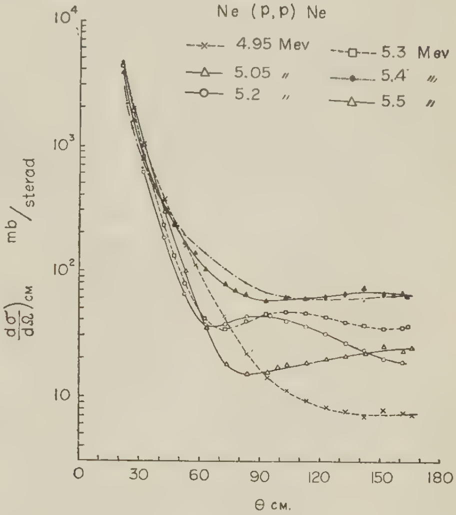

Fig. 4. The angular distributions of the elastic scatterings of protons from neon.

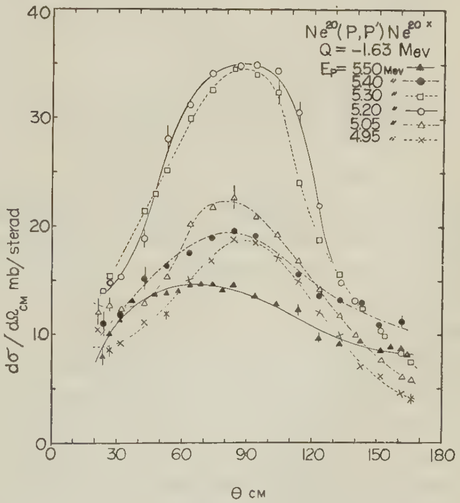

Fig. 5. The angular distributions of the reactions $Ne^{20}(p, p')Ne^{20*}$, $Q=-1.63$ Mev .

Next, as is seen in Fig. 6, the angular distributions of the inelastic scattering groups of Ne^{22} show the different shapes from those of Ne^{20} at the same enegy. The distribution shapes also change with energy.

All these features seem to support that our reactions proceed mainly through the formation of the compound nucleus. This arguments would be reasonable from the following two points. First, the energy region studied is not much higher than the so-called resonance region[12]. Thus the situations of both regions would not be different greatly. Second, the occurrence of resonance phenomena in our energy region seems to arise from the fact that the excitation energies of the compound nucleus Na^{21} are relatively low. As the separation energy of proton in Na^{21} is only 2.45 Mev, the excitation energy of Na^{21} corresponding to the proton energy of 5.5 Mev in nearly 7.8 Mev and is little higher than the excitation energy of 6.76 Mev in the mirror nucleus Ne^{21} formed by the Ne^{20} nucleus with zero energy neutron.

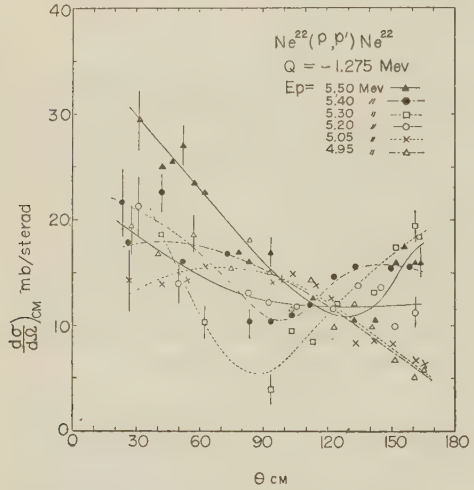

Fig. 6. The angular distributions of the reactions $Ne^{22}(p, p')Ne^{22*}$, $Q = -1.275$ Mev .

Here we should like to argue the shapes of the angular distributions of the inelastic scattering from Ne^{20}. The overall shapes of six results obtained are similar to each all and especially they are not so different from that obtained at 9. 51 Mev. As has been stated in introduction, the latter distribution shape has been interpreted by the direct interaction theory and the distribution shape is expected to vary slowly with energy. Thus, in spite of the many materials supporting the possible dominance of the compound nucleus formation process, this apparent insensitivity of the shapes to energy make ones fear that the direct process might play the main role in the energy region mentioned above. This argument is however, denied by our measurements of angular distributions which have been made at higher energies of 8.0, 9.5, 11.0, 12.5 and 14.0 Mev[13]. Among these results, the one at 9.5 Mev has showed the same distribution shape with that by Freemantle, et al. This distribution shapes at other energies have been, however, quite different from that at 9.5 Mev and also from that obtained by us in the neighborhood of 5.25 Mev. Therefore the distribution shape at 9.5 Mev is not the one which varies slowly with energy but the one which is seen rather especially in the restricted region of energy.

Now standing on the point of view that our reactions proceed through the formation of the compound nucleus, we shall discuss further our results.

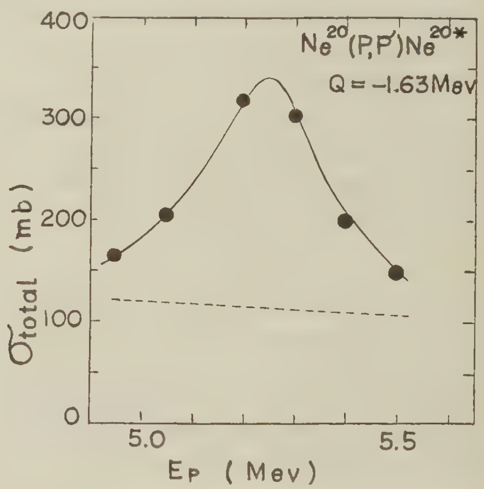

Fig. 7. The evergy dependence of the total cross sections for the reactions $Ne^{20}(p, p')Ne^{20*}$, $Q = -1.63$ Mev .

It must be emphasized that the anomaly found has a broad energy width of nearby 300 Kev. The experiments at energies below 4.4 Mev referred show that the mean level distance is about 0.2 Mev and the half widths of the nine levels observed are ranging from 12 Kev to 100 Kev, being usually some tens kilo volts[12]. The energy width observed by us is quite broader than those of lower levels. Here, we consider that this anomaly is due to a single level because the excitation curve for total cross sections vary with energy in the usual resonance behaviour as is shown in Fig. 7 and also the angular distributions do not change their shapes during the course.

Then it seems that the most parts of total cross sections are attributed to this anomaly. Fig. 7 shows that at the resonance energy of 5.25 Mev the cross section of this resonance stands for at least more than two third of the total cross section. The rest part may be attributed to the effects of some far levels or the direct process if possible. The extents to which the resonance parts amount in the total cross sections are, however, not so definite. In Fig. 7, the dotted line represents the part which varies slowly with E_p^{-1} dependence and the rest shows the resonance part which has a peak cross section of 230 mb at 5.25 Mev and a level width of 300 Kev.

The total cross section for the inelastic scattering of nucleons from a nucleus of a spin zero through a compound nucleus of spin J is given at resonance by the following well-known formula:

$$\sigma(p, p')=\frac{\pi}{k^2}\left(J+\frac{1}{2}\right)\frac{4\Gamma_{pJ}\Gamma_{p'J}}{\Gamma_J{}^2}. \qquad (1)$$

Where k is the wave number and Γ_J, Γ_{pJ} and $\Gamma_{p'J}$ are the total width, the partial width for the incident protons and that for the outgoing protons of the relevant compound level. Now $\pi/k^2=137$ mb and we may put approximately $\Gamma_J=\Gamma_{pJ}+\Gamma_{p'J}$. The factor $\pi(J+\frac{1}{2})/k^2$ in equation (1) represents the maximum value of the cross section for the reaction which proceeds through an intermediate state of spin J. Thus comparing the values of the experimental and theoretical cross sections, we can first eliminate the case $J=1/2$. In our case, the some fraction of resonance peak cross section, say 230 mb, is thought to be the result of a single level resonance. However, we must retain the possibility of $J=3/2$. As $3\pi/k^2$ is larger than $\sigma_t=340$ mb above, the cases $J\geq 5/2$ have the general possibility that even the whole of the peak total cross section are yet in the limit of the theoretical value due to a single level resonance process.

On the other hand, general consideration of the nuclear size and the incident proton energy limits the orbital angular momentum l in the incident state to $l\leq 3$ or 4 at most. Therefore $J=l\pm\frac{1}{2}$ would be limited to $J\leq 7/2$ probably.

Further selection of J among these values and assignment of parity π of the compound state must be performed under inquiring of the results for the angular distribution. The general theory of the angular distribution of product particles in a nuclear reaction which is applicable to our problem has been given in reference⁵⁾. The theoretical predictions are compared with our results, which is given by the following formula for the case of $E_p=5.20$ Mev:

$$\sigma(\theta)=\frac{\pi}{k^2}\frac{1}{2\pi}(1.14P_0+0.13P_1-0.88P_2 -0.18P_3+0.16P_4). \qquad (2)$$

Here P_n means the Legendre polynomial $P_n(\cos\theta)$. As contribution of the odd n part is relatively small, let us study tentatively one process through a compound nucleus level which can respond to the whole even parity part of the distribution formula and therefore seems to be dominant in our resonance phenomenon.

When we take into account the term P_4, we must exclude all processes with $J\leq 3/2$ because of the Yang's rule for the complexity of the angular distribution of the reaction¹⁴⁾. Then the process in which

$l=2$, $J(\pi)=5/2(+)$, $l'=0$ and 2, and $s'=5/2$

seems to be preferable. Here s' is the channel spin after the reaction, and the interference between outgoing waves has been taken into account. Next when we neglect the term P_4, the distributions of type $A-BP_2(\cos\theta)$ are reproduced respectively by the processes through $J(\pi)=3/2(-)$, $3/2(+)$ or $5/2(-)$.

Here, let us turn to the results for the elastic scattering. In order to search its anomaly, we rearrange our data shown in Fig. 4 into excitation curves at fourteen angles. Then the anomaly is found to vary with angle roughly according to the angle dependence of $-P_2(\cos\theta)$. The feature seems to support $l=2$ for the incident waves as the dominant process.

Concluding these arguments, we recommend $5/2(+)$ as the most possible state of the compound nucleus for the anomaly. As the phenomena are, however, rather complicate, the assignments $3/2(+)$, $5/2(-)$ and $3/2(-)$ have also some possibilities.

Acknowledgements

The authors would like to thank Professor T. Wakatsuki for his continued interest in the problem. We acknowledge their indebtedness to the Osaka University Cyclotron crew.

References

1) S. Kikuchi et al: Ann. Rep. Scient. Works, Fac. Sci. Osaka Univ. **3** (1955) 1.
2) H. Heitler, A. N. May and C. F. Powell: Proc. Roy. Soc. London **A**, **190** (1947) 180.
3) R. G. Freemantle, D. J. Prowse, A. Hosian and J. Rotblat: Phys. Rev. **96** (1954) 1270.
4) N. Bohr: Nature **137** (1936) 344. For example, J. Blatt and V. Weisskopf: *Theoretical Nuclear Physics* (John Wiley and Sons, Inc., 1952) chap. 8.
5) J. M. Blatt and L. C. Biedenharn: Rev. Mod. Phys. **24** (1952) 258. L. Wolfenstein: Phys. Rev. **82** (1951) 690. W. Hauser and H. Feshbach: Phys. Rev. **87** (1952) 366.
6) N. Austern, S. T. Butler and H. McManus: Phys. Rev. **92** (1953) 350. S. Hayakawa and S. Yoshida: Proc. Phys. Soc. **A**, **68** (1955) 656; Progr. Theor. Phys. **14** (1955) 1. D. M. Brink: Proc. Phys. Soc. **A**, **68** (1955) 994.
7) H. McManus: Report of the Brookhaven Conference on the Statistical Aspects of Nucleus (1955). S. T. Butler: Phys. Rev. **106** (1957) 272.
8) S. Yoshida: Proc. Phys. Soc. **A**, **69** (1956) 668.
9) S. Yamabe et al: J. Phys. Soc. Japan **12** (1958) 237.
10) C. W. Reich, G. C. Phillips and J. L. Russel: Phys. Rev. **104** (1956) 143.
11) M. Kondo and T. Yamazaki: J. Phys. Soc. Japan **13** (1958) 237.
12) W. Haeberli, A. Galonsky, E. Goldberg and R. Douglas: Phys. Rev. **91** (1953) 438. A. Galonsky, W. Haeberli, E. Goldberg and R. Douglas: Phys. Rev. **91** (1953) 439. W. C. Cox, J. J. Van Loef, P. M. Endt and J. C. Kluyver: Rev. Mod. Phys. **26** (1954) 95.
13) K. Matsuda, K. Kikuchi, S. Kobayashi, Y. Nagahara, Y. Oda, M. Takeda, C. Hu, T. Yamazaki and N. Takano: To be published in this Journal. This experiment was done in July 1958 with the 60″ cyclotron of Institute for Nuclear Study, University of Tokyo.
14) C. N. Yang: Phys. Rev. **74** (1948) 764.

JOURNAL OF THE PHYSICAL SOCIETY OF JAPAN, Vol. 14, No. 4, APRIL, 1959

On the Coefficients of Irreversible Processes in a Highly Ionized Gas

By Taro KIHARA

Department of Physics, Faculty of Science,
University of Tokyo

(Received December 4, 1958)

An effective interparticle potential, which is a modified Debye-Hückel potential, is introduced and discussed in order to eliminate simultaneous interactions between three particles or more in an ionized gas. For this potential weak-interaction asymptotes of collision cross sections necessary for the theory of irreversible processes are calculated without making further approximations. These cross sections are applied to relaxation between ion and electron temperatures and to the coefficient of viscosity.

§ 1. Introduction

In a previous paper¹⁾ by the same author phenomenological thermodynamics of irreversible processes was applied to plasmas. In the present paper the coefficients of irreversible processes in a gaseous plasma are treated in molecular terms.

Transport and relaxation phenomena in a highly ionized gas were treated recently by many authors. Their methods can be divided into two types. The one is the treatment by Cowling²⁾, Landshoff³⁾ and Chapman⁴⁾. It starts from the Boltzmann equation for dilute gases. The other is due to Spitzer and his coworkers⁵⁾,⁶⁾ who treat the problem as a stochastic process. To avoid divergence of cross sections these authors use a cut-off procedure or similar. When the cut-off is made at a length of the order of Debye shielding length, conclusions drawn from these two types are the same so far as the weak-interaction limits are concerned which do not depend on the length of cut-off.

In the present paper we are interested not only in the weak-interaction limits but in the asymptotic forms for weak interaction.

It is impossible at present to obtain exact expressions of the asymptotes. Hence all we can do is to make calculations in a least arbitrary way. Use of an effective interparticle potential is less arbitrary than the cut-off procedure, when the effective potential seems to be adequate.

In §§ 2 and 3 a model of effective interparticle potential will be discussed. By use of the model, weak-interaction asymptotes of cross section necessary for the theory of relaxation and transport phenomena will be calculated in § 4 without making further approximations. These cross sections will be applied, in § 5, to the relaxation between ion and electron temperatures. They will further applied, in § 6, to the coefficient of viscosity, for which accurate value even at the weak-interaction limit was not obtained before.

§ 2. Potential of Average Force between Two Particles

We first consider a highly ionized gas in thermal equillibrium composed of several species of particles with electric charges e_j and number densities n_j ($j=1, 2, \cdots$). The gas is supposed to be neutral

$$\sum n_j e_j = 0 \,. \tag{2.1}$$

All the particles is assumed to have no internal structure.

The charge of any particle in the plasma is shielded by surrounding charged particles. Our essential assumption is that the shielding is shared by many particles within a sphere of shielding radius. In other words, the plasma is assumed to be close to an ideal gas; or the absolute value of potential energy between two particles at the mean distance is assumed to be much smaller than the particle kinetic energy.

Then the electrostatic potential φ around a particle in the plasma satisfies, in the time average, the linear differential equation (the Poisson-Boltzmann equation)[7),8)]

$$\nabla^2\varphi = \kappa^2\varphi \tag{2.2}$$

with the Debye-Hückel characteristic constant κ defined by

$$\kappa^2 = 4\pi \sum n_j e_j^2 / kT \,, \tag{2.3}$$

kT being the Boltzmann constant times the temperature. The electrostatic potential around a particle with charge e_1 is given by its well-known solution

$$\varphi = e_j \exp(-\kappa r)/r \,, \tag{2.4}$$

r being the distance from the particle.

Now, let us consider the potential of average force between two charged particles shielded in the plasma. Relative position of the two particles is assumed to be fixed. Then the electric potential φ in the time average around the two-particle system is a solution

$$\varphi = \frac{e_1}{r_1}\exp(-\kappa r_1) + \frac{e_2}{r_2}\exp(-\kappa r_2)$$

of the equation (2.2). Here e_1 and e_2 are particle charges; r_1 and r_2 are distances from 1 and 2, respectively. If we multiply the φ at the position 1 by e_1 and the φ at 2 by e_2, sum up these, divide the sum by two, and take out the term depending on the distance r between the two particles, then we obtain

$$e_1 e_2 \exp(-\kappa r)/r \tag{2.5}$$

as the potential of average force. This is an elementary derivation of the result obtained by Kirkwood and Poirier[8)].

§ 3. Mayer's Theory and Effective Interparticle Potential

The free energy of an ordinary gas composed of N particles in volume V can be expanded into

$$F = F_{\text{ideal}} - NkT \sum_{\nu=1}^{\infty} \frac{\beta_\nu}{\nu+1} v^{-\nu} \,, \tag{3.1}$$

where $v=V/N$, and F_{ideal} means the free energy of an ideal gas. The coefficients β_ν's are given by Mayer's irreducible cluster integrals. When the interparticle potential is a function of the interparticle distance r only, β_1 in particular is given by

$$\beta_1 = 4\pi \sum_i \sum_j \frac{N_i}{N}\frac{N_j}{N} \int_0^\infty \left[\exp\left(-\frac{\psi_{ij}(r)}{kT}\right) - 1\right] r^2\,dr \,, \tag{3.2}$$

where N_j/N is the mole fraction of jth species and $\psi_{ij}(r)$ is the potential between ith and jth species.

In our case of plasma $\psi(r)$ is a Coulomb potential; hence the integral (3.2) for β_1 and corresponding integrals for $\beta_2, \beta_3, \cdots$ all diverge. Replacing first the Coulomb potential $1/r$ by $\exp(-\alpha r)/r$ with $\alpha>0$ and taking the limit $\alpha\to 0$ at the end, Mayer, in his paper on ionic solutions[9], found however that the asymptotic form of (3.1) for weak interaction agrees with the Debye-Hückel law

$$F=F_{\text{ideal}}-\frac{V}{3}\frac{\kappa^3 kT}{4\pi}\,, \qquad (3.3)$$

κ being the Debye-Hückel characteristic constant.

As a trial let us put

$$\Phi_{ij}(r)=e_i e_j \exp(-\kappa' r)/r \qquad (3.4)$$

in pace of $\psi_{ij}(r)$ in (3.2) and replace the right-hand side of (3.1) by its first two terms

$$F_{\text{ideal}}-NkT\cdot 2\pi v^{-1}\sum_i\sum_j \frac{N_i}{N}\frac{N_j}{N}$$
$$\times\int_0^\infty\left[\exp\left(-\frac{\Phi_{ij}(r)}{kT}\right)-1\right]r^2\,dr\,.$$

Here κ' is a positive constant. This becomes, when we take the weak interaction limit and use (2.1),

$$F_{\text{ideal}}-\frac{2\pi N}{vkT}\sum_i\sum_j\frac{N_i}{N}\frac{N_j}{N}$$
$$\times\int_0^\infty\frac{1}{2}\left(\frac{e_i e_j}{r}\right)^2\exp(-2\kappa' r)r^2\,dr$$

or

$$F_{\text{ideal}}-NkTv\kappa^4/32\pi\kappa'\,.$$

The last expression coincides with (3.3) when

$$\kappa'=3\kappa/8\,. \qquad (3.5)$$

Hence the Mayer series, the right-hand side of (3.1), is equal to the sum of its first two terms in which the Coulomb potential $e_i e_j/r$ are changed to $e_i e_j \exp(-\kappa' r)/r$ with an effective shielding constant $\kappa'=3\kappa/8$.

This fact may have some physical meaning. The νth term of the Mayer series comes from configurations in which ν particles interact simultaneously. *Interactions between three particles or more can be eliminated by use of a shielded interparticles potential instead of the Coulomb.* This effective interparticle potential (3.4) is not far from the potential (2.5) of the average force. The effective shielding constant is somewhat smaller than the Debye constant.

We have so far discussed in order to find a basis for using an effective interparticle potential in the calculation of coefficients of irreversible processes. For irreversible phenomena, unlike equilibrium properties, it is extremely difficult to calculate simultaneous interactions between three particles or more. Hence we shall neglect these interactions by use of an interparticle potential of the type

$$\Phi_{ij}(r)=e_i e_j \exp(-\kappa_{ij} r)/r\,. \qquad (3.6)$$

Here κ_{ij}'s are shielding constants which are assumed, for example, to be $3\kappa/8$. Although we can not exactly give the values of the shielding constants, final results do not sensitively depend on these values.

Only the case of weak interaction

$$\zeta_{ij}\equiv|e_i e_j|\kappa_{ij}/kT\ll 1 \qquad \text{for any } i, j \qquad (3.7)$$

will be treated in the following. In this case many particles may be present in a sphere of shielding radius. One might therefore think that, in such a situation, negligence of simultaneous interactions between three particles or more would not be permitted. This is not necessarily so. Let us consider, for example, diffraction of a light particle by two heavy particles according to a Coulomb field. Then it is true that in a configuration as shown in Fig. 1a the comming particles does not suffer diffraction although its effect will be counted twice in our approximation. However, there is also such a configuration as shown in Fig. 1b, where the scattering is four times as large as a single encounter. Since both configurations occur with equal probability, and since more general configurations are alike in this respect, the interference effect may be mostly cancelled in the average.

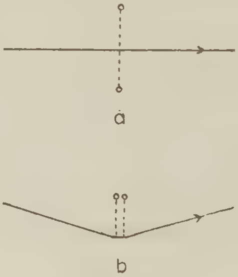

Fig. 1.

§ 4. Collision Cross Sections for the Shielded Potential

Having reduced the plasma to a "dilute" gas with the interparticle potential (3.6) we adopt Enskog-Chapman-Cowling's methods[10] of solving the Boltzmann equation. It is first necessary to calculate effective cross sections

$$\phi^{(l)}=\int_0^\infty(1-\cos^l\theta)gb\,db\qquad(l=1,2,\cdots)\quad(4.1)$$

for encounters between ith and jth species having particle masses m_i and m_j. Here θ is diffraction angle for the orbit of relative motion with the relative speed g and the impact parameter b. Then we have to know their statistical averages

$$\Omega_{ij}^{(l)}(r)=\sqrt{\pi}\int_0^\infty\phi^{(l)}\,\tilde{g}^{2r+2}\exp(-\tilde{g}^2)\,d\tilde{g}\,,\quad(4.2)$$

$(r=l,\ l+1,\cdots)$ where

$$\tilde{g}\equiv(m_{ij}/2kT)^{1/2}g\,,$$

and m_{ij} is the reduced mass,

$$m_{ij}=m_im_j(m_i+m_j)^{-1}\,.$$

The $\cos\theta$ in (4.1) is a function of

$$x\equiv\kappa_{ij}b\quad\text{and}\quad y\equiv m_{ij}g^2/2|e_ie_j|\kappa_{ij}\,.\quad(4.3)$$

By use of a dimensionless parameter

$$\zeta_{ij}\equiv|e_ie_j|\kappa_{ij}/kT=\tilde{g}^2/y\,,\qquad(4.4)$$

Ω can be expressed in the form

$$\Omega_{ij}^{(l)}(r)=\left(\frac{2\pi kT}{m_{ij}}\right)^{1/2}\left(\frac{e_ie_j}{2kT}\right)^2F_r^l(\zeta_{ij})\,,\qquad(4.5)$$

$$F_r^l(\zeta)=2\zeta^r\int_0^\infty\left[\int_0^\infty(1-\cos^l\theta)x\,dx\right]y^{r+1}\exp(-\zeta y)\,dy\,.\qquad(4.6)$$

What we need is the asymptotic forms of $F_r^l(\zeta)$'s for weak interaction, $\zeta\ll1$ (compare (3.7)). It will be shown in the following that these asymptotes are

$$F_r^l(\zeta)\approx(r-1)!\ \ l[\ln(3/4\zeta)-B_l+C_r]\,,\qquad(4.7)$$

where

$$B_1=0\,,\quad B_2=\frac{1}{2}\,,\quad B_3=\frac{2}{3}\,,\quad B_4=\frac{5}{6}\,,\ \cdots,$$

$$C_1=0\,,\quad C_2=1\,,\quad C_3=\frac{3}{2}\,,\quad C_4=\frac{11}{6}\,,\ \cdots.$$

The asymptote of the integral (4.6) is determined by the integrand with $y\gg1$. Hence the asymptote of $\int(1-\cos^l\theta)x\,dx$ for $y\gg1$ will be first evaluated. When two particles encounter with sufficiently large relative speed, effects of the shielding are negligible unless $\theta\ll1$. Hence we have

$$\tan(\theta/2)=e_ie_j/m_{ij}g^2b\qquad\text{unless}\quad\theta\ll1\,.$$

For $\theta\ll1$, a treatment similar to the perturbation method in classical dynamics can be applied:

$$\tan\frac{\theta}{2}=-\frac{1}{g}\int_b^\infty\frac{b}{r}\,\frac{1}{m_{ij}}\,\frac{d\Phi_{ij}}{dr}\left(\frac{dr}{dt}\right)^{-1}dr\,,$$

where t is the time and $dr/dt=g\sqrt{r^2-b^2}/r$. Hence

$$\tan\frac{\theta}{2}=-\frac{e_ie_j}{m_{ij}g^2}b\int_0^\infty\frac{d}{dr}\left(\frac{\exp(-\kappa_{ij}r)}{r}\right)(r^2-b^2)^{-1/2}\,dr=\frac{e_ie_j}{m_{ij}g^2b}f(x)\,,$$

where x is given by (4.3),

$$f(x)=-\int_1^\infty\frac{d}{d\rho}\left(\frac{\exp(-x\rho)}{\rho}\right)(\rho^2-1)^{-1/2}\,d\rho\,.$$

The function $f(x)$ decreases continuously from $f(0)=1$ to $f(\infty)=0$ as shown in Fig. 2. For all θ, therefore, we obtain, when $y\gg1$,

$$\tan\frac{\theta}{2}=\frac{e_ie_j}{m_{ij}g^2b}f(x)=\frac{f(x)}{2xy}$$

or

$$\cos\theta=\frac{(2xy)^2-f(x)^2}{(2xy)^2+f(x)^2}\,.$$

Let us choose an x_1 satisfying $y^{-1}\ll x_1\ll1$ and divide the domain of

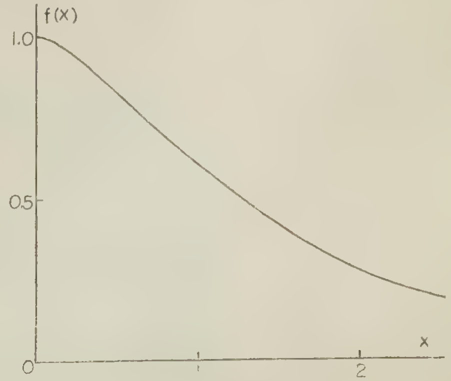

Fig. 2.

$$\int_0^\infty (1-\cos^l \theta) x\,dx \qquad \text{into} \qquad \int_0^{x_1} + \int_{x_1}^1 + \int_1^\infty .$$

Then

$$\int_0^{x_1} \approx \int_0^{x_1} \left[1-\left(\frac{(2xy)^2-1}{(2xy)^2+1}\right)^l\right] x\,dx$$

$$= \frac{1}{8y^2}\int_0^{(2x_1y)^2} \left[1-\left(\frac{\xi-1}{\xi+1}\right)^l\right] d\xi$$

$$= \frac{1}{8y^2}\int_0^{(2x_1y)^2} \sum_{p=1}^{l} (-1)^{p-1} \frac{l!}{p!(l-p)!}\left(\frac{2}{\xi+1}\right)^p d\xi$$

$$\approx \frac{l}{2y^2}[\ln(2x_1 y)-B_l]$$

where

$$B_1=0\,, \qquad B_l=\sum_{p=2}^{l}(-1)^p \frac{(l-1)!\,2^{p-2}}{p!\,(l-p)!\,(p-1)} \qquad \text{for} \quad l \geqq 2\,;$$

$$\int_{x_1}^1 \approx \int_{x_1}^1 2l\left[\frac{f(x)}{2xy}\right]^2 x\,dx = \frac{l}{2y^2}\int_{x_1}^1 \frac{f(x)^2}{x}dx$$

$$\approx \frac{l}{2y^2}\left[\ln\frac{1}{x_1} - \int_0^1 \frac{1-f(x)^2}{x}dx\right];$$

$$\int_1^\infty \approx \frac{l}{2y^2}\int_1^\infty \frac{f(x)^2}{x}dx .$$

Hence for $y \gg 1$ we obtain

$$\int_0^\infty (1-\cos^l\theta)x\,dx \approx \frac{l}{2y^2}\left[\ln\frac{2y}{\gamma'} - B_l\right],$$

where

$$\ln\gamma' = \int_0^1 \frac{1-f(x)^2}{x}dx - \int_1^\infty \frac{f(x)^2}{x}dx = 0.384 .$$

Substituting the result into (4.6) we have

$$F_r^l(\zeta) \approx l\zeta^r \int_0^\infty \left(\ln\frac{2y}{\gamma'} - B_l\right) y^{r-1}\exp(-\zeta y)\,dy$$

$$= (r-1)!\,l\left(\ln\frac{2}{\gamma'\zeta} - B_l\right) + l\int_0^\infty \ln\eta\cdot\eta^{r-1}\exp(-\eta)\,d\eta .$$

Let the last integral be $(r-1)!\,I_r$, then holds the recurrence formula

$$I_{r+1} = I_r + r^{-1} \qquad \text{for} \quad r \geqq 1\,,$$

and

$$I_1 = \lim_{\delta\to 0}\int_\delta^\infty \ln\eta\cdot\exp(-\eta)\,d\eta$$

$$= \lim\left[-\left\{\ln\eta\cdot\exp(-\eta)\right\}_\delta^\infty + \int_\delta^\infty \frac{\exp(-\eta)}{\eta}d\eta\right]$$

$$= -\int_0^1 \frac{1-\exp(-\eta)}{\eta}d\eta + \int_1^\infty \frac{\exp(-\eta)}{\eta}d\eta$$

$$= \ln(1/\gamma)\,,$$

where $\ln\gamma$ is the Euler constant 0.577. Our final result for the asymptotic form is, therefore,

$$F_r^l(\zeta) \approx (r-1)!\,l\,[\ln(2/\gamma\gamma'\zeta) - B_l + C_r]\,,$$

where

$$C_1=0\,,\qquad C_r=\frac{1}{r-1}+\frac{1}{r-2}+\cdots+1\qquad\text{for}\quad r\geqq 2\,.$$

This is equivalent to (4.7) since the constant $2/\gamma\gamma'$ is close to 3/4.

§ 5. Ion-Electron Relaxation

In this and next sections we consider a plasma composed of one type of positive ion (species 1) and electrons (species 2). The mass, charge and number density of the ion will be denoted by m_1, $e_1=Ze$ and n_1 and those of the electron by m_2, $e_2=-e$ and n_2, respectively. We assume $Zn_1=n_2$ and $Z\ll(m_1/m_2)^{1/2}$.

Since the mass ratio is far from unity, energy transfer per unit time is much smaller between an electron and an ion than between electrons or between ions. Hence the ion temperature T_1 and the electron temperature T_2 are often different although the velocity ditributions are both uniform and Maxwellian:

$$f_i(\boldsymbol{c}_j)=n_j\left(\frac{m_j}{2\pi kT_j}\right)^{3/2}\exp\left(-\frac{m_jc_j^2}{2kT_j}\right)\tag{5.1}$$

($j=1$ and 2) $\boldsymbol{c}_j$ being the particle velocities. These velocity distributions vary with time t through the temperatures only:

$$\frac{\partial f_j}{\partial t}=\left(\frac{m_jc_j^2}{2kT_j}-\frac{3}{2}\right)\frac{f_j}{T_j}\frac{dT_j}{dt}\,,\tag{5.2}$$

Our aim is to calculate the rate of relaxation between ion and electron temperatures.

The $\partial f_1/\partial t$ for ions is given by its time rate of increase due to encounters with electrons:

$$\left(\frac{m_1c_1^2}{2kT_1}-\frac{3}{2}\right)\frac{f_1}{T_1}\frac{dT_1}{dt}=\iiint(f_1'f_2'-f_1f_2)gb\,db\,d\varepsilon\,d\boldsymbol{c}_2\,,$$

in which $g=|\boldsymbol{c}_1-\boldsymbol{c}_2|$ as in § 4. Here $f_1'f_2'-f_1f_2$ is the abbreviation for $f_1(\boldsymbol{c}_1')f_2(\boldsymbol{c}_2')-f_1(\boldsymbol{c}_1)f_2(\boldsymbol{c}_2)$; $\boldsymbol{c}_1'$ and $\boldsymbol{c}_2'$ are the final velocities of an ion and an electron encountering with the initial velocities $\boldsymbol{c}_1$, $\boldsymbol{c}_2$, the impact parameter b and the diffraction azimuth ε for the orbit of relative motion. Multiplying both sides by $(m_1c_1^2/2kT_1)-(3/2)$ and integrating with respect to $\boldsymbol{c}_1$, we obtain

$$\frac{3}{2}n_1\frac{1}{T_1}\frac{dT_1}{dt}=\iiiint\left(\frac{m_1c_1^2}{2kT_1}-\frac{3}{2}\right)(f_1'f_2'-f_1f_2)gb\,db\,d\varepsilon\,d\boldsymbol{c}_1\,d\boldsymbol{c}_2\,.$$

The right-hand side can be transformed into

$$-\frac{m_1}{2kT_1}\iiiint(c_1^2-c_1'^2)f_1f_2\,gb\,db\,d\varepsilon\,d\boldsymbol{c}_1\,d\boldsymbol{c}_2$$

by use of the inverse encounters for $f_1'f_2'$. Introducing the center-of-mass velocity $\boldsymbol{G}$ and the relative velocity $\boldsymbol{g}$ by

$$\boldsymbol{G}=\frac{m_1}{m_1+m_2}\boldsymbol{c}_1+\frac{m_2}{m_1+m_2}\boldsymbol{c}_2\qquad\text{and}\qquad\boldsymbol{g}=\boldsymbol{c}_1-\boldsymbol{c}_2\,,$$

we have

$$c_1^2-c_1'^2=\frac{2m_2}{m_1+m_2}\boldsymbol{G}\cdot(\boldsymbol{g}-\boldsymbol{g}')\,,$$

where $\boldsymbol{g}'\equiv\boldsymbol{c}_1'-\boldsymbol{c}_2'$ is the relative velocity after encounter. Hence

$$\frac{3}{2}n_1k\frac{dT_1}{dt}=-\frac{m_1m_2}{m_1+m_2}\iiiint f_1f_2\boldsymbol{G}\cdot(\boldsymbol{g}-\boldsymbol{g}')gb\,db\,d\varepsilon\,d\boldsymbol{c}_1\,d\boldsymbol{c}_2\,.$$

Taking two unit vectors, $\boldsymbol{h}$ and $\boldsymbol{i}$, perpendicular to $\boldsymbol{g}$ and to each other, we can express $\boldsymbol{g}'$ as

$$\boldsymbol{g}'=\boldsymbol{g}\cos\theta+g\boldsymbol{h}\sin\theta\cos\varepsilon+g\boldsymbol{i}\sin\theta\sin\varepsilon\ .$$

Hence

$$\iint(\boldsymbol{g}-\boldsymbol{g}')gb\,db\,d\varepsilon=2\pi\int_0^\infty\boldsymbol{g}(1-\cos\theta)gb\,db=2\pi\phi^{(1)}\boldsymbol{g}$$

by the definition (4.1) for $\phi^{(1)}$. Thus we have

$$n_1k\frac{dT_1}{dt}=-\frac{4\pi}{3}\frac{m_1m_2}{m_1+m_2}\iint f_1f_2\boldsymbol{G}\cdot\boldsymbol{g}\phi^{(1)}\,d\boldsymbol{c}_1\,d\boldsymbol{c}_2\ .$$

Similarly

$$n_2k\frac{dT_2}{dt}=\frac{4\pi}{3}\frac{m_1m_2}{m_1+m_2}\iint f_1f_2\boldsymbol{G}\cdot\boldsymbol{g}\phi^{(1)}\,d\boldsymbol{c}_1\,d\boldsymbol{c}_2\ .$$

From these two relations we obtain

$$k\frac{d}{dt}(T_2-T_1)=\frac{4\pi}{3}\frac{n_1+n_2}{n_1n_2}\frac{m_1m_2}{m_1+m_2}\iint f_1f_2\boldsymbol{G}\cdot\boldsymbol{g}\phi^{(1)}\,d\boldsymbol{c}_1\,d\boldsymbol{c}_2\ . \tag{5.3}$$

The cross section $\phi^{(1)}$ is a function of the reduced mass $m_1m_2/(m_1+m_2)$ and the relative speed g. In the present case the former can be put equal to m_2, and the latter is

$$g=(c_1^2-2\boldsymbol{c}_1\cdot\boldsymbol{c}_2+c_2^2)^{1/2}\doteqdot c_2-\boldsymbol{c}_1\cdot\boldsymbol{c}_2/c_2\ ,$$

Hence the cross section becomes

$$\phi^{(1)}(g)=\phi^{(1)}(c_2)-\frac{\boldsymbol{c}_1\cdot\boldsymbol{c}_2}{c_2}\frac{\partial\phi^{(1)}}{\partial c_2}\ .$$

Inserting this into (5.3) with $\boldsymbol{G}$ and $\boldsymbol{g}$ expressed in terms of $\boldsymbol{c}_1$ and $\boldsymbol{c}_2$, denoting $\phi^{(1)}(\boldsymbol{c}_2)$ by $\phi^{(1)}$ anew, and neglecting small quantities we have

$$\begin{aligned}k\frac{d}{dt}(T_2-T_1)&=\frac{4\pi}{3}\frac{n_1+n_2}{n_1n_2}\frac{m_2}{m_1}\iint f_1f_2\left[(m_1c_1^2-m_2c_2^2)\phi^{(1)}+\frac{1}{3}m_1c_1^2c_2\frac{\partial\phi^{(1)}}{\partial c_2}\right]d\boldsymbol{c}_1\,d\boldsymbol{c}_2\\&=\frac{(4\pi)^2}{3}\frac{n_1+n_2}{n_2}\frac{m_2}{m_1}\int_0^\infty f_2\left[(3kT_1-m_2c_2^2)\phi^{(1)}+kT_1c_2\frac{\partial\phi^{(1)}}{\partial c_2}\right]c_2^2\,dc_2\ ,\end{aligned}$$

which can be reduced, after integration by parts, to

$$k\frac{d}{dt}(T_2-T_1)=-\frac{(4\pi)^2}{3}\frac{n_1+n_2}{n_2}\frac{(m_2)^2}{m_1}\frac{T_2-T_1}{T_2}\int_0^\infty f_2\phi^{(1)}c_2^4\,dc_2$$

or

$$-\frac{1}{T_2-T_1}\frac{d}{dt}(T_2-T_1)=\frac{32}{3}(n_1+n_2)\frac{m_2}{m_1}\sqrt{\pi}\int_0^\infty\exp(-\tilde{c}_2^2)\phi^{(1)}\tilde{c}_2^4\,d\tilde{c}_2$$

with $\tilde{c}=(m_2/2kT_2)^{1/2}c_2$. Hence, by the definition (4.2) for Ω, we finally obtain

$$-\frac{1}{T_2-T_1}\frac{d}{dt}(T_2-T_1)=\frac{32}{3}(n_1+n_2)\frac{m_2}{m_1}\Omega_{12}^{(1)}(1)\ . \tag{5.4}$$

Here $\Omega_{12}^{(1)}(1)$ is given by (4.2) with (4.7), but it refers to the electron temperature:

$$\Omega_{12}^{(1)}(1)=\left(\frac{2\pi kT_2}{m_2}\right)^{1/2}\left(\frac{Ze_2}{2kT_2}\right)^2\ln\frac{3kT_2}{4Ze^2\kappa_{12}}\ . \tag{5.5}$$

This is an improvement of the corresponding result by previous authors (Compare Spitzer's tract⁶⁾ Eq. (5.31)).

In the particular case where the temperature difference is small, the rate of relaxation, the right-hand side of (5.4), is independent of the time, and $|T_2-T_1|$ is proportional to exp $(-t/\tau)$ with a constant relaxation time τ.

Appendix to § 5.

It is interesting to note that a similar conclusion can be drawn from the viewpoint of the collective motion of plasma oscillation with the thermal energy. The collection of electrons is considered to make thermal oscillations of the wave length greater than the order of the Debye shielding length κ^{-1} (compare Pines and Bohm¹¹⁾). The collective motion in unit volume therefore has approximately κ^3 degrees of freedom. Since each mode of oscillation has the energy of order kT, the electric field due to one mode of oscillation is $(kT)^{1/2}$. Hence the total electric field acting on an ion is of the order of $(\kappa^3 kT)^{1/2}$, the acceleration being $(Ze/m_1)(\kappa^3 kT)^{1/2}$ with the ion mass m_1. The velocity which a rest ion has after one period τ_p of the plasma oscillation is therefore $(Ze/m_1)(\kappa^3 kT)^{1/2}\tau_p$, and after $N(\gg 1)$ periods, $N^{1/2}$ times this quantity. The relaxation time τ is given by the relationship

$$\frac{m_1}{2}\left[\left(\frac{\tau}{\tau_p}\right)^{1/2}\frac{Ze}{m_1}(\kappa^3 kT)^{1/2}\tau_p\right]^2 \sim \frac{1}{2}kT$$

or

$$\tau^{-1} \sim \frac{(Ze)^2}{m_1}\kappa^3\tau_p\,.$$

Since $\kappa^2 \sim ne^2/kT$ and $\tau_p \sim (m_2/ne^2)^{1/2}$ with the number density n and the mass m_2 of electrons, we finally obtain

$$\tau^{-1} \sim n(Ze^2)(kT)^{-3/2} m_2^{1/2} m_1^{-1}\,,$$

which agrees with the previous result so far as the order of magnitude is concerned.

§ 6. Viscosity

Chapman-Cowling's¹⁰⁾ scheme, slightly modified by the present author¹²⁾, of approximation to the coefficient of viscosity will be used in the following. We are to take into account the fact that the ion mass m_1 is much larger than the electron mass m_2, and hence the momentum is transported only through ions.

Thus, first approximation η_{I} to the viscosity η is given by

$$\eta_{\text{I}} = 5kT/8\Omega_{11}^{(2)}(2)\,.$$

Substituting our expression for Ω, (4.5) with (4.7), we obtain

$$\eta_{\text{I}} = \frac{5}{8}\left(\frac{m_1 kT}{\pi}\right)^{1/2}\left(\frac{kT}{Z^2e^2}\right)^2\left(\ln\frac{3kT}{4Z^2e^2\kappa_{11}}+\frac{1}{2}\right)^{-1}. \tag{6.1}$$

A second approximation η_{II} is of the form

$$\eta_{\text{II}} = \eta_{\text{I}}(1+\mathcal{E})\,, \tag{6.2}$$

where

$$\begin{aligned}\mathcal{E} &= \frac{3}{49}\left(\frac{7}{2}-\frac{\Omega_{11}^{(2)}(3)}{\Omega_{11}^{(2)}(2)}\right)^2\\ &= \frac{3}{49}\left(\frac{3}{2}-\frac{1}{\ln(3kT/4Z^2e^2\kappa_{11})+\frac{1}{2}}\right)^2.\end{aligned} \tag{6.3}$$

Since $\mathcal{E}$ is small, it is natural to expect that higher approximations are close to the second. In fact, at the weak-interaction limit where $\ln(kT/Z^2e^2\kappa_{11})\gg 1$, η is equal to $1.16\eta_{\text{I}}$, while $\eta_{\text{II}}=1.14\eta_{\text{I}}$.

Coefficients of other transport phenomena can be treated likewise, although first approximations are not accurate enough and higher ones are complicated.

The author wishes to thank Mr. Y. Midzuno for helpful discussions.

Note added in proof. Collision cross sections for the shielded Coulomb potential have just been treated in a similar manner by R.L. Liboff: Phys. Fluids **2** (1959) 40.

References

1) T. Kihara: J. Phys. Soc. Japan **14** (1959).
2) T. G. Cowling: Proc. Roy. Soc. London A, **183** (1945) 453.
3) R. Landshoff: Phys. Rev. **76** (1949) 904.
4) S. Chapman: Astrophys. J. **120** (1954) 151.
5) R. S. Cohen, L. Spitzer and P. McR. Routly: Phys. Rev. **80** (1950) 230. L. Spitzer and R. Härm: Phys. Rev. **89** (1953) 977.
6) L. Spitzer: *Physics of Fully Ionized Gases* (Interscience Publ., 1956).
7) P. Debye and E. Hückel: Phys. Z. **24** (1923) 185.
8) J. G. Kirkwood: J. Chem. Phys. **2** (1934) 767. J. G. Kirkwood and J. C. Poirier: J. Phys. Chem. **58** (1954) 591.
9) J. E. Mayer: J. Chem. Phys. **18** (1950) 1426.
10) S. Chapman and T. G. Cowling: *The Mathematical Theory of Non-Uniform Gases*, 2nd. ed. (Cambridge, 1952).
11) D. Pines and D. Bohm: Phys. Rev. **85** (1952) 338.

12) T. Kihara: *Imperfect Gases* (1949, Asakura, in Japanese). See also J. O. Hirschfelder, C. F. Curtiss and R. B. Bird: *Molecular Theory of Gases and Liquids* (Wiley, 1954).

JOURNAL OF THE PHYSICAL SOCIETY OF JAPAN, Vol. 14, No. 4, APRIL, 1959

The General Theory of Transport: The Difference between Electric Field and Density Gradient

By Tadao KASUYA

Physical Institute, Nagoya University

(Received August 4, 1958)

The difference between the electric currents due to the external electric field and the gradient of the chemical potential is discussed based on the general theory of transport coefficients. In the limit of weak magnetic field ($\hbar w \ll \kappa T$, where ω is Larmor frequency, κ Boltzmann constant, T absolute temperature) and weak collision ($\hbar/\tau \ll \kappa T$, where τ means the relaxation time), Einstein relation is applicable. In the limit of strong magnetic field, the current due to the gradient of the chemical potential exhibits the oscillatory behaviour similar to that of diamagnetism.

§ 1. Introduction

In the previous paper titled "A Theory of Impurity Conduction I1)" (hereafter refered to as [I] for brevity), we discussed the general theory of transport equation and emphasized that under the strong magnetic field the well-known Einstein relation is not applicable. That is, the electrical currents due to the external electric field and the gradient of the chemical potential are different in general, because the former is induced by the motion due to the external force and the latter is induced by that due to the internal strain of the system.

In this paper, we discuss this problem in more detail in the case that the Hamiltonian of the system is written by the sum of one electron Hamiltonian, namely in the case of impurity scattering. In the case that the many body correlation is essentially important, the situation is fairly complicated and is not treated in this paper.

§ 2. General Discussions

As was treated in [I], when the external force is written in terms of the potential $\varphi(\boldsymbol{r}, t)$, the expectation value of the electrical current density operator $\boldsymbol{j}(\boldsymbol{r})$ at position $\boldsymbol{r}$ and time t is given by

$$\langle \boldsymbol{j}(\boldsymbol{r}, t)\rangle = \mathrm{Tr}\exp(-\beta\mathscr{H})\left\{\boldsymbol{j}(\boldsymbol{r}) + \frac{1}{e}\int_0^t dt_1\int_0^\beta d\lambda\int d\boldsymbol{r}'\nabla'\varphi(\boldsymbol{r}', t)\cdot\boldsymbol{j}(\boldsymbol{r}')\boldsymbol{j}(\boldsymbol{r}, t_1 + i\hbar\lambda)\right\} \tag{1}$$

where

$$\beta = \frac{1}{\kappa T}, \tag{2}$$

$$\boldsymbol{j}(\boldsymbol{r}, t) = \exp(i\mathscr{H}t/\hbar)\frac{e}{2}\sum_i\{\boldsymbol{v}_i\delta(\boldsymbol{r}-\boldsymbol{r}_i) + \delta(\boldsymbol{r}-\boldsymbol{r}_i)\boldsymbol{v}_i\}\exp(-i\mathscr{H}t/\hbar), \tag{3}$$

and $\mathscr{H}$ is the Hamiltonian of the system.

When the potential is given by

$$\varphi(\boldsymbol{r}, t) = \varphi_k\exp(i\boldsymbol{k}\boldsymbol{r}), \tag{4}$$

it is convenient to use the Fourier component of the current density operator $\boldsymbol{j}(\boldsymbol{r})$, namely

$$\begin{aligned}\boldsymbol{j}_k &= \int \boldsymbol{j}(\boldsymbol{r}) \exp(i\boldsymbol{kr})\, d\boldsymbol{r} \\ &= \frac{e}{2} \sum_i (\boldsymbol{v}_i \exp(i\boldsymbol{kr}_i) + \exp(i\boldsymbol{kr}_i)\, \boldsymbol{v}_i)\,. \end{aligned} \tag{5}$$

Then, Eq. (1) becomes

$$\langle \boldsymbol{j}_{-k}(t)\rangle_{\text{force}} = \mathrm{Tr} \exp(-\beta \mathscr{H}) \left\{ \boldsymbol{j}_{-k} + ik\varphi_k e^{-1} \int_0^t dt_1 \int_0^\beta d\lambda \cdot \boldsymbol{j}_k \boldsymbol{j}_{-k}(t_1 + i\hbar\lambda) \right\}. \tag{6}$$

On the other hand, when there exists the internal strain and it is given by the potential of stress, that is, $-\varphi_k \exp(i\boldsymbol{kr})$, the expectation value of the current density operator is given as follows as is given in [I],

$$\langle \boldsymbol{j}_{-k}(t)\rangle_{\text{strain}} = \langle \boldsymbol{j}_{-k}(t)\rangle_{\text{ad}} + \langle \boldsymbol{j}_{-k}(t)\rangle_{\text{force}}\,, \tag{7}$$

$$\langle \boldsymbol{j}_{-k}(t)\rangle_{\text{ad}} = -\mathrm{Tr} \exp(-\beta \mathscr{H}) \int_0^\beta d\lambda\, \varphi_k n_k(i\hbar\lambda)\, \boldsymbol{j}_{-k}\,, \tag{7}$$

where

$$n_k(i\hbar\lambda) = \exp(\lambda \mathscr{H}) \sum_i \exp(i\boldsymbol{kr}_i) \exp(-\lambda \mathscr{H})\,. \tag{9}$$

In Eq. (7), the second term is the same as the expression (6) and the first term, that is given by Eq. (7), is the additive term characteristic of the strain. Our main problem is how to evaluate Eq. (8).

At first, we calculate Eq. (6). We assume here that the Hamiltonian $\mathscr{H}$ is written as the sum of the one electron Hamiltonian and rewrite the operators $\boldsymbol{j}_k$ and n_k by the second quantization method taking the eigenfunction of the one electron Hamiltonian as the basic wave function. Then performing the integrations with respect to t_1 and λ, Eq. (6) becomes

$$\begin{aligned}\langle \boldsymbol{j}_{-k}(t)\rangle_{\text{force}} = \frac{ik\varphi_k}{e\kappa T} \mathrm{Tr} \exp(-\beta \mathscr{H}) \Bigg[& \sum_{s \neq s'}\sum \cdot \langle s|\boldsymbol{j}_k|s'\rangle\langle s'|\boldsymbol{j}_{-k}|s\rangle \frac{\hbar}{E-E'} \frac{e^{\mathcal{E}-\mathcal{E}'}-1}{\mathcal{E}-\mathcal{E}'} \\ & \times \left\{ \frac{1}{i}\left(1-\cos\frac{E-E'}{\hbar}t\right) + \sin\frac{E-E'}{\hbar}t \right\} \boldsymbol{n}_s(1-\boldsymbol{n}_{s'}) \\ & + \sum_s \sum_{s'} \cdot \langle s|\boldsymbol{j}_k|s\rangle\langle s'|\boldsymbol{j}_{-k}|s'\rangle t \boldsymbol{n}_s \boldsymbol{n}_{s'} \Bigg]\,, \end{aligned} \tag{10}$$

where $\boldsymbol{n}_s$ is the operator of the occupation number of the state s and has the eigenvalue 0 or 1. Performing the trace as usual, $\boldsymbol{n}_s$ is replaced by the Fermi distribution function in thermal equilibrium $f(\mathcal{E})$, that is

$$\boldsymbol{n}_s \to f(\mathcal{E}) = [e^{\mathcal{E}}+1]^{-1}\,, \qquad \mathcal{E} = \frac{E_s - \zeta}{\kappa T}\,. \tag{11}$$

In the second term, when s' is the same state as s, the relation $\boldsymbol{n}_s\boldsymbol{n}_s = \boldsymbol{n}_s$ is used. Thus Eq. (10) becomes

$$\begin{aligned}\langle \boldsymbol{j}_{-k}(t)\rangle_{\text{force}} = \frac{ik\varphi_k}{e\kappa T} \Bigg[& \sum_{s \neq s'}\sum \cdot \langle s|\boldsymbol{j}_k|s'\rangle\langle s'|\boldsymbol{j}_{-k}|s\rangle \frac{\hbar}{E-E'} F(s, s') \\ & \times \left\{ \frac{1}{i}\left(1-\cos\frac{E-E'}{\hbar}t\right) + \sin\frac{E-E'}{\hbar}t \right\} \\ & + \sum_s \sum_{s'} \cdot \langle s|\boldsymbol{j}_k|s\rangle\langle s'|\boldsymbol{j}_{-k}|s'\rangle \{f(\mathcal{E})f(\mathcal{E}') + f_1(\mathcal{E})\delta_{ss'}\} t \Bigg]\,; \end{aligned} \tag{12}$$

where

$$F(s,s')=\frac{e^{\varepsilon}-e^{\varepsilon'}}{\varepsilon-\varepsilon'}f(\varepsilon)f(\varepsilon')=F(s',s)\,, \tag{13}$$

and

$$f_1(\varepsilon)=f(\varepsilon)\{1-f(\varepsilon)\}=[(e^{\varepsilon}+1)(1+e^{-\varepsilon})]^{-1}\,. \tag{14}$$

This equation is equivalent to Eq. (22) of [I] when $\boldsymbol{j}_k$ is replaced by $\boldsymbol{j}$.

Next, we evaluate Eq. (8) by the same method as the above, then we obtain the equation

$$\langle \boldsymbol{j}_{-k}(t)\rangle_{\mathrm{ad}}=-\frac{\varphi_k}{\kappa T}\Big[\sum_{s\neq s'}\sum\langle s|n_k|s'\rangle\langle s'|\boldsymbol{j}_{-k}|s\rangle F(s,s')$$
$$+\sum_{s}\sum_{s'}\langle s|n_k|s\rangle\langle s'|\boldsymbol{j}_{-k}|s'\rangle\{f(\varepsilon)f(\varepsilon')+f_1(\varepsilon)\delta_{ss'}\}\Big]. \tag{15}$$

Considering the relations

$$\sum_{s}\langle s|n_k|s\rangle f(\varepsilon)=0\,, \tag{16}$$

and

$$F(s,s)=\lim_{E'\to E}F(s,s')=f_1(\varepsilon)\,, \tag{17}$$

Eq. (15) becomes

$$\langle \boldsymbol{j}_{-k}(t)\rangle_{\mathrm{ad}}=-\frac{\varphi_k}{\kappa T}\sum_{s}\sum_{s'}\langle s|n_k|s'\rangle\langle s'|\boldsymbol{j}_{-k}|s\rangle F(s,s')\,. \tag{18}$$

Now we assume that the external potential $\varphi(\boldsymbol{r})$ varies very slowly in space and it is sufficient to take only the linear terms of k (hereafter we choose the direction of the gradient of the potential, $\boldsymbol{k}$, as the x-axis). Then we may expand n_k as $1+i\boldsymbol{k}\sum_i \boldsymbol{r}_i+\cdots$ and take only the linear terms of k. Further replacing the matrix element of $\boldsymbol{r}_i$ by that of $\boldsymbol{j}_i$, Eq. (18) becomes

$$\langle \boldsymbol{j}_{-k}(t)\rangle_{\mathrm{ad}}=-\frac{i\varphi_k}{e\kappa T}\Big[\sum_{s\neq s'}\sum\{\boldsymbol{k}\cdot\langle s|\boldsymbol{j}|s'\rangle\langle s'|\boldsymbol{j}|s\rangle-\langle s|\boldsymbol{j}|s'\rangle\boldsymbol{k}\cdot\langle s'|\boldsymbol{j}|s\rangle\}\frac{\hbar}{E-E'}\{F(s,s')-f_1(\varepsilon)\}\Big]. \tag{19}$$

The above expansion of n_k may be allowed when the extension of the electron wave function or the mean free path of the electron is smaller than k^{-1}.

From the above equation, we can obtain easily the following result that the additive current of x direction vanishes. This result implies that the well-known Kelvin relations concerning the thermoelectricity are satisfied in general.

The additive current perpendicular to the potential gradient does not vanish in general when the system has a particular direction (say the z-direction). The typical cases are such that the external magnetic field is applied in the z-direction, or the electron spins are ordered in the z-direction. Even in these cases, however, the additive current becomes very small if $F(s,s')$ and $\frac{1}{2}\{f_1(\varepsilon)+f_1(\varepsilon')\}$ are nearly equal. From Eq. (13), the above condition is equivalent to

$$\frac{E_s-E_{s'}}{\kappa T}\ll 1\,. \tag{20}$$

In the phenomena such as the anomalous Hall current in ferromagnetic metals, where the inter-band transition is essentially important, the above condition is not applicable. Concerning this current there were some disputes and detailed discussions may be given in another paper[2].

In the phenomena where the intra-band transition is important, the above condition is written approximately as

$$\frac{\hbar\omega}{\kappa T}\ll 1\,,\qquad \frac{\hbar}{\tau\kappa T}\ll 1\,, \tag{21}$$

where ω is the Larmor frequency

$$\omega=\frac{eH}{mc}\,, \tag{22}$$

and τ is the ordinary relaxation time, because the matrix element $\langle s|\boldsymbol{j}|s'\rangle$ is nearly zero when the energy difference $E_s - E_{s'}$ is larger than $\hbar\omega$ or $\hbar/\tau$. The conditions, (21), are just equivalent to the condition that the ordinary Boltzmann equation is applicable. As was discussed in [I], the condition that the Boltzmann-Bloch equation is applicable is approximately replaced by $\hbar/\tau\zeta \ll 1$ instead of $\hbar/\tau\kappa T \ll 1$, the same situation is also seen in Eq. (19). The more qualitative discussions in the case of strong magnetic field are given in the following section.

§ 3. Hall Current in a Strong Magnetic Field

As is discussed in the above section, the Hall currents induced by the electric field and the gradient of the chemical potential differ from each other when $\hbar\omega/\kappa T$ is much lager than unity. Here, we consider this problem in more detail. For simplicity, we consider the case that the collision effect is negligibly small and the system is treated as free electron system with effective mass m.

We choose the direction of the magnetic field as the z-axis, the direction of the force as the x-axis and consider the electrical current in the y-axis. We choose the gauge to write the vector potential $\boldsymbol{A}(\boldsymbol{r})$ as

$$A_x = A_z = 0\,, \qquad A_y = Hx\,. \tag{23}$$

Then, the Hamiltonian is written as

$$\mathscr{H} = \frac{1}{2m} \sum_i \left\{ p_{xi}^2 + \left(p_{yi} + \frac{e}{c} H x_i \right)^2 + p_{zi}^2 \right\}. \tag{24}$$

The eigenfunction of this Hamiltonian is

$$\psi_{k_z k_y n}(\boldsymbol{r}) = \exp(ik_y y + ik_z z) \exp\left(-\frac{(x-x_0)^2}{2a^2} \right) H_n\left(\frac{x-x_0}{a} \right), \tag{25}$$

where $H_n(x)$ represents the function of the n-th order harmonic oscillation with the centre at $x = x_0$, and

$$a^2 = \frac{\hbar c}{eH}\,, \qquad x_0 = -\frac{\hbar c}{eH} k_y\,. \tag{26}$$

The eigenvalue of the Hamiltonian is written as

$$E_{nk_z} = n\hbar\omega + \frac{\hbar^2 k_z^2}{2m}\,, \tag{27}$$

where

$$\omega = \frac{eH}{mc}\,. \tag{28}$$

In the steady state, the Hall currents due to the electric field and the gradient of the chemical potential are written from Eqs. (19) and (12) as

$$\langle j_{y,-k} \rangle_{\text{force}} = \frac{ik\varphi_k}{2e\kappa T} \sum_{s \neq s'}\sum \{ \langle s|j_x|s'\rangle\langle s'|j_y|s\rangle - \langle s|j_y|s'\rangle\langle s'|j_x|s\rangle \} \frac{\hbar}{E-E'} F(s, s')\,. \tag{29}$$

$$\langle j_{y,-k} \rangle_{\text{strain}} = \frac{ik\varphi_k}{2e\kappa T} \sum_{s \neq s'}\sum \{ \langle s|j_x|s'\rangle\langle s'|j_y|s\rangle - \langle s|j_y|s'\rangle\langle s'|j_x|s\rangle \} \frac{\hbar}{E-E'} f_1(\mathcal{E})\,. \tag{30}$$

because, considering the conditions mentioned above, the first term of Eq. (19) cancels out the current of Eq. (12) in steady state.

Using our model, the matrix elements of j_x and j_y become

$$\left. \begin{aligned} \langle s|j_x|s'\rangle &= ie\left(\frac{\hbar\omega}{2m} \right)^{1/2} \langle s|a_+ - a_-|s'\rangle\,, \\ \langle s|j_y|s'\rangle &= e\left(\frac{\hbar\omega}{2m} \right)^{1/2} \langle s|a_+ + a_-|s'\rangle\,, \end{aligned} \right\} \tag{31}$$

where the matrix elements of $a_\pm$ are written as

$$\langle n|a_+|n-1\rangle=\langle n-1|a_-|n\rangle=\sqrt{n}\ , \tag{32}$$

other elements being zero.

Eqs. (29) and (30) become

$$\langle j_{y,-k}\rangle_{\text{force}}=ik\varphi_k\frac{\hbar e}{2m\kappa T}\sum_s\{nF(s,s-1)+(n+1)F(s,s+1)\}\ , \tag{33}$$

$$\langle j_{y,-k}\rangle_{\text{strain}}=ik\varphi_k\frac{\hbar e}{2m\kappa T}\sum_s(2n+1)f_1(\mathcal{E})\ , \tag{34}$$

where $(s-1)$ means the state $(n-1, k_y, k_z)$.

At first, we consider Eq. (33). Performing the summation of k_y and k_z replaced by integration, Eq. (33) becomes

$$\langle j_{y,-k}\rangle_{\text{force}}=ik\varphi_k\frac{\sqrt{2}}{\pi^2}\frac{em^{1/2}}{\hbar^2}\sum_{n=0}^{[\zeta/\hbar\omega]}\sqrt{\zeta-n\hbar\omega}\ , \tag{35}$$

where $[x]$ means the integral part of x. On the other hand, the chemical potential ζ is determined by

$$\sum f(\mathcal{E})=N\ , \tag{36}$$

where N is the number density of the electron. Now performing integration over k_y and k_z one obtains from Eq. (36)

$$\frac{\sqrt{2}}{\pi^2}\frac{\omega m^{3/2}}{\hbar^2}\sum_{n=0}^{[\zeta/\hbar\omega]}\sqrt{\zeta-n\hbar\omega}=N\ . \tag{37}$$

Substituting this result into Eq. (35), we get

$$\langle j_{y,-k}\rangle_{\text{force}}=ik\varphi_k\frac{c}{H}N\ . \tag{38}$$

This result means the well-known fact that when the external electric field $F=k\varphi_k/e$ is applied in the direction perpendicular to the magnetic field, each electron moves in the direction perpendicular both to the magnetic and the electric field with the velocity Fc/H.

Next, we consider Eq. (34). To perform the integration over k_z easily, we approximate the function $f_1(\mathcal{E})$ as follows

$$\begin{aligned} f_1(\mathcal{E})&=1\ , && -\tfrac{1}{2}<\mathcal{E}<\tfrac{1}{2}\\ &=0\ , && \mathcal{E}<-\tfrac{1}{2}\ \text{ or }\ \tfrac{1}{2}<\mathcal{E}\ . \end{aligned} \tag{39}$$

Then Eq. (34) becomes

$$\langle j_{y,-k}\rangle_{\text{strain}}=ik\varphi_k\frac{\sqrt{2}}{\pi^2}\frac{e(m\zeta)^{1/2}}{\hbar^2}\sum_s G_n\ , \tag{40}$$

$$\begin{aligned} G_n=(n+\tfrac{1}{2})\frac{\hbar\omega}{\kappa T\zeta^{1/2}}&\{\sqrt{P(\zeta-n\hbar\omega+\kappa T/2)}\\ &-\sqrt{P(\zeta-n\hbar\omega-\kappa T/2)}\}\ , \end{aligned} \tag{41}$$

$$\begin{aligned} P(y)&=y\ , && 0\le y\\ &=0\ , && y<0\ . \end{aligned} \tag{42}$$

In Fig. 1, $\sum_n G_n$ is plotted as a function of $x=\zeta/\hbar\omega$. When $\zeta-n\hbar\omega$ is much larger than κT, G_n is written approximately as

$$G_n=\tfrac{1}{2}(n+\tfrac{1}{2})/\sqrt{x(x-n)}\ . \tag{43}$$

This approximation is equivalent to replacing $f_1(\mathcal{E})$ by $\delta(\mathcal{E})$-function as usual which is not a good approximation when $\zeta-n\hbar\omega$ becomes smaller than κT because in this range the state density of the system becomes infinity. When the broadening of each level by the collision mechanism, namely $\hbar/\tau$, becomes larger than κT, the height of each peak of $\sum_n G_n$ becomes $(1+(1/2n))\sqrt{\zeta\tau/\hbar}$ instead of $(1+(1/2n))\sqrt{\zeta/\kappa T}$. Thus, changing the value of the magnetic field H, $\langle j_{y,-k}\rangle_{\text{strain}}$ oscillates with sharp peaks at the points where the condition

$$\sum_n G_n=\frac{\zeta}{nT}\sum_n\left(n+\frac{1}{2}\right)x^{-3/2}\times\{\sqrt{p(x-n+xnT/2\zeta)}-\sqrt{p(x-n-xnT/2\zeta)}\}$$

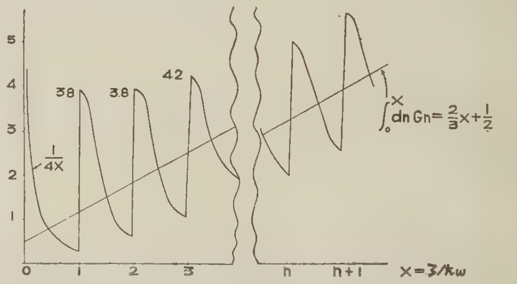

Fig. 1. The graph of $\Sigma_n G_n$ as a function of $\zeta/\hbar\omega$ $\Sigma_n G_n$ hanse peaks at points $x=n=$integer with the height of $\left(1+\frac{1}{2n}\right)\sqrt{\frac{\zeta}{nT}}$. In this graph we plot the curve by choosing the value of $\sqrt{\zeta_0/nT}$ as 3, where ζ_0 is the value of the Fermi energy when the external magnetic field is zero, and the value of ζ as a function of x is obtained in Fig. 2. The straight line is obtained by replacing Σ_n by integral $\int dn$.

$$x=\frac{\zeta}{\hbar\omega}=I=\text{integer} \tag{44}$$

is satisfied. The chemical potential ζ varies also with H as is seen from Eq. (37) and Fig. 2. When $\zeta/\hbar\omega$ is larger than unity, however, the change of ζ is much smaller than that of $\sum_n G_n$ and ζ is regarded nearly constant, namely

$$\zeta=\zeta_0=\frac{\hbar^2}{2m}(3\pi^2 N)^{2/3}, \tag{45}$$

which is the same as the value where the magnetic field is zero. When $\zeta/\hbar\omega$ becomes smaller than unity, however, the change of ζ becomes large and not negligible compared to $\sum_n G_n$. Then ζ is given by

$$\zeta=\frac{\pi^4}{2}N^2\frac{\hbar^4}{m^3\omega^2}=\frac{4}{9}\frac{\zeta_0{}^3}{(\zeta\omega)^2}, \tag{46}$$

and thus

$$\langle j_{y,-k}\rangle_{\text{strain}}=ik\varphi_k\frac{1}{2\pi^4}\frac{m^2\omega^2}{N\hbar^3}. \tag{47}$$

This character of the Hall current is recognized as follows. As is shown in Fig. 3, the current density flows in the y-direction when the magnetic field and the density gradient exist respectively in the z- and x-directions[3]. When the density gradient is induced by the gradient of the chemical potential $\nabla\zeta$, this current is proportional to the state density at the Fermi surface when the system is in Fermi degeneracy. Thus the oscillatory behaviour of the current density $j_y(\boldsymbol{r})$ is just the same as that of the state density at the Fermi surface. Thus the peculiar behaviour of $j_y(\boldsymbol{r})$ in a range of extremely strong magnetic field, namely $\zeta<\hbar\omega$, is also understandable such that the smaller N is, the smaller k_{z0} is, and the larger H is, the smaller the distance between the neighbouring states $2\pi\hbar c/eH$ is, and thus the larger the state density at the Fermi surface is.

$$\left(\frac{\zeta_0}{\zeta}\right)^{3/2}=\frac{3}{2}x^{-3/2}\sum_{n=0}^{[x]}\sqrt{x-n}$$

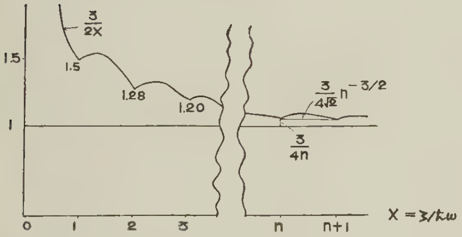

Fig. 2. The graph of $(\zeta_0/\zeta)^{3/2}$ as a function of $x=\zeta/\hbar\omega$.

$(\zeta_0/\zeta)^{3/2}$ has minima for integral values of x. If we replace the summation over n by integration, (ζ_0/ζ) becomes unity, that is, ζ becomes ζ_0. Which is the value corresponding to the case of zero external magnetic field. Each minimum of $(\zeta/\zeta^0)^{3/2}$ is larger than unity and the difference becomes $(3/4n)$ for sufficiently large value of n. The amplitude of the oscillation of $(\zeta/\zeta_0)^{3/2}$ becomes $(3/4\sqrt{2})n^{-3/2}$ for sufficiently large n as is shown in the above graph.

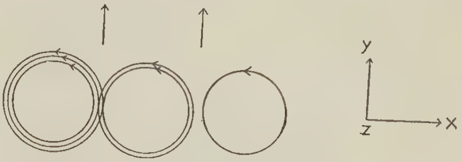

Fig. 3. A schematic explanation of the current density in the y-direction when the external magnetic field is applied in the z-direction and the density gradient exists in the x-direction.

§ 4. Concluding Remarks*

Knowing my conclusion concerning the Einstein relation S. Nakajima has reformulated this problem from the stand point of kinetic theory and obtained the same result as mine (Progr. Theor. Phys. **20** (1958) 948). Unfortunately publication of the present paper was unduly put off because of long delay in the process of reference after the receipt of the manuscript by the editorial committee.

References

1) T. Kasuya: J. Phys. Soc. Japan **13** (1958) 1096. Also see, for example, R. Kubo: J. Phys. Soc. Japan **12** (1957) 570.

2) R. Karplus and J. M. Luttinger: Phys. Rev. **95** (1954) 1154.
J. Smit: Physica **21** (1955) 877.

3) L. Spitzer: *Physics of Fully Ionized Gases* (Interscience Publ., New York, 1956).

---

* Added in February, 1959.

JOURNAL OF THE PHYSICAL SOCIETY OF JAPAN, Vol 14, No. 4, APRIL, 1959

Electrical and Thermal Conductivity of Monovalent Metals; The Influences of Coulomb Interaction

By Tadao KASUYA and Kazuo YAMADA

Physical Institute, Nagoya University

(Received October 8, 1958)

The electrical and thermal conduction phenomena are discussed by taking account of the effects of Coulomb interaction and Umklapp processes of electron-phonon collisions. The contributions of electron binary collisions through screened short range Coulomb potential to a relaxation processes are evaluated. The effect to the coupling parameter of electron-phonon interaction is also considered in the range of called Umklapp process. The effect of phonon drag is not considered in this paper.

§ 1. Introduction

The conduction phenomena of monovalent metals have been investigated by many authors, since Bloch. However, there are some ambiguous points even in alkali metals, where the theoretical treatment seems to be rather simple. In particular, how to evaluate the effects of the Coulomb interactions between electrons is one of the most serious problems and many attempts have been done so far. Recent works of D. Bohm—D. Pines[1)] and J. Bardeen—D. Pines[2)] have made it considerably clear by introducing the plasma mode. Our attempt in this paper is to see what effects should be caused by taking account of the Coulomb interactions between the conduction electrons on the conduction phenomena in metals. Here we shall confine ourselves to the case of sodium.

The problems considered are the following: i) The contribution of electron binary collisions by screened short range forces to the relaxation process. ii) The contribution of the Coulomb interactions to the effective coupling parameter of electron-phonon interactions, including the range of Umklapp process. iii) The deviation of energy spectrum from free electron approximation by the correlation effect between electrons. In turn, this may give rise to the change of electronic level density. In § 2, these problems are discussed in some detail.

In § 3 and Appendix II we shall obtain the concrete expressions for the electrical and thermal conductivity taking account of so called Umklapp process and finally these results will be compared with the experiments.

§ 2. Preliminary Discussions

i) *Electron binary collisions*

According to the theory of Bohm—Pines, the conduction electrons in metals exhibit both the collective and the individual particle motions. The long range part of the Coulomb force which corresponds to the long wave length part of the electronic density fluctuations causes the organized oscillation of the electron system as a whole. This mode is so called plasma oscillation. While, the motions corresponding to the short range part of the electronic density fluctuations are described by individual particle modes, and they interact with one another through the screened short range Coulomb forces. In this section, we shall consider the electron binary collisions by this short range potentials.

If the individual electronic state is described by a plane wave, the total wave vector is conserved in a process of electron binary collision, i.e., $\boldsymbol{k}_1+\boldsymbol{k}_2-\boldsymbol{k}_3-\boldsymbol{k}_4=0$ where the $\boldsymbol{k}_1$ and $\boldsymbol{k}_2$ mean the wave vectors of two initial electrons, $\boldsymbol{k}_3$ and $\boldsymbol{k}_4$ the wave vectors of final electrons. Therefore, these processes will not make any contribution to the electrical resistance in the first approximation. In higher approximation, of course, it might give rise to some effects even in this process because the distribution function of the electronic state undergoes a certain change by collision. However, in usual steady state in which the electrical resistance is mainly determined by electron-phonon collisions, the distribution function of Kramers type

$$[\{\exp(\hbar^2k^2/2m-\zeta)/kT+\boldsymbol{c}\cdot\boldsymbol{k}\}+1]^{-1},$$

where $\boldsymbol{c}$ is a constant vector and means a displacement of the gravity center of Fermi sphere, will be a good approximation. On the other hand, this Kramers distributions function represents the generalized equilibrium state of the system, where only the processes of electron binary collisions conserving the total energy and wave vector occurs. Thus this kind of effect also scarcely contributes to the electrical resistance. However, the electron is to be represented by Bloch's wave function, since it moves in a periodic crystalline field, and then there occur the so called Umklapp processes, say $\boldsymbol{k}_1+\boldsymbol{k}_2-\boldsymbol{k}_3-\boldsymbol{k}_4=\boldsymbol{K}_n$ where $\boldsymbol{K}_n$ means the principal wave vector of the reciprocal lattice. Thus only these Umklapp processes contributes to the electrical resistance through the electron binary collisions.

On the other hand, as to the thermal resistance, the circumstances are different, because it is determined by the relaxation mechanism of energy flow. When the electron system is in steady state under a given temperature gradient and the conditon of no electrical current, the distribution function becomes such as shown in Fig. 1. The electrons with wave vector of positive direction have a character of higher temperature range and those of negative direction have that of lower temperature range. Thus the electrons with energies higher than Fermi level flow in the positive direction and the electrons with lower energies flow in the negative directions. These two flows of the electrons are mixed together by the binary electron collision processes and the electron system approaches to the equilibrium. In consequence, these collision processes may contribute to the thermal resistance even in the plane wave approximation, as well as do the electron-phonon collision processes. It seems to us that Ginzburg and Silin³⁾, who discussed the effect of the electron binary collisions on the conduction phenomena, overlooked such a process as mentioned above.

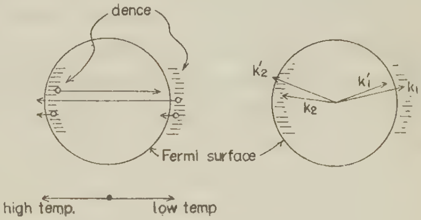

Fig. 1.

The electrons to take part in the collisions are those which fall in the energy range kT near Fermi level and hence we find that the frequency of binary collisions is proportional to T^2. On the other hand, that of the electron-phonon collisions is proportional to T at high temperature and to T^3 at low temperature. Accordingly, if we consider only the temperature tendency, the relaxation process by the electron binary collisions may dominate that of the electron-phonon collisions an sufficiently high or low temperature.

In order to calculate the resistance by the electron binary collision quantitatively, we asume the Hamiltonian of electron-electron interaction such as

$$H_{e-e}=\tfrac{1}{2}\sum_{s_1}\sum_{s_2}\sum_{s_3}\sum_{s_4}V(s_1s_2;\,s_3s_4)a_{s_1}{}^*a_{s_2}{}^*a_{s_3}a_{s_4}\delta_{\boldsymbol{k}_1+\boldsymbol{k}_2,\,\boldsymbol{k}_3+\boldsymbol{k}_4+\boldsymbol{K}_n} \tag{2.1}$$

where s means the electronic state of band l (including spin quantum number) and wave vector $\boldsymbol{k}$, $a_s{}^*$ and a_s means respectively the creation and annihilation operators of state s, and $\boldsymbol{K}_n$ the principal wave vector of the reciprocal lattice. We shall call hereafter the term of $\boldsymbol{K}_n=0$ as normal process (N-process) and one of $\boldsymbol{K}_n\neq0$ as Umklapp process (U-process). When $\boldsymbol{k}_1$, $\boldsymbol{k}_2$ and $\boldsymbol{k}_3$ are given, $\boldsymbol{k}_4$ and $\boldsymbol{K}_n$ are determined uniquely. The transition matrix element $V(s_1s_2;\,s_3s_4)$ is given by

$$V(s_1s_2;\,s_3s_4)=\sum_{\boldsymbol{K}_m}M_{\boldsymbol{k}_1-\boldsymbol{k}_4+\boldsymbol{K}_m}\left(\int_{\Omega_0}e^{-i\boldsymbol{K}_m\cdot\boldsymbol{r}}u_{s_1}{}^*(\boldsymbol{r})u_{s_4}(\boldsymbol{r})\,d\boldsymbol{r}\right)\times\left(\int_{\Omega_0}e^{-i(\boldsymbol{K}_n-\boldsymbol{K}_m)\cdot\boldsymbol{r}}u_{s_2}{}^*(\boldsymbol{r})u_{s_3}(\boldsymbol{r})\,d\boldsymbol{r}\right) \tag{2.2}$$

where Ω_0 is the volume of unit cell and M_q is the Fourier component of the interaction potential $V(|\boldsymbol{r}_i-\boldsymbol{r}_j|)$, that is

$$M_{\boldsymbol{q}}=\int e^{i\boldsymbol{q}\cdot\boldsymbol{r}}V(\boldsymbol{r})\,d\boldsymbol{r}\,. \tag{2.3}$$

If we assume that the system is represented by one band model and the electronic wave function of this band is represented by plane wave in a fairly good approximation, which means that $u_s(\boldsymbol{r})$ is nearly constant and will be applicable in monovalent metals, especially in alkali metals, then l means only the spin quantum number and in Eq. (2.2) the terms, say $\boldsymbol{K}_n=\boldsymbol{K}_m=0$ are most important. These terms, however, mean N-processes and hence no contribution to the electrical resistance. Amongst the terms corresponding to U-process, most important terms are these of $\boldsymbol{K}_n=\boldsymbol{K}_0$, $\boldsymbol{K}_m=0$ and $\boldsymbol{K}_m=\boldsymbol{K}_n=\boldsymbol{K}_0$. Then Eq. (2.2) becomes

$$(M_{k_1-k_4}+M_{k_1-k_4+K_0})A(\boldsymbol{K}_0) \tag{2.4}$$

where

$$A(\boldsymbol{K}_0)=\int_{\Omega_0} e^{-i\boldsymbol{K}_0\cdot\boldsymbol{r}}u_0^2(\boldsymbol{r})\,d\boldsymbol{r}\,, \tag{2.5}$$

where we substituted $u_0(\boldsymbol{r})$ for $u_k(\boldsymbol{r})$ by the above mentioned approximation, and the value of $A(\boldsymbol{K}_0)$ is estimated numerically by using $u_0(\boldsymbol{r})$ given by Wigner and Seitz[4].

Considering the effect of Fermi statistics, or spin quantum number of electron, the transition probability from the state $(k_1l_1;\,k_2l_2)$ to the state $(k_3l_2;\,k_4l_1)$ differs whether the spin directions of l_1 and l_2 is parallel. The squares of these matrix elements become such as

$$\left.\begin{aligned}&|W_p((\boldsymbol{k}_1\boldsymbol{k}_2);(\boldsymbol{k}_3\boldsymbol{k}_4))|^2\\&\quad=|V(\boldsymbol{k}_1\boldsymbol{k}_2;\boldsymbol{k}_3\boldsymbol{k}_4-V(\boldsymbol{k}_1\boldsymbol{k}_2;\boldsymbol{k}_4\boldsymbol{k}_3)|^2\,,\\&|W_a((\boldsymbol{k}_1\boldsymbol{k}_2);(\boldsymbol{k}_3\boldsymbol{k}_4))|^2=|V(\boldsymbol{k}_1\boldsymbol{k}_2;\boldsymbol{k}_3\boldsymbol{k}_4)|^2\,.\end{aligned}\right\} \tag{2.6}$$

The transition probability of parallel spin electrons becomes small by the effect of exchange correlation.

The main contribution to the thermal resistance comes from the N-process as mentioned above. Using again the approximation $u_k(\boldsymbol{r})\simeq u_0(\boldsymbol{r})$, Eq. (2.2) gives the matrix elements obtained by using the plane wave instead of the Bloch's function, and as well known the results agree with what computed by the Born approximation. However, as to the conduction electrons in a metal, it seems that the Born approximation is beyond the criterion of its validity, since their energies are at most a few e.v.. Therefore, we shall evaluate the exact probability of transition by using the partial wave method.

As the short-range potential we can consider the various forms as indicated in Fig. 2. Among them the following type is adopted because it is convenient for the calculation of the cross section.

$$\begin{aligned}V(r)&=\frac{e^2}{r}\left(1-\frac{r}{a}\right) &\quad r<a\\&=0 &\quad r>a\end{aligned} \tag{2.7}$$

where a is chosen as $2k_c^{-1}$. In sodium, $(k_c/k_0)\simeq 0.70$ where k_0 and k_c are respectively the magnitudes of the Fermi maximum and of

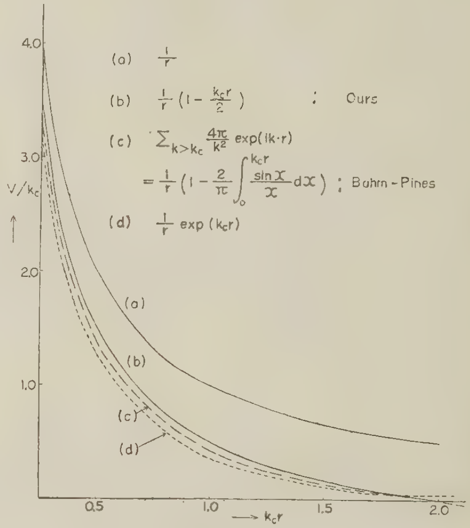

Fig. 2.

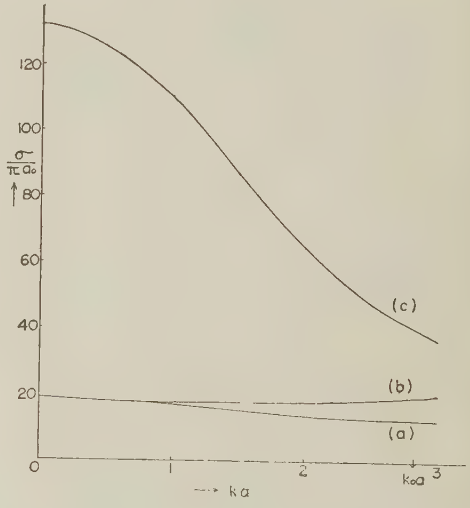

Fig. 3.

(a) Partial wave method neglecting spin effect

$$\frac{\sigma}{\pi a_0{}^2}=\frac{4}{(ka)^2}\left(\frac{a}{a_0}\right)^2(\sin^2\eta_0+3\sin^2\eta_1)$$

(b) Partial wave method

$$\frac{\sigma}{\pi a_0{}^2}=\frac{4}{(ka)^2}\left(\frac{a}{a_0}\right)^2(\sin^2\eta_0+9\sin^2\eta_1)$$

(c) Born approximation neglecting spin effect

$$\frac{\sigma}{\pi a_0{}^2}=\frac{2\pi}{(ka)^2}\left(\frac{a}{a_0}\right)^4\int_0^{2ka}\frac{(x-\sin x)^2}{x^5}dx$$

where a_0 is Bohr radius and $a/a_0=5.87$ in our case, η_0 and η_1 are respectively the phase shifts of s- and p-waves.

plasma cut-off wave vector. The calculation of cross section is given in Appendix I. The curves (c) and (a), shown in Fig. 3, represent respectively the total cross sections obtained by the Born approximation and by the partial wave method computing the phase shifts of s- and p-wave, where the spin effect is not considered. We find the Born approximation gives the larger cross section than that of the partial wave method. The curve (b) is the total cross section considering the spin direction (see Appendix I).

ii) *The effective coupling parameter of the electron-phonon interaction*

The Coulomb interactions between electrons contribute directly to the electrical resistance by their binary collisions, as mentioned above. In addition it has the effect of shielding the ionic field by the effective self field induced by coupling with the lattice vibrations. This was first investigated by J. Bardeen[6], who evaluated the probability for the electron to be scattered by the phonon, taking account of the Hartree's field; and Toya[7] furthermore considered the exchange interactions of the electrons in the simplified Hartree-Fock's approximation[8] and pointed out that this correlation between the parallel spins diminished the shielding effect given by J. Bardeen. One[9] of us also took into consideration the correlation between the anti-parallel spins in the same way as Toya did. Recently J. Bardeen and D. Pines discussed the problem of coupling between electrons and phonons by introducing the plasma mode and indicated that since the long range correlations between the electrons are included in the plasma mode, the coupling constant of electron-phonon interaction scarcely affected by the correlation effect of electrons when the wave vector of the phonon is smaller than k_c, and thus the effective matrix elements were in agreement with those obtained by J. Bardeen.

However, if the phonon wave length becomes comparable with or shorter than $2\pi/k_c$, the correlation between electrons through the screened Coulomb potential would have the appreciable influence on the electron-phonon interactions. In other words, the degree of shielding effect decreases when the correlation between electrons are considered, and hence the probability of electron-phonon collisions increases. Pines showed that this correlation of individual electrons was so large that it might contribute to the cohesive energy. Therefore, as to the formula of the matrix elements of electron-phonon interaction we use the following results. When the wave vector of phonon q is smaller than k_c, the result obtained by Bardeen is applicable. When q becomes larger than k_c, we calculate the correlation effect by using the simplified Hartree Fock's method, rewriting the correlation energy which depends only on the electron density into the form of the potential energy. The results are plotted in Fig. 4.

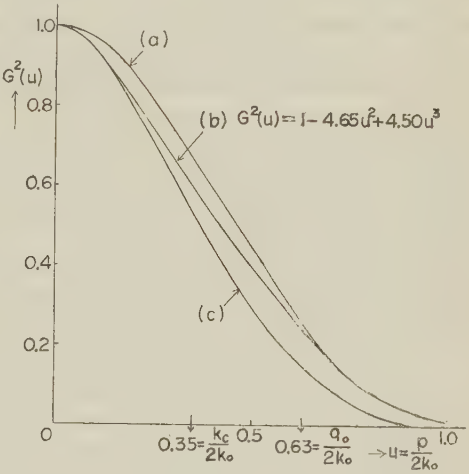

Fig. 4. (a) is the curve which was obtained by taking account of the correlation effect, which was calculated by using the simplified Hartree Fock's method, rewriting the correlation energy, which was evaluated by Pines(10) and depends only on the electron density, into the form of the potential energy. (b) is the curve which was obtained by interpolating the curves (a) and (c). (c) is the curve which was obtained by Bardeen(6).

According to the usual Bloch's theory, the probability that an electron emits or absorbs a phonon with wave vector $\boldsymbol{q}$ is given by

$$W(\boldsymbol{k}, \boldsymbol{k}', \boldsymbol{q}) = \left(\frac{2}{3} C\,|\boldsymbol{k}-\boldsymbol{k}'|\right)^2 \frac{\hbar}{2MN\omega_q} \delta_{\boldsymbol{k},\boldsymbol{k}'+\boldsymbol{q}+\boldsymbol{K}_n} \tag{2.8}$$

and the coupling parameter C is regarded as a constant of the same order as Fermi energy ζ and independent of the value of $|\boldsymbol{k}-\boldsymbol{k}'|$. However, as mentioned above, considering the shielding effect of electrons, C changes with $|\boldsymbol{k}-\boldsymbol{k}'|$. By using Bardeen's notation we write C as follows

$$C=\zeta G(u) \tag{2.9}$$

where

$$u=\frac{p}{2k_0}\,, \qquad \boldsymbol{p}=\boldsymbol{k}-\boldsymbol{k}'$$

and $G(u)$ is written by

$$G(u)=g(u)\,\frac{1+(V_0(r_s)-E_0)(3u^2/\beta\zeta)}{f(u)\{1-(3/2)(1-0.34)u^2\}+(2u^2/\beta)}\,. \tag{2.10}$$

This function differs from that of Bardeen only in a term $-(3/2)(1-0.34)u^2$ in the denominator. These terms $-(3/2)u^2$ and $(3/2)\times 0.34u^2$ come respectively from taking account of the correlation field of electrons with parallel and antiparallel spin. Fig. 4 shows that the quantity $|G(u)|^2$, which is proportional to the transition probability, becomes small markedly in the range where p is larger than k_c. We adopt in this paper the curve (b) which is obtained by the interpolation using both the curves (a) in the range of small value of p and the (c) in the range of large p.

In a range $u>(q_0/2k_0)\simeq 0.63$, U-process may occur, where q_0 is the magnitude of Debye's maximum wave vector.

In order to calculate $G(u)$ we require the matrix element of perturbing potential derived from electron clouds surrounding about a bare ion. Then we must evaluate the value of $(V_0(r_s)-E_0)$ in the numerator of Eq. (2.10), where $V_0(r_s)$ denotes the value of the undistorted potential on the surface of s-sphere and E_0 energy in the lowest state. As the value of $(V_0(r_s)-E_0)$, Bardeen[6)] took 0.2 e.v. and Toya[7)] 0.22 e.v., while Ziman[11)] used 1.3 e.v. reffering to Mott.

The equation to be solved by us is

$$-\frac{\hbar^2}{2m}\nabla^2\psi_0+(V_0(r)-E)\psi_0=0$$

$$V_0(r)=v+v_c+v_{\mathrm{cor}}$$

where v, v_c and v_{cor} denote respectively the potenial of bared ion, Coulomb potential by electron of uniform density and correlation potential, and ψ_0 the wave function of the ground state. Wigner and Seitz took the $-(\hbar/2m)\nabla^2+v$ as the unperturbed Hamiltonian and r_c as the perturbation. Mott's result correspond to the zeroth order, while Bardeen considered to the first order, namely

$$\bar{v}_c=4\pi\int_0^{r_s}\left(\frac{3}{2}\frac{e^2}{r_s}-\frac{e^2r^2}{2r_s^3}\right)r^2\,dr\bigg/\frac{4}{3}\pi r_s^3=1.2\,\frac{e^2}{r_s}$$

which was obtained with an approximation $u(r)\simeq 1$. In our case though v_{cor} also should be considered as a perturbation, we may consider that v_{cor} gives merely the constant energy of correlation independent of the position, because the Coulomb repulsion causes each electron to stay apart uniformly from point of view of the simplified Hartree Fock method, and also in sodium the wave function of the lowest state in nearly constant at the major portion of s-sphere. Therefore we adopted the Bardeen's result. It may be reasonable that we modify the Bardeen's result not by the alternation of the value of $(V_0(r_s)-E_0)$, but by taking account of the correlation field. However incidentally the interpolated curve, which is adopted by us, coincides fairly well with that which was used by Ziman[11)].

iii) *The energy spectrum*

The energy spectrum of electron deviates from that in the free electron approximation by the various factors. First, the crystalline field will be the most important cause. In alkali metals such as sodium, the wave function of electron may be expected to be nearly flat in the whole space except the points very near the ions, and hence a free electron model may be a good approximation. Second, the introduction of the plasma mode from the standpoint of Bohm and Pines brings the important effects. The effective mass of electron may be increased by the electron-plasma interaction and may be decreased by the restriction of the electronic states by the subsidiary conditions. The former has been estimated by D. Bohm and D. Pines, but the latter is the complicated problem. However, these effects may be not so important in Na because the freedom of phasma mode is not so large and they have the effects to cancel out each other. As for the rest of factors, one can consider the effects of the exchange energy through the screened short-range electron-electron interaction. In this case, we may expect not only the change of the effective mass of electron, but also the complicated change of the energy spectrum near the Fermi level (as well known, the state density near Fermi surface becomes abnormally small when we use the non-screened Coulomb potenial). F. J. Blatt and R. Barrie[12)] and Tuji[13)] have discussed the influences of exchange interactions through the screened Coulomb potentials on the level density and the relaxation time to determine the conductivities. If we consider this interaction between the electrons, then we also must take account of the effect of the electron-phonon interaction on the energy spectrum. However, the phenomena on which the structure of energy spectrum is supposed to affect delicately, particularly the thermoelectric phenomena at low temperature, will be reserved for another occasion, and in this paper we assume that the energy spectrum of electronic state is represented by the free electron model.

§ 3. Fundamental Transport Equation

To calculate the steady flow of the system under the external force or strain from the standpoint of the gas kinetic theory, we must obtain the velocity distribution function of one body in the steady state by solving the well known Boltzmann-Bloch equation. As is well known, there are two main mechanisms for the resistances with respect to the electron transport in metals, that is, the scattering of electrons by the thermal oscillation of the lattice (phonon) and by the static imperfection of the lattice. The latter mechanism is important at low temperature and in some substances causes a peculiar phenomenon of so called resistance minimum. In this paper we do not treat this mechanism but confine ourselves to the resistance by phonon scattering. In usual treatment to calculate ideal electrical conductivity one assume that the phonon distribution is in the thermal equilibrium. But since Peierls, there have been various comments for this problem and recently many authors have discussed the influences of the deviation of the phonon distribuion function from the equilibrium value on the transport properties in metals and semi-conductors, particularly on the thermo-electric phenomena. However, the treatments of this problem are compelled to be qualitative, because it is difficult to treat the relaxation processes of phonon system quantitatively. And as are pointed out by Sondheimer[14] and us[15], some incomplete points are involved in a few papers[16] of theirs. The detailed discussions about this problem will be given in another paper, and in this paper we assume that the phonon distribution is in thermal equilibrium. However, so far as the thermal conductivity is concerned, the results obtained in this paper may be applied without essential modification, even if the effect of so-called "phonon drag" is taken into account.

Provided that the deviation from the equilibrium distribution function of electron f_0 is small and the system is homogeneous, the electron distribution function $f(\boldsymbol{k})$ may be represented by

$$f(\boldsymbol{k})=f_0(\mathcal{E})-k_x\cdot c(\mathcal{E})\frac{\partial f_0(\mathcal{E})}{\partial \mathcal{E}} \tag{3.1}$$

where

$$f_0(\mathcal{E})=(e^{\mathcal{E}}+1)^{-1}\,, \qquad \mathcal{E}=(E-\zeta)/\kappa T\,. \tag{3.2}$$

To solve Bloch's integral equation with respect to $c(\mathcal{E})$, Sondheimer applied the variation method, in which the trial function $c(\mathcal{E})$ is expanded by the power series of $\mathcal{E}$. Now taking until the second term, it is

$$c(\mathcal{E})=c_1+c_2\cdot\mathcal{E}\,. \tag{3.3}$$

These terms mean respectively the uniform displacement of the Fermi sphere as a whole and the change of distribution in the neighborhood of the Fermi surface. For the electrical conductivity, we need only the first constant term, and if we regard the coupling parameter of the electron-phonon collision as a constant, then we have the Grüneisen formula for its ideal part. On the other hand, the thermal conductivity under the condition $\boldsymbol{j}=0$ is determined by the second term, the odd function of $\mathcal{E}$. However, it was pointed out by Kasuya[9] and Klemens[17] that this function $c_2\cdot\mathcal{E}$ could not be a good solution at the low temperature and furthermore the exact solution had to be a odd function of $\mathcal{E}$ which approaches to a constant value as $\mathcal{E}$ increases. Therefore, as a function with such a property we assume the following simple form

$$c(\mathcal{E})=c_1+c_2'\tanh\frac{\mathcal{E}}{2}\,. \tag{3.4}$$

In our case, though we must consider the distribution function under electron binary collisions as well as electron-phonon collisions, it will be allowed to assume that in the first approximation the electron distribution may be determined by electron-phonon collisions and given by Eq. (3.3) or (3.4).

In order to solve the equation of $c(\mathcal{E})$, we use the following method which is substantially equivalent to the variation method. Let us multiply on the both side of Bloch equation by $e\boldsymbol{v}(\boldsymbol{k})$, where $\boldsymbol{v}(\boldsymbol{k})$ is the electron belocity and e electronic charge, and sum over $\boldsymbol{k}$.

Then this equation represents that the changes of the electrical current density $\boldsymbol{j}$ per unit time by the external field and by the collision processes keep balance in a steady state. Similarly, if $\kappa T\mathcal{E}v(\boldsymbol{k})$ is multiplied, where $\mathcal{E}$ is given by Eq. (3.2), the equation means the balance of change of the thermal current density $\boldsymbol{Q}$ per unit time. Hereafter let us suppose that the directions of external fields are parallel to the x-axis for brevity and consider only these components of currents. Then the following two equations representing the total balance of the electrical and thermal flow are sufficient to determine two unknown constants c_1 and c_2 (or c_2').

$$\left(\frac{dj}{dt}\right)_{\text{drift}}+\left(\frac{dj}{dt}\right)_{\text{coll}}=0 \tag{3.5}$$

$$\left(\frac{dQ}{dt}\right)_{\text{drift}}+\left(\frac{dQ}{dt}\right)_{\text{coll}}=0\,. \tag{3.6}$$

Here the drift terms are

$$\left(\frac{dj}{dt}\right)_{\text{drift}}=-e\sum_{\boldsymbol{k}}v_x(\boldsymbol{k})\left\{\frac{e}{\hbar}F\frac{\partial f(\boldsymbol{k})}{\partial k_x}+v_x(\boldsymbol{k})\frac{\partial f(\boldsymbol{k})}{\partial x}\right\}, \tag{3.7}$$

$$\left(\frac{dQ}{dt}\right)_{\text{drift}}=-\kappa T\sum_{\boldsymbol{k}}\mathcal{E}(\boldsymbol{k})v_x(\boldsymbol{k})\left\{\frac{e}{\hbar}F\frac{\partial f(\boldsymbol{k})}{\partial k_x}+v_x(\boldsymbol{k})\frac{\partial f(\boldsymbol{k})}{\partial x}\right\}. \tag{3.8}$$

If we confine ourselves to the treatment linear concerning the fields, we may substitute $f_0(\mathcal{E})$ for $f(k)$ in the drift term and then can easily perform the summation by replacing with the integration over $\boldsymbol{k}$ as usual. Next the collision terms owing to the electron-phonon and electron-electron collisions are given by

$$\begin{aligned}-\left(\frac{dj}{dt}\right)_{\text{coll}}&=\frac{e2\pi}{\hbar}\sum_{\boldsymbol{k}}\sum_{\boldsymbol{k}'}\sum_{\boldsymbol{q}}W(\boldsymbol{k},\boldsymbol{k}',\boldsymbol{q})\{f_{\boldsymbol{k}}(1-f_{\boldsymbol{k}'})(N_q+1)-f_{\boldsymbol{k}'}(1-f_{\boldsymbol{k}})N_q\}(v_{\boldsymbol{k}'}-v_{\boldsymbol{k}})_x\delta(E_{\boldsymbol{k}'}-E_{\boldsymbol{k}}-\hbar\omega_q)\\&\quad+\frac{e2\pi}{\hbar}\sum\sum_{(\boldsymbol{k}_1\boldsymbol{k}_2)}\sum\sum_{(\boldsymbol{k}_3\boldsymbol{k}_4)}w(\boldsymbol{k}_1\boldsymbol{k}_2\boldsymbol{k}_3\boldsymbol{k}_4)f_{\boldsymbol{k}_1}f_{\boldsymbol{k}_2}(1-f_{\boldsymbol{k}_3})(1-f_{\boldsymbol{k}_4})(v_{\boldsymbol{k}_3}+v_{\boldsymbol{k}_4}-v_{\boldsymbol{k}_1}-v_{\boldsymbol{k}_2})_x\delta(E_{\boldsymbol{k}_1}+E_{\boldsymbol{k}_2}-E_{\boldsymbol{k}_3}-E_{\boldsymbol{k}_4})\,,\end{aligned} \tag{3.9}$$

$$\begin{aligned}-\left(\frac{dQ}{dt}\right)_{\text{coll}}&=\frac{2\pi\kappa T}{\hbar}\sum_{\boldsymbol{k}}\sum_{\boldsymbol{k}'}\sum_{\boldsymbol{q}}W(\boldsymbol{k},\boldsymbol{k}',\boldsymbol{q})\{f_{\boldsymbol{k}}(1-f_{\boldsymbol{k}'})(N_q+1)-f_{\boldsymbol{k}'}(1-f_{\boldsymbol{k}})N_q\}\\&\qquad\times(\mathcal{E}_{\boldsymbol{k}'}v_{\boldsymbol{k}'}-\mathcal{E}_{\boldsymbol{k}}v_{\boldsymbol{k}})_x\delta(E_{\boldsymbol{k}'}-E_{\boldsymbol{k}}-\hbar\omega_q)\\&\quad+\frac{2\pi\kappa T}{\hbar}\sum\sum_{(\boldsymbol{k}_1\boldsymbol{k}_2)}\sum\sum_{(\boldsymbol{k}_3\boldsymbol{k}_4)}w(\boldsymbol{k}_1\boldsymbol{k}_2\boldsymbol{k}_3\boldsymbol{k}_4)f_{\boldsymbol{k}_1}f_{\boldsymbol{k}_2}(1-f_{\boldsymbol{k}_3})(1-f_{\boldsymbol{k}_4})(\mathcal{E}_{\boldsymbol{k}_3}v_{\boldsymbol{k}_3}+\mathcal{E}_{\boldsymbol{k}_4}v_{\boldsymbol{k}_4}-\mathcal{E}_{\boldsymbol{k}_1}v_{\boldsymbol{k}_1}-\mathcal{E}_{\boldsymbol{k}_2}v_{\boldsymbol{k}_2})_x\\&\qquad\times\delta(E_{\boldsymbol{k}_1}+E_{\boldsymbol{k}_2}-E_{\boldsymbol{k}_3}-E_{\boldsymbol{k}_4})\end{aligned} \tag{3.10}$$

where $W(\boldsymbol{k},\boldsymbol{k}',\boldsymbol{q})$ is the square of the transition matrix element of electronphonon interaction and given by Eq. (2.8), while $w(\boldsymbol{k}_1\boldsymbol{k}_2\boldsymbol{k}_3\boldsymbol{k}_4)$ that of electron binary collision. As mentioned above, we assume that the phonon distribution is given by

$$N_q=N_0(x)=(e^x-1)^{-1}\,,\qquad x=\hbar\omega_q/\kappa T \tag{3.11}$$

where $N_0(x)$ is the thermal equilibrium distribution of phonon, and the electron energy spectrum is written by

$$E_k=\frac{\hbar^2}{2m}|\boldsymbol{k}|^2\,,\qquad v_k=\frac{\hbar k}{m} \tag{3.12}$$

where m means the effective mass of electron. In the following, we shall treat separately the electrical and thermal conductivity.

The electrical conductivity σ—For the electrical current, the odd part of $c(\mathcal{E})$ can be neglected since it gives only the higher orders of $\kappa T/\zeta$, while in the drift term $\partial T/\partial x$ is zero and thus we obtain

$$j=e\sum_k v_x(k)f(k)=\frac{en}{\hbar}\kappa Tc_1\,, \tag{3.13}$$

$$\left(\frac{dj}{dt}\right)_{\text{drift}} = -\left(\frac{e\hbar}{m}\right)^2 F \sum_{k} k_x^2 \frac{\partial f_0}{\partial E} = \frac{ne^2}{m} F . \tag{3.14}$$

Here it is convenient to introduce the average relaxation time τ_σ which is determined by the equation

$$\left(\frac{dj}{dt}\right)_{\text{coll}} = -\frac{j}{\tau_\sigma} . \tag{3,15}$$

Then it follows that using Eq. (3.13) to (3.15) and Eq. (3.5),

$$\sigma = j/F = \frac{ne^2}{m}\tau_\sigma . \tag{3.16}$$

Provided that two collision processes are independent of each other, we have

$$\frac{1}{\tau_\sigma} = \frac{1}{\tau_\sigma{}^p} + \frac{1}{\tau_\sigma{}^e} \tag{3.17}$$

where $\tau_\sigma{}^p$ and $\tau_\sigma{}^e$ denote respectively the average relaxation times of the electrical current by electron-phonon and electron binary collision processes. These calculations are performed in Appendix II.

The thermal conductivity κ—If we express the second term in Eq. (3.3) or (3.4) as $c_0(\mathcal{E})$, which indicates the odd function of $\mathcal{E}$, $c(\mathcal{E})$ is written by

$$c(\mathcal{E}) = c_1 + c_0(\mathcal{E}) \tag{3.18}$$

where

$$c_0(\mathcal{E}) = c_2 \cdot \mathcal{E} \qquad \text{or} \qquad c_2' \cdot \tanh\frac{\mathcal{E}}{2} . \tag{3.19}$$

Using Eqs. (3.1) and (3.18), j and Q are given by

$$j = e\sum_{k} v_x(\boldsymbol{k}) f(\boldsymbol{k}) = \frac{ne}{\hbar}\kappa T\left\{ c_1\left(1+\frac{\pi^2}{8}\gamma^2\right) - \frac{3}{2}\gamma\int_{-\infty}^{\infty} \mathcal{E} c_0(\mathcal{E}) \frac{\partial f_0}{\partial \mathcal{E}} d\mathcal{E}\right\} , \tag{3.20}$$

$$Q = \kappa T \sum_{k} \mathcal{E}_k v_x(\boldsymbol{k}) f(\boldsymbol{k}) = \frac{n\zeta}{\hbar}\kappa T\left\{ c_1\frac{\pi^2}{2}\gamma^2 - \gamma\int_{-\infty}^{\infty} \kappa c_0(\mathcal{E}) \frac{\partial f_0}{\partial \mathcal{E}} d\mathcal{E}\right\} , \tag{3.21}$$

in the approximation to take until the order of $(\kappa T/\zeta)^2 \equiv \gamma^2$.

Now we consider the thermal current density Q_0 under the condition $j=0$. By Eq. (3.20), this condition is equivalent to the relation

$$c_1 = \frac{3}{2}\gamma\left(1-\frac{\pi^2}{8}\gamma^2\right)\int_{-\infty}^{\infty} \mathcal{E}\cdot c_0(\mathcal{E}) \frac{\partial f_0}{\partial \mathcal{E}} d\mathcal{E} . \tag{3.22}$$

Substituting this relation into Eq. (3.21), we can easily see that the first term is negligibly smaller than the second. Therefore, in our approximation we may define Q_0 by

$$Q_0 = -\frac{n}{\hbar}(\kappa T)^2 \int_{-\infty}^{\infty} \mathcal{E} c_0(\mathcal{E}) \frac{\partial f_0}{\partial \mathcal{E}} d\mathcal{E} = \frac{n}{\hbar}(\kappa T)^2 c , \qquad c = \frac{\pi^2}{3}c_2 \quad \text{or} \quad \frac{1}{2}c_2' . \tag{3.23}$$

By the same consideration as the above, the drift term depends only on $\partial T/\partial x$ and the term proportional to $(eF+\partial\zeta/\partial x)$ becomes higher order with respect to γ and is negligible in our approximation, that is,

$$\left(\frac{dQ_0}{dt}\right)_{\text{drift}} = -\frac{\pi^2 n\kappa T}{3m}\frac{dT}{dx} . \tag{3.24}$$

If we introduce the average relaxation time τ_κ of the thermal flow by

$$\left(\frac{dQ_0}{dt}\right)_{\text{coll}}=-\frac{Q_0}{\tau_\kappa}, \tag{3.25}$$

the thermal conductivity κ becomes

$$\kappa=-Q_0\Big/\frac{dT}{dx}=\frac{\pi^2 n k^2 T}{3m}\tau_\kappa . \tag{3.26}$$

Corresponding to the case of electrical resistance, τ_κ is written by $\tau_\kappa{}^p$ and $\tau_\kappa{}^e$ by

$$\frac{1}{\tau_\kappa}=\frac{1}{\tau_\kappa{}^p}+\frac{1}{\tau_\kappa{}^e}. \tag{3.27}$$

Their evaluations are shown in Appendix II.

§ 4. Comparison with Experimental Results

In the first place we shall consider the thermal and electrical conductivities κ^p and σ^p which are attributed to the electron-phonon collisions and then compare them with the experimental results.

We obtain the full expressions for κ^p and σ^p by inserting $\tau_\kappa{}^p$, A(2.7) and $\tau_\sigma{}^p$, A(1.9) into the Eqs. (3.26) and (3.16). To compare with the experimental results at high and low temperatures, we have give the limiting formulas of the above expressions. Concerning κ^p, we use the expression of A(2.9) at low temperature. At high temperature, the both expressions of A(2.8) and A(2.8′) are equal.

$$\frac{1}{\kappa^p}=\begin{cases}\dfrac{3\pi}{4}\dfrac{\hbar^3 k_0}{M\kappa^3}\left\{72.7\dfrac{T^2}{\Theta^4}+\dfrac{0.18}{T^2}\left(1+\dfrac{\Theta'}{T}\right)\exp\left(-\dfrac{\Theta'}{T}\right)\right\}, & \dfrac{\Theta}{T},\ \dfrac{\Theta'}{T}\gg 1 \qquad (4.1)\\[2ex] \dfrac{3\pi}{4}\dfrac{\hbar^3 k_0}{M\kappa^3}\left\{\dfrac{0.41}{\Theta^2}+\dfrac{0.54}{\Theta'^2}\right\}, & \dfrac{\Theta}{T},\ \dfrac{\Theta'}{T}\ll 1 \qquad (4.2)\end{cases}$$

$$\frac{1}{\sigma^p}=\begin{cases}\dfrac{\pi^3}{4e^2}\dfrac{\hbar^3 k_0}{M\kappa}\left\{498\dfrac{T^5}{\Theta^6}+\dfrac{0.54}{T}\exp\left(-\dfrac{\Theta'}{T}\right)\right\}, & \dfrac{\Theta}{T},\ \dfrac{\Theta'}{T}\gg 1 \qquad (4.3)\\[2ex] \dfrac{\pi^3}{4e^2}\dfrac{\hbar^3 k_0}{M\kappa}\left\{\dfrac{0.41}{\Theta^2}T+\dfrac{0.54}{\Theta'^2}T\right\}, & \dfrac{\Theta}{T},\ \dfrac{\Theta'}{T}\ll 1 \qquad (4.4)\end{cases}$$

The experimental data of Na are listed in Table I.

Table I.

low temp.	high temp.
$\frac{T}{\kappa}=\begin{cases}0.42 \\ 0.06\end{cases}+3.8\times10^{-4}T^3$ (B.M.[18]) $3.5\times10^{-4}T^3$ (M.W.W.[19]) Watt$^{-1}\cdot$cm$\cdot$deg	$\kappa=1.38$ Watt$\cdot$cm$^{-1}\cdot$deg^{-1}
$\rho=\begin{cases}9.05\times10^{-9} \\ 1.52\times10^{-9}\end{cases}+5.37\times10^{-15}T^5$ (B.M.) $\Omega\cdot$cm 1.38×10^{-9} $8.4\times10^{-15}T^5$ (8∼15°K) (M.W.W.) $+8.6\times10^{-16}T^6$ (4∼9°K) (W.[20])	$\rho_{300°\mathrm{K}}=4.945\times10^{-6}$ $\rho_{196°\mathrm{K}}=2.916\times10^{-6}$ $\Omega\cdot$cm (B.P.[21])

As discussed at the beginning of § 3, the effects of the deviation of the phonon distribution function from the equilibrium value have not been considered in our treatment. This contributes to the thermal conductivity only in the higher order, but it may be expected that this has some contribution to the electrical conductivity though it depends on the relaxation process of phonon system. Therefore, first we shall fit Θ and Θ' by comparing with experimental results of thermal conductivity. However, it should be noticed that Θ^n in Eqs. (4.1)~(4.4) must be interpreted as a mean value over the variation of sound velocity, since the sound velocity which is one of factors determining Θ or Θ' is fairly anisotropic.

i) For κ^p at low temperature we can see that the contribution from U-processes is negligibly small. Thus by comparing the first term in Eq. (4.1) with experimental value, we obtain

$$\Theta \simeq 263^\circ\mathrm{K} \ (\mathrm{B.M.}) , \qquad (4.5)$$

$$\Theta \simeq 268^\circ\mathrm{K} \ (\mathrm{M.W.W.}) . \qquad (4.6)$$

The value of Θ depends on the from of the function $c_0(\mathcal{E})$ and the above result is obtained by using the c_2' term in Eq. (3.19) which is not the exact solution of Bloch equation at low temperature. According the Klemens[17], who solved the Bloch equation numerically in a limiting form at the low temperature, the numerical factor of the normal part in Eq. (4.1) is not 72.7 but 64.0. Hence, if we take account of this fact, Θ decreases about 9°K.

ii) For κ^p at high temperature we fit Θ' of Umklapp part to the experimental value by using Eq. (4.5) or (4.6) as Θ of N-part (i.e. first term) in Eq. (4.2). The value of Θ defined at low temperature is the mean value of Θ^{-4}. At higher temperature, however, the mean value of Θ^{-2} is aquired. These differences are, however, very small and we use the Eq. (4.5) or (4.6) for Θ. And it should be noticed that in the U-process both the longitudinal and transversal phonons contribute with nearly the same weight. For simplicity we here assume that both the modes participate in this process at the ratio 1:2. Then we have, using the Eq. (4.5)

$$\Theta \simeq 153^\circ\mathrm{K} . \qquad (4.7)$$

Even if we take Eq. (4.6) instead of Eq. (4.5), the above value scarcely changes. If we use Eq. (4.7) for the left hand side of A(3.3), we can estimate q' which is a parameter introduced in Appendix II and approximately evaluated as a mean wave vector of phonon concerning to U-process.

$$q'/q_0 \simeq 0.75 .$$

This value may be reasonable. In Fig. (5) the thermal resistance $(\kappa^p)^{-1}$ are plotted by using Eq. (4.5) as Θ and Eq. (4.7) as Θ'. (In our case, unknown parameters are reduced to two Debye temperatures Θ and Θ'.) As has been pointed out by many authors, the conductivity calculated by considering only a normal process has a fairly conspicuous minimum near $T/\Theta \simeq 0.2$ and the temperature dependence is in disagreement with experiment. Our normal part curve (a) has also same tendency. But Fig. (5) shows that this minimum is cancelled almost completely by the Umklapp part (b) and the coincidence with the experimental results is fairly good.

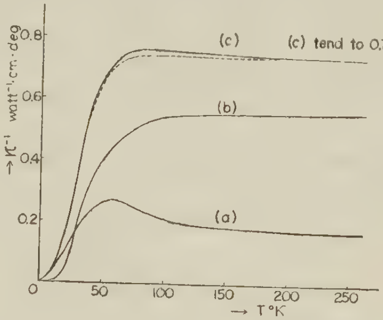

Fig. 5.

(a) Normal part which was fitted to experimental value at low temperature. (Θ=263°K)

(b) Umklapp part which was fitted to experimental value at high temperature. (Θ'=153°K)

(c) (a)+(b)

Dotted curve shows the experimental result. (B.M.[18])

iii) It is evident from Eqs. (4.2) and (4.4) that Wiedeman-Franz' law $\kappa/\sigma T = (\pi\kappa/e)^2/3$ is valid in the limits of high temperature. Therefore, σ^p at high temperature is in a good agreement with the experiment by using Θ and Θ' which are chosen to fit to κ^p for high temperature. However, experimentally this law is invalid near a melting point, for example in sodium it is near 370°K and the resistance is not proportional to T.* It seems to us that this increase of resistance is due to the self-diffusion of ions or the production of lattice-vacancy. Actually Gutowsky reported the motional narrowing of line width in nuclear magnetic resonance of sodium.

iv) Next, let us consider the electrical conductivity in low temperature. If we ignore the Umklapp part and consider only the normal part with Θ in **i**), the theoretical values of electrical conductivity becomes too large. As stated previously, the effect of non-equilibrium of the phonon distribution might be important in the electrical resistivity at low temperature. However, this effect has the tendency to decrease the electrical resistivity and thus no contribution to remove this discrepancy. Here we shall estimate roughly to what extent it can be adjusted by taking account of Umklapp process. Since the sound wave has fairly large anisotropy, we shall make use of the averaged one. (See Appendix III). Then, at low temperature, Umklapp part of $(\sigma^p)^{-1}$ results

---

* See Bradshaw and Pearson[21] for the resistivity of Na.

$$\overline{U}=\frac{1}{3}(\overline{U}_l+2\overline{U}_t)$$
$$=\frac{1}{3}\cdot\frac{0.54}{T}\left(0.54\frac{T}{\Theta_{l0}'}\exp\left(-\frac{\Theta_{l0}'}{T}\right)\right.$$
$$\left.+1.1\frac{T}{\Theta_{t0}'}\exp\left(-\frac{\Theta_{t0}'}{T}\right)\right)$$

by using Eqs. A(3.5) and A(3.6). From the comparison with the experimental value at $T=10$°K, we obtain

$$\Theta_{l0}'\simeq\Theta_{t0}'\simeq 85°\text{K} ,$$

if we substitute Θ of normal part for the value in Eq. (4.5). And we find that Umklapp part is about four times normal part. But the above evaluation is very rough and also the temperature dependence is not necessarily in agreement with experiment at low temperature, in which the electrical resistance is proportional to T^5 or T^6. However, since this temperature dependence is only valid in a very narrow range of temperature, our results seem to be not so unreasonable.

Lastly it remains to consider the contributions from the electron binary collisions σ^e and κ^e. Using $\tau_\sigma{}^e$ and $\tau_\kappa{}^e$ given by respectively A(1.23) and A(2.20), we obtain for Na

$$\frac{1}{\sigma^e}=0.01\frac{\hbar k_0}{e^2}\sigma_{t0t}\left(\frac{\kappa T}{\zeta}\right)^2$$
$$\simeq 1.1\times10^{-15}T^2\ (\Omega\cdot\text{cm}) , \tag{4.9}$$
$$\frac{1}{\kappa^e}=\frac{5.0}{\pi^2}\frac{\hbar k_0}{\kappa\zeta}\sigma_{t0t}\frac{\kappa T}{\zeta}$$
$$\simeq 6.0\times10^{-5}T\ (\text{watt}^{-1}\cdot\text{cm}\cdot\text{deg}) . \tag{4.10}$$

If we compare these results with the ideal part (i.e. that which the residural resistance is deducted from the experimental value), we find that both at 5°K and 300°K the thermal resistance (4.10) is smaller than ideal part by a factor of the order 10^{-2} and the electrical resistance (4.9) is smaller than the experimental value at low temperature by a factor of the order 10^{-3}, at high temperature by a factor of the order 10^{-4}. Hence, we may say that in monovalent metals the electron binary collisions may scarcely contribute to the resistances. In multivalent metals, however, the value of $A(K_0)$ becomes nearly unity in interband transitions. If we take $A(K_0)$ as unity, the electrical resistance by electron binary collisions becomes the same order of magnitude as that of electron-phonon collision in very low temperatures. The transport theory of multivalent metals has, however, many difficult problems and is not treated in detail in this paper.

Appendix I. Calculation of the Cross Section by the Partial Wave Method

The Schrödinger equation can be exactly solved for the potential given by Eq. (2.7). When the wave function is expanded into the partial waves, for $r<a$ its radial part $R_l(r)$ is so-called Coulomb function;

$$R_l(r)\propto F_l(Kr)/Kr ,$$

where

$$F_l(Kr)=(Kr)^{l+1}e^{iKr}f(l+1+in|2l+2|-2iKr)$$
$$K^2=k^2+(a_0a)^{-1} ,\qquad nK=(2a_0)^{-1} ,$$
$$a_0:\ \text{Bohr radius}$$
$$2k=k_1-k_2 ,\qquad 0<|k|<k_0$$

and f is the confluent hypergeometric function that is regular at the origin. For $r>a$,

$$R_l(r)\propto\cos\eta_l j_l(kr)-\sin\eta_l n_l(kr) ,$$

where j_l and n_l are respectively "spherical Bessel and Neumann" functions. The required phase shift η_l ($l=0, 1. 2, \cdots$) is computed by the boundary condition that the logarithmic derivative of $R_l(r)$ for $r\gtrless a$ be continuous at $r=a$, and then it follows

$$\tan\eta_l=\frac{\alpha_l j_l(ka)-j_l'(ka)}{\alpha_l n_l(ka)-n_l'(ka)} ,$$

where

$$\alpha_l=\left\{\left(\frac{r}{F_l}\frac{dF_l}{dr}\right)_{r=a}-1\right\}\Big/ka .$$

The values of $(r/F_l)(dF/dr)_{r=a}$ are tabulated on the reference (5) (Bloch, et al.) (in our case Ka falls in the range 2.4~3.8). η_l was calculated from $l=0$ to $l=2$. However, η_2 is very small and hereafter neglected. Thus the total cross section is given by

$$\sigma=\frac{4\pi}{k^2}(\sin^2\eta_0+3\sin^2\eta_1) . \tag{a}$$

As we consider the collisions of two identical particles with spin ½, we must take into account that collisions described by the symmetric and antisymmetric wave functions in the spacial part occur at the ratio 1:3, and so the differential cross section becomes

$$\sigma(\theta)=\frac{1}{4}(\sigma_s(\theta)+3\sigma_a(\theta))$$

where $\sigma_s(\theta)$ and $\sigma_a(\theta)$ are respectively symmetric and antisymmetric differential cross sections and are given by using the scattering amplitude $f(\theta)$ as follows

$$\sigma_s(\theta)=|f(\theta)+f(\pi-\theta)|^2=\frac{4}{k^2}\sin^2\eta_0$$

$$\sigma_a(\theta)=|f(\theta)-f(\pi-\theta)|^2=\frac{36}{k^2}\sin^2\eta_1\cos^2\theta$$

and so the total cross section becomes

$$\sigma_{tot}=\frac{4\pi}{k^2}(\sin^2\eta_0+9\sin^2\eta_1)\ . \tag{b}$$

In the range of larger ka, the contribution of p-wave becomes comparable order of that of s-wave. Abraham[22)] computed only the η_0 by the potential of type shown in Fig. 2 (d). In our case σ_{tot} depends scarcely on k as shown in Fig. 3 (b) and the constant value is about

$$\sigma_{tot}\simeq 19.0\pi a_0^2\ . \tag{b$'$}$$

Using the scattering amplitude

$$f(\theta)=-\frac{me^2}{\hbar^2K}\int_0^a\left(\frac{1}{r}-\frac{1}{a}\right)r\sin Kr\,dr$$

$$=-\frac{a^2}{a_0}\frac{1}{x^2}\left(1-\frac{\sin x}{x}\right),\quad x=Ka=2ka\sin\frac{\theta}{2},$$

and thus the cross section in the Born's approximation through the potential given by Eq. (2.7) is given by

$$\sigma=2\pi\int_0^\pi|f(\theta)|^2\sin\theta\,d\theta$$

$$=\frac{2\pi}{k^2}\left(\frac{a}{a_0}\right)^2\int_0^{2ka}\frac{(x-\sin x)^2}{x^5}dx\ . \tag{c}$$

This result was plotted in Fig. 3 in order to compare with the result (b) in which the spin quantum number is not taken into account.

Appendix II. Calculation of τ

1) *Electrical conductivity*

Calculation of $\tau_\sigma{}^p$—Using Eqs. (3.9), (3.13), (3.15) and (3.17), $\tau_\sigma{}^p$ becomes

$$\frac{1}{\tau_\sigma{}^p}=\frac{2\pi\hbar}{mn\kappa T}\sum_{\boldsymbol{k}}\sum_{\boldsymbol{k}'}\sum_{\boldsymbol{q}}W(\boldsymbol{k},\boldsymbol{k}',\boldsymbol{q})f_0(\mathcal{E}_{\boldsymbol{k}})f_0(\mathcal{E}_{\boldsymbol{k}'})N_0(x)\,e^{\mathcal{E}}{}_{\boldsymbol{k}'}(k_x-k_x)^2\,(E_{\boldsymbol{k}'}-E_{\boldsymbol{k}}-\hbar\omega_{\boldsymbol{q}})\ . \tag{A(1.1)}$$

Introducing the new variables by

$$\boldsymbol{k}'-\boldsymbol{k}=\boldsymbol{p}\ ,\qquad \mathcal{E}_{\boldsymbol{k}'}-\mathcal{E}_{\boldsymbol{k}}=\frac{\hbar\omega_{\boldsymbol{q}}}{\kappa T}=x \tag{A(1.2)}$$

A(1.1) may be rewritten as follows

$$\frac{1}{\tau_\sigma{}^p}=\frac{2\pi\hbar}{mn\kappa T}\sum_{\boldsymbol{k}}\sum_{\boldsymbol{P}(\boldsymbol{q})}W(|\boldsymbol{p}|,\boldsymbol{q})f_0(\mathcal{E})f_0(\mathcal{E}+x)\,e^{\mathcal{E}+x}N_0(x)\,p_x^2\,\delta(E'-E-\hbar\omega_{\boldsymbol{q}})$$

where for brevity we rewrite $\mathcal{E}_{\boldsymbol{k}'}$, $\mathcal{E}_{\boldsymbol{k}}$ and $E_{\boldsymbol{k}'}$, $E_{\boldsymbol{k}}$ by $\mathcal{E}'$, $\mathcal{E}$ and E', E and $\sum_{\boldsymbol{P}(\boldsymbol{q})}$ means the summation respect to Normal and Umklapp processes, as will be illustrated later. As usual these summations may be replaced by the integral over $\boldsymbol{k}$ and $\boldsymbol{p}$, furthermore the polar coordinates (k,θ_1,φ_1) with the polar axis in the direction $\boldsymbol{p}$ is used for the integration over $\boldsymbol{k}$ and (p,θ_2,φ_2) with the polar axis in the direction $\boldsymbol{x}$ (direction of field) is used for the integration by $\boldsymbol{p}$. Performing the integral over θ_1, θ_1 is determined by the property of δ-function such as

$$E'-E-\hbar\omega_{\boldsymbol{q}}=\frac{\hbar^2}{2m}(2pk\cos\theta_1-p^2)-\hbar\omega_{\boldsymbol{q}}=0\ , \tag{A(1.3)}$$

and for another slowely varying quantity of θ_1, θ_1 is substituted by

$$\cos\theta_1=\frac{m\omega_{\boldsymbol{q}}}{\hbar^2pk}-\frac{p}{2k}\ . \tag{A(1.4)}$$

Then one can readily perform other integrals apart from the integral over p and obtains

$$\frac{1}{\tau_\sigma{}^p}=\frac{m}{6\pi^3\hbar^3 n}\int_0^{2k_0}dp\,\frac{xp^3W(|\boldsymbol{p}|,\boldsymbol{q})}{(e^x-1)(1-e^{-x})}=\frac{m\zeta^2}{27\pi^3 MNn\hbar\kappa T}\int_0^{2k_0}dp\,\frac{p^5G^2(p/2k_0)}{(e^x-1)(1-e^{-x})} \qquad \text{A(1.5)}$$

where n and N are respectively the densities of electron and ion. We carry out the integration over p by separating the integral range into two parts as follows

$$0<p<q_0 \qquad \text{or} \qquad 0<u<\frac{q_0}{2k_0}=0{,}63 \qquad \text{A(1.6)}$$

$$q_0<p<2k_0 \qquad \text{or} \qquad 0.63<u<1 \qquad \text{A(1.6')}$$

where k_0 and q_0 denote respectively the magnitude of the Fermi maximum and Debye cut off wave vectors. In the range A(1.6) the Normal (or N-) process occurs, where the variable p may be replaced by the magnitude of phonon wave vector q, and $G^2(u)$ in A(1.5) is given by the approximate formula

$$\begin{aligned}G^2(u)&=1-4.65u^2+4.50u^3\\&=1-\frac{4.65}{4}\left(\frac{\delta}{t}\right)^2x^2+\frac{4.50}{8}\left(\frac{\delta}{t}\right)^3x^3\,, \qquad t=\frac{\Theta}{T}\,, \qquad \delta=\frac{q_0}{k_0}\end{aligned} \qquad \text{A(1.7)}$$

as shown in Fig. 3(b). On the other hand, in the range A(1.6′) the so-called Umklapp (or U-) process occurs, where $|\boldsymbol{p}|=p$ is determined by the relation $\boldsymbol{p}=\boldsymbol{q}+\boldsymbol{K}_0$ ($\boldsymbol{K}_0$ is a principal vector of the reciprocal lattice), depending on both the magnitude of $\boldsymbol{q}$ and angle $\widehat{\boldsymbol{q}\cdot\boldsymbol{K}_0}$. However, it is very difficult to perform the integration A(1.5) over this range rigorously by taking into account of this relation with $\boldsymbol{q}$. By using the approximation that q and x is constant, the integration over p is performable numerically such as

$$\int_{q_0}^{2k_0}dp\,p^5G^2\left(\frac{p}{2k_0}\right)=(2k_0)^6\int_{0.63}^{1}du\,u^5G^2(u)\simeq 0.0084(2k_0)^6 \qquad \text{A(1.8)}$$

which was obtained by using the curve for $u>0.63$ in Fig. 4. It is easily seen that the wave vector q of the phonons contributing to the U-process have the values close its maximum value and in contrast to the Normal process not only the longitudinal but also the transversal phonons play a equally important role. However when q becomes large, we shall be no able to distinguish these polarization modes and it will be also not a good approximation to use the relation $\omega_q=c_0q$, where c_0 represents the sound velocity (even if we allow this relation, practically c_0 depends on temperature and exhibits an anisotropy as mentioned in § 4). According to the facts stated above, we shall introduce a parameter Θ' defined by the relation $\hbar c_0q'=\kappa\Theta'$, in which q' means an averaged wave number of phonons contributing to Umklapp process, apart from Θ corresponding to q_0. Thus $\tau_\sigma{}^p$ is written with the two parameters, say $\Theta/T\equiv t$ and $\Theta'/T\equiv t'$, such as

$$\begin{aligned}\frac{1}{\tau_\sigma{}^p}&=\frac{m\zeta^2}{27\pi^3MNn\hbar\kappa T}\left[\left(\frac{q_0}{t}\right)^6\int_0^t dx\,\frac{x^5\left\{1-\frac{4.65}{4}\left(\frac{\delta}{t}\right)^2x^2+\frac{4.53}{8}\left(\frac{\delta}{t}\right)^3x^3\right\}}{(e^x-1)(1-e^{-x})}\right.\\&\qquad\qquad\left.+\frac{(2k_0)^6}{(e^{t'}-1)(1-e^{-t'})}\int_{0.63}^{1}du\,u^5G^2(u)\right]\\&=\frac{\pi m\zeta^2}{3M\hbar\kappa}\left[\frac{1}{\Theta}\frac{4}{t^5}\left\{\phi_5(t)-1.85\frac{\phi_7(t)}{t^2}+1.13\frac{\phi_8(t)}{t^3}\right\}+\frac{1}{\Theta'}\frac{0.54t'}{(e^{t'}-1)(1-e^{-t'})}\right].\end{aligned} \qquad \text{A(1.9)}$$

To obtain the last expression we used A(1.8) and relations

$$n=\frac{k_0{}^3}{3\pi^2}\,, \qquad N=\frac{q_0{}^3}{6\pi^2}\,, \qquad \delta^3=\left(\frac{q_0}{k_0}\right)^3=2 \quad \text{(for monovalent metal)} \qquad \text{A(1.10)}$$

and $\phi_n(t)$ is given by

$$\phi_n(t)=\int_0^t dx\frac{x^n}{(e^x-1)(1-e^{-x})} . \qquad \text{A(1.11)}$$

In A(1.9), if we ignore the Umklapp part and keep only the term $\phi_5(t)$ and replace ζ with the coupling constant C, we obtain the well known Grüneisen's formula.

Calculation of τ_σ^e—In order to compute the τ_σ^e defined by Eqs. (3.15) and (3.17) analytically we assume that the transition probability $w(\boldsymbol{k}_1\boldsymbol{k}_2\boldsymbol{k}_3\boldsymbol{k}_4)$ in Eq. (3.9) is not dependent on the wave number $\boldsymbol{k}$, but constant w. From Eqs. (2.4), (3.1) and Eq. (3.9), and taking account of the number of pairs 4 for the spin direction, we obtain

$$\frac{1}{\tau_\sigma^e}=\frac{\pi\hbar}{mn\kappa T}\sum_{\boldsymbol{k}_1}\sum_{\boldsymbol{k}_2}\sum_{\boldsymbol{k}_3} w f_0(\mathcal{E}_1)f_0(\mathcal{E}_2)f_0(-\mathcal{E}_3)f_0(-\mathcal{E}_4)\, K_{0x}{}^2\,\delta(E_1+E_2-E_3-E_4) \qquad \text{A(1.12)}$$

where since we allowed that the suffixes of this summation run over independently each other, we multiplied a factor $\frac{1}{4}$, and for simplicity denoted $\mathcal{E}_{\boldsymbol{k}_1}$ and $E_{\boldsymbol{k}_1}$ as $\mathcal{E}_1$ and E_1. Now we put

$$\boldsymbol{k}_1+\boldsymbol{k}_2=\boldsymbol{s}\ , \qquad \boldsymbol{k}_3+\boldsymbol{k}_4=\boldsymbol{r} \qquad \text{A(1.13)}$$

and use the approximation that for the calculation of summation in A(1.12) we consider only the processes of electron collisions in which both vectors $\boldsymbol{s}$ and $\boldsymbol{r}$ have the same directions as $\boldsymbol{K}_0$. This corresponds to the assumption that the system is homogeneous. Introducing the polar coordinates $(k_3, \theta_3, \varphi_3)$, polar axis being in the direction $\boldsymbol{r}$, $(k_2, \theta_2, \varphi_2)$, one being in $\boldsymbol{k}_1$ and $(k_1, \theta_1, \varphi_1)$, one being in $\boldsymbol{x}$, and then replacing the summation by the integration as follows

$$\left.\begin{aligned}&\sum_{\boldsymbol{k}_1}\sum_{\boldsymbol{k}_2}\sum_{\boldsymbol{k}_3}\rightarrow\left(\frac{1}{8\pi^3}\right)^3\int k_1{}^2\,dk_2\,d\Omega_1\int k_2{}^2\,dk_2\,d\Omega_2\int k_3{}^2\,dk_3\,d\Omega_3\ ,\\ &d\Omega_i=d(\cos\theta_i)\,d\varphi_i\ , \qquad i=1, 2, 3\end{aligned}\right\} \qquad \text{A(1.14)}$$

we can perform these integrations, using the following relations

$$|\boldsymbol{k}_1|\simeq|\boldsymbol{k}_2|\simeq|\boldsymbol{k}_3|\simeq|\boldsymbol{k}_4|\simeq k_0\ ,$$

$$E_4=\frac{\hbar^2}{2m}\cdot k_4{}^2=\frac{\hbar^2}{2m}(r^2+k_3{}^2+2rk_3\cos\theta_3)\ ,$$

$$\begin{aligned}E_1+E_2-E_3-E_4&=\frac{\hbar^2}{2m}(k_1{}^2+k_2{}^2-2k_3{}^2-r^2-2k_3r\cos\theta_3)\\ &\simeq-\frac{\hbar^2}{2m}(r^2+2k_0r\cos\theta_3)\ ,\end{aligned} \qquad \text{A(1.15)}$$

$$K_{0x}{}^2=\frac{K_0{}^2}{s^2}k_0{}^2(\cos\theta_1+\cos\alpha)^2\ , \qquad \text{A(1.16)}$$

$$s^2=2k_0{}^2(1+\cos\theta_2)\ , \qquad \text{A(1.17)}$$

$$\cos\alpha=\cos\theta_1\cos\theta_2+\sin\theta_1\sin\theta_2\cos\varphi_2\ . \qquad \text{A(1.18)}$$

Then as to the integration over θ_3, we notice only the δ-function and θ_3 is given by the relation A(1.15)=0. From the restriction $|\text{coo}\ \theta_3|<1$, the following relation

$$\left|\frac{r}{2k_0}\right|\leq 1 \qquad \text{or} \qquad s\geq K_0-2k_0\ ,$$

exists or in view of A(1.17) it becomes the restriction respect to $\cos\theta_2$; i.e.

$$\cos\theta_2\geq 2(b-1)^2-1\ , \qquad b=\frac{K_0}{2k_0}\ . \qquad \text{A(1.19)}$$

Then the integrations over solid angle Ω_i is performable using A(1.15)~(1.18) and becomes

$$\begin{aligned}
&\int K_{0x}^2\, \delta(E_1+E_2-E_3-E_4)\, d\Omega_1\, d\Omega_2\, d\Omega_3 \\
&= -\frac{2\pi m}{\hbar^2 k_0}\int \frac{K_{0x}^2}{K_0-s}\, d\Omega_1\, d\Omega_2 \\
&= -\frac{(2\pi)^3 m K_0^2}{2\hbar^2 k_0}\int_{2(b-1)^2-1}^{1} d(\cos\theta_2)\int_0^1 d(\cos\theta_1)\, \frac{\cos^2\theta_1(1+\cos\theta_2)^2+\frac{1}{2}\sin^2\theta_1\cdot\sin^2\theta_2}{(1+\cos\theta_2)(K_0-k_0\sqrt{2(1+\cos\theta)}\,)} \\
&= \frac{(2\pi)^3 32m}{3\hbar^2}\, b^2\left[1-\frac{b}{2}\{1+\log(b-1)\}\right]. \qquad \text{A(1.20)}
\end{aligned}$$

In the remaining integrals over k (k_1, k_2, k_3) we make use of $\mathcal{E}_i$ instead of k_i. Then we find that these integrations are transformed into a form of A(1.11) in which t is taken as infinity. Thus τ_σ^e becomes

$$\frac{1}{\tau_\sigma^e} = \frac{3}{8\pi}\frac{mk_0}{\hbar^3}n\left(\frac{\kappa T}{\zeta}\right)^2 \phi_2(\infty) w b^2\left[1-\frac{b}{2}\{1+\log(b-1)\}\right]. \qquad \text{A(1.21)}$$

For the transition probability w in above expression we may substitute $|2MA(K_0)|^2$ given in Eq. (2.4) when Born approximation is applicable. When Born approximation is not applicable, we assume that M can be replaced by the total cross section calculated in the case of the thermal conduction (see Appendix I and A(2.19)). As a result,

$$w \simeq \frac{4\pi\hbar^4}{m^2}\sigma_{tot}|A(K_0)|^2 . \qquad \text{A(1.22)}$$

Here $A(K_0)$, given in Eq. (2.5), were numerically calculated from Wigner-Seitz's result for sodium (using the wave function $u_0(r)$ at the ground state and $r_s=3.96$ Bohr unit) that is

$$A(K_0) \simeq 4.7\times 10^{-2} .$$

Substituting A(1.22) with this result, $\phi_2(\infty)\simeq 3.3$ and $b=(K_0/2k_0)\simeq 1.14$ (for sodium) for A(1.21), we obtain the final result

$$\frac{1}{\tau_\sigma^e} = 0.044\frac{\hbar k_0}{m} n\, \sigma_{tot}\left(\frac{\kappa T}{\zeta}\right)^2 . \qquad \text{A(1.23)}$$

Or if we define the mean free path by $l^e=\tau^e v_0=\hbar k_0\tau^e/m$,

$$l_\sigma^e = 0.044 n\, \sigma_{tot}\left(\frac{\kappa T}{\zeta}\right)^2 . \qquad \text{A(1.24)}$$

2) *Thermal conduction*

Calculation of τ_κ^p—From Eqs. (3.23), (3.28), (3.29) and (3.31), τ_κ^p is rewritten by the same way as that of τ_σ^p

$$\begin{aligned}
\frac{1}{\tau_\kappa^p} = \frac{2\pi\hbar}{mn\kappa Tc}\sum_{\boldsymbol{k}}\sum_{\boldsymbol{k}'}\sum_{\boldsymbol{q}} & W(\boldsymbol{k}, \boldsymbol{k}', \boldsymbol{q}) f_0(\mathcal{E}_k) f_0(\mathcal{E}_{k'}) e^{\mathcal{E}_{k'}} N_0(x)\{k_x' c_0(\mathcal{E}_{k'})-k_x c_0(\mathcal{E}_k)\} \\
& \times(\mathcal{E}_{k'}k_x'-\mathcal{E}_k k_x)\, \delta(E_{k'}-E_k-\hbar\omega_q) . \qquad \text{A(2.1)}
\end{aligned}$$

After the integration by solid angular variables, A(2.1) becomes

$$\frac{1}{\tau_\kappa^p} = \frac{m}{6\pi^3\hbar^3 nc}\int_0^{2k_0} dp\int_{-\infty}^{\infty} d\mathcal{E}\, W(|\boldsymbol{p}|, \boldsymbol{q})\, p N_0(x) f_0(\mathcal{E}_k) f_0(\mathcal{E}+x)\, e^{\mathcal{E}+x} K(\mathcal{E}, p) , \qquad \text{A(2.2)}$$

where

$$K(\mathcal{E},p)=xk^2\{c_0(\mathcal{E}+x)-c_0(\mathcal{E})\}+\frac{p^2}{2}\{\mathcal{E}c_0(\mathcal{E}+x)+(\mathcal{E}+x)c_0(\mathcal{E})\}+\frac{m\omega_q}{\hbar}\{(2x+\mathcal{E})c_0(\mathcal{E}+x)-(\mathcal{E}+x)c_0(\mathcal{E})\}\,. \tag{A(2.3)}$$

If we transform $c_0(\mathcal{E}+x)$ into $c_0(\mathcal{E})$ by means of the following relations for the odd-function $c_0(\mathcal{E})$ of $\mathcal{E}$,

$$\int_{-\infty}^{\infty}d\mathcal{E}\frac{c_0(\mathcal{E}\pm x)+c_0(\mathcal{E})}{(e^{-\varepsilon}+1)(e^{\varepsilon\pm x}+1)}=0\,,\qquad \int_{-\infty}^{\infty}d\mathcal{E}\frac{\mathcal{E}c_0(\mathcal{E}\pm x)-(\mathcal{E}\pm x)c_0(\mathcal{E})}{(e^{-\varepsilon}+1)(e^{\varepsilon\pm x}+1)}=0 \tag{A(2.4)}$$

and substitute Eq. (3.19) for $c_0(\mathcal{E})$ and then integrate over $\mathcal{E}$, A(2.2) and A(2.3) are reduced to

$$\frac{1}{\tau_\kappa{}^p}=\frac{m}{6\pi^3\hbar^3nc}\int_0^{2k_0}\frac{xpW(|\boldsymbol{p}|,\boldsymbol{q})}{(e^x-1)(1-e^{-x})}K'(p)\,, \tag{A(2.5)}$$

$$K'(p)=\begin{cases} c_2\left\{k_0{}^2x^2+p^2\left(\dfrac{\pi^2}{3}-\dfrac{x^2}{6}\right)\right\} & \text{(for high temp.)}\\[2ex] c_2'\left[k_0{}^2\left(\dfrac{x}{e^x-1}+\dfrac{x}{1-e^{-x}}-2\right)+p^2\left\{1-\dfrac{x}{4}\left(\dfrac{1}{e^x-1}+\dfrac{1}{1-e^{-x}}\right)\right\}\right] & \text{(for low temp.)}\end{cases} \tag{A(2.6)}$$

where c in A(2.5), being defined by Eq. (3.23), means c_2 or c_2' in accordance with that in $K'(p)$.

Now if one takes Eq. (2.8) for W and the term involving c_2 for $K'(p)$ and neglect the Umklapp process, one obtains the well-known expression for the thermal conductivity (Wilson[23]). In our treatment, Eq. (2.8) combined with Eq. (2.9) is substituted for W, then A(2.5) becomes

$$\frac{1}{\tau_\kappa{}^p}=\frac{m\zeta^2}{27\pi^3MNn\hbar\kappa Tc}\int_0^{2k_0}dp\,\frac{p^3G^2(p/2k_0)}{(e^x-1)(1-e^{-x})}K'(p)\,,$$

The integration over p can be performed by separating integral range into the regions defined by A(1.6) and A(1.6′) in the same way for $\tau_\sigma{}^p$. In the latter range we use the relation A(1.8) and

$$\int_{q_0}^{2k_0}dp\,p^3G^2\left(\frac{p}{2k_0}\right)=(2k_0)^4\int_{0.63}^{1}du\,u^3G^2(u)\simeq 0.014(2k_0)^4$$

to calculate the U-process.

As a result we have

$$\frac{1}{\tau_\kappa{}^p}=\frac{\pi mn\zeta^2}{3MN\hbar\kappa T}\begin{cases} g(t,t') & \text{(for high temp.)}\\ g'(t,t') & \text{(for low temp.)}\end{cases} \tag{A(2.7)}$$

where

$$g(t,t')=\frac{4}{t^6}\left\{(1+0.19t^2)\left(\phi_5(t)+\frac{1.13}{t^3}\phi_8(t)\right)-\left(0.40+\frac{1.85}{t^2}\right)\phi_7(t)+\frac{0.93}{t^2}\phi_9(t)-\frac{0.57}{t^3}\phi_{10}(t)\right\}$$
$$+\frac{0.54}{(e^{t'}-1)(1-e^{-t'})}(1+0.76t'^2)\,,$$

$$g'(t,t')=\frac{4}{t^6}\left\{2.52t^2\phi_3(t)-10.3\phi_5(t)+\frac{7.09}{t}\phi_6(t)+\frac{3.70}{t^2}\phi_7(t)-\frac{2.81}{t^3}\phi_8(t)-\frac{0.213t^6}{(e^t-1)(1-e^{-t})}\right\}$$
$$+\frac{0.180}{(e^{t'}-1)(1-e^{-t'})}\left\{1+\frac{t'(e^{t'}-e^{-t'})}{(e^{t'}-1)(1-e^{-t'})}\right\}.$$

These limiting expressions for the high and low temperatures are given by

$$g(t,t')=\begin{cases}\dfrac{0.413}{t^2}+\dfrac{0.540}{t'^2} & t,t'\ll 1 \qquad \text{A(2.8)}\\[2ex] \dfrac{95.2}{t^4}+0.540(1+0.76t'^2)\,e^{-t'} & t,t'\gg 1 \qquad \text{A(2.9)}\end{cases}$$

$$g'(t,t')=\begin{cases}\dfrac{0.413}{t^2}+\dfrac{0.540}{t'^2} & t,t'\ll 1 \qquad \text{A(2.8')}\\[2ex] \dfrac{72.7}{t^4}+0.180(1+t')\,e^{-t'} & t,t'\gg 1 \qquad \text{A(2.9')}\end{cases}$$

where we used $\phi_3(\infty)=7.212$ to obtain the first term in A(2.9′). The first terms of these equations indicate the contribution from Normal process and the second terms from Umklapp process. It is found from A(2.8) and A(2.8′) that in the limit at the high temperature they may attain to the same result whether c_2 is adopted for $c_0(\mathcal{E})$ in Eq. (3.19) or c_2', but for the Normal part at low temperature A(2.9′) become smaller than A(2.9).

Calculation of τ_κ^e—From the definition of τ_κ^e, Eqs. (3.25), (3.27), and (3.1) (3.23), τ_κ^e is calculated in the same way for τ_σ^e as follows:

$$\frac{1}{\tau_\kappa^e}=\frac{\pi\hbar}{mn\kappa Tc}\sum_{\boldsymbol{k}_1}\sum_{\boldsymbol{k}_2}\sum_{\boldsymbol{k}_3}\sum_{\boldsymbol{k}_4} w(\boldsymbol{k}_1\boldsymbol{k}_2\boldsymbol{k}_3\boldsymbol{k}_4)f_0(\mathcal{E}_1)f_0(\mathcal{E}_2)f_0(-\mathcal{E}_3)f_0(-\mathcal{E}_4)$$
$$\times\{k_{3x}c_0(\mathcal{E}_3)+k_{4x}c_0(\mathcal{E}_4)-k_{1x}c_0(\mathcal{E}_1)-k_{2x}c_0(\mathcal{E}_2)\}(k_{3x}\mathcal{E}_3+k_{4x}\mathcal{E}_4-k_{1x}\mathcal{E}_1-k_{2x}\mathcal{E}_2)\,\delta(E_1+E_2-E_3-E_4) \qquad \text{A(2.10)}$$

where for simplicity $\mathcal{E}_1$ and $\mathcal{E}_2$ denote $\mathcal{E}_{k_1}$ and $\mathcal{E}_{k_2}$. Here we consider only the process which conserves the total wave vector; i.e.

$$\boldsymbol{k}_1+\boldsymbol{k}_2-\boldsymbol{k}_3-\boldsymbol{k}_4=0 \qquad \text{A(2.11)}$$

and use for w the total cross section which was obtained by the partial wave method in Appendix I. Now if we put

$$\boldsymbol{k}_3-\boldsymbol{k}_1=\boldsymbol{k}_2-\boldsymbol{k}_4=\boldsymbol{l}\,, \qquad \text{A(2.12)}$$

four sums over $\boldsymbol{k}$'s are reduced to those over $\boldsymbol{k}_1$, $\boldsymbol{k}_2$ and $\boldsymbol{l}$. Then introducing three polar coordinates (k_1,θ_1,φ_1), (l,θ_2,φ_2) and (k_2,θ_3,φ_3), their poles being respectively the directions of $\boldsymbol{l}$, $\boldsymbol{k}_2$ and $\boldsymbol{x}$ (the direction of temperature gradient), and representing the angles that $\boldsymbol{x}$ makes with $\boldsymbol{k}_1$ and $\boldsymbol{l}$ respectively by α and β, we can make the following replacement,

$$\sum_{\boldsymbol{k}_1}\sum_{\boldsymbol{k}_2}\sum_{\boldsymbol{l}}\to\left(\frac{1}{8\pi^3}\right)^3\int l^2\,dl\,d\Omega_2\int k_2^2\,dk_2\,d\Omega_3\int k_1^2\,dk_1\,d\Omega_1\,,$$

$$d\Omega_i=d(\cos\theta_i)\,d\varphi_i\,;\qquad i=1,2,3\,,$$

$$k_{1x}=k_1\cos\alpha\,,\qquad k_{2x}=k_2\cos\theta_3\,,\qquad l_x=l\cos\beta\,,$$

$$\cos\alpha=\cos\theta_1\cos\beta+\sin\theta_1\sin\beta\cos\varphi_1\,,$$

$$\cos\beta=\cos\theta_2\cos\theta_3+\sin\theta_2\sin\theta_3\cos\varphi_2$$

and for the energy,

$$E_3+E_4-E_1-E_2=\frac{\hbar^2 l}{m}(k_1\cos\theta_1-k_2\cos\theta_2+l)\,, \qquad \text{A(2.13)}$$

$$\mathcal{E}_3-\mathcal{E}_1=\mathcal{E}_2-\mathcal{E}_4=z\,, \qquad \text{A(2.14)}$$

where

$$z=Al(2k_1\cos\theta_1+l)=Al(2k_2\cos\theta_2-l)\,, \qquad \text{A(2.15)}$$

$$A=\hbar^2/2m\kappa T\,. \tag{A(2.16)}$$

Furthermore transforming the variables θ_2 and k into z and $\mathcal{E}$ as follows,

$$d(\cos\theta_2)=\frac{dz}{2Alk_2}\,,\qquad k\,dk=\frac{d\mathcal{E}}{2A}\,,$$

it is easy to carry out the integration respect to the angles except θ_1, for which we need to notice only the variable $\cos\theta_1$ involved in the δ-function and to replace θ_1 in another slowly varying part with

$$\cos\theta_1=(k_2\cos\theta_2-l)/k_1\,,$$

which is derived from the condition of energy conservation, say A(2.13)=0. From A(2.15) and $|\cos\theta_1|\leq 1$, the range of z is restricted by

$$Al^2(1-2k_1/l)<z<Al^2(1+2k_1/l)\,. \tag{A(2.17)}$$

Since the range of l is in $0<l<2k_0$ from A(2.12) and hence the value of Al^2 falls into the range $0<Al^2<4\zeta/\kappa T$, we may be possible to approximate as follows

$$-\infty<z<+\infty\,,$$

instead of A(2.17). Thus after the integration of the angles except θ_2 we have

$$\frac{1}{\tau_\kappa^e}=(192\pi^5 n\hbar\kappa TA^3c)^{-1}w\int_0^{2k_0}dl\int_{-\infty}^{\infty}dz\int_{-\infty}^{\infty}d\mathcal{E}_1\int_{-\infty}^{\infty}d\mathcal{E}_2\,f_0(\mathcal{E}_1)f_0(\mathcal{E}_2)f_0(\mathcal{E}_1+z)f_0(\mathcal{E}_2-z)$$
$$\times e^{\mathcal{E}_1+\mathcal{E}_2}K(\mathcal{E}_1,\mathcal{E}_2,l,z)\,, \tag{A(2.18)}$$

where

$$K(\mathcal{E}_1,\mathcal{E}_2,l,z)=-\frac{z^2}{2A}\{c_0(\mathcal{E}_1)+c_0(\mathcal{E}_2)\}+\left(zl^2-2k_0^2z+\frac{z^3}{2A^2l^2}\right)\{c_0(\mathcal{E}_1)-c_0(\mathcal{E}_2)\}$$
$$+l^2\{\mathcal{E}_1c_0(\mathcal{E}_1)+\mathcal{E}_2c_0(\mathcal{E}_2)\}-\frac{z}{A}\{\mathcal{E}_1c_0(\mathcal{E}_2)-\mathcal{E}_2c_0(\mathcal{E}_1)\}\,, \tag{A(2.19)}$$

where to obtain A(2.18), A(2.19) we used A(2.4). We find that when we integrate over $\mathcal{E}_1$ and $\mathcal{E}_2$, the first and fourth term in A(2.19) vanish, if we remember that $c_0(\mathcal{E})$ is the odd-function of $\mathcal{E}$ and the Fermi function f_0 has form given by Eq. (3.2). Therefore it remains that we substitute the concrete form of $c_0(\mathcal{E})$, Eq. (3.19), for the second and third term (now since our attention lie in low temperature we take c_2' term) and integrate respect to the remaining variables. The final result is

$$\frac{1}{\tau_\kappa^e}=\frac{nmk_0}{\pi\hbar^3}\phi_2(\infty)w\left(\frac{\kappa T}{\zeta}\right)^2. \tag{A(2.20)}$$

Here as mentioned previously, replacing w with the total cross section σ_{tot} by

$$w=\frac{\pi\hbar^4}{m^2}\sigma_{tot} \tag{A(2.21)}$$

and using $\phi_2(\infty)\simeq 3.29$, we have

$$\frac{1}{\tau_\kappa^e}=6.6n\sigma_{tot}\frac{\hbar k_0}{m}\left(\frac{\kappa T}{\zeta}\right)^2 \tag{A(2.22)}$$

or writing by the mean free path

$$l_\kappa^e=6.6n\sigma_{tot}\left(\frac{\kappa T}{\zeta}\right)^2. \tag{A(2.23)}$$

Appendix III. Anisotropy of the Sound Velocity

The sound velocity of sodium was measured by Quimby-Siegel[24] and Bender[25]. Both results are fairly different, and Blackman[26] estimated $\overline{\Theta^n}$ by using the latter result. We here adopt the former. According to this result, the sound velocities of longitudinal and transversal waves c_l, c_t can be expressed approximately by the following experimental formulas;

$$c_l=\{1.4+4.0\sin^2\theta(\cos^2\theta+\tfrac{1}{4}\sin^2\theta\sin^2 2\varphi)\}\times 10^5\ \text{cm/sec}\ , \tag{A(3.1)}$$

$$c_t=\{2.4-4.7\sin^2\theta(\cos^2\theta+\tfrac{1}{4}\sin^2\theta\sin^2 2\varphi)\}\times 10^5\ \text{cm/sec}\ . \tag{A(3.2)}$$

It may be thought that only the longitudinal wave contributes to the Normal process, and hence all Θ^n in Eqs. (4.1)$\sim$(4.4) are to be understood as $(\hbar q_0/\kappa)\overline{c_l{}^n}$. To the Umklapp process we must consider the contribution from the phonons with two polarizations. Now if the both types of sound wave are mixed together at the ratio 1:2, those which we require are the following. First in high temperature,

$$\overline{\frac{1}{\Theta'^2}}=\frac{1}{3}\left(\frac{q_0}{q'}\right)^2\left(\frac{\kappa}{\hbar q_0}\right)^2\left\{\overline{\frac{1}{c_l{}^2}}+2\overline{\frac{1}{c_t{}^2}}\right\}, \tag{A(3.3)}$$

where q' is defined by the relation $\kappa\Theta'=\hbar cq'$ (see § 4 (ii)). Estimating roughly the mean values of $c_l{}^{-2}$ and $c_t{}^{-2}$ from the above experimental formulas these values are nearly equal; i.e.

$$\overline{c_t{}^{-2}}\simeq\overline{c_l{}^{-2}}\simeq 0.24\times 10^{-10}\,(\text{cm}\cdot\text{sec}^{-1})^{-2}\ . \tag{A(3.4)}$$

Next in low temperature, we need the mean value of the following quantity

$$\exp\left(-\frac{\Theta'}{T}\right)=\frac{1}{3}\left\{\exp\left(-\frac{\hbar q' c_l}{\kappa T}\right)+2\exp\left(-\frac{\hbar q' c_t}{\kappa T}\right)\right\}.$$

In order to evaluate the above quantity approximately, we shall expand c around its minimum point since we consider the case $\Theta'\gg T$. c_l has the minimum values in the six directions, that is, $\theta=0$, π and $\theta=\pi/2$; $\varphi=n\pi/2$ ($n=0, 1, 2, 3$). As each direction is equivalent, expanding around z-axis, we have

$$c_l\simeq(1.4+4\theta^2)\times 10^5\ \text{cm}\cdot\text{sec}^{-1}\ .$$

On the other hand, c_t has the minimum values in the eight directions, that is, $\cos\theta=\pm 3^{-1/2}$; $\varphi=\pi/4+n\pi/2$ ($n=0, 1, 2, 3$), and hence we must the original coordinate system into the new coordinate system with z'-axis, being in the direction $\cos\theta=3^{-1/2}$; $\varphi=\pi/4$, then the transformation matrix is given by

$$\sin\theta\cos\varphi=\frac{1}{\sqrt{2}}\sin\theta'\cos\varphi'+\frac{1}{\sqrt{6}}\sin\theta'\sin\varphi'+\frac{1}{\sqrt{3}}\cos\theta'\ ,$$

$$\sin\theta\sin\varphi=-\frac{1}{\sqrt{2}}\sin\theta'\cos\varphi'+\frac{1}{\sqrt{6}}\sin\theta'\sin\varphi'+\frac{1}{\sqrt{3}}\cos\theta'\ ,$$

$$\cos\theta=\qquad -\sqrt{\frac{2}{3}}\sin\theta'\sin\varphi'+\frac{1}{\sqrt{3}}\cos\theta'\ .$$

Hence we have

$$\sin^2\theta(\cos^2\theta+\sin^2\theta\cos^2\varphi\sin^2\varphi)\simeq\tfrac{1}{3}(1-2\theta'^2)$$

and using this result, c_t becomes

$$c_t\simeq(0.84+3.1\theta'^2)\times 10^5\ \text{cm}\cdot\text{sec}^{-1}\ .$$

Thus as the mean value of Umklapp part of electrical resistance at low temperature over the sound velocity we obtain

$$\begin{aligned}\overline{U_l}&=\frac{1}{4\pi}\frac{0{\cdot}54}{T}\int_{-1}^{1}dt\int_{0}^{2\pi}d\varphi\,\exp\left(-\frac{\hbar q'\,c_l(t,\varphi)}{\kappa T}\right)\\&\simeq\frac{0.54}{T}\cdot\frac{4.3}{8.0}\frac{T}{\Theta_{l0}'}\exp\left(-\frac{\Theta_{l0}'}{T}\right),\end{aligned}\tag{A(3.5)}$$

where

$$\kappa\Theta_{l0}'=\hbar q'\times1.4\times10^5$$

and

$$\overline{U_t}\simeq\frac{0.54}{T}\frac{3.4}{6.2}\frac{T}{\Theta_{t0}'}\exp\left(-\frac{\Theta_{t0}'}{T}\right),\tag{A(3.6)}$$

where

$$\kappa\Theta_{t0}'=\hbar q'\times0.84\times10^5\ .$$

References

1) D. Bohm and D. Pines: Phys. Rev. **92** (1953) 609.
2) J. Bardeen and D. Pines: Phys. Rev. **99** (1955) 1040.
3) V. L. Ginzburg and P. Silin: Sov. Phys. JETP **2** (1956) 46.
4) E. P. Wigner and F. Seitz: Phys. Rev. **43** (1933) 804; **46** (1934) 509.
5) I. Bloch et al: Rev. Mod. Phys. **23** (1951) 147.
6) J. Bardeen: Phys. Rev. **52** (1937) 688.
7) T. Toya: Busseiron-Kenkyu **59** (1953) 179.
8) J. C. Slater: Phys. Rev. **81** (1951) 385.
9) T. Kasuya: Progr. Theor. Phys. **13** (1955) 561.
10) D. Pines: *Solid State Physics.* (Academic Press. Inc. New York) Vol. **1**. Sec. 6 (1955).
11) J. M. Ziman: Proc. Roy. Soc. A, **226** (1954) 436.
12) F. J. Blatt: Phys. Rev. **99** (1955) 1735. R. Barrie: Phys. Rev. **103** (1956) 1581.
13) M. Tuji: Busseiron-Kenkyu **102** (1956) 127.
14) E. H. Sondheimer: Proc. Roy. Soc. **A, 234** (1956) 391. I. I. Hanna and E. H. Sondheimer: ibid **A, 239** (1957) 247.
15) T. Kasuya and K. Yamada: Busseiron-Kenkyu **100** (1956) 41.
16) D. ter Haar and A. Neaves: Proc. Roy. Soc. **A, 228** (1955) 568. S. Takeno: Busseiron-Kenkyu **96** (1956) 37; **108** (1957) 206; 227.
17) P. G. Klemense: Aust. J. Phys. **7** (1954) 64.
18) R. Berman and D. K. C. MacDonald: Proc. Roy. Soc. A, **209** (1951) 368.
19) D. K. C. MacDonald et al: Proc. Roy. Soc. A, **235** (1956) 358.
20) S. B. Woods: Canad. J. Phys. **34** (1956) 223.
21) E. J. Bradshaw and S. Pearson: Proc. Phys. Soc. **B, 69** (1956) Part 4.
22) E. Abraham: Phys. Rev. **95** (1954) 839.
23) A. H. Wilson: *The Theory of Metals.* (Cambridge Univ. Press., 1953).
24) S. Sielgel and S. L. Quimby: Phys. Rev. **54** (1938) 293.
25) O. Bender: Ann. Phys. (5), **34** (1939) 359.
26) M. Blackman: Proc. Phys. Soc. A, **64** (1951) 681.

JOURNAL OF THE PHYSICAL SOCIETY OF JAPAN, Vol. 14, No. 4, APRIL, 1959

On the Superstructure of the Ordered Alloy Cu_3Pd.
III. High Temperature Electron Diffraction Study

By Denjiro WATANABE

The Research Institute for Iron, Steel and Other Metals,
Tohoku University, Sendai, Japan

(Received October 9, 1958)

Using a high temperature electron diffraction camera, Cu_3Pd alloys have been investigated in thin oriented, evaporated films at temperatures below and above the critical point of order-disorder. The present work has elucidated that, in alloys of α''-phase, the line-up number of anti-phase domains and the degree of order inside domains decrease with increasing temperature in the range of 20∼40°C below the critical point, and an abrupt decrease of the line-up number of domains occurs at the critical point. In the range of 100∼150°C above the critical point, short chains of one-dimensional anti-phase domains with the same period of out-of-steps as in the ordered state remain randomly in an equilibrium state. On the other hand, anti-phase domains are absent in the alloys of α'-phase below as well as above the critical point.

§ 1. Introduction

In Part I of the present study[1)], the structure of ordered copper-palladium alloys has been investigated by electron diffraction in the composition range from 10 to 28 per cent Pd*, using thin single-crystalline films prepared by evaporation. It was shown that the alloys with compositions of 18 to 28 per cent Pd (α''-phase alloys) have a two-dimensional anti-phase domain structure in a fully ordered state, a fundamental cell of which is face-centred tetragonal with an atomic arrangement of the ordered Cu_3Au type. Alloys with palladium less than 18 per cent (α'-phase alloys) have the ordered Cu_3Au type structure with cubic symmetry, being consistent with the results obtained by Jones and Sykes[2)]. The two-dimensional anti-phase domain structure has been satisfactorily confirmed in bulk specimens in Part II[3)] and by Schubert, Kiefer, Wilkens and Haufler[4)], both using X-rays.

In Part I, weak diffuse maxima with peculiar splitting have been reported to remain at superlattice reflection positions, having more distinct contrast than those obtained from a quenched disordered CuAu alloy[5)], as shown in Fig. 6 of Part I, after quenching of the alloy films from temperatures above the critical point of order-disorder (T_c). As a relaxation time for ordering is considerably long in the present alloys[2)], the above splitting of superlattice reflections after quenching will reveal the actual state of the alloys above T_c and suggest the presence of anti-phase domains with nearly definite size. In order to obtain a distinct conclusion, however, it is necessary to observe diffraction patterns directly at high temperatures. According to Jones and Sykes[2)], there is a well-marked tail on the specific heat versus temperature curve of the alloy containing 24.9 per cent Pd above T_c (465°C), and in this respect, this alloy resembles Cu_3Au. On the electrical resistivity versus temperature curves of the present alloys, a peculiar anomaly has been found above T_c by Borelius, Johansson and Linde[6)] and by Kaya[7)]. These anomalous effects also seem to be attributed to the presence of some local order. Thus, the present work has been undertaken to elucidate the high temperature state of Cu_3Pd alloys up to 700°C, using a high temperature electron diffraction camera.

Until now, several high temperature diffraction studies on the alloys Cu_3Au and CuAu have been carried out by various authors, using X-rays[8)] as well as electrons[9)]. Raether's work of single-crystalline films of Cu_3Au gave an important information on the existence of anti-phase domains with various sizes at temperatures above T_c, 388°C, and is intimately connected with the present work. In the present paper, it will be shown that out-of-steps, classified into "the first kind"[1], with nearly definite period remain even at temperatures above T_c in the equilibrium state of α''-phase alloys, while such out-of-steps are absent in α'-phase alloys. The mode of line-up of anti-phase domains was studied also in the range of 20~40°C below T_c.

---

* In the present paper, all percentages refer to atomic per cent.

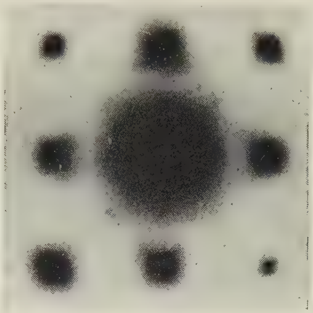

Fig. 1. Diffraction pattern obtained at 500°C from α'-phase film containing 13 per cent Pd.

§ 2. Experimental Method

Four kinds of single-crystalline films of copper-palladium alloys containing 13, 18, 25 and 28 per cent Pd respectively were prepared in the same way as described in Part I. These films were annealed for about 300 hours in the temperature range between critical points and 250°C and were cooled down to room temperature. This treatment was sufficient to complete the ordered state. Then, they were heated in the electron diffraction camera provided with a small high temperature furnace with heating velocity of 1~0.3°C/min. The diffraction patterns were observed on a fluorescent screen during heating and suitably recorded on dry plates.

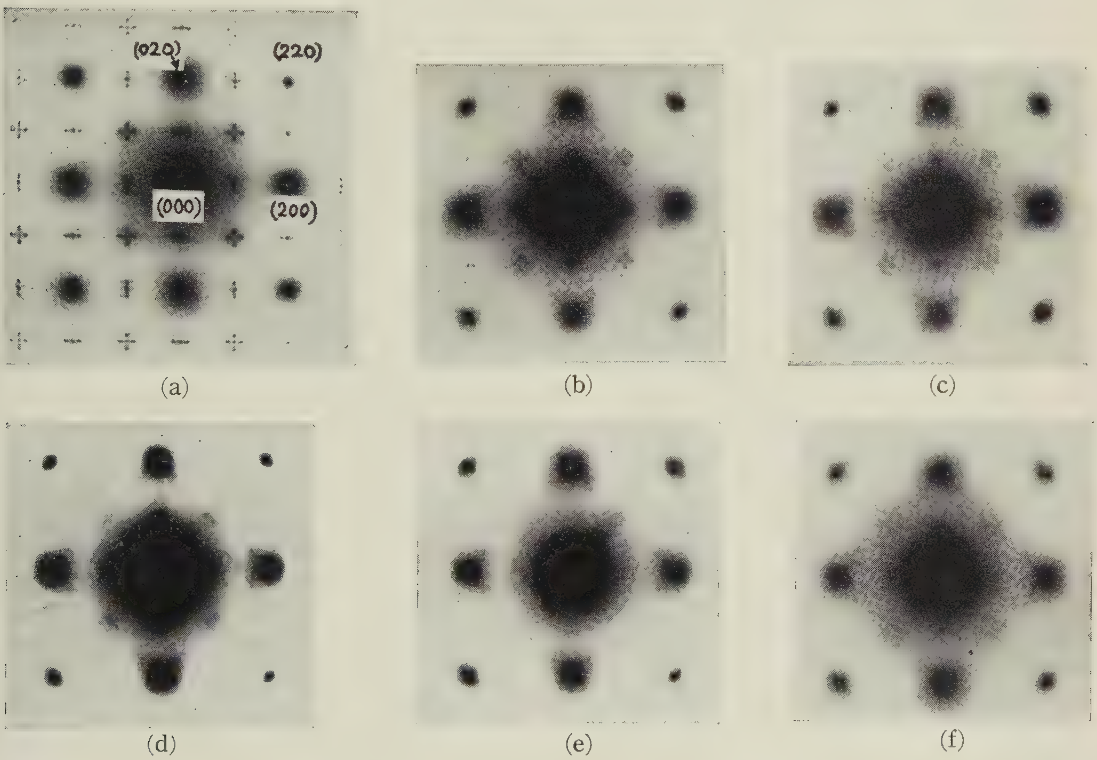

Fig. 2. Diffraction patterns obtained at various temperatures from α''-phase film containing 25 per cent Pd. (a) room temperature (fully ordered state), (b) 442°C, (c) 451°C, (d) 453°C, (e) 685°C, (f) 476°C (cooling case). Indices assigned to normal reflections are referred to the disordered cubic lattice.

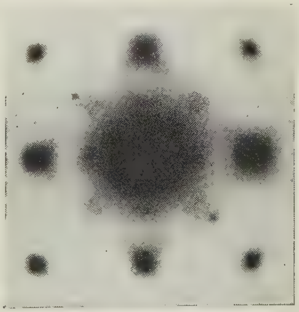

Fig. 3. Diffraction pattern obtained at 413°C from α''-phase film containing 28 per cent Pd.

The diffraction camera used was the same as described in Part I. The high temperature furnace was of a similar type to that used by Germer, Haworth and Lander10) in its construction and size, but was made of stainless steel instead of copper in order to avoid specimen contamination due to evaporation of copper at high temperatures. The heat loss by radiation was depressed by a shield made of stainless steel located around the furnace, and the conduction loss was estimated to be fairly low because both the furnace and the shield were connected with a supporting metal block only through a disk of steatite. A maximum temperature attained by a specimen film was about 750°C at 30 watt. The temperature was measured by means of a Pt-Pt·Rh thermocouple of 0.1 mm in diameter and a high resistance millivoltmeter. The temperature scale indicated on the latter was compared with critical points of order-disorder of the films of Cu_3Au and Cu_3Pd of known atomic compositions, and the apparent temperature was found to be about 10°C lower than the true temperature of a specimen film in the range between 380 and 500°C. In the present paper, temperatures indicated by the millivoltmeter are used for convenience' sake.

§ 3. Experimental Results

(1) *α′-phase alloy (13 per cent Pd)*

The sharpness and the intensity of diffraction spots did not change up to about 440°C (see Fig. 5 in Part I). Above 450°C, however, superlattice reflections gradually weakened with increasing temperature, their sharpness remaining scarcely changed. These reflections became diffuse abruptly and still fainter at 494°C, as shown in Fig. 1, but remained visible even at 600°C. The ordered structure known from the pattern is analogous to that of Cu_3Au, and the shape of the superlattice reflections shows that any kind of anti-phase domains is absent in this alloy below as well as above T_c.

(2) *α′′-phase alloys*

The ordered alloys of this phase have a two-dimensional anti-phase domain structure characterized by the two kinds of out-of-steps, as reported in Part I. According to the present high temperature study, the anti-phase domain characterized by the second kind of out-of-steps gradually faded away as the temperature approached T_c, while the other kind of anti-phase domain was preserved up to T_c throughout α′′-phase. It is remarkable that fairly well defined out-of-steps still persisted above T_c. Details of these aspects will be described about the sample of 25 per cent Pd as follows (see Fig. 2): While such a

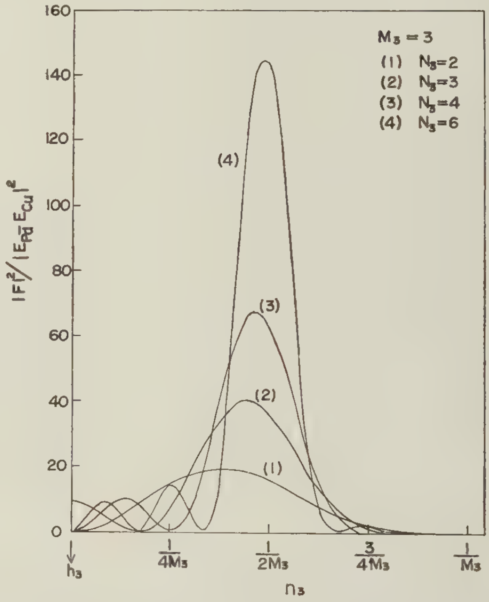

Fig. 4. The profile of split maximum along $[00h_3]$ in reciprocal space, given by numerical calculation.

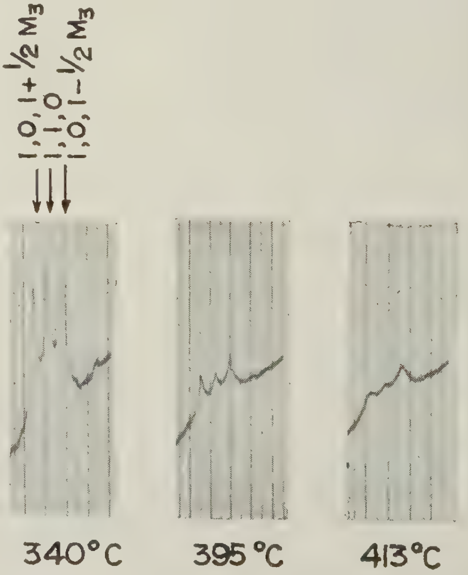

Fig. 5. Microphotometer curves of split superlattice reflections of the alloy containing 28 per cent Pd, at various temperatures.

pattern as shown in Fig. 2 (a) almost persisted up to about 420°C, the superlattice reflections exhibiting complex splits were gradually weakened with increasing temperature in the range between about 430 and 452°C, and, especially, the splits due to the second kind of out-of-steps almost faded away, as shown in Fig. 2 (b) and (c). The intensities of the splits due to the first kind of out-of-steps became far weaker immediately below 452°C than those of the splits in the fully ordered state, the sharpness being scarcely changed visually. At 452°C, these reflections became diffuse abruptly and fainter slightly, as the case of 13 per cent Pd, but diffuse maxima with peculiar splitting still remained, having far more distinct contrast than those in disordered CuAu alloy[5,11]. They were weakened gradually with increasing temperature and became very weak at about 490°C, but were visible even at about 600°C. Fig. 2 (d) shows the diffraction pattern at 453°C. At about 700°C, shapes of the faint diffuse maxima could no more be distinguished (Fig. 2 (e)). When the specimen was slowly cooled from 700°C with cooling rate of 1°C/min., the pattern changed almost reversibly (Fig. 2 (f)).

For 28 per cent Pd, the split sharp superlattice reflections were gradually weakened at temperatures above about 380°C and became very weak at 398°C. At 400°C, they became diffuse suddenly and fainter slightly, but separations of split maxima were scarcely changed though the splittings characterized by the second kind of out-of-steps disappeared. On further heating, the diffuse split maxima behaved themselves almost similarly to those of 25 per cent Pd (Fig. 3). For 18 per cent Pd, the behavior of superlattice reflections with rising temperature was essentially the same, except that the second kind of out-of-steps was not observed from the beginning.

The fact that the superlattice reflections in the alloy film of Cu_3Au decrease their intensities and become diffuse suddenly at T_c, 388°C, as reported by Raether[9], enables us to estimate the true temperature using this alloy film, which was found to be about 10°C higher than the apparent temperature as already described in § 2. Taking into account both this measurement and values of T_c for Cu_3Pd alloys determined by several investigators[2,12], we are able to regard the temperatures, at which the superlattice reflections become diffuse abruptly, as critical points of the present alloy films.

§ 4. Interpretations and Discussions for the Results

The following conclusions may be given from the above results about the mode of line-up of anti-phase domains in α''-phase alloys below and above T_c. The fact that the split superlattice reflections continue to be considerably sharp up to T_c seems to mean the keeping of a large line-up number of anti-phase domains, and the intensity decrease immediately below T_c may be mainly caused by the decreasing degree of order within each domain. Above T_c, diffraction maxima at superlattice reflection positions consist of diffuse split maxima with tolerable contrast, and the separations of their splits are much the same as in the ordered state, as shown in Table I. Therefore, we may have to consider that there remain anti-phase domains, characterized by the first kind of out-of-steps with nearly definite period, in a crystal where long range order vanishes. It seems that the model for such a state should be what is definitely distinguished from that below T_c in the line-up number of domains as well as in the degree of order within each domain, because the "disordered state" is treated.

Next, we shall examine the observed results in detail, considering the diffraction effect caused by the anti-phase domain structure on the basis of the one-dimensional structure characterized by the first kind of out-of-steps. If the line-up number of anti-phase domains along the z direction is N_3 and the period of out-of-steps, i. e., the size of anti-phase domain, measured in atomic distance, is M_3, the absolute value of the structure amplitude, $|F|$, is given for such a crystal by the following two equations, corresponding to even and odd values of N_3 respectively, at positions, h_1, h_2, $h_3 \pm n_3$, in reciprocal space*:

$$|F| = |E_{Pd} - E_{Cu}| \cdot \left| \frac{\sin M_3 n_3 \pi}{\sin n_3 \pi} \right| \cdot \left| \frac{\sin N_3 M_3 n_3 \pi}{\cos M_3 n_3 \pi} \right| \tag{1–1}$$

for N_3=even, and

---

* Here, h_1, h_2 and h_3 represent reciprocal lattice points, as usual.

$$|F|=|E_{Pd}-E_{Cu}|\cdot\left|\frac{\sin M_3n_3\pi}{\sin n_3\pi}\right|\cdot\left|\frac{\cos N_3M_3n_3\pi}{\cos M_3n_3\pi}\right| \tag{1-2}$$

for N_3=odd, where h_1 and h_2 are mixed, n_3 is continuous variable, and E_{Pd} and E_{Cu} are the atomic scattering factors for electron of palladium and copper respectively. If N_3 is of the same order of magnitude as M_3, the positions of maxima of $|F|^2$ are determined both by $|\sin N_3M_3n_3\pi/\cos M_3n_3\pi|^2$ or $|\cos N_3M_3n_3\pi/\cos M_3n_3\pi|^2$ and by $|\sin M_3n_3\pi/\sin n_3\pi|^2$, contrary to the case where N_3 predominates. Fig. 4 shows $|F|^2/|E_{Pd}-E_{Cu}|^2$ along the h_3 direction for small N_3 values, 2, 3, 4 and 6, M_3 being assumed to be 3. It can easily be seen from this figure that the peak of a split maximum shifts from the position, $h_3\pm(1/2M_3)$, toward the original superlattice reflection position, h_3, and its half value breadth increases as N_3 becomes small. On the other hand, it is located in the position, $h_3\pm(1/2M_3)$, when N_3 is larger than 6. The same holds for other M_3 values. If the collapse of order inside each domain occurs, the peak intensities of split spots decrease, since the scattering intensities of superlattice reflections are proportional to S^2, where S is the long range order parameter, but the sharpness will be unaffected.

Now, we can estimate N_3 values for various temperatures from the half value breadths of split maxima in the intensity curves obtained from microphotometer traces (Fig. 5). The results are given in Table II with mean sizes of chains of domains corresponding to them. From this measurement, it was found that N_3 is about 10 or more in the fully ordered state of 25~28 per cent Pd films and it gradually decreases with increasing temperature in the neighbourhood of T_c, reaching about 5~6

Table I. The separation of the split maxima in reciprocal space, m, and the period of out-of-steps, M_3.

18% Pd ($T_c\approx$483°C)			25% Pd ($T_c\approx$452°C)			28% Pd ($T_c\approx$400°C)		
Temperature (°C)	m	M_3	Temperature (°C)	m	M_3	Temperature (°C)	m	M_3
			fully ordered state	$\frac{2a_3^*}{7.2}$	3.6	fully ordered state	$\frac{2a_3^*}{6.1}$	3.0
440	$\frac{2a_3^*}{18.8}$	9.4	442	$\frac{2a_3^*}{7.6}$	3.8	395	$\frac{2a_3^*}{6.3}$	3.2
470	$\frac{2a_3^*}{21.5}$	10.8	451	$\frac{2a_3^*}{7.4}$	3.7	413	$\frac{2a_3^*}{6.2}$	3.1 (2.8)
			453	$\frac{2a_3^*}{7.7}$	3.9 (3.5)			
			462	$\frac{2a_3^*}{8.0}$	4.0 (3.6)			

In this table, m corresponds to the separation in superlattice reflections split along the h_3 direction in Fig. 11 of Part I, and a_3^* is the reciprocal lattice constant. M_3 has been calculated from the following relation: $m/2a_3^*=1/2M_3$. Parenthesized values have been estimated, assuming N_3 to be 3. In general measured values of M_3 are not integer, as in the fully ordered state[13].

Table II. N_3 values estimated from the half value breadths of split maxima and mean sizes of chains of domains corresponding to them.

25% Pd			28% Pd		
Temperature (°C)	N_3	Mean size (Å)	Temperature (°C)	N_3	Mean size (Å)
340	>9	>140	340	>10	>120
442	8~7	~100	395	7	~ 80
451	6~5	~ 70	398	6~5	~ 60
455	~3	~ 40	413	~3	~ 30

immediately below T_c. This decrease of N_3 causes peak intensities of split spots to be reduced approximately to one fourth. But the visually estimated intensities immediately below T_c are surely smaller than this expected value, as readily seen from Fig. 2. Therefore, some of the intensity decrease should be ascribed to a fall of the degree of order inside each domain. From the abrupt decrease of N_3 to about 3 immediately above T_c, it is suggested that a chain of anti-phase domains is cut to pieces by disordered regions appearing at T_c. In this case, however, an enormous change of intensity is not observed, as can be seen in Fig. 2. In order to explain the above-mentioned fact, the following model may be considered for the line-up of anti-phase domain structure in α''-phase alloys: The line-up number of domains, N_3, decreases almost to half with increasing temperature in the range of 40~20°C below T_c, and at the same time the degree of order inside each domain decreases rapidly, reaching the state with low ordering of atoms at T_c. Immediately above T_c, N_3 is diminished to about 3 which definitely distinguishes the state of the alloy from that below T_c, but a strong collapse of the degree of order seems not to occur within each domain. As the split maxima are visible even in the range of 100~150°C over T_c, it is certain that there is a sporadic random distribution of short chains of anti-phase domains in this temperature range. Inside a domain the degree of order is considerably lowered, but between domains the anti-phase relation yet remains.

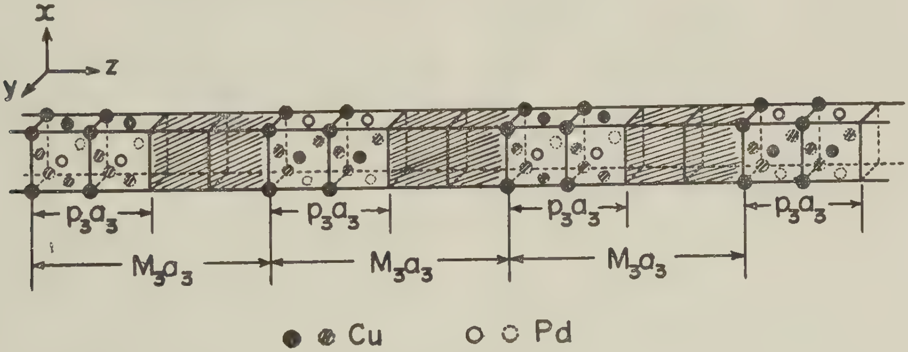

Fig. 6. Anti-phase domain structure including a disordered region at each domain boundary. The shaded regions indicate the disordered lattices.

A model shown in Fig. 6 is tentatively proposed for the anti-phase domain structure above T_c. It is a structure with a considerable size of a completely disordered region between comparatively ordered domains. The domain size and the period of out-of-steps are expressed by P_3a_3 and M_3a_3 respectively*. In the expression of the structure amplitude of superlattice reflections for such a lattice, the disordered region has nothing to do, and therefore the following expression is readily obtained for $|F|$ of superlattice reflections:

$$|E| = |E_{Pd} - E_{Cu}| \cdot \left| \frac{\sin P_3 n_3 \pi}{\sin n_3 \pi} \right| \cdot \left| \frac{\sin N_3 M_3 n_3 \pi}{\cos M_3 n_3 \pi} \right| \qquad (2)$$

for N_3=even, where N_3 and n_3 have the same significance as in equation (1). This equation leads to a similar result to that obtained from equation (1). That is to say, positions of split maxima are determined by $1/2M_3$ for N_3 larger than P_3, and a profile of splitting is similar to Fig. 4 for N_3 as small as P_3. But the peak intensity is much lowered in proportion to $|\sin P_3 n_3 \pi / \sin n_3 \pi|^2 / |\sin M_3 n_3 \pi / \sin n_3 \pi|^2$. It is chiefly the period of out-of-steps that determines the separation of split, while the intensity decreases with decreasing domain size. The present model seems to explain qualitatively the behavior of superlattice reflections at temperatures not too higher than T_c. For the intensity decrease of split maxima with further temperature rise, the decrease of P_3, N_3 and S inside domains will be responsible. Above 150°C over T_c, the peculiar shapes of diffuse maxima become indistinguishable, indicating the vanishing of domains, and faint superlattice reflections caused by the pure short range order are left.

---

* a_3 is the lattice constant along the z axis in terms of the fundamental cell.

An opinion might be given that the survival of anti-phase domain above T_c is not in equilibrium. However, the fact that when a film of 25 per cent Pd was cooled down from about 700°C the pattern reversibly changed denies this opinion. Because, if observed domains at rising temperature did not exist in an equilibrium state, the film cooled down should not have given peculiar forms of superlattice reflections. Thus, anti-phase domains characterized by the first kind are definitely present in an equilibrium state even above T_c in α''-phase alloys. The formation of anti-phase domains has been found in a Cu_3Au alloy[9] above T_c, but the split maxima were so diffuse that these were not regarded as separated. It is remarkable that diffuse split maxima in the present α''-phase alloys above T_c are sufficiently separated to enable us to recognize that the period of occurring out-of-steps is the same as that in the ordered state. The short chains of anti-phase domains formed above T_c are reasonably considered to be nuclei of anti-phase domains in the ordered state. Thus, the nucleation of ordering begins to occur in the range of 100∼150°C over T_c. In the X-ray study of CuAu alloy, Roberts[8] observed the outward shift of the (100) and (300) diffuse peaks above T_c, and suggested the existence of micro-regions of layered material similar to the ordered state. In the present alloy, however, the shift of split maxima corresponding to the tetragonality was not observed above T_c, as the axial ratio almost attains unity immediately below T_c.

In the following, some discussions will be given of the present result, in connection with the physical properties of Cu_3Pd alloy. Jones and Owen[14] concluded from the temperature dependence of the tetragonality that the long range order of the ordered alloy Cu_3Pd decreases with increasing temperature slowly at first but more rapidly above about 420°C, vanishing at 460°C. The change of anti-phase domain structure with increasing temperature below T_c revealed by the present work coincides fairly well with their conclusion. Moreover, the fact that the second kind of out-of-steps vanished in the temperature range of about 20°C below T_c in the heating case of the 25 per cent Pd alloy supports the suggestion given by Hirabayashi and Ogawa[3] that a well-marked maximum at about 400°C in the specific heat versus temperature curve obtained by Jones and Sykes[2] probably means the transition from the two-dimensional to the one-dimensional anti-phase domain structure. As is commonly known, a large change has been found to occur at T_c in physical properties of Cu_3Pd such as specific heat, electrical resistivity, etc[2],[6],[7]. According to the present experiment, on the other hand, the remarkable, crystallographical change at T_c in α''-phase alloys is the change of the line-up number of anti-phase domains rather than that of the degree of order inside domain. It should be remarked that such a structural change at T_c has not been found as yet on any alloy other than Cu_3Pd. According to Borelius, Johansson and Linde[6] and Kaya[7], the electrical resistivity of Cu_3Pd somewhat decreases with increasing temperature between 470 and 600°C, and normally increases above 600°C. They attributed this effect to the presence of a short range order and its collapse in connection with the corresponding anomaly on the specific heat versus temperature curve, but did not confirm these by X-rays. The short chains of anti-phase domains 30∼40Å long found by the present work in the temperature range of 100∼150°C above T_c may be responsible for the anomaly in electrical resistivity as well as in specific heat.

§ 5. Conclusion

According to the present high temperature electron diffraction work using thin single-crystalline films, the crystallographical states below and above the critical point of order in the Cu_3Pd alloys have been elucidated, concerning particularly the behavior of anti-phase domains. In α''-phase alloys, the line-up number of anti-phase domains decreases gradually with increasing temperature, reaching about 5∼6 immediately below the critical point, and the degree of order inside each domain decreases also. At the critical point, the abrupt decrease of the line-up number of domains takes place rather than that of the degree of order within domains. Diffuse scattering with peculiar splitting remains at superlattice reflection positions in the range of 100~150°C over the critical point. This means that in this temperature range the short chains of anti-phase domains, corresponding to the out-of-steps characterized by the first kind and with the same period as in the fully ordered state, are present, being scattered in the disordered state, in equilibrium. The above results seem to be consistent with the changes of physical properties accompanying the order-disorder transformation so far observed. In α'-phase alloy any kind of anti-phase domains is absent below as well as above the critical point.

Acknowledgement

The present author wishes to express his sincere thanks to Professor S. Ogawa for his kind guidance and encouragement. His thanks are also due to Mr. M. Hirabayashi whose discussion was very useful.

The present investigation has been supported partly by the fund of the Ministry of Education in Aid of Scientific Researches.

References

1) D. Watanabe and S. Ogawa: J. Phys. Soc. Japan **11** (1956) 226.
2) F. W. Jones and C. Sykes: J. Inst. Metals **65** (1939) 419.
3) M. Hirabayashi and S. Ogawa: J. Phys. Soc. Japan **12** (1957) 259.
4) K. Schubert, B. Kiefer, M. Wilkens and R. Haufler: Z. Metallk. **46** (1955) 692.
5) S. Ogawa and D. Watanabe: J. Phys. Soc. Japan **9** (1954) 475.
6) G. Borelius, C. H. Johansson and J. O. Linde: Ann. Physik **86** (1928) 291.
7) S. Kaya: Kikai-oyobi-Denki **6** (1947) 367.
8) J. M. Cowley: J. Appl. Phys. **21** (1950) 23. B. W. Roberts: Acta Met. **2** (1954) 597.
9) H. Raether: Z. angew. Phys. **4** (1952) 53.
10) L. H. Germer, F. E. Haworth ane J. J. Lander: Phys. Rev. **61** (1942) 614.
11) K. Sato, D. Watanabe and S. Ogawa: to be published.
12) F. E. Jaumot and A. Sawatzky: Acta Met. **4** (1956) 118.
13) K. Fujiwara: J. Phys. Soc. Japan **12** (1957) 7.
14) D. M. Jones and E. A. Owen: Proc. Phys. Soc. **B, 57** (1954) 297.

JOURNAL OF THE PHYSICAL SOCIETY OF JAPAN, Vol. 14, No. 4, APRIL, 1959

Electronmicroscopic Observation of the Additively Coloured KCl Crystal

By Tadatosi HIBI

Research Institute for Scientific Measurements,
Tohoku University, Sendai, Japan

and Tetsuhiko TOMIKI*

The Research Institute for Iron, Steel and other Metals,
Tohoku University, Sendai, Japan

(Received November 19, 1958)

The KCl single crystal which was grown from the melt, thermally quenched, and additively coloured with potassium metal were observed electronmicroscopically using replica technique. Growth of crystallites was seen both on the outer surfaces and in the interior of the crystal when it was thermally quenched or it was coloured additively. The crystallites grew more markedly in the latter case than in the former. The mechanism by which F centres are formed were considered.

§ 1. Introduction

Since Hedges and Mitchell[1)] succeeded in decorating the dislocations in AgBr crystal with printed out silver particles, many similar experiments have been carried out on the alkali-halide crystals[2)], divalent ionic crystals[3)] and silicon[4)]. These experiments have a characteristic feature that the dislocation patterns inside the crystal can be seen by an opitical microscope. This promotes the study about the possible arrangements of dislocations, the interaction between them, the movements of dislocations under various circumstances and the interaction between stoichiometric excess metal or segregated metal and dislocations.

One of the present authors has given attentions to the correlations between crystal growth and colouration of crystals, and carried out electronmicroscopic observations, using replica technique, for the alkali halide crystal coloured with X-ray[5)]. This experiment indicated that the crystallites appeared not only on the X-rayed (001) surface and side faces of the crystal, but also in the inner parts of this crystal as the irradiation of the crystal with X-ray proceeded, and that the grown crystallites disappeared in the reverse course of growth when the X-rayed crystal was bleached thermally and photochemically. These phenomena were also confirmed with the successive observations on the definite portion of the (001) plane of the same KCl crystal irradiated with X-ray and subsequently bleached photochemically, using the two-stage replica technique[6)]. This confirmation led to the conclusion that these phenomena could hardly be ascribed to the mere surface phenomena.

This article reports electronmicroscopic observations of the KCl single crystal which was coloured additively with excess potassium metal, here the observations were made with one-stage replica technique. Our main interests were directed upon the changes induced on the outer surfaces and in the inner parts of the crystal when it was coloured additively.

§ 2. Experimental Methods

Prior to the study of the crystal coloured with excess potassium metal, electronmicroscopic observations were made on the pure KCl single crystal which was heated and subsequently quenched to room temperature in vacuum. In this section, therefore, descriptions are given about the thermal treatment of KCl crystal in vacuum, the additive colouration of KCl crystal with potassium metal, and the preparation of replica.

2.1 *The heat treatment*

The KCl single crystal of about $1\times1\times2\,cm$ in the evacuated ($10^{-4}\,mmHg$) and sealed-off pyrex glass tube was heated in an electric furnace at the temperature of 520° to 580°C for 4 hours and then cooled very rapidly to room temperature. These conditions are the same as those of colouring the crystal additively except for one point, the lacking of potassium metal.

---

* The present Address: *Department of Physics, The Faculty of Science, Tohoku University, Sendai, Japan.*

2.2 *Additive colouration of crystal with potassium metal*

The KCl single crystal containing only *F* centres was obtained as usual by heating the crystal in the atmosphere of potassium vapour at the temperature of 520° to 580°C for 4 hours and then by cooling it very rapidly. Although the colouring agent, potassium metal, was more carefully distilled in vacuum than the case of usual optical study, it was difficult to avoid for the surface of distilled metal to be whitened slightly.

As is well known, when the amount of sealed potassium metal is too much, the surfaces of coloured crystal are covered with the residual metal. This metal film or drops of residual metal, together with the dark brown film usually enclosing the coloured crystal, disturbed the electronmicroscopic observation, because the replica was destroyed when it was removed from the surface of crystal in water (cf. Part **2.3** in this section) or because the replica became too thick to allow an electron-beam of an electron microscope to pass through it. After several trials, it was found that the appropriate amount of potassium metal to avoid these disturbances was obtainable, in the range of temperature employed, by distilling the metal the amount of which was that required to form *F* centres of density of about $10^{18}\ cm^{-3}$.

It was also confirmed that the coloured crystal showed only the *F* absorption band in the wavelength region of 2,300A to 10,000A.

2.3 *Preparation of replica*

Electronmicroscopic observations on the crystal surface were made using the one-stage replica technique. The methods for preparating replicas consist of two processes: (i) The crystal surface to be examined is obliquely

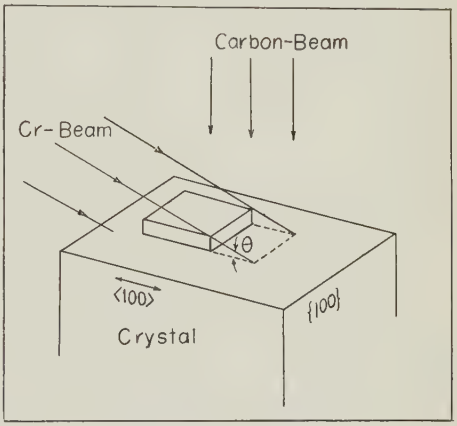

Fig. 1. The schematic diagram for the preparation of replicas.

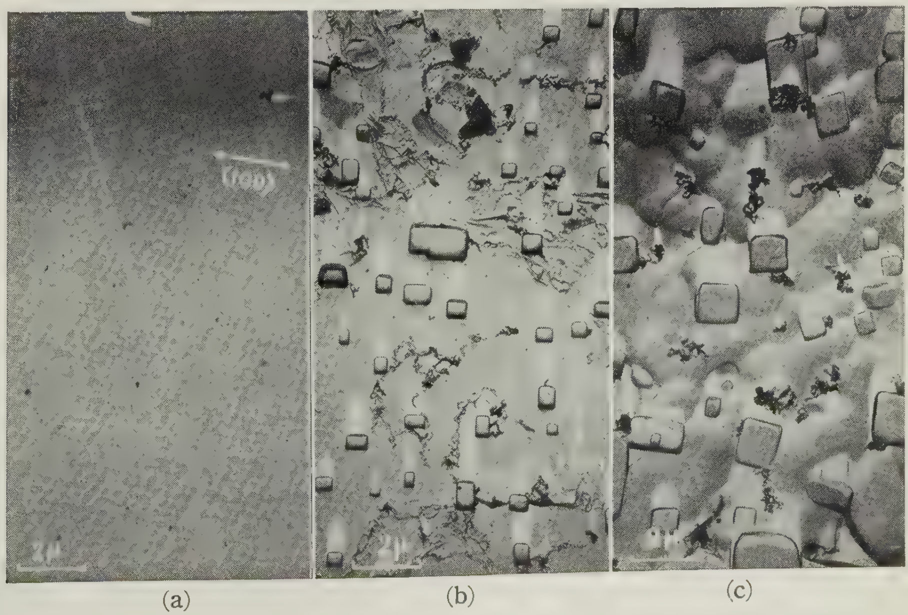

(a) (b) (c)

Fig. 2. (a): A fresh {100} cleavage plane of the KCl crystal grown from the melt. (b) and (c): {100} outer surfaces of the KCl crystal which was heated at 580°C for 4 hours and was quenched subsequently to the room temperature.

deposited with evaporated chromium in high vacuum. The direction of chromium-beam was chosen to be parallel to one of the ⟨100⟩ direction of the crystal and the angle between chromium-beam and the crystal surface θ was $\tan\theta = 1/3$. This chromium film was subsequently reinforced with carbon film. The schematic diagram of the apparatus for making a replica is shown in Fig. 1. (ii) The film was then removed from the replicated crystal surface by disolving the salt in water.

In order to observe the inner parts of the crystal, the replica was prepared on the fresh {100} cleavage surface of the crystal according to the procedures just described.

§ 3. Experimental Results

The descriptions are conveniently classified as follows:

3.1 The growth of crystallites on the surface of the KCl crystal which was quenched from high temperature in vacuum, and those on the surface of the KCl crystal which was coloured additively with excess potassium metal.

(a) The {100} cleavage surface of the KCl crystal cleaved from the block crystal.

(b) The {100} outer surface of the KCl crystal quenched thermally.

(c) The {100} outer surface of the KCl crystal coloured additively.

3.2 The inner part, *i.e.* the fresh {100} cleavage planes of the KCl crystal which was quenched from high temperature in vacuum and those of which was coloured additively with excess potassium metal.

(a) The fresh {100} cleavage planes of the KCl crystal quenched thermally.

(b) The fresh {100} cleavage planes of the KCl crystal coloured additively.

3.1 *The growth of crystallites on the surface of the KCl crystal which was quenched from high temperature in vacuum, and those on the surface of the KCl crystal which was coloured additively*

(a) *The {100} cleavage surface of the KCl*

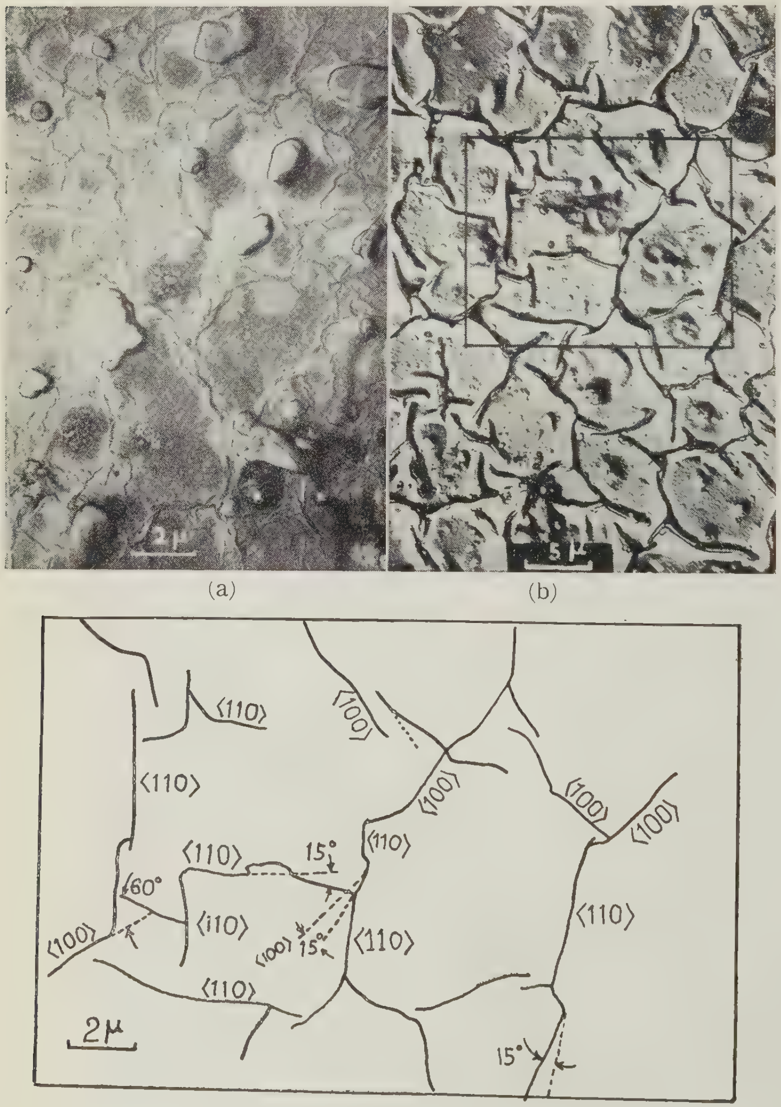

Fig. 3. (a) and (b): {100} outer surface of the KCl crystal which was coloured additively at 580°C for 4 hours. (c): The analysis of the crystallographic directions which appeared on the surface region enclosed by black lines in the figure 3 (b).

single crystal cleaved from the block crystal

Fig. 2 (a) shows one of the typical electron images of the freshly cleaved {100} surfaces of the KCl single crystal grown from the melt. In this figure, two linear cleavage steps can be seen on the flat and smooth surface. The step marked with white line makes an angle of 60° with the ⟨100⟩ direction of the KCl crystal (*i.e.* an angle of 15° with the ⟨110⟩) and the other step (dark line in the figure) makes an angle of 30° with the ⟨100⟩ direction of the crystal (*i.e.* an angle of 15° with the ⟨110⟩).

In general, the observed steps were straight and parallel to the crystallographic ⟨100⟩, ⟨100⟩±15°, ⟨110⟩ and ⟨110⟩±15° directions of the basal plane, though the steps composed of steps segments each of which is directed to one of the crystallographic directions just above (we term such a step as "composite step", for brevity) were rarely observable.

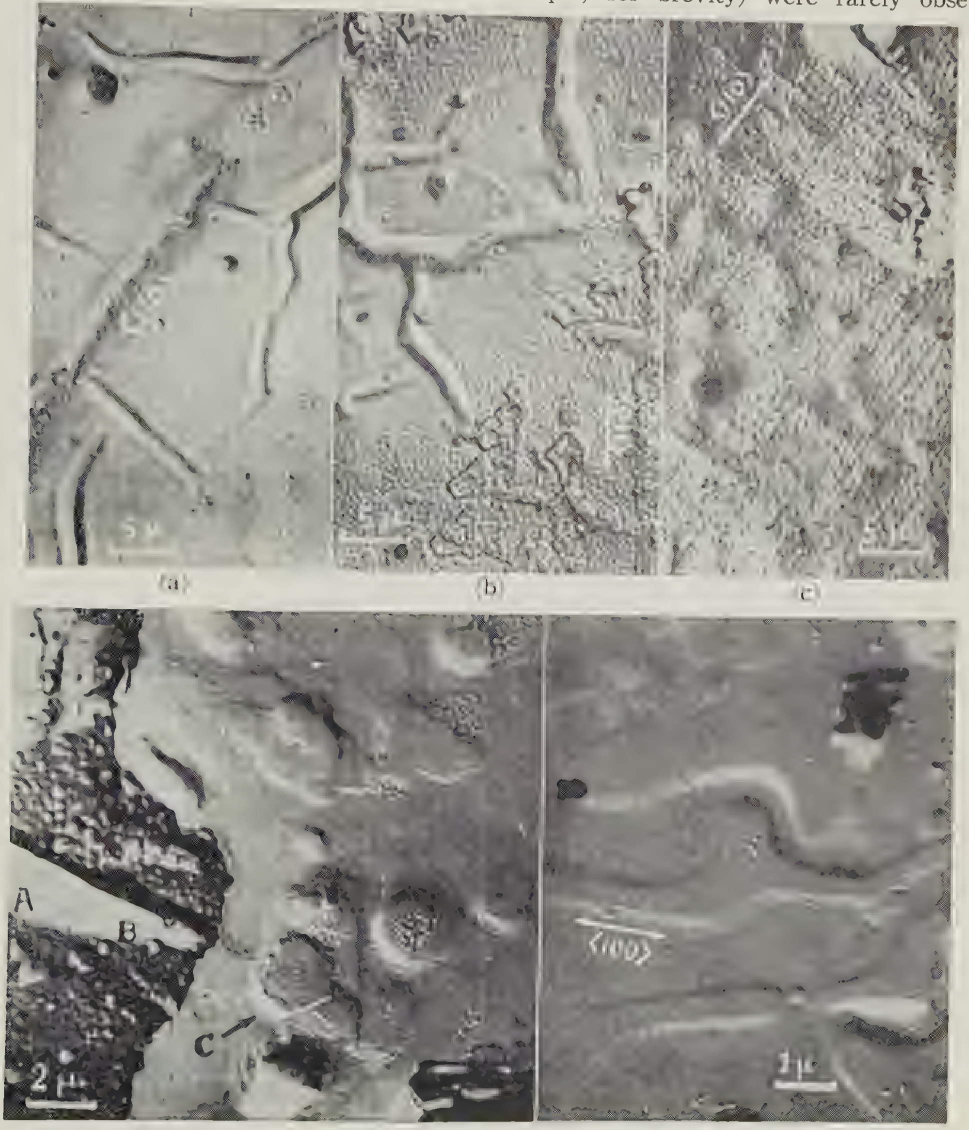

(a) (b) (c)

(d) (e)

Fig. 4. (a), (b) and (c): Three representative structures on the {100} outer surfaces of the KCl crystal which was coloured additively at 570°C±10°C. The surface area shown was covered with thin brownish film. (d) and (e): The outer surfaces of the KCl crystal coloured additively at 570°±10°C for 4 hours. The surface area shown corresponds to the real surface of the crystal not having the thin film.

The freshly cleaved {100} faces of KCl crystal were electronmicroscopically flat and smooth except for the cleavage steps. These characteristic features were used as a reference state in deciding whether the surface of crystal changed or not under the applied treatments.

(b) *The {100} outer surface of the KCl crystal quenched thermally*

When the KCl single crystal in the evacuated and sealed-off pyrex glass tube was quenched rapidly from 580°C to room temperature, the crystal surface became white visually.

Fig. 2 (b) is the photograph of the surface of this crystal. Many parallelopiped crystallites, the surface density of which was estimated as $10^7\ cm^{-2}$, can be seen on the flat {100} basal plane and they are about 0.4∼0.5 *microns* or less in heights. Their side planes are parallel to the ⟨100⟩ directions of the base crystal. In the case when the basal plane turns into a humpy state as shown in Fig. 2 (c), it can be seen that parallelopiped crystallites appear in the various crystallographic orientations. These humpy structures of the basal {100} plane are resulted from the network of the V-type grooves, which may be possibly corresponded to the *mosaic* structures (and the network of dislocations).

From Figs. 2 (b) and (c), it is sure that the parallelopiped crystallites came out on the {100} surface as the result of the thermal treatment, though their crystallographic orientations seem to depend closely on the microgeometry on the surface of the KCl crystal.

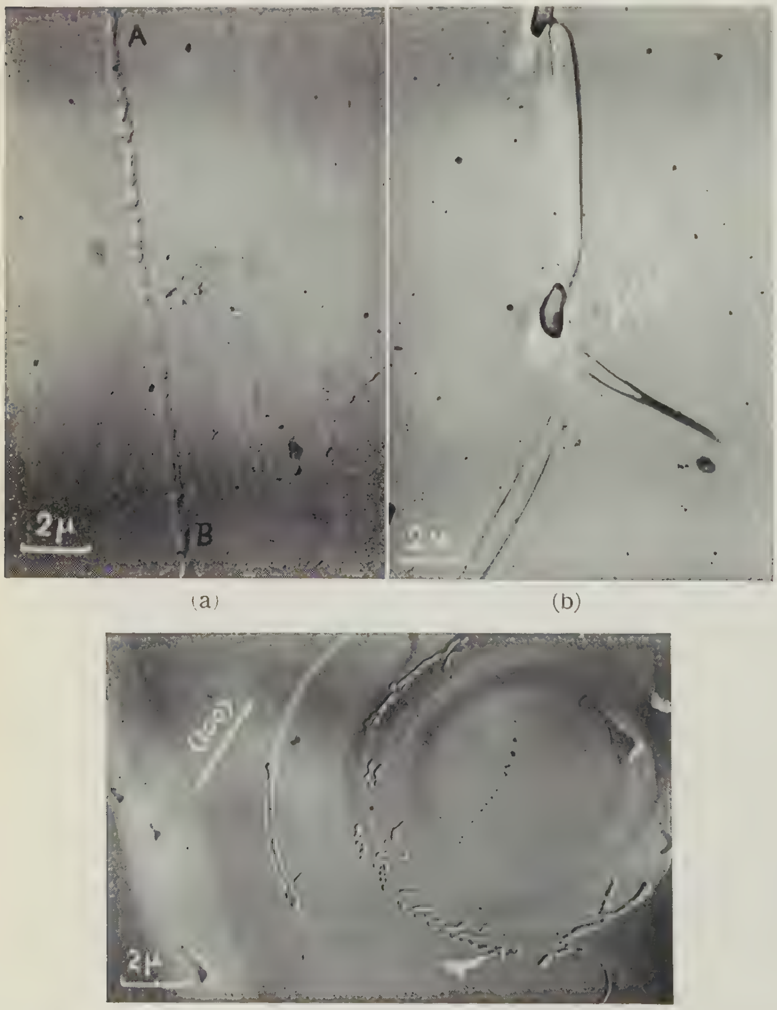

(a) (b)

(c)

Fig. 5. (a), (b) and (c): The fresh {100} cleavage surfaces of the KCl crystal which was heated in vacuum at 580°C for 4 hours and was then quenched to the room temperature.

(c) *The {100} outer surface of the KCl crystal coloured additively*

Fig. 3 (a), which was taken in the early stage of this experiment, shows the {100} surface of the KCl single crystal which was coloured additively by heating it in potassium vapour at the temperature of 580°C for 4 hours. Network patterns and many crystallites can be seen. As to the network patterns, we considered them to have appeared as a result of either (i) the wrinkles of the replica or (ii) the decorations of the netwerk imperfections with KCl molecules, *i.e.*, network structure of KCl layer newly built up preferentially along the imperfections on the surface.

Continuing observations to decide experimentally

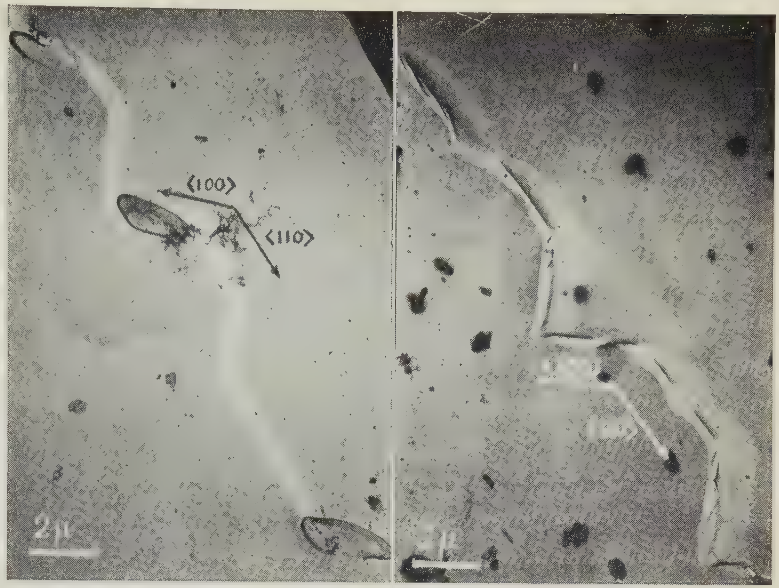

(a) (b)

Fig. 6. (a) and (b): The fresh {100} cleavage planes of the KCl crystal which was coloured additively at 580°C for 4 hours.

which of these two occurs are shown in the next series of photographs. The network patterns appeared on the KCl {100} surface are, as shown in Fig. 3 (b), composed of the mountain ranges whose directions are mostly directed to the ⟨100⟩, ⟨100⟩±15°, ⟨110⟩ and ⟨110⟩±15° of the basal {100} plane. The results of these analyses were also shown in Fig. 3 (c). Thus, it is hard to consider that the replica wrinkles in conformity to the crystallographic directions of the crystal, and so it is more natural to consider these patterns correspond directly to the changes on the surface of the crystal itself. Furthermore, these patterns vary from places to places depending on the microgeometries of the {100} surfaces of a crystal plate. They are roughly classified into the next three types:

(***I***) *The type of well-defined network patterns*

The network pattern of this type is shown in Fig. 4 (a). These network patterns are also composed of the protruding mountain-ranges whose directions are parallel to the ⟨100⟩, ⟨100⟩±15°, ⟨110⟩ and ⟨110⟩±15° of the base crystal. In this figure, the network patterns are larger in their size and more regularly arranged than those shown in Fig. 3 (b). The surface of the basal crystal is covered with many small grains.

On the surface region of the crystal having the features of this type, the parallelopiped crystallites, side planes of which were parallel to the ⟨100⟩ of the basal plane, could be occasionally observed. They grow usually at the kink sites of the protruding mountain ranges, or at the end points of the isolated segments of mountain ranges.

(***II***) *The type having the dendritic patterns and the network patterns*

The characteristic feature of this type is shown in Fig. 4 (b). The dendritic patterns can be seen on the right lower part and the network patterns grow on the left upper part of this figure. In general, it has been deduced from observations that these two patterns do not appear on the same portion of the surface of the crystal simultaneously and that the directions of the preferential growth of the dendrites are parallel to the ⟨110⟩ of the basal plane.

(***III***) *The type having a regular alignment of grains along the ⟨110⟩*

The characteristic feature of this type is shown in Fig. 4 (c). The grains of about 0.2 *microns* in size arrange regularly along the ⟨110⟩ directions of the basal plane and the network patterns do not develop markedly.

As was stated in § 2, the surfaces of KCl crystal coloured additively with excess potassium are usually covered with the dark brown thin film, even with the careful determination of the quantity of metal to be used. Figs. 3 and 4 are electron images showing the surface area covered with such film. But we have no needs to alter the preceding results and the analyses that the crystallites appear in the form of the network patterns or the isolated protuberances as shown in Fig. 3 (a) after the colouration of the KCl crystal. Fig. 4 (d) and Fig. 4 (e) will serve as these evidences. Fig. 4 (d) is the electron image of the surface area which was covered with the thin film (left side) and was not (right side). On the latter part of the surface, crystallites of about 2 *microns* in size grow and their shapes are very similar to those shown in Figs. 3 (a) and 4 (c). The lamellar structures can also be observed. Especially, the crystallites in a cross shape (marked as ***C*** in the figure) are continuously connected to the patterns of mountain range (***AB*** in the figure) on the surface area covered with the film. The surface structure ***AB*** is certainly the same type as the network pattern described above. The protuberances in the shape of mountain range in Fig. 4 (e) where the real surface of KCl crystal is shown are also corresponded to the network pattern and their directions can easily be assigned to the crystallographic directions such as the ⟨100⟩, ⟨110⟩ etc. of the basal plane. It is also observable in Fig. 4 (d) that the granular structures on the thin film, which have been already shown in Figs. 4 (a)—(c), disappear discontinously on the surface area not having the thin film. On the basis of these observations, we can safely conclude that the KCl crystallites grow either in the shape of the mountain range whose directions can be assigned to the crystallographic ⟨100⟩, ⟨110⟩ etc. directions of the basal plane or in the form of the isolated protuberances and the lamella structures, when the KCl crystal was coloured additively with excess potassium metal. We can also state that the granular structures are not related to the growth of KCl crystal. The dendrites and grains aligned along the ⟨110⟩ will probably be composed of potassium metal.

3.2 *The inner part, i.e., the fresh* {100} *cleavage planes of the KCl crystal which was quenched from high temperature in vacuum and those of which was coloured additively with excess potassium metal*

(a) *The fresh* {100} *cleavage planes of the KCl crystal quenched thermally*

The typical features of the fresh cleavage {100} planes normal to those shown in Figs. 2 (b) and (c) are represented in Fig. 5. The thermal conditions were already described in § **2.1.** The cleavage steps in Fig. 5 (a) are straight, but they have either the lamellar structures (perhaps it will be impossible to discern them in the reproduction) or the protuberances in the form of mountain range (step ***AB*** in the figure). In Fig. 5 (b), the step is not linear, but is composed of the step setments having

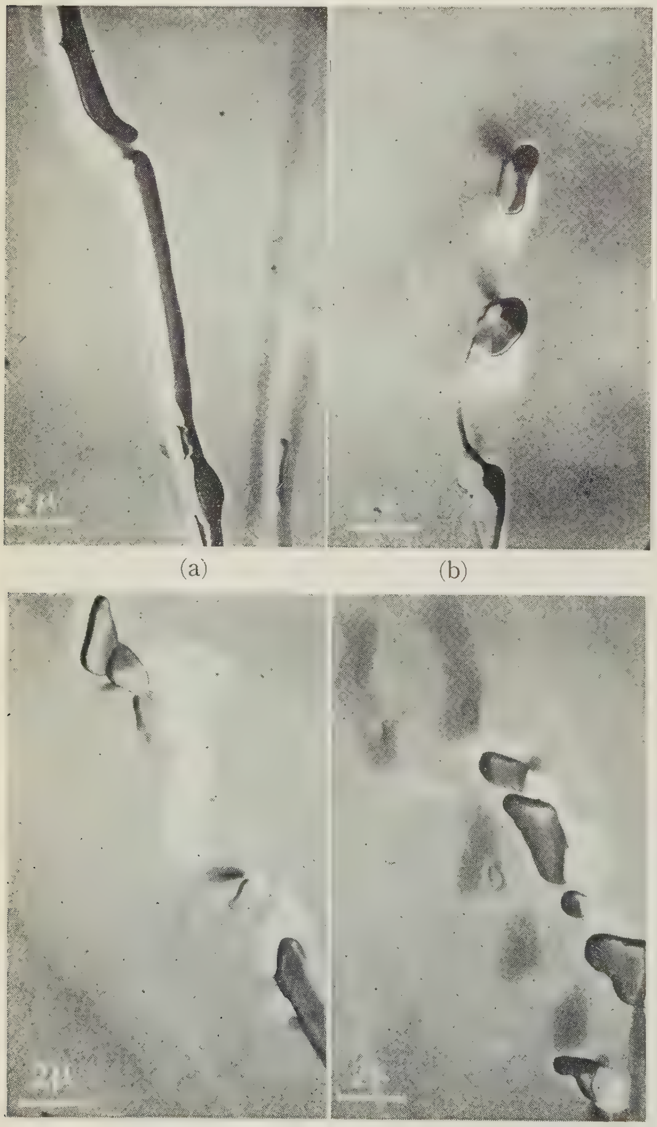

Fig. 7. (a), (b), (c) and (d): The fresh cleavage planes of the KCl crystal which was coloured additively with excess potassium metal. The colouration of the crystal becomes deeper in the alphabetic order.

the crystallographic ⟨100⟩ and ⟨110⟩±15° directions. At the kink sites of this step, a crystallite grows. The elliptical hills, as shown in Fig. 5 (c), were occasionally observed on the fresh {100} cleavage planes of the KCl crystal thermally quenched. The closed confocal elliptic steps forming this structure are decorated with many small elongated crystallites and are quite independent of the cleavage steps, for the latters are usually normal to the propagation front of the cleavage crack. It is deduced from observations that the mean value of the ratio of the major axis to the minor axis of these ellipses is about 1.3, and the lengths of the major axes vary from 0.5 to 0.7 *microns*.

(b) *The fresh* {100} *cleavage planes of the KCl crystal coloured additively*

Figs. 6 (a) and (b) show the fresh cleavage planes of the crystal coloured additively at the temperature of 580°C for 4 hours, and the {100} outer surfaces of this crystal were already shown in Fig. 3 (a). The steps are not linear, but are composed of the segments of step directed either to the ⟨110⟩ or to the ⟨100⟩. The crystallites can be seen at the kink sites of the step in Fig. 6 (a), and they are nearly parallel to the step directed to the ⟨100⟩ direction. These phenomena are quite analogous to those found in the crystal which was treated thermally (cf. Fig. 5 (b)), but it is clear that they appear in a larger scale than in Fig. 5 (b).

Since these changes of the inner parts of the crystal are decidedly caused by the colouration (or heat treatment), it is necessary to give attentions to the correlation between the changes of the inner parts of the coloured crystal and the degree of its colouration. When the comparisons were made, in achieving this experiment, betweeen the fresh cleavage planes of the crystals each of which had a different concentration of F centres and was coloured uniformly in itself, the results were too divergent to extract the correlation. This is probably due to the differences of the distribution of lattice imperfections inside each crystal, even when they were cleaved off from the same block of the crystal grown from the melt. We coloured, therefore, a single block of the KCl specimen in such a way as to produce inhomogeneity of colour inside the crystal. In this experiment, the colour was deeper in the central part of the crystal. Fig. 7 are the electron images of the fresh {100} cleavage surface of this crystal. The surface area corresponding to the inner part which is nearest to the outer surface of the block of the coloured crystal is represented by Fig. 7 (a) and the surface area corresponding to the central part of the coloured crystal is shown by Fig. 7 (d). Two intermediate parts, one of which is nearer to the region shown by Fig. 7 (a) and the other is nearer to the region shown by Fig. 7 (d), are represented by Fig. 7 (b) and (c), respectively. On the basis of the observations of these electron images, the followings can be summarized: As the degree of the colouration of the crystal proceeds, the zigzag steps and the crystallites appearing at the kink sites of steps become more numerous. These correlation between the degree of colouring of the crystal and the changes induced inside this crystal were quite identical with those found earlier in the NaCl and KBr crystals irradiated with X-ray⁵⁾. It is also remarkable that groups of wavy micro-steps, in addition to the zigzag steps, appear on the cleavage plane where the colouring was deeper and the zigzag steps with crystallites appear remarkably (see Figs. 7 (c) and (d), for example).

It must be mentioded that, although the crystallites coming out at the zigzag steps were observed frequently, the reverse structures of the fresh cleavage planes, *i.e.*, the hollow structures in which the crystallites are to be fitted to form the continuous crystal lattice were not observed. Furthermore, the shadows of the crystallites indicate that each crystallite is connected to the cleavage plane only at the kink sites of the step and the remainder sticks out upon the cleavage surface (see Fig. 7 (c), for example). Judging from these phenomena, the zigzag steps will probably be a kind of internal surfaces surrounded by the clusters of vacancy or cavities into which the crystallites come out (a kind or "crystal growth" inside the crystal).

From the observations of the fresh cleavage planes of KCl crystal which was thermally treated and which was coloured additively, it is concluded that these processes cause the changes inside the crystal, and that the effects are enhanced by the colouration.

§ 4. Interpretation of Experimental Results

In this paragraph, descriptions are given on the next three: 4.1, the fresh (100) cleavage planes of the KCl crystal grown from the melt; 4.2, the crystal growth of the KCl crystal which was thermally quenched and 4.3, the crystal growth of the KCl crystal coloured additively and the mechanism of additive colouration.

4.1 *The fresh* {100} *cleavage planes of the KCl crystal grown from the melt*

Many authors[7)-11)] have been interested in the cleavage surfaces of the crystals and have carried out the extensive experiments mainly with an optical microscope. Their main purposes were directed either to the propagation process of the cleavage crack or to the correlation between the patterns of the cleavage steps and the crystal imperfections. Confining these experiments to the ionic crystal, these works will be summarized as follows: The cleavage steps are usually perpendicular to the front of the cleavage crack and are the rough indication of the propagation direction of the crack. When a crack is propagating with velocity larger than a critical value ($\sim 6.10^3$ *cm/sec* in LiF crystal, for example[9)]), the cleavage steps appear relatively linear, and if the velocity of the propagation of the crack front is less than this, a crak proceeds unstably or stops sealing the loops of the dislocation into the crystal. In this case, the cleavage steps kink and new cleavage steps are formed at places where the dislocation loops were sealed in. Forty termed these places as "deformation zone"[10)]. On the other hand, when a cleavage crack meets a twist boundary, the same phenomena appear, and new cleavage steps are formed at screw dislocations. These observations with an optical microscope are not sufficient to interpret our results, because the detailed lineage of steps was not resolved optically.

According to the electronmicroscopic observations on the cleavage planes of the KCl single crystal grown from the melt (cf. **3.1** (a)), the cleavage steps were parallel to the crystallographic ⟨100⟩, ⟨110⟩, ⟨100⟩±15° and ⟨110⟩±15° directions and were straight, while the cleavage steps on the "deformation zone" became rather complicated. Taking account of the ambiguities of the *Cr*-shadow directions, ⟨100⟩±15° and ⟨110⟩±15° can reasonably be assigned to the ⟨120⟩, ⟨230⟩ and ⟨130⟩ directions of the basal crystal. Thus, we can conclude that the fresh cleavage {100} plane of the KCl crystal grown from the melt is flat and has steps having the directions of the ⟨100⟩, ⟨110⟩, ⟨120⟩, ⟨230⟩ and ⟨130⟩, provided that the crystal is perfect. This conclusion does not contradict to the observations that the cleavage steps run radially from the point at which the cleavage crack has been introduced, because they are considered to be composed of steps having the directions mentioned above.

4.2 *The crystal growth of the KCl crystal grown from the melt*

In the case of thermally treated KCl crystal in the evacuated and sealed off glass tube, many parallelopiped crystallites and the networks of V-type groove appeared on the outer surface of the specimen, while on the fresh cleavage plane of such a crystal composite steps and elliptic steps can be seen.

In genaral, when the KCl crystal in the evacuated, sealed off glass tube was heated, it is considerable that the KCl molecules evaporate from the surface of a sealed KCl crystal, thus the vapour pressures of solid phase and gas phase become equal at the prolonged heating at a given temperature. In this equilibrium state, the number of KCl molecules escaping from the surface and arriving at the surface must be equal. On the other hand, the KCl crystal kept at a higher temperature will acquire more vacancies than the crystal at room temperature. These vacancies can be supplied both from the outer surfaces and from the internal surfaces by diffusion process or from the dislocations by their climbing[16)].

Taking these situations into account, the present results can partly be explained. Concerning the growth of the parallelopiped crystallites on the outer surface of the specimen, three possible mechanisms may exist:

(i) The parallelopiped crystallites may have been resulted from the preferential flow of the matter from the interior, because if the vacancies diffuse uniformly from the outer surface into the crystal, outer surface must acquire a new layer of crystal. This preferential flow of matters may occur through dislocations or a kind of internal cracks.

(ii) The climb of composite dislocations sealed in beneath the surface during the cleaving process may also lead to the growth of crystallites, if the circumstances are available[16].

(iii) When the crystal in a pyrex glass tube was quenched to room temperature, the superfluous KCl molecules in gas phase may condense to form parallelopiped crystallites epitaxially grown on the outer surface of the specimen.

On the other hand, networks of V-type groove may result from the preferential thermal evaporation of KCl molecules from the subboundaries.

According to Figs. 5 (b) and (c), it is conceivable that internal surfaces and dislocations may serve as vacancy sources. We are inclined to consider that the composite step, or zigzag step such as shown in Fig. 5 (b) and Fig. 7, may correspond to such a kind of internal surfaces, because the crystallites at the kink sites grow sticking out on the fresh cleavage plane. Therefore, a zigzag step and a crystallite along it must be resulted from a crystal growth occurred on the internal surface, which associated with the flow of vacancies into the inner lattice sites. Especially, elliptic steps are quite independent of cleavage steps, and they are in a closed form. This is the reason why we consider an elliptic hill to correspond to the lattice misorientations which are quite independent of the cleaving process. One of the possible explanations for this structure may be the following: When an edge dislocation climbs delivering the vacancies into the interior to form dislocation rings, each rings will be pushed forwards by mutual repulsion, supposing that the edge dislocation is fixed at both ends. Then, if the cleavage crack happens to pass across this region, dislocation loops will come out on the fresh cleavage plane taking a shape of an elliptic hill because of easy cleave caused by the localized concentration of stress field arround the dislocation loops. Usually, these steps are decorated with crystallites as shown in Fig. 5 (b). The detailed explanation including these effects is impossible at present.

4.3 *The crystal growth of the KCl crystal coloured additively—the mechanism of additive colouration*

Colour centres in the alkali halide crystals have been an outstanding interest for many decades, and have been studied both from the theoretical and the experimental points of view[12)13)]. However, the electronmicroscopic studies have never been carried out on the additively coloured crystal (and also the thermally quenched crystal[14)]).

It is clear from the present observations that various kinds of changes appeared both on the outer surface and in the inner part of the KCl crystal which was quenched thermally and coloured additively, and that these changes occurred more markedly in the latter case: In the case of the KCl crystal coloured additively, crystallites grew on the outer surface of a coloured crystal block either in a form of mountain range or in a form of isolated protuberances; on the other hand, in the interior of the coloured crystal, the zigzag steps having crystallites at their kink site appeared more remarkably as the colouring of the crystal became deeper.

Now, the conditions of the additive colouration differ only one point from those of the thermal quenching in our experiment; the crystal was heated in the atmosphere of potassium vapour instead of KCl vapour.

Mott and Gurney[12)] discussed the mechanism by which F centres are formed additively: An atom of potassium metal is adsorbed on the surface, for example, at a point such as a kink site of the surface[17)]. Then an electron of the adsorbed atom is released into the conduction band; the positive ion left on the surface draws a negative ion beneath to form new layer of the crystal; the vacant lattice point then migrates to the interior and eventually traps the electron to form an F centre. In this case, the crystal is assumed to be ideal except for the surface.

In practice, however, an *ideal* crystal can hardly be obtainable, because the lattice imperfections can be sealed in the crystal in various modes both during crystal growth and during the process of cleavage. We consider that the growth of crystal having a lamella structure, such as shown in Fig. 4 (d), may corresprnd to the Mott and Gurney's case, approximately. Since the network patterns (cf. Figs. 4 (a) and (b)) grow preferentially on the outer surface of a coloured crystal, it is necessary to take these phenomena into account. In an alkali-halide crystal, slip takes place usually on the {110} along the ⟨110⟩, so the array of the screw dislocation appears along the ⟨110⟩ on the {100}, while the array of the edge dislocation lies along the ⟨100⟩ on the {100}. According to the analyses of the present observations, the directions of the above pattern were parallel to the ⟨100⟩, ⟨110⟩ and to the directions deviated 15° from them, as shown in Figs. 3 (c), 4 (a) and 4 (b). Therefore, the network patterns having a shape of mountain range correspond to the KCl layer preferentially built up along the array of dislocation emergences on the {100} outer surface. This fact indicates that ions can diffuse more freely through dislocations than through the perfect crystal lattice. In the *real* crystal, therefore, F centres can also be formed by potassium atoms which diffused into the interior of the KCl crystal through the internal surfaces or dislocations, in addition to the processes discussed by Mott and Gurney: Potassium atom is adsorbed not only on the outer surface, but also on the inner surface at a kink site or jogs of dislocations; electrons may be released from the potassium atoms to the conduction band, then, the positive ions are left at adsorbed places and draw the negative ions to form the KCl crystal lattice. This leads to either the crystal growth on the outer surface or the changes inside the crystal, i.e., the crystal growth interior of the crystal or changes of the shape of internal surface. The vacant lattice points migrate to the interior and trap eventually the released electrons to form F centres. The crystallites sticking out on the fresh cleavage planes and zigzag steps may probably be built up by the mechanism described above. These interpretations do not appear to contradict to the facts that the changes induced inside the crystal are enhanced in the coloured crystal relative to the thermally treated one.

Now, this crystal growth inside the crystal becomes more markedly as the colouration proceeds (cf. Fig. 7). If this can be served as a measure of a degree of colouration of the crystal, it would be reasonable to consider that F centres are formed preferentially in the region where imperfections exist: In the additive colouration of the KCl crystal by heating in the atmosphere of potassim vapour, F centres are produced uniformly at most in the localized region of the specimen.

§ 5. Summaries

Electronmicroscopic observations were made on the KCl single crystal either cleaved from the block, or quenched from high temperature to room temperature in the evacuated, sealed off glass tube or coloured additively with excess potassium metal, by means of replica technique. The important results obtained from these observations are summarized as follows:

(1) The cleavage steps on the fresh {100} cleavage plane of the KCl single crystal cleaved from the block are straight and parallel to the ⟨100⟩, ⟨110⟩, ⟨120⟩, ⟨130⟩ and ⟨230⟩ of the basal plane, if the crystal is perfect.

(2) When the KCl crystal in the evacuated, sealed off glass tube was heated, followed by the rapid quenching, the changes are induced not only on the outer surfaces, but also in the interior of the crystal. These phenomena are considered to be resulted from the formation of vacancies inside the crystal.

(3) In the case of the coloured crystal, the crystallites grew on the outer surface either in a form of mountain ranges or in a form of isolated protuberances, and the crystal growth occurred more markedly inside the crystal than the thermally treated one. The mechanism by which F centers are formed was considered.

Acknowledgements

It is a great pleasure to express the author's thanks to Prof. M. Ueta who gave us the detailed informations about the colouring procedure and checked the coloured crystal spectrophotometrically, and to Dr. T. Suzuki who read the manuscript and discussed with us with valuable suggestions. One of the authors (T. Tomiki) would like to express his thanks to Prof. S. Ogawa who provided him an opportunity to achieve this experiment at Research Institute for Scientific Measurements, Tohoku University.

References

1) J. M. Hedges and J. W. Mitchell: Phil. Mag. **44** (1953) 223, 357.
2) For example, see S. Amelinckx: Phil. Mag. **1** (1956) 269.
3) W. Bontinck and W. Dekeyser: Physica **22** (1956) 595, ibid. 607.

4) W. C. Dash: J. Appl. Phys. **27** (1956) 1387; **29** (1958) 705.
5) T. Hibi and K. Ishikawa: J. Phys. Soc. Japan **13** (1958) 717.
6) T. Hibi and K. Yada: J. Phys. Soc. Japan **14** (1959) 455.
7) P. B. Hirsch: *Progress of Metal Physics*, vol. 6 (Butterworths, London, 1956) 226.
8) J. J. Gilman: J Appl. Phys. **27** (1956) 1262; **27** (1956) 1018.
9) J. J. Gilman, C. Knudsin and W. P. Walsh: J. Appl. Phys. **29** (1958) 601.
10) A. J. Forty: Proc. Roy. Soc. **A, 242** (1957) 392.
11) C. A. Zapffe and C. O. Worden: Acta Cryst. **2** (1949) 377.
12) N. F. Mott and R. W. Gurney: *Electronic Processes in Ionic Crystals* (Oxford Clarendon Press, 1948).
13) F. Seitz: Rev. Mod. Phys. **26** (1954) 7; **18** (1946) 384.
14) E. Kern and H. Pick (Z. Physik **134** (1953) 610) observed with an optical and electron microscope the surfaces of the alkali-halide crystals when they were heated in the open air.
15) J. Bardeen and C. Herring: *Imperfections in nearly perfect crystals* (John Wiley and Sons, New York, 1952) 261.
16) S. Amelinckx, W. Bontinck, W. Dekeyser and F. Seitz: Phil. Mag. **2** (1957) 355.
17) J. W. Mitchell and N. F. Mott: Phil. Mag. **2** (1957) 1149.

JOURNAL OF THE PHYSICAL SOCIETY OF JAPAN, Vol. 14, No. 4, APRIL, 1959

Successive Electronmicroscopic Observation of Coloured and Bleached KCl Crystal

By Tadatosi HIBI and Keiji YADA

Research Institute for Scientific Measurements,
Tōhoku University, Sendai, Japan

(Received December 1, 1958)

The surface changes in a given part of the same KCl crystal during colouration by X-rays and in the process of bleaching by natural light have been successively observed by using two-stage replica. A slightly modified Bradley's method was used for making two-stage replica. By this method, the surface change at the definite position of the same KCl crystal was observed successively. According to the present results, it has been clearly confirmed that crystallites grown on the KCl crystal during X-ray colouration disappear during bleaching through the process quite reverse to the crystal growth in colouration and that the behaviour of the crystal growth and its disappearance are not simple, but very peculiar. Results obtained have been briefly discussed.

§ 1. Introduction

From electronmicroscopic observation of coloured NaCl and KBr crystals by X-ray irradiation and also of bleached crystals by natural light, one of the authors[1] observed the growth of crystallites on the front face, on the side face and on the new cleavage face of crystals with the progress in colouration. It was also observed that crystallites grown during colouration disappeared in bleaching by natural light through the process quite reverse to the crystal growth in colouration. A peculiar growth of crystallites was also observed on the front face with the progress in colouration. All these results were obtained by using ordinary one-stage replica. After making the deposited fims on the surfaces of many specimens irradiated by X-rays for different periods of time, alkali-halide crystals were dissolved in water and then deposited films were used as one-stage replica. However, crystallites appeared on the front face are not uniform in form and the behaviour of the crystal growth is not simple. Accordingly, after an exhaustive observation of several specimens obtained under the same experimental conditions, the ordinary method in which some characteristic properties are statistically determined was adopted. The result obtained by such a method should have some obscurities. Therefore, successive electronmicroscopic observations of the change in a given part of the same crystal are highly desired. In this experiment, the surface change in the given part of the same KCl crystal with colouration by X-rays and in the process of bleaching by natural light has been successively observed by using two-stage replica.

§ 2. Experimental Method

Direct electronmicroscopic observation of coloured and bleached alkali-halide crystal is impossible because of the change caused by electron bombardment in the course of its observation. So, replica method should be used and two-stage replica is also necessary for successive observation. However, it is difficult technically to locate the definite position of the same specimen always on the definite place of the definite hole of the fine mesh. A few methods[2] were hitherto presented for this purpose, and two electronmicrographs before and after a change in the specimen were shown by these methods. Only Bradley[3] reported on the possibility of successive observation of corrosion process of pearlitic steel, in which he succeeded in the illustration of the effect of etching time on a given field of a metallurgical specimen. Recently, Fourie[4] reported on the method for making successive replica based on Bradley's method to observe the successive change of slip lines appeared on the α-brass single crystal with plastic deformation. We first tried another method[5] to obtain a successive replica of the definite position of the specimen more accurately, though it was more difficult technically than Bradley's method. The defect of this method is in the difficulty of stripping one-stage replica from alkali-halide crystal. Therefore, in place of the above method a slightly modified Bradley's method was used in this experiment as described below.

The specimen was fixed on the glass plate by about 20% gelatin in water. After drying gelatin, some reference was marked on the surface of the specimen. A few scratched traces at right angle to each other along ⟨100⟩ direction were marked as reference by using fine tungsten wire 0.14 mm in diameter. The width of this scratch trace is several microns and it can be seen easily by optical microscope with 60 times magnification. After marking the reference on the crystal, a thin film of methylmethacrylate was cast on the surface from about 0.5% solution of benzene. As alkali-halide crystal is poisoned by chloroform which is solvent of Formvar, Formvar solution used by Bradley could not be used in this experiment.

Copper sheet mesh to 150 holes per inch having larger hole (0.15 mm in diameter) in the centre than other holes was used as the specimen grid. The position of this central hole can be found easily by the observation of intermediate image of electronmicroscope.

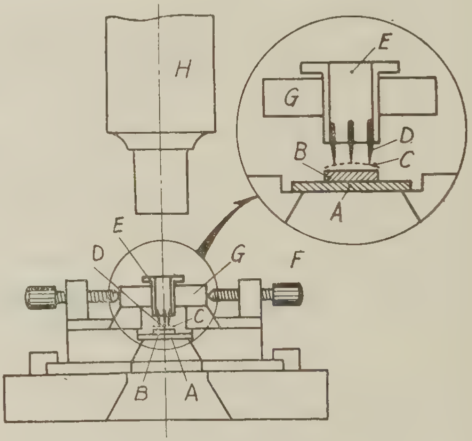

Fig. 1. The apparatus for obtaining successive two-stage replicas.

Fig. 1 illustrates the apparatus for the preparation of replicas as desired. In this figure A is glass plate, and B is the specimen. Sheet mesh C is attached to the tips of pins D which are soldered to holder E with a small amount of adhesive. Holder E is put in G which is movable in two directions horizontally by four screws F. To prevent the interest part of the specimen from being poisoned by mechanical contact when the mesh was displaced, the mesh was bent a little and only both ends touched to the thin film of methylmethacrylate. Observing by optical microscope H, reference mark of the specimen was brought into the marked opening of the

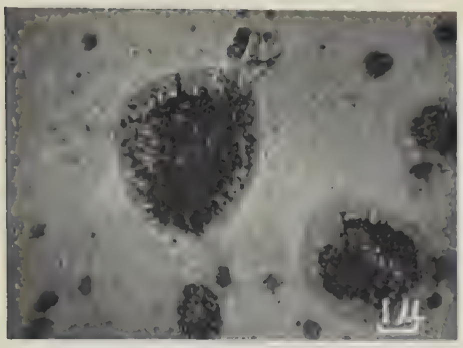

Fig. 2. Electron image of contamination which is supposed to be a substance removed from the specimen surface.

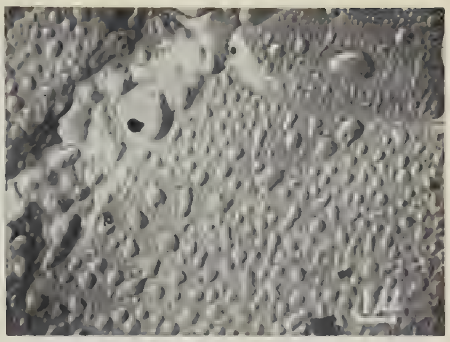

Fig. 3. Electron image of which the physical origin is not yet clear.

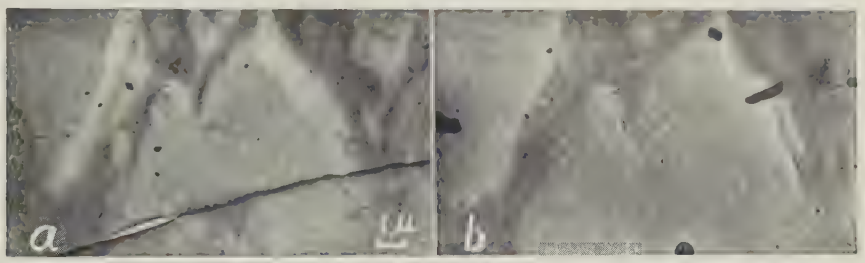

Fig. 4. The effect of humidity on KCl crystal: (a) the case of high humidity, (b) after drying it in a desiccator.

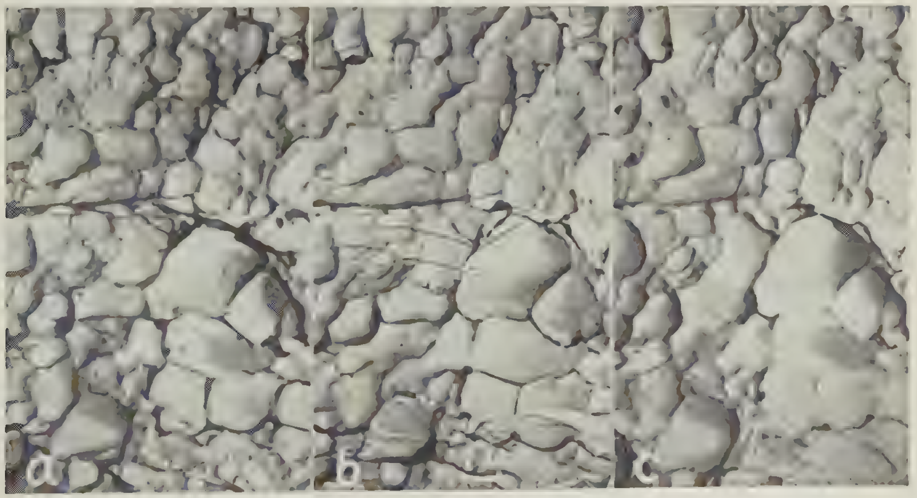

Fig. 5. Confirmation of reproducibility of successive replicas: (a) 1st replica, (b) 2nd replica, (c) 3rd replica.

mesh by four screws F. Next, one or two drops of a few percent, methylmethacrylate solution in benzene were droped on the mesh by using an injector, and then it was dried in air stream from a fan. After perfectly drying methylmethacrylate the mesh was removed from the specimen. And then Cr oblique two-stage replica reinforced by C was made. The evaporation angle of the replica was about $\tan^{-1}(1/3)$ for the front face. Special care was taken to cast the shadow perpendicularly to the cube edge of the crystal in the replication of the front face. After replication, the mesh was placed on the brass net with large squares and then it was immersed in the mixture of equal amount of benzene and chloroform. The brass net with the mesh was picked up gently from the

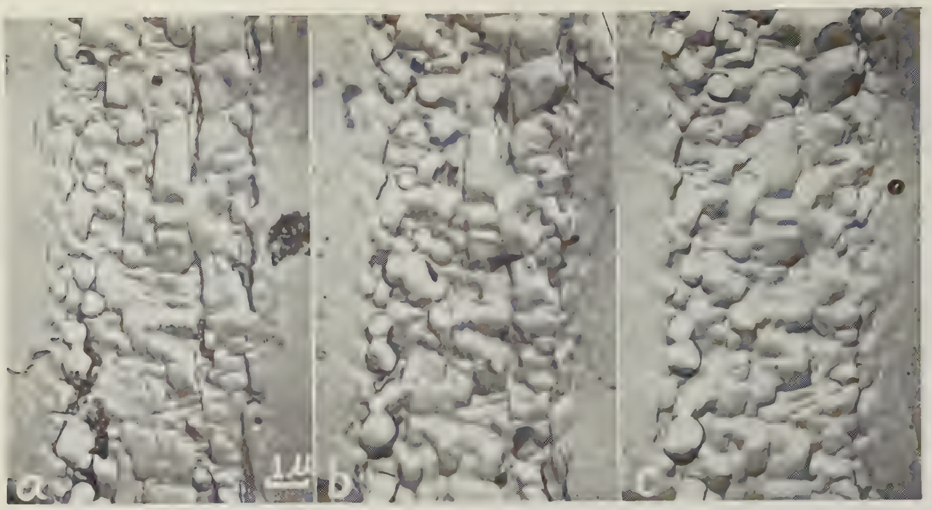

Fig. 6. The successive electron images of some crystallites appeared on the scratched trace on the surface of KCl crystal by holding it in air: (a) the standard crystal, (b) and (c) the same crystal held in air for 4 days and 7 days and after (a), respectively.

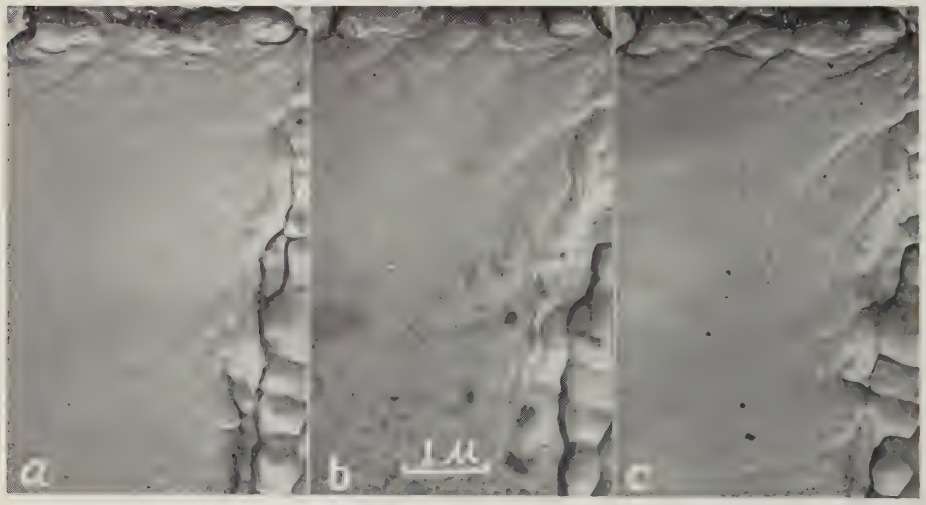

Fig. 7. The successive electron images of the smooth surface of KCl crystal by holding it in air: (a) the standard crystal, (b) and (c) the same crystal held in air for 4 days and 7 days after (a), respectively.

solution after dissolution of methylmethacrylate. The mesh was ready for examination under electronmicroscope.

When methylmethacrylate was dissolved, deposited thin film remained fixed in its original position, as pointed out by Bradley, and so it was not so difficult to obtain replicas of the definite position of the same specimen. However, we met with many other technical difficulties. It was necessary to choose the suitable tickness of deposited film, because rents would often occur in the film if the film was too thin, and the resolution of electron image would be lowered when the film was too thick. Besides, as contamination would often appear at the position to be observed, successive observations by replicas would be impossible. There were many kinds of contamination, namely, those clearly attributed to the dust and those to the residues of the methylmethacrylate. In addition, contamination due to the substance removed from the specimen surface was also observed, as shown in Fig. 2. Pattern shown in Fig. 3 also appeared, though it was still unknown whether it was attributed to adsorbed gas or moisture on the surface or to the change of crystal itself. When such an effect gave a

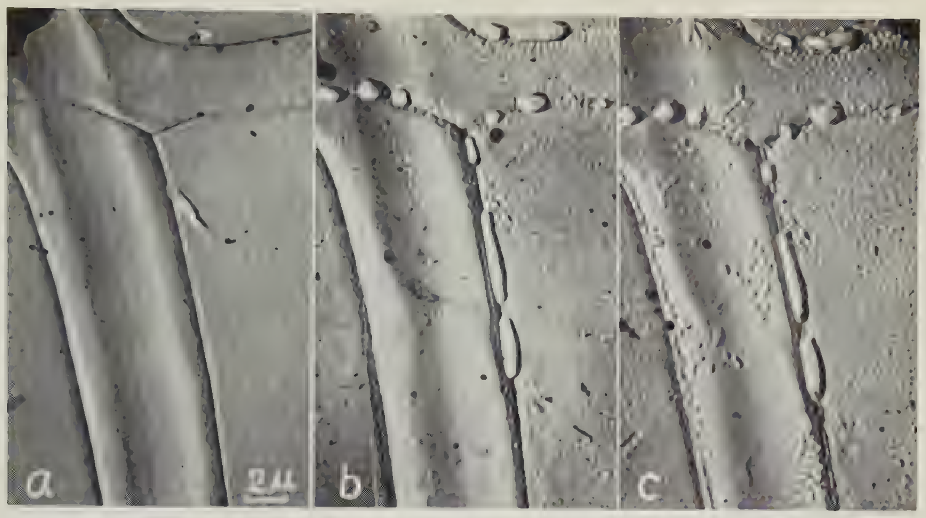

Fig. 8. The successive change caused by X-ray irradiation that appeared on the reference mark on the surface of KCl crystal: (a) the standard crystal, (b) the crystal coloured by X-ray irradiation for 4 hours and (c) the crystal coloured by X-ray irradiation for 3 hours in excess after (b).

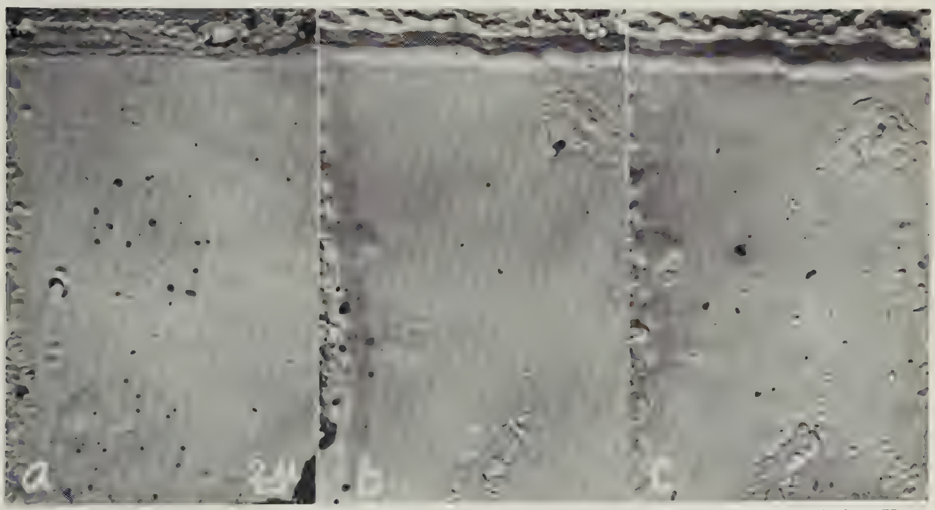

Fig. 9. The successive change on the smooth surface of KCl crystal coloured by X-ray irradiation: (a) the standard crystal, (b) and (c) the same crystal coloured by X-ray irradiation for 4 hours and for 10 hours after (a), respectively.

strong influence, successive observations became again impossible. However, these difficulties could be removed or minimized by technical training to the extent making successive observation possible. The largest technical difficulty was, however, the effect of humidity. When humidity was high, the contour of crystallites appeared on the surface became obscure, as shown in Fig. 4 (a), while clear crystal form shown in (b) could be obtained when observation was made as soon as possible after drying it in a desiccator. However, it was difficult to strip one-stage replica from the specimen when humidity was too low. It was found that the humidity of about 65% was the most suitable condition for replication.

In this experiment artificial KCl crystals were used as specimens, because they were comparatively insensitive to humidity and other conditions. The crystal was cloven in air into cubic pieces of about 4 mm × 5 mm × 0.5 mm and fixed on the slide glass by gelatin. The crystals were always used without pre-treatment such as water-polishing or annealing. They were also always irradiated by X-rays of 7 mA, 40 KV radiating from Fe target, and were kept in the dark during the X-ray irradiation. The distance between the specimen and the target was about 4 cm. Al foil of about 0.02 mm thickness was used as a window of X-ray tube. It took about 15 minutes to make the replication. In this experiment, therefore, coloured crystals were exposed to light only for this time interval.

§ 3. Experimental Results

To confirm whether the surface of KCl crystal will change or not by the casting of methylmethacrylate for making one-stage replica, some crystallite appeared on the surface of KCl crystal by scratch was selected as a standard to follow any change in the specimen. The result is shown in Fig. 5: (a), (b) and (c) are the electron images of the 1st, 2nd and 3rd replica. In this figure a little change is seen, but any essential change is hardly observable. Accordingly, it was confirmed that the specimen change due to casting of methylmethacrylate was very small. Whether the surface of KCl crystal will change or not by holding it in air for several days was also confirmed. Fig. 6 shows the electron image of some crystallites appeared on the surface of KCl crystal by scratch: (a) is the image of the standard specimen, (b) and (c) are the images of KCl crystal held in air for 4 days and for 7 days after (a), respectively. Fig. 7 also shows the electron images of the smooth surface of KCl crystal: (a) is the image of the standard specimen, (b) and (c) are the images of KCl crystal held in air for 4 days and for 7 days after (a), respectively. In these figure a little change is seen, but any essential change is hardly recognized. Therefore, it was also confirmed that the change on the surface of specimen due to humidity or contamination occured by holding it in air for several days was very small.

Fig. 8 shows the successive changes caused by X-ray irradiation that appeared on the reference mark on the surface of KCl crystal. (a) is the electron image of the standard KCl crystal, (b) that of the crystal coloured by X-ray irradiation for 4 hours, and (c) that of the crystal coloured by further X-ray irradiation for additional 3 hours after replication of (b). From this figure, it is clearly seen that in alkali-halide crystals coloured by X-ray ir-

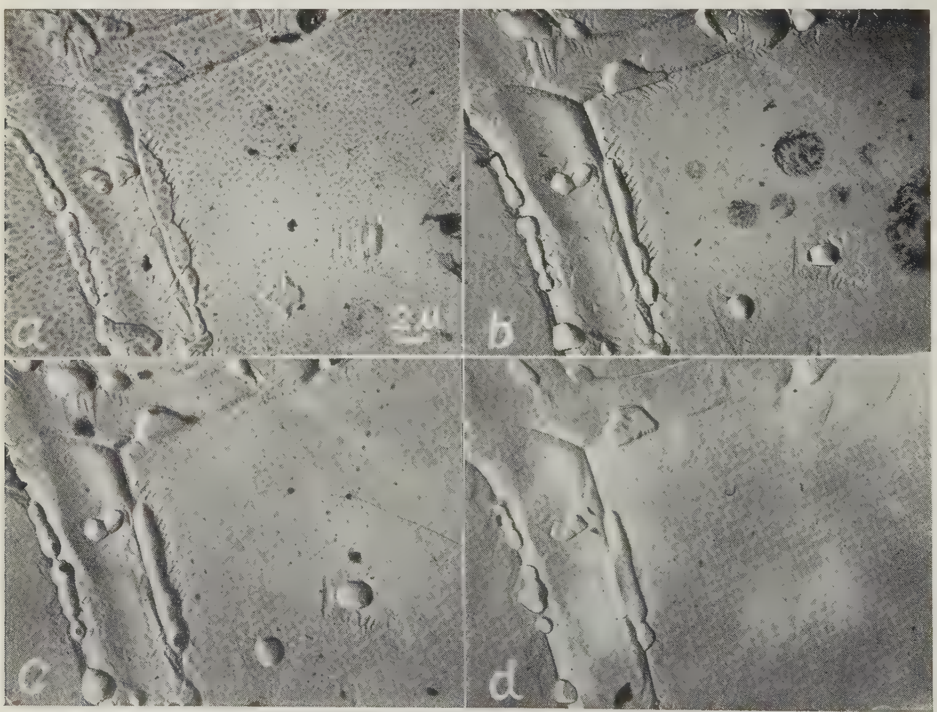

Fig. 10. The successive observation of the process of bleaching by natural light: (a) KCl crystal coloured by X-ray irradiation for 11 hours, (b), (c) and (d) the same crystal obtained 1 day, 2 days and 3 days after colouration, respectively.

radiation crystal growth appears on and along the reference mark. Fig. 9 shows the change on the smooth surface of KCl crystal coloured by X-ray irradition: (a) is the electron image of the standard specimen, (b) and (c) are the images of crystal coloured by X-ray

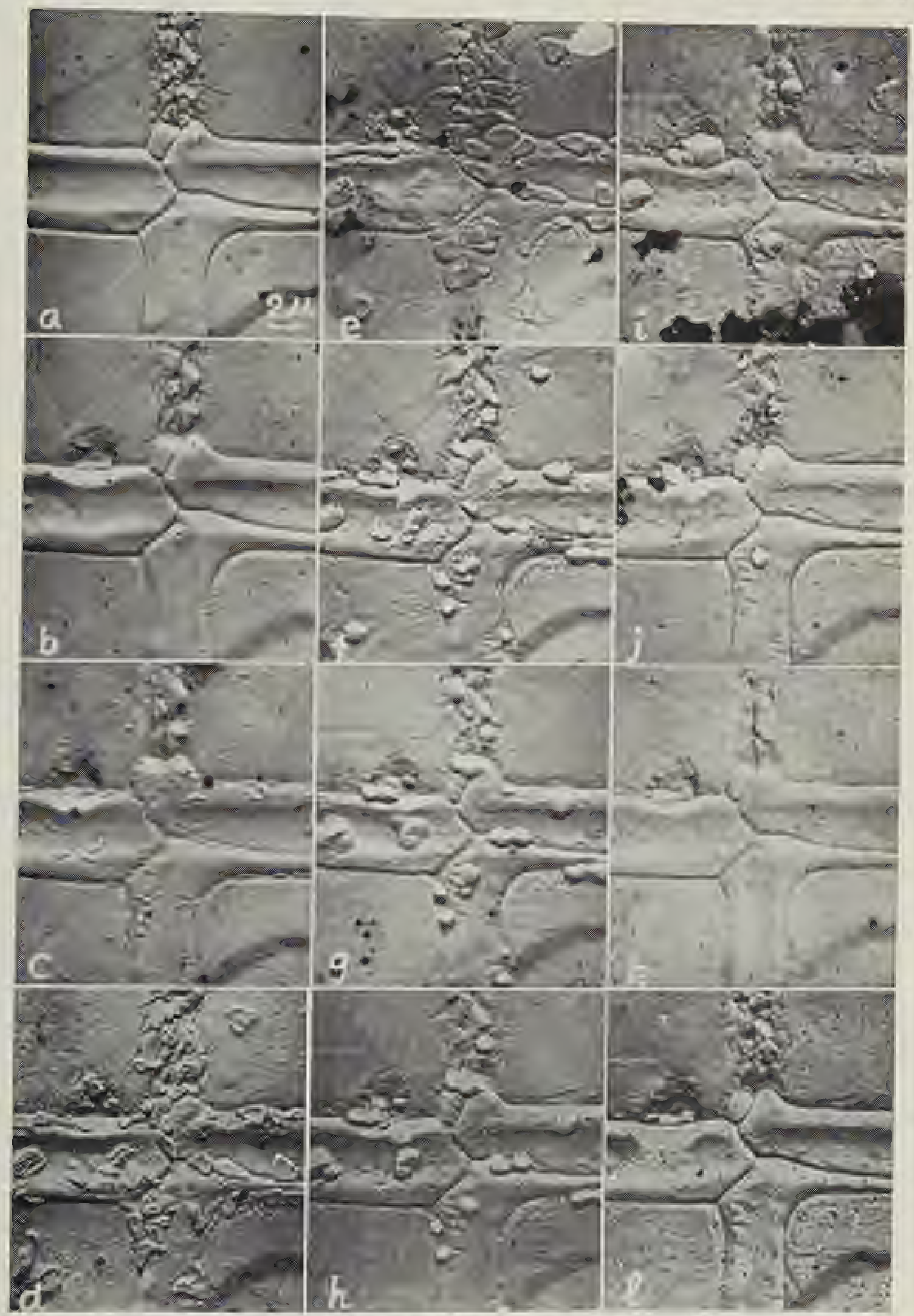

Fig. 11. The successive change of the definite position of the same KCl crystal coloured by X-ray irradiation and then bleached by natural light: (a) the standard crystal, and (b), (c) and (d) the crystal coloured by X-ray irradiation for 4, 7 and 11 hours respectively. From (e) to (l) shows the result of the process of bleaching by natural light after colouration by X-ray: (e) 30 minutes, (f) 1 day, (g) 2 days, (h) 3 days, (i) 23 days, (j) 24 days, (k) 29 days, and (1) 53 days, after (d) respectively.

irradiation for 4 hours and for 10 hours after (a), respectively. It was found in these images that crystal growth would also appear on the smooth surface by X-ray irradiation.

Fig. 10 shows the result of successive observations on the process of bleaching by natural light. (a) is the electron image of KCl crystal coloured by X-ray irradiation for 11 hours in which crystal growth is seen on both the reference mark and the smooth surface. (b), (c) and (d) are the images of the same specimen obtained 1 day, 2 days and 3 days after colouration, respectively. It is clearly seen from the results that the crystallites appeared either on the reference mark or on the smooth surface by X-ray irradiation disappear through the process of bleaching by natural light. It should be noted that the behaviour of disappearance of crystallites is not simple, but very peculiar

To obtain further confirmation of above-mentioned experimental results, the surface change of the definite position of the same KCl crystal coloured by X-ray irradiation and then bleached by natural light was observed successively. Fig. 11 shows the result: (a) is the electron image of standard specimen, and (b), (c) and (d) are the images of the same specimen coloured by X-ray irradiation for 4, 7 and 11 hours respectively. From these images it is clearly seen that a pronounced and peculiar crystal growth appears on the reference mark and also on the smooth surface. (e) to (l) illustrate the result of the process of bleaching by natural light after colouration by X-rays. (e), (f), (g), (h), (i), (j), (k) and (l) are the electron images of KCl crystal obtained 30 minutes, 1 day, 2 days, 3 days, 23 days, 24 days, 29 days and 53 days after (d), respectively. It is clearly seen from these that the crystallites grown during colouration disappear in a peculiar manner in bleaching by natural light and also that (k) and (l) obtained 29 days and 53 days after colouration are very similar to (b) coloured by X-ray irradiation for 4 hours. From this it was clearly confirmed that the crystallites grown during colouration disappeared in the course of bleaching through the reverse process to the crystal growth in colouration. These results agree with the previous experimental results[1).

§ 4. Consideration

From the above-mentioned results it was clearly confirmed that the crystallites grown on KCl crystal during colouration by X-rays disappeared during bleaching possibly by the process quite reverse to the crystal growth during colouration. It is difficult to explain this experimental fact as being the change of alkali-halide crystal only due to the surface evaporation or the surface migration. Accordingly, we must consider the mechanism of crystal growth due to ionic or atomic diffusion from the inner part of crystals for the explanation of the present phenomena and it will also be necessary to consider the reverse process for explaining the disapperance of crystallites during bleaching. In this experiment only surface observation was made. As seen in the previous experiment[1), it may naturally be anticipated that crystallites grow or disappear on mechanical imperfections (e. g., dislocations) in the crystals during colouring or bleaching process, respectively.

From this experiment it was found that the more pronounced crystal growth was seen on and along the artificial damage such as the scratched trace of the reference mark than that on the smooth surface. This fact is in agreement with the previous experimental result[1) that crystallites is easier to grow on the mechanical imperfections than on the smooth surface. It was also found in consistent with the previous experiment[1) that the behaviour of crystal growth and its disappearance were not simple, but very peculiar. The structure, similar to the one on the deposited thin film, that appeared in the cases of NaCl and KBr was not obtained from this experiment throughout the processes of colouring and bleaching. We did not also observe here such a special case as seen in previous experiment[1), in which the ⟨100⟩ direction of the crystallites was predominantly parallel either to the cube edge of the substrate or to the diagonal of the substrate. It seems that we missed observing such a stage in this experiment. Further successive observation is desirable to confirm clearly such phenomena and also to know finer changes in the crystals.

References

1) T. Hibi and K. Ishikawa: J. Phys. Soc. Japan **13** (1958) 709.

2) E. D. Hyam and J. Nutting: Brit. J. Appl. Phys. **3** (1952) 173. J. F. Nankivell: Brit. J. Appl. Phys. **4** (1953) 141. G. R. Booker: Brit. J. Appl. Phys. **5** (1954) 349.

3) D. E. Bradley: Brit. J. Appl. Phys. **6** (1955) 430.

4) J. T. Fourie: J. Appl. Phys. **29** (1958) 608.

5) T. Hibi and K. Yada: to be published.

JOURNAL OF THE PHYSICAL SOCIETY OF JAPAN, Vol. 14, No. 4, APRIL, 1959

Influence of Order-Disorder on Creep of a Superlattice Alloy*

By Taira SUZUKI and Mikio YAMAMOTO

The Research Institute for Iron, Steel and Other Metals,
Tohoku University, Sendai, Japan

(Received November 24, 1958)

A study has been made of the influence of order-disorder on the creep of a superlattice alloy Ni_3Fe. The results obtained strongly support the dislocation-climb mechanism. The activation energy for creep, independent of applied stress, slightly increases with the degree of order: 45.8 kcal/mol for disordered and 47.5 ± 2.0 kcal/mol for ordered phases. A discontinuity occurs at the critical temperature, *i.e.*, 505°C in the curves of creep rate *versus* the reciprocal of temperature. A remarkable acceleration of creep has been observed on the disordered alloys below T_C, which were obtained by quenching from 800°C, as compared with the rates expected from the values above T_C. A semi-quantitative theory has been proposed for such a configurational acceleration of creep in terms of order-disorder kinetics and dislocation processes in the superlattice alloy of AB_3 f.c.c. type.

In ordered alloys, the vacancy diffusion introducing the dislocation-climb is thought to be anisotropic with regard to the orientation of slip bands. This will result a significant difference in the stress dependence of creep rates in ordered phases from the one in disordered phases as observed here.

§ 1. Introduction

As the possible mechanisms for high temperature creep of close-packed metals the following are to be considered, (a) stress-induced diffusion of vacancies, (b) cross-slip, (c) intersection of other dislocations, (d) dislocation climb and (e) grain boundary flow. While (a) plays a predominant role in producing noncrystalline flow only near the melting point,[1] others are possible over a wide range of temperature, and all except (b) have more or less direct connections with the formation and the migration of the vacancy in those metals. The activation energy for creep, however, is thought to be different from each other in magnitude and in the dependence on applied stress. Mott has first discussed the importance of (d) and showed that the activation energy, independent of applied stress, should be close to that for the self-diffusion.[2] Many experimental works on high temperature creep of metals, *e.g.*, by Dorn *et al.*,[3] have since contributed to the promotion of theoretical surveys.

The most recent development of theories has been established by Weertman.[4] It has been understood that the steady-state creep occurs at a balanced state between hardening and recovery in metals concerned. The Weertman's model for the hardening and the recovery responsible for the creep is as follows: The slip dislocations are piled-up in front of barriers such as grain boundaries or the Lomer-Cottrell sessile dislocations, and introduce hardening. At high temperatures, where the equilibrium concentration of vacancies sets up near the lead dislocations, the vacancy flow along a concentration gradient between those dislocations will induce dislocation climb. The metals will thus recover from the hardened state and continue to flow. He obtained the creep rate at steady-state as

---

* The present experiments were performed in 1949 to 1950, and read at the Meeting of the Physical Society of Japan in 1951 (Bull. Phys. Soc. Japan **6** (1951) 321).

$$K=A\sigma^{m}\Psi/kT \quad \text{for } n\sigma b^{3}/kT<1\,, \quad (1)$$

where A is a constant, k is Boltzmann's constant, T is absolute temperature, σ is applied stress, b is the Burgers vector and n is the number of piled-up dislocations in one group. In this equation the exponent m is a factor to be determined by a detailed process of the dislocation climb, and Ψ has a form of $B\exp(-Q/kT)$, where B is a constant. If the stacking-fault energy is so large as to be able to maintain the equilibrium concentration of vacancies near the dislocation lines, Q is the activation energy for the atomic diffusion by vacancy mechanism in the metals. The above assumption will be valid in metals such as aluminium, lead and zinc. It is to be noted, however, that Franks and McLean,[5] and Semmel and Machlin[6] have found by etching technique such a dislocation climb to occur during creep at high temperatures even in copper or silver with the low stacking-fault energy.

In the following, we will draw attention to the creep in a superlattice alloy of AB_3 f.c.c. type. Since the rate of vacancy diffusion in such alloys is thought to depend upon the degree of order, the creep rate should be influenced by ordering if dislocation climb is rate-controlling for the creep as predicted by the theory. In beta brass, only one example in which tracer diffusion experiment has been done in an alloy with long-range order, the activation energy for the isotope diffusion has been found to be different from each other in the ordered state and in the disordered state.[7]* It is hence worth examining the variation of Q in Eq. (1) with atomic order not only from the points of the creep mechanism but from those of the order-disorder kinetics.

It is conceived that the vacancies in an well-ordered alloy diffuse by a highly correlated motion in such a way that the state of order is not destroyed by the movements of vacancies. Accordingly, the diffusion of vacancies resulting dislocation climb will be faster along the slip bands than in the perpendicular direction, since the slip dislocation introduces a disorder into the alloy along the slip bands. This situation is similar to the creep of tin crystals having anisotropic diffusion coefficients.[9] In such cases, it is expected that the dependence of creep rate on applied stress designated by the exponent m in Eq. (1) is different from what is expected for the case with the isotropic diffusion coefficient. In the present case, therefore, the value of m will depend on the initial degree of order.

As far as we know, there has been given one experiment on the creep of order-disorder alloy of beta brass done by Herman and Brown.[10] Although this is a pioneer work in this field, they interested only in the change of creep strength with temperature. They paid no attention to the problems as described above. Furthermore, beta brass is not necessarily adequate for the present aims, since the alloy equilibrated so rapidly that we cannot retain the disordered state by quenching.

§ 2. Experimental Procedure

An ingot of the alloy of about 10 cm length and 2 cm diameter was prepared by melting together of measured amounts of Mond nickel and electrolytic iron with 0.5% Mn in an alumina cruicible in vacuum. The ingot was hammered and drawn finally to the wire of 0.05 cm diameter for creep specimens. The specimen wires of 12 cm length were obtained and annealed in vacuum for about 1 day at 1000°C. The mean grain size thus obtained was smaller than the specimen diameter. The composition was checked by chemical analysis and found to be of 74.6 at. % Ni. Specimens for the measurements of specific heats were machined from the same ingot. They were obtained in a cylindrical form having a diameter of 1.5 cm and a length of 2.5 cm. Some were cold-worked in compression at room temperature and, then, a hole of 0.8

---

* Very recently, Goering and Nowick[8] have obtained a similar result in the alloy Cu_3Au by anelastic measurements.

cm diameter and 2 cm length was drilled with special care to avoid an excess heating, into which a heating coil of nichrome wire was inserted. One end of the differential thermocouple of Pt and Pt-Rh 13% was fixed to the specimen and the other end to the inner wall of a copper container surrounding the specimen. The apparatus and the methods were the same as one of the present authors used before for the measurements of heat emission associated with recovery of cold-worked copper.[11)]

The fully ordered specimens were obtained following Kaya's procedure,[12)] *i.e.*, by holding in vacuum for one week at 490°C (T_C=505°C) and then cooled to 450°C at a rate of 10° per day. The disordered specimens were quenched from 800°C in air as sealed in an evacuated quartz tube of 2 mm inner diameter and 0.5 mm wall-thickness.

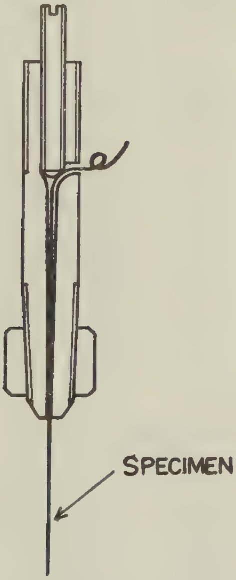

Fig. 1. A grip of specimen wire for creep testing.

The specimens were pulled in air at various temperatures and stresses in an apparatus with a special device,[13)] which applies a constant stress independent of the change of cross-section with elongation. Both ends of the specimen were gripped by pin-vices made of stainless steel after tightening each end by a bolt screwed into the vice as shown in Fig. 1. The effective length of the specimen between the grips was about 9 cm. The variable arm was set in a position to give a constant stress to the specimen during the test. The elongation was magnified by an optical lever system and it was read by telescope and scale. The sensitivity was 4.04×10^{-5} cm per millimeter of the scale at the distance of one meter.

The temperature of the specimen was kept constant within ±0.01°. Over most of the temperature range the specimen reached thermal equilibrium within eight minutes. The specimen were held for about thirty minutes at each temperature before the creep test being started.

§ 3. Results

Stress-strain curves for the ordered and disordered alloys were taken in compression at room temperature at the strain rate of 2×10^{-3} per second. As seen in Fig. 2, the disordred alloy (curve (a)) behaves similarly as most polycrystalline metals of face-centred cubic structure at relatively high temperatures. On the other hand, the stress-strain curve for the ordered alloy (curve (b)) is almost linear and has a high yield stress than that of the disordered alloy. It resembles to that of the above metals at low temperatures. It is very important, however, to remark that both polycrystals and single crystals of Cu_3Au behave in the opposite way such as the yield stress of the ordered alloy is lower than that of the disordered alloy.[14),15),16)] It is seen in Fig. 2 that after the rapid hardening stage the hardening rate of the disordered alloys decreases to the value smaller than that of the ordered alloys. Such a phenomenon is called dynamical recovery by Seeger *et al.*[17)]

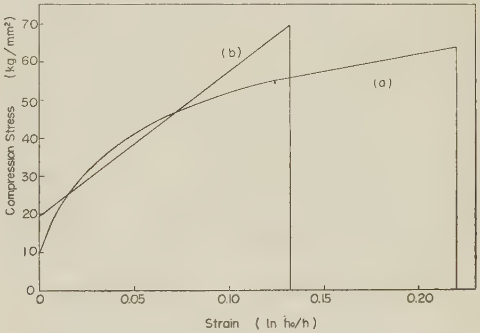

Fig. 2. Stress-strain curves in compression for the ordered and disordered alloys measured at room temperature: (a) disordered alloy which was quenched from 800°C in air; (b) ordered alloy.

The recovery in this case is induced by applied stress. At high temperatures, the corresponding recovery by the same or some other mechanism is greatly helped by thermal energy, which will have a close connection with creep to be studied here.

Before going further, it will be helpful to study the static recovery from a cold-worked state. We measured specific heats of cold-worked alloys at the heating rate of 1.5° per minute. Fig. 3 shows two cases; (a) an well-ordered alloy and (b) a disordered alloy. Curves (c) and (d) indicate specific heat *versus* temperature curves of undeformed alloys with the corresponding degree of order, respectively. The amounts of compression strain are shown in the figure. The recovery starts from about 300°C in both cases. There are two minima in both curves of (a) and (b). The corresponding minima are also found in the quenched specimen without cold-work. A similar result as shown by (d) was later obtained by Iida[18] and he studied it more in detail in connection with the ordering kinetics in Ni_3Fe. It is clearly seen from Fig. 3 that the heat generations corresponding to the two minima are accelerated by the presence of the dislocations. It suggests a close correlation between recovery and ordering through the atomic diffusion process. A peak in the specific heat *versus* temperature curves between 500° and 600°C relates to the atomic order-disorder and ferromagnetic transforma-

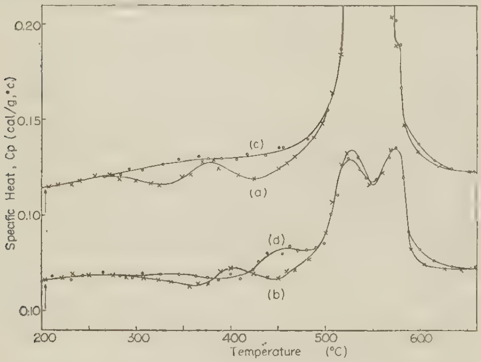

Fig. 3. Specific-heat *versus* temperature curves illustrating annealing process from quenched, disordered state or cold-worked state: (a) an well-ordered alloy deformed to $ln\ h_0/h = 0.132$; (b) a disordered alloy deformed to $ln\ h_0/h = 0.211$; (c) an well-ordered alloy without cold-work.

Table I. Creep data of ordered and disordered alloys of Ni_3Fe.

Temperature T (°K)	Applied stress (kg/mm²)	Creep rate K (sec⁻¹)	TK (°K·sec⁻¹)
(a) Disordered alloys			
573	26.1	2.18×10^{-8}	5.10×10^{-6}
	28.2	3.15×10^{-8}	1.81×10^{-5}
	29.9	4.76×10^{-8}	2.70×10^{-5}
	32.1	4.67×10^{-8}	2.67×10^{-5}
613	24.1	2.65×10^{-7}	1.68×10^{-4}
	28.1	3.74×10^{-7}	2.29×10^{-4}
	32.1	6.32×10^{-7}	3.88×10^{-4}
653	18.1	8.21×10^{-9}	5.36×10^{-5}
	21.8	4.00×10^{-7}	2.61×10^{-4}
	24.3	8.75×10^{-7}	5.75×10^{-4}
	26.3	9.40×10^{-7}	6.13×10^{-4}
	28.2	1.56×10^{-6}	1.02×10^{-3}
	28.7	1.67×10^{-6}	1.09×10^{-3}
693	10.1	2.91×10^{-9}	2.02×10^{-6}
	13.3	1.05×10^{-8}	2.02×10^{-6}
	20.6	3.48×10^{-7}	2.41×10^{-4}
	21.4	5.84×10^{-7}	4.04×10^{-4}
	23.6	2.14×10^{-6}	1.48×10^{-3}
	24.1	2.44×10^{-6}	1.69×10^{-3}
	28.2	5.77×10^{-6}	4.00×10^{-3}
813	10.1	6.77×10^{-7}	5.50×10^{-4}
	12.7	1.28×10^{-6}	1.04×10^{-3}
	13.8	1.46×10^{-6}	1.19×10^{-3}
	15.0	2.00×10^{-6}	1.63×10^{-3}
	16.8	3.42×10^{-6}	2.78×10^{-3}
853	9.5	2.14×10^{-6}	1.83×10^{-3}
	10.7	3.22×10^{-6}	2.75×10^{-3}
	11.8	3.28×10^{-6}	2.80×10^{-3}
	12.8	4.85×10^{-6}	4.13×10^{-3}
	13.9	7.04×10^{-6}	6.01×10^{-3}
891	3.1	5.98×10^{-7}	5.32×10^{-4}
	4.9	1.65×10^{-6}	1.47×10^{-3}
	8.0	4.76×10^{-6}	4.27×10^{-3}
	10.4	9.82×10^{-6}	8.75×10^{-3}
	12.5	1.36×10^{-5}	1.21×10^{-2}
(b) Ordered alloys			
643	26.1	1.09×10^{-8}	6.98×10^{-6}
	28.2	1.58×10^{-8}	1.02×10^{-5}
	29.8	2.17×10^{-8}	1.35×10^{-5}
	32.1	4.49×10^{-8}	2.88×10^{-5}
673	21.3	1.49×10^{-8}	1.01×10^{-5}
	24.1	5.20×10^{-8}	3.50×10^{-5}
	28.2	1.08×10^{-7}	7.29×10^{-5}
	29.8	1.93×10^{-7}	1.30×10^{-4}
733	21.3	2.54×10^{-7}	1.86×10^{-4}
	24.4	5.02×10^{-7}	3.68×10^{-4}
	26.8	4.04×10^{-7}	2.96×10^{-4}
	28.2	1.65×10^{-6}	1.21×10^{-3}
	30.5	3.40×10^{-6}	2.49×10^{-3}
753	19.9	2.69×10^{-7}	2.03×10^{-4}
	23.6	6.06×10^{-7}	4.56×10^{-4}
	26.0	1.00×10^{-6}	7.53×10^{-4}
	28.1	2.97×10^{-6}	2.24×10^{-3}
773	16.8	1.91×10^{-7}	1.47×10^{-4}
	19.9	6.28×10^{-7}	4.84×10^{-4}
	24.4	2.21×10^{-6}	1.70×10^{-3}
	26.8	4.98×10^{-6}	3.85×10^{-3}
	28.2	6.88×10^{-6}	5.32×10^{-3}

tions, which is not of interest in the present paper.

Creep curves of the ordered or disordred alloys were found to be quite similar to those of other metals like aluminium. The creep rate was constant over a large portion of the strain investigated. The observed steady-state creep rates of all the specimens have been listed in Table I along with the test temperatures and initial stresses.

The activation energy of creep can be found from a plot of the logarithm of the creep rate K times the absolute temperature T against the reciprocal of absolute temperature. Such plots are shown in Fig. 4. The two curves below the critical temperature T_C correspond to the specimens of ordered and disordered alloys, respectively. Each point was obtained at the stress of 28.2 kg/mm². Above T_C, however, creep rate at this level of stress is too fast to be observed by the present method. The plot in this region therefore was obtained at the stress of 12.5 kg/mm². Although the points at 380° and 420°C for the quenched specimens deviate appreciably, the linear part of the curve below T_C has approximately the same inclination as that of the curve above T_C. The activation energy thus obtained is 45.8 kcal/mol. On the other hand, the curve for the ordered alloy runs almost linearly up to 460°C and it gives the activation energy of 49.5 kcal/mol, slightly higher than that for the disordered alloy. No information of the activation energy for the atomic diffusion in Ni_3Fe to be compared with the above results has been given so far, however.

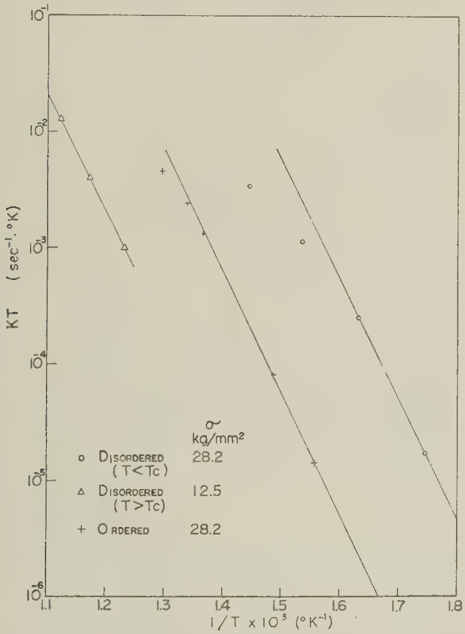

Fig. 4. Logarithm of KT *versus* inverse absolute temperature.

The last column of Table I lists the values of TK of all the specimens. Since a precise determination of Q below T_C seems to be rather difficult, the following tests were undertaken. Fig. 5 gives the plot of $TK \exp(Q/RT)$ *versus* the logarithm of stress for the disordered alloys. The points obtained at 300° and 340°C are on a straight line almost parallel to the one above T_C. This suggests that the estimated value of Q is sufficiently appropriate over the whole range of stress investigated. The inclination of the curves gives the value of m in Eq. (1) to be 3.1.

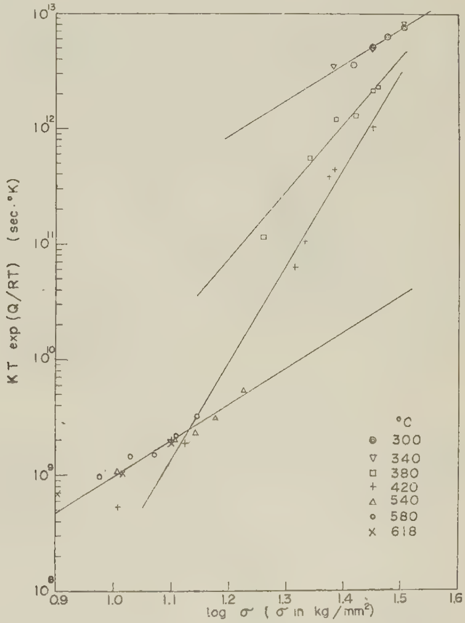

Fig. 5. Plot of $TK \exp(Q/RT)$ *versus* logarithm of stress for the disordered alloy.

The points at either 380° or 420°C are, however, on different straight lines with larger slopes, respectively. It appears that the slope of the curve in this region of temperature near T_C increases with testing temperature. It will be related to the increase of the degree of order in the specimen alloys by annealing before and during the tests. The similar plot on the ordered alloys in Fig. 6 must be compared with the above cases. Fig. 6 shows one example of the plot with $Q=49.5$ kcal/mol. The points are scattered as compared with those for the disordered alloy above T_C or at lower temperatures. The minimum scattering was obtained for $Q=47.5\pm2.0$ kcal/mol. It is conceivable that all the points are not on a single line, because the degree of order will change at temperatures such as 480° and 500°C in the neighbourhood of T_C. The slope of the straight lines shown in Fig. 6 gives $m=7.1$, which is remarkably larger than that for the disordered alloy.

The creep rates are plotted on a semi-logarithmic scale *versus* the reciprocal of absolute temperature for (a) $\sigma=31.6$ kg/mm², and (b) $\sigma=15.9$ kg/mm² in Fig. 7. The points in the figure are obtained by the relatively unambiguous extrapolation of the measured creep rates listed in Table I. There are a few points to be remarked:

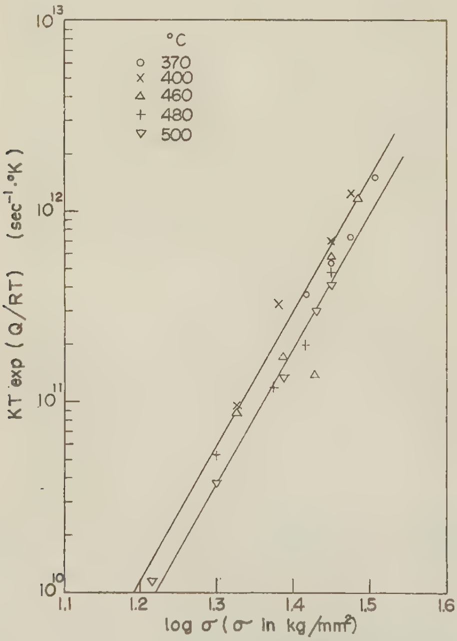

Fig. 6. Plot of $TK \exp(Q/RT)$ *versus* logarithm of stress for ordered alloy, using $Q=49.5$ kcal/mol.

(1) The activation energy Q, independent of applied stress, slightly increases with the degree of order.

(2) A discontinuity occurs in the curves of creep rate *versus* $1/T$ at the critical temperature, *i.e.*, 505°C.

(3) A remarkable acceleration of creep is found below T_C for both ordered and disordered alloys. The creep rate of the ordered alloy is lower for the stress of 15.9 kg/mm², but higher for the stress of 31.6 kg/mm² than the extrapolated values from above T_C corresponding to each stress, respectively where the creep is free from the configurational acceleration. Regarding this it should be added that the consistent dependence of creep rate on stress observed in the alloy, originally well-ordered, suggests an appreciable degree of order still maintained during creep over the whole range of stress investigated.

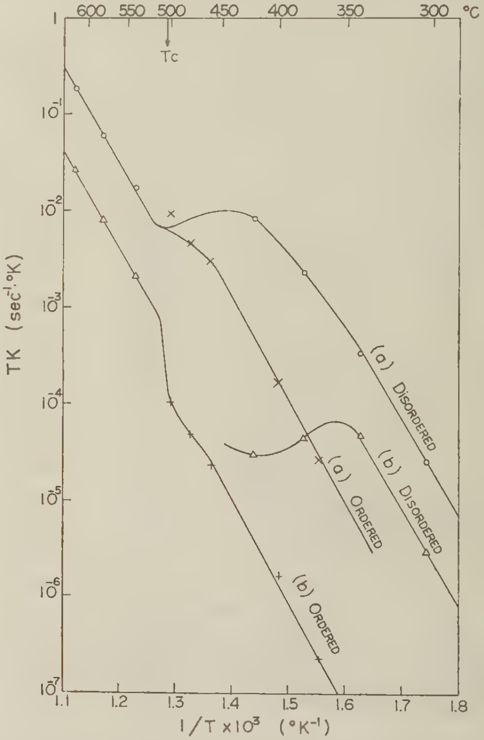

Fig. 7. Logarithm of creep rate times absolute temperature *versus* inverse absolute temperature; (a) $\sigma=31.6$ kg/mm² and (b) $\sigma=15.9$ kg/mm².

(4) For creep of the disordered alloy below T_C, the increase of stress appears to suppress the development of order above 360°C. This is not unconceivable, since the dislocations, increasing in number with applied stress, bring forth essentially the effect of disordering on atomic arrangements. The qualitative difference on this point from what we described in the last paragraph in (3) for the order-

ed alloy may be caused by a significant difference in the way of slip deformation, *i.e.*, the resulting distribution of the dislocations between both cases. This will be discussed below.

§ 4. Discussion

(a) Configurational acceleration of creep

The present results strongly support the theory that the observed creep is controlled by the process of dislocation climb through the vacancy diffusion. Such an influence of order-disorder on creep that gives rise to a configurational acceleration of creep (Fig. 7) is hardly expected from other mechanisms for high temperature creep such as, for instance, cross-slip. The activation energy of cross-slip is mainly determined by the stacking-fault energy according to Schoeck and Seeger.[19] It may give the variation of the activation energy for creep with atomic order, but it does not appear to result such a configurational acceleration as observed. It also does not seem to be significant to take into account non-crystalline flow through the vacancy diffusion such as stress-induced diffusion or grain boundary diffusion. There is an evidence concerning the crystalline nature of the observed creep, which will be discussed later in connection with the stress dependence of creep rates in the ordered and disordered alloys.

In the disordered alloy of AB_3 f.c.c. type a vacancy will jump preferentially to one of the neighbouring sites so as to reduce the configurational energy and the jump frequency is thus influenced by the configuration of its environment. The first problem is to find the total number of vacancy movements occuring in unit time, in which a vacancy moves from one lattice site to another at a given temperature and with a given environment. Using this result, it is possible to express the flux of vacancies along the concentration gradient of vacancies between two climbing dislocations. It will be taken that the total number of vacancy movements in unit time is linearly related with the net change of the degree of order. In doing this we assume the system to be homogeneous and describable solely by means of a long-range order parameter S. Accordingly, if the distribution of vacancies is not so heterogeneous, the rate of flow of vacancies will be given by

$$2\pi r(D+\alpha f_v^{-1}dS/dt)(\partial N/\partial r)\ ,$$

where α is a proportional factor equal to a^2N_0, a is the lattice constant, f_v is the fraction of vacancies, dS/dt is the rate of change of the long-range order parameter, $\partial N/\partial r$ is the concentration gradient of vacancies along the perpendicular distance from the dislocation line and D is the diffusion coefficient of the vacancies in a symmetrical environment, taking $D=D_A=D_B$. Following Weertman we assume that the lead dislocation in a piled-up group of n dislocations is the one to climb. Then, the vacancy concentration N_e in equilibrium with the lead dislocation is

$$N_e=N_O\exp(\pm n\sigma b^3/kT)\ ,$$

where N_O is the equilibrium concentration in a dislocation free crystal. Under steady-state conditions,

$$2\pi r\,\partial N/\partial r=N_0 n\sigma b^3/kT$$

when $n\sigma b^3/kT<1$. It thus follows that the rate of flow of vacancies P is

$$P=2\pi N_0(D+\alpha f_v^{-1}dS/dt)n\sigma b^3/kT\ . \tag{2}$$

The ordering rate dS/dt has been given analytically by Vineyard[20] as a function of S. According to him, it can be written as

$$F(S)=\frac{3(1-S)^2\exp(6VS/RT)-(3+S)(1+3S)\exp(-6VS/RT)}{6(1-S)\exp(3VS/RT)+2(5+3S)\exp(-3VS/RT)}\ .$$

In this expression, we simply assume $V=V_A=V_B$, where $V_A=\frac{1}{2}(V_{AA}-V_{AB})$, $V_B=\frac{1}{2}(V_{BB}-V_{AB})$, and V_{AA} *etc.* are the pairwise interaction energies between the nearest neighbours such as AA, BB and AB pairs, respectively. Inserting this into Eq. (2) one finds

$$P=2\pi N_O D(S)(1+16\alpha F(S))n\sigma b^3/kT\ . \tag{4}$$

It is clear from Eq. (4) that below T_C the climb rate of the dislocation, which is qual to b^2P, is larger by the factor $16\alpha F(S)$ than that above T_C, which is free from the influence of order. The above factor is an increasing function of S at $S\sim0$ at sufficiently low temperatures and it can be far larger than unity.* If the change of S during the observation of creep rate is small enough, which normally takes about one hour, the creep rate will be given as a function of the initial value of S. In fact, the creep rates shown in Table I were all obtained from the parts of creep curves with sufficiently constant slopes over the time of measurements. It is possible that $16\alpha F(S)$ is of the order of 100, which is the right order in magnitude in consistent with the observed results in taking account of a slight change of D with S. If we accept the Weertman's result, the creep rate K can be written as

$$K=(\text{climb rate}\times 1/h)MLL'b, \qquad (5)$$

where h is the climb height of the dislocation, which is determined by equality between the repulsive force given by the barrier in front of the piled-up group of dislocations and the applied force to induce the slip motion of the climbing dislocation. M is the number of the Frank-Read sources per unit volume, and L and L' are the slip distances of edge and screw parts of a dislocation loop, respectively. Eq. (5) is reduced to the form of Eq. (1), where A depends on S and changes slowly with temperature in the temperature range investigated.

The present experiments gave $m=3.1$ for the disordered alloy above T_C and at low temperatures below T_C. It is remarkable that the observed value of m on many metals except for a few examples like tin are almost 3 to 4. Theoretically Weertman has found m to be 3.6 for metals such as aluminium, although the theory is not so well established on this point.

(b) Dislocation climb and creep in an well ordered alloy

As well known, a single perfect dislocation in an well-ordered alloy of AB_3 f.c.c. type introduces an antiphase boundary along the half of slip plane through the crystal.[21),22)] Taking two neighbouring dislocations on the same slip plane, one may be called the disordering dislocation, while the other the ordering dislocation. The strips of disordered regions are arranged in parallel along the slip plane corresponding to the piled-up group of the dislocations which are illustrated in Fig. 8(a). In practice, however, the jogs formed rather at random in these dislocations by intersecting other dislocations will scatter the strips into irregular forms.* The scattered strips are illustrated schematically in Fig. 8(b), which shows the antiphase-domain boundaries by hatching in the same slip plane. These boundaries are distributed at random in the parallel planes, of which width depends on the distribution of positive and negative jogs and on their length. When slip occurs in the ordered alloy, therefore, the crystal region of certain width parallel to slip plane will become less-ordered.

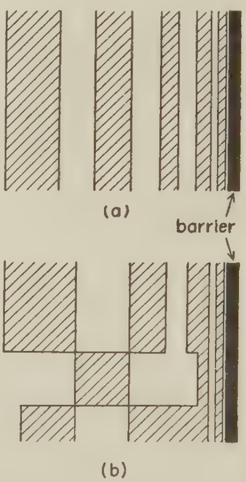

Fig. 8. Antiphase boundaries in a slip plane introduced by slip-dislocations piled up in front of a barrier. (a) An ideal pattern without any disturbance due to jogs; (b) random strips of antiphase boundaries formed by intersecting other dislocations, which are not rigidly fixed.

On the other hand, the vacancy in an well-ordered alloy is tightly bound to its original position, and any jump to the neighbouring position increases the configurational energy and such jumps will be immediately retraced. For the vacancy diffusion without creating disorder, therefore, it must need certain correlated processes as suggested by Elcock and McCombie.[23] The vacancy feels much more difficulty for its motion than in the disordered phase. As a result, the vacancy diffusion is faster within the slip bands than in the regions between the slip bands. In other words, the vacancy diffusion is anisotropic in this case. Therefore, a couple of the climb dislocations lying in the same slip band as close as possible will be preferentially chosen. The diffusion problem to be discussed now becomes effectively a one dimensional one.

---

* $F(S)$ has a zero at $S=0$. As discussed by Vineyard, the reason for this is that a completely disordered system has no preference for choosing any particular sublattice for A or B atom. We have to consider the effects of the short-range order to explain the acceleration of creep for $S=0$.

* The formation of jogs by intersecting other dislocations may explain a large part of the hardening in an ordered crystal by the same reason.

If we take the effective diffusivity of the vacancies within the slip band equal to D' and the diffusion length R, the rate of flow of vacancies from unit length of the dislocation through a volume along the slip band of width d is given by

$$P=(d/R)N_0D'F(S)16\alpha n\sigma b^3/kT \qquad (6)$$

instead of Eq. (4) for the isotropic diffusion case. The difference between the climb rates for the ordered and disordered phases is the factor (d/R) except for the diffusion coefficient. (d/R) should be of the order of $10^{-3}(D/D')$ at relatively low stress from the results shown in Fig. 7. Since it is reasonable to take $d=10b\sim100b$, R will be 10^4b to 10^5b. This is possible as the distance between the neighbouring piled-up groups of the dislocations in the same slip band.

The width d of slip bands must be a rapidly increasing function of stress so that the exponent m on the stress in Eq. (1) becomes larger than 3.6 for the isotropic diffusion if the stress dependence of other quantities is unchanged. Experimentally it is found that $m=7.1$ for the ordered alloy as already described. It is of interest to note that creep of tin crystals, where the diffusion coefficient in the c-direction is fairly smaller than that in the a-direction, has a similar stress dependence, *i.e.*, $m=4.6\sim5.0$,[9] although the situation such as the angle between the climb dislocation line and the c-axis is not necessarily 90 degrees renders the results more complex.

(c) Some note on stress-strain curves and specific heat-temperature curves

As Friedel[24] suggested, the initial part of stress-strain curve of polycrystalline metals resembles apparently to the second stage of that in single crystal of the same material. This will be reasonably explained by the fact that multiple slips take place in both cases and so the intersection between dislocations and the formation of the Lomer-Cottrell sessile dislocations occur to an appreciable extent, resulting the rapid hardening. While the stress-strain curve of the disordered alloy shows a typical form for the high temperature deformation of most face-centred cubic metals, the ordered alloy undergoes deformation typical for the low temperature deformation of those metals. Taking into account both facts, it will lead us to conclude that a dynamical recovery cannot easily set in the ordered alloy at room temperature as compared with that in the disordered alloy. This is possibly understood by the reason that either cross slip or breaking the sessile dislocations needs the additional activation energy, since it hardly expects the pairwise motion of the dislocations in such cases.

If such a recovery process takes place, slip lines becomes clustered and coarser. In fact, Taoka et al[25] have found electron-microscopically only fine slip lines in their ordered alloys of Cu_3Au and Ni_3Mn and coarse lines in their disordered alloys. The difficulty for the motion of jogs in an well-ordered phase, as discussed before, will of course strengthen the above tendency.

At the last on the stress-strain curves of Ni_3Fe alloys it remains to mention the yield stress of the ordered alloys. The change of yield stress with increasing degree of order in Ni_3Fe and Ni_3Mn is quite opposite to that in Cu_3Au alloys as described before. It seems to be difficult to explain the above disagreement between Ni_3Fe, Ni_3Mn and Cu_3Au at present.

Iida has studied the heat generations in Ni_3Fe quenched from various temperatures above T_C. His results are in consistent qualitatively with our results. He ascribes the first generation of heats to annealing and associated ordering of some lattice defects such as quenched vacancies and dislocations, and the second to the development of local order. The present investigation including additional works on cold-worked specimens supports in general his explanation. In more details, it should be added that with the increase of order and with the progress of recovery from the quenched state by the 'diffusion' of dislocations, it becomes harder gradually to advance such processes because of the increase of the activation energy for the vacancy diffusion as well as the decrease of the concentration gradient of the vacancies. The further development of order and recovery is therefore somewhat retarded to produce the second generation of heats, even though the reaction rate in the cold-worked specimen is still higher than in the quenched specimen without cold-work. The situation is well illustrated in Fig. 9, where the logarithm of electrical resistivity measured at room temperature is plotted against annealing time at 400°C. There are three stages of ordering and recovery. The first rapid change appears to correspond with the first generation of heats in the c_p-T curves and the next linear stage with the second generation of heats. The rates of the first and second changes are both faster in a cold-worked alloy than in the alloy without cold-work. It is seen, however, that the above relation becomes reverse at the third stage of ordering. The first rapid change of electrical resistivity in curve (a) shows an anomalous behaviour with a maximum typical for ordering of this alloy at relatively low temperatures, which may be caused by the nucleation of order.

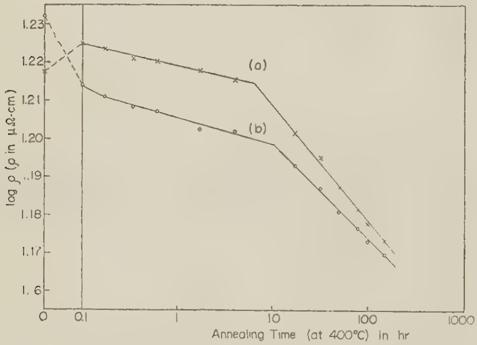

Fig. 9. Annealing curves of disordered alloys at 400°C. Electrical resistivity was measured at room temperature: (a) Without cold-work; (b) cold-worked in tension ($\ln l/l_0=0.137$). Specimen wires were originally quenched from 800°C in air.

References

1) F. R. N. Nabarro: Reports of a Conference on *the Strength of Solids*, Phys. Soc. London (1947) 75. C. Herring: J. Appl. Phys. **21** (1950) 437.
2) N. F. Mott: Proc. Phys. Soc. London **B, 61** (1951) 729; Phil. Mag. **43** (1952) 1151; **44** (1953) 741; Proc. Roy. Soc. **A, 220** (1953) 1.
3) J. E. Dorn: J. Mech. Phys. Solids **3** (1954) 85. T. E. Tietz and J. E. Dorn: AIME Trans. **206** (1956) 156.
4) J. Weertman: J. Appl. Phys. **26** (1955) 1213.
5) A. Franks and D. McLean: Phil. Mag. **1** (1956) 101.
6) J. W. Semmel and E. S. Machlin: Acta Met. **5** (1957) 582.
7) A. B. Kuper, D. Lazarus, J. R. Manning and C. T. Tomizuka: Phys. Rev. **104** (1956) 1536.
8) W. A. Goering and A. S. Nowick: AIME Trans. **208** (1958) 105.
9) J. Weertman and J. E. Breen: J. Appl. Phys. **27** (1956) 1189.
10) M. Herman and N. Brown: AIME Trans. **206** (1956) 604.
11) T. Suzuki: Sci. Rep. RITU **A1** (1949) 55.
12) S. Kaya: J. Fac. Sci. Hokkaido Univ. **2** (1938) 29.
13) E. N. da C. Andrade and B. Chalmers: Proc. Roy. Soc. **A, 138** (1932) 348.
14) W. D. Biggs and A. H. Cottrell: Phil. Mag. **45** (1954) 246.
15) G. W. Ardrey: Act. Met. **3** (1955) 525.
16) T. Suzuki, K. Sumino, M. Hirabayashi and M. Yamamoto: unpublished; see T. Suzuki, *Plastic Flow of Crystals* (Kaya et al, Solid State Physics **9**, Kyoritsu-sha, Tokyo, 1958) 311 (in Japanese).
17) A. Seeger, J. Diehl, S. Mader and H. Rebstock: Phil. Mag. **2** (1957) 323.
18) S. Iida: J. Phys. Soc. Japan **10** (1955) 9.
19) G. Schoeck and A. Seeger: Reports of a Conference on *Defects in Crystalline Solids*, Phys. Soc. London (1955) 340.
20) G. H. Vineyard: Phys. Rev. **102** (1956) 981.
21) A. H. Cottrell: *Relation of Properties to Microstructures*, ASM Monograph (1954) 131.
22) T. Suzuki: *Theory of Dislocation*, (Inst. Met. Japan 1951) (in Japanese).
23) E. W. Elcock and C. W. McCombie: Phys. Rev. **109** (1958) 605.
24) J. Friedel: Proc. Roy. Soc. **A, 242** (1957) 147.
25) T. Taoka and S. Sakata: Acta Met. **5** (1957) 61; T. Taoka and R. Honda: J. Electron Microscopy, Japan, **5** (1957) 19.

JOURNAL OF THE PHYSICAL SOCIETY OF JAPAN, Vol. 14, No. 4, APRIL, 1959

Effect of Electron Bombardment on Sodium Chloride

By Shigetomo YOSHIDA and Toshio IKEDA

Research Institute for Scientific Measurements, Tohoku University, Sendai

(Received November 28, 1958)

The absorption spectra ranging from 360 to 960 mμ were measured on rock salt crystals bombarded with electrons at various temperatures. Three types of color centers, namely F, 590 mμ and colloidal centers were formed as a function of specimen temperature during bombardment. The thermal bleaching of these three color centers was also investigated.

From these results it is supposed that the color center with an absorption peak at about 590 mμ may correspond to a precursor of colloidal sodium. It is also suggested that there may be a correlation between coloration and dissociation of sodium chloride by electron bombardment.

§ 1. Introduction

The effects of ionizing radiation on non-metals have been investigated mainly on silver and alkali halides irradiated with ultraviolet light and X-ray, respectively1)2). However, the effects of electron bombardment on these materials have scarcely been reported†. In this respect, following our previous works3) of the electron bombardment on alkali-earth oxides, we studied the effect of electron bombardment on rock salt. In alkali-earth oxides, it was found that the dissociation into constituent components occured under electron bombardment. In this paper we report the coloring of rock salt bombarded at various temperatures and the thermal bleaching of it*. We also considered the correlation between coloration and dissociation of sodium chloride by electron bombardment.

§ 2. Specimens and Experimental Procedure

All specimens used in this investigation were cleaved from rock salt crystal obtained from the Halle Company in Germany. After cleaving to the size of about 5×5×1 mm, platinum electrodes were applied to the both ends of the specimen by painting the aqueous platinum and baking it at about 750°C. After baking, the specimens were furnace-cooled to room temperature with a mean cooling rate of 4°C/min. This procedure was repeated three times for obtaining the well conductive electrodes.

The apparatus for electron bombardment is shown in Fig. 1. The electron gun was constructed with a hairpin tungsten filament F and a special Wehnelt electrode W4). On the interior wall of glass tube the colloidal graphite (Aquadag) was painted and used for the anode. The first anode A_1 was in contact with that wall. The specimen was supported by two thin copper plates L, which also served

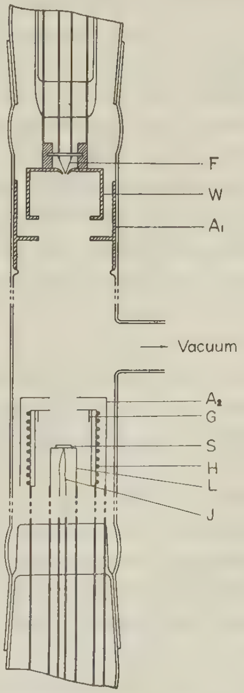

Fig. 1. Apparatus for electron bombardment. F: tungsten filament, W: Wehnelt electrode, A_1, A_2: first and second electrodes, G: secondary electron suppressor grid, S: specimen, H: heater, L: thin copper plate for lead and support, J: junction (Pt-PtRh).

---

* The preliminary results were already reported in the short note of this journal (J. Phys. Soc. Japan **12** (1957) 1422).

†

as the target leads, and placed in an electric furnace *H*. Between this furnace and glass wall the second anode A_2 was positioned and used as the thermal radiation shield. The Pt-PtRh junction *J* (0.08 mm ϕ) was attached to the opposite surface of the specimen. At the upper part of the specimen the grid *G* was placed and biased negatively so that the secondary electron from the specimen was suppressed. The sample, which was held at a distance of 35 cm from the filament, showed the blue fluorescent radiation under bombardment so that we could find the focusing condition of electron beam on the specimen. In order to obtain the fine adjustment of focusing we used a permanent magnet from the outside of the accelerating tube. In this arrangement, we could obtain the focal spot of about 0.1 cm² on the specimen at the bombarding voltage of 18 KV, the Wehnelt voltage of -60 V and the current density of about 40μA/cm².

The electron bombardment was carried out under the vacuum of $10^{-4} \sim 10^{-5}$ mm Hg. Before bombardment the sample was annealed in vacuo for 2 hours at about 450°C and then cooled slowly. The contamination of sample due to electron bombardment was produced especially at room temperature. Although the liquid air or dry ice trap was efficient for preventing the production of contamination, it was not possible to avoid it entirely. Under bombardment at higher temperature than about 200°C, the specimen was free from contamination.

The optical absorption spectra of the bombarded specimens were measured ranging from 360 mμ to 960 mμ by the photoelectric spectrophotometer (Hitachi EPU II).

§ 3. Experimental Results

(A) *Coloration at room temperature*

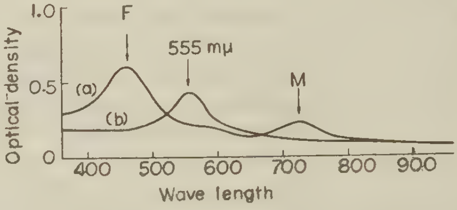

Fig. 2. Optical absorption curves for NaCl crystal bombarded with electrons at room temperature. Bombarding condition is $V=10$KV, $I=40\mu$A/cm² and $t=60$ minutes. (a) after bombardment (b) annealed at 200°C for 30 minutes.

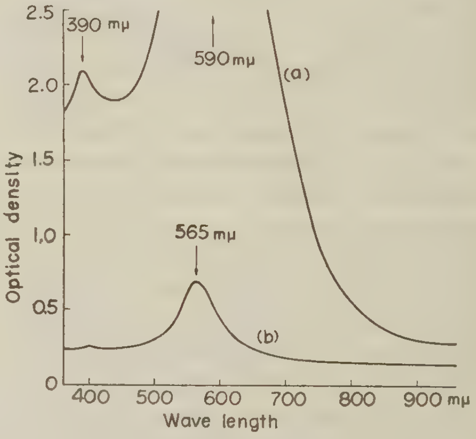

Fig. 3. Optical absorption curves for NaCl crystal bombarded with electrons at room temperature. Bombarding condition is $V=20$ KV, $I=40\mu$A/cm² and $t=60$ minutes. (a) after bombardment (b) annealed at 390°C for 60 minutes.

Initially electron bombardment was carried out at room temperature. The bombarding voltage employed ranged from 7 to 20 KV while the current density and bombarding time were fixed at 40μA/cm² and 60 minutes, respectively. The specimens were colored yellowish for the bombarding voltage below 13 KV. At the voltage higher than 16 KV, blue colored parts developed appreciably among yellowish ones. Under 20 KV bombardment the specimens acquired deep blue color. In these cases, the coloration was limited to the thin layers of bombarded surfaces. The absorption spectra of specimens bombarded at 10 KV and 20 KV are shown by the curve (a) of Figs. 2 and 3, respectively. The curve (a) in Fig. 2 shows distinct *F* and *M* bands familliar to sodium chloride. On the other hand the curve (a) in Fig. 3 shows the strong absorption band with a peak at about 590 mμ accompanied with the weak one at 390 mμ. The peak position of this strong absorption band was not constant and moved from 580 mμ to 600 mμ due to the difference of the bombarding condition. This absorption band was frequently observed in an asymmetrical form instead of the symmetrical bell shaped one. From these facts it is suggested that the blue coloration is due to the mixture of various degree of coloration centers which were probably generated owing to local non-uniformity of bombarding current on the specimen surface. For convenience we designated hereafter this absorption band as 590 mμ band. On the other hand, the peak position of 390 mμ band does not change appreciably.

Usually in the case of bombardment between 13 KV and 16 KV, the shape of absorption bands was not simple and it was difficult to obtain the reproducible results perhaps due to the coloration at the intermediate state between two conditions above mentioned. The absorption curve for the bombardment at 16 KV is shown in Fig. 4. As shown, it is characteristic of this absorption curve to spread over the wide wavelength range.

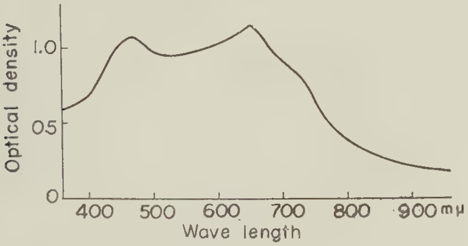

Fig. 4. Optical absorption curve for NaCl crystal bombarded with electrons at room temperature. Bombarding condition is $V=16$ KV, $I=40\mu A/cm^2$ and $t=60$ minutes.

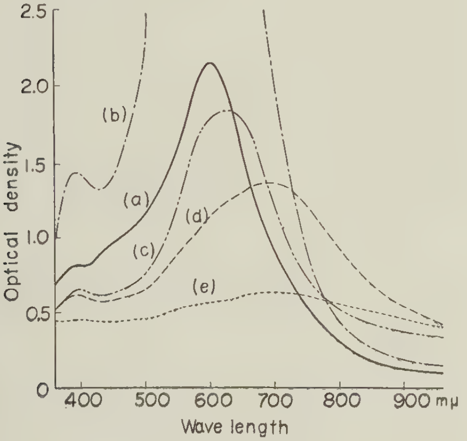

Fig. 5. Optical absorption curves for NaCl crystals bombarded with electrons at various temperatures. Bombarding condition is $V=18$ KV, $I=40\mu A/cm^2$ and $t=30$ minutes. The temperatures are as follows; (a) 15°C (b) 150°C (c) 234°C (d) 260°C (e) 283°C.

We also observed the coloration of specimens as a function of bombarding current. It was found that the blue coloration developed with increasing current density even at the low bombarding voltage. For example, the specimen bombarded at 10 KV and 40μA/cm^2 for 60 minutes displayed *F* and *M* bands as shown in the curve (a) of Fig. 2, but with the increase of current density to 140μA/cm^2 it acquired deep blue color corresponding to the strong absorption band at 590 mμ. From these results it is supposed that the blue coloration of sodium chloride bombarded with electrons is influenced greatly by the bombarding wattage. Although the rise of temperature was not noticed with the thermocouple attached to the back face of specimen, it may be considered that the increase in bombarding wattage is related to the rise of temperature on the bombarded surface.

(B) *Temperature dependence*

We next observed the coloration as a function of temperature. In these cases the bombarding condition was fixed as follows; voltage is 18 KV, current 40μA/cm^2 and time 30 minutes. The temperature during bombardment was changed from room temperature to about 400°C. In Fig. 5 the absorption spectra of the coloration at 15°C, 150°C, 234°C, 260°C and 283°C are shown. The peak position shifted towards longer wavelength and the shape of absorption bands became less sharp with increasing temperature. Above 300°C, the specimens did not show any coloration and became cloudy. In Fig. 6 microphotographs of these specimens are shown. It was seen that a number of cubic pits was formed on the bombarded surfaces and the size of these pits became larger with increasing temperature.

For the specimens showing the absorption peak at above 600 mμ which was produced under the bombardment at elevated temperature, we observed the scattering of dull red light from the bombarded surface. The dull red color corresponds to the complementary color of the pale blue one of the transmitted light. This behavior will be related to the scattering of light by colloidal particles. The weak absorption band with a peak at about 390 mμ was also found in this colloidal coloration but it seemed that the peak position shifted slightly towards the longer wavelength.

(C) *Effect of thermal bleaching*

The yellowish colored specimens which have *F* and *M* bands changed to reddish purple by heating them to 200°C in air. For example, the curve (b) in Fig. 2 is the absorption spectrum of the annealed specimen which changed thermally from curve (a). Heating to about 350°C, the specimen bleached out gradually without further alternation of coloration. In this process, the colloidal scattering from the colored part was not observed.

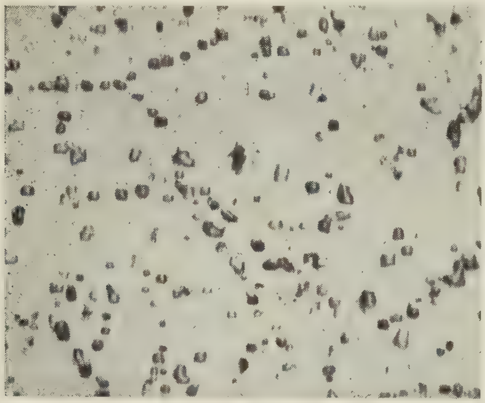

(a) Bombarded at 316°C.

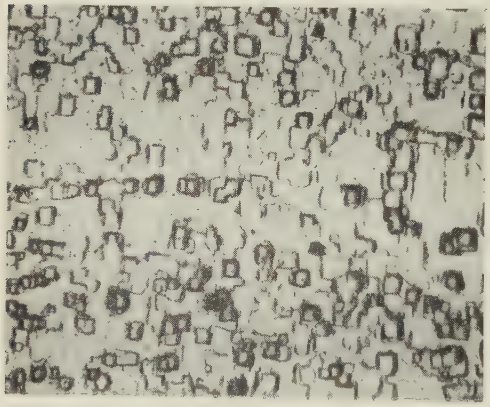

(b) Bombarded at 373°C.

Fig. 6. Microphotographs for NaCl crystals bombarded with electrons at high temperatures. Bombarding condition is $V=18$ KV, $I=40\mu\text{A/cm}^2$ and $t=30$ minutes. (×180)

Although the yellowish colored specimens showed the optical bleaching at room temperature, the blue colored specimens with 590 mμ band were very stable under the same condition. In Fig. 3, curve (b) shows the effect of thermal bleaching on blue colored specimen. As shown, the peak position shifted towards shorter wavelength by annealing and reached to 565 mμ after heating to 390°C. At the same time, the scattered light of green color, which is complementary one of reddish purple of the transmitted light, became to be observed. Consequently it was concluded that the blue coloration with 590 mμ band changed to the colloidal coloration with an absorption peak shifted towards shorter wavelength. On the other hand, the colloidal coloration which was produced under the bombardment at high temperature did not change by annealing, and bleached out entirely at about 450°C.

§ 4. Discussion

(A) *Colloidal coloration*

As previously mentioned, if the temperature during bombardment was high the scattered light from the colored surface of specimens was detected. Since the color of this scattered light was complementary to that of the transmitted light, it may be concluded that the origin of coloration was the scattering of light by the colloidal particles, that is, perhaps the metallic sodium particles. According to Savostianowa[5)] the peak position of the absorption band of natural blue rock salt shifts towards the longer wavelength with increasing diameter of colloidal particles. For example, the absorption peaks at 600 mμ and 650 mμ may be related to the scattering by the colloidal particles with diameter of 40 mμ and 70 mμ respectively. Consequently the results of Fig. 5 show that the colloidal particles with larger diameter would be produced with increasing temperature. It may be also concluded that the broad width of absorption band at high temperature will be related to the mixing state of the colloidal particles with various dimensions.

In additive coloration of potassium chloride, Scott and Smith[6)] observed that the colloidal coloration was produced by the coagulation of F centers during thermal treatment and the colloidal centers were in thermal equilibrium with F centers. However, our colloidal coloration which is produced by electron bombardment at high temperature is different in manner of thermal bleaching from the one which is produced by additive coloration. In our case the colloidal layer was formed immediately near the surface, so these excess sodium atoms may sublimate from the surface before they are converted into F centers.

(B) *Blue coloration*

The blue coloration which has the absorption peak at about 590 mμ was produced under the bombardment at intermediate temperature, *i.e.* at lower temperature than the one where the colloidal center is produced and at higher temperature than the one where the *F* center is produced. Therefore, the blue coloration may correspond to the transition state from the *F* coloration to the colloidal one. This color centers changed to the colloidal particles with the small diameter of about 10 mμ (according to Savostianowa⁵⁾) by heating. From these observations it is supposed that the center of blue coloration may correspond to the aggregate of excess sodium atoms, *i.e.* the precursor of colloidal sodium. As previously mentioned, it was considered that this coloration originated in the mixing state of the various coloration centers having the different absorption peaks. It may be considered that they may correspond to the difference of the degree of coagulation and have probably the same nature as the *R′* center observed by Scott and Bupp⁷⁾.

It is notable feature that the blue or colloidal coloration has always the weak absorption band at about 390 mμ. This band may correspond to the peak of the photoconducting current curve plotted against the wavelength in blue or violet rock salt containing colloidal sodium⁸⁾.

(C) *Bombardment effect*

It was known that three types of color centers above mentioned were respectively formed as a function of specimen temperature under bombardment. According to the results of electron bombardment on BaO, SrO and MgO⁹⁾, it was recognized that oxygen molecules evolved from those samples and excess metal atoms were produced near the surface. Taking these results into consideration it was supposed that the excess sodium atoms were obtained as a result of the evolution of chlorine atoms and aggregated into colloidal or 590 mμ centers according to the degree of coagulation. On the bombardment at elevated temperature only cubic pits were formed on the surface and no coloration was observed. This result may be explained by the sublimation of equal quantity of sodium and chlorine atoms.

In conclusion the authors wish to express their cordial thanks to Prof. T. Hibi for his stimulating discussions and to the Electrical Communication Laboratory of Nippon Telegraph and Telephone Corporation for the grant in aid.

References

1) J. W. Mitchell and N. F. Mott: Phil. Mag. **2** (1957) 1149.
2) F. Seitz: Rev. Mod. Phys. **26** (1954) 7.
3) S. Yoshida, N. Shibata, Y. Igarashi and H. Arata: J. Appl. Phys. **27** (1956) 497.
4) K. H. Steigerwald: Optik **5** (1949) 469.
5) M. Savostianowa: Z. Phys. **64** (1930) 262.
6) A. B. Scott and W. A. Smith: Phys. Rev. **83** (1951) 982.
7) A. B. Scott and L. P. Bupp: Phys. Rev. **79** (1950) 341.
8) Z. Gyulai: Z. Phys. **35** (1926) 411.
9) P. Wargo and W. G. Shepherd: Phys. Rev. **106** (1957) 694.

JOURNAL OF THE PHYSICAL SOCIETY OF JAPAN, Vol. 14, No. 4, APRIL, 1959

Configurational Coordinate Curves for Luminescence Center in $Ca_3(PO_4)_2$:Cu

By Keiji MAEDA

Matsuda Research Laboratory, Tokyo Shibaura Electric Co., Kawasaki, Japan

(Received December 5, 1958)

For $Ca_3(PO_4)_2$:Cu phosphor, measurements of spectral distributions of luminescence, reflectivity and quantum efficiency, temperature dependence of luminescence intensity and decay constants are carried out. The one-dimensional configurational coordinate curves for the luminescence center in this phosphor are determined by analysing spectral data. Some characteristics expected from these curves are compared with the observed; the agreement in the absorption band width and the disagreement in the activation energy for nonradiative transition are obtained. The relations between one- and many-dimensional models are investigated and the cause for the above disagreement is attributed to the simplicity of the assumed model. Discussions are also made on the nonradiative transitions in this center.

§ 1. Introduction

The configurational coordinate (hereafter abbreviated as C. C.) curves have been widely used to explain qualitatively some characteristics of the localized luminescence centers. Accompanying with the advance in our understanding, they have become to be discussed quantitatively[1)] and a review of the recent progress has been given by Klick and Schulman[2)].

The role of the C. C. diagram is quite important and it can be even said that the nature of luminescence center is thoroughly understood, if the C. C. diagram is completely determined for the center. There are two different ways of approach; one of these is by theoretical calculations and the other is by analysis of experimental results.

The first way is interesting in principle but very difficult in practice, because it requires to solve many electron systems accurately. Williams[3)] made detailed calculations for KCl: Tl and his results were in fair agreement with experiments. However, Knox and Dexter[4)] presented some critiques on his treatments suggesting that further improvements are necessary in calculations.

The second way is a very practical one, as it is to choose the C. C. curves so as to fit them with the measured characteristics. While this procedure becomes quite significant when we have other independent experimental values to be compared with those expected from the C. C. curves determined, because it is then possible to investigate the validity of the assumed model and the correlation among various characteristics. By this way, Klick and his colaborators derived the C. C. curves for the Mn-center in Zn_2SiO_4[5)] and the F-centers in several alkali halides[6)] and Hameka and Vlam[7)] derived those for the luminescence center in $CaWO_4$.

Following the second way we shall consider the C. C. diagram for the luminescence center in $Ca_3(PO_4)_2$:Cu phosphor, which has been extensively studied by Uehara and his colaborators[8)]. First we shall assume the one-dimensional model. Then we shall discuss the relations between the one- and many-dimensional models.

§ 2. C. C. Curves and Spectral Shape

As a large number of vibrational modes affect the energy of the luminescence center in solid, the C. C. space describing the center should be many-dimensional. To analyse experimental data, however, the many-dimensional treatment is too complex, so that we shall assume the simplified one-dimensional model, which is considered to represent the interaction of the center with the most important vibrational mode. Such a model has been adopted by all previous workers in their treatments of actual materials.[3),5)-7)]

In our simple model, the energies of the ground and excited states are represented by parabolic curves respectively. Accordingly, each state can be treated as a harmonic oscillator. Fig. 1 shows these C. C. curves. The vibrational frequencies are $\omega_g/2\pi$ in the ground state and $\omega_e/2\pi$ in the excited state respectively. The force constants are κ_g and κ_e for each of these two vibrations. The minimum point of the excited state curve is displaced by an amount U in the energy and by a distance x_0 in the coordinate from that of the ground state curve. The energy increase above the minimum at x_0 in the ground state is $X=\frac{1}{2}\kappa_g x_0^2$ and that at the origin of the coordinate in the excited state is $Y=\frac{1}{2}\kappa_e x_0^2$. These two curves intersect at the point, where the energy is W above the minimum of the excited state. Here W is the activation energy for the nonradiative de-excitation.

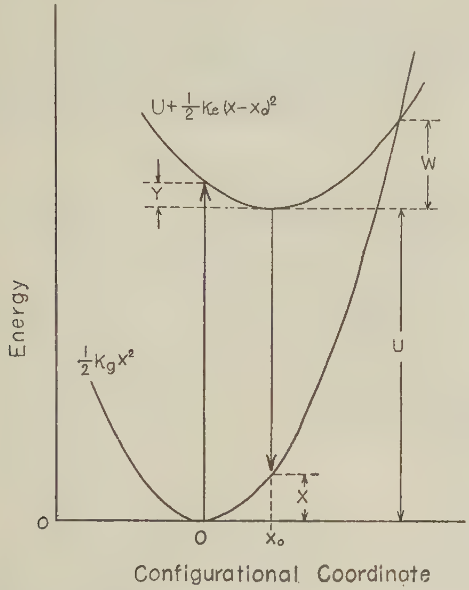

Fig. 1. One-dimensional configurational coordinate curves for a luminescence center. Arrows indicate optical transitions.

The energy difference between the m-th vibrational level in the ground state and the n-th vibrational level in the excited state is

$$E_{nm}=h\nu_{nm}=U+\hbar\omega_e(n+\tfrac{1}{2})-\hbar\omega_g(m+\tfrac{1}{2})\,. \quad (1)$$

When a transition occurs between these two levels, an absorption or emission of light is observed, the frequency of which is equal to ν_{nm} in Eq. (1). The absorption coefficient is proportional to $\nu_{nm}|M_{nm}|^2 w_m'$ and the luminescence intensity is proportional to $\nu_{nm}^4|M_{nm}|^2 w_n''$, where M_{nm} is the matrix element of dipole transition between these two levels and w_m' and w_n'' are the probabilities that the oscillator is in the m-th vibrational level in the ground state and that in the n-th vibrational level in the excited state respectively.

The wave function, from which the above matrix element is derived, may be decomposed into a product of electronic and nuclear wave functions. Here we assume the so-called Condon approximation; i.e., we neglect the dependence of electronic matrix element on nuclear positions. The observed absorption and emission bands consist of many line spectra with different combinations of m and n, overlapping one another. Considering all combinations of the vibrational levels, we obtain the distribution function for the absorption coefficient $\alpha(E)$ and that for the luminescence intensity $I(E)$;

$$\alpha(E)=\text{const}\times E\sum_n\sum_m\left|\int\psi_{en}^*(x)\psi_{gm}(x)\,dx\right|^2\exp\left\{-\left(m+\frac{1}{2}\right)\frac{\hbar\omega_g}{kT}\right\}\delta(E_{nm}-E)\,, \quad (2)$$

$$I(E)=\text{const}\times E^4\sum_n\sum_m\left|\int\psi_{gm}^*(x)\,\psi_{en}(x)\,dx\right|^2\exp\left\{-\left(n+\frac{1}{2}\right)\frac{\hbar\omega_e}{kT}\right\}\delta(E_{nm}-E)\,, \quad (3)$$

where ψ_{gm} and ψ_{en} are the vibrational wave functions of the m-th level in the ground state and that of the n-th level in the excited state respectively and x denotes the nuclear position.

In order to represent the shape of the normalized spectrum, $f(E)$, we shall use the semi-invariants. These are defined as the coefficients, λ_i, in the expansion

$$f(E)=\Phi_0(E)-\frac{\lambda_3}{6}\Phi_3(E)+\frac{\lambda_4}{24}\Phi_4(E)+\cdots\,, \quad (4)$$

where

$$\int f(E)\,dE=1\,,$$

$$\Phi_0(E)=\frac{1}{\sqrt{2\pi\lambda_2}}\exp\left\{-\frac{(E-\lambda_1)^2}{2\lambda_2}\right\},$$

$$\Phi_m(E)=\frac{d^m}{dE^m}\Phi_0(E).$$

By an ingenious method, Kubo and Toyozawa[9] derived the semi-invariants of the absorption band neglecting the E-dependency in Eq. (2). These are slightly modified when the E-dependency is taken into account. Making use of the relations among the semi-invariants and the moments, we have

$$\left.\begin{aligned}
\lambda_{1a}&=U+Y+\left\{\frac{1}{4}(\gamma^2-1)+\frac{\gamma^2 Y}{(U+Y)}\right\}\hbar\omega_g\coth\left(\frac{\hbar\omega_g}{2kT}\right)+\mathrm{O}\left\{\frac{(\hbar\omega_g)^2}{U}\right\},\\
\lambda_{2a}&=\gamma^2 Y\hbar\omega_g\coth\left(\frac{\hbar\omega_g}{2kT}\right)+\left\{\frac{1}{8}(\gamma^2-1)^2-\frac{\gamma^4 Y^2}{(U+Y)^2}+\frac{3}{2}(\gamma^2-1)\frac{\gamma^2 Y}{U+Y}\right\}\\
&\qquad\times(\hbar\omega_g)^2\coth^2\left(\frac{\hbar\omega_g}{2kT}\right)+\frac{\gamma^2 Y}{U+Y}(\hbar\omega_g)^2+\mathrm{O}\left\{\frac{(\hbar\omega_g)^3}{U}\right\},\\
\lambda_{3a}&=\gamma^2 Y(\hbar\omega_g)^2\left\{1+\frac{3}{2}(\gamma^2-1)\coth^2\left(\frac{\hbar\omega_g}{2kT}\right)\right\}+\mathrm{O}\{(\hbar\omega_g)^3\},
\end{aligned}\right\}\tag{5}$$

where

$$\gamma=\frac{\omega_e}{\omega_g}=\sqrt{\frac{\kappa_e}{\kappa_g}}.$$

In a similar way, the semi-invariants of the intensity distribution of luminescence given by Eq. (3) are calculated:

$$\left.\begin{aligned}
\lambda_{1f}&=U-X+\left\{\frac{4}{\gamma^2}\frac{X}{(U-X)}-\frac{1}{4}\left(\frac{1}{\gamma^2}-1\right)\right\}\hbar\omega_e\coth\left(\frac{\hbar\omega_e}{2kT}\right)+\mathrm{O}\left\{\frac{(\hbar\omega_e)^2}{U}\right\},\\
\lambda_{2f}&=\frac{X}{\gamma^2}\hbar\omega_e\coth\left(\frac{\hbar\omega_e}{2kT}\right)+\left\{\frac{1}{8}\left(\frac{1}{\gamma^2}-1\right)^2-\frac{6}{\gamma^2}\left(\frac{1}{\gamma^2}-1\right)\frac{X}{U-X}-\frac{4}{\gamma^4}\frac{X^2}{(U-X)^2}\right\}\\
&\qquad\times(\hbar\omega_e)^2\coth^2\left(\frac{\hbar\omega_e}{2kT}\right)-\frac{4}{\gamma^2}\frac{X}{(U-X)}(\hbar\omega_e)^2+\mathrm{O}\left\{\frac{(\hbar\omega_e)^3}{U}\right\},\\
\lambda_{3f}&=-\frac{X}{\gamma^2}(\hbar\omega_e)^2\left\{1+\frac{3}{2}\left(\frac{1}{\gamma^2}-1\right)\coth^2\left(\frac{\hbar\omega_e}{2kT}\right)\right\}+\mathrm{O}\{(\hbar\omega_e)^3\}.
\end{aligned}\right\}\tag{6}$$

The inclusion of the E- or E^4-dependency produces alterations of the second order terms in these expressions. Therefore, we may neglect these dependencies in a discussion of first order quantities of spectral shape when high accuracy is not required. But we must include them in a discussion of second order small quantities, e.g. the temperature dependence of the peak position. It should be noted that Eqs. (5) and (6) do not contain the mass of the harmonic oscillator. Accordingly, an ambiguous assumption about it is unnecessary in our later analysis of experimental results.

§ 3. Experimental Results

(1) *Sample preparation*

The sample is β-$Ca_3(PO_4)_2$:Cu powder phosphor which was fired at about 1100°C for 30 minutes in air and further 30 minutes in a reducing atmosphere (N_2+H_2)[8]. The activator concentration is 5×10^{-3} atoms of copper for three calcium atoms.

(2) *Luminescence spectrum*

Under excitation with 2537Å radiation this phosphor emits bright blue luminescence. The luminescence spectrum was measured at various temperatures. As an example the result taken at 284°K is shown in Fig. 2. The spectrum is nearly Gaussian in shape over all the temperature range, so that it is a single-component band.

The spectral width becomes broad with increasing temperature. In Fig. 3 the squared half-width is plotted against absolute temperature. According to Eq. (6), the squared width is proportional to $\hbar\omega_e \coth(\hbar\omega_e/2kT)$ in a first approximation. We can thus determine the vibrational frequency in the excited state by choosing it so as to fit the calculated temperature dependence with the observed. The curve in Fig. 3 is proportional to

$$\hbar\omega_e \coth(\hbar\omega_e/2kT)$$

with the frequency chosen, $6\times10^{12}\,\text{sec}^{-1}$, and the dotted line is its asymptote.

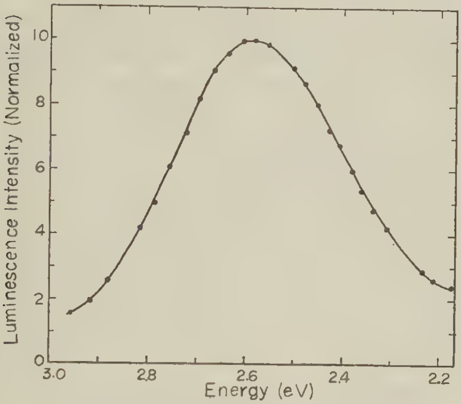

Fig. 2. Luminescence spectrum of $Ca_3(PO_4)_2$: Cu under 2537 A excitation at 284°K.

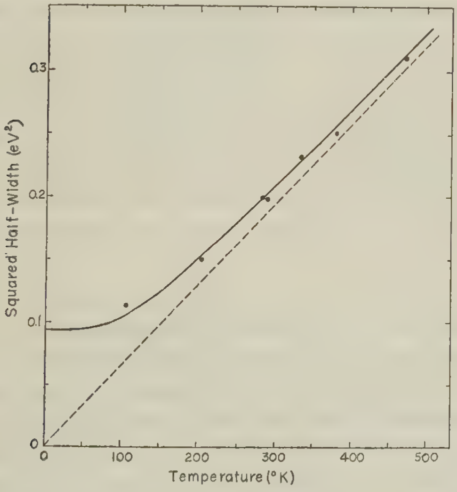

Fig. 3. Variation of the squared half-width of luminescence spectrum with temperature. Solid curve is calculated with the frequency 6×10^{12} sec^{-1} and dotted line is its asymptote.

The peak position of the luminescence band shifts to shorter wavelengths with increasing temperature and its variation is shown in Fig. 4 as a function of temperature.

The spectral shape is not strictly symmetric and in Fig. 5 the asymmetry defined by

$$S=\frac{h\nu_0-\frac{1}{2}(h\nu_++h\nu_-)}{h\nu_+-h\nu_-}\,, \tag{7}$$

is plotted against temperature, where $h\nu_0$ is the energy of the peak position and $h\nu_+$ and $h\nu_-$ are the energies of the half-maximum positions on the high- and low-energy side respectively.

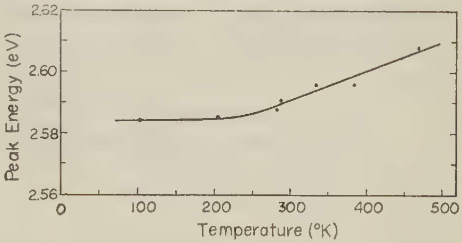

Fig. 4. Variation of the peak of luminescence spectrum with temperature.

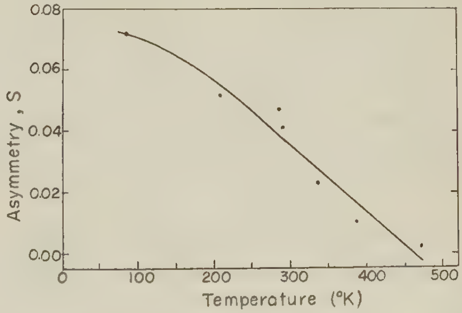

Fig. 5. Variation of the asymmetry of luminescence spectrum with temperature. The asymmetry S is defined by Eq. (7).

(3) *Spectral distributions of reflectivity and quantum efficiency*

The spectral distributions of the diffuse reflectivity and the quantum efficiency were measured for the phosphor and the pure host crystal by the apparatus made by Uehara and Masuda[10] in the writer's laboratory.* The results are shown in Fig. 6.

The quantum efficiency of luminescence is defined by the number of luminescence photons emitted per a photon absorbed by the center. The ratio of the energy absorbed by the luminescence center to that of the incident light is taken equal to the difference in the value of reflectivity between the phosphor and the host crystal without impurity. We make a correction, considering that the emission intensity measured on a thick layer of powder phosphor is $(1+R_l)/2$ of the total, where R_l is the diffuse reflectivity of the phosphor in the spectral region of the luminescence.**

---

* The method of measurement is as follows.[10] A layer of the powder sample of sufficient thickness, which do not transmit light through it, is placed before an exit slit of a monochrometer. The intensity ratios of the reflected light and the luminescent light to the incident light are measured separately by means of a combination of a filter and a photomultiplier, of which the spectral sensitivity is calibrated previously.

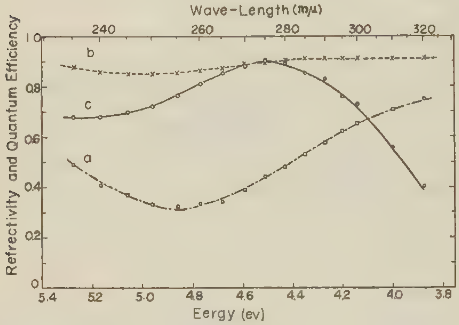

Fig. 6. Spectral distributions of (a) reflectivity of phosphor, (b) reflectivity of pure host crystal and (c) quantum efficiency of luminescence.

In Fig. 6 there is no characteristic absorption in the pure crystal and the reflectivity spectrum of the phosphor is symmetric in shape. On the contrary, the spectral distribution of the quantum efficiency is asymmetric, rapidly decreasing from the peak value on the low-energy side and slowly on the high-energy side. It should be noted that the peak position of the quantum efficiency curve is displaced by 0.35 eV to lower energy from the minimum position of the reflectivity curve.

(4) *Temperature dependence of luminescence intensity*

The temperature dependence of the luminescence intensity under 2537Å excitation is shown in Fig. 7. The luminescence intensity is nearly constant up to about 550°K and rapidly decreases above this temperature.

The probability of the nonradiative transition is given by $B\exp(-W/kT)$ and that of the radiative transition, A, is independent of temperature. Accordingly, the variation of the luminescence intensity with temperature is represented by

$$I=\frac{CA}{A+B\exp(-W/kT)}\,, \tag{8}$$

where C is a constant. For the best fit of Eq. (8) with the observed temperature dependence following values are chosen;

$$W=0.82\,\text{eV} \quad \text{and} \quad B/A=7.6\times10^5\,.$$

The calculated curve is shown in Fig. 7; here it is assumed that the gradual decrease observed in the lower temperature region superposes on the thermal quenching given by Eq. (8).

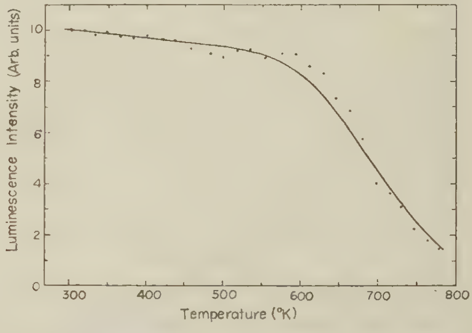

Fig. 7. Temperature dependence of luminescence intensity under 2537 A excitation. Solid curve is calculated to fit the experimental points.

(5) *Decay constant of luminescence*

The decay constants of luminescence were measured under the cathode ray pulse excitation. There are two exponentially decaying components; the fast component, being about a half of the total in intensity, has the time constant of 0.13 μsec and the slow component has the time constant of 1.5 μsec. From these results we can conclude that the radiative transition is the allowed and there is a trapping state from which a transition is easily made to the radiative state.

§ 4. Determination of C. C. Curves and Comparison with Experiments

From the conditions of preparation of the sample, we consider that the luminescence center is probably Cu^+ substituted for Ca^{++} in the lattice. The ground state of Cu^+ is

---

** As the phosphor particles emit light uniformly in all directions, a half of the emitted light appears directly from the surface of the phosphor layer but another half emitted backwards is reflected by the inner layers of the phosphor particles and then appears. Therefore, the observed luminescence intensity on the thick layer of phosphor is $(1+R_l)/2$ times of the total.

${}^1S_0(3d^{10})$ and the excited state is assumed to be ${}^3P_1(3d^94p)$.[8] The transition between these states is forbidden in the pure state by the spin selection rule but is allowed in the crystal due to the spin-orbit interaction.

We shall determine the C. C. curves for the luminescence center by analysing the experimental data on spectral shape. The values of U, X, Y and γ are calculated by Eqs. (5) and (6) using the following experimental values at 286°K;

position of maximum absorptance
4.85 eV,

position of maximum luminescence intensity
2.59 eV,

half-maximum width of luminescence spectrum 0.44_4 eV,

vibrational frequency in the excited state
$6\times10^{12}\,\mathrm{sec}^{-1}$.

The results are

$$U=3.49\,\mathrm{eV},\quad X=0.96\,\mathrm{eV},\quad Y=1.34\,\mathrm{eV}\quad \text{and}\quad \gamma^2=1.40.$$

Here, γ is surprisingly large. The energy diagram thus determined is shown in Fig. 8. Because the crystal structure of β-$Ca_3(PO_4)_2$ is unknown, the vibrational modes around the center are uncertain; even if the atomic configuration around the center is known, it is not unambiguous in detail what nuclear displacements are meant by the one-dimensional configurational coordinate. Accordingly, the values of x_0, κ_g and κ_e are not obtainable separately from X and Y.

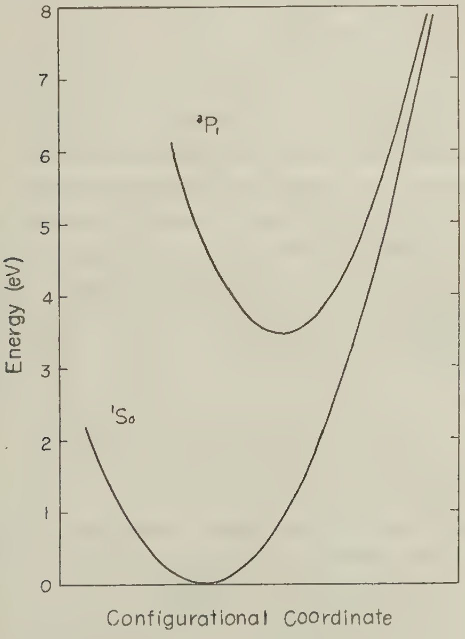

Fig. 8. One-dimensional configurational coordinate curves for the luminescence center, Cu^+, in $Ca_3(PO_4)_2$.

We shall compare the observed characteristics with those calculated from our C. C. curves by the help of Eqs. (5) and (6). In Section 3 we have made measurements of the diffuse reflectivity, since the sample is available only as powder. In order to obtain the shape of the absorption band, the following relation between the reflectivity, R, and the absorption coefficient, α, is used;

$$\alpha=\text{const}\times\frac{(1-R)^2}{R}.$$

This equation is derived by a crude approximation of a theory on the absorption and scattering and has been proved to hold within a wavelength range where the scattering is constant[11]. The spectral distribution of the relative absorption coefficient due to the luminescence center is calculated and is shown in Fig. 9.* The half-width of the absorption

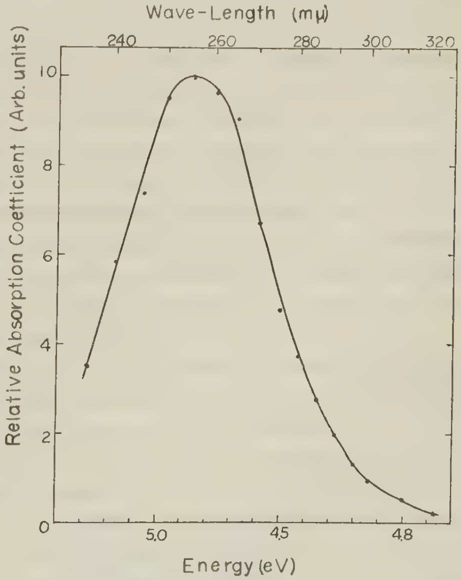

Fig. 9. Spectral distribution of relative absorption coefficient due to luminescence centers.

---

* The relative absorption coefficient shown is the difference between the calculated value from the reflectivity at the specified wavelength and that from the wavelength-independent reflectivity at longer wavelengths of the phosphor.

band is 0.71 eV in this figure whereas the expected value is 0.75 eV at room temperature. Thus the agreement is good.

Because the two curves do not intersect in Fig. 8, the activation energy for the nonradiative transition is expected to be infinitely large. On the other hand, the activation energy of 0.82 eV is obtained by analysing the temperature dependence of the luminescence intensity shown in Fig. 7. The variation of the peak of the luminescence band with temperature is 9×10^{-5} eV/deg by measurements and 1.7×10^{-4} eV/deg by the high temperature approximation of λ_{1f} in Eq. (6). The signs of variations with temperature are the same but the calculated value is about twice the observed. For the asymmetry of the luminescence spectrum, we expect the shape with slower decrease in the high-energy side than in the low-energy side at low temperatures and the opposite one at high temperatures. The experimental results in Fig. 5, however, show the asymmetry of the opposite direction at low temperatures, which diminishes as the temperature rises. The above disagreements are quite large.

§ 5. One-and Many-Dimensional Models

We shall consider possible reasons for the above discrepancies between the observed and calculated characteristics, especially, in the activation energy. (a) As there are several excited states in Cu^+ with comparable energy to $^3P_1$,[12] the nonradiative transition which contributes to the observed thermal quenching of luminescence may find an alternative way through another state from the excited to the ground state. However, we shall disregard here such a possibility because other disagreements than the activation energy are left unsettled. (b) Actually the potential energy would not be represented by a parabola up to a position where the nuclear displacement from the equilibrium position is large. The presence of anharmonic terms in the potential energy is suggested by the disagreement between the calculated and the observed asymmetry. By a qualitative calculation, however, it becomes clear that the anharmonic terms in the potential of the ground state, which lower the activation energy in the C. C. diagram, have an effect to increase the disagreement in asymmetry. (c) The assumption that the electronic matrix elements are independent of the nuclear positions may introduce an error. However, according to Dexter[13], the correction for this assumption introduces only a smaller change in the transition probability than the E^4-dependency which is proved in Section 2 to have no influence on the spectral shape to a first order approximation.

Fundamentally it is doubtful whether or not the many-dimensional C. C. shape can be replaced by the one-dimensional space for the sake of simplicity. The relations between one- and many-dimensional models will be investigated in the following. We assume that in the N-dimensional model, the energies of the ground and excited states are described by quadratic forms of the configurational coordinates with different origin, principal axis directions and curvatures respectively. The semi-invariants of the absorption band due to the optical transition between these two states are given by Kubo and Toyozawa[9] to a first approximation;

$$\left.\begin{aligned} \Lambda_{1a} &= \mathcal{E}_0 + \frac{1}{2}\Delta\Omega''^2\Delta\,, \\ \Lambda_{2a} &= \frac{\hbar}{2}\Delta\Omega''^2\Omega'^{-1}\coth\left(\frac{\hbar\Omega'}{2kT}\right)\Omega''^2\Delta\,. \end{aligned}\right\} \qquad (9)$$

In a similar way, the semi-invariants of the luminescence specrtum are also calculated;

$$\left.\begin{aligned} \Lambda_{1f} &= \mathcal{E}_0 - \frac{1}{2}\Delta\Omega'^2\Delta\,, \\ \Lambda_{2f} &= \frac{\hbar}{2}\Delta\Omega'^2\Omega''^{-1}\coth\left(\frac{\hbar\Omega''}{2kT}\right)\Omega'^2\Delta\,. \end{aligned}\right\} \qquad (10)$$

Here $\mathcal{E}_0$ is the energy separation between the minimum positions of the two electronic states, Δ is the N-dimensional vector denoting the the distance between these minimum positions and Ω'^2 and Ω''^2 are the N-dimensional tensors denoting the potentials of the ground and the excited state respectively. Since units are chosen here so as to the mass of the oscillators is unity, each element in Ω' and Ω'' is the vibrational frequency when these tensors are transformed into diagonal form.

If all the vibrational frequencies in the ground state and all those in the excited state are the same in their groups respectively while the former and the latter frequency are not necessarily equal, i.e. $\Omega'=\omega' I$ and $\Omega''=\omega'' I$, Eqs. (9) and (10) may be simplified to coincide with the first order terms in the corresponding Eqs. (5) and (6) of the one-dimensional model,* where we set Δ^2 equal to x_0^2. The same activation energy is also obtained in both models. Consequently the one-dimensional model in this special case represents the nature of the luminescence center correctly.

Although various vibrational frequencies would actually be involved, the experimental results on the temperature dependence of spectral width can usually be represented by assuming a single frequency. This is one of the reasons why the one-dimensional treatment has been used by many workers. However, the temperature dependence of the squared spectral width in the many-dimensional model as a sum of several hyperbolic cotangent terms of different vibrational frequencies can be approximated by a single hyperbolic cotangent term of suitably chosen frequency. We would not be able to discern experimentally the vibrational frequency spread within a range of several times in magnitude by measurements of the spectral width over the usual range of temperature. Consequently, the experimental results themselves cannot be the evidence supporting the one-dimensional treatment.

In the one-dimensional C. C. analysis, the vibrational frequency is determined by the ratio of the spectral width at 0°K to the rate of broadening at high temperatures. Thus the vibrational frequency in the ground state obtained from the analysis of the absorption band width is approximately equal to the following average of the actual frequencies; we have from Eqs. (5) and (9)

$$\omega_g=\frac{2k}{\hbar}\,\frac{A_{2a}(0^\circ\mathrm{K})}{(dA_{2a}/dT)_{T=\infty}}=\frac{\Delta\Omega''^2\Omega'^{-1}\Omega''^2\Delta}{\Delta\Omega''^2\Omega'^{-2}\Omega''^2\Delta}\,. \tag{11}$$

In the same way, the vibrational frequency in the excited state obtained from the analysis of the luminescence band width is approximately

$$\omega_e=\frac{2k}{\hbar}\,\frac{A_{2f}(0^\circ\mathrm{K})}{(dA_{2f}/dT)_{T=\infty}}=\frac{\Delta\Omega'^2\Omega''^{-1}\Omega'^2\Delta}{\Delta\Omega'^2\Omega''^{-2}\Omega'^2\Delta} \tag{12}$$

from Eqs. (6) and (10). Equating the expressions of the spectral width at 0°K in the two models to each other, the following relations among various quantities are obtained. We have for the absorption band width

$$x_0^2\frac{\omega_e^4}{\omega_g^2}=\Delta\Omega''^2\Omega'^{-2}\Omega''^2\Delta \tag{13}$$

from Eqs. (5), (9) and (11) and for the luminescence band width

$$x_0^2\frac{\omega_g^4}{\omega_e^2}=\Delta\Omega'^2\Omega''^{-2}\Omega'^2\Delta \tag{14}$$

from Eqs. (6), (10) and (12). It is clear from these equations that the value of each quantity in the one-dimensional model does not generally have any direct significance to the actual situation of the luminescence center.

The many-dimensional C. C. surfaces cannot be determined since the number of unknown parameters is larger than that of the experimental data even in the two-dimensional treatment. As an example indicating the validity of the one-dimensional treatment, the following procedures are adopted. Two-dimensional C. C. surfaces are arbitrarily assumed, from which similar characteristics result to those of the luminescence center in $Ca_3(PO_4)_2$:Cu. Then, by the help of Eqs. (5), (6), (9), (10), (12) and (14), the corresponding one-dimensional C. C. curves are determined, which give the same characteristics as those of the above two-dimensional C. C. diagram, i.e., the peak positions of the absorption and luminescence bands, the luminescence band width and its temperature dependence. Comparing other characteristics, which are not used in the determination of the one-dimensional diagram, we see that the absorption band width does not differ greatly in these two models but the activation energy for the nonradiative transition in the one-dimensional model is several times larger than that in the two-dimensional model.

Therefore it depends on the particularity of a center whether or not a one-dimensional model represents the nature of the luminescence center consistently. Even if it does, the configurational coordinate involved is the fictitious one. We must be rather satisfied with it when a spectral characteristic, e.g. the width of the absorption band in our case of $Ca_3(PO_4)_2$:Cu, is predicted reasonably. However, the activation energy for the nonradiative transition, which is the height of the lowest intersection point of two paraboloidal surfaces with different origins, principal axis directions and curvatures, cannot be generally predicted by the one-dimensional model. Further, the actual situation is more complex, when the anharmonicity of the potentials and the resonance between these two states in the vicinity of the intersection point are important.

---

* In the following discussions we shall be concerned with the first order terms alone in Eqs. (5) and (6).

§ 6. Nonradiative Transitions

We have obtained the ratio of the frequency factor in the nonradiative transition probability to the radiative transition probability by the analysis of the temperature dependence of the luminescence intensity. The latter is also determined in Section 3 by the measurement of the decay constant of luminescence. From these results the former is calculated to be $5.8 \times 10^{12}\,\mathrm{sec}^{-1}$. The frequency factor is generally considered to be the same order of or smaller than the vibrational frequency depending on the situations of the two electronic states near the lowest point where they intersect in the C. C. space. It is noteworthy that the frequency factor determined above is approximately equal to the vibrational frequency in the excited state ($6 \times 10^{12}\,\mathrm{sec}^{-1}$) obtained by the one-dimensional analysis of the thermal broadening of the luminescence spectrum.

The displacement of the peak of the quantum efficiency spectrum to the low-energy side by an amount of 0.35 eV from that of the absorption band and the asymmetry of the former curve in contrast to the latter as shown in Fig. 6 are considered due to the nonradiative transition mechanism proposed by Dexter et al.[10),14)] The position, to which the optical transition occurs from the ground state, is 1.34 eV above the minimum of the excited state in Fig. 8 and the height of the potential barrier for the nonradiative transition is experimentally 0.82 eV. Therefore, the former is probably higher than the latter in the many-dimensional C. C. diagram, when corrections are made to the one-dimensional value as discussed in the preceding section. In the way to the new equilibrium in the excited state after the absorption of light, the luminescence center may find itself in the vicinity of the intersection of these two electronic states. They considered that nonradiative return to the ground state occurs at this instant with so large probability that the luminescence efficiency becomes very low. In our measurements, however, the quantum efficiency at the peak of the absorption band is slightly smaller than the maximum value. Accordingly, if our interpretation is correct, their process does not seem to occur so frequently as they thought.

Acknowledgement

The author expresses his sincere thanks to Dr. Y. Uehara for his encouragements and informations indispensable to this research and to Prof. Y. Uemura of Tokyo University for his helpful discussions. The sample was prepared by Mr. Y. Kobuke and the temperature dependence of the luminescence intensity was measured by Mr. I. Masuda. The author is also grateful for their kindness.

References

1) For example, M. Lax: *Photoconductivity Conference* (John Wiley and Sons, New York, 1954) 111.
2) C. C. Klick and J. H. Schulman: *Solid State Physics*, vol. 5 (Academic Press, New York, 1957) 97.
3) F. E. Williams: J. Chem. Phys. **19** (1951) 457.
4) R. S. Knox and D. L. Dexter: Phys. Rev. **104** (1956) 1245.
5) C. C. Klick and J. H. Schulman: J. Opt. Soc. Amer. **42** (1952) 910.
6) G. A. Russel and C. C. Klick: Phys. Rev. **101** (1956) 1473.
7) H. F. Hameka and C. C. Vlam: Physica **19** (1953) 943.
8) Y. Uehara, I. Masuda and Y. Kobuke: J. Electrochem. Soc. **106** (1959) 200.
Y. Uehara: to be published in J. Electrochem. Soc.
9) R. Kubo and Y. Toyozawa: Progr. Theor. Phys. **13** (1955) 160.
10) Y. Uehara and I. Masuda: to be published.
11) F. Urbach, H. Hemmendinger and D. Pearlman: *Solid Luminescent Materials* (John Wiley and Sons, New York, 1948) 278.
12) C. E. Moore: *Atomic Energy Levels II* (Nat. Bur. Stand., Washington, 1952) 115.
13) D. L. Dexter: Phys. Rev. **96** (1954) 615.
14) D. L. Dexter, C. C. Klick and G. A. Russell: Phys. Rev. **100** (1955) 603.

JOURNAL OF THE PHYSICAL SOCIETY OF JAPAN, Vol. 14, No. 4, APRIL, 1959

Electron Diffraction Study on Polish Layers of Gold, II*

By Masao KURIYAMA**

Institute of Physics, College of General Education, University of Tokyo,
Komaba, Meguro-ku, Tokyo

(Received July 5, 1958)

Polish layer of gold was examined by means of the transmission method of electron diffraction. The diffraction pattern from the highly polished layer of gold (the Beilby layer) consists of three haloes, as reported in the previous paper (J. Phys. Soc. Japan **12** (1957) 151). The radial distribution function of atoms in the layer was calculated by Fourier transformation of the observed intensity. The observed intensity was compared with those calculated from appropriate models of atomic arrangement. It was found that the Beilby layer has an amorphous arrangement in which the first and the second coordination number are about 10 and 8, respectively.

§ 1. Introduction

In the previous paper,[1)]*** we reported the structure of polish layer of gold studied by the transmission method of electron diffraction. We found at advanced stages of polishing that the breadth of the Debye rings depends upon scattering angle. We concluded that the broadening is caused by both the small grain size and the inhomogeneous strain.

Two models have been proposed for the atomic arrangement in the Beilby layer.[2)] One is that the layer is composed of minute crystallites containing probably several unit cells, and another is that the layer is in the amorphous state. Raether and his collaborator[3)] supported the former and reported that the crystallites are not distorted. According to our result mentioned above, there is a considerable amount of strain in the polish layer even at the medium stage of polishing. We can suppose, therefore, that the crystallites in the Beilby layer which is obtained at more advanced stages of polishing are severely distorted. In this paper, we shall discuss the structure of the Beilby layer in detail.

The diffraction pattern from the Beilby layer obtained by the transmission method consists of three haloes: outer two have been observed by various authors[2)] and the first inner halo with the Bragg spacing 4.1Å have first been reported by Nonaka and Kohra.[4)] The Bragg spacing of the inner halo is nearly equal to (100) spacing of crystalline gold. So this inner halo may be explained by the non-vanishing structure factor violating the extinction rule for (100) reflection because of small grain size. Raether[5)] showed how subsidiary maxima of Laue's diffraction function became prominent when crystal size became very small. Boersch[6)] calculated the intensity for parallelepiped crystallites with the face centered cubic arrangement including 14 and 23 atoms. We also calculated the intensity for an octahedral crystallite, which was composed of a central atom surrounded by twelve nearest neighbours and six next nearest neighbours of the f.c.c. arrangement. However, the intensities of the first inner halo for these three models were too small to explain the observed intensity. Accordingly, the direct determination of the structure is desirable. We adopted in the present experiment the the radial distribution analysis.

Contaminations cannot be entirely eliminated even if the transmission method is adopted. Cochrane[7)] observed in his transmission pattern a sharp faint ring with the Bragg spacing 3.1Å and attributed it to some foreign substance on the film. Our first halo is neither sharp nor faint but diffuse and strong as much as the outer two haloes. The effect of contamination is, however, carefully studied in the present experiment and it is confirmed that the first inner halo is caused by polished gold, as will be described in § 5.

---

* The main parts of this article were read at the annual meeting of the Physical Society of Japan, Sendai, July 1956.

** Present address: Department of Physics, Faculty of Science, Tokyo Metropolitan University, Fukazawa, Setagaya-ku, Tokyo.

*** Reference 1) will be referred to as (I) hereafter.

§ 2. Experimental

The experimental procedures of preparing thin polished films of gold and obtaining the electron diffraction pattern were described in (I)***. Gold films electro-plated on copper or zinc were polished by chamois leather. The polished face was washed in benzene and then examined by the reflection method. After confirming the halo pattern, the polished film was removed from the substrate, rinsed in distilled water and then examined by the transmission method of electron diffraction. About ten specimens thus prepared produced the halo pattern characteristic of the Beilby layer. For three of the specimens prepared on Cu substrates, the intensity distribution of the pattern was measured in the following manner.

Five diffraction photographs were taken successively from each specimen with different exposures, and photographic density was measured by micro-photometry. For each pair or successive photographs, the density on a plate was plotted against the density at the corresponding position of another. The curve thus obtained was linear in the range of low density. With the repetition of this procedure for successive pairs, density on each plate was expressed in terms of the density on the plate with the shortest exposure time. The latter density is proportional to the intensity at any point except in the vicinity of the incident spot.[8]

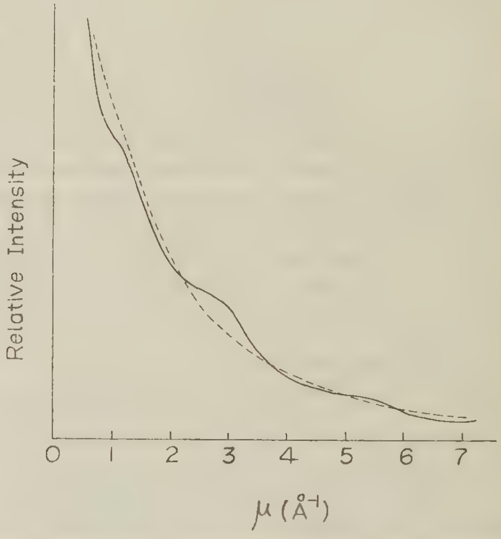

Fig. 1. Intensity distribution curve (solid curve) and background scattering curve (broken curve).

The average intensity distribution determined from three independent series of such photographs is shown in Fig. 1. The Bragg spacings corresponding to each halo are listed in Table I of (I).

Table I. The distances between neighbours and the numbers of coordination.

Number of spherical shell	Crystalline		Present results	
	Distances (Å)	Number of coordination	Distances (Å)	Number of coordination
1st	2.88	12	2.9	10
2nd	4.07	6	4.0	8
3rd	4.99	24	(5.0)*	(24)*

* Estimated values.

§ 3. Radial Distribution Function

The radial distribution function $4\pi r^2\rho(r)$ is obtained by the following formulae:

$$4\pi r^2\rho(r)=4\pi r^2\rho_0+\frac{2r}{\pi}\int_0^\infty \mu i(\mu)\sin\mu r d\mu\ , \quad (1)$$

$$\mu=4\pi\sin\frac{\phi}{2}\Big/\lambda\ ,$$

$$i(\mu)=I_{ia}/NE^2(\mu)$$

$$E(\mu)=\frac{8\pi^2me^2}{h^2}\ \frac{Z-F(\mu)}{\mu^2} \quad (2)$$

Here ρ_0 is the mean density of atoms; ϕ, the scattering angle; λ, the wave length of electrons; I_{ia}, the *interatomic* scattering given below; N, the number of atoms; Z, the atomic number and $F(\mu)$, the atomic scattering factor for X-rays. The observed intensity consists of the interatomic scattering and the background scattering,

$$I_{obs}=CI_{ia}+I_{bac}\,, \tag{3}$$

where C is a constant factor to be determined later, and I_{bac} is given by

$$I_{bac}=CNE^2(\mu)+x(\mu)+y(\mu)\,. \tag{4}$$

Here NE^2 is the atomic scattering: $x(\mu)$, the atomic inelastic scattering; $y(\mu)$, the multiple and instrumental scattering.

In the study of gas molecules[8], we can replace NE^2 in the denominator in (2) by I_{bac}, because $y(\mu)$ is negligible and $x(\mu)$ is almost similar to NE^2. So, we can put

$$i_{gas}(\mu)=(I_{obs}-I_{bac})/I_{bac}\,. \tag{5}$$

In the case of solid materials, however, this approximation can hardly be applicable, since $y(\mu)$ is not negligible and we must use

$$i(\mu)=(I_{obs}-I_{bac})/CNE^2\,. \tag{6}$$

The background scattering was separated from the observed intensity by the trial and error method first used by M. Takagi[9] in the study of liquid bismuth; trial background curves are improved by imposing the condition that the atomic distribution function should be zero for the values of r smaller than the atomic diameter d. From (1) this condition is expressed as

$$u(r)\equiv\int_0^\infty [C\mu i(\mu)]\sin\mu r\,d\mu\sim-2\pi^2Cr\rho_0 \qquad \text{for } r<d. \tag{7}$$

Fig. 2 shows $\mu i(\mu)$ curve obtained by the improved background curve.

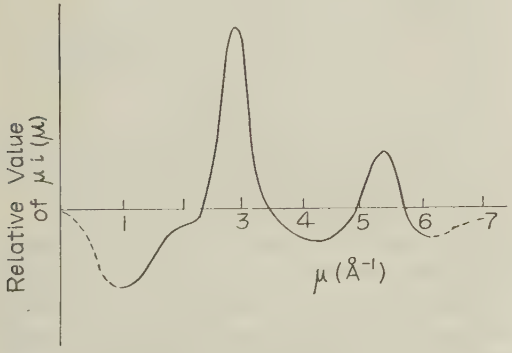

Fig. 2. $\mu i(\mu)$ curve obtained from the improved background curve.

For large values of μ, $\mu i(\mu)$ computed from the experimental value of $i(\mu)$ has large relative error. So, the values of $\mu i(\mu)$ beyond its fourth zero point, μ_0, was approximated by an analytic function $(\mu-\mu_0)I_0\exp\{-k^2(\mu-\mu_0)^2\}$. The constants I_0 and k are determined by taking into account the continuity relation of the function and its first derivative at the third minimum point (Fig.2). In the present experiment μ_0 is equal to 5.7Å^{-1}. This substitution does not cause a serious error in a few inner peaks of the radial distribution function and also this may exclude the effect caused by terminating $\mu i(\mu)$ abruptly.

In the range of small r, $u(r)$ must be proportional to the theoretical value $-2\pi^2r\rho_0$, as in (7). Assuming ρ_0 to be equal to the atomic density of the normal gold, the proportionality factor C is determined from the slope of the curve $u(r)$. The radial distribution curve can thus be obtained from (1). Fig. 3 shows the radial distribution curve.

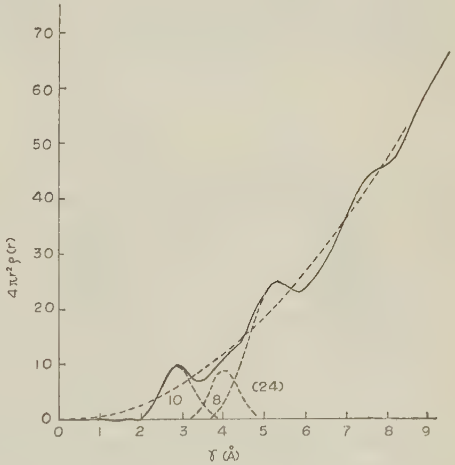

Fig. 3. Radial distribution function. Figures under each peak indicates the number of neighbours. The third coordination number is a estimated value.

The radial distribution curve can be divided into a few peaks, assuming a symmetrical profile for each peak (Fig. 3). Figures inscribed in Fig. 3 indicate the numbers of atoms under the peaks. The position of peaks and the number of atoms under each peak are summarized in Table I. It is noted that 1) the number of the first nearest neighbour is 10 and that of the second neighbour is 8, respectively, as compared with the values 12 and 6, respectively, of the face-centered arrangement, and 2) the radial distribution curve approaches the curve obtained from the random arrangement, with increase in r, as rapidly as in liquid.

§ 4. Intensity Distribution Calculated from Amorphous Models

The above mentioned result that the numbers of the first and second nearest neighbours in the Beilby layer are considerably different from those in the face-centered cubic arrangement is an important result of the radial distribution analysis. We now examine this point by a different method, *i.e.* by comparing the observed intensity with that calculated from appropriate models of atomic arrangement. If the intensity curves obtained from two models, one with the coordination numbers of normal gold and another with those obtained above, lie within the range of experimental errors, the above result may be spurious. If, on the contrary, two calculated intensity curves are distinctly different, we can decide which of the models represents the true atomic arrangement.

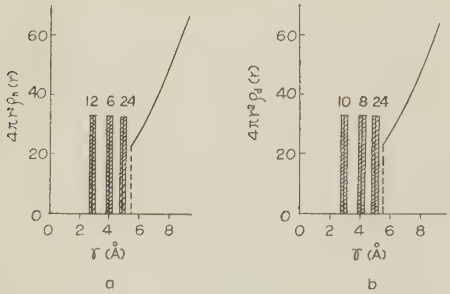

Fig. 4a and 4b. Schematic examples of the average radial distribution around an atom. *a* and *b* correspond to Model I and II, respectively, with $R=5.57$ Å.

It is assumed, for simplicity, that the atomic arrangement in the Beilby layer can be represented by the average radial distributions which are schematically shown in Fig. 4a and 4b. Within a sphere of radius R, atoms are situated on spherical shells with radii equal to the atomic distances in the perfect crystal, and in the range $r>R$, atoms are randomly distributed with the mean density ρ_0. The value of R is determined by the relation that the number of atoms in the sphere is equal to the mean density ρ_0 multiplied by the volume of the sphere. The number of atoms on each shell and the value of R are listed in Table II, for four models empolyed. The size effect corresponding to the extremly small size will be excluded by taking into account the average density of atoms for $r>R$.

Table II. The numbers of coordination in the amorphous models.

	Model I		Model II	
	a	b	a	b
No. of coordination 1st	12	12	10	10
No. of coordination 2nd	6	6	8	8
No. of coordination 3rd	24	—	24	—
No. of atoms within the sphere of radius R	43	19	43	19
Value of R (Å)	5.57	4.25	5.57	4.25

The intensity is calculated by the following formula:

$$I(\mu)=NE^2(\mu)\left\{1+\sum N_k\frac{\sin\mu r_k}{\mu r_k}-\frac{4\pi\rho_0}{\mu^3}(\sin\mu R-\mu R\cos\mu R)\right\},\quad (8)$$

where N_k is the number of atoms on the spherical shell of radius r_k. Fig. 5 shows the *interatomic* scattering curves for the above mentioned models. The first inner halo is not found in the curves for Model I a and b. Model II b shows the first inner halo resembling to the observed one. As R increases, the first inner halo becomes more intense, but other haloes split into crystalline reflection (Model I a). In the present calculation, the variation of the atomic distance is not taken into account. In the real substance, the displacement of atoms may alter not only

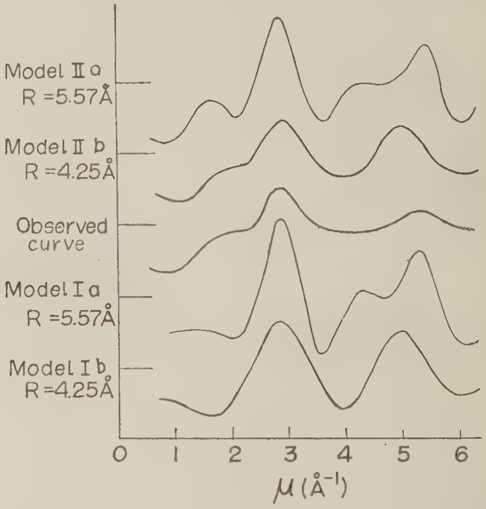

Fig. 5. Curves of $i(\mu)$ calculated by models and the observed curve of $i(\mu)$. $i(\mu)$ is derived from (8) by the relation; $i(\mu)=I(\mu)-NE^2(\mu)/NE^2(\mu)$.

the number of atoms on spherical shells, but also broaden the thickness of the shell. If the thickness of shells is taken into account in the model, the *interatomic* scattering curve for Model II will have more simillar appearance of the observed one. Thus, the coordination numbers obtained in § 3 is found to be reliable.

§ 5. Discussions

The effect of contaminations

The result given in §§ 3 and 4 concerning the numbers of coordination is mainly due to the exsistence of the first inner halo. So, the effect of contamination which might produce the observed first halo was examined carefully, and it was concluded that the present first halo was given by the polished film from the following reasons.

1) The diffraction pattern from debrises of chamois leather was intentionally obtained by the transmission method. The pattern obtained consists of two faint outer haloes and an intense diffuse one which resembles the present first halo. Careful examinations show, however, that the Bragg spacing of the intense halo differs from that of the present first halo by about 15%, and moreover, that the intensity profiles of the haloes are different from each other.

2) If the first inner halo was due to debrises of leather or other contaminations, it would appear also in the ring pattern obtained at medium stages of polishing. However, we have never observed the first inner halo superimposed on the ring pattern, though a *faint sharp* ring sometimes appeared in the ring pattern. This *faint sharp* ring, probably due to some contaminations, was entirely different from the present first halo.

3) All specimens yield the sharp ring pattern of gold, after annealing at various temperatures.

4) Oils contaminated on the surface might also be the origin of the first halo. However, the Bragg spacing of the present haloes did not coinside with those of oils.[10]

The effect of substrate

Atoms of the substrate metal may diffuse into gold film during polishing. However, if the solid solution of gold and copper gave the halo pattern obtained in the present experiment, we could have observed the pattern from copper or copper alloy after heat treatment. The same halo pattern was also obtained from the polished layer on zinc substrate. So, it is concluded that the halo pattern is not dependent on substrates.

Comparison with the results of liquid gold

Hendus[11] reported in the X-ray diffraction study of liquid gold at 1100°C that the nearest neighbour distance was 2.86 Å and the first coordination number was eleven. This result resembles the result of the present experiment. The intensity distribution, however, differs from the present result, especially in that the first halo was not observed. Suzuki[12] observed the first halo in the electron diffraction pattern from super-cooled liquid gold. The atomic arrangement may rather resemble that in the super-cooled liquid gold than that in liquid gold.

§ 6. Conclusions

The diffraction pattern from the Beilby layer of gold which is obtained at the highly advanced stage of polishing consists of three haloes. The intensity distribution of this halo pattern cannot be explained by the small size of crystallites. The radial distribution function obtained from the observed intensity distribution has a similar feature to that for liquid metals. However, the number of the first and second coordinations are about 10 and 8, respectively, while 12 and 6 for the f.c.c. arrangement.

It is, therefore, concluded that the Beily layer is in an *amorphous* state rather than the *micro-crystalline* state. The result given in (I) shows that the polish layer obtained at medium stages of polishing is composed of small crystallites with large amount of strain. So, the layer obtained at highly advanced stages may be composed of extremely minute crystallite with severe distortion, if the *micro-crystalline* view is preserved. An aggregate of such crystallites, however, cannot be discriminated from an amorphous state. Therefore, the result in (I) supports the present conclusion.

It is, moreover, noted that the Beilby layer, of the thin foil, easily recrystallizes at room temperature as well as at elevated temperatures. The amorphous state is found to be unstable, particularly when the Beily layer is removed from substrates.

The present auther wishes to express his sincere thanks to Prof. S. Takagi for his kind advice and encouragement throughout this work, and to Prof. K. Kohra for his continued interest and discussion. His thanks are also due to Prof. Y. Morino for allowing him to use punched cards and to Dr. K. Kuchitsu for his advice and his work in computation of Fourier integrals. This work was partly supported by a research grant of the Ministry of Education.

References

1) M. Kuriyama, K. Kohara and S. Takagi: J. Phys. Soc. Japan **12** (1957) 151.
2) See for instance, G. P. Thomson and W. Cochrane: *Theory and Practice of Electron Diffraction* chap. 8 (Macmillan, London 1939).
3) W. Kranert and H. Raether: Ann. Physik. **43** (1945) 520.
4) K. Nonaka and K. Kohra: J. Phys. Soc. Japan **9** (1954) 512.
5) H. Raether: Z. Phys. **126** (1949) 185.
6) H. Boersch: Z. Phys. **119** (1942) 154.
7) W. Cochrane: Proc. Roy. Soc. **A, 166** (1938) 228.
8) I. L. Karle and J. Karle: J. Chem. Phys. **17** (1949) 1052. J. Karle and I. L. Karle: J. Chem. Phys. **18** (1950) 957.
9) M. Takagi: J. Phys. Soc. Japan **11** (1956) 396.
10) C. W. Lufcy, F. S. Palubinskas and L. R. Maxwell: J. Chem. Phys. **19** (1951) 217.
11) H. Hendus: Z. Naturforsch. **2a** (1947) 505.
12) T. Suzuki: J. Phys. Soc. Japan **10** (1955) 1026.

JOURNAL OF THE PHYSICAL SOCIETY OF JAPAN, Vol. 14, No. 4, APRIL, 1959

Nuclear Magnetic Double Resonance Experiment on Two Proton System

By Junkichi ITOH and Riichiro KUSAKA

Department of Physics, Faculty of Science, Osaka University

(Received July 7, 1958)

Nuclear magnetic double resonance studies were done on two proton system in $K_2HgCl_4 \cdot H_2O$ single crystal. Applying a strong r.f. field with the frequency nearly equal to that of one line in the doublet of two proton resonance, the line shape of the other line of the doublet was measured for various values of the intensity and frequency of the strong r.f. field. Generally, the observed line shape shows further doublet structure, and the separation and relative intensities of this doublet depend upon the intensity and frequency of the strong r.f. field. Some calculations were made for the line structure of two proton system under the influence of a strong r.f. field. The experimental results agree qualitatively with the calculation, but there exist some descrepancies in the absolute magnitudes of the splitting of the induced doublet.

§ 1. Introduction

In recent years, double nuclear magnetic resonance has called much attentions, and several works have been done both theoretically and experimentally[1)-8)]. Generally, the magnetic resonance intensity, line shape and also spin-lattice relaxation time for one species of spins will change when another r.f. field having the resonance frequency of other species is applied.

In a two proton system, the characteristic feature lies in the fact that the resonance line shows doublet structure, split by the dipolar interaction between two protons, and a r.f. field with a frequency nearly equal to the resonance frequency of one line of the doublet will have several interesting effects on the other line. Bloembergen[9)] treated the problem theoretically, but no experiment has been done.

We made extensive investigations on two

proton system with single crystals of $K_2HgCl_4 \cdot H_2O$. In this report, we shall describe the results of the double resonance experiments using strong r.f. field. The results of our works concerning temperature dependence of the spin-lattice relaxation time and doublet separation, nuclear Overhauser effect, and also their correlation with the motions of the water molecules will be reported in near future.

The resonance figure of one of the doublet in a two proton system changed appreciably when another strong r.f. field having a frequency close to the other line of the doublet was applied. This occurs by the mixing of the Zeeman levels induced by this r.f. field. In the case of a single spin system, Bloch²⁾ showed that, by a strong r.f. field, single resonance line will split into doublet, whose separation and relative intensities depend upon the frequency difference between Zeeman frequency and the frequency of the applied strong r.f. field, and also upon the intensity of the r.f. field. Bloch also treated more general cases of multiple spin system with exchange coupling among them.

However, since the problem concerning two proton system is of a special one, we made some calculation, which will be shown in § 2. In § 3, the experimental results of the double resonance studies will be presented together with comparison with the calculation.

§ 2. Theoretical Calculation

The Hamiltonian of an isolated two proton system, mutually interacting by magnetic dipolar interaction, under a strong static field, H_0, and a r.f. field, $2H_1 \cos \omega t$, which is perpendicular to the static field, is given by

$$\begin{aligned}\mathscr{H} = &-(\mu/I)H_0(I_{1z}+I_{2z})\\ &-(\mu/I)\cdot 2H_1 \cos \omega t \cdot (I_{1x}+I_{2x})\\ &+(\mu/I)^2[(\boldsymbol{I}_1\cdot\boldsymbol{I}_2)r^{-3}-3(\boldsymbol{I}_1\cdot\boldsymbol{r})(\boldsymbol{I}_2\cdot\boldsymbol{r})r^{-5}] \qquad (1)\end{aligned}$$

where the direction of the static field is taken as the z-axis, that of the r.f. field as the x-axis, $\boldsymbol{r}$ is the interproton vector, $\boldsymbol{I}_1$ and $\boldsymbol{I}_2$ are the spin vectors of the proton 1 and 2, respectively, and μ and I are the magnetic moment and spin of the proton.

The r.f. field $2H_1 \cos \omega t$ can be devided into two circularly rotating field about the z-axis with frequencies ω and $-\omega$, and one of them with the frequency $-\omega$ alone can have perturbing effect on the magnetic resonance line. Hence we can discard the rotating field with the frequency ω which has little effect on the resonance line. We now transform the coordinate system (x, y, z) to (ξ, η, ζ), the latter being rotating about the z-axis with angular frequency $-\omega$. The ζ-axis is taken so as to coincide with the z-axis, and the ξ-axis is taken to have a phase to coincide with the rotating r.f. field. Then the Hamiltonian is transformed to the following form:

$$\begin{aligned}\mathscr{H}_r = &-(\mu/I)(I_{1\zeta}+I_{2\zeta})(H_0-\omega/\gamma)\\ &-(\mu/I)(I_{1\xi}+I_{2\xi})H_1+(\mu/I)^2(\tfrac{3}{2}\cos^2\theta-\tfrac{1}{2})r^{-3}\\ &\times(\boldsymbol{I}_1\cdot\boldsymbol{I}_2-3I_{1\zeta}\cdot I_{2\zeta})+(\text{time dependent}). \qquad (2)\end{aligned}$$

In this Hamiltonian, (time dependent) represents terms which depend upon time, and can be neglected in the following calculation as Redfield discussed already¹⁰⁾. γ is the gyromagnetic ratio of proton, and θ is the angle between the static field and the $p-p$ direction.

Then, the Hamiltonian (2) is time independent one, and the eigen-values and the corresponding eigen-functions can be obtained by solving the wave equation

$$i\hbar(\partial\phi/\partial t) = \mathscr{H}_r\phi\,. \qquad (3)$$

Now, with the Hamiltonian (2), one can show easily that two spins from one singlet and one triplet states, which are mutually independent and no transition can be realized between them. Therefore the singlet state has no contribution to the magnetic resonance phenomena as far as we deal with an isolated two proton system and it is suffice to solve triplet levels alone. The zero order spin functions of three levels of the triplet are $\phi_1=\alpha(1)\alpha(2)$, $\phi_0 = 1/\sqrt{2}\,[\alpha(1)\beta(2)+\beta(1)\alpha(2)]$, and $\phi_{-1}=\beta(1)\beta(2)$, respectively, where α and β represent the states having the ζ-component of the spin of 1/2 and $-1/2$, respectively. The secular equation with respect to this representation is given by

$$\begin{vmatrix} -Z-D-W & -\sqrt{2}R & 0 \\ -\sqrt{2}R & 2D-W & -\sqrt{2}R \\ 0 & -\sqrt{2}R & Z-D-W \end{vmatrix} = 0 \qquad (4)$$

where, W is the eigen-value of the energy, and, for simplicity, we denote that

$$\left.\begin{aligned} Z&=(\mu/I)(H_0-\omega/\gamma)\,,\\ D&=(1/4)(\mu/I)^2(3\cos^2\theta-1)r^{-3}\,,\\ R&=(\mu/I)\cdot H_1/2\,. \end{aligned}\right\} \qquad (5)$$

Further, if we denote $Z/D=A$, $R/D=B$, and $W/D=X$, the secular equation is transformed into

$$(X+A+1)(X-2)(X-A+1)=4B^2(X+1)\,. \tag{6}$$

Though D depends upon the orientation of the static field with respect to the proton-proton direction, equation (6) does not explicitly include this angle and is useful for the general discussions of the problem.

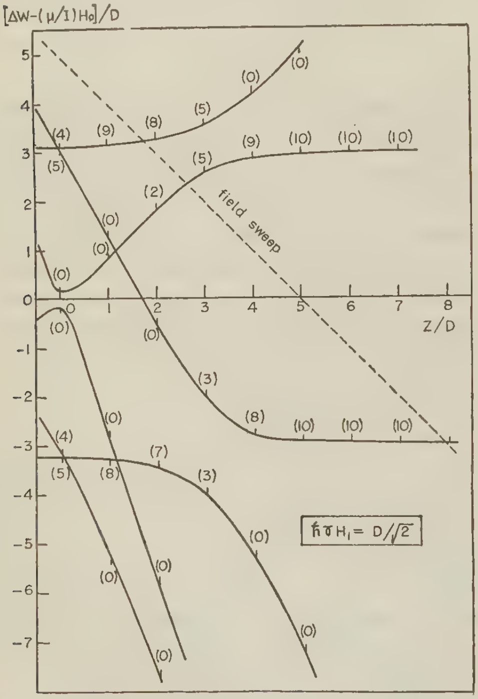

Fig. 1. Theoretical resonance energies, ΔW, of two proton system measured from the Zeeman energy of proton under a strong static and a r.f. magnetic fields, as a function of the difference between the energy of photons of the applied r.f. field and the Zeeman energy of proton, both in the unit of D (one-sixth of the doublet separation of two proton resonance). In the case shown in the figure, the intensity of the applied field, H_1, is equal to $D/\hbar\gamma\sqrt{2}$. Relative intensities are shown in the brackets.

Equation (6) cannot be solved analytically, and to get numerical values of the eigen-values, (6) must be solved numerically for given values of A and B.

Corresponding to the three eigen-values of the energy, E_a, E_b, E_c, the eigen-functions can be expressed by linear combinations of three spin functions ϕ_1, ϕ_0, and ϕ_{-1}. The time dependent Schrödinger wave functions are given by

$$\left.\begin{aligned}\phi_a&=(a_1\phi_1+a_0\phi_0+a_{-1}\phi_{-1})\exp(i\Delta\omega_a t)\,,\\ \phi_b&=(b_1\phi_1+b_0\phi_0+b_{-1}\phi_{-1})\exp(i\Delta\omega_b t)\,,\\ \phi_c&=(c_1\phi_1+c_0\phi_0+c_{-1}\phi_{-1})\exp(i\Delta\omega_c t)\,,\end{aligned}\right\}\tag{7}$$

where a_i, b_i, and c_i $(i=1, 2, 3)$ are normalized weights of the states 1, 0 and -1 for three eigen-states, respectively, and $\Delta\omega_j$ stands for $-E_j/\hbar$ $(j=a, b, c)$.

If we return to the original (x, y, z) system (laboratory coordinate system), ϕ_a, ϕ_b and ϕ_c are transformed into ψ_a, ψ_b and ψ_c, given by following equations:

$$\begin{aligned}\psi_a=a_1\phi_1\exp[i(\omega+\Delta\omega_a)t]+a_0\phi_0\exp[i\Delta\omega_a t]\\ +a_{-1}\phi_{-1}\exp[i(-\omega+\Delta\omega_a)t]\end{aligned} \qquad (8$$

and similar two equations.

When one more r.f. field is applied in the direction perpendicular both to H_0 and H_1, that is in the y-direction, transitions between these levels will occur. Let this r.f. field be $2H_2\cos\omega' t$. Then, since this field is harmonic in time, absorption will occur only when the exponential time factor of $\psi_i{}^*\psi_j$ $(i, j=a, b, c)$ is compensated by $\exp(\pm i\omega' t)$ of the applied field, and the intensity of the absorption is proportional to the square of the matrix element of I_y with respect to the initial and final states. Thus the resonance frequencies and relative intensities are given by

$$\left.\begin{array}{ll}\textit{resonance frequency} & \textit{relative intensity}\\ \omega+(\Delta\omega_a-\Delta\omega_b) & |a_1{}^*b_0+a_0{}^*b_{-1}|^2\\ \omega-(\Delta\omega_a-\Delta\omega_b) & |a_0{}^*b_1+a_{-1}{}^*b_0|^2\\ \omega+(\Delta\omega_a-\Delta\omega_c) & |a_{1*}c_0+a_0{}^*c_{-1}|^2\\ \omega-(\Delta\omega_a-\Delta\omega_c) & |a_0{}^*c_1+a_{-1}{}^*c_0|^2\\ \omega+(\Delta\omega_b-\Delta\omega_c) & |b_1{}^*c_0+b_0{}^*c_{-1}|^2\\ \omega-(\Delta\omega_b-\Delta\omega_c) & |b_0{}^*c_1+b_{-1}{}^*c_0|^2\end{array}\right\}\tag{9}$$

We solved the wave equation for several values of A and B. Fig. 1 shows calculated deviation of transition energies from Zeeman value as a function of A for the case $B=1/2\sqrt{2}$, or $\hbar\gamma H_1=D/\sqrt{2}$. Figures shown in the bracket are the relative intensities, the intensity of one of the doublet line in the case $H_1=0$ being taken as 10. As will be seen from this figure, doublet lines when $H_1=0$ split into six lines in general when $H_1\neq 0$. However, when H_1 is not very large, several lines have vanishing intensities, and when the frequency of the perturbing r.f. field is close to the resonance frequency of one of the doublet lines, the general feature of the resonance is as if each of the original doublet lines split into further doublets. Separation of these doublets and their relative intensities depend upon the values of Z and R. When R is small, the separation is also small, and the intensity of one of the doublet lines disappears when Z becomes large.

The above calculation is based upon the assumption that a two proton system is isolated from other nuclei, which is not the actual case. But general feature of the double resonance effect on two proton system in real crystal will be well represented by this simplified treatment. In next section, the calculation will be compared with the experimental results.

§ 3. Experimental Results and Discussions

a) *Experimental apparatus and procedure*

The detection of nuclear magnetic resonance was done by Pound-Watkins device. The detector coil was of usual solenoid type, while one more coil system, which was of Helmholtz coil type, was inserted so as to produce a perturbing r.f. field ($2H_1 \cos \omega t$) in the direction perpendicular both to the static and detecting fields. These Helmholtz coils were excited by a 807 oscillator and overall coil voltage amounted upto about 300 volt. But, because the gap of two coils was rather large, which was necessary to put the detector coil into this gap, H_1 amounted only about 2.8 gauss at its maximum.

The sample used was a single crystal of $K_2HgCl_4 \cdot H_2O$. Two proton character of water molecules in this crystal has been already investigated by us[11]. The separation of the doublet amounted about 86 kc/sec at its maximum, when the direction of the static field was parallel to $p-p$ direction within a water molecule. The width of each of the doublet lines originates mainly from magnetic dipolar interaction between protons, each belonging to the neighboring water molecules.

Though the detecting coil and Helmholtz coils were nearly perpendicular to each other, and moreover the relative orientation of the coils was adjusted to minimize stray field in the detector coil, pick-up of the perturbing r.f. field in the detector coil was considerably large, because the frequency difference between two r.f. frequencies was always less than 100 kc/sec. Therefore, in the out-put signal of the detector, there existed considerable amount of beat between two r.f. frequencies. Using a resonance amplifier tuned to the frequency of the static field modulation and a phase-sensitive detector, this could be almost eliminated. But when the intensity of the perturbing r.f. field was increased as large as 300 volts, the effect of the stray in the detecting system became so large that the nuclear magnetic resonance signal became unstable. So, the experiment was done upto the coil voltage of about 260 volts. It was preferable to keep the detecting r.f. field, H_2, as low as possible to avoid saturation effect. However, since the disturbing effect to the stray field increased as H_2 decreased, we could not use very low value of H_2 and the experiments were done with the value of H_2 by which the resonance signal saturated by a small amount. With this H_2 and when $H_1=0$, the signal intensity was about 75% of that in perfectly unsaturated condition. However, this may not affect the line structure appreciably.

It is preferable to sweep the frequency of the detector over the resonance range, fixing the static field and the frequency of the perturbing field. But, as the pick-up voltage changed violently with the change in the frequency difference between two r.f. systems, it was impossible to do the experiment with this procedure. Therefore, fixing the frequencies of the two r.f. fields, the static field was swept over the range of the expected resonances. In this case, the observed resonance figures correspond to those expected when A and B defined in § 2 are varied simultaneously with the value of the static field, or, the expected resonance fields are given by the intersections of a line which inclines $-45°$ with the ordinate axis with the curves given in Fig. 1. An example of this line was shown in Fig. 1. The A coordinate of the intersection of this line with the A-axis, transformed to the frequency scale, corresponds to the frequency difference between the two r.f. fields. In the example shown in Fig. 1, the frequency difference between the two fields is $5D/h$, and the reasonance figure consists of one singlet and one doublet. In the latter case, the frequency of the perturbing field is very close to that of the other line of two proton doublet and the perturbation of the energy levels occurs, while in the case of the singlet, the frequency of the perturbing field is very much apart from the two proton lines and no effect is expected.

A single crystal of $K_2HgCl_4 \cdot H_2O$ which was cut in the *c*-plane was used, and the experiments were done with the static field in the direction of interamolecular proton-proton line in one case, and in the direction of the *a*-axis in the other case. In the former case, the the separation of the doublet is about 86 Kc/sec, while in the latter case, about 65 Kc/sec. There exist two types of water molecules in the unit cell, having different orientations with respect to the crystal axes. In the case of the static field along each one of the crystallographic axis, proton-proton directions of these two types of water molecules make equal angles with the static field. Therefore, the resonance intensity is doubled in these cases and the measurements can be done more accurately than in other cases.

b) *Experimental results and discussions*

Fig. 2 shows the results of the measurements of derivatives of the absorption curves in the case of the static field in the direction of the *a*-axis. As shown in § 2, one line of the two proton doublet is not disturbed by the perturbing field; hence in this figure we only show the other line which is affected by the perturbing field. The top curve shows the resonance figure for the $H_1=0$. The lower curves correspond to the resonance curves when $H_1=1.7$ gauss. Here, the magnetic field was swept slowly over the region of the resonance, keeping both frequencies of two r.f. fields constant. $\Delta\nu$, the difference in frequency between the perturbing and detecting fields was taken as a parameter, and was shown in each curve. When $\Delta\nu$ was equal to the separation of the two proton doublet, the perturbing r.f. frequency just coincided with one line of the doublet at the static field strength which brought the detecting frequency to coincide with the other line, and then two lines with nearly equal intensities were seen in both sides of the original position of the two proton line. As $\Delta\nu$ was increased from the frequency difference of the two proton doublet, one line came closer to the original position with increasing intensity, while the other line displaced further from the original position with decreasing intensity.

By analysing each of the curves in Fig. 2 into two lines, the exact positions of these two lines were determined. To compare with the calculated values, the displacement of the resonance positions from the original one was plotted against $\Delta\nu-\Delta\nu_0$, where $\Delta\nu_0$ is the doublet separation of the two proton line, both in the unit of D (which is equal to $\nu_0/6$ in frequency scale). When the oscillation intensity of the perturbing coil was increased over 100 volts in terminal voltage, the tem-

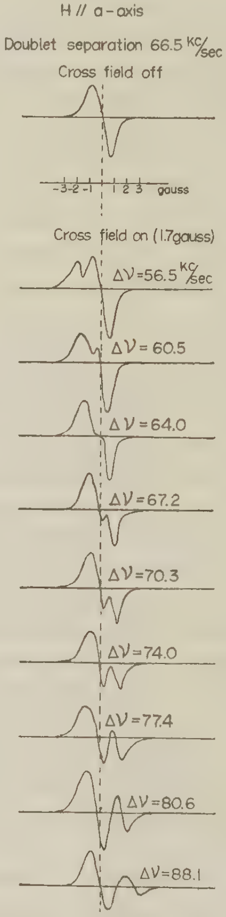

Fig. 2. Line shapes of one of the doublet lines in two proton system when a r.f. field with the frequency close to that of the other line of the doublet is applied. $\Delta\nu$ is the frequency difference of the detecting and perturbing fields. The direction of the static field is parallel to the *a*-axis.

perature of the Helmholtz coil rised and soon the temperature of the sample also rised considerably. Since the two proton doublet separation slightly decreases when the temperature rised, the value $\varDelta\nu_0$ and D in the above discussions should correspond to those at the equilibrium temperature, somewhat higher than room temperature. We estimated the temperature of the crystal and the plots in Fig. 3 were drawn with the corrected values of $\varDelta\nu_0$ and D. Though this correction was negligible for D, it had some effect on $\varDelta\nu-\varDelta\nu_0$, as this value was alway less than about 1/6 of $\varDelta\nu_0$ itself. To avoid this slight ambiguity, we plotted the separation of two lines in Fig. 4, which was scarcely affected by small possible error in determining the value of $\varDelta\nu_0$. Both in Figs. 3 and 4, two typical examples of the calculated curves were also shown. General tendency of the experimental plots is quite well represented by the calculation, but the experimental line-displacement or separation is somewhat smaller than the calculated one. This may be due to errors in the evaluation of the values of H_1, the uncertainty in the analyses of curves shown in Fig. 2, the effects on the transition mataices coming from the finite line width, and/or the change in the line shape by the perturbing field.

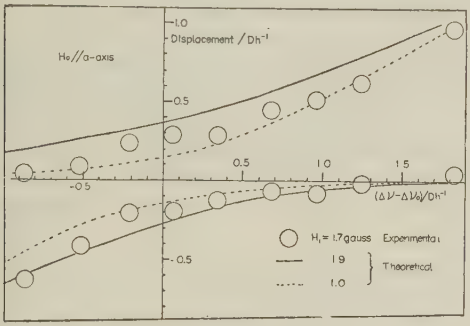

Fig. 3. Displacement of the resonance frequencies from the unperturbed frequency of one of the doublet lines, when a perturbing r.f. field is applied, as a function of the difference in frequency between the perturbing field and the other line of the doublet, both in the unit of $D/\hbar$. In this case the direction of the static field is parallel to the a-axis. Circles: the experimental values, solid and dotted curves: the calculated curves for different values of H_1.

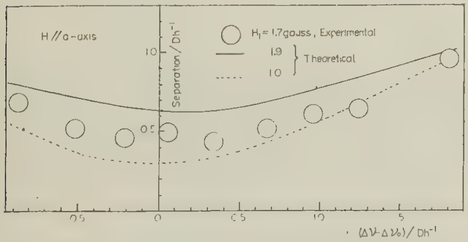

Fig. 4. Separation of two lines shown in Fig. 3, as a function of the difference in frequencies of the perturbing field and one of the doublet lines, both in the unit of $D/\hbar$. In this case, the static field is parallel to the a-axis. Circles: the experimental values, solid and dotted curves: the calculated curves for two different values of H_1.

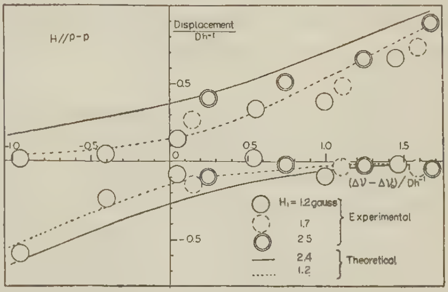

Fig. 5. Displacement of the resonance frequencies from the unperturbed frequency of one of the doublet lines, similar to Fig. 3, in the case where the static field is parallel to p-p direction.

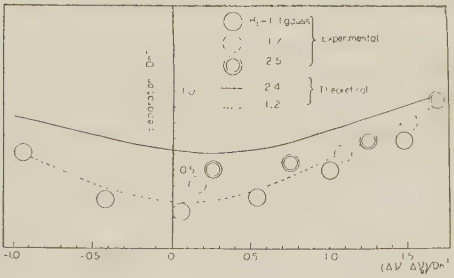

Fig. 6. Separation of two lines shown in Fig. 5.

In the case when the static field is in the direction of $p-p$ line, we made the experiments with three values of H_1, from 1.1 gauss to 2.5 gauss. The results of the experiments were shown in Figs. 5 and 6. Fig. 5 shows positions of the resonance fields, and Fig. 6 shows the separation of two lines. It can be seen from these figures that the separations or displacements increase with increasing H_1. In both figures the calculated curves for $H_1=1.2$ and 2.4 gauss were shown. Again the general tendency of the experimental plots is quite in agreement with the calculation, but a slight disagreement in the absolute values is recognized, as in the case of the static field in the direction of the *a*-axis.

As for relative intensities of the separated lines, quantitative comparison with the calculation seems to be difficult, because the line shape and the population difference of the levels in concern are difficult to be calculated, and also the analyses of the measured resonance curves cannot be carried out without ambiguity. However, general tendency of the calculation is well demonstrated by the experiments.

It seems more difficult to evaluate the line shape or width. The width of the resonance lines under strong r.f. perturbing field will be narrowed by the narrowing effect due to the perturbing field on the dipolar interaction from the neighboring water molecules having the same $p-p$ orientation, and at the same time the width will be broadened by the short life time of each Zeeman level due to the induced transitions by the perturbing field. The situation seems quite complicated and more detailed consideration will be needed for further discussions of the problem.

The authors would like to express their thanks to Professor K. Tomita for his valuable discussions.

References

1) R. V. Pound: Phys. Rev. **79** (1950) 685.
2) F. Bloch: Phys. Rev. **102** (1956) 104.
3) W. A. Anderson: Phys. Rev. **102** (1956) 15
4) I. Solomon: Phys. Rev. **99** (1955) 559.
5) A. L. Bloom and J. N. Shoolery: Phys. Rev. **97** (1955) 1261.
6) B. Herzog and E. L. Hahn: Phys. Rev. **103** (1956) 148.
7) I. Solomon and N. Bloembergen: J. Chem. Phys. **25** (1956) 261.
8) Y. Saito: J. Phys. Soc. Japan **13** (1958) 72.
9) N. Bloembergen: Phys. Rev. **104** (1956) 154
10) A. G. Redfield: Phys. Rev. **98** (1955) 1787.
11) J. Itoh, R. Kusaka, Y. Yamagata, R. Kiriyama, H. Ibamoto, T. Kanda and Y. Masuda: J. Phys. Soc. Japan **8** (1953) 287.

JOURNAL OF THE PHYSICAL SOCIETY OF JAPAN, Vol. 14, No. 4, APRIL, 1959

The Electronic Structure of the Protonated Methane CH_5^+

By Masatoshi YAMAZAKI

Department of Physics, Faculty of Science, Kanazawa University, Kanazawa, Japan

(Received November 12, 1958)

The electronic structure of the ground state of the protonated methane CH_5^+ is studied by the Heitler-London-Slater-Pauling method extended by Voge and by Kotani and Siga. The wave functions are constructed without the assumption of the electron pair bond and with taking $(2s)^2(2p)^2$, $(2s)(2p)^3$, and $(2p)^4$ configurations of the carbon atom into account. Assuming a probable model for this ion, we obtain seventeen $^1A_1'$ states. The energy matrix for these states is computed by means of the representation matrices of the symmetric group. By solving the secular equations thus obtained for two different sets of parameters, the binding energy (or the proton affinity) and the equilibrium proton-carbon distance are estimated.

§1. Introduction

The stable protonated methane CH_5^+ has been found by mass spectrometer and by other means[1]. This ion shows the simplest prototype of the intermediate transient state for the substitution reaction of the methyl compounds, (in general

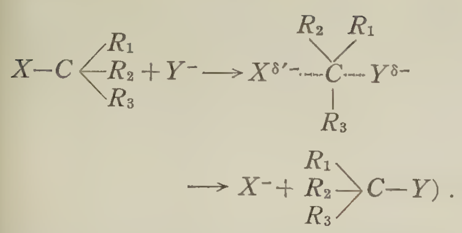

$$X-C\begin{smallmatrix}R_1\\R_2\\R_3\end{smallmatrix}+Y^-\longrightarrow X^{\delta'-}\cdots\overset{R_2\ \ R_1}{\underset{R_3}{C}}\cdots Y^{\delta-}\longrightarrow X^-+\begin{smallmatrix}R_1\\R_2\\R_3\end{smallmatrix}C-Y)\,.$$

The methane molecule is a saturated hydrocarbon, and CH_5^+ ion is an interesting example of the electron deficient compounds. The geometrical structure of this cation has not been established, but those for diborane and H_3 suggest the possibility of three hydrogen atoms and a carbon atom being coplanar, the remaining two hydrogen atoms being situated on the equivalent sites before and behind this plane, and the latter two hydrogen atoms making the so-called three-center bond with the carbon atom and sharing with the positive charge of the ion*. Little is known experimentally about this ion, so a detailed theoretical study of it would be of some interest.

In this paper we assume the symmetry group D_{3h} for this ion, and calculate the energy of the ion as the function of the carbon-proton distance by means of the atomic orbital method. If we wish to know the potential energy curve for the nuclear distance larger than the equilibrium value, internal energies of atoms become more and more important. These intratomic energies are not duly taken into account by the usual electron pair bond approximation. So we follow the general method similar to Voge[2) and Kotani and Siga[3) for the methane molecule, and Itoh, Ohno, and Kotani[4) for the methyl radical. Moreover in this general method, there is no need to worry about the choice of hybridized orbitals of the carbon atom, since the result by this method is invariant against any unitary transformation of the carbon orbitals.

§ 2. Construction of Wave Functions

A rectangular coordinate system is taken in such a way that the carbon nucleus C and the five hydrogen nuclei H_a, H_b, H_c, H_d, H_e have coordinates $(0, 0, 0)$, $(R, 0, 0)$, $(-\frac{1}{2}R, \frac{1}{2}\sqrt{3}R, 0)$, $(-\frac{1}{2}R, -\frac{1}{2}\sqrt{3}R, 0)$, $(0, 0, \overline{R})$, $(0, 0, -\overline{R})$, respectively (See Fig. 1.). We call H_a, H_b, and H_c the covalent hydrogen atom, and H_d, H_e the ionic hydrogen atom, as we assume all ionic structures except those which involve ionic H_d and H_e can be disregarded. Besides that, we assume the value of the $C-H$(covalent) internuclear distance R is kept to be 1.09A (the value for CH_4). Electrons in the K shell of the carbon atom are not taken explicitly in our calculations, and we treat the CH_5^+ ion as a eight-electron problem. The ground state of the ion is considered to be ${}^1A_1'$, so that the ${}^1A_1'$ part of the energy matrix is to be constructed in the present study.

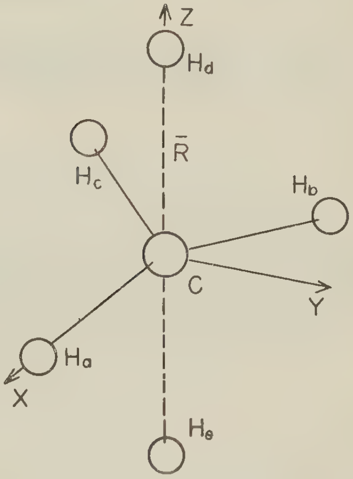

Fig. 1. Notations for CH_5^+

The number of basic ${}^1A_1'$ was functions is found as follows: In order to take account of the symmetry of the ion, we divide the ion into three zones C, H_3, and H_2^+. The C-zone has a spherical symmetry, but its atomic states can be reduced as the representation of D_{3h}. The H_3-zone gives ${}^2E'$ and ${}^4A_2'$, and the H_2^+-zone gives ${}^2A_1'$ and ${}^2A_2''$, if all hydrogen atoms are in the normal state. Combining these three zones, we find that each of $sp^3\ {}^3S^0$, ${}^5S^0$, ${}^1P^0$, ${}^3P^0$ states of the carbon atom gives rise to one ${}^1A_1'$ state of CH_5^+, each of $s^2p^2\ {}^1D$, ${}^3P$, $sp^3\ {}^1D^0$, $p^4\ {}^1D$, ${}^3P$ two, and $sp^3\ {}^3D^0$ three. Thus there are seventeen ${}^1A_1'$ states in all. This situation is the same as that of the ${}^2A_1$ state of the methyl radical with the C_{3v} symmetry.[4)

In order to calculate the matrix elements of the hamiltonian we construct the wave function as follows.[3),4),5),6) We denote by κ

---

* This suggestion is due to Prof. S. Nagakura.

(and λ), μ (and ν), and σ $(=2)$ (and ρ $(=2)$) the spin multiplicity of the C-, H_3-, and H_2^+-zone. We denote by $U_{\kappa;kl}(P)$ ($U_{\mu;mn}(Q)$) the k, l (m, n) matrix element for the permutation $P(Q)$ in the irreducible representation corresponding to spin multiplicity $\kappa(\mu)$ for the C-(H_3-) zone. The wave functions for the C-zone are

$$\Phi^{C,\alpha}_{\kappa M;k}=\Phi^{C,\alpha}_{S,M,k}=\frac{1}{\sqrt{f_\kappa}}\sum_l \Psi^{C,\alpha}_{\kappa;kl}\Theta_{S,M,l}$$

$$\Psi^{C,\alpha}_{\kappa;kl}=\sqrt{\frac{f_\kappa}{2^{\eta_\alpha}4!}}\sum_P U_{\kappa;kl}(P^{-1})P\phi_{\alpha_1}(1)\phi_{\alpha_2}(2)\phi_{\alpha_3}(3)\phi_{\alpha_4}(4)^*,$$

(f_κ=the dimension of the representation U_κ)

where α_1, α_2, α_3, α_4 are a set of orbitals taken from the available orbitals $2s$, $2px$, $2py$, and $2pz$, η_α is the number of orbitals in that set which are occupied by two electrons, and 1, 2, 3, 4 denote the position coordinates of four electrons in the carbon atom. These functions belong to a definite multiplicity κ, but generally they do not transform according to a definite irreducible representation of D_{3h}. Actually examining the transformation properties of $\Psi^{C,\alpha}_{\kappa;kl}$, we can construct appropriate linear combinations of them

$$\Psi^{C}_{\kappa\mu;hl}=\sum_{k\alpha} C_{\kappa\mu h;k\alpha}\Psi^{C,\alpha}_{\kappa;kl}\ ,$$

which form the bases of irreducible representations of D_{3h}. The wave functions for the H_3-zone are

$$\Phi^{H_3}_{\mu M;m}=\Phi^{H_3}_{S,M,m}=\frac{1}{\sqrt{f_\mu}}\sum_n \Psi^{H_3}_{\mu;mn}\Theta_{S,M,n}$$

$$\Psi^{H_3}_{\mu;mn}=\sqrt{\frac{f_\mu}{3!}}\sum_Q U_{\mu;mn}(Q^{-1})Q\phi_a(6)\phi_b(7)\phi_c(8)\ ,$$

---

* The forms of the matrices $U(P)$, which are used in the present study, correspond to the following definitions of the bases of the matrices $V(P)$ $(U(P)V(P)=\varepsilon_P)$.

for the C-zone: $\Theta_{S,M,l}$

$$S=2,\ M=2\qquad \Theta_{l=1}=\alpha(1)\alpha(2)\alpha(3)\alpha(4)\ ,$$

$$S=1,\ M=1\begin{cases}\Theta_{l=1}=\frac{1}{2}\{\alpha(1)\alpha(2)\alpha(3)\beta(4)+\alpha(1)\alpha(2)\beta(3)\alpha(4)-\alpha(1)\beta(2)\alpha(3)\alpha(4)-\beta(1)\alpha(2)\alpha(3)\alpha(4)\}\\ \Theta_{l=2}=\frac{1}{\sqrt{2}}\{\alpha(1)\beta(2)\alpha(3)\alpha(4)-\beta(1)\alpha(2)\alpha(3)\alpha)\}\\ \Theta_{l=3}=\frac{1}{\sqrt{2}}\{\alpha(1)\alpha(2)\beta(3)\alpha(4)-\alpha(1)\alpha(2)\alpha(3)\beta(4)\}\ ,\end{cases}$$

$$S=0,\ M=0\begin{cases}\Theta_{l=1}=\frac{1}{2}\{\alpha(1)\beta(2)-\beta(1)\alpha(2)\}\{\alpha(3)\beta(4)-\beta(3)\alpha(4)\}\\ \Theta_{l=2}=\frac{1}{\sqrt{3}}\Big[\frac{1}{2}\{\alpha(1)\beta(2)+\beta(1)\alpha(2)\}\{\alpha(3)\beta(4)+\beta(3)\alpha(4)\}\\ \qquad\qquad -\alpha(1)\alpha(2)\beta(3)\beta(4)-\beta(1)\beta(2)\alpha(3)\alpha(4)\Big]\ ,\end{cases}$$

for the H_3-zone: $\Theta_{S,M,n}$

$$S=\frac{3}{2},\ M=\frac{3}{2}\qquad \Theta_{n=1}=\alpha(6)\alpha(7)\alpha(8)\ ,$$

$$S=\frac{1}{2},\ M=\frac{1}{2}\begin{cases}\Theta_{n=1}=\frac{1}{\sqrt{2}}\{\alpha(6)\alpha(7)\beta(8)-\alpha(6)\beta(7)\alpha(8)\}\\ \Theta_{n=2}=\frac{1}{\sqrt{6}}\{2\beta(6)\alpha(7)\alpha(8)-\alpha(6)\alpha(7)\beta(8)-\alpha(6)\beta(7)\alpha(8)\}\ .\end{cases}$$

where ϕ_a, ϕ_b, ϕ_c denote the 1*s* orbitals of the hydrogen atoms H_a, H_b, H_c, respectively, and 6, 7, 8 denote the position coordinates of three electrons in three covalent hydrogen atoms. These wave functions belong to a definite multiplicity μ, and transform according to a definite irreducible representation of the point group D_{3h} ($\Psi_{\mu;mn}$'s are ${}^2E'$ for $\mu=2$ and ${}^4A_2'$ for $\mu=4$). The wave functions for the H_2^+-zone are

$$\Phi^{H_2^+,\beta}_{\sigma M;t} = \phi_d(5)\alpha(5) \quad \text{or} \quad \phi_e(5)\alpha(5)\ ,$$

where ϕ_d, ϕ_e denote the 1*s* orbitals of the hydrogen atoms H_d, H_e, respectively, and 5 denotes the position coordinate of the electron in the so-called ionic hydrogen atoms. The linear combinations

$$\frac{1}{\sqrt{2}}(\phi_d(5)+\phi_e(5))\ ,\quad \frac{1}{\sqrt{2}}(\phi_d(5)-\phi_e(5))$$

will form the bases of irreducible representations of D_{3h}.

The ${}^1A_1'$ wave functions of the whole system CH_5^+ are constructed as follows: We denote by $W_{pq}(S)$ the irreducible representation of the symmetric group $\mathfrak{S}_8$ corresponding to the singlet state, which is reduced with respect to the subgroup $\mathfrak{S}_4(1, 2, 3, 4)\times\mathfrak{S}_3(6, 7, 8)$**. Thus for any element of the subgroup $G=PQ$ ($P\in\mathfrak{S}_4(1, 2, 3, 4)$, $Q\in\mathfrak{S}_3(6, 7, 8)$),

$$W_{pq}(G)=W_{\kappa\mu km,\lambda\nu ln}(PQ)=\delta_{\kappa\lambda}\delta_{\mu\nu}U_{\kappa;kl}(P)U_{\mu;mn}(Q)\ .$$

The singlet wave functions of CH_5^+ are

$$\Phi^{\alpha,\beta}_{\kappa\mu\sigma(=2)M;\,km\jmath(=1)}=\Phi^{\alpha,\beta}_{S=0,M=0,km\jmath(=1)}=\sqrt{\frac{1}{14}}\sum_q \Psi^{\alpha,\beta}_{\kappa\mu\sigma(=2)km\jmath(=1),q}\,\Theta_{S-0,M=0,q}$$

$$\Psi^{\alpha,\beta}_{\kappa\mu\sigma(=2)km\jmath(=1),q}=\sqrt{\frac{14}{2^{\eta_\alpha}8!}}\sum_S W_{\kappa\mu km,q}(S^{-1})S\phi_{\alpha_1}(1)\phi_{\alpha_2}(2)\phi_{\alpha_3}(3)\phi_{\alpha_4}(4)\phi_\beta(5)\phi_a(6)\phi_b(7)\phi_c(8)\ .$$

Using the same coefficients as defined above for the *C*-zone and the H_2^+-zone, we obtain the ${}^1A_1'$ wave functions of CH_5^+ as follows:

$$\Phi_{\kappa\mu km}=\Phi_{S=0,M-0,km}=\sqrt{\frac{1}{14}}\sum_q\sqrt{\frac{1}{f_\mu}}\sum_{k\alpha\beta h}C_{\kappa\mu h;k\alpha\beta}\Psi^{\alpha,\beta}_{\kappa\mu kh,q}\Theta_{S,M,q}=\sum_q\sqrt{\frac{1}{14}}\Psi_{\kappa\mu,q}\Theta_{S=0,M=0,q}$$

$$\Psi_{\kappa\mu,q}=\sqrt{\frac{1}{f_\mu}}\sum_{k\alpha\beta h}C_{\kappa\mu h;k\alpha\beta}\Psi^{\alpha,\beta}_{\kappa\mu kh,q}\ .$$

These functions are given explicitly in Table I. These are similar to those for the methyl radical.[4)]

§ 3. Calculation of Matrix Elements

The elements of the hamiltonian are computed by the formula

$$\int\Psi^{\alpha,\beta}_{p,q}H\Psi^{\bar\alpha,\bar\beta}_{r,q}d\tau=\frac{1}{\sqrt{2^{\eta_\alpha+\eta_{\bar\alpha}}}}\sum_S W_{p,r}(S^{-1})\int(S\Psi^{\alpha,\beta})H\Psi^{\bar\alpha,\bar\beta}d\tau$$

$$\Psi^{\alpha,\beta}=\phi_{\alpha_1}(1)\phi_{\alpha_2}(2)\phi_{\alpha_3}(3)\phi_{\alpha_4}(4)\phi_\beta(5)\phi_a(6)\phi_b(7)\phi_c(8)$$

$$\Psi^{\bar\alpha,\bar\beta}=\phi_{\bar\alpha_1}(1)\phi_{\bar\alpha_2}(2)\phi_{\bar\alpha_3}(3)\phi_{\bar\alpha_4}(4)\phi_{\bar\beta}(5)\phi_a(6)\phi_b(7)\phi_c(8)\ .$$

** The irreducible representation of $\mathfrak{S}_8$ corresponding to the singlet state is given explicitly in Serber's paper (J. Chem. Phys. **2** (1934) 697). The transformation matrix ***T*** between Serber's matrix and *W*(*S*), which is reduced with respect to $\mathfrak{S}_4(1, 2, 3, 4)\times\mathfrak{S}_3(6, 7, 8)$, is also given explicitly in Itoh, Ohno, and Kotani's paper.[4)]

Table I. Wave function

Number of the eigenfunction	Parent state of the carbon atom	$^1A_1{}'$ wave function of $CH_5{}^+$
1	s^2p^2 ^1D	$\frac{1}{2\sqrt{2}}\psi^{xxssd}_{1211,q}+\frac{1}{2\sqrt{2}}\psi^{xxsse}_{1211,q}-\frac{1}{2\sqrt{2}}\psi^{yyssd}_{1211,q}-\frac{1}{2\sqrt{2}}\psi^{yysse}_{1211,q}-\frac{1}{2}\psi^{xyssd}_{1212,q}-\frac{1}{2}\psi^{xysse}_{1212,q}$
2	^1D	$\frac{1}{2}\psi^{xzssd}_{1211,q}-\frac{1}{2}\psi^{xzsse}_{1211,q}+\frac{1}{2}\psi^{yzssd}_{1212,q}-\frac{1}{2}\psi^{yzsse}_{1212,q}$
3	^3P	$\frac{1}{2}\psi^{xzssd}_{3231,q}-\frac{1}{2}\psi^{xzsse}_{3231,q}+\frac{1}{2}\psi^{yzssd}_{3232,q}-\frac{1}{2}\psi^{yzsse}_{3232,q}$
4	^3P	$-\frac{1}{\sqrt{2}}\psi^{xyssd}_{3431,q}-\frac{1}{\sqrt{2}}\psi^{xysse}_{3431,q}$
5	sp^3 $^3P^0$	$\frac{1}{2\sqrt{2}}\psi^{yyxsd}_{3221,q}+\frac{1}{2\sqrt{2}}\psi^{yyxse}_{3221,q}+\frac{1}{2\sqrt{2}}\psi^{zzxsd}_{3221,q}+\frac{1}{2\sqrt{2}}\psi^{zzxse}_{3221,q}+\frac{1}{2\sqrt{2}}\psi^{xxysd}_{3222,q}+\frac{1}{2\sqrt{2}}\psi^{xxyse}_{3222,q}$ $+\frac{1}{2\sqrt{2}}\psi^{zzysd}_{3222,q}+\frac{1}{2\sqrt{2}}\psi^{zzyse}_{3222,q}$
6	$^1P^0$	$\frac{1}{2\sqrt{2}}\psi^{yyxsd}_{1211,q}+\frac{1}{2\sqrt{2}}\psi^{yyxse}_{1211,q}+\frac{1}{2\sqrt{2}}\psi^{zzxsd}_{1211,q}+\frac{1}{2\sqrt{2}}\psi^{zzxse}_{1211,q}+\frac{1}{2\sqrt{2}}\psi^{xxysd}_{1212,q}+\frac{1}{2\sqrt{2}}\psi^{xxyse}_{1212,q}$ $+\frac{1}{2\sqrt{2}}\psi^{zzysd}_{1212,q}+\frac{1}{2\sqrt{2}}\psi^{zzyse}_{1212,q}$
7	$^3D^0$	$\frac{1}{2\sqrt{2}}\psi^{yyxsd}_{3221,q}+\frac{1}{2\sqrt{2}}\psi^{yyxse}_{3221,q}-\frac{1}{2\sqrt{2}}\phi^{zzxsd}_{3221,q}-\frac{1}{2\sqrt{2}}\phi^{zzxse}_{3221,q}+\frac{1}{2\sqrt{2}}\phi^{xxysd}_{3222,q}+\frac{1}{2\sqrt{2}}\phi^{xxyse}_{3222,q}$ $-\frac{1}{2\sqrt{2}}\phi^{zzysd}_{3222,q}-\frac{1}{2\sqrt{2}}\phi^{zzyse}_{3222,q}$
8	$^3D^0$	$\frac{1}{2\sqrt{2}}\phi^{xxzsd}_{3221,q}-\frac{1}{2\sqrt{2}}\phi^{xxzse}_{3221,q}-\frac{1}{2\sqrt{2}}\phi^{yyzsd}_{3221,q}+\frac{1}{2\sqrt{2}}\phi^{yyzse}_{3221,q}-\frac{1}{2}\phi^{xyzsd}_{3222,q}+\frac{1}{2}\phi^{xyzse}_{3222,q}$
9	$^3D^0$	$\frac{1}{\sqrt{3}}\phi^{xyzsd}_{3411,q}-\frac{1}{\sqrt{3}}\phi^{xyzse}_{3411,q}+\frac{1}{\sqrt{6}}\phi^{xyzsd}_{3431,q}-\frac{1}{\sqrt{6}}\phi^{xyzse}_{3431,q}$
10	$^1D^0$	$\frac{1}{2\sqrt{2}}\phi^{yyxsd}_{1211,q}+\frac{1}{2\sqrt{2}}\phi^{yyxse}_{1211,q}-\frac{1}{2\sqrt{2}}\phi^{zzxsd}_{1211,q}-\frac{1}{2\sqrt{2}}\phi^{zzxse}_{1211,q}+\frac{1}{2\sqrt{2}}\phi^{xxysd}_{1212,q}+\frac{1}{2\sqrt{2}}\phi^{xxyse}_{1212,q}$ $-\frac{1}{2\sqrt{2}}\phi^{zzysd}_{1212,q}-\frac{1}{2\sqrt{2}}\phi^{zzyse}_{1212,q}$
11	$^1D^0$	$\frac{1}{2\sqrt{2}}\phi^{xxzsd}_{1211,q}-\frac{1}{2\sqrt{2}}\phi^{xxzse}_{1211,q}-\frac{1}{2\sqrt{2}}\phi^{yyzsd}_{1211,q}+\frac{1}{2\sqrt{2}}\phi^{yyzse}_{1211,q}-\frac{1}{2}\phi^{xyzsd}_{1212,q}+\frac{1}{2}\phi^{xyzse}_{1212,q}$
12	$^5S^0$	$\frac{1}{\sqrt{2}}\phi^{xyzsd}_{5411,q}-\frac{1}{\sqrt{2}}\phi^{xyzse}_{5411,q}$
13	$^3S^0$	$\frac{1}{\sqrt{6}}\phi^{xyzsd}_{3411,q}-\frac{1}{\sqrt{6}}\phi^{xyzse}_{3411,q}-\frac{1}{\sqrt{3}}\phi^{xyzsd}_{3431,q}+\frac{1}{\sqrt{3}}\phi^{xyzse}_{3431,q}$
14	p^4 ^1D	$\frac{1}{2\sqrt{2}}\psi^{xxzzd}_{1211,q}+\frac{1}{2\sqrt{2}}\phi^{xxzze}_{1211,q}-\frac{1}{2\sqrt{2}}\phi^{yyzzd}_{1211,q}-\frac{1}{2\sqrt{2}}\psi^{yyzze}_{1211,q}-\frac{1}{2}\phi^{xyzzd}_{1212,q}-\frac{1}{2}\phi^{xyzze}_{1212,q}$
15	^1D	$\frac{1}{2}\phi^{yyxzd}_{1211,q}-\frac{1}{2}\phi^{yyxze}_{1211,q}+\frac{1}{2}\phi^{xxyzd}_{1212,q}-\frac{1}{2}\phi^{xxyze}_{1212,q}$
16	^3P	$-\frac{1}{2}\phi^{yyxzd}_{3221,q}+\frac{1}{2}\phi^{yyxze}_{3221,q}-\frac{1}{2}\phi^{xxyzd}_{3222,q}+\frac{1}{2}\phi^{xxyze}_{3222,q}$
17	^3P	$\frac{1}{\sqrt{2}}\phi^{zzxyd}_{3421,q}+\frac{1}{\sqrt{2}}\phi^{zzxye}_{3421,q}$

In constructing these matrix elements, we have neglected the non-orthogonality integrals between atomic orbitals belonging to different atoms, except that we take these integrals into account in the numerical values of the exchange integrals. The assumption of the atomic orbitals being orthogonal is indeed crude, so there seems to be some ambiguity about the definition of $H^{(1,2)}$. Under these circumstances, a strict non-empirical calculation is out of question but we may obtain better results by using good semi-empirical values for the various parameters. Although we cannot judge what kind of experimental results we should most reliably depend upon, we use the semi-empirical values existing in the literatures for some parameters (see § 4).

The parameters which appear in the present study are defined as follows:

1) intracarbon integrals

$$F^0(s,\ s),\ F^0(s,\ p),\ F^0(p,\ p),\ G^1(s,\ p),\ F^2(p,\ p)\ \text{and}\ I_p-I_s\ ,$$

(These notations are due to Slater.[7])

2) $C-H$ (covalent) integrals

$$M_{\alpha\beta}=\iint\phi_\alpha(1)\,\phi_a(2)\left(\frac{1}{r_{12}}+\frac{1}{R_{CHa}}-\frac{1}{r_{Ha1}}-\frac{1}{r_{C2}}\right)\phi_\beta(1)\phi_a(2)d\tau_1d\tau_2$$

$$N_{\alpha\beta}=\iint\phi_\alpha(2)\,\phi_a(1)\left(\frac{1}{r_{12}}+\frac{1}{R_{CHa}}-\frac{1}{r_{Ha1}}-\frac{1}{r_{C2}}\right)\phi_\beta(1)\phi_a(2)d\tau_1d\tau_2\ ,$$

3) H(covalent)$-H$(covalent) integrals

$$K_{HH}=\iint\phi_a(1)\phi_b(2)\left(\frac{1}{r_{12}}+\frac{1}{R_{HaHb}}-\frac{1}{r_{Ha2}}-\frac{1}{r_{Hb1}}\right)\phi_a(1)\phi_b(2)d\tau_1d\tau_2$$

$$J_{HH}=\iint\phi_a(2)\phi_b(1)\left(\frac{1}{r_{12}}+\frac{1}{R_{HaHb}}-\frac{1}{r_{Ha2}}-\frac{1}{r_{Hb1}}\right)\phi_a(1)\phi_b(2)d\tau_1d\tau_2\ ,$$

4) $C-H$(ionic) integrals

$$\overline{M}_{\alpha\beta}=\iint\phi_\alpha(1)\phi_d(2)\left(\frac{1}{r_{12}}+\frac{1}{R_{CHd}}+\frac{1}{R_{CHe}}-\frac{1}{r_{Hd1}}-\frac{1}{r_{He1}}-\frac{1}{r_{C2}}\right)\phi_\beta(1)\phi_d(2)d\tau_1d\tau_2$$

$$\overline{N}_{\alpha\beta}=\iint\phi_\alpha(2)\phi_d(1)\left(\frac{1}{r_{12}}+\frac{1}{R_{CHd}}+\frac{1}{R_{CHe}}-\frac{1}{r_{Hd1}}-\frac{1}{r_{He1}}-\frac{1}{r_{C2}}\right)\phi_\beta(1)\phi_d(2)d\tau_1d\tau_2\ ,$$

5) H(covalent)$-H$(ionic) integrals

$$\overline{K}_{HH}=\iint\phi_a(1)\phi_d(2)\left(\frac{1}{r_{12}}+\frac{1}{R_{HaHd}}+\frac{1}{R_{HaHe}}-\frac{1}{r_{Hd1}}-\frac{1}{r_{He1}}-\frac{1}{r_{Ha2}}\right)\phi_a(1)\phi_d(2)d\tau_1d\tau_2$$

$$\overline{J}_{HH}=\iint\phi_a(2)\phi_d(1)\left(\frac{1}{r_{12}}+\frac{1}{R_{HaHd}}+\frac{1}{R_{HaHe}}-\frac{1}{r_{Hd1}}-\frac{1}{r_{He1}}-\frac{1}{r_{Ha2}}\right)\phi_a(1)\phi_d(2)d\tau_1d\tau_2\ ,$$

6) $C-H_d-H_e$ integrals

$$\overline{\overline{M}}_{\alpha\beta}=\iint\phi_\alpha(1)\phi_d(2)\left(\frac{1}{r_{12}}+\frac{1}{R_{CHd}}+\frac{1}{R_{CHe}}-\frac{1}{r_{Hd1}}-\frac{1}{r_{He1}}-\frac{1}{r_{C2}}\right)\phi_\beta(1)\phi_e(2)d\tau_1d\tau_2$$

$$\overline{\overline{N}}_{\alpha\beta}=\iint\phi_\alpha(2)\phi_d(1)\left(\frac{1}{r_{12}}+\frac{1}{R_{CHd}}+\frac{1}{R_{CHe}}-\frac{1}{r_{Hd1}}-\frac{1}{r_{He1}}-\frac{1}{r_{C2}}\right)\phi_\beta(1)\phi_e(2)d\tau_1d\tau_2\ ,$$

7) H(covalent)$-H_d-H_e$ integrals

$$\overline{K}_{HH}=\iint\phi_a(1)\phi_d(2)\left(\frac{1}{r_{12}}+\frac{1}{R_{HaHd}}+\frac{1}{R_{HaHe}}-\frac{1}{r_{Ha2}}-\frac{1}{r_{Hd1}}-\frac{1}{r_{He1}}\right)\phi_a(1)\phi_e(2)d\tau_1d_2$$

$$\bar{J}_{HH}=\iint\phi_a(2)\phi_d(1)\left(\frac{1}{r_{12}}+\frac{1}{R_{HaHd}}+\frac{1}{R_{HaHe}}-\frac{1}{r_{Ha2}}-\frac{1}{r_{Hd1}}-\frac{1}{r_{He1}}\right)\phi_a(1)\phi_e(2)d\tau_1 d\tau_2\ ,$$

8) $$\bar{\bar{K}}=\int\phi_d(1)\left(\frac{1}{R_{HdHe}}-\frac{1}{r_{He1}}\right)\phi_d(1)d\tau_1+3\int\phi_a(1)\left(\frac{1}{R_{HaHe}}-\frac{1}{r_{He1}}\right)\phi_a(1)d\tau_1\ .$$

The explicit forms of the energy matrix are given in Table II.

Table II. Elements of energy matrix.

Any element $\boldsymbol{H}_{ij}$ may be devided into three parts H_{ij}, $\bar{H}_{ij}$, and $\bar{\bar{H}}_{ij}$. ($\boldsymbol{H}_{ij}=H_{ij}+\bar{H}_{ij}+\bar{\bar{H}}_{ij}$), where H_{ij} are those containing $W(C)$, $W(H)$, $M_{\alpha\beta}$, $N_{\alpha\beta}$, K_{HH} and J_{HH}, $\bar{H}_{ij}$ containing $\bar{M}_{\alpha\beta}$, $\bar{N}_{\alpha\beta}$, $\bar{K}_{HH}$ and $\bar{J}_{HH}$, and $\bar{\bar{H}}_{ij}$ containing $\bar{\bar{M}}_{\alpha\beta}$, $\bar{\bar{N}}_{\alpha\beta}$, $\bar{\bar{K}}_{HH}$ and $\bar{\bar{J}}_{HH}$. ($\bar{\bar{K}}_{HH}$ are contained only in the diagonal elements.) They are all zero but those given in the following.

1) H_{ij}. The explicit forms for H_{ij} are given in Itoh, Ohno, and Kotani's paper[4] for the methyl radical. By putting $\theta=90°$ in their Appendix III, our H_{ij} are obtained. Our definition of $M_{\alpha\beta}$, $N_{\alpha\beta}$ are opposite in sign to theirs. $4W_H(^2S)$ must be added to each diagonal element instead of $3W_H(^2S)$.

2) $\bar{H}_{ij}$

$\bar{H}_{1,1}=2\bar{M}_{\pi\pi}+2\bar{M}_{ss}-\bar{N}_{\pi\pi}-\bar{N}_{ss}+3\bar{K}_{HH}$

$\bar{H}_{2,2}=\bar{M}_{\pi\pi}+\bar{M}_{\sigma\sigma}+2\bar{M}_{ss}-\frac{1}{2}\bar{N}_{\pi\pi}-\frac{1}{2}\bar{N}_{\sigma\sigma}-\bar{N}_{ss}+3\bar{K}_{HH}$

$\bar{H}_{3,3}=\bar{M}_{\pi\pi}+\bar{M}_{\sigma\sigma}+2\bar{M}_{ss}+\frac{1}{2}\bar{N}_{\pi\pi}+\frac{1}{2}\bar{N}_{\sigma\sigma}-\bar{N}_{ss}+3\bar{K}_{HH}-2\bar{J}_{HH}$

$\bar{H}_{4,4}=2\bar{M}_{\pi\pi}+2\bar{M}_{ss}-2\bar{N}_{\pi\pi}-\bar{N}_{ss}+3\bar{K}_{HH}+\bar{J}_{HH}$

$\bar{H}_{5,5}=2\bar{M}_{\pi\pi}+\bar{M}_{\sigma\sigma}+\bar{M}_{ss}-\frac{1}{2}\bar{N}_{\sigma\sigma}+\frac{1}{2}\bar{N}_{ss}+3\bar{K}_{HH}-2\bar{J}_{HH}$

$\bar{H}_{6,6}=2\bar{M}_{\pi\pi}+\bar{M}_{\sigma\sigma}+\bar{M}_{ss}-\bar{N}_{\pi\pi}-\frac{1}{2}\bar{N}_{\sigma\sigma}-\frac{1}{2}\bar{N}_{ss}+3\bar{K}_{HH}$

$\bar{H}_{7,7}=2\bar{M}_{\pi\pi}+\bar{M}_{\sigma\sigma}+\bar{M}_{ss}-\frac{1}{2}\bar{N}_{\sigma\sigma}+\frac{1}{2}\bar{N}_{ss}+3\bar{K}_{HH}-2\bar{J}_{HH}$

$\bar{H}_{8,8}=2\bar{M}_{\pi\pi}+\bar{M}_{\sigma\sigma}+\bar{M}_{ss}-\bar{N}_{\pi\pi}+\frac{1}{2}\bar{N}_{\sigma\sigma}+\frac{1}{2}\bar{N}_{ss}+3\bar{K}_{HH}-2\bar{J}_{HH}$

$\bar{H}_{9,9}=2\bar{M}_{\pi\pi}+\bar{M}_{\sigma\sigma}+\bar{M}_{ss}-\frac{5}{3}\bar{N}_{\pi\pi}-\frac{1}{3}\bar{N}_{\sigma\sigma}-\bar{N}_{ss}+3\bar{K}_{HH}+\bar{J}_{HH}$

$\bar{H}_{10,10}=2\bar{M}_{\pi\pi}+\bar{M}_{\sigma\sigma}+\bar{M}_{ss}-\bar{N}_{\pi\pi}-\frac{1}{2}\bar{N}_{\sigma\sigma}-\frac{1}{2}\bar{N}_{ss}+3\bar{K}_{HH}$

$\bar{H}_{11,11}=2\bar{M}_{\pi\pi}+\bar{M}_{\sigma\sigma}+\bar{M}_{ss}-\bar{N}_{\pi\pi}-\frac{1}{2}\bar{N}_{\sigma\sigma}-\frac{1}{2}\bar{N}_{ss}+3\bar{K}_{HH}$

$\bar{H}_{12,12}=2\bar{M}_{\pi\pi}+\bar{M}_{\sigma\sigma}+\bar{M}_{ss}+\frac{1}{2}\bar{N}_{\pi\pi}+\frac{1}{4}\bar{N}_{\sigma\sigma}+\frac{1}{4}\bar{N}_{ss}+3\bar{K}_{HH}-3\bar{J}_{HH}$

$\bar{H}_{13,13}=2\bar{M}_{\pi\pi}+\bar{M}_{\sigma\sigma}+\bar{M}_{ss}-\frac{11}{6}\bar{N}_{\pi\pi}-\frac{11}{12}\bar{N}_{\sigma\sigma}-\frac{1}{4}\bar{N}_{ss}+3\bar{K}_{HH}+\bar{J}_{HH}$

$\bar{H}_{14,14}=2\bar{M}_{\pi\pi}+2\bar{M}_{\sigma\sigma}-\bar{N}_{\pi\pi}-\bar{N}_{\sigma\sigma}+3\bar{K}_{HH}$

$\bar{H}_{15,15}=3\bar{M}_{\pi\pi}+\bar{M}_{\sigma\sigma}-\frac{3}{2}\bar{N}_{\pi\pi}-\frac{1}{2}\bar{N}_{\sigma\sigma}+3\bar{K}_{HH}$

$\bar{H}_{16,16}=3\bar{M}_{\pi\pi}+\bar{M}_{\sigma\sigma}-\frac{1}{2}\bar{N}_{\pi\pi}+\frac{1}{2}\bar{N}_{\sigma\sigma}+3\bar{K}_{HH}-2\bar{J}_{HH}$

$\bar{H}_{17,17}=2\bar{M}_{\pi\pi}+2\bar{M}_{\sigma\sigma}-2\bar{N}_{\pi\pi}-\bar{N}_{\sigma\sigma}+3\bar{K}_{HH}+\bar{J}_{HH}$

$\bar{H}_{2,5}=\bar{H}_{7,15}=\bar{H}_{5,15}=\bar{H}_{3,10}=-\bar{H}_{3,6}=-\bar{H}_{2,7}=-\bar{H}_{6,16}=-\bar{H}_{10,16}=-\frac{1}{2}\sqrt{\frac{3}{2}}\bar{N}_{s\sigma}$

$\bar{H}_{2,6}=-\bar{H}_{2,10}=-\bar{H}_{6,15}=-\bar{H}_{10,15}=-\frac{1}{\sqrt{2}}\bar{M}_{s\sigma}+\frac{1}{2\sqrt{2}}\bar{N}_{s\sigma}$

$\bar{H}_{1,8}=-\bar{H}_{8,14}=\sqrt{\frac{3}{2}}\bar{N}_{s\sigma}$

$$\overline{H}_{5,16}=\overline{H}_{7,16}=-\frac{1}{\sqrt{2}}\overline{M}_{s\sigma}-\frac{1}{2\sqrt{2}}\overline{N}_{s\sigma}$$

$$\overline{H}_{1,11}=\overline{H}_{11,14}=\sqrt{2}\,\overline{M}_{s\sigma}-\frac{1}{\sqrt{2}}\overline{N}_{s\sigma}$$

$$\overline{H}_{2,3}=\overline{H}_{15,16}=-\frac{\sqrt{3}}{2}\overline{N}_{\pi\pi}+\frac{\sqrt{3}}{2}\overline{N}_{\sigma\sigma}$$

$$\overline{H}_{5,6}=\overline{H}_{7,10}=\frac{\sqrt{3}}{2}\overline{N}_{\pi\pi}-\frac{\sqrt{3}}{2}\overline{N}_{ss}$$

$$\overline{H}_{3,5}=-\overline{H}_{3,7}=\frac{1}{\sqrt{2}}\overline{M}_{s\sigma}-\frac{3}{2\sqrt{2}}\overline{N}_{s\sigma}$$

$$\overline{H}_{4,12}=-\overline{H}_{12,17}=\frac{\sqrt{5}}{2}\overline{N}_{s\sigma}$$

$$\overline{H}_{5,7}=\overline{H}_{6,10}=\overline{M}_{\pi\pi}-\overline{M}_{\sigma\sigma}-\frac{1}{2}\overline{N}_{\pi\pi}+\frac{1}{2}\overline{N}_{\sigma\sigma}$$

$$\overline{H}_{4,9}=-\sqrt{\frac{2}{3}}\overline{M}_{s\sigma}$$

$$\overline{H}_{4,13}=\frac{2}{\sqrt{3}}\overline{M}_{s\sigma}-\frac{\sqrt{3}}{2}\overline{N}_{s\sigma}$$

$$\overline{H}_{8,11}=\frac{\sqrt{3}}{2}\overline{N}_{\sigma\sigma}-\frac{\sqrt{3}}{2}\overline{N}_{ss}$$

$$\overline{H}_{9,12}=\sqrt{\frac{5}{6}}\overline{N}_{\pi\pi}-\sqrt{\frac{5}{6}}\overline{N}_{\sigma\sigma}$$

$$\overline{H}_{9,13}=\frac{\sqrt{2}}{6}\overline{N}_{\pi\pi}-\frac{\sqrt{2}}{6}\overline{N}_{\sigma\sigma}$$

$$\overline{H}_{9,17}=-\sqrt{\frac{2}{3}}\overline{M}_{s\sigma}+\sqrt{\frac{2}{3}}\overline{N}_{s\sigma}$$

$$\overline{H}_{12,13}=\sqrt{\frac{5}{12}}\overline{N}_{\pi\pi}+\sqrt{\frac{5}{48}}\overline{N}_{\sigma\sigma}-\sqrt{\frac{45}{48}}\overline{N}_{ss}$$

$$\overline{H}_{13,17}=\frac{2}{\sqrt{3}}\overline{M}_{s\sigma}-\frac{1}{2\sqrt{3}}\overline{N}_{s\sigma}$$

3) $\overline{\overline{H}}_{ij}$

$$\overline{\overline{H}}_{1,1}=2\overline{\overline{M}}_{\pi\pi}+2\overline{\overline{M}}_{ss}-\overline{\overline{N}}_{\pi\pi}-\overline{\overline{N}}_{ss}+3\overline{\overline{K}}_{HH}$$

$$\overline{\overline{H}}_{2,2}=-\overline{\overline{M}}_{\pi\pi}-\overline{\overline{M}}_{\sigma\sigma}-2\overline{\overline{M}}_{ss}+\frac{1}{2}\overline{\overline{N}}_{\pi\pi}+\frac{1}{2}\overline{\overline{N}}_{\sigma\sigma}+\overline{\overline{N}}_{ss}-3\overline{\overline{K}}_{HH}$$

$$\overline{\overline{H}}_{3,3}=-\overline{\overline{M}}_{\pi\pi}-\overline{\overline{M}}_{\sigma\sigma}-2\overline{\overline{M}}_{ss}-\frac{1}{2}\overline{\overline{N}}_{\pi\pi}-\frac{1}{2}\overline{\overline{N}}_{\sigma\sigma}+\overline{\overline{N}}_{ss}-3\overline{\overline{K}}_{HH}+2\overline{\overline{J}}_{HH}$$

$$\overline{\overline{H}}_{4,4}=2\overline{\overline{M}}_{\pi\pi}+2\overline{\overline{M}}_{ss}-2\overline{\overline{N}}_{\pi\pi}-\overline{\overline{N}}_{ss}+3\overline{\overline{K}}_{HH}+\overline{\overline{J}}_{HH}$$

$$\overline{\overline{H}}_{5,5}=2\overline{\overline{M}}_{\pi\pi}+\overline{\overline{M}}_{\sigma\sigma}+\overline{\overline{M}}_{ss}-\frac{1}{2}\overline{\overline{N}}_{\sigma\sigma}+\frac{1}{2}\overline{\overline{N}}_{ss}+3\overline{\overline{K}}_{HH}-2\overline{\overline{J}}_{HH}$$

$$\overline{\overline{H}}_{6,6}=2\overline{\overline{M}}_{\pi\pi}+\overline{\overline{M}}_{\sigma\sigma}+\overline{\overline{M}}_{ss}-\overline{\overline{N}}_{\pi\pi}-\frac{1}{2}\overline{\overline{N}}_{\sigma\sigma}-\frac{1}{2}\overline{\overline{N}}_{ss}+3\overline{\overline{K}}_{HH}$$

$$\overline{\overline{H}}_{7,7}=2\overline{\overline{M}}_{\pi\pi}+\overline{\overline{M}}_{\sigma\sigma}+\overline{\overline{M}}_{ss}-\frac{1}{2}\overline{\overline{N}}_{\sigma\sigma}+\frac{1}{2}\overline{\overline{N}}_{ss}+3\overline{\overline{K}}_{HH}-2\overline{\overline{J}}_{HH}$$

$$\overline{\overline{H}}_{8,8}=-2\overline{\overline{M}}_{\pi\pi}-\overline{\overline{M}}_{\sigma\sigma}-\overline{\overline{M}}_{ss}+\overline{\overline{N}}_{\pi\pi}-\frac{1}{2}\overline{\overline{N}}_{\sigma\sigma}-\frac{1}{2}\overline{\overline{N}}_{ss}-3\overline{\overline{K}}_{HH}+2\overline{\overline{J}}_{HH}$$

$$\overline{\overline{H}}_{9,9}=-2\overline{\overline{M}}_{\pi\pi}-\overline{\overline{M}}_{\sigma\sigma}-\overline{\overline{M}}_{ss}+\frac{5}{3}\overline{\overline{N}}_{\pi\pi}+\frac{1}{3}\overline{\overline{N}}_{\sigma\sigma}+\overline{\overline{N}}_{ss}-3\overline{\overline{K}}_{HH}-\overline{\overline{J}}_{HH}$$

$$\overline{\overline{H}}_{10,10}=2\overline{\overline{M}}_{\pi\pi}+\overline{\overline{M}}_{\sigma\sigma}+\overline{\overline{M}}_{ss}-\overline{\overline{N}}_{\pi\pi}-\frac{1}{2}\overline{\overline{N}}_{\sigma\sigma}-\frac{1}{2}\overline{\overline{N}}_{ss}+3\overline{\overline{K}}_{HH}$$

$$\overline{\overline{H}}_{11,11}=-2\overline{\overline{M}}_{\pi\pi}-\overline{\overline{M}}_{\sigma\sigma}-\overline{\overline{M}}_{ss}+\overline{\overline{N}}_{\pi\pi}+\frac{1}{2}\overline{\overline{N}}_{\sigma\sigma}+\frac{1}{2}\overline{\overline{N}}_{ss}-3\overline{\overline{K}}_{HH}$$

$$\overline{\overline{H}}_{12,12}=-2\overline{\overline{M}}_{\pi\pi}-\overline{\overline{M}}_{\sigma\sigma}-\overline{\overline{M}}_{ss}-\frac{1}{2}\overline{\overline{N}}_{\pi\pi}-\frac{1}{4}\overline{\overline{N}}_{\sigma\sigma}-\frac{1}{4}N_{ss}-3\overline{\overline{K}}_{HH}+3\overline{\overline{J}}_{HH}$$

$$\overline{\overline{H}}_{13,13}=-2\overline{\overline{M}}_{\pi\pi}-\overline{\overline{M}}_{\sigma\sigma}-\overline{\overline{M}}_{ss}+\frac{11}{6}\overline{\overline{N}}_{\pi\pi}+\frac{11}{12}\overline{\overline{N}}_{\sigma\sigma}+\frac{1}{4}\overline{\overline{N}}_{ss}-3\overline{\overline{K}}_{HH}-\overline{\overline{J}}_{HH}$$

$$\overline{\overline{H}}_{14,14}=2\overline{\overline{M}}_{\pi\pi}+2\overline{\overline{M}}_{\sigma\sigma}-\overline{\overline{N}}_{\pi\pi}-\overline{\overline{N}}_{\sigma\sigma}+3\overline{\overline{K}}_{HH}$$

$$\overline{\overline{H}}_{15,15}=-3\overline{\overline{M}}_{\pi\pi}-\overline{\overline{M}}_{\sigma\sigma}+\frac{3}{2}\overline{\overline{N}}_{\pi\pi}+\frac{1}{2}\overline{\overline{N}}_{\sigma\sigma}-3\overline{\overline{K}}_{HH}$$

$$\overline{H}_{16,16}=-3\overline{\overline{M}}_{\pi\pi}-\overline{\overline{M}}_{\sigma\sigma}+\frac{1}{2}\overline{\overline{N}}_{\pi\pi}-\frac{1}{2}\overline{\overline{N}}_{\sigma\sigma}-3\overline{\overline{K}}_{HH}+2\overline{\overline{J}}_{HH}$$

$$\overline{\overline{H}}_{17,17}=2\overline{\overline{M}}_{\pi\pi}+2\overline{\overline{M}}_{\sigma\sigma}-2\overline{\overline{N}}_{\pi\pi}-\overline{\overline{N}}_{\sigma\sigma}+3K_{HH}+\overline{\overline{J}}_{HH}$$

$$\overline{\overline{H}}_{2,3}=\overline{\overline{H}}_{15,16}=\frac{\sqrt{3}}{2}\overline{\overline{N}}_{\pi\pi}-\frac{\sqrt{3}}{2}\overline{\overline{N}}_{\sigma\sigma}$$

$$\overline{\overline{H}}_{5,7}=\overline{\overline{H}}_{6,10}=\overline{\overline{M}}_{\pi\pi}-\overline{\overline{M}}_{\sigma\sigma}-\frac{1}{2}\overline{\overline{N}}_{\pi\pi}+\frac{1}{2}N_{\sigma\sigma}$$

$$\overline{\overline{H}}_{5,6}=\overline{\overline{H}}_{7,10}=\frac{\sqrt{3}}{2}\overline{\overline{N}}_{\pi\pi}-\frac{\sqrt{3}}{2}\overline{\overline{N}}_{ss}$$

$$\overline{\overline{H}}_{8,11}=-\frac{\sqrt{3}}{2}\overline{\overline{N}}_{\sigma\sigma}+\frac{\sqrt{3}}{2}\overline{\overline{N}}_{ss}$$

$$\overline{\overline{H}}_{9,12}=-\sqrt{\frac{5}{6}}\overline{\overline{N}}_{\pi\pi}+\sqrt{\frac{5}{6}}\overline{\overline{N}}_{\sigma\sigma}$$

$$\overline{\overline{H}}_{9,13}=-\frac{\sqrt{2}}{6}\overline{\overline{N}}_{\pi\pi}+\frac{\sqrt{2}}{6}\overline{\overline{N}}_{\sigma\sigma}$$

$$\overline{\overline{H}}_{12,13}=-\sqrt{\frac{5}{12}}\overline{\overline{N}}_{\pi\pi}-\sqrt{\frac{5}{48}}\overline{\overline{N}}_{\sigma\sigma}+\sqrt{\frac{45}{48}}\overline{\overline{N}}_{ss}$$

§ 4. Estimations of Integrals

The values in *ev* of intracarbon integrals used are as follows:

$$F^0(s,\ s)=17.82,\quad F^0(s,\ p)=16.07$$
$$F^0(p,\ p)=14.75,\quad G^1(s,\ p)=2.18,$$
$$F^2(p,\ p)=0.188,\quad I_p-I_s=12.79.$$

These are taken from Van Vleck's paper.[8] The coulomb integrals $M_{\alpha\beta}$, $\overline{M}_{\alpha\beta}$, $\overline{\overline{M}}_{\alpha\beta}$ are obtained from Kotani-Amemiya's table[9] by using the carbon effective charge 3.18. (For $\overline{M}_{\alpha\beta}$ and $\overline{\overline{M}}_{\alpha\beta}$, we have also used some approximate values of the various three-center integrals. See below). The empirical values for $C-H$(covalent) integrals $N_{\alpha\beta}$ have been given by Van Vleck[10], Penney[11], and Voge[2], but we have no such information for $\overline{N}_{\alpha\beta}$ and $\overline{\overline{N}}_{\alpha\beta}$. Therefore we carry out in the present study two parallel calculations with two different sets of parameters, i.e., (a) with the exchange integrals $N_{\alpha\beta}$, $\overline{N}_{\alpha\beta}$, $\overline{\overline{N}}_{\alpha\beta}$ being computed from Kotani-Amemiya's table[9] and, if necessary, incorporated with approximate values of the various three-center integrals, and (b) with the exchange integrals $\overline{N}_{\alpha\beta}$, $\overline{\overline{N}}_{\alpha\beta}$, $N_{\alpha\beta}$ being those computed in "case (a)" multiplied by certain factors. The factors are determined from the ratios of the empirical values to those computed from the table for $N_{\alpha\beta}$ (i.e., 0.6831 for N_{ss}, $\overline{N}_{ss}$, N_{ss}, 1.288 for $N_{\sigma\sigma}$, $\overline{N}_{\sigma\sigma}$,

Table III. Estimated values in *ev* of three-center iutegrals.

$\overline{R}$	0.8174A	0.9196A	1.022A	1.124A	1.226A	1.328A
$(de:ss)$	4.42	3.41	2.49	2.08	1.57	1.16
$(de:\pi\pi)$	5.15	3.94	2.83	2.25	1.69	1.23
$(de:\sigma\sigma)$	5.20	3.98	2.92	2.27	1.71	1.25
$(H_e:ds)$	8.81	7.44	6.26	5.19	4.15	3.28
$(H_e:d\sigma)$	2.58	2.86	2.93	3.07	3.00	2.56
$(ds:es)$	7.27	6.16	5.13	4.22	3.42	2.75
$(d\sigma:e\sigma)$	−1.08	−1.25	−1.36	−1.44	−1.34	−1.22
$(d\pi:e\pi)$	0.40	0.37	0.34	0.30	0.28	0.20
$(C:de)$	6.56	4.80	3.48	2.85	2.20	1.69
$(H_e:ad)$	4.21	3.66	3.18	2.83	2.43	2.09
$(H\ :de)$	3.87	2.96	2.21	1.69	1.27	0.94
$(aa:de)$	3.25	2.49	1.78	1.42	1.05	0.78
$(ad:ae)$	2.31	1.94	1.64	1.33	1.08	0.86

$\bar{\bar{N}}_{\sigma\sigma}$, 0.8322 for $N_{\pi\pi}$, $\bar{N}_{\pi\pi}$, $\bar{\bar{N}}_{\pi\pi}$, and 0.6238 for $N_{s\sigma}$, $\bar{N}_{s\sigma}$). The coulomb and exchange integrals between hydrogen atoms are, as usual, assumed to be 1/10 and 9/10 of the Morse function, respectively.

There appear some three-center integrals to be evaluated. We estimate their values by the same method as that of Ellison,[12] which he has used in his calculation of the water molecule. The estimated values of three-center integrals are given in Table III. The values of various integrals used are given in Table IV.

Table IV. Valves in *ev* of various integrals.

M_{ss}	−0.6333	N_{ss}	a	−2.93	$N_{\pi\pi}$	a	0.72	K_{HH}	−0.106
$M_{\sigma\sigma}$	−2.036		b	−2.0		b	0.60	J_{HH}	−0.951
$M_{\pi\pi}$	0.069	$N_{\sigma\sigma}$	a	−1.75	$N_{s\sigma}$	a	−2.69		
$M_{s\sigma}$	−1.708		b	−2.25		b	−1.69		

$\bar{R}$		0.8174A	0.9196A	1.022A	1.124A	1.226A	1.328A
$\bar{M}_{ss}$		1.55	0.60	0.08	−0.15	−0.23	−0.24
$\bar{M}_{\sigma\sigma}$		−4.40	−4.58	−4.28	−3.77	−3.21	−2.68
$\bar{M}_{\pi\pi}$		4.52	3.14	2.25	1.66	1.26	0.98
$\bar{M}_{s\sigma}$		3.37	3.33	3.23	3.09	2.92	2.74
$\bar{N}_{ss}$	a	−1.08	−1.67	−1.79	−1.65	−1.34	−1.04
	b	−0.74	−1.14	−1.22	−1.12	−0.92	−0.71
$\bar{N}_{\sigma\sigma}$	a	1.39	0.59	0.08	−0.32	−0.49	−0.44
	b	1.79	0.76	0.10	−0.41	−0.63	−0.57
$\bar{N}_{\pi\pi}$	a	1.31	1.06	0.85	0.67	0.52	0.40
	b	1.09	0.88	0.70	0.55	0.43	0.33
$\bar{N}_{s\sigma}$	a	−0.36	−0.96	−1.21	−1.27	−1.16	−0.92
	b	−0.22	−0.60	−0.76	−0.80	−0.73	−0.58
$\bar{K}_{HH}$		−0.03	−0.06	−0.07	−0.08	−0.09	−0.09
$\bar{J}_{HH}$		−2.05	−1.83	−1.63	−1.48	−1.30	−1.14
$\bar{\bar{M}}_{ss}$		−0.80	−0.74	−0.68	−0.62	−0.56	−0.50
$\bar{\bar{M}}_{\sigma\sigma}$		−2.32	−1.80	−1.37	−1.18	−0.91	−0.73
$\bar{\bar{M}}_{\pi\pi}$		1.09	0.60	0.22	−0.07	−0.19	−0.27
$\bar{\bar{N}}_{ss}$	a	−1.92	−2.34	−2.34	−2.07	−1.66	−1.27
	b	−1.31	−1.60	−1.60	−1.41	−1.14	−0.87
$\bar{\bar{N}}_{\sigma\sigma}$	a	3.98	4.16	3.97	3.62	3.21	2.63
	b	5.12	5.35	5.11	4.66	4.14	3.39
$\bar{\bar{N}}_{\pi\pi}$	a	0.40	0.37	0.34	0.30	0.28	0.20
	b	0.33	0.31	0.28	0.25	0.23	0.17
$\bar{\bar{K}}_{HH}$		−0.47	−0.37	−0.30	−0.24	−0.20	−0.15
$\bar{\bar{J}}_{HH}$		−2.40	−2.20	−2.00	−1.82	−1.62	−1.44

§ 5. Solution of Secular Equations

The secular equation is of the seventeenth degree. We have solved them for six values of the $C-H$(ionic) distance $\bar{R}$, i.e., for $\bar{R}=$ 0.8174, 0.9196, 1.022, 1.124, 1.226, and 1.328A by the iteration method.

The electronic energy of the ground state is given in Table V for various values of $\bar{R}$ and illustrated by curve a (using parameters $N_{\alpha\beta}$, $\bar{N}_{\alpha\beta}$, $\bar{\bar{N}}_{\alpha\beta}$ without factor) and b (using parameters $N_{\alpha\beta}$, $\bar{N}_{\alpha\beta}$, $\bar{\bar{N}}_{\alpha\beta}$ with factor) in Fig. 2., from which we can see that the value of the equilibrium $C-H$(ionic) distance is nearly equal to that of the covalent $C-H$ distance for both (a) and (b). The calculated dissociation energy from the potential minimum is 21.98 ev for (a) "using parameters $N_{\alpha\beta}$, $\bar{N}_{\alpha\beta}$, $\bar{\bar{N}}_{\alpha\beta}$ without factor" and 19.75 eV for (b)

“ using parameters $N_{\alpha\beta}$, $\overline{N}_{\alpha\beta}$, $N_{\alpha\beta}$ with factor ”. If we subtract 16.9 eV, the experimental dissociation energy of the methane molecule from it, we obtain the proton affinity of the methane molecule to be 5.08 eV for (a) and 2.85 eV for (b). There is the difference of about 2.2 eV.

Table V. Binding energy in *ev*.

$\overline{R}$	a	b
0.8174A	15.921	14.685
0.9196A	20.222	18.372
1.022A	21.910	19.709
1.124A	21.974	19.742
1.226A	21.444	19.184
1.328A	20.397	18.037

a: using parameters $N_{\alpha\beta}$, $\overline{N}_{\alpha\beta}$, $\overline{\overline{N}}_{\alpha\beta}$ without factor

b: using parameters $N_{\alpha\beta}$, $\overline{N}_{\alpha\beta}$, $\overline{\overline{N}}_{\alpha\beta}$ with factor

The wave functions of the ground state are given in Table VI for various values of the *C—H*(ionic) distance and for two different sets of parameters. The contributions of s^2p^2, sp^3 and p^4 configurations of the carbon atom are shown in Table VII, where the results for the methane molecule and the methyl radical are also given for the sake of comparison.

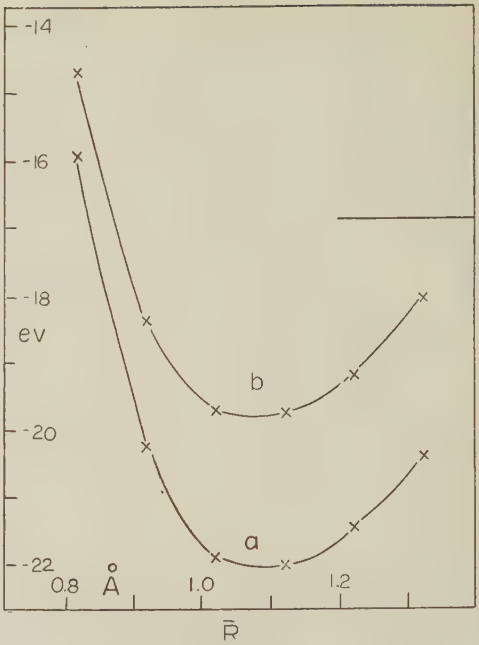

Fig. 2. Electronic energies of the ground state $^1A'_1$ of CH_5^+

a) using parameters $N_{\alpha\beta}$, $\overline{N}_{\alpha\beta}$, $\overline{\overline{N}}_{\alpha\beta}$ without factor.

b) using parameters $N_{\alpha\beta}$, $\overline{N}_{\alpha\beta}$, $\overline{\overline{N}}_{\alpha\beta}$ with factor.

The horizontal line indicates the dissociation limit into CH_4+H^+. We take $C(s^2p^2\ ^3P)+4H(^2S)+H^+$ as the origin of energy.

Table VI. Squares of coefficients of wave function.

a) using parameters $N_{\alpha\beta}$, $\overline{N}_{\alpha\beta}$, $\overline{\overline{N}}_{\alpha\beta}$ without factor.

No. of the eigenfunction	parent state of the carbon atom	$\overline{R}$ =0.8174A	$\overline{R}$ =0.9196A	$\overline{R}$ =1.022A	$\overline{R}$ =1.124A	$\overline{R}$ =1.226A	$\overline{R}$ =1.328A
1	$s^2p^2\ ^1D$	000	000	000	000	000	001
2	^1D	055	068	075	078	079	079
3	^3P	129	180	209	226	235	238
4	^3P	000	000	000	000	001	001
5	$sp^3\ ^3P^0$	101	089	069	056	040	028
6	$^1P^0$	057	039	026	019	012	008
7	$^3D^0$	093	082	062	048	031	018
8	$^3D^0$	050	068	085	095	108	119
9	$^3D^0$	078	087	095	101	108	114
10	$^1D^0$	053	036	023	016	009	005
11	$^1D^0$	026	030	033	035	038	039
12	$^5S^0$	084	118	148	170	194	216
13	$^3S^0$	015	016	016	016	018	017
14	$p^4\ ^1D$	057	043	032	024	019	012
15	^1D	010	010	014	015	017	020
16	^3P	024	026	039	045	052	060
17	^3P	168	108	074	056	039	025

Table VI.

b) using parameters $N_{\alpha\beta}$, $\bar{N}_{\alpha\beta}$, $\bar{\bar{N}}_{\alpha\beta}$ with factor.

No. of the eigenfunction	parent state of the carbon atom	$\bar{R}$ =0.8174A	$\bar{R}$ =0.9196A	$\bar{R}$ =1.022A	$\bar{R}$ =1.124A	$\bar{R}$ =1.226A	$\bar{R}$ =1.328A
1	$s^2p^2\ {}^1D$	000	000	000	000	001	002
2	${}^1D$	049	079	094	102	105	106
3	${}^3P$	117	214	272	303	320	327
4	${}^3P$	000	000	001	001	002	004
5	$sp^3\ {}^3P^0$	142	118	087	068	048	035
6	${}^1P^0$	091	057	035	025	016	010
7	${}^3D^0$	143	115	080	060	038	024
8	${}^3D^0$	021	041	060	070	083	092
9	${}^3D^0$	038	057	070	079	087	094
10	${}^1D^0$	093	056	032	021	012	007
11	${}^1D^0$	013	019	024	026	029	030
12	${}^5S^0$	038	079	115	137	163	184
13	${}^3S^0$	010	012	013	013	015	014
14	$p^4\ {}^1D$	054	035	025	017	013	008
15	${}^1D$	003	004	007	008	009	011
16	${}^3P$	007	011	020	024	029	033
17	${}^3P$	181	103	065	046	030	019

Table VII. Contributions of s^2p^2, sp^3, and p^4 configurations.

	s^2p^2	sp^3	p^4
a) $\bar{R}$=0.8174A	0.18	0.56	0.26
$\bar{R}$=0.9196A	0.25	0.56	0.19
$\bar{R}$=1.022A	0.28	0.56	0.16
$\bar{R}$=1.124A	0.30	0.56	0.14
$\bar{R}$=1.226A	0.32	0.55	0.13
$\bar{R}$=1.328A	0.32	0.56	0.12
b) $\bar{R}$=0.8174A	0.17	0.58	0.25
$\bar{R}$=0.9196A	0.29	0.56	0.15
$\bar{R}$=1.022A	0.37	0.51	0.12
$\bar{R}$=1.124A	0.41	0.49	0.10
$\bar{R}$=1.226A	0.43	0.49	0.08
$\bar{R}$=1.328A	0.44	0.49	0.07
CH_4	0.41	0.52	0.07
CH_3	0.42	0.52	0.06

§ 6. Discussion

According to the experiences in similar calculations of molecular energies the computed binding energies, when we use the parameters $N_{\alpha\beta}$, $\bar{N}_{\alpha\beta}$, $\bar{\bar{N}}_{\alpha\beta}$ without factor – "case (a)" – (not with factor – "case (b)" –), are generally larger than those experimentally known. This is due to the neglects of the non-orthogonalities of the atomic orbitals and the higher order permutations of electrons. So we can suppose the value for "case (a)" may be a little too large to be accepted. According to the experiences, too, we obtain rather surprising good results when we use good semi-empirical values for intermolecular integrals. In our treatment "case (b)", the values used for $N_{\alpha\beta}$ are the empirically better ones, but we do not know wether it is true for $\bar{N}_{\alpha\beta}$ and $\bar{\bar{N}}_{\alpha\beta}$. So there remains a little uncertainty in our confidence on the result for the "case (b)". Besides, in our calculation there are some questions about the neglects of overlap integrals and of ionic structures except those which involve ionic H_a and H_e. In this respect, Itoh, Ohno, and Kotani[4] have obtained the dissociation energy of 12.97 ev by the treatment of the methyl radical similar to our treatment "case (b)". The experimental value of it is 13.12 eV. The agreement is very good. Stevenson and Schissler have experimentally obtained the value more than 5.0 eV for the proton affinity of the methane molecule.[1]

Woods[13] has obtained the value 1.01A for the equilibrium $C-H$ distance for the methane molecule with using sp^3 hybridized orbitals and with considering the non-orthogonalities of the atomic orbitals and the higher order permutations of electrons, and Nakamura and Kakiuchi[14] have obtained the value 0.98A by performing more detailed calculations than that of Woods. The experimentally known value is 1.09A. Accordingly there may be the possibility of our value 1.10A obtained for the $C-H$(ionic) distance being smaller by about 0.1A than the truth. It is interesting that the resulted values of the $C-H$(ionic) distance are nearly the same for two different sets of parameters.

The contributions of s^2p^2, sp^3, and p^4 configurations of the carbon atom in the "case (b)" are very similar to those for the methane molecule and the methyl radical as seen from Table VII.

If we want to know the behaviour at large values of the $C-H$ distance, where the ion has the type C_{3v} of symmetry, each of the seventeen eigenfunctions is separated into two, one containing ϕ_d, the other ϕ_e, and we must solve the thirty-fourth degree secular equation (numbering: 1d, 1e, 2d, 2e, $\cdots$, 17d, 17e). Then our matrix elements H_{ij} and $\overline{H}_{ij}$ become $H_{id,jd}$, $\overline{H}_{id,jd}$ or $H_{ie,je}$, $\overline{H}_{ie,je}$, and $\overline{H}_{ij}$ become $H_{id,je}$. Our formulae of matrix elements can be used in this general case.

In the present study, we have assumed that the ground state of the protonated methane is ${}^1A_1'$ state, disregarded ionic structures except those which involve ionic H_a and H_e and overlap integrals, and chosen some arbitrary values for the various parameters. These points are open to questions.

The author wishes to express his sincere thanks to Professor K. Niira and Professor S. Nagakura for their kind guidances and suggestions. This work is indebted to the Ministry of Education for its research grant.

References

1) G. C. Eltenton: unpublished (1940). V. L. Tal'roze and A. K. Lyubimova: Dokl. Akad. Nauk SSSR **86** (1952) 909. D.P. Stevenson and D.O. Schissler: J. Chem. Phys. **23** (1955) 1353.
F. H. Field, J. L. Franklin and F. W. Lampe: J. Amer. Chem. Soc. **79** (1957) 2419.
2) H. H. Voge: J. Chem. Phys. **4** (1936) 581.
3) M. Kotani and M. Siga: Proc. Phys.-Math. Soc. Japan **19** (1937) 471.
4) T. Itoh, K. Ohno and M. Kotani: J. Phys. Soc. Japan **8** (1953) 41.
5) R. Serber: Phys. Rev. **45** (1934) 461.
6) T. Yamanouchi: Proc. Phys.-Math. Soc. Japan **18** (1936) 623.
7) J. C. Slater: Phys. Rev. **34** (1929) 1293.
8) J. H. Van Vleck: J. Chem. Phys. **2** (1934) 297.
9) M. Kotani and A. Amemiya: Proc. Phys.-Math. Soc. Japan **22** (1940) Extra No.
10) J. H. Van Vleck: J. Chem. Phys. **2** (1934) 20.
11) W. G. Penney: Trans. Faraday Soc. **31** (1935) 734.
12) F. O. Ellison: J. Chem. Phys. **23** (1955) 2358.
13) H. J. Woods: Trans. Faraday Soc. **28** (1932) 877.
14) J. Nakamura and Y. Kakiuchi: Spoken at the meeting of the Phys. Soc. Japan (October 1951).

JOURNAL OF THE PHYSICAL SOCIETY OF JAPAN, Vol. 14, No. 4, APRIL, 1959

Thermo-Remanent Magnetism in the Systems La_2O_3-Fe_2O_3 and Nd_2O_3-Fe_2O_3

By Hiroshi WATANABE

The Research Institute for Iron, Steel and Other Metals,
Tohoku University, Sendai

(Received December 3, 1958)

$LaFeO_3$, which is reported to be antiferromagnetic at room temperature, has, however, a small amount of remanent magnetization. By measuring the hysteresis loops of a sample before and after a thermomagnetic treatment, it is found that the hysteresis loop is shifted along the magnetization axis, especially for specimens cooled in a magnetic field below the magnetic transition temperature, *ca* 450°C. The phenomenon can well be interpreted as a sort of thermo-remanent magnetization. A similar phenomenon has also been found for $NdFeO_3$.

§ 1. Introduction

In the course of study on the thermomagnetic properties of perovskite-like compounds, it has been found that $LaFeO_3$, which is reported to be antiferromagnetic at room temperature, still has weak ferromagnetism and its hysteresis loop shows a quite unusual behavior; the hysteresis loop is shifted along the magnetization axis.

Hysteresis loops which are asymmetrical with respect to the coordinate axes have recently been reported in a few cases; Meiklejohn and Bean[1] found that an oxide-coated cobalt or iron particle had a hysteresis loop displaced along the field axis, if it had been cooled from temperatures above the antiferromagnetic Curie temperature of the relevant oxide; they attributed the anomalous magnetic behavior observed to the exchange contact of the metal particle with the oxide-coating.

Lin and Kaufmann[2] studied the magnetic properties of UMn_2, which, in spite of its several antiferromagnetic behaviors, showed a small remanence below 230°K if it had been cooled in a magnetic field. Samples so-treated showed an asymmetry in their hysteresis loop, although the displacement along the magnetization axis was very small.

These data are extremely interesting because ordinary ferromagnetics always show symmetrical hysteresis loops. In the exceptional cases as cited above, the phenomenon seems to be associated with antiferromagnetism or with some interaction between antiferromagnetic and ferromagnetic regions. The phenomenon dealt with here could also be closely related to the antiferromagnetism of $LaFeO_3$, although it can, in principle, be understood on the basis of Néel's theory of thermo-remanent magnetism[3].

$LaFeO_3$ is a magnetic compound with perovskite-like structure, in which the larger cation, La^{3+}, is nonmagnetic, and the smaller one, Fe^{3+}, is magnetic. Its crystal structure has been studied by a few authors[4][5] and reported to be cubic, but Geller and Wood[6] in a more precise measurement using single crystals have determined the crystal symmetry to be orthorhombic with $a=5.556$Å, $b=5.565$Å, $c=7.862$Å, and the probable space-group to be D_{2h}^{16}-Pbnm.

Its magnetic structure has been investigated by Koehler and Wollan[7]; each Fe^{3+} ion is surrounded by six Fe^{3+} neighbors whose spins are antiparallel to the given ion, superexchange interaction between near-neighboring Fe^{3+} ions *via* the intervening 0^{2-} ion being negative.

Weak ferromagnetism in $LaFeO_3$ was first reported by Forestier and Guiot-Guillain[8], who located its Curie temperature at 465°C. Paramagnetic susceptibility above the Curie temperature was measured by the author[9] and it was found that in some cases some amount of thermal hysteresis was present* immediately above the Curie temperature (450°C).

---

* The hysteresis could be reduced by annealing the sample at temperatures lower than the sintering temperature. At present, however, it is still doubtful whether the hysteresis is related to some complicated nature of the phase diagram, or not.

Jonker[10] considered the Curie temperature to be identical with the Néel temperature. Although it was felt that magnetization at room temperature was dependent on thermal or magnetic-field treatment, no systematic study concerning this point has ever been undertaken. The problem has not been solved completely, but the displacement of the hysteresis loop is a definite conclusion of the present study.

An attempt has been made to see if a similar phenomenon would be observed in other compounds. It is known from the work of Geller and Wood[6] that $YFeO_3$ as well as many rare-earth orthoferrites are isomorphous with $LaFeO_3$. An experiment on $NdFeO_3$ has, actually, given a positive result.

§ 2. Experimental

2.1. *Preparation of samples*

In view of the importance of the purity of the constituent oxides, powders of high purity La_2O_3 of different sources has been used and the results were compared. Experimental data varied slightly with different sources of constituent reagents. Nevertheless it was seen that this was not serious in the final conclusion. Fe_2O_3, prepared by calcination of FeC_2O_4 at 1200°C in air was used as the other constituent. Intimate mixtures of these constituent oxides were sintered, mostly in air, at various temperatures and then quenched or furnace-cooled or annealed.

X-ray powder photographs have been taken of some of the samples and were seen to be insensitive to heat-treatment. For stoichiometric $LaFeO_3$, the patterns were compatible with the crystallographic data reported in references. For samples richer in Fe_2O_3, lines of α-Fe_2O_3 appeared. Films of samples richer in La_2O_3 contained, besides the lines of $LaFeO_3$, additional lines, but no analysis of them has been intended.

2.2. *Thermomagnetic curves*

Thermomagnetic curves were taken with samples of various compositions (molar ratios of La_2O_3 to Fe_2O_3) and of various sintering temperatures. Typical examples of this series of measurements are shown in Fig. 1. The measuring field was about 6500 Oe.

As can be seen from the Figs. 1 (b) and 1 (c), $LaFeO_3$ and $La_{0.8}Fe_{1.2}O_3$ sintered at 1300°C are contaminated with α-Fe_2O_3 (Fig. 1 (d)),

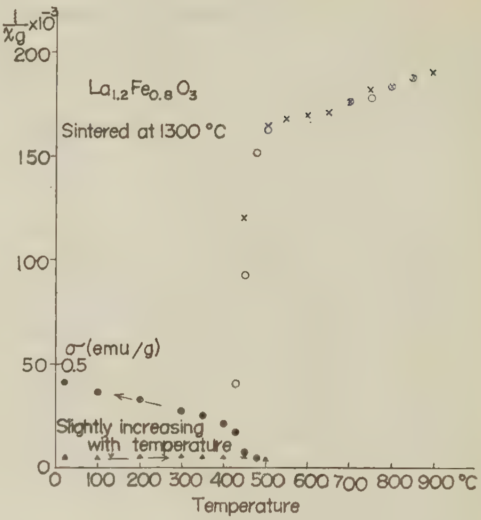

Fig. 1 (a)

Fig. 1. Thermomagnetic curves of $La_2O_3-Fe_2O_3$ system.
× and ⊙ are the experimental points for $(1/\chi_g)\times10^{-3}$ measured during heating and subsequent cooling, respectively. ▲ and ● those for magnetization σ.

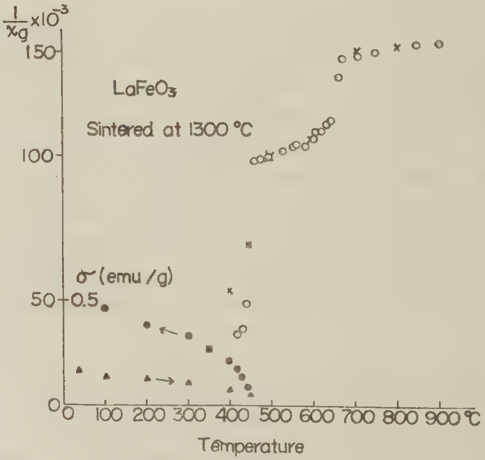

Fig. 1 (b)

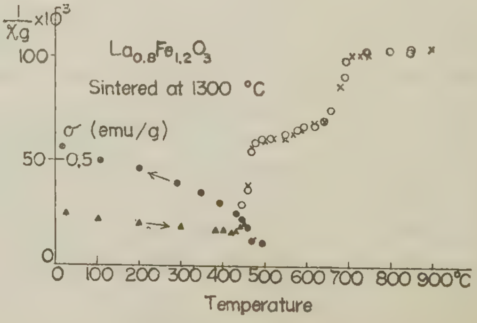

Fig. 1 (c)

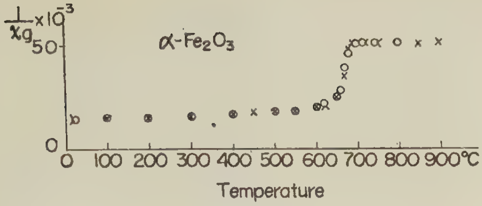

Fig. 1 (d)

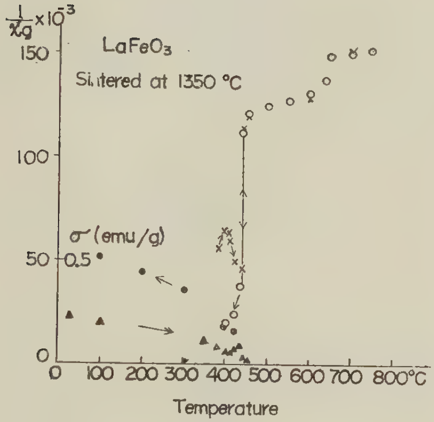

Fig. 1 (e)

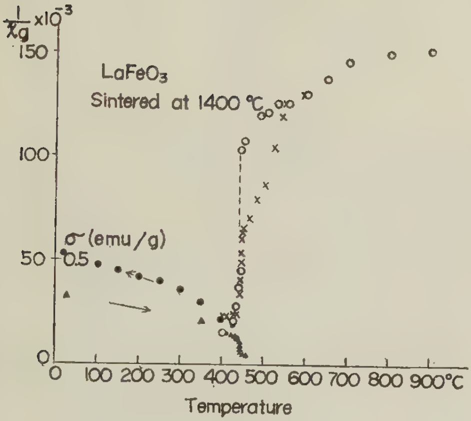

Fig. 1 (f)

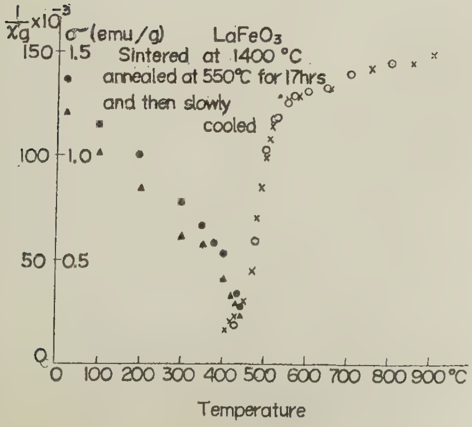

Fig. 1 (g)

since they have a magnetic transition at 680°C, which corresponds to the Curie temperature of the parasitic ferromagnetism of α-Fe_2O_3. From Fig. 1 (g) it may be seen that α-Fe_2O_3-free $LaFeO_3$ is only possible when it is sintered at 1400°C*. This was corroborated with the X-ray powder patterns.

Thermal hysteresis as is found in $LaFeO_3$ sintered at 1400°C (Fig. 1 (f)) usually occurs when the sample has been quenched from the sintering temperature. In this case the susceptibity in the cooling run undergoes a very sharp increase at 440°C. If this sample is annealed above the transition temperature, say at 550°C, the thermal hysteresis disappears and at the same time the magnetic transition becomes less sharp, the transition temperature becoming slightly higher. For this sample only can we calculate a reliable number of Bohr magnetons per Fe^{3+} ion in the paramagnetic region. It is, if the susceptibilities are corrected for diamagnetism of ion cores, equal to 5.80, slightly lower than the predicted spin-only value of 5.92. The paramagnetic Curie temperature, then, is about-1270°K.

All of the samples in Fig. 1 have a lower magnetization, in the initial heating (the initial state is the virgin state, *viz.*, the sample has never been treated in magnetic field at high tempepatures), and higher magnetization in the subsequent cooling. It was established in a separate experiment that this increase in magnetization was due to the presence of the remanent magnetic field (~30 Oe) of the electromagnet. Probably the field was most effective immediately below the magnetic transition temperature. This can be seen, *e.g.*, from the unusual behavior of the magnetization during heating of the sample in Figs. 1 (a), 1 (c), 1 (e) or 1 (g). Since the phenomenon was much like the Hopkinson effect usually met with in ferromagnetic materials, except that here the measuring field was exceptionally high, it was decided to compare the hysteresis loop of the virgin sample with that of the thermomagnetically treated one.

2.3. *Displaced hysteresis loops*

Hysteresis-loop measurement was made with the pendulum magnetometer which was also used for the thermomagnetic measurement.

---

* Strictly speaking, even this sample had a trace of α-Fe_2O_3.

In Fig. 2 are shown the loops of samples with and without magnetic heat-treatment. Although these data were taken with powdered samples, they were checked with cylindrically-pressed specimens with substantially the same results, so that it is impossible that the abnormal effect should have originated from any mechanical motion of the powders with the application of a magnetic field.

As can be seen from the figures, even the loops of virgin samples are slightly shifted along the magnetization axis. The sign of this shift is determined by the direction of the field applied first; if the field is applied in the +direction in the first place, then the loop becomes shifted in the +direction. The shift is usually less than 0.1 emu/g.

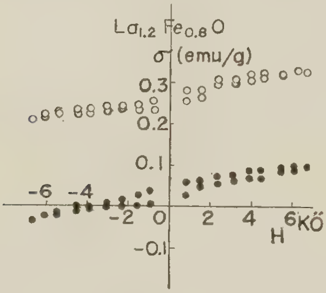

Fig. 2 (a)

Fig. 2. Hysteresis loops of samples of $La_2O_3-Fe_2O_3$ system.

● Experimental points for the virgin state.

⊙ Experimental points for a thermomagnetically treated state.

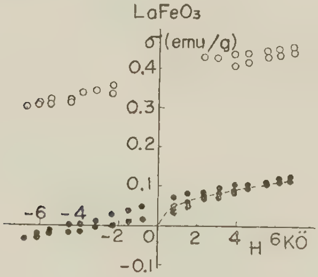

Fig. 2 (b)

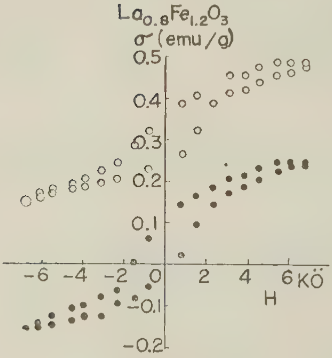

Fig. 2 (c)

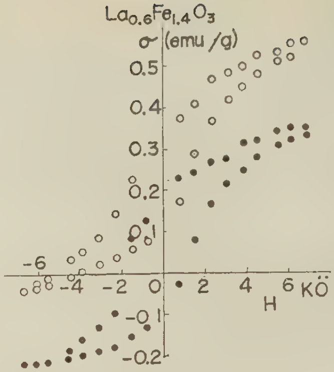

Fig. 2 (d)

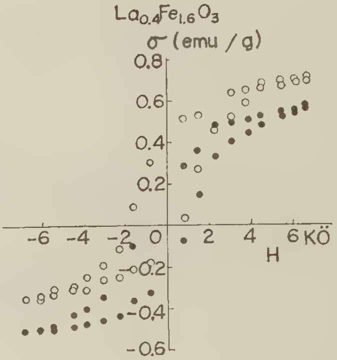

Fig. 2 (e)

When the sample has been cooled from temperatures above the magnetic transition temperature, *ca* 450°C, in a magnetic field of 30 Oe or stronger, apparently greater shifts result. The direction of the shift is in the direction of the magnetic field applied at high temperatures. The amount of this shift is maximum near the composition $LaFeO_3$, and decreases as the Fe^{3+} content increases, vanishing completely for α-Fe_2O_3. On the other hand, the richer the sample in Fe^{3+}, the greater the height of the hysteresis loop (here the height is defined as $\sigma_{H=H_{max}}-\sigma_{H=-H_{max}}$, where σ is magnetization per gram of the sample). Probably α-Fe_2O_3 which is not soluble in the perovskite phase is mostly responsible for the height of the hysteresis loop. Since both the amount of shift and the height of the hysteresis loop vary with the lanthanum oxide used in the sample preparation, and since there seems to be no correlation between them, it should be noted that the curves in Fig. 2 are pertinent to a particular series of samples. The phenomenon of the shift itself, however, is very common to these materials.

2.4. *The system* Nd_2O_3-Fe_2O_3

High purity Nd_2O_3 and Fe_2O_3 were mixed in equimolar proportion and the mixture was sintered at 1300°C. Thermomagnetic curves in Fig. 3 indicate that the Curie temperature of the weak ferromagnetism is about 450°C. As in La_2O_3-Fe_2O_3 system, the magnetization measured during cooling is higher than that measured during heating, and the hysteresis loops are displaced as well (Fig. 4).

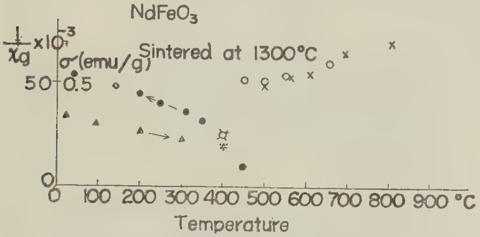

Fig. 3. Thermomagnetic curves of $NdFeO_3$.

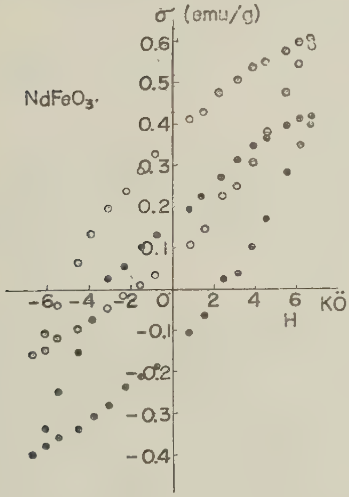

Fig. 4. Hysteresis loops of $NdFeO_3$. The symbols are the same as those in Fig. 2.

§ 3. Discussion

Weak ferromagnetism in antiferromagnetic compounds has been considered by several workers. Some of them attribute it to an intrinsic nature of the material[11], while others to some structure-sensitive character of the material, *e.g.*, domain boundaries[12], free surfaces at grain boundaries[13], dislocations[14] *etc.* It is very difficult to select the correct one out of these possibilities. The same is the case with the matter presented in the present study but some tentative discussion will be given below.

Hysteresis loops as shown in Fig. 2 will result if the material is composed of two magnetically independent parts, one with a usual (symmetric) hysteresis loop (A) and the other with a very hard magnetization in one direction (B) (Fig. 5). As already stated it is very probable that (A) is caused by the α-Fe_2O_3, non-soluble in the perovskite-like $LaFeO_3$ phase; the height of the hysteresis curve (A) is of the right order of magnitude if it corresponds to the parasitic ferromagntism of α-Fe_2O_3[15]. Then the essential problem is how the curve (B) is caused. This can be understood on the basis of Néel's theory of thermo-remanent and isothermal remanent magnetization. The small amount of magnetization (B) of a sample in the virgin state is due to grains with coercive forces less than the maximum field applied, which is far smaller than the overall coercive force. To remove this magnetization a field in the opposite direction slightly higher than that first applied will be sufficient. Indeed its magnetization can be reduced if, instead of applying from the outset a strong field in one direction, we apply a field with alternating

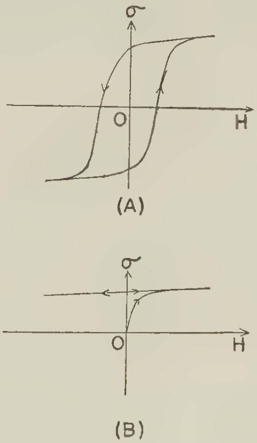

Fig. 5. Displaced hysteresis loop as decomposed into two components, (A) a normal one, and (B) an extremely hard one.

directions and increasing amplitude. In any case, comparing the magnitudes of thermoremanent and isothermal remanent magnetizations, one may recognize how large the overall coercive force is in this case.

The ferromagnetic meterial concerned here, however, is still in quesion. If we consider it to be orthoferrite, not completely antiferromagnetic but with small, uncompensated, parasitic ferromagnetism, the exceedingly large coercive force mentioned above should be interpreted as due to smallness of the saturation magnetization; with the formula for intrinsic coercive force

$$H_c \sim 0.64\, K/I_s\,,$$

where K and I_s, are the anisotropy constant and the saturation magnetization respectively, and with the values of $I_s \sim 0.5 \times$(X-ray density ~ 7)~ 3.5 gauss and $K \sim 10^6$ ergs/cc which is reasonably expected for a substance with magnetic ions in d^5 configuration, H_c becomes 2×10^4 Oe. With this picture, the Curie temperature of the parasitic ferromagnetism in $LaFeO_3$ should be coincident with the Néel temperature. Bozorth$^{16)}$ has recently considered the weak ferromagnetism of rare-earth and yttrium orthoferrites on the basis of an idea similar to Dzyaloshinsky's$^{11)}$, and has concluded that the net magnetic moment in most of the ferrites is directed along the c-axis of the orthorhombic crystal. Since this moment is very hard against rotation away from this axis, the value of K in the above expression should be taken to be much greater and we expect an even larger value of H_c.

An alternative picture which attributes the ferromagnetism (B) to small crystals of α-Fe_2O_3, in the form of thin films and closely attached to the lattice of orthoferrite seems to contradict the observations of domain patterns by Sherwood *et al.*,$^{17)}$ who have produced strong evidence for the fact that the weak ferromagnetism in many orthoferrites is a uniform body property of these substances.

Acknowledgments

I should like to express my hearty thanks to Dr. R. M. Bozorth for giving me the opportunity of knowing his recent work and experimental studies on orthoferrites by Sherwood *et al.* prior to publication, and also for helpful discussion. Thanks are also due to Prof. T. Nagamiya, Dr. E. P. Wohlfarth and Dr. S. Iida for stimulating discussions, to Mr. K. Ito for assistance in the measurements, and to members of the X-ray research laboratory of this Institute for taking powder photographs of the samples. A part of the expenditure of this study has been defrayed from the Scientific Research Funds of the Ministry of Education.

References

1) H. Meiklejohn and C. P. Bean: Phys. Rev. **105** (1957) 904.
2) S. T. Lin and R. Kaufmann: Phys. Rev. **108** (1957) 1171.
3) Reviewed in: L. Néel: Advances in Physics **4** (1955) 191.
4) St. V. Náray-Szabó: Nature **31** (1943) 466.
5) H. L. Yakel: Acta Cryst. **8** (1955) 394.
6) S. Geller and E. A. Wood: Acta Cryst. **9** (1956) 563.
7) W. C. Koehler and E. O. Wollan: J. Phys. Chem. Solids **2** (1957) 100.
8) H. Forestier and G. Guiot-Guillain: Compt. rend. **230** (1950) 1844.
9) H. Watanabe: Sci. Rep. RITU **A8** (1956) 14.
10) G. H. Jonker: Physica **22** (1956) 707.
11) I. Dzyaloshinsky: J. Phys. Chem. Solids **4** (1958) 241.
12) Y-Y. Li: Phys. Rev. **101** (1956) 450.
13) Prof. T. Nagamiya proposed a mechanism for weak ferromagnetism in α-Fe_2O_3 originating from grain boundaries (Kagaku **26** (1956) 415 (in Japanese)), but has expressed an opinion in a private talk that this problem has never been settled as yet.
14) I. S. Jacobs and C. P. Bean: J. Appl Phys. **29** (1958) 537.
15) L. Néel and R. Pauthenet: Compt. rend. **234** (1952) 2172.
16) R. M. Bozorth: Phys. Rev. Letters **1** (1958) 362.
17) R. C. Sherwood, J. P. Remeika and H. J. Williams: J. Appl. Phys. **30** (1959) 217.

JOURNAL OF THE PHYSICAL SOCIETY OF JAPAN, Vol. 14, No. 4, APRIL, 1959

Stabileco de du-dimensia fluo de Szymański

De Hideo TAKAMI

Departemento de Fiziko, Fakultato de Scienco, Universitato de Tokio

(Received January 8, 1959)

Stability of two-dimensional Szymański flow

Stability of a two-dimensional transient flow of an incompressible viscous fluid is investigated by the method of small oscillations. The basic flow is such that the fluid begins to move from rest between two parallel and infinitely large planes under a pressure of constant gradient applied along them and eventually attains the parabolic velocity distribution.

By the use of Lin's procedure the relation between the Reynolds number of the basic flow and the wave number of the antisymmetrical neutral oscillation (the neutral curve of stability) and also the minimum critical Reynolds number are calculated numerically for each of five representative stages of the transient flow, and the variation of its stability characteristics is discussed.

§ 1. Enkonduko

La problemo de la stabileco de fluo estas diskutita de multaj esplorantoj. Ĝenerala metodo de malgrandaj osciloj estas starigita pri fluo preskaŭ konstanta laŭlonge de ĝia direkto kaj en tempo, kaj ankaŭ estas kalkulitaj la karakterizaĵoj de stabileco de kelkaj konkretaj fluoj.

En ĉi tiu traktato ni konsideras la stabilecon de du-dimensia transira fluo de nekunpremebla viskoza fluido inter du paralelaj senlime larĝaj ebenoj sub premo de konstanta gradiento aplikata laŭlonge de ili.

Pri ĉiu de kvin apartaj specimenoj el la transira fluo estas nombre kalkulata, per la procedo de Lin²⁾, la rilato inter la nombro de Reynolds de la baza fluo kaj la ondnombro de la neŭtrala oscilo (t.e. la neŭtrala kurbo de stabileco) kaj ankaŭ estas kalkulata la minimuma kriza nombro de Reynolds. Per ĉi tiuj rezultoj ni esploras la laŭtempan ŝanĝiĝon de la stabileco de la fluo ĉe malgrandaj osciloj.

Koncerne nian problemon ni menciu precipe la esploron de Hahneman k.a.¹⁾ pri la stabileco de du-dimensia fluo ĉe la enirejo de ŝanelo.

§ 2. Bazaj fluoj

Ni konsideru nekunpremeblan viskozan fluidon kiu ripozas inter du paralelaj senlime larĝaj ebenoj $y=\pm h$ (Fig. 1). Se, post iu momento $t=0$, ni aplikados al la fluido premon de konstanta gradiento laŭlonge de la ebenoj (ekzemple en x-direkto), ĝi komencos kaj daŭros flui ŝanĝante la distribuon de rapido (U, V) laŭ sekvantaj ekvacioj:

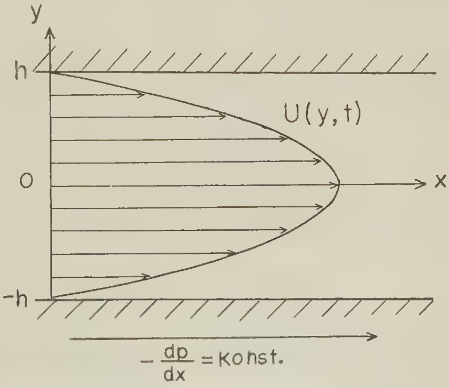

Fig. 1. Baza fluo.

$$\left\{\begin{aligned} &\frac{\partial U}{\partial t}+U\frac{\partial U}{\partial x}+V\frac{\partial U}{\partial y}=-\frac{1}{\rho}\frac{dp}{dx}+\nu\left(\frac{\partial^2 U}{\partial x^2}+\frac{\partial^2 U}{\partial y^2}\right), &(2.1)\\ &\frac{\partial V}{\partial t}+U\frac{\partial V}{\partial x}+V\frac{\partial V}{\partial y}=\qquad\qquad\nu\left(\frac{\partial^2 V}{\partial x^2}+\frac{\partial^2 V}{\partial y^2}\right), &(2.2)\\ &\frac{\partial U}{\partial x}+\frac{\partial V}{\partial y}=0, &(2.3)\end{aligned}\right.$$

kun la kondiĉo ĉe la komenco:

$$(U, V)=0 \qquad \text{ĉe} \quad t=0\,, \tag{2.4}$$

kaj la kondiĉoj ĉe la muroj:

$$(U, V)=0 \qquad \text{ĉe} \quad y=\pm h\,, \tag{2.5}$$

en kiuj U kaj V estu respektive la x- kaj y-komponantoj de rapido de la fluo, ρ la denseco, ν la koeficiento de kinematika viskozeco, p la premo kies gradiento estu konstanta, kaj la fluo estu du-dimensia.

Se ni supozas ke la rapido ne dependas de x, ni vidas el (2.3) ke $V=V(t)$, el ĉi tio kaj (2.5) ke $V\equiv 0$, sekve (2.2) estas bagatela kaj ni havas la ekvacion por $U(y, t)$:

$$\frac{\partial U}{\partial t}=-\frac{1}{\rho}\frac{dp}{dx}+\nu\frac{\partial^2 U}{\partial y^2}\,, \tag{2.6}$$

kun

$$\begin{cases} U(y, 0)=0\,, & (2.7)\\ U(\pm h, t)=0\,. & (2.8)\end{cases}$$

Ni difinu sendimensiajn kvantojn:

$$\left.\begin{aligned} &\tau\equiv\frac{\nu}{h^2}t\,, \qquad \eta\equiv\frac{y}{h}\,, \qquad u(\eta,\tau)\equiv\frac{h}{\nu}U\left(h\eta, \frac{h^2}{\nu}\tau\right),\\ &P\equiv-\frac{h^3}{\rho\nu^2}\frac{dp}{dx}=\text{konst.}>0\,,\end{aligned}\right\} \tag{2.9}$$

kaj nia ekvacio fariĝas

$$\frac{\partial u}{\partial \tau}-\frac{\partial^2 u}{\partial \eta^2}=P\,, \tag{2.10}$$

kun

$$\begin{cases} u(\eta, 0)=0\,, & (2.11)\\ u(\pm 1, \tau)=0\,, & (2.12)\end{cases}$$

kies solvo estas akirata en serio de Fourier:

$$u(\eta,\tau)=\frac{P}{2}\left[1-\eta^2-4\sum_{n=0}^{\infty}\frac{(-1)^n}{(n+\frac{1}{2})^3\pi^3}\cos\{(n+\tfrac{1}{2})\pi\eta\}\exp\{-(n+\tfrac{1}{2})^2\pi^2\tau\}\right], \tag{2.13}$$

aŭ, por malgranda τ, u estas ankaŭ esprimata en rapide konverĝanta serio:

$$u=P\tau\left[1-4\sum_{n=0}^{\infty}(-1)^n\left(\mathbf{i}^2\operatorname{erfc}\frac{2n+1+\eta}{2\sqrt{\tau}}+\mathbf{i}^2\operatorname{erfc}\frac{2n+1-\eta}{2\sqrt{\tau}}\right)\right] \tag{2.14}$$

kiel estus montrate per transformigo de Laplace; en (2.14) staras

$$\begin{aligned}\mathbf{i}^2\operatorname{erfc} x&=\frac{2}{\sqrt{\pi}}\int_x^\infty dt\int_t^\infty ds\int_s^\infty e^{-r^2}\,dr\\ &=\frac{1}{2\sqrt{\pi}}\left\{(2x^2+1)\int_x^\infty e^{-t^2}\,dt-x\,e^{-x^2}\right\}.\end{aligned} \tag{2.15}$$

En Fig. 2 estas montrataj la profiloj de rapido respondaj al diversaj valoroj de τ, kaj en Fig. 3 la maksimuma rapido kiel funkcio de τ. Ni vidas ke la profilo proksimiĝas al tiu de du-dimensia fluo de Poiseuille kiam τ senlime pligrandiĝas. Ni rememoru ke la responda tri-dimensia transira fluo tra ronda tubo estas kalkulita de Szymański[3].

§ 3. Stabileco ĉe malgrandaj osciloj

Nun ni esploru la stabilecon de la supre kalkulita fluo ĉe malgrandaj osciloj surmetitaj al ĝi.

Kiel oni ofte faras, ni supozas ke la rapido (u', v') de la malgranda oscilo estas esprimata per la flufunkcio ψ kiel

$$\left\{\begin{aligned} u' &= \frac{1}{\rho}\frac{\partial\psi}{\partial y}\,, \\ v' &= -\frac{1}{\rho}\frac{\partial\psi}{\partial x}\,, \end{aligned}\right. \tag{3.1}$$

en kiuj ψ havu la sekvantan formon (la ondo de Tollmien-Schlichting):

$$\psi = \phi(y)\exp\{i\tilde{\alpha}(x-\tilde{c}t)\}\,, \tag{3.2}$$

tiam ni havas la ekvacion por la amplekso $\phi(y)$:

$$(U-\tilde{c})\left(\frac{d^2\phi}{dy^2}-\tilde{\alpha}^2\phi\right)-\frac{\partial^2 U}{\partial y^2}\phi = \frac{\nu}{i\tilde{\alpha}}\left(\frac{d^4\phi}{dy^4}-2\tilde{\alpha}^2\frac{d^2\phi}{dy^2}+\tilde{\alpha}^4\phi\right), \tag{3.3}$$

kun la kondiĉoj ĉe la muroj:

$$\phi=0 \quad \text{kaj} \quad d\phi/dy=0 \qquad \text{ĉe} \quad y=\pm h\,. \tag{3.4}$$

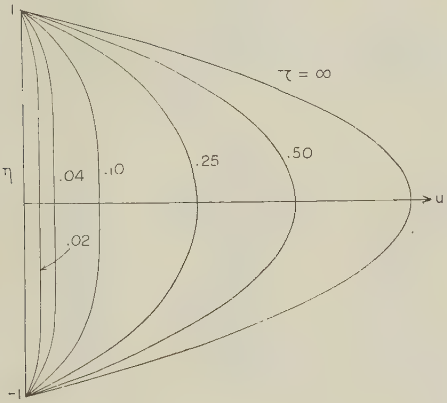

Fig. 2 (a). Profiloj de rapido $u(\eta,\tau)$ por diversaj valoroj de τ (vidu (2.9)).

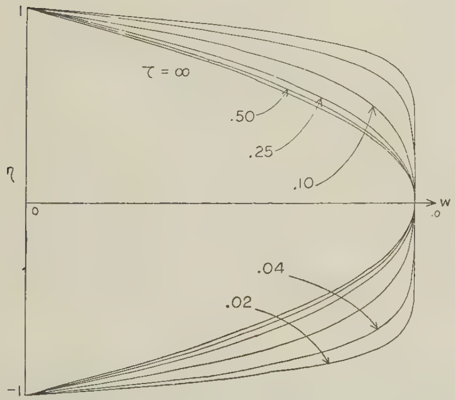

Fig. 2 (b). Profiloj de rapido $w(\eta,\tau)$ por diversaj valoroj de τ (vidu (3.5)).

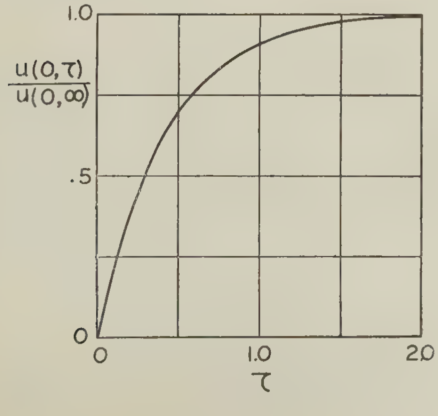

Fig. 3. La maksimuma rapido kiel funkcio de τ.

Metinte (3.2), ni supozas ke la relativa vario de la baza fluo $(\partial U/\partial t)/U$ estas multe pli malgranda ol la frekvenco $\tilde{\alpha}\tilde{c}$ de la surmetita oscilo, kaj ni rigardas la tempan variantan t en U kiel parametron nur karakterizantan la bazan fluon, kiu, ni postulas, daŭru senŝanĝa dum granda nombro da periodoj de la konsiderata oscilo. Ni memoru ke ĉi tiu kondiĉo ne povus esti realigata por malgrandega τ, t.e. dum la komenca tempo de la movo de fluido (vidu § 4).

Per sendimensiaj kvantoj:

$$w \equiv \frac{U}{U_m}\,, \quad \eta = \frac{y}{h}\,, \quad \alpha \equiv h\tilde{\alpha}\,, \quad c \equiv \frac{\tilde{c}}{U_m}\,, \tag{3.5}$$

en kiuj

$$U_m = \max_y U(y,t) = U(0,t)\,, \tag{3.6}$$

ekvacio (3.3) transformiĝas en la ekvacion de Orr-Sommerfeld:

$$(w-c)\left(\frac{d^2\phi}{d\eta^2}-\alpha^2\phi\right)-\frac{\partial^2 w}{\partial\eta^2}\phi = -\frac{i}{\alpha R}\left(\frac{d^4\phi}{d\eta^4}-2\alpha^2\,\frac{d^2\phi}{d\eta^2}+\alpha^4\phi\right), \tag{3.7}$$

kun

$$\left.\begin{aligned} \phi &= 0\,, \\ \frac{d\phi}{d\eta} &= 0 \end{aligned}\right\} \qquad \text{ĉe} \quad \eta=\pm 1\,, \tag{3.8}$$

en kiu R estu la nombro de Reynolds $U_m h/\nu$ de la fluo ĉe la momento τ.

Ekvacio (3.7), kun la kondiĉoj (3.8), donas kompleksvaloran rilaton inter realvaloraj R, α kaj kompleksvalora c. Se ni konsideras neŭtralan oscilon kies amplekso ne pliiĝos nek malpliiĝos, t.e. ni metas la imagan parton de *c* kiel nulon, tiam ni havas realvaloran rilaton inter R kaj α (neŭtralan kurbon de stabileco) kun la reala parto de c kiel parametro. Ĝi estas tio, kion ni kalkulas en ĉi tiu traktato.

§ 4. Nombraj rezultoj kaj diskutoj

La bone starigita procedo de Lin[2] estas aplikata por kalkuli la rilaton inter la nombro de Reynolds R kaj la ondnombro α de la neŭtrala oscilo antisimetria pri la ebeno $y=0$. Nombraj kalkuloj estas farataj por $\tau=0.02$, 0.04, 0.10, 0.25, 0.50 kaj ∞.* Tabelo. I kaj Fig. 4 montras niajn rezultojn. Per ĉi tio ni nun povas diskuti la laŭtempan ŝanĝiĝon de stabileco de la transira fluo komencinta de ripozo.

Tabelo. I. La rilato inter c, α kaj R de la neŭtrala oscilo.

$\tau=0.02$

c	α	R
0.077	0.664	30.7 $\times 10^5$
.150	1.147	3.14 〃
.157	1.210	2.70 〃
.164	1.278	2.34 〃
.171	1.357	2.04 〃
.178	1.449	1.79 〃
.184	1.581	1.59 〃
.188	1.715	1.50 〃
.188	1.872	1.56 〃
.184	1.951	1.77 〃
.178	1.995	2.14 〃
.171	2.000	2.61 〃
.164	1.982	3.17 〃
.157	1.954	3.90 〃
.150	1.908	4.85 〃
.077	1.134	97.5 〃

$\tau=0.04$

c	α	R
0.133	0.853	2.79 $\times 10^5$
.158	1.006	1.59 〃
.178	1.172	1.11 〃
.183	1.230	1.03 〃
.187	1.316	0.97 〃
.187	1.446	1.05 〃
.183	1.491	1.23 〃
.178	1.506	1.41 〃
.158	1.482	2.48 〃
.133	1.355	5.46 〃

$\tau=0.10$

c	α	R
0.070	0.457	11.9 $\times 10^5$
.136	0.726	1.26 〃
.168	0.882	6.48 $\times 10^4$
.174	0.920	5.83 〃
.184	0.988	5.07 〃
.190	1.076	4.68 〃
.190	1.164	5.17 〃
.184	1.170	6.41 〃
.174	1.178	8.35 〃
.168	1.173	9.95 〃
.136	1.084	2.59 $\times 10^5$
.070	0.731	43.4 〃

$\tau=0.25$

c	α	R
0.200	0.890	2.08 $\times 10^4$
.206	0.932	1.94 〃
.210	0.964	1.89 〃
.210	1.037	2.15 〃
.206	1.048	2.39 〃
.200	1.056	2.84 〃

$\tau=0.50$

c	α	R
0.204	0.814	1.38 $\times 10^4$
.214	0.852	1.20 〃
.223	0.893	1.06 〃
.242	1.027	0.906 〃
.242	1.057	0.961 〃
.223	1.075	1.57 〃
.214	1.067	1.95 〃
.204	1.052	2.41 〃

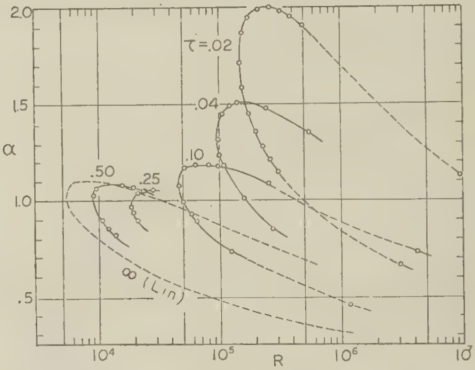

Fig. 4. Neŭtralaj kurboj de stabileco por diversaj valoroj de τ.

Ni povas rigardi la nombron de Reynolds R kiel funkcion de P kaj τ:

$$R(P,\tau)=\frac{hU_m}{\nu}=u(0,\tau)=\frac{P}{2}\{1-f(\tau)\}\,, \tag{4.1}$$

en kiu

$$f(\tau)=4\sum_{n=0}^{\infty}\frac{(-1)^n}{(n+\frac{1}{2})^3\pi^3}\exp\{-(n+\tfrac{1}{2})^2\pi^2\tau\}\,, \tag{4.2}$$

kaj

$$f(\infty)=0\,.$$

---

* Kalkulo pri $\tau=\infty$ nur servas por kontroli nian kalkulan procedon, ĉar oni jam havas rezulton kalkulitan de Lin pri ĉi tiu fluo.

Tabelo. II. La minimumaj krizaj nombroj de Reynolds $R_{kr}^{(\tau)}$ kaj respondaj krizaj ondnombroj $\alpha_{kr}^{(\tau)}$ por diversaj valoroj de τ.

τ	$R_{kr}^{(\tau)}$	$\alpha_{kr}^{(\tau)}$
0.02	15.0 $\times 10^4$	1.808
.04	9.54 〃	1.385
.10	4.63 〃	1.095
.25	1.88 〃	0.988
.50	0.906 〃	1.027
∞ (Lin)	0.531 〃	1.041

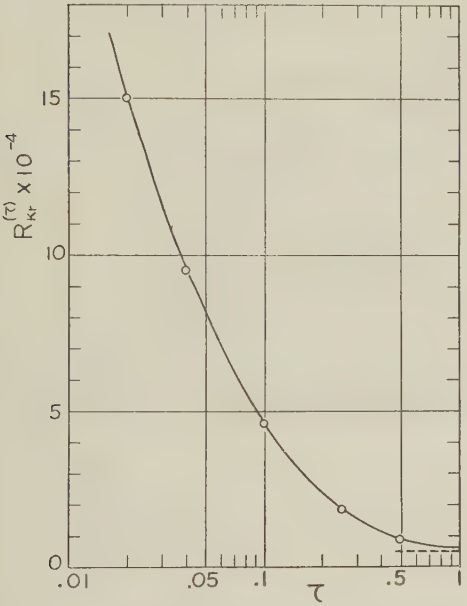

Fig. 5. La minimuma kriza nombro de Reynolds kiel funkcio de τ.

Por fiksa P, $R(P,\tau)$ pligrandiĝas paralele kun τ, dum la kriza nombro de Reynolds $R_{kr}^{(\tau)}$ (la plej malgranda valoro de R sur la kurbo de neŭtrala stabileco de la fluo karakterizata de τ) primalgrandiĝas (Tabelo. II aŭ Fig. 5). Sekve, la ekvacio

$$R(P,\tau)=R_{kr}^{(\tau)} \tag{4.3}$$

donas la rilaton inter la gradiento P de la aplikata premo kaj la kriza momento τ, antaŭ kiu la fluo estas absolute stabila sed post kiu ĝi ne estas tia. Ni atingos ĉi tiun rilaton, aŭ prefere la rilaton inter P kaj la maksimuma rapido $u_m(\tau)$ $(=u(0,\tau))$ ĉe la kriza momento, kiel jene. El ekvacioj:

$$R(P,\tau)=\frac{P}{2}\{1-f(\tau)\}=R_{kr}^{(\tau)}\,, \tag{4.4}$$

$$R(P_\infty,\infty)=\frac{P_\infty}{2} \qquad =R_{kr}^{(\infty)} \doteqdot 5.3\times 10^3\,, \tag{4.5}$$

kaj (4.1), ni ricevas

$$\frac{P}{P_\infty}=\frac{R_{kr}^{(\tau)}}{R_{kr}^{(\infty)}}\frac{1}{1-f(\tau)}=\frac{R_{kr}^{(\tau)}}{R_{kr}^{(\infty)}}\frac{u_m(\infty)}{u_m(\tau)}\,. \tag{4.6}$$

Ĉi tio estas montrata en Fig. 6. En (4.5) kaj (4.6), P_∞ estu tia valoro de P, ke sub la premo de konstanta gradiento P_∞ la fluo fariĝos ne absolute stabila unuafoje ĉe $\tau=\infty$.

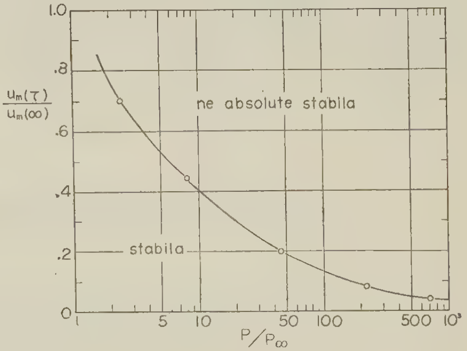

Fig. 6. La rilato inter la gradiento de premo kaj la maksimuma rapido ĉe la kriza momento.

Kiel estis jam rimarkite en § 3, nia kalkula procedo estus pravigita nur por osciloj multe pli rapidaj ol la ŝanĝiĝo de la baza fluo. Oni vere vidos ke ĉi tiu kondiĉo estas plenumita pri niaj kalkulitaj ekzemploj.

La periodo T de la oscilo estas:

$$T=\frac{2\pi}{\tilde{\alpha}\tilde{c}}=\frac{2\pi}{(\alpha/h)U_m c}=\frac{2\pi h}{\alpha c U_m}\,, \tag{4.7}$$

tial la proporcio de ŝanĝiĝo de la maksimuma rapido de la baza fluo al la rapido mem dum unu periodo de la surmetita oscilo estas kalkulata proksimume:

$$\begin{aligned}\frac{1}{U_m}\frac{dU_m}{dt}\cdot T&=\frac{\nu}{h^2}\frac{1}{U_m}\frac{dU_m}{d\tau}\cdot\frac{2\pi h}{\alpha c U_m}\\&=\frac{2\pi}{\alpha c R}\frac{d(\log U_m)}{d\tau}\,.\end{aligned} \tag{4.8}$$

Ni povas meti por malgrandega τ:

$$\frac{d(\log U_m)}{d\tau}=\frac{1}{\tau}\,, \tag{4.9}$$

ĉar tiam U_m estas proporcia al τ pro (2.14).

Kunkonsiderante ke U_m pligrandiĝas pli kaj pli malrapide kiam τ pliiĝas (Fig. 3), ni havas

$$\frac{1}{U_m}\frac{dU_m}{dt}\cdot T \lesssim \frac{2\pi}{c\tau}\frac{1}{\alpha R}\,. \tag{4.10}$$

La dekstra flanko de (4.10) prenas valorojn pli malgrandajn ol 0.7×10^{-2} en ĉiuj niaj ekzemploj, kaj tial estas pravigita nia procedo.

Aliflanke, iu nesimila aliro estus necesa por pli malgrandaj τ aŭ por pli malrapidaj osciloj.

Dankesprimo

Mi kore dankas profesoron Isao Imai por liaj gvidado kaj multvaloraj konsiloj tra la tuta esplorado, kaj ankaŭ la membrojn de lia laboratorio kaj profesoron Tomomasa Tatsumi por diskutoj kun ili. Ĉi tiu esploro povis esti efektivigita per la subvencio de la Ministerio de Eduko.

Referencoj

1) E. Hahneman, J. C. Freeman and M. Finston: J. Aero. Sci. **15** (1948) 493.
2) C. C. Lin: Quart. Appl. Math. **3** (1945) 117, 218; (1946) 277; aŭ *The theory of hydrodynamic stability* (Cambridge, 1955).
3) P. Szymański: Proc. 3rd Internat. Congr. Appl. Mech. **1** (Aug. 1930) 249.

JOURNAL OF THE PHYSICAL SOCIETY OF JAPAN, Vol. 14, No. 4, APRIL, 1959

The Forces experienced by a Lattice of Elliptic Cylinders in a Uniform Flow at Small Reynolds Numbers

By Sinzi* KUWABARA

Department of Physics, Faculty of Science, University of Tokyo

(Received January 8, 1959)

Using Imai's general method of solving two-dimensional Oseen's equations, the drag and lift coefficients for a lattice of parallel, equal and equidistant elliptic cylinders in a uniform flow at small Reynolds numbers are calculated. When the stagger is not present and the thickness ratio of the elliptic cylinders is taken to be unity, the expressions for these coefficients reduce to the case of a lattice of equal and equidistant circular cylinders which has been investigated by Tamada and Fujikawa.

§1. Introduction

The flows past a lattice consisting of equal and equidistant cylinders have been investigated for the case of circular cylinders by Tamada and Fujikawa[1] and by Miyagi[2] and for the case of flat plates by Hasimoto[3] and by the present author[4] on the basis of Oseen's or Stokes' approximation. In this paper, we shall deal with the problem of the same type as mentioned above for the case of a lattice of elliptic cylinders on the basis of Oseen's approximation.

As for the mathematical procedures use will be made of Imai's general method[5] of solving Oseen's equation, which the author has successfully applied to solve the cases of two circular cylinders[6] and two elliptic cylinders[7].

§2. Application of Imai's Method to the Case of a Lattice of Elliptic Cylinders

We consider a flow past lattice of infinitely many equal and equidistant elliptic cylinders. All the elliptic cylinders are placed parallel to each other and at an angle of attack β to the upstream uniform flow. Their mutual dis-

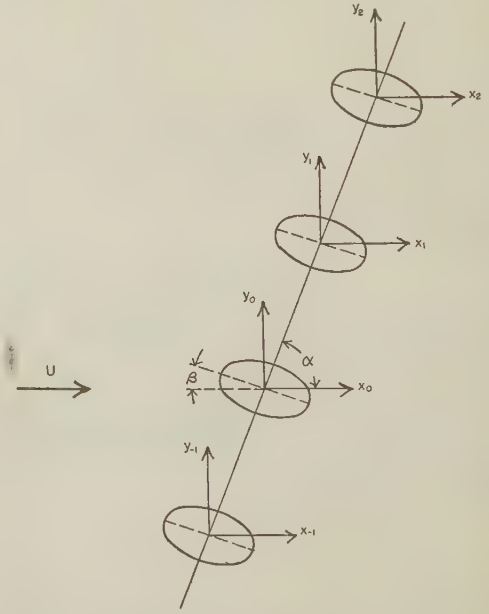

Fig. 1. The general configuration of a lattice of elliptic cylinders.

---

* Sinẓi=Ṣhinji

tance is d and their semi-major and semi-minor axes are $1+\sigma^2$ and $1-\sigma^2$ respectively. We introduce complex variables

$$z_p=x_p+y_p=r_p e^{i\theta_p}\ , \tag{2.1}$$

$$W=u-iv\ , \tag{2.2}$$

where (x_p, y_p) are the cartesian coordinates with the origin at the centre of the pth elliptic cylinder and with the x_p-axis taken parallel to the upstream uniform flow, (u, v) are the velocity components and (r_p, θ_p) the polar coordinates (cf. Fig. 1).

As in the previous paper[6], we can assume the complex velocity W as

$$W=U+\mathcal{E}+\sum_{p=-\infty}^{\infty} W_p\ , \tag{2.3}$$

with

$$W_p(z_p)=e^{kx_p}\sum_{n=0}^{\infty} k^n\{F_{n+1}(z_p)-G_n(z_p, \bar{z}_p)\} \tag{2.4}$$

near the pth elliptic cylinder E_p and

$$W_p(z_p)=\frac{i}{2k}\,e^{kx_p}\left\{A_1K_0(kr_p)+\sum_{n=0}^{\infty}(A_{n+1}\,e^{ni\theta_p}-\bar{A}_n\,e^{-ni\theta_p})K_n(kr_p)\right\}+\frac{df}{dz_p} \tag{2.5}$$

far from E_p. Here U is the velocity of the upstream uniform flow, $\mathcal{E}$, $2k=U/\nu$ (ν being the kinematic viscosity) and A_n are constants and $F_n(z_p)$, $G_n(z_p, \bar{z}_p)$ and $f(z_p)$ are known functions with arbitrary coefficients.

By the transformation function

$$z_p=C(Z_p+\sigma^2/Z_p)\ , \qquad (0\leq\sigma^2\leq 1,\ C=e^{-i\beta}) \tag{2.6}$$

the unit circle $Z_p=e^{i\theta}$ in the Z_p-plane is mapped onto the pth ellipse. In view of the periodicity of the configuration we may employ the boundary conditions:

$$W=U \qquad \text{for} \quad x=-\infty\ , \tag{2.7}$$

$$W=U+\mathcal{E}+\sum_{p=-\infty}^{\infty} W_p(z_p)=0\ , \qquad \text{on the surface of } E_0\,. \tag{2.8}$$

In this paper we shall confine ourselves to the first approximation. Thus we take only the terms of $O(k^0)$ in the complex velocity. Then (2.4) reduces to

$$W_0(z_0)=F_1(z_0)-G_0(z_0, \bar{z}_0)\ , \tag{2.9}$$

where

$$F_1(z_0)=-\tfrac{1}{4}i\bar{a}_0(\ln CZ_0-2S)+P(Z_0^{-1})\ , \tag{2.10}$$

$$G_0(z_0, \bar{z}_0)=\tfrac{1}{4}ia_0(1+\sigma^2\bar{C}^2)-\tfrac{1}{4}i\bar{a}_0\ln CZ_0+2i\{\bar{g}_0'(\bar{z}_0)-\tfrac{1}{8}\bar{a}_0\ln\bar{C}\bar{Z}_0\}+P(Z_0^{-1})\ , \tag{2.11}$$

with

$$\bar{g}_0'(\bar{z}_0)=\tfrac{1}{8}\bar{a}_0\ln\bar{C}\bar{Z}_0+P(Z_0^{-1})\ , \tag{2.12}$$

$$S=\ln(2/k)-\gamma\ , \qquad (\gamma \text{ is Euler's constant}) \tag{2.13}$$

and $P(Z)=\sum_{n=0}^{\infty} C_nZ^n$ where C_n's are arbitrary constants.

We now assume that $kd\geq O(1)$ so that $K_n(kd)\leq O(1)$. Taking the terms of $O(kd)$ in (2.5), we have

$$W_q(z_q)=\pm\frac{i}{2}\left\{K_1(|q|kd)\,e^{-qkd\cos\alpha}-\frac{1}{|q|kd}\right\}e^{-i\alpha}a_0+\tfrac{1}{2}e^{-qkd\cos\alpha}K_0(|q|kd)\bar{a}_0+P(Z_p) \tag{2.14}$$

near E_p. The double sign denotes that the upper sign is to be taken when $q>0$ and the lower sign when $q<0$.

Introducing (2.3) into (2.7) determines $\mathcal{E}$ as follows:

$$\mathcal{E}=-\lim_{z_n\to-\infty}\sum_{n=-\infty}^{\infty}\frac{ia_0}{2k}\frac{1}{z_n}=\lim_{z\to-\infty}\left(\frac{\pi}{de^{i\alpha}}\cot\frac{\pi z}{de^{i\alpha}}-\frac{1}{z}\right)=-\frac{i\pi}{d}e^{-i\alpha}\,. \tag{2.15}$$

Substituting from (2.7). (2.14) and (2.15) into (2.8), we obtain

$$\begin{aligned}&\bar{g}_0'(\bar{z}_0)-\tfrac{1}{8}\bar{a}_0\ln\bar{C}\bar{Z}_0+P(Z_0^{-1})\\&=\frac{1}{4}\left[2iU+\left\{\tfrac{1}{2}(1+\sigma^2\bar{C}^2)-\frac{i\pi}{kd}\cdot e^{-i\alpha}+2T_1e^{-i\alpha}\right\}a_0-(S+2T_0)\bar{a}_0\right]+P(Z_0)\end{aligned}\tag{2.16}$$

on the profile $Z_0=e^{i\theta}$.

For brevity we introduce two constants

$$R=2(1+\sigma^2)U/\nu=4(1+\sigma^2)k\ ,\tag{2.17}$$

and

$$h=d/(1+\sigma^2)\ ,\tag{2.18}$$

in place of k and d. R is the Reynolds number based on the major-axis of the elliptic cylinder. From (2.12) we find that the left-hand side of (2.16) is $P(Z_0^{-1})$ while the right-hand side of (2.16) is $P(Z_0)$. Hence both sides must be separately equal to zero. Thus we have

$$g_0(z_0)=\tfrac{1}{8}a_0\ln CZ_0\ ,\tag{2.19}$$

$$2iU=\left\{-\tfrac{1}{2}(1+\sigma^2\bar{C}^2)+\frac{4\pi i}{Rh}e^{-i\alpha}-2T_1e^{-i\alpha}\right\}a_0+(S+2T_0)\bar{a}_0\ ,\tag{2.20}$$

$$T_0=\sum_{n=1}^{\infty}K_0(nRh/4)\cosh(nRh\cos\alpha/4)\ ,\tag{2.21}$$

$$T_1=\sum_{n=1}^{\infty}K_1(nRh/4)\sinh(nRh\cos\alpha/4)\ ,\tag{2.22}$$

and

$$S=\ln 8(1+\sigma^2)/R-\gamma\ .\tag{2.23}$$

From (2.20) and its complex conjugate, we can determine a_0 as follows:

$$\begin{aligned}a_0=-\frac{2iU}{J}\Big[&S-\tfrac{1}{2}(1+\sigma^2\cos 2\beta)+\frac{4\pi}{Rh}\sin\alpha+2T_0\\&-2T_1\cos\alpha+i\left\{\tfrac{1}{2}\sigma^2\sin 2\beta-\frac{4\pi}{Rh}\cos\alpha-2T_1\sin\alpha\right\}\Big]\ ,\end{aligned}\tag{2.24}$$

where

$$\begin{aligned}J=&\left\{S-\tfrac{1}{2}(1+\sigma^2\cos 2\beta)+\frac{4\pi}{Rh}\sin\alpha+2T_0-2T_1\cos\alpha\right\}\\&\times\left\{S+\tfrac{1}{2}(1+\sigma^2\cos 2\beta)-\frac{4\pi}{Rh}\sin\alpha+2T_0-2T_1\cos\alpha\right\}\\&-\left(\tfrac{1}{2}\sigma^2\sin 2\beta-\frac{4\pi}{Rh}\cos\alpha-2T_1\sin\alpha\right)^2 .\end{aligned}\tag{2.25}$$

Let us define the drag coefficient C_D and the lift coefficient C_L for one of the elliptic cylinders by

$$C_D=\frac{X}{\tfrac{1}{2}\rho U^2\cdot 2(1+\sigma^2)}\ ,\qquad C_L=\frac{Y}{\tfrac{1}{2}\rho U^2\cdot 2(1+\sigma^2)}\ ,\tag{2.26}$$

where X and Y are the drag and lift on the elliptic cylinder. As was shown in the previous paper[8] (cf.Eq. (2.29) there) we have

$$C_D+iC_L=4\pi i a_0/UR\ .\tag{2.27}$$

Hence, substituting from (2.24) into (2.27) and separating real and imaginary parts, we have

$$C_D=\frac{8\pi}{RJ}\left[S-\tfrac{1}{2}(1+\sigma^2\cos 2\beta)+\frac{4\pi}{Rh}\sin\alpha+2T_0-2T_1\cos\alpha\right], \tag{2.28}$$

$$C_L=\frac{8\pi}{RJ}\left[\tfrac{1}{2}\sigma^2\sin 2\beta-\frac{4\pi}{Rh}\cos\alpha-2T_1\sin\alpha\right]. \tag{2.29}$$

§ 3. Special Cases of $\alpha=\pi/2$

These are the cases in which the flow impinges normally upon the surface of the lattice.

(A) *Elliptic cylinders*

i) β=arbitrary (axes of elliptic cylinders included to the lattice surface)

If we put $\alpha=\pi/2$, the expressions (2.28), (2.29), (2.25) and (2.21) reduce respectively to

$$C_D=\frac{8\pi}{RJ}\left\{S-\tfrac{1}{2}(1+\sigma^2\cos 2\beta)+\frac{4\pi}{Rh}+2T_0\right\}, \tag{3.1}$$

$$C_L=\frac{8\pi}{RJ}\tfrac{1}{2}\sigma^2\sin 2\beta\,, \tag{3.2}$$

$$J=\left\{S+\tfrac{1}{2}(1+\sigma^2\cos 2\beta)-\frac{4\pi}{Rh}+2T_0\right\}\left\{S-\tfrac{1}{2}(1+\sigma^2\cos 2\beta)+\frac{4\pi}{Rh}+2T_0\right\}-\tfrac{1}{4}\sigma^4\sin^2 2\beta\,, \tag{3.3}$$

$$T_0=\sum_{n=0}^{\infty}K_0(nRh/4)=\frac{1}{8}\frac{16\pi}{Rh}+\tfrac{1}{2}\ln\frac{Rh}{16\pi}+\frac{\gamma}{2}-\zeta(3)\left(\frac{Rh}{16\pi}\right)^2+\frac{3}{8}\zeta(5)\left(\frac{Rh}{16\pi}\right)^4-\cdots, \tag{3.4}$$

where ζ is Riemann's zeta function.

ii) $\beta=0$ (minor axis parallel to the lattice surface)

$$C_D=\frac{8\pi}{R}\left\{S+\tfrac{1}{2}(1+\sigma^2)-\frac{4\pi}{Rh}+2T_0\right\}^{-1}, \qquad C_L=0\,, \tag{3.5}$$

iii) $\beta=\pi/2$ (major axis parallel to the lattice surface)

$$C_D=\frac{8\pi}{R}\left\{S+\tfrac{1}{2}(1-\sigma^2)-\frac{4\pi}{Rh}+2T_0\right\}^{-1}, \qquad C_L=0\,. \tag{3.6}$$

(B) *Circular cylinders*

$$C_D=\frac{8\pi}{R}\left\{S+\tfrac{1}{2}-\frac{4\pi}{Rh}+2T_0\right\}^{-1}, \qquad C_L=0\,, \tag{3.7}$$

$$S=\ln(8/R)-\gamma\,, \qquad R=2U/\nu\,. \tag{3.8}$$

This expression coincides with the first approximation of Tamada and Fujikawa's corresponding formula for the case of a lattice of circular cylinders.

(C) *Flat plates*

i) β=arbitrary

$$C_D=\frac{8\pi}{RJ}\left\{S-\tfrac{1}{2}(1+\sigma^2\cos 2\beta)+\frac{4\pi}{Rh}+2T_0\right\}, \tag{3.9}$$

$$C_L=\frac{8\pi}{RJ}\tfrac{1}{2}\sin 2\beta\,, \tag{3.10}$$

$$J=\left\{S+\tfrac{1}{2}(1+\cos 2\beta)-\frac{4\pi}{Rh}+2T_0\right\}\left\{S-\tfrac{1}{2}(1+\cos 2\beta)+\frac{4\pi}{Rh}+2T_0\right\}-\tfrac{1}{4}\sin^2 2\beta\,, \tag{3.11}$$

$$S=\ln(16/R)-\gamma\ , \qquad R=4U/\nu\ . \tag{3.12}$$

ii) $\beta=0$ (flat plates perpendicular to the lattice surface)

$$C_D=\frac{8\pi}{R}\left\{S+1-\frac{4\pi}{Rh}+2T_0\right\}^{-1}=\frac{8\pi}{R}\left\{P-2\zeta(3)\left(\frac{Rh}{16\pi}\right)^2+\cdots\right\}^{-1}, \qquad C_L=0\ , \tag{3.13}$$

where

$$P=1-\ln(\pi/h)\ . \tag{3.14}$$

Only the first term of the expression (3.13) coincides with the corresponding formula of the author's previous paper[4] (Eq. (3.14)), which was obtained by Stokes' approximation.

iii) $\beta=\pi/2$ (flat plates lying on the lattice surface)

$$C_D=\frac{8\pi}{R}\left(S-\frac{4\pi}{Rh}+2T_0\right)^{-1}=\frac{8\pi}{R}\left\{\ln(h/\pi)-2\zeta(3)\left(\frac{Rh}{16\pi}\right)^2+\cdots\right\}^{-1}, \qquad C_L=0\ . \tag{3.15}$$

Only the first term of the expression of (3.15) coincides with the corresponding formula of Hasimoto's paper[3] (Eq. (4.36)), which was obtained by Stokes' approximation.

§ 4. Numerical Discussions

We have five parameters to determine the flow, that is, $\alpha, \beta, h, t=(1-\sigma^2)/(1+\sigma^2)$ (the thickness ratio of the elliptic cylinder) and R. Numerical calculations were carried out only for the case when $\alpha=90°$ and $h=10$. The other parameters β, t and R are taken as follows: $\beta=0°$, $18°$, $36°$, $54°$, $72°$, $90°$; $t=0$ (flat plates), 0.1, 0.5, 1.0 (circular cylinders) and $R=0.08$, 0.4, 1.0 (cf. Fig. 2 and Table I).

It is to be noted that by lattice formation the drag of the elliptic cylinder is increased and the lift is reduced in comparison with the

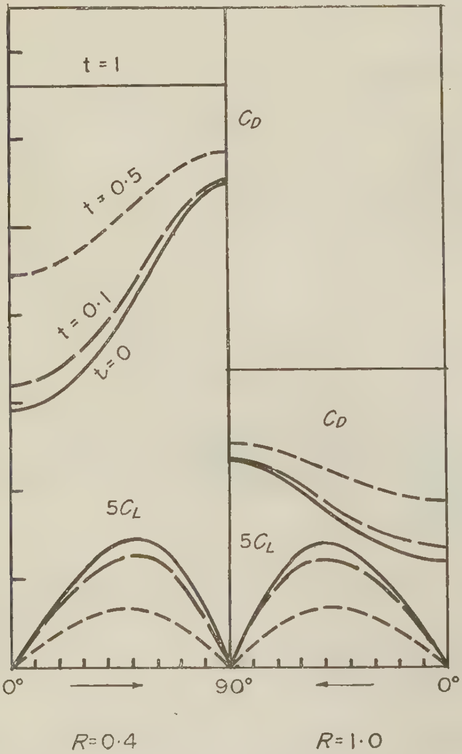

Fig. 2. C_D and C_L vs. β when $h=10$, $\alpha=\frac{\pi}{2}$ and $R=0.4$ and 1.0.

Table I. Calculated values of C_D and C_L for various values of β and R when $\alpha=90°$ and $h=10$.

(a) Flat plates

C_D

R \ β	0°	18°	36°	54°	72°	90°
0.08	145.63	152.58	174.08	210.04	251.31	271.47
0.4	29.32	30.89	35.62	43.14	51.22	54.98
1.0	12.13	12.93	15.24	18.66	22.01	23.46

C_L

0.08	0	1.416	2.593	3.099	2.274	0
0.4	0	1.392	2.501	2.897	2.054	0
1.0	0	1.418	2.474	2.739	1.854	0

(b) Elliptic cylinders with the thickness ratio $t=0.1$.

C_D

R \ β	0°	18°	36°	54°	72°	90°
0.08	159.39	166.13	186.60	219.57	255.58	275.51
0.4	32.11	33.61	38.05	44.90	51.99	55.19
1.0	13.33	14.08	16.22	19.32	22.29	23.56

C_L

0.08	0	1.262	2.279	2.661	1.902	0
0.4	0	1.243	2.208	2.511	1.746	0
1.0	0	1.273	2.204	2.412	1.614	0

(c) Elliptic cylinders with the thickness ratio $t=0.5$.

C_D

R \ β	0°	18°	36°	54°	72°	92°
0.08	221.48	226.61	241.20	261.91	281.34	289.52
0.4	44.75	45.84	48.90	53.15	57.06	58.68
1.0	18.86	19.38	20.81	22.74	24.46	25.15

C_L

R \ β	0°	18°	36°	54°	72°	92°
0.08	0	0.7040	1.209	1.309	0.8666	0
0.4	0	0.7032	1.198	1.282	0.8399	0
1.0	0	0.7461	1.255	1.320	0.8514	0

(d) Circular cylinders.

R	C_D
0.08	325.86
0.4	66.16
1.0	28.62

case of a single elliptic cylinder in the same condition, that is, with the same values of α, β, t and R.

Acknowledgement

The author wishes to express his sincere thanks to Professor Isao Imai for his continual guidance and encouragement throughout this study. He is also indebted to Dr. Mitutosi Kawaguti, Professor Hidenori Hasimoto and Mr. Hideo Takami for their invaluable discussions.

References

1) K. Tamada and H. Fujikawa: Quart. J. Mech. Appl. Math. **10** (1957) 425.
2) T. Miyagi: J. Phys. Soc. Japan **13** (1958) 493.
3) H. Hasimoto: J. Phys. Soc. Japan **13** (1958) 633.
4) S. Kuwabara: J. Phys. Soc. Japan **13** (1958) 1516.
5) I. Imai: Proc. Roy. Soc. **A**, **224** (1954) 141.
6) S. Kuwabara: J. Phys. Soc. Japan **12** (1957) 291.
7) S. Kuwabara: J. Phys. Soc. Japan **13** (1958) 506.

JOURNAL OF THE PHYSICAL SOCIETY OF JAPAN, Vol. 14, No. 4, APRIL, 1959

The Forces experienced by Randomly Distributed Parallel Circular Cylinders or Spheres in a Viscous Flow at Small Reynolds Numbers

By Sinzi* KUWABARA

Department of Physics, Faculty of Science, University of Tokyo

(Received January 8, 1959)

The forces experienced by parallel circular cylinders or spheres which are distributed at random and homogeneously in a viscous flow are investigated on the basis of Stokes' approximation. The results for the case of spheres are applied to the problem of sedimentation and compared with several experimental data.

§ 1. Introduction

Recently a number of investigations have been made on the interference effects submerged in a viscous flow at small Reynolds numbers. However, they have been mostly concerned with the case of two bodies or a regular lattice of infinitely many cylinders. In this parer, we extend such a treatment to the case of infinitely many circular cylinders or spheres which are distributed at random and homogeneously in a viscous flow. These results can be readily applied to the problem of sedimentation of particles of cylindrical or spherical shape. In § 4, we consider the application of our theory to the case of spherical particles, in comparison with other theories and experimental results.

In order to simulate the condition of random and homogeneous distribution of bodies, we take a model such that, in the coordinate system moving with the mean flow velocity U, each one of the bodies is moving with the negative velocity $-U$ in a certain closed surface on which both the normal fluid velocity and the vorticity vanish. The closed surface is taken to be a coaxial circular cylinder or a concentric sphere according as the body is a circular cylinder or a sphere.

---

* Sinzi=Shinji

§ 2. The Case of Parallel Circular Cylinders

In this case, we assume that i) all the circular cylinders have the same radius and the same velocity, ii) they are parallel to each other and perpendicular to the mean flow and iii) they are distributed at random and homogeneously.

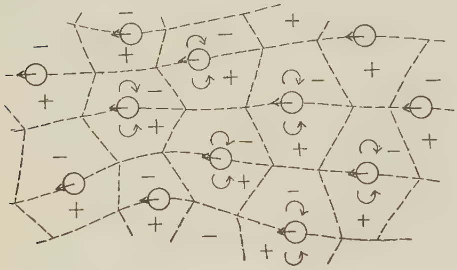

Fig. 1 (a)

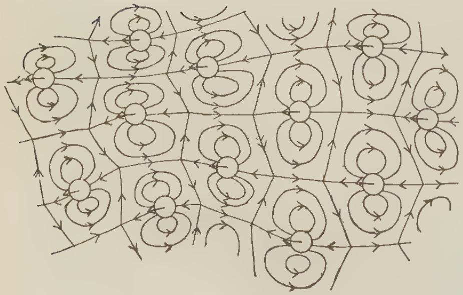

Fig. 1 (b)

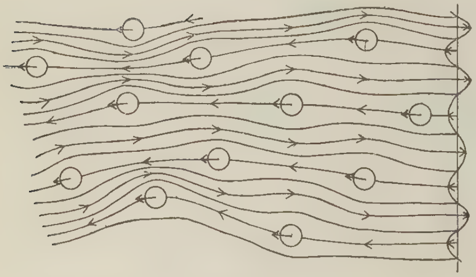

Fig. 1 (c)

Let us assume that the mean flow is directed from left to right. On the upper side of a cylinder the vorticity would be negative and on the lower side positive. Thus, midway between the neighbouring cylinders there will be lines of zero vorticity (the broken lines in Fig. 1 (a)). We may imagine that the streamlines are closed in the neighbourhood of the cylinder in the reference system which is moving at the mean flow velocity (cf. Fig. 1 (b)). In fact, otherwise, we should have a flow pattern consisting of a series of infinitely long strips of fluid with alternating flow direction located side by side (cf. Fig. 1 (c)). It seems however that such a flow would be improbable.

From the above consideration, we take the following mathematical model. We consider an imaginary circular cylinder of radius b enclosing and coaxial with the given circular cylinder of radius a. On the imaginary circular cylinder, the vorticity and the normal component of velocity are assumed to be zero, while on the solid circular cylinder the velocity should be equal to minus the mean flow velocity U (cf. Fig. 2). We take the cross-sectional area πb^2 of the imaginary circular cylinder to be equal to the "free" area corresponding to each solid cylinder, namely

$$\pi b^2 = 1/n \,, \tag{2.1}$$

where n is the number of the solid cylinders per unit area.

To Stokes' approximation the fundamental equation for the two-dimensional steady motion is written as

$$\Delta\Delta\psi = 0 \,, \tag{2.2}$$

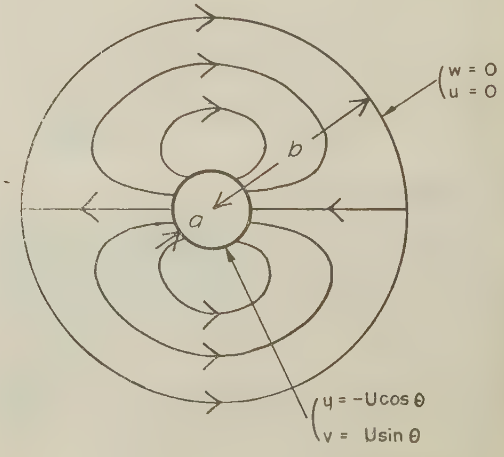

Fig. 2. The model of flow.

where ψ is the stream function such that, using cylindrical coordinates (r, θ), the velocity (u, v) and the vorticity ω are given by

$$u=\frac{1}{r}\frac{\partial\psi}{\partial\theta}\,, \qquad v=-\frac{\partial\psi}{\partial r}\,, \tag{2.3}$$

$$\omega=\frac{\partial v}{\partial r}-\frac{1}{r}\frac{\partial u}{\partial\theta}+\frac{v}{r}=-\varDelta\psi\,, \tag{2.4}$$

where

$$\varDelta=\frac{\partial^2}{\partial r^2}+\frac{1}{r}\frac{\partial}{\partial r}+\frac{1}{r^2}\frac{\partial^2}{\partial\theta^2}\,.$$

The boundary conditions of our model become as follows:

$$u=v=0 \qquad \text{for} \quad r=1\,, \tag{2.5}$$

$$u=U\cos\theta \qquad \text{for} \quad r=l\equiv b/a\,, \tag{2.6}$$

$$\omega=0 \qquad \text{for} \quad r=l\,, \tag{2.7}$$

in the reference system in which the cylinders are at rest*, where U is the velocity of the mean flow parallel to the original line $\theta=0$, and r has been made non-dimensional by taking a as unit.

We have a particular solution of (2.2) in the form

$$\psi=\left(A\frac{1}{r}+Br+Cr\ln r+Dr^2\right)\sin\theta\,, \tag{2.8}$$

where A, B, C and D are arbitrary constants which can be determined so as to satisfy the boundary conditions. Thus, by the boundary conditions (2.5)–(2.7), we have

$$A=\tfrac{1}{2}(U/K)(1-\tfrac{1}{2}l^{-2})\,, \tag{2.9}$$

$$B=-\tfrac{1}{2}(U/K)(1-l^{-2})\,, \tag{2.10}$$

$$C=U/K\,, \tag{2.11}$$

$$D=-\tfrac{1}{4}U/(l^2K)\,, \tag{2.12}$$

where

$$K=P+l^{-2}-\tfrac{1}{4}l^{-4}\,, \tag{2.13}$$

$$P=\ln l-\tfrac{3}{4}\,. \tag{2.14}$$

The drag X experienced by the solid cylinder can be calculated by use of Imai's formula (given as (12.13) in his paper[1]), which is an extension of the Blasius formula to the case of a viscous flow. In our case, the formula can be written simply as

$$X=-2\mu\int_C\frac{\partial\omega}{\partial\bar{z}}\bar{z}\,d\bar{z}\,, \tag{2.15}$$

where $\bar{z}=re^{-i\theta}$ and C signifies the contour of the cross section of the solid cylinder. Thus, we hove

$$X=4\pi\mu C\,. \tag{2.16}$$

The drag coefficient C_D can be obtained as follows:

$$C_D=\frac{X}{\frac{1}{2}\rho U^2\cdot 2}=\frac{8\pi}{RP}\left(1+\frac{1}{l^2P}-\frac{1}{4l^4P}\right)^{-1}$$

$$=\frac{8\pi}{RP}\left\{1-\frac{1}{l^2P}+\frac{1}{l^4P^2}(1+\tfrac{1}{4}P)-\cdots\right\}\,. \tag{2.17}$$

When l tends to infinitely, we have $C_D=0$. This is nothing other than the well-known paradox of Stokes.

§ 3. The Case of Spheres

In this case, we also assume that i) all the spheres have the same radius and the same velocity and ii) they are distributed at random and homogeneously. We use a model similar to the one used in § 2, except that we take, in place of (2.1),

$$\frac{4}{3}\pi b^3=\frac{1}{n}\,, \tag{3.1}$$

where b is the radius of the imaginary spherical surface concentric with the solid sphere.

To Stokes' approximation the fundamental equation for the axisymmetric steady flow is written in terms of Stokes' stream function ψ as

$$\left\{\frac{\partial^2}{\partial r^2}+\frac{\sin\theta}{r^2}\frac{\partial}{\partial\theta}\left(\frac{1}{\sin\theta}\frac{\partial}{\partial\theta}\right)\right\}^2\psi=0\,, \tag{3.2}$$

and the velocity and the vorticity are given by

$$u=-\frac{1}{r^2\sin\theta}\frac{\partial\psi}{\partial\theta}\,, \qquad v=\frac{1}{r\sin\theta}\frac{\partial\psi}{\partial r}\,, \tag{3.3}$$

$$\omega=\frac{\partial v}{\partial r}+\frac{v}{r}-\frac{\partial u}{r\partial\theta}\,. \tag{3.4}$$

where (r, θ, ϕ) are the polar coordinates, $(u, v, 0)$ the velocity components and $(0, 0, \omega)$ the vorticity components. Because of symmetry, the ϕ-component of the velocity and the r- and θ-components of the vorticity vanish.

The boundary conditions of our model become

$$u=v=0 \qquad \text{for} \quad r=1\,, \tag{3.5}$$

$$u=U\cos\theta \qquad \text{for} \quad r=l\equiv b/a\,, \tag{3.6}$$

$$\omega=0 \qquad \text{for} \quad r=l\,, \tag{3.7}$$

---

* By the invariance of the Navier-Stokes equations with respect to the Galilei transformation, we can choose any coordinate system suitable for the boundary conditions to be applied.

where U is the velocity of the mean flow parallel to the original line $\theta=0$, and r has been made non-dimensional by taking the radius of the solid sphere a as unit.

We have a particular solution of (3.2)[2] in the form:

$$\psi=\left(A\frac{1}{r}+Br+Cr^2+Dr^4\right)\sin^2\theta\,, \tag{3.8}$$

where A, B, C and D are arbitrary constants. Applying the boundary conditions (3.5)–(3.7) to (3.8), we have

$$A=-\tfrac{1}{4}U\{1-(2/5)l^{-3}\}/K\,, \tag{3.9a}$$

$$B=\tfrac{3}{4}U/K\,, \tag{3.9b}$$

$$C=-\tfrac{1}{2}U(1+\tfrac{1}{2}l^{-2})/K\,, \tag{3.9c}$$

$$D=\tfrac{3}{2}U/(l^3K)\,, \tag{3.9d}$$

where

$$K=\left(1-\frac{1}{l}\right)^3\left(1+\frac{6}{5}\frac{1}{l}+\frac{3}{5}\frac{1}{l^2}+\frac{1}{5}\frac{1}{l^3}\right). \tag{3.10}$$

By (3.3) and (3.4), we have

$$u=-2\left(\frac{A}{r^3}+\frac{B}{r}+C+Dr^2\right)\cos\theta\,, \tag{3.11}$$

$$v=-\left(\frac{A}{r^3}-\frac{B}{r}-2C-4Dr^2\right)\sin\theta\,, \tag{3.12}$$

$$\omega=-2\left(\frac{B}{r^2}-5Dr\right)\sin\theta\,. \tag{3.13}$$

The drag on a sphere may be calculated from the rate of dissipation of energy. The dissipation function Φ has the form

$$\begin{aligned}\Phi=\mu\Bigg\{&2\left(\frac{\partial u}{\partial r}\right)^2+2\left(\frac{\partial v}{r\partial\theta}+\frac{u}{r}\right)^2\\ &+2\left(\frac{u}{r}+\frac{v}{r\tan\theta}\right)^2+\left(\frac{\partial u}{r\partial\theta}+\frac{\partial v}{\partial r}-\frac{v}{r}\right)^2\Bigg\}\\ =12\mu&\left(\frac{3A}{r^4}+\frac{B}{r^2}-2Dr\right)^2\cos^2\theta\\ &+36\mu\left(\frac{A}{r^4}+Dr\right)^2\sin^2\theta\,.\end{aligned} \tag{3.14}$$

Total rate of dissipation of energy in the fluid becomes

$$\begin{aligned}&\int_0^\pi\int_1^l \Phi 2\pi r^2\cdot\sin\theta\,d\theta\cdot dr\\ &=\frac{16\pi\mu}{l^5}\{3A^2(l^2-1)+2ABl^2(l^3-1)\\ &\quad+B^2l^4(l-1)-2BDl^5(l^2-1)+2D^2l^5(l^5-1)\}\,.\end{aligned} \tag{3.15}$$

This is equal to XU where X is the drag experienced by the sphere. Substituting (3.9) into (3.15), we can find the drag and the drag coefficient C_D as

$$X=6\pi\mu U\cdot L(\xi)\,, \tag{3.16}$$

$$C_D=\frac{24}{R}L(\xi) \tag{3.17}$$

where

$$\begin{aligned}L(\xi)=&\left(1+\frac{51}{50}\xi+\frac{3}{50}\xi^2-\frac{7}{25}\xi^3+\frac{2}{5}\xi^4+\right.\\ &\left.+\frac{12}{25}\xi^5+\frac{6}{25}\xi^7+\frac{2}{25}\xi^8\right)(1-\xi)^{-3}\\ &\times\left(1+\frac{6}{5}\xi+\frac{3}{5}\xi^2+\frac{1}{5}\xi^3\right)^{-2}\\ =&1+\frac{81}{50}\xi+\frac{324}{125}\xi^2+\frac{13783}{1250}\xi^3+\cdots\end{aligned} \tag{3.18}$$

and

$$\xi=1/l=a/b\,. \tag{3.19}$$

If we let ξ tend to zero, we have $L=1$. Hence (3.16) reduces to the Stokes formula for the drag of a sphere (of radius 1) in an unlimited viscous flow.

§ 4. Application to the Problem of Sedimentation

This problem has been discussed by a number of authors.[3],[4],[5] Recently Kawaguti dealt with this problem by use of a model such that each one of the particles is represented by a sphere placed in a circular tube with frictionless wall[6]. More recently Hasimoto obtained such solutions of Stokes' equations that are triply periodic and represent the flow past a system of spheres placed at the simple cubic or the body-centred lattice points[7].

We can find the terminal settling velocity of homogeneously distributed sphere by equating the gravitational force to the viscous drag on one of them. The gravitational force is

$$X=(\sigma-\rho)\frac{4}{3}\pi a^3g\,, \tag{4.1}$$

and the drag is, from (3.17),

$$X=6\pi\mu Ua\cdot L(\xi)\,, \tag{4.2}$$

where σ is the density of the particle, ρ that of fluid and a the radius of the particle. Thus, the terminal settling velocity V is given by

$$V/V_0=1/L(\xi)\,, \tag{4.3}$$

where

$$V_0=\frac{2}{9}(\sigma-\rho)ga^2/\mu \tag{4.4}$$

is the terminal velocity of a single particle as given by the Stokes law.

The volume concentration c of particles (the ratio of the volume of particles to the volume of the system) can be related to ξ by

$$c=\frac{4}{3}\pi a^3\bigg/\left(\frac{4}{3}\pi b^3\right)=\left(\frac{a}{b}\right)^3=\xi^3\,. \tag{4.5}$$

Hence we can express (4.3) in terms of c as follows:

$$\begin{aligned}V/V_0&=1/L(c^{1/3})\\&=1-1.62c^{1/3}+0.012c^{2/3}\\&\quad+0.464152c+\cdots\,.\end{aligned} \tag{4.6}$$

For the case of circular cylinders, we can define the volume concentration as follows:

$$c=\pi a^2/(\pi b^2)=(a/b)^2=l^{-2}\,. \tag{4.7}$$

Table I. Calculated values of RC_D for various values of c for the case of circular cylinders by use of (4.8).

c	0.001	0.002	0.003	0.005	0.007	0.01	0.02	0.03	0.05	0.07	0.1
$l=b/a$	31.623	22.361	18.257	14.142	11.952	10.000	7.071	5.774	4.472	3.780	3.162
RC_D	9.292	10.653	11.649	13.199	14.462	16.084	20.501	24.329	31.525	38.761	50.387

Table II. Calculated values of V/V_0 for various values of c for the case of spheres by use of (4.6).

c	0.001	0.002	0.003	0.005	0.007	0.01	0.02	0.03	0.05	0.07	0.1
$l=b/a$	10.000	7.937	6.934	5.848	5.228	4.642	3.684	3.218	2.714	2.426	2.154
V/V_0	0.8388	0.7973	0.7687	0.7263	0.6945	0.6571	0.5719	0.5137	0.4308	0.3703	0.3015

Then (2.17) becomes

$$\begin{aligned}RC_D&=\frac{8\pi}{P}\left(1+\frac{c}{P}-\frac{c^2}{4P}\right)^{-1}\\&=\frac{8\pi}{P}\left\{1-\frac{c}{P}+\frac{c^2}{P^2}(1+\tfrac{1}{4}P)+\cdots\right\},\end{aligned} \tag{4.8}$$

where

$$P=-\frac{1}{2}\ln c-\frac{3}{4}\,. \tag{4.9}$$

§ 5. Numerical Discussions

For the case of circular cylinders, the relation between RC_D and $c=(a/b)^2=1/(\pi n)$ has been numerically calculated and is shown in Fig. 3 and tabulated in Table I. Unfortunately we have no experimental data for this case, so that we cannot compare our theory with experiment.

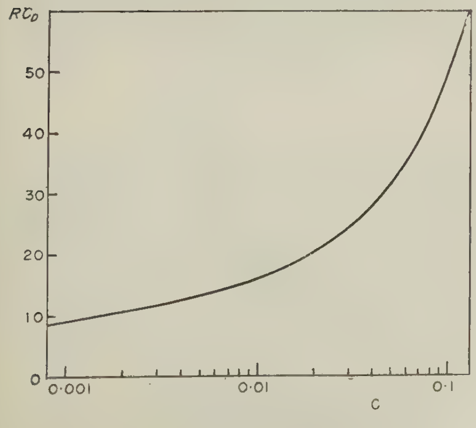

Fig. 3. RC_D vs. volume concentration.

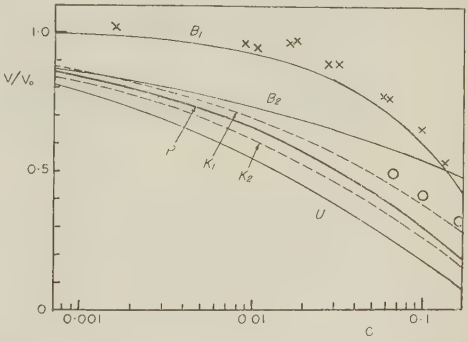

Fig. 4. Sedimentation velocity vs. volume concentration.

P	Present theory	theory
B_1	Burgers (lattice)	
B_2	Burgers (at random)	
U	Uchida	
K_1	Kawaguti (body-centred)	
K_2	Kawaguti (simple-cubic)	
○	Happel and Epstein	experiment
×	Noda	

For the case of spheres, the relation between V/V_0 and c is obtained as shown in Fig. 4 and tabulated in Table II. In Fig. 4 are also included the theoretical results due to Burgers[5], Uchida[6] and Kawaguti[7], as well as the experimental data of Happel and Epstein[8] and Noda[9]. It is to be noted that the curve V/V_0 against c of our theory lies between Kawaguti's curves for the simple cubic lattice and for the body-centered lattice approximation.

Acknowledgement

The author wishes to express his sincere thanks to Professor Isao Imai for his continual guidance and encouragement throughout this study. He is also indebted to Dr. Mitutosi Kawaguti who kindly furnished him with the data concerning the problem of sedimentation, and to Professor Hidenori Hasimoto and Mr. Hideo Takami for their invaluable discussions.

References

1) I. Imai: Proc. Roy. Soc. **A**, **208** (1951) 487.
2) H. Lamb: *Hydrodynamics* (Cambr. Univ. Press, 1932). § 338, p. 602.
3) E. Cunningham: Proc. Roy. Soc. **A**, **83** (1909) 357.
4) J. M. Burgers: Proc. Ned. Acad. Wet. **44** (1941) 1045, 1177; **45** (1942) 9, 126.
5) S. Uchida: Rept. of Inst. Sci. Tech. **3** (1949) 97.
6) M. Kawaguti: J. Phys. Soc. Japan **13** (1958) 209.
7) H. Hasimoto: Read before the 12th Annual meeting of the Physical Society of Japan held at Faculty of Culture, Univ. of Tokyo, Oct. 1957.
8) J. Happel and N. Epstein: Industr. and Engng. Chem. **46** (1954) 1187.
9) H. Noda: Bull. Chem. Soc. Japan **30** (1957) 495.

JOURNAL OF THE PHYSICAL SOCIETY OF JAPAN, Vol. 14, No. 4, APRIL, 1959

The Generation of Static Charge on High Polymer

By Shigeyoshi KITTAKA

Department of Physics, Tokyo College of Science, Shinjuku-ku, Tokyo

(Received November 5, 1958)

The generation of static electricity by the contact and seperation between high polymer substances and metals has been studied. The couples of polystyrene-Pt, Acrylite (polymethylmethacrylate)-Pt, and Teflon (polytetrafluoroethylene)-Pt were examined. It was observed that the surrounning conditions have serious effects on the quantity and sign of generated static charge.

The mechanism of generation of electro-static charge has been proposed assuming the energy levels of the localized electrons on the surface of high polymer substances and the change of these energy levels by the absorption of different gases. It was estimated that work functions of polystyrene, Acrylite, and Teflon are 5.74 eV, 5.48 eV and 6.04 eV, respectively.

§ 1. Introduction

The generation of static charge is one of the oldest problems in physics. The electrostatic series of many substances have already been established, and it has been recognized that these may be dependent on some intrinsic properties of insulating materials. However, the exact explanation of these series is not yet established even in recent solid state physics[1-6]. Therefore, we have performed the experiment of generation of static charge by the contact and separation between high polymer substances and metals. The effects of surrounding conditions (oxygen content of air and relative humidity) have been especially carefully studied in the present experiment. The analysis of these experimental results with the idea of surface energy levels[7,8] both on high polymers and metals can give the rough informations of work function of electrons on the high polymer surface, and their change in accompanying with the absorption of various gases in different conditions.

§ 2. Experimental Procedure

The special equipment designed for this experiment is shown in Fig. 1 and 2. The high polymer substances and the metals are brought into contact and then separated gradually. The generated charge on the high polymer test piece is measured in Faraday cylinder (F). The contact potential difference of metal test piece against a standard metal surface (Pt) is also measured. These measurements are repeated several times with successive contact and separation, and whole cycles of experiment are performed in a closed vessel by remote control system. The metal test piece (M) is a small rod of 4 mm in diameter and 2 mm in length, and the high polymer test picece (I) is also a rod of 6 mm in diameter and 100 mm in length. Both test pieces are moved back and forth by servo-motor and brought into contact with same contact force (3.8×10^4 dynes). The bending angle of phosphor bronze plate (P) is measured by reading microscope from the outside of the vessel for the control of contact force.

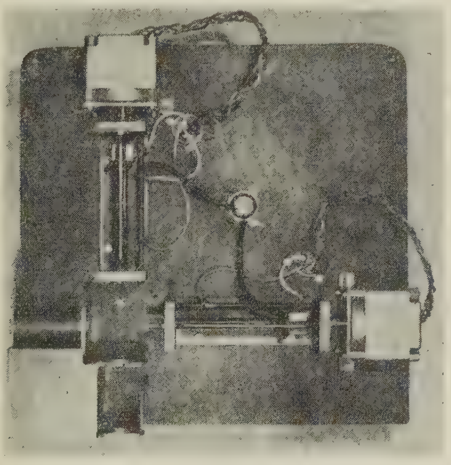

Fig. 1. Contact charging apparatus.

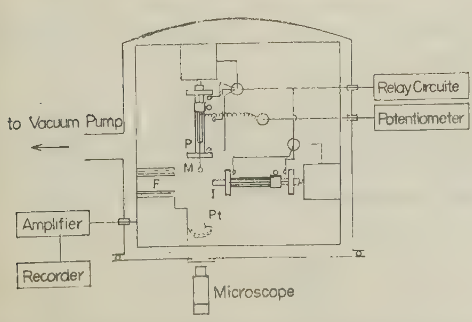

Fig. 2. Schematic diagram of the experimental equipment.

The quantity of electric charge on the high polymer is measured by transporting the high polymer test piece into the Faraday cylinder (F). When the top of the (high polymer) test piece reaches the center of F, the vacuum tube electrometer reading is V_1. In this position almost 95% of the electric lines of force are captured in the cylinder. When the test piece moves back to the original position, the reading of vacuum tube electrometer becomes V_0. Only 1% of the electric lines of force is captured in the cylinder in such a situation.

The absolute quantity of static charge, Q, will be $Q=CV$ $(V=V_1-V_0)$, in which C is electro-static capacity of Faraday cylinder to the earth. The contact potential difference of the metal test piece against the standard metal which is platinum in this experiment, is measured by Kelvin method. The metal test piece is moved to the platinum and the contact potential difference is measured by the potentiometer and vacuum tube electrometer; the latter is the same one as used for the measurement of the charge in Faraday

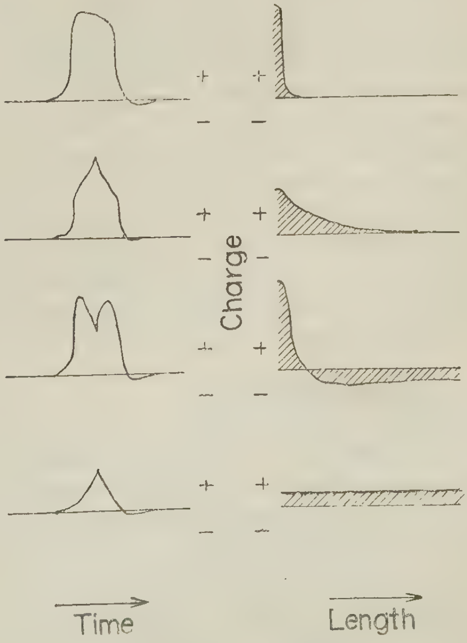

Fig. 3. Relation between the recorded wave form and distribution of charge on sample.

cylinder. The input resistance of vacuum tube electrometer is $10^{12}\Omega$ and connects with the first stage vacuum tube 956. The calibration voltage is applied to the first stage vacuum tube. The total capacity of electrometer is $(50\pm1)\ \mu\mu F$ and the time constant is 50 sec. The measuring period (during which the test piece is moved back and forth) is 12.5 sec. The noise level of the amplifier is 0.2 mV. The accuracy of charge measurement becomes 1×10^{-14}coul. The accuracy of contact potential difference measurement is about 10 mV. This is because the potential difference is divided into the capacity between test piece and standard platinum plate (say $1\ \mu\mu F$) and the input capacity (say $50\ \mu\mu F$).

The charged piece of high polymer is placed in the vessel until all the charges vanish. However, if the dielectric constant of the sample is large enough, the change of input capacitance by inserting the sample affects the voltage of Faraday cylinder. Also the electric conductive sample affects the voltage of electrometer by changing the contact potential. Polystyrene, Teflon and Acrylite have a little effect on input capacity and show regular behaviour in this point. However, the test piece of fused silica shows somewhat different behaviour and the zero point of output signal is hardly obtained.

The form of electrometer reading in the course of experiment gives some informations of distribution of electric charges on the test piece. Square waveform is observed when the charges are concentrated on the top of the test piece. However, in generally, the distribution of charges on the other place of sample gives a more complicated pattern. Typical curves are shown in Fig. 3. These curves also depend on the mechanism of leakage, i.e., leakage through surface conduction or through the surrounding.

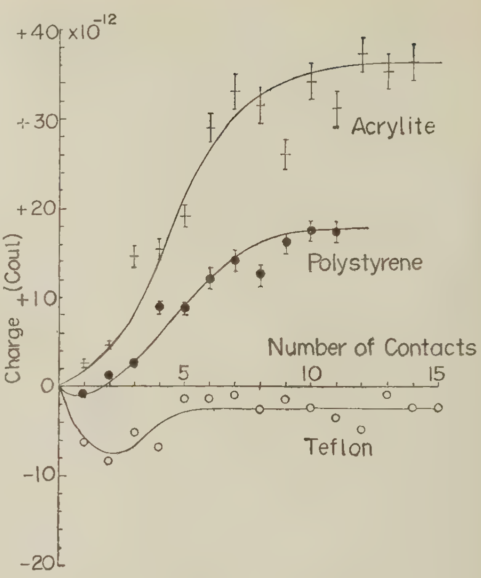

Fig. 4. Static charge on polystyrene, Acrylite and Teflon against Pt vs. contact numbers. at 1 mm Hg.

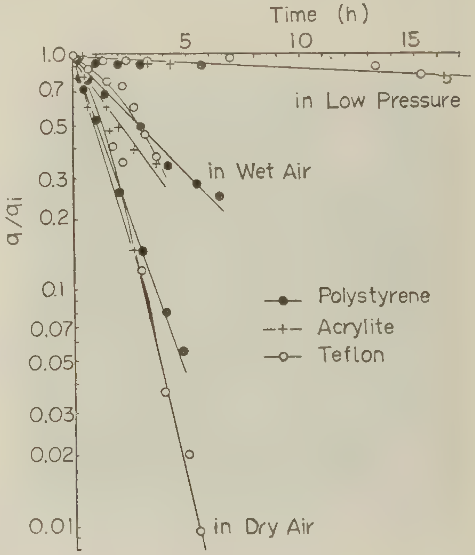

Fig. 5. Leakage curves of charge on high polymer substance. log q/q_i vs. time, q_i is the initial charge.

§ 3. Experimental Results

a) *General*

Fig. 4 shows the results of the experiment performed in vacuum. The generation of static charge showed saturation after 10 times contact and separation. Fig. 5 shows the leakage of electro-static charge in each case. The rate of generation of charge, dq/dt, is

$$\frac{dq}{dt}=\alpha(q_s-q)\ , \qquad (1)$$

were q_s is saturated charge and α is constant. From the results of Fig. 4, α is determined as 0.25 on the high polymer in vacuum.

The leakage of charge by conduction is given by

$$-\frac{dq}{dt}=\beta q\ , \qquad (2)$$

where β is constant which can be determined from the results of Fig. 5, and its value for high polymer is 2×10^{-4} in low pressure air.

From equations (1) and (2) we obtain

$$\frac{dq}{dt}=\alpha(q_s-q)-\beta q\ . \qquad (3)$$

Since the actual value of β is very small compared with α, one can use equation (1) instead of (3) for the analysis of this experiment.

b) *The effect of absorption of water*

Fig. 6 shows the experimental results of polystyrene in dry and wet air.

It is seen that in the dry air the sign of charge on polystyrene is positive, whereas in the 60% R.H. air the sign of charge on polystyrene is negative. This tendency is also confirmed by the experiment in the low pressure 1 mmHg as shown in Fig. 7. In this case the first several contacts and separations produce negative charge, which reaches the maximum. If the experiment is repeatedly performed under this condition, only positive charge is produced from the first contact and separation.

The experimental results of Acrylite are shown in Fig. 8. The sign of charge on Acrylite in the 60% R.H. is positive. But the charging decreases with increasing relative humidity. This we can attribute to decrease in the charge transfered, rather than to increase of surface conductivity.

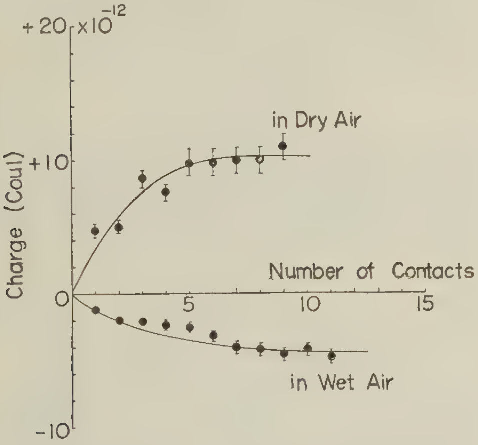

Fig. 6. Effect of absorbed water. Charge on polystyrene against Pt vs. contact numbers in dry air and wet air (60% R.H.)

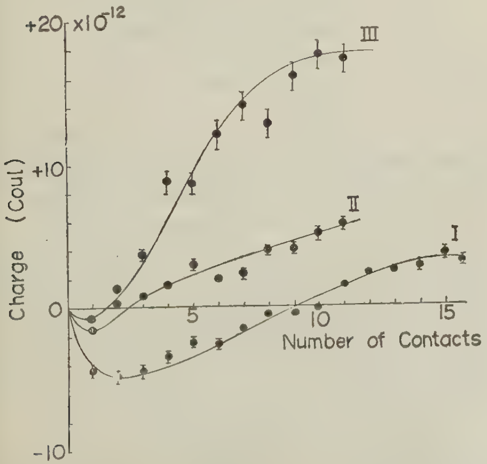

Fig. 7. Effect of absorbed gases. I, II, III, show the order of experiments.

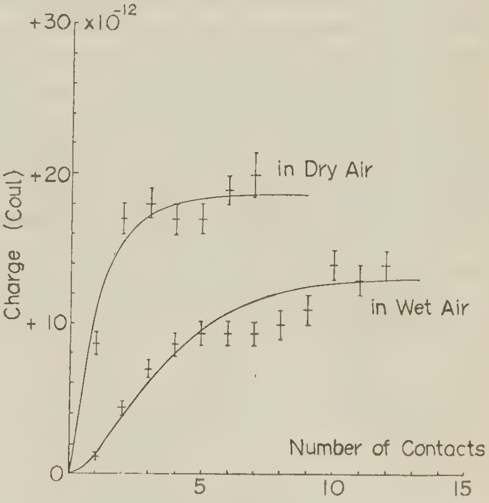

Fig. 8. Effect of absorbed water. Charge on Acrylite against Pt vs. contact numbers in dry air and wet air.

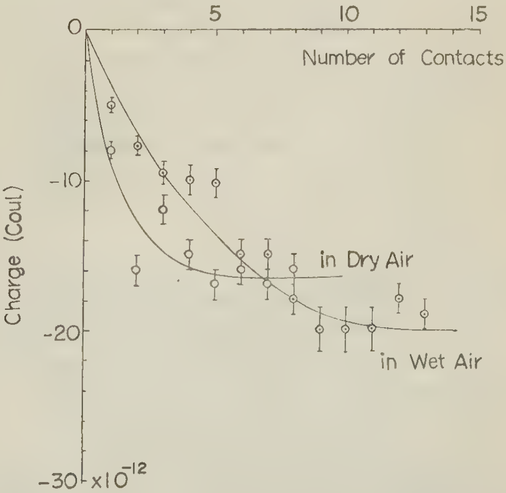

Fig. 9. Effect of absorbed water. Charge on Teflon against Pt vs. contact numbers in dry air and wet air.

The experimental results of Teflon are shown in Fig. 9. In this experiment the sign of charge on Teflon in low pressure is negative. In 60% R.H. air negative charges increase. From these results it seems that the charging on high polymers is shifted to the negative direction with increasing relative humidity.

c) *The effect of the gases*

In the experimental results described in the above sections it is noted that there is a systematic difference between the dry air condition and low pressure condition.

In Teflon-Pt system the negative charge of Teflon is greater in dry air than in low pressure, whereas in case of polystyrene and Acrylite the positive charge of high polymer is greater in low pressure than in dry air.

The experiments in the dry nitrogen gas are carried out and the results are shown in Fig. 10. These results are quite similar to the results in the condition of low pressure. Therefore, the charge difference between the dry air condition and low pressure condition seems to depend on oxygen.

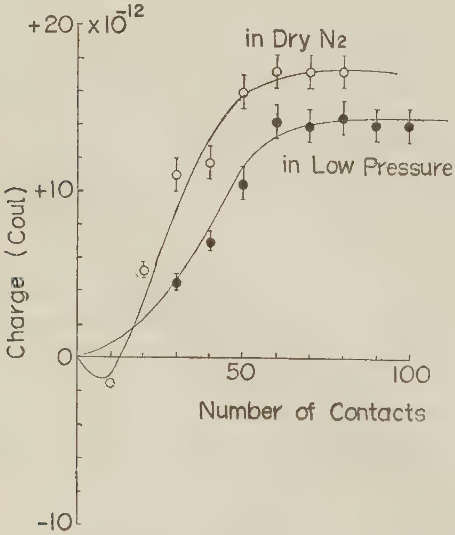

Fig. 10. Charge on polystyrene against Pt vs. contact numbers in dry nitrogen and low pressure.

§ 4. Discussion

a) *The generation of static charges*

Therefore the saturation of static charge in equation (1) will be explained in the following way: We suppose that both metal and high polymer have surface energy levels of electrons which are characterized by work function χ_1 and χ_2 respectively.

The surface energy levels of high polymer are localized and denoted by the dotted line in Fig. 11.

When these two surfaces are brought into contact, the transfer of electrons from one to another occurs and this makes the surface potential barrier which prevents the further transfer of electrons. When the two surfaces are separated, the transfered electrons carry static charge q. In the course of successive contact and separations the contact point of metal and high polymer is moved and the accumulation of static charge is increased.

However, when the potential barrier induced by transfered charges becomes high enough, further contact and separation has no more effect on accumulation of charge.

The saturation charge q_s in this state will be

$$q_s=\frac{A\varepsilon_0}{4\pi d_0}(\chi_1-\chi_2) \qquad (4)$$

were d_0 is average contact distance, A is area of contact and ε_0 is dielectric constant of high polymer. Using this equation we can estimate the relative magnitude of $(\chi_1-\chi_2)$ from the experimental values of saturation charge q_s. The analysis of experimental results in vacuum by equation (4) is tabulated in Table I.

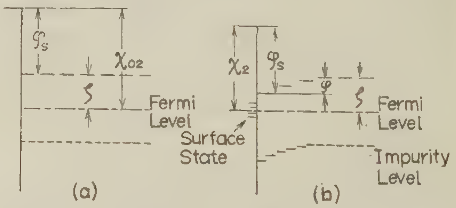

Fig. 11. (a) Energy level diagram of high polymer.
(b) Energy level diagram of polymer surface with absorbed water.

χ_{02} and χ_2 represent the work function, $\chi_2=\chi_{02}-\varphi$. φ is a potential energy change at the surface with absorbed water.

Table I. The charge obtained for high polymer vs. Pt, and estimated work function of high polymer. Assuming that the work function of Pt surface is 6.00 eV and is shifted by about 0.10 eV in wet air.

	q_s($\times10^{-12}$ coulomb)	χ_2 (eV)
Acrylite	36	5.48
polystyrene	18	5.74
Teflon	−2.5	6.04

b) *The effect of absorption of water*

The sign of charge on polystyrene tends to shift toward negative with increasing relative humidity, and the positive charge on Acrylite tends to decrease with increasing relative humidity.

From these experimental results it is concluded that the absorption of water molecule on surfaces of both platinum and polystyrene is the necessary condition for the production of negative charge on the polystyrene. There are several experimental studies[9] in which the absorption of water on the surfaces of metals and semiconductors decreases the surface work function. Hence, one can expect that the surface work function of high polymer will be changed by absorption of water on the surface.

From equation (4)

$q_s \propto \chi_1 - \chi_2$ in 60% R.H. air

$q_{s0} \propto \chi_{01} - \chi_{02}$ in desorbed state,

where

χ_1 is the work function of Pt

χ_2 is the work function of high polymer

The negative sign of q_s means that $\chi_1 < \chi_2$ and further when q_{s0} is positive,

$$\chi_{01} > \chi_{02} .$$

Therefore

$$\chi_{01} - \chi_1 > \chi_{02} - \chi_2 .$$

It follows that the decrease of surface work function of platinum can be greater than the decrease of surface work function of polystyrene, as shown in Fig. 12 schematically.

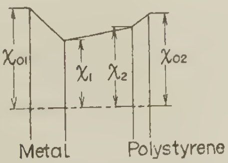

Fig. 12. Schematic diagram of the effect of absorbed water on the work functions of metal and polystyrene.
χ_{01}, χ_{02} are the work function of metal and polystyrene before absorption, χ_1, χ_2 after absorption.

From the experimental results of Acrylite as shown in Fig. 8, positive sign of q_{s0} in dry air means $\chi_{01} > \chi_{02}$. Even in 60% R.H. air q_s is smaller than q_{s0}, but not negative. $\chi_{01} - \chi_{02} > \chi_1 - \chi_2$. These results are explained by the schematic diagram of Fig. 13. The experimental results of Teflon are given in Fig. 9. In this experiment q_{s0} in dry air is negative and it means $\chi_{01} < \chi_{02}$. In 60% R.H. air negative charge is increased; $\chi_{02} - \chi_{01} < \chi_2 - \chi_1$. The results are described by the following schematic energy diagram in Fig. 14.

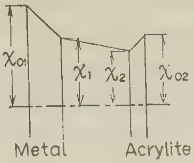

Fig. 13. Schematic diagram of the effect of absorbed water on the work functions of metal and Acrylite.

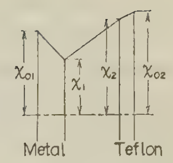

Fig. 14. Schematic diagram of the effect of absorbed water on the work functions of metal and Teflon.

c) *The effects of the absorption of* O_2

In the cases of polystyrene and Acrylite, the positive charge of high polymer is greater in low pressure than in dry air, and the negative charge of Teflon is greater in dry air than in low pressure.

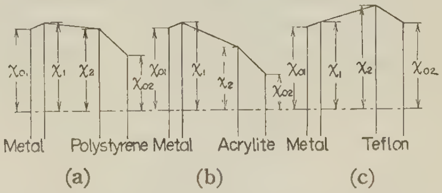

Fig. 15. Schematic diagram of the effect of absorbed O_2 on the work functions of metal and high polymer.
(a) Pt and polystyrene. (b) Pt and Acrylite
(c) Pt and Teflon.

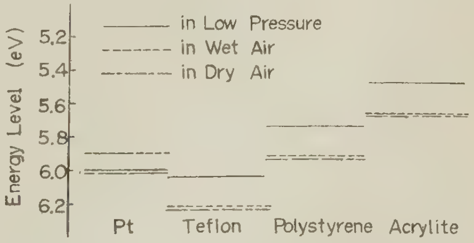

Fig. 16. Schematic energy diagrams of the work function on Acrylite, polystyrene and Teflon. These work functions were calculated from experimental data assuming the work functions of Pt and Pt with absorbed water are 6.00 eV and 5.90 eV respectively.

As shown in Fig. 10 the experimental results in the dry nitrogen gas are quite similar to the results in the condition of low pressure. This suggests that the absorption of oxygen by both surfaces will affect static charges.

There are several studies in which in accompanying with absorption of oxygen on metals and semiconductors surfaces the increase of surface work function was observed⁽¹⁰⁾.

The absorption of oxygen by high polymer can cause the increase of surface work function of high polymer, too.

The difference between q_s in dry air and q_{s0} in low pressure can be explained by the following schematic diagram Fig. 15. It is assumed that there is no appreciable increase of the surface work function by absorption of oxygen on platinum exposed for a long time in room air.

§ Summary

It has been shown in this report that the generation of static charges on high polymers varies with the surrounding conditions. Fig. 16 shows a schematic energy diagram by which the experimental results can be interpreted. From this diagram the work functions of the high polymers are estimated. Moreover, this schematic energy diagram will be applicable to predict the charging of the other high polymer substances.

Acknowledgments

The author wishes to express his cordial thanks to Dr. Jiro Furuichi and Dr. Masatami Takeda for helpful discussions and criticism. He is also grateful to Mr. Akinari Kasai for his assistance in performing the experiment.

References

1) W. R. Harper; Proc. Roy. Soc. **A, 205** (1951) 83.
2) V. E. Vick: Brit. J. Appl. Phys. Suppl. **2**, (1953) 1.
3) W. R. Harper: Phil. Mag. Suppl. **6** (1957) 365.
4) S. M. Skinner, R. H. Savage and J. E. Rutzler: J. Appl. Phys. **24** (1954) 438.
5) J. W. Peterson: J. Appl. Phys. **25** (1954) 501.
6) P. E. Wagner: J. Appl. Phys. **27** (1956) 1300.
7) J. Bardeen: Phys. Rev. **71** (1947) 717.
8) R. H. Kingston: J. Appl. Phys. **27** (1956) 101.
9) J. T. Law: J. Phys. Chem. **59** (1955) 67.
10) W. H. Brattain and J. Bardeen: Bell Syst. Tech. J. **32** (1953) 1.

Short Notes

This section is intended to secure prompt publication of important discoveries in physics. The reports should not exceed 800 words in length. A figure of size 7 cm × 7 cm will be counted as 150 words.

J. PHYS. SOC. JAPAN **14** (1959) 539

On the Low Lying Levels of Mn^{55}, II

By Sadaaki YANAGAWA

Department of Applied Physics, Faculty of Engineering, University of Tokyo, Tokyo

(Received February 24, 1959)

In the previous paper[1], we have discussed the low lying levels of Mn^{55} from the standpoint of the configurational mixings. In that case, the proton configurations for Fe^{56} were assumed to be the mixings of $\{(f_{7/2})^2 J\}$, $\{(f_{7/2} f_{5/2}) J\}$, and $\{(f_{7/2} p_{3/2}) J\}$; and for Mn^{55}, $\{(f_{7/2})^3 J\}$, $\{(f_{7/2})^2 J', f_{5/2} : J\}$ and $\{(f_{7/2})^2 J', p_{3/2} : J\}$. The group of neutrons were frozen to the seniority zero state, though it might be questionable.

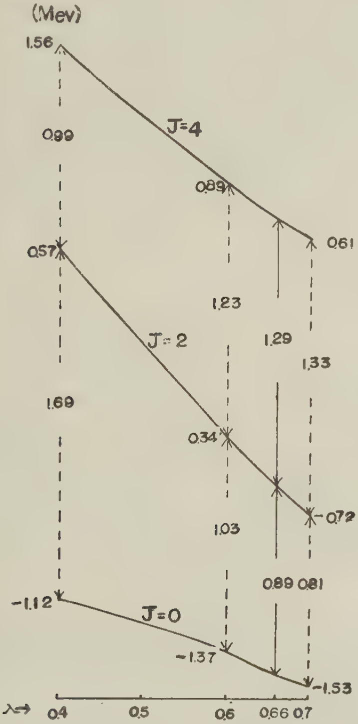

Fig. 1. Fe^{56} $a=0.2$.

We have found it illegitimate however, strictly speaking, to compute them as two and three body problems in the configurational mixings, but we have to calculate them as six and five body problems for Fe^{56} and Mn^{55} respectively. In this paper we assume that the following configurations are mixed with the main configuration $\{(f_{7/2})^{6,5} J\}$.

Fe^{56} $\{(f_{7/2})^4 0, (f_{5/2})^2 0 : 0\}$, $\{(f_{7/2})^4 0, (p_{3/2})^2 0 : 0\}$,
$\{(f_{7/2})^5 J', f_{5/2} : J\}$, $\{(f_{7/2})^5 J', p_{3/2} : J\}$,

where only $J'=3/2$, $5/2$ and $7/2$ are taken into account.

Mn^{55} $\{(f_{7/2})^4 J', f_{5/2} : J\}$, $\{(f_{7/2})^4 J', p_{3/2} : J\}$,

where $J'=0$, 2, 4, 6; and in $J'=2$, 4, the seniority number is assumed to be limited to 2 to simplify the computations.

The method of calculation is completely analogous to the previous one. The two-body interaction is assumed to be of the form $V(r_{12})[1+a(\sigma_1 \cdot \sigma_2)]$, where $V(r)$ is Gaussian potential. For the wave functions, the harmonic oscillator functions are used. The excitation energies of a single nucleon from $f_{7/2}$ to $f_{5/2}$ and $p_{3/2}$ are taken from the new experimental values of the 1st and 2nd excited states of Co^{57}. They are 1.9 Mev and 1.4 Mev respectively[2].

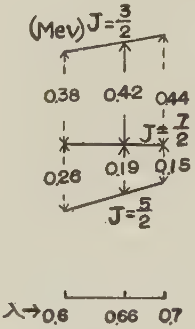

Fig. 2. Mn^{55}.

The results of the calculations for Fe^{56} show that the energy diagrams plotted against the range parameter λ give almost the same features as the previous ones obtained for the same value of the parameter a. (λ is the ratio of the potential range to the constant which determines the extension of the wave function.) It is not surprising that the values of a and λ for both cases, do not differ so much, because the configurations $(f_{7/2})^{\pm 2}$ are reasonably considered to be main for respective case. For $a=0.2$, $\lambda=0.66$, we have solved the secular equations for $J=3/2$, $5/2$ and $7/2$ states of Mn^{55}. The state $J=5/2$ is calculated to be the lowest and the energy splitting between $J=5/2$ and $J=7/2$ is about 0.19 Mev, but the level $J=3/2$ does not agree with the observed value of about 1.5 Mev[3].

References

1) S. Yanagawa: J. Phys. Soc. Japan **13** (1958) 323.
2) J. Konijn et al: Physica XXIV (1958) 129.
3) M. A. Rothman et al: Private communication.

J. PHYS. SOC. JAPAN **14** (1959) 540

Studies on Mercury Fulminate

By Surjit SINGH
TDE(ME) Kirkee, Poona-3 (India)†

(Received December 24, 1958)

Sekiguchi[1] prepared samples of mercuric fulminate at various temperatures by reacting mercury with nitric acid and alcohol in various proportions and observed that at lower temperatures larger proportions of crystals had acute angles of rhomb. Endo and Mashima studied the same reaction and concluded that the reaction product at 45–55°C was mercurous fulminate[2].

This letter describes the extensive study of this reaction in our laboratories and concludes that the end product is a mixture of mercury and mercuric fulminate and not mercurous fulminate as claimed by Endo and Mashima.

The reaction of mercury with nitric acid and alcohol at different temperature ranges (40° to 55°C) was studied and the reaction product was found to consist of crystals of mercuric fulminate with more acute angles of rhomb with occasional pyrimidal crystals (which confirms the observations of Sekiguchi) contaminated with varying quantity of free metallic mercury*. The impure product was crystallised from a 2 : 1 : 1 mixture of ice cold Ammonia (Sp. gr. .88): water: Alcohol and the purified material on analysis gave- Hg=70.40 percent (Hg as HgS): Purity**=99.8 percent.

This clearly shows that the product is mercuric fulminate and not mercurous fulminate.

We have attempted to produce mercurous fulminate by an alternative method. Equimolecular proportions of cold solutions (at −5°C) of sodium or potassium fulminate in methyl alcohol and mercurous nitrate (free from mercuric ion) in dilute nitric acid were mixed together. Immediately an grey amorphous precipitate was obtained. The crude material was dried for one week in an $CaCl_2$ dessicator and on analysis gave, Hg=82.6 percent, purity**=57.6 percent. However, during subsequent purification and crystallisation from Ammonia: Alcohol: water mixture, very large quantities of free metallic mercury were observed as residue. Crystals obtained from the above filtrate on analysis yielded the following results; Hg=70.4 percent; purity**=99.7 percent. This data can only be true for mercuric fulminate. Free mercury in the crude synthetic product was separately estimated and was found to be 41.05 percent. This clearly points out that the crude product was a mixture of equimolecular proportion of free mercury and mercuric fulminate.

Confirmatory evidence as to the above grey compound, even in the solid state being a mixture of free metallic mercury*** and mercuric fulminate is provided by the extreme ease with which a gold wire is amalgamated on passing it a few times through the sample whereas under identical conditions no amalgamation resulted with mercuric fulminate, mercurous nitrate or mercurous chloride.

Some comments on the work of Endo and Mashima will be useful. The presence of mercurous ions in their product was inferred due to the formation of of green mercurous iodide, on addition of potassium iodide to a solution of the substance in dilute nitric acid. It appears that this deduction is not valid, since the free metallic mercury present in the crude product will give rise to mercurous ions with dilute nitric acid and the latter react with potassium iodide to give a green precipitate.

It is well known that some mercurous salts are unstable and decompose into corresponding mercuric state with the liberation of free mercury[3]. Mercurous fulminate also appears to be very unstable and passes spontaneously to mercuric fulminate and free metallic mercury, according to the following reactions.

$$2Na(ON{=}C)_2+Hg_2(NO_3)_2 \longrightarrow 2NaNO_3+Hg_2(ON{=}C)_2$$

$$Hg_2(ON{=}C)_2 \longrightarrow Hg+Hg(ON{=}C)_2$$

Full details will be published elsewhere.

The author is grateful to Prof. D. S. Kothari, Scientific Adviser to the Minister of Defence, for his encouragement and interest throughout the progress of this work. Thanks are also due to Prof. S. Uda for deciphering the paper in Japanese by Endo and Mashima.

References

1) M. Sekiguchi: J. Phys. Soc. Japan **6** (1951) 541.
2) S. Endo and M. Mashima: J. Chem. Soc. Japan **73** (1952) 454.
3) M. C. Sneed and R. C. Brasted: *Comprehensive Inorganic Chemistry* **4** (Van. Nostrand Princeton, 1955) 97.

---

† This work was partly done at Institute of Armament Studies, Kirkee.

* Tiny globules of mercury can be readily seen under a microscope. A gold wire is also readily amalgamated.

** Calculated as mercuric fulminate by sodium thiosulphate titration.

*** Freshly prepared mercurous oxide Hg_2O, also amalgamates gold wire readily. Fricke and Ackerman, Z. anorg. Chem. **211** (1933) 233 have shown by X-Ray analysis that so called mercurous oxide Hg_2O is actually a mixture of $HgO+Hg$.

J. PHYS. SOC. JAPAN **14** (1959) 541

Low Temperature Thermoelectric Power of Cu–Mn Alloys

By Seiichi TANUMA

The Research Institute for Iron, Steel and Other Metals, Tohoku University, Sendai

(Received February 20, 1959)

It is known that the dilute alloys of copper with manganese show a minimum in the resistance-temperature curve in the low temperature region followed by a maximum at the lower temperatures[1)-3)]. We have measured the thermoelectric power of these alloys in this range of temperatures. The ingots which were made by melting oxygen-free copper (99.997% purity) and electrolytic manganese in vacuum were forged and cold-drawn to the wires of 0.3 mm in diameter and then annealed at 700°C for 5 hours. The thermoelectric power was measured by constructing a thermocouple with each alloy wire as an arm and a pure annealed copper wire as the reference arm. Thermoelectric voltage (E) of each couple was obtained as a function of the temperature difference between the hot junction immersed in melting ice and the cold junction in the cryostat, temperature (T) of which was varied from 4.2°K to about 200°K. The relation between E and T was plotted in Fig. 1. In all specimens, the sign of thermovoltage was such that the current flows from the copper wire to the alloy wire at the cold junction. Graphical determinations of the gradients of the $E-T$ curves at various temperatures gave the thermoelectric powers relative to copper as shown in Fig. 2. The absolute thermoelectric power (S) of the alloy can be obtained by adding algebraically the absolute thermoelectric power of copper[4),5)] which is denoted by the curve 0_A in Fig. 2. As an example, the curve 1_A is thus obtained for the absolute thermoelectric power of specimen No. 1.

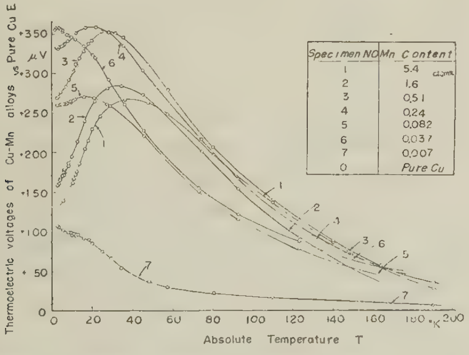

Fig. 1. Thermoelectric voltages of Cu–Mn alloys *versus* pure copper between the abscissa temperatuer and 0°C.

The absolute thermoelectric powers of Cu–Mn alloys, at intermediate temperatures, have negative sign and coincide generally with the values measured by Otter[6)] above the temperature of liquid air. In the $S-T$ curve at low temperatures, however, there appears a minimum followed by a maximum with lowering temperature. This seems to be a characteristic feature of these alloys which display a minimum and a maximum in the resistance (ρ)-temperature curves. The temperature where the maximum or the minimum appears in the $\rho-T$ curve and this point in the $S-T$ curve vary regularly with solute concentration respectively, but the coincidence between them is not necessarily observed. The thermoelectric minimum in these alloys is similar to the anomalous minimum reported in Cu–Sn alloys[4)]. Taking into account of the fact that Cu–Sn alloys show a maximum neither in resistance nor in thermoelectric power, the existence of the maximum in Cu–Mn alloys suggests some complicated factor entering into the nature of the *resistance minimum*. Perhaps this relates to the magnetic properties of solute ions in this alloys[7)].

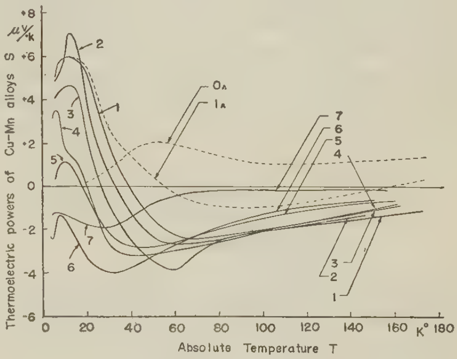

Fig. 2. Thermoelectric powers of Cu–Mn alloys.

The author wishes to express his sincere thanks to Prof. T. Fukuroi and to Assist. Prof. Y. Shibuya for their kindness of giving experimental facilities and stimulating discussions. A part of this work owes to the Scientific Research Fund of the Ministry of Education.

References

1) A. N. Gerritsen and J. O. Linde: Physica **18** (1952) 877.
2) R. W. Schmitt and I. S. Jacobs: Canad. J. Phys. **34** (1956) 1285.
3) Y. Shibuya, Y. Tawara, S. Tanuma, Y. Saito, Y. Muto and T. Fukuroi: Physica **24** (1958) 176.
4) D. K. C. MacDonald and W. B. Pearson: Acta Met. **1** (1955) 392.
5) G. Borelius, W. H. Keesom and C. H. Jacobson: Proc. Acad. Amsterdam **31** (1928) 1046.
6) F. A. Otter: J. Appl. Phys. **27** (1956) 197.
7) K. Yoshida: Phys. Rev. **107** (1958) 396.

J. PHYS. SOC. JAPAN **14** (1959) 542

Simplified Representations on the Firing Characteristics of Vibrational-Ignitor Tubes

By Setsuo OKANISHI and Hitoshi KANAMORI
Shimadzu Seisakusho Ltd., Kyoto

(Received February 10, 1959)

We have measured the firing probabilities of vibrational-ignitor tubes, in regard to several variables which are shown in Fig. 1. It was found, however, that such many variables could be reduced to three variables i, L_e and E^n/L $(1<n<2)$, and that general firing characteristics might be simply composed as in Fig. 2, as a conclusion. Where i is the instantaneous value of ignitor current, immediately before an ignitor is pulled up from the surface of a mercury cathode. Those characteristic curves have been explained by considering next two steps as firing process, as same as an ignitron[2)-4)] i.e., production of a cathode spot and stabilization of anode arc. In Fig. 2, abscissa takes i and ordinate takes the firing probability. Curve A shows the probability of cathode spot production, which may be reckoned as a function of i and fixed in such coordinates. Other variables influence it very little. Curve B shows the probability of stabilization of anode arc caused by a cathode spot. It is a function of i, L_e and E^n/L, where $1<n<2$, so that the last two variables are taken as parameters. And, the greater L_e and the greater E^n/L make probability the greater. Finally, curve C shows the probability of production of the arc between an ignitor and a cathode, added to curve B. It is also a function of i, L_e and E^n/L, in the case of greater i and L_e than those of curve B. Actual firing characteristics must be composed as 1–2–3 in Fig. 2, because a tube fires when those two conditions are filled. E_e only influences curve C at small L_e and large i; except that, E_e may be neglected compared with the voltage spike being proportional to L_ei, which produces arc between an ignitor and a cathode. E_e, L_e, R_e and R should not be considered directly.

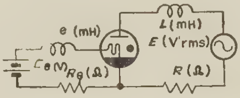

Fig. 1. The circuit and its parameters.

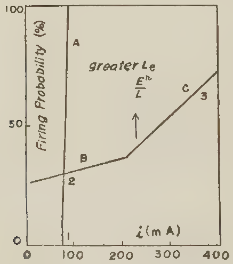

Fig. 2. The typical characteristics composed by 3 curves.

Some actual data are shown in the case of resistive load (Fig. 3). The characteristic curves are occupied by curve A, except upper part near 100%. In that of inductive load, curve B and C appear (Fig. 4). Thus, the possibility to simply represent the characteristics is found, instead of using many parameters in Fig. 1.

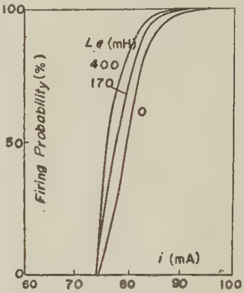

Fig. 3. The firing characteristics in the case of pure resistive load $E=200\sim600$ V, $R=10\sim160\,\Omega$, $E_e=6\sim30$ V.

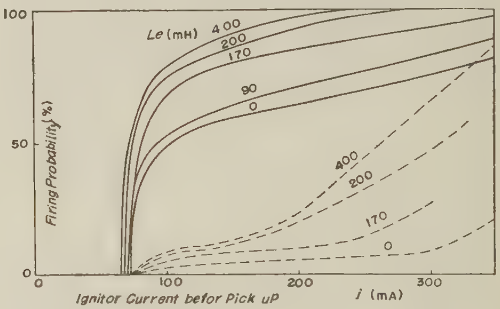

Fig. 4. The firing characteristics in the case of inductive load. Solid lines show the case of $E=600$ V, $L=370$ mH. Broken lines, $E=200$ V, $L=370$ mH.

References

1) Y. Hatta: Electronics **28** (1955) 248.
2) J. Slepian and D. R. Ludwig: A.I E.E. Trans. **52** (1933) 693.
3) J. M. Cage: Gen. Elect. Rev. **38** (1935) 464.
4) Mierdel: Siemeans Work **15** (1936) Part II 35.

J. Phys. Soc. Japan **14** (1959) 543

Cyclotron Resonance in Gas Discharge

By Kuniya FUKUDA, Hiroaki MATUMOTO,
Yoichi UCHIDA and Hisamitsu YOSHIMURA

*Department of Physics, Faculty of Science,
Kyoto University*

(Received February 19, 1959)

The dispersion of cyclotron resonance in gas discharge was measured at microwave frequency of 24,000 MCPS[1)-3)]. Discharge of air was held between a fine kovar wire ($\phi_a=0.5$ mm) inserted coaxially into the cylindrical cavity ($\phi_b=8$ mm) and the cavity wall. Magnetic field was applied perpendicular to the axis of the cylindrical cavity. Pressure of gas was monitored by an oil manometer and a thermister vacuum meter.

The TEM mode of cavity is perturbed only slightly for the exciting wavelength $\lambda<\pi(\phi_a+\phi_b)$[4)]. It may be, however, allowed to use the Langevin equation of motion of electrons in constant homogeneous magnetic field (along z-axis) and oscillating electric field (in xz-plane), which leads to the following equation for the imaginary part of the complex conductivity corresponding to microwave dispersion:

$$\sigma^x_{\mathrm{imag}}=\frac{Ne^2\tau}{m}\,\frac{\omega\tau(\omega_c{}^2\tau^2-\omega^2\tau^2-1)}{(1-\omega^2\tau^2+\omega_c{}^2\tau^2)^2+4\omega^2\tau^2}\,,$$

where ω is microwave frequency, τ mean free time of electron, ω_c cyclotron frequency and N electron density.

Experimental curves of dispersion I, II, and III show in Fig. 1 correspond to those at 1.4 mmHg, 1 mmHg and 0.5 mmHg of gas pressure respectively. They approximately fit the above Lorentzian expression with $\omega\tau\geq 1$. It is possible, therefore, to determine τ-values from the magnitude of magnetic field, giving the dispersion maximum: $\tau=3.9\times10^{-11}$ sec for 1.4 mmHg, 4.6×10^{-11} sec for 1 mmHg and 8.1×10^{-11} sec for 0.5 mmHg respectively. On the other hand, mean free time can also be estimated from the quality factor Q and the resonance frequency shift at zero field $\Delta\omega$ of the cavity under gas discharge, using the relation: $\omega\tau=2Q\Delta\omega/\omega$ $(=\sigma_{\mathrm{real}}/\sigma_{\mathrm{imag}})$. In our case $Q\approx1{,}000$ at each pressure, so that the values of τ are in the range of $3\sim1\times10^{-11}$ sec.

These values of τ derived in two different ways are in good agreement in the order of magnitude with each other, though experimental curves have somewhat complex behaviors in the region near zero field. Electron density in gas discharge is estimated to be of the order of 10^{10}/cc from the dispersion at zero field with $\tau\approx10^{-11}$ sec[6)-8)].

In our experiments the applied electrostatic field, together with the magnetic field, may cause considerable disturbances on the distribution of electron density. It may be preferable for the discharge current to have the same direction as that of the magnetic field. The investigations on other gases over wider pressure range, as well as the refinements of experimental conditions, are now in progress in our laboratory.

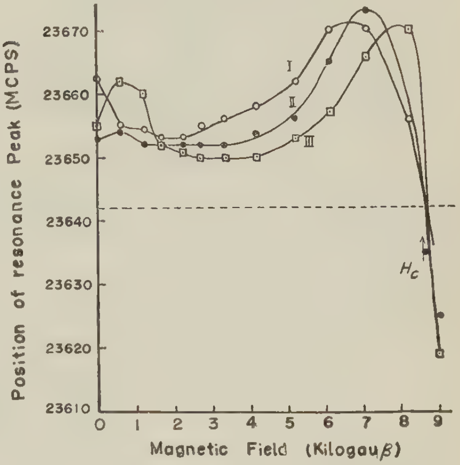

Fig. 1. Curves of the shift of microwave resonance frequency *versus* applied magnetic field. H_c is magnetic field at cyclotron resonance frequency, which is connected with cyclotron frequency ω_c as $\omega_c=eH_c/mc$. Dashed line shows the resonance frequency without discharge.

References

1) D. J. E. Ingram and J. G. Tapley: Rhys. Rev. **97** (1955) 238.
2) D. J. E. Ingram: Microwave and radio frequency spectroscopy (Discussion of the Faraday Society, No. 19 (1955) 104).
3) D. C. Kelly, H. Margenau and S. C. Brown: Phys. Rev. **108** (1957) 1367.
4) N. Marcuvitz: *Waveguide Handbook* (Rad. Lab. Series, Vol. 10) 77.
5) G. Dresselhaus, A. F. Kip and C. Kittel: Phys. Rev. **100** (1955) 618.
6) D. J. Rose and S. C. Brown: J. Appl. Phys. **23** (1952) 1028.
7) S. J. Buchsbaum and S. C. Brown: Phys. Rev. **106** (1957) 196.
8) K. B. Pearson: Phys. Rev. **106** (1957) 191.

J. Phys. Soc. Japan **14** (1959) 544∼545

Effects of γ-Rays on Aqueous Solutions of Synthetic Polymers

By Shintaro SUGAI, Mitsuo ISHIKAWA
and Jiro FURUICHI
Physics Department, Faculty of Science,
Hokkaido University, Sapporo,
Hokkaido, Japan

(Received February 20, 1959)

There has been as yet only a few researches concerning the effects of ionizing radiation on synthetic polymer solutions[1].

In the studies herewith reported, observations were made of the effects of γ-rays from Co^{60} on aqueous solutions of synthetic poly electrolyte Na-CMC, of which the average degrees of polymerization and etherification are respectively 560 and 0.685.

According to ultracentrifugal figures of considerably concentrated solutions, Na-CMC used in the present case seems to be a mixture of two group, one of which has a larger average molecular weight than the other.

Oxygen was not excluded from water and methyl-alcohol used as solvents and the irradiation was carried out under atomospheric pressure.

In Table I, decreases of specific viscosity due to irradiation are tabulated. Changes of molecular weights calculated from the intrinsic viscosity and those of ultracentrifugal coefficients respectively are indicated in Table I and II.

Table I. Decreases of specific viscosity of Na-CMC aqueous solutions under various conditions of irradiation.

c	solvent	dose-rate	dose	$-\Delta\eta_{sp}$	R	R/c
gr/cc	gr/cc	r/min	r	%	r	$10^6 r$ cc/gr
Type I Viscometer						
6.7×10^{-3}		600	18000	8.2	22500	3.2
1.4×10^{-3}		85	3000	10.0	3000	2.2
6.7×10^{-4}		190	4300	71.2	610	0.9
5.6×10^{-4}		85	1500	19.0	800	1.4
2.4×10^{-4}		170	850	26.6	320	1.3
〃	0.05 Me-OH	〃	〃	8.5		
〃	0.48 Me-OH	〃	〃	5.6		
6.7×10^{-5}		190	210	23.0	610	1.4
〃		85	420	39.0	110	1.7
〃		170	850	42.1	200	2.9
〃	0.051 NaCl	〃	〃	5.4		
〃	0.134 NaCl	〃	〃	0.5		
Type II Viscometer						
1.7×10^{-4}		33	220	15.0	150	0.9
〃		9	〃	17.5	125	0.8
2.3×10^{-5}		85	600	18.3	330	14
7.5×10^{-6}		33	220	17.0	130	20
〃		9	〃	19.0	120	20
2.3×10^{-6}		85	300	9.2	320	140

c: concentration of aqueous solution.
$-\Delta\eta_{sp}$: decrease of the specific viscosity.
R: dose required for producing $-\Delta\eta_{sp}=10\%$.

Table II. Changes of molecular weight.

c	dose	P/P_0	N
gr/cc	r		
2.0×10^{-3}	2200	0.97	0.031
6.7×10^{-4}	1700	0.92	0.086
〃	4300	0.75	0.333
6.7×10^{-5}	210	0.88	0.136
〃	420	0.71	0.408
〃	850	0.56	0.785

P, P_0: degrees of polymerization of irradiated and original molecules.
N: number of scissons per original molecules.

It seems that the main results in the present studies may be put in order as follows:

1) The molecular degradation only is an essential process in irradiated Na-CMC aqueous solutions.

2) Except in the extremely dilute, cases, typical kinetics of the indirect effect through the activated solvents is clearly observed[2]. The effective protection due to presence of methyl-alcohol and dependency of degradation upon molecular extension seem also to be symptomatic of the indirect effect.

3) From the change of the ratio of two components due to irradiation as shown in Table III.

the random fractures of polymer chains may be reasonably assumed³⁾.

Table III. Changes of ultracentrifugal figures.

c	dose	s_1	s_2	f_1/f_2
gr/cc	r	sved.	sved.	
2.4×10^{-3}	0	2.0	7.9	2.0
〃	6800	1.8	6.3	2.4
6.7×10^{-4}	0	2.5		∞
〃	3800	2.1		∞

s_1, s_2: sedimentation coefficients of two groups.
f_1, f_2: percentage of components of two groups.

Effect of irradiation on the electrical conductivity was also observed⁴⁾. At low temperatures, the conductivity of the irradiated solution is clearly greater than that of non-irradiated one, however that difference is very small at higher temperatures.

The details will soon be published.

References

1) P. Alexander and A. Charlesby: J. Poly. Sci. **23** (1957) 355. P. Alexander and M. Fox: Nature **170** (1952) 1022. A. Danno: J. Phys. Soc. Japan **13** (1958) 722.
2) P. Alexander and M. Fox: Trans. Faraday Soc. **50** (1954) 605.
3) F. A. Bovey: *The Effect of Ionizing Radiation on Natural and Synthetic High Polymers* (Interscience Publ., 1957).
4) M. Ishikawa and S. Sugai: Busseiron Kenkyu **4** (1959) 735 (in Japanese).

J. PHYS. SOC. JAPAN **14** (1959) 545

Maximum Principles for Vorticity in Viscous Fluid

By Tosio KATO and Hiroshi FUJITA
Department af Physics, University of Tokyo

(Received February 24, 1959)

The object of the present note is to point out that *maximum principles* hold for the vorticity in any two-dimensional flow, stationary as well as non-stationary, of an incompressible viscous fluid. These principles are analogous to the familiar ones for the Laplace and heat equations.

The vorticity is given by $\omega=\partial v/\partial x-\partial u/\partial y$ in terms of the velocity components u, v of the fluid and satisfies the differential equation

$$\frac{\partial\omega}{\partial t}-\nu\Delta\omega+u\frac{\partial\omega}{\partial x}+v\frac{\partial\omega}{\partial y}=0 \tag{1}$$

in the free space, where ν is the kinematic viscosity coefficient. If the flow is stationary, (1) reduces to

$$-\nu\Delta\omega+u\frac{\partial\omega}{\partial x}+v\frac{\partial\omega}{\partial y}=0\,. \tag{2}$$

Note that (1) and (2) can be regarded as *linear* differential equations for ω, whenever a definite flow u, v is being considered.

The maximum principles are given by the following theorems, in which D denotes an arbitrary domain of the x, y plane occupied by the fluid and C is the boundary of D.

Theorem I. *If the flow is stationary, the maximum and the minimum of ω in D are attained on C.*

Theorem II. *If the flow is non-stationary, the maximum and the minimum of ω in the cylindrical domain of the x, y, t space with (x, y) in D and $t_0\leq t\leq t_1$ are attained either on the "bottom" ($t=t_0$) or on the "vertical side" ((x, y) on C).*

If follows from Theorem I, for example, that the vorticity ω of a stationary flow always lies between its maximum ω_+ and minimum ω_- taken on the surface of the obstacle (assuming that $\omega\to0$ at infinity and that $\omega_-\leq0\leq\omega_+$).

The proof of these theorems are rather simple. To prove Theorem I, let ω_+ be the maximum of ω on C. Then $\omega'=\omega-\omega_+$ satisfies the same linear differential equation (2) as ω and its boundary values on C are non-positive. It follows from a standard argument¹⁾ that ω cannot take positive values in D. Thus $\omega\leq\omega_+$ and ω_+ is the maximum of ω in D. The minimum can be dealt with similarly. To prove Theorem II, let ω_+ be the maximum of ω on the bottom and the vertical side of the domain considered. Then $\omega'=\omega-\omega_+$ satisfies the same linear differential equation (1) as ω. Set $\omega''=e^{-ct}\omega'$ with an arbitrary $c>0$. ω'' satisfies the linear differential equation

$$\frac{\partial\omega''}{\partial t}+c\omega''-\nu\Delta\omega''+u\frac{\partial\omega''}{\partial x}+v\frac{\partial\omega''}{\partial y}=0$$

and its values are non-positive on the bottom and the vertical side. From this it follows again²⁾ that ω'' cannot take positive values in the domain of x, y, t space in question. This proves that $\omega'=e^{ct}\omega''\leq0$ and therefore that $\omega\leq\omega_+$. Thus ω_+ is the maximum of ω. The minimum can be treated similarly.

It appears that these maximum principles cannot in general be extended to three-dimensional flows. They are valid, however, in some special cases. In a stationary, axially symmetric flow, for example, analogues of Theorems I and II are seen to hold for the maximum of $|\omega|$ in any domain in which the radial velocity is non-positive.

References

1) R. Courant und D. Hilbert: *Methoden der Mathematischen Physik*, II (Berlin, 1937) chap. IV, § 5.
2) I. G. Petrovsky: *Lectures on Partial Differential Equations* (English Translation) (New York, 1954) § 38.

J. PHYS. SOC. JAPAN **14** (1959) 546

Interaction of Exciton with *R* Center in KCl Crystal

By Masayasu UETA and Masamitsu HIRAI
Department of Physics, Faculty of Science, University of Tohoku, Sendai

(Received February 27, 1959)

For the investigation of energy transfers which take place between the exciton and electron or hole trapping centers, the interaction with color centers in alkali halide crystals will be one of the most appropriate subjects on account of the fact that the structures of color centers and exciton have been studied so far extensively in these crystals. In the previous report[1] the effects of the exciton upon *F* and *U* centers in KCl and KBr crystals were described and it has been observed the quantum efficiencies for the bleaching of *F* centers and for the conversion of *U* centers to *F* centers by the ultra violet lights, of which wavelengths are in the region of the fundamental absorption tail, are greater than unity and thus the thermal effect of the exciton was discussed.

If the KCl crystal containing only *F* centers are illuminated with *F* absorption light, the complex centers of *R*, *M*, *N* and *K* are enhanced with the consumption of *F* centers. When this crystal is heated in dark, R_1 and R_2 bands are the first to disappear at the temperature slightly below 100°C. Thus, it is clear that *R*-center is most thermally unstable among these centers though it is stable optically. Therefore, assuming that the exciton produce the thermal spike as suggested by Seitz[2] and the thermal effect on *F* and *U* centers discussed in our previous report is correct, *R* center will be destroyed first of all when the crystal containing complex centers are irradiated by the ultra violet light in the exciton absorption band. The following result is considered to provide one possibility of this evidence.

A KCl crystal containing *F* centers with the density of 1.5×10^{17} per cubic centimeters was irradiated at room temperature with a high pressure mercury lamp through a green filter which transmits only the monochromatic light of Hg 5461 A. The irradiation period was so long that, equilibrium state between *F* centers and other complex centers was established and any more irradiation did produce no change in the absorption curve. The absorption curve of the crystal in the equilibrium state is shown in Fig. 1 (a). For the ultra violet light to form excitons a hydrogen discharge tube was used. The window material of the tube was a crystal-quartz plate which is transparent down to 1700 A.

At first, the crystal of which absorption curve is shown in Fig. 1 (a) was irradiated at room temperature for one minute with the hydrogen lamp through a filter of pure KBr crystal-plate of thickness $d=0.9$ mm, but any appreciable change of the absorption curve was not observed. However, against the same period of irradiation through a filter of pure KCl crystal-plate, a large change was detected: namely, *R* bands decreased and *F* band increased. Successive irradiations of ultra violet light with the KCl filter destroyed *R* bands completely and the electrons were transfered to *F* centers as shown in Fig. 1 (b). It is shown from the figure that *K* and *N* bands also decreased, but with a slower rate compared to *R* bands.

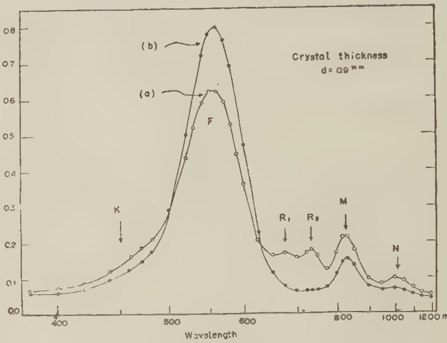

Fig. 1. a) The equilibrium state between *F* and complex centers. b) After the irradiation with exciton light for 20 minutes at 17°C.

From the fact that the ultra violet light filtered with KBr crystal has no appreciable effect, the wavelength of the photon which is effective upon the bleaching of *R* centers is shorter than that of the edge absorption of KBr crystal: i.e. 205 mμ. On the otherhand the KCl crystal ($d=0.7$ mm) is transparent down to 185 mμ and the tail of the fundamental absorption band extends to 210 mμ[1]. The total photon number of the ultra violet lights included in the region between the wavelengths of transmission limits of KCl and KBr crystals: (185 mμ–205 mμ) were measured with a thermopile as 8×10^{14} quanta per cm^2 per sec. at the position of irradiated crystal. From these facts, it is safely concluded that the observed photo chemical reaction can be attributed to the exciton.

To obtain the quantum efficiency for the reaction and the quantitative discussion, investigation on the thermal stability of *R* bands and the detailed absorption spectrum of the exciton absorption tail of the crystal containing the complex centers have being carried out.

References

1) M. Ueta, M. Hirai and H. Watanabe: J. Phys. Soc. Japan **14** (1959) 253.
2) F. Seitz: Rev. Mod. Phys. **26** (1954) 80.

Errata

Oxide-Cored Cathode

By Keiichi ANDO, Osami KAMIGAITO, Yoshihiro KAMIYA,
Shigetoshi TAKAHASHI and Ryozi UYEDA

J. Phys. Soc. Japan **14** (1959) 180

Page		line		
180	right	foot-note	Prof. S. Sasaki should be read Prof. N. Sasaki	
184	left	28	exide-coated	oxide-coated
184	right	2	event	evident
185	right	3	not only from the conical side	not only from the tip but from the conical side
185	right	35	Tras–50D	TRS-50D

On Quantitative Measurement of Turbulence by Means of a Constant Resistance Hot-wire Anemometer

By Nisiki HAYASI

J. Phys. Soc. Japan **14** (1959) 360

All α's and B's in the lines from 10 to 23 on page 362 should be replaced by $\hat{\alpha}$'s and $\hat{B}$'s, where $\hat{\alpha}=\alpha r_0/r_1$.

Page	Column	Line		(should be read)
362		26	B	β/α
362		28	$\bar{I}^2 r_0 R_3^2$	$\bar{I}^2 \bar{r} R_3^2$
363		3	$-i_e R_1 R_G/G$,	$-i_e R_1 R_G/G$.
364	right	9	this effect	these effects

Preparation of Anodic Oscillator Tube using Glow Discharge

By Kazuyuki OGAWA

J Phys. Soc. Japan **14** (1959) 385

In Fig. 3 the ordinate scale belonging to tube drop should be shifted down by 10 volts, i.e., 115 volt, 110 volt and 105 volt are respectively rewritten as 125 volt, 120 volt and 115 volt.

PROGRESS OF THEORETICAL PHYSICS

CONTENTS

Progress of Theoretical Physics Vol. 20, No. 3, September 1958

On the Concept of Potential in Quantum Field Theory..........Abraham KLEIN..257
A Comparison of Plane Wave Solutions in General Relativity with Those in Non-Symmetric Theory ....Hyôitirô TAKENO..267
The Magnetic Properties of the Praseodymium and the Neodymium Metals ....Tsuyoshi MURAO..277
Parity Nonconservation and the Beta-Spectrum of RaE.................... ....J. FUJITA, M. YAMADA, Z. MATUMOTO and S. NAKAMURA..287
Mesic Correction to the Beta-Decay in a Nucleus........................ ....J. FUJITA, Z. MATUMOTO, E. KUROBOSHI and H. MIYAZAWA..308
Spontaneous Fission Half-Lives .... Tatuya SASAKAWA and Masaru YASUNO..315
Effects of Defects on Lattice Vibrations—*Thermodynamical Properties*—.... ....Kaoru YAMAHUZI and Tomoyasu TANAKA..327
Composite Model of Pion and Pion-Nucleon Interaction..................... ....Chiaki IHARA and Shigeaki HATANO..356
Vibrational Thermodynamic Properties of Lattices with Defects, I —*The Linear Lattice*—............J. MAHANTY, A. A. MARADUDIN and G. H. WEISS..369
Letters to the Editor:
On the Consistency between the P-Wave Dispersion Relation and the Experiment.......................T. TSUCHIDA and A. KANAZAWA..395
On the Radiative Corrections to the Scattering of Mesons in an External Electromagnetic Field ....A. K. BHATIA and J. SUCHER..397
On Parity Nonconservation..................................T. TATI..398
On the Positronium in Metals .... H. KANAZAWA..400
Contents of Journ. Phys. Soc. of Japan, Vol. 13, No. 8 402

Price $ 1.25 per copy
$ 15.00 per year (postage inclusive)
Annual dues for foreign members (individual subscribers)
$ 12.00 (postage inclusive)
" for foreign members of the Physical Society of Japan
$ 10.00 (postage inclusive)

Application for members, subscriptions and orders for back numbers should be sent, directly or through book-dealers, to

The Publication Office
in
Yukawa Hall, Kyoto University, Kyoto, Japan

. . . .

ANNOUNCEMENT

REVISED Price List of Back Numbers (for subscribers abroad)

*Vols. 1–4	$ 6.40 each
*Vols. 5 & 6	$13.00 each (single copy: $2.50)
*Vols. 7 and succeeding ones	$ 8.00 each (single copy: $1.50)

Back number prices are effective for volumes other than last four (4) volumes (the current volume inclusive).

Thus, volumes 1 through 16 will be regarded as back numbers while volume 20 is being published.

The revised prices will be effective on and after August 1, 1958.

. . . .

JOURNAL OF THE PHYSICAL SOCIETY OF JAPAN, Vol. 14, No. 5, MAY, 1959

Elastic and Inelastic Scattering of 22 Mev Alpha Particles by Light Elements

By Chuin HU, Shohei KATO, Yukiyasu ODA
and Minoru TAKEDA

Department of Physics, Faculty of Science,
Osaka University, Osaka, Japan

(Received December 8, 1958)

The scattering of 22 Mev alpha particles from carbon, magnesium and silicon has been studied with scintillation counter technique. The elastic scatterings from carbon and magnesium have shown the characteristic diffraction pattern, which can be obtained from the theory of diffraction by an opaque sphere. The observed inelastic angular distributions could be approximated by the squares spherical Bessel function of second order as predicted by direct interaction theory. The agreement is appreciably good for our elements. However, the cross sections do not tend toward small values in the forward direction for magnesium and silicon.

§ 1. Introduction

Recently many experiments on the elastic and the inelastic scattering of alpha particles by various elements have been reported[1),2)]. The angular distributions of elastically scattered alpha particles by light nuclei in these experiments have been characterized by the appearance of diffraction patterns. It seems that these features can be interpreted well in terms of the optical model analysis, and many calculations were carried out[3)]. These calculations uses generally the depth of real and imaginary potentials, nuclear radius and boundary diffuseness, and they are appreciably complicated. But, in some cases, these diffraction patterns are also interpreted more simply by the classical point of view to give the interaction radius of incident particles and target nucleus. Because of short wave length and spinless properties of incident alpha particles, the elastic scattering of alpha particles has some analogy with the diffraction of light scattered by sphere[4)]. In order to calculate the differential cross sections, it is convenient to assume that the target nucleus can be represented as an opaque sphere, then one may find

$$\frac{d\sigma}{d\Omega}=k^2R^4\left[\frac{J_1(2Rk\sin(\theta/2))}{2Rk\sin(\theta/2)}\right]^2. \qquad (1)$$

The range of validity of this expression is restricted by some conditions on the scattering angle θ. On the other hand, the differential cross sections of inelastically scattered alpha particles were found to vary strongly with scattering angle, suggesting a direct interaction process of nuclear reaction. The form of the angular distribution based on the direct interaction proposed by Austern, Butler and McManus[5)] is found to be

$$\sigma(\theta)=\sum_l a_l[j_l(qa)]^2 \qquad (2)$$

and the interaction radius, which is chosen so as to make the curve of and angular distribution best fit, is determined. It is an interesting problem to compare the magnitudes of interaction radii obtained from both analysis of the elastic and inelastic sacttering data.

An another interesting feature of inelastic scattering of alpha particles is related with the isotopic spin selection rule. According to this prediction, bombardment of alpha particles cannot lead to any state of intermediate nucleus with different isotopic spin from that of the target nucleus, and in the case of inelastic scattering of alpha particles, only states with the same isotopic spin as the ground state can be excited. In fact, it has been shown experimentally[2)] that the probabilities of excitation forbidden by this selection rule are smaller than few percents of those of the allowed levels.

In the present experiment, the target of C^{12}, Mg^{24} and Si^{28} were bombarded by 22 Mev alpha particles accelerated by Osaka University cyclotron and the differentical cross sections of elastically and inelastically scattered alpha particles were measured by the scintillation counter. The appeared levels in our experiment have the same isotopic spin with the ground state.

§ 2. Experimental

The alpha particles were produced in Osaka University 44″ cyclotron by accelerating doubly ionized helium atoms to an energy of 22 Mev. A schematic diagram of the cyclotron, scattering chamber, and NaI scintillation counter was illustrated in our previous paper⁶⁾.

In the present experiment we did not use any particle selection technique, since the yield of protons from (α, p) reaction was very small compared with those of alpha particles scattered elastically or inelastically by light nuclei⁷⁾, and furthermore the (α, d) reaction has very large negative Q-value for the present case.

All targets, used above, were self-supported one and holded in aluminum target frames of $2\,\text{cm} \times 2\,\text{cm}$ in size. The carbon target of about $1\,\text{mg/cm}^2$ thickness was obtained by painting a soot dispersion in alcohol on a thin collodion film of several $\mu\text{g/cm}^2$. For the case determining the absolute cross sections, a 20 μ thick polyethylene foil was used. The magnesium target of $0.78\,\text{mg/cm}^2$ thickness prepared by evaporation method, and fused quartz foil of $1.4\,\text{mg/cm}^2$ thickness was used as silicon target.

The pulse height distributions of scattered alpha particle groups from the 22 Mev alpha particle bombardment on C, Mg and SiO_2 are shown in Figs. 1, 2 and 3, respectively.

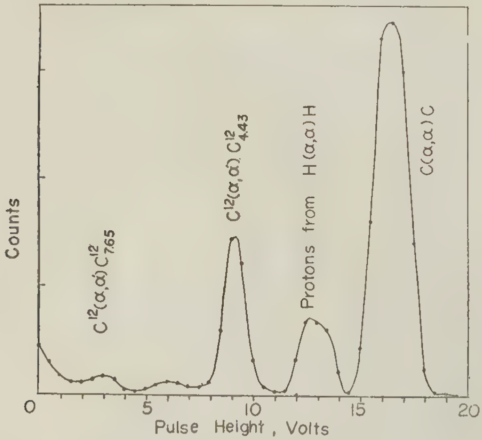

Fig. 1. The pulse height distribution of scattered particles from carbon target at $\theta=30°$. The first excited group is separated from recoil protons, due to hydrogen contamination, by Inserting a alminium foil in front of detector.

In the case of carbon we observed appreciable hydrogen contamination in the target. The group of this hydrogen contamination and the alpha group excited to the first excited level of carbon overlapped unfortunately, at about 25°. However, by inserting an aluminium absorber in front of the counter aperture, we could separate these groups. On the other hand, in the inelastic scattering from silicon we could not measure the differential cross sections at the angular region larger than 50° since the alpha group from the first excited level of silicon was masked by that of elastic scattering by oxygen.

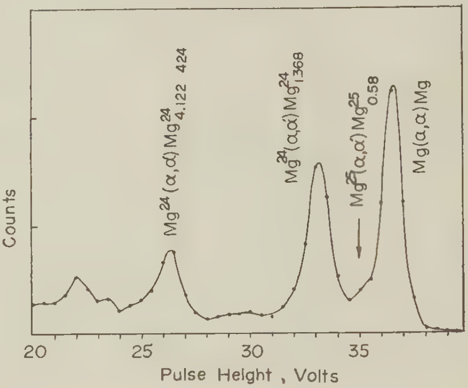

Fig. 2. The pulse height distribution of alpha particles from magnesium target at $\theta_{\text{lab}}=32.5°$.

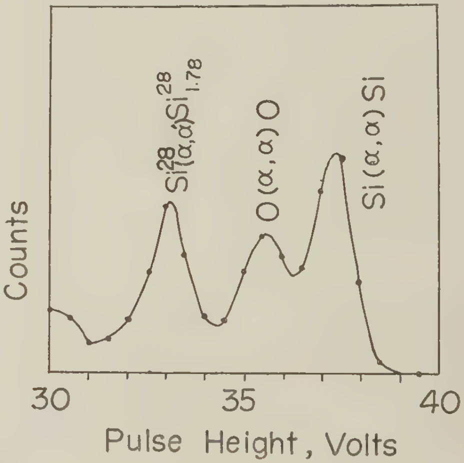

Fig. 3. The pulse height distribution of alpha particles from SiO_2 target at $\theta_{\text{lab}}=30°$.

§ 3. Results

1) *Elastic scattering*

The angular distributions of alpha particles elastically scattered by C^{12} and Mg^{24} are illustrated in Figs. 4 and 5, where the calculated Rutherford cross section are indicated by a dashed curve.

Diffraction patterns appear evidently in the forward direction in both cases. For the case of C^{12}, the smooth variation of the cross section from 60° to 78° which appeared in Watter's 31.5 Mev alpha particle experiments[2], is not observed in our 22 Mev experiments. This phenomena may be considered to be an energy dependent effect such as the dependence of the angular positions of maxima (or minima).

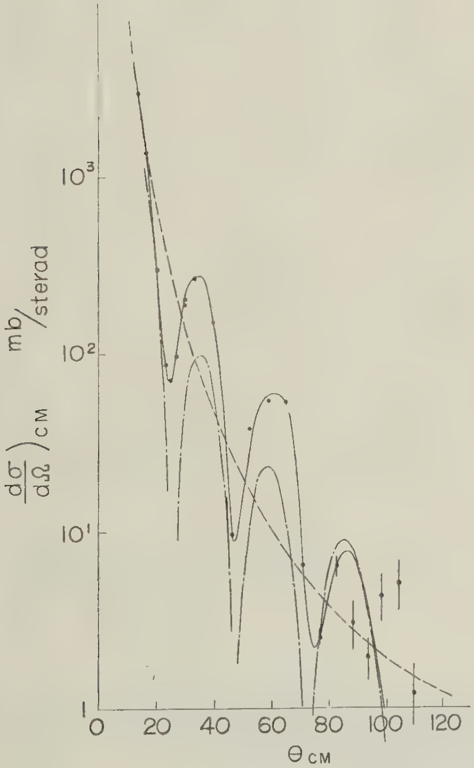

Fig. 4. The angular distribution of elastically scattered alpha particles from carbon.

As is shown in Fig. 4, the calculated curve assuming the scattering from an opaque sphere is in fair agreement with the experimental one, and it is true for the case of Mg^{24} also. In this calculation, we used expression (1) and the interaction radii have been adjusted to 5.5 and 6.0 fermis (1 fermi$=10^{-13}$ cm) for C^{12} and Mg^{24}, respectively, and they will be compared below with those fitted to inelastic scattering data.

The angular dependence of the deviations from the Rutherford scattering are different for the both cases, i.e., the experimental points are distributed around the Rutherford cross sections in the case of C^{12}, while for Mg^{24}, the diffraction pattern appears below the Rutherford curve. This situation is similar to that of 31.5 Mev work[2].

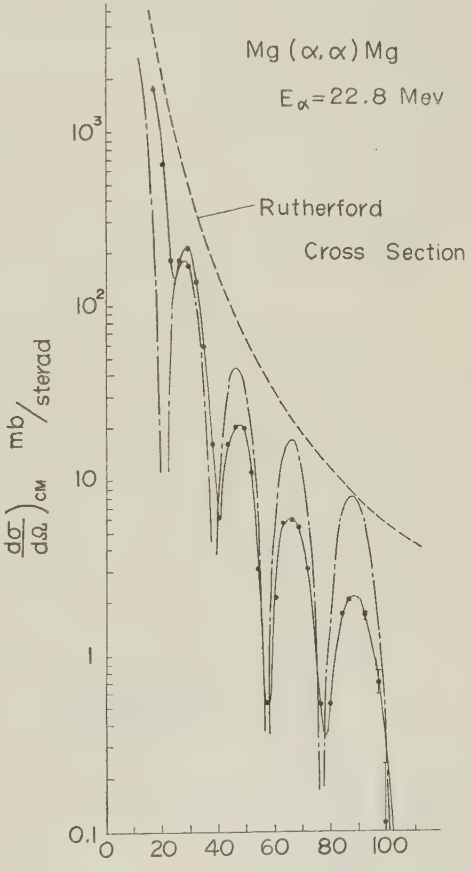

Fig. 5. The angular distribution of elastically scattered alpha particles from magnesium.

2) *Inelastic scattering*

In our case the spins and parities of the ground and excited state are respectively 0(+) and 2(+).

a) $C^{12}(\alpha, \alpha')C^{12*}$, $Q=-4.43$ Mev. The most pronounced feature of the angular distribution for this case is that the first maximum is at about 28°, though in the 31.5 Mev data[2] the cross section increase linearly at small angles. The theory predicts an angular distribution of the form of $[j_2(|\boldsymbol{k}_{\alpha}-\boldsymbol{k}_{\alpha'}|a)]^2$ for this case, and this is illustrated in Figs. 6 with the present experimental result. The interaction radius has been adjusted as 5.08 fermis and the agreement between the theoretical and experimental results is very good.

b) $Mg^{24}(\alpha, \alpha')Mg^{24*}$, $Q=-1.368$ Mev. Since the spins and parities of the ground state and the first excited level are 0(+) and 2(+), respectively, one may expect an angular distribution varying as $[j_2(|\boldsymbol{k}_\alpha-\boldsymbol{k}_{\alpha'}|a)]^2$. As illustrated in Fig. 7, the theoretical curve reproduces the experimental angular distribution fairly well, assuming the interaction radius of 6.3 fermis.

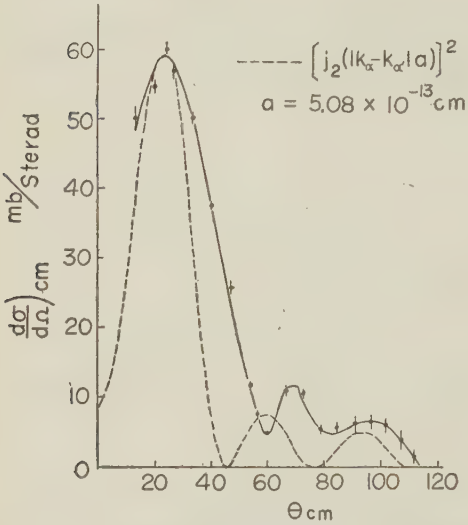

Fig. 6. The angular distribution of inelastically scattered alpha particles from carbon, $Q=-4.43$ Mev.

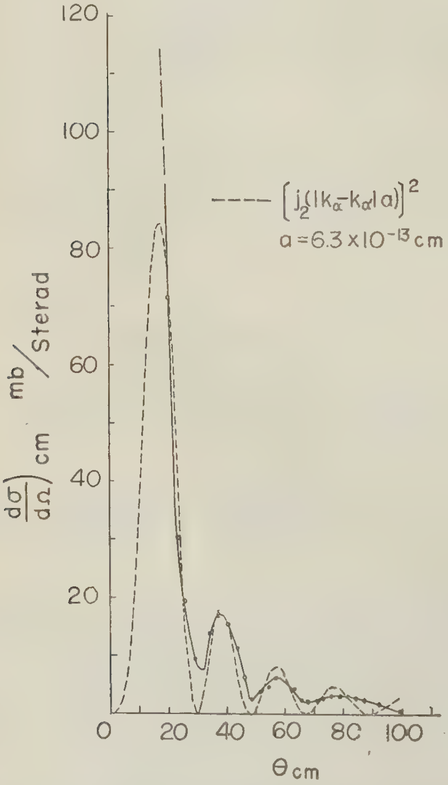

Fig. 7. The angular distribution of inelastically scattered alpha particles from the first excited states of magnesium, $Q=-1.368$ Mev.

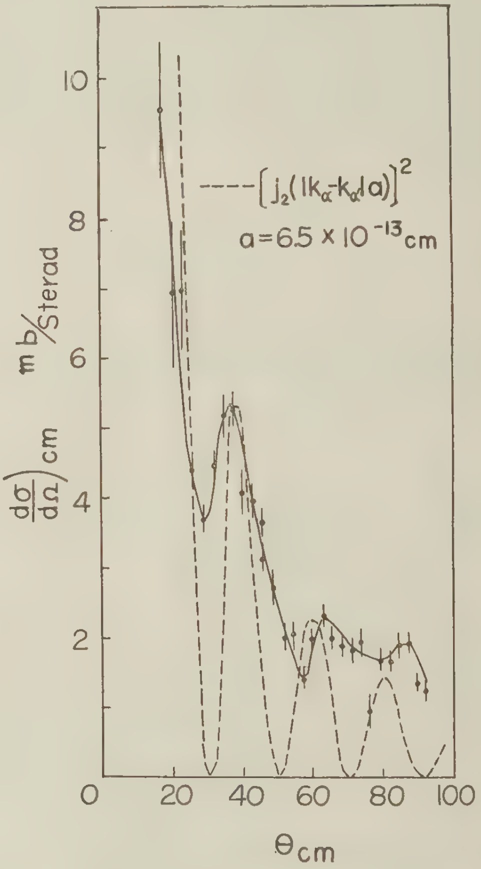

Fig. 8. The angular distribution of inelastically scattered alpha particles from the second and third excited states of magnesium, $Q=-4.12$ and -4.23 Mev together.

c) $Mg^{24}(\alpha, \alpha')Mg^{24*}$, $Q=-4.2$ Mev. The experimental differential cross section for this process is shown in Fig. 8.

Although the second excited levels of Mg^{24} has doublet structure of 2(+) and 4(+), the angular distribution of Fig. 8 seems to be contributed from the 2(+) level only since theoretical $[j_2]^2$ curve can reproduce the experimental results with a reasonable magnitude of interaction radius $a=6.5$ fermis.

d) $Si^{28}(\alpha, \alpha')Si^{28*}$, $Q=-1.78$ Mev. In Fig. 9, the experimental and calculated $[j_2|\boldsymbol{k}_\alpha-\boldsymbol{k}_{\alpha'}|a)]^2$

curves are illustrated together. Chosing the interaction radius as 6.16 fermis, the agreement between experimental and theoretical results is good, though the range of the scattering angles is only from 17° to 46°.

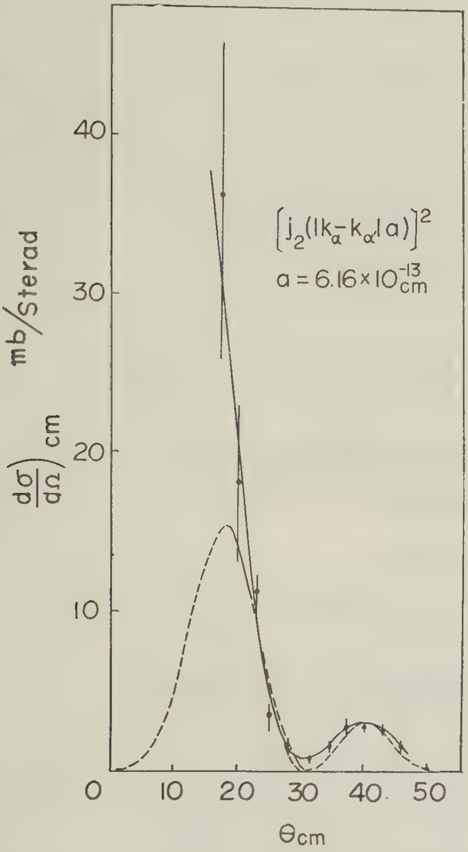

Fig. 9. The angular distribution of inelastically scattered alpha particles from the first excited state of silicon, $Q=-1.78$ Mev.

§ 4. Discussion and Conclusion

It is interesting to compare the nuclear radii determined by the elastic scattering of alpha particles with that deduced from inelastic scattering, although the two mechanisms of scattering of alpha particles are quite different each other. In the case of C^{12}, we have chosen the interaction radius as 5.5 fermis for the elastic scattering from the opaque sphere model and 5.08 fermis for the inelastic scattering from the direct interaction theory. In the case of Mg^{24}, we have taken the interaction radii as 6.0 and 6.3 fermis for elastic and inelastic scattering respectively. These agreements are rather good and they also agree with the radii which were determined by the sharp cut off model analysis⁹⁾. But these radii are larger than that obtained by optical model analysis³⁾.

The recent experiments about the inelastic scattering of nucleons from light nuclei have revealed some complexities in the angular distributions of the scattered particles which can not be explained by either the simple compound or direct theory of nuclear reactions. While the results for inelastic scattering of alpha particles described here are well interpreted by the simple direct theory of Austern, Butler and McManus. The angular distributions for the elastic scattering show that the nucleus would be almost black for the impinging of alpha particles. The existence of sharply defined boundary surface between the inside and outside of nucleus would play a role to exhibit the diffraction phenomena.

Almost all parts of our experimental results of the inelastic scattering are on the first excited states of even-even nuclei. The angular distributions predicted by the collective excitation theory also have the form of $[j_2(qa)]^2$ for these cases quite similarly to that of the former direct theory. Therefore, we can not argue which theory is more preferable as long as we concern only to the experimental results of the angular distributions. Now the above formal expression gives a small cross section at 0°. This feature has been recognized well in our result for C^{12}. Large forward peaks are, however, observed for Mg and Si, although the experimental error are somewhat large. This is explained by neither of the theories mentioned above.

As the yields of the reactions observed in our experiments are appreciable, it will be reasonable to say that the excited states studied have the same isotopic spin with that of the ground state. It is worthwhile to note here that the yield of second excited state of C^{12} is so small as we could not measure the angular distribution. This feature seems not to depend seriously on the incident energy²⁾. Similar results has been also found in the case of the inelastic scattering of protons from C^{12}.⁸⁾ Probably these features suggest that the nature of the second excited state would be greatly different from that of the ground state, and the transition would be highly suppressed.

Acknowledgements

The authors are indebted to Professor T. Wakatsuki for his continued interest in the problem. We also would like to express thanks to members of Osaka University Cyclotron.

References

1) R. M. Eisberg, G. Igo and H. E. Wegner: Phys. Rev. **99** (1955) 1606. P. C. Gugelot and M. Rickey: Phys. Rev. **101** (1956) 1613. L. Seidlitz, E. Blenler and D. J. Tendam: Phys. Rev. **110** (1958) 682.
2) H. J. Watters: Phys. Rev. **103** (1956) 1763.
3) G. Igo and R. M. Thaler: Phys. Rev. **106** (1957) 126.
4) L. Wayne Swenson, Ulrich Schindewolf and N. S. Wall: Nucl. Phys. **6** (1958) 203.
5) N. Austern, S. T. Butler and H. MacManus: Phys. Rev. **92** (1953) 350.
6) Y. Oda et al: J. Phys. Soc. Japan **14** (1959) 396.
7) C. H. Hunting and N. S. Wall: Phys. Rev. **108** (1958) 901. S. Yamabe: private communication.
8) R. W. Peele: Phys. Rev. **105** (1957) 1311. V. K. Rasmussen, D. W. Miller and M. B. Sampson: Phys. Rev. **100** (1955) 181.
9) D. D. Kerlee, J. S. Blair and G. W. Farwell: Phys. Rev. **107** (1957) 1343.

Journal of the Physical society of Japan, Vol. 14, No. 5, May, 1959

$Be^9(n,2n)Be^8$ and $B^{11}(n,\alpha)Li^8(\beta)Be^8$ Reactions by 14 Mev Neutrons

By Masakatsu Sakisaka

Department of Physics, Kōnan University, Kōbe

(Received December 19, 1958)

$Be^9(n, 2n)Be^8$ and $B^{11}(n, \alpha)Li^8(\beta)Be^8$ reactions induced by 14 Mev neutrons were studied by the method of beryllium and boron loaded nuclear emulsions.

In the former reaction, the angular distributions of Be^8 nuclei were strongly peaked backward in the center-of-mass system, suggesting that the direct interaction of the incident neutrons with beryllium—an inelastic scattering process before second neutron emission and a pick-up process probably—had a major contribution to the reaction. The cross sections were measured as 0.18±0.07, 0.03±0.02, 0.11±0.04 and 0.05±0.03 barns for the 3, 5, 7.5 and more than 9 Mev excited states of Be^8 respectively. When 0.17±0.03 barns was cited to the cross section with respect to its ground state, the total $(n, 2n)$ cross section was estimated as 0.54±0.09 barns.

The cross section of the latter reaction was measured as 35±7 millibarns in which the contribution of Be^8 in the ground state was not included. Most Li^8 nuclei were found to be left at the states lower than 2.5 Mev in the reaction. The decaying rates of Li^8 to the Be^8 states of 3, 5 and more than 8 Mev were about 75, 15 and 10% respectively and the mixing of the allowed transitions of such rates was consistent with the known β-spectrum of Li^8.

§ 1. Introduction

The interactions of various nuclei with fast neutrons have been studied and many informations about the reaction processes have been obtained, but there remain much ambiguities even in the phenomena concerning light nuclei.

$Be^9(n, 2n)Be^8$ reaction by 14 Mev neutrons was investigated by some workers$^{1)-4)}$ by observing the emitted neutrons from beryllium. Though these experiments gave important knowledges about the reaction cross section and the energy spectrum of the emitted neutrons, the angular distributions of the neutrons or recoil Be^8 nuclei have not yet been observed. Recently Anderson *et al.*5) have given the angular distribution of inelastically scattered neutrons corresponding to the 2.43 Mev level of Be^9 by a time-of-flight method.

$B^{11}(n, \alpha)Li^8(\beta)Be^8$ reaction at 14 Mev neutron energy has been studied by Heiberg6) and Armstrong and Frye7), but there still remain many uncertainties because of the small cross section of the reaction.

The final product of the above reactions is Be^8 nucleus. This nucleus has been most frequently investigated both theoretically and experimentally owing to its interesting nuclear character, but the existence of the excited states between 3 and 7.5 Mev has not yet been decisive. More precise experiments about these reactions are therefore desirable.

In this paper the two reactions induced by the 14 Mev neutrons were investigated by the method of the beryllium and boron loaded nuclear emulsions.

§ 2. Experimental Procedures

(1) *Neutron irradiations and monitoring*

The deuteron beam was accelerated to 170 Kev by a Cockcroft-Walton type accelerator. The magnetically analysed beam of a few μA bombarded to a thick tritium-titanium target producing 14 Mev neutrons of $T(d, n)\alpha$ reaction. The irradiation of nuclear plates by neutrons was performed as follows. Several Sakura NR-Ml nuclear plates (1″×3″ in size and 90 μ and 170 μ in thickness) were cut in half. The fellows of the halves were loaded with beryllium or boron by the procedures described in Appendixes I and II. The contents of beryllium and boron were determined by means of chemical and activation analysis respectively. The loaded plates and the unloaded ones for the background measurements wrapped by black papers separately were arranged abreast and 10 cm apart from the target on a plane perpendicular to the deuteron beam. The cadmium covers of 0.2 mm in thickness were used for both plates in order to filter the probable thermal neutrons. Their glacing angles were chosen as 5°.

To obtain the number of neutrons impinged on the nuclear plates, the recoil alpha-particles of $T(d, n)\alpha$ reaction emitted in the perpendicular direction with respect to the deuteron beam were counted by a CsI(Tl) crystal of 1/16″ in thickness viewed with a photomultiplier RCA 6810. The surface of the crystal was screened by two sheets of aluminium foils of 0.13 mg/cm^2 in thickness to prevent scattered deuterons and beam glow from reaching the crystal. The counting error was estimated to be less than 2%. The experimental arrangements are shown in Fig. 1.

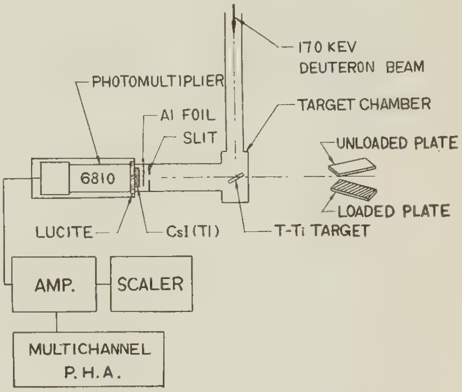

Fig. 1. Experimental arrangements.

The recoil alpha-particles of the neutrons used to irradiate the emulsions were emitted in the direction of 84° to the deuteron beam at the bombarding energy of 170 Kev. Therefore the counts of alpha-particles in this arrangement did not give directly the correct number of the neutrons falling on the emulsions, but the correction could be easily made, because the angular distribution of the neutrons in $T(d, n)\alpha$ reaction was found to be isotropic8) in the center-of-mass system at such a low deuteron energy.

The neutron energy was 14.1±0.2 Mev and the number of the irradiated neutrons at the plates was $(3.77 \pm 0.08) \times 10^7$ neutrons/cm^2 in each experiment.

(2) *Plate analysis*

The exposed plates were processed by the procedures shown in Appendixes I and II. The scannings of the processed emulsions were performed with two Tiyoda binocular microscopes at a magnification of 1350 for the beryllium loaded and the unloaded emulsions, while a magnification of 900 was adopted for the boron loaded ones, since the stars attributed to the boron disintegration reaction could be easily perceptible. Some typical examples are shown in Fig. 2.

The measurements of the following three quantities were made on each prong of an observed track or a star:

(a) horizontally projected length of the prong,
(b) dip of the prong,
(c) angle between the prong and the direction of the incident neutron.

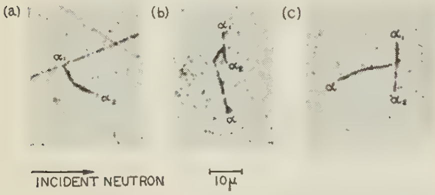

Fig. 2. Typical track and stars in beryllium and boron disintegrations respectively.
(a): Track of $Be^9(n, 2n)Be^8$ reaction:
E_1=2.09 Mev, E_2=2.54 Mev, E^*=4.10 Mev, Θ=147°
(b), (c): Stars of $B^{11}(n, \alpha)Li^8(\beta)Be^8$ reaction:
(b) E_1=1.23 Mev, E_2=1.23 Mev, E^*=2.36 Mev
(c) E_1=2.48 Mev, E_2=2.56 Mev, E^*=4.94 Mev
Both Li^8 are left at the ground state in the (n, α) reaction.

The errors of these quantities were estimated as ±0.5 μ, ±0.3 μ and ±2° respectively.

Since the range-energy relations for alpha-particles have not been given in the NR-Ml emulsion, they were determined experimentally as stated in Appendix III. The energy of each prong was obtained from the measured range-energy relations, from which the energies and the angular distributions in the center-of-mass system could be calculated about the reaction products.

§ 3. Results and Discussions

(1) $Be^9(n, 2n)Be^8$ *reaction*

It was found that even in the unloaded emulsions there were found many tracks similar to those due to Be^8 disintegration. These background tracks would be attributed to the followings:

(a) bent tracks of scattered low energy protons which are difficult to discriminate from those of alpha-particles,
(b) bent tracks of alpha-particles,
(c) 3-alpha stars from carbon whose one prong is too short to be detected or two of them are too close together to be resolved,
(d) tracks of light nuclei accompanied by the emission of a charged particle—the recoil atoms sometimes give the tracks indistinguishable from those of alpha-particles,
(e) tracks attributed to the emission of two charged particles.

At first the same areas of the beryllium loaded and unloaded pair were scanned and all the tracks in question were measured. When the energies of two alpha-particles were denoted as E_1 and E_2, there were the difference of the E_1+E_2 histograms between both plates near the energies of 3.5, 7.5 and more than 9 Mev. Moreover, when the number of tracks per Mev of E_1+E_2 was plotted against the energy ratio γ of the two alpha-particles (defined as $\gamma \geq 1$), it became clear that the differences were found only for the low γ region of $1 \leq \gamma \lesssim 2.5$. Therefore the subsequent scannings were performed so as to choose only the tracks of γ less than 3, that is, the tracks whose range of the longer prong did not exceed about three times of the other were chosen. By such a selection the scanning labour was greatly reduced.

In the track analysis, the length between the end of two alpha-particle prongs (P_1 and P_2 in Fig. 3) was first measured, from which

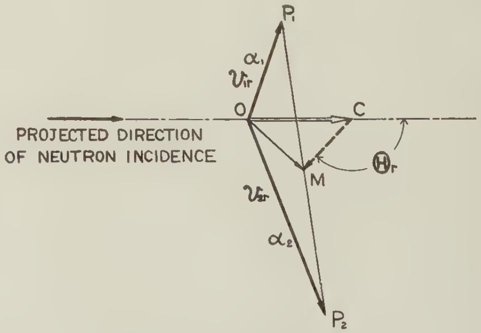

Fig. 3. Velocity vector diagram of the $Be^9(n, 2n)Be^8$ reaction on the projected plane.
Suffix r means the horizontal projection of the respective vector. Solid arrows show the vectors in the laboratory system and broken arrow gives the vector in the center-of-mass system. White arrow is the projected vector of the center of mass.

M: middle point of $\overline{P_1P_2}$,
$\overrightarrow{OM}$: projected velocity vector of Be^8

the excitation energy E^* of Be^8 could be calculated. The tracks in both emulsions were analysed in this way and the net histogram of E^* distribution is shown in Fig. 4. Besides the well-known ground, 3 and 7.5 Mev states, a level near 5 Mev and unresolved levels above 9 Mev are seen to be probable.

The angular distributions of Be^8 were obtained for the 3 and 7.5 Mev states from the direction $\overrightarrow{CM}$, which showed the strongly backward predominance in the center-of-mass system, as shown in Fig. 5. The reliable results were not given to the 5 Mev and above 9 Mev states owing to the small number of the net events.

In the $Be^9(n, 2n)$ reaction by 14 Mev neutrons, Rosen and Stewart[3] have reported the existence of the 2.43 and 7.9 Mev states of Be^9 and also found the emission of many neutrons of low energies. This indicates that the reaction proceeded mainly by an inelastic scattering of the incident neutron with beryllium at first and then the excited Be^9 nucleus disintegrated into a second neutron and Be^8 residual. Such a two-step process of the reaction has been found by Fowler *et al.*[9], Fischer[10], and Wagner and Huber[11] at the lower incident neutron energies.

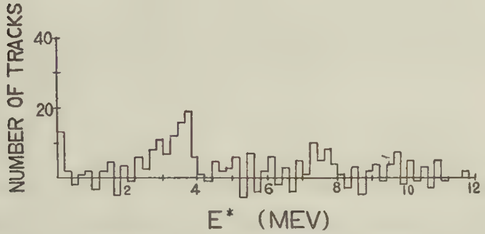

Fig. 4. Histogram of the excitation energy of Be^8 obtained from the $Be^9(n, 2n)Be^8$ reaction.

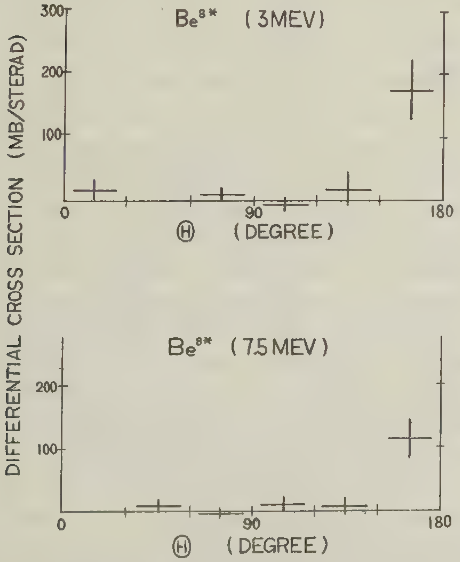

Fig. 5. Angular distributions of Be^8 from the $Be^9(n, 2n)Be^8$ reaction in the center-of-mass system.

The angular distribution of the neutrons inelastically scattered by the 2.43 Mev state Be^9 has recently been observed to be peaked forward[5]. Unfortunately, those for other levels of Be^9 have not yet been given. However the sharp and forward angular distributions of the inelastically scattered neutrons have been shown in the same paper by Rosen, though they were concerned with other nuclei of Ta and Bi.

To explain the present experimental results according to the two-step process alone, the following assumption would be necessary, that is, the inelastically scattered neutrons by Be^9 proceeded sharply and forwardly in the center-of-mass system (the recoil Be^9 are peaked backward) and the energy release† in the second process was small. Then the angular distributions of the residual Be^8 would resemble to those of the recoil Be^9. But it seems to be difficult that this assumption is correct.

Another quite different assumption might be admitted to the reaction mechanism; namely an incident neutron picked up the other neutron of Be^9 just as (n, d) or (p, d) reactions. In this process the residual Be^8 nucleus has an appreciable probability of backward predominance in its angular distribution. Again, the pick-up process alone is not satisfactory for explaining the energy spectrum of the emitted neutrons obtained by Rosen and Stewart. Rather, some mixing of the two-step process and the pick-up process seems adequate for the present investigation. But, since the further details cannot be derived at the present state of knowledge, more experiments are necessary.

Quite recently Remy and Winter[12] have investigated the $Be^9(n, 2n)$ reaction by time-of-flight method and obtained the complex energy distribution of the neutrons, showing that the reaction was not considered to be due to the simple two-step process alone—the various levels of Be^9 and Be^8 were not only concerned in the two-step process but also the pick-up process was expected from the angular correlation of the emitted neutrons. However the mixing ratio of the processes has not been given and, at this time, their investigation is correlated to the present study only qualitatively.

---

† If the excited Be^9 was at rest, one ninth of the energy release of $E_0^* - E^* - 1.67$ is given to Be^8 where E_0^*, E^* and -1.67 are the excitation energies of Be^9, Be^8 and the Q-value of $Be^9(n, 2n)$ reaction respsectively.

To obtain the reaction cross sections some corrections were necessary. First, the correction of the escaping probability of tracks from the emulsions was made by the ordinary method. Next, the effect of the increase of light nuclei in the loaded emulsions was corrected. It amounted to about 10±5%. And finally the contribution of a few tracks of γ greater than the chosen value was taken into account, which was estimated to be less than 5%.

Table I. Cross section of Be^9+n reactions (barns).

References	Level of Be^8 (Mev)					$\sigma_{n,2n}$	σ_n*
	0	3	5	7.5	>9		
Taylor *et al.*[1]							0.37±0.08
Flerov *et al.*[2]							0.64±0.02**
Rosen and Stewart[3]						0.42±0.07	0.42±0.07
MacGregor *et al.*[4]							0.49±0.02
Ashby *et al.*[13]						0.54±0.04	
Present author	>0.03±0.01	0.18±0.07	0.03±0.02	0.11±0.04	0.05±0.03	0.54±0.09	

* σ_n means the nonelastic cross section, which is tabulated for the sake of comparison.

** $E_n=14.5$ Mev.

The results are tabulated in Table I for the reactions proceeding *via* various levels of Be^8 nucleus. The value of 0.03±0.01 b for the Be^8 ground state is only a lower limit, because the tracks due to the disintegration of Be^8 in this state are difficult to be detected and liable to be missed. The total $(n, 2n)$ cross section is also shown in the table. It was obtained by summing up the cross sections corresponding to the respective levels of Be^8. But, in the summation, the value for the Be^8 ground state was chosen as 0.17±0.03 b† according to Anderson *et al.*[5]. The present value agrees well with the recent result of Ashby[13]. Comparing with some of the nonelastic cross sections, it may be concluded that the $(n, 2n)$ cross section is the major part of the nonelastic cross section.

The semi-empirical model of this reaction presented by Sachs[14] affords isotropy in the center-of-mass angular distributions of the neutrons and Be^8. This model seems inadequate so far as the reaction mechanism concerns, since the isotropical contributions was small in the present experiment. Bnt the behaviour of the $(n, 2n)$ cross sections measured by many workers up to 14 Mev of neutron energy fits well with Sachs' theory.

(2) $B^{11}(n, \alpha)Li^8(\beta)Be^8$ *reaction*

Of the neutron-induced disintegrations in boron, $B^{11}(n, \alpha)Li^8(\beta)Be^8(2\alpha)$ reaction gives rise to the hammer-shaped star, since the Li^8 does not decay until it has come to rest in the emulsion. This characteristic star could easily be found in the scanning, but that in which Be^8 was left in the ground state was hardly observed. The star is also indistinguishable from the 3-alpha star from carbon having one bent prong and two collinear equilateral ones, because the prongs of alpha-particles and recoil Li^8 atom would be short enough, if Li^8 would be left at the highly excited states. But the latter case was found to be rare as described later.

Fig. 6 gives the spectrum of the excitation energy E^* which was obtained by measuring the break-up of the final Be^8. In addition to the broad 3 Mev state a level of 5 Mev is seen. Armstrong and Frye⁷⁾ showed the slight indications of 2.2 and 4.0 Mev levels as well as the broad 3 Mev state but did not find the 5 Mev, though the number of their observed events was more than those of the present investigation.

---

† This value was obtained for the inelastic scattering of the neutrons proceeding *via* the 2.43 Mev level of Be^9 which was considered to decay to the Be^8 ground state only by neutron emission, since no gamma rays were found in the reaction. Therefore, Anderson's value may be taken to be equal to the disintegration cross section of Be^8 in the ground state.

The relative decaying rates of Li^8 to the 3, 5 and more than 8 Mev levels of Be^8 were about 75, 15 and 10% respectively. From the alpha-particles energy spectrum of the (n, α) reaction most Li^8 nuclei were found to be left in the states less than 2.5 Mev as shown in Fig. 7, but these states were not well resolved.

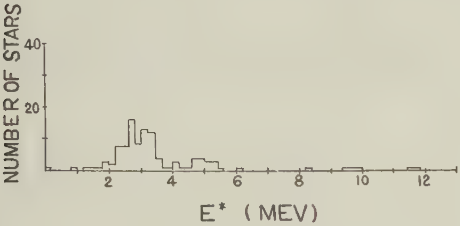

Fig. 6. Excitation energy of Be^8 obtained from the $B^{11}(n, \alpha)Li^8(\beta)Be^8$ reaction.

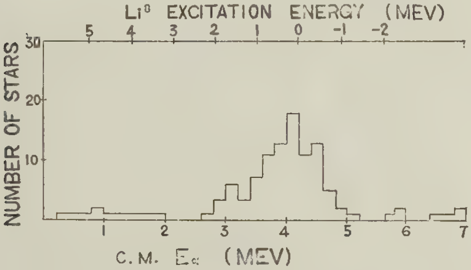

Fig. 7. Alpha-energy spectrum of the $B^{11}(n, \alpha)Li^8$ reaction in the center-of-mass system.

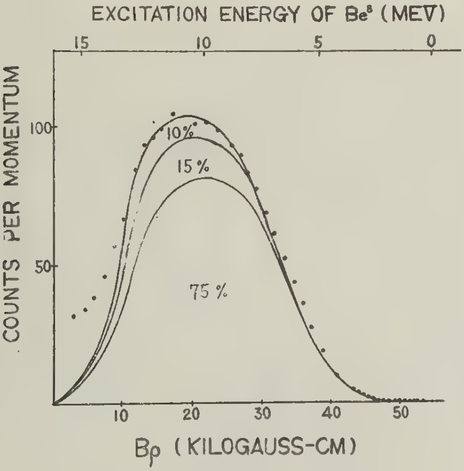

Fig. 8. β-spectrum of Li^8.

The dots show the measurement by Hornyak and Lauritsen¹⁵⁾.

The broadness of the respective levels of Be^8 is taken into account.

The cross section was 35±7 mb but it does not include the events of Be^8 in the ground state. Heiberg⁶⁾ gave about 30 mb to the reaction cross section at 14 Mev neutron energy, while Armstrong and Frye showed the cross section as 38.4±7.4 mb at 13.0 Mev and 30.9±6.3 mb at 14.7 Mev, both of which are in good agreement with the present observation.

The excited levels of Be^8 between 3 and 7.5 Mev have not yet been sufficiently decisive. But the present study has given a more reliable indication that at least one level exsists near 5 Mev.

According to Hornyak and Lauritsen¹⁵⁾, the β-ray spectrum of Li^8 indicated that about 90 per cent of the β-transitions occured to the 3 Mev state of Be^8 and 10 per cent to the states at nearly 10 and 13 Mev. However, the spectrum can be equally well explained, as shown in Fig. 8, by the superposition of the transitions obtained in the present experiment, namely; 75 and 15 per cent of the decays to the 3 and 5 Mev states respectively and 10 per cent to the state above 8 Mev. Here all the transitions are taken to be of the allowed type.

Burchum *et al.*¹⁶⁾ and Inall¹⁷⁾ have shown that in the $Li^7(p, \gamma)Be^8(2\alpha)$ reaction the weakly excited states were found near 4.2 and 5.4 Mev of Be^8 whose spins were assigned as $J=2^+$ by the $\gamma-\alpha$ angular correlation. It is reasonable that their 5.4 Mev is taken to be the same as the present 5 Mev one. Then, since the ground state of Li^8 is 2^+, the β-transition to the 5 Mev state of Be^8 is of the allowed type as assumed above. It is not inconsistent with the observations of Hanna *et al.*¹⁸⁾ and Bunbury¹⁹⁾ that the $\alpha-\beta$ angular correlation was isotropic within a few per cent in the $Li^8(\beta)Be^8(2\alpha)$ decay.

The reaction $B^{10}(n, t)Be^8$ was also observed. The cross section was estimated as 42±16 mb which did not include the contribution from the Be^8 ground state. Further results could not be obtained because of the very small number of the events.

Frye and Gammel²⁰⁾ found the total (n, t) cross section to be 102±17 mb for the 14.1

Mev neutrons. Comparing with the present result, the Be^8 ground state has nearly the same contribution as the excited states. According to Ribe and Seagrave[21], however, the ratio was 1:10. The more precise experiments would be desirable.

Acknowledgements

The author wishes to express his hearty thanks to Profs. B. Arakatsu and S. Kawata for their valuable discussions and continuous encouragements and to Mr. K. Yuasa and Mr. B. Saeki for their cooperative efforts during the experiments. He is indebted to Miss K. Ikeda, Miss A. Sukeno and Mr. K. Hanamoto for their scannings and calculations. He also wishes to thank Mr. Y. Kusaka for the advice in the chemical analysis of beryllium and Mr. S. Morita and others of the Kyūshū University for their cordial cooperation in the preliminary experiments.

This work was partly supported by The Scientific Research Expenditure of the Ministry of Education.

Appendix I. Preparations of the Beryllium Loaded Nuclear Emulsions

Since the supplies of the beryllium loaded nuclear plates have been stopped by the manufacturers owing to the poisoneous character of beryllium, one is obliged to try the loading by himself.

The 22% solution of beryllium acetate whose pH was about 5 was prepared. The Sakura NR-Ml nuclear plates of 90 μ and 170 μ in thickness were soaked in the solution for an hour at 11±1°C and dried in the ordinary atmosphere.

The plates were processed by the temperature method with amidol developer (pH=7.2) the emulsions were imprignated by a 2% glycerine solution after washing. The time of each stage in the course of the processing was the same as that[22] given to the Ilford C2 nuclear plates. However, 2 hours were adopted for the presoaking stage to remove the loaded beryllium in the emulsion which had a bad influence on the processing. The shrinkage factor of the loaded emulsions (~15 mg/cc of Be) was measured as 2.09±0.05 whereas that of the unloaded ones was 2.19±0.04.

Since pH of the loading solution was low, it is feared that the sensitivity decrease and the faster fading of the loaded emulsions may occur. By the grain counting of the tracks both in the loaded and unloaded plates irradiated by fast neutrons and alpha-particles from polonium, it was found that the loaded emulsions processed by the developer (pH=7.2) were as sensitive as the unloaded ones processed by the developer whose pH was adjusted to about 6.3. Therefore in the actual processing, pH of the developer was chosen as 7.2 for the loaded emulsions and 6.3 for the unloaded ones. The fading factors were measured for both plates and plotted in Fig. 9 against the time after irradiation. They were obtained for the alpha-particle tracks on the emulsion surfaces by counting the grain density. Since the irradiation time of the plates was less than an hour and the processing was done immediately after the irradiation in the present experiment, the effects of the fading would be negligible.

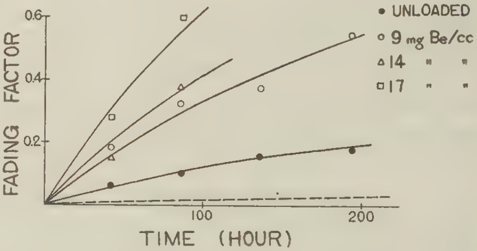

Fig. 9. Surface fading factor of the unloaded and beryllium loaded NR-M1 nuclear emulsions. The broken line shows the internal fading predicted for the unloaded emulsion.

The content of beryllium loaded in the emulsion was determined by the usual gravimetric analysis. The known quantity of the loaded emulsion was put into perchloric acid solution and warmed for an hour on water bath. After adding NH_4OH until pH of the solution came to about 9 the precipitate produced was filtered. Then the precipitate was dissolved in HCl solution and again NH_4OH was poured up to pH$\approx$9. The re-precipitated $Be(OH)_2$ was washed with hot water and changed to BeO by ignition in a porcelain crucible. The weight of BeO thus obtained was measured, from which the beryllium content could be determined within the error of about 5%. The contents of beryllium were 19.8 mg/cc and 13.5 mg/cc for the emulsions of 90 μ and 170 μ in thickness respectively.

Appendix II. Preparations of the Boron Loaded Nuclear Emulsions

The 5% solution of ammonium borate whose pH was 7.5 was used in the loading. The NR-M1 plates were soaked in the solution for two hours at 15±1°C.

The method of ordinary temperature processing was adopted in this case but the fixing was somewhat difficult. No significant difference of the sensitivlty was found between the loaded and unloaded plates. The shrinkage factor was about 1.8.

To obtain the content of boron in the emulsions the activation analysis method was chosen, since the chemical analysis was rather difficult. As shown in Fig. 10, a 50 mg Ra-Be neutron source was sunk in a paraffin block of 20 cm in diameter and 31 cm in height. The silver and indium foils of various thicknesses with and without cadmium covers were placed in a hole of the paraffin block and irradiated by thermal neutrons.

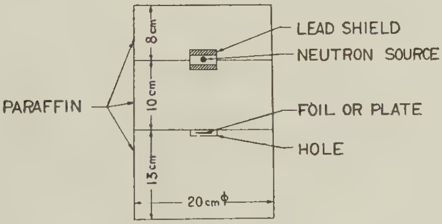

Fig. 10. Irradiation by thermal neutrons.

The induced activities of the foils by the reactions of $Ag^{107}(n, \gamma)Ag^{108}$ and $In^{115}(n, \gamma)In^{116}$ were measured by an end-window G-M counter. From the curve of foil thickness *vs* specific activity the propor thickness of the foil† necessary to obtain the total hot atoms in the sample was known.

If the foil is irradiated in the time interval 0 to t_0 by the constant flux of thermal neutrons and the induced activity is measured from time t_1 to t_2 after the end of the irradiation, the flux ϕ at the hole of the paraffin is derived by the following expression:

$$\phi = \frac{\lambda C \rho G}{N_0 \sigma_0 w_0 (1-e^{-\lambda t_0})(e^{-\lambda t_1}-e^{-\lambda t_2})} ,$$

where

λ : decay constant,
C : net count of the foil of proper thickness,
ρ : density of the foil,
G : factor involving the geometrical conditions and the effects of the absorption and the scattering of β-rays,
N_0: number of Ag^{107} or In^{115} atoms in unit volume of the foil,
σ_0 : activation cross section by thermal neutrons,
w_0 : weight of the foil of proper thickness for absolute β-counting.

The data in the flux measurements are shown in Table II. The neutron flux was estimated to be $\phi=(3.21\pm0.30)\times10^2$ neutrons/cm²·sec as a mean of the results for silver and indium.

Table II. Data of the neutron flux measurements.

Sample	Silver	Indium
t_0 (min)	5	30
t_1 (min)	0.5	2
t_2 (min)	5	30
λ (min^{-1})	0.295	0.01285
σ_0 (b)	44 ± 9[23]	145 ± 15[23]
C	369 ±4%	3650 ±2%
G	4.72 ±3%*	4.70 ±4%*
w_0 (mg)	337**	170**
ϕ (cm^{-2}·sec^{-1})	$(3.44\pm0.72)\times10^2$	$(2.97\pm0.33)\times10^2$

* The G-M counter used is the same as that used in the experiment by Yasumi[24].

** These values were not equal to the exact weights of the foils of proper thickness but were rather approximate ones, since the foils of exact weight were hardly preparable. The corrections were introduced to the results.

Secondly the boron loaded nuclear plates with and without cadmium covers were placed for 30 minutes in the hole and the short tracks attributed to $B^{10}(n, \alpha)Li^7$ reaction were counted. The number of boron atoms in the emulsion was derived by an equation as:

$$0.188 N\sigma\phi t = \nu ,$$

where N and ν are the number of boron atoms and the tracks in unit volume of the emulsion respectively and 0.188 is the abundance ratio of B^{10}. t is the exposure time and σ is the (n, α) cross section of B^{10} which is taken as 4010±22 b[23]. Referring to the obtained value of ϕ the boron content in the 170 μ emulsion was found to be 27.6±3.1 mg/cc.

---

† The proper thickness is meant as the thickness of the foil which has the same specific activity as that of zero thickness.

Appendix III. Range-Energy Relations of the NR-Ml Nuclear Emulsions for Alpha-Particles and Tritons

The range-energy relations of the NR-Ml emulsions for protons up to the energy of 14 Mev were measured by Nonaka *et al.*[25], but the relations for alpha-particles and tritons have not been given. In the present experiment they were determined as follows.

By measuring the range of alpha-particles from a polonium source attached to the surfaces of the unloaded and beryllium loaded NR-Ml plates, the mean ranges of 22.4 μ and 21.6 μ respectively were obtained from their range histograms. Since the range for the Ilford C2 emulsion is given as 22.2 μ[26][†], its standard range-energy relations for alpha-particles up to about 10 Mev were found to be also available for the NR-Ml unloaded emulsion and even for the loaded ones.[††] This is supported by the measurements of the recorded tracks when the source was placed 0.5 cm apart from the surfaces of the emulsions. The observed range-position relations were the same as those expected from the range-energy curve for the C2 emulsion.

As for tritons, the equation[27]:

$$E = \text{const} \cdot M^{1-n} R^{n}$$

was applied, where E, M and R are the energy, the mass and the corresponding range of a charged particle respectively and n is a constant characteristic of the emulsion. The equation holds for protons, deuterons and tritons. Since the NR-Ml emulsion does not differ greatly from other emulsions, n is assumed to be 0.575 in the energy range from 4 to 10 Mev when M is given in terms of the proton mass, R in microns and E in Mev. Then the range-energy relations for tritons could be obtained in the same energy region from the curve for protons measured by Nonaka[25].

Additional data were given by the slightly lithium loaded emulsion[†††] irradiated by thermal neutrons. The tracks due to $Li^6(n, t)\alpha$ reaction were measured and the range of 33.2 μ was obtained for the 2.73 Mev triton. Therefore, the whole range-energy relations for tritons up to 10 Mev could be obtained by extrapolating smoothly the above-mentioned curve so as to pass through the observed point at 2.73 Mev.

The range-energy relations for the three particles in the NR-Ml emulsions are shown in Fig. 11.

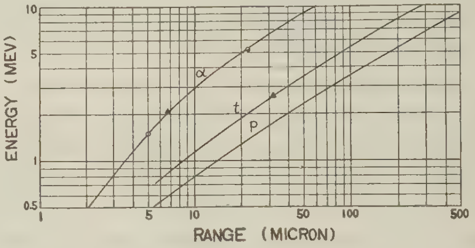

Fig. 11. Range-energy relations for protons, tritons and alpha-particles in the NR-Ml nuclear emulsion.

●: measurement by Po-α,
▲: measurement by $Li^6(n, \alpha)t$,
○: measurement by $B^{10}(n, \alpha)$

[†] The range obtained in the present experiment was 22.1 μ.

[††] It was shown that the same range-energy relations could be applicable to the boron loaded emulsions by observing the range of the alpha-particles from the reaction $B^{10}(n, \alpha)Li^7$.

[†††] A 2% solution of lithium acetate was used in the loading.

References

1) H. L. Taylor, O. Lönsjö and T. W. Bonner: Phys. Rev. **100** (1955) 174.
2) N. N. Flerov and V. M. Talyzin: Atomic Energy (U.S.S.R.) (English Translation) **4** (1956) 617.
3) L. Losen and L. Stewart: Phys. Rev. **107** (1957) 824.
4) M. H. MacGregor, W. P. Ball and R. Booth: Phys. Rev. **108** (1957) 726.
5) J. D. Anderson, C. C. Gardner, J. W. McClure, M. P. Nakada and C. Wong: Phys. Rev. **111** (1958) 572.
6) S. A. Heiberg: Phys. Rev. **96** (1954) 856 (A).
7) A. H. Armstrong and G. M. Frye, Jr.: Phys. Rev. **103** (1956) 335.
8) H. V. Argo, R. F. Taschek, H. M. Agnew, A. Hemmendinger and W. T. Lenard: Phys. Rev. **87** (1952) 612.
9) J. M. Fowler, S. S. Hanna and G. E. Owen: Phys. Rev. **98** (1955) 249 (A).
10) G. J. Fischer: Phys. Rev. **108** (1957) 99.
11) R. Wagner and P. Huber: Helv. Phys. Acta **31** (1958) 89.
12) E. Remy and K. Winter: Nuovo Cimento **9** (1958) 664.
13) V. J. Ashby, H. C. Catron, L. L. Newkirk and C. J. Taylor: Phys. Rev. **111** (1958) 616.

14) M. Sachs: Phys. Rev. **103** (1956) 671.
15) W. F. Hornyak and T. Lauritsen: Phys. Rev. **77** (1950) 160.
16) W. E. Burchum and J. M. Freeman: Phil. Mag. **41** (1950) 921.
17) E. K. Inall: Phil. Mag. **45** (1954) 768.
18) S. S. Hanna, E. C. LaVier and C. M. Class: Phys. Rev. **95** (1954) 110.
19) D. StP. Bunbury: Phys. Rev. **90** (1953) 1121.
20) G. M. Frye, Jr. and J. H. Gammel: Phys. Rev. **103** (1956) 328.
21) F. L. Ribe and J. D. Seagrave: Phys. Rev. **94** (1954) 934.
22) E. Segre: *Experimental Nuclear Physics*, vol. 1, (John Wiley, New York, 1953) 70.
23) D. H. Hughes and J. A. Harvey: *Neutron Cross Sections* (McGraw-Hill, New York, 1955).
24) S. Yasumi: J. Phys. Soc. Japan **12** (1957) 443.
25) I. Nonaka, S. Morita, N. Kawai, T. Ishimatsu, K. Takeshita, Y. Nakajima and N. Takeno: J. Phys. Soc. Japan **11** (1956) 1.
26) J. Rotblat: Nature **167** (1951) 550.
27) A. Beiser: Rev. Mod. Phys. **24** (1952) 273.

JOURNAL OF THE PHYSICAL SOCIETY OF JAPAN, Vol. 14, No. 5, MAY, 1959

Cell Theory of Classical Liquids. Phase Transition between Gas, Liquid and Solid. Part III. Yvon's Method and its Generalization

By Tohru MORITA

Physics Department, Tokyo Institute of Technology

(Received January 26, 1959)

The Method, proposed by Yvon, to start with the cluster expansion formulae and to classify the contributions of the clusters according to the form of the figure showing the coordinates of particles in the summand is fully developed for uniform and non-uniform lattice systems and compared with the cluster variation method. The cell theory of liquids is investigated from the standpoint of this method. It is shown that the cell-pair approximation developed in Parts I and II from the standpoint of the cluster variation method is shown to be identical to the approximation in which the figures that are contained in a cell or a pair of cells are taken into account correctly and the others are neglected, again in our present standpoint.

§ 1. Introduction

As shown in a seperate paper1) by the author and used in Part II2), continuous systems—fluids and solids—may be considered to be equivalent to lattice systems of infinitesimal lattice constant. Therefore, to investigate the phase transition of continuous system, we may take the procedure, first to construct a method for lattice systems and then to apply it to the lattice system of infinitesimal lattice constant. This procedure will be taken in this part. So that, our main interest in this part is to find a method for a lattice system, applicable to a lattice system of infinitesimal lattice constant. The investigation will be made about the cluster expansion method for a lattice system.

Let us consider a lattice system, of L lattice sites of a regular lattice, composed of N identical particles: the density is $\rho=N/L$. The potential energy of the system is assumed to be of the form:

$$\sum_{N\geq i>j\geq 1} V^{(2)}(R_i, R_j)\ , \qquad (R_i, R_j=1, \cdots, L)\ . \tag{1}$$

The cluster expansion formula of the free energy A of this system is:3),1)

$$\frac{A}{kT}=L\rho \ln \frac{\rho}{e}-\sum_{n=2}^{\infty} \frac{\rho^n}{n!} \sum_{R_1=1}^{L} \cdots \sum_{R_n=1}^{L} \sum_{n\geq i>j\geq 1}^{(A)} \Pi F_{ij} \tag{2}$$

with

$$F_{ij}=\exp[-V^{(2)}(R_i, R_j)/kT]-1\,, \qquad (3)$$

where (A) on $\sum^{(A)}$ implies the specification by Mayer[4] that the sum is to be taken over all products which are more than singly connected.

When we start with the continuous counterpart of this expansion formula for the case of continuous system, the following two kinds of approximation are usually adopted. Namely, we take account either of first few terms of small n, entirely neglecting the terms of large n, or of the terms which can be evaluated by means of the Fourier transformation, neglecting the other terms, namely considering the terms of ring[5], of watermelon[6], of netted rings[7] or of hyper-netted chains or rings[8]. It is obvious that the former method will not be available for fluids of not small density. When the latter method is used, it generally leads to a divergence of sum at a density. The theory of radial distribution function by Born, Green and Rodriguez[9] suggests that the results at the densities higher than the density of divergence may be obtained from this expansion by continuing the function analytically to that region. However, if we apply the latter method to the one-dimensional Ising system, for which the rigorous solution is known, there appears a point of divergence and no reasonable results at higher densities than this point can be obtained by the analytical continuation[10]. Therefore, the latter method seems to be valid only for fluids of not too high density. Furthermore, these methods do not give the rigorous result even for a lattice system in which the interaction of particles is such as only to exclude two or more particles to be at the same lattice site[10].

On the contrary, quite a different method of collecting the contributions is presented for a lattice system. That is, Yvon[11] has proposed to group the contributions by the number or the type of the figures of the lattice sites occupied by particles in the summand, and has shown that the consideration only of the pairs of lattice sites leads to the Bethe approximation. Then, for the case of binary mixtures of occupation probabilities ρ near 1/2, he considered the figures of square up to the first order of $\rho-1/2$. Rushbrooke and Scoins[12] starting with the similar standpoint as Yvon, have shown that clusters of lattice sites which contribute to the sum are those of point, bond and closed polygons and presented a systematic method of calculating the sum, for the case of Ising system. In this method, the approximation of point gives the rigorous results for the case of the potential such as only to exclude two or more particles to exist at the same lattice site. The approximation of bond leads to the Bethe approximation, which gives the rigorous results for one-dimensional Ising system, and the calculations in the higher approximations can comparatively easily be performed.

From the results obtained when applied to the one-dimensional Ising system, we expect that the method by Yvon, Rushbrooke and Scoins is superior to the methods developed especially for a continuous system, for fluids of not small density. The reason why the former could give a reasonable results in the region of high densities where the latter could not, will be due to the fact that the correlations of short range could be considered sufficiently in the former method. Therefore, we expect that we can obtain an approximation method applicable to fluids of high densities or solids if we take into account the short range correlations in a similar way. In this paper, we develop the method of Yvon. Rushbrooke and Scoins from the standpoint of the Ursell expansion for both uniform and non-uniform systems and compare it with the cluster variation method developed by Kikuchi et al.[13], in § 2, and then apply it in the "cell and cell pair approximation" to classical liquids in § 3. The results obtained in the cell and cell pair approximation in this formalism are shown to be identical to those developed in Parts I and II from the standpoint of the cluster variation method.

§ 2. Expansion of the Free Energy by Means of "Clusters of Lattice Sites"

We present here the method of Yvon, Rushbrooke and Scoins for a uniform lattice system in a compact form, and then generalize it to the case of non-uniform systems.

2a. *Uniform lattice system*

For the present, we consider a uniform lattice system of L lattice sites composed of $N=L\rho$ particles. The cluster expansion formula of the free energy A of this system is given by (2). The sums over lattice sites in the right hand side of (2) can be decomposed into sums over the clusters of lattice sites occupied by particles as

$$A=\sum_{m=1}^{L}\sum_{L\geq i_m>\cdots>i_2>i_1\geq 1}\sum\sum B(i_1,\cdots,i_m) \tag{4}$$

with

$$\frac{B(i)}{kT}=\rho\ln\frac{\rho}{e}-\sum_{n=2}^{\infty}\frac{\rho^n}{n!}\sum_{n\geq i>j\geq 1}^{(B)}\Pi F_{ij} \tag{5}$$

and

$$\frac{B(i_1,\cdots,i_m)}{kT}=-\sum_{n=m}^{\infty}\frac{\rho^n}{n!}\sum_{R_1=i_1}^{i_m}\cdots\sum_{R_n=i_1}^{i_m}\sum_{n\geq i>j\geq 1}^{(B)}\Pi F_{ij} \tag{6}$$

for $m\geqq 2$, where (B) on $\Sigma^{(B)}$ implies that the sum is to be taken over all products which are more than singly connected and for which every site of $(i_1,\cdots,i_m)$ is occupied by at least one particle.

(5) and (6) with (4) suggest us to define $A(i_1,\cdots,i_m)$ by*

$$A(i)=B(i) \tag{7'}$$

$$A(i,j)=B(i)+B(j)+B(i,j) \tag{7''}$$

$$A(i,j,k)=B(i)+B(j)+B(k)+B(i,j)+B(i,k)+B(j,k)+B(i,j,k) \tag{7'''}$$

. . . .

$$A(1,\cdots,L)=\sum B(i)+\sum_{L\geq i>j\geq 1}^{L}B(i,j)+\sum B(i,j,k)+\cdots+B(1,\cdots,L)\,. \tag{7^L}$$

From the comparison of (4) and (7^L) we see that $A(1,\cdots,L)=A$, and further that $A(i,\cdots,i_m)$ is the free energy per system of the ensemble of M ($M\rightarrow\infty$) replicas of system $(i_1,\cdots,i_m)$;** the potential energy between two particles in different replicas is assumed to be zero.

$A(1,\cdots,m)$ can then be calculated by obtaining the grand partition function per replica by

$$\Xi(1,\cdots,m)=\sum_{N=0}^{\infty}z_{1,\ldots,m}^{N}\sum_{R_1=1}^{m}\cdots\sum_{R_N=1}^{m}\exp\left[-\sum_{N\geq i>j\geq 1}V^{(2)}(R_i,R_j)/kT\right] \tag{8}$$

and determining the value of the fugacity $z_{1,\ldots,m}$ by

$$m\rho=\frac{\partial\ln\Xi(1,\cdots,m)}{\partial\ln z_{1,\ldots,m}}\,, \tag{9}$$

as

$$\frac{A(1,\cdots,m)}{kT}=m\rho\ln z_{1,\ldots,m}-\ln\Xi(1,\cdots,m)\,. \tag{10}$$

When the potential energy has a core: $V^{(2)}(R,R)=\infty$, then the sum in (8) becomes a finite power series of $z_{1,\ldots,m}$: the terms retained are those of $N\leq m$ and (9) may be solved explicitly. For instance, for the case of $V^{(2)}(R,R)=\infty$, for $m=1$

$$\Xi(1)=1+z_1\,,\qquad \rho=\frac{z_1}{1+z_1}\,,\qquad z_1=\frac{\rho}{1-\rho}\,,$$

---

* Note that we could start with the definition of $A(i_1,\cdots,i_m)$ as the free energy per system of M replicas of $(i_1,\cdots,i_m)$ and this Ursell expansion of $A(i_1,\cdots,i_m)$ defining $B(i_1,\cdots,i_m)$ as the correlations. When we have adopted this starting point, we would not need to use the cluster expansion formula (2) which is divergent for condensed phases when seen to be the expansion in powers of ρ.

** For large m, we may say that $A(i_1,\cdots,i_m)$ is the free energy of the system $(i_1,\cdots,i_m)$ when the number of particles in the system is $m\rho$, but for small m we may not say so.

thence

$$\frac{A(1)}{kT}=\rho\ln\rho+(1-\rho)\ln(1-\rho)\,, \tag{11}$$

and for $m=2$,

$$\Xi(1,2)=1+2z_{12}+z_{12}^2\exp[-\phi(a)/kT]\,,$$

$$2\rho=\frac{2z_{12}+2z_{12}^2\exp[-\phi(a)/kT]}{1+2z_{12}+z_{12}\exp[-\phi(a)/kT]}\,,$$

$$z_{12}=\frac{2\rho}{1-2\rho+\beta}\,,\qquad \beta\equiv\sqrt{1+4\rho(1-\rho)\{\exp[-\phi(a)/kT]-1\}}\,,$$

thence

$$\frac{A(1,2)}{kT}=\rho\frac{\phi(a)}{kT}+\rho\ln\frac{(\beta-1+2\rho)\rho}{kT}+(1-\rho)\ln\frac{(\beta+1-2\rho)(1-\rho)}{1+\beta}\,, \tag{12}$$

where $\phi(a)=V^{(2)}(1,2)$.

For the Ising system:

$$V^{(2)}(i,j)=\begin{cases}\infty & |i-j|=0\\ \phi(a) & |i-j|=a\\ 0 & |i-j|>a\,,\end{cases} \tag{13}$$

a denoting the distance of the nearest neighbor lattice sites; if we use the approximation only to consider up to $B(i,j)$ neglecting the higher terms in Eq. (7^L), then we get as an approximation for the free energy

$$\frac{A}{LkT}=\frac{c}{2}\rho\frac{\phi(a)}{kT}+\rho\ln\rho+(1-\rho)\ln(1-\rho)+\frac{c}{2}\left\{\rho\ln\frac{\beta-1+2\rho}{(1+\beta)\rho}+(1-\rho)\ln\frac{\beta+1-2\rho}{(1+\beta)(1-\rho)}\right\} \tag{14}$$

by the help of (7′) and (7″) with (11) and (12). This is just the result of the Bethe approximation$^{14)}$. Here, c is the coordination number of the lattice. In an analogous way, we will be able to proceed to the higher order terms. In that case is useful the theorem of Rushbrook and Scoins that $B(i_1,\cdots,i_m)$ for $m>2$ is zero except when the figure of $i_1,\cdots,i_m$ with bonds drawn between pair i_j and i_k for which $V^{(2)}(i_j,i_k)\neq 0$, is more than singly connected. If we want to estimate the error of the approximation for high temperature region, the theorem teaches that the contribution of the figures neglected in the Bethe approximation is $0(-\phi(a)/kT)^4$ or $0(-\phi(a)/kT)^3$ according as the smallest closed polygon neglected is □ or △; as $F_{ij}\sim-\phi(a)/kT$ for $|i-j|=a$.

2b. *Non-uniform lattice system*

Since we are to consider the system in the solid state where the one particle distribution function is not constant in the system as well as the system in the fluid states, we have to use the expansion formula of the free energy in terms of the one particle distribution function$^{1),15)}$:

$$\frac{A}{kT}=\sum_{R=1}^{L}\rho(R)\ln\frac{\rho(R)}{e}-\sum_{n=1}^{\infty}\frac{1}{n!}\sum_{R_1=1}^{L}\cdots\sum_{R_n=1}^{L}\rho(R_1)\cdots\rho(R_n)\sum^{(A)}\prod_{n\geq i>j\geq 1}F_{ij}\,. \tag{15}$$

This snm can be decomposed as (4) with

$$\frac{B(i)}{kT}=\rho(i)\ln\frac{\rho(i)}{e}-\sum_{n=2}^{\infty}\frac{1}{n!}\rho(i)^n\sum^{(B)}\prod_{n\geq i>j\geq 1}F_{ij} \tag{16}$$

and

$$\frac{B(i_1,\cdots,i_m)}{kT}=-\sum_{n=m}^{\infty}\frac{1}{n!}\sum_{R_1=i_1}^{i_m}\cdots\sum_{R_n=i_1}^{i_m}\rho(R_1)\cdots\rho(R_n)\sum^{(B)}\prod_{n\geq i>j\geq 1}F_{ij} \tag{17}$$

for $m \geqq 2$.

Again, we define $A(i_1, \cdots, i_m)$ by (7')–(7^L) in terms of $B(i_1, \cdots, i_n)$ given by (16) and (17). Then, $A(1, \cdots, L) = A$, and $A(i_1, \cdots, i_m)$ is the free energy per system of the ensemble of M $(M \to \infty)$ replicas of system $(i_1, \cdots, i_m)$ under the restriction that the one particle distribution function is the one prescribed: $\rho(R_i)$; the potential energy between two particles in different replicas is assumed to be zero.

$A(1, \cdots, m)$ can be calculated by using the relations

$$\Xi(1, \cdots, m) = \sum_{N_1=0}^{\infty} \cdots \sum_{N_m=0}^{\infty} z_{1,\ldots,m}(1)^{N_1} \cdots z_{1,\ldots,m}(m)^{N_m} \exp[-\Phi(N_1, \cdots, N_m)/kT] , \tag{18}$$

$$\rho(i) = \frac{\partial \ln \Xi(1, \cdots, m)}{\partial \ln z_{1,\ldots,m}(i)} \tag{19}$$

and

$$\frac{A(1, \cdots, m)}{kT} = \sum_{i=1}^{m} \rho(i) \ln z_{1,\ldots,m}(i) - \ln \Xi(1, \cdots, m) , \tag{20}$$

where $\Phi(N_1, \cdots, N_m)$ denotes the potential energy of the system when $N_1, N_2, \cdots, N_m$ particles are on the lattice site $1, 2, \cdots, m$, respectively, i.e.

$$\Phi(N_1, N_2, \cdots, N_m) = \sum_{m \geq i > j \geq 1} N_i N_j V^{(2)}(i, j) + \sum_{i=1}^{m} \frac{N_i(N_i-1)}{2} V^{(2)}(i, i) . \tag{21}$$

Here we have had to introduce the fugacity $z_{1,\ldots,m}(i)$ for each lattice site i, because the density $\rho(i)$ is prescribed for each lattice site separately.

For instance, we can calculate $B(1, 2)$ for the case when $V^{(2)}(i, i) = \infty$ as follows:

$$\Xi(1, 2) = 1 + z_{12}(1) + z_{12}(2) + z_{12}(1) z_{12}(2) u , \qquad u \equiv \exp[-V^{(2)}(1, 2)/kT] ;$$

$$\rho(1) = \frac{z_{12}(1) + z_{12}(1) z_{12}(2) u}{1 + z_{12}(1) + z_{12}(2) + z_{12}(1) z_{12}(2) u} ,$$

$$\rho(2) = \frac{z_{12}(2) + z_{12}(1) z_{12}(2) u}{1 + z_{12}(1) + z_{12}(2) + z_{12}(1) z_{12}(2) u} ,$$

$$z_{12}(1) = \frac{1}{2(1-\rho(1))u} [-1 + \rho(1) + \rho(2) - (\rho(2) - \rho(1))u + \beta] ,$$

$$z_{12}(2) = \frac{1}{2(1-\rho(2))u} [-1 + \rho(1) + \rho(2) + (\rho(2) - \rho(1))u + \beta] ,$$

$$\beta \equiv \sqrt{(1-\rho(1)-\rho(2))^2 + 2\rho(1)(1-\rho(1))u + 2\rho(2)(1-\rho(2)) + (\rho(2)-\rho(1))^2 u^2} .$$

Thence, we have

$$\begin{aligned} \frac{B(1, 2)}{kT} &= \frac{A(1, 2)}{kT} - \frac{A(1)}{kT} - \frac{A(2)}{kT} \\ &= -(1-\rho(1)-\rho(2)) \ln \frac{1}{2u} [-1 + \rho(1) + \rho(2) + (2-\rho(1)-\rho(2))u + \beta] \\ &\quad - \rho(1) \ln \frac{1}{2} [1 + (\rho(1)-\rho(2))(1-u) + \beta] \\ &\quad - \rho(2) \ln \frac{1}{2} [1 + (\rho(2)-\rho(1))(1-u) + \beta] . \end{aligned} \tag{22}$$

$A(1, \cdots, m)/kT$ can be evaluated also by the variational principle (cf. Ref. 16):

$$A(1, \cdots, m) = \text{Min}\, \mathscr{A}(1, \cdots, m) , \tag{23}$$

$$\frac{\mathscr{A}(1, \cdots, m)}{kT} = \sum_{N_1=0}^{\infty} \cdots \sum_{N_m=0}^{\infty} \rho^{[m]}(N_1, \cdots, N_m) \left\{ \frac{\Phi(N_1, \cdots, N_m)}{kT} + \ln \rho^{[m]}(N_1, \cdots, N_m) \right\} ; \tag{24}$$

the minimum is to be taken by the variation with respect to $\rho^{[m]}(N_1, \cdots, N_m)$ under the restriction that

$$\rho(i) = \sum_{N_1=0}^{\infty} \cdots \sum_{N_m=0}^{\infty} N_i \rho^{[m]}(N_1, \cdots, N_m) \,. \tag{25}$$

The calculation of $A(1, \cdots, m)$ by this variational principle is more powerful for large m than that by the grand partition function, if we are to be satisfied with the approximate evaluation.

The standpoint to cut the series (7^L) at a point and to calculate $A(i_1, \cdots, i_m)$ by the variational methods (23)–(25), can be formulated in the form of the Ursell expansion as we define $\mathscr{B}(i_1, \cdots, i_m)$ by

$$\mathscr{A}(i) = \mathscr{B}(i) \tag{26$'$}$$

$$\mathscr{A}(i, j) = \mathscr{B}(i) + \mathscr{B}(j) + \mathscr{B}(i, j) \tag{26$''$}$$

$$\mathscr{A}(i, j, k) = \mathscr{B}(i) + \mathscr{B}(j) + \mathscr{B}(k) + \mathscr{B}(i, j) + \mathscr{B}(i, k) + \mathscr{B}(i, k) + \mathscr{B}(i, j, k) \tag{26$'''$}$$

$$\cdots\cdots\cdots\cdots$$

$$\mathscr{A}(1, \cdots, L) = \sum_{i=1}^{L} \mathscr{B}(i) + \sum_{L \geq i > j \geq 1} \mathscr{B}(i, j) + \sum \mathscr{B}(i, j, k) + \cdots + \mathscr{B}(1, \cdots, L) \tag{26^L}$$

and consider only $\mathscr{B}(i_1, \cdots, i_m)$ with suitable figure of $(i_1, \cdots, i_m)$ dropping the other $\mathscr{B}(i_1, \cdots, i_m)$ and take the variation with respect to $\rho_{i_1, \ldots, i_m}^{[m]}(N_1, \cdots, N_m)$ under the restriction of (26).

Following the terminology used in the development of the cluster variation method by the author[16)], we call cluster of lattice sites $(i_1, \cdots, i_m)$ a preserved cluster if we retain $\mathscr{B}(i_1, \cdots, i_m)$ and a net-preserved cluster if we neglect $\mathscr{B}(i_1, \cdots, i_m)$. Then the approximation is decided by which clusters of lattice sites are to be preserved.

In this method the variations by $\rho^{[2]}, \cdots, \rho^{[m]}, \cdots$ are independent, while they are dependent on each other in the case of the cluster variation method[13),16),17)]. It is to be noted here that this is the only difference of these two methods. For the case in which the potential energy is such that $\Phi(N_1, \cdots, N_m) = \infty$ if one of N_i's is equal to or larger than two, the approximations to preserve the terms of $\mathscr{B}(i)$ and $\mathscr{B}(i, j)$ are identical for both method; leading to the Bethe approximation. When the terms of larger cluster of lattice sites are preserved, the cluster variation method is expected to give better results. However, the calculations will be far easier for our method developed in this section.

§3. Cell and Cell Pair Approximation

As in Parts I and II, we introduce the cell and cell pair approximation where clusters of lattice sites are preserved if and only if they are conceived in a cell or a pair of neighboring cells.

Let us divide L lattice sites into C cells, each with $s = L/C$ lattice sites, and denote μth lattice site of the ith cell by $i\mu$. Then, in the cell and cell pair approximation (7) is collected into

$$A(\text{cell}: i) = B(\text{cell}: i) \tag{27$'$}$$

$$A(\text{cells}: i, j) = B(\text{cell}: i) + B(\text{cell}: j) + B(\text{cells}: i, j) \tag{27$''$}$$

$$A = A(\text{cells}: 1, \cdots, C) = \sum_{i=1}^{C} B(\text{cell}: i) + \sum_{C \geq i > j \geq 1} B(\text{cells}: i, j) \tag{27^C}$$

where

$$A(\text{cell}: i) = A(i_1, \cdots, i_s) \,, \tag{28$'$}$$

$$A(\text{cells}: i, j) = A(i_1, \cdots, i_s, j_1, \cdots, j_s) \,, \tag{28$''$}$$

etc. Then, $A(\text{cells}: i_1, \cdots, i_m)$ is the free energy per system of the ensemble of M ($M \to \infty$) replicas of the system composed of the set of cells $(i_1, \cdots, i_m)$. With this interpretation, (27) can be taken also as the formulae for the case of a continuous system.

If the calculation of (27) is performed by the variational method analogous to (23) and if the size of a cell is such as not to contain two particles at a time, then the calculation becomes identical to that undertaken in Parts I and II.

As the result, the cell and cell pair approximation developed from the standpoint of the cluster variation method has been found to be an approximation which takes into account those parts of the factors $\Pi_{n\geq i>j\geq 1}F_{ij}$ correctly that the coordinates i and j are all conceived in a cell and a pair of neighboring cells and neglects the other parts. The reason why we could obtained the phase transition between solid and fluids seems to rest on the fact that we could consider the short range correlation for all clusters, may it be however large. From the standpoint in this paper, we can improve the approximation by taking into account also the long range parts of small clusters—2nd virial, rings, etc.—correctly besides short range parts of large clusters: In this way the approximation will be improved at low density region.

We will now conclude this section with a comment on the terms neglected. If the cell is of the size not to allow two of more particles to come in a cell at a time, the theorem by Rushbrooke and Scoins or its generalization teaches us that the clusters of lattice sites or space coordinates neglected are those which are over three or more cells, between which potential energies are not negligible, and on the other hand if we look at these terms from the standpoint of the cluster variation method, the neglect of these terms is allowed when the superposition approximation or its generalization is acceptable between particles in these cells.

§ 4. Conclusion

We have formulated the method of Yvon, Rushbrooke and Scoins to classify the contributions to the free energy according to the clusters of lattice sites schematically, generalized it to non-uniform systems and related with the cluster variation method. The cell and cell pair approximation in our method was shown to be identical to that in the cluster variation method: the practical calculations were performed by the author in Parts I and II. The analysis of this paper allows us to consider the approximation in the calculations in Parts I and II from another somewhat more clear standpoint of the cluster expansion method.

From our analysis in this paper, I believe that the essential parts of the contributions in the cluster expansion formula of the free energy responsible for solid and liquid phases and their phase transitions have been considered in our cell theory. Further improvements in the calculations will be discussed in the following papers in this series.

Acknowledgement

I would like to express my cordial thanks to Prof. J. Yvon for his kind disposal which made me acquainted with his theory in Ref. 11. My thanks are also due to Dr. K. Hiroike for his helpful discussions.

References

1) T. Morita: to be published in Progr. Theor. Phys. **21** (1959) 501.
2) T. Morita: J. Phys. Soc. Japan **12** (1957) 1195; of which Parts I and II are referred to as Parts I and II.
3) K. Fuchs: Proc. Roy. Soc. **A, 179** (1942) 340.
4) J. E. Mayer and M. G. Mayer: *Statistical Mechanics* (J. Wiley, New York, 1940) chap. 13.
5) E. W. Montroll and J. E. Mayer: J. Chem. Phys. **9** (1941) 626.
6) R. Abe: J. Phys. Soc. Japan **14** (1959) 10.
7) K. Hiroike: J. Phys. Soc. Japan **13** (1958) 1497.
8) T. Morita: Progr. Theor. Phys. **20** (1958) 920.
9) H. S. Green: Proc. Roy. Soc. **A, 189** (1947) 103. A. E. Rodriguez: Proc. Roy. Soc. **A, 196** (1949) 73. H. S. Green: *The Molecular Theory of Fluids* (North-Holland Publishing Co., 1952) chap. 3, § 6.
10) T. Morita: D. Sc. thesis, Tokyo Institute of Technology, 1959 (unpublished).
11) J. Yvon: Cahiers de Physique **28** (1945) 1; **31-32** (1948) 12.
12) G. S. Rushbrooke and H. I. Scoins: Proc. Roy. Soc. **A, 230** (1955) 74.
13) R. Kikuchi: Phys. Rev. **81** (1951) 988. M. Kurata, R. Kikuchi and T. Watari: J. Chem. Phys. **21** (1953) 434.

14) For example, E. A. Guggenheim: *Mixtures* (Oxford, 1952), Eq. (4.10.8).
15) E. A. Arinstein: Dokl. Akad. Nauk SSSR **112** (1957) 615.
16) T. Morita: J. Phys. Soc. Japan **12** (1957) 753.
17) J. Hijmans and J. De Boer: Physica **21** (1955) 471.

JOURNAL OF THE PHYSICAL SOCIETY OF JAPAN, Vol. 14, No. 5, MAY, 1959

Cell Theory of Classical Liquids. Phase Transition between Gas, Liquid and Solid. Part IV. F. C. C. Lattice Gases

By Tohru MORITA

Physics Department, Tokyo Institute of Technology

(Received January 26, 1959)

The method developed in Part III is applied in the approximation of the "statues of 6 points" to the face-centered cubic lattice gases, of nearest neighbor lattice sites distance $a/2$, composed of particles with hard core of diameter somewhat smaller than a, with and without attractive part. The results obtained are that these lattice gases will exhibit the solid-gas phase transition, while the liquid phase will not appear for systems of particles either with or without attractive interactions. Qualitative discussions are given of the reason why the difference that our lattice gases will not become liquid and the real gas condenses to liquid, arises.

§ 1. Introduction

As models for the theoretical investigation of the phase transition of liquid, some efforts have been made to investigate lattice gases, which can be treated more easily[1)-3)]. Since the later investigations[2),3)] have been made for the two-dimensional lattice gases, their results seem to be not suitable to make comparisons with the data for three-dimensional ordinary liquid. As early as 1939, Lennard-Jones and Devonshire[1)] investigated the simple cubic lattice gas, assuming the potential energy between a pair of particles to be positive infinity and a finite positive value when two particles are on the same lattice site and on the nearest neighbor lattice sites respectively and zero thereafter. The system was shown to exhibit a solid-gas phase transition. In their theory, the solid state is characterized as the state where, when we divide the lattice sites into two sublattices (○ and ●) as in Fig. 1, the lattice sites of one of sublattices (e.g. ○) are more populated by particles than the others (●), and gaseous state corresponds to the state where all the lattice sites are equally populated: The one particle distribution function is periodic in the solid state and constant in the gaseous state, in accordance with our physical intuition discriminating solid and gas. This point of view of discriminating the solid from the fluids is adopted in this series of work, both for lattice and continuous systems. Since the liquid —the continuous system— is equivalent to a lattice system of infinitesimal lattice constant, the lattice system with a smaller lattice constant will behave more similarly to the con-

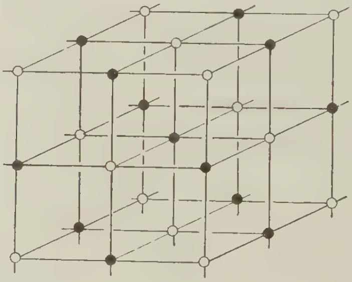

Fig. 1.

tinuous system. In this paper, we will improve the calculation by investigating the three-dimensional lattice gases, of lattice constant smaller than that in Ref. 1, composed of particles with hard core, with and without attractive part, respectively. Then, since these systems can be regarded as the continuous systems, of which the potential energy is determined by the distribution of the lattice sites, the volumes attached to which are occupied, independently of the detailed positions of particles in the volumes⁵⁾, our results can be compared with the phase transitions of ordinary liquids and we will reach some knowledges about what factors cause the phase transitions between gas, liquid and solid.

In § 2, we will apply the formalism of Part III⁴⁾ to our system in the approximation of the "statues of 6 points". In § 3, the detailed calculations will be made for lattice gases of hard spheres. In § 4, the calculations for lattice gases with both hard core and attractive part are given. In § 5, the results obtained will be compared with the phase transitions of ordinary gas, liquid and solid.

§ 2. Approximate Free Energy

The system to be considered in this part is such a lattice system that N identical particles are on $L=8C$ lattice sites, constituting a face-centerted cubic lattice of lattice constant $a/\sqrt{2}$ or nearest neighbor distance $a/2$, and the potential energy is given by

$$\sum_{N\geq i>j\geq 1} V^{(2)}(R_i, R_j) \tag{1}$$

where

$$V^{(2)}(R_i, R_j)=\phi(|R_i-R_j|)$$

$$\phi(r)\begin{cases} =\infty & r=a/2,\ \sqrt{2}\,a/2,\ \sqrt{3}\,a/2 \\ \leq 0 & r\geq a \\ =0 & r\rightarrow\infty; \end{cases} \tag{2}$$

the particle has a hard core of diameter $>\sqrt{3}\,a/2$, $<a$, and moreover we assume that $\phi(r)$ is smallest when $r=a$.* As the consequence, the system at 0°K becomes the crystal in which one of 8 f.c.c. sublattices** of lattice constant $\sqrt{2}\,a$ or nearest neighbor distance a is occupied by particles and others unoccupied. Thence, we may assume that the solid state is the state where one of sublattices is more populated than the others. In fact, we will proceed the discussions in the following taking such standpoint.

We can consider our system to be composed of the cells of Fig. 2 arranged in a f.c.c. lattice of lattice constant $\sqrt{2}$. Then, the lattice sites with $\nu=1, 2, \cdots, 8$ each in Fig. 2 constitutes a f.c.c. sublattice of lattice constant $\sqrt{2}\,a$. A sectional view is shown in Fig. 3.

In Parts I and II, we have considered the correlations of occupations in a cell and pairs of cells and used the generalized superposition approximation for the correlations be-

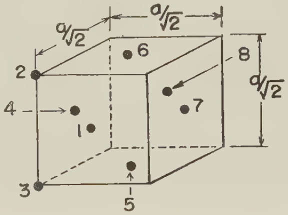

Fig. 2. A cell.

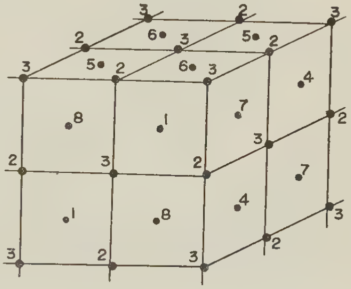

Fig. 3. A sectional view of our lattice. Lattice sites with $\nu=1, 2, \ldots, 8$ each constitutes a f.c.c. sublattice.

---

* In order to understand clearly the distribution of the lattice sites in our lattice, let us consider neighboring lattice sites as seen from a lattice site of $\nu=1$ in Fig. 3. It is as follows:

	distance	number	values of ν in Fig. 3
1st neighbor	$a/2$	12	$2\times(2, 3, 5, 6, 4, 7)$
2nd 〃	$\sqrt{2}\,a/2$	6	$6\times(8)$
3rd 〃	$\sqrt{3}\,a/2$	24	$4\times(2, 3, 5, 6, 4, 7)$
4th 〃	a	12	$12\times(1)$
5th 〃	$\sqrt{5}\,a/2$	24	$4\times(2, 3, 5, 6, 4, 7)$
6th 〃	$\sqrt{6}\,a/2$	8	$8\times(8)$
. . . . . .			

Here, for example, $2\times(2, 3, 5, 6, 4, 7)$ at the last column for the 1st neighbor denotes that 12 lattice sites of the 1st neighbor consist of 2 lattice sites each of $\nu=2$, 3, 5, 6, 4 and 7.

** Note that any regular lattice is composed of $8=2\times2\times2$ sublattices of the same lattice structure but with lattice constant twice of the original one.

tween three cells, even for clusters of lattice sites in a cell displaced, from the stand point of the cluster variation method. The approximation, if we see from the standpoint based on the cluster expansion method developed in Part III, seems to be imperfect in the respect that if a cluster of lattice sites is taken into account, then the clusters of the same form of figures should be taken account of in any stage of approximation. If physically seen, the standpoint of Parts I and II has not so much difficulties while it seems more statisfactory to take into account the clusters of lattice sites which have the same form, at the same time. With this consideration, we may make the calculations either by the formalism of the cluster variation method or by the formalism of the Part III. Here we will use the latter.

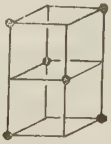

Fig. 4. A statue of 6 points.

Our approximation in the present article is to preserve the clusters of lattice sites inclusive in a "statue of 6 points" as shown in Fig. 4 or its rotated ones and those composed of two lattice sites and to neglect the others. In this approximation, we calculate the free energy and the equation of state of our lattice system, where the solid state will be assumed to be the state where one of the sublattices (e.g. taken to be 1) is the most populated and one (e.g. taken to be 8) is the worst populated and the others are equally populated, that is

$$\rho_1 \geqq \rho_2 = \rho_3 = \cdots = \rho_7 \geqq \rho_8; \tag{3}$$

ρ_ν, $\nu=1, \cdots, 8$, means the number density for each lattice site of the sublattice ν.

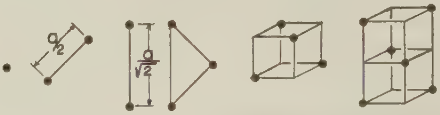

Fig. 5.

Here we are to write Eq. (III. 7^L)* retaining the contributions of the preserved clusters in our approximation. However it can easily be seen that the contributions from the clusters inclusive in the statues of 6 points can be collected to those from the clusters which are the intersections of two statues or the intersections of two intersections just obtained or of a intersection obtained and a statue$\cdots$: the total of which is shown in Fig. 5. Then, we introduce $B(i_1, \cdots, i_m)$ corresponding to these clusters of lattice sites by

$$A(i)=B(i)$$
$$A(i, j)=B(i)+B(j)+B(i, j)$$
$$A(i, j, k)=B(i)+B(j)+B(k)+B(i, j)+B(i, k)+B(j, k)+B(i, j, k)$$
$$A(i, j, k, l; \text{tetrahedron})=B(i)+B(j)+B(k)+B(l)+B(i, j)+B(i, k)+B(i, l)$$
$$+B(j, k)+B(j, l)+B(k, l)+B(i, j, k, l; \text{tetrahedron})$$

$A\Big($ 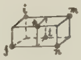 $\Big)$ $=B(i)+B(j)+B(k)+B(l)+B(m)+B(n)+B(i, j)+B(i, k)$

$$+B(i, l)+B(i, m)+B(j, k)+B(j, l)+B(j, n)+B(k, l)+B(k, m)+B(k, n)$$
$$+B(l, m)+B(l, n)+B(m, n)+B(i, k, m)+B(i, l, m)+B(j, k, n)+B(j, l, n)$$

$+B(i, j, k, l; \text{tetrahedron})+B(k, l, m, n; \text{tetrahedron})+B\Big($ 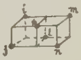 $\Big)$. (4)

Then we have for the free energy in our approximation as follows:

$$[A(1, \cdots, L)/kT]_{\text{up to statues of 6 pts.}}=(A/kT)_{\text{h.c.}}+(A/kT)_{\text{a.p.}}\,, \tag{5}$$

$$A_{\text{h.c.}}=\sum_{i=1}^{L} B(i)+\sum B(i, j; R_{ij}=a/2)+\sum B(i, j; R_{ij}=\sqrt{2}a/2)+\sum B(i, j, k; \triangle)$$
$$+\sum B(i, j, k, l; \text{tetrahedron})+\sum B(i, j, k, l, m, n; \text{statue of 6 pts.})\,, \tag{5'}$$

---

* (III-7^L) denotes Eq. (7^L) of Part III[4].

$$A_{\text{a.p.}}=\sum B(i,\ j;\ R_{ij}\geqq a)\ ;$$

where $(A/kT)_{\text{a.p.}}=A_{\text{a.p.}}/kT$ is the part of $A|kT$ which vanishes when the attractive part is absent and $(A/kT)_{\text{h.c.}}=A_{\text{h.c.}}/kT$ is the part which is independent of the attractive part, and hence we have separated into two parts: a. p. (attractive part) and h. c. (hard core part).

For our system, $A(i)$, $A(i,\ j;\ R_{ij}<a)$, $A(i,\ j,\ k;\ \triangle)$, $A(i,\ j,\ k,\ l;$ tetrahedron and $A(i,\ j,\ k,\ l,\ m,\ n;$ statue of 6pts.) are

$$\left.\begin{aligned}
&A(i)/kT=\rho_i\ln\rho_0+(1-\rho_i)\ln(1-\rho_i)\\
&A(i,\ j)/kT=\rho_i\ln\rho_i+\rho_j\ln\rho_j+(1-\rho_i-\rho_j)\ln(1-\rho_i-\rho_j)\qquad\text{for } R_{ij}<a\ ,\\
&A(i,\ j,\ k;\ \triangle)/kT=\rho_i\ln\rho_i+\rho_j\ln\rho_j+\rho_k\ln\rho_k+(1-\rho_i-\rho_j-\rho_k)\ln(1-\rho_i-\rho_j-\rho_k)\\
&A(1,\ 2,\ 3,\ 4;\ \text{tetrahedron})/kT=\sum_{s=1}^{4}\rho_{\nu_s}\ln\rho_{\nu_s}+\left(1-\sum_{s=1}^{4}\rho_{\nu_s}\right)\ln\left(1-\sum_{s=1}^{4}\rho_{\nu_s}\right)\\
&A(1,\ 2,\ \cdots,\ 6;\ \text{statue of 6 pts.})/kT=\sum_{s=1}^{6}\rho_{\nu_s}\ln\rho_{\nu_s}+\left(1-\sum_{s=1}^{6}\rho_{\nu_s}\right)\ln\left(1-\sum_{s=1}^{6}\rho_{\nu_s}\right).
\end{aligned}\right\}\tag{6}$$

These $A(i_1,\ \cdots,\ i_m)$ are determined by the relative positions of the sites of 1 and 8.

A lengthy but straightforward calculation gives

$$\begin{aligned}
(A/CkT)_{\text{h.c.}}=&\rho_1\ln\rho_1+\rho_8\ln\rho_8+6\rho_2\ln\rho_2-13(1-\rho_1)\ln(1-\rho_1)-13(1-\rho_8)\ln(1-\rho_8)\\
&-78(1-\rho_2)\ln(1-\rho_2)+48(1-\rho_1-\rho_2)\ln(1-\rho_1-\rho_2)+48(1-\rho_8-\rho_2)\ln(1-\rho_8-\rho_2)\\
&+114(1-2\rho_2)\ln(1-2\rho_2)+6(1-\rho_1-\rho_8)\ln(1-\rho_1-\rho_8)-12(1-\rho_1-2\rho_2)\ln(1-\rho_1-2\rho_2)\\
&-12(1-\rho_8-2\rho_2)\ln(1-\rho_8-2\rho_2)-48(1-3\rho_2)\ln(1-3\rho_2)-24(1-\rho_1-\rho_8-\rho_2)\ln(1-\rho_1-\rho_8-\rho_2)\\
&-40(1-\rho_1-3\rho_2)\ln(1-\rho_1-3\rho_2)-40(1-\rho_8-3\rho_2)\ln(1-\rho_8-3\rho_2)\\
&+24(1-\rho_1-\rho_8-4\rho_2)\ln(1-\rho_1-\rho_8-4\rho_2)+12(1-\rho_1-5\rho_2)\ln(1-\rho_1-5\rho_2)\\
&+12(1-\rho_8-5\rho_2)\ln(1-\rho_8-5\rho_2)\ .
\end{aligned}\tag{7}$$

As stated in Part III, we should determine the values of ρ_ν's by the condition

$$\frac{\partial A/CkT}{\partial\rho_\nu}=\text{a const. indep. of }\nu\ ,\tag{8}$$

which is the condition of A/CkT minimum under the condition of $\rho=\sum_{\nu=1}^{8}\rho_\nu$ given. We will minimize A/CkT under the restriction that

$$\rho_1=\frac{\rho e^{\alpha}}{2(3+\cosh\alpha)}\ ,\qquad\rho_2=\cdots=\rho_7=\frac{\rho}{2(3+\cosh\alpha)}\ ,\qquad\rho_8=\frac{\rho e^{-\alpha}}{2(3+\cosh\alpha)}\ ,\tag{9}$$

reducing the number of variational variable to one, α. If we substitute these in (7), the condition to determine ρ_ν's is

$$\frac{\partial A/CkT}{\partial\alpha}=0\ .\tag{10}$$

One of the roots is $\alpha=0$. Whether this state corresponds to the stable state or not is determined according as

$$\left[\frac{\partial^2}{\partial\alpha^2}\frac{A}{CkT}\right]_{\alpha=0}=\frac{\rho}{4}\zeta+\frac{1}{C}\left[\frac{\partial^2}{\partial\alpha^2}\sum_{R_{ij}\geqq a}B(i,\ j)\right]_{\alpha=0}\tag{11}$$

with

$$\zeta=1-\frac{13}{8l-1}+\frac{48}{8l-2}-\frac{12}{8l-3}-\frac{40}{8l-4}+\frac{12}{8l-6},\qquad l\equiv1/\rho\ ,\tag{12}$$

is positive or negative. ζ as a function of l is drawn in Fig. 6, which shows that $\alpha=0$ corresponds to a minimum for all values of ρ for a high temperature system where $B(i, j)$ for $R_{ij}\geqq a$ is small or for a system of hard spheres where the second term of the righthand side of (11) is zero. The detailed discussions will be given of the possible roots of (12) in the respective cases in the following sections.

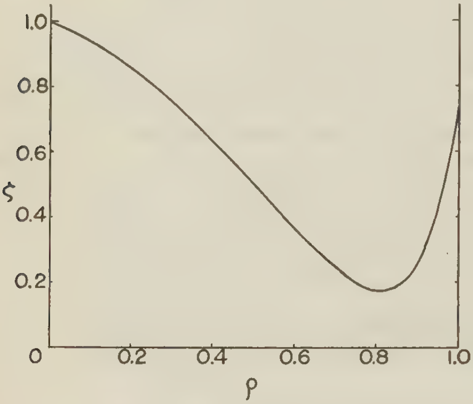

Fig. 6. $\zeta=\frac{4}{\rho}\left(\frac{\partial^2}{\partial\alpha^2}\frac{A}{CkT}\right)_{\text{h.c.},\ \alpha=0}-\rho$ curve.

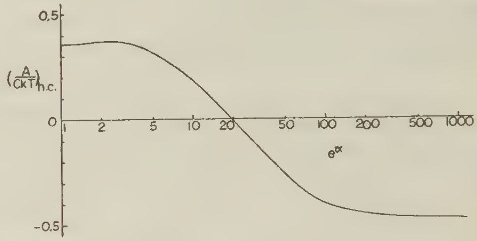

Fig. 7. $(A/CkT)_{\text{h.c.}}-\alpha$ for $\rho=0.8$.

Table I.

ρ	1.0	0.9	0.8	0.7
$\rho_2=\rho_8$	0	0.00001	0.00026	0.00170
$\Delta(A/CkT)_{\text{s.h.c.}}$	0	−0.00006	−0.00179	−0.01191
$(A/CkT)_{\text{s.h.c.}}$	0	−0.3251	−0.5004	−0.6109

§ 3. System of Hard Spheres

Here we will investigate the system of hard spheres, where the potential energy is assumed to be

$$\phi(r)=\begin{cases}\infty & r<a\\ 0 & r\geqq a\,,\end{cases} \tag{13}$$

then the equation for the free energy $(A/CkT)_{\text{h.c.}}$ is given by Eq. (7).

For this case.

$$\left[\frac{\partial^2}{\partial\alpha^2}\left(\frac{A}{CkT}\right)_{\text{h.c.}}\right]_{\alpha=0}=\frac{\rho}{4}\zeta>0 \qquad \text{for } 0\leqq\rho\leqq 1\,, \tag{14}$$

and so the state with $\alpha=0$ corresponds to the stable state for all values of ρ. In order to investigate the possibility of another minimum or another solution of (10), we have drawn $(A/CkT)_{\text{h.c.}}$ as a function of α for $\rho=0.8$ as an instance, which is shown in Fig. 7. It shows that another minimum will exist at $\alpha=\infty$ or $\alpha\sim\infty$; where $(A/CkT)_{\text{h.c.}}$ can be expanded in powers of ρ_2 and ρ_8 as

$$(A/CkT)_{\text{h.c.}}=(A/CkT)_{\text{s.h.c.}}+\Delta(A/CkT)_{\text{s.h.c.}} \tag{15}$$

$$(A/CkT)_{\text{s.h.c.}}=\rho\ln\rho+(1-\rho)\ln(1-\rho) \tag{16}$$

$$\begin{aligned}\Delta(A/CkT)_{\text{s.h.c.}}=&6\rho_2[\ln\rho_2-1-\ln\rho-5\ln(1-\rho)]\\&+\rho_8[\ln\rho_8-1-\ln\rho-5\ln(1-\rho)]+O(\rho_2{}^2,\ \rho_8{}^2,\ \rho_2\rho_8)\ .\end{aligned} \tag{17}$$

A minimum appears at

$$\rho_2=\rho_8=(1-\rho)^5 \tag{18}$$

where

$$\Delta(A/CkT)_{\text{s.h.c.}}=-7\rho(1-\rho)^5\ . \tag{19}$$

For several values of ρ, they are calculated and given in Table I where $(A/CkT)_{\text{s.h.c.}}$ is also given. The correction $\Delta(A/CkT)_{\text{s.h.c.}}$ is seen to be negligible. Then it will be sufficient to calculate $(A/CkT)_{\mathrm{h.c.}}$ for two cases: $\rho_1=\rho_8=\rho_2=\rho/8$ corresponding to the fluids state and $\rho_1=\rho$, $\rho_2=\rho_8=0$ corresponding to the solid state.

For the fluid state, we substitute $\rho_1=\rho_8=\rho_2=\rho/8$ in $(A/CkT)_{\mathrm{h.c.}}$, then we have

$$\begin{aligned}(A/CkT)_{\mathrm{f.h.c.}}=&\rho\ln\frac{\rho}{8}-104\left(1-\frac{\rho}{8}\right)\ln\left(1-\frac{\rho}{8}\right)+216\left(1-\frac{\rho}{4}\right)\ln\left(1-\frac{\rho}{4}\right)\\&-96\left(1-\frac{3}{3}\rho\right)\ln\left(1-\frac{3}{8}\rho\right)-80\left(1-\frac{\rho}{2}\right)\ln\left(1-\frac{\rho}{2}\right)\\&+48\left(1-\frac{3}{4}\rho\right)\ln\left(1-\frac{3}{4}\rho\right).\end{aligned}\tag{20}$$

The pressure and the chemical potential are given by

$$\begin{aligned}\left(\frac{\mu}{kT}\right)_{\mathrm{f.h.c.}}=&\frac{\partial}{\partial\rho}\left(\frac{A}{CkT}\right)_{\mathrm{f.h.c.}}=\ln\frac{\rho}{8}+13\ln\left(1-\frac{\rho}{8}\right)-54\ln\left(1-\frac{\rho}{4}\right)\\&+36\ln\left(1-\frac{3}{8}\rho\right)+40\ln\left(1-\frac{\rho}{2}\right)-36\ln\left(1-\frac{3}{4}\rho\right)\end{aligned}\tag{21}$$

$$\begin{aligned}\left(\frac{p}{kT}\right)_{\mathrm{f.h.c.}}=&\rho\left(\frac{\mu}{kT}\right)_{\mathrm{f.h.c.}}-\left(\frac{A}{CkT}\right)_{\mathrm{f.h.c.}}=104\ln\left(1-\frac{\rho}{8}\right)-216\ln\left(1-\frac{\rho}{4}\right)\\&+96\ln\left(1-\frac{3}{8}\rho\right)+80\ln\left(1-\frac{\rho}{2}\right)-48\ln\left(1-\frac{3}{4}\rho\right).\end{aligned}\tag{22}$$

For the solid state, they are

$$(A/CkT)_{\mathrm{s.h.c.}}=\rho\ln\rho+(1-\rho)\ln(1-\rho)\,,\tag{23}$$

$$(\mu/kT)_{\mathrm{s.h.c.}}=\ln\rho-\ln(1-\rho)\,,\tag{24}$$

$$(p/kT)_{\mathrm{s.h.c.}}=-\ln(1-\rho)\,.\tag{25}$$

They are drawn in Fig. 8 and Fig. 9. They show that our lattice gas of hard spheres exhibits a phase transition of first order between solid and gas. The coexistence densities, pressure and chemical potential are

$1/\rho_{\mathrm{solid}}=1.21$, $1/\rho_{\mathrm{gas}}=2.00$,

$p_{\mathrm{coexistence}}=1.74$, $\mu_{\mathrm{coexistence}}=1.54$,

the heat of sublimation is

$$\Delta S/NkT=\Delta A/NkT=1.35\,.$$

It is of interest to compare this phase transition with that for the continuous system of hard spheres, obtained by Wood, Jacobson, Alder and Wainwright⁶⁾: For the latter system, the metastable regions of gas and solid extend to the volume $v/v_0=1.55$ where their pressures are $pv_0/kT=7.1$ and 5.5 respectively. The corresponding values for our lattice system are calculated as $v=1.65$ and $p/kT=2.75$ and 0.95

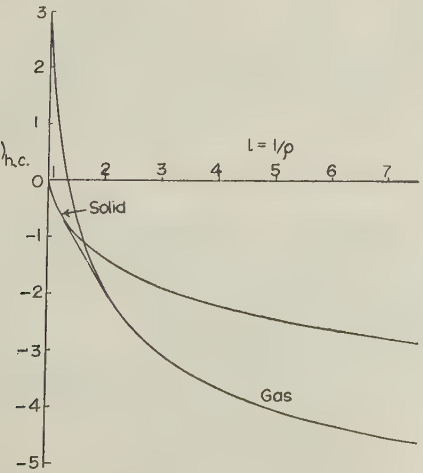

Fig. 8. $(A/C\rho kT)_{\mathrm{h.c.}}-1/\rho$ curve.

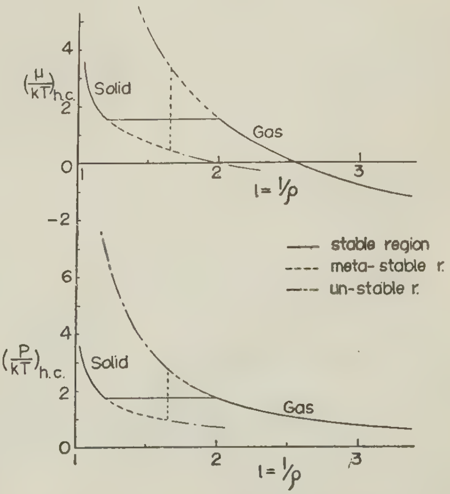

Fig. 9. $(\mu/kT)_{\mathrm{h.c.}}-1/\rho$ and $(p/kT)_{\mathrm{h.c.}}-1/\rho$ curves.

§ 4. System of Particles with Both Hard Core and Attractive Part

In this section we will investigate the system of which the potential energy is given by (1) and (2) with

$$\phi(r)=\begin{cases}\infty & r<a \\ 4\left(\dfrac{1}{r^{12}}-\dfrac{1}{r^{6}}\right) & r\geqq a\end{cases} \tag{26}$$

with $a=2^{1/6}$.

Here we will evaluate $B(i, j)$ for $R_{ij}\geqq a$ as

$$B(i, j)=\rho_i\rho_j\frac{\phi(R_{ij})}{kT}\,. \tag{27}$$

We might calculate it by (III–22), taking fully account of the products of f_{ij}. But, if j and k are neighbors and $B(i, j)$ and $B(i, k)$ are calculated by (III–22 , then the presence of a particle at i tends to make the presence of particles both at j and k favorable while if $B(i, j, k)$ were correctly considered the tendency for the presence of particles at i and j would reduce the tendency for i and k to be occupied at the same time. That is, the use of (III–22) seems to be physically unreasonable. Because of this we have decided to use the coarse approximation of the random mixing, which is not subjected to such an objection.

Then, the attractive part of the free energy becomes

$$\begin{aligned}\left(\frac{A}{CkT}\right)_{\text{a.p.}}&=\frac{1}{C}\sum_{R_{ij}\geqq a}B(i, j)\\ &=6(\rho_1{}^2+\rho_8{}^2+6\rho_2{}^2)\frac{\varphi_a}{kT}\\ &\quad+24(\rho_1\rho_2+\rho_8\rho_2+2\rho_2{}^2)\frac{\varphi_b}{kT}\\ &\quad+8(\rho_1\rho_8+3\rho_2{}^2)\frac{\varphi_c}{kT}\,.\end{aligned} \tag{28}$$

Here,

$$12\varphi_a=\sum_{j=1}^{0}{}^{*}\,V^{(2)}(|R_{i1}-R_{j1}|)\,, \tag{29a}$$

$$24\varphi_b=\sum_{j=1}^{0}{}^{*}\sum_{\nu=2}^{7}V^{(2)}(|R_{i1}-R_{j\nu}|)\,, \tag{29b}$$

$$8\varphi_c=\sum_{j=1}^{0}{}^{*}\,V^{(2)}(|R_{i1}-R_{j8}|)\,, \tag{29c}$$

where * on the summations means that in the summation j for which $V^{(2)}(|r_{i1}-r_{j\nu}|)=\infty$ should be omitted. These values for our potential are calculated as

$$12\varphi_a=-16.7760\,,\qquad 8\varphi_c=-8.7173\,,$$

$$12\varphi_a+24\varphi_b+8\varphi_c=-82.9921\,,$$

by the help of the table of Lennard-Jones and Ingham[7].

The region where $\alpha=0$ can be stable state:

$$\left(\frac{\partial^2}{\partial\alpha^2}\frac{A}{CkT}\right)_{\alpha=0}=\frac{\rho^2}{32}\left\{\frac{8\zeta}{\rho}+\frac{1}{kT}(12\varphi_a-8\varphi_c)\right\}>0\,,$$

is calculated as shown in Fig. 10, under the approximation (27) for $B(i, j)$.

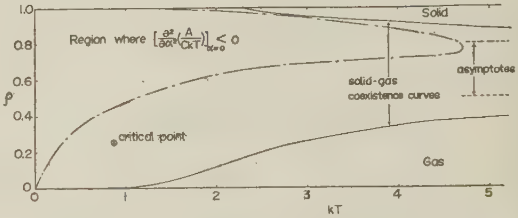

Fig. 10. Phase diagram ($\rho-kT$).

In the following, we calculate A/CkT for $\rho_1=\rho_8=\rho_2=\rho/8$ and $\rho_1=\rho$, $\rho_8=\rho_2=0$ respectively and take the smaller to be our approximate free energy and satisfy ourselves by confirming that the state $\rho_1=\rho_8=\rho_2=\rho/8$ does not come into the region where $\partial^2(A/CkT)/\partial\alpha^2<0$. This is justified so far as there will not appear a new minimum between $\alpha=0$ and $\alpha\sim\infty$. Here, note that the minimum near $\alpha=\infty$ will approach to ∞ where the potential energy is smaller.

For the uniform state, the free energy is

$$(A/CkT)_{\text{f.}}=(A/CkT)_{\text{f.h.c.}}+(A/CkT)_{\text{f.a.p.}} \tag{30}$$

$$\left(\frac{A}{CkT}\right)_{\text{f.a.p.}}=\frac{\rho^2}{16}\frac{12\varphi_a+24\varphi_b+8\varphi_c}{kT}\,. \tag{31}$$

The pressure is given by

$$\left(\frac{p}{kT}\right)_{\text{f.}}=\left(\frac{p}{kT}\right)_{\text{f.h.c.}}+\frac{\rho^2}{16}\frac{12\varphi_a+24\varphi_b+8\varphi_c}{kT}\,. \tag{32}$$

The critical point, then, is easily calculated in this approximation, as the solution of

$$\begin{aligned}-\frac{1}{8kT}&(12\varphi_a+24\varphi_b+8\varphi_c)\\ &=-\frac{104}{(8-\rho)\rho}+\frac{216\times2}{(8-2\sigma)\rho}-\frac{96\times3}{(8-3\rho)\rho}\\ &\quad-\frac{80\times4}{(8-4\rho)\rho}+\frac{48\times6}{(8-6\rho)\rho}\\ &=-\frac{104}{(8-\rho)^2}+\frac{216\times4}{(8-2\rho)^2}-\frac{96\times9}{(8-3\rho)^2}\\ &\quad-\frac{80\times16}{(8-4\rho)^2}+\frac{48\times36}{(8-6\rho)^2}\end{aligned} \tag{33}$$

as

$$\rho_c=0.2557\,,$$
$$kT_c=-\frac{12\varphi_a+24\varphi_b+8\varphi_c}{8\times 12.1970}=0.8505\,.$$

The free energy for the solid state is

$$\left(\frac{A}{CkT}\right)_{\mathrm{s.}}=\rho\ln\rho+(1-\rho)\ln(1-\rho)+6\rho^2\frac{\varphi_a}{kT}\,. \tag{34}$$

$A/C\rho kT$ as a function of $1/\rho$, calculated for $kT=0.8$ and 3.0, are drawn in Fig. 11. It shows that our system will not exhibit the liquid state. The coexistence curves between solid and gas are also drawn in Fig. 10: they have been obtained by drawning $A/C\rho kT-1/\rho$ curves for various values of kT. It is seen that the gaseous region does not come, surely, in the region where $\partial^2(A/CkT)/\partial\alpha^2<0$.

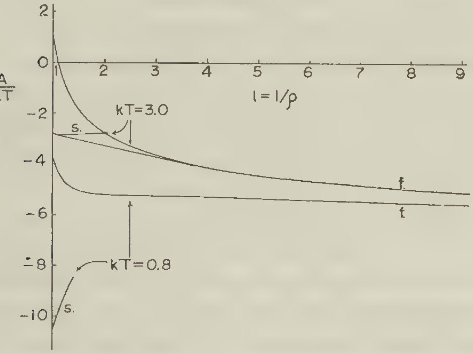

Fig. 11. $A/C\rho kT-1/\rho$ curve for $kT=0.8$ and 3.0.

The result obtained by calculating the hard core part of A/NkT by the approximation of "the statues of 6 points" and the attractive part by the approximation of the random mixing, is such as to exclude the appearance of the liquid state: the free energy for the solid state mixed by gas is lower than that of the liquid state. The phase equilibrium exists between solid of perfect order ($\rho=1$) and gas of comparatively low density, at low temperature region.

§ 5. Discussions

Our lattice gas seems not to exhibit the liquid state, while the ordinary continuous gas condenses to the liquid. Let us investigate the cause by which the difference arises. For this purpose, we consider an equivalent continuous system to our lattice gas. It is a continuous system of which the potential energy is determined only by the distribution of the lattice sites, the cells belonging to which are occupied, independently of the detailed positions of particles in the cells. Then, in such a system, even in the solid state as well as in fluid state, the molecules in a cell exist equally probably in the cell, because of the indifference of the potential energy; while in the ordinary continuous system, in the solid state the probability in a cell will be more restricted to smaller region than in the fluid state. This effect to the free energy is to reduce it for the fluid states and reduces the curve for the fluid state, perhaps until the stable liquid to be possible.

As the result, in order to get the results for the continuous system by using the calculation for a lattice system, we have either to reduce the lattice constant to a value which is small compared with the distance by which the one particle distribution function in the solid state varies or to evaluate the entropy due to the localization of the particles in a cell suitably. Such investigations will be the subject of a future publication.

The author wishes to express his cordial thanks to Dr. K. Hiroike for his helpful discussions.

References

1) J. E. Lennard-Jones and A. F. Devonshire: Proc. Roy. Soc. **A**, **169** (1939) 317; **A**, **170** (1939) 464.
2) R. Kikuchi: J. Chem. Phys. **19** (1951) 1230.
I. Shimose: J. Phys. Soc. Japan **10** (1955) 860.
3) T. Morita: J. Phys. Soc. Japan **12** (1957) 1195; which consists of Parts I and II of this series of work.
4) T. Morita: J. Phys. Soc. Japan **14** (1959) 563; which is Part III of this series.
5) T. Morita: to be published in Progr. Theor. Phys. **21** (1959) 501.
6) W. W. Wood and J. D. Jacobson: J. Chem. Phys. **27** (1957) 1207. B. J. Alder and T. E. Wainwright: J. Chem. Phys. **27** (1957) 1208.
7) J. E. Lennard-Jones and A. E. Ingham: Proc. Roy. Soc. **A**, **107** (1925) 636. see also, R. H. Fowler: *Statistical Mechanics* (Cambridge Univ. Press, 1936) 319.

JOURNAL OF THE PHYSICAL SOCIETY OF JAPAN, Vol. 14, No. 5, MAY, 1959

Study of Reorientational Motion in Solid State of 1, 2, 3-trichlorobenzene and Hexachlorobenzene by Pure Quadrupole Resonance

By Itaru TATSUZAKI

Research Institute of Applied Electricity, Hokkaido University, Sapporo

(Received December 26, 1958)

Abrupt increases accompanying the elevation of temperature were observed in the line widths of pure quadrupole resonance spectrum of 1, 2, 3-trichlorobenzene and hexachlorobenzene. The results suggest a possibility of reorientational motion of these molecules in temperature ranges far lower than the melting points. In consideration of hexagonal symmetry of hexachlorobenzene, it was concluded that there was occurring a reorientational motion around the hexagonal axis of this molecule. Its hindering potential barrier was estimated at $12.6 > W \geqslant 9.9$ Kcal/mole by means of pure quadrupole resonance alone. Although 1, 2, 3-trichlorobenzene has no symmetry about the normal axis of the molecular plane, measurements of proton magnetic resonance and dielectric constant, in addition to the pure quadrupole resonance suggested the possibility of the reorientational motion around the normal axis of the molecule, which covers only two neighboring equilibrium positions. From temperature dependence of the line width of pure quadrupole resonance spectrum, the mean height of its hindering potential barrier was estimated at $6.0 > W \geqslant 5.0$ Kcal/mole.

§ 1. Introduction

Molecular rotations in the solid states have been studied by several methods: X-ray analysis, measurement of a specific heat, dielectric measurement and a method of nuclear magnetic resonance. In cases where each molecule rotates almost freely, information about molecular rotations can be obtained either by X-ray analysis or by measurement of the specific heat. In the nuclear magnetic resonance experiment, on the contrary, the line width is affected even though the moleules cannot rotate freely, but can execute so-called reorientational motion. Dielectric measurement can also give information about the reorientational motion, and is however applicable only to polar molecules. In case a nucleus composing a molecule has a large nuclear quadrupole coupling constant, and yet the molecule is non-polar, both methods are not applicable. It is known that a molecule which has a symmetry axis executes a reorientational motion around the axis in temperature ranges far lower than the melting point. The number of molecules with sufficient energy to surmount the potential barrier W is proportional to $\exp(-W/kT)$. Such a motion produces a fluctuating electric field gradient at the nucleus[1)-3)]. This induces the transition between nuclear quadrupole levels, which limits the life time of the levels and accordingly broadens the line width of the pure quadrupole resonance spectrum. Study on this phenomenon was done by Bodin[1)] for the first time, using ethane derivatives. Prior to the present work, the present writer and colleague studied the phenomena for $Cl_3C \cdot CCl_3$[4)] and estimated the height of the hindering potential barrier.

Studies of pure quadrupole resonance spectra of multichlorobenzenes were made by Bray and Barnes[5)]. They reported that 1, 2, 3-trichlorobenzene showed clean signals on oscilloscope with a signal to noise ratio of about 8 to 1 at 77°K but no resonance was detectable at room temperature, even with elaborate recording techniques. Stimulated by this fact, the writer studied the temperature dependence of the line width of 1, 2, 3-trichlorobenzene.

§ 2. Experimental Procedures and Results

A. *Preparation of materials*

A commercial polycrystalline 1, 2, 3-trichlorobenzene was purified by recrystalization from ethyl alcohol solution and further by vacuum evaporation. The measured melting point of 1, 2. 3-trichlorobenzene was 52.6～52.7°C. Hexachlorobenzene used was commercial reagent grade powdered material with a melting point of 226°C.

B. *Pure quadrupole resonance spectroscopy*

As was done in the previous work[4)], a spectrometer of superregenerative type was used. It gave constantly reproducible absorption curves if both quench frequency and quench voltage were adjusted suitably. Quench frequency of 80～100 Kc/s and quench voltage of 1～2 volts were used throughout the present experiments. The sweep rates of frequency of the spectrometer were calibrated by Kōi's method[6)]. It was 0.02～0.04 Kc/s per second. The time required to sweep over absorption curves was about ten minutes. By integrating the differential curve taken on a recorder, measurement was made of the line width, which is defined as the interval between the two points of the curve where the integrated curve falls to half of the maximum value. The values obtained in repeated measurements agreed within an experimental error of 10%.

To obtain the temperature down to −130°C a cryostat was used. Its main part was a petroleum ether bath. Liquid nitrogen was introduced through a serpentine copper tube immersed in petroleum ether, by means of a water aspirator. The temperature was controlled through varying manually the quantity of liquid nitrogen flowing through the tube. By this method, it was possible to limit the temperature fluctuation in the cryostat within ±0.1°C. Measurements of the temperature were made with a calibrated copper-constantan thermocouple. Only after the desired temperature had been held for at least thirty minutes, were the measurements of quadrupole resonance started. Even though the stirrer had to be stopped to avoid an unfavourable fluctuation of the frequency during the sweeping of the absorption line, no remarkable drift of the temperature was recognized. This was probably associated with a large heat capacity of the cryostat. It is well known that a line width is broadened owing to distribution of resonance frequency caused by a non-uniformity of temperature in the sample. For chlorine nucleus (Cl^{35}, $\nu \simeq 30 \sim 40$ Mc/s), if it be assumed that there is a non-uniformity of 0.1°C in the sample, this broadening should be of the order of 0.3～0.4 Kc/s because the temperature coefficient of resonance frequency $-(d\nu/\nu dT)$ is of the order of magnitude 10^{-4}°K^{-1}. To examine the non-uniformity of temperature in the sample, measurements of the line width were made at several temperatures for para-dichlorobenzene, whose line width is explained by dipole-dipole interactions, which are almost independent of temperature. All values obtained were 1.40±0.05 K/cs, in agreement with those reported by Wang[7)]. This result seems to give assurance that the non-uniformity of temperature in the sample is less than 0.1°C in the course of sweeping of the absorption line. Some of the derivative curves of absorption lines in 1, 2, 3-trichlorobenzene are shown in Fig. 1.

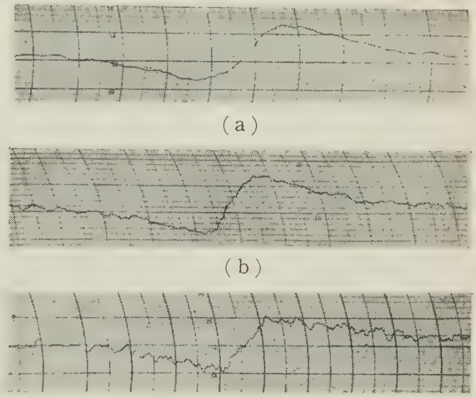
(a)
(b)
(c)

Fig. 1. Examples of the derivative curves obtained for 1, 2, 3-trichlorobenzene. a) 209.5°K, sweep rate of frequency: 0.027 Kc/s per second, half width: 1.75 Kc/s b) 225°K, 0.041 Kc/s per second, 2.3 Kc/s c) 230°K, 0.036 Kc/s per second, 2.6 Kc/s. Paper speed was one division per ten seconds.

1, 2, 3-trichlorobenzene

Six absorption lines were observed by Bray and Barnes[5)]. In the present study measurements were made of the width of the spectrum of the highest absorption frequency assigned to benzene-ring position 2 on the basis of frequency versus sigma value[5)]. Results are plotted in Fig. 2 together with those of hexachlorobenzene.

The broadening of the line width became so remarkable above 225°K that no reliable measurement could be made at temperatures above 240°K. Fig. 2 shows that the line width increases exponentially with the elevation of temperature. This broadening is probably due to the reorientational motion, which is the only possible origin of the increase of the line width accompanying the elevation of temperature. The temperature dependence of the line width is expressed by the formula:

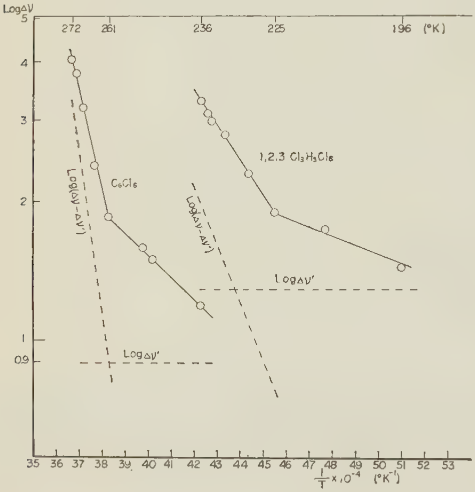

Fig. 2. Behavior of Cl^{35} line width $\varDelta\nu$ as a function of the inverse of the absolute temperature. Solid line: $\log \varDelta\nu$ *vs* $1/T$ Dotted line: $\log(\varDelta\nu - \varDelta\nu')$ *vs* $1/T$ and $\log \varDelta\nu'$ *vs* $1/T$, where $\varDelta\nu'$ is the contribution to the line width from origins other than the reorientational motion.

$$(\varDelta\nu-\varDelta\nu') \propto \exp\left(-\frac{W}{RT}\right) \qquad (1)$$

where $\varDelta\nu'$ is the line width due to the origins other than the reorientational motion. $\varDelta\nu'$ is assumed to be independent of temperature. Though this assumption may not be correct, it would not affect the conclusion seriously. W is the height of hindering potential barrier. The plotted line is now separated into two parts: $\log(\varDelta\nu-\varDelta\nu')$ and $\log(\varDelta\nu')$. From the slope of $\log(\varDelta\nu-\varDelta\nu')$, W is estimated at 6.0±0.1 Kcal/mole. It is reasonable to believe that the reorientational motion is occurring around the normal axis of the molecular plane. As the molecule has no symmetry about this axis, however, one can hardly consider that the reorientational motion becomes a rotation when the temperature is raised further. In order to examine the reorientational motion in this region in detail, the proton magnetic resonance experiment and the measurement of dielectric constant were carried out. Procedures and results will be given below in section 3.

Hexachlorobenzene

The quadrupole resonance frequencies of Cl^{35} were observed as functions of the temperature by Duchesne and Monfils[8]. The hexagonal symmetry of the molecule suggests a possibility of the reorientational motion occurring around the symmetry axis. The line widths of three components coincide with one another within the limits of experimental error. The broadening becomes remarkable above 261°K. From Fig. 2, the value 12.6±0.2 Kcal/mole was obtained for the height of the hindering potential barrier, under the same hypothesis as that adopted for the case of 1, 2, 3-trichlorobenzene.

§ 3 Additional Experiments

A. *Proton magnetic resonance spectroscopy*

The proton magnetic resonance experiment was carried out, in order to examine whether the reorientational motion which causes the broadening of the line width of the quadrupole resonance for 1, 2, 3-trichlorobenzene becomes a rotation at higher temperatures. If a complete rotation should occur at higher temperature, the phenomenon called motional narrowing would be observed, owing to the averaging-out of local magnetic fields at the positions of protons.

The spectrometer used was the same as that used by Odajima et al.[9),10)]. A narrow band amplifier and phase sensitive detector were used to observe the derivative of the absorption line as a function of applied magnetic field. The cryostat employed was one similar to that described by Gutowsky

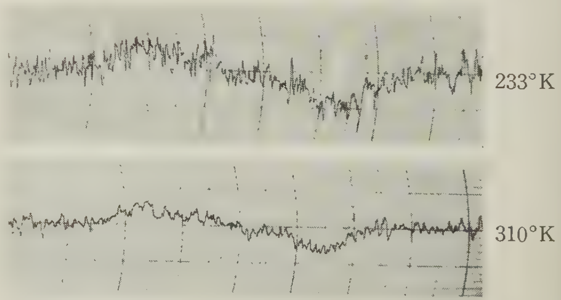

Fig. 3. Typical curves of the proton magnetic resonance for 1, 2, 3-trichlorobenzene. The mean peak-to-peak interval is 6.8±0.5 gauss.

et al.[11]. The constancy of temperature in the course of sweeping of the absorption line was maintained carefully within ±1°C in the vicinity of room temperature and ±3°C in the range 270～220°K. Fig. 3 shows the typical curves recorded for protons. The peak-to-peak intervals of the derivative curves versus temperature are plotted in Fig. 4. No remarkable temperature dependences of the derivative curves of the absorption line are found, up to the melting point. There is however a small reduction in the vicinity of the melting point, which presumably is due to pre-melting of the sample.

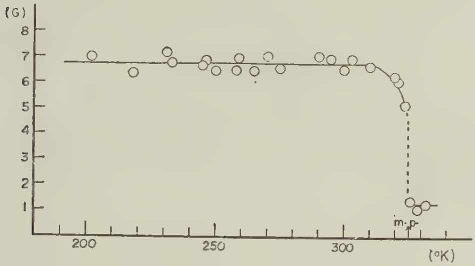

Fig. 4. Peak-to-peak interval of the proton magnetic resonance versus temperature for 1, 2, 3-trichlorobenzene.

It can therefore be concluded that the reorientational motion never becomes such a complete rotation that it can average out the local magnetic fields at the positions of the protons. From the result of the proton magnetic resonance experiment alone, however, another explanation may be possible: neither the rotation nor the reorientational motion does occur below the melting point. This explanation is, however, quite inconsistent with the result of the quadrupole resonance experiment.

B. *Measurement of dielectric constant*

In order to confirm with more certainty the existence of the reorientational motion, the dielectric constant was also measured. 1, 2, 3-trichlorobenzene is polar; the dipole moment lies in the molecular plane. If the reorientational motion occurs around the normal axis of the molecular plane, the dispersion of the dielectric constant ε' has to be observable. The measurement was made at 1 Kc/s with the alternating current bridge. The unbalanced voltage from the detector terminals of the bridge was provided with a sufficient amount of amplification and then led to a cathode ray oscilloscope. The type of the cell by which the dielectric constant ε' was measured was similar to the one described by White and Bishop[12]. The capacity of the cell was 30 pF, whose error was found to be within 3%. Fig. 5 shows the temperature dependence of ε'. From the behavior of ε', it becomes clear that the reorientational motion in fact does occur in the solid state.

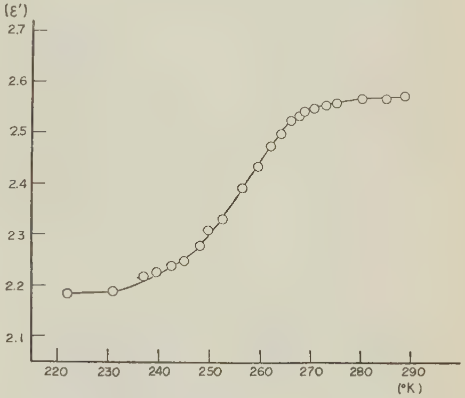

Fig. 5. Dielectric constant ε' of 1, 2, 3-trichlorobenzene *vs.* temperature.

§ 4. Discussions

A. *1, 2, 3-trichlorobenzene*

From the herein described series of experiments, it may be concluded that the reorientational motion occurs around the normal axis of the molecular plane in a temperature range far below the melting point which does not become a complete rotation so long as the substance exists in the solid state. The hindering potential energy of a polar molecule in a solid state depends in general on the magnitude as well as the asymmetry of all the intermolecular forces involved. The effect of various types of crystalline fields on the dipole direction has been considered by Frank[13] and White[14]. In 1940 White et al[15] measured the dielectric properties of hexasubstituted methylchlorobenzenes. They found that these substances possess a more or less restricted rotation freedom for temperatures sufficiently below the melting point. Especially they noticed an abnormal reduction of static polarizability with the decrease of temperature for 1, 2, 3-trimethyl-4, 5, 6-trichlorobenzene. This phenomenon was explained by a model of the hindering potential barrier, which is shown in Fig. 6, in which the reorientational motion occurs from one to another of two equilibrium orientations separated from each other by an angle of 72°C.

Though the methyl radical and proton differ from each other, the symmetry of both molecules is the same. If the analogous model on the hindering potential described above is employed for the analysis of the reorientational motion of 1, 2, 3-trichlorobenzene, the results of the experiments will be explained reasonably—the reorientational motion which occurs from one to another of two equilibrium orientations causes a line broadening of the pure quadrupole resonance spectrum and also causes a dispersion of dielectric constant; this motion can not induce motional narrowing, because the angle between two equilibrium positions is too small to average out the local magnetic fields. From the slope of $\log(\Delta\nu-\Delta\nu')$, W is estimated at 6.0 Kcal/mole under the assumption that $\Delta\nu'$ is independent of the temperature (§ 2). There is, however, also a broadening of the line width due to the molecular oscillation, which was studied by Bayer[16]. This broadening increases with temperature. If this broadening be taken into account, W would become smaller than 6 Kcal/mole. Since the value of 5 Kcal/mole is obtained from the slope of the experimental line in Fig. 2, it can safely be supposed that the height W of the hindering potential barrier lies between 6 Kcal/mole and 5 Kcal/mole. This seems to be reasonable in comparison with the values of 5740 cal/mole and 4610 cal/mole obtained for 1, 2, 3-trimethyl-4, 5, 6-trichlorobenzene.

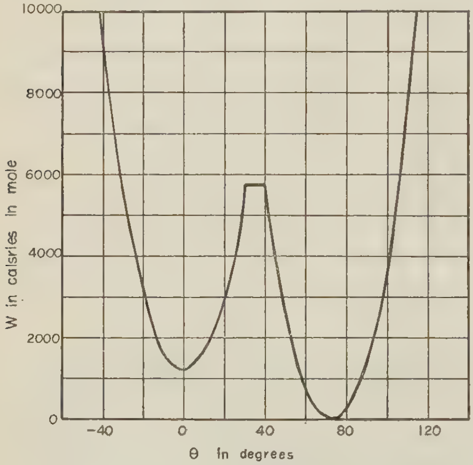

Fig. 6. Potential function assumed for the rotational motion of 1, 2, 3-trimethyl-4, 5, 6-trichlorobenzene. (After White et al[15]).

B. *Hexachlorobenzene*

It is shown through the experiment on the proton magnetic resonance[17] that benzene and hexamethylbenzene reorientate in solid state around a normal axis of the molecular plane. If it is permissible to consider that the hexachlorobenzene is a plane hexagon of carbon atoms, each of which possesses a side-bond chlorine atom in the plane, this molecule can also be considered as a plane hexagon of chlorine. It seems most reasonable, therefore, to associate the broadening of the line width with the six-fold reorientational motion. From the slope of $\log(\Delta\nu-\Delta\nu')$ W is estimated at 12.6 Kcal/mole (§ 2). If the additional broadening of the line width is taken into account, as was done in 1, 2, 3-trichlorobenzene, the reasonable value of W will become $12.6\ \text{Kcal/mole} > W \geqslant 9.9\ \text{Kcal/mole}$. Let it be considered how reliable these values are. Assume that, considering the hexagonal symmetry of the molecule, the hindering potential of the reorientational motion in the solid state has the form

$$V=\frac{1}{2}W(1-\cos 6\theta)\,. \qquad (2)$$

Then the rotational-vibrational frequency is given by

$$\nu_r=\frac{6}{2\pi}\sqrt{\frac{W}{2I}} \qquad (3)$$

where I is the moment of inertia about the axis of hexagonal symmetry. If use is made of the values of $12.6 > W \geqslant 9.9$ Kcal/mole and $I=36.83\times10^{-38}\,\text{gr cm}^2$, ν_r is found to be $1.03\times10^{12} > \nu_r \geqslant 0.91\times10^{12}\,\text{sec}^{-1}$. For polar molecules, the relaxation time τ obtained by the dielectric measurement is given, for any temperature, by

$$\tau=\frac{\varepsilon_\infty+2}{\varepsilon_s+2}\frac{1}{2\pi f_m} \qquad (4)$$

where ε_∞ and ε_s have the usual meanings. f_m is the frequency at which $\varepsilon=(\varepsilon_s+\varepsilon_\infty)/2$. According to the Eyring-Frank theory of an anomalous dispersion, on the other hand, $1/\tau$ is given by

$$\frac{1}{\tau}=\nu_r\exp\left(-\frac{W}{RT}\right) \qquad (5)$$

From the results of dielectric measurements made by White et al.[15] for chlorobenzene derivatives, the temperature at which f_m becomes 1 Kc/s can be estimated as listed in Table I.

Table I. Temperature at which f_m=1 Kc/s, estimated from the experimental results of White et al[15].

Sample	Numbers of Cl	T(°K)
1, 2, 3, 4-tetramethyl-5, 6-trichlorobenzene	2	165
1, 2, 4-trimethyl-3, 5, 6-trichlorobenzene	3	188
tetrachloro-o-xylene	4	203
methylpentachlorobenzene	5	229

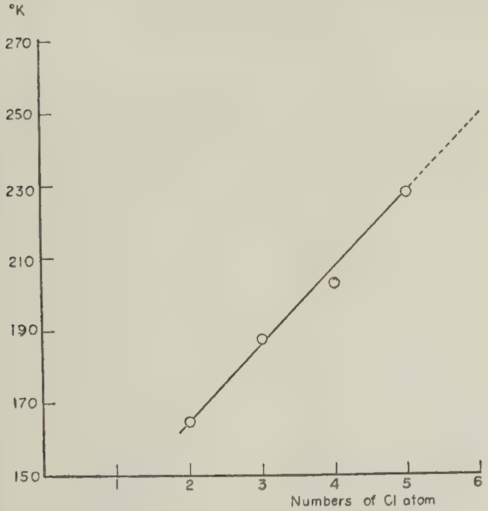

Fig. 7. Temperature T at which f_m=1Kc/s *vs.* number of chlorine atoms.

In Fig. 7 the values of T are plotted versus the number of chlorine atoms in the molecule. There is a remarkable regularity, which was also confirmed for the temperatures at which $\tau=10^{-6}$ sec by White et al.[15].

The temperature for Cl=6 can be determined by extrapolation to be 251°C. From the numerical values given above the value of W can be determined, using Eq. (4), (5) and the relation $(\varepsilon_\infty+2)/(\varepsilon_s+2)=1$ valid for non-polar substances. It becomes $9.41 > W \geqslant 9.33$ Kcal/mole, in good agreement with 9.9 Kcal/mole, the lower limit obtained from the present measurements.

Acknowledgment

The author wishes to express his sincere thanks to Professor Y. Yokozawa for his kind encouragement throughout the course of the present work. He is also grateful to Professor K. Higasi for his useful advices and to Assist. Prof. A. Odajima for his stimulating discussions. Thanks are also due Mr. J. Hori for his valuable criticisms. The present work was supported in part by a Grant of Aid for Developmental Scientific Research in the Ministry of Education.

References

1) Y. Ayant: Ann. Physique **10** (1955) 487.
2) M. B. Bodin: Ann. Physique **10** (1955) 533.
3) J. Seiden: Compt. rend. **242** (1956) 763.
4) I. Tatsuzaki and Y. Yokozawa: J. Phys. Soc. Japan **12** (1957) 802.
5) P. J. Bray and R. J. Branes: J. Chem. Phys. **25** (1956) 813.
6) Y. Kōi: J. Phys. Soc. Japan **12** (1957) 49.
7) T. Wang: Phys. Rev. **99** (1955) 566.
8) J. Duchesne and A. Monfils: J. Chem. Phys. **22** (1954) 562.
9) A. Odajima, J. Sohma and M. Koike: J. Phys. Soc. Japan **12** (1957) 272.
10) A. Odajima: J. Appl. Phys. Japan **27** (1958) 261.
11) H. S. Gutowsky, L. H. Meyer and R. E. McClure: Rev. Sci. Instr. **24** (1953) 644.
12) A. H. White and W. S. Bishop: J. Amer. Chem. Soc. **62** (1940) 8.
13) F. C. Frank: Trans. Faraday Soc. **A, 42** (1946) 24.
14) A. H. White: J. Chem. Phys. **7** (1939) 58.
15) A. H. White, B. S. Biggs and S. O. Morgan: J. Amer. Chem. Soc. **62** (1949) 16.
16) H. Bayer: Z. Phys. **130** (1951) 227.
17) E. R. Andrew: J. Chem. Phys. **18** (1950) 607.

Journal of the Physical Society of Japan, Vol. 14, No. 5, May, 1959

Electronic Structure of Bismuth Type Crystals, II

By Shoichi Mase

Department of General Education, University of Nagoya

(Received January 8, 1959)

Further study of the electronic structure of bismuth type crystals is made by calculating the energies along some directions in the reduced zone in more detail than in the previous paper, and a discussion is made on the location of electrons and holes in the Brillouin zone. We propose that in the case of bismuth the electrons are located at each centre of upper and lower inclined planes of Jones' zone and the holes are located at a particular point on each cross line of side-planes parallel to the c-axis, while in the case of antimony the electrons are located at the same places as in bismuth and the holes at different places which are defined in the text. On this model some electric and magnetic properties of the metals and alloys are discussed.

§ 1. Introduction

In the previous paper[1] (to be referred to as I), we calculated energy curves along some directions in the wave number space and discussed the relation between the energy bands and the observed values of diamagnetic susceptibility. The calculation was, however, performed only along two directions in the reduced zone. While the electronic properties of bismuth were discussed by Jones[2] basing upon a Brillouin zone which can contain five electron states per atom, Jones' ellipsoids for electrons and holes do not locate at the points equivalent to ours in the reduced zone. Exact knowledge of the energy surfaces is in need in order to see whether existing theories of diamagnetic susceptibility, cyclotron resonance, galvanomagnetic effect and others are appropriate or not to these metals in which considerable anomalies in these properties are observed.

In the present paper, we complement our previous calculation and make clearer on the relation between the energy bands and the electronic properties of the metals and alloys. In section 2, the correspondence between the reduced and Jones' Brillouin zones is discussed. The energy curves in some interesting symmetry directions are also calculated in more detail and it is shown that Jones' location of ellipsoids of electrons and holes is unjustified by our energy band calculation. In section 3, an explanation is given for some experimental results of electronic properties of bismuth, antimony, and bismuth-antimony alloys.

§ 2. Brillouin Zones and Energy Curves

Bismuth crystal has comparatively low symmetry (the space group symmetry D_{3d}^5), but the crystal structure is very similar to that of the simple cubic. It is almost clear that the anomalous properties of bismuth crystal are related to this resemblance, because the first Brillouin zone of the simple cubic lattice contains two electron states per atom while bismuth type metals have five valence electrons per atom. In other words, very small number of conduction electrons with small effective mass should be located somewhere on the zone boundaries which disappear in the case of the simple cubic lattice.

We choose the trigonal axis as z-axis (Fig. 1). The positions of representative atoms of two sublattices are

$$\left.\begin{aligned}
a_0&=(0,0,0)u\,,\\
a_1&=\left(0,\ \frac{\sqrt{6}}{3},\ \frac{2\sqrt{3}}{3}(1+3\omega)\right)u\,,\\
a_2'&=\left(\frac{\sqrt{2}}{2},\ \frac{\sqrt{6}}{6},\ -\frac{2\sqrt{3}}{3}(1+3\omega)\right)u\,,\\
b_2&=\left(\frac{\sqrt{2}}{2},\ \frac{\sqrt{6}}{6},\ \frac{\sqrt{3}}{3}(1+3\omega+3\varepsilon)\right)u\,,\\
b_1'&=\left(0,\ \frac{\sqrt{6}}{3},\ -\frac{\sqrt{3}}{3}(1+3\omega-3\varepsilon)\right)u\,.
\end{aligned}\right\}\tag{1}$$

The primitive translation vectors of the lattice are $\overrightarrow{a_0a_1}$, $\overrightarrow{a_0a_2}$ and $\overrightarrow{a_0a_3}$, then foundamental reciprocal lattice vectors are given by

$$\left.\begin{aligned} \boldsymbol{f}_1&=\left(0,\ \frac{\sqrt{6}}{3},\ \frac{\sqrt{3}}{6}\frac{1}{1+3\omega}\right)u^{-1},\\ \boldsymbol{f}_2&=\left(\frac{\sqrt{2}}{2},\ -\frac{\sqrt{6}}{6},\ \frac{\sqrt{3}}{6}\frac{1}{1+3\omega}\right)u^{-1},\\ \boldsymbol{f}_3&=\left(-\frac{\sqrt{2}}{2},\ -\frac{\sqrt{6}}{6},\ \frac{\sqrt{3}}{6}\frac{1}{1+3\omega}\right)u^{-1}. \end{aligned}\right\} \tag{2}$$

General vector $\boldsymbol{n}$ denoting one of the points of the reciprocal lattice is then given by

$$\boldsymbol{n}=n_1\boldsymbol{f}_1+n_2\boldsymbol{f}_2+n_3\boldsymbol{f}_3\ . \tag{3}$$

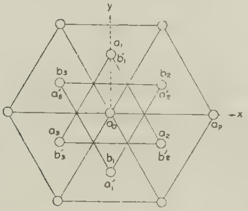

Fig. 1. The lattice structure of bismuth type crystal.

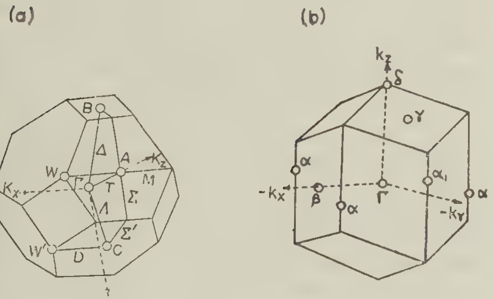

Fig. 2. The reduced zone (a) and the zone which can accommodate five electrons per atom (b).

Fig. 2(a) is the Brillouin zone surrounded by the planes such as (1, 0, 0), (1, 1, 1) and (1, 1, 0). Upper and lower hexagonal faces (the planes (1, 1, 1) and (−1, −1, −1)) and six side hexagonal like faces (the planes such as (1, 0, 0)) disappear in the simple cubic lattice. Fig. 2(b) is the Brillouin zone surrounded by the planes such as (1, −1, 0) (six side planes) and the planes such as (1, 2, 2) (six inclined planes). The latter planes disappear in the simple cubic lattice but the former do not. The points α_1, β and γ in Fig. 2(b) are transformed from the points A, B and C in Fig. 2(a) by the translation vectors given by $\boldsymbol{n}(-2, 0, 0)$, $\boldsymbol{n}(0, -2, 0)$ and $\boldsymbol{n}(0, 2, 2)$ respectively, i.e. these points are given by

$$\left.\begin{aligned} \alpha_1&=\left(0,\ -\frac{2\sqrt{6}}{3},\ \frac{\sqrt{3}}{6}\frac{1}{1+3\omega}\right)\frac{1}{2u},\\ \beta&=(-\sqrt{2},\ 0,\ 0)\frac{1}{2u},\\ \gamma&=\left(0,\ -\frac{\sqrt{6}}{3},\ \frac{5\sqrt{3}}{6}\frac{1}{1+3\omega}\right)\frac{1}{2u}. \end{aligned}\right\} \tag{4}$$

We proposed in I that the electrons occupying the states near the points A and C are responsible for the conduction phenomena of bismuth. While Jones proposed that in bismuth there are energy surface pockets of electrons at β and those of holes at δ. As was expressed already, the structure factor of the planes through β is not zero but two, irrespective of the crystal lattice being simple cubic or rhombohedral. Energy discontinuity should usually be large at such planes and the curvature of the energy curve along the perpendicular direction usually be small.

In Fig. 3 we give the energy curves along some symmetry directions. Fig. 3(a) was obtained with use of the secular equation in I (but by evaluating only few points). Fig. 3(b) and (c) were obtained by solving the secular equations in the case without spin, which were set up with use of the basis functions listed in Appendix. The notation used in the present paper is the same as in

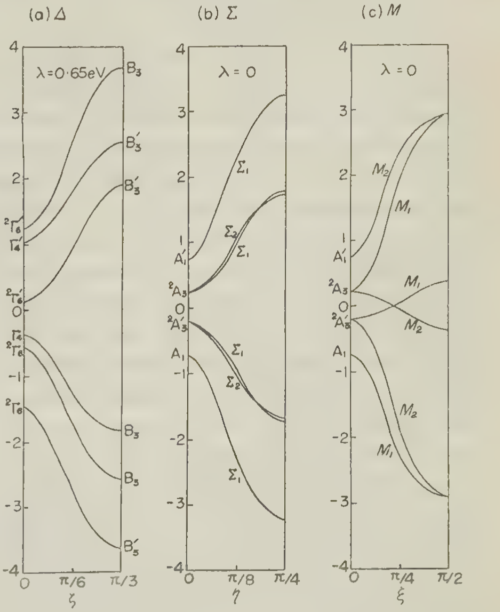

Fig. 3. Energy *versus* $\boldsymbol{k}$ curves along Δ, Σ and and M. The origin of the energy is arbitrary but the same in three cases. (Units ev).

I. The lattice parameters, energy integrals and others are taken the same as in I, i.e.

$$\left.\begin{array}{ll} \omega=0.0173\ , & \mathcal{E}=0.0548\ , \\ (pp\sigma)=1.1\,\mathrm{ev}\ , & (pp\pi)=-0.35\,\mathrm{ev}\ , \\ r_1=3\ , & r_2=6\ . \end{array}\right\} \quad (5)$$

The magnitude of the spin-orbit interaction parameter λ is shown in each figure. As was expected, the energy at β is far from the Fermi surface. In the case of $\lambda=0$, the energy curves along Σ are also far from the Fermi surface except in the immediate neighbourhood of the point A. This result may be unchanged even in the case of $\lambda \doteqdot 0$. Then we would have no interest in the present study, but it is not so along the line M. Without spin the bands M_1 and M_2 cross, but this crossing is got rid of by the spin-orbit interaction and the two bands are separated (see Table II (e) in I). This separation is small if λ is small. The energy curves along Σ' and D should be very similar to those along Σ and M respectively. If the electrons or holes are located somewhere on the lines M or D, we must consider six ellipsoids. If the maxima exist slightly in the zone, we have twelve ellipsoids.

We see the shift of the energy curves due to the change of the magnitude of λ. Since the lattice constants of bismuth and antimony are nearly equal (see Wilson: *The Theory of Metals* (1953) p. 63), the crystal field in the intermediate region of lattice points may not be modified so largely by alloying antimony in bismuth. The largest change in the crystal field should be the decrease in the average of the spin-orbit interaction energy. Although bismuth-antimony alloy is a disordered alloy, we will substitute the crystal potential of a disordered alloy by an average periodic potential, i.e. we neglect the dimness of the energy band due to the random distribution of atoms. Then we can to some extent express the effect of the alloying by the decreasing of the magnitude of λ, so far as we are interested in only the band shape. We show the result in Fig. 4. By decreasing the value of λ, the level $A_4'+A_5'$ goes down drastically but the level ${}^2A_6$ is almost constant, while the levels C_3+C_4 and $C_3'+C_4'$ go down more slowly than the level $A_4'+A_5'$. The energy gaps at A and C increase gradually.

§ 3. Discussion

On the present calculation together with the previous one we suppose that the electrons in bismuth may be located near the point γ (i.e. the point C), while the holes may be near the point α (i.e. A). This supposition is not in accord with Jones' speculation. In order to confirm our supposition, we will examine further whether our theory can explain various electronic properties relating to the energy surfaces.

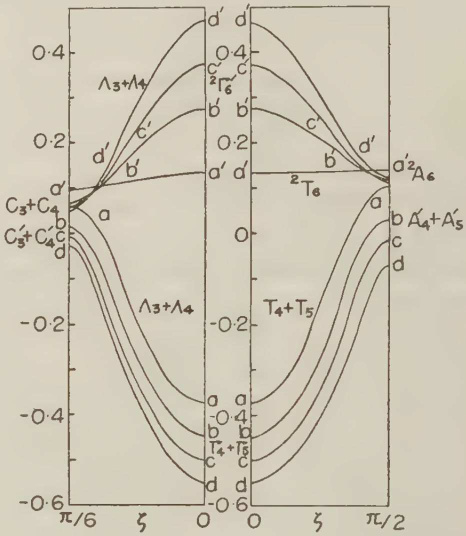

Fig. 4. Energy *versus* **k** curves. a, a′: $\lambda=0.65$ ev, b, b′: $\lambda=0.5$ ev, c, c′: $\lambda=0.4$ ev and d, d′: $\lambda=0.3$ ev. The origin of the energy is the same as that of Fig. 3. (Units ev).

As is known from early, the electrical conductivity, Hall coefficient, thermal conductivity, and thermoelectric power of bismuth-antimony alloy at room temperatures have respective extremum at the composition of about 16 atomic % antimony[3]. The diamagnetic susceptibility of this alloy changes monotonically with the concentration of antimony in the experiment up to 6 atomic %[3]. Recently Tanuma[4] studied these properties from the liquid helium to room temperatures and found similar behavior as in usual semiconductors in a certain range of the concentration of antimony. This behavior can be explained as follows. In the case of bismuth, the location of the electrons and holes was specified above. By alloying antimony having small value of the spin-orbit coupling parameter, the energy level $A_4'+A_5'$ at A gradually goes down relatively to the energy level C_3+C_4 at C. At some small percentage of antimony, the electrons at C and also the holes at A will be completely depleted and then various properties should become semiconductor like* (see the case of $\lambda=0.5$ ev in Fig. 4). By further alloying of antimony, the alloy will again become metallic, since pure antimony is a metal. For the alloy there are two possibilities of recovering metallic nature. One is that somewhere on the line M or D an unoccupied level M_3+M_4 or D_3+D_4 goes down under the level $C_3'+C_4'$ at C. Then the electrons at $C_3'+C_4'$ transfer into the level M_3+M_4 or D_3+D_4, i.e. the holes are produced at C. The other is that on the contrary to the above an occupied energy level on the line M or D is raised up relatively to the unoccupied level C_3+C_4 at C. Then the electrons at M or D transfer into the level C_3+C_4, i.e. the electrons are produced at C. As was already expressed, the levels C_3 and C_3' go down with the decrease of the value of λ. Then the former level becomes more favourable to be occupied by electrons and the latter becomes, on the contrary, more unfavourable to be occupied by holes. This result makes us prefer the second possibility. A natural deduction for the way of the moving of the energy levels in the alloying process is then that the extremum at or in the immediate neighbourhood of the point A moves away along the line M. The height of six or twelve maxima may be comparatively unmoving during this process (because of the crossing of two levels in the case of $\lambda=0$) and at a certain concentration (not so far from 16 atomic %) of antimony, the height of the extrema may again be raised up relatively to the level C_3. Thus, purely semiconductive region with a energy gap between the level C_3 and the maxima on the line M, even if possible, will be restricted in certain narrow range of the concentration of antimony and its energy gap should also be very small. We cannot rule out the possibility that the maxima do not go down under the level C_3, i.e. that there is no energy gap in any concentration, according to the following: If we assume the values of λ in bismuth and antimony to be 0.6 ev and 0.3～0.4 ev respectively and λ of this alloy to be that given by the ratio of the concentration, necessary quantity of antimony to deplete the electrons and holes at C and A is estimated to be more than 12～18 atomic %. This number is approximate, of course, but this result together with the experimental data of the electrical conductivity of the alloy at low temperatures⁴⁾ are rather favourable for this view.

The absence of the de Haas-van Alphen effect due to holes in bismuth remains unexplained. Our theory predicts that the energy surface near the point A has well defined effective mass and the magnitude of the effective mass is favourable order to observe the de Haas-van Alphen effect, if this part is the only energy surface of holes. This prediction is, however, not supported by experiments. Recent experiment of cyclotron resonance in bismuth⁵⁾ reports that there are majority carrier to be corresponded to the de Haas-van Alphen electrons and minority carrier with isotropic energy in the trigonal plane, and other broad lines in higher magnetic field region and comparatively narrow lines in lower field region which may be attributed to subharmonics of the minority carrier peak. Then we would modify a little the band structure near the point A as follows: The point A or slightly lower point is occupied by the minority carrier and along the line M six warped majority carrier surfaces are distributed in the immediate neighbourhood about the minority carrier surface. The former is minority holes with very small definite mass in the trigonal plane and the latter is majority holes which may have vaguely defined larger mass. This supposition of warped surfaces is not based upon the calculation, but is plausible according to Fig. 3(c). In high temperatures (for example above the liquid air temperature) or in samples having large excess of holes, this separation into seven hights is immaterial and the holes will behave like single surface with isotropic mass in the trigonal plane. This view is well suited to fair successes of Abeles-Meiboom's analysis⁶⁾ for galvanomagnetic effect and Lax *et al*'s analysis⁷⁾ for the cyclotron resonance data by Galt *et al*⁸⁾ and also to the experimental results of the de Haas-van Alphen effect and the cyclotron resonance mentioned above.

---

* Some interesting results on the deviation from typical semiconductor due to the random distribution of atoms or due to very slight overlapping of energy bands are reported by Tanuma (reference 4).

In the case of antimony, only one type of the de Haas-van Alphen period due to the energy pocket at C is observed. In order to fit this observation we consider that the hole energy surfaces on or near the line M will be warped surfaces or those with small curvature. Since, however, the energy separation between occupied and unoccupied bands should be fairly small on this line and the Hall coefficient of pure sample is positive, we must rule out the second possibility. In arsenic the situation may be very similar to that of antimony as deduced from Figs. 3 and 4. In this case, however, the overlapping is more pronounced and the Fermi level may pass just on the level ${}^2A_6$. Then we suppose that the long period in arsenic is due to the minority electrons.

The change of the magnetic susceptibility of the alloy is to be noted. In the diamagnetic susceptibility of bismuth (and also of antimony), the non-diagonal terms may be primarily important but the Landau diamagnetism is not, since we can estimate that the contribution of the conduction electrons to the Landau susceptibility is less than 20% of the experimental value as follows: First because of small concentration of carrier the contribution to the susceptibility due to the minority carrier should be negligible. This can be deduced from the present band calculation, the value of the effective mass estimated from the cyclotron absorption, and the absence of the de Haas-van Alphen effect. Secondly the ratio of the Landau susceptibility of majority holes to that of electrons is a little smaller than unity, if we approximate the hole surfaces with six or twelve maxima to be ellipsoidal and assume to be $m_\perp^{(h)}/m_\perp^{(e)} \gtrsim 3$ (basing upon the fact that the structure of the cyclotron absorption curve in high magnetic field mentioned above may be due to the majority holes) and $m_\parallel^{(h)} \sim m_\parallel^{(e)}$ in the magnetic field parallel to the bisectrix axis. This hole mass $m_\parallel^{(h)}$ parallel to the field is overestimated, since $m_\parallel^{(e)} \sim m_0$ and there is some evidence for $m_\parallel^{(h)} < m_0$.[5),7)] Then the contribution to the Landau susceptibility due to the holes is overestimated in the above evaluation. On the other hand the Landau susceptibility of the de Haas electrons is only 10% of the experimental value. These are all of the bases of our estimation. By alloying antimony in bismuth, three effects are to be considered. The energy gaps at C and A are broadened monotonically, the relative height varying as mentioned above, and the extrema where the holes are located may move away along the line M. The number of conduction electrons *versus* the concentration of antimony curve has a minimum about 16 atomic %, or there is a narrow region about this concentration in which electrons and holes are missing. The susceptibility due to filled band with small energy gaps at special points in $\boldsymbol{k}$-space may be strongly diamagnetic and may decrease monotonically with the concentration of antimony, because the effect from the points C and A are not probably counterbalanced by the other effect from points such as the maxima along M. If and only if we assume with Heine[9)] that total contribution of the conduction electrons is strongly paramagnetic, we can explain the susceptibility curve in small concentration of antimony given by Shoenberg and Uddin[3)]. In such an assumption, we expect that $-\chi$ curve will have a maximum about the concentration of 16 atomic % antimony, though there is not yet such an experimental report.

The author wishes to thank Professor K. Ariyama for his valuable advice of the manuscript.

Appendix. Basis Functions for Irreducible Representations of Single Groups of $\boldsymbol{k}$

We use the same notation as in I. $\nu = \mathcal{E}\pi/2(1+3\omega)$.

(i) Γ, A: $p=1$ for Γ, $p=-i\exp(-3\nu i)$ for A

$$\left.\begin{matrix}\psi(\Gamma_1)\\ \psi(\Gamma_1')\end{matrix}\right\} = \frac{\sqrt{2}}{2}(z \mp p\bar{z}) ,$$

$$\left.\begin{matrix}\psi({}^2\Gamma_3)\\ \psi({}^2\Gamma_3')\end{matrix}\right\} = \frac{\sqrt{2}}{2}(x \mp p\bar{x}) , \qquad \left.\begin{matrix}\psi'({}^2\Gamma_3)\\ \psi'({}^2\Gamma_3')\end{matrix}\right\} = \frac{\sqrt{2}}{2}(y \mp p\bar{y}) .$$

(ii) T

$$\psi_1(T_1)=z\ ,\qquad \psi_2(T_1)=\bar{z}\ ,$$

$$\psi_1({}^2T_3)=x\ ,\quad \psi_1'({}^2T_3)=y\ ,\qquad \psi_2({}^2T_3)=\bar{x}\ ,\quad \psi_2'({}^2T_3)=\bar{y}\ .$$

(iv) $\Lambda, \Delta, \Sigma, \Sigma'$

$$\psi_1(\Lambda_1)=y\ ,\qquad \psi_2(\Lambda_1)=\bar{y}\ ,$$

$$\psi_3(\Lambda_1)=z\ ,\qquad \psi_4(\Lambda_1)=\bar{z}\ ,$$

$$\psi_1(\Lambda_2)=x\ ,\qquad \psi_2(\Lambda_2)=\bar{x}\ .$$

(iii) B, C: $p=\exp(-2\nu i)$ for B, $p=-i\exp(-\nu i)$ for C

$$\left.\begin{matrix}\psi_1(B_1)\\ \psi_1(B_1')\end{matrix}\right\}=\frac{\sqrt{2}}{2}(y\mp p\bar{y})\ ,$$

$$\left.\begin{matrix}\psi_2(B_1)\\ \psi_2(B_1')\end{matrix}\right\}=\frac{\sqrt{2}}{2}(z\mp p\bar{z})\ ,$$

$$\left.\begin{matrix}\psi(B_2)\\ \psi(B_2')\end{matrix}\right\}=\frac{\sqrt{2}}{2}(x\mp\bar{x})\ .$$

(v) M, D: $p=\exp(-3\nu i)$ for M, $p=\exp(-\nu i)$ for D

$$\left.\begin{matrix}\psi_1(M_1)\\ \psi_1(M_2)\end{matrix}\right\}=\frac{\sqrt{2}}{2}(x\mp ip\bar{x})\ ,$$

$$\left.\begin{matrix}\psi_2(M_1)\\ \psi_2(M_2)\end{matrix}\right\}=\frac{\sqrt{2}}{2}(y\pm ip\bar{y})\ ,$$

$$\left.\begin{matrix}\psi_3(M_1)\\ \psi_3(M_2)\end{matrix}\right\}=\frac{\sqrt{2}}{2}(z\pm ip\bar{z})\ .$$

References

1) S. Mase: J. Phys. Soc. Japan **13** (1958) 434.
2) H. Jones: Proc. Roy. Soc. **A**, **147** (1934) 396.
3) W. Haken: Ann. Physik [4] **32** (1910) 326. A. W. Smith: Phys. Rev. **32** (1911) 183. G. Gehlhoff and F. Neumeier: Verh. deut. physik. Ges. **15** (1913) 88, 876. D. Shoenberg and M. Z. Uddin: Proc. Roy. Soc. **A**, **156** (1936) 687.
4) S. Tanuma: read on March 29 and October 19, 1958, at the Meeting of the Physical Society of Japan.
5) B. Lax: Rev. Mod. Phys. **30** (1958) 122.
6) B. Abeles and S. Meiboom: Phys. Rev. **101** (1956) 544.
7) B. Lax, K. J. Button, H. J. Zeiger and L. M. Roth: Phys. Rev. **102** (1956) 715.
8) J. K. Galt, W. A. Yagar, F. R. Merritt, B. B. Cetlin and H. W. Dail: Phys. Rev. **100** (1955) 748.
9) V. Heine: Proc. Phys. Soc. London **A**, **69** (1956) 513.

JOURNAL OF THE PHYSICAL SOCIETY OF JAPAN, Vol. 14, No. 5, MAY, 1959

Internal Friction of Lead, II

By Yosio HIKI

The Government Mechanical Laboratory, Suginami-ku, Tokyo, Japan

(Received February 7, 1959)

The experimental results on the internal friction of lead single crystals were discussed on the basis of the dislocation theory. At low temperatures, the dependences of the internal friction on the strain amplitude and the frequency are well explained with the pinned-down dislocation model. The pinning of dislocations by point defects is also varified to exist through analyzing the change of the amplitude dependence of the internal friction produced by annealing the specimen. The exponential increase of the internal friction with increasing temperature is considered to be due to the thermal break-away of the dislocations from the pinning points. On the assumption that the Cottrell's force acts between the pinning impurity atom and the dislocation, some of the unknown quantities of a crystal can be determined as follows: dislocation density is $1.03 \times 10^8\,\mathrm{cm}^{-2}$, loop length of dislocation network 1.71×10^{-4} cm, and mean distance between impurities on dislocation 2.85×10^{-5} cm. Above a certain temperature (about 300°K) the internal friction decreases with increasing strain amplitude, being the reverse of the behavior at low temperatures. This phenomenon is interpreted as the impurity pinning becomes ineffective at high temperatures and the formation of jogs at the network pinning points of the dislocations contributes to the internal friction.

§ 1. Introduction

The internal friction of lead single crystals has been measured as a function of the strain amplitude, frequency and temperature, and the results were described in the earlier paper$^{1)}$ (hereafter called part I). The following is an analysis of these experimental data by the dislocation theory of internal friction. As will be shown in § 2–§ 5, the behavior of the internal friction at low temperatures is well understood by the "pinned-down" dislocation theory established by Granato and Lücke$^{2)}$. In § 6 and § 7, the temperature dependence of the internal friction will be taken into account and another mechanism will be proposed as an origin of the internal friction at high temperatures. Some transient phenomena will also be discussed briefly (§ 8).

§ 2. Pinned-down Dislocation Theory

The "pinned-down" dislocation theory of internal friction of Granato-Lücke$^{2)}$ can be summarized as follows. Crystalline solid contains a network of dislocations, their intersections being usually immovable. The network loops of dislocations are further pinned down or fixed by point defects which exert forces on the dislocation lines. The internal friction originated from the vibration of dislocation lines may have two types. The first is the dynamic one due to the damping force against the movement of the dislocation. The expression for this internal friction is obtained by solving the equation of motion of a dislocation line segment between pinning points which vibrates under the influence of the external alternating stress. The damping force is assumed to be proportional to the velocity of the dislocation though its origin has not been well understood. The second is one of the static hysteresis type due to the break-away of the dislocation line from the pinning by point defects. The dissipation of energy corresponds to the area of the hysteresis loop in the stress—dislocation strain diagram during one cycle of the external vibration. If the frequency of the external force is in the kilocycle range, the internal friction of a single crystal is expressed as a sum of these two losses, δ_i and δ_h, the former being frequency dependent and amplitude independent while the latter frequency independent and amplitude dependent. When the point defects are arranged randomly along the dislocation lines, these are given by$^{2)}$

$$\delta_i = \frac{5!\,\Omega\Delta_0}{\pi^2 c}\Lambda L_e{}^4 B\omega\ ; \qquad L_e = 3.31 L_c\ , \tag{1}$$

$$\left.\begin{aligned} \delta_h &= \frac{c_0}{\mathcal{E}^{1/2}}\exp(-c_1/\mathcal{E})\ ; \\ c_0 &= \frac{2\Omega\Delta_0}{\pi^2}\left(\frac{F}{bsE}\right)^{1/2}\frac{\Lambda L_n{}^3}{L_c{}^{3/2}}\ , \\ c_1 &= \frac{2F}{\pi bsE}\cdot\frac{1}{L_c}\ . \end{aligned}\right\} \tag{2}$$

There is also an associated change of the elastic modulus. The fractional changes of Young's modulus are given by

$$(\Delta E/E)_i = \frac{6\Omega\Delta_0}{\pi}\Lambda L_c{}^2\ , \tag{3}$$

$$(\Delta E/E)_h = \frac{c_0}{\mathcal{E}^{1/2}}\exp(-c_1/\mathcal{E})\ . \tag{4}$$

In these equations, the main variables are the angular frequency of the vibration ω and the strain amplitude of the specimen $\mathcal{E}$. E is Young's modulus along specimen axis, G shear modulus along slip direction, ν Poisson's ratio, b Burgers vector, Ω orientation factor, s resolved shear stress factor and $\Delta_0 = 4(1-\nu)/\pi^2$, $c = 2Gb^2/\pi(1-\nu)$. In a f.c.c. lattice, $s = \cos\theta\cos\varphi$ and $\Omega = (E/G)(s^2/12)$, where θ is the angle between the specimen axis and the normal to the slip plane, and φ the angle between the specimen axis and the slip direction. Λ is the total length of dislocation lines per unit volume of the specimen, L_n loop length of dislocation network, L_c mean distance between point defects on the dislocation line, F the maximum binding force between point defect and dislocation, and B damping constant for dislocation movement. Among the above quantities, Λ, L_n, L_c, F and B are unknown, which may be determined by comparing the theory with experiments. The value of L_c takes the exponential distribution in the present case while L_n is assumed to be constant throughout a specimen.

§ 3. Qualitative Confirmations of the Theory

At low temperatures, the experimental results on the internal friction of lead are well explained by the pinned-down dislocation theory as follows:

(i) δ increases with increasing $\mathcal{E}$ [Fig. 2 in part I], and there is a linear relationship between $\log \mathcal{E}^{1/2}\delta_h$ and $\mathcal{E}^{-1}$ as shown in Fig. 1, fitting to Eq. (2). The values of c_0 and c_1 can be determined by the intercept and the slope of this straight line, respectively.

(ii) The plots of δ_h against $\mathcal{E}$ for the same specimen measured with different frequencies lie on the same curve [Fig. 3 in I], namely, δ_h is independent of the frequency.

(iii) The fractional change of Young's modulus associated with the change of the strain amplitude, $(\Delta E/E)_h$, is proportional to δ [Fig. 4 in I], as expected by comparing Eqs. (2) and (4).

(iv) In the low temperature region, δ measured with small strain amplitude seems to be proportional to the frequency [Fig. 9 in I], being consistent with Eq. (1).

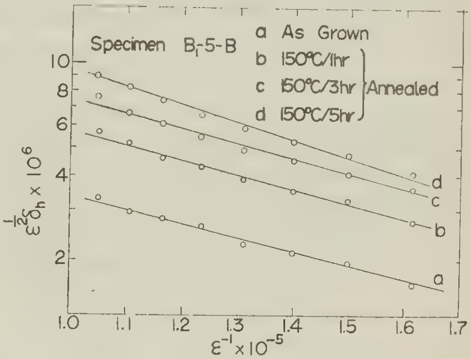

Fig. 1. Analysis of amplitude dependence of internal friction.

§ 4. Migration of Point Defects to Dislocations

In order to inspect the pinned-down model, the effect of annealing upon the amplitude dependence of the internal friction is to be examined. Cottrell and Bilby[3] offered a theory of strain ageing of metals and calculated the migration velocity of impurity atom to dislocation line under the influence of its stress field. According to them, in the early stage of ageing, the number of solute atoms which arrive at the unit length of dislocation line within time t is given by

$$n(t) = \alpha n_0\left(\frac{ADt}{kT}\right)^{2/3}\ , \tag{5}$$

where $\alpha = 3(\pi/2)^{1/3}$, n_0 is the total number of atoms in solution, $A = [4(1+\nu)/3(1-\nu)]Gber^3$, $e = (r-r')/r$, r and r' are the radii of solvent and solute atoms, $D\ (= D_0\exp(-Q/RT))$ is the diffusion coefficient and kT has its usual meaning. Using the theory described in § 2, the following relation is obtained from Eq. (2):

$$n(t)=\frac{1}{L_c(t)}-\frac{1}{L_c(0)}=\frac{\pi bsE}{2F}\,[c_1(t)-c_1(0)]\ ,$$

if there exists one point defect at a pinning point. Combining this with Eq. (5), we obtain

$$[c_1(t)-c_1(0)]=\beta\left[\frac{\exp(-Q/RT)}{T}\right]^{2/3}t^{2/3}\ , \qquad (6)$$

where β is a temperature-independent constant, Q is the activation energy for the diffusion of the point defect and t corresponds to the annealing time.

The amplitude dependence of the internal friction of a lead crystal received successive annealing has been measured at 8°C. From the analysis of the experimental data, the values of c_1 for the crystal as grown and annealed at 150°C for 1, 3 and 5 hours can be determined as shown in Fig. 1. Using these values, $[c_1(t)-c_1(0)]$ are plotted against $t^{2/3}$ in Fig. 2. These lie on a straight line as asserted by Eq. (6). The same specimen was also annealed at 135°C for 1, 3 and 5 hours; at 120°C for 1, 3 and 5 hours; at 105°C for 2, 4 and 7 hours, successively. Similar straight lines are also obtained for each annealing temperature as shown in Fig. 2. The activation energy can be calculated from these results with the usual method as shown in Fig. 3: $Q=26.6\pm0.8$ kcal/mol·deg.

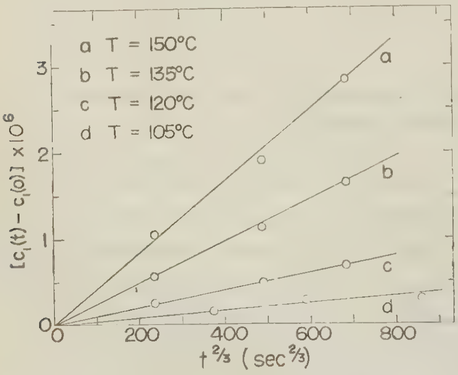

Fig. 2. Analysis of effect of annealing upon amplitude dependence.

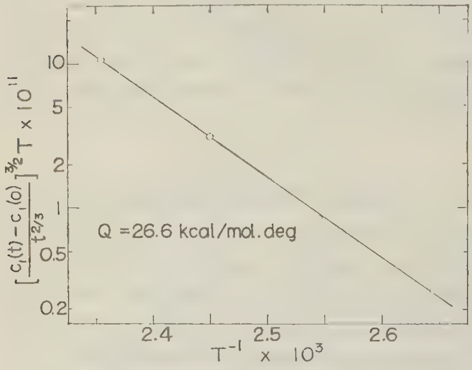

Fig. 3. Determination of activation energy for diffusion of point defect.

It is concluded that, in the present case, the dislocation are certainly pinned down by some point defects. The pinning agents may probably be impurity atoms. This has been suggested from the result of etch pits observation by the present author[4]. The number of etch pits per unit area on the lead single crystal made from the same material increases with increasing annealing time. This is explained by the fact that the impurity atoms migrate to the dislocation with prolonged annealing, because etch pit is considered to be produced by the combination of dislocation with impurity. The impurity atom acting as the pinning agent may be carbon, because it is the main impurity detected in the material [Table I in part I]. Although the direct measurement of the diffusion coefficient of carbon in lead has not yet appeared, the value of the activation energy obtained above ($Q=26.6$ kcal/mol·deg) seems to be quite reasonable. For the purpose of comparison the activation energies for diffusion of various elements determined by usual method are listed in Table I.

Table I. Activation energies for diffusion of various elements in lead. (in kcal/mol·deg)

I	II	III	IV	V
Ag	Cd	In	Sn	Sb
15.2	15.4	—	26.2	—
Au	Hg	Tl	Pb	Bi
14.0	19.0	19.4–24.6	27.9	18.4

§ 5. Numerical Evaluation of Unknown Quantities

The quantities appearing in Eqs. (1) and (2), A, L_n, L_c, F and B, can be calculated using some assumptions.

The crystal is considered to be broken up into blocks, dislocation lines forming the edges of these blocks. It is assumed that there is one dislocation per block face. This is fairly confirmed by X-ray experiments in the case of well-annealed crystals[5]. In this case, the following relation holds:

$$A=3L_n^2\ . \qquad (7)$$

Further assumptions are that the pinning agents are carbon atoms in the present case and that the force between the pinning atom and the dislocation line is that of Cottrell's⁶⁾. The binding energy between an impurity atom and a dislocation line is given by

$$U_0=\frac{4}{3}\frac{(1+\nu)}{(1-\nu)}\frac{Gber^3}{r_0}=A/r_0\ , \tag{8}$$

where A is the same constant as that in Eq. (5), and r_0 is the distance between a dislocation line and an impurity atom at the equilibrium position, being several times the Burgers vector. The maximum binding force between a dislocation line and an impurity atom is also given by

$$F=(3\sqrt{3}/8)A/r_0^2\ . \tag{9}$$

From the amplitude dependence of the internal friction of the specimen B₁–5–B annealed at 150°C for 60 hours, c_0 and c_1 in Eq. (2) are determined as stated in § 3. Inserting these values together with the value of δ_i at low temperatures into Eqs. (1), (2), (7) and (9), and regarding r_0/b as a parameter, the values of A, L_n, L_c, F and $B\,(\equiv B_1+B_2T)$ can be calculated. The value of δ_i in the region where the internal friction increases slightly with increasing temperature is used in the present case. The value of U_0 is also known from Eq. (8). The results are listed in Table II.

Table II.

r_0/b	$r_0\times10^8$ cm	$A\times10^{-7}$ cm^{-2}	$L_n\times10^4$ cm	$L_c\times10^5$ cm	$F\times10^6$ dyne	$B_1\times10^3$ gr/sec·cm	$B_2\times10^5$ gr/sec·cm·deg	U_0 kcal/mol·deg
1	3.50	0.08	18.9	31.5	9.13	0.11	0.03	7.30
2	7.00	1.33	4.74	7.90	2.29	1.80	0.45	3.65
3	10.5	6.73	2.11	3.52	1.02	9.00	2.25	2.44
5	17.5	52.5	0.76	1.26	0.37	70.7	17.7	1.46
7	24.5	200	0.39	0.65	0.19	269	67.3	1.05

§ 6. Effect of Temperature

The temperature dependence of the internal friction was not taken into account explicitly until now. At low temperatures, the internal friction of lead increases slightly with increasing temperature. This can be explained by the change of the damping constant B with temperature. As temperature is raised further, the internal friction increases steeply [Fig. 6 in part I], and this has been also observed by Bordoni *et al.*⁷⁾ and Weertman *et al.*⁸⁾ The phenomenon can be found in other metal single crystals, and some theories have been proposed to interpret it, by taking account of thermal motion of dislocations⁹⁾,¹⁰⁾.

The experimental results on the temperature dependence of the internal friction of lead will be analyzed as follows. The temperature-dependent part of the internal friction δ_T measured with small strain amplitude varies as $\exp(-U/RT)$, as shown in Fig. 4. The values of U of some specimens are listed in Table III. This behavior is considered to be due to the rate-controlling process so that the dislocations are thermally activated and broken away from the impurity pinning. Then U corresponds to the work to tear away the dislocation loop between network pinning points from impurity atoms. When the interaction between them is of Cottrell type, U is approximately U_0 times the number of impurity atoms on the dislocation loop, namely,

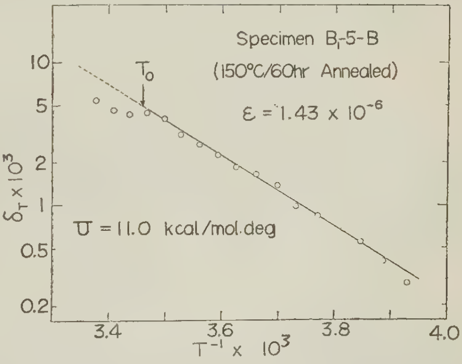

Fig. 4. Temperature dependence of internal friction at $T<T_0$.

$$U=U_0\times\left(\frac{L_n}{L_c}-1\right)\ . \tag{10}$$

As can be seen in Table III, the values of U

Table III.

Specimen	Purity	Treatment	$f(T_0)$ kc	U kcal/mol·deg	T_0 °K	ν_0	Ref.
B_1-5-B (single)	99.99%	150°C/60 hr annealed	64.9	11.0	289	1.4×10^{13}	1)
B_2-6-C (single)	99.99%	as grown	63.0	10.7	>306	$<3.0\times10^{12}$	1)
B_2-6-C (single)	99.99%	150°C/40 hr annealed	64.9	13.2	318	7.7×10^{13}	1)
Pb (single)	0.003 at. % C	—	30	22.2	520	6.8×10^{13}	8)
Pb-Sn (single)	0.058 at. % Sn	—	30	11.5	536	1.4×10^{9}	8)
n 1 (poly.)	Merk C.P.	machined	26.2	8.57	400	1.3×10^{9}	7)

are different in different specimens, probably due to the different impurity contents. In the same specimen, the value of U increases by prolonged annealing, as expected from the migration of the impurities to the dislocations.

In the above discussion, it is assumed that the concentration of the impurity atoms on the dislocation line, a/L_c, does not change during the measurement (a means the lattice parameter). This assumption seems to be reasonable because the migration velocity of the impurity is small even at 150°C [cf. §4]. The measuring temperature is lower than 70°C and long time is not wanted for measurement. On the contrary, if sufficient time is allowed for the atomic migration to occur, the concentration of impurities on dislocation is given by[6)]

$$C=C_0\exp(U_0/RT)\ , \qquad (11)$$

where C_0 is the average concentration in the crystal. From Eqs. (1) and (11), it is derived that δ_i is proportional to $\exp(-4U_0/RT)$. But this argument is not available to the analysis of the present experiment.

At higher temperatures, impurity atoms cannot pin down the dislocation line effectively. This occurs when the time required for a dislocation loop is broken away from impurity pinning by thermal fluctuations becomes smaller than the period of the external alternating stress, as stated by Weertman[11)], namely,

$$f\leqq\nu_0\exp(-U/RT)\ , \qquad (12)$$

where f is the frequency of the external stress, ν_0 the frequency of the thermal vibration of the dislocation loop. The critical temperature which corresponds to the equality in Eq. (12) may be the anomalous temperature T_0 which appears near 300°K in Figs. 6 and 7 in part I. This can be understood from the fact that δ decreases with increasing ε at temperatures higher than T_0. At lower temperatures, on the other hand, δ increases with increasing ε and this is the characteristic feature of the internal friction originated from the pinned-down dislocations [Fig. 8 in I]. The similar anomalous point can also be seen in the δ *vs* T curves observed by other authors [Figs. 6 and 11 in Weertman's[8)] and Fig. 2 in Bordoni's[7)]]. The reversal of the amplitude dependence near that temperature, however, did not seem to be examined by them. The frequency ν_0 can be calculated by Eq. (12), using the experimental values of U and T_0. These are summarized in Table III. The values of ν_0 are in the range between 10^9 and 10^{13}, which are in agreement with the usually accepted values of the frequency of the thermal vibration of dislocation.

Using the results obtained in §5 and Eq. (10) together with the experimental value of U, the various quantities for the specimen B_1-5-B, annealed at 150°C for 60 hours, can be determined without any undetermined parameter:

$$A=1.03\times10^{8}\ \mathrm{cm}^{-2}\ ,$$

$$L_n=1.71\times10^{-4}\ \mathrm{cm}\ ,$$

$$L_c=2.85\times10^{-5}\ \mathrm{cm}\ ,$$

$$F=8.25\times10^{-7}\ \mathrm{dyne}\ ,$$

$$B=(1.38\times10^{-2}+2.46\times10^{-5}T)\ \mathrm{gr/sec\cdot cm}\ ,$$

$$U_0=2.21\ \mathrm{kcal/mol\cdot deg}=0.093\ \mathrm{eV}\ ,$$

$$r_0=1.17\times10^{-7}\ \mathrm{cm}=3.33\times b\ .$$

The values of A, L_n and r_0 seem to be quite reasonable.

If the impurity atoms are in thermal equilibrium in the crystal, the average concentration of the impurity in the specimen can be calculated through inserting the values of U_0, $C=a/L_c$, and the annealing temperature $T=$

423°K into Eq. (11). It follows that $C_0=1.25\times10^{-4}$ while the concentration of carbon in lead determined by chemical analysis is 1.2×10^{-3}. This discrepancy may be explained as follows. (i) The solubility of carbon in lead is small and solute atoms are only a little part of the total carbon atoms. (ii) The specimen is not annealed perfectly yet. (iii) The material is purified in the course of making the single crystal.

Regarding the damping constant B, Leibfried[12] has analyzed the mechanism of damping, considering the scattering of phonons which impinge on the moving dislocations. From his formula, $B=9.5\times10^{-6}T$ is obtained for lead. Damping mechanisms proposed by other authors offer smaller values of B.

§ 7. Higher Temperature Region

As shown in Fig. 5, the internal friction in the temperature region higher than T_0 is expressed as

$$\delta=\delta_0+K/\mathcal{E}\ . \tag{13}$$

δ_0 is amplitude-independent and almost temperature-independent and K is sensitively dependent on temperature. The factor K varies as $\exp(-U'/RT)$ as shown in Fig. 6. The value of U' for the specimen B$_1$–5–B is found to be 13.5 kcal/mol·deg. These experimental facts will be explained as follows.

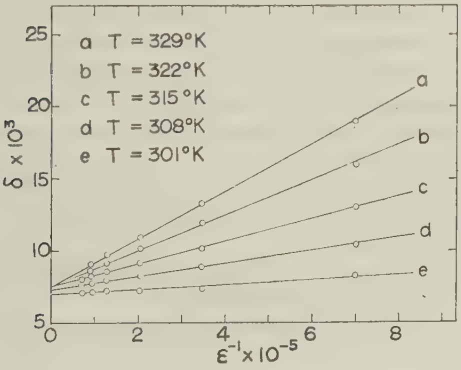

Fig. 5. Amplitude dependence of internal friction at $T>T_0$.

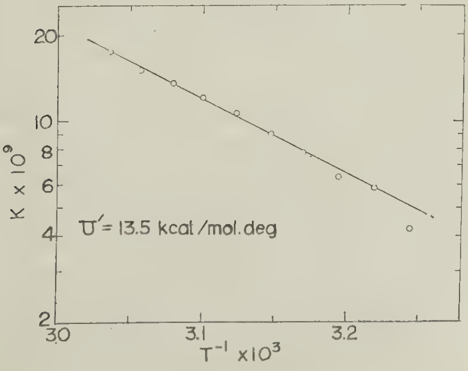

Fig. 6. Temperature dependence of factor K.

At temperatures higher than T_0, dislocations are not effectively pinned down by impurity atoms but pinned only by the intersections with other dislocation lines. The dislocation loop vibrates rather freely and produces a jog at the intersecting point. The formation of the jog is essentially an irreversible process of energy dissipation, since interstitial atoms or vacancies must be created and destroyed. According to Cottrell, the activation energy to form a jog is given by[13)]

$$U_0'=\gamma Gb^3-\sigma(t)L_n b^2\ , \tag{14}$$

where $\sigma(t)$ is the resolved shear stress of external force and γ is a constant of the order unity. The total increment of shearing strain produced by dislocation in the time interval dt is given by

$$d\mathcal{E}=K'\exp(-U_0'/RT)\,dt\ , \tag{15}$$

where K' is proportional to the frequency of vibration of dislocation and also depends on the geometry of dislocation. By definition, the internal friction is calculated as

$$\delta=\Delta W/2W=\int_{\text{cycle}}\sigma\, d\mathcal{E}/(\sigma_0^2/E)\ , \tag{16}$$

where σ_0 is the maximum shear stress. In the present case, the second term in U_0' given by Eq. (14) is estimated to be negligible in comparison with the first. Accordingly, the internal friction can be calculated from Eqs. (14), (15) and (16):

$$\delta=(K''/\mathcal{E})\exp(-U_0'/RT)\ , \tag{17}$$

where K'' is a constant. This conclusion is in good agreement with the experimental facts. If the value of U' is compared with U_0', γ is calculated to be about 0.3.

§ 8. Transient Phenomena

The internal friction of single crystal is markedly structure-sensitive and affected by slight cold-work. The change of the internal friction just after mounting the specimen [Fig. 1 in part I] may be due to recovery process associated with some unstable imperfections produced by handling the crystal. The large peak, which is also observed in the case of other pure metals[14], may be caused by the rearrangement of unstable dislocations. The smaller peak appearing in the earlier stage of the recovery of the quenched specimen may be originated from other kinds of imperfections.

Some of the irreproducible peaks at low temperatures on the internal friction *vs.* temperature curves, which vanish away when the specimen is annealed well [Fig. 6 in I], may be the result of "avalanche" process, namely, sudden movements of unstable dislocations provoked by the external vibrating stress[15],[16].

The apparent hysteresis in the internal friction *vs.* strain amplitude curve and the relating recovery-like phenomena [Fig. 5 in I] cannot be explained by the impurity-pinning model of dislocations. The model predicts that the dislocations, which break away from the impurity-pinning points and bow out during the increasing part of the stress cycle, collapse completely and are again pinned down by impurities in the other half-cycle. There must be one-to-one correspondence between the internal friction and the strain amplitude, being in disagreement with the present experimental facts. The activation energy of the recovery can be estimated from the curve of Fig. 5(b) in I. The value obtained is 8.8 kcal/mol·deg, being nearly one third of the activation energy for the self-diffusion of lead. The recovery may be attributed to the migration of vacancies[17] and these phenomena may be related to the vacancies formed by the vibrating dislocations.

Acknowledgements

The author wishes to express his sincere gratitudes to Dr. T. Kawada for his encouragement during the course of this work. He is also greatly indebted to Professor Y. Tomono and Professor R. R. Hasiguti for their kind advices. Thanks are also due to Mr. A. Hikata for his valuable discussions.

References

1) Y. Hiki: J. Phys. Soc. Japan **13** (1958) 1138.
2) A. Granato and K. Lücke: J. Appl. Phys. **27** (1956) 583, 789.
3) A. H. Cottrell and B. A. Bilby: Proc. Phys. Soc. London **A**, **62** (1949) 49.
4) Y. Hiki: J. Phys. Soc. Japan **13** (1958) 970.
5) G. K. Williamson and R. E. Smallman: Phil. Mag. **1** (1956) 34.
6) A. H. Cottrell: *Report of a Conference on Strength of Solids.* (Univ. Bristol, Phys. Soc., London, 1948) 30.
7) P. G. Bordoni and M. Nuovo: Nuovo Cimento **11** (1954) 127.
8) J. Weertman and E. I. Salkovitz: Acta Met. **3** (1955) 1.
9) W. P. Mason: J. Acoust. Soc. Amer. **27** (1955) 643.
10) J. Weertman: J. Appl. Phys. **28** (1957) 193.
11) J. Weertman: J. Appl. Phys. **26** (1955) 202.
12) G. Leibfried: Z. Phys. **127** (1950) 344.
13) A. H. Cottrell: *Dislocations and Plastic Flow in Crystals.* (Oxford Univ. Press, Oxford, 1953) 174.
14) A. S. Darling: J. Inst. Metals **85** (1957) 489.
15) H. Birnbaum and M. Levy: Acta Met. **4** (1956) 84.
16) A. J. Filmer, G. J. Hutton and T. S. Hutchison: J. Appl. Phys. **29** (1958) 146.
17) J. A. Manintveld: Nature **169** (1952) 623.

JOURNAL OF THE PHYSICAL SOCIETY OF JAPAN, Vol. 14, No. 5, MAY, 1959

Precipitation Process of Carbon in Alpha-Iron

By Tetsuro SUZUKI* and Yuzo TOMONO

Department of Physics, Faculty of Science, Tokyo University

(Received February 7, 1959)

The precipitation process of carbon in alpha-iron was studied by measuring the internal friction, and by observing the precipitates by electron microscope. The experimental results are expressed fairly well by the formula which expresses the sum of the two processes, one being the absorption of carbon atoms by the precipitates by way of dislocations and the other being the absorption of carbon atoms through the surfaces of the precipitates by the diffusion-limited process. The observation of the precipitates supports this explanation of the precipitation process.

§ 1. Introduction

The internal friction of alpha-iron containing carbon and nitrogen as solute atoms has been exhaustively studied by Snoek[1)] and Dijkstra[2)]. They have found that the internal friction arising from the stress-induced interstitial diffusion of solute atoms has a maximum at the temperature, at which the jumping frequency of interstitial atoms coincides with 2/3 of the measuring frequency, and that the amount of the maximum internal friction is proportional to the number of atoms in solid solution. By measuring the internal friction caused by the jumping of solute atoms, it is possible to estimate the amount of solute atoms at each stages of the aging treatment.

We have estimated the fraction of precipitated carbon atoms from the measurement of the internal friction, and have observed the shape of the precipitates by means of electron microscope.

§ 2. Aging Experiment on Wire Specimens

The specimens in the form of wire about 1 mm in diameter and 14 cm in length were used in this experiment. In order to eliminate both carbon and nitrogen atoms completely from the initial specimens, they were heated at 800°C for a few days within an atmosphere of dry hydrogen. Wert[3)] has shown that the precipitation process of carbon is correlated intimately with the precipitation of nitrogen if nitrogen is present. Therefore, it is necessary to check the nitrogen content in studying the precipitation process of carbon. For this purpose, the internal friction was measured at various temperatures. In case the peak of internal friction caused by the diffusion of carbon or nitrogen was detectable, decarburizing and denitriding treatment was repeated. By this procedure the contents of carbon and nitrogen were reduced to less than 5×10^{-4} wt. per cent. In the next step, the specimen was heated up to 700~800°C in an atmosphere of dry hydrogen and cyclohexane and then was quenched from 720°C on a copper plate, in order to dissolve appropriate amount of carbon atoms into the specimen.

The specimens containing carbon atoms about 0.009 wt. per cent in solid solution were cold-worked by 0, 0.93, 2.2, 3.3 and 4.3 per cent respectively after quenching. These specimens were aged at 100°C. The internal friction, the magnitude of which is proportional to the amount of carbon in solid solution, was measured at proper aging intervals by torsion pendulum. We can thus obtain the quantity q, the relative amount of carbon atoms which has precipitated during the aging

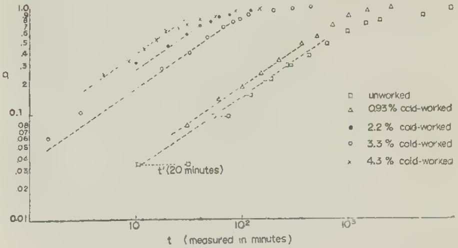

Fig. 1. Aging of cold-worked and unworked specimens at 100°C.

---

[*] Present address: The Toshiba Transistor Plant. 1, Komukai-Toshiba-cho, Kawasaki-shi, Kanagawa-ken, Japan.

time t. $\log q$ vs. $\log t$ is plotted in Fig. 1. In the worked specimens, q was found to be proportional to $t^{2/3}$ in the initial stages of the precipitation process. On the other hand, in the unworked specimens, q was found to be proportional to $(t-t')^{2/3}$, where t' is constant, in the initial stages of the precipitation process.

§ 3. Analysis of the Aging Experiment

If the precipitation process is to be described as the formation of Cottrell atmosphere[4)], the relative amount of precipitated carbon atoms, as Harper has shown[5)], will be given by the formula

$$q=1-\exp\left[-3L\left(\frac{\pi}{2}\right)^{1/3}\left(\frac{ADt}{kT}\right)^{2/3}\right] \tag{1}$$

where L is the dislocation density, D is the diffusion coefficient of interstitial carbon atoms in alpha-iron and A is a constant that depends on the elastic constants of the matrix, on the volume change caused by a solute atom, and on the magnitude of the Burgers vector of the dislocation. For the initial stages of the precipitation process, Eq. (1) reduces to

$$q\sim 3L\left(\frac{\pi}{2}\right)^{1/3}\left(\frac{ADt}{kT}\right)^{2/3}$$

As shown in Fig. 1, this $t^{2/3}$ law for the precipitation process holds for the worked specimens in the initial stages of the precipitation process. Also for the unworked specimen, if the effective aging time is taken to be $t-t'$, where t is the aging time and t' is about 20 minutes, the relative amount of precipitated carbon atom q is proportional to $(t-t')^{2/3}$ in the initial stages of the precipitation process.

If the experimental results obey Eq. (1), $\ln(1-q)$ plotted vs. t will be on a straight line. In our experiment, the experimental results of the unworked specimen plotted in $\ln(1-q)$ vs. $(t-t')^{2/3}$ are nearly on a straight line. However, the experimental results of the worked specimen plotted in $\ln(1-q)$ vs. $t^{2/3}$ are not on a straight line, but on a curved line concave downwards. This fact indicates that the precipitation rate becomes faster than Eq. (1) indicates in the later stages of the precipitation process.

According to Eq. (1), the rate of precipitation will be given as follows:

$$\left.\begin{aligned}\frac{1}{1-q}\frac{dq}{dt}&=\frac{2}{3}\frac{1}{\tau_d}\left(\frac{t}{\tau_d}\right)^{-1/3}\\ \tau_d&=(3L)^{-3/2}\left(\frac{\pi}{2}\right)^{-1/2}\frac{kT}{AD}\end{aligned}\right\} \tag{2}$$

Taking into account that the Cottrell atmosphere will be saturated with carbon atoms of 10^{-4} wt. per cent for density of dislocation as high as 10^{10}, the carbon atoms gathered by the attractive force of the dislocations are considered to be absorbed by the precipitates nucleated at some favourable point on the dislocation lines, for example at dislocation jogs. The carbon atoms absorbed by the dislocation will be drifted to the precipitates in negligible time which absorb carbon atoms also directly through their surfaces by the rate as is given by the following expression[6)]:

$$\left.\begin{aligned}\frac{1}{1-q}\frac{dq}{dt}&=\frac{3}{2}\frac{1}{\tau_c}q^{1/3}\\ \tau_c&=\left(\frac{3}{4\pi N}\right)^{2/3}\frac{1}{2D}\left(\frac{n_0-n_1}{n_\infty(0)-n_1}\right)^{1/3}\end{aligned}\right\} \tag{3}$$

where N is the density of precipitates nucleus and n_0, $n_\infty(0)$ and n_1 are the concentration of solute carbon in precipitates, in alpha-iron before aging and in alpha-iron after aging process has completed itself, respectively. Although the shape of the precipitate is assumed to be spherical in this expression, the shape of the precipitate is found not to be spherical but plate-like as described in § 4. The exact relation describing the growth of the plate-like precipitate by the diffusion limited process is not known, but Eq. (3) is expected to be the approximate expression for the rate of precipitation process due to absorption of carbon atoms by the precipitates through their surfaces.

Then, the total rate of precipitation is given by the sum of right hand sides of Eq. (2) and Eq. (3) as follows:

$$\frac{1}{1-q}\frac{dq}{dt}=\frac{2}{3}\frac{1}{\tau_d}\left(\frac{t}{\tau_d}\right)^{-1/3}+\frac{3}{2}\frac{1}{\tau_c}q^{1/3} \tag{3}$$

Assuming proper value of τ_c and τ_d, and integrating the differential equation numerically, the experimental plots for the worked specimens are fitted by the calculated curve. These plots are shown in Fig. 2. The experimental data are fairly reproduced by the calculated curve. From τ_c and τ_d, the density of precipitates and the density of dislocations in the worked specimens were estimated as shown in Table I. For the unworked specimen, effective aging time is taken to be $t-t'$, where t' is a constant and Eq. (4) was integrated for this effective aging time, and was fitted to the experimental plots as shown also in Fig. 2. In this procedure, τ_c and τ_d for the unworked specimen were calculated and also shown in Table I.

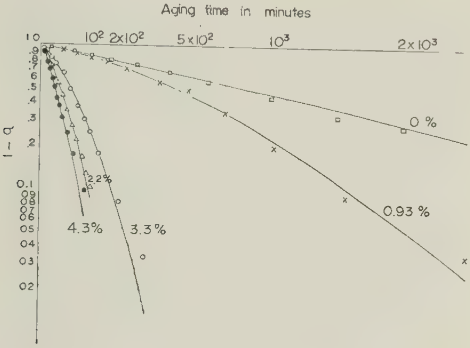

Fig. 2. log $(1-q)$ plotted *vs.* $t^{2/3}$.

Table I.

Cold-work (%)	τ_d (minutes)	τ_c (minutes)	dislocation density (lines/cm²)	precipitate density (1/cm³)
0	1500	27100	2.1×10^9	1.7×10^{11}
0.93	1480	1380	2.1×10^9	1.6×10^{13}
2.2	70	106	1.7×10^{10}	6.3×10^{14}
3.3	160	149	1.0×10^{10}	4.4×10^{14}
4.3	40	100	2.2×10^{11}	7.3×10^{14}

§ 4. Observation of Precipitates by Electron Microscope

It was found difficult to prepare replicas for electron microscope observation from wire specimens. Specimens in the form of rectangular bars 0.2 cm in thickness, 2 cm in width and 18 cm in length were prepared for the convenience of replica technique. Decarburizing and denitriding treatments and solution treatment of carbon of these specimens were performed by the same method as that of wire specimens.

The internal friction of specimens of this type was measured by suspending the specimen at the node of fundamental mode of flexual vibration. The vibration of the specimens was detected by using the circuit as shown in Fig. 3. The frequency of fundamental mode of flexual vibration of the bar is about 600 cps. The internal friction peaks due to diffusion of carbon and nitrogen appear at 110°C and 100°C, respectively, in this measuring frequency.

The aging treatment of these specimens were carried out by keeping them at the temperature of internal friction peak and this peak value of internal friction was measured

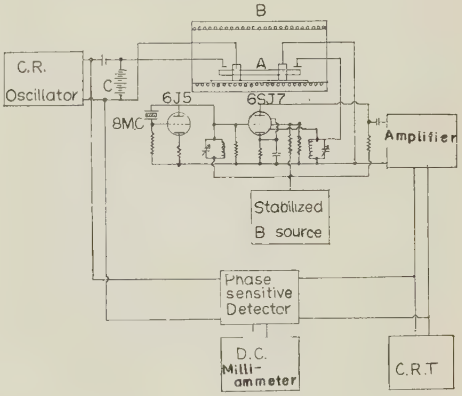

Fig. 3. Arrangement for measuring internal friction at 600 cps.

A. Specimen which is suspend at the node of flexual vibration.

B. Aging furnace controlled by the regulator.

C. Biasing voltage about 800 V.

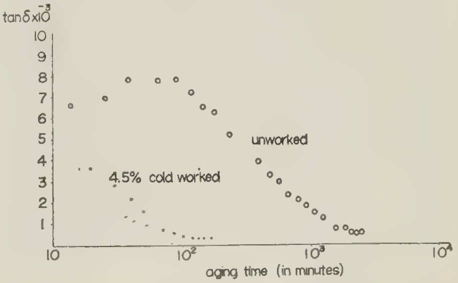

Fig. 4. Aging plots of bar specimens.

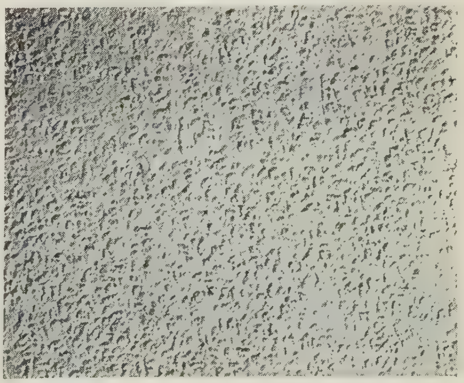

Fig. 5. Specimen aged for 150 minutes after 4.5% cold-working. ×12000.

at appropriate intervals. The internal friction of the worked and the unworked specimen was plotted vs. aging time in Fig. 4. The relatively low value of the internal friction in the initial stages of the aging process is due to the fact that it takes several minutes for the temperature of the specimen to attain to 110°C, at which the internal friction due to solute carbon is maximum.

As shown in Fig. 4, the precipitation process of the 4.5 per cent worked specimen have finished within 150 minutes. On the other hand, the precipitation process of the unworked specimen have scarcely begun within 150 minutes.

The photomicrographs of the specimens were taken by electron microscope using acetyl-cellulose-carbon replicas. The photo-

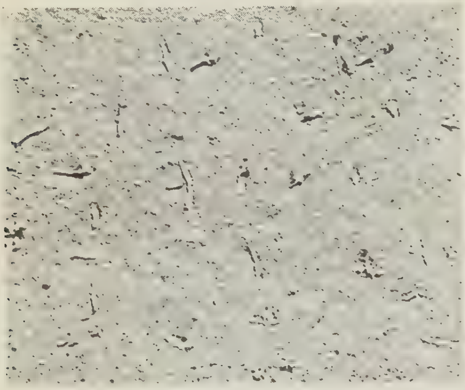

Fig. 6. Specimen aged for 150 minutes without working. ×12000.

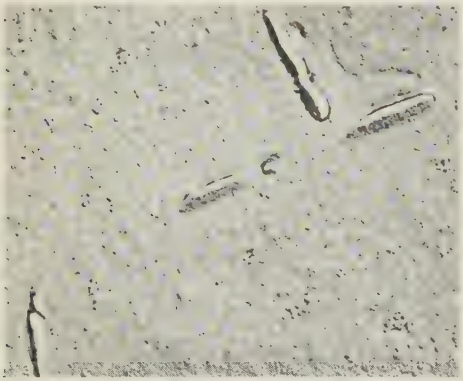

Fig. 7. Specimen aged for 870 minutes after 4.5% cold-working. ×12000.

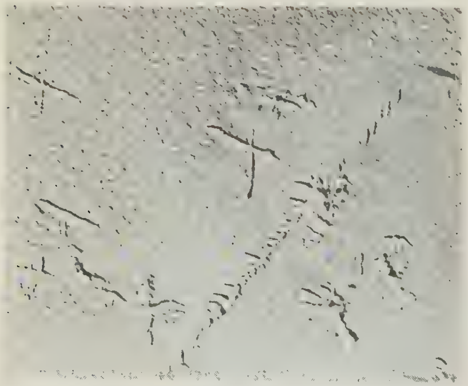

Fig. 8. Specimen aged for 870 minutes without working. ×12000.

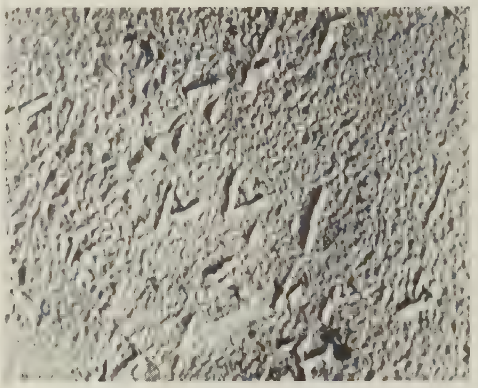

Fig. 9. Precipitates on (111). ×15000.

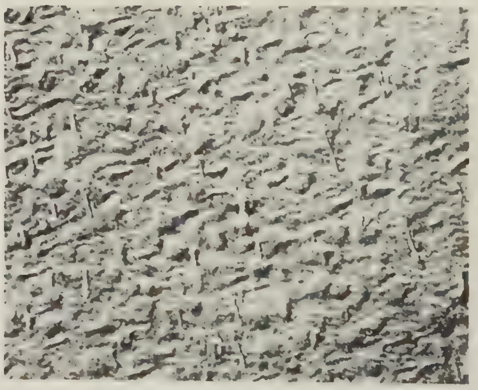

Fig. 10. Precipitates on (110). ×15000.

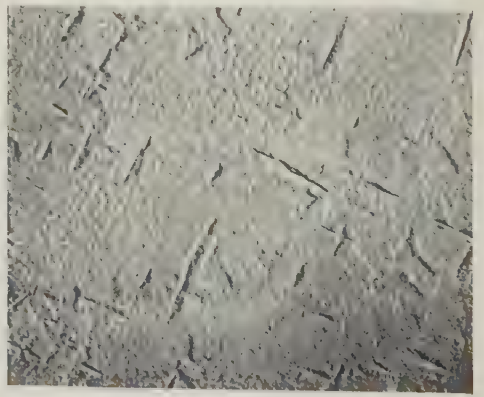

Fig. 11. Precipitates on (100). ×15000.

micrographs of the specimens aged for 150 minutes after 4.5 per cent cold-working and without working were shown in Fig. 5 and Fig. 6, respectively. In Fig. 5, there are a number of small plate-like precipitates and in Fig. 6 there are a relatively small number of precipitates. The photomicrographs of the specimens aged for 870 minutes after 4.5 per cent cold-working and without working were shown in Fig. 7 and Fig. 8, respectively. In Fig. 8, there are larger plate-like precipitates compared with the precipitates shown in Fig. 5. The precipitates in the unworked specimen were quite the same shape as published by W. Pitsch[7].

The photomicrographs of the specimens aged for 1800 minutes at 110°C without working were shown in Fig. 9, Fig. 10 and Fig. 11. The surfaces of the specimens shown in Fig. 9, Fig. 10 and Fig. 11 are (111), (110) and (100) planes, respectively. From these photomicrographs, it may be concluded that the carbon atoms in alpha-iron aged at about 100°C precipitate in plate-like shape on the (100) plane of the matrix iron.

§ 5. Discussions

As shown in Table I, the density of precipitates estimated from τ_c of Eq. (4) increases with the degree of the cold-working. The photomicrographs of the specimens also show that the density of the precipitates is higher in the cold-worked specimen than in the unworked specimen. On the other hand, it is known that the dislocation jogs increase due to intersection of dislocation lines in the course of plastic deformation. The density of the precipitates on the dislocation lines estimated from τ_c and τ_d is 3.32×10^4 per cm for the 4.5 per cent cold-worked specimen and 8 per cm for the unworked specimen. These value are not unreasonable value to be taken as the density of dislocation jogs. These data suggest that the precipitates nucleate at dislocation jogs.

In § 3, for the unworked specimen the effective aging time was taken to be $t-t'$. Hence, the precipitated fraction of carbon atoms q, in the unworked specimen was expressed to be proportional to $(t-t')^{2/3}$ in the initial stages of the precipitation process. However, as many authors have found[8],[9], q would be taken to be proportional to t^{α} in the initial stages of the precipitation process, where α is a constant between 1 and 1.15. This expression may be rather natural. By writing that q is proportional to $(t-t')^{2/3}$ in the initial stages of the precipitation process, we suggest that the precipitation process in the unworked specimen proceed also by way of dislocations and t' means a incubation time for the formation of precipitation nuclei. The density of dislocation lines estimated by assuming that the effective aging time is given by $(t-t')$ in the unworked specimen is the order of 10^9 lines/cm^2. This value of the dislocation density is not to be unexpected for the unworked specimen. It may be not unreasonable to consider that major part of the precipitation process of carbon in the unworked specimen also proceed by way of dislocation short circuit, because the mean distance between precipitation nuclei is too large for carbon atoms to be directly absorbed.

Acknowledgement

The authors wish to express their sincere gratitude to Prof. S. Kaya for his constant encouragement and discussions. The authors are also indebted to Dr. T. Taoka for his interests to this work and to Mr. S. Sakata for his cooperation in electron microscope technique.

References

1) J. L. Snoek: Physica **8** (1941) 711.
2) L. J. Dijkstra: Philips Res. Rep. **2** (1947) 357.
3) C. Wert: Acta Met. **2** (1954) 361.
4) A. H. Cottrell and B. Bilby: Proc. Phys. Soc. London **A**, **62** (1949) 49.
5) S. Harper: Phys. Rev. **83** (1951) 709.
6) C. Wert and C. Zener: J. Appl. Phys. **21** (1950) 5.
7) W. Pitsch: Acta Met. **5** (1957) 175.
8) W. Pitsch and K. Lücke: Arch. Eisenhüttenwesen **27** (1956) 45.
9) W. Dahl and K. Lücke: Arch. Eisenhüttenwesen **25** (1954) 241.

JOURNAL OF THE PHYSICAL SOCIETY OF JAPAN, Vol. 14, No. 5, MAY, 1959

Electronmicroscopic Observations of the KCl Single Crystal Irradiated with Ultra-Violet Light

By Tetsuhiko TOMIKI*
The Research Institute for Steel, Iron and other Metals,
Uuiversity of Tohoku
and Masayasu UETA
Department of Physics, The Faculty of Science,
University of Tohoku, Sendai

(Received November 21, 1958)

Electronmicroscopic observations were made for the KCl single crystal which was irradiated with light emitted from a hydrogen discharge tube, using the replica technique. Growth of crystallites occurred on the irradiated surface, and the irradiated effects could also be detected inside the crystal to the depth of 5 to 7 microns beneath the irradiated surface. It was confirmed experimentally that the growth of crystallites was induced by the ionic motions inside the irradiated crystal. The mechanism by which crystallites were formed is discussed in relation to the action of excitons.

§ 1. Introduction

The exciton has been one of the outstanding interests for both experimental and theoretical workers since Hilsch and Pohl measured at first the fundamental absorption bands of alkali-halides in the ultra-violet region. Hilsch and Pohl have found that the fundamental absorption bands of an alkali-halide crystal in a form of thin film consist of a series of relatively sharp bands[1),2)], and that free electrons are not produced by irradiating the crystals in the tail of the first fundamental absorption band when they are uncoloured[3)]. These facts indicate that the particles produced by this excitation are neutral. This neutral particle is believed as an electron coupled with a positive hole, and is called as an "*exciton*". Smakula[4)] has also observed that colour centres are produced in the alkali-halide crystals by irradiation with light lying in the tail of this band with quantum yield of unity at the initial stage. The numerous extensions of these measurements have been accumulated[5)]. Recently, Apker and Taft[6),7)] measured the photoelectric emission of alkali-halide crystals (both of single crystals and of thin films) and confirmed that the peak of photoelectric yield appears in the spectral region of the first fundamental absorption band, if the crystal contains F centers. This phenomenon was interpreted in a way that electrons associated with F centers are freed as a result of collision with excitons produced with light in this band, and are ejected outside the crystal. Thus, an exciton has a dual property to produce or destroy F centres.

On the other hand, Hibi and his coworkers have found electronmicroscopically that the growth of crystallites occurs both on the surfaces and in the inner parts of the alkali-halide crystals, when they are irradiated with X-ray[8)] or coloured with excess metal[9)].

The present article concerns with the growth of crystallites of the KCl single crystal that was illuminated with ultra-violet light. The observations were also made with an electron microscope using replica technique. The growth of crystallites was observable on the irradiated outer (001) surface and some effects induced by irradiation could be detected in the interior beneath the irradiated surface. These phenomena are discussed in relation to excitons.

§ 2. Experimental Methods

2.1 *Irradiation with ultra-violet light*

The (001) surface of the KCl single crystal cleaved from the block was illuminated in the open air with light from the hydrogen discharge tube through the LiF window. The separation between the (001) irradiated surface and the LiF window was chosen to be either 1 mm or 3 mm. According to optical measurements, the first fundamental absorption band of the KCl crystal has a peak at 1,625 A[1] at the room temperature and the long wavelength tail of the first fundamental absorption band of LiF single crystal rises steeply from the wavelength of nearly 1,500A*. In addition to these affairs, since the oxygen molecules in the air absorb strongly the ultraviolet light of which wavelength is shorter than 1,800 A, it could safely be concluded that the light quanta absorbed by the KCl crystal are those of long wavelength tail of the first fundamental band (exciton band).

---

* The present address: *Department of Physics, The Faculty of Science, University of Tohoku, Sendai.*

2.2 *Preparation of replicas*

The procedures for the preparation of replicas have been described in the previous papers[8)-10)]: The electron microscopic object is a replica of the crystal surface to be examined. The replica is the obliquely deposited Chromium film reinforced subsequently with Carbon film in a high vacuum. Here, the direction of chromium beam was parallel to the ⟨100⟩ of the KCl crystal and made an angle $\theta=\tan^{-1}(1/3)$ to its (001) surface.

Since it is considerable that the irradiation effects will be introduced most markedly into the interior directly beneath the irradiated surface, we made one sheet of replica which casts both the irradiated (001) surface and the fresh (010) cleavage plane of the crystal obtained after the illumination, when the inner parts of the crystal are to be examined[10)].

2.3 *The purity of KCl crystal*

The optical absorption spectra of the KCl single crystal employed show a slight impurity band whose absorption peak is located at 2,500 A.

§ 3. Experimental Results

In this section, the descriptions are given for the fresh {100} cleavage surface, the (001) surface irradiated with light emitted from a hydrogen discharge tube, and the interior beneath the irradiated surface of the KCl single crystal.

3.1 *The {100} plane*

Many investigators[11)] have been interested in the process of cleaving the crystal and the numerous observations have been made for the relation between the pattern of cleavage steps and the imperfections of the crystal. These works are mainly achieved with an optical microscope. Here, there is no need to describe them in detail, but it is sufficient to call attentions to the general feature of the freshly cleaved {100} plane: When the cleavage crack either propagates across a twist boundary or ceases to propagate during the crack front seals the loops of dislocation into the crystal (these regions were called as "deformation zones" by Forty[12)]), the new cleavage steps are formed at screw dislocations lying in this boundary or the "deformation zone"[12),13)]; however, between these zones, the cleavage crack propagates steadily with a constant velocity leaving straight cleavage steps on the cleavage plane.

Electronmicroscopically, on the other hand, the fresh {100} planes of KCl single crystal are flat and smooth and have straight cleavage steps whose crystallographic directions can be assigned to the ⟨100⟩, ⟨110⟩, ⟨120⟩, ⟨130⟩ and ⟨230⟩ directions[9)], when the crystal is perfect. The feature of this plane can be represented by Fig. 1(a). However, on the "deformation zone" the pattern of these cleavage steps turns into the complicated one. Since these zones occupy, as a whole, only small portions of the cleavage plane obtainable in usual cleaving processes, so general features of the freshly cleaved plane are well illustrated by Fig. 1(a) and these can be refered as the initial state of the irradiated surface of KCl single crystal.

For observations of an interior of a crystal, it has been usual to make the replica of a fresh cleavage plane which was produced by cutting the crystal plate normal to its (001) plane[8)9)]. In order to unify the experiment, however, it is necessary to observe an interior of a crystal by means of a replica which has informations both of the (001) and of the (010) cleavage surface (cf. § **2.2**). Fig. 1(b) is the electron micrograph obtained with such a replica. The (001) outer plane corresponds to the right half and the (010) plane to the left half of the photograph. The latter is flat and smooth, except for the straight cleavage steps running quite parallel to the intersection, marked with arrows, of the two cleavage planes, i.e. the [100] direction. This feature is also served as the initial state of an interior of the KCl crystal irradiated with light from a hydrogen discharge tube.

---

* Absorption of the LiF crystal, which was purchased from the Harshaw Chemical Company, was measured with the spectrophotometer constructed in our laboratory.

3.2 *The (001) outer surface of the KCl crystal irradiated with light from the hydrogen discharge tube*

Fig. 2 is the electron micrograph of the (001) outer surface of the KCl single crystal which was illuminated with light emitted from hydrogen discharge tube for 15 minutes. In this case, the crystal was apart 3 mm from the light source. It can be seen that crystallites appear densely all over the irradiated surface. When a crystal was placed at the distance of 1 mm from the hydrogen discharge tube and was illuminated with it for 15 minutes, appearances of the (001) surface turn into those such as shown in Figs. 3(a) and 3(b). The crystallites grow on the irradiated (001) surface with surface density of the order of $5 \cdot 10^7\,\mathrm{cm}^{-2}$, and their edges are directed to the $\langle 110 \rangle$ of the basal plane. In addition to these regular crystallites, we can also observe that tiny droplets of crystallites appear either at random (Fig. 3(a)) or in a regular alignement (Fig. 3(b)) on the irradiated (001) surface. Especially, in the latter case, this regular arrangement of droplets is parallel to the $\langle 110 \rangle$ of the basal plane, and come out either as satellites associated with larger crystallites of the regular shape or independently of them.

Fig. 4 is the (001) surface of the KCl crystal which was illuminated for 30 minutes at distance of 1 mm from the light source. In this case, the shape of crystallites are not so regular as shown in Fig. 3(a). These crystallites are estimated as 0.3 microns or less in heights.

Figs. 2–4 confirm that the crystallites come out on the (001) surface as the illumination with a hydrogen discharge tube proceeds, although it is quite sure that the shape or the growth mode of the grown up crystallites are closely related to both the microgeometry of the irradiated surface and the imperfections included in the interior beneath it, or the irradiation time.

According to the preliminary experiment carried out in vacuum, crystallites grew also on the irradiated surface. In this case, the KCl specimen was illuminated with monochromatic light ($\lambda = 1650$ A) near the peak of the first fundamental absorption band. The intensity of the incident beam was so weak that growth of crystallites was observed after the irradiation for 180 minutes. Fig. 5 shows the crystallites grown on the (001) of KCl specimen illuminated with light of 1650 A in vacuum for 180 minutes. One sees that they appear mainly along cleavage steps of the (001) irradiated surface. This corresponds to the first stage of crystal growth. Thus, it may be concluded that growth of crystallites was caused by the energy of incident light transferred to the crystal, and not by humidity or by atmosphere surrounding the specimen. In other words, these phenomena correspond to what might be termed *volume effect* and not to surface effect merely. These situations may well be illustrated by the phenomena induced inside the crystal by irradiation with ultra-violet light. This is described in the next section.

3.3 *The interior beneath the irradiated (001) surface*

Fig. 6 shows both the irradiated (001) surface and the fresh (010) cleavage plane of KCl crystal. The irradiated surface corresponds to the upper part and the cleavage plane to the lower part of the photograph. Here, irradiation time was 15 minutes and the separation between the crystal and the light source was 1 mm. The feature of the irradiated (001) surface in Fig. 6(a) corresponds to those shown in Fig. 3(a), and the (010) plane has groups of wavy cleavage steps.

The other interesting phenomena induced in the interior of the crystal by irradiation with ultra-violet light are shown in the Fig. 6(b). The crystallites (indicated in the figure with markings **A1** and **A2**) on the (010) plane come out from the interior to the outer (001) irradiated plane. Then, it is quite sure that the growth of crystallites on the (001) surface is induced as a result of the redistribution of ions inside the crystal, as was suggested by Hibi et al[8]. Furthermore, Fig. 6 indicates that the appearance of these wavy steps is a characteristic phenomenon which is associated with growth of crystallites as reported in the earlier paper[8],[9]. In addition to this, the step **BC** is not a cleavage step, because this is perpendicular to the direction of cleavage

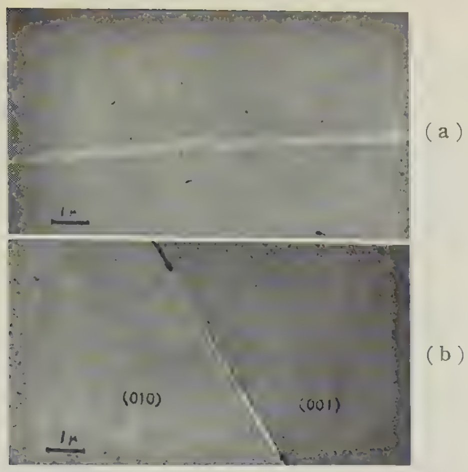

Fig. 1. Electron microphotographs of the KCl single crystal cleaved from the block crystal.
(a): The fresh {100} cleavage plane of the perfect crystal.
(b): The fresh (001) and (010) cleavage planes. The arrows indicate the intersection of the two planes.

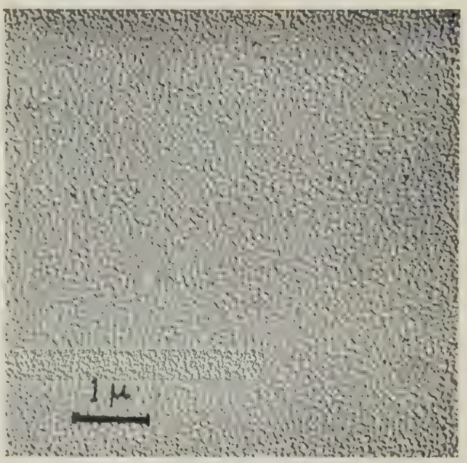

Fig. 2. Electron image of the (001) surface on which ultra-violet light illuminated for 15 minutes. The distance of the (001) plane and the light source was 3 mm.

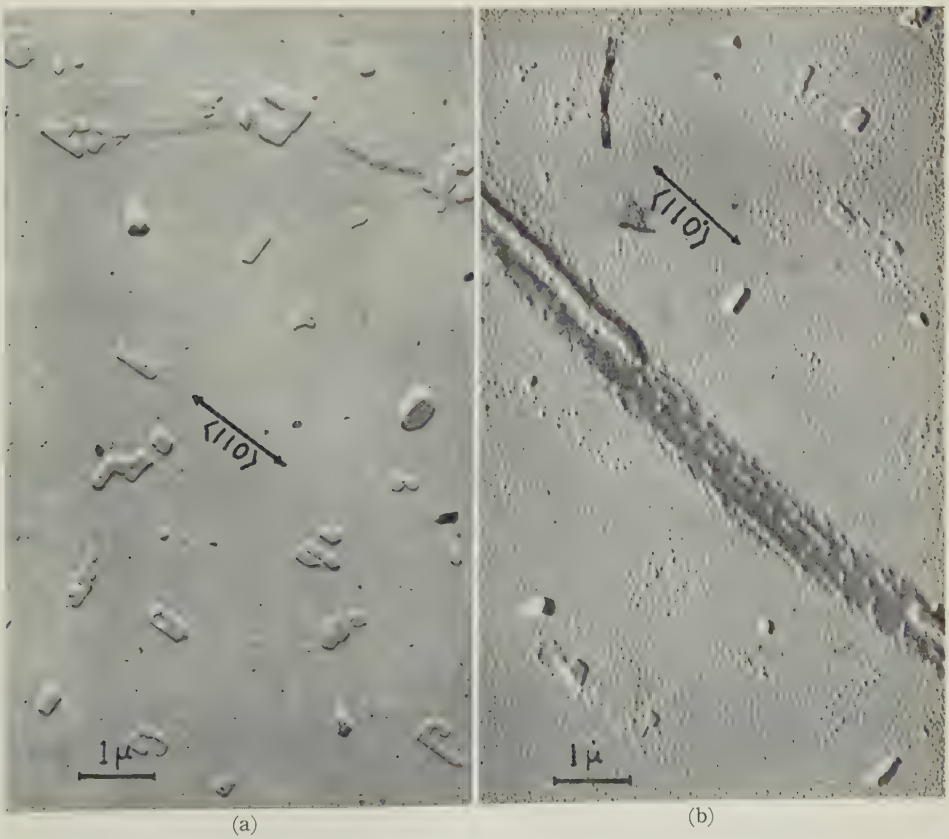

(a) (b)

Fig. 3. Electron image of the front (001) surface of the KCl crystal which was illuminated with ultra-violet light for 15 minutes at the distance of 1 mm from the light source.

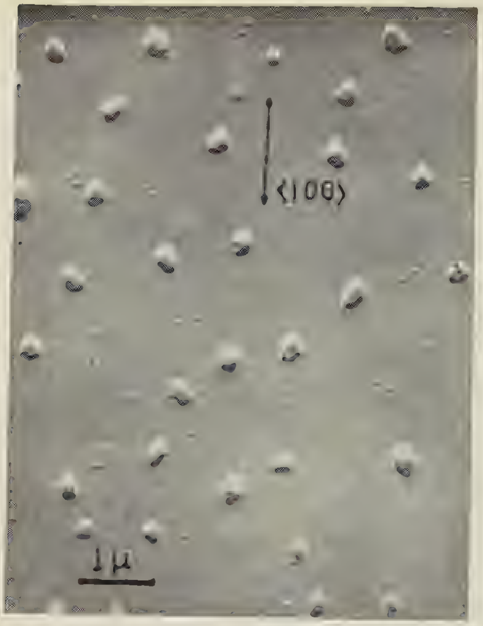

Fig. 4. Electron micrograph of the irradiated (001) surface of the KCl crystal which was illuminated with ultra-violet light for 30 minutes at the distance of 1 mm from the light source.

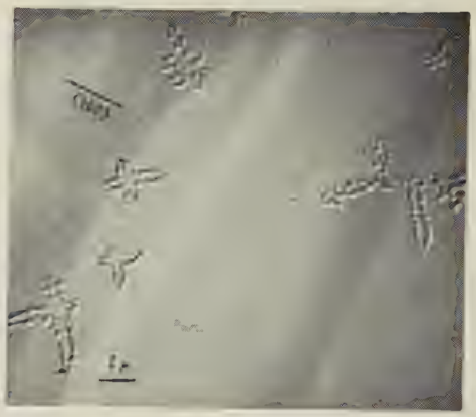

Fig. 5. Crystallities grown on the (001) of KCl specimen illuminated in vacuum with light of 1650 A for 180 minutes.

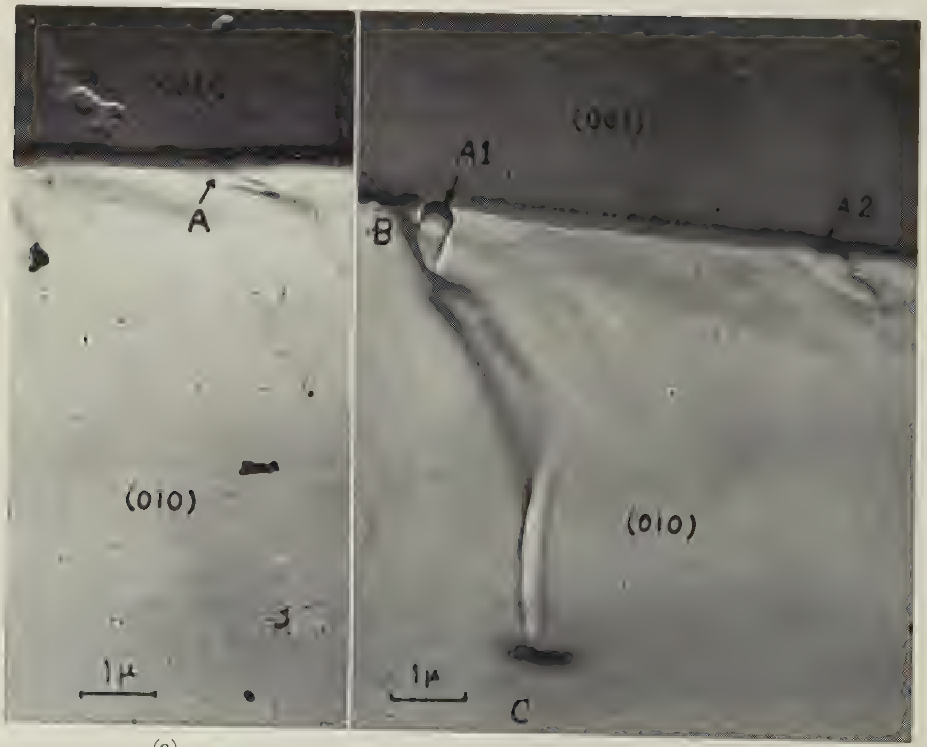

(a) (b)

Fig. 6. Electron micrograph both of the irradiated (001) plane and of the (010) plane which was obtained after the illumination with ultra violet-light for 15 minutes at the distance of 1 mm from the light source. **A** (Fig. 6 (a)), and **A1** and **A2** (Fig. 6 (b)) show the crystallites coming out to the outer (001) plane from interior.

steps.

From Fig. 6, it is confirmed that the wavy steps appear on the (010) plane down to the depth of 5 to 7 microns from the intersection of the (010) and (001) planes.

It is interesting to note that growth of crystallites or of the wavy steps did not occur when the KCl crystal was irradiated with X-ray for 60 minutes, even though it was coloured deeply. On the contrary, the results described here were obtained when the crystal was coloured only slightly.

§ 4. Interpretations of Experimental Results

According to the present observations, it is clear that crystallites grow on the (001) irradiated surface and they become larger and larger with irradiation time.

These phenomena have a close relationship to the change inside the crystal. Growth of crystallites have never been observed electronmicroscopically on the alkali halide crystals irradiated with visible light if they did not contain colour centers[8),19)]. Thus, it is conceivable that crystal growth on the irradiated plane and changes inside the crystal are induced by the light quanta absorbed in the tail of the first fundamental absorption band of KCl crystal, i.e. excitons.

4.1 *Changes inside the irradiated crystal*

One of the characteristic features which have been observed so far with an electron microscope is the following: When crystallites grow inside an alkali halide crystal, numerous zigzag steps appear on the fresh cleavage plane, and they are always accompanied both with crystallites at their kink sites and with a bundle of wavy steps[8),9)]. Suggestions were made for the zigzag step in a way that this may correspond to a kind of internal surface[9)].

According to Fig. 6, the same phenomena are also observed: The step **BC** in Fig. 6(b) is quite different from the cleavage step, for it is perpendicular to the direction of cleavage step. Furthermore, the step **BC** is in a form of zigzag only down to the depth of 5 to 7 microns beneath the irradiated surface and becomes then linear on the deeper region where wavy steps vanish. Then it is probable that the step **BC** is a kind of internal surface or a crystal imperfection which has no relation to the cleavage process, and that it turns into the zigzag one as the irradiation proceeds, even though it was originally straight before irradiation. The origin of this change is considered to be the action of excitons, such as thermal spikes, by which the redistribution of ions are induced inside the crystal accompanying the movement of internal surfaces such as the step **BC**. Fig. 6 seems to indicate that these processes are connected to growth of crystallites either along such a step or on the outer surface (see, the crystallite **A1** in Fig. 6(b)). This behaviour is quite similar to the nonconservative motion of dislocation[17),18)]. It is conceivable that crystallites **A** (Fig. 6(a)) and **A2** (Fig. 6(b)) are also resulted from the preferential diffusion of ions through some kind of crystal imperfection—dislocation, though this is not detected electronmicroscopically. These processes are favourable to the production of colour centres by excitons as proposed by Seitz[16)].

The nature of wavy steps is unknown at present. Though it is conceivable that they might indicate the internal stresses caused by the redistribution of ions, the sufficient confirmation is not obtained experimentally yet. They appear only down to the depth of 5 to 7 microns. Though this value corresponds to 1/10 of the minimum value of the penetration depth of incident light employed in this experiment, it may be possible to obtain the information regarding to the diffusion length of migrating exciton[16)], if the experiment is carried out with monochromatic light, especially with light at the peak of the first fudamental absorption band where the penetration depth of light is estimated as several hundreds angstrom.

4.2 *Crystallites on the irradiated surface*

If the above interpretation is correct, it is conceivable that distribution of crystallites on the outer surface must correspond directly to those of emergences of crystal imperfections on the (001). But, it will be rather difficult to accept this idea without restriction, if one sees the appearance of the irradiated plane as shown in Fig. 2. Nevertheless, we cannot deny the preferential diffusion of ions through imperfections as shown in Fig. 6. These peculiar behaviour of the irradiated surface were first discovered by Hibi and Ishikawa[8)] on the KBr and NaCl single crystals irradiated with X-ray and discussed by them [See Fig. 9 in their paper[8], for example]. They observed electronmicroscopically that in earlier stage of colouration of a crystal crystallites appear preferentially along steps, in the next stage crystallites cover uniformly on the irradiated surface and finally, distinct larger crystallites grow on it. Judging from experimental circumstances, it is conceivable that Figs. 5, 2, 3 and 4 show every stage of crystal growth in this order in a schematic representation.

From the present observations, these characteristic behaviours of the irradiated surface may be considered to be caused by the followings:

(i) Mode of crystal growth differs from places to places closely depending both on microgeometry and on the population of imperfections of the irradiated surface. Some evidences appear to support this. (ii) In addition to this, it is also acceptable that surface migration of ions occurred in some stage of crystal growth. This concept was already adopted in the explanation of the peculiar behaviours of the surface irradiated with X-ray by Hibi et al[8], because of the strong similarity to those of aggregation of a deposited film. (iii) The pattern of imperfection including the internal surface may be changed as the irradiation with ultra-violet light proceeds. (iv) Finally, transient departure from the normal composition may be induced locally on the surface by high energy radiation. It is difficult to attempt to make a further detailed explanation on the irradiated surface how these respective mechanisms affect on the every stage of crystal growth. It is considered to be most important and certain that the crystallites appear in the course of irradiation with ultraviolet light as a " volume effect " and become larger and larger with irradiation time.

Acknowledgement

It is a great pleasure to express the authors' thanks to Prof. S. Ogawa who was kindly interested in this experiment and also to Prof. Hibi who gave us the valuable suggestions. One of the authors (T. Tomiki) would like to express his sincere thanks to Prof. S. Ogawa who provided him an opportunity to achieve this experiment.

References

1) R. Hilsch and R. W. Pohl: Z. Phys. **57** (1929) 145.
2) R. Hilsch and R. W. Pohl: Z. Phys. **59** (1930) 812.
3) R. Hilsch and R. W. Pohl: Z. Phys. **68** (1931) 721.
4) A. Smakula: Z. Phys. **63** (1930) 762.
5) W. Martienssen: J. Phys. Chem. Solids **2** (1957) 257. P. L. Hartman, J. R. Nelson and J. G. Siegfried: Phys. Rev. **105** (1957) 123. F. Fischer: Z. Phys. **139** (1954) 328. H. M. O'Bryan and E. G. Schneider: Phys. Rev. **51** (1939) 293.
6) L. Apker and E. Taft: *Imperfections in nearly perfect crystals* (John Wiley and Sons, New York, 1952) 246.
7) E. A. Taft and H. R. Philipp: J. Phys. Chem. Solids **3** (1957) 1.
8) T. Hibi and K. Ishikawa: J. Phys. Soc. Japan **13** (1958) 709. T. Hibi and K. Yada: J. Phys. Soc. Japan **14** (1959) 455.
9) T. Hibi and T. Tomiki: J. Phys. Soc. Japan **14** (1959) 444.
10) T. Tomiki: J. Phys. Soc. Japan **14** (1959) 304.
11) The brief account for their works is summarized in the reference 9.
12) A. J. Forty: Proc. Roy. Soc. **A, 242** (1957) 392.
13) S. Amelinckx: Phil. Mag. **3** (8) (1958) 653.
14) F. Seitz: Rev. Mod. Phys. **26** (1954) *pp*. 80. *ff*.
15) F. Seitz: *Imperfections in nearly perfect crystals* (John Wiley and Sons, New York, 1952) 3.
16) F. Seitz: Rev. Mod. Phys.: loc. cit. p. 29.
17) J. Bardeen and C. Herring: *Imperfections in nearly perfect crystals* (John Wiley and Sons, New York, 1952) 261.
18) S. Amelinckx, W. Bontinck, W. Dekeyser and F. Seitz: Phil. Mag. **2** (8) (1957) 355.
19) T. Hibi and T. Tomiki: Sci. Rep. Res. Inst. Tohoku Univ. (to be published)

JOURNAL OF THE PHYSICAL SOCIETY OF JAPAN, Vol. 14, No. 5. MAY, 1959

On the Diamagnetism of Graphite, I. Energy Levels of π-electrons

By Hisanao SATO

Department of Physics, Nagoya University

(Received January 8, 1959)

The energy levels of the conduction electrons in graphite, in the presence of a magnetic field, are calculated by the method of the tight binding approximation, taking into account the effect of band-to-band transitions which is not included in the Landau-Peierls treatment. The present theory is a natural extension of the Luttinger-Kohn and McClure theories for the band structure of graphite. The relation to the diamagnetic susceptibility is discussed.

§1. Introduction

The effect of a uniform magnetic field on the orbital motion of free electrons was first studied by Landau¹⁾. He showed that the magnitude of the diamagnetic susceptibility of the free electron gas is equal to one-third of the spin paramagnetic susceptibility. For the diamagnetic susceptibility from the electrons in the periodic field of the lattice, Peierls²⁾ obtained a formula by a method which did not involve a detailed knowledge of the stationary states. Using wave functions in the tight binding approximation, he deduced the formula:

$$\chi_{\mathrm{dia}}=-\frac{1}{6}\left(\frac{e}{\hbar c}\right)^2\int\left\{\frac{\partial^2 E}{\partial k_x^2}\frac{\partial^2 E}{\partial k_y^2}-\left(\frac{\partial^2 E}{\partial k_x \partial k_y}\right)^2\right\}\frac{\partial f_0}{\partial E}\frac{dk}{(2\pi)^3}\,. \qquad (1)$$

This formula reduces to Landau's result when $E=\hbar^2k^2/2m$. Later Luttinger³⁾ proved the so-called effective mass theory using the Wannier functions. His result is that the Hamiltonian of the quasi-bound electrons is given by changing the argument of the function $E_m(\boldsymbol{k})$, energy of the mth band as a function of the wave vector $\boldsymbol{k}$, into a vector $\bar{\boldsymbol{k}}$ whose components are operators, satisfying the commutation law

$$[\bar{k}_x, \bar{k}_y]=i\frac{eH}{\hbar c}\,, \qquad (2)$$

where H is the magnetic field in the z-direction. The most questionable approximation in the effective mass theory consists in neglecting the interband transitions caused by the magnetic field.

Wilson⁴⁾ deduced the formula (1) by the direct calculation of the density matrix as a power series in H. In his calculation he neglected terms of the order of $kT/(E_m-E_{m'})$ compared with unity; this approximation corresponds to neglecting the interband elements in the effective mass theory. Besides (1), terms arising from the $\boldsymbol{k}$-dependence of the periodic part $u_{\boldsymbol{k}}(\boldsymbol{r})$ of the Bloch functions also contribute to the susceptibility. The magnitude of these terms are not clear since in general we do not have knowledges about $u_{\boldsymbol{k}}(\boldsymbol{r})$.

Adams⁵⁾ criticized the above mentioned theories in the case where two bands are near each other energetically at the same point in $\boldsymbol{k}$-space, and pointed out that the interband elements could make large contributions to the susceptibility.

The band structure of graphite was studied in detail by several authors⁶⁾⁻⁹⁾. Using the Peierls formula (1), Hove¹⁰⁾ calculated the diamagnetic susceptibility on the basis of the Wallace model⁶⁾ and showed that the magnitude of the theoretical susceptibility is about forty times too small. Mase⁹⁾ investigated the band structure by the Bloch tight binding method more precisely than Wallace did. He also found that one cannot explain the diamagnetism of graphite by means of the formula (1). Therefore it seems interesting to clarify the effect of the interband elements on the diamagnetism of graphite, in which the valence and conduction bands are degenerate.

Recently we have had some progress in searching the magnetic energy levels of electrons in the degenerate bands. Because the top of the valence bands for silicon and germanium are degenerate, the interband elements should be included in the theory of the cyclotron resonance of holes. Luttinger and Kohn[11] solved this problem making use of the fact that holes in question have small wave numbers. McClure[12] applied the method of Luttinger and Kohn to the two dimensional graphite layer and succeeded in accounting for the large diamagnetism, but the method is not adequate to the graphite crystal.

Corresponding to Wallace's calculation of the band structure, we shall solve the one electron Schrödinger equation by the tight binding approximation and investigate the effect of the band-to-band transitions caused by the magnetic field. In section 2 we shall discuss our approximations in detail. It is shown that our method gives the same result as McClure's in the case of hexagonal layer. In section 3 we shall apply our method to graphite. In section 4 the method of Luttinger and Kohn will be discussed concerning the application to graphite.

§ 2. Method of Tight Binding for Hexagonal Layer

In our tight binding approximation there is no essential distinction between the two and three dimensions. In this section, however, we shall investigate the energy levels for a hexagonal layer because of the simplicity and clearness of the calculation and for the convenience of comparison of our theory with McClure's one.

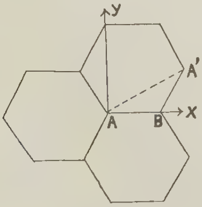

Fig. 1.

Fig. 1 shows hexagonal layer of graphite and our coordinate axes x and y. The unit cell contains two atoms, A and B, the distance between which being $1.42A$. The first Brillouin zone is a hexagon and a corner C indicated in Fig. 2 has $k_x=2\pi/\sqrt{3}\,a$ and $k_y=2\pi/3a$, where $a=1.42\times\sqrt{3}=2.46A$ is the distance between A and A' (Fig. 1). The valence and the conduction bands are degenerate at point C (and other equivalent points).

Assuming that a homogeneous magnetic field H is perpendicular to the plane of the hexagonal layer, we shall choose for the vector potential A

$$A_x=-H_y\,,\qquad A_y=A_z=0\,. \tag{3}$$

with this gause, the Hamiltonian becomes

$$\mathscr{H}=\mathscr{H}_0-\omega y p_x+\frac{m}{2}\omega^2y^2\,, \tag{4}$$

where

$$\omega=\frac{eH}{mc}\,,\qquad p_x=-i\hbar\frac{\partial}{\partial x}\,, \tag{5}$$

and $\mathscr{H}_0$ is the Hamiltonian of an electron in the lattice field. Then the eigen-value problem which we must solve is

$$\mathscr{H}\Psi=E\Psi\,. \tag{6}$$

Let $X(\boldsymbol{r})$ be the normalized $2p_z$ orbital function for an isolated carbon atom, then the wave function in the tight binding approximation becomes the linear combination of $\varphi_1(\boldsymbol{k})$ and $\varphi_2(\boldsymbol{k})$, which are defined by

$$\left.\begin{aligned}\varphi_1(\boldsymbol{k})&=\frac{1}{\sqrt{N}}\sum_A e^{i\boldsymbol{k}\cdot\boldsymbol{r}_A}X(\boldsymbol{r}-\boldsymbol{r}_A)\,,\\ \varphi_2(\boldsymbol{k})&=\frac{1}{\sqrt{N}}\sum_B e^{i\boldsymbol{k}\cdot\boldsymbol{r}_B}X(\boldsymbol{r}-\boldsymbol{r}_B)\,,\end{aligned}\right\} \tag{7}$$

where N is the number of unit cells and the sum is taken over all the equivalent lattice points which are designated by A or B.

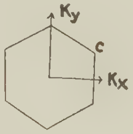

Fig. 2.

In the magnetic field a stationary state of an electron is no longer represented by a point in $\boldsymbol{k}$-space, but an electron forms a wave packet spreading over $\sqrt{eH/\hbar c}$. Therefore, we assume

$$\Psi=\int B_1(\boldsymbol{k}')\varphi_1(\boldsymbol{k}')\,d\boldsymbol{k}'+\int B_2(\boldsymbol{k}')\varphi_2(\boldsymbol{k}')\,d\boldsymbol{k}'\,, \tag{8}$$

the integration being taken over the first Brillouin zone. $B_1(\boldsymbol{k})$ and $B_2(\boldsymbol{k})$ are required to be periodic functions with the periodicity of the reciprocal lattice. The reason why we have neglected higher atomic states in Eq. (8) will be stated later on.

We substitute (8) into (6), multiply it by $\varphi_1{}^*(\boldsymbol{k})$ and integrate over the entire crystal. First let us consider the integral

$$\iint d\boldsymbol{k}'\, d\boldsymbol{r}\, B_2(\boldsymbol{k}')\varphi_1^*(\boldsymbol{k})\mathscr{H}\varphi_2(\boldsymbol{k}')=\mathrm{I}_0+\mathrm{I}_1+\mathrm{I}_2\,, \tag{9}$$

where

$$\mathrm{I}_0=\iint d\boldsymbol{k}'\, d\boldsymbol{r}\, B_2(\boldsymbol{k}')\varphi_1^*(\boldsymbol{k})\mathscr{H}_0\varphi_2(\boldsymbol{k}')\,,$$

$$\mathrm{I}_1=\iint d\boldsymbol{k}'\, d\boldsymbol{r}\, B_2(\boldsymbol{k}')\,\varphi_1^*(\boldsymbol{k})(-\omega y p_x)\,\varphi_2(\boldsymbol{k}')\,,$$

$$\mathrm{I}_2=\iint d\boldsymbol{k}'\, d\boldsymbol{r}\, B_2(\boldsymbol{k}')\,\varphi_1^*(\boldsymbol{k})\left(\frac{m}{2}\omega^2 y^2\right)\varphi_2(\boldsymbol{k}')\,.$$

I_0 may easily be evaluated as follows:

$$\begin{aligned}\mathrm{I}_0&=\int d\boldsymbol{k}' B_2(\boldsymbol{k}')\left(\frac{1}{N}\sum_{A,B} e^{-i\boldsymbol{k}\cdot\boldsymbol{r}_A+i\boldsymbol{k}'\cdot\boldsymbol{r}_B}\int X^*(\boldsymbol{r}-\boldsymbol{r}_A)\mathscr{H}_0\, X(\boldsymbol{r}-\boldsymbol{r}_B)\, d\boldsymbol{r}\right)\\&=\int d\boldsymbol{k}' B_2(\boldsymbol{k}')\left(\frac{1}{N}\sum_{A} e^{-i(\boldsymbol{k}-\boldsymbol{k}')\cdot\boldsymbol{r}_A}\right)\left(\sum_{\rho_{AB}} e^{i\boldsymbol{k}'\cdot\boldsymbol{\rho}_{AB}}\int X^*(\boldsymbol{r})\mathscr{H}_0 X(\boldsymbol{r}-\boldsymbol{\rho}_{AB})\, d\boldsymbol{r}\right)\\&=\mathrm{H}_0^{12}(\boldsymbol{k})B_2(\boldsymbol{k})\,,\end{aligned} \tag{10}$$

where

$$\left.\begin{aligned}\mathrm{H}_0^{12}(\boldsymbol{k})&=\sum_{\rho_{AB}} e^{i\boldsymbol{k}\cdot\boldsymbol{\rho}_{AB}}\int X^*(\boldsymbol{r})\mathscr{H}_0 X(\boldsymbol{r}-\boldsymbol{\rho}_{AB})\, d\boldsymbol{r}\,,\\ \boldsymbol{\rho}_{AB}&=\boldsymbol{r}_B-\boldsymbol{r}_A\,.\end{aligned}\right\} \tag{11}$$

Integral I_1 can be written as a sum of two terms I_1' and I_1'', where

$$\mathrm{I}_1'=-\omega\int d\boldsymbol{k}' B_2(\boldsymbol{k}')\left(N^{-1}\sum_{A,B} e^{-i\boldsymbol{k}\cdot\boldsymbol{r}_A+i\boldsymbol{k}'\cdot\boldsymbol{r}_B}\int X^*(\boldsymbol{r}-\boldsymbol{r}_A)(y-y_B)\,p_x X(\boldsymbol{r}-\boldsymbol{r}_B)\, d\boldsymbol{r}\right),$$

the magnitude of which may be of the order of $\omega B_2 a(\hbar/a)$. The other term I_1'' can be transformed into a simple form:

$$\begin{aligned}\mathrm{I}_1''&=\int d\boldsymbol{k}' B_2(\boldsymbol{k}')\left(N^{-1}\sum_{A,B} e^{-i\boldsymbol{k}\cdot\boldsymbol{r}_A+i\boldsymbol{k}'\cdot\boldsymbol{r}_B}\int X^*(\boldsymbol{r}-\boldsymbol{r}_A)(-\omega y_B p_x)X(\boldsymbol{r}-\boldsymbol{r}_B)\, d\boldsymbol{r}\right)\\&=-\omega\int d\boldsymbol{k}' B_2(\boldsymbol{k}')N^{-1}\sum_{A,B} e^{-i\boldsymbol{k}\cdot\boldsymbol{r}_A}\left(-i\frac{\partial e^{+i\boldsymbol{k}\cdot\boldsymbol{r}_B}}{\partial k_y'}\right)\int X^*(\boldsymbol{r}-\boldsymbol{r}_A)\,p_x X(\boldsymbol{r}-\boldsymbol{r}_B)\, d\boldsymbol{r}\\&=-i\omega\int d\boldsymbol{k}'\frac{\partial B_2}{\partial k_y'}\,N^{-1}\sum_{A,B} e^{-i\boldsymbol{k}\cdot\boldsymbol{r}_A+i\boldsymbol{k}'\cdot\boldsymbol{r}_B}\int X^*(\boldsymbol{r}-\boldsymbol{r}_A)\,p_x X(\boldsymbol{r}-\boldsymbol{r}_B)\, d\boldsymbol{r}\\&=-i\omega\, p_x^{12}(\boldsymbol{k})\frac{\partial B_2}{\partial k_y}\,.\end{aligned} \tag{12}$$

The integration by parts with respect to $\boldsymbol{k}'$ gives immediately the third line of the above equation, the surface integrals over the surface of the first Brillouin zone vanishing since all the functions are periodic functions of the reduced wave vector. In Eq. (12) $p_x^{12}(\boldsymbol{k})$ is defined by

$$p_x^{12}(\boldsymbol{k})=\sum_{\rho_{AB}} e^{i\boldsymbol{k}\cdot\boldsymbol{\rho}_{AB}}\int X^*(\boldsymbol{r})\,p_x X(\boldsymbol{r}-\boldsymbol{\rho}_{AB})\, d\boldsymbol{r}\,. \tag{13}$$

As will be shown below, $p_x^{12}(\boldsymbol{k})$ is of the order of $\hbar/a$ in the neighborhood of $\boldsymbol{k}=\boldsymbol{k}^c$, where $\boldsymbol{k}^c$ is a wave vector represented by point C. It will also be seen that the wave function $B_i(\boldsymbol{k})$ becomes wave functions of a harmonic oscillator. Therefore $\partial B_2/\partial k_y$ in (12) is nearly equal to $B_2/\bar{k}_y$, in which $\bar{k}_y$ means the value of k_y averaged with $B_i(\boldsymbol{k})$ and may approximately be given by $\sqrt{neH/\hbar c}$ (n is a quantum number of the harmonic oscillator). Then we shall see that the ratio I_1'/I_1'' will be very small compared with unity at least for small n. As a result of the above considerations we obtain

$$I_1 = I_1'' = -i\omega p_x^{12}(\boldsymbol{k})\frac{\partial B_2}{\partial k_y}\,. \tag{14}$$

To estimate the integral I_2 we substitute $y^2 = y_B^2 + 2y_B(y-y_B) + (y-y_B)^2$ in its integrand. Then I_2 will be given as a sum of three terms:

$$I_2 = I_2' + I_2'' + I_2''' \,,$$

where

$$I_2' = \iint d\boldsymbol{k}'d\boldsymbol{r}\, B_2(\boldsymbol{k}')\varphi_1^*(\boldsymbol{k})\left(\frac{m}{2}\omega^2 y_B^2\right)\varphi_2(\boldsymbol{k}')\,,$$

$$I_2'' = \iint d\boldsymbol{k}'d\boldsymbol{r}\, B_2(\boldsymbol{k}')\varphi_1^*(\boldsymbol{k})\left\{\frac{m}{2}\omega^2 2y_B(y-y_B)\right\}\varphi_2(\boldsymbol{k}')\,,$$

$$I_2''' = \iint d\boldsymbol{k}'d\boldsymbol{r}\, B_2(\boldsymbol{k}')\varphi_1^*(\boldsymbol{k})\left\{\frac{m}{2}\omega^2(y-y_B)^2\right\}\varphi_2(\boldsymbol{k}')\,.$$

Integral I_2' can be evaluated in the similar manner to I_1'' and the order of its magnitude may be given by

$$I_2' \simeq m\omega^2\frac{\partial^2 B_2}{\partial k_y^2} \simeq \omega\frac{eH}{c}\frac{B_2}{\bar{k}_y^2} \simeq \omega\hbar B_2\,.$$

Then we have

$$I_2'/I_1 \simeq a\bar{k}_y \ll 1\,.$$

Similarly it can be found that I_2'' and I_2''' are much smaller than I_2'. In this way we obtain the following equation to a good approximation:

$$\iint d\boldsymbol{k}'d\boldsymbol{r}\, B_2(\boldsymbol{k}')\,\varphi_1^*(\boldsymbol{k})\mathscr{H}\varphi_2(\boldsymbol{k}') = H_0^{12}(\boldsymbol{k})B_2(\boldsymbol{k}) - i\omega p_x^{12}(\boldsymbol{k})\frac{\partial B_2}{\partial k_y}\,. \tag{15}$$

Similarly we have

$$\iint d\boldsymbol{k}'d\boldsymbol{r}\, B_1(\boldsymbol{k}')\varphi_1^*(\boldsymbol{k})\mathscr{H}\varphi_1(\boldsymbol{k}') = H_0^{11}(\boldsymbol{k})B_1(\boldsymbol{k})\,, \tag{16}$$

where

$$H_0^{11}(\boldsymbol{k}) = \sum_{\rho_{AB'}} e^{i\boldsymbol{k}\cdot\boldsymbol{\rho}_{AB'}}\int X^*(\boldsymbol{r})\mathscr{H}_0 X(\boldsymbol{r}-\boldsymbol{\rho}_{AA'})\,d\boldsymbol{r}\,. \tag{17}$$

On the right hand side of (16) only $\mathscr{H}_0$ is retained since the diagonal element of the momentum is negligible compared with the nondiagonal element:

$$\int\varphi_1^*(\boldsymbol{k})\,p_x\,\varphi_1(\boldsymbol{k})\,d\boldsymbol{r} \ll \int\varphi_1^*(\boldsymbol{k})\,p_x\,\varphi_2(\boldsymbol{k})\,d\boldsymbol{r}\,.$$

Now we return to the problem concerning Eq. (8), in which we assumed Ψ as a linear combination of the atomic $2p_z$ functions. The contribution of higher states j, for instance, to the state 1 or 2 can be estimated by the perturbation method. The important matrix element which connects the states 1 and j may be $i\omega p_x^{1j}\partial/\partial k_y$. By the diagonalization we have the following term in our Hamiltonian;

$$\omega^2\frac{|p_x^{1j}|^2}{\Delta E_{1j}}\frac{\partial^2}{\partial k_y^2} \simeq m\omega^2\frac{\partial^2}{\partial k_y^2}\,,$$

which is of the same order of magnitude as I_2' which we neglected.

As a result of the above discussions we obtain the following differential equations for $B_1(\boldsymbol{k})$ and $B_2(\boldsymbol{k})$:

$$\left.\begin{aligned} &\mathrm{H}_0^{11}(\boldsymbol{k})\,B_1(\boldsymbol{k})+\left\{\mathrm{H}_0^{12}(\boldsymbol{k})-i\omega\, p_x^{12}(\boldsymbol{k})\frac{\partial}{\partial k_y}\right\}B_2(\boldsymbol{k})=EB_1(\boldsymbol{k})\,, \\ &\left\{\mathrm{H}_0^{21}(\boldsymbol{k})-i\omega\, p_x^{21}(\boldsymbol{k})\frac{\partial}{\partial k_y}\right\}B_1(\boldsymbol{k})+\mathrm{H}_0^{22}(\boldsymbol{k})\,B_2(\boldsymbol{k})=EB_2(\boldsymbol{k})\,, \end{aligned}\right\} \tag{18}$$

where $\mathrm{H}_0^{11}=\mathrm{H}_0^{22}$, $\mathrm{H}_0^{21}=\mathrm{H}_0^{12*}$ and $p_x^{21}=p_x^{12*}$. In order to obtain solutions for the set of equations (18) in the neighborhood of point C, we expand $\mathrm{H}_0^{11}(\boldsymbol{k})$, $\mathrm{H}_0^{12}(\boldsymbol{k})$ and $p_x^{12}(\boldsymbol{k})$ as power series of $k_x-k_x^c$ and $k_y-k_y^c$. Taking the origin of $\boldsymbol{k}$ at $\boldsymbol{k}^c$, we get to order linear in ak_x and ak_y:

$$\left.\begin{aligned} &\mathrm{H}_0^{11}=\mathrm{H}_0^{22}=E_0\,, \\ &\mathrm{H}_0^{12}=\frac{\sqrt{3}}{4}\gamma_0 a(lk_x+mk_y)\,, \\ &p_x^{12}=lp_0\,, \end{aligned}\right\} \tag{19}$$

where

$$\left.\begin{aligned} &l=\sqrt{3}+i\,, \\ &m=1-\sqrt{3}\,i\,, \\ &\gamma_0=-\int X^*(\boldsymbol{r})\mathscr{H}_0X(\boldsymbol{r}-\boldsymbol{\rho}_{AB})\,d\boldsymbol{r}\,, \\ &-\frac{4}{3}ip_0=\int X^*(\boldsymbol{r})\left(-i\hbar\frac{\partial}{\partial x}\right)X(\boldsymbol{r}-\boldsymbol{r}_{AB})\,d\boldsymbol{r}\,, \\ &\boldsymbol{r}_{AB}=(a/\sqrt{3}\,,0)\,. \end{aligned}\right\} \tag{20}$$

Substituting Eqs. (19) into (18), we have

$$\left.\begin{aligned} &\left(lk_x+mk_y-ils\frac{\partial}{\partial k_y}\right)B_2=\lambda B_1\,, \\ &\left(l^*k_x+m^*k_y-il^*s\frac{\partial}{\partial k_y}\right)B_1=\lambda B_2\,, \end{aligned}\right\} \tag{21}$$

where

$$\lambda=\frac{E-E_0}{(\sqrt{3}/4)\gamma_0 a}\,,\qquad \frac{\hbar}{m}p_0=\frac{\sqrt{3}}{4}\gamma_0' a\,,\qquad s=\frac{\gamma_0'}{\gamma_0}\frac{eH}{\hbar c}\,. \tag{22}$$

The set of equations (21) is the fundamental result of our method which determine the exact energy levels for small quantum numbers near the degeneracy point. Eqs. (21) are identical with Eqs. (2.7a) and (2.7b) in McClure's paper[12] if $\gamma_0=\gamma_0'$, which we can prove as below.

Following Kitano[13] we make use of the operator identity in order to verify $\gamma_0=\gamma_0'$;

$$p_x=\frac{mi}{\hbar}[\mathscr{H}_0, x]\,.$$

Adopting the $2p_z$ functions $X(\boldsymbol{r}-\boldsymbol{r}_A)$, $X(\boldsymbol{r}-\boldsymbol{r}_{A'})$,—and $X(\boldsymbol{r}-\boldsymbol{r}_B)$, $X(\boldsymbol{r}-\boldsymbol{r}_{B'})$,—as the bases, we calculate the matrix element of the above equation as follows:

$$\begin{aligned} p_{xAB}&=\frac{mi}{\hbar}(\mathscr{H}_{0AA}x_{AB}-\gamma_0 x_{BB}-x_{AB}\mathscr{H}_{0BB}+x_{AA}\gamma_0) \\ &=-\frac{mi}{\hbar}\gamma_0(x_{BB}-x_{AA}) \\ &=-\frac{mi}{\hbar}\frac{\gamma_0 a}{\sqrt{3}}\,. \end{aligned}$$

From (20) and (22) we have

$$p_{xAB} = -\frac{4}{3} i p_0 = -\frac{mi}{\hbar} \frac{\gamma_0' a}{\sqrt{3}} ,$$

and therefore

$$\gamma_0 = \gamma_0' .$$

Because the system of the $2p_z$ functions is not complete, our proof is an approximate one, but seems reasonable within the scope of our theory. As we are interested in wave functions which are localized in the Brillouin zone, we may replace the periodic boundary conditions for $B_i(\boldsymbol{k})$ by the requirement that they vanish for large values of $\boldsymbol{k}$. Then the solutions $B_1(\boldsymbol{k})$ and $B_2(\boldsymbol{k})$ for the set of the equations (21) are given by wave functions for the harmonic oscillator and the energy $\mathcal{E} = E - E_0$ becomes with $\gamma_0' = \gamma_0$

$$\mathcal{E} = E - E_0 = \pm \sqrt{\alpha n} , \tag{23}$$

$$\alpha = \tfrac{3}{2} \gamma_0^2 a^2 s , \tag{24}$$

where n takes all the positive integers. Putting $H=0$ in (21), we get the energy levels which Wallace has given:

$$\mathcal{E}(H=0) = \pm \sqrt{\tfrac{3}{4} \gamma_0^2 a^2 (k_x^2 + k_y^2)} . \tag{25}$$

In this section we obtained the same result as McClure's, but analyzed the approximations used by him precisely in view of the tight binding method. On the basis of this two-dimensional model McClure studied the diamagnetism of graphite. He noted that $n=0$ levels are responsible for the most part of the large diamagnetism and that a good agreement with the observed value of the normal susceptibility can be obtained.

§ 3. Method of Tight Binding for Graphite

Graphite lattice is built up of hexagonal layers, whose relation to each other is illustrated in Fig. 3. Dotted lines indicate one layer and the full lines the one 3.37A above it. The points A, B, C and D represent the four atoms of a unit cell. The first Brillouin zone for graphite is a hexagonal pill-box of height $4\pi/c_L$, as is indicated in Fig. 4, where c_L is the spacing between identical layers, 3.37×2=6.74A. The degenerate points are on the six vertical edges of the zone (H–H).

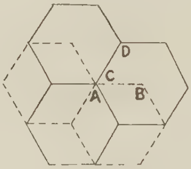

Fig. 3.

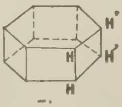

Fig. 4.

As in the case of a single layer we shall define $\varphi_i(\boldsymbol{k})$ in the form:

$$\varphi_i(\boldsymbol{k}) = \sum_{\nu} \exp[i\boldsymbol{k} \cdot \boldsymbol{r}_i^{\nu}] X(\boldsymbol{r} - \boldsymbol{r}_i^{\nu}), \tag{26}$$

where $i=1, 2, 3, 4$ correspond to atoms of the types A, B, C, D, respectively, and ν enumerates the different atoms of a given type in the crystal.

Assuming

$$\Psi = \sum_{i=1}^{4} \int B_i(\boldsymbol{k}') \varphi_i(\boldsymbol{k}') \, d\boldsymbol{k}' , \tag{27}$$

we shall proceed exactly in the same way as in the case of the hexagonal layer. If we suppose that the integrals connecting (A, D), (B, C) and (B, D) are zero, we obtain the following equations with the same approximation as that in section 2:

$$\left.\begin{aligned}
&\mathrm{H}_0^{11} B_1 + \left(\mathrm{H}_0^{12} - i\omega p_x^{12} \frac{\partial}{\partial k_y}\right) B_2 + \gamma_1 \Gamma B_3 && = E B_1 , \\
&\left(\mathrm{H}_0^{21} - i\omega p_x^{21} \frac{\partial}{\partial k_y}\right) B_1 + \mathrm{H}_0^{22} B_2 && = E B_2 , \\
&\gamma_1 \Gamma B_1 \qquad + \mathrm{H}_0^{33} B_3 + \left(\mathrm{H}_0^{34} - i\omega p_x^{34} \frac{\partial}{\partial k_y}\right) B_4 && = E B_3 , \\
&\qquad \left(\mathrm{H}_0^{43} - i\omega p_x^{43} \frac{\partial}{\partial k_y}\right) B_3 + \mathrm{H}_0^{44} B_4 && = E B_4 ,
\end{aligned}\right\} \tag{28}$$

where

$$\gamma_1 = \int X^*(\boldsymbol{r}) \mathscr{H}_0 X(\boldsymbol{r} - \boldsymbol{\rho}_{Ac})\, d\boldsymbol{r} \ ,$$

$$\Gamma = 2 \cos \frac{c_L}{2} k_z \ ,$$

and H_0^{ij} and p_x^{ij} have the same meanings as Eqs. (11), (13) and (17).

In the absence of a magnetic field, we can find that $B_3 = \pm B_1$, where the choice of the sign is immaterial. Therefore we choose $B_3 = -B_1$ in (28); then the upper two equations will become equivalent to the lower two. It will be shown in the next section that this choice does not give any limitation to the result.

Since we are interested in the solutions near the zone edge, we can expand H_0^{ij} and p_x^{ij} with regard to k_x and k_y. Then we can rewrite the upper two equations of (28) as follows:

$$\left.\begin{aligned} \frac{\sqrt{3}}{2} \gamma_0 a \left(l k_x + m k_y - i l s \frac{\partial}{\partial k_y} \right) B_2 &= (E - E_0 + \gamma_1 \Gamma) B_1 \ , \\ \frac{\sqrt{3}}{2} \gamma_0 a \left(l^* k_x + m^* k_y - i l^* s \frac{\partial}{\partial k_y} \right) B_1 &= (E - E_0) B_2 \ , \end{aligned}\right\} \tag{29}$$

which correspond to (21) in the case of the single layer. Substituting $H=0$ in (29), we find the energy levels which agree with Wallace's result:

$$E - E_0 = -\tfrac{1}{2}\gamma_1\Gamma \pm \sqrt{\tfrac{1}{4}\gamma_1^2\Gamma^2 + \tfrac{3}{4}\gamma_0^2 a^2 (k_x^2 + k_y^2)} \ . \tag{30}$$

As in the preceding section, the energy $E - E_0$ in (29), may be found to be

$$E - E_0 = -\tfrac{1}{2}\gamma_1\Gamma \pm \sqrt{\tfrac{1}{4}\gamma_1^2\Gamma^2 + \alpha n} \ . \tag{31}$$

for $n \geq 1$. For $n=0$, B_2 is interpreted to be zero and therefore we have

$$E - E_0 = -\gamma_1 \Gamma \ , \qquad (n=0) \ . \tag{32}$$

The lack of symmetry between B_1 and B_2 is due to our choice of gauge for the vector potential. The solution for the H′–H′ edge is symmetric in the opposite sense to (29), and for this case we have

$$E - E_0 = 0$$

for $n=0$. γ_0 in this section takes a different value from that for a single layer since the lattice fields are not identical, but for simplicity we do not use different notations. The results (31) and (32) is similar to (23) in the two-dimensional case with the difference that the zero point energy is missing in (23).

McClure has concluded on the basis of the two-dimensional model that $n=0$ levels play the dominant role for the diamagnetism. This is explained schematically in Fig. 5, which shows the level density g versus $E - E_0$ curve in a hexagonal layer. When $H=0$, there is no state having $E = E_0$, while $n=0$ levels are induced by the magnetic field. Hence in the magnetic field the electrons, which occupy the states of the valence and the conduction bands having the energy near $E = E_0$, assemble on this $n=0$ levels. This circumstance is indicated by arrows in Fig. 5. Consequently the average energy of the electrons is raised by the magnetic field provided that the number of electrons below E_0 is larger than that above it; this results from the thermal agitation of the Fermi distribution. The smaller the level density becomes, the larger this effect will be. As a result the Fermi energy will become so large as capable of explaining the observed periodicity of the de Haas-van Alphen effect. In the three-dimensional case the situation is not so simple. Unless we compute the susceptibility using the energy levels (31) and (32), we cannot compare our theory with the calculation based on the Peierls formula (1).

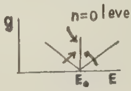

Fig. 5.

§ 4. Extension of Luttinger-Kohn Theory

In the preceding section we have calculated the energy levels of the conduction electrons in the magnetic field, which are correct in the neighborhood of the edge of the Brillouin zone. But the calculation depends so much on the tight binding approximation that it seems difficult to improve it more precisely.

In this section, therefore, we shall try to extend the method of Luttinger and Kohn in the form which will be suitable for the band structure of graphite. For this purpose we shall define the functions ϕ_{nk} as our bases:

$$\begin{aligned}\phi_{nk}&=\exp(i\boldsymbol{k}\cdot\boldsymbol{r})\,u_{nk_x{}^0k_y{}^0k_z}\\&=\exp(i(k_x-k_x{}^0)x+i(k_y-k_y{}^0)y)\psi_{nk_x{}^0k_y{}^0k_z}\,,\end{aligned}\tag{33}$$

where $k_x{}^0$ and $k_y{}^0$ are the values of k_x and k_y at the zone edge.

$$\psi_{nk_x{}^0k_y{}^0k_z}=\exp(ik_x{}^0x+ik_y{}^0+ik_zz)u_{nk_x{}^0k_y{}^0k_z}$$

is the Bloch function on this edge and satisfies

$$\mathscr{H}_0\psi_{nk_x{}^0k_y{}^0k_z}=E_n(k_x{}^0k_y{}^0k_z)\,\psi_{nk_x{}^0k_y{}^0k_z}\,. \tag{34}$$

It is apparent that functions ϕ_{nk} form an orthonormal system.

For simplicity we use u_{nk_z}, ψ_{nk_z} and $E_n(k_z)$ for $u_{nk_x{}^0k_y{}^0k_z}$, $\psi_{nk_x{}^0k_y{}^0k_z}$ and $E_n(k_x{}^0k_y{}^0k_z)$. Then the matrix elements of our Hamiltonian can easily be calculated:

$$\begin{aligned}(n\boldsymbol{k}|\mathscr{H}_0|n'\boldsymbol{k}')=\delta_{nn'}\delta(\boldsymbol{k}'-\boldsymbol{k})&\left[\frac{\hbar'}{2m}\{(k_x'-k_x{}^0)^2+(k_y'-k_y{}^0)^2\}+E_n(k_z)\right]\\&+\delta(\boldsymbol{k}'-\boldsymbol{k})\frac{\hbar}{m}\{(k_x'-k_x{}^0)\,p_x{}^{nn'}+(k_y'-k_y{}^0)\,p_y{}^{nn'}\}\,.\end{aligned}\tag{35}$$

$$(n\boldsymbol{k}|-\omega y p_x|n'\boldsymbol{k}')=i\omega\frac{\partial\delta(\boldsymbol{k}'-\boldsymbol{k})}{\partial k_y'}\{\hbar(k_x'-k_x{}^0)\delta_{nn'}+p_x{}^{nn'}\}\,, \tag{36}$$

$$\left(n\boldsymbol{k}\left|\frac{m}{2}\,\omega^2y^2\right|n'\boldsymbol{k}'\right)=-\frac{m}{2}\,\omega^2\frac{\partial^2(\boldsymbol{k}'-\boldsymbol{k})}{\partial k_y'^2}\,, \tag{37}$$

where

$$p_{x,y}^{nn'}=\int\psi_{nk_z}^*(-i\hbar\nabla_{x,y})\psi_{n'k_z}\,d\boldsymbol{r}\,. \tag{38}$$

With the assumption

$$\Psi=\sum_n\int d\boldsymbol{k}\,B_n(\boldsymbol{k})\,\phi_{nk}\,, \tag{39}$$

we have the set of differential equations for $B_n(\boldsymbol{k})$ from (35), (36) and (37), as before:

$$\begin{aligned}&\left[\frac{\hbar^2}{2m}\{(k_x-k_x{}^0)^2+(k_y-k_y{}^0))\}+E_n(k_z)\right]B_n(\boldsymbol{k})\\&\qquad+\frac{\hbar}{m}\sum_{n'}\{(k_x-k_x{}^0)\,p_x{}^{nn'}+(k_y-k_y{}^0)\,p_y{}^{nn'}\}B_{n'}(\boldsymbol{k})\\&\qquad-i\omega\sum_{n'}\{\hbar(k_x-k_x{}^0)\delta_{nn'}+p_x{}^{nn'}\}\frac{\partial B_{n'}}{\partial k_y}-\frac{m}{2}\,\omega^2\frac{\partial^2B_n}{\partial k_y{}^2}=EB_n(\boldsymbol{k})\,.\end{aligned}\tag{40}$$

In order to solve (40), we must simplify it by making use of the result of § 2. Putting $k_x{}^0=k_y{}^0=0$ and neglecting terms which can be thought to be small we have

$$\sum_{n'}\left\{\frac{\hbar}{m}(k_xp_x{}^{nn'}+k_yp_y{}^{nn'})-i\omega\,p_x{}^{nn'}\frac{\partial}{\partial k_y}\right\}B_{n'}(\boldsymbol{k})=\{E-E_n(k_z)\}B_n(\boldsymbol{k})\,, \tag{41}$$

where n and n' means the four bands which are near each other energetically at the zone edge, higher bands being negligible because their effects may only change the mass in (40) to the effective mass.

Putting $\omega=0$, Eqs. (41) become the ordinary secular equation which determines the energy band structure. According to the result of the tight binding method, this secular equation is reduced to the two-dimensional one if we neglect the energy integrals connecting (A, D), (B, C) and (B, D) as in § 3.[14] In this case the matrix elements of the momentum was already calculated by McClure[14]:

$$p_x^{12}=-ip_0\ ,\qquad p_y^{12}=p_0\ ,\qquad p_x^{11}=p_x^{22}=p_y^{11}=p_y^{22}=0\ , \tag{42}$$

where p_0 is a constant of the order of the magnitude $\hbar/a$ and plays the same role as γ_0. Therefore with the same approximations we can write from (41) as follows:

$$\left.\begin{aligned}\{E-E_1(k_z)\}B_1(\boldsymbol{k})&=\frac{\hbar}{m}p_0\left(-ik_x+k_y-s\frac{\partial}{\partial k_y}\right)B_2(\boldsymbol{k})\ ,\\ \{E-E_2(k_z)\}B_2(\boldsymbol{k})&=\frac{\hbar}{m}p_0\left(ik_x+k_y+s\frac{\partial}{\partial k_y}\right)B_1(\boldsymbol{k})\ .\end{aligned}\right\} \tag{43}$$

Provided that $E_1(k_z)=E_0-\gamma_1\Gamma$, $E_2=E_0$, the above equations become identical with (29).

§5. Remarks on the Diamagnetism of Graphite

The diamagnetic susceptibility of graphite shows a remarkable anisotropy[15]. $\chi_\perp$ is nearly equal to the diamagnetic susceptibility of diamond and is independent of temperature, but $\chi_\parallel$ is large and varies with temperature ($\parallel$ or $\perp$ means that the direction of the magnetic field is parallel or perpendicular to the *c* axis). It is expected that the behavior of $\chi_\parallel$ is caused by the π electrons. The temperature dependence of $\chi_\parallel$ can be evaluated correctly because we have calculated the energy levels near the Fermi surface, while we can say nothing about the magnitude of $\chi_\parallel$ to which all electrons may contribute. In connection with the latter we may point out that the k-dependence of u_k or the band structure is neglected in the Peierls formula (1).

Hove[10] studied the temperature variation of $\chi_\parallel$ in detail using the Peierls formula (1) with the Wallace model (30). He found that γ_1 had to be equal to 0.5 ev in order to obtain the agreement with the experiment. This value is five times as large as that estimated by Coulson[6]. We must study the variation of the susceptibility with temperature using the energy levels (31) and compare the result with Hove's calculation. But this program is left in future on account of laborious numerical computation.

The author wishes to thank Dr. F. Nakano and Mr. S. Mase for their valuable discussions, Prof. Ariyama and Dr. S. Nakajima for their helpful advice and encouragement during the course of this work.

References

1) L. Landau: Z. Phys. **64** (1930) 629.
2) R. Peierls: Z. Phys. **80** (1933) 763.
3) J. M. Luttinger: Phys. Rev. **84** (1951) 814.
4) A. H. Wilson: Proc. Cambr. Phil. Mag. **49** (1953) 292.
5) E. N. Adams: Phys. Rev. **85** (1952) 41; **89** (1953) 633.
6) P. R. Wallace: Phys. Rev. **71** (1947) 622.
7) C. A. Coulson and R. Taylor: Proc. Phys. Soc. London **A, 65** (1952) 815.
8) D. F. Johnston: Proc. Roy. Soc. **A, 227** 349.
9) S. Mase: Busseiron-Kenkyu no. 98 (1956) 101 (in Japanese).
10) J. E. Hove: Phys. Rev. **100** (1955) 645.
11) J. M. Luttinger and W. Kohn: Phys. Rev. **97** (1955) 869.
12) J. W. McClure: Phys. Rev. **104** (1956) 666.
13) Y. Kitano: private communication.
14) J. W. McClure: Phys. Rev. **108** (1957) 612. J. C. Slonczewski and P. R. Weiss: Phys. Rev. **109** (1958) 272.
15) N. Ganguli and K. S. Krinshnan: Proc. Roy. Soc. **A, 177** (1941) 168.

JOURNAL OF THE PHYSICAL SOCIETY OF JAPAN, Vol. 14, No. 5, MAY, 1959

The Thermoelectric, Galvanomagnetic and Thermomagnetic Effects of Monovalent Metals, IV. Effect of the Non-equilibrium Distribution of the Phonons

By Mikio TSUJI

General Education Department, Kyushu University, Fukuoka

(Received January 8, 1959)

The effects of the non-equilibrium distribution of the phonons on the electrical and thermal conductivities, thermoelectric power, and transverse galvano- and thermomagnetic effects of metals are calculated. It is shown that Onsager's reciprocal relation holds, actually, in the case of the non-equilibrium distribution of the phonons with presence of a magnetic field. For the spherical band model, the effect on the Ettingshausen-Nernst coefficient is not so large as appeared in literatures. For an anisotropic band model, the phonon drag terms appear in the Ettingshausen, Ettingshausen-Nernst and Righi-Leduc coefficients.

§ 1. Introduction

In the previous papers of this series¹⁾ (I, II and III), we have calculated the thermoelectric power and the transverse galvano- and thermomagnetic effects of the monovalent metals, by assuming the equilibrium distribution of the phonons. In I, it has been shown that the positive signs of the thermoelectric powers and the negative signs of the Ettingshausen and Ettingshausen-Nernst coefficients of the noble metals at high temperatures are interpreted qualitatively by assuming a simple model of the spherical energy band of the conduction electrons. In II and III, the calculations have been generalized to the case of low temperatures and to the anisotropic energy band, and we have derived the relations between the coefficients which hold irrespective of the scatting mechanism. Now the distribution of the phonons deviates, actually, from its equilibrium value, and the effects of this non-equilibrium phonons on the thermoelectric powers of metals²⁾ and semiconductors³⁾ below room temperature are, in fact, not necessarily small.

Assuming the quasi-free electron model, Hanna and Sondheimer⁴⁾ solved the simultaneous Boltzmann equations for the distribution functions of the electrons and the phonons by a method of successive approximations and obtained a set of interpolation formulae. A more rigorous solution was obtained by the author in another paper⁵⁾, in which the distribution function of the phonons was eliminated at first, and then the resultant equation was solved by using a variation principle. An identical method was adopted by Bailyn⁶⁾ independently*. In these articles so far mentioned, only the cases of no magnetic field have been treated. Recently, Parrott⁷⁾, Appel⁸⁾ and V. L. Gurevich (son of L. E. Gurevich) and Obraztsov⁹⁾ have calculated the effect of the non-equilibrium distribution of the phonons on the Ettingshausen-Nernst effect of the semi-conductors. The measurement of the effect has also been done by Herring *et al*¹⁰⁾. However, the effect for metals has not yet been calculated in detail except for a simple considerations of L. E. Gurevich¹¹⁾ who initially calculated the "phonon drag effect" on the thermoelectric power and also suggested the effect on the Ettingshausen-Nornst coefficient. Recently, Paul¹²⁾ has calculated the effects of the non-equilibrium distribution of the phonons on the thermal conductivity and the thermomagnetic effects of metals. However, unfortunately, there are many important errors in his article, and especially his conclusion on the Ettingshausen-Nernst effect is qualitatively invalid.

In this article, we consider the effect of the non-equilibrium distribution of the phonons on the transverse galvano- and thermo- magnetic effects of the monovalent metals, and give the corrections due to this effect for the results obtained in I, II and III. At first, in § 2, we show formally that the general reciprocal relations of Onsager hold for any conductor in a magnetic field, even if we consider the non-equilibrium distribution of the phonons. This fact has been shown by Sondheimer[13] for a special case of no magnetic field. The discussion given in § 2 holds not only for the monovalent metals but also for any conductors. In § 3 we write down the Boltzmann equations for a metal strip which has the spherical energy band and is placed in a transverse magnetic field. At first, we eliminate the distribution function of the phonons from the simultaneous Boltzmann equations, and then we solve the resultant equation by a variational method used in III. From the solution, we obtain the electrical and thermal conductivities, the thermoelectric power, and the Hall, Ettingshausen, Ettingshausen-Nernst and Righi-Leduc coefficients. We discuss, in § 4, the results obtained in § 3 and derive certain relations between the coefficients which hold irrespective of the scattering mechanism. It is shown that the "phonon drag" effect appears in the thermoelectric power, but it does not appear in the galvanomagnetic and thermomagnetic effects. However, the corrections due to the lattice thermal conductivity appear in the latter quantities. The effects for an anisotropic media are considered in § 5 and § 6. In § 5 we show that the phonon drag term of the thermoelectric power of a metal having cubic anisotropy is of the same order of magnitude as that of a metal having spherical energy band. In the presence of a magnetic field, however, the non-equilibrium distribution of the phonons give the phonon drag terms to the Ettingshausen, Ettingshausen-Nernst and Righi-Leduc coefficients of anisotropic metals if the departures from the spherical band are significant. These phonon drag terms disappear in the isotropic metals. These facts are shown in § 6.

---

* I am very grateful to Dr. Bailyn for sending me a copy of his manuscript before publication.

§ 2. Onsager's Reciprocal Relations

Assuming the equilibrium distribution of the phonons, Meixner[14] and Kohler[15] have shown that Onsager's reciprocal relations actually hold in the presence of a magnetic field. For the case of no magnetic field, Sondheimer[13] has shown that the reciprocal relations hold even if we take into account the departure from the equilibrium distribution of the phonons. In this section, we show that the relations also hold for the case where a magnetic field exists in a conductor and the distribution of the phonons deviates from equilibrium value. The proof is easily performed by using a method similar to that used by Kohle[15] in the case of the equilibrium distribution of the phonons. We put the distributions of the electrons and the phonons in the form

$$f(\boldsymbol{k})=f_0(E_{\boldsymbol{k}})-\Phi(\boldsymbol{k})\frac{\partial f_0}{\partial E}\,, \tag{1}$$

and

$$N(\boldsymbol{q})=N_0(h\nu_q)-\frac{\Psi(\boldsymbol{q})}{\kappa T}\frac{\partial N_0}{\partial z}\,, \tag{2}$$

respectively, where f_0 and N_0 are the equilibrium distributions, $\boldsymbol{k}$ and $\boldsymbol{q}$ are the wave numbers of an electron and of a phonon, ν_q is the frequency of the phonon, and $z=h\nu_q/\kappa T$. We assume that there are an electric field $\boldsymbol{F}$, a magnetic field $\boldsymbol{H}$ and a temperature gradient ∇T in any directions. Then we may write the Boltzmann equations schematically in the forms

$$\{L_1+M(\boldsymbol{H})\}\Phi(\boldsymbol{k})+L_2\Psi(\boldsymbol{q})$$
$$=\left(e\boldsymbol{F}-T\nabla\frac{E-\zeta}{T}\right)\cdot\boldsymbol{v}\frac{\partial f_0}{\partial E}\,, \tag{3}$$

$$L_3\Phi(\boldsymbol{k})+L_4\Psi(\boldsymbol{q})=-\boldsymbol{u}\cdot\nabla T\frac{\partial N_0}{\partial T}\,, \tag{4}$$

where $\boldsymbol{v}$ and $\boldsymbol{u}$ are the group velocities of an electron and a phonon respectively and ζ is the Fermi level. The definitions of the linear operators L_1, L_2, L_3 and L_4 are given in the article of Sondheimer[13] and they satisfy the symmetry relations

$$\int F(\boldsymbol{k})L_1(G)d\boldsymbol{k}=\int G(\boldsymbol{k})L_1(F)d\boldsymbol{k}\,, \tag{5}$$

$$2\int F(\boldsymbol{k})L_2(G)d\boldsymbol{k}=\int G(\boldsymbol{q})L_3(F)d\boldsymbol{q}\,, \tag{6}$$

$$\int F(\boldsymbol{q})L_4(G)d\boldsymbol{q}=\int G(\boldsymbol{q})L_4(F)d\boldsymbol{q}\,, \tag{7}$$

where F and G are arbitrary functions of $\boldsymbol{k}$ or $\boldsymbol{q}$. $M(\boldsymbol{H})$ is an operator which gives the effect of the Lorentz force due to the magnetic field and is defined by

$$M(\boldsymbol{H})\equiv\frac{e}{\hbar c}\frac{\partial f_0}{\partial E}\nabla_k E\cdot\boldsymbol{H}\times\nabla_k\,. \tag{8}$$

$M(\boldsymbol{H})$ satisfies the relation[14),15)]

$$\int F(\boldsymbol{k})M(\boldsymbol{H})G(\boldsymbol{k})d\boldsymbol{k}=\int G(\boldsymbol{k})M(-\boldsymbol{H})F(\boldsymbol{k})d\boldsymbol{k}\,. \tag{9}$$

Now if we put

$$\varPhi(\boldsymbol{k})=\left(e\boldsymbol{F}+T\nabla\frac{\zeta}{T}\right)\cdot\boldsymbol{\phi}+\frac{1}{T}\nabla T\cdot\boldsymbol{\psi}\ , \tag{10}$$

$$\varPsi(\boldsymbol{q})=\left(e\boldsymbol{F}+T\nabla\frac{\zeta}{T}\right)\cdot\boldsymbol{\mu}+\frac{1}{T}\nabla T\cdot\boldsymbol{\nu}\ , \tag{11}$$

the Boltzmann equations may be written in the forms

$$v_i\frac{\partial f_0}{\partial E}=\{L_1+M(\boldsymbol{H})\}\phi_i+L_2(\mu_i)\ , \tag{12}$$

$$v_iE\frac{\partial f_0}{\partial E}=\{L_1+M(\boldsymbol{H})\}\psi_i+L_2(\nu_i)\ , \tag{13}$$

$$0=L_3(\phi_i)+L_4(\mu_i)\ , \tag{14}$$

$$-u_iT\frac{\partial N_0}{\partial T}=L_3(\psi_i)+L_4(\nu_i)\ , \tag{15}$$

where the suffices $i=1,\ 2,\ 3$ denote the x, y, z components respectively. The electric and heat current densities are given by

$$\left.\begin{aligned} J_i&=\sum_j\left\{S_{ij}^{(1)}\left(e^2F_j+eT\frac{\partial}{\partial x_j}\frac{\zeta}{T}\right)+S_{ij}^{(2)}\frac{e}{T}\frac{\partial T}{\partial x_j}\right\}\ ,\\ w_i&=\sum_j\left\{S_{ij}^{(3)}\left(-eF_j-T\frac{\partial}{\partial x_j}\frac{\zeta}{T}\right)-S_{ij}^{(4)}\frac{1}{T}\frac{\partial T}{\partial x_j}\right\}\ ,\end{aligned}\right\} \tag{16}$$

respectively, where

$$S_{ij}^{(1)}=\frac{1}{4\pi^3}\int v_i\phi_j\frac{\partial f_0}{\partial E}d\boldsymbol{k}\ , \tag{17}$$

$$S_{ij}^{(2)}=\frac{1}{4\pi^3}\int v_i\psi_j\frac{\partial f_0}{\partial E}d\boldsymbol{k}\ , \tag{18}$$

$$S_{ij}^{(3)}=\frac{1}{4\pi^3}\int v_iE\,\phi_j\frac{\partial f_0}{\partial E}d\boldsymbol{k}-\frac{1}{8\pi^3}\int u_iT\mu_j\frac{\partial N_0}{\partial T}d\boldsymbol{q}\ , \tag{19}$$

$$S_{ij}^{(4)}=\frac{1}{4\pi^3}\int v_iE\,\psi_j\frac{\partial f_0}{\partial E}d\boldsymbol{k}-\frac{1}{8\pi^3}\int u_iT\nu_j\frac{\partial N_0}{\partial T}d\boldsymbol{q}\ . \tag{20}$$

The reciprocal relations are

$$S_{ij}^{(1)}(\boldsymbol{H})=S_{ji}^{(1)}(-\boldsymbol{H})\ , \tag{21}$$

$$S_{ij}^{(4)}(\boldsymbol{H})=S_{ji}^{(4)}(-\boldsymbol{H})\ , \tag{22}$$

$$S_{ij}^{(2)}(\boldsymbol{H})=S_{ji}^{(3)}(-\boldsymbol{H})\ . \tag{23}$$

Here we give the proof of (21). The proof of the remaining relations can be performed in a similar way.

Now we write the solutions of the equations (12) through (15) as ϕ_i^+ and μ_i^+, and the solutions of the equations with the magnetic field reversed in the directions as ϕ_i^- and μ_i^-. Using (12), we have

$$\begin{aligned} 4\pi^3S_{ij}^{(1)}(\boldsymbol{H})&=\int\phi_j^+\{L_1+M(\boldsymbol{H})\}\phi_i^+d\boldsymbol{k}+\int\phi_j^+L_2(\mu_i^+)d\boldsymbol{k}\\ &=\int\phi_j^+\{L_1+M(-\boldsymbol{H})\}\phi_i^-d\boldsymbol{k}+\int\phi_j^+L_2(\mu_i^-)d\boldsymbol{k}\ . \end{aligned} \tag{24}$$

Now using (5), (6), (7), (9) and (14), we have

$$\int\phi_j^+L_1(\phi_i^-)d\boldsymbol{k}=\int\phi_i^-L_1(\phi_j^+)d\boldsymbol{k}\ , \tag{25}$$

$$\int\phi_j^+M(-\boldsymbol{H})\phi_i^-d\boldsymbol{k}=\int\phi_i^-M(\boldsymbol{H})\phi_j^+d\boldsymbol{k}\ , \tag{26}$$

$$\begin{aligned} \int\phi_j^+L_2(\mu_i^-)d\boldsymbol{k}&=\frac{1}{2}\int\mu_i^-L_3(\phi_j^+)d\boldsymbol{q}=-\frac{1}{2}\int\mu_i^-L_4(\mu_j^+)d\boldsymbol{q}\\ &=-\frac{1}{2}\int\mu_j^+L_4(\mu_i^-)d\boldsymbol{q}=\int\phi_j^-L_2\mu_j^+d\boldsymbol{k}\ , \end{aligned} \tag{27}$$

Putting (25), (26) and (27) into (24), we have

$$4\pi^3 S_{ij}^{(1)}(\boldsymbol{H})=\int\phi_i^-\{L_1+M(\boldsymbol{H})\}\phi_j^+dk+\int\phi_j^-L_2(\mu_j^+)dk=4\pi^3 S_{ji}^{(1)}(-\boldsymbol{H})\,.$$

Now certain symmetry relations such as $\sigma(\boldsymbol{H})=\sigma(-\boldsymbol{H})$ (σ=the electrical conductivity) have been derived from (21), (22) and (23) by Meixner[14] and Kohler[15]. Here, it has been proved that these relations also remain valid even if the distribution of the phonons deviates from the equilibrium.

§ 3. Calculation on the Spherical Energy Band Model

In this section we consider only the case of a transverse magnetic field, $\boldsymbol{E}$, and ∇T being in x–y plane and $\boldsymbol{H}$ along z-axis. We assume that the energy of an electron $E(k)$ depends only on $k=|\boldsymbol{k}|$, and assume the Debye model for the phonons. In this case, $\Phi(\boldsymbol{k})$ and $\Psi(\boldsymbol{q})$ can be written in the form

$$\Phi(\boldsymbol{k})=k_xc_x(\eta)+k_yc_y(\eta)\,,\qquad \Psi(\boldsymbol{q})=q_xb_x(z)+q_yb_y(z)\,, \tag{28}$$

where $\eta=(E-\zeta)/\kappa T$. The collision operators can be written also in the form

$$L_1(\Phi)=\hbar^{-1}\{k_x\mathscr{L}_1(c_x)+k_y\mathscr{L}_1(c_y)\}\partial f_0/\partial E\,, \tag{29}$$

$$L_2(\Psi)=\hbar^{-1}\{k_x\mathscr{L}_2(b_x)+k_y\mathscr{L}_2(b_y)\}\partial f_0/\partial E\,, \tag{30}$$

$$L_3(\Phi)=\{q_x\mathscr{L}_3(c_x)+q_y\mathscr{L}_3(c_y)\}\partial N_0/\partial z\,, \tag{31}$$

$$L_4(\Psi)=\{q_x\mathscr{L}_4(b_x)+q_y\mathscr{L}_4(b_y)\}\partial N_0/\partial z\,. \tag{32}$$

The definite forms of $\mathscr{L}_1$, $\mathscr{L}_2$, $\mathscr{L}_3$ and $\mathscr{L}_4$ are given in the reference (5). From the symmetry relations (5), (6) and (7), we easily obtain the relations

$$\int k^4\left(\frac{dE}{dk}\right)^{-1}c(\eta)\mathscr{L}_1\{d(\eta)\}\frac{\partial f_0}{\partial\eta}d\eta=\int k^4\left(\frac{dE}{dk}\right)^{-1}d(\eta)\mathscr{L}_1\{c(\eta)\}\frac{\partial f_0}{\partial\eta}d\eta\,, \tag{33}$$

$$2h^{-1}\int k^4\left(\frac{dE}{dk}\right)^{-1}c(\eta)\mathscr{L}_2\{b(z)\}\frac{\partial f_0}{d\eta}d\eta=q_0^5\left(\frac{T}{\Theta}\right)^5\int z^4b(z)\mathscr{L}_3\{c(\eta)\}\frac{\partial N_0}{\partial z}dz\,, \tag{34}$$

$$\int z^4a(z)\mathscr{L}_4\{b(z)\}\frac{\partial N_0}{\partial z}dz=\int z^4b(z)\mathscr{L}_4\{a(z)\}\frac{\partial N_0}{\partial z}dz\,, \tag{35}$$

where q_0 is the maximum wave number of the phonons, Θ is the Debye characteristic temperature, d and c are arbitrary functions of η, and a and b are arbitrary functions of z.

Now the Boltzmann equations can be writted in the forms

$$\mathscr{L}_1(c_x)+\mathscr{L}_2(b_x)=\left(eF_x-T\frac{\partial}{\partial x}\frac{\zeta}{T}+\frac{E}{T}\frac{\partial T}{\partial x}\right)\frac{1}{k}\frac{dE}{dk}+\frac{eH}{\hbar c}\frac{1}{k}\frac{dE}{dk}c_y\,, \tag{36}$$

$$\mathscr{L}_1(c_y)+\mathscr{L}_2(b_y)=\left(eF_y-T\frac{\partial}{\partial y}\frac{\zeta}{T}+\frac{E}{T}\frac{\partial T}{\partial y}\right)\frac{1}{k}\frac{dE}{dk}-\frac{eH}{\hbar c}\frac{1}{k}\frac{dE}{dk}c_x\,, \tag{37}$$

$$\mathscr{L}_3(c_x)+\mathscr{L}_4(b_x)=\frac{\kappa}{\hbar q_0^2}\left(\frac{\Theta}{T}\right)^2\frac{\partial T}{\partial x}\,, \tag{38}$$

$$\mathscr{L}_3(c_y)+\mathscr{L}_4(b_y)=\frac{\kappa}{\hbar q_0^2}\left(\frac{\Theta}{T}\right)^2\frac{\partial T}{\partial y}\,. \tag{39}$$

Eliminating b_x and b_y from (36) through (39), we have

$$\mathscr{L}(c_x)=\left(eF_x-T\frac{\partial}{\partial x}\frac{\zeta}{T}+\frac{E}{T}\frac{\partial T}{\partial x}\right)\frac{1}{k}\frac{dE}{dk}+\frac{eH}{\hbar c}\frac{1}{k}\frac{dE}{dk}c_y-\frac{\partial T}{\partial x}\frac{\kappa}{\hbar q_0^2}\left(\frac{\Theta}{T}\right)^2\mathscr{L}_2\mathscr{L}_4^{-1}(1)\,, \tag{40}$$

$$\mathscr{L}(c_y)=\left(eF_y-T\frac{\partial}{\partial y}\frac{\zeta}{T}+\frac{E}{T}\frac{\partial T}{\partial y}\right)\frac{1}{k}\frac{dE}{dk}-\frac{eH}{\hbar c}\frac{1}{k}\frac{dE}{dk}c_x-\frac{\partial T}{\partial y}\frac{\kappa}{\hbar q_0^2}\left(\frac{\Theta}{T}\right)^2\mathscr{L}_2\mathscr{L}_4^{-1}(1)\,, \tag{41}$$

where

$$\mathscr{L}\equiv\mathscr{L}_1-\mathscr{L}_2\mathscr{L}_4^{-1}\mathscr{L}_3\,. \tag{42}$$

In (42), $\mathscr{L}_4^{-1}$ denotes the inverse operator of $\mathscr{L}_4$ and have the same symmetry as the original operator $\mathscr{L}_4$.

The last terms of the right sides of (40) and (41) give the effect of the deviation of the the phonon distribution produced by the thermal gradient, and these termes enter in the equation in the forms of "drift" terms. The "reaction" of the effect of the deviation of the electron distribution from equilibrium on the phonon distribution is included in the operator $\mathscr{L}$ as the second term of the right side of (42). This "reaction" has an effect that makes the rate of change of the electron distribution due to collision smaller than the case without the deviation of the distribution of the phonons.

Now we can show that the operator $\mathscr{L}$ has also the same symmetric character as $\mathscr{L}_1$. Bailyn[6] has proved this for a special case in which the term $\mathscr{L}_4(b)$ can be written down by using a relaxation time. Here we give a more general proof by using the relations (33), (34) and (35). For arbitrary functions $c(\eta)$ and $d(\eta)$ we have, by using (34),

$$\int k^4\left(\frac{dE}{dk}\right)^{-1}c(\eta)\mathscr{L}_2\mathscr{L}_4^{-1}\mathscr{L}_3\{d(\eta)\}\frac{\partial f_0}{\partial\eta}d\eta=q_0^5\left(\frac{T}{\Theta}\right)^5\int z^4[\mathscr{L}_4^{-1}\mathscr{L}_3\{d(\eta)\}]\mathscr{L}_3\{c(\eta)\}\frac{\partial N_0}{\partial z}dz\,. \tag{43}$$

Now from (35), we have

$$\int z^4a(z)\mathscr{L}_4^{-1}\{b(z)\}\frac{\partial N_0}{\partial z}dz=\int z^4b(z)\mathscr{L}_4^{-1}\{a(z)\}\frac{\partial N_0}{\partial z}dz\,. \tag{44}$$

Using (44), we can rewrite the right side of (43) as

$$q_0^5\left(\frac{T}{\Theta}\right)^5\int z^4[\mathscr{L}_4^{-1}\mathscr{L}_3\{c(\eta)\}]\mathscr{L}_3\{d(\eta)\}\frac{\partial N_0}{\partial z}dz\,.$$

Therefore, using again (34), we have

$$\int k^4\left(\frac{dE}{dk}\right)^{-1}c(\eta)\mathscr{L}_2\mathscr{L}_4^{-1}\mathscr{L}_3\{d(\eta)\}\frac{\partial f_0}{\partial\eta}d\eta=\int k^4\left(\frac{dE}{dk}\right)^{-1}d(\eta)\mathscr{L}_2\mathscr{L}_4^{-1}\mathscr{L}_3\{c(\eta)\}\frac{\partial f_0}{\partial\eta}d\eta\,. \tag{45}$$

Thus it has been shown that $\mathscr{L}_2\mathscr{L}_4^{-1}\mathscr{L}_3$ and so $\mathscr{L}$ satisfy the same symmetry relation as $\mathscr{L}_1$. More generaly we can prove easily that $L_2L_4^{-1}L_3$ satisfies the same symmetry relation as L_1.

Now, considering that (40) and (41) have the forms similar to the equations derived with the assumption of the equilibrium phonon distribution, we can solve these equations by using the varation principle used in III. Since the procedure is almost the same as in III, we write below only the outline of the procedure. If we put the solutions of (40) and (41) in the forms

$$c_x=c_{x,0}+c_{x,1}\eta\,,\qquad c_y=c_{y,0}+c_{y,1}\eta\,, \tag{46}$$

the coefficients of the right sides of (46) can be determined by the following equations

$$\left.\begin{aligned}&\sum_s c_{x,s}d_{rs}-\sum_s c_{y,s}\gamma_{r+s}-\left(eF_x+T\frac{\partial}{\partial x}\frac{\zeta}{T}\right)\alpha_r^{(1)}-\frac{1}{T}\frac{\partial T}{\partial x}\{\alpha_r^{(2)}+\beta_r^{(2)}\}=0\,,\\&\sum_s c_{y,s}d_{rs}+\sum_s c_{x,s}\gamma_{r+s}-\left(eF_y+T\frac{\partial}{\partial y}\frac{\zeta}{T}\right)\alpha_r^{(1)}-\frac{1}{T}\frac{\partial T}{\partial y}\{\alpha_r^{(2)}+\beta_r^{(2)}\}=0\,,\end{aligned}\right\} \tag{47}$$

where

$$d_{rs}=\int_{-\infty}^{\infty} k^4\left(\frac{dE}{dk}\right)^{-1}\eta^r\mathscr{L}(\eta^s)\frac{\partial f_0}{\partial\eta}d\eta\ , \tag{48}$$

$$\gamma_r=\frac{eH}{\hbar c}\int k^3\eta^r\frac{\partial f_0}{\partial\eta}d\eta=\frac{eH}{\hbar c}\alpha_r{}^{(1)}\ , \tag{49}$$

$$\alpha_r{}^{(n)}=\int E^{n-1}k^3\eta^r\frac{\partial f_0}{\partial\eta}d\eta\ , \tag{50}$$

$$\beta_r{}^{(n)}=-(n-1)\frac{\kappa T}{\hbar q_0{}^2}\left(\frac{\Theta}{T}\right)^2\int k^4\left(\frac{dE}{dk}\right)^{-1}\eta^r\frac{\partial f_0}{\partial\eta}\mathscr{L}_2\mathscr{L}_4{}^{-1}(1)d\eta\ . \tag{51}$$

Putting the solution (46) into (38) and (39), we have the solutions b_x and b_y as

$$\left.\begin{aligned} b_x&=-\mathscr{L}_4{}^{-1}\mathscr{L}_3(c_x)+\frac{\kappa}{\hbar q_0{}^2}\left(\frac{\Theta}{T}\right)^2\frac{\partial T}{\partial x}\mathscr{L}_4{}^{-1}(1)\ ,\\ b_y&=-\mathscr{L}_4{}^{-1}\mathscr{L}_3(c_y)+\frac{\kappa}{\hbar q_0{}^2}\left(\frac{\Theta}{T}\right)^2\frac{\partial T}{\partial y}\mathscr{L}_4{}^{-1}(1)\ .\end{aligned}\right\} \tag{52}$$

The electric and heat current densities are calculated by using the solution (46) and (52) and the results can be written in the same form as (37) in III, with the coefficients K_{mn}'s shown below. Using the notations of (31) in III, we have

$$\left.\begin{aligned}
K_{11}&=\frac{1}{3\pi^2\hbar}(c_0{}^{(1)}\alpha_0{}^{(1)}+c_1{}^{(1)}\alpha_1{}^{(1)})\ ,\\
K_{12}&=\frac{1}{3\pi^2\hbar}(c_0{}^{(2)}\alpha_0{}^{(1)}+c_1{}^{(2)}\alpha_1{}^{(1)})\ ,\\
K_{13}&=-\frac{1}{3\pi^2\hbar}(\bar{c}_0{}^{(1)}\alpha_0{}^{(1)}+\bar{c}_1{}^{(1)}\alpha_1{}^{(1)})\ ,\\
K_{14}&=-\frac{1}{3\pi^2\hbar}(\bar{c}_0{}^{(2)}\alpha_0{}^{(1)}+{}_1\bar{c}^{(2)}\alpha_1{}^{(1)})\ ,\\
K_{21}&=\frac{1}{3\pi^2\hbar}\{c_0{}^{(1)}(\alpha_0{}^{(2)}+\beta_0{}^{(2)})+c_1{}^{(1)}\alpha_1{}^{(2)}\}\ ,\\
K_{22}&=\frac{1}{3\pi^2\hbar}\{c_0{}^{(2)}(\alpha_0{}^{(2)}+\beta_0{}^{(2)})+c_1{}^{(2)}\alpha_1{}^{(2)}+\mathcal{E}\}\ ,\\
K_{23}&=-\frac{1}{3\pi^2\hbar}\{\bar{c}_0{}^{(1)}(\alpha_0{}^{(2)}+\beta_0{}^{(2)})+\bar{c}_1{}^{(1)}\alpha_1{}^{(2)}\}\ ,\\
K_{24}&=-\frac{1}{3\pi^2\hbar}\{\bar{c}_0{}^{(2)}(\alpha_0{}^{(2)}+\beta_0{}^{(2)})+\bar{c}_1{}^{(2)}\alpha_1{}^{(2)}\}\ ,
\end{aligned}\right\} \tag{53}$$

where

$$\frac{1}{3\pi^2\hbar}\mathcal{E}\equiv\frac{(\kappa T)^2q_0}{6\pi^2\hbar}\frac{T}{\Theta}\int z^4\frac{\partial N_0}{\partial z}\mathscr{L}_4{}^{-1}(1)dz\ , \tag{54}$$

and $c_r{}^{(n)}$ and $\bar{c}_r{}^{(n)}$ are given by (32) through (36) in III, by replacing $\alpha_r{}^{(2)}$ by $\alpha_r{}^{(2)}+\beta_r{}^{(2)}$. In the calculation of the phonon parts of K_{2m}'s we used the symmetry relations (34) and (35). From (53) it is easily shown that the following relations hold,

$$K_{21}=K_{12}\ ,\qquad K_{23}=K_{14}\ . \tag{55}$$

In the calculations of K_{mn}'s given by (53), we retain only up to the linear terms of H and the second order terms of $\kappa T/\zeta$. Here we note that $c_1{}^{(n)}$, $\bar{c}_1{}^{(n)}$ and $\alpha_1{}^{(n)}$ are of the orders of magnitudes of $(\kappa T/\zeta)^2$ times $c_0{}^{(n)}$, $\bar{c}_0{}^{(n)}$ and $\alpha_0{}^{(n)}$ respectively, and $\beta_0{}^{(2)}$ and $\beta_1{}^{(2)}$ are of the orders of magnitudes of $\kappa T/\zeta$ times $\alpha_0{}^{(2)}$ and $\alpha_1{}^{(2)}$ respectively. The estimations of the orders of magnitudes of $\beta_r{}^{(2)}$ are easily carried out by putting the definite forms of $\mathscr{L}_2$ and

$\mathscr{L}_4$ given below into (51). By using the values of K_{mn}'s, we can calculate all the quantities by the usual way described in I, and we have the following results. (In the following equations, k_0 is the radius of the Fermi sphere and $\alpha=(dE/dk)_{E=\zeta}$.)

(i) Electrical Conductivity

$$\sigma=\frac{e^2k_0^6}{3\pi^2\hbar d_{00}} . \tag{56}$$

(ii) Thermal Conductivity

$$\kappa_T=\kappa_1+\kappa_2 , \tag{57}$$

where

$$\kappa_1=\frac{\pi^2k_0^6\kappa^2T}{27\hbar d_{11}} , \tag{58}$$

$$\kappa_2=\frac{1}{3\pi^2\hbar}\mathcal{E} . \tag{59}$$

(iii) Absolute Thermoelectric Power

$$S=S_1+S_2 , \tag{60}$$

where

$$S_1=-\frac{\kappa}{e}\left\{\frac{\pi^2\kappa T}{\alpha k_0}-\frac{\pi^2d_{01}}{3d_{11}}+\frac{\pi^4\kappa Td_{00}}{3\alpha k_0d_{11}}\right\} , \tag{61}$$

$$S_2=\frac{\beta_0{}^{(2)}}{eTk_0^3} . \tag{62}$$

(iv) Hall Coefficient

$$R_H=-\frac{3\pi^2}{k_0^3ce}=-\frac{1}{nec} . \tag{63}$$

(v) Ettingshausen Coefficient

$$A_E=\frac{3\pi^2\left(\frac{\pi^2\kappa T}{\alpha k_0}d_{00}-d_{01}\right)}{c\kappa k_0^3d_{11}}\left(1+\frac{\kappa_g}{\kappa_e}\right)^{-1} . \tag{64}$$

(vi) Isothermal Ettingshausen-Nernst Coefficient

$$B^i_{EN}=\frac{\pi^4\kappa k_0^3\left(\frac{\pi^2\kappa T}{\alpha k_0}d_{00}-d_{01}\right)}{9\hbar cd_{11}^2} . \tag{65}$$

(vii) Righi-Leduc Coefficient

$$B_{RL}=-\frac{e\pi^2k_0^3}{3\hbar cd_{11}}\left(1+\frac{\kappa_g}{\kappa_e}\right)^{-1} . \tag{66}$$

It is to be noted that each of d_{rs} is defined by (48) and includes two terms; one of them comes from the first term of (42) and the other comes from the second term of (42). The former is identical with d_{rs} defined by (25) in I and the latter represents the effect of the "reaction". The second term of d_{00}, $d_{10}=d_{01}$ and d_{11} are identical with $\hbar$ times β_0, $\beta_1=\gamma_0$ and γ_1 defined in (35) and (36) in the reference (5). Now the second terms of d_{00} and d_{01} are of the same orders of magnitudes of the first terms of them respectively and become important at low temperatures for pure metals. The second term of d_{11} is of the order of magnitude of $(\kappa T/\zeta)^2$ times the first term, and so is negligible always.

Now the definite forms of $\mathscr{L}_1$, $\mathscr{L}_2$, $\mathscr{L}_3$ and $\mathscr{L}_4$ are given by the formulae[5]

$$\mathscr{L}_1(c)=-\frac{1}{\Lambda}\left(\frac{T}{\Theta}\right)^3\left(\frac{dE}{dk}\right)^{-1}\int_{-\theta/T}^{\theta/T}\left\{1+\left(\frac{1}{\alpha k_0}-\frac{\beta}{\alpha^2}\right)\kappa Tz\right\}$$
$$\cdot\left[c(\eta)-c(\eta+z)\left\{1+\frac{\kappa Tz}{kdE/dk}-\frac{q_0^2}{2k^2}\left(\frac{T}{\Theta}\right)^2 z^2\right\}\right]\frac{e^\eta+1}{e^{\eta+z}+1}\frac{z^2dz}{|1-e^{-z}|}-\frac{\hbar}{\tau_i}, \tag{67}$$

$$\mathscr{L}_2(b)=-\frac{1}{\Lambda}\left(\frac{T}{\Theta}\right)^3\left(\frac{dE}{dk}\right)^{-1}\int_{-\theta/T}^{\theta/T} b(|z|)\left\{1+\left(\frac{1}{\alpha k_0}-\frac{\beta}{\alpha^2}\right)\kappa Tz\right\}$$
$$\cdot\left\{\frac{\kappa Tz}{kdE/dk}-\frac{q_0^2}{2k^2}\left(\frac{T}{\Theta}\right)^2 z^2\right\}\frac{e^\eta+1}{e^{\eta+z}+1}\frac{z^2dz}{|1-e^{-z}|}, \tag{68}$$

$$\mathscr{L}_3(c)=\frac{2\Delta}{3\pi h\Lambda q_0^2}\left(\frac{\Theta}{T}\right)^2\frac{1-e^{-z}}{z^2}\left\{1+\left(\frac{1}{\alpha k_0}-\frac{\beta}{\alpha^2}\right)\kappa Tz\right\}$$
$$\cdot\int_{-\infty}^{\infty} k^4\left(\frac{dE}{dk}\right)^{-2}c(\eta)\left\{\frac{\dfrac{\kappa Tz}{kdE/dk}+\dfrac{q_0^2}{2k^2}\left(\dfrac{T}{\Theta}\right)^2 z^2}{(e^{-\eta}+1)(e^{\eta-z}+1)}-\frac{\dfrac{\kappa Tz}{kdE/dk}-\dfrac{q_0^2}{2k^2}\left(\dfrac{T}{\Theta}\right)^2 z^2}{(e^{-\eta}+1)(e^{\eta}+e^{-z})}\right\}d\eta, \tag{69}$$

$$\mathscr{L}_4(b)=-\frac{2\Delta k_0^2}{3\pi h\Lambda\alpha^2}(z+\Gamma)\left\{1+2\left(\frac{1}{\alpha k_0}-\frac{\beta}{\alpha^2}\right)\kappa T\frac{z^2}{z+\Gamma}\right\}, \tag{70}$$

where $\beta=(d^2E/dk^2)_{E=\zeta}$, Λ is the interaction parameter defined in I, τ_i denotes the relaxation time for the scattering of electrons by the impurity atoms and the lattice defects in the metal, Δ is the volume of the unit cell and Γ is given by

$$\Gamma=\frac{3\pi h\Lambda\alpha^2 u_0}{2\Delta L k_0^2\kappa T}, \tag{71}$$

in which u_0 is the sound velocity and L is the mean free path of the phonons due to the phonon-phonon scattering and phonon-impurity scattering etc. Here we have assumed, for simplicity, that only the longitudinal phonons interact with the electrons. A generalization to the case in which the transverse phonons also interact with the electrons is easy if we compare the results in this article with those given in the reference (5).

Putting (67), (68), (69) and (70) into (48), (51) and (54), we have

$$d_{00}=\frac{k_0^2q_0^2}{\Lambda\alpha^2}\left(\frac{T}{\Theta}\right)^5 J_5+\frac{\hbar k_0^4}{\tau_i\alpha}-\frac{k_0^2q_0^2}{\Lambda\alpha^2}\left(\frac{T}{\Theta}\right)^5 P_6, \tag{72}$$

$$d_{01}=d_{10}=\frac{\kappa Tk_0^4}{\Lambda\alpha^2}\left(\frac{T}{\Theta}\right)^3\left\{\frac{1}{\alpha k_0}+\frac{2\pi^2q_0^2}{3k_0^2}\left(\frac{T}{\Theta}\right)^2\left(\frac{1}{\alpha k_0}-\frac{\beta}{\alpha^2}\right)\right\}J_5+\frac{\hbar\pi^2\kappa Tk_0^4}{3\tau_i\alpha}$$
$$\cdot\left(\frac{4}{\alpha k_0}-\frac{\beta}{\alpha^2}-\frac{1}{\tau_i}\frac{d\tau_i}{dE}\right)-\frac{\kappa Tk_0^4}{\Lambda\alpha^2}\left(\frac{T}{\Theta}\right)^3\left\{\frac{1}{\alpha k_0}+\frac{2\pi^2q_0^2}{3k_0^2}\left(\frac{T}{\Theta}\right)^2\left(\frac{1}{\alpha k_0}-\frac{\beta}{\alpha^2}\right)\right\}P_6, \tag{73}$$

$$d_{11}=\frac{k_0^4}{\Lambda\alpha^2}\left(\frac{T}{\Theta}\right)^3\left\{1+\frac{\pi^2q_0^2}{3k_0^2}\left(\frac{T}{\Theta}\right)^2\right\}J_5+\frac{\pi^2\hbar k_0^4}{3\tau_i\alpha}, \tag{74}$$

$$\beta_0^{(2)}=-\frac{3\pi^2\kappa T}{\Delta}\left(\frac{T}{\Theta}\right)^3 P_5, \tag{75}$$

and

$$\varepsilon=\frac{\kappa^2T^2k_0^4}{q_0^2}\left(\frac{T}{\Theta}\right)P_4, \tag{76}$$

where

$$J_n\equiv\int_0^{\theta/T}\frac{z^ndz}{(e^z-1)(1-e^{-z})}, \tag{77}$$

$$P_n\equiv\int_0^{\theta/T}\frac{1}{z+\Gamma}\frac{z^ndz}{(e^z-1)(1-e^{-z})}. \tag{78}$$

If we put (72), (73) and (74) into (56) through (66), we find

$$\sigma=\frac{\sigma_e}{1-\delta_1}\,, \qquad \rho=\rho_e(1-\delta_1)\,, \tag{79}$$

$$\kappa_T=\kappa_e+\kappa_g\,, \tag{80}$$

$$S=S_e(1+\delta_2)+S_g\,, \tag{81}$$

$$R_H=R_{H,e}\,, \tag{82}$$

$$A_E=A_{E;e}\frac{1-\delta_3}{1+\kappa_g/\kappa_e}\,, \tag{83}$$

$$B^i_{EN}=B^i_{EN,e}(1-\delta_3)\,, \tag{84}$$

$$B_{RL}=\frac{B_{RL,e}}{1+\kappa_g/\kappa_e}\,, \tag{85}$$

where suffices e's denote the values of respective quantities in the case of the equilibrium distribution of the phonons (they have been given in I and III), κ_g is the lattice thermal conductivity in the case of the equilibrium electron distribution, S_g is the thermoelectric power produced by the "phonon drag" and δ_1, δ_2, δ_3 show the effect of the "reaction" term in Eq. (42). δ_1, δ_2, δ_3, S_g and κ_g/κ_e are given by

$$\delta_1=\frac{\Lambda^{-1}q_0{}^2(T/\Theta)^5P_6}{\tau_i{}^{-1}\hbar\alpha k_0{}^2+\Lambda^{-1}q_0{}^2(T/\Theta)^5J_5}\,, \tag{86}$$

$$\delta_2=\frac{\Lambda^{-1}\left(\frac{T}{\Theta}\right)^3\left\{\frac{1}{\alpha k_0}-\frac{\pi^2q_0{}^2}{3k_0{}^2}\left(\frac{T}{\Theta}\right)^2\left(\frac{1}{\alpha k_0}+\frac{2\beta}{\alpha^2}\right)\right\}P_6}{\frac{\pi^2\hbar\alpha}{3\tau_i}\left(\frac{2}{\alpha k_0}+\frac{\beta}{\alpha^2}+\frac{1}{\tau_i}\,\frac{d\tau_i}{dE}\right)+\frac{1}{\Lambda}\left(\frac{T}{\Theta}\right)^3\left\{\frac{2}{\alpha k_0}+\frac{2\pi^2q_0{}^2}{3k_0{}^2}\left(\frac{T}{\Theta}\right)^2\left(\frac{2}{\alpha k_0}+\frac{\beta}{\alpha^2}\right)\right\}J_5}\,, \tag{87}$$

$$\delta_3=\frac{\frac{1}{\Lambda}\left(\frac{T}{\Theta}\right)^3\left\{\frac{1}{\alpha k_0}-\frac{\pi^2q_0{}^2}{3k_0{}^2}\left(\frac{T}{\Theta}\right)^2\left(\frac{1}{\alpha k_0}+\frac{2\beta}{\alpha^2}\right)\right\}P_6}{\frac{\pi^2\hbar\alpha}{3\tau_i}\left(\frac{1}{\alpha k_0}-\frac{\beta}{\alpha^2}-\frac{1}{\tau_i}\,\frac{d\tau_i}{dE}\right)+\frac{1}{\Lambda}\left(\frac{T}{\Theta}\right)^3\left\{\frac{1}{\alpha k_0}-\frac{\pi^2q_0{}^2}{3k_0{}^2}\left(\frac{T}{\Theta}\right)^2\left(\frac{1}{\alpha k_0}+\frac{2\beta}{\alpha^2}\right)\right\}J_5}\,, \tag{88}$$

$$S_g=-\frac{\kappa}{e}\left(\frac{T}{\Theta}\right)^3P_5\,, \tag{89}$$

$$\frac{\kappa_g}{\kappa_e}=\left[\frac{9\hbar^2}{\tau_i\kappa^2Tk_0{}^2\alpha}+\frac{27\hbar}{\pi^2\Lambda\kappa^2Tk_0{}^2\alpha^2}\left(\frac{T}{\Theta}\right)^3\left\{1+\left(\frac{T}{\Theta}\right)^2\frac{\pi^2q_0{}^2}{3k_0{}^2}\right\}J_5\right]\frac{\Lambda k_0{}^4\alpha^2\kappa^2\Theta}{3\pi^2\hbar q_0{}^2}\left(\frac{T}{\Theta}\right)^2P_4\,, \tag{90}$$

respectively.

§ 4. Discussion

For a special case of the quasi-free electron model, we put $\alpha=\hbar^2k_0/m^*$ and $\beta=\hbar^2/m^*$, m^* being the effective mass, and then (79) and (80) coincide prefectly with the interpolation formulae derived by Hanna and Sondheimer⁴⁾. However, Eq. (81) differs from the result of Hanna and Sondheimer, in the point that the latter does not have the term δ_2S_e. For an ideally pure metal ($\tau_i\to\infty$) and at low temperatures, if we assume that the phonons were scattered only by the electrons, P_6 would tend to J_5 and so $\delta_1\to1$, $\delta_2\to1/2$ and $\delta_3\to1$. However, in reality, in most cases, P_6 is smaller than J_5 and $1/\tau_i$ does not vanish, and so δ_1, δ_2 and δ_3 are considerably smaller than unity. Therefore the effects of the "reaction" can be neglected in many cases*. On the contrary, as pointed out by L. E. Gurevich¹¹⁾ and Hanna and Sondheimer[4], the phonon drag term of the thermoelectric power S_g may become considerably large, at low temperatures.

---

* An Approximation used by Parrott⁷⁾ in the calculation of the Ettingshausen-Nernst effect in the semiconductors is equivalent to the neglect of the "reaction" effect.

Eq. (80) shows that the change of the lattice part of the thermal conductivity due to the non-equilibrium electrons is perfectly cancelled out by the change of the electronic part of the thermal conductivity due to the non-equilibrium phonons. Therefore the calculation of the change of the lattice part of the thermal conductivity by Paul[12] is meaningless and Paul's discussion on the change of the thermomagnetic effects due to the change of the lattice part of the thermal conductivity is also invalid.

Eq. (82) shows that the Hall coefficient is not altered by the phonon drift due to the electric current J_x. This may easily be understood as follows. If $F_y=0$, the magnetic field will produce the Hall current $J_{y,H}$ which is proportional to J_x and H. In reality, as an experimental condition, we put $J_y=0$ and so there appeares F_y which is given by the product of $-J_{y,H}$ and the transverse resistivity ρ_y. Now, the total current is in the x-direction and so ρ_x is modified as shown by (79), but ρ_y remains to be ρ_e. Therefore the Hall constant R_H $(=F_y/HJ_x)$ is not modified by the phonon drift in the x-direction.

The factor $(1+\kappa_g/\kappa_e)^{-1}$ in (83) is explained as follows. The magnetic field H produces a heat current $w_{y,H}$ which is proportional to J_x and H. Experimentally, we put $w_y=0$, and so there appeares a temperature gradient $\partial T/\partial y$ which is proportional to $w_{y,H}$ and inversely proportional to the thermal conductivity $\kappa_T=\kappa_e(1+\kappa_g/\kappa_e)$. Therefore, the Ettingshausen coefficient A_E $(=-(\partial T/\partial y)/HJ_x)$ becomes proportional to $(1+\kappa_g/\kappa_e)^{-1}$.

In the case of the Ettingshausen-Nernst effect, the magnetic field produces an electric current J_y which is proportional to the electronic part of the heat current w_x (i.e., proportional to $\kappa_e\partial T/\partial x$ and not $\kappa_T\partial T/\partial x$), and so $B^i_{EN}(=-F_y/H(\partial T/\partial x))$ does not depend on κ_g. Finally, in the case of the Righi-Leduc effect, the magnetic field produces an electronic heat current $w_{y,H}$ which is proportional to $\kappa_e\partial T/\partial x$. Experimentally, we put $w_y=0$, and so there appear a temperature gradient $\partial T/\partial y$ which is proportional to $w_{y,H}$ and inversely proportional to $\kappa_T=\kappa_e+\kappa_g$. Therefore the Righi-Leduc coefficient B_{RL} $(=(\partial T/\partial y)/H(\partial T/\partial x))$ is proportional to $(1+\kappa_g/\kappa_e)^{-1}$. The factor $(1+\kappa_g/\kappa_e)^{-1}$ appeared in (83) and (85) shows the effect of the fact that the heat current is carried by the phonons as well as by the electrons. We shall call the effect simply "the lattice conductivity effect". The "phonon drag" effect does not appear in (83), (84) and (85) (See § 6). Now for the pure metals, κ_g is usually very smaller than κ_e[16], and so we may conclude that, in the spherical band model, the non-equilibrium distribution of the phonons does not give so large contributions to the transverse galvanomagnetic and thermomagnetic effects as the contribution S_g in the thermoelectric power. This conclusion differs from those of Paul[12] and L. E. Gurevich[11] on the Ettingshausen-Nernst effect. Paul's calculation of A_{EN} $(=B^i_{EN}/\kappa_T)$ starts from a first order approximation

$$eF_y=-\frac{\pi^2}{2}\frac{eH\tau}{mc}\frac{\zeta}{T}\frac{\partial T}{\partial x}, \tag{91}$$

which gives as a first order approximation of B^i_{EN},

$$B^i_{EN}=\frac{\pi^2\tau\zeta}{2mcT}. \tag{92}$$

However, the exact first order approximation is given by

$$B^i_{EN}=\frac{\pi^2\kappa^2T}{3mc}\frac{\partial\tau}{\partial\zeta}=\frac{\pi^2\kappa^2\tau T}{2mc\zeta}, \tag{93}$$

where we put $\tau\propto E^{3/2}$ (high temperature and free electron approximation). Therefore Paul's result on the Ettingshausen-Nernst coefficient is not valid. L. E. Gurevich[11] calculated the electric current $\boldsymbol{J}$ from a Boltzmann equation in which usual drift term was replaced by a phonon drift term (corresponds to the last terms of (40) and (41)), expanded $\boldsymbol{J}$ in a power series of $\boldsymbol{H}$ and derived the "Nernst's current" $\boldsymbol{J}_N$ from the first order term of $\boldsymbol{H}$. In actuality, the experimental condition of the Ettingshausen-Nernst effect is $J_x=J_y=0$, and so the derivation of L. E. Gurevich seems to be invalid.

We have derived, in I and III, certain relations between the coefficients. Here we shall reexamine these relations in the case of the non-equilibrium distribution of the phonons. From (83) and (84) of this paper and (47) of III, we see that Bridgmann's relation

$$\frac{B_{EN}^{i}}{\kappa_T}\equiv A_{EN}^{i}=\frac{A_E}{T}\,, \tag{94}$$

holds also in the case of the non-equilibrium distribution of the phonons. This is a natural consequence of the Onsager relations (21), (22) and (23)[17]. (Paul's results do not satify this relation. See his Eqs. (38) and (43).) From (82), (83), (84) and (85), we see that the relation (48) of III is modified as

$$\frac{R_H B_{EN}^{i}}{A_E B_{RL}}\left(=\frac{R_H \kappa_T}{T B_{RL}}\right)=\frac{\pi^2}{3}\left(\frac{\kappa}{e}\right)^2\left(1+\frac{\kappa_g}{\kappa_e}\right)^2. \tag{95}$$

Further, if we neglect the small corrections δ_2 and δ_3 in (81) and (83), we have

$$\frac{1}{T}\left\{ncA_E\left(1+\frac{\kappa_g}{\kappa_e}\right)+\frac{3e}{\pi^2\kappa^2}S\right\}=-\frac{3}{\alpha k_0}-\frac{3e}{\pi^2\kappa^2 T}S_g\,, \tag{96}$$

which is a corrected formula of (61) of III.

Now for the impure metals or alloys at low temperatures, κ_g may become comparable with κ_e[16], and then the correction due to the "lattice conductivity effect" in A_E and B_{RL} may become important.

The results derived in this section is based on the spherical band model. In the next section, we show that the cubic anisotropy in the band structure does not alter the general situation of the electrical and thermal conductivities and the thermoelectric power. Therefore, Eqs. (79), (80) and (81) may be good approximation for the alkali metals such as sodium and potasium in which the band structures are thought to be fairly spherical. As will be shown in § 6, however, the anisotropy gives the "phonon drag" effects for A_E, B_{EN}^{i} and B_{RL}, and this may become important at low temperatures. Therefore the spherical band model of the metals may be useless for the discussion of the "phonon drag" effects of these quantities.

§ 5. Cubic Anisotropic Band Model without Magnetic Field

In III, we have seen that the transverse galvano- and thermomagnetic effects of an anisotropic crystal having cubic symmetry can be calculated approximately by using the variation principle. Hence, at first, it is thought that the calculation described in the preceding section might be generalized to any cubic anisotropic band by replacing the function (28) by the function (15) of III. However, in reality, as shown in the following section, the departure of the distribution of the phonons from the equilibrium gives new contributions (phonon drag terms) to the Ettingshausen, Ettingshausen-Nernst and Righi-Leduc coefficients, which appear only in anisotropic media. Of course these new terms have not appeared in the calculation in § 3. Moreover, if we generalize the calculation in § 3 simply by replacing the function (28) by the function (15) of III, we can not obtain the new terms. This is due to the fact that our method used in III is useless for the calculation of the quantities such as magnetoresistance to which the anisotropy is essentially important, namely the quantities which vanish for isotropic media.

Therefore, in this section we shall limit our calculation only to the case with no magnetic field. This is a simple generalization of the calculations in the reference (5), and so we write only the final results. Let the electric field F and the temperature gradient be in the x-direction. The Boltzmann equations can be written in the forms

$$L_1(\Phi_k)+L_2(\Psi_q)=\frac{1}{\hbar}\left(eF-T\frac{\partial}{\partial x}\,\frac{E-\zeta}{T}\right)\frac{\partial E}{\partial k_x}\,\frac{\partial f_0}{\partial E}\,, \tag{97}$$

$$L_3(\Phi_k)+L_4(\Psi_q)=-u_x\frac{\partial T}{\partial x}\frac{\partial N_0}{\partial T}\,. \tag{98}$$

Eliminating Ψ_q from (97) and (98), we have

$$L(\Phi_k)=\frac{1}{\hbar}\left(eF-T\frac{\partial}{\partial x}\frac{E-\zeta}{T}\right)\frac{\partial E}{\partial k_x}\frac{\partial f_0}{\partial E}+\frac{\partial T}{\partial x}L_2L_4^{-1}\left(u_x\frac{\partial N_0}{\partial T}\right), \tag{99}$$

where

$$L\equiv L_1-L_2L_4^{-1}L_3\,, \tag{100}$$

and L satisfies the symmetry relation (5). The second term of the right side of (100) represents the "reaction" and the second term of the right side of (99) represents the "phonon drag". As an approximate trial function, we put

$$\Phi_k=\frac{\partial E}{\partial k_x}(c_0+c_1\eta)\,. \tag{101}$$

After a calculation similar to that in § 3, we find

$$\sigma=\frac{e^2(\alpha_0^{(1)})^2}{4\pi^3\hbar d_{00}}\,, \tag{102}$$

$$\kappa_T=\kappa_e+\kappa_g\,, \tag{103}$$

$$\kappa_e=\frac{\{\alpha_1^{(1)}\alpha_0^{(2)}-\alpha_0^{(1)}\alpha_1^{(2)}\}^2}{4\pi^3\hbar T(\alpha_0^{(1)})^2 d_{11}}\,, \tag{104}$$

$$\kappa_g=\frac{\mathcal{E}}{4\pi^3\hbar T}\,, \tag{105}$$

$$S=S_e+S_g\,, \tag{106}$$

$$S_e=-\frac{\kappa}{e}\left\{\frac{\alpha_1^{(1)}}{\alpha_0^{(1)}}-\frac{\alpha_2^{(1)}d_{01}}{\alpha_0^{(1)}d_{11}}+\frac{\alpha_1^{(1)}\alpha_2^{(1)}d_{00}}{(\alpha_0^{(1)})^2 d_{11}}\right\}, \tag{107}$$

$$S_g=-\frac{1}{eT}\frac{\beta_0^{(2)}}{\alpha_0^{(1)}}\,, \tag{108}$$

where

$$\alpha_r^{(n)}=\int\left(\frac{\partial E}{\partial k_x}\right)^2E^{n-1}\eta^r\frac{\partial f_0}{\partial E}dk\,, \tag{109}$$

$$d_{rs}=\hbar\int\frac{\partial E}{\partial k_x}\eta^r L\left(\frac{\partial E}{\partial k_x}\eta^s\right)dk\,, \tag{110}$$

$$\mathcal{E}=-\frac{(\kappa\Theta)^2}{2\hbar q_0^4}\left(\frac{\Theta}{T}\right)^2\int q_x L_4^{-1}\left(q_x\frac{\partial N_0}{\partial z}\right)\frac{\partial N_0}{\partial z}dq\,, \tag{111}$$

$$\beta_0^{(2)}=-\frac{\kappa T}{q_0^2}\left(\frac{\Theta}{T}\right)^2\int\frac{\partial E}{\partial k_x}L_2L_4^{-1}\left(q_x\frac{\partial N_0}{\partial z}\right)dk\,. \tag{112}$$

Eq. (104) is identical with Eq. (22) of II, and if we neglect the small effect of the "reaction", σ and S_e given by (102) and (107) become identical with (21) and (23) of II, respectively. Eq. (108) gives the "phonon drag effect" on the thermoelectric power.

It is shown, in the following section, that Eqs. (102) through (108) give the exact results, if the collision operator L is represented by a relaxation time depending only on the electronic energy E_k. Further, in the case of the spherical energy band, these equations reduce to those derived in § 3. There appeares no essentially new term by the introduction of the cubic anisotropy.

§6. Special Case with Magnetic Field

In this section, we treat only a special case in which the collision operator L is represented by a relaxation time which depends only on the energy of the electron E_k. Assuming the equilibrium distribution of the phonons, we have calculated the transverse galvanomagnetic and thermomagnetic effects for the metals having the energy dependent relaxation time (§5 of III). We show below that, if we take into account the departure of the distribution of the phonons from equilibrium, new terms which vanish in the case of the spherical band, appear in the Ettingshausen, Ettingshausen-Nernst and Righi-Leduc coefficients. Now the Boltzmann equations (3) and (4) can be rewritten in the forms

$$L_1(\varPhi_k)+L_2(\varPsi_k)=\frac{1}{\hbar}\left(eF_x+T\frac{\partial}{\partial x}\frac{\zeta}{T}+\frac{E}{T}\frac{\partial T}{\partial x}\right)\frac{\partial E}{\partial k_x}\frac{\partial f_0}{\partial E}+\frac{1}{\hbar}\left(eF_y+T\frac{\partial}{\partial y}\frac{\zeta}{T}+\frac{E}{T}\frac{\partial T}{\partial y}\right)\frac{\partial E}{\partial k_y}\frac{\partial f_0}{\partial E}+\frac{eH}{\hbar^2 c}\frac{\partial f_0}{\partial E}\varOmega_3\varPhi_k\,, \tag{113}$$

$$L_3(\varPhi_k)+L_4(\varPsi_q)=-u_x\frac{\partial T}{\partial x}\frac{\partial N_0}{\partial T}-u_y\frac{\partial T}{\partial y}\frac{\partial N_0}{\partial T}\,, \tag{114}$$

where

$$\varOmega_3=\frac{\partial E}{\partial k_x}\frac{\partial}{\partial k_y}-\frac{\partial E}{\partial k_y}\frac{\partial}{\partial k_x}\,. \tag{115}$$

Eliminating $\varPsi(\boldsymbol{q})$ from (113) and (114), we have

$$L(\varPhi_k)=\frac{1}{\hbar}\left(eF_x+T\frac{\partial}{\partial x}\frac{\zeta}{T}+\frac{E}{T}\frac{\partial T}{\partial x}\right)\frac{\partial E}{\partial k_x}\frac{\partial f_0}{\partial E}+\frac{1}{\hbar}\left(eF_y+T\frac{\partial}{\partial y}\frac{\zeta}{T}+\frac{E}{T}\frac{\partial T}{\partial y}\right)\frac{\partial E}{\partial k_y}\frac{\partial f_0}{\partial E}+\frac{eH}{\hbar^2 c}\frac{\partial f_0}{\partial E}\varOmega_3\varPhi_k+\frac{\partial T}{\partial x}L_2L_4^{-1}\left(u_x\frac{\partial N_0}{\partial T}\right)+\frac{\partial T}{\partial y}L_2L_4^{-1}\left(u_y\frac{\partial N_0}{\partial T}\right)\,. \tag{116}$$

where L is given by (100).

Now we shall consider a special case in which $L(\varPhi)$ is given by

$$L(\varPhi)=-\frac{1}{\tau}\frac{\partial f_0}{\partial E}\varPhi\,, \tag{117}$$

where we assume that the relaxation time τ depends only on the energy of the electron E_k. By the method of the successive approximations, we can obtain the solution of (116) in a power series of H. Here we need to calculate only up to the first order term of H. From the solution $\varPhi_k$, we easily obtain the contribution of the electrons to K_{mn}. In the calculation, we use the fact that, for a cubic crystal, K_{11}, K_{22}, $K_{12}=K_{21}$ are the even functions of H and K_{13}, K_{21}, $K_{11}=K_{23}$ are the odd functions of H. This can be proved easily, by using the relations (21), (22) and (23). Putting the solution $\varPhi_k$ into (114), we have $\varPsi_k$. Then we can calculate the phonon contribution to K_{2n}, by using the formula of the lattice heat current

$$\boldsymbol{w}=\frac{1}{8\pi^3}\int \boldsymbol{u}T\varPsi_q\frac{\partial N_0}{\partial T}d\boldsymbol{q}\,. \tag{118}$$

The final results are

$$K_{11}=-\frac{1}{4\pi^3\hbar^2}\int\left(\frac{\partial E}{\partial k_x}\right)^2\tau\frac{\partial f_0}{\partial E}d\boldsymbol{k}\,, \tag{119}$$

$$K_{12}=K_{21}=-\frac{1}{4\pi^3\hbar^2}\int\left(\frac{\partial E}{\partial k_x}\right)^2 E\tau\frac{\partial f_0}{\partial E}d\boldsymbol{k}-\frac{T}{4\pi^3\hbar}\int\left(\frac{\partial E}{\partial k_x}\right)\tau L_2L_4^{-1}\left(u_x\frac{\partial N_0}{\partial T}\right)d\boldsymbol{k}\,, \tag{120}$$

$$K_{13}=-\frac{eH}{4\pi^3\hbar^4 c}\int\left(\frac{\partial E}{\partial k_x}\right)\tau\varOmega_3\left(\tau\frac{\partial E}{\partial k_y}\right)\frac{\partial f_0}{\partial E}d\boldsymbol{k}\,, \tag{121}$$

$$K_{14}=K_{23}=-\frac{eH}{4\pi^3\hbar^4c}\int\frac{\partial E}{\partial k_x}\tau\Omega_3\left(\tau E\frac{\partial E}{\partial k_y}\right)\frac{\partial f_0}{\partial E}d\boldsymbol{k}$$
$$-\frac{TeH}{4\pi^3\hbar^3c}\int\frac{\partial E}{\partial k_x}\tau\Omega_3\left\{\tau L_2L_4^{-1}\left(u_y\frac{\partial N_0}{\partial T}\right)\right\}d\boldsymbol{k}\,, \tag{122}$$

$$K_{22}=-\frac{1}{4\pi^3\hbar^2}\int\left(\frac{\partial E}{\partial k_x}\right)^2E^2\tau\frac{\partial f_0}{\partial E}d\boldsymbol{k}-\frac{T}{2\pi^3\hbar}\int\frac{\partial E}{\partial k_x}E\tau L_2L_4^{-1}\left(u_x\frac{\partial N_0}{\partial T}\right)d\boldsymbol{q}$$
$$+\frac{T^2}{8\pi^3}\int u_xL_4^{-1}\left(u_x\frac{\partial N_0}{\partial T}\right)\frac{\partial N_0}{\partial T}d\boldsymbol{q}\,, \tag{123}$$

$$K_{24}=-\frac{eH}{4\pi^3\hbar^4c}\int\frac{\partial E}{\partial k_x}E\tau\Omega_3\left(\tau E\frac{\partial E}{\partial k_y}\right)\frac{\partial f_0}{\partial E}d\boldsymbol{k}$$
$$-\frac{TeH}{2\pi^3\hbar^3c}\int\frac{\partial E}{\partial k_x}E\tau\Omega_3\left\{\tau L_2L_4^{-1}\left(u_y\frac{\partial N_0}{\partial T}\right)\right\}d\boldsymbol{k}\,. \tag{124}$$

The second terms of K_{12} and K_{14} are the phonon drag terms of the electric current. Using (119) through (124), we can calculate all the quantities required. The results for σ, κ_e and S are identical with (102) through (108) if we replace only the operator L by $-(1/\tau)\partial f_0/\partial E$. This fact guarantees that the procedure used in § 4 is an useful approximation. For the galvano- and thermomagnetic coefficients, we have

$$R_H=-\frac{4\pi^3}{ec}\frac{f_5}{f_1^2}\,, \tag{125}$$

$$A_E=\frac{4\pi^2T}{c}\frac{\left[f_5\left(\frac{1}{\tau}\frac{d\tau}{dE}-\frac{1}{f_1}\frac{\partial f_1}{\partial E}+\frac{1}{f_5}\frac{\partial f_5}{\partial E}\right)-\frac{3}{\pi^2\kappa^2T^2f_1}(f_1\xi_0^{(2)}-f_5\beta_0^{(2)})\right]}{f_1^2\left(1+\frac{\kappa_g}{\kappa_e}\right)}\,, \tag{126}$$

$$B_{EN}^{i}=\frac{\pi^2\kappa^2T\tau}{3\hbar^2cf_1}\left[f_5\left(\frac{1}{\tau}\frac{d\tau}{dE}-\frac{1}{f_1}\frac{\partial f_1}{\partial E}+\frac{1}{f_5}\frac{\partial f_5}{\partial E}\right)-\frac{3}{\pi^2\kappa^2T^2f_1}(f_1\xi_0^{(2)}-f_5\beta_0^{(2)})\right]\,, \tag{127}$$

$$B_{RL}=-\frac{e\tau}{\hbar^2c}\frac{\left[f_5-\frac{6\zeta}{\pi^2\kappa^2T^2f_1}(f_1\xi_0^{(2)}-f_5\beta_0^{(2)})\right]}{f_1\left(1+\frac{\kappa_g}{\kappa_e}\right)}\,, \tag{128}$$

where f_1 and f_5 are given by (29) and (28) of III, and

$$\beta_0^{(2)}=-T\hbar\int\frac{\partial E/\partial k_x}{|\mathrm{grad}_{\boldsymbol{k}}E|}L_2\left\{L_4^{-1}\left(u_x\frac{\partial N_0}{\partial T}\right)\right\}\left(\frac{\partial f_0}{\partial E}\right)^{-1}dS\,, \tag{129}$$

$$\xi_0^{(2)}=-T\hbar\int\frac{1}{|\mathrm{grad}_{\boldsymbol{k}}E|}\Omega_3\left(\frac{\partial E}{\partial k_y}\right)L_2\left\{L_4^{-1}\left(u_x\frac{\partial N_0}{\partial T}\right)\right\}\left(\frac{\partial f_0}{\partial E}\right)^{-1}dS\,. \tag{130}$$

where the integrations are carried over the Fermi surface. (Note that L_2 has a factor $\partial f_0/\partial E$ and (129) is identical with (112).) The second terms of the numerators of (126), (127) and (128) give the phonon drag effects. If we neglect these phonon drag terms, κ_g/κ_e in (126) and (128) and the "reaction term" in $1/\tau$, (125) through (128) become identical with (40), (52), (53) and (54) in III. Now for the spherical band model we can show easily that

$$f_1\xi_0^{(2)}-f_5\beta_0^{(2)}=0\,, \tag{131}$$

and if we replace $\mathscr{L}$ in § 3 by $-\hbar/\tau$, we see that the results obtained in § 3 are identical with those obtained in this section. Therefore the procedures used in § 3 are justified to be approximately valid for the spherical band model. Eq. (131) shows that the phonon drag effects do not appear in the transverse galvano- and thermomagnetic effects of the isotropic metals. In the case of the spherical band model, we have

$$\frac{\beta_0^{(2)}}{f_1}=-\kappa T\left(\frac{T}{\Theta}\right)^3P_5\,. \tag{132}$$

Therefore, if the second terms of the numerators of (126), (127) and (128) do not cancell out for a cubic anisotropic band, the ratios of the second terms to the first terms are of the order of magnitude of

$$\sim \frac{\zeta}{\kappa\Theta}\left(\frac{T}{\Theta}\right)^2 P_5 . \tag{133}$$

From the definition of P_n, we see that P_5 is always smaller than J_4. However, if the phonons are scattered predominantly by the electrons, P_5 becomes to be of the same order of magnitude as J_4 and so, at low temperatures, (133) becomes $\sim\zeta/\kappa T$. Therefore, there is a possibility that for a cubic anisotropic metal, the non-equilibrium distribution of the phonons gives fairly large contributions to the Ettingshausen, Ettingshausen-Nernst and Righi-Leduc effects, at low temperatures. This may be detected experimentally for the pure noble metals at low temperatures.

As a matter of course, (126) and (127) satisfy the Bridgmann relation (94). The relations (95) and (96), however, do not hold for the anisotropic media in which the cancelation (131) does not hold.

The cancellation of (131) is based on the Fermi statistics. Exactly speaking, the left side of (131) is of the order of $(\kappa T/\zeta)^2$ times $f_1\zeta_0^{(2)}$ or $f_5\beta_0^{(2)}$, for highly degenerate Fermi gas. For the non-degenerate semiconductors, owing to the Boltzmann statistics, the phonon drag terms do not vanish, even if the band structures are spherical, and so the phonon drag effects do appear in the Ettingshausen-Nernst coefficient *etc.* of the semi-conductors[7),8),9)]. If the band structure of the semiconductor is anisotropic, however, the phonon drag effects become larger than those of the isotropic semiconductor. The significan of the anisotropy in the cubic semiconductor has been pointed out by Herring *et al.*[1)]

Unfortunately, the measurements of the Ettingshausen, Ettingshausen-Nernst and Righi-Leduc coefficients of the monovalent metals at low temperatures have never been worked out, and so we can not, at present, compare our results with experiment.

Added Note. After communication to the editors, I became aware of the paper of G. E. Tauber (Canad. J. Phys. **36** (1958) 1308), in which he formulated a generalized variational principle by taking into account the phonon distribution functions and the external magnetic field. His formulation is a generalization of that of Dorn (Z. Naturforsch. **12a** (1957) 739) in the case of the presence of the magnetic field. We discussed the relation between our method and Dorn's one in ealier paper[5)]. The discussion would also hold for the relation between the Tauber's method and the method described in this paper.

References

1) M. Tsuji: J. Phys. Soc. Japan **13** (1958) 133; 818; 979.
2) See for instance, F. Blatt: *Solid State Physics*, vol. **4**, ed. by F. Seitz and D. Turnbull (Academic Press, New York, 1957) 357.
3) See for instance, V. A. Johnson: *Progress in Semiconductors* vol. **1**, ed. by A. F. Gibson, P. Aigrain and R. E. Burges (Heywood & Company, London, 1956) 63.
4) I. I. Hanna and E. H. Sondheimer: Proc. Roy. Soc. **A**, **239** (1957) 247.
5) M. Tsuji: Mem. Fac. of Sci. Kyushu Univ. Ser. **B**, **2** (1958) 119.
6) M. Bailyn: Phys. Rev.
7) J. E. Parrott: Proc. Phys. Soc. London **71** (1958) 82.
8) J. Appel: Z. Naturforsch. **13a** (1958) 386.
9) V. L. Gurevich and Iu. N. Obraztsov: Zh. Eks. Teor. Fiz. **32** (1957) 390; translated in Sov. Phys. JETP **5** (1957) 302.
10) C. Herring, T. H. Geballe and J. E. Kunzler: Phys. Rev. **111** (1958) 36.
11) L. E. Gurevich: J. Phys. Moscow **10** (1946) 174.
12) D. I. Paul: Phys. Rev. **111** (1958) 1086.
13) E. H. Sondheimer: Proc. Roy. Soc. **A**, **234** (1956) 391.
14) J. Meixner: Ann. Physik (5) **40** (1941) 165.
15) M. Kohler: Ann. Physik (5) **40** (1941) 601.
16) See for instance, P. G. Klemens: *Encyclopedia of Physics* vol. **14**, ed. by S. Flügge (Springer, Berlin, 1959) 259.
17) H. B. Callen: Phys. Rev. **73** (1948) 1349.

JOURNAL OF THE PHYSICAL SOCIETY OF JAPAN, Vol. 14, No. 5, MAY, 1959

Theoretical Treatment of the Movement of 180° Domain in $BaTiO_3$ Single Crystal

By Ryuji ABE

Faculty of Science, Nagoya University, Nagoya, Japan

(Received January 8, 1959)

A theoretical treatment was proposed for the movement of wedge-shaped 180° domains in $BaTiO_3$ single crystal. It was proved that the experimental relations found by Merz can be explained satisfactorily by considering this new mechanism of the domain motion. Further a few quantitative examinations were made and it was ascertained that there is no clear quantitative inconsistency between the theoretical relations and Merz's experimental relations.

§ 1. Introduction

A few years ago Merz observed 180° domains of $BaTiO_3$ single crystal by his original means, and with his cooperator[1] he succeeded in creating single crystals composed of only 180° domains. Using these crystals he studied their dynamic characteristics[2] by electrical means and found that there are simple relations between applied field and maximum of the induced current. To explain these relations, he assumed that at high fields the maximum of the current is determined by the growth process of nuclei while at low fields the maximum is determined mainly by the nucleation process of these nuclei. Then he proved that if the shape of a nucleus is a long flat dagger, the latter relation can be explained.

This experimental result and his explanation are very interesting because they are useful to study the properties of 180° wall. His explanation, however, is not satisfactory, because it contains a few questionable points. Furthermore no detailed explanation is given for the simple relation found at high fields. Therefore to explain these relations satisfactorily a more precise investigation on the movement of 180° domain should be made.

In the present paper a new treatment of the movement of 180° domain will be proposed, after Merz's explanation is examined. Then it will be proved that Merz's experimental relations can be explained saisfactorily by using this new treatment.

§ 2. Examination of Merz's Explanation

To fascilitate the later explanation, a brief review of Merz's experimental result and his explanation will be given at first. He applied square pulses to crystals and observed the induced current by cathode ray tube (Fig. 1). Then he plotted maximum of the current *versus* applied field (Fig. 2) and found from such figures that the current changes linearly with field at high fields, while it changes proportionally to $\exp(-(1/E))$ at low fields.

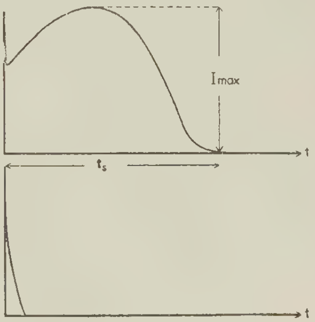

Fig. 1. Switching current *versus* time (after Merz).
Upper: when a field against the polarization is applied.
Lower: when a field for the polarization is applied.

To explain the former relation he assumed simply that the wall velocity changes linearly with the change of applied field, while to explain the latter relation he assumed that the maximum of the current is proportional to the nucleation rate of the new domain with antiparallel polarization and that the shape of the domain is a long flat dagger with a length l (in the direction of field) and a cross dimension $t \times w$ ($l \gg w > t$). The free energy of the new domain is then given by

$$\Delta F = -2EP_s lwt + \sigma_{W'}(wl + tl) + \sigma_{W''}wt \quad (1)$$

where P_S is the spontaneous polarization, $\sigma_{W'}$ is the wall energy/cm² of the side walls and $\sigma_{W''}$ is the wall energy/cm² of the front wall. The effects of the depolarizing field are neglected here because the new domain is very long and thin. Then assuming further that the nucleation rate is proportional to

$$\exp(-(\Delta F^*/kT))$$

and a width of the domain w is constant during the nucleation process, it can be obtained that

$$i_{\max} \propto \exp\left(-\frac{\Delta F^*}{kT}\right) = \exp\left(-\frac{w}{2}\frac{\sigma_{W'}\sigma_{W''}}{kTEP_S}\right) \tag{2}$$

where ΔF^* is the maximum of the free energy.

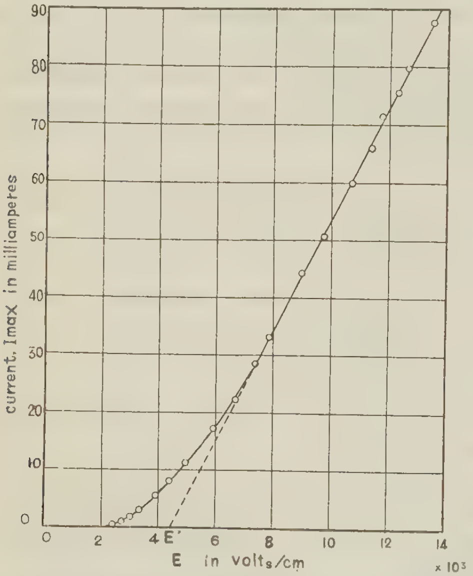

Fig. 2. Switching current *versus* applied field (after Merz).

Merz's explanation, however, contains a few questionable points. The first point is that Merz assumes that the free energy of a nucleus changes continuously with the change of its volume. Certainly this assumption is correct for the very large nucleus of which free energy can be considered to change continuously against the discontinuous change of the radius or the length by an unit lattice spacing. For the BaTiO$_3$ crystal, however, such a large nucleus can not appear within a few seconds, because the free energy of the nucleus is much higher than kT. This can be seen as follows: suppose that the nucleus is a long prolate spheroid with the radius r and the length l. The free energy of the nucleus is given by

$$\Delta F = -\frac{4}{3}\pi P_S E r^2 l + 4\pi\sigma_W r l + \frac{d}{2}\frac{4}{3}\pi\frac{r^4}{e}P_S^2 \dagger \tag{3}$$

where $d=4\pi(\log(l/r)-1)$. This free energy becomes maximum at $r=r^*$ and the maximum value is given by

$$\frac{4}{3}\pi P_S(d\sigma_W)^{1/2}(r^*)^{5/2} .$$

Since this maximum free energy must be of the order of kT in order that the new domain can be nucleated within a few seconds, the radius of the domain should be restricted to be

$$r^* \lesssim \left(\frac{3}{4\pi}\frac{kT}{P_S(d\sigma_W)^{1/2}}\right)^{5/2} . \tag{4}$$

Putting that $P_S=7.8\times10^4$ esu, $kT=4\times10^{-14}$ esu, $\sigma_W=1.40$ esu (according to Kinase and Takahasi's result4)) and $d=16\pi$, this condition becomes

$$r^* \lesssim 1\times10^{-9}\ \text{cm} .$$

This result indicates that Merz's assumption is not appropriate for the BaTiO$_3$ crystal. The second point is that Merz neglects the energy due to the depolarizing field. Certainly this neglection is correct for the nucleus of which length is much longer than the cross diameters. For such long nucleus, however,

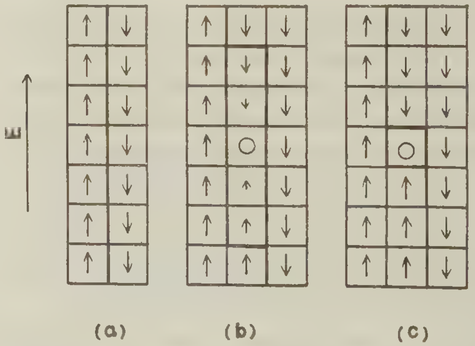

Fig. 3. Side wall and Front wall of 180° domain.
(a) 180° wall.
(b) Front wall with the thickness of 5 lattice spacings.
(c) Front wall with the thickness of one lattice spacing.

[†] The depolarizing energy is underestimated by the factor of $1/\varepsilon$ by Landauer3), because he assumes that the crystal is a linear dielectric, where ε is the dielectric constant of the crystal.

the wall energy of the front wall (the last term in Eq. (1)) may be also much smaller than the energy of the side walls (the second term in Eq. (1)). In fact it can be proved for a long prolate spheroid that the former is much smaller than the latter whenever the depolarizing energy is much small than the wall energy of the front wall.† Thus Merz's explanation by the dagger model may be also inappropriate to explain the relation $I_{\max}\propto e^{-(1/E)}$. The third points is that Merz uses two different mechanisms i.e. both nucleation and growth in explainning his experimental relations. Namely he explains the relation $I_{\max}\propto e^{-(1/E)}$ at low fields by the nucleation of new domains, while he explains the relation $I_{\max}\propto(E-E')$ at high fields by the growth of the nucleated domains. His explanation, however, seems to be rather artificial. As stated before, Merz assumes that at high fields the wall velocity of every nucleus is proportional to $(E-E')$. If this relation should be also kept at low fields, no growth of nuclei would occur by applying a field lower than the critical field E'. It will be easily seen that little current could be induced by applying the field, because, as proved above, by nucleation little current can be induced within a few seconds. This fact suggests that the observed relation at low fields should be also explained by considering the growth of 180° domains.

§ 3. Theoretical Treatment of the Movement of 180° Domain

Recently it has been proved by Kinase and Takahasi⁴⁾ that the 180° wall in the $BaTiO_3$ crystal has no thickness (Fig. 3(a)). On the other hand the front wall in the wedge-shape domain may have some thickness (Fig. 3(b)), because near the front wall the dipolar field acting on each Ti ion is quite different from the field near the 180° wall. The detailed study on the front wall is yet in progress by Kinase⁵⁾, and some informations were kindly given me by his private communication. Following discussions, accordingly, will be made by using these informations.

It has been proved by Kinase and Takahasi that Ti ion at the boundary of 180° wall can shifts its position to another stable position only when the applied field acting on the Ti ion satisfies the condition

$$3.246E\cdot e_{\mathrm{eff}}\geq\frac{\partial U^{i}}{\partial x}\qquad(5)$$

where e_{eff} is the effective charge of the Ti ion and $\partial U^{i}/\partial x$ is the gradient of the potential at the inflection point. The coefficient of E is determined by considering the modification of applied field in the crystal. The critical field satisfying this condition is evaluated to be 5.79×10^{6} volts/cm. This field is much higher than the field usually used in experiments ($\lesssim10^{4}$ volts/cm), hence the shift of Ti ion at the 180° boundary can not be caused only by the application of an outer field. Well then how high is the critical field for the front wall? In Fig. 4 the potentials in and near the front wall are shown schematically, assuming that the thickness of the front wall is 4 lattice spacings according to Kinase. Since the polarization should be continued fairly smoothly in the front wall,†† it will be correct to the rough approximation to

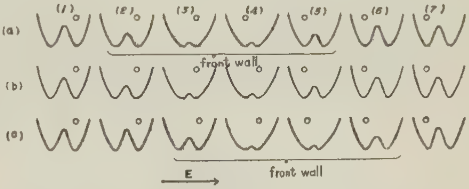

Fig. 4. Movement of front wall.
(a) When the field is abscent. (b) and (c) After applying the critical field. ○ Position of Ti ion.

---

† For a long prolate spheroid the free energy can be written approximately to be

$$\Delta F=4\pi\sigma_{W'}rl+2\pi r^{2}\sigma_{W''}+\frac{d}{2}\frac{4}{3}\pi\frac{r^{4}}{l}P_{S}^{2}\,.$$

In order that the depolarizing energy can be neglected in comparison with the wall energy of the front wall, the length should be limited to be

$$l\gg\frac{d}{3\sigma_{W''}}r^{2}P_{S}^{2}\,.$$

Then putting that $\sigma_{W'}=1.40$ esu⁴⁾, $\sigma_{W''}=80$ esu⁵⁾ and $d=16\pi$, it results in

$$\frac{\text{energy of the front wall}}{\text{energy of the side wall}}\ll7\times10^{-8}r^{-1}\,.$$

It will be seen from this relation that the energy of the front wall is negligible for real domains, because the right hand side of this relation is only of the order of unity even when $r=4\times10^{-8}$ cm.

†† This is caused by the fact that the dipoles, which are in head-to-tail relation, interact strongly with each other as proved by Kinase and Takahasi¹⁾.

assume that the polarization in the front wall changes linearly from lattice to lattice. Then the dipole moments in the front wall are given by $e_{\text{eff}}x' = \frac{1}{5}e_{\text{eff}}x_S$ for cells (3) and (4) and by $e_{\text{eff}}x'' = \frac{3}{5}e_{\text{eff}}x_S$ for cells (2) and (5) (Fig. 4(a)), where $e_{\text{eff}}x_S$ is the dipole moment in a cell that does not belong to the front wall and x', x'' and x_S are the displacements of each Ti ion from the center of each cell. According to Kinase and Takahasi, this displacement can be written in general to be

$$x = \sqrt{\frac{(-a'-a)}{2b}} \tag{6}$$

where a' is a negative constant relating with the dipole interaction, while a and b are positive constants relating with the van der Waal's and overlap interactions. Then using the relation

$$\frac{\partial U^i}{\partial x} = \frac{8}{3\sqrt{3}} x^3 b \tag{7}$$

and considering that b for the cell (4) is larger by about 10% than b for the normal cell e.g. cell (1),[†] the critical field for the Ti ion in cell (4) becomes

$$E^{(4)} \sim 5 \times 10^4 \text{ volts/cm}$$

which is still higher than the field usually applied in experiments. In Fig. 4(b) and Fig. 4(c) the displacements of Ti ions by applying this critical field are shown in dividing the process into two steps. It will be seen from Fig. 4(c) that a new front wall has been formed in cells (3), (4), (5) and (6). This fact indicates that the front wall can shift its position by applying this field and so the critical field for the Ti ion in cell (4) can be identified with the critical field for the front wall itself. Further this fact suggests that at ordinary fields the front wall can not move at all without the effects of thermal vibration of Ti ion. Therefore in treating the movement of the front wall the effects of thermal vibration should be introduced precisely into calculation. In Fig. 5 and Fig. 6 the movements of a part of the front wall are shown schematically. It will be seen from Fig. 6 that the wall should have the high energy state on the way of proceeding by one lattice spacing in the direction of applied field. This fact implies that the front wall will move most rapidly as a whole when a certain volume of the wall reverses its polarization simultaneously in a single vibration of Ti ion. To consider the intermediate high energy state, let us denote the increase of the energy of front wall from the normal state by σ^* per unit area. Further let us assume that the domain grows by the successive formation of small steps in the front wall such as the shaded part in Fig. 5. For brevity call the part "local wall". Then the changes of free energy of the local wall in the intermediate state, ΔF^M, and in the final state, ΔF^F, are given respectively by

$$\Delta F^M = -EP_S\Delta V + \frac{\sigma^*}{u}\Delta F \tag{8}$$

and by

$$\Delta F^F = -2EP_S\Delta V + \sigma_W\Delta S \tag{9}$$

where ΔV and ΔS denote the increases of

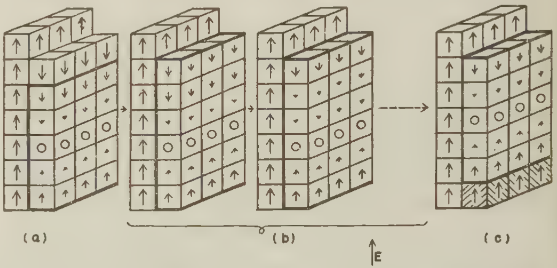

Fig. 6. Movement of local wall.
It is assumed here that the thickness of the front wall is 5 lattice spacings in making the movement clear. (a) Initial state. (b) Intermediate states. (c) Final state.

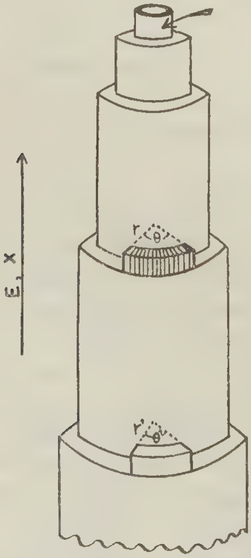

Fig. 5. Spike-shaped 180° domain.

[†] These can be easily proved using Kinase and Takahasi's result.

volume and surface of the domain respectively, u is the unit lattice spacing and σ_W is the wall energy/cm² of 180° wall. The probability by which the local wall proceeds by one unit lattice spacing in the direction of applied field is then given approximately by

$$p=\nu\left(\exp\left(-\frac{((\sigma^*/u)-EP_S)}{kT}\right)\Delta V-\exp\left(-\frac{\{((\sigma^*/u)+EP_S)\Delta V-\sigma_W\Delta S\}}{kT}\right)\right) \tag{10}$$

where ν is the frequency of the thermal vibration of Ti ion. The free energy ΔF^M must be of the order of kT in observing the wall motion within a few minutes. Further at an ordinary field both $EP_S\Delta V$ and $\sigma_W\Delta S$ are much smaller than $(\sigma^*/u)\Delta V$. Then Eq. (10) can be expanded, resulting in

$$p=\frac{\nu}{kT}(2EP_S\Delta V-\sigma_W\Delta S)\exp\left(-\frac{\sigma^*\cdot\Delta V}{kT\cdot u}\right) \tag{11}$$

where the smaller terms are neglected. The current induced by this wall motion is then given by

$$i_{\text{local}}=\frac{2P_S}{d_0}p\Delta V\,, \tag{12}$$

where d_0 is the thickness of the crystal. Neglecting the curvature of the local wall[†] and putting that $\Delta V=su^2$ and $\Delta S=2u^2$, above relation becomes

$$i_{\text{local}}=\frac{4P_S\nu u^4 s}{d_0kT}(sEP_S-\sigma_W)\exp\left(-\frac{\sigma^* su}{kT}\right). \tag{13}$$

This equation represents the relation between the applied field and the current caused by the movement of a local wall with the width s. It will be easily seen that this current becomes maximum when

$$s=s^*=\frac{2A+BC+\sqrt{4A^2+B^2C^2}}{2AC}\qquad\left(s>\frac{\sigma_W}{EP_S}\right), \tag{14}$$

where

$$A=\frac{4EP_S^2\nu u^4}{d_0kT}\,,\qquad B=\frac{4P_S\nu u^4\sigma_W}{d_0kT}$$

and

$$C=\frac{\sigma^* u}{kT}\,,$$

and the maximum current is given by

$$i^*_{\text{local}}=\frac{4P_S\nu u^4 s^*}{d_0kT}(s^*EP_S-\sigma_W)\exp\left(-\frac{\sigma^* s^* u}{kT}\right), \tag{13′}$$

In case of either $2A\gg BC$ (which is satisfied when applied field is fairly high) or $2A\ll BC$ (which is satisfied when applied field is low) this relation can be simplified to be

$$i^*_{\text{local}}=\frac{16P_S^2\nu u^2kT}{d_0(\sigma^*)^2}\left(E-\frac{\sigma_W\sigma^* u}{2kTP_S}\right)e^{-2} \tag{15}$$

or

$$i^*_{\text{local}}=\frac{4P_S\nu u^3\sigma_W}{d_0\sigma^*}\exp\left(-\frac{\sigma_W\sigma^* u}{kTEP_S}\right). \tag{16}$$

respectively. These dependences of the local current on applied field are analogous to the dependences of the observed maximum current on applied field. Therefore if the total maximum current[††] can be represented in terms of this local current, Merz's experimental relations will be explained favorably using above relations. Although this is not satisfied in general, it can be proved as shown in Appendix that in case of either $2A\gg BC$ or $2A\ll BC$ the total maximum current can be represented by the forms similar to the maximum local current. Later in § 5 this consideration will be used.

For the BaTiO₃ crystal, however, the depolarizing field may have severe effects on the movement of whole wall. Further, at the top of wedge-shaped domain the behaviors of the local walls may be different. Therefore in trying to explain Merz's relations it should be further tried to clarify how large these effects are. These examinations will be given in the following sections.

§ 4. Formation of New Steps

It will be seen in Fig. 5 that the top of a spike-shaped domain is formed by a small cylindrical step, indicated by arrow in the figure. This step can be newly formed in the way similar to the growth of a local wall in the lower steps. The new step, however, can not be formed so fast as other local walls, because as seen in Fig. 7 at the final state the whole side wall of the new step should be added and so the transition probability for the new step becomes smaller than the probability for the local wall of the same dimension. In the following, accordingly, some examination will be done for the movement of the new step. Suppose that the new step is a disk with the radius r and the height n.

[†] If the local wall is assumed to be an arc with the radius r and the angle θ (Fig. 5), above relations $\Delta V=su$ and $\Delta S=2u^2$ should be replaced by $\Delta V=r\theta u^2$ and $\Delta S=2u^2+\theta u^2$ respectively. This difference, however, will be negligible for a fairly large r.

[††] Some confusion may be caused by the use of the term "maximum". "Maximum" in the maximum local current means that the current becomes maximum when a local wall has a certain valume s^*u^2. On the other hand "maximum" in the total maximum current means that the current becomes maximum in the process of the switching of all domains. Accordingly, there is no direct connection between the two terms.

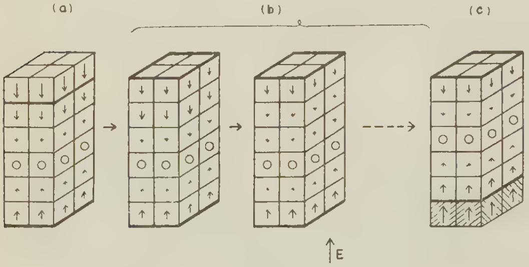

Fig. 7. Movement of step.
It is assumed here that the thickness of the front wall is 5 lattice spacings in making the movement clear. (a) Initial state. (b) Intermediate states. (c) Final state.

The probability by which the new step is formed per unit time is given analogously to Eq. (11) by

$$p=\frac{2\pi r u\nu}{kT}(rEP_S-\sigma_W)\exp\left(-\frac{\pi\sigma^* r^2}{kT}\right). \qquad (11')$$

This probability becomes maximum for a certain radius $r=r^*$ which satisfies the equation

$$r^3-\frac{B'}{A'}r^2-\frac{1}{C'}r+\frac{B'}{2AC'}=0$$

where

$$A'=\frac{2\pi u\nu EP_S}{kT}, \qquad B'=\frac{2\pi u\nu\sigma_W}{kT}$$

and

$$C'=\frac{\pi\sigma^*}{kT},$$

and the maximum probability is given by

$$p_{\max}=\frac{2\pi r^*\nu u}{kT}(r^*EP_S-\sigma_W)\exp\left(-\frac{\pi\sigma^*(r^*)^2}{kT}\right)$$
$$\left(r^*>\frac{B'}{A'}\right). \qquad (17)$$

In case of $r^*\gg(B'/A')$ (which is satisfied when the applied field is fairly high) this probability reduces approximately to be

$$p_{\max}=\frac{2\nu uP_S}{\sigma^*}\left(E-\frac{\sqrt{\pi\sigma^*}\,\sigma_W}{\sqrt{kT}\,P_S}\right)e^{-1}, \qquad (18)$$

while in case of $r^*\simeq(B'/A')$ (which is satisfied when the applied field is low) it reduces approximately to be

$$p_{\max}=\frac{2u\nu EP_S}{\sigma^*}\exp\left(-\frac{\pi\sigma_W{}^2\sigma^*}{E^2P_S{}^2kT}\right). \qquad (19)$$

These probabilities correspond respectively to the maximum probabilities for the local wall

$$p_{\max}=\frac{2u\nu P_S}{\sigma^*}\left(E-\frac{\sigma_W\sigma^* u}{kTP_S}\right)e^{-1} \qquad (20)$$

and

$$p_{\max}=\frac{2u\nu EP_S}{\sigma^*}\exp\left(-\frac{\sigma_W\sigma^* u}{EP_SkT}\right). \qquad (21)$$

It will be easily seen from these relations that at high fields the probability for the new step is not so different from the probability for the local wall, while at low fields the former becomes much smaller than the latter. The slower motion of the step at low fields, however, will little affect on the movement of the whole front wall, owing to the effects of dipolarizing field as discussed in the following section. Accordingly, we will neglect at all the particular motion of the step in the latter calculation.

§ 5. Effects of Depolarizing Field

In the previous sections the effects of the depolarizing field on the wall motion have been neglected thoroughly. This effects, however, may be quite large for the $BaTiO_3$ crystal in which the very large spontaneous polarization is caused. For example it can be seen as follows: suppose that the domain has a shape of a long prolate spheroid with the radius r and the length l. When the field is abscent, the free energy of the domain is given by[†]

$$\Delta F=4\pi\sigma_W rl+\frac{2}{3}\pi d\frac{r^4}{l}P_S{}^2. \qquad (22)$$

This energy becomes minimum at a certain length

[†] The present expression of depolarizing energy is correct when the thickness of the crystal is much larger than the length of the domain. If the length becomes comparable with the thickness, the effects of depolarizing field will be much changed.

$$l=l_{\min}=\left(\frac{d}{6}r^3\frac{P_S{}^2}{\sigma_W}\right)^{1/2}$$

for a certain radius r. Assuming that $d=16\pi$, $P_S=7.8\times10^4$ esu and $\sigma_W=1.40$ esu, the length becomes about 2×10^{-1} cm, 6×10^{-3} cm and 2×10^{-4} cm for $r=10^{-4}$ cm, 10^{-5} cm and 10^{-6} cm respectively. Since in the minimum the depolarizing energy of the domain is of the same order as the wall energy, in case of Merz's 180° domains, which have the length of about 10^{-3} cm and the radius of about 10^{-4} cm, the depolarizing energy will be much higher than the wall energy. This seems to mean that for the observed domain the movement of the front wall should be determined mainly by the effects of depolarizing field. On the contrary the switching current observed in experiments is sensitively dependent on applied field and so the movement of the front wall may be determined rather by the strength of applied field. Why does this discrepancy appear ? How can this inconsistency be resolved ?

One way to answer this question is to consider that the actual depolarizing field is much weaker than the depolarizing field expected from the calculation. In fact this may be realized for a standing or very slowly moving domain, because the depolarizing change on the front wall will be neutralized gradually by the floating charge. For a rapidly moving domain, however, such neutralization is not expected at all, because the $BaTiO_3$, crystal is not a good conductor, but may be only a little conductive. Accordingly, in explaining Merz's experimental result this seems to be inappropriate. The other way to answer the question is to consider again the proposal in § 3 that the front wall of a domain should have a high energy state on the way of each proceeding by one lattice spacing. This assumption indicates that the whole front wall can not shift its position simultaneously even when large amount of decrease of the depolarizing energy will be caused and further suggests that the effects of applying field may be predominant in the movement of the whole front wall in spite of the large effects of depolarizing field, if the movement of each local wall would be little affected by the depolarizing field. Although it is very difficult to treat this problem precisely, the effects of applying field on the real domain can be introduced into calculation as follows: in Fig. 8 a part of a real domain is shown two-dimensionally. The dotted line in this figure represents the surface of the ideal ellipsoid having an uniform depolarizing field. It will be seen from this figure that the real domain wall can not fit at all with the ideal surface. This fact implies that for a number of Ti ions in the front wall the two possible states of polarization may be nearly equally probable, because the departure of a small part of the wall from the ideal surface may cause the increase of depolarizing energy. In other words the whole domain wall may be deformed a little by the application of an outer field, in spite of the large effects of depolarizing field. In addition, it is known that an uniform deformation of the whole front wall may cause the gradual decrease of depolarizing energy. Therefore if a certain uniform deformation of the front wall is attained by the application of an outer field, the whole front wall will continue to proceed in the direction of applied field in decreasing the total free energy of the domain. The features of the movement are shown schematically in Fig. 9.

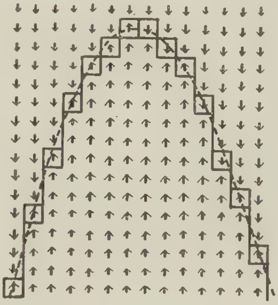

Fig. 8. A part of a domain.
The dotted line indicates the ideal surface of the domain.

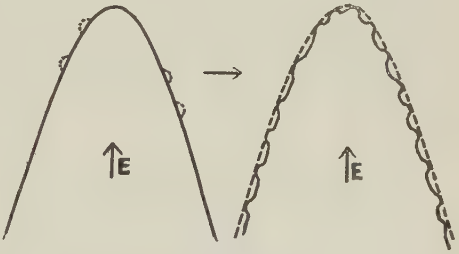

Fig. 9. Movement of the domain caused by the local shift. The dotted lines indicate the shifts of wall with the lapse of time.

To consider this movement, let us assume now that (1) when a certain number of the local walls, which have the two possible stable states, have shifted their positions in the direction favorable to the applied field—accurately speaking when the shifted front area of the original wall reaches a certain magnitude—the whole front wall can proceed to form a new front surface which fits nearly to a new ideal ellipsoid, (2) the shifts of these local walls are not affected at all by the effects of the depolarizing field and (3) owing to the change of depolarizing field the other local walls which have only one stable state at first also can shift their positions very rapidly according to the shifts of the easily movable local walls. Then the transition time necessary for the whole front wall to shift its position by the least distance is given by

$$\Delta t=\frac{n}{p^*} \tag{22}$$

where p^* is the transition probability of the local wall and n is the number of times of the transition when the shifted front area becomes a certain critical area, S_0. Here it is assumed that all the local walls have the constant front area of s^*u. Since n can be written to be

$$n=\frac{S_0}{ms^*u}$$

the transition time becomes

$$\Delta t=\frac{S_0}{ms^*up^*} \tag{23}$$

where m is the number of the local walls which can shift simultaneously. Thus the effects of the depolarizing field can be introduced into calculation to the rough approximation. In the following section Merz's experimental relations will be explained using this relation.

§ 6. Explanation of Merz's Experimental Result

Before trying to explain Merz's experimental relations we will study how a wedge-shaped domain grow or decay. In Fig. 10 the process is shown two dimensionally. It will be seen from this figure that there are three stages of movement of every domain i.e. the first stage of the growth of each domain, the second stage of the apparent sidewise motion of each wall and the third stage of the decay of remanent domain. It should be noticed here that the remanent domain may have a fairly complicated shape at first, because real three-dimensional domains may be arranged in a more complicated way. Among these three stages some different movements of the wall may be appeared. For example at the first stage a new step should be formed successively to continue the growth, while at the third stage a step which is already existing may immediately disappear by the movement of the other local walls. As supposed by the discussion in the previous section such differences will be little important on the movement of the whole front wall. Accordingly, we will neglect them at all now. Then from Eq. (23) the current induced by the movement of a domain can be written to be

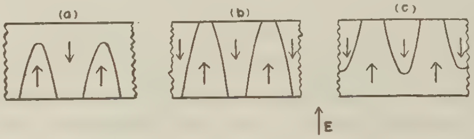

Fig. 10. Growth and decay of 2-dimensional domains.
(a) 1st stage. (b) 2nd stage. (c) 3rd stage.

$$i_{\text{domain}}=\frac{2P_S}{d_0}\frac{\Delta V_{\text{domain}}}{\Delta t}$$

where ΔV_{domain} is the volume change caused by the displacement of the domain. This can be reduced using the relation

$$s^*up^*=\frac{d_0}{2P_S}\,i^*_{\text{local}}$$

to be

$$i_{\text{domain}}=\frac{m\Delta V_{\text{domain}}}{S_0u}\,i^*_{\text{local}}\,, \tag{24}$$

Then summing this current over all domains in the crystal, the total current becomes

$$I=\sum_{i=1}^{N}\frac{m^i\Delta V^i_{\text{domain}}}{S_0{}^iu}\cdot i^*_{\text{local}}\,. \tag{25}$$

It will be seen from this equation that the total current is proportional to the maximum local current at any instant and it becomes when the term $\sum(m^i\Delta V^i_{\text{domain}}/S_0{}^iu)$ is maximum. To the first approximation let us assume that all the domains have a same dimension and takes a similar behavior with the lapse of time. Then the total maximum current is given by

$$I_{\max}=\frac{N^*m^*\varDelta V^*_{\mathrm{domain}}}{S_0^*}\cdot i^*_{\mathrm{local}} \tag{26}$$

where N^*, m^*, S_0^* and $\varDelta V^*_{\mathrm{domain}}$ represent respectively N, m, S_0 and $\varDelta V_{\mathrm{domain}}$ in the maximum current. Substituting Eqs. (15) or (16) into Eq. (26), this becomes

$$I_{\max}=\frac{16N^*m^*\varDelta V^*_{\mathrm{domain}}}{S_0^*}\cdot\frac{P_S^2\nu ukT}{d_0(\sigma^*)^2}\left(E=\frac{\sigma_W\sigma^*u}{2kTP_S}\right)e^{-2} \tag{27}$$

at fairly high fields or

$$I_{\max}=\frac{4N^*m^*\varDelta V^*_{\mathrm{domain}}}{S_0^*}\cdot\frac{P_S\nu u^2\sigma_W}{d_0\sigma^*}\exp\left(-\frac{\sigma_W\sigma^*u}{kTEP_S}\right) \tag{28}$$

at low fields. It will be seen from these relations that Merz's experimental relations can be explained satisfactorily, considering that N^*, m^*, S_0^* and $\varDelta V^*_{\mathrm{domain}}$ will be little dependent on the strength of applied field.

The relations between applied field and switching time can be also obtained from Eq. (23). That is, from Eq. (23) the switching time can be written to be

$$t_S=\int_0^{t_S}dt=\frac{2P_Su}{i^*_{\mathrm{local}}\cdot d_0}\sum_t\frac{S_0^t}{m^t}\,. \tag{29}$$

To the first approximation let us assume that (S_0^t/m^t) is not changed at all through the switching process and it is equal to (S^{0*}/m^*). Then the switching time can be written approximately to be

$$t_S=\frac{d_0}{u}\cdot\frac{2P_Su}{i^*_{\mathrm{local}}\cdot d_0}\frac{S_0^*}{m^*}=\frac{2P_SS_0^*}{m^*i^*_{\mathrm{local}}}\,. \tag{29'}$$

Then using the previous result, the reciprocal of the switching time is given by

$$\frac{1}{t_S}=\frac{8m^*P_S\nu u^2kT}{S_0^*d_0(\sigma^*)^2}\left(E-\frac{\sigma_W\sigma^*u}{2kTP_S}\right)e^{-2} \tag{30}$$

at fairly high fields and by

$$\frac{1}{t_S}=\frac{2m^*\nu u^3\sigma_W}{S_0^*d_0\sigma^*}\exp\left(-\frac{\sigma_W\sigma^*u}{kTEP_S}\right) \tag{31}$$

at low fields. It will be seen from these relations that Merz's experimental relations⁶⁾ (Fig. 11) can be explained satisfactorily, considering that m^* and S_0^* are little dependent on the strength of applied field.

§ 7. Discussions

To construct the preceeding theory it has been assumed that a front wall must pass across a certain potential barrier to move by an unit lattice spacing in the direction of appried field. This assumption is essentially important to determine whether the theory is appropriate to explain Merz's result or not. One way to judge this assumption is to examine the theoretical relations quantitatively. If a clear quantitative inconsistency appears in them, the present model should be abandoned. Below a few quantitative examinations will be given.

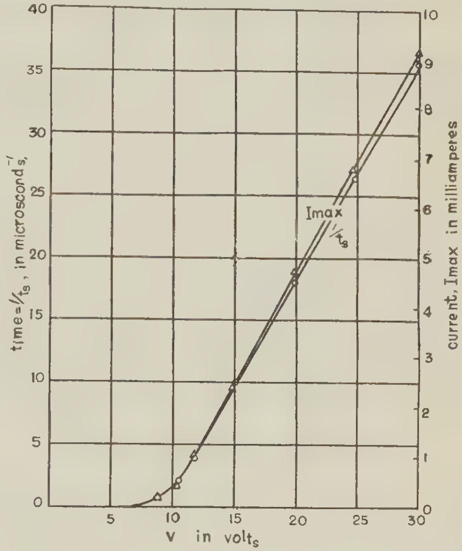

Fig. 11. Switching current and reciprocal switching time *versus* applied field (after Merz).

(1) We will determine at first the value of σ^* in comparison with Merz's experimental result. Using the data that $E'=14.3$ esu† at 23°C and $P_S=7.8\times10^4$ esu and putting that $kT=4\times10^{-14}$ esu and $\sigma_W=1.40$ esu it can be obtained that

---

† This value was determined from Merz's figure (Fig. 2).

†† If the thickness of the wall is n lattice spacings, the wall can proceed by one lattice spacing in the direction of applied field by passing through the intermediate high energy state which corresponds to the state of wall with $(n+1)$ lattice spacing. According to Kinase⁵⁾ the thickness of the front wall is about 4 lattice spacing and the wall energy is about 80 erg/cm². Using these values and assuming as done by Merz²⁾ that the anisotropy energy of wall is proportional to the number of lattice in the wall, while the dipole interaction energy of wall is proportional to the reciprocal of the number, it can be obtained that

$$\sigma^*\simeq2\ \mathrm{erg/cm^2}\,.$$

$$\sigma^*=1.6\ \mathrm{erg/cm^2}\ .$$

This value will be plausible, considering that by another calculation†† the value of σ^* is given to be about 2 erg/cm².

(2) The restriction for the thermal frequency of Ti ion can be deduced from Eq. (30) in comparison with Merz's experimental result. Namely, using the data that $t_S=0.4\times10^{-6}$ sec at $E=40$ esu and $d_0=5\times10^{-3}$ cm, it can be obtained that

$$\frac{S_0^*}{m^*\nu}=4.3\times10^{-27}\ \mathrm{cm^2\ sec}\ . \qquad (32)$$

Using the relations that $n=(S_0^*/m^*s^*u)\geqq1$ and $s^*u=(2kT/\sigma^*)$† the restriction reduces to be

$$\nu\geqq1.2\times10^{13}\ \mathrm{sec^{-1}}\ .$$

This result indicates that the magnitude of ν will be plausible if n is of the order of one.

(3) The term $N^*\Delta V^*_{\mathrm{domain}}/u$ can be determined from Eq. (27) in comparison with Merz's experimental result; using Eq. (32) and the result that $I_{\max}=75\times10^{-3}$ amperes$=22.5\times10^7$ esu at $E=40$ esu, it can be seen that

$$\frac{N^*\Delta V^*_{\mathrm{domain}}}{u}=5.6\times10^{-4}\ \mathrm{cm^2}\ .$$

Since $\Delta V^*_{\mathrm{domain}}/u$ is of the order of the cross section of the domain, $N^*(\Delta V^*_{\mathrm{domain}}/u)$ will be of the order of the electrode surface. This expectation seems to be satisfied, reminding the fact that the electrode surface of Merz's crystal is about 10^{-4} cm².

Thus above quantitative analysis shows that no apparent inconsistency appears between the present theory and Merz's experimental result.

Finally the author wishes to express his thanks to Dr. S. Marutake and Dr. T. Nakamura for their valuable advices and to Dr. W. Kinase for his kind communications.

Appendix

For the movement of the front wall of which front area is much larger than the area of s^*u, the current can be written approximately to be

$$i_{\mathrm{front}}=\alpha\int_0^\infty i_{\mathrm{local}}(s)\,ds \qquad (1)$$

where α is a certain constant. Using the relations that

$$i_{\mathrm{local}}(s)=f(s)(E-E'(s))\exp\left(-\frac{\sigma^*su}{kT}\right) \qquad (2)$$

and $s_0=(\sigma_W/EP_S)$, the current becomes

$$i_{\mathrm{front}}=\alpha E\int_{\sigma_W/EP_S}^\infty f(s)\exp\left(-\frac{\sigma^*su}{kT}\right)ds$$
$$-\alpha\int_{\sigma_W/EP_S}^\infty f(s)E'(s)\exp\left(-\frac{\sigma^*su}{kT}\right)ds\ . \qquad (3)$$

For the sufficiently large E which satisfies the condition $2A\gg BC$ the lower limit of each integral can be replaced approximately by 0. Then it will be easily seen that the current has the same dependence on applied field as i^*_{local}.

For the small E which satisfies the condition $2A\ll BC$ the current becomes maximum when s is nearly equal to σ_W/EP_S and it decreases abruptly with the increase of s. Since both $f(s)$ and $E'(s)$ changes slowly with the change of s in comparison with $\exp(-(\sigma^*su/kT))$, the current can be written approximately to be

$$i_{\mathrm{front}}=\alpha f(s^*)(E-E'(s^*))\int_{s^*}^\infty\exp\left(-\frac{\sigma^*su}{kT}\right)ds \qquad (4)$$

which reduces to be

$$i_{\mathrm{front}}=\frac{4\alpha kTP_S\nu u^2\sigma_W}{d_0(\sigma^*)^2}\exp\left(-\frac{\sigma^*\sigma_Wu}{kTEP_S}\right)\ . \qquad (5)$$

This result indicates that at low fields the current also has the same dependence on applied field as i^*_{local}.

By the way, the total maximum current can be written to be

$$I_{\max}=\alpha_{\max}\int i_{\mathrm{local}}(s)\,ds \qquad (6)$$

if the effects of depolarizing field is neglected thoroughly. Then from above relations it will be seen that in case of $2A\gg BC$ or $2A\ll BC$ the total maximum current has the form similar to Eq. (15) or Eq. (16).

References

1) J. P. Remeika: J. Amer. Chem. Soc. **76** (1954) 940.
2) W. J. Merz: Phys. Rev. **95** (1954) 690.
3) R. Landauer: J. Appl. Phys. **28** (1957) 227.
4) W. Kinase and H. Takahasi: J. Phys. Soc. Japan **12** (1957) 464.
5) W. Kinase: read at the Meeting of the Phys. Soc. Japan, April 1958; Busseiron-Kenkyu, Ser. 2, **4** (1958) 721 (in Japanese).
6) W. J. Merz: J. Appl. Phys. **27** (1956) 938.

---

† This relation is satisfied at fairly high fields.

JOURNAL OF THE PHYSICAL SOCIETY OF JAPAN, Vol. 14, No. 5, MAY, 1959

Nuclear Magnetic Resonance in Dilute Copper Alloys at Low Temperatures, I.
Experimental Aspects*

By Tadashi SUGAWARA

The Research Institute for Iron, Steel and Other Metals,
Tohoku University, Sendai

(Received January 8, 1959)

The nuclear magnetic resonance of Cu^{63} in dilute copper alloys has been studied in order to make clear the origin of their anomalous magnetic, electric and thermal behaviors observed at low temperatures. The specimens were the dilute solid solutions of Ti, Cr, Mn, Fe, Co, Ni, Zn and Sn in Cu. From the temperature dependence of the observed line width, it was concluded that Ti, Ni, and Zn behave as non-magnetic ions while the others do as paramagnetic ions. Sn in Cu-alloy showed temperature dependent paramagnetism in spite of its temperature independent paramagnetism in the metal. The solute contribution to the widths in Cu–Cr, Cu–Mn, Cu–Fe and Cu–Co in weak field showed a Curie-Weiss behavior. The Weiss temperatures obtained indicated increasing ferromagnetic interaction with increasing solute concentration. The width in Cu–Mn was proportional to the magnetic field except at very low temperatures, while those in Cu–Cr and Cu–Fe showed anomalous field dependence at temperatures below 20°K. The Knight shift in these paramagnetic alloys was larger than that in pure Cu, but the deviation was very small at high temperatures. At very low temperatures the spin-lattice relaxation times in Cu–Cr, Cu–Mn and Cu–Fe became shorter than those in pure Cu and in non-magnetic alloys such as Cu–Zn.

§ 1. Introduction

Recently the low temperature property of the dilute alloys of iron group elements in noble metals has received considerable attention by experimental and theoretical physicists. Particularly the magnetic, electric, and thermal properties of Cu–Mn system have been studied in detail1)-5). The alloy is paramagnetic at high temperatures and becomes antiferromagnetic as the temperature is lowered. The electron spin resonance at high temperatures shows a single absorption line with $g \simeq 2.00$, suggesting the existence of of Mn^{2+} or Mn^{0}. Below the Néel temperature the resonance shows some characteristics of the antiferromagnetic resonance. The line width of Cu^{63} nuclear resonance is broad and temperature-dependent in the paramagnetic state, while the Knight shift is nearly the same as that in pure Cu. A broad peak in the specific heat curve has also been observed near the Néel point6). In addition to these magnetic anomalies, very dilute alloys show resistance maximum and minimum at low temperatures and also anomalous magnetoresistance which depends upon the magnetization of the sample.

Some of these anomalous properties of Cu–Mn have been explained theoretically in terms of the *s–d* exchange interaction7)-9). However, there remain many problems to be solved such as the resistance maximum and minimum and the mechanism of spin ordering in Cu–Mn. In addition, no satisfactory explanation has been made of the fact that the other alloys of transition elements show different magnetic and electric behaviors as compared with Cu–Mn10),11). For instance, only a minimum has been observed in the resistance *vs.* temperature curve in dilute Cu–Fe12) which is paramagnetic like Cu–Mn12),13). For the better understanding of the nature of the dilute alloys, a detailed experimental study concerning the electronic structure of them seems to be required. The present work was undertaken for this purpose.

The electron spin resonance of the solute ion and the nuclear spin resonance of the solvent nuclei provide powerful means for the present purpose. The former has an advantage over the latter as it gives a direct information on the electronic state of the solute ion and the magnetic interaction effects. However, its application to the present problem seems to be limited because of the fact that no resonance has been observed in alloys other than Cu–Mn and other Mn alloys2). The nuclear spin resonance gives informations on the state of the localized unpaired spin through the line broadening and the charge density of the *s*-electrons through the Knight shift. In this work, the Cu^{63} resonance was studied in dilute copper alloys containing iron group metals such as Ti, Cr, Mn, Fe, Co and Ni, and from the result it was intended to draw a conclusion about the electronic structure of these alloys. Cu–Zn and Cu–Sn, each containing nonmagnetic element as the solute, were also studied for comparison. The resonance behavior of Cu–Sn attracted much interest as it shows a resistance minimum14) and an anomalous magnetic behavior at low temperature15).

---

* A preliminary report of this work has been published previously. T. Sugawara: J. Phys. Soc. Japan **12** (1957) 309.

In this paper (Part I) only the experimental result is described, and theoretical considerations of the result as well as of the electronic structure of the dilute alloys will be published in a subsequent paper (Part II).

§ 2. The Apparatus

A block diagram of the experimental arrangement is shown in Fig. 1. An electromagnet of the Bitter type provided magnetic fields up to 10^4 oersted in a 40 mm air gap. The pole faces were 165 mm in diameter and the inhomogeneity of the field across the sample of about 1 cm^3 was less than 0.1 oersted at 5000 oersted. The field was modulated at 50 cps from a low frequency oscillator. The resonance signal was detected with a marginal oscillator of the Pound-Knight-Watkins type. The derivative of the absorption line was displayed on a recorder by sweeping the magnetic field at a constant frequency or by sweeping the frequency of the oscillator at a constant field. The sample coil were wound with silver wire. Special care was taken to avoid mixing of the external Cu signal with that from the sample.

A metal cryostat was used throughout this work. The temperatures of liquid hydrogen and helium range were determined by measuring the vapor pressure of the bath liquid or the resistance of a carbon resistor placed near the sample.

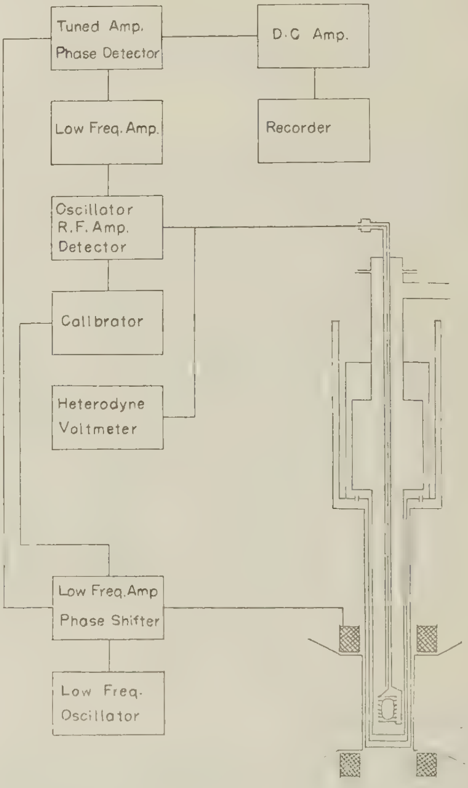

Fig. 1. Experimental arrangement.

Table I. Composition of the specimen.

	Concentration (atom. %)			Concentration (atom. %)	
Alloy	Solute	Fe	Alloy	Solute	Fe
Cu–Ti	0.014	0.003	Cu–Co	0.038	
Cu–Cr	0.016	0.005		0.080	0.005
	0.065			0.15	0.007
Cu–Mn	0.021		Cu–Ni	0.080	
	0.026	0.005		1.45	0.010
	0.055	0.006		3.79	
Cu–Fe	0.040		Cu–Zn	4.15	0.004
	0.11		Cu–Sn	0.35	0.003
	0.20		Cu		0.005

§ 3. Preparation of Samples

The compositions of the alloys studied are collected in Table I. The concentration of the solute and impurities was determined by chemical analysis.

The alloy was prepared by melting electrolytic copper of about 99.99% purity and the mother alloy containing solute metal of about 10% in an induction furnace *in vacuo*. The melt was held at 1200°C for about 30 minutes and then casted into a cold ingot case. The ingot was cold-worked into a rod of about 11 mm indiameter and pickled in a 50% solution of nitric acid to a diameter of 8 mm to remove surface contamination. The ingot was sealed in a quartz tube under vacuum and annealed at about 950°C for 30 hours. The effect of annealing period upon the homogeneity of the alloy was tested by comparing the Cu^{63} resonance in two Cu–Mn samples of the same concentration annealed for 20 hours and 100 hours respectively. A period of 30 hours proved to be sufficient as the widths were the same within the experimental error. The annealed sample was quenched into water to avoid precipitation. This procedure was necessary for obtaining a good solid solution as the solubility of Fe, Co, Cr, and Ti in Cu are rather small at room temperature[16]. Finally the rod was pickled in a nitric acid solution and then powdered.

For magnetic resonance work on conductors the grain size of the sample should be smaller than the skin depth[17]-[19], given by

$$\delta=(\rho\times10^9/\mu f)^{1/2}(2\pi)^{-1}\,, \qquad (1)$$

where ρ is the specific resistance in Ω-cm, μ is the permiability, and f is the frequency in cps. δ's of pure Cu at 4.2°K and of 0.03% Cu–Mn at the temperature of resistance maximum are 1.5 micron and 6 micron respectively for the frequency of 10 Mc/sec. Therefore, the mean diameter of the sample should be smaller than 1 micron for pure copper and also smaller than 5 micron for most of the alloys. Preparation of such a fine powder was not easy. After trying various methods a rather teadous but primitive method, in which the alloy was rubbed with a finely grained oil stone in liquid paraffine, was proved to be satisfactory. Very fine powders were separated from the product by use of the difference of the falling velocity in benzene. The yield of powders less than 2 micron in

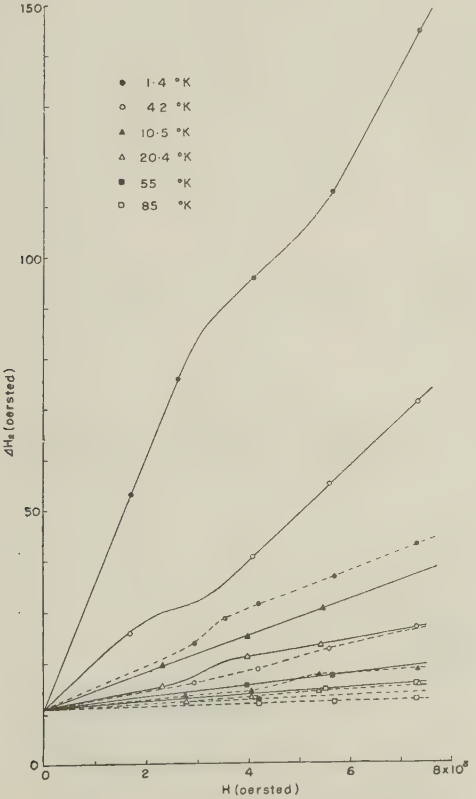

Fig. 2. Line width ΔH_2 *versus* field strength in Cu–Cr at various temperatures. Solid line: 0.065% Cr, Dotted Line: 0.016% Cr.

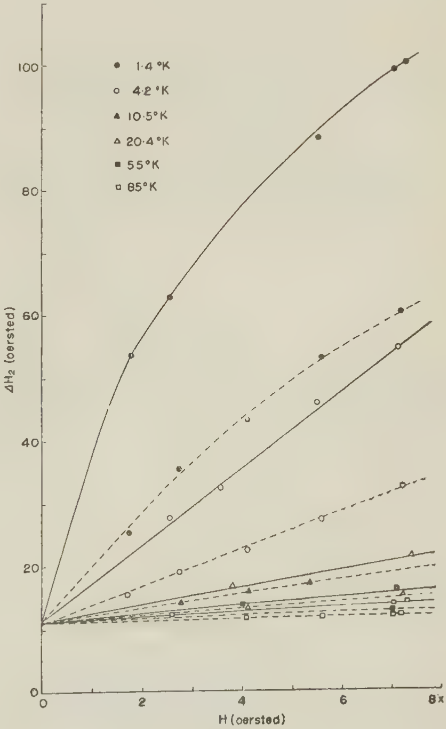

Fig. 3. Line width ΔH_2 *versus* field strength in Cu–Mn at various temperatures. Solid line: 0.056% Mn, dotted line: 0.026% Mn.

diameter was about a few per cent of the coarse powder. Finally about 0.5 gr of fine powders thus obtained was suspended in molten paraffine and mold into a thin walled glass tube.

§ 4. Line Width and its Field Dependence

The derivatives of Cu^{63} absorption line in the sample were measured at various magnetic fields and temperatures. The separation ΔH_1 between points of extreme deflection and the separation ΔH_2 between points where the deflection had fallen to half of the peak value of the derivative curve were both used as measures of the line width. In this work, the latter was used frequently as it was more sensitive to the effect of the solute than the former. The observed ΔH_2 of Cu^{63} in various samples are shown in Figs. 2 through 7.

In most of the alloys of transition metals the line width increased as the temperature was decreased or the field was increased. The effect, among the alloys of the same concentration, was largest for Cr and Mn and was not observed for Ni and Ti. Non-transition metal alloys showed, in general, no excess broadening as compared with pure Cu. However, Cu–Sn be haved like Cu–Mn alloy though the broadening was smaller.

The shape of the broad line, observed at

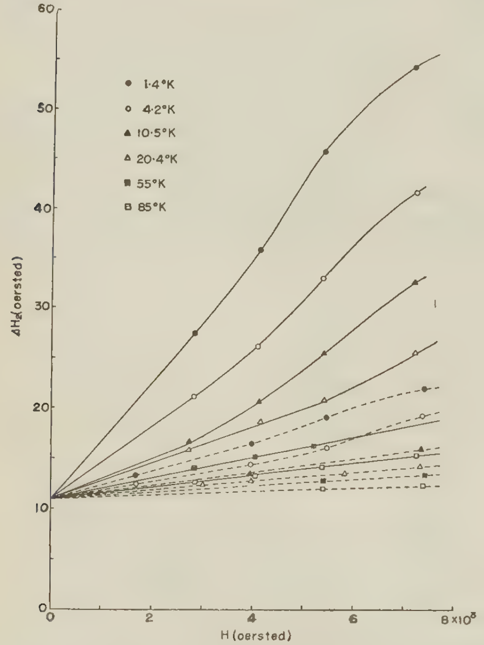

Fig. 4. Line width ΔH_2 *versus* field strength in Cu–Fe at various temperatures. Solid line: 0.11% Fe, dotted line 0.040% Fe.

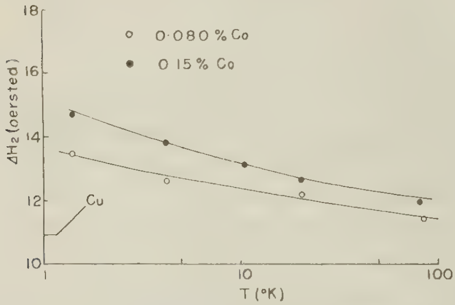

Fig. 5. Line width ΔH_2 *versus* temperature in Cu–Co at 7350 oersted.

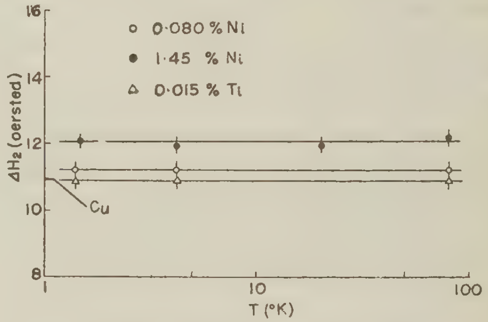

Fig. 6. Line width ΔH_2 *versus* temperature in Cu–Ti and Cu–Ni at 7350 oersted.

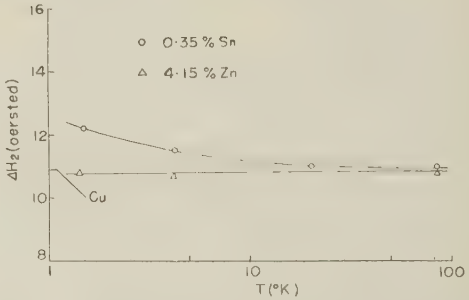

Fig. 7. Line width ΔH_2 *versus* temperature in Cu–Sn and Cu–Zn at 7350 oersted.

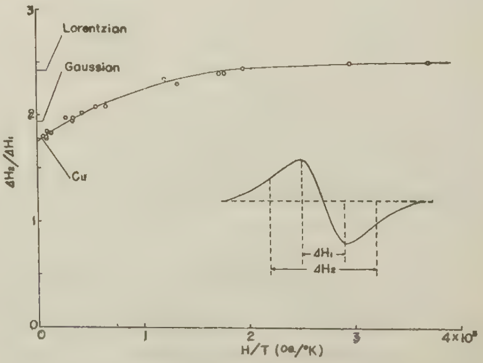

Fig. 8. Ratio $\Delta H_2/\Delta H_1$ in 0.026% Cu–Mn.

low temperatures, was nearly Lorentzian in shape and became nearly Gaussian as the temperature was increased. As an example of this change the ratio $\Delta H_2/\Delta H_1$ of Cu^{63} resonance in Cu–Mn has been plotted against H/T in Fig. 8. The ratio is 1.94 for a Gaussian line and 2.40 for a Lorentzian line.

Broadening of the line width is expected when the solute atoms or ions have a localized 3d state with unpaired spins. The effect of the solute spins is simply to give a local field at a nucleus due to its dipolar and indirect exchange coupling with Cu nuclear spins, as the relaxation time of the 3d spin is considered to be short compared with the nuclear spin-spin relaxation time of Cu. The local field at a nucleus is given by[7),9)]

$$H_{\mathrm{loc},i}=-\langle S_Z\rangle\left(\frac{3n}{N}\right)^2\frac{2\pi}{E_f}\frac{AJ_{sd}}{g_N\mu_N}\Sigma_kF(2k_mr_{ik})$$
$$-g\mu_B\langle S_z\rangle\Sigma_kr_{ik}{}^{-3}(1-3\gamma_{ik}{}^2)\ , \qquad (2)$$

where $\langle S_z\rangle$ is the average of the z component of the 3d spin, N is the total number of atoms, n is the total number of conduction electrons, E_F is the Fermi energy of Cu, A is the hyperfine interaction constant, J_{sd} is the s–d exchange constant and γ_{ik} is the direction cosine of the radius vector r_{ik} between the kth solute atom and the ith nucleus under consideration with respect to the external field direction (z-axis), and F is a complex function of the maximum wave vector k_m and r_{ik}. This local field will have different values for different Cu sites and, therefore, the distribution of them will give a line broadening mechanism of inhomogeneous type[23)]. The spectrum of this local field for a system of randomly diluted spins becomes in general Lorentzian as was shown by Kittel and Abrahams[20)] and by Behringer[9)]. In fact, such broadening of the line width in Cu–Mn was originally observed by Owen et al and has been discussed theoretically by Behringer[9)]. The spin-spin interaction between Cu nuclei will give the broadening of the component line of the local field spectrum. Then the total line shape will be expressed by

$$I(H)=\int_{-\infty}^{+\infty}g(H-H_0)\,p(H_0)\,dH_0\ , \qquad (3)$$

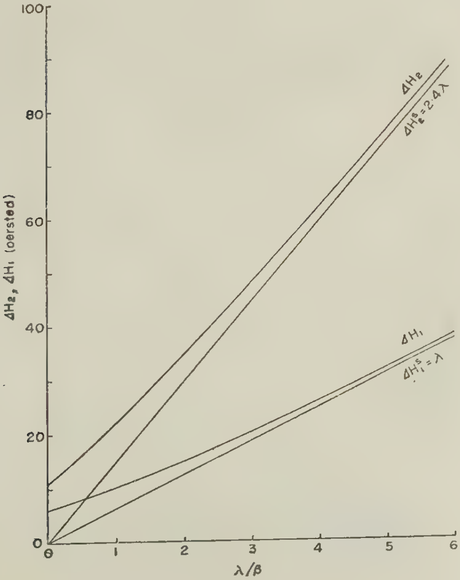

Fig. 9. Calculated line width, ΔH_2 and ΔH_1, for paramagnetic alloys. The straight line shows the contribution of the solute to the width.

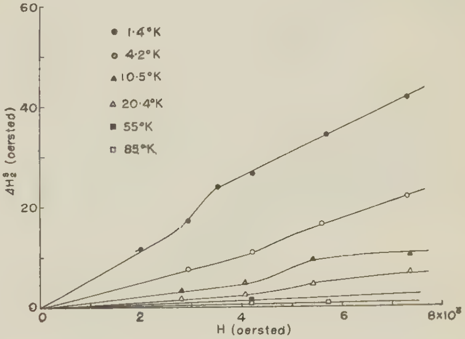

a) 0.016% Cr.

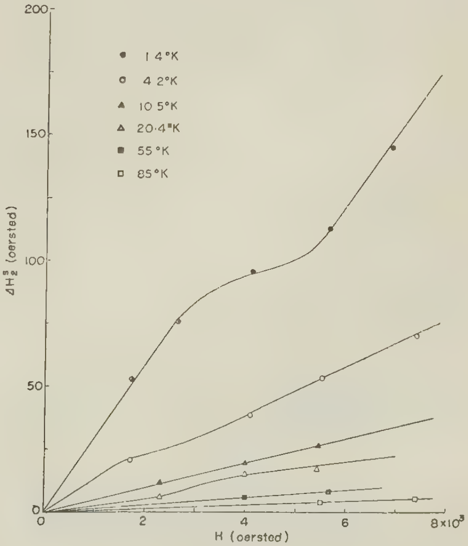

b) 0065% Cr.

Fig. 10. Field dependence of $\Delta H_2{}^s$, the contribution of the solute to ΔH_2, in Cu–Cr.

where $g(H)$ is the shape function for pure Cu and $p(H_0)$ is the intensity distribution function of the local field given by Eq. (2).

Informations about the magnetic behavior of the solute have been derived from the line width data by the following procedure. Assuming a cut-off Lorentzian shape for $p(H_0)$* and the line shape of pure Cu for $g(H)$, the derivative of $I(H)$ has been calculated for various values of a parameter λ/β, where λ is the width of $p(H_0)$ and β is that of $g(H)$. The theoretical line widths which should correspond to the measured width ΔH_1 and ΔH_2 respectively, have been plotted in Fig. 9 as functions of λ/β. The line widths of $p(H_0)$, ΔH_1^s and ΔH_2^s, which are just the solute contributions to the width ΔH_1 and ΔH_2, have been plotted in the same figure using the relation

$$\Delta H_1^s = \lambda\,, \qquad \Delta H_2^s = 2.40\lambda\,.$$

From the figure ΔH_2^s (or ΔH_1^s) corresponding to the observed line width ΔH_2 (or ΔH_1) has been obtained easily. In Figs. 10, 11 and 12 ΔH_2^s's for Cu–Cr, Cu–Mn, and Cu–Fe at various temperatures have been plotted as functions of the field strength.

For a cut-off Lorentzian, λ is given by

$$\lambda = \frac{\pi}{\alpha\sqrt{3}}\langle \Delta H^2 \rangle\,, \qquad (4)$$

where α is the cut-off frequency large compared with λ and $\langle \Delta H^2 \rangle$ is the second moment given by

$$\langle \Delta H^2 \rangle = \Sigma_i (H_{\mathrm{loc},i})^2\,. \qquad (5)$$

The cut-off frequency α can be regarded as the frequency corresponding to the maximum value of the local field given by Eq. (2).

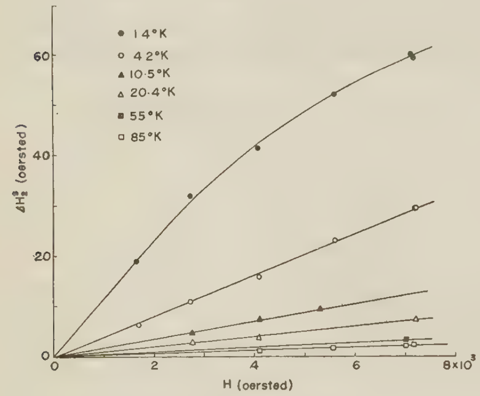

a) 0.026% Mn.

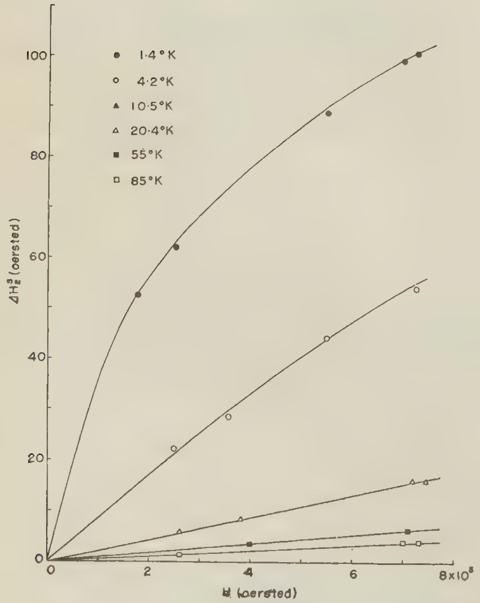

b) 0.055% Mn.

Fig. 11. Field dependence of ΔH_2^s, the contribution of the solute to ΔH_2, in Cu–Mn.

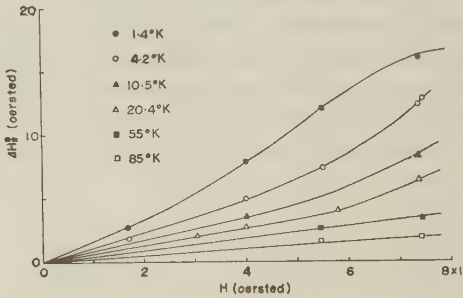

a) 0.040% Fe.

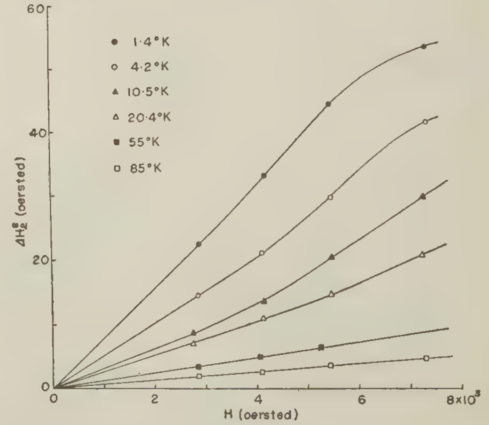

b) 0.11% Fe.

Fig. 12. Field dependence of ΔH_2^s, the contribution of the solute to ΔH_2, in Cu–Fe.

---

* This assumption has been justified experimentally as is seen from Fig. 8. See also Ref. 9).

Combining Eqs. (4) and (5) and using the summation method of Kittel and Abrahams[20], one obtains an expression for ΔH_2^s,

$$\Delta H_2^s = 2.40 \frac{\pi}{\alpha\sqrt{3}} f \Sigma'(H_{\text{loc}})^2$$
$$= 4.35 \frac{f}{\gamma (H_{\text{loc}})_{\max}} \Sigma'(H_{\text{loc}})^2 \qquad (6)$$

where Σ' means the sum over the whole lattice points, and f is the fractional concentration of the solute. Eq. (6) shows that ΔH_2^s (and also ΔH_1^s) should be proportional to $\langle S_z \rangle$ and consequently should have the same temperature and field dependence as the magnetization of the alloy. In fact that field dependence of ΔH_2^s in Cu–Mn was in agreement with the magnetization curves reported by Schmidt and Jacobs[4]. However, Cu–Cr and also Cu–Fe showed anomalous field dependences as seen in Figs. 10 and 12. The deviation from the linear relation at 7000 oersted was maximum at about 5°K in 0.040% Cu–Fe and at about 15°K in 0,11% Cu–Fe.

From the foregoing it is concluded that $\Delta H_2^s/H$ should be proportional to the susceptibility of the alloy. Fig. 13 is a plott of the reciprocal of $\Delta H_2^s/H$, obtained from the slope of the low field part of the ΔH_2^s curve, as a function of temperature. As is seen from the figure, the Curie-Weiss law,

$$\Delta H_2^s/H = C_2^s/(T-\Theta) \qquad (7)$$

holds fairly well in Cu–Cr, Cu–Mn and Cu–Fe. Deviations from the Curie-Weiss law occur only at very low temperatures in Cu–Cr and in Cu–Mn, but at temperatures below 20°K in Cu–Fe. In Table II, Θ and C_2^s for various alloys are collected and compared with Θ obtained from the susceptibility data found in the literatures.

The foregoing analysis of the line width is based upon a phenomenological theory of the line broadening and therefore requires more rigorous theoretical foundation. This will be made in Part II of this paper in conjunction with the electronic state of the solute and the *s–d* exchange interaction in dilute alloys.

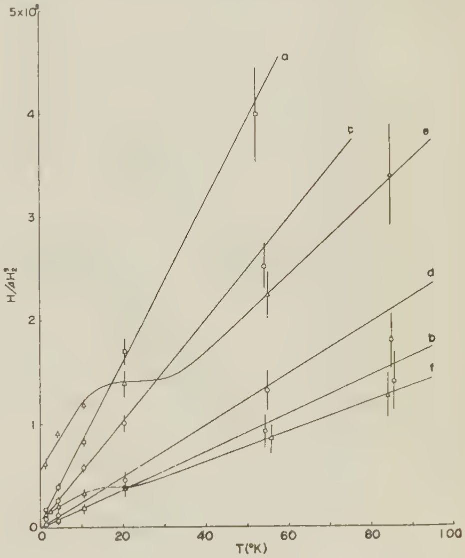

Fig. 13. $H/\Delta H^s_2$ *vs.* temperature in Cu–Cr, Cu–Mn, and Cu–Fe. This is equivalent to the reciprocal susceptibility *vs.* temperature diagram. a) 0.016% Cr, b) 0.065% Cr, c) 0.026% Mn, d) 0.055% Mn, e) 0.040% Fe, f) 0.11% Fe.

Table II. Curie-Weiss Law in Cu–Cr, Cu–Mn, Cu–Fe and Cu–Co.

Solute	%	Θ (deg.) line width	Θ (deg.) susceptibility	C_2^S (10^{-3}) line width
Cr	0.016	−0.6±0.5	—	13.0±1.0
	0.065	0 ±0.5	—	57 ±3
Mn	0.026	−0.3±0.5	0±2[a]	20.5±1.5
	0.055	0 ±0.5	0±2	45 ±3
Fe	0.040	−10 ±5	−14[b]	26 ±3
	0.11	−3 ±2	−7	68 ±4
Co	0.080	∼−70	∼−1000[c]	
	0.15	∼−50	∼−1000	

a) Ref. 4).
b) Ref. 13).
c) E. Hildebrand: Ann. Phys. **30** (1937) 593.

§ 5. The Knight Shift

The Knight shift was obtained by measuring the difference between the resonance field of the alloy and of the reference sample at a same frequency. As the reference a small amount of CuBr was sealed in the sample tube, so that the resonance field could be compared at the same temperature. The measurements were carried out mostly at a frequency of about 8.3 Mc but sometimes at lower frequencies. Temperature dependence of the shift of Cu^{63} resonance in various alloys is illustrated in Fig. 14. Alloys containing non-magnetic or weakly magnetic solutes show nearly the the same shift as compared with pure Cu. On the other hand, Cu–Cr, Cu–Mn and Cu–Fe, which are paramagnetic, show slightly larger shift than pure Cu in contradiction to the previous results on Cu–Mn by Owen *et al*2) and by van der Lugt *et al.*22)

When the dimension of a metallic specimen is not small compared with the skin depth, the absorption signal contains the real and imaginary components, i.e.

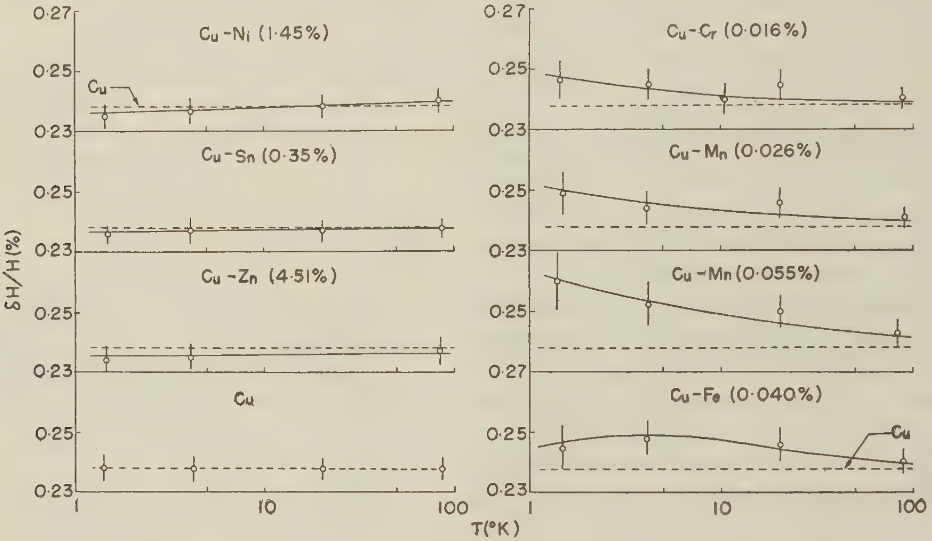

Fig. 14. Knight shifts of Cu^{63} in dilute alloys and in pure copper.

$$dI/dH=a(d\chi'/dH)+b(d\chi''/dH)\,, \qquad (8)$$

where χ' and χ'' are the real and imaginary parts of the nuclear susceptibility. Consequently the signal is asymmetric and the apparent Knight shift measured at the point of zero derivative becomes smaller thanthe true Knight shift18). The grain size of samples used in this work was smaller than the skin depth, so the effect was considere dto be negligible as compared with the experimental error.

The line shift δH of the host nucleus in paramagnetic alloys can be expressed by the sum of two components of different origin, one due to the hyperfine interaction of the nucleus with conduction electrons and the other due to the interaction of the nuclear spin with the localized spins as discussed before Therefore, it follows that

$$\delta H=(\delta H)_\sigma+(\delta H)_S\,. \qquad (9)$$

The first term is proportional to the conduction electron magnetization and, if a uniform polarization of the conduction electron spin due to *s–d* exchange exists, it will depend upon the magnetization of the solute spin1). According to Yoshida7), however, the polarization is localized in the vicinity of the solute atom and, therefore, the shift should not differ from that for the solvent metal. Similarly the variation of the shift due to a change in the electron charge density upon alloying has been shown negligible as the extra charge is also highly localized23). The second term contains the first order shift due to the z-component of the solute spin and the second order shift due to the perpendicular component. The first order shift is equal to the first moment of the local field given by Eq. (2), in which the dipolar contribution vanishes for a powdered sample and the indirect exchange contribution gives a small negative value⁷⁾. The second order effect, which produces a paramagnetic shift, is negligible in dilute alloys.

The above consideration gives no satisfactory explanation of the observed temperature dependent shift in the alloys with Cr, Mn and Fe. Therefore the extra shift must be attributed to the uniform polarization of s-electrons due to s–d exchange in contrast with the theory⁷⁾. It is also interesting to note that the shift in Cu–Ni have the same value as that of pure Cu. The alloy shows fairly large increase of the temperature independent paramagnetism with increasing Ni concentration²⁴⁾. The present data will be useful for understanding the anomalous magnetic behavior of the system Cu–Ni.

§ 6. The Spin-Lattice Relaxation Time

The saturation curve method was used for the determination of the nuclear spin-lattice relaxation time T_1 of Cu^{63} nucleus. The experiments were carried out mostly at a frequency of about 8.3 Mc. Determination of T_1 from the saturation curve of the paramagnetic alloys was made as follows. As has been mentioned in the previous section, the line broadening in these alloys is of inhomogeneous type. The saturation behavior of the derivative of the inhomogeneously broadened line can be expressed by²⁵⁾

$$dI(H, H_1)/dH$$
$$=\frac{d}{dH}\int_{-\infty}^{+\infty} p(H_0)\frac{g(H-H_0)}{1+\frac{1}{4}\pi\gamma^2H_1^2T_1g(H-H_0)}\,dH_0 \tag{10}$$

where $p(H_0)$ and $g(H-H_0)$ have the same meanings as in Eq. (3) respectively, and H_1 is the radio frequency magnetic field at the sample. Eq. (10) is varid only when the homogeneous saturation occurs over the narrow interval limitted by the width of the component line $g(H)$. It is not certain whether this condition is realized in the paramagnetic alloys or not. Therefore Eq. (10) has been assumed tentatively,* and the line shape function of pure Cu has been taken for $g(H)$ as a limiting case. Using Eq. (8) theoretical saturation curves have been constructed for various values of the parameter λ/β as has been done in § 4. The curve for the case $\lambda=0$ has been made to coincide with the observed saturation curve in pure Cu. T_1 has been calculated by fitting the observed saturation data with the theoretical curve having the same λ/β or $\Delta H_1^s/\beta$. Values of T_1 thus obtained have been plotted against temperature in Fig. 15.

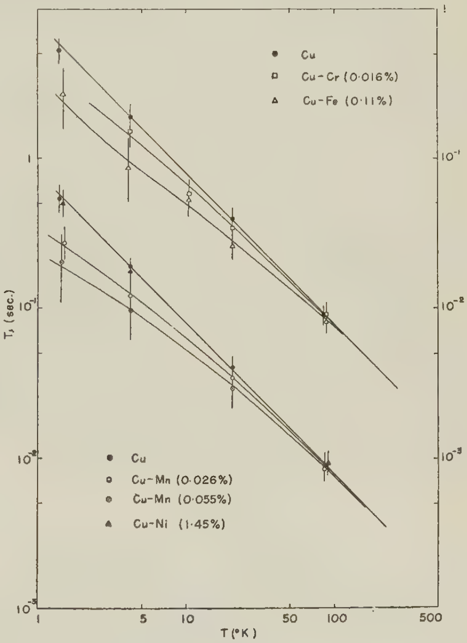

Fig. 15. Spin-lattice relaxation time T_1 of Cu^{63} in dilute alloys and in pure copper.

As is seen from Fig. 15, T_1 in paramagnetic alloys becomes shorter than that in pure Cu when the temperature is lowered. The deviation is large for alloys containing Mn and Cr, in which the line width is also large at low temperatures. In alloys containing non-magnetic solute such as Ni or Zn, T_1 is nearly the same as that of pure Cu. In general, $(1/T_1)$ can be expressed by the sum of transition probabilities of various relaxation mechanisms,

$$1/T_1=(1/T_1)_\sigma+(1/T_1)_S+(1/T_1)_D \tag{11}$$

where $(1/T_1)_\sigma$ is the contribution from the Heitler-Korringa relaxation²⁶⁾, $(1/T_1)_S$ is that due to the interaction of the nuclear spins with the solute spins and $(1/T_1)_D$ is that due to the spin diffusion[27]. It is not possible to derive the contribution of $(1/T_1)_S$ and of $(1/T_1)_D$ separately from the observed data. But the present result shows that $(1/T_1)_S$ or $(1/T_1)_D$ is comparable in magnitude with $(1/T_1)_\sigma$ in paramagnetic alloys such as Cu–Mn. At present the origin of such short T_1 is not clear, though the spin diffusion seems to be responsible in part for this.

---

* However, this assumption was proved to be not a poor approximation from the fact that the theoretical saturation curve agreed with experimental data fairly well and also the whole line shape did not change appreciably with increasing degree of saturation.

The foregoing analysis has been made on the assumption that the homogeneous saturation occurs only over the region determined by the width of pure Cu. If the homogeneous region is more broad than that assumed, T_1 of paramagnetic alloys at low temperatures will become shorter than the value shown in Fig. 15.

Acknowledgements

The author would like to express his thanks to Prof. E. Kanda for his continued interest and encouragement. He is also grateful to Dr. T. Moriya, Mr. Y. Obata, Mr. H. Hasegawa, Dr. Y. Shibuya, Mr. T. Otsuka, and Mr. S. Nagasaki for their helpful suggestions and discussions. This work has been supported in part by the Scientific Research Expenditure from the Ministry of Education.

References

1) J. Owen, M. Brown, W. D. Knight and C. Kittel: Phys. Rev. **102** (1956) 1501.
2) J. Owen, M. E. Brown, V. Arp and A. F. Kip: J. Phys. Chem. Solids **2** (1957) 85.
3) C. J. Gorter, G. J. van den Berg and J. de Nobel: Canad. J. Phys. **34** (1956) 1281.
4) R. W. Schmidt and I. S. Jacobs: J. Phys. Chem. Solids **3** (1957) 324.
5) Y. Shibuya et al: presented at the Kamerlingh-Onnes Conference on Low Temperature Physics, Leiden, June 1958.
6) Y. Mutô: private communication.
7) K. Yoshida: Phys. Rev. **106** (1957) 893.
8) K. Yoshida: Phys. Rev. **107** (1957) 396.
9) R. Behringer: J. Phys. Chem. Solids **2** (1957) 209.
10) J. Friedel has given an explanation of the magnetic behavior.
J. Friedel: Canad. J. Phys. **34** (1956) 1190.
11) J. Korringa and A. N. Gerritsen: Physica **19** (1953) 457.
12) D. K. C. MacDonald and W. B. Pearson: Proc. Roy. Soc. **A**, **219** (1953) 373. C. K. White: Canad. J. Phys. **33** (1955) 119.
13) F. Bitter, A. R. Kaufman, C. Starr and S. T. Pan: Phys. Rev. **60** (1941) 134.
14) K. K. C. MacDonald and W. B. Pearson: Acta Met. **3** (1955) 392.
15) F. T. Hedcock: Phys. Rev. **104** (1956) 1964.
16) M. Hansen: *Constitution of Binary Alloys* (McGraw-Hill, New York, 1958).
17) N. Bloembergen: J. Appl. Phys. **23** (1952) 1383.
18) A. C. Chapman, P. Rhodes and E. F. W. Seymour: Proc. Phys. Soc. London **B**, **70** (1957) 345.
19) Y. Masuda: J. Phys. Soc. Japan **12** (1957) 523.
20) C. Kittel and E. Abrahams: Phys. Rev. **90** (1953) 238.
21) N. Bloembergen and T. J. Rowland: Phys. Rev. **97** (1955) 1679. M. A. Ruderman and C. Kittel: Phys. Rev. **96** (1954) 99.
22) W. van der Lugt, N. J. Poulis, G. E. G. Hardeman and W. P. A. Hass: Physica **23** (1957) 798.
23) J. Friedel: J. phys. radium **16** (1955) 444.
24) E. Wm. Pugh, B. R. Coles, A. Arrott and J. E. Goldman: Phys. Rev. **105** (1957) 814.
25) A. M. Portis: Phys. Rev. **91** (1953) 1071.
T. Sugawara: Sci. Rep. RITU **A**, **8** (1956) 95.
26) J. Korringa: Physica **16** (1950) 601.
27) N. Bloembergen: Physica **15** (1949) 386.

Journal of the Physical Society of Japan, Vol. 14, No. 5, May, 1959

Theory of Spatially Growing Plasma Waves

By Masao Sumi

Electrical Communication Laboratory,
Musashino-shi, Tokyo

(Received January 26, 1959)

The linearized theory of spatially growing waves in a uniform plasma is investigated in detail. By solving the dispersion relation in this case, characteristics of excited waves are presented. Behaviors of the growth-rate and the phase-velocity of amplified wave are examined in connection with the frequency and various conditions of the medium plasma and the directed beam. It is seen that the theory is in good agreement with some features of experimental results.

§ 1. Introduction

Longitudinal plasma waves which increase with distance have been discussed by many authors. The amplification process in double-stream discovered by Haeff and others[1)] is a simple example of this kind. Two groups of electrons with different velocities interact with each other, as a result of which, under some favorable circumstances, a disturbance located at some point increases in the direction of streams as it propagates. It is found that an amplified wave receives energy from the faster stream and has a phase-velocity which lies almost midway between two velocities in the double-stream. If the plasma consists of electrons with distributed velocities, the simple theory of double stream is not appropriate. This case has also been discussed to some extent in several papers by taking approximate velocity distribution in the thermal plasma. Feinstein and Sen[2)] took the square velocity distribution of thermal electrons and established the region over which the wave is amplified, but they did not give the magnitude of amplification. A dispersion relation equivalent to theirs was also examined by Lampert[3)], who disclosed a part of features of its solution.

The present paper, which solves fundamental equations as a boundary value problem, completes the more detailed investigation for beam excitation of plasma waves in linear approximation, together with our latest work[4)] (abbreviated hereafter as I), in which characteristics of solutions for an initial value problem were examined. The procedure in analysis employed here will follow that adopted in I: the Fourier-Laplace transform of fundamental equations will lead to a dispersion relation, the solution of which will yield characteristics of growing waves in space.

§ 2. Dispersion Relation

Fundamental equations used here are the same as those in part I; namely, the Boltzmann equation and the Poisson equation.

As usual the linearized equations for oscillating components are obtained, neglecting short range collisions, as below

$$\frac{\partial f_1}{\partial t}+\boldsymbol{v}\frac{\partial f_1}{\partial \boldsymbol{x}}-\frac{e}{m}\boldsymbol{E}\frac{\partial f_0}{\partial \boldsymbol{v}}=0\,, \tag{2.1}$$

and

$$\frac{\partial \boldsymbol{E}}{\partial \boldsymbol{x}}=-\frac{e}{\varepsilon_0}\int f_1 d\boldsymbol{v}\,. \tag{2.2}$$

To deal with a boundary-value problem, let the equations above be Fourier-analysed in time and Laplace-transformed in space. In one dimensional case. they become

$$i(\omega-ku)F(u,\,k,\,\omega)+uf(u,\,0,\,\omega)+\frac{e}{m}\mathcal{E}(k,\,\omega)\frac{df_0}{du}=0\,, \tag{2.3}$$

$$ik\mathcal{E}(k,\,\omega)-E(0,\,\omega)=-\frac{e}{\varepsilon_0}\int_{-\infty}^{\infty}F(u,\,k,\,\omega)du\,, \tag{2.4}$$

where $E(u,\,k,\,\omega)$ and $\mathcal{E}(k,\,\omega)$ are the Fourier-Laplace transforms of $f(u,\,z,\,t)$ and $E(z,\,t)$ respectively,

$$\begin{Bmatrix} F(u,\,k,\,\omega) \\ \mathcal{E}(k,\,\omega) \end{Bmatrix}=\frac{1}{2\pi}\int_0^\infty dz\int_{-\infty}^{\infty}dt e^{-i(kz-\omega t)}\begin{Bmatrix} f(u,\,z,\,t) \\ E(z,\,t) \end{Bmatrix}\,. \tag{2.5}$$

While $f(u,\,0,\,\omega)$ and $E(0,\,\omega)$ represent the Fourier components for the boundary value of respective quantity.

From Eqs. (2.3) and (2.4) we obtain the transformed electric field component

$$\mathcal{E}(k,\omega)=\frac{-iE(0,\omega)+\dfrac{e}{\varepsilon_0 k}\displaystyle\int_{-\infty}^{\infty}\frac{uf(u,0,\omega)}{(u-\omega/k)}du}{k\left[1-\dfrac{e^2}{m\varepsilon_0 k^2}\displaystyle\int_{-\infty}^{\infty}\frac{df_0/du}{(u-\omega/k)}du\right]}\,, \tag{2.6}$$

for Im$(k)<0$. The expression which is valid for the whole k plane can be defined by means of analytical continuation of Eq. (2.6). The result is that the path of integration along the real axis of u-plane in Eq. (2.6) has to be replaced by the contour C or C′, according to whether the value of ω is positive or negative, respectively. The contour C, as argued in I, goes from $-\infty$ to $+\infty$ making a downward detour in the lower half u-plane in order to avoid all singularities; and the contour C′ takes the similar path in the upper half-plane.

To find $E(z,t)$, $\mathcal{E}(k,\omega)$ must be transformed inversely to the original coordinates. Then it becomes necessary to get roots of the denominator of $\mathcal{E}(k,\omega)$ which, in turn, are determined by the dispersion relation

$$D(k,\omega)\equiv 1-\frac{e^2}{m\varepsilon_0 k^2}\int_{\mathrm{C\ or\ C'}}\frac{df_0/du}{u-\omega/k}du=0\,. \tag{2.7}$$

Thus the solution of the relation (2.7) for ω real and k complex, such as $k=k_0-i\gamma$, gives characteristics of plasma waves in a boundary value problem.

In our case of beam excitation, it is supposed that the stationary distribution function $f_0(u)$ is composed of one part for uniform plasma and the other for a directed beam; the former has a Maxwellian form and the latter a δ-functional form corresponding to a single velocity. Hence we may write

$$f_0(u)=(n_p/\sqrt{\pi}\,u_T)\exp\left[-(u/u_T)^2\right]+n_b\delta(u-u_b)\,, \tag{2.8}$$

where n_p and n_b are electron densities in the plasma and the beam respectively, and u_T denotes the mean thermal velocity in the plasma: $u_T=(2\kappa T/m)^{1/2}$. With this distribution function, the dispersion relation (2.7) becomes

$$D(k,\omega)=1+\left[2\beta_p^2\{1\pm i\sqrt{\pi}\,\beta e^{-\beta^2}[1\pm\Phi(i\beta)]\}-\frac{\beta_b^2}{(\xi-\beta)^2}\right]=0\,, \tag{2.9}$$

(+sign for $\omega>0$, $-$sign for $\omega<0$)

where $\beta_p=\omega_p/ku_T$, $\beta_b=\omega_b/ku_T$, $\beta=\omega/ku_T$, $\xi=u_b/u_T$, $\omega_p^2=n_pe^2/m\varepsilon_0$, $\omega_b^2=n_be^2/m\varepsilon_0$ and

$$\Phi(x)=\frac{2}{\sqrt{\pi}}\int_0^x e^{-t^2}dt\,.$$

If the value of ω/k_0 is positive, k_0 being the real part of complex k, the excited wave propagates in the same direction as that of beam velocity; or it is a forward wave. If it is negative, the wave propagates in the reverse direction, or a backward wave. Accordingly the double signs in Eq. (2.9) can be rewritten as follows

$$D(k,\omega)=1+\left[2\beta_p^2\{1+i\sqrt{\pi}\,\beta e^{-\beta^2}[1+\Phi(i\beta)]\}-\frac{\beta_b^2}{(\xi\mp\beta)^2}\right]=0\,, \tag{2.10}$$

where the minus sign corresponds to forward waves and the plus one to backward waves. Solutions of Eq. (2.10) for Im$(k)\gtreqless 0$ will give features of spatially growing, stationary or decaying waves, respectively. They will be examined in later sections.

§ 3. Characteristics of Growing Waves

On the physical ground it may be inferred that a growing wave will occur in the forward direction and not in the backward, since a forward wave alone couples closely with the beam and receives energy from it. Hence in this section only forward waves will be considered.

Now the dispersion relation for a forward wave will be solved for $Im(k)>0$. We are mainly interested in the case when the electron velocity in the beam is much greater than the mean thermal velocity of electrons in the medium plasma, or $\xi\gg 1$. As an amplified wave has a phase velocity a little below the beam velocity, $|\beta|$ may also be greater than 1. For $|\beta|\gg 1$, $\Phi(i\beta)$ is expanded as a power series in β^{-2}. Thus the dispersion relation (2.10) can be written as

$$1=\frac{\beta_p^2}{\beta^2}\left(1+\frac{3}{2\beta^2}+\frac{15}{4\beta^4}+\cdots\right)+\frac{\beta_b^2}{(\xi-\beta)^2}\,. \tag{3.1}$$

After some manipulations we devide Eq. (3.1) into a real and an imaginary part by putting $k=k_0-i\gamma$ ($\gamma>0$), in order to seek solutions for growing waves. Then we get

$$\left(\frac{\omega}{\omega_p}\right)^2=\left[1+\frac{3}{2\xi^2}\frac{(1-\varepsilon^2)}{(1-\chi)^2}+\frac{15}{4\xi^4}\frac{\{(1-\varepsilon^2)-4\varepsilon^2\}}{(1-\chi)^4}+\cdots\right]+\sigma\frac{(1-\chi^2)(\chi^2-\varepsilon^2)}{(\chi^2+\varepsilon^2)^2}\,. \tag{3.2}$$

$$\frac{3}{2\xi^2}\frac{(\chi^2+\varepsilon^2)^2}{(1-\chi)^4}\left[1+\frac{5}{\xi^2}\frac{(1-\varepsilon^2)}{(1-\chi)^2}+\cdots\right]=\sigma\chi\,, \tag{3.3}$$

where $\sigma=n_b/n_p$, $\varepsilon=\gamma/k_0$ and $\chi=1-(\omega/k_0u_b)$. Solutions of these two equations will give characteristics of growing waves of the form $\exp(\gamma z)\exp[i(k_0z-\omega t)]$; namely, relations between the frequency ω, the growth-rate γ and the phase-velocity of the wave ω/k_0.

Consider first the extreme case of $u_T\rightarrow 0$, or the case without thermal motions in the medium plasma. Then ξ tends to infinity, giving solutions of Eq. (3.3), $\chi=0$ or 1. From the definition $\chi=1$ implies the wave phase velocity $u_w=\omega/k_0=0$. It is indeed a physically trivial solution. For $\chi=0$, $u_w=u_b$; the wave is entirely synchronized with the beam. Hence we can obtain from Eq. (3.2) the growth-rate

$$(\gamma u_b/\omega_p)^2=\sigma/[(\omega_p/\omega)^2-1]\,. \tag{3.4}$$

In the frequency range $0<\omega<\omega_p$, it gives $0<\gamma<\infty$ and ω_p is a sort of resonant frequency. It is this situation that was early discussed by Pierce[1].

In general cases, Eqs. (3.2) must be solved numerically. With two parameters of ξ and σ, Eq. (3.3) gives a function of $\chi(\varepsilon;\,\xi,\,\sigma)$. Inserting it into the right hand side of Eq. (3.2), ω/ω_p is obtained as a function of ε, too. From these both the growth-rate γ and the phase velocity u_w of the wave are traced against a variable ε, by the use of relations such that $\gamma u_b/\omega_p=\varepsilon(\omega/\omega_p)/(1-\chi)$ and $u_w/u_b=1-x$. Then we get finally Figs. 1–4.

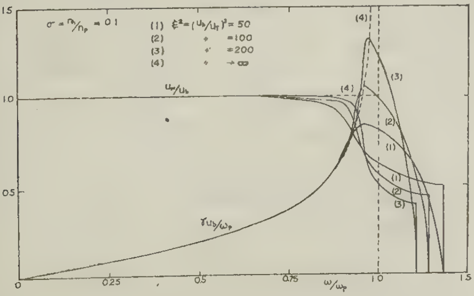

Fig. 1. Characteristics of amplified wave *versus* the frequency, when the mean thermal velocity of electrons in the plasma is varied.

Fig. 1 represents the rate of growth and the phase-velocity of the amplified wave versus the modulating frequency with a parameter ξ, σ being held constant: a typical value 0.1. In the frequency range far below the plasma frequency ω_p, γ increases slowly with ω, but remains small. The wave phase velocity is nearly equal to the beam velocity. As ω approaches ω_p, γ rises sharply and reaches its maximum at a frequency a little below ω_p, beyond which it falls steeply to zero. The phase velocity u_w decreases rapidly near the maximum point of γ, where the energy transfer from the beam to the wave also reaches its maximum proportional to γ. If we suppose u_b to be kept constant and u_T to be varied, the peak value becomes larger with decreasing u_T or increasing ξ, until it tends fo infinity at vanishing u_T as was mentioned in the preceding paragraph. This limiting case for $\xi^2\rightarrow\infty$ is also shown in Fig. 1 by a broken line.

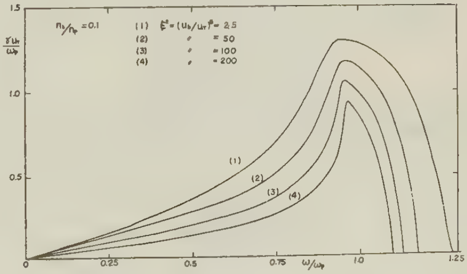

Fig. 2. The growth-rate of amplified wave *versus* the frequency, when the beam velocity is changed.

On the contrary to the above, when u_T holds constant and u_b becomes greater, curves for the rate of growth $\gamma u_T/\omega_p$ are plotted in Fig. 2. As u_b or ξ increases, the magnitude of peak value of γ gets smaller. In the limit of $\xi^2\rightarrow\infty$, the curve for γ is flattened; it implies that the amplification is reduced to infinitecimal. The reason is that the faster is the beam velocity, the shorter becomes the interaction time per unit length, resulting the reduction of growth-rate.

In Fig. 3 the behavior for varying beam density with a definite beam velocity is represented. With increasing density, the peak of the growth-rate curve is more elevated and more apart from the plasma frequency.

Finally Fig. 4 presents several curves of amplification rate, $\gamma u_b/\omega_b$ with a parameter of modulating frequency ω, when the plasma density is varied and the beam is unvaried. Each curve shows an abrupt rise beyond the critical density until it reaches its peak-value at a density such that ω_p is slightly over ω. Beyond the peak, the curve falls off rather gradually. In the next section this feature will be compared with that observed.

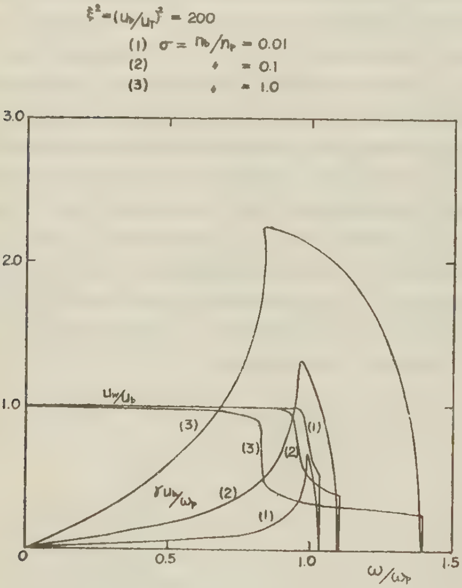

Fig. 3. Wave characteristics for varying beam density with a constant beam velocity.

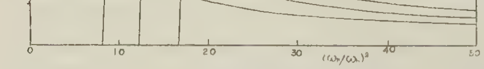

Fig. 4. The rate of amplification for the variation of plasma density, the beam being unaltered.

§4. Comparison with Experimental Results and Discussions

Recently an experiment corresponding to the excitation of spatially growing waves as discussed above has been successfully performed[5]. A fast electron beam, passed through a plasma in gaseous discharges with a definite depth, was modulated near the incident boundary by a microwave signal. Then an output signal was picked up from the modulated beam after leaving the opposite boundary of the plasma. Thus the amplification of the signal was observed; curves for relative output gain versus arc current were obtained at several frequencies. These may be compared with the theory in the following.

An electric field of amplified wave can be written as $E=E_0 \exp(\gamma z)$, so that the output gain expressed by decibels is found to be proportional to γ. On the other hand it is known that the plasma arc current is proportional to the electron density, or to ω_p^2. Consequently, experimental curves in this case should correspond to theoretical curves given in Fig. 4. Indeed it is the case as expected, since the rapid rise on one side of the peak and the gradual fall on the other side can be seen in both groups of curves and besides the shift of each curve with respect to the variation of frequency occurs in a quite similar way. This can be regarded as a satisfactory verification for qualitative agreements between theory and experiment.

The experimental value of output gain, about 8 db per cm for the beam voltage of 400 volts and the modulating frequency of about 3000 Mc/sec, has been obtained*. The theoretical value is now expressed as $8.69\,\gamma$ db. The maximum γ for different values of σ are estimated from Fig. 3; the value of $\gamma_{\max} u_b/\omega$ are about 1.3, 0.7 and 0.3 for $\sigma=0.1$, 0.01 and 0.001, respectively. We see that the calculated gain is much greater than that observed, since it amounts to about 40 db per cm even at $\sigma=0.001$. The reason for this discrepancy has not yet been clarified. If a high gain such as predicted by the theory is realized, it will cause a saturation effect of amplification, although it is beyond the validity of linear theory.

The approximation for $|\beta|\gg 1$ in which the error integral can be expanded as a power series does not hold good as $|\beta|$, or ξ, approaches 1. In the range of $|\beta|\sim 1$, the expansion cannot be applied and a numerical table for the error integral must be used. As seen in Fig. 2, the decrease of u_b or ξ gives rise to a higher peak-value of $\gamma u_T/\omega_p$. However as $|\beta|$ approaches one, it would not be so. It would be inferred that the peak-value begins to reduce and finally to zero somewhere u_b is nearly equal to u_T, although the detailed knowledge of it cannot be obtained unless we have exact solutions for $|\beta|\sim 1$.

---

* This result was reported at the Brooklyn Polytechnic Symposium in April 1958. In this report the calculation for gain similar to that we developed here was carried out independently and its result agrees with a part of ours. The author is indebted to Dr. Boyd for his communication.

So far we have considered only the case for growing waves. Now some remarks will be given concerning stationary or decaying waves. For a stationary or undamped wave, we may suppose both ω and k as real. Hence so is β, and the function $\Phi(i\beta)$ becomes pure imaginary. The imaginary part of Eq. (2.10) can then be written as

$$2\sqrt{\pi}\,\beta_p{}^2\beta e^{-\beta^2}=0\,. \tag{4.1}$$

Thus we get

$$\beta=0 \quad \text{or} \quad \beta\to\infty\,, \tag{4.2}$$

which, for ω non-zero and finite, yields

$$k\to\infty \quad \text{or} \quad k\to 0\,,$$

respectively. We find that the real part of Eq. (2.10) is not satisfied in the former case, whereas in the latter it gives the frequency $\omega=(\omega_p{}^2+\omega_b{}^2)^{1/2}$. It is to be noted that this is the only stationary wave. The wave which seems to exist in the limit of vanishing amplification, $\gamma\to 0$, cannot be realized, since the limit of $\varepsilon\to 0$ should be excluded in the case of amplification. This consequence is, of course, in accord with that derived by Berz6), in which the only stationary wave was that for $k=0$ and $\omega=\omega_p$ in the absence of beam.

For decaying waves, the dispersion relation can be expanded in Taylor's series with respect to γ in the case of smallest damping. Retaining only the first order terms for γ, we obtain a result

$$\frac{\gamma u_b}{\omega}\sim -\sqrt{\pi}\left(\frac{u_w}{u_T}\right)^2\left(\frac{\omega_p}{\omega_b}\right)^2 e^{-(u_w/u_T)^2}\,, \tag{4.3}$$

for $u_w \gg u_b$. The damping described by Eq. (4.3) is seen to behave in a similar way as the Landau damping7), which depends on the continuous velocity distribution of electrons in the plasma. In the limit of $k_0\to 0$, γ tends to zero, corresponding to the stationary wave. It may be concluded, at any rate, that the stationary and decaying waves discussed above would be practically unimportant for the beam excitation of plasma waves.

The spatially growing waves described in the present theory as well as in the double-stream theory have so far been observed only when the beam or beams were artificially modulated by a signal in the injection side. Without such a modulation, it will be impossible to get amplified waves propagating along the beam in a homogeneous plasma. In a usual gaseous discharge where a directed beam exists, it may be possible to get an amplified wave because of the inhomogeneity in the electron density. This phenomenon has recently been discussed by Emeleus et al8). In the case of a homogeneous plasma, on the contrary, it can be expected that plasma waves of a standing-wave form are excited9). The detailed comparison between theory and experiment with respect to it will be developed in the forthcoming paper.

Acknowledgment

The author wishes to express his gratitude to Professors T. Kihara and S. Kojima, and also to Dr. K. Takayama for their valuable remarks and discussions.

References

1) A. V. Haeff: Phys. Rev. **74** (1948) 1932; Proc. Inst. Radio. Eng. **37** (1954) 4. L. S. Nergaard: RCA Rev. **9** (1948) 585. J. R. Pierce: J. Appl. Phys. **20** (1949) 1060.
2) J. Feinstein and H. K. Sen: Phys. Rev. **83** (1951) 405.
3) M. A. Lampert: J. Appl. Phys. **27** (1956) 5.
4) M. Sumi: J. Phys. Soc. Japan **13** (1958) 1476.
5) G. D. Boyd, L. M. Field and R. W. Gould: Phys. Rev. **109** (1958) 1393.
6) F. Berz: Proc. Phys. Soc. London **B, 68** (1956) 939.
7) L. Landau: J. Phys. USSR **10** (1946) 25.
8) D. W. Mahaffey, G. McCullagh and K. G. Emeleus: Phys. Rev. **112** (1958) 1052.
9) M. Sumi: Phys. Rev. Letters **2** (1959) 37.

JOURNAL OF THE PHYSICAL SOCIETY OF JAPAN, Vol. 14, No. 5, MAY, 1959

High Subsonic Flow with Normal Shock Wave at Nearly Critical Mach Number

By Takeo SAKURAI*

Department of Aeronautical Engineering, Faculty of Engineering, Kyoto University

(Received October 22, 1958)

High subsonic flow past a biconvex circular arc aerofoil with a pair of normal shock waves at nearly critical Mach number is discussed by a very simple approximation procedure. The shock waves are assumed to be the normal shock waves which start from the surface of the aerofoil and stand perpendicularly to the direction of the uniform flow. The locations of the sonic line and the shock waves are treated as unknown parameters to be determined in the course of analysis. The results show that these parameters have real physical meaning only when the Mach number exceeds the usual critical Mach number calculated by means of Prandtl-Glauert approximation. The results also suggest that the curvature of the profile must change discontinuously at its intersection with the shock wave. This fact is also confirmed by applying Lin's exact consideration. Thus, it is concluded that there can exist no high subsonic flow of ideal fluid with normal shock waves starting from the surface past a profile having continuous curvature.

§ 1. Introduction

The study of the high subsonic flow past a profile with shock waves is very important from the practical as well as the academic viewpoints. The analytic solution of the problem is, however, very difficult, because there is no simple fundamental solution for the mixet subsonic and supersonic flow field in the presence of shock waves. A few examples which have hitherto been attacked with success are all based on tedious numerical calculations. Emmons[1)] analysed the flow past a profile with a pair of shock waves originating from the surface by the relaxation method, and obtained the results which seemed to agree well with experiments. His results also suggest that there is a singular point of the flow field on the profile immediately behind the shock wave. The details of the structure of the singularity, however, have not been worked out, because the meshes used by him are too coarse. Recently, Oswatitsch[5)] proposed a method based on an integral equation which is deduced from the basic equations of transonic flow. He solved the integral equation by using a very rough approximation, and obtained the results which agreed qualitatively with experiments. Later on, Gullstrand[2)] and Spreiter[6)] improved his analysis, and obtained the results which seemed to be reliable quantitatively as well as qualitatively. They solved the integral equation assuming a kind of the velocity distribution in the y-direction all over the field, such that the length of the shock wave is infinite. The procedure of the numerical calculations is still very tedious in spite of the above simplifications. Thus, it may be said that their results are indeed useful, but not at all completely satisfactory. Because of these circumstances, it seems worthwhile to reconsider the problem of the high subsonic flow, and to complement the results hitherto obtained.

In this paper, the writer proposes a new simple approximation procedure to treat the high subsonic flow past a profile with shock waves at nearly critical Mach number, and applies this procedure to the flow past a biconvex circular arc aerofoil.

§ 2. Basic Equations

Following Oswatitsch,[4)] the basic equations of the high subsonic flow past a thin aerofoil are represented as follows,

$$(1-u)\frac{\partial u}{\partial x}+\frac{\partial v}{\partial y}=0 \tag{1}$$

---

* This work was done at the Department of Physics, Faculty of Science, University of Tokyo. This is abstracted from the thesis presented in partial fulfilment of the requirements for the degree of the Doctor of Science at the University of Tokyo.

$$\frac{\partial u}{\partial y}-\frac{\partial v}{\partial x}=0 \tag{2}$$

with

$$x=\hat{x}\,, \quad y=\beta_\infty\hat{y}\,, \quad \beta_\infty=\sqrt{1-M_\infty^2} \tag{3}$$

$$u=\frac{\hat{u}-\hat{u}_\infty}{\hat{c}_*-\hat{u}_\infty}\,, \quad v=\frac{1}{\beta_\infty}\frac{\hat{v}}{\hat{c}_*-\hat{u}_\infty} \tag{4}$$

Here $(\hat{x}, \hat{y})$ are the Cartesian coordinates of a point in the plane of fluid motion in which the $\hat{x}$-axis is taken parallel to the direction of the uniform flow. $(\hat{u}, \hat{v})$ are the velocity components and M_∞, $\hat{u}_\infty$ and $\hat{c}_*$ are respectively the Mach number, the magnitude of the velocity and the critical velocity of the uniform flow. Letters with circumflex indicate variables in the physical plane.

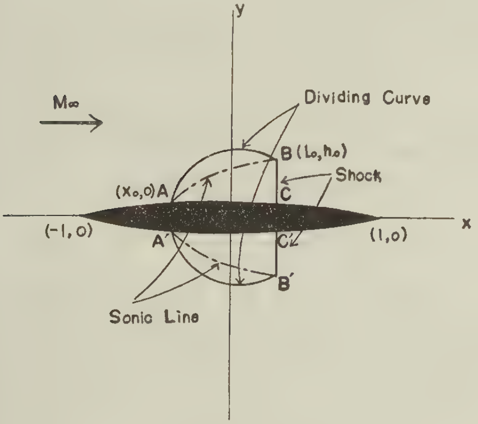

Fig. 1.

Let us divide the flow field into two regions, inner and outer, such that the latter corresponds to the purely subsonic flow while the former to the partly supersonic flow. (Fig. 1). From Eq. (4), it is clear that u is everywhere smaller than 1 in the purely subsonic region. Hence, we can obtain the crudest approximation to Eqs. (1) and (2) in the outer region by neglecting the nonlinear term of Eq. (1). This is, of course, equivalent to the well-known Prandtl-Glauert approximation:

$$\frac{\partial u}{\partial x}+\frac{\partial v}{\partial y}=0 \tag{5}$$

$$\frac{\partial u}{\partial y}-\frac{\partial v}{\partial x}=0 \tag{6}$$

If the Mach number of the uniform flow exceeds the critical value only slightly, it is expected that the partly supersonic region is very small and u is almost equal to 1 in and near the region. Then, to the crudest approximation, we can neglect the first term of Eq. (1) in the inner region. It is equivalent to the Prandtl-Glauert equation at Mach number 1, and the equation is of parabolic type having characteristic curves perpendicular to the x-axis:

$$\frac{\partial v}{\partial y}=0 \tag{7}$$

$$\frac{\partial u}{\partial y}-\frac{\partial v}{\partial x}=0 \tag{8}$$

Boundary conditions are similar to those in the usual thin wing theory:

1) (u, v) is one-valued and finite all over the flow field,

2) $(u, v)\to 0$ as $|x+iy|\to\infty$,

3) $\hat{v}=\hat{u}_\infty \frac{d\hat{y}}{d\hat{x}}\Big|_{\hat{y}=0}$ on the surface of the profile, which lies approximately on $\hat{y}=0$

$$v=\frac{M_\infty^*}{\beta_\infty^2(1-M_\infty^*)}\frac{dy}{dx}\Big|_{y=0} \quad \text{with} \quad M_\infty^*=\frac{\hat{u}_\infty}{\hat{c}_*}\,. \tag{9}$$

§ 3. The Method of Solution

Before proceeding to the discussion of the new method of solution, we must consider the relation which connects the inner and the outer solutions. The boundary curve between the inner and the outer regions is assumed to be composed of the shock wave and some suitable curve (e.g. a circular arc). On the portion of the boundary corresponding to the shock wave, two solutions are related by the shock condition:

$$1-u_i=u_o-1 \tag{10}$$

As will be shown below, the relation on the remaining part of the boundary may be taken simply as

$$u_i=u_o\,, \qquad v_i=v_o \tag{11}$$

where (u_i, v_i) and (u_o, v_o) are respectively the inner and the outer solutions. Indeed, if we could have obtained the exact solutions of the original equations (1) and (2) for the two regions, the above relations would obviously ensure the coincidence of the derivatives of u and v of any arbitrary order on both sides of the boundary curve. In our case, however, different approximate equations have been adopted in the two regions, so that we could not expect the coincidence of the values of derivatives of u and v calculated in the respective regions, even if we adjust the solutions so as to satisfy the relations (11). Such discrepancies are, however, expected to become smaller, if we adopt higher approximations to the original equations (1) and (2). Thus it appears that the above relations (11) are suitable for our purpose.

The procedure of solving the problem is as follows: First, we assume the location of the sonic line which represents the boundary of the supersonic region. We next divide the flow field, as mentioned above, into the inner and the outer regions by a curve which is composed of the shock wave and the other part wholly lying in the purely subsonic region (Fig. 1).

Now, the inner solution is uniquely determined by the boundary condition on the surface of the profile and the location of the sonic line already assumed. Then the connecting relations (11) together with the shock conditions (10) afford the u_o-distribution over the dividing curve. The outer solution is determined uniquely by means of this u_o-distribution and the remaining boundary conditions.

Comparing the solutions thus obtained, on the dividing curve, we find of course $u_i=u_o$ but in general $v_i\neq v_o$. Unknown parameters relating to the location of the sonic line are then adjusted by the requirement $v_i=v_o$ on the dividing curve.

Since the boundary condition (9) is satisfied in our approximation, (u_i, v_i) already coincide with (u_o, v_o) at the connecting point on the profile. There exist, however, discrepancy of the velocity gradient at that point. Such a discrepancy is undesirable, because the velocity gradient is one of the most important quantities from the physical viewpoints. Hence, let us require further that the velocity gradients of both solutions must be equal on the profile though it may appear to be an over-determinate condition in the exact treatment of the original equations (1) and (2).

§ 4. Application to the Flow past a Biconvex Circular Arc Aerofoil

Let us consider the flow past a biconvex circular arc aerofoil. The shock wave is assumed to be normal to the x-axis, extending from the point B to B′ (Fig. 1). The shape of the sonic line is assumed to be parabola passing points A, B(A′, B′) with its axis of symmetry on the line $x=l_0$:

$$y=\pm h_0\left\{1-\left(\frac{x-l_0}{x_0-l_0}\right)^2\right\}$$

+: upper half plane
−: lower half plane (12)

The dividing curve is assumed to be a circle passing points BA(A′)B′:

$$\left\{x-\frac{l_0^2-x_0^2+h_0^2}{2(l_0-x_0)}\right\}^2+y^2=\left\{\frac{(l_0-x_0)^2+h_0^2}{2(l_0-x_0)}\right\}^2 \tag{13}$$

From the assumed shape of the sonic line and the boundary condition on the profile the inner solution is obtained immediately:

$$\left.\begin{aligned} u_i&=1+2\nu\left[h_0\left\{1-\left(\frac{x-l_0}{x_0-l_0}\right)^2\right\}-y\right]\\ v_i&=-2\nu x\end{aligned}\right\} \tag{14}$$

where

$$\nu=\frac{tM_\infty^*}{\beta_\infty(1-M_\infty^*)}$$

and t is the thickness ratio of the profile. Here the boundary condition (9) for the circular arc aerofoil is expressed as follows;

$$v=-2\nu x \tag{15}$$

In order to obtain the outer solution, let us decompose the solution as follows:

$$w_o=u_o-iv_o=w_o^{(1)}+w_o^{(2)} \tag{16}$$

$$w_o^{(1)}=\frac{2\nu}{\pi}\left(2+z\log\frac{z-1}{z+1}\right),\qquad z=x+iy \tag{17}$$

$w_o^{(1)}$ is nothing but the usual Prandtl-Glauert solution. $w_o^{(2)}$ represents the distortion of the outer solution imposed by the existence of the shock wave, and must satisfy the following boundary conditions:

(A) $w_o^{(1)}$ is one-valued and continuous throughout the outer region,

(B) $w_o^{(2)}\to 0$ as $|z|\to\infty$,

(C) $v_o^{(2)}=0$ on the surface of the profile,

(D) on the dividing curve the following conditions must be satisfied:

(a) on the shock wave:

$$u_o^{(2)}=1-\frac{4\nu}{\pi}(1-l_0^2)+2\nu(2y-h_0) \tag{18}$$

(b) on the dividing circle:

$$u_o^{(2)}=1-\frac{4\nu}{\pi}(1-x^2+y^2)+2\nu h_0\left\{1-\left(\frac{x-l_0}{x_0-l_0}\right)^2\right\} \tag{19}$$

In these expressions, we have assumed that the Mach number of the uniform flow is nearly critical, that is, $x_0, l_0, h_0\ll 1$, and retain only the terms of the lowest order of these quantities. Also, inspecting these conditions, we find that

$$l_0 \sim x_0\,, \qquad h_0 \sim x_0^2 \tag{20}$$

provided that x_0, h_0, l_0 contributed simultaneously to the value of $u_o^{(2)}$ on the dividing curve. From the above relations (20) we can show that the shape of the sonic line of our solution is similar to that of the continuous solution $w_o^{(1)}$. Thus, the above relation seems to be plausible from the physical viewpoint, for it is expected that the shape of the sonic line does not change suddenly even if a shock wave appears. We assume, therefore, the above relation (20), and take the lowest order of x_0.

Further, since $l_0 \ll 1$, the trace of the shock wave can be safely replaced by the circular arc BB′, so that the problem reduces to a very simple form, that is, to obtaining a harmonic function, the value of which is given over a small circle and which becomes 0 at ∞. The condition on the profile is satisfied automatically by the symmetry of the solution.

The point (x, y) on the dividing circle is represented, by the assumption (20), as follows,

$$\left.\begin{aligned} x &= \frac{l_0+x_0}{2} + \frac{l_0-x_0}{2}\cos\theta \\ y &= \frac{l_0-x_0}{2}\sin\theta \end{aligned}\right\} \tag{21}$$

where $0 \leq \theta \leq 2\pi$. Inserting (21) into Eqs. (18) and (19), these conditions are rewritten as follows:

on the unit circle of the ζ-plane,

$$u_o^{(2)} = u_o^{(2),1} + u_o^{(2),2} \tag{22}$$

$$\begin{aligned} u_o^{(2),1} = 1 &- \frac{4\nu}{\pi} + \frac{\nu}{\pi}(l_0+x_0)^2 + \frac{5}{4}\nu h_0 \\ &+ \left\{\frac{2\nu}{\pi}(l_0^2-x_0^2) + \nu h_0\right\}\cos\theta \\ &+ \left\{\frac{\nu}{\pi}(l_0-x_0)^2 - \frac{\nu h_0}{4}\right\}\sin 2\theta \\ &\qquad 0 \leq \theta \leq 2\pi \end{aligned} \tag{23}$$

$$u_o^{(2),2} = \begin{cases} -4\nu h_0 + 4\nu h_0 \dfrac{\theta}{\theta_0} & 0 \leq \theta \leq \theta_0 \\ 0 & \theta_0 \leq \theta \leq 2\pi - \theta_0 \\ -4\nu h_0 + 4\nu h_0 \dfrac{2\pi-\theta}{\theta_0} & 2\pi - \theta_0 \leq \theta \leq 2\pi \end{cases} \tag{24}$$

where

$$\zeta = \left(z - \frac{l_0+x_0}{2}\right) \bigg/ \left(\frac{l_0-x_0}{2}\right) \tag{25}$$

the analytic function $w_o^{(2)}$ which satisfies the above conditions is easily obtained by the formula in the theory of functions:[7)]

$$\begin{aligned} w_o^{(2)} = 1 &- \frac{4\nu}{\pi} + \frac{\nu}{\pi}(l_0+x_0)^2 + \frac{5}{4}\nu h_0 \\ &+ \left\{\frac{2\nu}{\pi}(l_0^2-x_0^2) + \nu h_0\right\}\frac{1}{\zeta} \\ &+ \left\{\frac{\nu}{\pi}(l_0-x_0)^2 - \frac{\nu h_0}{4}\right\}\frac{1}{\zeta^2} \\ &+ \frac{2\nu h_0}{\pi}\int_0^{\theta_0}\left(-1+\frac{\theta}{\theta_0}\right)\frac{\zeta e^{i\theta}+1}{\zeta e^{i\theta}-1}d\theta \\ &+ \frac{2\nu h_0}{\pi}\int_{2\pi-\theta_0}^{2\pi}\left(-1+\frac{2\pi-\theta}{\theta_0}\right)\frac{\zeta e^{i\theta}+1}{\zeta e^{i\theta}-1}d\theta \end{aligned} \tag{26}$$

It is clear that this solution already satisfies the conditions (A), (C) and (D). However, the first term (constant) as well as the integral terms do not vanish in general at ∞, contrary to the condition (B). Because the contributions from the integral terms are $O(x_0^3)$ and may be neglected, the condition (B) then requires the first constant term to vanish, i.e.

$$1 - \frac{4\nu}{\pi} + \frac{\nu}{\pi}(l_0+x_0)^2 + \frac{5}{4}\nu h_0 = 0 \tag{27}$$

On the other hand, from Eqs. (14), (16), (17) and (26), the condition that the velocity gradients of the inner and outer solutions must coincide at $(x_0, 0)$ is represented as follows:

$$\frac{16x_0}{\pi} + \frac{3h_0}{l_0 - x_0} = \frac{4h_0}{x_0 - l_0} \tag{28}$$

Also it is required, as already mentioned, that $v_i = v_o$ on the dividing circle. But, because two conditions (27) and (28) have already been assigned for three parameters x_0, l_0 and h_0, we can satisfy the condition: $v_i = v_o$ at only one point or in the mean on the circle. The latter procedure gives

$$\frac{4}{\pi}(l_0^2 - x_0^2) + h_0 = 0 \tag{29}$$

The same relation would also be obtained by satisfying the condition at the top of the circle ($\theta = \pi/2$). Hence, we shall adopt (29) as the third condition for determining the parameters x_0, l_0 and h_0.

Solving (27), (28) and (29), we obtain the following expressions for x_0, l_0, h_0:

$$\left.\begin{aligned} &x_0=-\frac{7\sqrt{\pi}}{\sqrt{216}}\sqrt{\frac{4\nu/\pi-1}{\nu}}, \qquad l_0=-\frac{3}{7}x_0 \\ &h_0=\frac{160}{216}\frac{4\nu/\pi-1}{\nu} \end{aligned}\right\} \tag{30}$$

§ 5. Results and Discussions

The manner of variation of x_0, l_0 and h_0 with Mach number is shown in Table I, for the case when the thickness ratio of the profile is 0.06.

Table I.

M_∞	x_0	l_0	h_0
0.85	positive	negative	negative
0.8526	−0.0438	0.0188	0.00199
0.853	−0.0772	0.0331	0.00620
0.854	−0.1266	0.0543	0.01666
0.856	−0.1897	0.0813	0.03742
0.86	−0.2745	0.1176	0.07892

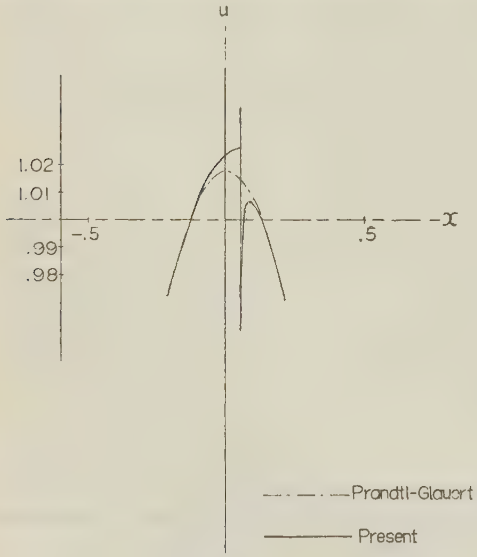

Fig. 2.

When the Mach number of the uniform flow is below the critical value corresponding to Prandtl-Glauert solution (0.8524), all x_0, l_0 and h_0 take values without any physical meaning. But as soon as the Mach number exceeds this critical value, these parameters become significant and their absolute values increase with Mach number. This is a very remarkable feature of our result, which gives a new meaning to the concept of the usual critical Mach number. The rapid change of l_0 near the critical Mach number also agrees qualitatively with Spreiter's results.

Fig. 2 gives the velocity distribution over the profile for the case $t=0.06$, $M_\infty=0.854$, where the neighbourhood of the supersonic region is magnified in order to reveal the fine structure of the distribution. Comparing our result with Spreiter's, we find that in our case the velocity changes very rapidly behind the shock wave and becomes partly supersonic. Especially the velocity gradient becomes infinite, immediately behind the shock wave, suggesting that it is a singular point of the solution. This is due to the fact that we have used the normal shock condition to obtain u_o on the back side of the shock wave. Let us now discuss this point in some detail.

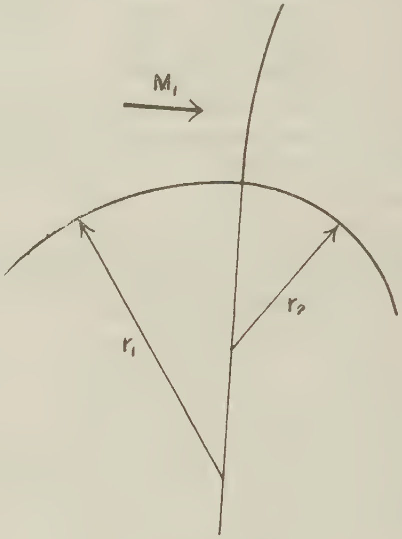

Fig. 3.

From the irrotationality $\partial v_i/\partial x=\partial u_i/\partial y$, $\partial v_o/\partial x=\partial u_o/\partial y$ and the shock condition $1-u_i=u_o-1$, we obtain

$$-(\partial v_i/\partial x)=\partial v_o/\partial x \tag{31}$$

In the thin-wing expansion method, $\partial v/\partial x$ represents the curvature of the profile, so that Eq. (31) represents the fact that there must be a discontinuity of the curvature of the profile through the shock wave. This result is clearly of general nature and can be applied to the case of Spreiter and Gullstrand. Their results seem at first sight to be plausible because of the moderate behaviour of velocity distribution behind the shock wave. However, this is wholly due to their erroneous assumption for the form of the velocity distribution normal to the aerofoil surface immediately after the shock wave. The velocity gradient there must be infinite as in the present case. C. C. Lin[3] discussed in an exact manner the case of the normal shock wave on the curved profile, and deduced the following relation,

$$\frac{2}{\gamma+1}\left\{M_1^2-\frac{\gamma+3}{2}\right\}\cdot\left(-\frac{1}{r_1}\right) - \frac{1}{\gamma+1}\left\{\frac{2}{M_1^2}+(\gamma-1)\right\}\cdot\left(-\frac{1}{r_2}\right)=0 \qquad (32)$$

where M_1 is the Mach number in front of the shock wave, r_1 and r_2 are the radii of curvature of the profile in front and after the shock wave respectively (Fig. 3). In this equation, if we assume $M_1 \simeq 1$, we obtain $r_1 \simeq -r_2$, which is equivalent to the relation (31).

From the above discussions, it is concluded that there can exist no high subsonic flow with shock waves past a profile having continuous curvature. The only exceptional case is that of zero curvature, e.g. the case of flow past a wedge or a diamond profile. The former case has recently been discussed by H. Yoshihara.[8] The existence of approximately normal shock waves observed in experiments seems to be due to the interference of the shock wave and the boundary layer. Full explanation of the phenomenon will be the subject of the future work.

Acknowledgement

The writer wishes to express his cordial thanks to Professor Isao Imai for his hearty guidance and encouragements throughout this work. He is also indebted to Professor Ko Tamada and Professor Hidenori Hasimoto for their encouragements and kind inspection of the manuscript of this paper.

References

1) H. W. Emmons: NACA Tech. Note no. 1746 (1948).
2) T. R. Gullstrand: KTH-Aero. Tech. Note no. 20 (1952).
3) C. C. Lin and S. I. Rubinov: J. Math. Phys. **27** (1948) 105.
4) K. Oswatitsch: *Gasdynamics* (Academic Press, New York, 1956) 468.
5) K. Oswatitsch: Z. angew. Math. Mech. **30** (1950) 17.
6) J. R. Spreiter and A. Alksne: NACA Tech. Note no. 1217 (1955).
7) M. Tsuji: *Kansuron* (*Theory of Functions*), vol. **2** (Asakura Press, Tokyo, 1952) 36.
8) H. Yoshihara: J. Aero. Sci. **24** (1957) 661.

JOURNAL OF THE PHYSICAL SOCIETY OF JAPAN, Vol. 14, No. 5, MAY, 1959

Flash X-Ray Radiography for the Density Measurement in a Hypersonic Air Flow

By Fumio TAMAKI
Institute of Industrial Science, University of Tokyo
and KIM, Chul-Soo
Department of Physics, Faculty of Science, University of Tokyo

(Received January 30, 1959)

Soft X-ray radiograph method using a flash X-ray tube was developed as a means of measuring air density in a hypersonic flow in a shock tube. The method was applied to the measurement of the density distribution between a circular cylinder and the detached shock wave at a free-stream Mach number of 5.5 and a free-stream density of about one-tenth of the normal atmosphere. Results suggest that the method is promising for the investigation of hypersonic flow fields, especially for the measurement of narrow regions with steep density gradients, because the effect of refraction can be neglected without error in the wavelength range of X-rays.

§ 1. Introduction

The technique most frequently used for the quantitative measurement of density in a high-speed air flow is the optical interferometry. The method is simple and has sufficient accuracies in most applications to the studies of transonic and supersonic flows in wind tunnels and shock tubes. However, it has certain disadvantages inherent in itself. Due to the refraction of light rays passing through the testing medium, the accuracy decreases when the measurement is made over a long path length in the neighbourhood of a model surface or in the region with a steep density gradient. Furthermore, the sensitivity of the method decreases seriously at low air density.

An alternative method which utilizes the absorption of soft X-rays has been introduced by Arnold.1) In his method, a narrow beam of X-rays normal to the direction of the flow is used, and the intensity of the transmitted X-rays as measured by an ionization chamber furnishes a measure for the integrated gas density across the test section. Considerable improvements in the techniques have been made by Winkler,2) Weltman, Fairweather and Papke,3) and Dimeff, Hallett and Hansen,4) using Geiger-Müller counters and improved X-ray tubes. A general survey of the X-ray techniques has also been made by Winkler.5)

In comparison to the usual optical methods, refraction and diffraction phenomena can be neglected with X-rays because of the small deviation of the index of refraction from unity and the short wavelength. Moreover, the method can be used at fairly low density if the wavelength of the X-rays is sufficiently long. Therefore, the method is considered to be particularly useful for the studies of such phenomena as occur near the body nose or within the boundary layer in a hypersonic, low-density air stream.

As to the technique of obtaining absorption data of a flow field, it is usual to make point-by-point measurements by moving the X-ray tube and the receiver. An alternative way is the so-called radiography, that is to photograph a certain portion of the flow field by the transmitted X-rays and measure the film density by a photodensitometer. This method has been proposed by Weltman, Fairweather and Papke in Ref. 3. Main difficulties in this procedure are that the photographic film is less sensitive to small X-ray intensities than ionization chamber or counter, and the production of strong X-rays of long wavelengths is a very difficult matter. Recently, we have noticed that the radiograph method with a continuously operating X-ray tube has been used successfully by Stine, Wagoner and Lugn6) for the studies of the transonic flow about a sharp leading edge.

In the present work, a technique for the soft X-ray radiography using a flash X-ray tube has been developed and applied to the hypersonic flow in a shock tube. The flash tube is of the type which has been developed by Prof. M. Hirata and Dr. F. Tachibana.[7] Air density of the free stream treated in our experiments is about one-tenth of the normal atmosphere, and the path length is 5.8 cm. In the X-ray range suitable for such measurements, a large portion of the X-rays produced in the flash tube is absorbed in its window material, so that at present a single flash is not sufficient for obtaining sufficient film densities. Accordingly, photographs are taken by repeating two or more times the operations of both the X-ray tube and the shock tube. However, the authors consider that the production of stronger X-rays by a single flash will be possible by improving the design of the X-ray tube and the discharge circuit.

§ 2. Theory of Density Determination by X-Ray Radiography

Theory of density determination by X-ray radiography has been developed by Weltman and others in Ref. 3. Outlines of the theory will be given in the following.

Assume that the X-rays are emitted conically from a point source, and after passing through an absorbing medium, reach a photographic film situated at a distance r from the source. Then the ratio of the intensity I of the X-rays remaining after absorption to the intensity I_0 of the X-rays incident on the absorber is expressed as

$$\frac{I}{I_0}=\frac{cA}{4\pi r^2}e^{-B\rho L} \qquad (1)$$

where B is the total mass absorption coefficient, ρ the density of the absorber, L the path length in the absorber, A the cross-sectional area of the X-ray beam at the distance r, and c a factor which accounts for the absorption before entering and after leaving the absorber.

Sensitivity in density measurement is given by the minimum detectable density change $\Delta\rho$ divided by the density ρ. This ratio can be calculated from Eq. (1) as

$$\frac{\Delta\rho}{\rho}=-\frac{\Delta I}{IB\rho L} \qquad (2)$$

where ΔI is the minimum detectable change in the X-ray intensity.

The characteristic curve of a photographic material, representing the film density as a function of the logarithmic exposure, is a straight line over a considerable portion. The equation of this straight line is expressed as

$$D=\gamma\{\log(I/A)+\log t-\log i\} \qquad (3)$$

where D is the film density, γ the slope of the line, t the exposure time and i the inertia of the film.

Substituting Eq. (1) into Eq. (3), we have

$$\rho=-\frac{D}{0.434\gamma BL}+K \qquad (4)$$

where

$$K=\gamma\left(\log\frac{I_0c}{4\pi r^2}+\log t-\log i\right)\Big/(0.434\gamma BL) \qquad (5)$$

is a constant for a given experimental arrangement and exposure time.

From Eq. (4), the sensitivity in air-density measurement is written as

$$\frac{\Delta\rho}{\rho}=-\frac{\Delta D}{0.434\gamma B\rho L} \qquad (6)$$

where ΔD is the minimum detectable change in film density. This equation shows that a high sensitivity can be obtained when the total mass absorption coefficient is large.

Total mass absorption coefficient is expressed by the empirical relation

$$B=CZ^4\lambda^3+\sigma(Z,\lambda) \qquad (7)$$

The first term accounts for the true absorption and the second term for the scattering. In the first term, C is a constant which changes its value at the critical absorption wavelengths, Z is the atomic number of the absorbing element and λ is the wavelength of the X-rays. As mentioned by Winkler,[5] the above formula represents the value of B for air with fair accuracy up to 5 Å, but gives too large values for longer wavelengths, and the formula of Victoreen,[8]

$$B=(C'\lambda^3-D'\lambda^4)+\sigma(Z,\lambda) \qquad (8)$$

is better for wider range of wavelengths. Here C' and D' are constants which may be calculated from the atomic energy states of the absorbing element.

The scattering term $\sigma(Z,\lambda)$ increases slowly with Z and λ. However, in the wavelength range of soft X-rays, σ is negligible compared with the first term.

In our experiments, X-rays with a continuous spectrum are used. In this case, the effective wavelength is controlled by the operating voltage of the X-ray tube. When the anode voltage is V kilovolts, the shortest wavelength in Ångstrom unit is expressed by the formula

$$\lambda_0 = 12.405/V \qquad (9)$$

and the effective wavelength λ_{eff} is approximately equal to $1.3\lambda_0$, so that we have

$$\lambda_{\text{eff}} \fallingdotseq 16.13/V \qquad (10)$$

It can be concluded from Eqs. (6), (7) and (10) that a high sensitivity in air-density measurement can be realized by operating the X-ray tube at a sufficiently low voltage.

§ 3. Shock Tube and Flash X-Ray Tube

The shock tube used in the experiments is the same type as previously used by the present authors.[9),10)] The schematic diagram of the tube is shown in Fig. 1. The pressure in the high pressure chamber is raised to 12 atms by supplying the air from a reservoir, the low pressure chamber is evacuated to the pressure of 2 mm Hg, and a cellophane diaphragm separating these chambers is ruptured by a steel needle installed in the high pressure chamber. Then the air in the high pressure chamber expands through the divergent nozzle in the low pressure chamber, and a quasi-steady flow of Mach number of 5.5 is obtained at the test section. Duration of the uniform flow is about 1 millisecond, and the density of this flow is $1.0\times10^{-4}\,\text{g/cm}^3$.

The flash X-ray tube is shown in Figs. 1 and 2. Photo. 1 shows its parts disassembled, and Photo. 2 shows the tube attached to the shock tube wall.

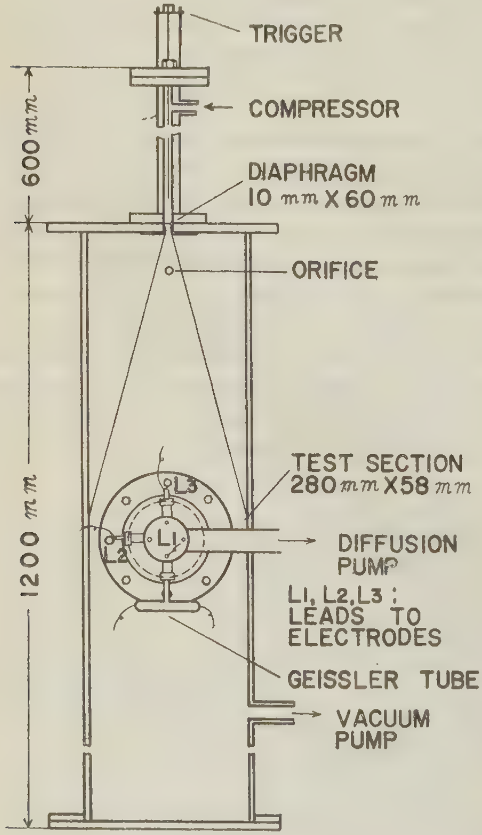

Fig. 1. Shock tube and X-ray tube.

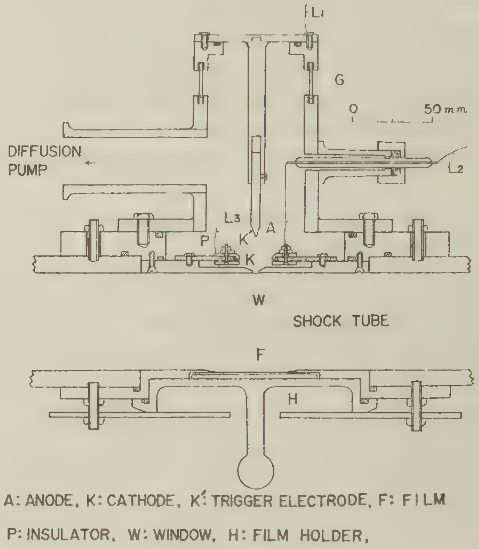
L1
G
0
50 mm
DIFFUSION PUMP
L2
L3
A
P
K'
K
W
SHOCK TUBE
F
H
A: ANODE, K: CATHODE, K': TRIGGER ELECTRODE, F: FILM
P: INSULATOR, W: WINDOW, H: FILM HOLDER,

Fig. 2. X-ray tube.

The anode A is made of a tungsten rod of 6 mm diameter, its end being sharpened to a 30° total-angle cone. Two ring plates of stainless steel are used as the cathode K and the trigger electrode K′. They are set on each side of an insulator plate P of polyetrafluoroethylene. Inner edges of the electrode plates face each other with a clearance of 0.1 mm, so as to form a ring-shaped spark gap.

The distance between the anode and the plane of the cathode is adjusted to 20 mm. A voltage of 1.65∼2.75 kV is applied to the anode, and about 4 kV is applied to the trigger electrode. Electric circuits are shown in Fig. 3.

A discharge between the trigger electrode and the cathode through the ring-shaped gap is made to occur at a desired instant by the aid of a timing device shown in Fig. 3. This trigger discharge induces the main discharge between the anode and the cathode. With this discharge, soft X-rays of high intensity are emitted from the anode during a very short time interval.

The timing device consists of an auxiliary spark gap S in the trigger discharge circuit and a thyratron circuit for triggering a spark discharge through S. This circuit has an automobile ignition coil in the plate side of the thyratron and a metallic contact element in the grid side. This contact element, utilizing the deformation of a thin aluminium foil by pressure, is attached to the end of a glass tube which is connected to the orifice on the shock tube wall (see Fig. 1), and made to act by the pressure wave propagating through the glass tube.

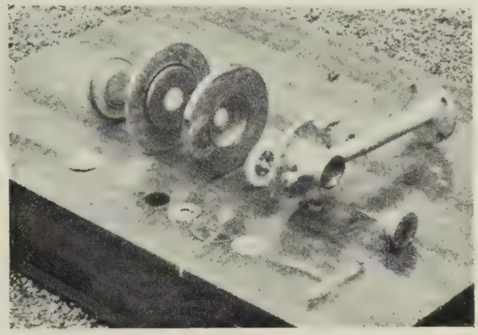

Photo. 1. Parts of X-ray tube.

Photo. 2. X-ray tube mounted on shock tube wall.

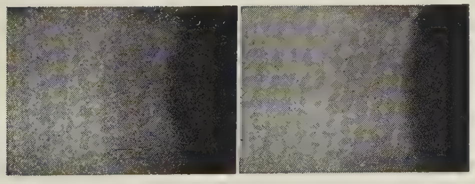

Photo. 3. Radiographs of flow with detached shock wave, taken by: (a) two flashes at $V_a=2.75$ kV; (b) eight flashes at $V_a=1.65$ kV.

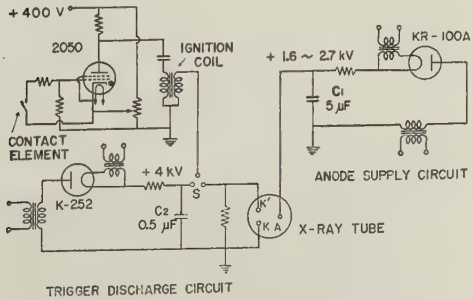

Fig. 3. Electric circuits.

The X-ray tube has a window W of 5 mm diameter, and a thin cellophane of 2 micron thickness is used as a window material. As the discarges in the tube are accompanied with the radiation of visible rays, it is required for the window material to pass only the X-rays and cut off all the visible rays. For this purpose, special black ink "Cello-Colour 7694 Black", made by Toyo Ink Co., is painted on the cellophane. This window permits higher transmission of soft X-rays than other materials, such as beryllium or aluminium foils.

Since the window cannot keep a high vacuum of the tube permanently, it is evacuated continuously to the pressure below 10^{-5} mm Hg by using a rotary and an oil diffusion pump. The latter is seen in the right part of Photo. 2.

§ 4. Experiments and Results

We attempted to apply the above-mentioned apparatus to the measurement of the hypersonic flow past a circular cylinder, in particular, to the measurement of the density distribution between the detached shock and the nose of the cylinder.

In order to determine the wavelength suitable for our purpose and to obtain the relation betweent the air density in the test section and the photographic density of the film exposed to the X-rays transmitted through the test section, low pressure chamber of the shock tube was evacuated to various values of pressure between 20 and 450 mm Hg, and for each case, the film held on the shock tube wall was exposed to the X-rays emitted from the flash tube.

The effective wavelength of the X-rays was varied by varying the anode voltage V_a. Trigger electrode voltage V_t, capacitances C_1 and C_2 and the distance s from the anode to the plane of the cathode-ring were varied systematically until the maximum intensity of the X-rays could be attained. It was shown by these experiments that, (1) a sufficient sensitivity could be obtained with V_a below 3 kV; (2) the quantity of the X-rays produced by a single discharge was a little insufficient, so that two or more discharges were necessary for obtaining film densities sufficient for photodensitometry; (3) the most satisfactory results were obtained with $V_t = 4$ kV, $s = 20$ mm, $C_1 = 5\ \mu$F and $C_2 \fallingdotseq 0.5\ \mu$F for the case of $V_a = 1.65 \sim 2.75$ kV. The use of larger capacitances might increase the X-ray intensity, but it was not possible in the present tube, because, when C_2 was large, the trigger discharge was followed by a detrimental discharge between the cathode and some other metallic parts in the tube due perhaps to an electric oscillation in the discharge circuit, and this made the intensity of the X-rays emitted from the anode quite indefinite. The authors consider that this can be avoided by improving the design of the tube and minimizing the inductance in the trigger discharge circuit, and then it will be possible to produce X-rays strong enough for taking a photograph by a single flash.

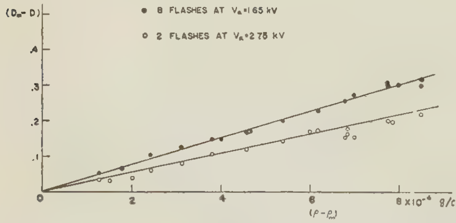

Fig. 4. Relation between air density and film density.

After these preliminary experiments, the apparatus was used for the measurement of the density distribution between the detached shock and the nose of a circular cylinder, placed in the hypersonic flow established in the shock tube. Mach number M_∞ of the free stream as determined from schlieren observation of Mach waves was 5.5, and the corresponding density ρ_∞ of the free stream was estimated to be 1.0×10^{-4} g/cm³. The diameter of the cylinder was 6 mm, and the span was 55 mm. Clearances of 1.5 mm were left between both ends of the cylinder and the tube walls in order to avoid the end effects due to the shock-boundary-layer interaction. Reynolds number based on the cylinder diameter and the free-stream condition was 1.6×10^5. Operations of both the shock tube and the X-ray tube were repeated two or more times for obtaining a radiograph.

Radiographs of the flow with a detached shock wave are shown in Photos. 3(a) and (b). The one was obtained by two flashes at $V_a = 2.75$ kV and the other by eight flashes at $V_a = 1.65$ kV. Following Eq. (10), these values of V_a correspond to the wavelengths of 6 and 10Å, respectively.

Fig. 4 shows calibration curves which represent the relation between air density and film density for these cases. Both quantities are referred to the free-stream values ρ_∞ and D_∞. Here, D_∞ was determined by evacuating the test section to the density ρ_∞.

Fig. 5 shows the density distribution behind the detached shock wave. Interferometric results obtained by the junior author for $M_\infty = 1.8$ and 4.0 are also reproduced in the

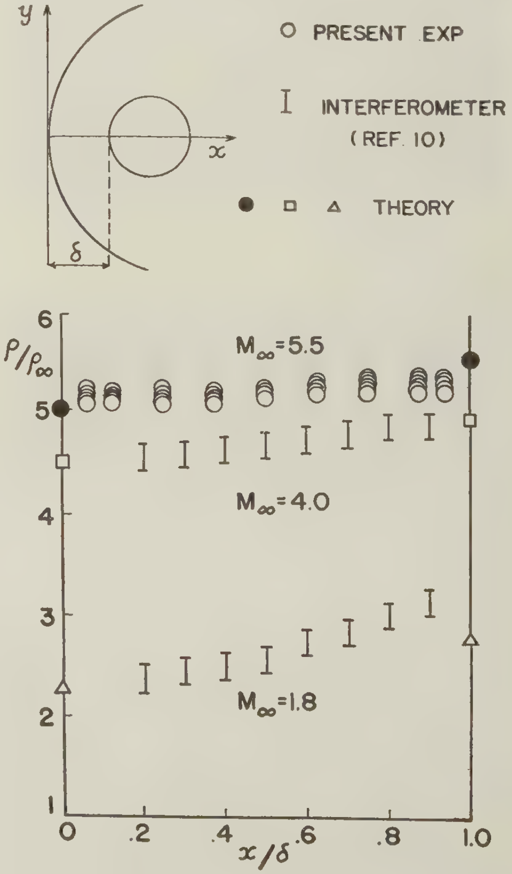

Fig. 5. Density distribution between shock wave and stagnation point.

figure. It can be seen that the present method gives good quantitative density data.

The stand-off distance δ between the shock wave and the stagnation point is shown in Fig. 6, together with the previous data obtained by optical methods.

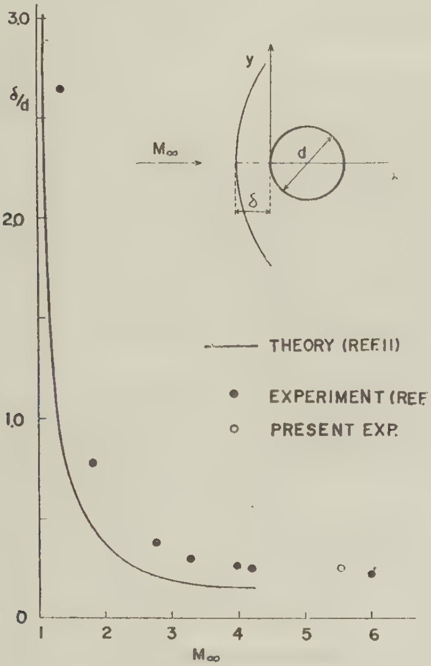

Fig. 6. Stand-off distance between shock wave and stagnation point.

As photographic materials, "Fuji High Speed X-Ray Film, Type 200" and "Fuji Developer, Rendol" were used, developing time of 5 minutes being strictly kept throughout the experiments. Measurements of film densities were made by using a photo-cell type microphotometer with a slit pick-up of 0.01 mm width.

It is concluded from these experiments that the present radiograph method is very promising for the density measurement in low-density hypersonic flows, especially for the investigation of a narrow region with a steep density gradient, such as the region near the body nose or the boundary layer.

The authors wish to express their cordial thanks to Prof. Hirata and Dr. Tachibana for their valuable advices in the course of the present experiments.

References

1) G. Arnold: Aerodynamisches Inst., Peenemünde Heeresversuchsstelle, Archiv. 66/124 (1944).
2) E. M. Winkler: NOL Memo. **10** (1949) 118.
3) R. N. Weltman, S. Fairweather and D. Papke: NACA Tech. Note 2406 (1951).
4) J. Dimeff, R. K. Hallett and C. F. Hansen: NACA Tech. Note 2845 (1952).
5) E. M. Winkler: *Physical Measurements in Gas Dynamics and Combustion*, ed. by R. W. Ladenberg et al. (Princeton Univ. Press, 1954) art. A, 6.
6) H. A. Stine, C. B. Wagoner and A. L. Lugn, Jr.: Paper for Presentation at the 1958 Summer Meeting of the American Physical Society at the University of British Columbia, Aug. 1958.
7) F. Tachibana: Nippon Buturi Gakkai-si **10** (1956) 404 (in Japanese).
8) J. A. Victoreen: J. Appl. Phys. **19** (1948) 855; **20** (1949) 1141.
9) F. Tamaki: J. Phys. Soc. Japan **11** (1956) 434.
10) C. S. Kim: J. Phys. Soc. Japan **11** (1956) 439.
11) K. Hida: J. Phys. Soc. Japan **8** (1953) 740.

Journal of the Physical Society of Japan, Vol. 14, No. 5, May, 1959

On the New Reverberation Chamber with Nonparallel Walls (Studies on the Measurement of Absorption Coefficient by the Reverberation Chamber Method, II)

By Kozi Sato and Masaru Koyasu

Kobayasi Institute of Physical Research, Kokubunji, Tokyo, Japan

(Received August 18, 1958)

The details of the new reverberation chamber are given. It has a volume of 513 m^3 and is surrounded by nonparallel walls. The results of model room experiments previously reported have been used to determine the shape and volume of this chamber. At 500 cps., the reverberation time of empty chamber was 22 seconds. The position of the microphone and the sound absorbing material did not affect the reverberation time of this chamber. This fact would show that the sound field of this chamber would fulfill the requisite for the diffuse sound field which is the premise of the reverberation chamber method.

§ 1. Introduction

From the fundamental researches described in the Report I$^{1)}$, it has come to be clear that to make the shape of a reverberation chamber irregular is one of the effective means to get diffuse sound field which is indispensable for a reverberation chamber. Furthermore, relation between the size of the chamber and the uniformity of the sound field has been investigated. Based upon the results of these researches, a new reverberation chamber was constructed. This chamber has a volume of 513 m^3 and is surrounded by nonparallel walls.

We inquired into the various characteristics of this chamber without sound absorbing materials. Further we pursued the effects of the warble tone and the loudspeaker upon the above characteristics. It was experimentally proved that the reverberation time of the chamber was longer than 20 seconds at 500 cps. and that the fluctuation of repeatedly measured reverberation time under the same condition was quite small. It was also confirmed that this was true in any part of the chamber.

However, when a sound absorbing material is put into the chamber to measure the absorption coefficient, the sound field would be different from that when the chamber is empty. Thus, special regard has been paid to the position of the sample material and the arrangement of the microphone in the conventional reverberation chambers.

The effect of the several factors affecting the sound field of our new reverberation chamber was investigated. As for the sample materials, we selected fibrous acoustic tiles and mineral wool board as typical examples from the viewpoint of the magnitude of absorption coefficient and its frequency characteristics. The results of these experiments showed that the position of the microphone and the sample material did not affect the absorption coefficient. This fact would show that the sound field of this chamber would fulfill the requisite for the diffuse sound field which is the premise of the reverberation chamber method.

§ 2. Construction of the Reverberation Chamber

2.1. Design and construction of the reverberation chamber

Since the irregular chamber used in the three-dimensional model room experiments was found more suitable as a reverberation chamber than a rectangular one, we designed a chamber after this irregular model. Next, the dimensions of the chamber was determined by consideration of the lowest frequency to be measured, which was around 60 cps. in this case. For this purpose, it was decided to make the frequency of 2000 cps. in the model chamber correspond to 100 cps. in the actual chamber. Accordingly the length of each side of the chamber was made 20 times as long as that of the model chamber, and thus the chamber of about 500 m³ became necessary. On the other hand, if the volume of the chamber is V, and the surface area is S, the number of normal modes $\varDelta N$ in the frequency range between ν and $\nu+\varDelta\nu$ is approximately given by[2)]

$$\varDelta N \doteqdot \left(\frac{4\pi V}{c^3}\nu^2+\frac{\pi S}{2c}\nu\right)\varDelta\nu\,.$$

If the number of normal modes is calculated in the rectangular chamber (the ratio of the sides is 1.00 : 0.80 : 0.64) under the conditions of $V=500\ \mathrm{m}^3$, the number of normal modes included within a 1/3 octave band with center frequencies of 60 and 100 cps. are 9.5 and 38.4 respectively. This shows that the chamber dimensions as large as these are necessary from the viewpoint of the number of normal modes.

Next, the finish of the interior of the reverberation chamber offers an important problem as to the accuracy in measurement. Conventionally, the wall surfaces are finished with concrete (plastered or painted), parquet tiles, etc. We decided to adopt the polished concrete, taking into consideration the fact that its sound absorption is small and its maintenance is easy due to small quality change caused by time element.

Table I. Details of the reverberation chamber

Volume	513 m³
Surface area	382 m²
Shape	Nonparallel Walls
Wall thickness	40 cm
Wall surface material	Steel-framed concrete with polished concrete

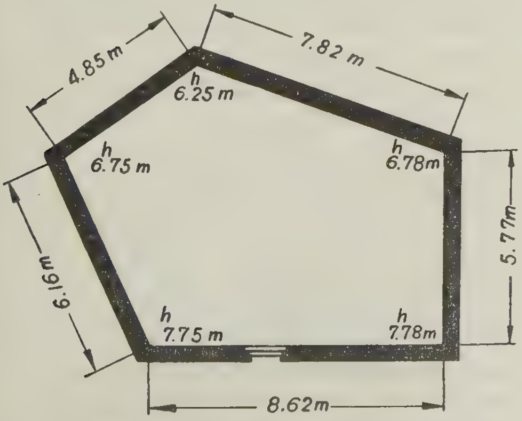

Fig. 1. Plan of the reverberation chamber. h shows the height of each corner.

Important data for this chamber which was made so as to match the previously mentioned conditions are shown in Table I. Dimensions of the chamber is given in Fig. 1 and photo Fig. 2 shows the interior of the chamber.

2.2. Reverberation time measuring apparatus

The most important section of the rever-

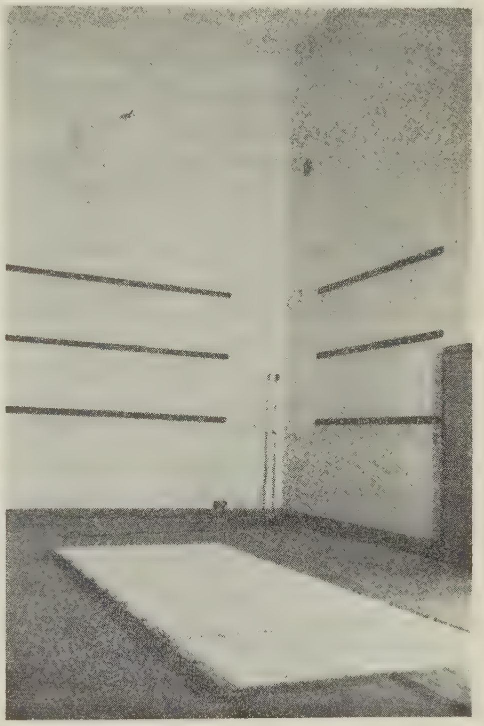

Fig. 2. Interior of the reverberation chamber.

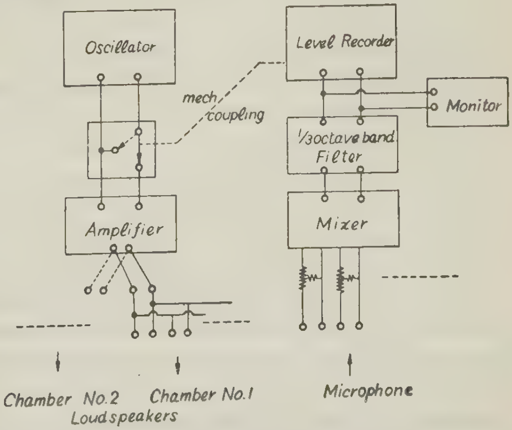

Fig. 3. Block diagram of the apparatus for the measurements of reverberation time.

beration time measuring apparatus is the one which measures or records the decay process of sound. Here, we used a high speed level recorder for this purpose. Furthermore, since the reverberation time to be measured is relatively long, the make and break of the simple mechanical contact point, which work in linkage with the level recorder, were adopted for the switching-on and -off of the oscillator. The block diagram of the measuring apparatus is shown in Fig. 3.

§ 3. Characteristics of the Empty Reverberation Chamber

3.1. Researches on measuring system

(i) *Characteristics of warble tone*

When the center frequency is ν_0, modulation swing $\pm\varDelta\nu$ and the modulation frequency α, the warble tone given by them has a spectrum consisting of $2\varDelta\nu/\alpha$ components lined up at intervals of α cycles within the range of $\nu_0\pm\varDelta\nu$[3]. If the dimensions of the chamber and the center frequency are given, the minimum permissible value of $\varDelta\nu$ is given by the condition that it should include sufficient number of normal modes to uniformize the sound field. Under the given conditions that ν_0 equals 100 cps. and the number of normal modes equals 30, an inequality $\varDelta\nu>9$ results. It was also found that if $\varDelta\nu$ is made larger, unevenness in absorption within the range becomes sometimes intolerable. In the present experiments, $\varDelta\nu$ was made 10 percent of center frequency at lower frequencies and 50 cps. at higher frequencies.

Next, for the purpose of exciting all the normal modes within the range, the interval α of spectrum offers a problem. In the chamber with sharp resonant characteristics (that is, long reverberation time), some of the normal modes are not excited unless the intervals are sufficiently small. On the other hand, if α is so small that one sweep takes too long a time, the normal modes at the far end of frequency range are considerably decayed, and accordingly it means little to use warble tone. Such being the case, α must be decided in connection with the reverberation time of the chamber. A conventional rule for the suitable range of α is given by an inequality $8/T>\alpha>4/T$[4]. However, as will be mentioned later, our reverberation chamber has far longer reverberation time than the ordinarily used ones, and consequently we thought it necessary to confirm the above inequality by the experiments as the first step.

An example of decay curves obtained by observing the variation with modulation frequency α is shown in Fig. 4. The reverberation time T was 22 seconds. When α became more than 8, fluctuation of sound pressure level in the steady state became small and minute changes on the way of decay were not observed. However, large undulations were seen over the whole decay curves. When α is small, the fluctuation in the steady state became large but the decay showed a perfectly logarithmic curve (The ordinate in the records is a decibel scale and so the ideally exponential decay is recorded as the straight line.) From these results, we came to the conclusion that the modulation frequency must be around $10/T\sim20/T$.

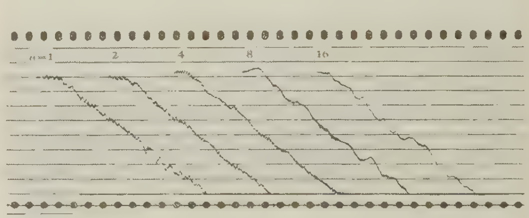

Fig. 4. Variation of decay curve with modulation frequency of warble tone.
$\nu_0=500$ c/s, $\varDelta\nu=30$ c/s

(ii) *Selection of loudspeakers*

A loudspeaker was selected by considering the following two points. That is, it has a sufficient power output so as to show at least the decay curve of 40 decibels before reaching the noise level, and also it is intended to decrease the added absorption due to the loudspeaker.

At first, we used a 25 cm cone type loudspeaker which was housed in a closed enclosure of $0.18\ \mathrm{m}^3$ cubical content. In this condition, the minimum resonant frequency of the loudspeaker is around 50 cps. There was observed an absorption around 100 cps. caused probably by the vibration of the closed enclosure panels. As a result, the decay curve showed a slight bend around this frequency and the reverberation times derived from the decay curves measured under the same conditions showed inconsistent values.

In the second experiment, a horn-speaker driver unit was used. It did not produce any trouble regarding the measurement of the decay curve at the frequencies higher than about 100 cps., though the power output was a bit insufficient. Further, the reverberation time showed about the same values in each experiment, and the reverberation time became remarkably longer, especially at frequencies below 300 cps.

Then the reverberation time was measured at 125 cps. with several types of loudspeakers.

Table II. Effects of loudspeaker on the reverberation time. $\nu_0=125$ cps., $\Delta\nu=15$ cps., $\alpha=1$.

Type of loudspeaker	Average of 10 measurements	Standard deviation
Horn-speaker unit	46.0 sec	0.35 sec
25 cm cone (naked)	40.0	0.90
25 cm cone (with buffle board of 50 cm × 50 cm)	39.0	1.2
20 cm cone (built in a closed cubical enclosure of 0.027 m³)	35.5	1.5
25 cm cone (built in a closed enclosure of 0.18 m³)	25.7	1.2

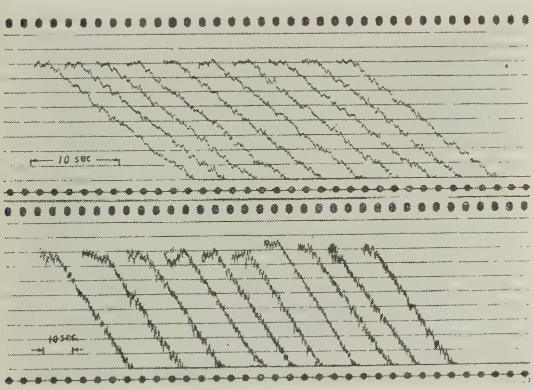

Fig. 5. Decay curve for empty chamber.
Upper: $\nu_0=500$ c/s, $\Delta\nu=30$ c/s, $\alpha=1$
Lower: $\nu_0=125$ c/s, $\Delta\nu=15$ c/s, $\alpha=1$

The results of these experiments are shown in Table II which includes the average and standard deviation of reverberation times for ten measurements. From these experiments, it was decided to use the horn-speaker driver unit in most experiments.

3.2. Reverberation time and sound pressure distribution

(i) *Reverberation time*

Firstly, we measured the reverberation time of the chamber, using the horn-speaker unit as the source of sound. The examples of the decay curves measured respectively at 500 and 125 cps. are shown in Fig. 5. These show an almost perfect logarithmic decay. Though we moved the microphone to five corners (including the position of the loudspeaker) and then to the center of the chamber, reverberation times were scarecely affected by the changes of the position of the microphone at any frequency between 125 and 4000 cps.

Table III. Reverberation time of empty chamber (measured in June 21, 1956)

Frequency	Average	Standard deviation
125 cps.	46.0 sec	0.5 sec
250	37.0	0.5
500	22.5	0.2_5
1000	14.0	0.1_0
2000	10.0	0.1_0
4000	5.3_8	0.0_7

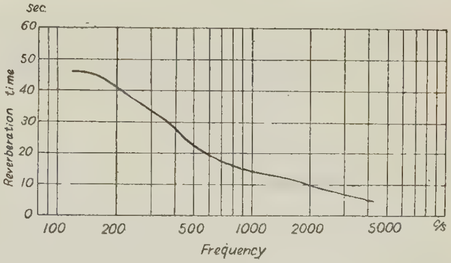

Fig. 6. Reverberation times for empty chamber.

Table IV. Sound pressure distribution in the chamber. Microphone position; M_1.

Frequency	Position of microphone					
	M_1	M_2	M_3	M_4	M_5	M_c
125 cps.	5 db	2 db	0 db	2 db	1 db	0 db
250	1	1	1	0	2	0
500	1	−1	−1	−1	0	0
1000	1	−2	−2	−1	0	0
2000	0	−1	−1	−1	0	0
4000	0	−2	−2	−2	0	0

Table III and Fig. 6 show the results. Each row in Table III shows the average and standard deviation of the reverberation times for five measurements. Reverberation times at high frequencies depend largely on weather conditions. We shall report the detailed results on this subject in the near future.

(ii) *Sound pressure distribution*

The unevenness in sound pressure level in the steady state which are measured at six positions used previously for measuring the reverberation time, is shown in Table IV. The marks which indicate the positions of the microphone in Table IV correspond to those of Fig. 7 and will be used in all subsequent experiments. The difference of sound pressure level in different positions is quite small, being about 2 decibels even at 125 cps. except at the position of the loudspeaker.

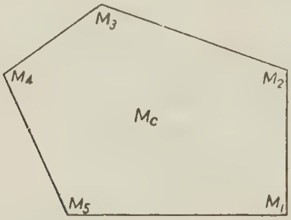

Fig. 7. Positions of microphone for reverberation measurements.

§ 4. Examinations of Various Factors that have an Influence upon the Measuremens of Absorption Coefficient

As was discussed in Report I, the sound field in the reverberation chamber must fulfill the assumption of the diffuse sound field. The effect of several factors which might affect the sound field, was investigated in our reverberation chamber. We used the fibrous acoustic tiles and mineral wool board, as the sample materials for these experiments. The former has a large absorption at low frequencies, and on the contrary, the latter has a large absorption at high frequencies.

4.1. Patterns of decay curves

First, we examined the influence upon decay curves of two kinds of sample materials up to 30 m² fixed respectively on three or four faces of the reverberation chamber. The decay was completely logarithmic in this case as in the empty chamber, within the frequency range of 125 to 4000 cps. Thus it was made clear that we could determine the reverberation time uniquely from this result. No extraordinary decay was observed at 200 cps. corresponding to the maximum absorption of the fibrous acoustic tiles and neither at high frequencies where a large absorption occured in case of the mineral wool. Fig. 8 are examples of respective decay curves.

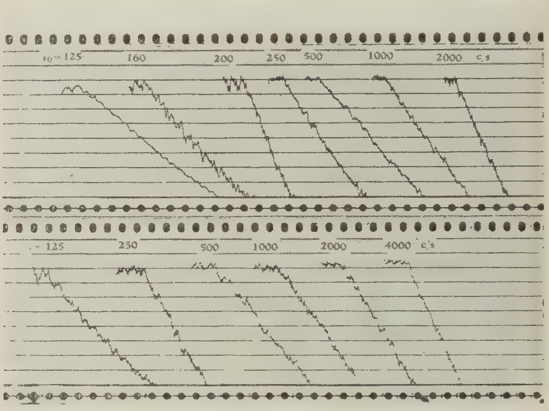

Fig. 8. Decay curves for the chamber, sample material present.
Upper: fibrous acoustic tiles, 10 m² (floor)
Lower: mineral wool, 16.5 m² (floor and two walls)

4.2. Effect of the position of the microphone

Using the sample material of 25 or 30 m², we investigated the effect of the position of the microphone on the absorption coefficient. The results are shown in Figs. 9 and 10. It was found that, for any sample material used, the position of the microphone exerted little influence upon the absorption coefficient. It is conspicuous that no effect upon absorption coefficient was found not only in any corner of the chamber but even in the center.

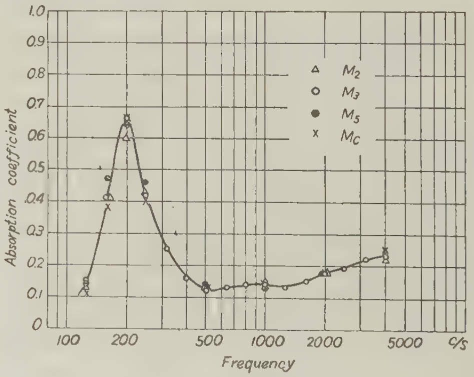

Fig. 9. Effect of microphone position on absorption coefficient of fibrous acoustic tiles. Sample area 25 m² (floor and two walls)

The uniformity of the reverberation time is the most important property of the reverberation chamber, and so we investigated this in detail. At the seven microphone positions which were arbitrarily chosen in the chamber, we measured twenty decay curves at each position. The average and standard deviation of reverberation times thus obtained are shown in Table V. Consequently, one microphone placed in an optional position may be enough for this kind of measurements.

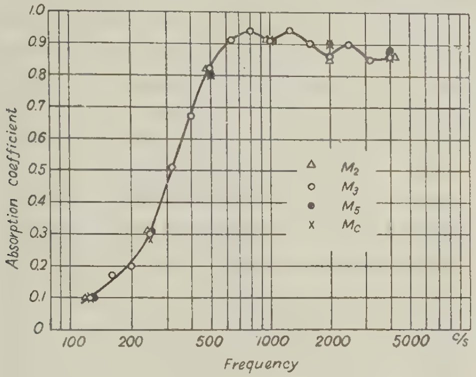

Fig. 10. Effect of microphone position on absorption coefficient of mineral wool. Sample area 30 m² (floor and three walls)

Table V. Reverberation time of the chamber when the mineral wool 10 m² was placed on the center of the floor. Seven microphone positions were chosen arbitrarily in the chamber and twenty decay curves were measured at each position.

Frequency	Average	Standard deviation
125 cps.	28.9 sec	0.97 sec
250	14.4	0.22
500	7.0_1	0.05
1000	5.8_0	0.07_2
2000	4.8_7	0.09_3
4000	2.8_3	0.08_4

4.3. Effect of area of the sample material

Next, placing the microphone in a fixed position, we examined the effect of the sample area upon absorption coefficient. Fibrous acoustic tiles having areas from 10 to 25 m² were fixed on three faces of the reverberation chamber. In case of mineral wool, the areas were from 3.3 to 30 m². The one with 30m² area was fixed on four faces of the chamber, the one with 3.3 m² area was fixed on the floor only, and all others were fixed on three faces of the chamber. The measured results of absorption coefficient are shown in Figs. 11 and 12.

In case of mineral wool, the absorption coefficient obtained for the sample area of 3.3 m² became larger than that of other sample areas for the frequencies above 500 cps. This is considered to be the area effect explained by Chrisler's experiments⁵⁾. However, when the area is reduced to this extent, the measuring accuracy falls off extremely. Therefore, we are furthering a more precise investigation. However, in either of sample materials, no significant difference in absorption coefficient was found against the area change of more than 10 m².

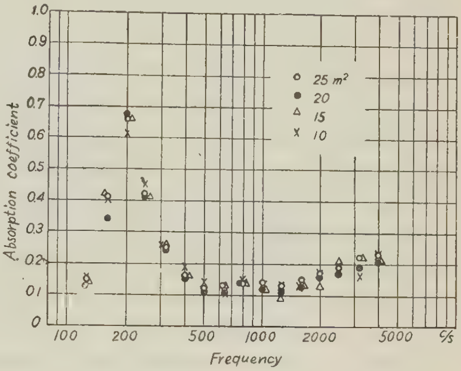

Fig. 11. Effect of sample area on absorption coefficient of fibrous acoustic tiles.

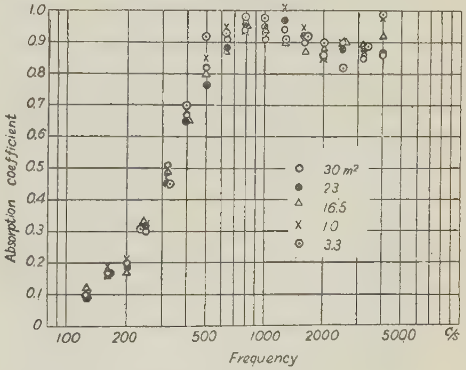

Fig. 12. Effect of sample area on absorption coefficient of mineral wool.

4.4. Effect of the mounting position of sample materials

We compared the absorption coefficients obtained respectively in three mounting positions of sample materials. In one case the sample material of 10 m² was separated on three faces, while in the other two cases the sample material of the same area was concentrated only on the floor (at floor center and edge). The results are shown in Figs. 13 and 14. We found out that, in case of areas in this experiment, the absorption coefficient was not affected by the mounting position of sample material at any frequency.

4.5. Case of a large quantity of sample material being placed only on the floor

When mineral wool of 30 m² was placed on the floor, decay curves showed a bend for the frequencies between 1000 and 2000 cps. So, we measured the decay curves for various areas, within the range of 400 to 4000 cps. at intervals of 1/3 octave. The results are shown in Fig. 15. As the area decreases, the range of frequency for which a bend takes place becomes narrower and it is not discernible below 16.5 m². We showed in the same figure the results obtained when the sample material was placed on three faces separately. In this case, the decay curves were all straight

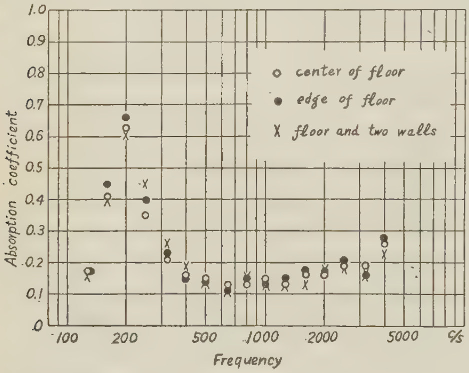

Fig. 13. Effect of sample position on absorption coefficient of fibrous acoustic tiles. Sample area 10 m².

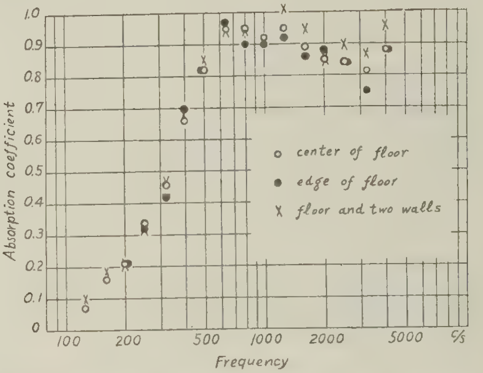

Fig. 14. Effect of sample position on absorption coefficient of mineral wool. Sample area 10 m².

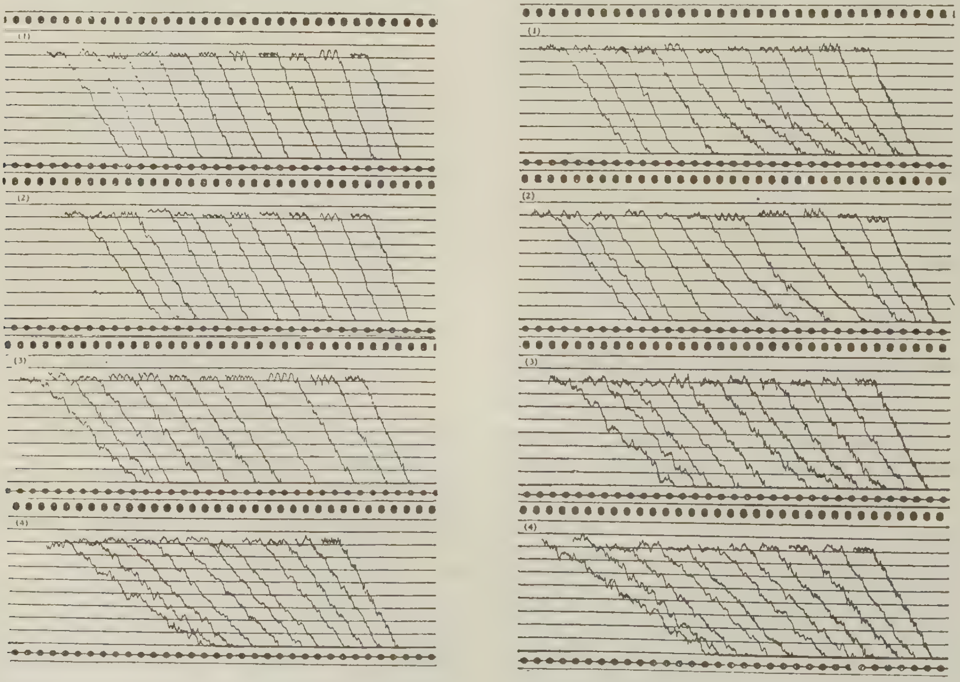

(a)

(b)

Fig. 15. Decay curves for various frequencies. Curves obtained by changing the frequency from 400 to 4000 cps. in $^1/_3$ octave step.

(a) mineral wool, floor and two walls.
(1) 30 m² (2) 23 m² (3) 16.5 m²
(4) 10 m²

(b) mineral wool, floors only.
(1) 30 m² (2) 23 m² (3) 16.5 m²
(4) 10 m²

lines, without any influence of area and frequency.

When the decay curve shows a bend, we can no longer assume that the sound field in the chamber is diffuse. However, we tentatively determined the absorption coefficient using the slope at the beginning part of the decay curve. Above 500 cps., where the absorption coefficient is large, it decreases as the area increases (Fig. 16). This is rather an expected matter, because the sound field in the chamber differs from that in the empty chamber.

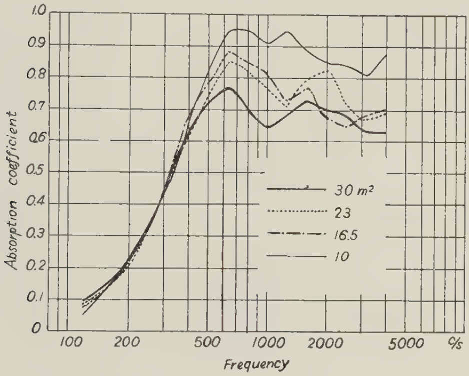

Fig. 16. Effect of sample area on absorption coefficient of mineral wool (sample placed on the floor only)

§ 5. Conclusion

The outline of our newly constructed reverberation chamber and the various characteristics of this chamber concerning the absorption coefficient measurements are presented. The shape of the chamber was decided by the experiments conducted with the model rooms described in Report I, in order to fulfill the essential condition of diffuse sound field. The volume of the chamber was decided upon 513 m³ for the purpose of measurements down to 60 cps.

Investigation on measuring system using the empty chamber, has shown that the absorption by the loudspeaker has a considerable effect on reverberation time at low frequencies and that the modulation frequency in warble tone has a considerable effect on decay curves. The reverberation time at 500 cps. is 22 seconds when the chamber is empty.

We investigated the various factors which were supposed to have influences upon the absorption coefficient measurements. The decay curve showed the logarithmic decay even when the sample material was present. The position of microphone was found immaterial in the measurements and also, when the sample material was about 10 m², the mounting position of the sample had no effect upon the absorption coefficient. These results would show that the sound field of this chamber would fulfill the requisite for the diffuse sound field, and that this chamber would have characteristics as expected from the fundamental experiments. This will bear witness to the fact that the sound field in our reverberation chamber has been much more improved than in the conventional ones, in which a special regard had to be paid in such things as to use several microphone positions and also to choose proper mounting position of sample materials.

This chamber was completed by the cooperation of Shimizu Construction Co., Ltd. Members of the Acoustical Material Association of Japan provided us with sample materials used for these researches. The fundamental experiments were conducted in cooperation with Mr. J. Sakagami. We should like to express our sincere appreciation for their cooperation.

This work was partly supported by the Scientific Research Fund of the Ministry of Educations.

References

1) K. Sato and M. Koyasu: J. Phys. Soc. Japan **14** (1959) 365.
2) D. Y. Maa: J. Acoust. Soc. Amer. **10** (1939) 235.
3) W. L. Barrow: Ann Physik **11** (1931) 174.
4) P. V. Brüel: *Sound Insulation and Room Acoustic* (Chapmann and Hall Ltd., 1951) 190.
5) V. L. Chrisler: J. Res. Nat. Bur. Stand. **13** (1934) 169.

This section is intended to secure prompt publication of important discoveries in physics. The reports should not exceed 800 words in length. A figure of size 7 cm × 7 cm will be counted as 150 words.

J. Phys. Soc. Japan **14** (1958) 678

A Visualizing Method of Electron Temperature and Plasma Density

By Hajime TAMAGAWA and Junji FUJITA
Department of Physics, Faculty of Science, University of Tokyo

(Received March 6, 1959)

On the measurement of a transient plasma, it is desirable to obtain the informations about the plasma within a sufficiently short time interval during which the plasma quantities may be regarded to remain constant. The usual single probe method is unsuitable for the investigations of a rapidly changing plasma. A floating double probe method was devised[1] for a research of decaying plasmas, it fits, however, only for the measurements of repeatable and reproducible phenomena. Some trials were made[2,3] to get informations from the oscillograms of probe characteristics.

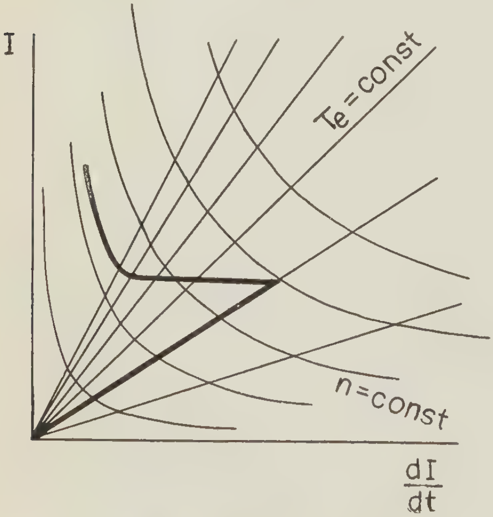

Fig. 1.

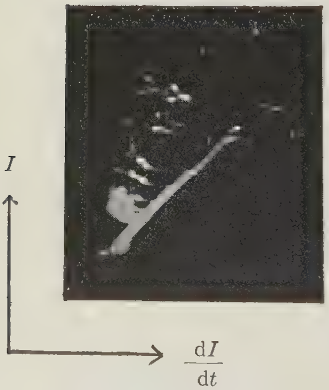

Fig. 2.

The authors succeeded to visualize electron temperatures as well as plasma densities of a transient plasma directly on the pattern of cathode-ray-tube. The principle is based on the Langmuir's single probe method. Electron temperature is obtained by differentiating a logarithm of the probe current with respect to the probe potential, that is

$$\frac{e}{kT_e}=\frac{\mathrm{d}}{\mathrm{d}V}(\log I)=\frac{1}{I}\frac{\mathrm{d}I}{\mathrm{d}V}=\frac{1}{I}\frac{\mathrm{d}I}{\mathrm{d}t}\Big/\frac{\mathrm{d}V}{\mathrm{d}t}$$

Then, if the probe potential is changed linearly with time, electron temperature is given by the ratio of probe current to its time-derivative. Above quantities are represented on the pattern of cathode-ray-tube as the slopes of straight lines which start from the origin, when the probe current is introduced to the Y-axis, and the time-derivative to the X-axis.

When the prove potential exceeds the space potential, electron current to the probe no longer increases with probe potential and saturation occurs, which results abrupt discontinuity of $\mathrm{d}I/\mathrm{d}t$ at the space potential. Once electron temperature is determined, plasma density is obtainable from the electron current density at the space potential.

$$n=\frac{J_{es}}{e}\sqrt{\frac{2\pi m}{kT_e}}$$

Fig. 1 will be helpful for understanding this principle, and an example of oscillograph pattern is shown in Fig. 2.

One of the chief difficulties of this method is to need extremely wide-band amplifiers and a high-fidelity oscilloscope. Next, the output impedance of the saw-tooth-wave generator should be as low as possible, otherwise the linearlity of voltage is affected by the drain of the probe current, and $\mathrm{d}V/\mathrm{d}t$=constant is no longer valid. These difficulties are, however, purely technical problems.

The authors wish to express their sincere thanks to Prof. K. Honda for the valuable discussions, and Japan Atomic Energy Research Institute for the instrumental facility. This work is supported by the Scientific Research Expenditure of the Ministry of Education.

References

1) E. O. Johnson and L. Malter: Phys. Rev. **80** (1950) 58.
2) S. Togo: J. Inst. Elec. Eng. (Japan) **53** (1933) 109.
3) T. Sakaguchi and R. Itadani: Kakuyugo-Kenkyu **1** (1958) 431 (in Japanese).

J. PHYS. SOC. JAPAN **14** (1959) 679

An Abnormal Saturation Behavior in High Resolution Proton Magnetic Resonance Spectra

By Michihiko NAGUMO and Yoshinobu KAKIUCHI
Institute for Solid State Physics, University of Tokyo

(Received March 20, 1959)

In the experiments of high resolution nuclear magnetic resonance, asymmetry of the line shapes depending on the sweep direction is often experienced[1].

A remarkable anomaly in saturation behavior, however, which is essentially different from the usual ones is observed in the spectra of some benzene substituents.

The apparatus used is Varian V-4300 N. M. R. Spectrometer at 40 mc, and the measurements were conducted at room temperature. The magnetic field is swept slowly as usual

Spectra of nitrobenzene, for example, are of multiplet structure due to the indirect I-I coupling between ring protons. It is diluted to less than about twenty per cent with cyclohexane, acetone, etc., the proton resonance line of each solvent being in higher field side compared with that of nitrobenzene.

No saturation is observed under moderate radiation field when the magnetic field is swept from lower to higher value, whereas the decrease of the *signal intensity as a whole* as well as the distortion of the line shape *does* appear when the field is swept from higher to lower value.

This phenomenon becomes the more conspicuous, the stronger H_1, the intensity of the radiation field, and the slower the rate of the sweep through the solute signal as is naturally expected, but is quite independent of the H_1 while the field is swept through the solvent signal.

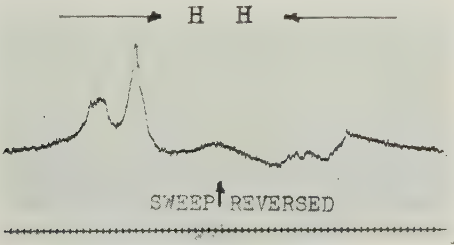

Fig. 1. Proton Resonance Spectra of Nitrobenzene Diluted in Cyclohexane.

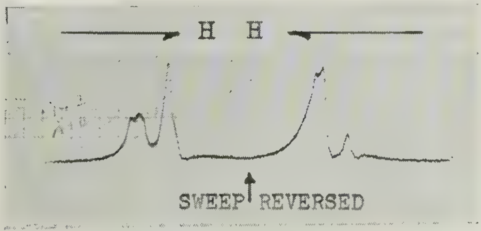

Fig. 2. Proton Resonance Spectra of Nitrobenzene Diluted in Carbon Tetrachloride.

The choice of the solvent is immaterial in so far as it contains protons, and its proton resonance line appears in higher field side with respect to that of the solute.

On the other hand, in concentrated solutions or with solvent which contains no protons, carbon tetrachloride for example, such an asymmetry in the total area of the signal for the forward and reversed sweep directions does not appear.

Similar phenomena are also found in many other substances; say aniline, pyridine, p-nitrochlorobenzene, etc., which have at least two kinds of non-equivalent ring protons as is the case in nitrobenzene, thus forming multiplet spectra, whereas in benzene, or monochlorobenzene, whose spectra consist of almost a single line, such an anomaly is not observed. This abnormal saturation behavior occurs irrespective of the relative positions of each proton group with respect to the substitute groups.

Examples are illustrated in the figures. The figure 1 is the data for 9.7 mole per cent solution of nitrobenzene in cyclohexane with $H_1=84$ microgauss, and the sweep rate 1.0 milligauss per second. The line of cyclohexane is out of the sweep range, and locates in higher field. The figure 2 is contrasted with the former. It is the spectra of the same substance, when diluted with carbon tetrachloride to 15.9 mole percent, with $H_1=84$ microgauss and the sweep rate 1.0 milligauss per second.

Wertz et al previously reported[1] an asymmetry of the proton magnetic resonance spectra of methyl alcohol in backward sweep following the initial.

The total area of the signal as a whole in that case, however, is almost unchanged by reversing the sweep direction. In this respect, the phenomena here reported differ essentially from theirs.

Their case is rather similar to the result of our observation with stronger H_1 in concentrated solutions or in non-protonic solvents, and the interaction within the spin system seems to be the dominant mechanism in this case.

For the mechanism of the abnormal saturation phenomena stated above, however, it is quite plausible that the solvent spins play an important rôle through some interaction with solute spin systems. Further studies are now in progress.

The authors wish to express their sincere thanks to Professors G. Hazato, T. Ikenoue and T. Isobe of Tohoku University, who enabled the authors to use the apparatus and gave them great helps throughout the experiment.

References

1) J. E. Wertz, P. L. Jain and R. L. Batdorf; Phys. Rev. **102** (1956) 920.

J. Phys. Soc. Japan **14** (1959) 680~681

Phase Transition in Tungsten Trioxide

By Sigetosi Tanisaki
Faculty of Literature and Science, Yamaguchi University

(Received March 7, 1959)

The dielectric constant-temperature curve of the ceramics of tungsten trioxide WO_3 exhibits a maximum near 20°C1), and there is a possibility that this material might be ferroelectric below this temperature. On the other hand, it has been shown by the X-ray investigation that this material has a monoclinic structure in room temperature in which ions are arranged in an antiparallel manner2) and it transforms to an orthorhombic phase near 350°C on heating and transforms near −40°C on cooling to a lower temperature form which has been supposed to be trigonal3). The phase transition of this material near 20°C has not been known. In the present note the phase transition from monoclinic to triclinic near 17°C is described.

The tabular crystal of WO_3 with c-surfaces well developed has usually two kinds of domains whose walls are (110) and (100) in room temperature, but sometimes another kind of domains which are formed by twinning on (010) plane is found below 17°C. This (010) domain structure can be easily observed with the polarizing microscope between crossed nicols as shown in Fig. 1 (a), because, when c-surface of the crystal is observed, the extinction position of each domain differs from those of its adjacent domains by about 6°. And also the difference of the extinction positions of neighbouring domains is observed on a-surface of the crystal. These facts suggest that the crystal constructed by (010) domains may have a triclinic structure, and this suggestion is ascertained by the X-ray method. The lattice constants of the triclinic phase determined from X-ray rotational photographs are as follows:

$$a=7.30\text{Å},\quad b=7.52\text{Å}\quad c=7.69\text{Å}$$
$$\alpha=88°50',\quad \beta=90°55',\quad \gamma=90°56'.$$

The triclinic crystal transforms to the monoclinic phase near 17°C on heating and the monoclinic crystal thus obtained has few or no (100) walls (Fig. 1 (b)). The transition from the triclinic phase to the lower temperature phase is observed near −40°C on cooling (Fig. 1 (c)). These two phase transitions can be repeatedly observed with the polarizing microscope showing a thermal hysteresis in some extent.

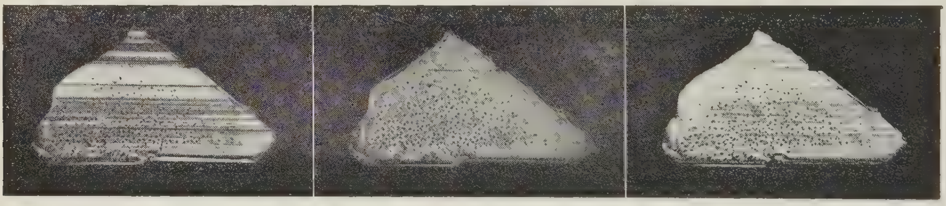
(a) (b) (c)

Fig. 1. (a) Triclinic phase observed between crossed nicols (10°C).
(b) Monoclinic phase (25°C). Only one (100) wall is seen near the right corner of the crystal.
(c) Lower temperature phase (−55°C).

The monoclinic crystal which has many fine (100) domains is hard to transform to triclinic even in low temperature below 0°C and an apparently direct phase transition from the monoclinic phase to the lower temperature phase is frequently observed near −40°C, but the transition from the lower temperature phase to the triclinic phase on heating is always observed. The monoclinic multidomain crystal can be changed to the single domain crystal easily by the external stress4), and the obtained single domain crystal always shows the monoclinic-triclinic transition near 17°C. On the other hand, whenever the crystal which shows the monoclinic-triclinic transition is heated once above 350°C, the monoclinic-orthorhombic transition temperature, it has many fine (100) domains in room temperature and does not show the monoclinic-triclinic transition near 17°C. It seems to be due to this effect of (100) domains that the existence of the triclinic phase between the monoclinic phase and the lower temperature phase has been overlooked by many investigators.

The dielectric properties of this triclinic phase should be studied in future.

The author wishes to express his sincere thanks to Prof. K. Tanaka for his continual encouragement.

References

1) S. Nagasawa: Denki-Kagaku **16** (1948) 13, 57; **17** (1949) 174.
T. Okada, K. Hirakawa and F. Irie: Busseiron-Kenkyu **15** (1949) 49.
S. Sawada: Rep. Inst. Sci. and Tech. Univ Tokyo **4** (1950) 223.

2) R. Ueda and J. Kobayashi: Phys. Rev. **91** (1953) 1565.
3) M. Foëx: Compt. rend. **228** (1949) 1335.
B. T. Matthias and E. A. Wood: Phys. Rev. **84** (1951) 1255.
K. Hirakawa: J. Phys. Soc. Japan **7** (1952) 331.
S. Sawada: J. Phys. Soc. Japan **11** (1956) 1237, 1246.
4) S. Tanisaki: J. Phys. Soc. Japan **13** (1958) 363.

J. PHYS. SOC. JAPAN **14** (1959) 681

Absorption Spectrum of Copper-Coloured Cuprous Oxide

By Masakazu HAYASHI

Department of Physics, Faculty of Science, Hokkaido University, Sapporo

(Received March 4, 1959)

By heating a cuprous oxide film 0.1 mm thick in a vacuum electric furnace maintained at 900°C, a copper-coloured specimen of partially reduced cuprous oxide was obtained. The absorption spectrum of the specimen revealed an interesting band as will be described in the following.

The spectrograph of Hilger's constant deviation type was used with an incandescent lamp as the light source. The transparency of the specimen was so poor that very long exposure was necessary to obtain the clear absorption spectrum.

In Fig. 1, two spectrograms taken at room temperature are shown: (*a*) is the spectrogram of the normal cuprous oxide film of 0.1 mm thickness and (*b*) is the spectrogram of the copper-coloured specimen obtained by the above-mentioned procedure.

In (*a*), we can observe three absorption edges at the wavelengths 637 mμ, 628 mμ and 607 mμ. The writer has already given the interpretation of these as follows¹⁾:

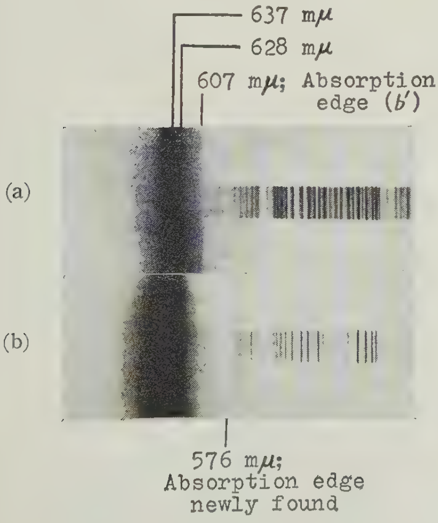
637 mμ
628 mμ
607 mμ; Absorption edge (b')
(a)
(b)
576 mμ; Absorption edge newly found

Fig. 1.

1) The two sharp absorption edges at 637 mμ and 628 mμ correspond to the transitions from the doublet states ^2P of O^- to the empty band;

2) The third at 607 mμ is the limit of the long wavelength tail of the characteristic absorption of the cuprous oxide film of 0.1 mm thickness. (The shift of the edge towards the shorter wavelength side is always observed not only with the decrease of temperature, but also with the decrease of film thickness. In the previous work²⁾, this edge was called "the absorption edge (b')".)

In (*b*) of Fig. 1, we can also identify two sharp absorption edges at 637 mμ and 628 mμ, but cannot observe the absorption edge corresponding to that designated as (b') in (2). Instead a new absorption edge is found at the wavelength 576 mμ where a broad band starts towards the longer wavelength side extending over the two sharp edges stated in (1). The disappearance of the absorption edge (b') can be explained by assuming that the reduction process makes the cuprous oxide film so thin that the absorption edge (b') moves towards the wavelength shorter than 607 mμ and is missed there.

Lange³⁾ measured extensively the spectral sensitivity of photo-e.m.f. of copper-cuprous oxide photo-cells at various temperatures. According to his results for the room temperature, (i) the maximum sensitivity is obtained at about 630 mμ; (ii) the long wavelength limit of sensitivity is about 1.4μ; and (iii) towards the wavelength shorter than 630 mμ, the sensitivity rapidly decreases and beyond 575 mμ no photo-e.m.f. can be detected. This sharp drop at 575 mμ has hitherto been interpreted⁴⁾ as due to the increase of the absorption coefficient of cuprous oxide to values so large that the light cannot penetrate the material.

The broad absorption band newly found in the present study might be inferred to be responsible for the photo-e.m.f. of the copper-cuprous oxide photo-cells mentioned above. This consideration comes from the circumstances that the shortest wavelength of the new absorption band happens to coincide with that of the spectral distribution of photo-e.m.f. at room temperature.

The writer is now preparing further experiment to see if the above experiment can be asserted to be valid.

References

1) M. Hayashi: J. Fac. Sci. Hokkaido Univ. (II), **4** (1952) 107.
2) M. Hayashi: *loc. cit.*; M. Hayashi and K. Katsuki: J. Phys. Soc. Japan **7** (1952) 599.
3) B. Lange: Naturwiss. **19** (1931) 529.
4) B. Lange: *loc. cit.*; N. F. Mott and R. W. Gurney: *Electronic Processes in Ionic Crystals* (Clarendon Press, Oxford, 1940) 195.

J. Phys. Soc. Japan **14** (1959) 682

Visible Light Emission from Metal-Silicon Contact

By Makoto Kikuchi
Electrotechnical Laboratory, Tokyo, Japan

(Received March 12, 1959)

It has so far been observed that visible light was emitted from a reverse biased p-n junction in silicon crystals[1]. On the course of study on this kind of phenomena, we have found out that the light was emitted even from a metal-silicon contact. When a small electrode is formed on a silicon crystal surface with silver paste as shown in Fig. 1, the contact shows strongly rectifying characteristic, and small bright radiating spots appear on the periphery of the electrode in the hard flow direction of the characteristic (Fig. 2).

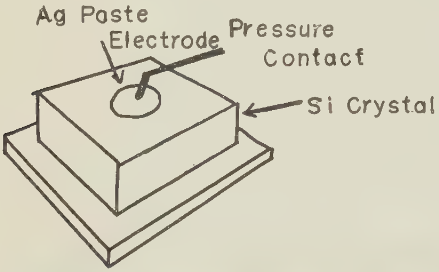

Fig. 1. The sample preparation.

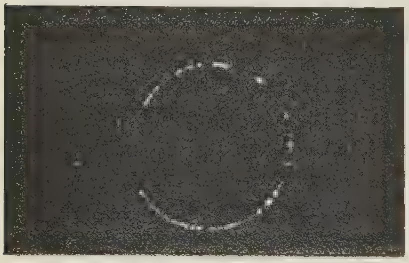

Fig. 2. Photograph of the visible light emission from the Ag-paste electrode on the silicon crystal.

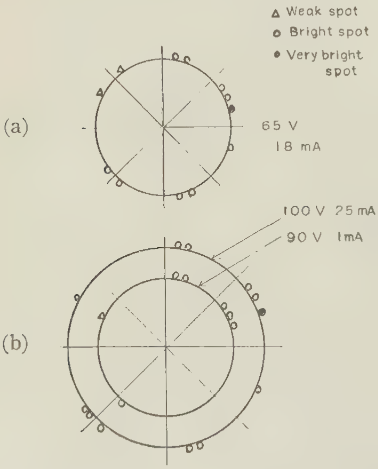

Fig. 3. Appearance of the radiating spots (a) before, and (b) after the application of castor oil.

Many kinds of experiments have been performed to clarify whether these light spots are of the same nature as those observed in the p-n junctions (i.e. microplasma). Fig. 3. (b) shows the appearance of the spots on the periphery of the electrode when it is immersed in castor oil. As is shown, the spots appear at the same positions as before applying the castor oil (Fig. 3 (a)), although the backward current is reduced and the voltage necessary to get the same pattern is increased. This result may serve as an evidence to deny the possibility that the spots are small discharge in the air gap between silver particle and silicon surface.

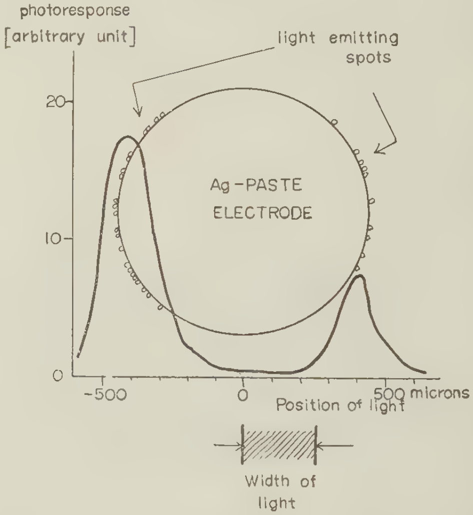

Fig. 4. The local photoresponse of the contact when the spots are being observed. The light is chopped at 245 cps, and the width of the light is 250 microns.

In Fig. 4 is shown the result of the measurement of the local photoresponse of the contact when the spots are being observed. A chopped light from a slit is focused and scanned in one direction on the electrode. As is shown, remarkable multiplication is observed at the light emitting spots.

Some of the spots are reddy and blue, but most are yellow or white. Almost the same pattern could be observed down to the liquid oxygen temperature. The appearance of the spots seems to have strong correlation with the magnitude of the current and also with its fluctuation.

The experimental details and the discussion will be reported in the near future.

References

1) R. Newmann: Phys. Rev. **100** (1955) 700. A. G. Chynoweth et al: Phys. Rev. **102** (1956) 369. A. G. Cynoweth et al: J. Appl. Phys. **29** (1958) 1103.

J. PHYS. SOC. JAPAN **14** (1959) 683～684

Nuclear Spin-Spin Coupling between Protons in Vinyl Derivatives

By Tatsuo SHIMIZU, Shin-ichi MATSUOKA,
Shuzo HATTORI and Kantaro SENDA
Department of Physics, Kanazawa University, Kanazawa

(Received March 24, 1959)

In order to examine the spin-spin coupling constants between protons in vinyl group, we have chosen styrene and trans-cinnamic aldehyde by the reason that the shift between protons in their vinyl groups is relatively large. We have assigned their proton spectra as 3-spin system, neglecting the interactions with protons in benzene ring*. We have taken the Hamiltonian for such a system as follows:

$$\mathscr{H}=\sigma_1 I_{z1}+\sigma_2 I_{z2}+\sigma_3 I_{z3}+J_1\mathbf{I}_1\cdot\mathbf{I}_2+J_2\mathbf{I}_2\cdot\mathbf{I}_3+J_3\mathbf{I}_3\cdot\mathbf{I}_1\ ,$$

where

$$\sigma_i=(\gamma/2\pi)H_i\ .$$

We rewrite this as the sum of the following $\mathscr{H}^{(0)}$ and $\mathscr{H}^{(1)}$,

$$\mathscr{H}^{(0)}=\sigma_1(I_{z1}+I_{z2}+I_{z3})\ ,$$

$$\mathscr{H}^{(1)}=\sigma' I_{z2}+\sigma I_{z3}+J_1\mathbf{I}_1\cdot\mathbf{I}_2+J_2\mathbf{I}_2\cdot\mathbf{I}_3+J_3\mathbf{I}_3\cdot\mathbf{I}_1\ ,$$

were

$$\sigma'=\sigma_2-\sigma_1,\qquad \sigma=\sigma_3-\sigma_1\ .$$

Considering J_1, J_2, J_3 as perturbations, we have determined the parameters as follows: $\sigma'=20.6$ cps, $\sigma=59.8$ cps; $J_1=1.6$ cps, $J_2=17.2$ cps, $J_3=10.6$ cps for styrene, and $\sigma'=-117.8$ cps, $\sigma=-93.0$ cps; $J_1=7.4$ cps, $J_2=15.2$ cps, $J_3<0.5$ cps for trans-cinnamic aldehyde.

The calculated patterns with these values reproduce the experimental spectra which are shown in Fig. 1 and Fig. 2. The signs of J's have not been able to be determined at all in this approximation.

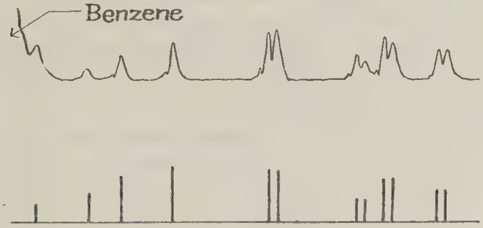

Fig. 1. Calculated and experimental spectra of styrene.

In order to make the assigned coupling constants correspond to the chemical structures, we first consider trans-cinnamic aldehyde. In this case, the shift between aldehyde group and benzene group is known¹⁾ approximately and the coupling constant between the farthest protons is considered to be nearly zero. So we have been able to make them correspond to the chemical structures as shown in Fig. 3 (a), where the cis-form of CHO is shown, but the coupling constants obtained above are average values of the spectra in the cis- and the trans-form. From this, it is inferred that the coupling constant between protons in vinyl group in the trans-position is approximately 15 cps.

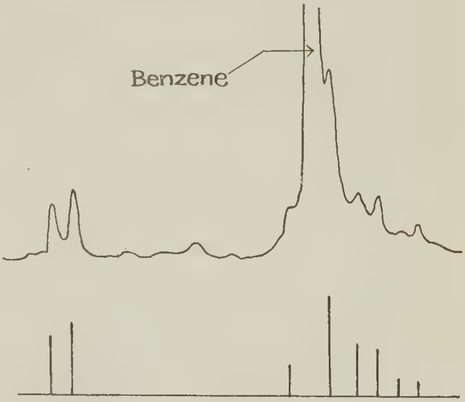

Fig. 2. Calculated and experimental spectra of trans-cinnamic aldehyde.

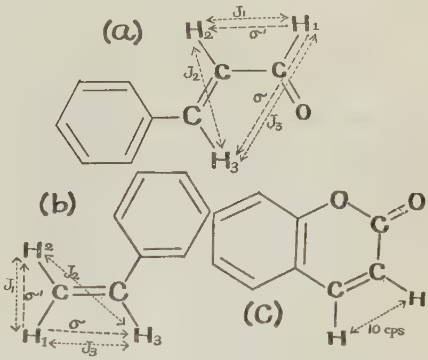

Fig. 3.

Further we have examined the spectrum of coumarine (see Fig. 3 (c)) and have found the coupling constant between protons in the cis-position to be approximately 10 cps. From these results, we have made the assigned coupling constants of styrene correspond to the chemical structures as shown in Fig. 3 (b). From the results obtained above, we have ascertained that the coupling constant between protons bonded to the same carbon atom in vinyl group is small²⁾,³⁾, and that the coupling constants between protons in the cis- and trans-positions separated by two carbon atoms are far larger than this[4].

---

* In trans-cinnamic aldehyde, the coupling J_3, between H_1 and H_3 (see Fig. 3 (a)) is expected to be very small in the same order as the coupling between H_1 and ortho proton in benzene ring, but only J_3 is taken into accunt formally to treat this spectra as 3-spin system.

The coupling constants, J_1, J_2 and J_3 of styrene obtained above are in very good agreement with the corresponding values, 1.4, 17.5 10.8 cps and 1.9, 17.4, 10.4 cps, for 3,3-dimethyl-1-butene and 1-butene respectively which Alexander has reported[4]. Though the assignment of the observed coupling constants to the cis- and trans-coupling was not made clear in his paper, we have been able to distinguish the cis- and trans-coupling constants. And the values of the cis- and trans-coupling constants we obtained are consistent with the theory of Karplus[5], appeared after this work was carried out.

The good agreement of the coupling constants among styrene, 3,3-dimethyl-1-butene and 1-butene shows that the substitutional radical does not alter coupling constants appreciably, while it has an effect on chemical shifts considerably.

The measurements were performed at Japan Electron Optics Laboratory Co., Ltd. using JNM-3 type NMR spectrometer operated at 40 Mc.

References

1) L. H. Meyer, A. Saika and H. S. Gutowsky: J. Amer. Chem. Soc. **75** (1953) 4567.
2) H. M. McConnell, A. D. McLean and C. A. Reilly: J. Chem. Phys. **23** (1955) 1152.
3) W. A. Anderson: Phys. Rev. **102** (1956) 151.
4) S. Alexander: J. Chem. Phys. **28** (1958) 358.
5) M. Karplus: J. Chem. Phys. **30** (1959) 11.

J. Phys. Soc. Japan **14** (1959) 684

Fine Structures of Proton Resonance Spectra of Fluorobenzene Derivatives

By Minoru KIMURA, Shin-ichi MATSUOKA, Shuzo HATTORI and Kantaro SENDA
Department of Physics, Kanazawa University, Kanazawa

(Received March 20, 1959)

We have studied the high resolution proton resonance spectra of *p*-bromo-fluorobenzene and *p*-iodo-fluorobenzene.

Their spectra show the fine structures due to spin-spin couplings, and we have analyzed them as 5 spin system of XA_2B_2 type with C_{2v} symmetry. In this analysis, we have adopted the notations as shown in Fig. 1 in which the symmetrical property has been taken into account, and have neglected $J_p(\mathrm{HH})$, as reported to be approximately zero by Richards and Schaefer[1], Bak et al[2], and by Gutowsky et al[2]. Then, if we neglect $J_m(\mathrm{HH})$, the secular equation of the Hamiltonian for this system have been able to solve exactly. To such approximation that $J_m(\mathrm{HH})$ has been neglected, the main intense lines are expected to be eight lines, divided into two groups each having four lines. The separations of these two groups are due to the chemical shift between the protons at the *ortho*- and the *meta*-position.

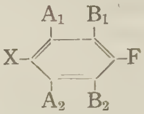

$$J(\mathrm{F}-\mathrm{A}_1)=J(\mathrm{F}-\mathrm{A}_2)\equiv J_o(\mathrm{FH})$$
$$J(\mathrm{F}-\mathrm{B}_1)=J(\mathrm{F}-\mathrm{B}_2)\equiv J_m(\mathrm{FH})$$
$$J(\mathrm{A}_1-\mathrm{A}_2)=J(\mathrm{B}_1-\mathrm{B}_2)\equiv J_m(\mathrm{HH})$$
$$J(\mathrm{A}_1-\mathrm{B}_1)=J(\mathrm{A}_2-\mathrm{B}_2)\equiv J_o(\mathrm{HH})$$
$$J(\mathrm{A}_1-\mathrm{B}_2)=J(\mathrm{A}_2-\mathrm{B}_1)\equiv J_p(\mathrm{HH})$$

Fig. 1.

The contribution of $J_m(\mathrm{HH})$ to the energy shift has been calculated by making use of a perturbation theory to the first order. In the observed spectra, it happened that the two lines in the intense ones overlapped. These intense lines in the observed spectra have enabled us to determine the coupling constants $J_o(\mathrm{FH})$, $J_m(\mathrm{FH})$, $J_o(\mathrm{HH})$ and the chemical shift, σ. Their values thus obtained are:

$\sigma=18.97$ cps; $J_o(\mathrm{FH})=9.47$ cps, $J_m(\mathrm{FH})=6.11$ cps, and $J_o(\mathrm{HH})=9.65$ cps for p-bromo-fluorobenzene; $\sigma=32.6$ cps; $J_o(\mathrm{FH})=9.35$ cps, $J_m(\mathrm{FH})=6.08$ cps and $J_o(\mathrm{HH})=9.30$ cps for *p*-iodo-fluorobenzene.

$J_m(\mathrm{HH})$ is to be determined by performing the assignments of the other weaker lines which are separated from the intense lines by the effect of $J_m(\mathrm{HH})$. In our estimation, it is probable that the value of $J_m(\mathrm{HH})$ is approximately 2 cps in both molecules and has the same sign with $J_o(\mathrm{HH})$. However, in order to determine the value of $J_m(\mathrm{HH})$ accurately, the resolving power of the spectrometer must be improved a little more.

The investigations about the benzene derivatives have been reported by Richards and Schaefer[1], Bak et al[2], and Gutowsky et al[3]. They investigated *p*-fluoro-aniline, deuterium substituted fluorobenzenes and other substituted fluorobenzenes and found the chemical shift between protons in the *ortho*- and the *meta*-position, and determined the values of the spin-spin coupling constants between nuclei. The coupling constants obtained here agree almost with their results.

The spectra were observed with JNM-3 type NMR spectrometer of Japan Electron Optics Laboratory Co., Ltd. operated at the fixed frequency 40 Mc.

References

1) R. E. Richards and T. Schaefer: Proc. Roy. Soc. A, **246** (1958) 429.
2) B. Bak, J. N. Shoolery and G. A. Williams: J. Mol. Spectroscopy **2** (1958) 525.
3) H. S. Gutowsky, C. H. Holm, A. Saika and G. A. Williams: J. Amer. Chem. Soc. **79** (1957) 4596.

J. PHYS. SOC. JAPAN **14** (1959) 685~686

A Metastable Phase in Sn-Mg Alloy Film

By Ryōji SUGANUMA
Physical Institute, Kyōto Prefectural Medical College

(Received February 5, 1959)

Through the electron diffraction study of Sn-Mg alloy films, a new phase was observed which seemed to be metastable.

The thin films were made in vacuum (about 10^{-5} mmHg) by successive evaporation of Sn and Mg on Formvar films at room temperatures. The compositions of films as a whole were 7~55 at. % Sn and the total amount of the evaporated metals was about 10 mg.

The diffraction pattern of the films whose compositions as a whole are Mg-rich compared with that of Mg_2Sn is composed of the patterns of Sn, Mg, Mg_2Sn and an unknown new phase at room temperatures. When these films are heated in the electron diffraction apparatus, the new phase immediately disappeared at about 150°C and the diffraction patterns of these specimens only show the existence of Mg and Mg_2Sn, which do not show any change even after the cooling to the room temperatures. While, in the case of Mg-poor specimens which are composed of Sn, Mg_2Sn and the new phase at room temperatures, the most part of the film indicates only two phases of Sn and Mg_2Sn at about 150°C, but a part of the same film remains in the state of three phases, namely, the melt of Sn, Mg_2Sn and the new phase, at about 315°C. The diffraction patterns of these specimens show no changes by the cooling to the room temperatures as the case of Mg-rich ones. The unknown new phase was always observed for the specimens before heat treatments, independently of the compositions of films as a whole and no matter which constituent metal was deposited as the primary layer. The specimens, which are composed of two phases of Sn and Mg_2Sn by the heating up to 150°C, do not show the existence of the new phase even after the annealing for about one hour at the temperatures of about 100°C, 150°C and 240°C (the melting point of Sn being 232°C), respectively, and in addition, the bulk specimens prepared by the vacuum melting of Sn and Mg (about 65 at. % Sn) only show two phases of Sn and Mg_2Sn, but not the new phase. From these facts, the new phase seems to be metastable at least in the temperature ranges studied (i.e. from room temperatures to about 150°C for the Mg-rich specimens and to about 315°C for the Mg-poor ones).

The diffraction rings of the new phase and Sn mostly overlap each other. But, in the diffraction patterns obtained at the temperatures higher than the melting point of Sn, the halo pattern of Sn appears in place of the ring pattern of Sn so that the diffraction pattern of the new phase can be easily distinguished from that of Sn.

The diffraction pattern of this new phase could not be compatibly explained by assuming the tetragonal or hexagonal systems. Therefore, Lipson's method[1] for the orthorhombic crystals was applied. It was successful in this case and approximate values of three axes of the orthorhombic unit-cell were obtained graphically. After refined numerical calculations, the three axes were determined to be a=15.23Å b=8.90Å and c=13.10Å. For example, the observed and calculated spacings for the specimen of about 50 at. % Sn, which was made by the deposition of Mg on the primary Sn deposit, are tabulated in Table I. The spacings of Mg_2Sn observed with the specimens, which indicate

Table I.

New phase				Mg_2Sn		
(hkl)	d(calc.)	d(obs.)	I(obs.)	(hkl)	d	I
013	3.91_0Å	3.90_9Å*	s	111	3.91_2Å	s
400	3.80_7	3.80_7	s			
022	3.68_1	3.68_5	s			
411	3.38_1	3.37_9*	w	200	3.38_4	w
023	3.11_2	3.11_8	w			
420	2.89_3	2.89_8	m			
421	2.82_5	2.82_7	vvw			
422	2.64_6	2.65_3	m			
323	2.65_3					
128	2.59_8	2.59_2	w			
503	2.49_5	2.50_4	w			
414	2.39_1	2.39_5*	s	220	2.39_0	s
025	2.25_8	2.27_4	vw			
040	2.22_5	2.22_5	m			
006	2.18_3	2.18_3	m			
042	2.10_7	2.11_6	w			
216	2.04_2	2.04_5*	s	311	2.04_2	m
604	2.00_5	2.00_1	vvw			
614	1.95_7	1.95_3*	w	222	1.95_0	vw
800	1.90_4	1.91_3	w			
044	1.84_0	1.84_8	vvw			
150	1.76_8	1.77_2	vvw			
426	1.74_2	1.74_1	vw			
822	1.69_0	1.69_2*	m	400	1.68_8	w
910	1.66_2	1.66_5	m			
008	1.63_6	1.63_4	vw			
218	1.57_5	1.57_2	m			
046	1.55_6	1.55_6*	w	331	1.55_2	w
060	1.48_3	1.48_7	w			
446	1.44_2	1.44_2	m	420	—	—
816	1.41_6	1.41_7	vw			
432	1.35_2	1.35_5	vw			
646	1.32_8	1.32_9	vvw			
464	1.27_3	1.27_5	w			

* These lines are superposed on the reflections of Mg_2Sn, so that they might have to be disregarded.

two phases of Sn and Mg_2Sn, are also shown in Table I. These values agree well with the data obtained from the X-ray diffraction.

When the systematic absence in the diffraction lines, except the (013) reflection superposed on the (111) reflection of Mg_2Sn, is considered, the space group of the new phase may be supposed to be P_{bnn} and the symmetry does not become higher than P_{bnn} even though all the reflections superposed on those of Mg_2Sn are neglected. However because only powder diffraction data with thin films are available in the present stage, further studies will be required for the accurate determination of the space group.

Reference

1) H. S. Peiser et al: *X-Ray Diffraction by Polycrystalline Materials* (The Institute of Physics, London, 1955) 350.

J. PHYS. SOC. JAPAN **14** (1959) 686

Anomalous Hall Effect due to an s-d Interaction in the Dilute Alloys Containing the Transition Elements

By Mikio TSUJI

General Education Department, Kyushu University, Otsubo-machi, Fukuoka

(Received March 30, 1959)

Since the discovery of the anomalous behaviour of the electrical resistivity of noble metal alloys by Geritsen and Linde¹⁾, the mechanism causing the anomaly has been the subject of a number of investigation. Recently Yosida²⁾ has presented a theory in which the anomalous decrease of the electrical resistivity at low temperature and the anomalous negative magnetoresistance of the noble metals containing traces of the transition elements have been interpreted as an effect of the s-d exchange interaction between the conduction electrons and the magnetic ions. Here, we shall show that, if the mechanism of Yosida is true, the alloys would show also an anomalous Hall effect*.

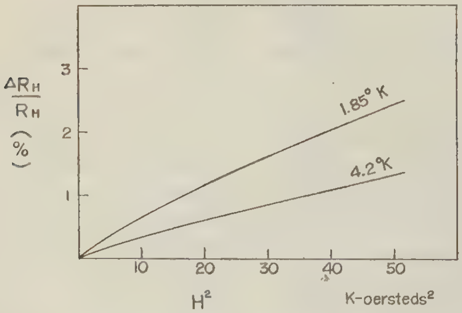

Fig. 1. Change in Hall coefficient vs. square of magnetic field for the 0.2 at. per cent Mn in Cu. (Estimated from Schmitt and Jacobs' data and Eq. (5)).

Now, in a dilute alloys having total magnetization of the transitions ions M, the relaxation times $\tau_\pm$ of the conduction electrons of + and − spins are,

$$\tau_\pm \propto 1/(W_0 \mp wM)\ , \tag{1}$$

respectively²⁾. Here $W_0 \mp wM$ is the transition probability of the electrons. From (1), Yosida has obtained the resistivity of the alloys as

$$\rho \propto (\tau^+ + \tau^-)^{-1} = \frac{W_0}{2} - \frac{w^2}{2W_0} M^2\ . \tag{2}$$

The Hall coefficient R_H is given by

$$R_H = 2R_0 \frac{\tau_+{}^2 + \tau_-{}^2}{(\tau_+ + \tau_-)^2}\ , \tag{3}$$

where R_0 is the Hall coefficient in the limit of small magnetic field ($\tau_+ = \tau^-$). Inserting (1) into (3), we have

$$R_H = R_0\left(1 + \frac{w_2}{W_0{}^2} M^2\right)\ . \tag{4}$$

Eq. (4) shows that an anomalous Hall effect $\Delta R_H = R_0(w^2/W_0{}^2)M^2$ would appear in the alloys, which is proportional to the square of the total magnetization and causes an increase of the absolute value of the Hall coefficient. From (2) and (4), we have a relation

$$\frac{\Delta R_H}{R_H} = -\frac{\Delta\rho}{\rho}\ . \tag{5}$$

Schmitt and Jacobs³⁾ have measured the magnetoresistance of the dilute Cu-Mn alloys at low temperatures. Therefore, we can estimate the order of magnitude of the expected anomaly in the Hall effect and its temperature dependence by using the relation (5). As an example, the estimated values $\Delta R_H/R_H$ for 0.2 at % Cu-Mn alloys are shown in Fig. 1.

We should like to thank Prof. Y. Sibuya, Tohoku University, who called this problem to our attention.

References

1) A. N. Gerritsen and J. O. Linde: Physica **17** (1951) 573; 584.
2) K. Yoshida: Phys. Rev. **107** (1957) 396.
3) R. W. Schmitt and I. S. Jacobs: J. Phys. Chem. Solids **3** (1957) 324.

---

* The similar results as ours have obtained, independently, by K. Yosida and T. Kasuya. (Private communication)

J. PHYS. SOC. JAPAN **14** (1959) 687~688

Changes of Ultrasonic Attenuation during Creep of Aluminum

By Akira HIKATA and Masayoshi TUTUMI

Government Mechanical Laboratory,
132 Sumiyoshi-cho, Suginamiku, Tokyo

(Received December 2, 1958)

It has been reported[1-4] that ultrasonic attenuation is very sensitive to the plastic deformations of metals. On this basis, changes of ultrasonic attenuation during creep experiments of aluminum (99.97 per cent purity) at room temperature were investigated.

Ultrasonic pulses of 5 MC/sec are transmitted to the specimen at its one end using a quartz transducer and multiple echoes reflected from the other end of the specimen are received by the same transducer. The electric signals thus obtained are then amplified and displayed on the screen of the synchronized oscilloscope. The specimens are subjected to a constant load, and attenuation of the ultrasonic waves and strain are measured as a function of time.

One of the results is shown in Fig. 1. Curve *S* shows the usual strain-time relation of this experiment in which the load was increased or decreased several times by a small amount during the creep process. Curve *R* is for the strain rate-time relation calculated from the curve *S*. Curve α is for the corresponding attenuation-time relation.

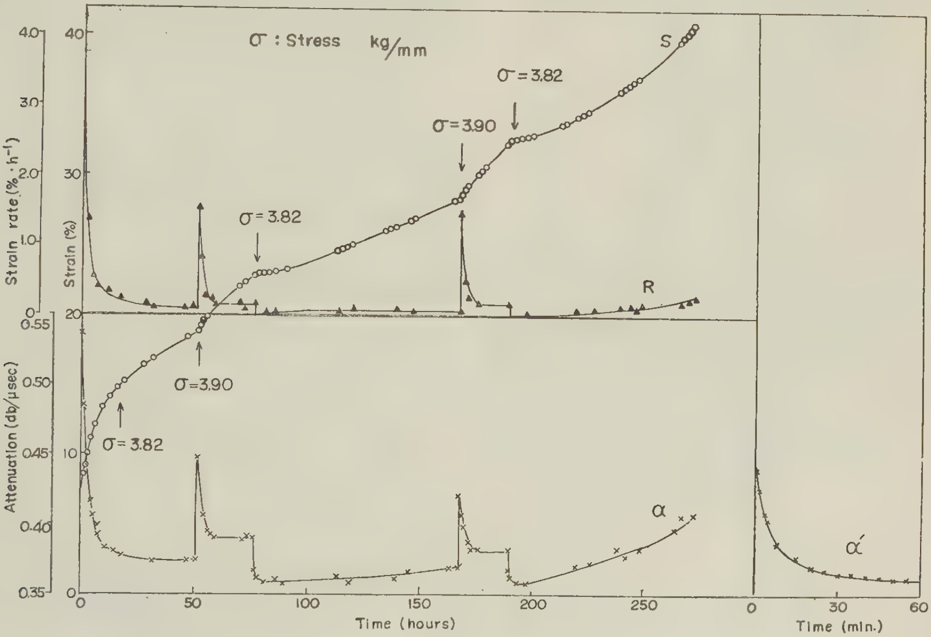

Fig. 1. Curve S: Creep strain-time relation. Curve R: Creep rate-time relation.
Curve α: Attenuation-time relation. Curve α': Recovery of attenuation.

It becomes clear from this experiment that there is a close relationship between the strain rate and ultrasonic attenuation.

According to Granato and Lücke[5),6)] ultrasonic attenuation is determined by the effective loop length and density of dislocations. It is plausible that during the creep process, the effect which increases the attenuation, such as the increase of dislocation density and bulging out of dislocation loops, and the effect which decreases the attenuation, such as the pinning of those dislocations by vacancies created during the deformation, are always competing each other. When there is any disturbance between these two effects by changing the load slightly, the balance will not be held anymore and sharp increase or decrease of attenuation is observed until it reaches the new equilibrium state. The details of this mechanism together with the experiments now undergoing will be published later.

Curve α' of the Fig. 1 is for the recovery of the attenuation when the load is completely removed at the end of the experiment. This curve clearly shows that the increase of attenuation at the final stage of the creep process does not come from the decrease of the cross sectional area of the specimen by necking.

References

1) G. Alers: Phys. Rev. **97** (1955) 863.

2) A. Hikata, R. Truell, A. Granato, B. Chick and K. Lücke: J. Appl. Phys. **27** (1956) 396.
3) A. Hikata and R. Truell: J. Appl. Phys. **28** (1957) 522.
4) A. Granato, A. Hikata and K. Lücke: Acta Met. **6** (1958) 470.
5) A. Granato and K. Lücke: J. Appl. Phys. **27** (1956) 583.
6) A. Granato and K. Lücke: J. Appl. Phys. **27** (1956) 789.

J. Phys. Soc. Japan **14** (1959) 688~689

Size Effects on the Ferrimagnetic Resonance Absorption of Polycrystalline Ferrites and Garnets

By Hiroo Yonemitsu

Matsuda Research Laboratories,
Tokyo Shibaura Electric Co.,
Kawasaki, Japan

(Received January 19, 1959)

Polycrystalline ferrites and garnets are prepared by the usual ceramic technique, and their size effects on ferrimagnetic resonance absorptions are investigated. Samples are ground in the form of sphere by the Bond's method and put into the rectangular cavity resonator having the TE_{101} mode. Measuring apparatus is composed of the source modulation balanced bridge type spectrometer using the magic-tee, and operates at the frequency of 9,345 Mc.

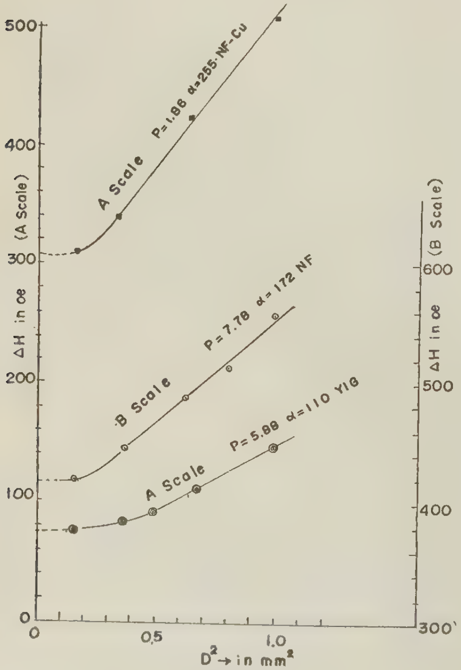

Fig. 1.

Effects of size on the microwave properties of ferrites have been already investigated by several authors[1-6]. But most of their works chiefly dealed with the shift in resonance field.

This paper deals with the size effect which is defined here as the variation of resonance line-width ΔH with the diameter D of sample.

The typical data are shown in Fig. 1, where one may notice that ΔH has a certain constant value provided D^2 is sufficiently small, while ΔH increases linearly with D^2 if D^2 is rather large. It can be approximated by the following empirical formula

$$\Delta H = a + \alpha D^2$$

where α is the proportional constant.

Since α is strongly dependent upon the porosity

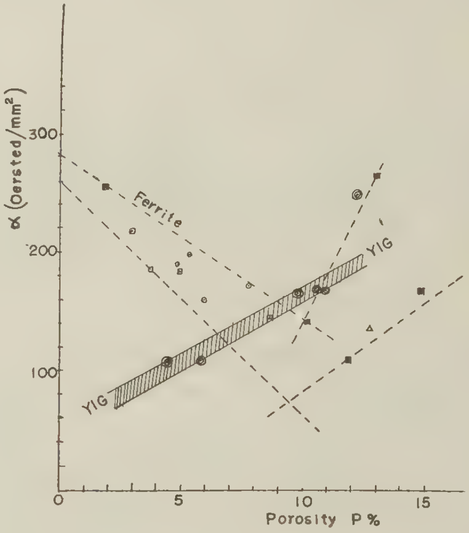

Fig. 2.

⊙ Nickel ferrite $Ni_{1.0}Fe_{2.0}Co_{0.0147}O_4$
1200~1400°C (2 hrs)

■ Nickel-copper ferrite $\begin{cases} Fe_2O_3 = 50 \text{ mol } \% \\ NiO = 50 \text{ mol } \% \\ CuO = 0 \sim 10 \text{ mol } \% \end{cases}$
added;
1150~1400°C (2~6 hrs)

⊡ Nickel-copper ginc ferrite $\begin{cases} Fe_2O_3 \ (48 \text{ mol } \%) \\ NiO \ (34 \text{ mol } \%) \\ ZnO \ (18 \text{ mol } \%) \\ CuO = 0 \sim 10 \text{ mol } \% \end{cases}$
added;
1200~1250°C (2 hrs)

△ Nickel-cobalt ferrite $\begin{cases} Fe_2O_3 \ (48 \text{ mol } \%) \\ NiO \ (34 \text{ mol } \%) \\ ZnO \ (18 \text{ mol } \%) \\ CoO = 0 \sim 1.0 \text{ mol } \% \end{cases}$
added;
1200~1250°C (2 hrs)

◎ YIG $5Fe_2O_3 \cdot 3YeO_3$

p (in %) of each sample, an attempt is made here that α is plotted against p. Several such results are shown in Fig. 2.

In most ferrite samples α decreases with p until p is equal to about 10%. Since these materials were fired at high temperatures with long keeping times, they should contain many ferrous ions. It is verified by their very high conductivities. While in the garnet samples α is initially small and increases gradually with p. As for the yttrium iron garnet (YIG), it is verified by X-ray and thermomagnetic analysis that the possibility of the presence of ferrous ions is very small. This difference in the content of the ferrous ions between the two materials might have some contribution to the observed different character of the two materials.

Further considerations will be presented soon later.

References

1) W. A. Yager, J. K. Galt, F. R. Merritt and E. A. Wood: Phys. Rev. **80** (1950) 744.
2) H. G. Beljers and D. Polder: Nature **165** (1950) 800.
3) P. A. Miles: Nature **174** (1954) 177.
4) Y. Kojima: Sci. Rept. Res. Inst. Tohoku Univ. Ser. A **6** no. 6 (1954) 614.
5) T. R. McGuire: Conference on Magnetism and Magnetic Materials (Pittsburg, Pennsylvania, June 14–16, 1955).
6) J. O. Artman: J. Appl. Phys. **28** (1957) 92.

J. PHYS. SOC. JAPAN **14** (1955) 689~690

An Application of the FA-Modified TF Model to the Singly Ionized Negative Ion

By Shigehiro KOBAYASHI

Department of Physics, Kagawa University, Takamatsu

(Received February 9, 1959)

It is well known[1)] that the Thomas-Fermi (TF) model modified by Fermi and Amaldi (FA), taking as its TF function the ordinary one φ_0 with the modified unit μ^*, enables us to treat the free states of singly ionized negative ions as well as atoms and positive ions.

By the use of this model, Jensen[2)] has already calculated the values of molar diamagnetic susceptibilities of neon-like negative ions and obtained fairly good results.

As another application of this model, we have calculated the mean excitation energy and the X-ray scattering factor with the use of our table of $\varphi_0(x)$[3)].

Fig. 1 shows the nearly linear dependence of the mean excitation potential V_M and energy E_M on atomic number Z, both in logarithmic scale.

Fig. 2 shows the variation of the coherent scattering factor $\mathfrak{f}_0$ and the incoherent scattering factor s_0^2 per electron† *versus* $\sin\theta/\lambda$.

Fig. 3 shows the coherent scattering factor f_0 for several negative ions. As there has been no calculated values of f_0 using the Hartree-Fock (HF)

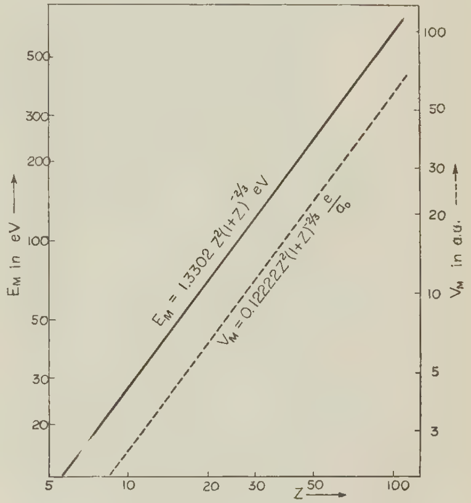

Fig. 1.

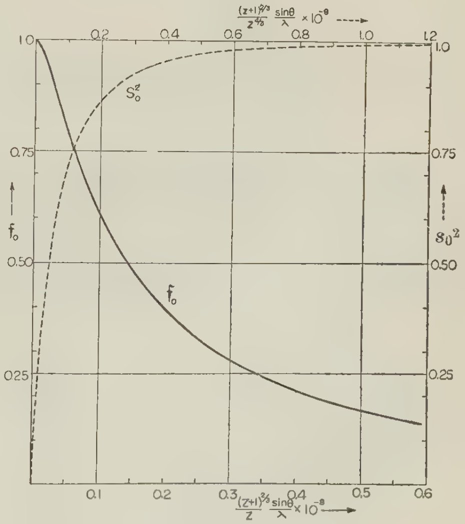

Fig. 2.

---

† Definition of $\mathfrak{f}_0$ and s_0^2 are due to Bethe [Ann. Physik V **5** (1930) 325] and Heisenberg [Phys. Zs. **32** (1931) 737] and these quantities have been obtained as definite functions of $\frac{(Z+1)^{2/3}}{Z}\frac{\sin\theta}{\lambda}$ and $\frac{(Z+1)^{2/3}}{Z^{4/3}}\frac{\sin\theta}{\lambda}$ only, respectively.

field for heavy negative ions, we have plotted those values for F^- and Cl^-, for comparison[4]. Though these are not heavy enough, we did so because we found no better means. It is noticeable that the discrepancy changes its sign alternately with the increase of $\sin\theta/\lambda$ for both ions.

The author wishes to express his sincere thanks to Professor K. Umeda of Okayama University for his continued guidance and kind encouragement throughout this work.

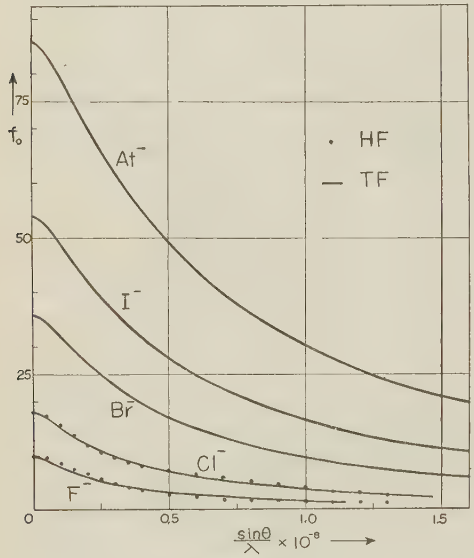

Fig. 3

References

1) P. Gombás: *Die statistische Theorie des Atoms und ihre Anwendungen* (Springer, Wien, 1949) 68.
2) H. Jensen: Z. Phys. **101** (1936) 141.
3) S. Kobayashi and T. Taima: Mem. Fac. Liberal Arts & Educ., Kagawa Univ., II no. 33 (1956).
4) J. Berghuis, IJ. M. Haanappel, M. Potters, B. O. Loopstra, C. H. MacGillavry and A. L. Veenendaal: Acta Cryst. **8** (1955) 478.

J. PHYS. SOC. JAPAN **14** (1959) 690~691

Evaluation of the Nuclear Quadrupole Moment of N^{14}

By Yoshifumi KATO
Osaka Municipal Technical Research Institute, Osaka
and Osamu NAKAHARA
Department of Physics, Kyoto University,

(Received March 20, 1959)

The nuclear quadrupole moment of N^{14} nucleus evaluated from the eQq coupling energy in molecules by several people seems to have disagreed values. Owing to the lack of the datum by the atomic beam experiment for this atom, we are forced to evaluate the quadrupole moment from the molecuar data using the calculated field gradient.

Townes et al[1] have estimated $Q(N^{14})=2\times10^{-26}$ cm² from the experimental datum on cyanide, while Sheriden et al[2] $Q(N^{14})=1\times10^{-26}\,\mathrm{cm}^2$ from the experimental datum on NF_3. These are derived from the field gradient calculated by the simple approximation which was offered by Townes and Dailey[3]. Recently, Bassompierre[4] has calculated the field gradient by LCAO SCF MO which was set up by him for the HCN molecule and obtained $Q(N^{14})=0.71\times10^{-26}\,\mathrm{cm}^2$ from the experimental datum on HCN.

In views of these facts, it seems worthwhile for us to estimate $Q(N^{14})$ from the experimental datum on the NH_3 molecule by calculating the field gradient at the N nucleus, using the LCAO SCF MO set up by Duncan[5] for this molecule. Duncan's function gives 99.2% and 72% of the experimental total and binding energy respectively. This seems a fairly good result as the quantum-mechanical calculation of this kind[6]. The NH_3 molecule has three-fold symmetry around the principal axis of symmetry, so that we only have to calculate the mean value of $\delta^2V/\delta Z^2(=q)$, where Z is taken along the principal axis of symmetry and V is the electrostatic potential in the molecule. Now q can be divided into two parts; $q=q_n+q_e$, where q_n and q_e respectively represent the contribution to the field gradient from the three protons all the electrons in the molecule. q_e can be written in the scheme of LCAO MO as follows,

$$
\begin{aligned}
q_e&=-2e\sum_{i.p.q}\alpha_{ip}\alpha_{iq}\int\chi_p{}^*\frac{3\cos^2\theta_z-1}{r_N{}^3}\chi_q dV\\
&=-2e\sum_i q'_{\phi i\phi i}\ , \qquad (1)
\end{aligned}
$$

where i stands for the suffix of the occupied MO; $\phi_i=\sum_p \alpha_{ip}\chi_p$, χ's represent Slater AO and r_N, θ_Z are the distance from the N nucleus and the polar angle from the Z axis. e is the protonic change. For the evaluation of the integrals in Eq. (1), we have made use of the Barnett-Coulson method[7] which enables us to expand 1s orbitals centered on three protons in terms of r_N, θ_Z and φ. A three-center integral is also expanded in the same manner and its radial part is reduced to a doubly infinite series; $\sum_{n,n'}^{\infty}\int\zeta_{1,n}(1,r_N:R)\times\zeta_{1,n'}(1,r_N:R)r_N{}^{-2}dr_N$. The convergence is rather poor, yet we think it is sufficient to take several terms because of the small contribution to q_e from this integral. The contributions to q_e from each occupied MO (ϕ_i) are as follows;

$$\begin{aligned} q'_{\phi_1\phi_1} &\quad +0.03164\ 38\ \text{a.u.},\\ q'_{\phi_2\phi_2} &\quad +1.65281\ 69\ \text{a.u.},\\ q'_{\phi_3\phi_3} &\quad +0.00001\ 604\ \text{a.u.},\\ q'_{\phi_5\phi_5}=q'_{\phi_7\phi_7} &\quad -0.49257\ 03\ \text{a.u.}, \end{aligned} \tag{2}$$

here the number of suffix i is the same as Duncan's one. Then we obtain $q_e=1.39467e$ a.u..

For the field gradient q_n due to protons, we have taken into account of the effect of the nuclear vibration in the molecule. A study of the normal modes of vibration in this molecule[8] shows that at ordinary temperature, we have only to take an average value over symmetric bending vibration of protons corresponding $\nu_2(a_1)=950\,\text{cm}^{-1}$, and therefore we have estimated the average regarding this mode as the simple harmonic oscillation. Following these considerations, we have obtained $q_n=-0.224115e$ a. u.. If all the nuclei are assumed to be fixed in the equilibrium positions, q_n becomes $-0.246876e$ a.u.. In order to take the effect of the nuclear vibrations on q_e into accunt, we must know the adiabatic dependence of q_e on the normal coordinates of vibration. However this is a very difficult task and therefore we have assumed that q_e is independent on the nuclear vibrations. This is probably allowed since the electrons, which give a great effect to the field gradient, are in vicinity of the N nucleus and they would be scarcely perturbed by small vibration of protons.

Now the total field gradient q becomes $-1.61879e$ a.u. for the vibrating nuclei and $-1.64155e$ a.u. for the static nuclei. The nuclear quadrupole coupling energy of the NH_3 molecule is known to be -4.10Mc.[9], from which we obtain $Q(\text{N}^{14})=1.08\times10^{-26}\,\text{cm}^2$ for the vibrating nuclei and $1.06\times10^{-26}\,\text{cm}^2$ for the static nuclei. It is interesting to note that our estimated value has fallen into the intermediate value between Townes et al's and Bassompierre's estimation.

References

1) C. H. Townes, A. N. Holden and F. R. Merritt; Phys. Rev. **74** (1948) 1113.
2) G. Sheriden and W. Gordy: Phys. Rev. **79** (1950) 513.
3) C. H. Townes and B. P. Dailey: J. Chem. Phys. **17** (1949) 782.
4) A. Bassompierre: Compt. rend. **240** (1955) 285.
5) A. B. F. Duncan: J. Chem. Phys. **27** (1957) 423.
6) For example, F. O. Ellison and H. Shull: J. Chem. Phys. **21** (1953) 1420 (H_2O). C. W. Scherr: ibid. **23** (1955) 569 (N_2). R. C. Sahni: ibid. **25** (1956) 332 (BH).
7) M. P. Barnett and C. A. Coulson: Trans. Roy. Soc. (London) **243** (1951) 221.
8) D. C. Mckean and P. N. Schatz: J. Chem. Phys. **24** (1956) 316.
9) B. T. Feld: Phys. Rev. **72** (1947) 1116.

Errata

A Note on the Theories Underlying the Polarimetric Study of Very Thin Dielectric Surface Layers

By Sadao NOMURA and Koreo KINOSITA

J. Phys. Soc. Japan **14** (1959) 297

Page	Column	Line		Should be read
297	left	7	light fall on···	light to fall on···
299	the line just above Eq. (15), and Eq. (15)		φ_p	$\varphi_{\rm p}$
301	right	Eq. (36)	$\rho_{\rm B}=\pm[\boldsymbol{L}_R'(0)\boldsymbol{N}(0)]_{\rm B}=\rho_{\rm p}$	$\rho_{\rm B}=\pm[\boldsymbol{L}_R'(0)\boldsymbol{N}(0)]_{\rm B}\,x=\rho_{\rm p}$
302	left	Eq. (39)	$\pm\frac{\pi}{\lambda}\frac{\sqrt{1+\varepsilon_2}}{\sqrt{1-\varepsilon_2}}\eta$	$\pm\frac{\pi}{\lambda}\frac{\sqrt{1+\varepsilon_2}}{1-\varepsilon_2}\eta$
303	the equation just above Eq. (53)			numbered (52)
303	left	Eq. (53)	$\left[\frac{\partial\boldsymbol{L}(0)}{\partial\varphi}\right]_{\rm B}$	$\left[\frac{\partial\boldsymbol{L}(0)}{\partial\varphi_1}\right]_{\rm B}$
303	left	8 from the bottom	Eq. (51)	Eq. (52)

PROGRESS OF THEORETICAL PHYSICS

CONTENTS

Progress of Theoretical Physics Vol. 20, No. 4, October 1958

Dispersion Relation for *K* Meson-Nucleon Scattering and its Application .... Keiji IGI..403
Hypothesis of Invariance of CP Alone and Conservation of Parity in Strong Interactions ....Chikashi ISO..410
Quantum Statistical Mechanics of Electron-Phonon System, II—*Specific Heat and Spin Paramagnetic Susceptibility*— ....Hiroshi ICHIMURA..415
Relativistic Wave Equations with Maximum Spin Two..................... ....T. TSUNETO and I. FUJIWARA..439
Possible Experimental Tests on the Decay Interactions of Hyperons ....Kiyomi ITABASHI..457
Perturbational Calculations of Propagators of the Elementary Particles interacting with the Gravitational Field ....Yoshio MIYATAKE..476
Effect of the Non-Relativistic Recoil of a Source Particle in Quantum Field Theories...................................J. OSADA and H. FUJINO..487
Tensor and Spin-Orbit Forces in Nucleon-Nucleon Scattering..Ryozo TAMAGAKI..505
On the Wave Propagation in the Non-Linear Fields, II ....Tosiya TANIUTI..529
Indirect Coupling of Nuclear Spins in Antiferromagnet with Particular Reference to MnF_2 at Very Low Temperatures ....Tuto NAKAMURA..542
Quasi-Chemical Equilibrium Theory, Part II....J. M. BLATT and T. MATSUBARA..553

Letters to the Editor:

Meson-Meson Interaction................K. IGI and K. KAWARABAYASHI..576
Baryon Mass Spectrum ....H. KATSUMORI and K. SHIMOURA..578
First Excited State in Ca^{42} and Ca^{44}......................T. KOMODA..580

Price $ 1.25 per copy
$ 15.00 per year (postage inclusive)
Annual dues for foreign members (individual subscribers)
$ 12.00 (postage inclusive)
〃 for foreign members of the Physical Society of Japan
$ 10.00 (postage inclusive)

Application for members, subscriptions and orders for back numbers should be sent, directly or through book-dealers, to

The Publication Office
in
Yukawa Hall, Kyoto University, Kyoto, Japan

. . . .

ANNOUNCEMENT

REVISED Price List of Back Numbers (for subscribers abroad)

*Vols. 1–4	$ 6.40 each
*Vols. 5 & 6	$13.00 each (single copy: $2.50)
*Vols. 7 and succeeding ones	$ 8.00 each (single copy: $1.50)

Back number prices are effective for volumes other than last four (4) volumes (the current volume inclusive).

Thus, volumes 1 through 16 will be regarded as back numbers while volume 20 is being published.

The revised prices will be effective on and after August 1, 1958.

. . . .

JOURNAL OF THE PHYSICAL SOCIETY OF JAPAN, Vol. 14, No. 6, JUNE, 1959

Absolute Cross Sections of the (γ, n) Reaction for Cu^{63}, Zn^{64} and Ag^{109}

By Teruo NAKAMURA, Kunio TAKAMATSU, Kiyoji FUKUNAGA,
Minoru YATA and Shinjiro YASUMI

Department of Physics, Faculty of Science, University of Kyoto

(Received January 14, 1959)

The photonuclear reaction cross section of $Cu^{63}(\gamma, n)Cu^{62}$ has been frequently used as the standard for the (γ, n) reactions, but the measured values by many workers do not agree with one another and can be roughly divided into two groups, namely, about 100 mb group and about 50 mb group. It appears that the former group contains the values obtained mainly by measurements by use of bremsstrahlungs, while the latter those obtained mainly with Li–p γ-rays.

We attempted to re-determine the (γ, n) cross section for copper, zinc and silver by Li–p γ-ray. Absolute measurement of γ-quanta was performed by Hough's method, and reaction yields were determined by the activation method in which the absolute numbers of activated nuclei in samples were determined by measuring the β-ray with a 4π-proportional counter and applying the "method of extrapolation". The cross sections of Cu^{63}, Zn^{64} and Ag^{109} for 17.6 Mev γ-rays were found to be 42.5 mb±15%, 23.3 mb±18% and 61.5 mb±16% respectively. Experimental cross sections so far obtained by many workers are compiled in Table II and some discussions are given.

§ 1. Introduction

The absolute cross sections of (γ, n) reactions have been studied by many workers.$^{1)-13)}$ Especially, for Cu^{63}, its cross section has been customarily used as the standard of (γ, n) reaction cross sections and has been frequently measured for both lithium-gamma rays and bremsstrahlungs by using various methods as indicated in Table II.

It seems curious, however, that experimental cross section values of this reaction never agree with one another and the discrepancies between them sometimes exceed over about 100%. So far as the $Cu^{63}(\gamma, n)Cu^{62}$ reaction cross section value is used as the standard, this uncertainty introduces directly the ambiguities of the same order into the integrated cross section value $\int \sigma dE$ which is often compared with the sum rule of the photonuclear reaction. Therefore further investigation on the cross section seems to be extremely desirable. For this reason, we have attempted to re-determine the (γ, n) absolute cross sections of Cu^{63}, Zn^{64} and Ag^{109} for Li–p γ-rays.

§ 2. Experimental Procedure

The γ-rays were produced by the $Li^7(p, \gamma)Be^8$ reaction. Li metal targets of 0.5 mm thick were bombarded with magnetically analysed protons which were accelerated to 500 Kev by a Cockcroft generator and whose intensities were about 50 μA～100 μA. Sample discs made of copper, zinc and silver were irradiated by these γ-rays, and (γ, n) cross sections were determined by the activation method.

The size of the proton beam spot was about 8 mm in diameter, and the distance between the sample disc and the γ-ray source was 14.5 mm, the former having been fixed on the target box with an aluminium jig$^{14)}$.

Sample discs used were all 20 mm in diameter and 1 mm thick for copper and silver, and 0.6 mm thick for zinc respectively. These dimensions were the same as those of the monitor discs, which had been used by one of authors (S. Y.) in the measurement of the 14 Mev neutron reaction cross section$^{15)}$.

The γ-ray intensities were measured by using an end-window Geiger counter with a 5 mm lead converter on the front and its counting efficiency for Li–p γ-ray was calibrated by

Hough's method16). Hough's method may be summarized as follows: When a thin metal foil is placed in front of a Geiger counter on the passage of γ-rays, the counting rate of the counter will increase due to secondary electrons from metal foil produced by γ-rays. From this excess counting rate and the electronic cross section of γ-ray for a converter metal, we can obtain the γ-ray flux at the position of the converter foil. In our case, when the counter was situated at a distance of 31.7 cm from the target, one count of this counter corresponds to $(1.63\pm0.20)\times10^4\ \gamma$ quanta per 4π steradians14).

Produced activities were measured by use of an end-window Geiger counter with the disc in front of the window. To hold the disc, a jig was used, which is the same one as that used in the β-counting described in ref. 15).

Using the activation method, the cross section is obtained as follows. γ-quanta were measured for every one minute interval for copper and zinc, and for every half a minute interval for silver, and we considered that the γ-ray intensity was kept constant in that interval and the fluctuation of the intensity was considered as errors. Then the cross section σ for copper and zinc is given by*

$$\sigma=\frac{M\left[N\Big/\sum_{i=1}^{T} n_{\gamma i}\exp\{-(T-i+t_0)\lambda\}\right]S\cdot G_G\cdot C_k}{N_0\eta[(1-e^{-\lambda})(1-e^{-\lambda t'})/\lambda]}.$$

and that for silver is given by

$$\sigma=\frac{M\left[N\Big/\sum_{i=1}^{2T} 2n_{\gamma i}\exp\{-(T-i/2+t_0)\lambda\}\right]S\cdot C_G\cdot C_k}{N_0\eta[(1-e^{-\lambda/2})(1-e^{-\lambda t'})/\lambda]},$$

where

N_0: Avogadro's number,

M: molecular weight of the sample,

η: isotopic abundance ratio,

λ: decay constant of the activity,

S: correction factor related to the self-absorption and scattering of the sample, which was measured by the method of extrapolation,

C_G: geometrical correction factor for the β-counting concerning the absorption by the air and the mica window, the back scattering and the solid angle, which was measured by a 4π-proportional counter,

C_k: correction factor concerning the branching ratio between the positron emission and the orbital electron capture, namely

$C_k=1$ for the case of β^- activity

$C_k>1$ for the case of β^+ activity,

i: number of the order of each time interval during bombardment (integer),

$n_{\gamma i}$: number of photons reaching the sample disc in one minute or half a minute of i-th interval,

N: β-counts per t' minute on the sample disc,

T: time of irradiation (minute),

t_0: time elapsed from the end of irradiation to the beginning of the beta counting (minute),

t': time of beta counting (minute).

For the correction factors S and C_G, we used the values measured in ref. 15). Then the identity of the properties of both G–M tubes must be assured. So it was checked with the calibration disc of KCl and it was found that they were identical with each other within the statistical error.

The time of the irradiation of γ-rays was about twice the half life for each sample and the time of β-counting was ten minutes for copper and silver, and thirty minutes for zinc respectively.

---

* For the derivation of this formula, see the appendix in ref. 15). Since sample discs used in this experiment, as mentioned above, have the same dimension as those of the monitor discs used in ref. 15), N in this equation corresponds to N_M in ref. 15). In the present case, however, measurements determining S-value were not performed, but we adopted S measured by the method of extrapolation in ref. 15) for that in this equation, because both $(n, 2n)$ and (γ, n) reactions should produce the same residual nucleus.

Consequently, we may regard S-value as the "correction factor" by which counts of comparatively thick sample N can be converted to a value proportional to the specific activity.

§ 3. Results

The cross sections obtained are shown in Table I. As these decay constants, we used the value for copper which was determined in our measurement with Peierls' method and the values from King's table[17] for zinc and silver.

Table I. Results obtained.

Reaction	λ (min^{-1})	σ(Li–$p\gamma$) (mb)	σ(17.6 Mev)** (mb)
$Cu^{63}(\gamma, n)Cu^{62}$	0.0695*±2%	37.7±15%	42.5
$Zn^{64}(\gamma, n)Zn^{63}$	0.018	20.7±18%	23.3
$Ag^{109}(\gamma, n)Ag^{108}$	0.295	54.6±16%	61.5

* The decay constant of Cu^{62} was determined in our measurement.

** For the reduction to 17.6 Mev monochromatic γ-ray, we used the ratio 1:2 as the intensity ratio of 14.8 Mev to 17.6 Mev γ-ray, and the results of bremsstrahlung experiments as the excitation curve for each elements.

For the reactions $Cu^{63}(\gamma, n)Cu^{62}$ and $Ag^{109}(\gamma, n)Ag^{108}$, the contributions of $Cu^{65}(\gamma, n)Cu^{64}$ (half life ~12 hour) and $Ag^{107}(\gamma, n)Ag^{106}$ (half life 24 min) must be considered respectively. In the case of copper, the contribution of β-activity of Cu^{64} for the β counting of Cu^{62} can be neglected because of the long half life, so that the correction was not made but was included in the counting errors.

In the case of silver, on the contrary, the contribution of Ag^{106} β-activity cannot be neglected because of the comparatively short half life. Thus, using the experimental value as obtained by Uemura *et al.*[18] for the ratio of the cross section of $Ag^{109}(\gamma, n)Ag^{108}$ to that of $Ag^{107}(\gamma, n)Ag^{106}$ for Li–p γ-rays, and considering that the geometrical factor C_G and specific activity S are of the same values for both Ag^{108} and Ag^{106} β-activities, the cross section of $Ag^{109}(\gamma, n)Ag^{108}$ becomes as follows:

$$\sigma=\frac{M\cdot S\cdot C_k}{N_0}\,\frac{N}{\Sigma}\ ,$$

with

$$\Sigma=\eta_1[\{1-\exp(-\lambda_1/2)\}\{1-\exp(-\lambda_1 t')\}/\lambda_1]$$
$$\times\sum_{i=1}^{2T}2n_{\gamma i}\exp[-(T-i/2+t_0)\lambda_1]\frac{1}{C_{k1}}$$
$$+\ \frac{\sigma_2}{\sigma_1}\eta_2[\{1-\exp(-\lambda_2/2)\}\{1-\exp(-\lambda_2 t')\}/\lambda_2]$$
$$\times\sum_{i=1}^{2T}2n_{\gamma i}\exp[-(T-i/2+t_0)\lambda_2]\frac{1}{C_{k2}}\ ,$$

$$\frac{\sigma_2}{\sigma_1}=0.903\ ,$$

where suffixes 1 and 2 correspond to Ag^{109} and Ag^{107} respectively.

The source of error was mainly in the measurement of the absolute gamma quanta, being 13%[14], and in the estimation of other errors the upper limits were used if they could not be estimated accurately. They were as follows: ±1% from the calculation of the solid angle of the sample subtended to the γ-source, ±4% from the shift of the position of the γ-source, less than 1.5% from an additional error concerning geometrical factor C_G due to the difference of the irradiation geometry between the present work and ref. 15), and some errors for each sample. The last errors mentioned here were for Cu, the statistical error of β-counting : ±1%; the fluctuation of γ-ray intensities during the irradiation : below ±2.5%; decay constant λ : ±2%; specific activity S : ±3%; geometrical factor C_G : ±2% and the contamination of beta activities of Cu^{64} for the beta counting : below 2%; while for Zn, the statistical error of the beta counting : ±4%; the fluctuation of γ-ray intensities during the irradiation : below 0.2%; the error of λ negligibly small; S : ±10% and C_G : ±4%; and for Ag, the statistical error of the beta counting : 4%; the fluctuation of γ-ray intensity during the irradiation : below ±2%; λ : ±1%; S : ±7% and C_G : ±3%. The errors shown in Table I are the roots of square sums of them.

§ 4. Discussions

Making a list of the experimental values of the reaction cross section of $Cu^{63}(\gamma, n)Cu^{62}$ for 17.6 Mev photons as summarized in Table II, it appears that they are divided into two groups i.e. one group of about 100 mb and the other of about 50 mb. The experiments belonging to the former were all performed by using the bremsstrahlungs of betatrons or a linear accelerator except those of Wäffler and Hirzel[1] and Carver and Kondaiah[10], and (γ, n) excitation curves were obtained from the yield curves with the photon difference

Table II. Summary of absolute

Author	γ-ray		
	Source (Spectrum)	Monitor	Monitor calibration
H. Wäffler und O. Hirzel (1948)	Li–*p*	thick walled Al G. M. counter	cal. F. L. L.[a]
S. Shimizu (1949)	Li–*p*	lead G. M. counter	cal. Sonoda[b]
B. D. McDaniel, R. L. Walker and M. B. Stearns (1950)	Li–*p*	lead G. M. counter	exper. Hough[c]
H. E. Johns, L. Katz, R. A. Dauglas and R. N. H. Haslam (1950)	24 Mev Betatron (Schiff)	roentgen meter	cal. F. L. L.
B. C. Diven and G. M. Almy (1950)	22 Mev Betatron (Schiff)	roentgen meter	cal. F. L. L.
P. R. Byerly and W. E. Stephens (1951)	24 Mev Betatron (Schiff)	γ-monitor	Victoreen roentgen meter
V. F. Krohn and E. F. Shrader (1952)	21 Mev Betatron (exper.)	pair spect. meter	D_2O emulsion D_2-photodis. σ
H. Glättli, O. Seippel and P. Stoll (1952)	Li–*p*	G. M. counter	exper. Hough
R. Montalbetti, L. Katz and J. Goldenberg (1953)	23 Mev Betatron (Schiff)	roentgen meter	cal.
J. H. Carver and E. Kondaiah (1954)	Li–*p*	brass G. M. counter	exper. Barnes[d]
A. I. Berman and K. L. Brown (1954)	36 Mev Linac (Bethe-Heitler)	incident electron beam intensity	
W. H. Hartley, W. E. Stephens and E. J. Winhold (1956)	Li–*p*	NaI Scintillation counter	cal. White[e], incident proton beam intensity
B. I. Gavrilov and L. E. Lazareva (1956)	Synchrotron 27 Mev (Schiff)	Al ionization chamber	cal. F. L. F.[f]
Present Work (1959)	Li–*p*	G. M. counter	exper. Hough

a) ref. 19.
b) ref. 22.
c) ref. 16.
d) ref. 20.
e) G. R. White: National Bureau of Standards Reports (1952) 1003.
f) Flower, Lawson and Fossey: P. P. S. **65B** (1952) 286.
g) The electron attenuation factor in the counter wall $e^{-\mu x}$ was used in calculation.
h) Specific activity *S* and geometrical factor *G* of β counting were obtained by the extrapolation method.
i) Specific activity *S* and geometrical factor *G* were measured. See ref. 4.

method in which the shapes of spectra of bremsstrahlungs were needed for the analysis of data, and in almost all the cases the theoretical curves were used for the spectrum of bremsstrahlungs. For the measurements of the intensity of bremsstrahlung, a roentgen-meter or an ionization chamber was usually used and its response was theoretically calculated.

Among the measurements with bremsstrahlungs, however, it is noticeable that Krohn and Shrader[7] determined the energy spectra of bremsstrahlungs by the D_2O emulsion and monitored these intensities by the γ-ray pair spectrometer which was calibrated with the cross section of the photodisintegration of deuteron, and Berman and Brown[11] used directly the incident electron intensity from a linear accelerator to determine the intensity of the bremsstrahlung.

In addition, as mentioned above, there are only two measurements by Li–*p* γ-ray in the 100 mb group. Wäffler and Hirzel[1] obtained 120 mb with Li–*p* γ-ray who used a thick aluminium counter for the measurement of the γ-ray intensity and its counting efficiency (γ, *n*) cross sections.

neutron detector	Neutron yield			(γ, *n*) cross section of copper. Author results (mb)	$\sigma_{Cu^{63}}(17.6)$ [o] (mb)	relative cross section [p]		
	neutron detector calibration	β-counting	β-counting calibration			Cu	Zn	Ag
BF₃+paraffin	Ra+Be, Po+Be	Al G. M. counter (cylindrical)	cal. $-e^{-\mu x}$ [g]	$120\pm30\ ^{63\ \mathrm{k)}}_{17.6\ \mathrm{l)}}$	120	100	62^{64}	176^{109}
		G. M. counter (end window)	extrap. S [h] extrap. G	$77\pm13\ ^{63}_{17.6}$	33*			
				$55\pm12\ ^{\mathrm{nat\ m)}}_{\mathrm{Li}-p\ \mathrm{n)}}$	55	100	86	24.5
		G. M. counter	exper. S [i] exper. G	$110\ ^{63}_{17.6}$	110			
		G. M. counter (end window)	RaE	$100\ ^{63}_{17.6}$	100	100		190^{109}
		G. M. counter	RaD+E	$100\ ^{63}_{17.6}$	100			
		G. M. counter (end window)	extrap. S RaD+E, P^{32}	$90\ ^{63}_{17.6}$	90			
		G. M. counter	exper. S RaD+E	$48\pm8\ ^{63}_{\mathrm{Li}-p}$	54			
BF₃+paraffin				$110\ ^{\mathrm{nat}}_{17.6}$	95	100	95	251
Szilard-Chalmers	D(γ, *n*) Ra+Be			$85\pm15\ ^{\mathrm{nat}}_{\mathrm{Li}-p}$	85			
		4π-scintillation counter	extrap. S	$97\ ^{63}_{17.6}$	97			
BF₃+paraffin	Ra+Be, Sb+Be			$75\ ^{\mathrm{nat}}_{17.6}$	65	100	88	270
BF₃+paraffin	Ra+Be			$120\ ^{\mathrm{nat}}_{17.6}$	104			
		G. M. counter (end window)	extrap. S 4π. G [j]	$38\pm6\ ^{63}_{\mathrm{Li}-p}$	43	100	55^{64}	145^{109}

j) Geometrical factor *G* was measured by the 4π-counter.
k) The cross section of $Cu^{63}(\gamma, n)$.
l) The cross section by 17.6 Mev photons.
m) The cross section of natural copper.
n) The cross section by Li–*p* γ-ray.
o) The following values were used to reduce the cross section of $Cu^{63}(\gamma, n)$ by 17.6 Mev photons: the intensity ratio of 17.6 Mev and 14.8 Mev photons in the Li–*p* γ-ray is 2:1, $\sigma_{17.6\,\mathrm{Mev}}(\mathrm{Cu})/\sigma_{14.8\,\mathrm{Mev}}(\mathrm{Cu})=1.67$ and $\sigma_{17.6\,\mathrm{Mev}}(\mathrm{Cu}^{65})/\sigma_{17.6\,\mathrm{Mev}}(\mathrm{Cu}^{63})=1.5$.
p) Suffix numbers show the mass number of the isotopes.
* See § 4. Discussions or ref. 14.

was calculated by Fowler *et al.*[19] Carver and Kondaiah[10] measured neutron yields with the Szilard-Chalmers' method and determined the γ-flux with the brass Geiger counter calibrated experimentally by Barnes *et al.*[20] They calibrated this counter using a thick-walled ionization chamber made of graphite which contained a cylindrical cavity filled with pure nitrogen, whose ionization current was translated into the γ-ray flux by the theory of Lax[21] and the validity of this theory was accertained by the α-counting from the reaction $F^{19}(p, \alpha, \gamma)O^{16}$.

On the other hand, experiments belonging to the 50 mb group were all done with Li–*p* γ-rays including the present work, and the γ-ray intensities were all determined with G–M counters calibrated by Hough's method.

Previously, $Cu^{63}(\gamma, n)Cu^{62}$ reaction cross section had been measured by Shimizu[2] at our laboratory, and with Hough's method we calibrated the γ-intensity monitor which had been used by him and whose efficiency was calculated by Sonoda.[22] This result reduced the cross section value reported by Shimizu to 33 mb as shown in Table II.

It is seen in Table II that in each group the relative cross sections agree fairly well with one another. For this reason, it seems reasonable to us that these discrepancies may be due to the uncertainty of determination of photon intensities.

It should be emphasized that the cross section values belonging to 50 mb-group are obtained by purely experimental methods and therefore considered to be more reliable than 100 mb group.

It is very desirable, however, to find the reason why there are such large discrepancies in the experimental determinations of (γ, n) cross section.

Acknowledgement

The authors wish to express their cordial thanks to Prof. K. Kimura for his continual interest and encouragements. They are also greatly indebted to Prof. S. Shimizu for valuable discussions and to Mr. Y. Saji of Institute for Nuclear Study, University of Tokyo for private communication. Further, they are grateful to Miss T. Hirata for preparing the manuscript.

References

1) H. Wäffler und O. Hirzel: Helv. Phys. Acta **21** (1948) 200.
2) S. Shimizu: Mem. Coll. Sci. Kyoto Univ. **A**, **25** (1949) 193.
3) B. D. McDaniel, R. L. Walker and M. B. Stearns: Phys. Rev. **80** (1950) 807.
4) H. E. Johns, L. Katz, R. A. Dauglas and R. N. H. Haslam: Phys. Rev. **80** (1950) 1062.
5) B. C. Diven and G. M. Almy: Phys. Rev. **80** (1950) 407.
6) P. R. Byerly and W. E. Stephens: Phys. Rev. **83** (1951) 54.
7) V. F. Krohn and E. F. Shrader: Phys. Rev. **87** (1952) 685.
8) H. Glättli, O. Seippel and P. Stall: Helv. Phys. Acta **25** (1952) 491.
9) R. Montalbetti, L. Katz and J. Goldenberg: Phys. Rev. **91** (1953) 659.
10) J. H. Carver and E. Kondaiah: Phil. Mag. **45** (1954) 988.
11) A. I. Berman and K. L. Brown: Phys. Rev. **96** (1954) 83.
12) W. H. Hartley, W. E. Stephens and E. J. Winhold: Phys. Rev. **104** (1956) 178.
13) B. I. Gavrilov and L. E. Lazareva: Soviet Phys. **3** (1957) 871.
14) T. Nakamura, K. Fukunaga, K. Takamatsu and S. Yasumi: Mem. Coll. Sci. Kyoto Univ. (to be published).
15) S. Yasumi: J. Phys. Soc. Japan **12** (1957) 443.
16) P. V. C. Hough: Phys. Rev. **80** (1950) 1069.
17) R. W. King: Rev. Mod. Phys. **26** (1954) 327.
18) Y. Uemura, M. Sonoda, Y. Saji, S. Yasumi, Y. Ishizaki and Y. Ohno: Bull. Inst. Chem. Res. Kyoto Univ. **29** (1952) 66.
19) W. A. Fowler, C. C. Lauritsen and T. Lauritsen: Rev. Mod. Phys. **20** (1948) 236.
20) C. A. Barnes, J. H. Carver, G. H. Stafford and D. H. Wilkinson: Phys. Rev. **86** (1952) 359.
21) M. Lax: Phys. Rev. **72** (1947) 61.
22) M. Sonoda: J. Phys. Soc. Japan **5** (1950) 53, 403, 408.

JOURNAL OF THE PHYSICAL SOCIETY OF JAPAN Vol. 14, No. 6, JUNE, 1959

Gamma Rays from Neutron Inelastic Scattering of Magnesium, Aluminum, Iron and Bismuth

By Masanao HOSOE and Shoji SUZUKI

Department of Physics, St. Paul's University, Tokyo, Japan

(Received February 23, 1959)

The gamma rays resulting from the ring scatterers of Mg, Al, Fe and Bi bombarded with 2.95 MeV neutrons have been investigated. The cross sections for the 0.845 MeV gamma ray from Fe^{56} and for the 1.37 MeV gamma ray from Mg^{24} were 1.10 ± 0.13 and 0.66 ± 0.10 in barns respectively. The angular distributions of the gamma rays relative to the direction of the incident neutrons were both symmetric around 90°. These cross sections and angular distributions were compared with the statistical theory by the optical model. Our results were fairly well interpreted by using a diffuse potential well.

§ 1. Introduction

Hauser and Feshbach1) developed the statistical theory by which the inelastic scattering of neutrons could be accounted for. But their theory is not capable of interpreting the details which are shown up in the recent experiments. The fine structure in the excitation curves obtained by Kiehn and Goodman2) would not be interpreted by the statistical theory which assumes a continuous level scheme of the compound nucleus, though this theory holds for an excitation curve smoothed out over energy. Cranberg and Levin3) and Muehlhause et al4) found the asymmetric angular distributions of inelastically scattered neutrons. The associated gamma rays were also found as being asymmetrically distributed by the recent experiment5). These facts show that the statistical assumption fails in some cases.

However, there are some other experimental results which can be accounted for by the statistical theory. For these cases one can calculate the transmission coefficients in the Hauser and Feshbach's formula1), being based on some model. Van Loef and Lind6) have measured the excitation curves of inelastic scattering for neutrons with energies up to 2 MeV and the angular distribution of the 0.845 MeV gamma ray from iron for the 1.77 MeV incident neutrons. Using the statistical theory they calculated the transmission coefficients by the optical model7) to fit their results, and obtained 0.2 for the absorption coefficient for the case of a square well potential. This result is nearly equivalent to that reduced from the continuum theory, and this figure is not consistent with the value determined from the total and elastic scattering cross sections. Cranberg and Levin3) and Muehlhause et al4) measured also the angular distributions of gamma ray from iron for the neutrons of 2.45 and 1.66 MeV respectively. According to our calculation8) which is shown in Appendix, the diffuse potential fits satisfactorily to their results with the values of parameters determined by Beyster et al9), while it could not interprete the Van Loef and Lind's experiment6).

This paper presents the study on the gamma rays from the ring scatterers of Mg, Al, Fe and Bi bombarded by neutrons of energy of 2.85 to 3.00 MeV, and particularly the measurement of angular distributions for the 0.845 MeV gamma ray from Fe^{56} and for the 1.37 MeV gamma-ray from Mg^{24}. By comparing the cross sections and the angular distributions with our calculation using the Hauser and Feshbach's and Satchler's formulas10) respectively, we aimed to determine the most appropriate model and its nuclear parameters for both nuclei.

§ 2. Experimental Procedure and Correction

We used the D–D neutrons produced by a 200 kV Cockcroft-Walton accelerator. Their energies were 2.85 ± 0.10, 2.90 ± 0.10, 2.95 ± 0.10 and 3.00 ± 0.10 MeV. The scatterers used were of doughnut type with the outer diameter of 13 cm and the inner diameter of 7 cm and their diameter of the cross section was 3 cm. They were made of iron, magnesium, aluminum and bismuth all with purity of 99.9%. A carbon ring was used for making correction of the effect of elastically scattered neutrons from the scatterer.

We used a gamma ray spectrometer with a NaI(Tl) scintillator (1″φ×1″) mounted on a Du Monte 6292 photomultiplier with a magnetic shield of mu-metal. Pulses from the photomultiplier were amplified by an A-1 amplifier and analyzed by a single channel pulse height analyzer of Johonstone type or a Gray-Wedge analyzer. Neutron flux was monitored by a calibrated scintillation counter with a stilbene crystal (1″φ×½″).

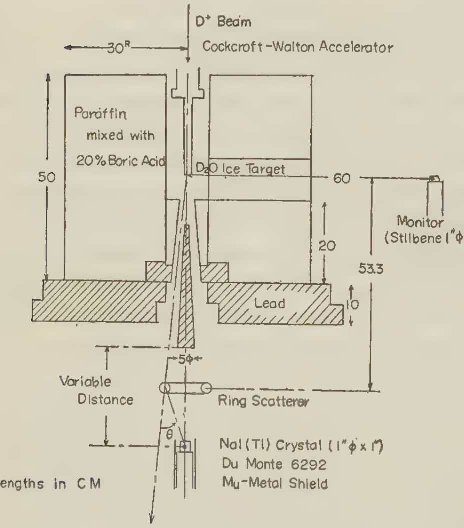

Fig. 1. Experimental arrangement.

The experimental arrangement is shown in Fig. 1. The detector was set at different positions on the central axis of the scatterer for the measurement of the angular distribution of gamma rays. The numerical calculation of the angular resolution of our geometry gave about ±7° at the 90° position, which was the worst case.

The background counting was due to stray neutrons and gamma rays incident on the crystal. The neutrons gave rise to the $I^{127}(n, n')I^{127*}(\gamma)$ and $I^{127}(n, \gamma)I^{128}(\beta)$ reactions which contributed considerably to the background. In order to keep the background from the room wall at a low level, the incident neutrons were canalized by a block of paraffin mixed with 20% boric acid. For example at the 90° position, this shielding reduced the stray neutrons of 1–2.5 MeV to about 4% of the direct neutrons, while this figure was about 9% without the shielding, and the ratio of the counts of the 0.845 MeV gamma ray from the $Fe^{56}(n, n')Fe^{56*}$ reaction to the background counts was increased from 2 to 5 at the 90° position. The background counts due to induced activity in the crystal, mostly attributed to I^{128} with the half-life of 25 minutes, were measured for 4 minutes after every neutron exposure of 4 minutes. The induced background amounted about 15% of the total background. We stopped continuous repetition of measurements before the induced background increased to 40% of the total background.

The net counts N due to the gamma ray for each angle is calculated as

$$N = N_s - C(N_d - N_n) - N_n ,$$

where N_s, N_d and N_n are the counting rates respectively with the sample scatterer, with the dummy scatterer (carbon for the iron sample and aluminum for the magnesium sample) and without the scatterer; the induced background counts have been subtracted from N_s, N_d and N_n. C is the correction factor for the difference of the number of atoms and cross sections of neutron scattering by the dummy and the scatterer. For the determination of the differential cross section of inelastic scattering $\sigma(\theta)$, we took into account the following three factors: multiple scattering of the incident neutrons, absorption of gamma rays in the scatterer, and detection efficiency of the crystal detector.

We assumed that the directional deviation of incident neutron, which might be caused by multiple scattering, is negligiblly small because of great probability of the forward elastic scattering. $\sigma(\theta)$ can be calculated from the equation:

$$N = \sum_j N_j = \sum_j \sum_i Q_i \exp(-\mu_1 l_{ij})\, dV_i n \sigma(\theta_0 + \Delta\theta_{ij}) \frac{\eta_j}{4\pi r_{ij}^2} \exp(-\mu_2 l_{ji}')\, dV_j , \qquad (1)$$

where N_j is the counts given in an elementary volume dV_j in the crystal, η_j the detection efficiency per unit volume for the gamma rays incident on dV_j, Q_i the neutron flux at an elementary volume dV_i in the scatterer which contains n nuclei per unit volume, r_{ij} the distance between dV_i and dV_j, θ_0 the angle between the direction of the incident neutron and the line from the geometrical center of the scatterer to the effective center of the crystal, $\theta_0+\Delta\theta_{ij}$ the angle between the directions of r_{ij} and the incident neutrons, and l_{ij} and μ_1 are the path length and absorption coefficient of the gamma ray in the scatterer and l_{ji}' and μ_2 are the corresponding quantities in the crystal. Day[11] calculated Eq. (1) numerically by using an Analogue Computer. We used the following method of approximation:

Expanding $\sigma(\theta_0+\Delta\theta_{ij})$ at the point θ_0 we get from Eq. (1)

$$N\propto\sigma(\theta_0)\left\langle\frac{Q_i\exp(-\mu_1 l_{ij}-\mu_2 l_{ji}')\eta_j}{4\pi r_{ij}^2}\right\rangle_{AV}+\sigma'(\theta_0)\left\langle\frac{\Delta\theta_{ij}Q_i\exp(-\mu_1 l_{ij}-\mu_2 l_{ji}')\eta_j}{4\pi r_{ij}^2}\right\rangle_{AV}+\cdots. \tag{2}$$

Then we rewrite

$$\left\langle\frac{Q_i\exp(-\mu_1 l_{ij}-\mu_2 l_{ji}')\eta_j}{4\pi r_{ij}^2}\right\rangle_{AV}\equiv\gamma(\theta_0)\left\langle\frac{\exp(-\mu_2 l_{ji}')\eta_j}{4\pi r_{ij}^2}\right\rangle_{AV}. \tag{3}$$

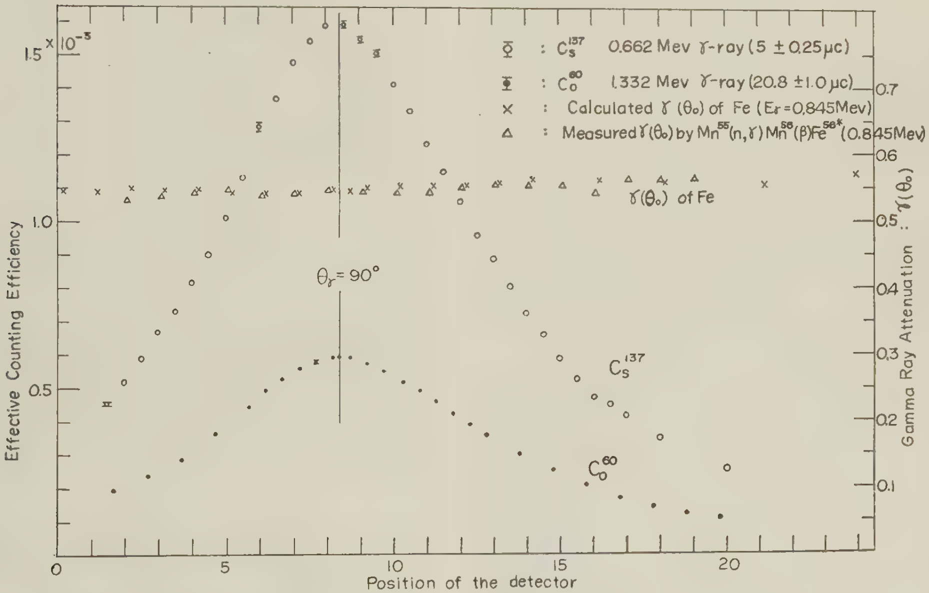

Fig. 2. Variation of the effective counting efficiency for the gamma rays of 0.662 MeV (Cs^{137}) and 1.332 MeV (Co^{60}) with the positions of NaI(Tl) crystal, and the gamma ray attenuation in the doughnut ring of iron: $\gamma(\theta_0)$.

The factor $\left\langle\frac{\exp(-\mu_2 l_{ji}')\eta_j}{4\pi r_{ij}^2}\right\rangle_{AV}$ means the effective counting efficiency of the detector system. We determined this value experimentally by using a dummy source of Cs^{137} ($5\pm0.25\,\mu c$) or Co^{60} ($20.8\pm1.0\,\mu c$) which was contained in a polyethylene container with the same size as the scatterer. The experimental results are shown in Fig. 2. The effective center of the crystal was also determined from these curves. The factor $\gamma(\theta_0)$ is a function of $Q_1, Q_2, \cdots$ beside θ_0 and means correction for the attenuations of the gamma ray by self-absorption and of the incident neutrons in the scatterer. This factor would be expected to be nearly constant against θ_0 for the case of uniform value of Q_i, because of circular cross section of the scatterer, but in general $\gamma(\theta_0)$ is larger for backward angles than forward on account of flux attenuation of the incident neutrons. In order to estimate variation of $\gamma(\theta_0)$ with θ_0, and to make use of the value for calculation of the differential cross section, we calculated numerically $\gamma(\theta_0)$ by the following approximated formula:

$$\left\langle\frac{Q_i\exp(-\mu_1 l_{i0})}{r_{i0}^2}\right\rangle_{AV}\Big/1/r_0^2\,, \tag{4}$$

where r_0 is the distance between the geometrical center of the cross section of the scatterer and the effective center of the crystal. We calculated the formula (4) for the following three cases of Q_i. For the first case, the neutron flux was assumed to be constant throughout the scatterer[11]; this means no attenuation of the incident neutrons. As seen in Fig. 2, the value obtained was independent of θ_0 within the error of the calculation. For the second case, the neutron flux decreased by the total cross section of neutron[6] along its incident direction; this means complete neglect of multiple scattering. The variation of $\gamma(\theta_0)$ with the angle θ_0 was, for example, $+9\%$ for 140° and -9% for 40° relative to the 90° value. The above assumptions might be the two extreme cases. For the third case, the calculation was made for the assumption that the neutron flux decreased only by the inelastic scattering cross section, giving the result that the variation of $\gamma(\theta_0)$ was $\pm 4\%$ for the both angles mentioned above relative to the 90° value. For the determination of the cross section we took the third case.

In order to test the reliability of the calculated values of $\gamma(\theta_0)$, we activated uniformly by thermal neutrons a ring of iron alloy containing 30% manganese with the same size as the scatterer. The division of the count of the 0.845 Mev gamma ray from the $Mn^{55}(n, \gamma)Mn^{56}(\beta)Fe^{56*}$ reaction by the count for the dummy gamma ray source gave $\gamma(\theta_0)$ for the first case according to the formula (4). The result is presented in Fig. 2, being normalized to the calculated value at 90°, and is in good agreement with the calculation within 3%. This implies that the approximation under which the formula (4) was derived was satisfactorily accurate for uniform Q_i. For the case of ununiform Q_i, the formula (4) may be used also as a good approximation since $\partial\gamma(\theta_0)/\partial Q_i$ is nearly equal to the differential coefficient of formula (4) with regard to Q_i.

We evaluated also the second term of Eq. (2) in the same way. The contribution to N was only $\pm 0.7\%$ which could be neglected.

In order to estimate the neutron energies and their widths, we measured the differential cross sections and the excitation curve for the elastically scattered neutrons by carbon by using a plastic phosphor ($1''\phi \times 1''$) as a neutron detector in the same geometry. The differential cross sections of carbon are given in Fig. 3, together with the exprimental data of Meier et al[12] and Budde and Huber[13]. It is seen that the large anisotropy due to $D_{3/2}$ resonance of C^{13} at the 2.95 MeV neutron energy is fairly smoothed out in our experiment. This was considered as due to the large energy width of the neutrons ($\Delta E_n \simeq$ 0.10 MeV) and not due to poor angular resolution of the detector. The symmetrical distribution about 90°, together with the manganese test, shows that our experimental arrangement was competent to measure the angular distribution.

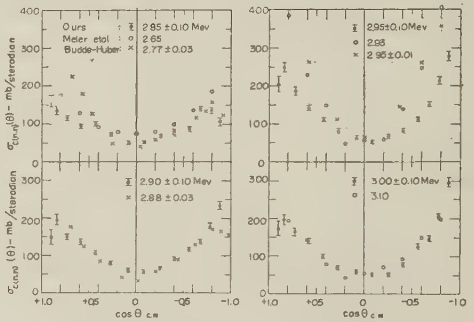

Fig. 3. Differential cross sections of the elastically scattered neutrons by carbon at the 2.85, 2.90, 2.95 and 3.00 MeV neutron energies (full circles). The open circles show the results obtained by Meier et al and the crosses show that by Budde and Huber.

§ 3. Results and Discussion

(1) The inelastic cross section of Mg, Al, Fe and Bi:

Figs. 4, 5, 6 and 7 show the typical pulse height distributions of the gamma rays from inelastic scattering and the detector background. The energy of gamma rays ranged from about 0.5 MeV to 2.2 MeV except for background gamma rays. As we used a small NaI(Tl) crystal to have a good angular resolution, we could not detect gamma rays of higher energies. The results are shown in Table I. The gamma rays from the scatterer and the background are in good agreement in energy with those found by other authors[2), 6),11),14),15),16] except a few points. In the background, several peaks which were not in other authors' results are found. According to Kiehn and Goodman[2], the third excited state of Fe^{56} was 2.25 MeV, but Poppema et al[17] and Morgan[14] assigned it to 2.65 MeV.

The present authors' result agreed with the latter's. This is due to the fact that Kiehn and Goodman might have missed the 1.81 MeV gamma ray resulting from the transition between the third and the first levels. Although Shapiro and Higgs[16] assigned a 2.07 MeV gamma ray to the transition from the second level to the ground state of Fe^{56}, our result indicated that it might come from the transition from the fourth level to the first. For Al^{27}, Morgan has found two gamma rays of 1.45 MeV and 1.75 MeV corresponding to the transitions from the third level to the first and from the fourth level to the second. These gamma rays were missing in our experiment, probably because of being masked by the background.

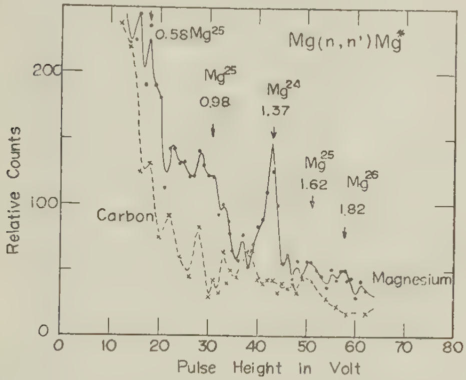

Fig. 4. The pulse height distributions of the gamma rays from magnesium and the background due to a carbon ring at the 2.95 MeV neutron energy. Channel width=1 Volt.

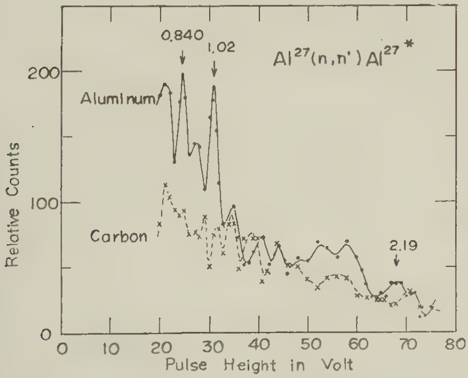

Fig. 5. The pulse height distributions of the gamma rays from aluminum and the background due to a carbon ring at the 2.95 MeV neutron energy. Channel width=1 Volt.

The differential cross sections at 90° for the 2.95±0.10 MeV neutrons were measured only for the cases in which the associated gamma rays had distinct photopeaks. The result is included in Table I. By measuring the angular distributions of the 0.845 MeV gamma ray of Fe^{56} and the 1.37 MeV gamma ray of Mg^{24}, we found the inelastic scattering cross sections $\sigma_{(n,n')}$; $\sigma_{Fe^{56}(n,n')}$ were 1.14±0.13, 1.19±0.14, 1.10±0.13 and 1.06±0.12 in barns at E_n=2.85±0.10, 2.90±0.10, 2.95±0.10 and 3.00±0.10 in MeV respectively, and $\sigma_{Mg^{24}(n,n')}$ was 0.66±0.10 barn at E_n=2.95±0.10 MeV. The errors were computed from the uncertainties of the neutron flux (±9%), of the effective counting efficiency (±5%), of the calculation of $\gamma(\theta_0)$ (±2%), and finally of the geometrical setting, the statistical errors of the counting rate and the fluctuation of the electrical instruments (the last three total

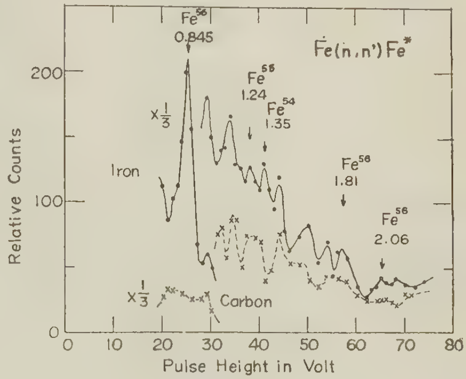

Fig. 6. The pulse height distributions of the gamma rays from iron and the background due to a carbon ring at the 2.95 MeV neutron energy. Channel width=1 Volt.

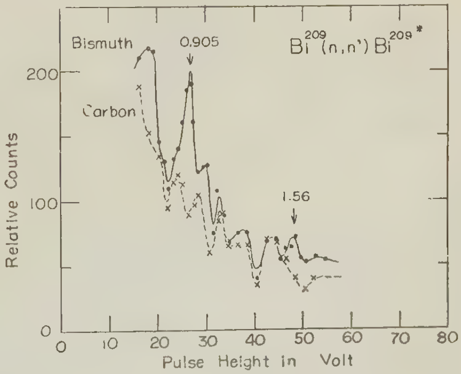

Fig. 7. The pulse height distributions of the gamma rays from bismuth and the background due to a carbon ring at the 2.95 MeV neutron energy. Channel width=1 Volt.

Table I. The gamma rays resulting from Mg, Al, Fe and Bi bombarded by the 2.95±0.10 MeV neutrons and the background gamma rays produced in a NaI(Tl) crystal.

Element	Gamma ray energy (E_γ) in Mev	$d\sigma(90°)/d\omega$ in mb/ster	Production and probable transition	References
Magnesium	(0.58)		Mg^{25}(1st→0)	
	(0.98)		Mg^{25}(2nd→0)	
	1.37±0.02	44±4	All$(n, n')Mg^{24}$(1st→0)	3) 11) 15)
	1.62±0.04		Mg^{25}(3rd→0)	
	1.82±0.04		Mg^{26}(1st→0)	
Aluminum	0.840±0.01	8±2	Al^{27}(1st→0)	2) 3) 11) 14) 15)
	1.02 ±0.03	20±2	All$(n, n')Al^{27}$(2nd→0)	
	2.19 ±0.06	7±1	Al^{27}(3rd→0)	
Iron	0.845±0.01	70±7	Fe^{56}(1st→0)	2) 3) 4) 6) 11) 14) 15) 16)
	1.24 ±0.03		Fe^{56}(2nd→0)	
	1.35 ±0.03		All$(n, n')Fe^{54}$(1st→0)	
	1.81 ±0.04		Fe^{56}(3rd→1st)	
	2.06 ±0.06		Fe^{56}(4th→1st)	
Bismuth	0.905±0.01	48±5	All$(n, n')Bi^{209}$(1st→0)	2) 3) 11) 14) 15)
	1.56 ±0.03	12±2	Bi^{209}(2nd→0)	
NaI(Tl) crystal	0.134±0.006		$I^{127}(n, \gamma)I^{128}$(2nd→0)	2) 6) 11) 14) 15) 16)
	0.200±0.01		$I^{127}(n, n')$	
	0.352±0.02		$I^{127}(n, n')$	
	0.429±0.02		$I^{127}(n, \gamma)I^{128}\rightarrow Xe^{128}$(1st→0)	
	0.486±0.02		$Na^{23}(n, n')Na^{23}$(1st→0)	
	(0.550±0.03)*			
	0.631±0.03		$I^{127}(n, n')$	
	0.750±0.04		$I^{127}(n, n')$	
	(0.97 ±0.05)*			
	1.02 ±0.05		$I^{127}(n, n')$	
	1.20 ±0.05*			
	1.25 ±0.05*			
	1.39 ±0.05*		$Na^{23}(n, \gamma)Na^{24}\rightarrow Mg^{24}$(1st→0)	
	1.44 ±0.06		$I^{127}(n, n')$	
	1.63 ±0.06		$Na^{23}(n, n')Na^{23}$(2nd→0)	
	1.76 ±0.06		$I^{127}(n, n')$	
	1.96 ±0.08*		$Na^{23}(n, n')Na^{23}$(3rd→0)	

* These gamma rays were not found in the references.

±3%).

We compared our experimental values of the inelastic scattering cross section for Fe^{56} and Mg^{24} with our calculated values[8)] based on the Hauser and Feshbach theory. The calculation was made on the four assumptions listed in Table II. The calculated values of $\sigma_{Fe^{56}(n,n')}$ were 0.803 barn for assumption (I), 0.468 barn for (II), 0.466 barn for (III) and 1.176 barn for (IV) at $E_n=2.90$ MeV and those of $\sigma_{Mg^{24}(n,n')}$ were 0.768 barn for (I) and 0.700 barn for (IV) at $E_n=2.95$ MeV. The comparison of the experimental data with the calculated values shows that our results could be interpreted fairly well by a diffuse potential well with the parameters which were derived from the experiment of Beyster et al.[19)]

(2) The angular distribution of the gamma rays from Fe^{56} and Mg^{24}:

Figs. 8 and 9 show the relative values of

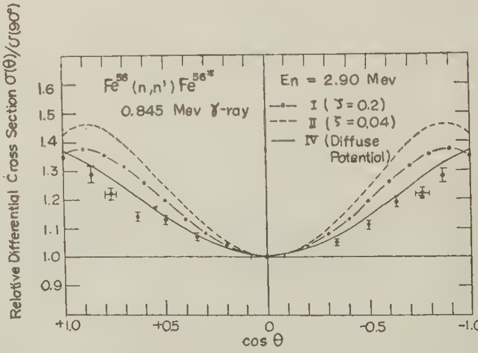

Fig. 8. Angular distribution of the 0.845 MeV gamma ray from the inelastic scattering of iron at the 2.90 MeV neutron energy. The full and dashed curves are the theoretical angular distributions calculated using a diffuse potential (Assumption IV) and a square well potential (Assumption I, $\zeta=0.2$ and II, $\zeta=0.04$) respectively.

Table II. Nuclear parameters used in our calculation.[8)]

Assumption	Absorption coefficient (ζ) in optical model		V_0 in MeV	Nuclear radius (R) and Diffuseness parameter (a)	Type of a potential well	References
	Incidental, $T_{l_0}(E)$	Scattered, $T_{l_i}'(E_i)$				
I	0.2	0.2	42	$R=(1.27A^{1/3}+0.6)\times10^{-13}$ cm*	Square well	*Weisskopf[18)]
II	0.04	0.04	42	〃	〃	
III	0.04	0.2	42	〃	〃	
IV	Mg Fe 0.05 0.07 | | 0.15 0.2	Mg Fe 0.05 0.07 | | 0.15 0.2	Mg Fe 40 39 | | 46 40	$R=1.450A^{1/3}\times10^{-13}$ cm $a=0.350\times10^{-13}$ cm	Diffuse surfaced well	Beyster et al[9)]

the differential cross section of the gamma rays of 0.845 MeV from Fe^{56} and 1.37 MeV from Mg^{24} respectively, being normalized to the values at 90° for the 2.95 MeV neutrons. The points refer to the experimental results and the curves to the theoretical values. The corrections which we mentioned before have been applied to these data. The angular distributions are symmetric around 90° and are in the best agreement with the theoretical calculation on the assumption of the diffuse potential well. Our calculation showed that the same conclusion was drawn with the other experimental data of iron which have been published already by Muehlhause et al[4)] using the 1.66 MeV neutrons and by Cranberg and Levin[3)] using the 2.45 MeV neutrons.

If the assumption of the statistical model is not satisfied, we could expect an asymmetry around 90° by using a neutron beam with the narrow energy width. However, it might be due to the broadness of energy of neutrons that our experiment failed to find any significant change in the angular distribution by using the neutrons of energy from 2.85 MeV to 3.00 MeV, if this existed any.

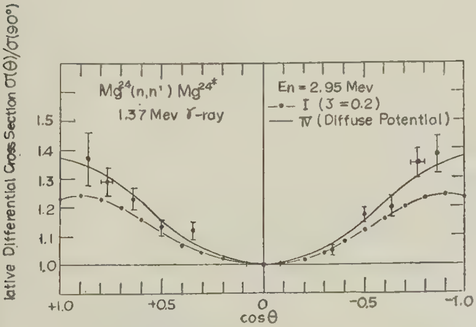

Fig. 9. Angular distribution of the 1.37 MeV gamma ray from the inelastic scattering of magnesium at the 2.95 MeV neutron energy. The full and dashed curves are the theoretical angular distributions calculated using a diffuse potential (Assumption IV) and a square well potential (Assumption I, $\zeta=0.2$).

Acknowledgements

The authors wish to express their great gratitude to Professor E. Tajima and Assistant Professors I. Ogawa and M. Hattori for their encouragement and many useful discussions. Also they wish to thank Assistant Professor M. Tsukuda for the electric equipment and Mr. T. Sasaki of Tokai Electrode Ltd. for his offer of pure carbon rings. They are grateful to Mr. T. Hamada of Scientific Research Institute who offered them calibrated liquid Cs^{137} and Co^{60} gamma ray sources.

This study was supported in part by the Scientific Research Expenditure of the Ministry of Education.

Appendix

Here are appended the outline of the theoretical calculation which we quoted in this text[8)].

We calculated numerically (1) the Hauser and Feshbach's formula of the inelastic scattering cross section of neutrons and (2) the modified Satchler's formula of the angular distribution of the gamma ray resulting from the inelastic scattering of the even-even nuclei for the four assumptions about the transmission coefficients $T_l(E)$ and the other nuclear parameters which are shown in Table II in the text.

In this calculation, we assumed the orbital angular momenta l_0 (incidental) and l_i (scattered) less than 3 for the cross section and less than 2 for the angular distribution on account of avoiding complexity. For the case of Fe^{56}, we took into consideration the contribution of the 2nd and 3rd excited states in our calculation. We used the level scheme of Fe^{56} which was assigned by Poppema et al.[17] For Mg^{24}, there are no contribution from the 2nd and higher excited states for the energy region used in this experiment.

The following are the statistically averaged scattering matrix, according to Satchler[10],

$$\begin{aligned}&\langle S(J;\, j_i l_i;\, j_0 l_0) S^*(J';\, j_i' l_i';\, j_0' l_0')\rangle_{AV}\\&\quad = S(J;\, j_i l_i;\, j_0 l_0) S^*(J;\, j_i' l_i';\, j_0' l_0')\delta(JJ')\delta(l_i l_i')\delta(l_0 l_0')\\&\quad \simeq \frac{T_l(E)T_{l_i}'(E_i)}{\Sigma \varepsilon_{l'}{}^J T_l'(E_q)}\delta(JJ')\delta(l_i l_i')\delta(l_0 l_0')\,,\end{aligned} \tag{5}$$

where J is the nuclear spin of the compound nucleus, $j = l \pm \frac{1}{2}$, $\varepsilon_{l'}{}^J$ is the factor defined by Hauser and Feshbach, and summation Σ extends over all channels (l', E_q) through J. We denoted the energy of neutron scattered leaving the nucleus to the i-th level as E_i.

The differential cross section is given by

$$\frac{d\sigma(\theta)}{d\omega} = \frac{\lambda^2}{4(2J_0+1)(2s+1)} W(\theta, \varphi)\,, \tag{6}$$

where s is the spin of incident neutron, J_0 is the ground state spin of target nucleus, and $W(\theta, \varphi)$ is the angular distribution function between the associate gamma ray and the incident neutron. Neglecting the contribution of channels higher than the 4th excited state and the effect of interferences between channels, $W(\theta)$ can be written as follows,

$$W(\theta) = \frac{1}{2\pi}\int_0^{2\pi} W(\theta, \varphi)\, d\varphi = W(\theta)_{1st} + W(\theta)_{2nd} + W(\theta)_{3rd}\,. \tag{7}$$

(a) Contribution of the channel through the 1st excited state (2^+):

$$\begin{aligned}W(\theta)_{1st} = 2\Bigg[&\frac{2T_0(E)T_2'(E_1)}{T_0(E)+2T_2'(E_1)+2T_2'(E_3)} + \frac{T_1(E)T_1'(E_1)}{T_1(E)+T_1'(E_1)+T_1'(E_3)}\\&+\frac{T_1(E)T_1'(E_1)}{T_1(E)+2T_1'(E_1)+2T_1'(E_3)}\{4+P_2(\cos\theta)\} + \frac{T_2(E)T_0'(E_1)}{A}\{2+P_2(\cos\theta)\}\\&+\frac{T_2(E)T_0'(E_1)}{B}\{3+1.711P_2(\cos\theta)-1.713P_4(\cos\theta)\}\\&+\frac{T_2(E)T_2'(E_1)}{A}\{4-0.7148P_2(\cos\theta)\}+\frac{T_2(E)T_2'(E_1)}{B}\{6+0.8598P_4(\cos\theta)\}\Bigg]\,,\end{aligned} \tag{8}$$

where

$$A = T_2(E)+T_0'(E_1)+2T_2'(E_1)+T_2'(E_2)+T_0'(E_3)+2T_2'(E_3)$$

and

$$B = T_2(E)+T_0'(E_1)+2T_2'(E_1)+2T_2'(E_2)+T_0'(E_3)+2T_2'(E_3)\,.$$

(b) Contribution of the channel through the 2nd excited state (4^+):

$$W(\theta)_{2nd} = 2\left[\frac{T_2(E)T_2'(E_2)}{A}\{2+0.5612P_2(\cos\theta)\} + \frac{T_2(E)T_2'(E_2)}{B}\{6+2.436P_2(\cos\theta)\}\right]. \tag{9}$$

(c) Contribution of the channel through the 3rd excited state (2^+):

$$W(\theta)_{3rd} = \{\text{Eq. (8) with permutation of } E_1 \text{ and } E_3\}\,. \tag{10}$$

The Satchler's formula[10] is a special case of Eq. (7).

References

1) W. Hauser and H. Feshbach: Phys. Rev. **87** (1952) 366.
2) R. M. Kiehn and C. Goodman: Phys. Rev. **95** (1954) 989.
3) L. Cranberg and J. S. Levin: Phys. Rev. **103** (1956) 343.
4) C. O. Muehlhause, S. D. Bloom, H. E. Wegner and G. N. Glasoe: Phys. Rev. **103** (1956) 720.
5) Proceedings of the International Conference on the Neutron Interactions with the Nucleus, held at Columbia University, TID-7547 (1957). V. Naggiar, G. C. Phillips, M. Roclawski-Conjeaud and D. Szteinsznaider: Compt. rend. **245** (1957) 668.
6) J. J. Van Loef and D. A. Lind: Phys. Rev. **101** (1956) 103.
7) H. Feshbach, C. E. Porter and V. F. Weisskopf: Phys. Rev. **96** (1954) 448.
8) S. Suzuki and M. Hosoe: Genshikaku-Kenkyu vol. **3** (1958) 1 (in Japanese).
9) J. R. Beyster, R. G. Schrandt, M. Walt and E. W. Salmi: LA-2099 (1957).
10) G. R. Satchler: Phys. Rev. **104** (1956) 1198; **111** (1958) 1747.
11) R. B. Day: Phys. Rev. **102** (1956) 767.
12) R. W. Meier, P. Scherrer und G. Trumpy: Helv. Phys. Acta **27** (1954) 577.
13) R. Budde und P. Huber: Helv. Phys. Acta **28** (1955) 49.
14) I. L. Morgan: Phys. Rev. **103** (1956) 1031.
15) V. E. Scherrer, B. A. Allison and W. R. Faust: Phys. Rev. **96** (1954) 386.
16) P. Shapiro and R. W. Higgs: Phys. Rev. **108** (1957) 760.
17) O. J. Poppema, J. G. Siekman, R. Van Wageningen and H. A. Tolhoek: Physica **21** (1955) 223.
18) V. F. Weisskopf: Rev. Mod. Phys. **29** (1957) 174.
19) J. R. Beyster, M. Walt and E. W. Salmi: Phys. Rev. **104** (1956) 1319.

JOURNAL OF THE PHYSICAL SOCIETY OF JAPAN, Vol. 14, No. 6, JUNE, 1959

Angular Distributions of the Reaction $F^{19}(p, \alpha)O^{16}$ at 8.0~14.2 Mev*

By Hiroshi OGATA

Department of Nuclear Science, Faculty of Science, Kyoto University

(Received February 16, 1959)

The alpha particles from the reaction $F^{19}(p, \alpha)O^{16}$ resulting in the ground state of O^{16} have been measured, making use of a proportional counter method.

The excitation curve has been measured at a laboratory angle of 50° from 12.9 to 14.1 Mev. The curve changes smoothly with incident proton energy. The angular distributions of the alpha particles have been measured at 14.2, 13.5, 13.0, 12.0, 11.0, 10.0, 9.0, and 8.0 Mev, which can be qualitatively explained by the simple triton pickup theory. Although fairly good agreements with the theory can be seen at 14.2, 13.5 and 9.0 Mev, the angular distributions for the other energies deviate from the theory to some extent. The deviation is generally larger for backward angles and especially at 11.0 and 8.0 Mev striking backward peaks are observed. It is considered that for detailed explanation of the results, refinement of the theory or introduction of other processes of the reaction or both are required.

§ 1. Introduction

It is considered that most of the nuclear reactions which are induced by high energy particles and result in a low-lying level of the final nucleus are predominantly direct reactions. One good example of such a reaction is the well known deuteron stripping or pick-up reaction, for which Butler's stripping theory[1] has been proved to be very useful. Also it is expected that the reactions such as (n, p), (p, p'), (p, α), (α, α'), etc. can be treated in a similar way and show stripping-like angular distributions.

---

* Experiments were performed using the 160 cm cyclotron at the Institute for Nuclear Study, Univ. of Tokyo.

For (p, α) reactions resulting in the low-lying levels of the final nucleus at about 10 or 20 Mev measurements have been reported by several authors. Maxson and Terrell[2)] and Fischer *et al.*[3)] have observed the reaction $C^{12}(p, \alpha)B^9$ at 15.6 and 18.6 Mev and the reaction $Al^{27}(p, \alpha)Mg^{24}$ at about 11 Mev, respectively, and found that the ground state angular distributions for these reactions can be qualitatively fitted by curves obtained from the triton pickup or exchange theories. By Brady[4)] and by Fulmer and Cohen,[5)] (p, α) reactions have been studied for Rh at 18 Mev and for many targets at 23 Mev, respectively. They have reported that the high energy parts of the spectra, which correspond to low-lying levels of the final nuclei, are strongly forward directed and indicate that they are produced by direct interaction reactions.

For the reaction $F^{19}(p, \alpha)O^{16}$ resulting in the ground state of O^{16}, triton pickup behavior is expected to occur because of the structure of F^{19} which has a proton and two neutrons outside the closed O^{16} core. Likely and Brady[6)] have measured the differential cross sections for the reaction $F^{19}(p, \alpha)O^{16}$ resulting in the ground state of O^{16} at 18.5 and 16.0 Mev. It has been shown that the angular distributions can be fitted approximately by the Born approximation for triton pickup. Their measurements have been performed only at 18.5 and 16.0 Mev for rather forward angles up to 120° and 100°, respectively. It is interesting to observe the behaviors of the angular distributions, extending the measurements to larger angles, and to see if these can be explained in terms of triton pickup, as the incident proton energy varies in a wide range in our case. In this paper it is intended to describe the results of the measurement of the reaction $F^{19}(p, \alpha)O^{16}$ at several energies between 8.0 and 14.2 Mev.

§ 2. Experimental Procedures

The angular distribution of the alpha particles emitted from the $F^{19}(p, \alpha)O^{16}$ reaction was measured in a 100 cm scattering chamber[7)] of the Institute for Nuclear Study, University of Tokyo.

Proton beam obtained from a variable energy 160 cm cyclotron[7)] at the Institute for Nuclear Study passes through two collimating apertures of 5.0 mm in diameter at distances 34.3 cm and 114.3 cm from the target, respectively, and several antiscattering apertures, and then is admitted to the scattering chamber. The beam spot in the center of the chamber was about 0.5 cm in diameter.

A teflon foil, 1.58 mg/cm², served as the target, which was placed at an angle of 45° to the incident beam.

As the detector of the alpha particles, a proportional counter method was employed. Equal energy losses of an alpha particle and a proton in a proportional counter produce pulses of approximately equal height, while for a scintillation counter the alpha particle gives much smaller pulse than the proton. Therefore, even in the present measurement of the reaction for which the emitted alpha particles to be detected have much higher energy than elastically scattered protons, if a conventional scintillation counter be employed, it is considered that the pulse height distributions cannot be free from the disturbances of these protons.

A proportional counter of a finite length can be employed to obtain energy spectra of alpha particles, making use of the difference in energy loss between protons and alpha particles. Now let us consider that an alpha particle or a proton enters into a proportional counter and stops just at the end of its sensitive volume. If the window and the insensitive volume of the counter have no significant effects, the energy ($E_{\alpha\,\max}$) of such an alpha particle is much larger than that of such a proton ($E_{p\,\max}$), which produces the maximum pulse among the protons entering the counter. If there are no alpha particles with so high energy that pass through the counter, one can obtain the energy distribution of the alpha particles with energies between $E_{\alpha\,\min}$ and $E_{\alpha\,\max}$, where $E_{\alpha\,\min}$ is the energy of the alpha particles which produce the same ionization in the sensitive volume of the counter as the protons having $E_{p\,\max}$ and is somewhat larger than $E_{p\,\max}$ owing to the effect of the counter part preceding the sensitive volume. Moreover, as compared with a detector of a practically infinite length such as a conventional scintillation counter the finite length proportional counter method enables one to diminish greatly the pile-up effect of the pulses due to the elastically scattered protons which are predominant at smaller angles. Naturally, these effects can be reduced considerably by using a scintillation counter with a thin crystal, but this is accompanied by a technical difficulty of making very thin crystals. Further with the proportional counter, an energy range of the alpha particle desired to be measured can be easily adjusted by changing the counter pressure.

In this experiment, a counter telescope which consists of two proportional counters as shown in Fig. 1 was used. The telescope was prepared to discriminate the low energy alpha particles from the protons, deuterons and high energy alpha particles by a method of anti-coincidence. For this purpose, the proportional counter has some advantage over the scintillation counter. In this experiment, however, the second proportional counter was not required to be used, because alpha particles to be detected are the most energetic particles among the particles emitted when teflon is bombarded with protons.

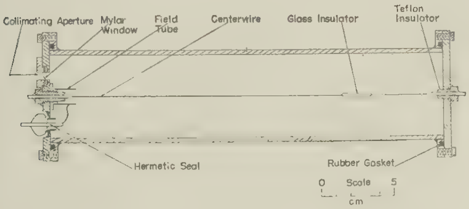

Fig. 1. Proportional counter telescope used for the detection of the alpha particles.

The telescope was mounted on the turn table of the scattering chamber together with the head amplifiers and could be placed at any angle with respect to the proton beam. The distance from the inner surface of the collimator to the target was 18.1 cm. The aperture of the collimator was 0.48 cm in diameter, and the solid angle subtended by the collimator at the target was calculated to be 5.52×10^{-4} steradian. The counter was filled with argon and 5% CO_2 at a pressure of 98 cm Hg. The field tube was prepared to define the sensitive volume of the counter by a plane perpendicular to the counter axis. The mylar window is 1.28 mg/cm² in thickness. The energy loss in the mylar window and the insensitive part of the counter is about 1.4 Mev for 15 Mev alpha particles.

When the incident proton energy is so high and the measurement is carried out at smaller angle, it takes place that the alpha particles pass through the counter volume and give smaller pulses, and pulses of less energetic alpha particles or protons become comparable with the desired ones. In order to be free from this disturbance, an Al absorber of about 50 μ in thickness was attached in front of the collimator for proton energies above 13.0 Mev at angles between 15° and 80°.

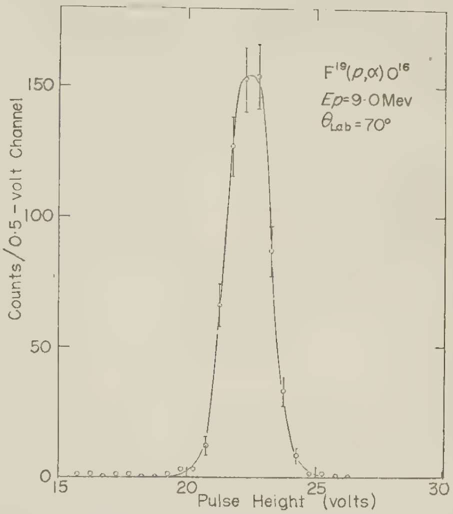

Fig. 2. Typical pules height distribution of alpha particles from the reaction $F^{19}(p, \alpha)O^{16}$ at a laboratory angle of 50° for 9.0 Mev protons.

Pulses from the first counter were amplified and fed into a 20-channel pulse height analyzer. Fig. 2 shows a typical pulse height distribution of alpha particles emitted from $F^{19}(p, \alpha)O^{16}$ resulting in the ground state of O^{15} at a laboratory angle of 70° for 9.0 Mev protons. Owing to the large Q-value of the reaction (+8.12 Mev[8)]) and the large level distance between the ground and first excited states of O^{16}(6.06 Mev[8)]), the background and the overlapping between the alpha particle groups are not observed in the energy spectrum.

After bombarding the target and passing through the scattering chamber, the beam was collected in a Faraday cup connected to a current integrator, which was used to determine the absolute cross sections.

To normalize the angular distributions a CsI scintillation counter was used as a monitor at 90° to the incident beam. The detector bias was chosen to count only the pulses due to the protons scattered elastically by carbon and fluorine in the teflon target and those scattered inelastically by carbon through the first excited state.

§ 3. Results and Discussions

The excitation curve for the reaction $F^{19}(p, \alpha)O^{16}$ resulting in the ground state of O^{16} was measured at a laboratory angle of 50°. The proton energy spread was estimated to be about 50 Kev. The result is shown in Fig. 3. It can be seen that the curve changes smoothly with incident proton energy.

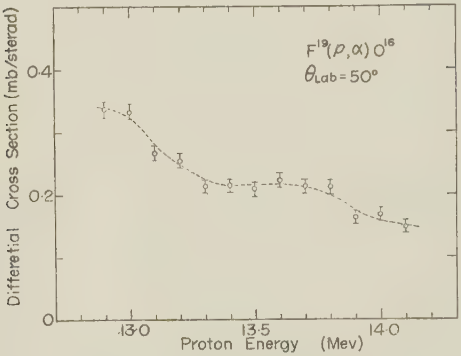

Fig. 3. Excitation curve for the reaction $F^{19}(p, \alpha)O^{16}$ resulting in the ground state at a laboratory angle of 50°.

The angular distributions of this reaction were measured at 14.2, 13.5, 13.0, 12.0, 11.0, 10.0, 9.0, and 8.0 Mev. These results are shown in Fig. 4.

The angular distribution changes gradually with incident proton energy, this can be expected by the smooth excitation curve. These angular distributions show undoubtedly evidence for a surface direct interaction and it is very difficult to explain these behaviors by compound nucleus process.

For the simplest explanation of these behaviors one can consider that the reaction occurs through the triton pickup process because F^{19} has a proton and two neutrons outside the closed O^{16} core. In the pickup process, the incident proton captures these nucleons which would be virtually separated from F^{19} as a triton with $l=0$, the only possible value consistent with the spins and parities of the triton $(1/2^+)$, $F^{19}(1/2^+)$, and $O^{16}(0^+)$.

According to the simple theory[9] of the triton pickup reaction the angular distribution

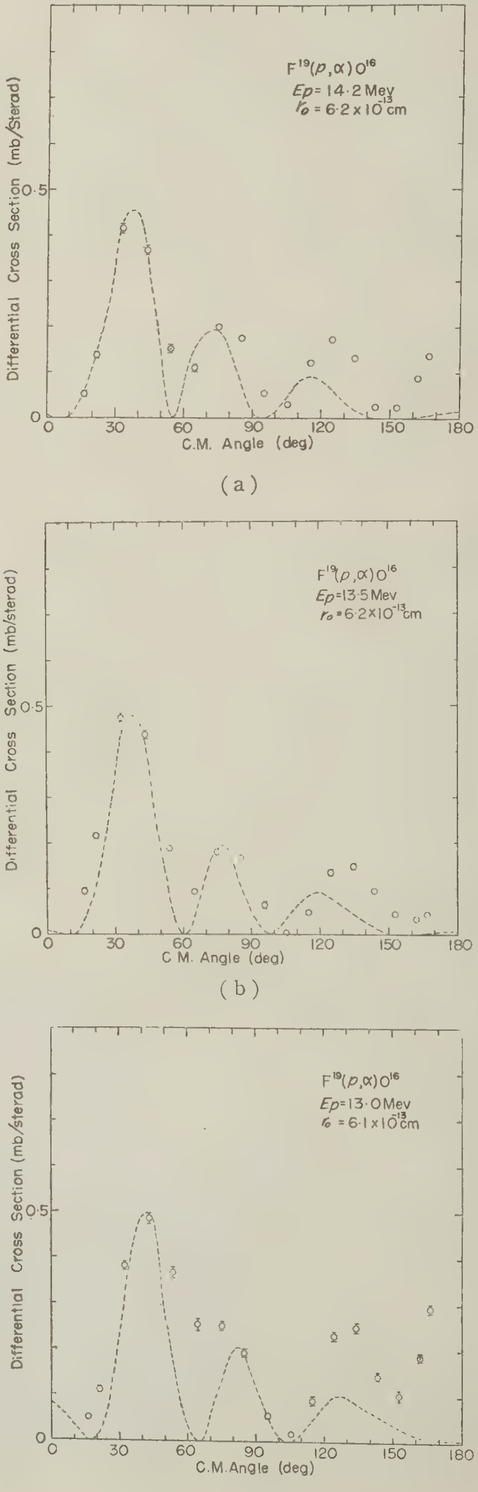

(a)

(b)

(c)

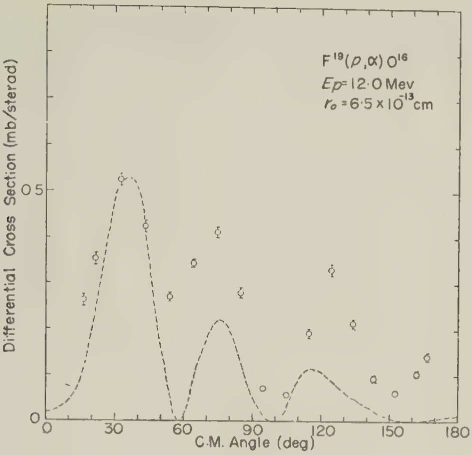

(d)

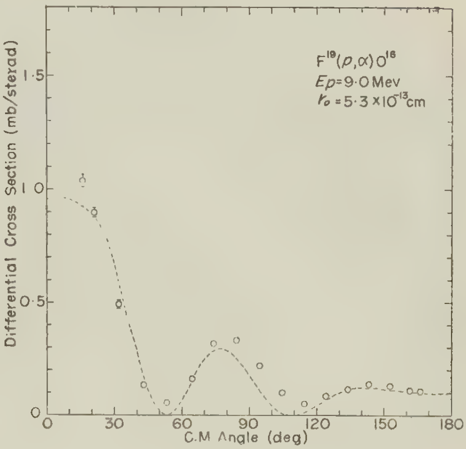

(g)

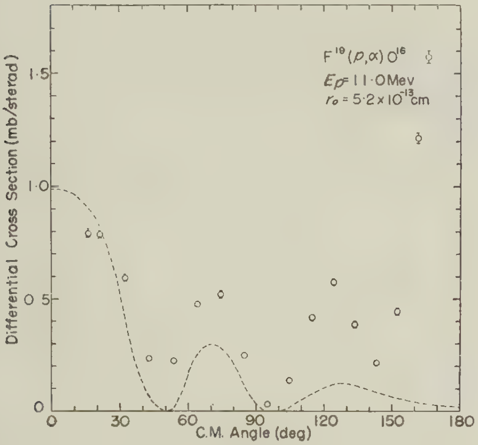

(e)

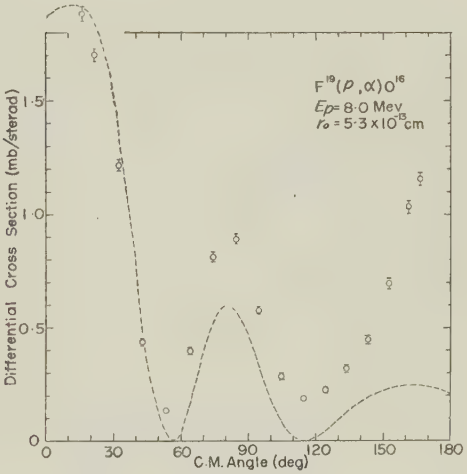

(h)

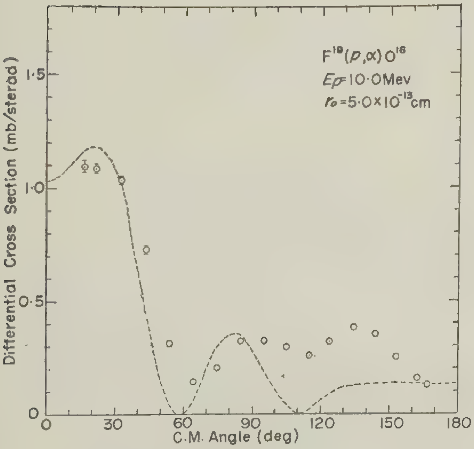

(f)

Fig. 4. Angular distributions of the reaction measured at 14.2, 13.5, 13.0, 12.0, 11.0, 10.0, 9.0, and 8.0 Mev. Dashed curves were calculated from the triton pickup theory.

of the reaction $F^{19}(p, \alpha)O^{16}$ can be expressed as follows:

$$\frac{d\sigma}{d\Omega} \propto \left[\frac{1}{Q^2+k^2} W\{j_0(Qr),\ h_0(i\kappa r)\}_{r_0}\right]^2, \quad (1)$$

where

$$Q=\left|\boldsymbol{k}_\alpha-\boldsymbol{k}_p \frac{m_f}{m_i}\right| \qquad (2)$$

is the characteristic momentum transfer, $\boldsymbol{k}_p$ and $\boldsymbol{k}_\alpha$ are relative momenta in units of $\hbar$ for the incident proton and the outgoing alpha particles respectively, m_i and m_f are masses of F^{19} and O^{16} respectively; κ is related to the triton binding energy $\mathcal{E}_t$ of F^{19} with the following expression:

$$\mathcal{E}_t=\left(\frac{\hbar^2}{2\mu}\right)\kappa^2, \qquad (3)$$

μ is the reduced mass of the triton and O^{16}; and

$$W\{j_0, h_0\}_{r_0} = \left\{ j_0 \frac{\partial h_0}{\partial r} - \frac{\partial j_0}{\partial r} h_0 \right\}_{r_0}, \qquad (4)$$

j_0 and h_0 being the spherical Bessel and Hankel functions of the first kind of order 0 respectively and r_0 the interaction radius between the triton and O^{16}.

The dashed curves in Fig. 4 were calculated from Eq. (1) for radii of 6.2, 6.2, 6.1, 6.5, 5.2, 5.0, 5.3, and 5.3×10^{-13} cm at the eight incident proton energies from 14.2 to 8.0Mev, respectively. These values of r_0 were chosen rather arbitrarilly to give the best agreement with the experimental results by visual fitting.

For all of the energies at which the angular distributions were measured, it can be seen that the general behaviors of the angular distributions can be reproduced by the triton pickup theory. At 14.2, 13.5, and 9.0 Mev, the angular distributions show fairly good agreement with the theory, but it is noticeable that difference exists between the interaction radii of 6.2×10^{-13} cm for 14.2 and 13.5 Mev and of 5.3×10^{-13} cm for 9.0 Mev. Likely and Brady⁶⁾ have shown that the angular distributions observed at 18.5 and 16.7 Mev are reproduced fairly well by the theoretical curves calculated from Eq. (1) for radii of 7.05 and 7.53×10^{-13} cm respectively, but the periods of oscillation of theoretical curves are too small. Considering the effect of nuclear interaction, they obtained $r_0=6.5\times10^{-13}$ cm for both energies semi-empirically by shifting the phase. Any of these values are not in agreement with the present results.

The angular distributions for the other energies deviate from the theory to some extent. The deviation is generally large for the backward angle, and especially at 11.0 and 8.0 Mev striking backward peaks are observed.

The simple expression (1) was calculated with the plane wave Born approximation assuming the triton-proton interaction of zero range, and neglecting the Coulomb effect, nuclear interactions between the incident and outgoing particles with the final nucleus, and any contribution from the region $r<r_0$. By refining the stripping theory, it is considered that better agreements with the experimental results may be obtained. As Likely and Brady carried out, the discrepancy in the interaction radii may be removed by considering the Coulomb effect¹⁰⁾ or nuclear interaction. Also the variation of the angular distribution with the incident energy may be explained by distorting the incident and outgoing waves.¹¹⁾

For the reaction $F^{19}(p, \alpha)O^{16}$, exchange or knockout process can be considered in analogous to that proposed by Austern *et al.*.¹²⁾ In this process, the incident proton scatters out the alpha particle from the target and is captured to form the final nucleus. The angular distribution from this exchange proceses is essentially expressed also by Eq. (1). In another process for the reaction, the incident proton is captured by the interaction with the core of the initial nucleus while the alpha particle is stripped off from the initial nucleus. This heavy particle stripping process gives the angular distribution having backward peaks for emitted alpha particles. Owen and Madansky¹³⁾ explained their $B^{11}(d, n)C^{12}$ angular distribution, which shows a large energy dependence, including the heavy particle stripping reactions. For the reaction $F^{19}(p, \alpha)O^{16}$, it is considered that the contribution from these processes other than the triton pickup process cannot be neglected. Indeed the backward peakings appeared in the 11.0 and 8.0 Mev results show possibly the evidence for considerable contribution of the heavy particle stripping process.

In conclusion, the simple triton pickup theory can explain the general features of the angular distributions of the present reaction. For detailed explanation of the results, however, refinement of the theory of the triton pickup reaction or introduction of other processes of the reaction or both are necessary.

Acknowledgements

The author wishes to express his sincere thanks to Professor K. Kimura, Professor S. Yasumi and Dr. I. Kumabe for their valuable suggestions, continual encouragements and many discussions. He is also indebted to the cyclotron crew of the Institute for Nuclear Study, University of Tokyo, for their kind hospitality and patient cooperation. His thanks are also due to Mr. C. L. Wang, Mr. M. Kawashima, and Mr. M. Yada for their cooperative efforts throughout this work.

References

1) S. T. Butler: Proc. Roy. Soc. **A, 208** (1951) 559.

2) D. R. Maxson and J. G. Terrell: Bull. Amer. Phys. Soc. Ser. II, **3** (1958) 381.
3) G. E. Fischer, V. K. Fischer, E. A. Remler, and M. D. Tatcher: Phys. Rev. **110** (1958) 286 (L).
4) These data were introduced by P. C. Gugelot in Physica **22** (1956) 1019.
5) C. B. Fulmer and B. L. Cohen: Phys. Rev. **112** (1958) 1672.
6) J. G. Likely and F. P. Brady: Phys. Rev. **104** (1956) 118.
7) K. Kikuchi, S. Kobayashi, and K. Matsuda: J. Phys. Soc. Japan **14** (1959) 121.
8) F. Ajzenberg and T. Lauritsen: Rev. Mod. Phys. **27** (1955) 77.
9) S. T. Butler: Phys. Rev. **106** (1957) 272.
10) W. Tobocman and M. H. Kalos: Phys. Rev. **97** (1955) 132.
11) R. Kajikawa, T. Sasakawa and W. Watari: Progr. Theor. Phys. **16** (1956) 152.
12) N. Austern, S. T. Butler and H. McManus: Phys. Rev. **92** (1953) 350.
13) G. E. Owen and L. Madansky: Phys. Rev. **105** (1957) 1766.

JOURNAL OF THE PHYSICAL SOCIETY OF JAPAN, Vol. 14, No. 6, JUNE, 1959

Excitation Functions and Angular Distributions of the Reactions $Al^{27}(p, \alpha)Mg^{24}$ at 12.7~14.1 Mev and $Cr^{52}(p, \alpha)V^{49}$ at 9.0~14.2 Mev*

By Isao KUMABE, Ching Ling WANG, Maumi KAWASHIMA,
Minoru YADA

Department of Physics, Faculty of Science, Kyoto University

and Hiroshi OGATA

*Department of Nuclear Science, Faculty of Science,
Kyoto University*

(Received February 16, 1959)

Making use of a proportional counter, alpha particles have been observed from the reactions $Al^{27}(p, \alpha)Mg^{24}$ resulting in the ground and first excited states of Mg^{24} and $Cr^{52}(p, \alpha)V^{49}$ resulting in the lowest three and a few higher states. Excitation curves have been measured at a laboratory angle of 50° with respect to the bombarding beam, from 12.7 to 14.1 Mev for $Al^{27}(p, \alpha)Mg^{24}$ and from 9.0 to 14.8 Mev for $Cr^{52}(p, \alpha)V^{49}$. The former shows a sharp energy dependence, while the latter shows a fairly smooth structure. Angular distributions have been measured at 14.1, 13.0 and 12.8 Mev for $Al^{27}(p, \alpha)Mg^{24}$ and at 14.2, 13.0, 12.0, 11.0, 10.0, 9.5 and 9.0 Mev for $Cr^{52}(p, \alpha)V^{49}$. Although the $Al^{27}(p, \alpha_0)Mg^{24}$ data can be partially fitted by $[j_2(Qr_0)]^2$ of Butler's theory, some angular distributions show strong backward peaking. Either interference between various direct interaction processes or between direct interaction and compound nuclear precesses, or both are responsible for this reaction. The approximate 90° symmetry of $Cr^{52}(p, \alpha)V^{49}$ angular distribution does not appear to be inconsistent with the statistical theory of nuclear reactions. However, the conspicuous forward peak at higher energies, especially at 14.2 Mev, is considered to indicate the increasing contribution of direct interaction processes.

§1. Introduction

The angular distributions of alpha particles resulting from the bombardment of various elements with high energy photons, especially when the incident proton energy varies in a wide region, are expected to be an important source of information regarding the basic mechanism of nuclear reactions. While the (n, α) reactions of medium weight nuclei at 14.8 Mev in our previous work[1] appeared to be in favor of the compound mechanism, it has been of interest to investigate the (p, α) reactions of these elements also as an analogous nuclear reaction in the same energy region.

---

* Experiments were performed using the 160 cm cyclotron of the Institute for Nuclear Study, Univ. of Tokyo.

For (p, α) reactions, measurements have been carried out by several workers. For a light element, Maxson and Terrell[2] have observed the reactions $C^{12}(p, \alpha)B^9$ resulting in the ground state and a level at 2.39 ± 0.08 Mev. It has been reported that $C^{12}(p, \alpha)B^9$ ground state angular distributions at 15.6 and 18.6 Mev are qualitatively in agreement with the triton pickup or Butler knockon theories. Likely and Brady[3] have measured the angular distributions of alpha particles from the reaction $F^{19}(p, \alpha)O^{16}$ at 18.5 and 16.0 Mev resulting in the ground state of O^{16}. They have found that the angular distribution shows three maxima, which can be fitted approximately by the Born approximation for triton pickup. Similar prominent characteristics of the direct interaction of the reaction $F^{19}(p, \alpha)O^{16}$ have also been reported at $8.0 \sim 14.2$ Mev proton energies in the preceding paper[4].

For a heavy element, Brady[5] has measured the angular distribution of alpha particles from the reaction $Rh^{103}(p, \alpha)Ru^{100}$. The particles "evaporating" with low energy show almost isotropic angular distributions. However, the angular distribution of fast particles resulting in the ground state of Ru^{100} is strongly forwark directed and is considered to be the product of direct interaction. By Fulmer and Cohen[6], the (p, α) reactions induced by 23 Mev protons in targets of a wide range of atomic number have been studied. They have reported that, for targets of atomic number $\lesssim 50$, the energy spectra and angular distributions indicate that most of the alpha particles are produced in compound nucleus reaction as observed by us for the (n, α) reactions, while the alpha particles from the heaviest elements and the high energy parts of the spectra from lighter targets are strongly forward peaked, indicating that they are produced by direct interaction reactions.

Fischer *et al.*[7] have reported an anomalous behavior of $Al^{27}(p, \alpha)Mg^{24}$ differential cross sections, in spite of the partial success of Butler's direct interaction theory in fitting the experimental $C^{12}(\alpha, p)N^{15}$ angular distributions. They have measured the angular distributions of the reactions $Al^{27}(p, \alpha)Mg^{24}$ resulting in the ground and the first excited states of Mg^{24} at about 11 Mev, as well as the excitation curves for these reactions in the energy region between 9.6 and 11 Mev. The sharp energy dependence of these excitation curves observed by them is entirely unexpected from the view-point of direct interaction theories. Their result suggests an additional interest in observing the same reaction in the higher energy region.

The reaction $Cr^{52}(p, \alpha)V^{49}$ has been of special interest, because the atomic weight of Cr is between those of Al and Rh, and these nuclei of intermediate mass are expected to give results which are more closely related to the result of the (n, α) reaction. It is also of interest to see how the angular distribution changes as the energy of the incident proton varies in a wide region.

In the present paper, the results of measurements on angular distributions as well as excitation curves of alpha particles from proton bombardment of Al and Cr are given.

§ 2. Experimental Arrangement and Procedure

Proton beam was obtained from a 160 cm variable energy cyclotron[8] at the Institute for Nuclear Study, University of Tokyo. The detector is a proportional counter filled with argon and 5% CO_2 at such pressures that the fast alpha particles from the individual (p, α) reaction lose their energy completely inside the sensitive volume of the counter. In this way, alpha particle groups were easily separated from proton and deuteron groups. Although no detailed calculation was made, the multiple Coulomb scattering in the mylar foil window and A–CO_2 gas is expected to have a a negligible effect on the proportional counter spectra. Since the general experimental method has been described in the preceding paper[4], we will mention only procedures which were peculiar to individual targets.

For the study of the reaction $Al^{27}(p, \alpha)Mg^{24}$, a foil of aluminum having a thickness of 0.68 mg/cm² was used as the target. In order to stop completely the alpha particles resulting in the ground state of Mg^{24}, the counter was filled with A–CO_2 up to 97 cm Hg.

For the reaction $Cr^{52}(p, \alpha)V^{49}$, the target used was a self-supporting foil of Cr metal having a thickness of 0.366 mg/cm², obtained by an electrolytic method. The proportional counter pressure was 98 cm, 52 cm, 28 cm and 22 cm Hg for 14.2 Mev, 13.0∼12.0 Mev, 11.0∼10.0 Mev, and 9.5∼9.0 Mev incident proton energies, respectively.

§ 3. Results and Discussion

(1) Case of $Al^{27}(p, \alpha)Mg^{24}$

A typical pulse height distribution of the alpha particles from the reaction $Al^{27}(p, \alpha)Mg^{24}$ measured at a laboratory angle of 60° for a proton energy of 14.1 Mev is shown in Fig. 1.

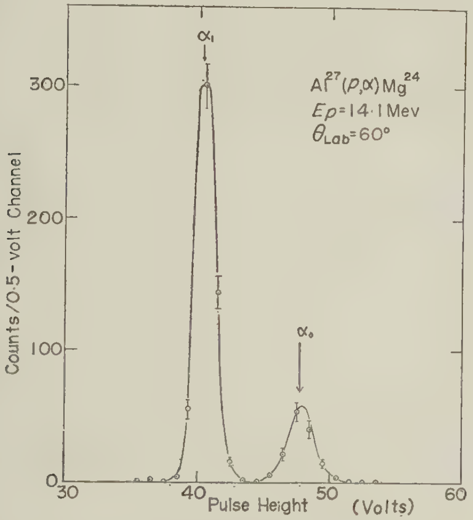

Fig. 1. Typical spectrum of alpha particles from the reactions $Al^{27}(p, \alpha)Mg^{24}$ resulting in the ground and first excited states of Mg^{24} at a laboratory angle of 60° for 14.1 Mev protons.

Two peaks appeared in Fig. 1 correspond to the reaction $Al^{27}(p, \alpha_0)Mg^{24}$ ($Q=+1.593$ Mev[9]) resulting in the ground state and the reaction $Al^{27}(p, \alpha_1)Mg^{24*}$ ($Q=+0.225$ Mev[9]) in the first excited state of Mg^{24}. The energy resolution is about 5%, and complete separation of these two peaks is obtained. Although the separation is slightly worse for larger angles and the analysis of the peaks should be imposed on the spectra, the ambiguity accompanied by this analysis is rather small. Background due to oxygen and carbon contamination and reactions other than (p, α) reactions, for instance (p, p') reaction, are expected to have no influence upon the spectra, considering the Q values ($Q=-5.204$ Mev for $O^{16}(p, \alpha)N^{13}$ and $Q=-7.559$ Mev for $C^{12}(p, \alpha)B^{9}$[10]) and the energy losses in the counter volume.

Fig. 2 shows the excitation curves at a laboratory angle of 50° for the reactions $Al^{27}(p, \alpha_0)Mg^{24}$ and $Al^{27}(p, \alpha_1)Mg^{24*}$. The dashed curves were obtained merely by connecting smoothly the data, so it must not be considered that these represent the true excitation curves. However, no doubt these data provide evidence for the sharp energy dependence of these differential cross sections in the energy region between 12.7 and 14.1 Mev.

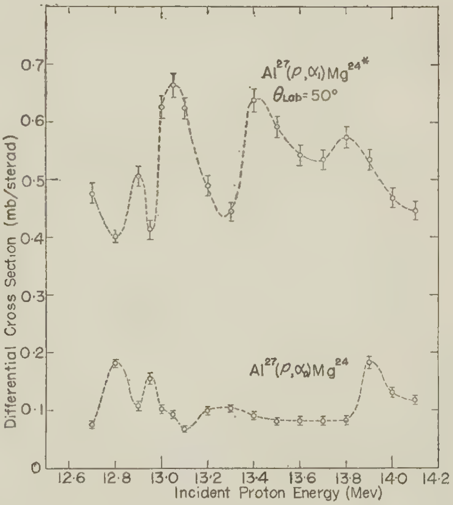

Fig. 2. Excitation functions for $Al^{27}(p, \alpha_0)Mg^{24}$ and $Al^{27}(p, \alpha_1)Mg^{24*}$ at a laboratory angle of 50°.

Fig. 3 shows the angular distributions of alpha particles from these reactions at 14.1, 13.0 and 12.8 Mev incident proton energy. Comparing the results at 12.8 and 13.0 Mev, where the excitation curves seem to show the sharpest energy dependence in the measured energy region, it should be remembered that a mere 200 Kev change in incident proton energy results in a remarkable change of the angular distribution for $Al^{27}(p, \alpha_0)Mg^{24}$, that is, the angular distribution shows a strong backward peaking at 12.8 Mev but a low backward tail at 13.0 Mev, while for $Al^{27}(p, \alpha)Mg^{24*}$ the angular distribution is not so much affected as for $Al^{27}(p, \alpha_0)Mg^{24}$ by this change of incident proton energy except for larger angles where an appreciable difference can be seen.

It is interesting to compare these results with the triton pickup or exchange theories. According to the simple theories of these surface direct interactions11), the angular distribulion for $Al^{27}(p, \alpha_0)Mg^{24}$ is found to be essentially expressed as follows:

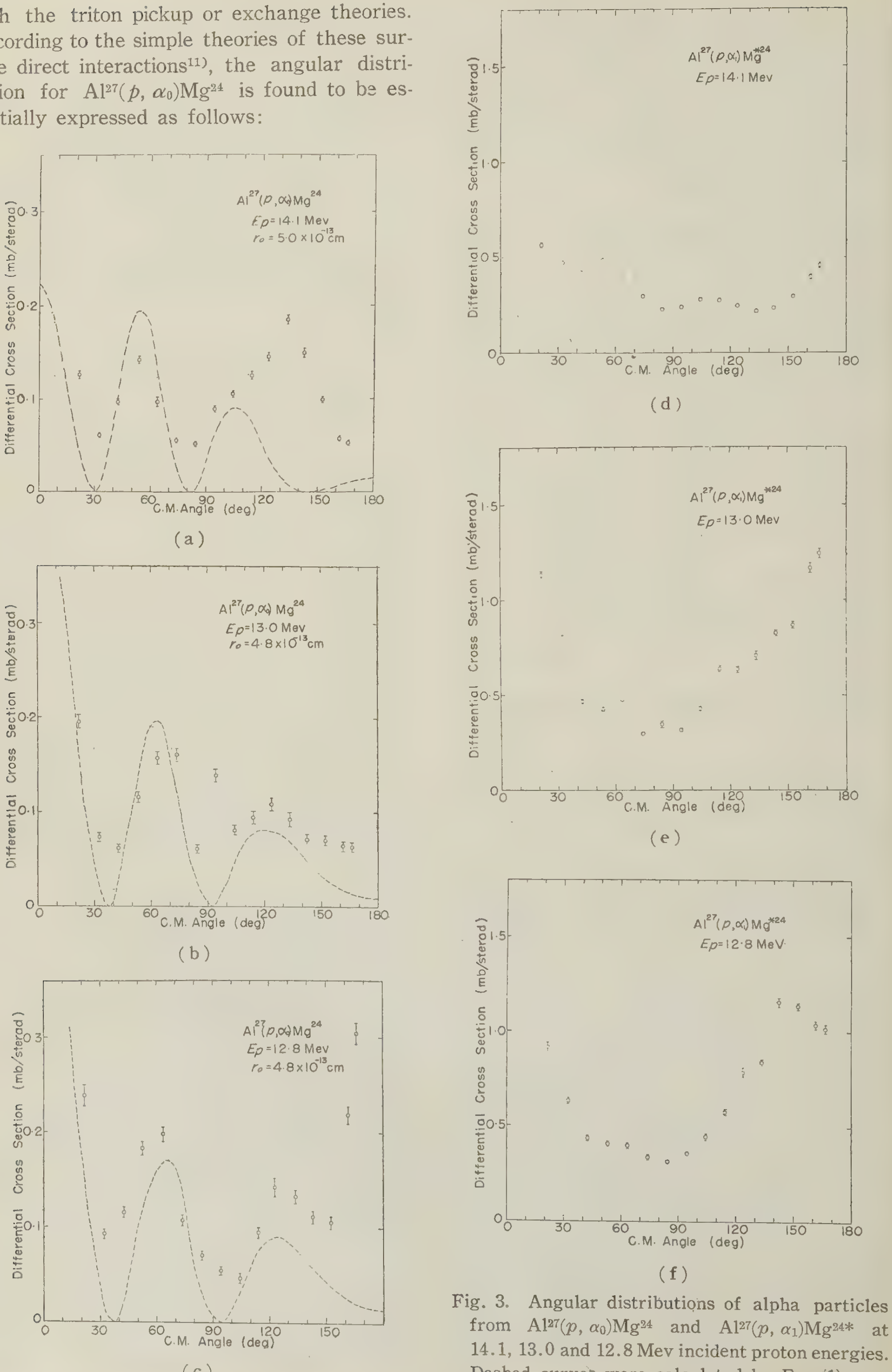

(a)

(b)

(c)

(d)

(e)

(f)

Fig. 3. Angular distributions of alpha particles from $Al^{27}(p, \alpha_0)Mg^{24}$ and $Al^{27}(p, \alpha_1)Mg^{24*}$ at 14.1, 13.0 and 12.8 Mev incident proton energies. Dashed curves were calculated by Eq. (1).

$$\frac{d\sigma}{d\Omega} \propto [j_2(Qr_0)]^2 \,, \qquad (1)$$

where j_2 is the spherical Bessel function of order 2, and Q is the momentum transfer as obtained by following equation:

$$Q = \left| \boldsymbol{k}_p - \frac{M_i}{M_f} \boldsymbol{k}_\alpha \right| ,$$

where $\boldsymbol{k}_p$ and $\boldsymbol{k}_\alpha$ are the center of mass momenta in units of $\hbar$ of the incident protons and the emergent alpha particles, respectively, and M_i and M_f are the masses of Al^{27} and Mg^{24}, respectively, and r_0 is the interaction radius. The dashed curves in Fig. 3 were calculated from Eq. (1) for the reaction $Al^{27}(p, \alpha_0)Mg^{24}$. No theoretical curves from direct interaction theories can be expected to fit the angular distributions for $Al^{27}(p, \alpha_1)Mg^{24*}$, because of the absence of the characteristic maxima and minima in the experimental results.

As having been observed by Fischer *et al.* in the energy region between 9.6 and 11.0 Mev, the rapid change of angular distribution for $Al^{27}(p, \alpha_0)Mg^{24}$ with the incident energy, as well as the sharp energy dependent excitation curve for either reaction was observed. Also the angular distributions can be partially fitted by Eq. (1) with radii of 5.0, 4.8 and 4.8×10^{-13} cm at 14.1, 13.0 and 12.8 Mev, respectively. Fischer *et al.* have used a radius of 4.50×10^{-13} cm for a fit to their data. It must be noted that these values for the radius are not very different from one another. For $Al^{27}(p, \alpha_1)Mg^{24*}$ it is noteworthy that although for smaller angles the angular distribution does not seem to change so rapidly as for $Al^{27}(p, \alpha_0)Mg^{24}$, an appreciable difference can be seen between the angular distributions at 12.8 and 13.0 Mev for larger angles than 140° where measurements have not been performed by Fischer *et al.* at 10.87 and 10.97 Mev. By Kobayashi *et al.*12), very sharp energy dependence of the differential cross section has been observed also for the reaction $Ne^{22}(p, p')Ne^{22}$ resulting in the first excited state in the incident energy region between 8.6 and 9.7 Mev at laboratory angles of 45° and 60°.

The partial fit of the $Al^{27}(p, \alpha_0)Mg^{24}$ data by a curve of the general form $[j_2(Qr_0)]^2$ suggests that the surface direct interaction such as the triton pickup or exchange reaction plays an important role.

The observed sharp energy dependence cannot be explained by the simple theories of direct interaction which predict very slowly changing differential cross sections. Modification of the direct interaction theories,13),14) including the distorted wave treatments, would probably also not produce such a sharp energy dependence. Owen and Madansky15) have obtained good qualitative agreement with their angular distributions for $B^{11}(p, n)C^{12}$, which show a large energy dependence, extending the ordinary deuteron stripping theory to include the effect of heavy particle stripping. By an analogous treatment, the present results of the reaction $Al^{27}(p, \alpha)Mg^{24}$ may be explained. On the other hand, assuming that the reaction $Al^{27}(p, \alpha)Mg^{24}$ occurs through the compound nucleus formation, the sharp energy dependence cannot be expected from the statistical theory16), which is based on the assumptions that there are many levels of all types at the excitation energy of the compound nucleus (continuum assumption), and the corresponding wave functions have a random phase so that when phase averages are performed all interference terms will vanish (statistical assumption). Therefore the continuum or statistical assumption must not be satisfied. However, in this case, since the continuum assumption is probably satisfied, the statistical assumption might be considered to be violated. Then it is considered that either interference between various direct interaction processes or between direct inter-

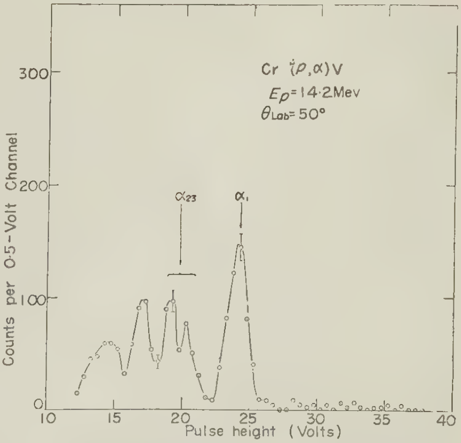

Fig. 4. Typical spectrum of alpha particles from the reaction $Cr(p, \alpha)V$ at a laboratory angle of 50° for 14.2 Mev protons.

action and compound nucleus processes, or both are responsible for the present reaction.

(2) Case of $Cr^{52}(p, \alpha)V^{49}$

In Fig. 4, a typical pulse height distribution of the alpha particles from the reaction $Cr(p, \alpha)V$, measured at a laboratory angle of 50° and 14.2 Mev proton energy is shown. Natural chromium has four stable isotopes of mass number 50, 52, 53 and 54 and their abundance ratios are 4.31, 83.75, 9.55 and 2.3%, respectively, among which Cr^{52} is the most abundant. Then the peaks appeared in Fig. 4 are probably responsible for the reaction $Cr^{52}(p, \alpha)V^{49}$. The level scheme of V^{49} remains almost unknown except the first three states, that is, ground, 0.08 Mev and 0.152 Mev states[17], which are very close to one another. From the energetics by comparing the pulse height of the present reaction with that of the reaction $Al^{27}(p, \alpha)Mg^{24}$, the first peak of the alpha particle spectrum is considered to correspond to the reactions resulting in these states of V^{49}, while it is not known to which levels of V^{49} the second or third peaks of the pulse height distribution refers. The small but discernible tail which appears at the high energy side of the first peak is probably attributed to alpha particles from the (p, α) reactions of Cr^{50}, Cr^{53} and Cr^{54}. Supposing that the (p, α) cross sections are of the same order for all Cr isotopes, the background of these isotopes is considered to have no significant effect on the spectra, since these isotopic abundance ratios are small as compared with Cr^{52}. Background due to carbon or oxygen contamination does not effect the measurement as in the case of Al, since the Q value of $Cr^{52}(p, \alpha)V^{49}$ is merely -2.59 Mev, which was calculated from mass data[18].

Fig. 5 shows the excitation curve at a laboratory angle of 50° for the first peak of the pulse height spectrum corresponding to the reaction $Cr^{52}(p, \alpha_1)V^{49}$ resulting in the first three states of V^{49}. Since no sharp energy dependence but smooth structure was observed in the energy region between 13.6 and 14.8 Mev, the angular distribution was measured at intervals of about 1 Mev for the proton energy.

Fig. 6 shows the angular distribution of this reaction at 14.2, 13.0, 12.0, 11.0, 10.0, 9.5 and 9.0 Mev proton energies. The angular distributions of alpha particles (α_{23}) responsible for the unsufficiently resolved second and third peaks of the pulse height spectrum, which correspond to the levels of V^{49} up to about 1 Mev excitation except the first three levels, was measured at 14.2, 13.0 and 12.0 Mev proton energies. These are also shown in Fig. 6.

In Fig. 6, it can be seen that, though a forward peak is discernible prominently at 14.2 Mev and slightly at 13.0 and 12.0 Mev, the angular distribution for the reaction $Cr^{52}(p, \alpha_1)V^{49}$ is nearly symmetrical about 90°

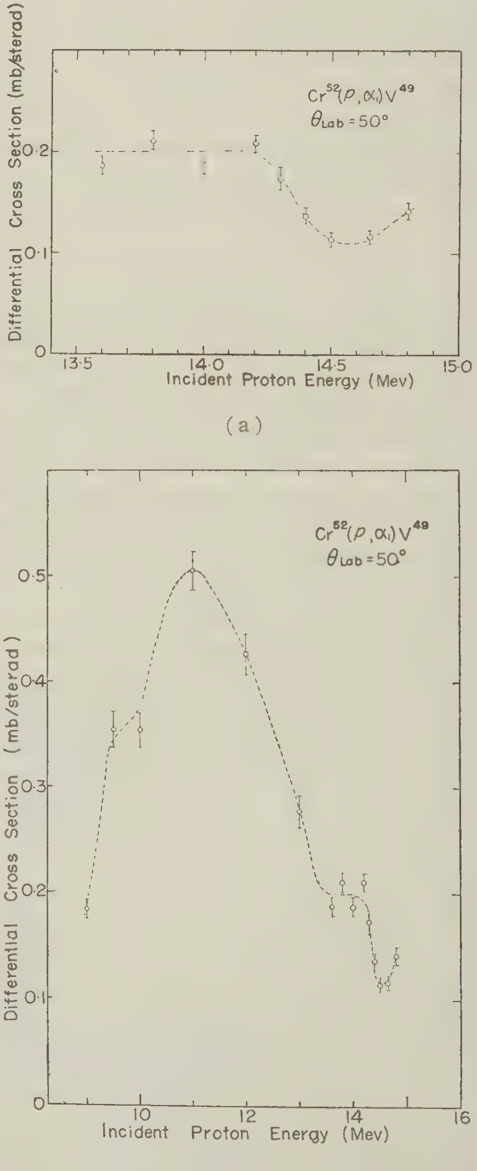

(a)

(b)

Fig. 5. Excitation function for $Cr^{52}(p, \alpha_1)V^{49}$ at a laboratory angle of 50°.

except at 14.2 Mev. Also for $Cr^{52}(p, \alpha_{23})V^{49}$, the angular distributions do not deviate appreciably from 90° symmetry.

The approximate symmetry about 90° of the angular distribution is consistent with the prediction of the statistical theory of nuclear reactions[16], and suggests that most of the reactions occur through the compound nucleus

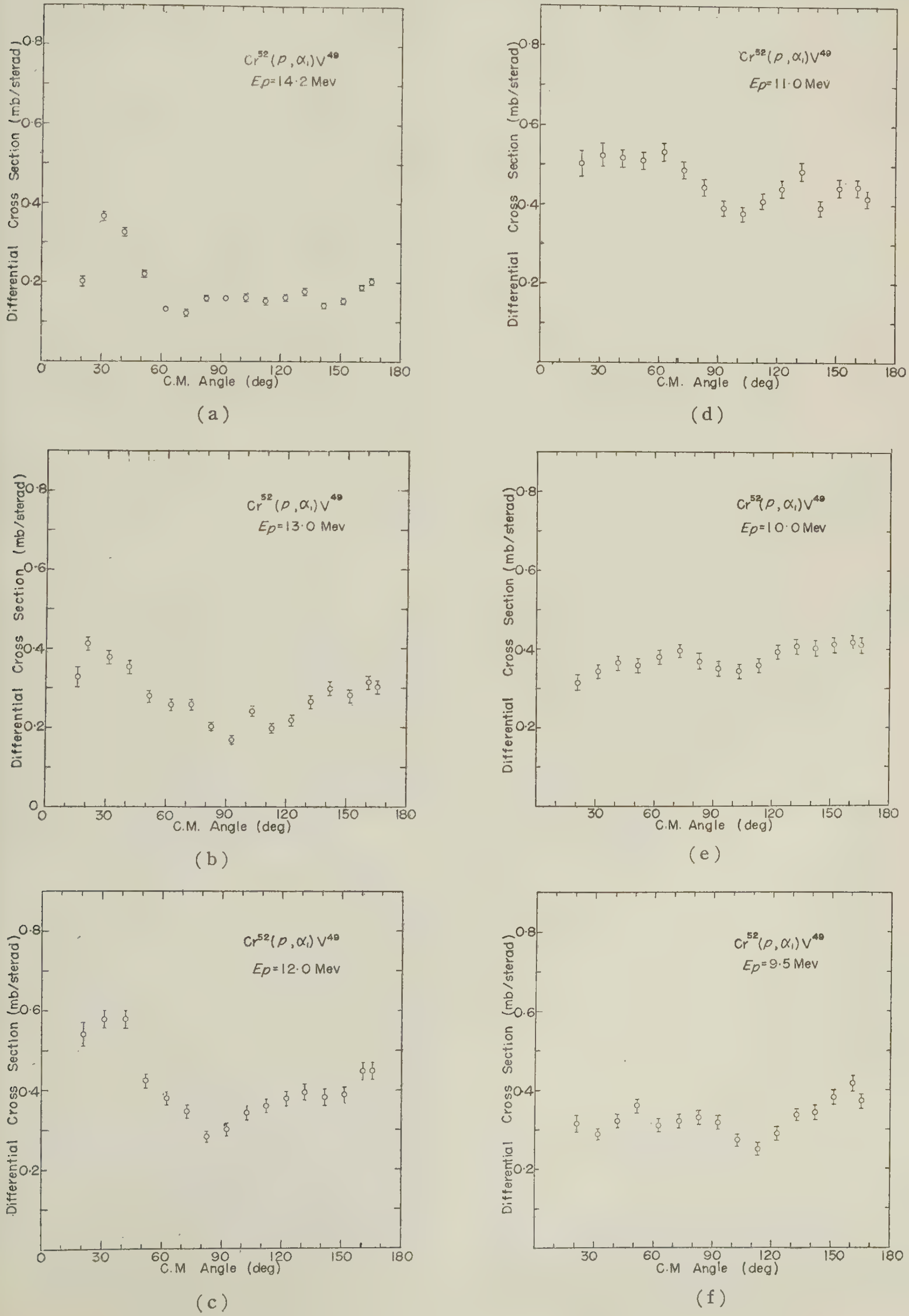

(a) (d)

(b) (e)

(c) (f)

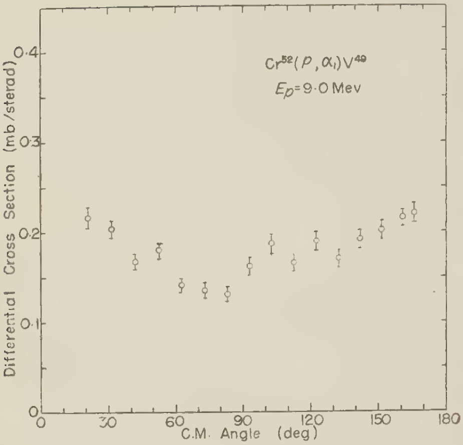

(g)

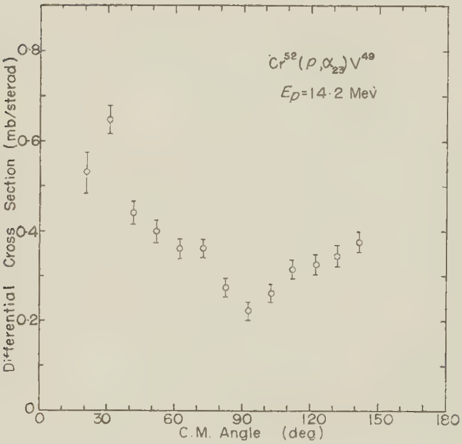

(h)

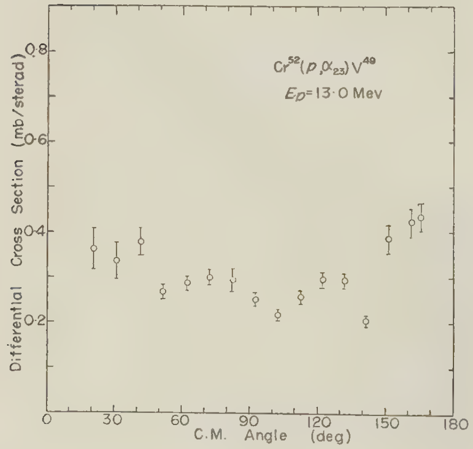

(i)

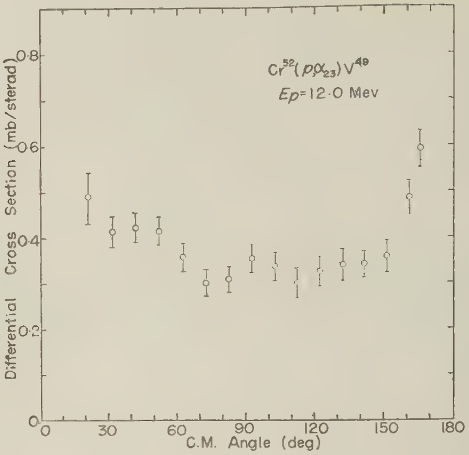

(j)

Fig. 6. Angular distributions of alpha particles from $Cr^{52}(p, \alpha_1)V^{49}$ at 14.2, 13.0, 12.0, 11.0, 10.0, 9.5, and 9.0 Mev proton energies and from $Cr^{52}(p, \alpha_{23})V^{49}$ at 14.2, 13.0 and 12.0 Mev proton energies.

formation. From the view-point of the compound nucleus theory, the cross section for the reaction to a particular state of the final nucleus varies with incident energy depending upon the number of the competing open channels, including that of other types of reactions such as (p, n) or (p, p') reaction, and upon the Coulomb barrier penetrability of the emergent particles. Therefore, the cross section is expected to reach its maximum value near the Coulomb barrier height for the emergent particles and to decrease with either increasing or decreasing incident energy from there. Indeed, for the reaction $Cr^{52}(p, \alpha_1)V^{49}$, we can see in Figs. 5 and 6 that the cross section can be seen to have its maximum at an incident energy of about 11.0 Mev which corresponds to an emergent alpha particle energy of 8.13 Mev, whereas the Coulomb barrier is 9.9 Mev for a radius of $1.5\times10^{-13}\,A^{1/3}$ cm. This behavior of the cross section is not inconsistent with the compound nucleus process for this reaction.

On the other hand, the forward peak discernible in the angular distribution for the reaction $Cr^{52}(p, \alpha_1)V^{49}$ above 12 Mev proton energy seems to suggest an appreciable contribution of direct interaction at these energies.

Fulmer and Cohen have measured the energy distribution of alpha particles from (p, α) reactions induced by 23 Mev protons at several angles in elements from Al to Au. It has been reported that for Ni, the nearest element to Cr among the elements measured by them, the high energy part of the spectrum is strongly forward peaked and suggests to be produced by direct interaction reactions.

It may be said that the reaction $Cr^{52}(p, \alpha_1)V^{49}$ occurs mostly through the compound nucleus formation at lower incident energies below 11 Mev and then the contribution from the direct interaction becomes significant gradually.

In conclusion, for the reactions $Al^{27}(p, \alpha)Mg^{24}$ and $Cr^{52}(p, \alpha)V^{49}$ resulting in the lower excited states of the final nuclei, the opposite aspects of the nuclear interactions, that is, the direct interaction and the compound process, are observed, which is considered to be due to the difference in the structures of the target. However, the behaviors of the emergent alpha particles are not explained merely by the simple theory of direct interaction or by the statistical theory of the nuclear reaction but it is considered that the various direct interactions and compound processes contribute in a complicated manner. It is hoped that further meassurements of (p, α) reactions for other elements will be carried out.

Acknowledgements

The authors wish to express their sincere thanks to Professor K. Kimura and Professor S. Yasumi for their valuable suggestions and continual encouragements throughout this work. Their thanks are also due to the cyclotron crew of the Institute for Nuclear Study, University of Tokyo, for their kind hospitality and patient cooperation.

References

1) I. Kumabe, E. Takekoshi, H. Ogata, Y. Tsuneoka and S. Ōki: Phys. Rev. **106** (1957) 155. I. Kumabe, E. Takekoshi, H. Ogata, Y. Tsuneoka and S. Ōki: J. Phys. Soc. Japan **13** (1958) 129. I. Kumabe: J. Phys. Soc. Japan **13** (1958) 325.
2) D. R. Maxson and J. G. Terrell: Bull. Amer. Phys. Soc. Ser. II, **3** (1958) 381.
3) J. G. Likely and F. P. Brady: Phys. Rev. **104** (1956) 118.
4) H. Ogata: preceding paper.
5) These data were introduced by P. C. Gugelot in Physica **22** (1956) 1019.
6) C. B. Fulmer and B. L. Cohen: Phys. Rev. **112** (1958) 1672.
7) G. E. Fischer, V. K. Fischer, E. A. Remler and M. D. Tatcher: Phys. Rev. **110** (1958) 286 (L).
8) K. Kikuchi, S. Kobayashi and K. Matsuda: J. Phys. Soc. Japan **14** (1959) 121.
9) P. M. Endt and J. C. Kluyver: Rev. Mod. Phys. **26** (1954) 95.
10) F. Ajzenberg and T. Lauritsen: Rev. Mod. Phys. **27** (1955) 77.
11) S. T. Butler: Phys. Rev. **106** (1957) 272.
12) S. Kobayashi: private communication.
13) W. Tobocman and M. H. Kalos: Phys. Rev. **97** (1955) 132.
14) S. Hayakawa and S. Yoshida: Progr. Theor. Phys. **14** (1955) 1.
15) G. E. Owen and L. Madansky: Phys. Rev. **105** (1957) 1766.
16) W. Hauser and H. Feshbach: Phys. Rev. **87** (1952) 366.
17) R. H. Nussbaum, A. H. Wapstra, G. J. Nijgh, L. T. M. Ornstein and N. F. Verster: Physica **20** (1954) 165.
18) C. F. Giese and J. L. Benson: Phys. Rev. **110** (1958) 712.

Journal of the Physical Society of Japan, Vol. 14, No. 6, June, 1959

On the Brownian Motion of a Classical Oscillator

By Morikazu Toda

Department of Physics, Tokyo University of Education

(Received March 6, 1959)

The Brownian motion of a classical harmonic oscillator is treated mechanically throughout. The oscillator is coupled with thermostat which is composed of a great number of harmonic oscillators. By use of a transformation which eliminates the coupling to the first order, the second order quantities like the friction force in obtained. Correlation of random force is also discussed.

§1. Introduction

Brownian motion is usually treated by the theory of stochastic processes[1], which has quite wide applicability providing us with one of the most beautiful and powerful methods in many problems. In this theory, however, we have to assume several hypothesis, e.g. the existence of the friction force and the nature and the correlation of random force. The friction force and the random force come from the same origin, namely the interaction with other part of the system. But they are introduced by separate assumptions and the relation between them is derived by use of *ad hoc* assumption that the system is to approach the state of thermal equilibrium if it is left undisturbed. And this kind of theory has no direct connection to the general theory of irreversible processes.

There were several attempts to formulate the theory of irreversible processes or of random processes on purely mechanical basis. Kirkwood[2] derived friction constant and the Fokker-Planck equation in classical mechanics. Zwanzig[3] wanted to have the Fokker-Planck equation in quantum mechanics. Callen and Welton[4] treated quantum mechanics of dissipative system. In these calculations, it was necessary, in principle, to solve the equation of motion for a suitable time interval, which must not be too small and not too large. Evolution of the system was then given by connecting the time intervals. Kubo[5] developed a method which deals with systems not far from equilibrium.

One of the aims of this paper is to get rid of and to clarify the nature of the stochastic theory. We start with a well defined system with definite interaction. We show that the interaction gives rise to friction and that the remaining force is random force. We employ a method similar to that used in the general theory of irreversible processes[6],[7]. The method used in this paper is applicable to more complicated systems. To avoid ambiguity, however, we shall here confine ourselves to the simplest system we can consider. Indeed there are many controversial points in the general theory of irreversible processes, and it is hoped to give more or less sound footings to it, because by so doing we can test some of the concepts and clarify the nature of approximation used in the general theory. We shall treat more complicated problems (relaxation of two-oscillators, spin relaxation, etc.) in the near future.

The system we treat here is an assembly of harmonic oscillators and interaction force is assumed to be linear with respect to displacements. The interaction, assumed small, is introduced from infinite past, and the equations of motion are solved therefrom. We go over to coordinate systems (ξ, η) which rotate with proper frequencies, and then transform to $(\bar{\xi}, \bar{\eta})$ by eliminating the first order terms of the interaction. We take an oscillator and regard the rest of the system as thermostat, for which we assume certain equilibrium properties.

The system is the same as that treated in a previous paper[7] dealt with quantum mechanical density matrix. Though the present paper supplements, in some respects, what were missing in the previous one, the main purpose is to give a very elementary but sound footing to the problem.

It seems worth noting the origin of the friction force. Consider that we displace an oscillator; this implies a work against the other oscillators. A part of this work will give rise to a shift in oscillation frequency and will be conservative, but as there is naturally a tendency to equalize energy of oscillators some part of that work has to be dissipated in the form of friction.

§ 2. Interacting Oscillators

First we shall consider a harmonic oscillator under an external force F. The canonical equations of motion are

$$\dot{x}=p/m\ , \qquad \dot{p}=-m\omega^2x+F\ . \tag{2.1}$$

As is well known if $F=0$ the oscillator describes a circle in the phase space $(x, p/m\omega)$ with angular velocity $-\omega$. It is therefore convenient to refer to a rotating coordinate system and use

$$\left.\begin{aligned}\xi&=x\cos\omega t-(p/m\omega)\sin\omega t\ ,\\ \eta&=m\omega x\sin\omega t+p\cos\omega t\ .\end{aligned}\right\} \tag{2.2}$$

The equations of motion (2.1) then go over into

$$\left.\begin{aligned}\dot{\xi}&=-F\sin\omega t/m\omega\ ,\\ \dot{\eta}&=F\cos\omega t\ .\end{aligned}\right\} \tag{2.3}$$

We see that if there were no external force both ξ and η stay constant.

Now we consider an assembly of harmonic oscillators. We assume that the interaction energy is of the form

$$\lambda V=\sum\lambda_{ij}x_ix_j\ , \tag{2.4}$$

where λ_{ij} is the coupling constant between the i-th and the j-th oscillators, λ stands for the magnitude of the interaction: $\lambda\sim O(\lambda_{ij})$. Let m_i and ω_i the mass and the frequency of the i-th oscillator and define ξ_i and η_i by equations analogous to Eqs. (2.2). The force acting on the i-th oscillator is

$$\begin{aligned}F_i&=-\sum{}'\lambda_{ij}x_j\\ &=-\sum_{j\neq i}{}'\lambda_{ij}\left(\xi_j\cos\omega_jt+\frac{\eta_j}{m_j\omega_j}\sin\omega_jt\right)\ .\end{aligned} \tag{2.5}$$

We shall suppose that the interaction is introduced adiabatically from the past. Under this supposition we replace λ_{ij} by $\lambda_{ij}e^{st}$ and afterwords take the limit $s\to 0$. Then the equations of motion for the oscillator i are combined into

$$\begin{pmatrix}m_i\omega_i\dot{\xi}_i\\ -\dot{\eta}_i\end{pmatrix}=\sum{}'\lambda_{ij}{}^{st}\left(\xi_j\cos\omega_jt+\frac{\eta_j}{m_j\omega_j}\sin\omega_jt\right)\begin{pmatrix}\sin\omega_it\\ \cos\omega_it\end{pmatrix}\ . \tag{2.6}$$

We assume that the coupling constants λ_{ij} are small and solve the above equation using the following method. We notice the fact that if λ were zero ξ and η would stay constant, and put

$$\left.\begin{aligned}\xi_i&=\overline{\xi}_i+\xi_i'(\overline{\xi},\overline{\eta},t)\ ,\\ \eta_i&=\overline{\eta}_i+\eta_i'(\overline{\xi},\overline{\eta},t)\ ,\end{aligned}\right\} \tag{2.7}$$

in which $\overline{\xi}=(\overline{\xi}_1,\overline{\xi}_2,\cdots)$ and $\overline{\eta}=(\overline{\eta}_1,\overline{\eta}_2,\cdots)$ are defined in such a way that their rate of change is of second order in λ:

$$\dot{\overline{\xi}}_i=O(\lambda^2)\ , \qquad \dot{\overline{\eta}}_i=O(\lambda^2)\ . \tag{2.8*}$$

Accordingly the rate of change in ξ' and η' are of first order in λ. Though the way of splitting thus ξ and η is not at all unique, the result is however independent of the way as can be seen easily. In particular we demand that ξ' are of the order λ. The simplest way is to define them by

$$\left.\begin{aligned}m_i\omega_i\xi_i'&=\sum{}'\lambda_{ij}\left\{\overline{\xi}_ic_{ji}(t)+\frac{\overline{\eta}_j}{m_j\omega_j}S_{ji}(t)\right\}\ ,\\ -\eta_i'&=\sum{}'\lambda_{ij}\left\{\overline{\xi}_iC_{ji}(t)+\frac{\overline{\eta}_j}{m_j\omega_j}s_{ji}(t)\right\}\ .\end{aligned}\right\} \tag{2.9}$$

and choose the function c_{ji}, S_{ji}. C_{ji} and s_{ji} in such a way that their time derivative coincide the time factors in the right hand side of Eqs. (2.6). That is

---

* In the previous paper7) an inappropriate terminology "systematic" was used for $\overline{\rho}$, which corresponds to $\overline{\xi}$ or $\overline{\eta}$. These quantities have oscillatory behavior as well.

$$\dot{c}_{ji}(t)=e^{st}\cos\omega_j t\sin\omega_j t\ ,\qquad \text{etc.} \tag{2.10}$$

We may understand change of variables from (ξ,η) to $(\bar{\xi},\bar{\eta})$ as a transformation which is canonical if λ^2 terms are neglected, and c_{ij} etc. as action integrals corresponding to the transformation.

We may also understand the variables $\bar{\xi}$ and $\bar{\eta}$ as follows: When an oscillator is displaced the rest positions of other oscillators will be shifted also. In virture of the interaction, therefore, each oscillator will be seen to oscillate around instantaneous rest position. According to this interpretation $\bar{\xi}$ stands for the displacement from the instantaneous rest position ξ'.

Now we have

$$\left.\begin{aligned} m_i\omega_i\xi_i' &= \sum{}'\lambda_{ij}\left\{\bar{\xi}_j\int_{-\infty}^{t}dt'e^{st'}\cos\omega_j t'\sin\omega_i t'+\frac{\bar{\eta}_j}{m_j\omega_j}\int_{-\infty}^{t}dt'e^{st'}\sin\omega_j t'\sin\omega_i t'\right\}\ ,\\ -\eta_i' &= \sum{}'\lambda_{ij}\left\{\bar{\xi}_j\int_{-\infty}^{t}dt'e^{st'}\cos\omega_j t'\cos\omega_i t'+\frac{\bar{\eta}_j}{m_j\omega_j}\int_{-\infty}^{t}dt'e^{st'}\sin\omega_j t'\cos\omega_i t'\right\}\ ,\end{aligned}\right\} \tag{2.11}$$

If we insert these expressions into Eqs. (2.7) and then into (2.6) we shall see that the rate of change in $\bar{\xi}$ and $\bar{\eta}$ are of the order λ^2 as required (c.f. Eqs. (2.15) below).

It is important for our calculation that ξ' and η' do not increase with time and oscillate in the limit $s\rightarrow 0$. In actual, for $\omega, \omega'>0$,

$$c_{ij}=s_{ji}=\lim_{s\to 0}\int_{-\infty}^{t}dt'e^{st'}\cos\omega_i t'\sin\omega_j t'=-\frac{\cos(\omega_i+\omega_j)t}{2(\omega_i+\omega_j)}+\frac{\cos(\omega_j-\omega_j)t}{2(\omega_i-\omega_j)}\ ,$$

$$\left.\begin{matrix}C_{ij}\\ S_{ij}\end{matrix}\right\}=\lim_{s\to 0}\int_{-\infty}^{t}dt'e^{st'}\left\{\begin{matrix}\cos\omega_i t'\cos\omega_j t'\\ \sin\omega_i t'\sin\omega_j t'\end{matrix}\right\}=\frac{\pi}{2}\delta(\omega_i-\omega_j)\pm\frac{\sin(\omega_i+\omega_j)t}{2(\omega_i+\omega_j)}+\frac{\sin(\omega_i-\omega_j)t}{2(\omega_i-\omega_j)}\ .$$

And we have

$$\left.\begin{aligned} \xi_j' &= \frac{1}{m_j\omega_j}\sum{}'\lambda_{jk}\left[\frac{\bar{\eta}_k}{m_k\omega_k}\left\{\frac{\pi}{2}\delta(\omega_k-\omega_j)-\frac{\sin(\omega_k+\omega_j)t}{2(\omega_k+\omega_j)}+\frac{\sin(\omega_k-\omega_j)t}{2(\omega_k-\omega_j)}\right\}\right.\\ &\qquad\left.+\bar{\xi}_k\left\{-\frac{\cos(\omega_k+\omega_j)t}{2(\omega_k+\omega_j)}+\frac{\cos(\omega_k-\omega_j)t}{2(\omega_k-\omega_j)}\right\}\right],\\ \eta_j' &= -\sum{}'\lambda_{jk}\left[\bar{\xi}_k\left\{\frac{\pi}{2}\delta(\omega_k-\omega_j)+\frac{\sin(\omega_k+\omega_j)t}{2(\omega_k+\omega_j)}+\frac{\sin(\omega_k-\omega_j)t}{2(\omega_k-\omega_j)}\right\}\right.\\ &\qquad\left.+\frac{\bar{\eta}_k}{m_k\omega_k}\left\{-\frac{\cos(\omega_k+\omega_j)t}{2(\omega_k+\omega_j)}-\frac{\cos(\omega_k-\omega_j)t}{2(\omega_k-\omega_j)}\right\}\right].\end{aligned}\right\} \tag{2.12}$$

In virtue of these equations, after inserting Eqs. (2.7) into the right hand side of (2.6), we get

$$\begin{pmatrix} m_i\omega_i\dot{\xi}_i\\ -\dot{\eta}_i\end{pmatrix}=-F_i(t)\begin{pmatrix}\sin\omega_i t\\ \cos\omega_i t\end{pmatrix} \tag{2.13}$$

where

$$F_i(t)=-\sum\lambda_{ij}\left(\bar{\xi}_j\cos\omega_j t+\frac{\bar{\eta}_j}{m_j\omega_j}\sin\omega_j t\right)+\tilde{F}(t)\ , \tag{2.13'}$$

$$\begin{aligned}\tilde{F}(t)=-\sum_{j\neq i}{}'\frac{\lambda_{ij}}{m_j\omega_j}\sum_{k\neq j}{}'\lambda_{jk}&\left[\bar{\xi}_k\left\{-\frac{\pi}{2}\delta(\omega_k-\omega_j)\sin\omega_j t+\frac{\omega_j}{\omega_k^2-\omega_j^2}\cos\omega_k t\right\}\right.\\ &\left.+\frac{\bar{\eta}_k}{m_k\omega_k}\left\{\frac{\pi}{2}\delta(\omega_k-\omega_j)\cos\omega_j t+\frac{\omega_j}{\omega_k^2-\omega_j^2}\sin\omega_k t\right\}\right].\end{aligned} \tag{2.13''}$$

This is the equation of fundamental importance in the present calculation.

Further we have to prove Eqs. (2.8) that $\dot{\xi}$ and $\dot{\bar{\eta}}$ are second order in λ. To verify this we make $\dot{\xi}$ and $\dot{\eta}$ from Eqs. (2.7) and (2.11) or (2.9) and insert them into the left-hand side of (2.13) to get

$$m_i\omega_i\dot{\bar{\xi}}_i-\sum \lambda_{ij}\{\dot{\bar{\xi}}_j c_{ji}+(\dot{\bar{\eta}}_j/m_j\omega_j)S_{ji}\}=-\tilde{F}_i(t)\sin\omega_i t \tag{2.14}$$

and similar equations for $\dot{\bar{\eta}}_i$. In these simultaneous equations $\tilde{F}_i(t)$ is of second order in λ and does not contain $\dot{\bar{\xi}}$ nor $\dot{\bar{\eta}}$. So except for very unusual cases we may replace the set of simultaneous equations by

$$\begin{pmatrix} m_i\omega_i\dot{\bar{\xi}}_i \\ -\dot{\bar{\eta}}_i \end{pmatrix}=-\tilde{F}(t)\begin{pmatrix} \sin\omega_i t \\ \cos\omega_i t \end{pmatrix} \tag{2.15}$$

where $\tilde{F}_i(t)$ is give by Eq. (2.13″). Therefore the rate of change in $\bar{\xi}$ and $\bar{\eta}$ is second order in λ, and stays very small all the time.

In the following it is sometimes convenient to use the notations,

$$\left.\begin{aligned} \bar{x}_i&=\bar{\xi}_i\cos\omega_i t+\frac{\bar{\eta}_i}{m_i\omega_i}\sin\omega_i t\ , \\ \bar{p}_i&=-m_i\omega_i\bar{\xi}_i\sin\omega_i t+\bar{\eta}_i\cos\omega_i t\ . \end{aligned}\right\} \tag{2.16}$$

§ 3. Damped Oscillation

Let us pay special attention to the oscillator $i=0$ (central oscillator) and consider the assembly of other oscillators $1, 2, \cdots, j, \cdots, k, \cdots$ $(\neq 0)$ as forming thermostat.

Further, we assume that the thermostat is always in the state of thermal equalibrium with temperature T. The most logical way to introduce this *ad hoc* assumption is to take an ensemble of systems of the same construction and energy (each system is what we have considered in § 2). We are to follow the motion of the central oscillators $i=0$ in all the systems; the representative points belonging to the central oscillators are expected to suffer Brownian motion and to diffuse in a certain way in the phase space (x_0, p_0). The other oscillators $1, 2, \cdots, j, \cdots, k, \cdots$ are the thermostat oscillators and their motion is supposed to be in perfect randomness at every instant. Under this supposition we can speak of the average taken over the configuration of the thermostat.

As to the thermostat in equilibrium state the average of fluctuations, ξ_j' and η_j', will vanish. On the other hand $\bar{\xi}_j$ and $\bar{\eta}_j$ will be distributed symmetrically, their averages being zero. Thus

$$\left.\begin{aligned} \langle\bar{\xi}_j\rangle&=\langle\xi_j'\rangle=\langle\xi_j\rangle=0\ , \\ \langle\bar{\eta}_j\rangle&=\langle\eta_j'\rangle=\langle\eta_j\rangle=0\ . \end{aligned}\right\} \tag{3.1}$$

We see that these requirements are consistent with Eqs. (2.15). Now

The difference between $\langle\xi_j^2\rangle$ and $\langle\bar{\xi}_j^2\rangle$, for instance, is of second order in λ^2. We shall neglect λ^2 terms and formulate the ensemble average:

$$\langle\bar{\xi}_j^2\rangle=\langle\bar{\eta}_j^2\rangle/(m_j\omega_j)^2=kT/m_j\omega_j^2\ . \tag{3.2}$$

Further we assume that

$$\langle\bar{\xi}_j(t)\bar{\xi}_k(t')\rangle=0 \quad (j\neq k)\ , \qquad \langle\bar{\xi}_j(t)\bar{\eta}_k(t')\rangle=0\ . \tag{3.2′}$$

We see again that these requirements are consistent with Eqs. (2.15). Now

$$\left.\begin{aligned} \dot{x}&=p_0/m_0\ , \\ \dot{p}_0&=-m_0\omega_0^2x_0-m_0\omega_0\dot{\xi}_0\sin\omega_0 t+\dot{\eta}_0\cos\omega_0 t\ . \end{aligned}\right\} \tag{3.3}$$

Taking average over the thermostat oscillators we get from Eqs. (2.13),

$$\langle \dot{p}_0\rangle = -m_0\omega_0^2\langle x_0\rangle - \sum \frac{\lambda_{0j}^2}{m_j\omega_j}\frac{\pi}{2}\delta(\omega_0-\omega_j)\left\langle -\bar{\xi}_0\sin\omega_0 t + \frac{\bar{\eta}_0}{m_0\omega_0}\cos\omega_0 t\right\rangle$$
$$-\sum \frac{\lambda_{0j}^2}{m_j\omega_j}\frac{\omega_j}{\omega_0^2-\omega_j^2}\left\langle \bar{\xi}_0\cos\omega_0 t + \frac{\bar{\eta}_0}{m_0\omega_0}\sin\omega_0 t\right\rangle . \tag{3.4}$$

The averages in the right-hand side of this equation are $-\langle\bar{p}_0\rangle/m_0\omega_0$ and $\langle\bar{x}_0\rangle$. Therefore we may write

$$\langle\dot{p}_0\rangle + m_0\omega_0^2\langle x_0\rangle = \Lambda\langle\bar{x}_0\rangle - \zeta\langle\bar{p}_0\rangle/m_0 , \tag{3.5}$$

where

$$\left.\begin{aligned} \Lambda &= \sum_j \frac{1}{m_j}\frac{\lambda_{0j}^2}{\omega_j^2-\omega_0^2} , \\ \zeta &= \frac{\pi}{2}\frac{1}{m_0}\sum_j \frac{\lambda_{0j}^2}{m_j\omega_0^2}\delta(\omega_0-\omega_j) . \end{aligned}\right\} \tag{3.6}$$

As Λ and ζ are of the order λ^2, we may replace $\langle\bar{x}_0\rangle$ and $\langle\bar{p}_0\rangle$ by $\langle x_0\rangle$ and $\langle p_0\rangle$ in the right-hand side of (3.5), because we are neglecting higher orders in λ.

We obtain finally the damping equation,

$$m_0\frac{d^2}{dt^2}\langle x_0\rangle + \zeta\frac{d}{dt}\langle x_0\rangle + (m_0\omega_0^2-\Lambda)\langle x_0\rangle = 0 , \tag{3.7}$$

where ζ is the friction constant and Λ stands for the shift in frequency. If there are

$$g(\omega')\,d\omega'$$

oscillators in the thermostat within the frequency range $\omega'\sim\omega'+d\omega'$, and if their masses are the same,

$$m' = m_j .$$

we have[7)]

$$\Lambda = \frac{1}{m'}\int\frac{\lambda^2(\omega)g(\omega)\,d\omega}{\omega^2-\omega_0^2} ,$$

$$\zeta = \lambda^2(\omega)\frac{\pi}{2}g(\omega_0)/mm'\omega_0^2 .$$

in which we have written $\lambda(\omega_j)$ for λ_{0j}, that is, we look λ_{0j} as a function of the frequency ω_j of the thermostat oscillator. As in the case of a radiation field[8)] or the like, if $g(\omega)\propto\omega^2$ then ζ would become independent of ω, provided if $\lambda(\omega)$ were constant[7)]. In this case, however, Λ would diverge, and we have to cut off high frequency range or to renormarize the frequency of the central oscillator. This is the situation frequently called as the ultraviolet divergence. But in our case we may think of appropriate forms for $\lambda(\omega)$ and $g(\omega)$.

It is easy to see that the term $\Lambda\langle x_0\rangle$ actually represent the reaction due to thermostat oscillator on the central oscillator: Suppose that the central oscillator is oscillating with amplitude a_0. The oscillator j of the thermostat coupled with the central oscillator is then subject to forced oscillation and its motion is given by

$$x_j = a_j\sin(\omega_j t+\delta_j) + \frac{1}{\omega_j^2-\omega_0^2}\frac{-\lambda_{0j}}{m_j}a_0\sin(\omega_0 t+\delta_0) .$$

The influence of the second term on the central oscillator is the reaction force given by

$$f_{0\to j\to 0} = -\lambda_{j0}\frac{1}{\omega_j^2-\omega_0^2}\frac{-\lambda_{0j}}{m_j}a_0\sin(\omega_0 t+\delta_0) = \frac{\lambda_{0j}^2}{\omega_j^2-\omega_0^2}\frac{1}{m_j}x_0 .$$

The summation of this force over j gives $\Lambda\langle x_0\rangle$.

§ 4. Langevin Equation and Correlation of Random Force

Going back to Eq. (3.3) we see that the equation for p_0 is of the form

$$\dot{p}_0+m_0\omega_0{}^2x_0=-\sum\lambda_{0j}\left(\bar{\xi}_j\cos\omega_jt+\frac{\bar{\eta}_j}{m_j\omega_j}\sin\omega_jt\right)+(\Lambda\bar{x}_0-\zeta\bar{p}_0/m)$$
$$+(\text{terms linear in } \bar{\xi}_j \text{ and } \bar{\eta}_j \text{ of thermostat})\,. \tag{4.1}$$

The last term on the right-hand side is fluctuating, but of the order λ^2. The second term is of the order λ^2, but it is not fluctuating and gives rise to the frequency shift and the friction after replacing $\bar{x}_0$ and $\bar{p}_0$ by x_0 and p_0. The fluctuating force is therefore

$$f(t)=-\sum\lambda_{0j}\left(\bar{\xi}_j\cos\omega_jt+\frac{\bar{\eta}_j}{m_j\omega_j}\sin\omega_jt\right)+\mathrm{O}(\lambda^2)$$
$$=-\sum\lambda_{0j}\langle\bar{x}_j\rangle+\mathrm{O}(\lambda^2)\,. \tag{4.2}$$

Consequently we get the Langevin equation,

$$m_0\ddot{x}_0+\zeta\dot{x}_0+(m_0\omega^2-\Lambda)x_0=f(t)\,. \tag{4.3}$$

The correlation function of the fluctuating force is

$$\langle f(t)f(t+\tau)\rangle=\sum\sum\lambda_{0j}\lambda_{0k}\langle\bar{x}_j(t)\bar{x}_k(t+\tau)\rangle\,, \tag{4.4}$$

in which

$$\bar{x}_j(t)\bar{x}_k(t+\tau)=\bar{\xi}_j(t)\bar{\xi}_k(t+\tau)\cos\omega_jt\cos\omega_k(t+\tau)$$
$$+\frac{\bar{\eta}_j(t)\bar{\eta}_k(t+\tau)}{m_jm_k\omega_j\omega_k}\sin\omega_jt\sin\omega_k(t+\tau)$$
$$+\frac{\bar{\xi}_j(t)\bar{\eta}_k(t+\tau)}{m_k\omega_k}\cos\omega_jt\sin\omega_k(t+\tau)$$
$$+\frac{\bar{\eta}_j(t)\bar{\xi}_k(t+\tau)}{m_j\omega_j}\sin\omega_jt\cos\omega_k(t+\tau)\,. \tag{4.5}$$

Now we shall evaluate quantities like $\langle\bar{\xi}_j(t)\bar{\xi}_j(t+\tau)\rangle$. To do this we make the derivative with respect to τ. Replacing t by $t+\tau$ in Eq. (2.15) and multiplying by $\bar{\xi}_i(t)$ we get

$$\langle\bar{\xi}_j(t)\dot{\bar{\xi}}_j(t+\tau)\rangle=\sum_l\frac{\lambda_{jl}\lambda_{lj}}{m_j\omega_jm_l\omega_l}\langle\bar{\xi}_j(t)\bar{\xi}_j(t+\tau)\rangle\left\{-\frac{\pi}{2}\delta(\omega_j-\omega_l)\sin\omega_l(t+\tau)\right.$$
$$\left.+\frac{\omega_l}{\omega_j{}^2-\omega_l{}^2}\cos\omega_j(t+\tau)\right\}\sin\omega_j(t+\tau)\,. \tag{4.6}$$

We take time average of the ensemble average and designate it by $\overline{\langle\ \rangle}$. We have

$$\frac{d}{d\tau}\overline{\langle\bar{\xi}_j(t)\bar{\xi}_j(t+\tau)\rangle}=\frac{\zeta(\omega_j)}{2}\langle\bar{\xi}_j(t)\bar{\xi}_j(t+\tau)\rangle \tag{4.7}$$

where ζ is the friction constant given by Eq. (3.6). We have a similar equation for $\overline{\langle\eta_j(t)\eta_j(t+\tau)\rangle}$. Thus

$$\left.\begin{aligned}\overline{\langle\xi_j(t)\xi_j(t+\tau)\rangle}&=\langle\bar{\xi}_j{}^2\rangle e^{-\zeta\tau/2}\,,\\ \overline{\langle\eta_j(t)\eta_j(t+\tau)\rangle}&=\langle\bar{\eta}_j{}^2\rangle e^{-\zeta\tau/2}\,.\end{aligned}\right\} \tag{4.8}$$

Analogously we can prove that $\overline{\langle\bar{\xi}_j(t)\bar{\xi}_k(t+\tau)\rangle}$ $(j\neq k)$ and $\overline{\langle\bar{\xi}_j(t)\bar{\eta}_k(t+\tau)\rangle}$ vanish if they are zero initially. So that Eqs. (3.2′) are consistent in this sense.

Inserting Eq. (4.8) into (4.5) we get

$$\overline{\langle \bar{x}_j(t)\bar{x}_k(t+\tau)\rangle}=\langle \bar{\xi}_j^2\rangle \delta_{jk} e^{-\zeta\tau/2}\cos(\omega_j\tau)\ . \tag{4.9}$$

The factor $\cos(\omega_j\tau)$ on the right-hand side comes from the nature of the oscillator.

The force acting on the central oscillator under Brownian motion is $f(t)=-\sum \lambda_{0j}\bar{x}_j+O(\lambda^2)$. The correlation of the random force is therefore

$$\overline{\langle f(t)f(t+\tau)\rangle}=\sum \lambda^2(\omega_j)\langle \xi_j^2\rangle e^{-\zeta(\omega_j)\tau/2}\cos\omega_j\tau\ , \tag{4.10}$$

where, as before, we have written $\lambda(\omega_j)$ for λ_{0j}. The spectrum is

$$\begin{aligned}&\int_0^\infty d\tau \cos\omega\tau\overline{\langle f(t)f(t+\tau)\rangle}\\ &\quad=\sum \lambda^2(\omega_j)\langle \bar{\xi}_j^2\rangle\ \frac{1}{2}\left\{\frac{\zeta/2}{(\omega-\omega_j)^2+(\zeta/2)^2}+\frac{\zeta/2}{(\omega+\omega_j)^2+(\zeta/2)^2}\right\}\\ &\quad=\sum \lambda^2(\omega)\langle \bar{\xi}^2(\omega)\rangle\frac{\pi}{2}\{\delta(\omega-\omega_j)+\delta(\omega+\omega_j)\}\ , \qquad (\zeta\to 0)\ .\end{aligned}$$

Thus, in terms of the friction constant ζ of (3.6), we have

$$\int_0^\infty dt \cos\omega\tau\overline{\langle f(t)f(t+\tau)\rangle}=mkT\zeta(\omega)\ . \tag{4.11}$$

This agrees with the Wiener-Khintchine theorem[9]. In particular for $\omega=\omega_0$ Eq. (4.11) is the relation between the correlation of random force and the friction constant for the harmonic oscillator under consideration. In the special case $\omega=0$, Eq. (4.11) reduces to the well-known relation,

$$\int_0^\infty d\tau\overline{\langle f(t)f(t+\tau)\rangle}=mkT\zeta(0)\ . \tag{4.12}$$

§ 5. Concluding Remarks

The essential point of the method of treatment is made clear for a simple example, in which one might understand the physical meaning of every line of the calculation.

We might have used, instead of ξ and η, the variables defined by

$$a=\sqrt{m\omega/2}\,(\xi+i\eta/m\omega)\ ,$$
$$a^*=\sqrt{m\omega/2}\,(\xi-i\eta/m\omega)\ .$$

Then the calculation will admit direct translation into quantum mechanics, which will be discussed in a later article.

The present study was partially financiated by the Scientific Research Fund of the Ministry of Education.

References

1) S. Chandrasekhar: Rev. Mod. Phys. **15** (1943) 2. M. C. Wang and G. E. Uhlenbeck: Rev. Mod. Phys. **17** (1945) 323.
2) J. G. Kirkwood: J. Chem. Phys. **14** (1946) 180.
3) R. Zwanzig: J. Chem. Phys. **28** (1958) 365.
4) H. B. Callen and T. A. Welton: Phys. Rev. **83** (1951) 134.
5) R. Kubo: J. Phys. Soc. Japan **12** (1957) 570. R. Kubo et al: ibid **12** (1957) 1203.
6) I. Prigogine and M. Toda: Mol. Phys. **1** (1958) 48.
7) M. Toda: J. Phys. Soc. Japan **13** (1958) 1266.
8) W. Heitler: *The Quantum Theory of Radiation*, (Oxford, 1954) 32.
9) for example, C. Kittle: *Elementary Statistical Physics*, (John Wiley & Sons, New York, 1958).

JOURNAL OF THE PHYSICAL SOCIETY OF JAPAN, Vol. 14, No. 6, JUNE, 1959

Thermoelectric Power of AgCl

By Yasumasa SUSUKI, Shigeaki ENDŌ
and Eijirō HAGA
Department of Physics, Faculty of Science,
Niigata University

(Received February 11, 1959)

The thermoelectric power of AgCl doped with several concentrations of $CdCl_2$ is measured and compared with the theory.

§ 1. Introduction

Recently the theory of thermoelectric power of ionic crystals[1,2] has been developed as a help of understanding of the electrical property and the Soret phenomenon. The purpose of the present paper is to give an information on thermoelectric properties of AgCl crystals by combining the available theory with measurements on AgCl doped with several concentrations of $CdCl_2$.

§ 2. Experimental Arrangements

We prepared specimens of silver chloride by adding hydrochloric acid to a solution of silver nitrate, and well washing the precipitate away from violet light. The impurities in samples were analysed by a spectroscopic method. Iron, silicon and magnesium were barely detected, so that we estimate that the amount of these impurities is below 10^{-3} Mol-%. Also we used specimens of silver chloride offered from the laboratory of Fuji Photo Film Co., and the both samples showed no material differences.

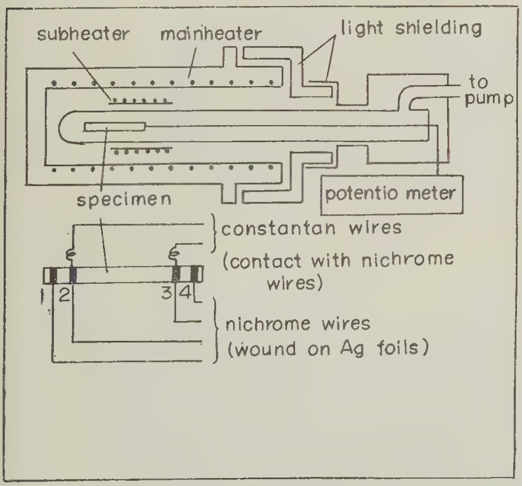

1, 2, 3, 4: Conductivity measurement probes.
2, 3: Thermoelectric voltage measurement probes.

Fig. 1. The schematic diagram of the experimental arrangements.

After being washed and dried, the precipitate is mixed well with a proper amount of $CdCl_2$ and is put in a hard glass tube with a capillary.[3] The tube is heated up to 580°C while evacuating and then sealed. We shake the tube slowly in order to mix AgCl with $CdCl_2$ uniformly and at the same time, in order to avoid adhesion of sample to glass wall and to eliminate bubbles. The molten salt is cooled with a speed of the order of 1°C/min near the melting point of AgCl. The speed at which crystal is cooled to room temperature may be larger than that at the melting point, because the quenching has an effect only at lower temperature than the range of our measurements (100∼400°C).[4] The sample thus obtained, was cut with a silicon carbide cutter and ground to a proper size (its typical dimension is $2\times2\times20\,\mathrm{mm}^3$). In some cases, the ground specimens were immersed in concentrated ammonia for a minute to remove the contaminated layers; in other cases, glass knife was used. There are no significant differences in thermoelectric power for both treatments.

The experimental arrangements are shown in Fig. 1. Four silver foils are wound on the specimen. The conductivity is measured as a function of the temperature making use of the four silver probes. We determine $CdCl_2$ concentrations from such conductivity measurements by refering the published data of Teltow.[6] The results are shown in Table I as c. Here c^* denotes $CdCl_2$ concentrations mixed at the beginning.

Temperature gradient is set up by a movable subheater, the position of which determines the magnitude of the temperature gradient and its sign. (The temperature difference between two ends is chosen to be smaller than 15°C.) In practice, in order to save the time necessary for steady state to attain, the main- and sub-heater was fixed and the sample was moved: in this way, the sign of the gradient could be reversed in twenty minutes or shorter than that.

Table I. $CdCl_2$ concentrations.

c^* (Mol-%)	c (Mol-%)	Remark
0.20	0.068	The tube was not shaked
0.20	0.16	
0.026	0.022	The tube was shaked slowly
0.20	0.2_0	
0.010	0.008_0	

§ 3. Result

The result is shown in Fig. 2. For pure samples, the results agree well with Reinhold's one.[5)] In most specimens, if measurements are made in the run of low- high- low temperature, they are not reproducible in low temperature range; that is, the magnitude of the thermoelectric voltage becomes smaller in the second run than in the first run. In the case of the pure samples, this deviation from the theoretical value at low temperature may be explained by an unavoidable contamination during the measurement and may be interpreted by the divalent impurity concentration of about 1×10^3 Mol-% (pure No. 4). But in the case of the doped specimens, it is not possible to give such a simple interpretation.

Now, the thermoelectric power, Q, is given by[2,1)]

$$eQ=-\frac{t_i}{T}(h_F+Q_i{}^*+Q_V{}^*) -k\ln c_v+Q_v/T+\alpha\,, \tag{1}$$

$$\alpha=k\sum\ln\nu_P/\nu_v-(s_P-s_{\mathrm{Ag}}^{\mathrm{Ag}})\,.$$

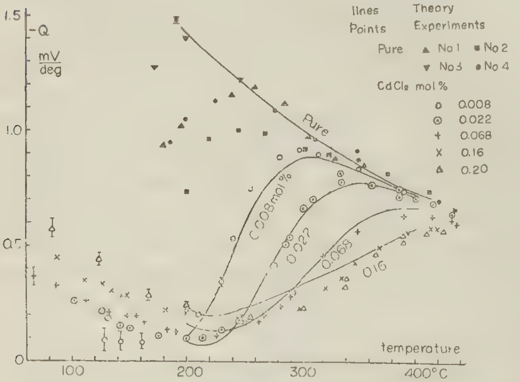

Fig. 2. The thermoelectric power *versus* temperature.

Here, the transport number of Ag interstitial ions, t_i, and the concentration of Ag^+ vacancies, c_v, can be obtained from the conductivity data of Teltow:[5)]

$$t_i=\frac{\varphi}{\varphi+\xi^2},\quad c_v=x_0\xi,\quad z=\frac{\xi+\varphi/\xi}{1+\varphi}\,. \tag{2}$$

One value of $h_F+Q_i{}^*+Q_v{}^*$ is obtained from the difference of Q between a pure sample and an impure sample at each temperature.[1)] Next, the value of $-Q_v{}^*/T-\alpha$ at each temperature is obtained by making use of the mean value of $h_F+Q_i{}^*+Q_v{}^*$ for five impure samples so that Eq. (1) fits experimental value for a pure sample. The values of $h_F+Q_i{}^*+Q_v{}^*$ and $-Q_v{}^*/T-\alpha$ thus obtained are shown in Fig. 3. By making use of these values, the theoretical curves are given in Fig. 2. It is seen from Fig. 2 that the theory fits experiments pretty well. It is seen from Fig. 3 that $h_F+Q_i{}^*+Q_v{}^*$ varies severely with temperature and the value of $-Q_v{}^*$ is larger than the activation energy of the mobility of Ag^+ vacancies.* The simple model of Wirtz[7)] can not explain these results. This theoretical difficulty will be discussed in future.

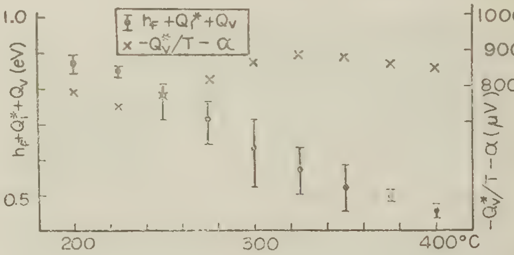

Fig. 3. The values of $h_F+Q_i{}^*+Q_v{}^*$ and $-Q_v{}^*/T-\alpha$.

The writers wish to express their sincere thanks to Dr. Y. Mizuki of Fuji Photo Film Co. for the kind supply of the AgCl samples, and to Mr. T. Ninomiya and Dr. H. Kanzaki of Bussei Laboratory for their kind helps. The writers also are indebted to Dr. A. B. Lidiard and Dr. W. Christy for informing

---

* According to the private communication of Dr. A. B. Lidiard, W. Christy found the similar behaviors in AgBr.

them the results on AgBr before publication, and to Mr. T. Suzuki of the department of chemistry in our university for the spectrographic investigation.

The present work was partly supported by the Scientific Research Fund of the Ministry of Education.

References

1) R. E. Howard and A. B. Lidiard: Phil. Mag. **2** (1957) 1462.
2) E. Haga: J. Phys. Soc. Japan **13** (1958) 1090.
3) F. C. Brown: J. Phys. Chem. Solids **4** (1958) 206.
4) R. Matejec: Z. Phys. **148** (1957) 454.
5) J. Teltow: Ann. Physik **15** (1955) 268.
6) H. Reinhold: Z. Anorg. Allg. Chem. **171** (1928) 181.
7) K. Wirtz: Z. Phys. **44** (1943) 221,

Journal of the Physical Society of Japan, Vol. 14, No. 6, June, 1959

Internal Friction of KCl Crystals at Low Temperatures

By Taira SUZUKI,* Katsumi SUZUKI and Tomoo KAMIGAKI

The Research Institute for Iron, Steel and Other Metals,
Tohoku University, Sendai, Japan

(Received March 4, 1959)

Ultrasonic attenuation in megacycle range for cold-worked and for quenched KCl crystals has been measured against temperature between 200°K and room temperature. A very broad relaxation band appears below 240°K for cold-worked crystals. The experiments on the anisotropy of attenuation in crystals cold-worked by uniaxial compression demonstrate that the attenuation is caused by the motion of the dislocations. The activation energy is found to be 0.44 eV. Quenched crystals show also a similar band. The following are very unique features: As quenching temperature is raised the attenuation band shifts to higher temperature. This shift is accompanied by the increase of the activation energy. Another significant nature is the ageing effect, which results also a band-shift to higher temperature with increasing ageing time after quenching.

It has been discussed that the effects of vacancies in the dislocation core upon the activation energy for the motion of dislocations and the concurrent motion of vacancies in the cores of oscillating dislocations both give rise to such a broad band as observed.

§ 1. Introduction

Most of the work on low-temperature internal friction has been concerned with metals[1)–5)] and a few with germanium[6),7)] and silicon[8)]. Many interesting features of dislocation dynamics have been revealed so far. However, there are several respects in which ionic crystals such as NaCl are of special significance. First, for the comprehensive understanding of dislocation dynamics in crystalline solids it is naturally desired to extend the investigation to the ionic crystals, since no work has been done so far on such crystals. Besides, theoretical aids seem to be possible in the ionic crystals much more than in metals. Indeed, the energy of dislocation cores has been calculated for the first time for NaCl by Huntington, Dickey and Thomson[9)], and Bassani and Thomson[10)] have discussed the electrical interaction between a dislocation and a vacancy in its core. It overwhelms the elastic field interaction, which is most important in metals.

A second point of interest in connection with the alkali halides relates to a question on the nature of low-temperature relaxation peak: In the discussion of the Bordoni peak in face-centred cubic metals Seeger[11] has stated his opinion that the impurities present in the crystals give no effect on the peak temperature for a fixed frequency. This is the feature really found in most metals such as aluminium and copper. However, it is questionable if we believe the Seeger-Mason mechanism based on the oscillation of a dislocation line in a potential well. This is because even fresh dislocations introduced by cold-working in specimen crystals have a sufficient time to be trapped by the impurities in most experiments before starting the measurements of ultrasonic attenuation and these impurities will modify the activation energy for the oscillatory motion of the dislocations. It is desired to do experiments with respect to the above question. It seems most appropriate for this aim to study the effect of vacancies on low-temperature internal friction of the alkali halides because of their strong interaction with dislocations as mentioned above.

---

* Now at the Institute for Solid State Physics, Tokyo University, Tokyo.

The results obtained by the present experiment have been discussed in connection with the recent proposal on the minimum stress required for the motion of charged dislocations in the alkali halides made by Eshelby, Newey and Pratt[12] and with the experimental results on critical shear stress of KCl studied by Doyama and one of the present authors[13].

§ 2. Experimental Procedure

Measurements were made with the pulsed ultrasonics[14]. The system for the measurement consists of a pulse generator and a receiver to produce and to detect the megacycle-frequency pulses which are impressed on the x-cut quartz crystal. The quartz crystal used is about 1 cm in diameter and the thickness corresponds to the fundamental frequency of 5 Mc/sec. The multiply reflected pulses are received by the quartz crystal and observed by a cathode-ray oscilloscope. The smallest reading of a variable attenuator inserted in series in the circuit was 0.1 db, which corresponds to 0.05 db/cm for a specimen of 1 cm in length.

Prior to mounting the crystal a metal foil of copper of five microns in thickness was cemented carefully to the cleavage surface of a specimen crystal by means of beeze-wax or rosin. This metal foil was connected to the detecting system. It is very important to find out appropriate cementing materials for the test of brittle specimens such as the present crystals, otherwise fine cracks are formed at low temperatures. Since we could not make a success in finding such a material, the temperature range investigated is from 200°K to room temperature. Further studies on acoustic spectra of KCl crystals at sufficiently low temperatures will be done in near future. The transducer crystal was then cemented on the above metal foil by the Bond cement and its opposite face was also cemented to another metal foil serving as the input electrode. A sufficient damping of the transducer was given by means of an ebonite block. The assembly was enclosed in a container made of copper block wound by an insulated resistance wire for heating and inserted into a glass tube. The whole assembly was then evacuated and cooled in the liquid nitrogen bath. Temperature of a specimen was measured by a copper-constantan thermocouple mounted in a very close distance from the specimen.

The attenuation was measured at temperature intervals of 2° to 5° on heating run. The maximum strain amplitude was less than 10^{-7} and the frequencies used were 5 and 15 Mc/sec. Within this strain range the attenuation proved independent of strain. The absolute accuracy of measured attenuations from one run to the next is mainly determined by the mounting conditions and is approximately ± 0.3 db/cm.

Specimen crystals were KCl obtained from the Harshaw Chemical Company, which were annealed normally at 550°C in air for 5 hours and, then, slowly cooled to room temperature in taking care to avoid thermal strain. The specimens were cleaved to about $1.5 \times 1.5 \times 1.5$ cm^3 before the final anneal. Cold work was given by a compression testing machine at room temperature. An appropriate lubricant was used to give a deformation as uniform as possible. Quenching was made by pulling out a thin SB glass tube opened to air containing the specimen from a resistance-furnace at a desired temperature onto a copper plate at room temperature.

§ 3. Experimental Results

1. *General*

Attenuation was measured on specimen crystals which were slowly cooled and then cold-worked by compression. The general features will be seen in Fig. 1. Attenuations for crystals quenched from 550° and 700°C are also plotted in this figure. Since measurements were all made above 200°K, it is not clear whether a sharp peak corresponding to the Bordoni peak such as found in metals appears below this temperature or not. A question arises on the origin of the attenuation band near 240°K. Since there has been no indication of any similar side-peak on the higher temperature side of the Bordoni peak in face-centred cubic metals, it may be possible that the phenomenon is based on some characteristics of the dislocations or other imperfections in ionic crystals of NaCl type.

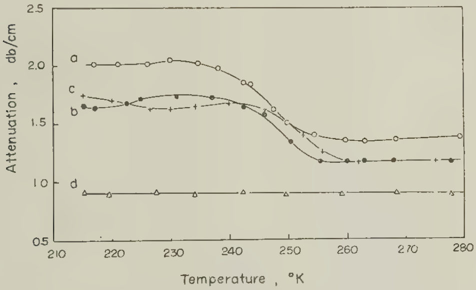

Fig. 1. Attenuations plotted against temperature for cold-worked and for quenched crystals.
(a) Cold-worked by 0.26 precent in compression (specimen No. 29E).
(b) Quenched from 550°C (specimen No. 22A–1).
(c) Quenched from 700°C (specimen No. 27E).
(d) Slowly cooled (specimen No. 9).

The general features of the observed band are:

(1) The band-edge position is independent of strain amplitudes in the range investigated here.

(2) The band-height increases with plastic strain less than 4 percent. For higher strains it does not seem so sensitive to plastic strain as before.

(3) The band-edge shifts to higher temperature with increasing quenching temperature.

(4) The shift of the band-edge also occurs in the case of holding crystals at room temperature after quenching (ageing effect).

(5) The attenuation is sensitive to the frequency of ultrasonics. Curves in Fig. 1 were obtained at 5 Mc/sec. More detailed descriptions for each case will be given in the following.

2. *Anisotropy of attenuation in cold-worked crystals*

When the crystals are compressed in the direction parallel to a cubic axis, the four glide systems, $\{\langle\bar{1}01\rangle/(101)\}$, are equally oriented to the applied stress. It is known that as long as plastic strain is not so large the crystals occasionally deform by the action of a single glide system or double glide systems whose Burgers vectors are perpendicular to each other[15]. If the longitudinal wave excited by the x-cut quartz crystal directs in the direction normal to the Burgers vector of the dislocation concerned, no contribution to the dislocation damping should be expected, since it gives no effective shearing stress acting on it. Therefore, the respective attenuations parallel to three directions normal to each other such as shown in Fig. 2 will constitute an arithmetic relation. A hatching indicated in the inset in the same figure corresponds to the birefringence bands observed by polarizing microscope. We tried to observe the predicted relation on different specimens and obtained

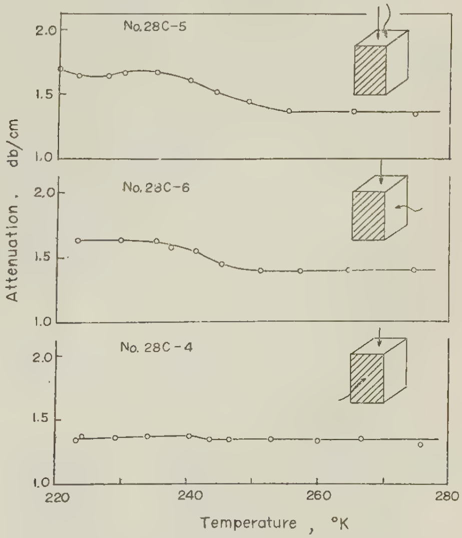

Fig. 2. Orientation dependence of attenuations in cold-worked crystals. A hatching corresponds to the birefringence bands observed by polarizing microscope. Solid arrows indicate the direction of compression and wavy arrows designate the one of incident pulsed waves.

a consistent result in every case as expected. Solid arrows designate the compression axis and wavy arrows correspond to the direction of propagation of longitudinal pulsed waves. The peak attenuation for the specimen No. 28C–5 is approximately equal to the sum of the ones at respective peaks for other two. A very small step can be seen at about 243°K in the case of No. 28C–4. This would be caused either by a small number of the dislocations introduced by cold-working whose Burgers vectors are not normal to the oscillation direction of pulsed waves, or by the possibility that the acoustic waves have a small component of stress parallel to the specimen surface on which the transducer crystal was cemented.

The above observations give doubtlessly an evidence that the attenuation observed is related to the motion of dislocations in crystals. A similar anisotropy of the logarithmic decrement has been observed on zinc single crystals by Read[16], Alers[17], and Waterman[18]. The observations of this sort can offer a most beautiful demonstration of dislocation damping.

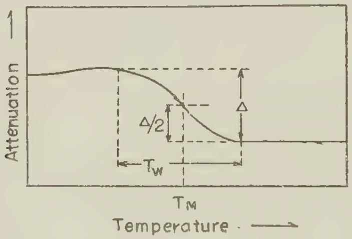

Fig. 3. A schematic illustration for the definition of T_M.

The observed attenuation forms a very broad band showing a spectrum of activation energies. For the sake of brevity, however, we assume the following working hypothesis that the largest activation energy W of the relaxation process is to be determined by using the following equation, i.e.,

$$\frac{W}{R}\left(\frac{1}{T_{M1}}-\frac{1}{T_{M2}}\right)=\log\left(\frac{f_2}{f_1}\right), \qquad (1)$$

for a change in frequency from f_1 to f_2, where R is the gas constant. T_{M1} and T_{M2} are the temperatures for frequencies f_1 and f_2, respectively, corresponding to the half maximum at the band edge. This is schematically illustrated in Fig. 3. Table I sums up all the results of cold-worked crystals in the range of plastic strain 0.2 to 4 percent. The band-edge position is rather independent of ageing time at room temperature after cold work. It must be remembered here that it spent at least one hour for mounting the specimen and lowering temperature before starting measurements. Taking average of T_M shown in Table I, it gives 242°K for 5 Mc/sec and 251°K for 15 Mc/sec. The activation energy thus obtained is 0.44 eV.

3. *Attenuation of quenched crystals*

The attenuation band obtained from crystals quenched from the temperature range of

Table I. Attenuation data for cold-worked crystals.

Specimen No.	Strain (%)	Direction of pulses*	Time after cold-work (hrs)	T_M (°K)	T_W (°K)	Peak height Δ (db/cm)
5 Mc/sec						
10	0.48	∥	—	240	60	0.85
13	0.90	⊥	—	—	15	0.67
28A–1	0.79	∥	3	244	31	0.73
28A–2	0.79	⊥	24	242	13	0.20
28C–2	0.36	⊥	23	240	4	0.05
28C–4	0.36	⊥	35	242	5	0.03
28C–5	0.36	∥	80	243	25	0.30
28C–6	0.36	⊥	90	241	10	0.25
28C–8	0.36	⊥	288	246	16	0.25
29E	0.26	∥	24	246	27.5	0.70
15 Mc/sec						
15A–2	3.64	∥	31	253	32	1.10
14	3.88	∥	5	250	18	1.35
28A–3	0.79	∥	45	250	25	0.33

* Relative to the compression axis.

Table II. Attenuation data for quenched crystals.

Specimen No.	Quenching temperature (°C)	Time after quenching (hrs)	T_M (°K)	T_W (°K)	Peak height Δ (db/cm)
5 Mc/sec					
11	550	5	242	13	0.30
16A-3	550	34	245	32	0.60
18	550	3	249	36	0.57
22A-1	550	2	248.5	20	0.55
22A-2	550	50	247.5	10	0.10
22A-3	550	75	250	15	0.43
15 Mc/sec					
20	550	2	(254)	30	0.90
21	550	4	262	22	1.00
5 Mc/sec					
30	700	38	260	8	0.44
31	700	2	253.5	8	0.40
27E	700	10	252.5	16	0.50
28D-1	700	3	257	10	0.18
28D-3	700	24	263	3	0.19
15 Mc/sec					
28D-2	700	6	264	12	0.70
28D-4	700	27.5	270.5	12	0.27

intrinsic conductivity is very similar to that observed in cold-worked specimens as already shown in Fig. 1. One of the most remarkable features will be the shift of the band edge with increasing quenching temperature. Table II includes all the data on quenched crystals from 550° and 700°C. Another remarkable feature seen in Table II is the shift of the band edge with increasing ageing time at room temperature. The results are illustrated in Fig. 4 for crystals quenched from 700°C. Such effects have not been observed in other materials.

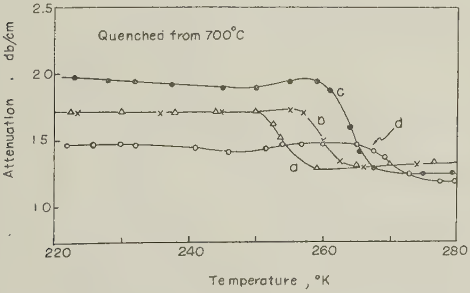

Fig. 4. Frequency dependence of attenuation and its variation with ageing time at room temperature for crystals quenched from 700°C. (a) specimen No. 31 at 5 Mc/sec after 2 hours; (b) specimen No. 30 at 5 Mc/sec after 38 hours; (c) specimen No. 28D-2 at 15 Mc/sec after 6 hours; (d) specimen No. 28D-4 at 15 Mc/sec after 27.5 hours.

In our crystals quenched from 550°C, T_M is 248°K for 5 Mc/sec after about one hour from quenching and it shifts to 250°K after one day at room temperature. For crystals quenched from 700°C, the temperature shifts from 252° to 262°K for 5 Mc/sec with increasing ageing time. This phenomenon is accompanied by a remarkable increase of the activation energy. The following Table III will show such a variation of the activation energy. An increase in the activation energy also occurs when quenching temperature is raised as seen in the same table. The frequency ν_0 in Table III is obtained from the relation $\nu=\nu_0 \exp(-W/kT_M)$, where ν is taken to be the frequency of applied ultrasonics.

Quenching from the temperature range of

Table III. Variation of the activation energy with quenching temperature and with ageing time after quenching.

Treatment	ν_0 (sec)$^{-1}$	Activation energy (eV)
Cold-worked	4.4×10^{13}	0.44
Quenched from 550°C	1.7×10^{13}	0.43
Quenched from 700°C		
(a) short time	1.1×10^{14}	0.49
(b) long time at r. t.	$10^{15\pm1}$	0.61 ± 0.07

intrinsic conductivity will introduce dislocations and vacancies into the crystal. The above effects are hardly explained by a separate action either of the dislocations or of the vacancies. The activation energy for the motion of paired vacancies in KCl is 0.38 eV according to Dienes' calculation[19] and it does not seem to depend upon quenching temperature. Therefore, the motion of paised vacancies is hardly responsible for the observed relaxation. It will be necessary to take account of some correlation characteristic of the ionic crystals between the dislocations and the vacancies for the explanation of the observed phenomena.

§ 4. Discussions

1. *The Bordoni peak*

It has been shown in most experiments concerning the Bordoni peak in metals that the peak temperature for a fixed frequency is independent of the concentration and the nature of the impurities present. Seeger[11] has thus developed his theory of the Bordoni peak in face-centred cubic metals without taking account of the influence of impurities present. It seems to be quite questionable, however, that the impurities attached to the dislocations do not give any influence on the oscillatory motion of dislocations which causes the relaxation to be considered. In fact, the following discussion will lead us to conclude that the low-temperature internal friction peak should generally depend on the point defects present. The degree of the dependence is determined by the nature and the magnitude of interaction between the defects and the dislocation, however.

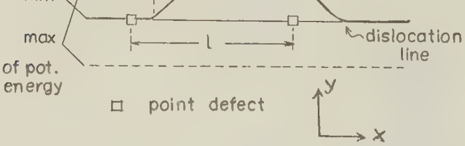

Fig. 5. Transition state in the formation of a kink pair according to Seeger. The effect of point defects attached to the dislocation line is described in the present paper.

Following Seeger and Mason[20] we consider the relaxation process due to the oscillation of a dislocation lying along its potential minimum. The activation energy is given by the formation energy of a half-kink pair. Fig. 5 illustrates the transition state corresponding to the position of maximum energy through which a dislocation segment is thrown to the neighbouring potential minimum. For practical purpose the potential energy of the dislocation line may be given by

$$E(y)=E_0-\alpha\cos\frac{2\pi y}{a}\,, \tag{2}$$

where 2α is the amplitude of the potential and a is the lattice constant. Using this one obtains the activation energy as

$$W=W_k+2\alpha d\,, \tag{3}$$

where W_k is the energy of a kink of width w and d is the optimum length of the dislocation segment at the transition state. Both are given by Seeger as increasing functions of α.

To examine the effect of point defects attached to the dislocation line we will begin with the case where the point defects are elastically bound to an edge dislocation. The interaction potential is given by Bilby (see Cottrell)[21] as

$$U=-A(\sin\theta)/|\boldsymbol{r}|\,, \tag{4}$$

where $|\boldsymbol{r}|$ is the magnitude of the radius vector from the dislocation line to the defect, θ is the angle between $\boldsymbol{r}$ and the Burgers vector of the dislocation, and A is a parameter depending on the elastic constants of the crystal, the lattice constant, and the relative degree of misfit of the defect. $|\boldsymbol{r}|$ should be larger than the core-radius r_0 of the dislocation. Suppose the defects pinning the dislocation line at the points separated by l from each other. Taking the displacement of the dislocation to be $\boldsymbol{\delta}$, the change of the potential will be $-\boldsymbol{\delta}\cdot\nabla U(\boldsymbol{r})$ when $|\boldsymbol{r}|>|\boldsymbol{\delta}|$. One easily finds that the increase of the activation energy is at most one tenth of $|U|_{\max}$ when $l\approx(d_0+w)$. The maximum value of $|U|$ in most cases is taken to be 0.2 eV or less, whereas the activation energy W is found experimentally to be 0.1 eV for aluminium and 0.07 eV for copper. Here the suffix 0 denotes the values for the dislocations free from point defects. Since the Bordoni peak is thought to be caused by fresh dislocations introduced by cold-working, the mean separation l between the pinning points should be large as compared to an equilibrium value, which is attained by the diffusion process. l can be estimated as $4a$ for $|U|_{\max}=0.2$ eV and $200a$ for $|U|_{\max}=0.1$ eV for copper of 99.99 percent purity in equilibrium at room temperature. On the other hand, (d_0+w) is found to be about $60a$ in copper for the applied shear stress smaller by one order of magnitude than the Peierls-Nabarro stress.

At any rate, it is doubtless that the activation energy for the motion of edge dislocations is very sensitive to the impurities. Therefore, the main Bordoni peak in such metals should be thought to be caused by the relaxation associated with the motion of screw dislocations which are less sensitive to the impurities. Besides, it is possible that the activation energy W_0 for the screw dislocations are large as compared with that for the dislocations of other orientation in such metals. This makes much simpler the appearance of the Bordoni peak as observed than in the opposite case.*

The situation is probably more complex in the case of ionic crystals. According to Bassani and Thomson[10], the positive-ion vacancy in NaCl is bound to the dislocation core with the binding energy equal to 0.4 eV. The binding energy of the negative-ion vacancy should be at least as large as that of the positive-ion vacancy. Fig. 6 illustrates the configuration of ions and the negative-ion vacancy in the core of a (110) edge dislocation. When the dislocation proceeds a distance of b in the direction [$\bar{1}10$], the ion configuration (a) changes to the one (b), in which the vacancy is left behind. The core-radius of a (110) edge dislocation in NaCl has been estimated to be $0.75b$ by Huntington *et al*[9]. It may be about the same in KCl. When the dislocation proceeds a unit distance b, therefore, the vacancy is left at the edge of the core. If we apply Eq. (4) to this case, the binding energy is found to be negative and equal to -0.06 eV using Bassani-Thomson's estimate of the relative misfit of the *positive-ion vacancy*. Accordingly, the activation energy for the motion of the dislocation increases by at least 0.4 eV as long as $l<(d_0+W)$. It should be noted that Bassani and Thomson have estimated l at room temperature for annealed NaCl of high purity as about $20a$. While, (d_0+W) can be assumed to be of the same order as that for copper, i.e., $60a$.

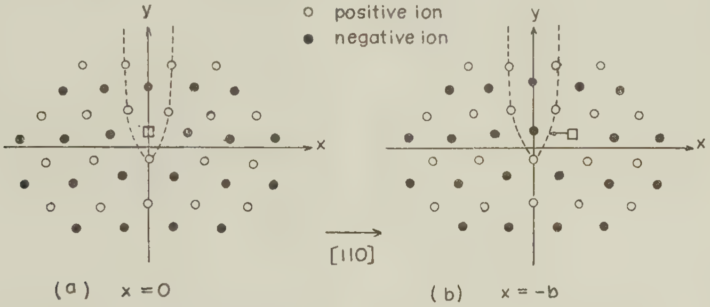

Fig. 6. Ion configuration of a (110) edge dislocation.

(a) illustrates the configuration of the dislocation at $x=0$, and the position of the vacancy in the core according to Bassani and Thomson.

(b) corresponds to the same dislocation proceeded a distance of b to the negative direction of the x-axis. The vacancy left behind tends to follow this motion.

Since the activation energy W_0 is thought to be about 0.1 eV for the crystals concerned, it is quite reasonable to expect a great influence of the vacancies in the dislocation core upon the low-temperature internal friction. It is also natural to expect a spectrum of activation energies depending on various l in cold-worked or quenched crystals, and the ageing effect is also easily understood in taking account of a variation of l with ageing time.

The predicted spectrum of attenuations in KCl is illustrated in Fig. 7(a), whereas the corresponding spectrum for metals of face-centred cubic structure is shown in (b). The main peak in (a) is due to the dislocations free from vacancies. It may happen in cold-worked crystals. The spectrum shown in (b) has been found in copper²⁾,³⁾. It is possible that the impurities elastically bound to the 30°-dislocations is responsible for the subsidiary peak with the activation energy smaller than that of the main peak. Caswell has indeed observed that the subsidiary peak in copper is sensitive to impurities present. A question may be raised in his observation, that is, a slight shift of the main peak to lower temperature with increasing concentration of impurities. A similar observation has also been made by Einspruch and Truell⁴⁾ in aluminium. These facts may be explained by the present prediction as due to the shift of the subsidiary peak to higher temperature.

---

* The above discussion neglected the effects of the separation of a dislocation into two partials.

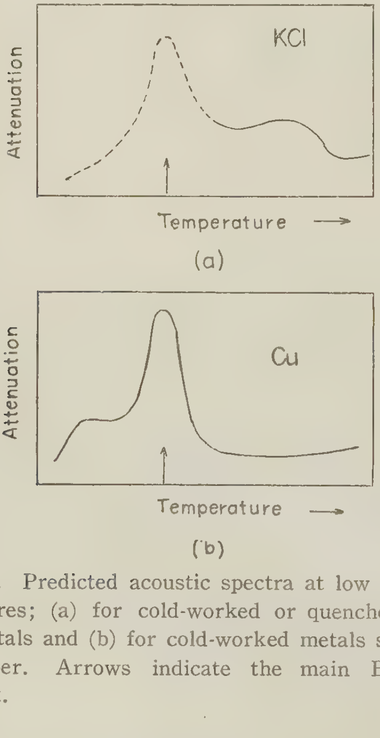

Fig. 7. Predicted acoustic spectra at low temperatures; (a) for cold-worked or quenched KCl crystals and (b) for cold-worked metals such as copper. Arrows indicate the main Bordoni peak.

Although the experimental results on KCl seem to be explained satisfactorily by the above theory, there remains one difficulty, that is, the magnitude of ν_0 corresponding to the value at the attenuation edge as listed in Table III. They are too large to be the frequency with which a rigid dislocation line oscillates in its potential well. The corresponding frequency for copper is calculated as 10^{11} sec^{-1} using Seeger's estimate and 10^{10} sec^{-1} using Mason's estimate. Experimentally, it is obtained as 8×10^{7} sec^{-1} for copper²⁾ and 4×10^{10} sec^{-1} for aluminium⁴⁾. In KCl it will not be much different from these values, even if the strong binding of vacancies to the dislocations is taken into account. It thus appears worth while examining the following possibility to solve the difficulty.

2. *The concurrent motion of vacancies with dislocations*

The possibility to be discussed here is the concurrent motion of vacancies with the dislocation motion. Other possibilities independent of the dislocation motion such as the motion of paired vacancies or vacancy-multivalent impurity pair encounter difficulties in explaining the magnitude of the observed activation energy and its variation with quenching temperature and with ageing time at room temperature.

Kessler⁶⁾ has explained the peak of logarithmic decrement in germanium by the vacancy-drag model following the idea of Cottrell and Jaswon²²⁾. In his theory the vacancies are bound to an edge dislocation by the elastic interaction. The logarithmic decrement is thus predicted to be proportional to the vacancy concentration in the lattice and to the lattice diffusion coefficient of vacancies. These predictions, accordingly, encounter the same difficulties as mentioned above. However, the vacancies in KCl are trapped in the dislocation core and behave quite differently from the above case. It may be possible to alter the general nature of the vacancy-drag process.

When the vacancies are trapped in the dislocation core, the dislocation will be charged either positively or negatively depending upon the effective charge of those vacancies. If crystals such as NaCl are annealed at high temperatures in the range of intrinsic conductivity, the positive-ion vacancies are more easily introduced. Consequently, the dislocations acting as internal sources for vacancies will be oppositely charged to compensate the excess charge introduced. Then the Debye-cloud will be formed around the charged dislocation. This is what Eshelby, Newey and Pratt¹²⁾ have recently discussed as an important origin of critical shear stress of such crystals

Following the above theory, it is expected that as quenching temperature increases the electrostatic potential hill opposing the motion of the vacancies in the dislocation core is raised on account of the increase in the line charge of the dislocation. The motion of dislocation jogs carrying a net charge will also induce a relaxation peak. However, the motion of the jogs with gliding edge dislocation does not need the vacancy diffusion. Accordingly, the potential barrier will be small as compared with that for the above process.

We will discuss following the above interpretation a few points with respect to the activation energy obtained. Although the activation energy for the crystals quenched from 700°C increases appreciably with ageing time at room temperature, the one obtained for the crystals plastically deformed or quenched from 550°C does not seem to alter with ageing time. This will be explained partly because the density of excess vacancies introduced is too low to form the effective Debye-cloud and partly because the ageing process is almost over before starting the measurements. In fact, Fischbach and Nowick[23] have found that the Gyulai-Hartly effect supposed to be caused by the excess free vacancies introduced into NaCl by plastic deformation at room temperature completely dissapeared within about one hour. The number of the vacancies generated by applied stress of 10^7 dynes/cm^2 is estimated to be 10^{15} cm^{-3}. The number of free vacancies in equilibrium at 550°C for KCl is larger only by one order of magnitude than the above value.

According to the above discussions, the activation energy 0.44 eV obtained from cold-worked crystals can be taken to be equal to the one for the motion of the negative-ion vacancy in the dislocation core. This is about one third of the activation energy for the motion of the negative-ion vacancy in the lattice if it is taken to be almost equal to the value in NaCl, which has been directly measured recently[24]. The activation energy to overcome the potential hill due to the Debye-cloud formed at 700°C is thus estimated from Table III as $(0.49-0.44)=0.05$ eV. The increase of the activation energy with ageing time at room temperature after quenching from 700°C, which is equal to (0.12 ± 0.07)eV, may be explained by the increase of the barrier height due to a change in the Debye-radius during the ageing. The phenomenon is then thought to be similar to the one found in additively coloured KCl[13]. The activation energy to overcome the potential barrier is proportional to the inverse root of temperature and other variables are taken to be constant. The increase of the activation energy concerned is thus estimated as

$$0.49\times(\sqrt{700/300}-1)=0.26\,\mathrm{eV}\,.$$

This is not unreasonable as compared with (0.12 ± 0.07) eV as obtained above, if we take into account of the possibility that the crystals are not effectively quenched from 700°C but the number of quenched-in vacancies will correspond to the equilibrium number at lower temperature.

The phenomena are thus qualitatively well explained and the magnitude of the frequency ν_0 is most plausible according to the above mechanism. At present, however, it seems reasonable to conclude that both mechanisms mentioned above in (1) and (2) produce the broad attenuation band in the temperature range investigated.

Finally we would like to remark the effects of the vacancy-drag process upon critical shear stress. They must be known before we discuss the effects of the Debye-Cloud upon critical shear stress. If we take the density of the dislocations ρ and the speed of the dislocations v, then shearing rate is given by

$$\dot{\varepsilon}=b\rho v\,. \tag{5}$$

Since $\dot{\varepsilon}$ is the order of 10^{-3} sec^{-1} under usual conditions and ρ is taken to be the order of 10^6 cm^{-2}, it follows for very small strain as concerned here that

$$v=2.3\times10^{-2}\,\mathrm{cm\cdot sec^{-1}}\,.$$

While, if we consider seriously the present mechanism, it gives from the present measurements as

$$v'=2.2\times10^{-2}\,\mathrm{cm\ sec^{-1}}$$

at about 240°K for the speed of a vacancy in the dislocation core. Accordingly, it will be possible that the vacancies in the dislocation core can follow the motion of the dislocation over some critical distance important for determining critical shear stress. It may be expected, therefore that even in the case where the line charge of dislocations is caused by the vacancies in the cores, not by jogs, critical shear stress of the crystals at relatively high temperatures is influenced by the presence of the Debye-cloud.

Acknowledgements

The present authors wish to express their sincere appreciation to Professor M. Yamamoto and Professor T. Hirone for providing them various experimental facilities during the course of this work.

A part of this work was supported by the Scientific Research Grant of the Ministry of Education in 1958.

References

1) P. G. Bordoni: J. Acoust. Soc. Amer. **26** (1954) 495.
2) D. H. Niblett and J. Wilks: Phil. Mag. **1** (1956) 415.
3) H. L. Caswell: J. Appl. Phys. **29** (1958) 1210.
4) N. G. Einspruch and R. Truell: Phys. Rev. **109** (1958) 652.
5) T. S. Hutchison and G. J. Hutton: Canad. J. Phys. **36** (1958) 82.
6) J. O. Kessler: Phys. Rev. **110** (1957) 646, 654.
7) P. D. Southgate: Phys. Rev. **110** (1958) 855.
8) P. D. Southgate: Proc. Phys. Soc. London **B**, **70** (1957) 804.
9) H. B. Huntington, J. E. Dickey and R. Thomson: Phys. Rev. **100** (1955) 1117.
10) F. Bassani and R. Thomson: Phys. Rev. **102** (1956) 1264.
11) A. Seeger: Phil. Mag. **1** (1955) 651. A. Seeger, H. Donth and F. Pfaff: Discussion Faraday Soc. **23** (1957) 19.
12) J. D. Eshelby, C. W. A. Newey and P. L. Pratt: Phil. Mag. **4** (1958) 75.
13) T. Suzuki and M. Doyama: J. Phys. Chem. Solids (in press).
14) T. Hirone and T. Kamigaki: Sci. Rep. RITU **7** (1955) 456.
15) T. Suzuki: *Dislocations and Mechanical Properties of Crystals*, ed. by J. C. Fisher (John Wiley, New York, 1957) 215.
16) T. A. Read: Phys. Rev. **58** (1940) 371; Trans. AIME **143** (1940) 30.
17) G. Alers: Phys. Rev. **97** (1955) 863.
18) P. C. Waterman: J. Appl. Phys. **29** (1958) 1190.
19) G. J. Dienes: J. Chem. Phys. **16** (1948) 620.
20) W. P. Mason: Phys. Rev. **97** (1955) 557; Bell Syst. Tech. J. **34** (1955) 903.
21) B. A. Bilby: see A. H. Cottrell, *Dislocations and Plastic Flow in Crystals* (Oxford Univ. Press, London, 1953) 56.
22) A. H. Cottrell and M. A. Jaswon: Proc. Roy. Soc. **A**, **199** (1949) 104.
23) D. B. Fischbach and A. S. Nowick: J. Phys. Chem. Solids **5** (1958) 302.
24) L. G. Harrison, J. A. Morrison and R. Rudham: Trans. Faraday Soc. **54** (1958) 106. J. A. Morrison and R. Rudham: J. Phys. Chem. Solids **5** (1958) 403.

JOURNAL OF THE PHYSICAL SOCIETY OF JAPAN, Vol. 14, No. 6, JUNE, 1959

Defects in Ionic Crystals,
II. An Analysis of F and V_1 Centers

By Tatsumi KUROSAWA

The Institute for Solid State Physics, University of Tokyo

(Received December 18, 1958)

The deformation of the lattice around F and V_1 (the Seitz' model) centers in alkali halides is determined from the experimental data on the difference between two ionization energies (optical and thermal) of these centers. In the process of the determination, we apply the method which has been developed in the previous paper (J. Phys. Soc. Japan **13** (1958) 153). We find that the lattice deformation is rather small in the case of the F centers, but very large in the case of the V_1 centers.

§ 1. Introduction

Recently, the investigation of the electronic structure of color centers has been developed by many authors. Nevertheless, we know very little about the lattice deformation around the centers. In general, it is very difficult to determine the lattice deformation around a center either experimentally or theoretically. In some cases, however, the following consideration may give a useful information for this purpose, if only the necessary experimental data are available.

As is well-known, the optical ionization energy I_{op} of a center in a crystal is not always equal to its thermal ionization energy I_{th}. This is due to the electron-lattice interaction, and is explained schematically by such a diagram as Fig. 1. Generally, it is very difficult to construct this kind of a diagram with reasonable accuracy. In the cases of F and V_1* centers in alkali halide crystals, however, the construction of the diagram for the ionized state can be performed with reasonable accuracy, because this state is a simple vacancy in an otherwise perfect crystal. Therefore, if the experimental data on the energy difference $(I_{op}-I_{th})$ are available, we can guess the equilibrium configuration of these centers by using the theoretical diagram. Since the problem is to determine the equilibrium configuration in a multi-dimensional space with only one available datum $(I_{op}-I_{th})$, some suitable assumptions are necessary.

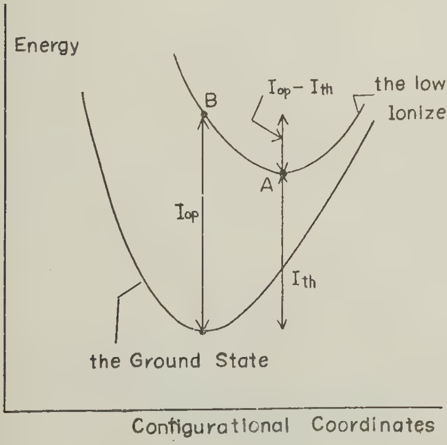

Fig. 1.

In the present paper, the method developed in the previous paper[1)] is applied to compute the energy-configuration diagram of the ionized F and V_1 centers. It is to be noted that the method of Mott and Littleton[2)] is not applicable to the defect which is not in the equilibrium configuration. Using the available data of $(I_{op}-I_{th})$, we determine the ground state configurations of these centers; the deformation of the lattice around the center is small in the case of the F centers, but very large in the case of the V_1 centers.

§ 2. Assumptions and Approximations

In this section we shall summarize assumptions and approximations which we shall adopt throughout this paper.

(1) We calculate the energy-configuration diagrams of the ionized centers by using the method which has been developed in the previous paper. However, since it is difficult to calculate the energy for an arbitrary configuration of the lattice around the center, we adopt an approximate method (see Appendix).

---

* We adopt the model of the V_1 center as suggested by Seitz.

(2) We use the ionic model, where the interionic potentials, the polarizabilities and the short range effect of electronic polarization have been determined in the previous paper.

(3) We assume that the ionic arrangement does not change at the optical transition (the Franck-Condon principle), and that the motion of electrons (for instance, the electronic polarization of the ions around the center) follows any change instantaneously.

(4) We consider only the displacement of the nearest neighbor ions around the center when the F or V_1 center is at the state of the minimum energy. Since these centers are neutral, this assumption may be approximately allowable.

§ 3. *F* Center

As is well-known, an F center consists of a V_- and a trapped electron. Therefore, the state A in Fig. 1 corresponds to the state where a V_- is at its equilibrium configuration and an electron is at the bottom of the conduction band (more precisely, at the lowest polaron state), and in the state B a V_- is surrounded by the ions of the same arrangement as the F center in the equilibrium and an electron is at the bottom of the conduction band (not a polaron state). The energy difference between the state B and A is equal to $(I_{op}-I_{th})$.

Gurney and Mott[3] have calculated the values of I_{th} by using the experimental data of Pohl. Here, we recalculate them by using new data of the formation energy of the Schottky defect. On the other hand, the data of I_{op} are not available except the case of KBr, where the threshold energy $h\nu_{thres}$ of photoconduction due to direct optical ionization of the F center has been measured by Inchauspé.[4]

Now, let us assume that in the state B the nearest neighbour (1, 0, 0) ions are displacing symmetrically around the vacancy, which is situated at the point (0, 0, 0). (This assumption may not be far from truth.) Then, we compute the energy of the V_- of NaCl and KBr crystals in displaced configurations $(1+\xi, 0, 0)$ etc. as a function of the displacement ξ, where the energy is measured from its lowest energy state (Fig. 2). Here we assign the outward displacement positive sign of ξ. As mentioned previously, the displacement of the other ions is assumed to be zero and the electronic polarization is supposed to take its equilibrium value at each displacement ξ.

According to the theory of Lee, Low and Pines,[6] the energy E_p which is necessary to bring an electron from the lowest polaron state to the bottom of the conduction band is given by $\alpha\hbar\omega_l$, where α is the coupling constant between an electron and the polarization field and ω_l is the angular frequency of the longitudinal optical vibration. The numerical values of E_p are shown in Table I, where the effective mass of the conduction band is assumed to be equal to the free electron mass. From these values we may expect that E_p is rather small as compared with the amount of uncertainty of the other quantities, so that we disregard it.

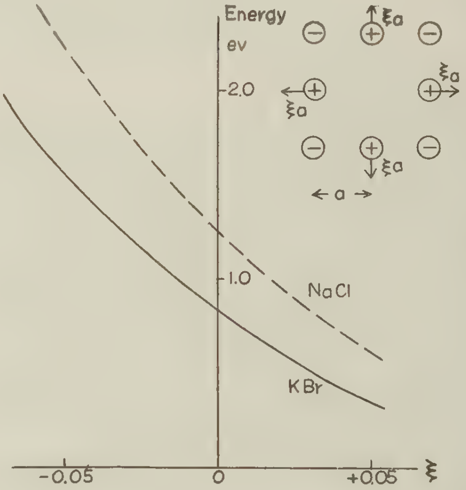

Fig. 2. Energy of a V_- as a function of the displacement of the nearest neighbour ions.

Table I. Energies in eV (F center)

	I_{th}	$h\nu_F$	$h\nu_{thres}$	E_p
NaCl	1,97	2,74		0,18
KCl	2,13	2,31		0,15
KBr	1,88	2,07	3,6	0,12

If we neglect the energy E_p, the energy illustrated in Fig. 2 is to be equal to $(I_{op}-I_{th})$ when ξ takes the value corresponding to the state B. By using the observed data of KBr we estimate: $I_{op}-I_{th}\simeq 1{,}7$ eV and $\xi\simeq -0.06$. We see that the nearest neighbor ions displace inwards in some extent. This result is qualitatively in agreement with the theoretical calculation by Kojima[6] concerning the structure of the F center in LiF; according to his calculation $\xi=-0{,}074$. In the case of NaCl the value of I_{op} is not available. However, it is almost certain that the energy I_{op} is larger than the F band absorption energy $h\nu_F$. That is, $I_{op}-I_{th}>h\nu_F-I_{th}\simeq 0.77$ eV and $\xi<0.04$. At any rate, we find that the deformation of the lattice around the F center seems to be small*.

§ 4. V_1 Center

We assign the Seitz' model to the observed V_1 band,[7] although there are some ambiguities in this assignment. The V_1 center is a peculiar center in the sense that optically it has a deeper level than the F center, but thermally it seems to be very shallow. It is bleached thermally at 128°K in KCl and at 115°K in KBr.[8] Here we shall follow the usual interpretation that the V_1 center is so shallow that the trapped hole is released thermally at such low temperatures, although this interpretation is not unique at present. It is also probable that an electron released from a certain shallow trap annihilates the hole of the V_1 center.[9]

According to the estimation by Dutton and Maurer,[8] the thermal depth of the V_1 center is 0,26 eV in KCl and 0,23 eV in KBr. We assume that these depths correspond to I_{th}, i.e., the energy necessary to decompose a V_1 center into a V_+ in its equilibrium configuration and a hole at the lowest polaron type state.** There remains another possibility, however, that the above-mentioned depth is the barrier height between the lowest state of the V_1 center and the decomposed state. In this case, the values of I_{th} are still more diminished. The energy I_{op} may be larger than the photon energy of the V_1 band absorption $h\nu_V$.

Table II. Energies in eV (V_1 center)

	I_{th}	$h\nu_V$
KCl	0,26	3,48
KBr	0,23	3,02

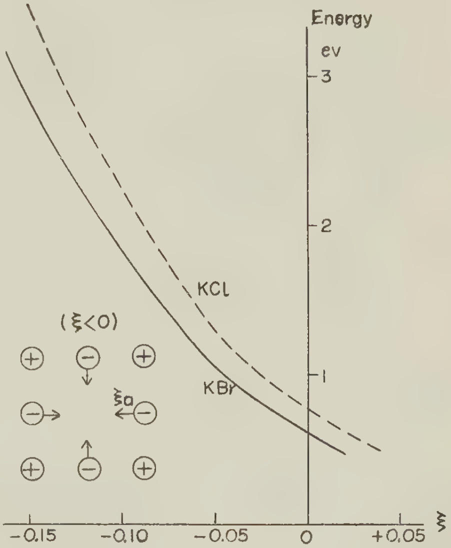

Fig. 3. Energy of a V_+ as a function of the displacement of the nearest neighbour ions (the first model).

In the same way as the case of the F center, we calculate the energy of a V_+ as a function of the displacement of the nearest neighbour ions (Fig. 3). If we take the values, $I_{op}-I_{th}\simeq h\nu_V-I_{th}\simeq 3{,}22$ eV (KCl) and 2,79 eV (KBr), the displacement becomes $-0{,}15a$ and $-0{,}14a$, respectively. We see that the deformation around the V_1 center is quite large as compared with that of the F center.

On the other hand, we think that the

---

* So far we have neglected the displacement of the ions except the nearest neighbor ions. However, the displacement of the other ions may be quite small, because the F center is a neutral one and the orbit of its electron is well localized. Therefore, it would be sufficient to consider the displacement of the second neighbour ions in addition to the nearest neighbours. If the second neighbour ions displace outwards, the energy curve in Fig. 2 goes upwards and the value of ξ where the energy is equal to the observed $(I_{op}-I_{th})$ becomes algebraically larger, and vice versa. In KBr, the displacement of the second neighbour ions around the V_- is estimated to be about $-0.02a$. It is not probable that the displacement would be much larger than this value in the case of the F center. From these considerations we estimate the error in the calculated value of the ξ due to the neglection of the displacement of the other ions as about $0{,}01a$, at most $0{,}02a$.

** Dutton and Maurer have observed a current burst at the thermal bleaching, so that the released hole may not be in such a state as the immobile Känzig's center.

earlier model of Känzig center[10] which was a (halogen$_2$)$^-$ molecular ion accompanied with a V_+, is also possible for the model of the V_1 center. In Fig. 4, the energy contours of a V_+ in KCl are illustrated as a function of the displacement of the two nearest neighbour ions, where all the other ions are fixed at their original sites of the undeformed lattice. In this case, the displacement is about 0,3a. In KBr the situation is nearly the same.

Several points must be mentioned about the reliability of the above results.

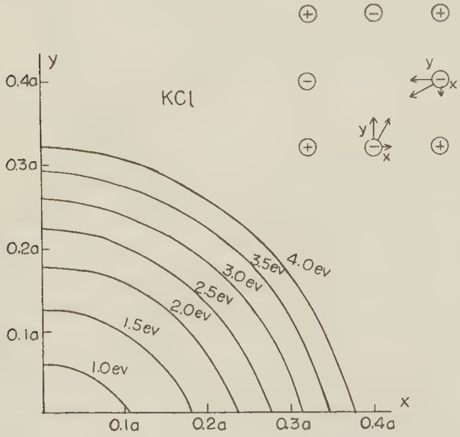

Fig. 4. Energy of a V_+ as a function of the displacement of the two nearest neighbour ions (the second model).

First, the deformation is very large, so that the interionic potentials which have been determined from the data of perfect crystals, may be doubtful. For instance, the short range interaction energy between halogen ions is neglected in our calculations, but it should not be neglected, especially in the case of the second model, because the distance between the relevant halogen ions is very small (about 2,7A in KCl and 2,8A in KBr). However, the determination of the short range energy between two halogen ions with a reliable accuracy is very difficult.

Secondly, the accuracy of our energy form, which is explained in the Appendix, is reduced when the deformation is large. Moreover, we have introduced several simplifying assumptions in the case of the second model so as to avoid cumbersome calculations due to its low symmetry.

Thirdly, the displacement of the other ions may not be small in the case of such a large deformation.

However, all these things get into trouble only when the deformation is large. Therefore, it is certain that the lattice deformation around the V_1 center is large, even if the inaccuracy of the theory affects the detailed results mentioned previously.

Here, we neglect the energy E_p of the hole, which will be larger than that of the electron, because the effective mass of the valence band is heavier than that of the conduction band. But the upper limit of this energy may be of the order of $(1/2)\{1/\mathcal{E}_0)-(1/\mathcal{E})\}(e^2/a)\simeq 0.5$ eV. This does not modify our results considerably.

It is hard to interpret the reason why the lattice deformation around the V_1 center is so large. Although it is out of the scope of our paper to discuss this problem, we shall point out some possibilities.

The first possibility is that the Seitz' model or the interpretation of Dutton and Maurer is incorrect*. In this case, our calculation is meaningless.

Table III. V_1 band absorption (eV).

NaCl	3,59		
KCl	3,48	KBr	3,02
RbCl	3,45	RbBr	2,95

On the other hand, if the Seitz' model and the interpretation of Dutton and Maurer are correct, we are forced to accept the result that the lattice deformation around the V_1 center is large. In the latter case, however, the second model seems to be more favorable than the first to interpret the large deformation. If the model of the Känzig center is true, the existence of the (halogen$_2$)$^-$ molecular ion accompanied with a V_+ is not unreasonable. The second model is also favorable to interpret the fact that $h\nu_V$ depends only on the kind of halogen ions and hardly on alkali ions[11] (Table III). Lambe and West[12] have failed to detect dichroism of the V_1 band. However, if the transition time to convert a V_1 center from a (halogen$_2$)$^-$ configuration to the other (halogen$_2$)$^-$ configuration around the V_+ is sufficiently short*, the dichroism can not be detected. As the transition time depends quite sensitively on the height of the potential barrier to be surmounted, it is possible that the (halogen$_2$)$^-$ state is mobile in the case of the V_1 center but not in the case of the Känzig center.

---

* Delbecq and others[13] have found that the V_1 band is bleached at lower temperature than the Känzig center. If the V_1 center is bleached by the electrons released from the other centers, it is strange that the Känzig center is not bleached at the same time.

We are greatly indebted to Professor J. Yamashita for his helpful discussions.

Appendix

According to the discussion in the previous paper, the energy of a defect is formally given by

$$W(X,\ P,\ x,\ p)=\frac{1}{2}\sum_{\kappa,\lambda} a_{\kappa\lambda}p_\kappa p_\lambda+\sum_{\kappa,\mu} b_{\kappa\mu}p_\kappa x_\mu+\frac{1}{2}\sum_{\mu,\nu} c_{\mu\nu}x_\mu x_\nu+\sum_\kappa f_\kappa(X,\ P)p_\kappa$$
$$+\sum_\mu g_\mu(X,\ P)x_\mu+A(X,\ P)+\phi_0+\sum_\kappa \phi_\kappa{}^p p_\kappa+\sum_\mu \phi_\mu{}^d x_\mu+\Phi(X,\ P)\,, \qquad (\mathrm{A}\cdot 1)$$

where $P\ (\equiv P_1,\ P_2,\ \cdots,\ P_k,\ \cdots)$ and $X\ (\equiv X_1,\ X_2,\ \cdots,\ X_m,\ \cdots)$ represent the electronic polarizations and displacements of the ions in the region near the defect, and $p\ (\equiv p_1,\ \cdots,\ p_\kappa,\cdots)$ and $x\ (\equiv x_1,\ \cdots,\ x_\mu,\ \cdots)$ represent those of the ions in the outer region. In our case, we take the former ions to be the nearest neighbor ions and the latters to be the other ions. The first six terms are the energy necessary to deform the lattice and ions up to a state $(x,\ p,\ X,\ P)$ without the defect, and the last four terms represent the energy necessary to remove the central ion from the lattice to infinity with the fixed state $(x,\ p,\ X,\ P)$.

According to the assumptions in § 2,

$$x_\mu=0 \qquad \text{for all } \mu, \qquad (\mathrm{A}\cdot 2)$$

and the electronic polarizations take their equilibrium values $p_\kappa(X)$'s and $P_k(X)$'s for a given X, that is,

$$\left(\frac{\partial W}{\partial p_\kappa}\right)_{p=p(X),P=P(X)}=0\,, \qquad (\mathrm{A}\cdot 3)$$

or

$$\sum_\lambda a_{\kappa\lambda}p_\lambda(X)+f_\kappa(X,\ P(X))+\phi_\kappa{}^p=0 \qquad \text{for all } \kappa, \qquad (\mathrm{A}\cdot 4)$$

and

$$\left(\frac{\partial W}{\partial P_k}\right)_{p=p(X),P=P(X)}=0 \qquad \text{for all } k. \qquad (\mathrm{A}\cdot 5)$$

If we insert the above x, $p(X)$ and $P(X)$ into $W(x,\ p,\ X,\ P)$, it becomes as follows,

$$W(0,\ p(X),\ X,\ P(X))=\frac{1}{2}\sum_\kappa \{f_\kappa(X,\ P(X))+\phi_\kappa{}^p\}p_\kappa(X)$$
$$+\phi_0+A(X,\ P(X))+\Phi(X,\ P(X))\,. \qquad (\mathrm{A}\cdot 6)$$

It is difficult to solve $p_\kappa(X)$'s for a given value of X. However, when the displacement of the nearest neighbor ions is zero (i.e., no lattice deformation), we can solve $p_\kappa(X)$'s at least approximately. According to the first approximation by Mott and Littleton, $p_\kappa(0)$'s are given by

$$p_\kappa(0)=\frac{ea^3}{2\pi r_\kappa{}^2}\left(1-\frac{1}{\varepsilon_0}\right)\frac{\alpha_\kappa}{\alpha_+ +\alpha_-}\,, \qquad (\mathrm{A}\cdot 7)$$

where r_κ is the distance of the κth ion from the origin, α_κ, α_+ and α_- is the polarizability of the κth, positive and negative ion respectively. Inserting these $p_\kappa(0)$'s into the Eq. (A·6), we can calculate $W(0,\ p(0),\ 0,\ P(0))$. When $X \neq 0$, we avoid the above-mentioned difficulty in the following ways.

---

* If this is true, the strong electric field along the (110) direction may cause a sort of dichroism.

1) In general,

$$|\phi_\kappa{}^p| \gg |f_\kappa(X,\ P(X)) - f_\kappa(0,\ P(0))|\ , \tag{A·8}$$

at least when X is not so large. Therefore we put

$$p_\kappa(X) \simeq p_\kappa(0) \tag{A·9}$$

and then

$$\begin{aligned} W(0,\ p(X),\ X,\ P(X)) &\simeq W(0,\ p(0),\ X,\ P^*(X)) \\ &= \frac{1}{2}\sum_\kappa \{f_\kappa(X,\ P^*(X)) + \phi_\kappa{}^p\} p_\kappa(0) + \phi_0 + A(X,\ P^*(X)) + \Phi(X,\ P^*(X))\ , \end{aligned} \tag{A·10}$$

where $P^*(X)$ are given by

$$\left(\frac{\partial W}{\partial P_k}\right)_{p=p(0),P=P^*(X),x=0} = 0\ . \tag{A·11}$$

2) From Eq. (A·4), we see that

$$\frac{1}{2}\sum_{\kappa,\lambda} a_{\kappa\lambda} p_\kappa(X) p_\lambda(X) = -\frac{1}{2}\sum_\kappa \{f_\kappa(X,\ P(X)) + \phi_\kappa{}^p\} p_\kappa(X)\ . \tag{A·12}$$

Putting $X=0$ in the above equation, we obtain

$$\begin{aligned} W(0,\ p(0),\ X,\ P) = \sum_\kappa p_\kappa(0)\left[\frac{1}{2}\phi_\kappa{}^p + f_\kappa(X,\ P) - \frac{1}{2} f_\kappa(0,\ P(0))\right] \\ + A(X,\ P) + \phi_0 + \Phi(X,\ P) > W(0,\ p(X),\ X,\ P(X))\ . \end{aligned} \tag{A·13}$$

In virtue of this inequality, we can compute the upper bound of the energy. The difference between the above two energy forms (A·10) and (A·13) is very small.

References

1) T. Kurosawa: J. Phys. Soc. Japan **13** (1958) 153.
2) N. F. Mott. and M. J. Littleton: Trans. Faraday Soc. **34** (1938) 485.
3) N. F. Mott and R. W. Gurney: *Electronic Processes in Ionic Crystals*, (Clarendon Press, Oxford, 1948), chap. 4.
4) N. Inchauspé: Phys. Rev. **106** (1957) 898.
5) T. D. Lee, F. E. Low and D. Pines: Phys. Rev. **90** (1953) 297.
6) T. Kojima: J. Phys. Soc. Japan **12** (1957) 918.
7) F. Seitz: Rev. Mod. Phys. **26** (1954) 7.
8) D. Dutton and R. J. Maurer: Phys. Rev. **90** (1953) 126.
9) T. G. Castner and W. Känzig: J. Phys. Chem. Solids **3** (1957) 178.
10) W. Känzig: Phys. Rev. **99** (1955) 1890.
11) G. Miessner and H. Pick: Z. Phys. **134** (1953) 604.
12) J. Lambe and E. J. West: Phys. Rev. **108** (1957) 634.
13) C. J. Delbecq, B. Smaller and P. H. Yuster: Phys. Rev. **111** (1958) 1235.

JOURNAL OF THE PHYSICAL SOCIETY OF JAPAN, Vol. 14, No. 6, June, 1959

A Semi-empirical Theory of the Conjugated Systems, III. Bond Alternation and Electron Fixation

By Yuzuru OOSHIKA*

Polytechnic Institute of Brooklyn, Broolyn, New York

(Received December 15, 1958)

Extending the previous treatment of the author on the bond alternation in infinite conjugated systems to finite systems, it is investigated why the wave-lengths of some homologous series appear to tend to infinity while those of others to finite limits when the number of carbon atoms increases. It is concluded that the bond alternation does not occur in shorter symmetrical or slightly unsymmetrical chains, while, in strongly unsymmetrical chains, the bond alternation always occurs and that it always occurs in longer chains according to the result in the previous paper.

In the previous paper[1)], the author showed by using his semi-empirical s.c.f. method that the bond alternation in the conjugated polyene chain can actually occur by a bulk effect, not by an end effect as considered earlier. But the treatment there applies only to an infinitely long conjugated chain, and cannot distinguish the difference in the light absorption of symmetrical and unsymmetrical cyanine dyes. Labhart[2)], almost simultaneously with the author, discussed the same problem using the free electron model. His method applies also to chains of finite length, and he showed that, in symmetrical cyanines, the bond alternation does not occur up to about 30 carbon-atom chains. Huzinaga and Hasino[3)], too, discussed the absorption spectra and the bond alternation in conjugated chains by their "bond-orbital" method and obtained agreement between many experimental data and the results calculated from their theoretical formula by adjusting two parameters. In the latter two papers, however, the consideration of the electronic interaction is not very well-formulated. In this note, the author should like to extend his treatment to conjugated chains with finite length and to show the difference between the symmetrical cyanines on one hand and the unsymmetrical cyanines, merocyanines and polyenes on the other.

Consider, at first, an even-membered polyene chain with $2n$ carbon atoms and $2n$ π-electrons. Let the interaction integrals $\left(\beta-\frac{p}{2}\frac{e^2}{R}\right)^{4)}$ be $-\gamma_1, -\gamma_2, -\gamma_1, -\gamma_2, \cdots, -\gamma_1$ $(\gamma_1>\gamma_2>0)$ from the left and alternately. The bond orders are to be different from bond to bond in this case, because all the bonds are not equivalent to each other as contrast to the conjugated ring. But, for simplicity, we shall calculate only the average bond orders for the alternate double (short) and single (long) bonds, respectively. The (average) partial π-bond order for the short and long bonds due to a single molecular orbital

$$p_d(k)=\frac{\sqrt{1+z^2+2z\cos 2k}}{n}\,\frac{(2n+2)+2nz\cos 2k}{(2n+2)+2nz^2+2(2n+1)\cos 2k} \qquad (1)$$

$$p_s(k)=\frac{\sqrt{1+z^2+2z\cos 2k}}{n-1}\,\frac{(2n+z)\cos 2k+2nz}{(2n+2)+2nz^2+2(2n+1)z\cos 2k} \qquad (2)$$

$$z=\gamma_2/\gamma_1\ ,$$

respectively, where k, the value characterizing the molecular orbital, is given by the following simultaneous equations

$$(2n+1)k+2\theta=m\pi\ , \qquad m=1,\cdots,2n \qquad (3)$$

$$\tan 2\theta=\frac{1-z}{1+z}\tan k\ . \qquad (4)$$

The total π-bond orders, P_d and P_s, are calculated by summing up $p_d(k)$ and $p_s(k)$ over filled orbitals, respectively. Then we can obtain approximate s.c.f. orbitals (approximate because of the non-equivalence of different bonds) by the same way as in the previous paper, i.e. calculating p_d and p_s for any given $z(<1)$, deducing z again from the calculated p_d and p_s, and repeating such procedures till s.c.f. orbitals are attained. It may be interesting to calculate the bond order and, hence, the bond length of the particular polyenes and to compare the results with available experimental data. But, here, we need not actually carry out the above procedure, because that the bond alternation occurs in such even-membered polyene chains is self-evident from the result in the previous paper[1]. We shall not discuss these even-membered polyene chain further.

---

* On leave from Kobayashi Institute of Physical Research.

Now we shall consider how the situation is different in odd-membered ($2n+1$-carbon) chain. Let the interaction integrals be $-\gamma_1$, $-\gamma_2, -\gamma_1, \cdots, -\gamma_2$, alternately from the left end of the chain ($\gamma_1>\gamma_2>0$). The molecular orbitals are

$$\psi_k=\frac{1}{n+1}\left[\sum_{s=1}^{n+1}\sin\{(2s-1)k+2\theta\}\psi_{2s-1}\right]$$
$$+\sum_{s=1}^{n}\sin 2sk\psi_{2s} \qquad (5)$$

where ψ_{2s-1} is the atomic orbital on the $2n-1$-th carbon atom, $\tan 2\theta$ is as in Eq. (4), and

$$k=\frac{m}{n+1}\frac{\pi}{2} \qquad m=1, \cdots, n, n+2, \cdots, 2n+1\,. \qquad (6)$$

In addition to the $2n$ molecular orbitals above, we obtain a "surface" (or end) orbital,

$$\psi_0=\frac{1}{\sigma}\left\{\sum_{s=1}^{n+1}\left(-\frac{\gamma_2}{\gamma_1}\right)^{n+1-s}\psi_{2s-1}\right\}\,. \qquad (7)$$

This end orbital is of non-bonding character, and the electron in that orbital is almost localized in one end, which may be called the electron fixation, to distinguish from the electron localization used in the electronic theory of organic reactions. It does not occur in the ordinary treatment of allyl radicals where $\gamma_1=\gamma_2$. The average partial bond orders by orbital k are very simply

$$\left.\begin{aligned} p_d(k)&=\frac{1}{n}\cos(k-2\theta)\\ p_s(k)&=\frac{1}{n}\cos(k+2\theta)\end{aligned}\right\} \qquad (8)$$

for the double and single bonds, respectively.

Then we can calculate bond orders by summing up $p_d(k)$'s and $p_s(k)$'s, respectively. If we neglect the effect of the net charge, the number of electrons in the non-bonding end orbitals does not matter, and the bond orders are the same for $2n$, $2n+1$, and $2n+2$ electrons, i.e. for the cation, the radical and the anion. The actual numerical calculations were carried out by using the values of parameters and the method in the previous paper[4], and it is found that for $n=2$ or 3, i.e., for 5 or 7-membered chain, $z=1$ is the only solution and the bond alternation and the resulting electron fixation cannot occur, and for $n=3$ or 4 it actually occurs. The precision of our numerical calculation prevents our predicting exactly the chain length at which the bond alternation actually begins. In addition, it is sensitive to the values of the parameters. But, in any case, it may be concluded that the bond alternation and the electron fixation do not occur for the shorter chain with carbon atoms less than 7 or 9. The electron fixation and the bond alternation in odd-membered chain are closely related to each other, and if one of them occurs, the other also occurs if we remove one π-orbital and one π-electron from the allyl radical, the remainder is similar to the polyene chain. Then if we can make the electron fixation to occur by a certain method and the remaining system to be polyene-like, the bond alternation may occur for short chains. The electron fixation has previously been pointed out by Nikitiné[5] in his free electron treatment of cyanine dyes, but its connection with the bond alternation was not clear.

Now, the cyanine dye cations have nitrogen-containing nuclei at both ends, where the potential is deeper than at the intermediate portion of the chain. If the coulomb integral (in the sense of the s.c.f. method) at one end is sufficiently more negative than those in the intermediate portion, it may be expected that the two electrons are fixed at the end and that the remaining $2n$ centers and $2n$ electrons constitute a system just like the polyene chain, and then the bond alternation may occur in rather short chains. This is shown as follows.

Let the coulomb integral of the left end atom be α'; those of other atoms be α ($\alpha'<\alpha<0$), and the interaction integrals be $-\gamma$ for all bonds. The simultaneous linear equations for determining the molecular orbitals are now

$$\left.\begin{aligned}&(\alpha'-\mathcal{E})c_1-\gamma c_2=0\\&-\gamma c_1+(\alpha-\mathcal{E})c_2-\gamma c_3=0\\&-\gamma c_2+(\alpha-\mathcal{E})c_3-\gamma c_4=0\\&\cdots\cdots\cdots\cdots\end{aligned}\right\}\qquad(9)$$

If these equations have a solution which damps out towards the right of the chain, i.e.,

$$\left.\begin{aligned}&c_1=1\,,\quad c_2=e^{-k}\,,\quad c_3=e^{-2k}\,,\\&Re(k)>0\end{aligned}\right\}\qquad(10)$$

for a half-infinite chain, e^k is to be equal to $(\alpha-\alpha')/\gamma$. Then, if $\alpha-\alpha'>\gamma$, there exists an end orbital even when the bond alternation does not occur, and the energy of the end orbital is the lowest of all the molecular orbitals. By a similar method, for a symmetrical finite odd-membered chain ($2n+1$-centers, and equal coulomb integrals for both end atoms), it is shown that

$$\frac{\cosh(n+1)k}{\cosh nk}=\frac{\alpha-\alpha'}{\gamma}\qquad(11)$$

or

$$\frac{\sinh(n+1)k}{\sinh nk}=\frac{\alpha-\alpha'}{\gamma}\,.\qquad(12)$$

Then, in the case also, we may consider that the electron fixation occurs if the equations above have solutions with real values of k though the end orbital is not non-bonding. With increasing ratio of $\alpha-\alpha'$ to γ, we, at first, obtain a solution of a real k value by Eq. (11) when the ratio exceeds unity, and then another one by Eq. (12) for a slightly higher value of $(\alpha-\alpha')/\gamma$. Thus, whether the electron fixation does occur or not depends upon the value of $(\alpha-\alpha')/\gamma$. For unsymmetrical odd-membered chains, where the coulomb integrals are α' and α'' for the left and right end atoms, respectively, we cannot carry out such an exact calculation as above, but we may expect that $(\alpha-\alpha')/\gamma$ (or $(\alpha-\alpha'')/\gamma$) is a measure of whether the electrod fixation occurs or not at the left (or right) end. From these discussions, the conclusions below may be deduced:

1. If $(\alpha-\alpha')/\gamma>1$ and $(\alpha-\alpha'')/\gamma>1$, the electron fixation occurs at both ends. The remaining system is of $2n-1$-center and $2n-2$-electron, and just like to an allyl cation with a shorter chain-length than that of the parent cyanine cations. The bond alternation does not occur up to $n=4$ or 5 as shown in the preceding paragraph, and, hence, the absorption wave length seems to increase linearly with the number of carbon atoms.

2. If $(\alpha-\alpha')/\gamma<1$ and $(\alpha-\alpha'')/\gamma<1$, the electron fixation does not occur at both ends, and the system is in itself like to an allyl anion of $2n+1$-center and $2n+2$-electron. The bond alternation does not occur up to $n=3$ or 4, and the absorption wave length is somewhat longer than that in case 1, because the effective chain length is larger by one C–C bond.

The two cases above correspond to symmetrical or slightly unsymmetrical dyes.

3. If $(\alpha-\alpha')/\gamma>1$ and $(\alpha-\alpha'')/\gamma<1$ (or $(\alpha-\alpha')\gamma<1$ and $(\alpha-\alpha'')/\gamma>1$), the electron fixation occurs at the left (or right) end only, and the remaining system is of $2n$-center and $2n$-electron, just like to polyene chains. Hence, the bond alternation does occur even for the shortest chain. This behavior corresponds to that of the strongly unsymmetrical cyanine dyes.

It is now clear from the above conclusion why the absorption wave length of strongly unsymmetrical dyes appears to be convergent while those of symmetrical and slightly unsymmetrical dyes appear to be non-convergent. It depends wholly on the electron fixation and the resulting bond alternation. Using the discussions in this note and the previous one, we need no longer introduce the shady concept that an end effect survives even in an infinitely long chain. The end effect works only at shorter chains.

References

1) Y. Ooshika: J. Phys. Soc. Japan **12** (1957) 1246.
2) H. Labhart: J. Chem. Phys. **27** (1957) 957.
3) S. Huzinaga and T. Hasino: Progr. Theor. Phys. **18** (1957) 649.
4) Y. Ooshika: J. Phys. Soc. Japan **12** (1957) 1238, 1246.
5) B. Nikitiné: J. chim. phys. **49** (1952) 175.

JOURNAL OF THE PHYSICAL SOCIETY OF JAPAN Vol. 14, No. 6, JUNE, 1959

Galvano- and Thermomagnetic Effects in α-Ag_2Te

By Shin-ya MIYATANI and Isaaki YOKOTA

Department of Physics, Faculty of Science, Niigata University

(Received December 20, 1958)

Nernst coefficient, magnetoresistance, and magnetothermoelectric power together with electrical conductivity, Hall coefficient, and thermoelectric power of α-Ag_2Te are measured as functions of the e.m.f., E of the galvanic cell Ag|AgI|Ag_2Te|Pt, where E may be considered to represent the relative position of the Fermi level in the Ag_2Te specimen. The experimental results exhibit consistent agreement with the Lorentz-Sommerfeld theory for degenerate two-band semiconductors with energy independent mean free paths of carriers. Relative thermal conductivity is also measured, showing minimum at a E value expected from the theory.

§1. Introduction

In the recent work[1] on semiconducting properties of α-Ag_2Te by one of the present authors, it has been shown that electrical conductivity, Hall coefficient, thermoelectric power, and the amount of silver removed from (or supplied to) Ag_2Te specimen across the galvanic cell Ag|AgI|Ag_2Te|Pt as functions of the e.m.f., E, of the cell, while temperature is kept constant, can be consistently interpleted in terms of the Lorentz-Sommerfeld theory, the e.m.f. of the cell being assumed to represent the relative position of the Fermi level in the Ag_2Te specimen. As pointed out there, there has remained some indefiniteness on the energy dependence of the mean free path, l, of carriers. Namely, assuming $l=l_0x^r$ where x is the reduced carrier energy, the two assumed values, $r=0$ (energy independent mean free path) and $r=1/2$ (energy independent relaxation time), have been as well able to account for the experimental results.

In the present work, Nernst coefficient, magnetoresistance, and magnetothermoelectric power of α-Ag_2Te have been measured also as functions of the e.m.f. of the cell, E, for the purpose to determine more accurately the energy dependence of mean free paths of carriers, since these quantities are rather sensitive to the scattering mechanism. As will be seen later, the assumption of energy independent free path length ($r=0$) yields better agreement between theory and experiment for these quantities than that of energy independent relaxation time ($r=1/2$).

By the way, in the β-form of Ag_2Te (stable below ~140°C) there exsist rather complicated situations, that is, the e.m.f. of the galvanic cell seems not to represent the relative position of the Fermi level in the Ag_2Te specimen, indicating that the chemical potential of Ag ion in β-Ag_2Te depends rather sensitively on the composition, and, moreover, the experimental results cannot be accounted for by energy independent mean free paths even when appropriate corrections to the e.m.f. of the cell is made so as to deduce the relative position of the Fermi level. The details will be reported elsewhere.

§2. Theoretical

Here, we summarize the theoretical formulae for the transport coefficients in two-band semiconductors which can be obtained from the Boltzmann equation[2~8]. In the present case of Ag_2Te, the energy gap is so narrow as several kT and effective mass of conduction electrons is so small as $0.1\,m$ (see Table I) that one must take into account the degeneracies of both electrons and holes. The assumptions made are as follows:

(i) The energy momentum relations are of standard form for both electrons and holes $\mathcal{E}=\hbar^2k^2/2m^*$[5].

(ii) There exists the time of relaxation for carriers, τ, which is a function of carrier energy only.

(iii) The mean free path, l, of carriers defined as $l=\tau v$, where v is the carrier velocity, depends on carrier energy as $l=l_0(\mathcal{E}/kT)^r$.

In this paragraph we confine ourselves to the effects which have been measured in the present work. As for other related effects such as Ettinghausen effect and Righi-Leduc effect see the Appendix I.

For convenience of description we first summarize the formulae for single carrier semiconductors²⁾.

(A_1) The electrical conductivity, σ:

$$\sigma=e\mu N\frac{4}{3\sqrt{\pi}}(r+1)F_r(\eta)\,. \tag{1}$$

(B_1) The thermoelectric power, Θ:

$$\Theta=\mp\frac{k}{e}(\beta-\eta)\,. \tag{2}$$

(C_1) The Hall coefficient, R:

$$R\sigma=\mp\mu\alpha\,. \tag{3}$$

(D_1) The Nernst coefficient, Q:

$$Q=\frac{k}{e}\mu(\alpha\beta-\gamma)\,. \tag{4}$$

(E_1) The thermal conductivity, κ.

$$\kappa=\left(\frac{k}{e}\right)^2 T\sigma(\delta-\beta^2)+\kappa_{ph}\equiv\kappa_e+\kappa_{ph}\,. \tag{5}$$

where κ_e is the electronic thermal conductivity and κ_{ph} is the phonon term.

(F_1) The magnetoresistance, B:

$$B=\frac{\Delta\rho}{\rho H^2}=\mu^2(\varphi-\alpha^2)\,. \tag{6}$$

(G_1) The magneto-thermoelectric power, W:

$$W=\frac{\Delta\Theta}{H^2}=\mp\frac{k}{e}\mu^2\{\beta(\varphi-\alpha^2)+\alpha\gamma-\psi\}\,. \tag{7}$$

In Eqs. (2), (3) and (7) the upper sign applies to n-type material and the lower to p-type material. The meenings of the notations above used are as follow:

$$\mu=\frac{el_0}{\sqrt{2m^*kT}} \tag{8}$$

which differs from the ordinary mobility in the classical limit by the factor $3\sqrt{\pi}/4\Gamma(r+2)$.

$$N=2(2\pi m^*kT)^{3/2}h^{-3}\,. \tag{9}$$

η is the reduced Fermi level measured from the edge of the band, i.e. ζ/kT for n-type materials and $(-\zeta-E_g)/kT$ for p-type materials where ζ is the Fermi level measured from the bottom of the conduction band and E_g is the energy gap. $F_r(\eta)$ is Fermi-Dirac function of order r: $F_r(\eta)=\int_0^\infty x^r\,dx/(e^{x-\eta}+1)$. α, β, γ, δ, φ and ψ are functions of η and are defined as ratios of two Fermi-Dirac functions:

$$\left.\begin{array}{lll}\alpha=\dfrac{(2r+\frac{1}{2})F_{2r-(1/2)}}{(r+1)F_r}\,, & \beta=\dfrac{(r+2)F_{r+1}}{(r+1)F_r}\,, & \gamma=\dfrac{(2r+\frac{3}{2})F_{2r+(1/2)}}{(r+1)F_r}\,,\\[2ex] \delta=\dfrac{(r+3)F_{r+2}}{(r+1)F_r}\,, & \varphi=\dfrac{3rF_{3r-1}}{(r+1)F_r}\,, & \psi=\dfrac{(3r+1)F_{3r}}{(r+1)F_r}\,,\end{array}\right\} \tag{10}$$

(Remark: $(s+1)F_s(\eta)$ with $s=-1$ means $(1+e^{-\eta})^{-1}$).

It is straightforward but in some cases rather tedius to generalize above formulae to two-band semiconductors. In doing with the non-isothermal effects, the temperature dependence of the energy gap has been taken into consideration⁷⁾, though it does not explicitly enter into the final expressions. In the followings the suffices 1 and 2 refer to electrons and holes respectively. Especially

$$t_1=\frac{\sigma_1}{\sigma_1+\sigma_2}\,,\qquad t_2=\frac{\sigma_2}{\sigma_1+\sigma_2} \tag{11}$$

are the transport numbers of electrons and holes respectively. We have

(A_2) The electrical conductivity, σ:

$$\sigma=\sigma_1+\sigma_2\,. \tag{12}$$

(B_2) The thermoelectric power, Θ:

$$\Theta=t_1\Theta_1+t_2\Theta_2\,. \tag{13}$$

(C_2) The Hall coefficient, R:

$$R\sigma=t_1(R\sigma)_1+t_2(R\sigma)_2\,. \tag{14}$$

(D_2) The Nernst coefficient, Q:

$$Q=t_1Q_1+t_2Q_2-t_1t_2\frac{k}{e}(\beta_1+\beta_2+g)(\mu_1\alpha_1+\mu_2\alpha_2)\,, \tag{15}$$

where g is the reduced energy gap: $g=E_g/kT$.

(E$_2$) The electronic thermal conductivity, κ_e:

$$\kappa_e=\kappa_{e,1}+\kappa_{e,2}+t_1t_2\left(\frac{k}{e}\right)^2 T\sigma(\beta_1+\beta_2+g)^2\ . \tag{16}$$

(F$_2$) The magnetoresistance, B:

$$B=t_1B_1+t_2B_2+t_1t_2(\mu_1\alpha_1+\mu_2\alpha_2)^2\ . \tag{17}$$

(G$_2$) The magneto-thermoelectric power, W:

$$W=t_1W_1+t_2W_2+t_1t_2\frac{k}{e}\{(\beta_1+\beta_2+g)(\mu_1{}^2\varphi_1-\mu_2{}^2\varphi_2)$$
$$-(\mu_1\alpha_1+\mu_2\alpha_2)[(t_1\mu_1\alpha_1-t_2\mu_2\alpha_2)(\beta_1+\beta_2+g)+\mu_1(\alpha_1\beta_1-\gamma_1)-\mu_2(\alpha_2\beta_2-\gamma_2)]\}\ . \tag{18}$$

In the above, σ_1 and σ_2 are given by Eq. (1) with appropriate respective parameters, and so on. It is easy to see that these agree with those derived by Putley[3] in the limit of Boltzmann statistics with energy independent mean free path of carriers except Eq. (18) to which the corresponding equation is missing in his paper.

We notice that for $r=1/2$ (energy independent relation time) $\alpha=\varphi=1$ and $\beta=\gamma=\psi$, and hence Nernst coefficient, magnetoresistance and magnetothermoelectric power vanish except for the mixed conduction region where both electrons and holes contribute to the conduction.

§ 3. Comparison with Experiment

The experimental arrangements are same as previously reported[1]. In α-Ag$_2$Te the electron mobility is far larger than the hole mobility ($\mu_1\sim 80\mu_2$, see Table I) and hence we are allowed to neglect all terms involving μ_2 in Eqs. (14) to (18). We then rewrite Eqs. (13) to (18) in the forms which will be convenient for comparing with experiment in the present work. We have:

(B$_2$) Thermoelectric power:

$$\theta\equiv\Theta\frac{e}{k}=-(\beta_1-\eta_1)+t_2(\beta_1+\beta_2+g)\ . \tag{13a}$$

(C$_2$) Hall coefficient:

$$R\sigma=t_1\mu_1\alpha_1\ . \tag{14a}$$

(D$_2$) Nernst coefficient:

$$q\equiv Q\frac{e}{k\mu_1}=t_1\{(\eta_1-\theta)\alpha_1-\gamma_1\}\ . \tag{15a}$$

(E$_2$) Electronic thermal conductivity:

$$\bar{\kappa}_e\equiv\kappa_e\left(\frac{e}{k}\right)^2\frac{1}{T}$$
$$=\bar{\kappa}_{e,1}+\bar{\kappa}_{e,2}+t_1t_2\sigma(\beta_1+\beta_2+g)^2\ . \tag{16a}$$

(F$_2$) Magnetoresistance

$$b\equiv\frac{B}{\mu_1{}^2}=t_1(\varphi_1-t_1\alpha_1{}^2)\ . \tag{17a}$$

(G$_2$) Magneto-thermoelectric power

$$w=\frac{We}{k\mu_1{}^2}=-t_1\{(\eta_1-\theta)(\varphi_1-t_1\alpha_1{}^2)$$
$$+\alpha_1\gamma_1t_1-\psi_1\}\ . \tag{18a}$$

Fig. 1 shows σ/μ_1, t_1, $R\sigma/\mu_1$ and θ vs eE/kT

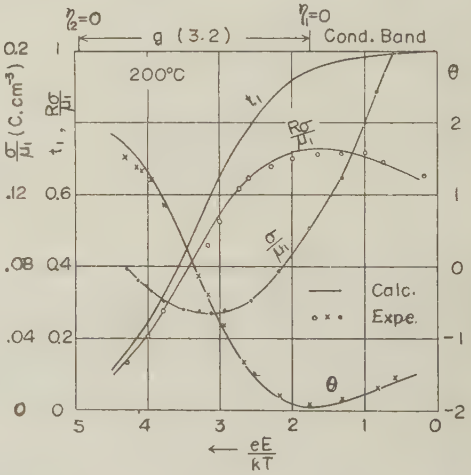

Fig. 1. σ/μ_1, t_1, $R\sigma/\mu_1$ and θ vs eE/kT at 200°C. $\mu_1=1700$ cm^2 sec^{-1} volt^{-1}.

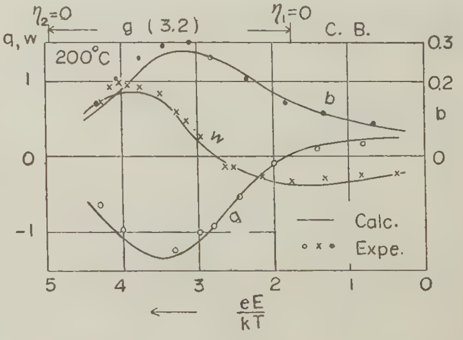

Fig. 2. q, b, and w vs eE/kT at 200°C.

plots at 200°C (see also Figs. 3, 10 and 12 in the reference (1)), and Fig. 2 shows q, b and w vs eE/kT plots at the same temperature where E is the e.m.f. of the galvanic cell Ag|AgI|Ag_2Te|Pt. As noted at the end of the preceding paragraph, if $r=1/2$ is valid then q, b and w should vanish in the limit of $t_1=1$ (at the right-hand parts of the plots). As seen in Fig. 2, this is not the case, indicating that $r=1/2$ is not valid. Therefore, we construct the theoretical curves assuming $r=0$ in the following way. At first, comparing log σ vs eE/kT plot with log F_0 vs η curve we determine the position of the bottom level of the conduction band (eE/kT value corresponding to $\eta_1=0$) and $\mu_1 N_1$ so as to give the best fit at the right-hand part of the plot where electron conduction is far predominant. Thus we determine the electron conductivity σ_1 and accordingly the transport number, t_1, of electrons as functions of η_1.

Next, E_g/kT and accordingly the top level of the valence band are determined from the eE/kT value (η_1 value) at the reversal of experimental Θ by making use of Eq. (13a). Further μ_1 is determined from $R\sigma$ by making use of Eq. (14a). Then we have all parameters necessary for calculating θ, $R\sigma/\mu_1$, q, b and w. The numerical values of α, β, γ, δ and φ, as functions of η for $r=0$ are tabulated in the Appendix (II). Calculated curves are shown in the figures in full lines. As seen in the figures, the agreement between the experimental plots and the calculated curves is satisfactorily good, indicating that $r=0$ (energy independent mean free paths of carriers) is valid for α-Ag_2Te.

Table I.

Temperature (°C)	$\frac{4\mu_1}{3\sqrt{\pi}}$ (cm² s⁻¹v⁻¹)	m_1^*/m	$\frac{4}{3\sqrt{\pi}}\mu_2$	m_2^*/m	E_g (mv)
165	1.5×10^3	0.077	18	1.5	95
220	1.1 〃	0.093	16	1.7	140
300	0.76 〃	0.11	13	1.7	180

The effective mass of electron can be obtained from μ_1 and $\mu_1 N$ above determined. As for the effective mass and μ_2 of holes, we can determine them from the analysis of the amount of silver removed from Ag_2Te specimen across AgI vs eE/kT plot and conductivity vs eE/kT plot; the former should represent $n_2-n_1=2/\sqrt{\pi}\cdot(N_2F_{1/2}(\eta_2)-N_1F_{1/2}(\eta_1))$ vs η_1 apart from an additive constant. For the details, refer to the reference (1). In Table I, being the revision of the table in the reference (1) where $r=1/2$ is assumed, the effective masses and the mobilities of carriers thus determined are tabulated together with energy gap for three temperatures in the α-range.

We have measured also the relative value of the thermal conductivity which may be determined from the ratio of the temperature drops across the two specimens, one to be measured and the other to be refered (see Fig. 3). The measured relative thermal conductivity shows a minimum at eE/kT value just expected from the theoretical expression for electronic thermal conductivity, Eq. (16a).

This work was supported by the research grant of the Ministry of Education.

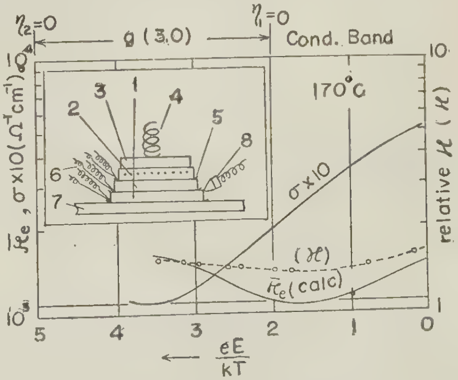

Fig. 3. 1. two specimens, 2. heater, 3. porcelain, 4. steel spring, 5. Pt foil, 6. constantan Nichrome couple, 7. Cu plate, 8. AglAgI.

Appendix I.

For single carrier semiconductors:

(H₁) The Ettinghausen coefficient, P:

$$P=\frac{QT}{\kappa}\ .$$

(I₁) The Righi-Leduc coefficient, S:

$$S=\mp\left(\frac{k}{e}\right)^2\frac{\sigma T}{\kappa}\mu(\mathcal{E}+\alpha\beta^2-2\beta\gamma)\ .$$

where

$$\mathcal{E}=\left(2r+\frac{5}{2}\right)F_{2r+3/2}\Big/(r+1)F_r\ .$$

For two-band semiconductors:

(H₂) The Ettinghausen coefficient, P:

$$P=\frac{QT}{\kappa}\ .$$

(I₂) The Righi-Leduc coefficient, S:

$$S=-\left(\frac{k}{e}\right)^2\frac{T}{\kappa}\{s_1-s_2+t_1t_2[(g+\beta_1+\beta_2)^2(-\sigma_1\mu_2+\sigma_2\mu_1)$$

$$+2(g+\beta_1+\beta_2)\sigma(-\mu_1(\alpha_1\beta_1-\gamma_1)+\mu_2(\alpha_2\beta_2-\gamma_2))]\}\ .$$

where

$$s=\sigma\mu(\mathcal{E}+\alpha\beta^2-2\beta\gamma)\ .$$

Appendix II.

η	α	β	γ	δ	ε	φ
Classical limit	$\frac{\sqrt{\pi}}{2}$	2	$\frac{3\sqrt{\pi}}{4}$	6	$\frac{15\sqrt{\pi}}{8}$	1
−2	.86339	2.0643	1.3542	6.2933	3.4626	.93910
−1	.83179	2.1621	1.3910	6.7528	3.6777	.85851
0	.77343	2.3732	1.4674	7.8036	4.1579	.72135
1	.69284	2.7498	1.5944	9.8469	5.0650	.55648
2	.61011	3.3037	1.7653	13.322	6.5083	.41410
3	.53880	3.9989	1.9568	18.569	8.4905	.31246
4	.48211	4.7915	2.1542	25.828	10.968	.24439
5	.43773	5.6476	2.3482	34.825	13.882	.19839
High degen. limit	$\eta^{-1/2}(1-a)$	$\eta(1+8a)$	$\eta^{1/2}(1+3a)$	$\eta^2(1+24a)$	$\eta^{3/2}(1+15a)$	η^{-1}

where $a=\pi^2/(24\eta^2)$.

References

1) S. Miyatani: J. Phys. Soc. Japan **13** (1958) 341.
2) R. W. Wright: Proc. Phys. Soc. London **A**, **64** (1951) 984.
3) E. H. Putley: Proc. Phys. Soc. London **B**, **68** (1957) 35.
4) O. Madelung: *Handbuch der Physik* **20** (1957) 53.
5) F. J. Blatt: Solid State Physics **4** (1957) 199.
6) A. H. Wilson: *The Theory of Metals* (Cambridge Univ. Press, 1953) chap. 8.
7) E. Haga: J. Phys. Soc. Japan **14** (1959) 35.
8) J.-P. Jan: Solid State Physics **5** (1957) 1.

JOURNAL OF TEH PHYSICAL SOCIETY OF JAPAN, Vol. 14, No. 6, JUNE, 1959

On the X-Ray Diffuse Scattering by 1-3-5-Triphenylbenzene

By M. Shehata FARAG

National Research Centre, Dokki, Cairo-Egypt

(Received May 6, 1958)

In crystalline 1-3-5-triphenylbenzene every four molecules form a pseudo-hexagonal *orthorhombic* unit cell with the [100] as the pseudo-hexagonal axis. The deviation from hexagonal symmetry which is only 0° 19′ is discussed in terms of both the crystal structure and the diffuse scattering reflections shown by a Laue photograph taken with the X-ray beam parallel to the [100] axis. Two other Laue photographs with the X-ray beam parallel to the [010] and [001] axes are given. All the diffuse scattering reflections in the three photographs are indexed and the types of elastic waves (of thermal origin) affecting the crystal lattice are revealed.

§ 1. Introduction

1-3-5-Triphenylbenzene $C_6H_3\ (C_6H_5)_3$ crystallises in the orthorhombic system. It has been crystallographically studied by Knopp and Arzruni; their results have been quoted by Groth[1]. The a-and c-axes given in Groth are now interchanged and the original c-axis is halved. This interchange is necessary, because the crystal, as shown by Lonsdale and Orelkin[2], is polar.

The crystal structure was completely solved by the author by the method of double Fourier series and three dimensional line syntheses. The unit cell dimensions are:

$a=7.47\pm0.02$ Å, $b=19.66\pm0.05$ Å,
$c=11.19\pm0.03$ Å.

The space group is $Pna2_1$, with four molecules per unit cell.

§ 2. Pseudo-Hexagonal Symmetry

From the values of "b" and "c". ($c/b\approx\tan 30°$) it is clear that the crystal is pseudo-hexagonal with "a" as the pseudo-trigonal axis. The deviation from pseudo-hexagonal symmetry is 0° 19′.

Fig. 1 shows, in projection, the orthorhombic unit cell (of sides ob and oc) with its pseudo-hexagonal dimensions. The crystal structure analyses show that the molecules are arranged in two layers apporximately at $x=1/4$, $3/4$ and are nearly parallel to the (200) planes. The fractional coordinates of the centre of the molecules as given by the author[3], are (0.250, 0.169,–0.011). For the sake of the present argument these are approximately (1/4, 1/6, 0). This approximation will not upset the final conclusion. According to the space group symmetry the coordinates of the centres of the molecules in the two layers are approximately:

First layer: (1/4, 1/6, 0); (1/4, 4/6, 1/2)
Second layer: (3/4, 2/6, 0); (3/4, 5/6, 1/2)

If these coordinates are referred to a hexagonal unit cell, they show clearly the presence of a trigonal axis perpendicular to each layer as can be seen in Fig. 1. These axes, although parallel to the a-axis of the orthorhombic unit cell, are not coincident, the lateral shift being $b/6=3.28$ Å as we go from layer to layer. Had there been no shift, the unit cell would have been a true hexagonal one. This difference being 3.28 Å is quite considerable, and is presumably associated with the absence of a true trigonal axis in both the crystal and molecule.

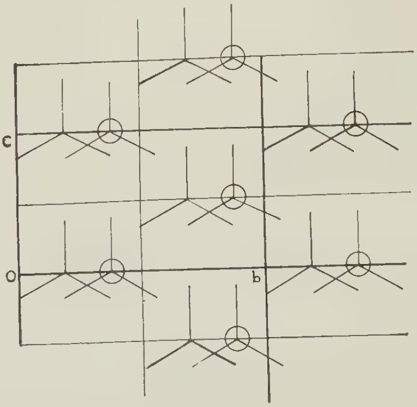

Fig. 1.

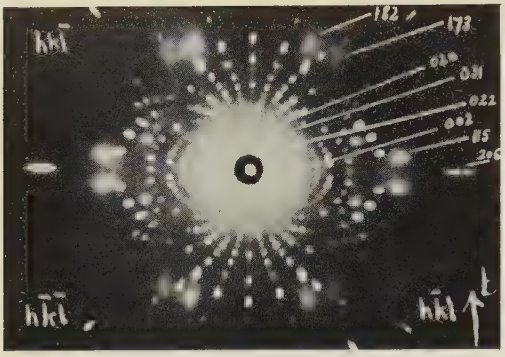

Fig. 2-a. The beam is along [100], the [010] is vertical.

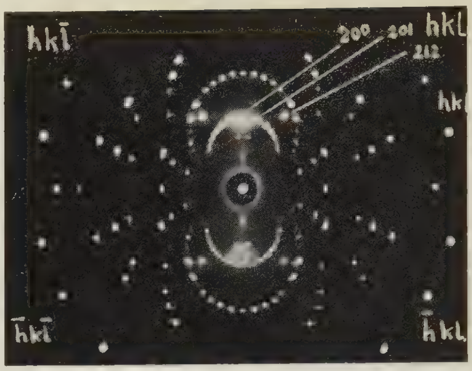

Fig. 3. The beam is along [010], the [100] is vertical.

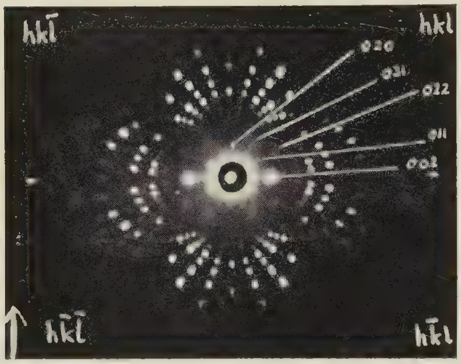

Fig. 2-b.

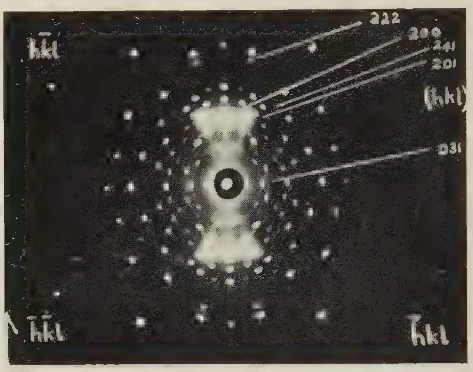

Fig. 4. The beam is along the [001], the [100] is vertical.

Table I.

Direction of X-ray beam	Diffuse reflection observed		
	Index	Shape	Intensity
[100]	(020)	very small, circular	weak
	(002)	small, circular	very strong
[010]	(200)	large, elliptical	very strong
	(002)	absent	absent
[001]	(200)	large, elliptical	very strong
	(020)	absent	absent

Figs. 2-a and -b, 3 and 4 show three Laue photographs taken with the X-ray beam parallel to [100], [010], and [001] axes respectively. The Laue spots in them show that the crystal has an mmm symmetry, while the extra spots, i.e., the diffuse scattering reflections in photograph Fig. 2 show a well marked pseudo-hexagonal symmetry.

The diffuse scattering reflections in each photograph were indexed by comparing the Laue photographs with 10° oscillation photographs taken on flat films at the same crystal-film distance (3 cm.) and with the Laue positions as centres of oscillations, Bernal[4)], Lonsdale and Smith[5)]. The indices of the Bragg reflections corresponding to the diffuse scattering reflections are shown on the photographs.

The striking similarity between Fig. 2-a and Fig. 1 is evident. The signs of pseudo-hexagonal symmetry exhibited in photograph Fig. 2 are shown by the following groups of diffuse reflections:

(a) The diffuse scattering pattern of (182), $(18\bar{2})$, $(1\bar{8}\bar{2})$, $(1\bar{8}2)$, (173), $(17\bar{3})$, $(1\bar{7}\bar{3})$, $(1\bar{7}3)$ and

(115), (11$\bar{5}$), ($\bar{1}\bar{1}$5), (1$\bar{1}$5) shows a well marked hexagonal symmetry. It is of interest to consider the (0kl) planes which pass through the intersections of the previous planes and the (100), i.e. the (082), (08$\bar{2}$), (0$\bar{8}\bar{2}$), (0$\bar{8}$2), (073), ···; and (015), ···. These planes have nearly the same spacings, lie at 60° approximately to each other if taken in a cyclic order (as will be shown) and the reflections from them are relatively of large amplitudes as can be seen from the following data:

Plane:	(082)	(073)	(015)	
Spacing:	2.28	3.25	2.22 Å	
$\lvert F(\text{obs})\rvert$:	42	71	70,	on the absolute scale, cf. F (000)=648

The angle between (082) and (073)=60° 20′ and
The angle between (073) and (015)=59° 41′

(b) The diffuse reflections of (011), (01$\bar{1}$), (0$\bar{1}\bar{1}$), (0$\bar{1}$1) and (020), (0$\bar{2}$0) show also signs of hexagonal symmetry, which could be seen in Fig. 2-a and not in Fig. 2-b. This is due to the central halo in the latter. The spacings and $\lvert F(\text{obs})\rvert$'s of the corresponding Bragg reflections are:

Plane:	(011)	(020)	
Spacing:	9.74	9.83 Å	
$\lvert F(\text{obs})\rvert$:	46	48,	on the absolute scale.

The angle between (011) and (020)=60° 19′

(c) There are diffuse reflections for the (002), (022), ··· and none at all for their pseudo-hexagonal repetitions, i.e. for the (040) and (0$\bar{4}$0); but the Bragg reflections have nearly the same structure amplitudes as shown by the following data:

Plane:	(022)	(040).	
Spacing:	4.87	4.92 Å	
$\lvert F(\text{obs})\rvert$:	41	44,	on the absolute scale.

The angle between (022) and (040)=60° 19′

(d) The diffuse reflections of the (002), (00$\bar{2}$) and their pseudo-hexagonal repetitions, the (031), (03$\bar{1}$), ··· form another group, but the diffuse scattering reflection of the (002) *is much stronger* than that of the (031). This corresponds to the amplitudes of the Bragg reflections which are of very different values. The spacing and $\lvert F(\text{obs})\rvert$'s of these planes are:

Plane:	(002)	(031)	
Spacing:	5.60	5.70 Å	
$\lvert F(\text{obs})\rvert$:	140	8,	on the absolute scale.

The angle between (002) and (031)=59° 40′

§ 3. Types of Diffuse Reflections

a) *Large elliptical or circular diffuse reflections*

In photographs Figs. 3 and 4, there are large elliptical and circular diffuse spots associated with the (200) and (201). They indicate that the structure is of a layer type (Lonsdale and Smith⁵⁾), the (200) being the molecular plane rather than the (201). This is the case as shown by the author³⁾.

b) *Diffuse streaks*

Diffuse streaks characteristic of chain structures, can be seen in photograph Fig. 3, associated with the Bragg reflections (135), (13$\bar{5}$), ($\bar{1}$3$\bar{5}$) and ($\bar{1}$35). This indicates that the atoms form a chain-like-arrangement in planes perpendicular to the previous planes. There are other chains in the structure which should produce similar diffuse streaks on Laue photographs if the crystal has the proper orientation to show them. To reveal all such chains, a series of increasingly mis-set Laue photographs would be necessary.

c) *Small circular diffuse reflections* (*anisotropic*)

It may be seen that although the diffuse scattering reflection of the (002) is very strong in photograph Fig. 2, where the X-ray beam is parallel to the [100] axis, no traces of any diffuse scattering for it are present in photograph Fig. 3 where the X-ray beam is parallel to the [010] axis. The fact is noticeable since in reciprocal space the point corresponding to the (002) lies symmetrically to both the a^*- and b^*-axes. Had the distribution of the diffuse reflecting power about the 002 reciprocal lattice point been spherical or nearly so, one would expect a diffuse reflection corresponding to it to appear in both photographs, Figs. 2 and 3.

These two photographs show that the reflecting power of that plane is extended considerably in the "a^*" direction only in the (a^*–c^*) plane but not in the "b^*" nor in the "c^*" directions in the (b^*–c^*) plane. One concludes from the photographs that the diffuse reflecting power about the 002 reciprocal lattice point is of *a needle* shape whose length is parallel to the a^*-axis and its cross section is circular. In terms of the crystal structure, and according to Born⁶⁾ and Lonsdale⁷⁾

this implies that there are elastic waves of large amplitude affecting the (001) planes and travelling only along the [100] axis.

It should be mentioned here that it is a general rule that elastic waves propagated along a given direction in the crystal cause an extension of the reflecting power of each reciprocal lattice point along the direction of propagation. The diffuse reflections of (011), (022), (031), ⋯ are also such that the diffuse reflecting powers of the points corresponding to these planes in reciprocal space are extended along the [100] axis only.

§ 4. Atomic Movements

To picture the kind of elastic waves, of thermal origin, that affect the crystal lattice, we have to consider the diffuse reflections corresponding to the axial planes. These are sufficient since in the orthorhombic system, the axes of the triaxial ellipsoid representing the physical properties coincide with the crystallographic axes. These are given in Table I. These diffuse reflections show that:

(i) There are *transverse* elastic waves of large amplitude travelling along the crystal [100]-axis such that the (001) planes are strongly affected and the arrangement of the atoms in these planes along the [010] direction is relatively unaffected. Such waves give a strong diffuse reflection for the (002) when the X-ray beam is parallel to the [100]-axis and none for that plane if the X-ray beam is parallel to the [010]-axis.

(ii) Since the (200) gives large elliptical diffuse reflections when the beam is parallel to the [010] and [001] axes, then it implies the presence of waves strongly affecting those planes and travelling in all directions in the crystal. These waves include *transverse*, *longitudinal* and other combinations of them.

(iii) Waves travelling along the [100]-axis such that the (010) planes are affected are highly damped.

(iv) Waves causing oscillational vibrations of the molecules in the (100) planes are forbidden. Such waves, if exist, would affect the relative arrangement of the atoms along the [010]-axis, and would produce a diffuse reflection for the (002) when the beam is along the [010] axis.

All such waves are of thermal origin, and it would be interesting to study the thermal conductivities of the crystal along its three crystallographic axes.

In conclusion the author wishes to record his sincere thanks to Professor Dame Kathleen Lonsdale F.R.S., D.B.E. for her help, criticism and encouragement while this work was in progress.

References

1) P. Groth: Chemische Kryst. **6**, 34.
2) K. Lonsdale and B. Orelkin: Proc. Roy. Soc. A, **144** (1934) 630.
3) M. S. Farag; Acta Cryst. **7** (1954) 117.
4) J. D. Bernal: Proc. Roy. Soc. A, **113** (1926) 117.
5) K. Lonsdale and H. Smith: Proc. Roy. Soc. A, **179** (1941) 8.
6) M. Born: Rep. Progr. Phys. (Phys. Soc. London) **9** (1942–3) 294.
7) K. Lonsdale: Proc. Phys. Soc. London **54** (1942) 314.

JOURNAL OF THE PHYSICAL SOCIETY OF JAPAN, Vol. 14, No. 6, JUNE, 1959

Metamagnetism of Methylamine Chrome Alum

By Kazuo MOTIZUKI

Department of Physics, Osaka University, Japan

(Received February 18, 1959)

Methylamine chrome alum shows an antiferromagnetic ordering below 0.015°K–0.02°K and it is known that this ordering results from the magnetic dipole-dipole interaction among the chromic ions. The present paper investigates, on the basis of the molecular field approximation, the phenomenon of transition below the Néel point from the antiferromagnetic state to the paramagnetic state caused by an applied field, at constant temperature or at constant entropy. Depending on the direction of the applied field relative to the crystalline axes and also on the shape of sample, different behaviours of the transition are obtained. For a spherical sample three are studied, namely, the cases of $\boldsymbol{H}//[111]$, $\boldsymbol{H}//[100]$ and $\boldsymbol{H}//[10\bar{1}]$, and for an infinitely long sample two cases, i.e., the axis of the sample and $\boldsymbol{H}$ are both parallel to either [111] or [100]. In Appendix is given a summary of the previous theoretical study by Kanamori, Motizuki and Yosida of the same kind of antiferro-paramagnetic transition in two-sublattice antiferromagnet, in relation to the present investigation.

§ 1. Introduction

Methylamine chrome alum is a well-known substance used for adiabatic demagnetization.[1] The magnetic and thermal properties of this salt below 1°K have been studied by several authors, with powder samples[2),3] or with single crystals,[4)-8] and an antiferromagnetic transition has been discovered at about 0.015°K–0.02°K.[4),7] Van Vleck[9] and Hebb and Purcell[10] investigated theoretically the paramagnetic properties of this substance at relatively high temperatures, by the moment expansion method, and O'Brien[11] extended their studies to the antiferromagnetically ordered state, using the molecular field approximation, and has shown that the antiferromagnetic ordering results mainly from the magnetic dipole-dipole interaction among the chromic ions.

In this alum, the chromic ions are situated on the face-centred cubic lattice and the symmetry of the crystalline field at each chromic ion is trigonal, with its trigonal axis pointing along one of the body diagonals. In this crystalline field, the electronic state of the free chromic ion, ^4F, is split in such a way that the ground orbital state is non-degenerate and the two Kramers doublets belonging to it have spin components ±3/2 and ±1/2 along the trigonal axis, the ±3/2 doublet lying lower. The energy difference between these two doublets, δ, has been estimated to be about 0.25°K[12] (in temperature scale), which is about ten times as large as the antiferromagnetic transition temperature, T_N. Therefore, near or T_N, only the lower Kramers doublet should be populated and the spin is to be tightly bound along the trigonal axis. We shall confine ourselves to this temperature range.

The face-centred cubic lattice of the chromic ions can be divided into four simple cubic sublattices whose crystalline fields have their trigonal axes pointing along [111], $[1\bar{1}\bar{1}]$, $[\bar{1}1\bar{1}]$ and $[\bar{1}\bar{1}1]$. We shall denote their magnetizations by J, K, L and M respectively. For a spherical sample, the interaction energy between these four sublattices can be written, according to O'Brien, as

$$\mathscr{H}=-\mu(JK+JL+JM+KL+KM+LM) \quad (1)$$

where μ is the interaction constant and we understand by J, K, L and M the thermal average values of the atomic magnetic moments of the sublattices, measured respectively along their unique axes. The interaction is mainly of the magnetic dipole character and μ is therefore positive according to O'Brien, so that the state with $J=K=L=3\mu_B$ or $-3\mu_B$ is the most stable state at absolute zero in the absence of any external field. The corresponding ordering of the spins is antiferromagnetic in the sense that the total magnetic moment is zero, although the four spin directions are not antiparallel to one another.

The purpose of the present paper is to investigate, on the basis of the interaction energy (1) and the approximation of the molecular field, the phenomenon of the transition from antiferromagnetic state to paramagnetic state due to applied field. Depending on the direction of the applied field relative to the crystalline axes, different behaviours of the transition will be predicted. We shall treat particularly the cases in which the external field is applied parallel to [111], [100] and [10$\bar{1}$].

The antiferro-paramagnetic transition by application of a magnetic field has been studied by several authors for the ordinary two-sublattices antiferromagnet. Garrett[13] has studied this phenomenon for the case where the exchange interaction acts only between different sublattices and has shown that the transition is always of the second kind. The present author, in collaboration with Kanamori and Yosida,[14] has extended Garrett's theory to the case where there exist exchange interactions not only between different sublattices but also within the same sublattice. The exchange interactions have been assumed to be anisotropic. It was found, for instance, that the antiferro-paramagnetic transition for a field applied along the easy axis of magnetization is not always of the second kind; if antiferromagnetic interaction acts not only between different sublattices but also in the same sublattice, the type of the transition changes from the second kind to the first kind with lowering temperature. Gorter and Van Peski-Tinbergen[16] studied independently the same problem and arrived at the same results. Since, however, our study was published in Japanese and treats the problem a little more in detail than Gorter et al. do, we shall summarize in Appendix the most essential part of it which is intimately connected with the present problem.

§ 2. Change of Magnetization due to Application of a Magnetic Field

In the presence of an external magnetic field, $\boldsymbol{H}$, the effective magnetic field acting on each ion of sublattice J is given, corresponding to (1), by

$$H_{J,eff}=\mu(K+L+M)+H\cos\theta_J \tag{2}$$

where θ_J is the angle between the external magnetic field and the trigonal axis of this sublattice. Similar expressions are given for sublattices K, L and M. In (2), the demagnetizing field is included in $\mu(K+L+M)$, assuming the sample to be spherical. Later in § 3 we shall consider the case of an infinitely long sample, in which case $\mu(K+L+M)$ must be corrected for different demagnetizing field.

In the effective field (2), the chromic ion takes energy values $-3\beta H_{J,eff}$ and $+3\beta H_{J,eff}$, where β is the Bohr magneton. Therefore the molecular field theory gives the equation

$$\tanh\frac{3\beta}{kT}\left[\mu(K+L+M)+H\cos\theta_J\right]=\frac{J}{3\beta}. \tag{3}$$

For the sake of simplicity, we shall use the following reduced quantities:

$$\begin{aligned}&a=J/3\beta,\ b=K/3\beta,\ c=L/3\beta,\ d=M/3\beta;\\&x=9\beta^2\mu/kT=T_N/3T;\\&h=H/3\beta\mu,\ h_J=h\cos\theta_J,\quad\text{etc.}\end{aligned} \tag{4}$$

Here $T_N=27\beta^2\mu/k$ is the Néel temperature when there is no external field. Then, Eq. (3) and the corresponding equations for K, L and M can be written

$$\begin{aligned}x(b+c+d+h_J)&=\tanh^{-1}a,\\x(a+c+d+h_K)&=\tanh^{-1}b,\\x(a+b+d+h_L)&=\tanh^{-1}c,\\x(a+b+c+h_M)&=\tanh^{-1}d.\end{aligned} \tag{5}$$

We shall solve these equations for the following three special cases.

a) The external field is parallel to [111].

In this case Eqs. (5) become

$$\begin{aligned}x(b+c+d+h)&=\tanh^{-1}a,\\x(a+c+d-h/3)&=\tanh^{-1}b,\\x(a+b+d-h/3)&=\tanh^{-1}c,\\x(a+b+c-h/3)&=\tanh^{-1}d.\end{aligned} \tag{6}$$

From these equations it follows that $b=c=d$, since b, c and d are uniquely determined from these equations by giving a, x and h, as one can verify easily, and $b=c=d$ is compatible with these equations. Thus Eqs. (6) reduce to

$$\begin{aligned}x(3b+h)&=\tanh^{-1}a\,,\\x(a+2b-h/3)&=\tanh^{-1}b\,.\end{aligned} \tag{7}$$

These equations can be solved easily at absolute zero and the result for the total magnetization, a–b, is plotted against h in Fig. 1.

At an arbitrary temperature, it is convenient to use a graphical method to solve Eqs. (7). Curves of constant temperature, x, and curves of constant field, h, are drawn in the a, b-plane, and the intersecting points are looked for. These curves are given in Fig. 2 and Fig. 3. The total magnetization, a–b, as a function of h, at two temperatures $T=(2/3)T_N$ and $T=T_N$, is given in Fig. 4. It is seen that there are three different solutions, (A), (B), (C), on the lower field side. Two of them, (B) and (C), join smoothly with each other at a certain field, above which they cease to exist. This field is $h=9$ at 0°K; since the unit of the field is $3\beta\mu=34.0$ oe., $h=9$ corresponds to 306 oe.. When the temperature is raised, it shifts towards the lower field side and the area enclosed by (B) and (C) decreases. At $T=T_N$ the area vanishes and (A) becomes a broken curve shown in Fig. 4. Fig. 5 shows schematically the vari-

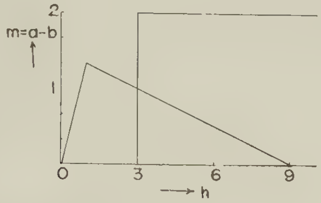

Fig. 1. Magnetization, $m=a-b$, versus applied field along [111] at 0°K.

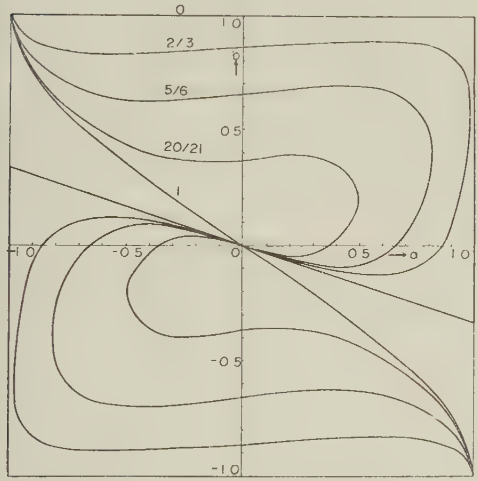

Fig. 2. Curves of constant temperature in the a, b-plane. $\boldsymbol{H}$//[111].

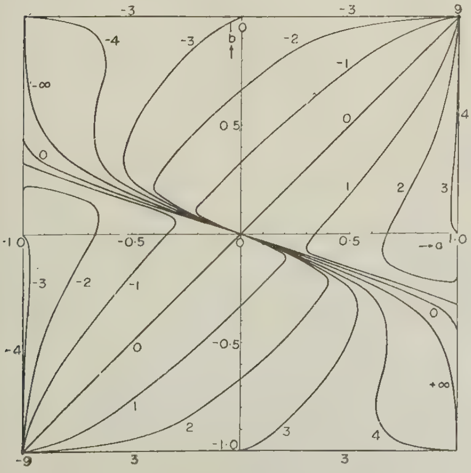

Fig. 3. Curves of constant field in the a, b-plane. $\boldsymbol{H}$//[111].

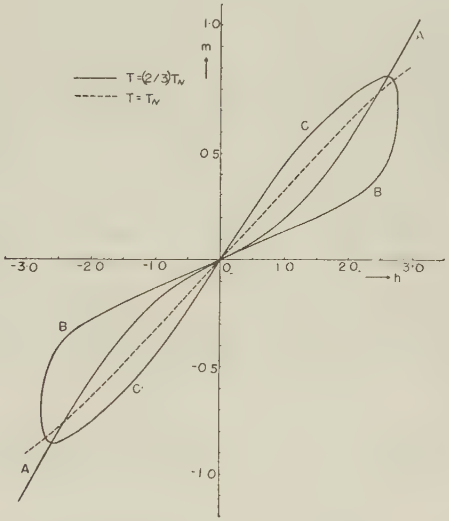

Fig. 4. Magnetization, $m=a-b$, versus applied field along [111] at $T=(2/3)T_N$ and $T=T_N$.

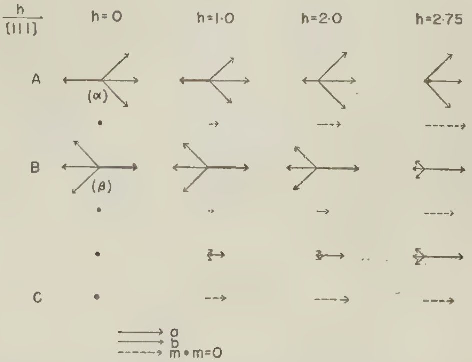

Fig. 5. Behaviours of a, b and $m=a-b$ with applied field.
Three cases A, B and C correspond, respectively, to the solutions (A), (B) and (C) given in Fig. 4.

ations of a, b and $m=a-b$ with varying external field, corresponding to the three solutions. If the field is reversed, the signs of a and b are reversed.

At $T=0$, a and b are zero for the solution (C). Therefore this solution corresponds to the paramagnetic state which must be unstable. Corresponding to (A) and (B), there are two states which are degenerate at $h=0$. In one of them, the spin directions of the four sublattices are $[111]$, $[1\bar{1}\bar{1}]$, $[\bar{1}1\bar{1}]$, $[\bar{1}\bar{1}1]$, as shown in Fig. 5, (β), and in the other all the spin directions are reversed, (α). The crystal may consist of antiferromagnetic domains of these two states at $h=0$ and $T=0$. However, when the field is applied along [111], the domain structure will vanish and the magnetization will follow the curve (A) starting from (α), as this curve will give a higher magnetization than the curve (B). Decreasing the field and further reversing its direction, one will perhaps observe the following hysteresis effect: the magnetization will first come back along (A), then, after passing through the origin, will follow the curve (B) since the sudden change from (α) to (β) at the origin might not take place easily, and finally at a certain negative field it will change over to the curve (A).

b) The external field is parallel to [100].

Evidently, $a=b$ and $c=d$ in this case. Thus Eqs. (5) become

$$\begin{aligned} x(a+2c+h/\sqrt{3})&=\tanh^{-1} a,\\ x(c+2a-h/\sqrt{3})&=\tanh^{-1} c. \end{aligned} \tag{8}$$

At absolute zero, the relation between h and $a-c$ ($=\sqrt{3}/2$ times the total magnetization in the direction of the external field) is easily obtained and is shown in Fig. 6. Our previous theory[14] of the two-sublattices model can be applied for the present case, taking the molecular field coefficients A and Γ in the ratio 2:1 (A is the coefficient of the molecular field in one sublattice due to the other sublattice and Γ that due to the same sublattice). Then equations determining the sublattice magnetizations of the two-sublattices model become equivalent to Eq. (8). For the details, the reader is referred to Appendix, where different cases are classified according to different values of $\lambda=\Gamma/(A+\Gamma)$, including $\lambda=1/3$. Here we only summarize our results:

1) At temperatures above t_1 (measured in units of T_N), defined in 3) of Appendix, the antiferro-paramagnetic transition due to application of a magnetic field is of the second kind, as predicted by Garrett.[13]

2) At low temperatures below t_2 ($<t_1$), defined also in Appendix, the antiferro-paramagnetic transition is of the first kind.

3) In the temperature range between t_1 and t_2, transition occurs twice. The first transition occurs from an antiferromagnetic state to another antiferromagnetic state and it is of the first kind. A further transition occurs from the latter to the paramagnetic state at a higher field and it is of the second kind.

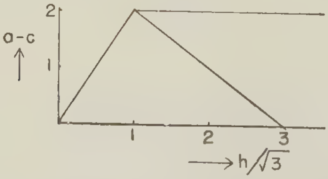

Fig. 6. Magnetization, a-c, versus applied field along [100] at 0°K.

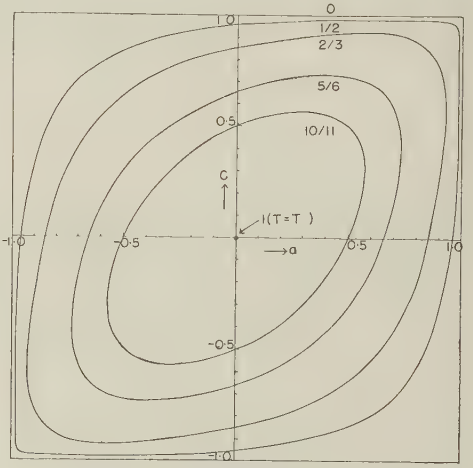

Fig. 7. Curves of constant temperature in the a, c-plane. $\boldsymbol{H}$//[100].

To estimate temperatures t_1 and t_2, a graphical method was used. Curves of constant temperature, x, and curves of constant field, h, corresponding to Eqs. (8) are drawn as given in Fig. 7 and Fig. 8; their intersecting points correspond to antiferromagnetic and paramagnetic solutions. The antiferromagnetic solution coincides with the paramagnetic solutions ($a=-c$) at the following critical curve (see Fig. 9)

$$1/x_c=3(1-a^2)\,,$$
$$h_c/\sqrt{3}=a+3(1-a^2)\tanh^{-}a. \qquad (9)$$

According to our previous theory (given in Appendix), there exists in the temperature range $t>t_1$ ($t=1/3x=T/T_N$) only one antiferromagnetic solution below h_c and none above h_c (Fig. A. 4 (e)). On the other hand, between t_1 and t_2 there exist two or three antiferromagnetic solutions in a certain narrow field range which lies below h_c (Fig. A. 5 (2)).

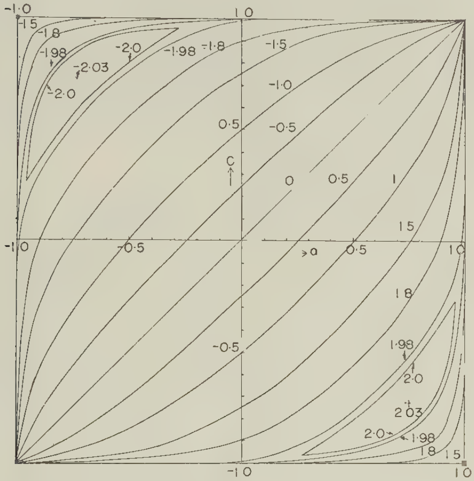

Fig. 8. Curves of constant field in the a, c-plane. $\boldsymbol{H}$//[100].

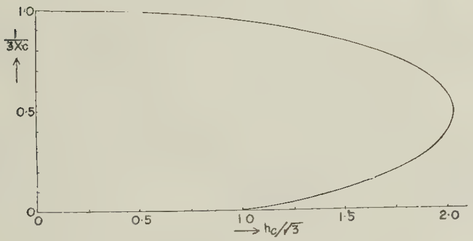

Fig. 9. Critical curve, $1/3x_c$ vs. $h_c/\sqrt{3}$.

From the intersecting points of curves of Fig. 7 and Fig. 8 above $t=0.467$ (at which h_c attains its maximum) we find only one antiferromagnetic solution for $h\leq h_c$. We see therefore that t_1 is lower than 0.467. As an example the magnetization curve at $t=0.564$ is shown in Fig. 10(a). As another example, we took $t=0.360$ and made a numerical calculation, and found that at this temperature there is only one solution at $h=h_c$ ($=1.9865$) but there are three solutions at $h=h_c-0.0013$. Fig. 10(b) shows the magnetization curve at this temperature. Therefore, t_1 must lie in the range $0.360<t_1<0.467$, and probably very close to 0.360.

Next we estimate t_2. At this temperature, there exist three antiferromagnetic solutions at $h=h_c$, one of which coinciding with the paramagnetic solution; a transition of the first kind must occur at h_c. According to our previous theory, t_2 is greater than $4/3-1/3\lambda$, which is equal to 1/3 in the present case of $\lambda=1/3$. The magnetization curve at $t=0.340$ is shown in Fig. 10(c); it can be seen that at this temperature the antiferro-paramagnetic transition is of the first kind but occurs at a field a little higher than h_c (a little to the right of the vertical broken line, as the two areas enclosed by this line and the curve are unequal). Therefore, t_2 must be between 0.340 and 0.360.

The temperature range between t_1 and t_2 may be too narrow to be of practical interest.

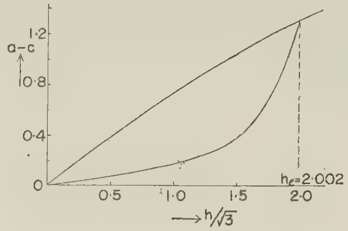

a) $T=0.564T_N$,

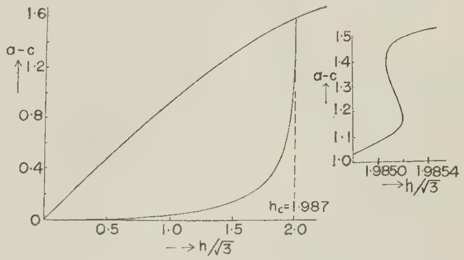

b) $T=0.360T_N$

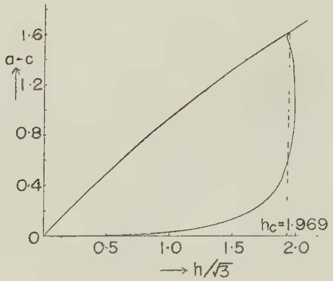

c) $T=0.340T_N$.

Fig. 10. Magnetization, $a-c$, versus applied field along [100] at constant temperature.

c) The external field is parallel to $[10\bar{1}]$.

In this case the external field is perpendicular to a and c, and Eqs. (2) become

$$\begin{aligned} &x(b+c+d)=\tanh^{-1} a, \\ &x(a+c+d+2h/\sqrt{6})=\tanh^{-1} b, \\ &x(a+b+d)=\tanh^{-1} c, \\ &x(a+b+c-2h/\sqrt{6})=\tanh^{-1} d. \end{aligned} \tag{10}$$

Subtracting the third equation from the first one, we obtain $xc+\tanh^{-1} c=xa+\tanh^{-1} a$, so that $a=c$. Therefore Eqs. (10) reduce to

$$\begin{aligned} &x(a+b+d)=\tanh^{-1} a, \\ &x(2a+d+2h/\sqrt{6})=\tanh^{-1} b, \\ &x(2a+b-2h/\sqrt{6})=\tanh^{-1} d. \end{aligned} \tag{11}$$

As a is perpendicular to the external field, the total magnetization in the direction of the external field is $b-d=m$ times $\sqrt{2/3}$. Writting $b+d=m'$, Eqs. (11) can be written as follows:

$$\begin{aligned} &m^2=m'^2+4-4m' \Big/ \tanh\left[\frac{m'+4a}{m'+a}\tanh^{-1} a\right], \\ &x=\frac{\tanh^{-1} a}{m'+a}, \\ &\frac{4}{\sqrt{6}}h=m+(m'+a)\tanh^{-1}\left[\frac{m}{1-(m'^2-m^2)/4}\right] \\ &\qquad \Big/ \tanh^{-1} a. \end{aligned} \tag{12}$$

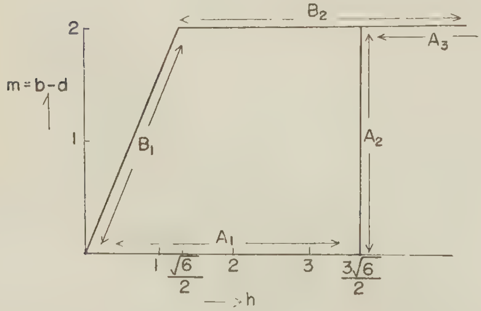

Fig. 11. Magnetization, $m=b-d$, versus applied field along $[10\bar{1}]$ at 0°K.

The relation between h and m at absolute zero is shown in Fig. 11. The portions of this curve denoted by A_1, B_1, etc. correspond to the following states:

A_1: two states, $a=c=1$, $b=1$, $d=1$ and $a=c=-1$, $b=-1$, $d=-1$, of an equal energy.

A_2: two states, $a=c=1$, $b=1$, $-1\leq d\leq 1$ and $a=c=-1$, $-1\leq b\leq 1$, $d=-1$.

A_3: two states, $a=c=1$, $b=1$, $d=-1$ and $a=c=-1$, $b=1$, $d=-1$.

B_1: one state, $a=c=0$, $b=(\sqrt{6}/3)h$, $d=-(\sqrt{6}/3)h$.

B_2: one state, $a=c=0$, $b=1$, $d=-1$.

A_3 and B_2 have an equal total magnetization but the respective values of a and c are different. The energy value is lower in A_3 than in B_2. Therefore the magnetization, m, changes along A_1, A_2 and A_3 with increasing external field.

At an arbitrary temperature the relation between m and h cannot be obtained analytically. However, the paramagnetic solution at finite temperatures which joins B_1 and B_2 at absolute zero can easily be obtained putting $b=-d$ $(m'=0)$. Then the relation between m, h and x becomes

$$h=\frac{\sqrt{6}}{2}\left[\frac{1}{x}\tanh^{-1}\frac{m}{2}+\frac{m}{2}\right]. \tag{13}$$

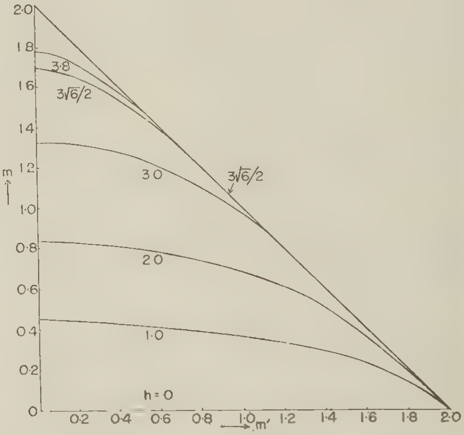

Fig. 12. Curves of constant temperature in the m, m'-plane. $\boldsymbol{H}//[10\bar{1}]$.

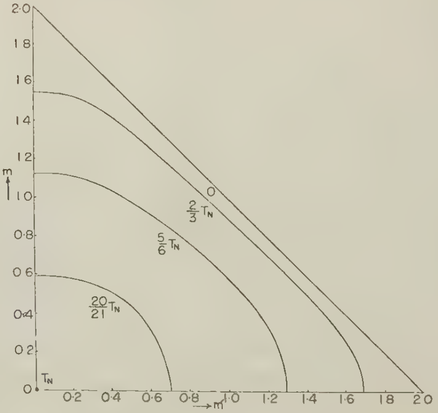

Fig. 13. Curves of constant field in the m, m'-plane. $\boldsymbol{H}//[10\bar{1}]$.

Next, in order to obtain antiferromagnetic solutions ($m'\neq 0$), curves of constant temperature and curves of constant field in the $m\sim m'$ plane were calculated with the use of Eqs. (12) (Fig. 12 and Fig. 13). (In this calculation, a was calculated as a function of m and m' from the first equation of (12) and then x and h were calculated.) At $T=T_N$ the curve of constant x shrinks to the origin and at $T\fallingdotseq 0$ the curve becomes a straight line, $m=2-m'$. The limiting value of m for $m'\to 0$ is given, as a function of x, by

$$m^2=4-\frac{4(1-x)}{x(1+3x)} \qquad \text{for } \frac{1}{3}\leq x\leq 1 \quad \left(\frac{T_N}{3}\leq T\leq T_N\right),$$

$$m=2 \qquad \text{for } 1\leq x \left(T\leq\frac{T_N}{3}\right).$$

In Fig. 13, all curves for $h\leq 3\sqrt{6}/2$ go through a point $m=0$, $m'=2$; at $h=3\sqrt{6}/2$, there are two branches, one of which is a straight line, $m=2-m'$, and the other is a curve bending downwards, both starting from $m=0$, $m'=2$; for $h>3\sqrt{6}/2$, the curve starts at a point $m=2$, $m'=0$, goes down almost along the straight line $m=2-m'$, down to certain point, and then returns in the region enclosed by the two curves for $h=3\sqrt{6}/2$ to a point on the m-axis. In Fig. 13, only the returning part is shown, since the first part is not discriminable from that straight line. At $h=\infty$, the curve becomes a point ($m=2$, $m'=0$).

Looking for the intersecting points of these sets of curves, we obtain the $m\sim h$ relation corresponding to antiferromagnetic solution. In the temperature range $T_N/3\leq T\leq T_N$, there is one antiferromagnetic solution below h_c, at which it coincides with the paramagnetic solution and the transition is of the second kind. As an example, the curve of $m\sim h$ at $T=(2/3)T_N$ is shown in Fig. 14. The transition field h_c is given by

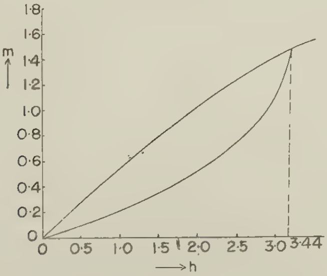

Fig. 14. Magnetization, $m=b-d$, versus applied field along $[10\bar{1}]$ at $T=(2/3)T_N$.

$$\frac{2}{\sqrt{6}}h_c=\left[1-\frac{T(3T-T_N)}{T_N(T+T_N)}\right]^{1/2} +3\frac{T}{T_N}\tanh^{-1}\left[1-\frac{T(3T-T_N)}{T_N(T+T_N)}\right]^{1/2}. \tag{14}$$

When the temperature approaches $T_N/3$, the transition field increases indefinitely. Below $T_N/3$, the antiferromagnetic and paramagnetic solutions do not meet at a finite field strength, so that we have no sharp antiferro-paramagnetic transition.

§ 3. The Case of Infinitely Long Sample

In this section we shall consider the case of an infinitely long sample. The field is assumed as applied parallel to its axis.

If the axis of the sample is parallel to one of the symmetry axes of the crystal, the demagnetizing field is zero. In such a case, the effective field given by Eq. (2) must be corrected as

$$\begin{aligned} H_{J,eff}&=\mu(K+L+M)+H\cos\theta_J \\ &\quad+\frac{4\pi}{3}\left[J-\frac{1}{3}(K+L+M)\right]\times\frac{N}{4} \\ &=\mu[k\{J-(K+L+M)/3\}+(K+L+M)] \\ &\quad+H\cos\theta_J\,, \end{aligned} \tag{15}$$

where $k=\pi N/3\mu=1.71$, if the value of μ given by O'Brien[11] is used. We shall study how the magnetization curve undergoes a change for the present case. Comparing Eq. (15) with Eq. (2), it will be seen that, in the case of $\boldsymbol{H}//[111]$ and $\boldsymbol{H}//[100]$, the correction due to the absence of the demagnetizing field in the present case can be made by altering the scale of the applied fild; namely, one has only to use $h-km$ instead of h for the curves of Fig. 4 and Fig. 10, respectively.

In the case of $\boldsymbol{H}//[111]$, the behavior of the magnetization curve in qualitatively the same as that of Fig. 4. However, in the case of $\boldsymbol{H}//[100]$, for which we have now $\lambda=0.71$ ($\lambda=1/3$ in the spherical case), we are in the region $1/2<\lambda<1$ (see Appendix). Therefore the feature of the transition becomes simpler. Namely, at temperatures below $0.87T_N$ the transition is of the first kind and above $0.87T_N$ it is of the second kind.

§ 4. Magnetization Versus Applied Field at Constant Entropy

At temperatures as low as 0.01°K, experiment at constant temperature may not be practicable. Therefore, we shall calculate the magnetization curve at constant entropy.

In the molecular field approximation, the entropy of system is represented by the sum of the entropy of each spin:

$$\frac{S}{R}=\ln 2-\frac{1}{8}[(1+a)\ln(1+a)+(1-a)\ln(1-a)]$$
$$-\text{similar terms in } b,\ c \text{ and } d, \tag{16}$$

where a, b, c and d are the sublattice magnetizations. We shall consider the case of spherical sample and treat the cases of $\boldsymbol{H}//[111]$ and $\boldsymbol{H}//[100]$, but not the case of $\boldsymbol{H}//[10\bar{1}]$ which requires a more laborious calculation. We look for the intersecting points of curves of constant entropy and curves of constant field, the latter being given in Fig. 2 and Fig. 8.

a) $\boldsymbol{H}//[111]$

Curves of total magnetization, $m=a-b$, at different entropy values are shown in Fig. 15. There are three critical entropy values, $S_1>S_2>S_3$, which are calculated to be $0.52R$, $0.44R$ and $0.17R$, respectively. For $S>S_1$, there are three different solutions, (A), (B) and (C), up to a certain field, but only (A) beyond it. (B) and (C) join smoothly with each other (Fig. 15(1)). At maximum value of entropy, $S=\ln 2$, the loop consisting of (B) and (C) shrinks to nothing and (A) coincides with the abscissa. In the entropy range between S_1 and S_2, (B) and (C) do not join (Fig. 15(2)) and with decreasing entropy from S_1 to S_2, (C) diminishes and finally vanishes at $S=S_2$. Between S_2 and S_3 there are two solutions, (A) and (B), (B) ceasing to exist beyond a certain field (Fig. 15(3)). Below S_3, (A) shows a discontinuity at $h=3$ (Fig. 15(4)). At zero entropy, solution (A) jumps from $m=0$ to $m=2$ at $h=3$ (Fig. 15(5)).

These three solutions correspond to those at constant temperature in Fig. 4. Two of them, (A) and (B), have an equal energy at $h=0$ and (C) has a higher energy. It might be noted that, when S and H are taken as independent variables, differential enthalpy $dH=TdS-MdH$ is to be considered, instead of differential Gibbs free energy $dF=-SdT-MdH$, to treat the thermodynamical equilibrium; thus, for $dS=0$ the state of minimum

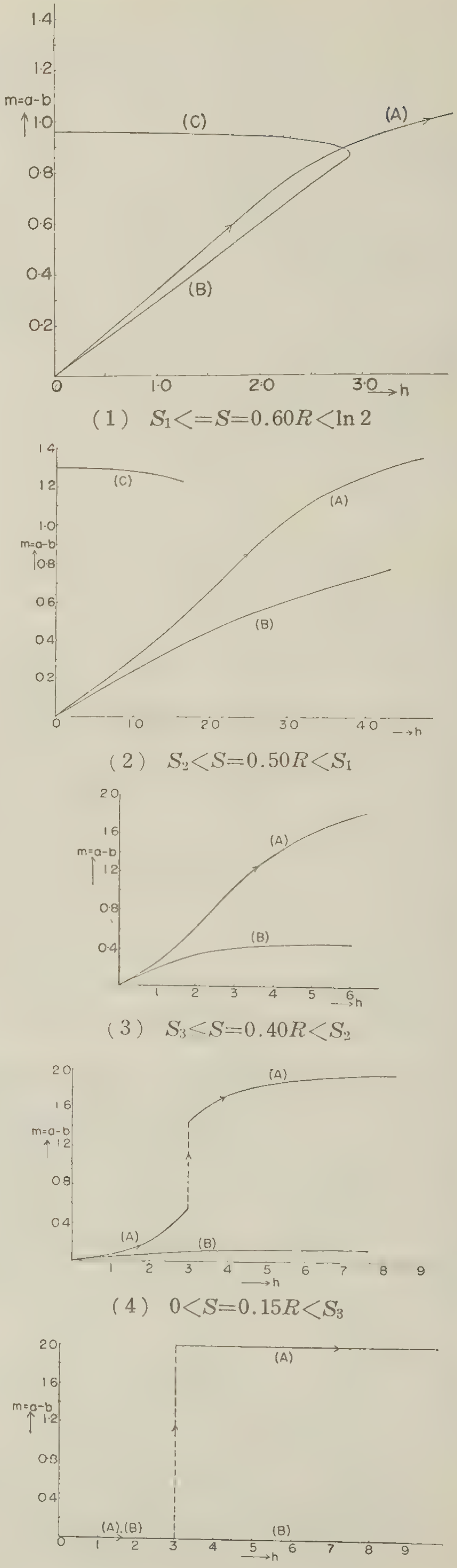

(1) $S_1<=S=0.60R<\ln 2$

(2) $S_2<S=0.50R<S_1$

(3) $S_3<S=0.40R<S_2$

(4) $0<S=0.15R<S_3$

(5) $S=0$

Fig. 15. Magnetization, $m=a-b$, versus applied field along [111] at constant entropy.

magnetization energy $\left(=-\int MdH\right)$ will be realized. So the magnetization will follow the curve (A). The same kind of hysteresis effect as that described in § 2 a) is expected in this case.

b) ***H***//[100]

The intersecting points of curves of constant entropy and curves of constant field give antiferromagnetic solutions ($a \neq -c$) and a paramagnetic solution ($a=-c$). One of these antiferromagnetic solutions coincides with the paramagnetic solution at the critical field h_c given by Eq. (9). For the paramagnetic solution, the magnetization curve at constant entropy is a horizontal line, $a-c=2a=$ constant. The antiferromagnetic solutions behave in the following way.

There are again three critical values of S, $S_1>S_2=0.35R>S_3$. In the entropy range $\ln 2>S>S_1$, there exists only one antiferromagnetic solution below h_c and none above h_c. (At $S=\ln 2$, it disappears.) In the range $S_1>S>S_2$, which is probably very narrow, there exist two or three antiferromagnetic solutions in a certain narrow field range which is below h_c. The magnetization curves for $S=0.60R$ ($>S_1$) and $S=0.35R$ ($=S_2$) are shown in Fig. 16(a).

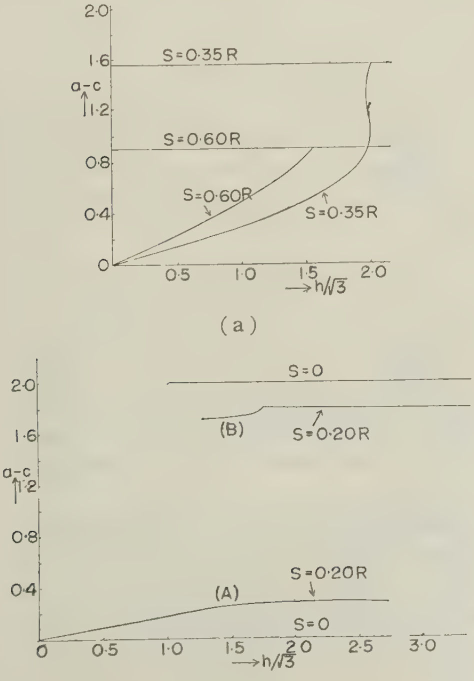

(a)

(b)

Fig. 16. Magnetization, $a-c=(\sqrt{3}/2)m$, versus applied field along [100] at constant entropy.

Below S_2, the magnetization curve separates into two branches. As an example the magnetization curve at $S=0.20R$ is shown in Fig. 16(b); (A) and (B) represent these two branches. The gap between these two curve may have been caused by our use of the molecular field approximation. If we could calculate the entropy to a better approximation, they might have joined smoothly to each other. For $S=0$, curve (A) coincides with the ordinate for $0 \leq h \leq 3$ and curve (B) becomes one point, $a-c=2$, $h=1$, as shown in Fig. 16(b).

The antiferro-paramagnetic transition is of the second kind at entropies above S_1. In a narrow range between S_1 and S_3, we have two transitions. The first transition occurs from an antiferromagnetic state to another antiferromagnetic state and is of the first kind. A further transition occurs from the latter to the paramagnetic state at a higher field and it is of the second kind. At entropies below S_3, antiferro-paramagnetic transition is of the first kind. These features are similar to those at constant temperature.

§ 5. Conclusion

We have calculated the magnetization curve versus external field at constant temperature and at constant entropy to study the nature of the antiferro-paramagnetic transition.

Interesting results obtained are different behaviors of the transition depending on the direction of the applied field.

The results at constant temperature for spherical sample can be summarized as follows:

a) When the field is parallel to [111], the total magnetization follows the curve (A) in Fig. 4; there is no sharp transition. One expects a hysteresis effect that on reversing the field direction the magnetization will follow curve (B) for a while and then jump over to curve (A).

b) When the field is parallel to [100], there is an antiferro-paramagnetic transition. At temperatures above t_1 (t_1 is between 0.360 and 0.467 and close to 0.360), the transition of the second kind, and below t_2 ($0.340<t_2<0.360$) it is of the first kind. In the temperature range between t_1 and t_2, transition occurs twice. The first transition is from an antiferromagnetic state to another antiferromagnetic state and it is of the first kind. The second transition which occurs at a higher field is from the second antiferromagnetic state to the paramagnetic state and is of the second kind.

c) When the external field is parallel to $[10\bar{1}]$, which is perpendicular to two of the four sublattice spin axes, the antiferro-paramagnetic transition is of the second kind and it occurs only at temperatures above $(1/3)T_N$; there is no transition below $(1/3)T_N$.

Very similar results are predicted for the magnetization at constant entropy.

Calculations at constant temperature have also been made for infinitely long sample to which a field is applied parallel to its axis. In this case we have the following results:

a) When the axis is parallel to [111], the magnetization curve is qualitatively the same as that for spherical sample.

b) When the axis is parallel to [100], the antiferro-paramagnetic transition is of the first kind below $0.87T_N$ but it is of the second kind above $0.87T_N$.

We have assumed that the sublattice spins are tightly bounded along the respective trigonal axes of the crystalline fields (the three-fold axes of the crystal). However, at high field, where the Zeeman energy becomes comparable to or larger than the Kramers doublet separation, δ, there will be a thermal excitation to the upper Kramers doublet and the spin direction will be able to deviate from the trigonal axis. In such a case our conclusion has to be modified.

The writer would like to express her sincere thanks to Professor T. Nagamiya for suggesting this problem and for his help and encouragement. She is also indebted to Dr. J. Kanamori for valuable discussion.

Appendix.

Transition from Antiferromagnetic to Paramagnetic State by an Applied Field

We introduce the following effective field acting on each spin of the positive and negative sublattices:

$$H_{eff}^{\pm}=H-AM^{\mp}+\Gamma M^{\pm}, \qquad \text{(A.1)}$$

where H is the external field applied along the easy axis of the spins, $M^{\pm}$ are the sublattice magnetizations (positive when they are parallel to the applied field, negative when antiparallel) and A and Γ are the molecular field coefficients. $M^{\pm}$ are determined by the equations

$$M^{\pm}=\frac{Ng\beta}{2}B_S\left[\frac{Sg\beta}{kT}(H-AM^{\mp}+\Gamma M^{\pm})\right], \qquad \text{(A.2)}$$

where N is the total number of spins, S the magnitude of each spin and B_S the Brillouin function. The Néel temperature, T_N, is given by

$$T_N=\frac{C}{2}(A+\Gamma)$$

where

$$C=Ng^2\beta^2S(S+1)/3k\,.$$

Using the reduced quantities,

$$M^{\pm}\Big/\frac{N}{2}g\beta S=\sigma^{\pm}\,,$$

$$\frac{T}{T_N}=t\,,$$

$$H\Big/(A+\Gamma)\frac{N}{2}g\beta S=h\,,$$

(A.2) is written

$$\sigma^{\pm}=B_S\left[\frac{3S}{S+1}\frac{h-(1-\lambda)\sigma^{\mp}+\lambda\sigma^{\pm}}{t}\right], \qquad \text{(A.3)}$$

where

$$\lambda=\frac{\Gamma}{A+\Gamma}\,.$$

A is assumed to be positive, Γ either positive or negative and $A+\Gamma>0$, as otherwise the stability of the two-sublattice antiferromagnetism will be invalidated. Therefore $1>\lambda>-\infty$.

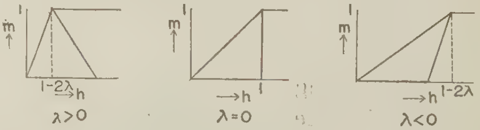

Fig. A1. Magnetization, m, versus applied field at 0°K in the cases of $\lambda>0$, $\lambda=0$ and $\lambda<0$.

At absolute zero, the relation between the external field and the total magnetization, $m=(\sigma^{+}+\sigma^{-})/2$, is as shown in Fig. A.1. In the case of $\lambda\leq0$, the antiferromagnetic state continues up to $h=1$, then a ferromagnetic state starts and at $h=1-2\lambda$ the ferromagnetic state is realized. In the case of $\lambda>0$, the ferromagnetic state is unstable and at $h=1-\lambda$ a transition of the first kind occurs from the antiferromagnetic state to the ferromagnetic state.

To investigate the transition at the arbitrary temperature, we shall confine ourselves to the case of $S=1/2$. Perhaps we may expect similar results for any value of S. For $S=1/2$, Eq. (A.3) reduces to

$$\sigma^{\pm}=\tanh\left[\frac{h-(1-\lambda)\sigma^{\mp}+\lambda\sigma^{\pm}}{t}\right]. \qquad \text{(A.4)}$$

If we use $m=(\sigma^{+}+\sigma^{-})/2$ and $m'=(\sigma^{+}-\sigma^{-})/2$ instead of σ^{+} and σ^{-}, Eqs. (A.4) become

$$m^2=1-2m'\coth(2m'/t)+m'^2, \qquad \text{(A.5)}$$

$$h=\frac{t}{2}\tanh^{-1}\left[\frac{\{1-2m'\coth(2m'/t)+m'^2\}^{1/2}}{1-m'\coth(2m'/t)}\right] +(1-2\lambda)\{1-2m'\coth(2m'/t)+m'^2\}^{1/2}. \qquad \text{(A.6)}$$

It can be shown that m is a monotonously decreasing function of $|m'|$ in the allowable range of m', $-\sigma_0<m'<\sigma_0$ (σ_0 represents the magnitude of σ^{+} and σ^{-} of the antiferromagnetic state at $h=0$). The $h\sim m'$ curve representing the antiferromagnetic solution will appear in three types as shown in Fig. A.2, corresponding to different values of t and λ. At the field h_c, which corresponds to $m'=0$, the antiferromagnetic solution joins the paramagnetic solution, which is the vertical line passing through $m'=0$. In order to examine the ranges of λ and t which give rise to these three types, we calculate dh/dm' and expand it in the neighbourhood of $m'=0$. Using another variable $y=2m'/t$, we have

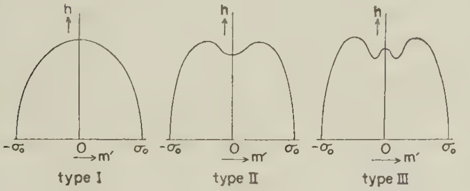

type I type II type III

Fig. A2. Three types of h vs. m' curve.

$$\frac{dh}{dy}=\frac{t}{2\{1-ty\coth y+(ty/2)^2\}^{1/2}}\left[\lambda\left(\frac{4}{3}-\frac{1}{3\lambda}-t\right)y +\frac{1}{15}\left(1-\frac{8}{3}\lambda\right)y^3 +\frac{2}{63}\left(-\frac{1}{3}+\frac{4}{5}\lambda\right)y^5+\cdots\right]. \qquad \text{(A.7)}$$

If the coefficient of the linear term of y, $\lambda(4/3-1/3\lambda-t)$, is positive, the $h\sim m'$ curve is of type II, and if it is negative, the curve is either of type I or of type III. The temperature at which the transition from type II to type I or III occurs is determined by $4/3-1/3\lambda-t=0$, i.e., $t=4/3-1/3\lambda$. This t is greater than 1 (higher than the Néel temperature) if $\lambda<0$, in which case we have no finite value of σ_0 and thus Eq. (A.7) has no meaning. In this case, one sublattice magnetization increases and the other decreases monotonically with increasing field below the Néel temperature, as $\Gamma<0$ and $A>-\Gamma$, and we have a $h\sim m'$ curve of type I; thus, a transition of the second kind occurs at $h=h_c$. If $1/4<\lambda<1$, $t=4/3-1/3\lambda$ lies between 0 and 1, and a transition between type II and type I or III occurs below the Néel temperature. We further distinguish between two cases, $1/4<\lambda<3/8$ and $3/8<\lambda<1$, the former corresponding to the positive coefficient of y^3 in Eq. (A.7) and the latter to the negative coefficient. Furtheremore, if $0<\lambda<1/4$, the $h\sim m'$ curve is always of type I or III because the coefficient of y in Eq. (A.7) is negative. We shall investigate these cases separately.

1) $1/2<\lambda<1$

This case is the same as the next case ($3/8\leq\lambda\leq1/2$) except for the existence of a ferromagnetic solution. However, the ferromagnetic Curie point at $h=0$ is $2\lambda-1$ and is lower than the transition point from type II to type I or III, therefore the ferromagnetic solution will not be realized.

2) $3/8\leq\lambda\leq1/2$

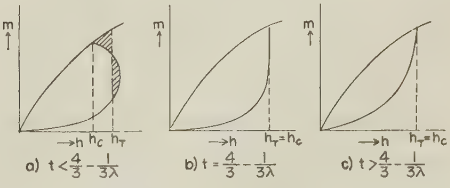

a) $t<\frac{4}{3}-\frac{1}{3\lambda}$ b) $t=\frac{4}{3}-\frac{1}{3\lambda}$ c) $t>\frac{4}{3}-\frac{1}{3\lambda}$

Fig. A3. Magnetization versus external field for the case of $3/8<\lambda<1/2$. h_T represents the transition field from antiferromagnetic state to paramagnetic state.

At a temperature $t=4/3-1/3\lambda$, the top of the $h\sim y$ curve is flat and, since the coefficient of y^3 in (A.7) is negative, the curve looks like type I but it is flat at the top. Above this temperature, the curve is of type I, which diminishes to a point as t approaches 1. Below this temperature, the curve must be of type II. Since m is a decreasing function of

m' or y, as mentioned before, the relation between m and h must be as shown by Fig. A.3 in this temperature range; an antiferro-paramagnetic transition of the first kind must occur at a certain field at which the area of the shaded portions of the curve become equal. In the higher temperature region the transition is naturally of the second kind.

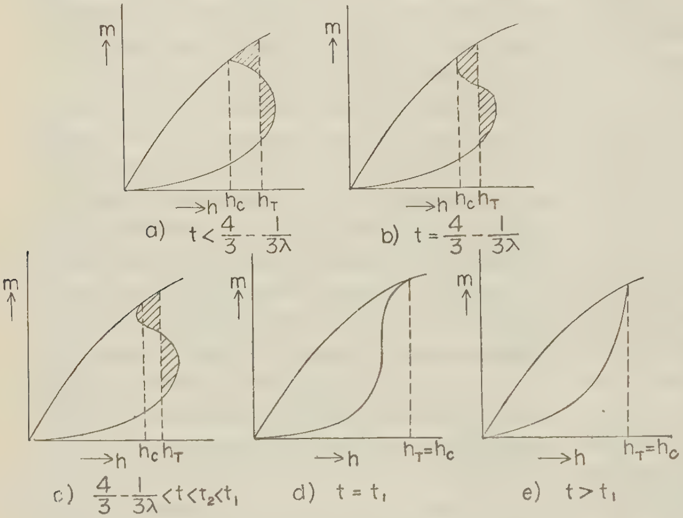

a) $t<\frac{4}{3}-\frac{1}{3\lambda}$ b) $t=\frac{4}{3}-\frac{1}{3\lambda}$

c) $\frac{4}{3}-\frac{1}{3\lambda}<t<t_2<t_1$ d) $t=t_1$ e) $t>t_1$

Fig. A4. Magnetization versus external field for the case of $1/4<\lambda<3/8$.

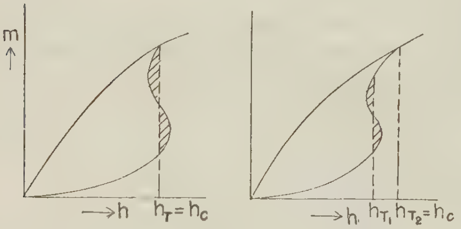

Fig. A5. Magnetization versus external field for the case of $1/4<\lambda<3/8$.

3) $1/4<\lambda<3/8$

Since the coefficient of y^3 in Eq. (A.7) is positive in this case, the curve of h versus y at $t=4/3-1/3\lambda$ looks like type II but it is flat at the bottom of the concave part. For $t<4/3-1/3\lambda$, the carve first changes to type III and then to type I with increasing temperature. The temperature at which the curve changes from type III to type I will be denoted by t_1. The change of the $m\sim h$ curve with varying temperature is shown in Fig. A.4. Just below t_1, a transition of this first kind from an antiferromagnetic state to another antiferromagnetic state must occur, as shown in the second figure of Fig. A.5, at a field which is lower than the field of the antiferro-paramagnetic transition. The latter is of the second kind. The first figure of Fig. A.5 represents the transition at another temperature, t_2, at which the character of the antiferro-paramagnetic transition changes from the first kind to the second kind. A double transition occurs in the range $t_2<t<t_1$. An example of determing these temperatures, t_1 and t_2, is given in the text.

4) $0<\lambda\leq1/4$

In this case the coefficient of y in Eq. (A.7) is always negative and so the curve $h\sim y$ is of type I or type III. However, considering the behaviour of the curve at absolute zero, the curve must be of type III at sufficiently low temperatures. There exists a temperature, t_1, at which change from type III to type I occurs, and also t_2, as in the previous case (see Fig. A.5).

5) $\lambda\leq0$

In this case m is a monotonously increasing function of h, as mentioned before, and the antiferro-paramagnetic transition is always of the second kind. The transition field is that given by Garrett.[13)]

References

1) De Klerk and R. P. Hudson: Phys. Rev. **91** (1953) 278.
2) J. M. Daniels and N. Kurti: Proc. Roy. Soc. A, **221** (1954) 243.
3) W. E. Gardner and N. Kurti: Proc. Roy. Soc. A, **223** (1954) 543.
4) R. P. Hudson and C. M. Mclane: Phys. Rev. **95** (1954) 932.
5) E. Ambler and R. P. Hudson: Phys. Rev. **96** (1954) 907.
6) J. A. Beun, J. M. Steenland, D. De Klerk and C. J. Gorter: Physica **21** (1955) 767.
7) J. A. Beun, A. R. Miedema and J. M. Steenland: Physica **23** (1957) 1.
8) C. W. Dempesy and R. C. Sapp: Phys. Rev. **110** (1958) 332.
9) J. H. Van Vleck: J. Chem. Phys. **5** (1937) 320.
10) M. H. Hebb and E. M. Purcell: J. Chem. Phys. **5** (1937) 338.
11) C. M. O'Brien: Phys. Rev. **104** (1956) 1573.

12) B. Bleaney: Proc. Roy. Soc. A, **204** (1950) 213.
13) C. G. B. Garrett: J. Chem. Phys. **19** (1951) 1154.
14) J. Kanamori, K. Motizuki and K. Yosida: Buseiron-Kenkyu **63** (1953) 28 (in Japanese).
15) C. J. Gorter and Van Peski-Tinbergen: Physica **22** (1956) 273.

JOURNAL OF THE PHYSICAL SOCIETY OF JAPAN, Vol. 14, No. 6, JUNE, 1959

Crystal Structure of 2-Amino Azulene

By Yoshito TAKAKI, Yoshio SASADA and Isamu NITTA

Faculty of Science, Osaka University

(Received February 26, 1959)

A systematization was proposed for the determination of the crystal structure when the crystal consists of the molecules with known shape. The main feature of this method is to separate the refinements by the least squares at an early stage into (1) successive improvements of the position and orientation of the molecule and (2) correction of the molecular shape fixing the molecular position and orientation.

The result of the application of this method to the crystal of 2-amino azulene (a=11.62, b=10.76, c=6.32 Å, Z=4, space group $Pbn2_1$) was given.

§1. Introduction

While several systematic procedures, such as Fourier methods, have been used for the refinements of structure in the X-ray crystal analysis, there remains unsolved an important problem, how to obtain systematically the approximate parameters as the starting point of the refinement. If, for example, a molecule without centre of symmetry contains light atoms only, it is often difficult to obtain satisfactory results by the so-called direct methods proposed heretofore. Such being the case, instead of applying these methods, the authors have attempted to use fully the information given by the intensity data for individual reflexions as well as known molecular shape.

The present account will describe a systematization of the method of this kind, applied to the crystal of 2-amino azulene which was taken up as a part of the serial investigations of crystal structures of the compounds containing planar seven-memberd carbon rings1)−7).

§2. Experimental

Crystals are obtained as very fine reddish violet needles elongated along the direction of the c axis.

Crystallographic and physical data are obtained as follows.

2-Amino azulene; $C_{10}H_9N$, m.p. 93–94°C.
Orthorhombic; $a=11.62\pm0.04$, $b=10.76\pm0.04$, $c=6.32\pm0.03$Å.
Absent spectra; $(0kl)$ when k is odd, $(h0l)$ when $h+l$ is odd.
Space group; $Pbn2_1-C_{2v}^9$.
Four molecules per unit cell.
Volume of unit cell; 790.2Å^3.
Density (by floatation); 1.20 g.cm^{-3}.
Density (calculated); 1.20 g.cm^{-3}.
Linear absorption coefficient for CuK_α radiation, μ=6.5 cm^{-1}.
Total number of electrons per unit cell, $F(000)=304$.

For the structure analysis, a complete set of relative intensities for $(hk0)$, $(hk1)$, $(hk2)$ and $(hk3)$ were obtained by the integrated Weissenberg procedure. The specimen used has the following maximum and minimum dimensions at right angle to the axis of rotation: 0.01×0.006 cm.

Intensities were estimated by visual comparison with a calibrated scale. The multiple-film technique was used to correlate strong and weak reflexions, ranging in relative intensities from 5100 to 1. Reflexions from only 96 planes were observed out of 163 possible $(kh0)$'s. The corrections for polarization and Lorentz factors were made in the usual way, and that of absorption was neglected.

§ 3. Structure Determination of (001) Projection

Analysis was made in the following sequence:

a) The molecule of 2-amino azulene was assumed to possess the dimensions as shown in Fig. 1.

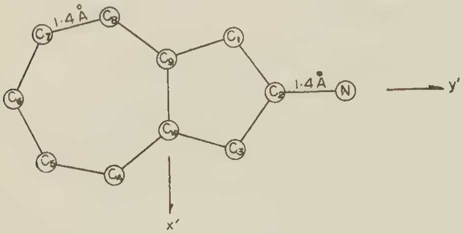

Fig. 1. Assumed model of the molecule.

b) The approximate position and orientation of the molecule were chosen by using the structure factor maps[4].

c) At such stage, the application of the ordinary least squares, sometimes leads to false structures (see Appendix). In order to avoid such confusions, the authors allowed for the shape of the molecule as the limiting conditions in the application of this method.

Let

(x_i, y_i, z_i) the coordinates of the i-th atom in the molecule with respect to the crystal axes a, b and c,

$(x_i', y_i', 0)$ the coordinates of the same atom with respect to the molecular axes as shown in Fig. 1,

$(p, q, 0)$ the coordinates of the origin of the molecular axes in the (001) projection,

$(\lambda_1, \mu_1, \nu_1)$, $(\lambda_2, \mu_2, \nu_2)$, $(\lambda_3, \mu_3, \nu_3)$ the direction cosines of the molecular axes x', y' and z' with respect to the crystal axes a, b and c respectively,

Δx_i, Δy_i, Δp, Δq corrections,

F_0, F_c observed and calculated structure factors,

w weight.

From simple consideration of the analytical geometry,

$$\left.\begin{aligned} x_i &= x_i'\lambda_1 + y_i'\lambda_2 + p \\ y_i &= x_i'\mu_1 + y_i'\mu_2 + q \end{aligned}\right\} . \tag{1}$$

Then

$$\left.\begin{aligned} \Delta x_i &= x_i'\Delta\lambda_1 + y_i'\Delta\lambda_2 + \Delta p \\ \Delta y_i &= x_i'\Delta\mu_1 + y_i'\Delta\mu_2 + \Delta q \end{aligned}\right\} . \tag{2}$$

If $F = \sum_i F_i(x_i, y_i)$, where the summation is taken over all the atoms in the cell, each structure factor gives observational equation,

$$\begin{aligned} w\Delta F = w \sum_i \{&(\partial F/\partial x_i)(x_i'\Delta\lambda_1 + y_i'\Delta\lambda_2 + \Delta p) \\ &+ (\partial F/\partial y_i)(x_i'\Delta\mu_1 + y_i'\Delta\mu_2 + \Delta q)\} . \end{aligned} \tag{3}$$

To find the most probable values, usual procedures of the least squares are applied.

d) After several successive applications of the above-mentioned method, there remain some comparatively large discrepancies between observed and calculated structure factors, even for the reflexions with lower order indices, although the values of the corrections decrease with advancing refinement processes. This is mainly due to the insufficiency of the parameters contained in the assumed model.

In the following step of refinement, the authors tried to shift each atom in the molecule, so as to keep the molecular symmetry of C_{2v} with all the atoms except the nitrogen. From equation (1), it follows

$$\left.\begin{aligned} \Delta x_i &= \lambda_1\Delta x_i' + \lambda_2\Delta y_i' + \Delta p \\ \Delta y_i &= \mu_1\Delta x_i' + \mu_2\Delta y_i' + \Delta q \end{aligned}\right\} . \tag{4}$$

Then the observational equation is written as

$$\begin{aligned} w\Delta F = w\sum_i \, [&\{(\partial F/\partial x_i)\lambda_1 + (\partial F/\partial y_i)\mu_1\}\Delta x_i' \\ &+ \{(\partial F/\partial x_i)\lambda_2 + (\partial F/\partial y_i)\mu_2\}\Delta y_i' \\ &+ (\partial F/\partial x_i)\Delta p + (\partial F/\partial y_i)\Delta q] \end{aligned} \tag{5}$$

where there are thirteen independent parameters and $\sum_i$ means the summation over all these independent parameters. These parameters were corrected by the successive three least squares processes. Discrepancy index, $R = \sum||F_0| - |F_c||/\sum|F_0|$, decreased by about 0.1. Agreement between the observed and calculated structure factors showed remarkable improvement, especially for some reflexions with relatively lower indices.

e) Finally, the coordinates obtained in this way were refined by means of least squares without keeping the symmetry C_{2v} among atoms in the molecule.

In the application of the least squares, the authors have experienced difficulties due to the effect that the higher order reflexions decreased rapidly owing to large temperature factor.

The magnitudes of the coefficients in the observational equation are proportional to $hf \cdot \exp(-B\xi^2/4\lambda^2)$ if $\sin 2\pi(hx_i+ky_i)$ is assumed to be constant. As the maximum h for a given ξ is $a\xi/\lambda$, they can be considered to be proportional to $\xi f \cdot \exp(-B\xi^2/4\lambda^2)$, as shown in Fig. 2 for several B. In the present case, magnitudes of coefficients corresponded to those shown by the lowest curve in Fig. 2, and the effect from the reflexions with larger ξ than 1.0 were very small. In order to accelerate convergence, $\exp(+0.7\xi^2)$ was taken as the weight in the least squares. Using this value, the coefficients in the observational equation were adjusted to be of almost equal magnitudes in the range of higher angle than $\xi=0.5$. By this means, it was possible to obtain the satisfactory solution which gave fair agreement between observed and calculated structure factors over all the range of ξ.

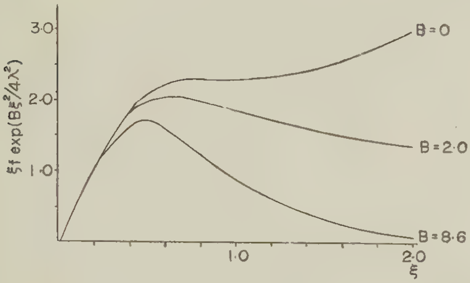

Fig. 2. Variation of magnitudes of the coefficients in the observational equation with ξ.

The final discrepancy index became 0.18

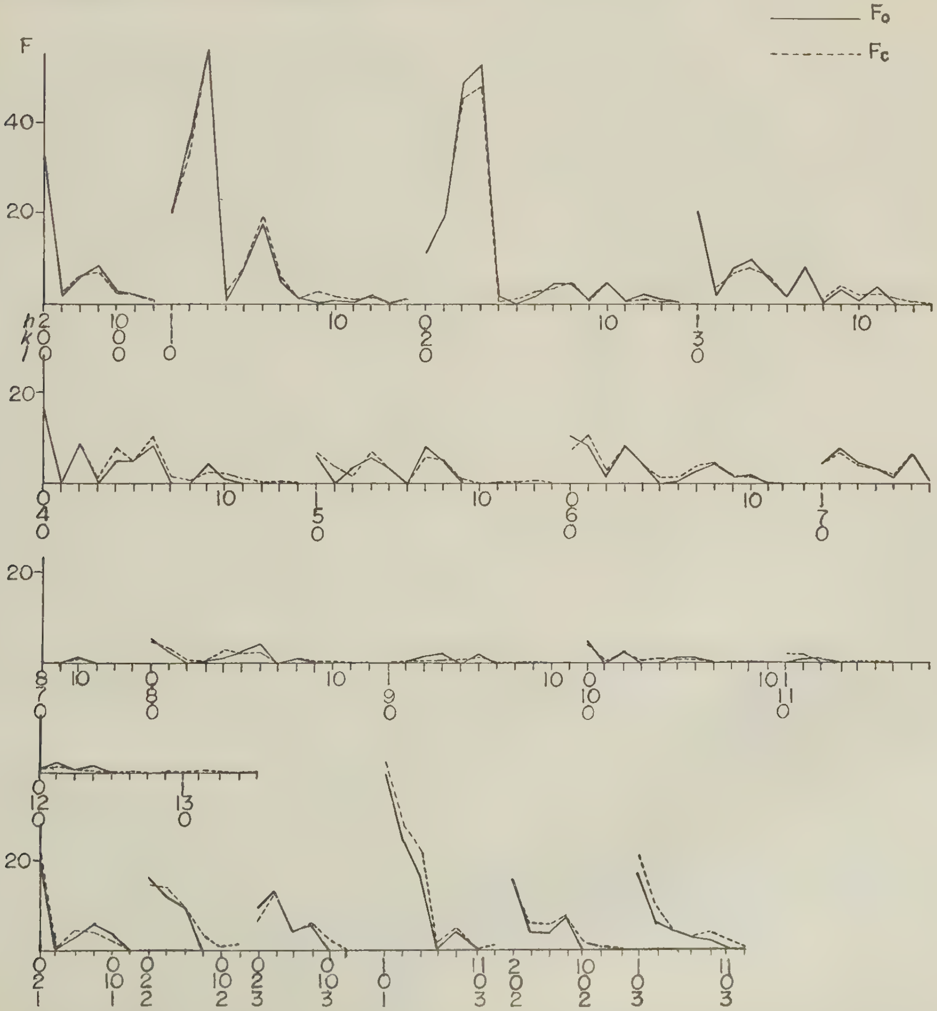

Fig. 3. Observed and calculated structure factors for $(hk0)$, $(0kl)$ and $(h0l)$.

Table I. Atomic coordinates.

Atom	x/a	y/b	z/c
N	0.226	0.615	0.010
C_1	0.092	0.442	0.000
C_2	0.180	0.507	0.093
C_3	0.201	0.452	0.285
C_4	0.133	0.271	0.503
C_5	0.058	0.169	0.528
C_6	−0.030	0.116	0.409
C_7	−0.064	0.161	0.212
C_8	−0.028	0.259	0.086
C_9	0.059	0.345	0.132
C_{10}	0.134	0.348	0.328

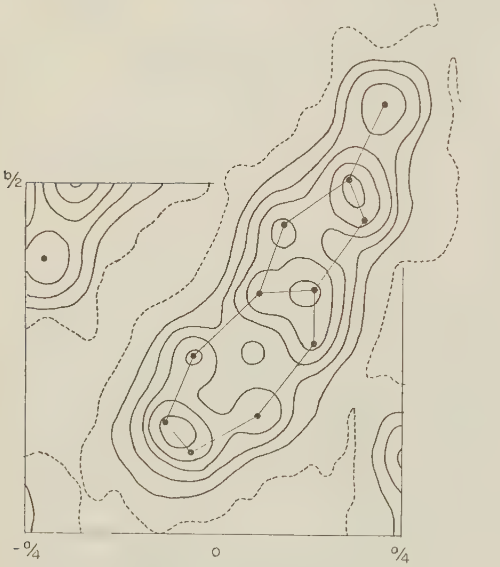

Fig. 4. The final electron-density projection along the c axis. Contours at intervals of 1 $e\text{Å}^{-2}$ with the lowest solid contour at 2 $e\text{Å}^{-2}$. The broken one shows 1 $e\text{Å}^{-2}$ level.

($R=0.13$ if non-observed reflexions were omitted in the calculation). Throughout these calculations, the atomic scattering factors were taken from McWeeny[8], using for carbon the values for 'valence states'. The best B factor was 8.6. In Table I are listed the final atomic coordinates. Fig. 3 shows the comparison between observed and calculated structure factors $F(hk0)$ and Fig. 4 the final Fourier projection of the electron density on the (001) plane.

§ 4. Determination of z Coordinates

Structure factors $F(0kl)$ and $F(h0l)$ were taken from the equi-inclination Weissenberg photographs about the c axis for the first, second and third layer lines. As the accuracy of intensity measurements is rather low and moreover the data is small in number, ordinary procedure of the analysis could not be applied. Therefore, approximate z coordinates were first estimated on the basis of x and y coordinates already obtained and the assumed planarity of the molecule. It is noted that any one of the atoms can take its z value equal to zero as the c axis is polar. Ten parameters were refined by the trial method. The final values are also listed in Table I and the comparison between observed and calculated structure factors $F(0kl)$ and $F(h0l)$ is shown in Fig. 3.

§ 5. Description of the Structure and Conclusion

Crystal structure projected on the (001) plane is shown in Fig. 5. Intra-molecular distances are between 1.37 and 1.41Å except C_9–C_{10} for which a value of 1.52Å is found. Intermolecular distances in contact with each other are between 3.6 and 4.0Å. It may be concluded that the crystal is formed mainly by van der Waals forces, and the crystal structure as a whole can be taken as one somewhat modified from the structure of naphthalene[9]. This is probably due to the similar shape and small dipole moment of this substance (2.09 D[10]). Recently it becomes clear[11] that, although azulene (an isomer of naphthalene) belongs to the same space group as that of naphthalene, a simple random reversal of direction of successive azulene molecules was observed in the crystal. It is interesting to note that, while the orientation of azulene molecules (with smaller dipole moment (1.0 D)) is random, the present structure shows the regular reversal of direction of successive molecules.

In conclusion, the authors wish to make some comments for the method described in this paper. At the present stage of development of the phase problem, it is necessary to use fully and systematically the definitely known physical and chemical evidences, in order to solve the structure of a crystal with minimum efforts. The process mentioned above, which is an attempt of this kind, consists of two parts, that is, the first is the

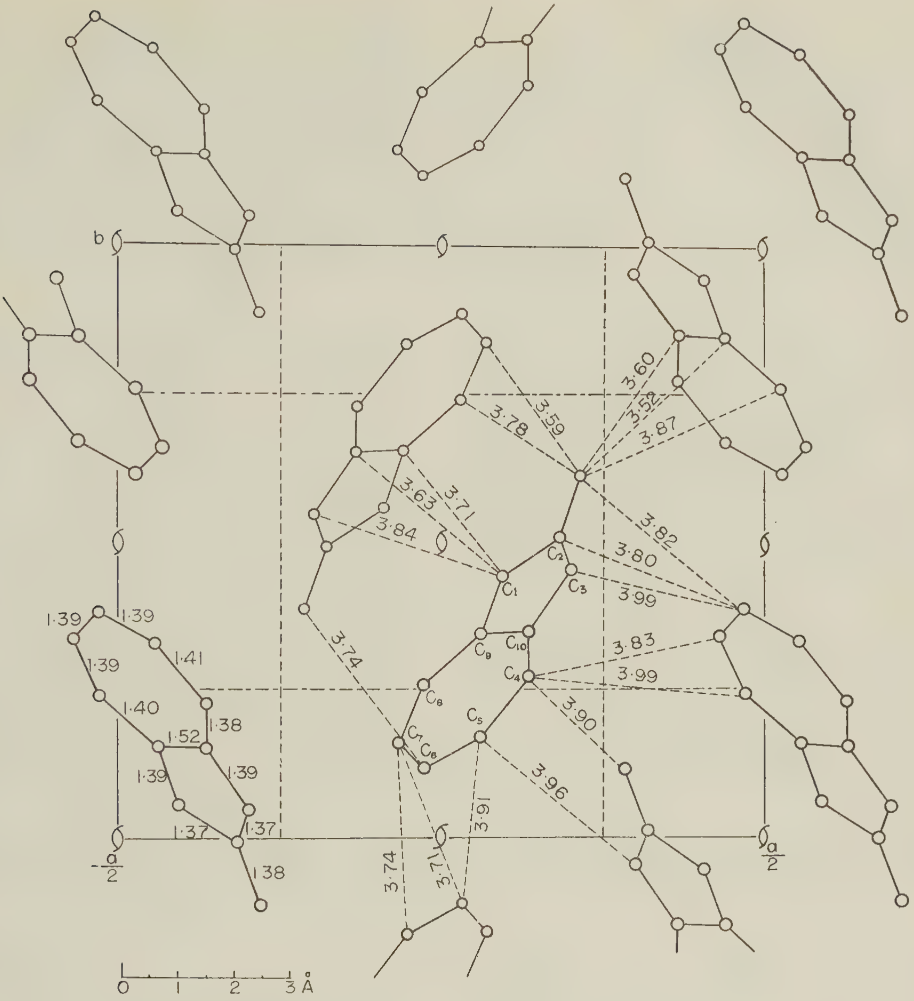

Fig. 5. Arrangement of molecules in the (001) projection.

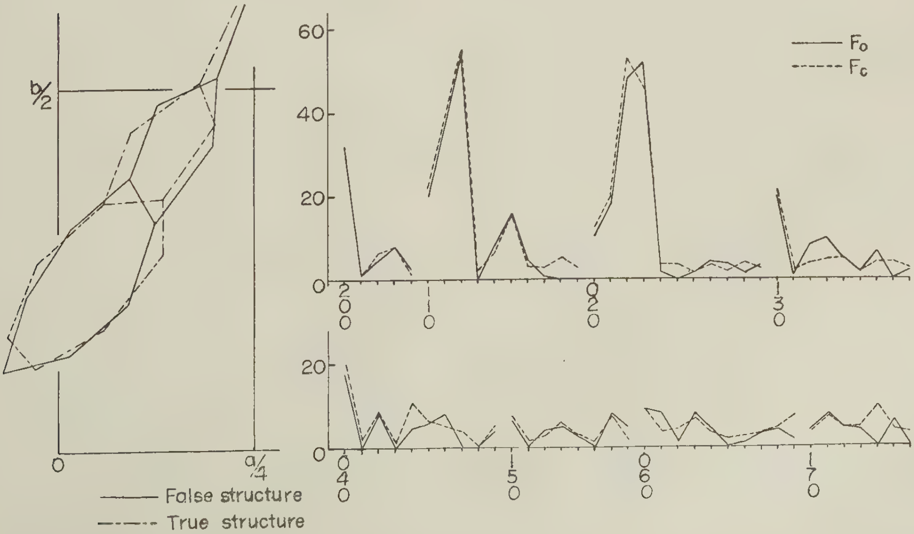

Fig. 6. Observed and calculated structure factors $F(hk0)$ calculated for the false structure (a part).

determination of approximate position and orientation of the molecule using the structure factor map and the second is the improvement by the least squares with the limiting conditions. It is possible in many cases to limit allowable sets of molecular positions and orientations severely enough to apply the second process, as far as the molecule is not of too large magnitude. On the other hand, we can avoid by the second process any false structures which often appear in routine applications of the least squares and lead the structure which is sufficiently enough to achieve further refinement by the orthodox procedure. The authors think that the procedure described in this paper is simple and practical, even for the cases with molecules having no centre of symmetry provided that their molecular shapes are roughly known.

The authors wish to express their sincere thanks to Professor T. Nozoe for supplying the sample and for continued interest. The authors are also indebted to Professor T. Watanabé for kind discussion of the results of this investigation.

Appendix. Example of False Structure

The authors drew attention elsewhere about the fact that the routine application of any systematic processes sometimes leads to false structures. An example of the false structures which was derived starting from a crude structure by the least squares without consideration of molecular shape is shown in Fig. 6 in the form of comparison between observed and calculated structure factors with corresponding false molecular position.

References

1) Y. Sasada and I. Nitta: Acta Cryst. **9** (1956) 205.
2) Y. Sasada and I. Nitta: Bull. Chem. Soc. Japan **30** (1957) 62.
3) Y. Sasada, K. Osaki and I. Nitta: Acta Cryst. **7** (1954) 113.
4) Y. Sasada: Bull. Chem. Soc. Japan **32** (1959) 165.
5) Y. Sasada: Bull. Chem. Soc. Japan **32** (1959) 171.
6) C. Tamura, Y. Sasada and I. Nitta: Bull. Chem. Soc. Japan **32** (1959) 458.
7) K. Furukawa, Y. Sasada and T. Watanabé: to be published.
8) R. McWeeny: Acta Cryst. **4** (1951) 513.
5) S. C. Abrahams, J. M. Robertson and J. G. White: Acta Cryst. **2** (1949) 238.
10) Y. Kurita and M. Kubo: to be published.
11) J. M. Robertson, H. M. M. Shearer, G. A. Sim and D. G. Watson: Nature **182** (1958) 177.

JOURNAL OF THE PHYSICAL SOCIETY OF JAPAN, Vol. 14, No. 6, JUNE, 1959

Study of Segmental Motion in Polymer Solutions by Nuclear Magnetic Resonance

By Akira ODAJIMA

Research Institute of Applied Electricity,
Hokkaido University Sapporo

(Received March 4, 1959)

Experimental and theoretical considerations of segmental motion in chain molecules were studied from the view point of nuclear mognetic resonance.

By using the high resolution type spectrometer of NMR, it was verified that the line widths of phenyl group and CH_2 group in polystyrene-CCl_4 solutions were almost all independent of chain lengths in dilute solutions. These values of line widths indicate that the so-called segmental motion in a chain is performed in the unit of about ten monomers.

The segmental motion hindered by the potential field was discussed by using the generalized theory of Brownian motion. The influences of restricted motion upon T_1 and T_2 in polyisobutylene-CCl_4 solution are examined. The results of our theory are as follows. The activation energy of segmental motion tends to the activation energy of solvent when the concentration of polymer decreases. The value of activation energy increases with the increase of concentration of polymer. These results are in a good agreement with these of mechanical and dielectric measurements. Furthermore, the values of hindering potential are calculated from the data of T_1 and T_2 in PIB solutions.

Finally, it is verified that the rigidity of polymer solution in the high frequency measurement should be caused by the potential field hindering the micro-Brownian motion of segment.

§1. Introduction

The development of experimental methods[1),2)] of observing nuclear magnetic resonance (NMR) has brought a renewed interest in the theory of high polymer solutions. Although only a few experiments have been reported, they have revealed a posibility of certain connections between the motions indicated by NMR and the mechanical and dielectric properties of high polymer solutions.

Hitherto, theoretical treatments of the motion of chain molecules have been introduced by Kirkwood et al[3)] and by Rouse[4)] and Bueche[5)]. In the Kirkwood theory, it is assumed that the bond lengths and the bond angles of each polymer molecule are constant, but that the azimuth angles are free to rotate. Thus, they introduced the coordinates describing the configuration of a molecule, and gave the equation of diffusion in the multidimensional space defined by these coordinates. On the other hand, more simplified theories by Rouse and Bueche assume that a polymer molecule is divided into a number of submolecules whose end-to-end distance shows the Gaussian distribution. That is to say, it is assumed that the molecules are replaced by a number of beads of submolecules linked by Hookean springs, and a frictional constant ζ of the bead is taken into consideration.

In NMR measurements, the micro-motions of individual group in the chain molecules are observed in detail. In this meaning, the models proposed by Rouse and Bueche may not be suitable, unless they are modified with some devices.

On the contrary, the rigorous method of Kirkwood seems to be helpful to apply to the NMR theory concerning to the internal motions of polymer solutions. Recently, Miyake[6)] developed a theory based on the statistical mechanical theory of irreversible processes given by Kirkwood[7)]. However, a great difficulty[8)] has been pointed out in the derivation of an actual distribution of correlation times of segmental motions from the Kirkwood equation[3].

Moreover, the experimental results[9] in dielectric dispersion in the polar polymer solutions were in disagreement with the Kirkwood theory[3]. According to this theory[3], the average relaxation time $\bar{\tau}_D$ is proportional to α power of the degree of polymerization. In Gaussian chain $\alpha=1/2$, but α may be larger than 1/2 as a result of the excluded volume effect. However, the experimental data[9] showed that $\bar{\tau}_D$ did not change systematically with the molecular weight, and its observed variation was less rapid than the one predicted by the theory in the dilute concentrations.

In the Kirkwood theory[3] hydrodynamic interactions between the segment in molecules are considered, but no interactions between polymer molecules are included. Therefore, the predicted dependence should be applied in the case of very dilute solutions.

It is worth while to study by NMR method whether the spin-lattice relaxation time T_1 and the spin-spin relaxation time T_2 in the polymer solution also depend upon the molecular weight or not. According to our measurements and the one by Nolle[2], T_2 is independent of the degree of polymerization, in the dilute range. In the concentrated region of the solutions, T_2 seems to be dependent upon the degree of polymerization. However, in such a concentrated region, the Kirkwood theory is rather inapplicable and the molecular weight dependency of T_2 should be explained by a different mechanism*.

Further, Nolle[10] has recently made a detailed measurement of T_1 and T_2 in polyisobutylene (PIB)–CCl_4 solutions by means of the spin-echo transient method, which is not yet published**. Herein, the present author finds interesting problems in the T_1 and T_2 behaviors concerning to the temperature and concentration as well as the molecular weights.

In the aspect of theoretical study, on the other hand, a great progress has been achieved in the magnetic resonance absorption since the BPP theory[11] was proposed. Kubo-Tomita[12] presented a theory which treated the motion of spins by a quantum-statistical method based on the linear theory of irreversible process. Another theories essentially similar to this were also presented by Solomon[13] and Red-field[14].

Strictly speaking, however, these theories do not take sufficiently the complicated motions of segments in polymer systems into consideration. Therefore they may not be suitable to explain the mechanisms of T_1 and T_2 in polymer solutions. In this paper, the author will deal with the relaxation problem of NMR in polymer solutions on the basis of new theoretical approach concerning to the Brownian motion of segments in chain molecules.

§ 2. Experimental Results

I. *NMR methods*

When the molecular motion becomes rapid and its correlation time is small, a high homogeneity of the magnetic field is required for the measurement of the line width of absorption line. Accordingly, few attempt[1] has been made to obtain the absorption lines in polymer solutions.

By employing a high resolution magnet of Varian Association Spectrometer***, measurements of absorption line of polystyrene (PS) and polyisobutylene (PIB) in solutions were undertaken. In order to obtain their high resolution spectra, it is necessary to select a solvent without containing a proton. This requirement was satisfied by using CCl_4 and CS_2 as the solvent.

Samples were placed in 5 mm O.D. glass tube. The portion of the magnetic field occupied by the samples was found to be uniform within about 2 c/s or about 0.5 milligauss. All measurements were carried out at room temperature.

---

* The experimental result that the motional narrowing of line width is related with the molecular weight was found in polystyrene, solid polymer, by Guth et al. (L. V. Holroyd, R. S. Codrington, B. A. Mrowca, and E. Guth: J. Appl. Phys. **12** (1951) 696). As well known in the thermal properties of solid polymer, owning to the fact that the free volume for segmental motion is related with molecular weight, the line width transition temperature of polystyrene may depend upon molecular weight. So, this dependency should be caused by a mechanism different from the one in the Kirkwood theory.

** A copy of Nolle's paper unpublished was privately sent through Mr. Sohma who was now at Department of Physics, University of Maryland.

*** Measurements were carried out at the Chemical Research Institute of Non-Aqueous Solutions, Tohoku University.

II. *Effects of molecular weight and concentration on T_1 and T_2*

The proton spectra of PS and PIB solutions are shown in Fig. 1. The multiple structures of these lines are in accord with the chemical shifts predicted from the structures of $(-CH\cdot C\cdot(C_6H_5)\cdot CH_2-)_n$ and $(-C\cdot(CH_3)_2\cdot CH_2-)_n$, respectively.

In four samples of fractionized PS used in the measurements*, the half widths of their each groups are obtained over the concentration range of 2.7 g/100 cc to 11 g/100 cc, as shown in Table I.

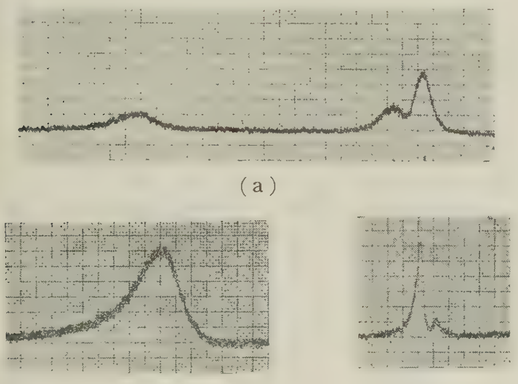
(a)

(b) (c)

(a) PS (d.p.$=1.1\times10^3$)-CCl_4 solution (6.5 g/10 cc). Reading from left to right the peaks corresponding to resonance absorption in CH_2, CH, and C_6H_5 groups.

(b) Absorption line of CH_2 group in the spectrum of PS (d.p.$=1.02\times10^4$)–CCl_4 solution (11 g/100 cc).

(c) PIB–CCl_4 solution (6.5 g/100 cc). Reading from left to right the peaks corresponding to CH_3 and CH_2 groups.

Fig. 1. Example of spectra of the proton resonance absorption in PS and PIB solutions. (Resonance frequency, 40 Mc/s. Sweep rate, 4 c/s per second).

The half line widths of the CH_2 group in PS are larger than those of the phenyl group. It is supposed that the two lines of CH_2 group and CH group in PS may have fine structures due to the $I-I$ coupling with the CH group and CH_2 group in the neighbour on the chain, respectively. The large widths of CH_2 group and CH group lines are probably caused by a multiple structure of lines, the splitting of which is unseparable.

The widths of phenyl group are almost independent of the concentrations in the range mentioned above, It is also verified that the line width of phenyl group is not dependent on the molecular weight in dilute solutions as well as the dielectric relaxation time of polar polymer solutions⁹⁾. On the other hand, it is presumed that the values of the width of CH_2 group increase as the concentration

Table I.

	Degree of polymerization	Concentration (g/100 cc)	Half width (c/s)	
			phenyl group	CH_2-group
	10^4	11.0	16	35
		4.1	15	28
PS	4×10^3	2.7	15	27
	10^3	6.5	15	28
	7×10^2	10.0	16	30
			CH_3-group	CH_2-group
PIB	2×10^4	6.5	6.5	~10
		3.0	6	~10

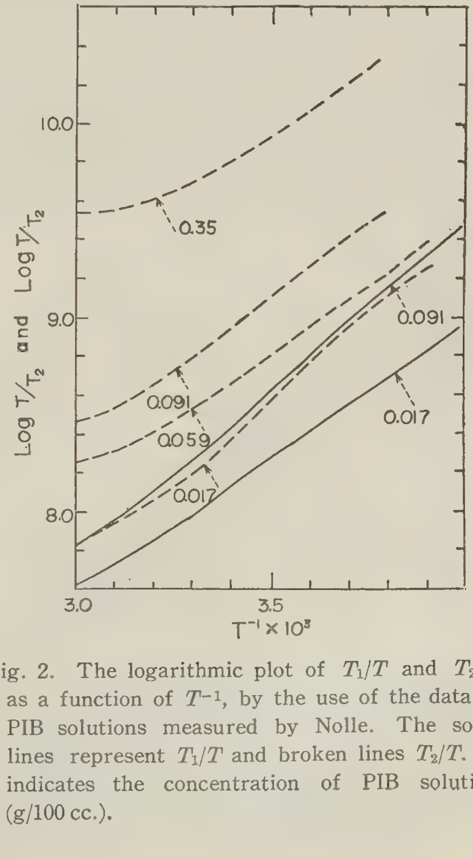

Fig. 2. The logarithmic plot of T_1/T and T_2/T as a function of T^{-1}, by the use of the data of PIB solutions measured by Nolle. The solid lines represent T_1/T and broken lines T_2/T. **c** indicates the concentration of PIB solution (g/100 cc.).

---

* The fractionation of PS was performed by Mr. Miyake, Dept. of Phys., Hokkaido University.

increases.

One kind of PIB sample, the molecular weight of which is about 10^6 is used*. The half widths of CH_2 ond CH_3 groups seem to be almost constant under the concentration of 6.5 g/100 cc, and they are smaller than those of the CH_2 and CH groups in PS.

It is interesting that Nolle[10] also found both T_1 and T_2 in PIB–CCl_4 solutions became substantially independent of concentrations and molecular weights in sufficiently dilute solutions. But he found further that they fell rapidly with increasing concentration above a fairely well defined critical value. This point will be discussed in section 6.

III. *Effects of on T_1 and T_2 temperature*

By the use of Nolle's data of the T_1 and T_2 vs. temperature curves in PIB solution, both T/T_1 and T/T_2 are plotted against the inverse of temperature T^{-1} in Fig. 2. Here, it is found that the T_1 curves are approximately linear. The T_2 curves, however, are less linear in higher region of temperature when the solution becomes dense.

§ 3. Brownian Motion in the Potential Field

We shall now consider, in the classical theory, the general Brownian motion under the influence of the potential field[15].

When it is assumed that the Brownian movement can be idealized as a Markoff process, the probability distribution $W(\Delta\vec{r}, \Delta\vec{u}; \Delta t)$ in a phase space can be derived from the following equation:

$$\frac{\partial W}{\partial t}+(W, \mathscr{H})=\eta\, \mathrm{div}_u (W\vec{u})+q\nabla_u{}^2 W\,, \quad (1)$$

where ( ) means the Poisson's blacket. The coefficients η and q are given by

$$\left\{\begin{aligned} -\eta\vec{u}&=\frac{\langle\Delta\vec{u}\rangle}{\Delta t} && \text{(2a)}\\ q&=\frac{\langle\Delta u^2\rangle}{\Delta t}\,. && \text{(2b)}\end{aligned}\right.$$

However, if we are interested only in time interval very large compared to the "time of relaxation" η^{-1}, we can reduce Eq. (1) to the Fokker-Planck equation in configuration space independently of the velocity space.

We shall also suppose that the force $-\mathrm{grad}\, U$ does not change appreciably over a distance of the order of $(q/\eta^3)^{1/2}$. With this assumption, the transition probability $\omega(\Delta\vec{r}; \Delta t)$ that suffers an increment $\Delta\vec{r}$ in the coordinate space in time $\Delta t \gg \eta^{-1}$ is obtained from the equation in the form

$$\frac{\partial\omega}{\partial t}=\mathrm{div}\,(q/\eta^2\, \mathrm{grad}\, \omega+\omega/\eta\cdot \mathrm{grad}\, U)\,, \quad (3)$$

where q and η are related to the diffusion constant D as

$$D=q/\eta^2\,. \quad (4)$$

Here we draw attention to the fact that this equation is valid only if we ignore the effects which happen in time intervals of the order of η^{-1} and space intervals of the order of $(q/\eta^3)^{1/2}$. When such effects are of interest, we should go back to Eq. (1) which is rigorously valid in the phase space.

We think, however, the approach by Eq. (3) is helpful to explain the motions of segments in polymer solutions as will be desbribed in section. The entanglment between the chain molecules is considered to give a steric hinderance to the rotational motion of the segment. And it may be supposed that such a hindrance is expressed by the potential barrier against the segmental motion.

In this case, we start from the motions of proton pairs isolated in the chain molecule which rotate under a hindering potential. However, these results should be applicable not only to those of the chain molecules but to the other rotational motions in general.

From Eq. (3), the differential equation of the rotational Brownian motion of proton pair is given as

$$\frac{\partial f}{\partial t}=\frac{k_0T}{\eta}\left\{\frac{1}{\sin\theta}\frac{\partial}{\partial\theta}\sin\theta\left(\frac{\partial f}{\partial\theta}+\frac{1}{k_0T}\frac{\partial U}{\partial\theta}f\right)+\frac{1}{\sin^2\theta}\frac{\partial^2}{\partial\varphi^2}f+\frac{1}{k_0T\sin^2\theta}\frac{\partial}{\partial\varphi}f\frac{\partial U}{\partial\varphi}\right\}. \quad (5)$$

The spherical coordinate system-(θ, φ) is defined so that the hindering potential of rotation is expressed by

$$U(\theta)=-W\cos\theta\,. \quad (6)$$

---

* This sample was supplied through the kindness of Dr. Iwayanagi, Scientific Research Institute, Tokyo.

Substituting Eq. (6) into Eq. (5) and putting $\cos\theta=v$, we get

$$\frac{\partial f}{\partial t}=\frac{k_0T}{\eta}\left\{\frac{\partial}{\partial v}(1-v^2)\frac{\partial f}{\partial v}+\frac{1}{1-v^2}\frac{\partial^2}{\partial\varphi^2}f-\frac{W}{k_0T}\frac{\partial}{\partial v}(1-v^2)f\right\}. \tag{7}$$

In order to solve Eq. (7), we consider the operator

$$L_0=\frac{d}{dv}(1-v^2)\frac{d}{dv}-\left(\frac{W}{2k_0T}\right)^2(1-v^2)+\frac{W}{k_0T}v-\frac{m^2}{1-v^2}. \tag{8}$$

By supposing that L_0 is self-adjoint, let us consider the eigenvalue problem,

$$L_0X+\lambda X=0. \tag{9}$$

L_0 will possess a set of eigenvalues $-\lambda_{mn}$ and eigen functions X_{mn} forming a complete orthogonal set.

Thus, a solution of Eq. (7) may be written in a series of the orthogonal set as

$$f=\sum_{mn}c_{mn}e^{(W/2k_0T)v}\cdot X_n{}^m\cdot e^{-\lambda_{mn}t}. \tag{10}$$

At $t=0$, the direction of nucleus pair is in the position (θ_0, φ_0), and the distribution function in the initial state is

$$f(0)=\delta(\theta-\theta_0)\cdot\delta(\varphi-\varphi_0). \tag{11}$$

From this condition, the expansion coefficient is determined as

$$c_{mn}=\frac{e^{-im\varphi_0}X_n{}^{m*}(v_0)e^{-(W/2k_0T)v_0}}{\int_{-1}^{1}|X_n{}^m|^2dv\cdot\int_{-1}^{1}e^{(W/k_0T)v}dv}. \tag{12}$$

§ 4. Spin-Lattice Relaxation Time and Spin-Spin Relaxation Time for the Rotations Restricted

By following the Solomon's theory[13], the relaxation of two-spin systems was treated by a random semiclassical perturbation.

Though his theory may be not rigorous enough, it was verified to be correct[14] when the fluctuations of the dipolar field are rapid as in liquids. Therefore, it may be reasonable to apply this method for the rubbery state of polymers.

The Hamiltonian of an interacting pair of like spins, in a magnetic field H_0 along the z' direction is

$$\mathscr{H}=\mathscr{H}_m-\hbar\gamma H_0(I_{1z'}+I_{2z'})+\mathscr{H}', \tag{13}$$

$\mathscr{H}_m$ is the Hamiltonian of the motion of the particles and commutes with the spin operators. The next terms are the Zeeman energies of two spins in the constant magnetic field H_0. We will consider only spin of value $\frac{1}{2}$ so that there is no quadrapole interaction. H' is the spin-spin interaction term considered as a perturbation which is expressed by

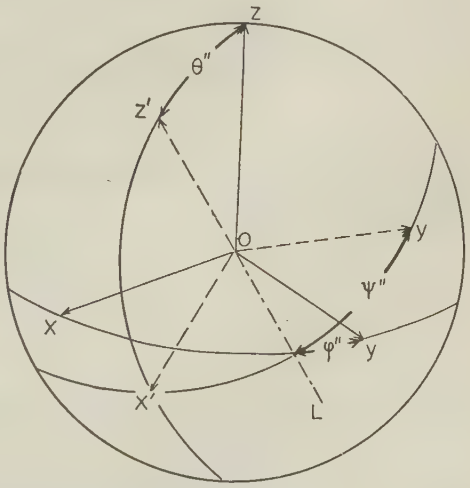

Fig. 3. Diagram illustrating the transformation between (θ, ϕ, ψ)-coordinate and $(\theta'\ \phi', \psi')$-coordinate. The magnetic field H is applied to the z'-direction. The Eulerian angles are illustrated by θ'', ϕ'', and ψ'', respectively.

$$\mathscr{H}'=[I_{1z'}\cdot I_{2z'}-\tfrac{1}{4}(I_{1+}\cdot I_{2-}+I_{1-}\cdot I_{2+})]F_0+[I_{1+}\cdot I_{2z'}+I_{1z'}\cdot I_{2+}]\cdot F_1$$
$$+[I_{1-}\cdot I_{2z'}+I_{1z'}\cdot I_{2-}]\cdot F_1{}^*+(I_{1+}\cdot I_{2+})\cdot F_2+(I_{1-}\cdot I_{2-})F_2{}^*\ , \tag{14}$$

where

$$\left\{\begin{aligned} &F_0(t)=k(1-3\cos^2\theta'(t)) && \text{(15a)}\\ &F_1(t)=-\tfrac{3}{2}k\sin\theta'(t)\cos\theta'(t)e^{i\varphi'(t)} && \text{(15b)}\\ &F_2(t)=-\tfrac{3}{4}k\sin^2\theta'(t)e^{2i\varphi'(t)}\ , && \text{(15c)}\end{aligned}\right.$$

and

$$k=\hbar^2\gamma^2/b^3\ , \tag{16}$$

and $I_\pm$ are the raising and lowering operators of the nuclear spin and $I_{z'}$ is the longitudinal component of the magnetic moment.

Now, as is shown in Fig. 3, the transformation of the coordinate system-(θ,φ) given in the preceding section into the coordinate system-(θ',φ') with the z' axis in the direction of the magnetic field, gives the following relations:

$$\left\{\begin{aligned} &\sin\theta'\cos\varphi'=(\cos\psi''\cos\varphi''\cos\theta''-\sin\psi''\sin\varphi'')\sin\theta\cos\varphi+(\cos\psi''\sin\varphi''\cos\theta''\\ &\qquad+\sin\psi''\cos\varphi'')\sin\theta\sin\varphi-(\cos\psi''\sin\theta'')\cos\theta\ . && \text{(17a)}\\ &\sin\theta'\sin\varphi'=(-\sin\psi''\cos\varphi''\cos\theta''-\cos\psi''\sin\varphi'')\sin\theta\cos\varphi+(-\sin\psi''\sin\varphi''\cos\theta''\\ &\qquad+\cos\psi''\cos\varphi'')\sin\theta\cdot\sin\varphi+(\sin\psi''\sin\theta'')\cos\theta\ . && \text{(17b)}\\ &\cos\theta'=(\cos\varphi''\sin\theta'')\sin\theta\cos\varphi+(\sin\varphi''\sin\theta''\cos\theta'')\sin\theta\cos\theta\sin\varphi\ . && \text{(17c)}\end{aligned}\right.$$

Transforming (θ',φ')-representations of F_0, F_1 and F_2 in Eqs. (15) into (θ,φ)-representations, we get

$$\left\{\begin{aligned} F_0/k=&-\tfrac{1}{2}(1-3\cos^2\theta)(1-3\cos^2\theta'')-\tfrac{3}{4}\sin 2\theta\,(e^{i\varphi}+e^{-i\varphi})\sin 2\theta''\\ &-\tfrac{3}{4}\sin^2\theta(e^{2i\varphi}+e^{-2i\varphi})\sin^2\theta'' && \text{(18a)}\\ F_1/k=&-\tfrac{3}{8}(1-3\cos^2\theta)\sin 2\theta''e^{-i\psi''}-\tfrac{3}{8}\sin 2\theta e^{i\psi}(\cos 2\theta''+\cos\theta'')e^{-i\psi''}\\ &-\tfrac{3}{8}\sin 2\theta e^{-i\psi}(\cos 2\theta''-\cos\theta'')e^{-i\psi''}-\tfrac{3}{8}\sin^2\theta\cdot e^{2i\varphi}\sin\theta''(1+\cos\theta'')e^{-i\psi''}\\ &+\tfrac{3}{8}\sin^2\theta e^{-2i\varphi}\sin\theta''(1-\cos\theta'')e^{-i\psi''}\ . && \text{(18b)}\\ F_2/k=&\tfrac{3}{8}(1-3\cos^2\theta)\sin^2\theta''e^{-2i\psi''}+\tfrac{3}{8}\sin 2\theta e^{i\varphi}\sin\theta''(1+\cos\theta'')e^{-2i\psi''}\\ &-\tfrac{3}{8}\sin 2\theta e^{-i\varphi}\sin\theta''(1-\cos\theta'')e^{-2i\psi''}+\tfrac{3}{16}\sin^2\theta e^{2i\varphi}(1+\cos\theta'')^2e^{-2i\psi''}\\ &+\tfrac{3}{16}\sin^2\theta\cdot e^{-2i\varphi}(1-\cos\theta'')^2e^{-2i\psi''} && \text{(18c)}\end{aligned}\right.$$

According to Solomon[13)], we have a couple of transition probabilities for the longitudinal component $I_{z'}$ as follows:

$$\left\{\begin{aligned} &w_1=\frac{1}{t\hbar^2}\left|\int_0^t\frac{1}{2}F_1(t')e^{-i\omega t'}dt'\right|^2\ . && \text{(19a)}\\ &w_2=\frac{1}{t\hbar^2}\left|\int_0^t\frac{1}{2}F_2(t')e^{-2i\omega t'}dt'\right|^2\ . && \text{(19b)}\end{aligned}\right.$$

In order to perform the integration of Eqs. (19), the following correlation functions corresponding to Eqs. (18) have to be determined.

$$K_i(\tau)=\langle F_i(t)\cdot F_i{}^*(t+\tau)\rangle\ . \qquad (i=0,\,1,\,2) \tag{20}$$

If we apply the distribution function of the Brownian motion expressed by Eq. (10), with the initial condition given by Eq. (11), to the correlation functions $K_i(\tau)$, and when the average over the initial values (θ_0,φ_0) and the average over Eulerian angles (θ'',φ'') are taken, the transition probabilities become

$$\left\{\begin{aligned} w_1&=\frac{3}{20}\left(\frac{k}{\hbar}\right)^2\left\{\frac{1}{4}\sum_n\frac{A_n\tau_n}{1+\omega^2\tau_n{}^2}+\frac{3}{4}\sum_n\frac{B_n\tau_n}{1+\omega^2\tau_n{}^2}+\frac{3}{4}\sum_n\frac{C_n\tau_n}{1+\omega^2\tau_n{}^2}\right\} &&\text{(21a)}\\ w_2&=\frac{3}{20}\left(\frac{k}{\hbar}\right)^2\left\{\sum_n\frac{A_n\tau_n}{1+4\omega^2\tau_n{}^2}+3\sum_n\frac{B_n\tau_n}{1+4\omega^2\tau_n{}^2}+3\sum_n\frac{C_n\tau_n}{1+4\omega^2\tau_n{}^2}\right\}, &&\text{(21b)}\end{aligned}\right.$$

where

$$\left\{\begin{aligned} A_n&=\left\{\int_{-1}^{1}(3v^2-1)X_n{}^0\exp\left(\frac{W}{2k_0T}\,v\right)dv\right\}^2\Big/\int_{-1}^{1}|X_n{}^0|^2dv\cdot\int_{-1}^{1}e^{(W/k_0T)v}dv &&\text{(22a)}\\ B_n&=\left\{\int_{-1}^{1}2v\sqrt{1-v^2}\,X_n{}^1\exp\left(\frac{W}{2k_0T}\,v\right)dv\right\}^2\Big/\int_{-1}^{1}|X_n{}^1|^2dv\cdot\int_{-1}^{1}e^{(W/k_0T)v}dv &&\text{(22b)}\\ C_n&=\left\{\int_{-1}^{1}(1-v^2)X_n{}^2\exp\left(\frac{W}{2k_0T}\,v\right)dv\right\}^2\Big/\int_{-1}^{1}|X_n{}^2|^2dv\cdot\int_{-1}^{1}e^{(W/k_0T)v}dv\,, &&\text{(22c)}\end{aligned}\right.$$

and A_n, B_n ,and C_n correspond to $m=0$, ±1, and ±2, respectively. When these values in Eq. (21) are used, the spin-lattice relaxation time T_1, the derivation of which is given in Appendix, is expressed as follows:

$$T_1{}^{-1}=2(w_1+w_2)=\frac{3}{8}\left(\frac{k}{\hbar}\right)^2\sum(A_n+3B_n+3C_n)\left(\frac{\tau_n}{1+\omega^2\tau_n{}^2}+\frac{4\tau_n}{1+4\omega^2\tau_n{}^2}\right). \tag{23}$$

On the other hand, the expressions of the transition probabilities of the transversal components are

$$\left\{\begin{aligned} u_1&=\frac{1}{t\hbar^2}\left|\frac{1}{4}\int_0^t\{e^{-i\omega t'}F_1(t')+e^{i\omega t'}F_1{}^*(t')-e^{-2i\omega t'}F_2(t')+e^{2i\omega t'}F^*(t')\}dt'\right|^2 &&\text{(24a)}\\ u_2&=\frac{1}{t\hbar^2}\left|\frac{1}{4}\int_0^t\left\{\frac{3}{2}F_0(t')+2e^{-\omega t'}F_1(t')-2e^{i\omega t'}F_1{}^*(t')+e^{-2i\omega t'}F_2(t')+e^{2i\omega t'}F_2{}^*(t')\right\}dt'\right|^2. &&\text{(24b)}\end{aligned}\right.$$

Following the similar procedure, we get the transition probabilities as follows:

$$\left\{\begin{aligned} u_1&=\frac{3}{20}\left(\frac{k}{\hbar}\right)^2\sum_{n=1}\left(\frac{A_n+3B_n+3C_n}{8}\right)\left(\frac{\tau_n}{1+\omega^2\tau_n{}^2}+\frac{\tau_n}{1+4\omega^2\tau_n{}^2}\right) &&\text{(25a)}\\ u_2&=\frac{3}{20}\left(\frac{k}{\hbar}\right)^2\sum_{n=1}\left(\frac{A_n+3B_n+3C_n}{8}\right)\left(3\tau_n+\frac{4\tau_n}{1+\omega^2\tau_n{}^2}+\frac{\tau_n}{1+4\omega^2\tau_n{}^2}\right). &&\text{(25b)}\end{aligned}\right.$$

As will be shown in Appendix, the spin-spin relaxation time T_2 can be represented with the above transition probabilities as

$$T_2{}^{-1}=2(u_1+u_2)=\frac{3}{10}\left(\frac{k}{\hbar}\right)^2\sum_{n=1}\frac{(A_n+3B_n+3C_n)}{8}\left(3\tau_n+\frac{5\tau_n}{1+\omega^2\tau_n{}^2}+\frac{2\tau_n}{1+4\omega^2\tau_n{}^2}\right). \tag{26}$$

However, we have to take the contribution of the term of $\lambda_{mn}=0$ to T_2 into account. This term in Eq. (10) is

$$\psi_{00}(v)=e^{(W/2k_0T)v}X_0{}^0=\exp\{W/(k_0T)\cdot v\}\,, \tag{27}$$

and

$$C_{00}=\left(\int_{-1}^{1}e^{(W/k_0T)v}dv\right)^{-1}. \tag{28}$$

This indicates that starting from an arbitary initial distribution $f(\theta_0,\varphi_0:0)$, the Boltzmann distribution in the potential $U(\theta)$ will be established after the time interval of $\Delta t\gg\eta^{-1}$. Hereafter we call $\psi_{00}(v)$ the stationary component. It is emphasized that the stationary component is obtained from the local magnetic field fluctuating rapidly due to the thermal motions restricted in the potential field but is independent of time.

As will be easily seen from the form of Fourier integral in Eqs. (19), the stationary component gives no contribution to T_1. But it contributes to T_2 through the term of $F_0(t)$ in Eq. (25b). The contribution must be calculated by a different method from the one described above. By using Eq. (27), the function corresponding to Eq. (20) is obtained from F_0 in Eq. (18a) by

$$K_s=\frac{1}{5}\frac{\left\{\int_{-1}^{1}(1-3v^2)e^{(W/k_0T)v}dv\right\}^2}{\left\{\int_{-1}^{1}e^{(W/k_0T)v}dv\right\}^2}\,. \tag{29}$$

This corresponds to the time-independent component in the local magnetic field. Therefore, according to BPP theory[11)], K_s is related to the term of $(T_2)_s$ that is the contribution of the stationary component to T_2. The relation between K_s and $(T_2)_s$ is

$$(T_2)_s^{-1}=\frac{\sqrt{3}}{2}\sqrt{I(I+1)}\left(\frac{k}{\hbar}\right)K_s^{1/2}\,. \tag{30}$$

Hence, the spin-spin relaxation time for the rotation hindered by the given potential barrier is expressed as the sum of two contributions mentioned above. That is,

$$T_2^{-1}=(T_2)_m^{-1}+(T_2)_s^{-1}\,, \tag{31}$$

where $(1/T_2)_m$ is obtained as Eq. (27).

§ 5. Case of $W/k_0T<1$

Although it is generally rather difficult to solve Eq. (9), the solutions of the case we shall deal become easy, because the assumption of the hindering potential W is assumed to be $W/k_0T<1$. In this case, X_n^m and λ_{mn} in Eq. (9) can be expanded as a power series of W/k_0T as follows:

$$\left\{\begin{aligned} &X_n^m=\exp\left(\frac{W}{2k_0T}v\right)\cdot\left(X_n^{m(0)}+\left(\frac{W}{k_0T}\right)X_n^{m(1)}+\left(\frac{W}{k_0T}\right)^2X_n^{m(2)}+\cdots\right) && \text{(32a)}\\ &\lambda_{mn}=\lambda_{mn}^{(0)}+\left(\frac{W}{k_0T}\right)\lambda_{mn}^{(1)}+\left(\frac{W}{k_0T}\right)^2\cdot\lambda_{mn}^{(2)}+\cdots\,. && \text{(32b)}\end{aligned}\right.$$

The zero-order approximations of Eqs. (32) are

$$\left\{\begin{aligned} &X_n^{m(0)}=\hat{P}_n^m(v) && \text{(33a)}\\ &\lambda_{mn}^{(0)}=n(n+1)\cdot k_0T/\eta\,, && \text{(33b)}\end{aligned}\right.$$

where $\hat{P}_n^m(v)$ is the normalized Legendre function. Moreover, $\lambda_{mn}^{(1)}$ is given by the equation

$$\lambda_{mn}^{(1)}=\int\hat{P}_n^m v\hat{P}_n^{m*}dv=0\,. \tag{34}$$

Therefore, the eigenvalue is not influenced by the existence of the hindering potential for the first order approximation.

On the other hand, using the first order approximation of X_n^m, we get the following equations for the coefficients A_n, B_n and C_n in Eqs. (22).

$$\left\{\begin{aligned} &A_1^{(1)}=\frac{3}{25}\left(\frac{W}{k_0T}\right)^2\left[1+\left\{\frac{1}{6}+\frac{3}{5}+\frac{1}{3^2}\left(1+\frac{1}{5^2}\right)\right\}\left(\frac{W}{k_0T}\right)^2\right]^{-1}\\ &A_2^{(1)}=\frac{4}{5}\left[1+\left\{\frac{1}{6}+\frac{11}{21}+\frac{1}{5^2}\left(\frac{1}{3^2}+\frac{1}{7^2}\right)\right\}\left(\frac{W}{k_0T}\right)^2\right]^{-1}\\ &A_3^{(1)}=\frac{7}{27}\left(\frac{W}{k_0T}\right)^2\left[1+\frac{23}{45}+\left\{\frac{1}{6}+\frac{1}{7^2}\left(\frac{1}{5^2}+\frac{1}{9^2}\right)\right\}\left(\frac{W}{k_0T}\right)^2\right]^{-1}\\ &A_l^{(1)}=0 \qquad (l\neq 1,2,3)\end{aligned}\right. \tag{35}$$

$$\left\{\begin{aligned} B_1^{(1)}&=\frac{3}{50}\left(\frac{W}{k_0T}\right)^2\left[1+\frac{1}{5}+\left(\frac{W}{k_0T}\right)^2\left(\frac{1}{6}+\frac{1}{5^2}\right)\right]^{-1}\\ B_2^{(1)}&=\frac{8}{15}\left[1+\left(\frac{W}{k_0T}\right)^2\left\{\frac{1}{6}+\frac{4}{7}+\frac{1}{5^2}\left(1+\frac{8^2}{7^2}\right)\right\}\right]^{-1}\\ B_3^{(1)}&=\frac{14}{27}\times\frac{4^2}{5^2}\left[1+\left(\frac{W}{k_0T}\right)^2\left\{\frac{1}{6}+\frac{7}{15}+\frac{1}{7^2}\left(\frac{8^2}{5^2}+\frac{9^2}{3^2}\right)\right\}\right]^{-1}\\ B_l^{(1)}&=0\qquad (l\neq 1,\, 2,\, 3) \end{aligned}\right. \tag{36}$$

$$\left\{\begin{aligned} C_2^{(1)}&=\frac{8}{15}\left[1+\left(\frac{W}{k_0T}\right)^2\left\{\frac{3}{28}+\frac{1}{6}+\frac{8^2}{7^2}\right\}\right]^{-1}\\ C_3^{(1)}&=\frac{14}{135}\left(\frac{W}{k_0T}\right)^2\left[1+\frac{1}{3}+\left(\frac{W}{k_0T}\right)^2\left\{\frac{1}{6}+\frac{1}{7^2}(8^2+20^2)\right\}\right]^{-1}\\ C_l^{(1)}&=0\qquad (l\neq 2,\, 3)\,. \end{aligned}\right. \tag{37}$$

For the term corresponding to $n=0$, that is, the stationary component, we get the following equation neglecting the higher decimals than the order of three in the expansion:

$$K_{0s}=\frac{1}{5}\left(\frac{2}{15}\right)^2\left(\frac{W}{k_0T}\right)^4\left\{1-\frac{4}{21}\left(\frac{W}{k_0T}\right)^2\right\}\,. \tag{38}$$

Then we can estimate both T_1 and T_2 according to the following expressions with the first order approximation of X_n^m and λ_{mn}:

$$\left\{\begin{aligned} T_1^{-1}&=\frac{\eta}{k_0T}\left(\frac{k}{\hbar}\right)^2\left\{0.25-0.033\left(\frac{W}{k_0T}\right)^2\right\} && \text{(39a)}\\ T_2^{-1}&=0.045\left(\frac{k}{\hbar}\right)\left(\frac{W}{k_0T}\right)^2+\frac{\eta}{k_0T}\left(\frac{k}{\hbar}\right)^2\left\{0.25-0.033\left(\frac{W}{k_0T}\right)^2\right\}\,. && \text{(39b)} \end{aligned}\right.$$

For the case of $W/k_0T>1$, the perturbation theory is not applicable. Thus, it is difficult to get the solutions of X_n^m and λ_{mn}, but we can obtain the average value $\langle\lambda_{mn}\rangle$. The detailed discussion on this point will be reported in near future.

§ 6. Discussions

I. *Some properties of T_1 and T_2 in PIB solutions*

(I) *A note of the critical concentration in polymer solution.*

Before attempting to apply our theory described in the preceding sections to the results of T_1 and T_2 measured in polymer solutions, it must be noted that both T_1 and T_2 tend to have certain values which are independent of the molecular weight as the concentration decreases. As mentioned in the preceding section, both T_1 and T_2 fall rapidly with increasing concentration above a fairly well defined critical value. Fig. 4 shows the critical concentration, corresponding to the knee in T_2 curve at 25°C, as a function of the molecular weight. The critical concentration is presumably the concentration above which each polymer molecule has a kind of entanglement each other as Nolle[10] pointed out. From this presumption, he estimated the critical concentration theoretically as follow:

$$W_c=7.1M_s^{3/2}/\alpha^3Al^3M^{1/2}\,, \tag{40}$$

where M_s stands for molecular weight of the basic unit, α for "excluded volume", A for Avogadro's number, l for the length of segment, and M for the Molecular weight of the chain molecule.

Nolle[10] thought that Eq. (40) was not satisfied with his experimental data, as is shown in the solid line in Fig. 4, but it is supposed that the experimental data is in fairly good agreement with Eq. (40) in the range of the molecular weight higher than 10^5, as is shown by the broken line in Fig. 4. Under the molecular weight of 10^5, the assumption that each long chain molecule coils up in a sphere and α can be taken as unity does not presumably hold, and then the curve of W_c would shift from the proportional line to $M^{-1/2}$.

The dependency of viscosity of liquid polymers and concentrated solutions on the molecular weight[16) is known to change at the molecular weight 10^3, that is, to show a different characteristic beyond this boundary of polymerization. This might essentially have a connection with the phenomenon of polymer solutions mentioned above.

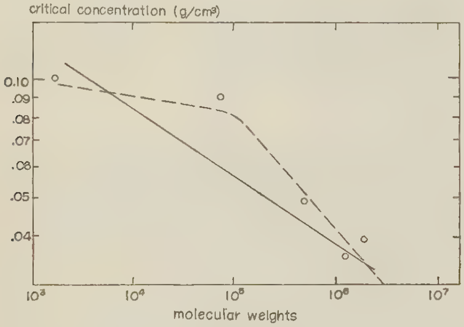

Fig. 4. Critical concentration of PIB solution, corresponding to the knee in T_2 curve at 25°C, as a function of molecular weight (obtained by Nolle). The solid line plotted by Nolle represents critical concentration proportional to the $-1/6$ power of molecular weight. The broken line added by the author represents $-1/2$ power of molecular weight, above that of 10^5.

(II) *A kinematic unit of segmental motions.* There is another important connection between the properties of liquid polymers and the polymer solutions. In the viscous flow of liquid polymers[17), it has been suggested that the elementary process of flow consists of the displacement or jump of only a small segment of molecule rather than the displacement of the entire molecules as a unit. As the evidence of supporting this hypothesis for long chain polymers, it was found that the values of the activation energy were low (only several times the values of their monomer unit) and independent of chain length.

On the other hand, the half widths shown in Table I or T_1^{-1} and T_2^{-1} in the Nolle's data[10) are independent of the molecular weights. And their values are more than ten times of the order of the monomer molecules, for instance, T_1 of PIB solutions (C=0.0173 g/cm³) at 20°C is 0.09 sec[10) and T_1 of distilled water (η=1.02 centi-poise) at 20°C is 2.3 sec[11). Consequently, it is readily interpreted that the reorientation or the displacement is carried out by such a small segment with about ten monomer units as the segment in liquid polymers*.

(III) *A mechanism of segmental motions.* It is found from the above mentioned data that the frictional constants of segmental motions in the high frequency region are not related to the chain length. This frequency region is correspondent to more than O(10^6 c/s). Below this frequency, spectral lines are unobservable by the Varian Spectrometer.

The result that the relaxation times are independent of the molecular weight suggests us that the motional behavior of each segment is not so markedly influenced by the interaction of other segments on the same chain that the Kirkwood theory[3) predicted. This theory gives the mobility of segments a large inhomogeneity for their positions on the chain so that the theoretical result does not become to agree with the experimental results.

From NMR data, it may reasonably be assumed that the mobilities of segments in the high frequency motions are homogeneous concerning to the position on the chain to which the segments belong. When the concentration increases, however, the entanglement among the chain molecules must be considered. The entanglement may give a kind of steric hinderance to the reorientation and the displacement of the segments. Herein, we assume for simplicity that such a hinderance can be expressed independently of each molecular group in the segment by equation:

$$V(\theta_{i\lambda}) = -W\cos\theta_{i\lambda}\,, \tag{41}$$

where the suffix means i-th gronp in λ-th segment. The Eulerian angles (θ'', ψ'') given in Eq. (17) are expressed on coordinates defined in each molecular group, in each segment, respectively.

It should be noted that such hindering potentials can not in general be assumed to be

---

[*] It is well known in experimental results of T_1[11) that the correlation time τ of molecular motion is given by

$$\tau = 4\pi\eta a^3/3k_0T\,. \tag{53}$$

In the above PIB-CCl_4 solution, the viscosity coefficient of CCl_4 is 0.97 centi-poise[4 at 20°C, so effective volume of PIB for segmental motion is approximately twenty five times of that of water molecule.

fixed in the space. The potential field should be understood to fluctuate because of the motion of the chain molecule or the large group of segments as a whole. According to the dynamical study, for instance, in PIB (molecular weight, 3.87×10^{6})-cychlohexane solution (1%)[18], the characteristic frequency of the motion of large group of segments is 550 c/s.

Therefore, in polymer solutions, the stationary component in Eq. (27) gives the contribution to T_2 in somewhat modified form. That is to say, the contribution of motion due to the segment group to T_2 becomes as follows when the motional effect derived from the Kubo-Tomita equation[12], are taken into consideration:

$$(T_2^{-1})_g=\frac{2}{\pi}(T_2^{-1})_s\cdot\tan^{-1}\left(\frac{\pi\tau_g}{4\log 2\cdot T_2}\right), \quad (42)$$

where $(T_2^{-1})_s$ was given in Eq. (30) and τ_g is the correlation time of motion of submolecule group as a whole.

In conclusion, the present model is divided into two parts for the segmental motions: the one is the micro-rotational motion of segment, and the other the motion of segment group as a whole.

II. *Some notes concerning application of theory of T_1 and T_2 to polymer solutions*

Based on the above described assumptions, the NMR in PIB solution can be treated as the problem of NMR in the system in which two-spin system of CH_2 groups and three-spin system of CH_3 groups exist independently each other. The theory concerning to this problem was discussed in the former sections.

First, the following points must be taken into consideration. One is the point that an absorption line of PIB solution in Fig. 1 consists of two lines and each of them comes from the CH_3 and the CH_2 groups. Hence Nolle's values of both T_1 and T_2 measured by "spin-echo" method should be considered as a kind of average value of the two groups. The average is assumed to be

$$\frac{1}{T_i}=\frac{1}{4}\left(\frac{1}{T_i}\right)_{CH_2}+\frac{3}{4}\left(\frac{1}{T_i}\right)_{CH_3}, \quad (i=1,\ 2) \qquad (43)$$

where the coefficients 3/4 and 1/4 come from the ratio of the number of protons in the CH_3 and the CH_2 groups in PIB molecule.*

The next problem is the estimation of influence of the interaction due to inter-group protons upon T_1 and T_2. Powles[1] found from the measurement of the second moment of PIB that the spin-spin interaction due to the inter-groups was unexpectedly large. In a solution, however, each group rotates with a sufficient rapidness about the $C-C$ axis so that the local magnetic field due to the inter-group interaction would be more remarkably averaged than due to the intra-group interaction. In other words, it may be able to assume, by neglecting the inter-group interaction, that only the intra-group interaction contributes to both T_1 and T_2 in a solution.

Furthermore, it must be noted that the Solomon's theory[13] is not generally applicable to the system with more two spins. Kubo-Tomita's theory[12] shows, however, that T_1 and T_2 can be given by similar equations with the relations obtained from Solomon's theory[13] even for the systems with many spins, when the correlation function is expressed by

$$K(\tau)=\exp(-|t|/\tau_c)\ .^{**} \qquad (46)$$

---

* The reasonability of T_1 and T_2 that can be computed from Eq. (43) will be examined compared with the experimental data in PIB-solutions. The half widths of the CH_3 and CH_2 groups in the PIB solution (6.5 g/100 cc) are 6.5 c/s and about 10 c/s, respectively, as shown in Table I. By subtracting the width of the inhomogeneous magnetic field $\Delta\nu'$ of 2 c/s, and by using the relation of $T_2^{-1}=\pi(\Delta\nu_{1/2}-\Delta\nu')$, Eq. (43) gives the value of T_2^{-1} as

$$T_2^{-1}\approx 17\ \text{sec}^{-1}\ . \qquad (44)$$

On the other hand, the Nolle's data give the following value of T_2^{-1} at $c=0.059$ g/cm³ and $T=20$°C.

$$T_2^{-1}\approx 20\ \text{sec}^{-1}\ . \qquad (45)$$

Thus, T_2 calculated from the line width in the present measurements is in fairly good agreement with that in Nolle's data.

** In this theory, T_1 and T_2 are

$$\begin{cases} T_1^{-1}=\sigma_P{}^2B\left(\dfrac{2}{5}\dfrac{\tau_c}{1+\omega^2\tau_c{}^2}+\dfrac{8}{5}\dfrac{\tau_c}{1+4\omega^2\tau_c{}^2}\right) & (47a)\\ T_2^{-1}=\sigma_P{}^2B\left(\dfrac{3}{5}\tau_c+\dfrac{\tau_c}{1+w^2\tau_c{}^2}+\dfrac{2}{5}\dfrac{\tau_c}{1+4\omega^2\tau_c{}^2}\right), & (47b)\end{cases}$$

where

$$\begin{cases} \sigma_P{}^2=I(I+1)(k/\hbar)^2 & (48a)\\ B=\sum_j (b/r_{ij})^\gamma\ . & (48b)\end{cases}$$

When Eqs. (47) are applied to two-spin systems, the same solutions as Solomon's equation can be described.

And, in case of such a modified correlation function as Eq. (10), it is assumed that Eqs. (27) and (31) obtained in the preceding section are applicable, by substituting $\sigma_P{}^2B$ for $I(I+1)(k/\hbar)^2$, in three-spin systems, too. The $\frac{3}{5}\tau_P{}^2B$ in Eqs. (47) is the second moment of rigid state[12)], and is given by

$$\tfrac{3}{5}\sigma_P{}^2B=\gamma^2\langle \Delta H^2\rangle_{\text{rig}}\ . \tag{49}$$

Therefore, $\frac{3}{5}\sigma_P{}^2B$ in Eq. (49) is

$$\tfrac{3}{5}\sigma_P{}^2B=\tfrac{3}{4}(\gamma^2\langle \Delta H^2\rangle_{\text{rot}})_{\text{CH}_3}+\tfrac{1}{4}(\gamma^2\langle \Delta H^2\rangle)_{\text{CH}_2}=5.03\times 10^9(\text{sec}^{-2})\ .^{*} \tag{50}$$

III. *Comparison of the present theory with the experimental results*

Nolle's measurements of both T_1 and T_2 were carried out at the resonance frequency $\omega/2\pi$ of 28 Mc/s. Therefore, as shown in Fig. 2, the small values of $T_1{}^{-1}$ and $T_2{}^{-1}$ of PIB solutions in his data indicate the condition of $\tau_n \ll \omega^{-1}$ for the correlation times in Eqs. (39). Hence, by using Eq. (50), Eqs. (39) are applicable to this case in such forms as

$$\left\{\begin{aligned} &T_1{}^{-1}=\frac{\eta}{k_0T}\sigma_P{}^2B\left\{0.33-0.044\left(\frac{W}{k_0T}\right)^2\right\} && \text{(52a)}\\ &T_2{}^{-1}=0.052\sqrt{\sigma_P{}^2B}\left(\frac{W}{k_0T}\right)^2\frac{2}{\pi}\tan^{-1}\frac{\pi\tau_g}{4\log 2\cdot T_2}+\frac{\eta}{k_0T}\sigma_P{}^2B\left\{0.33-0.044\left(\frac{W}{k_0T}\right)^2\right\}\ , && \text{(52b)}\end{aligned}\right.$$

where the mobility of segmental motion is expressed by

$$\beta=\eta^{-1}=\beta_0\exp(-U/k_0T)\ . \tag{54a}$$

It is clear, from $\log T/T_1$ curves represented approximately with a straight line in Fig. 2, that Eq. (52a) is in a good agreement with the experimental curve, if the hindering potential W in Eq. (52a) is understood to satisfy $W/k_0T<1$.

Table II. The activation energies of segmental motion.

Concentration (g/cm³)	(A) from T_1 curves	(B) from T_2 curves in the consideration of stationary component	(C) from T_2 curves without the stationary component
0.017	2.6		3.2
0.059		3.8	2.9
0.091	3.6	4.1	2.9
0.350		5.4	2.7

As is shown in Table II (A), for the solution of lower concentration (0.017 g/cm³), the activation energy U estimated from the the gradient of $\log T/T_1$ curve in Fig. 2 is

$$U=2.6\ \text{Kcal/mol}\ . \tag{54b}$$

It is note-worthy that this value is approximately same with 2.4 Kcal/mole of the activation energy of the solvent, CCl_4**.

For the solution of higher concentration (0.091 g/cm³), the gradient of the curve becomes steeper and less linear. On the other hand, $\log T/T_2$ curves shown in Fig. 2 are less linear than the curve of $\log T/T_1$. When the solution becomes more dense, the deviation of the curve from the straight line becomes appreciable. This tendency is especially remarkable in the region of high temperature.

Another noticeable result is that T_1 is larger than T_2 in dilute solutions in spite of the other theoretical prediction[11)-13)] of $T_1\approx T_2$ when $\tau_N<\omega^{-1}$. According to the present theory, however, Eq. (52b) is also in a good agreement with the experimental curves of T_2.

---

* The second moments of both methylene and methyl groups in PIB molecule can be calculated as follows, by assuming the tetrahedral structure:

$$\left\{\begin{aligned} &(\langle \Delta H^2\rangle)_{\text{CH}_2}=11.3\ \text{gauss}^2 && \text{(51a)}\\ &(\langle \Delta H^2\rangle)_{\text{CH}_3}=22.5\ \text{gauss}^2\ . && \text{(51b)}\end{aligned}\right.$$

However, the CH_3 groups in PIB solutions rotate more rapldly about C_3-symmetric axis than motions with the other freedoms in a molecule. According to Gutowsky and Pake[20)], in a C_3-rotation, the effective value of the second moment of CH_3 group is one forth of the second moment in a irrotational state. Namely,

$$(\langle \Delta H^2\rangle_{\text{rot}})_{\text{CH}_3}=5.6\ \text{gauss}^2\ . \tag{51c}$$

** The value of activation energy for CCl_4 was calculated from the temperature variation of the viscosity of CCl_4 which was tabulated on the chemical table in "Kagaku-Binran", (Maruzen press, 1958) 476.

Thus the author is inclined to consider that this agreement is due to the stationary component in Eq. (52b).

Since the temperature variation of the stationary component in Eq. (52b) is less than that of the other terms, the contribution of the stationary component to T_2 should become effective at high temperature.

Even at lower concentration of C=0.017 g/cm³, at which individual chain molecule is supposed to be independent and separated, as was described in the preceding section, the $\log T/T_2$ curve also deviated considerably from a linearity and is not equal to $\log T/T_1$. The reason of this trend is not clear at the present state.

Table III. The hindering potential energies.

Concentration (g/cm³)	W/k_0T
0.017	1.2×10^{-2}(50°C)
0.091	2.5×10^{-2}(60°C)

The values of hindering potential can be determined from the ratio of T_1 and T_2 by using the Eqs. (52), if the correlation time τ_g of submolecular group in Eq. (42) is known. Assuming $\tau_g > T_2$ in Eq. (52b), for simplicity, we obtain the value of W as shown in Table III. It is supposed that the small values of hindering potential energy in Table III are due to the flexible rotation of each molecular group around the $C-C$ axis in a chain molecule in spite of the fact that the translational motion of molecule as a whole is hindered by the entanglements among chains in solutions.

Further, the relation

$$T\left\{T_2^{-1}-0.052\sqrt{\sigma_P{}^2 B}\left(\frac{W}{k_0T}\right)^2\right\} = 0.33\frac{\sigma_P{}^2 B}{k_0\beta_0}\exp\left(\frac{U}{k_0T}\right) \tag{55}$$

is plotted against the inverse of temperature T^{-1} in Fig. 5 for three cases of C=0.059, 0.091, and 0.35 (g/cm³). Here, the values of W are assumed as $2.1\times10^{-2}\,k_0T$, $2.3\times10^{-2}\,k_0T$, and $4.6\times10^{-2}\,k_0T$, respectively.

When the approximation introduced in the above discussion is considered, the linearity of the curve shown in Fig. 5 is satisfactory. The activation energy U obtained from T/T_2 curves by Eq. (55) is tabulated for various concentrations in Table II (A and B). As are shown in Table II, both W and U increase with the concentration.

On the other hand, the values of activation energy which are calculated, by following the conventional way, in an approximation of neglecting the contribution of the stationary component in Eq. (52b) are added in Table II(C). It can be seen that the activation energy decreases as the concentration increases, if the conventional way is employed. In many studies of NMR, for instance, concerning to valcanized rubbers[1] and plasticized PIB[19], it is also reported that an opening the freedom of segmental motions introduces an increases of activation energy.

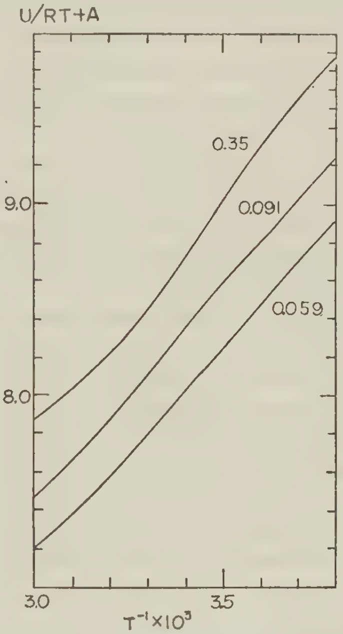

Fig. 5. Plot of U/k_0T against $1/T$ obtained by the use of Eq. (55), at the three concentrations (g/100 cc) of PIB solution which are indicated in the curves, respectively.

In the other measurements of mechanical[17] and dielectric relaxations[21], however, it is well known that the activation energy decreases with the concentrations of solvents. As the freedom of segmental motion depends upon the entanglement among chain molecules, it is rather acceptable that the activation energy would decrease with the increase of solvents. Thus, in this case, above mentioned results which is derived from Eq. (52b) with the stationary component, may seem to be plausible.

Table IV. The correlation times and the relaxation times in polymer solutions.

Method	Sample	Solvent	(sec)	Concentration	Temperature (°C)
NMR	PIB	CCl_4	2×10^{-9}	6.5 g/100 cc	20
	PS	CCl_4	4.6×10^{-9}	6.5 g/100 cc	20
Dielectric	PVAc	toluene	7×10^{-9}	6 g/100 cc	−10
	PMA	toluene	1.6×10^{-8}	6 g/100 cc	−10
Ultrasonic	PIB	cyclohexane	4.5×10^{-7}	1%	25

IV. *Correlation time and hindering potential*

The correlation time τ_N* and the relaxation times τ_D and τ_M are presented in Table IV, respectively. The τ_M used in Table IV is the value which is obtained from the dispersion of ultrasonic shear wave in the PIB-cyclohexane solution (1%). It has been explained that the ultrasonic relaxation time in this case is related to the twisting motion of the smallest segment group in a chain, since the stiffness of PIB-cyclohexane solution becomes from 890 dyne/cm² to 84,000 dyne/cm² in the frequency region of $\omega>\tau_N^{-1}$.[18] The τ_N is the value of PIB–CCl_4 solution obtained from our measurement. The value of τ_N is remarkably smaller than τ_M. This suggests to us that the mechanism of segmental motion observed by the ultrasonic relaxation is different from the one detected by NMR.

As shown in Table IV, however, τ_N may be of the same order of τ_D at the same concentration and temperature which is obtained by extrapolating from the experimental data[9], even if the samples employed are not same in both cases.

These data seem to be very interesting and important facts in making clear the mechanisms of segmental motions in a chain molecule.

Next, it is very desirable to verify how the hindering potential W described in the present theory is connected with the other physical quantities characterising the motions of polymer molecule. As mentioned above, the stiffness of polymer solutions is markedly large in the regions of high frequency. Hence, it is supposed that in this case the flow of segment group as a whole is quenched but the micro-Brownian motions of segments are occured in a certain restricted region. That is to say, the rigidity of polymer molecule depends upon the so-called energy effect rather than the so-called entropy effect concerning the rotational motion of segment around each C–C bond, even if the entropy effect is an origin of the rubber elasticity in polymer systems in static case.

Following the above consideration, the rigidity of polymer system in the high frequency field can be simply estimated as follows. It may be reasonable to adopt Eq. (6) as the potential energy concerning the rotational displacement of each segment.

Hence, for a small displacement, the potential energy per 1 cc of polymer systems, for example, PIB solutions (1 g/100 cc) is given by

$$E=\frac{1}{2}W\theta^2\frac{N}{M}\times0.01\,, \tag{56a}$$

where M is the molecular weight of the monomer and N is Avogadro's number.

If we assume $W=10^{-2}\,k_0T$, in the consideration of our results shown in Table III, the value of energy at 300°K becomes

$$E=\frac{4.3}{2}\times10^{4}\cdot\theta^2\,. \tag{56b}$$

On the other hand, the energy of this should be same as the elastic energy in the system caused by the ultrasonic shear wave, that is

$$E=\frac{1}{2}G\cdot\theta^2\cdot V\,, \tag{57}$$

where G is the rigidity and V the volume in the system. Therefore, in the above case, G is

$$G=4.3\times10^4\ \text{dyne/cm}^2\,. \tag{58}$$

This value is in a pretty good agreement with the experimental value of rigidity, 8.4× 10 dyne/cm², in PIB-cyclohexane solution (1%) which has the similar condition with the one assumed in Eq. (56b).

---

* τ_N was calculated from the data of line width shown in Table I, by using Eqs. (47). Here we assumed a single correlation time in the polymer solutions.

In conclusion, it may be sure that the potential field hindering the motions of segments in a chain exists even in fairly dilute solutions of polymer, and the results that the hindering potential has an effect on segmental motions become more and more marked in high frequency measurements.

It seems to us, that the present theory of the segmental motion is more proper in such a case than the Kirkwood[3)] or the Rouse[4)] and Bueche[5)] theories, though it has not been applied to a number of problems concerning relaxational phenomena other than NMR one in polymer solutions.

Acknowledgement

The author would like to express his sincere thanks to Professor Y. Yokozawa for his continuous interests in this study. Grateful thanks are also due to Professor G. Hazato and his coworkers at Tohoku University for their kind cooperations to carry out the measurements. The author would also like to extend his thanks to my friends Dr. M. Arie, Assistant Professor J. Sohma, and Mr. Y. Miyake, Hokkaido University for invaluable discussions and helps.

Appendix. Relaxation Processes in Two-Spin System

According to the Solomon's paper[13)], we define two eigenstates $|+\rangle$ and $|-\rangle$ of the unperturbed Hamiltonian for spin I_1 of value $\frac{1}{2}$ corresponding to both energies E_+ and E_-, respectively.

Similar two eigenstates of spin I_2 of value $\frac{1}{2}$ are defined as $|+)$ and $|-)$.

Thus we define four eigenstates of two spins by the following relations

$$\left\{\begin{aligned} &I_{1\zeta}|+\rangle=\tfrac{1}{2}|+\rangle \\ &I_{1\zeta}|-\rangle=-\tfrac{1}{2}|-\rangle \\ &I_{2\zeta}|+)=\tfrac{1}{2}|+) \\ &I_{2\zeta}|-)=-\tfrac{1}{2}|-)\ . \end{aligned}\right. \tag{A1}$$

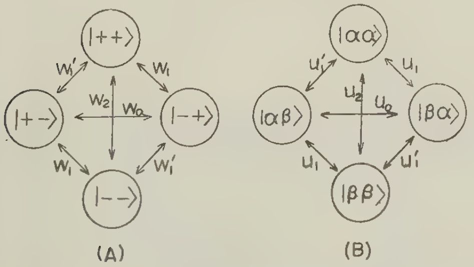

Fig. 6. (A) Transition probabilities between the eigenstates of the longitudinal components of the spin operators. (B) Transition probabilities between the eigenstates of the transverse components of the spin operators.

Therefore the four unperturbed eigenstates of two-spin system become $|+,+\rangle$, $|+,-\rangle$, $|-,+\rangle$ and $|-,-\rangle$ with the respective occupation members N_{++}, N_{+-}, N_{-+} and N_{--}. The transition probabilities between these four states shown in Fig. 6(a) are represented by w_0, w_1, w_1' and w_2.

Next, four eigenstates of the transverse components of the magnetic moment must be also defined. These four eigenstates of the spins are expressed by

$$\left\{\begin{aligned} &I_{1\xi}|\alpha\rangle=\tfrac{1}{2}|\alpha\rangle \\ &I_{1\xi}|\beta\rangle=-\tfrac{1}{2}|\beta\rangle \\ &I_{2\xi}|\alpha)=\tfrac{1}{2}|\alpha) \\ &I_{2\xi}|\beta)=-\tfrac{1}{2}|\beta)\ . \end{aligned}\right. \tag{A2}$$

Hence the four states of a pair, $|\alpha,\alpha\rangle$, $|\alpha,\beta\rangle$, $|\beta,\alpha\rangle$ and $|\beta,\beta\rangle$, are not eigenstates of the energy. According to Solomon's theory, however, we can define the occupation numbers $N_{\alpha\alpha}$, $N_{\alpha\beta}$, $N_{\beta\alpha}$ and $N_{\beta\beta}$, and the transition probabilities u_0, u_1, u_1' and u_2 between these states, as are indicated on Fig. 6(b).

The macroscopic magnetic moments of $\bar{I}_{1\zeta}$ and $\bar{I}_{2\zeta}$ are given by the following equations:

$$\left\{\begin{aligned} &K\bar{I}_{1\zeta}=(N_{++}+N_{+-})-(N_{-+}+N_{--}) && \text{(A3a)} \\ &K\bar{I}_{2\zeta}=(N_{++}+N_{-+})-(N_{+-}+N_{--})\ . && \text{(A3b)} \end{aligned}\right.$$

Similar equations are also given for the transverse components $\bar{I}_{1\xi}$ and $\bar{I}_{2\xi}$.

Thus, the equations of motion of the longitudinal component and the transverse one in the two spin system lead to the following equations, respectively:

$$\left\{\begin{aligned} &\frac{d(\bar{I}_{1\zeta}+\bar{I}_{2\zeta})}{dt}=-2(w_1+w_2)(\bar{I}_{1\zeta}+\bar{I}_{2\zeta}-2\bar{I}_0) && \text{(A4a)} \\ &\frac{d(\bar{I}_{1\xi}+\bar{I}_{2\xi})}{dt}=-2(u_1+u_2)(\bar{I}_{1\xi}+\bar{I}_{2\xi})\ . && \text{(A4b)} \end{aligned}\right.$$

In conclusion, the longitudinal relaxation time T_1 and the transverse one T_2 are given respectively by

$$\left\{\begin{aligned} &1/T_1=2(w_1+w_2) && \text{(A5a)} \\ &1/T_2=2(u_1+u_2)\ . && \text{(A5b)} \end{aligned}\right.$$

References

1) H. S. Gutowsky, A. Saika, M. Takeda and D. E. Woessnes: J. Chem. Phys. **27** (1957) 534.
2) A. W. Nolle: Phys. Rev. **98** (1955) 1560.
3) J. C. Kirkwood and R. M. Fuoss: J. Chem. Phys. **9** (1941) 329. W. G. Hammerle and J. G. Kirkwood: ibid. **23** (1955) 1743.
4) P. E. Rouse: J. Chem. Phys. **21** (1953) 1272.
5) F. Bueche: J. Chem. Phys. **22** (1954) 603.
6) A. Miyake: J. Polymer Sci. **28** (1958) 476.
7) J. G. Kirkwood: J. Polymer Sci. **12** (1954) 1.
8) Y. Ikeda: Bull. Kobayasi Inst. Phys. Res. **6** (1956) 44 (in Japanese).
9) L. de Bronckere, D. Buess and L. K. H. Van Beek: J. Polymer Sci. **23** (1957) 233.
10) A. W. Nolle: unpublished.
11) N. Bloembergen, E. M. Purcell and R. V. Pound: Phys. Rev. **73** (1948) 679.
12) R. Kubo and K. Tomita: J. Phys. Soc. Japan **9** (1954) 888.
13) I. Solomon: Phys. Rev. **99** (1955) 559.
14) A. G. Redfield: I. B. M. Journal **1** (1957) 19.
15) S. Chandrasekhar: Rev. Mod. Phys. **15** (1953) 1.
16) T. G. Fox and S. J. Loshack: J. Appl. Phys. **26** (1955) 1080.
17) F. R. Eirich: *Rhoeology* vol. **1**, (Academic Press, New York, 1956) chap. 12, 431.
18) W. P. Mason and H. J. Mcskimin: Bell Syst. Tech. J. **31** (1952) 122. W. O. Baker and J. H. Heiss: ibid. **31** (1952) 306.
19) J. G. Powles: Proc. Phys. Soc. London **69** (1956) 281.
20) H. S. Gutowsky and G. E. Pake: J. Chem. Phys. **18** (1950) 162.
21) W. Kauzmann: Rev. Mod. Phys. **14** (1942) 12.

JOURNAL OF THE PHYSICAL SOCIETY OF JAPAN, Vol. 14, No. 6, JUNE, 1959

Effects of Gamma Rays on Aqueous Solution of Polyvinyl Alcohol

By Osamu SAITO

Faculty of Engineering, Chuo University, Bunkyo-ku, Tokyo

(Received March 4, 1959)

The general treatment developed in previous papers is applied to the case where the aqueous solution of polyvinyl alcohol is irradiated by gamma rays and the results are compared with Danno's measurements. The behaviours of irradiated aqueous solution of polyvinyl alcohol before and after gelation are well explained by the author's general theory. It is concluded from the analysis that end-linking instead of cross-linking occurs in the solution and also that only one molecular end out of the two which are produced by molecular scission of a polymer links with a monomer unit of another polymer molecule. It is also shown that if any impurity, especially oxygen, is not contained, the intrinsic viscosity of polyvinyl alcohol increases with radiation dose.

§ 1. Introduction

The author developed in his previous papers$^{1)-3)}$ a general theory concerning the effects of high energy radiation on polymers. In this paper the theory will be applied to the case where the aqueous solution of polyvinyl alcohol is irradiated by gamma rays. A. Danno measured the intrinsic viscosity and the gel point of polyvinyl alcohol irradiated by gamma rays$^{4)}$. These results are shown in Figs. 1 and 2. The change in viscosity-average degree of polymerization with increasing amount of radiation dose is represented in Fig. 1, and the dose for the incipient gel formation shown in Fig. 2 has a minimum at a certain value of concentration. The properties shown in these figures must be accounted for by a general theory.

When a polymer is irradiated by ionizing radiation, the intrinsic viscosity $[\eta]$ will change its value with the radiation dose R. It has been shown in the previous paper[3] that in the early period of irradiation we have the relation:

$$[\eta]/[\eta]_0=1+A_1R+A_2R^2+\cdots\,, \qquad (1)$$

where $[\eta]_0$ is the intrinsic viscosity before irradiation. The viscosity-average degree of polymerization $\bar{p}$ is likewise expressible in the following form:

$$\bar{p}/\bar{p}_0=1+B_1R+B_2R^2+\cdots\,, \qquad (2)$$

where $\bar{p}_0$ is the initial value of $\bar{p}$ and

$$B_1=A_1/\alpha,\ B_2=(A_2/2)+(1-\alpha)A_1^2/2\alpha,\ \cdots. \qquad (3)$$

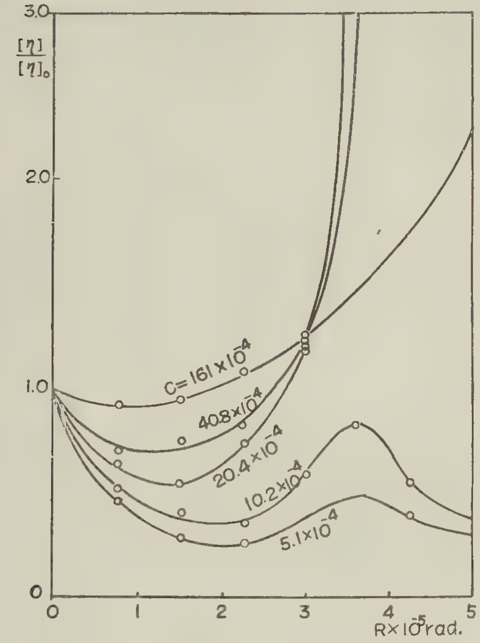

Fig. 1.

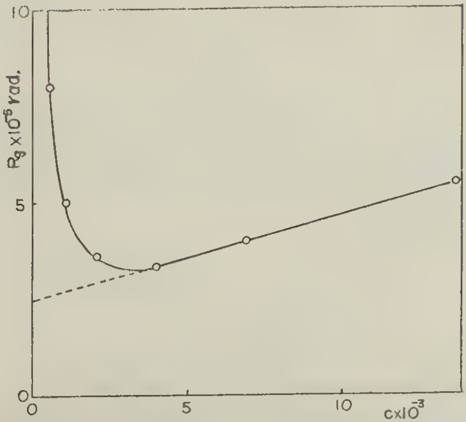

Fig. 2.

If cross-linking and degration occur in the irradiated polymer, the coefficients are given by the following formulas:

$$A_1=u\dot{c}\alpha\left\{\frac{(\alpha+2)(\alpha+7)}{6}-\lambda\right\}, \qquad (4)$$

$$A_2=\frac{u^2\dot{c}^2\alpha(\alpha+1)}{2}\left\{\frac{(\alpha+2)(\alpha+3)(\alpha+7)(\alpha+14)}{90}-\frac{(\alpha+2)(\alpha+7)}{3}\lambda+\lambda^2\right\}, \qquad (5)$$

where u is the number-average degree of polymerization before irradiation, α is the exponent in the relation between the intrinsic viscosity and number-average molecular weight, $\dot{c}$ is the probability that a monomer unit irradiated by radiation of unit dose will cross-link with a monomer unit of another molecule, and $\lambda=\dot{r}/\dot{c}$, where $\dot{r}$ is the probability that a monomer unit irradiated by radiation of unit dose will be scissored. The value of α may vary with radiation dose. In the early period of irradiation, however, it may not differ greatly from the value before irradiation. We may, therefore, use 0.62[5] for the value of α of polyvinyl alcohol.

If the polyvinyl alcohol whose number-average degree of polymerization is u is irradiated by gamma rays and the change of intrinsic viscosity is measured, the values of A_1 and A_2 will easily be calculated from the viscosity curve. Then we obtain $\dot{c}$ and λ by solving Eqs. (4) and (5). And the radiation dose necessary for the incipient gel formation is given by

$$R_g=1/u\dot{c}(4-\lambda)\,. \qquad (6)$$

It is usually difficult to get the accurate value of A_2. When the value of $\dot{c}$ is very small, the values of $\dot{c}$ and λ cannot be accurately calculated from Eqs. (4) and (5). We must then use Eq. (6) instead of Eq. (5).

When the end-linking occurs in the irradiated polymer, the coefficients A_1 and A_2 are given by the following formulas[3]:

$$A_1=u\dot{r}\alpha\{(\alpha+3)\sigma-1\}\,, \qquad (7)$$

$$A_2=\frac{u^2\dot{r}^2\alpha(\alpha+1)}{2}\left\{\frac{3}{4}\sigma^2(\alpha+2)(\alpha+3)-2\sigma(1-\sigma)(\alpha+2)+(1-\sigma)^2\right\}, \qquad (8)$$

where σ is the probability that a molecular end prouced by a main chain scission will link with a monomer unit of another molecule. We get $\dot{r}$ and σ by solving these equations.

Then the radiation dose necessary for the incipient gel formation is given by

$$R_g=1/\dot{r}(4\sigma-1)\,. \tag{9}$$

When the value of $\dot{r}$ is very small, we must calculate $\dot{r}$ and σ from Eqs. (7) and (9).

These results were derived for polymers not in solution. However, if we consider the fact that the probabilities $\dot{c}$, $\dot{r}$ and σ are determined by the circumstances around the ploymer molecule, they may be expected to be applicable to the cases where polymers are in solution or contain impurities.

§ 2. Cross-linking and Degration

As is shown in Fig. 2 gel is formed in the irradiated aqueous solution of polyvinyl alcohol. This fact indicates that cross-linking or end-linking is produced in the solution. Let us now assume that cross-linking occurs in it. In Fig. 2 the curve for larger concentration is linear. When the linear portion is extended back to lower concentration, it does not go through the origin. Danno[4] showed that the product uR_{gi} is independent of the value of u, where u is the initial degree of polymerization of polyvinyl alcohol and R_{gi} is the dose corresponding to the intersection of the extended line and the ordinate axis. This fact can be accounted for by the consideration that a fraction of radiation energy is consumed by some impurity perhaps oxygen, and R_g-R_{gi} is the net dose necessary for the incipient gel formation. We should notice the fact that the coefficients A_1 and A_2 of Eq. (1) are much influenced by impurity. On the contrary, if we use R_g-R_{gi} instead of R_g of Eq. (6), the right hand side of the equation must be independent of the effect of impurity.

When the aqueous solution of polyvinyl alcohol is irradiated, the following two cases may be conceivable. The first is that the radiation reacts upon polymer molecules directly and produces active centres, for example free redicals, which cross-link with monomer units of other molecules. The second is that the radiation reacts upon water molecules and dissociates some of them. The products give active centres to polymer molecules, and the active centres cross-link with monomer units of other molecules. Let us call the former the direct action and the latter the indirect action of radiation. For the case where the polymer is degraded by radiation, the direct and indirect action are also conceivable. Let us denote by $\dot{c}_0$ the probability that a monomer unit irradiated by radiation of unit dose will cross-link directly with a monomer unit of another polymer molecule. $\dot{c}_0$ is independent of the concentration of polymer. If we denote by $\dot{a}_1$ the probability that a water molecule will be dissociated by radiation of unit dose, the probability that a monomer unit irradiated by radiation of unit dose will indirectly cross-link is

$$\dot{a}_1(1-c)/c\,, \tag{10}$$

where the effect of impurity is neglected and the ratio of the total number of monomer units and the number of water molecules is expressed as $c:1-c$. When the effect of impurity is not neglected, the probability becomes

$$\dot{a}_1\frac{1-c}{c}\,\frac{c}{c+k_1}=\dot{a}_1\frac{1-c}{c+k_1}\,, \tag{11}$$

where k_1 is proportional to the amount and the reaction rate of impurity, but it does not depend on the concentration c. Thus the total probability that a monomer unit irradiated by radiation of unit dose will cross-link is given by

$$\dot{c}=\dot{c}_0+\dot{a}_1\frac{1-c}{c+k_1}\,. \tag{12}$$

Similarly the total probability that a monomer unit irradiated by radiation of unit dose will be ruptured is given by

$$\dot{r}=\dot{r}_0+\dot{a}_2\frac{1-c}{c+k_2}\,, \tag{13}$$

where $\dot{r}_0$ is the probability that a monomer unit will be directly ruptured by radiation of unit dose, $\dot{a}_2$ is the probability that a water molecule will be dissociated by radiation of unit dose, and k_2 is proportional to the amount and the reaction rate of impurity. In general, $\dot{a}_1$ will not have the same value as $\dot{a}_2$. Substituting Eqs. (12) and (13) into Eqs. (3) and (4), we obtain

$$B_1=u\left[\{\beta(\dot{c}_0-\dot{a}_1)-(\dot{r}_0-\dot{a}_2)\}+\beta\dot{a}_1\frac{1+k_1}{c+k_1}\right.$$
$$\left.-\dot{a}_2\frac{1+k_2}{c+k_2}\right], \tag{14}$$

where $\beta=(\alpha+2)(\alpha+7)/6$. Since the effect of impurity is not included in the radiation dose R_g-R_{gi}, we obtain from Eq. (6) the relation:

$$\frac{1}{R_g+R_{gi}}=u(4\dot{c}\psi-\dot{r})$$
$$=u\left\{4(\dot{c}_0-\dot{a}_1)\phi-(\dot{r}_0-\dot{a}_2)+\frac{4\dot{a}_1\phi-\dot{a}_2}{c}\right\}, \tag{15}$$

where ϕ has been introduced for the following reason. It is very difficult for polymer molecules in lower concentration to interact upon each other. The larger are the polymer molecules, the smaller are their mobilities. When the polymer concentration is very small, large molecules will hardly interact upon each other, and the probability of cross-linking $\dot{c}$ will be diminished. ϕ is a factor expressing this property, and it varies with the concentration c and becomes unity for larger concentration. If we plot $1/(R_g-R_{gi})$ against $1/c$, we must obtain a straight line for the smaller values of $1/c$. This is the case for Fig. 3, where the values of $1/(R_g-R_{gi})$ for the aqueous solution of polyvinyl alcohol is plotted against $1/c$. From this linear portion we obtain the relations:

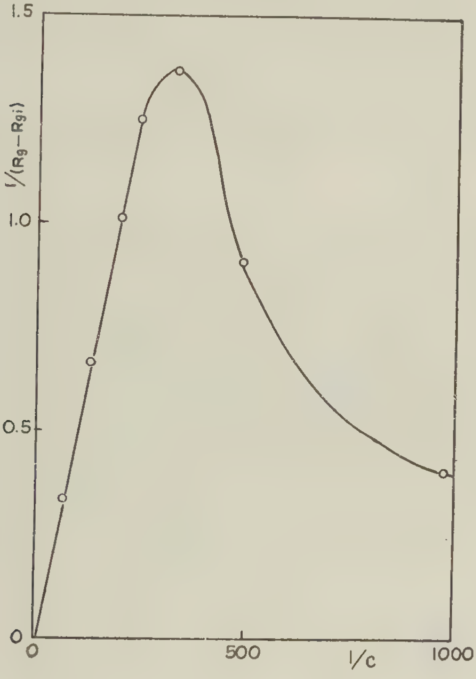

Fig. 3.

$$4(\dot{c}_0-a_1)-(\dot{r}_0-\dot{a}_2)=0\ , \tag{16}$$
$$4\dot{a}_1-\dot{a}_2=5.51\times10^{-6}\ . \tag{17}$$

It is shown by Eq. (14) that if we plot B_1 against $1/c$, a straight line must be obtained for smaller values of $1/c$. This is the case for Fig. 4. From the slope of this line we get the relation:

$$\beta\dot{a}_1(1+k_1)-\dot{a}_2(1+k_2)=3.10\times10^{-3}\ . \tag{18}$$

And for $c=0$ we also get the following values from extrapolating the measured values in Fig. 5.

$$B_1=-1.11 \quad \text{and} \quad dB_1/dc=-177\ . \tag{19}$$

By solving Eqs. (16)~(19), we obtain

$$\dot{a}_1=0\ , \quad \dot{a}_2=-5.51\times10^{-6}\ ,$$
$$k_1=0\ , \quad k_2=-2.8\times10^{-3}\ .$$

These results are unreasonable. On the other hand, by determining the parameters of Eq. (14) so that it may well represent all the measured values of B_1, the following values are obtained:

$$\dot{a}_1=0.855\times10^{-5}\ , \quad \dot{a}_2=2.58\times10^{-5}\ ,$$

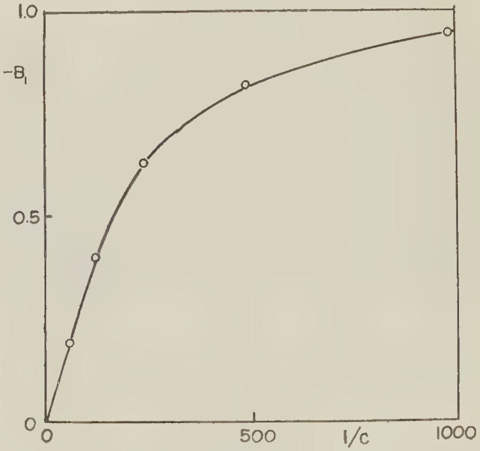

Fig. 4.

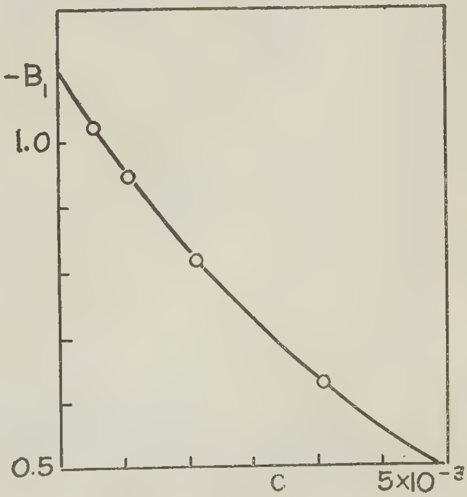

Fig. 5.

$$k_1=2.0\times10^{-2}\ , \qquad k_2=1.0\times10^{-2},$$

From these results we get

$$4\dot{a}_1-\dot{a}_2=8.40\times10^{-6}\ .$$

This is contradictory to Eq. (17). We may, therefore, conclude that cross-linking does not occur in the irradiated aqueous solution of polyvinyl alcohol.

§ 3. End-linking

Now we assume that end-linking occurs in the irradiated aqueous solution of polyvinyl alcohol. Linkage and scission are independent of each other in cross-linking, but they are correlated with each other in end-linking. In end-linking the probabilities $\dot{r}$ and σ are the fundamental parameters. Since $\dot{r}$ is the same as that in the preceding section, it is expressed as follows:

$$\dot{r}=\dot{r}_0+\dot{a}\frac{1+c}{c+k_1} \tag{20}$$

where $\dot{r}_0$ is the probability that a monomer unit will be directly ruptured by radiation of unit dose, $\dot{a}$ is the probability that a water molecule will be dissociated by radiation of unit dose, and k_1 is proportional to the amount and the reaction rate of impurity, but not dependent on the polymer concentration. The probability σ that an active end produced by molecular scission will link with a monomer unit of another molecule is expressed as

$$\sigma=\sigma_0\frac{c}{c+k_2}\ , \tag{21}$$

where σ_0 is the value of the probability σ for large polymer concentration and negligibly small amount of impurity, and k_2 is proportional to the amount and the reaction rate of impurity which inhibits the end-linking. The value of σ_0 is the same as that of σ for solid polyvinyl alcohol. Substituting Eqs. (20) and (21) into Eqs. (3) and (7), we get

$$B_1=u\left\{\dot{r}_0+\dot{a}\frac{1-c}{c+k_1}\right\}\left\{\frac{(\alpha+3)\sigma_0 c}{c+k_2}-1\right\}\ , \tag{22}$$

and hence Eq. (9) gives

$$\frac{1}{R_g-R_{gi}}=u\left\{\dot{r}_0+\dot{a}\frac{1-c}{c}\right\}(4\sigma_0\phi-1)\ , \tag{23}$$

where ϕ is the same factor as that considered in the preceding section. If we determine the parameters in Eqs. (20) and (21) by considering the linear portion in Fig. 3 and the measured values of B_1, the following results are obtained:

$$\dot{r}_0=2.28\times10^{-5}\ , \quad \dot{a}=2.28\times10^{-5}\ , \quad \sigma_0=0.31\ ,$$
$$k_1=2.0\times10^{-2}\ , \qquad k_2=1.0\times10^{-2}\ .$$

The value of σ_0 is larger than $1/(\alpha+3)=0.276$. We know[3], therefore, that the viscosity-average molecular weight of polyvinyl alcohol irradiated in aqueous solution increases with radiation dose, if no impurity is contained.

The G-value of the dissociation of water molecules is given by the formula:

$$G_a=\frac{(\text{Avogadro number}/18)\,\dot{a}}{\text{absorbed energy in e.v./gram/dose}}\times100$$
$$=12\ ,$$

the G-value of main chain rupture of solid polyvinyl alcohol by

$$G_r=\frac{(\text{Avogadro number}/44)\,\dot{r}_0}{\text{absorbed energy in e.v./gram/dose}}\times100$$
$$=5.0\ ,$$

and the G-value of end-linking for solid polyvinyl alcohol by

$$G_{\text{e.l.}}=\frac{(\text{Avogadro number}/44)\,2\dot{r}_0\sigma_0}{\text{absorbed energy in e.v./gram/dose}}\times100$$
$$=3.1\ .$$

Therefore, the energy for producing an end-linkage is 32 e.v.. It is assumed in this case that two ends produced by a molecular scission are active. If we assume that only one of the two ends is active, the G-value becomes a half of the above-mentioned value, and the energy for producing an end-linkage is 62 e.v., which agrees with Danno's experimental result.

Thus it is concluded that end-linking occurs in the irradiated aqueous solution of polyvinyl

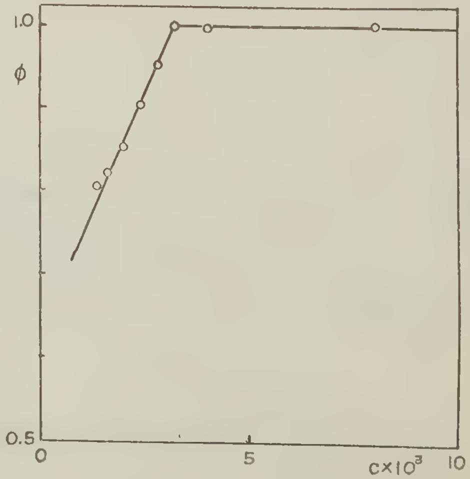

Fig. 6.

alcohol and that only one of the two molecular ends produced by a molecular scission is active and links with a monomer unit of another molecule.

The factor ϕ in Eq. (23) is equal to unity for larger value of c. Comparing Eq. (23) with the curve in Fig. 3, we should obtain the relation between ϕ and c. However, there being only a few observed values, we could not hope to find correct relation. Therefore, in order to know the approximate behaviour of ϕ, we have calculated the values of ϕ, by interpolating the values of $1/(R_g-R_{gi})$ in Fig. 3. The result is shown in Fig. 6. It will be seen that the curve of ϕ against c is approximately linear. From this fact it may be considered that the probability that an active centre will end-link with a monomer unit of another molecule is proportional to the number of polymer molecules contained in a sphere of definite radius with centre at the active centre. The more correct measurments are, however, necessary in order to know the details.

§ 4. Summary

Effects of radiation on aqueous solution of polymers have been discussed by a few authors. There has, however, been no successful attempt to explain the properties before and after gelation at a single stroke. The author applies his theory to the irradiated aqueous solution of polyvinyl alcohol and shows that end-linking instead of cross-linking occurs in the solution. He also calculates G-values of molecular scission and end-linking, the values thus obtained being in good agreement with those obtained by A. Danno. The author concludes that only one molecular end out of the two which are produced by molecular scission links with a monomer unit of another polymer molecule. It is also shown that if no impurity is present, the intrinsic viscosity and the viscosity-average molecular weight of irradiated polyvinyl alcohol in aqueous solution increase with radiation dose. When the concentration of polymer is very low, linking between large molecules is hindered and the gel formation suppressed. This is the reason why the radiation dose necessary for the incipient gel formation has a minimum. In order to know the details, more accurate experiments are desired.

Acknowledgement

The author wishes to express his sincere thanks to Professor A. Amemiya, for his continued interest and support in all phases of this research. He wishes to thank Professor A. Harasima, Dr. K. Shinohara and Mr. A. Danno for their valuable suggestions as well as guidances and also the members of the Group for the Study of Irradiated Polymers in Tokyo for discussions.

References

1) O. Saito: J. Phys. Soc. Japan **13** (1958) 198.
2) O. Saito: J. Phys. Soc. Japan **13** (1958) 1451.
3) O. Saito: J. Phys. Soc. Japan **13** (1958) 1465.
4) A. Danno: J. Phys. Soc. Japan **13** (1958) 722.
5) H. Staudinger and H. Warth: J. Prak. Chem. **155** (1940) 261.

JOURNAL OF THE PHYSICAL SOCIETY OF JAPAN, Vol. 14, No. 6, JUNE, 1959

Effect of Impurity on Molecular Linking of Irradiated Polymer

By Osamu SAITO

Faculty of Engineering, Chuo University Bunkyo-ku, Tokyo

(Received March 4, 1959)

The effect of impurity on cross-linking or end-linking of an irradiated polymer is discussed theoretically. It is shown that the radiation effect on a pure polymer can be found by measuring the intrinsic viscosity and the gel point of an irradiated polymer containing an impurity. The theory is compared with Chapiro's measurements. One of the important results is that when impurity hinders cross-linking, all the relations between physical quantities of an irradiated polymer containing impurity can be reduced to those of the polymer containing no impurity, if use is made of a reduced radiation dose instead of the real dose. This is not the case for the effect of impurity on end-linking. Such a difference is expected to enable us to distinguish between cross-linking and end-linking.

§ 1. Introduction

The author has developed in his previous papers[1)-3)] a theory concerning the effects of high energy radiation on polymers. In this paper the theory will be extended to cover the effect of impurity. Polymers contain usually some impurity, for example, oxygen. Polymer in the market contain more or less additives, the effect of which may not be neglected. The effect of oxygen is especially important, because a little amount of oxygen gives a fairly large effect on polymers and it is very difficulty to remove oxygen completely out of them. On the contrary, if we know how it reacts upon polymers, we may be able to know the radiation effects on pure polymers by analyzing the experimental results for various pressure of oxygen.

§ 2. Effect of Impurity on Cross-linking

When a polymer contains some radical scavenger, radiation cross-linking will be hindered by it. The mechanism is considered as follows. Active centres will be produced by radiation on some of monomer units.

This probability will be denoted by $\dot{c}$ as in the previous paper. When a polymer contains some impurity, $\dot{c}$ is lowered by the effect. Let us denote by $n(p, R)$ the number of polymer molecules which give the degree of polymerization p and are irradiated by radiation of dose R. When the radiation dose is increased from R to $R+dR$, the increment of $n(p, R)$ is given by

$$dn(p, R) = -pn(p, R)\dot{c}dR\left(\frac{kN}{kN+k'n_i}\right) - N\dot{c}\left(\frac{kpn(p, R)}{kN+k'n_i}\right)dR + \int_0^p ln(l, R)\,dl\,\dot{c}\,dR\left\{\frac{k(p-l)n(p-l, R)}{kN+k'n_i}\right\}, \tag{1}$$

where N is the total number of monomer units, n_i is the number of impurity molecules, k is the reaction rate constant for the active centre and monomer unit, and k' is the constant for the active centre and impurity. If we write

$$m(p, R) = n(p, R)/N, \quad m_i(R) = n_i(R)/N, \quad k_i = k'/k,$$

Eq. (1) becomes

$$\frac{\partial m(p, R)}{\partial R} = \frac{1}{(1+k_i m_i)}\left\{-2pm(p, R) + \int_0^p l(p-l)m(l, R)m(p-l, R)\,dl\right\}. \tag{2}$$

If we introduce a new variable

$$\bar{R} = \int_0^R \frac{dR}{1+k_i m_i}, \tag{3}$$

Eq. (2) becomes

$$\frac{\partial m(p,\ \overline{R})}{\partial \overline{R}}=-2pm(p,\ \overline{R})+\int_0^p l(p-l)m(l,\ \overline{R})m(p-l,\ \overline{R})dl\,. \tag{4}$$

This is the same as the equation for the polymer containing no impurity, which has been considered in detail in our previous papers.[1)-3)]

The increment of the number of impurity molecules is given by

$$dn_i(R)=-N\dot{c}dR\left(\frac{k'n_i}{kN+k'n_i}\right)+N\phi dR\,, \tag{5}$$

where ϕ represents the amount of impurity which is supplied from outside per monomer unit and per unit radiation dose. This equation can be written in another form:

$$\frac{dm_i}{dR}=-\frac{\dot{c}k_i m_i}{1+k_i m_i}+\phi\,, \tag{6}$$

where $m_i=n_i/N$. This can be easily solved, when ϕ is known.

Case A. m_i=const. When the supply of impurity from outside is enough, m_i takes a constant value, say A. In this case Eq. (3) gives

$$R/\overline{R}=1+k_iA. \tag{7}$$

$\overline{R}$ can be easily obtained from the experimental curves as shown in Fig. 1, where the abscissa is the radiation dose and the ordinate is any one of physical quantities, for example, viscosity, molecular weight, melting point and so forth. The relation between R and $\overline{R}$ is linear. The slope varies with A. The radiation dose R_g necessary for the incipient gel formation is related to the dose R_g for the polymer containing no impurity by the following formula:

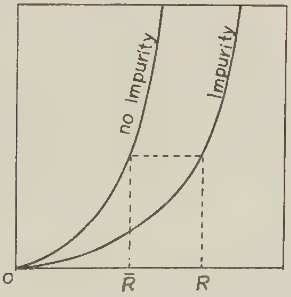

Fig. 1.

$$(R_g-\overline{R}_g)/\overline{R}_g=k_iA \tag{8}$$

The left hand side must, therefore, by proportional to the amount of impurity A. When a thin film of polymer is irradiated in air by radiation of low dose rate, the amount of oxygen in the polymer will always be constant. If we perform experiments under various pressures of oxygen, $(R_g-\overline{R}_g)/\overline{R}_g$ plotted against the pressures of oxygen will give a straight line, because A will be proportional to the pressure.

Case B. $\phi\equiv0$. This is the case where there is no supply of impurity from outside and this is more easily realized by experiment than the preceding case. When the initial value of m_i is A, Eq. (6) gives

$$R=\overline{R}+(A/\dot{c})\{1-\exp(-k_i\dot{c}\overline{R})\}\,. \tag{9}$$

Then we get

$$\left(\frac{dR}{d\overline{R}}\right)=1+k_iA\exp(-k_i\dot{c}\overline{R}) \tag{10}$$

and after a certain value of R, we get the following relation

$$\frac{dR}{d\overline{R}}=1\,. \tag{11}$$

Chapiro[4)] measured the change in melting point of polyethylene film irradiaed in air. The relation between R and $\overline{R}$ deduced form the measurement is represented is Fig. 2. The initial slope of the curve is 7.5. The slope decreases gradually to the ultimate value unity. For larger values of $\overline{R}$ Eq. (9)

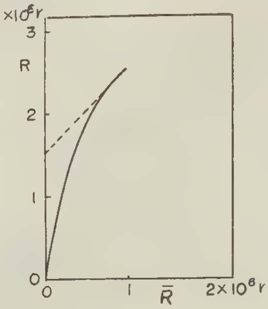

Fig. 2.

is reduced to

$$R=\overline{R}+A/\dot{c}\,. \tag{12}$$

This is a linear relation. If we extend the line back to $\overline{R}=0$, the intersection of the line and the ordinate axis gives

$$\frac{A}{\dot{c}}=1.54 \quad (10^6\mathrm{r})^{-1}.$$

If we assume that the G-value of cross-linking of irradiated polyethylene is 6.8,⁵⁾ we obtain

$$\dot{c}=1.8\times10^{-4} \quad (10^6\mathrm{r})^{-1},$$

so that

$$A=2.8\times10^{-4}.$$

This value means that there existed initially 2.8 oxygen molecules per 10^4 monomer units. Since ϕ is not zero in Chapiro's experiment, the abovementioned value of A will be a little larger than the true value.

At the gel point Eq. (9) becomes

$$R_g=\overline{R}_g+(A/\dot{c})\{1-\exp(-k_i\dot{c}\overline{R}_g)\}\,. \tag{13}$$

This shows that the radiation dose necessary for the incipient gel formation is a linear function of the amount of impurity. We can calculate the parameters A, $\dot{c}$, R_g and k_i form Eq. (10) and (13) and the value of $A/\dot{c}$ which is obtained from Eq. (12).

Case C. $k_i m_i \ll 1$. In this case Eq. (6) becomes

$$\frac{dm_i}{dR}+\dot{c}k_i m_i=\phi\,, \tag{14}$$

When ϕ is a known function of R, the solution is

$$m_i=\exp(-k_i\dot{c}R)\left\{\int_0^R \phi\exp(k_i\dot{c}R)dR+A\right\}. \tag{15}$$

Let us consider the case where m_i is equal to A for $0\leqq R\leqq R_1$, and then $\phi\equiv0$ for $R>R_1$, then Eq. (15) gives

$$m_i=\begin{cases}A\,, & \text{for } 0\leqq R\leqq R_1\,,\\ A\exp\{-k_i\dot{c}(R-R_1)\}\,, & \text{for } R_1<R\,,\end{cases} \tag{16}$$

and Eq. (3) becomes

$$\overline{R}=\begin{cases}R/(1+k_iA)\,, & \text{for } 0\leqq R\leqq R_1\,,\\ R-R_1-(A/\dot{c})[1-\exp\{-k_i\dot{c}(R-R_1)\}]\,, & \text{for } R_1<R\,.\end{cases} \tag{17}$$

For large R it becomes

$$\overline{R}=R-R_1-A/\dot{c}\,. \tag{18}$$

If ϕ is proportional to $A-m_i$, that is

$$\phi=\kappa(A-m_i)\,, \tag{19}$$

then Eq. (14) becomes

$$\frac{dm_i}{dR}+(\dot{c}k_i+\kappa)m_i=\kappa A\,, \tag{20}$$

which can be integrated to give

$$m_i=\frac{\kappa A}{\kappa+\dot{c}k_i}\left[1+\left(2+\frac{\dot{c}k_i}{\kappa}\right)\exp\{-(\kappa+\dot{c}k_i)R\}\right], \tag{21}$$

and hence from Eq. (3) we get

$$\overline{R}=\left(1-\frac{\kappa k_iA}{ck_i+\kappa}\right)R+\frac{k_iA(2\kappa+\dot{c}k_i)}{(\dot{c}k_i+\kappa)^2}\left[\exp\{-(\dot{c}k_i+\kappa)R\}-1\right]. \tag{22}$$

For large R it becomes

$$\overline{R}=\left(1-\frac{\kappa k_iA}{ck_i+\kappa}\right)R-\frac{k_iA(2\kappa+\dot{c}k_i)}{(\dot{c}k_i+\kappa)^2} \tag{23}$$

This is a linear relation but the slope is not equal to unity. Thus the behaviour is not the same as that in the preceding cases.

§ 3. Effect of Impurity on Cross-linking with Degradation

When degradation as well as cross-linking occurs in an irradiated polymer, the effects of impurity must be considered at the same time.

(i) Let us first consider the case where cross-linking is hindered by impurity, but degradation is not affected at all. In this case the following equations are derived

$$\frac{\partial m(p,\ \overline{R})}{\dot{c}\partial R}=-2pm(p,\ \overline{R})+\int_0^p l(p-l)m(l,\ \overline{R})m(p-l,\ \overline{R})dl\ , \tag{24}$$

$$\overline{R}=\int_0^R \frac{dR}{1+k_i m_i}\ . \tag{25}$$

However, the distribution function for $\overline{R}=0$ must be given by[1]

$$\left\{m(p,\ 0)+2\dot{r}p\int_p^\infty m(p,\ 0)dp+\dot{r}^2p^2\int_p^\infty dp\int_p^\infty m(p,\ 0)dp\right\}\exp(-p\dot{r}R)\ . \tag{26}$$

When the molecular weight distribution before irradiation is of the Poisson type, Eq. (26) becomes

$$\left(\frac{1}{u}+\dot{r}R\right)^2\exp\left\{-\left(\frac{1}{u}+\dot{r}R\right)p\right\}\ , \tag{27}$$

where u is the number-average degree of polymerization before irradiation.

When the supply of impurity is enough, m_i is equal to a constant, say A.

Then the relation between R and $\overline{R}$ becomes

$$\overline{R}=R/(1+k_iA) \tag{28}$$

if we assume

$$\dot{c}_i=\dot{c}/(1+k_iA) \tag{29}$$

Eq. (24) becomes equal to that for the polymer containing no impurity. Therefore, if we use rupturing probability $\dot{r}$ and reduced cross-linking probability $\dot{c}_i$, the behaviour of irradiated polymer including impurity is reduced to that for the polymer containing no impurity. For instance, the number and the weight-average molecular weight are given respectively by

$$M_n(R)=M_n(0)/\{1+(\dot{r}-2\dot{c}_i)nR\}\ , \tag{30}$$

$$M_w(R)=M_w(0)/\{1+(\dot{r}-4\dot{c}_i)uR\}\ , \tag{31}$$

and the intrinsic viscosity is given by[3]

$$\frac{[\eta]}{[\eta]_0}=\frac{2\sin(\alpha\pi)}{\pi\alpha(\alpha+1)(1+u\dot{r}R)^\alpha}\int_0^1\frac{y^{\alpha+1}dy}{(1-y)^\alpha\{1-Ky(y+1)\}^\alpha}\ , \tag{32}$$

where

$$K=2u\dot{c}_iR/(1+u\dot{r}R)\ . \tag{33}$$

When R is sufficiently small

$$[\eta]/[\eta]_0=1+a_1R+a_2R^2+\cdots\ , \tag{34}$$

where

$$a_1=u\alpha\left\{\frac{(\alpha+2)(\alpha+7)}{6}c_i-r\right\}\ ,\qquad \text{etc.} \tag{35}$$

The radiation dose necessary for the incipient gel formation is given by

$$R_g=1/\{u(4\dot{c}_i-\dot{r})\}\ . \tag{36}$$

The relation between R_g and A is not linear. When A is very small, Eq. (36) becomes

$$1/R_g=u(4\dot{c}-\dot{r})-4u\dot{c}k_iA\ . \tag{37}$$

If the initial slope a_i in Eq. (34) is measured, and the value and the slope of $1/R_g$ at $A=0$ are determined, the parameters $\dot{c}$, $\dot{r}$ and k_i can all be calculated from Eq. (35) and (37). When there is no supply of impurity during irradiation, the following formula is derived:

$$R=\overline{R}+(A/\dot{c})\{1-\exp(-k_i\dot{c}\overline{R})\}\ . \tag{38}$$

The number- and the weight-average molecular weight are repectively

$$M_n(R)=M_n(0)/\{1+u\dot{r}R-2u\dot{c}\overline{R}\}\ ,$$

$$M_w(R)=M_w(0)/\{1+u\dot{r}R-4u\dot{c}\overline{R}\}\ . \tag{39}$$

We know from the last formula that if there hold inequalities

$$4/(1+R_iA)<\dot{r}/\dot{c}<4\ , \tag{40}$$

the weight-average molecular weight has a minimum. Such a behaviour never occurs for polymers containing no impurity. We must, however, remember the fact that the viscosity-average molecular weight for a polymer including no impurity may have also a minimum.

The dose for incipient gel formation is given by

$$R_g=(1+4u\dot{c}\overline{R}_g)/u\dot{r} \tag{41}$$

where $\overline{R}_g$ satisfies the equation:

$$1+u\overline{R}_g(\dot{r}-4\dot{c})+(u\dot{r}A/\dot{c})\{1-\exp(-k_i\dot{c}\overline{R}_g)\}=0\ . \tag{42}$$

When A is not small, the relation between R_g and A is not linear. On the contrary, when A is sufficiently small, $1/R_g$ becomes a linear function of A, that is

$$\frac{1}{R_g}=u(4\dot{c}-\dot{r})-4u^2(4\dot{c}-\dot{r})A\left[1-\exp\left\{-\frac{k_i\dot{c}}{u(4\dot{c}-\dot{r})}\right\}\right]. \tag{43}$$

On the other hand, the intrinsic viscosity is given by

$$\frac{[\eta]}{[\eta]_0}=\frac{2\sin(\alpha\pi)}{\pi\alpha(\alpha+1)(1+u\dot{r}R)^\alpha}\int_0^1\frac{y^{\alpha+1}dy}{(1-y)^\alpha\{1-Ky(y+1)\}^\alpha}\ , \tag{44}$$

where

$$K=2u\dot{c}\overline{R}/(1+u\dot{r}R)\ . \tag{45}$$

When $\overline{R}_g$ is sufficiently small, Eq. (44) can be expanded in a series

$$\frac{[\eta]}{[\eta]_0}=1+u\alpha\left\{\frac{(\alpha+2)(\alpha+7)}{6(1+k_iA)}\dot{c}-\dot{r}\right\}R+\cdots\ . \tag{46}$$

If we measure the initial value and the slope of intrinsic viscosity $[\eta]$ as well as the value and the slope of $1/R_g$ at $A=0$, we can calculate the values $\dot{c}$, $\dot{r}$ and k_i from Eqs. (43), (46).

(ii) Let us next consider the case in which an impurity molecule not only combines with a molecular end produced by a molecular scission but also it hinders cross-linking. In this case the equation corresponding to Eq. (5) is given by

$$\frac{dm_i}{dR} = -\dot{c}\frac{k_c m_i}{1+k_c m_i} - 2\dot{r}\frac{k_r m_i}{1+k_r m_i} + \phi\,, \tag{47}$$

where k_c and k_r are the ratios of reaction rate constants and correspond respectively to cross-linking and rupture. When $k_c m_i \ll 1$ and $k_r m_i \ll 1$, Eq. (47) becomes

$$\frac{dm_i}{dR} = -(\dot{c}k_c + 2\dot{r}k_r)m_i + \phi\,. \tag{48}$$

Now let us divide m_i into two fractions m_i' and m_i'', where m_i' is the fraction of impurity which hinders cross-linking and m_i'' is the fraction of impurity which combines with molecular ends produced by scission. Then we obtain the relation:

$$dm_i' : dm_i'' = \dot{c}\frac{k_c m_i}{1+k_c m_i} : 2\dot{r}\frac{k_r m_i}{1+k_r m_i}\,. \tag{49}$$

Therefore

$$\frac{dm_i'}{dm_i} = \dot{c}\left(\frac{1}{k_r} + m_i\right)\Big/\left\{\frac{\dot{c}}{k_r} + \frac{2\dot{r}}{k_c} + (\dot{c} - 2\dot{r})m_i\right\}. \tag{50}$$

Since $k_c m_i \ll 1$ and $k_r m_i \ll 1$, Eq. (50) becomes

$$\frac{dm_i'}{dm_i} = \frac{k_c\dot{c}}{k_c\dot{c} + 2k_r\dot{r}} = \frac{1}{1 + 2\lambda\mu} \tag{51}$$

where $\lambda = \dot{r}/\dot{c}$ and $\mu = k_r/k_c$, so that

$$m_i' = m_i/(1+2\lambda\mu)\,. \tag{52}$$

Case A. When the supply of impurity during irradiation is enough, m_i has a constant value, say A. Then

$$m_i' = A/(1+2\lambda\mu)\,. \tag{53}$$

Accordingly

$$\frac{R}{\overline{R}} = 1 + \frac{k_c A}{1+2\lambda\mu}\,. \tag{54}$$

If we put

$$c_i = \dot{c}/(1+k_i A) \qquad \text{and} \qquad k_i = k_c/(1+2\lambda\mu)\,, \tag{55}$$

we can made the same discussions as those about Eqs. (30)∼(36).

Case B. When there is no supply of impurity, Eq. (48) gives

$$m_i = A\exp\{-(k_c\dot{c} + 2k_r\dot{r})R\} \tag{56}$$

and then

$$m_i' = A(1+2\lambda\mu)^{-1}\exp\{-(k_c\dot{c} + 2k_r\dot{r})R\}\,. \tag{57}$$

Therefore, we get

$$\overline{R} = R + \frac{1}{k_c\dot{c} + 2k_r\dot{r}}\log\left[1 - \frac{k_c A}{1+2\lambda\mu+k_c A}\left[1 - \exp\{-(k_c\dot{c} + 2k_r\dot{r})R\}\right]\right]. \tag{58}$$

Since $k_i A$ is very small, the following relation is derived:

$$R = \overline{R} + \frac{A}{\dot{c}(1+2\lambda\mu)^2}[1 - \exp\{-k_c\dot{c}(1+2\lambda\mu)R\}]\,. \tag{59}$$

Comparing Eq. (38) with (56), we know that if we replace $\dot{c}(1+2\lambda\mu)$ by $\dot{c}$ and $A/(1+2\lambda\mu)$ by A, Eq. (59) becomes the same as Eq. (38). Therefore, the same discussion as those about (38)$\sim$(46) can be repeated here.

(iii) Let us assume lastly that the scission of polymer molecules occurs at the same time in two ways, one way is that a monomer unit is directly ruptured by radiation and the other is that a cross-linking unit produced by radiation combines with an impurity and then ruptures instead of making cross-linking. In this case the equation for degradation becomes

$$\frac{\partial m(p,\ R)}{\partial R}=-p\left(\dot{r}+\frac{\dot{c}k_i m_i}{1+k_i m_i}\right)m(p,\ R)+2\int_p^\infty\left(\dot{r}+\frac{\dot{c}k_i m_i}{1+k_i m_i}\right)m(l,\ R)dl\,. \tag{60}$$

If we put

$$\overline{\overline{R}}=\int_0^R\left\{1+\frac{\dot{c}k_i m_i}{\dot{r}(1+k_i m_i)}\right\}dR\,, \tag{61}$$

Eq. (60) becomes

$$\frac{\partial m(p,\ \overline{\overline{R}})}{\dot{r}\partial\overline{\overline{R}}}=-pm(p,\ \overline{\overline{R}})+2\int_p^\infty m(l,\ \overline{\overline{R}})dl\,. \tag{62}$$

This is the same as for the polymer containing no impurity. When the initial molecular weight distribution is of the Poisson type, the degradation changes the distribution into the following form:

$$m(p,\ \overline{\overline{R}})=\left(\frac{1}{u}+r\overline{\overline{R}}\right)^2\exp\left\{-\left(\frac{1}{u}+\dot{r}\overline{\overline{R}}\right)p\right\}\,. \tag{63}$$

The effect of cross-linking on the molecular weight distribution is represented by Eqs. (24) and (25), and the change of the number of impurity molecules is given by Eq. (6).

Case A. When the supply of impurity is enough, m_i will have a constant value, say, A. If we replace $\dot{r}$ in the formulas for the case of no impurity by $\dot{r}+\dot{c}k_iA/(1+k_iA)$ and $\dot{c}$ in them by $\dot{c}/(1+k_iA)$, we obtain the formulas which take into account the effect of impurity.

Case B. When there is no supply of impurity during irradiation, the relations among R, $\overline{R}$ and $\overline{\overline{R}}$ are given by

$$R=\overline{R}+(A/\dot{c})\{1-\exp(-\dot{c}k_i\overline{R})\}\,, \tag{64}$$

$$R=A\exp(-\dot{c}k_iR)\{A-\dot{r}(\overline{\overline{R}}-R)\}\exp\{-\dot{c}k_i(\overline{\overline{R}}-R)\}\,. \tag{65}$$

The number- and the weight-average molecular weight are given respectively by

$$M_n(R)=M_n(0)/(1+u\dot{r}\overline{\overline{R}}-2u\dot{c}\overline{R})\,, \tag{66}$$

$$M_w(R)=M_w(0)/(1+u\dot{r}\overline{\overline{R}}-4u\dot{c}\overline{R})\,. \tag{67}$$

When A is sufficiently small, we get

$$\overline{R}=R+(A/\dot{c})\{1-\exp(-\dot{c}k_iR)\}+\cdots\,, \tag{68}$$

$$\overline{\overline{R}}=R+(A/\dot{r})\{1-\exp(-\dot{c}k_iR)\}+\cdots\,, \tag{69}$$

and the radiation dose for the incipient gel formation R_g is given by

$$1/R_g=u(4\dot{c}-\dot{r})-3u^2(4\dot{c}-\dot{r})A[1-\exp\{-k_i\dot{c}/(4\dot{c}-\dot{r})u\}]+\cdots\,. \tag{70}$$

The intrinsic viscosity is given by[3)]

$$\frac{[\eta]}{[\eta]_0}=\frac{2\sin(\alpha\pi)}{\pi\alpha(\alpha+1)(1+u\dot{r}\overline{\overline{R}})^\alpha}\int_0^1\frac{y^{\alpha+1}dy}{(1-y)^\alpha\{1-Ky(y+1)\}^\alpha}\,, \tag{71}$$

where

$$K=2u\dot{c}\overline{R}/(1+u\dot{r}\overline{\overline{R}})\,. \tag{72}$$

Where R is sufficiently small,

$$\frac{[\eta]}{[\eta]_0}=1+u\alpha\left\{\frac{(\alpha+2)(\alpha+7)}{6(1+k_iA)}\dot{c}-\dot{r}\right\}R+\cdots. \tag{73}$$

By comparing the measured values with Eqs. (70) and (73), we obtain the values of $\dot{c}$, $\dot{r}$ and k_i.

§ 4. Effect of Impurity on End-linking

The fundamental parameters in end-linking of an irradiated polymer are $\dot{r}$ and σ; the former is the same as the degrading probability $\dot{r}$ in degradation and the latter is the probability that an end produced by molecular scission will link with a monomer unit of another polymer molecule. The effect of impurity will reduce the value of σ. By the same consideration as that mentioned in the previous sections, σ will be expressed as follows:

$$\sigma=\sigma_0/(1+k_im_i)\,, \tag{74}$$

where σ_0 is the probability σ for no impurity.

Case A. When the supply of impurity from outside is sufficient, m_i is equal to a constant, say A. Then σ has also a constant value, that is

$$\sigma_i=\sigma_0/(1+k_iA)\,. \tag{75}$$

If we use the reduced probability σ_i instead of σ in the case where no impurity is contained, the radiation effect could be estimated. For instance, the number- and the weight-average molecular weight are respectively

$$M_n(R)=M_n(0)/\{1+(1-2\sigma_i)u\dot{r}R\} \tag{76}$$

$$M_w(R)=M_w(0)/\{1+(1-4\sigma_i)u\dot{r}R\} \tag{76}$$

where the initial molecular weight distribution is assumed to be of the Poisson type.

The radiation dose R_g necessary for the incipient gel formation is given by

$$R_g=\frac{1}{u\dot{r}(4\sigma_i-1)}\,, \tag{78}$$

when $k_iA\ll1$

$$\frac{1}{R_g}=u\dot{r}\left(\frac{4\sigma_0}{1+k_iA}-1\right)=u\dot{r}\{(4\sigma_0-1)-4\sigma_0k_iA\}\,. \tag{79}$$

The intrinsic viscosity is given by

$$\frac{[\eta]}{[\eta]_0}=\{1+(1-\sigma_i)u\dot{r}R\}^{-\alpha}\int_0^1\frac{y^{\alpha+1}dy}{(1-y)^{\alpha}(1-Ky)^{\alpha}}\,, \tag{80}$$

where

$$K=\frac{1+u\dot{r}R}{1+(1-\sigma)u\dot{r}R}\,. \tag{81}$$

When R is sufficiently small

$$[\eta]/[\eta]_0=1+\alpha\{\sigma_i(\alpha+3)-1\}u\dot{r}R+\cdots\,. \tag{82}$$

If we measure the value and the slope of $1/R_g$ at $A=0$ and also the slope of intrinsic viscosity at $R=0$, we can calculate the values of $\dot{r}$, σ_0 and k_i.

Case B. When there is no supply of impurity from outside, the variation of the number of impurity molecules is expressed by

$$\frac{dm_i}{dR} = -\frac{2\dot{r}\sigma_0 k_i m_i}{1+k_i m_i} . \tag{83}$$

The solution satisfying the initial condition $m_i(0)=A$ is given by

$$2k_i\dot{r}\sigma_0 R = k_i(A-m_i)+\log(A/m_i) . \tag{84}$$

When A is sufficiently small, it becomes

$$m_i = A\exp(-2k_i\dot{r}\sigma_0 R)[1+Ak_i\{1-\exp(-2k_i\dot{r}\sigma_0 R)\}+\cdots] , \tag{85}$$

therefore, we obtain

$$\sigma_0/\sigma = 1+k_iA\exp(-2k_i\dot{r}\sigma_0 R)+\cdots . \tag{86}$$

The radiation dose R_g for the incipient gel formation is given by

$$1/R_g = u\dot{r}\{(4\sigma_0-1)-4k_iA\sigma_0\exp(-2k_i\dot{r}\sigma_0 R_g)\} . \tag{87}$$

On the other hand, when the radiation dose and the amount of impurity are both small, the intrinsic viscosity is given by

$$\begin{aligned}[\eta]/[\eta]_0 &= 1+\alpha\{\sigma_0(\alpha+3)-1+\sigma_0(\alpha+3)k_iA\exp(-2k_i\dot{r}\sigma_0 R)+\cdots\} \\ &= 1+\alpha\{(\alpha+3)\sigma_0-1\}+\alpha(\alpha+3)\sigma_0 k_iA\exp(-2k_i\dot{r}\sigma_0 R)+\cdots .\end{aligned} \tag{88}$$

If we measure the value and the slope of $1/R_g$ at $A=0$ and also the initial slope of the intrinsic viscosity, we can calculate the values of $\dot{r}$, σ_0 and k_i from Eqs. (87) and (88).

It is important to note that when impurity hinders cross-linking the reduced radiation dose $\overline{R}$ can be defined in such a manner that, in terms of $\overline{R}$ instead of R, all the relations between physical quantities of an irradiated polymer containing impurity, for example, average molecular weights, viscosity, and melting point, can be reduced to those of the polymer containing no impurity. This is not the case for the effect of impurity in end-linking. Such a difference in character may be expected to enable us to distinguish between cross-linking and end-linking.

§ 5. Summary

The effect of impurity on irradiated polymer is discussed. Polymer contains usually some impurities or additives. Among many impurities oxygen is the most important, because it gives a large effect on irradiated polymers and it is difficult to remove completely out of polymers. It is, however, concluded from our discussion that the radiation effect on pure polymers is known from the measurements of intrinsic viscosity and gel point of irradiated polymers containing impurities.

In the case where molecular linking is accompanied by degradation the analysis is performed by assuming that the statistical result is not altered by exchanging the order of molecular linking and molecular scission. The validity of this assumption is not verified. However, even if the assumption might not be correct the error would not be large in the period before the gel point, because an intial polymer molecule had, in the average, less than one linking unit before the incipient gel formation. The validity of our results will be justified by experiments.

Acknowledgements

The author wishes to express his sincere thanks to Professor A. Amemiya for his continued interest and support in all phases of this research. The author wishes to thanks Professor. A. Harasima and Dr. K. Shinohara for their kind guidance and also the members of the Group for the Study of Irradiated Polymer in Tokyo for their discussions.

References

1) O. Saito: J. Phys. Soc. Japan **13** (1958) 198.
2) O. Saito: J. Phys. Soc. Japan **13** (1958) 1451.
3) O. Saito: J. Phys. Soc. Japan **13** (1958) 1465.
4) A. Chapiro: J. chim. phys. **52** (1955) 246.
5) R. M. Black and B. J. Lyons: Nature **180** (1957) 1346.

JOURNAL OF THE PHYSICAL SOCIETY OF JAPAN, Vol. 14, No. 6, JUNE, 1959

A New Type of Antiferromagnetic Structure in the Rutile Type Crystal

By Akio YOSHIMORI

Department of Physics, University of Osaka Prefecture,
Mozu-Higashi, Sakai

(Received March 6, 1959)

A new type of antiferromagnetic spin arrangement, which is theoretically possible in the rutile type crystal and seems to be realized in polianite, MnO_2, is proposed. This spin arrangement, which will be named the *screw-type structure*, consists of spins screwing along the four-fold crystalline axis. The stability ranges of this and other spin structures are studied, assuming three different exchange interactions. The magnetic properties of the screw-type structure, including the anisotropy energy due to dipolar interaction and that due to crystalline field, the susceptibility, the spin waves, and the neutron diffraction pattern, are studied. Neutron diffraction data for polianite obtained by Erickson (unpublished) can well be accounted for by the screw-type structure with a pitch of $(7/2)c$. The magnetic properties of the MnO_2 crystal are discussed on the basis of this 7/2-pitch-structure.

§ 1. Introduction

The purpose of the present paper is to find out possible antiferromagnetic spin arrangements in the rutile type crystal and to study their magnetic properties. In this crystal we expect three different superexchange interactions with exchange integrals J_1, J_2 and J_3, the first being the exchange integral between neighboring corner cation and body-center cation, the second that between two cations neighboring along the c-axis, and the third that between two cations neighboring along the a- or b-axis. It will be shown on the basis of a classical energy consideration that, if the first two exchange interactions act in antiferromagnetic way ($J_1>0$, $J_2>0$), three types of spin superstructure will be possible, the relative stability of which depending on the relative magnitudes of the three exchange integrals. One of them is the MnF_2-type structure[1], in which the corner spins and body-center spins point antiparallel, the second is the structure suggested by Bizette[2], Erickson[3] and Yosida[4], in which the corner spins and the body-center spins form uncorrelated antiferromagnetic sublattices, and the last is a new spin arrangement which we propose and in which positive spins on the corner sites and negative spins on the body-center sites screw along the c-axis. This arrangement will be called the "screw-type" structure; the pitch of the screw depends on the value of J_2/J_1.

In the MnF_2-type spin structure, the exchange coupling between neighbors along the c-axis and that along the a-axis or b-axis act unfavorably, if $J_2>0$ and $J_3>0$, but the exchange coupling between neighboring corner and body-center cations acts favorably ($J_1>0$) and this stabilizes the structure. In the Bizette-Erickson-Yosida-structure, the first two couplings act favorably if $J_2>0$, $J_3>0$, while the third (J_1) is inactive. Therefore, if J_2 is large compared with J_1, both being assumed to be positive, and J_3 is small compared with J_1 and J_2, or J_3 is negative, these two structures will not be stable, and it can be shown that the new screw-type structure becomes more stable when $J_2/J_1>1$.

The screw-type structure seems to be realized in polianite, MnO_2. Bizette and Tsai[6] (1949) measured the powder susceptibility of polianite and found that its Néel temperature is at 84°K. Bizette[2] (1950) measured χ_a and χ_c of a single crystal of it and suggested that spins in this crystal might form two mutually uncorrelated antiferromagnetic sublattices whose spin axes are along [110] and [1$\bar{1}$0], respectively. Erickson[3] (1952) carried out a neutron diffraction experiment with a powder sample and found that the corner spins and the body-center spins separately form antiferromagnetic sublattices. Yosida[4] (1952) calculated the dipolar anisotropy energy assuming the Bizette-Erickson structure, and qualitatively explained the anisotropy of the susceptibility below and above the Néel temperature. A recent neutron diffraction experiment by Erickson[6] with a single crystal indicates, however, a different spin structure: the spins are in the c-plane but the magnetic unit cell is seven times as large as the chemical unit cell along the c-axis. It will be shown that the screw-type structure of a pitch of $(7/2)c$ will account for the lines observed by him.

By calculating the classical dipolar anisotropy energy in the screw-type structure, it was found for MnO_2 lattice that when the unit turning angle of the spins, corresponding to the unit c-axis, is less than about 100°, the spins are in an arbitrary plane which contains the c-axis, and that when the unit turning angle is greater than 100°, the spins become perpendicular to the c-axis. It was found further that the crystalline field anisotropy energy stabilizes, to a certain extent, the structures of pitches of simple rational numbers in units of c.

The ratio of the susceptibility in the easy plane to that perpendicular to the easy plane is found to be finite at absolute zero and to depend on the value of J_2/J_1. For a pitch of $(7/2)c$ a qualitative agreement with the experimental results obtained by Bizette[2] is found.

Spin waves in the screw-type structure are also calculated and two non-degenerate branches of the spin wave modes are obtained. It will be shown that there are three modes of antiferromagnetic resonance. Finally, neutron diffraction pattern expected from the screw-type structure will be discussed.

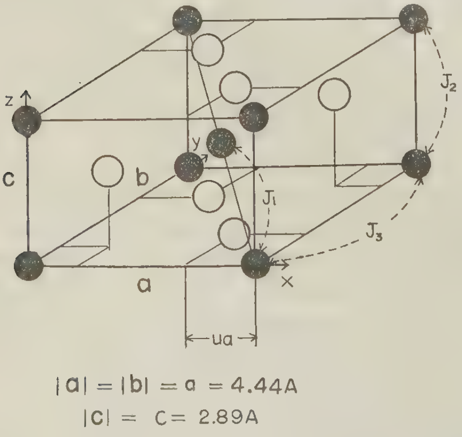

Fig. 1. The rutile type crystal structure of MnO_2. Solid circles are cations, open circles anions. The value of u is unknown for MnO_2. For MnF_2, NiF_2, $u=0.31$.

§ 2. Derivation of the Screw-type Structure

As mentioned in the preceding section, we shall assume three different exchange integrals J_1, J_2 and J_3 (see Fig. 1), and start with a Hamiltonian,

$$H_{\mathrm{ex}}=2J_1\sum_{<ii'>_1}\boldsymbol{S}_i\cdot\boldsymbol{S}_{i'}+2J_2\{\sum_{<ij>_2}\boldsymbol{S}_i\cdot\boldsymbol{S}_j+\sum_{<i'j'>_2}\boldsymbol{S}_{i'}\cdot\boldsymbol{S}_{j'}\}+2J_3\{\sum_{<ij>_3}\boldsymbol{S}_i\cdot\boldsymbol{S}_j+\sum_{<i'j'>_3}\boldsymbol{S}_{i'}\cdot\boldsymbol{S}_{j'}\}\,, \tag{1}$$

where i and j run over $N/2$ corner cations and i' and j' over $N/2$ body-center cations, $<\ >_1$ means pairs of neighboring corner and body-center cations, $<\ >_2$ pairs of cations neighboring along the c-axis, and $<\ >_3$ those along the a- or b-axis. For a while, we shall treat the spins as classical vectors and look for the minimum of H_{ex}. For this purpose we perform Fourier transformations on $\boldsymbol{S}_i$ and $\boldsymbol{S}_{i'}$:

$$\boldsymbol{S}_i=\sum_{\boldsymbol{k}}\boldsymbol{S}(\boldsymbol{k})\exp(i\boldsymbol{k}\cdot\boldsymbol{r}_i),\quad \boldsymbol{S}(-\boldsymbol{k})=\boldsymbol{S}^*(\boldsymbol{k}),$$
$$\boldsymbol{S}_{i'}=\sum_{\boldsymbol{k}}\boldsymbol{S}'(\boldsymbol{k})\exp(i\boldsymbol{k}\cdot\boldsymbol{r}_{i'}),\quad \boldsymbol{S}'(-\boldsymbol{k})=\boldsymbol{S}'^*(\boldsymbol{k}), \tag{2}$$

where $\boldsymbol{k}$ runs over $N/2$ wave vectors in the Brillouin zone corresponding to the chemical cell. Then, we have

$$H_{\mathrm{ex}}\cdot(2/N)=16J_1\sum_{\boldsymbol{k}}\gamma_{\boldsymbol{k}1}\boldsymbol{S}(\boldsymbol{k})\cdot\boldsymbol{S}'(-\boldsymbol{k})+\sum_{\boldsymbol{k}}(2J_2\gamma_{\boldsymbol{k}2}+4J_3\gamma_{\boldsymbol{k}3})(\boldsymbol{S}(\boldsymbol{k})\cdot\boldsymbol{S}(-\boldsymbol{k})+\boldsymbol{S}'(\boldsymbol{k})\cdot\boldsymbol{S}'(-\boldsymbol{k}))\,,$$

where

$$\gamma_{\boldsymbol{k}1}=\cos(k_xa/2)\cos(k_ya/2)\cos(k_zc/2),$$
$$\gamma_{\boldsymbol{k}2}=\cos(k_zc), \tag{3}$$
$$\gamma_{\boldsymbol{k}2}=\{\cos(k_xa)+\cos(k_ya)\}/2\,.$$

Since $\boldsymbol{S}_i^2=\boldsymbol{S}_{i'}^2=S^2$, we have

$$\sum_{\boldsymbol{k},\boldsymbol{k}'}\boldsymbol{S}(\boldsymbol{k})\cdot\boldsymbol{S}(\boldsymbol{k}')\exp\{i(\boldsymbol{k}+\boldsymbol{k}')\cdot\boldsymbol{r}_i\}=S^2,$$
$$\sum_{\boldsymbol{k},\boldsymbol{k}'}\boldsymbol{S}'(\boldsymbol{k})\cdot\boldsymbol{S}'(\boldsymbol{k}')\exp\{i(\boldsymbol{k}+\boldsymbol{k}')\cdot\boldsymbol{r}_{i'}\}=S^2\,.$$

Under conditions (4), we vary $\boldsymbol{S}(\boldsymbol{k})$ and $\boldsymbol{S}'(\boldsymbol{k})$ so as to make H_{ex} stationary. Then, equations determining these vectors are found to be as follows:

$$(4J_2\gamma_{\boldsymbol{k}2}+8J_3\gamma_{\boldsymbol{k}3})\boldsymbol{S}(\boldsymbol{k})+16J_1\gamma_{\boldsymbol{k}1}\boldsymbol{S}'(\boldsymbol{k})=\lambda\boldsymbol{S}(\boldsymbol{k}), \tag{5}$$

$$16J_1\gamma_{\boldsymbol{k}1}\boldsymbol{S}(\boldsymbol{k})+(4J_2\gamma_{\boldsymbol{k}2}+8J_3\gamma_{\boldsymbol{k}3})\boldsymbol{S}'(\boldsymbol{k})=\lambda\boldsymbol{S}'(\boldsymbol{k}), \tag{6}$$

where λ is the Lagrange multipier which we have assumed to be common to all the N conditions of (4) (for different $\boldsymbol{r}_i$ and $\boldsymbol{r}_{i'}$). This assumption means that we are here concerned with a simple sinusoidal change of the spin components in space, with a wave vector $\boldsymbol{k}$, only distinguishing between the corner and body-center sites, since without this assumption different $\boldsymbol{k}$ vectors will mix in the equations for $\boldsymbol{S}(\boldsymbol{k})$ and $\boldsymbol{S}'(\boldsymbol{k})$. We are therefore imposing only one condition

$$\sum_i \boldsymbol{S}_i{}^2+\sum_{i'} \boldsymbol{S}_{i'}{}^2=(N/2)\sum_{\boldsymbol{k}}(\boldsymbol{S}(\boldsymbol{k})\cdot\boldsymbol{S}(-\boldsymbol{k})$$
$$+\boldsymbol{S}'(\boldsymbol{k})\cdot\boldsymbol{S}'(-\boldsymbol{k}))=NS^2, \tag{7}$$

in place of N conditions (4). We have thus to test later whether or not the obtained solution will satisfy all the N conditions (4). $(N/2)\lambda S$ is the energy of the total system, H_{ex}, as one can see by multiplying both the sides of (5) by $\boldsymbol{S}(-\boldsymbol{k})$ and both the sides of (6) by $\boldsymbol{S}'(-\boldsymbol{k})$ and summing them over $\boldsymbol{k}$*.

In order to obtain a non-vanishing solution of (5) and (6), λ must take the following eigenvalues:

$$\lambda=\mp 16J_1\gamma_{\boldsymbol{k}1}+4J_2\gamma_{\boldsymbol{k}2}+8J_3\gamma_{\boldsymbol{k}3} \tag{8}$$

The corresponding eigen-vectors satisfy

$$\boldsymbol{S}(\boldsymbol{k})=\mp\boldsymbol{S}'(\boldsymbol{k})\ , \tag{9}$$

if $\gamma_{\boldsymbol{k}1}\neq 0$. If $\gamma_{\boldsymbol{k}1}=0$, $\boldsymbol{S}(\boldsymbol{k})$ and $\boldsymbol{S}'(\boldsymbol{k})$ are uncorrelated to each other. Now (4) can be written as

$$\boldsymbol{S}(\boldsymbol{k})^2\exp(2i\boldsymbol{k}\cdot\boldsymbol{r}_i)+\boldsymbol{S}(-\boldsymbol{k})^2\exp(-2i\boldsymbol{k}\cdot\boldsymbol{r}_i)$$
$$+2\boldsymbol{S}(\boldsymbol{k})\cdot\boldsymbol{S}(-\boldsymbol{k})=S^2,$$
$$\boldsymbol{S}'(\boldsymbol{k})^2\exp(2i\boldsymbol{k}\cdot\boldsymbol{r}_{i'})+\boldsymbol{S}'(-\boldsymbol{k})^2\exp(-2i\boldsymbol{k}\cdot\boldsymbol{r}_{i'})$$
$$+2\boldsymbol{S}'(\boldsymbol{k})\cdot\boldsymbol{S}'(-\boldsymbol{k})=S^2. \tag{10}$$

In order that the right-hand sides of these equations are independent of $\boldsymbol{r}_i$ and $\boldsymbol{r}_{i'}$, either k_xa, k_ya and k_zc must be integral multiples of π or $\boldsymbol{S}(\boldsymbol{k})^2=\boldsymbol{S}'(\boldsymbol{k})^2=0$. If k_xa, k_ya and k_zc are zero and $\boldsymbol{S}(\boldsymbol{k})=-\boldsymbol{S}'(\boldsymbol{k})$, we have the MnF$_2$-type antiferromagnetic structure; if $\boldsymbol{S}(\boldsymbol{k})=\boldsymbol{S}'(\boldsymbol{k})$, we have the ferromagnetic structure. If k_xa, k_ya and k_zc are all π, in which case $\gamma_{\boldsymbol{k}1}=0$, we have the Bizette-Erickson-Yosida structure. Now, if $\boldsymbol{S}(\boldsymbol{k})^2=\boldsymbol{S}'(\boldsymbol{k})^2=0$,

$$\boldsymbol{S}(\boldsymbol{k})=\mp\boldsymbol{S}'(\boldsymbol{k})=(\boldsymbol{u}_1-i\boldsymbol{u}_2)S/2, \tag{11}$$

where $\boldsymbol{u}_1$ and $\boldsymbol{u}_2$ are real unit vectors which are perpendicular to each other. For this solution, (2) becomes

$$\boldsymbol{S}_i=\{(\boldsymbol{u}_1-i\boldsymbol{u}_2)\exp(i\boldsymbol{k}\cdot\boldsymbol{r}_i)+\text{conj. comp.}\}S/2,$$
$$=\{\boldsymbol{u}_1\cos(\boldsymbol{k}\cdot\boldsymbol{r}_i)+\boldsymbol{u}_2\sin(\boldsymbol{k}\cdot\boldsymbol{r}_i)\}S, \tag{12}$$
$$\boldsymbol{S}_{i'}=\mp\{\boldsymbol{u}_1\cos(\boldsymbol{k}\cdot\boldsymbol{r}_{i'})+\boldsymbol{u}_2\sin(\boldsymbol{k}\cdot\boldsymbol{r}_{i'})\}S\ .$$

The corresponding spin structure is such that it can be derived from the MnF$_2$-type antiferromagnetic structure (for the $-$ sign in (12)) or from the ferromagnetic structure (for the $+$ sign) by rotating the spins in the $\boldsymbol{u}_1$, $\boldsymbol{u}_2$-plane in such a way that they screw along the direction of $\boldsymbol{k}$ with a pitch of $2\pi/k$. This may be called the screw-type structure.

The energy of the system, i.e., λ $(=(\text{total energy})\ (2/NS^2))$, is given as follows. For the MnF$_2$-type antiferromagnetic structure:

$$\lambda=-16J_1+4J_2+8J_3\ , \tag{13}$$

for the B. E. Y.-structure:

$$\lambda=-4J_2-8J_3\ , \tag{14}$$

and for the screw-type structure, λ is given by the minimum of (8). This minimum value and the corresponding $\boldsymbol{k}$-value are obtained from the equations

$$\sin(k_xa/2)\{\pm J_1\cos(k_ya/2)\cos(k_zc/2)$$
$$-J_3\cos(k_xa/2)\}=0,$$
$$\sin(k_ya/2)\{\pm J_1\cos(k_zc/2)\cos(k_xa/2)$$
$$-J_3\cos(k_ya/2)\}=0\ . \tag{15}$$
$$\sin(k_zc/2)\{\pm J_1\cos(k_xa/2)\cos(k_ya/2)$$
$$-J_2\cos(k_zc/2)\}=0.$$

There are several solutions of these equations, of which the following three are new:

(a) Spins in the same xy-plane are parallel, i. e., k_xa and k_ya are zero, and they screw along the z-axis with a unit screwing angle equal to k_zc (see Fig. 2), where k_zc satisfies.

$$\cos(k_zc/2)=J_1/J_2,$$
$$\text{provided that } |J_2|>|J_1|, \tag{16}$$

(see Fig. 3). The corresponding λ-value is

$$\lambda=-8(J_1{}^2/J_2)-4J_2+8J_3. \tag{17}$$

(b) Spins in the same yz-plane are parallel and they screw along the x-axis, with a unit screwing angle of k_xa, where

---

* More generally, we can replace λ of the right-hand of (6) by a different Lagrange multiplier λ', imposing two conditions: $\sum_i S_i{}^2=(N/2)S^2$ and $\sum_i S_{i'}{}^2=(N/2)S^2$. Then, the energy of the system becomes $(\lambda+\lambda')S^2/2$. λ and λ' are related to each other by the vanishing of the determinant of the equations, and it can be shown that the energy is a minimum when $\lambda=\lambda'$.

$\cos(k_x a/2) = J_1/J_3$, provided that $|J_3| > |J_1|$.

The corresponding λ-value is

$$\lambda = -8(J_1^2/J_3) + 4J_2 \,. \tag{19}$$

The x and y axes may be interchanged.

(c) A three-dimentional screw, with

$$\cos(k_x a/2/2) = \cos(k_y a/2) = \sqrt{J_2 J_3}/J_1,$$

$$\cos(k_z c/2) = J_3/J_1,$$

$$(|J_1| > \sqrt{J_2 J_3},\ J_2 J_3 > 0,\ |J_3| > |J_1|) \,.$$

The corresponding λ-value is given by

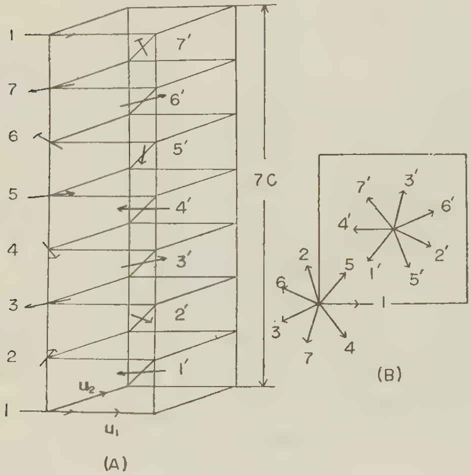

Fig. 2. (A) The screw-type structure with a pitch of 7/2 (proper screw-type structure). (B) Projection on the c-plane.

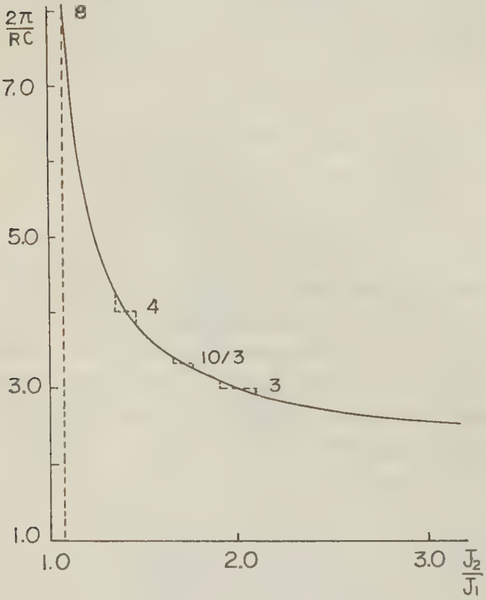

Fig. 3. Relation between the pitch of the screw and J_2/J_1. Dotted lines indicate (schematically) the modification in certain ranges of J_2/J_1 when the anisotropy energy is considered.

$$\lambda = 8J_2 J_3^2/J_1^2 - 4J_2 - 8J_3 \,. \tag{19}$$

It is interesting to note that the energy λ is the same for both the screwed ferromagnetic ($J_1 < 0$) and screwed MnF$_2$-type antiferromagnetic ($J_1 > 0$) structures in the above three cases, as it should be since J_1 appears only as J_1^2.

Now we compare the energy values of the various structures derived above. Comparing (13) with (14), it can be seen that the boundary of the relative stability of the correspond ing two structures is given by

$$J_2 + 2J_3 = 2J_1 \,. \tag{20}$$

If $J_2 + 2J_3 < 2J_1$, the MnF$_2$-type structure is more stable, but if $J_2 + 2J_3 > 2J_1$, the B. E. Y.-structure becomes more stable. The structure which screws along the c-axis appears when $J_2 > J_1$ (we assume $J_1 > 0$), and it can be shown that its stability range is bounded by

$$J_2 = J_1 \quad \text{and} \quad 2J_2 J_3 = J_1^2 \,. \tag{21}$$

The other two screw-type structures have no stability range. Therefore, the whole J_2/J_1, J_3/J_1-plane can be divided into four parts as shown in Fig. 4. In this figure, the structure for $J_2 < 0$ and $J_3 > J_1$ (>0) is such that the spins are parallel to each other along the c-axis and antiparallel along the a and b-axes while the corner spins and body-center spins are uncorrelated.

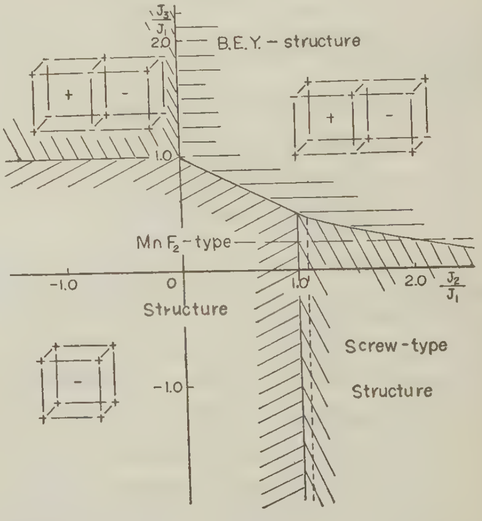

Fig. 4. The stability boundaries of various spin structures in the J_2/J_1, J_3/J_1-plane. Dotted vertical line shows the shift of the boundary due to dipolar anisotropy energy (assuming the calculated dipolar interaction in MnO$_2$ and estimating J_1, J_2, J_3 for the same crystal).

In the molecular field approximation, the Néel temperature, T_N, in the screw-type structure with a screw axis along the c-axis, is obtained through a simple calculation as

$$k_B T_N = \{S(S+1)/3\}(8J_1^2/J_2 + 4J_2 - 8J_3), \qquad (22)$$

(k_B: the Boltzmann constant) and the paramagnetic Curie temperature, Θ_p, as

$$k_B \Theta_p = \{S(S+1)/3\}(16J_1 + 4J_2 + 8J_3)\ . \qquad (23)$$

Their ration, Θ_p/T_N, is

$$\frac{\Theta_p}{T_N} = \frac{4+(J_2/J_1)+2(J_3/J_1)}{2(J_2/J_1)^{-1}+(J_2/J_1)-2(J_3/J_1)}\ . \qquad (24)$$

The maximum allowable value of Θ_p/T_N in the screw-type structure of a given pitch occurs at $2(J_3/J_1)=(J_2/J_1)^{-1}$, which is the largest allowable value of $2(J_3/J_1)$ in this structure, and

$$\left(\frac{\Theta_p}{T_N}\right)_{\max} = \frac{4+(J_2/J_1)^{-1}+(J_2/J_1)}{(J_2/J_1)^{-1}+(J_2/J_1)}\ .$$

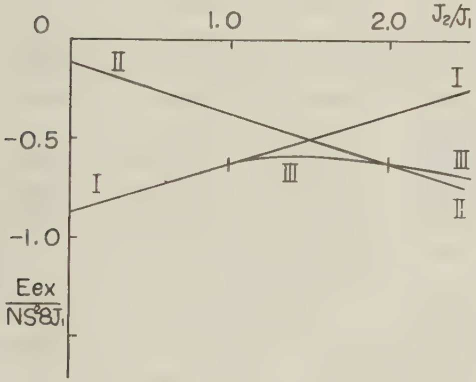

Fig. 5. The energy diagram for the various structures along the dashed line in Fig. 4 ($J_3/J_1 = 1/4$)
I MnF$_2$-type structure,
II B. E. Y.-structure,
III Screw-type structure.

The energies of the three superstructures are shown as functions of J_2/J_1 for $J_3/J_1=0.25$ in Fig. 5. It is noted that the energy curve of the screw-type structure makes a contact of the second order with that of the MnF$_2$-type structure at $J_2/J_1=1$.

Since the anisotropy energy has not yet been considered, the spins in the screw-type structure can be parallel to an arbitrary plane. If the spins are parallel to a plane which contains the c-axis, we may call the structure the "cycloidal structure" (Fig. 6). If the spins are perpendicular to the c-axis, i.e., the screw axis, the structure may be called the "proper screw-type structure". Whether the latter or the former is realized depends on the anisotropy energy, which will be the subject of the next section.

The "proper" 7/2-pitch-structure (Fig. 2) is expected as realized in MnO$_2$ from our analysis of the neutron diffraction data (unpublished) by Erickson⁶⁾. If we assume this, we expect from the conditions of stabilizing the screw-type structure, i.e. from Eq. (16) and $2J_2J_3 < J_1^2$, that in MnO$_2$ J_2/J_1 is 1.60 and J_3/J_1 smaller than 0.31. On the other hand, we can also determine J_3/J_1 from Eq. (24) and the observed ratio of Θ_p (316°K) to T_N (84°K) by Bizette and Tsai⁵⁾, and have $J_3/J_1 \approx 0.56$. This discrepancy will be discussed in section 7. We give here a rough estimate of J_1 for our later purpose assuming somewhat arbitrary $J_3/J_1=0.25$: using Eq. (22) and putting $S=3/2$ and $T_N=84$°K, we have $16J_1 \sim 90\ \mathrm{cm}^{-1}$.

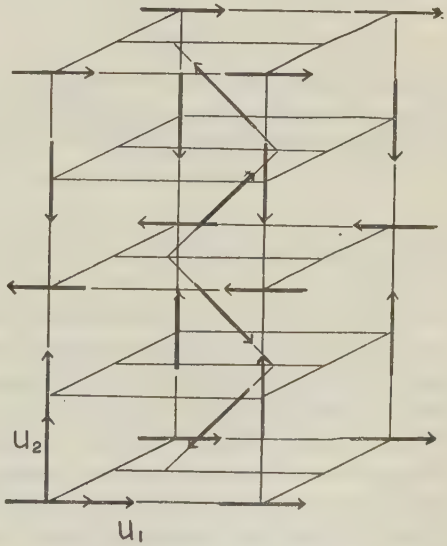

Fig. 6. The cycloidal structure with a pitch of 4.

§ 3. Role of the Anisotropy Energy in the Screw-type Structure

(A) *Anisotropy energy due to magnetic dipolar interaction*

The magnetic field at each cation due to the magnetic moments of other cations can be expressed as follows:

$$\boldsymbol{H}_n{}^{\mathrm{dip}} = \sum_l \Phi_{nl}\boldsymbol{\mu}_l + \sum_{l'} \Phi'_{nl'}\boldsymbol{\mu}_{l'},$$

$$\boldsymbol{H}_{n'}{}^{\mathrm{dip}} = \sum_{l'} \Phi_{n'l'}\boldsymbol{\mu}_{l'} + \sum_l \Phi'_{n'l}\boldsymbol{\mu}_l, \qquad (26)$$

where we number layers of corner cations and body-center cations successively along the c-axis, and denote by n and l the layers of corner cations and by n' and l' the layers of body-center cations; $\boldsymbol{H}_n{}^{\mathrm{dip}}$ and $\boldsymbol{H}_{n'}{}^{\mathrm{dip}}$ therefore mean, respectively, the field at a corner cation on the nth net-plane and the field at a body-center cation on the n'th net-plane, and $\boldsymbol{\mu}_l$ and $\boldsymbol{\mu}_{l'}$ are the magnetic moments of cations on the lth net-plane and l'th net-plane. $\boldsymbol{\Phi}_{nl}$ and $\boldsymbol{\Phi}'_{nl'}$ are tensors, and evidently

$$\boldsymbol{\Phi}_{nl}=\boldsymbol{\Phi}_{|n-l|},\quad \boldsymbol{\Phi}'_{nl'}=\boldsymbol{\Phi}'_{|n-l'|}.$$

When the principal axes of the crystal are taken to be the coordinates axes (Fig. 1), it is evident from the crystalline symmetry that $\boldsymbol{\Phi}_{nl}$ and $\boldsymbol{\Phi}'_{nl'}$ are diagonal, and the following relations hold between their principal values;

$$\Phi_{|n-l|,x}=\Phi_{|n-l|,y}=-(1/2)\Phi_{|n-l|,z}\ ,$$
$$\Phi'_{|n-l'|,x}=\Phi'_{|n-l'|,y}=-(1/2)\Phi'_{|n-l'|,z}\ ,$$

Here $\Phi_{|l|,z}$ for instance, is given by

$$\Phi_{|l|,z}=\sum_i r_{li}{}^{-3}\{3(z_l/r_{li})^2-1\}\ ,$$

where r_{li} means the distance from a given cation on the zeroth layer to the ith cation on the lth layer, and the summation extends over all i if $l\neq 0$, but it excludes $r_{0i}=0$ if $l=0$.

$$\boldsymbol{\mu}_l=g\mu_{\mathrm{B}}\boldsymbol{S}_l=g\mu_{\mathrm{B}}<S_\xi>\{\boldsymbol{u}_1\cos(kz_l)+\boldsymbol{u}_2\sin(kz_l)\}\ ,$$
$$\boldsymbol{\mu}_{l'}=g\mu_{\mathrm{B}}\boldsymbol{S}_{l'} \tag{27}$$
$$=g\mu_{\mathrm{B}}<S_\xi>\{-\boldsymbol{u}_1\cos(kz_{l'})-\boldsymbol{u}_2\sin(kz_{l'})\}\ ,$$

where S_ξ is the component of spin in the direction of the molecular field to which it is subjected and is common to all the spins. We take out two layers which are on the opposite sides of the nth layer at the same distance and combine their $\boldsymbol{\mu}$'s together in the sum of the first eqation of (26). Since the sum of these $\boldsymbol{\mu}$'s is a vector which is parallel to the magnetization of the nth layer, we can simplify the calculation of (26). It can be shown that $\boldsymbol{H}_n{}^{\mathrm{dip}}$ is expressed as

$$\boldsymbol{H}_n{}^{\mathrm{dip}}=(N/2)g\mu_{\mathrm{B}}<S_\xi>\varphi_A(\theta)\{(\boldsymbol{c}/c)(\boldsymbol{c}/c)-\boldsymbol{I}\}$$
$$\cdot\{\boldsymbol{u}_1\cos(kz_n)+\boldsymbol{u}_2\sin(kz_n)\}\ , \tag{28}$$

where $3(\boldsymbol{c}/c)(\boldsymbol{c}/c)-\boldsymbol{I}$ is a dyadic whose diagonal elements are -1, -1, 2, and

$$\varphi_A(\theta)=\{\varphi(\theta)-\varphi'(\theta)\}/2, \tag{29}$$
$$\varphi(\theta)=(2/N)\sum_l \Phi_{|l|,z}\cos(kz_l), \tag{30}$$
$$\varphi'(\theta)=(2/N)\sum_{l'} \Phi_{|l'|,z}\cos(kz_{l'}), \tag{31}$$

where $2\theta(=k_zc)$ is the unit screwing angle. $\boldsymbol{H}_{n'}{}^{\mathrm{dip}}$ can be expressed in a similar manner. Denoting by n_z the number of net-planes, the dipolar energy per unit volume, E_{dip}, is calculated as follows:

$$E_{\mathrm{dip}}=(N/2n_z)\{-\sum_n \boldsymbol{\mu}_n\cdot\boldsymbol{H}_n{}^{\mathrm{dip}}-\sum_n \boldsymbol{\mu}_{n'}\cdot\boldsymbol{H}_{n'}{}^{\mathrm{dip}}\},$$
$$=\{1-(3/2)(u_{1z}{}^2+u_{2z}{}^2)\}\varphi_A(\theta)(N\mu/2)^2,$$
$$\mu=g\mu_{\mathrm{B}}<S_\xi>.$$

If $\boldsymbol{u}_3$ is defined by $\boldsymbol{u}_3=\boldsymbol{u}_1\times\boldsymbol{u}_2$ and Θ is the angle between $\boldsymbol{u}_3$ and the c-axis, it follows that

$$u_{1z}{}^2+u_{2z}{}^2=1-u_{3z}{}^2=1-\cos^2\Theta.$$

Thus

$$E_{\mathrm{dip}}=(1/2)(3\cos^2\Theta-1)\varphi_A(\theta)(N\mu/2)^2. \tag{32}$$

The values of $\varphi(\theta)$ and $\varphi'(\theta)$ were calculated

Table I.

θ^0	$-\varphi(\theta)$	$-\varphi'(\theta)$	$\varphi_A(\theta)$
0	1.27	11.78	5.26
15	1.91	11.26	4.68
30	3.64	9.83	3.10
45	5.94	7.74	0.90
51.4	6.96	6.72	−0.12
60	8.20	5.29	−1.46
75	9.81	2.68	−3.57
90	10.39	0	−5.20

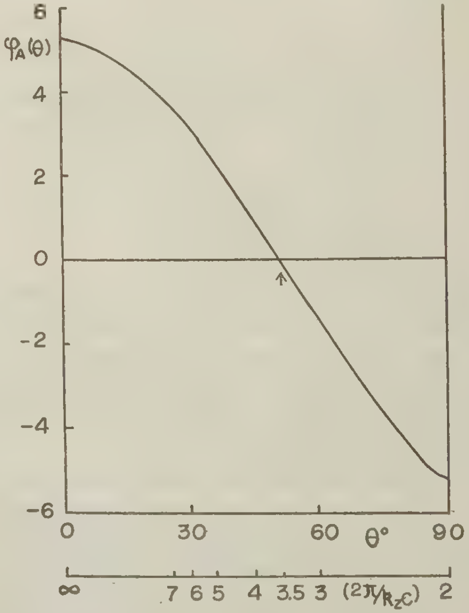

Fig. 7. The variation of $\varphi_A(\theta)$ versus θ in MnO$_2$. A small arrow indicates the point corresponding to a pitch of 3.5.

by the direct sum method first summing over cations on each net-plane and then summing over different net-planes. The results are shown in Table I and Fig. 7 for the lattice of MnO_2. Putting $S=3/2$ and $g=2$, E_{dip}/N becomes

$$E_{\mathrm{diq}}/N=0.0169\varphi_A(\theta)(<S_\xi>/S)^2(3\cos^2\Theta-1)\mathrm{cm}^{-1}. \tag{33}$$

If $\varphi_A(\theta)$ is positive, the easy planes of the spins is parallel to the c-axis ($\Theta=90°$), i.e., the cycloidal structure becomes stable, but if $\varphi_A(\theta)$ is negative, the proper screw-type structure ($\Theta=0°$) becomes stable. In Fig. 7 it is seen that $\varphi_A(\theta)$ changes sign at $\theta=50.8°$. In the 7/2-pitch-structure for which $\theta=51.4°$, θ is a little above this value and so the magnetizations are stabilized in the c-plane. E_{dip}/N of the 7/2-pitch-structure is

$$E_{\mathrm{dip}}/N=-0.002(<S_\xi>/S)^2(3\cos^2\Theta-1)\ \mathrm{cm}^{-1}. \tag{34}$$

This anisotropy energy is very small and may not be important compared with the crystalline field anisotropy energy which will be discussed later.

The dipolar energy of the MnF_2-type structure, in which spins point parallel to the c-axis, is $-(1/2)\varphi_A(0)(N\mu/2)^2$. This is twice as large as that of the cycloidal structure for vanishing θ. On the other hand, the difference in the exchange energy for the MnF_2-type and screw-type structures is very small when $J_2/J_1\sim1$, as mentioned in section 2. Therefore, if J_2 exceeds J_1 only a little, the MnF_2-type structure will remain to be more stable than the cycloidal structure, since the corresponding increase in exchange energy will be over-compensated by dipolar energy; in other words, the stability boundary shifts a little towards a larger value of J_2/J_1. For MnO_2, the difference in dipolar energy per cation corresponding to these two possible structure, namely $(1/2N)\varphi_A(0)(N\mu/2)^2$, is about $0.09\ \mathrm{cm}^{-1}$. In order to estimate the order of magnitude of the shift in this case, we assume $16J_1\sim90\ \mathrm{cm}^{-1}$ (see the preceding section), then the boundary value of J_2/J_1 turns out to be 1.08 (Fig. 4). The pitch corresponding to this new boundary is about 8, i.e., screw-type structures with larger pitches than about 8 are unstable (Fig. 3). The stability boundary shifts also due to the crystalline field anisotropy energy, which will be treated in the next subsection.

(B) *Anisotropy energy due to crystalline field*

The Mn^{4+} ions in polianite may have an anisotropy energy due to the crystalline field. Let us consider the orthorhombic anisotropy energy of the lowest order:

$$\begin{aligned}&D'\beta_3^2-E'\beta_1\beta_2,\\ &\qquad\text{for the corner cations,}\\ &D'\beta_3^2+E'\beta_1\beta_2,\\ &\qquad\text{for the body-center cations,}\end{aligned} \tag{35}$$

where β_1, β_2, β_3 are the direction cosines of the spins referred to the principal axes of the crystal. These energies are derived from the effective spin Hamiltonian,

$$\sum_i\{DS_{iz}^2-E(S_{ix}S_{iy}+S_{iy}S_{ix})\}+\sum_{i'}\{DS_{i'z}^2+E(S_{i'x}S_{i'y}+S_{i'y}S_{i'x})\}. \tag{36}$$

Making use of the molecular field approximation, we have

$$D'/D=E'/E=\{3<S_\xi>^2-S(S+1)\}/2. \tag{37}$$

Treating (35) as a classical perturbation to the exchange energy, one can easily obtain the first order crystalline anisotropy energy (per cation) to be

$$(D'/2)\sin^2\Theta, \tag{38}$$

(the terms with E' are averaged out to zero). Hence, for positive D' the proper screw-type and for negative D' the cycloidal structure are stabilized. For negative D', the stability boundary between the MnF_2-type structure and screw-type structure shifts in the same way as in the case of dipolar anisotropy energy.

The anisotropy energy in the easy plane of the proper screw-type structure will vary discontinuosly as a function of pitch due to E'-terms, if we go over to higher order perturbation calculation. Due to the E'-terms of (35), the corner spins tend towards [110] and the body-center spins towards [1$\bar{1}$0], assuming $E'>0$, and it can be shown that a structure with a pitch of a simple rational number is stabilized by this effect. For example, the anisotropy energy in the c-plane of the 6-pitch-structure is expressible as a combination of $\sin6\theta^*$ and $\cos6\theta^*$ and that of the 4-pitch-structure as a combination of $\sin8\theta^*$ and $\cos8\theta^*$, where θ^* specifies the angle of rotation of tne spins as a whole in the c-

plane, the minima of which these anisotropy energies depressing the total energy. The anisotropy energy in the easy plane may also come from the orthorhombic anisotropy energy of a higher order (for example, a higher order quantum-mechanical perturbation of the spin-orbit coupling). In any case, the anisotropy energy in the easy plane must appear at lower orders for simple pitches than for complex pitches. In particular, for irrational pitches we have no anisotropy energy. As a result, the pitch as a function of J_2/J_1 will become as shown schematically in Fig. 3. However, the width of each part of constant pitch in this figure may be very small, as it arises from a higher order perturbational calculation. We find a similar situation in the cycloidal structure considering only the dipolar interaction.

§4. Susceptibility

In calculating the susceptibility, we shall neglect the dipolar interaction, which will be of minor importance compared with the exchange interaction, if the Néel temperature of the substance is high ($\gg 1°$K). The crystalline field anisotropy energy will be taken into account through an anisotropic g-factor. By applying an external field, the pitch of of the screw will be slightly changed if the field is applied in the plane of the spins, but it can be shown that the change does not occur to first order in $\boldsymbol{H}$. Therefore, we shall assume that the pitch is a given constant.

When the external field $\boldsymbol{H}$ is applied perpendicularly to the plane in which the spins lie, we obtain a temperature-independent susceptibility, $\chi_{s\perp}$, as we shall show below. In this case, all the $\boldsymbol{\mu}_n$ and $\boldsymbol{\mu}_{n'}$ must make the same angle, τ ($<90°$), with $\boldsymbol{H}$. The torque on, say, $\boldsymbol{\mu}_n$ must vanish, i.e.

$$\boldsymbol{\mu}_n \times (\boldsymbol{H}_n^{\mathrm{ex}} + \boldsymbol{H}) = 0 \tag{39}$$

where

$$\boldsymbol{H}_n^{\mathrm{ex}} = -(\alpha_1/2)(\boldsymbol{\mu}_{n'} + \boldsymbol{\mu}_{n'-1}) - (\alpha_2/2)(\boldsymbol{\mu}_{n+1} + \boldsymbol{\mu}_{n-1}) - \gamma \boldsymbol{\mu}_n,$$

$$\alpha_1 = 16 J_1 (g\mu_{\mathrm{B}})^{-2}, \qquad \alpha_2 = 4 J_2 (g\mu_{\mathrm{B}})^{-2}, \qquad \gamma = 8 J_3 (g\mu_{\mathrm{B}})^{-2}. \tag{40}$$

If the z'-axis is taken along $\boldsymbol{H}$, x'-axis along the original $\boldsymbol{\mu}_n$-direction (for no external field) and the y'-axis perpendicular to the both, we have from the y'-component of (39),

$$\mu \cos\tau(\alpha_1 \mu \sin\tau \cos\theta - \alpha_2 \mu \sin\tau \cos 2\theta) - \mu \sin\tau(-\alpha_1 \mu \cos\tau - \alpha_2 \mu \cos\tau + H) = 0,$$

or

$$\mu \cos\tau = H / \{\alpha_1(1+\cos\theta) + \alpha_2(1-\cos 2\theta)\} .$$

The magnitude of the total magnetization is

$$N\mu_{z'} = N\mu\cos\tau = H/\{A_1(1+\cos\theta) + A_2(1-\cos 2\theta)\} ,$$

$$A_1 = \alpha_1/N, \quad A_2 = \alpha_2/N$$

so that the susceptibility is given by

$$\chi_{s\perp} = 1/\{A_1(1+\cos\theta) + A_2(1-\cos 2\theta)\} . \tag{41}$$

It might be remined that $\cos\theta = J_1/J_2 = A_1/4A_2$.

When $\boldsymbol{H}$ is applied in the spin plane, we have a different susceptibility, $\chi_{s//}$. In this case, we denote the angle between the equilibrium direction of $\boldsymbol{\mu}_n$ in the field and $\boldsymbol{H}$ itself by θ_n and similarly the angle between $-\boldsymbol{\mu}_{n'}$ and $\boldsymbol{H}$ by $\theta_{n'}$. Then we have

$$\begin{aligned} |\boldsymbol{\mu}_n \times (\boldsymbol{H}_n^{\mathrm{ex}} + \boldsymbol{H})| = -\alpha_1 \mu_n \{ & \mu_{n'} \sin(\theta_{n'} - \theta_n) \\ & - \mu_{n'-1} \sin(\theta_n - \theta_{n'-1})\} + \alpha_2 \mu_n \{\mu_{n+1} \sin(\theta_{n+1} - \theta_n) \\ & - \mu_{n-1} \sin(\theta_n - \theta_{n-1})\} - \mu_n H \sin\theta_n = 0 , \end{aligned} \tag{42}$$

and a similar equation for $\boldsymbol{\mu}_{n'}$. Here $\boldsymbol{H}_n^{\mathrm{ex}}$, given by (40), is different from that without external field since $\boldsymbol{\mu}_n$ and $\boldsymbol{\mu}_{n'}$ have changed, not only as regards their directions but also as regards their lengths. The latter is determined by

$$\mu_n = g\mu_B \langle S_\xi \rangle = g\mu_B S B_S(y_n)\,, \qquad y_n = (g\mu_B S/k_B T)|\boldsymbol{H}_n^{\text{ex}} + \boldsymbol{H}|\,, \tag{43}$$

and similar equations for $\mu_{n'}$, where $B_S(y)$ is the Brillouin function. When no external field is present, $\theta_{n+1}{}^{(0)} - \theta_n{}^{(0)}$ and $\theta_{n'}{}^{(0)} - \theta_n{}^{(0)}$ are given by

$$\theta_{n+1}{}^{(0)} - \theta_n{}^{(0)} = 2\theta, \qquad \theta_{n'}{}^{(0)} - \theta_n{}^{(0)} = \theta\,, \tag{44}$$

and all the μ_n and $\mu_{n'}$ are equal to

$$\mu = g\mu_B S B_S(y_0), \qquad y_0 = (g\mu_B S/k_B T)\mu(\alpha_1 \cos\theta - \alpha_2 \cos 2\theta - \gamma)\,.$$

If angular shifts, $\Delta\theta_n = \theta_n - \theta_n{}^{(0)}$, $\Delta\theta_{n'} = \theta_{n'} - \theta_{n'}{}^{(0)}$, and variations of μ_n and $\mu_{n'}$, denoted as $\mu\mathcal{E}_n$ and $\mu\mathcal{E}_{n'}$, due to the external field are considered to the first order in H, Eqs. (42) and (43) can be linearized, and the following difference equations are obtained for $\mathcal{E}_n$, $\mathcal{E}_{n'}$ and $\Delta\theta_n$, $\Delta\theta_{n'}$:

$$\begin{aligned}
&(\alpha_1/2)(\mathcal{E}_{n'} - \mathcal{E}_{n'-1}) \sin\theta - (\alpha_2/2)(\mathcal{E}_{n+1} - \mathcal{E}_{n-1}) \sin 2\theta \\
&\quad + (\alpha_1/2)(\Delta\theta_{n'} + \Delta\theta_{n'-1} - 2\Delta\theta_n) \cos\theta - (\alpha_2/2)(\Delta\theta_{n+1} + \Delta\theta_{n-1} - 2\Delta\theta_n) \cos 2\theta \\
&\quad - (H/\mu) \sin(2n\theta + \theta_0{}^{(0)}) = 0\,,
\end{aligned} \tag{45}$$

$$\begin{aligned}
&-(\alpha_1/2)(\mathcal{E}_{n'} + \mathcal{E}_{n'-1}) \cos\theta + \{t\mathcal{E}_n + (\alpha_2/2)(\mathcal{E}_{n+1} + \mathcal{E}_{n-1}) \cos 2\theta\} \\
&\quad - (\alpha_1/2)(\Delta\theta_n - \Delta\theta_{n'-1}) \sin\theta + (\alpha_2/2)(\Delta\theta_{n+1} - \Delta\theta_{n-1}) \sin 2\theta \\
&\quad + (H/\mu) \cos(2n\theta + \theta_0{}^{(0)}) = 0\,,
\end{aligned} \tag{46}$$

where

$$t = k_B T\{(g\mu_B)^2 B_S'(y_0)\}^{-1} + \gamma$$

The following solutions are easily found from these difference equations:

$$\begin{aligned}
\Delta\theta_n &= -d_1 \sin(2n\theta + \theta_0{}^{(0)}), & \Delta\theta_n &= d_1 \sin\{(2n+1)\theta + \theta_0{}^{(0)}\}\,, \\
\mathcal{E}_n &= d_2 \cos(2n\theta + \theta_0{}^{(0)}), & \mathcal{E}_n &= -d_2 \cos\{(2n+1)\theta + \theta_0{}^{(0)}\}\,,
\end{aligned} \tag{47}$$

where

$$Nd_1 = (H/\mu)(V - W)/(UV - W^2), \qquad Nd_2 = (H/\mu)(U - W)(UV - W^2),$$

$$U = (t/N) + A_1 \cos^2\theta + A_2 \cos^2 2\theta, \qquad V = A_1 \cos\theta(1 + \cos\theta) - A_2 \cos 2\theta(1 - \cos 2\theta),$$

$$W = A_1 \sin^2\theta + A_2 \sin^2 2\theta,$$

The magnitude of the total magnetization is

$$(N/n_z)\{\sum_n \mu_n \cos\theta_n - \sum_{n'} \mu_n \cos\theta_{n'}\} = (N\mu/2)(d_1 + d_2)\,,$$

so that the susceptibility is given by

$$\chi_{s//} = (1/2)(U + V - 2W)/(UV - W^2)\,. \tag{48}$$

This $\chi_{s//}$ has a finite value at absolute zero. For $T \to 0$, t becomes infinite and so $U \to \infty$, so that

$$(\chi_{s//})_{T=0} = 1/(2V) = (1/2)\{A_1 \cos\theta(1 + \cos\theta) - A_2 \cos 2\theta(1 - \cos 2\theta)\}^{-1}. \tag{49}$$

The ratio of $\chi_{s//}$ to $\chi_{s\perp}$ at absolute zero is a function of θ only (see Fig. 8), and is given by

$$(\chi_{s//})_{T=0}/\chi_{s\perp}=(1/2)\{(1+\cos\theta)+(A_2/A_1)(1-\cos 2\theta)\}$$
$$\times\{\cos\theta(1+\cos\theta)-(A_2/A_1)\cos 2\theta(1-\cos 2\theta)\}^{-1}, \tag{50}$$

where

$$\cos\theta=A_1/(4A_2)\ .$$

$\chi_{s//}$ increases monotonically with rising temperature up to T_N. At $T=T_N$, t becomes

$$(t/N)_{T=T_N}=A_1\cos\theta-A_2\cos 2\theta,$$

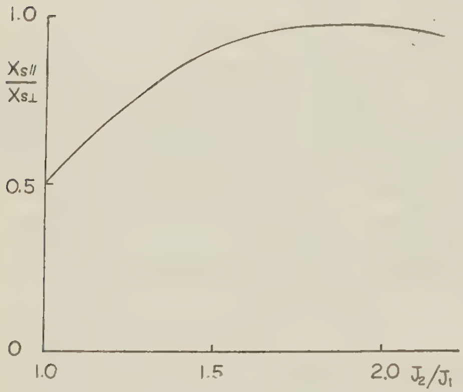

Fig. 8. Variation of $\chi_{s//}/\chi_{s\perp}$ against J_2/J_1.

and it can be shown that $\chi_{s//}$ coincides with $\chi_{s\perp}$.

When the anisotropy of the g-factor and the anisotropic crystalline field are taken into consideration, Eq. (39) will be replaced by

$$\boldsymbol{\mu}_n\times(\boldsymbol{H}_n^{\mathrm{ex}}+\boldsymbol{H}_n^{\mathrm{c.a}}+\boldsymbol{H}^*)=0\ ,$$

and y_n in Eq. (43) by

$$y_n=(g\mu_B S/k_B T)|\boldsymbol{H}_n^{\mathrm{ex}}+\boldsymbol{H}_n^{\mathrm{c.a}}+\boldsymbol{H}^*|\ .$$

Here $\boldsymbol{H}_n^{\mathrm{c.a}}$ (effective field due to crystalline anisotropy) is given, corresponding to (35), by

$$\boldsymbol{H}_n^{\mathrm{c.a}}=-(D'/\mu)\beta_{3n}(\boldsymbol{c}/c)-(E'/\mu)(\beta_{2n}\boldsymbol{a}/a+\beta_{1n}\boldsymbol{b}/a)\ ,$$

and $\boldsymbol{H}^*$, $\boldsymbol{H}^{*\prime}$ are defined by

$$\boldsymbol{g}^2\boldsymbol{H}=g^2\boldsymbol{H}^*,\qquad \boldsymbol{g}'^2\boldsymbol{H}=g^2\boldsymbol{H}'^*,$$

where $\boldsymbol{g}$ and $\boldsymbol{g}'$ are g-tensors for the corner and body-center cations, respectively. Their principal values will be denoted as g_1, g_2, g_3 corresponding to the axes [110], [1$\bar{1}$0], [001] for the corner sites and [1$\bar{1}$0], [$\bar{1}\bar{1}$0], [001] for the body-center sites. Assuming the proper screw-type structure, we obtain, in place of $\chi_{s\perp}$ and $\chi_{s//}$,

$$\chi_c=(g_3/g)^2\{A_1(1+\cos\theta)+A_2(1-\cos 2\theta)+(D'/\mu^2)(2/N)\}^{-1}, \tag{51}$$

$$\chi_a=(1/2)\{(g_1^2+g_2^2)/2g^2\}(U+V-2W)/(UV-W^2)\ . \tag{52}$$

At absolute zero, χ_a reduces to

$$(\chi_a)_{T=0}=(1/2)\{(g_1^2+g_2^2)/2g^2\}(1/V)\ . \tag{53}$$

We shall calculate the principal susceptibilities for the proper screw-type structure of pitch 7/2 and compare them with those measured by Bizette[2] with a single crystal of MnO_2. As $4A_2/A_1=J_2/J_1=1.60$ for this pitch, we obtain $(\chi_{s//})_{T=0}/\chi_{s\perp}=0.94$ from (50), neglecting the anisotropy of the g-factor and $\boldsymbol{H}_n^{\mathrm{c.a}}$. However, the experimental value of $(\chi_a)_{T=0}/(\chi_c)_{T=0}$ is 0.79. Furthermore, χ_a is smaller than χ_c above the Néel temperature according to Bizette. These discrepencies may perhaps be explained by the anisotropy of the g-factor, crystalline anisotropy field and dipolar interaction.

It was already pointed out by Yosida[1] that an observed value of χ_a/χ_c larger than 1/2 at absolute zero can be qualitatively accounted by the B.E.Y.-structure and the anisotropic property of the susceptibility above the Néel temperature by dipolar interaction. However, the dipolar interaction does not seem to be suficient to account for the latter quantitatively.

If we assume $g_1/g_3\approx 0.84$ (putting $g_1=g_2$ for simplicity and neglecting D' in expression (51) for χ_c), we can account for the difference between 0.94 and 0.79 for $(\chi_{s//})_{T=0}/\chi_{s\perp}$. D is related with g-values by

$$D\sim\lambda(g_3-g_1)/2\ ,$$

where λ is the spin-orbit coupling constant and is $140\,\mathrm{cm}^{-1}$ 7) for the free Mn^{4+}. Since $g_3 > g_1$, D is positive, which means that the crystalline anisotropy energy, in addition to the dipolar energy, stabilizes the proper screw-type structure. This is consistent with our assumption made at the beginning. If we adopt 1.49 for the value of $\{(2g_1^2+g_3^2)/3\}^{1/2}$, as Bizette and Tsai5) found from their powder susceptibility measurments above the Néel temperature assuming $S=3/2$ for Mn^{4+}, we find $D \sim 9\,\mathrm{cm}^{-1}$. This is somewhat too large to be expected from data on other salts and may not be reliable, but the positive sign of D will be certain.

Finally, it may be noted that, when a strong field is applied in the c-plane for the proper screw-type structure, we expect flopping of the spin direction as in the usual antiferromagnet. Namely, above a certain critical field, spins as a whole will turn and become perpendicular to the applied field, in other words, the proper screw-type structure will change to a cycloidal structure. This critical field can easily be derived from (33) and (38), as

$$H_c^2=\{ND'-3\varphi_A(\theta)(N\mu/2)^2\}/(\chi_{s\perp}-\chi_{s//}) \, .$$

H_c is about 10^6 oe at absolute zero for the above value of D ($D'=3D/2$ for $S=3/2$).

§ 5. Spin Waves and Antiferromagnetic Resonance in the Proper Screw-type Structure

We start with the exchange Hamiltonian (1). First, we perform an orthogonal coordinate transformation for spin components which is different for different positions of the spin:

$$\begin{aligned} S_{ix}&=S_{i\xi}\cos(kz_i)-S_{i\eta}\sin(kz_i), & S_{iy}&=S_{i\xi}\sin(kz_i)+S_{i\eta}\cos(kz_i), \\ S_{i'x}&=-S_{i'\xi'}\cos(kz_{i'})+S_{i'\eta'}\sin(kz_{i'}), & S_{i'y}&=-S_{i'\xi'}\sin(kz_{i'})-S_{i'\eta'}\sin(kz_{i'}) \, . \end{aligned} \tag{54}$$

ξ and ξ' are the equilibrium directions of the spins at the corner sites and body-center sites, respectively. Quantizing the spins along ξ and ξ' and using Holstein-Primakoff's technique8), we can derive the following spin-wave Hamiltonian:

$$\begin{aligned} H_{\mathrm{sw}}=&-N8J_1S^2\cos\theta+N2J_2S^2\cos 2\theta+N4J_3S^2 \\ &+2J_1S\sum_{<ii'>1}[(a_i^*a_i+b_{i'}^*b_{i'})\cos\theta+(a_i^*b_{i'}+a_ib_{i'}^*) \\ &\times(1-\cos\theta)/2-(a_ib_{i'}+a_i^*b_{i'}^*)(1+\cos\theta)/2] \\ &+2J_2S[\sum_{<ij>2}\{-(a_i^*a_i+a_j^*a_j)\cos 2\theta+(a_i^*a_j+a_ia_j^*) \\ &\times(1+\cos 2\theta)/2-(a_ia_j+a_i^*a_j^*)(1-\cos 2\theta)/2\} \\ &+\sum_{<i'j'>2}\{-(b_{i'}^*b_{i'}+b_{j'}^*b_{j'})\cos 2\theta+(b_{i'}^*b_{j'}+b_{i'}b_{j'}^*) \\ &\times(1+\cos 2\theta)/2-(b_{i'}b_{j'}+b_{i'}^*b_{j'}^*)(1-\cos 2\theta)/2\}] \\ &+2J_3S[\sum_{<ij>3}\{-(a_i^*a_i+a_j^*a_j)+(a_ia_j^*+a_i^*a_j)\} \\ &+\sum_{<i'j'>3}\{-(b_{i'}^*b_{i'}+b_{j'}^*b_{j'})+(b_{i'}^*b_{j'}+b_{i'}b_{j'}^*)\}] \, , \end{aligned}$$

where a_i, $b_{i'}$, a_i^*, $b_{i'}^*$ are the annihilation and creation operators and are connected with the spin operators by the following equations:

$$S_{i\xi}=S-a_i^*a_i\,, \qquad S_{i\eta}+iS_{iz}=(2S)^{1/2}\{1-(a_i^*a_i/2S)\}^{1/2}a_i\approx(2S)^{1/2}a_i\,,$$

$$S_{i'\xi'}=S-b_{i'}^*b_{i'}\,, \qquad S_{i'\eta'}+iS_{i'z}\approx(2S)^{1/2}b_{i'}\,.$$

We perform Fourier transformations on a_i and $b_{i'}$:

$$a_{\boldsymbol{q}}=(2/N)^{1/2}\sum_i a_i\exp(i\boldsymbol{q}\cdot\boldsymbol{r}_i)\,, \qquad b_{\boldsymbol{q}}=(2/N)^{1/2}\sum_i b_{i'}\exp(i\boldsymbol{q}\cdot\boldsymbol{r}_{i'})\,,$$

where $\boldsymbol{q}$ runs over the $N/2$ wave vectors in the Brillouin zone, referred to the chemical unit cell. Furthermore, the following new operators, $A_{q\mathrm{I}}$ and $A_{q\mathrm{II}}$, will be introduced:

$$\begin{aligned} A_{q\mathrm{I}} &= (1/8)[\{(A^-/B^+)^{1/4}+(B^+/A^-)^{1/4}\}(a_q+b_q) \\ &\qquad +\{(A^-/B^+)^{1/4}-(B^+/A^-)^{1/4}\}(a_q{}^*+b_q{}^*)] , \\ A_{q\mathrm{II}} &= (1/8)[\{(A^+/B^-)^{1/4}+(B^-/A^+)^{1/4}\}(a_q-b_q) \\ &\qquad +\{(A^+/B^-)^{1/4}-(B^-/A^+)^{1/4}\}(a_q{}^*-b_q{}^*)] , \end{aligned} \tag{56}$$

where

$$\begin{aligned} A^\pm &= 16J_1S\cos\theta(1\pm\gamma_{q1})-4J_2S\cos 2\theta(1-\gamma_{q2})-8J_3S(1-\gamma_{q3}) , \\ B^\pm &= 16J_1S(\cos\theta\pm\gamma_{q1})-4J_2S(\cos 2\theta-\gamma_{q2})-8J_3S(1-\gamma_{q3}) , \end{aligned} \tag{57}$$

$$\begin{aligned} \gamma_{q1} &= \cos(q_xa/2)\cos(q_ya/2)\cos(q_zc/2) , \\ \gamma_{q2} &= \cos(q_zc), \qquad \gamma_{q3}=\{\cos(q_xa)+\cos(q_ya)\}/2 , \end{aligned} \tag{58}$$

(see (3)). Using these operators, we can derive the diagonalized spin wave Hamiltonian:

$$\begin{aligned} H_{\mathrm{sw}} &= -N8J_1S(S+1)\cos\theta+N2J_2S(S+1)\cos 2\theta \\ &\quad +N4J_3S(S+1)+\sum_q \hbar\omega_{q\mathrm{I}}(N_{q\mathrm{I}}+(1/2))+\sum_q \hbar\omega_{q\mathrm{II}}(N_{q\mathrm{II}}+(1/2)) , \end{aligned} \tag{59}$$

where

$$\begin{aligned} N_{q\mathrm{I}} &= A_{q\mathrm{I}}{}^*A_{q\mathrm{I}} , \qquad N_{q\mathrm{II}}=A_{q\mathrm{II}}{}^*A_{q\mathrm{II}} , \\ \hbar\omega_{q\mathrm{I}} &= \{A^-B^+\}^{1/2}, \qquad \hbar_{q\mathrm{II}}=\{A^+B^-\}^{1/2} . \end{aligned} \tag{60}$$

As can be seen from (57), (58) and (60), $\omega_{q\mathrm{I}}$ vanishes at $\boldsymbol{q}=0$ and $\omega_{q\mathrm{II}}$ vanishes at $\boldsymbol{q}=\pm\boldsymbol{k}$ (where $\boldsymbol{k}$ is the wave vector of the screw). In the neighborhood of these points, $\omega_{q\mathrm{I}}$ and $\omega_{q\mathrm{II}}$ can be expanded as

$$\begin{aligned} (\hbar\omega_{q\mathrm{I}})^2 &= 8S^2\{4J_1(1+\cos\theta)-J_2(1-\cos 2\theta)\}\{(J_1\cos\theta-J_3)(q_x{}^2+q_y{}^2)a^2 \\ &\qquad +(J_1\cos\theta-J_2\cos 2\theta)q_z{}^2c^2\} , \\ (\hbar\omega_{q\mathrm{II}})^2 &= 8S^2\{4J_1\cos\theta(1+\cos\theta)-J_2\cos 2\theta(1-\cos 2\theta)\} \\ &\qquad \times\{(J_1\cos\theta-J_3)(q_x{}^2+q_y{}^2)a^2+(J_1\cos\theta-J_2\cos 2\theta)(q_z\mp k)^2c^2\} . \end{aligned} \tag{61}$$

A sketch of the variation of these frequencies against q_z is shown in Fig. 9.

The modes of oscillation of the spins in branch I at $\boldsymbol{q}=0$ and branch II at $\boldsymbol{q}=\pm\boldsymbol{k}$, are illustrated by Fig. 10. They must be detectable by antiferromagnetic resonance at zero field, as the matrix elements of $\sum_i S_{iz}+\sum_{i'} S_{i'z}$ and $\sum_i S_{ix}+\sum_{i'} S_{i'x}$, for branch I and II respectively, do not vanish. The first mode can be excited when an oscillating field is applied along the the c-axis, and the second doubly degenerate modes by an oscillating field in the c-plane. Taking into account the crystalline anisotropy energy, (36), as well as the dipolar interaction, the frequency of the doubly degenerate modes for $\boldsymbol{q}=\pm\boldsymbol{k}$ is calculated to be as follows:

$$(\hbar\omega_{\mathrm{II}})^2=4S^2\{4J_1\cos\theta(1+\cos\theta)-J_2\cos 2\theta(1-\cos 2\theta)\}\{(D/2)-(3N/8)\varphi_A(\theta)g^2\mu_{\mathrm{B}}{}^2\} , \tag{62}$$

$$(\omega_{\mathrm{II}}/\gamma)^2=2D_1/\chi_{s//} ,$$

where $\chi_{s//}$ is given by (49), and D_1 is defined by the total anisotropy energy, E_a,

$$E_a=D_1\sin^2\Theta=\{N(D'/2)-(3/2)\varphi_A(\theta)(N\mu/2)^2\}\sin^2\Theta .$$

In the case of $\mathrm{MnO_2}$, the wavelength corresponding to the frequency of this mode is calculated to be about 200 μ, assuming $16J_1\sim 90\ \mathrm{cm}^{-1}$, $J_2/J_1\approx 1.60$ (see section 2) and $D\sim 90\ \mathrm{cm}^{-1}$ (see section 4), thus it comes into the far infra-red region.

The mode of $q=0$ belonging to branch I is such that the spins oscillate as illustrated in Fig. 10 (A); the spins make a small oscillation as a whole in the c-plane, as well as out-of plane motions. Hence, its frequency is expected to be proportional to the geometrical mean between $1/\chi_{s\perp}$ and the anisotropy constant in the c-plane. The anisotropy energy in the c-plane may be very small, as discussed in section 3 (B), so that frequency of this mode may also be very low.

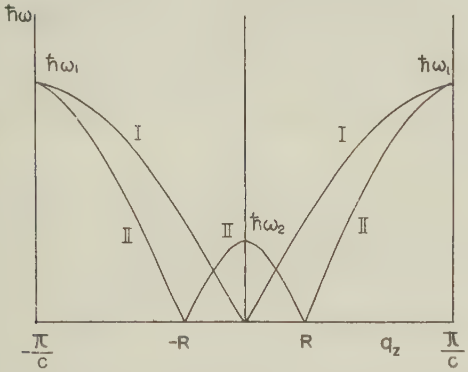

Fig. 9. Sketch of the frequency spectra.
$\hbar\omega_1 = S[(16J_1\cos\theta - 8J_2\cos\theta)\{16J_1\cos\theta - 4J_2(\cos 2\theta + 1)\}]^{1/2}$
$\hbar\omega_2 = S[32J_1\cos\theta\{16J_1(\cos\theta - 1) + 4J_2(1 - \cos 2\theta)\}]^{1/2}$

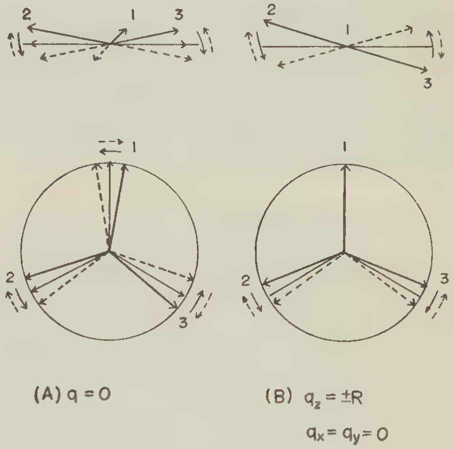

(A) $q=0$

(B) $q_z=\pm R$ $q_x=q_y=0$

Fig. 10. The modes of the spin wave of $q=0$ in branch I (A) and $q_z=k$. ($q_x, q_y=0$) in branch II (B) (the 3-pitch-structure).

The upper figures are projections perpendicular to the c-axis. The lower figures those on the c-plane.

§ 6. Neutron Diffraction Pattern

The scattering cross-section of neutrons from the screw-type structure is calculated from the standered formula[9)] as

$$d\sigma/d\Omega \propto f(\kappa)^2\{1+(\kappa_\perp/\kappa)^2\}(<S^\xi>/S)^2\{\Delta(\kappa-\boldsymbol{k}+\boldsymbol{K})+\Delta(\kappa+\boldsymbol{k}+\boldsymbol{K})\}\sin^2\{((K_1+K_2)a+K_3c)/2\}\,, \qquad (63)$$

where $d\sigma/d\Omega$ is the differential cross-section, $f(\kappa)$ the form factor, κ the scattering vector, $\kappa_\perp$ the component of κ perpendicular to the plane to which the spins are parallel, $\boldsymbol{K}$ the reciprocal lattice vector referred to the chemical unit cell, K_1, K_2, K_3 are its components, and

Table II.

Indices	$\kappa=4\pi\sin\theta_B/\lambda$ (A^{-1})	$1+(\kappa_z/\kappa)^2$	$f(\kappa)^2$ *	I/I_{005}
102	1.54	1.16	.71	.60
005	1.55	2	.69	1
115	2.54	1.38	.34	.34
009	2.80	2	.27	.39
212	3.22	1.04	.19	.14
205	3.23	1.23	.19	.17
119	3.44	1.65	.15	.18
209	3.98	1.49	.06	.06
1012	3.98	1.87	.06	.08
302	4.29	1.02	.04	.03
225	4.29	1.13	.04	.03

* The normalized form factor for Mn^{2+} (not for Mn^{4+}) by Shull et al. used. (C. G. Shull, W. A. Strauser, and E. O. Wollan: Phys. Rev. **83** (1951) 334).

$$\Delta(\boldsymbol{X})=(2/N)|\sum_i \exp(\mathrm{i}\boldsymbol{X}\cdot\boldsymbol{r}_i)|^2, \qquad |X_x|,\ |X_y|<\pi/a, \qquad |X_z|<\pi/c.$$

As easily seen from (63), the Bragg condition for the magnetic reflection is that κ is equal to $\boldsymbol{K}\pm\boldsymbol{k}$ and $\{(K_1+K_2)a+K_3c)\}/\pi$ is odd. Hence, if p is the reciprocal of the screw pitch in units of c, we expect reflections $1, 0, p$, $0, 0, 1\pm p$, $1, 1, 1\pm p$, $2, 0, 1\pm p$, etc..

Through private correspondences the writer has been informed by Prof. Erickson[6] of his experiment of neutron diffraction with a single crystal of polianite. He has observed five relations 102, 005, 115, 009, and 205, at 80°K, where his indices refer to the magnetic unit cell which is seven times large along the c-axis compared with the chemical unit cell. These reflections are just what we expect for the screw-type structure of pitch 7/2. The calculated relative intensities of the reflections expected for the proper 7/2-pitch-structure are shown in Table II.

§ 7. Concluding Remarks

By a Fourier method, possible arrangements of classical vector spins in rutile-type crystal were studied, and it was found that the screw-type structure is energetically favorable under certain conditions imposed on the values of J_2/J_1 and J_3/J_1. A similar method of "the normal mode" has been independently used by Gersch and Koehler[10] in their study of the spin arrangement in some simple lattices, but they assumed scalar spins which have only two discrete values, $+S$ and $-S$, so that they could not find a configuration in which the spin direction varies gradually in space.

The stability conditions for the screw-type structure with a pitch of 7/2, which seems to be realized in polianite, are that $J_2/J_1=1.60$ and $J_3/J_1<0.31$, as described in section 2. The range of J_2/J_1, in which the 7/2-pitch-structure is stabilized by the crystalline field anisotropy, is extremely narrow, as discussed in section 3. It would therefore be accidental that the pitch of the screw in polianite at 80°K be exactly 7/2; to account for the neutron diffraction data, the pitch can be approximately 7/2. The pitch can vary in the neighborhood of 7/2 if J_2/J_1 varies due, for instance, to thermal expansion or an applied stress. It might be interesting to perform a neutron diffraction experiment at lower temperatures or under stress to detect such a variation in pitch.

If $J_3/J_1>0.31$, the 7/2-pitch screw-type structure cannot be realized, and the theoretical value of Θ_p/T_N cannot exceed 2.8. If we determine J_3/J_1 using Eq. (24) from the observed ratio of Θ_p (316°K) to T_N (84°K), that is, $\Theta_p/T_N=3.8$, we obtain $J_3/J_1\sim 0.56$. This discrepancy may partly be due to a crude approximation of the molecular field theory.

If θ is put equal to zero in (57), (60) and (61), we have the frequencies of the spin waves in the $\mathrm{MnF_2}$-type structure. According to these frequency formulae, some modes with small $\boldsymbol{q}$ have imaginary frequencies when J_2 is greater than J_1, as clearly seen from (61). This situation has been pointed out by Nagai and Nakamura[11]. However, the $\mathrm{MnF_2}$-type structure is less stable than the screw-type structure for $J_2>J_1$. Therefore we see that, as soon as the spin superstructure becomes energetically unstable, some of the spin wave excitations become also unstable. This statement is also true when the screw-type structure becomes less stable than the B.E.Y.-structure ($2J_2J_3>J_1^2$, $J_2/J_1>1$), in which case the frequencies of modes with $\boldsymbol{q}$ in the neighborhood of $q_x, q_y=\pm\pi/a$, $q_z=\pm\pi/c$ become imaginary. It can be shown that if only exchange energy is considered, the stability boundaries in the J_2/J_1, J_3/J_1-plane derivable from the instability of the spin waves are the same with those which can be derived by comparing the energy values of the various spin superstructures. When the anisotropy energy is also taken into consideration, this becomes no longer true; for example, in the region where the $\mathrm{MnF_2}$-type structure has just become unstable, all the spin waves of the same structure remain still stable.

The writer would like to express his deep thanks to Professor T. Nagamiya of Osaka University for suggesting this study as well as his continual advice in the course of the work and to Dr. J. Kanamori of Osaka University and Mr. Y. Kitano of University of Osaka Prefecture for their helpful discussions.

He is also indebted to Professor R. A. Erickson of Ohio State University for kindly supplying his experimental data prior to publication.

References

1) P. W. Anderson: Phys. Rev. **79** (1950) 705. J. H. Van Vleck: J. phys. radium **12** (1951) 262.
2) H. Bizette: J. phys. radium **12** (1951) 161.
3) R. A. Erickson: Phys. Rev. **85** (1952) 745.
4) K. Yosida: Progr. Theor. Phys. **8** (1952) 259.
5) H. Bizette and B. Tsai: *Colloque sur la polarisation de la matière* cited by Lidiard (Paris, C.N.R.S. 1949) 164, (Reports on Progr. in Phys. **17** (1954) 201).
6) R. A. Erickson: private communication.
7) Charlotte E. Moore: *Atomic Energy Levels* vol. **1**, (Nat. Bur. Stand. 1952).
8) T. Holstein and H. Primakoff: Phys. Rev. **58** (1940) 1908.
9) O. Halpern and M. H. Johnson: Phys. Rev. **55** (1939) 898.
10) H. A. Gersch and W. C. Koehler: J. Phys. Chem. Solid **5** (1958) 180.
11) O. Nagai and T. Nakamura: private communication.

JOURNAL OF THE PHYSICAL SOCIETY OF JAPAN, Vol. 14, No. 6, JUNE, 1959

Oscillations in Plasma II

By Shoji KOJIMA, Kiyoe KATO, Shigeo HAGIWARA
and Ri'ichi MATSUZAKI

Tokyo University of Education, Otsuka, Tokyo

(Received March 2, 1959)

As previously reported, two or three plasma-electron oscillations of slightly different frequencies are simultaneously generated in a hot cathode discharge. The filled gas is mercury vapour at pressures of order of 1 micron. These oscillations can be observed by a Yagi antenna set apart from the discharge tube as well as by a probe in it. In the discharges the primary electrons form convergent and divergent beams. The oscillation of the highest frequency is generated by the convergent beam in the central part of the tube and this is that observed by many authors. The oscillation of the lowest frequency seems to be generated near the wall of tube by the divergent beam. Another oscillation having a middle frequency is often observed. This is generated at the periphery of the convergent beam.

§ 1. Introduction

In a previous paper[1], hereafter refered to as **I**, it was reported that a discharge at low pressure generates simultaneously two or three plasma oscillations of different frequencies. The frequency of plasma-electrons oscillation, f_p, is related to the concentration of electrons, N, by the well known expression

$$f_p=\sqrt{Ne^2/\pi m}\,, \tag{1}$$

where e is the charge and m the mass of electron. Therefore the oscillation of unique frequency will be expected. If the concentration of electrons is not uniform, frequencies of oscillations will be distributed continuously. The observation, however, indicated that there are discrete oscillations having different frequencies. In the present work the origin of the oscillations has been studied.

An experiment described in **I** showed that the plasma oscillation could be observed outside a discharge tube by a small antenna. Since the plasma oscillation is a longitudinal wave, it will give rise to no electromagnetic wave. In the preliminary experiment the antenna received the oscillation by electrostatic interaction because of small range of investigated distance whose maximum was less than a wave length. In the present work the investigation has been extended to a region where the induction field would vanish.

§ 2. Procedure of Experiments

In the previous work three types of discharge tube were used. The types A and C were similar to that described by Merrill and Webb[2)] and to that by Looney and Brown[3)] respectively. The type B was same as the type A except having no probe. In the present work somewhat modified tubes are used. However, the types are essentially same as before. All the discharge tubes are hot cathode tubes filled with mercury vapour at pressures of the order of 10^{-3} mm Hg.

The oscillations whose frequencies are in a region between 500 Mc and 1000 Mc are detected by a super-regenerative detector through a probe inserted in the discharge tube or through an antenna set outside the tube. The frequency of the detector can be controlled by changing the plungers of coaxial cavities as described in **I**. In most of the experiments, however, the detector is used at a fixed frequency and the frequency of oscillation is adjusted to it by changing a discharge current.

By means of superimposing an a.c. current of a suitable amplitude on a d.c. discharge current, generation of the oscillation whose frequency agrees with that of detector is visualized with an oscilloscope. A block diagram of this experimental method is shown in Fig. 1. The oscilloscope display which was obtained for the tube described below (§ 5) is reproduced in Fig. 2.

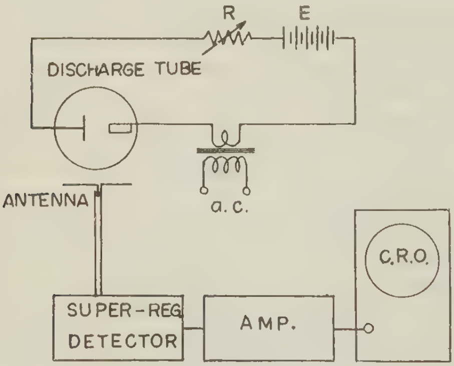

Fig. 1. Block diagram illustrating the method of displaying plasma oscillations on a cathode-ray oscilloscope.

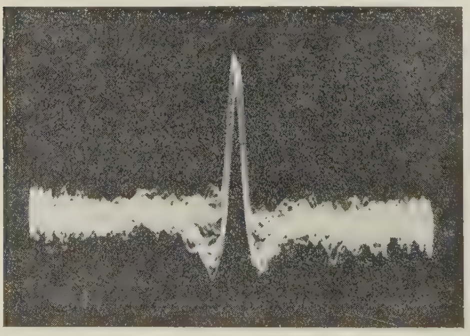

Fig. 2. A typical oscillogram. The time base of the oscilloscope runs in synchronism with the discharge current. The frequency of the detector is 833 Mc. The d.c. discharge current is 21 mA, on which a.c. current of 6 mA is superimposed.

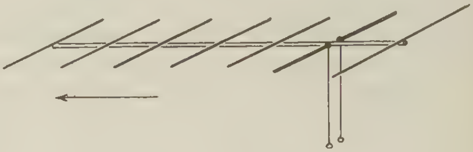

Fig. 3. Yagi antenna.

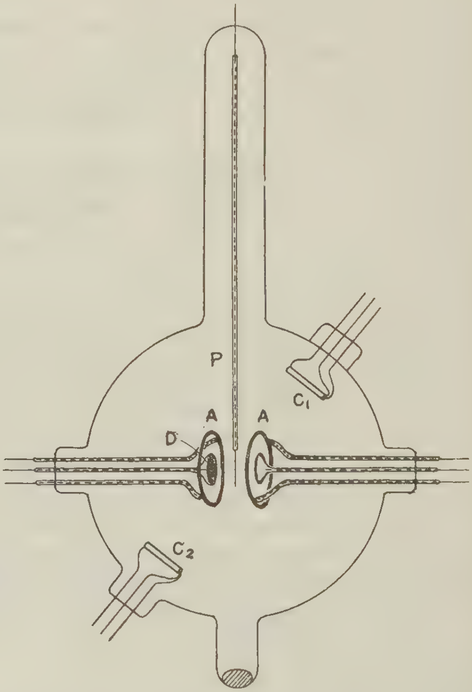

Fig. 4. Discharge tube having two cathodes. A: Pair of ring anodes, D: Pair of plane probes, C_1 and C_2: Cathodes, P: Movable needle probe.

A Yagi antenna which consists of five guiding elements and one reflector is used for receiving. The construction is shown in Fig. 3.

§ 3. Oscillations in a Tube having Two Cathodes

In **I** it was shown that the auxiliary electron beam in the discharge tube of type C was not essential to generate the oscillations. The discharge tubes used here were same as the type C in **I**, but they had no auxiliary electron gun. A diagram of the tube is shown in Fig. 4. As previous experiments a relation between the frequency and the discharge current was studied. The obtained plots of frequency of oscillation *vs*. the discharge current are shown in Fig. 5. In this case too, three groups of oscillations, *a*, *b* and *c* groups were observed. The oscillations of the *c* group were very weak compared with those of other groups. On this tube an effect of pair of cathodes could be studied by changing the currents through the each cathode independently. A circuit diagram of the experiments is shown in Fig. 6. In order to generate the oscillation of a fixed frequency there are some relations between the currents I_1 and I_2. Such relations were searched. The result is reproduced in Fig. 7. The points P_1 and P_2 in the figure correspond to the points indicated in Fig. 6 where the two cathodes were connected together. Even if one of the cathode currents is decreased, I_1 form P_1 to P_1' for example, the other cathode current I_2 is almost constant. This suggests that the origin of the oscillations of group *a* is related to the cathode C_2. Similary the origin of the oscillations of group *b* is related to the cathode C_1. It is interesting that both oscillations originated from the pair of cathodes are observed by a probe at the center of discharge tube. If the cathodes were made identically, the groups *a* and *b* would coincide with each other. On the group *c* a discussion will be given in the next section.

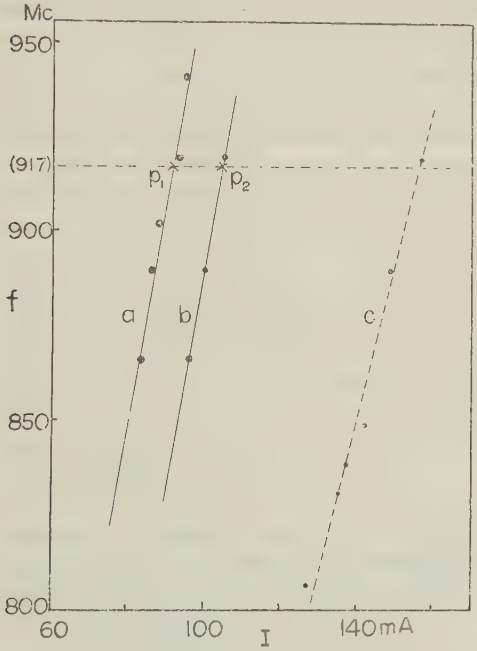

Fig. 5. Plots of frequencies of oscillations *vs*. discharge currents.

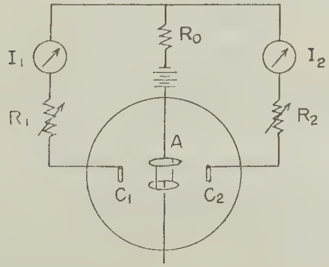

Fig. 6. Circuit diagram of experiment for a tube having two cathodes.

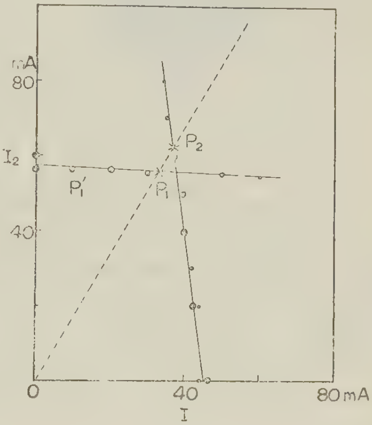

Fig. 7. Plots showing relation of two currents which generate the oscillation of 917 Mc. The intensity of oscillation is illustrated by the size of point.

§ 4. Detailed Characters of Oscillations

In order to determine the concentration of electrons a discharge tube was equiped with a pair of plane probes. Its diagram is shown in Fig. 8. In the discharge tube the primary electrons form two beams. One is converging and the other diverging*. The central region α where the convergent electron beam is present is brighter than the neighbouring plasma. The structure of discharge is also shown schematically in Fig. 8. In addition to the plane probes this tube has a pair of needle probes which are movable across the beam of electrons. From one of these probes the oscillations were picked up. A relation between the frequency of oscillation and the discharge current was studied. The result with a probe at the center of region α is shown in Fig. 9 with full circles. The plots form into two groups as the case shown in Fig. 4 in **I**. When the pick-up probe was set at the periphery of region α the oscillations mentioned above became somewhat weak and newly the third group appeared. These oscillations are shown in Fig. 9 with open circles. The results shown in Fig. 9 indicate that two or three oscillations with different frequencies can be generated simultaneously at a fixed discharge current.

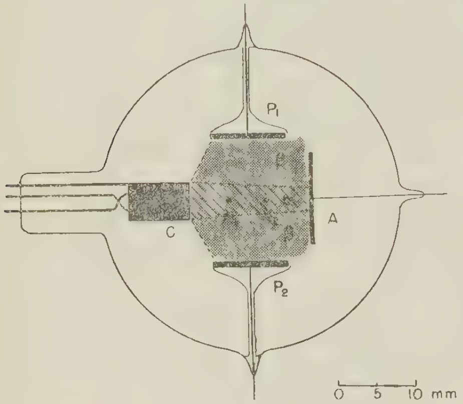

Fig. 8. Discharge tube having plane probes. A: Anode, C: Cathode, P_1 and P_2: Pair of plane probes, N_1 and N_2: Pair of needle probes, α: Bright region, β: Faint region.

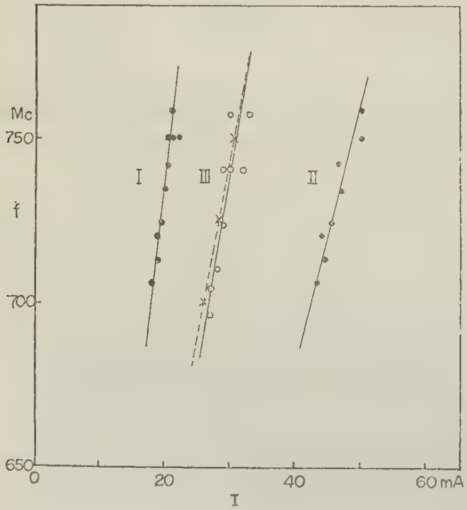

Fig. 9. Plots of frequencies of oscillations *vs.* discharge currents. Closed circles indicate the results with a probe at the center and open circles the results at the periphery of region α. Crosses represent the results calculated from measured densities.

The simultaneous generation of the oscillations was verified more directly with an experiment where two super-regenerative detectors working with different frequencies were used.

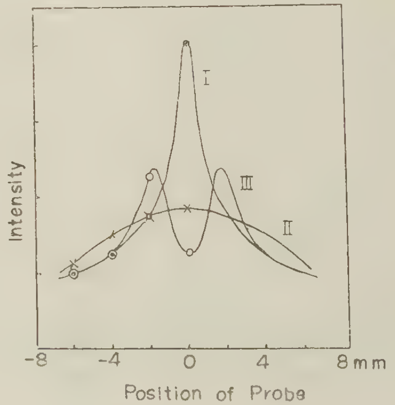

Fig. 10. Intensity as a function of position of the probe. The distance is measured from the center to the wall. I, II and III indicate the groups of oscillation shown in Fig. 9.

The concentrations of electrons were determined from measurements with the plane probes. An ion-saturation current of the probe, I_s, is expressed by Boyd[3] and Shultz-Brown[4] as follows:

$$I_s=0.61eN\sqrt{kT_e/M}\,S \tag{2}$$

where k is Boltzmann constant, T_e the electron temperature, M the mass of ion and S the area of the plane probe**. From the measurement of I_s the electron concentration N was determined by using Eq. (2) and then the frequency of the plasma oscillation was calculated by the aid of Eq. (1). The calculated frequencies are shown in Fig. 9 by crosses. The straight line through the calculated points agrees with the line representing the third group of the oscillations. Since the measured concentrations give certain average values, the agreement should not be interpreted strictly. It means only that all the observed oscillations are reasonable to attribute to the plasma electron oscillation.

---

* The convergent and divergent beams start from near the cathode. In the present case the meniscus which is described by Allen et al. (British J. Appl. Phys. **6** (1955) 320) was not seen.

** In I, the usual expression $I_s=\frac{1}{4}eN\sqrt{8kT_p/\pi M}\,S$ was used, where T_p is the ion temperature. In the present case at which the pressure is low enough the expression (2) seems to be more adequate.

When the pick-up probe was moved from the center to the wall, the intensity of the oscillations of each group varied in different manner as shown in Fig. 10. Since the oscillations belonging to the third group have a maximum intensity at the boundary between the regions α and β, they seem to be generated at this boundary. The oscillations of the first group, which are generated strongly at the center of plasma, seem to be the main plasma oscillations that are reported by many authors[2),3)]. The oscillations of the second group are observed in a very wide region which extends to the wall. The convergent and divergent beams presumably play roles analogous to those from two cathodes mentioned in the last section. Then, the oscillation of the second group seems to be a plasma oscillation which is generated by the divergent electron beam.

The frequencies of oscillations of the first and the second groups may be determined from the electron concentration in the regions α and β respectively. The Eq. (1) yields the following frequencies:

$$f_1=\sqrt{e^2N_\alpha/\pi m} \text{ and } f_2=\sqrt{e^2N_\beta/\pi m}\,, \qquad (3)$$

where N_α and N_β are the concentrations in the regions α and β. By using needle double probes the concentrations were measured. The obtained values were not accurate in absolute scale because of the effect of sheath around the probes, but useful for comparison between them. The results supported above relations.

In view of the location of oscillation the third group may attribute to the sheath resonance which occurs at the boundary between the regions α and β. If a discontinuity in concentration is assumed, the frequency of the resonance is expressed by

$$f_3=\sqrt{f_1^2-f_2^2}\,. \qquad (4)$$

The results shown in Fig. 9 give the ratio $f_1 : f_2 : f_3$ to be about $\sqrt{54} : \sqrt{23} : \sqrt{35}$ which satisfy the relation expressed by Eq. (4) approximately.

The groups a and b in the discharge tube having two cathodes which are mentioned in the last section correspond to the first group in the present case. The group c to which belonging oscillation is very weak, corresponds probably to the second group in the present case.

§ 5. Radiation having the Frequency of Plasma Oscillation

The oscillations of the three groups mentioned in the last section were also observed outside the discharge tube by a Yagi antenna. In this case the probe is unnecessary. Sometimes, however, the probe affected the oscillations. When the probe was inserted at the periphery of region α, the oscillations of the third group became strong. It may be considered that the probe works as a sending antenna. It was tested with a discharge tube whose probe was made from non-conducting material. The effect of the probe, however, was same as the case of conducting probe. So that the action of probe is to disturb the plasma and to strengthen the oscillation.

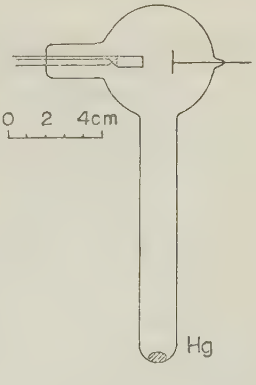

Fig. 11 Discharge tube having no probe.

Radiation was further studied with a tube having no probe. A diagram of the used tube is shown in Fig. 11. Since the Yagi antenna had large gain, the oscillation could be detected at a distance of 300 cm from the tube. The decrease of the observed intensity was less than that given by the inverse square law. As shown in Fig. 12, the field strength was almost inversely proportional to the distance. This suggests that the oscillation propagates as an electromagnetic radiation. The intensity of radiation depended on its direction. The curve shown in the figure was a result when the direction of antenna was set at perpendicular to the axis of the discharge tube and the plane of the antenna was parallel to the axis.

The angular dependency of the radiation was measured by changing the direction of antenna. The results in two cases where the elements of Yagi antenna are parallel and perpendicular to the axis of discharge tube are shown in Fig. 13. On the direction perpendicular to the axis of tube the intensity of radiation was very different in the two cases. Such polarization effect was studied by rotating the antenna around its axis. The results of measurements are shown in Fig. 14.

The angular distribution and polarization are not same for three groups of oscillations. The results mentioned above are refered to the first group of the oscillations. The oscillations of the second and third groups did not show remarkable polarization as those of the first group*.

Since the super-regenerative detector emits oscillations from itself, it may receive change of impedance of distant plasma. In order to prove the presence of radiation a detector of pure absorption type is preferable. Fortunately, when the a.c. modulation of the discharge current was applied, a method of crystal detector and amplifier was usable. The radiation from the oscillation of the first group could be verified by this method.

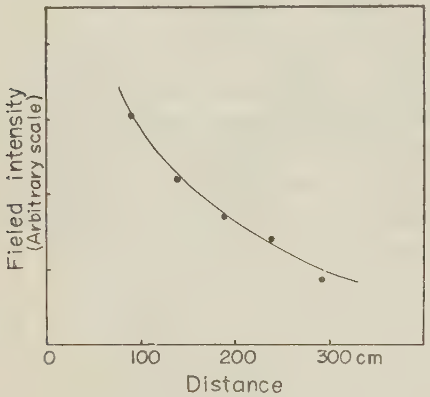

Fig. 12. Intensity as a function of distance from the centre of discharge tube.

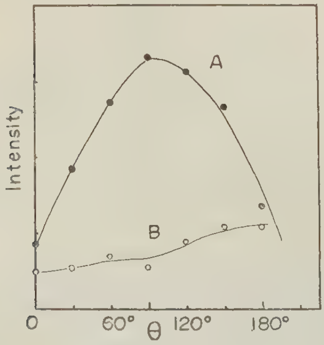

Fig. 13. Angular distribution of radiation. θ is the angle between the direction of Yagi antenna and the direction from the anode of discharge tube towards the cathode. A. The elements of the antenna are parallel to the axis of discharge tube. B. They are perpendicular to the axis.

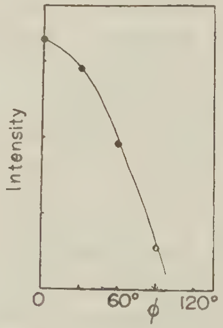

Fig. 14. Polarization of radiation. ϕ is the rotation angle of the antenna around its axis. 0° is the direction where the elements of the antenna are parallel to the axis of discharge tube.

§ 6. Conclusion

In **I**, many plasma oscillations having slight different frequencies were detected. In the present work details of the oscillations are studied. Generally, a discharge tube yields two plasma oscillations. One is generated in the central region of discharge tube by a convergent electron beam from the cathode. The other is generated in the region near the wall by a divergent electron beam from the cathode. The frequency of the latter is lower than that of the former. When the main electron beam has a clear boundary, another oscillation is generated.

---

* The third group of oscillations was scarcely observed for the tube having no probe. Only when the convergent beam had sharp periphery, it appeared.

These plasma oscillations can be radiated as electromagnetic waves.

This work was financed by the Scientific Research Fund of the Ministry of Education.

References

1) S. Kojima, K. Kato and S. Hagiwara: J. Phys. Soc. Japan **11** (1957) 1276.
2) H. J. Merrill and H. W. Webb: Phys. Rev. **55** (1939) 1191.
3) D. H. Looney and S. C. Brown: Phys. Rev. **93** (1954) 965.
4) R. L. F. Boyd: Proc. Roy. Soc. **A**, **201** (1950) 329.
5) G. J. Schulz and S. C. Brown: Phys. Rev. **98** (1955) 1642.

JOURNAL OF THE PHYSICAL SOCIETY OF JAPAN, Vol. 14, No. 6, JUNE, 1959

Experimental Studies on the Hypersonic Flow past Plane, Convex and Concave Wedges

By KIM, Chul-Soo*

Department of Physics, Faculty of Science,
University of Tokyo

(Received January 30, 1959)

In this paper, the phenomena of viscous-inviscid interaction effects at $M_\infty=6.2$ over the front part of bodies have been investigated. The models tested are a flat plate and wedges having a plane, a convex or a concave surface, respectively. A uniform flow of $R_\infty=2.0\times10^5$ per cm was established using a divergent shock tube. The measurements of the flow field were made by optical methods (interferometer and schlieren photograph), and in order to supplement the data the X-ray technique was employed near the leading edge of the model.

The results are as follows. (1) For a flat plate: i) the pressure distribution on the sharp-nosed plate is about 5 per cent higher than Nagakura-Naruse's theoretical values; ii) the boundary layer thickness agrees almost perfectly with Naruse's theoretical values; iii) the shock wave location is in good agreement with the empirical formulae of Kendall and of Bogdonoff and Hammitt. (2) For wedges: i) near the leading edge, the boundary layer growth on a concave wedge is more rapid than that either on a plane or a convex wedge; ii) except in the region close to the leading edge, the influence of leading edge bluntness on boundary layer growth is significant in the order of convex wedge, plane wedge and concave wedge; iii) except in the region very close to the leading edge, the pressure distributions at the front parts of the plane and convex wedges are in fairly good agreement with the values predicted by inviscid theories (characteristic method, tangent-wedge approximation, Newtonian-plus-centrifugal-force approximation and hypersonic small disturbance theory), but considerable discrepancies are found at the rear parts; iv) for the concave wedge, agreement is rather better at the rear part of the body than at its front part.

§ 1. Introduction

When the flight Mach number greatly exceeds unity, linearized theory breaks down for a very slender body because non-linearity becomes an essential feature of the flow. This is due to the fact that the kinetic energy of the hypersonic flow is much larger than that of the subsonic or the supersonic flow. Therefore, the exact equations are in general very difficult to be handled even when the viscosity and the real gas effects associated with the hypersonic flow are neglected. Approximate solutions were obtained by Van Dyke1) and Cole2) on the assumption that the entire flow field involves only small disturbances. But, for slender or thin bodies, the shock wave lies relatively close to the surface of the body and the so-called viscous-inviscid interaction may be generally more significant than that for blunt bodies. When this interaction is strong3)–4) or weak6)–9), many theoretical studies have been performed assuming that the flow between the shock wave and the body surface consists of the boundary layer and the inviscid external flow. Quite recently, Nagakura and Naruse10) obtained an excellent approximate solution which covers the whole region including strong and weak interaction regions, in the case of the flow over a flat plate.

---

* Present address: Department of Physics, National Seoul University, Tongsung-Dong, Seoul, Korea.

Theoretical studies are mostly limited to the sharp-nosed simple bodies, so far as the present author is aware, but it is, in practice, impossible to make such a sharp nose. Thus, in particular, the interest of an experimental study seems to be in the problem of the effect of leading edge bluntness on the hypersonic flow field over the body. For the hypersonic flow over a flat plate, several experiments were carried out by Bogdonoff and Hammitt11), by Kendall12) and by Bertram13). In these experiments, blunt leading edges of various thickness were obtained by cutting the leading edge of the wedge normal to the plane surface. They emphasized that the Reynolds number R_t based on the thickness of the leading edge behaved as a very important parameter in the study of viscous-inviscid interaction of the hypersonic flow.

The main aim of the present experiment is to study how the small disturbances propagate in the hypersonic flow. For this purpose, three groups of models are used: plane wedge, convex wedge and concave wedge (see Fig. 2). The choice of these models is physically significant in the following respects. For the plane wedge and the convex wedge, disturbances due to the boundary layer add a negative pressure gradient to the pressure for the inviscid flow past a plane wedge, whereas for the concave wedge it adds a positive pressure gradient. Therefore, the former has a tendency to make the boundary layer thin and the latter has an opposite tendency. What has prompted this experiment is, in short, the expectation that there will be different modes of the viscous-inviscid

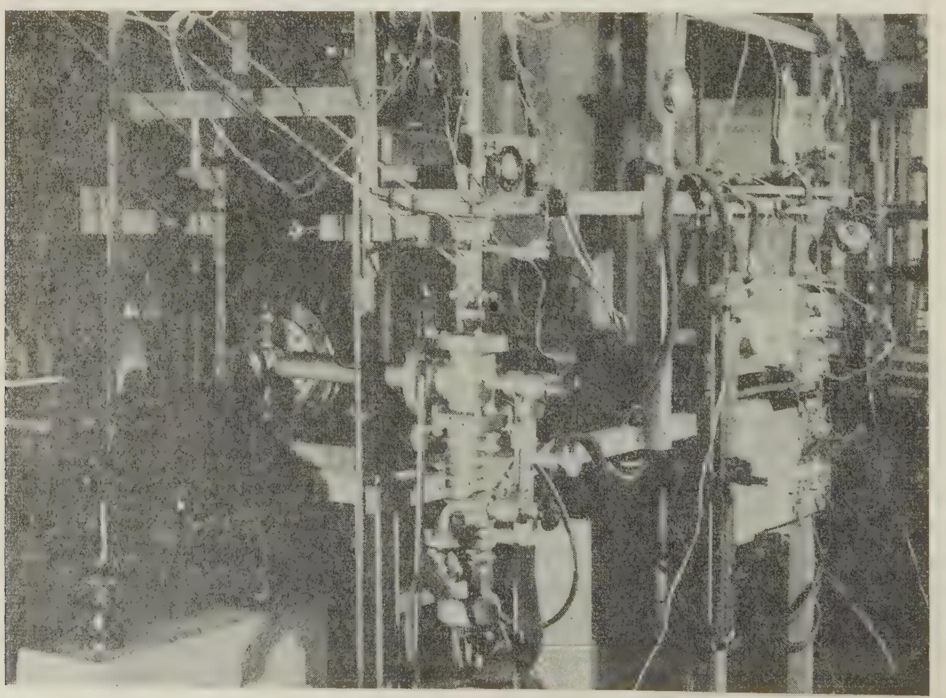

Fig. 1. Photograph of apparatus.

interaction in the accelerating (for plane wedge and convex wedge) and the decelerating (for concave wedge) hypersonic flow. For the detailed study of the problem, the effects of leading edge bluntness were also investigated. All the experiments were carried out at the free stream Mach number of $M_\infty=6.2$, utilizing the shock tube. The Reynolds number of the uniform flow was $R_\infty=2.0\times10^5$ per cm, and the duration of the uniform flow was about 1 milli-second. The measurements of the flow field were made by optical methods (interferometer and schlieren photograph), and near the leading edge of the model, the X-ray technique was employed for determining the air density. Experimental results will be compared with Van Dyke's hypersonic small disturbance theory[1] which assumes ideal gas flow. Experiments for the flat plate will also be compared with those of Bogdonoff and Hammitt[11] and of Kendall[12].

§ 2. Apparatus

Full explanation of the divergent shock tube, optical apparatus and X-ray tube has already been made by Professor F. Tamaki and the present author in Refs. 14, 15 and 16. Accordingly, only a photograph of the essential parts of the apparatus will be presented in Fig. 1. Divergent nozzle used in the present experiments has a throat section of 5 mm × 58 mm and a test section of 230 mm × 58 mm. Models tested are shown in Fig. 2. For the sake of convenience, each model is called $W_{P2.5}$, W_{E1}, W_{C0}, etc. First subscripts P, E and C denote plane, convex (expansion) and concave wedge, respectively, and second subscripts 0, 1 and 2.5 represent the cutting distance L from the sharp leading edge in millimeter scale.

In order to make the comparison of the experimental results with Van Dyke's hypersonic small disturbance theory, the leading edge of W_{P0}, W_{E0} and W_{C0} are sharpened as sharp as possible, and they are examined several times throughout the experiments to keep R_t $(=\rho_\infty u_\infty t/\mu_\infty$, t being the thickness of the leading edge) below 200. For these

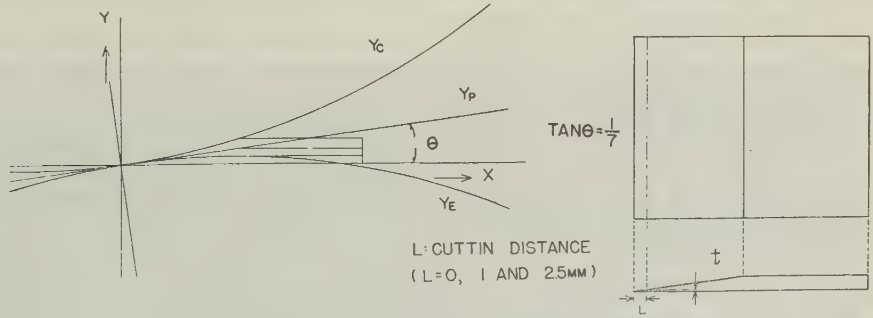

	PLANE WEDGE	CONVEX WEDGE	CONCAVE WEDGE
MODEL	W_{P0} 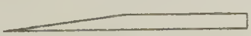	W_{E0} 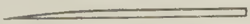	W_{C0} 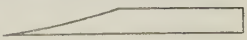
Rt　L: MM	200　0MM	200　0MM	200　0MM
EQUATION OF WEDGE-SURFACE	$Y_P=\frac{1}{7}X$	$Y_E=-247.48+\sqrt{(250)^2-(X-35.36)^2}$	$Y_C=+247.48-\sqrt{(250)^2-(X+35.36)^2}$
MODEL	W_{P1} 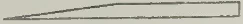	W_{E1} 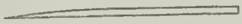	W_{C1} 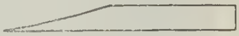
Rt　L: MM	2800　1MM	2700　1MM	2900　1MM
MODEL	$W_{P2.5}$ 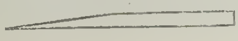	REYNOLDS NUMBER OF THE UNIFORM FLOW PER CENTIMETER $R_\infty=2.0\times10^5$ Rt · REYNOLDS NUMBER BASED ON LEADING EDGE THICKNESS t OF THE WEDGE	
Rt　L: MM	6400		

Fig. 2. Models.

models, the hypersonic similarity parameter defined by $k = M_\infty \tau$ is of the order of unity, where M_∞ is the Mach number of the uniform flow and τ expresses either the thickness of the model or the inclination of the shock wave emanating from the leading edge of the model. For the study of the effects of the leading edge bluntness on the propagation of small disturbance in the hypersonic flow, W_{P1}, $W_{P2.5}$, W_{E1} and W_{C1} are made by cutting the leading edges of W_{P0}, W_{E0} and W_{C0} normal to their flat surfaces. All the models are made of stainless steel. The span is 58 mm and the length of the uncut models is 80 mm.

§ 3. Results and Discussions

3.1) *Uniform flow*

If one uses a continuously running wind tunnel, the aerodynamic heating due to the hypersonic flow is much more significant at the front part of the body than at its rear part. Therefore, in order to keep the uniform temperature over the entire surface of the body, the surface must be partly heated or cooled. Thus, it is rather difficult to obtain the uniform surface temperature in actual experiments, although this condition makes theoretical analysis easy. Since a shock tube runs in a short time interval (about 1 millisecond) this difficulty dissolves itself. The shock tube was operated under the initial condition of $p_0/p_1 = 10$ atms/2 mm Hg and $T_0/T_1 = 325°\text{K}/295°\text{K}$, where p_0, T_0 and p_1, T_1 denote the initial pressures and temperatures in the high and the low pressure chamber respectively. The Mach number M_∞ of the free stream at the test section was 6.2. This value was determined by observing Mach waves generated by small disturbing elements attached to the divergent walls of the shock tube. Temperature of the free stream was estimated to be about 37°K, and Reynolds number R_∞ of the free stream was 2.0×10^5 per cm.

3.2) *X-ray technique: radiographic method*

Except Bogdonoff-Hammitt's experiment, most of the measurements of the hypersonic flow past a flat plate were carried out with static pressure holes and Pitot tubes. However, the probe methods encounter an unavoidable difficulty in bringing the probe very close to the leading edge without disturbing the surrounding flow. In our experiments, measurements of the flow field were made mainly by optical methods. Even with these methods the accuracies of the measurements were not satisfactory near the leading edge of the model, because of the indistinctness of the interferogram and the schlieren photograph, and of the decrease in accuracy due to the refraction of light rays near the leading edge. Accordingly, the soft X-ray radiography described in the previous report (Ref. 16) was used in order to supplement the density data near the leading edge.

The same flash X-ray tube as in Ref. 16 was used in the present experiments. The anode voltage was 1800 volts, and the potential for the triggering discharge was 2400 volts. In order to sensitize the X-ray film it was exposed to three flashes of X-rays at the initial condition of the low pressure chamber of the shock tube ($p_1 = 2$ mm Hg, $T_1 = 295°\text{K}$) before experiments. Then it was exposed to three flashes by repeating three times the operation of the shock tube.

Fig. 3 shows the typical radiograph of the flow near the leading edge of the model W_{P1} whose leading edge thickness is about 10 microns. As seen in this photograph, the shock wave coincides with the outer edge of the boundary layer in the immediate neighbourhood of the leading edge. Such a distinct flow pattern cannot be observed by ordinary optical methods, as shown in Fig. 4. Quantitative results obtained from these radiographs will be presented in the following subsections.

3.3) *Boundary layer*

Interferograms and schlieren photographs of the flow past a plane wedge, a convex wedge and a concave wedge are shown in Figs. 4a, 4b and 4c, respectively.

Let us consider first the boundary layer growth on the surface of the flat plate. As seen from these photographs, the region between the plate surface and the shock wave except in the neighbourhood of the leading edge is distinctly separated into the boundary layer and the isentropic external flow, when the Reynolds number R_t based on the leading edge thickness t is 200 approximately. Boundary layer having finite thickness already exists at the leading edge of the body. Thus, in its immediate neighbourhood, the outer edge of the boundary layer coincides with the shock wave. Because of this abrupt growth of the boundary layer even with such a small value of R_t, the shock wave is slightly curved near the leading edge. In this region, the flow field between the shock wave and the boundary layer is not isopicnal laterally, i.e. in the direction normal to the surface of the flat plate. This phenomenon seems to be due not to the bluntness of the leading edge but to the viscous effect (see 3.5)).

Fig. 4a shows that the flow region affected by the leading edge increases with increasing R_t. At R_t of approximately 6400, the bound-

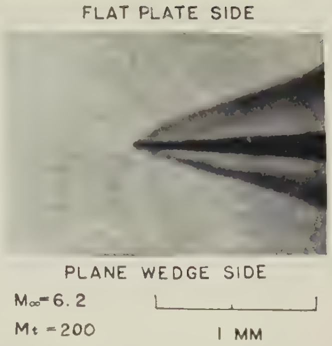

Fig. 3. Radiograph of the flow near the leading edge.

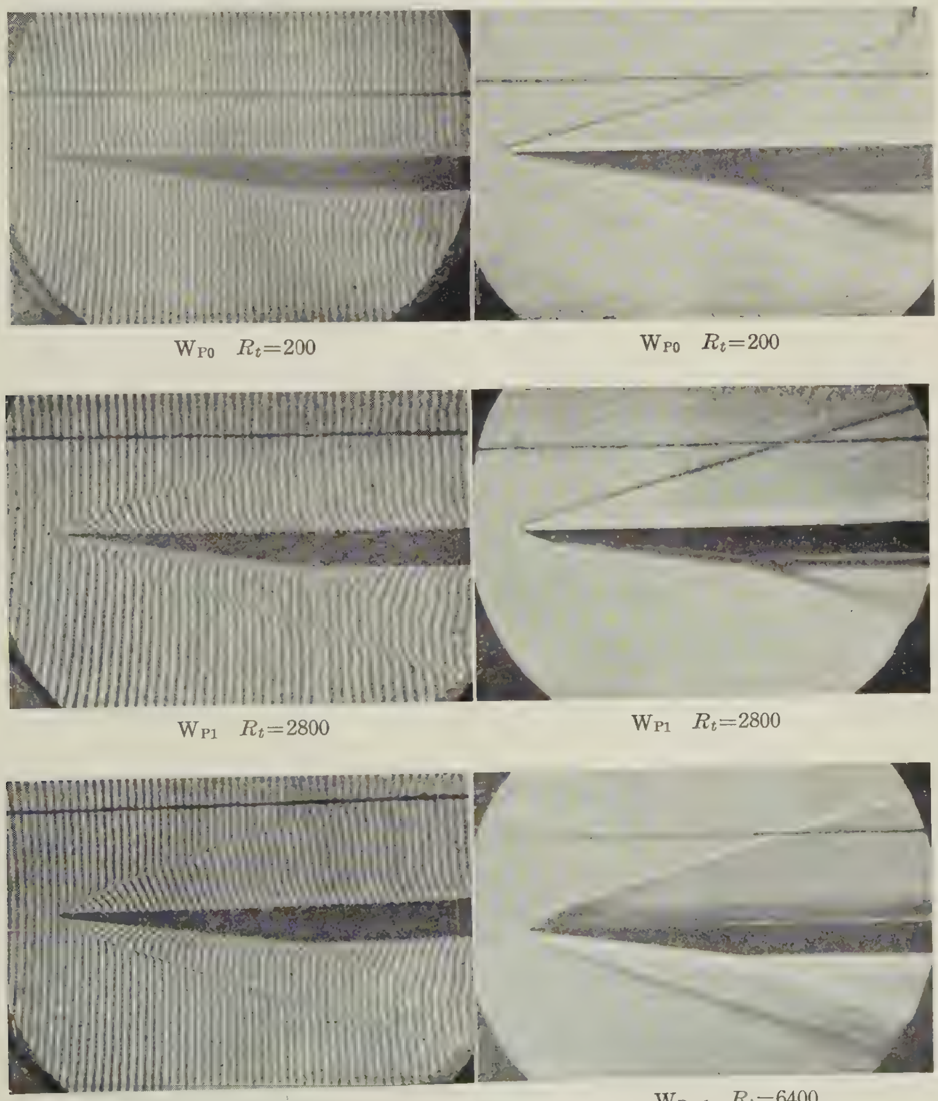

W_{P0} R_t=200 W_{P0} R_t=200

W_{P1} R_t=2800 W_{P1} R_t=2800

$W_{P2.5}$ R_t=6400 $W_{P2.5}$ R_t=6400

Fig. 4. Interferograms and schlieren photographs.

(a). plane wedge.

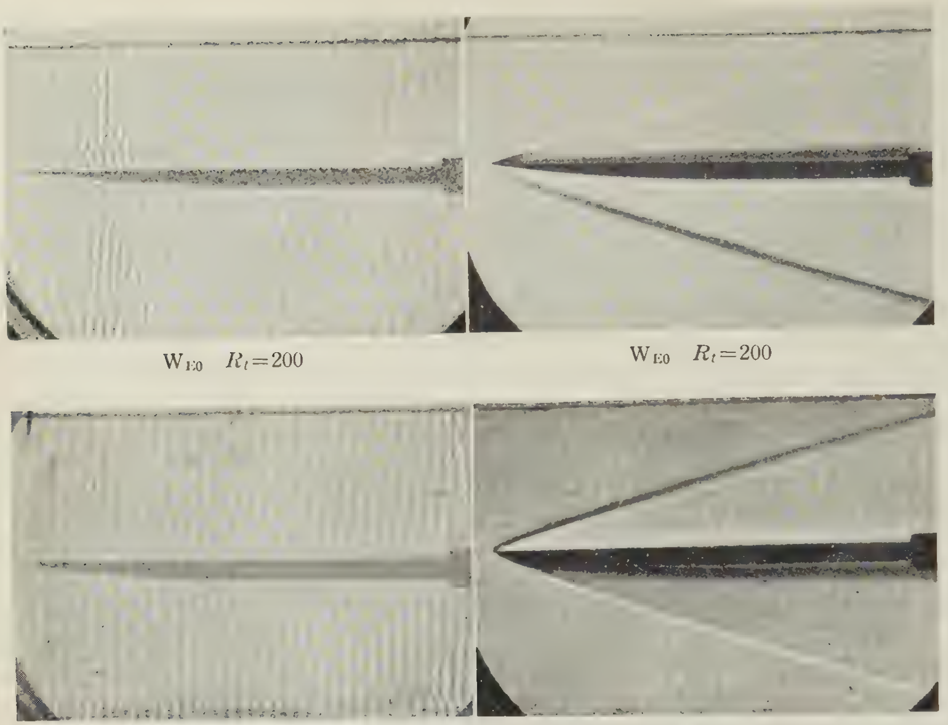

W_{E0} $R_t=200$ W_{E0} $R_t=200$

W_{E1} $R_t=2700$ W_{E1} $R_t=2700$

Fig. 4 (b). convex wedge.

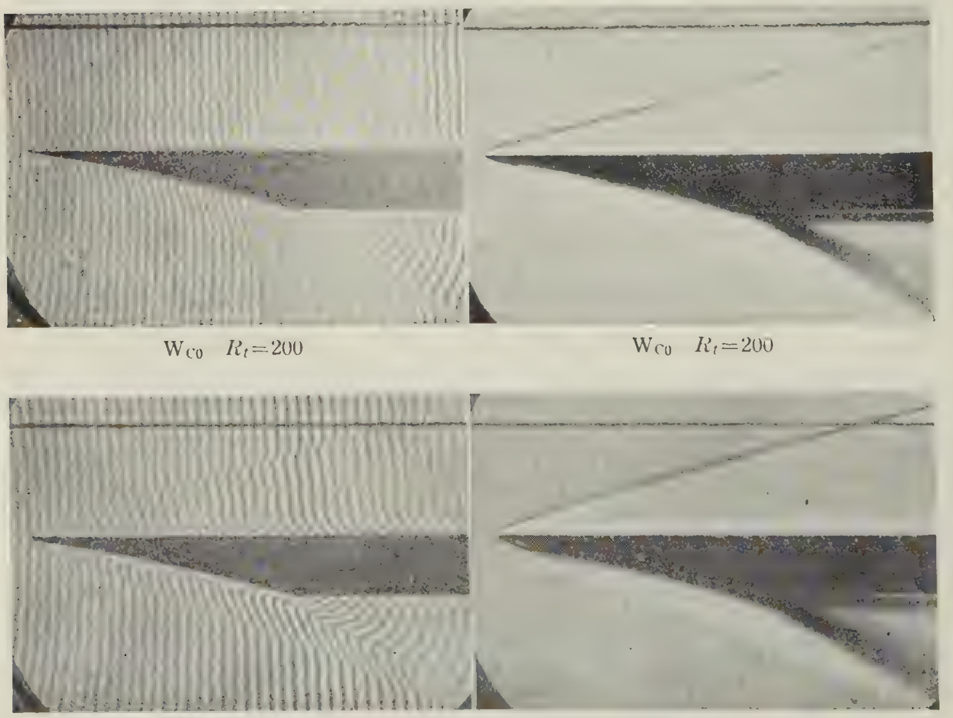

W_{C0} $R_t=200$ W_{C0} $R_t=200$

W_{C1} $R_t=2900$ W_{C1} $R_t=2900$

Fig. 4 (c). concave wedge.

ary layer cannot be distinguished from external flow with an interferogram. Here, the measurements of the boundary layer thickness δ were made by tracing the sharp bents of the interferometer fringes. Boundary layer thickness along the flat plate at various R_t is shown in Fig. 5. Utilizing the helium tunnel at Princeton, Bogdonoff and Hammitt carried out similar experiments for the flat plate of various leading edge thicknesses t with an interferometer. The influence of bluntness upon the boundary layer growth in their experiments appears much stronger than that of the present experiments. Although this may be mainly due to the larger values of M_∞ in their experiments, it may be partly due to the use of helium as a working gas.

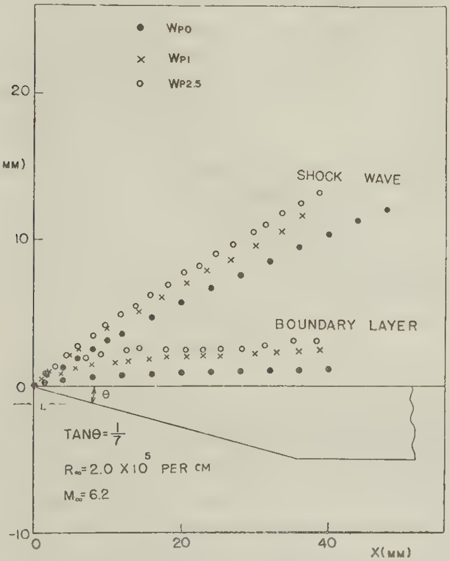

Fig. 5. Shock wave and boundary layer for the flat surface.

In Fig. 6, the boundary layer thickness δ on the flat plate for $R_t=200$ is given by a chain line, and the theoretical values δ_{N-N} calculated by the following formula of Nagakura and Naruse are given by a dotted line:

$$\delta^2_{N-N}\approx\delta^{*2}=K\left(\frac{p}{p_\infty}\right)^{-\alpha}\int_{x_J}^{x}\left(\frac{p}{p_\infty}\right)^{\alpha-1}dx+\text{const}\,,$$

where K and α are constants. Difference between the thickness δ and the displacement thickness δ^* is neglected in the present comparison, since it is of the order of M_∞^{-2} in the hypersonic region. The values of p/p_∞, the ratio of static pressure on the plate to that of the free stream, are determined from interferograms and radiographs (see 3.5)). These two curves show similar shapes in boundary layer growth along the x-axis, the ratio δ/δ_{N-N} being about 1.3 throughout the entire surface. It was revealed through a private communication from H. Naruse to the author that he obtained a more precise theoretical formula for the boundary layer thickness without neglecting the order of M_∞^{-2}. When his refined formula is applied, our experimental values are found to agree almost perfectly with the theoretical ones (see double-dotted chain line in Fig. 6).

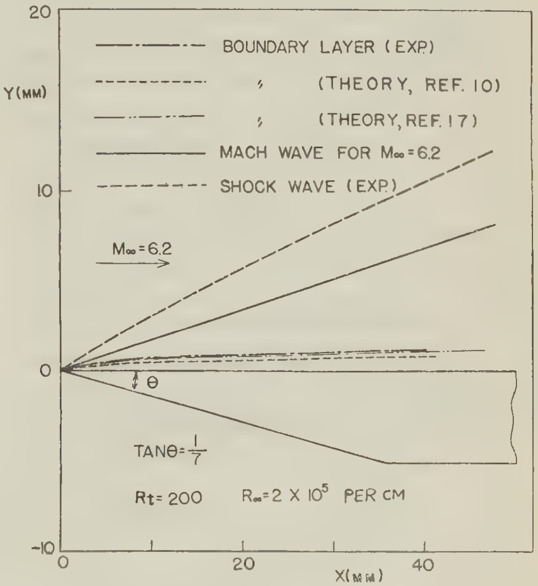

Fig. 6. Boundary layer growth along the flat surface.

The shapes of the boundary layer on a plane wedge, a convex wedge and a concave wedge are shown in Figs. 7a, 7b and 7c, respectively. Compared with the boundary layer shapes on W_{P0} and W_{E0}, a boundary layer of a different shape grows on W_{C0}: 1) boundary layers of parabolic shapes grow on W_{P0} and W_{E0}, while in the case of W_{C0}, the boundary layer growth is more rapid near the leading edge and is more gradual in the rear part; 2) the boundary layer grown on the front part of W_{C0} has the effect to fill up the cave of the surface; 3) in the neighbourhood of the shoulder, the boundary layer thicknesses on W_{P0}, W_{E0} and W_{C0} are nearly the same. These phenomena seem to depend on the effects of Reynolds number, stability of boundary layer, leading edge bluntness and others. However, it seems to the author that: 1) the fundamental feature of the leading edge effects for plane, convex and concave wedges is the same as for the flat plate; 2) except in the region close to the leading edge, the influence of R_t on boundary layer growth is significant in the order: convex wedge, plane wedge and concave wedge.

3.4) *Shapes of shock waves*

Since the shock wave location is closely related to the effective shape of the body (the geometrical shape of the body plus the boundary layer displacement thickness), it is as important as the boundary layer on body surface for the study of viscous-inviscid interaction. Here, the author considers only the front portion of the shock wave which is not influenced by the shoulder of the model.

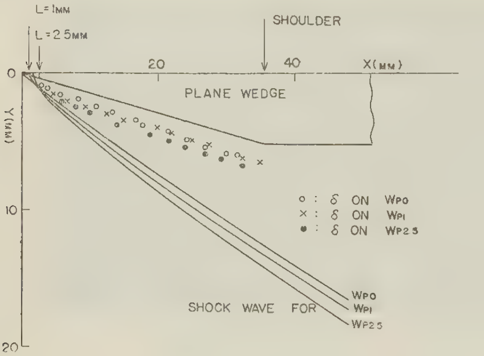

(a) plane wedge.

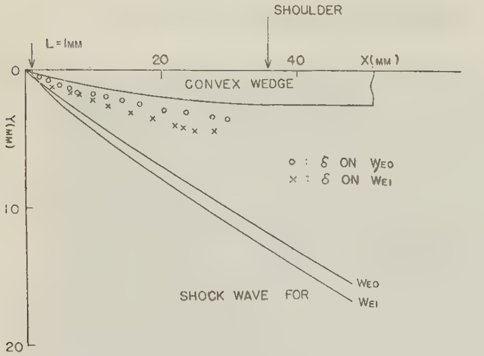

(b) convex wedge.

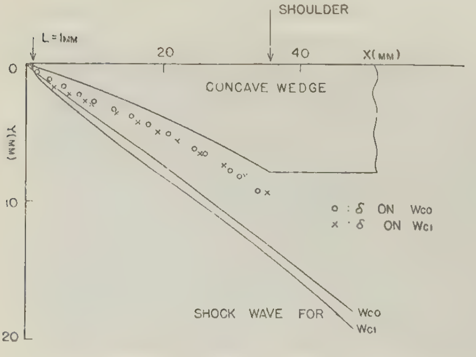

(c) concave wedge.

Fig. 7. Shock wave and boundary larger for wedge surfaces.

Fig. 6 and Fig. 8 show the shapes of shock wave originating from the flat plate and from W_{P0}, W_{E0} and W_{C0}. In Fig. 8, the dotted lines show the shapes of theoretical shock waves obtained by characteristic method[17], neglecting the reflection at the shock wave of the waves generated from the body surface (compression and expansion waves). The chain lines in the same figure show those calculated according to the hypersonic small disturbance theory[1], considering only the first order of the body curvature. In the present experiments, optical methods (interferometer and schlieren method) are mainly employed for determining the shapes of the shock waves, but near the leading edge where they become not clear, X-ray technique is employed. The steepness of the experimental shock location compared with the above theoretical curves is, of course, due to the growth of the boundary layer. It is interesting, however, that shock waves for W_{E0} and W_{C0} are very close to that for W_{P0}, though the geometrical shapes of these bodies are fairly different. This fact seems to show the importance of the leading edge effect in the hypersonic flow.

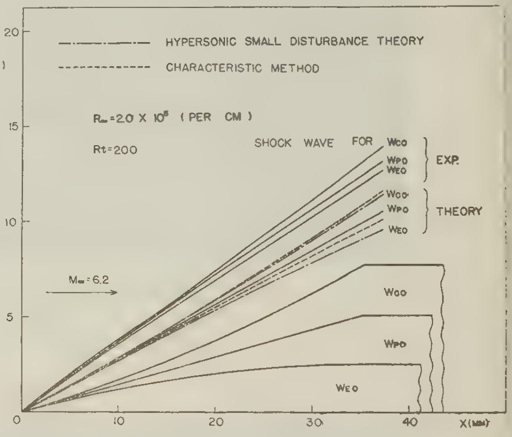

Fig. 8. Shock shapes.

As the thickness of the leading edge increases, the shapes of the shock waves become increasingly fat. The corresponding shock shapes for a flat plate, a plane wedge, a convex wedge and a concave wedge are shown in Figs. 5, 7a, 7b and 7c, respectively. The characters of the shock shapes are listed in the following Table.

	Flat plate	Plane wedge	Convex wedge	Concave wedge
$L=0$ mm	×	×	×	○
$L=1$ mm	×	○	×	○
$L=2.5$ mm	×	○		

○: with inflection point
×: without inflection point

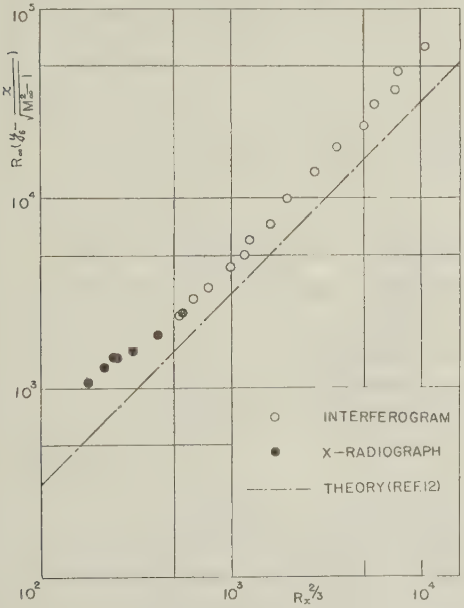

Fig. 9. Relation between $R_x^{2/3}$ and $R_\infty(y_s - x/\sqrt{M_\infty^2-1})$.

The appearance of an inflexion point in the shock wave for W_{C0} even when the leading edge is the sharpest in our experiments, i.e. as sharp as $R_t=200$, seems to be due to the peculiar boundary layer growth on the front part of the body (see 3.3)).

For the comparison with Kendall's theoretical shock shapes[12] for a flat plate, the experimental values shown in Fig. 6 are replotted in Fig. 9, representing the relation between $R_x^{2/3}$ and $(y_s - x/\sqrt{M_\infty^2-1})$, where y_s is the ordinate of the shock wave.

It should be remarked here that the shock location in Fig. 6 is also represented as $R_{ys} \sim R_x^{0.91}$, where R_{ys} is the Reynolds number based on y_s. It is shown in Ref. 12 that the shock locations for a flat plate with $R_t=119$ $(M_\infty=14)$[11], and with $R_t \doteqdot 100$ $(M_\infty=5.8)$[12] may be expressed as $R_{ys} \sim R_x^{0.88}$ and $R_{ys} \sim R_x^{0.90}$, respectively. The agreement of the shock shapes in the present experiments with those in Refs. 11 and 12 is very good.

3.5) *Pressure distribution*

The distribution of the non-dimensional pressure p/p_∞ over a flat plate for various R_t is plotted against x in Fig. 10, and against the hypersonic interaction parameter $s=(c\mu_\infty/\rho_\infty u_\infty)^{1/2} M_\infty^3 x^{-1/2}$ in Fig. 11, where c is a constant related to temperature ratio T/T_∞ and viscosity ratio μ/μ_∞, ρ is the density, and ∞ denotes the free-stream condition. In order to determine the pressure from the density measured by the interferometry, it is necessary to assume the entropy change across the shock wave. For the cases of $L=0$ and 1 mm, the entropy change was estimated from the mean value of the inclinations of the shock wave at the leading edge and the shoulder, while for the case of $L=2.5$ mm, it was estimated from the normal shock relation.

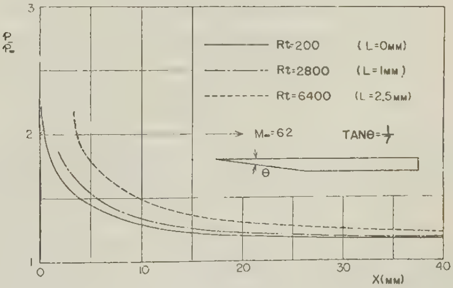

Fig. 10. Pressure distribution on flat plate (leading edge effect).

The pressure rise at the leading edge is evident even in the case of sharp-nosed flat plate ($L=0$ mm), for which inviscid theory predicts no pressure rise (see Fig. 10). This pressure rise at the leading edge may be caused either by the bluntness of the edge or by the viscous effects. Therefore, it seems to be desirable to determine, if possible, the relative importance of these effects under the various flow conditions. It is thus necessary to investigate the flow in the neighbourhood of the leading edge. But the investigation is very difficult by using the static pressure holes or the interferometer, as already mentioned in 3.3). Here, the pressure distribution near the leading edge (to the distance of 1 mm from the leading edge) was measured by the X-ray technique. In this case, the entropy change for the derivation of the pressure distribution p/p_∞ from the measured values of ρ/ρ_∞ was determined by the shock wave inclination at the leading edge in the radiograph.

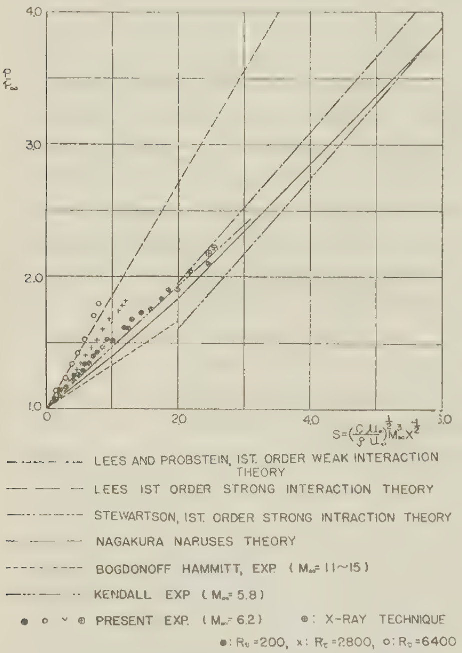

Fig. 11. Relation between p/p_∞ and hypersonic interaction parameter s.

As seen in Fig. 10, the leading edge thickness of the flat plate causes a pressure rise but not seriously. For instance, at the forward part of the flat plate (in the region of about 8 mm from the leading edge), the values of p/p_∞ become merely 1.4 times, as the leading edge thickness t increases from 10 microns ($L=0$ mm) to 320 microns ($L=2.5$ mm). Since the value of t in cases of W_{P0}, W_{E0} and W_{C0} did not exceed 10 microns, the pressure rise due to the leading edge thickness is small, and thus, the leading edge thickness cannot be considered as a major cause for the pressure rise. The pressure rise seems mainly due to the viscous effects near the leading edge of the flat plate. This fact is also confirmed by Bertram's calculation[13].

Fig. 12 presents experimental values of pressure for plane, convex and concave wedges of $L=0$ and 1 mm. In the same figure are also included theoretical values for these wedges with infinitely sharp nose, assuming inviscid flow. The full lines, the chain lines and the dotted lines denote the values calculated by characteristic method[17], tangent-wedge approximation[5] and Newtonian-plus-centrifugal force approximation[18], respectively. The broken lines show the value calculated by Van Dyke's first order approximation of the hypersonic small disturbance theory (considering only the first order of the curvature of the body). The pressure distribution on the surface of W_{C0} is somewhat different from that for W_{P0} and W_{E0}, that is: 1) at the front part of W_{C0}, values of p/p_∞ are nearly the same over a fairly wide range, whereas they decrease gradually on W_{E0} and more gradually on W_{P0}; 2) approaching the shoulders of W_{P0} and W_{E0} there are considerable discrepancies between the theoretical and the measured values of p/p_∞, but these discrepancies become small on the surface of W_{C0} as the distance from the leading edge increases; 3) the pressure rise due to the leading edge thickness is not so severe on the concave wedge as on the plane and the convex wedge (see Fig. 12). These facts are, of course, closely related to the boundary

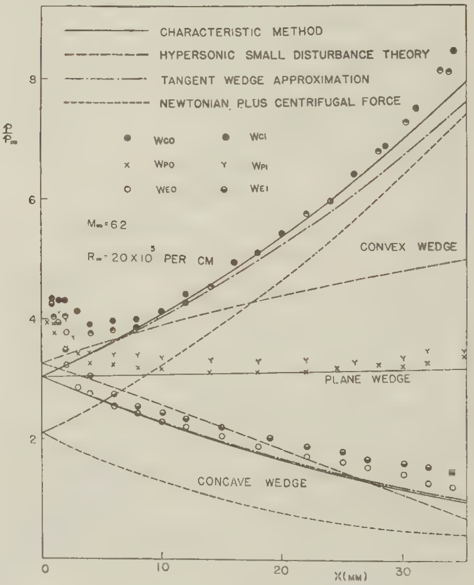

Fig. 12. Pressure distribution on wedge surfaces.

layer growth on the models.

The author wishes to express his sincere gratitude to Professor Fumio Tamaki for the valuable guidance and advice in conducting the experimental work. The author expresses his cordial thanks to Professor Isao Imai for his continual encouragement throughout this work. His cordial thanks are also due to Dr. M. Kawaguti and Mr. H. Naruse for their kind informations and eager discussions.

References

1) D. Van Dyke: NACA Tech. note 3173 (1954).
2) J. D. Cole: J. Aero. Sci. **24** (1957) 448.
3) L. Lees and R. F. Probstein: Princeton Univ. Aero. Eng. Rep. 195 (1952).
4) M. H. Bertram: NACA Tech. note 2773 (1953).
5) L. Lees: IAS-RAeS Proc. (1955) 241.
6) K. Stewartson: J. Aero. Sci. **22** (1955) 303.
7) L. Lees: J. Aero. Sci. **20** (1953) 143.
8) T. Y. Li and H. T. Nagamatsu: J. Aero. Sci. **20** (1953) 345.
9) M. Yasuhara: J. Phys. Soc. Japan **12** (1957) 177.
10) T. Nagakura and H. Naruse: J. Phys. Soc. Japan **12** (1957) 1298.
11) S. M. Bogdonoff and A. G. Hammitt: J. Aero. Sci. **23** (1956) 108.
12) J. M. Kendall: J. Aero. Sci. **24** (1957) 47.
13) M. H. Bertram: J. Aero. Sci. **21** (1954) 430.
14) F. Tamaki: J. Phys. Soc. Japan **11** (1956) 434.
15) C. S. Kim: J. Phys. Soc. Japan **11** (1956) 439.
16) F. Tamaki and C. S. Kim: J. Phys. Soc. Japan **14** (1959) 664.
17) A. J. Eggers, R. C. Saving and C. A. Syverston: J. Aero. Sci. **22** (1955) 231.
18) H. R. Ivey, E. G. Klunker and E. N. Bowen: NACA Tech. note 613 (1948).

JOURNAL OF THE PHYSICAL SOCIETY OF JAPAN Vol. 14, No. 6, JUNE, 1959

The Drag of Lattice of Many Parallel Circular Cylinders at Low Reynolds Number

By Takashi SAWADA

Department of Physics, Asahigawa College, Hokkaido Gakugei University, Asahigawa, Hokkaido, Japan

(Received January 29, 1959)

The relations between the drag coefficient C of lattice of many parallel circular cylinders and Reynolds number R were studied experimentally. The drag of the specimen falling in a tower was measured in the region of R=ca 0.25~1.0. If C vs R curve of a cylinder by Wieselsberger is used as standard, C vs R relations of lattice are approximately the same as Wieselsberger's, when $h/d=250$ and 125, with d being the diameter of the cylinder, and h the distance of the centers of the two cylinders. Accordingly it is seen that Imai's formula on the basis of the combination of Stokes' and Oseen's approximations is better than Tomotika and Aoi's formula on the basis of Oseen's. The C vs R relations of lattice, when $h/d=50$, 25 and 12.5, are somewhat similar to Fujikawa's C vs R curves of two parallel cylinders.

§ 1. Introduction

In nature we can see some hairy bodies such as pappi of dandelion or thistle. Formerly the properties of drag of these bodies falling in air were studied by the author[1]. The pappi are assemblages of many thin cylinders in spatial configurations, so the hydrodynamical analysis of their drag should be very complicated. But the simplest of them may be subjected to theoretical analysis. Some years ago, H. Fujikawa[2] calculated the drag of two parallel circular cylinders on the basis of Oseen's approximation. The drag of lattice of infinitely many parallel circular cylinders was studied by K. Tamada and H. Fujikawa[3] on the same basis, and by T. Miyagi[4] on the basis of Stokes'. In this paper the author presents the results of experimental study on the drag of lattice of many parallel circular cylinders of finite length arranged in a plane. Further, he can determine the most credible curve of drag coefficient C vs Reynolds number R relation of an isolated cylinder at low Reynolds number.

§ 2. Specimens and Experimental Method

To make specimens of lattice of parallel cylinders, the author used thin glass filaments of ca 20 μ in diameter. They were measured by the optical microscope with the dissolving power of 0.2 μ and therefore the accuracy of measurement was not so good with regard to each one filament, but the mean value of many may be fairly accurate. For example, if the number of filaments is 10, then the probable error may be 0.06 μ.

To set the specimen, a square-shaped framework made of glass filaments of 30~70 μ in diameter was used, the length of its one side being 6 cm. The drag of the specimen was calculated from its final falling velocity in a tower of square cross section whose height and side length are respectively 420 cm and 50 cm. The effective length of the tower to measure velocity is 250 cm. Because the plane of specimen must be kept horizontal in falling, at eace corner of the framework was attached a filament of 8.0 cm in length and 30~70 μ in diameter, and their opposite ends were joined together at one point. Furthermore, to protect the thin filaments of lattice, 1~3 supporting filaments are attached perpendicular to them. The distances between centers of adjacent filaments, h, were varied as 5.0, 2.5, 2.0, 1.5, 1.0, 0.5 and 0.25 mm. As the diameter of filament, d, is 20 μ, the ratios h/d are respectively 250, 125, 100, 75, 50, 25 and 12.5. The coefficient of viscosity of air was calculated by Sutherland's formula:

$$\eta=\eta_0\left(\frac{T}{T_0}\right)^{3/2}\frac{C+T_0}{C+T},$$

where $\eta_0=1.722\cdot10^{-4}$ poise, $T_0=273.15°\text{K}$ and $C=105.6°\text{K}$.

The density of air was calculated taking into consideration its humidity.

§ 3. Determination of Standard C vs R Curves of Isolated Cylinder Set Perpendicular or Oblique to Uniform Flow

If the drag of the framework, legs and supporting filaments is subtracted from the total drag of the specimen, then we can obtain the drag of lattice, from which we can find the mean drag coefficient of each cylinder per unit length. The drag of the framework and supporting filaments is calculated by means of the drag coefficient of a circular cylinder perpendicular to uniform flow. In our experiments, the Reynolds number used in the above calculation lies between ca 0.3 and 3.0. In this region, C vs R relations are given by several authors. S. Tomotika and T. Aoi[5] gave theoretical formula according to Oseen's approximation, and I. Imai[6] by suitable combination of Oseen's and Stokes' approximations. Further F. Eisner[7] and C. Wieselsberger[8] gave respectively semiempirical curves. Lately R. Finn[9] reported numerous experimental data, in which are to our regret considerable fluctuations. See Fig. 1.

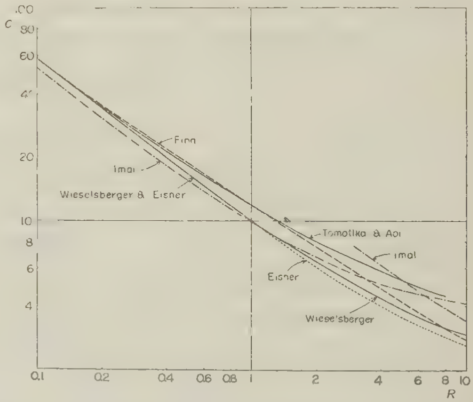

Fig. 1. Theoretical or experimental C vs R curves of an isolated circular cylinder by several authors.

But these curves are different from each other, so we could not decide definitely which of them is the best. Therefore the author determined the most suitable curve by the method of trial and error. It is as follows:

In case of large value of $h/d\geq125$, the interference of each cylinder may be negligibly small. Let us assume any curve of the above as standard, and by means of a suitable method which will be shown later, determine C vs R curve of a cylinder set oblique to the main flow. Next we calculate the drag of framework, supporting filaments and legs, then subtract them from the total drag of the specimen. Finally we obtain the C vs R curve of the lattice. If the latter coincides approximately with the assumed C vs R curve of a cylinder set perpendicular to the main flow, we can say that the assumed C vs R curve is true.

As shown later, it resulted that C vs R curves in the region $0.3<R<3.0$ by Eisner, Wieselsberger or Imai are better than that by Tomotika and Aoi or Finn, but the value of drag coefficient by Imai in the region $R<1$ is slightly less than reality. But the difference between Wieselsberger's and Eisner's curves is small in this region, so the author could not determine which of them is the better. In the present work, he adopted temporarily Wieselsberger's curve as standard and could obtain satisfactory results.

The force acting on a cylinder set obliquely in a uniform flow has been studied by Tomotika, Aoi and Yosinobu on the basis of Oseen's approximation. Let us represent the transverse and longitudinal components as

$$N=1/2\cdot\rho v^2 dC_N\ ,$$

$$L=1/2\cdot\rho v^2 dC_L\ .$$

Here ρ is the density of fluid, v the velocity of the uniform flow, and C_N and C_L are non-dimensional force coefficients. Then the resultant drag on unit length of the cylinder in the direction of uniform flow is given by

$$D=1/2\cdot\rho v^2 d\sin i(C_N+C_L\cot i)\ ,$$

where i is the angle of incidence, i.e. the angle between the axis of the cylinder and the direction of the uniform flow. In our experiment, the angle of incidence is determined by the length of the leg of the specimen. Because the effective length of the leg was 7.8 cm, the angle of incidence was 33°. In Fig. 2 the values of $(C_N+C_L\cot i)$ are given against Reynolds number.

First we experimented on the specimens constructed of framework and legs only. As stated above, the drag of framework was calculated according to Wieselsberger's curve and was subtracted from the total drag. Then we obtain the drag coefficient of the leg; here the projected length of legs is taken as 17.2 cm. Because of difficulty in obtaining the exact values of mass and dimension of specimen, the number of data is only three. But as seen in Fig. 2 these data lie on one curve slightly above Wieselsberger's. Comparing this with theoretical curves by Tomotika, Aoi and Yoshinobu it is seen that there is a remarkable similarity between them. Thus we may assume that the absolute values of drag coefficient of a cylinder by Tomotika, Aoi and Yoshinobu are larger than reality, but the ratios between drag coefficients of a cylinder set perpendicular and oblique are correctly expressed. In our specimens there are 5 singular points, i.e. 4 corners of the square and the lower center. To determine the C vs R curve of a cylinder set oblique, we must take into consideration this singularity. Let us denote the ratios of drag coefficients of a cylinder for $i=90°$ and 33° at the same Reynolds number by A_0 and A, where the former is the theoretical value by Tomotika, Aoi and Yoshinobu and the latter the experimental value. The mean value of A/A_0 with regard to 3 experimental data was 1.037. We may suppose that the value 0.037 originated from the above singularity, but the exact meaning of this number cannot be explained by these experiments only.

The process of drawing the curve is as follows: At any Reynolds number the drag coefficient C_1 is read from Wieselsberger's curve. At the same Reynolds number the drag coefficients C_{10} at $i=90°$ and C_{20} at $i=33°$ are read from the theoretical curve by Tomotika, Aoi and Yosinobu. $A_0=C_{20}/C_{10}$ is multiplied by the factors 1.037 and C_1. The re-

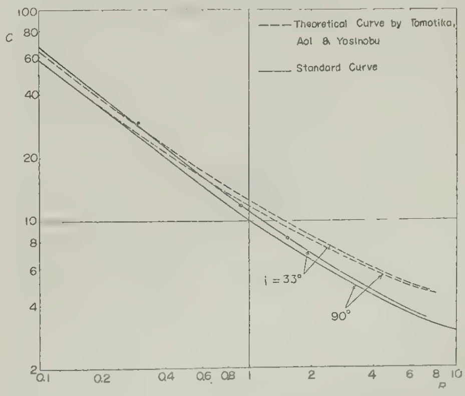

Fig. 2. C vs R curves of an isolated circular cylinder set perpendicular and oblique to main flow.

sult is C_2, which is considered to be the most reliable of the drag coefficient of the legs.

By this method we obtained the standard curves for calculation of drag of framework, supporting filaments and legs as shown in Fig. 2.

§ 4. Relation between Drag Coefficient and Reynolds Number of Lattice

The general method of experiment has already been mentioned. To vary the Reynolds number, a small weight of lead was hung at the lower ends of legs by means of a thin nylon filament. The drag of the weight is very small in comparison with the other parts of specimen, so we can neglect it. The symbols necessary to show experimental data are as follows:

$D_0=mg$	total drag of specimen
n	number of cylinders of lattice
l	length of cylinder
suffix 1	framework
2	legs
3	supporting filaments
4	lattice

1. $h/d=250$ ($h=5.0$ mm, $n=11$)

In this case the magnitudes of D_1, D_2 and D_3 are of the same order as D_4, so the errors by use of unsuitable standard curve may be quite large. But as shown in Fig. 4 we obtained quite satisfactory results. An example of experimental data is as follows:

Specimen No. V–4 (Fig. 3)

$d_1=5.31\cdot10^{-3}$cm $l_1=24.7$ cm
$d_2=5.13$ 〃 $l_2=32.0$
$d_3=2.0$ 〃 $l_3=6.2$
$d_4=2.00$ 〃 $l_4=67.9$
$v=36.54$ cm·sec^{-1} $D_0=3.548$ dyn
$R_1=1.270$ $C_1=8.58$ $D_1=0.890$
$R_2=1.227$ $C_2=9.61$ $D_2=0.670$
$R_3=0.478$ $C_3=17.35$ $D_3=0.170$
$R_4=0.478$ $C_4=16.9$ $D_4=1.82$

2. $h/d=125$ ($h=2.5$ mm, $n=23$)

To obtain the specimen as light as possible, we used the cylinders of nearly 2.0 μ in diameter as framework and legs. By use of this, we obtained data at very low Reynolds

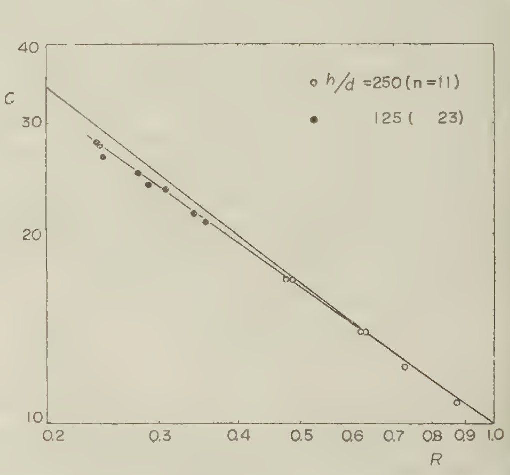

Fig. 4. Relation between C and R of lattice of parallel circular cylinders, in which h/d is 250 and 125.

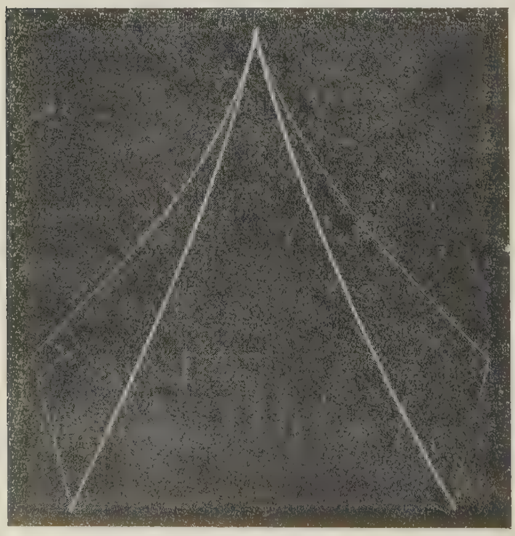

Fig. 3. Specimen of $h/d=250$. Side view.

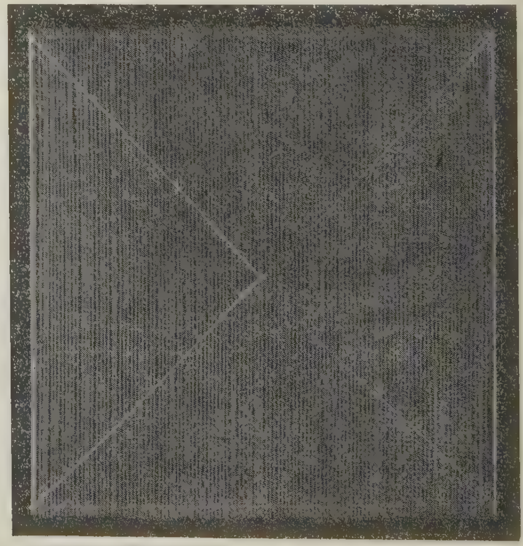

Fig. 5. Specimen of $h/d=25$. Plan view.

number, but data beyond $R=0.4$ were not accurate because of flexion of framework in falling. The C vs R relation is shown in Fig. 4, which on the whole is the same as in $h/d=250$.

3. $h/d=100$ ($h=2.0$ mm, $n=29$)
4. $h/d=75$ ($h=1.5$ mm, $n=39$)

In these two cases we could not perceive any distinct effects of interference of cylinders. The C vs R curves are nearly the same as in the previous cases.

5. $h/d=50$ ($h=1.0$ mm, $n=59$)

An example of experimental data is as follows:

Specimen No. V-3

$d_1=4.02\cdot10^{-3}$cm $l_1=24.8$ cm
$d_2=5.23$ 〃 $l_2=32.0$
$d_3=2.0$ 〃 $l_3=6.2$
$d_4=2.00$ 〃 $l_4=368$
$v=20.66$ cm·sec^{-1} $D_0=5.485$ dyn
$R_1=0.546$ $C_1=15.7$ $D_1=0.398$
$R_2=0.711$ $C_2=14.2$ $D_2=0.325$
$R_3=0.272$ $C_3=27.0$ $D_3=0.085$
$R_4=0.272$ $C_4=25.0$ $D_4=4.68$

The C vs R relation is shown in Fig. 6.

6. $h/d=25$ ($h=0.5$ mm, $n=119$)

In this case the effects of interference of cylinders are remarkable. An example of experimental data is as follows:

Specimen No. V-2 (Fig. 5)

$d_1=6.0\cdot10^{-3}$cm $l_1=24.7$ cm
$d_2=6.8$ 〃 $l_2=32.0$
$d_3=2.0$ 〃 $l_3=12.4$
$d_4=1.98$ 〃 $l_4=739$
$v=22.42$ cm·sec^{-1} $D_0=10.42$ dyn
$R_1=0.887$ $C_1=10.9$ $D_1=0.483$
$R_2=1.005$ $C_2=11.15$ $D_2=0.389$
$R_3=0.296$ $C_3=25.3$ $D_3=0.188$
$R_4=0.293$ $C_4=21.4$ $D_4=9.36$

On account of interference of cylinders, strictly speaking we ought not to use the standard curve of isolated cylinder to calculate the drag of framework and supporting filaments. But as seen above, D_1, D_2 and D_3 are small compared with D_4, so their errors may be neglected. The C vs R relation is shown in Fig. 6, in which the curve tends asymtotically to coincide with the standard curve of isolated cylinder at higher Reynolds number.

7. $h/d=12.5$ ($h=0.25$ mm, $n=239$)

An example of experimental data is as follows:

Specimen No. V-8

$d_1=6.9\cdot10^{-3}$cm $l_1=24.7$ cm
$d_2=7.6$ 〃 $l_2=32.0$
$d_3=2.0$ 〃 $l_3=18.4$
$d_4=2.00$ 〃 $l_4=1480$
$v=27.1$ cm·sec^{-1} $D_0=17.89$ dyn
$R_1=1.197$ $C_1=8.9$ $D_1=0.65$
$R_2=1.318$ $C_2=9.3$ $D_2=0.52$
$R_3=0.347$ $C_3=22.3$ $D_3=0.35$
$R_4=0.347$ $C_4=12.9$ $D_4=16.4$

The C vs R relation is shown in Fig. 6. The effects of interference of cylinders are very remarkable, so the apparent drag coefficient of lattice $C_{ap}=Cd/h$ cannot exceed the value of the drag coefficient of square plate, i.e. 1.16.

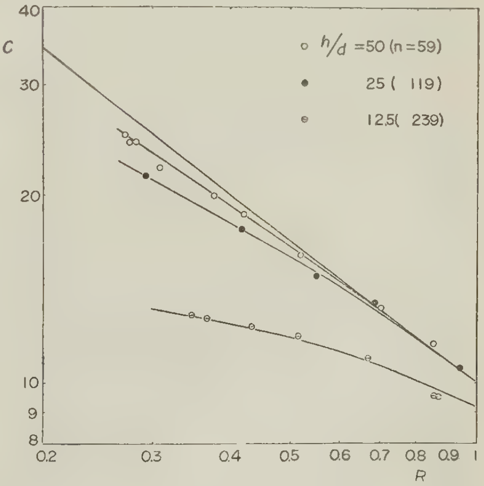

Fig. 6. Relation between C and R of lattice of parallel circular cylinders, in which h/d is 50, 25 and 12.5.

§ 5. Discussion of the Results

According to Fujikawa's calculation the C vs R curves of two parallel cylinders are as Fig. 7. The features of these are very similar to our results. In general the smaller the value of h/d, the more deviates the C vs R curve from that of the isolated cylinder, but the former approaches asymtotically to the latter at higher Reynolds number.

The C vs R curves of lattice of infinitely many parallel circular cylinders calculated by Tamada and Fujikawa are shown in Fig. 8. The relations between these curves and that for an isolated cylinder are in the opposite trend to our results. If, however, we use not the falling velocity of specimen but the actual velocity of flow through the lattice to calculate the drag coefficient, we would obttain the curves similar to Fig. 8.

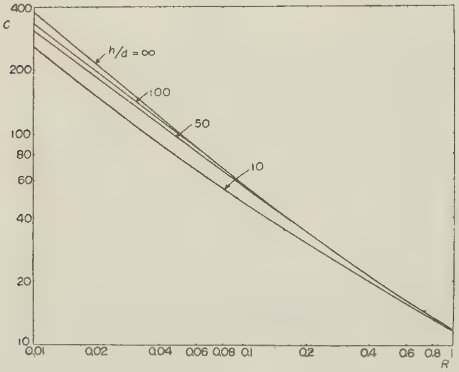

Fig. 7. C vs R curves of two parallel circular cylinders calculated by H. Fujikawa.

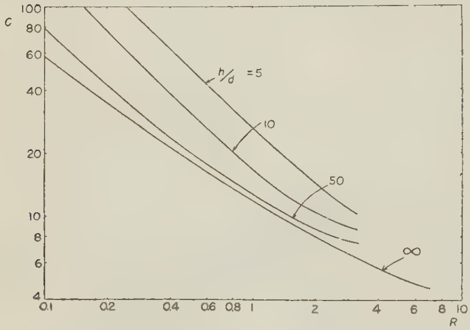

Fig. 8. C vs R curves of lattice of infinitely many parallel circular cylinders calculated by K. Tamada and H. Fujikawa.

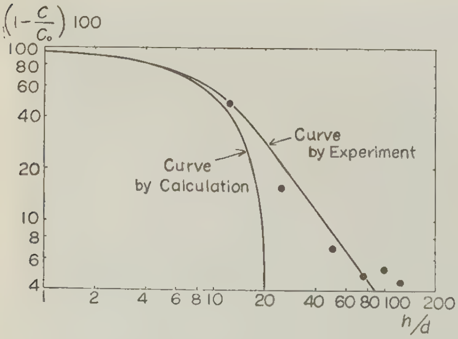

Fig. 9. Relation between $(1-C/C_0)\cdot 100$ and h/d, where C and C_0 represent respectively drag coefficient of a lattice and of an isolated circular cylinder at $R=0.3$.

The value of the drag coefficient of an isolated cylinder at $R=0.3$, C_0, is 25.0. Let us represent as C the experimental value of drag coefficient of lattice at the same Reynolds number. In Fig. 9 are shown the $(1-C/C_0)\cdot 100$ vs h/d relations, where the curve by calculation is as follows: We assume that the apparent drag coefficient of lattice cannot exceed 1.16, i.e. the value of the drag coefficient of square plate no matter how small the value of h/d is. The drag coefficient of lattice which gives $C_{ap}=1.16$, i.e. $C'=1.16h/d$ will become larger with increasing h/d, but cannot exceed 25.0, that is, the value of the drag coefficient of an isolated cylinder. If $h/d=21.55$, then $C'=25.0$. By means of the above formula we calculate C' for $h/d<21.55$, and plot $(1-C'/C_0)\cdot 100$ against h/d. Thus we obtain the curve by calculation. It may be supposed that the curve by experiment will approach asymtotically to it at smaller value of h/d.

Acknowledgement

The author wishes to express his sincere thanks to Prof. U. Nakaya for his continued encouragement throughout this work, and to Profs. I. Imai, K. Tamada, Y. Takaisi and H. Fujikawa for their kind interest and discussions.

References

1) T. Sawada: J. Hokkaido Gakugei Univ. **7** (1956) 63 (in Japanese).
2) H. Fujikawa: J. Phys. Soc. Japan **11** (1956) 558.
3) T. Tamada and H. Fujikawa: Quart. J. Mech. Appl. Math. **10** (1957) 423.
4) T. Miyagi: J. Phys. Soc. Japan **13** (1958) 493.
5) S. Tomotika and T. Aoi: Mem. Coll. Sci. Univ. Kyoto **A, 26** (1950) 183.
6) I. Imai: Univ. Maryland, Inst. Fluid Dyn. and Math., Tech. Note BN-104 (1957).
7) W. Müller: *Einführung in die Theorie der zähen Flüssigkeiten* (Leipzig, 1932).
8) C. Wieselsberger: Phys. Z. **22** (1921) 321.
9) R. Finn: J. Appl. Phys. **24** (1953) 771.
10) S. Tomotika, T. Aoi and H. Yosinobu: Proc. Roy. Soc. **A, 219** (1953) 233.

JOURNAL OF THE PHYSICAL SOCIETY OF JAPAN, Vol. 14, No. 6, JUNE, 1959

Downstream Development of the Wakes behind Cylinders

By Sadatoshi TANEDA

Kobe University of Mercantile Marine

(Received March 4, 1959)

Wake development behind circular cylinders and flat plates was investigated in the research water tanks. The aluminium dust method was used to observe the flow patterns.

At the intermediate Reynolds number range the Kármán vortex streets are formed in the wakes behind cylindrical obstacles. But these primary Kármán vortex streets are not stable. They are more and more deformed as the distance from the obstacle is increased, and finally break down.

Thereafter, however, the wake in most cases begins to rearrange itself again into a configuration of the Kármán vortex street. The dimension of the secondary Kármán vortex street thus produced is much larger than that of the primary one. For the circular cylinder, when Reynolds number is lower than about 150, the ratio of the wave length of the secondary vortex street to that of the primary one is about 1.8 to 3.6, while it is about 10 when Reynolds number is higher than about 150.

Sometimes the secondary Kármán vortex street simply decays by viscous diffusion as it moves downstream, but in most cases it rearranges itself again to the next Kármán vortex street.

§ 1. Introduction

Since the time of Bénard[1)], the wake produced by a two dimensional body has been investigated by many experimenters. Especially the Kármán vortex street has long been a matter of interests to hydrodynamicians. All the observations, however, have been made only near the body, and we have no information relating to the flow at a great distance downstream from the body.

On the other hand, owing to the extreme mathematical difficulties of the problem, there has been little theoretical investigation of the wake, and the problem is still left unsolved, in spite of its importance.

In order to investigate the wake more closely, it seems to be necessary to observe the behaviour of the flow not only at the neighbourhood of the body but also at a great distance downstream.

In the present paper a description is given of the observations on the wake development far downstream behind circular cylinders and flat plates, at Reynolds numbers between 10^1 and 10^3 for the circular cylinder and between 10^3 and 10^5 for the flat plate. (The Reynolds number R is Ud/ν for the circular cylinder and Ul/ν for the flat plate, where U is the model speed, d is the cylinder diameter, l is the plate length and ν is the kinematic viscosity of the fluid.)

§ 2. Apparatus and Experimental Method

The experiments were made with the glass sided water tanks of three different sizes. They are 300 cm long, 20 cm deep and 20 cm wide; 400 cm long, 30 cm deep and 30 cm wide; and 2500 cm long, 150 cm deep and 200 cm wide respectively.

The carriage to which a model was fixed upright was moved uniformly along rails mounted horizontally over each water tank. Circular cylinders and thin flat plates of various size were used as models. All the flat plates were carefully tapered smooth to sharp edges. Sizes of the models used are given in Table I. The Reynolds number could be varied from 10^1 to 10^3 for the circular cylinder and from 10^3 to 10^6 for the flat plate.

In order to visualize the motion of water below the free surface, aluminium dust was suspended uniformly in the water. Then the movement of the suspended aluminium dust, which was illuminated horizontally from a side of the tank by a sheet of intense light from incandescent lamps behind a narrow slit, was photographed from above with a

Table I. Sizes of the models used.

Circular cylinder

d (mm)	L (mm)	L/d
2.0	180	90
2.0	280	140
3.0	180	60
3.0	280	93
3.2	180	56
3.2	280	88
4.8	280	58
9.8	1000	102

Flat plate

l (mm)	t (mm)	L (mm)	L/l
101	0.5	180	1.8
101	0.5	280	2.8
140	1.0	180	1.3
140	1.0	280	2.0
223	1.0	180	0.8
223	1.0	280	1.3
1580	2.0	1200	0.8

d: Diameter of the cylinder.
L: Span of the model.
l: Length of the flat plate.
t: Thickness of the flat plate.

camera. From these pictures, the wave length and the spacing ratio of the vortex street were determined.

On the other hand, it was attempted to use the hot wire technique for determing the frequency of the velocity fluctuations in the wake. Pt wire of 30 μ in diameter and about 5 mm in length, which was heated electrically by 250 cycle a. c., was used in the water as the hot wire. It was quite easy to determine the frequency of the velocity fluctuations in the primary Kármán vortex street with the hot wire, as was reported in the previous paper[2]. However, it was not easy to detect the frequency of the secondary Kármán vortex street, because the velocity of the flow in the secondary vortex street was extremely small. In the present experiments, therefore, the measurements of the secondary Kármán vortex street were made chiefly by means of photography.

§ 3. Results

In the first place, observations were made on the wake behind circular cylinders.

Many photographs of the wake were taken at various Reynolds numbers. From these photographs it was confirmed that, at the intermediate range of the Reynolds number, the wake behind a cylinder oscillates and arranges itself into a configuration corresponding to that of the Kármán vortex street some distance downstream.

The Kármán vortex street thus produced, however, can not keep its regular arrangement for a long distance. It gradually changes its shape with the distance from the cylinder, and finally breaks down at a distance of about 50 diameters behind the cylinder. The point at which the breakdown of the Kármán vortex street occurs depends on the Reynolds number. The distance from the cylinder to the transition point seems to be decreased as R is increased. Moreover, it was found that the way in which the wake develops downstream is quite different in the two ranges, $R<150$ and $R>150$.

When R is lower than about 150, the flow is always the typical viscous flow and there is no further possibility for the fluid to become turbulent. After the primary Kármán vortex street breaks down, there follows at once a secondary Kármán vortex street, the wave length of which is much larger than that of the primary one. The secondary Kármán vortex street is always somewhat irregular at the beginning of its appearance. It, however, gradually becomes regular and is finally completed at about 10^3 diameters behind the cylinder.

If λ_1 and λ_2 are the wave lengths of the primary and the secondary Kármán vortex street respectively, λ_2/λ_1 depends on the Reynolds number. The values of λ_2/λ_1 for various Reynolds numbers are shown in Table II. As is seen from the table, there seems to be a general relation that the lower is the Reynolds number, the larger is the value of λ_2/λ_1. At $R=60$ the value of λ_2/λ_1 is about 3.3, while at $R=125$ it is about 1.8.

When R is lower than about 50, it is rather difficult to determine the wave length of the secondary Kármán vortex street from the photographs, since the image of the secondary Kármán vortex street is not clear at such low Reynolds numbers. At $R<50$ the existence of the secondary vortex street is somewhat in doubt.

An example of the wake for $R<150$ is shown in the photographs of Fig. 1. They are the photographs of one part of the field, taken successively by a camera fixed to the water tank at a Reynolds number of 73.5, up to a distance of about 500 diameters behind the cylinder.

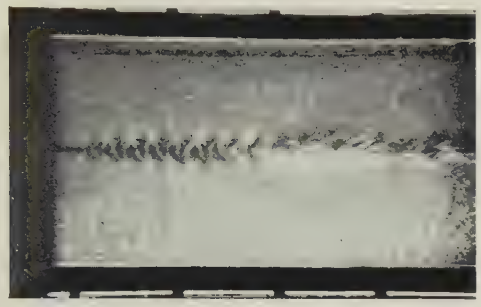

(a) Oscillating wake immediately behind the cylinder. $\lambda_1=19$ mm.

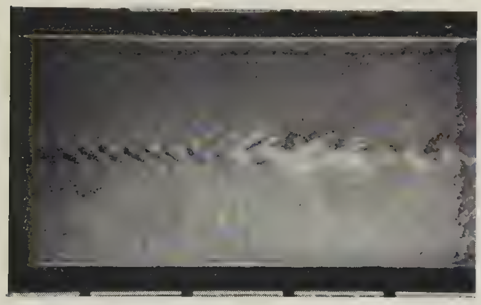

(b) about 10 cm to 50 cm behind the cylinder.

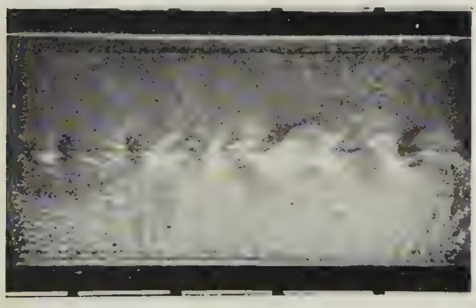

(c) about 30 cm to 70 cm behind the cylinder.

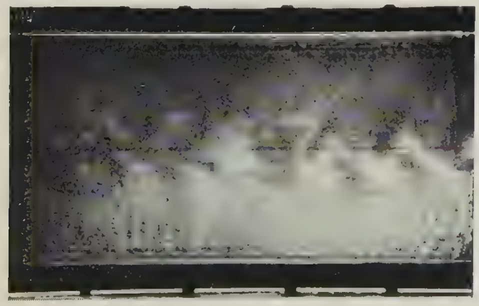

(d) about 70 cm to 110 cm behind the cylinder.

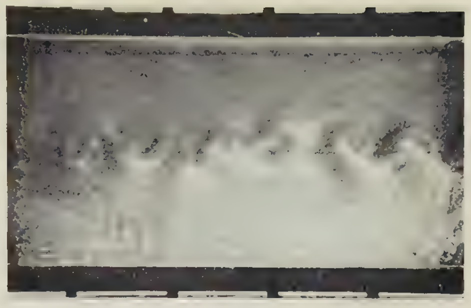

(e) about 110 cm to 150 cm behind the cylinder. $\lambda_2=56$ mm, $\lambda_2/\lambda_1=2.9$.

Fig. 1. Photographs showing downstream wake development behind a circular cylinder for $U=2.22$ cm/s, $d=3.0$ mm and $R=73.5$.

λ_1: Wave length of the primary vortex street.

λ_2: Wave length of the secondary vortex street.

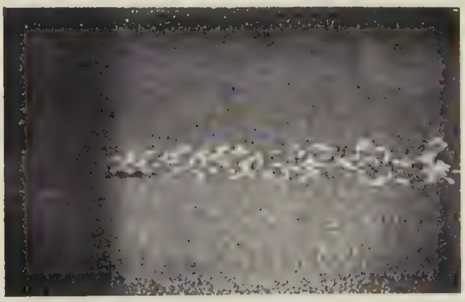

(a) Oscillating wake immediately behind the cylinder. $\lambda_1=13$ mm.

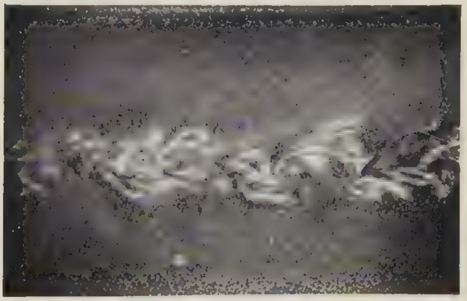

(b) about 80 cm to 120 cm behind the cylinder.

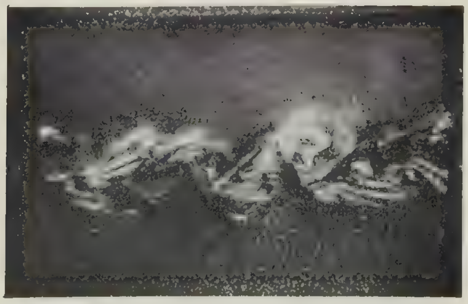

(c) about 180 cm to 220 cm behind the cylinder,

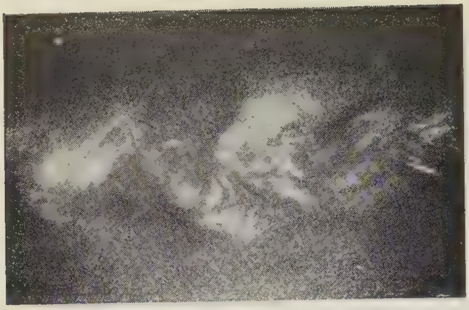

(d) about 270 cm to 310 cm behind the cylinder.

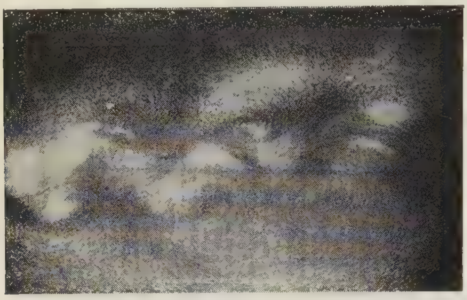

(e) about 460 cm to 500 cm behind the cylinder. $\lambda_2=110$ mm, $\lambda_2/\lambda_1=8.5$.

Fig. 2. Photographs showing downstream wake development behind a circular cylinder for $U=9.53$ cm/s, $d=3.0$ mm and $R=304$.

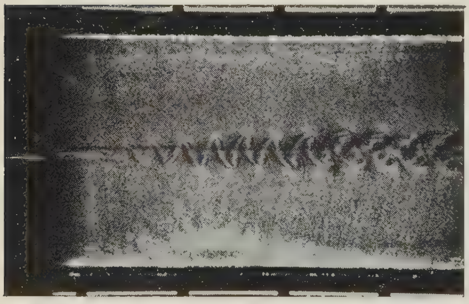

(a) Oscillating wake immediately behind the flat plate. $\lambda_1=27$ mm.

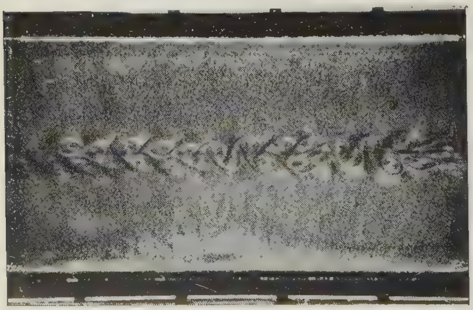

(b) about 20 cm to 60 cm behind the flat plate.

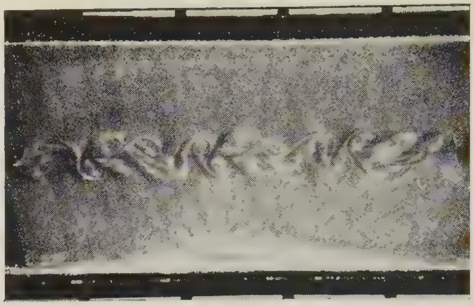

(c) about 50 cm to 90 cm behind the flat plate.

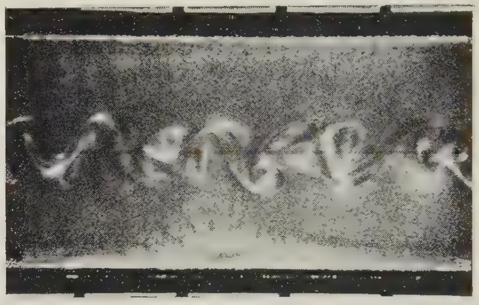

(d) about 100 cm to 140 cm behind the flat plate.

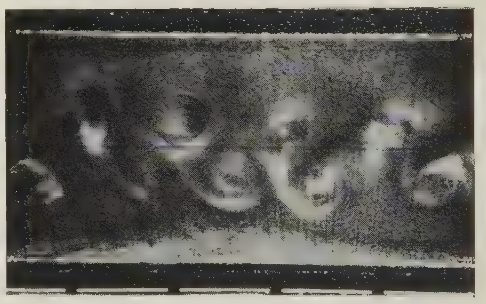

(e) about 200 cm to 240 cm behind the flat plate. $\lambda_2=80$ mm, $\lambda_2/\lambda_1=3.0$.

Fig. 3. Photographs showing downstream wake dovelopment behind a flat plate placed at zero incidence for $U=5.0$ cm/s, $l=140$ mm and $R=8150$.

On the other hand, when R is higher than about 150, the way in which the secondary vortex street is formed is quite different from that at R lower than about 150. At $R>150$, after the primary Kármán vortex street breaks down, the wake becomes turbulent, as was already pointed out by Roshko[3] in 1953. The turbulent wake continues to exist for a considerable distance, then there appear again a new Kármán vortex street. The ratio of the wave length of the new vortex street to that of the primary one scatters largely and cannot be determined precisely, but it is of order of magnitude of 10. This value is much larger than that for $R<150$.

Table II. Values of λ_2/λ_1 for various test Reynolds numbers.

d (mm)	U (cm/s)	R	λ_1 (mm)	λ_2 (mm)	λ_2/λ_1
2.0	2.66	61.0	14	46	3.3
3.0	1.87	63.8	21	65	3.1
3.0	1.94	67.0	20	62	3.1
3.0	1.94	67.0	19	67	3.5
3.0	2.22	73.5	19	60	3.2
3.0	2.22	73.5	19	56	2.9
2.0	3.26	74.0	13	33	2.5
3.0	2.50	78.5	18	41	2.3
3.0	2.73	82.7	19	43	2.3
2.0	3.61	84.0	12	24	2.0
3.0	2.91	93.5	17	42	2.5
3.0	2.91	93.5	18	45	2.5
2.0	4.14	94.7	12	29	2.4
3.0	3.57	108.0	17	34	2.0
3.2	3.57	108.0	19	40	2.1
4.8	2.22	115.0	25	47	1.9
3.0	3.16	115.0	17	31	1.8
3.0	3.16	115.0	17	42	2.5
4.8	2.50	125.0	23	41	1.8
4.8	2.91	149.0	23	46	2.0

d: Diameter of the cylinder.
U: Model speed.
R: Reynolds number (Ud/ν).
λ_1: Wave length of the primary vortex street.
λ_2: Wave length of the secondary vortex street.

Fig. 2 shows an example of the wake at $R=304$.

Sometimes the secondary Kármán vortex street is observed to decay simply by viscous diffusion as it moves downstream. But, in most cases, it breaks down at some distance downstream, then the formation of the next Kármán vortex street begins again, and in this way the formation and the breakdown of the vortex street are repeated alternately, the wave length becoming larger and larger with every transition from one vortex street to the next.

In the second place, the experiments similar to those described above were also made for the flat plate placed at zero incidence. And it was found that the manner of the formation of the secondary Kármán vortex street and the subsequent history are substantially similar to those for the circular cylinder. An example of the wake development behind a flat plate at $R=8150$ is shown in Fig. 3.

As is well known, the boundary layer of the flat plate is turbulent when R is larger than about 5×10^5. Even in this range of Reynolds number, however, the appearance of the primary and the secondary Kármán vortex street could be observed up to $R=10^6$ or more, although their periodicity was somewhat irregular.

§ 4. Discussion

It is believed that the Kármán vortex street is stable for the perfect fluid. However, the actual vortex street which appears in the wake of real fluid is not stable. It continuously changes its shape with the distance from the body and finally breaks down. After this, however, the wake shows a strong tendency to rearrange itself again into the configuration of the Kármán vortex street. In this way the formation and the breakdown of the regular vortex street occur alternately as the distance from the obstacle is increased, the wave length becoming larger and larger with every transition from one vortex street to the next. Even when the regular vortex street is not formed, the dimension of the predominant discrete vortices which appear in the wake always increases as the distance from the body increases.

These results show that the dimension of the Kármán vortex street which is formed in the wake is the function not only of the Reynolds number of the body but also of the distance from the body.

Thus, we are led to the following questions: (1) why the vortex street with a fixed wave length cannot exist for a long distance, (2) why the periodicity of the wake can appear again after it has broken down once. It appears that the answer lies in the hydrodynamical stability problem. A Kármán vortex street which is stable at one position in the wake may be no longer stable at the other position. Then the wake may begin to rearrange itself into the next Kármán vortex street which is stable in the new position. And in this way the formation and the breakdown of the vortex street may occur alternately. Further investigations on this possibility are being carried out.

In conclusion, the author wishes to express his thanks to Professor Hikoji Yamada of Research Institute for Applied Mechanics, for his valuable advice and encouragement in the course of this work. The present investigation was supported by the Scientific Research Grant of the Ministry of Education.

References

1) H. Bénard: Compt. rend. **147** (1908) 970.
2) S. Taneda: J. Phys. Soc. Japan **13** (1958) 418.
3) A. Roshko: NACA Tech. Note no. 2913 (1953).

Errata

Internal Friction of Lead. II

By Yosio HIKI

J. Phys. Soc. Japan **14** (1959) 590

Page	Column	Line		Should be read
592	right	Eq. (7)	$\Lambda=3L_n^2$	$\Lambda=3L_n^{-2}$

The Proton Magnetic Resonance Absorption of the Trichloroacetic Acid in Solid Phase

By Masashi YAGI and Masayasu UETA

J. Phys. Soc. Japan **14** (1959) 377

Column	Line	Wrong	Corrected
right	24	2.6_7	1.6_7

Short Notes

This section is intended to secure prompt publication of important discoveries in physics. The reports should not exceed 800 words in length. A figure of size 7 cm × 7 cm will be counted as 150 words.

J. PHYS. SOC. JAPAN **14** (1959) 849

On the Anomalous Magnetoresistance Effect in n-InSb

By Wataru SASAKI and Chikako YAMANOUCHI
Electrotechnical Laboratory, Nagatacho, Tokyo

(Received May 1, 1959)

It has been pointed out by Broom[1] that n type InSb containing less than 10^{16} carriers per cc shows oscillatory magnetoresistance effect at liquid helium temperature. We have prepared various InSb crystals containing less than 10^{16} carriers per cc, and have measured the magnetoresistance effect in these crystals.

It has been found that the crystals containing nearly same amount of carriers show either oscillatory or non-oscillatory magnetoresistance such as observed in heavily doped n-Ge[2] or p-InSb[3], and that the oscillatory effect is found in crystals in which conduction electrons have higher mobility values.

Fig. 1 shows the distribution of the crystals in regard to their carrier concentration and the relaxation time determined from their conductivity and Hall constant at liquid helium temperature. △ represents the crystals which show non-soscillatory effect, while ⊙ and ● represent the crystals which show oscillatory effect at the magnetic field higher than 1 koe and 2 koe respectively. This figure contains the results obtained by Frederikse and Hosler[4] as well as those by us.

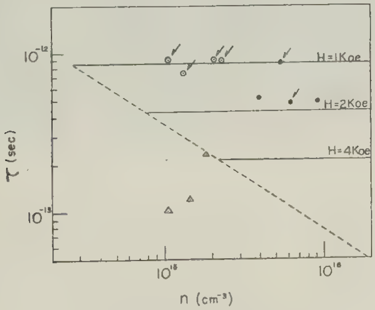

Fig. 1. Relaxation time τ and carrier concentration n of various crystals of n-InSb. △ represents crystals with non-oscillatory magnetoresistance, and ⊙ and ● represent crystals with oscillatory magnetoresistance at magnetic fields higher than 1 koe and 2 koe respectively. The points attached with small arrows represent the observation by Frederikse and Hosler.

If the oscillatory magnetoresistance effect is caused by the same origin as de Haas van Alphen effect, we can expect that this effect will occur when the relaxation time of conduction electrons is longer than the cyclotron period, $\tau_c = m^*c/eH$, and when the carrier concentration is large enough so that the Fermi energy is higher than the diamagnetic energy difference $\varepsilon_d = e\hbar H/m^*c$ for the magnetic field where the oscillatory effect is observable. We can define a region in Fig. 1 where these two conditions for de Haas van Alphen effect are satisfied. We draw horizontal lines at τ values equal to τ_c for various magnetic field strength with $m^* = 0.015\,\mathrm{m}$[5], and draw a broken line which consists of points on the horizontal lines where the Fermi energy corresponding to the concentration is equal to ε_d for each magnetic field strength. The conditions for de Haas van Alphen effect are satisfied for crystals represented by points on the right side of this broken line at the magnetic field with τ_c values shorter than their relaxation time.

As is seen in Fig. 1, the points representing crystals which do not show oscillatory effect are situated on the left side of the broken line, while the points for the oscillatory crystals are situated on the other side of the broken line, and the magnetic field where the oscillation begins corresponds to the parameter of the horizontal lines.

These facts show that the oscillatory magnetoresistance effect and de Haas van Alphen effect are caused by the same mechanism and that the assumed m^* value is well fitted for these InSb crystals.

References

1) R. F. Broom: Proc. Phys. Soc. London **71** (1958) 470.
2) W. Sasaki and Y. Kanai: J. Phys. Soc. Japan **11** (1956) 894.
3) H. Fritzsche and K. Lark-Horovitz: Phys. Rev. **99** (1955) 400.
4) H. P. R. Frederikse and W. Hosler: Phys. Rev. **108** (1957) 1146.
5) H. J. Hrostowski, F. J. Morin, T. H. Geballe, and G. H. Wneatley: Phys. Rev. **99** (1955) 635

J. PHYS. SOC. JAPAN **14** (1959) 850~851

Synthesis of Large CdS and ZnS Crystals

By Jiro NISHIMURA
Faculty of Art and Literature, Iwate University, Morioka, Japan
and Yasaku TANABE
Research Institute for Scientific Measurements, Tohoku University, Sendai, Japan

(Received May 11, 1959)

In spite of several outstanding methods,[1][2][3] it is not easy to synthesize large CdS and ZnS crystals. We have succeeded, with sufficient reproducibility, in synthesizing large single crystals from a charge of sulfide powder by the following procedure.[4] Polycrystals of easy grain growth are first prepared from a charge of powder by sublimation and recrystallization process. Special lattice plane of these polycrystals is prevailing at their growth front when the vapor of CdS and ZnS is cooled and recrystallized in the zone with large temperature gradient. These polycrystals are a bundle of needle like or rod-like grains with the growth plane of the same Miller index. C-axis of these grains are all parallel in the case of CdS to and make an angle of 25° in the case of ZnS with the normal direction of the substrate surface. Single crystals are then grown from these polycrystals by heat treatment under saturated vapor. The above-mentioned procedure, namely, recrystallization and grain growth, can be done by a single run of the furnace.

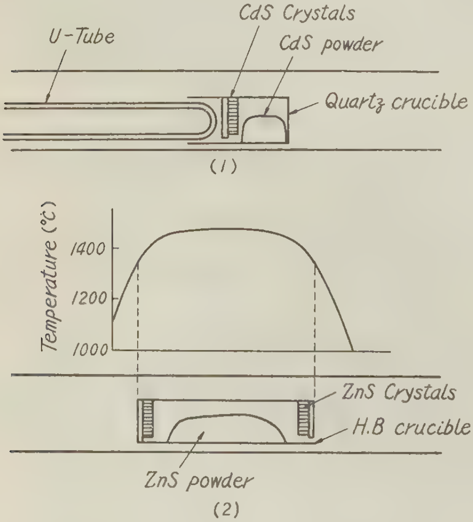

Fig. 1. Furnaces with contents in place.

Experimental furnaces are shown in Fig. 1. A charge of CdS powder is placed in a quartz tube 30 mm in diameter with cups at its both ends (Fig. 1, (1)). One end of the tube is situated in the sublimation zone. The cup of the other end serves as substrate upon which single crystals are formed. It has a small hole for exchanging the ambient gas and is attached to the head of U tube by which steep temperature gradient is formed there. CdS vapar produced in the sublimation zone is cooled and recrystallized on the substrate, and one or several single crystals are synthesized by grain growth. In the case of ZnS, another furnace with steep temperature gradient is used without U-tube (Fig. 1, (2)), and H. B. combustion tube (>57% Al_2O_3) together with S. S. A. crucible (>95% Al_2O_3) are inserted in it.

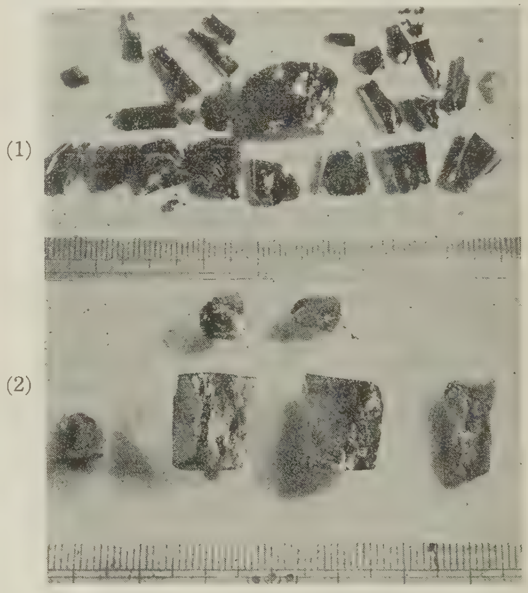

Fig. 2. (1) CdS single crystals cleaved from a polycrystal.
(2) ZnS single crystals cleaved from a polycrystal.

Table 1. Conditions for growing CdS and ZnS Crystals.

	CdS	ZnS
A charge of powder (g)	40	60
Temperature of sublimation zone (°C)	1150	1430
Temperature of recrystallization zone (°C)	1050	1350
Temperature gradient (°C cm⁻¹)	20	50
Time of treatment (hr)	70	80

Fig. 2 and Table 1 show some examples of CdS and ZnS crystals and their growing conditions. Large CdS block in the center consists of several single crystals of about 3×3×12 mm³ which grow parallel to one another. The other CdS blocks are separate single crystals. Two large ZnS crystals in the center, cleaved from the middle part of one single crystal are both about 5 g in weight and their crystal structure is of Wurtzite type and have stacking faults. The larger the quantity of a charge and the higher the furnace temperature, the larger single crystals may grow. Remarkable grain growth in ZnS was observed when the temperature of recrystallization zone was higher than 1400°C.

A detailed description will be published later.

References

1) S. J. Czyzak, D. J. Craig, D. E. McCain and D. C. Reynolds: J. Appl. Phys. **23** (1952) 932.
2) S. Ibuki and K. Awazu: J. Phys. Soc. Japan **11** (1956) 1297.
3) S. J. Czyzak, D. C. Reynolds, R. C. Allen and C. C. Reynolds; J. Opt. Soc. Amer. **44** (1954) 864.
4) J. Nishimura and Y. Tanabe: Bull. Res. Inst. Sci. Measur. Tohoku Univ. **7** (1959) 215.

J. PHYS. SOC. JAPAN **14** (1959) 851~852

Double Proton Magnetic Resonance by a Side Band Method

By Junkichi ITOH and Siro SATO
Department of Physics, Osaka University

(Received March 28, 1959)

If, in an organic liquid, the chemical shifts of NMR lines from equivalent protons in atomic groups A and B differ considerably from each other, well-resolved two lines will be observed in high resolution spectrum, each of which will split further into several multiplet components in the presence of an indirect spin-spin coupling between these protons.

Suppose we are observing the A resonance by an usual method, and an additional rf field with amplitude H_{1B} is applied, whose frequency is equal to that of the B resonance. When γH_{1B} (γ is the gyromagnetic ratio of proton) is made considerably larger than the equivalent frequency of the indirect coupling, the multiplet will be smeared out into a single line with the intensity given by the sum of the intensities of the normal multiplet lines.

This type of double resonance has been analysed by Bloch⁽¹⁾, and Anderson⁽²⁾ has demonstrated the effect by his successful experiment. However, since the difference between these two frequencies is usually less than a few hundred cycles per second, a fairly large beating makes it rather difficult to apply this method to extensive investigation of indirect coupling in complex organic compounds.

We have carried out similar experiments by making use of a side band technique. It is well known that when the static field is modulated slightly by audiofrequency $\omega_m/2\pi$, small side band peaks appear at the magnetic fields $\pm\omega_m/\gamma$ distant from the main resonance field. The intensity of the side band peaks is determined by the degree of the modulation. So, making the degree of the modulation quite small, the main resonance can be strongly saturated while the side band peaks are always kept in unsaturated state. If we choose $\omega_m/2\pi$ equal to the frequency difference between the A and B resonances, one of the side band peaks of the A resonance will then appear exactly at the B resonance, and *vice versa*. When H_1 is very weak, this side band peak is hardly recognized, being completely hidden in the main line. But, when H_1 is increased to saturate the main resonance, keeping the side band peak in unsaturated condition, this side band peak will become to be seen on a broad peak of the saturated main line. If γH_1 overcomes the indirect spin-spin conpling frequency considerably, this indirect interaction will be ineffective to form normal multiplet and the side band peak will become a single line with the intensity equal to the sum of the intensities of the multiplet lines.

We have examined this consideration on CH_3CHO. A Varian 4300 B high resolution NMR spectrometer was used. The frequency difference between the proton resonances from CH_3 and CHO groups in this molecule at 40 mc/sec was 303 cps. By the indirect spin-spin coupling, they have doublet and quartet structures, respectively. Keeping $\omega_m/2\pi$ constant, 303 cps, H_1 was increased upto such a value as to wash out the indirect interaction, and the side band line from CH_3 group was observed which appeared just at the main B resonance. Fig. 1 shows the result of the observation. As is predicted by the foregoing argument, only a single line appears in this figure, instead of the normal doublet. When $\omega_m/2\pi$ was altered slightly from 303 cps, the normal doulet structure appeared again as shown in Fig. 2.

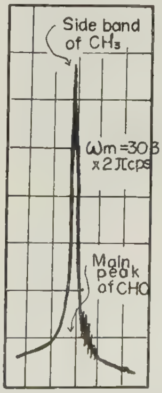

Fig. 1.

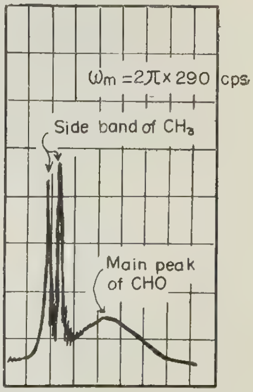

Fig. 2.

This method of double resonance may be found useful for analysing complex spectra in nuclear magnetic resonance of organic molecules.

References

1) F. Bloch: Phys. Rev. **102** (1956) 104.
2) W. A. Anderson: Phys. Rev. **102** (1956) 151.

J. Phys. Soc. Japan **14** (1959) 852

Avalanche Electroluminescence in CdS Single Crystal

By Makoto KIKUCHI and Sigeru IIZIMA
Electrotechnical Laboratory, Tokyo, Japan

(Received April 11, 1959)

CdS single crystal having an ohmic evaporated In electrode and a non-ohmic Ag-paste electrode generally shows N-type rectifying characteristic.[1] CdS rectifying cells whose construction is shown in fig. 1 are made with flaky single crystals. With these cells, when the forward voltage is increased up to 25∼50 volts, the forward current increases rapidly and light is emitted as shown in fig. 2.

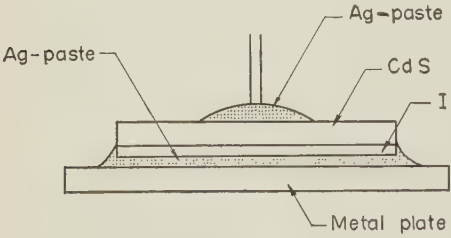

Fig. 1. The construction of the rectifying cell.

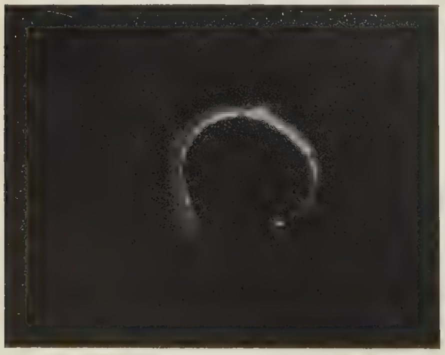

Fig. 2. Photograph of light emission from the Ag-paste electrode.

The relationship between the current through the cell and the light intensity is shown in fig. 3. Since the creep of the light intensity occurs with DC steady current, voltage pulse is used for the measurement. The repetition frequency is 5,000 cps, and the pulse width is 20 microseconds. The current which passes through the cell is read on an oscilloscope and the average current of photomultiplier is measured by a DC microammeter.

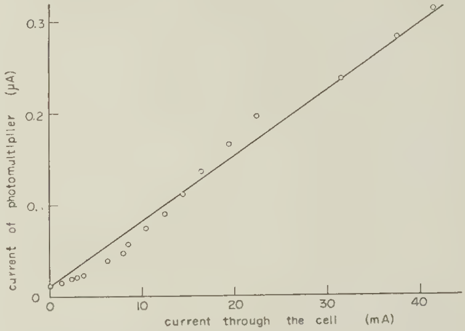

Fig. 3. The light intensity versus the current through the cell.

V-I characteristic of the cell is shown in fig. 4. Again, the voltage pulse is used to eliminate the creep effect. The repetition frequency is 100 cps and the pulse width is 20 microseconds. When the voltage reaches a critical value, current increases rapidly. This behavior is quite similar to that of the gas discharge tube.

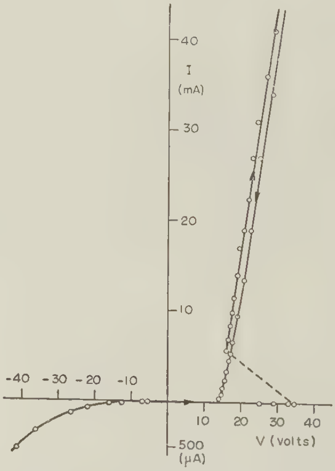

Fig. 4. The V-I characteristic of the cell.

It is believed that when the forward voltage reaches a certain value, the avalanche breakdown occurs in the bulk of the crystal, taking the low differential resistance in on-state (about 400 ohms) into account. The emission of the light is due to the recombination of electrons and holes generated in the above process.

Reference

1) R. W. Smith: Phys. Rev. **97** (1955) 1525.

J. PHYS. SOC. JAPAN **14** (1959) 853

Ferrimagnetic Resonance Line Width in Polycrystalline $Y_3Fe_{5-x}In_xO_{12}$

By Tomonao MIYADAI, Yuzo SHICHIJO
Electrical Communication Laboratory,
Nippon Telephone and Telegraph Public
Corporation, Tokyo
and Ichiro TSUBOKAWA
Research Institute for Iron,
Steel and Other Metals,
Tohoku University, Sendai

(Received April 9, 1959)

Since the discovery by Bertaut et al[1], intense interests have been taken to the ferrimagnetic oxides with garnet structure, having a general formula, $M_3Fe_5O_{12}$. The discovery by Dillon[2] of an extremely narrow ferrimagnetic resonance line width in an yttrium-iron garnet (YIG) single crystal, strengthened these interests. In this connection, it is interesting to investigate the change in line width in the indium-substituted YIG, $Y_3Fe_{5-x}In_xO_{12}$.

The mixtures of Y_2O_3 (99.9%), Fe_2O_3 and In_2O_3 powders in desired proportions were pressed into disk form, sintered at 1400°C in air for about six hours and cooled in the furnace. The samples for resonance absorption were spheres of 0.32 to 0.49 mm in diameter which had been ground by Bond's method[3]. The microwave frequency was 20080 Mc/sec and a rectangular cavity of transmission type with H_{105} mode was used.

The experimental results are shown in Fig. 1. Each point for the half line width plotted in this figure is the minimum value among those obtained for several samples with the same indium concentration, x. As shown in this figure, at $x=0$ the line width takes a value of 130 Oe and increases rapidly with increasing x to c.a. 900 Oe at $x=1.3$. Beyond this point it decreases slightly. The absorption intensity, however, first increases, passes through a maximum at nearly $x=0.3$, then decreases monotonically and reaches zero at about $x=2$. As is shown in the figure, this variation corresponds exactly to the variation of saturation magnetization, Ms, with x. The g-values of these samples were between 2.01 and 2.03.

According to X-ray analysis, the samples consist only of garnet phase for $0 \leq x \leq 0$, of three phases (Garnet+$YFeO_3$+In_2O_3) for $1.0<x<2.0$ and at $x=2.0$, of two phases ($YFeO_3$+In_2O_3).

The reason for the increase in line width with increasing indium content is not clear since our samples were polycrystals. Schlömann[4] studied the ferrimagnetic resonance in polycrystalline ferrites and concluded that the line width is broadened by $|K_1|/Ms+1.5(4\pi Ms)\Delta V/V$ in a polycrystalline specimen, where K_1 is the 1st order anisotropy constant, Ms the saturation magnetization at a given temperature and $\Delta V/V$ the ratio of the pore-volume in the sample to its apparent volume. Since all our samples have a relative density of more than 90%, the fluctuation through the samples in the value of $\Delta V/V$ will be within a few percent. The saturation magnetization at room temperature varies with x as shown in the figure. This initial increase of Ms in c.a. 15% and, for x greater than 0.3, Ms decreases considerably. Therefore, the amount of increase of the second term, $1.5(4\pi Ms)\Delta V/V$ resulting from the In-substitution will not exceed 20%. It may be certain that $|K_1|/Ms$ will not increase since the ferromagnetic Curie temperature decreases with increasing x. Therefore, so long as depending on the Schlömann's result, the line broadening due to polycrystallinity should be of the same magnitude for all our samples. It might be possible that the greater part of the increase in line width for the single phase region ($0 \leq x \leq 1.0$) results from the irregularities[5] in 16(a) and 24(d) sites caused by the indium substitution for Fe.

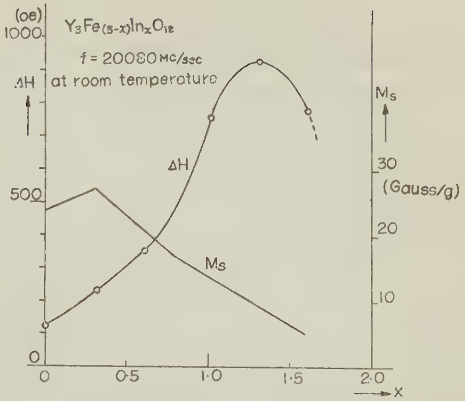

Fig. 1. Variations of the full half line width, ΔH, and of the saturation magnetization at room temperature, Ms, with x in $Y_3Fe_{5-x}In_xO_{12}$.

References

1) F. Bertaut et F. Forrat: Compt. rend. **242** (1956) 382.
2) J. F. Dillon, Jr.: Phys. Rev. **105** (1957) 759.
3) W. L. Bond: Rev. Sci. Instr. **22** (1951) 344.
4) E. Schlömann: Conference on Magnetism and Magnetic Materials, Boston, Oct. 1956 (A.I.E.E.), 600.
5) For example, A. M. Clogston, H. Suhl, L. R. Walker and P. W. Anderson: J. Phys. Chem. Solids **1** (1956) 129.

J. Phys. Soc. Japan **14** (1959) 854

Electric Resistance and Cation Distribution of Fe-Mn Ferrite System

By Zenya Funatogawa, Nahonori Miyata and Seiji Usami
Department of Physics, Yokohama National University, Yokohama

(Received April 13, 1959)

By means of the electrical resistance measurements of $Mn_xFe_{3-x}O_4$ ($0 \leqq x \leqq 1.14$) the distribution of Mn-ions on the crystal lattice points was estimated. It was concluded that Mn-ions should occupy the B-sites of the spinel lattice at least in the region of low Mn-ion content.

Specimens (3×3×8 mm) were cut from large blocks solidified from the melt in the air. Dependence of the specific electrical resistance (ρ) on absolute temperature (T) (100°K–280°K) was measured by the four probes method with two In-amalgam electrodes on both sides of the specimen for the current flow and two brass electrodes, 4 mm apart, for measuring the potential between them. $\log \rho$ depends linearly on $1/T$ between 120°K and 200°K ($x \geqq 0.1$), and a knick is observed at about 120°K in the region $0.2 \leqq x \leqq 0.6$. Linear dependency mentioned above tells us that specific resistance is expressed by $\rho = \rho_0 \exp(\varepsilon/kT)$. Two constants ε and ρ_0 are plotted against x in Fig. 1 and 2. Experimental values of ρ_0 represented by open circles in Fig. 2 are expressed by a simple relation, $\rho_0 = 6 \times 10^{-3} (x/1-x)$, which is shown by a curve in the figure.

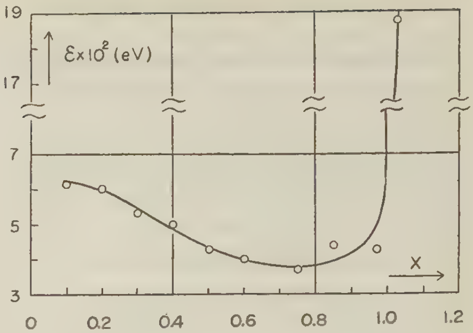

Fig. 1. Activation energy ε *vs.* Mn-ion concentration x.

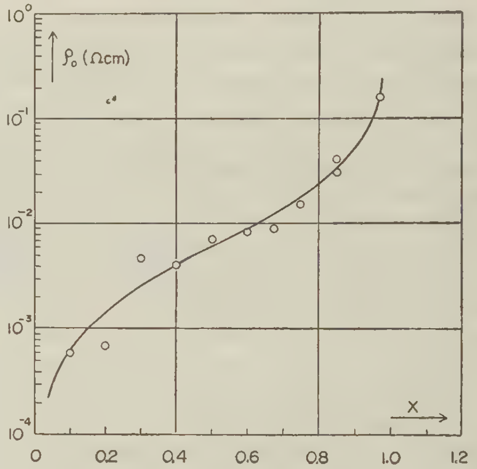

Fig. 2. ρ_0 *vs.* x; open circles represent experimental values and a curve shows $\rho_0 = 6 \times 10^{-3}(x/1-x)\ \Omega$ cm.

Conduction mechanism of these ferrites is understood as the motion of electrons between Fe^{2+} and Fe^{3+} on the B-site of the spinel lattice. Also $\rho_0 = 1/n_0 \mu e$, where n_0 is the concentration of charge carrier at the condition that T is extrapolated to infinity, μ is the mobility, and e is the charge. n_0 is proportional to $(1-x)$, the number of Fe^{2+} ion which is always at the B-sites, and independent of the distribution of Mn-ions. But as for μ, there are two possibilities; (1) it does not depend on x if Mn-ions occupy the A-sites because there are only Fe^{2+} and Fe^{3+} on the B-sites and μ is determined by scattering by thermal motion of crystal lattice, or (2) it is reciprocally proportional to x if Mn-ions are distributed on the B-sites because scattering by Mn-ions is predominant. Then ρ_0 depends on x as const.$\times(1/1-x)$ or const.$\times(x/1-x)$ when Mn-ions occupy A-sites or B-sites respectively. The experiment shows the latter case is actually true. But it must be noted that their difference is not clear in the region of low Fe^{2+} concentration where $1/1-x$ in both expressions is predominant. It is now believed by the neutron diffraction experiment that Fe_3O_4 and $MnFe_2O_4$ have inverse and nearly normal spinel structure respectively¹⁾. Then we should recognize that by substitution for Fe^{2+} in magnetite by Mn^{2+} the latter occupy B-sites in the region of low concentration while normal type spinel is stable in the region of large concentration.

We are now investigating the magnetic crystalline anisotropy of these ferrites and pronounced valley in the curve $-K_1/M$ *vs.* composition x is observed. $-K_1/M$ is a minimum in the region $0.6 < x < 0.7$ and changes its sign. The relation between these facts and distribution of ions mentioned above will be discussed in the paper of this journal very soon.

Reference

1) G. G. Shull, E. O. Wollan and W. C. Koehler: Phys. Rev. **84** (1951) 912. J. M. Hastings and L. M. Corliss: Phys. Rev. **104** (1956) 328.

J. PHYS. SOC. JAPAN **14** (1959) 855~856

Magnetic Annealing Effect in α Fe_2O_3

By Takao IWATA, Masako IWATA
and Mikio YAMAMOTO

*The Research Institute for Iron, Steel
and Other Metals,
Tôhoku University, Sendai*

(Received March 11, 1959)

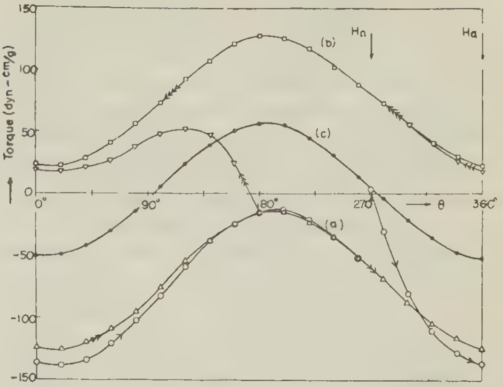

Fig. 1. Torque curves for the rotating field of 1320 Oe of an α Fe_2O_3 disc cooled in magnetic field (H_a) and then placed in a perpendicular field (H_n). The curve (c) is the averge of the curves (a) and (b).

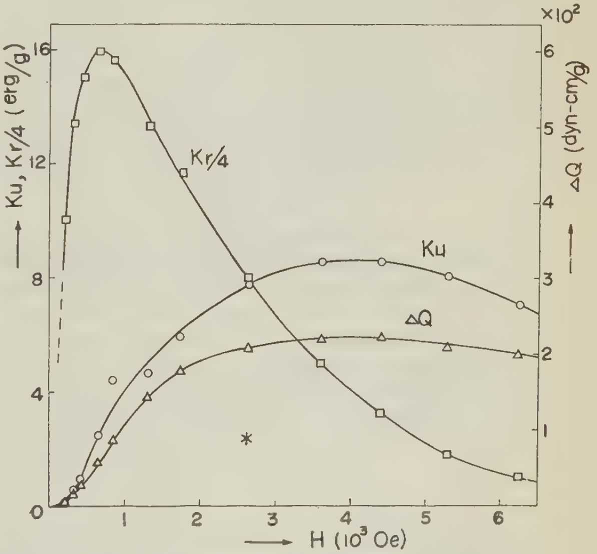

Fig. 2. The measured values of K_u, K_r, and ΔQ as dependent on the measuring field (H) in an α Fe_2O_3 disc. $*$ is the value of measured K_u at the liquid air temperature.

We have studied the magnetic annealing effect in α Fe_2O_3, which is an antiferromagnetic with superposed parasitic ferromagnetism of unknown origin[1].

The disc specimen, 1.62 gr in weight, was made from pure αFe_2O_3 powder (produced from $Fe(NO_3)_3 \cdot 9H_2O$ by heating in air) by sintering at 1000°C in oxygen. It was cooled in air from 750°C (the Néel temperature is about 675°C) in magnetic field (H_a) of moderate intensity (440 Oe), the direction of which is denoted as $\theta=360°$. The magnetic torque measurements of the specimen in this state could not detect any effect of magnetic annealing; the torque curves can be interpreted simply by the presence of the thermo-remanence remaining in the direction of the annealing field. Then, in order to eliminate the effect of the thermo-remanence, the magnetically annealed specimen was magnetized along the $\theta=270°$ direction by an intense field of 6700 Oe (H_n), and the torque of thus treated specimen was measured in the rotating field (H) applied parallel to its disc surface. Typical torque curves as obtained for $H=1320$ Oe are shown in Fig. 1. As is seen clearly, the curve (a) which was measured by the clockwise rotation of H shifts greatly from the curve (b) which was measured by the counter-clockwise rotation of H. This shows that the parasitic ferromagnetism has a large rotational hysteresis in accordance with the observation by Jacobs and Bean[2]. The curve (c) as determined by averaging the curves (a) and (b) cuts the abscissa at a point shifted slightly from $\theta=270°$ towards $\theta=360°$, the deviation angle of this intersecting point being nearly proportional to H.

The Fourier analysis of the averaged torque curves shows that the energy associated with them can be expressed by a formula

$$E=-K_r\cos(\theta+\pi/2)-K_u\cos\theta\ .$$

This formula indicates that the first term is due to the remanent magnetization remaining in the direction of $\theta=270°$ as a result of the application of H_n and the second term is an unidirectional magnetic anisotropy induced by magnetic annealing which stabilizes the magnetization vectors lying in the direction of H_ι ($\theta=360°$). The dependence on H of K_r, K_u, and the magnitude of the rotational hysteresis, ΔQ, which is the difference between the clockwise and counter-clockwise measured torque curves, is shown in Fig. 2. It is to be noted that the value of K_u measured at the liquid air temperature is considerably low, as shown in Fig. 2, which corresponds to the already known experimental fact that the parasitic ferromagnetism of α Fe_2O_3 reduces considerably at low temperatures[1].

The observed unidirectional anisotropy may be explained by assuming, as an origin of the parasitic ferromagnetism, the existence of ferromagnetic layers such as the β phase[3], which are parallel to the basal plane of α Fe_2O_3 crystal and in exchange contact with the antiferromagnetic matrix. When the specimen is cooled from above the Néel temperature in magnetic field of moderate intensity, spins in the antiferromagnetic regions near the ferromagnetic layers aligne themselves parallel to spins in the ferromagnetic layers so as to lower the energy of the exchange contact instead of aligning perpendicularly to the annealing field, and thus an unidirectional effective anisotropy energy is produced within the ferromagnetic layers and brought to the room temperature. The antiferromagnetic spins aligned parallel to the spins in the ferromagnetic layers will not be affected by the normally applied field H_n. Then the unidirectional magnetic anisotropy will be observed only by the above-stated special procedure. In an intense measuring field ($H>4000$ Oe) the stabilizing action of the antiferromagnetic spins will be weakened, so that the unidirectional anisotropy and the rotational hysteresis of the torque will begin to decrease (cf. Fig. 2). Here, it is assumed that the direction of antiferromagnetic spins can rotate in a basal plane so as to become perpendicular to the applied field and the critical field strength for such a rotation is about 2000 Oe after the magnetization measurements of Bizette et al.[4] Finally, it should be remarked that the observed unidirectional anisotropy can not be explained by the uniform body parasitic ferromagnetism such as proposed by Dzyaloshinsky[5].

References

1) L. Néel: Rev. Mod. Phys. **25** (1953) 58.
2) I. S. Jacobs and C. P. Bean: J. Appl. Phys. **29** (1958) 537.
3) G. I. Finch and K. P. Sinha: Proc. Roy. Soc. **A, 241** (1957) 1.
4) H. Bizette, R. Chevallier and B. Tsaï: Compt. rend. **236** (1953) 2043.
5) I. Dzyaloshinsky: J. Phys. Chem. Solids **4** (1958) 241.

J. PHYS. SOC. JAPAN **14** (1959) 856

Quenching Effect of the Photoconductivity Decay in CdS

By Makoto KIKUCHI and Sigeru IIZIMA
Electrotechnical Laboratory, Tokyo, Japan

(Received April 11, 1959)

On one face of the flaky CdS single crystal is evaporated In, and on the opposite face Ag-paste is applied. The cell having such a configuration shows relatively good rectifying characteristic.[1] The decay of photocurrent in forward direction after having been irradiated with very weak light is much faster than that in backward direction. In fig. 1, the time required for the photocurrent to decay down to one fifth of stationary value, $T_{1/5}$, is plotted as a function of applied voltage. The relation between the applied voltage and the stationary photocurrent is also shown.

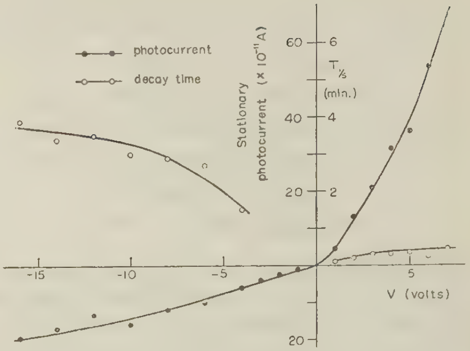

Fig. 1. The stationary value of photocurrent and its decay time versus applied voltage.

When the cell is biased forward, photocurrent and its decay are governed by the photoconductivity and its decay in the bulk of crystal. On the other hand, when biased backward, they are governed by the photoconductivity and its decay in the barrier layer near the surface where Ag-paste is applied. Since the free carriers are exhausted in the barrier, the rate of recombination process is low, and the recovery after the light is removed may be expected to be slow.

The slow decay of the photocurrent in the backward direction is accelerated by temporarily removing the bias voltage or reversing it to forward as shown in fig. 2. The cell on which backward bias (7 volts) is applied is illuminated with a very weak light, and after the photocurrent reaches the stationary value, the light is removed. In the course of the decay of photocurrent, applied bias voltage is reduced to zero, and after 10 seconds raised again to 7 volts. The current is rapidly settled down to original dark value by this process.

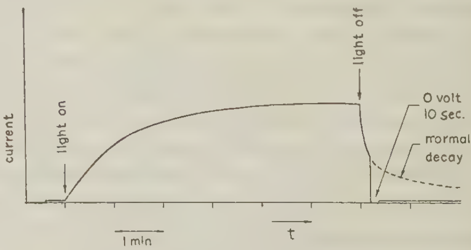

Fig. 2. The quenching effect of photocurrent decay by temporarily reducing the voltage to zero.

A possible explanation is as follows: reducing the voltage to zero, the barrier layer is shrinked, then the region in which the free carriers has been exhausted or nearly exhausted is made to have more free carriers, and the recovery is accelerated.

Reference

1) R. W. Smith: Phys. Rev. **97** (1955) 1525.

J. PHYS. SOC. JAPAN **14** (1959) 857~858

Luminescence of KI:Tl Induced by Far Ultraviolet Light*

By Masayasu UETA and Takehiko ISHII

Department of Physics, The Faculty of Science, University of Tohoku, Sendai

(Received May 9, 1959)

Luminescence of Tl ion in alkali halide crystals has been investigated so extensively since early decades from both the theoretical and experimental sides, because of the fact that the electronic transition involved in either emission and absorption is considered to take place within the Tl ion, and the model of the luminescence center is quite simple. The emission of the pure and activated crystals was studied in NaI crystal and the fluorescence which is likely attributed to the exciton has been reported[1].

The investigations of Tl emission with irradiations of lights in the fundamental absorption bands of host crystals, will provide valuable informations to the process of the energy transfer in crystals.

This note describes a preliminary results on the quantum yield of Tl-fluorescence in KI crystal when it is excited at room temperature with lights in the far ultraviolet absorption bands. Teegarden[2] has obtained the similar results independently, using a KI crystal containing much smaller concentration of Tl ion (one part in 10^5), hence the comparison is also described.

The KI crystal was grown from the melt containing three mol. per cent thallium, and one tenth of the initial concentration of Tl is considered to be introduced in a single crystal. For the illumination, the monochromatic lights (band pass is 6 mμ) from a hydrogen discharge tube through the previously reported vacuum monochromator[3] was used. The relative intensities of monochromatic lights in the region from 300 mμ to 150 mμ incident upon the crystal surface were obtained by measuring the fluorenscence of a sodium salicylate fluorescent screen which was placed close to the crystal. The fluorescent screen is confirmed to have same uniform quantum efficiency to the lights down to 100 mμ[4].

The fluorescent screen was removed out of the light path by means of rotation mechanism, then the monochromatic lights illuminated the crystal and made it luminesce. The luminescence from the crystal and from the screen were measured alternatively for each monochromatic light with a photomultiplier tube. The direction for receiving the luminescence from the crystal was set to take a proper angle against the path of monochromatic lights to avoid the stray light from the monochromator.

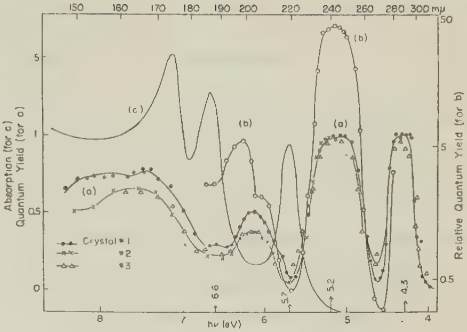

Fig. 1. Quantum yield of Tl emission in KI crystal at room temperature as a function of photon energy. The concentration of Tl is about 0.3% for (a) and 0.001% for (b). Curve (b) is the results by Teegarden. Curve (c) is absorption bands of thin film of KI crystal by Schneider and O'Bryan.

The relative quantum yield thus obtained is shown in Fig. 1 (a). For the comparison, the result by Teegarden is given by (b). Two peaks at $h\nu=4.3$ eV and 5.2 eV are the direct excitation of Tl and correspond to absorption maxima of Tl ion itself. As cleary shown in the absorption curve of pure KI film (c)[5], minima at $h\nu=5.7$ eV and 6.6 eV correspond to the maxima of absorption coefficient of the host crystal, hence they are attributed mainly to the reflection loss.

It is well known that the yield of Tl emission is unity[6] with a light in the region of its absorption bands. Comparing the relative height in Fig. 1 (a), the yield for lights below 175 mμ is determined to have the value of 0.8.

On the other hand, when the host crystal is irradiated in this spectral region, it shows a photoconduction and free electrons and holes are generated. Therefore, the emission in this spectral region is considered to be due to the energy transfer through the recombination of electron and hole.

There is no definite information where the photoconducting region starts, however, it may be considered to extend to the excition peak at $h\nu=5.7$ eV. Therefore, the peak of yield at $h\nu=6.2$ eV will be the superposition of the emission induced by the exciton and the recombination of electron and hole. From these facts, the efficiency of emission of Tl ion induced by only the exciton will be lower than that indicated in Figure, at room temperature.

The quantum yield of the induced emission by exciton or recombination of electron and hole depends on the Tl concentration as seen from figures of (a) and (b). Therefore, with measuring the yield as a function of Tl concentration, the mechanism of energy transfer will be discussed.

---

* This work was talked at physics meeting in October, 1958.

References

1) W. van Sciver and R. Hofstadter: Phys. Rev. **97** (1956) 1181.
2) K. Teegarden: unpublished. The authors are deeply indebted to Dr. Teegarden who showed them his results before publication.
3) M. Ueta, M. Hirai and H. Watanabe: J. Phys. Soc. Japan **14** (1959) 253.
4) F. S. Johnson, K. Watanabe and R. Tousey: J. Opt. Soc. Amer. **41** (1951) 702.
5) E. G. Schneider and H. M. O'Bryan: Phys. Rev. **51** (1937) 293.
6) W. Bünger: Z. Phys. **66** (1930) 311.

J. Phys. Soc. Japan **14** (1955) 858

Distortion of the Octahedral Charge Distribution in Some Cobalt Complexes

By Tadashi Sugawara
The Research Institute for Iron, Steel,
and Other Metals,
Tohoku University, Sendai

(Received April 14, 1959)

Study of the electric quadrupole interaction of the nucleus of an iron group ion with the local field gradient in crystals gives informations on the nature of the crystalline electric field as the local field gradient has a close relation to the electric local field.1) We studied the quadrupole effect in the nuclear magnetic resonance of Co^{59} in $K_3[Co(CN)_6]$ and $[Co(NH_3)_6]Cl_3$, which are diamagnetic.

Rotation patterns about the a, b and c axes of the pseudo-orthorhombic crystal (twin) of $K_3[Co(CN)_6]$ were measured at 4.2°K. The quadrupole coupling constant e^2qQ/h, the asymmetry parameter η, and the orientation of the principal axes of the field gradient tensor were determined by the usual method. The obtained values were $e^2qQ/h=7.3\pm0.1$ MC and $\eta=0.75\pm0.03$. The orientations of the principal axes for the two equivalent $Co(CN)_6$ groups in an unit cell are shown in Fig. 1. This asymmetric field gradient seems to have its main origin in the asymmetry of charge distribution in the group $Co(CN)_6$, as the directions of the principal axes can not be related to the arrangement of K^+ and $[Co(CN)_6]^{3-}$ ions in the monoclinic unit cell.2) It must be noted that the orientation of the principal axes of the g-tensor of $K_3[Fe(CN)_6]$,3) which is isomorphous with $K_3[Co(CN)_6]$, differs appreciablly from this.

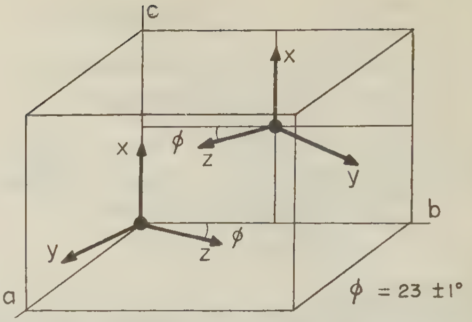

Fig. 1. Orientation of the principal axes of the field gradient tensor in $K_3[Co(CN)_6]$. The z axis lies along the direction of maximum and the x axis along the direction of minimum field gradient. The x axis is parallel to the crystallographic c-axis.

The powdered specimen of $[Co(NH_3)_6]Cl_3$ showed an asymmetrically broadened resonance line at low temperatures. Its shape was quite similar to the second order powder pattern of the central component ($m=+\frac{1}{2}\leftrightarrow-\frac{1}{2}$) for the field gradient of axial symmetry.1) Assuming $\eta=0$, e^2qQ/h was found as 1.5 ± 0.1 MC at 4.2°K. The symmetry axis will probably lie in the [111] direction of the $Co(NH_3)_6$ octahedron.

The above results show that there exists considerable distortion of the octahedral charge distribution around the Co nucleus. Such a distortion will be related to the anisotropy of the crystalline electric field in paramagnetic complexes such as $K_3[Fe(CN)_6]$ and $[Cr(NH_3)_6]Cl_3$. More interesting result will be obtained from the nuclear resonance of Mn^{55} in $K_3Mn(CN)_6$ (paramagnetic) at very low temperatures.

References

1) M. H. Cohen and F. Reif: *Solid State Physics*, vol. **5** ed. by F. Seitz and D. Turnbull (Academic Press, New York, 1957) 321.
2) V. Barkhatov and H. Zdanov: Z. Fiz. Khim. SSSR. **18** (1944) 437. *Structure Reports* **9** (1942–1944) 209.
3) J. M. Baker, B. Bleaney and K. D. Bowers: Proc. Phys. Soc. London **B**, **69** (1956) 1205.

BACK NUMBER

SUPPLEMENT

Progress of Theoretical Physics

No. 1. **(1955)**, $ 1.50
Collected Papers on Meson Theory. I—*Formalism and models*—

No. 2. **(1955)**, $ 1.50
Collected Papers on Meson Theory. II—*Intermediate and strong coupling theories*—

No. 3. **(1956)**, $ 1.50
Meson Theory. III—*Nuclear forces*—
1. Development of pion theory nuclear forces ....Iwadare, Otsuki, Tamagaki, Machida, Toyoda & Watari
2. Verification of pion theory of nuclear forces ....Iwadare, Otsuki, Tamagaki & Watari
3. Construction of nuclear potential from pion theory....Machida & Toyoda
4. Definition of nuclear potential............................K. Nishijima
5. On the method of the theory of nuclear forces ....Taketani, Nakamura & Sasaki

No. 4. **(1957)**, $ 1.00
Relativistic Hydrodynamics of the Dirac Matter. I—*General theory*— ....**T. Takabayasi**

No. 5. **(1958)**, $ 1.00
Anomalous Magnetic Moment of the Nucleon...................**E. Yamada**
Pion Theory of the Anomalous Magnetic Moment of the Nucleon .... **H. Hasegawa**
Phenomenological Theory of Pion-Nucleon Reactions ....**S. Hayakawa, M. Kawaguchi** & **S. Minami**
A New Mathematical Formulation of Quantum Mechanics in the Framework of Wave-Packet Theory.—*Transformation theory, theory of scattering and functional differentiation*— ....**M. Namiki** & **R. Iino**

No. 6. **(1958)**, $ 1.00
Origin of Cosmic Rays................**S. Hayakawa, K. Ito** & **Y. Terashima**
Lateral and Angular Structure Functions of Electron Showers ....**K. Kamata** & **J. Nishimura**

No. 7. **(1959)**, $ 1.00
Theory of Scatterings and Reactions.........................**Y. Yamaguchi**
Conservation Laws in the Isotopic Spin Space and Their Violation by the Electromagnetic Interaction ....**M. Kato** & **G. Takeda**
On the Structure of Interactions...............................**H. Umezawa**

No. 8. (In printing), $ 1.00
Hypothetical Velocity Measurements of a Dirac Particle...........**Z. Koba**
Some Feasible Tests of Quantum Electrodynamics at Small Distances .... **S. C. Frautschi**
Nuclear Moments and Configuration Mixing ....**A. Arima, H. Horie** & **H. Noya**

PROGRESS OF THEORETICAL PHYSICS

CONTENTS

Progress of Theoretical Physics Vol. 20, No. 5, November 1958

New Interpretation of Hyperonic Charge and its Generalization to Leptons ......Takao OKABAYASHI..583

Bose-Einstein Lattice Gases equivalent to the Heisenberg Model of Ferro-, Antiferro, and Ferri-Magnetism ......Tohru MORITA..614

Nitrogen Induced Nuclear Reactions in Sodium......Ryuzo NAKASIMA..625

The Interaction between Two Normal Helium Atoms —*A Consistent Treatment*— ......T. HASINO and S. HUZINAGA..631

The First Forbidden β-Decay......T. KOTANI and M. ROSS..643

Dispersion Relations and Vertex Properties in Perturbation Theory..K. SYMANZIK..690

On the Tests of Gravitational Theories in terms of an Artificial Satellite ......H. NARIAI and Y. UENO..703

Equilibrium Properties of Classical Electron Gas in Uniform Positive Ion Distribution......Y. H. Ichikawa..715

Bose-Einstein Lattice Gas Theory of Ferromagnetism......Tohru MORITA..728

Notes on the Magnetic Mirror Effect ......Masatomo SATO..737

A General Theory of Magnetic Double Resonance ......Kazuhisa TOMITA..743

Letters to the Editor:

- On the Absorptive Range in the Pion-Nucleon Collision at High Energies......K. ISHIDA..774
- An Illustrative Example of the Nuclear Collective Motion..F. IWAMOTO..776
- Molecular Processes induced by μ^- Mesons in Hydrogen Bubble Chamber, I—*Transfer Process of μ^- Meson from Proton to Deuteron*—......M. SHIMIZU, Y. MIZUNO and T. IZUYAMA..777
- Absorption Effects in Antinucleon Phenomena, II ......Y. KAKUDO, T. KAMMURI and R. NAKASIMA..779
- The Meissner-Ochsenfeld Effect in the Bogoliubov Theory ...... J. M. Blatt and T. MATSUBARA..781

Errata: A Comment on Bardeen's Theory of Superconductivity ......S. NAKAJIMA and T. KASUYA..783

Contents of J. Phys. Soc. of Japan Vol. 13, No. 9......784

Price $ 1.25 per copy
$ 15.00 per year (postage inclusive)
Annual dues for foreign members (individual subscribers)
$ 12.00 (postage inclusive)
〃 for foreign members of the Physical Society of Japan
$ 10.00 (postage inclusive)

Application for members, subscriptions and orders for back numbers should be sent, directly or through book-dealers, to

The Publication Office
in
Yukawa Hall, Kyoto University, Kyoto, Japan

. . . .

ANNOUNCEMENT

REVISED Price List of Back Numbers (for subscribers abroad)

*Vols. 1–4	$ 6.40 each
*Vols. 5 & 6	$13.00 each (single copy: $2.50)
*Vols. 7 and succeeding ones	$ 8.00 each (single copy: $1.50)

Back number prices are effective for volumes other than last four (4) volumes (the current volume inclusive).

Thus, volumes 1 through 16 will be regarded as back numbers while volume 20 is being published.

The revised prices will be effective on and after August 1, 1958.

. . . .

JOURNAL OF THE PHYSICAL SOCIETY OF JAPAN, Vol. 14, No. 7, JULY, 1959

Elastic and Inelastic Scatterings of Protons from Ti, Cr, Ni, Zn, and O at 8 to 14 MeV

Chuin HU*, Ken KIKUCHI**, Shinsaku KOBAYASHI*** Kazuhisa
MATSUDA***, Yukio NAGAHARA****, Yukiyasu ODA*,
Naoyuki TAKANO*****, Minoru TAKEDA*
and Takashi YAMAZAKI*

Institute for Nuclear Study, University of Tokyo,
Tanashi-machi, Tokyo

(Received March 27, 1959)

The elastic and inelastic (leading to the first excited states of target nuclei) scatterings of protons by medium weight nuclei (Ti, Cr, Ni, and Zn) were studied by observing the dependence of their angular distributions on bombarding energies from 8 MeV to 14 MeV. The angular distributions of protons elastically scattered from oxygen were also measured in the same energy range. There are appreciable regularities in the elastic scatterings by medium weight nuclei as regards the dependence of their angular distributions on the bombarding energy and on the atomic number except in the case of the bombarding energy of 8 MeV. The elastic scatterings from oxygen show an anomalous behaviour at energies about 9 MeV. The angular distributions of protons inelastically scattered from medium weight nuclei can be fitted by the predictions of the direct interaction theory with Born approximation at about 14 MeV, but at the lower bombarding energies they seem not to do so, although they have the prominent forward peaks. The distorted Born approximation or the admixture of amplitudes due to compound process seems to be necessary to explain the angular distributions. In addition, it is found that the yield of the inelastic scattering varies with the bombarding energy appreciably.

For Ni target, the dependence of the yield of the inelastic scattering leading to the first excited state on the bombarding energy was measured in detail by changing the incident proton energy finely at intervals of about 50 KeV. We recognized that there were resonance-like behaviours with spacing of about several hundred KeV.

§ 1. Introduction

Recently rather many experimental investigations have been reported upon the angular distributions of elastic and inelastic (leaving the residual nuclei in discrete states) scatterings of intermediate energy protons by nuclei. The results on elastic scatterings are fitted by optical model analysis. While the results on inelastic scatterings, leaving the residual nuclei in low-lying states, show rather complicated aspects, and do not allow us to make any clear interpretation of the reaction mechanism. The data of most investigations† were, however, confined to some light nuclei and limited to narrow region of incident energy. In this situation, we consider, the accumulation of more experimental data is desirable for further developments.

The experiment reported here is a part of our studies along this line. The whole plan of our study includes the measurements of angular distributions of the elastic and the inelastic scatterings from almost all the even-even nuclei from oxygen to zinc (including

---

* Department of Physics, Osaka University.

** University of Minnesota, on leave from INS.

*** Institute for Nuclear Study, University of Tokyo.

**** Department of Physics, Yokohama National University.

***** Department of Physics, Kyushu University.

† The works of B. L. Cohen[1] on anomalous inelastic scattering cover a wide range of mass number or that of R. W. Peele[2] on Carbon covers a wide range of incident energy.

nitrogen) in their natural isotopic abundances. The energies of incident protons were varied between 8 MeV and 14 MeV. The present report forms the Part I of our studies and concerns with the experiments with the foil targets of medium weight nuclei; titanium, chromium, nickel and zinc, and also with the gas target of oxygen.

Among the present authors the members of Osaka University had performed systematic investigations³⁾ of inelastic scatterings of protons near 5.5 MeV and had an intension to extend their works using gas targets to the higher energies.

The experimental method and procedure of the present experiment are similar to those of the previous work reported by some of us.⁴⁾

§ 2. Experimental

The proton beam of the INS cyclotron⁵⁾ was brought to the scattering chamber of 100 cm in diameter through a pair of magnetic quadrupole lens, a sector magnet and a collimator. Then the proton beam was scattered by a target mounted at the centre of the scattering chamber and then detected by a NaI (Tl) scintillation crystal and a photomultiplier (RCA 6342), which were located on the turning table in the scattering chamber. Output pulses were amplified and feed to a Johnstone type 20-channel pulse height analyser. Details of the scattering system, beam integration, beam energy measurement and the scintillation counter have all been described in Reference 4. As the gas target, we used a gas chamber, which was made of a brass cylinder of 9 cm in a diameter and of 6 cm in height and had a window extending along the angle of more than 180°, including the beam entrance and the beam exit. This window was covered with a sheet of aluminium foil of 20 μ in thickness.

The thicknesses of the self-supporting foils used as the targets were; Ti (2.09 mg/cm²), Cr (0.37 mg/cm²), Ni (1.02 mg/cm²) and Zn (4.48 mg/cm²), respectively. As the oxygen target we used the gas of 1/2 atom. When excitation curves were measured, the beam energy was varied at intervals of 50 KeV by changing the magnetic field and the frequency of the cyclotron. The energy spread of the incident beam was not determined precisely but it seemed to be less than 50 KeV. Although technique used for continuous changing of the energy was rather preliminary, the agreement between the results of two independent runs were good.

The typical energy spectra of the emitted protons are shown in Fig. 1. Fig. 1 displays also that most parts of the errors in differential cross sections, especially at forward angles, are caused by background subtraction.

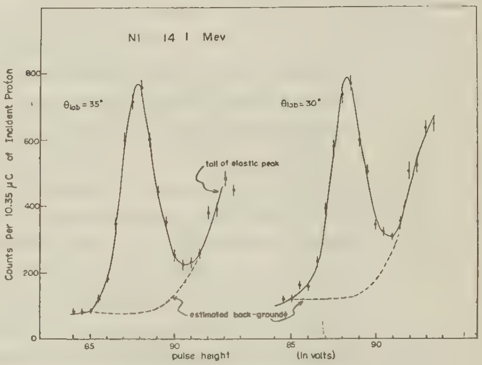

Fig. 1. Examples of pulse height spectrum of inelastic peak at for ward angles.

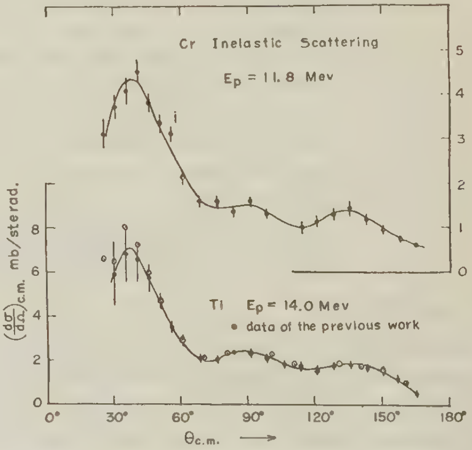

Fig. 2. Differential cross sections with estimated errors (1).

Examples of differential cross sections of inelastic scatterings containing errors due to counting statistics and background subtraction are shown in Figs. 2 to 5. At the bombarding energy of 14 MeV, the figures also include the results of Reference 4. The agreement between both measurements is fairly good.

The errors of the absolute values of cross sections come mainly from the uncertainty in target thickness and were less than 10% for foil targets and less than 5% for gas targets. The relative errors of the cross sections of elastic scattering may be 5% or less. The total cross sections of inelastic scattering, obtained by numerical integration of angular distribution curves, will have the errors less than 20%.

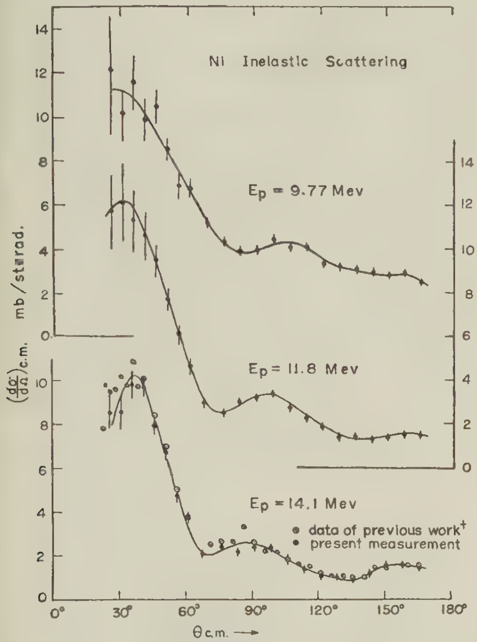

Fig. 3. Differential cross sections with estimated errors (2).

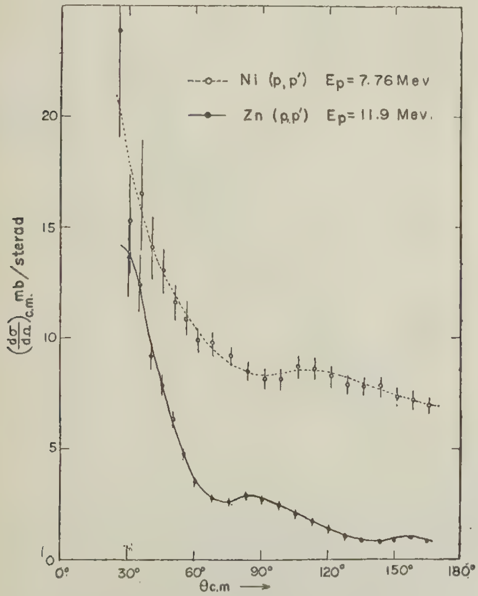

Fig. 4. Differential cross sections with estimated errors (3).

The elastic scattering from oxygen was measured especially for the purpose of subtraction of background due to oxygen contamination in the cases of chromium and magnesium.

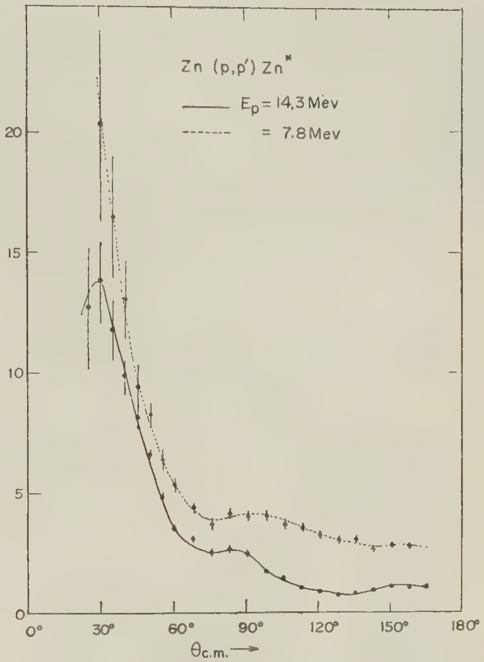

Fig. 5. Differedtial cross sections with estimated errors (4).

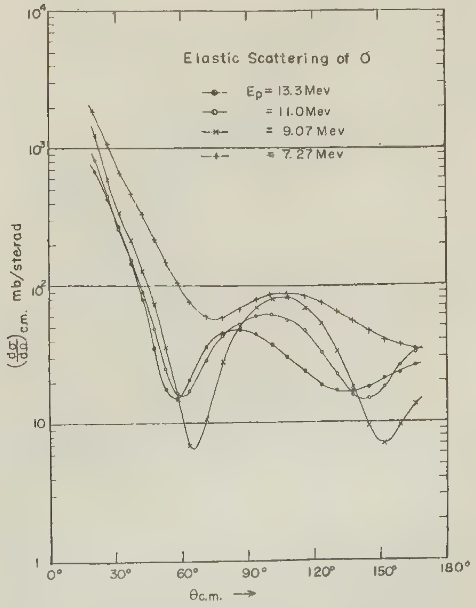

Fig. 6. Angular distributions of elastic scattering on Oxgen.

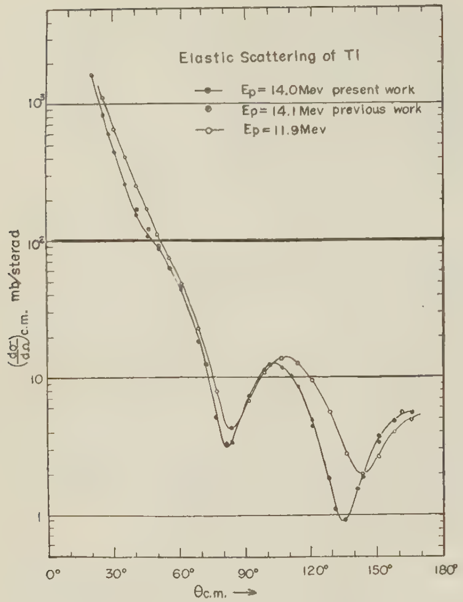

Fig. 7. Angular distributions of elastic scattering on Titanium.

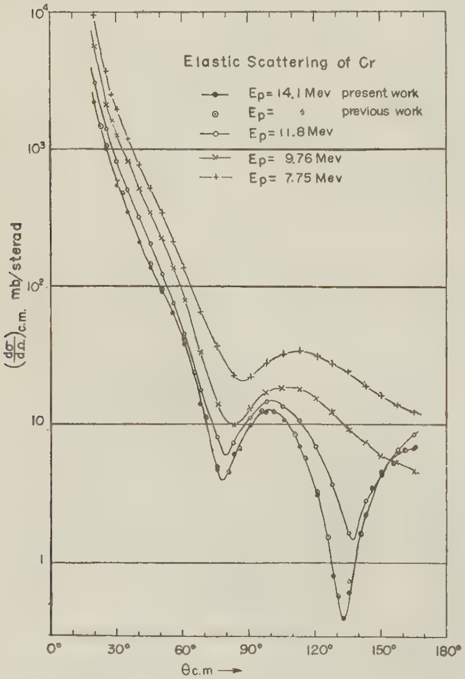

Fig. 8. Angular distributions of elastic scattering on Chromium.

§ 3. Results and Discussion

A. *Elastic scattering*

The absolute differential cross sections of elastic scatterings were measured at energies of 14, 12, 10, and 8 MeV for oxygen; 14, and

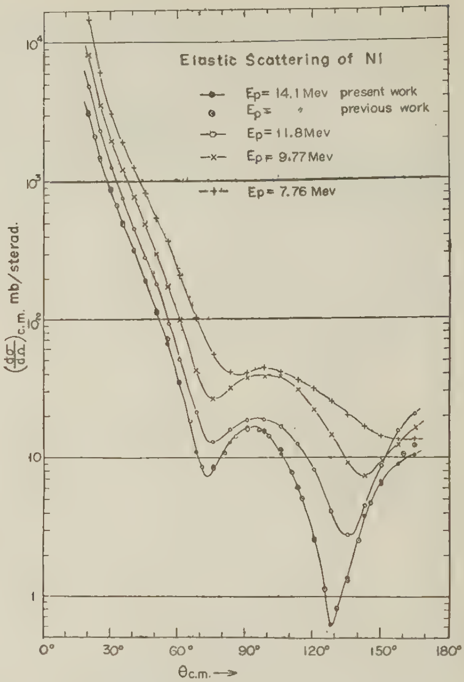

Fig. 9. Angular distributions of elastic scattering on Nickel.

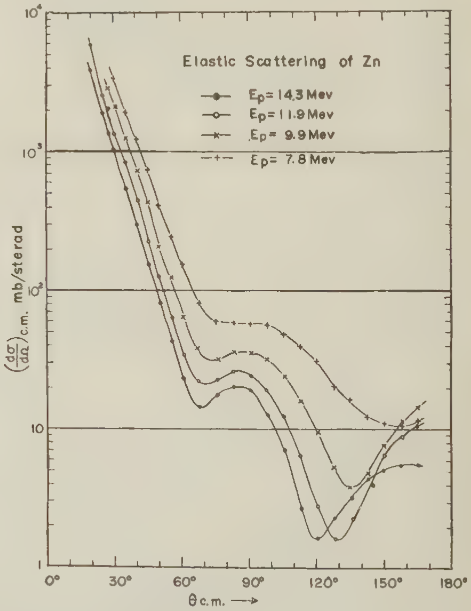

Fig. 10. Angular distributions of elastic scattering on Zinc.

12 MeV for Ti; 14, 12, 10, and 8 MeV for Cr, Ni and Zn. These results are shown in Figs. 6 to 10*. They show that, except the case of

---

* The numerical tables of the differential cross sections of elastic and inelastic scatterings will be reported elsewhere.

oxygen, there exist smooth variations with the bombarding energy and with the atomic number. The latter dependence is shown in Fig. 11. Fig. 12 shows the plots of the positions of the first maxima as a function of $A^{-1/3}$. This figure shows that there exist marked regularities at energies more than 10 MeV, but at 8 MeV the behaviour is somewhat different. Simple calculation shows that there is not the relation that $kR\theta_{\min}$ is constant. For the lighter nucleus; Ti, we recognize a hump at forward angles but it disappears as the atomic number is increased or the bombarding energy is decreased. This hump becomes clear for argon*.

In the case of nuclei from argon* to zinc, the minima in angular distributions are smeared out as the incident energy decreases. But in the case of oxygen, the minima become sharper at about 9 MeV. Such a marked energy dependence in elastic scatterings does not appear in the case of nitrogen** but similar effects occur in the case of neon** from 10 MeV to 14 MeV. This behaviour in oxygen or in neon seems to be anomalous. The angular distribution at 9.07 MeV in the case of oxygen resembles fairly to that obtained by W. E. Burnham et al.[6] at $E_{\text{lab}}=9.5$ MeV. This shows that the above-mentioned anomaly is not confined to narrow region of incident energy. All through this report, we express energies in the centre of mass system.

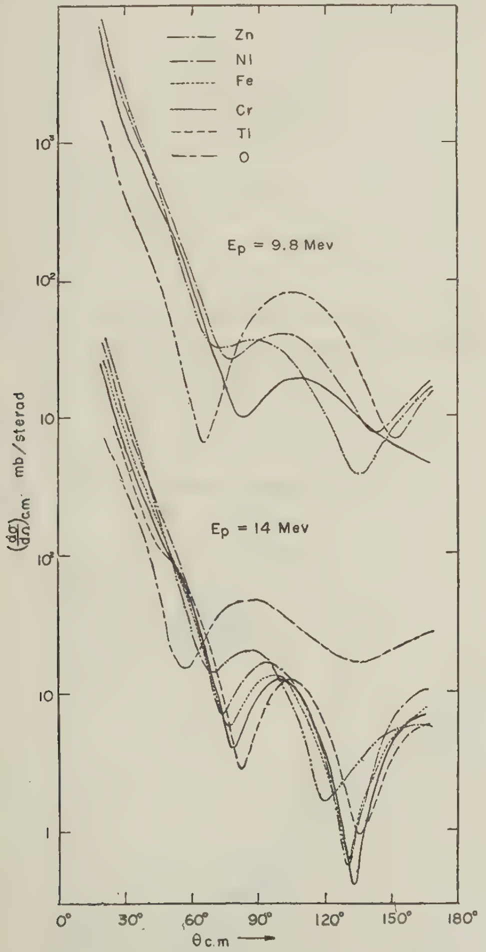

Fig. 11. Comparison of elastic scattering.

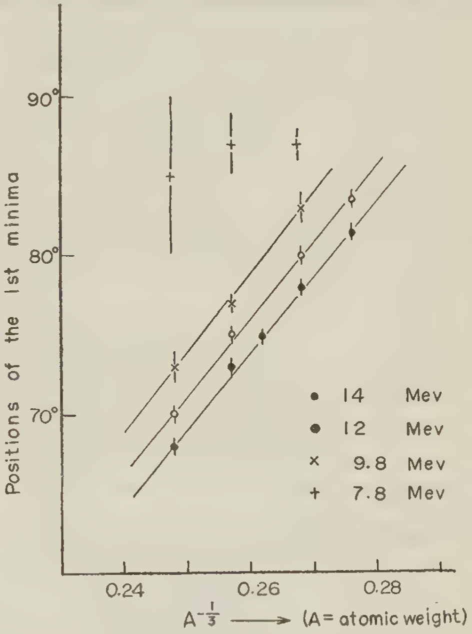

Fig. 12. Regularities in the elastic scattering.

B. *Inelastic scattering*

The angular distributions of inelastic scatterings from Ti, Cr, Ni, and Zn were measured in the same energy region as the elastic scattering, and are shown in Figs. 13 to 16. The curves in these figures are drawn smoothly among experimental points as shown in Figs. 2 to 5. The levels which take part in the measured cross sections are also shown in these figures. The results are not so regular as was in the case of elastic scattering. This circumstance may indicates that the inelastic scattering concerns with details of the structure of nucleus.

We may make some general discussions on the inelastic scatterings of proton, observed in this experiments, leading to the first excited states of even-even nuclei. There are following features in these cases. First, we have a common spin-parity relation between the levels, even though natural elements are used as targets and the first levels of individual isotopes are admixed. Secondly, we may assume the energy spread of the beam cover so many levels of the compound nuclei in these medium weight nuclei and at our bombarding energies.

---

* The results for lighter nuclei will be published in another report.

As reported in reference 4, the angular distributions can be fitted well by the simple theory of the surface-direct reaction based on the Born approximation at about 14 MeV.

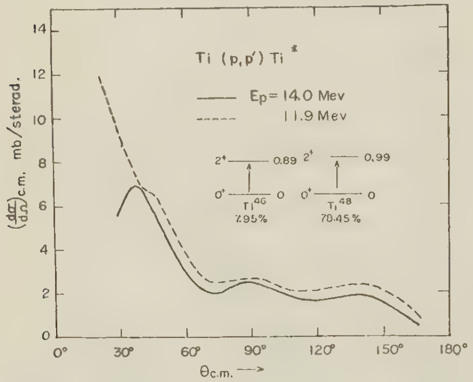

Fig. 13. Angular distributions of inelastic scattering (1st excited state) on Titanium.

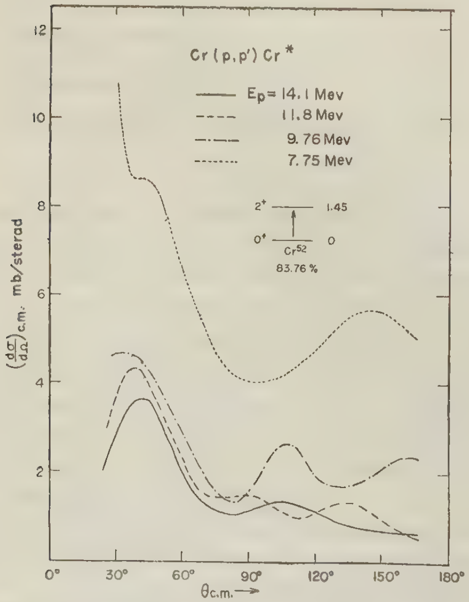

Fig. 14. Angular distributions of inelastic scattering (1st excited state) on Chromium.

However, when the energy is decreased, the first maximum seems to shift to the smalle angle or to disappear, although the prominen formard peaking is preserved all over the energy range.

At present, however, a decisive conclusio on the angular distribution at very small angles might involve some vulnerabilities. W

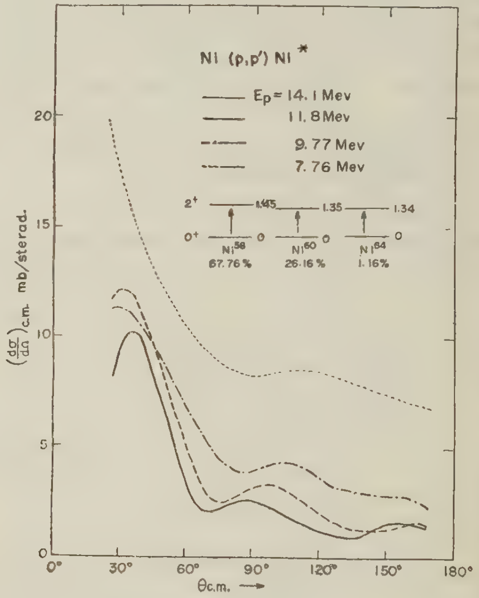

Fig. 15. Angular distributions of inelastic scattering (1st excited state) on Nickel.

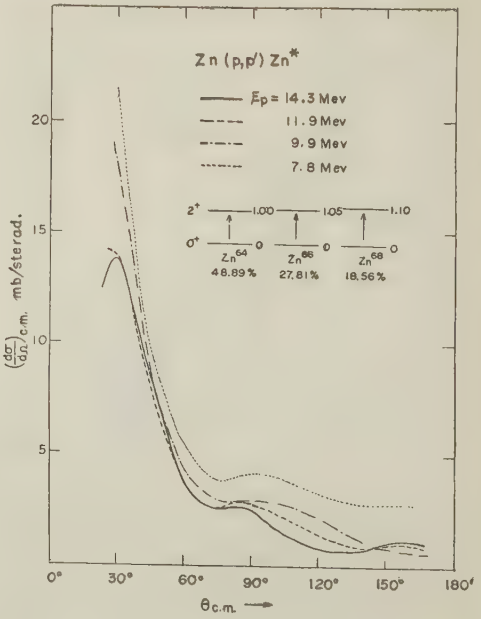

Fig. 16. Angular distributions of inelastic scattering (1st excited statate) on Zinc.

expect further studies with a magnetic reaction particle analyser.

The total cross sections obtained by numerical integration of angular distribution curves are shown in Fig. 17. In performing the integration, the cross sections at forward angles were estimated by extrapolation. The total cross section increases as the incident energy decreases. In the cases of nickel and chromium, this increase becomes steeper from a certain energy.

For nickel, the excitation curves for elastic and for inelastic scattering at laboratory angles of 45° and 90° were measured near 9 MeV and 12 MeV. The bombarding energies were changed at intervals of about 50 KeV. The results shown in Figs. 18 to 19 reveal a very interesting phenomena. The general tendency of forward peaking is preserved all through the energy range. Near 9 MeV, however, $(d\sigma/d\Omega)_{45^\circ}/(d\sigma/d\Omega)_{90^\circ}$ varies violently with bombarding energy; e.g. the angular distribution changes remarkably with small variation of the incident energy. The percentage change at 45° is much larger than that at 90°. In addition, there seems to be no correlation between peaks of inelastic scattering and those of elastic scattering. The resonance at 9.3 MeV has a full width at half maximum of 150 KeV and the spacing of the peaks is several hundred KeV.

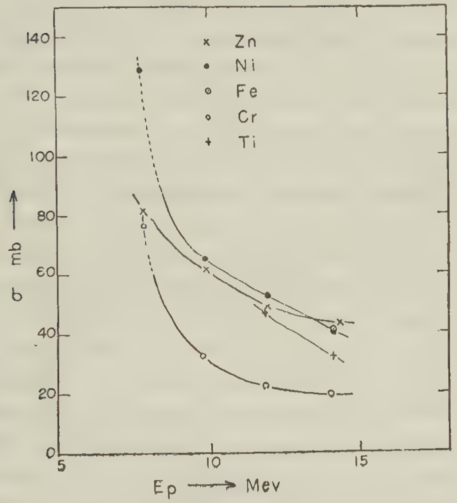

Fig. 17. Total cross sections of inelastic scattering (1st excited state).

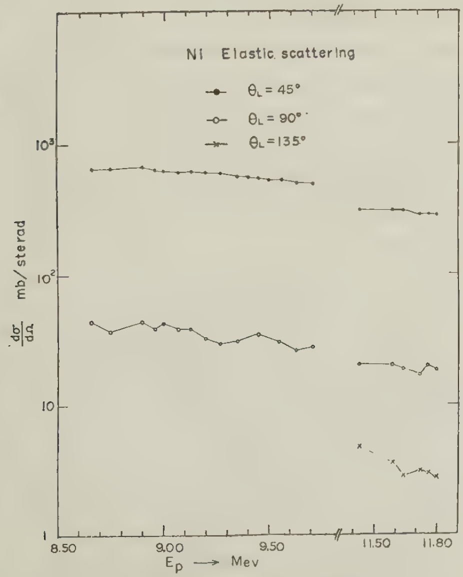

Fig. 18. Excitation curve of elastic scattering on Ni.

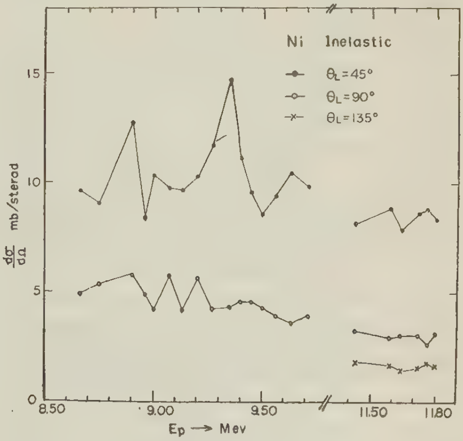

Fig. 19. Excitation curve of inelastic scattering (1st excited state) on Ni.

Some of discussions on the experimental results will be given as follows:

a) The behaviour of angular distributions with decreasing energy may be explained with the distorted Borm approximation. The mean free path of nucleon in nuclear matter is reduced as the incident energy is increased, and so, at higher energy ($E_p>10$ MeV), the direct interaction occurs mainly at the surface of the target nucleus and the nucleon which enter into the nucleus forms a compound nucleus and contributes little to the scattering to the low-lying state as the excitation energy is high and many channels are open. Thus these scatterings could fit well the simple theory of surface interaction with the Born approximation. At the lower energy ($E_p <$ 10 MeV), the above assumption will be violated and the wave will be more distorted. Moreover, as pointed out in c), the admixtures of the compound nucleus formation or some effects like it, may not be neglected as the number of open channel decreases.

b) Sudden increase of total cross sections with decreasing of the incident energy cannot be explained by the simple Born approximation, but it may be conceivable$^{7)}$ in the distorted wave approximation. Alternatively, this may be explained by the compound nucleus formation and the decrease of the number of open channels. It should be noted that such a sudden increase is chiefly due to the increase of nearly isotropic parts of the angular distribution.

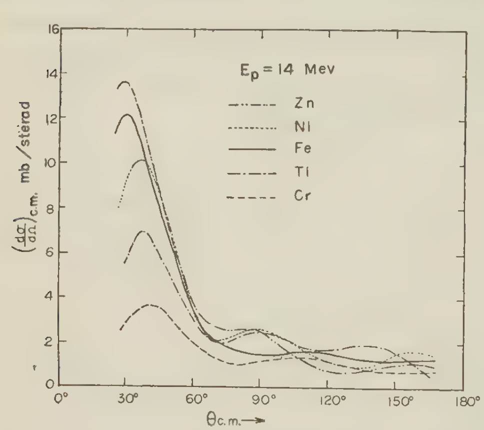

Fig. 20. Comparison of inelastic scattering at $E_p = 14$ Mev.

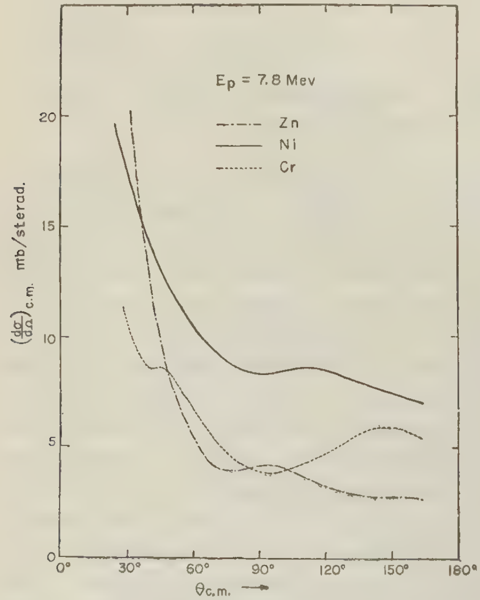

Fig. 21. Comparison of inelastic scattering at 7.8 Mev.

c) Total cross sections and, in particular, the yields of forward peak which are perhaps due to the direct interaction are very different among neighbouring elements. The yield from chromium is very small. The difference between the yield from Cr^{52} (which has the magic neutron number) and that from Ni (which has the magic proton number) suggests some information about the reaction mechanism. (cf. Figs. 20, 21).

d) We did not expect such a variation of differential cross sections as occur in the excitation curves of Ni in these energy range and in such a medium weight nuclei*. These resonance-behaviours are very similar to that have been found in the (d, p) reactions from light nuclei$^{8)}$ (lighter than Ca^{40}). The excitation energies of compound nuclei formed by proton are generally much lower than that formed by deuteron when the bombarding energies are same. In (d, p) reactions, these phenomena are in general regarded as the admixture of the amplitude due to compound process or the resonance interaction between the emitted proton and the residual nucleus. It should be noted that the excitation energy of the Ni$+p$ system is low as compared with that of neighbouring elements. K. Izumo$^{9)}$ has proposed an explanation for such resonances with large spacings. His idea bases on some kind of partial heating of the nucleus. The similar resonance phenomena with large spacings have also been found in our measurements in the case of the inelastic scattering from lighter nuclei, which will be reported in our paper to be published. More exhaustive studies may be necessary to clarity these phenomena.

Acknowledgement

The author wish to thank Professor I. Nonaka for his constant encouragements, and to Professor S. Yoshida and Dr. M. Sano for their suggestions about theoretical interpretation.

They also express their thanks to Mr. H. Ogawa and Mr. T. Miyazawa for their excellent operation of the cyclotron.

---

* As regards the level density of Cu^{59} at the lower excitation energies, see reference 10).

References

1) B. L. Cohen: Phys. Rev. **105** (1957) 1959. B. L. Cohen and S. W. Mosko: ibid. **106** (1957) 995. B. L. Cohen and A. G. Rubin: ibid. **111** (1958) 1968.
2) R. W. Peelle: Phys. Rev. **105** (1957) 1311.
3) Y. Oda, M. Takeda, C. Hu and S. Kato: Phys. Soc. Japan **14** (1959) 396; **14** (1959) 549. M. Kondo and T. Yamazaki: ibid. **13** (1958) 771. S. Yamabe: ibid. **13** (1958) 237. S. Yamabe, M. Kondo, T. Yamazaki and T. Toi: ibid. **13** (1958) 777.
4) K. Kikuchi, S. Kobayashi and K. Matsuda: J. Phys. Soc. Japan **14** (1959) 121.
5) S. Kikuchi et al.: to be published.
6) W. E. Burcham, W. M. Gibson, R. Muller and J. Rotblat: Phys. Rev. **92** (1953) 1266.
7) C. A. Levinson and M. K. Banerjee: Annals of Physics **3** (1958) 670.
8) T. F. Stratton et al.: Phys. Rev. **98** (1955) 629. T. W. Bonner et al.: ibid. **101** (1956) 209. M. T. McEllistrem et al.: Phys. Rev. **104** (1957) 1008. I. A. Nemilov and V. F. Litvin: Soviet Physics **4** (1957) 606. S. A. Cox and R. M. Williamson: Phys. Rev. **105** (1957) 1799. H. A. Hill and J. M. Blair: ibid. **111** (1958) 1142. M. T. McEllistrem: ibid. **111** (1958) 596.
9) K. Izumo: Progr. Theor. Phys. **21** (1959) 468.
10) J. R. Schiffer, M. S. Moore and C. M. Class: Phys. Rev. **104** (1956) 1661.

JOURNAL OF THE PHYSICAL SOCIETY OF JAPAN, Vol. 14, No. 7, JULY, 1959

$C^{12}(n,n')3\alpha$ Reaction induced by 14.8 MeV Neutrons

By Yoshikazu TSUNEOKA

Department of Physics, Faculty of Science,
University of Kyoto, Kyoto

(Received September 22, 1958)

The probable mechanism of the $C^{12}(n, n')3\alpha$ reaction when induced by d-T neutrons has been deduced from a study of 403 stars in nuclear emulsions. The angular distribution of the inelastically scattered neutrons show a forward peak, and it is concluded that the reaction occurred mainly through the compound nucleus and that the asymmetry at about 90° is caused by the interference of several levels. The possible decay mode of the C^{12} nucleus was also investigated, and an approximate branching ratio was obtained, assuming that the decay mode via Be^9 was negligible. Then, comparing the angular distributions of the inelastically scattered neutrons which correspond to the different decay modes, Sacks's model for the direct break-up of C^{13*} was found to be in disagreement with the present experimental results.

§ 1. Introduction

Chadwick, Feather and Davies[1] discovered the neutron-induced break-up of C^{12} in a methane filled cloud chamber exposed to Po-Be neutrons. Green and Gibson[2] studied this reaction using d-D neutrons, d-Li neutrons, d-B^{10} neutrons, d-B^{11} neutrons and d-N neutrons, and established that these reactions are $C^{12}+n\rightarrow 3\alpha+n-7.34$ MeV and $N^{14}+n\rightarrow Li^7+2\alpha-8.8$ MeV. These events form " stars " apparently radiating from the points of disintegration, because all the processes under investigation occur within a very short interval. This fact introduces certain difficulties into the task of identifying intermediate stages of the reactions.

The cross section of this reaction was measured by Green and Gibson using d-Li neutrons ranging from 108. to 14.5 MeV, and by Kellog[3] using 90 MeV neutrons, and by Frye *et al.*[4] using d-T neutrons ranging from 12 to 20 MeV. The values of the cross section measured by Frye *et al.* are 78 mb at 12.6 MeV, 265 mb at 16.9 MeV and 223 mb at 20.1 MeV. These values of the cross section were calculated semi-empirically by Sacks[5] and agree well for low energy reactions.

The angular distribution of the inelastically scattered neutrons was measured by Green and Gibson for the first time, and found to be isotropic within the limits of experimental error. O'Neill[6)] was able to show that the angular distribution for all inelastically scattered neutrons was isotropic within about 15% using the time-of-flight technique. And Frye *et al.* observed that all scattered neutrons which made "carbon stars" in nuclear emulsions have isotropic angular distributions when the energies of the incident neutrons were mixed from 12.3 to 13.5 MeV, from 14.1 to 16.9 MeV and from 17.6 to 20.1 MeV.

The decaying mode of this reaction has also been investigated by many authors. Perkin[7)] analyzed 700 stars in nuclear emulsions exposed to *d*-Li neutrons with a maximum energy of 24 MeV, and found indications for Be^8 levels at 2.65, 4.0, 7.25 and 9.8 MeV. He found that the 485 stars correspond to the $C^{12}(n, n')3\alpha$ reaction, but it seems that the carbon stars which involve the ground state of Be^8 were missed in scanning. And the angular distribution of alpha particles was found to be isotropic in the center-of-mass system. Jackson and Wanklyne[8)] studied these events using the cloud chamber and *p*-Be neutrons ranging from 8 to 40 MeV. They found that the evidence based on the energy distribution of the emerging particles shows that the reaction proceeds to an appreciable extent by the formation of a compound nucleus at neutron energies less than 20 MeV, while at higher energies the mechanism is that of excitation of C^{12} by inelastic collision. And they found that in 40% of the events, Be^8 occurs in its ground state, and that in less than 25% of the events involving the 9.6 MeV level of C^{12} decay occurs directly into there alpha particles. Frye *et al.* also found evidence for C^{12} levels at 9.6, 7.7 MeV and for Be^8 levels at 0, 3 MeV. And the processes via Be^9 were estimated to be less than 25% of the events. But the center-of-mass energy spectrum of the scattered neutrons may be fitted by a four-particle phase space distribution.

In the present work, using nuclear emulsions and *d*-T neutrons, the angular distributions of the inelastically scattered neutrons are studied in more detail, and probable mechanisms for neutron interaction and break-up of the carbon nucleus are deduced. Sacks's model for the direct break-up of C^{13*} is also compared with the present experimental results.

§2. Experimental Procedure

The experimental arrangement is shown schematically in Fig. 1. 1″×1(1/2)″ Ilford C2 nuclear emulsions (200 μ) were irradiated by 14.8 MeV neutrons which were produced by the *d*-T reaction, employing magnetically analyzed molecular deuterium of 220 keV from a Cockcroft-Walton machine. The tritium target consisted of 0.5 curies absorbed in a 0.2 mg/cm² zirconium foil and was bombarded with a steady beam of about 100 μA. The distance from the tritium target to the center of the emulsions was 4″ and the direction of the incident neutrons lies in the *y*-*z* plane, and the total flux of neutrons on the emulsions was 9.42×10^8 neutrons/cm².

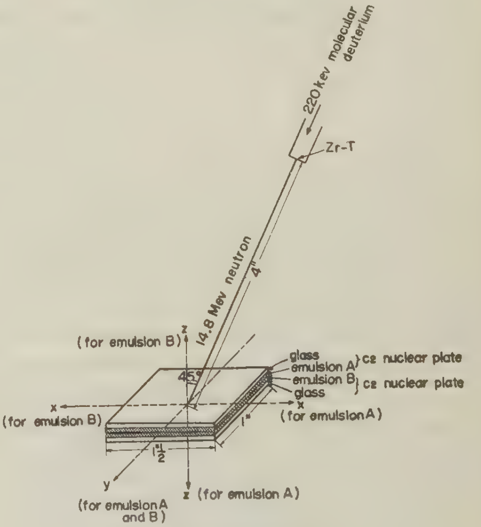

Fig. 1. Experimental Arrangement. The direction of the incident neutrons lies in the $y-z$ plane.

An incident angle of 45° was chosen to minimize the error arising from the variation of shrinkage factor from day to day. The error is averaged over all angles in this case, but the disadvantage of this angle are that more complicated calculations are needed, and that the half width of the calculated curve in Fig. 4 becomes broader owing to a larger error introduced in measuring the depth of tracks. But the advantage of obtaining more accurate angular distributions of inelastically scattered neutrons is essential for the present experimental aims.

Two emulsions A and B were placed face to face as shown in Fig. 1. This setting and the choice of the incident angle has other advantages, *i.e.*, the effects of the neutron attenuation in the glass and emulsion becomes nearly the same for the whole observing volume.

The emulsions were processed by the temperature method[9] using a low *p*H (6.6) amidol developer, and during the hot stage the conditions of 15 minutes and 18°C were chosen as suitable to reduce background fogs and recoil proton tracks.

The processed emulsions were scanned with the " Tiyoda LCM bi " microscope and the " Nippon Kogaku KUG bi " microscope at a magnification of 1350 and 1500 respectively. In the microscopic field, the x, y, z coordinates relative to the vertex of each carbon star were chosen in a right hand system, and the z axis had the direction from the interior region of the emulsion toward the surface. And a nuclear plate was attached to the stage of the microscope so that the direction of the incident neutrons lies in the y-z plane. The x, y, z coordinates of the end point of alpha prongs relative to the vertex of the carbon star were measured in the microscopic field with a eye-piece graticle and a scale of a fine focus screw. As the diameter of the microscopic field is about 100 μ in both types of microscopes, the measurements could be made near the center of the field where the curvature of the field can be neglected. Each depth measurement was subject to about $\pm 0.5\ \mu$ standard deviation. Errors in horizontal projections were about $\pm 0.3\ \mu$.

To determine the shrinkage factor, the Po^{210}-α source was placed on a small portion of emulsion surface, and by measuring the horizontal and vertical components of the length of Po^{210}-α tracks the shrinkage factor was determined graphically[10] to be 2.2. The range-energy relation for the C2 emulsion was obtained from the range-energy relation of Rotblat[11] calibrated for the humidity of laboratory conditions according to the measured range of Po^{210}-α tracks. More discussion

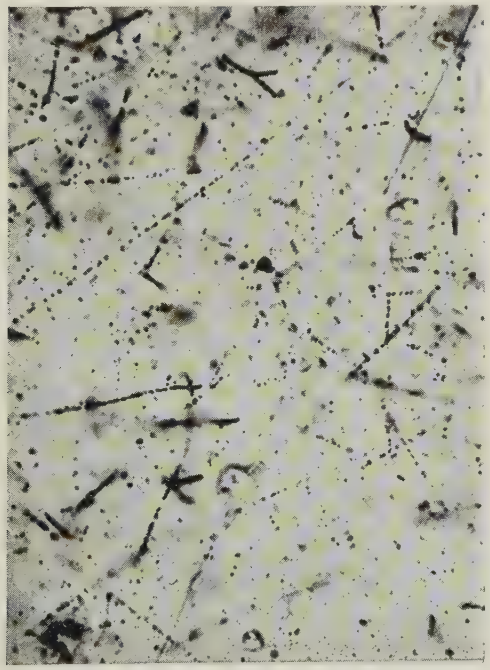

Fig. 2. Microphotograph of carbon star and recoil protons and alpha particles from (n, α) reaction of C, N, O.

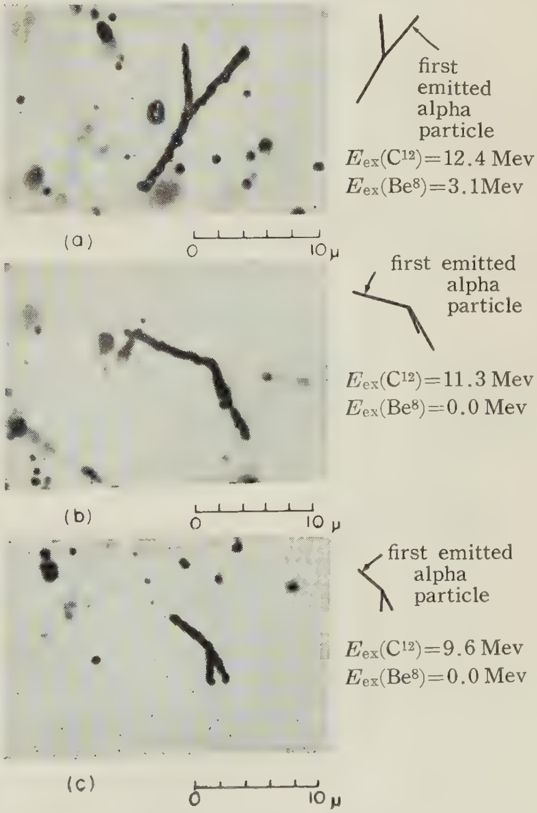
first emitted alpha particle
$E_{ex}(C^{12})=12.4$ Mev
$E_{ex}(Be^8)=3.1$Mev
(a)
0
10 μ
first emitted alpha particle
$E_{ex}(C^{12})=11.3$ Mev
$E_{ex}(Be^8)=0.0$ Mev
(b)
0
10 μ
first emitted alpha particle
$E_{ex}(C^{12})=9.6$ Mev
$E_{ex}(Be^8)=0.0$ Mev
(c)
0
10 μ

Fig. 3. Microphotographs of typical carbon stars.
(a): cascade break-up that involves the first excited state of Be^8.
(b), (c): cascade break-up that involves the ground state of Be^8.

on the measurement of shrinkage has been reported in another paper.[12]

Data were obtained in two emulsions A and B, and analyzed separately. After it was established that the two sets displayed the same general features, the data were combined. This confirms that there was not a systematic error arising from the measurement of depth and that the method of calculations was not in error. (The depth was measured using the scale of a fine focus screw with attention given to the backrash of gears. But there may exist a personal error and an error arising from the fact that the end point of the track near the surface of the emulsion appears sharp compared to the end point which lies deep within the emulsion.)

Fig. 2 shows the typical microscopic field. The three pronged star is the carbon star, and the single tracks of short range and large grain density are produced by alpha particles emitted probably by the (n, α) reaction of carbon, nitrogen or oxygen. And long tracks with low grain density are produced by the neutron-recoiled protons. Fig. 3 shows the typical carbon stars which are considered (a): cascade break-up that involves the first excited state of Be^8, (b) (c): cascade break-up that involves the ground state of Be^8. The analysis described in § 3 ($E_{ij}^*-E_k$ graph) must be used to determine the decay mode.

§ 3. Star Calculations and Results

As the direction of the incident neutron is known, the energy of the incident neutrons as well as the energy and direction of the inelastically scattered neutrons can be calculated from the measured energy and momentum of the three alpha particles as follows.

Using the conservation law of energy and momentum, we get

$$\left.\begin{aligned} E_n+Q=E_{n'}+\sum E_i \\ X_n=X_{n'}+\sum X_i\,, \quad Y_n=Y_{n'}+\sum Y_i\,, \quad Z_n=Z_{n'}+\sum Z_i \end{aligned}\right\} \tag{1}$$

where E_i $(i=1, 2, 3)$ is the energy of the ith alpha particles in the laboratory system, E_n and $E_{n'}$ are the energy of the incident and the inelastically sattered neutrons, respectively, $Q(=-7.28\,\mathrm{MeV})$ is the Q value for the break-up of C^{12} into three alpha particles, and X_n, Y_n, Z_n; $X_{n'}, Y_{n'}, Z_{n'}$; X_i, Y_i, Z_i $(i=1, 2, 3)$ are the x, y, z component of the momentum of the incident and the inelastically scattered neutrons and the ith alpha particles, respectively. Momentum is taken as $(mE)^{1/2}$, with m in atomic mass units and E in MeV.

Since the incident angle of the neutron is 45° as in Fig. 1,

$$X_n=0\,, \qquad Y_n=\pm Z_n\,, \tag{2}$$

where the double sign is plus for emulsion A and minus for emulsion B, and the energy of the neutrons can be expressed in momentum by,

$$\left.\begin{aligned} E_n=X_n^2+Y_n^2+Z_n^2\,, \\ E_{n'}=X_{n'}^2+Y_{n'}^2+Z_{n'}^2. \end{aligned}\right\} \tag{3}$$

From these formulae (1), (2) and (3), we get

$$E_n=\frac{1}{2}\left[\frac{(\Sigma E_i)-Q+(\Sigma X_i)^2+(\Sigma Y_i)^2+(\Sigma Z_i)^2}{(\Sigma Y_i)\pm(\Sigma Z_i)}\right]^2, \tag{4}$$

where the double sign is the same as in formula (2). Fig. 4 shows the results thus calculated

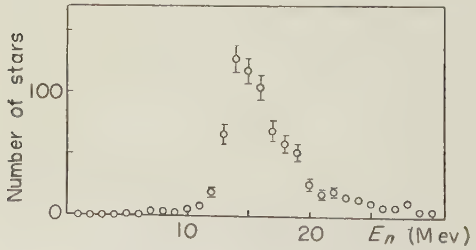

Fig. 4. Calculated energy of the incident neutrons.

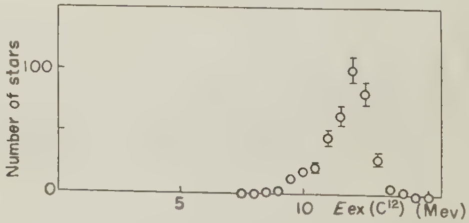

Fig. 5. Excitation energy of C^{12}.

for 889 stars. Some contribution from the $N^{14}(n, 2\alpha)Li^7$ reaction appeared on the higher energy side. Then, 403 stars that gave calculated values in the region of $12.8 \leq E_n < 16.8$ MeV were selected as $C^{12}(n, n')3\alpha$ stars produced by 14.8 MeV monochromatic neutrons.

The excitation energies of C^{12} for these 403 stars were calculated by the following formula, and the results are shown in Fig. 5.

$$E_{ex}(C^{12}) = (\Sigma E_i) - Q - \frac{1}{12}[(\Sigma X_i)^2 + (\Sigma Y_i)^2 + (\Sigma Z_i)^2] \tag{5}$$

where $E_{ex}(C^{12})$ is the excitation energy of C^{12} and the other notations are the same as in the preceding formulae. Figs. 6 and 7 show the energy distribution of the inelastically scattered neutrons and the three alpha particles which made a carbon star in the laboratory system.

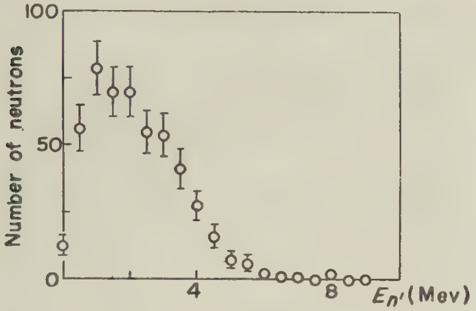

Fig. 6. Energy distribution of the inelastically scattered neutrons in the laboratory system.

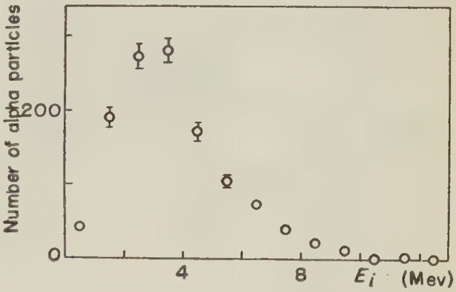

Fig. 7. Energy distribution of the alpha particles in the laboratory system.

The energy $E_{n'}$ and the angle θ_0 of the scattered neutrons in the laboratory system can be obtained by the following formulae, where the double sign is plus for emulsion A and minus for emulsion B:

$$E_{n'} = (\Sigma X_i)^2 + \left[\left(\frac{E_n}{2}\right)^{1/2} - \Sigma Y_i\right]^2 + \left[\pm\left(\frac{E_n}{2}\right)^{1/2} - \Sigma Z_i\right]^2 \tag{6}$$

$$\cos\theta_0 = (2E_{n'})^{-1/2}\left[\left\{\left(\frac{E_n}{2}\right)^{1/2} - \Sigma Y_i\right\} \pm \left\{\pm\left(\frac{E_n}{2}\right)^{1/2} - \Sigma Z_i\right\}\right] \tag{7}$$

To get the angular distribution of the inelastically scattered neutrons in the C^{13} center-of-mass system, Figs. 8 and 9 were drawn using the following formulae (8) and (9) respectively*:

$$\gamma \equiv \frac{v''}{v'} = [1 + 11.42E_{n'} - 6.76(E_{n'})^{1/2}\cos\theta_0]^{-1/2}, \tag{8}$$

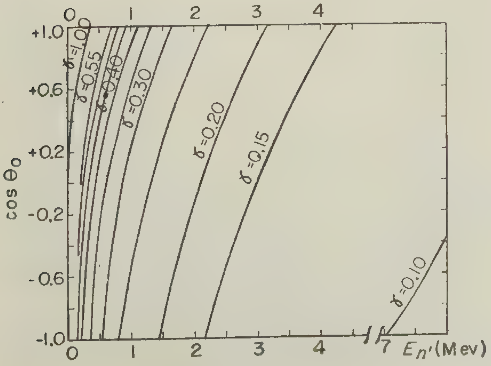

Fig. 8. A plot $E_{n'}$ vs. $\cos\theta_0$.

---

* From kinematical considerations,

$$\gamma = \left[\frac{m_n m_{n'} E_n}{m_{C^{12}}(m_{C^{12}} + m_{n'})Q' + m_{C^{12}}(m_{C^{12}} + m_{n'} - m_n)E_n}\right]^{1/2}$$
$$= \left(\frac{E_n}{12 \cdot 13Q' + 12^2 E_n}\right)^{1/2} \tag{10}$$

and $Q' \equiv Q - E_{ex}(C^{12})$

$$= E_{n'}\left(1 + \frac{m_n}{m_{C^{12}}}\right) - E_n\left(1 - \frac{m_n}{m_{C^{12}}}\right)$$
$$- \frac{2}{m_{C^{12}}}(m_n m_{n'} E_n E_{n'})^{1/2}\cos\theta_0$$
$$= \frac{13}{12}E_{n'} - \frac{11}{12}E_n - \frac{1}{6}(E_n E_{n'})^{1/2}\cos\theta_0, \tag{11}$$

where Q' is the experimental Q value13) and $m_n, m_{n'}$ and $m_{C^{12}}$ are the mass of the incident neutron, the inelastically scattered neutron and the C^{12} nucleus, respectively. Then, substituting the formula (11) into the formula (10) we can obtain the formula (8) using $E_n = 14.8$ Mev.

$$\tan\theta_0 = \frac{\sin\theta}{\gamma + \cos\theta}\,, \tag{9}$$

where θ is the angle, v' and v'' are the velocities of the incident neutron and the C^{12} nucleus respectively, in the C^{13} center-of-mass system.

We can determine γ from $E_{n'}$ and $\cos\theta_0$ using Fig. 8, and θ from γ and $\cos\theta_0$ using Fig. 9. These calculations were made for each star individually and we got the angular distribution of the inelastically scattered neutrons in the C^{13} center-of-mass system, which is shown in Fig. 10.

Then, we divided the scattered neutrons into three regions according to their energy.

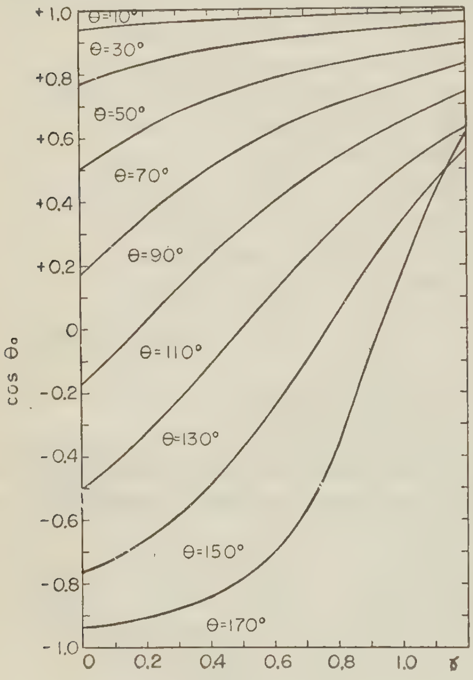

Fig. 9. A plot γ vs. $\cos\theta_0$.

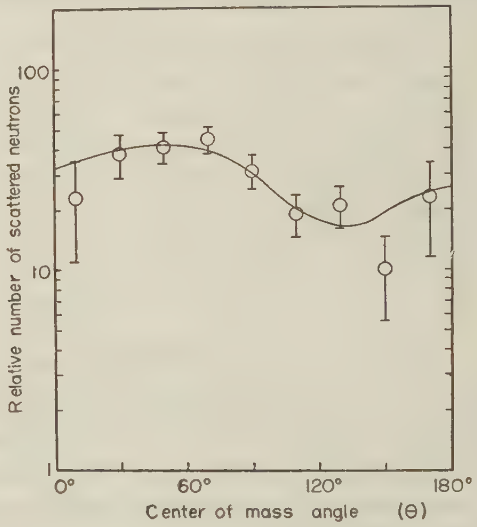

Fig. 11. Angular distribution of the inelastically scattered neutrons (higher energy part)

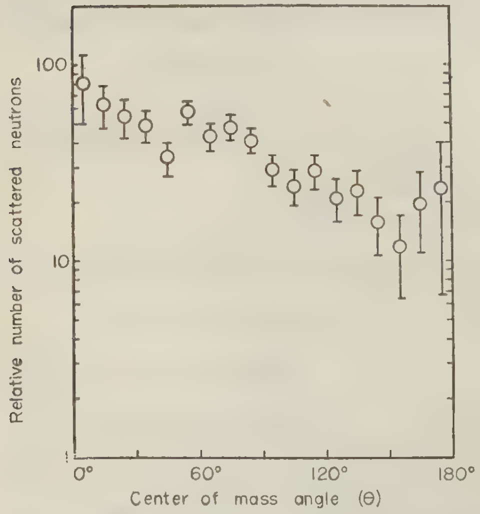

Fig. 10. Angular distribution of the inelastically scattered neutrons.

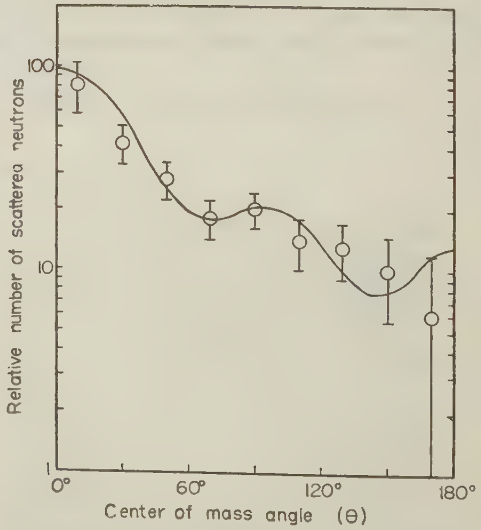

Fig. 12. Angular distribution of the inelastically scattered neutrons (lower energy part).

Figs. 11 and 12 show the angular distributions of the inelastically scattered neutrons for $8.5 \leqq E_{ex}(C^{12}) < 11.75$ MeV and $12.25 \leqq E_{ex}(C^{12}) < 13.7$ MeV respectively. The resulting curves have the following equations when fitted by the method of least squares,

$$\sigma(\theta) = 30 + 15P_1(\cos\theta) - 0.6P_2(\cos\theta) - 11P_3(\cos\theta)\,, \qquad (12)$$
$$\text{for } 8.5 \leqq E_{ex}(C^{12}) < 11.75\ \text{MeV}\,,$$

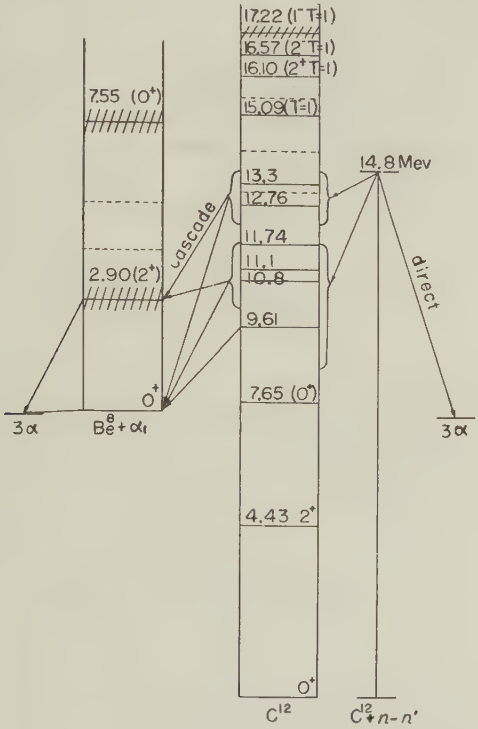

Fig. 13. The energy-level diagram for Be^8 and C^{12} (taken from Ajzenberg and Lauritsen[14]).

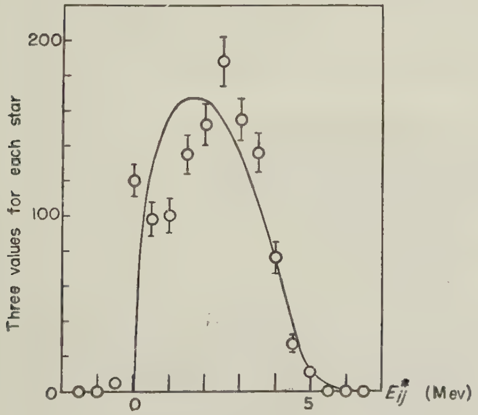

Fig. 14. Distribution of E^*_{ij} values. (three values for each star, *i.e.*, E^*_{12}, E^*_{23} and E^*_{31}). Two peaks at 0 Mev and 3 Mev correspond to the levels of Be^8, and the solid curve shows the theoretical distribution of E^*_{ij} values when the decay mode is the tripartition of C^{12*} directly into three alpha particles.

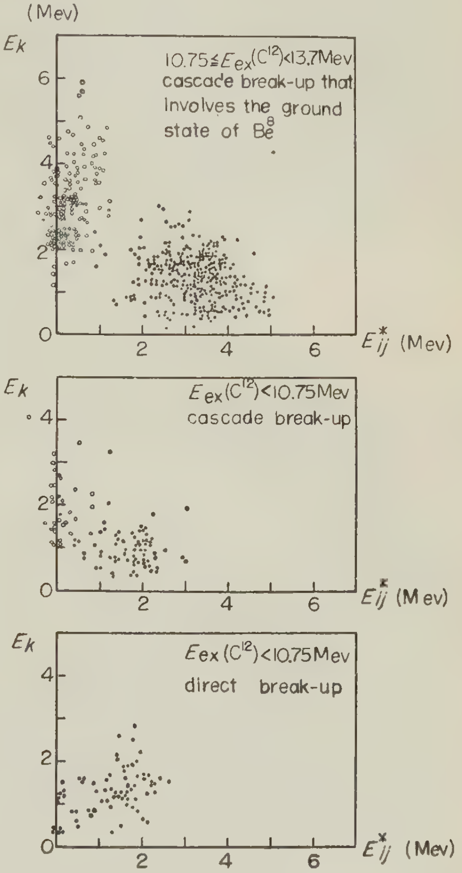

Fig. 15. Some examples of $E^*_{ij} - E_k$ graphs, where the open circles show the "real" values and the closed circles show the "spurious" values.

	star (a)	star (b)	star (c)
$E_{ex}(C^{12})$	12.4 Mev	11.3 Mev	9.6 Mev
$E_{ex}(Be^8)$	3.1	0.0	0.0
E^*_{12}	3.9	2.5	1.7
E^*_{23}	0.4	0.0	0.0
E^*_{31}	3.1	3.2	1.5
E_1	2.0	2.1	1.1
E_2	2.0	1.0	0.8
E_3	1.5	1.9	0.9

$$\sigma(\theta)=22+21P_1(\cos\theta)+16P_2(\cos\theta)+20P_3(\cos\theta)+16P_4(\cos\theta)\,, \quad \text{for } 12.25 \leqq E_{ex}(C^{12}) < 13.7\ \text{MeV}\,, \tag{13}$$

where $P_l(\cos\theta)$ is the Legendre polynomial of the l th degree. As can be seen from Fig. 13, there are four levels in the region of $8.5 \leqq E_{ex}(C^{12}) < 11.75$ MeV, and two levels in the region of $12.25 \leqq E_{ex}(C^{13}) < 13.7$ Mev. The angular distribution for the region of $11.75 \leqq E_{ex}(C^{12}) < 12.25$ MeV shows the intermediate character of Figs. 11 and 12 ; and there is no level in this region of the excitation energy as can be seen from Fig. 13.

If the cascade break-up of C^{12*} that involves the intermediate Be^8 nucleus is more predominant than the direct break-up of C^{12*} into three alpha particles, evidence for Be^8 levels would appear when the excitation energy of Be^8 was calculated. As no one can decide, from the shape of the carbon stars, which two of the three alpha particles came from the break-up of Be^8, three calculations must be made for each star giving at most one third " real " values superimposed upon a two thirds background of spurious values. The excitation energy of Be^8 nucleus E^*_{ij} is given by

$$E^*_{ij}=E_i+E_j-0.1-\frac{1}{8}[(X_i+X_j)^2+(Y_i+Y_j)^2+(Z_i+Z_j)^2]\,, \quad (i, j=1, 2, 3) \tag{14}$$

where 0.1 is the Q value for the break-up of Be^8 into two alpha particles. Fig. 14 shows the distribution of E^*_{ij} values, there being three values for each star as described above. If the C^{12} nucleus does not break-up in a cascade form but directly into three alpha particles, these E^*_{ij} values are all suprious. But, as can be seen from Fig. 14, there is good evidence for the mechanism involving the ground state and the first excited state of Be^8. As for the possible decay mode, Frye *et al.* showed that the mode involving Be^9 was negligible compared with the mode involving Be^8 or direct break-up, and we assumed that all the stars undergo the Be^8 or direct break-up.

Then, we plotted the $E^*_{ij}-E_k$ graph $(i, j, k=1, 2, 3)$, and selected the stars which had nearly zero E^*_{ij} which may correspond to cascade break up involving the ground state of Be^8 and having large E_k value. Similiarly the stars that involve the first excited state of Be^8 were selected. Fig. 15 shows some of these $E^*_{ij}-E_k$ graphs, open circles show the " real " values and closed circles show the " spurious " values. For example, analysis of the carbon stars shown in Fig. 3 gives the following values, where $E_{ex}(Be^8)$ is the " real " excitation energy of Be^8.

From this analysis, the branching ratio of the various disintegration modes was found as follows :

$$\begin{pmatrix}\text{direct}\\ \text{break-up}\end{pmatrix} : \begin{pmatrix}\text{cascade break-up}\\ \text{via the ground}\\ \text{state of } Be^8\end{pmatrix} : \begin{pmatrix}\text{cascade break-up}\\ \text{via the first ex-}\\ \text{cited state of } Be^8\end{pmatrix} = 148 \text{ events} : 193 \text{ events} : 62 \text{ events} \approx 2:3:1 \tag{15}$$

§ 4. Discussion

Carbon 12 is a very tightly bound nucleus, and (p, p') experiments on this nucleus can be accounted for by the direct interaction mechanism, according to Austern, Butler and Mc Manus[15], when the residual nucleus is in the lower excited state. Therefore we expected at first that the contribution from the direct interaction would appear in the angular distributions of the inelastically scattered neutrons, but as can be seen in Figs. 6, 10, 11 and 12 there is no high energy group of inelastically scattered neutrons and the angular distribution of the " lower " energy group of the inelastically scattered neutrons shows the stronger forward peak. If the forward peaks in Figs. 11 and 12 arise from the mixing of the direct interaction process, the " higher " energy group of the inelastically scattered neutrons ought to show a stronger forward peak; and in addition to this result, Frye *et al.* showed that all scattered neutrons which made carbon star had isotropic distribution when the energies of the incident neutrons were mixed from 14.1 to 16.9 MeV. Therefore we should conclude that the reaction occurred mainly through the compound nucleus, and the angular distributions in the present experiment were probably due to the interference effect of several levels.

As for the decay modes, disintegration of the compound nucleus C^{13*} may be considered mainly as follows.

(a): the cascade break-up that involves Be^8($C^{13*}\rightarrow C^{12*}+n'\rightarrow Be^{8*}+\alpha_1+n'\rightarrow 2\alpha+\alpha_1+n'$),

(b): the direct break-up of C^{12*} into there alpha particles ($C^{13*}\rightarrow C^{12*}+n'\rightarrow 3\alpha+n'$),

(c): Sacks's model ($C^{13*}\rightarrow 3\alpha+n'$).

According to Fig. 5 there is evidence for the 9.6 MeV level of C^{12}, but the peak at about 12 MeV cannot be considered as a peak which corresponds to a single level, since the peak shifts with increasing neutron energy[4] and the level spacing of C^{12} near 12 MeV is less than the resolution of the present experiments. Therefore the peak at about 12 MeV can be accounted for by either (a), (b) or (c). On the other hand, if the direct break-up of C^{12*} into three alpha particle occurs as the main process and the statistical assumption of equal probability in phase space is made for these three alpha particles, the distribution of E_{ij}^* values can be calculated by,

$$P(E_{ij}^*)dE_{ij}^*=\frac{8}{\pi[E_{ex}(C^{12})-Q]}(E_{ij}^*)^{1/2}\times[E_{ex}(C^{12})-Q-E_{ij}^*]^{1/2}dE_{ij}^* \qquad (16)$$

where $P(E_{ij}^*)dE_{ij}^*$ is the probability for finding E_{ij}^* values in the domain of $(E_{ij}^*, E_{ij}^*+dE_{ij}^*)$, and for $E_{ex}(C^{12})$ we used the experimental result. The solid curve in Fig. 14 was calculated in this way, but the experimental results cannot be fitted by this curve. Therefore good evidence for the ground and the first excited state of Be^8 can be obtained, which is in good agreement with the result by Frye *et al.*

Further, as the analysis using the $E_{ij}^*-E_k$ graph shows that the cascade break-up that involves Be^8 is about twice the rest of the other decay modes as indicated by the formula (15), we can conclude that the possible decay mode is the cascade break-up of C^{12*} that involves Be^8, superimposed by the small amount of direct break-up of C^{12*} or/and C^{13*}. To determine which process of direct break-up occurs, the inelastically scattered neutrons were divided into two groups. Fig. 16 shows the angular distribution of the inelastically scattered neutrons for direct break-up, and the angular distribution of the inelastically scattered neutrons for the cascade break-up that involves Be^8. Even the ambiguity of classifying the decay mode by Fig. 15 is taken into account, the angular distribution for the direct break-up of C^{13*} is expected to be more isotropic than the angular distribution for the cascade break-up or the direct break-up C^{12*}, because the semi-empirical theory of Sacks[5] predicts the isotropic angular distribution for neutrons and alpha particles. But the present experimental results show that both the angular distributions in Fig. 16 are similar in shape, and the angular distribution for direct break-up is peaked forward rather strongly. Therefore we can conclude that the angular distribution for direct break-up

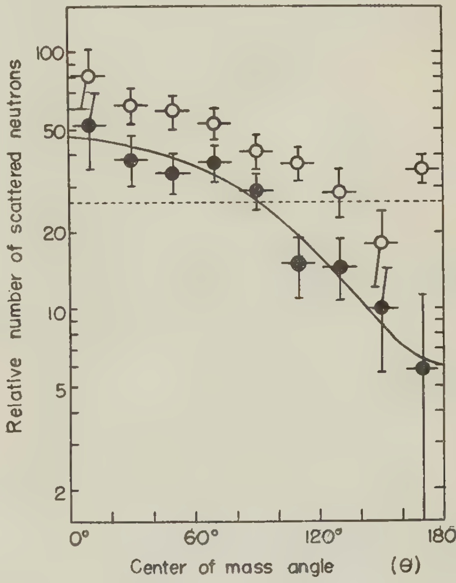

Fig. 16. Angular distribution of the inelastically scattered neutrons, where the open circles correspond to the carbon stars that break-up in cascade form, while the closed circles correspond to the carbon stars that break-up directly into three alpha particles. The solid curve is the experimental curve corresponds to the closed circles, while the dotted curve is the theoretical curve when the decay mode is Sacks's type.

corresponds not to the direct break-up of C^{13*}, but to the direct break-up of C^{12*} superimposed by some amount of the cascade break-up of C^{12*} that involves Be^8. In this case, the intermediate state of Be^8 is probably the first excited state, because the classification of direct and cascade break-up using $E^*_{ij}-E_k$ values is easier for the cascade break-up that involves the ground state of Be^8. The solid curve in Fig. 16 corresponds to the cabon stars that break-up directly into three alpha particles, which has the following equations when fitted by the method of least squares:

$$\sigma(\theta)=26+20P_1(\cos\theta) \tag{17}$$

and the dotted curve shows the prediction by Sacks's model.

Although the cross section calculated by Sacks agrees very well for low energy reactions, we could not find evidence for this process. The disagreement with Sacks's model in the angular distribution measurement was also fount by Sakisaka[16] in his recent experiments on the reaction $Be^9(n, 2n)2\alpha$ using 14 MeV neutrons.

The present experimental results for the decay mode of carbon nucleus is also reasonable, if we compare this result with the other experiments[17] for the break-up of C^{12*}, for which the excitation energy is about the same and the mechanism of excitation is different than that in the present experiment. In these experiments, the disintegration of excited C^{12*} nucleus proceeds in most cases by successive emissions of alpha particles rather than by tripartition of C^{12*} directly into three alpha particles. The branching ratio of direct break-up given in the formula (15) seems rather too large compared with such other experiments; for example, we did not obtain the evidence of tripartition of C^{12*} by p-Li γ rays even though the excitation was higher than the present experiment, and the peak or shoulder that corresponds to the first emitted alpha particles cannot be seen in Fig. 7, while it can be clearly seen in the experiment by Cook *et al.* on the study of $B^{12}(\beta^-)C^{12*}\cdot(\alpha_1)Be^{8*}(2\alpha)$, $E_{ex}(C^{12})\leq 13.4$ MeV. But this small discrepancy for the branching ratio of direct break-up is not so important because the mechanisms for exciting C^{12*} are different in these cases.

Fig. 17 shows the angular distribution of the inelastically scattered neutrons for the carbon stars that break-up in cascade form. The solid curves have the following equations when fitted by the method of least squares:

$$\sigma(\theta)=16+3P_1(\cos\theta)-P_2(\mathrm{cor}\,\theta)-8P_3(\cos\theta)\,,\quad \text{for } 8.5\leq E_{ex}(C^{12})<11.75\text{ MeV}, \tag{18}$$

$$\sigma(\theta)=16+14P_1(\cos\theta)+10P_2(\cos\theta)+10P_3(\cos\theta)\,,\quad \text{for } 12.25\leq E_{ex}(C^{12})<13.7\text{ MeV}. \tag{19}$$

The difference of two angular distributions in Fig. 17 is more conspicuous than that of the angular distributions in Figs. 11 and 12.

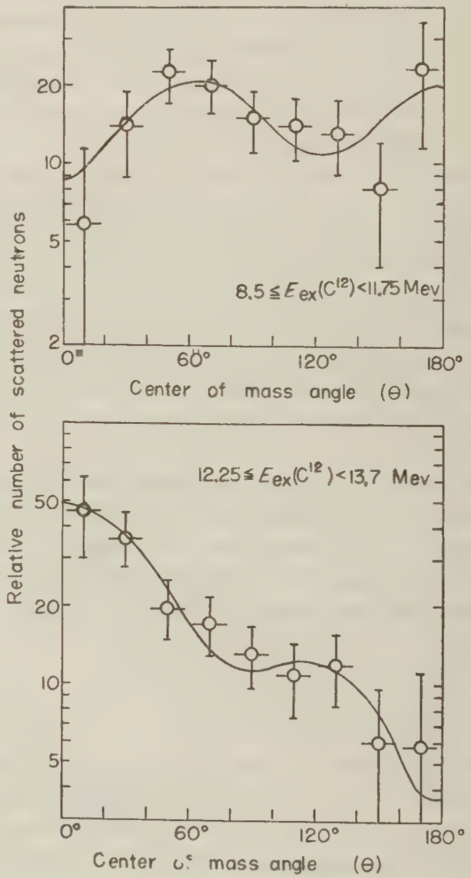

Fig. 17. Angular distribution of the inelastically scattered neutrons for the carbon stars that break-up in cascade form.

§ 5. Conclusion

The results of the present experiment can be summarized schematically as follows, where the double arrows represent the predominant processes.

Acknowledgement

The author wishes to express his sincere

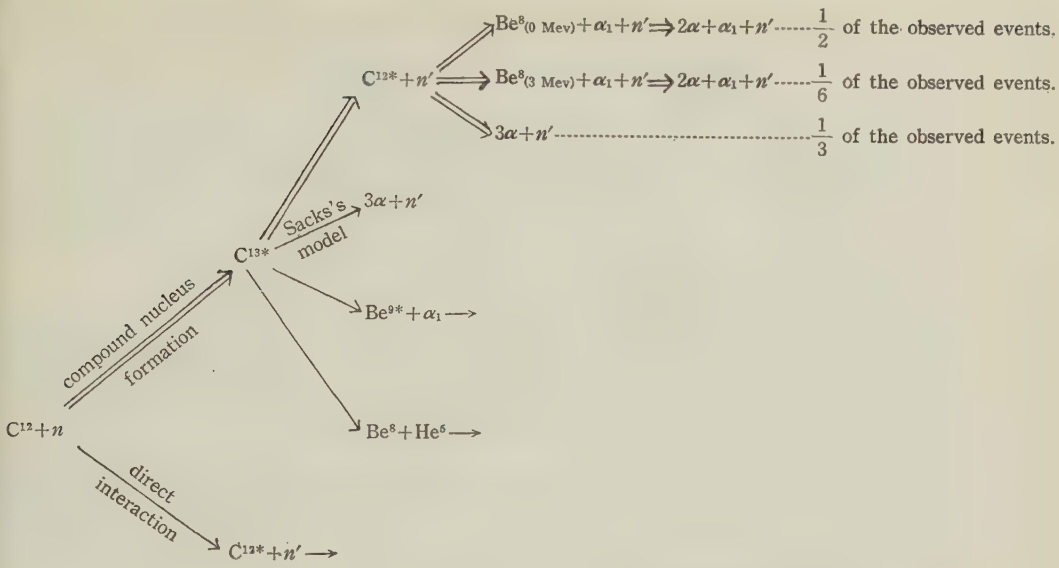
$Be^8{}_{(0\ Mev)}+\alpha_1+n' \Rightarrow 2\alpha+\alpha_1+n'$ ------ $\frac{1}{2}$ of the observed events.
$C^{12*}+n'$
$Be^8{}_{(3\ Mev)}+\alpha_1+n' \Rightarrow 2\alpha+\alpha_1+n'$ ------ $\frac{1}{6}$ of the observed events.
$3\alpha+n'$ ------ $\frac{1}{3}$ of the observed events.
Sacks's model
$3\alpha+n'$
C^{13*}
$Be^{9*}+\alpha_1 \rightarrow$
compound nucleus formation
$Be^8+He^6 \rightarrow$
$C^{12}+n$
direct interaction
$C^{12*}+n' \rightarrow$

thanks to Profs. K. Kimura and S. Yasumi for thier suggestions and continual encouragement throughout the present work. Thanks are also due to Dr. I. Kumabe for the neutron irradiation and to Mrs. E. Takekoshi and Miss. N. Shiomi for their help in scanning, calculations and discussions. This work has been supported by the Scientific Research Fund of the Ministry of Education.

References

1) J. Chadwick, N. Feather and W. T. Davies: Proc. Camb. Phil. Soc. **30** (1934) 357.
2) L. Green and W. M. Gibson: Proc. Phys. Soc. London **A**, **62** (1949) 296.
3) D. A. Kellog: Phys. Rev. **90** (1953) 244.
4) G. M. Frye, L. Rosen and L. Stewart: Phys. Rev. **99** (1955) 1375.
5) M. Sacks: Phys. Rev. **103** (1956) 671.
6) G. K. O'Neill: Phys. Rev. **95** (1954) 1235.
7) J. L. Perkin: Phys. Rev. **81** (1951) 892.
8) J. D. Jackson and D. I. Wanklyn: Phys. Rev. **90** (1953) 381.
9) C. C. Dilworth, G. P. S. Occhialini and R. M. Payne: Nature **162** (1948) 102. A. D. Dainton, A. R. Gattiker and W. O. Lock: Phil. Mag. **42** (1951) 396.
10) J. Rotblat and C. T. Tai: *Fundamental Mechanism of Photographic Sensitivity*, ed. by J. W. Mitchell (Butterworths Sci. Publ. London, 1951) 331.
11) J. Rotblat: Nature **167** (1951) 550.
12) Y. Tsuneoka, E. Takekoshi, I. Kumabe, H. Ogata, S. Oki and N. Shiomi: Genshikaku-Kenkyu **3** (1958) 25 (in Japanese).
13) A. E. S. Green: *Nuclear Physics* (McGraw Hill, New York, 1955) 212.
14) F. Ajzenberg and T. Lauritsen: Rev. Mod. Phys. **27** (1955) 77.
15) N. Austern, S. T. Butler and H. McManus: Phys. Rev. **92** (1953) 350.
16) M. Sakisaka: private communication.
17) For example,
D. L. Liversey and C. L. Smith: Proc. Phys. Soc. London **A**, **66** (1953) 689. J. Muto, E. Takekoshi, T. Nakamura, A. Imamura and Y. Tsuneoka: J. Phys. Soc. Japan **12** (1957) 109. C. W. Cook, W. A. Fowler, C. C. Lauritsen and T. Lauritsen: Phys. Rev. **111** (1958) 567.

JOURNAL OF THE PHYSICAL SOCIETY OF JAPAN, Vol. 14, No. 7, JULY, 1959

A Jet Shower with Energy of 5×10^{13} eV found in Emulsion Chamber

By Kiyoshi NISHIKAWA

Institute of Physics, Wakayama University, Wakayama

(Received January 11, 1959)

A high energy jet shower suitable for detailed analysis was found in one of the emulsion chambers flown in 1956 as the "Emulsion Chamber Project". The charged secondary particles of this jet were analysed in the usual way and especially the energy of π^0-mesons was determined by making use of the cascade showers developed from the γ-rays decayed from these π^0-mesons. The energy of incident particles was obtained by the use of usual median angle method, and was estimated to be 5×10^{13} eV ($\gamma_c = 165$).

Next, by making use of the fact that transverse momenta of points are constant and by analysing cascade showers developed from γ-rays produced by the decay of π^0-mesons, the energy of secondary particles was estimated. It was thus found that the differential momentum spectrum obtained is of the form dP/P^3. Also inelasticity coefficients K', K'' and K in the definition of the Bristol group were estimated to be 0.15, 0.10 and 0.5 respectively.

Further, the results of the present analysis were compared with various theories.

§ 1. Introduction

In recent years a great number of works on cosmic ray jet showers in nuclear emulsions have been performed. In order to study the detailed mechanism of multiple meson production at extremely high energy, the "Emulsion Chamber Project"[1] was carried out in 1956 with a collaboration of several laboratories in Japan. One of the most important results obtained is that the value of the transverse momentum of π-mesons is several hundred MeV/c over the wide ranges of both primary and secondary energies. The emulsion chamber has an advantage over ordinary emulsion stacks in that it is possible to estimate the energy of π^0-mesons accurately by the use of separate cascade showers developed from the γ-rays from π^0-mesons.

In the present paper we shall report the results of a detailed analysis of one jet shower "*ST 2*" which was found in one of the emulsion chambers and seemed to be favourable for the detailed study. In this case, not only many cascade cores from secondary π^0-mesons but also charged particles were clearly observed.

For the study of extremely high energy phenomena the emulsion chamber seems to be more preferable to ordinary emulsion stacks, because in the case of usual stack the electron pairs converted from γ-rays mix with the charged secondary particles in the inner core of the extremely high energy jet, thus making the detailed analysis of these secondary particles difficult. Therefore, it is desirable to accumulate much data about the extremely high energy jet by the use of emulsion chambers which have better arrangement than those in the present experiment.

§ 2. Experimental Procedure

a) The balloon flight and the arrangement of the experiment

Our emulsion chambers were flown at an altitude of 23 Km by polyethylene balloons (5600 m^3) launched from Kobe in summer 1956. The emulsion chamber, in which the jet we are going to report was found, is of the type B[1]. Its arrangement is shown in Fig. 1. It consists of seventeen G 5 200 microns plates (6″×8″), ten plates of carbon with thickness of 8 mm, eight plates of lead with thickness of 5 mm and two air gaps of 2 cm. In this chamber the upper part, which is consisted of material with low atomic number, acts as a jet producing layer, while the lower part of material with high atomic number acts as a detecting layer of cascade showers developed from γ-rays which are the decay products of π^0-mesons resulting from jets.

b) **Observation and measurement**

Scanning was carried out to search for cascade showers in the emulsion plate at the bottom of the emulsion chamber. A shower having 11 cascade corres, as shown in Fig. 2, was found in the course of this scanning. By tracing the tracks of the shower back to the upper plates a jet was found, in which one heavily ionized track and 53 shower particles could be seen. Fig. 3 shows the target diagram of the charged shower particles. The origin of the jet was in the top carbon plate, so that the primary particle could not be seen. The axis of the jet was determined in two ways, namely from the analysis of the cascade showers[1)] and from the center of mass of the charged particles. These two determinations were in very good accord, and it was found that the said axis makes an angle of 76° with the emulsion surfaces.

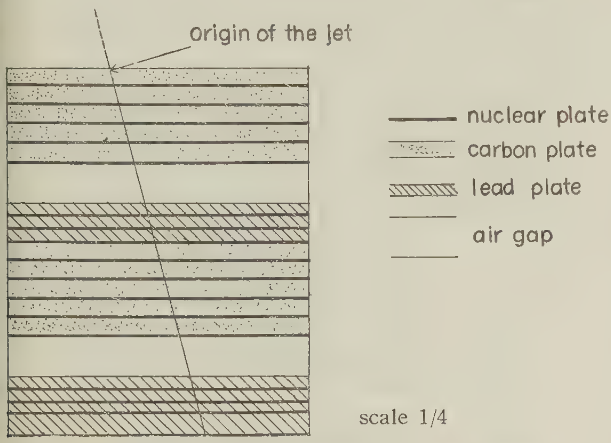

Fig. 1. Elevation of the type **B** of the emulsion chamber, showing the arrangement of plates and air gaps.

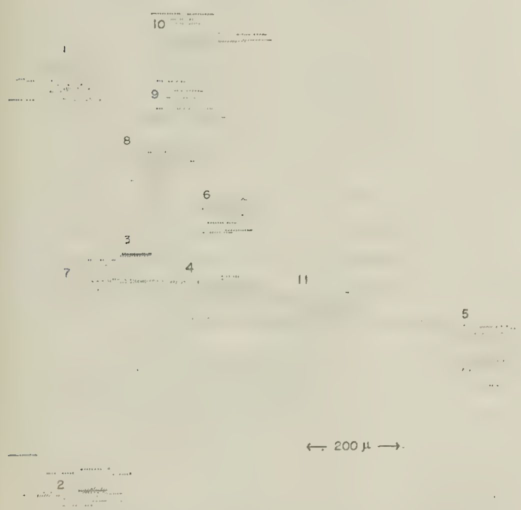

Fig. 2. Illustration of the cascade showers having 11 cores observed at the bottom of the emulsion chamber.

From an analysis of the cascade showers[1)] developed in the inner cone, the energy of π^0-mesons, $E\pi^0$, was estimated by the use of Nishimura-Kamata's distribution function[1)]. The angles, $\theta\pi^0$, which π^0-mesons make with the shower axis were also estimated from the analysis of the cascade showers. The results are tabulated in Table I. Over wider region outside the inner cone, electron pairs and cascade showers were scanned. These γ-rays are also considered to be due to the π^0-mesons belonging to the outer cone of this jet, because the γ-rays from the bremsstrahlung by the charged particles are estimated to be negligible[2)]. The angles θ_γ, between the γ-rays and the shower axis were measured by making use of the target diagram, obtaining the results as tabulated in Table II.

Table I. Values of energy E_{π^9}, transverse momentum P_T and angle θ_{π^0} of π^0, and those of E_γ and θ_γ of γ-rays decayed from π^0, both in the inner cone of the jet.

No. of γ	θ_γ (rad)	E_γ (eV)
3	0.53×10^{-3}	10.0×10^{11}
7	1.43	0.5
8	1.84	1.0
4	1.93	0.5
6	2.01	0.5
9	3.38	0.2
11	4.13	0.2
1	4.62	1.0
10	5.04	0.1
2	6.28	0.5
5	8.41	0.4

No. of γ	θ_{π^0} (rad)	E_{π^0} (eV)	P_T (MeV/c)
1-9	4.11×10^{-3}	1.09×10^{11}	450
4-10	1.35	0.58	78
3-7	0.73	7.75	561
6-8	1.41	1.41	198
5-11	7.03	0.68	476
2	6.28	0.5	314

Table II. Angles between the jet axis and γ-rays produced by π^0 in the outer cone of the jet.

θ(rad)	θ(rad)	θ(rad)
7.05×10^{-3}	16.5×10^{-3}	31.2×10^{-3}
7.1	17.6	31.8
8.25	19.4	32.4
8.8	23.6	33.0
9.4	25.9	36.5
9.4	26.5	38.8
10.6	27.1	38.8
14.1	29.4	45.3
14.1	30.0	47.1
14.1	30.6	50.6
16.1		

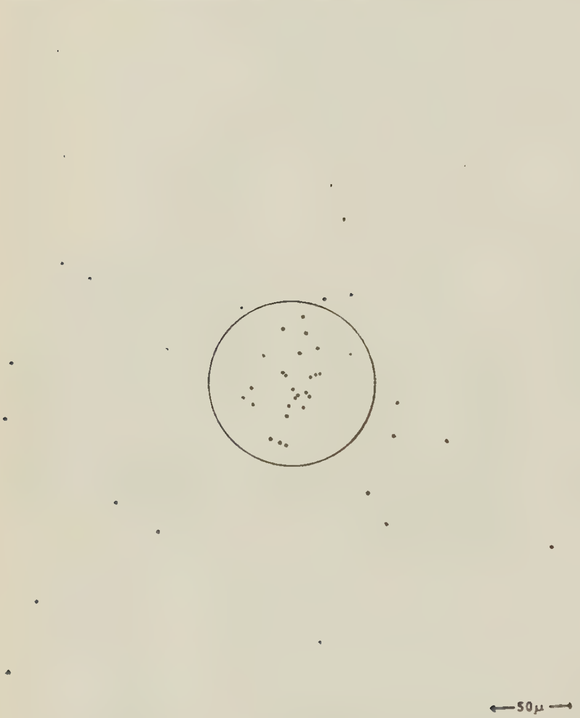

Fig. 3. The target diagram of charged shower particles at 8.5 mm beneath the origin of the jet.

Charged shower particles were observed in several plates near the origin. The angles, θ, which these shower particles make with the shower axis are given in Table III. The target diagram (Fig. 3) used for measuring these angles is that in the emulsion plate just beneath the production point of the jet shower, because the number of electron pairs from the γ-rays of π^0-mesons is estimated to be negligible.

§ 3. Estimation of the Incident Energy

An estimation of the energy of the primary particle is made by kinematical method due to Castagnoli *et* al.,[3] assuming that the interaction is a nucleon-nucleon collision. From the data of charged shower particles, the Lorentz factor γ_c of the center of momentum system is obtained from the equation:

$$\frac{1}{n_s}\sum_{i=1}^{n_s}\log\tan\theta_i=\log\frac{1}{\gamma_c}, \qquad (1)$$

where n_s is the number of the charged shower particles, and θ_i the angle of the ith shower particle with the shower axis in the laboratory system (L. system). Then, the energy E_0 of the primary nucleon in the L. system is

$$E_0=(2\gamma_c^2-1)Mc^2, \qquad (2)$$

where Mc^2 is the rest mass of a nucleon. Plotting the values of $\tan\theta_i$ on the logarithmic scale as in Fig. 4, the following results are obtained:

$$\gamma_c=165.4^{+26.6}_{-19.9},$$

$$E_0=(5.10\,^{+1.83}_{-1.14})\times10^{13}\ \mathrm{eV},$$

Table III. Angles between charged shower particles and the jet axis.

θ(rad)	θ(rad)	θ(rad)	θ(rad)	θ(rad)	θ(rad)
0.43×10^{-3}	1.98×10^{-3}	4.21×10^{-3}	8.60×10^{-3}	16.0×10^{-3}	22.0×10^{-3}
0.86	2.24	4.48	9.81	16.1	23.0
0.95	2.42	4.56	10.0	17.3	23.1
1.03	2.50	4.65	12.4	18.6	25.5
1.10	3.00	5.09	12.7	19.7	26.2
1.27	3.02	5.16	13.1	19.8	31.3
1.57	3.27	6.89	15.2	21.2	32.2
1.58	3.35	6.95	15.5	21.4	
1.72	3.79	8.02			
1.94	4.05	8.15			

the errors estimated above being merely statistical.

According to the theory of the multiple meson production by Landau[4] or Fermi[5], the relation between the multiplicity and the the energy of primary particle of mass number A is given by[6]

$$n_s=2Al\sqrt{\gamma_c}\ , \qquad (3)$$

where l is the ratio of the length of column in target nuclear matter to that in incident nuclear matter. In the present jet l is estimated as 2.1 if A is 1 and as 1.0 if A is 2. Therefore, three nucleons are considered to be involved in the collision. Then, the energy of incident particle will be

$$E_0=2l\gamma_c^2Mc^2=10^{14}\ \text{eV}\ .^{7)}$$

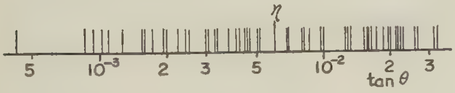

Fig. 4. Tan θ plot of charged shower particles.

§ 4. Multiplicity and Ratio of Numbers of Neutral and Charged Particles

The number of the shower particles obtained from the above-mentioned observations is shown in Table IV. In this table "charged" contains not only $\pi^{\pm}$-mesons but also the more heavy particles, *i.e.*, "x-particles" as mentioned by the Bristol group.[8] The ratio of the number of π^0-mesons to that of $\pi^{\pm}$-mesons plus x-particles is shown in the last row of the table. It will be seen that the ratio of the numbers of neutral and charged particles emitted in both the inner and outer cones is 0.45, in agreement with the results hitherto obtained. However, it is to be noticed that the said ratio in the inner cone is somewhat less than that in the outer cone.

Table IV. Number of shower particles and ration of numbers of neutral and charged particles.

	inner cone	outer cone	total
charged	26	27	53
π^0	7	17 (31 cascades)	24
total	33	44	77
$\dfrac{\pi^0}{\pi^{\pm}+x^{\pm}}$	0.27	0.63	0.45

§ 5. Angular Distribution of the Shower Particles

If we transform the angle θ in the L. system, which the shower particle makes with the jet axis, to the angle $\bar{\theta}$ in the C. M. system by the use of the relation:

$$\gamma_c \tan\theta=\tan(\bar{\theta}/2)\ , \qquad (4)$$

the angular distribution in the C. M. system of the charged shower particles and π^0-mesons emitted in the inner cone becomes as shown in Fig. 5 (a) and (b).

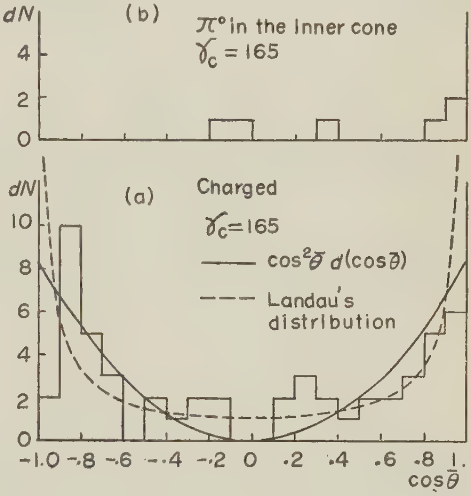

Fig. 5. The angular distribution of shower particles in the C. M. system.
(a) Charged secondary particles
(b) π^0 in the inner cone

Following B. Edwards *et al.*[8], this angular distribution may be represented approximately by an expression $\cos^m\bar{\theta}d(\cos\bar{\theta})$, with m positive even integer, and a convenient parameter specifying the degree of anisotropy is $(\text{cosec}\ \bar{\theta})_{\text{av.}}$, which for the above expression becomes

$$(\text{cosec}\ \bar{\theta})_{\text{av.}} \simeq 1.25\sqrt{m} \qquad (\text{for large } m).$$

In our jet m is nearly equal to 2, so that the anisotropy is of rather low degree in comparison with that obtained by other authors for such a high energy collision. The angular distribution is also compared with that given by Landau's theory in Fig. 5 (a), by normalizing the total number of mesons with the experimental values.

The integral angular distribution in the L. system for charged shower particles is shown in Fig. 6 by plotting $\log[F(\theta)/\{1-F(\theta)\}]$

against los $(\gamma_c \tan\theta)$, where $F(\theta)$ is a fraction of the number of tracks with angles less than θ making with the jet axis.[9] It will be seen that a straight line with slope 1.3 fits the observed values fairly well. In this connection it may be noted that in a similar representation, the isotropic distribution in the C. M. system is expressed by a straight line with slope 2,[10] while in the extremely anisotropic distribution of Heisenberg a straight line has slope 1.[11]

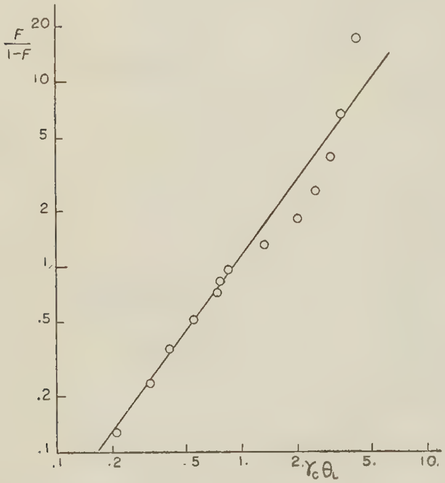

Fig. 6. $\log [F(\theta)/\{1-F(\theta)\}]$ *versus*. $\log \gamma_c \tan\theta$ plot of charged particles.

Also, it is found that the integral distribution in cosec $\bar{\theta}$ for charged shower particles is represented by a relation of the form $N(>\operatorname{cosec}\bar{\theta}) \propto (\operatorname{cosec}\bar{\theta})^{-2}$. This implies that the differential momentum spectrum of the shower particles subject to the assumption $P_T =$ const. is, on the average, of the form dP/P^3. This result does not agree with the form dP/P^2 as assumed by Heisenberg[12] and the experimental results obtained by the Bristol group[8] as well as an estimation made by S. Hasegawa *et al.*[13] Further, it is found that as shown in Fig. 7, the differential momentum spectrum falls off fairly rapidly with increasing pion energy as in the form dP/P^4 from the point at which the momentum of pion is about 0.8 GeV/c.

§ 6. Energy Estimation of the Shower Particles

The energy of π^0-mesons emitted in the inner cone can be determined in the same way as in our previous experiment[1] and the results obtained are shown in Table I. The energy for charged particles was estimated assuming that their transverse momenta P_T are all of the same value 0.38 ± 0.02 GeV/c as obtained for π^0-mesons in our previous experiment cited above. For π^0-mesons emitted in the outer cone the total energy was estimated as the total sum of energies of γ-rays produced by the decayed π^0-mesons, using the result that their transverse momenta $P_{T\gamma}$ are one half of those of π^0-mesons, namely $P_{T\gamma} = 0.19 \pm 0.01$ GeV/c.[8] The ratio of the energy of neutral particles to that of charged ones in the L. system was calculated using the values above estimated. The results are shown in Table V, where $E_{\pi^\pm}$ denotes the total enrgy of the π^+- and π^--mesons and E_{charged} is that of all the charged particles, which was

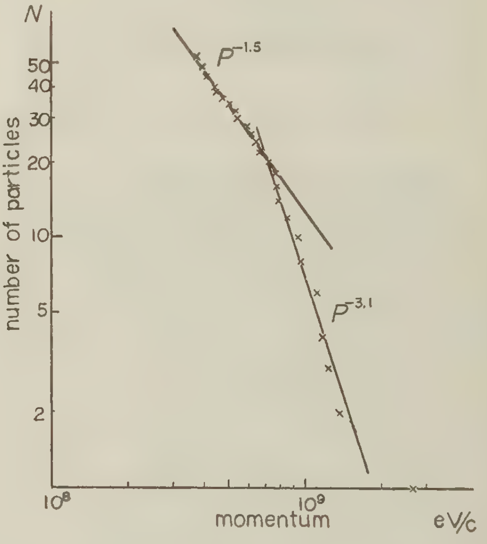

Fig. 7. (a) Integral momentum distribution of charged shower particles in the C. M. system.

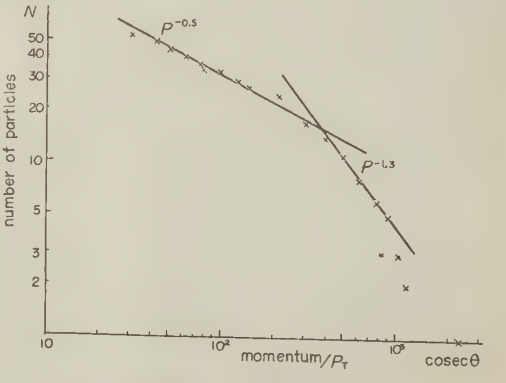

Fig. 7. (b) Integral momentum distribution of charged shower particles in the L. system.

Table V. Energy in GeV of secondary particles.

In the C. M. system

	inner cone	outer cone	total
charged	20.3 ±4.1 (12.8±2.8)	15.1±3.0 (9.71±2.16)	35.4±5.1 (22.5±3.6)
π^0	4.25±1.74	4.25*±1.74	8.5*±2.5
total	24.55±4.4 (17.05±3.33)	19.35*±3.47 (13.96*±2.77)	43.9*±5.6 (31.0*±4.4)

In the L. system

	inner cone	outer cone	total
charged	5460±1098 (3030±673)	727±145 (645±143)	6187±885 (3675±588)
π^0	1198±76	339±63	1537±90
total	6658±1101 (4228±677)	1066±158 (984±153)	7724±890 (5212±596)

Here, errors indicated are merely statistical.

The ratio of the energy of neutral particles to that of charged ones in the *L.* system.

	inner cone	outer cone	total
E_{π^0}/E charged	0.22	0.47	0.25
$E_{\pi^0}/E_{\pi^\pm}$	0.40	0.53	0.42

calculated by regarding them as pions. In this table, the value in parentheses are those calculated for the shower particles by excluding x-particles, being 20 per cent of all the particles, emitted forwards and backwards near the axis in the C. M. system. Also, the values with asterisk are those estimated under a conventional assumption that for the same kind of particles the energy emitted in the outer cone in the C. M. system is equal to that emitted in the inner cone.

As will be seen from the table, the values of the ratio $E_{\pi^0}/E_{\pi^\pm}$ in the inner and outer cones are nearly equal to each other, namely ~0.4 and ~0.5 respectively. It is to be noted, however, that the values of the ratio of the total energy of π^0-mesons to that of all the charged particles, including x-particles, $E_{\pi^0}/E_{\text{charged}}$ are different, being ~0.2 for the inner cone and ~0.5 for the outer cone. These results seem to suggest that both the percentage here adopted for the x-particles, *i.e.* 20 per cent, and their angular distribution are not far from reality.

§ 7. Inelasticity

The inelasticity coefficient, K', defined as the ratio between the total energy of secondary particles and the kinetic energy of nucleons before collision in the C. M. system assuming all the shower particles as pions, was estimated in three different ways:

(1) Thus, in the first place, by making use of the fact that the transverse momentum P_T of pions is constant and assuming charge independence in meson creation, the value of K' was estimated by the formula:

$$K' = \frac{1.5\, P_T \times \Sigma \operatorname{cosec} \bar{\theta}}{2\gamma_c},$$

obtaining the result that $K' = 0.16 \pm 0.03$.

(2) Secondly, estimating the energy of charged pions by the same method as above as well as the energy of neutral pions from the analysis of cascade showers developed from γ-rays which decayed from them, the value of K' was determined, and it was found that $K' = 0.13 \pm 0.02$.

(3) Thirdly, the value of K' was also estimated by estimating, by the same method as in the second case, the energies of charged pions as well as of neutral pions emitted only in the inner cone, obtaining the result that $K' = 0.15 \pm 0.03$.

On the other hand, the value of the inelasticity coefficient K'', i.e., a fraction of the available energy radiated as points, was calculated, assuming that 20 per cent of the secondary particles are x-particles and are emitted with the smallest forward and backward angles in the C. M. system. It was thus found that $K'' = 0.10 \pm 0.02$, 0.09 ± 0.02 and 0.10 ± 0.02 corresponding to each K' in the above three cases respectively.

The values of K' and K'' in reference to the L. system were also calculated, obtaining the result that

$$K_L'=0.14\pm0.03,\ K_L''=0.10\pm0.02\ .$$

It is seen that the values of K' and K_L' determined in the above four different ways are in good agreement with each other, and similar situation can be found in the values of K''.

Since the transverse momentum P_T of x-particles is estimated to be 1.8 ± 0.5 GeV/c and according to the results of the Bristol group[8], the number of x^0-particles is 1.25 ± 0.5 times as large as that of charged x-particles, the energy of various particles in reference to the C. M. system are calculated as follows:

Energy of $\pi^\pm$: $22.5\pm\ 3.6$ GeV .
Energy of $x^\pm$: 60.7 ± 24.7 GeV .
Energy of x^0 : 75.8 ± 43.2 GeV .
Energy of π^0 : $8.5\pm\ 2.5$ GeV .

Total : 167.5 ± 50.0 GeV .

Thus, the value of the inelasticity coefficient K, *i. e.*, a fraction of the energy radiated as secondary shower particles, becomes 0.51 ± 0.17.

Also, in reference to the L. system we find that

energy of $\pi^\pm$: $(\ 3.68\pm0.59)\times10^3$ GeV ,
energy of $x^\pm$: $(11.94\pm4.86)\times10^3$ GeV ,
energy of x^0 : $(14.92\pm8.50)\times10^3$ GeV ,
energy of π^0 : $(\ 1.54\pm0.09)\times10^3$ GeV ,

total : $(32.08\pm9.81)\times10^3$ GeV .

Therefore, the value of the inelasticity coefficient K_L in reference to the L. system corresponding to the above K becomes 0.59 ± 0.20. All the errors estimated in this section are merely statistical.

Judging from the above results it may be considered that fairly appropriate and reliable values for K'' and K are respectively

$K''\sim0.1$ for pions only,

$K\sim0.5$ for all the secondary particles.

All the above values of the inelasticity coefficients have been calculated assuming that the event is caused by a nucleon-nucleon collision. However, in case when the value of l is 2 and the target is a nucleus with two proton mass, each of the above values should be divided by 2. In this case the comparatively reliable values of K'' and K are respectively

$$K''\sim0.05,\quad K\sim0.3\ .$$

§ 8. Conclusion and Discussion

The results of our present experiment may be summarized as follow:

(a) A jet found in one of the emulsion chambers has 53 shower particles and 24 π^0-mesons created in the interaction, and the ratio R of neutral to charged particles is 0.45.

(*b*) The value of γ_c is 165, and the incident energy in the L. system is $(5.10^{+1.83}_{-1.14})\times10^{13}$ eV when the event is assumed to be due to a nucleon-nucleon collision.

(c) The angular distribution is anisotropic in the C. M. system and agrees to some degree with Landau's distribution. The indication of anisotropy is as follows:

(i) If we approximate the angular distribution in the C. M. system by an expression $dn=\cos^m\bar{\theta}d(\cos\bar{\theta})$, the value of m becomes 2.

(ii) In the L. system, the slope of a straight line obtained by plotting $\log[F/(1-F)]$ against $\log(\gamma_c\theta)$ is 1.3.

(d) The differential momentum distribution of secondary particles in the C. M. system is, on the average, of the form dP/P^3, and it falls off sharply with increasing pion energy in the form dP/P^4.

(e) The inelasticity coefficients estimated are respectively as follows:

$K'=0.15$	regarding all shower particles as pions,
$K''=0.1$	for pions only,
$K=0.5$	for pions plus x-particles.

(f) The value of l in Eq. (3) is 2.

It was shown by previous experiments by the Bristol group[8] and other workers[14,15] that in general the higher is the energy of the primary particle of the nuclear collision, the larger the degree of anisotropy of the angular distribution. It is interesting to note, however, that although our jet is of high energy (5×10^{13} eV), the degree of anisotropy is comparatively small as indicated by the results that the value of m is 2 and the slope of the F-plot is 1.3. Further, it is to be noted that as indicated by the result that the value of l is 2, the present jet has high multiplicity for its energy, and is not considered to be an event caused by a single nucleon-nucleon collision.

The value of the inelasticity coefficient K is nearly 0.5, but not unity as suggested by the theory of Fermi[5] or Landau[4], in spite of taking account of an appreciable error in the results by the Bristol group on x-particle. By adjusting the value of P_T of x-particles it is able to make the value of K unity, but the adjusted value of P_T of 25 x-particles (charged: 11 and neutral: 14) is, on the average, as high as 4 GeV/c. Judging from the results by the Bristol group, however, it is not reasonable to consider that all the x-particles have such a high P_T as 4 GeV/c. Therefore, about one half of the incident energy may be carried away by a nucleon or nucleons involved in the collision, or may not contribute to the collision.

These experimental results do not agree with the theory of Fermi or Landau as to the inelasticity coefficient K, but they are considered to be in fairly good agreement with Landau's theory in respect of the angular distribution in the C. M. system of shower particles. It will be important to compare the experimental results with various theories by using the parameters essential to the theories. This can be done when more experimental results will be accumulated and one can then clarify what is really essential to a particular theory.

Acknowledgement

The author wishes to express his hearty gratitude to Professor K. Kimura and Professor O. Minakawa for their sustained interest and encouragement throughout the course of the present work. His sincere appreciation and thanks are also due to Professor S. Tokunaga and Miss. T. Ishii for their cooperative efforts, and to the staff of the Institute for Nuclear Study, University of Tokyo, and the Emulsion Research Group in Japan for making the balloon flight possible.

This work was financially supported by a grant-in-aid for scientific research of the Ministry of Education for the 1956 fiscal year.

References

1) O. Minakawa, Y. Nishimura, M. Tsuzuki, H. Yamanouchi, H. Aizu, H. Hasegawa, T. Ishii, S. Tokunaga, Y. Fujimoto, S. Hasegawa, J. Nishimura, K. Niu, K. Nishikawa, K. Imaeda and M. Kazuno: Suppl. Nuovo Cimento **8** (1958) 761 and INSJ-7, preprint, Tokyo, March 1958.
2) M. F. Kaplon and D. M. Ritson: Phys. Rev. **88** (1952) 386.
3) C. Castagnoli, G. Cortini, C. Franzinetti, A. Manfredini and D. Moreno: Nuovo Cimento **10** (1953) 1539.
4) S. Z. Belen'kji and L. D. Landau: Suppl. Nuovo Cimento **3** (1956) 15.
5) E. Fermi: Progr. Theor. Phys. **5** (1950) 570.
6) G. B. Ždanov, E. A. Zamčalova, M. I. Tretjakova and M. N. Ščerbrkova: Suppl. Nuovo Cimento **8** (1958) 726.
7) I. A. Ivanovskaya and D. S. Chernavsky: Nucl. Phys. **4** (1957) 29.
8) F. A. Brisbout, C. Dahanayake, A. Engler, Y. Fujimoto and D. H. Perkins: Phil. Mag. **1** (1956) 605. B. Edwards, J. Losty, D. H. Perkins, K. Pinkau and J. Reynolds: Phil. Mag. **3** (1958) 237.
9) G. Bertolino and D. Pescetti: Nuovo Cimento **12** (1954) 630.
10) N. M. Duller and W. D. Walker: Phys. Rev. **93** (1954) 215.
11) P. Ciok, T. Coghen, J. Gierula, R. Holyński, A. Jurak, M. Mięsowicz, T. Saniewska, O. Stanisz and J. Rernegr: Nuovo Cimento **8** (1958) 166.
12) W. Heisenberg: Z. Phys. **133** (1952) 65.
13) S. Hasegawa, J. Nishimura and Y. Nishimura: Nuovo Cimento **5** (1957) 979.
14) S. Tokunaga, K. Nishikawa and T. Ishii: J. Phys. Soc. Japan (in press).
15) P. Ciok, T. Coghen, J. Gierula, R. Holyński, A. Jurak, M. Mięsowicz, T. Saniewska and J. Pernegr: P. A. N. I. B. J. -30/VI, preprint, Warsaw, June 1958.

JOURNAL OF THE PHYSICAL SOCIETY OF JAPAN, Vol. 14, No. 7, JULY, 1959

An Experimental Investigation on the Mode of Slip in Face-Centered Cubic Metals

By Tadami TAOKA*, Kō YASUKŌCHI, Ryūkichi HONDA*
and Isao ŌYAMA**

Department of Physics, Faculty of Science, University of Tokyo

(Received January 8, 1959)

The changes of saturation of magnetization of the ordered Ni_3Mn and Pt_3Co alloys caused by plastic deformation were used as the criterion to decide whether the slip in metals is "homogeneous" or "inhomogeneous", i.e., whether it takes place in atomic steps on many successive atomic planes or in large steps on widely separated single atomic planes. It was found that in the ordered Ni_3Mn alloy, the saturation magnetization decreases with the amount of elongation at room temperature, while in the ordered Pt_3Co alloys, the intensity of magnetization at temperature near the Curie point increases with the amount of compression. These changes, which are roughly proportional to the amount of deformation, are probably understood only from the point of view that new disordered regions with Curie point different from that of the ordered state are produced during the deformation, being associated with homogeneous slip on successive atomic planes.

§ 1. Introduction

During recent years, following the original work of Heidenreich and Shockley[1] which was undertaken to get a clear understanding of slip mechanism within crystals, many observations on the surface structures of deformed metals have been accumulated by Brown,[2] Kuhlman-Wilsdorf and Wilsdorf,[3] Thomas and Nutting,[4] Seeger et al.[5] and others.[6] They are mainly concerned with the dependence of the fine structures of slip bands on the stages of deformation, the alloying elements of the specimen, and temperature. In the above investigations, it has been usually presupposed that the slip, in the course of slip band formation, takes place in large steps on single atomic planes separated by laminae of undeformed regions. In the following, the term "inhomogeneous" slip will be used for the slip on widely separated single atomic planes, as schematically shown in Fig. 1 (a). This assumption has been supported by Mott's theoretical description[7] given of the edge and screw dislocation net-works on {111} planes in a face-centered cubic lattice. These net-works lead to an account of Frank-Read sources multiplying dislocations in single atomic planes. Recently H. Wilsdorf and J. T. Fourie[8] succeeded in showing directly by an electron microscope using high resolution replica techniques that there does not exist angular difference between the slip plane and the surface exposed within the slip zones. This result might be doubtless so far as concerned with the slipbands on the surface of deformed α-brass.

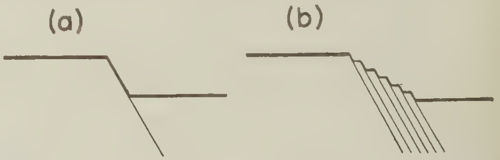

Fig. 1. Two schematical modes of slip: (a) "Inhomogeneous" slip on one plane. (b) "Homogeneous" slip on a number of neighbouring planes.

On the other hand, Yakutovitch et al.,[9] who repeated the work of Heidenreich and Shockley on aluminium, failed to confirm their results. They arrived at a conclusion that each elementary slip band is a region of finite width in which localized deformation of the amount of order of one atomic distance per successive slip plane is concentrated. This type of slip is called "homogeneous" slip which is schematically shown in Fig. 1

---

* Now at National Research Institute for Metals, Nakameguro, Meguro-ku, Tokyo.

** Now at the Central Inspection Institute of Weights and Measures, Itabashi-ku, Tokyo.

(b). H. Suzuki and F. E. Fujita[10] observed the fine surface structures of α-brass before and after cold-work by electron microscope and were also led to the same view. T. Suzuki and H. Suzuki[11] have pointed out that Frank-Read sources on {111} planes multiplying dislocations on only one atomic plane proposed by Mott seem to be very rare as compared with those on {113} planes multiplying dislocations in successive atomic planes. They also pointed out that the surface structures of deformed crystals might be produced rather by the operation of the surface sources which are different from those in the interior of metals.

Brown and Honeycombe[12] and others have experimentally shown that the slip structure observed on specimen surface depends on the difference of surface structures obtained after various preparations of the surface. These results are summarized in "Surface Effect in Plastic Deformation of Metals" by Brown.[12] There remains more or less a distorted layer after mechanical polishing, an oxide layer after an electropolishing and a fine surface structure after chemical polishing. The slip structures on the crystal surfaces sensitively depend on these surface structures. It is extremely difficult to decide whether any one of different observations described above reveals the true state of affaiars in the interior of crystal or not. It will be necessary to develope the techniques other than the surface observations to understand the correct process of slip in the interior of crystals. The experiment of Blewitt and Koehler[14] on slip in ordered alloy Cu_3Au seems hopeful to get some answer on the slip mode in the interior of crystals. The significant point of this work is that the disordering process in deformation is a direct result of atomic slip. The residual resistance was used as the criterion of the order and it was found possible to calculate the degree of order in a semiquantitative way. The result shows that there are three stages of deformation and it can be understood by using the same mechanism of slip as that proposed by Heidenreich and Shockley, namely an inhomogeneous slip. In spite of their good idea, we are doubtful of their conclusions because the assumptions presupposed in their calculations are too simple to deduce their results. Moreover, the electric resistance is structure sensitive and depends not only on the degree of order but also on the various types of lattice defects which would be introduced during the cold work.

Now, we will focus our attension to make clear which mode of slip actually takes place inhomogeneous or homogeneous slip. It is likely that the spontaneous magnetization of ferromagnetic order-disoder alloys is a favourable physical quantity to decide the mode of slip, because it is structure insensitive. For this purpose we have picked up two alloys, Ni_3Mn and Pt_3Co of which the saturation magnetization largely depends on the degree of order. In case of Ni_3Mn,[15] it is ferromagnetic in ordered state, but is paramagnetic in disordered state at room temperature, while Pt_3Co is paramagnetic in ordered state and ferromagnetic in disordered state at room temperature, as is recently found by Simpson and Tredgold.[16]

Let us consider the changes of spontaneous magnetization produced during the deformation of these ordered alloys in both cases of slip modes. In homogeneous slip, the saturation magnetization of Ni_3Mn will gradually decrease, while that of Pt_3Co will increase, with a formation of slip bands which are assumed as the disordered regions. On the other hand, in inhomogeneous slip, any appreciable change might not be expected in both alloys. Then this circumstance will be utilized for the criterion whether the slip mode is "homogeneous" or "inhomogeneous".

§ 2. Specimens and Experimental Methods

2.1 Ni_3Mn

The materials investigated were prepared by melting together electrolytic nickel and electrolytic manganese in vacuum and the alloys were drawn to a wire of 1.0 mm in diameter after a homogenizing heat treatment at 1200°C for 6 hours. It was cut in rods of 200~250 mm length and further annealed at 1200°C for 2 hours to remove the mechanical strain, and then they were sealed in evacuated quartz tubes. Different states of order of this alloy were obtained by quenching, in a course of slow cooling, from 600°C (disorder), 460°C, 400°C (intermediate order) and by slow cooling to room temperature (perfect order), following the suggestion by S. Kaya.[15] As a measure of ordering, the electrical resistance and saturation magnetization measured at room temperature are tabulated in Table I. After these heat treatments, the alloy was chemically analysed and was found to be about 1% richer in nickel compared with the stoichiometric composition Ni_3Mn. The size of grains was larger than the diameter of rods. The specimens were carefully electropolished to produce a clean surface before extension of them. They were extended up to several percent at a rate of one percent per second. After various stages of elongation, the magnetization curves and saturation magnetization were measured by the usual ballistic method at room temperature.

Table I. Electrical resistivity and saturation magnetization measured at room temperature of Ni_3Mn alloy quenched from various temperatures.

Specimen number	1	2	3	4
Quenching Temperture, °C	600	460	400	20
Electrical Resistivity, Ω-cm	72.7	42.7	26.6	19.8
Saturation Magnetization, gauss/cc	30	699	852	916

2.2 Pt_3Co

The alloy was prepared by melting together the known amounts of pure (99.99%) platinum and (99.99%) cobalt in vacuum to give the Pt_3Co composition. The alloy was cold-rolled after a homogenizing annealing at 1200°C and was cut into the form of rectangular parallelepiped, about 2 mm × 2 mm × 4 mm. The polycrystalline specimens were sealed in evacuated quartz tubes, and annealed at 1200°C for 2 hours and some of them were quenched into cold water. These specimens were at the disordered state. An intermediate state of order was obtained by quenching the specimens from 600°C, in the course of slow cooling from 800°C to room temperature for 18 days. The electrical resistivity and saturation magnetization of these specimens measured at room temperature are tabulated in Table II.

For the purpose of slip formation within the specimens, they were compressed up to several percent at a rate of one precent per second. To measure their saturation magnetization in the temperature range from liquid oxygen temperature to 400°C, a modified Domenicali type magnetometer was used. The details of this apparatus will be described elsewhere.[17] The saturation values of magnetization of specimens with various stages of deformation were measured in a magnetic field of 7500 Oe. The values were actually found to be independent of the field strength between 4100 Oe and 8900 Oe. The temperature of specimens could be changed up to room temperature in an evacuated quartz tube which was initially immersed into liquid oxygen. For the measurements at higher temperatures, the liquid oxygen vessel was replaced by an electrical furnace. The heating rate was about 2°C per minute through the whole temperature range.

Table II. Electrical resistivity and saturation magnetization measured at room temperature of Pt_3Co alloys with various order.

Specimen Number	1	2	3
Quenching Temperature, °C	1200	600	20
Electrical Resistivity, Ω-cm	42.7		40.3
Saturation Magnetization, gauss/g	18.9	9.6	2.5
Curie Temperature, °C	12	52	209

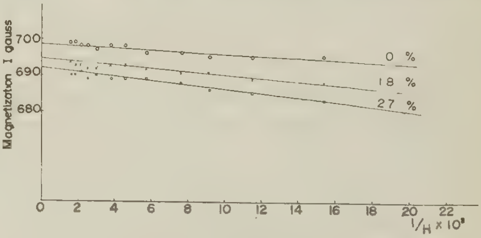

Fig. 2. Variation of magnetization intensity as a reciprocal function of field for the specimen quenched from 460°C. The amounts of elongation are indicated on the curves.

§ 3. Experimental Results and Discussions

3.1 Ni_3Mn

Some examples of magnetization curves are shown in Fig. 2, which represent the variation of magnetization as a function of reciprocal of field, I/H, for the specimens quenched from 460°C. They can be represented by straight lines in the range of considerably large field, namely a simple from $I=I_s(1-a/H)$ where I and I_s are the magnetization at field intensity H and infinity respectively and a is a constant, showing the inclination of the straight line. As W. F. Brown[18] has already explained, the inclination a increases with the amount of cold work. The saturation values of magnetization I_s can be determined by extrapolating the lines to an extremely large field. As can be seen in the figure, the saturation values so determined decrease with the amount of elongation. Fig. 3 (a) shows the decrease of the saturation magnetization, ΔI_s, measured at room temperature, as function of elongation for the specimens quenched from various temperature. In Fig. 3 (b), ΔI_s is replaced by $\Delta I_s/I_s$. As can be seen in these figures, the decrease of saturation magnetization is approximately proportional to the amount of elongation in the range of extension smaller than about 6%.

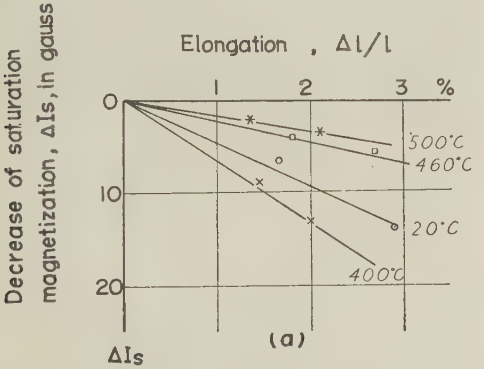

Fig. 3. Variation of decrease of saturations magnetization, ΔI_s and $\Delta I_s/I_s$, as a function of elongation. The quenching temperatures are indicated on the curves.

These results must be attributed to either a uniform decrease of ordering within the whole specimen or discrete disordered regions created by the cole work. Considering that the disordering process is a direct result of atomic slip, the latter case is reasonable, because the slip in metals is concentrated on widely spaced regions. If a lamina of crystal glide relative to its neighbour by an odd number of atomic distances, the effect is to disorder the atomic arrangement between these two neighbouring planes. Now, let us return to the slip mode. In the inhomogeneous slip, the disordering occurs only between two neighbouring atomic planes. Then one can not expect the appreciable decrease of the saturation magnetization due to cold work. Moreover, such a disordering occurs only when the slip distance is an odd number of atomic spacings. From energy consideration, such a slip seems to be rare compared with the slip of an even number of atomic spacings which does not accompany the disordering process. While, in the homogeneous slip, the disordered regions the thickness of which is more than a few hundreds A would be produced and accordingly the magnetization will decrease with the increase of the disordered region.

In the above discussion, only single dislocations are considered. However, in the ordered alloy, pairs of dislocations seem to appear and the number of them will increase with degree of order, because the slip plane is in anti-phase in either side of single dislocation being accompanied by high energy, which is reduced by the pair of dislocations. In case of pairs of dislocations, disordering does not occur as the direct results of the propagation of such dislocations. In inhomogeneous slip, the conclution mentioned above need not be changed. Moreover, even in the case of homogeneous slip, disordering process will not occur and appreciable decrease of magnetization is not expected after the cold work.

The present experimental results, i.e. the decrease of magnetization in Ni_3Mn proportional with the extension, lead to the conclusion that the slip takes place on many successive atomic planes by the movement of an appreciable number of single dislocations, even though the existence of pairs of dislocations might not be deniable. Under the extension smaller than about 3%, only one system of the slip planes within each crystal grain will be active, as was already shown by our electronmicroscopic observations.[19] In the homogeneous slip caused by single dislocations, the disordered regions and accordingly the change of magnetization as well will be proportional to the amount of elongation, in agreement with our experimental results. Moreover, the other experimental result that the decrease of magnetization caused by the cold work is larger in intermediate order than in ordered state might be explained by the facts that energy contained in anti-phase boundary is lower in intermediate order and consequently single dislocation is likely to be more probable to exist than in perfectly ordered state. The above argument leads one to believe that the slip in Ni_3Mn crystal takes place in atomic steps extending on many successive atomic planes, namely by the "homogeneous" slip.

However, there exists another factor which may affect the apparent saturation value of magnetization measured by ballistic method, that is, the deviation of shape of specimens from the ideal cylindrical from which is introduced during the cold work. It is difficult to estimate theoretically the amount of this effect. One experimental estimation of this effect is given by considering the same experiment on Ni_3Fe alloy of which saturation value scarecely changes due to the disordering (nearly 4%). The result on Ni_3Fe is indicated in Fig. 3 (b) by a mark, ⊙. The amount of this change can not be neglected, but is still small compared with that of Ni_3Mn.

Because of the difficulties to measure the absolute value of saturation magnetization more acurately, it seems favourable to assume that the distorted specimen consists of two kinds of regions with different Curie points. Unfortunately, as the magnetic intensity of the disordered Ni_3Mn alloy falls very gradually with increasing temperature, it is not easy to apply such an analysis to this case. While, in the case of Pt_3Co, the value of saturation magnetization falls so sharply with increasing temperature that one can apply this analysis. Moreover, as this alloy has higher Curie point in disordered state than in ordered state a small portion of disordered region embedded in the matrix of ordered phase gives a comparatively large contribution to total intensity of magnetization at a temperature near the Curie point of ordered state. This is a very favourable fact to our present purpose.

3.2 Pt_3Co

The magnetization-temperature curves of Pt_3Co with various stages of order are shown by full lines in Fig. 4, which were measurred at 7500 Oe from liqued oxygen temperature to 400°C using the magnetic belance described in Section 2.2. These curves are typical saturation magnetization-temperature curves for ferromagnetic substances of single phase, the Curie points of which are about 12°C, 51°C and 209°C respectivery, and these curves seem to tend the same saturation value at 0°K. The saturation value of disordered state is about 18.9 gauss/g at room temperature, while that of ordered state is about 2.5 gauss/g.

The ordered specimen was compressed by a specially devised small compressor. Fig. 5 shows the saturation magnetization-temperature curves of the ordered alloy of various stages of compression measured at temperatures near their Curie points. The differences between these curves are represented in Fig. 6. As shown in this figure, a considerable amount of difference can be seen between the curves of undeformed and deformed specimen, especially in temperature above the Curie point of the undeformed alloy. Roughly speaking, this result may be understood as a formation of new regions, of which the Curie point is higher than that of original phase, in argeement with the result on Ni_3Mn alloy.

To make clear this situation, it will be appropriate to replace Fig. 6 by Fig. 7. Fig. 7 represents the ratios of $\sigma_5/\Delta\sigma_2$ and $\Delta\sigma_8/\Delta\sigma_5$ in temperature above the Curie point of undeformed

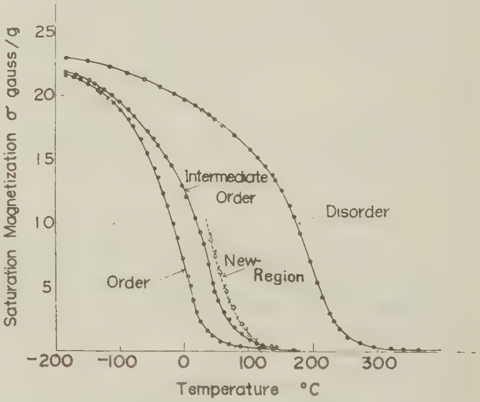

Fig. 4. Magnetization-temperature curves of Pt_3Co alloy with various stages of order. The dotted line represents the estimated curve for the new disordered region produced after slight compression; for 4% elongation and for 7% elongation.

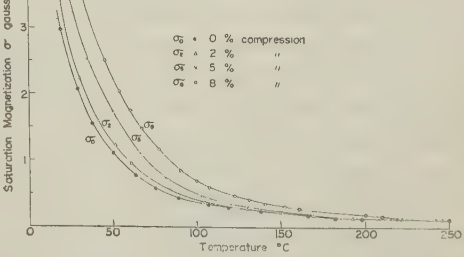

Fig. 5. Magnetization-temperature curves of the ordered Pt_3Co alloy of various states of compression near the Curie point. The amounts of compression are indicated in the figure.

formed ordered alloy, where $\Delta\sigma_2$, $\Delta\sigma_5$ and $\Delta\sigma_8$ are the differences between magnetization values of 2%, 5% and 8% compressed specimens and that of undeformed alloy respectively. As can been seen, the values of $\Delta\sigma_5/\Delta\sigma_2$ and $\Delta\sigma_8/\sigma_5$ are approximately constant over wide range of temperature. This result is reasonable quantitatively from the point of view that any amount of compression is associated with the creation of new disordered region with higher Curie point than that of the original ordered phase. The constant value 3.2 and 2.0 obtained from the figure are slightly larger than the simply expected values 5/2 and 8/5. This may be attributed to the following two factors; one is the experimental error in the measurment of amount of compression, the other is the appearance of multiplicated slip system associated with the increase of deformation.

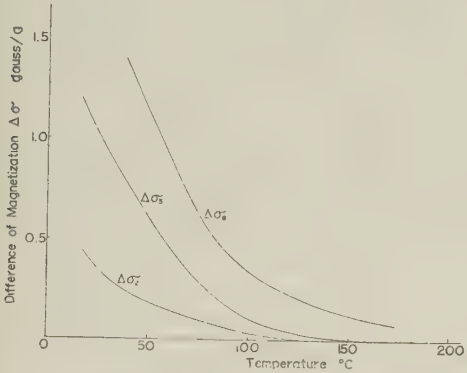

Fig. 6. Difference of magnetization between deformed specimens and undeformed one in the temperature near the Curie point for ordered state of Pt_3Co alloy. The amount of elongation are indicated on the curves.

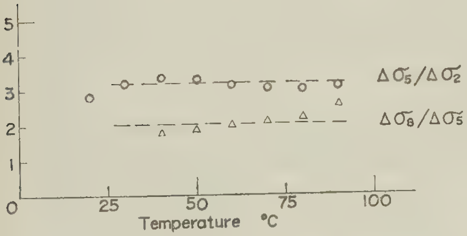

Fig. 7. $\Delta\sigma_5/\Delta\sigma_2$ and $\Delta\sigma_8/\Delta\sigma_5$ as a function of temperature.

The saturation magnetization-temperature curves of the new disordered region produced after 2% and 5% compression can be estimated and represented by a dotted line in Fig. 4. The difference between Curie points of the mechanically disordered region and that of thermally disordered phase would be reasonable because the new region is in a directional order, namely ordering in a perpendicular direction to the slip plane is broken away but that on the slip plane is maintained constant. This curve is nearly the same as one of intermediate state of order as shown in this figure. Thus the increase of magnetization of the deformed alloy may be explained due to the new disordered regions produced during the deformation where the slips take place by an amount of order of one atomic distance on many successive planes, namely by the "homogeneous" slip.

§ 4. Summary and Acknowledgment

The experimental results can be summarized as follows:

1) In the ordered Ni_3Mn alloy, of which the Curie point is higher than that of disordered state, the saturation magnetization decreases with an amount of elongation at room temperature.

2) In the ordered Pt_3Co alloy, of which the Curie point is lower than that of disordered state, the intensity of magnetization in temperature near the Curie point increases with an amount of compression.

3) These changes of magnetization are roughly proportional to an amount of deformation.

These results can be only understood from the point of view that a new disordered phase of which the Curie point is different from that of original phase is produced during the deformation, in which the slips take place by an amount of order of one atomic distance on successive plane, namely by the "homogeneous" slip.

It is great pleasure for the authors to thanks Prof. S. Kaya for his valuable suggestions, discussions and encouragement throughout this work. The authors also wish to express hearty thanks to prof. R. R. Hashiguchi, Prof. S. Chikazumi, Dr. T. Suzuki, Dr. Y. Tomono, and Dr. S. Iida for their kind discussions.

References

1) R. D. Heidenreich and W. Shockley: *The Strength of Solids* (London, Phys. Soc., 1948) 57.

2) A. F. Brown: Nature **163** (1949) 961; Advances in Physics **1** (1952) 427.
3) D. Kuhlmann-Wilsdorf and H. Wilsdorf: Acta Met. **1** (1953) 394. D. Kuhlmann-Wilsdorf, J. H. van der Merwe and H. Wilsdorf: Phil. Mag. **43** (1952) 632.
4) G. Thomas and J. Nutting: J. I. Metals **85** (1956-7) 1.
5) A. Seeger, J. Diehl, S. Mader and H. Rebstock: Phil. Mag. 8 series **2** (1957) 323.
6) T. Nagashima and T. Yamamoto: Acta Met. **4** (1956) 94. T. Taoka and S. Sakata: Acta Met. **5** (1957) 61.
7) N. F. Mott: Proc. Phys. Soc. London **B, 64** (1951) 729.
8) H. Wilsdorf and J. T. Fourie: Acta Met. **4** (1956) 271.
9) N. V. Yakutovich, E. S. Ykovleva, R. M. Leriman and N. N. Bujnov: Izv. Akad. Nauk. SSSR. **15** (1951) 382. A. F. Brown: Advances in Physics **1** (1952) 455.
10) H. Suzuki and F. E. Fujita: J. Phys. Soc. Japan **9** (1954) 428.
11) T. Suzuki and H. Suzuki: Crystal Dislocation (Proc. of Int. Conf. of Theor. Phys. Kyoto and Tokyo 1953) 571. Sci. Rep. Res. Inst. Tohoku Univ. **A, 6** (1954) 574. T. Suzuki: Sci. Rep. Res. Inst. Tohoku Univ. **A, 6** (1954) 309. H. Suzuki: J. Phys. Soc. Japan **9** (1954) 531.
12) A. F. Brown and R. W. K. Honeycombe: Phil. Mag. **42** (1951) 1146.
13) A. F. Brown: Advances in Physics **1** (1952) 427.
14) T. H. Blewitt and J. S. Koehler: Synposium on Plastic Deformation of Crystallin Solids (Pittsburgh 1950) 77.
15) S. Kaya and M. Nakayama: Proc. Phys. Math. Soc. Japan **22** (1940) 126. T. Taoka and T. Ohtsuka: J. Phys Soc. Japan **9** (1954) 723.
16) A. W. Simpson and R. H. Tredgold: Proc. Phys. Soc. London **B, 67** (1954) 38.
17) K. Yasukochi: to be Published.
18) W. F. Brown: Phys. Rev. **60** (1941) 139.
19) T. Taoka and R. Honda: J. of Electronmicroscopy Japan **5** (1957) 19.

Journal of the Physical Society of Japan, Vol. 14, No. 7, July, 1959

Photoconduction and Darkening of AgCl Crystals at Low Temperatures

By Noriaki Itoh

Department of Electrical Engineering, College of Engineering, Osaka University

and Tokuo Suita

Department of Nuclear Engineering, College of Engineering, Osaka University

(Received February 9, 1959)

Photocurrent of AgCl was measured using light and voltage pulses of about 50 μsec duration between −150°C and −50°C. Experimental results show that the life time of electrons has a maximum between −80°C and −110°C depending on the treatments of the samples. Darkening of the crystals was also measured at lower temperatures, showing that the darkenability increases with temperature higher than −80°C. The results were discussed with models containing sensitivity centers and recombination centers and it seems to be clear that the temperature dependence of the life time is concerned with the darkening properties of the crystals.

§ 1. Introduction

According to Gurney and Mott theory[1] on photographic processes in silver halide crystals, there are two fundamental stages in it, namely the electronic stage and the ionic stage. In the first stage, pairs of conduction electrons and holes are created by absorbing photons and these charge carriers are trapped at some trapping sites after wandering in the crystals. In the second stage, the negatively charged centers attract interstitial silver ions which combine with the trapped electrons to form silver atoms. This principle was verified by Haynes and Shockley[2], who showed that photolytic silvers were displaced by voltage pulses and showed that electrons are participating in the photolytic processes,

Gurney and Mott theory, however, explained nothing about the detailed mechanisms involved, for example, about the nature of the trapping centers nor about the behaviors of holes. In these connections Seitz[3] and Mitchell[4] gave another theories, although the principle by Mott and Gurney remained unchanged. Seitz explained that the photolytic silvers are formed at the incipient vacancies which have half charge and attract electrons and silver ions alternately. By Mitchell's theory holes are trapped with the production of interstitial silver ions and this silver ions combine with liberated electrons at so-called sensitivity centers.

In order to clarify the mechanism of photographic processes, it is necessary to study the nature of trapping centers. Although most of the features of trapped electrons and holes in alkali halide crystals have been studied by optical methods[5], these methods are not so powerful in silver halide crystals. Kaiser[6] found a peak at 375 mμ in AgCl having excess silver at low temperatures. This center changed into colloidal silver when crystals were warmed to room temperatures, and Seitz considered it to be a kind of F-center.[7]

Another method of obtaining some knowledges of trapping centers for electrons and holes is to measure photocurrent. Gilleo[8] measured photocurrent by monochromatic light after filling up trapping centers by photoemission from electrodes. His results showed that there are five bands for electrons and two bands for holes. Van Heyningen and Brown[9] have studied current glow curve of AgCl after illumination at 9°K, and showed that there are three kinds of electron traps having glow peaks at 15°K, 35°K and 170°K. It has also been cleared that photolytic silvers are formed preferentially near dislocation lines by the observation of Hedges and Mitchell[10], showing that the sensitivity centers are located near dislocation lines. In spite of these studies, the detailed nature of trapping centers have not been specified yet.

The purpose of the present investigation is to study the behavior of photoelectrons by measuring photocurrent and darkening at various temperatures. Crystals used in the present experiments were grown by Kyropoulos method in air and they may contain a certain amount of oxygen and have some effects on photoelectric and photolytic properties as pointed out by Brown[11] and Mithcell[12]. Therefore, our results may be concerned with the presence of oxygen. Studies on these points and effects of impurities are now in progress.

§ 2. Experimental Procedures

As silver chloride crystals are good ionic conductors, it should be avoided to apply them D. C. voltages, especially at higher temperatures. It also should be avoided to illuminate the crystals for overly long period to prevent their photographic reactions. Therefore, both voltage and light pulses were used for the measurement of photocurrent. The length of both pulses was about 50 μsec, and their repeatness was 30 cycles/sec.

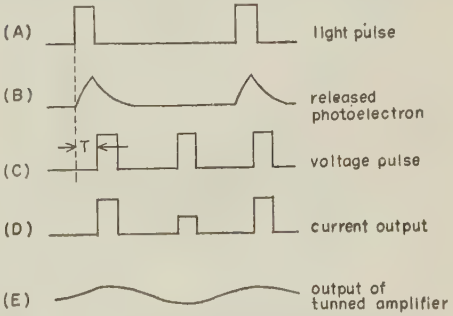

Fig. 1. Waveforms of the measuring system.

In order to obtain higher sensitivity and to measure the time response of photocurrent, we used the methods shown schematically in Fig. 1. Some devises have been made in order to separate photocurrent component from dark current and charging current component. The similar methods were utilized in the measurements of optical absorption change of gasses.[13] The crystal was illuminated by light pulses (A) (Fig. 1), having frequency of 30 cycles/sec, by which photoelectrons will be released as shown in (B). The rectangular voltage pulses (C) of 50 μsec, were applied to the specimens at a frequency of 60 cycles/sec, and the current output would be as shown by (D). The difference between the magnitude of any current pulses and the following ones coinsides with the conductivity change induced by light pulses. This difference was amplified by a narrow band amplifier, which has the center frequency of 30 cycles/sec. By changing the delay time, T, of the voltage pulses to the light pulses, the time dependence of photocurrent was also measured. Measurements were also done using 800 cycles/sec light pulses instead of 30 cycles/sec light pulses.

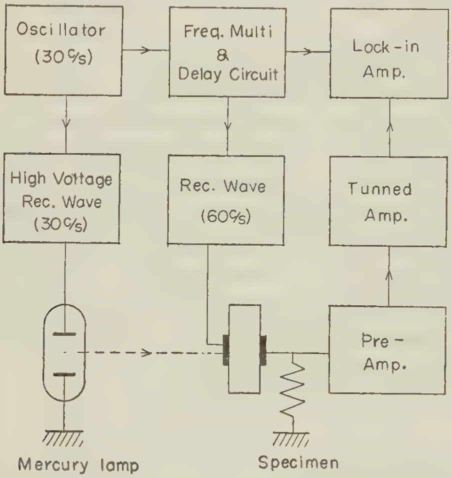

Fig. 2. Block diagram of the measuring apparatus.

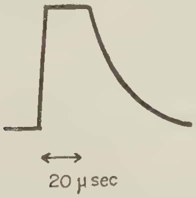

Fig. 3. Waveform of light pulses.

The block diagram of the apparatus is shown in Fig. 2. The light pulses were generated by applying rectangular high voltage pulses to a mercury arc lamp with V-V1A filter. The waveform of the light pulses is shown in Fig. 3, and its decay time constant was 50 μsec. The delay circuit between the 60 cycles/sec rectangular wave generator and the master oscillator could change the time interval between light pulses and voltage pulses. The tunned amplifier contained a rejection filter of 60 cycles/sec, so that the gain at 60 cycles/sec was at least some thousandths of that at 30 cycles/sec.

For the darkening experiments, the high pressure mercury lamp of 100 watt with V-VIA filter were used as a light source and the absorption coefficients were measured by Beckman type spectrophotometer (Shimazu, QB-50) at room temperature.

The crystals of AgCl were grown by Kyropoulos method in air. Recrystallization was repeated three or four times in order to get pure specimens. The specimens were cut from large crystal blocks. For the measurement of photocurrent the specimens were $1\times20\times20$ mm^3 plates and for the measurement of optical absorption the specimens were $1\times10\times10$ mm^3 plates. After being cut the specimens were ground by sand paper, polished on dry oil stone and washed by distilled water, which served a good optical surface. The electrode were thin silver plates made by development on the surface of the specimens with photographic developer, and through these electrodes the specimens were illuminated. The measurements were done in a vacuum cell with quartz windows.

§ 3. Experimental Results

We measured the temperature dependence of photocurrent using voltage and light pulses, the results of which are shown in Fig. 4. In this case every light pulses were superimposed on the voltage pulses, and there was no delay between the light pulses and voltage pulses. These results did not depend on the duration of both voltage and light pulses, showing that they are free from space charge effects.

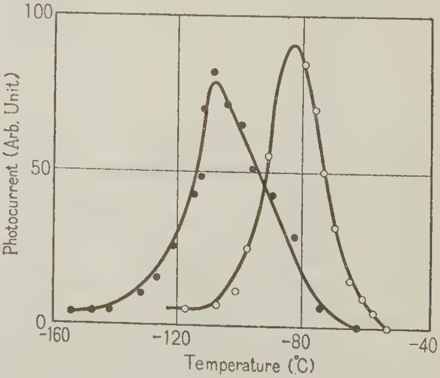

Fig. 4. Temperature dependence of photocurrent of AgCl measured by light and voltage pulses of 50 μsec duration. Applied voltage, 650V/cm; —○—○— with specimens not pre-illuminated; —●—●— with specimens pre-illuminated for 30 min at room temperature.

They also did not depend upon the repeatness of both pulses except at the lowest temperatures where decay time constant of photocurrent is near the time interval of voltage pulses (Fig. 7). As shown in Fig. 4, the photocurrent temperature curve takes a maximum and the temperature of the maximum photocurrent shifts to lower temperature side by pre-illumination at room temperature. In the case of virgin specimen the photocurrent takes a maximum at about −80°C, and this results are almost reproducible during several runs as long as the measurements were limited below −50°C. But in order to avoid the complication due to changes of the results during the measurements for virgin specimens, we used the specimens pre-illuminated for 30 minutes at room temperature in the following measurements of photocurrents.

As the photocurrent depends on the quantum yield of free electrons and holes formation η, mobility of electrons μ, and mean life time of electrons τ as $i=Ie\eta\mu\tau$ (holes are not expected to move), where I is the number of incident photons per second, it is necessary for us to know which factors are the most important to explain the photocurrent temperature curve shown above. Therefore, the voltage current curve were measured at several temperatures, the results of which are shown in Fig. 5. From these curves the Schubweg of electrons[14] $w=\mu\tau$ can be calculated. At −106°C we obtained the Schubweg of 5×10^{-4} cm^2/volt and from which we get the life time of 5×10^{-6} sec using the mobility of 100 cm^2/volt sec.[15] The Schubweg at −80°C and −128°C is about one tenth of the value at −106°C, showing that the Schubweg takes a maximum near −108°C. We can conclude qualitatively from these results that the temperature dependence of the photocurrent is determined mainly by the temperature dependence of Schubweg and not of quantum yield.

It can be shown that the dependence of mobility on temperature obtained by various authors[15] is quite small comparing with that of photocurrent obtained by us. Therefore the rapid change in photocurrent with temperature seems to be almost entirely due to

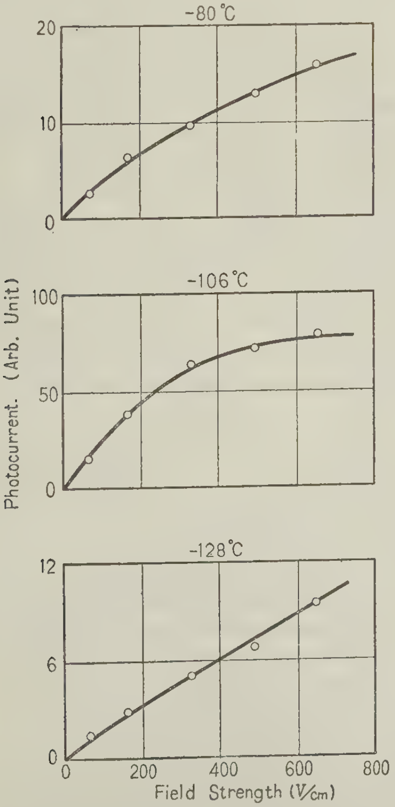

Fig. 5. Photocurrent vs. field strength measured with light and voltage pulses

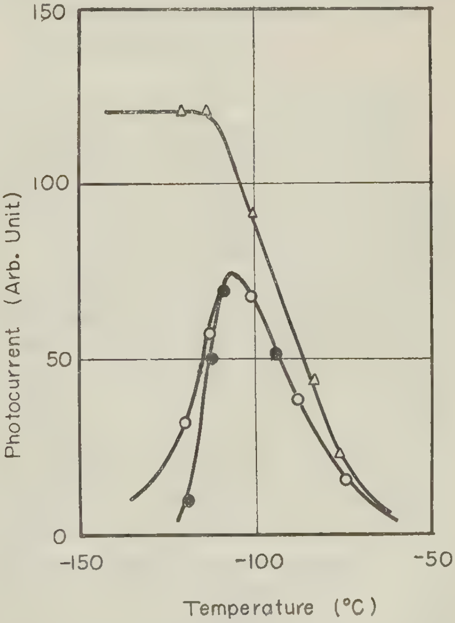

Fig. 6. Effect of continuous illumination on pulse photocurrent: —○—○—, without continuous illumination; —●—●—, with continuous illumination of 600 mμ; —△—△—, with continuous illumination of 400 mμ. Applied pulse voltage, 650 v/cm.

the change of life time of electrons with temperature.

In order to get some knowledges about the nature of the trapping centers which may cause such a temperature dependence of photocurrent, measurements were done on the change of pulse photocurrent due to constant illumination. These additional illumination may vacant the trapping centers if its wavelength corresponds to the energy depth of trapping centers, and may fill up the trapping centers if its wavelength corresponds to the energy of the forbidden gap. The effect of additional continuous illumination are shown in Fig. 6. The additional light was illuminated from the side wall. Photocurrent due to continuous illumination can be discriminated from that due to light pulses because the amplifier is sensitive only to 30 cycles/sec signals. When the wavelength of continuous light was 400 mμ, the photocurrent increased at lower temperatures and showed no maximum. When it was near 600 mμ, the photocurrent decreased a little at lower temperatures.

The decay characteristic of photocurrent was also measured at several temperatures, the results of which are shown in Fig. 7, where the abscissa is the time interval T between voltage pulse and light pulse (see Fig. 1). At higher temperatures than −108°C the decay time constant was lower than 50 μsec. However, at −120°C the decay time constant was about 1 msec. Measurements were also done on the build-up of photocurrent by 1 msec light pulses and obtained the results showing slow build-up at lower temperatures than −108°C.

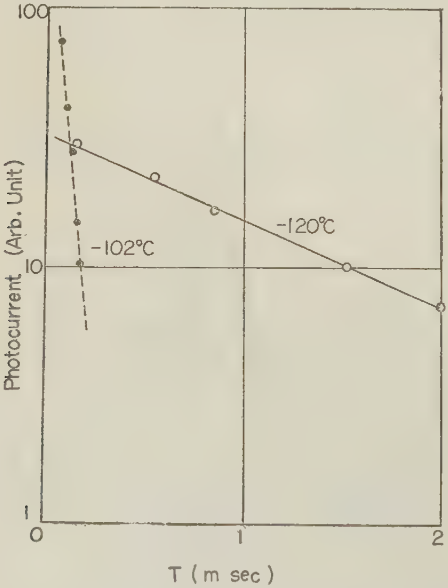

Fig. 7. Decay curve of photocurrent after light pulses. T, time difference between light pulses and voltage pulses; applied voltage, 650 V/cm (The result at −102°C is shown by a dotted line because it is the same as the decay of light pulse)

In the case of photographic film, it was shown that photographic sensitivity increased rapidly with increasing temperature.[16] It is interesting to know if there are any relations between the photocurrent-temperature curve and the temperature dependence of the rate of formation of photolytic silver in silver chloride crystals. In order to examine the rate of formation of photolytic silver with various temperatures, the change of absorption coefficient at room temperatures were

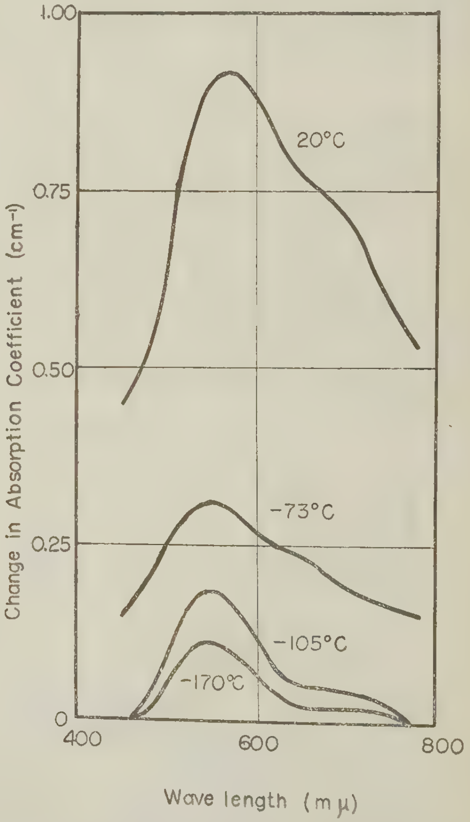

Fig. 8. Change of absorption coefficient measured at 20°C, after low temperature illumination. Illumination was done from lower temperature subsequently, that is, −170°C, −105°C, −73°C, and 20°C.

measured after illuminations at lower temperatures. Wainfan[17] showed that optical absorption changes did not occur by illumination at −100°C, but they occured after warming to room temperature by our results. It may be possible because silver ions will be attracted to trapped electrons during warming up. In Fig. 8 the change of absorption coefficient after subsequent illumination from lower temperatures for virgin specimens is shown. The results for 20°C are just the same as Wainfan's results, but for lower temperature illumination the peak is rather narrow. Fig. 8 shows that at higher temperatures than −73°C the change of absorption coefficient due to illumination becomes considerable although at −105°C it was just the same as that at −170°C. It may be concluded from this results that the formation of photolytic silver becomes considerable at higher temperatures than −80°C.

In order to know the concentration of sensitivity centers, it is useful to investigate the relation between the darkening and the illumination period at low temperatures. At low temperatures only a few silver atoms are formed in each sensitivity centers because Ag^+ ions move very slowly in these temperatures. As shown in Fig. 9 the absorption change is independent on the illumination period more than 1 hour illumination, which seems to indicate that all sensitivity centers are filled up by about 1 hour illumination at −170°C. From the absorption curve for three hours illumination we can estimate* the concentration of sensitivity centers by Smakula's formula[18], getting the value of the order of 10^{16}, if we take the oscillator strength about 0.1.

§ 4. Discussion

As explained in the previous sections, it seems to be clear that the abrupt change of photocurrent observed in the present experiments seems likely to be due to the temperature dependence of life time of electrons. We are going to discuss the nature of the trapping centers in silver chloride crystals from the experimental results obtained.

The types of trapping centers which we should take into consideration are as follows;
(1) shallow trapping centers, the depth of which is comparable with kT,
(2) recombination centers in which recombination of electrons and holes occurs, and
(3) sensitivity centers in which photographic silver are formed.

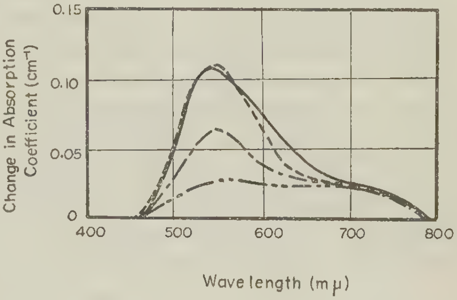

Fig. 9. Change of absorption coefficient measured at 20°C, after illumination at −170°C. ———, 3 hours illumination; - - - - -, 1 hour illumination; —·—· 10 min. illumination; and —··—··, 2 min. illumination.

In discussing our results it should be noted that we are measuring by repeated light pulses whose interval was about 30 msec. By each pulse, photoelectrons are released which will be trapped at several kinds of trapping centers within less than 10 μsec. These trapped electrons will redistribute themselves in the following time interval, and photocurrent for the next light pulse is dependent upon the number of vacant trapping centers at the start of the light pulse. As the measurement was done after the steady state was established, the magnitude of our photocurrent depends upon the rate of neutralization of trapped electrons.

It seems clear that the increase of photocurrent with temperature can be explained by the presence of shallow trapping centers as discussed in the case of alkali halide[19]. At lower temperatures electrons trapped by these centers can hardly be released from them within the termination of light pulse, whereas at higher temperatures they are released instantaneously by thermal agitation which serves to increase the photocurrent. This consideration is consistent with the results of decay time measurement; decay time is long when the thermal release occurs slowly. The depth of shallow trapping centers from the conduction band bottom is estimated to be about 0.3 eV, if we assume that the frequency factor is about 10^{13}.

---

* It is not clear that the Smakula's formula are applicable to the case of this center. However it seems reasonable that the equation can be used for order estimation, if we consider the facts obtained by F. C. Brown and N. Wainfan[17] that the absorption band due to the coloration at room temperature can be bleached by illuminating the crystal by the light near the peak of the band. Moreover, the center causing the absorption peak of Fig. 9 seems to be composed of a few silver atoms because the illumination was done at low temperatures.

The decrease of photocurrent with temperature has not been reported in other insulating crystals. In semiconductors such as CdS these phenomena were observed[20]. It can be explained if we assume that the number of effective trapping centers for electrons increases with temperature. In the case of CdS these phenomena are explained by the increase of recombination velocity of free electrons and holes with increasing temperature. In extremely low temperatures holes are trapped by shallow hole traps which can trap only holes. Therefore, recombination do not occur, and recombination center are all filled with electrons during the measurement. With increasing temperature the trapped holes begin to be released thermally and recombine with electrons at recombination centers. Thus the rate of trapping electrons at recombination centers increases with temperature.

The explanation above may be applicable in the case of silver halide crystals. We can, however, make another explanation taking sensitivity centers into consideration. It is suggeseted by the theory of photographic sensitivity that the photographic silvers are formed by the neutralization of trapped electrons by interstitial silver ions at sensitivity centers. With increasing temperature the mobility of silver ions increases and the formation of photographic silver occurs with higher rate. As sensitivity center can trap electrons again after neutralization, the photocurrent will decrease with temperature because the number of effective trapping centers increases with increasing temperature.

Energy diagram for the both explanation are shown in Fig. 10. In any case we should assume the existence of deep lying centers besides the shallow trapping centers, which are filled with electrons generated by successive light pulses at low temperatures. In our measurement by repeated voltage and light pulses, it takes several seconds to reach a stational value of photocurrent after illumination is begun. This fact supports the existence of such deep lying trapping centers. Another evidence of such trapping centers is given by the results of Fig. 6. The fact that the photocurrent decreases by the illumination with 600 mμ light at lower temperatures shows that these trapping centers are filled at lower temperatures. These phenomena occur by the illumination near 600 mμ, so that the depth of these centers can be estimated near 1.5 eV below the conduction band.

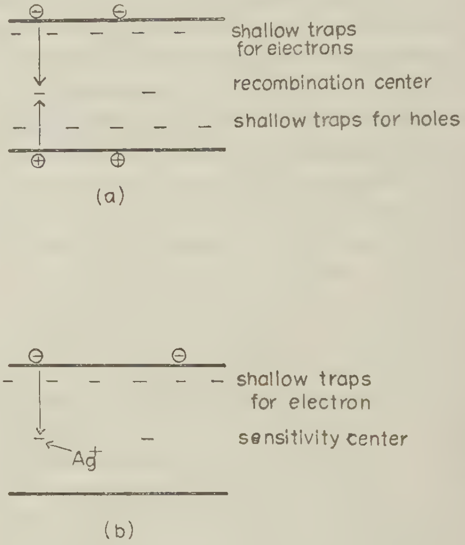

Fig. 10. Energy diagram of models, containing (a) recombination centers and (b) sensitivity centers.

The effect of illumination with 400 mμ light can be explained considering shallow trapping centers. Electrons are always released from valence band by constant illumination, which are trapped by shallow trapping centers at low temperatures. Therefore, current response due to light pulse is much higher in the presence of continuous illumination at these temperatures. With increasing temperatures, the neutralization with silver ions or positive holes become more frequent which *surpasses* the rate of electron liberation by continuous illumination.

Considering the facts that the photographic sensitivity increases with temperature, second explanation seems to be more reasonable. That is because if recombination rate increases with temperature the photographic sensitivity should decrease with temperature.

The following fact seems to support the above explanation. If we plot the decreasing part of our photocurrent-temperature curve by log (photocurrent) and $1/T$, we get a straight line, the slope of which shows the activation energy of 0.5 eV. It can be easily seen that the effective number of trapping centers is proportional to the velocity of neutralization of trapped electrons, which will be proportional to the diffusion velocity of silver ions. The activation energy obtained from the conductivity-temperature curve in these temperature regions[21)] is approximately the same as that obtained from the photocurrent-temperature curve.

The results of our experiments seems to be explained by considering two kinds of trapping centers. The one is shallow trapping centers whose depth is about 0.3 eV. The another is rather deep one whose depth is about 1.5 eV and the density is estimated to be of the order of 10^{15}/cc. The nature of these centers is not known clearly. From the results of Fig. 4 they are sure to depend on the existence of large silver aggregates formed by pre-illumination at room temperature. We are now proceeding the experimental study to know the effect of impurity and imperfections on the photocurrent and darkening.

We would like to express our gratitude to Dr. E. Mizuki and other staffs of the Research Laboratory of Fuji Photo Film Co. for their valuable discussions and their supplying raw material. We are also thankful to Dr. Y. Inuishi and other staffs of our Laboratory for their helpful discussions.

References

1) N. F. Mott and Gurney: *Electronic Processes in Ionic Crystals* (Oxford, 1948).
2) J. R. Haynes and W. Shockley: *Reports on Conference of Strength of Solids* (Phys. Soc., London, 1948) 151; Phys. Rev. **82** (1951) 935.
3) F. Seitz: Rev. Mod. Phys. **23** (1951) 328. F. Seitz and F. C. Brown: *Photographic Sensitivity* ed. by S. Fujisawa vol. **2** (Maruzen, Tokyo, 1958) 11.
4) J. W. Mitchell: J. Phot. Sci. **5** (1957) 49; *Photographic Sensitivity*, vol. **2** (Maruzen, Tokyo, 1958) 47.
5) F. Seitz: Rev. Mod. Phys. **26** (1954) 7.
6) W. Kaiser: Z. Phys. **132** (1953) 497.
7) F. Seitz: *Photographic Sensitivity*, ed. by S. Fujisawa, vol. **1** (Maruzen, Tokyo, 1956) 5.
8) M. A. Gilleo: Phys. Rev. **91** (1953) 534.
9) R. S. Van Heyningen and F. C. Brown: Phys. Rev. **111** (1958) 462.
10) J. R. Hedges and J. W. Mitchell: Phil. Mag. (7) **44** (1953) 223. See also H. Kanzaki: J. Phys. Soc. Japan **11** (1956) 120, 126.
11) F. C. Brown: J. Phys. Chem. Solids **4** (1958) 206.
12) J. W. Mitchell: Phil. Mag. (8) **2** (1957) 1276.
13) A. V. Phelps and J. L. Pack: Rev. Sci. Instr. **26** (1955) 45.
14) Ref. 1, p. 122.
15) F. C. Brown: Phys. Rev. **99** (1955) 355. C. Yamanaka, E. Sakai and T. Suita: J. Phys. Soc. Japan **10** (1955) 238.
16) J. H. Webb and C. H. Evans: J. Opt. Soc. Amer. **28** (1938) 249.
17) F. C. Brown and N. Wainfan: Phys. Rev. **105** (1957) 93. N. Wainfan: Phys. Rev. **105** (1957) 100.
18) A. Smakula: Z. Phys. **59** (1930) 603.
19) R. W. Pohl: Ann. Physik **29** (1937) 239. Von Gericke: Nachr. Akad. Wiss. (Göttingen, 1950) 1.
20) R. H. Bube: *Photoconductivity Conference*, ed. by R. G. Breckenridge, B. R. Russel and E. E. Hahn (Wiley, New York, 1956) 575.
21) W. Lehfeldt: Z. Phys. **85** (1933) 717.

JOURNAL OF THE PHYSICAL SOCIETY OF JAPAN, Vol 14, No. 7, JULY, 1959

On the Non-Isothermal Diffusion Theory of Rectifiers*

By Tadasi NUMATA

Nagasaki University, Ohasi-Machi, Nagasaki, Japan

(Received February 26, 1959)

The general non-isothermal diffusion theory of rectifiers has been derived by using the non-isothermal diffusion equation deduced from the formal theory of conduction. The rectification equation obtained depends clearly upon temperature distribution in a barrier. If a temperature difference exists between the both ends of the barrier, then the appearance of thermoelectromotive force is predicted from the present theory. Taking into account the non-isothermal property of the barrier, the present theory shows the tendency that the values of the dielectric constants of barrier materials for Cu_2O and Se rectifiers determined from the capacitance-voltage characteristics seem to approach those of the bulk materials of Cu_2O and Se, respectively.

§ 1. Introduction

The diffusion theories of rectifiers which were first presented by Wagner[1] have been later developed by Mott[2], Schottky[3], and many other authors.[4] Especially Billig[5] and Landsberg[6] have recently developed the theory further in a general way. But all these theories have been so constructed as to be essentially isothermal since these theories had been developed by using the well-known isothermal diffusion equation established by Wagner.

While an electric current flows through a rectifier disk, the heat generation occurs necessarily in a barrier region. Therefore the barrier and its neighbour playing an important part in respect of rectification phenomena should become non-isothermal, and this tendency would become more conspicuous with increased applied voltage in both forward and reverse directions. So it is desirable from the theoretical point of view to construct a non-isothermal diffusion theory of rectifiers taking into account the non-isothermal property of the barrier. Of course, in order to construct such a theory, it is necessary to introduce the non-isothermal diffusion equation which is a starting-point for non-isothermal theories.

In this paper, we shall first introduce a general non-isothermal diffusion equation of rectifier theory by generalizing a non-isothermal diffusion equation deduced from the formal theory of conduction, and next construct generally a non-isothermal diffusion theory on the same line as the isothermal theory presented by Landsberg.[7]

§ 2. A General Non-Isothermal Diffusion Equation

We shall presuppose a simple n-type semiconductor. Results derived on this assumption can be applied to a p-type semi-conductor by making some modifications for the charge and the mass of charge carriers and for the energy, etc..

Supposing first that the Maxwell-Boltzmann distribution function applies to conduction electrons in a conduction band of a semiconductor, electrical conduction by those electrons in the absence of magnetic fields is given by

$$j = eK_1\left\{eE - kT\frac{\partial}{\partial x}\left(\ln\frac{n}{T^{3/2}}\right)\right\} - \frac{e}{T}K_2\frac{\partial T}{\partial x} \tag{1}$$

from the formal theory of conduction,[8] where j is the current density which flows in the direction of the positive x-axis, e the (algebraic) charge on the electron, n the volume density of the conduction electrons, k the Boltzmann's constant, T the absolute temperature, E the electric field applied parallel to the x-axis, and K_s is given by the following equation :

$$K_s = \frac{2^{\frac{1}{2}p+2}\mu n}{3\pi^{1/2}m^{\frac{1}{2}p+1}}(kT)^{S+\frac{1}{2}p-1} \cdot \Gamma\left(S + \frac{1}{2}p + \frac{3}{2}\right), \tag{2}$$

in which m is the effective mass of electron,

---

* A part of this paper was published in Science Bulleín of the Faculty of Liberal Arts and Education, Nagasaki University, **7** (1958) 13 (in Japanese).

Γ the gamma function, and the electron energy has been measured from the bottom of the conduction band. In obtaining Eq. (1) it has been assumed that a time of relaxation is given by $\tau=\mu c^p$, where μ is a constant, c the velocity of an electron, and p a suitable parameter.[9]

Provided we put as follows:

$$v\equiv-\frac{eK_1}{n}, \tag{3. a}$$

$$D\equiv\frac{K_1kT}{n}, \tag{3. b}$$

$$\delta\equiv\left(\frac{K_2}{T}-\frac{3}{2}kK_1\right), \tag{3. c}$$

then Eq. (1) yields

$$j=-envE-eD\frac{\partial n}{\partial x}-e\delta\frac{\partial T}{\partial x}. \tag{4}$$

For $\partial T/\partial x=0$, we get the isothermal diffusion equation

$$j=-envE-eD\frac{\partial n}{\partial x}, \tag{5}$$

which has been used hitherto for rectifier theories. Here v and D are the mobility and the diffusion coefficient, respectively.

Dividing the both sides of Eq. (4) by eD, we obtain

$$-\frac{j}{eD}=\lambda n\frac{\partial V}{\partial x}+\frac{\partial n}{\partial x}+\Lambda\frac{n}{T}\frac{\partial T}{\partial x}, \tag{6}$$

where V is the potential energy of an electron.

By using Eqs. (2), (3. a), (3. b), and (3. c), we get

$$\lambda=-\frac{v}{eD}=\frac{1}{kT}, \tag{7. a}$$

$$\Lambda=\frac{T}{n}\frac{\delta}{D}=\left(1+\frac{1}{2}p\right). \tag{7. b}$$

Eq. (7. a) represents the validity of Einstein's relation under the above assumptions. Eq. (7. b) shows that Λ is a constant including p as a parameter.

In the case that the Fermi-Dirac distribution function applies to the conduction electrons, we get the same expression for the current density j as Eq. (4), where v, D, and δ are, respectively, given by[10]

$$v\equiv-\frac{eK_1}{n}, \tag{8. a}$$

$$D\equiv\frac{2kT}{n}K_1\frac{F_{1/2}(\zeta^*)}{F_{-1/2}(\zeta^*)}, \tag{8. b}$$

$$\delta\equiv\left(\frac{K_2}{T}-3kK_1\frac{F_{1/2}(\zeta^*)}{F_{-1/2}(\zeta^*)}\right), \tag{8. c}$$

where K_s and $F_\xi(\zeta^*)$ are, respectively, the following integrals

$$K_s=-\frac{16\sqrt{2}\pi m^{1/2}}{3h^3}\int_0^\infty\tau E^{s+\frac{1}{2}}\frac{\partial f_0}{\partial E}dE, \tag{9}$$

$$F_\xi(\zeta^*)=\int_0^\infty\frac{x^\xi dx}{1+e^{x-\zeta^*}}, \quad (\xi>-1), \tag{10}$$

here h is the Planck's constant, f_0 the Fermi-Dirac distribution function in a thermal equilibrium state, ζ^* the thermodynamic potential divided by kT. In the equation corresponding to Eq. (6) we obtain

$$\lambda=-\frac{v}{eD}=\frac{1}{2kT}\frac{F_{-1/2}(\zeta^*)}{F_{1/2}(\zeta^*)}, \tag{11. a}$$

$$\Lambda=\frac{\delta T}{nD}=\frac{1}{2}\frac{5+p}{3+p}\frac{F_{-1/2}(\zeta^*)}{F_{1/2}(\zeta^*)}\frac{F_{3/2+p/2}(\zeta^*)}{F_{1/2+p/2}(\zeta^*)}-\frac{3}{2}, \tag{11. b}$$

according to

$$n=\frac{8\sqrt{2}\pi(mkT)^{3/2}}{h^3}F_{1/2}(\zeta^*).$$

The values of ζ^* should in general be negative, so that we can expand the denominator of the integrand in $F_\xi(\zeta^*)$ in terms of $\exp[-x+\zeta^*]$. Then we get

$$F_\xi(\zeta^*)=\Gamma(\xi+1)\sum_{s=1}^{\infty}(-1)^{s-1}\frac{e^{s\zeta^*}}{S^{\xi+1}}. \tag{12}$$

Using this equation, Eqs. (11. a) and (11. b) yield approximately

$$\lambda=\frac{1}{kT}\left(1-\frac{e^{\zeta^*}}{2^{3/2}}\right), \tag{13. a}$$

and

$$\Lambda=\left[\left(\frac{5}{2}+\frac{p}{2}\right)\left\{1-\frac{(2^{p/2}-1)e^{\zeta^*}}{2^{3/2+p/2}}\right\}-\frac{3}{2}\right], \tag{13. b}$$

respectively. For $e^{\zeta^*}\ll1$, Eqs. (13. a) and (13. b) tend, respectively, to

$$\lambda=\frac{1}{kT} \tag{14. a}$$

and

$$\Lambda=\left(1+\frac{1}{2}p\right). \tag{14. b}$$

Eqs. (13. a) and (13. b) show that λ and Λ are weak functions of ζ^*. But for $e^{\zeta^*}\ll1$, Λ tends to a constant, and also the Einstein's relation is approximately established.

From the above considerations, we have seen that if we denote v, D, δ, λ, and Λ by the above equations, respectively, we can express the non-isothermal diffusion equation in the same form as (4) or (6) in both of Maxwell-Boltzmann and Fermi-Dirac statistics, though slight differences exist between the two cases.

§ 3. Barriers

The potential energy of current carriers in a rectifying barrier has a maximum $V_m (= V(b))$ at some plane $x=b$ and drops to zero at a plane $x=a$ close to a metal electrode, due to the image force (see Fig. 1). x is measured into the semiconductor from the metal-semiconductor interface and the zero of potential energy is taken at the bottom of the conduction band of the semiconductor in the absence of applied voltages. a is very small compared to b which depends on an applied voltage.

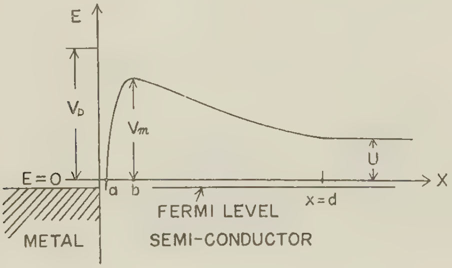

Fig. 1. Potential barrier of an n-type semiconductor in the presence of an applied voltage U/e.

The thickness, d, of the barrier is defined b

$$n(d)=n(x)=\text{const.} \quad \text{for } x \geqq d ,$$

where $n(d)$ is the volume density of the cur rent carriers in the bulk semiconductor, bein assumed to be independent of applied voltages The volume density of the current carriers $n(a)$, at the plane $x=a$ may be assumed to b nearly equal to the one at the surface of th metal and to be independent of applied vol tages. Defining an applied voltage $U/e >$ for a forward voltage, we have $V(x, U) = U$ for $x \geqq d$.

The potential energy of the current carrier in the heterogeneous barrier, $V(x, U)$, can b obtained by adding the term due to the imag force to the solution of the differential equa tion

$$\frac{d}{dx}\left\{\varepsilon(x)\frac{dV}{dx}\right\}=4\pi e^2 N(x) , \tag{15}$$

where $\varepsilon(x)$ is the dielectric constant of the barrier material, which is a function of since the temperature in the barrier is function of x, $N(x)$ the volume density of the ionized impurity centres in the barrier. W have $n(x)=N(x)$ for $x \geqq d$ since the net charg in the interior of the bulk semiconducto must vanish.

Integrating Eq. (15) twice with respect t x over the region $[x, d]$ and reducing the double integral by a partial integration, we obtain

$$V(x)=U-\varepsilon(d)\tilde{\varepsilon}(x)V'(d)+4\pi e^2\int_x^d \{\tilde{\varepsilon}(x)-\tilde{\varepsilon}(y)\}N(y)\,dy-\frac{e^2\varphi(x)}{4\varepsilon(b)x} , \tag{16}$$

where

$$\tilde{\varepsilon}(x)=\int_x^d \frac{dt}{\varepsilon(t)} . \tag{17}$$

In the last added term, which is due to the image force, $\varphi(x)$ is the function introduced as a correction coefficient by taking into account the temperature dependence of the dielectric constant. Let V_D be the diffusion potential in the absence of the image force, then V_D has the form

$$V_D=U-\varepsilon(d)\tilde{\varepsilon}(0)V'(d)+4\pi e^2\int_0^d \{\tilde{\varepsilon}(0)-\tilde{\varepsilon}(y)\}N(y)\,dy . \tag{18}$$

Inserting the condition $dV/dx=0$ at $x=b$ into the equation obtained by differenting Eq. (16 with respect to x, we obtain

$$\frac{1}{b^2}=\frac{16\pi}{\nu(b)\varphi(b)}\int_b^d N(y)dy-\frac{4\varepsilon(d)V'(d)}{e^2\nu(b)\varphi(b)} , \tag{19}$$

where

$$\nu(b)=1-\frac{\varphi'(b)}{\varphi(b)}b\approx 1 . \tag{20}$$

Since b is in general small (of order 10^{-7} cm.), ν is of order unity.

By using Eqs. (16), (17), (18), and (19), we obtain

$$V_D - V(b) = \frac{e^2\eta(b)\varphi(b)}{2\varepsilon(b)b}, \tag{21}$$

where

$$\begin{aligned}\eta(b) &= \frac{1}{2}\left[1 + \frac{\nu(b)\varepsilon(b)}{b}\int_0^b \frac{dt}{\varepsilon(t)} + \frac{16\pi\varepsilon(b)b}{\varphi(b)}\int_0^b \{\tilde{\varepsilon}(0) - \tilde{\varepsilon}(y)\}N(y)\,dy\right] \\ &\approx \frac{1}{2}\left(1 + \frac{\nu(b)\varepsilon(b)}{b}\int_0^b \frac{dt}{\varepsilon(t)}\right),\end{aligned} \tag{22}$$

and by Eq. (16)

$$-V''(b) = \frac{e^2\varphi(b)\phi(b)}{2\varepsilon(b)b^3}, \tag{23}$$

where

$$\begin{aligned}\phi(b) &= 1 - \left(\frac{1}{2}\frac{\varepsilon'(b)}{\varepsilon(b)} + \frac{\varphi'(b)}{\varphi(b)}\right)b + \frac{1}{2}\left(\frac{\varepsilon'(b)\varphi'(b)}{\varepsilon(b)\varphi(b)} + \frac{\varphi''(b)}{\varphi(b)}\right)b^2 - 8\pi\frac{N(b)}{\varphi(b)}b^3 \\ &\approx 1.\end{aligned} \tag{24}$$

§ 4. Derivation of Rectification Equation

In order to obtain a rectification equation, we must integrate the non-isothermal diffusion equation (6) over the barrier. As a heat generation by an electric current occurs in the barrier, the temperature distribution should depend on an applied voltage U/e. Let the temperature and the electrical potential energy in the barrier be, respectively,

$$T = T(T_d, U, x) \quad \text{and} \quad V = V(T_d, U, x), \tag{25}$$

where T_d is the temperature at $x=d$, and it will be assumed to be equal to the temperature in the interior of the bulk semiconductor.

The diffusiom equation (6) is a linear differential equation with respect to n, since D, λ, and A can be expressed as some functions of a variable x only by means of Eq. (25), respectively. Integrating Eq. (6) in the region $[x, d]$ using an integrating factor

$$\exp\left[-\int_x^d\left(\lambda\frac{dV}{dz} + \frac{A}{T}\frac{dT}{dz}\right)dz\right],$$

we have

$$-\int_x^d \frac{j}{eD}\exp\left[-\int_y^d\left(\lambda\frac{dV}{dz} + \frac{A}{T}\frac{dT}{dz}\right)dz\right]dy + n(x)\exp\left[-\int_x^d\left(\lambda\frac{dV}{dz} + \frac{A}{T}\frac{dT}{dz}\right)dz\right] = n(d) \tag{26}$$

Now putting $n(a)$ as

$$n(a) = An(d), \tag{27}$$

then Eq. (26) yields

$$j = \frac{en(d)}{j_0}\left[A\exp\left\{-\int_a^d\left(\lambda\frac{dV}{dx} + \frac{A}{T}\frac{dT}{dx}\right)dx\right\} - 1\right], \tag{28}$$

where

$$j_0 = \int_a^d \frac{1}{D}\exp\left[-\int_y^d\left(\lambda\frac{dV}{dz} + \frac{A}{T}\frac{dT}{dz}\right)dz\right]dy. \tag{29}$$

In the case of isothermal barriers, inserting the condition $j=0$ when $U=0$ into Eq. (28), we have

$$A = \exp\left(\int_a^d \lambda\frac{dV}{dx}\,dx\right). \tag{30}$$

Furthermore, if the Einstein's relation holds, A becomes unity being independent of temperature.

In the case of non-isothermal barriers, supposing that both metal and bulk semiconductor are to be in thermal equilibrium, and at low temperatures $n(d)$ is simply given by[11)]

$$n(d)=(2)(2\pi mkT/h^2)^{3/4}N_0^{1/2}e^{-(\Delta E/2kT)}\ , \tag{31}$$

and at high temperatures $n(d)$ tends to the value N_0 which is the density of impurity centres in the bulk semiconductor, the value of A can be easily given by

$$A(T_a,T_d)=\begin{cases} 1 & \text{for high temperatures,} \quad (32.a) \\ \left(\dfrac{T_a}{T_d}\right)^{3/4}\exp\left[-\dfrac{\Delta E}{2k}\left(\dfrac{1}{T_a}-\dfrac{1}{T_d}\right)\right] & \text{for low temperatures,} \quad (32.b) \end{cases}$$

where T_a and T_d are the temperatures at $x=a$ and $x=b$, respectively, and $\Delta E(>0)$ the energy difference between the bottom of the conduction band of the semiconductor and the impurity level.

The exponent in Eq. (29) can be integrated by a partial integration:

$$\int_y^d\left(\lambda\frac{dV}{dz}+\frac{A}{T}\frac{dT}{dz}\right)dz=\int_y^d\lambda\frac{dV}{dz}dz+\ln\frac{T_d^{A(d)}}{T_y^{A(y)}}-\int_{T_y}^{T_d}(\ln T)\frac{dA}{dT}dT\ . \tag{33}$$

The third term on the right-hand side of Eq. (33) will be generally small in camparison with the others, hence in the following calculation we shall neglect this term. Substituting Eq. (33) into Eq. (29) we get

$$j_0=\Psi\int_a^b\left[\frac{1}{D}\left(\frac{T_x^{A(x)}}{T_d^{A(d)}}\right)\exp\left\{-\int_x^d\lambda\frac{dV}{dy}dy\right\}\right]dx\ , \tag{34}$$

where

$$\Psi\equiv1+\frac{\displaystyle\int_b^d\left[\frac{1}{D}\left(\frac{T_x^{A(x)}}{T_d^{A(d)}}\right)\exp\left\{-\int_x^d\lambda\frac{dV}{dy}dy\right\}\right]dx}{\displaystyle\int_a^b\left[\frac{1}{D}\left(\frac{T_x^{A(x)}}{T_d^{A(d)}}\right)\exp\left\{-\int_x^d\lambda\frac{dV}{dy}dy\right\}\right]dx} \tag{35}$$

The value of the dimensionless factor Ψ depends upon applied valtages and temperatures of the barrier, and is limited usually for variation of temperature as follows:

$$\Psi\geqq\lim_{kT\to0}\Psi\ (\approx2) \tag{36}$$

Figs. 2 and 3 show the variation of Ψ calculated for special barriers by assuming an isothermal barrier, a constant mobility, Eqs. (7. *a*) and (7. *b*).

The potential energy in the region $[a, b]$ has a steep slope for both the reverse and the

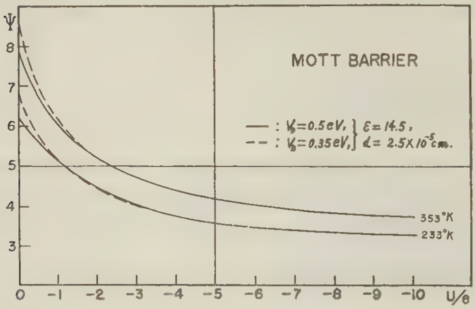

Fig. 2. Ψ as function of applied voltage U/e for an isothermal Mott barrier. Calculations have been done using Simpson's 1/3 rule.

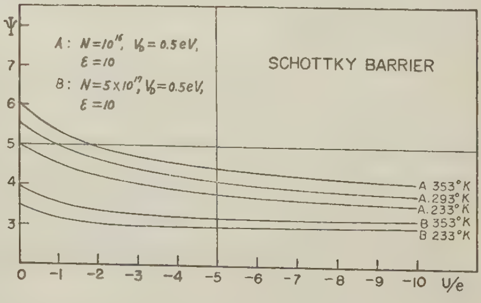

Fig. 3. Ψ as function of applied voltage U/e for an isothermal Schottky barrier.

small forward applied voltages (see Fig. 1), hence we shall use Laplace's approximation to calculate the integral in Eq. (34) in this region, but not use Laplace's approximation in the region $[b, d]$ where the slope of the potential energy is not so steep excepting high reverse applied voltages. If Laplace's approximation would be used for both of these two regions of the barrier as has been done by Landsberg, then we get $\Psi=2$, but this value of Ψ is smaller than its true value, since Laplace's approximation is applicable in the limit kT (which λ involves) → zero.

The theorem of Laplace's approximation[12] to be used is

$$\int_a^b \phi(x)\exp[h(x)]dx \approx \left(-\frac{\pi}{2h_m''}\right)^{1/2}\phi_m \exp[h_m]\,, \tag{37}$$

where the subscript m denotes the values at the maximum of $h(x)$. Since the variation of the electric field is likely to be larger than that of the temperature in the barrier, the maximum h_m will occur at the plane at which the potential energy V reaches its maximum (at $x=b$). Hence by a partial integration

$$h_m = \int_d^b \lambda \frac{dV}{dx}dx = \lambda(b)V(b) - \lambda(d)V(d) - \int_d^b V\frac{d\lambda}{dx}dx\,. \tag{38}$$

Making use of Eqs. (21), (23), (34), (37), and (38), we obtain

$$j = J\Psi^{-1}y^{3/2}\left(\frac{T_d^{\Lambda(d)}}{T_b^{\Lambda(b)}}\right)e^y\left\{A\frac{T_a^{\Lambda(a)}}{T_d^{\Lambda(d)}}\exp\left(-\int_a^d \lambda\frac{dV}{dx}dx\right)-1\right\}\exp\left[\left(\int_d^b V\frac{d\lambda}{dx}dx\right)+\lambda(d)U\right], \tag{39}$$

where

$$J = 2\left(\frac{2}{\pi}\right)^{1/2}\frac{\phi^{1/2}(b)\varepsilon(b)}{\eta^{3/2}(b)\varphi(b)}n(d)\frac{D(b)}{e\lambda(b)}\exp[-\lambda(b)V_D]\,, \tag{40}$$

and

$$y = \frac{e^2\eta(b)\varphi(b)\lambda(b)}{2\varepsilon(b)b}\,. \tag{41}$$

Eq. (39) may be rewritten as follows:

$$j = J\Psi^{-1}y^{3/2}\left(\frac{T_d^{\Lambda(d)}}{T_b^{\Lambda(b)}}\right)e^y\left\{A\frac{T_a^{\Lambda(a)}}{T_d^{\Lambda(d)}}\exp\left(\int_a^b V\frac{d\lambda}{dx}dx\right)-\exp\left(\lambda(d)U-\int_a^d V\frac{d\lambda}{dx}dx\right)\right\}. \tag{42}$$

Eqs. (39) and (42) are the general formulas which give the characteristics for reverse and small forward applied voltages.

When the values of $d\lambda/dx$ is so small to satisfy the conditions $\int_a^b V\frac{d\lambda}{dx}dx\approx 0$ and $\int_d^b V\frac{d\lambda}{dx}dx\approx 0$, Eq. (42) becomes

$$j = J\Psi^{-1}y^{3/2}\frac{T_d^{\Lambda(d)}}{T_b^{\Lambda(b)}}e^y\left\{A\frac{T_a^{\Lambda(a)}}{T_d^{\Lambda(d)}}-e^{\lambda(d)U}\right\}, \tag{43}$$

Further, assuming Eqs. (14. *a*) and (14. *b*), that is $\lambda=1/kT$ and Λ=constant, Eq. (43) takes the form

$$j = J_E\Psi^{-1}y^{3/2}\left(\frac{T_d}{T_b}\right)^\Lambda e^y\left\{A\left(\frac{T_a}{T_d}\right)^\Lambda - e^{U/kT_d}\right\}, \tag{44}$$

where

$$J_E = -2\left(\frac{2}{\pi}\right)^{1/2}\frac{\phi^{1/2}(b)\varepsilon(b)}{\eta^{3/2}(b)\varphi(b)}n(d)\frac{v(b)}{e^2}k^2T_b^2\exp\left[-\frac{V_D}{kT_b}\right], \tag{45}$$

and

$$y = \frac{e^2\eta(b)\varphi(b)}{2\varepsilon(b)b}\frac{1}{kT_b}\,. \tag{46}$$

§ 5. Special Cases of the Rectification Equation

a) Isothermal barriers

In this case, $T_a=T_b=T_d$ and $A(T_a,\ T_d)=1$, so that Eq. (42) yields

$$j=J\Psi^{-1}y^{3/2}T^{\Lambda(d)-\Lambda(b)}e^{y}\left[T^{\Lambda(a)-\Lambda(d)}\exp\left(\int_a^b V\frac{d\lambda}{dx}dx\right)-\exp\left(\lambda(d)U-\int_b^d V\frac{d\lambda}{dx}dx\right)\right] \tag{47}$$

If, furthermore, $\lambda=1/kT$ and $\Lambda=$ constant, Eq. (47) leads to

$$j=J_E\Psi^{-1}y^{3/2}e^{y}\left[1-\exp\left(\frac{U}{kT}\right)\right]. \tag{48}$$

In this case, $\varphi(b)$ and $\phi(b)$ in j and J_E are equal to unity, respectively. When $\Psi=2$, Eq. (48) is just the same as obtained by Landsberg,[13] but the value of Ψ does not usually become equal to 2 excepting the limit of $T\to 0$ as seen from Figs. 2 and 3 or Eq. (36).

b) Characteristics for zero applied voltage

Putting $U=0$ into Eqs. (42) and (44), we obtain, respectively,

$$j=J\Psi^{-1}_{U=0}\,y^{3/2}_{U=0}\frac{T_d^{\Lambda(d)}}{T_b^{\Lambda(b)}}e^{y_{U=0}}\left[A\frac{T_a^{\Lambda(a)}}{T_d^{\Lambda(d)}}\exp\left(\int_a^b V\frac{d\lambda}{dx}dx\right)_{U=0}-\exp\left(-\int_b^d V\frac{d\lambda}{dx}dx\right)_{U=0}\right] \tag{49}$$

and

$$j=J_E\,\Psi^{-1}_{U=0}\,y^{3/2}_{U=0}\left(\frac{T_d}{T_b}\right)^{\Lambda}e^{y_{U=0}}\left[A\left(\frac{T_a}{T_d}\right)^{\Lambda}-1\right]. \tag{50}$$

If $T_a\neq T_d$, the insides of the brackets in Eqs. (49) and (50) are not generally equal to zero. Hence, if the rectifier is in series with a negligible resistance in a circuit, then a thermoelectric current given by Eq. (49) or (50) flows in the circuit. According to Eq. (50), if $\Lambda>0$, then

$$\left.\begin{matrix} j<0 \\ j>0 \end{matrix}\right\}\ \text{as}\ \left\{\begin{matrix} T_a>T_d \\ T_a<T_d \end{matrix}\right.. \tag{51}$$

For an open circuit, according to Eq. (42) or (44), a thermoelectromotive force

$$\frac{U}{e}=\frac{1}{e\lambda(d)}\left\{\ln\frac{n(a)}{n(d)}+\ln\frac{T_a^{\Lambda(a)}}{T_b^{\Lambda(b)}}+\int_a^d V\frac{d\lambda}{dx}dx\right\} \tag{52}$$

or

$$\frac{U}{e}=\frac{kT_d}{e}\left\{\ln\frac{n(a)}{n(d)}+\Lambda\ln\frac{T_a}{T_d}\right\} \tag{53}$$

takes place between the both ends of the barrier, respectively.

c) Characteristics for reverse applied voltage

In this case, $\exp[U/kT]\ll 1$, then Eqs. (42) and (44) yield, respectively,

$$j=J\Psi^{-1}Ay^{3/2}\frac{T_a^{\Lambda(a)}}{T_b^{\Lambda(b)}}e^{y}\exp\left(\int_a^b V\frac{d\lambda}{dx}dx\right) \tag{54}$$

and

$$j=J_E\,\Psi^{-1}Ay^{3/2}\left(\frac{T_a}{T_d}\right)^{\Lambda}e^{y}. \tag{55}$$

If the temperature gradient due to self-heating in the barrier is such as $T_b>T_a>T_d$, the larger reverse current than that expected from the isothermal theory will flow through the barrier, nevertheless the factor $\exp\left(\int_a^b V\frac{d\lambda}{dx}dx\right)$ acts usually to decrease j. When $A(T_a,\ T_d)\approx 1$, the magnitude of the reverse current is mainly dominated by the magnitude of J which ncreases exponentially as increasing of the temperature T_b. But it should be noted that the factor $\Psi(T_d, U)$ acts to increase in some degree the magnitude of the reverse current with decreasing temperature of the rectifier as seen from Figs. 2 and 3, and that the nobility of charge carriers is temperature-dependent. Therefore the reverse current may, n some special cases, increase with decreasing temperature of the barrier.

§ 6. Barrier Capacitance

If the lower limit in the integral in Eq. (19) is put equal to zero,[13] the charge, q, per unit area of the heterogeneous barrier layer is approximately given by

$$q=e\int_0^a N(x)\,dx=\frac{e\nu(b)\varphi(b)}{16\pi}\frac{1}{b^2}+\frac{\varepsilon(d)V'(d)}{4\pi e}\,, \tag{56}$$

the contribution of the current carriers to this charge being neglected compared with the charge due to the ionized impurity centres.

Using Eqs. (56) and (41), the capacitance, C, per unit area is given by

$$C=e\frac{dq}{d(V_D-U)}=\frac{1}{4\pi e^2}\left\{\Sigma(b)\frac{d(y^2)}{d(V_D-U)}+y^2\frac{d(\Sigma(b))}{d(V_D-U)}\right\} \tag{57}$$

where

$$\Sigma(b)=\frac{\nu(b)\varepsilon^2(b)}{\eta^2(b)\varphi(b)\lambda^2(b)}\,, \tag{58}$$

The term $V'(d)$ in Eq. (56) has been assumed to be negligible or at least to be approximately independent of V_D-U, so that the following considerations do not apply to a Mott barrier.

On integrating Eq. (57), we obtain

$$\frac{\Sigma_U(b)}{\Sigma_0(b)}y^2(U)-y^2(0)=4\pi\left(\frac{e\lambda(T_a)}{\varepsilon(T_a)}\right)^2\int_U^0 C(U)dU\,, \tag{59}$$

where $\Sigma_U(b)$ and $\Sigma_0(b)$ are the values of $\Sigma(b)$ at the applied voltages U/e and at the zero applied voltage, respectively, and also $\Sigma_0(b)$ is equal to $\varepsilon^2(T_a)/\lambda^2(T_a)$ since the temperature at the zero applied voltage is constant through the barrier and equal to the ambient temperature T_a.

Eq. (59) is slightly different from that obtained for isothermal barriers by Landsberg[13] in the point that the coefficient of $y(U)$ is not unity, but $\Sigma_U(b)/\Sigma_0(b)$.

§ 7. Analysis of Experimental Characteristics

Assuming Eqs. (7.a) and (32.a) (the latter corresponds to the the case where all impurities are ionized; this seems to hold for Se.[14]), and neglecting $\ln(T_a^{\Lambda(a)}/T_b^{\Lambda(b)})$, Eq. (54) can be rewritten as follows (see Appendix):

$$\frac{3}{2}\ln y(U)+y(U)=\ln j(U)-\ln J_E(T_a)+\ln\Psi-\frac{1}{kT_a^2}(V_D-\theta V(b))\Delta T\,, \tag{60}$$

where

$$J_E(T_a)=2\left(\frac{2}{\pi}\right)^{1/2}\frac{\phi^{1/2}(a)\varepsilon(a)}{\eta^{3/2}(a)\varphi(a)}n(d)\frac{v(a)}{e^2}k^2T_a^2\exp\left[-\frac{V_D}{kT_a}\right], \tag{61}$$

and

$$\Delta T=T_b-T_a\,,\qquad 0<\theta<1\,. \tag{62}$$

The last term on the right-hand side of Eq. (60) represents the effect due to temperature rise of the barrier.

On the other hand, from Eq. (59) we can obtain approximately

$$\ln[y^2(U)-y^2(0)]=\ln\left[4\pi\left(\frac{e}{kT_a}\right)^2\int_U^0 C(U)dU\right]-2\ln\varepsilon(T_a)\,, \tag{63}$$

since $\ln\left[\frac{\Sigma_{U}(b)}{\Sigma_0(b)} y^2(U)-y^2(0)\right]$ may be approximately equal to $\ln[y^2(U)-y^2(0)]$ except for the case of large reverse applied voltages.

As seen from Eqs. (60) and (63), we can draw the theoretical curves of $3/2 \ln y(U)+y(U$ as function of $\ln[y^2(U)-y^2(0)]$ for given suitable values of $y(0)$, since $3/2 \ln y(U)+y(U)$ and $\ln[y^2(U)-y^2(0)]$ are connected through the parameter $y(U)$. On the other hand, using the measured j and C values for each reverse voltages, we can plot the experimental curves o $\ln j$ as function of

$$\ln\left[4\pi\left(\frac{e}{kT_a}\right)^2\int_U^0 C\,dU\right].$$

The latter experimental curve should coincide with one of the theoretical curves by parallel displacements of $2\ln\varepsilon(T_a)$ horizontally and $\ln J_E(T_a)-\ln\Psi+\frac{1}{kT_a^2}(V_D-\theta V(b))\Delta T$ vertically. This type of analysis in the isothermal cases was first used by Lees[15] and next by Moriguchi and Okazaki.[16]

Table I. The values of $y(0)$, $\varepsilon(T_a)$, $J_E(T_a)$, and $b(0)$ for the Se rectifier (No. 11-1). Ambient temperature $T_a=160$°K.

Authors	Maximum temperature rise ΔT_m (°K)	$y(0)$	$\varepsilon(T_a)$	$J_E(T_a)$ (μA cm^{-2})	$b(0)$ (Å)
Moriguchi and Okazaki	0	1.0	4.5	4*	116
Present author	0	1.0	4.8	9.5	109
〃	5	1.0	5.7	12	88
〃	10	1.0	6.7	14	79
〃	20	1.0	12	21	45

* : twice the value of Moriguchi and Okazaki's data.

Table II. The values of $y(0)$, $\varepsilon(T_a)$, $J_E(T_a)$, and $b(0)$ for the Cu_2O rectifier (No. 20-2). Ambient temperature $T_a=176$°K.

Authors	Maximum temperature rise ΔT_m (°K)	$y(0)$	$\varepsilon(T_a)$	$J_E(T_a)$ (μA cm^{-2})	$b(0)$ (Å)
Moriguchi and Okazaki	0	0.25	4.6	1.7×10^{-1}*	412
Present author	0	0.35	4.6	3.3×10^{-1}	295
〃	5	0.35	5.7	4.5×10^{-1}	237
〃	10	0.35	6.4	4.8×10^{-1}	211
〃	20	0.35	9.5	6.6×10^{-1}	143

Now from the above non-isothermal theoretical point of view, it may be desired to analyse the experimental results obtained by Moriguchi and Okazaki to check up how the temperature rise of the barrier affects experimental results. But we can not find the values of Ψ, θ, $V(b)$, and ΔT necessary for the analysis, because the temperature distribution in the barrier is not yet given and we can not analyse the experimental results along the same lines as Moriguchi and Okazaki have taken. Under the present situation we should be obliged to do a very rough analysis under the following assumptions:

(1) The value of $V(b)$ is that for a Schottky barrier;

(2) $V_D=0.5$ eV, $\theta=0.5$ for both Cu_2O and Se rectifiers;

(3) The temperature-and voltage-dependences of Ψ are approximately of the form of the curve A illustrated in Fig. 3;

(4) ΔT is zero at the lowest applied voltage and has a maximum value, ΔT_m, at the highest applied voltage (the assumed values of ΔT_m are shown in Tables I and II).

From the above assumptions we get only two experimental values for the lowest and highest applied voltages. Therefore, we can not get an experimental *curve* to fit one of the above-mentioned theoretical curves. To get a rough knowledge on the effect of the temperature rise in the barrier, we may make the above two experimental points, for which the correction due to the temperature rise is applied, fit the same curve as the theoretical one, which is first determined by neglecting the temperature rise, (this is, under the isothermal condition), by suitable parallel displacements. From the values of these parallel displacements we can find the values of $y(0)$, $\varepsilon(T_a)$, and $J_E(T_a)$. Some of the results obtained by the present analysis are shown in Tables I and II, which include the results by Moriguchi and Okazaki. By the above parallel displacements, the experimental points, for which the correction due to the temperature rise is not applied, should displace from the above theoretical curve. From the vertical component of this displacement for each experimental point, we may estimate the temperature rise of the barrier at each applied voltage except the lowest and highest ones.

Under the isothermal condition, the overlap of each experimental curve with one of the theoretical curves after suitable parallel displacements is found to be better than that obtained by Moriguchi and Okazaki. The reason may be possibly due to the fact that the factor Ψ modifies, especially, the low reverse characteristics. The results for the isothermal condition are also given in the third line of Tables I and II.

§ 8. Discussion

In the preceding sections, we have developed generally the non-isothermal diffusion theory of metal rectifiers by integrating the general non-isothermal diffusion equation newly introduced here. In the development of the theory, the assumption of temperature-and voltage-independences of mobility and diffusion coefficient have not been made with dropping of the Einstein mobility relation. Hence the present theory has been constructed under fewer theoretical restrictions. The rectification equation obtained shows clearly how rectification current depends upon the temperature distribution in the barrier layer since it containe T_a, T_b, and T_d in addition to the values of D, λ, and Λ at the various positions in the barrier layer. Therefore, if the temperature distribution in the barrier layer changes as rectification current flows through the barrier, thermal creep may be able to occur. Furthermore, owing to a temperature difference between both ends of the barrier, thermoelectric current flows in a circuit or thermoelectromotive force generates at both ends of the barrier according to whether the circuit is closed or not. These effects can not be expected explicitly by the usual isothermal theories. In order to obtain further knowledges on the above effects or to analyse experimental results in detail, it is necessary to solve a differential equation of heat conduction with heat generation source under suitable boundary conditions. But this has not been done in this paper.

The value of Ψ generally depends upon temperature and voltage distributions in the barrier layer and several quantities of the barrier. Hence it is practically not easy to obtain the accurate value of Ψ of a special rectifier under a given applied voltage and ambient temperature. But the tendency of the variation of Ψ may be, in general, similar to those indicated in Figs. 2 and 3 obtained for the special cases of Mott and Schottky barriers. It should be noted that the value of Ψ is larger than 2 over the usual temperature range, and the value of Ψ in the vicinity of zero bias voltage changes rapidly with variation of applied voltage and ambient temperature. These properties of Ψ may affect effectively the low voltage characteristics and zero bias resistance.

As seen from Tables I and II, the values of the dielectric constants determined by Moriguchi and Okazaki are pretty smaller than those of the bulk materials of Cu_2O (10.5, Højendahl(17); and 8, Wright(11)) and Se (6.13, Vonwiller and Mason;(18) 6.60, Schmidt;(19) 7.44, Pirani; and 6.31, Tammann and Boehme,(20) for vitreous Se. 8∼20, Eckart and Rabenhorst;(21) Jaumann and Neckenbürger;(22) and 14.5, Numata and Isami,(23) for hexagonal Se). But taking into account the temperature rise of the barrier, the Tables show that the values of the dielectric constants determined in the present analysis tend to approach those of the bulk materials. This fact seems to be in favour of the present non-isothermal theory.

Finally, the author expresses his sincere thanks to Professor A. Okazaki of Kyusyu University for his continual advice and encouragement and to Mr. Y. Moriguchi for lending of the experimental data. The present investigation was finacially spported by the Scientific Research Expenditure of the Ministry of Education.

Appendix

Making a logarithm of Eq. (54), we obtain

$$\frac{3}{2}\ln y(U)+y(U)=\ln j(U)-\ln J_E(T_b)+\ln\Psi-\int_a^b V\frac{d}{dx}\left(\frac{1}{kT}\right)dx\,, \tag{A.1}$$

under the above-mentioned assumptions.

Expressing $J_E(T_b)$ given by Eq. (45) in terms of the values of the quantities at the plane $x=a$ by using Taylor's theorem, we obtain approximately

$$\ln J_E(T_b)=\ln J_E(T_a)+\frac{V_D}{kT_a^2}\Delta T\,. \tag{A.2}$$

The function $V(x)$ is a monotonous increasing function in the interval $a\leqq x\leqq b$. Hence, if $dT/dx>0$ in the above interval, we have the following inequality relation:

$$0<-\int_a^b V\frac{d}{dx}\left(\frac{1}{kT}\right)dx<-\int_a^b V(b)\frac{d}{dx}\left(\frac{1}{kT}\right)d\,x. \tag{A.3}$$

By Taylor's expansion, Eq. (A.3) can be written as

$$0<-\int_a^b V\frac{d}{dx}\left(\frac{1}{kT}\right)dx<\frac{V(b)}{kT_a^2}\Delta T\,.$$

On the other hand,

$$0<\theta\frac{V(b)}{kT_a^2}\Delta T<\frac{V(b)}{kT_a^2}\Delta T\,,\qquad 0<\theta<1$$

Hence, selecting a suitable value of θ $(0<\theta<1)$, we can obtain

$$-\int_a^b V\frac{d}{dx}\left(\frac{1}{kT}\right)dx=\theta\frac{V(b)}{kT_a^2}\Delta T\,,\qquad 0<\theta<1. \tag{A.4}$$

By Eqs. (A.1), (A.2), and (A.4), we get Eq. (60).

References

1) C. Wagner: Z. Phys. **32** (1931) 641.
2) N. F. Mott: Proc. Roy. Soc. **A, 171** (1939) 27.
3) W. Schottky: Z. Phys. **113** (1939) 367.
4) H. K. Henisch: *Rectifying Semi-Conductor Contacts* (Oxford, 1957); *Metal Rectifiers* (Oxford, 1948).
5) E. Billig: Proc. Roy. Soc. **A, 207** (1951) 156.
6) P. T. Landsberg: Proc. Roy. Soc. **A, 206** (1951) 463; ibid. **206** (1951) 477; ibid. **213** (1952) 266; Proc. Phys. Soc. London **B, 65** (1952) 397; ibid. **68** (1955) 366; Z. Phys. Chem. **198** (1951) 75.
7) P. T. Landsberg: Proc. Phys. Soc. London **B, 68** (1955) 366.
8) A. H. Wilson: *The Theory of Metals* (Cambridge, 1953) 7.
9) A. H. Wilson: ibid. p. 10.
10) P. T. Landsberg: Proc. Roy. Soc. **A, 213** (1952) 266. A. H. Wilson: *The Theory of Metals* (Cambridge, 1953) 17.
11) D. A. Wright: *Semi-Conductors* (London: Methuen, 1950) 43.
12) D. V. Widder: *The Laplace Transform* (Oxford, 1946) 278, Theorem 2b.
13) P. T. Landsberg: Proc. Roy. Soc. **A, 206** (1951) 477.
14) K. W. Plessner: Proc. Phys. Soc. London **B, 64** (1951) 671.
15) J. Lees: Ph. D. Thesis, University of Aberdeen; Proc. Phys. Soc. London **B, 66** (1953) 622.
16) Y. Moriguchi and A. Okazaki: Proc. Phys. Soc. London **B, 70** (1957) 991.
17) K. Hϕjendahl: Z. Phys. Chem. **B, 20** (1933) 54.

18) O. U. Vonwiller and W. H. Mason: Proc. Roy. Soc. **A**, **79** (1907) 177.
19) W. Schmidt: Ann. Physik **4** (1903) 11, 119.
20) G. Tammann and W. Boeme: Z. anorg. Chem. **197** (1931) 1.
21) F. Eckart and J. Rabenhorst: Ann. Physik **19** (1957) 381.
22) J. Jaumann and E. Neckenbürger: Z. Phys. **151** (1958) 72.
23) T. Numata and A. Isami: read at the regular meeting of Kyusyu branch of Physical Society of Japan in June 1958.

JOURNAL OF THE PHYSICAL SOCIETY OF JAPAN, Vol. 14, No. 7, JULY, 1959

Study on Vacuum Deposition of Metals, I
On the Formation of Alloys by Successive Deposition of Constituent Metal Vapours in Vacuum

By Yoshibumi FUJIKI

Institute of Physics, Kyōto Prefectural Medical College

(Received March 6, 1959)

The formation of alloy phases by successive deposition of constituent metal vapours in vacuum was investigated by electron diffraction method for some binary alloy systems. It was concluded that the temperature of the surface layer of primary deposit is raised by the deposition of secondary metal vapour. This temperature rise, which contributes to the formation of alloy phases, is mainly due to the latent heat of condensation of the metal vapour which deposits on the substrate, and consequently metal pairs which have larger latent heat of condensation may form alloys easier than those which have smaller ones. It was also suggested that some structural defects in the substrate layer would contribute to the formation of alloy phases.

§ 1. Introduction

When the vapours of two metals are deposited successively on any substrate in vacuum, alloys of these two metals are formed for some pairs of metals, but not for other pairs. Michel$^{1)}$ examined Ag–Zn, Ag–Sn, Al–Sb, Al–Cu and other pairs by electron diffraction method and found the formation of alloys for the first two pairs, but not for other pairs. He considered these phenomena as the problem of inter-diffusion similar to the case of bulk specimens, and calculated the depth to which inter-diffusion had occurred for a day using the diffusion constants of the chemical diffusion extrapolated from values at high temperatures to room temperature. His conclusion is that alloy formations are observed for pairs whose diffusion constants at room temperature are larger than the order of 10^{-20} cm^2/sec, and not for pairs whose diffusion constants are smaller than this.

The writer observed almost instantaneous formation of alloy phase by the deposition of secondary metal vapour in electron diffraction camera for Pb–Bi system, and the rate of formation of alloy seemed too large for the order of diffusion constant at room temperature (10^{-16} cm^2/sec). When Sn vapour was deposited on Cu deposit (the weight ratio of Sn and Cu having been 60:40), an alloy of the nickel arsenide type (hexagonal, a=4.19Å, c=5.08Å) was observed. The diffusion constant at room temperature in this case is of the order of 10^{-32} cm^2/sec. The writer supposed that these facts depend upon two main factors, namely, the temperature rise of the surface of primary deposit by the deposition of the secondary constituent metal vapour and the crystal texture or the condition of the surface of the primary deposit. To confirm these conjectures the writer examined some metal pairs by the electron diffraction method.

§ 2. Temperature Rise of the Primary Deposit by the Secondary Vapour Deposition

The temperature of the deposit is supposed to be considerably high just after the deposition of vapour, and then is lowered rapidly to room temperature, and so the temperature of the surface layer of the primary deposit would be risen by the deposition of secondary constituents. The temperature of the secondary deposit should be higher at the surface layer than the bottom during the deposition, and so the diffusion should occur upwards. The alloy thus formed should be those whose composition is rich in secondary element compared with the composition of films as a whole. To assure this the writer examined first the Au–Pb alloy system. Au–Pb alloy system has three intermetallic compounds, Au_2Pb (cubic, a=7.93Å), $AuPb_2$ (tetragonal, a=7.31Å, c=5.644Å) and $AuPb_3$[2] (tetragonal, a=11.958Å, c=5.878Å), and this alloy system is suitable for this aim. Each constituent metal was heated in a spiral of tungsten wire (about 0.22 mm in diameter) and deposited on a Formvar film successively in vacuum (about 2×10^{-5} mm Hg). Total amount of two constituent metals was 10 mg and the distance between filaments and substrate was 6 cm. The rate of evaporation was about 25 mg per minute. After two constituent metals were vaporized, specimen was examined by electron diffraction method. The ratio of the amount of two constituent metals, the alloy phases observed and the intensities of their diffraction patterns are listed in Table I. These results show that compositions of alloys formed are rich in the later deposited element compared with the compositions of films as a whole. These diffraction patterns changed to those which correspond to the alloy phases of the composition of film as a whole when suitably heat-treated in vacuum (see Table I).

When the amount of Pb for the secondary element was reduced to about 2 mg (i.e. 20 wt. % Pb), no alloy phase appeared but only Pb and Au. This specimen showed the diffraction pattern of Au_2Pb and Au after heat-treatment. This phenomenon may be understood by considering that the amount of deposited Pb vapour is very small, so that the latent heat of Pb vapour is insufficient for the temperature rise of the surface of Au necessary to form alloys.

Table I.

	Composition of films as a whole Au:Pb in wt. %		Alloy phase formed				
			Au	Au_2Pb	$AuPb_2$	$AuPb_3$	Pb
Au deposited on Pb	80:20	a	s	m			w
		b	m	s			
	66:34	a	vw	m	w		
		b		s			
	32:68	a	vw	m	w		vw
		b			s		
	27:73	a			m	w	m
		b			m	m	vw
Pb deposited on Au	80:20	a	s				w
		b	m	m			
	66:34	a	s		s		
		b		s			
	32:68	a	vw		s	w	tr.
		b			s		
	15:85	a				s	w
		b				s	w

a: before annealing
b: after annealing at about 200°C for a suitable time
Intensities of diffraction lines
(s: strong m: medium strong
w: weak vw: very weak tr.: trace)

Thin films prepared by the deposition of Sn vapour showed the fibre structure which persisted up to the melting point of Sn. But this fibre structure was destroyed by the deposition of Zn vapour on it at room temperature. (Sn–Zn system has no compound but eutectic; eutectic point is 199°C.)

This suggests that the temperature of Sn layer was elevated to near the eutectic point by the deposition of Zn vapour. These results show the temperature rise of films during the deposition of the vapour of the secondary constituent metals.

To estimate the temperature rise, Cd–Sn system was investigated. This system has β-phase (hexagonal) which is stable at temperatures higher than 133°C only. The β-phase was observed when Cd vapour was deposited on Sn layer. It is estimated from this result that the temperature of the surface layer of Sn deposit rose at least above 133°C in this case.

§ 3. Source of the Heat Energy

The source of the heat energy producing the temperature rise should be composed of two parts, namely, the radiation heat from the filament, and the kinetic energy of vapour atoms and the latent heat of condensation by the deposition. To determine which of these is more effective, an experiment of deposition was carried out, shielding the radiation heat. A small rectangular aluminium mirror, whose width was a little larger than the diameter of filament coil, was placed between the filament and substrate at the distance about 1 cm apart from the former. A fraction of Pb vapour swerved in the shadow of radiation shield excepting the case when the vapour density was very low, and thus Pb was deposited on Au film which was prepared by the deposition of Au vapour previously. The formation of alloys was also observed when the vapour density was comparatively high. Compared with the fact that the alloys were not formed when the amount of evaporated Pb was about 2 mg with no radiation shielding because of the insufficiency of the total latent heat as previously mentioned, it is concluded that the latent heat of condensation is more effective for the temperature rise of the surface. If this conclusion is correct, alloys will not be formed if the speed of evaporation of secondary constituent metal is very slow, even though the amount of it is sufficient to form alloys when the evaporation speed is suitably high. To examine this, Pb, 5 mg in weight, was evaporated on Au deposit in about 20 minutes with no radiation shield. The heating current of filament was carefully controlled to keep the uniform evaporation rate. Alloys were not formed in this case.

Then it is presumed that alloys will be formed easier when metals having larger latent heats of evaporation per mole are deposited on the primary deposits than when those having smaller ones are deposited. (Since the kinetic energy of vapour atoms, the latent heat of solidification and the specific heat are small compared with the latent heat of condensation, only the latter has been taken up.) As mentioned above, no alloy was formed when small quantity of Pb vapour was deposited on Au, and therefore it seems suitable for the confirmation of the above-mentioned presumption to examine whether the alloys are formed or not by the deposi-

Table II.

Secondary deposit	Base deposit	Alloy phase formed	Latent heat of vaporization of secondary deposit
Pb	Au	none	42,400 cal/mole
Au	Pb	$AuPb_2$	81,800
Pb	Bi	none	42,400
Bi	Pb	none	42,600
Sn	Ag	γ–Ag–Sn	70,000
Ag	Sn	γ–Ag–Sn	60,720

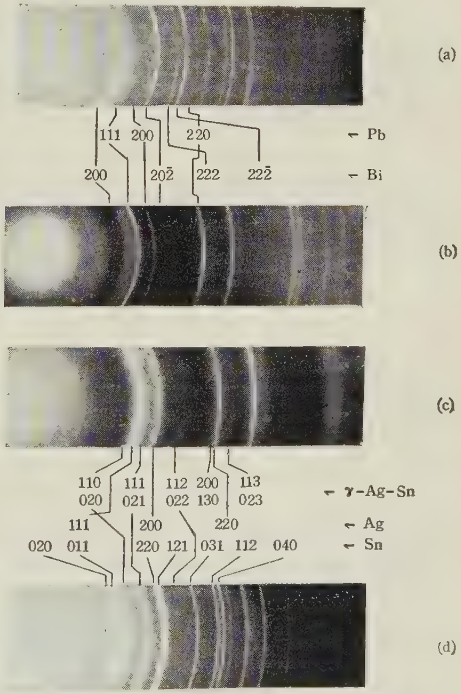

Fig. 1. Thin metal films deposited on various base metals.
(a) Pb was deposited on Bi film.
(b) Bi was deposited on Pb film.
(c) Sn was deposited on Ag film.
(d) Ag was deposited on Sn film.

tion of small quantities of the same mole of the secondary constituents having various latent heats of condensation per mole. The latent heats of condensation of Au, Pb, Bi, Sn and Ag are listed in Table II[3]. Experiments were carried out for Au–Pb, Pb–Bi and Ag–Sn systems. The quantity of each metal used for the second vaporization was between $8\sim10\times10^{-6}$ mole. In the case of Au deposited on Pb layer the alloy phase was formed, but the case of Pb deposited on Au layer showed no alloy formation. The formation of alloy was observed for the Ag–Sn system but no alloy phase was observed for Pb–Bi system independently of the order of evaporation (see Fig. 1). Latent heats of condensation of Pb and Bi are smaller than those of Ag and Sn (see Table II). Considering that diffusion constant at room temperature is of the order of 10^{-16} cm²/sec for Pb–Bi and 10^{-20} cm²/sec for Ag–Sn and the activation energy is 18.6 and 21.4 kcal per mole respectively, it is concluded that the latent heat of condensation is a main cause for the temperature rise of the substrate layer.

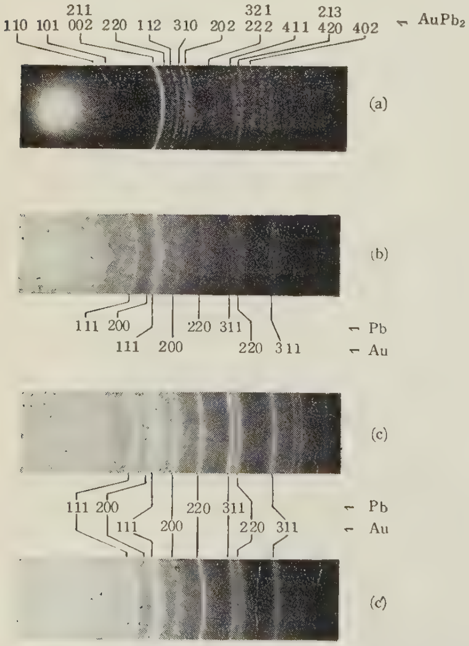

Fig. 2. Pb deposited on Au films (ratio of Pb and Au in weight is 50:50).
(a) Au film is fresh.
(b) Au film is aged for a week at room temperature.
(c) Au film is annealed for an hour at about 200°C. This diffraction pattern shows the state immediately after Pb was evaporated.
(c′) One day after of (c).

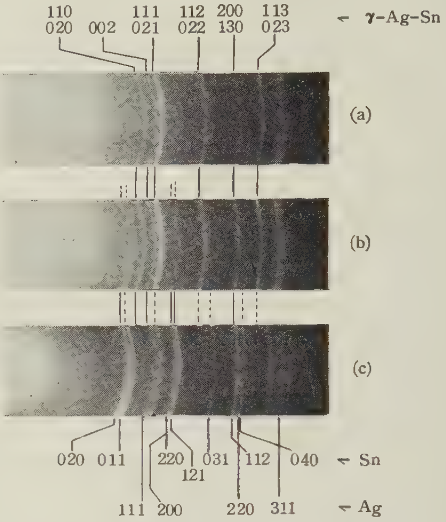

Fig. 3. Sn deposited on Ag films (ratio of Sn and Ag in weight is 50:50).
(a) Ag film is fresh.
(b) Ag film is annealed for 2 hours at about 100°C.
(c) Ag film is annealed for 2 hours at about 200°C.

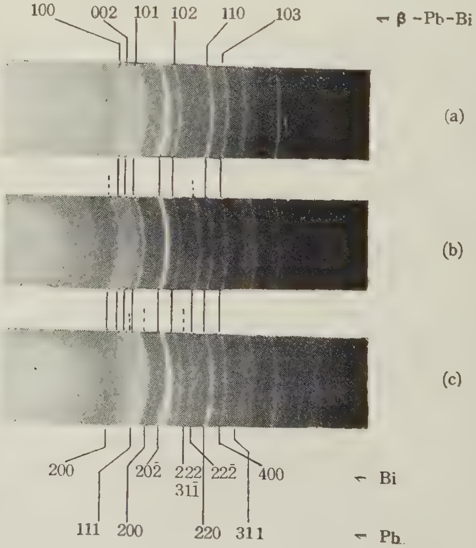
100 002 101 102 110 103 ← β-Pb-Bi
(a)
(b)
(c)
200 202 222 311 222 400 ← Bi
111 200 220 311 ← Pb

Fig. 4. Pb deposited on Bi films (ratio of Pb and Bi in weight is 50:50).
(a) Bi film is fresh.
(b) Bi film is annealed for 2 hours at about 100°C.
(c) Bi film is annealed for 2 hours at about 200°C.

§ 4. Effect of the Texture or Surface Condition of Primary Deposit on the Formation of Alloys

As mentioned above, alloys were formed when Au and Pb vapours were deposited successively. But when the Pb vapour was deposited on Au layer which was annealed at 200°C for an hour or at room temperature for a week in vacuum, alloy phases did not appear. These specimens showed no change after annealing for a day at room temperature (see Fig. 2). This was the same when in place of Au deposit the commercial Au foil was used as substrate layer. The diffusion constant at room temperature is about 10^{-10} cm^2/sec in this case and alloy formation should occur according to the interpretation of Michel. To verify that the cause of no alloy formation in the case of annealed Au deposit or foil lies in the contamination of surface or not, the annealed Au deposit or foil was immersed in benzen, distilled water and absolute alcohol successively and the Pb vapour was then deposited on it. No alloy formation was observed yet, however. A fresh Au deposit treated as annealed one was also examined, and in this case the formation of alloy was observed. This shows that a fresh one is not affected by such treatments. These facts show that the cause of no alloy formation in the former case does not lie in the contamination of surface and alloy formation depends not only upon the temperature rise of the surface but also upon the texture or structure of the substrate layer.

To test this, the substrate layers of Ag and Bi were annealed for appropriate time and then the vapour of Sn was deposited on Ag film and Pb vapour on Bi film, respectively. The results are shown in Figs. 3 and 4. As is seen in these figures, alloys were formed contrary to the case of Pb–Au, but the amount of alloys formed diminished as the temperature of annealing became higher. In short, annealing of the substrate layers promotes the tendency to prevent the formation of alloy phases. The grain size of the substrate layer would become large by annealing and as the result the contact area of the substrate with the secondary deposit would diminish, thus reducing the rate of formation of alloys. The tendency of the grain growth would be larger at about these temperatures for Bi and Ag than for Au, but the diminution of the formation of alloy is larger for Au than for Ag or Bi. Especially, the appreciable grain growth of Au by the annealing for a week at room temperature was not observed. Consequently, the grain size is not the ultimate factor, but some structural defects, which have been investigated by many authors, would contribute to the formation of alloy phases.

§ 5. Summary

The formation of alloy phases by successive deposition of constituent metal vapours in vacuum was investigated by electron diffraction method for Au–Pb, Bi–Pb, Cu–Sn, Ag–Sn and Cd–Sn alloy systems. It was concluded that the temperature of the surface layer of the primary deposit is elevated by the deposition of the secondary metal vapour, and this temperature rise contributes to the formation of alloy phases. This temperature rise is mainly due to the latent heat of condensation of the metal vapour which deposits on the substrate layer, and the radiation heat from the filament contributes little to this phenomenon compared with the latent heat of condensation. Consequently, metal pairs having larger latent heat of condensation may form alloys easier than those having smaller ones. The degree of this temperature rise was at least 133°C for Cd–Sn system. It was also suggested that some structural defects in the substrate layer would contribute to the formation of alloys.

Acknowledgement

The writer wishes to express his sincere thanks to Professor K. Tanaka of Kyoto University for his kind advice and discussions and the encouragement throughout the present investigation. The writer is also grateful to Mr. R. Suganuma and Mr. T. Yoshida in our Institute for their assistance.

References

1) P. Michel: Ann. Physique, Sér. 13, **1** (1956) 719.
2) Y. Fujiki: Mem. Coll. Sci., Univ. Kyoto (in press). Y. Fujiki *et al.*: J. Phys. Soc. Japan **13** (1958) 969.
3) S. Dushman: *Scientific Foundation of Vacuum Technique*, (John Wiley, New York, 1949) 756.

JOURNAL OF THE PHYSICAL SOCIETY OF JAPAN, Vol. 14, No. 7, JULY, 1959

Effects of Heat Treatment upon the Electrical Properties of Silicon

By Yasuo MATUKURA

Electrotechnical Laboratory, Tokyo, Japan

(Received March 19, 1959)

Experimental studies have been made of the processes in which the changes of the carrier concentration and minority carrier lifetime are introduced into silicon by heat treatment at the temperature range 400–1200°C. In the low temperature heat treatment, the formed denors are less in the vicinity of crystal defects. In the high temperature heat treatment, the decrease of carrier density in *p*- and *n*-type crystals is observed in addition to the annihilation of the formed donors. These behaviors are closely related to the crystal defects. The characteristics of the processes involved are discussed and explained by the introduction of the recombination centers with a capture cross section of 2×10^{-15} cm^2 for hole (at 300°K).

§1. Introduction

It has been observed[1)–4)] that the donor formation is quite large in silicon crystals after heating between 400°C and 500°C, and these denors can be annihilated by a subsequent heat treatment above 600°C. The details of this phenomena depend on the parameters of the crystal growth such as gaseous ambient, rotation rate, and crystal diameter. W. Kaiser[4),5)] has shown that silicon crystals pulled from a quartz crucible contain oxygen as much as 10^{18} cm^{-3}, and some heat treatment effects are caused by the presence of oxygen. Some other investigators have reported[6)–8)] that lifetime of minority carriers in silicon may be influenced by heat treatment, and S. Lederhandler and J. R. Patel[9)] have shown that oxygen atoms can pricipitate at dislocations in crystal. As the correlation between the denor formation, the change in lifetime, and the presence of dislocation has not yet been studied, it is interesting for us to study the electrical properties of heat treated silicon having deliberately introduced defects in order to understand the behaviors of oxygen in silicon.

Here, observations are made on the changes of carrier density and minority carrier lifetime in pulled silicon crystals by heat treatment between 400 and 1200°C, and the results are explained by both the defects in silicon and the recombination centers introduced by heat treatment.

§2. Experimental Results

Several silicon crystals are sulled from a quartz crucible in argon atmosphere with various rotation rates. In order to produce a grain boundary parallel to the pulled axis, some other crystals are pulled with two seeds which have the same ⟨111⟩ axis and are put together side by side.

Samples are ground with silicon carbide powder, and rinsed in a mixture of HNO_3 and HF and then in deionized water. Throughout heat treatment, samples are put upon a quartz boat in a quartz tube using argon as a gas ambient unless stated otherwise.

Resistivity is measured by four point probe method or by potentiometer on the bridge shape samples, and carrier concentration is determined by the value of Hall coefficient or resistivity using the mobility data. Lifetime of minority carriers of the surface treated silicon is measured by Morton Haynes method under an ambient *dc* illumination.

A. *General features*

A typical variation of carrier concentration change measured at room temperature with treating temperature is shown in Fig. 1. This is found in *p*-type specimens cut from the same ingot pulled at 60 rpm. Heating time in hydrogen is about 50 min in each treatment. It is seen that the hole density in silicon decreases by heating at the temperatures in the range of 400 to 600°C and increases at above 600°C. This change results from the donor formation and annihilation. The values of the activation energies of such induced donor centers have been determined by measurements of the variations of Hall coefficient with temperature on arsenic doped silicon which is heated at 470°C for 50 hours. Two levels at 0.14 eV and 0.31 eV below the conduction band are evaluated, in a good agreement with F. J. Morin's data[10]. Since the shallow level may be completely ionized at room temperature, it has been assumed in this work that the change in carrier concentration by heat treatment below 600°C is a measure of the number of the induced donor.

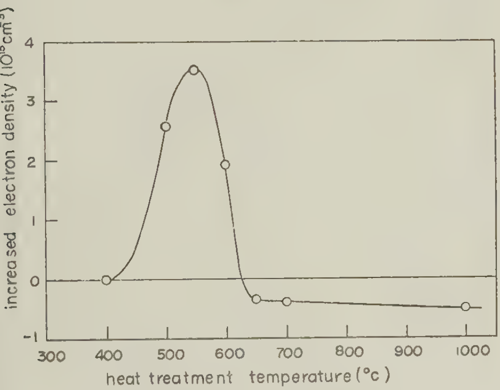

Fig. 1. The change of carier density as a function of heat treatment temperature in p-type silicon pulled at 60 RPM.

The formed donor denters are annihilated by subsequent heat treatment for short period above 600°C, and appeared again below 600°C[2),3)]. It has been known that the donor concentration formed by heating in the temperature range of 400 to 600°C is larger in the crystals pulled at high rotation rate than at low. As the crystal experiences the temperature of the donor formation during the pulling, the formed donors exist originally in every pulled crystal. The decrease in donor density, shown in Fig. 1, by the heat treatment above 600°C is due to the annihilation of the donors formed during the pulling at high rotation rate, 60 rpm.

The formed donor density depends much on the period of heat treatment. It is observed that the denor density induced by heat treatment at 450°C increased with the heating period and approached some value which may be related to the pulling condition. These results agree with Fuller's[3)] and Kaiser's[4)]. The specimens are also heated in various sorts of ambient gas at 500°C. It is seen that the heat treatment in vacuum of 1×10^{-5} mm Hg induces the denors a little less than the other treatments in hydrogen, argon, and air. The induced donor density is not influenced by cooling rate from 500°C. This is examined by the following experiments. The specimens were quickly dropped into the diffusion pump oil at room temperature from the treating temperature and other specimens were slowly cooled. In both treatments, the difference in the formed donor density is not seen.

In the high temperature treatment, it is observed that in addition to the annihilation of the formed donors, both electron density in n-type and hole density in p-type crystal decrease, independent of the crystal growth condition. Such decreases of carrier density are not affected by the variation of cooling rate* from high temperature, but little affected by the sorts of ambient atmosphere including vacuum.

Lifetime of minority carriers decreases by the heat treatment in the temperature range of 400 to 1200°C. This is similar to the characteristic of the decrease of carrier density by the high temperature treatment mentioned above.

B. *Heat treatment at low temperature*

Specimens of about 7×2 mm^2 cross section are cut along the radial direction in some round slices from n-type crystal pulled at 10 rpm. After heat treatment for 30 hours at 450°C, the induced donor concentration varies along the rod. One of these radial variations is shown in Fig. 2, where etch pit density and lifetime of minority carriers before and after the heat treatment are shown together. It is seen that the induced donor concentration decreases at the edge of the slice where the etch pit density is large compared with at the center, and that the decreases of the lifetime are striking at the center.

---

* More rapid cooling experiment were performed by quenching the p-type specimens by dropping into the room temperature oil from 1000°C for about 3 sec. The decrease of hole density in order of 5×10^{14} cm^{-3} was observed. As this results will be related to the lattice defects made by quenching, it will be reasonable to discuss this phenomena in other place.

A *p*-type specimen having an artificial grain boundary pulled at 10 rpm as shown in Fig. 3 is heated at 470°C for 25 hours. The changes of the hole concentration along the rod are also shown in Fig. 3. It is explicitly shown that in the neighbourhood of the grain boundary the formed donor concentration is small compared with that at the other portions.

In order to make precise of the influence of crystal defects on the concentration of the formed donors, the following experiments are also performed. Two specimens are cut along the radial direction from the adjacent slices of the *n*-type ingot. One is etched by CP–4, and another is ground by 600 mesh silicon carbide and carefully rinsed in deionized water. After both specimens are heated for 25 hours at 470°C, the radial variations of increased electron density are measured along the rod. The results are shown in Fig. 4. At the edge where a large number of dislocations are expected, the difference in the formed donor density between both specimens

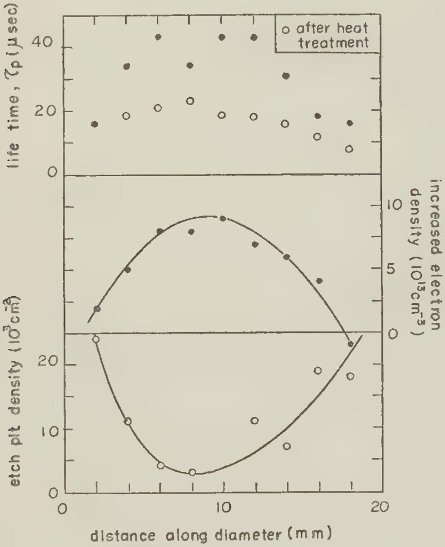

Fig. 2. Increased electron density, etch pit density, and lifetime as a function of distance along the diameter in *n*-type silicon heated at 450°C.

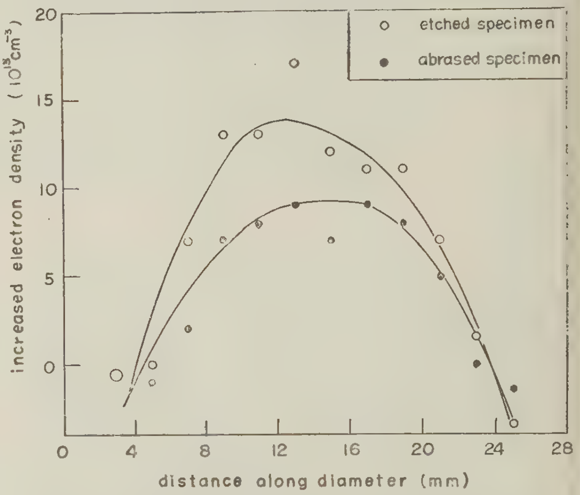

Fig. 4. Increased electron density as a function of distance along the diameter in *n*-type silicon having a etched or abrased surface by heat treatment at 470°C.

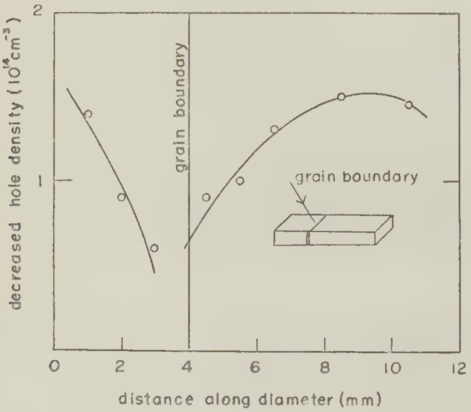

Fig. 3. Decreased hole density as a function of distance along the diameter in *p*-type silicon having a grain boundary by heat treatment at 470°C.

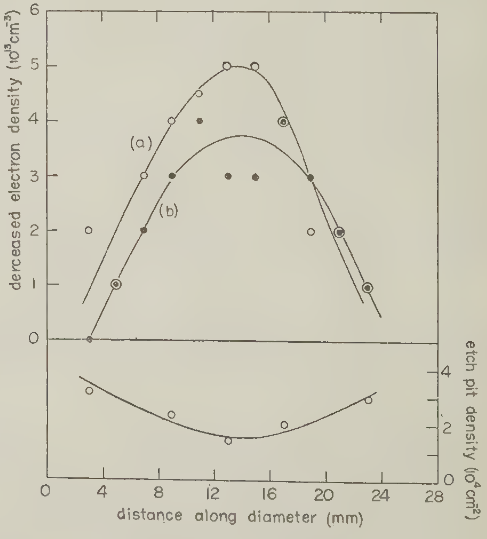

Fig. 5. Decreased electron density and etch pit density as a function of distance along the diameter in *n*-type silicon heated at 1000°C. (a): etched specimen, (b): abrased specimen.

is not clearly observed, but at the center the formed donor density in the etched specimens is distinctly higher than that in the ground.

From the above mentioned results, it is seen that the donor formation depends strongly on the degree of crystal perfection.

C. *Heat treatment at high temperature*

Both silicon specimens, one cut from a pulled ingot and another from vacuum floating zone refined crystal, exhibit a number of interesting effects by heat treatment in the temperature range of 600 to 1200°C.

Specimens of $7\times2\,\text{mm}^2$ cross section are cut along the radial direction from some round slices of an n-type crystal pulled at 10 rpm. After heat treatment for 8 hours at 1000°C, electron densities decrease as a function of the radial distance as shown by curve (a) in Fig. 5, where the dislocation density along the sample is also shown. Another specimen having the same dimensions is prepared from the adjacent slice of the crystal, and ground by 600 mesh silicon carbide and then carefully rinsed in deionized water. This specimen is heated with the etched one, the results of which is already shown by curve (a). The radial variations of the decreased electron density are shown by curve (b) in Fig. 5. It is seen that the decreases of electron density are contrary to the results caused by a low temperature heat treatment and are striking in the center of the rods where etch pit densities are low. In Fig. 5, it is also seen that the decreases of electron density in the abrased specimen is less than that in the etched one. Such decreases of carrier density are accompanied by the decreases of minority carrier lifetime.

In order to investigate the correlation between the changes of the carrier density and the crystal defects, p-type specimens having a grain boundary are heated for 8 hours at 1000°C. An example of the results is shown by curve (a) in Fig. 6, where the decrease of hole density is plotted along the sample. It is seen that the decreases of hole density are small at the grain boundary. Measurements of thermoelectromotive force by hot probe method show an n-type property along the grain boundary. The similar features are also observed in the following experiments: Among the two p-type specimens cut from a vacuum floating zone refined crystal, one is etched and another is ground, and after a heat treatment at 1000°C for 8 hours, it is observed that only the surface of the abrased specimen has an n-type layer of 1×10^{-2} mm thickness which is determined by angle lapping and hot probe technique. The decreases of the hole density are also observed in these specimens which may be expected to have a lower concentration of oxygen atoms.

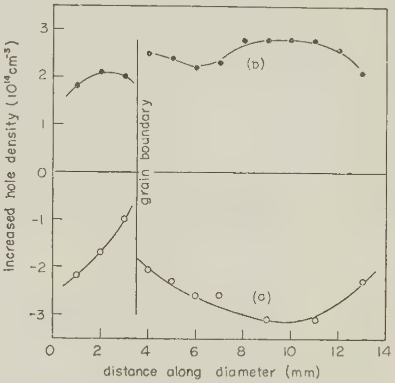

Fig. 6. Changes of hole density as a function of distance along the diameter in p-type silicon having a grain boundary. (a): after heat treatment at 1000°C, (b): after subsequent heat treatment at 470°C.

The p-type sample heated at 1000°C is again heated at 470°C for 25 hours. The change of hole density before and after the heat treatment at 470°C is shown by curve (b) in Fig. 6. In spite of the heat treatment by which the large amount of the donors should be formed, it is observed that the hole density on the contrary increases only in the order of the decreases by the heat treatment at 1000°C.

The decrease of carrier density in p- and n-type silicon by a high temperature heat treatment is accompanied by the decrease of the minority carrier lifetime. Such phenomena depend on the temperature at which the specimens are heated. Some n-type specimens are cut from a crystal pulled at low rotation rate and the values of lifetime are found to be 30 to 50 μsec. These specimens are heated for 6 hours at various temperatures. Fig. 7 shows the variations of the decreased electron density and the lifetime after the heat treatment with the reciprocal of the treating temperature. If it is assumed that the logarithm of the decreased electron density and the lifetime after the heat treatment vary linearly with the reciplocal of the treating temperature, the activation energy may be obtained as 0.36 eV for the changes of electron density and 0.34 eV for the lifetime. It is also observed that the decreases in carrier density and the lifetime after a heat treatment depend neither on the heating period, nor on the resistivity and the lifetime before the heat treatment.

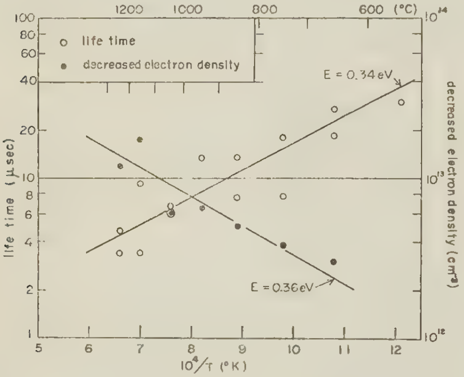

Fig. 7. Lifetime after heat treatment and decreased electron density as a function of reciprocal of heat treatment temperature in *n*-type silicon.

§ 3. Discussion

Discussion is separated into two parts; first, the donor formation by low temperature heat treatment and second, the decreases of carrier density and the annihilation of the formed donors by high temperature's one.

About the phenomena of donor formation, Kaiser[5] has shown that the oxygen atoms included in silicon cause the absorption at 9 μ by Si–O molecular vibration, and that oxygen atoms sensitive with the 9 μ absorption are mostly present at the center of pulled ingot, contributing to the donor formation by a heat treatment at 450°C. The results given in Fig. 2 and 3 show that the formed donor density depends in a very sensitive way on the dislocation density of the materials. Edge portions of pulled crystal and the neighborhood of grain boundary have a higher dislocation density than at the center. The formed donor density is distinctly small at the grain boundary and the edge portion. From these data, it may be reasonable to assume that, when a crystal is cooled during the pulling, the oxygen atoms introduced into the crystal are frozen at the dislocations and the grain boundary, and that the frozen oxygen atoms do not contribute to the donor formation by a low temperature hert treatment. Such assumptions that the oxygen atoms in crystal may be captured by the crystal defects are consistent with the results of low temperature heat treatment on the specimens having an abrased layer as shown in Fig. 4, that is, as the oxygen atoms in crystal diffuse and precipitate in the abrased surface layer, the density of oxygen atoms to contribute to the donor formation is smaller in the abrased specimens than in the etched one. At the edge of crystal, as the oxygen atoms are nearly frozen at dislocations during the pulling, the influence of surface abrasion may be expected to be very small. Lederhandler and Patel[9] have used nearly the same assumption and clearly explained their data on the fast decrease of the absorption coefficient at 9 μ by high temperature heat treatment on the plastically deformed silicon.

The phenomena induced in silicon by a high temperature heat treatment can be explained by the following two processes; (a) annihilation of the formed donors and (b) decrease of carrier density in *p*- and *n*-type silicon. The former may be related to the oxygen atoms included in crystal, but the latter should not be related to oxygen since the decrease of hole density is also observed on a vacuum floating zone refined silicon which is believed to include less oxygen atoms.

Process (a) is explained by Kaiser's assumption that the oxygen atoms, originally active in donor formation, group together into clusters of high oxygen concentration during the heat treatment at 1000°C and then the formed donors are annihilated. In such process, electron density in *n*-type crystal decreases and hole density in *p*-type increases. In Fig. 1, the increases of hole density by a heat treatment at above 600°C show that the donors induced during the pulling are annihilated by this process.

Most of the high temperature heat treatment effects are hardly explained by the process (a). Reduction of the density of majority carriers shown by the curve (a) and (b) in Fig. 5 and the curve (a) in Fig. 6 may be explained by a new assumption that heat treatment introduces some deep trapping centers into both n- and p-type silicons. By further assumption for these trapping centers to play another important role, the recombination center, when the minority carrier is present, the observed reduction of the lifetime after heat treatment may easily be explained. To explain the correlation between the decreased majority carriers density and the lattice imperfection and to explain the n-type character of the grain boundary and the abrased surface, these centers should be assumed to be captured by dislocations quite easily after high temperature heat treatment and to become new donors. If these centers may have a temperature dependent solubility11) and may aggregate each other by low temperature heat treatment, the behavior of the curve (b) in Fig. 6 will be reasonably understood. Also, the facts that the minority carrier lifetime is slightly recovered by the subsequent low temperature heat treatment will be reasonably explained.

If the energy necessary to introduce this center into silicon is E eV, the density of this center Δn, will be given by the following equation,

$$\Delta n = N_0 \exp(-E/kT) .$$

Value of E determined by the slope in Fig. 7 is about 0.35 eV, and N_0 is $2\times10^{14}\,\mathrm{cm}^{-3}$. The lifetime τ_p in the n-type crystal heated at high temperature may be nearly determined by the number and the capture cross section σ of the introduced recombination center,

$$\sigma = \frac{1}{\Delta n \cdot v \cdot \tau_p} .$$

The value of σ obtained from Fig. 7 is $2\times10^{-15}\,\mathrm{cm}^2$ for hole at 300°K. Same estimation of σ for electron in p-type silicon were performed by some experiments. The value of σ is order of about $10^{-15}\,\mathrm{cm}^2$ for electron at 300°K.

The value of the formation energy estimated from the data does not agree with the B. Ross's value6) and the Bemski's one8) which have determined by the quench experiments. It seems that this discrepancy results from the difference in the cooling rate from a treated temperature. Recently, Bemski12) has reported that at high temperature gold is introduced in a concentration of $10^{14}\,\mathrm{cm}^{-3}$ into silicon from the surface and formed a donor level at 0.34 eV from the conduction band. It is interesting to notice that the density of the recombination centers introduced in our experiments is of the order of 10^{12} to $10^{14}\,\mathrm{cm}^{-3}$ at 600 to 1200°C and that the capture cross sections for hole and electron are similar to Bemski's results13). If these centers are introduced from the surface, the concentration of centers must be proportional to the ratio of surface area to volume of the specimen. Studies on the energy level of the centers and on the variation of their concentration with the surface-to-volume ratio seems to be helpful for getting information about what they actually are.

Acknowledgements

The author wishes to thanks Prof. Dr. A. Okazaki and Dr. T. Momota for their continual encouragements, Dr. M. Shibuya for helpful discussions, Mr. K. Hashimoto for the measurements of Hall effect, and Mr. T. Suzuki for assistance in experiments.

References

1) C. S. Fuller et al.: Phys. Rev. **96** (1954) 833. C. S. Fuller, J. A. Ditzenberger, N. B. Hannay and E. Buehler: Acta Met. **3** (1955) 97.
2) Y. Matukura: J. Phys. Soc. Japan **12** (1957) 103.
3) C. S. Fuller and R. A. Logan: J. Appl. Phys. **28** (1957) 1427.
4) W. Kaiser: Phys. Rev. **105** (1957) 1751.
5) W. Kaiser, P. H. Keck and C. F. Lange: Phys. Rev. **101** (1956) 1264.
6) B. Ross and J. R. Madigan: Phys. Rev. **108** (1957) 1428.
7) L. M. Nijland and L. J. Van der Pauw: J. Electronics and Controls **3** (1957) 391.
8) G. Bemski: Phys. Rev. **103** (1956) 567.
9) S. Lederhandler and J. R. Patel: Phys. Rev. **108** (1957) 239.
10) F. J. Morin et al: Phys. Rev. **96** (1954) 833.
11) R. J. Hodgkinson: Physica **20** (1954) 1000.
12) G. Bemski and J. D. Struthers: J. Electrochem. Soc. **105** (1958) 588.
13) G. Bemski: Phys. Rev. **111** (1958) 1515.

Journal of the Physical Society of Japan, Vol. 14, No. 7, July, 1959

Electronmicroscopic Observations of the Cleavage Plane of KCl Crystal

—the Deformation Zone—

By Tetsuhiko Tomiki*

The Research Institute for Steel, Iron and other Metals,
Tohoku University, Sendai, Japan

(Received February 17, 1959)

The *deformation zone* of KCl single crystal decorated with potassium colloid particles is investigated with electron microscope using a replica technique. The deformation zone is formed independently on the imperfections contained originally in the crystal. The slip lines near the deformation zone observed with light microscope are consisted of a number of fine slip lamellae. The thickness D of the slip lamella, the slip distance s and the height h of the slip step were estimated as $D=720$A, $s=270$A and $h=240$A for three adjacent slip lines. It is suggested that several hundreds of screw type dislocations are attached to every new cleavage step at the deformation zone. The attempts were made for the explanation of the mechanism by which new cleavage steps are formed at the deformation zone.

§ 1. Introduction

When an alkali halide single crystal is coloured either with x-ray[1),2)] or with excess alkali metals introduced additively,[3)] growth of crystallites is observed electronmicroscopically not only on the outer surface, but also in the interior of the crystal. One of the most important markings in analysing the effects induced inside the crystal has been the pattern of steps revealed on the freshly cleaved plane obtained after the colouration, and the characteristic features observed so far with electron microscope are summarized in the following: On the fresh cleavage plane of the coloured crystal, it is observed a zigzag step at the kink site where crystallites grow and, in some cases, a bundle of wavy steps converges at such a kink site. This phenomenon was interpreted as follows: The zigzag step may correspond to a kind of internal surface which was originally straight before colouration and was made to turn into the zigzag shape as a result of ion redistributions caused by the colouring processes. It is also considered that such a motion of the internal surface causes growth of crystallites at kink sites. The bundle of wavy steps attached to the kink site may indicate the internal stress produced by the process stated above.[1),3),4)] These situations are quite similar to those which could be expected on the nonconservative motion of dislocations. At present, we have not a sufficient experimental confirmation to interpret the phenomenon in languages of the current dislocation theory, except for a few remarkable cases.

On the other hand, it has been generally accepted, on the basis of the observations with optical microscope, that when the cleavage crack front travels across a twist boundary, new cleavage steps are formed at screw dislocations whose Burgers vectors are not parallel to the cleavage plane.[5)] Recent investigation by Forty[6)] showed that when the cleavage crack front ceased its propagation, the two halves of the crystal plate have plastically deformed by absorption of the kinetic energy of the crack front, and that the new cleavage steps are formed there when the cleavage crack front is made to move forwards again. He observed also the ⟨100⟩ slip lines attached to every cleavage steps which were created anew, and called this special region "*deformation zone*", which can also be produced when the cleavage crack front propagates with a velocity under a critical value.[6),7)] It was suggested that the array of dislocation loops are nucleated along the deformation zone, and this was proved by decorating the dislocation loops with excess metal particles.[8] Another experiment was carried out independently on LiF single crystal with using a successive etch technique, and this gave the same confirmation, too.[9]

---

* Present Address: *Department of Physics, Faculty of Science, Tohoku University.*

If the above relation between the cleavage step and the screw dislocation were applicable to the bundle of wavy steps which converges at the crystallite grown at the kink site of a zigzag step, there must exist a screw dislocation whose Burgers vector is not parallel to the cleavage plane. But, this would be too favourable to be true. It is desired to observe the deformation zone or a twist boundary with electron microscope, if the attempts are made for the interpretation of the characteristic features of step patterns.

As the first step to see the relationship between the cleavage steps and the crystal imperfections such as dislocations, the deformation zone of KCl single crystal was observed with electron microscope.

§ 2. Experimental

2·1 *KCl crystal employed in the experiment*

KCl specimen employed here was not a

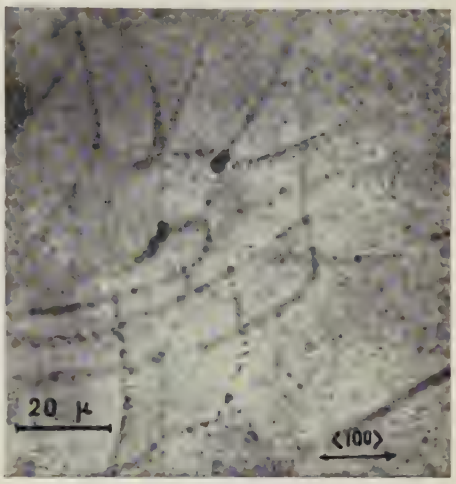

Fig. 1. An optical microscopic image of KCl crystal decorated with colloid particles along dislocation lines.

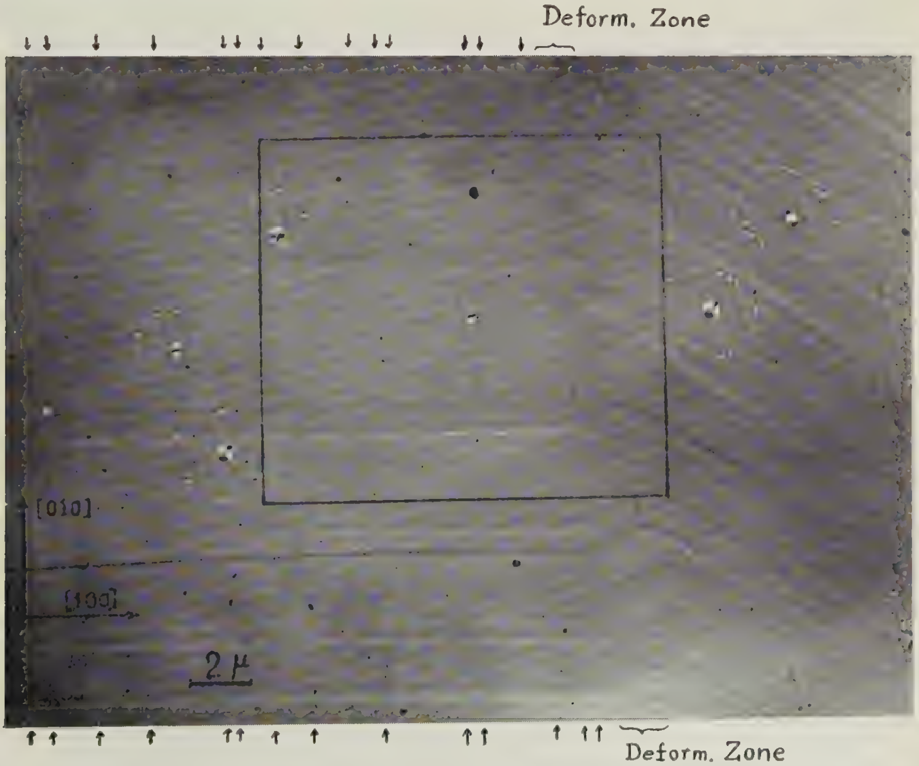

Fig. 2. An electron image of the deformation zone and the cleavage plane adjacent to it. The [100] and [010] direction are chosen as shown in the figure, and the [001] axis is directed upwards normally to the paper. *Cr*-shadow is directed to the [010], and the cleavage crack front propagated from left to right. Every arrow indicates the spots where the slip lamellae are predominant.

pure single crystal cleaved from the block, but was one decorated with potassium colloid particles along the dislocation networks. The reason why the decorated crystal was adopted is based on the following facts: The electronmicroscopic observations on the freshly cleaved {100} planes of the decorated crystal showed that a pit is produced at the spot on the cleavage plane where colloid particle precipitated[10]; this means that we can obtain the surface markings which are closely related to the crystal imperfections without smearing out the fine steps of an electronmicroscopic scale, for the application of the usual etch technique to the fresh cleavage plane to produce the etch pits leads to the simultaneous and inevitable removal of the surface layer of few microns in thickness.

In the present experiment, the undeformed KCl single crystal was heated in the atmosphere of potassium vapour at 550°C for 4 hours, followed by the furnace cooling to room temperature in 12 hours. By this pro-procedure, it was possible to obtain the crystal that was decorated with potassium colloid particles along the dislocation lines as shown in Fig. 1. If the crystal is quenched to room temperature instead of the furnace cooling, it will acquire the atomic dispersed ***F*** centres, as is well known. The procedure adopted in this experiment is slightly different from Rexer's method by which greater parts of the experiments for decorating dislocations of alkali halides with colloid particles were carried out,[11] nevertheless the phenomena that the crystal becomes to contain colloid particles by this procedure are not quite new in themselves.[12]

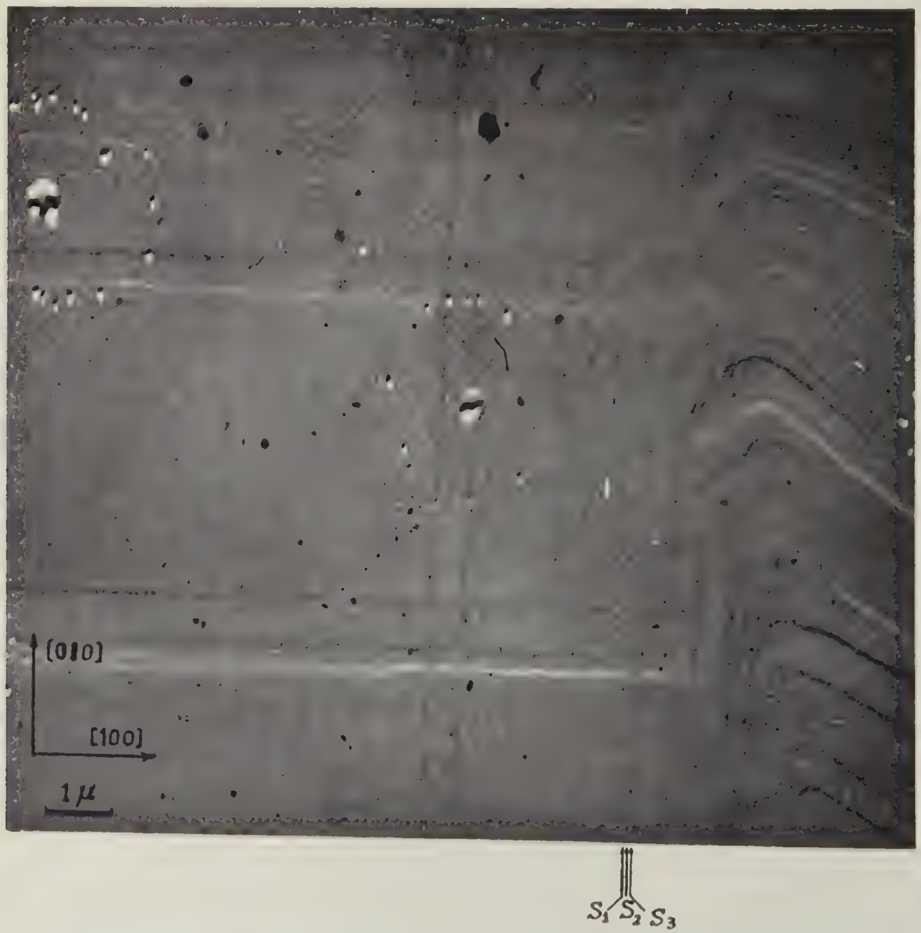

Fig. 3. An electron image of fine slip lamellae on the cleavage plane adjacent to the deformation zone. The coordinate system is identical with that of Fig. 2. The slip lines S_1, S_2 and S_3 are estimated as about 240A in heights.

2·2 *Cleavage planes and a reprica*

The (001) cleavage plane of the crystal was obtained with a sharp razor by tapping it with pincette at room temperature. The special attentions were not put on the cleaving process as were done in the previous workers.[6),7)] This fresh cleavage plane was observed with the electron microscope using the one stage replica which was consisted of obliquely deposited ***Cr*** film subsequently reinforced with ***C*** film in high vacuum, where the ***Cr***-beam was directed parallel to one of the ⟨100⟩ of the specimen and made an angle $\theta = \tan^{-1}(0.4)$ to the cleavage plane to be observed.

§ 3. Experimental Results

The electron image of the deformation zone described above and the surface area adjacent to it are shown in Fig. 2 which illustrates the general features of cleavage steps on this surface area. The shadow direction indicates that the cleavage crack front propagated from left to right leaving the straight cleavage steps directed to the [100] of the basal plane behind, until it reached to the defor-

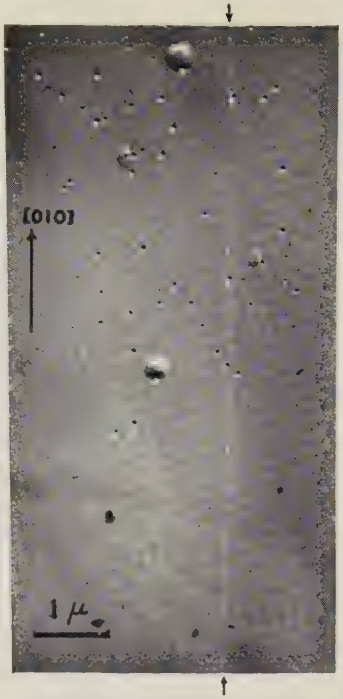

Fig. 4. An electron image showing the single slip line on the flat cleavage plane. The arrow indicates the [010] slip line.

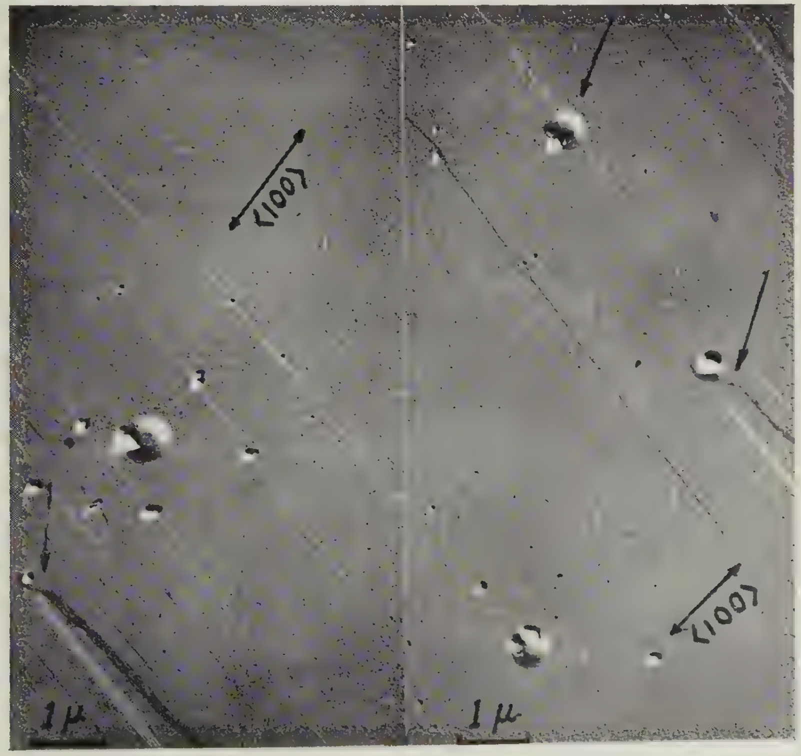

(a) (b)

Fig. 5. An electron micrograph showing the effect of imperfections on the cleavage step.

mation zone. When the cleavage crack front passed across this zone, the new cleavage steps were produced and their running direction was suffered a sudden change from the older [100] to the direction making an angle of about 30° to it after the short passage along the direction making an angle of about 20° to the [010].

The small semispherical pits of about 0.5 microns in diameter encircled with tiny drops are observable on the cleavage plane. They are considered to be resulted from the potassium colloid particles.[10] Since they indicate probably the place where imperfections were located before cleaving process, it is conceivable that a deformation zone can be formed independently of the imperfections contained originally in the crystal, provided that all of the imperfections are to be decorated with colloid particles.

Another interesting phenomenon is that the fine slip lines having the [010] direction of the basal plane are observed chiefly on the surface area where only the [100] cleavage steps appear. Every arrow in the figure indicates the spots where the slip lamellae are predominant.

Fig. 3 shows the detailed structure on the surface region enclosed with black lines in Fig. 2. One sees here clearly a kind of fluctuation in the density and strength of the fine slips. To every new cleavage step a number of fine slip lines whose directions are slightly deviated (about 20°) from the [010] are attached. The sum of their slipped distances represents roughly the height of the new cleavage step to which they are attached. Furthermore, the [100] cleavage step are segmented by the [010] slip lines. The shape of the intersection of the cleavage step and slip planes indicates that the resolved slip processes are mainly due to the (101)/$[10\bar{1}]$ slip system. It should be pointed out, however, that the slip lines are not always so simple as stated above, but mixed with other glide systems.

Fig. 4 is the electron micrograph which shows the single slip line on the cleavage plane. We could occasionally observe slip lines of this type on the cleavage plane.

Finally, it must be mentioned the effect of the "colloid" pit on the cleavage step. Though it is observed that a new cleavage step is rarely created behind the spot where colloid particle precipitated, its definite influences on the cleavage step could not be observed as shown in Figs. 2, 3 and 4. If a fine cleavage step happened to proceed against the pit, its passage was forced to curve leaving a semicircular locus of the cleavage step around the pit. The radius of curvature of the semicircular step was slightly larger than that of the pit by 300 A to 1,000 A. This is considered to be caused by the stress around the imperfection. These phenomena are shown in Fig. 5.

§ 4. Discussion

4·1 *Estimation of the number of screw dislocations*

The resolved [010] slip lines on Figs. 2 and 3 probably correspond to the (101)/$[10\bar{1}]$ slip system, taking the orthogonal coordinates system such as shown in Fig. 2. It is conceivable that this configuration causes the slip lines to have the dark contrast against

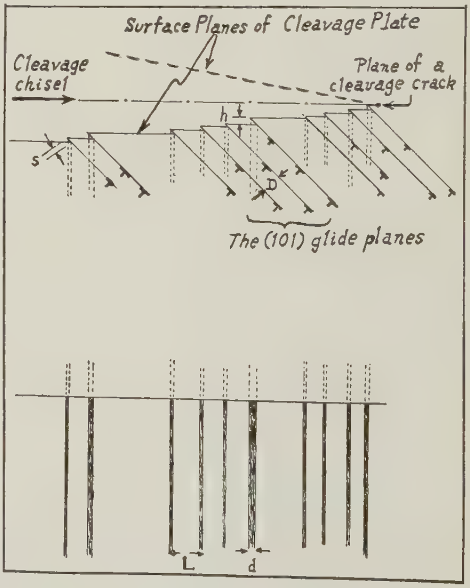

Fig. 6. (a): A schematic diagram of slip lamella and plastic bending of the half crystal. This configuration was obtained on the basis of Fig. 2 (or 3). The slip distance s of a slip lamella, the step height h and the lamella width D are defined. (b): The darkening of an electron image obtained from the replica which casts the surface represented by Fig. 6 (a). The width d of a slip line and the lamella length L measured along the [100] on the (100) are defined.

the slip lamellae even though the ***Cr***-shadow was parallel to the [010] direction. Fig. 6 is the schematic diagram obtained from Fig. 2 (or 3). Then, the step height h due to the slip motion of each lamella is equal to the breadth d of the slip line, and the slip distance s along the [101] is $\sqrt{2}\cdot d$. The thickness D of a slip lammella is given by $L/\sqrt{2}$, where L is the breadth of the lammella measured along the [100] on the (001) plane (see, Fig. 6). For the slip system S_1, S_2 and S_3 indicated in Fig. 2, the following values can be obtained:

	Slip			Lamella	
	S_1	S_2	S_3	S_2S_1	S_3S_2
h	240 A	>240 A	240 A	—	—
s	270 A	>270 A	270 A	—	—
D	—	—	—	720 A	720 A

These values will give a rough picture for the slip system observable in the region near the deformation zone. To each new cleavage step created along the deformation zone five to ten resolved slip lines are attached, so we can calculate the number N of the screw dislocations per new cleavage step according to the next equation:

$$N=(s/\boldsymbol{b})\cdot n \tag{1}$$

where,

n=the number of slip lines attaching to a new cleavage step

$\boldsymbol{b}$=Burgers Vector$=a\cdot[110]/2$

Taking $s=270$ A, the relation $N=120\cdot n$ is obtained. Thus, it is estimated that 5.10^2 to 10^3 screw dislocations are created at or near the every new cleavage step along the deformation zone.

4·2 *The mechanism of the creation of new cleavage steps*

According to the present investigation, the deformation zone was formed independently of the imperfections originally included in the crystal plate, because Fig. 2 shows that the deformation zone is located on the region of the cleavage plane which has not any relationship to the colloid pit. Thus, it is certain that the slip lines observed in Figs. 2 and 3 were produced by the applied external force by which the cleavage crack front was driven.

As to the mechanism of formation of the deformation zone, the previous investigators[6),7)] infered as following: When the cleavage crack was introduced into the crystal and driven by the external force, the elastic energy in the crystal is stored up in addition to the increment of the surface energy accompanied with the crack propagation; this elastic energy is released possibly by the plastic work, hence the dislocation loops are spontaneously introduced into the crystal region near the front of a propagating cleavage crack. This special region is the so called deformation zone, as stated in § **1**. This problem has been investigated on the standpoint of crack propagation. Nevertheless, the mechanism by which new cleavage steps are created along the narrow strip of deformation zone was not taken up so far as we know. In this paragraph, some discussions are given on this point.

When the cleavage crack was introduced into the crystal plate along the {100} so as to obtain two halves of the crystal plate with equal thickness, they separate each other with nearly equal amount of a plastic bending which is partly caused with glide processes extensively occurred on the deformation zone. In the other case when the thinner crystal plate was cleaved off from the thicker one, the former is severely deformed. It is considered here, therefore, the mechanism by which the new cleavage steps are created along the deformation zone only in the case when the two halves of the crystal plate are cleaved with equal thickness and under the same plastic bending. This may be applicable to the other cases with a slight modification.

Fig. 7 shows that the cleavage crack ***ABNM*** is introduced into the crystal plate to produce two halves of crystal plate ***I*** and ***II*** with equal thickness, here a cleavage crack front is located along the curve ***ASB***. It is assumed that the crystal plates ***I*** and ***II*** are equivalent in all respects. Now, let us suppose that the elastic energy in the crystal is stored up and happens to be elevated at a critical value at the instant when the cleavage crack front is located along the ***ASB***, and that the crystal plates ***I*** and ***II*** are consequently deformed by slip by the high stress concentration at the point, for example S, on the **ASB** in order to release it. For the easy comparison between Fig. 2 (or 3) with Fig. 7, the same coordinate system was adopted in both figures. The family of the [100] cleavage steps in Fig. 2 is considered to exist on the cleavage crack **ABNM** in Fig. 7. If the slip process in **I** is due to the $(101)/[10\bar{1}]$ system, as in Fig. 3, the crystal plate **II** must slip along the [101] on the $(\bar{1}01)$ at the same instance because of the assumption of equivalency. Consequently, dislocation loops may be nucleated both on the (101) and on the $(\bar{1}01)$, where the dislocation loops on the (101) may be easily located downwards in the region of the crystal plate **I**, and those on the $(\bar{1}01)$ upwards in the crystal plate **II**. The parts of dislocation loops near the free surface **ASBNM** may move to the surface, then cut it leaving the slip steps along the [010] to release the stress field. The configuration of the dislocation loops at this instance is represented in the figure as the curves of $SP_{\text{I}}E_{\text{I}}$ and $SP_{\text{II}}E_{\text{II}}$. The character P indicates that they have the positive edge character, and the character E for the end point of the dislocation loop. The shaded part in the figure indicates the slipped region. Near the point S, the excess of screw dislocations of the same sign may be concentrated locally. If the dislocation loop $SP_{\text{II}}E_{\text{II}}$ have a screw component near the region S whose sign is reverse to that of the $SP_{\text{I}}E_{\text{I}}$, the high concentration of the stress at the region S could not be released, thus such kind of combination of slip processes is meaningless. These special situations lead to raise the elastic energy in the neighbourhood of S, and give rise to the additional force $\boldsymbol{F}$ directed towards interior the crystal along the [010]. In accordance with Fig. 2, if we suppose the applied external force $\boldsymbol{f}$ to be directed along the [100], the cleavage crack front near the point S may be driven by the resultant force $(\boldsymbol{F}+\boldsymbol{f})$. This mechanism appears to explain the facts that the slip steps serve as the starting lamellae of every new cleavage step to which they are attached and that their directions are deviated slightly from the [010] direction (see § **3**; Fig. 3, for example). After the additional spontaneous force $\boldsymbol{F}$ around the point S as well as the other points along the deformation zone under the same condition as S vanishes by the movement of the crack front along the special direction stated above, the crack front should be driven solely by the external force along the direction favourable to it. Thus, the cleavage step may change its running direction suddenly. It is conceivable that the abrupt change of the direction of cleavage steps from that of the slip lamella making an angle 20° to the [010] in Fig. 3 may correspond to the above state of affairs.

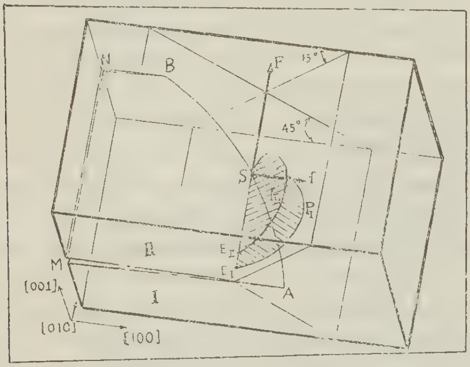

Fig. 7. Schematic diagram for the propagation of a cleavage crack front. **ABNM** is the cleavage crack, **ASB** is the front of a cleavage crack. The curve $SP_{\text{II}}E_{\text{II}}$ corresponds to a dislocation loop on the $(\bar{1}01)$ and $SP_{\text{I}}E_{\text{I}}$ to that on the (101). Shaded regions represent the slipped area (See the text).

Now, according to the above mechanism, it appears possible to understand the reason why the new cleavage steps are formed and suffered to the abrupt change of their running directions at the deformation zone **ASB** nearly independent of the older cleavage steps. As estimated in § **4·1**, it is easy to make the older cleavage steps of 0.1 microns or less in heights vanish by the slipping process. If any cleavage step is sufficiently high so that it is not made vanish by the slip process, it can across the deformation zone. However, its running direction is forced to change at the deformation zone to the direction which was determined by the force $\boldsymbol{F}$ to relieve the strain energy of the screw dislocations with same sign.

§ 5. Summaries

The cleavage plane of KCl single crystal containing colloid particles was investigated with electron microscope using one stage replica technique. The important results are summarized as follows:

(1) The deformation zone is formed independently of the imperfections contained originally in the crystal.

(2) The slip lines near the deformation zone observed with light microscope are consisted of a number of fine slip lamellae. Measurements were made on the thickness D of the slip lamella, the slip distance s and the height h of the slip step for three examples. They gave the following values: $D=720$ A, $s=270$ A and $h=240$ A. Thus, it was estimated that several hundreds of screw dislocation are attached to every new cleavage step at the deformation zone.

(3) It was found that new cleavage steps are created independent of the older cleavage steps at the deformation zone and that the height of a new cleavage step at the defortion zone and that the height of a new cleavage step is nearly equal to the sum of the slip lamellae attaching to it. Attempts were made for the explanation of the mechanism by which new cleavage steps are formed and made to change near the deformation zone their running direction from that of the older one.

(4) Some effects of crystal imperfection on the passage of a cleavage step was detected (Fig. 5).

Acknowledgements

This experiment was made in 1956 during the course of the experiment of the additively coloured crystal with the electron microscope[3),10)] at the *Research Institute for Scientific Measurement, Tohoku University*. The author would like to express his cordial thanks to Prof. S. Ogawa, *the Research Institute for Steel, Iron and other Metals*, who made this possible. He is very greateful to Prof. T. Hibi for his kind and instructive guidances to electronmicroscopy through experiments. His gratitudes are also due to Dr. T. Suzuki who kindly suggested the mechanism of the production of new cleavage steps and criticized the manuscript.

References

1) T. Hibi and K. Ishikawa: J. Phys. Soc. Japan **13** (1958) 709.
2) T. Hibi and K. Yada: J. Phys. Soc. Japan **14** (1959) 455.
3) T. Hibi and T. Tomiki: J. Phys. Soc. Japan **14** (1959) 444.
4) T. Tomiki: J. Phys. Soc. Japan **14** (1959) 304. T. Tomiki and M. Ueta: ibid. **14** (1959) 602.
5) P. B. Hirsch: *Progress in Metal Physics*, vol. **6**. (Butterworths London, 1956) 267.
6) A. J. Forty: Proc. Roy. Soc. **A, 242** (1957) 392.
7) J. J. Gilman and W. G. Johnston: J. Appl. Phys. **27** (1956) 1018. J. J. Gilman: ibid. **27** (1956) 1262. J. J. Gilman, C. Knudsen and W. P. Walsh: ibid. **29** (1958) 601.
8) S. Amelinckx: Phil. Mag. **3** (1958) 653.
9) J. J. Gilman and W. G. Johnston: *Dislocations and Mechanical Properties of Crystals* (Wiley, New York, 1956) 116.
10) T. Hibi and T. Tomiki: J. Phys. Soc. Japan **14** (1959) 375.
11) See, for example, S. Amelinckx: Phil. Mag. **1** (1956) 269.
12) See, for example, E. Mollwo: Z. Phys. **85** (1933) 56.

JOURNAL OF THE PHYSICAL SOCIETY OF JAPAN, Vol. 14, No. 7, JULY, 1959

β-Ferric Oxyhydroxide and Green Rust

By D. R. Dasgupta and A. L. Mackay

Birkbeck College Crystallographic Laboratory,
21, Torrington Square, London, W. C. 1

Evidence that the existence of crystalline $Fe(OH)_3$ has not been demonstrated by Abe[1)] is presented and doubts cast on the existence of β-FeOOH are dispelled. The green rust observed by Yoshioka[9)] is shown to be identical with that found by Keller[6)] and outline structures are suggested for these compounds.

§ 1. Introduction

In the course of a programme of work on magnetic iron minerals we have studied as many iron oxides and hydroxides as have been reported in the literature and in most cases have been able to characterise the various phases and elucidate their mutual relationships. Our experiments lead us to results which conflict with those of Yoshioka[9),10)] and Abe[1)] which are reported in Structure Reports, **15** (1951).

§ 2. β-FeOOH

Data on the material precipitated when ferric chloride solution is hydrolysed at about 90°C have been published by several authors, for example, Weiser and Milligan[3)], Kratky and Nowotny[7)] and ASTM cards numbers 1–0669, 3–0429 and 3–0446. All these observations are in substantial agreement with our own (Table I), except that Weiser and Milligan, presumably because of instrumental deficiencies, did not record the highest spacing in the diffraction pattern (at 7.40Å). Within experimental error our pattern can be indexed on the basis of a body-centred tetragonal unit cell with the dimensions $a=10.48\pm0.01$ and $c=3.023\pm0.005$Å. Small distortions from this symmetry are, of course, not excluded by a powder photograph.

We prepared our specimen by the hydrolysis of $FeCl_3$ but examined also the hydrolysis products of a number of other ferric salts. We found that FeF_3 gave a product identical with β-FeOOH. Ferric bromide, nitrate and sulphate, however, gave α-FeOOH on hydrolysis. Ferric alum gave jarosite, $(NH_4)Fe_3(OH)_6(SO_4)_2$. From a mixed solution of chloride or fluoride and sulphate, β-FeOOH was precipitated in preference to jarosite. All methods of preparation gave, to within 1%, the same spacings which did not vary with the Cl′ content. On very prolonged hydrolysis at 90° (for 144 hours) β-FeOOH transformed to α-Fe_2O_3 and not to α-FeOOH.

We think that the structure should be compared with that of hollandite or α-MnO_2 (Byström[3)]) where the unit cell is very similar (space group I4/m and cell dimensions $a=9.8$ and $c=2.86$Å) and where extra large ions are necessary for stabilising the structure. In the manganese oxide Ba^{++} ions occur statistically and analyses of β-FeOOH show variable quantities (up to 4%) of Cl′ ions. The Cl′ (or F′) cannot occur stoichiometrically as the diameter of the Cl′ ion (3.62Å) is greater than the c-dimension of the cell. Analysis also confirms that all the iron is in the ferric state.

On heating, β-FeOOH loses water and transforms to α-Fe_2O_3 at about 200° depending on the Cl′ content. (With less Cl′ the temperature of the decomposition is lowered). It is difficult to estimate the significance of the water loss, about 20% above 100°, because of the adsorption of water on small particles. The loss if the composition were FeOOH would be 10% and if $Fe(OH)_3$, 25%. There are good reasons for not believing the material to be $Fe(OH)_3$ because the latter is well known as a gel which on drying at room temperature goes to α-Fe_2O_3 and on ageing may give α-FeOOH. No reliable observations of crystalline $Fe(OH)_3$ have been made before.

Abe's data seem to correspond to a mixture of β-FeOOH and $FeCl_3\cdot 6H_2O$ (see Table I). Decomposition of the ferric chloride hydrate by the electron beam would account for the difference between the X-ray and electron diffraction observations.

The agreement between the observed and calculated values using the hydrargillite-type

Table I. Analysis of Abe's powder photographs of "$Fe(OH)_3$".

Abe's preparation			β-FeOOH (Mackay and Dasgupta)			$FeCl_3 \cdot 6H_2O$ (ASTM 1-0152)		Differences
I	d(Å)	Method	I	d(Å)	*hkl*	I	d(Å)	(Abe's less other)
w	6.95	X	vs	7.40	110			−0.45
vm	6.49	X				100	6.0	+0.46
mw	4.95	X	m	5.25	200			−0.30
w	4.43	X				38	4.40	+0.03
vw	4.10?	X				20	4.40	+0.10
			(vw	3.70	220)			
mw	3.39	X	vs	3.311	310	38	3.50	+0.08, −0.11
s	3.23	X E				75	3.14	+0.09
						50	2.76	
m	2.57	X E	m	2.616	400	31	2.57	−0.05, −0.00
vs	2.48	X E	s	2.543	211	38	2.42	−0.06, +0.06
			(w	2.343	420)			
s	2.23	X E	m	2.285	301	25	2.19	−0.05, +0.04
m	2.08	X E	{w	2.097	321			−0.02
			w	2.064	510			+0.02
sm	1.915	X E	ms	1.944	411	28	1.94	−0.03, −0.03
						20	1.90	+0.02
			(vw	1.854	440)	and weaker lines		
sm	1.72	X E	m	1.746	600			−0.03
			(vw	1.719	501, 431)			
vs	1.615	X E	vs	1.635	521			−0.02
s	1.490	X E	m	1.515	002			−0.03
			(w	1.497	611)			
			(w	1.480	112, 710; 550)			
			(vw	1.459	640)			
sm	1.418	X E	s	1.438	541			−0.02
m	1.356	X E	m	1.374	730, 312			−0.02
m	1.293	X E	w	1.310				−0.02
			(vw	1.290)				
			(vw	1.272)				
			(vw	1.229)				
			(vw	1.219)				
m	1.189	E	vw	1.189				0.00
			(vw	1.166)				
m	1.137	E	vw	1.158				−0.01
			m	1.138				0.00
			(vw	1.107)				
			(vw	1.085)				
sm	1.053	E	vw	1.064				
			vw	1.050				
			w	1.030				−0.02

* X=X-ray diffraction E=electron diffraction.

structure is certainly remarkable but if the latter really obtained the intensities should be similar to those in the powder pattern of $Al(OH)_3$. The extremely strong reflexion (002) corresponding to the layer structure should be outstanding but it appears to be only moderate while there are other serious intensity differences.

We conclude therefore, that the existence of crystalline $Fe(OH)_3$ has not been demonstrated and that the β-FeOH remains as a well-characterised and established compound.

§ 3. Green Rust

We have prepared green rust (Feitknecht and Keller[5]) in quantity both chemically, by the controlled oxidation of buffered ferrous solutions, and electrolytically. In the presence of Cl′ ions the rust produced has a rhombohedral cell with $a=3.198\pm0.01$ and $c=24.2\pm0.1$Å. This is called "green rust I" and has been described by Keller[6]. In the presence of SO_4'' ions the same material is also formed (with dimensions $a=3.23$ and $c=22.5$) but at a later stage another phase, which we have called "green rust II" appears. This has a hexagonal cell with dimensions $a=3.174$ and $c=10.94$Å. The green rust II is also formed in the electrolysis of N/10 $(NH_4)_2SO_4$ between iron electrodes at a high current density, air being excluded from the solution. Further details are in the press elsewhere.

Table II. Analysis of Yoshioka's powder data for green rust (1948).

$1/d^2$ Observed (Yoshioka)	*hkl* Orthorhombic indices (Yoshioka)	$1/d^2$ Calculated (Mackay)	*hkil* Hexagonal indices (Mackay)	$1/d^2$ calc. $-1/d^2$ obs.
0.1422	200	0.1425	$10\bar{1}2$	0.0003
0.1833	103	0.1834	$10\bar{1}5$	0.0001
0.2601	004	0.2596	$10\bar{1}8$	−0.0005
0.3295	301	0.3297	$10\bar{1}$, 10	0.0002
0.4005	020, 204	0.4035	$11\bar{2}0$	0.0030
0.420	310	0.421	$11\bar{2}3$	0.001
0.541	220	0.540	$20\bar{2}1$	−0.001
0.5835	123	0.587	$20\bar{2}5$	0.0035
0.661	024	0.663	$20\bar{2}8$	0.002
0.938	130	0.945	$21\bar{3}1$	0.007
0.988	026, 510	0.992	$21\bar{3}5$	0.004
1.061	231	1.068	$21\bar{3}8$	0.007
1.220	330	1.210	$30\bar{3}0$	−0.010
1.278	600	1.280	$30\bar{3}6$	0.002
1.621	040	1.614	$22\bar{4}0$	−0.007
1.751	240, 044	1.752	$31\bar{4}1$	0.001

$1/d^2$ is calculated for a rhombohedral cell with hexagonal cell dimensions $a=3.15$ and $c=22.6$Å. In the X-ray powder photograph the reflexion 0003 is very strong and 0006 is strong. There are other intensity differences consequent on the preferred orientation in the electron diffraction camera.

The material reported by Yoshioka[9] appears to differ from these two forms. Nevertheless spacings recorded by electron diffraction can be very satisfactorily indexed on a rhomdohedral cell with $a=3.15$ and $c=22.6$Å (see Table II). It is thus seen to be substantially the same as the green rust I which would be expected in the electrolysis of dilute NaCl with iron electrodes. However, the strongest lines, 0003 and 0006, found in the X-ray pattern are missing. It is also noticable that the 1 indices do not exceed 10. These observations would be consistent with the orientation of flakes of rust parallel to the mounting film and perpendicular to the electron beam.

There seems to be no simple transformation between Yoshioka's cell (body-centred orthorhombic with $a=5.30$, $b=3.16$ and $c=7.83$Å) and ours. This orthorhombic cell is not, therefore, an alternative description and coincidences between certain key spacing explain the satisfactory indexing of the spacings. It would be possible to use a monoclinic cell with $a=5.45$, $b=3.15$, $b=7.75$ and $\beta=103.6°$ ($d_{100}=5.30$ and $d_{001}=7.53$Å) which was centred on the c-face.

Some speculations can be made as to the structure of the green rusts I and II in terms of the packings of equal spheres, if some simplifying assumptions are made:

a) Hexagonal layers of anions (O″, OH′ or H_2O) are stacked so that regular tetrahedra fill space. The interlayer distance is thus 0.817a where a is the anion diameter.

b) There will be tetrahedral and octahedral vacancies available for cations. Assume that no great distortion of the structure is caused by filling these and restrict consideration to the octahedral holes.

c) Restrict consideration to hexagonal cells (P or R) with one anion per layer (a=approx.

3.16Å).

d) Reject as unlikely the sharing of faces by coordination octahedra (or tetrahedra) round the cations (Pauling's rules).

e) Assume the compounds are stoichiometric. There are then, only the following stackings for the numbers of layers indicated: (A, B, C denote anions at 0, 0, z; 1/3, 2/3, z; 2/3, 1/3, z and a, b, c denote cations with the same coordinates)

2-layers

Composition AO_2. Sequence A–BcA. ($c=1.633a$, hexagonal cell).

3-layers

Composition AO. Sequence AcBaCbA. (cubic with $a_{cub.}=1.414a$).

Composition A_2O_3. Sequence AcBaC–A. ($c=2.45a$, hexagonal).

Composition AO_3. Sequence AcB–C–A. ($c=2.45a$, hexagonal).

4-layers

Composition A_2O_4. Sequence AcB–AbC–A or A–BcAbC–A. ($c=3.27a$, hexagonal).

6-layer rhombohedral

Composition AO_2. Sequence AcB–CbA–BaC–A. ($c=4.90a$, rhombohedral)

9-layer rhombohedral

Composition A_2O_3. Sequence AcBaC–BaCbA–CbAcB–A

Composition AO_3. Sequence AcB–C–BaC–A–CbA–B–A or A–B–CaB–C–AbC–BcA. ($c=7.35a$, rhombohedral).

We suggest that as a first approximation the green rust I has the 9 layer rhombohedral structure (c/a obs.=7.2) and that the green rust II has the 4 layer structure A–BcAbC–A (c/a obs.=3.4). The 2 and 6 layer structures are exemplified by $Fe(OH)_2$ and $CdCl_2$ respectively⁴⁾.

The formula $Fe^{++}Fe^{+++}O_2''\cdot OH'$ suggested by Deiss and Schikorr as the composition of the green rust I seems, therefore, not only compatible with the structure but likely, if the above assumptions are correct.

References

1) R. Abe: J. Phys. Soc. Japan **6** (1951) 345.
2) J. D. Bernal, D. R. Dasgupta and A. L. Mackay: Clay Minerals Bulletin (1959) (In press).
3) A. Byström and A. M. Byström: Acta Cryst. **3** (1950) 146.
4) E. Deiss and G. Schikorr: Zeit. anorg. allg. Chem. **172** (1928) 32.
5) W. Feitknecht and G. Keller: Zeit. anorg. allg. Chem. **262** (1950) 61.
6) G. Keller: Thesis (Bern, 1948).
7) O. Kratky and H. Nowotny: Zeit. Krist. **A**, **100** (1938) 356.
8) H. B. Weiser and W. O. Milligan: J. Amer. Chem. Soc. **57** (1935) 238.
9) H. Yoshioka: Kagaku **18** (1948) 413.
10) H. Yoshioka: J. Phys. Soc. Japan **4** (1949) 270.

JOURNAL OF THE PHYSICAL SOCIETY OF JAPAN, Vol. 14, No. 7, JULY, 1959

Anti-Phase Domains in Gold-Copper-Zinc Ordered Alloys Revealed by Electron Microscope

By Shiro OGAWA, Denjiro WATANABE

The Research Institute for Iron, Steel and Other Metals,
Tohoku University, Sendai

Hiroshi WATANABE and Tsutomu KOMODA

Hitachi Central Research Laboratory,
Kokubunji, Tokyo

(Received March 7, 1959)

Using thin evaporated films of gold-copper-zinc ternary ordered alloys, the line-up of anti-phase domains has been observed as parallel lines on transmission electron micrographs of bright field, down to a domain size of about 8Å.

The lattice modulation accompanying anti-phase domains, i.e. the periodic error of lattice spacing or scattering factor with the same period as a domain size, has again been verified to play an important role in forming the satellites around the direct spot on a diffraction pattern, and hence, in forming the parallel lines on electron-microscopic images. Two-thirds of the intensity of the satellites have been estimated in the present alloy films to arise from the modulation, and the rest probably from double diffraction.

§ 1. Introduction

In our previous work[1] it was reported that parallel lines spaced at intervals of about 20Å were observed on transmission electron micrographs from evaporated films of CuAu II and that they revealed the line-up of stable anti-phase domains in this ordered alloy. There are many ordered alloys with long period, i.e. with anti-phase domains of definite size[2], and most of them have considerably smaller domains than CuAu II. It is interesting and desirable to observe the domain structures also in such alloys with smaller domain size by means of electron microscopy. This observation will be useful in the following two points. First, it enables us to investigate into the details of distribution of anti-phase domains in many examples, and secondly, it affords data to the problem how far the fine structure of metals and alloys can be resolved by an electron microscope with the high resolving power.

K. Schubert *et al*[3],[4] studied many ordered alloys with long period by means of X-ray diffraction, especially, in detail those in the gold-copper-zinc system. According to them, the addition of zinc to CuAu makes a domain size smaller, keeping the crystal structure almost isomorphous to CuAuII. For example, an alloy containing 42.5 gold, 42.5 copper and 5 zinc in atomic per cent has a domain size of 3.7 a, i.e. about 14.7Å, a being the lattice constant along the line-up direction of domains. The more the zinc content is, the smaller this size, and for an alloy containing 31 gold, 31 copper and 38 zinc in atomic per cent a domain size is 1.4 a, i.e. about 5.5Å. Thus, the addition of a divalent metal makes the occurrence of out-of-steps more frequent and gives rise to a continuous decrease of the domain size. The present authors undertook to utilize this fact and to observe anti-phase domains far smaller than those in CuAuII. The observation was made on several ternary alloy films with different contents of zinc, and the line structures corresponding to the line-up of domains were successfully observed, the least resolved distance being 8Å. The details of observation and the discussion on them will be given in § 3 and § 4, respectively.

§ 2. Experimental

Specimen films were prepared as follows: Gold was first evaporated on to cleavage surfaces of rocksalt heated at 400°C and then equivalent copper in number of atoms was evaporated on gold films at room temperature. Composite films were homogenized and alloy-

Table I. Lattice constants and domain sizes of the Au–Cu–Zn alloy films.

No.	a (Å)	b (Å)	c (Å)	domain size (Å)	M=domain size/a
1	3.94		3.68	13.3	3.4
2	3.96		3.68	11.8	3.0
3	4.01	3.96	3.68	9.4	2.3
4	4.02	3.94	3.68	8.0	2.0

ed at 350°C, and after having been detached from the substrates, they were mounted on titanium plates with pin holes 0.1 mm in diameter. Electron diffraction proved these films to be composed of single-crystalline CuAu I. They were again put into the evaporation chamber, and after preheating at 350°C a small quantity of zinc was evaporated on to them, the temperature being maintained at about 100°C. The alloy films consisting of the three elements were then heated up to 350°C, kept at this temperature for 2 hours and slowly cooled. This treatment was sufficient to produce single-crystalline ternary alloy films of the crystal structure isomorphous to CuAuII. Thus, four kinds of specimens with different compositions were prepared, but the compositions were not immediately known. Domain sizes estimated from separations of split superlattice reflections of diffraction patterns were 13.3Å, 11.8Å, 9.4Å and 8.0Å, corresponding to 3.4 a, 3.0 a, 2.3 a and 2.0 a, respectively. According to X-ray measurements by Schubert *et al*, these data show compositions of the films to range between 47gold-47copper-6zinc and 38gold-38copper-24zinc in atomic composition. The lattice constants of these alloys are tabulated in Table I with the above data. Specimens No. 3 and 4 have orthorhombic unit cells, while No. 1 and 2 were observed from electron diffraction patterns not to be orthorhombic but to be tetragonal. The film thickness was always about 300Å.

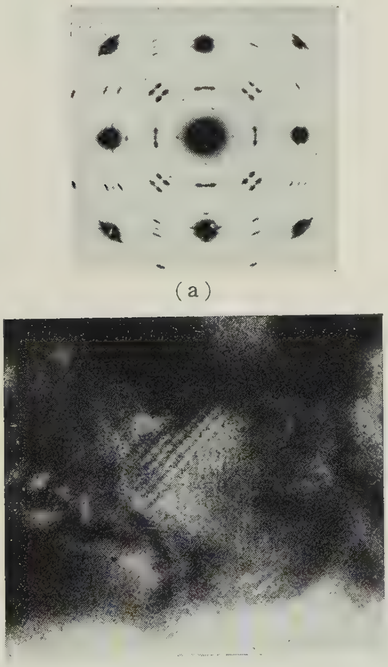
(a)

(b)

Fig. 1. (a): Electron diffraction pattern of a Au-Cu-Zn alloy film with M=3.4 (No. 1), normal incidence. (b): Its electron micrograph. (750,000×). The mean spacing of the lines is 13.3Å.

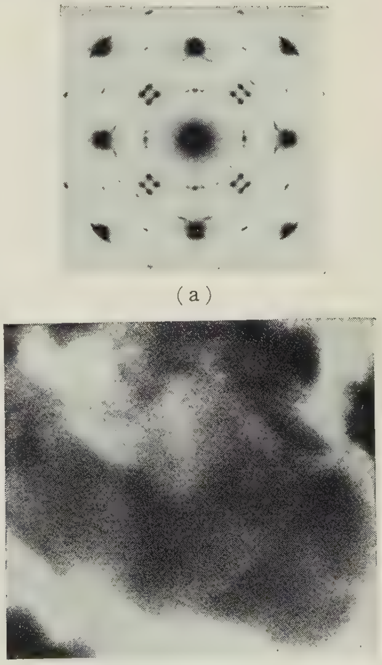
(a)

(b)

Fig. 2. (a): Electron diffraction pattern of a Au–Cu–Zn alloy film with M=3.0 (No. 2), normal incidence. (b): Its electron micrograph. (750,000×). The mean spacing of the lines is 11.8Å.

The electron microscope of Hitachi HU-10 type was used, as in the previous work[1]. The operating voltage, the focal length of the objective lens and the aperture size were 75 KV, 3 mm and 50 $\mu\phi$, respectively. The images were recorded on Fuji Process plates (hard) at a magnification of 80,000~120,000 x.

§ 3. Results

Electron diffraction patterns of four kinds of single-crystalline alloy films are shown in Figs. 1(a), 2(a), 3(a) and 4(a), respectively. They are quite similar to the pattern of CuAuII[5], the main difference between one another consisting in the separations of split superlattice reflections and of satellites around the direct spot and main reflections. The smaller the domain size is, the larger the separations, and the satellites of the first order which are very much close to the direct spot in case of CuAuII are here sufficiently separated from it. Some special remarks should be made about Fig. 4(a). First, spots in a {001} group of supperlattice reflections, Miller's indices being used in terms of the

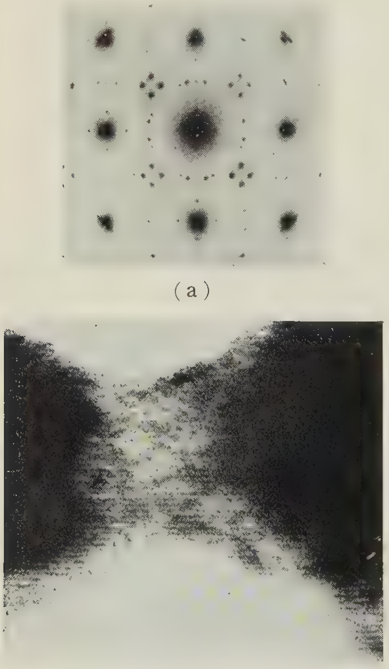
(a)

(b)

Fig. 3. (a): Electron diffraction pattern of a Au–Cu–Zn alloy film with $M=2.3$ (No. 3), normal incidence. (b): Its electron micrograph. (750,000 ×). The mean spacing of the lines is 9.4Å.

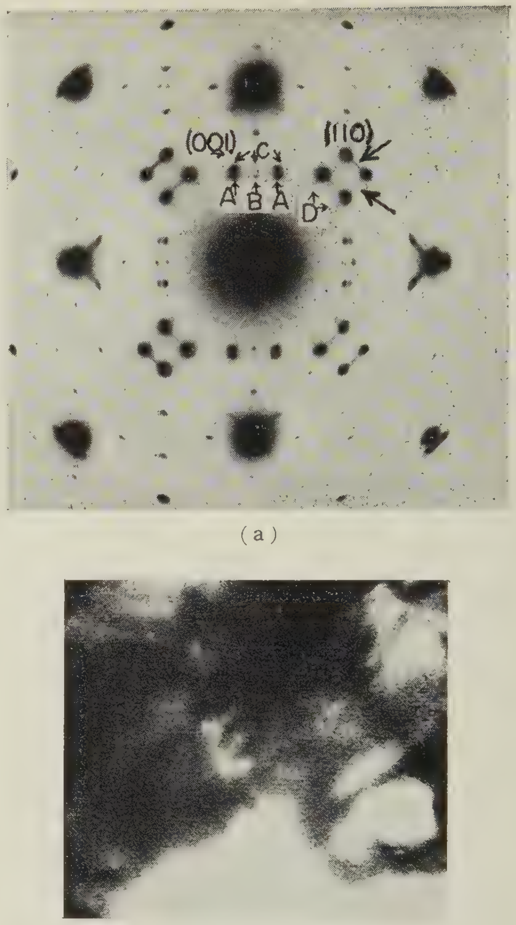

(a)

(b)

Fig. 4. (a): Electron diffraction pattern of a Au–Cu–Zn alloy film with $M=2.0$ (No. 4), normal incidence. (b): Its electron micrograph. (750,000 ×). The mean spacing of the lines is 8.0Å.

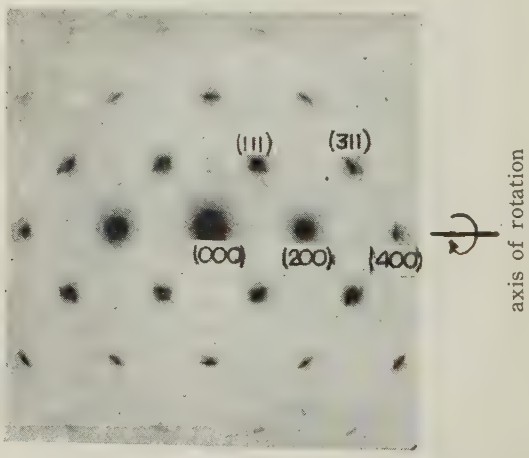

Fig. 5. Electron diffraction pattern of the same film as in Fig. 3 (a), [110] incidence.

disordered cubic lattice, appear to be doubled. The fact is, however, that there occurs nothing unusual. That is to say, owing to the special value of domain size, $2a$, both the second order splits of {110} superlattice reflections, A, and the second order satellite of the direct spot, B, just accompany the original three component spots of {001} group, C. Secondly, the nearest neighbors among four component spots forming a {110} cross are connected with each other by lines of fairly strong intensity, as indicated by arrows, and moreover, there are seen unusually diffuse spots, D, immediately inside the two inner component spots. The origin of these phenomena is not clear at present.

Utilizing the satellites around the direct spot to image formation, it was tried to observe the line structures on electron micrographs of the present alloy films of four kinds. The micrographs obtained are shown in Figs. 1(b), 2(b), 3(b) and 4(b) and are of very high magnification. Equally spaced parallel lines are seen on each of them. The instrumental magnification was calibrated against the $(20\bar{1})$ spacing of copper phthalocyanine. The mean spacings of the lines agree within about 10 per cent with the values deduced from the diffraction patterns, 13.3Å, 11.8Å, 9.4Å and 8.0Å, respectively.

The line structures were found only at a few places in the image on one photographic plate, and so the above electron micrographs were selected from not many examples. The little frequency of visibility of the line structure is probably caused by the lack of uniformity in the thickness of the present specimens. As shown on micrographs, they have a patch-like structure, and there may be appreciable unevenness even in one agglomeration. The preparation method of films by Bassett, Menter and Pashley⁶⁾ is probably better in obtaining the uniform thickness.

In Fig. 1(b) two sets of parallel lines are seen, one consisting of the lines with a smaller spacing and the other with a larger spacing. The former set is understood from the value of its spacing to correspond to the line-up of anti-phase domains, while the latter is inclined by 45° to the former and its spacing is about $\sqrt{2}$ times as large as the former. The nature of the set with the larger spacing will be elucidated in § 4. Any of the line structures seen on the micrographs except Fig. 1(b) is interpreted to represent the line-up of domains. As it is known from the diffraction patterns that there are two orthogonal directions of the line-up of domains in the film plane, the lines should be observed along two orthogonal directions also on the micrographs. These micrographs, however, do not show such two directions owing to the limited area where the lines are visible, although such two orthogonal sets of the lines were surely seen at some distance from each other on one photographic plate.

§ 4. Discussion

In the previous work¹⁾ the present authors ascribed the origin of the satellites around the main reflections to some periodic lattice modulation, accompanying anti-phase domains, with the same period as a domain size, provided that the modulation meant not the periodic occurrence of out-of-steps but the formation of a periodic error of lattice spacing or of scattering factor. There may be some contribution of secondary diffraction to the intensity of the satellites, but the present authors concluded experimentally that a greater part of the intensity is caused by the above modulation of the lattice. Glossop and Pashley⁷⁾ also tried to observe anti-phase domain boundaries in CuAuII by means of electron microscope and obtained the similar line structure in bright field images as well as in dark field images. According to them, the latter image is formed directly as a result of the phase change itself by utilizing two pairs of two component spots in a {110} cross, while the former is formed by combination between the direct spot and the satellites which are produced by double diffraction of two component spots in a cross. Thus, they neglected the effect of the periodic modulation in explanation of the image. Although the present authors were convinced that the said modulation plays an important role in producing the satellites, the experiment which involved the tilting of the specimen and was done in the previous work was repeated in the present case, in order to examine quantitatively the contribution of double diffraction. Fig. 5 shows that the satellites remained even when the film producing the diffraction pattern in Fig. 3(a) at normal incidence was tilted about the principal axis lying in the film plane until {110} groups of superlattice reflections vanished and {111} main reflections appeared. In this condition there are no split superlattice reflections located close to the sphere of reflection in reciprocal space, except those of the considerably higher order. It is highly improbable, therefore, that the remaining satellites are caused by double diffraction, and they should be considered as originated entirely from the periodic lattice modulation. They appear fairly strong, but a microphotometry showed their intensity to be about two-thirds of the original intensity in Fig. 3(a), {400} reflections on the tilting axis being taken as standard. The intensity of the remaining satellites was sensitive to an error in the direction of the tilting axis, and the above value is the maximum one in several examinations. Similar results were obtained also from the other kinds of films. About one-third of the original intensity, therefore, depends upon the appearance of split superlattice reflections and might arise from double diffraction. Double diffraction considered here, however, may mean not such one as given by two incoherent layers, which were previously discussed, but a dynamical one occurring in a coherent lattice, as suggested by Glossop and Pashley⁷⁾.

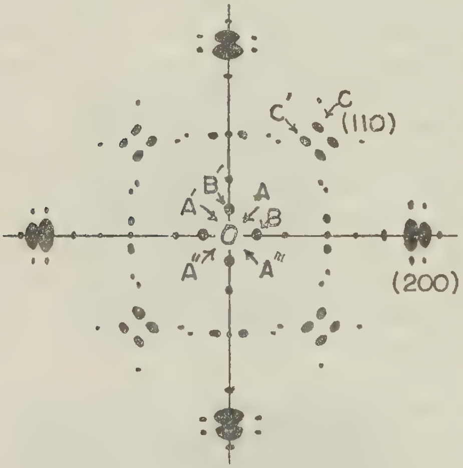

Fig. 6. Illustration of Fig. 1 (a).

Next, the lines with the larger spacing seen in Fig. 1(b) will be explained. In Fig. 6, which is an illustration of Fig. 1(a), OA corresponds to the spacing $\sqrt{2}$ times as large as the domain size which is represented by OB and OB', if a diffraction spot were observable at A. As OA is equal to CC' which is a distance between two neighboring spots in a {110} cross, it may be conceivable that A would be produced by double diffraction. However, diffraction spots, C and C', belong to different systems of anti-phase domains, and hence this double diffraction is caused not by dynamical interaction in a coherent lattice but by successive diffraction through two overlapped layers of different systems of anti-phase domains whose line-up directions are orthogonal to each other in the film plane. This idea explains well both the spacing and the direction of the lines in question which are thought as a kind of a rotational moiré pattern. Such lines as these have already been observed in CuAuII by Glossop and Pashley⁷⁾ and explained in the above-mentioned way by them. In their case, however, two sets of the lines crossing each other were observed. These sets are thought to be due to the occurrence of two component diffraction beams, e. g. A and A' in Fig. 6, at the same time by double diffraction. In the present case, however, only one of the two component diffraction beams was probably formed and hence only one set of the lines was observed. The fact is, however, that in the present diffraction patterns the diffracted intensity has never been observed at any of A, A', A'' and A'''. If the overlapping of two different systems of domains is so rare that it contributes very little intensity to the diffraction pattern, however, the circumstances will fully be understood.

The number M, a size of anti-phase domains measured in atomic distance, is given in general as a fractional number from diffraction patterns. This fact can be understood, if different domain sizes are assumed to be mixed in a coherent crystal lattice. This assumption was verified in the previous work¹⁾, where the line structure on electron micrographs of CuAuII was observed to contain surely two kinds of the spacing, i.e. two kinds of M values. The same should hold also for some of the present alloys, i.e. for those with M values, 3.4 and 2.3. Measurements of the spacing were carefully done on the line structures of the four kinds of alloys by means of a comparator as well as of a microphotometer. A positive evidence for a mixture of M values, however, could not be obtained from the electron micrographs in the present case, probably due to the obscurity based on too large magnification. But it will be worth while saying that the fluctuation of the measured spacing is larger in the alloys with M values of 3.4 and 2.3 and amounts to about ±15 per cent, while it is smaller in the alloys with M values of 3.0 and 2.0 and amounts to about ±8 per cent. The latter fluctuation is an error of measurements, because there should be the uniform spacing in the latter alloys. Thus, if further examples are required for a mixture of different domain sizes to be observed on electron micrographs, it may be disadvantageous to use ordered alloys with small domain sizes such as in the present work.

References

1) S. Ogawa, D. Watanabe, H. Watanabe and T. Komoda: Acta Cryst. **11** (1958) 872.
2) For example, D. Watanabe and S. Ogawa: J. Phys. Soc. Japan **11** (1956) 226. K. Fujiwara, M. Hirabayashi, D. Watanabe and S. Ogawa: J. Phys. Soc. Japan **13** (1958) 167.
3) K. Schubert, B. Kiefer, M. Wilkens und R. Haufler: Z. Metallkde. **46** (1955) 692.
4) M. Wilkens und K. Schubert: Z. Metallkde. **48** (1957) 550.
5) S. Ogawa and D. Watanabe: J. Phys. Soc. Japan **9** (1954) 475.
6) G. A. Bassett, J. W. Menter and D. W. Pashley: Proc. Roy. Soc. **A, 246** (1958) 345.
7) A. B. Glossop and D. W. Pashley: Proc. Roy. Soc. **A, 250** (1959) 132.

JOURNAL OF THE PHYSICAL SOCIETY OF JAPAN, Vol. 14, No. 7, JULY, 1959

Proton Magnetic Resonance in Hydrates of Halogen Compounds of Mg, Ca, Sr and Ba

By Syukuro YANO

Faculty of Engineering, Kyoto University, Kyoto

(Received September 12, 1958)

Proton resonance in crystal water of $Mg(H_2O)_6Cl_2$, $Mg(H_2O)_6Br_2$, CaI_26H_2O, SrI_26H_2O and MgI_28H_2O was studied in temperature range from −90°C to +110°C and the same in $CaCl_26H_2O$, $CaBr_26H_2O$, $SrCl_26H_2O$ and $SrBr_26H_2O$ was studied in the range above room temperature, all in powdered states. Line shapes were recorded by the radiofrequency spectrometer with an automatic field scanning apparatus connected to the sweeping coils of a permanent magnet. Transitions of second moment and line shapes were observed for all the above salts. Experiments on single crystals of $Mg(H_2O)_6Cl_2$ and CaI_26H_2O were also carried out at room temperature. In $Mg(H_2O)_6Cl_2$, $Mg(H_2O)_6Br_2$, CaI_26H_2O, SrI_26H_2O and BaI_26H_2O, water molecules of hydration have the states of hindered rotational motion below melting point, but in $CaCl_26H_2O$, $CaBr_26H_2O$, $SrCl_26H_2O$ and $SrBr_26H_2O$, these rotational states were not observed. The angle between the rotational axis of a water molecule and its inter-proton direction was estimated to be about 90° in the case of $Mg(H_2O)_6Cl_2$. In the cases of CaI_26H_2O and SrI_26H_2O these angles are calculated to be 45° or 60°, and these results suggest the precession of the rotational axis, if rotational motion of water molecules is assumed to occur about an axis perpendicular to the inter-proton axis. Sharp peaks appearing in chlorides and bromides of Ca and Sr are interpreted as the narrowing due to random re-orientation of the rotational axis.

§ 1. Introduction

The studies of structure and motion of water molecules in hydrated crystals are important for the information about the hydrogen bonds and chemical properties of compounds. The halogen compounds of the group II elements, Mg, Ca, Sr and Ba, have six water molecules as hydrates at normal temperature, and their chemical properties can be compared with each other because they are of the varied combinations of the metallic ions and halogen ions. One of the characteristic properties of these salts is the strongly hygroscopic nature in the dehydrated state and the strong deliquescence in the hydrated state. Therefore, it is interesting to obtain some informations about the state of the water molecules in these hydrates.

Nuclear magnetic resonance method in solid state explored by E. M. Purcell *et al.*[1] has been applied to the structural investigation of water molecules in hydrates by G. E. Pake[2] and others[3], or to the study of hindered rotational motion in solids[4]. The rotational motion of NH_4[4], or CH_4[5] molecules in solid has been observed by many workers. Since these molecules are non-polar and have symmetrical shapes, their hindering potentials are in general not high. However, water molecules are not expected to rotate easily because of larger electric dipole moment and less symmetrical shape. Therefore, the rotational motion of water molecules in solid has not been found yet as far as the author knows. Translational motion of proton along the hydrogen bonds in solid was found in several substances involving ferroelectric substances[6], and small torsional oscillation of water molecules in $K_2HgCl_4H_2O$ was also studied by J. Itoh *et al*[7].

It is reported, in the present paper, that proton magnetic resonance in hydrates examined here has been found to show two types of line shape transitions when temperature changes, and these will be discussed by rotational model of water molecules. Although the complex structure and strong deliquescence have not permitted the precise determination of hydrogen positions in these salts, experiments on small single crystals were used for the determination of motional state of water molecules. Besides above salts, resonance research has been made on beryllium salts, the results of which are not reported here because they are only on $BeCl_2 4H_2O$ and $BeSO_4 4H_2O$.

§ 2. Experimental Apparatus and Procedure

Experiments were performed using the modulation technique described by Bloembergen, Purcell and Pound[1]. A block diagram of the apparatus is shown in Fig. 1. The first measurement was made in $Mg(H_2O)_6Cl_2$ by the Weiss type electromagnet which was excited by currents from 24 volts batteries to give the gap field of about 3000 gauss with pole pieces 10 cm in diameter and 25 mm air gap length. The homogeneity of magnetic field within 0.2 gauss over the sample volume was obtained by providing the ring shim of 3 mm wide and 0.7 mm high around the periphery of each pole face, adjusting carefully parallelism and coaxiality of both pole caps with three brass spacers. For cooling experiments this magnet was not suited because of the intervening of the spacers and smallness of gap length.

A permanent magnet with pole face diameter of 140 mm and air gap length of 40 mm was constructed, which produces the magnetic field of 4140 gauss by NKS-3*, with a uniformity of 2×10^{-5} over the sample volume. Continuous variation of the static magnetic field linear with time was achieved by an automatic current scanning apparatus[8], which supplied current by ten 807 control tubes to the ten coils connected in series each coil having 250 turn windings around a pole. An error voltage which is the difference of the potential between that across the standard resistor R_S and that across reference rheostat, is amplified by a direct current amplifier and applied to the control tubes in such a phase that the error voltage may be reduced to zero. The rheostat is a 15-revolutions helipot which is driven continuously with time by a clock motor. The accuracy of the sweeping rate is larger than 10^{-4} and static stability is higher than 10^{-5} over 10 minutes.

For the detection of resonance signals, a

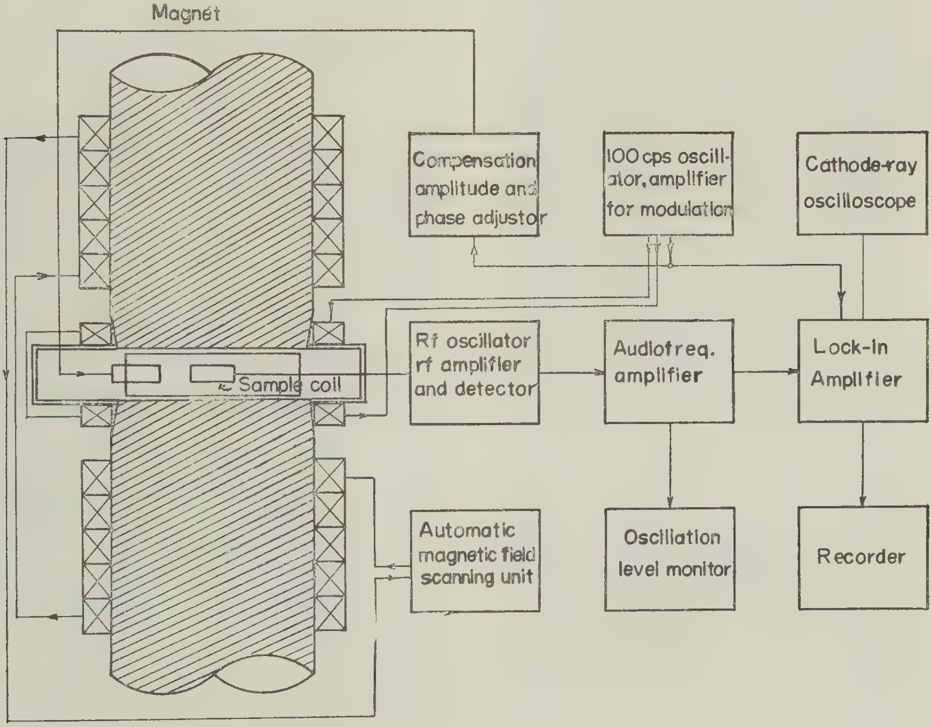
Magnet
Compensation amplitude and phase adjustor
100 cps oscillator, amplifier for modulation
Cathode-ray oscilloscope
Sample coil
Rf oscillator rf amplifier and detector
Audiofreq. amplifier
Lock-in Amplifier
Automatic magnetic field scanning unit
Oscillation level monitor
Recorder

Fig. 1. Block diagram of the apparatus.

---

* This magnet was constructed by Sumitomo Metal Industries, Ltd., Osaka.

6J6 cathode coupled oscillator developed by Pound and Knight[9] and an autodyne oscillating detector similar to Hopkins' circuit[10] were used. To study the temperature variation of resonance, cooling or heating of the high frequency probe was made by thermal conduction. A brass pipe for shielding of a radiofrequency coil was tightly inserted into a hole of the copper block to which a long copper rod was connected as shown in Fig. 2. This rod was inserted into a dewar vessel containing liquid oxygen or into a long heater coil. By suitably enclosing the air gap of the magnet, high temperature stablity was secured throughout a long period of time.

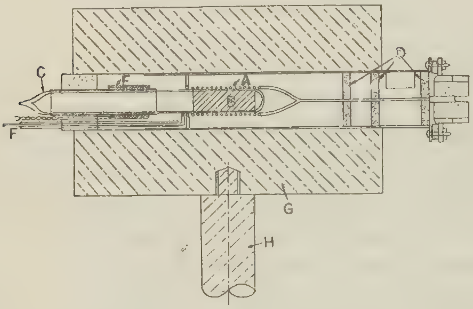

Fig. 2. Sample coil assembly.
A. Rf coil, B. Sample, C. Glass tube containing sample, D. Daiflon spacers, E. Coil for compensation, F. Cupper-constantan thermocouple, G. Cupper block, H. Cupper rod.

Sample temperature was varied by adjusting the position of the dewar or the current of the heater coil. Use of such conduction method is of great advantage in preventing noise generated by boiling of liquid oxygen or by both electric induction and mechanical vibrations produced by the heating current. A radiofrequency lead from the sample coil is supported by Daiflon spacers and the probe part within the shielding cylinder can be easily interchanged by removing it at a coaxial cable connector. The small coil inserted coaxially into this part was used to deliver ac voltage into the radiofrequency coil for the cancellation of constant zero drift due to the residual voltage induced directly by ac modulation which remains after careful positioning of this probe in the magnet gap. In most cases, however, signals obtained were strong enough at low level of magnetic field modulation, 0.5~1 gauss peak to peak, so that the use of this cancellation unit is not always necessary.

Samples were obtained from Maruwaka Chemical Company almost in powdered states. Iodides of Ca, Sr and Ba have the strongest deliquescence and magnesium salts come next to this. A small crystal of CaI_26H_2O with the size of about 1×1×1 mm^3 deliquesces and becomes liquid after exposed in ordinary atmosphere for several seconds. Instead of making a fine powder of CaI_26H_2O and $SrI_2 \cdot 6H_2O$, small crystals in a glass tube were dried by pumping in vacuum until it became transparent and sealed in vacuum, then these samples were heated to their melting point and quenched quickly. Slowly cooled samples of these salts show different shapes in their absorption curves when they are rotated in magnetic field, although their shape has a good symmetry. These effects are due to the crystallization by slow cooling. Chlorides and bromides of Ca, Sr and Ba have not so strong deliquescence that fine powders are easily compressed to form a small circular tablet and sealed in a glass tube after pumping in vacuum.

Single crystals of $Mg(H_2O)_6Cl_2$ were grown from aqueous solution by evaporation method or slow cooling method. A needle-like single crystal having the size of 25×3×3 mm^3 was grown by the latter method. This crystal was fixed in a test tube and sealed in vacuum. A plate-type crystal of CaI_26H_2O of the size of 1×5×7 mm^3 was selected from many crystals made by Maruwaka Co.

Resonance curves were recorded automatically every 3°~5°C in temperature range from −90°C to +110°C in almost all powdered samples, but for CaI_26H_2O and SrI_26H_2O a hundred curves were recorded. Temperature was measured by a copper-constantan thermocouple attached to the sample tube wall.

Melting point of the samples was measured in vacuum sealed test tube immersed in a water bath except in case of the magnesium salts, and the result was in good agreement with the values described in text-books on chemistry.

§ 3. Experimental Results and Discussion

In general proton resonance absorption derivatives in these hydrates have a line shape similar to Fig. 3. In some of them, however, the separation between peaks of doublet becomes narrower below room temperature, and in others a single peak appears overlapping the line at its center. The experimental results obtained in powdered samples are summarized in Table I with three characteristic separations and second moments calculated from experimental derivative curves. Chloride and bromide of Ca and Sr show rather broad absorption curves of two spin system with second moments of nearly 30 gauss² at room temperature. Chloride and bromide of Mg and iodide of Ca, Sr and Ba have very

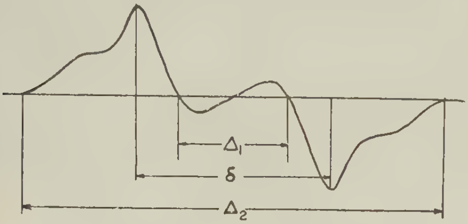

Fig. 3. Line shape and parameters of resonance line.

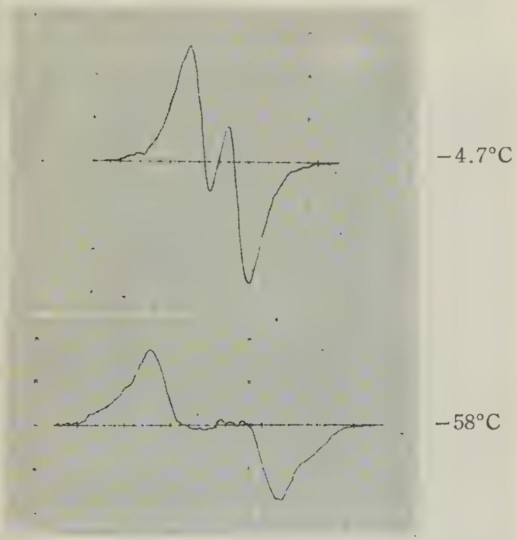

Fig. 4. Recorded derivatives of proton resonance in powdered $Mg(H_2O)_6Br_2$.

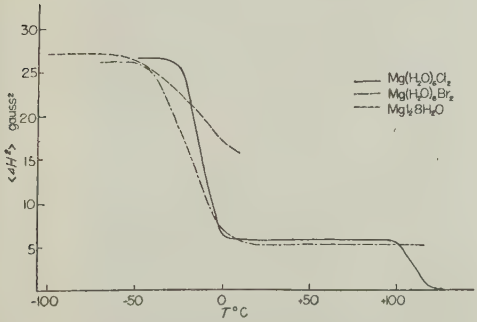

Fig. 5. Variations of second moments with temperature in $Mg(H_2O)_6Cl_2$, $Mg(H_2O)_6Br_2$ and MgI_28H_2O.

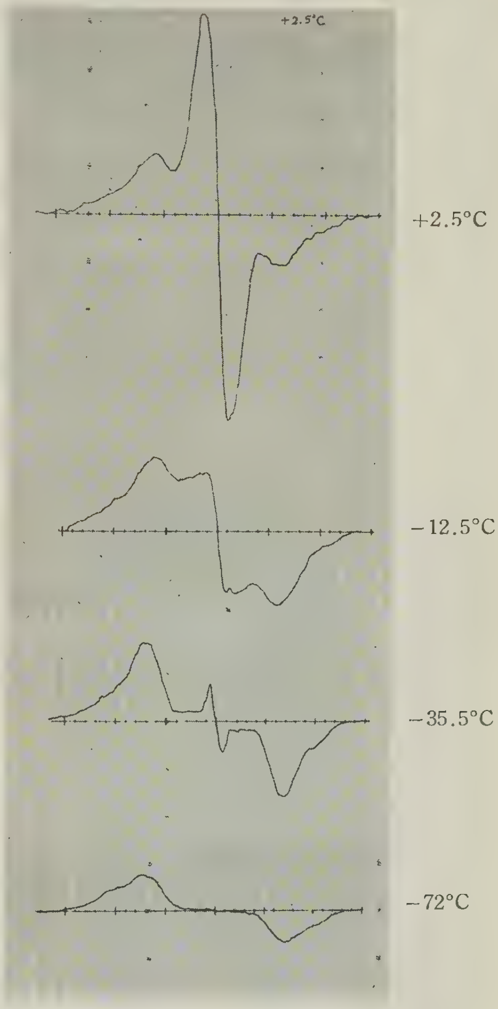

Fig. 6. Recorded derivatives of proton resonance in powdered MgI_28H_2O.

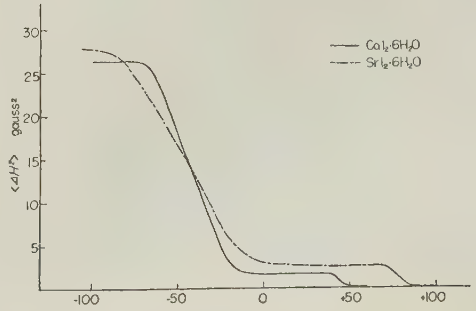

Fig. 7. Variation of second moments with temperature in CaI_26H_2O and SrI_26H_2O.

narrow curves with small second moments at room temperature. A narrow curve observed at room temperature seems to be due to some motion of water molecules, so the resonance curves were taken at different temperatures. At lower temperatures they became a broad and definite two spin system structure with second moments of about 26~28 gauss². Fig. 4 shows two photographs of absorption derivatives at two different temperatures selected from curves recorded by millivoltmeter charts in $Mg(H_2O)_6Br_2$. Nearly the same results had been obtained in $Mg(H_2O)_6Cl_2$[11].

Second moment variation with temperature of $Mg(H_2O)_6Cl_2$, $Mg(H_2O)_6Br_2$ and MgI_28H_2O is shown in Fig. 5. Chloride and bromide exhibit line width and second moment transitions at about 0°C and it seems to become rigid at about −30°C and −50°C respectively. At lower temperatures MgI_28H_2O has a broad and nearly flat resonance curve, but a sharp peak appears at −55°C which becomes larger as temperature rises, as shown in Fig. 6. The gradual decrease of second moment in Fig. 4 is due to the mixing of this sharp part. Strong signals with narrower separation between doublet than in the magnesium salts were observed in both iodide of Ca and that of Sr at room temperature. Variation of second moment and line shapes with temperature are also given in Figs. 7 and 8.

a) *Hindered rotation of water molecules in* $Mg(H_2O)_6Cl_2$ *and* $Mg(H_2O)_6Br_2$

The formula derived theoretically by Van Vleck[12] may be written for the case of these powdered hydrates as

$$\begin{aligned}\langle \varDelta H^2\rangle &= \langle \varDelta H^2\rangle_0 + \langle \varDelta H^2\rangle_1 \\ \langle \varDelta H^2\rangle_0 &= (4/5)\alpha^2 = 358.1\times10^{-48} r^{-6} \qquad (1) \\ \langle \varDelta H^2\rangle_1 &= 358.1\times10^{-48}\sum_j r_j^{-6} \\ &\quad + (4/15)\sum_k I_k(I_k+1) g_k^2 \beta^2 r_k^{-6}\end{aligned}$$

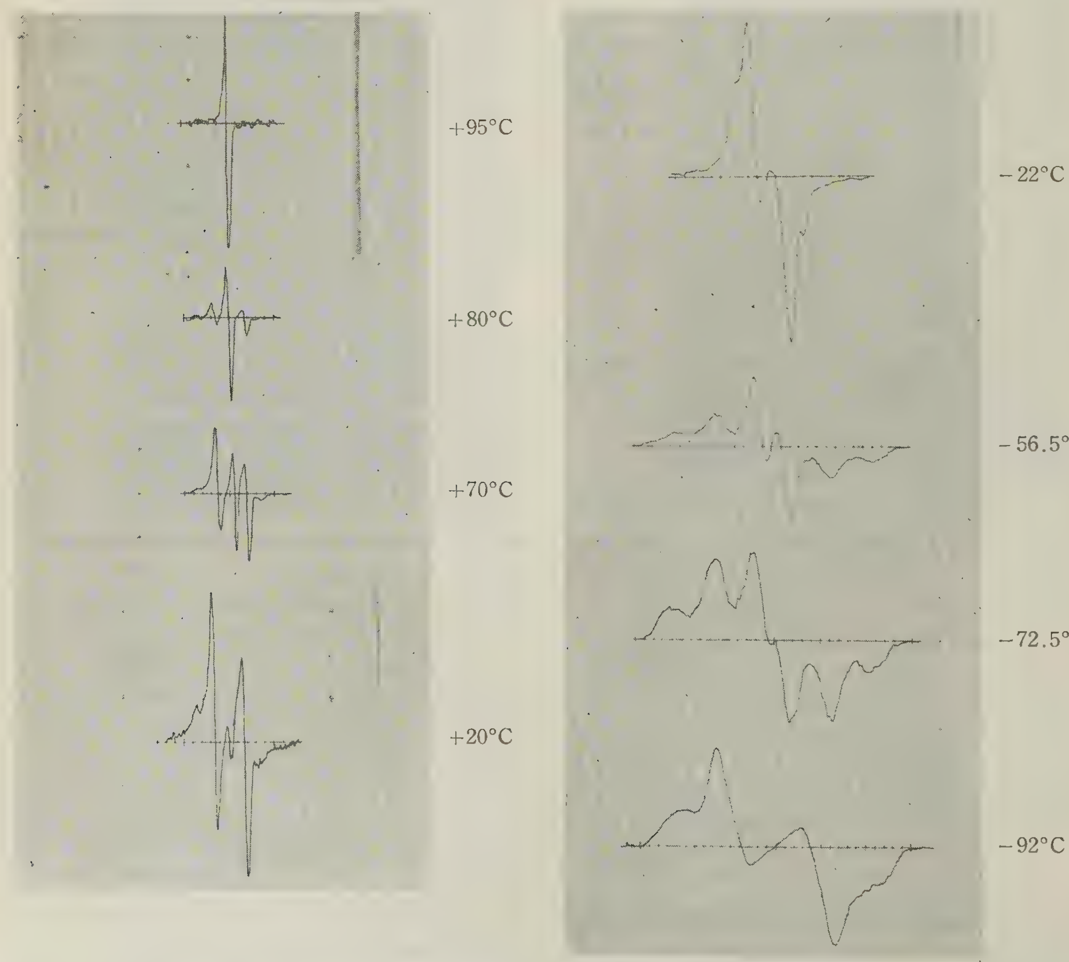

Fig. 8. Recorded derivatives of proton resonance in powdered SrI_26H_2O.

that is, total second moment, $\langle \Delta H^2 \rangle$, is divided into two parts, the intra-water molecular part $\langle \Delta H^2 \rangle_0$ and the interaction part due to other molecules $\langle \Delta H^2 \rangle_1$. r is the inter-proton distance in a given water molecule, $\alpha = (3/2)\mu r^{-3}$, $\mu = gI\beta$, r_j's are the distances to other protons, r_k's are the ones to other magnetic nuclei with the spin and the gyromagnetic ratio of I_k and g_k respectively, and β is the nuclear magneton. Eq. (1) is valid when the lattice is rigid. The structure of hexahydrated magnesium chloride and the corresponding bromide has the same type, but it is different from the one of $SrCl_2 6H_2O$ type. The unit cell contains two molecules: $a_0 = 9.90$A, $b_0 = 7.15$A, $c_0 = 6.10$A with the angle $\beta = 94°$ between positive a and c axes for the chloric salt, and $a_0 = 10.25$A, $b_0 = 7.40$A, $c_0 = 6.30$A, $\beta = 93°30'$ for the bromic salt. In both salts the magnesium ion is surrounded by six water molecules in the form of a regular octahedron and each halogen ion has eight H_2O neighbors. Projections of $Mg(H_2O)_6Cl_2$ on a b-face and an a-face are shown in Fig. 9[13].

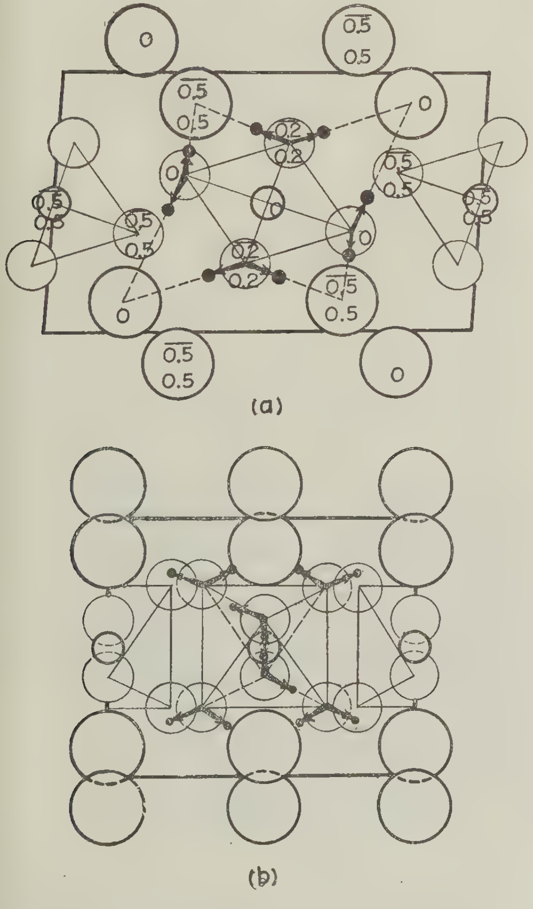

Fig. 9. (a) A projection of the monoclinic $Mg(H_2O)_6Cl_2$ structure on a b-face. The chlorine atoms are shown as the largest circles, the water molecules as middle-sized circles which surround octahedrally the central magnesium atom shown by the smallest circles. The assumed positions of hydrogens of water molecules are shown by the small black circles.
(b) A projection on an a-face.

Considering distances from water molecules to chlorine atoms or to other water molecules and also directions to chlorine atoms from oxygen positions, probable hydrogen bonds locations considered here are shown in Fig. 9 by arrows with black circles which indicate each hydrogen position. In this configuration the bond angles of H-O-H are 130°~140°. However, the bond angle of water molecule is to be nearly equal to tetrahedral angle. Therefore the intermolecular part of the second moment was calculated by assuming the water molecule which had the tetrahedral bond angle and the direction of one O-H coinciding with one of the directions of O-H····Cl shown in the figure. There are two possible arrangements for each of two water molecules just lying on b-plane, and also two for each of four water molecules which are lying above or below b-plane. By averaging the values of $\langle \Delta H^2 \rangle_1$ calculated for the combination of these configurations, we obtained the value of $\langle \Delta H^2 \rangle_1 = 5.95 \pm 0.6$ gauss^2. Using the value of $\langle \Delta H^2 \rangle_0$ which is obtained by subtracting $\langle \Delta H^2 \rangle_1$ from the observed value of the second moment 26.0 ± 0.5 gauss^2, the inter-proton distance in these water molecules is calculated to be 1.615 ± 0.015A.

The second moment obtained from the experimental records shows a transition at −30°~0°C as in Fig. 5. The data on the solubility of $MgCl_2$ in water show that twelve-hydrate is stable below −16.4°C, eight-hydrate is stable between −16.4°C and −3.4°C, and that hexahydrate is stable above −3.4°C to 117°C. The temperature of phase change, −16.4°C and −3.4°C, is nearly equal to the temperature of the second moment transition. However, it is not reasonable to consider that the transition of the second moment at −30°C~0°C originates from a phase change of the crystal or the change of the hydration

Table I.

		Δ_1	δ	Δ_2	$\langle \Delta H^2 \rangle$
$CaSO_4 2H_2O$*	(room temp.)	6.0	12.0	30	24.5
$CuCl_2 2H_2O$*	(room temp.)	6.5	11.5	26	22
$MgCl_2 6H_2O$	(below −30°C)	7.2	14.0	31	26.0±0.5
$MgBr_2 6H_2O$	(below −60°C)	7.0	13.6	30	25.7±0.5
$MgI_2 8H_2O$	(below −70°C)	—	14.5	30	27.2
$MgCl_2 6H_2O$	(room temp.)	3.0±0.2	6.0±0.2	16±2	6.0±0.5
$MgBr_2 6H_2O$	(room temp.)	3.0±0.2	6.0±0.2	16±2	5.5±0.8
$MgI_2 8H_2O$	(room temp.)	**	2.5	30	less than 15
$CaCl_2 6H_2O$	(room temp.)	7.0	13.0	30	30
$CaBr_2 6H_2O$	(room temp.)	5.0	12.0	30	30
$CaI_2 6H_2O$	(below −70°C)	7.8	12.0	29±1	26.1±0.5
$CaI_2 6H_2O$	(room temp.)	**	2.6±0.1	5±1	1.6
$SrCl_2 6H_2O$	(room temp.)	7.0	16.0	32	30
$SrBr_2 6H_2O$	(room temp.)	8.0	16.0	33	33
$SrI_2 6H_2O$	(below −90°C)	7.7	13.3	30	27.7±0.5
$SrI_2 6H_2O$	(room temp.)	3.0	3.7	12±2	2.5±0.3
$BaI_2 6H_2O$	(room temp.)	3.1±0.1	4.2	9.4	3.0
$BaI_2 2H_2O$	(room temp.)	3.1	4.1	9.6	2.7

* These salts are listed for comparison. ** Central peak.

number. But instead we regard it as originating from the onset of some motion of the water molecules. The reasons are as follows. (1) Because the samples used are the dried hexahydrated powder sealed at room temperature and absolute number of water molecules must be unchanged, some fraction of the hexahydrated molecules must be dehydrated below −30°C, if eight- or twelve-hydrate is produced by cooling. However, dehydration temperature of hexahydrates is about 117°C from the solubility data. Then our sample must keep a form of hexahydrate below −30°C. (2) If the inter-proton distance is calculated on the assumption that the doublet line with second moment of 6.0 gauss^2 observed at room temperature originates from rigid lattice, it becomes 1.96A or longer, and this is nearly equal to twice 0.98A of O-H distance in a water molecule in a gas phase. Also as seen in Table I, second moments for $SrI_2 6H_2O$, $CaI_2 6H_2O$ and $BaI_2 6H_2O$ are much smaller than those of magnesium salts at room temperature, so that the resulting inter-proton distance from rigid lattice model becomes longer than 2A. It is difficult to believe that the water molecule is distorted in these salts, although the structure of a water molecule in a solid is affected by their surrounding ions. (3) In the case of phase transformation, variations in second moment associated with a change of crystal structure cannot be so large as those observed. For example, $CuCl_2 2H_2O$ and $CaSO_4 2H_2O$ have nearly equal second moments and the same line shape. For iodide of barium, our experiment shows independence of line shape and second moment on the hydration number as seen in Table I. (4) The assumption of rotational motion of water molecule is consistent with other results obtained so far, as will be described below. Tunneling motion of the proton between an oxygen atom and a halogen ion is also discussed later.

The second moment for a proton pair in rotational motion about an arbitrary axis may be derived by the method used by Gutowsky and Pake⁴⁾,

$$\begin{aligned} \langle \Delta H^2 \rangle_0 &= (4/5)\alpha'^2 , \\ \langle \Delta H^2 \rangle_1 &= 358.1\times 10^{-48}[\langle r_j^{-3}\rangle_{\mathrm{AV}}]^2 \\ &\quad +(4/15)\sum_k I_k(I_k+1)g_k^2\beta^2[\langle r_k^{-3}\rangle_{\mathrm{AV}}]^2 . \end{aligned} \tag{2}$$

Here, $\alpha'=\alpha P_2(\cos\gamma)$, γ is the angle between the radius r and the axis of rotation of r and $\langle r_j^{-3}\rangle_{\mathrm{AV}}$ and $\langle r_k^{-3}\rangle_{\mathrm{AV}}$ denote the average value over the rotational position of the molecule. Eq. (2) may apply to the second moment for a powder on the assumptions that the rotation permit the use of a classical average over this motion and that the reorientational frequency of this motion is higher than the frequency width of the absorption curve.

To distinguish exactly $\langle \Delta H^2\rangle_0$ from $\langle \Delta H^2\rangle_1$ in the observed value of $\langle \Delta H^2\rangle$, the result of the experiment on single crystal is used. When a single crystal involving a proton pair P—P rotating about an axis OR is measured in various orientations, keeping external magnetic field H_0 in the xy-plane as shown in Fig. 10, the observed doublet separation δH of the proton signal may be written as

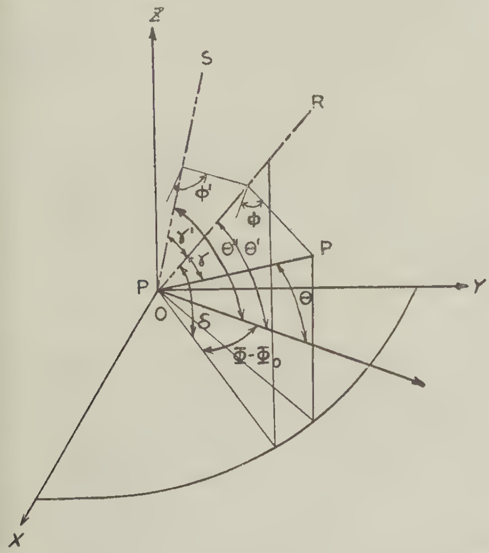

Fig. 10. Definition of various angles for the model of a rotating proton pair.

$$\begin{aligned}\delta H &= 4\alpha P_2(\cos\gamma)P_2(\cos\theta')\\ &= 2\alpha'\{3\cos^2\delta\cos^2(\Phi-\Phi_0)-1\}\,, \qquad (3)\end{aligned}$$

where θ', $\Phi-\Phi_0$ and δ are as shown in the figure. If δH is measured for various $\Phi-\Phi_0$, with a constant angle δ, and α' can be determined. Then from the known values of δ, γ will also be given.

Experimental plot of δH is shown in Fig. 11a, and the derivative curves for the special three orientations are reproduced in Fig. 11b. These experiments were performed using a needle-like single crystal with its long axis perpendicular to the static external magnetic field. Since the smaller one of the extreme values of δH is $2\alpha'$, the experiment gives $2\alpha'=5.10$ gauss, which is compared with $2\alpha=10.0$ gauss derived from $\langle \Delta H^2\rangle_0$ for the rigid lattice value. Two possible values 88°±2° and 35°±0.5° for γ follow. The former is easily accepted. The width of a component line of the doublet shown in Fig. 11b can be considered to originate from isotropic contribution of neighboring molecules. The smallest value among them is 2.2 gauss at room temperature. As the result, $\langle \Delta H^2\rangle_1$ becomes 0.60 gauss². $\langle \Delta H^2\rangle_0$ for the rotational motion can be calculated to be 5.05±0.28 gauss², using $r=1.615\pm0.015$A and $P_2(\cos\gamma)=0.5$. The sum of the two values, 5.65 gauss², is within the experimental error

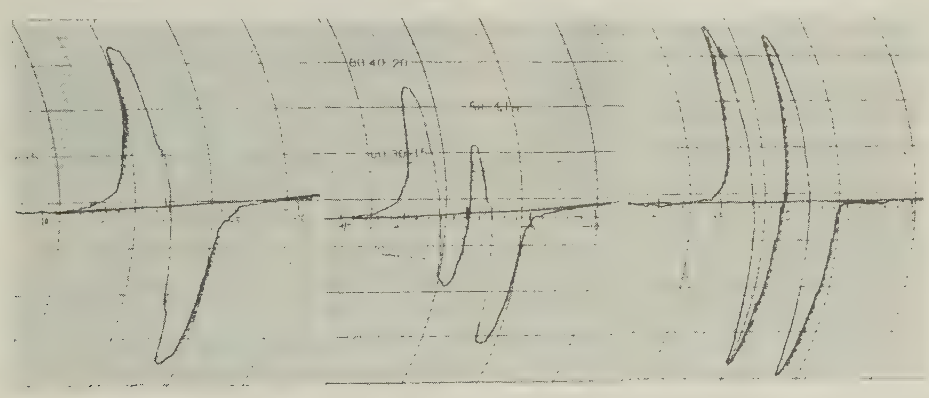

(b)

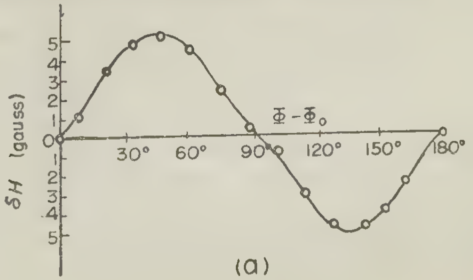

Fig. 11. (a) Line pair separation as a function of the angle $\Phi-\Phi_0$ as shown in Fig. 10 for a single crystal of $Mg(H_2O)_6Cl_2$.
(b) Recorded derivatives of proton resonance in a single crystal of $Mg(H_2O)_6Cl_2$ for three directions of $\Phi-\Phi_0$.

Table II.

salt	state	$\langle \Delta H^2 \rangle_0$	$\langle \Delta H^2 \rangle_1$	r	γ
$Mg(H_2O)_6Cl_2$	rigid	20.2±1.10	5.95	1.615±0.015	—
$Mg(H_2O)_6Cl_2$	rotation	5.2	0.8	—	88°±2°
$Mg(H_2O)_6Br_2$	rigid	20.5	5.2	1.61±0.02	—
$Mg(H_2O)_3Br_2$	rotation	5.0	0.5	—	88°±3°

of the observed value for the powder, 6.0±0.5 gauss^2.

Nearly the same results were obtained for $Mg(H_2O)_6Br_2$. Although the difference from the resuts of $Mg(H_2O)_6Cl_2$ was almost within experimental errors, it is quite certain that the second moment for Br-salt is a little smaller than that for Cl-salt. This fact corresponds to the expanded structure of Br-salt due to the larger size of Br ions. The second moment increase due to Br-nuclei in place of Cl-nuclei is about 0.4 gauss^2 and gives little contribution. These results are summarized in Table II.

b) *Hindered rotation of water molecules in* CaI_26H_2O *and* SrI_26H_2O

The crystal structure of CaI_26H_2O and SrI_26H_2O is determined by X-ray and this has a type of layer structure isomorphous with that of $SrCl_26H_2O$, in which the position parameters of oxygens of water molecules are also known. In these crystals a metallic ion is surrounded by nine water molecules, three of them in the equivalent positions on the same plane with the metallic ion, three on the upper and three on the lower planes respectively[15]. From various considerations on these crystals, the position of water molecules is determined, although it is not definitely known by the X-ray analysis, assuming that the distance from metallic ion to water molecule is the sum of ionic radii, for Ca^{++} and H_2O, being 2.39A, and for Sr^{++} and H_2O, being 2.53A. The distance between water molecules becomes equal to the sum of an ionic radius of the nearest neighbor halogen and the radius of the water molecules, using the same relative position for halogen as in $SrCl_26H_2O$. By the same method used previously for $Mg(H_2O)_6Cl_2$, experimental rigid lattice second moments 26.1 and 27.7 gauss^2 for CaI_26H_2O and SrI_26H_2O respectively, give the values of the intra-molecular part as $\langle \Delta H^2 \rangle_0 = 23.0$ and 25.0 gauss^2. The values of $\langle \Delta H^2 \rangle_1 = 3.0$ and 2.7 gauss^2, calculated for the Ca-salt and the Sr-salt respectively, consist of the part of proton-proton interaction between neighboring water molecules, 2.5 and 2.3 gauss^2, and that of proton-halogen interaction part of 0.5 and 0.4 gauss^2 respectively.

The inter-proton distance in the water molecule becomes 1.595±0.02 for the Ca-salt and 1.576±0.02A for the Sr-salt. Second moment transitions to very small value from rigid lattice value which occur at about −70°C∼−15°C and −85°C∼−5°C for the Ca-salt and the Sr-salt respectively as seen in Fig. 7, are considered to be also due to the motional narrowing as in the case of the Mg-salts. In these iodides the values of second moment at room temperature are about 6.5% and 9.5% of the rigid values respectively, while in $Mg(H_2O)_6Cl_2$ and $Mg(H_2O)_6Br_2$ the corresponding reductions have been 22% and 15% respectively.

Two types of experiments were performed at room temperature on the single crystal of a small plate type CaI_26H_2O. In one case resonance curves were recorded in various directions 7.5° apart, rotating the plane parallel to the crystal plate, keeping one axis on it perpendicular to the static magnetic field. In another case the axis normal to the crystal plate was held perpendicular to the external field, and the crystal was rotated about this axis. In the former case the maximum number of component lines resolved was 2 and these component lines of the doublets have maximum separation of 2.45 gauss and interchange their positions to give another extreme separation of 2.20 gauss after the rotation by 90°, as seen in Figs. 12a. and b. In the latter experiment maximum splitting number was 3. The further splittings with incomplete resolution were observed ambiguously at a certain angle of crystal rotation. The splitting shown in Fig. 12a indicates $2\alpha' = 2.2$ gauss. Using the same procedure in Eqs. (2) and (3), the angle γ

becomes about 63.5° or 46°. The inter-contribution $\langle\Delta H^2\rangle_1=0.6$ gauss² between neighboring molecules obtained by subtracting $\langle\Delta H^2\rangle_0=1.0\pm0.1$ gauss² from the experimental value $\langle\Delta H^2\rangle=1.6$ gauss² at room temperature is not so different from the value expected from $\langle\Delta H^2\rangle_1=2.5$ gauss² at rigid lattice. The minimum observed width of the component line is 0.6 gauss from Fig. 12b, which amounts to $\langle\Delta H^2\rangle_1$ of 0.05 gauss². In powdered $CaI_2 6H_2O$, two types of resonance were observed in samples of two kinds which differ mainly in the rate of evaporation at precipitation. One type has a central peak, and the second moment is 1.6 gauss². The other is a doublet and has the second moment of 0.6 gauss², but this was observed about the sample which later dissociated and could not be tested again. It is not certain that this type can exist always in a stable form. Although it is probable that HI molecules remained in these powders from chemical point of view, it is not reasonable to regard the central peak as originating from the HI molecules in so far as the resonance signal is taken into consideration, because the disappearance of central peak at low temperature may not correspond to HI model and the vacuum puming treatment would remove the residual HI molecules if they are adsorbed on the surfaces of these powders.

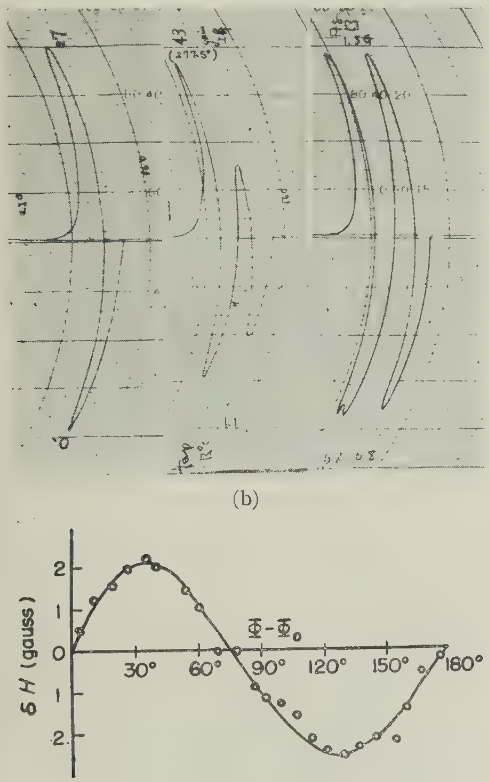

(b)

(a)

Fig. 12. (a) Line pair separation as a function of the angle $\Phi-\Phi_0$ as shown in Fig. 10 for a single crystal of $CaI_2 6H_2O$.
(b) Recorded derivatives of proton resonance in a single crystal of $CaI_2 6H_2O$ for three directions of $\Phi-\Phi_0$.

In $SrI_2 6H_2O$ the second moment observed at room temperature can be separated to $\langle\Delta H^2\rangle_0=2.0$ gauss² and $\langle\Delta H^2\rangle_1=0.5$ gauss², by assuming the model of rotating water molecules with $\gamma=67.5°$ or 43.5°. The variation of the selection of the ratio of $\langle\Delta H^2\rangle_0$ to $\langle\Delta H^2\rangle_1$ from 2.5/0 to 1.5/1.0 may change the angle by ±2° about the above values.

To avoid difficulties exist in the model of rotational motion of water molecules with such a value of the angle γ, the precessional motion of rotational axis around a definite direction is considered as a new model. In Fig. 10, if the rotational axis of OR precesses around an arbitrary axis OS with a constant angle between OR and OS, we have, denoting

$$\alpha''=\alpha' P_2(\cos\gamma')=\alpha P_2(\cos\gamma)P_2(\cos\gamma'),$$
$$\delta H=2\alpha''\{3\cos^2\delta'\cdot\cos^2(\Phi-\Phi_0)-1\}, \qquad (4)$$

since the average of $P_2(\cos\theta')$ over the angle ϕ' becomes $P_2(\cos\theta'')P_2(\cos\gamma')$ by the addition theorem of the Legendre functions. Therefore, the doublet separation in this case is given by writting α'' in place of α' in Eq. (3). Here δ' and $\Phi'-\Phi_0'$ are the angles for OS corresponding to δ and $\Phi-\Phi_0$ for OR.

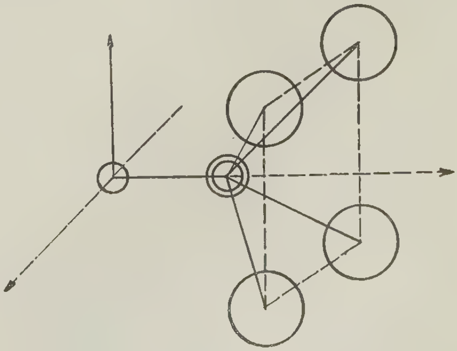

Fig. 13. Drawings showing the relative position of H_2O and the halogen ions in $CaI_2 6H_2O$ and $SrI_2 6H_2O$. Larger circles represent the iodine ions, a small circle represents a Ca or Sr ion, and a double circle shows a water molecule.

Table III.

salt	state	$\langle \Delta H^2 \rangle_0$	$\langle \Delta H^2 \rangle_1$	γ	γ'
$CaI_2 6H_2O$	rigid	23.0	3.0	1.595±0.02	—
$CaI_2 6H_2O$	rotation	1.0	0.6	—	40°
$SrI_2 6H_2O$	rigid	25.0	2.7	1.576±0.02	—
$SrI_2 6H_2O$	rotation	2.0	0.5	—	33°

The second moment for such a powder is given by the modification of Eq. (2) as follows:

$$\langle \Delta H^2 \rangle_0 = (4/5)\alpha''^2 = (4/5)\alpha^2\{P_2(\cos\gamma')P_2(\cos\gamma)\}^2 \,. \qquad (5)$$

In crystals having the structure of $SrCl_2 6H_2O$ type, the positions of water molecules can be shown by Fig. 13. This structure suggests the precessional motion of rotating axis, without discarding the model of rotational motion about C_2-axis of water molecules, because the second moment in this case takes a reduction due to $\{P_2(\cos\gamma')\}^2$ with $P_2(\cos\gamma)=0.5$. Thus γ' becomes 40° for $CaI_2 6H_2O$ and 33° for $SrI_2 6H_2O$. Theses results are tabulated in Table III.

c) *Results on other hydrates*

Powdered $CaCl_2 6H_2O$, $CaBr_2 6H_2O$, $SrCl_2 6H_2O$ and $SrBr_2 6H_2O$ have broad resonance lines of almost two spin type at room temperature, which correspond to the rigid lattice with second moment of about 30 gauss². Signal to noise ratios for these resonances are not so high as for the salts discussed in a) and b) because very low level of oscillation of the rf oscillator is used to avoid distortion of signals by a slight saturation. Although a sharp overlapping central peak with the broad line which originates from the adsorbed moisture on the surface of powders or from remaining HCI or HBr was eliminated by vacuum drying as much as possible, resonance signals in $CaCl_2 6H_2O$ and $CaBr_2 6H_2O$ had nevertheless a faint central peak, but those in $SrCl_2 6H_2O$ and $SrBr_2 6H_2O$ showed hardly any peaks. However, in enough lower temperature ranges which is above room temperature but under the melting points, a peak appeared at the center of the broad line in the latter salts, and it became large at elevated temperature with the decrease in intensity of broad lines. In the former salts the nearly same things occurred. This state must correspond to the transitions of resonance in $Mg(H_2O)_6Cl_2$ or $SrI_2 6H_2O$ at higher temperatures, but these hydrates melt into their own water without passing the state in which the water of hydration can rotate in their lattice. It is often said in chemistry that hydrogens will escape from these crystals as molecules HCI or HBr at melting. If it is assumed in this model that the hydrogen belonging to a water molecule is shifted to the neighboring halogen ion and forms a molecule HCl or HBr before melting, then this state must correspond to the narrower line. However, in $SrCl_2 6H_2O$, for example, when one proton of a water molecule moves to the chlorine atom to form HCI, interatomic distance of which is taken to be 1.27A, the second moment for such a model of the distorted water molecule is calculated to be 2.1 gauss², and the line becomes a doublet having a peak separation of 3.22 gauss. This is different from the observed one in $SrCl_2 6H_2O$, but it is similar to the reasonance of $SrI_2 6H_2O$ in the room temperature range. On the other hand, if HI molecules are formed in solid state of $SrI_2 6H_2O$ in the room temperature range, the bond formation of I–H····O–H gives the second moment of 2.65 gauss² for hydrogen-iodine interaction and 4.42 gauss² for proton-proton interaction. The sum of these two values is much larger than the observed value of the second moment at room temperature for $SrI_2 6H_2O$. The motion of the proton between two potential minima along O–H····I bond makes the second moment assume an intermediate value between the rigid lattice value, 23.5 gauss², and the above distorted value, 7.07 gauss². Thus in all cases, the reasonable account can be made only on the model that the proton moves out of the line joining the oxygen and the halogen ion.

As an explanation for a central peak, the following motional narrowing is considered. If the precessional motion occurs varying the angle between the axis of rotation and the axis of precession from γ_1' to γ_2', then the eduction of the approximate doublet separaion δH is shown to be proportional to the verage value of $P_2(\cos\gamma')$ over γ' from γ_1' o γ_2'. For example, a doublet separation of bout 10 gauss reduces to 0.65 gauss taking $_1'=45°$ and $\gamma_2'=60°$, and the doublet line nay not be distinguished from a single peak, vhen $\langle \Delta H^2\rangle_1 \geqq 0.2$ gauss². Moreover, the second noment can be reduced to zero, if the average of $P_2(\cos\gamma')$ is taken over the angle γ' rom 0° to 90°. Thus the rotational motion pproaches in such a manner to random rerientational motion, then the resonance line ives rise to a sharp central peak. Without assing the rotational motion or precession f a definite angle, the hydrates discussed in) go into the liquid-like structure.

4. Concluding Remarks

It should be concluded, from the above reults, that the water molecules of hydration n some halogen compounds of the second roup elements go into the hindered rotationl motion. However, detailed behavior of his motion such as rotational frequency, or he reasons why these motion should occur n some salts and not in others, is not certain, nd must be studied further.

Little is known about the thermal properies of these hydrates and we know the data bout the hydration of magnesium chloride nly. Energies of hydration of Mg^{++} ion nd $[Mg(H_2O)_6]^{++}$ ion are estimated to be 52 kcal/g.ion and 210 kcal/g.ion respectively16), nd heat of solution of $Mg(H_2O)_6Cl_2$ crystal s known to be 2.94 kcal/mole17). We may neglect the energies associated with entropy hanges in the reactions, because they are mall compared to these energies. By subracting the heat of solution of $Mg(H_2O)_6Cl_2$ rom the sum of hydration energies of $Mg(H_2O)_6]^{++}$ ion and two Cl^- ions, we obained 345 kcal/g.ion as the binding energies etween two Cl^- ion and $[Mg(H_2O)_6]^{++}$ ion. On the other hand, the energy of formation f $[Mg(H_2O)_6]^{++}$ ion from Mg^{++} ion and six H_2O molecules can be calculated as the diference between the energies of hydration f Mg^{++} ion and $[Mg(H_2O)_6]^{++}$ ion. This mounts to be 242 kcal/g.ion. Although hese values show that the attractive forces etween electric dipoles of the water moleules and chlorine negative ions are not so small, the arrangement of negative ions does not make the suitable angle of H–O–H as well as sufficiently shorter O–H····Cl distance for Cl····H–O–H····Cl binding to be possible, therefore the water molecule may take two or more equilibrium directions. Moreover, we believe that the coordination of water molecules to the central small metallic ion makes the interaction between charges of the electric dipoles reduce appreciably the hindering potential for rotation in the case of magnesium salts.

Possibility of hindered rotational motion of water molecules for the iodides will be due to the small electronegativity of iodine ion and it represents little contribution of covalency to these binding.

Acknowledgement

The author wishes to express his sincere thanks to Professor Tunahiko Sidei for his continual guidance and encouragement throughout this study. He is also indebted to Mr. Takenobu Higashimura for his invaluable advice, to Mr. Tadao Matsunami for preparing a single crystal of $Mg(H_2O)_6Cl_2$, and to Mr. Sōji Sasaki for his assistance in construction of the experimental apparatus.

References

1) N. Bloembergen, E. M. Purcell and R. V. Pound: Phys. Rev. **73** (1948) 679.
2) G. E. Pake: J. Chem. Phys. **16** (1948) 327.
3) H. S. Gutowsky, G. B. Kistiakowsky, G. E. Pake and E. M. Purcell: J. Chem. Phys. **17** (1949) 972. J. Itoh, R. Kusaka, Y. Yamagata, R. Kiriyama, H. Ibamoto, T. Kanda and Y. Masuda: J. Phys. Soc. Japan **8** (1953) 287.
4) H. S. Gutowsky and G. E. Pake: J. Chem. Phys. **18** (1950) 162.
5) N. L. Alpert: Phys. Rev. **75** (1949) 398. F. Bitter, D. N. Alpert, H. L. Poss, C. G. Leher and S. T. Lin: Phys. Rev. **71** (1947) 738.
6) R. Newman: J. Chem. Phys. **18** (1950) 669.
7) J. Itoh and R. Kusaka: Bull. Phys. Soc. Japan (April 1957) 6B19. (in Japanese)
8) T. Sidei, S. Yano and S. Sasaki: to be published in J. Appl. Phys. Japan (in Japanese).
9) R. V. Pound and W. D. Knight: Rev. Sci. Instr. **21** (1950) 219.
10) N. J. Hopkins: Rev. Sci. Instr. **20** (1949) 401.
11) T. Sidei and S. Yano: J. Chem. Phys. **23** (1955) 1554.
12) J. H. Van Vleck: Phys. Rev. **74** (1948) 1168.

13) R. W. G. Wyckoff: *Crystal Strucіures*, vol. **2** (Interscience Publishers, INC., N.Y. 1951). K. R. Andress and J. Gunderman: Z. Krist. **A, 87** (1934) 345.
14) *International Critical Tables*, vol. **4** (1928).
15) R. W. G. Wyckoff: *Crystal Siurciures*, vol. **2** (Interscience Publishers, INC., N.Y. 1951). A. Tovborg-Jensen: K. Danske Vidensk. Selsk. Mat. Fys. Medd. (1940) no. 17.
16) *Kagaku Butsuri II* (Bussei Butsurigaku Koza vol. **4**, 1957) chap. 7, (in Japanese).
17) *Iniernational Critical Tables*, vol. **5** (1928).

JOURNAL OF THE PHYSICAL SOCIETY OF JAPAN, Vol. 14, No. 7, JULY, 1959

Radiofrequency Spectroscopy Using Three-Level Maser Action

By Koichi SHIMODA

Department of Physics, Faculty of Science, University of Tokyo

(Received April 3, 1959)

A direct transition between l-type doublet of OCS molecule was observed either as emission or absorption using the three-level maser action. The pumping radiation was supplied by a klystron 2K33 at the frequency correspanding to $J=2\leftarrow1$, and the l-type doubling transition at 12.78 Mc/sec for $J=1$ was observed by a modified Pound-Knight circuit. Generally the low frequency transition of molecules is shown to be detectable using the bandwidth of about $1\,\mathrm{s}^{-1}$, if the corresponding microwave transition at 24,000 Mc/sec has the absorption coefficient larger than $10^{-8}\,\mathrm{cm}^{-1}$. The line-width can possibly be reduced to several kc/sec at the sacrifice of sensitivity. The application of this type of spectrometer is also discussed.

§ 1. General Considerations

The absorption of electromagnetic waves by molecules in gases has widely been observed in the infrared and microwave range, but it has never been observed in the lower radiofrequency range. This is only because the absorption by molecules is approximately proportional to the square of the frequency and it becomes very weak at lower frequencies. Thus the radiofrequency spectroscopy of gases by conventional methods of microwave spectroscopy is not practicable in the range below 1000 Mc/sec, where only a few lines have been observed[1].

However, a variety of transitions is known to fall in still lower radiofrequency range which is too weak to be detected by a conventional absoption technique. It is the purpose of this paper to report the first success of observing low frequency transitions of molecules by the application of three-level maser technique[2][3].

Consider a three-level system where the low frequency transition to be observed may either be $\nu_0=(E_3-E_2)/h$ as in Fig. 1 (a) or $\nu_0=(E_2-E_1)/h$ as in Fig. 1 (b). In order to simplify the discussion only the case of Fig. 1 (a) will be described.

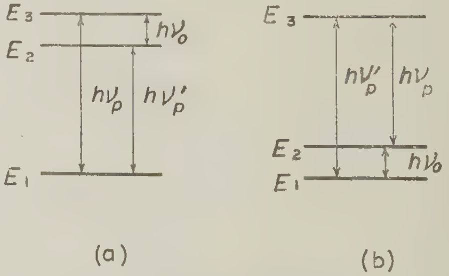

Fig. 1. Three level systems.

The power absorption coefficient at the frequency $\nu=\nu_0$ is given by

$$\alpha=(n_2-n_3)\frac{8\pi^2\nu_0}{3hc}\frac{|\mu_0|^2}{\Delta\nu}, \qquad (1)$$

where n_2 and n_3 are the number density of molecules in the energy levels E_2 and E_3 respectively, μ_0 the dipole matrix element between states E_2 and E_3, and $\Delta\nu$ the half-half-width of the line which is assumed to be mostly due to pressure broadening. In thermal equilibrium at temperature T, the Boltzmann distribution shows

$$n_2-n_3=\frac{h\nu_0}{kT}n_2 \qquad (2)$$

and the absorption coefficient is given by

$$\alpha_0=\frac{8\pi^2\nu_0^2 n_2}{3ckT}\frac{|\mu_0|^2}{\Delta\nu}. \qquad (3)$$

Therefore the absorption coefficient is proportional to the square of the frequency, assuming that other factors are constant.

If the transition between states E_1 and E_3 is allowed, pumping power at the frequency $\nu_p=(E_3-E_1)/h$ is used to saturate the transition, and then the induced emission at the frequency ν_0 will be observed. On the other hand, if the transition between states E_1 and E_2 is allowed, the pumping power at the frequency $\nu_p'=(E_2-E_1)/h$ will enhance the induced absorption at the frequency ν_0. In either case for complete saturation one obtains

$$|n_2-n_3|\cong\frac{h\nu_p}{2kT}n_2. \qquad (4)$$

The absorption coefficient or the coefficient of induced emission in this case becomes

$$\alpha_{0,\text{pump}}\cong\frac{4\pi^2\nu_0\nu_p n_2}{3ckT}\frac{|\mu_0|^2}{\Delta\nu} \qquad (5)$$

which is $\nu_p/2\nu_0$ times larger than α_0.

Since the low frequency transition can more conveniently be observed with a resonator cell than a transmission line cell, a better measure of the intensity is the quality factor of the molecules. It is denoted by $Q_m(\nu)$ and is given by

$$Q_m(\nu)=\frac{2\pi\nu_0}{c\alpha(\nu)} \qquad (6)$$

as a function of frequency. For $\nu=\nu_0$, $Q_m(\nu_0)$ will be simply written as Q_m, but it may be noted that Q^{-1} of the molecule in this paper does not represent the line-width but is equal to the loss factor of the gas.

When the molecule is completely saturated by the pumping radiation, the following equation is obtained from Eqs. (5) and (6).

$$\frac{1}{Q_m}=\frac{2\pi\nu_p n_2}{3kT}\frac{|\mu_0|^2}{\Delta\nu} \qquad (7a)$$

This equation may be expressed as

$$\frac{1}{Q_m}=\frac{\lambda_p\alpha_p}{4\pi}\left|\frac{\mu_0}{\mu_p}\right|^2 \qquad (7b)$$

where μ_p is the dipole matrix element of the pumping transition and α_p is the absorption coefficient at ν_p. It is noticeable that Eq. (7) is independent of ν_0. Assuming that the pumping frequency is about 24 Gc/sec and $\mu_0\approx\mu_p$, Eq. (7) can be written as

$$\frac{1}{Q_m}\approx\frac{\alpha_p}{10}. \qquad (8)$$

As the typical value of microwave absorption coefficient which has been measured arround 24 Gc/sec is $\alpha_p=10^{-5}\sim10^{-8}$ cm^{-1}, the above equation shows that Q of the molecule at the low frequency transition should be such that $1/Q_m=10^{-6}\sim10^{-9}$, which is of detectable magnitude as will be shown below.

§ 2. Line-Width and Sensitivity of Three-Level Maser Spectrometer

If the radiofrequency spectral lines are as broad as those in the microwave range, direct observation of low frequency transitions would be less worthy of study. The resolution of microwave spectrometer is largely limited by Doppler broadening, which is proportional to the transition frequency and the velocity of molecules. The Doppler width is approximately given by

$$\Delta\nu_D\approx\frac{v_m}{c}\nu_0\approx10^{-6}\nu_0, \qquad (9)$$

where v_m is the average velocity of molecules. For low frequencies, $\nu_0\approx10$ Mc/sec, the Doppler width, $\Delta\nu_D\approx0.01$ kc/sec, is so small as to allow very high resolution. However, other broadening factors will dominate in usual experimental conditions.

The broadening by collisions of molecules with cell walls or electrodes is given approximately by[4)]

$$\Delta\nu_w\cong\frac{0.1}{d}\sqrt{\frac{2RT}{M}}, \qquad (10)$$

where d is the distance between opposite walls, R the gas constant, and M the molecular weight. As an example take $d=2$ cm, $M=60$, and then Eq. (10) gives $\Delta\nu_w=1.45$ kc/sec.

The broadening by collisions of molecules with each other is known to be proportional to the gas pressure. In order to reduce it to 1 kc/sec for example, the gas pressure must be of the order of 10^{-4} mm Hg.

Saturation effect will be appreciable, when the field intensity at the frequency ν_0 is larger than the critical value E_c which is approximately given by

$$E_c^2 = 3h^2 \frac{(\varDelta\nu_0)^2}{|\mu_0|^2} \tag{11}$$

where $\varDelta\nu_0$ is the total line-width and h the Planck's constant. The critical field E_c may be written as

$$E_c(\text{V/cm}) = 3.44 \times 10^{-3} \frac{\varDelta\nu_0(\text{kc/sec})}{|\mu_0|(\text{Debye})} . \tag{12}$$

Therefore, the field intensity must be very weak in order to obtain high resolution. For example, when $\varDelta\nu_0 = 3$ kc/sec and $\mu_0 = 1$ Debye, the field intensity must be less than 10 mV/cm.

Now the sensitivity of the spectrometer is calculated. In order to detect electric dipole transition, the molecules of gas must be put in the r.f. electric field. The cell acts as a capacitor C, which forms a resonant circuit with an external inductance L. Assuming that the quality factor of the LC resonator is Q_0 at the absence of molecules in the capacitor, the impedance at the resonant frequancy is $R_0 = Q_0/2\pi\nu_0 C$. At the presence of molecular transition having Q_m the impedance at resonance becomes

$$R = \frac{Q_0 Q_m}{2\pi\nu_0 C(Q_0 + Q_m)} .$$

Therefore, when the LC resonator is driven by a constant current generator, the resonator r.f. voltage $V_0 = iR_0$ will change by $\varDelta V_0 = i(R - R_0)$ at the presence of molecules. For $Q_m \gg Q_0$ the signal voltage due to the transition of molecules is

$$\varDelta V_0 = K \frac{Q_0}{Q_m} V_0 , \tag{13}$$

where K is the filling factor.

On the other hand the effective noise voltage is expressed as

$$\overline{v_n^2} = 4FR_0 kT\varDelta f ,$$

where F is the noise figure of the r.f. spectrometer, and $\varDelta f$ the effective bandwidth of the detecting system.

Assume for simplicity that the signal voltage larger than r.m.s. noise voltage can be detected. Then the minimum detectable $1/Q_m$ is

$$\left(\frac{1}{Q_m}\right)_{\min} = \frac{2}{KV_0} \sqrt{\frac{FkT\varDelta f}{2\pi\nu_0 C Q_0}} . \tag{14}$$

This equation shows that the larger the r.f. voltage the higher the sensitivity, while equation (11) or (12) requires the lower r.f. voltage for the higher resolution.

As an example of high sensitivity let us take $V_0 = 0.2$V, $F = 2$, $\varDelta f = 1\,\text{s}^{-1}$, $K = 0.8$, $\nu_0 = 10$ Mc/sec $= 10^7\text{s}^{-1}$, $Q_0 = 100$, and $C = 200$ pF, one obtains

$$\left(\frac{1}{Q_m}\right)_{\min} = 1 \times 10^{-9} .$$

This sensitivity assures observation of r.f. transition having the intensity corresponding to the microwave absorption coefficient of $10^{-8}\,\text{cm}^{-1}$ as can be seen from Eq. (8).

However, higher resolution must be attained at the sacrifice of high sensitivity. The resonator voltage should be smaller than $V_0 = 3.44 \times 10^{-3} \varDelta\nu_0 d/\mu_0$ volts from Eq. (12), where d is the separation of r.f. electrodes in centimeters. For example, take $\varDelta\nu_0 = 3$ kc/sec, $\mu_0 = 1$ Debye, $d = 2$ cm, and $V_0 = 2 \times 10^{-2}$V is obtained. This results in the sensitivity as

$$\left(\frac{1}{Q_m}\right)_{\min} = 1 \times 10^{-8} ,$$

if other factors are the same as before.

§ 3. Experimental Results

A three-level radiofrequency spectrometer has been constructed and tested to observe direct l-type doubling transitions of ICN and OCS. The spectrometer was first operated for ICN. The rotational spectrum of ICN, corresponding to the transition $J = 2 \leftarrow 1$, shows l-type doublets, which were measured by Oka, Hirakawa, and Miyahara, although they were not reported in their paper[5] because of the inadequacy of these lines in determining the quadrupole coupling constants.

The rotational transition of ICN at 13,094 Mc/sec or 13,083 Mc/sec, corresponding to $J = 2 \leftarrow 1$, $F = 9/2 \leftarrow 7/2$, and $v_2 = 1$, was employed to increase the intensity of direct l-type doubling transition at 5.4 Mc/sec, for $J = 1$. The experiment turned out to be a failure, and the reasons of its negative result are considered as follows. The pumping radiation supplied by a crystal doubler was not sufficiently strong to achieve appreciable saturation. Moreover, the presence of hyperfine structures due to I^{127} and N^{14} made each component weaker, and the sample used was not pure.

Then the three-level spectrometer was

tested with carbonyl sulfide which shows no hyperfine structure. The pumping transition was $J=2\leftarrow1$ in $v_2=1$ state, and the direct l-type doubling transition for $J=1$ could be observed either as emission or as absorption at 12.78 Mc/sec. The accurate frequency was not measured, but it seemed to be only a little smaller than this value.

The energy level diagram of OCS for $J=1$ and 2 is shown in Fig. 2, and the frequencies of allowed transitions between these levels are:

$\nu_{12}=12.78$ Mc/sec
$\nu_{34}=38.35$ Mc/sec
$\nu_{13}=24{,}355.50$ Mc/sec
$\nu_{24}=24{,}381.07$ Mc/sec

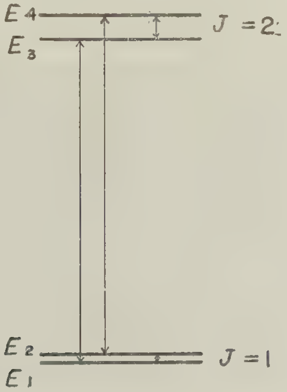

Fig. 2. Energy level diagram of OCS in the first bending vibrational mode.

In thermal equlibrium at room temperature the absorption coefficient of $J=1$ line at 12.78 Mc/sec is calculated to be $\alpha_0=4.0\times10^{-13}\,\mathrm{cm}^{-1}$, which is many orders of magnitude smaller than the detectable absorption without pumping.

The dipole matrix element[6] for the transition $J+1\leftrightarrow J$ is

$$|\mu_{ij}|^2=\mu^2\frac{(J+1)^2-l^2}{(J+1)(2J+1)} \tag{15}$$

and for $\Delta J=0$

$$|\mu_{ij}|^2=\mu^2\frac{l^2}{(J+1)(2J+1)}\,. \tag{16}$$

Thus for the pumping transition $J=2\leftarrow1$ at the frequency ν_{13} or ν_{24}, $|\mu_p|^2=\frac{1}{2}\mu^2$, and for direct l-type doubling transition of $J=1$ $|\mu_0|^2=\frac{1}{6}\mu^2$. As the absorption coefficient at the frequency ν_p is $\alpha_p=4.4\times10^{-6}\,\mathrm{cm}^{-1}$, the intensity of l-type doubling transition under complete saturation by pumping at the frequency $\nu_p=\nu_{13}$ or ν_{24} is calculated from Eq. (7b) as

$$\frac{1}{Q_m}=1.4\times10^{-7}\,. \tag{17}$$

The calculated intensity of the $J=2$ line is $1/Q_m=5.7\times10^{-8}$ because $|\mu_0|^2=\frac{1}{15}\mu^2$ in this case.

To achieve high resolution as well as high sensitivity, the separation of r.f. electrodes must be large, but then large pumping power is required. The optimum pumping power of a plane polarized wave can be approximately expressed as

$$P_{\mathrm{opt}}=\frac{3ch^2}{4\pi}\frac{(\Delta\nu_p)^2}{|\mu_p|^2}S\,, \tag{18}^*$$

where the relaxation time is taken as $\nu=1/2\pi\Delta\nu_p$, $\Delta\nu_p$ is the total line-width including Doppler effect of the pumping transition, and S is the cross-sectional area of the cell. It may be noted that although the Doppler broadening is not a power dissipating process, it must be taken into the calculation of saturation power, because only during the time interval $1/2\pi\Delta\nu_D$ the phase difference between molecules and waves is kept within one radian.

Taking the following values, $|\mu_p|^2=\frac{1}{2}(0.709)^2$, $\Delta\nu_p=70$ kc/sec, and $S=23\,\mathrm{cm}^2$, the optimum pumping power is calculated as

$$P_{\mathrm{opt}}=14\,\mathrm{mW}\,.$$

Microwave power of this order of magnitude at 24 Gc/sec was supplied by a klystron 2K33.

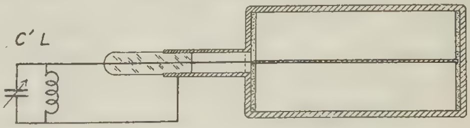

Fig. 3. Cross-section of the waveguide cell.

The absorption cell is made of 3,000 Mc/sec band waveguide of 2 meters length, whose cross-section is 72.0 mm×34.0 mm I.D. and the r.f. center electrode has been inserted in the same way as the Stark septum as shown in Fig. 3.

The r.f. voltage is applied to the center electrode which is connected to an external inductance L and a small variable capacitor to tune the resonant frequency.

---

* This corresponds exactly to $|y|^2\tau^2=\frac{1}{2}$ in ref. (7) or $|\mu_p|_x E\tau=h$, where E is the r.m.s. field intensity of the pumping radiation.

The r.f. oscillator and detector employed is of a modified Pound-Knight circuit.[8] The pumping radiation is frequency modulated at the frequency of $175\,\mathrm{s}^{-1}$, and the r.f. amplifier and detector is followed by a tuned $175\,\mathrm{s}^{-1}$ amplifier and a phase-sensitive detector. The time constant of the filter in the detector output can be varied from 0.005 to 0.25 sec. The output of the spectrometer can be observed with a d.c. oscilloscope as well as with a pen-and-ink recorder. A block diagram of the spectrometer is shown in Fig. 4.

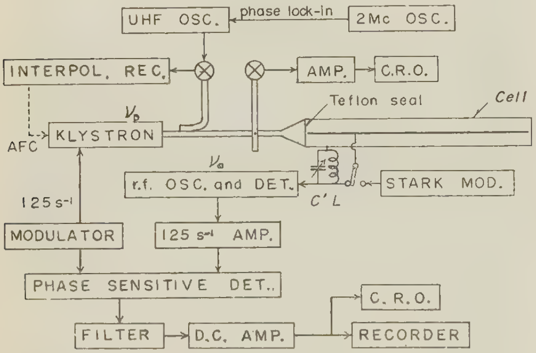

Fig. 4. Block diagram of the three level r.f. spectrometer. $125\,\mathrm{s}^{-1}$ should read $175\,\mathrm{s}^{-1}$.

The absorption cell is used as a Stark cell to observe and monitor the pumping transition by a crystal detector in an auxiliary waveguide.

The klystron 2K33 might be automatically frequency controlled with respect to the UHF oscillator at 358 Mc/sec which is locked in the harmonic of a 2 Mc/sec crystal oscillator[9], but actually it was manually tuned with respect to the 358 Mc/sec oscillator. To sweep the microwave frequency for pumping, frequency of the interpolation receiver was changed with time. When the pumping frequency was ν_{13}, emission of r.f. signal at $\nu_0=\nu_{12}$ could be observed, and when it was ν_{24}, absorption of r.f. signal could be observed.

The capacitance of the r.f. electrode of the cell is about 300 pF including capacitance of the lead, and Q of the resonant circuit is fairly low. Because the r.f. field is stronger at the edge of the electrode, the filling factor is supposed to be also small. Using the values, $\Delta\nu_0=10$ kc/sec, $|\mu_0|=0.709/6^{1/2}$ Debye, and $d=1.66$ cm, it is found from Eq. (12) or (15) that the resonator voltage should not exceed $V_0=0.2$ V. Then the minimum detectable intensity is calculated from Eq. (14), assuming $\nu_0=12.78$ Mc/sec, $C=3\times10^{-10}$ F, $Q_0=20$, $K=0.5$, $F=3$, and $\Delta f=1.3\,\mathrm{s}^{-1}$, corresponding to the filter time constant of 0.25 seconds, as

$$\left(\frac{1}{Q_{\mathrm{m}}}\right)_{\min}=3.6\times10^{-9}\,.$$

Therefore, the l-type doubling transition having the intensity as shown by Eq. (17) must be observed with the signal to noise ratio of

$$\frac{S}{N}=\frac{1.4\times10^{-7}}{3.6\times10^{-9}}=39\,.$$

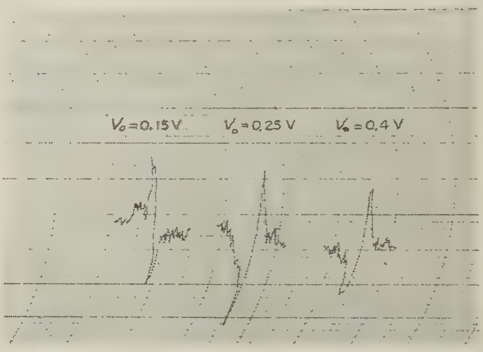

Fig. 5. Traces of records of the direct l-type doubling transition of OCS, where the left one was taken with sweep in the reverse direction.

By sweeping the pumping frequency through ν_{p}, the direct l-type doubling transition was observed and recorded as shown in Fig. 5, using the filter time constant of 0.25 seconds. The observed intensity of the line agrees fairly well with the calculated value, thus confirming the theoretical considerations given above. Saturation effect by r.f. field was observed when the r.f. amplitude was increased above 0.1 volt.

The spectrum could also be recorded by sweeping the r.f. frequency. However, the record was disturbed and blotted by interferences from other laboratories. The observed line-width at a pressure of about 10^{-3} mm Hg and with r.f. amplitude of about 0.25 volts was nearly 40 kc/sec. The line-width was found to decrease by reducing the pressure, but then the signal intensity also decreased and the pumping power could not considerably be reduced. It can be supposed that much higher sensitivity with slower sweep as well as smaller r.f. amplitude must be used in order to reduce the line-width below 10 kc/sec and observe the line with good signal to noise ratio.

§ 4. Applications

Most of the low frequency transitions of simple molecules might be studied by the three-level technique described above.

1. Direct transitions between K-type doublets, corresponding to $\Delta J=0$ and $\Delta K_1=1$ in case of a nearly symmetric prolate rotor, can be detected. The transition $\Delta J=1$ is used for pumping. A slightly asymmetric molecule such as CH_2CO or CH_2DC1 seems to be a good example of this type, and larger signal intensity than for l-type doubling transition is generally expected.
2. Direct hyperfine transitions corresponding to $\Delta J=0$ and $\Delta F=\pm1$ for a symmetric molecule may be studied. But the intensity is expected to be smaller, because the magnitude of the dipole matrix element is rather small in this case.
3. Transitions between Stark or Zeeman components under d.c. external field, corresponding to $\Delta J=0$ and $\Delta M=\pm1$, may also be observed.
4. Other low frequency transitions due to l-type doubling, inversion, or internal rotation may possibly be observed, if both the observation frequency and the pumping frequency fall in some convenient ranges.

In conclusion the author would like to express his thanks for the assistance of Messrs H. Takuma and T. Shimizu in carrying out the experiment. He also thanks for the financial help of the Ministry of Education.

References

1) Y. Beers et. al: J. Chem. Phys. **23** (1955) 1601. F. Sterzer and Y. Beers: Phys. Rev. **100** (1955) 1174.
2) N. Bloembergen: Phys. Rev. **104** (1956) 324.
3) A. L. McWhorter and J. W. Meyer: Phys. Rev. **109** (1958) 312.
4) M. Danos and S. Geschwind: Phys. Rev. **91** (1953) 1159.
5) T. Oka, H. Hirakawa, and A. Miyahara: J. Phys. Soc. Japan **12** (1957) 39.
6) C. H. Townes and A. L. Schawlow: *Microwave Spectroscopy* (McGraw-Hill, 1955).
7) A. Javan: Phys. Rev. **107** (1957) 1579.
8) R. V. Pound and W. D. Knight: Rev. Sci. Instr. **21** (1950) 219.
9) K. Shimoda: J. Phys. Soc. Japan **9** (1954) 378.

JOURNAL OF THE PHYSICAL SOCIETY OF JAPAN, Vol. 14, No. 7, JULY, 1959

Stationäre Temperaturverteilung in der Wand vielschichtiger Röhrenleitungen

Von Václav VODIČKA

Pilsen, ČSR

(Eingegangen am 19. März 1959)

The present paper solves completely the problem of stationary temperature distribution in a hollow n-layerd circular cylinder whose boundaries are kept at given temperatures varying both in the tangential and in the longitudinal direction. The first part of the paper takes into account heat transfer at the surfaces of separation, and the second part treats the case of a continuous variation of temperature at each surface of separation. The results are very complicated.

Dieser Aufsatz bringt fertige Formeln für stationäre Temperaturfelder in einem hohlen n-schichtigen Kreiszylinder, dessen beide Oberflächen auf vorgeschriebener Temperatur gehalten werden. Trotz ihrer technischen Bedeutung hat der Verfasser die fertigen Formeln in der Literatur nicht finden können.

Der ganze Aufsatz zerfällt in zwei Teile.

Im ersten rechnen wir mit endlichen Wärmeübergangsfaktoren an den Trennflächen einzelner Körperschichten, der zweite Teil setzt überall stetige Aenderung sowohl der Temperatur als auch des Wärmeflusses voraus.

I. Wärmesprünge an den Trennflächen

§ 1. Problemstellung. **Es seien**

$$0<\rho_1<\rho_2<\cdots<\rho_{n+1}\,, \quad h_i>0\,, \quad h_i'>0 \qquad (i=2,\,3,\,\cdots,\,n) \tag{1}$$

gegebene Konstanten, $f(\varphi, z)$ und $F(\varphi, z)$ zwei für alle reellen φ, z definierte Funktionen mit der Periode 2π bezüglich φ. Im Bereich $0\le\varphi\le 2\pi$ lassen sich $f(\varphi, z)$ und $F(\varphi, z)$ in Fourierreihen entwickeln, als Funktionen von z seien beide mit Hilfe vom Fourierschen Integraltheorem ausdrückbar.

Unter diesen Verhältnissen geht es um die in φ periodische Lösun $u_i(\rho, \varphi, z)$ folgender technisch und physikalisch leicht verständlichen Aufgabe:

$$\frac{\partial^2 u_i}{\partial\rho^2}+\frac{1}{\rho}\frac{\partial u_i}{\partial\rho}+\frac{1}{\rho^2}\frac{\partial^2 u_i}{\partial\varphi^2}+\frac{\partial^2 u_i}{\partial z^2}=0$$

$$(\rho_i<\rho<\rho_{i+1},\ 0\le\varphi\le 2\pi,\ -\infty<z<+\infty;\ i=1,\,2,\,\cdots,\,n)\,, \tag{2}$$

$$u_1(\rho_1, \varphi, z)=f(\varphi, z) \qquad (0\le\varphi\le 2\pi,\ -\infty<z<+\infty)\,, \tag{3.1}$$

$$\frac{\partial u_i}{\partial\rho}+h_{i+1}(u_i-u_{i+1})=\frac{\partial u_{i+1}}{\partial\rho}+h_{i+1}'(u_i-u_{i+1})=0$$

$$(\rho=\rho_{i+1},\ 0\le\varphi\le 2\pi,\ -\infty<z<+\infty;\ i=1,\,2,\,\cdots,\,n-1)\,, \tag{3.2}$$

$$u_n(\rho_{n+1}, \varphi, z)=F(\varphi, z) \qquad (0\le\varphi\le 2\pi,\ -\infty<z<+\infty)\,. \tag{3.3}$$

§ 2. Zurückführung auf zwei einfachere Fälle

Die Lösung unseres Problems (2)–(3.3) ergibt sich augenscheinlich durch Summierung der Lösungen zweier einfacheren Aufgaben, die dadurch zustandekommen, dass man sich in (2)–(3.3) das eine mal $F(\varphi, z)$ und das andere mal $f(\varphi, z)$ durch Null ersetzt denkt.

Ist $u_i^{(1)}(\rho, \varphi, z)$; $i=1, 2, \cdots, n$ die Lösung des ersten und $u_i^{(2)}(\rho, \varphi, z)$; $i=1, 2‘ \cdots, n$ des zweiten Teilproblems, so hat man also in

$$u_i(\rho, \varphi, z)=u_i^{(1)}(\rho, \varphi, z)+u_i^{(2)}(\rho, \varphi, z) \qquad (i=1,\,2,\,\cdots,\,n) \tag{4}$$

das verlangte Ergebnis für die Anfangsaufgabe (2)–(3.3).

§ 3. Die Bestimmung von $u_i^{(1)}(\rho, \varphi, z)$; $i=1, 2, \cdots, n$

Die mit noch unbestimmten Parametern β, γ und mit /im allgemeinen freilich von β, γ abhängigen/ beliebigen Konstanten A_{ik}, B_{ik}, C_{ik} und D_{ik} gebildeten Ausdrücke

$$\left.\begin{aligned}
&v_{ik}=R_{ik}(\beta\rho)(A_{ik}\cos k\varphi+B_{ik}\sin k\varphi)\cos\beta(\gamma-z) && (i=1,\,2,\,\cdots,\,n)\\
&R_{ik}(\beta\rho)=C_{ik}I_k(\beta\rho)+D_{ik}K_k(\beta\rho) && (i=1,\,2,\,\cdots,\,n-1)\,,\\
&R_{nk}(\beta\rho)=K_k(\beta\rho_{n+1})I_k(\beta\rho)-I_k(\beta\rho_{n+1})K_n(\beta\rho) && (k=0,\,1,\,2,\,\cdots)
\end{aligned}\right\} \tag{5}$$

sind für jedes k Lösungen von (2), haben die Periode 2π besüglich φ und darüber hinaus ist $v_{nk}(\rho_{n+1}, \varphi, z)=0$

Es ist leicht zu erzielen, dass auch noch die Uebergangsbedingungen (3.2) von den v_{ik} erfüllt werden. Dies wird dann und nur dann der Fall, wenn

$$\left.\begin{aligned}
&h_{i+1}(A_{i+1,k}\cos k\varphi+B_{i+1,k}\sin k\varphi)R_{i+1,k}'(\beta\rho_{i+1})=h_{i+i}'(A_{ik}\cos k\varphi+B_{ik}\sin k\varphi)R_{ik}'(\beta\rho_{i+1})\,,\\
&h_{i+1}\frac{R_{ik}(\beta\rho_{i+1})}{R_{ik}'(\beta\rho_{i+1})}=h_{i+1}'\frac{R_{i+1,k}(\beta\rho_{i+1})}{R_{i+1,k}'(\beta\rho_{i+1})}-1;\ R_{mk}'(\beta\rho_n)=\left[\frac{d}{d\rho}R_{mk}(\beta\rho)\right]_{\rho=\rho_n}\\
&\qquad\qquad(0\le\varphi\le 2\pi;\ i=1,\,2,\,\cdots,\,n-1,\ k=0,\,1,\,2,\,\cdots)\,.
\end{aligned}\right\} \tag{6}$$

Gebraucht man die Tatsache, dass sich aus

$$\frac{a+bx}{A+Bx}=\frac{1}{p}\left(-1+q\,\frac{a+by}{A+By}\right)$$

nach einiger Rechenarbeit

$$x=\frac{1}{N}\left(P-\frac{pq\Delta^2}{M+Ny}\right)$$

mit

$$\begin{aligned} &M=aBq-A(B+bp)\,, && N=-B[B+b(p-q)]\,,\\ &P=A[B+b(p-q)]+p\Delta\,, && \Delta=aB-Ab \end{aligned}$$

ergibt, so folgt aus der zweiten Gleichungsgruppe (6)-unter gleichzeitiger Berücksichtigung von (5) und von bekannten Wronskischen Beziehungen aus der Theorie der Zylinderfunktionen-leicht

$$D_{ik}=q_{ik}C_{ik} \qquad (i=1,\,2,\,\cdots,\,n-1;\ k=0,\,1,\,2,\,\cdots) \tag{7}$$

$$\left.\begin{aligned} q_{ik}=q_{ik}(\beta)= &\ \frac{1}{N_{i+1,k}(\beta)}\left\{P_{i+1,k}(\beta)-\frac{h_{i+1}h'_{i+1}}{\rho_{i+1}^2[M_{i+1,k}(\beta)+N_{i+1,k}(\beta)q_{i+1,k}(\beta)]}\right\},\\ &M_{i+1,k}(\beta)=-I_k'(\beta\rho_{i+1})K_k'(\beta\rho_{i+1})-h_{i+1}I_k'(\beta\rho_{i+1})K_k(\beta\rho_{i+1})+h'_{i+1}I_k(\beta\rho_{i+1})K_k'(\beta\rho_{i+1})\,,\\ &N_{i+1,k}(\beta)=-K_k'(\beta\rho_{i+1})[K_k'(\beta\rho_{i+1})+(h_{i+1}-h'_{i+1})K_k(\beta\rho_{i+1})]\,,\\ &P_{i+1,k}(\beta)=-\frac{h_{i+1}}{\rho_{i+1}}+I_k'(\beta\rho_{i+1})[K_k'(\beta\rho_{i+1})+(h_{i+1}-h'_{i+1})K_k(\beta\rho_{i+1}]\\ &\qquad\qquad\qquad\qquad\qquad\qquad (i=1,\,2,\,\cdots,\,n-2;\ k=0,\,1,\,2,\,\cdots)\\ q_{n-1,k}=q_{n-1,k}(\beta) = &-\frac{1}{\rho_nK_k'(\beta\rho_n)}\left\{\rho_nI_k'(\beta\rho_n)\right.\\ &\left.+\frac{h_n}{-h_nK_k(\beta\rho_n)+K_k'(\beta\rho_n)\left[-1+h_n'\,\dfrac{K_k(\beta\rho_{n+1})I_k(\beta\rho_n)-I_k(\beta\rho_{n+1})K_k(\beta\rho_n)}{K_k(\beta\rho_{n+1})I_k'(\beta\rho_n)-I_k(\beta\rho_{n+1})K_k'(\beta\rho_n)}\right]}\right\}\\ &\qquad\qquad\qquad\qquad\qquad\qquad (k=0,\,1,\,2,\,\cdots)\,. \end{aligned}\right\} \tag{7.1}$$

Geht man mit (7) und (7.1) in die erste Gleichungsgruppe (6) ein, so bekommt man daraus durch leichte Rechnung

$$\left.\begin{aligned} &A_{i+1,k}C_{i+1,k}=\delta_{i+1,k}A_{1k}C_{1k}\,, \qquad B_{i+1,k}C_{i+1,k}=\delta_{i+1,k}B_{1k}C_{1k}\\ &\qquad\qquad\qquad\qquad (i=1,\,2,\,\cdots,\,n-2;\ k=0,\,1,\,2,\,\cdots)\\ &\delta_{i+1,k}=\delta_{i+1,k}(\beta)=\frac{h_2'h_3'\cdots h'_{i+1}}{h_2h_3\cdots h_{i+1}}\prod_{\nu=1}^{i}\frac{I_k'(\beta\rho_{\nu+1})+q_{\nu k}K_k'(\beta\rho_{\nu+1})}{I_k'(\beta\rho_{\nu+1})+q_{\nu+1,k}K_k'(\beta\rho_{\nu+1})}\\ &A_{nk}=\delta_{nk}A_{1k}C_{1k}\,, \qquad B_{nk}=\delta_{nk}B_{1k}C_{1k} \qquad (k=0,\,1,\,2,\,\cdots)\\ &\delta_{nk}=\delta_{nk}(\beta)=\frac{h_n'}{h_k}\cdot\frac{I_k'(\beta\rho_n)+q_{n-1,k}K_k'(\beta\rho_n)}{K_k(\beta\rho_{n+1})I_k'(\beta\rho_n)-I_k(\beta\rho_{n+1})K_k'(\beta\rho_n)}\delta_{n-1,k}(\beta)\,. \end{aligned}\right\} \tag{8}$$

Unter Zuhilfenahme von bisherigen Ergebnissen erscheinen unsere partikuläre Lösungen (5) in der Form

$$v_{ik}=\delta_{ik}(\beta)C_{1k}V_{ik}(\beta\rho)\Phi_k(\varphi)\cos\beta(\gamma-z) \qquad (i=1,\,2,\,\cdots n;\ k=0,\,1,\,2,\,\cdots) \tag{9}$$

worin $\delta_{1k}=1$ $(k=0,\,1,\,2,\,\cdots)$ und die übrigen $\delta_{ik}(\beta)$ nach (8) zu berechnen sind. Weiter ist mit den durch (7.1) bestimmten Grössen q_{ik}

$$V_{ik}(\beta\rho)=I_k(\beta\rho)+q_{ik}K_k(\beta\rho)\,, \qquad V_{nk}(\beta\rho)=K_k(\beta\rho_{n+1})I_k(\beta\rho)-I_k(\beta\rho_{n+1})K_k(\beta\rho) \tag{9.1}$$
$$(i=1,\,2,\,\cdots,\,n-1;\;\; k=0,\,1,\,2,\,\cdots)$$

und endlich

$$\Phi_k(\varphi)=A_{1k}\cos k\varphi+B_{1k}\sin k\varphi \qquad (k=0,\,1,\,2,\,\cdots) \tag{9.2}$$

Die durch (9)–(9.2) definierten Ausdrücke $v_{ik}=v_{ik}(\rho,\,\varphi,\,z;\;\beta,\,\gamma)$ genügen allen Forderungen unseres ersten Teilproblems, bis auf (3.1). Dasselbe gilt dann natürlich auch für die Funktionen

$$u_{ik}(\rho,\,\varphi,\,z)=\int_0^\infty d\beta\int_{-\infty}^\infty v_{ik}(\rho,\,\varphi,\,z;\;\beta,\,\gamma)d\gamma \qquad (i=1,\,2,\,\cdots,\,n;\;\; k=0,\,1,\,2,\,\cdots)\,. \tag{10}$$

Die letzte noch zu befriedigende Bedingung (3.1) drückt sich mit geläufigem Ansatz

$$u_i^{(1)}(\rho,\,\varphi,\,z)=\sum_{k=0}^\infty u_{ik}(\rho,\,\varphi,\,z) \qquad (i=1,\,2,\,\cdots,\,n) \tag{11}$$

aus durch die Gleichung

$$\left.\begin{aligned}
&\frac{1}{\pi}\sum_{k=0}^\infty\int_0^\infty d\beta\int_{-\infty}^\infty[f_{k1}(\gamma)\cos k\varphi+f_{k2}(\gamma)\sin k\varphi]\cos\beta(\gamma-z)d\gamma\\
&=\sum_{k=0}^\infty\int_0^\infty[I_k(\beta\rho_1)+q_{1k}K_k(\beta\rho_1)]d\beta\int_{-\infty}^\infty C_{1k}(A_{1k}\cos k\varphi+B_{1k}\sin k\varphi)\cos\beta(\gamma-z)d\gamma\,,\\
&f_{01}(\gamma)=\frac{1}{2\pi}\int_0^{2\pi}f(\alpha,\,\gamma)d\alpha\,, \qquad \begin{matrix}f_{k1}(\gamma)\\ f_{k2}(\gamma)\end{matrix}=\frac{1}{\pi}\int_0^{2\pi}f(\alpha,\,\gamma)\cdot\begin{matrix}\cos k\alpha\\ \sin k\alpha\end{matrix}d\alpha \qquad (k\geq 1)\,.
\end{aligned}\right\} \tag{12}$$

Daraus entnimmt man sofort

$$\begin{matrix}A_{1k}C_{1k}\\ B_{1k}C_{1k}\end{matrix}=\frac{1}{\pi\Lambda_k}\cdot\begin{matrix}f_{k1}(\gamma)\\ f_{k2}(\gamma)\end{matrix}\,, \qquad \Lambda_k=\Lambda_k(\beta)=I_k(\beta\rho_1)+q_{1k}K_k(\beta\rho_1) \qquad (k=0,\,1,\,2,\,\cdots)\,, \tag{13}$$

wobei natürlich für das Endergebnis ganz belanglos ist, dass der Ausdruck $B_{10}C_{10}$ unbestimmt bleibt.

Fasst man die bisherigen Teilergebnisse (11), (10), (9)–(9.2) zusammen, so gelangt man zur folgenden fertigen Lösung unseres ersten Teilproblems:

$$u_i^{(1)}(\rho,\,\varphi,\,z)=\frac{1}{\pi}\sum_{k=0}^\infty\int_0^\infty\frac{\delta_{ik}(\beta)}{\Lambda_k(\beta)}V_{ik}(\beta\rho)\,d\beta\int_{-\infty}^\infty[f_{k1}(\gamma)\cos k\varphi+f_{k2}(\gamma)\sin k\varphi]\cos\beta(\gamma-z)d\gamma$$
$$(i=1,\,2,\,\cdots,\,n)\,. \tag{14}$$

Die in den Lösungsformeln (14) vorkommenden Grössen und Ausdrücke berechnen sich wie folgt: q_{ik} nach (7.1), $\Lambda_k(\beta)$ nach (13), $V_{ik}(\beta\rho)$ nach (9.1), $f_{k1}(\gamma)$ und $f_{k2}(\gamma)$ nach (12), $\delta_{1k}(\beta)=1$ und die anderen $\delta_{ik}(\beta)$ sind in (8) erklärt; I_k und K_k bedeuten modifizierte Besselsche Funktionen, mit Strich werden überall die Ableitungen nach ρ bezeichnet, sodass z. B.

$$I_k'(\beta\rho_n)=\left[\frac{d}{d\rho}I_k(\beta\rho)\right]_{\rho=\rho_n}\,.$$

§ 4. Die Bestimmung von $u_i^{(2)}(\rho,\,\varphi,\,z)$; $i=1,\,2,\,\cdots,\,n$

Nach dem, was im Abschnitt 2 gesagt wurde, geht es hier bloss um eine unwesentliche Abänderung der vorigen Aufgabe. Die gewünschte Lösung kann angenscheinlich direkt nach (14) ohne jede Rechnung aufgeschrieben werden, indem man in (14) die alten Symbole durch neue nach dem leicht verständlichen Schema

$$\left.\begin{array}{lllll} u_i^{(1)}(\rho, \varphi, z)\,, & \rho_i\,, & f(\varphi, z)\,, & h_i\,, & k_i' \\ u_{n+1-i}^{(2)}(\rho, \varphi, z)\,, & \rho_{n+2-i}\,, & F(\varphi, z)\,. & -h_{n+2-i}'\,, & -h_{n+2-i} \end{array}\right\} \tag{15}$$

ersetzt.

Dadurch erhält man

$$u_i^{(2)} = \frac{1}{\pi}\sum_{k=0}^{\infty}\int_0^{\infty}\frac{d_{ik}(\beta)}{L_k(\beta)}W_{ik}(\beta\rho)d\beta\int_{-\infty}^{\infty}[F_{k1}(\gamma)\cos k\varphi + F_{k2}(\gamma)\sin k\varphi]\cos\beta(\gamma - z)d\gamma$$

$$(i=1, 2, \cdots, n) \tag{16}$$

wobei die hier vorkommenden Abkürzungen folgende Bedeutung haben:

$$\left.\begin{array}{l} d_{1k}(\beta) = \dfrac{h_2}{h_2'}\cdot\dfrac{I_k'(\beta\rho_2) + r_{2k}K_k'(\beta\rho_2)}{K_k(\beta\rho_1)I_k'(\beta\rho_2) - I_k(\beta\rho_1)K_k'(\beta\rho_2)}d_{2k}(\beta)\,, \\ d_{i+1,k}(\beta) = \dfrac{h_{i+2}h_{i+3}\cdots h_n}{h_{i+2}'h_{i+3}'\cdots h_n'}\displaystyle\prod_{\nu=1}^{n-i-1}\dfrac{I_k'(\beta\rho_{n+1-\nu}) + r_{n+1-\nu,k}K_k'(\beta\rho_{n+1-\nu})}{I_k'(\beta\rho_{n+1-\nu}) + r_{n-\nu,k}K_k'(\beta\rho_{n+1-\nu})} \\ \qquad\qquad (i=1, 2, \cdots, n-2),\ d_{nk}(\beta) = 1;\ (k=0, 1, 2, \cdots) \end{array}\right\} \tag{16.1}$$

$$L_k(\beta) = I_k(\beta\rho_{n+1}) + r_{nk}K_k(\beta\rho_{n+1}) \qquad (k=0, 1, 2, \cdots) \tag{16.2}$$

$$W_{1k}(\beta\rho) = K_k(\beta\rho_i)I_k(\beta\rho) - I_k(\beta\rho_1)K_k(\beta\rho)\,, \qquad W_{ik}(\beta\rho) = I_k(\beta\rho) + r_{ik}K_k(\beta\rho)$$

$$(i=2, 3, \cdots, n;\ k=0, 1, 2, \cdots) \tag{16.3}$$

$$\left.\begin{array}{l} r_{2k} = r_{2k}(\beta) = -\dfrac{1}{\rho_2K_k'(\beta\rho_2)}\left\{\rho_2I_k'(\beta\rho_2) + \dfrac{h_2'}{-h_2'K_k(\beta\rho_2) + K_k'(\beta\rho_2)\left[1 + h_2\dfrac{K_k(\beta\rho_1)I_k(\beta\rho_2) - I_k(\beta\rho_1)K_k(\beta\rho_2)}{K_k(\beta\rho_1)I_k'(\beta\rho_2) - I_k(\beta\rho_1)K_k'(\beta\rho_2)}\right]}\right\}\,, \\ r_{ik} = r_{ik}(\beta) = \dfrac{1}{T_{ik}(\beta)}\left\{U_{ik}(\beta) - \dfrac{h_ih_i'}{\rho_i^2[S_{ik}(\beta) + r_{i-1,k}T_{ik}(\beta)]}\right\}\,. \\ \quad S_{ik}(\beta) = -I_k'(\beta\rho_i)K_k'(\beta\rho_i) - h_iI_k(\beta\rho_i)K_k'(\beta\rho_i) + h_i'I_k'(\beta\rho_i)K_k(\beta\rho_i)\,, \\ \quad T_{ik}(\beta) = -K_k'(\beta\rho_i)[K_k'(\beta\rho_i) + (h_i - h_i')K_k(\beta\rho_i)]\,, \\ \quad U_{ik}(\beta) = \dfrac{h_i'}{\rho_i} + I_k'(\beta\rho_i)[K_k'(\beta\rho_i) + (h_i - -h_i')K_k(\beta\rho_i)] \\ \qquad\qquad (i=3, 4, \cdots, n;\ k=0, 1, 2, \cdots) \end{array}\right\} \tag{16.4}$$

$$F_{01}(\gamma) = \frac{1}{2\pi}\int_0^{2\pi}(F(\alpha, \gamma)d\alpha\,, \qquad \begin{matrix}F_{k1}(\gamma)\\F_{k2}(\gamma)\end{matrix} = \frac{1}{\pi}\int^{2\pi}F(\alpha\gamma)\begin{matrix}\cos k\alpha\\ \sin k\alpha\end{matrix}d\alpha \qquad (k=1, 2, \cdots)\,. \tag{16.5}$$

§ 5. Die Lösung des ursprünglichen Problems (2)–(3.3)

Nach der Vorschrift (4) ergibt sich die gewünschte Lösung durch Summierung der beiden Teillösungen (14) und (16). Der Leser möge sich vom neuen direkt überzeugen, dass die so erhaltenen $u_i(\rho, \varphi, z)$ wirklich unsere ursprüngliche Aufgabe (2)–(3.3) befriedigen.

II. Stetige Aenderung der Temperatur und des Wärmeflusses

Das jetzige Problem unterscheidet sich von dem vorhergehenden nur in den Bedingungen (3.2), die jetzt durch die geläufigen Beziehungen

$$u_i = u_{i+1}\,, \qquad \lambda_i\frac{\partial u_i}{\partial\rho} = \lambda_{i+1}\frac{\partial u_{i+1}}{\partial\rho}(\rho = \rho_{i+1},\ 0 \leq \varphi \leq 2\pi,\ -\infty < z < +\infty;\ i=1, 2, \cdots, n-1) \tag{17}$$

zu ersetzen sind.

Die Lösung ergibt sich augenscheinlich aus dem Ergebnis des ersten Teiles durch den Grenzübergang

$$h_{i+1}\to+\infty\,,\qquad h'_{i+1}\to+\infty\,,\qquad \frac{h'_{i+1}}{h_{i+1}}=\frac{\lambda_i}{\lambda_{i+1}}\qquad (i=1,\,2,\,\cdots,\,n-1)\,,\tag{18}$$

wenn man wie üblich unter λ_i $(i=1,\,2,\,\cdots,\,n)$ die Wärmeleitfähigkeit der i-ten Körperschicht versteht.

Nach einiger Rechenarbeit kommt man so zum Ergebnis

$$\begin{aligned}u_i(\rho,\,\varphi,\,z)=&\frac{1}{\pi}\sum_{k=0}^{\infty}\int_0^\infty\frac{\delta_{ik}(\beta)}{\Lambda_k(\beta)}V_{ik}(\beta\rho)d\beta\int_{-\infty}^{\infty}[f_{k1}(\gamma)\cos k\varphi+f_{k2}(\gamma)\sin k\varphi]\cos\beta(\gamma-z)d\gamma\\&+\frac{1}{\pi}\sum_{k=0}^{\infty}\int_0^\infty\frac{d_{ik}(\beta)}{L_{1k}(\beta)}W_{ik}(\beta\rho)d\beta\int_{-\infty}^{\infty}[F_{k1}(\gamma)\cos k\varphi+F_{k2}(\gamma)\sin k\varphi]\cos\beta(\gamma-z)d\gamma\\&\qquad\qquad(i=1,\,2,,\,\cdots,\,n);\end{aligned}\tag{19}$$

$$\left.\begin{aligned}&\delta_{1k}(\beta)=1\,,\qquad \delta_{i+1,k}(\beta)=\frac{\lambda_1}{\lambda_{i+1}}\prod_{\nu=1}^{i}\frac{I_k'(\beta\rho_{\nu+1})+q_{\nu k}(\beta)K_k'(\beta\rho_{\nu+1})}{I_k'(\beta\rho_{\nu+1})+q_{\nu+1,k}(\beta)K_k'(\beta\rho_{\nu+1})}\\&\qquad\qquad\qquad(i=1,\,2,\,\cdots,\,n-2)\,,\\&\delta_{nk}(\beta)=\kappa_n\frac{I_k'(\beta\rho_n)+q_{n-1,k}(\beta)K_k'(\beta\rho_n)}{K_k(\beta\rho_{n+1})I_k'(\beta\rho_n)-I_k(\beta\rho_{n+1})K_k'(\beta\rho_n)}\delta_{n-1,k}(\beta)\\&\Lambda_k(\beta)=I_k(\beta\rho_1)+q_{1k}(\beta)K_k(\beta\rho_1)\,,\qquad V_{ik}(\beta\rho)=I_k(\beta\rho)+q_{ik}(\beta)K_k(\beta\rho)\\&V_{nk}(\beta\rho)=K_k(\beta\rho_{n+1})I_k(\beta\rho)-I_k(\beta\rho_{n+1})K_k(\beta\rho)\qquad(i=1,\,2,\,\cdots,\,n-1)\\&q_{ik}(\beta)=\frac{1}{N_{i+1,k}(\beta)}\left\{-P_{i+1,k}(\beta)+\frac{\kappa_{i+1}}{\rho_{i+1}^2[M_{i+1,k}(\beta)-q_{i+1,k}(\beta)N_{i+1,k}(\beta)]}\right\}\,,\\&\qquad M_{i+1,k}(\beta)=\kappa_{i+1}I_k(\beta\rho_{i+1})K_k'(\beta\rho_{i+1})-I_k'(\beta\rho_{i+1})K_k(\beta\rho_{i+1})\\&\qquad N_{i+1,k}(\beta)=(1-\kappa_{i+1})K_k(\beta\rho_{i+1})K_k'(\beta\rho_{i+1})\\&\qquad P_{i+1,k}(\beta)=-\frac{1}{\rho_{i+1}}+(1-\kappa_{i+1})I_k'(\beta\rho_{i+1})K_k(\beta\rho_{i+1})\qquad(i=1,\,2,\,\cdots,\,n-2)\,,\\&q_{n-1,k}(\beta)=-\frac{1}{\rho_nK_k'(\beta\rho_n)}\Bigg[\rho_nI_k'(\beta\rho_n)\\&\qquad+\frac{1}{-K_k(\beta\rho_n)+\kappa_nK_k'(\beta\rho_n)\dfrac{K_k(\beta\rho_{n+1})I_k(\beta\rho_n)-I_k(\beta\rho_{n-1})K_k(\beta\rho_n)}{K_k(\beta\rho_{n+1})I_k'(\beta\rho_n)-I_k(\beta\rho_{n+1})K_k'(\beta\rho_n)}}\Bigg]\\&\kappa_{i+1}=\frac{\lambda_i}{\lambda_{i+1}}\qquad(i=1,\,2,\,\cdots,\,n-1)\end{aligned}\right\}\tag{19.1}$$

$$\left.\begin{aligned}&d_{1k}(\beta)=\frac{1}{\kappa_2}\cdot\frac{I_k'(\beta\rho_2)+r_{2k}(\beta)K_k'(\beta\rho_2)}{K_k(\beta\rho_1)I_k'(\beta\rho_2)-I_k(\beta\rho_1)K_k'(\beta\rho_2)}d_{2k}(\beta)\,,\qquad d_{nk}(\beta)=1\,,\\&d_{i+1,k}(\beta)=\frac{\lambda_n}{\lambda_{i+1}}\prod_{\nu=1}^{n-i-1}\frac{I_k'(\beta\rho_{n+1-\nu})+r_{n+1-\nu,k}(\beta)K_k'(\beta\rho_{n+1-\nu})}{I_k'(\beta\rho_{n+1-\nu})+r_{n-\nu,k}(\beta)K_k'(\beta\rho_{n+1-\nu})}\\&\qquad\qquad\qquad(i=1,\,2,\,\cdots,\,n-2)\\&L_k(\beta)=I_k(\beta\rho_{n+1})+r_{nk}(\beta)K_k(\beta\rho_{n+1})\\&W_{1k}(\beta\rho)=K_k(\beta\rho_1)I_k(\beta\rho)-I_k(\beta\rho_1)K_k(\beta\rho)\,,\qquad W_{ik}(\beta\rho)=I_k(\beta\rho)+r_{ik}(\beta)K_k(\beta\rho)\\&\qquad\qquad\qquad(i=2,\,3,\,\cdots,\,n)\end{aligned}\right|$$

$$\left.\begin{aligned}
r_{2k}(\beta) &= -\frac{1}{\rho_2 K_k'(\beta\rho_2)}\Bigg[\rho_2 I_k'(\beta\rho_2) \\
&\quad + \frac{\kappa_2}{-\kappa_2 K_k(\beta\rho_2) + K_k'(\beta\rho_2)\dfrac{K_k(\beta\rho_1)I_k(\beta\rho_2) - I_k(\beta\rho_1)K_k(\beta\rho_2)}{K_k(\beta\rho_1)I_k'(\beta\rho_2) - I_k(\beta\rho_1)K_k'(\beta\rho_2)}}\Bigg], \\
r_{ik}(\beta) &= \frac{1}{T_{ik}(\beta)}\left\{-U_{ik}(\beta) + \frac{\kappa_i}{\rho_i^2[S_{ik}(\beta) - r_{i-1,k}(\beta)T_{ik}(\beta)]}\right\}, \\
S_{ik}(\beta) &= -I_k(\beta\rho_i)K_k'(\beta\rho_i) + \kappa_i I_k'(\beta\rho_i)K_k(\beta\rho_i) \\
T_{ik}(\beta) &= (1-\kappa_i)K_k(\beta\rho_i)K_k'(\beta\rho_i) \\
U_{ik}(\beta) &= \frac{\kappa_i}{\rho_i} + (1-\kappa_i)I_k'(\beta\rho_i)K_k(\beta\rho_i) \qquad (i=3, 4, \cdots n)\,.
\end{aligned}\right\} \quad (19.2)$$

Was endlich die in der Lösung (19) noch vorkommenden Fourierkoeffizienten $f_{k1}(\gamma)$, $f_{k2}(\gamma)$, $F_{k1}(\gamma)$ und $F_{k2}(\gamma)$ betrifft, so behalten diese ihre früheren Werte (12) und (16.5).

Errata

On the Viscosity of Irradiated Polymers I

By Mitio INOKUTI

J. Phys. Soc. Japan **14** (1959) 79

Page	Line		Should be read
83	19 Eq. (42)	$\frac{\alpha(\alpha+1)(\alpha+2)(\alpha+3)}{12}\zeta^4$	$\frac{\alpha(\alpha+1)(\alpha+2)(\alpha+3)}{48}\zeta^4$
83	22 Eq. (44)	$\frac{2^\alpha\alpha(\alpha+1)(\alpha+2)(2\alpha+5)}{6}\zeta^4$	$\frac{2^\alpha\alpha(\alpha+1)(\alpha+2)(5\alpha+11)}{24}\zeta^4$

Short Notes

This section is intended to secure prompt publication of important discoveries in physics. The reports should not exceed 800 words in length. A figure of size 7 cm × 7 cm will be counted as 150 words.

J. Phys. Soc. Japan **14** (1959) 966

Three-Level Maser Detector for Ultramicrowaves

By Koichi SHIMODA

Deparment of Physics, Faculty of Science, University of Tokyo

(Received May 12, 1959)

Conventional electronic detectors such as silicon diodes lose their sensitivity in the millimeter and sub-millimeter ranges. A device which was proposed by the author as a three-level maser detector* is described in this note.

Consider a system of molecules which have energy levels as shown in Fig. 1. Here a transition between levels E_2 and E_3 falls in the conventional microwave range where a good sensitivity is feasible. When the other transition between levels E_1 and either E_2 or E_3 is allowed, the system can be used to detect high frequency waves written as ν_p or ν_p' in Fig. 1.

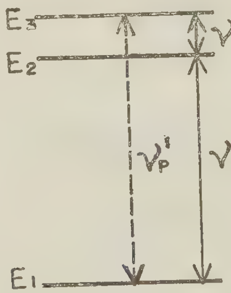

Fig. 1. Three levels.

Absorption of ultra-microwaves at the frequency ν_p or ν_p' changes the population of levels and results in the increase or decrease of microwave absorption at the frequency ν_0. The system is similar to that which has been studied as a three-level maser spectrometer[1] except that all transitions lie in much higher frequencies in this case.

Because the gas absorption coefficient is very large at higher frequencies, the ultra-microwaves at the frequency ν_p will be appreciably absorbed by a small amount of gas. Increase of population of the level E_2 is given by

$$\Delta n_2 = \frac{\tau}{Vh\nu_p}\Delta P\,, \tag{1}$$

where ΔP is the absorbed ultra-microwave power, V the volume of the gas, and $\tau \approx (2\pi\,\Delta\nu_p)^{-1}$ the time of relaxation. The microwave gas absorption coefficient at the frequency ν_0 is given by

$$\alpha_0 = (n_2 - n_3)\frac{8\pi^2\nu_0}{3hc}\frac{|\mu_0|^2}{\Delta\nu_0}\,, \tag{2}$$

where μ_0 is the dipole matrix element, and $\Delta\nu_0$ the half-width of the line. The change of α_0 when the ultra-microwave power is absorbed by ΔP is

$$\Delta\alpha_0 = \Delta n_2\frac{8\pi^2\nu_0}{3hc}\frac{|\mu_0|^2}{\Delta\nu_0} = \frac{\Delta P}{V}\frac{8\pi^2\nu_0\tau}{3h^2c\nu_p}\frac{|\mu_0|^2}{\Delta\nu_0}\,. \tag{3}$$

Then the absorbed ultra-microwave power is expressed as

$$\Delta P = \frac{3h^2c}{4\pi}\frac{\nu_p}{\nu_0}\frac{\Delta\nu_0\Delta\nu_p}{|\mu_0|^2}V\Delta\alpha_0\,. \tag{4}$$

It may be noted that this equation does not include n_2 nor n_3, and hence for the sensitive detection one choose molecules which have large $|\mu_0|$ and considerable absorption coefficient at the frequency ν_p.

Taking values as $\Delta\nu_0 = \Delta\nu_p = 100$ kc/sec, $|\mu_0|^2=$ D^2, Eq. (4) becomes

$$\Delta P = 10^{-4}V\frac{\nu_p}{\nu_0}\Delta\alpha_0 \text{ watts.}$$

A typical microwave spectrometer can observe the change of absorption as small as 10^{-8} cm^{-1}. Thus the minimum detectable power at $\lambda_p = \frac{c}{\nu_p} = 0.4$ mm is

$$\frac{\Delta P}{V} = 3 \times 10^{-11} \text{ W/cm}^3\,.$$

A long waveguide cell should not be used, since the ultra-microwave is absorbed in a short length of the path. A compromise is the use of a cavity cell tuned to the frequency ν_0, in which the ultra-microwave is radiated. With the cell volume of 10 cm^3 the ultra-microwave power of 3×10^{-10} watts might be detected.

It may be impossible to reduce the line-width of the ultra-microwave line to 100 kc/sec and may perhaps be some ten times larger. Nevertheless the three level maser detector is expected to be more sensitive than crystal detectors, minimum detectable power of which is estimated as 10^{-6} watt at the wavelength of 0.4 mm.

---

* This proposal was given at the annual meeting of the Physical Society of Japan in October 1958.

1) K. Shimoda: J. Phys. Soc. Japan **14** (1959) 954.

J. Phys. Soc. Japan **14** (1959) 967~968

Polaron Mobility in Potassium Bromide

By Masami Onuki and Hajimu Kawamura

Department of Applied Physics, Osaka City University, Osaka

(Received May 19, 1959)

The reliable value of electron mobility in alkali halide crystal have been desired in connection with the polaron problem.[1][2] We made experiment on the KBr crystal of high purity obtained by the recrystalization technique. The conductivity was afforded by illuminating the additive coloured crystal with 500 watts tungsten lamp through water filter. For the measurment we adopted the ac method after Macdonald,[3] in order to avoid the space charge effect, the frequency being 330 cycles/sec. The detecting device is composed of pre-amplifier, difference amplifier, main band pass amplifier, dc detector and cathode ray oscilloscope. The input impedance of the pre-amplifier was about 80 $M\Omega$ for 330 cycles/sec, the input capacitance being eliminated by feed back system. The push-pull output of about 100 volts from an oscillator is supplied to each current electrode. The relative amplitude and phase are adjusted so that the voltage at two Hall electrodes are just balanced when the magnetic field is absent. The temperature range was from 85°K to room temperature. The maximum intensity of the magnetic field was 4500 oersted.

Since the impedance between Hall electrodes which is about $1\sim3\times10^9\Omega$ under illumination at room temperature is much higher than the input impedance, the detected Hall voltage is reduced by the factor Z_{cry}/Z_{in}, where Z_{in} and Z_{cry} are the input and crystal impedance respectively. Hence it is necessary to measure Z_{cry} as well as appearent Hall voltage V'_H in order to get the true Hall voltage V_H. Fig. 1 shows the photoconductivity σ which is the reciprocal of Z_{cry}, V'_H and V_H in arbitrary scale as the function of temperature. The mobility μ is given by $(V_H/t)/(KV_l/l)=\mu H\cdot10^{-8}$, where l is the length of the specimen, t the width, V_l its applied voltge and K the numerical factor due to the non-uniformity of electric field near the Hall electrode. We determined this value to be 0.83 by mapping the pattern of the electric field by making use of conducting sheet.

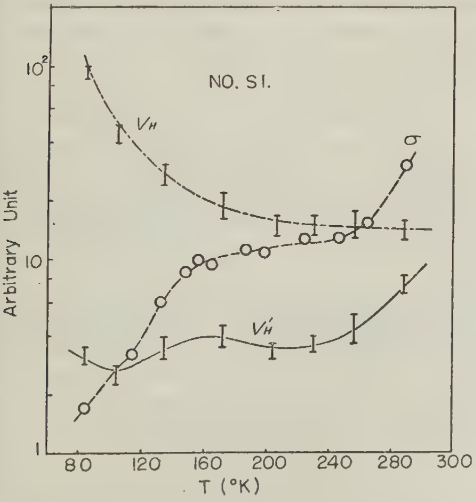

Fig. 1. V'_H, σ and V_H *vs* temperature, the ordinate being arbitrary scale.

The average values of μ for about ten specimens are plotted as the function of temperature in Fig. 2.

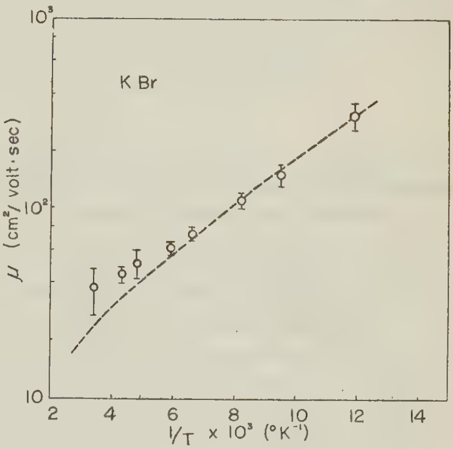

Fig. 2. Mobility in KBr as a function of temperature. The dotted line shows the theoretical curve $\mu=A$ $(\exp\Theta/T-1)$, with $A=16.4$ cm²/volt sec and $\Theta=255$°K.

These points better fit to $\mu=A$ $(\exp\Theta/T-1)$ rather than $\mu=BT^{-n}$. The best fit was obtained for $A=16.4$ cm²/volt sec and $\Theta=255$°K. According to Low and Pines,[1] μ is given by

$$\mu=\frac{1}{2\alpha\omega}\,\frac{e}{m^*}\left(\frac{m^*}{m_p}\right)^3 f(\alpha)\cdot(\exp\Theta/T-1),\ \Theta>T,$$

$$m_p=m^*\left(1+\frac{\alpha}{6}\right),\ \alpha=\frac{e^2}{\hbar}\left(\frac{m}{2\hbar\,\omega}\right)^{\frac{1}{2}}\frac{\varepsilon_s-\varepsilon_0}{\varepsilon_s\varepsilon_0}\left(\frac{m^*}{m}\right)^{\frac{1}{2}},$$

where m^* and m_p are the effective masses of conduction electron and polaron respectively. From the measured value of A we have $m_p=0.33m$, $m^*=0.23m$ and $\alpha=2.65$, where m is the free electron mass. The Debye temperature associated with the longitudinal optical vibration Θ is calculated from Reststrahl frequency ω_t by making use of the relation $k\Theta=\sqrt{\varepsilon_s/\varepsilon_0}\ \hbar\omega_t$ where ε_s and ε_0 are the static and optical dielectric constant respectively. We get $\Theta=246$°K for KBr, which is to be compared with the experimental value of 255°K. From this work we can conclude that the interaction of electron with the optical phonon is more dominant than with the acoustical phonon as well as with the impurity centers above 80°K. The acoustical mode may become effective below 50°K, if the deformation potential of KBr is the same order with that of KCl which was calculated by one of us.[4)]

It is our pleasure to thank Mr. H. Okura who furnished specimens and gave many valuable discussions.

References

1) F. E. Low and D. Pines: Phys. Rev. **98** (1955) 414.
2) H. Froelich: Advances in Physics **3** (1954) 325.
3) J. R. Macdonald and J. E. Robinson: Phys. Rev. **95** (1954) 44.
4) H. Kawamura: J. Phys. Chem. Solids **5** (1958) 256.

J. PHYS. SOC. JAPAN **14** (1959) 968

Connection Formulas for WKB Solutions with Two Turning Points

By Haruo MORIGUCHI

Department of Physics, Faculty of Liberal Arts, Shizuoka University, Shizuoka

(Received April 27, 1959)

In this note we shall give the connection formulas for the WKB solutions of a differential eqation

$$\frac{d^2y}{dx^2}+f(x)y=0\,, \tag{1}$$

where $f(x)$ is a smooth function of x which satisfies the following conditions:

$$f(a)=f(-a)=0\,, \tag{2}$$

$$f(x)<0 \qquad \text{for } x<-a \text{ and } x>a\,, \tag{3}$$

and for $b<x<c$, $f(x)$ can be approximated as

$$f(x)\sim\nu+\frac{1}{2}-\frac{x^2}{4}\,, \tag{4}$$

where

$$a=2(\nu+\tfrac{1}{2})^{1/2}\,, \qquad \nu\geqq-\tfrac{1}{2}\,,$$

and

$$b\ll-a\,, \qquad c\gg a\,.$$

Under these conditions, let us write the WKB approximate solutions for $|x|\gg a$ as

$$y\sim y_{\substack{1\\2}}=|f(x)|^{-1/4}\exp\left(\pm\int_x^{-a}\sqrt{|f(x)|}dx\right) \quad (x\ll-a)\,, \tag{5}$$

and

$$y\sim y_{\substack{3\\4}}=|f(x)|^{-1/4}\exp\left(\pm\int_a^{x}\sqrt{|f(x)|}dx\right) \quad (x\gg a) \tag{6}$$

Then we have the connection formulas

$$y_1\leftrightarrow-\cos\nu\pi\, y_3-\sqrt{\frac{\pi}{2}}\frac{\sin\nu\pi}{\Gamma(\nu+1)}(\nu+\tfrac{1}{2})^{\nu+1/2}e^{-\nu-1/2}y_4\,, \tag{7}$$

$$y_2\leftrightarrow\cos\nu\pi\, y_4-\sqrt{\frac{2}{\pi}}\sin\nu\pi\,\Gamma(\nu+1)(\nu+\tfrac{1}{2})^{-\nu-1/2}e^{\nu+1/2}y_3, \tag{8}$$

$$y_3\leftrightarrow-\cos\nu\pi\, y_1-\sqrt{\frac{2}{\pi}}\frac{\sin\nu\pi}{\Gamma(\nu+1)}(\nu+\tfrac{1}{2})^{\nu+1/2}e^{-\nu-1/2}y_2\,, \tag{9}$$

and

$$y_4\leftrightarrow\cos\nu\pi\, y_2-\sqrt{\frac{2}{\pi}}\sin\nu\pi\,\Gamma(\nu+1)(\nu+\tfrac{1}{2})^{-\nu-1/2}e^{\nu+1/2}y_1 \tag{10}$$

For the deduction of these formulas, let us consider an approximate solution

$$y\sim y_0=D_\nu(x) \tag{11}$$

in the region $b<x<c$. Here $D_\nu(x)$ is the parabolic cylinder function, for which we have the asymptotic expression

$$D_\nu(x)\sim\begin{cases} x^\nu\exp(-x^2/4) & (x\gg a)\\ \cos\nu\pi\,|x|^\nu\exp(-x^2/4) & \\ \quad -\sqrt{2/\pi}\,\Gamma(\nu+1)\sin\nu\pi\,|x|^{-\nu-1}\exp(x^2/4)\,. & (x\ll-a)\end{cases} \tag{12}$$

On the other hand, substituting (4) into (5) and (6) and expanding them, we have, for large values of $|x|$,

$$\begin{cases} y_1\sim\sqrt{2}(\nu+\tfrac{1}{2})^{\nu/2+1/4}e^{-\nu/2-1/4}|x|^{-\nu-1}\exp(x^2/4) \\ \hfill (x\ll-a) \\ y_2\sim\sqrt{2}(\nu+\tfrac{1}{2})^{-\nu/2-1/4}e^{\nu/2+1/4}|x|^{\nu}\exp(-x^2/4)\,, \end{cases}$$

and (13)

$$\begin{cases} y_3\sim\sqrt{2}(\nu+\tfrac{1}{2})^{\nu/2+1/4}e^{-\nu/2-1/4}x^{-\nu-1}\exp(x^2/4) \\ \hfill (x\gg a) \\ y_4\sim\sqrt{2}(\nu+\tfrac{1}{2})^{-\nu/2-1/4}e^{\nu/2+1/4}x^{\nu}\exp(-x^2/4)\,. \end{cases}$$

Now (12) and (13) should be the approximate solutions of the same order of accuracy for $b<x\ll-a$ or $a\ll x<c$. Hence, comparing them with each other we have the connection formula (10), and inverting the role of the sign of x we have (8). Other formulas (7) and (9) can be derived from (8) and (10). When ν is large, we have, for the coefficients in the expressions (7)—(10),

$$\sqrt{\frac{2}{\pi}}\Gamma(\nu+1)\sin\nu\pi(\nu+\tfrac{1}{2})^{-\nu-1/2}e^{\nu+1/2}\sim2\sin\nu\pi\,. \tag{14}$$

The corresponding formulas, in which the coefficients have such a simple asymptotic form can also be obtained by repeated use of the usual connection formula at the linear turning points a and $-a$.

More rigorous and extended discussions on the asymptotic solutions about turning points will be shortly published.

J. Phys. Soc. Japan **14** (1959) 969

F-centers in LiCl Crystals

By Kuniya FUKUDA, Hiroaki MATSUMOTO
and Akizo OKUDA*

*Department of Physics, Faculty of Science,
Kyoto University*

(Received May 23, 1959)

Optical and spin resonance absorptions were measured on the LiCl crystals irradiated by X- or γ-ray at room temperature.

In Fig. 1 are shown the optical absorption curves of the colored crystals; curve I shows the absorption of the crystal irradiated by X-ray at room temperature and curve II that obtained after the colored crystal showing curve I was bleached by F-light. LiCl crystals are so much hygroscopic that the optical measurements are very difficult. In our experiments the crystal could be kept transparent throughout the period of X-ray irradiation and optical measurements by holding it in a vacuum vessel, which has two quartz windows for optical measurements and one Al-foil window for X-ray irradiation; the cloudiness on the crystal surface caused by moisture could be removed by heating slowly the crystal during evacuation of the vessel. In curve I there exists no appreciable absorption except the absorption of F-center at 395 mμ, which has the half-width of about 0.65 eV. On the other hand, Ottmer1) measured the optical absorption of the X-ray irradiated crystal by immersing it into the saturated solution of LiCl and found out two small humps on the long wavelength side of F-absorption. These very small absorption bands at 580 and 650 mμ are tentatively assigned to R_2 and M centers respectively, but further investigations are necessary for conclusive assignments.

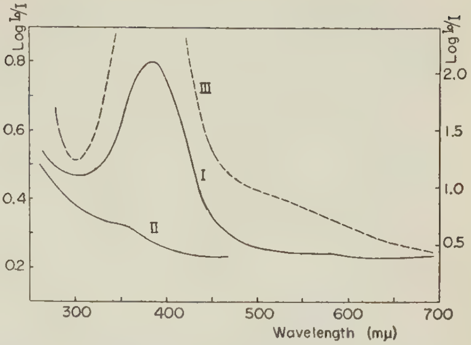

Fig. 1. The optical absorption curves of colored LiCl crystals. Curve I: after 5 hrs irradiation of X-ray (30 kV, 20 mA), curve-II: after F-light bleaching of the sample showing curve-I, curve-III: after 100 hrs irradiation of γ-ray (dosage: 2×10^5 r/hr).

Electron spin resonance measurements were carried out on the crystal irradiated by Co^{60} γ-ray at room temperature, the optical absorption of which is shown as curve III in Fig. 1. In this case the crystal shows also only F-absorption; and the absorption below 300 mμ results from the polyvinyl coating film, which protects the crystal from moisture for optical measurements. The density of F-centers is estimated as $10^{18}\mathrm{cm}^{-3}$ in the order of magnitude from Smakula's formula, provided that for LiCl the refractive index and the oscillator strength of F-center are approximated as 1.5 and unity respectively. The derivative curve of the spin resonance absorption was recorded, which centered at the external magnetic field $H=8{,}515\pm5$ gauss for the microwave frequency of 23,804 MCPS and had the peak to peak width of 50 gauss. Thus, for F-center of LiCl the g-value is 1.997 ± 0.002 and the half-width 60 gauss because of the Gaussian shape of absorption. This value of g is about the same as that of F-center in KCl2) and the half-width of 60 gauss considerably smaller than that of 90 gauss predicted by Kittel3). He calculated the widths of F-center resonance for various alkali-halides by making appropriate extrapolations from the results of KCl F-center, but it is likely that the discrepancy in the above extent, though it is smaller for LiF F-center3),4), occurs between the observed and the predicted width by his method based on the L.C.A.O. model of F-center wave function*. The half-width value of 60 gauss leads to the density of F-center electron $|\psi(\mathrm{Li})|^2=0.95\times10^{23}\mathrm{cm}^{-3}$ at the nucleus of a nearest neighbour Li ion, because the contributions from the nuclei of the next nearest neighbour Cl ions to the width may be neglected.

If the L.C.A.O. type wave function is assumed for LiCl F-center, the above value of F-electron density gives $\xi=0.36$ in $|\psi(\mathrm{Li})|^2=\frac{1}{6}\xi|\psi_{\mathrm{Li}}(0)|^2$ for LiCl in contrast to $\xi=0.6$ for KCl2), where $|\psi_{\mathrm{Li}}(0)|^2$ is the density of 2s electron at the nucleus for free atom.

References

1) R. Ottmer: Z. Phys. **46** (1928) 798.
2) A. F. Kip, C. Kittel, R. A. Levy and A. M. Portis: Phys. Rev. **91** (1953) 1066.
3) C. Kittel: *Defects in Crystalline Solids*, Report of 1954 Bristol Conference (Phys. Soc. London) p. 33.
4) N. M. Lord: Phys. Rev. **105** (1957) 756.

---

[*] Department of Mathematics and Physics, Faculty of Science and Engineering, Ritsumeikan University.

[*] The plausible errors introduced by this type of wave function into the calculation of hyperfine interaction energy were discussed by Gourary and Adrian (Phys. Rev. **105** (1957) 1180).

J. PHYS. SOC. JAPAN **14** (1959) 970~971

Observation of a Peculiar Type of Domain Structure of Triclinic Tungsten Trioxide

By Sigetosi TANISAKI

Faculty of Literature and Science, Yamaguchi University

(Received March 23, 1959)

Triclinic tungsten trioxide has usually the domain structure whose walls are (010) twin planes as shown in the previous note[1]. In the monoclinic-triclinic phase transition, (110) domain walls observed in the monoclinic phase change itself into the irregular boundaries rather than the domain walls in the triclinic phase, and each part of the crystal divided by the boundaries has a regular (010) domain structure which is sensitive to the external stress as well as in the monoclinic phase[2].

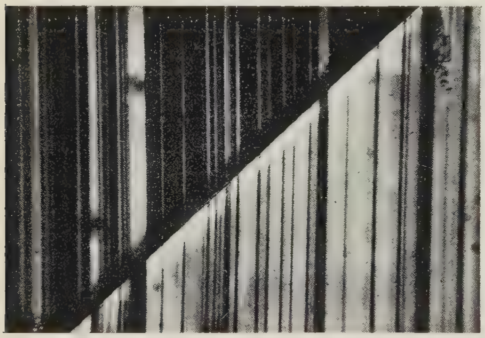

Fig. 1. Domain structure obtained by the pressure along *b*-axis.

The appearance of a peculiar type of domain structure under the pressure along *b*-axis is observed between crossed nicols (Fig. 1). In Fig. 1 the left upper part is the original (010) domains and the right lower part is the new domains induced by the stress, and the angle between a domain wall of the upper part and that of the lower part is about 178°. The boundary between upper and lower parts is not vertical to *c* surface of the crystal but inclined to it. Apparently the domain structure of this type is very similar to that obtained by the pressure along *c* axis in the monoclinic phase (Photo. 4 in the previous paper[2]) except the inclination of the boundary to the crystal surface, and similarly as in the previous paper it can be explained by taking into consideration the reversal of *a* and *b* axes by the pressure on either side of the boundary and the condition of continuity that the crystal must have the least strain at the boundary. It is supposed that the orientation of the crystallographic axes of each domain is as shown in Fig. 2 and the boundary plane is very close to $(\bar{6}61)$ and $(66\bar{1})$, or $(\bar{6}61)'$ and $(661)'$ for either side, where indices with a prime are used for the planes of lower part. Then the peculiar domain pattern observed between crossed nicols which is caused by the difference of the extinction position of each domain can be easily understood from this orientation of the crystallographic axes. The angles between (010) walls of the upper domains and (100) walls of the lower domains are calculated to be 178°16′ for the boundary of $(\bar{6}61)$ and $(\bar{6}61)'$ and 178°20′ for $(66\bar{1})$ and $(661)'$ from the lattice constants of the triclinic phase ($a=7.30$Å, $b=7.52$Å, $c=7.69$Å, $\alpha=88°50'$, $\beta=90°55'$, $\gamma=90°56'$)[1]. Though there is a difference of angle 5′ between them, the coincidence of these values with the measured one is satisfactory. In the side view of the crystal, if the boundary plane is assumed to be $(\bar{6}61)$ etc. themselves, l and l' in Fig. 2 (b) are corresponding lengths at the boundary on either side of it, whose values are calculated to be 46.59_9Å and 46.59_8Å respectively, and the calculated value of the angle between *a* axis and the direction of l is 81°54′ whose measured value is about 81°. The small difference between these values shows that the boundary is not $(\bar{6}61)$ etc. themselves but very close to them. Of course the fitness at the boundary is not perfect and there must be a strain in the crystal. The supposition for the orientation of the crystallographic axes of each domain is ascertained by taking X-ray rotational photographs of either side of the boundary.

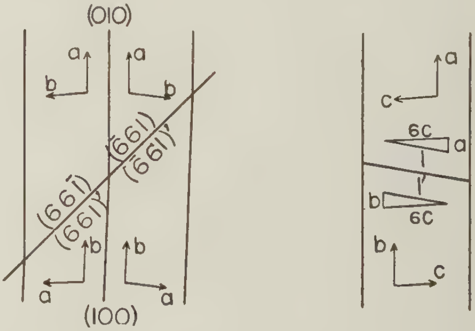

(a) (b)

Fig. 2. (a) top and (b) side views of supposed domain structure.

The (100) domain structure induced by the stress does not seem to be stable in the triclinic phase and the change to the (010) domain structure followed by a gradual displacement of the boundary takes place below the transition temperature to the monoclinic phase when heating up the crystal. In other words the orientation of the crystal axes reversed by the stress is not maintained in transforming from the triclinic phase to the monoclinic phase, but recovers the original orientation before the phase transition takes place.

The author wishes to thank Prof. K. Tanaka for his continual encouragement. This work was supported in part by the Grant in Aid for the Fundamental Scientific Research from the Ministry of Education.

References

1) S. Tanisaki: J. Phys. Soc. Japan **14** (1959) 680.
2) S. Tanisaki: J. Phys. Soc. Japan **13** (1958) 363.

J. Phys. Soc. Japan **14** (1959) 971

Dielectric Property of Triglycine Sulfate Single Crystal at 9000 Mc/s Region

By Atsuo NISHIOKA
Electrical Communication Laboratoyy, Musashino, Tokyo,
and Minoru TAKEUCHI
Fuji Electric Machine Manufacturing Company, Ltd., Tokyo

(Received May 28, 1959)

Ferroelectricity of triglycine sulfate was found by Matthias et al,[1] and studied in detail by Hoshino,[2] Kiyasu,[3] and Toyota,[4] but its dielectric property in the microwave region is not yet reported. Since it has been suggested that the ferroelectricity of this crystal may be contributed from the hydrogen bond, it is interesting to study how the hydorogen bond affect the dielectric property of this crystal at the microwave frequencies, and to compare with that of some other hydrogen-bonded crystals like rochelle salt, which had been studied in the microwave region by Akao et al.[5]

Firsty the dielectric constant, ε, and loss tangent, tan δ, were measured at room temperature in the ferroelectric b-axis by the standing wave method at 9600 Mc/s; $\varepsilon_b=19.7\pm0.2$ and tan $\delta=0.043\pm0.002$. This value of dielectric constant seems to be relatively high, compared with that of low frequency value, e.g., $\varepsilon_b=35$ at 10 kc/s measured by Hoshino et al,[2] and the medium value of tan δ suggest that the dielectric relaxation process is effective in the microwave region.

Then, we have measured the temperature dependence of the dielectric property of thin plate crystals by the cavity perturbation method, using H_{111} mode. A circular disk of 2.8 mm in diameter and 0.18 mm in thickns was suspended by a small Teflon rod at the center of H_{111} cavity with its ab-plane parallel to the high frequency electric field. Because the value of above quoted dielectric constant and the dimensions of the specimen were near the limit of the approximation of the cavity perturbation method, it was difficult to estimate the accurate value of the dielectric constant, and thus we show the temperature dependence of the observed frequency shift due to the insertion of crystal into the cavity above and below the Curie point, in place of the dielectric constant, in Fig. 1. The reduced frequency shift refered to 21°C which is purely contributed from the crystal, show the marked anomaly in the b-axis at 47°C, the Curie point, but no anomaly in the a-axis. These tendency is parallel to that observed at low frequency by Hoshino,[2] and therefore, we may suppose that the dielectric anomaly of triglycine sulfate crystal does not disappear in the microwave frequency, and is more sharp than that of rochelle salt at 10,000 Mc/s,[5] and so it would be necessary to cover wide frequency range extending to the shorter wave length, to clarify the mechanism of the dielectric relaxation of this crystal.

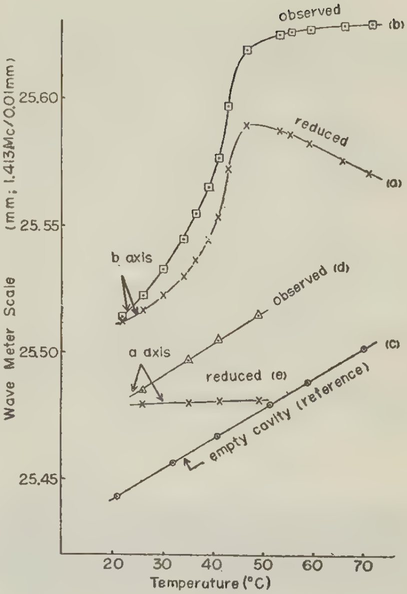

Fig. 1. Obserued frequency change of H_{111} cavity with temperature Curves (*a*) and (*e*) show values corrected for thermal expamsion of the cavity.

References

1) B. T. Matthias, C. E. Miller, and J. P. Remeika: Phys. Rev. **104** (1956) 849.
2) S. Hoshino, T. Mitsui, F. Jona and R. Pepinsky: Phys. Rev. **107** (1957) 1255.
3) Kiyasu, Z., K. Husimi and K. Kataoka: J. Phys. Soc. Japan **13** (1958) 661.
4) H. Toyota: J. Phys. Soc. Japan **14** (1959) 376.
5) H. Akao and T. Sasaki: J. Chem. Phys. **23** (1955) 2210.

J. Phys. Soc. Japan **14** (1959) 972

NMR Second Moment of a Radical under the Restricted Rotation

By Akira Miyake, Riichirô Chûjô
Faculty of Liberal Arts and Science, Shizuoka University, Shizuoka
and Hatsuko Adachi
Fujieda-Nishi High School, Shizuoka Prefecture

(Received May 25, 1959)

As we can assume the rotation of the side chain group, *e.g.* CH_3 radical, in the polymer is caused rapidly at higher temperatures under the restricting potential

$$V(\varphi)=\frac{u}{2}(1-\cos\varphi)+\frac{v}{2}(1-\cos 3\varphi)\ , \tag{1}$$

so we may have the second moment of NMR due to the group, according to Gutowsky *et al.*,1)

$$\varDelta H_2{}^2=3\hbar^2\gamma^2 I(I+1)\frac{1}{N}\sum_j\sum_k r_{jk}{}^{-6}\langle P_2(\cos\theta_{jk})^2\rangle \tag{2}$$

$$\langle P_2(\cos\theta_{jk})^2\rangle=\left\langle\left[\int_{-\pi}^{\pi}P_2(\cos\theta_{jk})\exp\{-V(\varphi)/kT\}d\varphi\Big/\int_{-\pi}^{\pi}\exp\{-V(\varphi)/kT\}d\varphi\right]^2\right\rangle_{\text{isotropic mean}}, \tag{3}$$

where

$$\begin{aligned}P_2(\cos\theta_{jk})=&P_2(\cos\theta')P_2(\cos\gamma_{jk})\\&-\frac{1}{3}P_2{}^1(\cos\theta')P_2{}^1(\cos\gamma_{jk})\cos(\varphi-\varphi_{jk}')\\&+\frac{1}{12}P_2{}^2(\cos\theta')P_2{}^2(\cos\gamma_{jk})\cos 2(\varphi-\varphi_{jk}')\ ,\end{aligned} \tag{4}$$

$P_2(z)$ and $P_2{}^m(z)$ $(m=1,\ 2)$ denote Legendre and associated Legendre polynomials of the second order respectively, γ_{jk} is the angle between the rotational axis and the internuclear vector connecting the jth nucleus with the kth, other notation is similar to that used in the previous article.2)

Eq. (3) results in3)

$$\begin{aligned}\langle P_2(\cos\theta_{jk})^2\rangle=&\frac{1}{5}\left\{P_2(\cos\gamma_{jk})\right\}^2\\&+\left\{I_0(u/2kT)I_0(v/2kT)+2\sum_{m=1}^{\infty}I_{3m}(u/2kT)I_m(v/2kT)\right\}^{-2}\\&\times\left[\frac{1}{15}\left\{P_2{}^1(\cos\gamma_{jk})\right\}^2\left\{I_1(u/2kT)I_0(v/2kT)\right.\right.\\&\left.+\sum_{m=1}^{\infty}(I_{3m-1}(u/2kT)+I_{3m+1}(u/2kT))I_m(v/2kT)\right\}^2\\&+\frac{1}{60}\left\{P_2{}^2(\cos\gamma_{jk})\right\}^2\left\{I_2(u/2kT)I_0(v/2kT)\right.\\&\left.\left.+\sum_{m=1}^{\infty}(I_{3m-2}(u/2kT)+I_{3m+2}(u/2kT))I_m(v/2kT)\right\}^2\right]\ ,\end{aligned} \tag{5}$$

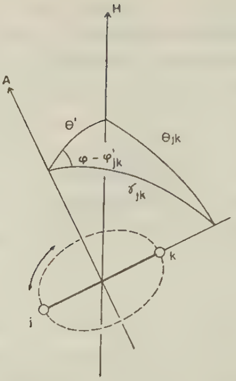

Fig. 1. Explanatory figure for angles θ_{jk}, θ', γ_{jk}, and $\varphi-\varphi_{jk}'$. H and A denote the static field and the rotational axis directions respectively.

which is reduced to

$$\frac{1}{4}f_1(T)=\frac{1}{20}+\frac{3}{20}\left\{\frac{I_2(u/2kT)}{I_0(u/2kT)}\right\}^2 \tag{6}$$

if $v=0$, and to

$$\frac{1}{4}f_3(T)=\frac{1}{20} \tag{6'}$$

if $u=0$, as shown in the previous article.2)

On the contrary, the theoretical second moment is given by Eq. (2) where in place of Eq. (3)

$$\langle P_2(\cos\theta_{jk})^2\rangle=\left\langle\int_{-\pi}^{\pi}\{P_2(\cos\theta_{jk})\}^2\exp\{-V(\varphi)/kT\}d\varphi\Big/\int_{-\pi}^{\pi}\exp\{-V(\varphi)/kT\}d\varphi\right\rangle_{\text{isotropic mean}}=\frac{1}{5} \tag{3'}$$

must be substituted. The theoretical one is constant, as already indicated.4) The case in which azimuths of one- and three-fold potential minima in Eq. (1) are distributed independently of each other is discussed by Odajima.5)

References

1) H. S. Gutowsky and G. E. Pake: J. Chem. Phys. **18** (1950) 162. J. G. Powles and H. S. Gutowsky: *ibid.* **21** (1953) 1695, 1704.
2) A. Miyake and R. Chûjô: J. Phys. Soc. Japan **14** (1959) 978.
3) R. Chûjô: Busseiron Kenkyû Ser. II, **2** (1957) 633. H. Adachi and R. Chûjô: *ibid.* **3** (1958) 150. A. Miyake: *ibid.* **3** (1958) 155.
4) P. W. Anderson: J. Phys. Soc. Japan **9** (1954) 316. R. Kubo and K. Tomita: *ibid.* **9** (1954) 888.
5) A. Odajima: Busseiron Kenkyû Ser. II, **3** (1958) 703.

J. PHYS. SOC. JAPAN **14** (1959) 973~974

Ferroelectricity in Potassium Ferrocyanide Trihydrate

By Shigeru WAKU, Hisao HIRABAYASHI,
Hiroo TOYODA and Hiroshi IWASAKI
Electrical Communication Laboratory, Nippon Telegraph and Telephone Public Corporation,
and Ryoichi KIRIYAMA
Department of Chemistry, Osaka University, Osaka

(Received June 8, 1959)

One of the authors has reported a study on the dielectric anomaly in [101] and [10$\bar{1}$] directions of potassium ferrocyanide trihydrate crystals. In investigating dielectric and hysteresis properties of this substance, we have discovered ferroelectric behavior below −22°C. Potassium ferro cyanide trihydrate, K_4 [Fe (CN)$_6$]. $3H_2O$, cristallizes with monoclinic symmetry and space group C 2/c, having cell constants $a=9.32A$, $b=16.84A$, $c=9.32A$ and $\beta=90°\pm5'$ at room temperature.[2] Due to its pseudotetragonal lattice structure, large crystals show usually lamellar twinning with twin axis along with twin axis along [010]. Cleavage is perfect perpendicular to b axis.

Dielectric measurements were made on plates cut perpendicular to [010], [101] and [10$\bar{1}$] directions. Fig. 1 shows the curves of the small signal dielectric constant of these plates. In [010] direction, there is no dielectric anomaly except a small peak at −22°C. In [101] and [10$\bar{1}$] directions, five peaks are seen at about −22, −26, −33, −43 and −80°C respectively. Height of the peaks along one of these two directions is far larger than the other. Ferroelectric hysteresis loop appears in [101] and [10$\bar{1}$] directions below −22°C down to −140°C, the lowest temperature of measurement. As the coercive field increases rapidly with decreasing temperature, saturated figures of ferroelectric hysteresis loop can be observed only in a narrow temperature range. In [010] direction, ferroelectric hysteresis does not appear over a whole range of measuring temperature. Feature of the spontaneous polarization at the ferroelectric transition, corresponding to the first dielectric peak at about −22°C, suggests that this transition is of a second order. Abrupt increase of spontaneous polarization at about −33°C corresponds to the third dielectric peak seen in Fig. 1. There are no distinguished differences in hysteresis characteristics between [101] and [10$\bar{1}$] directions, in contradiction to the dielectric anisotropy. This discrepancy may be partly due to the probable change of polarization direction caused by the high electric field in hysteresis measurement. The fact that the lower curve in Fig. 1 shifted to the higher one under the application of high field, seems to support this assumption. As it is certain that the ferroelectric axis lies in the cleavage (010) plane, the space group just below the Curie point may be Cc. Therefore, two independent directions of polarization may be possible. This possibility, together with the existence of lamellar twin, makes the determination of polarization axis quite difficult.

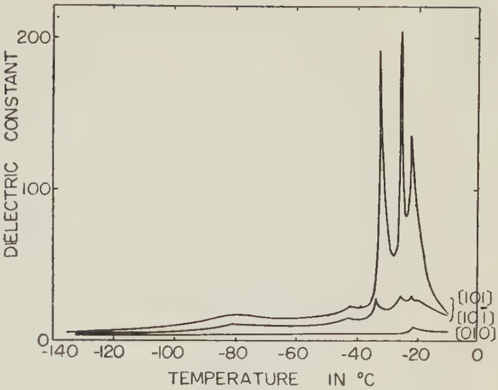

Fig. 1. Dielectric constant, measured along [010], [101] and [10$\bar{1}$] directions, as a function of temperature.

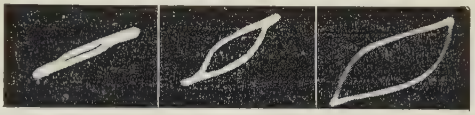

−25.0°C −31.4°C −55.6°C

Fig. 2. Hysteresis loops at three different temperetures.

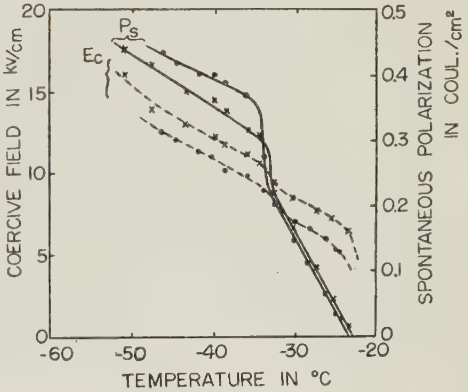

Fig. 3. Spontaneous polarization and coercive field along [101], [10$\bar{1}$] direction as a function of temperature.

We have also examined several isomorphous compounds, most of which show some anomalies above liquid nitrogen temperature. Detailed studies of these materials will be reported subsequently.

References

1) R. Kiriyama and K. Tabata: Symposium of Structural Chemistry, the Chemical Society of Japan, October, 1956.
2) V. A. Pospelov and G. S. Zudanov: J. fiz. chim. USSR **21** (1947) 405.

J. PHYS. SOC. JAPAN **14** (1959) 974~975

On the Structure of Green Rust of Iron

By Hide YOSHIOKA
Physical Institute, Nagoya University, Nagoya

(Received June 3, 1959)

Dasgupta and Mackay[1] proposed a structure of green rust which we previously studied by means of electron diffraction[2]. However, their analysis of our data on a rhombohedral cell seems to be unable to explain our observation that the rust sometimes produces a diffraction pattern as we denoted by S.R.S. (II) in our paper. The intensity of rings of the pattern is asymmetrically distributed as shown in Figs. 1 and 2. This fact indicates that the Intenzitätbereich in the reciprocal lattice is much elongated in one direction, namely, the crystal is nearly two-dimensional. Accordingly, we indexed rings which appear in the pattern S.R.S. (II) by ($hk0$). The hexagonal indices given by Mackay for our ($hk0$) rings do not belong to the same zone axis and conflict with the above fact.

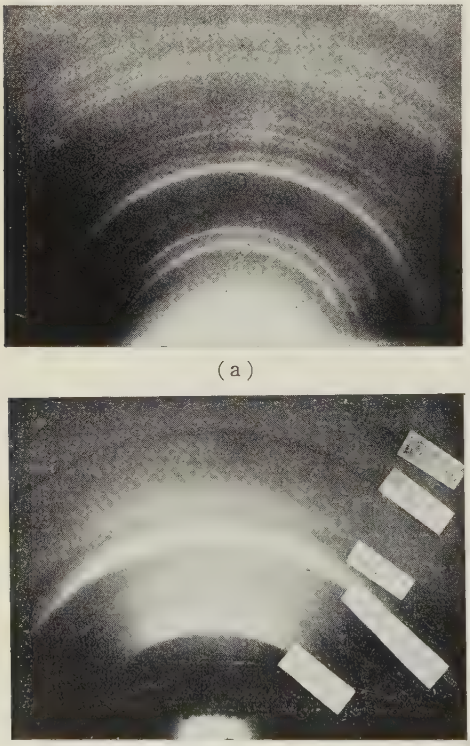
(a)
(b)

Fig. 1. Electron diffraction pattern of green rust.
(a) normal pattern (S.R.S. (I)).
(b) S.R.S. (II).

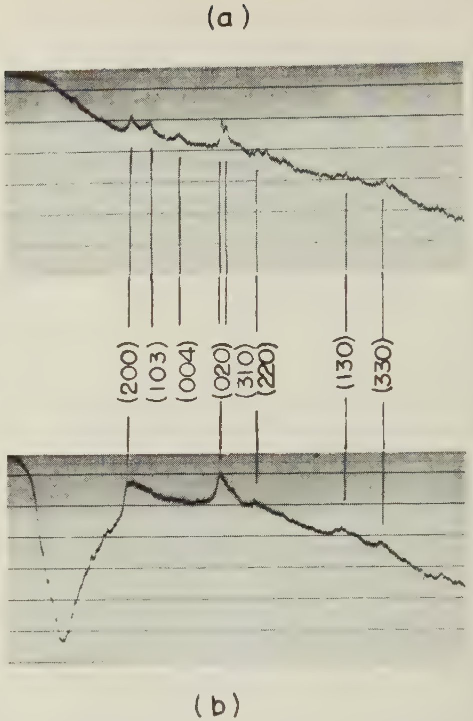

Fig. 2. Microphotometric trace of diffraction rings.
(a) normal pattern (S.R.S. (I)).
(b) S.R.S. (II).

We determined c-axis so as to index the other rings in green rust pattern as (hkl) with $l \neq 0$ on orthorhombic system. Therefore, it is not conclusive that c-axis is perpendicular to ab-plane. Thus, the monoclinic structure suggested by Dasgupta and Mackay may be possible. Their monoclinic cell gives the same index as ours when $l=0$.

Finally, it is worthwhile to note that the inner two rings which exist in X-ray data of Feitknecht and Keller[3] and are missing in our electron diffraction data can be indexed as (001) and (002) using our cell vectors. The fact that they are missing in our photograph seems to indicate that our crystals are very thin plates parallel to ab-plane. The small glancing angles to ab-plane make the reflexions (001) and (002) unfavorable in electron diffraction, as in the case of graphite where (002) ring is usually weak in electron diffraction[4].

The author wishes to express his thanks to Mr. H. Morimoto for the microphotometry of the diffraction rings.

References

1) D. R. Dasgupta and A. L. Mackay: J. Phys. Soc. Japan **14** (1959) 932.
2) H. Yoshioka and R. Uyeda: Proc. Japan Acad. **21** (1945) 340; **22** (1946) 198. H. Yoshioka: J. Phys. Soc. Japan **4** (1949) 270.
3) W. Feitknecht and G. Keller: Z. anorg. allg. Chem. **262** (1950) 61.
4) R. Uyeda, S. Ito and K. Kimoto: J. Phys. Soc. Japan **2** (1947) 9.

J. PHYS. SOC. JAPAN **14** (1959) 975~976

Extraordinary Hall Effect in Silicon-Iron Single Crystals

By Eiji TATSUMOTO and Tetsuhiko OKAMOTO

Department of Physics, Faculty of Science, Hiroshima University

(Received April 27, 1959)

The extraordinary Hall effect in ferromagnetic metals is observed in company with the ordinary Hall effect until the magnetization saturates, as is suggested by the empirical formula, $e_h = R_1 M + R_0 H_{eff}$.[1]. Here, e_h is the Hall resistivity or the Hall voltage per unit current density, $R_1 M$ the extraordinary Hall resistivity, R_1 the extraordinary Hall coefficient, M, the magnetization in the direction of the applied field, $R_0 H_{eff}$. the ordinary Hall resistivity, R_0, the ordinary Hall coefficient and H_{eff}. the effective field in the ordinary effect.

Usually, the extraordinary resistivity, $R_1 M$, is much larger than the ordinary resistivity, $R_0 H_{eff}$., except in extremely low temperatures. Even in such a case, in order to obtain the extraordinary Hall coefficient, R_1, we must take into consideration the size effect of the specimens, because the definite width and thickness of the specimens result in the difference between the magnetizations near the edge and in the central part of the specimens at a given applied field, until the magnetization saturates. The magnetization in the direction of the applied field is larger near the edge than in the central part in low applied fields because magnetic poles appear at the edge, so that the demagnetizing field in the direction of the applied field becomes smaller near the edge than in the central part.

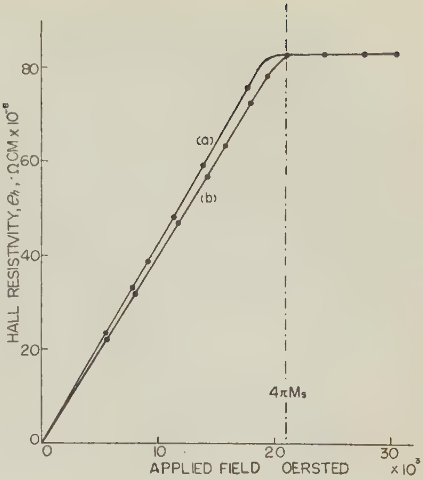

Fig. 1. Hall resistivities measured by contacting the probes, respectively, at the edges (a), and about 1.5 mm inside from the edges (b), of a 1.23% silicon-iron single crystal strip, 0.5 mm × 9 mm × 35 mm, with the (001)-[100] crystal orientation.

In Fig. 1, the two seemingly different Hall resistivities are given as an example. These are measured on the 1.23% silicon-iron single crystal strip,[2] 0.5 mm × 9 mm × 35 mm, with the (001)−[100] crystal orientation by contacting the probes, respectively, at the edges (a-curve) and about 1.5 mm inside from the edges at room temperature. This difference evidently results from the difference between the magnetizations near the edge and in the central part of the specimen, as is described above. Near the edge, magnetizing becomes suddenly hard as the magnetization reaches the saturation value as is inferred from a-curve. In a-curve, about 26,000 oersted in applied field is necessary to saturate the magnetization completely, while in b-curve it is about 23,000 oersted. The difference in amount of the field is mainly attributable to the difference in the magnetizing field that is normal to the specimen near the contacting probes, being caused by the appearance of magnetic poles at the edge. In b-curve, the applied field, H_0, is nearly proportional to the magnetization ($H_0 \simeq 4\pi M$), because the demagnetizing factor is nearly 4π in the whole magnetizing process ($H_0 \simeq B$) and the magnetizing field, H, is much smaller than $4\pi M$ ($B \simeq 4\pi M$). Here B is the magnetic induction of the specimen. Referring to the linearity of b-curve until the magnetization nearly saturates, the extraordinary Hall resistivity is regarded as proportional to the magnetization as is given by $R_1 M$ in Fig. 1. Thus we can obtain the extraordinary Hall coefficient, R_1, approximately from b-curve, not from a-curve. However, we can obtain R_1 more accurately even in the measurement in a-curve, by adopting the value at the intersection between the axis of $4\pi M_s$, 21,000 oersted, in the applied field and the backward extrapolation of the straight line in the ordinary effect in the applied fields larger than $4\pi M_s$, in Fig. 1. This is because the ordinary Hall effect is the same in a- and b-curves after the complete saturation magnetization. With this procedure, the ordinary Hall resistivity, $R_0 H_{eff}$., is eliminated, since experimentally the effective field in the ordinary effect is regarded as the magnetizing field, H. As for the effective field, it is to be published by the same authors simultaneously under the title, "Effective Field in the Ordinary Hall Effect in Ferromagnetics".

By adopting this procedure in the masurements on the $(001)-[100]$, $(001)-[110]$ and $(0\bar{1}1)-[111]$ specimens and polycrystals, the extraordinary Hall effect is confirmed to be isotropic as was ascertained by Webster[3] on iron single crystals. In this case the extraordinary Hall coefficient at room temperature is 49.2×10^{-11} volt cm/oersted amp.

References

1) E. M. Pugh and N. Rostoker: Rev. Mod. Phys. **25** (1953) 151.
2) E. Tatsumoto and T. Okamoto: J. Phys. Soc. Japan **14** (1959) 226.
3) W. L. Webster: Proc. Camb. Phil. Soc. **23** (1927) 800.

J. Phys. Soc. Japan **14** (1959) 976~977

Effective Field in the Ordinary Hall Effect in Ferromagnetics

By Eiji TATSUMOTO and Tetsuhiko OKAMOTO

Department of Physics, Faculty of Science, Hiroshima University

(Received April 27, 1959)

The nature of the effective field in the ordinary Hall effect in ferromagnetics has not yet been confirmed. From the empirical consideration Pugh and Rostoker[1] have suggested this to be the magnetizing field, H, while Wannier[2] has theoretically expected this to be $H+2\pi M(1+p)$, where M is the magnetization and p the relative probability of a conduction electron penetrating in the interior of a polarized electron ($p\leq 1$). On the other hand, Smit[3] has asserted this to be $B=H+4\pi M$. Now in this report the effective field is pointed out to be the magnetizing field, H, just as suggested by Pugh et al.

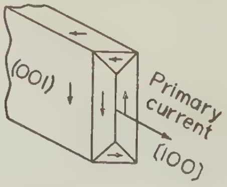

Fig. 1. Domain structure, in the iron single crystal strips with the $(001)-[100]$ crystal orientation, produced by the circular magnetic field due to the primary current.

The ordinary Hall effect has already been confirmed experimentally by the present authors to be anisotropic and to vary by the lattice deformation in the measurements on the 1.23% silicon-iron single crystal strips[4] and on the pure iron single crystal strips, though concerning the latter case it has not been published yet. However, the extraordinary Hall effect is isotropic[5,6] and hardly affected by the lattice deformation. The lattice deformation is made by applying tensions in the elestic range. In the $(001)-[100]$ specimens, the domain structure as shown in Fig. 1 is produced by the circular magnetic field due to the primary current when it is sufficiently strong.[7] Tensions applied to the direction of the primary current changes the domains perpendicular to the primary current into those parallel to the same direction. In both cases with and without tensions, the extraordinary Hall effect is almost not different. This means that the extraordinary Hall effect does not depend on the magnetizing process, but depends on the amount of the magnetization only.

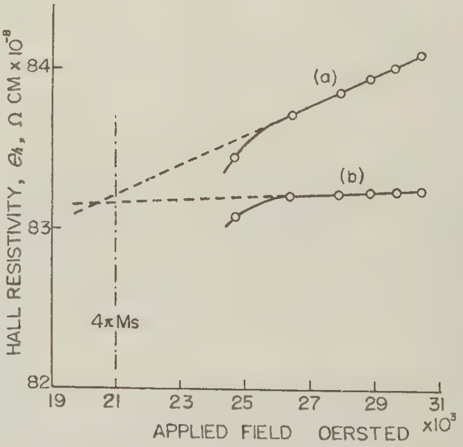

Fig. 2. Hall resistivities measured in high applied fields on the 1.23% silicon-iron single crystal strip, 0.5 mm × 9 mm × 35 mm, with the $(001)-[100]$ crystal orientation by contacting the probes at the edges: a- and b-curves stand for those measured when 0.25 kg/mm² and 1.9 kg/mm² are applied in the [100] direction, respectively.

In Fig. 2 are given the Hall resistivities measured, in high applied fields, on the 1.23% silicon-iron single crystal strip, 0.5 mm × 9 mm × 35 mm, with the $(001)-[100]$ crystal orientation, when 0.25 kg/mm² (a-curve) and 1.9 kg/mm² (b-curve) are applied in the direction of the primary current, i.e. in the [100] direction, respectively. These measurements were made by contacting the probes at the edges of the specimen. According to such a way of measurement, about 26,000 oersted in applied field is necessary to complete the extraordinary Hall effect, while about 21,000 oersted, $4\pi M_s$, is enough to saturate the magnetization technically if the demagnetizing factor is 4π. This fact is mainly due to the appearance of magnetic poles at the edge of the specimen[6]. When the linear parts in high applied fields, i.e. the ordinary Hall resistivities, are extrapolated backward, they intersect each other around $4\pi M_s$, 21,000 oersted, in the applied field. This means that the effective field is just the magnetizing field, H, and is neither $H+2\pi M(1+p)$ nor $B=H+4\pi M$, because if the effective field is $H+2\pi M(1+p)$ or $B=H+4\pi M$, the intersection point should be between zero and $2\pi M_s$, 10,500 oersted, or around zero in the applied field, respectively. Accordingly we may safely conclude that the effective field in the ordinary Hall effect is the magnetizing field.

References

1) E. M. Pugh and N. Rostoker: Rev. Mod. Phys. **25** (1953) 151.
2) G. H. Wannier: Phys. Rev. **72** (1947) 304.
3) J. Smit: *Thesis* (University of Leiden, 1956).
4) E. Tatsumoto and T. Okamoto: J. Phys. Soc. Japan **14** (1959) 226.
5) W. L. Webster: Proc. Camb. Phil. Soc. **23** (1927) 800.
6) E. Tatsumoto and T. Okamoto: J. Phys. Soc. Japan **14** (1959) 975.
7) E. Tatsumoto: Phys. Rev. **109** (1958) 658.

J. PHYS. SOC. JAPAN **14** (1959) 977~978

An Extended Form of Weyl-Laue Theorem and its Application to Surface Problems

By Akira SUGIYAMA

Nagoya Technical College, Nagoya

(Received March 16, 1959)

A metal is assumed simply to consist of a uniform distribution of positive charge with density ρ_0 ($=k_F{}^3/3\pi^2$, k_F the usual Fermi momentum* volume V_0 and area of boundary surface S_0 and of a number $N_0=\rho_0 V_0$ of electrons. The electrons are free in such a potential box with an infinitely high barrier that has similar shape as the positive charge, but whose volume V is not taken necessarily to be equal to V_0.

The free electrons are specified by wave vectors $\vec{k}$, and the number $N(k)$ of energy levels of the free electrons within $|\vec{k}|\leq k$ in the potential box of any shape with volume V and the area of the boundary surface $S\sim S_0$ is expressed in the form

$$N(k)=\frac{k^3 V}{3\pi^2}-\frac{k^2 S_0}{8\pi} \tag{1}$$

where the first term represents the Weyl-Laue[1] theorem, and the second term is the correction term considering effects of the boundary surfaces. The validity of the second term is inferable from a physical insight, though a mathematical proof is given only for particular cases of outer surfaces of cubic, platelike and spherical boxes and inner surfaces of spherical and cylindrical cavities in larger boxes.

The formula (1) gives a simple method of deriving in a general way some interesting properties of surfaces of any shape as given below.

At 0°K, the maximum momentum k_m of the occupied levels is determined by

$$N(k_m)=N_0=k_F{}^2 V_0/3\pi^2 \tag{2}$$

According to Friedel[2], the interior density of the free electrons $\rho_i=k_m{}^3/3\pi^2$ should be equal to ρ_0, or

$$k_m=k_F\ . \tag{3}$$

Then, from (1), (2) and (3), we obtain the relation

$$V=V_0+b_\infty S_0\ ,\quad b_\infty k_F=3\pi/8 \tag{4}$$

1. Using (2) and (3), ρ_i is rewritten in

$$\rho_i=(N_0/V)+(k_F{}^2/8\pi)(S_0/V)$$

which shows that the surface of an infinitely high barrier expels the free electrons into the interior by an amount of $k_F{}^2/8\pi$ per unit area, since the first term N_0/V is the average density. The same has been shown by Bardeen[3] and Swiatecki[4] for a particular case of the plane surface.

2. The total energy E of the electron system is given as

$$E=\int_0^{k_m}\frac{1}{2}k^2\frac{\partial N}{\partial k}dk=\frac{k_m{}^5 V}{10\pi^2}-\frac{k_m{}^4 S_0}{32\pi^2} \tag{5}$$

or

$$=\frac{k_F{}^5 V_0}{10\pi^2}+\frac{k_F{}^4 S_0}{160\pi}$$

by using (3) and (4). Now the second term shows the surface energy

$$E_S{}^{(0)}=k_F{}^4/160\pi \tag{6}$$

per unit area of any shape, which agrees with the result given by previous authors[4,5] for a particular case of the plane surface**.

The surface energy (6) is proved to be approximately valid even for inner surface of cavities with smaller radius in spite of an assumption made in deriving (1) that the boundary surface has a larger radius of curvature.

---

* Atomic units are used.

** On rough assumption $V=V_0$, we obtain $k_m=k_F+(\pi S_0/8V_0)$ from (2), instead of (3), and then the surface energy $E_S{}^{(1)}=k_F{}^4/32\pi$ from (5), instead of (6). $E_S{}^{(1)}$ agrees with the results given by Brager et al[6]. for the plane surface, and by Brager[7] for the spherical one.

For an example, the formation of an atomic vacancy in monovalent metals is equivalent to creating the cavity of Wigner-Seitz radius r_S in the positive charge distribution, and therefore we can estimate the formation energy of vacancy ΔE_v equal to $4\pi r_S^2 \cdot \beta E_S^{(0)}$, where β is a factor representing effects of curvature. On the other hand, Seeger and Bross[8] have carried out numerical calculation of ΔE_v based on the Friedel's sum rule and the assumption of infinitely high potential barrier, from which we obtain $\beta \sim 0.93$.

For another example, the formation energy of a vacancy-pair with the distance $2C$ is estimated to be $\Delta E_{v-p} = S(C) \cdot \beta E_S^{(0)}$, where $S(C)$ denotes the surface area of the rotational ellipsoid with foci separated by $2C$ and twice volume of single vacancy. From the numerical calculations of ΔE_{v-p} by Seeger et al.[8], we obtain $\beta \sim 0.95$ for the range.

These examples agree in showing approximate validity of (6), or $\beta \sim 1$, for surfaces of larger curvature. Then the association energy of a vacancy pair is interpreted as a gain in surface energy due to decrease in the total surface area when two single vacancies make a pair.

Detailed treatments will be discussed later.

References

1) H. Weyl: Math. Ann. **71** (1911) 441.
M. Laue: Ann. Physik **44** (1914) 1197.
2) J. Friedel: Phil. Mag. **43** (1952) 153.
3) J. Bardeen: Phys. Rev. **49** (1936) 654.
4) W. J. Swiatecki: Proc. Phys. Soc. London **64** (1951) 227.
5) H. B. Huntington: Phys. Rev. **81** (1951) 1035.
6) A. Brager and A. Schuchowitzky: Acta Physicochim. **21** (1946) 13.
7) A. Brager: J. Phys. Chim. USSR **21** (1947) 623.
8) A. Seeger and H. Bross: Z. Phys. **145** (1956) 161.

J. PHYS. SOC. JAPAN **14** (1959) 978~979

NMR Second Moment of a Radical Rotating in a Periodic Potential

By Akira MIYAKE and Riichirô CHÛJÔ

Faculty of Liberal Arts and Science, Shizuoka University, Shizuoka

(Received May 25, 1959)

The influence of the motion of a radical, *e.g.* NH_2, CH_3 or benzene ring, in a periodic potential upon the second moment of NMR was discussed by Gutowsky and Pake,[1] Andrew and Bersohn,[2] Powles and Gutowsky,[3] and Das.[4] Although the theoretical second moment is nearly unaffected by the motion, as indicated by Anderson,[5] Kubo and Tomita,[6] yet the observed one which is practically obtained through cutting off the tails of the absorption line is changed almost in parallel with the motional narrowing of the line width.[7]

The second moment due to the radical is given by

$$\Delta H_2{}^2 = \frac{3}{4}\hbar^2\gamma^2 I(I+1)\frac{1}{N}\sum_j\sum_k \langle r_{jk}{}^{-6}(3\cos^2\theta_{jk}-1)^2\rangle\,, \tag{1}$$

where γ is the gyromagnetic ratio of resonating nuclei, I their spin quantum number, N the number of resonating nuclei in the radical, r_{jk} the distance between the jth and the kth resonating nuclei, θ_{jk} the angle between the applied static field direction and the r_{jk} direction. Let the n-fold periodic potential for the rotational angle φ of the radical be

$$V_n(\varphi) = \frac{u}{2}(1-\cos n\varphi)\,. \tag{2}$$

When the n-fold symmetry axis is perpendicular to every r_{jk} direction, we can take

$$\cos\theta_{jk} = \sin\theta' \cos(\varphi - \varphi_{jk}')\,, \tag{3}$$

where θ' is the angle between the static field direction and the symmetry axis, φ_{jk}' azimuth of the r_{jk} direction.

As at high temperatures the motion is very rapid, we can consider the over-all motional average nuclear magnetic interaction, so that we may have

$$\Delta H_2{}^2 = \frac{3}{4}\hbar^2\gamma^2 I(I+1)\frac{1}{N}\sum_j\sum_k r_{jk}{}^{-6} f_n(T)\,, \tag{4}$$

$$f_n(T) = \left\langle\left[\int_{-\pi}^{\pi}(3\cos^2\theta_{jk}-1)\exp\{-V_n(\varphi)/kT\}d\varphi \Big/ \int_{-\pi}^{\pi}\exp\{-V_n(\varphi)/kT\}d\varphi\right]^2\right\rangle_{\text{isotropic mean}}, \tag{5}$$

where the isotropic mean is taken over θ' and φ_{jk}'. Eq. (5) gives

$$\left.\begin{aligned} f_1(T) &= \frac{1}{5}+\frac{3}{5}\left\{\frac{I_2(u/2kT)}{I_0(u/2kT)}\right\}^2 \simeq \frac{1}{5}+\frac{3}{320}(u/2kT)^4+\cdots, \\ f_2(T) &= \frac{1}{5}+\frac{3}{5}\left\{\frac{I_1(u/2kT)}{I_0(u/2kT)}\right\}^2 \simeq \frac{1}{5}+\frac{3}{20}(u/2kT)^2+\cdots, \\ f_n(T) &= \frac{1}{5} \qquad\qquad n \geqq 3 \qquad\qquad , \end{aligned}\right\} \tag{6}$$

where $I_n(x)$ is modified Bessel function of the nth order.

On the other hand, at low temperatures the motion is almost confined to the bottom of a potential trough, so we must have in place of $f_n(T)$

$$g_n(T) = \left\langle\left[\int_{-\pi/n}^{\pi/n}(3\cos^2\theta_{jk}-1)\exp\{-V_n(\varphi)/kT\}d\varphi\right.\right.$$

$$\Big/\int_{-\pi/n}^{\pi/n}\exp\{-V_n(\varphi)/kT\}d\varphi\Big]^2\Big\rangle_{\text{isotropic mean}}, \tag{5'}$$

provided the motion within the trough is rapid. Eq. (5′) gives

$$\left.\begin{aligned} g_1(T)&=f_1(T)\simeq\frac{4}{5}-\frac{12}{5}(2kT/u)+\cdots \qquad ,\\ g_2(T)&=f_2(T)\simeq\frac{4}{5}-\frac{3}{5}(2kT/u)+\cdots \qquad ,\\ g_n(T)&=\frac{1}{5}+\frac{3}{20}\frac{n^2}{\pi^2}\sin^2(2\pi/n)\\ &\quad\cdot\left\{1-8\sum_{r=1}^{\infty}\frac{(-1)^r}{(nr+2)(nr-2)}\frac{I_r(u/2kT)}{I_0(u/2kT)}\right\}^2\\ &\simeq\frac{4}{5}-\frac{12}{5n^2}(2kT/u)+\cdots \qquad n\geqq 3\,. \end{aligned}\right\} \tag{6'}$$

As

$$\langle V_n\rangle=\int_{-\pi/n}^{\pi/n}V_n(\varphi)\exp\{-V_n(\varphi)/kT\}d\varphi \Big/\int_{-\pi/n}^{\pi/n}\exp\{-V_n(\varphi)/kT\}d\varphi\simeq\frac{1}{2}kT+\cdots$$

at low temperatures, we can write

$$\frac{5}{4}g_n(T)\simeq 1-\frac{12}{n^2}\frac{\langle V_n\rangle}{u} \qquad n\geqq 1\,, \tag{7}$$

which is to be compared with that given by Das,[4] where factor 12 of the second term in the right side of Eq. (7) is substituted by 112/9.

The relation

$$f_n(\infty)/g_n(0)=1/4 \qquad n\geqq 1 \tag{8}$$

coincides with the conclusion already given by Gutowsky and Pake.[1] The diversity in the cases $n=1$, $n=2$ and $n\geqq 3$, as seen in Eqs. (6) and (6′), arises from the nature of symmetry in the nuclear magnetic dipolar interaction. $f_n(T)$ and $g_n(T)$ *vs.* $2kT/u$ are shown graphically in Fig. 1.

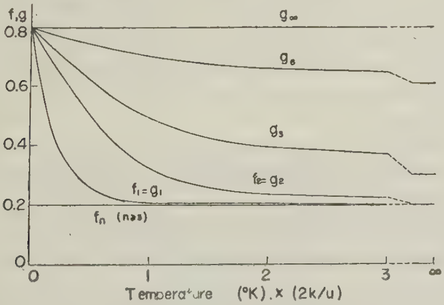

Fig. 1. $f_n(T)$ and $g_n(T)$ *vs.* $2kT/u$ for $n=1$, 2, 3, 6 and ∞.

References

1) H. S. Gutowsky and G. E. Pake: J. Chem. Phys. **18** (1950) 162.
2) E. R. Andrew and R. Bersohn: J. Chem. Phys. **18** (1950) 159.
3) J. G. Powles and H. S. Gutowsky: J. Chem. Phys. **21** (1953) 1695, 1704; **23** (1955) 1692.
4) T. P. Das: J. Chem. Phys. **27** (1957) 763.
5) P. W. Anderson: J. Phys. Soc. Japan **9** (1954) 316.
6) R. Kubo and K. Tomita: J. Phys. Soc. Japan **9** (1954) 888.
7) A. Miyake: J. Polymer Chem. (in Japanese) **16** (1959) 40.

J. PHYS. SOC. JAPAN **14** (1959) 979~980

New Cold Cathode Using Magnesium Oxide

By Tetsuji IMAI, Yoshihiko MIZUSHIMA
and Yoshitaka IGARASHI

Electrical Communication Laboratory
Nippon Telegraph
and Telehone Public Corporation,
Tokyo, Japan

(Received May 21, 1959)

It was reported by Jacobs[1),2)] that a target on which magnesium oxide was deposited emitted secondary electrons as much as one thousand times the primary ones. Although the phenomenon resembled Malter's Effect on a cathode of composition (Al)–Al_2O_3–Cs_2O, Jacobs emphasized that the phenomenon was quite different from that Effect and due to the avalanche process produced in the magnesium oxide layer. Furthermore, with proper

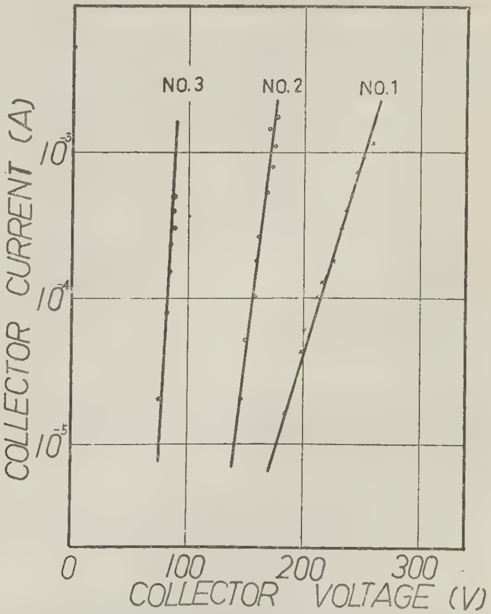

Fig. 1. Collector voltage—current characteristics of MgO cathodes. No. 1, 2 and 3 are test tubes having different electrode configurations.

disposition of the potential across the layer, the emission current could be made self-sustaining, with no primary current. This was first reported by Dobischek, Jacobs and Freely[3] and on BaO by Yoshida et al.[4]

We could prepare the magnesium oxide cathodes yielding self-sustaining emission current of the order of milliamperes in a quite simple way which will be given elswhere in detail. According to Jacobs, a rather complicated method is necessary to obtain the extremely high yield of secondary emission or self-sustaining emission, that is, both the evaporation of magnesium and the heat treatment of the deposit should be applied in an atmosphere of oxygen in order to get good results.

Some results obtained by us on the relation between the self-sustaining emission and the collector voltage are illustrated in Fig. 1, which implies the relation

$$I=I_0 \exp(NV),$$

where I is the emission current from the cathode, V collector voltage, I_0 and N constants depending on the cathode and electrode configurations. The cathode was not self-starting and required some external stimulus, such as electrons, photons or ions. Among others electron bombardment was the most effective to start the current. Illumination with light from incandescent lamp was also effective. Between the light intensity (L) and the time (t) which was required to start, we obtained a relation,

$$L\cdot t=\text{const}.$$

One of the most remarkable phenomena observed is an accumulation effect of light stimulation at the magnesium oxide cathode. Holding the distance between the cathode and the light source constant, the cathode was exposed to light of a constant flux intermittently. The integrated time of exposure until an electron emission sets in was found to be independent on the length of pause. One of these results is given in Fig. 2. The pause length between light exposures was chosen as 5 sec, 15 sec, 30 sec, 1 min, 2 min, 5 min and 10 min, but substantially constant total-exposure-time was required to start an emission. This implies that a physical phenomenon caused by light stimulation is able to maintain for a long time without appreciable decay. The light exposure will eject electrons, out of the MgO as the photo-emission, leaving the outside of the MgO layer positively charged and the positive charge on the MgO surface can not escape owing to the extreme high resistivity of the layer.

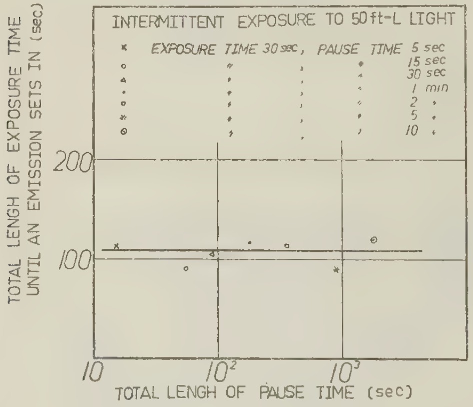

Fig. 2. The relation between the integrated time of exposure until an emission sets in and the length of pause at the intermittent exposure method.

It was found further that the photo-effect mentioned above had a cut-off-energy in the ultraviolet region. It was also found that the characteristic phosphorescent glow was violet or blue and in some cases redish violet.

References

1) H. Jacobs: Phys. Rev. **84** (1951) 877.
2) A. Jacobs, J. Freely and F. A. Brand: Phys. Rev. **88** (1952) 492.
3) D. Dobischek, H. Jacobs and J. Freely: Phys. Rev. **91** (1953) 804.
4) S. Yoshida, Y. Igarashi and H. Arata: J. Appl. Phys. Japan **23** (1954) 566.

J. PHYS. SOC. JAPAN **14** (1959) 980～981

Microwave Spectrum of Ethyl Iodide

By Takahiro KASUYA and Takeshi OKA
Department of Physics, Faculty of Science, University of Tokyo, Tokyo

(Received May 21, 1959)

The microwave spectrum of ethyl iodide C_2H_5I was observed in the frequency range from 5 to 30 kMc/sec. About fifty lines were assigned to the a-type transitios, and other twenty to the b-type transitions.

This molecule is a slightly asymmetric rotor with $b_p \doteqdot -0.003$, having a very large quadrupole coupling constant, and the calculated frequencies could not satisfactorily be fitted to the observed spectrum with the first order quadrupole treatment alone.

The second order quadrupole effect was calculated using the wave function expanded in the power series of b_p[1]. With the parameters listed in Table II, the discrepancies between the calculated and observed frequencies were less than 1 Mc/sec (Table I).

The hyperfine anomalies in $K=1$ lines reported by Wagner and Dailey in the case of C_2H_5Br[2]

Table I. Spectroscopic parameters of ethyl iodide.

A	29109.2±5 Mc/sec	$(eqQ)_{aa}$	−1481.9±0.5 Mc/sec
B	2979.2 ±0.5	$\eta=(\chi_{bb}-\chi_{cc})/\chi_{a}$	=0.22 (assumed)
C	2797.1 ±0.5	$\xi=\chi_{bc}/\chi_{aa}$	=0.60 (〃)

were also observed in this molecule. For example, the hyperfine component corresponding to 7/2→9/2 of $2_{12}\rightarrow3_{13}$ transition was found to show the splitting of 1.09 Mc/sec. This splitting was explained by taking into account of the internal rotation of CH_3 group (Table II).

Table II. An example of hyperfine anomaly.

$2_{12}\rightarrow3_{13}$	obs.	calc.
9/2→11/2	17096.08	17095.84
7/2→ 9/2	17034.84	17035.30 (E)
	17035.75	17034.21 (A)
3/2→ 5/2	16976.8	16976.6
1/2→ 3/2	17007.76	17007.14

The quadrupole interaction term averaged by the rigid asymmetric rotor wave function is known to be

$$eqQ=\frac{(eqQ)_{aa}}{(J+1)(2J+3)}\Big[\{3K^2-J(J+1)\}+(-1)^{\gamma}\frac{J(J+1)\eta}{2}\delta_{K,1}+\text{asymmetry correction}\Big].^{3)}$$

The second term $\pm[J(J+1)\eta]/2$ which does not vanish for $K=1$ must be multiplied by a factor ε, owing to the coupling of internal and overall rotation[4].

For A-state of internal rotation ε is one, but for E-state it is dependent sensitively on potential, which can be used to evaluate the barrier height[5]. Treating the internal rotation problem by the Hamiltonian developed by Kilb, Lin and Wilson[6], the potential value of about 2.4 kcal/mole was obtained. This should be compared with that of C_2H_5Cl and C_2H_5Br [7]*.

From the parameters listed in Table I, the structural constants were determined as follows

Table III. Microwave spectrum of ethyl iodide.

a-type transition				b-type transition	
$0_{00}\rightarrow1_{01}$		9/2→ 9/2	17070.40	$3_{03}\rightarrow3_{12}$	
5/2→ 3/2	5988.1	3/2→ 3/2	17382.34	11/2→11/2	26744
5/2→ 5/2	5542.08	$3_{30}\rightarrow4_{31}$, $3_{31}\rightarrow4_{32}$		9/2→ 9/2	26845
5/2→ 7/2	5852.44	11/2→13/2	23214.30	7/2→ 7/2	26837
$2_{10}\rightarrow3_{21}$		9/2→11/2	22968.75	5/2→ 5/2	26796
9/2→11/2	17443.60	7/2→ 9/2	22978.44	7/2→ 5/2	26928
7/2→ 9/2	17155.92	5/2→ 7/2	23116.56	5/2→ 3/2	26900
5/2→ 7/2	17227.84	$3_{21}\rightarrow4_{22}$		$4_{04}\rightarrow4_{1}^{3}$	
$2_{21}\rightarrow3_{22}$		11/2→13/2	23167.05	13/2→13/2	27108
9/2→11/2	17438.08	9/2→11/2	23059.77	11/2→11/2	27196
7/2→ 9/2	17152.32	7/2→ 9/2	23050.34	7/2→ 7/2	27166
$2_{02}\rightarrow3_{03}$		5/2→ 7/2	23090.64	5/2→ 5/2	27096
9/2→11/2	17342.28	$3_{22}\rightarrow4_{23}$		$5_{05}\rightarrow5_{14}$	
7/2→ 9/2	17354.96	11/2→13/2	23158.50	15/2→15/2	27595
5/2→ 7/2	17283.82	9/2→11/2	23050.34	13/2→13/2	27638
3/2→ 5/2	17212.40	7/2→ 9/2	23042.24	11/2→11/2	27663
		5/2→ 7/2	23083.38	5/2→ 5/2	27565

assuming the C–C bond length to be 1.555±0.005Å[2]

C–I 2.207±0.005Å, ∠CCI 112°1′±30″

More precise analysis especially of the b-type transition lines is now in progress considering the internal rotation effect.

The authors wish to express their thanks to Prof. K. Shimoda for his kind guidance and encouragement throughout this work.

References

1) D. R. Lide, Jr.: J. Chem. Phys. **20** (1952) 176.
2) R. S. Wagner and B. P. Dailey: J. Chem. Phys. **26** (1957) 1588.
3) C. H. Townes and A. L. Schawlow: *Microwave Spectroscopy* (McGraw-Hill Book Company, New York, 1955).
4) D. R. Lide, Jr.: J. Chem. Phys. **27** (1957) 343.
5) D. R. Herschbach: *Tables for the internal rotation problem* (Harvard Univ.)
6) R. W. Kilb, C. C. Lind and E. B. Wilson: J. Chem. Phys. **26** (1957) 1695.
7) D. R. Lide, Jr.: J. Chem. Phys. **30** (1959) 37.

---

* 3560±12 cal/mole for C_2H_5Cl and 3567±30 cal-mole for C_2H_5Br.

PROGRESS OF THEORETICAL PHYSICS

CONTENTS

Progress of Theoretical Physics Vol. 20, No. 6, December 1958

Ground State Energy of Bose Particle System .... Ryuzo ABE..785
The Clebsch-Gordan Coefficients .... S. Datta MAJUMDAR..798
Electronic Structure of the Exciton in Ionic Crystal—*Further Discussion of a Localized Exciton (Zero-th Order Description) and General Formulation of a Moving Exciton in Alkali Halides—* .... T. MUTO, S. OYAMA and H. OKUNO..804
A Theory of Clothee Unstable Particles, II .... Noboru NAKANISHI..822
The Dispersion Relation and the Pion-Nuclear Interaction Cross Section at Very High Energies .... T. SAKUMA, S. FURUI and A. KANAZAWA..835
An Analysis of Experimental Data on Extensive Air Showers ... Saburo MIYAKE..844
Theory of Unstable Particles in the Wave-Packet-Formalism .. Kunio YAMAMOTO..857
Quantum Theory in Pseudo-Hilbert Space .... G. KONISI and T. OGIMOTO..868
Derivation of the Two Nucleon Potential ...... A. KLEIN and B. H. McCORMICK..876
Magnetic Properties of the Iron-Group Anhydrous Chlorides .. Junjiro KANAMORI..890
Mass Reversal and Weak Interactions .... Tadashi OUCHI..909
Theory of Classical Fluids: Hyper-Netted Chain Approximation, I —*Formulation for a One-Component System*— .... Tohru MORITA 920
Meson Production in Meson-Nucleon Interaction .... S. K. KUNDU..939
On Quantum Theory of Transport Phenomena—*Steady Diffusion*— .... Sadao NAKAJIMA..948
Foundation of Deformed Potential Model for Nuclear Rotation .... K. IKADA, M. KOBAYASI, T. MARUMORI, S. NAGATA and T. SHIOZAKI..960
Letters to the Editor:
Influence of the Exchange and Correlation on the Electron-Phonon Interaction in Metals .... T. TOYA..971
Electrical Conductivity of Monovalent Metals .... T. TOYA..973
Normal Vibrations of Copper .... T. TOYA..974
A Note on the Elastic Scattering of High Energy Deuterons by Complex Nuclei .... Y. NISHIDA and H, TANAKA..976
Some Remarks on the Scattering Problem .... M. IDA..979
Superconductivity of Ferromagnetic Metals .... T. KASUYA..980
Proton-Proton Scattering in the Gev Region—*Criticism of the Blockhintsev-Bubelev Model—* .... J. OBA and T. GOTO..982
Errata: Dispersion Relations in Nucleon-Nucleon Scattering .... S. MATSUYAMA and H. MIYAZAWA..983
Contents of Journ. Phys. Soc. of Japan, Vol. 13, No. 10, 11 984
Contents and Authors Index to Volume 20 .... i–x

Price $ 1.25 per copy
$ 15.00 per year (postage inclusive)
Annual dues for foreign members (individual subscribers)
$ 12.00 (postage inclusive)
" for foreign members of the Physical Society of Japan
$ 10.00 (postage inclusive)

Application for members, subscriptions and orders for back numbers should be sent, directly or through book-dealers, to

The Publication Office
in
Yukawa Hall, Kyoto University, Kyoto, Japan

JOURNAL OF THE PHYSICAL SOCIETY OF JAPAN Vol. 14, No. 8, AUGUST, 1959

Angular Correlation of Gamma Rays from Xe^{126} and Te^{126}

By Mitsuo SAKAI, Hidetsugu IKEGAMI, Toshimitsu YAMAZAKI
Institute for Nuclear Study, University of Tokyo, Tanashimachi,
Kitatamagun, Tokyo, Japan

and Kazusuke SUGIYAMA
Department of Physics, Tohoku University, Sendai, Japan

(Received February 21, 1959)

The angular correlation of gamma rays in 2−2−0 cascade transitions in Xe^{126} and Te^{126} is measured from the decay of I^{126} in order to obtain the mixing ratio of competing E2 and M1 transitions in the 2−2 transition. The mixing ratio is found to have positive sign for both nuclei, as expected from the systematics of excited levels in even-even nuclei.

§ 1. Introduction

The systematics of excited levels in even-even nuclei revealed recently1) that the nuclei having 0−2−2 spin sequence[*] appear in three neutron-islands where the 1/2 orbit competes with the higher angular momentum orbit owing to the large pairing energy, namely $38 \leq N \leq 48$, $(2\,p_{1/2}, 1\,g_{9/2})$, $64 \leq N \leq 74$, $(3\,s_{1/2}, 1\,h_{11/2})$ and $110 \leq N \leq 120$, $(3\,p_{1/2}, 1\,i_{13/2})$[**]. Moreover it was pointed out from a rather poor statistics that the sign of mixing ratio δ of competing E2 and M1 transitions from the second 2+ to the first 2+ level alternates from one island to the other. The sign of the first and third islands is negative[***] and that of the second island is positive. This observation seems to be very important for understanding the physical meaning of the mixing ratio in even-even nuclei.

Since in the second island δ was measured only in Sn^{116} 3) and Te^{122} 4), it was considered worth while to measure the sign of δ in Xe^{126} and Te^{126} by using gamma rays from I^{126} (13 day) in order to put this interesting rule on the more solid experimental bases.

The decay scheme of I^{126} (Fig. 1) was very well established by beta and gamma spectroscopy5). Therefore the problem is now to measure the angular correlations between 0.75-MeV and 0.65-MeV gamma rays in Te^{126} and between 0.48-MeV and 0.386-MeV gamma rays in Xe^{126}.

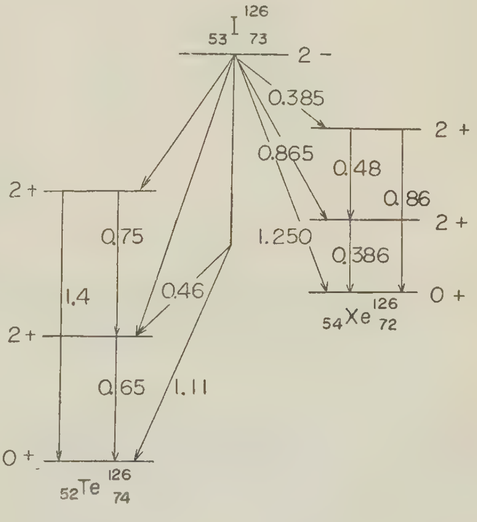

Fig. 1. Decay scheme of I^{126} proposed by Koert et al.

§ 2. Source Preparation

The I^{126} sample was prepared by bombarding a natural antimony layer with 200 microampere-hours of 30-MeV alpha particles in the 63-in. cyclotron of the Institute for Nuclear Study of University of Tokyo, leading to the reaction Sb^{123} (α, n) I^{126}. Since I^{124} (4.5 day) was produced at the same time, the measurement was started about 40 days after the bombardment. The scintillation spectrum of $\mathrm{I}^{124}+\mathrm{I}^{126}$ is presented in Fig. 2 with its time dependence. A radio active NaI solution of

---

[*] The nuclei having 4+ or 0+ level near the second 2+ level are included in this category.

[**] Notice that there exist proton islands originating from the competition of proton configurations $(2\,p_{1/2}, 1\,g_{9/2})$ and $(3\,s_{1/2}, 1\,h_{11/2})$. The last one and the third neutron island overlap each other.

[***] It was remarked recently2) that several nuclei in the third island have positive mixing ratio. However this may be explained by the fact that the second proton island overlaps just this region, so it is not inconsistent with the rule.

1 mm diameter and 4 mm long in a plastic container was served as the source for the correlation experiment for avoiding the influence of extra-nuclear fields.

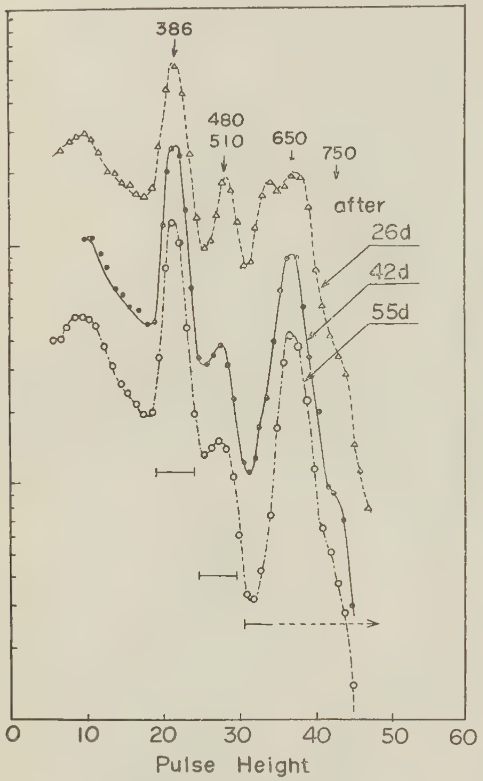

Fig. 2. Scintillation pulse height spectra of gamma rays in decay of $I^{126}+I^{124}$ taken 26 days, 42 days and 52 days after the bombardment.

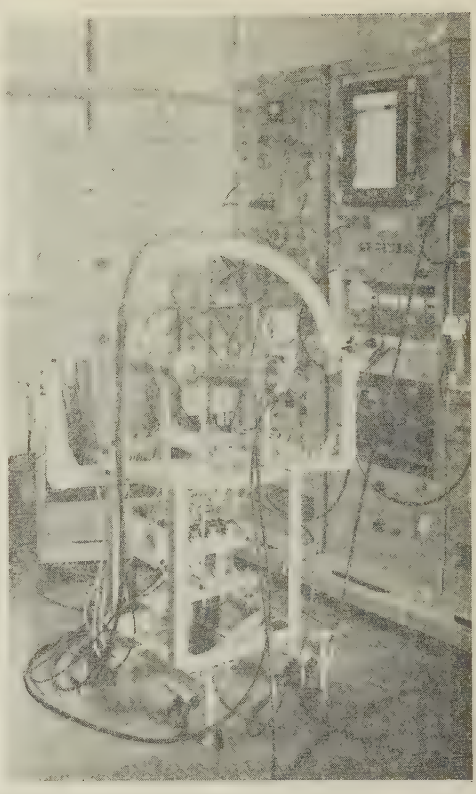

Fig. 3. The angular correlation apparatus.

§ 3. Results

The angular correlation apparatus is shown in Fig. 3, consisting of two detectors, one fixed and one movable, mounted on a table. NaI (TI) crystals, one 2-in. in diameter by 2-in. height and one 1¾-in. in diameter by 2-in. height from Harshaw Chemical Corporation, were coupled to Dumont 6292 photomultipliers. The coincidence circuit was a conventional one of which $2\tau \simeq 0.6\mu$ sec. Throughout the measurement, the accidental coincidence counts were about 10% of the total coincidence counts. The five measuring points, separated each other by 15°, were chosen from 90° to 150° for avoiding the false coincidence counts in region at 180° produced by annihilation radiation.

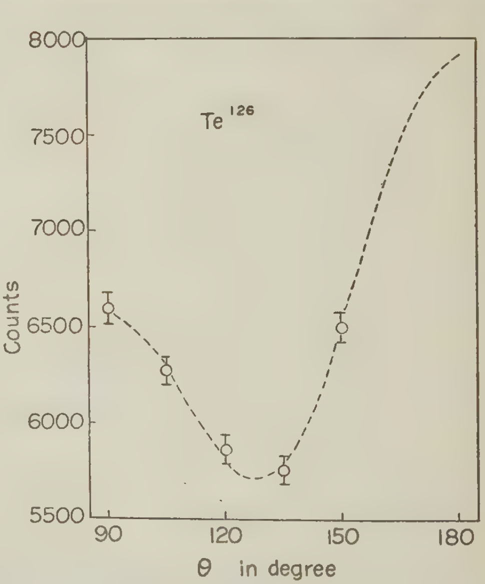

Fig. 4. Correlation curve in Te^{126}. The dashed curve is the calculated one.

1) *Angular correlation in* Te^{126}

The lower end of integral gate in each channel is set at 0.62-Mev pulse height as indicated in Fig. 2. In this gate setting, as known from the decay scheme, we can expected no other coincidences than that between 0.65-MeV and 0.75-MeV gamma rays. The result is presented in Fig. 4. Assuming the experimental correlation function $W'(\theta)$ as $1+A_2'P_2(\cos\theta)+A_4'P_4(\cos\theta)$, the least square fit has given $A_2'=0.055\pm0.008$ and $A_4'=0.214\pm0.012$. The calculated correlation curve with these A_2' and A_4' is presented also in Fig. 4. Since the energies of the gamma rays in Te^{126} and Xe^{126} are not so different from that of annihilation radiation, the correction for finite solid angle was made according to Church-Kraushaar's method⁶⁾, by measuring the angular resolution with annihilation radiation of Na^{22}. The correction coefficients Q_0/Q_2 and Q_0/Q_4 were, then, obtained to be 0.93 and 0.80, respectively. The correlation coefficients corrected for finite solid angle were the followings: $A_2=0.059\pm0.009$ and $A_4=0.268\pm0.014$.

2) *Angular correlation in* Xe^{126}

In this case the differential gates were used. The window setting in each channel, being at the photo-peaks of 0.386-MeV and 0.48-MeV respectively, was indicated in Fig. 2. The geometrical conditions were the same as that in Te^{126}. The following two points were carefully checked. The first point is the contribution of 0.51-MeV annihilation radiation to the coincidence counts because it gives excessive coincidence counts in position at 180°. Since in the present geometrical setting the overall angular resolution deduced by using annihilation radiation in Na^{22} was found to be 10.5° at half maximum, it was concluded that there was no such influence in region between 90° and 150°. The second point is the contribution of coincidence counts from the 0.65-MeV and 0.76-MeV gamma rays in Te^{126} to the correlation pattern in question. The estimation of this undesirable contribution was found to be about 10% in the present window setting, and since the observed correlation pattern was similar to that of Te^{126}, the subtraction of this contribution from the observed value could be expected to produce not so serious effect for getting the true correlation function of Xe^{126}. The corrected value is presented in Fig. 5 with the least squares curve. According to the same precedure as the preceding paragraph, the final result was obtained: $A_2'=0.066\pm0.023$, $A_4'=0.235\pm0.033$, $A_2=-0.071\pm0.025$ and $A_4=0.294\pm0.041$.

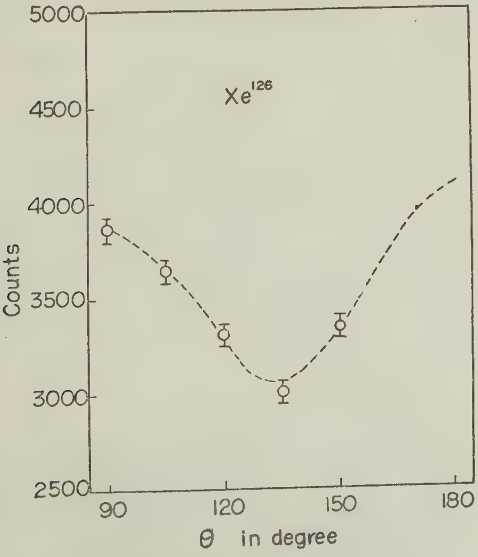

Fig. 5. Correlation curve in Xe^{126}. The dashed curve is the calculated one.

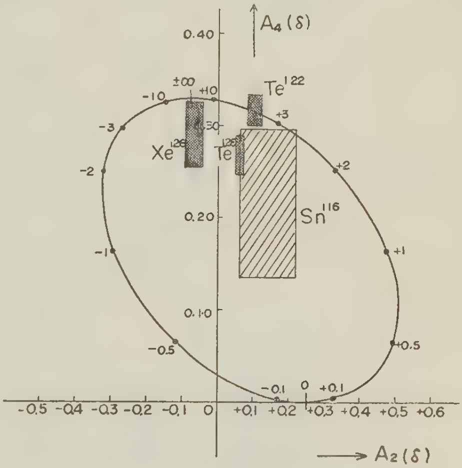

Fig. 6. Elliptical representation of A_2 and A_4 in cascade gamma transition for nuclei in 2nd S(2) island. The parameter on the ellipse indicates directly δ instead of $\delta'(=\delta(1+|\delta|)^{-1})$ used in reference 7.

§ 4. Discussion

The values of A_2 and A_4 obtained in § 3 are presented in the elliptical representation of A_2 and $A_4$⁷⁾. The A_2 and A_4 in Sn^{116} ³⁾ and Te^{122} ⁴⁾ are put also in the same figure. Parameters attached to the ellipse are mixing ratio δ in stead of $\delta'(=\delta(1+|\delta|)^{-1})$ used in reference⁷⁾. From this figure, it can be seen that the mixing ratio of these nuclei has positive sign as expected from the rule¹⁾. This rule seems to be very important for understanding the physical meaning of mixing ratio in even-even nuclei and for shedding light on the excitation mechanism of so-called vibrational levels.

Acknowledgement

We wish to thank Professor S. Kikuchi, Director of the Institute for Nuclear Study, and Professor I. Nonaka for their constant interest and encouragement. The help given by Dr. K. Saito of our Institute and Dr. H. Shimojima, Mr. H. Fukutomi and Mr. T. Nitta of the Tokyo Institute of Technology on the chemical separation of racioactive isotope is deeply appreciated.

References

1) M. Sakai: Rep. Inst. Nucl. Study, Univ. of Tokyo INSJ-6, Feb (1958).
2) V. R. Points and C. E. Mandeville: to be published in the report of the Franklin Institute.
3) R. P. Scharenberg, M. G. Stewart and M. L. Wiedenbeck: Phys. Rev. **101** (1956) 689.
4) C. F. Coleman: Nucl. Phys. **7** (1958) 488.
5) L. Koert, P. Macklin, B. Ferrelly, R. Van Lieshout and C. S. Wu: Phys. Rev. **98** (1955) 1230.
6) E. L. Church and J. J. Kraushaar: Phys. Rev. **88** (1952) 419.
7) C. F. Coleman: Nucl. Phys. **5** (1958) 495.

JOURNAL OF THE PHYSICAL SOCIETY OF JAPAN, Vol. 14, No. 8, AUGUST, 1959

Decay of I^{124}

By Kazusuke SUGIYAMA

Department of Physics, Tohoku University, Sendai

Hidetsugu IKEGAMI, Toshimitsu YAMAZAKI and Mitsuo SAKAI

Institute for Nuclear Study, University of Tokyo,
Kitatamagun, Tokyo

(Received May 1, 1959)

The gamma and beta rays following the decay of I^{124} which was produced by Sb (α, n) reaction have been studied with scintillation spectrometers both single and in coincidence, and with a beta-ray spectrometer. Three gamma rays at 2.74-MeV, 2.29-MeV and 1.50-MeV and probably 0.9-MeV which were not found in decay of Sb^{124} were observed. The beta-gamma coincidence experiments revealed that the first positron group decays to the ground level of Te^{124} so that the energy difference between I^{124} and Te^{124} becomes 3.22-MeV, being consistent with beta decay energy systematics. In addition this beta component was found to have an unique 1st forbidden type spectrum, showing the spin and parity of the ground state of I^{124} is $2-$. From these results we led to conclude the presence of two new levels at 2.88-MeV and 2.74-MeV which the spin value is probably 1 and the parity is negative. A doublet level at the second excited level previously reported was not confirmed in the present experiment. However a definite evidence of cross-over transition from the second level to the ground level was obtained which may indicate a presence of a $2+$ level at the second excited level. The tentative decay scheme is proposed.

§ 1. Introduction

The excited levels in Te^{124} were studied in detail by making use of the radiations from the decay of Sb^{124}.[1] Especially Dzelepov et al.[2] published very recently the level scheme of Te^{124}, showing the presence of a doublet at the second excited level. However the positron emitter I^{124} (4.5-day) decaying to the same daughter nucleus was not yet studied except the Michell's work[3] in 1949.

Since I^{124} belongs to the so-called 2nd $S(2)$ pattern[4] of which the systematic investigation of excited levels was taken as the central project of our group and since so little information on this isotope was available up to the present*, it was considered worth while to produce a sample of this isotope for studying the radiations from this isotope by scintillation counter techniques developed since the time of Michell's work.

§ 2. Source Preparation

The I^{124} sample was prepared by bombarding a natural antimony layer with 200 microampere-hours of 30–MeV alpha particles in the 63″ cyclotron of the Institute for Nuclear Study of the University of Tokyo, leading to the reaction $Sb^{121}(\alpha, n)I^{124}$. The antimony layer soft-soldered on the thin copper plate was fastened on the large copper block which was served as the head for the probe of 4″ in diameter. After the bombardment, the antimony layer was turn off from the backing copper plate, and dissolved in a mixture of sulfuric acid and potassium sulfate. The active iodine was warmed up to the temperature of about 300°C**.

Since the bombardment produces the radioactive I^{123}, I^{125} and I^{126} aside from I^{124} in question (see Table I), the measurement was started one week after the bombardment, avoiding the interference of the very strong 0.159 MeV gamma ray from I^{123}. The presence of radiations from I^{126} gave no significant disturbance in the following measurements.

Table I. Nuclear reaction in natural antimony by 30 MeV alpha particles.

57%	Sb^{121}	(α, n)	I^{124}	4.5d	
	〃	$(\alpha, 2n)$	I^{123}	13h	0.159 MeV γ and E. C.
	〃	$(\alpha, 3n)$	I^{122}	3.5m	no γ
	〃	(α, p)	Te^{124}	stable	
	〃	(α, pn)	Te^{123}	stable	
43%	Sb^{123}	(α, n)	I^{126}	13d	
	〃	$(\alpha, 2n)$	I^{125}	60d	0.035 MeV γ and E. C.
	〃	$(\alpha, 3n)$	I^{124}	4.5d	
	〃	(α, p)	Te^{126}	stable	
	〃	(α, pn)	Te^{125}	stable	

§ 3. Gamma Ray Spectrum

a) *Single spectrum analysis*

The gamma ray spectrum was taken by the scintillation counter which consisted of a cylindrical NaI (Tl) crystal, 4-in. long and 4-in. in diameter coupled with a Dumont type 6364 photo-multiplier and Sunvic 100-channel pulse-height analyser. In this measurement the gamma rays were collimated by a cylin-

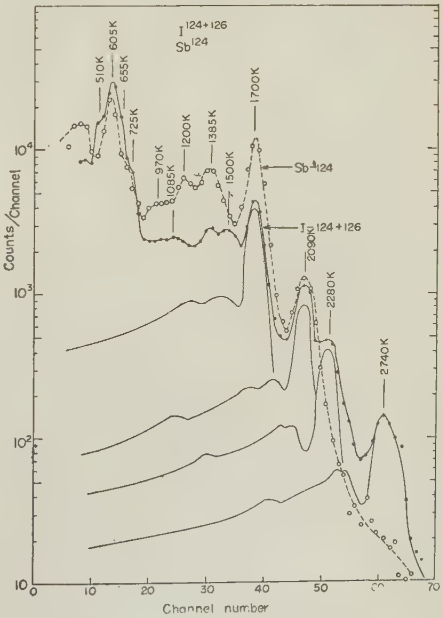

Fig. 1. Scintillation pulse-height spectrum in I^{124} $+I^{126}$ taken by the 100-channel pulse-height analyser. The spectrum in Sb^{124} is presented for comparison. The response-curve analysis is indicated by thin line curves.

---

* After this experiment was accomplished, the authors noticed that two groups have performed the same kind of experiment. The agreement of the present results with the others was found to be fairly well. (R. Van Lieshout: private comunication. Mitchell et al: Bull. Amer. Phys. Soc. Ser II **3** (1958) 357).

** The chemical procedure will be described in detail elsewhere by K. Saito et al.

Table II. Energy and relative intensity of gamma radiations in I^{124} and Sb^{124}.

I^{124}				Sb^{124}			
Present authors		R. Van Lieshout**		R. Van Lieshout**		B. S. Dzelepov et al.***	
Energy (KeV)	Relative Intensity	Energy (KeV)	Relative Intensity	Energy (KeV)	Relative Intensity	Energy	Relative Intensity
605	320±50	605	605±20	605	195±10	609	197
(655)	(45)*					646	15
720	(40)	725	110±5			714	7
900	(2)			725	29±2	723	20
970	(2)	970	10±2	970	4.4±1	969	5
1080±40	(3)	1040	10±2	1040	5.6±1	1047	5
1330 }	(47)	1380	30±10			1326	2.8
1380 }						1361	2
1500±60	(22)	1500	33±3	1380	16±5	1370	7
1700±20	100	1690	100			1450	4.2
2100±30	25±3	2090	15±2	1690	100	1692	100
2290±40	11±2	2280	12±2	2090	15±1.5	2088	12.6
2740 }	6±1	2750	5±1	2280	1.0±0.2		
(2880) }							

* Parentheses indicate an aproximate value which may have an error of order of 30%.

** Private comunication. To be published in Physica. Gamma Rays with weak intensity are omitted.

*** c.f. ref. 2).

Table III. Chart of gamma-gamma coincidence.

○ and × stand for yes and no coincidence respectively.

Energy (KeV)	605	655	720	900	970	1085	1380	1500	1700	2090	2290	2740
605	?	○	○	?	○	○	○	○	○	○	○	×
720	○	?	?	?	?	?	○	○	×	×	×	×
970	○	○	○	?	?	?	○	○	×	×	×	×
1300–1350	○	○	○	○	○	○	○	○	×	×	×	×

drical aperture of 0.8 cm and 10 cm long in the lead shield. This procedure was essentially useful for measuring higher energy gamma ray, reducing sum and escape peaks. For the purpose of comparison the spectrum of Sb ^{124} was also measured. In Fig. 1 the scintillation gamma ray spectra of these isotopes are presented and in Table II the energy of the gamma rays is tabulated with their relative intensity. The last value was obtained from the efficiency curve and photofraction curves for this detection system.

The new gamma rays at 1.50 MeV, 2.29 MeV and 2.74 MeV were observed. The last one was suspected to be a composite peak of 2.74 MeV and 2.88 MeV gamma rays but the definite conclusion was not obtained. Moreover, the comparison with the spectra of Sb^{124} indicated the presence of a gamma ray in region of energy 0.9 MeV. Both of pulse height peaks at 2.74 MeV and 2.29 MeV were observed to have the same decay time as that of 1.70 MeV gamma ray, having verified that these gamma rays belongs to I^{124}, since the 1.70 MeV gamma ray was found in the decay of Sb^{124}.

b) *Coincidence measurement*

The coincidence measurement was performed by making use of the multi-channel pulse-height analyser. Selection of a definite gamma ray from gate detector can be made with the single channel analyser and then gamma ray spectrum in coincidence with it via main detector may display on the multi-channel analyser. We have used three coincidence apparatus which had the following combination; $1\frac{1}{2}$-in. $\phi\times 1\frac{1}{2}$-in. height (gate)+4-in. $\phi\times 4$-in. height (main)+Sunvic 100 channels pulse-height analyser, $1\frac{1}{2}$-in. $\phi\times 1\frac{1}{2}$-in. height (gate)+$1\frac{1}{2}$-in. $\phi\times 1\frac{1}{2}$-in. height (main)+fast-slow coincidence circuit of which $2\tau\simeq 30$ mμs* and $1\frac{3}{4}$-in. $\phi\times 2$-in. height (gate)+2-in. $\phi\times 2$-in. height (main)+INS 10 channels pulse-height analyser** with slow gate circuit of which $2\tau\simeq 4\mu$s.

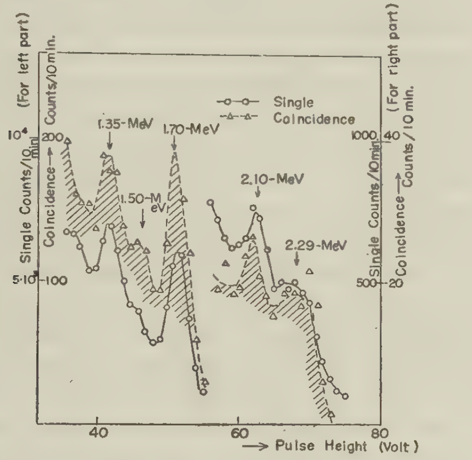

Fig. 2. Coincidence spectrum with 0-61-Mev photo-peak.

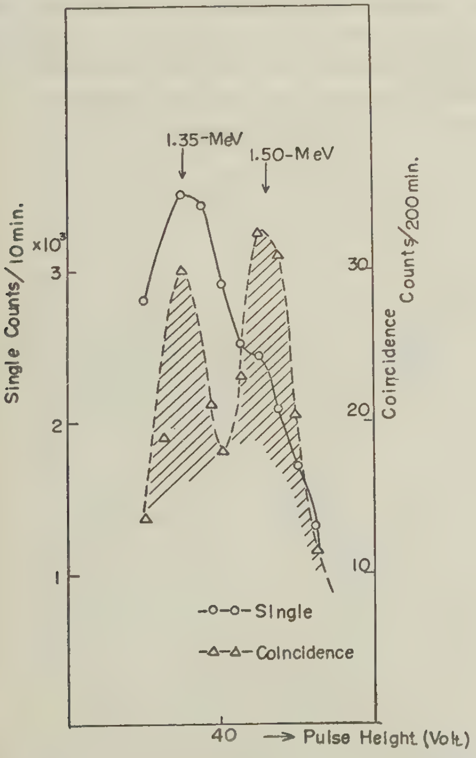

Fig. 3. Coincidence spectrum with 0.72-Mev photo-peak.

The results cross-checked by these two systems are tabulated in Table III. The typical coincidence spectra are presented in Fig. 2, Fig. 3 and Fig. 4. It should be mentioned that further careful examination of the coincidence spectrum with 1.35 MeV gamma ray in the region 0.9∼1.1 MeV indicates a presence of 0.9 MeV gamma ray. This fact is consistent with the observation in the preceding paragraph.

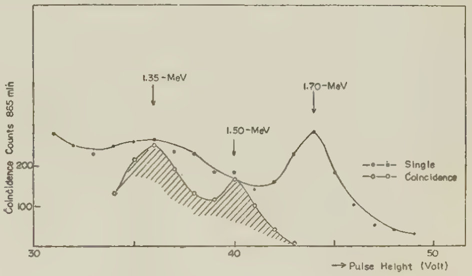

Fig. 4. Coincidence spectrum with about 1.35-Mev pulse-height region.

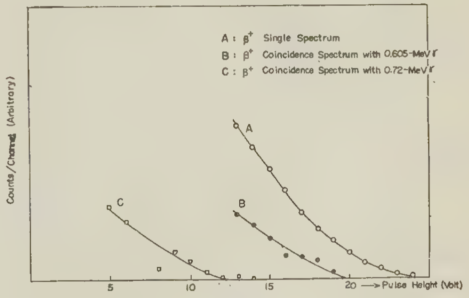

Fig. 5. $\beta^+-\gamma$ coincidence spectrum.

§ 4. Beta Ray Spectrum

a) *$\beta^+-\gamma$ coincidence spectrum*

In this case, the main detector was a beta ray detector which consisted of 1-in. $\phi\times 5$ mm thickness plastic scintillator coupled with a Dumont 6292 photomultiplier and the gate detector was a cylindrical NaI (Tl) crystal, 2-in. long. and 2-in. diameter attached to a Dumont 6292 photomultiplier. An INS 10 channels pulse-height analyser was used as the displaying apparatus for coincidence pulses. The total and coincidence spectra are presented in Fig. 5 which revealed the main beta component decays to the ground level and the 0.605 MeV gamma ray is in coincidence with the second beta component and 0.72 MeV gamma ray in coincidence with the third beta component. Since the maximum energy of the first beta component was known to be 2.20 MeV$^{3)}$, this fact indicates the energy difference between I^{124} and Te^{124} is 3.22 MeV, being consistent with the beta decay energy systematics. (see Fig. 6)

---

* M. Sugawara: to be published.

** INS 10-channels pulse-height analyser was developed by the electronics section of the Institute for Nuclear Study.

b) *Fermi plot analysis*

In order to get the Fermi plot of the first beta component, INS III beta spectrometer* (a sector type double focusing beta ray spectrometer of which $\rho=18$ cm) was used. The shape factor deduced from the Fermi plot is presented in Fig. 7, showing clearly a characteristic curve for the unique first forbidden type spectrum. Combining the result of the preceding paragraph, we concluded that the ground level of I^{124} has the spin value of 2 and negative parity.

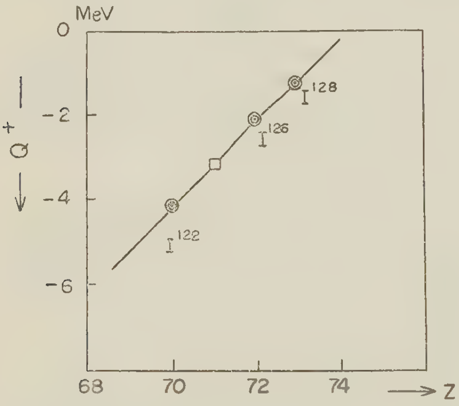

Fig. 6. Beta decay energy systematics.

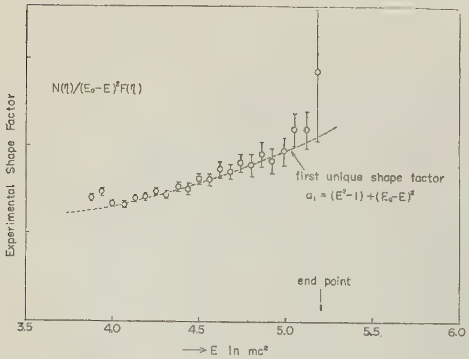

Fig. 7. Shape factor for the first positron component of I^{124}.

§ 5. Conclusion

The gamma ray spectrum showed the new photo-peaks at 2.74 MeV, 2.31 MeV, 1.50 MeV and probably at 0.9 MeV which were not observed in the decay of Sb^{124}. This fact indicates the presence of the new levels in Te^{124}. Since the 2.74 MeV gamma ray was found to decay directly to the ground level of Te^{124} and since the 2.28 MeV gamma ray was found to coincide with the 0.605 MeV gamma ray, we were led to assign the new excited level at 2.88 MeV and 2.74 MeV above the ground level.

The spin value of the ground level of I^{124} was definitely established as 2− by the shape of the 2.02 MeV first positron spectrum. Since the beta component decays to the ground level, the energy difference between I^{124} and Te^{124} should be 3.22 MeV which is consistent with the beta decay energy systematics. As the ground level of Sb^{124}, of which the spin and parity are known as 3−$^{5)}$ can not decay to the new levels by beta ray emission, we were led to conclude that the spin and parity of these levels is probably 1−.

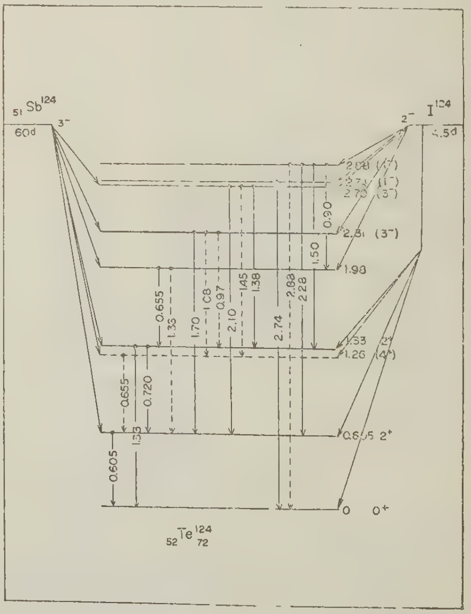

Fig. 8. Proposed decay scheme of I^{124}. The decay scheme of Sb^{124} proposed by B. S. Dzelepov et al. (ref. 2) is also shown in this figure.

---

* The details of this spectrometer will be soon published.

The 1.35 MeV gamma ray is in coincidence with the 1.50 MeV gamma ray and partially with 1.35 MeV gamma ray as shown in Fig. 4. This fact indicates; 1) the second 1.33 MeV level should be capable to de-excite to the ground level by cross-over gamma radiation and the spin and parity of this level may be 2+ as expected from the gamma ray energy relation and from the energy systematics of excited level of the S(2) pattern and 2) there must be a gamma ray of about 1.35 MeV which decays in parallel with these 1.35 MeV gamma rays and 3) the presence of a new excited level at 2.88 MeV of which the energy is the sum of 1.33 MeV and 1.50 MeV is evident, Fig. 8 shows a rather complicated decay scheme deduced from the present results and the information from the decay of Sb^{124}. Of course it is too complicated that we could not pretend it is a real one. Especially the interesting doublet at the second excited level reported by Dzelepov et al. can not be confirmed in the present experiment.

The only possibility of obtaining a negative parity for the I^{124} ground level lies in assigning on $h_{11/2}$ state to the 71st neutron which seems to be the same situation as that of I^{126}. So far as the spin of new levels are concerned, it may be understood as the following configurations from the single particle aspect

$$\{(1g_{7/2})^1(1h_{11/2})^1(3-)\}_p\{(2d_{3/2})^2(2+)\}_n(1-)$$

and

$$\{(2d_{5/2})^1(1h_{11/2})^1(3-)\}_p\{(2d_{3/2})^2(2+)\}_n(1-)$$

Therefore these two level seems to have the intimate relation to the two 3− levels just bellow these 1− levels, since the configuration of latter levels were thought as

$$\{(1g_{7/2})^1(1h_{11/2})^1(3-)\}\{(2d_{3/2})^2(0+)\}_n(3-)$$

and

$$\{(2d_{3/2})^1(1h_{11/2})^1(3-)\}_p\{(2d_{3/2})^2(0+)\}_n(3-)$$

respectively. Of course it may be possible to discuss these levels by the collective model. And in this case, the explanation as an appearance of octupole vibrational levels seems to be very attractive.

The present authors express their sincere thanks to Professor S. Kikuchi and Professor I. Nonaka for their encouragement and interest in the research. Their thanks are also due to Dr. K. Saito of the Institute for Nuclear Study and Dr. H. Shimojima, Mr. H. Fukutomi and Mr. T. Nitta of the Tokyo Institute of Technology for their skillful chemical separation of radioactive isotope and to the cyclotron crew of the Institute for Nuclear Study for their kindful cooperations. One of authors (K, S) is grateful to Prof. M. Kimura and the staff of the Laboratory of Nuclear Physics, Tohoku University, for encouragement in the experiment.

References

1) L. M. Langer and J. W. Starner: Phys. Rev. **93** (1954) 253. N. H. Lazar: Phys. Rev. **95** (1955) 292. A. V. Zolotavin, E. P. Grigoruev and M. A. Abroyav: Izv. Akad. Nauk. SSSR **20** (1956) 289. B. S. Dzelepov et al: Nucl. Phys. **2** (1956) 408.
2) B. S. Dzelepov et al: Nucl. Phys. **6** (1958) 655.
3) A. C. G. Michell et al: Phys. Rev. **76** (1949) 1450.
4) M. Sakai: Rep. Inst. Nucl. Study, Univ. of Tokyo, no. 6, Feb (1958).
5) J. J. Kraushaar and M. Goldhaber: Phys. Rev. **89** (1953) 1081. F. R. Metzger: Phys. Rev. **90** (1953) 328. T. Hayashi: J. Phys. Soc. Japan **13** (1958) 117.

JOURNAL OF THE PHYSICAL SOCIETY OF JAPAN, Vol. 14, No. 8, AUGUST, 1959

Theory of Thermoelectric Power of Ionic Crystals, II.

By Eijirō HAGA

Department of Physics, Faculty of Science, Niigata University

(Received December 25, 1958)

A theory of the thermoelectric power of the NaCl crystal doped with $CdCl_2$ is developed, when we measure it by using the chlorine gas electrode. We derive also the expressions of it by taking into account the Coulomb interaction between defects in NaCl and AgBr, and estimate the correction terms to the simple theory. Next the relation between the thermoelectric power with the metallic electrodes and that with the halogen electrodes is derived, and the theoretical result is compared with experiments in silver halides and lead halides.

§1. Introduction

There is only a qualitative theory[1] on the mechanism of thermal diffusion of ions in ionic crystals. The information about this is obtained from the thermoelectric power. The purpose of the present paper is to investigate the thermal properties of alkali halides from the knowledge of the thermoelectric power. In the previous paper (I) we have developed a theory of the thermoelectric effects in AgBr or AgCl, under the condition that the silver metal is used as electrode and defects distribute at random in it.[2] In the case of alkali halides, however, alkali metals are not available as electrode because of their low melting points. Therefore, we shall develope a theory of the thermoelectric power of NaCl with use of the chlorine gas electrode as devised by Reinhold.[3]

As is well known, the ionic conduction in alkali halides is due to the presence of the Schottky defects in contrast with silver halides. Etzel and Maurer have measured the ionic conduction in NaCl doped with $CdCl_2$, and estimated several important parameters making use of the simple theory in which the Coulomb interaction between defects is left out of consideration.[4] Their measurements show that below 400°C the intrinsic effects can be neglected in comparison with the impurity effects.

Further, the analyses of the ionic conduction have been carried out taking into account the Coulomb interaction between defects in AgBr by Teltow[5] and in NaCl at impurity range by Lidiard[6]. The values of parameters thus obtained are considerably different from those based on the simple theory. Therefore, it seems interesting to study the effect of the Coulomb interaction on the thermoelectric power. This effect will be considered in the Debye-Huckel approximation[7] for NaCl and AgBr.

§2. Thermoelectric Power of NaCl

Let us consider the following arrangement devised by Reinhold:

$$M\,|\,C,\ Cl_2\,|\,NaCl\,|\,Cl_2,\ C\,|\,M\,. \qquad (1)$$

Here, C is the graphite rod inserted ("eingeschmolzen") into a sample of NaCl, and M is the lead wire. We shall calculate the difference of the Fermi levels per degree, eQ, between the topps of two graphite rods in NaCl, which is equal to the thermoelectric power measured in the arrangement (1) times the magnitude of electronic charge if the thermoelectric powers of M and C are left out of consideration.

The chlorine atom in NaCl near the contact with C and that in the chlorine gas at the same temperature, are in thermal equilibrium through the process of generation of V-centers in NaCl, so that we have

$$\mu_{Cl}^{NaCl}=\mu_{Cl_2}^{Cl_2}/2\,, \qquad (2)$$

where μ_{Cl}^{NaCl} and $\mu_{Cl_2}^{Cl_2}$ are the chemical potential of a chlorine atom in NaCl and that of a chlorine molecule in the chlorine gas, respectively. Further, the following reaction takes place at the constact between NaCl and C:

$$Cl \leftrightarrows Cl^- - e^-\,. \qquad (3)$$

The above equilibrium will be established through the process in which electrons from C recombine with trapped holes in V-centers and the double layer is formed at the contact between NaCl and C, or through the inverse process. We have, from the reaction (3),

$$\mu_{\mathrm{Cl}}^{\mathrm{NaCl}}=\mu_{\mathrm{Cl}^-}^{\mathrm{NaCl}}-\zeta_{e^-}^{C}\,, \tag{4}$$

where $\zeta_{\mathrm{Cl}^-}^{\mathrm{NaCl}}$ and $\zeta_{e^-}^{C}$ are the electrochemical potential of a chlorine ion in NaCl and that of an electron in C, respectively. From Eqs. (2) and (4), we find the following fundamental equation for Q:

$$eQ=eQ_{\mathrm{Cl}^-}^{\mathrm{NaCl}}-s_{\mathrm{Cl}_2}^{\mathrm{Cl}_2}/2\,, \tag{5}$$

where $eQ_{\mathrm{Cl}^-}^{\mathrm{NaCl}}$ is the value obtained by subtracting the electrochemical potential of a chlorine ion in NaCl at a certain point from that at other point at lower temperature by 1°C, and $s_{\mathrm{Cl}_2}^{\mathrm{Cl}_2}$ is the entropy of a chlorine molecule in the chlorine gas. Now the problem is merely to calculate $eQ_{\mathrm{Cl}^-}^{\mathrm{NaCl}}$.

Let us now assume that positive and negative ion vacancies are distributed at random. The chemical potential of an Na^+ vacancy, μ_+, and that of a Cl^- vacancy, μ_-, which are defined as the Gibbs free energy of taking out a sodium ion and a chlorine ion in a normal site into the vacuum, respectively, are then given by

$$\left.\begin{aligned}\mu_+&=\mu_+{}^0+kT\ln c_+\\ \mu_-&=\mu_-{}^0+kT\ln c_-\end{aligned}\right\} \tag{6}$$

where $\mu_+{}^0$ and $\mu_-{}^0$ are the Gibbs free energies of taking out a sodium ion and a chlorine ion in a normal site in a perfect crystal of NaCl into the vacuum, respectively, c_+ and c_- are the mol fractions of sodium- and chlorine-ion vacancies, respectively. From Eqs. (5) and (6), we can derive an expression for the thermoelectric power:

$$eQ=-\frac{t_-}{T}(h_s+Q_+{}^*+Q_-{}^*)+\frac{Q_+{}^*}{T}-k\ln c_+ +\left(s_{\mathrm{Cl}^-}^{P}-\frac{1}{2}s_{\mathrm{Cl}_2}^{\mathrm{Cl}_2}\right)+k\Sigma\ln\frac{\nu_P}{\nu_+}\,. \tag{7}$$

Here t_- is the transport number of the chlorine ion, h_s is the enthalpy of formation of a pair of Schottky defects, $Q_+{}^*$ and $Q_-{}^*$ are the heat of transport of an Na^+- and a Cl^--vacancy, and $s_{\mathrm{Cl}^-}^{P}$ is the entropy of a sodium ion in a perfect crystal of NaCl. Further, ν_P and ν_+ are the frequency of a normal mode of lattice oscillations in a perfect crystal and that in a crystal including only an Na^+ vacancy as defect, and $\sum$ means the summation over all normal modes. The entropy of a pair of Schottky defects, s_s, is written as

$$s_s=k\Sigma\ln(\nu_P/\nu_+)+k\Sigma\ln(\nu_P/\nu_-)\,, \tag{8}$$

of which both terms are expected to be positive.[8] If we assume that they are equal, we have $k\ln\nu_P/\nu_+\sim 150\ \mu v$/degree according to Etzel and Maurer.[4] Further, the analysis of Etzel and Maurer gives $h_s\sim 2.02\ ev$. It may be assumed that $s_{\mathrm{Cl}^-}^{P}$ is equal to a half of the entropy of a pair of ions in a perfect crystal of NaCl which is obtained from the experiment on the specific heat. Then, we can find the values of $Q_+{}^*$ by comparing the theoretical expression (7) with the experiment on the thermoelectric power of NaCl at the impurity range ($t_-\sim 0$). It is to be noted that the diffusion of pairs of Cd^{++} and Na^+ vacancies, and of those of Na^+- and Cl^--vacancies, have no effect on Eq. (7), since they have no charge.

So far, we have neglected the Coulomb interaction between defects. We shall now consider this effect in the impurity range making use of the Debye-Hückel approximation. The chemical potential of an Na^+ vacancy, μ_+, is now written as[7]

$$\mu_+=\mu_+{}^0+kT\ln(c_+f_+)\,. \tag{9}$$

If the charge neutrality is assumed, the activity coefficient, f_+, is given by[7]

$$\ln f_+=-\frac{e^2}{2\varepsilon kT}\frac{\kappa}{1+\kappa R}\,,\qquad \kappa^2=\frac{8\pi e^2c_+}{v\varepsilon kT}\,, \tag{10}$$

where R is the effective shortest distance of approach of a Cd^{++} and an Na^+ vacancy without forming a complex, ε is the dielectric constant, and v is the volume per pair of ions of pure salt. Lidiard[6] has put $R\equiv\sqrt{2}\,a$ and $e^2/\sqrt{2}\,k\varepsilon a\equiv T_0$, where a is the normal anion-cation separation, and obtained $T_0=3900$°K from comparison with the experiment of Etzel and Maurer.[4] Further, he has obtained the expression of the degree of association of a Cd^{++} and an Na^+ vacancy, p, as

Table I. The value of Q_c in μv/°C in NaCl

°C	$c_0=10^{-4}$	$c_0=10^{-8}$	$c_0=10^{-2}$
200	+26	+59	+63
300	+ 4	+22	+25
400	− 4	+ 5	+ 9
500	− 7	− 3	+ 1
600	− 7	− 6	− 2
700	− 7	− 8	− 4

$$\frac{p}{(1-p)^2}=\exp\left[\frac{T_0}{T}+\ln(12c_0)-\frac{2(2\sqrt{2}\,\pi)^{1/2}(T_0/T)^{3/2}[c_0(1-p)]^{1/2}}{1+4(\sqrt{2}\,\pi)^{1/2}[(1-p)c_0T_0/T]^{1/2}}\right], \tag{11}$$

where c_0 is the mol fraction of doped cadmium. From Eqs. (10) and (11), $\ln f_+$ is written as

$$-kT\ln f_+=\frac{kT_0}{2}\left[1+\frac{T}{T_0}\ln(12c_0)-\frac{T}{T_0}\ln\frac{p}{(1-p)^2}\right]. \tag{12}$$

The electric field is obtainable from the condition that the current density due to Na^+ vacancies :[11]

$$j_+=\frac{\sigma_+}{e}\left(eE+\frac{\partial\mu_+}{\partial c_+}\frac{dc_+}{dx}+\frac{Q_+}{T}\frac{dT}{dx}\right) \tag{13}$$

vanishes. Here σ_+ is the partial conductivity due to Na^+ vacancies. From Eqs. (9), (11), (12) and (13), we find

$$eQ=\frac{Q_+{}^*}{T}-k\ln[c_0(1-p)]+\left(s^P_{Cl^-}-\frac{1}{2}s^{Cl_2}_{Cl_2}\right)+k\Sigma\ln\frac{\nu_P}{\nu_+}+eQ_c\,, \tag{14}$$

where eQ_c is obtained by differentiating Eq. (12) with respect to T as

$$eQ_c=\frac{k}{2}\,\frac{[1+p+p\ln\{12c_0(1-p)^2/p\}]\cdot[T_0/T+\ln\{12c_0(1-p)^2/p\}]}{p[T_0/T+\ln\{12c_0(1-p)^2/p\}]-2(1+p)[1+4(\sqrt{2}\,\pi)^{1/2}\{(1-p)c_0T_0/T\}^{1/2}]} \tag{15}$$

and represents the deviation from the simple theory. Table I. shows the values of Q_c in μv/degree at several temperatures and with several mol fractions of doped cadmium, where p has been obtained from Eq. (11). It is seen from Table I. that the correction term, Q_c, is so small that it need not to be taken into account in the analysis of the thermoelectric power of NaCl, at least, in the impurity range.

Nikitinskaya and Murin have measured the thermoelectric power of NaCl by making use of Pt etc. as the electrodes.[9] It is difficult to interprete their results, since we do not know what is the equilibrium condition at the junction between Pt and NaCl. The experiment with use of the chlorine electrode is desirable.

§ 3. The Effect of the Coulomb Interaction on the Thermoelectric Power of AgBr, and the Relations between Q_M and Q_H

Let us consider the effect of the Coulomb interaction also in the case of AgBr in the Debye-Hückel approximation, The ionic conduction in AgBr is due to both Ag^+ interstitial ions and vacancies. The chemical potential of an Ag^+ vacancy, μ_v, is given by Eqs. (9) and (10), where R means the effective shortest of approach of three kinds of ions (i.e. a Cd^{++} dissociated, an Ag^+ interstitial ion and an Ag^+ vacancy) without forming a complex, and the suffix v is used in place of $+$, in this section. The chemical potential of an Ag^+ interstitial ion, μ_i, is given by

$$\mu_i=\mu_i{}^0+kT\ln(c_if_i/2)\,, \tag{16}$$

where c_i and f_i are the mol fraction and the activity coefficient of an Ag^+ interstitial ion, respectively. The neutrality condition gives $f_i=f_v$. The current density due to Ag^+ vacancies, j_v, is given by Eq. (14). On the other hand, the current density due to Ag^+ interstitial ions, j_i, is given by[11]

$$j_i=\frac{\sigma_i}{e}\left(eE-\frac{\partial\mu_i}{\partial c_i}\frac{dc_i}{dx}-\frac{\partial\mu_i}{\partial c_v}\frac{dc_v}{dx}-\frac{Q_i{}^*}{T}\frac{dT}{dx}\right), \tag{17}$$

where σ_i is the partial conductivity due to Ag^+ interstitial ions. As f_i and accordingly μ_i depend on c_v, the third term in Eq. (17) represents the diffusion of Ag^+ interstitial ions in the presence of the concentration gradient of Ag^+ vacancies. From Eqs. (3) and (7) in (I), we find the thermoelectric power Q :

$$eQ=-\frac{t_i}{T}(h_F+Q_i{}^*+Q_v{}^*)-k\ln c_v+\frac{Q_v{}^*}{T}+\alpha+eQ_c\,. \tag{18}$$

Here t_i is the transport number of Ag^+ interstitial ions, α is the notation used in (I). Further, Q_c represents the deviation from the simple theory and is given by

$$eQ_c=-\frac{\partial}{\partial T}[kT\ln f_v]+2kTt_i\frac{\partial}{\partial T}\ln f_v\,, \tag{19}$$

$$\frac{\partial}{\partial T}[kT\ln f_v]=\frac{e^2\kappa}{4\varepsilon(1+\kappa R)^2}\left[\frac{1}{T}+(3+2\kappa R)\frac{1}{\varepsilon}\frac{d\varepsilon}{dT}+\frac{1}{v}\frac{dv}{dT}+2\kappa\frac{dR}{dT}-\frac{1}{c_v}\frac{dc_v}{dT}\right], \tag{20}$$

$$2kT\frac{\partial}{\partial T}\ln f_v=\frac{e^2}{\varepsilon T}\frac{\kappa}{1+\kappa R}+2\frac{\partial}{\partial T}[kT\ln f_v]\,. \tag{21}$$

Now, we roughly estimate the values of Q_c making use of the values of parameters obtained from the simple theory by Teltow.5) Table II shows the values of Q_c in μv/degre for AgBr+0.25%−CdBr$_2$ and pure AgBr. For comparison, the experimental values of Patrick and Lawson are also shown. Here, the value of ε is obtained from the extrapolation of the experimental values of Eucken and Büchner.10) It is seen from Table II that the correction due to the Coulomb interaction is small compared with the experimental values.

Reinhold3) has measured the thermoelectric powers of silver halides and lead halides in two different ways, one is with use of the metallic electrodes and the other with use of the halogen electrodes. We shall find the relations between the thermoelectric powers with the metallic electrodes, Q_M, and those with the halogen electrodes, Q_H. The assumption of local equilibrium in silver halides, AgX, leads to

$$\zeta_{\mathrm{Ag}^+}+\zeta_{\mathrm{X}^-}=\mu_L^P \tag{22}$$

where μ_L^P is the chemical potential of a pair of ions in a perfect crystal of AgX. From Eq. (5) and Eq. (3) in (I), we obtain

$$Q_H=Q_M+S \tag{23}$$

$$eS=s_L^P-s_{\mathrm{Ag}}^{\mathrm{Ag}}-s_{\mathrm{X}_2}^{\mathrm{X}_2}/2\,, \tag{24}$$

where s_L^P is the entropy of a pair of ions in a perfect crystal of AgX. Similarly we have, in the case of lead halides,

$$eS=(s_L^P-s_{\mathrm{Pb}}^{\mathrm{Pb}}-s_{\mathrm{X}_2}^{\mathrm{X}_2})/2\,, \tag{25}$$

where s_L^P is the entropy per molecule of PbX$_2$ in a perfect crystal of PbX$_2$. Table III shows the values of Q_H-Q_M in μv/degree obtained by Reinhold and those of S in μv/degree found from the experiment on the specific heat.

Table II. The value of Q_c and the experimental value of Q by Patrick and Lawson in AgBr (in μv/°C).

AgBr+0.25%-CdBr$_2$						Pure AgBr					
°C	$R=0$	$R=a$	$R=2a$	$R=3a$	Exp.	°C	$R=0$	$R=a$	$R=2a$	$R=3a$	Exp.
100	−20	−20	−20	−20	−400	200	−110	−80	−60	−50	−1240
150	−50	−40	−30	−30	−310	250	−110	−60	−30	−10	−1010
200	−60	−40	−30	−30	−290	300	− 80	−10	+10	+20	− 820
250	+10	+ 4	+ 3	+ 2	−430	350	− 40	+30	+40	+40	− 660

Table III. Q_H-Q_M and S in μv/°C.

	AgBr		AgCl		PbBr$_2$		PbBr$_2$	
°K	Q_H-Q_M	S	Q_H-Q_M	S	Q_H-Q_M	S	Q_H-Q_M	S
400	−660	−570	−180	−540	−850	−760	−700	−720
500	−680	−550	−380	−500	−790	−720	−700	−710
600	−680	−510	−580	−460	−740	−710	−700	−700

The present work was supported by the Scientific Research Fund of the Ministry of Education.

References

1) K. Wirtz: Phys. Z. **44** (1943) 221.
2) E. Haga: J. Phys. Soc. Japan **13** (1958) 1090.
3) H. Reinhold: Z. anorg. allg. Chem. **171** (1928) 181. H. Reinhold and A. Blachny: Z. Electrochem. **39** (1933) 290.
4) H. W. Etzel and R. J. Maurer: J. Chem. Phys. **18** (1950) 1003.
5) J. Teltow; Ann. Physik **5** (1949) 71.

6) A. B. Lidiard: Phys. Rev. **94** (1954) 29.
7) R. H. Fowler and E. A. Guggenheim: *Statistical Thermodynamics* (Cambridge Univ., 1939).
8) N. F. Mott and R. W. Gurney: *Electronic Processes in Ionic Crystals*, 2nd ed. (Oxford, 1848.)
9) T. I. Nikitiskaya and A. N. Murin: Zh. Tekh. Fiz. **25** (1955) 1198.
10) A. Eucken and A. Buchner: Z. phys. Chem. (B) **27** (1934) 321.
11) C. Wagner: Ann. Physik **3** (1929) 629.
S. R. de Groot: *Thermodynamics of Irreversible Processes* (Amsterdam, 1951.)

JOURNAL OF THE PHYSICAL SOCIETY OF JAPAN, Vol. 14, No. 8, AUGUST, 1959

Ionic Conduction in β-Ag_2Te and β-Ag_2Se

By Shin-ya MIYATANI

Department of Physics, Faculty of Science,
Niigata University

(Received March 17, 1959)

The ionic conductivity, σ_i, of β-Ag_2Te and β-Ag_2Se is estimated from the time constant of the ionic polarization with the help of the galvanic cell Ag|AgI|specimen|Pt, showing that σ_i depends on the composition (deviation from the stoichiometric ratio) in contrast with the composition-independent σ_i in their α phase. The chemical potential of Ag ion, ζ_i, known from the e.m.f., E, of the cell is also dependent on the composition in the β phase, and accordingly E does not represent the relative position of the Fermi level as in the α phase. This composition dependence of ζ_i and σ_i is accounted for by a simple theory. In addition, the electronic properties measured as functions of E are also compared with the theory with a correction to E by ζ_i.

§ 1. Introduction

As known from the measurements of the transport numbers by Tubandt, Wagner et al.[1], Ag ions are mobile in Ag_2S, Ag_2Se and Ag_2Te. The ionic conductivity, σ_i is fairly large in their α phases, while it is so small in their β phases that the measurement of the transport number becomes difficult except β-Ag_2S in which the electronic conductivity, σ_e, is also small as shown in Fig. 1. We have already reported about "polarization method" for measuring σ_i, which is available even in such a case of small transport number[2],[3]. The results for β-Ag_2Te and β-Ag_2Se obtained by this method will be reported in the present paper. Fig. 1 shows a somewhat schematic diagram of σ_e and σ_i thus obtained vs temperature[3].

Now, as used already in Tubandt-Wagner method, the galvanic cell Ag|AgI| Ag_2 VIb specimen Pt is very convenient, since Ag can be freely supplied to or removed from the specimen and e.m.f., E, of the cell gives us the information of the chemical potential of Ag, ζ_i, in the specimen[4],[5]. That is,

$$eE=\zeta_a{}^0-\zeta_a=\zeta_e{}^0+\zeta_i{}^0-(\zeta_e+\zeta_i)\ , \qquad (1)$$

where ζ_a, ζ_i and ζ_e are the chemical potentials of an Ag atom, Ag ion and electron in the specimen respectively, and the superscript 0 represents those in Ag-saturated state. In the α phase, $\zeta_i=\zeta_i{}^0$, namely ζ_i is composition-independent, since there are more than two available sites for each Ag ion (average crystal)[6], giving $eE=\zeta_e{}^0-\zeta_e$, that is, E representing the relative position of the Fermi level. In the β phase, on the contrary, $\zeta_i\neq\zeta_i{}^0$, namely composition-dependent, as seen later, which means that the character of average crystal becomes lost. Correspondingly, the ionic conductivity, σ_i, is composition-independent in the α phase, while it will be, in general, composition-dependent in the β phase as AgCl, AgBr etc. In fact, σ_i depends on the composition in β-Ag_2Se as seen later. Thus, the β phases of Ag_2Te and Ag_2Se are of interest in the sense that they are located in a transient region from the average type to non-average.

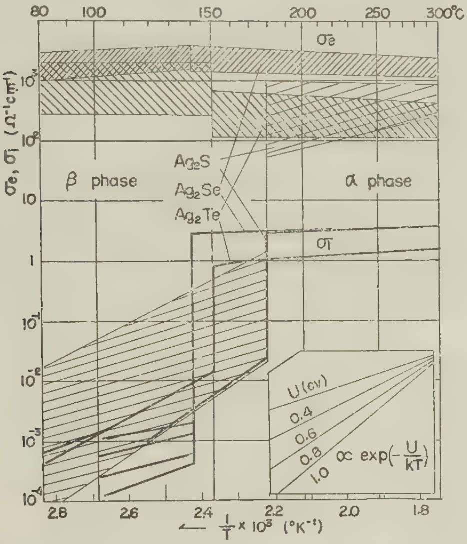

Fig. 1. σ_e and σ_i vs $1/T$ (somewhat schematic). The σ_e's are in the range shown by hatching, depending on the composition. $\exp(-U/kT)$ is also drawn for reference.

§ 2. Experimental and Comparison with Theory

(a) *The chemical potential of Ag ion*

Fig. 2 shows E and σ_e vs temperature for various x values where x represents the deviation from the stoichiometric ratio as $Ag_{2(1+x)}Te$ (or Se) and is equal to the concentration of excess Ag, D, divided by the concentration of Ag ion, N, ($eN=4.77\times10^3 C\ cm^{-3}$ for Ag_2Te and 5.25×10^3 for Ag_2Se). First, let us consider Ag_2Te. The E vs temperature curves (Fig. 2(a)) show that they become to separate from each other with decreasing temperature. Such a separation is not observed in the α phase and can not be attributed to the chemical potential of electron, ζ_e since the electrical properties such as thermoelectric power, Nernst coefficient etc. do not indicate the increase of degeneracy large enough to account for such a separation. It should be, therefore, attributed to the chemical potential of Ag ion, ζ_i, that is, ζ_i should be composition-dependent.

In order to obtain the theoretical expression for ζ_i, let us assume there are two available sites, a and b, of different occupation energies, E_a and E_b ($E_a>E_b$) for each Ag ion. In the limit of perfect average crystal ($E_a=E_b$) the two sites are equivalent, and in the other limit of $E_a\gg E_b$ the a-site corresponds to interstitial and the b-site to normal site.

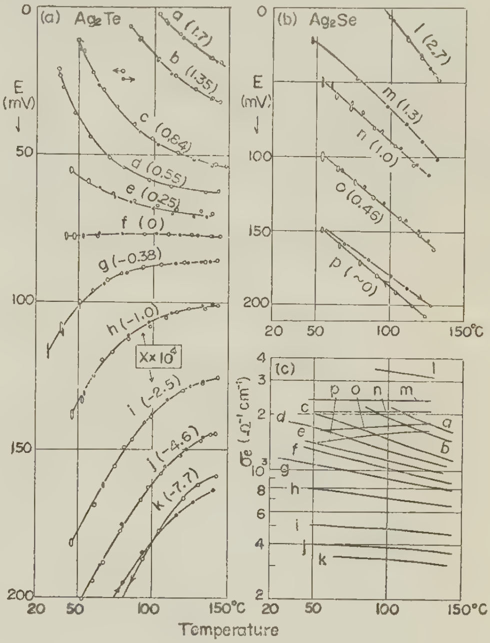

Fig. 2. (a) E vs temperature for Ag_2Te with various x values where the x values are known relative to a certain composition from the amount of Ag removed or supplied across AgI, and $x=0$ is determined by the analysis in the α phase. (b) The similar plots for Ag_2Se where $x=0$ is determined by the analysis of σ_i as seen later. (c) σ_e vs temperature corresponding to (a) and (b).

Then ζ_i is given, as seen in the next paragraph, by

$$\left.\begin{aligned}\zeta_i&=\frac{E_a+E_b}{2}-\frac{kT}{2}\log j+kT\log(\sqrt{1+z^2}+z)\,,\\ z&\equiv\frac{n-N}{2\sqrt{j}\,AN}=\frac{x}{2\sqrt{j}\,A}\,,\\ A&\equiv\exp\left(-\frac{E_a-E_b}{2kT}\right),\end{aligned}\right\}\qquad(2)$$

where n is the concentration of Ag ion, N is that in the stoichiometric composition which is equal to the concentration of the b-site, N_b, and j is the ratio of the number of a-site to b-site, N_a/N_b. Eq. (2) is reduced, if $|z|\gg 1$, to

$$\left.\begin{aligned}\zeta_i&=E_a+kT\log\frac{n-N}{N_a} &&(n>N)\,,\\ \zeta_v&=-\zeta_i=-E_b+kT\log\frac{N-n}{N} &&(n<N)\,,\end{aligned}\right\}\qquad(3)$$

which are the familiar expressions for single defect; interstitial only and vacancy only respectively. Fig. 3(a) shows $\log(\sqrt{1+z^2}+z)$ (the last term of Eq. (2) divided by kT) vs $\log A$, taking $x/\sqrt{j}$ as parameter. The abscissa can be regarded as $1/T$ in a certain scale because of $-\log A=(E_a-E_b)/(2kT)$. This function tends to $\log(x/\sqrt{j})-\log A$ for $z\gg 1$ as shown by broken lines, corresponding to Eq. (3). Further, since $\log(\sqrt{1+z^2}+z)$ is an odd function of z or x, the curves for negative x become same, exclusive of sign. For negative x, however, the curves in the figure may be regarded as $|-\log\sqrt{j}+\log(\sqrt{1+z^2}+z)|$ vs $\log A$ taking x itself as parameter if $|z|$ is large, since the latter function tends to $\log(x/A)$. Fig. 3(a) is rewritten as 3(b); $-(1/2)\log j+\log(\sqrt{1+z^2}+z)$ vs x, taking A and j as parameters, which represents how ζ_i changes with x at a fixed temperature.

Now, returning to the experimental, the change of E with varying temperature in Fig. 2(a) is constituted of three factors; the change of $\zeta_a{}^0$, of ζ_e, and of ζ_i. The first corresponds to the change of the saturation limit for Ag, and the second is due to the change of carrier densities and the energy

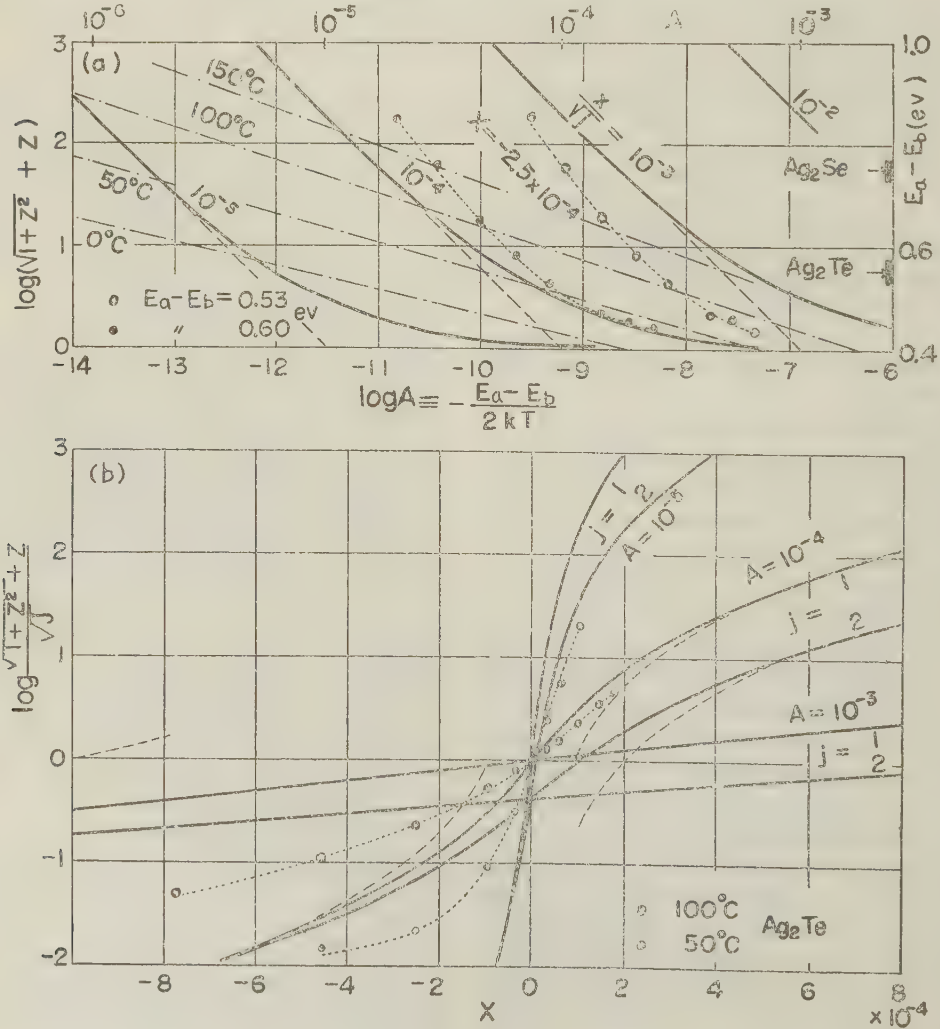

Fig. 3.

gap which may be taken as constant (composition-independent) in the present rough discussion, and the last will be due to the temperature dependent term in Eq. (2). One will see in Fig. 2(a) that the inclinations of E-curves decrease with increasing temperature and become almost zero at the neighborhood of the transition point, which may mean that the composition-dependent term of ζ_i tends to zero at such a temperature. Further the E curve for $x=0$ is almost horizontal and so we may take the curves in Fig. 2 (a) as representing the last term of Eq. (2), exclusive of the respective additive constants coming from the difference of ζ_e which will be nearly equal to the difference of E at a higher temperature e.g. 140°C. Thus, comparing Fig. 2(a) with 3(a), one will see that it may be possible to account for the experimental by Eq. (2). The value of E_a-E_b is accordingly obtainable, e.g. from the inclination of E curves for large z. Some of the experimental values are shown in Fig. 3(a) and (b); assuming two values of E_a-E_b for (a) and assuming the curve passes the origin for (b). From these plots, one will see that the experimental and theory show at least a qualitative agreement. The value of E_a-E_b thus estimated is shown on the ordinate axis at right. For convenience, E_a-E_b vs $\log A$ lines are also drawn as the chain lines, making use of which it is easy to know the A value from the E_a-E_b value.

Next, let us consider Ag_2Se (Fig. 2(b)). In

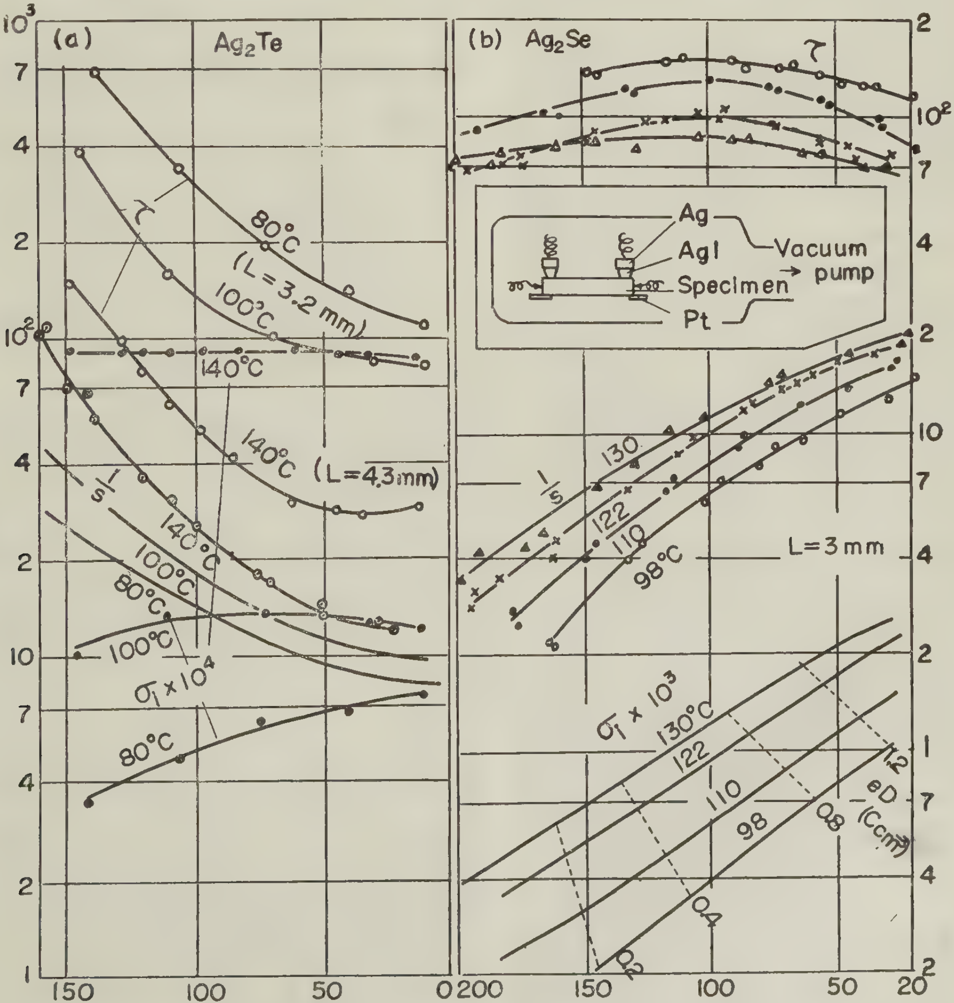

Fig. 4. τ (sec), $1/s$ (C v^{-1} cm^{-3}), and σ_i (Ω^{-1} cm^{-1}) vs E.

this case, the negative x is not realized owing to the evaporation (or precipitation) of Se, and so the separation as appears in Ag_2Te is not remarkable. However, the rapid increase of E with increasing temperature suggests also that it is due to ζ_i. The value of A will be estimated in the next section.

(b) *Ionic conductivity*

As mentioned in Introduction, the ionic conductivity, σ_i, is obtainable from the polarization as follows[2]: When a constant direct current is sent to the specimen through platinum electrodes, the polarization of Ag ions occurs along the specimen. The time constant, τ, for the polarization to build up or decay out is given by

$$\frac{1}{\tau}=\left(\frac{\pi}{L}\right)^2\frac{\sigma_i\sigma_e}{\sigma_i+\sigma_e}\frac{\partial(\zeta_e+\zeta_i)/e}{\partial(eD)}\approx\left(\frac{\pi}{L}\right)^2\sigma_i\left|\frac{\partial E}{\partial(eD)}\right|, \tag{4}$$

where L is the length of the specimen (see also the next paragraph (b)), The value of $|\partial E/\partial(eD)|\equiv s$ is known if one measures the change of E at the change of eD which is equal to the amount of electricity sent across AgI divided by the volume of the specimen. The time constant, τ, is also obtainable from the time rate of change of E at the polarization building up and decaying out (see the schematic diagram in Fig. 4). Thus σ_i is estimated with use of Eq. (4). When σ_i is as small as the present case, L should be chosen properly small so that τ is not too large. Besides, AgI–5%AgCl is used in place of pure AgI, since σ_i in the γ phase of pure AgI is very small.

Fig. 4 shows τ, $1/s$ and σ_i obtained from them vs E for different temperatures. As seen in the figure, σ_i of β-Ag_2Te is almost composition independent at least at higher temperatures, while σ_i of β-Ag_2Se depends remarkably on the composition. Then, let us consider such a composition dependence with the help of the simple model assumed in the preceding section. From a simple calculation (see § 3 (c)), σ_i is expected as

$$\sigma_i=eN\sqrt{j}\,A\{(a+b)\sqrt{1+z^2}+(a-b)z\}\,, \tag{5}$$

where a and b are the mobilities of Ag ion in the a-site and b-site respectively. If z is large, Eq. (5) is reduced to $\sigma_i=2eN\sqrt{j}\,Az=eaD$. In order to compare Eq. (5) with the experimental, σ_i of Ag_2Se is plotted against eD (relative) as Fig. 5, which shows that σ_i is, in fact, proportional to eD for large z only if the origin of eD is properly chosen as shown in the figure. From the inclination of the straight lines representing $\sigma_i=eaD$, the value of a is determined for each temperature as 0.9×10^{-3} cm² sec⁻¹ volt⁻¹ at 98°C, 1.1×10^{-3} at 110°C, 1.4×10^{-3} at 122°C and 1.6×10^{-3} at 130°C. Further, the deviation from this line is

$$\sigma_i-aeD=eN\sqrt{j}\,A(a+b)(\sqrt{1+z^2}-z)\,, \tag{6}$$

which is $eN\sqrt{j}\,A(a+b)\equiv\sigma_{i0}$ at $z=0$ $(D=0)$.

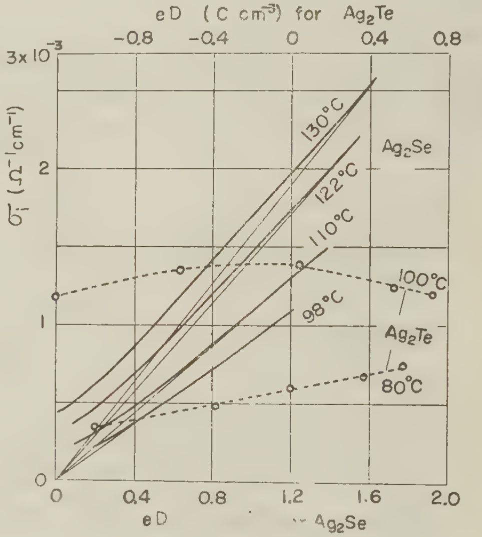

Fig. 5. σ_i vs eD.

The value of σ_{i0} is estimated by extrapolation to $D=0$, and hence we have $jA(1+b/a)$ as 3.2×10^{-5} (110°C), 4.0×10^{-5} (122°C) and 5.1×10^{-5} (130°C). Thus we see that A is order of 10^{-5} at these temperatures. On the other hand, the value of A is required to be $1\sim2\times10^{-5}$ at 124°C from the analysis of the electronic properties (see § 3 (d)). The value of E_a-E_b thus estimated is also shown in Fig. 3(a).

Next, let us consider σ_i of Ag_2Te. At temperatures higher than 140°C, where ζ_i is almost composition independent as mentioned in (a), σ_i is expected to be also composition independent just as in the α phase. This is in fact the case as mentioned already (Fig. 4). Regarding the composition dependence at lower temperatures (Fig. 5), we can not say anything sure since the measurement of τ is not too reliable.

In conclusion, one will see, from the description so far, that what determines the composition dependence of ζ_i and σ_i is A (or the reduced energy difference between two sites, $(E_a-E_b)/(kT)$) and x (or the amount of excess or deficit mobile ions). The α-phase of Ag_2Te, Ag_2Se and Ag_2S and the β phase of Ag_2S are average type, and β-Ag_2Se is almost non-average, and β-Ag_2Te is just intermediate.

§ 3. Theoretical and Electronic Properties

(a) *The chemical potential of an Ag ion*

If there are two available sites, a and b, of different occupation energies, E_a and E_b ($E_a>E_b$) for an Ag ion, then Ag ions will be distributed in these two kinds of sites with different concentration, n_a and n_b. From the condition of thermal equilibrium we have

$$\zeta_i=E_a+kT\log\frac{n_a}{N_a-n_a}\,, \tag{7}$$

$$\frac{n_a(N_b-n_b)}{n_b(N_a-n_a)}=\exp\left(-\frac{E_a-E_b}{kT}\right)\equiv A^2\,, \tag{8}$$

where N_a and N_b are the concentration of the a-sites and b-sites respectively. From Eqs. (7), (8) and $n=n_a+n_b$, ζ_i is, putting $N_b=N$, $N_a=jN$, expressed as

$$\left.\begin{aligned}\zeta_i&=\frac{E_a+E_b}{2}+kT\log\frac{\sqrt{1+z^2}+z-\sqrt{j}\,A}{\sqrt{j}-A(z+\sqrt{1+z^2})}\,,\\ z&\equiv\frac{1-A^2}{2\sqrt{j}\,A}\left(\frac{n}{N}-\frac{1-jA^2}{1-A^2}\right).\end{aligned}\right\} \tag{9}$$

Also, n_a and n_b are given by

$$n_a=\frac{\sqrt{j}\,NA}{1-A^2}(z+\sqrt{1+z^2}-\sqrt{j}\,A)\,, \tag{10}$$

$$n_b=\frac{N}{1-A^2}\{1-\sqrt{j}\,A(\sqrt{1+z^2}-z)\} \tag{11}$$

respectively. If $A\ll 1$, i.e. $(E_a-E_b)\gg kT$, then Eq. (9) is reduced to

$$\left.\begin{aligned}\zeta_i&=\frac{E_a+E_b}{2}-\frac{kT}{2}\log j+kT\log(\sqrt{1+z^2}+z)\,,\\ z&=\frac{1}{2\sqrt{j}\,A}\left(\frac{n}{N}-1\right).\end{aligned}\right\} \tag{12}$$

(b) *Polarization*

When a constant direct current is sent to the specimen through the platinum electrodes at the ends of the specimen, the current densities carried by electrons and ions, i_e and i_i, are given by

$$i_e=\sigma_e\frac{d}{dx}\left(\frac{\zeta_e}{e}-\Phi\right), \tag{13}$$

$$i_i=-\sigma_i\frac{d}{dx}\left(\frac{\zeta_i}{e}+\Phi\right), \tag{14}$$

where Φ is the electrostatic potential. Under the boundary condition that there is neither supply nor removal of Ag at the electrodes, these differential equations can be solved²⁾, resulting in the expression for the time constant, τ, as given by Eq. (4).

(c) *Ionic conductivity*

The ionic conductivity, σ_i, may be expressed as

$$\sigma_i=en_a\mu_a+en_b\mu_b\,, \tag{15}$$

where μ_a and μ_b are the mobilities of Ag ions in the a-site and b-site respectively. In particular, if $E_a=E_b$ (perfect average), then $\mu_a=\mu_b=\mu$ and hence $\sigma_i=en\mu\approx eN\mu$, that is, composition-independent σ_i. On the contrary, if $E_a-E_b\gg kT$, and $|x|$ is so large that Eq. (3) is valid, then Eq. (15) is reduced to $\sigma_i=en_a\mu_a$ for positive x and $\sigma_i=en_b\mu_b\equiv e(N-n_b)\mu_v$ for negative x. As seen by the latter equation, μ_a, μ_b, and so μ_v will be dependent of n_a and n_b as given by $\mu_a=a(N_a-n_a)/N_a$, $\mu_b=b(N-n_b)/N$, and so $\mu_v=bn_b/N$. Then σ_i may be given by

$$\sigma_i=ean_a\frac{N_a-n_a}{N_a}+ebn_b\frac{N-n_b}{N}\,, \tag{16}$$

which is rewritten, making use of Eqs. (10) and (11), as

$$\sigma_i=\frac{eN\sqrt{j}A}{(1-A^2)^2}\left(a+\frac{b}{y^2}\right)(y-\sqrt{j}\,A)\left(1-\frac{A}{\sqrt{j}}y\right), \tag{17}$$

where $y=\sqrt{1+z^2}+z$. If $A\ll 1$, it is reduced to

$$\begin{aligned}\sigma_i&=eN\sqrt{j}\,A\left(ay+\frac{b}{y}\right)\\ &=eN\sqrt{j}\,A\{(a+b)\sqrt{1+z^2}+(a-b)z\}\,,\end{aligned} \tag{18}$$

which is again reduced to $eN\sqrt{j}\,A2az=ea(n-N)$ for $n<N$, and $eb(N-n)$ for $N>n$, if $|z|\gg 1$. Here, it becomes meaningless to give a and b seperately according as A increases and approaches to unity where the a- and b-sites are equivalent.

(d) *Electronic properties*

Fig. 6(a) shows σ_e and $R\sigma_e$ vs eE/kT for Ag_2Se, where R is the Hall coefficient. As emphasized so far, E contains ζ_i beside ζ_e, and so the above plot is rewritten as the plot against $eE/kT+\log(\sqrt{1+z^2}+z)=$ const. $-\eta_1$ as (b), where $A=10^{-5}$ and $j=1$ are assumed and η_1 is the reduced Fermi energy. (c) is the similar plot for $\theta\equiv e\Theta/k$ (reduced thermoelectric power). The theoretical curves are drawn so as to fit with the experimental points as shown in (b) and (c), where the relaxation time is assumed constant, i.e. the mean free path $l=l_0(\mathcal{E}/kT)^{1/2}$ since $R\sigma_e$ is almost constant. We obtain, under such assumptions, the electron mobility $\mu=el_0/\sqrt{2m_1kT}$ as 1500 cm^2 s^{-1} v^{-1} and effective electron mass, m_1, as 0.11m at 124°C. Next, Fig. 7(a) and (b) are the similar plots against eE/kT corrected by $\log(\sqrt{1+z^2}+z)$ for Ag$_2$Te, where $A=2.7\times10^{-4}$ ($E_a-E_b=0.53$ eV) and $j=1$ are assumed; (a) is σ_e and $R\sigma_e$ vs η_1+const. and (b) is θ, q, $\sqrt{b}$, and w vs η_1+const., where $q\equiv eQ(kR\sigma_e)^{-1}$ is the reduced Nernst coefficient, $b\equiv(-\Delta\sigma)\sigma^{-1}(HR\sigma_e)^{-2}$ is the reduced magnetoresistance, and $w\equiv\Delta\Theta\Theta^{-1}(HR\sigma_e)^{-2}$ is the reduced magnetothermoelectric power. The theoretical expressions are as follows; $q=\eta-\theta-\gamma/\alpha$, $b=\varphi/(t\alpha^2)-1$, and $w=(\eta-\theta)b+\gamma/\alpha-\psi/(t\alpha^2)$, where $\eta=\eta_1$, $t=\sigma_1/(\sigma_1+\sigma_2)$ (σ_1; electron conductivity, σ_2: hole conductivity and α, γ, φ and ψ are the Fermi-Dirac integrals as defined in the reference 7). The theoretical curves are drawn as shown in the figure where the constant mean free path $l=l_0$ and the effective mass of hole $m_2=m$ are assumed. They agree with the experimental points fairly well except w, indicating the validity of our various assumptions. Thus we obtain the electron mobility $\mu_1=el_{01}/\sqrt{2m_1kT}$ as 5430 cm^2 s^{-1} v^{-1}, hole mobility μ_2 as 80 〃, m_1 as 0.06m, and the energy gap E_G as 1.5kT at 100°C. For both Ag$_2$Se and Ag$_2$Te, the agreement between experiment and theory as shown in Figs. 6 and 7 will be never obtained without the correction to E.

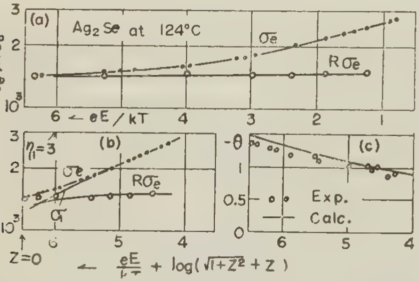

Fig. 6. An example of analysis of electronic properties for β-Ag$_2$Se.

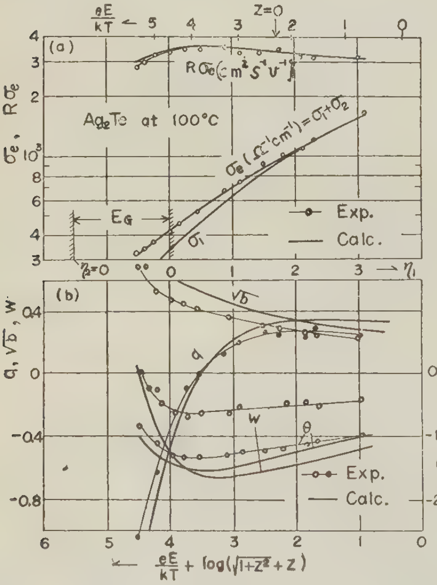

Fig. 7. An example of analysis for β-Ag$_2$Te.

The author wishes to express his sincere thanks to Mr. Suzuki, Mr. Yokota and Mr. Haga for their kind advices and discussions. This work was supported by the research grant of the Ministry of Education.

References

1) F. Seitz: *The Modern Theory of Solids* (McGraw-Hill Book Co., New York, 1940) 63.
2) I. Yokota: J. Phys. Soc. Japan **8** (1953) 595.
3) S. Miyatani: J. Phys. Soc. Japan **9** (1955) 786; **13** (1958) 317; **13** (1958) 341.
4) M. H. Hebb: J. Chem. Phys. **20** (1952) 185.
5) C. Wagner: J. Chem. Phys. **21** (1953) 1819.
6) P. Rahlfs: Z. phys. Chem. **B**, **31** (1935) 157.
7) S. Miyatani and I. Yokota: J. Phys. Soc. Japan **14** (1959) 750.

JOURNAL OF THE PHYSICAL SOCIETY OF JAPAN Vol. 14, No. 8, AUGUST, 1959

Structures of Ferroelectric Domains in Triglycine Sulfate

By Hiroo TOYODA, Shigeru WAKU and Hisao HIRABAYASHI
Nippon Telegraph and Telephone Public Corporation, Tokyo, Japan

(Received March 19, 1959)

Domain structures in ferroelectric glycine sulfate are studied by etching in various alcohols. Methyl alcohol etches the head of polarization more readily than the tail end, and gives, in a relatively short time, clear domain patterns. Moreover, this etchant etches the (001) surface very slowly and after a long time delineates the arranging manner of domains along the polarization axis. Domain boundaries have cylindrical surfaces parallel to b axis, but the sections perpendicular to the axis are quite indefinite in dimensition and direction. Domain terminated with a rounded tip in the antiparallell domain was observed. Crystal imperfection seems to have a considsrable effect on the domain structure of this crystal. Some preliminary studies of domain wall motion under the application of electric field are also reported.

§ 1. Introduction

since the discovery of ferroelectric glycine sulfate[1] many workers have had interests on this material. Crystal structure and optical properties[2], phase transition[3], dielectric and thermal properties[4], coercive field and spontaneous polarization[5],[6], switching properties[7]-[10], secondary electron emission[11], piezo-electric constants[12], conditions of crystal growth[13,14] have been studied. One of the authors has investigated the etch pits on the crystal by various liquids and discovered the difference of the etch pits between the tail and head of the polarization[15].

In order to visualize the domains, there are three principal techniques. The first one, the etching technique, is usually applied to barium titanate[16]-[20]. Phosphoric, nitric, chroric and fluoric acids etch the head of polarization of this material more easily than the tail end. The second one uses the polarized light and can reveal the domain structures by the displacement of optic planes. This is widely used for barium titanate[21]-[24] and other perovskite families[25]-[27], for rochelle salt[28]-[31], and potassium dihydrogen phosphate[32]. The third one takes advantage of the pyroelectric property of rochelle salt[33],[34]. Fine powder of sulphur, lycopodium and carmine, blown over a charged crystal, adheres to the surface and covers it with patches of red and yellow, indicating the polarity. The authors, in progress of the study, were informed that recently G. L. Pearson improved this technique and developed a colloical process applicable to all the ferroelectrics*.

Studies on the domain structure in triglycine sulfate (hereafter abbreviated as TGS) have not yet been reported. The reason exists, for one thing, in the fact that there are only 180° domain walls and that polarization reversal does not bring about any rotation of optic planes. Though Wood and Holden[2] noted the unsymmetrical etch pits to determine the crystal symmetry, precise description was omitted. The authors have investigated the domain structures of this material, using the etching technique and electron-microscope[35].

The crystal symmetry of TGS, $(NH_2CH_2COOH)_3H_2SO_4$, below its Curie point at 47°C, belongs to monoclinic space group, C_2^2 or $P2_1$. Wood and Holden[2] have presented two possible choices of axes. In this paper the authors adopt the one with β more close to 90°. Lattice parameters are

$$a_0=9.15\text{Å},\ b_0=12.69\text{Å},\ c_0=5.73\text{Å},\ \beta=105°40'.$$

An optic plane is inclined to (100) at an angle of 93° and approximately parallel to $(10\bar{2})$, Fig. 1 shows these relations.

§ 2. Experiments

Etch patterns on (010) surfaces

Etchants examined are water, acetic acid, acetone, ethyl ether, methyl alcohol, ethyl alcohol, n-buthyl alcohl, ethylene glycol, glycerine, ethylene glycol mono-methyl ether, and methyl alcohol containing various salts. All of these chemicals are of chemically pure grade.

---

* The authors are grateful to Dr. T. Nakamura for his kindness to show them a private communication from G. L. Pearson.

At first, etching results of naturally cleaved b face will be summarized. Water and acetic acid solve the surface very rapidly over the whole area, and no definite etch pattern can be found, while acetone, ethyl ether and glycerine do not etch the surface even after more than 24 hours at 30°C.

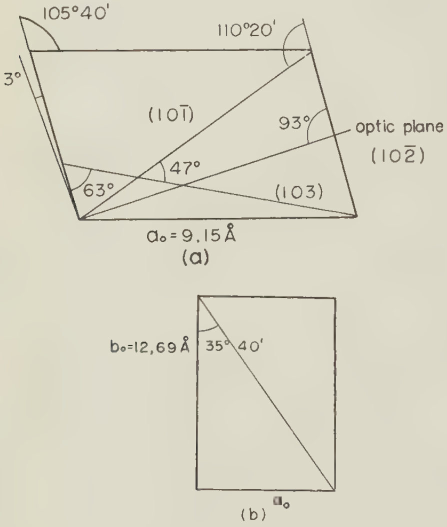

(a) (010) face,
(b) (001) face.

Fig. 1. Unit cell dimension and several relevant planes.

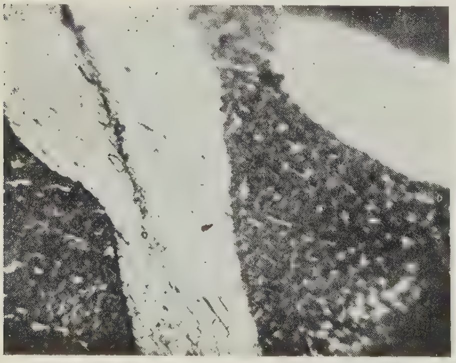
(×80)

Fig. 2. Etch pattern on (010) surface produced by methyl alcohol at 10°C for two days. Dark (uneven) area corresponds to the head of polarization, while light (flat) area corresponds to the tail.

Alcohols mentioned above, except glycerine, etch the surface in somewhat different manners. Monovalent alcohols examined all give similar etch pits, though the etching rate decreases with the increase of molecular weight. Etch pits due to methyl alcohol at 10°C for two days are shown in Fig. 2. Uneven part is found to correspond to the positive pole end of ferroelectric polarization, and the flat part to correspond to the negative pole. Etching rate increases with etching temperature. The pits at lower temperature are of the pyramidal shape, while those at higher temperature are long and of wave form. The results obtained at 27°C for two hours are shown in Fig. 3.

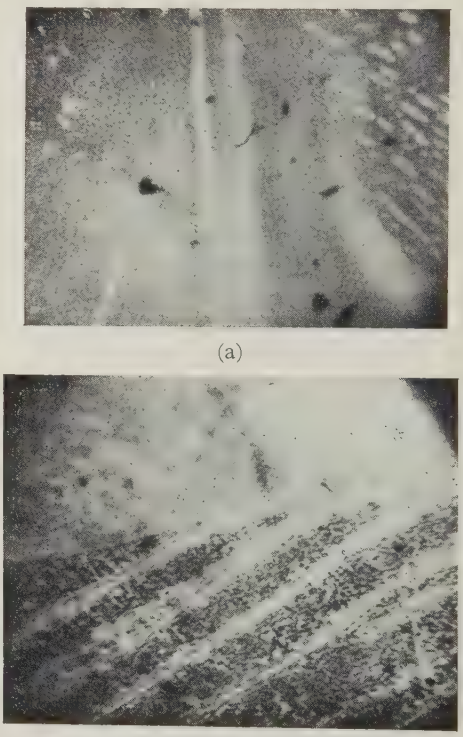
(a)

(b)

Fig. 3. Etch patterns on (010) surfaces produced by methyl alcohol at 27°C for two hours. (a) ×20, (b) ×70.

Fig. 4 shows the fine structure, revealed by electron microscope, of an etched surface. $(0\bar{1}0)$ faces overwhelm the negative pole end, while at positive end, considerable appearance of surfaces inclined to b axis, such as $\{1\bar{1}\bar{1}\}$ and $\{1\bar{1}0\}$, is characteristic.

Ethylene glycol etches the surface in a

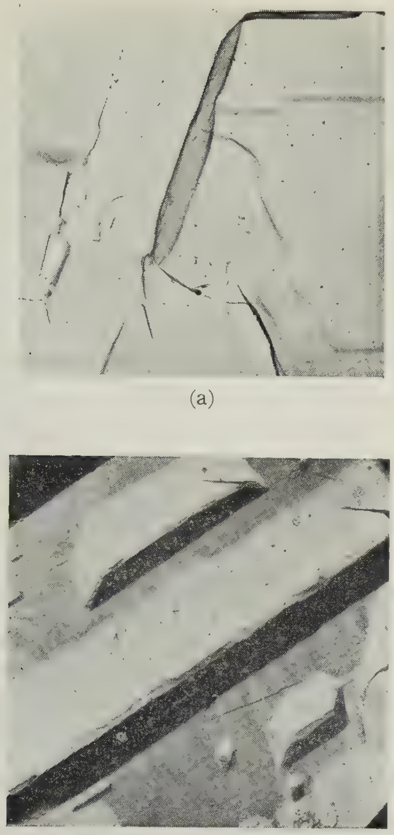

(a)

(b)

Fig. 4. Electronmicroscopic pictures of etch pits on (010) surface produced by methyl alcohol at 27°C for two hours. Negative replica shadowed by germanium at an inclination of 30°. (a) tail of polarization (×1000), (b) head (×800).

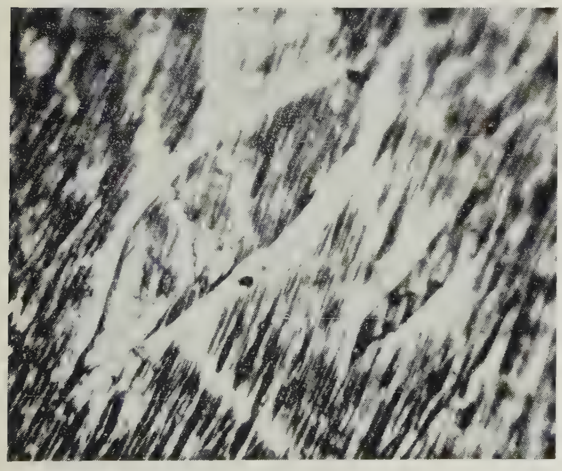

(×160)

Fig. 5. Etch pits on (010) surface produced by methyl cellosolve at 27°C for 30 hours.

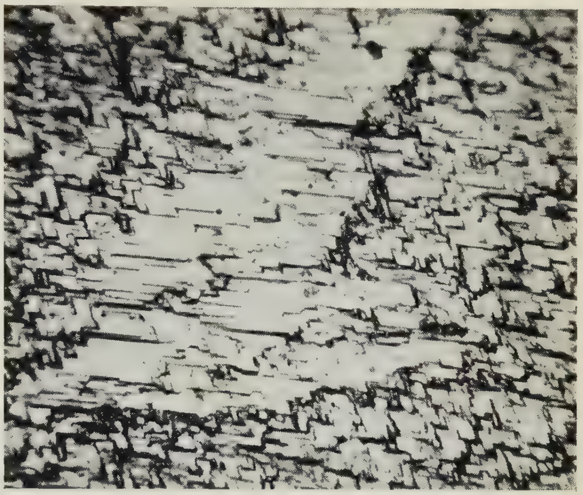

(×160)

Fig. 6. Etch pits on (010) surface produced by methyl cellosolve at 10°C for two weeks.

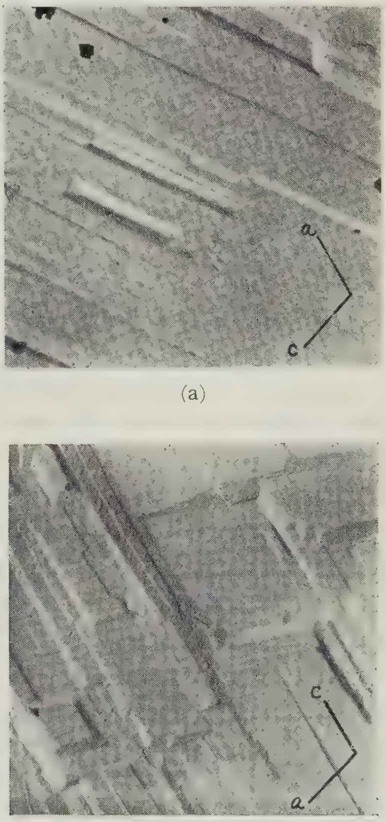

(a)

(b)

Fig. 7. Electronmicroscopic pictures of etch pits on (010) surface produced by methyl cellosolve at 10°C for two weeks. (×1000) (a) tail of polarization, (b) head.

stream-line pattern, which is nearly rectilinear. Ethylene glycol mono-methyl ether, the socalled methyl cellosolve, is one of the most interesting ethcants. At higher temperature, the etch pits are not very different from the ones by ethylene glycol. Fig. 5 shows the picture of the etched surface at 27°C for 30 hours. Though presence of domains of both polarities is evidenced by the boundaries seen in the figure, the difference of the appearance between the head and the tail of polarization is not readily recognized. Etching rate becomes, however, very slow at lower temperature. Etching at 10°C for more than two weeks produces a remarkably regular etch pattern. Fig. 6 and 7 are pictures of typical parts of etched surfaces. Most of the edges, as seen in the pictures, correspond to $\langle 10\bar{1} \rangle$ and $\langle 100 \rangle$. The part, which displays the long strip-shaped patterns in Fig. 6, corresponds to the tail of polarization, while the short figures represent the head. Fig. 6 and 8 contain some domain boundaries. Patterns on both sides of the boundary differs each other, but the directions of edge lines are common to both regions.

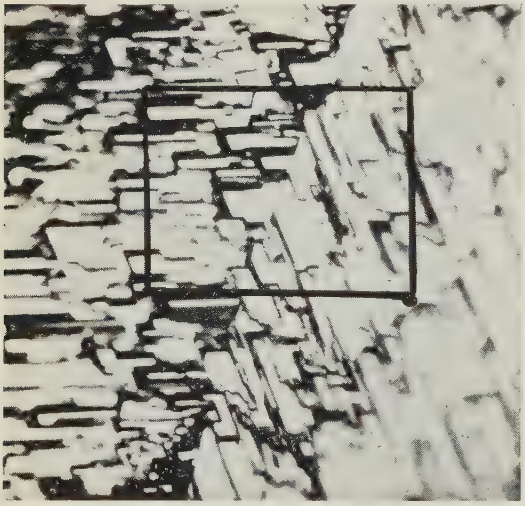
(a)

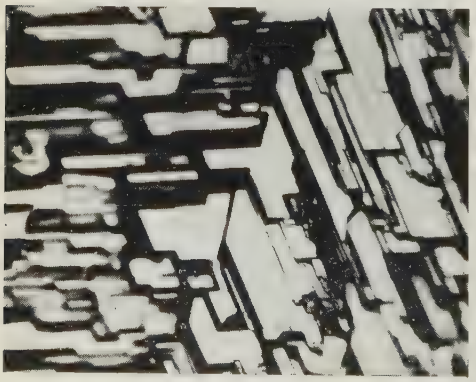
(b)

Fig. 8. Domain boundary reverled by methyl cellosolve on (010) surface. (a) ×180; (b) framed area in (a) enlarge; ×300.

Methyl alcohol containing some inorganic salts acts in a somewhat different manner, compared with pure alcohol. Methyl alcohol solves, to some degree, nitrates, hydroxides and halogenates, but it does not solve the sulfates to the same degree except in a few cases. When a crystal is immersed in methyl alcohol containing the salts other than sulfates, its whole surface is soon covered by numerous, small needlelike crystallites. No structural difference was found that might correspond to the difference of the polarization. In the methyl alcohol saturated with potassium hydroxide, a sharp striped pattern appears in addition to these crystallites. The stripes are completely linear and parallel to each other and shown in Fig. 9.

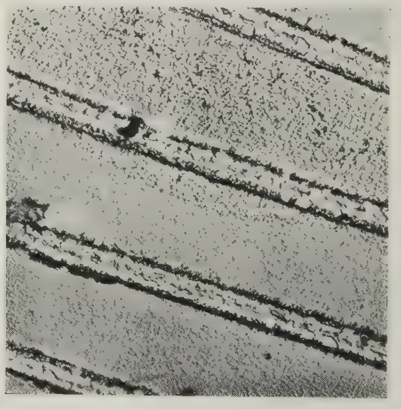
(×1000)

Fig. 9. Electronmicrospic eicture of the figure produced by methyl alcohol saturated with KOH on (010) surface.

Sulfates have completely different effect on etching. Methyl alcohol saturated with cupric sulfate did not gave any appreciable etch pits in 24 hours, while the saturated solution of ammonium sulfate gave a characteristic etch pattern, as shown in Fig. 10, with a marked difference for polarization. Etching advances more easily at the head of polarization and $\{0\bar{1}1\}$ and $\{1\bar{1}\bar{1}\}$ faces are observed distinctly in the picture.

The difference of the salts in the effect on etching may be accounted for by the fact that the salts other than sulfates can react with the sulfuric ion in TGS, and the resultant sulfate, which is less soluble in methyl alcohol, crystallizes on the surface. The significance of the characteristic etch pits given by methyl alcohol containing potassium hydroxide is not yet understood. (When the etched crystal was immersed in water, the surface dissolved, liberating some gas bubbles).

Etch patterns on the other surfaces

The effect of methyl alcohol and methyl cellosolve on the various surfaces of single crystal were investigated. Etching occurs more or less readily on all the surfaces. The etching proceeds very slowly on (001) surface, but it reveals the existence of domains. Herring-bones-shaped patterns obtained by etching in methyl alcohol for one month at room temperature are shown in Fig. 11. Characteristic [110] edges turn over to their mirror images across the domain boundaries. These boundaries are nearly parallel to b axis or direction of polarization, as is usual in 180° domain walls, but some domains have been found to terminate within the crystal with rounded end. An example is shown in Fig. 11 (b). Fig. 12 shows typical picture of several other surfaces etched in methyl alcohol for one month.

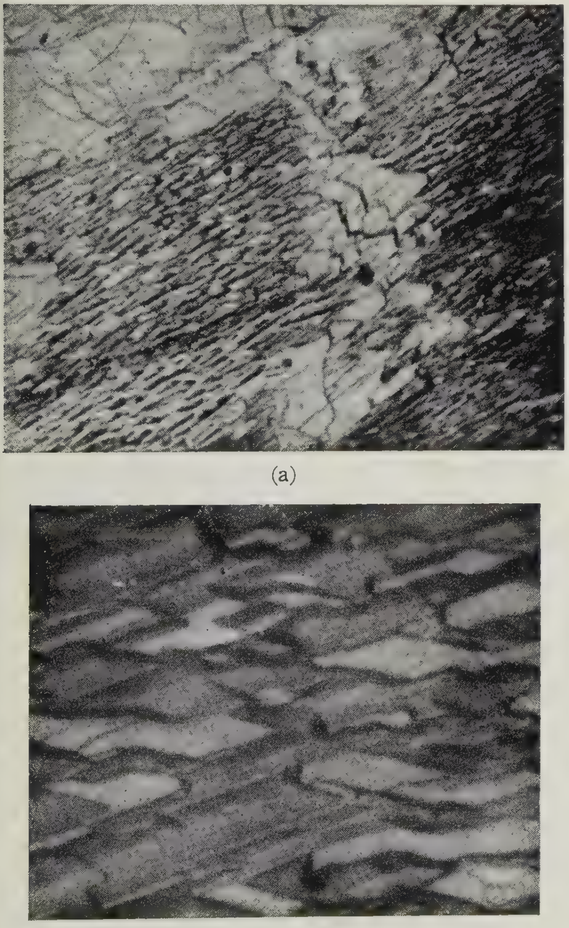

(a)

(b)

Fig. 10. Etch pits on (010) surface produced by methyl alcohol saturated with ammonium sulfate at 27°C for 30 hours. (a) ×50; (b) head of polarization; $\{1\bar{1}\bar{1}\}$ and $\{0\bar{1}1\}$ planes appear distinctly; ×350.

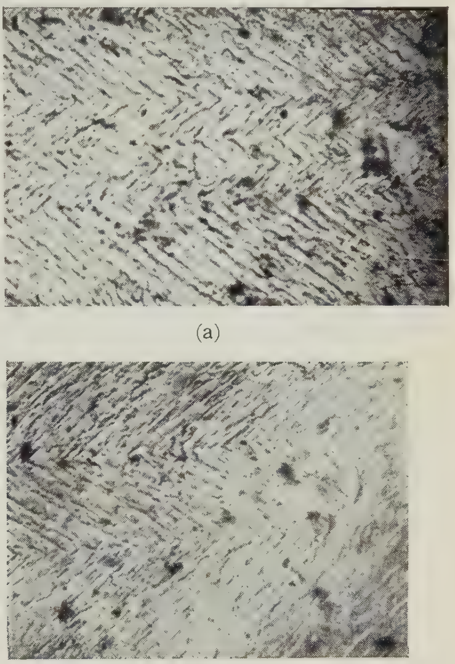

(a)

(b)

Fig. 11. Etch patterns on (001) surface produced by methyl alcohol at 10°C for one month. ×100. (b) shows a round-headed domain embeded in antiparallel domain. b-axis passes horizontally in the paper.

Shape of domains

The domain boundaries are cylindrical surfaces which are parallel to b axis, while their intersections with (010) face are rather indefinite. Spindle-shaped and rectilinear sections are most frequently observed, but their directions are not definite concerned with the crystal axes. There exist rarely domain side boundaries inclined to b axis. The angle of

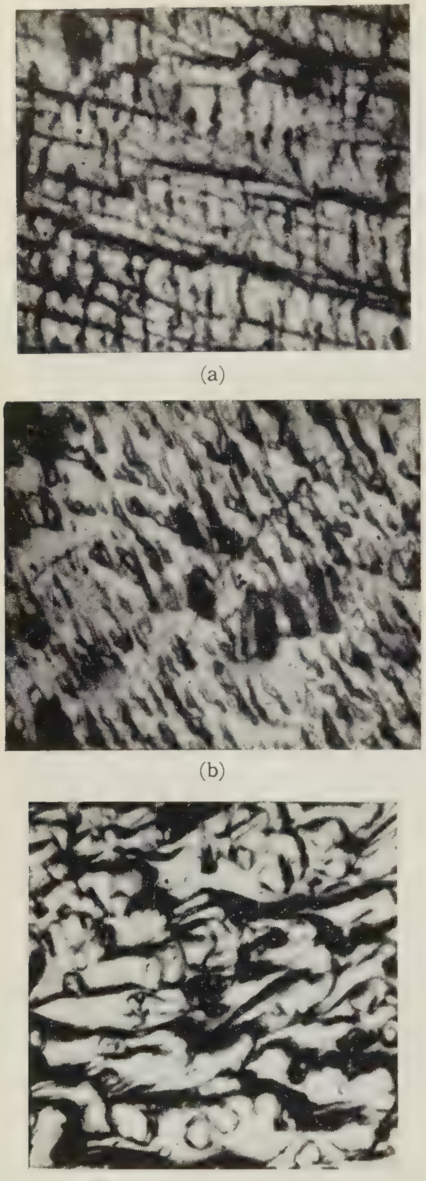

(a)

(b)

(c)

Fig. 12. Etch patterns produced by methyl alcohol at 10°C for one month. (a) (111) surface; ×270: (b) (121) surface; ×270: (c) (301) surface; ×190.

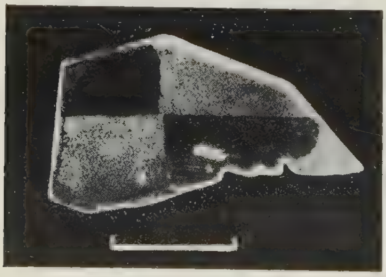

Fig. 13. Etch pattern after poling. Scale is 1 cm.

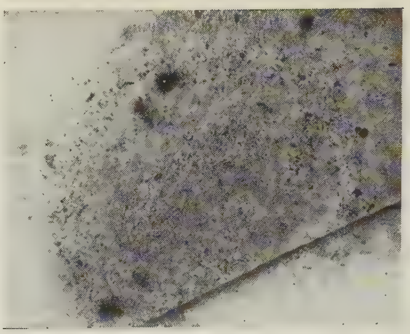

Fig. 14. Etch pattern on a crystal with an approximately vanishing average polarization, brought about by a relatively high field applied to a circular electrode. Domains completely penetrate to backside; ×25.

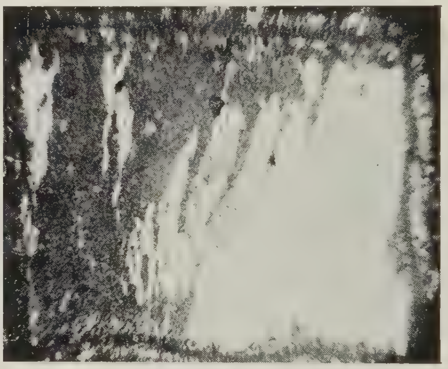

Fig. 15. Etch pattern on a crystal with an approximately vanishing average polarization, brought about by a lower field applied to a rectangular electrode. Domain penetration is not all complete; ×25.

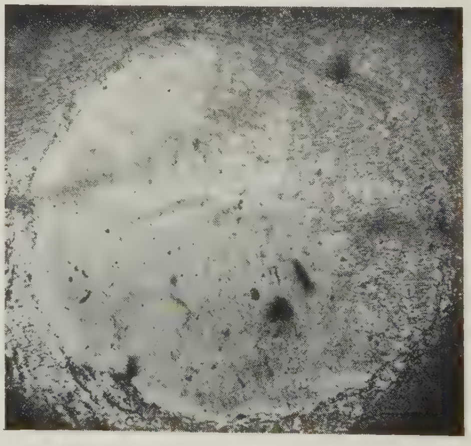

Fig. 16. Etch pattern on a crystal showing a remarkable anomaly under the application of electric field. The oppositely polarized domain has grown, after removal of the field in a certain limited region, as seen in right side: ×25.

inclination is not yet determined. Dimensions of domains also vary remarkably, ranging from few tenth of a millimeter to several millimeters.

Application of electric field

Cooling past the Curie point with application of D. C. electric field turns a crystal into a single domain, and the boundaries of various shapes, which have had existed before poling, completely disappear, as is found when re-etched in methyl alcohol. Also the domain patterns given by etching, after this single domain crystal is again heated over the transition without electric field, are quite different from the original domain patterns. Fig. 13 shows an etched crystal after poling by the field with opposite sign applied to two sets of diagonal quadrants respectively.

Some preliminary studies have been made on the dynamics of polarization reversal using etch technique, together with the supersonic method developed by K. Husimi[36] to measure the average polarization. Fig. 14 shows an etch pattern of a crystal with approximately vanishing average polarization, brought about by a pulse of 1.5 kv/cm and 100μ sec. at 10°C. It was assured by etch patterns that the domain penetrated completely through the crystal along b axis. Fig. 15 is also an example of a crystal with null polarization, reached by a lower field, 50 v/cm at 20°C. It was hard to say, in this case, that the domain penetration was complete. Though the electrode shape and temperature examined are not the same, this difference of penetration might be attributed to the field strength.

There are some exceptional crystals that display distinct unsymmetry in polarization reversal. In such a crystal, a low positive field E_1 brings about readily a 100 per cent polarization and the polarization does not decay after the removal of field. But in the negative direction, $-E_1$ brings about the polarization only to -50 per cent and thereafter, the polarization grows with successively growing negative field and arrives at -100 per cent by a quite higher field than E_1. When the negative field is lowered, the polarization falls off rapidly to -50 per cent at $-E_2$, the magnitude of which is far below E_1. Accordingly, a reversible pseudo-double hysteresis buckled at $-E_1$ and $-E_2$ is observed. This example may be understood as an extreme case of the phenomenon known as "lock-in". When this crystal was etched after application of high negative field, it was revealed that about one quarter of electroded area was polarized in positive direction (Fig. 16). Domain penetration was found to be complete. More detailed study on the effect of applied field are now in progress.

§ 3. Discussion

When one observes the plates of TGS along the b axis by polarized microscope, he can not find any displacement of extinction position across the domain boundaries. The fact is understood as follows. At the Curie point, crystal symmetry changes from $P2_1/m$ to $P2_1$ and two crystals with positive and negative polarization should be in the relation of mirror image against the mirror plane, which the crystal has had above Curie point. Alternatively said, two crystals are in the relation of inversion concerned with the center of symmetry of paraelectric phase. a and c axes are common to both crystals, while b axes are antiparallel to each other. Polarization reversal changes the crystal from a right handed one to a left handed one and does not displace the optic plane.

Above the Curie point, the glycine molecules have nearly flat sheetlike structures and one of them lies on the mirror plane, together with the inorganic anion, while two other glycines are situated symmetrically with re-

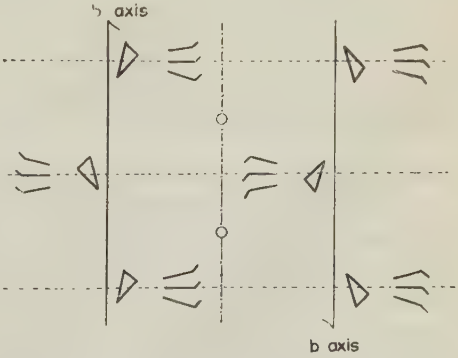

Fig. 17. A schematic picture of domain boundary;
dotted lines; mirror plane in the high temperature phase.
small circle; center of symmetry in the high temperature phase.
chained line; domain boundary.
scalene triangle; sulfate ion.
heavy full line; glycine molecule.

spect to the plane[4],[37]. Breakdown of the coplanarity of glycine molecule is believed to act as a trigger on the transition[1],[88]. Fig. 17 is a schematic picture of polarization reversal.

The absence of change of axial direction with polarization reversal explains the irregular shape of domain boundaries. Spindle-shaped sections may be favored since it lessens the wall energy. Imperfections may be playing the principal role to determine the various forms of boundaries. This assumption is supported by the anomaly observed under the application of electric field. Imperfections of some kinds seem to exist causing a strong crystalline field that aligns the polarization in one direction over a certain region of the crystal. Boundaries of domain terminated within the crystal as seen in Fig. 11 (b) and boundaries inclined to b axis should have higher energy because of the head-to-head coupling and they would be hard to be realized in a perfect crystal. The cause of existence may be also due to crystal imperfection.

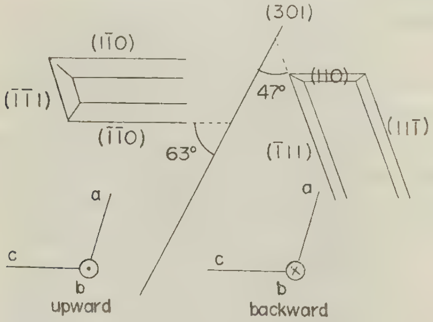

Fig. 18. A schematic picture of etch pits produced by methyl cellosolve.

Etched patterns produced by methyl cellosolve (Fig. 6 to 8) are explained in Fig. 18 on the basis of above-metinoned model. The boundary plane is taken as (301) according to an example in Fig. 8. b axis, which is perpendicular to the paper, points backwards in the right side of the boundary and upwards in the left side. Planes which appear readily by etching are shown on both sides. Difference in the etching rates for the planes with opposite indices results in different appearance of etch patterns, while the direction of intersecting lines of b faces with these planes is the same on both sides of the boundary.

Attempts have been made to reveal the twin structures in TGS by X-ray, but no result has been reached that differed in any way from the crystal of single domain. X-ray experiment showed that the change of β at the transition point was very little.

The results are summarized as follows;

1). Methyl alcohol and its solution saturated with ammonium sulfate etch more easily the head of polarization than the tail.

2). Methyl cellosolve gives a regular etch pattern closely related to the crystal axis.

3). Methyl alcohol etches other surfaces more or less readily and the etch pattern on (001) surface deilneates the domain structure.

4). Domains have cylindrical surfaces parallel to the polarization axis, while the sections normal to the axis are indefinite.

5). Crystal imperfections seem to have a large effect on the domain structure.

The authors are grateful to Mr. Y. Tanaka in preparation of the crystals of triglycine sulfate and to Mr. S. Hirota for electron microscopy. The authors wishes to express their sincere thanks to Mr. N. Niizeki for X-ray analysis and helpful discussions.

References

1) B. T. Matthias, C. E. Miller and J. P. Remika: Phys. Rev. **104** (1956) 849.
2) E. A. Wood and A. N. Holden: Acta Cryst. **10** (1957) 145.
3) S. Triebwasser: I. B. M. J. Res. Dev. **2** (1958) 212.
4) S. Hoshino, T. Mitsui, F. Jona and R. Pepinsky: Phys. Rev. **107** (1957) 1255.
5) S. Domanski: Proc. Phys. Soc. London **72**, **B** (1958) 306.
6) L. Taurel, E. Pourel and F. Thomassin: Compt. rend. **246** (1958) 70.
7) Z. Kiyasu, K. Husimi and K. Kataoka: J. Phys. Soc. Japan **13** (1958) 661.
8) C. F. Pulvari and W. Kuebler: J. Appl. Phys. **29** (1951) 1742.
9) E. Fatuzzo: Helv. Phys. Acta **31** (1958) 309.
10) H. Toyoda, S. Waku, S. Shibata and Y. Tanaka: J. Phys. Soc. Japan **14** (1959) 109.
11) R. C. Miller and R. D. Heidenreich: J. Appl. Phys. **29** (1958) 957.
12) K. Husimi and K. Kataoka: J. Phys. Soc. Japan **14** (1959) 105.
13) Y. Tanaka and S. Waku: J. Appl. Phys. Japan **27** (1958) 561.

14) R. Nitsche: Helv. Phys. Acta **31** (1958) 306.
15) H. Toyoda: J. Phys. Soc. Japan **14** (1959) 376.
16) J. A. Hooton and W. J. Merz: Phys. Rev. **98** (1955) 409.
17) D. S. Campbell and D. J. Stirland: Brit. J. Appl. Phys. **7** (1956) 62.
18) D. C. Cameron: I. B. M. J. Res. Dev. **1** (1957) 2.
19) R. C. Miller: Phys. Rev. **111** (1958) 736.
20) R. C. Miller and A. Savage: Phys. Rev. **111** (1958) 755.
21) H. Blattner, W. Känzig, W. J. Merz and H. Sutter: Helv. Phys. Acta **21** (1948) 207.
22) H. F. Kay: Acta Cryst. **1** (1948) 229.
23) P. W. Forsbergh Jr.: Phys. Rev. **76** (1949) 1187.
24) W. J. Merz: Phys. Rev. **88** (1952) 421.
25) R. Ueda and T. Ichinokawa: J. Phys. Soc. Japan **6** (1951) 122.
26) S. Tanisaki: J. Phys. Soc. Japan **13** (1958) 363.
27) J. Kobayashi: J. Appl Phys. **29** (1958) 866.
28) M. Marutake: J. Phys. Soc. Japan **7** (1952) 25.
29) T. Nakamura: J. Phys. Soc. Japan **11** (1956) 624.
30) E. Straubel-Fisher: Naturwiss. **44** (1957) 239.
31) H. E. Müser und H. Flunkert: Z. Phys. **150** (1958) 21.
32) J. Furuichi and T. Mitsui: Phys. Rev. **90** (1953) 193.
33) H. Mueller: Phys. Rev. **47** (1935) 175.
34) W. G. Cady: *Piezoelectricity* (McGraw-Hill, New York, 1946).
35) S. Hirota: Elect. Commun. Lab. Rep. 58–259 (1958). Methacrylate plastic film was used to prepare replica.
36) K. Husimi and K. Kataoka: J. Appl. Phys. **29** (1958) 1247.
37) R. Pepinsky, Y. Okaya, D. P. Eastman and T. Mitsui: Phys. Rev. **107** (1957) 1538.
38) B. T. Matthias and J. P. Remeika: Phys. Rev. **103** (1956) 262.

JOURNAL OF THE PHYSICAL SOCIETY OF JAPAN, Vol. 14, No. 8, AUGUST, 1959

On the Electronic Structure of the U_2-center in KCl Crystals, I.

By Hiroshi MIMURA* and Yasutada UEMURA**

** Department of Applied Physics, University of Tokyo*

*** Department of Physics, University of Tokyo*

(Received May 2, 1959)

The electronic structure of the U_2 center is studied by using the so called "point ion lattice model".

The wave function which is obtained for the ground state of the U_2 center by considering the effects of various kinds of interactions, is applied to analyze the observed data of E.S.R.[1]

The 1s wave function of the free hydrogen orthogonalized to the core orbitals of the surrounding ions gives us the interpretation of E.S.R. in the order of magnitude, however, there still remain some discrepancies between the calculated and the observed values. The physical origins of these discrepancies are considered. The large zero point vibration of the U_2 center suggests to us that the width of the absorption curve of E.S.R. is broadened about 20% by the vibration. Discussions on the effect of polarization, of crystalline field and on the optical absorption are made briefly by assuming the point ion and dipole approximation.

§ 1. Introduction

In the course of the study on the electronic structure of hydrogen in alkali halide crystals, the U_2 center, which is supposed to be an interstitial hydrogen atom, is studied theoretically in this paper.

The experiments of E. S. R. and the optical absorption by Delbecq, Smaller and Yuster have given us much interesting information on the electronic states of hydrogen in alkali halides. From their experiments in U_2 center of KCl crystals we learn the following. The separation $(\Delta H)_s$ between the two peaks in the absorption pattern of E. S. R. is 500±10 gauss which corresponds to the doublet structure owing to the hyperfine interaction of the electron spin in the U_2 center with the nuclear spin of the proton. The width of each branch of the absorption pattern is measured as 68±5 gauss in the peak to peak value of the differential curve of the absorption. This value gives the half width $(\Delta H)_w$ of 81 gauss if the absorption curve is assumed to be Gaussian. It has been suggested that the width $(\Delta H)_w$ comes from the Fermi-interaction between the electron in the U_2 center and the nuclei of the surrounding ions.

Apparently it is not clearly understood why the observed width $(\Delta H)_w$ is so broad as to be comparable with those of the F center, even though the separation $(\Delta H)_s$ shows a slight change from the value of the free hydrogen.

Therefore the main purpose of this paper is to find the wave function of the U_2 center by which we are able to explain both the separation $(\Delta H)_s$ and the width $(\Delta H)_w$ quantitatively.

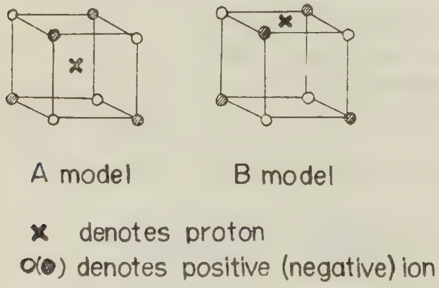

Fig. 1. Model of U_2 center.

As to the model of the U_2 center we assume that it is a hydrogen atom in the interstitial point A shown in Fig. 1. Strictly speaking it is not yet definitely established by the experiments that the hydrogen atom really exists at position A as in Fig. 1, however, it is highly probable because of the geometrically high symmetry of the point. Another possibility of the position of hydrogen, for example, is the position B as in Fig. 1, which is discussed briefly in Appendix I. The second assumption is made by confining our calculation to the range of the so called "point-ion-lattice approximation". Gourary and Adrain[(2)] have developed their theory of "point-ion-lattice approximation" and succeeded in explaining the experimental data of the optical absorption and E. S. R. which are observed in the F and M centers in alkali halides.

The results of their theoretical calculation seem to agree with the observed data, however, there remain some ambiguities in the treatment because it is difficult for this simple method of approximation to consider the effects of the displacement and polarization of the ions perfectly. In the case of the U_2 center these ambiguities are supposed to be smaller than in the cases of the F and M centers, for the crystal field arround the U_2 center has the high symmetry and there is no vacant lattice site, further more, the effect of the polarization is very small because of the localization of the trapped electron in the neighbourhood of the proton. Therefore we are able to clearly examine the applicability of this approximation. It is also believed that it will be easy to estimate the magnitudes of the complicated effects which are not included in this simple approximation.

In Chapter 1 we have tried to analyze the data of E. S. R. and to find the wave function for the ground state of U_2 center. It is shown in §4 that the wave function of the hydrogen orthogonalized to the orbitals of the core-electrons in the surrounding ions gives the correct order of magnitudes in $(\Delta H)_s$ and $(\Delta H)_w$. However, there still remain some discrepancies between the calculated and experimental values. In order to investigate the origins of the discrepancies, it is investigated in §6 to what extent the wave function is changed by the effects of the crystalline field, the polarization and the resonance to the outer orbitals in the alkali atoms. The limit of the applicability of the "point-ion-lattice approximation" is also discussed from the qualitative point of view. One of the characteristic features of U_2 center is the large amplitude of zero-point vibration of the proton in the interstitial point. The influence of this vibration on the absorption pattern of E.S.R. is estimated semi-empirically in §5 of Chapter 1.

In Chapter 2, the wave function and the

energy level for the first excited state of the U_2 center are studied by the same method as those in Chapter 1. We try to examine the three possible interpretations for the optical absorption of the U_2 center. The first, is that it corresponds to the transition between the ground and excited levels of hydrogen modified by the crystalline field, secondly that it corresponds to the exciton absorption disturbed by the U_2 center and thirdly that it corresponds to the electron transfer to the U_2 center from the four neighbouring halogen ions. In the actual crystal the latter two processes may not be clearly distinguished from each other and the observed excitation may be the mixture or in other words the resonance of the two processes. If we confine ourselves to the standpoint of the "point-ion-lattice approximation" it is not perfectly determined which of the three processes is really predominant in the crystal, and the agreement of the calculated values of the optical absorption with the observed ones seems worse than in the case of E. S. R. The reasons of the discrepancy are discussed qualitatively. As the result of whole discussions we can conclude that the hydrogen atom in alkali halides is a good tracer by which we are able to investigate the relation between the electronic structure of color centers and the many kinds of interactions which appear in the neighbourhood of centers.

I. Analysis of E. S. R.

—The electronic structure of the ground state—

§ 2. Expressions for the Separation and the Width

The absorbed microwave frequency ν corresponding to the transition between the Zeeman levels is given as follows:

$$h\nu = g\mu_B H + a_0 I_{0z} + \sum_i (a_i + b_i) I_{iz} \tag{1}$$

where H means the external magnetic field along the z axis, μ_B is the Bohr magneton, a_0 is the coupling constant of the hyperfine interaction between electron and proton, (a_i+b_i) is those between electron and i-th nucleous, and I_{0z} and I_{iz} means the nuclear spins of proton and i-th nucleus respectively. These coupling constants are expressed as follows

$$\left.\begin{array}{ll} a_0 = -\dfrac{16\pi}{3}\dfrac{\mu_B \mu_0}{I_0}|\Psi(0)|^2 & \text{Fermi interaction with proton} \\ a_i = -\dfrac{16\pi}{3}\dfrac{\mu_B \mu_i}{I_i}|\Psi(R_i)|^2 & \text{Fermi interaction with } i\text{-th nucleus} \\ b_i = 2\dfrac{\mu_B \mu_i}{I_i}\left\langle \dfrac{3\cos^2\theta - 1}{|\boldsymbol{r}-\boldsymbol{R}|^3} \right\rangle & \text{dipole-dipole interaction with } i\text{-th nucleus} \end{array}\right. \tag{2}$$

The values of μ_0, I_0 and μ_i, I_i which we use in the calculation are shown in Table I.(3)

Table I.3)

proton	$\mu_0=2.79$ (μ_N)	$I_0=1/2$
deuteron	$\mu_0=0.86$	$I_0=1$
K	$\langle\mu_K\rangle=0.38$	$I_K=3/2$
Cl	$\langle\mu_{Cl}\rangle=0.79$	$I_{Cl}=3/2$

$\mu_N = e\hbar/2MC = 5.05\times10^{-24}$ erg/gauß.

The separation $(\varDelta H)_s$ is estimated as

$$(\varDelta H)_s = \frac{a_0}{g\mu_B} \tag{3}$$

and the half width $(\varDelta H)_w$ is estimated by using the following relation.

$$(\varDelta H)_w = 2.35 \times \frac{1}{g\mu_B} \times \left[\sum_i (a_i^2 + b_i^2)\frac{1}{3}I_i(I_i+1)\right]^{\frac{1}{2}} \tag{4}$$

The g factor of U_2 center has been observed to be same as those of the free hydrogen. Therefore we assume in this paper that $g \doteqdot 2$ and avoid discussing the minor effect of spin-orbit coupling in the U_2 center. If we have the wave function $\Psi(\boldsymbol{r})$ for the ground state of U_2 center, we can estimate $(\varDelta H)_s$ and $(\varDelta H)_w$ by using (2) (3) and (4). The value of $|\Psi(0)|^2$ which is the electron density at the proton, concerns the separation $(\varDelta H)_s$ and the value of $|\Psi(\boldsymbol{R}_i)|^2$ which is the electron density at i-th nucleus is related to the width $(\varDelta H)_w$.

§ 3. The Most Primitive Model

—free hydrogen—

The fact that the doublet separation (500±10 gauss) is nearly equal to free hydrogen (506 gauss) suggests to us the estimated width, $(\varDelta H)_w$ by employing the 1s wave function of the free hydrogen $\psi_H(\boldsymbol{r})$ as the first approximation of $\Psi(\boldsymbol{r})$.

$$\Psi(\boldsymbol{r}) = \psi_H(\boldsymbol{r}) = \frac{1}{\sqrt{\pi}}e^{-r} \quad \text{(in a.u.)} \tag{5}$$

When the magnetic field H has the [1,0,0] direction, b_i vanishes and only the Fermi term a_i contributes to the width if we take into account the interaction of the trapped electron with only the eight nearest ions. The width $(\varDelta H)_w$ is estimated as about 0.01 gauss. When the direction of H is [1, 1, 1], $\sum_i b_i^2$ takes its maximum value and the width $(\varDelta H)_w$ is predicted as about 1 gauss. These values are far smaller than the experimental ones. Therefore, we have to modify $\Psi(\boldsymbol{r})$ of (5).

§ 4. Orthogonalization to the Core States

Gourary and Adrain have proposed a new method to treat the electron excess color center. They have evaluated the Zeeman energy with the trapped electron wave function orthogonalized to the core orbitals of the surrounding ions. The trapped electron wave function is obtained by the variation principle, assuming that the trial wave function is slowly varying near these ions, so that the charge distribution of ions can be replaced by that of point charge.

Applying this method to the U_2 center and taking the 1s like wave function $\psi_H(\mu r)$ in (5) as the trial function, we can easily see

$$(\psi_H|V_{cry}^0|\psi_H)=0$$

where V_{cry}^0 means the crystalline field caused by the point ion lattice. Therefore we directly orthogonalize the function $\psi_H(r)$ to the core orbitals and get the following $\Psi(\boldsymbol{r})$

$$\begin{aligned}\Psi(\boldsymbol{r})&=N[\psi_H-\sum_{ik}S_{ik}\phi_{ik}]\\ N&=[1-\sum_{ik}S_{ik}^2]^{-\frac{1}{2}}\qquad(6)\\ S_{ik}&=(\psi_H|\phi_{ik})\end{aligned}$$

where ϕ_{ik} means k-th orbital in i-th ion. In order to estimate the overlap integral S_{ik}, we use the Slater's type ϕ_{ik}, and to estimate $\phi_{ik}(0)$ we use the Hartree's function⁽⁴⁾ for ϕ_{ik}. These orbitals are as follows

$$\begin{aligned}&\phi_{ce^-,np}(\boldsymbol{r})=N_1r^{n-1}\,e^{-\nu_n r}\cos\theta\\ &\phi_{ce^-,ns}(\boldsymbol{r})=N_2r^{n-1}\,e^{-\nu_n r}\\ &\phi_{k^+,np}(\boldsymbol{r})=N_3r^{n-1}\,e^{-\mu_n r}\cos\theta\\ &\phi_{k^+,ns}(\boldsymbol{r})=N_4r^{n-1}\,e^{-\mu_n r}\qquad\text{(See Table II)}\end{aligned}$$

The estimated values of $(\varDelta H)_s$ and $(\varDelta H)_w$ by using these functions, are given as

$$\begin{aligned}&(\varDelta H)_s=550\ \text{gauss (obs. }500\pm10\text{ gauss)}\\ &(\varDelta H)_w=46\ \text{gauss (obs. 81 gauss)}\end{aligned}\qquad(7)$$

The main contribution to the width is due to the Fermi term of the trapped electron with the four Cl⁻ nuclei. The magnitude of the Fermi interaction with the K^+ nucleus is about 1/4 of that with the Cl⁻ nucleus. The magnitude of dipole-dipole interaction is estimated to be less than 1/15 of the Fermi term even though the direction of H is chosen as the most favourable one.

Table II.⁴⁾

n	μ_n (K⁺)	ν_n (Cl⁻)	$\sqrt{4\pi}\phi_{ns}^{\mathrm{K}^+}(0)$	$\sqrt{4\pi}\phi_{ns}^{\mathrm{Cl}^-}(0)$
1	18.7	16.7	161.7	136.5
2	$\frac{1}{2}$(14.85)	$\frac{1}{2}$(12.85)	46.41	38.24
3	$\frac{1}{3}$(7.75)	$\frac{1}{3}$(5.75)	15.29_5	11.31

ν, μ and ϕ in *a.u.*

The results obtained in (7) seem to be satisfactory in the order of magnitudes, but it should be remarked that the orthogonalization procedure necessarily accompanies the larger value of separation $(\varDelta H)_s$ than those of the free hydrogen whereas the observed $(\varDelta H)_s$ is nearly equal or slightly smaller than those of the free hydrogen. We have also to notice that the calculated value of $(\varDelta H)_w$ is smaller than the observed one, whereas the predicted value for the width of E. S. R. in the F and M centers by this method is always larger than the experimental one.

This tendency of discrepancy in the F and M centers is interpreted as to be plausible by the fact that the value of S_{ik} will decrease if we strictly carry out the variation of $\Psi(\boldsymbol{r})$ by including the exchange energy which is neglected in the simple treatment.

Considering the above mentioned circumstances we shall try in § 6 to discuss some possible effects which may cause the change of $\Psi(\boldsymbol{r})$ in (6).

§ 5. The Effect of the Vibration of the Hydrogen on E. S. R.

Before entering into the more detailed discussions of $\Psi(\boldsymbol{r})$, we shall consider in this section the effect of the vibration of the proton on E. S. R. Because of the light mass of the proton, it may have a considerably large amplitude of zero point vibration in the crystal and may be supposed to show some appreciable effects on E. S. R.

If the condition $h\nu_0\gg kT\gg\hbar\omega$ is satisfied, that is, the frequency ω of the fluctuation of the local magnetic field due to the hyperfine interaction is far smaller than the frequency ν_0 of the vibration, and the observed temperature T is sufficiently low to suppose that only the zero point vibration is predominant, we obtain the following equation

$$\bar{A}_i \doteqdot \int A_i(\boldsymbol{x})\chi_0^2(\boldsymbol{x})d\boldsymbol{x} \Big/ \int \chi_0^2(\boldsymbol{x})\,d\boldsymbol{x} \tag{8}$$

where $A_i(\boldsymbol{x})$ is the coupling constant of the hyperfine interaction with i-th ion when the proton is displaced by the distance $\boldsymbol{x}$ from the equilibrium point and $\chi_0(\boldsymbol{x})$ means the wave function of zeroth vibrational state of the proton or deuteron. If we assume that the adiabatic potential of the proton is given by $(\kappa/2)x^2$, the $\chi_0(\boldsymbol{x})$ is given as follows

$$\chi_0(\boldsymbol{x}) = N\exp\left(-\frac{\alpha}{2}x^2\right) : \quad \alpha = \frac{\sqrt{M\kappa}}{\hbar} \tag{9}$$

where M means the mass of the proton or deuteron.

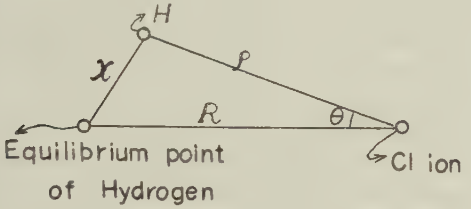

Fig. 2. Schematic representation of coordinates of proton.

By considering the fact that the width comes mainly from the Fermi interaction with four nearest Cl^- ions and it is proportional to $|\Psi(R_{Cl^-})|^2$, we further assume that $A_i(\boldsymbol{x})$ is proportional to the square of the overlap integral S between the ls orbital of hydrogen and the 3s orbital which belongs to one of the nearest Cl^- ion. As shown in Appendix II, S is well reproduced by the function $S_0 e^{-\beta\rho}$, $\beta=0.8$ in a. u. so that we have $A(\boldsymbol{x}) = A_0 e^{-2\beta\rho}$ and $A(0) = A_0 e^{-2\beta R}$, where we denote by ρ and R the distance between the chlorine nucleus and the proton and that between the chlorine nucleus and the equilibrium position of the proton respectively, as shown in Fig. 2. Using these relations we can estimate $\bar{A}$ to be as follows.

$$\begin{aligned}
\bar{A} &= A_0 \iint e^{-\alpha x^2 - 2\beta\rho}\,\rho^2 d\rho d(\cos\theta) \Big/ \iint e^{-\alpha x^2}\rho^2 d\rho d\,(\cos\theta) \\
&= A_0 e^{-2\beta R}\left[\left(1-\frac{\beta}{R\alpha}\right)e^{\frac{\beta^2}{\alpha}}\frac{1}{2}\left\{1+Erf\left[\sqrt{\alpha}\left(R-\frac{\beta}{\alpha}\right)\right]\right\}\right. \\
&\quad \left. +\left(1+\frac{\beta}{R\alpha}\right)e^{\frac{\beta^2}{\alpha}}e^{4\beta R}\frac{1}{2}\left\{1-Erf\left[\sqrt{\alpha}\left(R+\frac{\beta}{\alpha}\right)\right]\right\}\right] \\
&\doteqdot A(0)\left(1-\frac{\beta}{R\alpha}\right)e^{\frac{\beta^2}{\alpha}}
\end{aligned} \tag{10}$$

where $\quad Erf(x) = \frac{2}{\sqrt{\pi}}\int_0^x e^{-x^2}\,dx$

Therefore the width $(\Delta H)_w$ should be multiplied by the factor $\left(1-\frac{\beta}{R\alpha}\right)e^{\beta^2/\alpha}$ as the effect of the vibration. This correction factor is shown in Fig. 3 as the function of β^2/α.

In order to apply this relation to the U_2 center we have to know the value of α and to verify the assumption which was introduced to obtain the relation (10). This is a difficult problem and we have to content ourselves with a crude approximation only. We estimate semi-empirically the order of magnitude of α by using the data of thermal annihilation of the U_2-center. It has been suggested that a hydrogen atom which forms U_2-center migrates through the crystal to form a hydrogen molecule H_2 by the collision process $H+H \rightarrow H_2$. We assume that a hydrogen atom migrates in the potential field $V(x) = (1/2)V_0 \cos\left(\frac{\pi}{a}x\right)$ as shown in Fig. 5 with jumping frequency ν which is given as follows

$$\nu = \nu_j e^{-\frac{V_0}{kT}} \tag{11}$$

and we further assume that the force constant κ of the vibration can be related to this potential $V(x)$ in the following manner,

$$\kappa = \frac{1}{2}V_0\left(\frac{\pi}{a}\right)^2 \tag{12}$$

where 2a is the lattice distance and its numerical value is 5.93 (a. u.) for KCl crystal. Strictly speaking the relation (12) does not hold exactly but it may be applicable in estimating the order of magnitude. By employing (12) we can get the following relations,

$$\alpha=\frac{\sqrt{M\kappa}}{\hbar}=\frac{\pi}{\hbar a}\sqrt{\frac{MV_0}{2}} \tag{13}$$

$$h\nu_0=\frac{h}{2\pi}\sqrt{\frac{\kappa}{M}}=\frac{h}{2a}\sqrt{\frac{V_0}{M}} \tag{14}$$

On the other hand, the thermal bleaching process of the U_2-center is governed by the following kinetic equation of the *bi*-molecular reaction,

$$-\frac{dn}{dt}=\frac{\nu}{N_L}n^2 \tag{15}$$

where n is the number of U_2 centers, N_L is the number of the equilibrium points for the U_2 center and ν means the jumping frequency given by (11)*. By denoting n at $t=0$ as n_0 and integrating the equation (15), we get

$$\left(\frac{n_0}{n}-1\right)=\frac{n_0}{N_L}(t\nu_j)e^{-\frac{V_0}{kT}} \tag{16}$$

Delbecq, Smaller and Yuster mearured the decreasing of U_2 centers by the pulse annealing of $t=2$ minuits as the function of annealing temperature.(1) The initial concentration n_0 of the U_2 center is suggested as $n_0 \doteqdot 1/5\times 2\times 10^{18}$/c.c. by their experiment. In Fig. 5, we try to fit the curve (16) with their observed data. Unfortunately their experimental values are scattered, so that we can not decide the value of V_0 exactly, however, it seems to be in the range of 0.15~0.25 eV. If we assume that $V_0=0.19$ eV we obtain $\nu_0 \doteqdot 10^{13}$ sec^{-1} by using (14) and $\alpha=2.6$ by using (13). We can see that the condition $\hbar\omega \gg kT \gg \hbar\nu_0$ is satisfied. On the other hand we are able to decide ν_j as 10^{13} sec^{-1} by using Fig. 5. Of course ν_0 is not the same as ν_j, however, ν_0 and ν_j should be in the same order of magnitude. As shown in the above considerations, this condition is satisfied if we assume $V_0=0.19$ eV., on the other hand, it is not satisfied if we assume $V_0=0.25$ eV, because in this case we obtain $\nu_0 \doteqdot 10^{13}$ sec^{-1} from (14) and $\nu_j \doteqdot 10^{16}$ sec^{-1} from Fig. V.

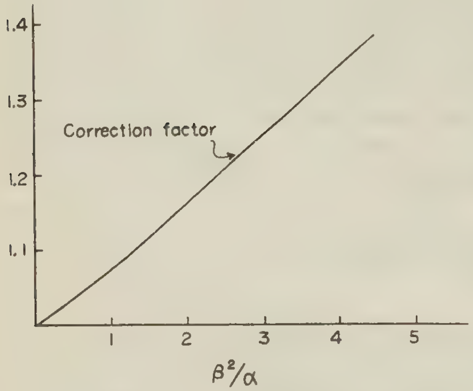

Fig. 3. Correction factor.

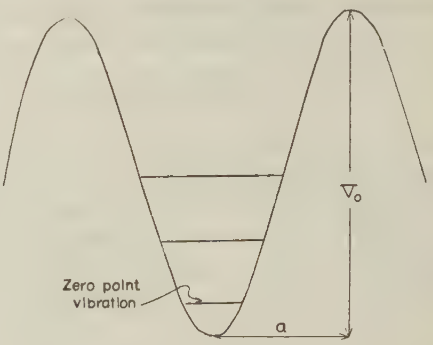

Fig. 4. Adiabatic potential for proton (schematic).

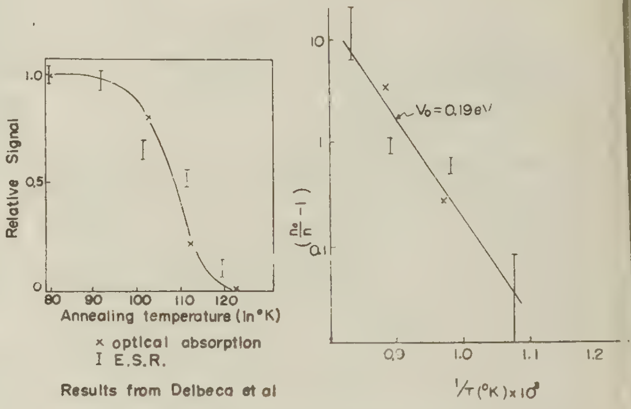

Fig. 5. Thermal bleaching behavior of U_2 center.

The experiment further shows that the maximum rate of decay of the U_2 center occurs near $n_0/n=2$ and at 108°K in the case of proton and at 113°K in the case of deuteron. This difference in the temperature is analized in Appendix III.

By considering these discussions, it is suggested that the approximate value of β^2/α is about $0.64/2.6=0.25$ in the case of proton and $0.25/\sqrt{2}=0.18$ in the case of deuteron. Therefore the correction factor is obtained as 1.21 in the case of the proton, the width $(\Delta H)_w$ of E. S. R. which is calculated in (7) by assuming the fixed center model should be multiplied by the factor of 1.21. By considering that the overlap integral is far smaller than 1, we can expand the normalization factor N in (6) as follows

---

* Strictly speaking, frequency ν may not be exactly the same as the jumping frequency (11). It may be multiplied by some numerical factor of the order 10^{-1}~10. However it has not the important meaning in the following discussions.

$$N^2=(1-\sum_{ik} S_{ik}^2)^{-1}\doteqdot 1+\sum_{ik} S_{ik}^2+\cdots$$

so that the deviation of the doublet separation from these of free hydrogen should also be multiplied by 1.21. As the correction factor is 1.15 in the case of deuteron, we may expect that the difference of $(\Delta H)_w$ in both cases is about 1/20 of $(\Delta H)_w$ itself. Unfortunately it is not clear whether the observed width $(\Delta H)_w$ is different in this order of magnitude between both cases or not, because the experiment by Delbecq, Smaller and Yuster is not sufficiently accurate to detect this small difference.

Finally it should be noticed that such an appreciable effect of the vibration on the absorption pattern of E. S. R. is the characteristic feature of the hydrogen because of its large amplitude of zero point vibration.

§ 6. Some Possible Effects Modifying $\Psi(r)$

6–A. In section 4, we considered the effect of the Pauli's exclusion principle by the orthogonalization which causes the decreasing of the electron density in the neighbourhood of ions (not at the nuclei of ions) accompanying the increasing of the electron density near the proton.

To remove the discrepancy in $(\Delta H)_s$ in (7) we have to investigate the possible effects which decrease the electron density near the proton. In order to explain the fact that $(\Delta H)_s$ is nearly equal to the value of the free hydrogen, $\psi_H=\frac{1}{\sqrt{\pi}}e^{-r}$ should be replaced by $\psi_H=\sqrt{\frac{\mu^3}{\pi}}e^{-\mu r}$ ($\mu=0.97$ in a. u.) if we take the hydrogen like ls wave function for ψ_H.

Contrary to the effect of Pauli's principle, the polarization and the crystalline field of the surrounding ion will be supposed to extend the electron distribution to the outer region of the proton. Therefore we will examine to what extent the decay constant μ of the hydrogen like wave function is decreased by these effects.

6–B. *Effect of the polarization*

We put the decay constant μ as $\mu=1+\varepsilon$ and assume that $\varepsilon\ll 1$. The total energy including polarization is as follows

$$H=H_0+H_{e.p}+H_p \tag{17}$$

where H_0 is the electronic energy and is given by $\frac{1}{2}\{-1+\varepsilon^2\}$. H_p is the self energy of polarization and $H_{e.p}$ is the interaction energy between the U_2 center and the induced polarization of the neighbouring ions. If we replace the approximate polarization by the induced point dipoles on the ions, we get the following equation

$$\begin{aligned} H_{e.p}&=-n\alpha q^2/R_i^4 \\ q&=1-4\pi\int_0^{R=R_i}\psi_H^2(r.\varepsilon)r^2dr \\ \psi_H&=Ne^{-(1+\varepsilon)r} \end{aligned} \tag{18}$$

where R_i is the distance between the proton and nearest neighbouring ions, α is the mean value of polarizabilities of the nearest ions, n is the number of the nearest ions, and q means the effective charge which induces the polarization of the nearest ions. H_p is given by $-\frac{1}{2}H_{e.p}$.⁽⁹⁾ We expand $H_p+H_{e.p}$ to the lst order in ε and minimize the value of H. The obtained value of ε is about $-\frac{1}{2}\alpha$(in a. u.)$\times 10^{-6}\doteqdot 7\times 10^{-6}$ and it is far smaller than 1.

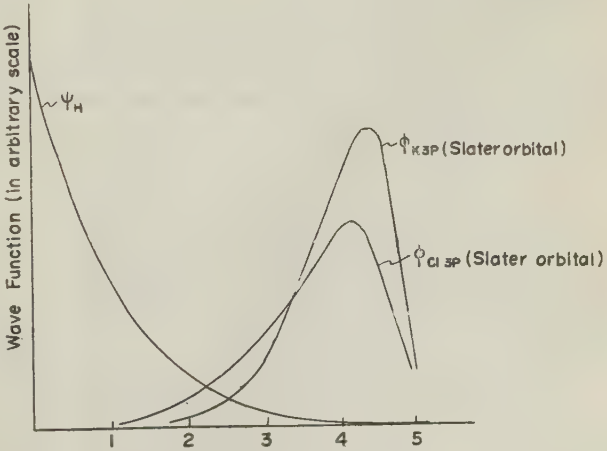

Fig. 6. Extention of wave functions.

Hence, the effect of ε on E. S. R. is quite small, so long as we confine ourselves to the point dipole approximation. However, it should be remarked that the point dipole approximation is not adequate to the U_2 center, because the effective charge q is not slowly varying near the lattice points of the neighbour ions. For example as calculated from Fig. 6, q is 50 times larger in value $R=\frac{1}{2}R_i$ than $R=R_i$, and the charge distribution of core electrons is still appreciable in this range of R. If we want to treat the polarization more in detail we have to discuss the many electron systems in which the orbitals of core electrons have variable freedom in precisely representing the polarization. Detailed discussions along these lines are not in the range of the present paper in which we assume the point ion lattice model. This problem will be discussed in a forthcoming paper.

6–C. *Effect of the mixing of f-type function owing to the crystalline field*

As shown in § 4, the expectation value of V^0_{cry} is zero so long as we confine ourselves to the use of ls like wavefunction as ψ_H, however the crystalline field V^0_{cry} causes the mixing of the $4f$ like wave function. We put ψ_H as follows

$$\begin{aligned}\psi_H&=\alpha\psi_{H1S}+\beta\psi_{H4}\\ \psi_{H1S}&=N(\varepsilon)e^{-(1+\varepsilon)r} \qquad (19)\\ \psi_{H4f}&=N(\nu)e^{-\nu r}x.y.z\ .\end{aligned}$$

and determine the variational parameters α, β, ε and ν to minimize the electronic energy of the U_2 center in the point ion lattice. The results are as follows

$$\alpha=1 \quad \beta=0.058 \quad \varepsilon=0.012 \quad \nu=1.0 \qquad (20)$$

By substituting the wave function (19) into (6) we recalculate the width and the separation. The results are as follows

$$\begin{aligned}(\varDelta H)_s&\doteqdot 525 \text{ gauss}\\ (\varDelta H)_w&\doteqdot 58 \text{ gauss}\end{aligned} \qquad (21)$$

Owing to the negative charge of Cl⁻ ion, the charge distribution of the trapped electron is reduced in the range of Cl⁻ so that it is natural that we have the smaller value of $(\varDelta H)_w$ than those obtained in (7).

Considering the limit of the point ion model it is not clear whether the values obtained in (21) are plausible or not because the degree of mixing of the f type function may depend on the detailed interactions with the core orbitals. Therefore it is necessary to treat the problem as many electrons system and the situation is similar to the case of 6–B.

6–D. *The effect of electron transfer*

So far we have considered that the trapped electron is localized in the neighbourhood of the proton. However the electron may transfer onto K⁺ ions or the electron which belongs to the Cl⁻ closed shell may transfer onto the hydrogen atom. The former process is interpreted in terms of the resonance between 4s orbitals of the nearest K atoms, and the latter is interpreted as a kind of configurational interactions. The problem to examine precisely those effects is not possible if we assume the point ion lattice, but by the following simple considerations it is suggested that these effects may not be significant.

In order to examine the resonance of the 4s orbitals of the nearest K⁺ ions, we take the L. C. A. O. procedure. In this procedure the most essential quantity is the non-diagonal matrix element of the following type $\left(\psi_{HIS}|V_{cry}|\sum_{K_i=1}^{4}\phi_{K_i 4S}\right)$. If we replace V_{cry} by $\sum_i \frac{\pm 1}{|\boldsymbol{r}-\boldsymbol{R}_i|}$ and $\sum\phi_{K_i 4s}$ by the slowly varying function, for example the Slater's one, this nondiagonal element is nearly equal to $\left(\psi_H\middle|\sum_i\frac{\pm 1}{|\boldsymbol{r}-\boldsymbol{R}_i|}\middle|\psi_f\right)$, in which ψ_f means the f symmetrical component of $\sum_{K_i}\phi_{K_i 4s}$ expanded around the proton. The effect of this term is the same as the one which has already been discussed in 6–C. The other essential point of L. C. A. O. method is that we use the A. O. of ϕ_{K4s} localizing near the ion potential field, $V_{K,\text{ion}}$, to gain the additional potential energy to those calculated by the point ion model. To estimate this effect we will compare the following two energies

$$\begin{aligned}E_A&\equiv\left(\psi_H\middle|-\frac{\varDelta}{2}-\frac{1}{r_H}-\frac{1}{r_K}\middle|\phi_{K4s}\right)\\ &=E_H(\psi_H|\phi_{K4s})+\left(\psi_H\middle|\frac{-1}{r_K}\middle|\phi_{K4s}\right)\\ E_B&\equiv\left(\psi_H\middle|-\frac{\varDelta}{2}-\frac{1}{r_H}+V_{K,\text{ion}}\middle|\phi_{K4s}\right)\\ &=E_K(\psi_H|\phi_{K4s})+\left(\psi_H\middle|\frac{-1}{r_H}\middle|\phi_{K4s}\right)\end{aligned}$$

where E_H or E_K represents the ionization energy of hydrogen (1s) or potassium (4s) electron respectively :

$$-E_K=0.1595$$
$$-E_H=0.5$$

E_A-E_B will give the energy gain of this kind. If we use the Slater's type function(5) as $\phi_{K4s}=Nr^2e^{-0.549r}$ we obtain $E_A=-0.1911$ a. u. and $E_B=-0.1912$ a. u. and the difference is very small. Thus it seems that the 4s orbital of K ion can hardly resonate with 1s orbital of hydrogen. As to the configuration interaction, the degree of mixing of the state in which a hole exists in a core orbital of Cl^- ion, can be examined by calculating the energy $E_g-\chi-I$ in the energy cycle principle. E_g means the band gap of KCl crystals, χ is the electron affinity of KCl crystals, and I is the electron affinity of the hydrogen. If we assume approximately $\chi\doteqdot0.5$ eV. and take the known values of $E_g=9.44$ eV and $I=0.71$ eV, $E_g-\chi-I$ becomes nearly equal to 9.2 eV. This energy seems too large to cause the appreciable effect of the electron transfer to the hydrogen from the Cl^- ion.

II. Brief discussions on the optical absorption

§ 7. The Wave Length of the Optical Absorption

The optical absorption peak of the U_2 band in KCl crystals appears at the wave length of 236 mμ i. e. about 5.2 eV. At present it is not clear what kind of electronic transition corresponds to this optical absorption. In this section we classify three typical types of the transition and estimate the absorption wave length or photon energy by means of the simple point ion lattice model.

7–A. *Transition of the trapped electron*

We take the wave function of 1s and 2p like state as follows

$$\Psi_{gr}=Ne^{-\nu r} \qquad \Psi_{ex}=Nxe^{-\mu r}$$

If we assume the point ion lattice model we can easily get the following relations,

$$(\Psi_{gr}|V^0_{cry}|\Psi_{gr})=(\Psi_{ex}|V^0_{cry}|\Psi_{ex})$$
$$=(\Psi_{gr}|V^0_{cry}|\Psi_{ex})=0$$

so that the absorbed energy of the photon is 10.2 eV which is the same as the energy gap between the 1s and 2p states of the free hydrogen.

In order to consider the effect of the crystalline field on the excited state, we take the following wave function,

$$\Psi_{ex}=N_1xe^{-\mu_1r}+N_2yze^{-\mu_2r}$$

where μ_1, μ_2, N_1, and N_2 are the variational parameters. If we minimize the energy of the excited state, this level appears to be about 0.18 (a. u.) lower than those of the continuum state and the corresponding absorption energy is 8.7 eV. It seems too large to be compared with the observed value of 5.2 eV. If we include the effect of exchange interaction between the trapped electron and those of the surrounding ions, the energy gap may be larger than the values obtained above. On the other hand the effect of polarization may contribute to decrease the energy gap.

In any case we can conclude that the transition of the trapped electron in the U_2 center may not take place near the energy of 5.2 eV if we confine ourselves to use the point ion lattice model.

7–B. *Exciton near the U_2 center*

There are other interpretations on the optical absorption in the U_2 center, the electron transfer model from the Cl^- ions near the U_2 center. The one is to interprete the exciton absorption near the U_2 center and the other is electron transfer to the U_2 center from the Cl^- ions. As has been already mentioned, these two processes may not be clearly distinguished from each other in the actual process.

To calculate the absorbed energy of the first process, we utilize the treatment by Bassani and Inchauspé(6) who succeeded in explaining the absorbed energies of α and β excitons. Their method is the semiclassical one, based on the electron transfer model of exciton, in which the charge distribution of the excited electron is ignored. The Coulomb field and the polarization are expressed approximately by the interaction between the point dipoles and the point charges and the complicated interaction caused by the exchange effect is neglected. A similar picture was used in this paper. According to the discussions by Bassani and Inchauspé, the difference between the excitation energy of free exciton and U_2 center is given by the difference of the following three kinds of energies Q, W, and P.

Q: Coulomb interaction energy between the charges of the point ion lattice

W: Repulsive interaction energy between

the ion cores*

P: Energy of polarization

Because of the neutrality of H atom, difference ΔQ vanishes. The difference ΔP is due to the polarization of the interstitial hydrogen and is given as follows (See Fig. 7)

$$\Delta P=\left[\frac{1}{r^4_{13}}+\frac{1}{r^4_{32}}-\frac{2\cos(r_{13}r_{23})}{r^2_{13}r^2_{32}}\right]\frac{\alpha_H}{2}\doteqdot 0.12\,\text{eV}$$

where α_H means the polarizability of the hydrogen atom and is 4.6 a. u. In this simple evaluation of ΔP, we neglect the shielding effect caused by the polarization of the other ions, and it leads us to overestimate the value of ΔP. In order to estimate ΔW, we assume approximtely that the repulsive energy W is given by⁽¹⁰⁾

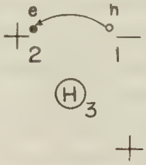

Fig. 7. Exciton model of U_2 band.

$$W\doteqdot C\frac{S^2}{R}$$

We further assume that the hydrogen migrates in the potential field given by W so that we are able to determine the constant factor C by using the known value of the height of this potential field (=0.19 eV as shown in § 5) and the estimated value of the overlap integral S.

The difference ΔW is estimated as 0.04 eV. The total energy difference $\Delta(h\nu)$ is

$$\Delta h\nu=(h\nu)_{free}-(h\nu)_{U_2}=\Delta W+\Delta P+\Delta Q\doteqdot 0.16\,\text{eV}$$

This value is far smaller than the value required, for the exciton peak appears at 7.6 eV in KCl which requires the difference $\Delta(h\nu)$ of 2.4 eV. The discrepancy seems to come from the simplified picture of the point ion and dipole model. We may have to study the effect of the polarization and the exchange interaction more precisely. As stated in §6–D. the required energy for another process is estimated to be 9.2 eV by energy cycle principle.

§ 8. Conclusions and Summary

(1) The 1s wave function of the free hydrogen which is orthogonalized to the core orbitals of the nearest ions, gives the separation $(\Delta H)_s$ and the width $(\Delta H)_w$ of E.S.R. as

$(\Delta H)_s=550$ gauss (obs. 500 gauss)

$(\Delta H)_w=46$ gauss (obs. 81 gauss)

(2) Owing to the large amplitude of zero point vibration of the interstitial hydrogen, the width $(\Delta H)_w$ spreads about 20% larger than those estimated by assuming the fixed model of hydrogen at the body diagonal interstitial point.

(3) The effects of the polarization and the crystlline field are considered by using the simple point ion lattice and the point dipole model. If we confine ourselves to this simple model, these effects on the wave function of U_2 center are very small.

(4) Brief discussions on the optical absorption are developed from the same standpoint. The estimated energy of the absorbed photon is considerably larger than the observed one. If we assume that the absorption corresponds to the transition between the ground and excited levels of hydrogen modified by the crystalline field, we get

$(h\nu)_{U_2}=8.7$ eV (obs. 5.2 eV)

If we assume that the absorption is the exciton absorption near the U_2 center, we get $(h\nu)_{U_2}=7.4$ eV (obs. 5.2 eV) and if we assume that it corresponds to the electron transfer to the U_2 center from the surrounding Cl^- ions we get

$(h\nu)_{U_2}=9.2$ eV (obs. 5.2 eV)

(5) In order to understand origin of the discrepancies between the calculated and observed values we have to take account of the core electrons more accurately, to esitimate the energy of the exchange interaction, to consider the effect of polarization more precisely and to notice further the effect of spin polarization of the core electrons,⁽⁷⁾ because the velocity of the electron in the U_2 center is nearly the same with those of the core electrons.

---

* Bassani and Inchauspé have neglected the energy difference in the process to bring back the neutral atoms into crystal.

If we take account of the difference in this process, it should be expected that the difference in the repulsive energy has only smaller effect on the absorption energy. Thus, the following estimation of ΔW should correspond to overestimation.

(6) Through all the discussions in this paper we conclude that the U_2 center is one of the best tracers which shows the physical characteristics of various kinds of interactions involved in the problem of colour centers.

Acknowledgement

The authors wish to express their hearty thanks to Professors T. Inui and R. Kubo for their encouragement. This work was supported by a grant in Aid for Fundamental Scientific Research from the Ministry of Education.

Appendix I. On the model *B* of U_2 center

Considering the geometrical symmetry only, the site *B* in Fig. 1 is possible as well as site *A*. However, the site *B* seems tentatively to be unacceptable because of the large repulsive energy. Further, the model *A* of the U_2 center is more favourable than the model *B* to interprete the observed data of E. S. R. If we assume the model *B* we may expect that the separation $(\Delta H)_s$ shows a larger deviation from the one of free hydrogen because the overlap integral S_{tk} shows the larger value than in the model *A*.

The line shape of each branch is suggested as to be a triangle if we take the primitive treatment of § 4.

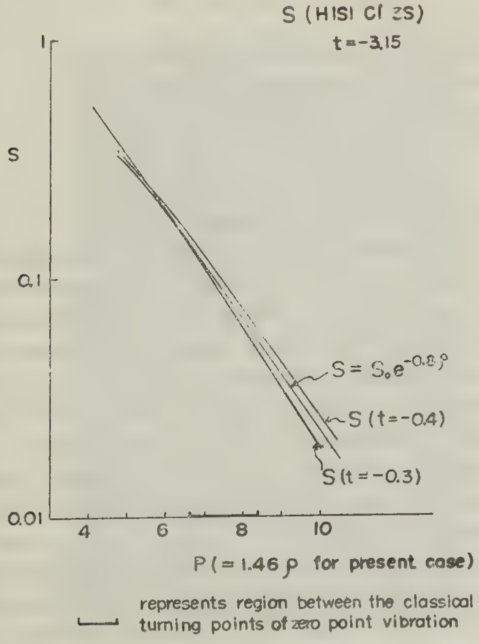

Fig. 8. Approximation for overlap integral.

The calculated results for the model *B* are as follows

$(\Delta H)_s \fallingdotseq 610$ gauss obtained by the same
$(\Delta H)_w \fallingdotseq 155$ gauss approximation in § 4
$(\Delta H)_s \fallingdotseq 560$ gauss obtained by the same
$(\Delta H)_w \fallingdotseq 127$ gauss approximation in § 6–C

Appendix II. Approximate formula for the overlap integral

We assume approximately the analytic form for the overlap integral $S(Cl\,3s|H\,1s)$ in $E_q(10)$ as follows.

$$S=S_0\,e^{-\beta\rho} \qquad \beta=0.8\text{ a. u.}$$

The value of β is determined as a tangent near the internuclear distance in Fig. 8, where the value of *S* is obtained from the Mulliken's table.⁽⁸⁾ $S(Cl\,3p\,\sigma|H\,1s)$ is also approximately given by nearly the same function as $S(Cl\,3s|H\,1s)$ in the required region of *r*.

Appendix III. On the difference of bleaching temperature between *D* and *H*

The experiments by Delbecq, Smaller and Yuster shows that the maximum rate of the decay caused by pulse annealing of 2 min. occurs at 108°K, $n/n_0=\frac{1}{2}$ in the case of proton U_2 center and at 113°K, $n/n_0=\frac{1}{2}$ in the case of deuteron U_2 center.

Using the equation (16) and the above data we can obtain the height of potential barrier for each case where ν_j is replaced approximately by ν_0 which is proportional to $M^{-1/2}$. We find that the height of potential barrier is different from each other by the value of 0.006 eV. The difference seems to come from the difference of the zero point energies in each cases.

If we estimate these energies by (14) and by assuming $V_0=0.19$ eV we obtain the following results.

$$\frac{1}{2}h\nu_0=0.02\text{ eV.} \qquad \text{for } H$$

$$\frac{1}{2}h\nu_0=\frac{0.02}{\sqrt{2}}\text{eV.} \qquad \text{for } D$$

Therefore the difference between above two values is to be 0.006 eV which is in agreement with the difference obtained from the barrier height.

References

1) C. J. Delbecq, B. Smaller and R. H. Yuster: Phys. Rev. **104** (1956) 599.
2) B. S. Gourary and F. J. Adrian: Phys. Rev. **105** (1957) 1180. B. S. Gourary and P. J. Luke: Phys. Rev. **107** (1957) 960. B. S. Gourary: Phys. Rev. **112** (1959) 337.
3) A. F. Kip et al: Phys. Rev. **91** (1950) 1066.
4) D. R. Hartree and W. Hartree: Proc. Roy. Soc. A, **156** (1936) 54; A, **166** (1938) 458.
5) H. Miyakawa and T. Muto: Rep. of Inst. Sci. Technol. Tokyo Univ. **9** (1955) 33 (in Japanese).
6) F. Bassani and N. Inchauspé: Phys. Rev. **105** (1954) 819.
7) Remarked by J. Kondo, who is now calculating of this effect.
8) R. S. Mulliken et al: J. Chem. Phys. **17** (1949) 1248.
9) T. Kojima: J. Phys. Soc. Japan **12** (1957) 908.
10) F. E. Williams: J. Chem. Phys. **19** (1951) 457.

JOURNAL OF THE PHYSICAL SOCIETY OF JAPAN, Vol. 14, No. 8, AUGUST, 1959

Etch Pits Corresponding to Dislocations in Ferroelectric Guanidinium Aluminum Sulfate Hexahydrate

By Terutaro NAKAMURA

Department of Physics, Ochanomizu University,
Otsuka, Tokyo.

(Received May 2, 1959)

Cleavage surface of ferroelectric G.A.S.H. crystal was etched with a mixture of water and ethyl alcohol, followed by rinsing in benzene. Identical etch pits were observed on matching cleavage faces. Density of the pits is $10^4/cm^2$ in the order of magnitude. Mechanical shock produces etch pits. Successive etching causes growth of pits at the unchanged locations. These facts lead us to conclude that the pits must correspond to dislocations. Patterns of etch pits on the upper and the lower cleaved faces of the crystal indicated that dislocation penetrates the crystal several hundred micron thick. Pair arrangements and linear arrays of etch pits were observed. Etch pits, of which the deepest points differ from the centers of triangles, correspond to dislocations not perpendicular to cleavage surface.

§ 1. Introduction

The polarization reversal of ferroelectric crystals is attained through the movement of the ferroelectric domain walls, and it is very plausible that the domain wall movement has interesting interactions with crystal imperfections especially with dislocations, as pointed out by a few authors.1) It will be much interesting to inquire the behavior of polarization reversal or domain switching in connection with the dislocation. However, the information on dislocations in ferroelectric crystals has been lacking, and even the observation of a dislocation itself has not yet been reported, except the observation of growth spirals on crystals of WO_3.2)

The present article describes the observation of etch pits on {0001} cleavage surfaces of guanidinium aluminum sulfate hexahydrate, $C(NH_2)_3\ Al(SO_4)_2\cdot 6H_2O$ (usually abbreviated as G.A.S.H.) which was first reported to be ferroelectric by Holden et al in 1955,3) and has been investigated by several authors.4)–6)

Holden et al4) reported that great many triangular pits were observed on {0001} surfaces of G.A.S.H. by etching with water, without questioning whether these pits had anything to do with crystal imperfections. Our present study has revealed several important characteristics of etch pits, leading us to the conclusion that the etch pits having pyramidal form correspond almost certainly to dislocations, existing in G. A. S. H. crystals.

Crystallographic description of G.A.S.H. was made by Wood,[5)] reporting that the space group is P-31 m, while she found by optical and X-ray examination that the etch pits differently "cocked" in different parts of crystals reported by Holden et al[6)] do not result from the deviation from the parallelism of crystal structure in these different part. Crystal structure of guanadinium gallium sulfate hexahydrate, isomorph to G.A.S.H., was recently determined by S. Geller et al.[6)]

§ 2. Preparation of the Crystals

Since the solubility curve of G.A.S.H. into water makes low angle with temperature axis, and the activation energy of the diffusion depends greatly upon temperature, it is not adequate to cultivate the crystals by cooling method but evaporation method is well applicable. Equimolar mixture of $(CH_5N_3)_2H_2SO_4$ and $Al_2(SO_4)_3$ were poured into water and stirred well at about 40°C, 30% solution of $(CH_5N_3)\ H_2SO_4 \cdot Al_2(SO_4)_3$ being obtained. This solution was kept in a thermostat at 30°C, water being evaporated quite gradually there. G.A.S.H. crystals of hexagonal prismatic form, every edge of the hexagon being a few cm, hight being from a few to a fraction of cm were obtained. Some crystals were obtained from aqueous solution of crystallized G.A.S.H., by a recrystallization process. Crystals obtained from aqueous solution of $(CH_5N_3)_2H_2SO_4$ and $Al_2(SO_4)_3$ were not free from flaws, but crystals obtained by recrystallization were quite transparent.

Specimens were made by cleavage along {0001} plane. Very good cleavages were obtained with a razor blade tapped sharply but lightly by a small hammer.

Etching, of which method is described in the following paragraph, revealed that the as grown crystals show different densities of etch pits piece by piece, ranging from less than 10^4 up to 10^5/cm^2.

Dielectric measurement revealed that the crystals show different P-E hysteresis loops place to place, some are biased, some are doubled, some are symmetrical, some are round-shouldered, and some are not ferroelectric without displaying any hysteresis loop.

§ 3. Etching Technique

G.A.S.H. crystal has a perfect cleavage parallel to {0001} face. Cleavage faces were etched by a mixture of ethyl alcohol and distilled water in the volume ratio 7:1, the duration of etching ranging from a few to several seconds. Immediately after etching

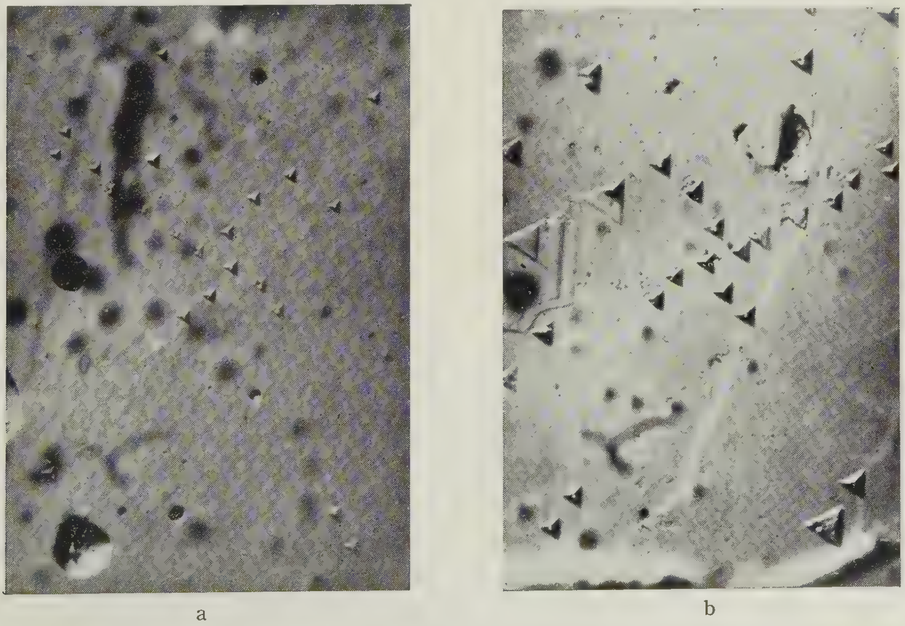
a b

Fig. 1. Mirror images on matched faces. (×125)

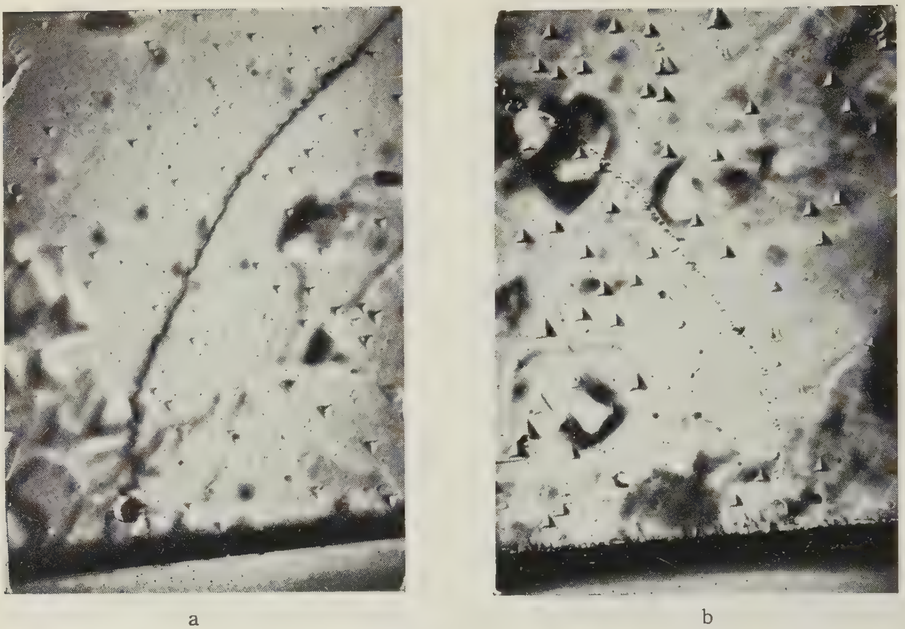

Fig. 2. Mirror images on matched faces. (×125)

in the solution, the crystal was rinsed in benzene, followed by drying the crystal, whose surface to be examined being in contact with a certain kind of blotting paper.

This method enabled us to observe triangular etch pits on uncontaminated faces, the cleavage steps remaining essentially unchanged before and after the etching. On the other hand, water as etchant, that was used by Holden et al, shows too much high speed of etchting, resulting in disappearance of cleavage steps and contamination of the surface, hence it was quite impossible to distinguish even the locality of etch pits.

§ 4. Experimental Results

(a) *Matching faces*

A piece of G.A.S.H. crystal, that had been cleaved from the crystal as grown, was cleaved into two halves. The matching cleavage faces of the crystal were etched and observed under a microscope. Some examples of couples of photomicrographs of etching surfaces are displayed in Figs. 1a, 1b, 2a, 2b, 10a and 10b. Reader will recognize that the patterns are mirror images apart from small detail.

These photographs clearly show that a certain crystal imperfection that causes preferential etching goes from one piece to another through the matching face as shown in Figs. 11 a and b. This imperfection is conceivably a dislocation, together with other experimental results reported below.

(b) *Density of etch pits*

Etch pits photographed were counted over 23 photomicrographs and distribution curve as shown in Fig. 3 was obtained. Counting of etch pits, of which density is less than $10^3/\text{cm}^2$ was not attempted, because of the limit of the visual field of microscope. The geometrical mean was calculated to be $0.7\times 10^4/\text{cm}^2$. This value $\sim 10^4/\text{cm}^2$ is reasonable, if we take these pits to correspond to dislo-

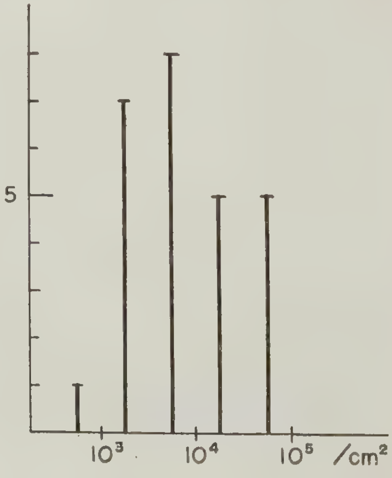

Fig. 3. Distribution of dislocation density.

cations, because the densities of etch pits corresponding to dislocations in LiF[7], KCl[8], NaCl[9] etc. have similar orders of magnitude.

(c) *Production of etch pits by mechanical shock*

If it is provided that the etch pits observed on the {0001} faces of G.A.S.H. correspond to dislocations, it will be expected that some etch pits should be observed after mechanical shock.

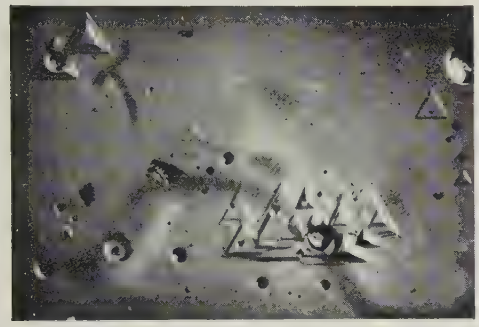

Fig. 4. Dislocation etch pits produced by dropping a steel bar onto the cleavage face. (×100)

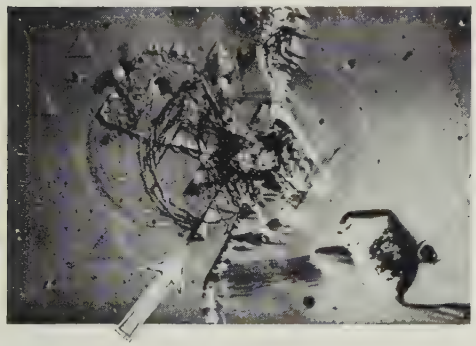

Fig. 5. Photomicrograph of needle contacted face, after a second etching. (×100)

It was easy to find a certain region of crystal, where etch pits were very few. This region was mechanically shocked by dropping a steel bar onto the surface, or by contact of point of a needle. The mechanillay shocked region underwent a second etching. The examples of results are illustrated in Figs. 4 and 5. The photomicrographs seem to indicate that dislocations were created by mechanical contacts. Flat bottomed pits observed in the photographs will be discussed in the next paragraph.

(d) *Successive etching*

The cleavage surface was successively etched. A piece of crystal was picked up, which showed a few etch pits. This crystal was etched successively. The very small pits, that were observed in the first etching, became larger and a little deeper at the unchanged locations, without producing new pyramidal pits, as shown in Figs. 6a∼d.

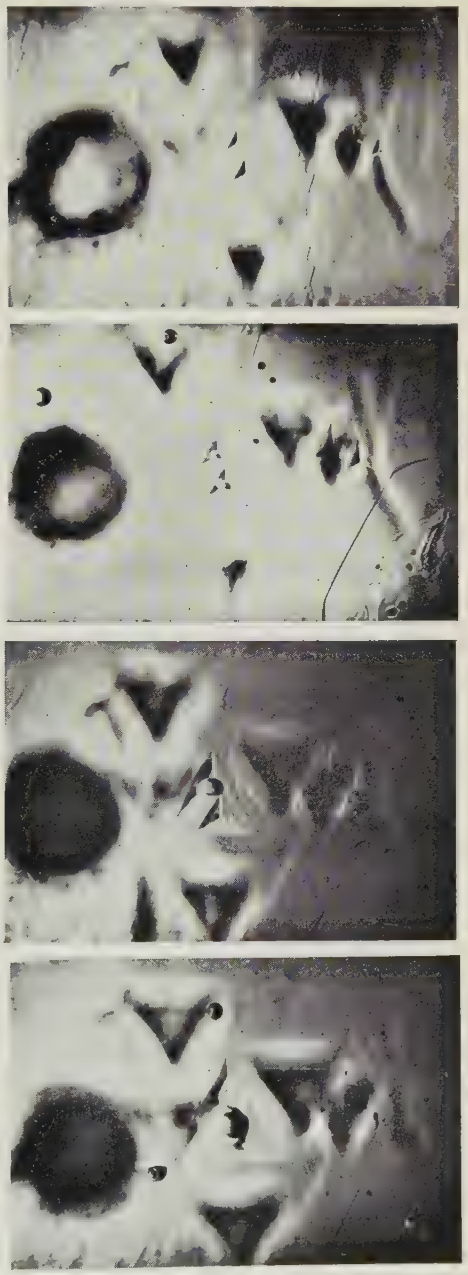

Fig. 6. Effect of successive etching. (×100)

When the state of Fig. 6d was reached, where couples of pyramidal pits became indistiguishable, pyramidal pits had deepness of several microns, indicating that the pits observed represent dislocations, of which length is at least about ten microns.

In the course of successive etching in Figs. 6 it was observable that flat-bottomed pits appeared or disappeared. These pits may correspond to emergence points of dislocation half loop, which is located or has been located extremely close to the surface. This situation is shown in Fig. 11c and discussed in § 5.

(e) *Regularity of etch pattern*

Inquiring a number of photomicrographs it is easily recognized that the distribution of etch pits are not quite at random, but pits have tendency to be arranged in a regular manner.

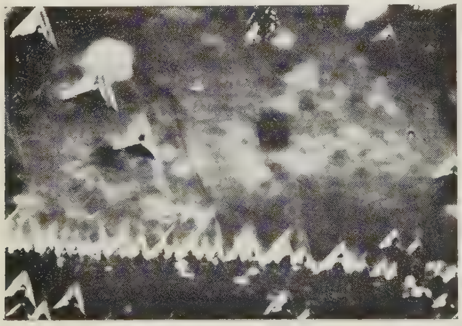

Fig. 7. Dislocation array forming grain boundary.
(×100)

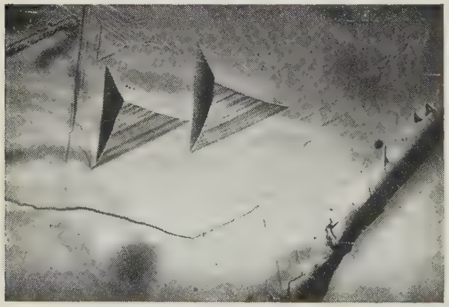

Fig. 8. Pair dislocations.
(×100)

Firstly, pairs of etch pits are very frequently observed, as shown in Figs. 1, 6 and 8. It will be very likely that a pair of pits correspond to a pair of emergence points of dislocations. This pair of points are probably both ends of dislocation half loop.

Secondly, etch pits have a tendency that they make a linear array, as seen for example in Figs. 1 and 9. Linear arrays of closely located pits as shown in the lower part of Fig. 7 is sometimes observed. It was confirmed that an array of pits were found on the grain boundary, which was observable by an optical mean.

(f) *Penetrating dislocation*

A piece of G.A.S.H. crystal, cleaved from a crystal as grown, was cleaved again into two halves. After the etching and the rinsing, both sides of every piece was dried in contact with the blotting paper simultaneously. Figs. 9 show patterns of etch pits on four faces. Patterns on matched faces are in the relation of mirror images, as seen from Figs. 9b and c. Patterns on the upper and the lower faces of piece (I), as shown in Figs. 9a and b, show that threee dislocation lines penetrate through the crystal. Since the thickness of the piece (I) was about 370μ, the dislocations corresponding to the etch pits will have a length of a few hundred microns.

Patterns on the upper and the lower faces of piece (II), as shown in Figs. 9c and d, show that one dislocation penetrate this piece, and the other two make a half loop.

Geometrical arrangement of the dislocation lines in this crystal is as shown in Fig. 9e.

§ 5. Discussion

G.A.S.H. crystal has an advantage that uncontaminated surface is easily obtained by cleavage. In these circumstances a suitable etchant is able to attack immediately the stressed region around the emergence point of the dislocation and produce an etch pit, without necessitating the presence of some concentration of impurities around it.

In the previous paragraph six experimental facts were shown, providing very strong supports of the view that the etch pit observed indicates the emergence point of a dislocation.

The density of etch pits in a good region of the crystal is as low as $10^4/\text{cm}^2$, while the density is large where linear array of dislocations that corresponds to grain boundary is observed (Fig. 7). The low value of the density, suggests that the pits do not correspond to impurities but dislocations.

As reported by Holden et al[4), some etch pits are "cocked", namely the deepest points of the pits are displaced with respect to the centers of triangular peripheries.

The angle that a dislocation makes with the {0001} cleaved surface can be estimated by the asymmetry of the etch pits. Fig. 10c indicates the relation between cocked pits on the matching faces, of which photomicrographs are shown in Figs. 10a and 10b. The identity of the etch pits on both matched faces does not necessarily mean the coincidence of the deepest point of pits, but, if we superpose every corresponding pit so as to make the total overlapping area maximum as in Fig. 10c, the deepest points of the matching etch pits displace almost the same amount with respect to the centers of the peripheries and in the opppsite directions. This is a strong support that some dislocations make certain angles with {0001} face going from one side to another through the cleavage surface as shown in Fig. 11b.

Shape of pyramical etch pits is rather shallow. Etch pits, of which edges are of the order of 1/10 mm, has a deepness of only a few microns, showing that the pyramidal faces are not crystallographic $\{11\bar{2}1\}$ plane, but form stepped walls.

In the case of "cocked" pits accordingly, small amount of displacement of the deepest point with respect to the center of triangle means rather remarkable inclination of dislocation line, some measured values of angle that the dislocations make with the {0001} basal plane amounted 15°~30° approximately.

It must be noted here that there observed are a few etch pits of triangular form, of which bottom is not pointed but very flat. Some examples of these pits are found in Figs. 1b, 4 and 12. Some of flat pits do not compose mirror images between matching faces, but they showed no positive evidence to be identified as dislocations existing there.

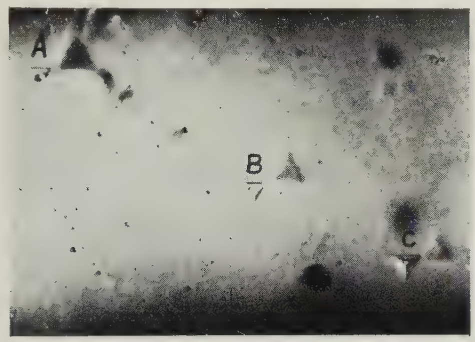

a

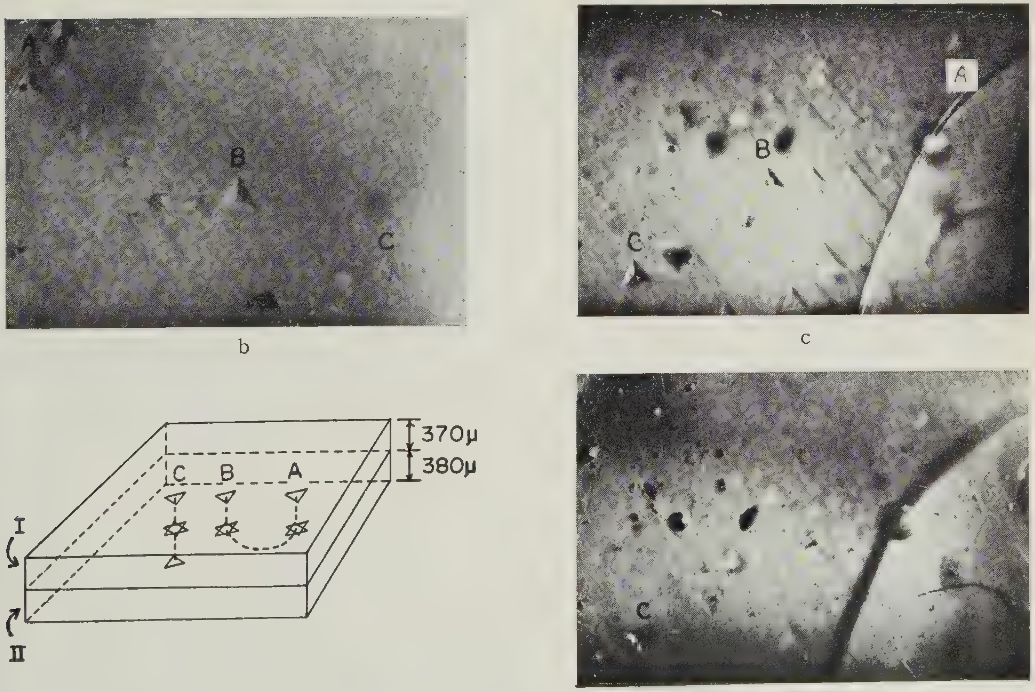

b

c

e

d

Fig. 9. Dislocation lines penetrating through a crystal.
(×100)

Neverthless some of the flat-bottomed pits are conceivable to correspond to emergence points of dislocations. If a dislocation line enters the crystal making very low angle with the cleavage face, and it lies extremely close to the surface, it is expected that the flat-bottomed pits are obtained as shown in Fig. 11c.

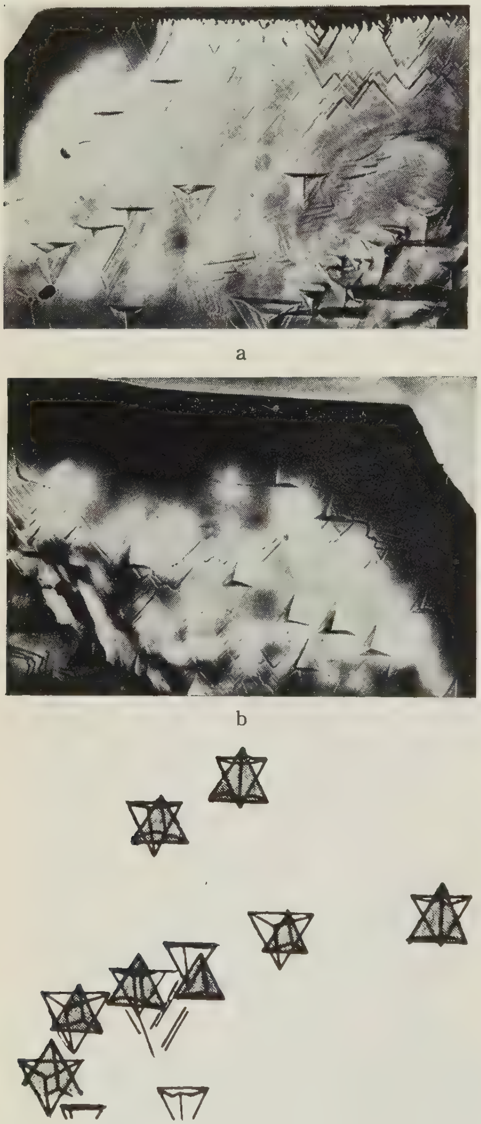
a

b

c

a, b: Mirror images of pits of which the deepest points differ from the centers of peripheries. (×100)

c: Superposition of cocked pits on matched faces.

Fig. 10.

An array of closely connected pits, as shown by an arrow in Fig. 5, is observed in the photomicrograph of etch figure produced by etching after mechanical shock. This figure may be accounted as a trace of moving dislocation.

Observations of etch pits on the upper and the lower cleavage faces indicated that the dislocations were existent penetrating through the crystal, a few or several hundred micron thick, as shown in Figs. 9. This experiment is expected to indicate a possible slip plane. Dislocation lines A, B, and C were perpendicular to the {0001} cleavage faces within the limits of experimental error. Slip plane seemed to be near {11$\bar{2}$0}, although precise measurement was not made.

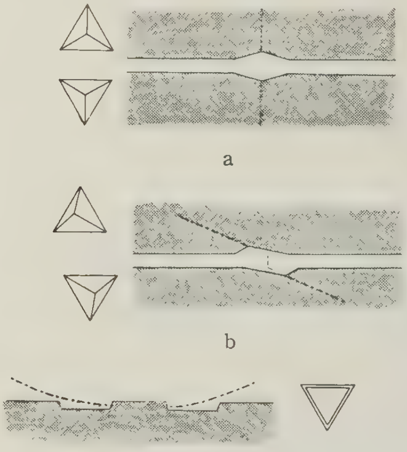
a

b

c

a: Dislocation perpendicular to matched faces.

b: Dislocation not perpendicular to matched faces causes etch pits of which deepest points differ from the center of the triangles.

c: Dislocation that causes a flat pit.

Fig. 11.

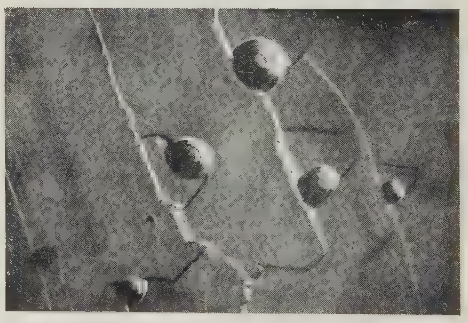
Fig. 12. Etch pits at contaminated cleavage step. (×100)

The etch pits are, however, sensitive not only to dislocations but also such crystal imperfections as contaminated points at cleavage steps and others. The etch pits produced at these defects are usually flat-bottomed as shown in Fig. 12., and easily distinguished from the dislocation pits, which are characteristic pointed ones.

Circular pits are sometimes observed, as in for example Figs. 4, 6, and 12. They are dislocation insensitive. These round pits may be due to unskilfulness of etching technique.

By the etching experiment it is found that the slip bands are difficult to produce, by compressing the specimen in the direction of $\langle 11\bar{2}0\rangle$. This seems at first glance disadvantageous to conclude for the etch pits to correspond to dislocations.

This phenomenon, however, is plausibly explained in taking into account that this substance is ferroelectric. If the compression along $\langle 11\bar{2}0\rangle$ is applied, polarization parallel to $\langle 0001\rangle$ occur by the piezoelectric effect because the space group is $P\text{–}31m$. Therefore ferroelectric domain boundary may move, resulting in the consumption of energy applied by the compression. Energy given by the compression is not used for the production of slip bands, but used for the displacement of the domain wall. This is a possible explanation that the slip bands are difficult to observe.

§ 6. Conclusion

Cleavage surface of G.A.S.H. was studied by etching technique. Identical etch pits were observed on matching faces. Density of the pits is $10^4/\text{cm}^2$ in the order of magnitude. This value supports the view that the etch pits do not correspond to impurities but emergence points of dislocations.

Mechanical shock produces etch pits. These pits show that dislocations were produced and probably moved during the etching process.

Etch pits of which deepest points displace with respect to the centers of the triangles correspond to dislocations inclined to the cleavage face.

Pairs of pits or linear arrays of pits are frequently observed.

Array of pits corresponding to grain boundary is observed.

Successive etching causes growth of pits at the unchanged locations.

Patterns of etch pits on the upper and the lower cleaved faces of the crystal indicated that dislocation penetrates the crystal, several hundred micron thick.

These experimental results lead us to the conclusion that the etch pits observed are emergence points of dislocation.

The author is much indebted to Prof. M. Sakamoto of Tokyo College of Science, for his illuminative discussions and valuable suggestions. He is also grateful to Prof. H. Takahasi of University of Tokyo, for interest and encouragement. The author is thankful to Miss M. Yamazaki, Miss Y. Nakao, Mr. K. Oi and Miss H. Kubota for their deligent and skilful assistance in the course of this work. This study was finantially supported in part by a Grant in Aid for Scientific Research from the Ministry of Education.

References

1) T. Nakamura: J. Phys. Soc. Japan **9** (1954) 425; **11** (1956) 624. W. Kinase and H. Takahasi: J. Phys. Soc. Japan **12** (1957) 464.
2) S. Tanisaki: J. Phys. Soc. Japan **11** (1956) 620.
3) A. N. Holden et al: Phys. Rev. **98** (1955) 546.
4) A. N. Holden et al: Phys. Rev. **101** (1956) 962. A. G. Chynoweth: Phys. Rev. **102** (1956) 1021.
5) E. A. Wood: Acta Cryst. **9** (1956) 618.
6) S. Geller et al: Z. Krist. **111** (1956) 117.
7) J. J. Gilman et al: Dislocations and Mechanical Properties of Crystals—An International Conference held at Lake Placid, Sep. 1956.
8) M. Sakamoto et al: J. Phys. Soc. Japan **13** (1958) 800.
9) S. Amelinckx: Acta Metall. **2** (1954) 848.

Journal of the Physical Society of Japan Vol. 14, No. 8, August, 1959

Nuclear Quadrupole Resonances of Nitrogen in Amino and Amido Compounds*

By Midori MINEMATSU

Department of Physics, Tokyo University of Education, Otsuka, Tokyo

(Received March 6, 1959)

Pure quadrupole spectra of N^{14} in para-bromoaniline, para-chloroaniline, para-phenylenediamine, and urea were obtained. From the spectra quadrupole coupling constants and asymmetry parameters were determined. The apparent intensity of the high frequency line was always greater than that of the low frequency line when the method of Zeeman modulation was applied. This fact was interpreted from the second-order perturbation theory of Zeeman effect. By using the method of frequency modulation, the intensity difference between two lines became so small as it was interpreted with the population-difference between each state. The principal axis system of nitrogen in para-bromoaniline was determined with Zeeman studies. Discussions supported that the three bonds about nitrogen in these compounds are coplanar with the plane of benzen ring.

§ 1. Introduction

Since the first successful experiments on nuclear quadrupole resonances of nitogen in BrCN, ICN, and $(CH_2)_6N_4$ were carried out by Watkins and Pound in 1952[1], a few work has been done with this nucleus. In recent years O'Konski and Flautt found the resonances in NH_3, ND_3, and $N(CH_3)_3$[2], and Casabella and Bray in ClCN[3], and then in CH_3CN, C_2H_5CN, and $CH_2(CN_2)_2$[4]**. The latter authors gave an important discussion on the shape of trace of the resonance line. Chiba, Toyama and Morino detected one of nitrogen resonances in $CO(NH_2)_2$[5]***.

The theory of nuclear quadrupole resonance predicts that in nitrogen, which has a spin of unity, a non-zero field gradient asymmetry parameter, η, gives rise to two resonance lines. Therefore, a pair of resonance lines would be expected in urea. If the pair of resonance lines were observed, the nuclear quadrupole coupling constant and the asymmetry parameter would be determined from their frequencies. Amino-compounds, such as para-bromoaniline, para-chloroaniline and para-phenylenediamine, seemed to have a relatively large asymmetry parameter. The present work has been attempted to detect pairs of resonance lines in those compounds. A brief account of this work was reported by Kojima, Tanaka and the present author[6]. In this paper, the method of detection and the analysis of the results are described in detail. Further experiments on the method of frequency modulation and discussions on the apparent intensity of the line are also reported here.

§ 2. Experimental Procedure

a) *Detection of the resonance lines*

The nitrogen resonances whose frequencies are in a region between 2 Mc and 4 Mc were detected with a recording spectrometer. The principle of the spectrometer was essentially same as the Pound-Watkins[7] type, but the circuit was somewhat modified[8]. An oscillator in the spectrometer was a cathode-coupled 6J6 type with a cathode resistance. A decoupling resistance which served to decouple the tuned circuit from the plate of the second half of the 6J6 was adjusted to the largest value that sustained oscillation. A single-stage r.f. amplifier followed the oscillator. Its output was rectified by a 6AL5 and a negative voltage was fed into the second grid of the 6J6 through a circuit of capacity and resistance with a time constant of one second. This feedback was useful to stabilize the amplitude of oscillation and to control the level of oscillation. In this experiment, the r.f. level was adjusted by the feedback control, and the bias control in the cathode of the 6J6 was shorted out. The sensitivity of the spectrometer was measured by a calibrator. A narrow band amplifier⁹⁾, a phase sensitive detector¹⁰⁾, and an integrating output circuit were used and the signal was displayed on a recording meter. As a Zeeman modulation an on-off square wave of magnetic field at 160 cps was applied on the sample. Since the compounds which were used in the present experiments were expected to have a large asymmetry parameter, the strength of the Zeeman modulation field was increased up to about 50 gauss. The most of the measurements were done at liquid nitrogen temperature, in order to avoid an effect of the internal rotation of the N-H bond and to improve the signal-to-noise ratio. Since a saturation effect, however, increased at a low temperature, the spectrometer had to be used at a sufficiently low power-level to avoid it. In the best condition of the spectrometer, the power-level of the oscillator was about 0.5 v (r.m.s.), and the frequency-sweep of the spectrometer was 4∼6 kc per minute. At

---

* A doctorial thesis submitted to Tokyo University of Education.

** When the present work had just been finished, we received the report of the experiment on CH_3CN, C_2H_5CN, and $CH_2(CN_2)_2$ by Casabella and Bray. They mentioned that in the compound having a large η the detection of resonance would be very difficult in the experimental technique.

*** The author wishes to thank to Professor Y. Morino, Dr T. Chiba, and Mr. M. Toyama who gave her the information of high frequency line of urea before publication.

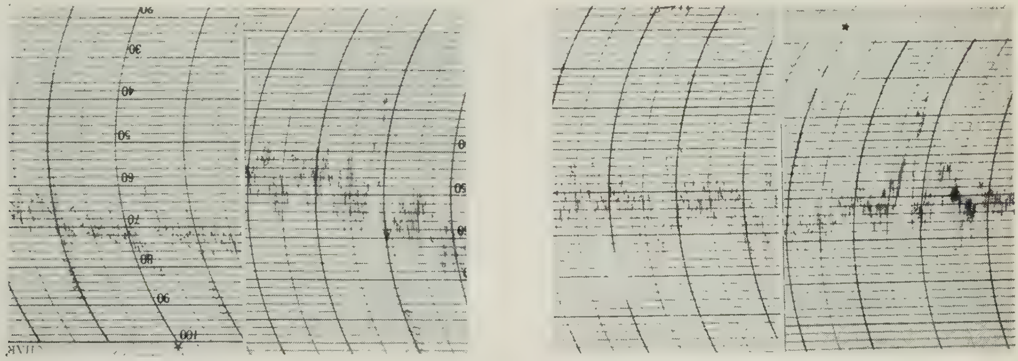

(a) p-$BrC_6H_4NH_2$; frequency sweep of 6 kc/min. (b) p-$ClC_6H_4NH_2$; frequency sweep of 6 kc/min.

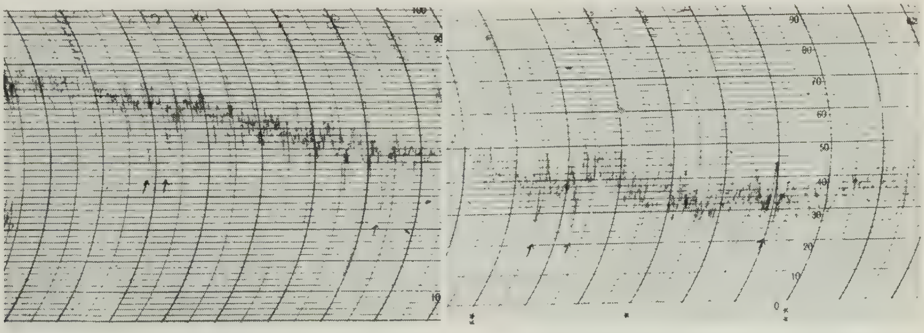

(c) p-$(NH_2)_2C_6H_4$; frequency sweep of 4 kc/min.

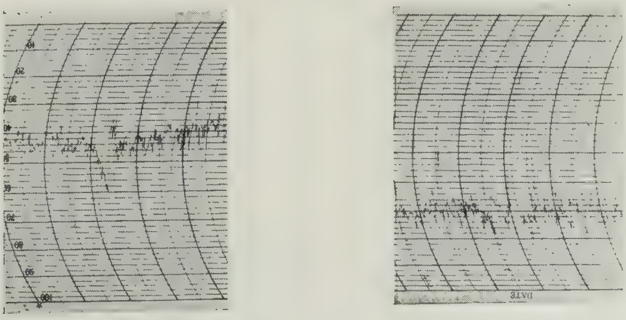

(d) $CO(NH_2)_2$; frequency sweep of 6 kc/min.

Fig. 1. N^{14} resonances.

such condition a slight saturation effect still remained. The frequency of resonance was measured by the method that frequency-markers from a signal generator whose frequency was calibrated with J. J. Y. were superposed on the resonance traces. The compounds investigated were commercial products*. As all compounds tend to decompose above the melting points, these were carefully melted in glass envelopes of about 10 cc. The results of measurements are given in Table 1, and the recorded spectra in these compounds are shown in Fig. 1.

Table. I. Observed resonance frequencies at liquid nitrogen temperature.

Compound	ν_1 (Mc/ sec)	ν_2 (Mc/sec)
p-$BrC_6H_4NH_2$	2.860 ± 0.001	3.3417 ± 0.0003
p-$ClC_6H_4NH_2$	2.837 ± 0.001	3.3382 ± 0.0003
p-$(NH_2)_2C_6H_4$	2.674 ± 0.001	3.1902 ± 0.0003
	2.690^a	3.2109 ± 0.0003
	2.694^a	3.2129 ± 0.0003
$CO(NH_2)_2$	2.347 ± 0.001	2.9137 ± 0.0003

^{a} Very week.

b) *Zeeman effect*

A single crystal of p-$BrC_6H_4NH_2$ could be prepared by the method of pointed-bottom crucible[11], then the Zeeman studies on bromine and nitrogen were attempted. A Helmholtz coil which was used to give a magnetic field could be rotated for full 360° in the horizontal plane. The crystal was mounted as the cylindrical axis was parallel to the r.f. field and to the horizontal plane. It could be rotated for full 360° about this axis, so that all orientations of the magnetic field with respect to the crystal would be obtained.

For Zeeman studies on the resonance line of 221.8 Mc of Br^{81}, the field strength of about 300 gauss was used. From the measured zero-splitting loci, the orientations of the principal axes of bromine were obtained. The results indicated that there are two principal axis systems x_1, y_1, z_1, and x_2, y_2, z_2, and that the angle between the Br-C bounds is $78°24'\pm30'$ and the axes, y_1 and y_2, which lie in a plane of the benzene ring, are parallel.

The Zeeman studies on the nitrogen resonance were carried out with respect to the high frequency line, by using frequency modulation. The magnetic field was applied on three special orientations, which correspond to a, b and c axes of the crystal. In this case a Helmholtz coil[12] used was larger than that of the previous experiment for Br^{81} in order to cool the sample with liquid nitrogen. From the shifts of the lines at the three orientations of the applied field, the principal axes of nitrogen were determined. Since the experiment was more difficult than that of bromine, the results of measurements had considerable experimental errors.

§ 3. Analysis

a) *Spectra*

The Hamiltonian for the interaction between the quadrupole moment Q and the electric field gradient q_{ii} is given by the following formula[13]:

$$\mathscr{H}=K[3\boldsymbol{I}_z^2-\boldsymbol{I}^2-\eta(\boldsymbol{I}_x^2-\boldsymbol{I}_y^2)]\ , \tag{1}$$

where

$$K=\frac{eQq_{zz}}{4\boldsymbol{I}(2\boldsymbol{I}-1)}$$

and

$$\eta=\left|\frac{q_{xx}-q_{yy}}{q_{zz}}\right| .$$

In nitrogen, which has a spin of unity, a non-zero asymmetry parameter removes the degeneracy of the $m=\pm1$ state, and causes the transition to split into two[7]. Thus a quadrupole spectrum of N^{14} consists of a pair of resonance lines. Their frequencies are given by

$$\nu_1=(3-\eta)K$$

and

$$\nu_2=(3+\eta)K\ . \tag{2}$$

A third transition exists at $2\eta K$, but usually occurs so low in frequency that it is unobservable. When a weak magnetic field is applied to the system, the perturbation term to be added to the Hamiltonian (1) is

$$\mathscr{H}^1=-\boldsymbol{\mu H}=D(\cos\theta\cdot\boldsymbol{I}_z+\frac{\sin\theta}{2}[e^{-i\phi}\boldsymbol{I}_+ +e^{i\phi}\boldsymbol{I}_-])\ . \tag{3}$$

When η is small, the frequencies of observable transitions are given by the followings[3]:

$$\left.\begin{aligned}\nu_1'&=3K-(\eta^2K^2+D^2\cos^2\theta)^{1/2}\\ \nu_2'&=3K+(\eta^2K^2+D^2\cos^2\theta)^{1/2}\ .\end{aligned}\right\} \tag{4}$$

---

* The sample of urea was provided by Toyo Koatsu Industries, Inc.

An upper limit on the values of η for which the small η approximation is valid is about 14%. For the case where η is larger than this value, the frequencies must be solved by the second-order perturbation theory. Then, the frequencies are given by

$$\left.\begin{aligned} \nu_1'' &= (3-\eta)K - \frac{D^2\cos^2\theta}{2\eta K} + \frac{2D^2\sin^2\theta\sin^2\phi}{(3-\eta)K} \\ &\quad + \frac{D^2\sin^2\theta\cos^2\phi}{(3+\eta)K} \\ \nu_1'' &= (3+\eta)K + \frac{D^2\cos^2\theta}{2\eta K} + \frac{2D^2\sin^2\theta\cos^2\phi}{(3+\eta)K} \\ &\quad + \frac{D^2\sin^2\theta\sin^2\phi}{(3-\eta)K} \end{aligned}\right\} \tag{4'}$$

In a single crystal, each resonance line shifts according to the angle, θ and φ, which are the usual spherical polar coordinates of the applied magnetic field referred to the principal axis system of the field gradient tensor. In a polycrystalline or a powdered sample it is smeared out, because the orientations of the Zeeman field to the principal axes are at random on each nucleus in the samples. In any cases the effects of the field on the lines, which split due to η, increase their separation. In the recorded spectra with Zeeman modulation, if $\eta \neq 0$, the high frequency line has a negative wing on the higher side and the low frequency line has it on the lower side as discussed by Casabella and Bray.

p-$BrC_6H_5NH_2$, p-$ClC_6H_4NH_2$, and $CO(NH_2)_2$ have a pair of lines with the shapes as shown in Fig. 1. Among these compounds the crystal structures of p-$BrC_6H_4NH_2$ and p-$ClC_6H_4NH_2$ are known by Zeeman studies of nuclear quadrupole resonance of bromine[14] and chlorine[15], and that of urea is well known by X-ray diffraction measurements[16], and all nitrogen atoms in the compounds are at equivalent positions in the crystals. Both facts suggest that these pairs are caused by the non-zero asymmetry parameters. Therefore, the values of eQq and η are obtained with Eqs. (2). The results are listed in Table II. If the crystal structure of p-$(NH_2)_2C_6H_4$ was similar to that of p-$BrC_6H_4NH_2$ and p-$ClC_6H_4NH_2$, the resonance lines of p-$(NH_2)_2C_6H_4$ in which the number of N atoms per molecule is twice would be strongest among them. The spectrum, however, is composed of three pairs of lines, whose intensity is weaker than that of others. This suggests that there are three non-equivalent positions of N atoms in a unit cell. Since the variations of eQq and η by the crystal effects seem to be small, the combinations of lines as described in Table I would be plausible. In Table II the constants, eQq and η for one pair are listed.

Table II. Quadrupole coupling parameters.

Compound	eQq (Mc/sec)	η (%)
p-$BrC_6H_4NH_2$	4.135	23.1
p-$ClC_6H_4NH_2$	4.117	24.3
p-$(NH_2)_2C_6H_4$	3.910	26.4
$CO(NH_2)_2$	3.507	32.3

On Zeeman powder pattern and on the shape of the negative wing, the detail discussions given by Casabella and Bray are applicable for the present cases.

b) *Strength of Zeeman modulation*

Since the Zeeman shift of the resonance frequency decreases when the asymmetry parameter increases, the Zeeman modulation of a large amplitude is necessary for the present cases. For an high frequency line in the powdered sample where η is 25 percent and K is about 1 Mc, the Zeeman modulation of amplitude of 100 gauss yields only an average shift of 1 kc, which is nearly equal to the line width. Therefore, the Zeeman modulation of amplitude of 50 gauss which was used in the present experiment should only give almost same intensity as the frequency modulation of amplitude of a half line width does. In fact, a comparison of the resonance lines of p-$BrC_6H_4NH_2$ between the Zeeman modulation and the frequency modula-

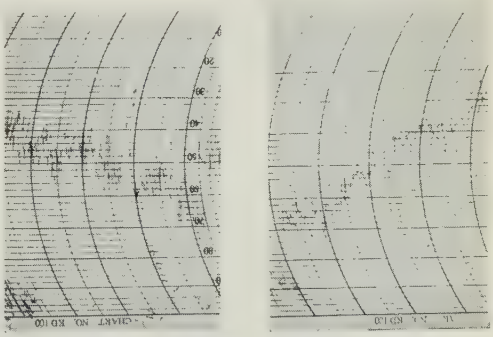
(a) Zeeman modulation. (b) Frequency modulation.

Fig. 2. Nitrogen resonances in p-$BrC_6H_4NH_2$.

tion shown in Fig. 2 indicates that the lines are nearly equal intensities. The more intense field will give the better signal-to-noise ratio. This will be also suggested from the intensity ratio between the negative wing and the positive main part, when the effect of saturation was removed. In the recording traces shown in Fig. 1, however, an extreme saturation appeares. For example, in urea, when the spectrometer was swept from low to high frequencies, the main positive part of the low frequency line and the negative wing of the high frequency line completely disappeared, and when the specrometer was swept from high to low frequencies, the situation was reversed. At room temperature where the relaxation time is short the negative wing appeared as shown in Fig. 3, even if the spectrometer was used at the same condition.

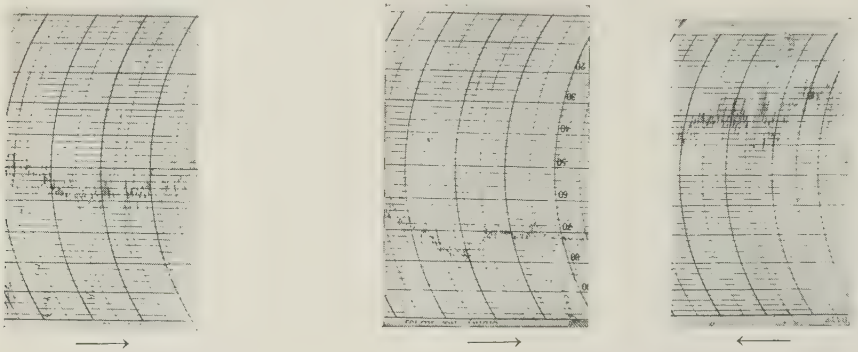
(a) Room temperature. (b) Liquid nitrogen temperature.

Fig. 3. Nitrogen resonances of high frequency lines in urea illustrating a saturation effects. The arrows indicates the direction of increasing frequency.

c) *Intensities of a pair of lines*

Under the same condition of spectrometer, in the same sensitivity, the same power level and the same rate of frequency sweep the intensities of a pair of lines were considerably different. The line of the high frequency was always stronger than the line of the low frequency. In the polycrystalline samples of the amino-compounds, the intensity ratio of the high frequency line to the low frequency line was from 1.5 to 1.7. In urea the ratio was about 2.5. The intensity difference can not be attributed simply to a saturation effect under the present experimental condition. The intensity difference sometimes comes from the difference of population of nuclei in the energy states. Since the ratio of the population-difference is approximately equal to the ratio of the resonance frequencies, a simple calculation yields that the intensity ratio of the two lines is about 1.25 for the case of urea. A large discrepancy between this value and the experimentally obtained value seems to depend on another mechanism. It may be an effect of the Zeeman modulation. When η is small enough, the Zeeman shifts are symmetrical as expressed by the second terms of Eqs. (4′). However, when η is large as the present cases, the third and fourth terms of the equations are not neglected. These terms result to asymmetrical shifts. The frequency shifts at the modulation field of 50 gauss were calculated for the polycrystalline samples of p-$BrC_6H_4NH_2$ and urea, where $\cos^2\theta$, $\sin^2\theta$, $\cos^2\varphi$ and $\sin^2\varphi$ in Eqs. (4′), were replaced by their average values,

$$\langle \cos^2\theta \rangle_{av} = \langle \sin^2\theta \rangle_{av} = 1/2$$
$$\langle \cos^2\varphi \rangle_{av} = \langle \sin^2\varphi \rangle_{av} = 1/2 \, .$$

Table III. Zeeman shifts in polycrystal.

Compound	$\Delta\nu_1$ (c/sec)	$\Delta\nu_2$ (c/sec)
p-$BrC_6H_4NH_2$	215	341
$CO(NH_2)_2$	159	361

The calculated results are summerized in Table III. It shows that the Zeeman modulation field is less effective for the low frequency line than for the high frequency line. The pronounced difference of the intensities in urea is attributed to the effectiveness of the Zeeman field.

If the method of frequency modulation is applied, such a large intensity difference will not appear. Fig. 4 shows the traces of the nitrogen resonances in urea by this way. The intensity ratio of the two lines became about 1:2. This value agrees with that obtained from the simple calculation of population-ratio mentioned above.

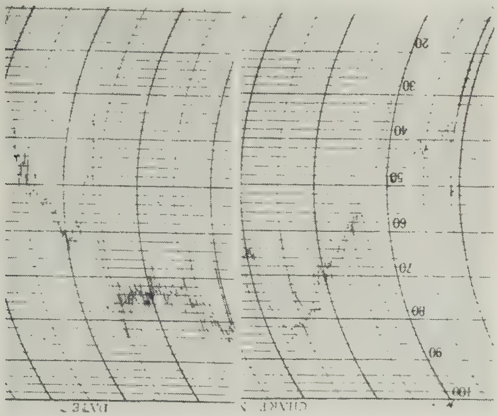

Low frequency line High frequency line

Fig. 4. Nitrogen resonances in urea with frequency modulation.

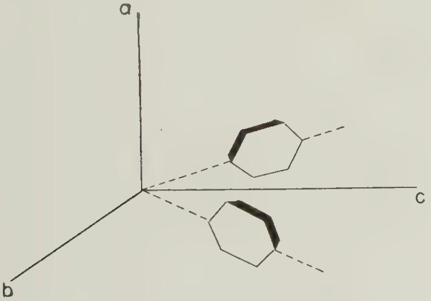

Fig. 5. Molecular arrangements in crystalline p-$BrC_6H_4NH_2$.

d) *Determination of principal axes*

If the r.f. field oriented to the x direction is applied to a single crystal, the high frequency line has the maximum intensity and the low frequency line vanishes. On the other hand, with the r.f. field in the y direction, the situation is reversed[17]. Therefore, the measurement of the intensity of resonance line in a single crystal is useful to determine the location of the principal axes. Beside this method the principal axes are also determined by Zeeman study. In this experiment both methods were applied for p-$BrC_6H_4NH_2$ which has two molecules with non-equivalent directions as shown in Fig. 5. The cylindrical axis of the single crystal prepared was nearly parallel to the a axis.

In this sample, the low frequency line was not detected while the high frequency line was stronger than that in other polycrystalline sample. This indicates that the orientation of the r.f. field to the cylindrical axis of the single crystal is nearly parallel to the x axis in the nitrogen atom.

The Zeeman studies on the nitrogen resonance were done at the three orientations described in the section 2 b, with the applied field of 68 gauss. The Zeeman shifts measured are listed in the last column of Table IV.

Table IV. Zeeman shifts in single crystal of p-$BrC_6H_4NH_2$.

Orientation			Frequency shift (c/sec)	
	θ	θ	calculated	observed
a	90°	0°	254	~100
b	39°12′	90°	700	~800
c	50°48′	90°	524	~500

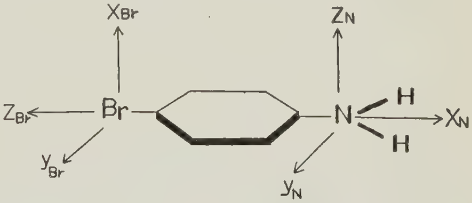

Fig. 6. Principal axis systems for bromine and nitrogen in p-$BrC_6H_4NH_2$.

The results are well interpreted by assuming that the z axis for the nitrogen atom is perpendicular to the plane of the benzene ring. The x and the y axes are discriminated from the intensity measurement of pair of lines. The principal axis system thus determined is shown in Fig. 6. Based upon this principal axis system, the Zeeman shifts at the three orintations were calculated with Eqs. (4′). In Table IV, the results are compared with the experimental results.

e) *Substituent Hammett's σ in amino-compounds*

In the cases of substituted chlorobenzenes, bromobenzenes and iodobenzenes, linear correlations between the resonance frequencies and the substituent parameters, sigma of

Hammett, have been noted[18)-22)]. The substituent constant is defined originally by the equation[23),24)]:

$$\log(K/K^\circ)\equiv\sigma \qquad (5)$$

where K° and K are the acid dissociation constants of benzoic acid and its monosubstituted derivatives, respectively. Eq. (5) implies an arbitrary definition of a reaction constant of unity for this reference series, and a substituent constant of zero for the unsubstituted compound. The relation between the resonance frequency and the substituent constant is attributed to the fact that the sigma value of substituent and quadrupole coupling constant of the halogen are both the measures of the electron density at the position of the halogen nucleus. Not only for halogen but also for nitrogen, that will be true. So the obtained coupling constants were compared with σ data in Table V. eQq increases as σ become greater. A correlation function as indicated by Bray and Barnes[22)] can not be determined accurately, because of small number of substances measured. However, it is shown that the tendency of the correlation function accords with that in case of halogen, although the nature of bonding in nitrogen differs considerably from that of halogen. According to the above correlation, the frequency of resonance line in p-$IC_6H_4NH_2$ is estimated to be somewhat higher than that in p-$BrC_6H_4NH_2$. The detection of the line has been carried out unsuccessfully.

Table V. Substituent constants at para position.

Substituent	σ_{para}	eQq (Mc/sec)
NH_2	−0.660	3.910
Cl	0.227	4.117
Br	0.232	4.135
I	0.276	

§ 4. Discussion

On amino-compound, it has not yet been established experimentally whether the bonds of nitrogen are strictly coplanar or not. However, the coplanarity is preferable for the arguments described in the following: Reaction constant at the para-position in the amino-compounds used, indicates the importance of the structure II shown in Fig. 7. If the valency angles at the nitrogen atom are the same as in ammonia, satisfactory resonance with the electron of the ring can not occur. In order to take account of the resonance structure the bonds of the nitrogen atom should be coplanar or nearly coplanar with the benzene ring. As Coulson has suggested[25)] it seems quite probable to consider the three bonds around the N atom as nearly coplanar.

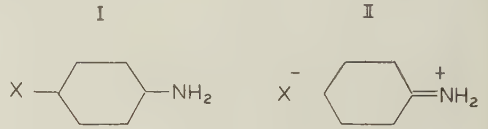

Fig. 7. Tetravalent resonance structure of nitrogen in aromatic molecules.

On urea, the evidence for the planar structure has been reported by Andrew and Hyndman[26)]. Though they assumed the three bonds of nitrogen are equivalent, the N-H bond and the N-C bond will be not necessarily equivalent. Therefore, the wave functions as the H-N-H angle is θ in a planar model are assumed. Then, they become

$$\left.\begin{aligned}
\psi_1&=p_z\\
\psi_2&=\sqrt{\alpha}\,s+\sqrt{1+\alpha}\,p_x\\
\psi_3&=\sqrt{\frac{1-\alpha}{2}}\,s-\sqrt{\frac{\alpha}{2}}\,p_x+\sqrt{\frac{1}{2}}\,p_y\\
\psi_4&=\sqrt{\frac{1-\alpha}{2}}\,s-\sqrt{\frac{\alpha}{2}}\,p_x-\sqrt{\frac{1}{2}}\,p_y
\end{aligned}\right\} \qquad (6)$$

where α is the s-character, being connected with θ as follows,

$$\tan\frac{\theta}{2}=\frac{1}{\sqrt{\alpha}}.$$

ψ_1 corresponds to the orbital of lone pair electron, ψ_2 to the N-C bond and ψ_3 and ψ_4 to the N-H bonds. The coordinate being chosen as shown in Fig. 8.

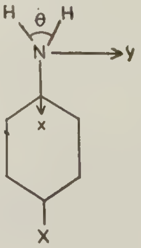

Fig. 8.

a) *Amino-compounds*

The bond structure can be considered to be made up of the five structures shown in Fig. 9, under which the fractional importance of each structure is described. β_1 and β_2 are assumed to be 13% and 35% respectively from electronegativity difference for the N-C and the N-H bonds[27]. The unbalanced electrons and the asymmetry parameter are calculated as follows;

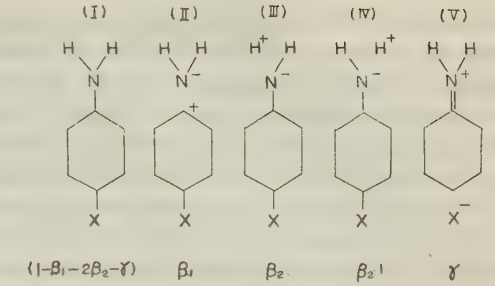

Fig. 9. Five resonance structures in p-$XC_6H_4NH_2$.

$$\left.\begin{aligned}
U_z&=-\left[1-\beta_1\left\{1-\frac{(1+\alpha)}{2(1+c)}\right\}-2\beta_2\left\{1+\frac{(3-\alpha)}{4(1+c)}\right\}-\gamma\right]\\
U_x&=\frac{1}{2}(1-\beta_1-2\beta_2-\gamma)-\frac{1}{2}(1-2\alpha)\frac{\beta_1}{1+c}+\frac{1}{2}(3-2\alpha)\frac{\beta_2}{1+c}\\
U_y&=\frac{1}{2}(1-\beta_1-2\beta_2-\gamma)+\frac{1}{2}(2-\alpha)\frac{\beta_1}{1+c}+\frac{\alpha\beta_2}{2(1+c)}\\
\eta&=\frac{U_x-U_y}{U_z}=\frac{3(1-\alpha)(\beta_2-\beta_1)}{2(1+c)U_z},
\end{aligned}\right\}\quad(7)$$

where c is the screening constant and estimated to be 0.32 for nitrogen[28]. Since the coupling constant for one unbalanced p-electron has not been measured for N^{14}, a value of 10 Mc was assumed[3]. The experimental values for eQq and η yield α and γ by the aid of Eqs (7). For p-$BrC_6H_4NH_2$ α is 0.6, corresponding to θ of 104°, and γ is 0.16. Table II indicates that eQq decreases gradually in the order of p-$BrC_6H_4NH_2$, p-$ClC_6H_4NH_2$, and p-$(NH_2)_2C_6H_4$ while η increases. If the atom X is substituted in p-$XC_6H_4NH_2$, the importance of the resonance structure V will vary with the atom X. As the atom X is more electron-attractive, the structure V is more important[28],[29]. Namely, when γ increases eQq decreases. This fact will be guessed from the substituent constants of Hammett's σ in the series of the side chain, for the constant indicates a measure of importance of the structure V depending on the atom X. Thus the results of amino-compounds can be reasonably interpreted.

b) *Urea*

For the reason as indicated before, discussions of the bonds around the nitrogen in urea can also be carried on with Eqs. (7). Using the experimental values for eQq and η, α is obtained to be 0.55 corresponding to θ of 107°, and γ to be 0.22. According to the analysis by X-ray, the length of the C-N bonds is 1.37 A[16], which indicates that the bonds have somewhat double bond character shown in Fig. 10. The fractional importance of this resonance structure calculated from the bond length is 0.27 which corresponds to γ. This agreement suggests that the consideration mentioned above seems to be reasonable.

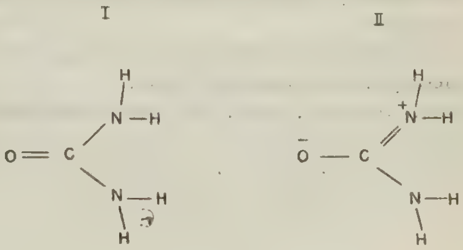

Fig. 10. Tetravalent resonance structure of nitrogen in urea.

§ 5. Conclusion

Pure quadrupole spectra of N^{14} in para-bromoaniline, para-chloroaniline, para-phenylenediamine, and urea were obtained. From the spectra, the quadrupole coupling constants and the asymmetry parameters were determined. The apparent intensity of the high frequency line was always greater than that of the low frequency line when the method of Zeeman modulation was applied. This was interpreted from the second-order perturbation theory of Zeeman effect. The principal axis system of nitrogen in p-$BrC_6H_4NH_2$ was determined, by using the method of frequency modulation. The results mentioned above seem to support that the three bonds about nitrogen in amino-compounds such as aniline are coplanar with the plane of benzene ring. The values of eQq and η for these compounds were analyzed by the aid of the planar model.

The author wishes to express her sincere thanks to Professor Shoji Kojima for his kind guidance and encouragement throughout the course of this work. She is also grateful to Mr. M. Tanaka for his helps on experiments and to other members of the laboratory for their valuable discussions.

References

1) G. D. Watkins and P. V. Pound: Phys. Rev. **85** (1952) 1062.
2) C. T. O'Konski and T. J. Flautt: J. Chem. Phys. **27** (1957) 815.
3) P. A. Casabella and P. J. Bray: J. Chem. Phys. **28** (1858) 1182.
4) P. A. Casebella and P. J. Bray: J. Chem. Phys. **29** (1958) 1105.
5) T. Chiba, M. Toyama and Y. Morino: J. Phys. Soc. Japan **14** (1958) 379.
6) S. Kojima, M. Minematsu and M. Tanaka: to be published.
7) G. D. Watkins: Thesis, Havard Univ. (1952).
8) M. Tanaka: Master's thesis, Tokyo Univ. of Education.
9) G. E. Valley and H. Wallman: *Vacuum Tube Amplifiers* (McGraw-Hill, 1948).
10) N. A. Schuster: Rev. Sci. Instr. **22** (1951) 254.
11) S. Kojima, K. Tsukada, A. Shimauchi and Y. Hinaga: J. Phys. Soc. Japan **9** (1954) 795.
12) S. Kojima, Y. Abe, M. Minematsu, K. Tsukada and A. Shimauchi: J. Phys. Soc. Japan **12** (1957) 1225.
13) H. Krüger: Z. Phys. **130** (1951) 371.
14) K. Shimomura: unpublished.
15) H. C. Meal: J. Chem. Phys. **24** (1956) 1011.
16) R. W. Wycoff and R. B. Corey: Z. Krist. **83** (1934) 462. P. Vaughan and J. Donohue: Acta Cryst. Camb. **5** (1952) 530.
17) T. P. Das and E. L. Hahn: *Nucler Quadrupole Resonance Spectroscopy*, in Solid State Physics (Academic Press, New York, 1958).
18) H. C. Meal: J. Amer. Chem. Soc. **74** (1952) 6121.
19) P. J. Bray and R. G. Barnes: J. Chem. Phys. **22** (1954) 2023; Phys. Rev. **99** (1955) 612.
20) P. J. Bray: J. Chem. Phys. **22** (1954) 950, 1787.
21) G. W. Ludwig: J. Chem. Phys. **25** (1956) 159.
22) P. J. Bray and R. G. Barnes: J. Chem. Phys. **27** (1957) 551.
23) L. P. Hammett: *Physical Organic Chemistry* (McGraw-Hill, 1940).
24) H. H. Jaffe: Chem. Rev. **53** (1953) 191.
25) C. B. Coulson: *Valence* (Oxford Univ. Press, 1953).
26) E. R. Andrew and D. Hyndman: Proc. Phys. Soc. London **A**, **66**, **11** (1953) 1187.
27) B. P. Dailey and C. H. Townes: J. Chem. Phys. **23** (1955) 118.
28) L. Pauling: *Nature of the Chemical Bond* (Cornell Univ. Press, 1939).
29) J. K. Wilmshurst: J. Chem. Phys. **28** (1958) 733.

JOURNAL OF THE PHYSICAL SOCIETY OF JAPAN, Vol. 14, No. 8, AUGUST, 1959

Thomas-Fermi Model of Positive Ion

By Shigehiro KOBAYASHI

Department of Physics, Kagawa University, Takamatsu

(Received March 9, 1959)

Exact solutions of the Thomas-Fermi equation for positive ion have been obtained including their derivatives by the inward numerical integration. The whole range of the ionization degree of physical interest has been covered in sufficient detail to permit accurate interpolation for intermediate regions. Using these numerical solutions, several physical quantities of free positive ions have been investigated.

§ 1. Introduction

The statistical model of Thomas[1]-Fermi[2] (to be referred to as TF hereafter) has provided an important means for obtaining qualitative as well as semi-quantitative estimates of atomic behavior. Since it needs tedious numerical integration to solve the fundamental equation, the so-called TF equation, the accurate solutions for neutral atoms in compressed states as well as free states have been reported only several years ago by Latter[3] and others[4]. For the case of positive ions there were hitherto only a few typical solutions reported by Fermi[5], by Miranda[6] and by Feynman, Metropolis and Teller[7]. These were obtained by the *outward* integration of the TF equation. This method is available for not too small values of ionization degree because the integral curves then cut the x-axis in a fairly large angle at a finite distance from the origin. For smaller values of ionization degree, however, the curves meet the x-axis nearly tangentially so that the values of the boundary radius and the tangential slope there (or the ionization degree) cannot be accurately determined. In consequence, we have had no exact relationship between the boundary radius and the ionization degree, and some uncertainties have followed in the calculation of the physical quantities of the TF positive ions. The object of this paper is to remove these uncertainties by the adoption of the *inward* numerical integration and to obtain accurate information about the TF positive ions.

First, we have calculated exact solutions of the TF equation for positive ions in a systematic sequence of ionization degree by the inward numerical integration method (§ 2), which has been employed successfully to overcome the similar difficulty occuring in the case of the Thomas-Fermi-Dirac (TFD) model[8] as well as the TF model[9] for free neutral atoms.

Using the values of the TF functions and their derivatives obtained as solutions of the TF equation, we have investigated systematically such quantities of positive ions as Fermi coefficient (§ 3), boundary radius (§ 4), ionic radius (§ 5), energy and ionization potential (§ 6), mean excitation potential and energy (§ 7), diamagnetic susceptibility (§ 8), scattering factors (§ 9) and electric field at the nucleus of polarized ions (§ 10) as functions of ionization degree and atomic number, respectively.

As seen from the calculated values of some physical quantities, *e.g.* diamagnetic susceptibility of neon-like ions[10] etc., the TF method provides a better approximation for positive ions than for neutral atoms owing to the large electron density caused by strong contraction of the electron cloud.

§ 2. Method of Solution of the TF Equation

It is well known[11] that the potential V and the electron density ρ at the distance

$$x=r/\mu \tag{1}$$

measured in the TF unit

$$\mu=\frac{1}{4}\left(\frac{9\pi^2}{2Z}\right)^{1/3}a_0\,, \qquad \left(a_0=\frac{h^2}{4\pi^2me^2}\right) \tag{2}$$

within the ion having atomic number Z, electron number N and boundary radius $r_0=\mu x_0$, are expressed as follows:

$$V=\frac{Ze}{r}\varphi+V_0\,, \tag{3}$$

$$V_0=(Z-N)e/r_0 \tag{4}$$

$$\rho=\frac{Z}{4\pi\mu^3}\left(\frac{\varphi}{x}\right)^{3/2}. \tag{5}$$

Here φ is the TF function and satisfies the TF equation

$$\varphi''=\varphi^{3/2}/x^{1/2} \tag{6}$$

subject to the boundary conditions

$$\varphi(0)=1 \tag{7}$$

and

$$\varphi(x_0)=0,\ -x_0\varphi'(x_0)=\frac{Z-N}{Z}\equiv q\ . \tag{8}$$

Eq. (7) corresponds to the singularity of the electrostatic potential $V(r)\sim Ze/r$ at the nucleus $r\sim 0$. Eq. (8) results from the values of the potential and field strength at the boundary $x=x_0$ of the free ion with the ionization degree q.

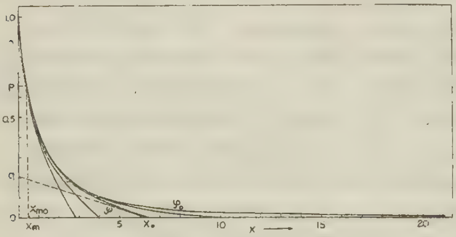

Fig. 1. Curves of the TF function $\varphi(x)$.
φ_0: for free neutral atom.
φ: for positive ion.
x_0: boundary radius.
q: ionization degree.
x_{m0}: atomic radius.
x_m: ionic radius. ($\overline{OP}:\overline{PQ}=3:1$)

To avoid the effect of the self-field of the electron from the original TF model represented by above Eqs. (1) to (8), Fermi and Amaldi[12] (FA) have proposed a modified TF model, by the use of which we can treat the free states of the singly ionized negative ions[13] as well as atoms and positive ions, as follows:

$$x=r/\mu^*\ , \tag{1'}$$

$$\mu^*=\left(\frac{N}{N-1}\right)^{2/3}\mu\ , \tag{2'}$$

$$V=\frac{Ze}{r}\varphi-\frac{e}{N}\int\frac{\rho}{r}dv+V_0^*\ , \tag{3'}$$

$$V_0^*=(Z-N+1)e/r_0\ , \tag{4'}$$

$$\rho=\frac{Z}{4\pi\mu^{*3}}\ \frac{N}{N-1}\left(\frac{\varphi}{x}\right)^{3/2}, \tag{5'}$$

$$\varphi''=\varphi^{3/2}/x^{1/2}, \tag{6'}$$

$$\varphi(0)=1\ , \tag{7'}$$

$$\varphi(x_0)=0,\ -x_0\varphi'(x_0)=q+\frac{1}{Z}\ . \tag{8'}$$

In order to solve, not outwardly but inwardly, the original TF Eq. (6) for positive ions subject to the boundary condition Eqs. (7) and (8) as stated above, we assume an appropriately chosen value of ionization degree for each of a number of starting points taken midway between $x=2$ and 36.5.

In accordance with the same numerical integration routine that we have used for free neutral atoms[9], the starting values of φ and its derivatives in the neighborhood of a chosen starting point x_0 were calculated with the use of series expansion

$$\begin{aligned}\varphi(x)=\ &q\left(1-\frac{x}{x_0}\right)+\frac{4}{35}(qx_0)^{3/2}\left(1-\frac{x}{x_0}\right)^{7/2}+\frac{2}{63}(qx_0)^{3/2}\left(1-\frac{x}{x_0}\right)^{9/2}\\&+\frac{1}{66}(qx_0)^{3/2}\left(1-\frac{x}{x_0}\right)^{11/2}+\frac{1}{175}q^2x_0^3\left(1-\frac{x}{x_0}\right)^{6}+\frac{5}{572}(qx_0)^{3/2}\left(1-\frac{x}{x_0}\right)^{13/2}\\&+\frac{1}{315}q^2x_0^3\left(1-\frac{x}{x_0}\right)^{7}+\frac{7}{1248}(qx_0)^{3/2}\left(1-\frac{x}{x_0}\right)^{15/2}+\frac{16}{8085}q^2x_0^3\left(1-\frac{x}{x_0}\right)^{8}\\&+\frac{1}{85}\left[\frac{21}{64}+\frac{22}{1225}qx_0^3\right](qx_0)^{3/2}\left(1-\frac{x}{x_0}\right)^{17/2}+\frac{4}{3003}qx_0^3\left(1-\frac{x}{x_0}\right)^{9}\\&+\frac{11}{17}\left[\frac{21}{4864}+\frac{1}{3675}qx_0^3\right](qx_0)^{3/2}\left(1-\frac{x}{x_0}\right)^{19/2}+\frac{128}{135135}q^2x_0^3\left(1-\frac{x}{x_0}\right)^{10}\\&+\cdots\cdots\cdots\ .\end{aligned} \tag{9}$$

The integral curve thus obtained, starting from an arbitrarily chosen point $x=\bar{x}_0$ with appropriately assumed ionization degree $\bar{q}$, cuts the φ-axis in a non-vanishing angle so that it is possible to determine accurately the point of intersection $\bar{\varphi}(0)$ as well as the slope $\bar{\varphi}'(0)$ there. Of course, $\bar{\varphi}(0)$ is not always unity as requested by the boundary condition

Table I. Values of $-\varphi'(0)$, $-\varphi'(x_0)$, $-k$, x_0, q, Z and $\int_0^{x_0}\varphi x dx$ for a sequence of different states of ionization of free positive ions.

No. of State	$-\varphi'(0)$	$-\varphi'(x_0)$	$-k$	x_0	q	Z				$\int_0^{x_0}\varphi x dx$
						$n=1$	$n=2$	$n=3$	$n=4$	
Limit	∞	∞	0	0	1 (bare ion)	1	2	3	4	0
....	....	....	....	....	....	....	....	....	....	....
1	1.650 00	0.32167	0.0619	2.00 135	0.6437 7	1.553	3.107	4.660	6.213	0.46864
2*	1.60	0.18662	0.0227	2.79 5	0.5216 0	1.917	3.834	5.752	7.669	0.77411
3	1.594 84	0.09615 00	$0.0^{2}677$	3.99 531	0.3841 49	2.603	5.206	7.809	10.413	1.2446
4*	1.589	0.03476	$0.0^{3}993$	6.42 3	0.2232 6	4.479	8.958	13.437	17.916	2.1186
5*	1.588 2	0.01243	$0.0^{3}141$	9.75 58	0.1212 6	8.247	16.493	24.740	32.987	3.0806
6	1.588 1832	0.01102 7993	$0.0^{3}112$	10.21 3420	0.1126 335	8.878	17.757	26.635	35.513	3.1935
7	1.588 1550	$0.0^{2}947$ 5908	$0.0^{4}840$	10.81 3890	0.1024 714	9.759	19.518	29.276	39.035	3.3357
8	1.588 1363	$0.0^{2}830$ 5484	$0.0^{4}653$	11.35 6993	0.0943 2533	10.602	21.203	31.805	42.406	3.4587
9	1.588 1158	$0.0^{2}690$ 2822	$0.0^{4}458$	12.15 3597	0.0838 9418	11.920	23.840	35.759	47.679	3.6301
10	1.588 1018	$0.0^{2}560$ 7422	$0.0^{4}308$	13.09 8890	0.0734 5100	13.615	27.229	40.844	54.458	3.8205
11	0911	449 2267	201	14.16 9079	636 5129	15.711	31.421	47.132	62.842	4.0210
12	0826	337 0924	116	15.65 5574	527 7376	18.949	37.898	56.846	75.795	4.2754
13	0784	265 6563	$0.0^{5}734$	16.97 9866	451 0808	22.169	44.338	66.507	88.676	4.4816
14	0758	212 7849	479	18.29 3373	389 2553	25.690	51.380	77.070	102.760	4.6693
15	0745	181 2041	352	19.29 4651	349 6269	28.602	57.204	85.806	114.408	4.8026
16	0733	145 7040	231	20.72 4758	301 9680	33.116	66.232	99.348	132.464	4.9792
17	0725	115 6380	148	22.33 4691	258 2739	38.719	77.437	116.156		5.1615
18	0720	$0.0^{3}951$ 3226	102	23.77 4059	226 1680	44.215	88.430	132.645		5.3113
19	0717	745 4886	$0.0^{6}636$	25.68 0252	191 4434	52.235	104.470			5.4929
20	1.588 07152	$0.0^{3}640$ 3459	$0.0^{6}474$	26.93 2856	0.0172 4634	57.983	115.967			5.6031
21	07137	539 5861	341	28.40 5138	153 2702	65.244	130.489			5.7242
22	07123	430 6665	221	30.44 8439	131 1312	76.260				5.8790
23	07119	379 7601	173	31.64 2325	120 1649	83.219				5.9631
24	07114	323 1015	127	33.23 4873	107 3824	93.125				6.0686
25	07112	293 0264	105	34.23 1189	100 3064	99.695		$(Z=n/q)$		6.1311
26	07111	281 1632	$0.0^{7}970$	34.66 0362	$0.0^{2}97$ 4522	102.614				6.1575
27	07108	231 0296	664	36.76 4521	84 3258	118.588				6.2790
28	07107	197 0675	488	38.54 9058	75 9677	131.635				6.3747
....	....	....	....	....	....	....				....
Limit	1.588 07102	0	0	∞	0 (neutral atom)	∞				9.1943

* is taken from Miranda[6].

Table II. Values of $-k$, x_0, x_m and their associated quantities for various q's.

q	$-k$			x_0			x_m		$\frac{x_m}{x_0}$	$\frac{\delta}{k}$
	exact	from (13)	from (13′)	exact	(14)	Fermi	exact	from (17)		
0.009	$0.0^{7}787$	$0.0^{7}765$	$0.0^{7}605$	35.795			0.3857 6430		0.010777	1.4
10	$.0^{6}103$	$.0^{6}103$	830	34.277	34.16	35.5	6426	0.3545 28	11254	1.5
11	136	136	$.0^{6}110$	32.888			6421		11730	1.5
12	173	174	144	31.661			6417		12184	1.3
13	215	219	182	30.565			6411		12621	1.4
14	265	270	228	29.576			6403		13043	1.4
15	321	330	280	28.680			6394		13451	1.4
16	384	396	340	27.861			6384		13846	1.5
0.018	$0.0^{6}535$	$0.0^{6}555$	$0.0^{6}484$	26.414			0.3857 636		0.014605	1.5
20	719	750	664	25.168	24.96	25.4	634	0.3545 27	15328	1.4
22	941	984	883	24.082			631		16019	1.4
24	$0.0^{5}120$	$.0^{5}126$	$.0^{5}115$	23.121			627		16685	1.4
26	151	159	146	22.264			623		17327	1.4
28	186	196	182	21.490			617		17951	1.5
30	227	239	224	20.790	20.53	21.1	612	0.3545 23	18555	1.4
0.035	$0.0^{5}353$	$0.0^{5}372$	$0.0^{5}356$	19.285			0.3857 59		0.020003	1.4
40	518	545	531	18.045			57		21378	1.4
45	729	762	757	17.001			54		22690	1.4
50	991	$.0^{4}103$	$.0^{4}104$	16.101	15.80	16.2	50	0.3545 09	23958	1.4
55	$.0^{4}131$	136	138	15.318			45		25182	1.4
60	169	174	179	14.625			41		26375	1.4
0.07	$0.0^{4}267$	$0.0^{4}270$	$0.0^{4}285$	13.452			0.3857 26		0.028674	1.4
8	397	395	425	12.486	12.15	12.9	7 07	0.3544 48	30891	1.4
9	566	553	605	11.672			6 84		33044	1.42
10	780	748	830	10.972	10.62	11.2	6 54	0.3543 74	35149	1.42
11	$.0^{3}104$	982	$.0^{3}110$	10.362			6 16		37214	1.42
12	136	$.0^{3}126$	144	9.820			5 74		39264	1.41

Eq. (7). But it is possible to make the solution $\bar{\varphi}(\bar{x})$ satisfy Eq. (7) and get the normalized TF function $\varphi(x)$, if we apply the scale factor transformation based on the Sommerfeld invariance property[14] of the TF equation, as:

$$
\begin{aligned}
&[\bar{\varphi}(0)]^{1/3}\bar{x} \to x\,, \\
&\bar{\varphi}(x)/\bar{\varphi}(0) \to \bar{\varphi}(x)\,, \\
&\bar{\varphi}'(x)/[\bar{\varphi}'(0)]^{4/3} \to \varphi'(x)\,,
\end{aligned}
\qquad (10)
$$

and

$$\bar{q}/\bar{\varphi}(0) \to q\,.$$

The full tables of the obtained values of the normalized TF functions and their derivatives of free positive ions for twenty-eight different degrees of ionization have been published in a separate paper[15] which is available on request.

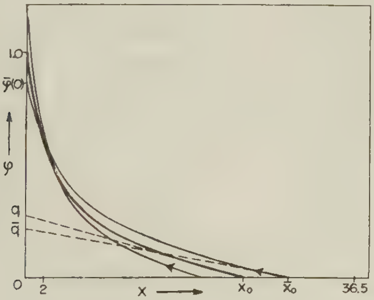

Fig. 2. Solution curves of the TF equation.

$\bar{x}_0$: starting point taken arbitrarily midway between $x=2$ and 36.5.
$\bar{q}$: ionization degree assumed appropriately for $\bar{x}_0$.
$\bar{\varphi}$: integral curve.
$\bar{\varphi}(0)$: final value ($\neq 1$).
φ: normalized TF function $\varphi=\bar{\varphi}/\bar{\varphi}(0)$.
x_0: boundary radius $x_0=[\bar{\varphi}(0)]^{1/3}\bar{x}_0$.
q: ionization degree $q=\bar{q}/\bar{\varphi}(0)$.

Two curves of $\varphi(x)$ and $\bar{\varphi}(\bar{x})$ always cross each other.

It is very convenient that these values for free positive original TF model can be directed to the FA-modified TF atoms and ions as well as compressed positive ions.

In Table I are columed the values of initial slope, Fermi coefficient, boundary radius, ionization degree and atomic number corresponding to the order of ionization from one to four for the calculated states mentioned above. For the sake of completeness the three states given by Miranda[6] are inserted. In Table II, we have these quantities as functions of ionization degree in a regular sequence.

§ 3. Fermi Coefficient

The TF function for positive ions can also be expressed approximately with the use the ordinary TF function φ_0 for free neutral atoms and the Fermi part η_0 as[6]

$$
\begin{aligned}
\varphi(x) &= \varphi_0(x) + k\eta_0(x)\,, \\
\varphi'(x) &= \varphi_0'(x) + k\eta_0'(x)\,.
\end{aligned}
\qquad (11)
$$

Since these values have been recently tabulated accurately by the present author[16], the inverted equation of Eq. (11)

$$k(x) = \frac{\varphi(x)-\varphi_0(x)}{\eta_0(x)} = \frac{\varphi'(x)-\varphi_0'(x)}{\eta_0'(x)} \qquad (12)$$

affords information about the constancy of the Fermi coefficient k, namely the validity of Eq. (11).

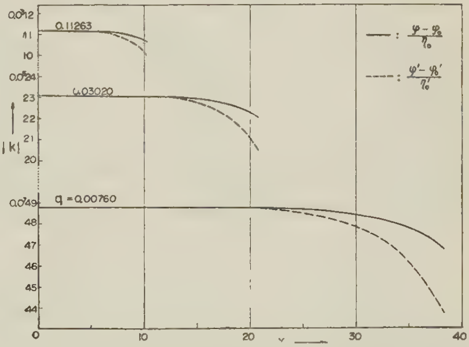

Fig. 3. Fermi coefficient $k(x, q=\text{const})$-curves. The turning point of two curves in each state corresponds to the position x where the value of $k\eta_0(x)$ equals to about 1/10 of $\varphi_0(x)$.

The values of k, thus obtained for three typical states, are plotted in Fig. 3 which shows that we can regard k as a constant in each state where the value of $k\eta_0(x)$ is small compared with that of $\varphi_0(x)$ by less than 1/10.

These constant values of k in each state are listed in Tables I and II. They are also plotted *versus* q in logarithmic scale in Fig. 4. In this figure, as Fermi and Amaldi[12] have pointed out, we find the existence of approximate linear relation between $\log|k|$ and $\log q$, which is determined by the method of least squares as

$$k = -0.0542\, q^{2.86}\,, \qquad (13)$$

while Fermi and Amaldi gave an expression with somewhat different numerical parameters

$$k=-0.083\,q^3\,. \tag{13'}$$

The exact relation Eq. (13) enables us to construct correctly the TF functions for positive ions with any ionization degree and to calculate easily various physical quantities concerned with positive ions. However, as it is an approximate expression, we cannot expect too much of the results evaluated along this line. All values of the physical quantities in the following sections have been directly calculated with the use of our tables[15] of the TF functions obtained as solutions of the TF equation for free positive ions. The full tables of them are available on request.

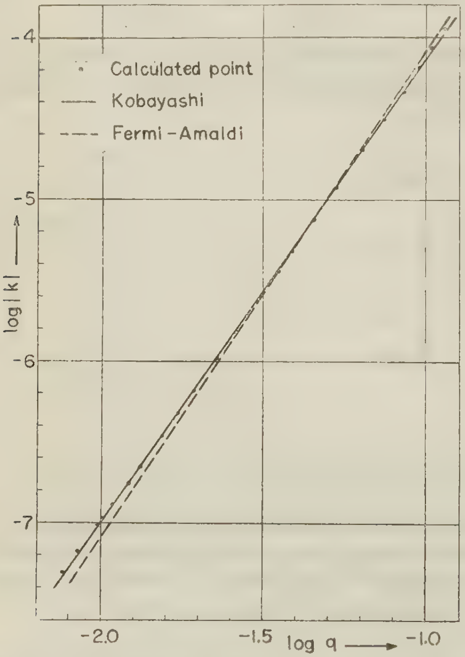

Fig. 4. Dependence on q of k.
The full line is determined by the method of least squares, while the dotted line by Fermi and Amaldi. Approximation degree of these lines is indicated by the numericals of the columns 3 and 4 in Table II.

§ 4. Boundary Radius

The dependence of boundary radius x_0 of free positive ions on initial slope $\varphi'(0)$, ionization degree q and atomic number Z is given by the numericals in Table I and II and shown in Figs. 5 and 6. In Table II, for reference, we have tabulated the values of boundary radius calculated by Fermi[6] and those recalculated by the present author with the Sommerfeld approximate formula[14]

$$\frac{z_0}{(1+z_0)^{1+\lambda_1/2}}=\frac{q}{\lambda_1}\,, \tag{14}$$

where

$$z_0\equiv(x_0/12^{2/3})^{\lambda_2}$$

and

$$\lambda_1\equiv7+\sqrt{73}\,,\quad \lambda_2\equiv-7+\sqrt{73}\,.$$

These values are also plotted in Fig. 5 which indicates that for smaller q the Sommerfeld approximate formula is better, and for larger q the calculated values by Fermi are nearer to the exact curve than the Sommerfeld formula. The reason for this fact lies in the circumstances that the Fermi values have been obtained by the outward integration which is applicable for larger q, while the Sommerfeld formula has an asymptotic

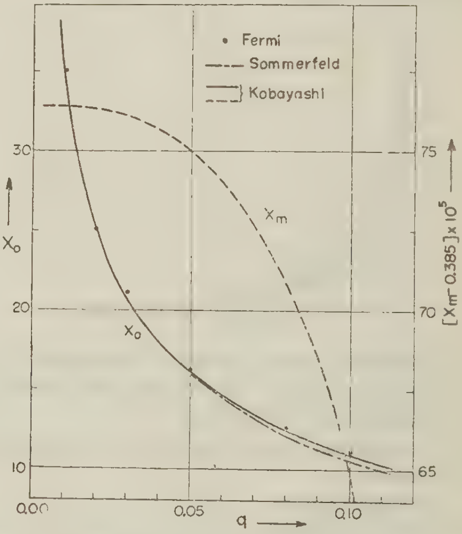

Fig. 5. Dependence of x_0 and x_m on q.

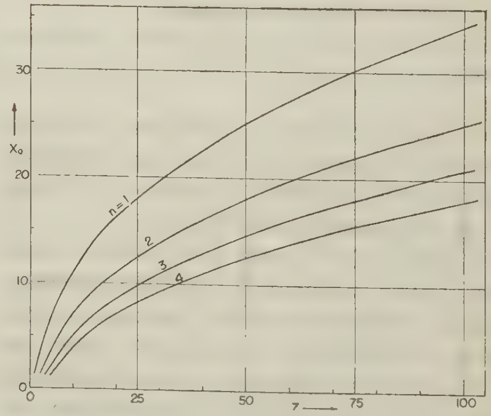

Fig. 6. Dependence on Z of x_0 for singly ($n=1$) to quadruply ($n=4$) ionized positive ions.

character valid for smaller q.

As seen in Figs. 5 and 6, the boundary radius x_0 of the TF ions monotonically decreases with the increase of ionization degree q and increases with the increase of atomic number Z for a fixed order of ionization n, and it is a defect of the TF model that it cannot explain the periodic properties.

In the FA-modified TF model, the above values of x_0 for free positive ions with atomic number $Z(n)$ turn out to be the boundary radius of free ions with atomic number $Z(n-1)$, and $Z(0)$ means the atomic number Z of free neutral atoms. Our numerical values of several atoms are given in Table III, with the Fermi coefficient k for them.

Table III. Values of x_0 and $-k$ of the FA-modified TF atoms.

Z	atom	x		$-k$	
		exact	FA[12]	exact	FA[12]
10	Ne	10.972	10.8	0.0^4780	0.0^48300
11	Na	11.604		584	
14	Si	13.303	13.0	283	3025
18	A	15.237		135	
19	K	15.678	15.4	115	1210
26	Fe	18.403	18.2	$.0^5463$	$.0^54722$
31	Ga	20.070	19.9	279	2786
36	Kr	21.572		182	
37	Rb	21.857	21.8	168	1639
42	Mo	23.208	23.2	0.0^5118	0.0^51120
47	Ag	24.458	24.5	$.0^6856$	$.0^67994$
53	I	25.852	26.1	610	5575
54	Xe	26.074		579	
58	Ce	27.936	27.2	474	4254
67	Ho	28.744	29.2	317	2760
74	W	30.045	30.6	240	2048
80	Hg	31.098	31.7	193	1621
92	U	33.060	34.1	131	1066

§ 5. Ionic Radius

By the radius corresponding to the maximum of radial electron density, we define ionic radius of the TF ions in the same manner as for neutral atoms[17]. Since the radial density is given by $4\pi\rho r^2=(\varphi^3x)^{1/2}Z/\mu$, the ionic radius x_m is the root of the equation

$$\varphi(x)+3x\varphi'(x)=0 \qquad (15)$$

which, as seen in Fig. 1, the geometrical meaning that $\varphi(x_m)=\overline{OP}=3\overline{PQ}=3x_m|\varphi'(x_m)|$.

The numerical values of the ionic radius of ions for various states of ionization follow from our tables of the TF functions, and are columned in Table II, which shows that the ionic radii x_m in different states of ionization differ only slightly from the atomic radius x_{m0} of free neutral atoms.*

Taking into consideration that this difference $\delta=x_m-x_{m0}$ and the Fermi coefficient k are both small quantities, we can also determine these values by the following approximate method. If we rewrite and expand Eq. (15) with the use of δ and k and neglect the higher order terms of small quantities, we obtain

$$\varphi_0(x_{m0})+3x_{m0}\varphi_0'(x_{m0})=0$$

and

$$k\eta_0(x_{m0})+\varphi_0'(x_{m0})\delta+3\varphi_0'(x_{m0})\delta$$
$$+3x_{m0}[k\eta_0'(x_{m0})+\varphi_0'(x_{m0})\delta]=0\,.$$

The former is the equation that gives the atomic radius and from the latter δ is determined as

$$\delta=-\frac{\eta_0(x_{m0})+3x_{m0}\eta_0'(x_{m0})}{4\varphi_0'(x_{m0})+3x_{m0}^{1/2}[\varphi_0(x_{m0})]^{3/2}}$$
$$=1.42\,k=-0.0770\,q^{2.86}. \qquad (16)$$

In Table II, there are columned the values of δ/k as well as x_m/x_0 as functions of ionization degree q. We have also listed the values of the ionic radius which are obtained by the same method applied to the Sommerfeld asymptotic solution for ions[14]

---

* The value of the atomic radius of free neutral TF atoms obtained by the present author is 0.3857 6441, while it is 0.3857 653 by Matsukuma[18].

$$\varphi=\frac{1}{(1+z)^{\lambda_1/2}}\left[1-\left(\frac{1+z}{1+z_0}\right)^{\lambda_1/\lambda_2}\right]. \tag{17}$$

The disagreement between these values and the exact ones results from the fact that the ionic radii are ordinarily small and the Sommerfeld solution does not give a good approximation for these small x owing to its asymptotic character.

The dependence of the ionic radius x_m on ionization degree q is also shown in Fig. 5. It is natural that the ionic radius of the TF ions decreases monotonically with the increase of ionization degree.

§ 6. Energy and Ionization Potential

The energies of n-ply ionized positive ions with atomic number Z[11]

$$E(Z,n)=\frac{12}{7}\left(\frac{2}{9\pi^2}\right)^{1/3}Z^{7/3}\left[\varphi'(0)+\frac{n^2}{Z^2x_0}\right]\frac{e^2}{a_0}$$
$$=13.172\left(\frac{n}{q}\right)^{7/3}\left[\varphi'(0)+\frac{q^2}{x_0}\right]eV \tag{18}$$

have been evaluated with the use of Table I. The values of $E(Z, n)$ obtained for various order of ionization n are, in spite of their small differences, on one straight line drawn in Fig. 7 in logarithmic scale.*

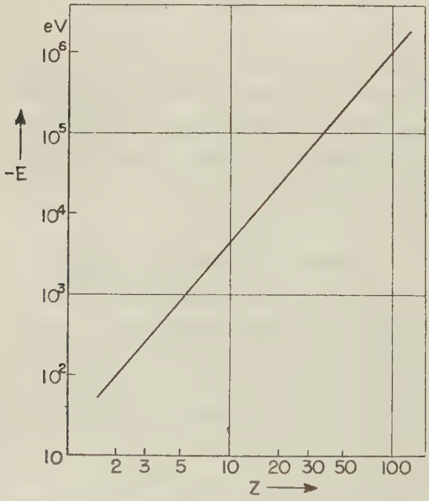

Fig. 7. Dependence on Z of E.
The energies $E(Z, n)$ for singly to quadruply ionized positive ions as well as atoms are shown by one straight line in spite of their small differences.

The total or successive ionization potential (that is, the energy required to remove n electrons in all, or the n-th electron alone, from the atoms or ions) is given respectively by

$$Q(Z,n)=E(Z,n)-E(Z,0)$$
$$=13.172\left(\frac{n}{q}\right)^{7/3}\left[\varphi'(0)+\frac{q^2}{x_0}\right]eV \tag{19}$$

or

$$J(Z,n)=Q(Z,n)-Q(Z,n-1)\,. \tag{20}$$

The results obtained for the former are shown in Fig. 8 and those for the latter are tabulated in Table IV. The excessive smallness of these values as compared with the experimental values[19] seems to be due to the omission of the exchange and correlation energies in the TF model.

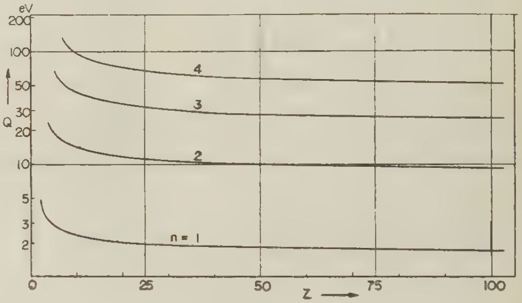

Fig. 8. Dependence on Z of Q.

§ 7. Mean Excitation Potential and Energy

Using our tables of the TF functions for free positive ions, we have calculated the mean excitation potential and energy which are defined by Bethe[20] and Sommerfeld[14] as a logarithmic mean

$$\log V_M=\int_0^{r_0}\log V\cdot\rho r^2\,dr\Big/\int_0^{r_0}\rho r^2 dr$$

and

$$\log E_M=\int_0^{r_0}\log|E|\cdot\rho r^2\,dr\Big/\int_0^{r_0}\rho r^2 dr\,.$$

Here V and E are the electrostatic potential and mean total energy per electron at distance r from the nucleus,

$$V=\frac{Ze}{r}\varphi+V_0=\frac{Ze}{\mu}\left[\frac{\varphi}{x}+\frac{q}{x_0}\right]$$

and

$$E=\frac{3e}{5}(V-V_0)-eV=-\frac{2Ze^2}{5\mu}\left[\frac{\varphi}{x}+\frac{5}{2}\frac{q}{x_0}\right],$$

respectively.

---

* Our value of energy for free atoms

$E(Z,0)=-0.76875\,Z^{7/3}=-20.917\,Z^{7/3}$ eV

is also represented with same line in Fig. 7.

Table IV. Ionization potential $J(n)$.

Z	atom	J $(n=1)$		J $(n=2)$		$J(3)$	$J(4)$
		cal.	exp.	cal.	exp.		
10	Ne	2.36	21.56	12.04	41.07	29.3	51.8
18	A	2.11	15.76	10.09	27.62	22.8	40.5
36	Kr	1.91	14.00	8.73	24.56	19.0	31.5
54	Xe	1.82	12.13	8.19	21.21	17.4	29.1

If we evaluate

$$\gamma_V(q)=\int_0^{x_0}\varphi^{3/2}x^{1/2}\log\left[\frac{\varphi}{x}+\frac{q}{x_0}\right]dx \div\int_0^{x_0}\varphi^{3/2}x^{1/2}dx$$

and

$$\gamma_E(q)=\int_0^{x_0}\varphi^{3/2}x^{1/2}\log\left[\frac{\varphi}{x}+\frac{5}{2}\frac{q}{x_0}\right]dx \div\int_0^{x_0}\varphi^{3/2}x^{1/2}dx$$

both of which depend only on ionization degree q, we can express the mean excitation potential and energy as

$$\left.\begin{aligned} V_M(Z,\ n)&=\frac{Ze}{\mu}\cdot 10^{\gamma_V}\\ &=4\left(\frac{2}{9\pi^2}\right)^{1/3}\cdot 10^{\gamma_V}Z^{4/3}\frac{e}{a_0}\\ \text{and}\qquad&\\ E_M(Z,\ n)&=\frac{2Ze^2}{5\mu}\cdot 10^{\gamma_E}\\ &=\frac{8}{5}\left(\frac{2}{9\pi^2}\right)^{1/3}\cdot 10^{\gamma_E}Z^{4/3}\frac{e^2}{a_0}\,. \end{aligned}\right\}\qquad(21)$$

Existence of the simple relations $V_M(Z,\ n)=n^{4/3}V_M(Z/n,\ 1)$ and $E_M(Z,\ n)=n^{4/3}E_M(Z/n,\ 1)$, which are characteristic of the TF model and cannot be found in the TFD model[21], makes it easy for us to calculate the values of V_M and E_M for larger n. The curves that indicate the dependence on Z of E_M for singly to quadruply ionized positive ions are shown in Fig. 9, in which we have drawn the line for free neutral atoms* for reference.

The V_M and E_M curves for n-ply ionized positive ions become infinite for $Z=n$, *i.e.* bare ions with no electron, as well as $Z=\infty$, and have the minimum for a definite intermediate value of Z, say $Z_{\min}$, while in the case of neutral atoms V_M and E_M vanish owing to the singularity of its bare states, *i.e.* $Z=0$. Fig. 9 shows that the values of $Z_{\min}$ and $E_M(Z_{\min})$ increase with the increase of n, respectively.

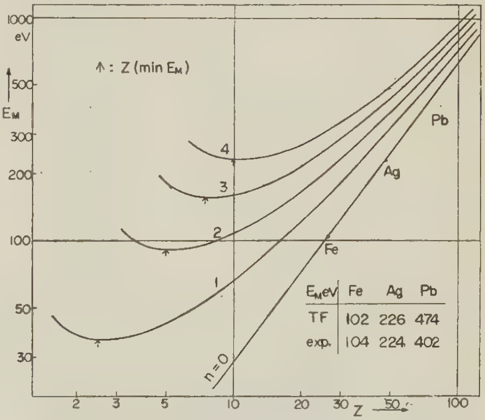

Fig. 9. Dependence on Z of E_M.

§ 8. Diamagnetic Susceptibility

The molar diamagnetic susceptibilities[11]

$$\chi=-\frac{Le^2}{6mc^2}\int_0^{r_0}4\pi\rho r^4dr$$

with L=Loschmidt number and c=light velocity, have been computed for positive ions. As is well known, the original TF model is inadequate for this purpose because of the overspreading of the electron cloud within the model. So we have calculated them with the use of the FA-modified TF model for free neutral atoms and for singly to quadruply ionized positive ions. Then, the formula to be used is given by

$$\chi(Z,\ n)=-0.62105Z^{1/3}\left(\frac{Z-n}{Z-n-1}\right)^{7/3}\times\left[6\int_0^{x_0}\varphi x dx-x_0^3\varphi'(x_0)\right]\times 10^{-6}\ \text{cm}^3,\quad(22)$$

---

* Our recalculated values using the exact table of the ordinary TF function for free neutral atoms

$$V_M(Z,\ 0)=0.12222\,Z^{4/3}\cdot e/a_0$$

and

$$M_M(Z,\ 0)=0.48887\,Z^{4/3}\cdot e^2/a_0 =1.3302\,Z^{4/3}\,\text{eV}$$

have reproduced Gombás' values[11].

and the term in the bracket depends on ionization degree q only. We have added to Table I the values of $\int_0^{x_0}\varphi x\,dx$, evaluated for the different states of ionization by the extended Simpson rule.*[,22)]

In comparison with the other theoretical[10),23)] and experimental values[24)], our numerical values are tabulated in Table V for the inert gas atoms and ions homologous to the inert gas, for which only the spherically symmetrical TF model is legitimately valid. As seen from the table, our results are fairly good. From the standpoint of the diamagnetic susceptibility, the FA-modified TF model seems to have a little more overspreading of the electron cloud than the TFD model[23)].

Table V. Comparison of the molar diamagnetic susceptibility $-\chi\times10^6$ cm^3.

Z	atom or ion	FA-modified TF	TFD	HF	exp.*
10	Ne	12.62	14.33	8.06	6.8
11	Na$^+$	7.22	7.83	5.08	4.1
12	Mg^{2+}	4.83	5.24	3.74	3.1
13	Al^{3+}	3.50	3.81	2.88	
14	Si^{4+}	2.69	2.92	2.29	
18	A	21.67	22.15		19.5
19	K$^+$	14.05	14.04		14.1
20	Ca^{2+}	10.24	10.26		11.1
21	Sc^{3+}	7.94	7.99		
22	Ti^{4+}	6.40	6.45		
36	Kr	37.34	35.51	31.10	28.0
37	Rb$^+$	26.95	25.53		25.1
38	Sr^{2+}	21.27	20.27		21.0
39	Y^{3+}	17.55	16.82		
40	Zr^{4+}	14.88	14.33		
54	Xe	49.53	45.96		42.4
55	Cs$^+$	37.54	34.92		38.7
56	Ba^{2+}	30.71	28.79		32.6
57	La^{3+}	26.09	24.62		
58	Ce^{4+}	22.68	21.52		

* The experimental values for ions are the estimated ones for compressed state in solid and liquid, while all theoretical values are for free ions.

§ 9. Scattering Factor

The X-ray scattering factors, coherent and incoherent, of the free positive TF ions at rest have been investigated.

The coherent scattering factor[25)] of positive ions is given by

$$f_0=\int_0^{x_0}\frac{\sin\kappa r}{\kappa r}4\pi\rho r^2dr$$

$$=Z\left[1-q\frac{\sin(\kappa\mu x_0)}{\kappa\mu x_0}-\kappa\mu\int_0^{x_0}\varphi\sin(\kappa\mu x)\,dx\right]\qquad(23)$$

with $\kappa=4\pi\sin\theta/\lambda$ and $\theta=$half scattering angle.

For very small scattering angles[20),26)], Eq. (23) can be approximated as

$$f_0\approx Z\left[1-q-(\kappa\mu)^2\int_0^{x_0}\varphi x dx\right]$$

the coefficient $\int_0^{x_0}\varphi x dx$ appears also in the calculation of the diamagnetic susceptibility Eq. (22) and is given as function of q in Table I.

For the convenience of comparison with the incoherent scattering factor, we do not use the scattering factor per electron $\mathfrak{f}_0=f_0/N$ defined by Bethe[20)], but rather the scattering factor per atomic number $\boldsymbol{f}_0=f_0/Z=N/Z\mathfrak{f}_0$. This quantity $\boldsymbol{f}_0$ depends only on the ionization degree q and on $\kappa\mu\propto Z^{-1/3}\sin\theta/\lambda$, and has been calculated for twenty eight different states of ionization degree q and for $\kappa\mu=0°$ (5°) 40°, 50° (12.5°) 200°. The dependence of $\boldsymbol{f}_0$ on $\kappa\mu$ (or $Z^{-1/3}\sin\theta/\lambda$) and on q is shown in Figs. 10 and 11. The numerical values are tabulated in Table VI for regular intervals of q.

---

* This rule may be used for numerical integrations with roughly divided intervals, and has also been applied to all other integrals in this paper.

As is seen in these figures and in the table, the coherent scattering factor per atomic number f_0 has the following features:

(1) $f_0(q=0,\ \kappa\mu=0°)=1$

(2) $f_0(q,\ \kappa\mu=0°)=1-q$,
$f_0(q,\ \kappa\mu=0°)=Z(1-q)=N$

(3) $f_0(q=1,\ \kappa\mu)=0$

(4) $f_0(q,\ \kappa\mu=\infty)=0$

(5) $f_0(q,\ \kappa\mu>50°)$ is nearly independent of small q or large x_0.

(6) $f_0(q=\text{const},\ \kappa\mu)$ is a monotonically decreasing function of $\kappa\mu$.

The comparison of the calculated values of f_0 with those[28)] calculated using the Hartree-Fock field for several positive ions is shown in Fig 12. We find the agreement is qualitatively sufficient.

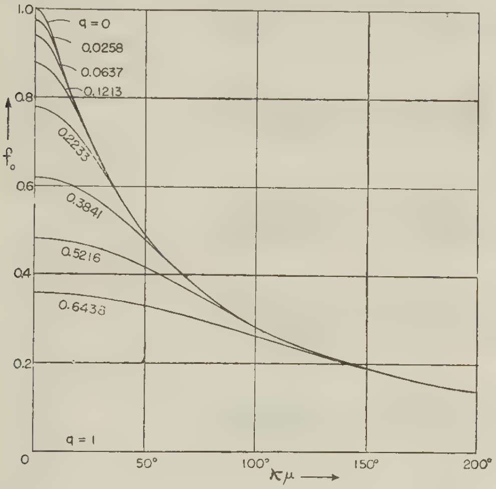

Fig. 10. $f_0(\kappa\mu,\ q=\text{const})$-curves.

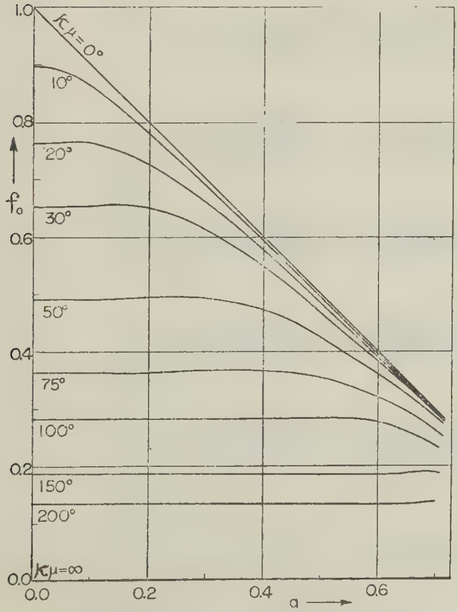

Fig. 11. $f_0(q,\ \kappa\mu=\text{const})$-curves.

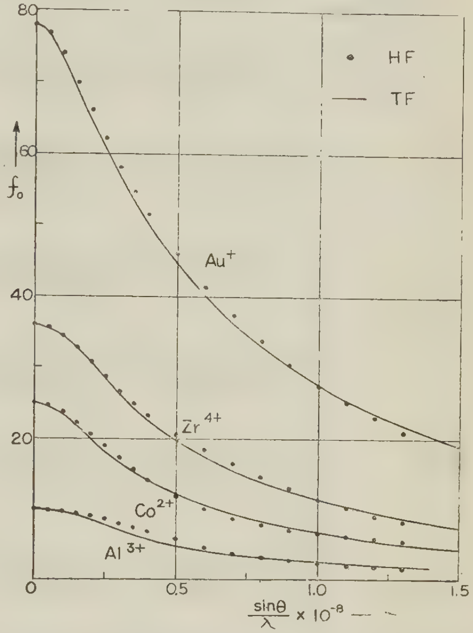

Fig. 12. Comparison of f_0 curves based on the TF model and Hartree-Fock field for singly to quadruply ionized positive ions.

The incoherent scattering factor per electron[29)] can be calculated from the expression

$$\begin{aligned} s_0^2(w) &= 1-\int_0^{\xi_0}[\sqrt{\varphi/x}-w]^2\left[\sqrt{\varphi/x}+\frac{w}{2}\right]x^2dx \\ &= 1-\frac{1}{6}(w\xi_0)^3+\int_0^{\xi_0}\left[\frac{3}{2}w\varphi x-\varphi^{2/3}\,x^{1/2}\right]dx \\ &= \varphi(\xi_0)-\xi_0\varphi'(\xi_0) \\ &\quad -\frac{1}{6}(w\xi_0)^3+\frac{3}{2}w\int_0^{\xi_0}\varphi x dx\ , \end{aligned} \tag{24}^*$$

where ξ_0 is the root of the equation

$$\sqrt{\varphi(\xi)/\xi}=w=\frac{\kappa\mu}{(6\pi Z)^{1/3}}\ .$$

The obtained numericals are given in Table VII and their dependence on w (or $Z^{-2/3}\sin\theta/\lambda$) and on q is shown in Figs. 13 and 14.

The incoherent scattering factor per electron

---

* For very small scattering angles,

$$S_0^2 \approx q+\frac{3}{2}w\int_0^{x_0}\varphi x dx\ .$$

Table VI. Values of coherent scattering factor per atomic number $\boldsymbol{f}_0(q, \kappa\mu)$.

q \ $\kappa\mu$	0°	5°	10°	15°	20°	25°	30°	35°	40°	50°	62.5°	75°	87.5°	100°	112.5°
0*	1.0000	0.9617	0.8959	0.8276	0.7633	0.7047	0.6521	0.6049	0.5627	0.4908	0.4195	0.3635	0.3187	0.2822	0.2521
...	....	....	....	....	....	....	....	....	....	....	....	....	....	....	....
0.009	0.9910	0.9611	0.8960	0.8275	0.7633	0.7047	0.6521	0.6049	0.5627	0.4908	0.4195	0.3635	0.3187	0.2822	0.2521
10	9900	9608	8962	8275	7633	7047	6521	6049	5627	4908	4195	3635	3187	2822	2521
11	9890	9605	8963	8275	7633	7047	6521	6049	5627	4908	4195	3635	3187	2822	2521
12	9880	9601	8964	8274	7633	7048	6521	6049	5627	4908	4195	3635	3187	2822	2521
13	9870	9597	8964	8274	7633	7048	6521	6049	5627	4908	4195	3635	3187	2822	2521
14	9860	9592	8967	8274	7633	7048	6521	6049	5627	4908	4195	3635	3187	2822	2521
15	9850	9587	8967	8275	7632	7048	6521	6049	5627	4908	4195	3635	3187	2822	2521
16	9840	9582	8967	8275	7632	7048	6521	6049	5627	4908	4195	3635	3187	2822	2521
0.018	0.9820	0.9571	0.8968	0.8276	0.7631	0.7048	0.6521	0.6049	0.5627	0.4908	0.4195	0.3635	0.3187	0.2822	0.2521
20	9800	9560	8969	8278	7631	7048	6521	6049	5627	4908	4195	3635	3187	2822	2521
22	9780	9547	8969	8279	7630	7048	6521	6049	5627	4908	4195	3635	3187	2822	2521
24	9760	9534	8967	8282	7630	7047	6521	6049	5627	4908	4195	3635	3187	2822	2521
26	9740	9521	8966	8284	7630	7046	6522	6049	5627	4908	4195	3635	3187	2822	2521
28	9720	9507	8963	8286	7631	7045	6522	6049	5627	4908	4195	3635	3187	2822	2521
30	9700	9493	8958	8288	7632	7045	6522	6050	5627	4908	4195	3635	3187	2822	2521
0.035	0.9650	0.9456	0.8946	0.8292	0.7635	0.7044	0.6521	0.6051	0.5627	0.4908	0.4195	0.3635	0.3187	0.2822	0.2521
40	9600	9418	8935	8295	7640	7043	6519	6051	5628	4908	4195	3635	3187	2822	2521
45	9550	9383	8917	8296	7645	7045	6519	6050	5628	4908	4196	3635	3187	2822	2521
50	9500	9340	8898	8294	7650	7048	6516	6048	5628	4908	4196	3635	3187	2822	2521
55	9450	9296	8876	8290	7654	7052	6516	6046	5628	4908	4196	3635	3187	2822	2521
60	9400	9253	8851	8284	7657	7056	6517	6045	5627	4909	4195	3636	3187	2822	2521
0.07	0.9300	0.9167	0.8798	0.8265	0.7662	0.7065	0.6521	0.6043	0.5622	0.4910	0.4195	0.3636	0.3187	0.2822	0.2521
8	9200	9079	8738	8239	7660	7073	6528	6045	5620	4910	4196	3635	3187	2822	2521
9	9100	8989	8673	8207	7653	7080	6536	6048	5620	4907	4197	3634	3187	2822	2520
10	9000	8898	8605	8167	7640	7083	6545	6054	5621	4905	4198	3634	3187	2822	2520
11	8900	8805	8533	8122	7621	7083	6552	6062	5624	4902	4197	3635	3186	2822	2521
12	8800	8712	8462	8073	7596	7078	6558	6070	5629	4899	4196	3636	3185	2822	2521

q \ $\kappa\mu$	125°	137.5°	150°	162.5°	175°	187.5°	200°
0~0.12	0.2269	0.2055	0.1873	0.1717	0.1580	0.1461	0.1355

[*] The values for atom as the limit are somewhat different from those calculated by Umeda and Tomishima[27] using the Miranda's table[6].

Table VII. Values of incoherent scattering factor per electron $s_0^2(q, w)$.

q \ w	0.00	0.025	0.05	0.1	0.2	0.3	0.4	0.5	0.6	0.7	0.8	0.9	1.0	1.5	2.0
0*	0.0000	0.1986	0.3228	0.4881	0.6743	0.7765	0.8394	0.8807	0.9091	0.9292	0.9440	0.9550	0.9633	0.9847	0.9924
...	....	....	....	....	....	....	....	....	....	....	....	....	....	....	....
0.009	0.0090	0.1986	0.3228	0.4881	0.6743	0.7765	0.8394	0.8807	0.9091	0.9292	0.9440	0.9550	0.9633	0.9847	0.9924
10	0100	1987	3228	4881	6743	7765	8394	8807	9091	9292	9440	9550	9633	9847	9924
11	0110	1987	3228	4881	6743	7765	8394	8807	9091	9292	9440	9550	9633	9847	9924
12	0120	1987	3228	4881	6743	7765	8394	8807	9091	9292	9440	9550	9633	9847	9924
13	0130	1988	3228	4881	6743	7765	8394	8807	9091	9292	9440	9550	9633	9847	9924
14	0140	1988	3228	4881	6743	7765	8394	8807	9091	9292	9440	9550	9633	9847	9924
15	0150	1988	3228	4881	6743	7765	8394	8807	9091	9292	9440	9550	9633	9847	9924
16	0160	1988	3228	4881	6743	7765	8394	8807	9091	9292	9440	9550	9633	9847	9924
0.018	0.0180	0.1989	0.3229	0.4881	0.6743	0.7765	0.8394	0.8807	0.9091	0.9292	0.9440	0.9550	0.9633	0.9847	0.9924
20	0200	1991	3229	4881	6743	7765	8394	8807	9091	9292	9440	9550	9633	9847	9924
22	0220	1992	3229	4881	6743	7765	8394	8807	9091	9292	9440	9550	9633	9847	9924
24	0240	1994	3229	4881	6743	7765	8394	8807	9091	9292	9440	9550	9633	9847	9924
26	0260	1995	3230	4881	6743	7765	8394	8807	9091	9292	9440	9550	9633	9847	9924
28	0280	1997	3231	4881	6743	7765	8394	8807	9091	9292	9440	9550	9633	9847	9924
30	0300	2000	3231	4881	6743	7765	8394	8807	9091	9292	9440	9550	9633	9847	9924
0.035	0.0350	0.2007	0.3232	0.4881	0.6743	0.7765	0.8394	0.8807	0.9091	0.9292	0.9440	0.9550	0.9633	0.9847	0.9924
40	0400	2016	3234	4882	6743	7765	8394	8807	9091	9292	9440	9550	9633	9847	9924
45	0450	2026	3237	4883	6743	7765	8394	8807	9091	9292	9440	9550	9633	9847	9924
50	0500	2038	3240	4884	6743	7765	8394	8807	9091	9292	9440	9550	9633	9847	9924
55	0550	2051	3244	4884	6743	7765	8394	8807	9091	9292	9440	9550	9633	9847	9924
60	0600	2066	3248	4885	6744	7765	8394	8807	9091	9292	9440	9550	9633	9847	9924
0.07	0.0700	0.2101	0.3258	0.4887	0.6745	0.7765	0.8394	0.8807	0.9091	0.9292	0.9440	0.9550	0.9633	0.9847	0.9924
8	0800	2140	3271	4890	6745	7765	8394	8807	9091	9292	9440	9550	9633	9847	9924
9	0900	2184	3288	4894	6746	7765	8394	8807	9091	9292	9440	9550	9633	9847	9924
10	1000	2232	3308	4898	6747	7765	8394	8807	9091	9292	9440	9550	9633	9847	9924
11	1100	2284	3331	4904	6748	7766	8394	8807	9091	9292	9440	9550	9633	9847	9924
12	1200	2338	3356	4910	6749	7767	8395	8807	9091	9293	9440	9550	9634	9847	9924

q \ w	3.	5.	∞
0~0.12	0.9974	0.9994	1.0000

* The values for atom as the limit are in good agreement with those calculated by Tietz[30] for various ξ_0's not for various w's as in our calculation.

s_0^2 has the following features:

(1) $s_0^2(q=0,\ w=0)=0$

(2) $s_0^2(q,\ w=0)=q$

(3) $s_0^2(q=1,\ w)=1$

(4) $s_0^2(q,\ w=\infty)=1$

(5) $s_0^2(q,\ w>0.2)$ is nearly indpendent of small q or large x_0.

(6) $s_0^2(q=\text{const},\ w)$ is a monotonically increasing function of w.

It is noticeable that the coherent scattering factor per atomic number f_0 and the incoherent scattering factor per electron s_0^2 have quite antagonistic characters as seen in the above tables and figures, *i.e.* one increases while the other decreases, or one is high while the other is low.

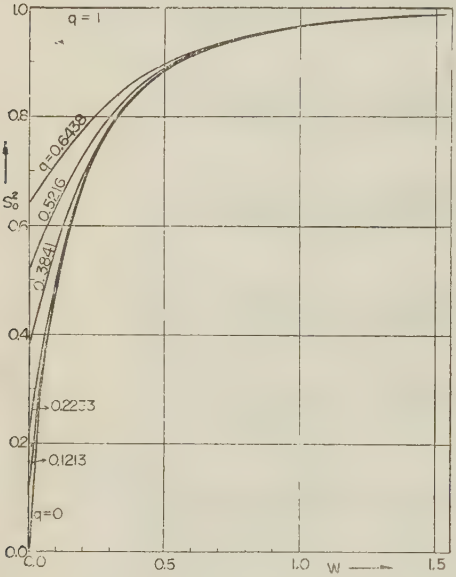

Fig. 13. $s_0^2(w, q=$bonst)-curves.

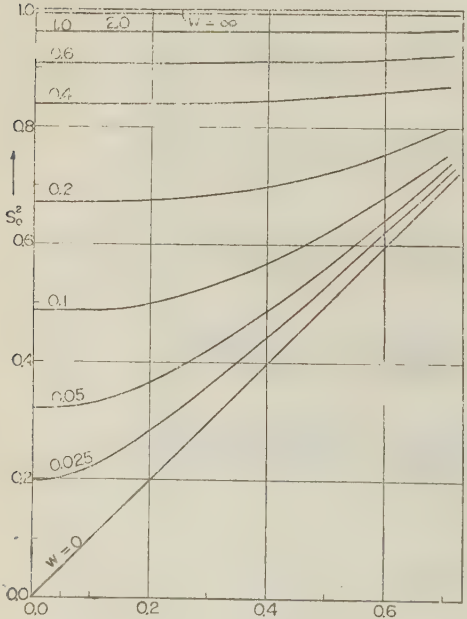

Fig. 14. $s_0^2(q, w=$const)-curves.

The total X-ray intensities scattered by an ion with atomic number Z and electron number N are proportional of $f_0^2+Ns_0^2=Zf^2{}_0^2+Ns_0^2$ and their values for Cs atom and ions, which is usually taken as the standard element for the calculation of the scattering factors, are shown in Fig. 15. We find that the scattered intensities are almost independent of the order of ionization n of ions except for the very small $\sin\theta/\lambda\times10^{-8}$ (<0.1) cm^{-1}.

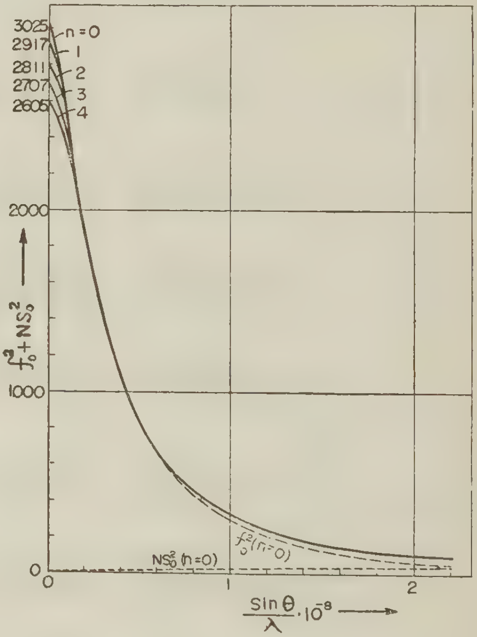

Fig. 15. Comparison of the factor $f_0^2+Ns_0^2$ proportional to the total X-ray intensity scattered by Cs ions, standard element, with order of ionization zero to four.

§ 10. Electric Field at the Nucleus

It was pointed out by Sternheimer[31)] that the electric field at the nucleus of the TF model polarized in the presence of the unit external electric field, is given by

$$\overline{E}_{\text{ind}}(0)=\frac{1}{2}\int_0^{x_0}\sqrt{\varphi x}\,dx \tag{25}$$

and that it does not allow us to calculate $\overline{E}_{\text{ind}}(0)$ for neutral TF atoms, because in this case the integral diverges logarithmically at the upper limit of the integral $x_0=\infty$. For positive ions as well as the FA-modified model, however, this integral does not diverge because of the finiteness of the upper limit x_0*.

We have investigated systematically the dependence of $\overline{E}_{\mathrm{ind}}(0)$ on ionization degree q and atomic number Z using our tables of the TF functions for free positive ions. The variation of the obtained values of $\overline{E}_{\mathrm{ind}}(0)$ values Z is shown in Fig. 16.

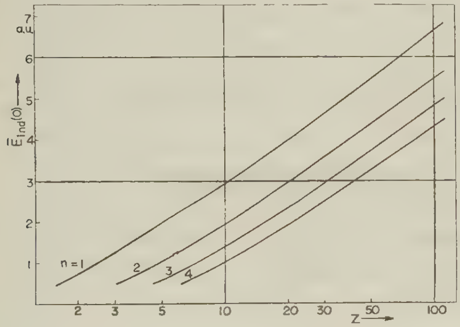

Fig. 16. Dependence on Z of $\overline{E}_{\mathrm{ind}}(0)$.

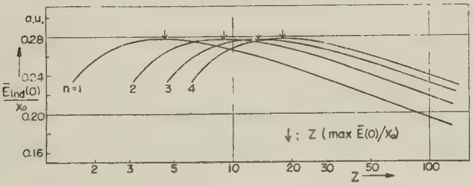

Fig. 17. Variation of $\overline{E}_{\mathrm{ind}}(0)/x_0$ *versus* Z.

Sternheimer, and later Umeda and the present author$^{32)}$ more definitely, remarked that the value of $\overline{E}_{\mathrm{ind}}(0)/x_0$ for the TFD ions are nearly constant, independent of Z, n and x_0. This seems to be also valid for the TF ions as indicated in Fig. 17, though the curves of $\overline{E}_{\mathrm{ind}}(0)/x_0$ versus Z have a weak maximum at an intermediate value of Z, say $Z_{\max}$, which increases with the increase of n.

Acknowledgements

The author wishes to express his sincere thanks to Professor K. Umeda of Okayama University for suggesting this problem, and for his continued guidance and encouragement throughout this work. His thanks are also due to Professors M. Kotani, P. Gombás and C. A. Coulson for their kind interests. He is also indebted to the Ministry of Education for the Scientific Research Fund granted to the Research Group for the Study of Atomic and Molecular Structure. Further thanks are due to the Matsudaira Fund at Takamatsu for the donation of an electric calculator which helped him very much in this investigation.

References

1) L. H. Thomas: Proc. Camb. Phil. Soc. **23** (1926) 542.
2) E. Fermi: Rend. Lincei **6** (1928) 48.
3) R. Latter: J. Chem. Phys. **24** (1956) 280.
4) S. Kobayashi and T. Taima: Mem. Fac. Liberal Arts and Educ., Kagawa Univ., II no. 33 (1956). R. A. Ballinger: Private communication.
5) E. Fermi: Mem. Accad. Italia **1** (1930) 149.
6) C. Miranda: Mem. Accad. Italia **5** (1934) 285.
7) R. P. Feynman, N. Metropolis and E. Teller: Phys. Rev. **75** (1949) 1561.
8) K. Umeda: Phys. Rev. **58** (1940) 92; J. Fac. Sci., Hokkaido Univ., II **5** (1942) 171.
9) S. Kobayashi, T. Matsukuma, S. Nagai and K. Umeda: J. Phys. Soc. Japan **10** (1955) 759.
10) S. Kobayashi: J. Phys. Soc. Japan **12** (1957) 737.
11) P. Gombás: *Die statistische Theorie des Atoms und ihre Anwendungen* (Springer, Wien, 1949); *Statistische Behandlung des Atoms*, Handbuch der Physik vol. **36** (Springer, Berlin, 1956).
12) E. Fermi and E. Amaldi: Mem. Accad. Italia **6** (1934) 117.
13) S. Kobayashi: J. Phys. Soc. Japan **14** (1959) 689.
14) A. Sommerfeld: Z. Phys. **78** (1932) 283.
15) S. Kobayashi: Mem. Fac. Liberal Arts and Educ., Kagawa Univ., II no. 62 (1958).
16) S. Kobayashi: J. Phys. Soc. Japan **11** (1956) 609. S. Kobayashi and T. Taima: Mem. Fac. Liberal Arts and Educ., Kagawa Univ., II no. 33 (1956).
17) N. F. Mott and H. S. W. Massey: *The Theory of Atomic Collisions*, 2nd. ed. (Oxford, 1949) 207.
18) K. Umeda: J. Fac. Sci., Hokkaido Univ., II **3** (1949) 255. In this paper the Matsukuma's value is reported.
19) D. E. Gray et al: *American Institute of Physics Handbook* (McGraw-Hill, New York, 1957) 7–14.
20) H. A. Bethe: Ann. Physik V **5** (1930) 325;

---

* The circumstances are similar for the induced quadrupole moment at the nucleus.

Z. Phys. **76** (1932) 293.

21) K. Umeda and S. Kobayashi: to be published.

22) S. Kobayashi: Mem. Fac. Liberal Arts and Educ., Kagawa Univ., II no. 55 (1957).

23) L. H. Thomas and K. Umeda: J. Chem. Phys. **24** (1956) 1113.

24) W. R. Myers: Rev. Mod. Phys. **24** (1952) 15.

25) R. W. Bragg and J. West: Z. Krist. **69** (1928) 118. B. v. Sz. Nagy: Z. Physik **91** (1934) 105; **94** (1935) 229; T. Derenzini: Nuovo Cimento **13** (1936) 341. L. H. Thomas and K. Umeda: J. Chem. Phys. **26** (1957) 293.

26) K. Umeda: to be published.

27) K. Umeda and Y. Tomishima: J. Phys. Soc. Japan **10** (1955) 753.

28) C. H. Macgillavry: to be published.

29) W. Heisenberg: Phys. Z. **32** (1931) 737. L. Bewilogua: Phys. Zs. **32** (1931) 740.

30) T. Tietz: Nuovo Cimento **8** (1958) 951.

31) R. M. Sternheimer: Phys. Rev. **96** (1954) 951.

32) K. Umeda and S. Kobayashi: to be published.

JOURNAL OF THE PHYSICAL SOCIETY OF JAPAN, Vol. 14, No. 8, AUGUST, 1959

Higher Order Transitions in Double Resonance

By Ko SUGIHARA

Physical Institute, Nagoya University, Nagoya

(Received March 13, 1959)

Saito et al have observed anomalous behaviours in the double resonances in metal halides in the early stage of saturational narrowing. They have reported following observations, which remained unexplained.

(1) The resonance line of the traced nucleus (B) becomes asymmetric and simultaneously shows shift, when the frequency of the nucleus (A) irradiated by the strong r.f. field is slightly off-resonant.

(2) In the case of the exact resonance, the intensity of the B-resonance decreases and the line disappears from observation. They called this phenomenon "collapsing".

(3) In some crystals (e.g. Li F) having short spin lattice relaxation time, anomalous effects (1) and (2) do not appear. Recently Bloembergen and Sorokin have observed a large dispersive polarization of the saturated Cs^{133} in Cs^{133} Br^{81} double resonance by applying a r.f. field precessing near the Br^{81} resonance. At first sight, above mentioned two phenomena appear to be very different, however, they are closely related to each other. It is the purpose of this paper to propose a general theory unifying the two different situations by taking into consideration the effect of the higher order transitions introduced by Bloembergen in discussing the "Overhauser Induction".

By using a generalized Solomon equation derived from a density matrix, the behaviours of the coupled spin system is discussed.

§1. Introduction

In a double resonance experiment in the coupled spin system A B, a weak resonance of the B-system is traced under an irradiation of a strong r.f. field resonating to the A-spin. Recently the technique of the double resonance has been used to investigate various problems. In these experiments two different phenomena appear according to the relative magnitudes of the intensity of the fluctuation of the lattice system and the spin coupling. One of them is the so-called Overhauser effect1) and is shown in lithium metal, remarkable enhancement of the nuclear polarization results from the increasing of the electron-spin resonance and the same effect is expected in nuclear double resonance although the magnitude of the induced polarization is much smaller[2)]. The other phenomenon is the saturational narrowing[3)]. The application of a strong r.f. field resonating to A nuclei induces rapid transitions between the A spin Zeeman levels, and averages out the local fields produced at the position of B nuclei by the magnetic moments of A nuclei. Then the narrowing of the B resonance line is observed.

Recently Bloch[4)] has proposed a theory of saturational narrowing. A general treatment unifying the two different situations has been proposed by Tomita[5)].

Above mentioned phenomena are the problems which can be treated in the frame of the second order perturbation of the mutual interaction. Recently, however, new effects, which can not be understood by these theories, have been observed experimentally.

Saito, Masuda and Kanda[6)*)] have found anomalous behaviours in the double resonances in metal halides in the early stage of saturation. They have reported following observations:

(1) The B resonance becomes asymmetric and simultaneously shows shift, when the r.f. frequency ω of the A-system is slightly off-resonant from the resonance frequency ω_A.

(2) In the exact resonance case $\omega=\omega_A$, the intensity of B resonance decreases and the line becomes broad. They called this phenomenon as "collapsing".

(3) In some crystal (Li F) having short spin-lattice relaxation time, anomalous effects (1) and (2) do not appear.

Bloembergen and Sorokin[7)†)] have observed a large transverse magnetization of the saturated nuclei Cs^{133} in $Cs^{133}Br^{81}$ nuclear double resonance by applying slightly off resonant frequency from the Br precessional frequency. The sign of the transverse magnetization reverses according to the difference of the r.f. frequency from the exact resonant one is positive or negative.

Purcell proposed the name "Overhauser Induction" to this effect[7)]. It will be shown that interesting phenomena discovered by B.S. and S.M.K. are both attributed to the higher order transitions in double resonances.

Bloembergen[8)] has proposed a simple theory to interpret the experiment of S.M.K. as follows:

In the process of sweeping the r.f. frequency ω', suppose that ω' is related to the resonance frequency ω_B by the following relation,

$$\omega'=\omega_B\pm\tilde{\omega}_A\,,\quad \tilde{\omega}_A=\sqrt{\Delta_A{}^2+\omega_{1A}{}^2}\,, \qquad (1.1)$$

where $\Delta_A=\omega_A-\omega$ and ω_{1A} is the amplitude in frequency scale of the r.f. field acting on A.

Here $\tilde{\omega}_A$ corresponds to the effective field in the rotating frame with angular velocity ω around the static field. If the condition (1.1) is satisfied, it is permissible energetically to induce the double transition in which A and B flip simultaneously and the total energy changes by $\hbar\omega'$.

Regarding the r.f. field energy of the B nuclei and the mutual interaction as together constituting the perturbation, the double transition results from a fourth order perturbation calculation. In the case $\Delta_A=0$, triple and more higher order processes will also become important, so the collapsing can be expected as a result of the line broadening by double and higher order transitions. In the case $\Delta_A\neq0$, there is a region in which $\tilde{\omega}_A$ surpass the mutual interaction and the double transition is responsible for the skewness of the absorption line, though it is not so intense to induce the collapsing. The author does not agree with the Bloembergen's simple discussion for the skewness of the absorption line. By our theory it is explained as follows: The absorption mode (or dispersion mode) of the B-system is proportional to its polarization which is composed of the three terms. The first is the proper contribution from the B-system and corresponds to the polarization to be realized when the A nuclei are in the thermal equilibrium state. The asymmetry does not result from this term. The other is the part produced by the double transition. Since this is proportional to the polarization of the A-system parallel to the effective field $\tilde{\omega}_A$, x-component in the rotating frame has non-vanishing value in the case of a exact resonance while z-component appears only in the case of a off-resonance.

In the case $\Delta_A\neq0$, the x-component is unimportant except in the case in which the dispersion mode is enhanced as a result of the Overhauser induction and the contribution of the z-component is rather important. Moreover this term reverses its sign according to whether ω' equals to $\omega_B+\tilde{\omega}_A$ or $\omega_B-\tilde{\omega}_A$, so that it will be responsible for the asymmetry of the resonance line around the center frequency ω_B.

---

*) Hereafter this work will be referred to as S.M.K.

†) Hereafter this work will be referred to as B.S.

When the spin-lattice relaxation process of the B-system is so rapid that the proper contribution from the B-system is predominant, then the anomalies should disappear. If the intensity of the double transition is comparable to that of the center line, then the resonance line will shift toward the more intense side among the two double transitions. If the double transition is so frequent that it determines the balancing between A and B, and B is approximately in a thermal equilibrium, the magnetization of the A-system parallel to the effective field $\tilde{\omega}_A$ should be very large and comparable to the thermal equilibrium value of the B-system.

This is the "Overhauser Induction". The theory given by B.S. in the case spin 1/2 is insufficient since they neglect the spin-relaxation process relevant to the A-system. In the following sections we will intend to construct a macroscopic Solomon equation which describes the coupled spin system A B. This is derived from a microscopic density matrix following the method developed by Wangsness-Bloch⁹⁾, Bloch¹⁰⁾ and Tomita⁵⁾ by taking into consideration the effect of the double transition.

§ 2. Equation of Motion of the Density Matrix

The Hamiltonian of the total system is given by

$$\mathscr{H}=\hbar(H_A+H_B+G+F)\,, \tag{2.1}$$

where

$$\left\{\begin{array}{l} H_A=E_A+D_A+G_A\,, \\ H_B=E_B+D_B+G_B\,. \end{array}\right. \tag{2.2}$$

Here E stands for the Zeeman energy

$$\left\{\begin{array}{l} E_A=-\gamma_A H_0 \sum\limits_j I_{Aj}{}^0=-\omega_A \sum\limits_j I_{Aj}{}^0\,, \\ E_B=-\gamma_B H_0 \sum\limits_k I_{Bk}{}^0=-\omega_B \sum\limits_k I_{Bk}{}^0\,, \end{array}\right. \tag{2.3}$$

and D is the energy associated with the radio-frequency field H_{1A} and H_{1B},

$$\left\{\begin{array}{l} D_A=-(\omega_{1A}/2) \sum\limits_j (I_{Aj}{}^+e^{i\omega t}+I_{Aj}{}^-e^{-i\omega t})\,, \\ D_B=-(\omega_{1B}/2) \sum\limits_k (I_{Bk}{}^+e^{i\omega' t}+I_{Bk}{}^-e^{-i\omega' t})\,, \end{array}\right. \tag{2.4}$$

where $\omega_{1A}=\gamma_A H_{1A}$ and $\omega_{1B}=\gamma_B H_{1B}$ and γ_A and γ_B gyromagnetic ratios of A and B spin respectively.

G_A and G_B are the proper interactions of A and B responsible for the spin-spin and spin-lattice relaxations and here let us assume for simplicity the local field picture

$$\left\{\begin{array}{l} G_A=\sum\limits_j \sum\limits_{\mu_j} I_{Aj}{}^{\mu_j}F_A{}^{\bar{\mu}_j}\,, \\ G_B=\sum\limits_k \sum\limits_{\mu_k} I_{Bk}{}^{\mu_k}F_B{}^{\bar{\mu}_k}\,, \quad (\mu_j,\ \mu_k=0,\ \pm 1) \end{array}\right. \tag{2.5}$$

where $\bar{\mu}_j$ and $\bar{\mu}_k$ denote $-\mu_j$ and $-\mu_k$ and I^μ stands for the spin operator corresponding to the quantum jump μ. G is the spin coupling between the two system and is written in the form,

$$G=\sum_j \sum_k \sum_{\mu_j} \sum_{\mu_k} I_{Aj}{}^{\mu_j} I_{Bk}{}^{\mu_k} F_{jk}{}^{\bar{\mu}_j\bar{\mu}_k}\,, \tag{2.6}$$

which includes an indirect exchange and a pseudo-dipolar coupling. Finally F is the energy of the lattice system. Then the density matrix ρ describing the whole system obeys the equation of motion

$$\frac{d}{dt}\rho=i[\rho,\ H_A+H_B+G+F]\,. \tag{2.7}$$

When a strong r.f. field is applied to the A-system, it is not permissible to regard D_A as a small perturbation so that it is convenient to make the transformation to the coordinate system which makes D_A as time-independent¹¹⁾.

They by way of the transformation

$$A^T=\exp(iE't)A\exp(-iE't)\,, \tag{2.8}$$

where

$$E'=-\omega(\sum_j I_{Aj}{}^0+\sum_k I_{Bk}{}^0)\,, \tag*{(2.8)$'$}$$

the density matrix ρ^T in the new frame is found to obey the following equation

$$\frac{d}{dt}\rho^T=i[\rho^T,\ E_A{}^{Te}+E_B{}^{Te}+D_B{}^T+G_A{}^T+G_B{}^T+G^T+F]\,, \tag*{(2.7)$'$}$$

where

$$\left\{\begin{array}{ll} E_A{}^{Te}=-(\varDelta_A \sum\limits_j I_{Aj}{}^0+\omega_{1A} \sum\limits_j I_{Aj}{}^x)\,, & (\varDelta_A=\omega_A-\omega) \\ E_B{}^{Te}=-\varDelta_B \sum\limits_k I_{Bk}{}^0\,, & (\varDelta_B=\omega_B-\omega) \end{array}\right. \tag{2.9}$$

$$D_B{}^T=-(\omega_{1B}/2)\sum_k (I_{Bk}{}^+\exp i(\omega'-\omega)t+I_{Bk}{}^-\exp -i(\omega'-\omega)t)\ , \tag{2.10}$$

$$G_A{}^T=\sum_j\sum_{\mu_j} I_{Aj}{}^{\mu_j}F_A{}^{\bar{\mu}_j}\exp(i\omega_{\mu_j}t)\ , \qquad (\omega_{\mu_j}=-\mu_j\omega) \tag{2.11}$$

$$G_B{}^T=\sum_k\sum_{\mu_k} I_{Bk}{}^{\mu_k}F_B{}^{\bar{\mu}_k}\exp(i\omega_{\mu_k}t)\ , \qquad (\omega_{\mu_k}=-\mu_k\omega) \tag{2.12}$$

$$G^T=\sum_j\sum_k\sum_{\mu_j}\sum_{\mu_k} I_{Aj}{}^{\mu_j}I_{Bk}{}^{\mu_k}F_{jk}{}^{\bar{\mu}_j\bar{\mu}_k}\exp i(\omega_{\mu_j}+\omega_{\mu_k})t\ . \tag{2.13}$$

In order to diagonalize $E_A{}^{Te}$, we will carry out a further transformation to a new coordinate system whose z-axis coincides with the effective field direction in the rotating system, and whose y-axis remains unchanged. This transformation corresponds to the rotation of angle $\Theta=\tan^{-1}(\omega_{1A}/\Delta_A)$ about y-axis. In this way we get

$$E_A{}^{Te}=-\tilde{\omega}_A\sum_j I_{Aj}(0) \tag{2.14}$$

In general the spin operators of the A-system are written in the form

$$I_{Aj}{}^{\mu_j}=\sum_{\nu_j=0,\pm1} a_{\mu_j\nu_j}I_{Aj}(\nu_j)\ , \tag{2.15}$$

where $I_{Aj}(\nu_j)$ is the spin operator associated with ν_j quantum jump in the new coordinate system and the explicit representation of (2.15) is

$$\begin{bmatrix} I^0 \\ I^+ \\ I^- \end{bmatrix}=\begin{bmatrix} \cos\Theta & -\sin\Theta/2 & -\sin\Theta/2 \\ \sin\Theta & (\cos\Theta+1)/2 & (\cos\Theta-1)/2 \\ \sin\Theta & (\cos\Theta-1)/2 & (\cos\Theta+1)/2 \end{bmatrix}\begin{bmatrix} I(0) \\ I(+) \\ I(-) \end{bmatrix}. \tag{2.16}$$

$G_A{}^T$ and G^T in the new coordinate system are given by

$$G_A{}^T=\sum_j\sum_{\mu_j}\sum_{\nu_j} a_{\mu_j\nu_j}I_{Aj}(\nu_j)F_A{}^{\bar{\mu}_j}\exp(\mathrm{i}\omega_{\mu_j}t)\ , \tag{2.17}$$

$$G^T=\sum_j\sum_k\sum_{\mu_j}\sum_{\mu_k}\sum_{\nu_j} a_{\mu_j\nu_j}I_{Aj}(\nu_j)I_{Bk}{}^{\mu_k}F_{jk}{}^{\bar{\mu}_j\bar{\mu}_k}\exp i(\omega_{\mu_j}+\omega_{\mu_k})t\ . \tag{2.18}$$

If H_{1A} is large (but still much less than the static field H_0), $D_B{}^T$, $G_A{}^T$, $G_B{}^T$ and G^T may be regarded as small perturbation as compared with the remaining parts in (2.7)′. Then we take the interaction representation using the operation

$$A^*=\exp i(E_A{}^{Te}+E_B{}^{Te}+F)tA\exp -i(E_A{}^{Te}+E_B{}^{Te}+F)t\ . \tag{2.19}$$

By way of (2.19), (2.7)′ is transformed into

$$(d/dt)\rho^{T*}=i[\rho^{T*},\ G_A{}^{T*}+G_B{}^{T*}+G^{T*}+D_B{}^{T*}]\ , \tag{2.20}$$

where

$$D_B{}^{T*}=-(\omega_{1B}/2)\sum_k \{I_{Bk}{}^+\exp i(\omega'-\omega_B)t+I_{Bk}{}^-\exp -i(\omega'-\omega_B)t\}\ , \tag{2.21}$$

$$G_A{}^{T*}=\sum_j\sum_{\mu_j}\sum_{\nu_j} a_{\mu_j\nu_j}I_{Aj}(\nu_j)F_A{}^{\bar{\mu}_j*}\exp i(\omega_{\mu_j}+\omega_{\nu_j})t\ , \quad (\omega_{\nu_j}=-\nu_j\tilde{\omega}_A)\ . \tag{2.22}$$

$F_A{}^{\bar{\mu}_j}$ is decomposed into the frequency spectrum as

$$F_A{}^{\bar{\mu}_j*}=\exp(iFt)F_A{}^{\bar{\mu}_j}\exp(-iFt)=\sum_\lambda F_A{}^{\bar{\mu}_j}(\lambda)\exp(i\omega_\lambda t)\ . \tag*{(2.22)′}$$

Similarly,

$$G_B{}^{T*}=\sum_k\sum_{\mu_k}\sum_\lambda I_{Bk}{}^{\mu_k}F_B{}^{\bar{\mu}_k}(\lambda)\exp i(\omega_{\mu_k}{}^0+\omega_\lambda)t\ , \tag{2.23}$$

where

$$\omega_{\mu_k}{}^0=-\mu_k\omega_B\ .$$

Since the lattice part of G is nearly rigid, $F_{jk}{}^{\bar{\mu}_j\bar{\mu}_k}$ may be regarded as constant, so that we have

$$G^{T*}=\sum_j\sum_k\sum_{\mu_j}\sum_{\mu_k}\sum_{\nu_j} a_{\mu_j\nu_j}I_{Aj}(\nu_j)F_{jk}{}^{\bar{\mu}_j\bar{\mu}_k}\exp i(\omega_{\mu_j}+\omega_{\mu_k}{}^0+\omega_{\nu_j})t\ . \tag{2.24}$$

To take into consideration the effect of tne double transition, it is necessary to develop up to the fourth order perturbation containing G^{T*} and D^{T*} in (2.20), but we can obtain the same result in the approximation of the second order perturbation by introducing the effective Hamiltonian like

$$K^T=(\omega_{1B}/2)\sum_j\sum_k\sum_{\nu_j\neq 0} a_{0\nu_j}F_{jk}{}^{00}\{I_{Bk}{}^+\exp i(\omega'-\omega)t+I_{Bk}{}^-\exp -i(\omega'-\omega)t\}I_{Aj}(\nu_j)I_{Bk}{}^0(\omega_{\nu_j})^{-1}\,, \tag{2.25}$$

$$K^{T*}=(\omega_{1B}/2)\sum_j\sum_k\sum_{\nu_j\neq 0} a_{0\nu_j}F_{jk}{}^{00}\{I_{Bk}{}^+\exp i(\omega'-\omega_B+\omega_{\nu_j})t+I_{Bk}{}^-\exp -i(\omega'-\omega_B+\omega_{\nu_j})t\}$$
$$\times I_{Aj}(\nu_j)I_{Bk}{}^0(\omega_{\nu_j})^{-1}\,. \tag{2.25$'$}$$

K^T, which is derived from the second order perturbational calculation regarding $D_B{}^T$ and G^T as small perturbation, has matrix elements which induces the double transition. The contributions from G_A, G_B and G up to the second order perturbation have been discussed in detail by Tomita[5] and here we shall not touch on these terms further in this section. Short time development of the density matrix regarding K^{T*} as a small perturbation is

$$\rho^{T*}(t)=\rho^{T*}(0)+\varDelta_1\rho^{T*}+\varDelta_2\rho^{T*}\,, \tag{2.26}$$

where

$$\left\{\begin{aligned}\varDelta_1\rho^{T*}&=-i\int_0^t dt_1[K^{T*}(t_1),\ \rho^{T*}(0)]\,,\\ \varDelta_2\rho^{T*}&=-\int_0^t dt_1\int_0^{t1} dt_2[K^{T*}(t_1),\ [K^{T*}(t_2),\ \rho^{T*}(0)]]\,,\end{aligned}\right. \tag{2.26$'$}$$

The contribution from $\varDelta_1\rho^{T*}$ may be neglected in (2.26), and inserting (2.25)′ into (2.26)′ the second order term is explicitly given by

$$\varDelta_2\rho^{T*}=-(\omega_{1B}/2)^2a_{01}a_{0\bar{1}}\sum_j\sum_k\sum_{\nu_j\neq 0}|F_{jk}{}^{00}|^2\int_0^t dt_1\int_0^{t1}dt_2\{\exp i(\omega'-\omega_B+\omega_{\nu_j})(t_1-t_2)$$
$$\times[I_{Bk}{}^+I_{Bk}{}^0I_{Aj}(\nu_j),\ [I_{Bk}{}^-I_{Bk}{}^0I_{Aj}(\bar{\nu}_j),\ \rho^{T*}(0)]]+\exp -i(\omega'-\omega_B+\omega_{\nu_j})(t_1-t_2)$$
$$\times[I_{Bk}{}^-I_{Bk}{}^0I_{Aj}(\nu_j),\ [I_{Bk}{}^+I_{Bk}{}^0I_{Aj}(\rho^{T*}(0)]]\}(\omega_{\nu_j}\omega_{\bar{\nu}_j})^{-1}\,. \tag{2.27}$$

By using (2.19), we shall again come back to the rotating coordinate system. Let us suppose that the density matrix describing the whole system can be factorized into the spin part σ—Bloch[9),10)] proposed the name "distribution matrix"—and the lattice part ρ_F which is practically independent of the behavior of the spin system and may be assumed as the canonical distribution corresponding to the lattice energy F.

Inserting the relation $a_{01}=a_{0\bar{1}}=-(\sin\Theta/2)$ obtained from (2.16) and averaging over the lattice part, it is easily shown that the time derivative of the second order term of σ^T is given by

$$\frac{d}{dt}\varDelta_2\sigma^T=t\left(\frac{\omega_{1B}}{\tilde{\omega}_A}\right)^2\frac{\sin^2\Theta}{16}\sum_j\sum_k\sum_{\nu_j\neq 0}\sum_{\lambda=\pm 1}\langle|F_{jk}{}^{00}|^2\rangle_F\delta_{\omega',\omega_B-\omega_{\nu_j}}$$
$$\times[I_{Bk}{}^{\lambda}I_{Bk}{}^0I_{Aj}(\lambda\nu_j),\ [I_{Bk}{}^{\bar{\lambda}}I_{Bk}{}^0I_{Aj}(\overline{\lambda}\nu_j),\ \sigma^T(0)]\,, \tag{2.28}$$

where $\langle\ \ \rangle_F$ denotes the operation averaging over the lattice states.

§ 3. Solomon Equation

In this section, the Solomon equation describing a macroscopic motion of the coupled spin system A B is derived on the basis of (2.28).

Taking an average the product of (2.28) and a spin function $Q_A(Q_B)$ over the B(A) system, the macroscopic equation of $Q_A(Q_B)$ due to the interaction K is easily obtained. At first we shall derive the equation of Q_B.

Coming back to the static coordinate system*), $\langle Q_B\rangle$ obeys the following equation

---

*) The term appearing due to coming back to the static system will be contained in considering the effects of G_A, G_B and G.

$$\left.\frac{d}{dt}\right)_k\langle Q_B\rangle=t\left(\frac{\omega_{1B}}{\omega_{1A}}\right)^2\frac{\sin^2\Theta}{16}\sum_j\sum_k\sum_{\nu j=\pm1}\sum_{\lambda=\pm1}\langle|F_{jk}{}^{00}|^2\rangle_F\delta_{\omega',\omega_B-\omega\nu_j}$$
$$\times\{\langle[[Q_B,\ I_{Bk}{}^{\lambda}I_{Bk}{}^0],\ I_{Bk}{}^{\bar\lambda}I_{Bk}{}^0]\rangle\langle I_{Aj}(\lambda\nu_j)I_{Aj}(\bar\lambda\nu_j)\rangle$$
$$+\langle I_{Bk}{}^{\bar\lambda}I_{Bk}{}^0[Q_B,\ I_{Bk}{}^{\lambda}I_{Bk}{}^0]\rangle\langle[I_{Aj}(\lambda\nu_j),\ I_{Aj}(\bar\lambda\nu_j)]\rangle\}\ . \tag{3.1}$$

We should be be remembered that the linear equation associated with the spin operator holds in the case of $I_B=1/2$ and in the approximation retaining the terms up to the first order in $\hbar\omega_A/kT$, $\hbar\omega_B/kT$ and $\hbar\omega_{1A}/kT$.

Putting $Q_B=I_{Bz}=\sum_k I_{Bk}{}^0$, the equation (3.1) becomes

$$\left.\frac{d}{dt}\right)_k\langle I_{Bz}\rangle=-t\frac{\sin^4\Theta}{24}I_A(I_A+1)\left(\frac{\omega_{1B}}{\omega_{1A}}\right)^2\sum_j\langle|F_{jk}{}^{00}|^2\rangle^2\langle I_{Bz}\rangle\sum_{\lambda=\pm1}\delta_{\omega'\omega_B+\lambda\tilde\omega_A}$$
$$-t\frac{\sin^4\Theta}{32}\left(\frac{\omega_{1B}}{\omega_{1A}}\right)^2\sum_j\langle|F_{jk}{}^{00}|\rangle_F\langle I_A(0)\rangle\sum_{\lambda=\pm1}\lambda\delta_{\omega',\omega_B+\lambda\tilde\omega_A}\ , \tag{3.2}$$

where j and k denote the suffixes of A and B respectively and $I_A(0)=\sum_j I_{Aj}(0)$.

In order to observe the qualitative behaviour, we may replace the Gaussian line constituted by the rigid lattices regularly distributed by the Lorentzian line which has an equal half value width. This simplification corresponds to the approximation using one operator T_2 in Bloch equation to represent the spin-spin relaxation process. Therefore, the following replacement is introduced

$$t\sum_j\langle|F_{jk}{}^{00}|^2\rangle_F(1/3)I_A(I_A+1)\to1.175[\langle\varDelta\omega_B\rangle^2]^{1/2}\ , \tag{3.3}$$

where $\langle\varDelta\omega_B\rangle^2=\sum_j\langle|F_{jk}{}^{00}|\rangle_F(1/3(I_A(I_A+1)$ is the second moment of the local field at the position of a B spin produced by the A nuclei.

A similar approximation as (3.3) is used like

$$t\sum_k\langle|F_{jk}{}^{00}|^2\rangle_F(1/3)(1/2)(3/2)\to1.175[\langle\varDelta\omega_A\rangle^2]^{1/2}\ , \tag*{(3.3)$'$}$$

where $\langle\varDelta\omega_A\rangle^2=\sum_k\langle|F_{jk}{}^{00}|^2\rangle_F(1/3)(1/2)(3/2)$ is the second moment of the local field at the position of an A spin produced by the B nuclei.

(3.3) and (3.3)′, (3.2) is simplified in Bloch type like

$$\left.\frac{d}{dt}\right)_k\langle I_{Bz}\rangle+\sum_{\lambda=\pm1}\delta_{\omega',\omega_B+\lambda\tilde\omega_A}\{s^4\varPhi_B{}'\langle I_{Bz}\rangle+\lambda s^4\varPhi_A{}'(s\langle I_{Ax}\rangle+c\langle I_{Az}\rangle)\}=0\ , \tag{3.2}$$

where

$$s=\sin\Theta\ ,\qquad c=\cos\Theta\ ,$$
$$\varPhi_A{}'=\frac{1.175}{2\sqrt{2}}\left|\frac{\omega_{1B}}{\omega_{1A}}\right|[\langle\varDelta\omega_A\rangle^2]^{1/2}\ ,\qquad \varPhi_B{}'=\frac{1.175}{2\sqrt{2}}\left|\frac{\omega_{1B}}{\omega_{1A}}\right|[\langle\varDelta\omega_B\rangle^2]^{1/2}\ .$$

It should be remembered that the A-system is described with regard to the rotating system. Then the differential equation governing the motion of the B-system becomes

$$\left.\frac{d}{dt}\right)_k\begin{bmatrix}\langle I_{Bx}\rangle\\ \langle I_{By}\rangle\\ \langle I_{Bz}\rangle\end{bmatrix}+\begin{bmatrix}(1/2)s^4\varPhi_B{}' & 0 & 0\\ 0 & (1/2)s^4\varPhi_B{}' & 0\\ 0 & 0 & s^4\varPhi_B{}'\end{bmatrix}\begin{bmatrix}\langle I_{Bx}\rangle\\ \langle I_{By}\rangle\\ \langle I_{Bz}\rangle\end{bmatrix}+\lambda\varPhi_A{}'\begin{bmatrix}0\\ 0\\ s^5\langle I_{Ax}\rangle+s^4c\langle I_{Az}\rangle\end{bmatrix}=0\ , \tag{3.4}$$

where for simplicity $\delta_{\omega',\omega_B+\lambda\tilde\omega_A}$ is omitted. It is worth noticing that the coupling terms with the A-system contain the sign λ. Similarly the equation governing the A-system is easily derived from (2.28)

$$\left.\frac{d}{dt}\right)_k\langle Q_A\rangle=t\left(\frac{\omega_{1B}}{\tilde\omega_A}\right)^2\frac{\sin^2\Theta}{16}\sum_j\sum_k\sum_{\nu j=\pm1}\sum_{\lambda=\pm1}\langle|F_{jk}{}^{00}|^2\rangle_F\delta_{\omega',\omega_B-\omega\nu_j}$$
$$\times\{\langle I_{Bk}{}^{\lambda}I_B{}^{k0}I_{Bk}{}^{\bar\lambda}I_{Bk}{}^0\rangle\langle[[Q_A,\ I_{Aj}(\lambda\nu_j)],\ I_{Aj}(\bar\lambda\nu_j)]\rangle$$
$$+\langle[I_{Bk}{}^{\lambda}I_{Bk}{}^0,\ I_{Bk}{}^{\bar\lambda}I_{Bk}{}^0]\rangle\langle I_{Aj}(\bar\lambda\nu_j)[Q_A,\ I_{Aj}(\lambda\nu_j)]\rangle\}\ . \tag{3.5}$$

the steady-state solution of (3.9)

$$\langle I_{Ax}\rangle=\frac{\Phi_{Ax}{}^{0}}{\Phi_{Ax}+\Phi_{A}'+\Phi_{A}'+a(\Phi_{B}'+\phi_{B}')}\langle I_{Ax}\rangle_{0}$$

$$-\lambda\frac{\Phi_{Bz}{}^{0}(\Phi_{B}'+\phi_{B}')}{(\Phi_{Bx}+\Phi_{B}'+\phi_{B}')\{\Phi_{Ax}+\Phi_{A}'+\phi_{A}'+a(\Phi_{B}'+\phi_{B}'\}}\langle I_{Bz}\rangle_{0}\,, \tag{4.4}$$

$$\langle I_{Az}\rangle=\frac{\Phi_{Az}{}^{0}\{\Phi_{Ax}+(1/2)(\Phi_{A}'+\phi_{A}')\}}{\{\Phi_{Ax}+(1/2)(\Phi_{A}'+\phi_{A}')\}\{\Phi_{Az}+(1/2)(\Phi_{A}'+\phi_{A}')\}+\omega_{1A}{}^{2}}\langle I_{Az}\rangle_{0}\,. \tag{4.4$'$}$$

The Overhauser induction is the effect in which the second term in (4.4) is much larger than the first and $\langle I_{Ax}\rangle$ becomes to be nearly equal to $\langle I_{Bz}\rangle_0$ in magnitude and the conditions to be satisfied in order to induce the effect is summarized as follows:

(i) The spin-lattice relaxation constant Φ_{Bz}*) is so large that the condition $\Phi_{Bz}\gtrsim\Phi_{B}'$\**) is satisfied and this condition means that $\langle I_{Bz}\rangle_e$ is nearly equal to $\langle I_{Bz}\rangle_0$.

(ii) The spin-spin relaxation of the A-system is supressed due to the strong resonant r.f. field and the condition $\Phi_{A}'\sim\Phi_{Ax}$ is satisfied.

Then

$$\langle I_{Ax}\rangle\approx-\lambda\langle I_{Bz}\rangle_0\,, \tag{4.5}$$

and $\langle I_{Ax}\rangle$ reverses its sign around the center frequency ω_B due to the existence of sign λ.

(2) *Experiment of* S.M.K.

In discussing the experiment of S.M.K., it is necessary to study the behaviour of $\langle v\rangle$. As is shown in (4.3) and (4.2), $\langle v\rangle$ is proportional to $\langle I_{Bz}\rangle$ which is composed of three parts. According to the relative magnitude between them, various situations are realized and the asymmetry of the line shape is ascribed to the term $\lambda s^4ca\langle I_{Az}\rangle$ which appears only in the off-resonant case. In the experiment on *TlF*, the asymmetry has been observed when $\Delta_A=\pm2\pi\times5$ kc and the amplitude of the r.f. field of the A-system is 1∼3 gauss. Suppose that H_{1A} equals to 3 gauss, since $s\doteqdot1$ and $c\doteqdot\Delta_A/\omega_{1A}=0.15$ in this case†), it may be permissible to replace by the quantities in exact resonance in evaluating $\langle I_{Bz}\rangle_e$, a, $\langle I_{Az}\rangle$ and $\langle I_{Ax}\rangle$.

Here we may classify three different cases:

(i) The case in which the spin-lattice relaxation of the B-system is sufficiently rapid.

In this case the term $\langle I_{Bz}\rangle_e$ is superior to the other terms among $\langle I_{Bz}\rangle$, and so the appearance of the normal line shape is expected. In lithium fluoride crystals it has been observed that the sample which has short relaxation time does not show any anomalous behaviour and the situation corresponds precisely to the case above mentioned.

(ii) The case in which the Overhauser induction occurs and the condition

$$\langle I_{Ax}\rangle\approx-\lambda\langle I_{Bz}\rangle_0\gg\langle I_{Az}\rangle\,, \tag{4.6}$$

holds.

Then, $\langle I_{Bz}\rangle$ is given by

$$\langle I_{Bz}\rangle\doteqdot\langle I_{Bz}\rangle_e-s^5a\langle I_{Bz}\rangle_e\,, \tag{4.6$'$}$$

and any skewness in the resonance line will not appear.

(iii) The case in which in (4.2) the term proportional to $\langle I_{Az}\rangle$ surpasses the term proportional to $\langle I_{Ax}\rangle$ and contributes to $\langle I_{Bz}\rangle$ in the same order magnitude as $\langle I_{Bz}\rangle_e$. In this case $\langle v\rangle$ depends upon the sign λ appreciably and the asymmetry will result from the differences of the absorption intensity around the center frequency ω_B and simultaneously the position of intensity maximum may be pulled up nearer to the side at which the absorption is more intense. This is the anomaly observed in the off-resonant case. In the exact resonance the asymmetry and the shift will disapper and, as has already been pointed out by Bloembergen in this region the relation $\omega_{1A}\lesssim|F_{jk}{}^{00}|$ is satisfied and the "collapse" results from a severe broadening of the line by second and higher order transitions.

§ 5. Conclusion

We have not made a quantitative analysis of the experiments, but it appears that they are in agreement qualitatively with the predictions of our theory. To represent the equation in Bloch type, we have been forced to use the approximations like (3.3) and (3.3)′

---

*) $\Phi_{Bz}\doteqdot\Phi_{Bz}{}^0$; **) Usually $(\Phi_A', \Phi_B')>(\phi_A', \phi_B')$.

†) A-system is F^{19} nucleus and the magnetic moment of F^{19} equals to 2.6273 nuclear magneton.

ut the treatment presented here should be mproved mathematically. The restriction ssuming $I_B=1/2$ is inevitable to represent he equation in linear form of spin operators. ince the experiment of S.M.K. has been one under the circumstance in which theoetical background is obscure, it is desirable o research further in this stage.

References

1) A. W. Overhauser: Phys. Rev. **91** (1953) 476; **92** (1953) 411. A. Abragam: Phys. Rev. **95** (1955) 1729. C. Kittel: Phys. Rev. **95** (1954) 589. T. R. Carver and C. P. Slichter: Phys. Rev. **92** (1954) 212.
2) I. Solomon: Phys. Rev. **99** (1955) 559.
3) A. L. Bloom and J. N. Shoolery: Phys. Rev. **97** (1955) 1261. J. N. Shoolery: Discussions of the Faraday Society no. 19 (1955) 215. W. A. Anderson: Phys. Rev. **102** (1956) 151. B. Herzog and E. L. Hahn: Phys. Rev. **103** (1956) 148. L. R. Sarles and R. M. Cotts: Phys. Rev. **111** (1958) 853.
4) F. Bloch: Phys. Rev. **111** (1958) 841.
5) K. Tomita: Progr. Theor. Phys. **20** (1958) 743.
6) Y. Saito, Y. Masuda and T. Kanda: Spoken at the annual meeting of the Physical Society of Japan (1955). Y. Saito: J. Phys. Soc. Japan **13** (1958) 72.
7) N. Bloembergen and P. P. Sorokin: Phys. Rev. **110** (1958) 865.
8) N. Bloembergen: J. Phys. Soc. Japan **13** (1958) 660.
9) R. K. Wangsness and F. Bloch: Phys. Rev. **89** (1953) 728.
10) F. Bloch: Phys. Rev. **102** (1956) 104; **105** (1957) 1206.
11) A. G. Redfield: Phys. Rev. **98** (1955) 1789. K. Tomita: Progr. Theor. Phys. **19** (1958) 541.

JOURNAL OF THE PHYSICAL SOCIETY OF JAPAN, Vol. 14, No. 8, AUGUST, 1959

On the Dynamic Mechanical Properties of Polymers at Ultrasonic Frequencies in Relation to Their Glass Transition Phenomena

By Yasaku WADA, Hidenori HIROSE, Taro ASANO
Department of Applied Physics, Faculty of Engineering,
University of Tokyo, Tokyo, Japan
and Seita FUKUTOMI
Department of Physics, Faculty of Liberal Arts,
University of Oita, Oita, Japan

(Received April 6, 1959)

Complex Young's modulus, rigidity and bulk modulus are measured at 33 kc/s, 66 kc/s and 1 Mc/s for polystyrene, polymethyl methacrylate, polyvinyl acetate and phenol resin. In each material, the storage modulus-temperature curve has a discontinuity in the slope, irrespective of frequency and type of modulus, at the glass transition temperature T_g determined from thermal expansion. This discontinuity takes place through a strong dependence of the modulus on the specific volume.

Besides, the first three materials exhibit secondary discontinuities at T_g', about thirty degrees below T_g, both in thermal expansion and modulus-temperature curve. Some possible interpretations are given to this secondary discontinuity, resulting in the conclusion that the glass transition occurs over a rather wide range of temperature and is completed at T_g with increasing temperature.

The ratio of the temperature coefficients of the modulus, taken below and above T_g, agrees well with that of volume expansion curve. This is also the case about T_g', being indicative of predominantly energetic nature of elasticity.

The loss factor begins to rise slightly at T_g', then rapidly at T_g as the temperature is elevated, suggesting that local motions of molecular chains are first encountered at T_g'.

The real part of Poisson's ratio seems nearly constant through the temperatures studied, including the glass transition temperature, whereas the imaginary part is found to vanish.

§ 1. Introduction

A very wide class of substances which fall in the supercooled state, such as silicate and selenium glasses, glucose, glycerine, and so on, exhibit glass transition phenomena. Among them, organic substances composed of long chain molecules have so far been most widely investigated.

As a high polymeric substance is cooled down from its rubbery state, the activation energy for the rotation of polymer chains increases as a consequence of decrease in the intermolecular free volume. When the critical temperature is attained where the activation energy for the free rotation of backbone chains becomes so large that the rotation can no more take place within the time of observation, the free volume is frozen in and kept unchanged below this temperature. This temperature is usually called "glass transition temperature" and is the dividing line between glass-like and rubber-like properties of a polymer. Experimentally, the glass transition temperature is in most cases determined from the discontinuity in thermal expansion.

The glass transition of a polymer is usually considered as a predominantly rate and not equilibrium phenomenon. The transition temperature, however, only slightly depends on the rate of cooling within the usual range of rate at least, apparently because the activation energy for molecular rotation, in the neighborhood of this temperature, very rapidly increases with decrease in the free volume. Probably, a change of 1°C corresponds to the change of an order of the magnitude in the relaxation time. From the same reason, this temperature also remains almost constant for either cooling or heating process. The description in a subsequent paper is always given for heating process, namely, for "loosening" of free volume, not for freezing-in.

It has been well confirmed by numerous investigators that a marked change is observed in many physical properties at the glass temperature. Fig. 1 illustrates an over-all behavior of the real and imaginary part of complex modulus, say complex rigidity, of a linear amorphous polymer at constant frequency, together with the volume expansion curve.

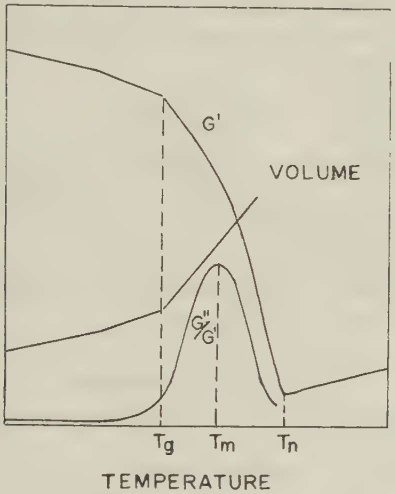

Fig. 1. Over-all behaviors of complex rigidity $G'+iG''$ and specific volume of a linear amorphous polymer near glass transition temperature.

As has been in recent years firmly established[1-7], the storage modulus-temperature curve exhibits a discontinuity in the slope at the glass transition temperature T_g. One of the present authors[4,5] and Work[3] have pointed out that this break takes place through a strong dependence of the modulus on the specific volume and is simply a manifestation of the break in volume-temperature curve at T_g. Consequently, as has been verified by many authors, the break temperature is independent of a wide range of time or frequency, from even the static measurement[6] up to the range of megacycles[5].

In many of the existing reports, the glass transition temperature has often been referred to the temperature where the loss modulus G'' or loss factor G''/G' becomes maximum (T_m in Fig. 1). This temperature is characteristic of the relaxational effect of segmental motions of polymer chains and essentially depends on frequency of observation. Some other authors[8] have given the name of glass transition temperature to the point where G' becomes minimum, in other words, equilibrium rubber elasticity is first encountered (T_n in Fig. 1). These scattered definitions of the transition temperature seem to come from the confusion between the loosening of free volume at T_g and the relaxational phenomena of segmental motions *above* T_g. In as much as the glass transition is a change of state of a substance, if not in the sense of thermodynamics, the transition temperature should be independent of the method or time scale of measurement, if it may depend on the rate of heating or cooling.

The purpose of this paper is, first, to investigate the temperature variation of various types of complex moduli, Young's modulus, rigidity, bulk modulus etc., and to afford a quantitative basis to the above discussions. Second, some suggestions will be given to the anomalies observed in the modulus-temperature curves below the glass transition temperature.

§ 2. Experimental

The real and imaginary parts of complex Young's modulus and rigidity were measured by the composite oscillator method at a frequency of 33 kc/s for all samples and at 66 kc/s for polystyrene alone. Details of experimental techniques of the method have been described in the previous papers.[5,9,10]

Fig. 2 shows a block diagram of the measuring apparatus at 33 kc/s. Essentially, it consists of a device for applying voltage of variable frequency to a composite oscillator system and observing the frequency depend-

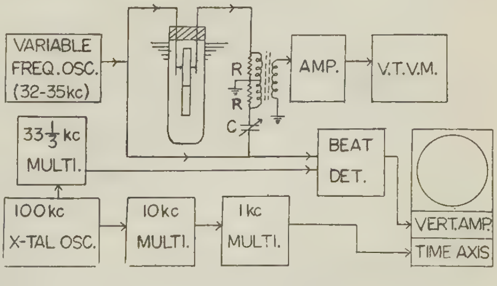

Fig. 2. Block diagram of composite oscillator method at 33 kc/s.

ence of the resultant current. A composite oscillator system was made by cementing a piezoelectric oscillator to a specimen rod of a similar resonant frequency and was set into vibration, the nodal points of the oscillator being supported. The bridge circuit including C and R eliminated the clamped admittance of the oscillator and only the motional admittance *vs.* frequency was read on the vacuum tube voltmeter. The storage modulus and loss factor of the specimen were evaluated from the resonant frequency and half-width of the composite system respectively. The frequency of the oscillator circuit was compared with a standard quartz oscillator and was calibrated to a few cycles by the beat method.

Measurements of Young's modulus were made by use of an ammonium dihydrogen phosphate (ADP) 45° Z-cut longitudinal oscillator, whereas a quartz torsional oscillator was employed in measurements of rigidity. An ADP oscillator has lower density and lower elastic modulus than quartz and consequently has a better acoustic matching with a polymer specimen⁽¹⁰⁾. In the case of measurements of rigidity, an ADP torsional oscillator was not advantageous over quartz on account of the complicated construction of the former.

The cross section of the specimen rod used in the composite oscillator method was identical with the piezoelectric oscillator, $3\times5\,\mathrm{mm}^2$ for longitudinal oscillation and 6 mm in diameter for torsion. The length of the specimen was adjusted so as to make the resonant frequencies of the piezoelectric oscillator and composite oscillator system lie within a few percent. The specimen was cemented to the oscillator by means of styrenated alkyd resin.

The real parts of bulk modulus and rigidity, K' and G', at 1 Mc/s were computed from longitudinal and transversal wave velocities, c_l and c_t respectively, by the following equations:

$$K'=\rho\left(c_l^2-\frac{4}{3}c_t^2\right), \qquad G'=\rho c_t^2, \tag{1}$$

where ρ=density.

Measurements of sound velocities were made using pulse technique (see Fig. 3). A pulsed compressional wave was generated and received in a water tank by a pair of transducers. The time shift of the received signal when a sample was inserted in the path of the beam was compensated by a calibrated delay circuit. From the time shift when the sample plate was set perpendicular to the sound beam, c_l was obtained by means of the relationship

$$c_l=\frac{dc_0}{d-c_0\Delta t}, \tag{2}$$

where d=sample thickness, c_0=velocity in water, and Δt=time shift. When the incident angle θ of sound to the plate was larger than the total reflection angle $\theta_t=\sin^{-1}(c_0/c_l)$, transversal wave alone is transmitted into the plate and c_t was calculated as

$$c_t=\frac{dc_0}{d\cos(\theta-\varphi)-c_0\Delta t\cos\varphi}, \tag{3}$$

where φ is refraction angle and given by

$$\sin\varphi=\frac{c_t}{c_0}\sin\theta\,. \tag{4}$$

The value of c_t was evaluated from Eqs. (3) and (4) by a successive approximation, first assuming an appropriate value for c_t. Δt in eq. (3) is numerically negative for polystyrene in water.

The longitudinal wave velocity was also obtained from the total reflection angle θ_t,⁴⁾,⁵⁾ being in good agreement with that from eq. (2).

Cubical thermal expansion was determined by placing a specimen in the bulb of a Pyrex dilatometer, surrounding it with mercury, and reading the level of mercury in the capillary of the dilatometer as the temperature was varied. The volume of the dilatometer bulb was ca. 15.6 cc and the diameter of the capillary was 2.52 mm. The freezing point of mercury imposed limitations on low temperature measurements.

Density at 15°C was measured by the floatation method in aqueous solutions of sugar.

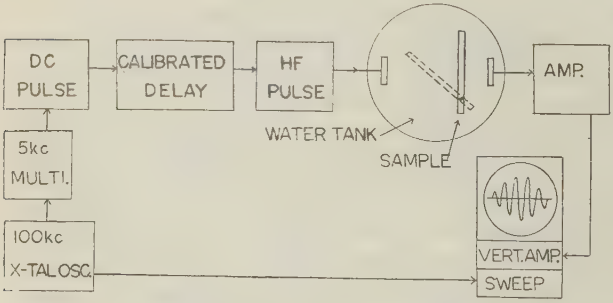

Fig. 3. Block diagram of pulse transmission method.

The rate of heating and cooling was kept almost constant, 10 deg/hr, both in the ultrasonic measurements and in the dilatometry. This rate was sufficient to ensure the uniformity of temperature in the specimen.

§ 3. Sample

Experiments were made on polystyrene (abridged by PS in the following), polymethyl methacrylate (PMMA), polyvinyl acetate (PVAc) and phenol-formaldehyde resin (PhF). PS sample was moulded from pellets, PMMA and PVAc were cast from monomer by block polymerization, PhF was prepared from phenol and formaldehyde of equal mole with ammonium catalyst. Another polystyrene sample (PSa), prepared by block polymerization, was used only in thermal expansion.

Original stocks of each sample except PVAc were in a form of plate, specimens being cut out of the central part of the plate and annealed at 100°C for several hours in order to avoid possible residual stress and volatile impurities. The stock of PVAc was of a form of a short circular rod, thus the measurement of Young's modulus was impossible.

Intrinsic viscosity $[\eta]$ of PS, PSa, PMMA and PVAc was measured at 30°C in benzene solutions. The results are tabulated in Table I, with the viscosity average molecular weight $\bar{M}$ computed by use of the conventional $[\eta]-\bar{M}$ relations.[11)-13)]

Table I. Viscosity average molecular weight and density of samples.

Substance	Symbol	$[\eta]$	$\bar{M}$ (10^5)	ρ (g/cc, 15°C)
Polystyrene	PS	1.15	3.2	1.056
	PSa	0.89	2.3	1.054
Polymethyl methrcrylate	PMMA	3.47	14	1.185
Polyvinyl acetate	PVAc	1.95	5.1	1.194
Phenol formaldehyde resin	PhF	—	—	1.273

Rigidity G' of the same lot of phenol-formaldehyde resin as used in the present experiment was obtained by Hideshima at 0.5 c/s[14)] and it was found that G' becomes proportional to absolute temperature above 120°C. Since $G'=2.8\times10^7$ dyn/cm^2 at 160°C, we can estimate the average molecular weight of a segment between neighboring crosslinks as $M=1.3\times10^3$, using the well known formula $G'=\rho RT/M$, where ρ=density, R=universal gas constant, T=absolute temperature.

§ 4. Volume-Temperature Relation

Fig. 4 shows the volume-temperature curves for five samples. Two samples of polystyrene (PS and PSa) caused no appreciable difference in thermal expansion.

Remarkable discontinuities in the slope of the curves are observed at 81°C for PS, 28°C for PVAc and 53°C for PhF. These points are the glass transition temperature T_g as listed in the literature[15)]. In the case of PMMA, the glass transition is said to be encountered at ca. 100°C,[14)] the high temperature end of this experiment.

The volume-temperature curves in Fig. 4

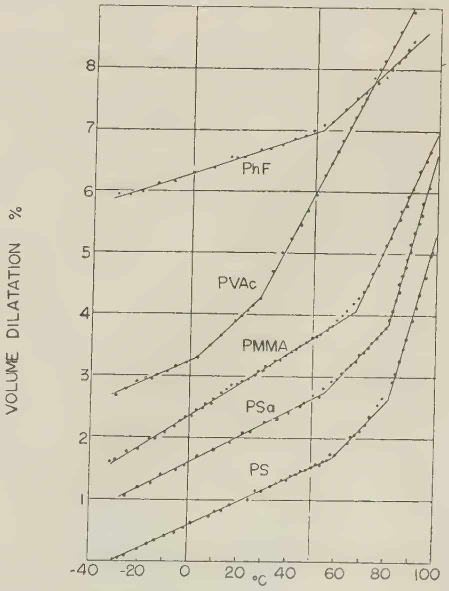

Fig. 4. Volume-temperature curves of five specimens.

are not entirely linear in the range below T_g, but less remarkable discontinuities in the slope can be found at 56°C for PS, 67°C for PMMA and 3°C for PVAc. Possible interpretations to these discontinuities, here named "secondary discontinuity temperature (T_g')," will be later referred to in detail. It might be noted, however, that T_g' lies about thirty degrees lower than T_g for the three polymers.

The behavior of PhF is somewhat different from other three and will be discussed in the last section.

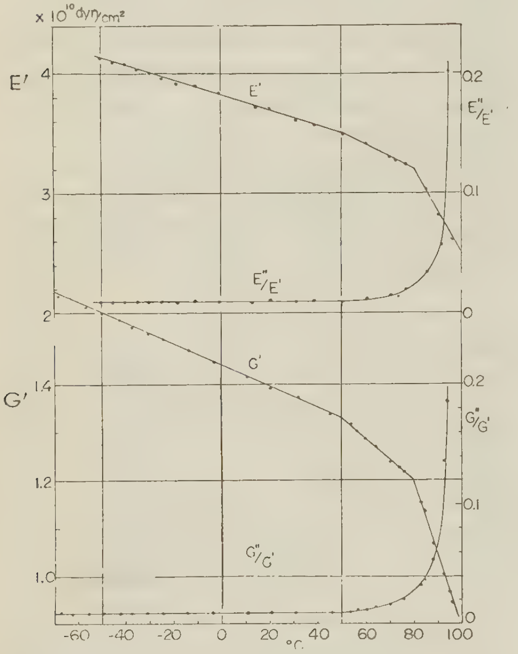

Fig. 5. Complex Young's modulus and rigidity of PS at 33 kc/s.

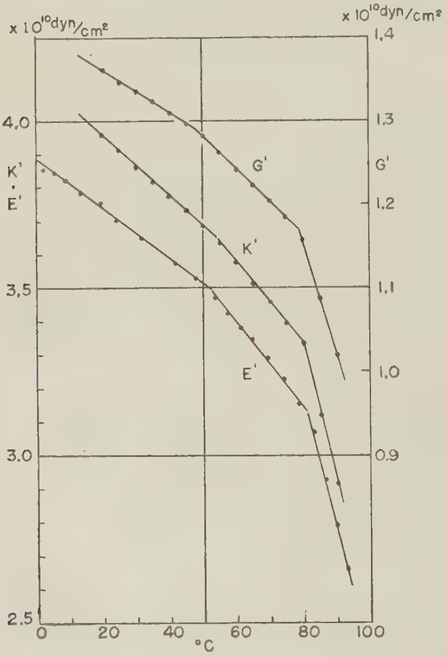

Fig. 6. Young's modulus at 66 kc/s, rigidity and bulk modulus at 1 Mc/s of PS.

§ 5. Temperature Dependence of Storage Modulus

Experimental results of the real part (sto-

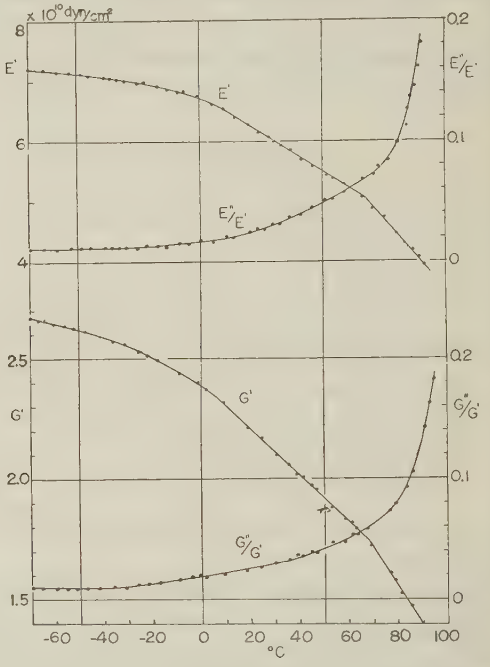

Fig. 7. Complex Young's modulus and rigidity of PMMA at 33 kc/s.

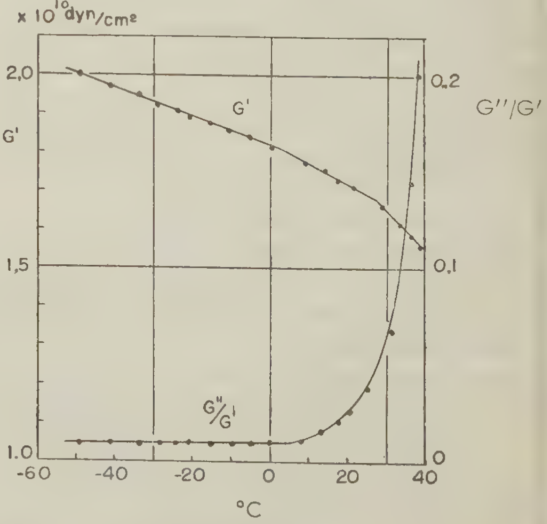

Fig. 8. Complex rigidity of PVAc at 33 kc/s.

rage modulus) of Young's modulus E', rigidity G', and bulk modulus K' are shown in Figs. 5, 6, 7, 8 and 9. K' and G' at 1 Mc/s were obtained only for PS, evaluated from the smoothed curves of c_l and c_t.

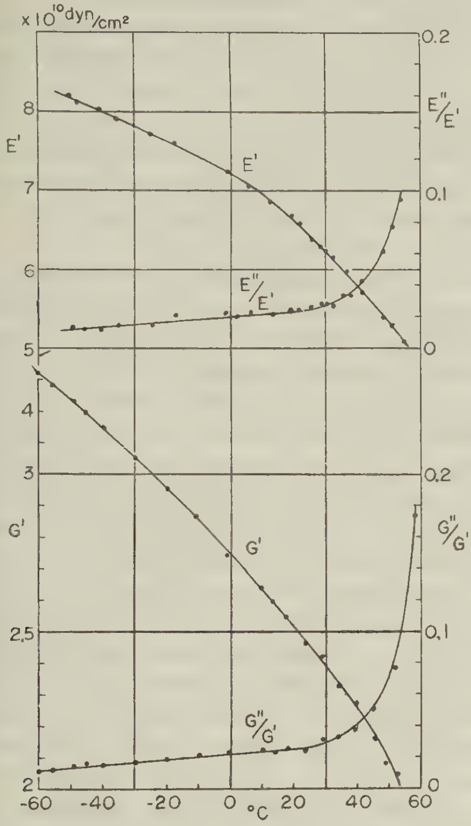

Fig. 9. Complex Young's modulus and rigidity of PhF at 33 kc/s.

As is readily seen in Figs. 5, 6, 7 and 8, E', G' and K' *vs.* temperature curves of PS, PMMA and PVAc all exhibit discontinuities at the temperatures which agree with T_g and T_g' within the experimental accuracy. In the case of PhF alone, a rapid increase in loss made the measurement of modulus impossible above T_g, so the discontinuity was not verified.

In Table II are listed these discontinuity temperatures, T_g and T_g', and the temperature coefficients, α, β and γ, of the linear portions of the curve below T_g', between T_g' and T_g, and above T_g, respectively.

Taking into account a rather large experimental error in the temperature coefficient, it may be permissible to deduce the following rules from the data in Table II. (1) The discontinuity occurs at the same temperature for thermal expansion and for ultrasonic measurement, irrespective of frequency and type of modulus. (2) The temperature coefficients α, β and γ respectively are common among three moduli, E', G' and K'. (3) The ratios β/α and γ/β are the same with volume as with modulus.

According to the simple theory Work[3] has developed, these three rules point to the conclusion that the three types of storage moduli are all of energetic nature and the temperature dependence of moduli is simply a mani-

Table II. Temperatures of discontinuity and temperature coefficients.

Sample	Observed quantity	Temp. of discontinuity (°C)		Temp. coefficients (10^{-3}/deg)			Ratio	
		T_g'	T_g	α	β	γ	β/α	γ/β
PS	volume	56	81	0.19	2.38	1.48	2.0	3.9
	E (33 kc)	50	81	1.7	2.7	13.4	1.6	4.9
	G (33 kc)	50	79	1.6	3.2	13.2	2.0	4.2
	E (66 kc)	53	81	2.0	3.9	13.0	1.9	3.3
	G (1 Mc)	48	79	2.0	3.1	14.3	1.6	4.6
	K (1 Mc)	54	80	2.4	3.2	13.3	1.4	4.2
PMMA	volume	67	—	0.25	0.70	—	2.8	—
	E (33 kc)	67	—	4.5	12.2	—	2.7	—
	G (33 kc)	68	—	5.2	11.1	—	2.2	—
PVAc	volume	3	28	0.19	0.35	0.75	1.8	2.2
	G (33 kc)	3	26	2.0	3.5	10.0	1.8	2.8
PhF	volume	—	53	—	0.13	0.39	—	3.0
	E (33 kc)	—	—	—	7.0	—	—	—
	G (33 kc)	—	—	—	7.8	—	—	—

festation of that of volume. Entropic elasticity and its relaxation effect might add an appreciable contribution to the modulus only well above the temperatures studied.

Fig. 10 shows the real part of Poisson's ratio σ' calculated from E' and G' and from K' and G' by the following equations which are valid for loss factor $\ll 1$ as is our case,

$$\sigma'=\frac{E'}{2G'}-1 \tag{5}$$

and

$$\sigma'=\frac{3K'-2G'}{3(3K'+G')}\,. \tag{6}$$

The σ'-temperature curves have no discontinuity at T_g as well as T_g', being a natural consequence of the rule (2) above mentioned.

As can be seen in the data for PS (Figs. 5, 6 and 10), no frequency dependence of E', G' and σ' is appreciable, being also characteristic of energetic elasticity.

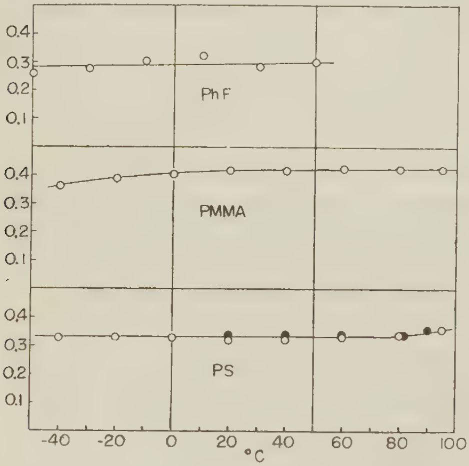

Fig. 10. Real part of Poisson's ratio calculated from E' and G' at 33 kc/s (circle) and from K' and G' at 1 Mc/s (point).

§ 6. Molecular Interpretation of Secondary Discontinuity

It has been suggested by many investigators that the glass transition arises from loosening of free volume accompanied by the free rotation of backbone chains of polymers. Besides this transition, as pointed out in the preceding sections, a secondary discontinuity temperature T_g' was observed below T_g in the case of PS, PMMA and PVAc. This discontinuity probably cannot be ascribed to any shortcomings of experimental procedures, because the discontinuity occurs in quite a similar way both in thermal expansion measurement as well as in measurement of various types of moduli.

In fact, this secondary discontinuity has been observed in most of the existing reports. In the case of polystyrene, for example, Hideshima and Okano[6] have found it in their study of creep compliance. A similar phenomenon is seen in the data of thermal expansion measured by Jenckel and Überreiter[16], Spencer and Boyer[17], though they took no special interest in it.

It is of course difficult to decide experimentally whether a true discontinuity in the slope occurs at T_g', or only a rapid but continuous increase takes place. It may be sure, however, that the partial loosening of free volume begins near T_g'.

There are two possible interpretations to the molecular mechanism involved with this phenomenon, namely, the rotation of side groups of chain polymers and the rotation of the end parts of backbone chains.

The concept of the rotation of side groups has frequently been employed in the interpretation of transitions below T_g. In the present case, this concept encounters some difficulties, if not decisive ones, as follows. First, the C–C bond between benzene ring and another radical has been considered as rigid in a molecule of low molecular weight at least. In the case of polystyrene, this conclusion should be altered, if the side group, benzene ring, actually rotates before the rotation of backbone chains begins. Second, in the case of polymethyl methacrylate, the existing interpretation[18] that the so-called "β-transition" comes from the rotation of side group as a whole should be revised, if $T_g'=$ ca 70°C is due to this rotation.

An alternative possibility to the secondary discontinuity is that a local loosening of free volume first appears at T_g' in regions surrounding chain ends. This idea was suggested by Meares[19] in a study of diffusion of gas in a polyvinyl acetate film. If so, the discontinuity at T_g' should be depressed for the fractionated sample including few number fraction of short chain molecules. In fact, the discontinuity does not take place so markedly in the thermal expansion measurement with well fractionated polystyrenes by Fox and Flory[20]. It may be reasonably assumed that the kinetic motions of segments first begins at T_g' in the vicinity of "network defects," chain ends for example, where the mobility of segments is larger than else, and then these rubber-like regions grow co-operatively as temperature is raised, until at T_g they constitute a continuous phase. This point of view results in the conclusion that the glass transition do not necessarily occur at a very narrow range of temperature, but in a rather wide range.

Anyway, more definite conclusions will probably have to await an investigation with samples of a wider range of chemical constitutions and of known molecular weight distributions. Precise measurements of certain other properties such as line-width of nuclear magnetic resonance will be also very desirable to this purpose.

§ 7. Temperature Dependence of Loss Factor

The data of loss factor are presented in Figs. 5, 6, 7, 8 and 9. For each polymer, two loss factors, E''/E' and G''/G', are almost equal to each other within the experimental error in the temperature studied. This results in the fact that the imaginary part of Poisson's ratio σ'' is nearly zero, following the equation below,

$$\sigma''=\frac{E'}{2G'}\frac{(E''/E'-G''/G')}{1+(G''/G')^2} . \qquad (7)$$

Temperature dependence of loss factor exhibits features quite different from that of storage modulus, because the energetic elasticity greatly contributes to the modulus, but very little to the loss. Therefore, the entropic elasticity in turn, if slightly intermixed with the energetic one, may be revealed clearly in the latter, but not in the former. The rapid increase of loss factor from T_g as found in the data may be safely regarded as a result of onset of segmental motions at T_g. A slow increase is also observed at T_g', affording an additional basis to the conclusion in the preceding section that the motions of chains locally starts at T_g'.

As mentioned in the introduction of this paper, the glass transition temperature has often been referred to the temperature of loss maximum. However, in our standpoint of view, it may be rather reasonable to say that the transition temperature corresponds to the point where the loss factor begins to rise, though this point is experimentally difficult to identify exactly.

Finally, some supplementary remarks will be given about PMMA and PhF. In the case of PMMA (see Fig. 7), a slight increase in the slope of the loss factor-temperature curve is observed at −40°C, which may presumably be allied with the so-called β-transition, though the corresponding maximum of the loss factor shifts to a much higher temperature at ultrasonic frequencies and becomes undistinguishable from the primary glass transition.

For the PMMA specimen, which was cut out of the same stock as the present study, but had been left for two months in an atmosphere of high humidity, a slight peak of the loss factor was observed as illustrated in Fig. 11. As Yamamoto and Wada have said in the previous report⁹⁾, this peak probably arises from water included in the specimen.

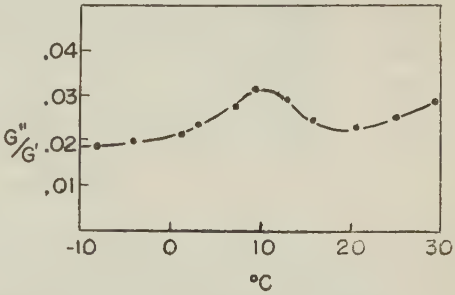

Fig. 11. G''/G' of PMMA including water at 33 kc/s.

The behaviors of PhF are somewhat different from other three samples both in the storage modulus and loss factor. The modulus-temperature curve of PhF (see Fig. 9) has no distinct discontinuity below T_g, but the slope continuously decreases with lowering temperature. The loss factor steadily decreases with decreasing temperature and shows no indication to level off, even at the lowest end of the temperature studied, in contradistinction to other samples. These behaviors may presumably be caused from permanent crosslinks in this polymer. The permanent crosslinks hinder the molecular motions above T_g, resulting in a rather large number of "network defects" in the glassy state and, as a consequence, a perfect freezing-in of free volume is not reached until the temperature is lowered far below T_g.

Acknowledgements

The authors are deeply indebted to Dr. S. Iwayanagi, Messrs. T. Hideshima and K. Okano at the Institute of Physical and Chemical Research for many valuable suggestions during the course of this work. The aid of Dr. K. Kawada at the same institute in obtaining the samples is gratefully acknowledged. Dr. Y. Kunisaki at the Nihon Denki Co. Ltd. furnished ADP oscillators used in in this work, for which we thank him.

References

1) J. L. Melchor and A. A. Petrauskas: Ind. Eng. Chem. **44** (1952) 716.
2) S. V. Subrahmanyam: J. Chem. Phys. **22** (1954) 1562.
3) R. N. Work: J. Appl. Phys. **27** (1956) 69.
4) Y. Wada: J. Appl. Phys. Japan **24** (1955) 159, 287.
5) Y. Wada and K. Yamamoto: J. Phys. Soc. Japan **11** (1956) 887.
6) T. Hideshima and K. Okano: J. Appl. Phys. Japan **27** (1958) 281.
7) L. Verdini: Nuovo Cimento, **5** (1957) 648.
8) R. S. Witte and R. L. Anthony: J. Appl. Phys. **22** (1951) 689.
9) K. Yamamoto and Y. Wada: J. Phys. Soc. Japan **12** (1957) 374.
10) Y. Wada and H. Hirose: J. Appl. Phys. Japan **27** (1958) 652; **28** (1959) 319.
11) T. G. Fox and P. J. Flory: J. Amer. Chem. Soc. **70** (1948) 2384.
12) J. Baxandale, S. Bywater and M. Evans: J. Polymer Sci. **1** (1946) 237.
13) A. Nakajima: Chemistry of High Polymers, Japan **11** (1954) 142.
14) T. Hideshima: private communication.
15) H. A. Stuart: Die Physik der Hochpolymeren vol. **3** (1955) 667.
16) E. Jenckel and K. Überreiter: Z. phys. Chem. A, **182** (1938) 361.
17) R. S. Spencer and R. F. Boyer: J. Appl. Phys. **17** (1946) 398.
18) K. Deutsch, E. A. W. Hoff and W. Redish: J. Polymer Sci. **13** (1954) 565.
19) P. Meares: Trans. Faraday Soc. **53** (1957) 31.
20) T. G. Fox and P. J. Flory: J. Appl. Phys. **21** (1950) 581.

JOURNAL OF THE PHYSICAL SOCIETY OF JAPAN, Vol. 14, No. 8, AUGUST, 1959

X-Ray Study on the Molecular Rotation in Cubic Ammonium Nitrate

By Yasuhiro SHINNAKA

Faculty of Literature and Science, Yamaguchi University

(Received February 27, 1959)

Molecular rotation in cubic ammonium nitrate was studied by using a single crystal obtained by slow cooling from the melt. The observed X-ray scatterings of two different kinds were used: one is the Laue-Bragg scattering and another the diffuse scattering. The first and the second order diffuse scatterings of disk-like shape $(\sin(\varphi/2)/\lambda\times10^{-8}=0.1945,\ 0.3089)$ perpendicular to the direction $\boldsymbol{a}^*$ and its equivalents in the reciprocal lattice were observed in addition to the diffuse scattering due to ordinary thermal vibration. These diffuse scatterings were considered to be due to the rotation of nitrate groups.

By the study on the Laue-Bragg scattering two models of the hindered rotation were selected and it was found by the study on the diffuse scattering that one of these two models is most probable. Further, the correlation among the individual rotating nitrate groups was considered for interpreting the characteristic intensity distribution of the first order diffuse scattering as well as the existence of the second order diffuse scattering. One type of the correlations which is specified by a parameter $\boldsymbol{P}$ denoting the degree of the randomness in the distribution of the rotation-axes was taken into consideration for the analysis of the diffuse scattering. The model thus obtained is closely connected with the model of the rotation in the tetragonal ammonium nitrate and it seems that there still exists correlation not only between the neighbouring nitrate groups but also between remoter ones.

§ 1. Introduction

It is known that ammonium nitrate has five modifications and among them the cubic modification is stable in the temperature range of 125.2°C～169°C (melting point). With respect to the cubic modification the rotation of nitrate groups has been considered by S. B. Hendricks and his coworkers1) from the fact that X-ray powder photographs have required the cubic unit cell containing a single molecule. But, on account of the unreliability of the intensity measurement due to the high rate of crystal growth, they could not obtain any appropriate model of the rotation. Also, with respect to the cubic modifications of other nitrates such as $RbNO_3$, $CsNO_3$ and $T1NO_3$ the rotation of nitrate groups has been considered in the same manner by other workers2),3). On the other hand, by the use of X-ray powder method U. Korhonen4) reported recently that the cubic nitrates $RbNO_3$ and $CsNO_3$ have the larger cubic unit cells containing eight molecules (space group Pa3) in which there does not exist the rotation of nitrate groups.

In a previous paper5) by the present author it was considered that the nitrate groups of ammonium nitrate are in hindered rotation in the tetragonal modification (84.2°C～125.2°C). And so it seems that the rotation is violent in the cubic modification. It is therefore interesting to study more in detail the behaviour of nitrate groups in cubic ammonium nitrate.

In order to avoid the difficulty of the intensity measurement in the powder method and further to get the pattern of X-ray diffuse scattering arising from the disorder of nitrate grougs, in case when the nitrate groups are in rotation, the present study was carried out by using a single crystal of the cubic modification. And the crystal structure of the cubic ammonium nitrate was studied by the Laue-Bragg scattering and the observed diffuse scattering.

In this paper the results derived from the Laue-Bragg scattering and the diffuse scattering will be shown in Parts **I** and **II** respectively.

I. Study on Laue-Bragg Scattering

§ 2. Preparation of Single Crystal

Since single crystals of the cubic modification could not be obtained from other modifications owing to the destruction of crystal in phase transitions, they were prepared as follows. Dry sample placed in a sealed small glass tube was mounted on the sample holder of camera and was repeated to melt and solidify in order to exclude the bubble in the sample. And the sample was melted carefully so as to remain a small crystal and then by slow cooling a crystal grew up along the direction of the axis of glass tube on account of the temperature gradient existing in that direction in the furnace. This procedure was observed with a telescope. After having annealed the sample for about one day at about 150°C a good single crystal was obtained. By such a method crystals with the direction ⟨001⟩ or ⟨011⟩ near the axis of glass tube were often obtained and by the help of Laue photographs the axis of the crystal was corrected so as to have the direction ⟨001⟩ or ⟨011⟩ along the rotation-axis of the camera.

§ 3. Determination of the Structure

The rotation photographs were taken with the direction ⟨001⟩ or ⟨011⟩ vertical by using X-ray Cu$K\alpha$ and Mo$K\alpha$ (filtered). The data require a cubic unit cell of the structure with $a=4.37$Å at 140°C containing a single molecule, and Bragg spots suggesting a larger unit cell could not be observed. The intensities measured by the microphotometer are shown in Table I under the heading $|\overline{F}|_{\mathrm{obs.}}$, the mean structure factor.

Such unit cell suggests that the nitrate groups are in rotation, where the term "rotation" means not only the dynamical rotation but also the statistical disorder. The structure factors were calculated for the assumed several models of the rotation. In all models it was assumed that a nitrate group holds the form of planar equilateral triangle with N–O distance of 1.22Å as found in other nitrates6) and that the atomic scattering factor f_{NH_4} for Cu$K\alpha$ is approximately the same as determined for Mo$K\alpha$ diffracted from NH_4Cl7), and f_{N} and f_{O} of the nitrate group are the same as those used for cubic $RbNO_3$4).

The centers of ammonium groups can be taken at 000 and those of the nitrate groups at $\frac{1}{2}\frac{1}{2}\frac{1}{2}$ statistically. If the correlation between each rotating group is neglected, the several modes of the rotation will be specified by the distribution of the rotation-axes.

At first, the following two models were considered on the basis of the assumption that N atoms of the nitrate groups are at $\frac{1}{2}\frac{1}{2}\frac{1}{2}$ and that the rotation-axes are perpendicular to NO_3 planes through the N atoms;

model (1): the rotation-axes are oriented at random,

model (2): the rotation-axes are parallel to three orthogonal directions ⟨100⟩ and its equivalents,

where the nitrate groups are rotating with constant angular velocity about the rotation-axes.

Table I.

(hkl)	$\lvert\overline{F}\rvert_{\mathrm{obs.}}$	$\overline{F}(1)$	$\overline{F}(2)$	$\overline{F}(3)$	$\overline{F}(4)$	$\overline{F}(5)$
(100)	8.7	−13.0	−10.1	−8.4	−8.7	−9.1
(110)	15.1	24.7	18.1	14.3	16.0	16.2
(111)	5.8	1.8	2.6	3.5	5.2	4.2
(200)	10.0	10.0	10.0	10.0	10.0	10.0
(210)	2.2	4.1	2.6	1.5	2.9	2.4
(211)	2.0	5.9	3.7	2.3	2.4	3.1
(220)	2.4	4.8	2.7	2.5	2.1	3.8
(300)	2.7	2.4	−1.1	−1.9	−1.5	1.4
(221)	3.4	2.4	2.9	3.3	4.3	2.7
(310)	3.5	4.5	4.7	4.2	4.6	2.3
(311)	0	1.4	0.6	0.7	0.8	3.0
(222)	0	4.3	2.5	0.7	0.3	3.2
(320)	0	0.8	1.0	0.4	0.9	1.3
(321)	*v.w.*	4.1	2.7	1.8	2.1	2.1
(400)	*v.w.*	3.8	4.5	3.3	2.6	2.0

$\overline{F}(i)$ represents the calculated mean structure factor for (i) model and all values are arranged relatively by taking $\overline{F}(200)=10.0$.

The calculated structure factors for these models are shown in Table I. They are not in good agreement with the observed ones and it is noticed that among the structure factors of the main reflection planes the calculated $\overline{F}(111)_{\mathrm{cal}}$ of both models are so weaker than the observed one. It is found from several further numerical trials that if the N atom is at $\frac{1}{2}\frac{1}{2}\frac{1}{2}$ such tendency is hold for the other models. Therefore the position of N atoms must be slightly displaced from the body center of cubic unit cell.

Then it was considered to be probable that the nitrate groups take successively some equivalent quasi-stable configurations with the same probability in each unit cell. As to the configurations of the nitrate group which seem to be quasi-stable, the configurations similar to those in the other modifications of ammonium nitrate were chosen as follows.

From the tetragonal modification, the model (3) with twelve equivalent configurations was considered and one of which is shown in Fig. 1. This model is similar to the model (2).

From the orthorhombic modification (32.3°C ~84.2°C) of the type NiAs, the model (4) having eight equivalent configurations was considered and one of which is shown in Fig. 2. This model is similar to that of cubic $RbNO_3$, that is, in cubic $RbNO_3$ these eight equivalent nitrate groups are arranged under the space group Pa3 in larger unit cell. Also it is considered that this model is similar to the model in which the rotation-axes are parallel to the direction $\langle 111 \rangle$ and its equivalents.

From the orthorhombic modification (32.3°C ~−18°C) of the type CsCl, the model (5) having twelve equivalent configurations was considered and one of which is shown in Fig. 3. This model is similar to the model in which the rotation-axes are parallel to the direction $\langle 110 \rangle$ and its equivalents.

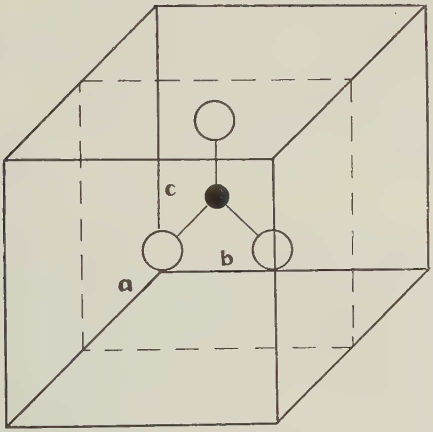

Fig. 1. One of the twelve equivalent configurations of the nitrate group for model (3). Positions of atoms in the nitrate group: N:(0.5, 0.5, 0.5+v); O:(0.5, 0.5, 0.779+v), (0.5, 0.742, 0.36+v), (0.5, 0.258, 0.36+v).

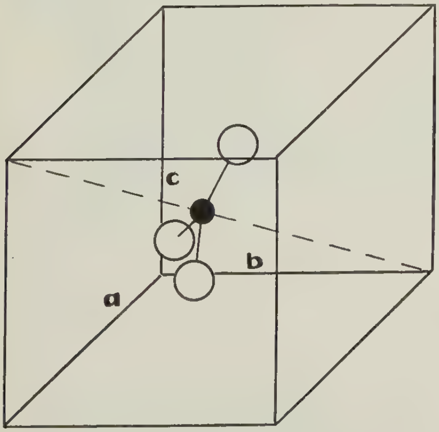

Fig. 2. One of the eight equivalent configurations of the nitrate group for model (4). Positions of atoms in the nitrate group: N:$(x, \bar{x}, x)$; O:$(u, \bar{u}, z)$, $(u, \bar{z}, u)$, $(z, \bar{u}, u)$.

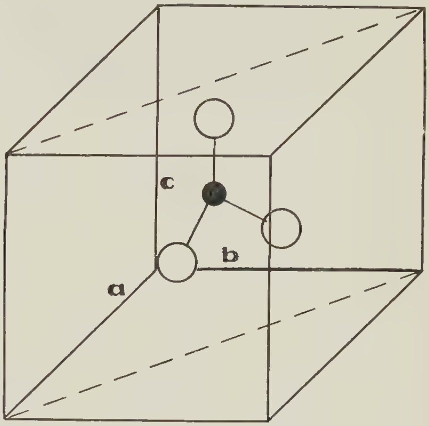

Fig. 3. One of the twelve equivalent configurations of the nitrate group for model (5). Positions of atoms in the nitrate group: N:(0.5, 0.5, 0.5+v); O:(0.5, 0.5, 0.779+v), (0.329, −0.329, 0.36+v), (−0.329, 0.329, 0.36+v).

Table II.

Model (3):	$v=0.05$		
Model (4):	$x=0.554$,	$u=0.44$,	$z=0.782$
Model (5):	$v=0.10$		

In these models the atomic positions were determined so as to be in agreement with the experimental data as good as possible. The atomic positions of each one of equivalent configurations for these models are shown in Table II and the corresponding calculated structure factors are shown in Table I. Among them both the calculated structure factors for models (3) and (4) were in fairly good agreement with the observed ones.

While, it may be still possible that as in the case of $RbNO_3$ the unit cell of ammonium nitrate is larger and contains eight molecules. However, no Bragg spots suggesting a larger unit cell could be observed in the present experiment.

Judging from the above results it can be considered that in the cubic modification the nitrate groups are in rotation and the mode of rotation is quite similar to either of the models (3) and (4). Of course the rotation will be more complex on account of several factors such as correlation, hindrance and thermal vibration. Therefore it is hard to say whether the structure of cubic modification is more closely connected with the structure of tetragonal modification or with that of orthorhombic modification (NiAs type). In order to obtain the more informations on the rotation the observed diffuse scattering will be discussed in the following Part **II**.

In closing this Part **I**, a few words should be added on an anistropic effect of extinction. In many rotation photographs taken with the good crystals annealed enough, it was found that the extinctions in the equatorial reflections, particularly those of {100} and {110}, were often stronger than the extinctions of the other layer lines (see Photo. 1). The ratios of intensity (I) between the reflections of each equivalent plane $\{hkl\}$ in zero layer line and first layer line were measured as follows:

situation of sample	$\{hkl\}$	$\frac{I(\text{zero layer})}{I(\text{first layer})}$
⟨001⟩ vertical	{110}	~1/2
⟨011⟩ vertical	{100}	~1/2

These ratios have been corrected by *rho* factor that depends upon the angle of inclination ρ of the reflecting planes to the vertical rotation-axis. Many factors may be supposed as the cause of this effect, for example, some imperfections in crystal growth, the strain which is likely caused easily by some weak forces on account of the softness of the crystal, and so on. The anisotropic effect of the extinction is now under investigation.

II. Study on Diffuse Scattering

According to the variety of crystal imperfections there are many types of the diffuse scattering[8),9)], so that the interpretation of the observed diffuse scattering is difficult. Among these types only a few experimental researches[10)] and theoretical discussions[11),12)] seem to have been carried out so far on the type corresponding to the molecular rotation in crystal.

The diffuse scatterings observed in the present experiment, in addition to the ordinary diffuse scattering due to thermal vibration, in cubic ammonium nitrate may be considered to be due to the rotation of the nitrate groups. Therefore, the present study may be of interest in that it gives us additional informations on the diffuse scatterings due to the molecular rotation in crystal.

§ 4. Observation of the Diffuse Scattering

Many Laue photographs were taken with cubic axis vertical at about 2° intervals over the whole rotational range by using filtered CuKα and MoKα on cylindrical films (camera radius = 50.7 mm). The interval between each photograph was calibrated by measuring the positions of Laue spots, and the distribution

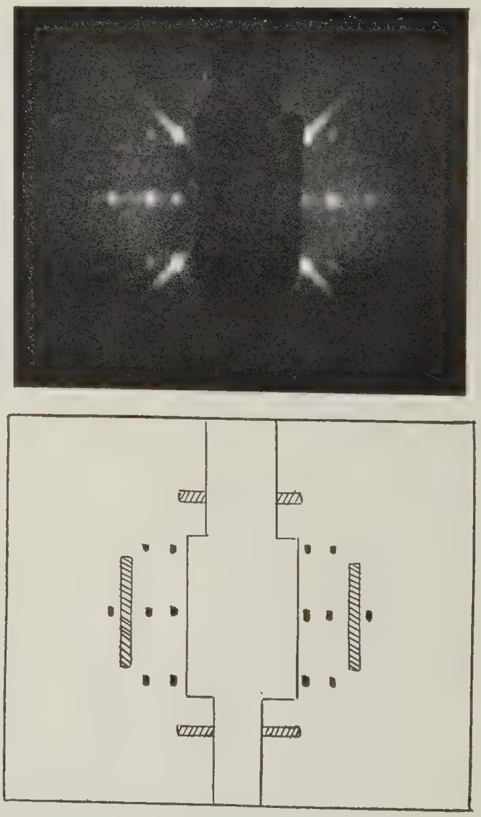

Photo. 1. Rotation photograph taken with cubic axis vertical by using filtered MoKα, showing the anisotropic extinction and the diffuse scattering.

of diffuse scattering in a reciprocal-lattice was obtained by the usual geometrical method.

Photographs 1 and 2 are typical examples of the photographs and Fig. 4 is the illustration of Photo. 2. The obtained reciprocal-lattice representation of the diffuse scattering is shown in Figs. 5 and 6; but the ordinary thermal vibration diffuse scatterings observed in the neighbouring region of the reciprocal-lattice points are omitted. The ordinary thermal diffuse scatterings in the neighbouring region of the reciprocal-lattice points {100}, {110}, {111} and {200} were remarkable, but they had no particular correlation with another disk-like diffuse scattering in question.

In each direction of three primitive translations of the reciprocal lattice ($\boldsymbol{a}^*$, $\boldsymbol{b}^*$ and $\boldsymbol{c}^*$) two disk-like diffuse scatterings were observed

(1)

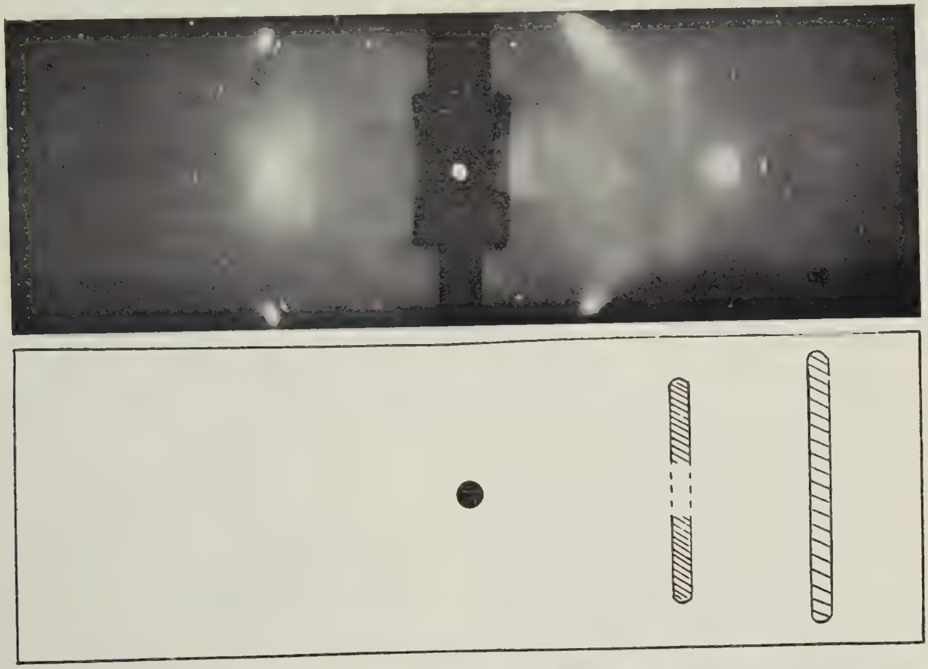

(2)

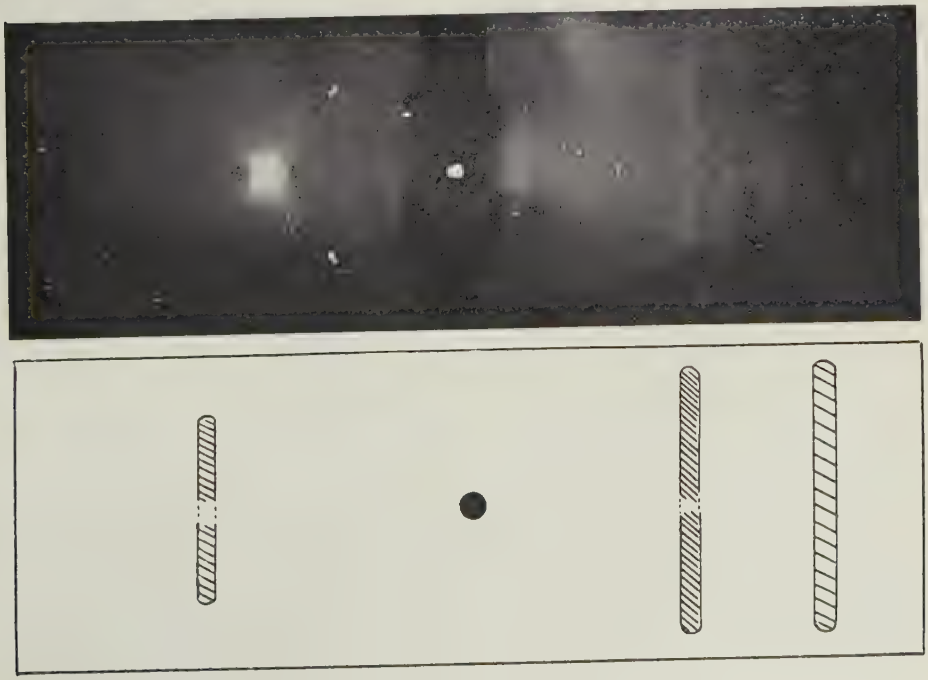

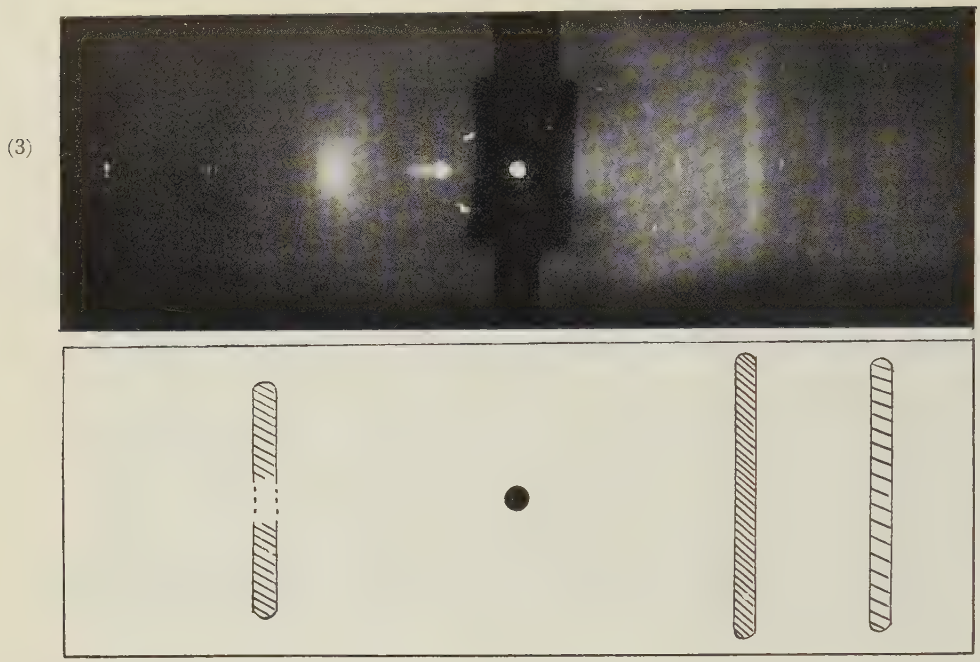

Photo. 2. Photographs showing the variety of the Laue spots and the diffuse maxima when the angle of incidence was changed. Filtered Cu radiation.

to be perpendicular to each direction and hereafter one of them will be called the first order diffuse scattering and the other the second order diffuse scattering. The values of $\sin(\varphi/2)/\lambda\times10^{-8}$ at the centers of the two disk-like diffuse scatterings are 0.1945 and 0.3089 respectively, where λ is the wave length of incident beam and φ an angle of scattering. Though the intensity distribution of these diffuse scatterings could not be determined in detail owing to the weakness of their intensities, it was noticed that the intensity distribution of the first order diffuse scattering was particularly characteristic: the intensity at its central part was weak.

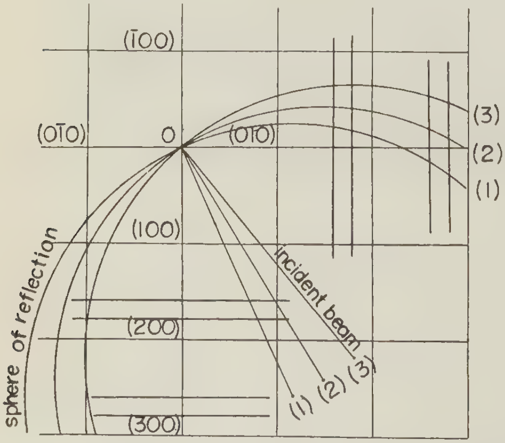

Fig. 4. The reciprocal-lattice diagram corresponding to Photo. 2.

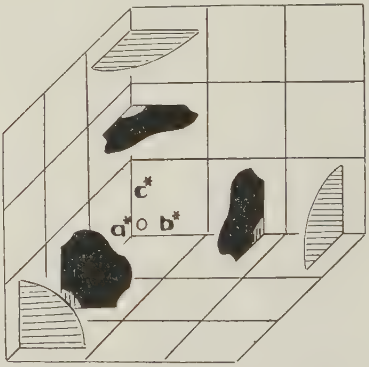

Fig. 5. Schematical reciprocal-lattice representation of the X-ray diffuse maxima.

It seems that the first and the second order diffuse scattering are due to the rotation of the nitrate groups.

§ 5. Interpretation of Diffuse Scattering

As the first step to analyze the observed diffuse scattering, any correlation among the individual rotating nitrate groups was neglected. In this case the intensity I of the diffuse scattering is given by[8),9)]

$$I=K[\overline{|F^n|^2}-|\overline{F}|^2](1+\cos^2\varphi)/2\ , \qquad (1)$$

where K is a constant for a given crystal and the same value of K will be used throughout this paper.

The distribution of the diffuse scattering in the reciprocal lattice were evaluated in several models. It was temporarily assumed for the convenience of the evaluation that the center of each N atom of the nitrate group is at body center in each cubic unit cell as assumed in the first part of Part **I**. In practice such simplification will be admitted, for it is clear from the several numerical trials that the distribution of the diffuse scattering derived from the above assumed models is not so different from the distribution of the similar models obtained in the latter part of Part **I**; the positions of diffuse maxima and the feature of the intensity distribution are not so different except for the absolute value of the intensity. General feature of the diffuse scattering is more sensitive to the kinds of models than to the approximation above mentioned.

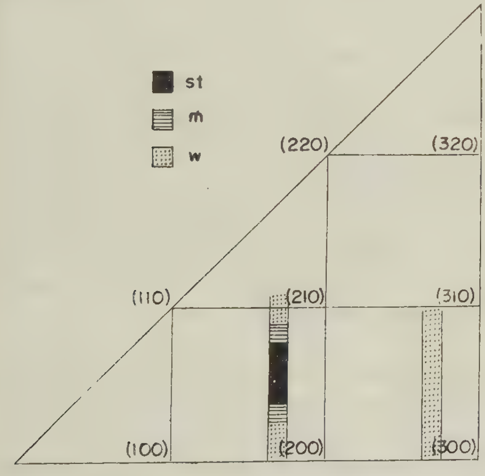

Fig. 6. Reciprocal net showing positions of diffuse maxima in central layer lines of Laue photographs taken with cubic axis vertical.

The models of the rotation evaluated are as follows.

a) When the rotation-axes of the nitrate groups are oriented at random, formula (1) becomes

$$I=Kf_0^2\left[3+6\frac{\sin sr'}{sr'}-9\left(\frac{\sin sr}{sr}\right)^2\right](1+\cos^2\varphi)/2\,, \tag{2}$$

$$s=4\pi\sin(\varphi/2)/\lambda\,, \tag{3}$$

where r is the N–O distance of 1.22Å and r' the O–O distance in a nitrate group. Equi-reflection contours in the reciprocal net $l=0$ is shown in Fig. 7 a).

b) When the rotation-axes are parallel to three directions ⟨100⟩ and its equivalents,

c) when the rotation-axes are parallel to four directions ⟨111⟩ and its equivalents,

d) when the rotation-axes are parallel to six directions ⟨110⟩ and its equivalents,

formula (1) for each model is given in the form:

$$I=Kf_0^2\left[3+\frac{1}{n}\sum_{i=1}^{n}6J_0(sr'\sin\psi^i)-\left\{\frac{1}{n}\sum_{i=1}^{n}3J_0(sr\sin\psi^i)\right\}^2\right](1+\cos^2\varphi)/2\,, \tag{4}$$

where n is the number of rotation-axes of each model, J_0 the Bessel function of order zero and ψ^i the angle between the rotation-axis and $\boldsymbol{h}=\boldsymbol{k}-\boldsymbol{k}_0$ ($\boldsymbol{k}_0$: the wave vector of the incident beam, $\boldsymbol{k}$: the wave vector of the scattered beam). Equi-reflection contours calculated for b), c) and d) models are shown in Figs. 7 b), 7 c) and 7 d).

Among these models, general feature of the diffuse scattering calculated for b) model is most similar to the observed one. Equi-reflection contours for the model (3), one of the two probable models obtained in Part **I** similar to b) model, are also calculated and shown in Fig. 7 e). However, the distributions represented in Fig. 7 b) and Fig. 7 e) are different from the observed one in the following two points: the characteristic distribution of the first order scattering is not represented and the second order diffuse scattering is absent.

It will be found from the above calculation that the diffuse maxima in the reciprocal net for each model appear in the direction of the rotation-axes of each model. And for the purpose of explaining the characteristic distribution of the first order, the steady precessional motion about each of the directions ⟨100⟩ and its equivalents was considered in order to make the directions of the rotation-axes run parallel with the directions of the observed diffuse maxima in the first order diffuse scattering. Moreover, the motions consisting of the combination of the nutation with the precession were considered. But the correspondency of the directions of the diffuse maxima to the rotation-axes exists only in b), c) and d) models, and the distribution obtained by the approximate calculation for these models is similar to that of the weighted mean of the distribution for b), c) and d) models. And any noticeable distribution comparable with that of b) model could not be obtained from these distributions.

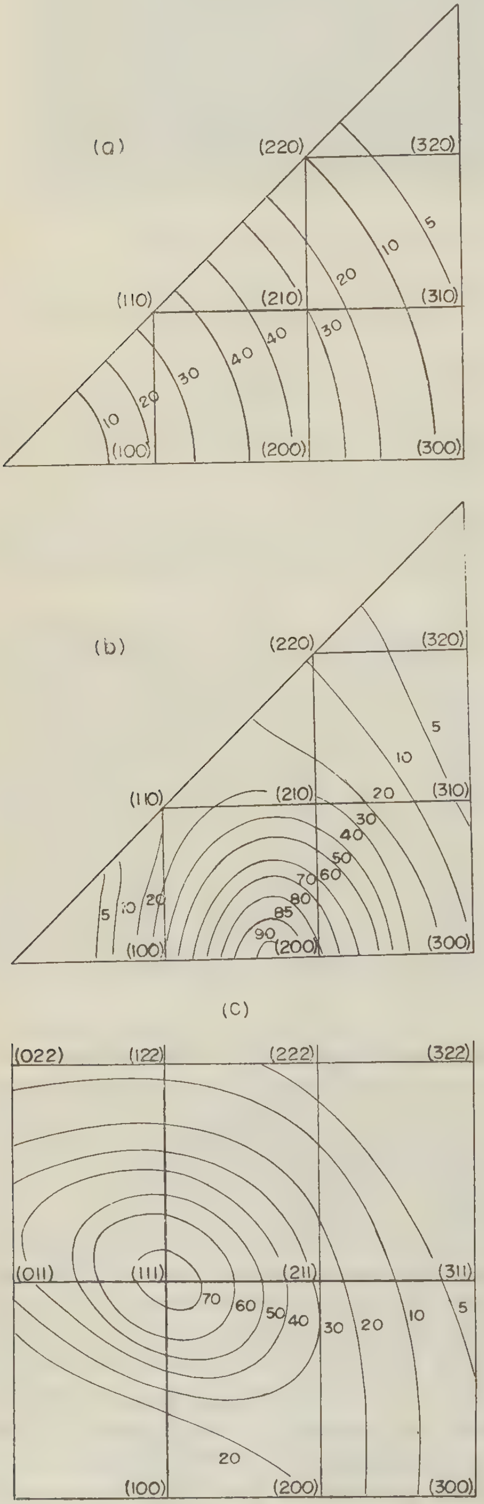

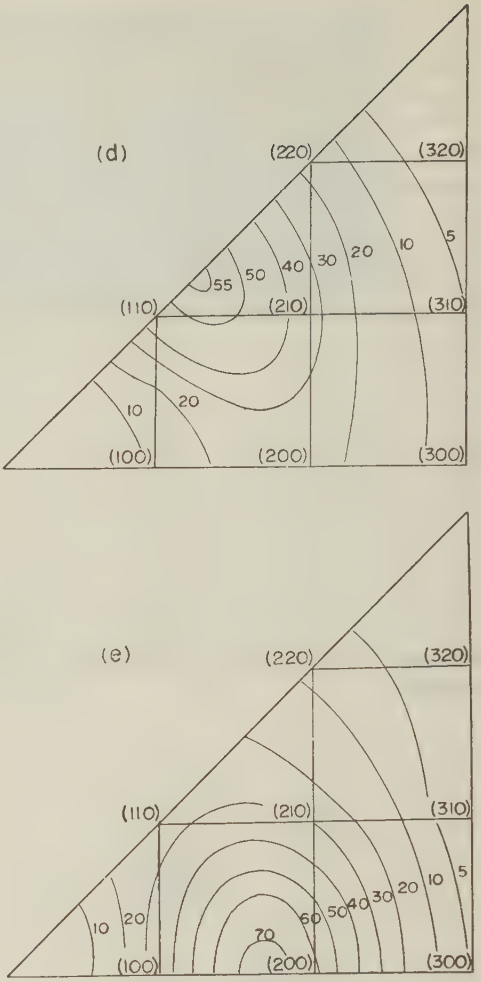

Fig. 7. A set of intensity contours of the models (a), (b), (c), (d) and (3).

The failure may be due to the neglect of the correlation. But it is supposed that b) model is to some extent close to the actual rotation judging from the similarity of the general feature and the position of the first order diffuse scattering in both of the diffuse scatterings. The b) model might be taken as the first approximate model.

As the second step to the analysis, the correlations among the individual nitrate groups were taken into consideration. When the observed diffuse scattering (Fig. 6) was compared with the calculated one for b) model (Fig. 7 b)), there seemed not to exist so strong correlation, but from the fact that the broadness of the observed diffuse maxima seems to be very narrow in contrast with that of the calculated one, it may be assumed that there still exists the correlation not only in the neighbouring nitrate groups but also in the remoter ones. Various types of correlation are supposed to exist, and only a simple case will be taken up here as an example to see how these correlations affect the diffuse scattering. Suppose that, in b) model, each adjacent nitrate group is more likely to have the rotation-axis of different direction than that of the same direction, the phase in the rotation about each axis being however assumed to be independent of one another. The degree of the correlation will be specified by mentioning that the probability of finding out that both nitrate groups in any n, n'th unit cells are rotating about the axes of the same direction, is $\boldsymbol{P}(|\boldsymbol{R}_n-\boldsymbol{R}_{n'}|)$ as a function of the interdistance $|\boldsymbol{R}_n-\boldsymbol{R}_{n'}|$, where $\boldsymbol{R}_n$, $\boldsymbol{R}_{n'}$ are the position vectors of n, n'th unit cells. Now it will be assumed as a temporary measure that the values of $\boldsymbol{P}(|\boldsymbol{R}_n-\boldsymbol{R}_{n'}|)$ at $|\boldsymbol{R}_n-\boldsymbol{R}_{n'}|=a$, $\sqrt{2}a$, $\sqrt{3}a$ are α, β, γ respectively, where a is the axis length of cubic ammonium nitrate, and that the nitrate groups at larger distances have independent directions each other ($\boldsymbol{P}=1/3$). The elementary model b), which has three directions of the rotation-axes and has not any correlation, corresponds to the model for $\alpha=\beta=\gamma=1/3$. Next, the models for $1/3>\alpha>0$, $1/3<\beta<1$ and $1/3>\gamma>0$ will be considered. Of course the model having such rotation is not considered to be so reasonable; even if only the ionic radii of atoms were taken into consideration, improbable arrangements occur in no small probability on account of disregarding the phase relation in rotation, although the chances of taking such improbable arrangements are much less than in b) model which has no correlation.

Now, the intensity of the coherent X-ray scattering for the disorder crystal is in general given by

$$I=I_e\sum_n\sum_{n'}\exp(2\pi i\boldsymbol{h}\cdot\boldsymbol{R}_n-\boldsymbol{R}_{n'})\langle F^n(F^{n'})^*\rangle\,, \tag{5}$$

where

I_e : the Thomson factor,

$\boldsymbol{R}_n$: the position vector of the nth lattice point,

F^n : the structure factor of the nth unit cell,

$\langle\ \rangle$: the mean process under the condition that $|\boldsymbol{R}_n-\boldsymbol{R}_{n'}|$ is fixed,

$\sum\limits_n\sum\limits_{n'}$: summation is taken over all the lattice points.

In the present problem this formula gives

$$\begin{aligned}I=I_e\Big[&\langle F^n(F^{n'})^*\rangle\sum_{\substack{n\ \ n'\\(|\boldsymbol{R}_i|>\sqrt{3}a)}}\exp(2\pi i\boldsymbol{h}\cdot R_n-\boldsymbol{R}_{n'})+\langle F^n(F^{n'})^*\rangle\sum_{\substack{n\ \ n'\\(|\boldsymbol{R}_i|=\sqrt{3}a)}}\exp(2\pi i\boldsymbol{h}\cdot\boldsymbol{R}_n-\boldsymbol{R}_{n'})\\&+\langle F^n(F^{n'})^*\rangle\sum_{\substack{n\ \ n'\\(|\boldsymbol{R}_i|=\sqrt{2}a)}}\exp(2\pi i\boldsymbol{h}\cdot\boldsymbol{R}_n-\boldsymbol{R}_{n'})+\langle F^n(F^{n'})^*\rangle\sum_{\substack{n\ \ n'\\(|\boldsymbol{R}_i|=a)}}\exp(2\pi i\boldsymbol{h}\cdot\boldsymbol{R}_n-\boldsymbol{R}_{n'})\\&+\langle F^n(F^{n'})^*\rangle\sum_{\substack{n\ \ n'\\(|\boldsymbol{R}_i|=0)}}\exp(2\pi i\boldsymbol{h}\cdot\boldsymbol{R}_n-\boldsymbol{R}_{n'})\Big]\,,\end{aligned}\tag{6}$$

where $\sum\limits_{\substack{n\ \ n'\\(|\boldsymbol{R}_i|=a)}}$ denotes the summation taken over the lattice points which satisfy the relation $|\boldsymbol{R}_n-\boldsymbol{R}_{n'}|=|\boldsymbol{R}_i|=a$ and so on.

These summations can be calculated for the given crystal. Each value of $\langle F^n(F^{n'})^*\rangle$ in (6) is given as follows:

$$\left.\begin{aligned}&\langle F^n(F^{n'})^*\rangle_{(|\boldsymbol{R}_i|>\sqrt{3}a)}=|\overline{F}|^2\,,\\&\langle F^n(F^{n'})^*\rangle_{(|\boldsymbol{R}_i|=\sqrt{3}a)}=\frac{(3\gamma-1)}{2}\left\{\frac{1}{3}(|F_1|^2+|F_2|^2+|F_3|^2)-|\overline{F}|^2\right\}+|\overline{F}|^2\,,\\&\langle F^n(F^{n'})^*\rangle_{(|\boldsymbol{R}_i|=\sqrt{2}a)}=\frac{(3\beta-1)}{2}\left\{\frac{1}{3}(|F_1|^2+|F_2|^2+|F_3|^2)-|\overline{F}|^2\right\}+|\overline{F}|^2\,,\\&\langle F^n(F^{n'})^*\rangle_{(|\boldsymbol{R}_i|=a)}=\frac{(3\alpha-1)}{2}\left\{\frac{1}{3}(|F_1|^2+|F_2|^2+|F_3|^2)-|\overline{F}|^2\right\}+|\overline{F}|^2\,,\\&\langle F^n(F^{n'})^*\rangle_{(|\boldsymbol{R}_i|=0)}=\overline{|F^n|^2}\,,\end{aligned}\right\}\tag{7}$$

where F_i $(i=1, 2, 3)$ is the mean structure factor of the unit cell with only i rotation-axis.

Thus the formula (6) becomes finally

$$I=I_1+I_2\ , \tag{8}$$

with

$$I_1=I_e|\overline{F}|^2\sum_{n}\sum_{n'}\exp(2\pi i\boldsymbol{h}\cdot\boldsymbol{R}_n-\boldsymbol{R}_{n'})\ , \tag{9}$$

$$\begin{aligned}I_2=I_eN\Big[\overline{|F^n|^2}-|\overline{F}|^2+\Big\{\frac{1}{3}(|F_1|^2+|F_2|^2+|F_3|^2)-|\overline{F}|^2\Big\}\Big\{(3\alpha-1)\sum_{\substack{i=1\\(|\boldsymbol{R}_i|=a)}}^{3}\cos 2\pi\boldsymbol{h}\cdot\boldsymbol{R}_i\\ +(3\beta-1)\sum_{\substack{i=1\\(|\boldsymbol{R}_i|=\sqrt{2}\,a)}}^{6}\cos 2\pi\boldsymbol{h}\cdot\boldsymbol{R}_i+(3\gamma-1)\sum_{\substack{i=1\\(|\boldsymbol{R}_i|=\sqrt{3}\,a)}}^{4}\cos 2\pi\boldsymbol{h}\cdot\boldsymbol{R}_i\Big\}\Big]\ ,\end{aligned} \tag{10}$$

where I_1 represents the lattice spectra and have been discussed in Part **I**; I_2 represents the diffuse scattering and N the total number of the lattice points. In the calculation of I_2, I_eN was replaced by $K(1+\cos^2\varphi)/2$ as done in formula (1).

Three parameters α, β and γ were chosen so as to satisfy the experimental data as best as possible. The calculated intensity contours are shown in Fig. 8 a) ($\alpha=0.13$, $\beta=0.37$, $\gamma=0.33$). And also the intensity contours were derived in the same way from the model (3) obtained in Part **I**. The obtained contours are shown in Fig. 8 b) ($\alpha=0.13$, $\beta=0.35$, $\gamma=0.33$).

These intensity contours as shown in Figs. 8 a), 8 b) have the characteristic feature of the intensity distribution of the observed first order diffuse scattering and show the possibility of the appearance of the second order diffuse maxima by taking such a correlation into consideration. From this point of view, the present model is considered to be more appropriate as the model of the rotation in cubic ammonium nitrate than the elementary b) model. However the positions of the first order and the second order maxima are slightly different from the observed ones. The cause of this discrepancy may be chiefly due to the approximation of the correlation. The correlation, especially, the phase differences among the individual rotating nitrate groups and the correlation between remoter ones will have to be taken into consideration. Therefore a significant meaning will not be given to the values of these parameters α, β and γ, but they will still be useful to see the degree of the correlation.

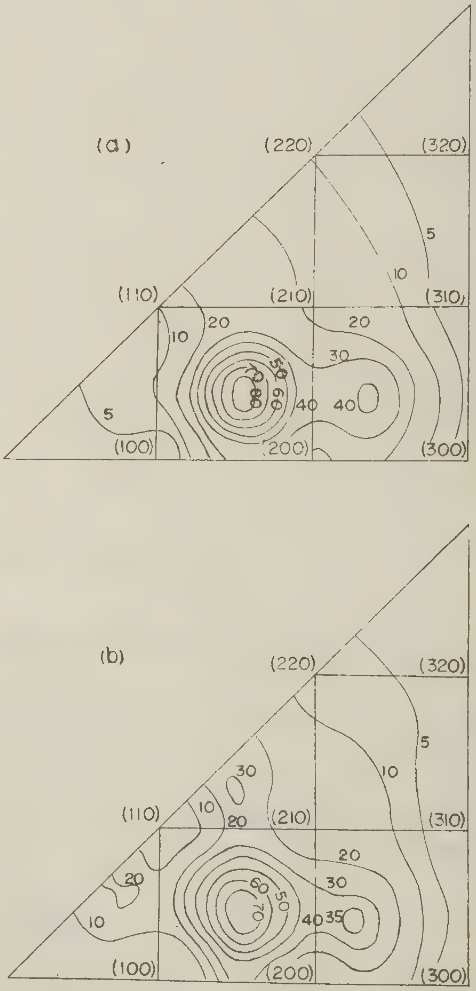

Fig. 8. A set of intensity contours of the models in which the correlation is taken into consideration by introducing three parameters α, β and γ.
(a) $\alpha=0.13$, $\beta=0.37$, $\gamma=0.33$.
(b) $\alpha=0.13$, $\beta=0.35$, $\gamma=0.33$.

§ 6. Discussion

From the analysis of the diffuse scattering in Part **II**, it is considered that the assumption that the diffuse scattering is due to the disorder of nitrate groups is correct. Therefore, with respect to the structure of the cubic ammonium nitrate, the model (3) in Part **I** which has a sort of correlation as discussed in § 5 of Part **II** is considered to be most probable between two models which had been left undetermined in Part **I**. This model is best connected with the tetragonal modification among various modifications in ammonium nitrate.

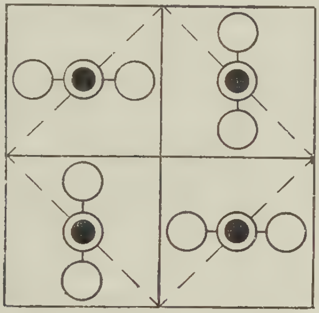

Fig. 9. Showing the arrangement of the nitrate groups in the tetragonal modification projected on (001). Full line represents the unimolecular pseudocell and broken line the true unit.

When, in the tetragonal modification, the unimolecular pseudocells are considered, the rotation-axes are arranged regularly as shown in Fig. 9, in which the rotation-axes of two directions ⟨100⟩ and ⟨010⟩ are arranged so as to have the different directions in each neighbouring unit cell. In the present model of the cubic modification the rotation-axes are arranged almost at random; namely, the rotation-axes of three directions ⟨100⟩, ⟨010⟩ and ⟨001⟩ are arranged under the weak correlation of the tendency similar to that in the tetragonal modification. Such behaviour of the nitrate group is very different from that in other nitrates such as $NaNO_3$⁶⁾ $KNO_3$⁶⁾, $RbNO_3$⁴⁾ and $CsNO_3$⁴⁾.

In general it cannot be expected that neighbouring groups will rotate independently of one another in crystals. The correlations among the rotators exert a great influence on the diffuse scattering. In the case of thermal vibration, the thermal diffuse scattering cannot be interpreted at all without taking the correlation into consideration, but it is considered from this study that the diffuse scattering due to the molecular rotation in most crystals will be able to find in itself some detectable amounts of the feature which will be expected to arise when correlation is neglected. Therefore, it is expected that the diffuse scattering is useful for determining the mode of the rotation and the correlation among the rotators.

With respect to the rotation of the nitrate groups, the more complex mechanism are to be considered in cubic ammonium nitrate. In order to obtain more informations about the rotation it is hoped to have the more detailed intensity measurement and the informations of interatomic forces. And also the study on an anistropic diffuse scattering expected in the tetragonal modification will be useful to find how the phase differences between the rotating nitrate groups affect the diffuse scattering. This subject is now under investigation.

The author expresses his cordial thanks to Prof. K. Tanaka of Kyoto University for his kind guidance and discussion throughout the course of this research. He also wishes to thanks Mr. M. Minami and Mr. G. Nakagawa for their assistance. A part of this work was supported by the Scientific Research Expenditure of the Ministry of Education.

References

1) F. C. Kracek, E. Posnjak and S. B. Hendricks: J. Amer. Chem. Soc. **54** (1932) 2766.
2) C. Finbak and O. Hassel: Z. phys. Chem. **B**, **35** (1937) 25.
3) S. Sato: J. Sci. Res. Inst. (Tokyo) **48** (1954) 59.
4) U. Korhonen: Ann. Acad. Sci. Fenn. **A**, **1** (1951) 102; **A**, **1** (1953) 150.
5) Y. Shinnaka: J. Phys. Soc. Japan **11** (1956) 393.
6) P. E. Tahvonen: Ann. Acad. Sci. Fenn. **A**, **1** (1947) 42; **A**, **1** (1947) 43; **A**, **1** (1947) 44.
7) R. W. G. Wyckoff and A. H. Armstrong: Z. Krist. **72** (1929) 319.
8) W. H. Zachariasen: *Theory of X-ray Diffraction in Crystal* (Wiley, New York, 1945).
9) S. Miyake: *Theory of X-ray Diffraction* (Asakura Press, Tokyo, 1949) (in Japanese).
10) T. Oda: X-rays **4** (1945) 2; **5** (1948) 26; **6** (1950) 15 (in Japanese).
11) T. Matsubara: X-rays **6** (1950) 7 (in Japanese).
12) M. Atoji, T. Watanabe and W. N. Lipscomb: Acta Cryst. **6** (1953) 62.

JOURNAL OF THE PHYSICAL SOCIETY OF JAPAN Vol. 14, No. 8, AUGUST, 1959

On the Anomalous Dispersion of n-Primary Alcohols

By Kenjiro ASAI

Department of Physics, Faculty of Science, Kyoto University

(Received May 2, 1959)

Mechanisms proposed for the dielectric anomaly observed in the low temperature form of *n*-primary alcohols are re-examined, considering especially the influence of thermal history of a sample. The slowly cooled sample gives the longer relaxation time τ and wider distribution of τ than the rapidly cooled one. The activation energy for the dipole orientation depends upon the number of carbons in the alcohol molecule. Results obtained are different from those of previous investigators, but a reasonable model is obtained for this Debye-type abnormal dispersion.

§ 1. Introduction

The dielectric properties of long-chain n-primary alcohols have been investigated by many researchers,[1~5] but they dealt only with the "waxy form" (i.e. α form). Systematic investigation on the low temperature form have done by Meakins and others[6~9] for a series of *n*-primary alcohols. These works are interesting on account of revealing the existence of the abnormal dispersion of Debye-type in the low temperature form, and offering a model of co-operative orientation of O–H···O chain formed by the hydroxyl groups of alcohol molecules. Dryden[8] obtained a value of about 15 Kcal/mol for the activation energy of dipolar orientation, irrespective of the number of carbon atoms in alcohol molecules.

Independently, Takamatsu[10] observed an abnormal dispersion of Debye-type in the low temperature form of C$_{32}$ alcohol, and gave a value of 26.4 Kcal/mol for the activation energy. He explained this result by torsional motion of alcohol molecules. Two different experimental results and corresponding models were presented, namely the co-operative orientation model and single molecule model.

In order to examine these apparently contradicting results, a study on the dielectric properties of n-primary alcohols has been carried out for a series of different carbon numbers which were obtained by synthesis.

§ 2. Experimental Procedure

The measurements were made on eleven *n*-primary alcohols (C$_{18}$, C$_{21}$, C$_{22}$, C$_{27}$, C$_{28}$, C$_{29}$, C$_{31}$, C$_{32}$, C$_{33}$, C$_{34}$, C$_{35}$). Methods of preparation of samples will be explained in another paper.[11]

The temperature and frequency dependencies of dielectric constant and loss were measured by bridge method for the frequency range 50 c/s∼50 Kc/s, and for the frequency range above 100 Kc/s Q meter was used. The phase transformation caused by temperature change was also examined by X-ray diffraction by other members in our laboratory. Dielectric measurements were done referring to the results of X-ray investigation. Data on the phase change of these alcohols are given in Table I, in which α form is a high temperature form and β, γ and δ forms are low temperature modifications. Hitherto α form has been considered to be vertical form with rotational molecular motion about the long axis of the molecule, but by the present structure analysis of a single crystal it was found to be a tilted form. β is a vertical form and γ is a tilted form, the latter having been often designated as β_2 by Smyth and others. Another tilted form δ exists in the odd members above C$_{31}$. More detailed informations about the crystal structures and polymorphism of these alcohols have been given in other papers[12~14]. The values in Table I were obtained by X-ray photographs recording continuously the phase changes of alcohols, so the accuracy of them is not so good, being about ±1°C, as restricted by the construction of X-ray camera. The value in the brackets are those obtained in cooling stage and the bars in the columns show that such transformations do not occur in either case of heating or cooling.

Sample was melted and solidified in a test condenser which was made from copper plated with nickel. Cooling speed from the

Table I.

Number of carbon atoms	Transformation temperature (°C)				
	$T(\rightleftarrows\alpha)$	$T(\gamma\rightleftarrows\alpha)$	$T(\delta\rightleftarrows\alpha)$	$T(\alpha\rightleftarrows\text{Liq.})$	$T(\gamma\rightleftarrows\text{Liq.})$
18	49 (46)	52 (—)		57 (55)	
21	60 (54)			68 (65)	
22		67 (61)		72 (67)	
27	75 (70)			80 (78)	
28		— (75)		— (80)	82 (—)
29	79 (72)			82 (80)	
31			81 (76)	86 (85)	
32		— (83)		— (86)	88 (—)
33			85 (80)	89 (87)	
34		— (86)		— (88)	90 (—)
35			87 (82)	90 (89)	

molten state to solid phase was varied from 0.5°C/min to about 100°C/min.

§ 3. Results and Discussion

Typical results on the frequency dependencies of dielectric constant and loss are given in Fig. 1. In this case, sample was cooled rather slowly. ϵ'' and ϵ' decrease gradually with increasing frequency in the frequency range of observation. This result is very different from the results reported by Meakins and others. Namely, the marked loss maximum reported by them was not observed in this frequency range. Such tendency did not change so remarkably by varying the temperature to transformation point. This characteristic was commonly observed for every n-primary alcohol in its low temperature form.

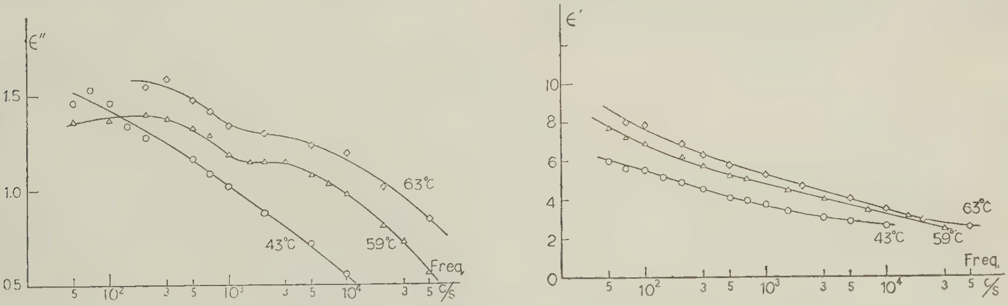

Fig. 1. Frequency dependencies of ϵ'' and ϵ' of $C_{34}H_{69}OH$. The cooling rate from the melt is about 0.5°C/min.

The discrepancy between the experimental results obtained by Meakins and by the present author seems to depend on the difference in the treatment of samples. Meakins and others pulverized the solidified alcohol and pressed it in the form of a circular disk, and measured with it between mercury electrodes. Such procedure does not seem to be adequate in considering a sample as uniform dielectric material. Moreover, the intimate contact at the interfaces between sample and electrodes will not always be secured. Heterogeneity in dielectrics and loose contact at the electrode surface give sometimes confusing results. It is known that *n*-alcohol gives occasionally several modifications of crystal structure with varieties in tilt angle of *c*-axis by rolling. In spite of these confusing factors in experimental procedure, the explanation given by Meakins and Sack[15), 16)] is very interesting and seems to be fruitful. They considered the co-operative rotation of dipoles, connected to each other by hydrogen bonds, as a cause of Debye-type abnormal dispersion observed in their measurements for the low temperature form of C_{18}, C_{22} and C_{26} alcohols.

The curves given in Fig. 1 are very different from the usual ε″–frequency curves indicating Debye-type dispersion. But quite different result was obtained in the case of a rapidly cooled sample of the same material (Fig. 2). Typical Debye-type dispersion curves were observed as in the case of the measurements by Meakins and others.

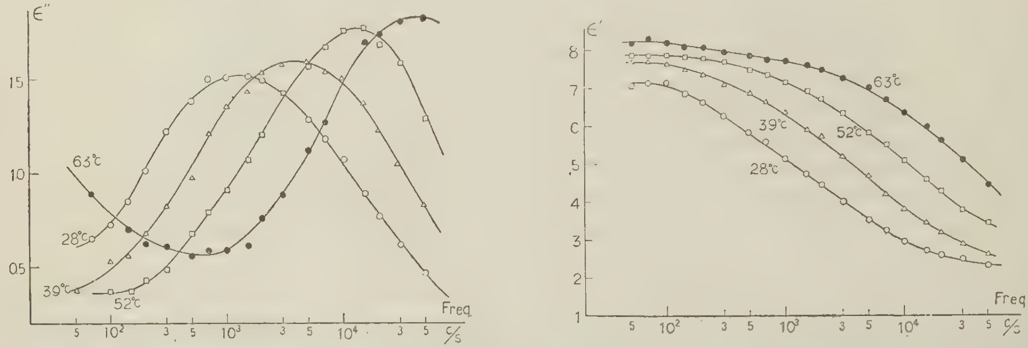

Fig. 2. Frequency dependencies of ε″ and ε′ of $C_{34}H_{69}OH$. The cooling rate from the melt is about 50°C/min.

Next, this sample was annealed at a temperature a few degrees below the melting point. The shift of maximum of ε″–frequency curve to low frequency side was observed by annealing (Fig. 3). Such influence of the heat treatment of the sample upon the dielectric properties of *n*-alcohols suggests the correctness of co-operative orientation mechanism. According to this models, a chain of hydroxyl groups of alcohol molecules connected to each other by hydrogen bonds changes its direction by successive orientation of neighbouring molecules. Therefore, the relaxation time of dipole orientation of a chain depends upon the number *n* of hydrogen bonds included in the chain. For example, Sack[16] gave a result that the relaxation time is proprotional to n^2 and polarization is proportional to n^3. He did not give any estimation on the size of the region in which co-operative orientation occurred. However, the length of the hydroxyl chain would not exceed at most the distance between the neighbouring defects in the chain. Hence the relaxation time seems to be controlled by the distribution of the lattice imperfections in a crystal. Moreover, the effect of the size of crystallites in a sample might be taken into account. These factors will be affected appreciably by the condition of crystal formation, e.g., the cooling speed from the melt. So the dependency of the dielectric behaviour on the thermal history of a sample will be explained by the change of the relaxation time. Namely, the curves illustrated in Fig. 1 seems to correspond to the high frequency parts of the Debye-type dispersion curve with long relaxation time, and they shift to high frequency side in Fig. 2 corresponding to the shortening of relaxation time, as a result of the increase of defects in a hydroxyl chain.

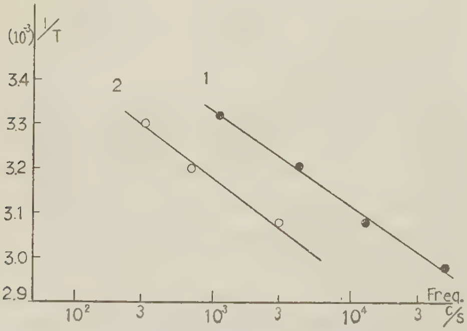

Fig. 3. Temperature dependency of f_m, the frequency of loss maximum, for $C_{34}H_{69}OH$. (1): Rapidly cooled sample. (2): Annealed sample.

In a word, the region of abnormal dispersion would exist at far below 50 c/s for slowly cooled sample, but it seems to come into the present measuring frequency region by rapid cooling. Some defects will be excluded by annealing. This in turn extends the O–H···O chain. The variation of relaxation times illustrated in Fig. 3 will be explained by such mechanism.

As a result of co-operative orientation, the distribution of the relaxation times will become broader than that in the case of single molecule orientation. The variation of Cole diagram is illustrated in Fig. 4 for quenched and annealed samples. Two remarkable effects brought by annealing are recognized in this figure. The first point is the increase of ϵ_s' and the second is the increase of α which expresses the distribution of relaxation times. For the slowly cooled samples ϵ_s' and α increased in more degree and $\epsilon'-\epsilon''$ diagram varied sometimes from Cole-Cole type to Davidson-Cole type. Namely, it is considered that the formation of a new group of relaxation times occurred.

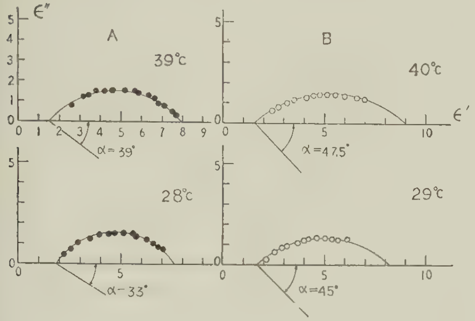

Fig. 4. Cole diagrams for $C_{34}H_{69}OH$. (A): rapidly cooled sample. (B): annealed sample.

The temperature dependencies of ϵ' and ϵ'' are also interesting. As an example, the curves for $C_{32}H_{65}OH$ are given in Fig. 5. The most remarkable feature is the rapid increase of dielectric constant with temperature, especially in the range above 60°C. Such temperature dependency might exist in the lower members of the series. But it was covered by the occurrence of the phase transformation from β or γ to α. As is seen in Table I, such phase transformation does not occur in heating stage for the higher members of even group than $C_{28}H_{57}OH$. So the above mentioned behaviour was fully developed without disturbance by phase transformation for such longer alcohols and it is recognized that such tendency is the characteristic to the low temperature forms of longer alcohols. Surely, the values of dielectric constant depend upon the frequency of the measurement corresponding to the Debye type dispersion mechanism explained previously. As is expressed in Fig. 4, a sample obtained by rather slow cooling from the melt gives a very wide distribution of relaxation times. Considering such fact, the temperature dependency of ϵ' may be expressed schematically as in Fig. 6. Namely the observed curve will be expressed by the superposition of different curves with different relaxation times. A comparison with two kinds of samples obtained by different cooling rates from the melt is also given in Fig. 7. This result supports the above explanation.

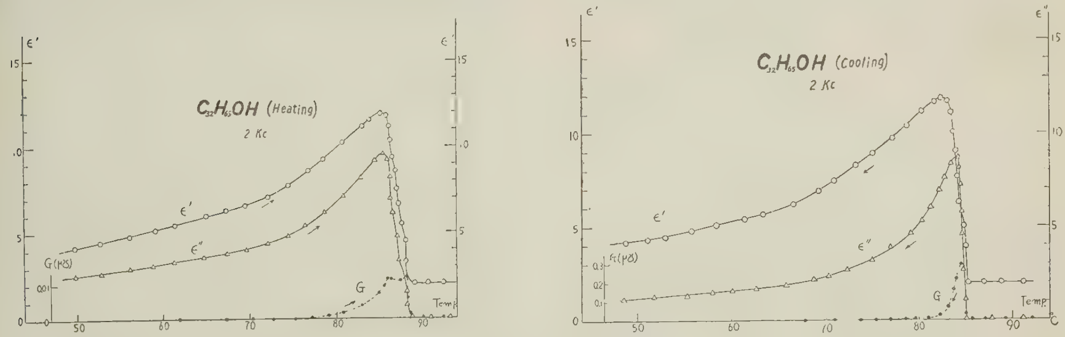

Fig. 5. Temperature dependencies of ϵ'' and ϵ'. Electric conductivity of the sample is also plotted in the figures by the notation G, but the scales are altered case by case, depending on the existence or non-existence of α-phase. The value of ϵ'' is A.C. value. (D.C. conductivity had been subtracted). (a): Heating stage, (b): Cooling stage.

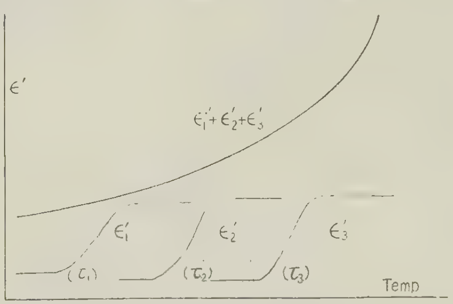

Fig. 6. Schematic diagram indicating the temperature dependency of dielectric constant of n-alcohols.

Namely, for rapidly cooled sample loss maximum shifts to low temperature side in temperature scale, corresponding to the shortening of τ, and therefore the rapid increase of ϵ' is not seen for this sample in contrast with the slowly cooled one.

As additional factors contributing to the increase of ϵ' with temperature rise, the partial break in hydroxyl chain and the usual thermal activation process may be considered. The former brings the shortening of relaxation time. In order to check the influence of such factors, the similar measurement was carried out at higher frequency of 1 Mc/s which is far away from the dispersion region (Fig. 8). The result for a single crystal of $C_{28}H_{57}OH$ also gives a similar curve (Fig. 9), though the accuracy of the measurement was not so good on account of the small size of the crystal (being about 30μ×0.5 mm×5 mm). Referring to these experimental results, the influence of the variation in the molecular freedom with the increase of temperature does not seem to play an important role at least up to the temperature close to the melting point.

The dielectric properties of n-primary alcohols have been noticed by previous investigators on account of the anomaly of α phase. But the high value of dielectric constant of this phase seems to be only apparent due to the high electric conductivity, and some discussion on this problem was made previously3). The high dielectric constant of the low temperature form is, however, the net value essential to n-higher alcohols. An interesting feature is shown in Fig. 10. The dielectric constant increases distinctly by the transformation to the low temperature form from the high temperature one, quite contrary

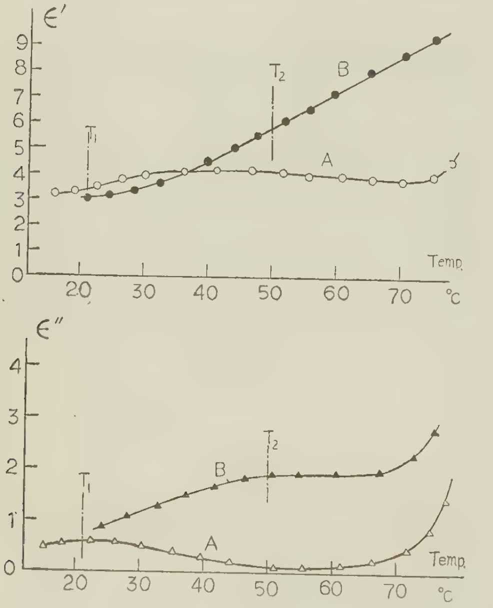

Fig. 7. Comparison of the dielectric properties between two different samples of $C_{35}H_{71}OH$. The temperature regions of low temperature form are only indicated. (A): Rapidly cooled sample. (B): Slowly cooled sample. T_1 and T_2 are the temperatures of loss maximum at this measuring frequency, 2 Kc/s, for (A) and (B) respectively, obtained by interpolation of f_m-1/T curves for each sample.

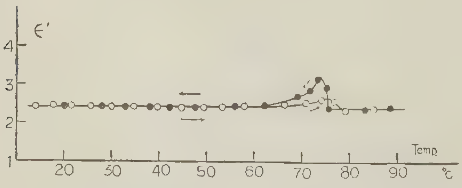

Fig. 8. Temperature dependency of ϵ' of $C_{34}H_{59}OH$ measured at 1 Mc/s.

● : Cooling ○ : Heating

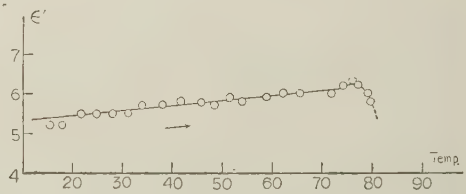

Fig. 9. Temperature dependency of a single crystal of $C_{23}H_{57}OH$ measured at 2 Kc/s. The direction of electric field is vertical to b–c plane of a crystal.

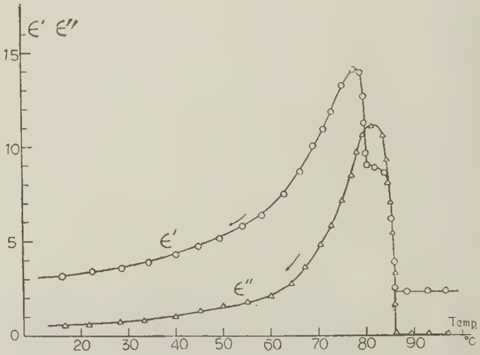

Fig. 10. Temperature dependencies of ϵ'' and ϵ' of $C_{31}H_{;}OH$ in cooling stage. The frequency of measurement is 2 Kc/s.

to the case of the lower members, for example, $C_{16}H_{33}OH$ (cetyl alcohol). O–H···O chain might be broken from place to place in α phase owing to the increased thermal motion of the individual molecules in more degree than in low temperature form. Hence the true dielectric constant must be smaller in α phase than in β or γ.

Lastly the detailed discussion should be made on the feature of co-operatively rotating dipoles. According to Sack[15), 16)] two models may be considered for it; one is such that each proton shifts co-operatively one potential minimum to another in a hydrogen bond connecting the neighbouring molecules. In this case molecules take successively the molecular state such as $\left(\begin{smallmatrix}\mathrm{O}\\ |\\ \mathrm{R}\end{smallmatrix}\right)^{-}$ and as a result of this process, a pair of positive and negative ions appear at each end of O–H···O chain. Another scheme given by Sack is the co-operative rotation of hydroxyl groups of alcohol molecules about their C–O bonds. In this case, there exists one pair of antiparallel neighbours of the type:

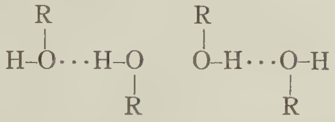

$$\begin{matrix}\mathrm{R} & & & \mathrm{R} & & \\ | & & & | & & \\ \mathrm{H{-}O\cdots H{-}O} & & & \mathrm{O{-}H\cdots O{-}H} & & \\ & | & & & | & \\ & \mathrm{R} & & & \mathrm{R} & \end{matrix}$$

and such a disorder can wander along the chain by means of reversals of individual dipoles. Thus the reversal of the whole chain can also be possible. But he did not give decisive conclusion in favour of any one of these two models.

In the high temperature form both mechanisms will be present together, giving the high electrical conductivity due to proton transfer. But the results on electrical conductivity show that this is not the case in the low temperature form. It may be inferred from the results of structure analysis[14)] that the chain of hydroxyl groups will run in the direction of a-axis in γ form, and b-axis in β form, respectively. And it is also known that the thermal motion of oxygen atoms is more remarkable than carbon atoms in the molecule. Hence there is a good reason to accept the model of rotation of hydroxyl group about C–O bond as true. But it is doubtful whether the dipole rotation occurs independently of the molecular motion as a whole, as explained by Meakins and others[7, 8, 15)]. As a foundation for it they stated that the relaxation time becomes short with increasing molecular weight. But the relaxation time is affected exceedingly by the number of hydroxyl groups in a chain as explained previously. So the relaxation time has not any important meanings in the discussion of molecular motion. It is not the relaxation time but the activation energy of dipole orientation that is important in the discussion of this problem. Dryden[8)] gave a value of 15 Kcal/mol commonly for three n-alcohols (C_{18}, C_{22} and C_{26}). But the dependency on the molecular weight of alcohol was observed in the present research for five odd alcohols and three even alcohols (Fig. 11). The activation energy increases with the molecular weight and the representative points for each alcohol in Fig. 11 seem to be classified into three groups according to the crystal structure. But it must be confirmed by a further study on more other kinds of n-alcohols.

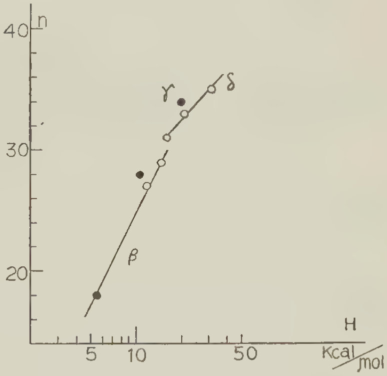

Fig. 11. The dependency of the activation energy of dipole orientation on the molecular size. n is the number of carbon atoms in an alcohol molecule.

The result is quite different from data by Dryden, but he also gave values dependent on the molecular weight for three symmetrical secondary alcohols in spite of considering the same orientation model. Moreover, the decisive information on the crystal structure was not obtained as a result of hard mechanical treatment of the sample material.

Anyhow, the activation of the dipole orientation of O–H···O chain must be considered at its ends. For example, the activation energy H may be the energy necessary for certain disorder such as described above to introduce into the chain. Here the molecular motion as a whole will play an important role. It is known by X-ray investigation[14] that the translational motion along the molecular long axis occurred in α phase so as to make impossible to decide the location of carbon atoms in the molecules. Indeed, the molecules are not so mobile in the low temperature forms, but the occasional possibility of such a motion will not be denied. It is difficult to propose a decisive model for the co-operative dipole orientation, but presumably it will be carried out by the successive elementary process which is a combination of small axial displacement of a molecule and the rotation of hydroxyl group about C–O bond.

The samples which was investigated by Takamatsu[10] seems to be a certain mixture of few neighbouring members, because even alcohols longer than $C_{28}H_{57}OH$ do not give a transformation point in heating process in spite of his result. Co-operative orientation would be disturbed in such a sample, so the results became different from others. In this case the hydroxyl chain would not be so developed as in the case of pure sample. But a value of 26.5 Kcal/mol is not so defferent from that of pure sample referring to Fig. 11, although τ is short consistent with the decrease of the number of dipoles in a chain.

Acknowledgement

The author wishes to express his sincere thanks to Professor K. Tanaka and Mr. T. Seto for their kind helps and fruitful discussions. He got much advantage by obtaining the detailed informations about the crystal structures of *n*-alcohols investigated by Seto. His thanks are also due to Professor R. Goto and Mr. A. Watanabe who gave him an opportunity of promoting the present work by synthesizing a series of pure *n*-alcohols.

References

1) J. D. Hoffman and C. P. Symth: J. Amer. Chem. Soc. **71** (1949) 431.
2) Y. Kakiuchi, T. Sakurai and T. Suzuki: J. Phys. Soc. Japan **5** (1950) 369.
3) K. Asai, E. Yoda and S. Yamanaka: J. Phys. Soc. Japan **10** (1955) 634.
4) M. Ida: J. Phys. Soc. Japan **11** (1956) 1121.
5) M. Takeyama: J. Phys. Soc. Japan **12** (1957) 1167.
6(R. J. Meakins and J. W. Mully: Aust. J. Sci. Res. A, **4** (1951) 365.
7) B. V. Hamon and R. J. Meakins: Aust. J. Sci. Res. **A, 5** (1952) 671.
8) J. S. Dryden: Aust. J. Sci. Res. **A, 5** (1952) 661.
9) B. V. Hamon and R. J. Meakins: Aust. J. Chem. **6** (1953) 27.
10) T. Takamatsu: J. Phys. Soc. Japan **10** (1955) 1049.
11) A. Watanabe: unpublished.
12) K. Tanaka, T. Seto and T. Hayashida: Bull. Inst. Chem. Res. Kyoto Univ. **35** (1957) 123.
13) K. Tanaka, T. Seto and T. Hayashida: unpublished.
14) T. Seto: unpublished.
15) R. J. Meakins and R. A. Sack: Aust. J. Sci. Res. A, **4** (1951) 213.
16) R. A. Sack: Aust. J. Sci. Res. **A, 5** (1952) 132.

JOURNAL OF THE PHYSICAL SOCIETY OF JAPAN, Vol. 14, No. 8, AUGUST, 1959

Measurement of Ion Sheath Thickness using the Double Probe with Fixed Potential

By Minoru SUGAWARA and Yoshisuke HATTA

Faculty of Engineering, Tohoku University, Sendai, Japan

(Received February 10, 1959)

When a negative potential is given to the double probe usually used as floating condition for gaseous discharge, two ion sheaths formed around the two single probes may overlap. Application is made of this phenomenon in measuring the thickness of ion sheath in a dark plasma.

§ 1. Introduction

The present paper is concerned with the probe method in the plasma of gaseous discharge. When a negative potential with respect to the potential of surrounding plasma is applied to a double probe which consists of two single probes and which is usually used as floating condition[1),2)], ion sheaths are formed around two probes. And when the absolute value of the negative potential is sufficiently large, these two ion sheaths overlap each other, which can be seen by observing the decrease in ion current which flows to one of these two single probes compared with that when the other probe is floating and no overlap occurs. These phenomena are useful in measuring the ion sheath thickness in a dark plasma.

§ 2. Experiments and Consideration

Fig. 1 illustrates the circuit diagram of the authors' experiments. P_1 and P_2 are two single probes fixed in parallel. They are made of W rods and are of the same size (radius; $r_p=0.25$ mm, length; $l=5$ mm). Ip_1 and Ip_2 are the ion currents flowing to P_1 and P_2 respectively. In Fig. 2, Ip_1 and Ip_2 are plotted against Vp_1 by using Vp_2 as parameter. Among those curves, the character of Ip_1, when Vp_2 is floating potential, is the normal ion current characteristic of a single probe. Compared with it, we can see that Vp_2 is capable of decreasing Ip_1 when it is high negative. We can also see that Vp_1 affects Ip_2. These phenomena are thought to be the effects of the overlapping of the two ion sheaths.

Let Fig. 3 represent the perpendicular cross section of the ion sheaths when they overlap.

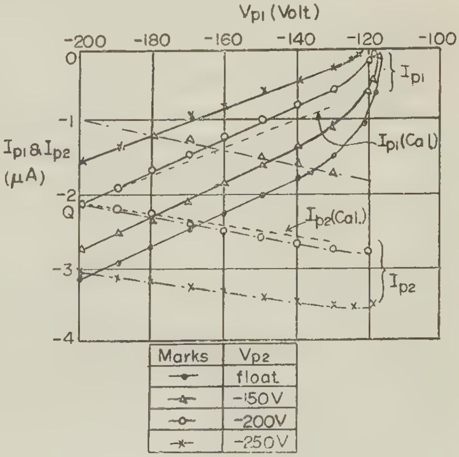

Fig. 2. Ip_1 and Ip_2 plotted against Vp_1. Anode current (I_a) is 2 ma.

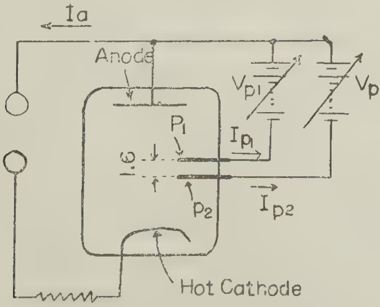

Fig. 1. The circuit diagram of the experiments. The test tube is filled with argon gas (21mmHg).

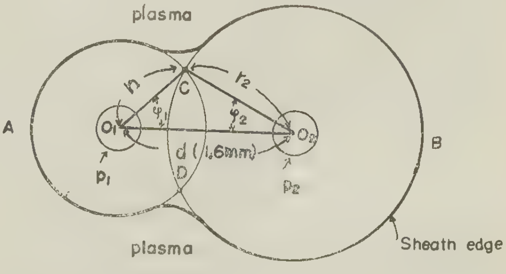

Fig. 3. The cross section of the overlapped ion sheaths.

In the figure, r_1 and r_2 are the radii of two ion sheaths when they are independent of each other, and C & D are the intersection of the two circles. The cross section of the overlapped ion sheaths is thought to be guitar-shaped, as shown by a solid line. Ions reaching the sheath edge by random motion flow to P_1 or P_2 according to boundary conditions. It is very difficult, however, to calculate the ratio Ip_2/Ip_1 accurately. Here, the authors assume the following as the first order approximation:

$$\frac{Ip_2}{Ip_1}=\frac{\text{length of arc } \overset{\frown}{\text{CBD}}}{\text{length of arc } \overset{\frown}{\text{CAD}}}=\frac{r_2(1-\varphi_2/\pi)}{r_1(1-\varphi_1/\pi)} \tag{1}$$

where

$$\left.\begin{aligned}\varphi_1&=\cos^{-1}\{(d^2+r_1^2-r_2^2)/(2dr_1)\}\\ \varphi_2&=\cos^{-1}\{(d^2+r_2^2-r_1^2)/(2dr_2)\}\end{aligned}\right\} \tag{2}$$

Now we shall check this assumption. The relation of r_1 to (Vp_1-V_s) where V_s is the space potential of the surrounding plasma in the case of a cylindrical probe and short mean free path was calculated by Kobayashi and Watanabe[3]. Using their results, we can calculate r_1 and r_2 as the function of Vp_1 and Vp_2 after determining V_s by the conventional single probe method. By putting these results in Eqs. (1) and (2), Ip_2/Ip_1 can be obtained. The broken lines shown in Fig. 2 are plotted by using the results of these calculations when Vp_2 is -200 Volts, the absolute value being adjusted so that both experimental and theoretical curves might agree at Q (where $Vp_1=Vp_2$). It can be said that the agreement is good in spite of rough approximation. The discrepancy is probably due to the potential difference between P_1 and P_2 which affects the path of ions and causes the drift current between them.

§ 3. Measurement of the Thickness of Ion Sheath

These results can be applied in measuring the thickness of an ion sheath. Owing to the above-mentioned considerations, the error of the calculation is considered to be minimum when $Vp_1=Vp_2$. So the authors made use of this case. First, P_1 and P_2 were directly connected and $Ip_1+Ip_2\,(=2Ip_1)$ was measured as $2Ip_1\,(\mathrm{D})$ at a certain negative value of Vp_1. Next, P_2 was put in the floating conditions. The sheath radius of the floating probe P_2 was so small as not to overlap with P_1. So P_1 behaved as a single probe. Vp_1 was kept unchanged. Under these conditions, Ip_1 was read as $Ip_1\,(\mathrm{S})$. Then, by the authors' assumption

$$M\equiv\frac{Ip_1(\mathrm{D})}{Ip_1(\mathrm{S})}=\frac{\pi-\varphi_1}{\pi}=1-\frac{1}{\pi}\cos^{-1}\left(\frac{d}{2r_1}\right) \tag{3}$$

or

$$r_1=\frac{d}{2\cos\{\pi(1-M)\}}\,. \tag{4}$$

By this method $r_1\,(=r_2)$ can be measured as the function of $Vp'\,(=Vp-V_s)$ as plotted in Fig. 4 in which it is stated that the following relation holds:

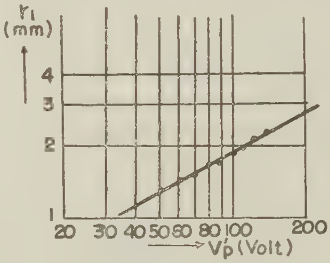

Fig. 4. Vp' vs. r_1.

$$r_1\propto(Vp')^{0.56}\,. \tag{5}$$

According to Kobayashi and Watanabe's calculation[3]

$$r_1\propto(Vp')^{0.6}\,. \tag{6}$$

The agreement is almost satisfactory.

Throughout these discussions, the authors assumed that the disturbance in the plasma condition by the ion sheath could be neglected.

§ 4. Conclusions and Acknowledgement

In the probe method, the measurement of the ion sheath thickness is an important mean to determine the ion density, because the sheath radius becomes an effective probe radius for ion collection. The shortcoming of this method is that it is practically useful only within the range of $0.5d<r_1<1.5d$, though the upper limit is not critical. So, we have to make use of the double probe whose d is adjustable when a previous estimation of r_1 is impossible. This may be troublesome, but it is the only mean to measure the thickness of the ion sheath in a dark plasma.

The authors wish to express their sincere thanks to Prof. Watanabe who directed the

work.

References

1) E. O. Jonson and L. Malter: Phys. Rev. **80** (1950) 58.
2) S. Kojima and K. Takayama: J. Phys. Soc. Japan **4** (1949) 349; **5** (1950) 357.
3) H. Kobayashi and Y. Watanabe: J. Inst. Elec. Eng. (Japan) **75** (Dec. 1955) 1469.

JOURNAL OF THE PHYSICAL SOCIETY OF JAPAN Vol. 14, No. 8, AUGUST, 1959

Excitation of Oscillations in a Plasma Layer

By Masao SUMI
Electrical Communication Laboratory
Musashino-shi, Tokyo, Japan

(Received April 30, 1959)

Theory of excitation of standing waves in a uniform plasma layer by an injected electron beam is presented. Various characteristics of excited waves are investigated; in particular, discontinuous jumps of frequency and mode can be expected with the variation of electron density, layer thickness and beam voltage. The consequences of the theory are compared with experimental results. It is seen that observed phenomena concerning standing plasma waves are satisfactorily illustrated in a quite natural way.

§1. Introduction

During the last thirty years a number of experiments on electron plasma oscillations have been performed in gaseous discharges. In recent years, particularly, various aspects of oscillation phenomena have been made clear in several observations.1)~5) These oscillations can be considered as arising from the interaction of an electron beam with a group of electrons in a medium plasma. The electron beam may be either emitted from a cathode in such a way as to create electrons in the medium by ionization or shot into the medium plasma from another source. Among observations quoted above, spatially growing plasma waves5) belong to a sort of double-stream amplification and have already been discussed in some detail by the author in a preceding paper.6) In the other works Wehner1) have successfully explained his results in terms of klystron-like mechanism. However, by means of this mechanism, it seems difficult to account for other experimental results as will be shown later. Therefore the range of validity of klystron-like mechanism remains still unestablished. In some observations there appeared standing plasma waves2)3) and in others much more complicated phenomena were observed3)4) probably in connection with the density gradient, for which reasonable explanations have not yet been given.

Recently the author has developed the more detailed theory of excited plasma waves,7) in which oscillations in a plasma layer bounded by thin sheaths have also been discussed.

The purpose of this paper is first to describe theoretical behaviours of standing plasma waves by use of a simple model of beam-excitation of oscillations in a uniform plasma layer and second to show that the consequences thus obtained are able to well-illustrate several phenomena characteristic of excited standing waves. Effects due to the non-uniformity of electron density will not be taken into account in this article.

§2. Theoretical Basis

As the details have been presented in the previous work,7) we shall describe here only the outline and the consequences of our theory. Basic equations are the Boltzmann equation for the distribution function of electron-velocity and the Poisson equation satisfied by an electric field in the plasma. The effect of short-range collisions for oscillating parts is neglected and that of long-range collisions is supposed to be included in the fluctuating electric field, as was earlier done by Vlasov.[8] These equations are linearized and solved by means of Fourier-Laplace transform method. Taking a Maxwellian velocity distribution function for the medium electrons and a single velocity one for the electron beam, we get the following dispersion relation

$$\left(\frac{\omega}{\omega_p}\right)^2=1+\frac{3}{2\beta^2}+\frac{15}{4\beta^4}\cdots+\sigma\frac{\beta^2}{(\xi-\beta)^2}, \quad (1)$$

where $\beta=\omega/ku_T$, $\xi=u_b/ku_T$, $\omega^2{}_p=n_pe^2/m\epsilon_0$ and $\sigma=n_b/n_p$. u_b and n_b denote the velocity and the number density of the beam respectively, while $u_T=(2\kappa T/m)^{1/2}$ and n_p are the thermal velocity and the number density of electrons in the plasma respectively. The relation (1) is obtained without any ambiguity by use of an approximation for $|\beta|\gg1$. Although similar dispersion relations have been derived and discussed to some extent by several authors,[9)-11)] more exact and detailed characteristics are needed for our purpose. Then Eq. (1) is solved for an excited wave, where $\mathrm{Im}(\omega)=\gamma>0$, a complex frequency being written as $\omega=\omega_0+i\gamma$. Each wave component builds up proportionally to $exp(\gamma t)\,exp[i(kx-\omega_0t)]$ from a ground level of initial disturbance, that is, a thermal fluctuating level. Except for very small values of σ ($\lesssim10^{-3}$), Eq. (1) cannot be solved analytically; hence it must be solved numerically for almost all practical cases. The typical case with the density ratio $\sigma=0.1$ is shown in Fig. 1, where the frequency ω_0 and the wave growth-rate γ, both normalized by plasma frequency ω_p, and the ratio of the plasma wave velocity $u_w=\omega_0/k$ to the beam velocity u_b are plotted against the wave number k. These characteristics are found to be not very sensitive to finite values of $\xi^2=(u_b/u_T)^2$, which implies that the effect of change of the beam velocity is not so great. Therefore, for simplicity, we shall consider only the case of $\xi^2\to\infty$ in later discussions. As is shown in Fig. 1, the phase velocity for an excited wave is always smaller than the beam velocity. Then the coupling between the beam and the wave is so strong that the kinetic energy of beam is transfered to the energy of excited wave. Both too fast and too slow waves cannot deprive the beam of enough energy to grow up. As a result, the excited wave has an upper limit of the wave number k, and the rate of wave growth becomes maximum at a value of k almost midway between zero and its critical limit, where the oscillation frequency is slightly lower than the plasma frequency in the medium.

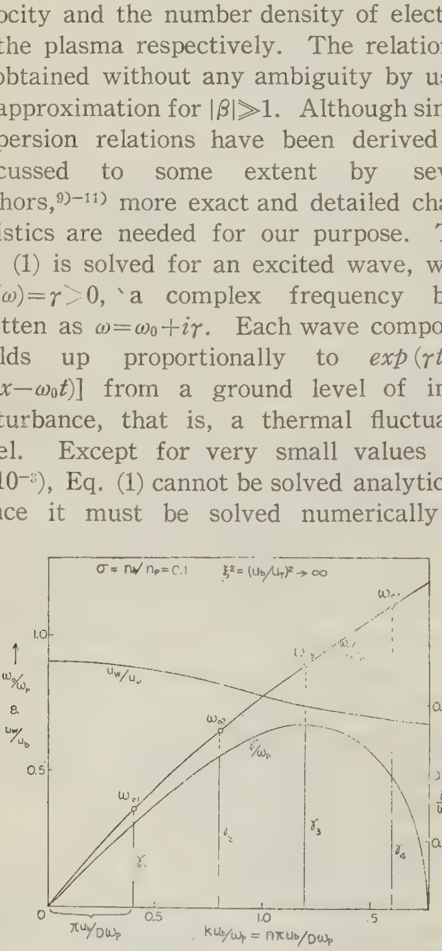

Fig. 1. Typical characteristics of excited waves in a plasma layer with a thickness *D*.

§ 3. Excitation of Standing Waves in a Uniform Plasma Layer[12]*

The theory described in the preceding section is applied to the excitation of a standing wave in a uniform plasma layer with a thickness D. Suppose that the layer is sharply bounded by extremely thin sheaths and that all the electrons in the medium plasma are reflected on both boundaries with negligible energy loss. There exist initially small density fluctuations due to thermal agitation in the layer. In such a disturbance there are wave-components which have wave-numbers and phase velocities appropriate for excitation as shown in the last section. They interact strongly with the beam which passes through the layer, and then receive energy from it. The waves thus excited are reflected on both boundaries, running back and forth. After a while only the waves which satisfy a condition for standing wave survive; Their wavelength λ must satisfy the relation

---

* A short note on this subject is seen in reference 12.

$D=n(\lambda/2)$, D being the layer thickness and n an integer. Then it is only to forward waves that the beam transfers its kinetic energy. On the other hand, backward waves play a role in the feedback of oscillatory energy to forward waves. Thus excited waves should have discrete wave numbers, $k_n=n\pi/D$, which must be less than the upper limit of k-value represented in Fig. 1. Corresponding to each value of k_n, it is possible to excite the wave with the frequency ω_{0n} and the growth rate γ_n as seen also in Fig. 1. Since the oscillatory energy W increases in proportion to $exp\,(2\gamma t)$, the rate of energy transfer from the beam to the plasma wave, $(1/W)\,(dW/dt)$, is proportional to γ. Therefore it may be right to consider γ_n as the relative intensity for each excited wave within the validity of linear approximation. If the transferred energy is not too large and the magnitude of parameter $\pi u_b/D\omega_p$ is not too small, it would be reasonable to suppose that the energy is concentrated exclusively in the mode corresponding to the maximum γ_n among possible modes. For example γ_3 is the maximum in Fig. 1; and therefore the wave with the mode of $n=3$ will be excited.

Now we consider the case when the parameter $\pi u_b/D\omega_p$ changes continuously. Letting it decrease, then in Fig. 1 γ_3 tends to be smaller, while γ_4 becomes larger; the frequency ω_{03} is gradually lowered, exhibiting a frequency-pulling phenomenon. As soon as γ_4 exceeds γ_3, the mode number of the excited plasma wave changes abruptly from $n=3$ to 4. At the same time, its frequency jumps from ω_{03} to ω_{04}. Further decrease of the parameter $\pi u_b/D\omega_p$ causes repeated jumps of wave-mode and frequency as shown in Fig. 2. Corresponding to the variation of magnitude of γ_n, the intensity of excited waves will become comparatively weak near the region where the mode-jumps occur and will attain its maximum almost midway between jumps. Since every combination of changes of the quantities u_b, D and ω_p brings about the variation of the parameter $\pi u_b/\mathrm{D}\omega_p$, yielding the frequency-pulling and the mode and frequency jumps, the pattern represented in Fig. 2 is of great importance for the prediction of various phenomena based on our theory. In the next section we will show how the observed phenomena can be explained on the basis of this pattern.

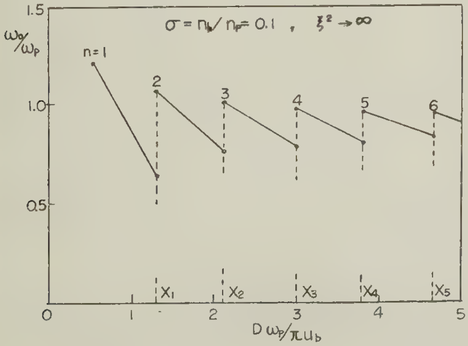

Fig. 2. The pattern of modes and normalized frequencies represented against the parameter $D\omega_p/\pi u_b$.

§ 4. Comparison between Theory and Experiments

In the theoretical pattern presented in Fig. 2, there are three simple cases in which the parameter $\pi u_b/\mathrm{D}\omega_p$ varies.

First is the case where ω_p and u_b hold constant and the thickness of the plasma layer D changes. It has been realized in experiments performed by Looney and Brown[2] and by Bailey and Emeleus[3] (abbreviated hereafter as L–B and B–E respectively). In the former, the existence and several features of a standing plasma wave were established; the successive jumps of frequency and mode were observed as the thickness of plasma sheath was varied. It corresponds to just what is shown in Fig. 2. In spite of the uncertain value of n_b/n_p, it is easy to see a good agreement in order of magnitude between theory and experiment. In the latter paper by B–E, similar phenomena of frequency jumps were displayed as a probe was moved away from the cathode. This can be well illustrated if we suppose that standing waves were excited in the region between the cathode and the probe. The intensity distribution in this case, too, is nicely checked by the theory. However we note that the measured intensity would not be picked up directly from the standing waves, but from the beam modulated proportionally to the intensity of standing waves.

A quantitative agreement will be found by comparing with their typical figure representing the frequency pulling. Denote observed distances from the cathode at which frequency jumps occur as D_n $(n=1, 2, \ldots)$. Assuming $\sigma=n_b/n_p=0.1$ and using the values of ω_p and u_b in their data, theoretical values of D_n are obtained from the relation $D_n\omega_p/\pi u_b=X_n$ where X_n is represented in Fig. 2. The calculated and observed values are listed in Table I, indicating a satisfactory agreement. The differences of them for n greater than 4 would be probably due to either the scattering of beam or the decrease in electron density with the distance away from the cathode.

Table I. The distances from the cathode where the successive mode-jump occurs.

	D_1	D_2	D_3	D_4	D_5
	mm				
cal.	2.0	3.2	4.5	5.7	7.1
obs.	2.1	3.2	5.0	6.4	9.2

Second case is that ω_p is varied, while u_b, D and σ are kept constant. It may be realized when the beam density is changed, the beam voltage being unchanged. Then D and σ may be practically regarded as constant. To see the variation of the frequency ω_0 with the plasma density, it is convenient to reform the pattern in Fig. 2 as that in Fig. 3. Likewise we can get Fig. 4 for $\sigma=1.0$. It is seen that discontinuous transitions of frequency and mode occur repeatedly as the plasma density increases. On each frequency plateau the intensity will become maximum nearly midway, since so behaves γ_n. Furthermore the inclination of frequency plateau is found to vary with the density ratio σ. For $\sigma=1.0$ it is entirely horizontal, but becomes inclined with the decrease of the value of σ.

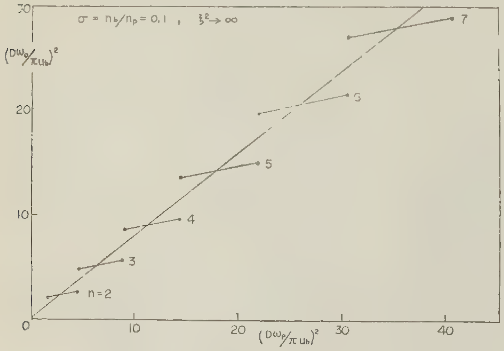

Fig. 3. The pattern of modes and frequencies for $n_b/n_p=0.1$ when the electron density in the medium is varied.

These behaviours of standing wave expected by the theory are qualitatively quite in accord with the results obtained by L–B. From Figs. 3 and 4 we can get calculated values of the centre frequency of each mode, using the observed values of D and u_b. They are compared with the observed centre frequencies in Table II. The calculated values are only slightly greater than the observed. It can be somewhat improved by taking into account of the velocity spread in the beam. Thus the quantitative agreement would also be almost satisfactory.

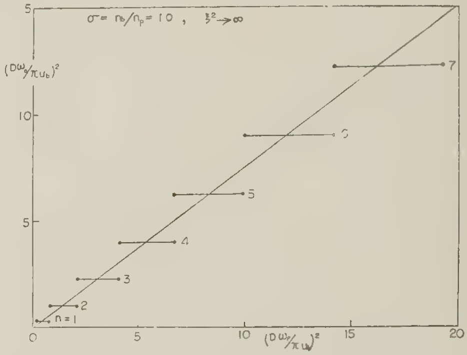

Fig. 4. The pattern of modes and frequencies for $n_b/n_p=1.0$ when the electron density in the medium is varied.

Table II. Centre frequency of each mode.

mode-number n	f_0 (cal.)		f_0 (obs.)
	$\sigma=0.1$	$\sigma=1.0$	
	Gc/s		
2	0.6	0.4	—
3	0.9	0.6	0.6
4	1.2	0.8	0.7
5	1.5	1.0	0.8
6	1.8	1.2	0.9
7	2.1	1.4	1.0

Third is the case where u_b is altered, whereas ω_p and D are unaltered. This can be also expected to give rise to the same phenomena as the first case. However no corresponding experiment has yet been known.

Looney and Brown applied the klystron-like mechanism in order to illustrate their experimental results. In fact Wehner has given an almost satisfactory explanation of his data by the use of this mechanism, in which the beam is velocity-modulated near the sheath-edge of injection side and the energy of this modulation is extracted at the sheath of opposite side, thus yielding the feedback mechanism to the uniformly oscillating medium plasma. Accordingly, the analogy to the klystron is very direct. Here it is to be noted that, for the medium plasma, oscillations do not exist in the intermediate region between sheaths, but only exist at both sheath-edges. In the case by L–B, on the contrary, the situation is somewhat different from Wehner's. It appears that the extraction point by L–B is not always in the region where the energy is actually extracted from the beam. For, the extraction planes calculated by them lie sometimes nearly midway between both sheaths, thus being unable to provide the oscillating energy to the medium plasma.

It was moreover shown by L–B that there was a relation such as $X_s+X_t=$constant, where X_s is the sheath thickness and X_t is the transit distance from the modulation point at the sheath edge to the extraction point. However it is easy to see that this relation can be interpreted in terms of our theory as $X_s+(D/2)=$constant, which has really a definite physical meaning of a half distance between two electrodes.

As a consequence, it may be concluded that the mechanism proposed by the author would be more reasonable for the excitation of standing plasma waves.

§ 5. Discussions

At first we assumed a model of a plasma layer with infinitely thin sheaths. Then it was verified that consequences derived from our theory based on this model could quite naturally explain observed phenomena concerning standing plasma waves. This indicates that the model adopted is very adequate for the present case. In actual cases, however, the sheath thickness is finite, so that electrons in the medium impinging on it are reflected after different penetrations into the sheath according to different electron energies. Hence reflected waves will be more or less distorted. But the distortion would be small if the sheath thickness is much thinner than the wavelength of excited plasma wave. Therefore in most practical cases the sheath thickness may be neglected, enabling the above model to be valid.

It will be interesting for some investigators to discuss a condition for the excitation of millimeter waves. For this, it is first necessary to realize a thin plasma layer with electron density higher than about 10^{13} per cubic centimeter. For the layer thickness of about 1 mm the theory predicts that an injected electron beam of nearly one thousand volts will excite a suitable mode of standing wave. For instance, the beam with 1600 volts will give the mode number of 4 or 5 for the layer of 1 mm in thickness and of 10^{13} in density. The intensity obtainable will increase with the current density of the beam, but is difficult to estimate by the present theory.

It will be the next problems to evaluate the intensity of oscillations as well as the effects due to inhomogeneity in plasmas.

The author is indebted to Professor S. Kojima and Dr. K. Takayama for illuminating discussions, in particular, concerning the comparison with experiments. He is also grateful to Professor T. Kihara for helpful remarks on this manuscript.

References

1) G. Wehner: J. Appl. Phys. **22** (1951) 761.
2) D. H. Looney and S. C. Brown: Phys. Rev. **93** (1954) 965.
3) R. A. Bailey and K. G. Emeleus: Proc. Roy. Irish Acad. **57** (1957) 1276.
4) S. Kojima, K. Kato and S. Hagiwara: J. Phys. Soc. Japan **12** (1957) 1276.
5) G. D. Boyd, L. M. Field and R. W. Gould: Phys. Rev. **109** (1958) 1393.
6) M. Sumi: J. Phys. Soc. Japan **14** (1959) 653.
7) M. Sumi: J. Phys. Soc. Japan **13** (1958) 1476.
8) A. Vlasov: J. Phys. USSR. **9** (1945) 25, 130.
9) D. Bohm and E. P. Gross: Phys. Rev. **75** (1949) 1851.
10) A. I. Akhiezer and I. Feinberg: Zh. Eks. Teor. Fiz. **21** (1951) 1262.
11) M. A. Lampert: J. Appl. Phys. **27** (1956) 5.
12) M. Sumi: Phys. Rev. Letters **2** (1959) 37.

JOURNAL OF THE PHYSICAL SOCIETY OF JAPAN Vol. 14, No. 8, AUGUST, 1959

High Subsonic Flow past a Wedge in a Two-Dimensional Wind Tunnel at its choked State

By Shigeki MORIOKA

Department of Aeronautics, Faculty of Engineering,
Kyoto University

(Received April 21, 1959)

The two-dimensional high subsonic flow at the choked state past a symmetrical double-wedge profile placed midway between two parallel walls is investigated. The subsonic flow field over the front half of the profile is given by the relaxation solution for a Tricomi's boundary value problem in the hodograph plane. The supersonic flow over the rear half is calculated by the method of characteristics. The results for the pressure distribution and the choking Mach number are found to agree well with Marschner's analytical results over fairly wide range of the transonic parameter.

§ 1. Introduction

The two-dimensional high subsonic flow at the choked state past a symmetrical double-wedge profile placed midway between two parallel walls has been studied analytically by B. W. Marschner1) and Z. Hasimoto.2) Though the problem is rather simple as a boundary value problem for Tricomi's equation, the analyses developed by these writers are fairly complicated and seem to contain some questions. The problem may also be solved numerically by the relaxation method formulated by W. G. Vincenti.3) This method is free from any restriction except for the transonic approximation and gives the data for the whole flow field. Therefore, it may be worth while to reconsider the problem by this method and to check the existing analytical results. The calculation is accomplished for three values of the transonic parameter; –0.703. –0.921, and –1.116. These correspond to the values of the choking Mach number: 0.869, 0.829, and 0.795, respectively, for a special wedge of thickness ratio 0.1. Marschner's parameter ρ_0/ρ_c takes the values 0.159, 0.353, and 0.608 for respective cases. This parameter measures the wall effect and is assumed to be small in Marschner's analysis. In the Appendix, the case of sonic unbounded flow is also treated by the numerical method.

§ 2. Boundary Value Problem and its Reduction to Finite Difference Equation

The flow in the physical plane and its image in the hodograph plane are shown in Figs. 2, 3 and Fig. 1, respectively. (In the following description only the flow in the upper half-plane will be described, since the flow is symmetrical about the chord line.) In this paper are used the same notations as in Ref. 3 except for the definition of the pressure coefficient. As for detailed formulation of the boundary value problem in the hodograph plane, its reduction to finite difference equations, and the transformation to the physical plane, reference may be made also to the cited paper. Here are listed only the relations necessary in the following discussion.

Notations

a^*	critical velocity
c	airfoil chord
H	width of the tunnel
M_0	choking Mach number
p	local pressure
p^*	pressure at the critical speed
t	airfoil thickness
V	local speed of the flow
x, y	Cartesian coordinates in the physical plane
γ	ratio of the specific heats (1.4 for air)
θ	local inclination of the flow relative to the x-axis
θ_w	half vortex-angle of the wedge, $=t/c$
ρ^*	fluid density at critical speed
ψ	stream function
ψ_w	value of ψ on the tunnel wall

Boundary value problem

Fundamental equation:

$$\psi_{\tilde{\eta}\tilde{\eta}}-2\tilde{\eta}\psi_{\tilde{\theta}\tilde{\theta}}=0 \qquad (1)$$

where $\tilde{\eta}=\eta/\eta_0$, $\tilde{\theta}=2^{\frac{1}{2}}\theta/\eta_0^{\frac{3}{2}}$, and

$$\eta=(\gamma+1)^{\frac{1}{3}}(V-a^{*})/a^{*}$$

Boundary conditions:

On basic streamline:

$$\begin{aligned}&\psi=0 \quad \text{for} \quad \tilde{\eta}<-1, \quad \tilde{\theta}=0\\ &\psi=0 \quad \text{for} \quad \tilde{\eta}\leqq 0, \quad \tilde{\theta}=\tilde{\theta}_w \qquad (2)\\ &\psi=0 \quad \text{for} \quad \tilde{\eta}\to-\infty, \quad 0\leqq\tilde{\theta}\leqq\tilde{\theta}_w\end{aligned}$$

On sonic line:

$$\eta_{\tilde{\eta}}(0,\theta)+\frac{2^{\frac{4}{3}}\pi}{3^{\frac{1}{6}}\Gamma^3(\frac{1}{3})}\int_{\tilde{\theta}_w}^{\tilde{\theta}}\frac{\psi_{\tilde{\theta}}(0,\tilde{\theta}')}{(\tilde{\theta}'-\tilde{\theta})^{\frac{3}{2}}}d\tilde{\theta}'=0$$

$$\text{for} \quad \tilde{\eta}=0, \quad 0\leqq\tilde{\theta}\leqq\tilde{\theta}_w \qquad (3)$$

On solid wall:

$$\psi=\psi_w(=1) \quad \text{for} \quad -1<\tilde{\eta}\leqq 0, \quad \tilde{\theta}=0 \qquad (4)$$

Transformation to the physical plane

$$d\left(\frac{x}{c}\right)=\frac{1}{4I_w}(2\tilde{\eta}\psi_{\tilde{\theta}}\,d\tilde{\eta}+\psi_{\tilde{\eta}}\,d\tilde{\theta})$$

$$d\left(\frac{y}{c}\right)=\frac{1}{4I_w}\left\{2\tilde{\theta}_w/(\gamma+1)\left(\frac{t}{c}\right)\right\}^{\frac{1}{3}}d\psi \qquad (5)$$

where

$$I_w=\int_{-\infty}^{0}\tilde{\eta}\psi_{\tilde{\theta}}(\tilde{\eta},\tilde{\theta}_w)d\tilde{\eta}$$

Pressure coefficient and its relation to Marschner's and Vincenti's ones:

$$\begin{aligned}\tilde{c}_p&=(\gamma+1)^{\frac{1}{3}}\left(\frac{t}{c}\right)^{-\frac{2}{3}}(p-p^*)\Big/\frac{1}{2}\rho^*a^{*2}\\ &=[c_p]_{\text{Vincenti}}-2\xi_0 \qquad (6)\\ &=(\gamma+1)^{\frac{1}{3}}[\theta_0{}^{-\frac{2}{3}}c_p]_{\text{Marschner}}\end{aligned}$$

Singular point

In the vicinity of the singular point $\tilde{\eta}=-1$, $\tilde{\theta}=0$ (source type for the present problem) corresponding to the uniform flow, Tricomi's equation can be approximated by Laplace's equation. This gives an approximate solution

$$\psi=\psi_w\left\{1-\frac{1}{\pi}\tan^{-1}\frac{\tilde{\theta}}{2^{\frac{1}{2}}(\tilde{\eta}+1)}\right\} \qquad (7)$$

Then, $d\left(\frac{x}{c}\right)=-\frac{\psi_w}{2^{\frac{1}{2}}\pi I_w}d\left\{\tilde{\eta}-\log(\tilde{\eta}+1)\right\}$ (8)

But, in the present method, the singularity may be represented simply by taking $\psi=\frac{\psi_w}{2}$ at the lattice point $\tilde{\eta}=-1$, $\tilde{\theta}=0$.

§ 3. Hodograph Solution and Flow in the Physical Plane

Fig. 1 shows the hodograph pattern for $\xi_0=-0.921$. Figs. 2 and 3 show the flow in the physical plane for $\xi_0=-0.921$ and -1.116. It may be seen that the patterns of the equi-speed line for both cases are very similar.

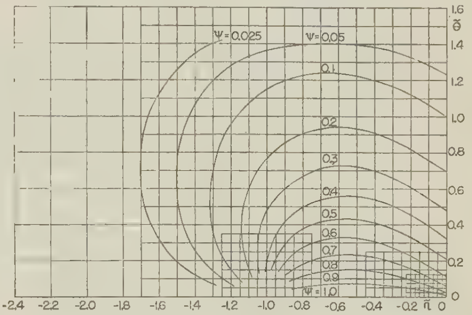

Fig. 1. Distribution of lattice points and stream-lines pattern in $\tilde{\eta}-\tilde{\theta}$ plane ($\xi_0=-0.921$)

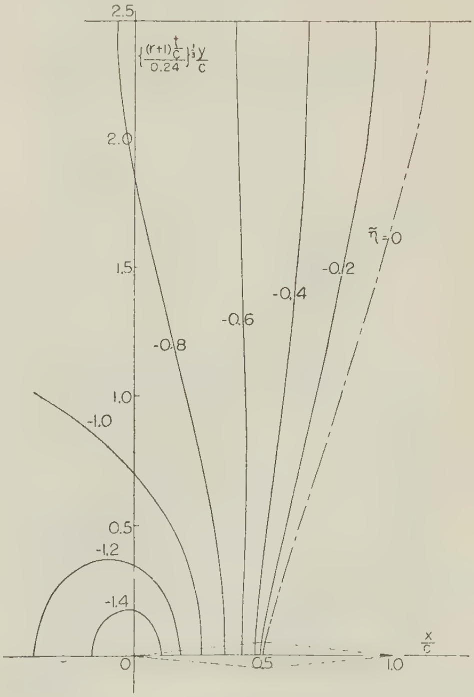

Fig. 2. Equi-speed line and sonic line relative to wedge profile and tunnel wall ($\xi_0=-0.921$)

The change of $\psi_{\tilde{\eta}}$ along the sonic line and the streamline pattern near the origin of the hodograph plane suggest that the shape of the sonic line near the wall is similar to that near the axis of a Laval nozzle, where[2] $\psi\propto\tilde{\theta}^{\frac{1}{3}}$, $\psi_{\tilde{\eta}}\propto\tilde{\theta}^{-\frac{1}{3}}$ along $\tilde{\eta}=0$, and hence $x\propto y^2$, i.e. it is parabolic.

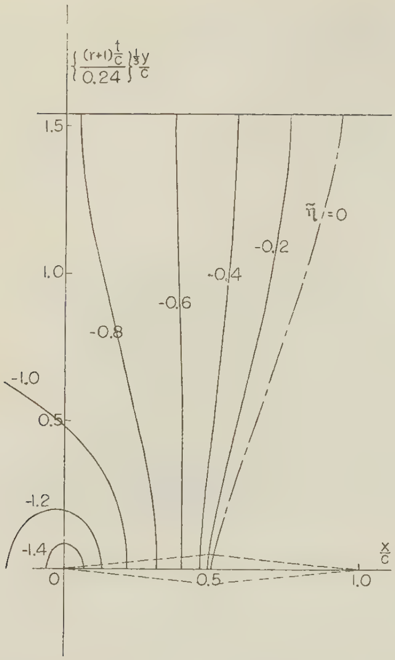

Fig. 3. Equi-speed line and sonic line relative to wedge profile and tunnel wall ($\xi_0=-1.116$)

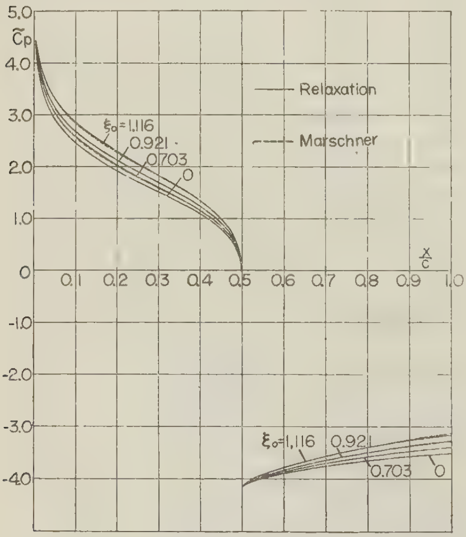

Fig. 4. Chordwise distribution of pressure coefficient.

§ 4. Pressure Coefficient

Fig. 4 shows the distribution of the pressure coefficient on the profile. The dotted line in the figure represents for comparison the result calculated by Marschner's formula. It will be seen that the agreement of the present and analytical results is fairly good even for $\xi_0=-1.116$. In this connection it should be mentioned that Marschner's formula predicts only the difference from the resul for the unbounded sonic flow. As to th latter there exists well known study due t Guderley and Yoshihara.[5] The presen writer has, however, recalculated the sai case also by the relaxation technique. Th details are given in the Appendix of th present paper. The curve for $\xi_0=0$ in Fig 4 shows the result of calculation. As is see in the Appendix, the curve has small bu systematic deviation from Guderley an Yoshihara's one. The cause of discrepanc is not clear to the present writer. In th present paper, however, the numerical one is used as the basis of Marschner's correctio formula, since it gives better agreemen Also it seems preferable in view of the so-called sonic freeze.

§ 5. Choking Mach Number

The values of choking Mach number are plotted in Fig. 5 against the ratio t/H of the airfoil thickness to the width of the tunnel, for the said three values of ξ_0 assuming $t/c=0.1$. The results due to Marschner and to the one-dimensional theory are also plotted for the sake of comparison.

Now, the transonic parameter is usually defined as

$$\xi_0=(\gamma+1)^{\frac13}\left(\frac{V_0}{a^*}-1\right)\left(\frac{t}{c}\right)^{\frac23} \tag{9}$$

where $\frac{V_0}{a^*}=(\gamma+1)^{\frac12}M_0/\{2+(\gamma-1)M_0^2\}^{\frac12}$

Since (M_0-1) is small, this can be approximated by.

$$\xi_0=(M_0^2-1)\Big/\left\{(\gamma+1)\frac{t}{c}\right\}^{\frac23} \tag{10}$$

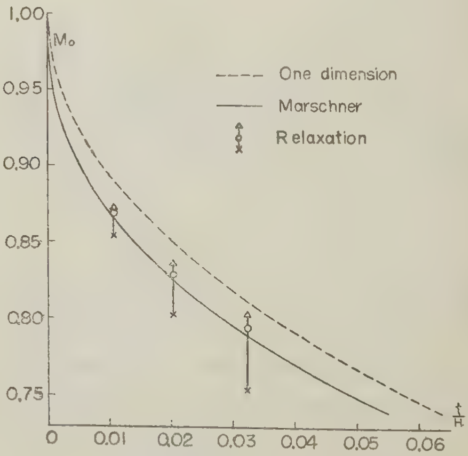

Fig. 5. t/H vs. choking Mach number for $t/c=0.1$

Eqs. (9) and (10) are equivalent within the transonic approximation. There occur, however, numerical difference when we calculate M_0 from these formulas with given γ, ξ_0 and t/c. Small circles in Fig. 5 represent the values as computed by Eq. (9). These are seen to lie near to Marschner's curve. While, Eq. (10) gives the values indicated by crosses in the figure, which suggest fairly lower choking Mach numbers than Marschner's values. On the other hand, the present flow may also be regarded as produced by a normal shock at infinity upstream from a supersonic uniform flow with the transonic parameter $-\xi_0$. Then, evaluating the Mach number of the supersonic flow by Eq. (10), and applying the transonic normal shock condition (symmetric jump in Mach number), we get the values denoted by small deltas in Fig. 5. These values indicate higher values of the choking Mach number. From these results it seems that the determination of the choking Mach number for a given configuration is a delicate problem to the transonic approximation theory.

The writer wishes to express his hearty thanks to Prof. K. Tamada and to Prof. Z. Hasimoto for their encouragement and valuable discussion.

Appendix. *Sonic flow past a wedge profile at zero angle of attack.*

The equations (1) to (6) have been derived by the transformation $\tilde{\eta}=\eta/\eta_0$, $\tilde{\theta}=2^{\frac{1}{3}}\theta/\eta_0^{\frac{3}{2}}$. For the sonic flow, the transformation cannot be used because the upper boundary in the hodograph plane runs away to infinity. In this case, we take the transformation

$$\tilde{\eta}=\tilde{\theta}_w^{\frac{2}{3}}\eta/2^{\frac{1}{3}}\theta_w^{\frac{2}{3}}$$
$$\tilde{\theta}=\tilde{\theta}_w\theta/\theta_w$$

By this transformation, the equations (1) to (6) are invariant in their forms. But, the singular point corresponding to the uniform flow is shifted on the sonic line, i.e. $\tilde{\eta}=0$, $\tilde{\theta}=0$, and the upper boundary in the hodograph plane remains at $\tilde{\theta}=\tilde{\theta}_w$.

As the values of ψ at the lattice points facing the singular point, we take the following

$$\psi=\sum_{m=-\infty}^{\infty}\psi_w$$

where $\psi_m=-f_m/(2f_m^2-\tilde{\eta})^3$

$$f_m^3-\frac{3}{2}\tilde{\eta}f_m+\frac{3}{4}(\tilde{\theta}-2m\tilde{\theta}_w)=0$$

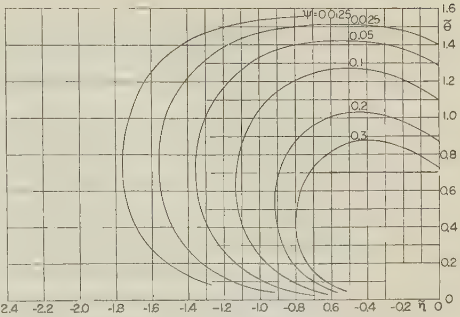

Fig. 6. Distribution of lattice points and streamlines pattern in $\tilde{\eta}-\tilde{\theta}$ plane (sonic unbounded flow).

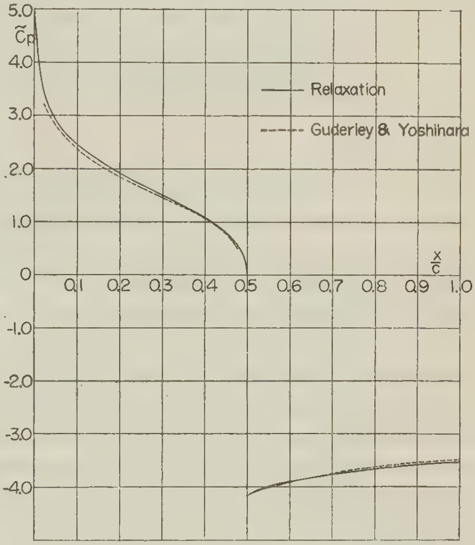

Fig. 7. Distribution of pressure coefficient on wedge profile at sonic unbounded flow.

It can easily be shown that $\psi_m(\tilde{\eta}, \tilde{\theta})$ is a fundamental solution of Eq. (1) representing the sonic uniform flow at infinity in the physical plane. Further, it is obvious that $\psi(\tilde{\eta}, \pm\tilde{\theta}_w)=0$.

Fig. 6 shows the calculated hodograph pattern. In Fig. 7 is given a comparison of the present result and Guderley's one for the distribution of pressure coefficient on the profile.

References

1) B. W. Marschner: J. Aero. Sci. **23** (1956) 368.
2) Z. Hasimoto: unpublished.
3) W. G. Vincenti and C. B. Wagoner: N.A.C.A. Tech. Rep. no. 1095 (1952).
4) S. Tomotika and K. Tamada: Quart. Appl. Math. **7** (1950) 381.
5) G. Guderley and H. Yoshihara: J. Aero. Sci. **17** (1950) 723.

Journal of the Physical Society of Japan, Vol. 14, No. 8, August, 1959

Rheological Equation of Voigtian Material

By Wataru Segawa

Faculty of Literature and Science, Nihon University, Tokyo

(Received April 11, 1959)

In this paper, the well-known classical one-dimentional rheological equation of Voigtian material having a single retardation time is extended so as to be applicable to three-dimentional and large deformation, and Lagrange's and Euler's representations are explicitly used.

Our rheological equation in Euler's representation is reduced to the most general stress-strain relation which was described by Rivlin and is derived by general procedure using the elastic theory of finite deformation, when its terms relating to viscosity are eliminated, and is reduced to the most general stress-strain rate relation which was derived by Reiner and Rivlin, when its terms relating to elasticity are omitted.

Then, the above equation is applied to simple elongation and simple shear, with satisfactory results.

§ 1. Introduction

It is well known that the theory of hydrodynamics is well expressed by two representations, Lagrange's and Euler's, which are, whether explicitly or not, used also in the theory of finite elastic deformation[1]. But, we can seldom find the theory of viscoelasticity or elastico-viscosity, where the above two representations are explicitly used. In this paper, we will use the two representations explicitly and effectively to derive three-dimentional rheological equation of a Voigtian material.

The most general stress-strain relation in finite elastic deformation can be derived by a general procedure in the elastic theory of finite deformation, and its Euler's representation was described by Rivlin[2], and the most general stress-strain rate relation of isotropic viscous liquid was derived by Reiner[3] and Rivlin[4]. As it is well known, the classical Voigt model[5] having a single retardation time is a parallel combination of a Hookian spring and a Newtonian dashpot. Thus, if we want to seek the three-dimentional extention of the one-dimentional model, we should replace the Hookian spring and the Newtonian dashpot by the spring whose behavior is ruled by the most general stress-strain law and the dashpot whose behavior is ruled by the most general stress-strain rate law, respectively. In other words, the general equation of Voigtian material in Euler's representation should be reduced to Rivlin's equation of the finite elastic deformation if its viscous terms are omitted, and to Reiner-Rivlin's equation if its elastic terms are eliminated. In this article, we will derive such general equations of Voigtian material.

For the simplicity of mathematical description, we will use Einstein's convention throughout this article. We will denote the quantities relating to Lagrange's and Euler's representations by the suffixes of Latin letters (i, j, k etc.) and of Greek letters (λ, μ, ν etc.) respectively.

§ 2. Strain, Strain Rate and Stress

Let us regard a Voigtian material as a system of particles. Let the position of a material point be P for $t=0$ (undeformed state) and P^* for time t (deformed state), and let the coordinates of P and P^* be x^i and x^{*i} ($i=1, 2, 3$), respectively, on a rectangular coordinate system X^i ($i=1, 2, 3$) fixed in space. Then, we have

$$x^{*i}=x^{*i}(x^1, x^2, x^3, t)\,, \quad x^{*i}(x^1, x^2, x^3, 0)=x^i \tag{2.1}$$

or

$$x^i=x^i(x^{*1}, x^{*2}, x^{*3}, t)\,, \quad x^i(x^{*1}, x^{*2}, x^{*3}, 0)=x^{*i} \tag{2.1$'$}$$

where we assume that the function x^{*i} and x^i are one valued and continuous functions and are differentiable by the respective independent variables as many times as necessary. The Lagrange's representation of the strain in P^* is given by

$$\varepsilon_{ij}=\tfrac{1}{2}(g_{ij}-\delta_{ij}) \tag{2.2}$$

where

$$g_{ij}=x^{*k}_{,i}x^{*k}_{,j} \quad (x^{*k}_{,j}=\partial x^{*k}/\partial x^i) \tag{2.2$'$}$$

and δ_{ij} is Kronecker's δ. Then, we have

$$\varepsilon_{ij}=\varepsilon_{ij}(x^1, x^2, x^3, t)\ , \quad \varepsilon_{ij}(x^1, x^2, x^3, 0)=0 \qquad (2.3)$$

The displacement u^k ($k=1, 2, 3$) is defined by

$$x^{*k}-x^k=u^k \qquad (2.4)$$

If we substitute Eq. (2.4) into Eq. (2.2) and Eq. (2.2′), we have

$$\begin{aligned}\varepsilon_{ij}&=\tfrac{1}{2}\{(x^k+u^k)_{,i}(x^k+u^k)_{,j}-\delta_{ij}\}\\ &=\tfrac{1}{2}\{(\delta_{ki}+u^k_{,i})(\delta_{kj}+u^k_{,j})-\delta_{ij}\}\\ &=\tfrac{1}{2}\{\delta_{ij}+u^i_{,j}+u^j_{,i}+u^k_{,i}u^k_{,j}-\delta_{ij}\}\\ &=\tfrac{1}{2}(u^i_{,j}+u^j_{,i}+u^k_{,i}u^k_{,j}) \qquad (2.5)\end{aligned}$$

From Eq. (2.5), we can see that the values of the shearing components of the strain in this paper are one half of the values of the corresponding shearing components of the strain ordinarily used.[1)]

From Eq. (2.3), we can define the strain rate in Lagrange's representation $d\varepsilon_{ij}/dt$. Denoting the strain rate in Euler's representation by $f_{\lambda\mu}$, we have the following relation between $\dot{\varepsilon}_{ij}$ and $f_{\lambda\mu}$:

$$f_{\lambda\mu}=x^i_{,\lambda}\,x^j_{,\mu}\,\dot{\varepsilon}_{ij} \qquad (x^i_{,\lambda}=\partial x^i/\partial x^{*\lambda}) \qquad (2.6)$$

or

$$\dot{\varepsilon}_{ij}=x^{*\lambda}_{,i}\,x^{*\mu}_{,j}\,f_{\lambda\mu} \qquad (2.6')$$

Let the X^λ-component of the velocity $\boldsymbol{v}$ of a material particle in time t be v^λ, then $f_{\lambda\mu}$ is also defined by

$$f_{\lambda\mu}=\tfrac{1}{2}(v^\lambda_{,\mu}+v^\mu_{,\lambda}) \qquad (2.7)$$

as ordinarily done. We can prove that the right hand side of Eq. (2.6) is equivalent to that of Eq. (2.7), as follows:

$$\begin{aligned}&x^i_{,\lambda}\,x^j_{,\mu}d/dt\tfrac{1}{2}(g_{ij}-\delta_{ij})\\ &=x^i_{,\lambda}\,x^j_{,\mu}d/dt\tfrac{1}{2}(x^{*k}_{,i}\,x^{*k}_{,j})\\ &=\tfrac{1}{2}x^i_{,\lambda}\,x^j_{,\mu}(\dot{x}^{*k}_{,j}\,x^{*k}_{,i}+\dot{x}^{*k}_{,i}\,x^{*k}_{,j})\\ &=\tfrac{1}{2}(\dot{x}^{*k}_{,\mu}\,\delta_{k\lambda}+\dot{x}^{*k}_{,\lambda}\,\delta_{k\mu})\\ &=\tfrac{1}{2}(\dot{x}^{*\lambda}_{,\mu}+\dot{x}^{*\mu}_{,\lambda})=\tfrac{1}{2}(v^\lambda_{,\mu}+v^\mu_{,\lambda}) \qquad (2.8)\end{aligned}$$

where we have used following relations:

$$x^{*k}_{,i}\,x^i_{,\lambda}=\frac{\partial x^{*k}}{\partial x^1}\frac{\partial x^1}{\partial x^{*\lambda}}+\frac{\partial x^{*k}}{\partial x^2}\frac{\partial x^2}{\partial x^{*\lambda}}+\frac{\partial x^{*k}}{\partial x^3}\frac{\partial x^3}{\partial x^{*\lambda}}=\delta_{k\lambda}\ , \quad \text{etc.}$$

$$\frac{dx^{*\lambda}}{dt}=v^\lambda\ , \quad \text{etc.}$$

Let the Lagrange's and Euler's representation of stress be σ^{ij} and $T^{\lambda\mu}$ respectively, then we have

$$DT^{\lambda\mu}=x^{*\lambda}_{,i}\,x^{*\mu}_{,j}\,\sigma^{ij} \qquad (2.9)$$

or

$$\sigma^{ij}=D\,x^i_{,\lambda}\,x^j_{,\mu}\,T^{\lambda\mu} \qquad (2.9')$$

where D is the volume magnification ratio. In the sequel, we assume that the above relations can be hold relating to elastic stress and viscous stress, separately. $T^{\lambda\mu}$ is the stress relating to the unit area in deformed state and often called *actual stress*. So-called *conventional stress*, that is, the stress relating to the unit area in undeformed state is not σ^{ij}, but σ^{ij} multiplied by extention ratio in x^i-direction or x^j-direction[1)].

We can define many sets of invariant quantities of strain, strain rate and stress in Lagrange's and Euler's representation, but the followings will be used in this article:

$$I_1^*=\varepsilon_{ii}\ , \quad I_2^*=\tfrac{1}{2}\varepsilon_{ij}\,\varepsilon_{ij}\ , \quad I_3^*=\tfrac{1}{3}\varepsilon_{ij}\,\varepsilon_{jk}\,\varepsilon_{ki} \qquad (2.10)$$

$$I_1=g_{ii}\ , \quad I_2=D^2g^{ii}=D^2g_{\lambda\lambda}'\ ,$$
$$I_3=D^2=\det|g_{ij}|=\det|g'^{\lambda\mu}| \qquad (2.11)$$

where

$$\left\{\begin{aligned}g^{ij}&=x^i_{,\lambda}\,x^j_{,\lambda} &&(2.12)\\ g'_{\lambda\mu}&=x^i_{,\lambda}\,x^i_{,\mu} &&(2.13)\\ g'^{\lambda\mu}&=x^{*\lambda}_{,i}\,x^{*\mu}_{,i} &&(2.14)\end{aligned}\right.$$

$$K_1^*=f_{\lambda\lambda}\ , \quad K_2^*=\tfrac{1}{2}f_{\lambda\mu}f_{\lambda\mu}\ , \quad K_3^*=\tfrac{1}{3}f_{\lambda\mu}f_{\mu\nu}f_{\nu\lambda} \qquad (2.15)$$

§ 3. Derivation of Rheological Equation

Let the free energy of Helmholtz and the dissipation function per unit volume in undeformed state be A and W', respectively, then we have, from the first law of thermodynamics, for isothermal rheological process,

$$\frac{dA}{dt}+W'=\sigma^{ij}\frac{d\varepsilon_{ij}}{dt} \qquad (3.1)$$

Denote the quantities relating to elasticity (spring) and viscosity (dashpot) by the suffixes e and v respectively. Extending the assumptions which hold in one-dimentional Voigt model, we assume that next relations can hold in three-dimentional Voigt model:

$$\sigma^{ij}=\sigma_e^{ij}+\sigma_v^{ij} \qquad (3.2)$$

$$\dot{\varepsilon}_{ij}=\dot{\varepsilon}_{eij}=\dot{\varepsilon}_{vij} \qquad (3.3)$$

Substituting Eq. (3.2) into Eq. (3.1) and taking Eq. (3.3) into account, we obtain

$$dA/dt=\sigma_e^{ij}\,\dot{\varepsilon}_{ij} \qquad (3.4)$$

$$W'=\sigma_v^{ij}\,\dot{\varepsilon}_{ij} \qquad (3.5)$$

i) *elastic stress*

From (3.4), we have

$$\sigma_e^{ij}=\partial A/\partial\varepsilon_{ij} \qquad (3.6)$$

If the body is isotropic in undeformed state ($t=0$), we have

$$A=A(I_1^*, I_2^*, I_3^*) \qquad (3.7)$$

then, we obtain

$$\sigma_e^{ij}=\frac{\partial A}{\partial I_1^*}\delta_{ij}+\frac{\partial A}{\partial I_2^*}\varepsilon_{ij}+\frac{\partial A}{\partial I_3^*}\varepsilon_{ik}\,\varepsilon_{kj} \tag{3.8}$$

Further, if the body is incompressible, we have

$$D=1$$

then, we have

$$\partial D/\partial\varepsilon_{ij}=D^2g^{ij}=g^{ij} \tag{3.9}$$

where g^{ij} is defined by (2.12). Let the undetermined multiplier be φ', then we have, using Eq. (3.8) and Eq. (3.9), and taking $\partial A/\partial I_3^*=1$ into account,

$$\sigma_e^{ij}=\varphi' g^{ij}+\frac{\partial A}{\partial I_1^*}\delta_{ij}+\frac{\partial A}{\partial I_2^*}\varepsilon_{ij} \tag{3.10}$$

Then, if we put as follows:

$$\begin{aligned}\varphi'&=\varphi+\frac{1}{2}(2I_1^*-4I_2^*+4I_1^*+3)\frac{\partial A}{\partial I_1^*}\\&=\varphi+\frac{1}{2}I_2\frac{\partial A}{\partial I_1^*}\end{aligned}$$

where I_2 is defined by (2.11), Eq. (3.10) can be rewritten as follows:

$$\sigma_e^{ij}=\left(\varphi+\frac{1}{2}I_2\frac{\partial A}{\partial I_1^*}\right)g^{ij}+\frac{\partial A}{\partial I_1^*}\delta_{ij}+\frac{\partial A}{\partial I_2^*}\varepsilon_{ij} \tag{3.11}$$

If we apply Eq. (2.9) to elastic stress, we have

$$DT_e^{\lambda\mu}=x^{*\lambda}{}_{,i}\,x^{*\mu}{}_{,j}\,\sigma_e^{ij} \tag{3.12}$$

Substituting Eq. (3.8) and Eq. (3.11) into Eq. (3.12), we have following equations.[7]

$$\begin{aligned}T_e^{\lambda\mu}=\frac{2}{D}\Big\{&g'^{\lambda\mu}\frac{\partial A}{\partial I_1}(g'^{\nu\nu}g'^{\lambda\mu}-g'^{\nu\lambda}g'^{\nu\mu}-I_2\delta_{\lambda\mu})\\&\cdot\frac{\partial A}{\partial I_2}+I_2\delta_{\lambda\mu}\frac{\partial A}{\partial I_2}+I_3\delta_{\lambda\mu}\frac{\partial A}{\partial I_3}\Big\}\end{aligned} \tag{3.13}$$

and

$$\begin{aligned}T_e^{\lambda\mu}=2\Big\{&g'^{\lambda\mu}\frac{\partial A}{\partial I_1}+(g'^{\nu\nu}g'^{\lambda\mu}-g'^{\nu\lambda}g'^{\nu\mu}-I_2\,\delta_{\lambda\mu})\\&\cdot\frac{\partial A}{\partial I_2}+\varphi\,\delta_{\lambda\mu}\Big\}\end{aligned} \tag{3.14}$$

respectively, where I_1, I_2, and I_3 are defined by (2.11) and $g'^{\lambda\mu}$ is defined by Eq. (2.14).

ii) *viscous stress*

If we apply Eq. (2.9′) for viscous stress, we have

$$\sigma_v^{ij}=D\,x^i{}_{,\lambda}\,x^j{}_{,\mu}\,T_v^{\lambda\mu} \tag{3.15}$$

substituting Eq. (2.6′) and Eq. (3.15) into Eq. (3.5), we have

$$W'=D\,T_v^{\lambda\mu}f_{\lambda\mu} \tag{3.16}$$

Let the dissipation function relating to deformed state be W, then we have

$$DW=W' \tag{3.17}$$

From Eq. (3.16) and Eq. (3.17), we have

$$W=T_v^{\lambda\mu}f_{\lambda\mu} \tag{3.18}$$

If we assume that the process of viscous flow does not yield anisotropy, then we have

$$W=W(K_1^*,K_2^*,K_3^*) \tag{3.19}$$

moreover, if we assume that W can be expanded as the power series of K_1^*, K_2^* and K_3^*, we have (using Einstein's notation)

$$\begin{aligned}W&=a_i\,K_i^*+b_{ij}\,K_i^*\,K_j^*+c_{ijk}\,K_i^*\,K_j^*\,K_k^*+\cdots\\&=a_1\,K_1^*+b_{1j}K_1^*\,K_j^*+c_{1jk}\,K_1^*\,K_j^*\,K_k^*+\cdots\\&\quad+a_2\,K_2^*+b_{2j}\,K_2^*\,K_j^*+c_{2jk}\,K_2^*\,K_j^*K_k^*+\cdots\\&\quad+a_3\,K_3^*+b_{3j}\,K_3^*\,K_j^*+c_{3jk}\,K_3^*\,K_j^*K_k^*+\cdots\\&=(a_1+b_{1j}\,K_j^*+c_{1jk}\,K_j^*\,K_k^*+\cdots\cdot)K_1^*\\&\quad+(a_2+b_{2j}\,K_j^*+c_{2jk}\,K_j^*\,K_k^*+\cdots\cdot)K_2^*\\&\quad+(a_3+b_{3j}\,K_j^*+c_{3jk}\,K_j^*\,K_k^*+\cdots\cdot)K_3^*\end{aligned}$$

Putting as follows:

$$\begin{aligned}\eta_1&=a_1+b_{1j}\,K_j^*+c_{1jk}\,K_j^*\,K_k^*+\cdots\cdot\\2\eta_2&=a_2+b_{2j}\,K_j^*+c_{2jk}\,K_j^*\,K_k^*+\cdots\cdot\\3\eta_3&=a_3+b_{3j}\,K_j^*+c_{3jk}\,K_j^*\,K_k^*+\cdots\cdot\end{aligned}$$

we have

$$W=\eta_1\,K_1^*+2\eta_2\,K_2^*+3\eta_3\,K_3^* \tag{3.20}$$

(As $W\geqq 0$ always, some of the coefficients $a_i, b_{ij}, c_{ijk}, \cdots$, $(i, j, k=1, 2, 3)$ will become zero.) From Eq. (3.18) and Eq. (3.20), taking Eq. (2.15) into account, we have

$$T_v^{\lambda\mu}=\eta_1\,\delta_{\lambda\mu}+\eta_2\,f_{\lambda\mu}+\eta_3\,f_{\lambda\nu}f_{\nu\mu} \tag{3.21}$$

where η_1, η_2, and η_3 are functions of K_1^*, K_2^*, and K_3^*. If incompressible, $K_1^*=\operatorname{div}\boldsymbol{v}=0$, then η_2 and η_3 will become the function of K_2^* and K_3^*, and η_1 will become arbitrary hydrostatic pressure. Then, if we rewrite K_2^* and K_3^* by K_2 and K_3 which are strain rate invariants ordinarily used, we can obtain the equation of Reiner and Rivlin.

The Euler's representation of Eq. (3.2) is expressed by

$$T^{\lambda\mu}=T_e^{\lambda\mu}+T_v^{\lambda\mu} \tag{3.22}$$

From Eq. (3.13), Eq. (3.14), Eq. (3.21) and Eq. (3.22), we can obtain the rheological equations of Voigtian material which is isotropic in undeformed state as follows (filing $\eta_1\,\delta_{\lambda\mu}$ into $\varphi\delta_{\lambda\mu}$ in Eq. (3.24)):

$$\begin{aligned}T^{\lambda\mu}=\frac{2}{D}\Big\{&g'^{\lambda\mu}\frac{\partial A}{\partial I_1}+(g'^{\nu\nu}g'^{\lambda\mu}-g'^{\nu\lambda}g'^{\nu\mu}-I_2\,\delta_{\lambda\mu})\\&\cdot\frac{\partial A}{\partial I_2}+I_2\,\delta_{\lambda\mu}\frac{\partial A}{\partial I_2}+I_3\,\delta_{\lambda\mu}\frac{\partial A}{\partial I_3}\Big\}\\&+\eta_1\,\delta_{\lambda\mu}+\eta_2\,f_{\lambda\mu}+\eta_3\,f_{\lambda\nu}f_{\nu\mu}\end{aligned} \tag{3.23}$$

for a compressible material, and

$$T^{\lambda\mu}=2\left\{g'^{\lambda\mu}\frac{\partial A}{\partial I_1}+(g'^{\nu\nu}\,g'^{\lambda\mu}-g'^{\nu\lambda}\,g'^{\nu\mu}\right.$$
$$\left.-I_2\,\delta_{\lambda\mu})\frac{\partial A}{\partial I_2}\right\}+\varphi\,\delta_{\lambda\mu}+\eta_2 f_{\lambda\mu}+\eta_3 f_{\lambda\nu}f_{\nu\mu} \quad (3.24)$$

for an incompressible material.

§ 4. Simple Elongation

Let us consider uniform elongation of incompressible rod-like material which is homogeneous and initially isotropic, in the direction of its length, which we select as the direction of X^1-axis. This deformation is specified by

$$x^{*1}=\alpha x^1\,,\quad x^{*2}=\frac{1}{\sqrt{\alpha}}x^2\,,\quad x^{*3}=\frac{1}{\sqrt{\alpha}}x^3\,,\qquad \alpha=\alpha(t) \quad (4.1)$$

or

$$x^1=\frac{1}{\alpha}x^{*1}\,,\quad x^2=\sqrt{\alpha}\,x^{*2}\,,\quad x^3=\sqrt{\alpha}\,x^{*3}\,,\qquad \alpha=\alpha(t) \quad (4.2)$$

where α is an extention ratio, and

$$T^{22}=T^{33}\,,\quad T^{12}=T^{23}=T^{31}=0 \quad (4.3)$$

Substituting (4.1) into (2.14), we have

$$g'^{11}=\alpha^2\,,\quad g'^{22}=g'^{33}=1/\alpha\,,\quad \text{all others}=0 \quad (4.4)$$

From the second equation of (2.11), (2.12) and (4.2), we have

$$I_2=g^{11}+g^{22}+g^{33}=\frac{1}{\alpha^2}+2\alpha \quad (4.5)$$

From (4.1) and (4.2), we have

$$\left.\begin{aligned} v^1&=\frac{dx^{*1}}{dt}=\dot\alpha\,x^1=\frac{\dot\alpha}{\alpha}x^{*1}\\ v^2&=\frac{dx^{*2}}{dt}=-\frac{1}{2}\alpha^{-3/2}\dot\alpha\,x^2=-\frac{1}{2}\frac{\dot\alpha}{\alpha}x^{*2}\\ v^3&=-\frac{1}{2}\frac{\dot\alpha}{\alpha}x^{*3}\end{aligned}\right\} \quad (4.6)$$

Then, if we substitute (4.6) into (2.7), we have

$$f_{11}=\frac{\dot\alpha}{\alpha}\,,\quad f_{22}=f_{33}=-\frac{1}{2}\frac{\dot\alpha}{\alpha}\,,\quad \text{all others}=0 \quad (4.7)$$

If we substitute (4.3), (4.4), (4.5) and (4.7) into (3.24), we have

$$\left.\begin{aligned} T^{11}&=2\left\{\alpha^2\frac{\partial A}{\partial I_1}+\left(-\frac{1}{\alpha^2}\right)\frac{\partial A}{\partial I_2}\right\}\\ &\qquad+\varphi+\eta_2\frac{\dot\alpha}{\alpha}+\eta_3\left(\frac{\dot\alpha}{\alpha}\right)^2\\ 0\;&=2\left\{\frac{1}{\alpha}\frac{\partial A}{\partial I_1}+(-\alpha)\frac{\partial A}{\partial I_2}\right\}\\ &\qquad+\varphi+\eta_2\left(-\frac{1}{2}\frac{\dot\alpha}{\alpha}\right)+\eta_3\left(-\frac{1}{2}\frac{\dot\alpha}{\alpha}\right)^2\end{aligned}\right\} \quad (4.8)$$

From (4.8), we have

$$T^{11}=2\left(\alpha^2-\frac{1}{\alpha}\right)\left(\frac{\partial A}{\partial I_1}+\frac{1}{2}\frac{\partial A}{\partial I_2}\right)+\frac{3}{2}\eta_2\frac{\dot\alpha}{\alpha}+\frac{5}{4}\eta_3\frac{\dot\alpha^2}{\alpha^2} \quad (4.9)$$

According to Neo-Hookian theory of rubber elasticity,

$$A=\frac{1}{2}\mu(I_1-3)$$

then, we have

$$\frac{\partial A}{\partial I_1}=\frac{1}{2}\mu\,,\qquad \frac{\partial A}{\partial I_2}=0$$

Corresponding to the above relations, if we assume as follows:

$$\tfrac{1}{2}\eta_2=\eta=\text{const}\,,\quad \eta_3=0$$

then (4.9) becomes

$$T^{11}=\mu\left(\alpha^2-\frac{1}{\alpha}\right)+3\eta\frac{\dot\alpha}{\alpha} \quad (4.10)$$

If we put as follows:

$$\alpha=1+\varepsilon$$

then (4.10) becomes

$$T^{11}=\mu\{(1+\varepsilon)^2-(1+\varepsilon)^{-1}\}+3\eta\frac{\dot\varepsilon}{1+\varepsilon}$$
$$=3\mu\,\varepsilon\left(1+\frac{\varepsilon^2}{3}-\frac{\varepsilon^4}{3}+\cdots\cdots\right)+3\eta\frac{\dot\varepsilon}{1+\varepsilon}$$

If $\varepsilon\ll 1$ and terms of higher orders of ε can be neglected, the above equation becomes

$$T^{11}=3\mu\,\varepsilon+3\eta\,\dot\varepsilon \quad (4.11)$$

which is equivalent to the classical equation of Voigt model.

§ 5. Simple Shear

Let us consider incompressible simple shearing flow parallel to the X^1X^3-plane. This motion is specified by

$$x^{*1}=x^1+kx^2\,,\quad x^{*2}=x^2\,,\quad x^{*3}=x^3\,,\quad k=k(t) \quad (5.1)$$

or

$$x^1=x^{*1}-kx^{*2}\,,\quad x^2=x^{*2}\,,\quad x^3=x^{*3}\,,\quad k=k(t) \tag{5.2}$$

where $\frac{1}{2}\dot{k}$ is the shear velocity.

Substituting (5.1) into (2.14), we have

$$\left.\begin{aligned} &g'^{11}=1+k^2\,,\quad g'^{22}=1\,,\quad g'^{33}=1\\ &g'^{12}=k\,,\qquad g'^{23}=g'^{31}=0 \end{aligned}\right\} \tag{5.3}$$

and from the second equation of (2.11), (2.12) and (5.2) we have

$$I_2=g^{11}+g^{22}+g^{33}=k^2+3 \tag{5.4}$$

Differentiating (5.1) with respect to time t and taking (5.2) into account, we obtain

$$v^1=\dot{k}\,x^{*2}\,,\quad v^2=v^3=0 \tag{5.5}$$

Substituting (5.5) into (2.7), we have

$$f_{12}=\tfrac{1}{2}\dot{k}\,,\quad \text{all others}=0 \tag{5.6}$$

And substituting (5.3), (5.4) and (5.6) into (3.24), we can obtain

$$\left.\begin{aligned} &T^{11}=2\left\{(1+k^2)\frac{\partial A}{\partial I_1}-\frac{\partial A}{\partial I_2}\right\}+\varphi+\eta_3\left(\frac{1}{2}\dot{k}\right)^2\\ &T^{22}=2\left\{\frac{\partial A}{\partial I_1}-(k^2+1)\frac{\partial A}{\partial I_2}\right\}+\varphi+\eta_3\left(\frac{1}{2}\dot{k}\right)^2\\ &T^{33}=2\left(\frac{\partial A}{\partial I_1}-\frac{\partial A}{\partial I_2}\right)+\varphi\\ &T^{12}=2\left(k\frac{\partial A}{\partial I_1}+k\,\frac{\partial A}{\partial I_2}\right)+\eta_2\left(\frac{1}{2}\dot{k}\right)\\ &T^{23}=T^{31}=0 \end{aligned}\right\} \tag{5.7}$$

Then, if we assume that $T^{33}=0$, we obtain

$$\left.\begin{aligned} &T^{11}=2k^2\frac{\partial A}{\partial I_1}+\eta_3\left(\frac{1}{2}\dot{k}\right)^2\\ &T^{22}=-2k^2\frac{\partial A}{\partial I_2}+\eta_3\left(\frac{1}{2}\dot{k}\right)^2\\ &T^{12}=2k\left(\frac{\partial A}{\partial I_1}+\frac{\partial A}{\partial I_2}\right)+\eta_2\left(\frac{1}{2}\dot{k}\right)\\ &\text{all others}=0 \end{aligned}\right\} \tag{5.8}$$

We can see, from (5.8) that there appears so-called second-order effects (Poynting effect and cross viscosity,) and the third equation of (5.8) will be reduced to the corresponding classical equation if appropriate approximations similar as in § 4 are done.

§ 6. Discussions

We have assumed isotropy of the material in undeformed state, when we derive elastic stress-strain relation in § 3. This assumption does not mean that the material must be isotropic always, in other words, the material may become anisotropic in the process of elastic large deformation even if it is isotropic in its initial state. (Such material may be called *quasi-isotropic material.*[6]) At the same time, we have assumed that the process of viscous flow will not yield any anisotropy. Moreover, we assume that the above-mentioned two assumptions are not inconsistent with each other. In the actual process of deformation of our Voigtian material, both elastic and viscous process take place at the same time, and the material which is isotropic in initial state will become anisotropic as the deformation proceeds.

As far as we stay in the Voigt model having single retardation time, our rheological equations, Eq. (3.23) and Eq. (3.24), seem to be the most general possible equations under the assumptions of isotropy as above and the others mentioned in § 3. As we have already mentioned, their elastic terms are equivalent to the corresponding terms in Rivlin's equation of large elastic deformation, and their viscous terms to those in Reiner-Rivlin's equation. The results of application of Eq. (3.24) to simple deformations are reasonable and satisfactory, as we have seen in § 4 and § 5. Eq. (3.23) and Eq. (3.24) are given in Euler's representation but, if necessary, we can derive their Lagrange's representation by virtue of Eq. (2.9′).

References

1) For instance, V. V. Novozhilov: *Foundation of the Nonlinear Theory of Elasticity* (Graylock Press, New York, 1953).

2) R. S. Rivlin: *Large Elastic Deformations,* Rheology vol. I, ed. by F. R. Eirich (Academic Press, New York, 1956) chap. 10.

3) M. Reiner: Amer. J. Math. **67** (1945) 350. I. Braun and M. Reiner: Quart. J. Mech. Appl. Math. **5** (1952) 42.

4) R. S. Rivlin: Proc. Roy. Soc. **A, 193** (1948) 260.

5) For instance, T. Alfrey: *Mechanical Behaviors of High Polymer* (Interscience. Publ, New York, 1948).

6) M. Reiner: *Phenomenological Macrorheology,* Rheology vol. I, ed. by F. R. Eirich (Academic Press, New York, 1956) chap. 2, p. 11.

7) W. Segawa: Reports on Progress in Polymer Physics in Japan (1959) 36.

JOURNAL OF THE PHYSICAL SOCIETY OF JAPAN, Vol. 14 No. 8, AUGUST, 1959

Surface Cracks of Sheet Glass Produced by Sodium Vapor Treatment

By Junn NAKAYAMA

Ceramic Division,
Research Laboratory of Asahi Glass Co., Yokohama

(Received April 28, 1959)

Observation was made on the surface cracks of soda-lime-silica sheet glass produced by sodium vapor treatment in vacuum at 350°C. It was suggested first by Andrade and Tsien and recently concluded by Gordon *et al* that these surface cracks are developed from latent Griffith cracks through some etching action (the so-called decoration by Gordon *et al*) of sodium vapor. According to the present experiment, there are several phenomena on the surface cracks which are difficult to explain by the latent crack theory. The correlations of surface cracks to the drawing mark or to the direction of the periphery of the specimen, for instance, can be more reasonably explained by the cracking mechanism due to the shrinkage of transmuted surface layers after the sodium vapor attack. In this connection, it should rather be prefered that the surface cracks are newly originated by the treatment.

§1. Introduction

It has been known that the treatment of a piece of glass by sodium vapor in vacuum at high temperatures produces visible cracks on the surface. This was first reported by Andrade and Tsien¹⁾, who considered that the cracks were developed from the latent cracks, the so-called Griffith cracks²⁾, through the *etching* action of sodium vapor. Levengood and Butler³⁾ also seem to insist the presence of the latent cracks in their experiment on the adhesive strength of glue to glass surface and show the surface cracks produced by the sodium treatment. Recently Gordon *et al*⁴⁾ have published a work with conclusion similar to that made by Andrade and Tsien.

We have reached, however, to the conclusion different with the previous workers'. According to the present experiment, it is believed that the cracks are mostly not developed from latent cracks but newly created by the sodium treatment. The mechanism of the formation of these cracks might be attributed to the contraction of sodium treated surface layer against mother glass in the process of cooling after heating at 350°C.

§2. Experimental Procedures

The method for making the surface cracks is similar to that of Levengood and Butler, with some small modifications. Specimen container in which the reaction takes place is an ordinary glass tube, 2 to 3 cm in diameter and about 20 cm in length, with a "neck" as shown in Fig. 1. The specimens are cut from soda-lime-silica sheet glass of 2, 3 and 5 mm thicknesses, and a rod of 5 mm diameter of fused quartz is added for com-

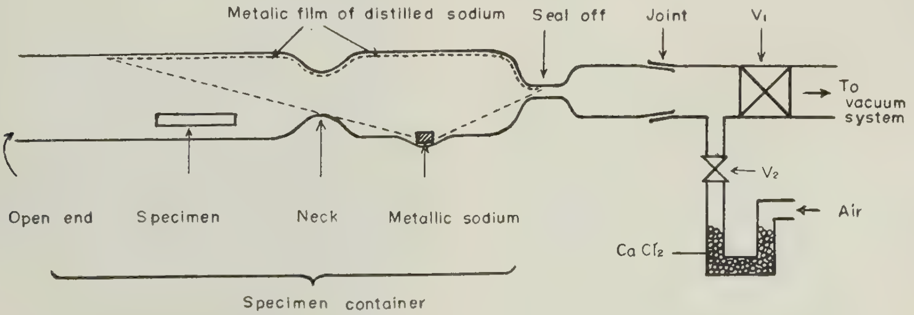

Fig. 1. Schematic diagram of the apparatus.

parison. Details of the procedure are as follows:

1) The specimen (*ca.* $1\times2\,\mathrm{cm}^2$) is cleaned by soaking with soap and distilled water.
2) The container is attached to the vacuum system with the valve V_1 closed and V_2 opened.
3) The dried air is kept to pass through the container from V_2 to the "open end" while the whole container is heated by a hand burner for about one minute to remove the adsorbed water from the inner surface.
4) After the container has been cooled down to the room temperature, a metallic sodium cube with edges of 5 to 10 mm length is inserted into the hollow of the tube from the "open end" without wiping off the kerosene which has protected the metallic sodium during storation.
5) The "open end" is sealed after the specimen is set in the container.
6) The valve V_2 is closed and V_1 is opened to evacuate the container to 1×10^{-3} mm Hg. In this process the kerosene vaporizes and is removed from the surface of sodium.
7) By heating the hollow in which the sodium block is located whole sodium melts and gradually evaporates to make a mirror of metallic sodium on the inner surface of the container. The neck in the tube protects the specimen from a direct deposition of metallic sodium on it.
8) When the vacuum reaches to 1×10^{-4}mm Hg, the container is sealed off from the the vacuum system.
9) The container is heated in an electric furnace and kept at 350°C for one hour or more. In this process, the specimen and the container wall get colored yellow or brown.
10) After the container has been cooled to the room temperature, it is broken and the surface of the specimen is observed.

§ 3. Experimental Results

1) *Surface cracks*

(*a*) Fig. 2 shows typical cracks produced. Cracks have a tendency to run perpendicularly to the edges of the specimen, in spite of the fact that the edges can have arbitrary directions relative to the drawing direction of the sheet glass.

(*b*) Cracks appear not only on the origina glass surface but also on the surfac newly produced by cutting or breaking (See Figs. 3 and 4.)

(*c*) A contaminated spot due to incomplete cleaning often becomes a starting poin of surface cracks. (See Fig. 5.)

(*d*) Cracks can appear even when the specimen is fire-polished just before the

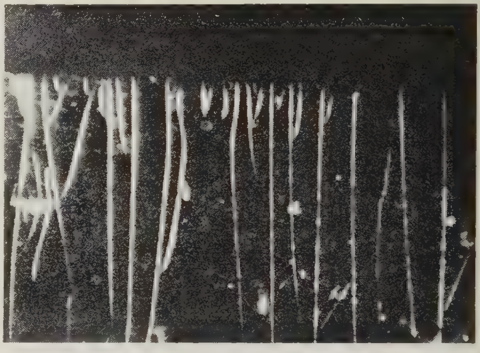

Fig. 2. Typical surface cracks developed perpendicularly to the edge of the specimen. (40×).

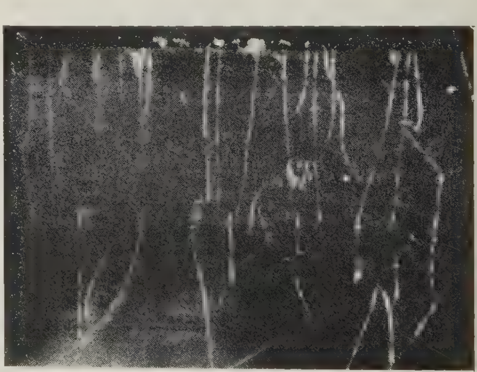

Fig. 3. Surface cracks on the cut side. (40×).

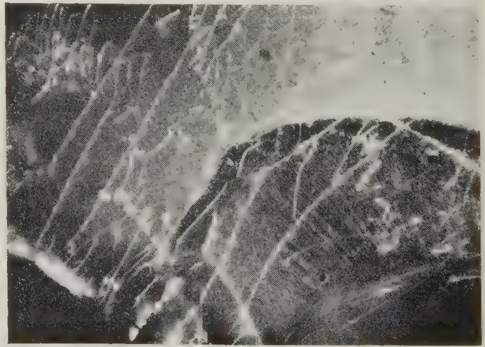

Fig. 4. Surface cracks on the original surface and the newly fractured shell-shaped surface of the specimen, showing the continuity of cracks at the boundary. (40×).

sodium treatment.

(*e*) By the sodium treatment, the surface crack which had disappeared with the lapse of time after its appearance by chilling could not be reproduced.

(*f*) The number of cracks increases with the treating time approaching to some ultimate value which probably depends on the quantity of sodium used.

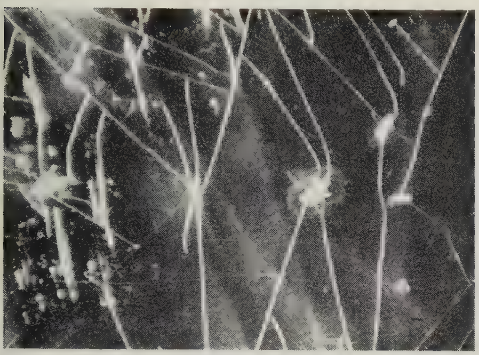

Fig. 5. Surface cracks observed when cleaning is incomplete. Cracks start from the contamination spots. (40×).

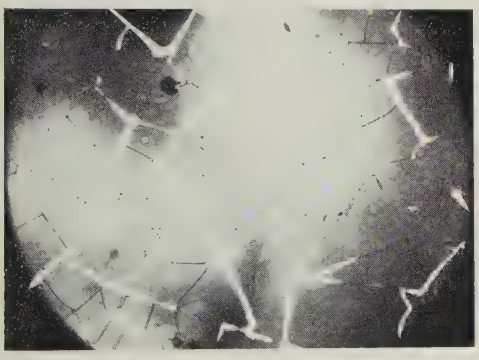

Fig. 6. Surface cracks produced by prolonged treatment. Each domain surrounded by the cracks shows Newton's rings. (30×)

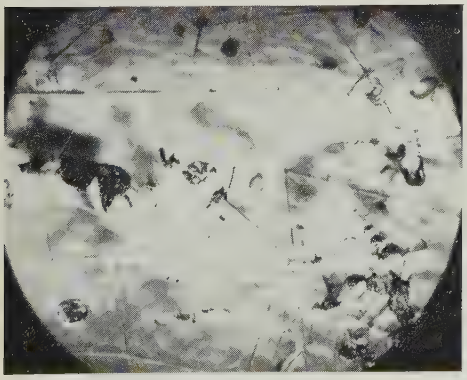

Fig. 7. The surface of specimen after the original surface layer has been flaked off. (30×)

(*g*) Treating with 0.3 g of sodium for 14 hours produces many cracks which are visible with the naked eyes. In Fig. 6, each domain surrounded by the cracks shows Newton's rings indicating that the surface is going to flake off. In this photograph, some cracks look like white lines showing that the light from the source comes directly through the cracks which are to some extent widely opened. The surface layer which is going to flake off can easily be removed by rubbing mechanically, and the new surface shows a roughened structure as is illustrated in Fig. 7.

(*h*) In a rod of fused quartz, cracks are more easily produced with less sodium and less treating time than in the ordinary soda-lime-silica glass. When pieces of soda-lime-silica glass and of fused quartz are treated at the same time in one container, the latter shows definitely darker color and more numerous cracks than the former.

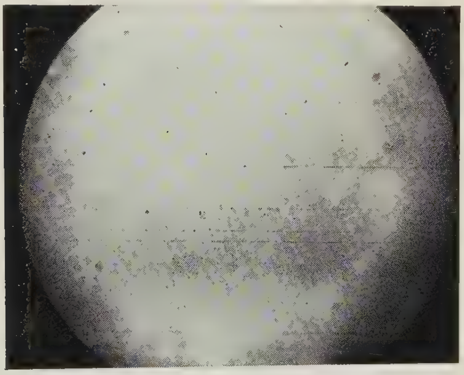

Fig. 8. Drawing marks (parallel straight lines) produced by sodium treatment. (30×)

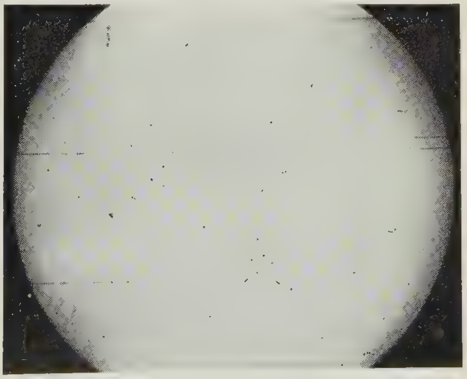

Fig. 9. Drawing marks after the water soaking of the specimen in Fig. 8. (30×)

2) *Drawing marks*

If a large quantity of sodium, say 1 g, is used, there frequently appears a group of lines with low contrast resembling to the so-called "drawing marks" which usually are observed by etching with hydrofluoric acid. (See Fig. 8.)

These lines, however, are made very clear by soaking the treated specimen in water above *ca.* 70°C (Fig. 9). In this photograph, a drawing mark forms a hair-curled shape. This indicates that these lines are not the "etched" parts but rather the "unetched" parts. The cross sectional view of the surface layer before and after the soaking would be as illustrated in Fig. 10.

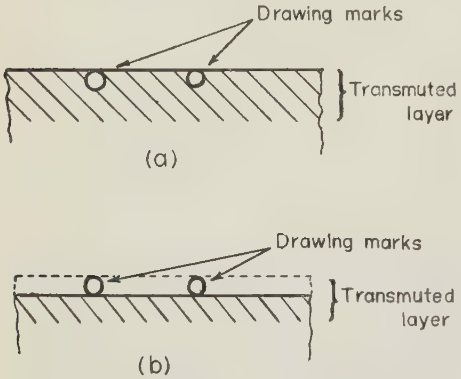

Fig. 10. Cross-sectional view of sodium treated surface layer with drawing marks. (a) Before, and (b) after soaking in water.

The difference in composition between mother glass and the drawing marks may result in the difference in reaction with sodium vapor and causes a difference in refractivity between the drawing marks and the rest of the surface film which makes these lines visible. Before soaking in water, these lines are fairly faint, as was the case in hydrofluoric acid etching, probably due to the small difference in refractivity. By soaking in water, however, surface layer except the portion of drawing marks seems to be carried away. The thread-like drawing marks are left on the new surface, which of course are more easily observed.

3) *Relation between the surface cracks and the drawing marks*

The surface of the specimen treated with a large amount of sodium (*ca.* 1.5 g) for about 15 hours looks dark brown or almost black and the observation by transmitted light is impossible. By reflected light, however, one can easily find out many drawing marks and very rough cracks as shown in Fig. 11. The parallel straight lines running obliquely in the left-half of the photograph are the drawing marks, and the other irregular lines are the surface cracks. The circular cracks which are seen left below are due to the contamination in the cleaning process. By soaking in water of *ca.* 70°C, both the surface layer and the drawing marks which have been especially developed by the "black" treatment can be thoroughly removed as flaked small pieces, but the surface cracks remain unchanged as seen in the right half of Fig. 11.

The flakes of the surface layer precipitated in this case were examined by X-ray and spectral analysis. The X-ray diffraction pattern was very complicated, and it was difficult to determine the structure. The result of the spectral analysis is given in Table I. It is interesting that the quantity of sodium is unexpectedly small. From this it is considered that the sodium atoms enter

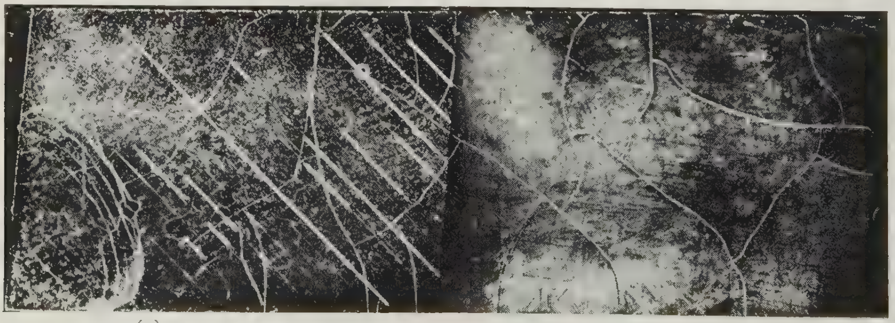

(a) (b)

Fig. 11. Surface cracks and drawing marks produced by prolonged treatment with a large amount of sodium. (4×) (a) Before, and (b) after soaking in water.

into the network of glass, and destroy the glass structure. The sodium ions are then easy to move and dissolve into water exhaustedly.

The observation of the intersecting point of a drawing mark and a surface crack (circle mark in the left half of Fig. 11) reveals that the drawing mark is shifted aside when it crosses the surface crack as in Fig. 12. The width of the crack is measured, in this case, directly on the photograph to be about 30μ. From these results a geometric model is proposed as illustrated in Fig. 13. The drawing marks lie exclusively in the surface layer, whereas the cracks reach a further depth.

Table I. Spectral analysis of precipitated flakes from the treated layer into water.

Si	Mg	Ca	Al	Ti	Cu	Fe	Na
+++	+++	++	+	+	tr	tr	tr

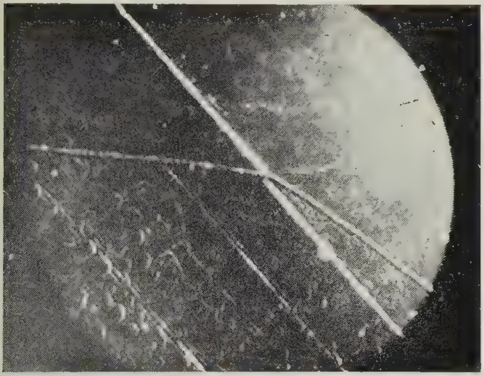

Fig. 12. Intersecting point of a surface crack and a drawing mark. The drawing mark (white line running obliquely) is shifted aside by the surface crack. (30×)

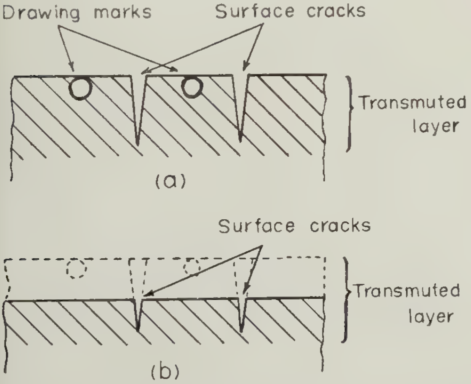

Fig. 13. Cross-sectional view of sodium treated surface layer with surface cracks and drawing marks. (a) Before, and (b) after soaking in water.

4) *Other natures of surface layer*

The color of the surface of the specimen changes from yellow through brown to black depending on the degree of treatment, especially on the quantity of the sodium used. Being soaked in water of about 50°C, or warmer, the color faids out producing bubbles, and the wet surface at this state shows alkalinity and the color of interference probably due to the flowing out of sodium ions from the surface layer.

The volume of the surface layer treated by sodium increases in contrast to the hydrofluoric acid etching. According to the measurement by the interference microscope, the treated layer is higher than the original surface by 5000Å in the extreme case, but it gets lower than the latter by 1000Å after soaking in water. The increment of height might be due to the sodium atoms entering into the network of glass structure and destroying the Si–O structure as was mentioned before. As the result of the destruction of the glass structure, the surface layer becomes very fragile, and is easily flaked off by rubbing. When soaked in water, the sodium flows out from the destroyed network into the water, resulting in the decrement of volume or level.

§ 4. Discussion

It would not be useless to elucidate the conclusions and discussions of the previous workers before discussing the present experiment. Andrade and Tsien, who first reported the detailed behaviour of the surface cracks produced by sodium treatment, tried the experiments on several sorts of glasses with different compositions. They concluded that the surface cracks produced by the sodium treatment are the *latent Griffith cracks* from the following experimental results.

1) The cracks are well developed in the situations where systematic scratching is improbable.
2) The cracks (latent cracks) develop with age which are almost completely absent on fresh glass immediately after drawing, and get frequent on the same glass some hours after drawing.

3) They are well developed in hard glasses, and hardly found in soft soda glasses.

4) A piece of plate glass exposed to sodium vapor showed no typical Griffith cracks. A fine diamond scratch was then made on another specimen from the same piece. Etching (sodium treatment) revealed typical cracks running out on both sides from the scratch in directions approximately normal to its length.

5) Other surface markings, such as scratches and drawing marks, can be developed by the attack of hydrofluoric acid; the Griffith cracks cannot be so brought to light.

6) The nature of the attack by the sodium vapor is not studied.

Gordon *et al* are led to the same conclusion as to the intrinsic nature of the surface cracks in the meaning that the cracks which are made visible by the sodium treatment are the *pre-existent* cracks. They derived the conclusion from the following results.

1) There is a relationship between the frequency of surface cracks and the mechanical weakness of the glasses from the same test rods; and it may be supposed that the more numerous the cracks, the greater the chance of a lethal defect.

2) Two Pyrex rods were twisted in opposite senses and were then clamped together at the ends so that they maintained mutually opposing torsional strains when decorated (*i.e.* sodium treated). For both rods the primary cracks run nearly normal to the tensional component of the shear, and many of the secondary cracks have been opened against the compressive stress. The same result was obtained with a silica rod subjected to bending, with the normal and parallel cracks to the axis of the piece on the tensile and compressive side, respectively.

3) In the accidental scrape, the pattern of cracks produced by the scrape is entirely contained by the pre-existent crack pattern. In the artificial scrape, there appear the primary cracks intersecting the scrape line, and the secondary cracks which run from the scrape normal to it are stopped by the pre-existent primary cracks.

4) In many cases cracks start from the surface devitrifications. If such a process were to take place on a smaller scale in the surface of glass, it might account for some of the observed behavior of glass surfaces. That is to say, it would explain both the origin of the cracks and perhaps the existence of surface tension.

Apart from the discussion about the existence of Griffith cracks, there no doubt are weak points on the glass surface. The weak points might be of various kinds, such as mechanical scratches, devitrifications around which the stress concentration is inevitable, and corrosion of glass surface by the so-called weathering in which the glass structure at the surface layer gets changed mainly due to dissolution of metallic ions into the adsorbed moisture. We consider, however, that the cracks produced by sodium treatment are mostly not the latent cracks but are newly originated or grown from the weak points mentioned above.

It is clear, first, from Fig. 12 that the nature of the attack by sodium vapor of which previous workers have not given any explanation, is not a simple etching. If it were the etching, the drawing mark which intersects the surface crack would have to lie on a straight line however wide the gap of the crack may be after the crack is made. Actually, however, as shown in Fig. 12, the drawing mark is shifted aside to each other by the surface crack. This shows that the mechanism might be attributed to the shrinkage of surface layer against mother glass. In the case of hydrofluoric acid etching the surface crack except the scratches cannot be developed, as was also already pointed out by the previous workers.

Observations on the surface cracks in the present experiment show the validity of the assumption that the cracking takes place after the treatment. If the surface cracks did pre-exist, the crack pattern would be independent of the direction of the periphery of the specimen, and to the contaminated spot which could be cleaned up by soaking process. Moreover, if the surface cracks appeared on the new surface of shell-shaped fracture, the cracks would have to be independent to the cracks on the original surface. However, these demands which arise from the assumption of the pre-existent racks are not realized as have been stated n the previous section. These results show hat the surface cracks are mostly produced y the sodium treatment. The mechanism f cracking after the treatment has not yet een made clear strictly, but a possibility is roposed that the difference in shrinkage etween the surface layer and the mother lass is responsible for this.

Almost all the experimental results of the revious workers can well be understood by he "subsequent cracking" mechanism. With he hard glasses the cracks are easy to appear ecause of a large difference in shrinkage. The statement made by Andrade and Tsien that the cracks are hardly found in soft soda glass would probably be due to the short duration of treating time: they treated the specimen for half an hour at most. The results that the cracks develop with age and that a diamond scratch makes many cracks may be attributed to the increase of weak points with age and to the presence of fine cracks which are usually observed in the friction of glass on hard substance, respectively. The selective appearance of primary cracks on the specimens subjected to the torsional or bending stress, as was found by Gordon *et al*, is naturally understood by the present mechanism. In this case, the surface layer which is made fragile by the attack of sodium vapor may easily be broken by the applied stress in a direction normal to the maximum tension. They showed a photograph of intersection of a surface crack (primary crack) and a scratch made by steel needle in which the primary crack preceded the surface cracks grown from the scratch, and this fact seems to be a key-point of the "pre-existent" crack theory of Gordon *et al*. In this case, it is supposed by the subsequent cracking theory that the originating point of the primary crack was weaker than the fine cracks which existed at the scratch. It is often experienced that an artificially made scratch does not become the starting point of fracture in the breaking tests of glass, and it is possible for the primary crack to precede the cracks which grow from the fine cracks at the scratches.

§ 5. Conclusions

It is concluded that the surface cracks produced by the sodium treatment are mostly not the latent cracks but the newly originated or grown ones by the treatment from the flaws of various kinds. The difference in shrinkage between the surface layer and the mother glass is proposed to be a possible assumption as to the cracking mechanism.

The nature of the attack by the sodium vapor is not yet clear, but it has been proved that the structure of glass in the surface layer is destroyed and is made very fragile by the sodium treatment.

Acknowledgements

The author should like to express his sincere thanks to President Dr. S. Suetoshi, Vice President Dr. T. Uekawa, and Chief Researcher Dr. E. Kanai of the Res. Lab. of Asahi Glass Co., and President Dr. M. Funaoka of the Iho Factory of Asahi Glass Co. for their kind advices. He is also indebted to Prof. K. Kinosita of Gakushuin University for his kind discussion and recommendation to publish this work.

References

1) E.N. da C. Andrade and L. C. Tsien: Proc. Roy. Soc. **A**, **159** (1937) 346.
2) A. A. Griffith: Phil. Trans. Roy. Soc. **A**, **221** (1920) 163.
3) W. C. Levengood and E. B. Butler: Amer. Ceram. Soc. J. **36** (1953) 257.
4) J. E. Gordon, D. M. Marsh and Margaret E. M. L. Parratt: Proc. Roy. Soc. **A**, **249** (1959) 65.

Note added 30 June 1959. An interesting paper was reported by A. S. Argon (Proc. Roy. Soc. **A**, **250** (1959) 472), which dealt with the surface cracks developed by sodium treatment on flat chemical Pyrex glass. He used the ball indentation method to distinguish the "real" (pre-existent) cracks from the artificial ones. That is, he made the Hertz fracture on the specimen before the sodium treatment. After the treatment, if a crack intersects the Hertz fracture at two points, it can be considered to have existed originally as a real crack; but, if not, it is artificial. He found a few "real" long cracks in this way on one single specimen, but vast majority of cracks were found to be artificial.

Short Notes

This section is intended to secure prompt publication of important discoveries in physics. The reports should not exceed 800 words in length. A figure of size 7 cm×7 cm will be counted as 150 words.

J. PHYS. SOC. JAPAN **14** (1959) 1114

Thermal Stability of the R, N and M Centres and the Oscillator Strength of the M Band of KCl Crystal

By Tetsuhiko TOMIKI

Department of Physics, The Faculty of Science, Tohoku University, Sendai, Japan

(Received June 4, 1959)

Okura[1)] measured the oscillator strength of the *M* band f_M of KCl crystal and obtained the relation $f_M=0.42f_F$, where $f_F=0.83$ is the oscillator strength of the ***F*** band of KCl. In this experiment, the assumption was made that only the transformation in the form of $\boldsymbol{F}\rightarrow\boldsymbol{M}$ occurred by irradiation with ***F*** light at beginning. Unfortunately, this basic assumption is not valid strictly: Firstly, the ***A*** band comes out at first on the red tail of the ***F*** band during the course of illumination with ***F*** light, as pointed out by Petroff[2)]; secondly, the ***R*** and ***N*** centres are also created simultaneously as the ***M*** band is developed; furthermore, in general, the half-width of the ***F*** band varies as the illumination with ***F*** light proceeds, and the ***K*** band is enhanced. Therefore, it is conceivable that $f_M=0.42f_F$ was underestimated.

In order to determine the oscillator strength of the ***M*** band experimentally, it is necessary to exclude these complexities. It is confirmed that this necessary condition is satisfactorily fulfilled when the additively coloured KCl crystal, which was exposed to ***F*** light so as to produce the ***M*** centre (together with the undesired ***A*** and ***R*** centres) a room temperature, is heated slowly up to 115°C followed by a slow cooling to room temperatur (see the curve (2) in Fig. 1 (b)), because the photochemical products except for the ***M*** centre ar thermally unstable and decompose according t the next forms: $\boldsymbol{R}\rightarrow\boldsymbol{N}$ and ***F*** (above 50°C), an $\boldsymbol{N}\rightarrow\boldsymbol{F}$ and ***M*** (above 100°C). The ***M*** centre is the most stable and decomposes thermally into the ***F*** centre above 130°C according to the equatio $1/\tau=2\cdot10^{12}\exp(-1.31\,(\text{ev})/kT)\,(\text{sec}^{-1})$. Thus, it is possible to realize the necessary condition that the crystal contains only ***F*** and ***M*** centres (see, Fig. 1 (a) and (b)). This fact enables us to determin the oscillator strength of the ***M*** band with high precision.

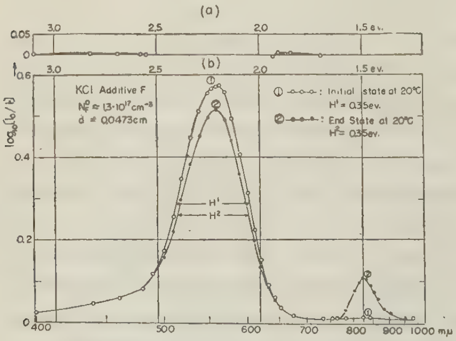

Fig. 1 (a): The increment of the absorption in the spectral region except the ***M*** band.

Fig. 1 (b): Curve (1) is the initial state, curve (2) shows the absorption spectra when the specimen was cooled to room temperature after the ***M*** band was developed at room temperature following by the temperature elevation to 115°C.

When the density of the ***F*** centres are determined with Kleinschrod-Smakula equation[3)] $1.31\cdot10^{16}\,K_FH_F$ and that of the ***M*** centres with Smakula equation[4)] $1.06\cdot10^{16}\,K_MH_M$, it is found that 2***F*** centres are required to creat one ***M*** centre. This indicates that the oscillator strength of the ***M*** band is formally equal to 0.5. In this case, it is *assumed* that the second absorption of the ***M*** centre does not exist in the region of the ***F*** band, because the bleaching curve of the ***F*** band caused by illumination with ***F*** light does not exhibit any anomaly even when the ***M*** band decreases at later stage. Furthermore, that the ***M*** centre carries only one electron is also assumed. To test this assumption, the quantum yield η_F defined by (Number of created ***F*** centres)/(Quanta absorbed by ***M*** band) was studied as a function of temperature. The result shows that η_F reaches a maximum value 0.56 above 130°C where the photochemical reaction occurred in the pure form $\boldsymbol{M}+(\text{photon})_M\rightarrow\boldsymbol{F}$, *i.e.*, $\eta_F=2\eta_M$. On the other hand, η_M was an order of 10^{-2} at room temperature.

The detailed description of this experiment will be reported in this journal. To Prof. M. Ueta, the author is very grateful for his kind interest and stimulating discussions.

References

1) H. Okura: J. Phys. Soc. Japan **12** (1957) 1315.
2) St. Petroff: Z. Phys. **27** (1950) 443.
3) F. G. Kleinschrod: Ann. Physik (5) **27** (1936) 97.
4) A. Smakula: Z. Phys. **59** (1930) 603.

J. Phys. Soc. Japan **14** (1959) 1115

Antiferromagnetism in $KMnF_3$

By Shinji Ogawa

Research Institute of Applied Electricity,
Hokkaido University

(Received May 28, 1959)

The magnetic susceptibility of $KMnF_3$ has been easured from room temperature down to 77°K ıd an antiferromagnetic behavior has been found. Martin *et al.*1) have reported on the antiferromagnetm in compounds of the type KMF_3 (where M=Mn, e, Co, Ni and Cu), in which the investigations of MnF_3 and $KCuF_3$ were not complete, however.

Specimens were prepared in two different ways; ne from the aqueous solutions of KF and $MnCl_2$ ollowing Nuka's method2), and the other by preipitating $KMnF_3$ in KCl from the melts of $MnCl_2$ nd 3KF at about 900°C in a platiumm crucible. he former specimen (A) was a fine powder of hite color with a dash of pink, and the latter pecimen (B) was transparent pale brown cubic rystals. An X-ray analysis revealed that both pecimens crystalize in the cubic perovskite strucures with lattice parameters a_0=4.190Å and 4.186Å or A and B respectively.

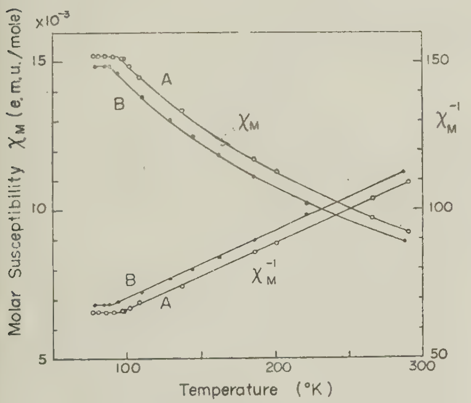

Fig. 1. Molar susceptibilities of specimens A and B of $KMnF_3$ versus temperature. (Inverse susceptibilities were also plotted.) These curves were corrected for the diamagnetism of -0.03×10^{-3} e.m.u./mole.

The temperature dependence of the susceptibility s shown in Fig. 1, and the magnetic data are summarized in Table I together with the X-ray data.

The measured susceptibilities obey fairly well to he Curie-Weiss law above about 100°K, and become onstant below 95° and 89°K for specimens A and B respectively, showing the presence of an antierromagnetic order in these temperature ranges. The antiferromagnetism should be mainly caused by an superexchange interaction through an intermediate fluorine ion, and this will be suggested by the fluorine hyperfine structure in the paramagnetic resonance of Mn^{2+} in a $KMgF_3$ single crystal3).

In the NMR of F^{19} in $KMnF_3$, Shulman *et* al.4) have recently observed a shift of resonance line by which the presence of a fairly large superexchange interaction is suggested, and have found a transition temperature 88.3°K which is in good agreement with T_N of our specimen B within the experimental error.

Table I. Lattice parameter a_0, Néel temperature T_N, asymptotic Curie temperature Θ, Curie constant C_M, effective number of Bohr magnetons p and molar susceptibility at Néel temperature $\chi_M(T_N)$ of $KMnF_3$.

	Specimen A	Specimen B
a_0	4.190±0.001Å	4.186±0.001Å
T_N	95±3°K	89±1°K
Θ	202±2°	204±2°
C_M	4.52±0.04	4.38±0.04
p	6.04±0.03	5.94±0.03
$\chi_M(T_N)$	15.2×10^{-3}	14.9×10^{-3}

References

1) R. L. Martin, R. S. Nyholm and N. C. Stephenson: Chemistry and Industry (1956) 83.
2) P. Nuka: Z. anorg. Chem. **180** (1929) 235.
3) S. Ogawa and Y. Yokozawa: to be published.
4) R. G. Shulman, K. Knox and B. J. Wyluda: Bull. Amer. Phys. Soc. **4** (1959) 166.

Note added in proof: Dr. K. Hirakawa have recently measured the magnetic susceptibilities of the compounds of type KMF_3. His result on $KMnF_3$ is: a_0=4.190Å, T_N=90°K, Θ=167° and C_M=4.438. I am grateful to Dr. Hirakawa for informing me of his results before publication.

J. PHYS. SOC. JAPAN **14** (1959) 1116

Paramagnetic Resonance of Manganese in $KMgF_3$

By Shinji OGAWA and Yasaburo YOKOZAWA

Research Institute of Applied Electricity, Hokkaido University

(Received May 28, 1959)

In connection with the antiferromagnetism in $KMnF_3$ [1], a paramagnetic resonance of Mn^{2+} ions has been observed in a single crystal of $KMgF_3$ containing about a few hundred parts per million manganese ions, at room temperature and 3.2 cm wave length.

As to the crystal structure of $KMgF_3$, there have been reported two types; a cubic perovskite[2),3)] and a monoclinic[4),5)]. The sample used in the resonance experiment had a cubic perovskite structure with a lattice parameter $a_0=3.987\pm0.002$Å.

The observed paramagnetic resonance spectrum consisted of many extra lines in addition to the usual fs and hfs lines of a Mn^{2+} ion. These extra lines may be due to the hyperfine interaction between manganese electrons and surrounding fluorine nuclei as in the case of Mn^{2+} in ZnF_2[6)] and CaF_2[7)]. Thus the observed spectra at various crystal orientations are all described by the spin Hamiltonian;

$$\mathscr{H}=g\beta\boldsymbol{H}\cdot\boldsymbol{S}+(1/6)a[S_x{}^4+S_y{}^4+S_z{}^4 -(1/5)S(S+1)(3S^2+3S-1)]+A\boldsymbol{S}\cdot\boldsymbol{I}+\mathscr{H}'$$

and

$$\mathscr{H}'=\sum_N \boldsymbol{S}\cdot A^N\cdot\boldsymbol{I}^N\ ,$$

where N runs over the six nearest neighbor fluorine ions, $\boldsymbol{I}^N$ is the nuclear spin of the Nth nearest neighbor fluorine ion and A^N the hyperfine interaction tensor between the manganese electronic spin and the fluorine nuclear spin. In our case of cubic symmetry, $\mathscr{H}'$ produces a shift δH of the resonance field;

$$\delta H=A_s\sum_N I_z{}^N+A_p\sum_N I_z{}^N(3\cos^2\theta^N-1)\ ,$$

where A_s is the isotropic part of A^N, A_p the anisotropic part and θ^N is the angle between the external magnetic field and the σ-bonding axis to the Nth fluorine ion. If use is made of Tinkham's notation[6)], our A_p is equal to his $(A_{p\sigma}-A_{p\pi})$. That is, one can know only a difference between cont butions from σ- and π-bondings of p electron.

Parameters determined from the observed spect are summarized in Table I.

From the above value of A_s, one can estimat in the same way as Tinkham[6)] and Baker *et al* have done, the amount of time the magnetic electrons spend in s orbitals on the fluorine ion, a suming that they are all in $2s$ orbitals. We co clude that the magnetic electrons have 0.58 ± 0.03 $2s$ character at each fluorine nucleus and 1.74 0.09% in each two $d\gamma$ orbitals. To estimate th amount of time in p orbitals, the contribution from direct dipole-dipole interaction, 3.6×10^{-4} cm must be subtructed from the observed A_p. Afte this has been done, we conclude that the $2p$ character is more than 1.2 ± 1.0% at each fluorin nucleus and more than 3.7 ± 3.0% in each $d\gamma$ orbita

Recently, Shulman *et al.*[8)] have observed a nuclea magnetic resonance of F^{19} in $KMnF_3$. From th shifts of resonance lines, they estimated A_s an A_p (A_σ in their notation) to be 15.5 ± 0.5 and 1.2 $\pm0.13\times10^{-4}$ cm^{-1} respectively. If the differenc of Mn^{2+}–F^- distances in $KMgF_3$ and $KMnF_3$ i taken into account, the results of electron para magnetic and nuclear magnetic resonances are ra ther in good agreement. This point will be dis cussed in a future paper.

Similar resonances of Mn^{2+} ions have been ob served in $KCdF_3$ and K_2MgF_4. Details will be published in this journal.

Table I. g-factor, cubic crystal field splitting parameter a and hfs parameter A of Mn^{2+} ion, and hf interaction parameters between manganese electrons and surrounding fluorine nuclei, A_s and A_p, in $KMgF_3$.

g	1.999 ± 0.002
a	$(+)\ 8.5\pm1.0\times10^{-4}$ cm^{-1}
A	$(-)\ 91.2\pm1.0\times10^{-4}$ cm^{-1}
$\lvert A_s\rvert$	$18.2\pm0.9\times10^{-4}$ cm^{-1}
$\lvert A_p\rvert$	$4.7\pm0.9\times10^{-4}$ cm^{-1}

References

1) S. Ogawa: to be published.
2) A. E. van Arkel: Physica **5** (1925) 162.
3) R. C. DeVries and R. Roy: J. Amer. Chem. Soc. **75** (1953) 2479.
4) H. Remy and W. Seeman: Rec. trav. chim. Pays-Bas **59** (1940) 516.
5) W. L. W. Ludekens and A. J. E. Welch: Acta Cryst. **5** (1952) 841.
6) M. Tinkham: Proc. Roy. Soc. **A**, **236** (1956) 535, 549.
7) J. M. Baker, B. Bleaney and W. Hays: Proc. Roy. Soc. A, **247** (1958) 141.
8) R. G. Shulman, K. Knox and B. J. Wyluda: Bull. Amer. Phys. Soc. **4** (1959) 166.

J. PHYS. SOC. JAPAN **14** (1959) 1117~1118

Fine Structure in the Giant Resonance for Cu^{63} and $Ag^{107}(\gamma, n)$ Reactions

By Teruo NAKAMURA, Kiyoji FUKUNAGA,
Kunio TAKAMATSU, Minoru YATA
and Shinjiro YASUMI

Department of Physics, Faculty of Science,
Kyoto University

(Received June 6, 1959)

Hitherto the investigations on the fine structure ı the giant resonance for the nuclear photoreaction ave been carried out by many authors. For medi- m weight nuclei, any fine levels were not detected y Saskatchewan group1) although they found many vels for several light nuclei, but Phillips2) de- cted more than ten breaks in the $Cu^{63}(\gamma, n)$ acti- ation curve in the energy range from 13.5 Mev 17.5 Mev with a 20 Mev betatron.

By the experiments with capture γ rays also, the xistence of fine structures in the Cu and $Zn(\gamma, n)$ xcitation curves has been reported by Bunbury3) nd Campbell4). We have investigated for medium veight nuclei such as Cu and Ag whether there xist fine structures or not, utilizing the energy ariation of Li-*p* γ rays by the Doppler effect.

The Li-*p* γ rays emitted from a thick lithium nethal bombarded with 500 kev protons consist of 17.6 Mev line with 10.7 kev half-width (in C.M. ystem) and a broad spectrum of 14.8 Mev com- onent. In the laboratory system, the energy of γ ays varies depending on the "Doppler angle" that s defined as the angle between proton beams and rays, since the excited nuclei of Be^8 have some elocities ranging from 1.23 to 1.28×10^8 cm/sec vithin the resonance width and can be considered o maintain those velocity vectors until they emit rays. (For the life-time of Be^{8*} to ground state ransition is estimated as 4×10^{-17} sec from $\Gamma_\gamma=$ 6.7 ev, and so the running distance of Be^{8*} nuclei vithin this life-time is about 5×10^{-9} cm). The ange of energy variation due to the Doppler effect is ±65 kev for 17.6 Mev line, while the photons of 14.8 Mev component could not contribute to produce fine structures because those energy spread is very broad (~2 Mev) compared to the width of fine structures as far reported.

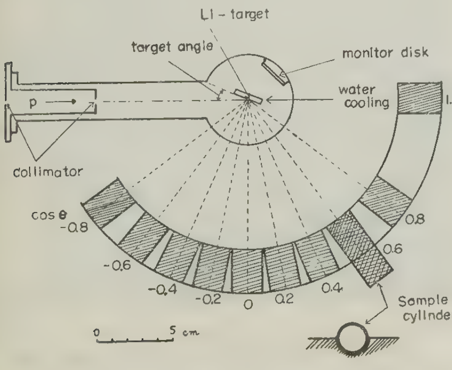

Fig. 1. Irradiation system of γ rays.

The target assembly is shown schematically in Fig. 1. The distance between a sample and γ-ray source was 10 cm. The form of a sample was a hollow cylinder with 5 cm length, 1.64 cm inner diameter and 1 mm thick. Eighteen cylinders made of copper and two cylinders made of silver were used, and the dimension of each sample was equal within 0.3% error.

The energy distribution of γ-rays irradiated on a sample is determined by the resonance formula with 10.7 kev half-width (in C.M. system) and the Doppler spread of photon energy due to the finite angle subtended by the sample cylinder at the γ-source. In our experimental arrangement it can be shown by calculations that a half of the total activities produced in a sample was produced by the γ-rays with about ±7 kev energy spread.

The samples were irradiated for about 20 minutes for copper and for about 25 minutes for silver at nine Doppler angles in front of a lithium target. β activities of irradiated samples were measured with two cylindrical G.M. counters of thin brass wall (0.125 mm thick). The counting efficiencies of both counters were mutually checked by Ra γ-source placed at the fixed position. In addition, in order to avoid the systematic errors due to the lack of uniformity of sample dimensions and slight inequality on the counting efficiencies of two counters, the combination of sample and counter at a given angle was interchanged. γ-ray intensities were

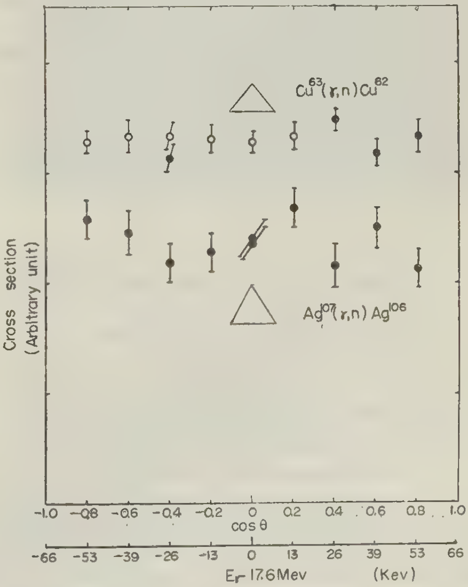

Fig. 2. Excitation curves of $Cu^{63}(\gamma, n)Cu^{62}$ and $Ag^{107}(\gamma, n)Ag^{106}$ reactions.

monitored with the β activities of a copper or silver disk irradiated simultaneously with sample cylinders.

The relative cross sections for Cu^{63} and $Ag^{107}(\gamma, n)$ reactions are plotted as a function of Doppler angles in Fig. 2. (The contributions from activities of Ag^{108} were eliminated by using the decay curve.) For copper the data of target angle 60° and 25° are shown with open and closed circles respectively, and for silver only the data of target angle 25° are plotted. The errors indicated in the figures are only statistical, and other errors are negligibly small.

In the present experiment, the lower limits of detectable magnitude of a fine level were considered as roughly three times of statistical errors, and they were evaluated as about 0.2 Mev-mb for copper and 0.7 Mev-mb for silver using the cross section values recently determined by us5) and so it was concluded from Fig. 2 that in $Cu^{63}(\gamma, n)$ reaction there was no fine level larger than 0.2 Mev-mb, while in $Ag^{107}(\gamma, n)$ reaction there was no fine level larger than 0.7 Mev-mb but some fine levels less than 0.7 Mev-mb seem to exist in the energy region of 17.6 Mev ± 65 kev. These conclusions do not agree with Bunbury's results3), but for the case of copper they agree with the result reported by Foster6) that there was no fine level for Cu by the method of Li-p γ-rays and neutron detection.

References

1) L. Katz, R. N. H. Haslam, R. J. Horsley, A. G. W. Cameron and R. Montalbetti: Phys. Rev. **95** (1954) 464.
2) K. Phillips: Phil. Mag. **44** (1953) 533.
3) D. St. P. Bunbury: Proc. Phys. Soc. London A, **67** (1954) 1106.
4) J. G. Campbell: Aust. J. Phys. **8** (1955) 449.
5) T. Nakamura, K. Takamatsu, K. Fukunaga, M. Yata and S. Yasumi: J. Phys. Soc. Japan (in press).
6) D. G. Foster: Doctoral Thesis of Cornell Univ. (1956).

J. PHYS. SOC. JAPAN **14** (1959) 1118

Hot Holes in Tellurium

By Yasuo KANAI

Electrical Communication Laboratory,
Musashinoshi, Tokyo

(Received June 16, 1959)

Current-voltage character and Hall coefficient of Te single crystals were measured in the pulsive high electric field at 77°K. Typical result of our samples is shown in Fig. 1. The direction of current flow was parallel to the c-axis, and the sample had the following character at 77°K; resistivity $\rho = 1.04 \times 10^{-1}$ ohm-cm and Hall coefficien $R = +412$ cm³/coul., hence the hole density $p = 3\pi/8Re = 1.78 \times 10^{16}$/cc and the hole mobility $\mu_0 = 8R/3\pi\rho = 3.37 \times 10^3$ cm²/V sec. As shown in Fig. 1 in the high electric field the current density was not proportional to the electric field but proportional approximately to the square root of it. In the same region of electric field, there was no change in the value of Hall coefficient. Hence we might believe that the decrease of current density of Te in high electric field was caused by the reduction of hole mobility.

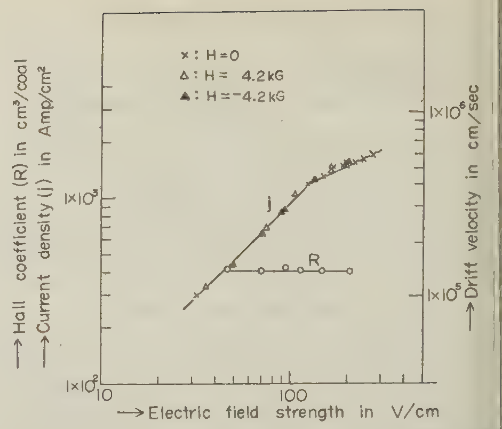

Fig. 1. Current-voltage character with and without transverse magnetic field and Hall coefficien at 4.2 kG of Te crystal at 77°K.

Following the Shockley's calculation1), E_c, the critical value of the electric field, where the Ohm's law ceases to be valid, is given approximately by the formula

$$\mu_0 E_c \equiv v_{dc} = 1.51\, v_s$$

where

μ_0: low field mobility
v_{dc}: critical value of drift velocity
v_s: sound velocity in crystal.

If we assume2) 0.5×10^{12} c.g.s. for the value of c_{ii}, the elastic constant, in Te, we get 2.83×10^5 cm/sec for the value of v_s in Te. So we can estimate 1.27×10^2 V/cm as the theoretical value of E_c. This value is in good agreement with the experimental value, i.e. 1.2×10^2 V/cm. Hence, if it is allowed to neglect the anisotropy of Te crystal, we may conclude that the main part of the energy loss of holes in Te is acoustic-phonon scattering, and the contribution from optical-phonon scattering seems to be negligible.

References

1) W. Shockley: Bell Syst. Tech. J. **30** (1951) 990.
2) J. Bardeen and W. Shockley: Phys. Rev. **80** (1950) 72.

J. PHYS. SOC. JAPAN **14** (1959) 1119~1120

Anomalous Transmission of Electrons in a Film of Molybdenite

By Kazutake Kohra
Institute of Physics, College of General Education, University of Tokyo, Komaba, Meguro, Tokyo
and
Hiroshi Watanabe
Hitachi Central Research Laboratory, Kokubunji, Tokyo

(Received June 13, 1959)

It is known from pretty long ago that the transmission of X-rays abnormally increases when the diffraction takes place in a nearly perfect crystal with sufficient thickness[1]. This phenomenon was explained with the dynamical theory taking account of absorption[2].

The present note reports that the similar effect has been observed also in case of electrons. The Hillier patterns from a film of molybdenite crystal were taken at several regions with various thickness, the accelerating voltage being 75 kv.

From relatively thin parts of the film, usual net patterns were obtained, where many diffraction streaks form diffraction images (Fig. 1). Corresponding to most of the diffraction streaks the extinction (dark) streaks were ascertained in the incident image, as usually expected. (In practice, such correspondence could not be ascertained for all diffraction streaks probably because of the complicated nature of the pattern. However, any bright, not dark, streaks in the incident image were not found corresponding to the diffraction streaks).

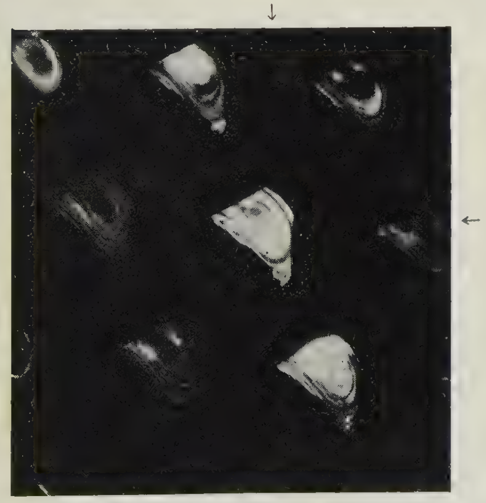

Fig. 1. Hiller pattern from a thin part of molybdenite film.
(The incident pattern is indicated by the arrows.)

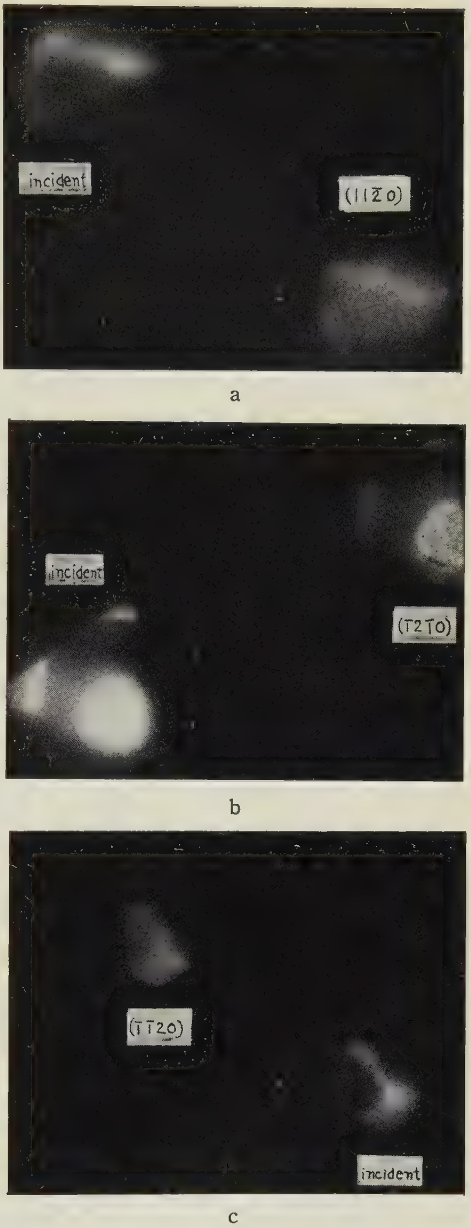

Fig. 2. Hillier patterns from thickparts of molybdenite film.

When the irradiated part is appropriately thick, the patterns as shown in Fig. 2 were obtained. Besides the incident image, only one diffraction image is remarkable, the index of which is (11$\bar{2}$0) or equivalent to it for all cases*. Although the pattern is not sharply defined and of weak contrast because of the strong backgrornd, it can be clearly seen that the *bright*, *not dark*, streak in the incident image corresponds to some bright streak in the diffraction image. They are almost same to each other in shape and intensity. This phenomenon means that the transmitted intensity does not decrease, but increases when the diffraction takes place, being no more than that of anomalous transmission which is known for X-rays.

---

* In the original photographic plate, another diffraction (10$\bar{1}$0) and the Kikuchi band, although faint, were sometimes observed.

The phenomenon of anomalous transmission for electrons can be explained analogously to for X-rays. According to the theory, this phenomenon is observed only when the crystal is sufficiently thick. This is consistent with our observation that the anomalous transmission appears only when the film is so thick that the net pattern disappears and the Kikuchi band appears.

It is also to be noted that the streaks are not straight, but curved. This is probably caused by that the film is curved. Then it might be said that the anomalous transmission is observed even if the crystal is not so perfect.

References

1) For example, G. Borrmann: Phys. Z. **42** (1940) 157; Z. Phys. **127** (1950) 297. H. N. Cambell: J. Appl. Phys. **22** (1951) 1139. G. L. Rogosa and G. Schwarz: Phys. Rev. **87** (1952) 995. G. Brogren and O. Adell: Ark. Fys. **8** (1953) 97; **8** (1954) 401. Refer to K. Kohra: Nippon Buturi Gakkai-si **13** (1958) 762 (in Japanese).
2) M. v. Laue: Acta Cryst. **127** (1950) 297. W. H. Zachzriassen: Proc. Nat. Acad. Sci. **38** (1952) 378.

J. Phys. Soc. Japan **14** (1959) 1120

On the Magnetic Property of Iron Telluride

By Ichiro TSUBOKAWA and Shoko CHIBA

The Research Institute for Iron, Steel and Other Metals, Tohoku University, Sendai, Japan

(Received May 15, 1959)

Magnetic properties and the phase diagram of the system of iron and tellurium in the range of the vicinity of stoichiometric composition (fifty atomic percent) were investigated by one of the present authors[1] as well as by Kondoh and Uchida[2]. The former author showed that there exists a single phase domain of iron telluride (α-phase) extending from 46 to 49 atomic percent of tellurium ($FeTe_{0.85}$~$FeTe_{0.96}$) in this binary system. Grϕnvold, Haraldsen and Vihovde[3] reported also that this phase has a cyrstal structure intermediate between PbO and Fe_2As structures. Recently, Westrum, Chou and Crϕnvold[4] reported a lumda-shaped anomalous heat absorption at 63°K for the compound with the composition $FeTe_{0.90}$. From the specific heat vs. temperature curve obtained by them, the excess heat absorption and the total entropy change were estimated to be afout 60 cal per mol of iron atom and 0.57 cal/mol°K respectively.

In order to clarify the origin of the heat absorption above mentioned, the magnetic susceptibility for an α-phase compound, $FeTe_{0.95}$ was measured by the present authors from the boiling point of of helium to room temperature. The measuremen was made by means of a magnetic balance in the magnetic field of 3.0 kOe. The result obtained is shown in Fig. 1. As seen from the figure, the susceptibility reaches its maximum at about 63°K, which coincides with the lumda point in the specific heat vs. temperature curve. On the higher temperature side of this maximum point (200°~750°K), the susceptibility is represented quite well by an equation $\chi=(0.0042)/(T+130)$*. From this Curie constant, the corresponding effective Bohr magneto nnumber is found to be 2.44. Assuming $\mu_{eff}=\sqrt{g^2S(S+1)}$ and $g=2$, $S=1.64/2$ is obtained. (S is the average spin quantum number and g the Landé factor). If the change at 63°K is antiferro → paramagnetic transition, the total entropy change and excess heat absorption are estimated to be $\Delta s=R\log(2S+1)=1.94$ cal/mol°K and $\Delta Q=103$ cal/mol. Although these figures are slightly greater than the results from the measurement of the specific heat mentioned above, the lumda point of susceptibility may be considered to be the antiferromagnetic Néel point.

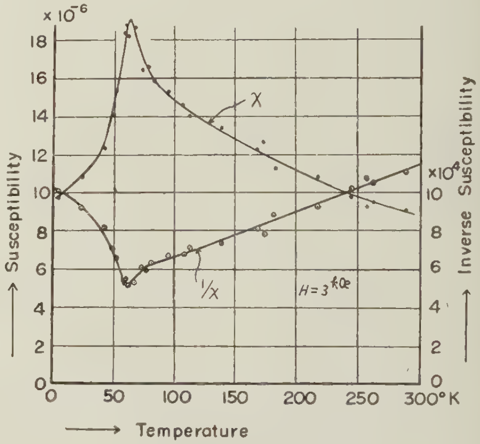

Fig. 1. The susceptibility or the inverse susceptibility versus temperature curves for $FeTe_{0.95}$.

The authors wish to express their hearty thanks to Profs. T. Hirone, S. Maeda and N. Tsuya for their encouragement and valuable discussion.

---

* The Curie constant differs from the value in the previous paper[1]. It has been found for the chech by Chiba that the absolute values of the susceptibility in the preveous measurements were not correct and they were smaller than the correct value by about 20%.

References

) S. Chiba: J. Phys. Soc. Japan **10** (1955) 837.
) H. Kondoh, and E. Uchida: J. Phys. Soc. Japan **10** (1955) 357.
) F. Grϕnvold, H. Haraldsen and J. Vihovde: Acta Chem. Scand. (1954) **8** 1927.
) E. F. Westrum, C. Chou and F. Grϕnvold: J. Chem. Phys. **30** (1959) 761.

J. Phys. Soc. Japan **14** (1959) 1121~1122

Thomas-Fermi Model of Compressed Positive Ion

By Shigehiro Kobayashi

Department of Physics, Kagawa University, Takamatsu

(Received June 8, 1959)

For the following three cases 1 to 3, the TF nethod was established previously by the corresponding investigators.

	neutral atom	positive ion
free state	1. Thomas-Fermi[1)	2. Guth-Peierls[2)
compressed state	3. Slater-Krutter[3)	3.

We have made a calculation of the remaining (most general) case 4, namely the TF method for positive ons in compressed state. We wish to report about ts method briefly in the following short note.

The TF equation of a compressed positive ion akes also the ordinary form

$$\phi''=\phi^{3/2}/x^{1/2}\,. \tag{1}$$

ts solution, so-called the TF function denoted by $\phi_{q,X}(x)$ for the case of ionization degree $q\equiv$ $Z-N)/Z$ (Z=atomic number, N=electron number) nd boundary radius X (in TF unit μ), is subject o the conditions at the nucleus ($x=0$)

$$\phi_{q,X}(0)=1 \quad : \quad \text{nucleus predominates} \tag{2}$$

nd at the boundary ($x=X$)

$$\phi_{q,X}(X)\neq 0 \quad : \quad \text{finite pressure} \tag{3}$$

nd

$$\phi_{q,X}(X)-X\phi'_{q,X}(X)=q \quad : \quad \text{net charge}=(Z-N)e\,. \tag{3a}$$

n the case of free state (boundary radius $x_0>X$), he last conditions are replaced by the following onditions

$$\phi_{q,x_0}(x_0)=0 \quad : \quad \text{zero pressure} \tag{4}$$

nd

$$-x_0\phi'_{q,x_0}(x_0)=q \quad : \quad \text{net charge}=(Z-N)e\,. \tag{4a}$$

These circumstances can be seen from Fig. 1, where four tangent lines [1] to [4] correspond to the boundary conditions of the above four cases 1 to 4, respectively.

Then, it has been established that for a definite value of q the decreasing boundary radius (the increasing compression) takes the TF curve with the decreasing initial slope (shifted more upwards), the relations of which are shown in Fig. 2.

In our case characterized by (q, X), also, the electron density and the potential distribution are given by

$$\rho=\frac{Z}{4\pi\mu^3}\left[\frac{\phi_{q,X}(x)}{x}\right]^{3/2} \tag{5}$$

and

$$V=V_0+\frac{Ze}{\mu}\,\frac{\phi_{q,X}(x)}{x} \tag{6}$$

respectively, as functions of x. Here, V_0 is the maximum potential for the electrons in the ion and can be determined, following Slater and Krutter, in such a way that the potential V in the immediate neighborhood of the nucleus has a value independent

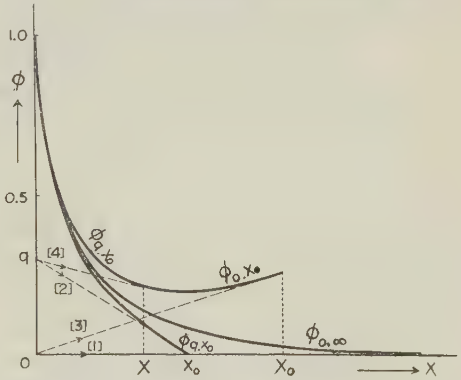

Fig. 1. The boundary conditions of the TF function $\phi(x)$.

$\phi_{o,\infty}$: free } neutral atom
ϕ_{o,x_0}: compressed } neutral atom
ϕ_{q,x_0}: free } positive ion
$\phi_{q,X}$: compressed } positive ion

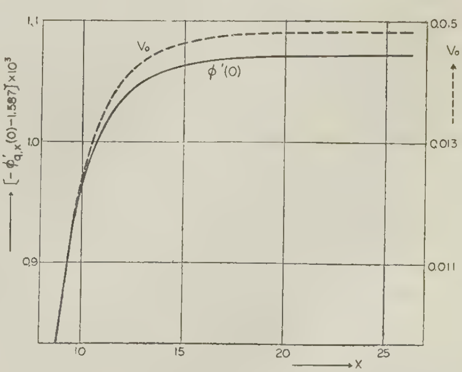

Fig. 2. The initial slope of the associated TF curve $\phi'_{q,X}(0)$ and maximum potential V_0 as functions of the boundary radius X for Cs ion.

of the boundary radius as

$$V_0=\left[\frac{q}{x_0}+\phi'_{q,x_0}(0)-\phi'_{q,X}(0)\right]\frac{Ze}{\mu} \tag{7}$$

dependent on q and X. (Cf. Fig. 2)

As our case is most general, this expression (7) is reduced for the three cases naturally to the familiar ones[4];

$$\begin{aligned} V_0&=0 && \text{for free neutral atoms}\\ &=(Z-N)e/\mu x_0 && \text{for free ions}\\ &=[\phi'_{0,\infty}(0)-\phi'_{0,X_0}(0)]\frac{Ze}{\mu} && \text{for compressed atoms.} \end{aligned}$$

These expressions (5) to (7) have enabled us to calculate various physical quantities for positive ions in compressed state, for example, equation of state, compressibility and so on.

The details of the calculation and the evaluated values of these quantities for Cs ion will be soon published in a separate paper[5].

The author wishes to express his sincere thank to professor K. Umeda of Okayama University fo his continued guidance and kind encouragemen throughout this work.

References

1) L. H. Thomas: Proc. Camb. Phil. Soc. 2 (1926) 542. E. Fermi: Rend. Lincei **6** (1928) 4
2) E. Guth and R. Peierls: Phys. Rev. **37** (1931 217.
3) J. C. Slater and H. M. Krutter: Phys. Re **47** (1935) 559.
4) P. Gombás: *Die statistische Theorie des Ato und ihre Anwenduugen* (Springer, Wien, 1949
5) S. Kobayashi: Mem. Fac. Liberal Arts & Educ., Kagawa Univ., II no. 82 (1959).

Errata

An Experimental Investigation on the Mode of Slip in Face-Centered Cubic Metals

By Tadami TAOKA, Kō YASUKŌCHI, Ryūkichi HONDA and Isao ŌYAMA

J. Phys. Soc. Japan **14** (1959) 888

The following figure (Fig. 3, b) should be inserted in next to Fig. 3, a in P. 891.

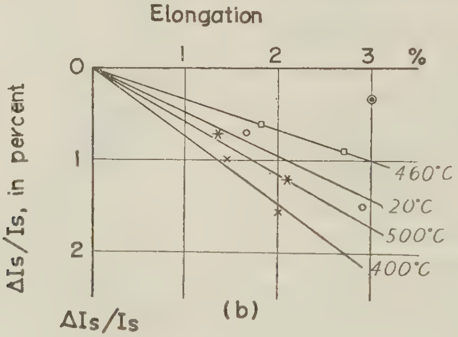

Fig. 3, b.

Internal Friction of KCl Crystals at Low Temperatures

By Taira SUZUKI, Katsumi SUZUKI and Kazuo KAMIGAKI

J. Phys. Soc. Japan **14** (1959) 731

Page	Erratum	Corrected
731～740	Author's Name: Tomoo KAMIGAKI	Kazuo KAMIGAKI

On the Non-Isothermal Diffusion Theory of Rectifiers

By Tadasi NUMATA

J. Phys. Soc. Japan **14** (1959) 902

Page	Line		Should be read
904	Eq. (16)	$\frac{e^2\varphi(x)}{4\varepsilon(b)x}$	$\frac{\boldsymbol{e}^2\varphi(x)}{4\varepsilon(b)x}$
906	14	camparison	comparison
	20	valtages	voltages
907	Eq. (42)	$\exp\left(\lambda(d)U-\int_a^d V\frac{d\lambda}{dx}dx\right)$	$\exp\left(\lambda(d)U-\int_b^d V\frac{d\lambda}{dx}dx\right)$
908	Eq. (52)	$\ln\frac{T_a^{\Lambda(a)}}{T_b^{\Lambda(b)}}$	$\ln\frac{T_a^{\Lambda(a)}}{T_a^{\Lambda(a)}}$

JOURNAL OF THE PHYSICAL SOCIETY OF JAPAN, Vol. 14, No. 9, SEPTEMBER, 1959

Electroluminescence of ZnS Phosphors Excited by Short Field Pulses

By Shoji TANAKA

Department of Applied Physics, University of Tokyo,
Tokyo, Japan

(Received February 7, 1959)

The electroluminescence in ZnS:Cu, Pb phosphors excited by short field pulses are investigated and excitation and recombination mechanisms of luminescent centers are discussed. The exciting pulse fields used in these experiments are rectangular pulses having durations of 1 to 40 microseconds. From the experimental results about emission spectra, brightness waveforms, dependences of light outputs on the applied voltages and pulse durations, decay times, build-up characteristics and their temperature dependences, the following considerations are made: the local intense field generated at the cathode region of phosphor particle accerelates the primary electrons and the luminescent centers are impact-ionized by these electrons. The field strength may be smaller than in the case of sinusoidal field excitation and then the excitation efficiency of primary electron greatly decreases compared with the latter case. The primary electrons are partly generated thermally and partly by the direct field-ionization. The decay of electroluminescence obeys the bimolecular law and is affected by the electron traps in the region of long pulse durations. The build-up characteristics are also affected by the deeply lying electron traps.

§ 1. Introduction

The electroluminescence phenomena in ZnS phosphors have been greatly investigated recently. Voltage dependences, brightness waveforms, frequency and temperature dependences and other associated characteristics have been reported. Above all, the intrinsic electroluminescence, which is obtained with the powder phosphor dispersed in dielectric medium, has been exclusively studied.

The mechanism of electroluminescence, however, is not clear enough even now, since the phenomena generated in phosphors are very complicated and can hardly be separated into elementary processes experimentally. Curie1), Piper and Williams2), Zalm3) and others proposed the fundamental considerations based on the impact ionization mechanism. The impact ionization of luminescent centers by primary electrons which are accerelated in the intense field is the most reasonable excitation mechanism, but the source of the primary electrons, effects of electron traps and donors, and the reason of formation of local intense field have been discussed from the several points of view.

The aim of this paper reported here is the study of the excitation and recombination mechanisms of the luminescent centers in ZnS powder phosphors by means of high speed pulse fields. As explained in a previous report4), the excitation by the short field pulse is more useful than usual sinusoidal field excitation for the study of the electroluminescence phenomena, since the waveforms are very simple, and the processes of the excitation and recombination can be separated and moreover the troublesome trapping of electrons may greatly decrease compared with the sinusoidal field excitations. Matossi and Nudelman5), Zalm3), and Hahn and Seemann6) investigated the electroluminescence by using the pulse fields. Matossi and Nudelman used relatively slow pulses and other nonsinusoidal fields, and discussed the effects of the inner polarization fields from the electroluminescence waveforms. Zalm studied the brightness waveforms and analysed them under the assumption of the recombination process of the excited luminescent centers and free electrons. These studies, however, seem to have payed little care on the waveform of exciting pulse. On the other hand, Hahn and Seemann used high speed pulses and discussed the effects of boundary layers between phosphors and electrodes, and polarization charges qualitatively.

According to our studies, it is evident that the brightness waveforms of electroluminescence are greatly affected by the waveforms of exciting fields, and so the rise and fall times of the exciting pulse fields must have as small values as possible. In the following sections, the emission spectra, brightness waveforms, voltage dependences and other associated characteristics of the electroluminescence of ZnS:Cu, Pb phosphors excited by short field pulses will be mentioned, and discussed with the excitation and recombination mechanisms.

§ 2. Experimental Procedure

The samples used in this experiment are ZnS:Cu, Pb powder phosphors being especially made for the electroluminescence, and are prepared as follows: ZnS powder is mixed with Cu and Pb of about 0.1% and baked at 900°C (with NaCl as flux material), 1 hour in air, and after baking washed in NaCN solution.

These samples are dispersed in silicone oil and pressed between metal plate and conducting glass. They are, however, separated from the both electrodes by Mylar sheets of 12μ thick. These Mylar sheets are used to avoid the contact effects between the samples and the electrodes, because the contact phenomena influence the electroluminescence brightness waveforms as indicated by Hahn and Seemann. Therefore, the cell is completely symmetric in its construction. The dimension of the cells are $5\times5\times0.025\ \text{mm}^3$ and their electric capacities are about 30 PF (for the pulse method, the smaller the cell capacity is the better).

The exciting electric pulse fields obtained from the pulse generator are always negative DC pulses and their rise and fall times are 0.2 and 0.3 microseconds respectively. The heights of the electric pulses are 1500 volts at maximum and repeating frequencies are 25 c/s to 1 kc/s, and pulse durations are 1 to 40 microseconds.

The luminescence generated by the exciting pulse field in the sample is detected by RCA 931–A multiplier phototube which is shielded by metal case from the disturbance of outer electric fields. The output signal from the multiplier phototube is observed by a synchroscope which can resolve the transient phenomena shorter than 0.1 microsecond. On the other hand, in the case of measuring the integrated light output the direct current amplifier is used to measure the integrated output current of multiplier phototube.

§ 3. Experimental Results

(a) *Emission spectra*

ZnS:Cu, Pb phosphors used in this experiment have two emission bands in green and

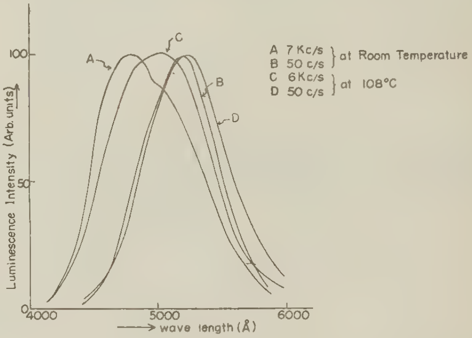

Fig. 1. Emission spectra of electroluminescence excited by sinusoidal fields.

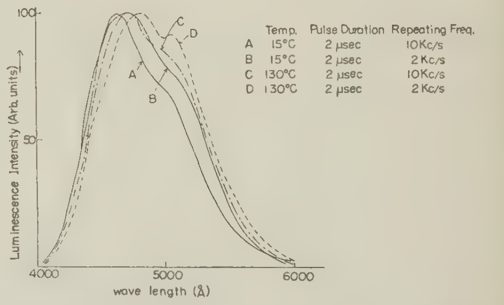

Fig. 2 (a). Emission spectra of electroluminescence excited by short field pulses.

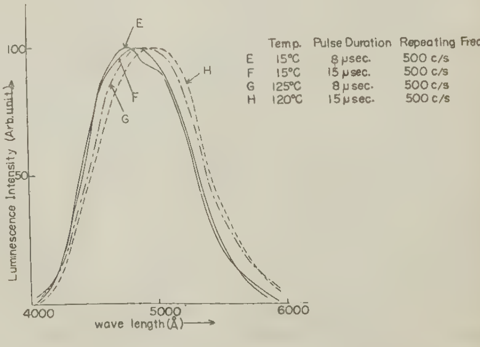

Fig. 2 (b). Emission spectra of electroluminescence excited by short field pulses.

blue regions. The green band is observed by excitation with ultraviolet irradiation or low frequency sinusoidal field at room temperature and seem to have a peak output at 520 mμ in wavelength. The blue band, on the other hand, is observed by excitation with high frequency sinusoidal field and seems to have a peak at 460 mμ. (Fig. 1)

When these samples are excited by short field pulses used in this experiment, the blue band emissions are predominantly observed even at low repeating frequencies, though the emission peaks tend to shift to longer wavelength slightly at high temperatures or long pulse durations, as indicated in Fig. 2. Considering that the decay time of luminescence is short enough—a few microseconds—in the case of short field pulse excitation as indicated in the following section, it may be expected that the hole migrations from blue to green centers hardly affect the emission spectra contrary to the case of sinusoidal field excitation.

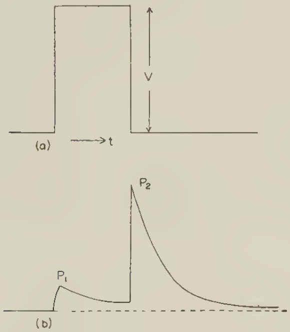

Fig. 3. Brightness waveform of electroluminescence.
(a) Waveform of exciting pulse field.
(b) Brightness waveform.

(b) *Brightness waveforms*

The brightness waveforms of electroluminescence excited by short field pulses have two peaks, and the first and the second peaks are in phase with the rise and fall of the rectangular exciting pulse. The typical one is shown in Fig. 3, but the ratio of heights of two peaks and luminescent decay following these peaks depend on the kinds of phosphors considerably (three kinds of phosphors other than that reported here are observed by the same experimental apparatus).

In our samples, the first peaks are much smaller than the second peaks (Fig. 4), though the former tend to increase compared with the latter at high repeating frequencies or long pulse durations.

Furthermore, the polarity of the emission of electroluminescent cell is observed, because the DC pulses are used for the excitation. The multiplier phototube faces to the transparent conducting glass of the cell, and when the conducting glass electrode is negative to the metal electrode, the obtained brightness is 1.25 times larger than the reverse case (Table I). Since the construction of the cell is symmetric as above mentioned, this polarity of the emission is caused from the absorption or scattering of the emitted light by the sample material itself.

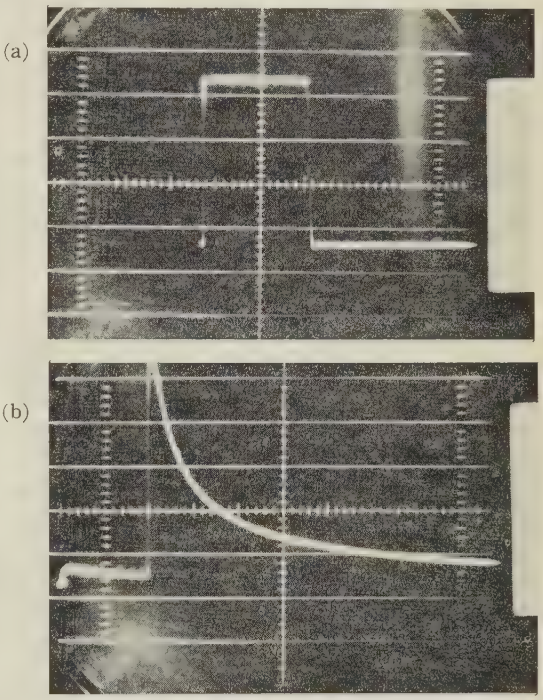

Fig. 4. Brightness waveform of electroluminescence.
(a) Waveform of applied field pulse, duration 10 microseconds.
(b) Waveform of electroluminescence excited by the pulse field indicated by (a). Time mark is 1 microsecond.

These results indicate that the excitation of electroluminescence in the phosphor by electric field is generated in the cathode region of phosphor particles, in accordance with results obtained by several other workers.

Table I. Polarity of light output with direction of field.

Exciting condition			P_2'/P_2''
Voltage	Rep. freq.	Pulse duration	
900V	2 Kc/s	2μ sec	$\frac{2.3}{1.8}$
1500V	2 Kc/s	5μ sec	$\frac{2.6}{2.1}$
1200V	50 c/s	30μ sec	$\frac{3.2}{2.2}$
900V	50 c/s	30μ sec	$\frac{2.6}{2.1}$

P_2': Second peak height when conducting glass is negative.

P_2'': Second peak height when conducting glass is positive.

(c) *Decay of electroluminescence*

It is very interesting to analyse the decay character of electroluminescence, for the initial decay which is difficult to be observed in usual photoluminescence, can be observed. In this experiment the decay of the electroluminescence is measured only in the one which follow the second peak, because the first peak is very small and hence it is difficult to analyse it accurately.

The luminescent decay of ZnS type phosphors should obey the bimolecular law in principle: that is

$$I=\frac{I_0}{(1+An_0t)^2}\,, \tag{1}$$

or

$$\frac{\sqrt{I_0}}{\sqrt{I}}=(1+An_0t)\,, \tag{2}$$

where I is the brightness of phosphorescence during the decay, I_0 is the initial value of I at $t=0$, A is a recombination constant of the excited centers and free electrons, n_0 is the initial value of the density of the excited centers, and

$$A=\sigma v\,, \tag{3}$$

where σ is the recombination cross section of luminescent centers and v is the thermal velocity of free electrons.

One of our results is illustrated in Fig. 5 and 6 according to the equations (1) and (2) respectively. From these figures it is evident that the bimolecular law is valid in the beginning of decay up to 20% of the initial value, that is, the slope of log-log plot in Fig. 5 is equal to 2, and in Fig. 6 the curve of inverse square root values of I is nearly straight line at the beginning of decay. Furthermore semi-log plot of decay is shown

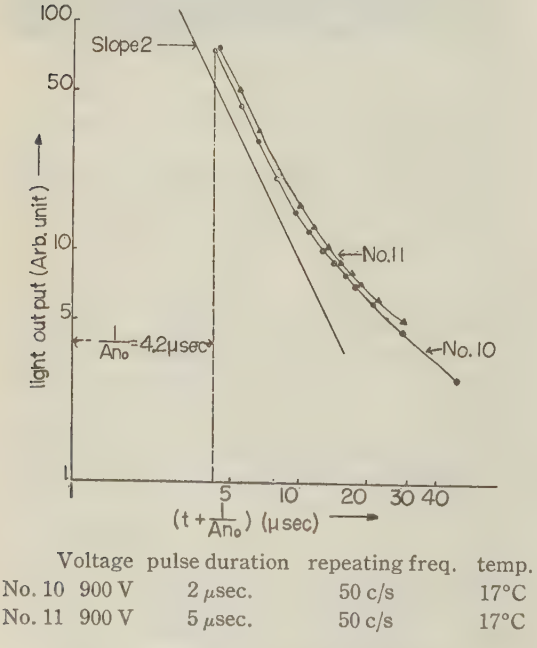

Fig. 5. Decay of electroluminescence.

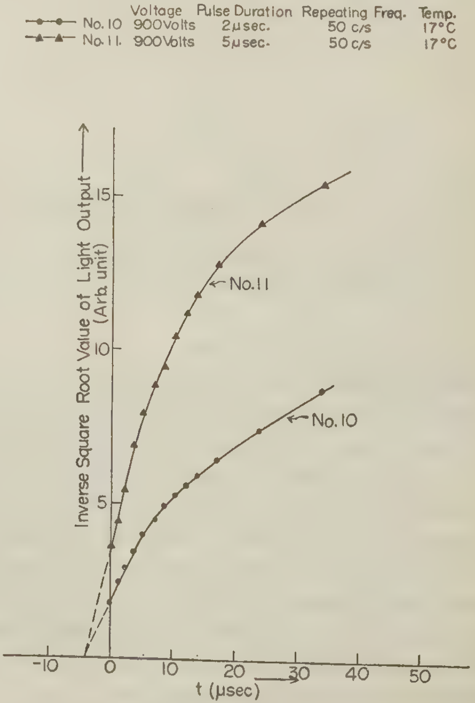

Fig. 6. Decay of electroluminescence.

in Fig. 7 to compare the experimental result with the monomolecular law, and this plot does not coincide with the straight line. The value of An_0 is obtained from the intersection of extrapolated straight line of $\sqrt{I_0}/\sqrt{I}$ on the horizontal time scale line in Fig. 6 or the time necessary to decay to 0.25 I_0 in Fig. 7. The obtained values of An_0 and the corresponding excitation conditions are shown in Table II. From Table II we can find that the decay times (in this paper it is defined as the time which is necessary for decay to one quater of initial value i.e. $1/An_0$) of these electroluminescence are in the region of 4 to 10 microseconds. The nature of the decay is very interesting especially at high tempera-

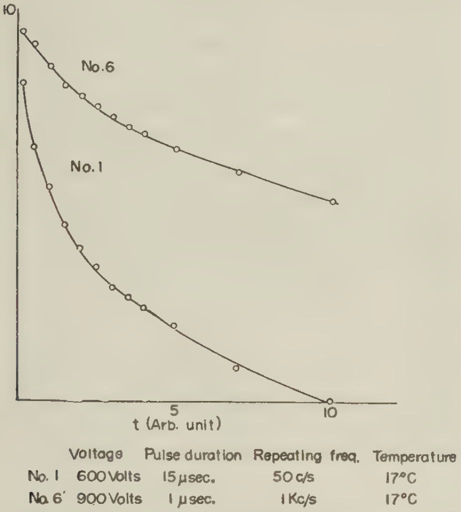

Fig. 7. Decay of electroluminescence.

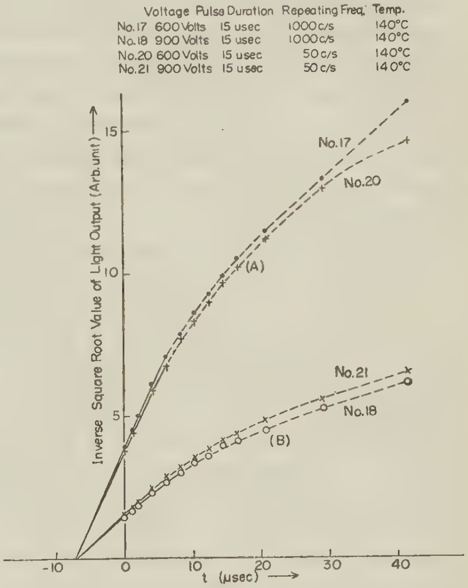

Fig. 8. Decay of electroluminescence.

Table II. Decay times of electroluminescence in various exciting conditions.

No.	Exciting conditions				Decay time	
	Temp.	Voltage	Rep. freq.	Pulse duration	A n_0	Decay time
1	17°C	600 V	50 c/s	15μ sec	1.05×10^5 sec^{-1}	9.55×10^{-6} sec
2		900	50		1.77	5.64
3		600	1000		1.16	8.61
4		900	1000		1.16	8.62
11		900	50	5μ	1.62	7.93
12		900	1000		2.08	4.80
9		900	1000	2μ	1.01	9.89
10		900	50		2.26	4.41
5		900	50	1μ	2.41	4.15
6		900	1000		1.25	8.02
17	140°C	600	1000	15μ	1.42	7.06
18		900	1000		1.44	6.96
20		600	50		1.41	7.09
21		900	50		1.41	7.09
14		900	50	5μ	1.85	5.40
15		900	1000		1.85	5.40
16		600	1000		1.85	5.40
22		900	50	2μ	2.61	3.84
23		900	1000		2.48	4.03
24		900	1000	1μ	2.51	3.98
25		900	50		2.49	4.02

ture, that is, the values of An_0 in these data are almost equal even in various exciting voltages. The two curves illustrated in Fig. 8 indicate this feature: that is, although the peak values of the brightness of case (B) is about six times larger than the case (A) as explained in a later section, the values of An_0 are nearly equal in two cases. Moreover, at high temperature the decay times tend to increase with the pulse durations as shown in Fig. 9. On the contrary, the decay times at room temperature fluctuate considerably even for same exciting conditions: this might be due to the effects of electron traps as discussed later.

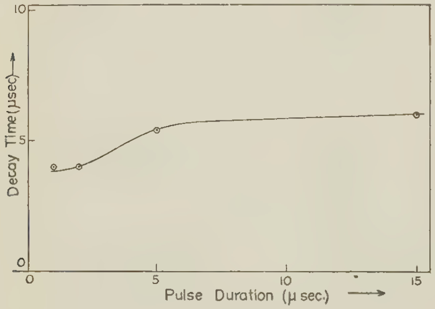

Fig. 9. Dependence of electroluminescent decay on pulse duration at 140°C.

These decay characters seem to be important to understand not only the electroluminescent mechanism, but also the nature of the luminescent centers, as will be discussed later.

(d) *Voltage dependences of brightness*

The voltage dependences of the electroluminescent brightness can be measured by the peak value of the brightness waveforms because of the invariance of the wave forms with the applied voltages. The integrated light outputs are also measured by DC amplifier, when it is necessary to compare two cases, i.e. pulse and sinusoidal field excitations. The typical results are illustrated in Fig. 10, and these voltage dependences seem to obey the law which is proposed by Taylor and Alfrey[7], and Zalm[3], at least under 1000 volts, that is

$$B=B_0 \exp\left(-\frac{c}{\sqrt{V}}\right), \tag{4}$$

where B is the brightness, V is the applied voltage to the cell, B_0 and c are constants. The values of c are obtained from the slope of Fig. 10, and the results obtained in the same cell under various exciting conditions are listed in Table III. These results illustrate that the c-values are nearly independent of exciting conditions except for the case of high repeating frequency and are about $2.6\times 100\ (\text{volts})^{1/2}$. In the region of voltages higher than 1000 volts, however, the dependences become slightly steeper than in the low vol-

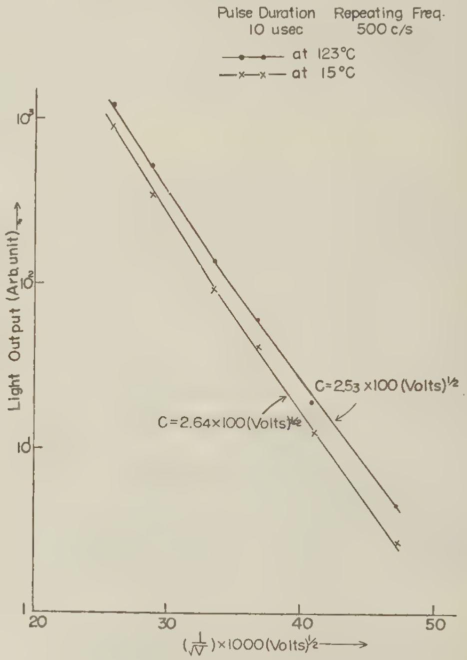

Fig. 10. Voltage dependences of electroluminescence.

Table III. c-values in various exciting conditions.

Pulse duration	Repeating freq.	Temperature	c-value
2μ sec	50 c/s	15° C	$2.5_3\times 10^2$ (volts)$^{1/2}$
		123° C	2.5_3
	500 c/s	15° C	2.5_9
		123° C	2.6_8
5μ sec	50 c/s	15° C	2.5_6
		123° C	2.6_4
	500 c/s	15° C	2.5_6
		123° C	2.5_0
10μ sec	50 c/s	15° C	2.5_3
		123° C	2.5_6
	500 c/s	15° C	2.6_4
		123° C	2.5_0
20μ sec	50 c/s	15° C	2.4_8
		123° C	2.4_0
50μ sec	50 c/s	15° C	2.5_3
		123° C	2.4_5

tage region.

The comparison of exciting efficiencies in two cases of sinusoidal and pulse field excitations (in the same cell) are made by measuring the integrated light outputs by DC amplifier in low voltage region and the results are shown in Fig. 11. In this figure the applied voltage V of sinusoidal field means the peak voltage of the field. The interesting features in this results are as follows: first, the integrated light output is much smaller in the pulse field excitation than in the case of sinusoidal field excitation, and second, the voltage dependence is steeper in the case of pulse field excitation and the c-value is nearly twice as much as in the case of sinusoidal field excitation. (The slight difference of c-value between in Fig. 10 and 11 might be due to the using of different cells in each case.)

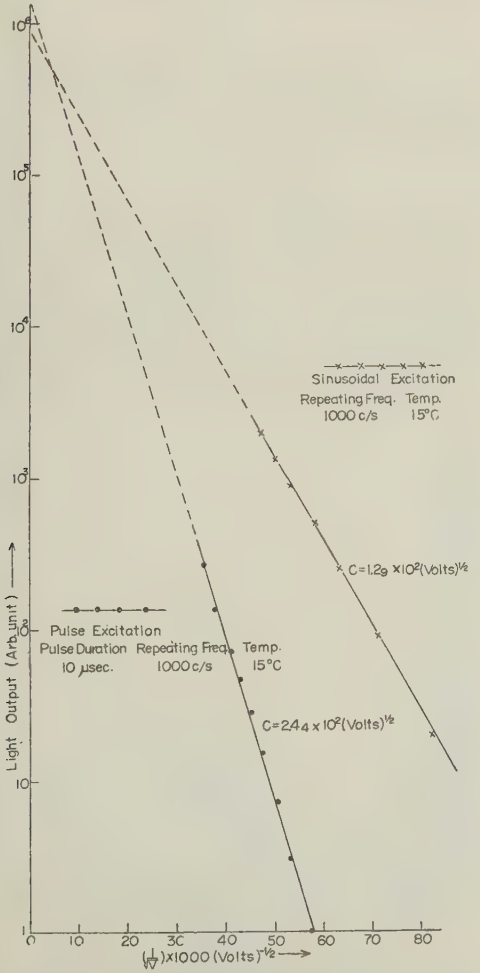

Fig. 11. Voltage dependences of electroluminescence.

The constant factor B_0 in Eq. 4, which is determined from the intersection point of the extrapolated straight line with the light output scale in Fig. 11, is about three times larger in the case of pulse field excitation than in the sinusoidal case. (The light outputs indicated in this figure must be divided by two in the case of sinusoidal excitations to compare with the ones in the case of pulse excitation, because in the former case the excitation raises up twice in each cycle.) The emission bands of luminescence in each case, however, are considerably different, *i.e.*, the blue band in pulse case and the green band in sinusoidal case are predominant respectively as indicated in Sect. 3 (a). Therefore, speaking of the number of photons emitted from the phosphors, the difference of the constant factor B_0 between two cases may become smaller, because the photosensitivity of multiplier phototube is smaller in the green band than in the blue band. These facts indicate that the excitation efficiency is almost completely determined in both cases by the exponential factor in Eq. 4, which involves the inner field generation, and not the constant factor B_0, which may involve the primary electron generation, at least over the room temperature.

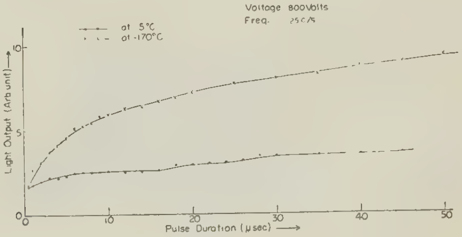

Fig. 12. Dependence of electroluminescence on pulse duration.

(e) *Dependences on the pulse durations*

The light output of electroluminescence tends to increase with the pulse duration of exciting field, and this feature is larger at room temperature than at higher or lower temperatures. Fig. 12 shows this character, where the light outputs are measured with DC amplifier as mentioned in the previous section. In the region up to 20 microseconds, the approximately exponential increases are observed, and in the region longer than 20 microseconds the slower increases are observ-

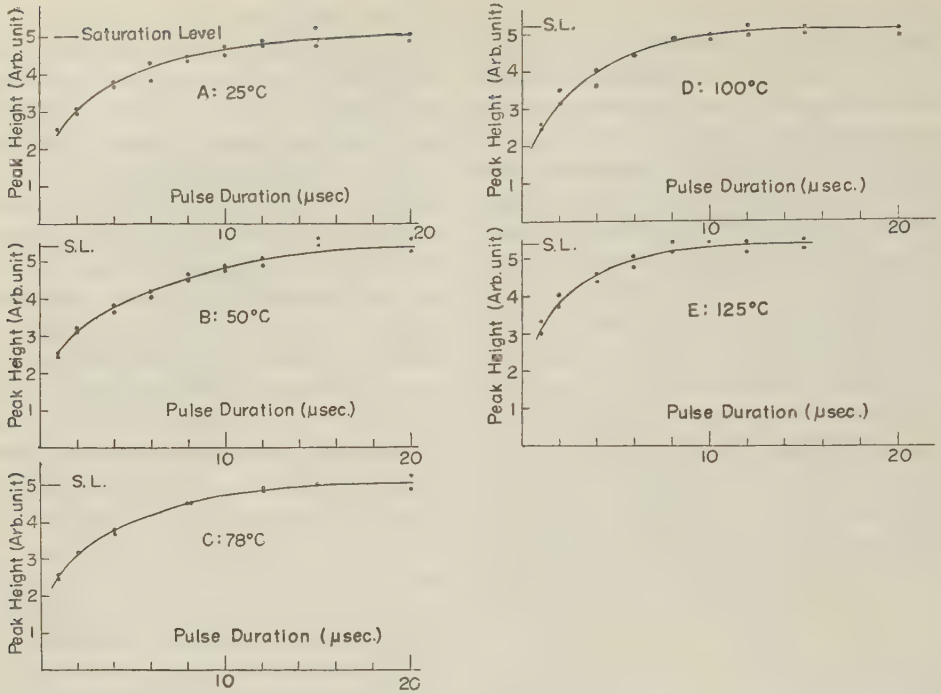

Fig. 13. Dependences of electroluminescence on pulse duration at different temperatures.

Voltage	Repeating freq.
900 Volts	50 c/s

ed at room temperature. At liquid air temperature, on the other hand, the sharp rise of light output with the pulse duration is hardly observed and the output increases slowly up to over 40 microseconds. The sharp rise at temperature higher than room temperature is measured up to 170°C in the region of 1 to 15 microseconds (to keep the constancy of temperature, longer pulse durations are not used). The results are shown in Fig. 13 and if we assume the suitable saturation values of light outputs with the pulse durations (this assumption means that the sharp and slow rises may be due to different mechanisms), these curves are all expressed by exponential form as shown in Fig.

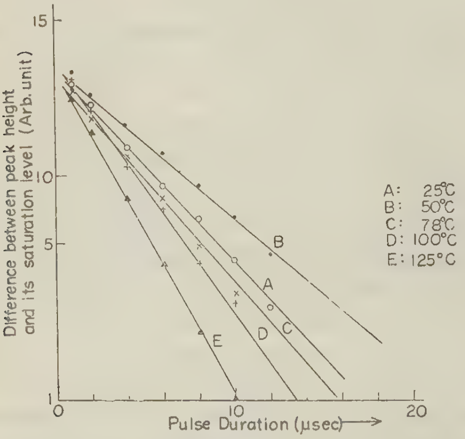

Fig. 14. Semi-log plot of curves in Fig. 13 for each temperature.

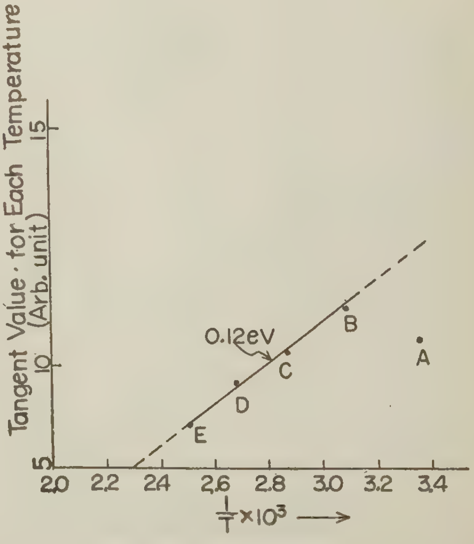

Fig. 15. Temperature dependence of slope in Fig. 14.

14. The logarithmic values of slopes of these curves in Fig. 14 are plotted in Fig. 15 against temperature and we obtain the activation energy of about 0.12 eV except only one point corresponding to room temperature. The variation of this activation energy with the applied voltage can not be observed between 600 to 900 volts.

Comparing with the results of the voltage dependences of the intensity mentioned above, these results are very interesting and will be discussed later.

(f) *Dependences on the repeating frequencies of exciting pulse*

The luminescent brightness are nearly independent of the repeating frequencies of exciting pulse up to 1 kc/s, therefore the repeating frequencies under 1 kc/s are used throughout in this experiment except that of the build-up characteristics mentioned in the next section.

(g) *Build-up characteristics*

The build-up phenomena is important to understand the mechanism of electroluminescence. That is, the processes of the formation of local intense field in the phosphor powder, and the trapping of excited electrons in the anode region, take parts in this phenomenon as mentioned by Zalm. The electrons trapped elesewhere may not be able to escape for considerably long time after electric excitations at room temperature, and so the preheating of the sample up to high temperature is necessary to obtain the precise results of the build-up characteristics. In our experiment, these phenomena are observed by the single sweep method using a synchroscope and the considerably high repeating frequencies of the exciting pulse are used, since the precise observations are obtained only at high frequencies by this method.

The samples are heated at about 120°C for half an hour and cooled to room temperature in the dark, and then the measurements are made at room temperature. The first and the second runs of the measurements after preheating give clearly different results as shown in Fig. 16. The measurements are made at 116°C and 25°C, and when the exciting pulse of duration of 2 microseconds and of 50 kc/s frequency is used, the obtained results are as follows:

(1) In all cases the first peaks are smaller than the second ones, and at first application of the exciting pulse the first peaks are too small to be measured accurately.

(2) At 116°C the second peaks saturate at fifth pulse, and the first peaks grow more slowly and saturate at eighth pulse. The saturated values of the first peaks are about 80% of those of the second peaks. On the other hand, the first peaks are only few percent of the second ones in the case of low repeating frequencies as explained in the preceding sections. These differences of the brightness waveforms with the repeating frequencies may be interesting problem, though the detailed discussions are not made in this paper.

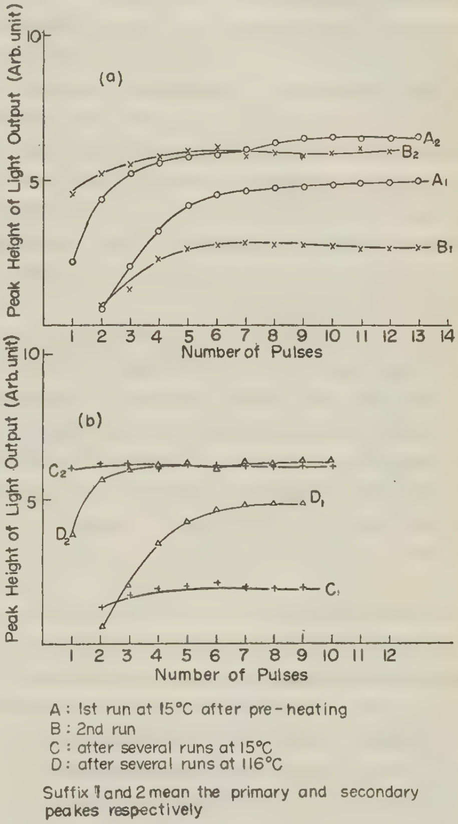

Voltage	Pulse duration	Repeating freq.
900 Volts	2 μsec.	50 Kc/s

Fig. 16. Build-up of electroluminescence excited by pulse field.

(3) At room temperature the results from the preheated samples are similar with the former case, at least in the first run, except the slower build-up than at 116°C, but in the second run of the measurement the results

are considerably different. In the second run, the first peaks are smaller by a factor of two than the first run, and the second peaks grow faster, although the values of the saturated peaks are almost equal to the ones in the first runs. Thus the saturated first peaks are becoming smaller with the measurement runs, while the saturated secondary peaks are almost constant.

In the case of another exciting condition, (duration of 10 microseconds and repeating frequency of 5 kc/s), the general features are similar to the former case, but the ratio of the saturated values of the first and the second peaks is smaller than the former case even in the first run, and this might be due to the exciting conditions which are similar to the continuous excitations mentioned in the preceding sections.

From the above results, we can conclude that the build-up characteristics of electroluminescence are greatly affected by the trapping of excited electrons, and the brightness waveforms are also considerably sensible to this electron trapping (or the space charges formed by the positively charged excited centers).

§ 4. Discussions

The experimental results described in the previous sections are closely connected one another and therefore the unified discussions about these results are necessary to clarify the mechanism of electroluminescence. The mechanism of the electroluminescence has been discussed by many workers from different points of view, and the favourable theories are proposed at least in the basic points. Piper and Williams[2] compared theoretically the possible cases of the excitation mechanism and concluded that the impact ionization of luminescent centers by fast electrons is the most acceptable.

We are going to settle the mechanism of the excitation and recombination processes in electroluminescence as follows and will discuss the experimental results in later sections.

To obtain the electroluminescence, the primary electrons have to be accerelated by the externally applied electric field until they get enough optical energy i.e. the energy corresponding to the forbidden gap or the one from the ground state to the conduction band. We assume that the local intense field is generated just near the surface of phosphor particle dispersed in dielectric medium as proposed by Piper, Williams[2], Curie[1] and Zalm[3], and the excitation processes are raised up only in this region. Moreover an extensive low field region in series with this high field region permits operation over a broader range of applied voltages without creation of unstable breakdown condition. Schematic diagram of this situation is shown in Fig. 17. In the first region (cathode side of the particle) the primary electrons are generated from the donors or traps by the field- or thermal-ionization processes, and these electrons risen in the condition band are accerelated in the second region, in which the local intense field stronger than mean field about by a factor of ten is generated. The electrons in the ground states of the centers or in the filled band are excited up to the conduction band by inelastic collisions with the fast primary electrons. It may be possible that the 1st and 2nd regions overlap each other in some phosphors. The secondary electrons ejected up to the conduction band flow with the primary electrons by the external field to the third, low field region, and stay there during the application of the external field. When the applied field is off, the electrons in the 3rd region begin to come back to the 2nd region, and recombine with the ionized centers to emit the light. As the ionized centers left in the 2nd region are positively charged, the positive space charge layer grows in the second region and therefore the inner field is strengthened, until the steady state is established.

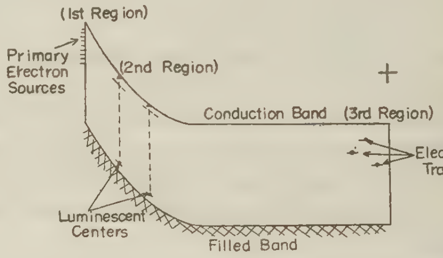

Fig. 17. Band model of electroluminescence in ZnS:Cu, Pb phosphor.

The excitation probability (multipication factor) in the 2nd region is roughly estimated as follows: the probability that an electron in electric field is accerelated to ionization energy without a collision with the crystal lattice is given by Seitz[8)] as

$$p=\exp\left(-\frac{c'}{F}\right), \tag{5}$$

where c' is a constant, and this factor is estimated by Callen[9)] as about 2.3×10^6 volts/cm at room temperature. Therefore the number of secondary electrons produced while n primary electrons move dx, is given by

$$dn=\frac{n}{\mu\tau F}\exp\left(\frac{-c'}{F}\right) \tag{6}$$

where μ is the electron mobility and τ is the collision time of electron with the lattice and F is the field strength.

Therefore the total number of centers excited during the excitation process is

$$n-n_0=n_0\left\{\exp\left(a\int_0^{F_{\max}}\frac{\exp(c'/F)}{F}dF\right)-1\right\} \tag{7}$$

where a is dx/dF, n_0 is the number of primary electrons, and $F_{\max}$ is the maximum field strength in the barrier.

Zalm indicated that the multiplication factor is smaller than 1 and then the Eq. 7 is approximately expressed by

$$n-n_0\sim\exp\left(\frac{-c'}{F_{\max}}\right) \tag{8}$$

in the case of ZnS single crystal, in which the primary electrons penetrate through the potential barrier between crystal and metal electrode and the inner field is calculated simply under assumption of Mott-Schottky type exhaustion layer as discussed by Piper and Williams.

In the case of intrinsic electroluminescence, on the other hand, the source of primary electrons and the situation of the inner field are not clear enough. But according to Zalm the strength of the inner field in the 2nd region is nearly expressed as follows:

$$F=A\sqrt{V}, \tag{9}$$

where A is a constant, and this expression is the same as in the case of single crystal above mentioned. Therefore the voltage dependence of electroluminescent brightness is

$$B=B_0\exp\left(-\frac{c}{\sqrt{V}}\right) \tag{10}$$

from Eqs. 8 and 9 where B_0 and c are constants. This equation is the same as Eq. 4 and is the suitable expression for experimental results in the wide range of applied voltages as reported by many investigators.

The problem of the primary electron source seems to be fairly critical, as the electroluminescence is the field-dominated phenomenon. Piper and Williams[2)] proposed a model in which the deep lying donors are the source of them, and calculated the voltage dependences under the assumption of the field ionization of these donors. On the other hand, Taylor and Alfrey[7)] assumed that the primary electrons are generated thermally from the electron traps and analysed their experimental data of frequency dependences of electroluminescence. Moreover Zalm assumed that the donors in the interface layer between ZnS and Cu_2S which exists on the surface of the phosphor particle, are the primary electron sources, and the variation of the distribution of these donors hardly affects the voltage dependences of electroluminescence mentioned in Eq. 10. It seems, however, that the effects of electron traps and donors on the excitation of electroluminescence are considerably complex. Actually Johnson, Piper and Williams[10)] explained the temperature dependences of electroluminescence under the assumption that the traps may supply the primary electrons by field ionization at low temperature and on the other hand they are thermally emptied, enhancing the field strength in the 2nd region at high temperature.

In this paper we compare these mechanisms of the primary electron generation in detail in Sect. 4 (d).

The processes of the excitation and recombination above mentioned are only outlines of the electroluminescent phenomena, which are very complex and give diverse results in various samples. In the following sections, the detailed considerations about the experimental results in our samples will be made and some mechanisms will be proposed.

(a) *Emission spectra and luminescent centers*

In our experimental results described in Sect. 3 (a) the spectral distributions of electroluminescence excited by short field pulses shift considerably to the shorter wavelength compared with the case of sinusoidal field excitations even at very low repeating frequencies. As the emission peak of the electroluminescence excited by sinusoidal field shifts to the shorter wavelength with frequency as shown in Fig. 1, the pulse excitation might be considered corresponding to the sinusoidal excitation of considerably high frequency. Phenomenologically speaking, the pulse excitation used in this experiment might correspond to the sinusoidal excitation of the frequencies of 100 to 50 kc/s, since the luminescent decay times are 5 to 10 microsecond in the case of pulse excitation (Sect. 3 (b)).

Now we must consider the luminescent centers in ZnS:Cu, Pb phosphors. From the photoluminescent data the emission peaks of ZnS:Cu phosphors lie at the wavelengths of about 460, 520 and 670 mμ[11]. On the other hand, another peak might exist due to lead activators as indicated by Fonda[12]. In the case of electroluminescence of our samples, however, it is considered that the luminescent centers corresponding to the first two emission bands emit the light prepominantly (blue and green centers), and these features coincide with the results obtained by Waymouth[13] and other workers. Green peaks are predominantly observed at the low frequency sinusoidal excitations and at high temperatures, and blue peaks at high frequencies and low temperatures. Besides, these temperature dependences of the spectral distribution are similar to the case of photoluminescence of ZnS:Cu phosphors (e.g. Tomlinson)[14]. Though the several mechanisms about the problem of colour shift in electroluminescence above mentioned are proposed by Zalm, Curie, Tomlinson, and Goffaux[15] based on some assumptions about luminescent centers, it seems that the critical evidence does not exist yet. Moreover, Burns[16], and Nudelman and Matossi[5] indicated that the color shift of electroluminescence in ZnS phosphor can be explained with the assumption of the different excitation mechanisms in the blue and green centers. They assumed that the blue luminescence is due to the excitation of electron from the ground level to some excited level within this center, followed by an almost immediate direct transition to ground level, and the green luminescence, on the contrary, is due to some phosphorescence processes with a delaying mechanism such as traps or metastable states and with transitions involving the conduction band. In our experiments, however, these excitation processes are not the case, since the most excited electrons may be risen to the conduction band as indicated in the following section.

Therefore the color shift in our samples is probably due to the difference of the recombination process in two types of centers, or the hole migration mechanism. If we assume the hole migration mechanism from blue to green centers as Zalm and others (Klasens and Schön's theory)[17], the followings are necessary to explain the experimental results. (1) the cross section of blue centers for impact ionization is much larger than that of green centers, or (2) the cross section of the filled blue centers for the hole trapping is much larger than that of green centers, if the ionizing process is attained only by the collisions of lattice atoms and fast electrons.

(b) *Brightness waveforms*

As described in Sec. 3 (b) the brightness waveforms of the electroluminescence excited by the short pulse fields are considerably different from the ones excited by the sinusoidal fields. In the brightness waveforms excited by pulse fields the first peaks are much smaller than the second ones, and this result indicates that the recombination process is raised up mainly after the excitation is cut off but not during the excitation. Because the short pulses used in this experiment are the DC pulses, it may be impossible that the reverse field generated by the polarization charges overcomes the externally applied fields.

We can expect also from the smallness of the first peaks that the probability of the excitation, in which electrons transit from the ground state to the excited state and drop immediately to the ground state, is very small. The recombination probability where the accerelated electrons in the 2nd region recombine with the excited centers in this region, may also be small. The transit time of fast electrons necessary to pass the 2nd region might be estimated as:

$$T=\frac{d}{\mu F}, \tag{11}$$

where d is the depth of the 2nd region which is about 10^{-3} cm, μ is the electron mobility which is about 100 cm^2/volt. sec., and

F is the field strength of about 10^6 volt/cm, and so T is about 10^{-11} sec.. As the decay time of the electroluminescence is over 5 microseconds as described in Sec. 3 (d), it may be considered that the greater part of the free electrons are moved to the 3rd region without recombinations.

The asymmetry of the brightness due to the polarity of field applied to the cell may be considered as follows: the luminescence occurs always in the 2nd region which is in the cathode side of the particle, and the emitted light is absorbed or scattered by phosphor powder going through the cell. Therefore if the emission is observed from the cathode side, the brightness may be larger than the reverse case.

From these points of view, this experiment is the direct evidence for the excitation and recombination mechanisms settled in the previous section.

(c) *Voltage dependences of brightness*

The voltage dependences of electroluminescent brightness are closely connected to the voltage dependences of excitation probability of the luminescent centers, which involve the relation between the inner and externally applied fields.

If we assume that the exponential factor in Eq. 10 is independent of the the mechanism of the generation of the primary electrons, the constant factor c is

$$c = c'/A, \tag{12}$$

introducting Eq. 9 to Eq. 10. Therefore the larger the c-value is, the weaker the inner field is.

In our experiments, the c-value in the case of sinusoidal excitation is about 130 $(\text{volts})^{1/2}$ at room temperature, and this value is of the same order as that of Zalm's data. On the other hand, the c-value in the case of pulse excitation is about 250 $(\text{volts})^{1/2}$, and this value is nearly twice as much as in the sinusoidal case. These results seem to be due to the difference of the emitting particles, or the difference of the inner field strength of the same particle in each cases. The c-values of the individual particle of phosphor may be distributed in certain wide range and the particles which have small c-values contribute mainly to the luminescence. There are, however, no reasons why particles having large c-values can emit the light predominantly even in the case of pulse excitations. In any case, it might be considered that the c-values in all particles become larger in the case of pulse excitation than in the sinusoidal case. If the inner field in the 2nd region is weaker in the pulse excitation than in the sinusoidal case even at the same peak voltage, the c-value becomes larger and the luminescent brightness becomes lower in the forme case. This is just the case of our experimental results. That is to say, the strength of the inner field as smaller by about a factor of two in the pulse excitations.

The strength of the inner field might vary with the frequency of applied field, if the dielectric relaxation of dielectric medium of the electroluminescent cell occurs in the frequency range of applied field. In our case, however, this is not true, for in the silicone oil the relaxation may occur only above 10 Mc/s and furthermore the preliminary experiments using binderless cell gave the same results as reported here.

In any case, it might be sure that the reason for the weakness of inner field in the case of pulse excitation is the electronic phenomena in the phosphor particle, that is, the positive space charges in the 2nd region or the polarization field consisting of the trapped electrons in the deep traps in the 3rd region. Assuming the Mott-Schottky type exhaustion barrier in the 2nd region, the maximum field strength is

$$F_{\max} = -AV^{1/2} \tag{13}$$

and

$$A = (8\pi Ne/\mathcal{E})^{1/2}, \tag{14}$$

where V is the applied voltage, N is the space charge density in the barrier and $\mathcal{E}$ is the dielectric constant of the crystal. The field strength is proportional to the square root of the space charge density in this region. Therefore the space charge density in the case of pulse excitation might be one-forth of the density in the case of sinusoidal excitation.

Maeda[18) calculated the strength of the inner field under special assumptions, and indicated that a field strong enough for electroluminescent phenomenon can be obtained, even if there are no space charges in the 2nd region. From our discussions, however, the positive space charges in the 2nd region seem to play an important role in the generation of local intense field, because it seems that there might be no difference of the field strength in two cases according to the Maeda's considerations.

(d) *Dependences of brightness on the pulse duration*

The dependences of the electroluminescent brightness on the pulse duration mentioned in Sect. 3 (e) may involve essentially the transient phenomena in electroluminescent mechanism. It may be considered that the increase of the brightness with the pulse duration is due to the increase of the number of primary electrons. The reason for the increase of primary electrons with the pulse duration may be considered in two cases as follows. First, if we assume that the primary electrons are generated thermally from the donors or traps in the 1st region which may be in the interface layer between the surface conductive layer and ZnS, the number of paimary electrons generated per unit time at the time t after the application of field is expressed by

$$n=n_0 p \exp(-pt) , \tag{15}$$

where

$$p=s \exp\left(-\frac{E}{kT}\right) , \tag{16}$$

where n_0 is the number of electrons in the donors or traps before the application of the field and s is the frequency factor and E is the depth of the donors or traps. Therefore, the electroluminescent brightness increase with the pulse duration τ as

$$\int_0^\tau n dt=n_0(1-\exp(-p\tau)). \tag{17}$$

This equation seems to coincide with our experimental results illustrated in Figs. 13 and 15. The depth of donor or trapping level obtained from the experimental results, however, seem to be too small compared with the trap depth usualy obtained from the glow curve data.[4] Therefore, it might be considered that the shallow donors in the interface, in which the band gap might be considerably smaller than the one of ZnS, are the sources of primary electrons.

Second, if we assume that the primary electrons are generated from the donors or traps by the field-ionization directly, it must be concluded that the field strength in the 1st region increases with the time while the pulse field is applied, and so the longer the time is, the deeper the emptied level is. The analysis of this process is so complex that we consider some simple case. For simplicity we assume that if the field strength overcomes F, the levels lying at depth E are ionized immediately, and the relation between E and F is[13]

$$F=\text{const.}\, E^{3/2}. \tag{18}$$

Moreover, assuming that the distribution of levels in the 1st region is

$$n(E)dE=g(F)dF , \tag{19}$$

and F increases with time as

$$F(t)=F_0+f(t) , \tag{20}$$

where F_0 is the field strength generated instantaneously and $f(t)$ is the one increasing after the application of external field. The electroluminescent brightness may increase as

$$B(t)=B_1\int_0^F g(F)\cdot\exp(-c/F)dF . \tag{21}$$

Putting $F_0 \gg f(t)$, the above equation becomes

$$B(t)=B_2\int_0^f g(F_0+f)\exp(cf)df+B_2' . \tag{22}$$

Now we assume that the function $g(F_0+f)$ is the slowly-varying one, and so Eq. 22 may become

$$B(t)=B_3\int_0^t \exp(cf(t))\cdot\frac{df}{dt}\cdot dt+B_2' . \tag{23}$$

The function $F(t)$, which indicates the process of space charge formation, might be estimated as follows. If we assume that the space charges in the *2nd* region increase by the thermal releasing of the trapped electrons, the space charge density increases as

$$N=N_0+N_T(1-\exp(-pt)) , \tag{24}$$

where N_0 is the space charge density being generated instantaneously and N_T is the density of trapped electrons at $t=0$. As the field strength is expressed in Eq. (13) and (14), the field strength in this case is

$$F=F_0+apt , \tag{25}$$

where a is a constant.

Therefore, the brightness is

$$B(t)=B_0'\int_0^t \exp(capt)dt+B_0'' = B_0\exp(capt)+B_0'' . \tag{26}$$

This equation is clearly inconsistent with our experimental results, and so the mechanism assumed in the former case may contribute to this phenomenon at least in this phosphors. Moreover the experimental results which indicate the invariance of the curve shape with the applied voltages as indicated in Sec. 3 (e), may confirm this conclusion.

The latter case, however, seems to play a certain role in electroluminescent phenomena. For the light output excited by the 0.5 microseconds pulse in duration at room temperature is almost the same as that excited at liquid air temperature; and in the further investigations now in progress,[20] in which very short pulses (almost 30 millimicroseconds in duration) are used, considerable light outputs are still observed. These facts indicate that the primary electrons generated by the direct field-ionization may be effective in some parts of excitation of electroluminescence as discussed by Piper and Williams.

(e) *Decay of electroluminescence*

The study of the luminescent decay in this paper gives us the interesting results in considering not only the recombination process but also the excitation process. As explained in Sec. 3 (c) the luminescent decay obeys the bimolecular law at least in the beginning, and furthermore the constant factors An_0 are almost the same in spite of the different exciting voltages. From the formal interpretation it means that the initial density of the ionized centers at $t=0$ in the 2nd region is nearely independent of the exciting conditions.

The alternative interpretation, in which it is assumed that these decay times are composed of the time necessary to come back to the 2nd region from the 3rd region and the time staying at the excited states of the blue centers, will lead to the inconsistent results with experiments. First, the time necessary to come back to the 2nd region is estimated from the equation similar to Eq. 11, though the field strength by the polarization charges can not be determined precisely. If we assume that the polarization field is as low as 10 volts/cm and the particle size is about 10μ, the transit time is about 1 microsecond. Furthermore, if we assume that the process in which the electrons flow back to the 2nd region is the rate-determining process, the monomolecular law may predominate in the recombination processes as indicated by Zalm. This problem will be discussed later again. Second, if the optical transition of electron from the excited state to the ground state of the luminescent center is the rate-determining process, the luminescent decay must obey the monomolecular law, and moreover the life time of the excited state may be considerably shorter than 1 microsecond as indicated by Mott and Gurney[19].

In any case we shall have to consider more precisely the reason why the bimolecular mechanism predominates the recombination process. Zalm indicated that the phase shift of the peak in the brightness waveform excited by sinusoidal field can be explained under the assumption of monomolecular law. This means that the free electron density flowing back from the 3rd region is considerably smaller than the density of ionized positive centers in the 2nd region and so the electron flow to the 2nd region is the rate-determining process. His assumption, however, loses its validity in the case of small excitation intensity. As indicated in Sec. 4 (d), the excitation probability in the case of pulse field is much smaller than in the case of sinusoidal excitation, although the number of primary electrons seems to be the same order in both cases as shown in Fig. 11. Furthermore, the trapping effect in the 3rd region during the application of the external field may decrease, if the pulse duration is considerably short as discussed later, and so the electrons staying in the 3rd region may come back to the 2nd region instantaneosely as soon as the external field is removed even in the low polarization field.

From these points of view, it may not be impossible that the bimolecular recombination process between the free electrons and ionized centers is the rate-determining one in the case of short pulse field excitations.

Surely it is an interesting fact that the decay time is nearly independent of the voltages of applied field. This fact, however, is explained under the assumptions as follows: (1) the number of primary electrons is greatly larger than the secondary ones generated by impact ionization of luminescent centers, and (2) the recombination cross section of the ionized center is the same as that of primary electron sources which are ionized thermally or directly by the externally applied field. The assumption (1) is justified from Eq. 7 in Sec. 4 even in the case of pulse excitations. On the contrary, there are no foundations to insist on the assumption (2), because the structure of primary electron source is not clarified up to date.

If we assume that there are two kinds of ionized centers and the number of the one is considerably greater than the other, the recombination process is expressed by the following equations,

$$-\frac{dn_1}{dt}=An_1(n_1+n_2)\ ,$$

$$-\frac{dn_2}{dt}=Bn_2(n_1+n_2)\ , \tag{27}$$

where n_1, n_2 and A, B are the densities and the recombination factors of two kinds of centers respectively, and from the above assumption $n_1 \gg n_2$. Therefore we can write approximately,

$$-\frac{dn_1}{dt}=An_1^2\ ,$$

$$-\frac{dn_2}{dt}=Bn_1n_2\ . \tag{28}$$

The solutions of these differential equations are

$$n_1=\frac{N_1}{N_1At+1}\ ,$$

$$n_2=\frac{BN_1N_2}{(N_1At+1)^{B/A}}\ , \tag{29}$$

where N_1, N_2 are the initial values of n_1 and n_2 at $t=0$ respectively. Therefore, the light output from the second centers may decay as:

$$L=\frac{BN_1N_2}{(N_1At+1)^{(B/A)+1}}\ . \tag{30}$$

This Eq. 30 indicates that the decay of light output from the second centers may obey the bimolecular law if the recombination factors A and B are equal under the assumption (2). Furthermore, the decay time becomes independent of the initial density of the second ionized centers, N_2. This means that the decay time does not vary with the applied voltages, if the number of primary electrons N_1 are independent of the applied voltages. As stated in Sec. 4 (c) and (d), it seems that the number of available primary electrons in the excitation is the same, if the temperature and the pulse duration have the definite values.

Of course, the luminescence decay might obey also the bimolecular law, if the recombination factor A is considerably greater than B and the decay of n_1 is very rapid comparing with that of n_2. Furthermore, as the width of exhaustion barrier which coincides with the 2nd region spreads with the applied voltage proportional to its square root, the density of ionized centers may not increase as expected from the light outputs. If we assume that the density of ionized centers is uniform in the 2nd region, the decay time may be expressed as

$$\tau \propto \sqrt{\frac{\sqrt{V}}{I_0}} \tag{31}$$

(for $I_0 \propto n_0^2\sqrt{V}$),

where V is the applied voltage and I_0 is the initial value of light output at $t=0$. As the light output I_1 excited by the pulse of 900 volts in height is 6.5 times larger than I_2 excited by the 600 volts pulse from Fig. 10, so

$$\tau_2 \doteqdot 2.3\tau_1\ , \tag{32}$$

where τ_1 and τ_2 are the decay times corresponding to I_1 and I_2 respectively. The Table II indicates that the decay time does not vary as expected from the above equation especially at high temperature.

In any case, we can estimate the density of centers which plays a role mainly in determining the decay time from Eq. 3. If we assume that the thermal velocity of free electron is 10^7 cm/sec, and the recombination cross section of centers is 10^{-18} cm^2, the density of ionized centers is of the order of 10^{16} cm^{-3}. This value is rather too small and it seems that the recombination cross section is slightly smaller than the value given here.

The trapping effect in the 3rd region may appear in some cases. The free electrons in the 3rd region may decrease with time during the application of field by trapping phenomena as the following equation,

$$-\frac{dn}{dt}=\sigma_T vnN_T\ , \tag{33}$$

where σ_T is the trapping cross section of electron traps, v is the thermal velocity of free electrons and N_T is the trap density. Assuming that $n \ll N_T$,

$$n=n_0\exp(-\sigma vN_Tt)\ . \tag{34}$$

When the externally applied field is removed, the remaining electrons in the conduction band begin to come back to the 2nd region, and the number of free electrons coming back to the 2nd region may decrease with the pulse duration as expected from Eq. 34. Therefore the decay time may be longer for longer pulse duration, as the luminescent decay obeys the bimolecular law. The results illustrated in Fig. 9 may be the case.

The analysis of electroluminescent decay seems to be interesting but considerably difficult problem, as the ionized centers and the electrons are not always distributed uniformly in the material, and the space charge layers and polarization fields might affect the decay time as discussed by Matossi[5] and Frankl[21].

(f) *Build-up characteristics*

As explained in Sec. 3 (g), the build-up of electroluminescence might be due to the trapping phenomena of excited electrons. That is, some part of secondary electrons excited by electron impacts may be trapped in the deep traps in the 3rd region and then they can not come back to the 2nd region for certainly long time comparing with the time from pulse to pulse. Therefore the ionized centers may be left without the radiative recombinations in the 2nd region, and the field strength in this region and so the light output may grow gradually with the number of the repeating pulses, until the stationary state is established.

From the glow experiment of photoluminescence reported before[4], it is clarified that there are two types of electron traps, the depths of which are about 0.35 eV and 0.47 eV respectively (the frequency factor is estimated as $10^{10}\,\text{sec.}^{-1}$ in both traps). The other types deeper than these traps might exist in this phosphor, i.e. surface traps and etc., as the build-up character as illustrated in Fig. 17 (a) could not be observed for a long time after several runs of measurements at room temperature unless the preheating is made.

It is likely, however, the two types of traps above mentioned are effective enough to build-up the electroluminescence at the repeating frequency of 50 kc/s. The results shown in Fig. 17 (b) indicate that the build-up character can be observed still after several runs of measurements at 125°C. This means that the traps, from which the electrons can scape thermally within a comparatively short time at this temperature, may be effective to this character. The probability that an electron escapes to the conduction band from the trap of 0.47 eV depth at 120°C, is estimated as

$$p=s\cdot\exp\left(-\frac{E}{kT}\right)\doteqdot 3\times10^{+3}\,\text{sec}^{-1}\,. \qquad (35)$$

Then these traps seem to be effective in this repeating frequency of exciting pulse of 50 kc/s, though the probability of electron trapping is not determined precisely.

§ 5. Summary

The electroluminescence phenomena in ZnS: Cu, Pb phosphors excited by the short field pulses are investigated and the excitation and the recombination mechanisms are discussed. From the experimental results of emission spectra, brightness waveforms, dependences of light outputs on the applied voltages and pulse durations, decay times, build-up characteristics and their temperature dependences, the following considerations are made: the local intense field generated at the cathode region of particle accerelates the primary electrons and the luminescent centers are impact-ionized by these primary electrons. The field strength may be smaller than in the case of sinusoidal fied excitation and then the excitation efficiency of primary electrons greatly decreases compared with the latter case. The primary electrons are partly generated thermally and partly by the direct field-ionization. The blue luminescent centers are mainly excited and they emit the light predominantly without the hole migration mechanism. Besides, the decay times and the build-up characteristics are affected by the trapping effects in the anode region of phosphor particle.

The author considers that the electroluminescence excited by short field pulse has the complementary nature to the one excited by the sinusoidal field, and further experiments are now in progress.

§ 6. Acknowledgments

The author wishes to thank Professors Y. Suge and T. Inui for their continuous and helpful encouragements, and Mr. K. Sugiyama and M. Wakatuki for their helpful assistances, and Mr. M. Kobayashi for his advices in the measuring equipments.

The author also wishes to thank Mr. T. Toriu of Dai-Nippon Toryo Company for giving him the phosphor samples, and Mr. S. Kawashima of NHK Technical Laboratory for his helpful discussions.

References

1) D. Curie: J. phys. radium **14** (1953) 510.
2) W. W. Piper and F. E. Williams: Phys. Rev. **98** (1955) 1809; Brit. J. Appl. Phys., Suppl. no. 4 (1955) 39.
3) P. Zalm: Philips Res. Rep. **11** (1956) 353, 471.
4) S. Tanaka: J. Appl. Phys. Japan **11** (1957) 594.
5) S. Nudelman and F. Matossi: J. Electrochem. Soc. **101** (1954) 546. F. Matossi and S. Nudelman: Phys. Rev. **99** (1955) 1100.
6) D. Hahn and F. W. Seemann: Z. Phys. **149** (1957) 486.
7) J. B. Taylor and G. Alfrey: Brit. J. Appl. Phys., Suppl. no. 4 (1955) 44.
8) F. Seitz: Phys. Rev. **76** (1949) 1376.
9) H. Callen: Phys. Rev. **76** (1949) 1394.
10) P. D. Johnson, W. W. Piper and F. E. Williams: J. Electrochem. Soc. **103** (1956) 201.
11) R. Bowers and N. T. Melamed: Phys. Rev. **99** (1955) 1781.
12) G. R. Fonda: J. Opt. Soc. Amer. **36** (1946) 382.
13) K. H. Butler and J. F. Waymouth: Brit. J. Appl. Phys., Suppl. no. 4 (1955) 33.
14) T. B. Tomlinson: J. Electronics **2** (1956) 166.
15) R. Goffaux: J. phys. radium **17** (1956) 763; **18** (1957) 1.
16) L. Burns: J. Electrochem. Soc. **100** (1953) 572.
17) H. A. Klasens: Nature **158** (1946) 306. M. Schön: Z. Phys. **119** (1942) 463.
18) K. Maeda: J. Phys. Soc. Japan **13** (1958) 1352.
19) N. F. Mott and R. W. Gurney: *Electronic Processes in Ionic Crystals*, 1st ed. (Oxford Press, 1940) chapt. 6.
20) S. Tanaka: to be published.
21) D. R. Frankl: Phys. Rev. **111** (1958) 1540.

JOURNAL OF THE PHYSICAL SOCIETY OF JAPAN, Vol. 14, No. 9, SEPTEMBER, 1959

Dielectric Susceptibility Tensor of Cadmium Sulfide

By Taizō MASUMI*

Department of Applied Physics, University of Tokyo, Tokyo, Japan

(Received March 27, 1959)

The components of static dielectric tensor $\|\kappa_{s_{ij}}\|$ of wurtzite cadmium sulfide have been examined. An anisotropy of κ_s was found between the two crystal orientations [$2\bar{1}\bar{1}0$] and [0001], that provides some suggestive knowledges on the lattice vibration spectra of cadmium sulfide and on the scattering mechanisms of electrons in several semiconductors.

A systematic examination on the dielectric susceptibilities over several semiconductors gives us various knowledges about the nature of the binding between constituent atoms of the crystals. Homopolar binding is more important in usual semiconductors than in inoic crystals. In such cases, the dielectric constant measurement provides a sensitive test of the natures of the binding1),2) as well as the elastic constants measurement1),3).

Cadmium sulfide single crystals have been studied up to now about flaky crystals with prefered crystal orientations prepared by vapour phase or sublimation processes at near atmospheric pressures. Kroeger et al4). had performed the capacitance measurements for ribbon-shaped cadmium sulfide crystals at 1 and 100 kc/sec and obtained the low frequency dielectric constant $\kappa_s=11.6\pm1.5$ for insulating specimens. However, it is supposed that the applied field $\boldsymbol{E}$ in their measurements may

---

* Present Address: Institute of Physical and Chemical Research, 31, Kamifujimae-Cho, Bunkyo-Ku, Tokyo, Japan.

Table I.

Dielectric constant	Direction of field	T (°C)	Frequency				
			300 cps	1 kc	10 kc	50 kc	10 Mc
$\kappa_{s[2\bar{1}\bar{1}0]}$	$[2\bar{1}\bar{1}0]$	14°C	10.1	10.1	10.1	9.86*	9.78
$\kappa_{s[01\bar{1}0]}$	$[01\bar{1}0]$	14°C				9.77*	
$\kappa_{s[0001]}$	[0001]	14°C	7.87	7.87	7.13	6.12*	7.13
Anisotropy Parameter	$K_{\kappa_s}=\frac{\kappa_{s[0001]}}{\kappa_{[2\bar{1}\bar{1}0]}}$	14°C	0.78	0.78	0.71	0.62*	0.74

An example of experimental values of static dielectric constants of hexagonal cadmium sulfide at room temperatures. * By resonant circuit and at 20°C. (After Taizō Masumi)

have a direction parallel to the crystal orientation $[2\bar{1}\bar{1}0]$ for flaky crystals. Medcalf and Fahrig[5)] have recently developed a method of growing cadmium sulfide single crystals of uniform size, shape and homogeneity from the melt at high pressures and temperatures By using such specimens, the author has been able to find the anisotropy in static dielectric constant of cadmium sulfide single crystals. The present re-examination on the dielectric susceptibility tensor supported by the progresses in crystal growing technique[6)] has an aim to study the lattice vibration spectra and scattering mechanism of electrons in cadmium sulfide.

Samples used for our experiment are not ribbon-shaped crystals, but specimens cleaved, machined and polished from cadmium sulfide ingots produced by the Eagle-Picher Company. Sizes of specimens are of about $0.5\sim0.8\,\mathrm{cm}^2$ in area and $0.07\sim0.5$ cm in thickness (parallel to the $[2\bar{1}\bar{1}0]$ or [0001] direction). Static dielectric constant κ_s is determined by the lumped circuits, that is, by the null method involving some types of capacitance bridge in the medium frequency range or by a resonant circuit for the dielectric measurement in higher region. The whole frequency range extends from 10^2 cps to 50 Mc/sec in our experiments. Particular attentions should be paid on photoconductivity phenomena in the crystal as remarked by Kroeger et al.[4)]. We also used the crystals kept in dark for at least a day before observations.

An example of experimental results on a specimen is shown in Table I for κ_s, where the loss factor $\tan\delta$ has not been studied. These values may involve some degrees of errors because no correction were made for edge effects. Slight increases in observed dielectric constants at lower frequency region may be due to the inhomogeneity in resistivity.

The amounts of impurity atom in the specimens are of the orders of 10^{-4} for zinc and indium and 10^{-5} for silicon. We neglected also the temperature effect that is unlikely to be large.

As shown in Table I, the observed dielectric constants of cadmium sulfide single crystals show a remarkable difference between the $[2\bar{1}\bar{1}0]$ and [0001] directions, while we have not observed any appreciable anisotropy in the (0001) plane. Frequency dependence of κ_s scarecely has been recognized for each direction. The probable values of κ_s over several specimens are found to be as follows;

$$\kappa_{s[2\bar{1}\bar{1}0]}=10.8\pm1.6 \quad \text{at } 15°\text{C}$$

$$\kappa_{s[0001]}=7.8\pm1.4 \quad \text{at } 15°\text{C}$$

$$K_{\kappa_s}=\frac{\kappa_{s[0001]}}{\kappa_{s[2\bar{1}\bar{1}0]}}=0.73 \quad \text{at } 15°\text{C}\,.$$

These results on the dielectric susceptibility tensor of wurtzite type cadmium sulfide suggest us that there exist some anisotropies in the effective charge of constituent ions and/or in the restoring force against their displacements, from which we can easily derive the dispersion relation for the longitudinal optical branch depending on (σ/σ) and also imagine an anisotropic energy surface $\hbar\omega(\sigma)=$const. in σ-space, where σ denotes the phonon wave vector. It may be possible that these situation play some roles in the scattering mechanism anisotropy of electrons in some types of semiconductors[7)-10)]*.

---

*) Some situations parallel with those for cadmium sulfide had been recognized also for semiconducting rutile TiO_2, although they have been rather neglected up to now.

The author would like to express his sincere gratitudes to Professor Y. Suge and Professor T. Inui of Tokyo University for their continual encouragements, and to Professor Y. Uemura of the University for his kind critiques and discussions. Sincere thanks are also, especially, due to Dr. H. Mimura, Dr. T. Tanaka and Dr. M. Kobayashi for their helpful discussions.

References

1) N. F. Mott and R. W. Gurney: *Electronic Processes in Ionic Crystals*, 2nd ed., (Oxford, 1950).
2) Z. I. Kir'iashkina, F. M. Popov, D. N. Bilenko and V. I. Kir'iashkin: J. Tech. Phys. USSR, **27** (1957) 85 (Original); **2** (1957) 69 (in English).
3) T. Masumi and T. Tanaka: to be published on those of cadmium sulfide.
4) F. A. Kroeger, H. J. Vink and J. Volger: Philips Res. Rep. **10** (1955) 39.
5) W. E. Medcalf and R. H. Fahrig: J. Electrochem. Soc. **105** (1958) 719.
6) H. Yamashita and S. Ibuki: J. Phys. Soc. Japan **13** (1958) 226. D. C. Reynolds and L. C. Greene: J. Appl. Phys. **29** (1958) 559. L. C. Greene, D. C. Reynolds, S. J. Czyzak and W. M. Baker: J. Chem. Phys. **29** (1958) 1375. D. R. Boyd and Y. T. Sihvonen: J. Appl. Phys. **30** (1959) 176.
7) Y. Suge, S. Tanaka, and T. Masumi: to be published in the Proceedings of the International Conferences on Solid State Physics and Electronics and Telecommunications at Brussels in June 1958.
8) T. Masumi: J. Phys. Soc. Japan **14** (1959) 47.
9) D. C. Cronemeyer: Phys. Rev. **87** (1952) 876.
10) R. G. Breckenridge: Phys. Rev. **91** (1953) 793.

JOURNAL OF THE PHYSICAL SOCIETY OF JAPAN, Vol. 14, No. 9, SEPTEMBER, 1959

On the Screening of Impurity Potential by Conduction Electrons

By Noboru TAKIMOTO

*Department of Physics, University of Tokyo**

(Received April 15, 1959)

A detailed investigation is made on self-consistent impurity potential in a charge cloud of conduction electrons. It is shown first that the Thomas-Fermi method can be used so as to include a certain correlation effect between the conduction electrons which is ignored in customary theories. The same problem is then treated by the method of Nakajima and Bardeen and Pines and it is shown that it leads to essentially the same result as that obtained by the Thomas-Fermi method. The obtained potential differs from the usual one in the fact that the screening parameter now depends on the way of the scattering. Some discussion is given about the equivalence of the two methods and further possible improvement. The potential thus derived is then used for the calculation of the electric resistance governed by the impurity scattering.

§1. Introduction

The method of Thomas-Fermi (T.F.) has often been used in deriving self-consistent potential due to a lattice imperfection embedded in a sea of conduction electrons. This method is of statistical nature and is based on the assumption that when one is interested in the interaction between one particular electron and a certain lattice imperfection, all the other conduction electrons are in local thermal equilibrium in the field of the imperfection as well as of the particular electrons*, i.e., the heaping up of screening electrons (or holes) is partly due to the thermal contact of these electrons (or holes) with the other degrees of freedom localized around the imperfection. It can also be shown that if the conduction electrons and the imperfection are treated as isolated from any other systems, the same result is obtained for the screening. In this case the screening arises entirely from the adiabatic deformation of the charge distribution of the conduction electrons. However, when the assumption of the local equilibrium or of the adiabatic motion of the screening electrons ceases to be valid**, the T.F. method allows no further refinement. Thus one needs some other method which treats the same problem from a dynamical point of view. A great deal of work has been done from such a point of view for the problem of the electron-phonon interaction, but nothing so far for the problem of the impurity scattering***. In early investigation of the electron-phonon interaction, two alternative assumptions were adopted with regard to the charge distribution of the conduction electrons in the field of thermally distored lattice: Nordheim[1)] assumed it rigid, while Bloch and Bethe[2)] assumed it deformable. However, the difference between the potentials they adopted was only formal.

---

* Present Address: Research Institute for Iron, Steel and Other Metals, Tohoku University, Sendai, Japan.

Later, this problem was treated in more detail by Bardeen[3)], who noticed the adiabatic deformation of the charge distribution in the distorted lattice and thus confirmed Bloch-Bethe's assumption. At the same time he derived the self-consistent scattering potential with use of the T.F. method.

More recently, Fröhlich[4)] used a field theoretical technique to treat the adiabatic part of the electron-phonon interaction systematically, and showed that the adiabatic motion of the conduction electrons reduces the phonon velocity to what is actually observed. Fröhlich's work was then extended by Nakajima[5)], who showed that Bardeen's potential can be derived in a more straightforward manner from the original Hamiltonian through a certain transformation. He showed also that Fröhlich's renormalization procedure of the phonon velocity can be extended to include the interaction between the electrons.

Finally, Bardeen and Pines[6)] superposed on the Nakajima's method the collective treatment of Bohm and Pines[7)], and eliminated a great part of the e-e interaction which makes the collective modes. The previous results, however, remained essentially unaltered.

It is clear that the same arguments can be applied to the problem of the impurity scattering, which will be treated in the following. The adiabatic motion of the conduction electrons which reduces the phonon velocity in the electron-phonon case now results in the deformation of their charge distribution in the field of impurity atoms, and this gives rise to the screening effect. The mathematical parallelism between these two cases is almost perfect, and the formulae derived later in this paper can be derived from those for the electron-phonon case by putting ω, the phonon frequency, equal to zero.

This method of obtaining the self-consistent potential resembles the Hartree-Fock's method, but differs from it in that here the method takes account of a certain correlation between electrons automatically. It is shown that the new potential, obtained after some simplifying assumptions, contains the simplest result of the T. F. Method in a certain limit, and that the method can be applied to more general problems to which the T.F. method is hardly applicable.

In § 2, the T.F. method will be recapitulated in such a way available for the later discussions, and all the essential result will be obtained there. In § 3, Nakajima's method will be used to renormalize the impurity potential, and one will see the coincidence of the result with that of § 2. In § 4, the collective treatment will be given along the line similar to that of Bardeen and Pines. The properties of the effective impurity potential thus derived will be discussed fully in two cases where the screening electrons are degenerate (in § 5), and where these are non-degenerate (in § 6). These will be used then for the calculation of the relaxation time of the electric current for both cases (in § 7), and it will be shown that the residual resistance changes only slightly: In metals it is raised a little from the value given by older theories in which the impurity potential is simply screened coulombic. In semi-conductors it will be concluded that the truth lies between two assumptions adopted by Conwell-Weisskopf and Brooks-Herring.

---

* In this statement, the T. F. method is meant not to be the customary one, but one which will be developed in § 2 of this paper. In the customary T. F. method, the effect of the particular electron is ignored.

** At absolute zero of temperature, both assumptions may be equivalent and valid.

*** Unfortunately, the established method at present is not yet so successful as to include the non-adiabatic motion of the screening electrons in an unambiguous manner.

In appendix it will be shown that by the Nakajima's method one can get the screening of the coulomb interaction between conduction electrons without introducing the plasma explicity.

§ 2. The Thomas-Fermi Method

Suppose that an impurity atom is introduced substitutionally into a certain metal and that some of the valence electrons of the atom are released from the atom and itinerate over the crystal as members of the conduction electrons, leaving thus Ze excess ionic charges at the atom. The conduction electrons of the metal are perturbed by this impurity atom.

The perturbations which destroy the periodicity of the crystal are primarily due to the coulomb interaction between the electron in consideration (the Aufelektron) and the excess ionic charges, the excess coulomb interaction between the Aufelektron and those electrons or holes which heap up around the impurity atom. Here the " excess interaction " means the difference in the interaction of the Aufelektron with other electrons when there is the impurity atom and when there is none. Other minor effects are: the difference of Hartree-Fock field of the ionic charges of the impurity atom from that of the mother crystal atom, local strain around the impurity atom and so on.

The first of these is the coulomb interaction $U(r_0)$

$$U(r_0)=-\frac{Ze^2}{r_0} \tag{2.1}$$

with the origin at the impurity atom. The charge distribution of the conduction electrons is affected by the ionic charges Ze and the modified charge distribution which is determined by the potential itself. Thus self-consistency is required between the potential and the charge distribution.

Let $f(H)$ be the distribution function of a conduction electron with one particle Hamiltonian H. The Poisson equation requires

$$\begin{aligned}\Delta U(\boldsymbol{r}_0)=-4\pi e^2\boldsymbol{Tr}[\{f(H_0+U)\\ -f(H_0)\}\delta(\boldsymbol{r}-\boldsymbol{r}_0)]+4\pi Ze^2\delta(\boldsymbol{r}_0),\end{aligned} \tag{2.2}$$

where H_0 is the kinetic energy of a conduction electron, and $\boldsymbol{Tr}$ means the operation

$$\boldsymbol{Tr}[A]=\sum_{k\sigma}\int\psi_k{}^*(\boldsymbol{r})A\psi_k(\boldsymbol{r})\,d\boldsymbol{r}$$

where $\psi_k(\boldsymbol{r})$ is the eigen function of H_0 specified by the wave vector $\boldsymbol{k}$ and σ is the spin coordinate. The first term on the right hand side of (2.2) except the factor $-4\pi e$ represents the difference of the charge density in the presence of the impurity atom from that in its absence. If U in the curely bracket is taken for c-number and only the first term in the expansion of $f(H_0+U)$with the respect to U is retained, Eq. (2.2) gives the well-known formula

$$U(r_0)=-\frac{Ze^2}{r_0}e^{-qr_0}, \tag{2.3}$$

with

$$q^2=4\pi e^2n(\zeta)\ , \tag{2.4}$$

where $n(\zeta)$ is the state density at the Fermi level ζ.

In obtaining (2.3), the Fermi distribution is assumed to be perfectly degenerate. It is reported that the inclusion of the exchange interaction in Eq. (2.2) raises the screening factor q about one half[8]. This seems not to be acceptable, for it is hardly understandable why the exchange term should have any connection with the Poisson equation (2.2). Furthermore, it is probable that the exchange interaction will greatly be reduced if the correlation is included from the start. This will be demonstrated in § 4.

Reflecting the procedure by which it is derived, U given by Eq. (2.3) is to be used only as a c-number, or, what amounts to be the same, as diagonal elements. In other words, it is a potential, as it were, for a test charge, that is, no deformation on the side of the screening electrons in the field of the Aufelektron is considered. Actually, any electron may be picked up from whole conduction electrons as Aufelektron in question, so that this particular electron will be screened by the remaining charges with a hole scooped out by itself, that is, the screening charges are polarized by the Aufelektron, the effect of the screening thus being somewhat diminished. Mathematically, this polarization arises from the off-diagonal elements of U which are ignored in deriving (2.3).

This can be taken care of if U in the function $f(H_0+U)$ is treated as a q-number. In order to expand $f(H_0+U)$ into a power series of U, one writes $f(H_0+U)$ as

$$f(H_0+U)=\frac{1}{2\pi i}\int_{c-i\infty}^{c+i\infty} e^{(H_0+U)s}\phi(s)ds\ , \tag{2.5}$$

where $\phi(s)$ is the Laplace transformation of the distribution function:

$$\phi(s)=\int_0^\infty e^{-sE}f(E)dE\ . \tag{2.6}$$

The integral of (2.5) is performed along the so-called Bromwich path. Now, one can expand $\exp(H_0+U)$ into the ordered exponential series:

$$e^{(H_0+U)s}=e^{H_0 s}+\int_0^s ds' e^{H_0(s-s')}Ue^{H_0 s'}+\cdots\ . \tag{2.7}$$

Then one obtains in the linear approximation,

$$\begin{aligned}&\boldsymbol{Tr}[\{f(H_0+U)-f(H_0)\}\delta(\boldsymbol{r}-\boldsymbol{r}_0)]\\&\quad=\sum_{\boldsymbol{k}\sigma}\sum_{\boldsymbol{k}'}\frac{1}{2\pi i}\int_{c-i\infty}^{c+i\infty}ds\cdot\phi(s)\int_0^s ds'\langle\boldsymbol{k}/e^{H_0(s-s')}Ue^{H_0 s'}/\boldsymbol{k}'\rangle\times\langle\boldsymbol{k}'/\delta(\boldsymbol{r}-\boldsymbol{r}_0)/\boldsymbol{k}\rangle\ ,\end{aligned}$$

where

$$\langle\boldsymbol{k}/\boldsymbol{A}/\boldsymbol{k}'\rangle=\int\psi_{\boldsymbol{k}}^*(\boldsymbol{r})\boldsymbol{A}\psi_{\boldsymbol{k}'}(\boldsymbol{r})\,d\boldsymbol{r}\ ,$$

Let E_k be an eigen value of H_0 with an eigen function ψ_k, then the above expression can be manipulated as follows:

$$\begin{aligned}&\sum_{\boldsymbol{k}\sigma}\sum_{\boldsymbol{k}'}\frac{1}{2\pi i}\int_{c-i\infty}^{c+i\infty}ds\phi(s)\int_0^s ds' e^{E_k(s-s')}\langle\boldsymbol{k}|U|\boldsymbol{k}'\rangle e^{E_{k'}s}\langle\boldsymbol{k}'|\delta(\boldsymbol{r}-\boldsymbol{r}_0)|\boldsymbol{k}\rangle\\&\qquad=\sum_{\boldsymbol{k}\sigma}\sum_{\boldsymbol{k}'}\int_{c-i\infty}^{c+i\infty}ds\phi(s)\frac{e^{E_{k'}s}-e^{E_k s}}{E_{k'}-E_k}\langle\boldsymbol{k}|U|\boldsymbol{k}'\rangle\langle\boldsymbol{k}'|\delta(\boldsymbol{r}-\boldsymbol{r}_0)|\boldsymbol{k}\\&\qquad=\sum_{\boldsymbol{k}\sigma}\sum_{\boldsymbol{k}'}\frac{f(E_{k'})-f(E_k)}{E_{k'}-E_k}\langle\boldsymbol{k}|U|\boldsymbol{k}'\rangle\langle\boldsymbol{k}'|\delta(\boldsymbol{r}-\boldsymbol{r}_0)|\boldsymbol{k}\rangle\ .\end{aligned}\tag{2.8}$$

In the free electron approximation,

$$\langle\boldsymbol{k}|U|\boldsymbol{k}'\rangle=U(\boldsymbol{k}-\boldsymbol{k}')$$

and

$$\langle\boldsymbol{k}'|\delta(\boldsymbol{r}-\boldsymbol{r}_0)|\boldsymbol{k}\rangle=e^{i(\boldsymbol{k}-\boldsymbol{k}')\cdot\boldsymbol{r}_0}\ , \tag{2.9}$$

where $U(\boldsymbol{k}-\boldsymbol{k}')$ is defined by the Fourier transformation of U:

$$U(\boldsymbol{r}_0)=\frac{1}{(2\pi)^3}\int e^{i\kappa\cdot\boldsymbol{r}_0}U(\kappa)d\kappa\ . \tag{2.10}$$

From Eqs. (2.8), (2.9) and (2.10), the Poisson equation is transformed to

$$-\kappa^2U(\kappa)=-4\pi e^2\sum_{\boldsymbol{k}}\frac{f(E_{k-\kappa})-f(E_k)}{E_{k-\kappa}-E_k}U(\kappa)+4\pi Ze^2\ ,$$

whence

$$U(\kappa) = -\frac{4\pi Ze^2}{\kappa^2 + \boldsymbol{H}(\kappa)} ,$$

where

$$\boldsymbol{H}(\kappa) = -4\pi e^2 \sum_{k\sigma} \frac{f(E_{k-\kappa}) - f(E_k)}{E_{k-\kappa} - E_k} . \tag{2.11}$$

A detailed investigation of the potential (2.11) will be postponed to §§ 5 and 6. It is easily shown that in the limit of $\kappa \to 0$, where the polarization effect mentioned above becomes negligible, (2.11) reduces to the screened coulombic form with a screening "constant" (2.4), but for larger κ or for the smaller impact parameter, $\boldsymbol{H}(\kappa)$, the screening parameter, depends on the way of the scattering.

It is reported that the method of Gell-mann and Brueckner leads the same result (2.11) for the impurity potential*). It is interesting to see that a phenomenological theory is equivalent in essence to the orthodox formalism of the many-body problem. This implies that the method of the next section has a very intimate connection with the Gell-mann and Brueckner's method.

§ 3. The Nakajima's Method

This section will be devoted to a formulation of the dynamical method of obtaining the effective impurity potential. Although the method yields after all the same result as obtained by the T.F. method, the procedure is not so straight-forward as the statistical method and there remains a problem unsolved in connection with the invalidity of the adiabatic assumption described in the introduction.

In the following, the problem is treated in the number representation. The Hamiltonian of the electronic system with a proper choice of the base is

$$H^{(1)} = \sum_{k\sigma} E_k n_{k\sigma} + \frac{1}{2} \sum_{\kappa \neq 0} M_\kappa{}^2 \rho_\kappa \rho_{-\kappa} + \sum_{\kappa \neq 0} U_{-\kappa} \rho_\kappa , \tag{3.1}$$

where E_k is the unperturbed energy of a conduction electron with the wave vector $\boldsymbol{k}$ and $n_{k\sigma}$ is the occupation operator of the state specified by $\boldsymbol{k}$, σ. The effective mass expression

$$E = \frac{1}{2m^*} \hbar^2 k^2 , \tag{3.2}$$

is used throughout this paper. ρ_κ is the Fourier component of the density fluctuation

$$\rho_\kappa = \sum_{k\sigma} c_{k-\kappa\sigma}{}^* c_{k\sigma} , \tag{3.3}$$

where $c_{k\sigma}{}^*$ and $c_{\ \sigma}$ are respectively the creation and annihilation operator of the electron $\boldsymbol{k}$, σ, satisfying the anticommutation relations:

$$[c_{k\sigma}{}^*, c_{k'\sigma'}]_+ = \delta_{kk'} \delta_{\sigma\sigma'} , \qquad [c_{k\sigma}{}^*, c_{k'\sigma'}{}^*]_+ = [c_{k\sigma}, c_{k'\sigma'}]_+ = 0 , \tag{3.4}$$

and the relation

$$n_{k\sigma} = c_{k\sigma}{}^* c_{k\sigma} .$$

$M_\kappa{}^2$ is the matrix element of the e-e interaction e^2/r_{12}**) and $U_{-\kappa}$ is that of the bare impurity potential $-Ze^2/r$:

---

*) T. Izuyama, Dissertation. The author is indebted to Dr. T. Izuyama for very valuable discussions about this problem.

**) Actually, the whole e-e interaction should not be included, since a certain part of it is included already for the modification of the electron mass in the crystal. In relation to this, there seems to exist an ambiguity in the choice of the mass of the screening electrons, for, though the effective mass expression (3.2) is adopted here, it can also be considered that the periodic potential of the crystal has little effect on the screening electrons when they are in the limited range around the impurity atom. A detailed investigation of it, however, is beyond the scope of this paper. It is expected that the qualitative conclusions obtained in this paper is not far from the truth.

$$M_\kappa^2=\int\psi_{k-\kappa}^*(\boldsymbol{r}_1)\psi_{k'}^*(\boldsymbol{r}_2)\frac{e^2}{r_{12}}\psi_k(\boldsymbol{r}_1)\psi_{k'-\kappa}(\boldsymbol{r}_2)d\boldsymbol{r}_1d\boldsymbol{r}_2\,,$$

$$U_{-\kappa}=\int\psi_{k-\kappa}^*(\boldsymbol{r})\frac{-Ze^2}{r}\psi_k(\boldsymbol{r})d\boldsymbol{r}\,, \tag{3.5}$$

where $\psi_{\boldsymbol{k}}(\boldsymbol{r})$ is the Bloch function. These matrix elements will be assumed in the following to depends only on the difference κ of wave vectors of initial and final states. In the free electron approximation, they are:

$$M_\kappa^2=\frac{4\pi e^2}{\kappa^2}\quad\text{and}\quad U_{-\kappa}=-\frac{4\pi Ze^2}{\kappa^2}\,, \tag{3.6}$$

which are normalized over the unit volume.

$H^{(1)}$ is divided into three parts:

$$H^{(1)}=H_0+H_c+H_I\,,$$

where

$$H_0=\sum_{k\sigma}E\,n_{k\sigma},\quad H_c=\frac{1}{2}\sum_{\kappa\neq0}M_\kappa^2\rho_\kappa\rho_{-\kappa}\quad\text{and}\quad H_I=\sum_{\kappa\neq0}U_{-\kappa}\rho_\kappa\,. \tag{3.7}$$

Now, it is required to obtain the eigenvalue in a form

$$H^{(1)}e^{iS/\hbar}\Psi_0=Ee^{iS/\hbar}\Psi_0\,, \tag{3.8}$$

where Ψ_0 is the eigenfunction of the unperturbed system H_0, and $\exp(iS/\hbar)$ is a transformation operator. Two transformations can be considered, one associated with H_c and the other with H_I. In this section it is assumed that the former transformation has little effect in determining the effective impurity potential. This is the assumption which Nakajima made tacitly in his derivation of the effective electron-phonon interaction. In the next section both transformations will be carried out in parallel.

The transformed Hamiltonian is expanded in a series of the undetermined operator S:

$$e^{-iS/\hbar}H^{(1)}e^{iS/\hbar}=H^{(1)}-\frac{i}{\hbar}[S,\ H^{(1)}]-\frac{1}{2\hbar^2}[S[S,\ H^{(1)}]]+\cdots\,. \tag{3.9}$$

Now, the first term of the right hand side is written as

$$H^{(1)}=H_0+H_c+H_I^0+(H_I-H_I^0)\,, \tag{3.10}$$

where H_I^0 is the effective impurity potential to be determined.

S is required to satisfy the equation

$$H_I^0-\frac{i}{\hbar}[S,\ H_0]=0 \tag{3.11}$$

and H_I^0 is to be obtained by another equation

$$-\frac{i}{\hbar}[S,\ H_c]+H_I-H_I^0=0\,. \tag{3.12}$$

This can be solved only after making an approximation which will be described later. Two equations (3.11) and (3.12) are combined into a single one:

$$-\frac{i}{\hbar}[S,\ H_0+H_c]+H_I=0$$

This equation implies that one is proceeding with a perturbation calculation with system H_0+H_c as the unperturbed. The effect of the impurity atom is displayed by the operator S which, as Eq. (3.11) indicates, is determined by the renormalized interaction $H_I{}^0$, and the term $-i/\hbar[S, H_c]$ is interpreted as the change of e-e interaction energy in the presence of the impurity atom. The screening effect of the conduction electrons arises from this change. The self-consistency of the treatment is implied by Eq. (3.12), which can be read as follows: The effective potential $H_I{}^0$ is determined by the bare potential H_I together with the correction term $-i/\hbar[S, H_c]$ which arises as a result of the deformation of the charge distribution determined by the effective potential itself.

Let the effective potential be expressed as

$$H_I{}^0=\sum_{k\sigma}\sum_{\kappa} U^0(\boldsymbol{k}-\kappa,\ \boldsymbol{k})c_{k-\kappa\sigma}{}^*c_{k\sigma}\ . \tag{3.13}$$

It turns out that the single parameter κ does not suffice this time to specify the effective potential.

It can easily be shown that the operator

$$-\frac{i}{\hbar}S=\sum_{k\sigma}\sum_{\kappa}\frac{U^0(k-\kappa,\ k)}{E_{k-\kappa}-E_k}c_{k-\kappa\sigma}{}^*c_{k\sigma}\ , \tag{3.14}$$

satisfies Eq. (3.11). Substitution of this into the commutator of (3.12) gives

$$\begin{aligned}\frac{i}{\hbar}[S,\ H_c]=&\sum_{k\sigma}\sum_{\kappa}\frac{U^0(\boldsymbol{k}-\kappa,\ \boldsymbol{k})}{E_{k-\kappa}-E_k}\frac{1}{2}\sum_{\kappa'}M_{\kappa'}{}^2\\&\times\{(c_{k-\kappa\sigma}{}^*c_{k+\kappa'\sigma}-c_{k-\kappa-\kappa'}c_{k\sigma})\sum_{k'\sigma'}c_{k'\sigma'}{}^*c_{k'-\kappa'\sigma'}\\&+\sum_{k'\sigma'}c_{k'-\kappa'\sigma'}{}^*c_{k'\sigma'}(c_{k-\kappa\sigma}{}^*c_{k-\kappa'\sigma}-c_{k+\kappa'-\kappa\sigma}c_{k\sigma})\}\ .\end{aligned} \tag{3.15}$$

According to Bardeen and Pines, the approximation to retain only the diagonal terms in the round bracket in (3.15) gives the Hartree's approximation[*]. In addition to this, there are two other diagonal combinations which represent the exchange effect. These three terms give the final equation which must be solved to give the self-consistent potential $U(\boldsymbol{k}-\kappa,\ \boldsymbol{k})$. This is

$$\begin{aligned}M_\kappa{}^2\sum_{k'\sigma'}&\frac{U(\boldsymbol{k}'-\kappa,\ \boldsymbol{k}')}{E_{k'-\kappa}-E_{k'}}(n_{k'-\kappa'\sigma'}-n_{k'\sigma'})+\sum_{\kappa'}M_{\kappa'}{}^2\frac{U^0(\boldsymbol{k}-\kappa,\ \boldsymbol{k})}{E_{k-\kappa}-E_k}\\&\times(n_{k-\kappa-\kappa'\sigma}-n_{k-\kappa'\sigma})+\sum_{k'}M_{k'-\kappa}{}^2\frac{U^0(\boldsymbol{k}'-\kappa,\ \boldsymbol{k}')}{E_{k'-\kappa}-E_{k'}}(n_{k'\sigma}-n_{k'-\kappa\sigma})\\&+U_{-\kappa}-U^0(\boldsymbol{k}-\kappa,\ \boldsymbol{k})=0\ .\end{aligned} \tag{3.16}$$

This is a set of algebraic equation with infinite variables, actually the integral equation, so that it is hopeless to obtain its general solution. If two exchange terms are omitted, it is simplified to

$$M_\kappa{}^2\sum_{k'\sigma'}\frac{U^0(\boldsymbol{k}'-\kappa,\ \boldsymbol{k}')}{E_{k'-\kappa}-E_{k'}}(n_{k'-\kappa\sigma}-n_{k'\sigma})+U_{-\kappa}-U^0(\boldsymbol{k}-\kappa,\ \boldsymbol{k})=0\ .$$

In this approximation, indices other than κ can be suppressed from U^0:

$$M_\kappa{}^2\sum_{k'\sigma'}\frac{n_{k'-\kappa\sigma'}-n_{k'\sigma'}}{E_{k'-\kappa}-E_{k'}}U_{-\kappa}{}^0+U_{-\kappa}-U_{-\kappa}{}^0=0\ , \tag{3.17}$$

whence one obtains finally

---

[*] Bohm and Pines[7] remarked also that this is nothing but the random phase approximation adopted by themselves in deriving the equation of motion for the density fluctuation ρ_κ.

$$U_{-\kappa}{}^{0}=\frac{U_{-\kappa}}{1-M_{\kappa}{}^{2}\sum\limits_{k\sigma}(n_{k-\kappa\sigma}-n_{k\sigma})/(E_{k-\kappa}-E_{k})} \qquad (=U_{\kappa}{}^{0})\,. \tag{3.18}$$

When the distribution function is substituted into operator $n_{k\sigma}$ (3.18) reduces to (2.11). As for the convergence of the series expansion (3.9), the same argument as given in the electron-phonon case holds here, too, that is, one can choose an energy interval ΔE in such a way that the energy denominator in (3.14) is restricted to be larger than this, but the omission of terms with denominators smaller than this has little influence on the result, while the series (3.9) converges rapidly. ΔE can properly be chosen if the alloy is dilute enough.

The above argument has, however, no physical base and ΔE has been chosen only for the mathematical convenience. According to the method developed in this section, one cannot treat the screening of that part of interaction which, in the form of the matrix elements, connects any two states whose wave vectors differ very little from each other, or, in other words, which associates with nearly forward scattering. For such a mode of scattering, the assumption of the adiabatic motion of the screening electrons will be invalid, and it is required to investigate in detail the mechanisms which cause the non-adiabatic motion. Unfortunately, no theory is established at present which allows to treat such a ploblem. Up to the second order perturbation which is a main object of this paper, the ambiguity in the choice of ΔE has no direct concern with the results.

After all, the transformed Hamiltonian is written as:

$$\begin{aligned} e^{-iS/\hbar}H^{(1)}e^{iS/\hbar}= & \sum_{k\sigma}E_{k}n_{k\sigma}+\sum_{\langle k\sigma,\kappa\rangle}\sum U_{\kappa}{}^{0}c_{k-\kappa\sigma}c_{k\sigma} \\ & +\frac{1}{2}\sum_{\kappa}M_{\kappa}{}^{2}\rho_{\kappa}\rho_{-\kappa}-\frac{i}{\hbar}[S,\ H_{I}]+\text{higher order terms}, \end{aligned} \tag{3.19}$$

where $\langle k\sigma,\ \kappa\rangle$ means to take summation over those $\boldsymbol{k}$ and σ for which

$$|E_{k-\kappa}-E_{k}|<\Delta E\,, \tag{3.20}$$

or, in other words, only those processes which corresponds to the real scattering are retained in the summation. This term cannot be eliminated by transformation without causing divergence of the seried (3.9)*).

Thus for not too small κ's, one has seen the coincidence of the results of the two methods. This is reasonable, because for such κ's, the screening is mainly determined by the dynamical properties of the system consisting of the conduction electrons and the impurity atom. It is for smaller κ's that each method, the satistical one of § 2 and the dynamical one of § 3, has its own feature and will yield different result from each other.

Similar procedures employed in this section can be applied to eliminate or to renormalize the higher order term $-i/\hbar\ [S,\ H_I]$ and so on, but this will not be done here.

§ 4. The Collective Treatment

The effective potential (3.18) is derived as a solution of Eq. (3.12) after making the random phase approximation and on the supposition that exchange terms would have no essential effects. The latter supposition is highly probable, because the coulomb interaction will reduce to a great extent the chance for any two electrons to get near each other. In case of the electron-phonon interaction, Bardeen and Pines[6] showed this by introducing the collective coordinates. This method will be use here for the problem in hand in a somewhat different manner, but of course the principle is the same. The starting Hamiltonian is

---

*) Strictly speaking, the summation in the denominator of Eq. (3.18) must be carried out under the restriction:

$$|F_{k-\kappa}-E_{k}|>\Delta E$$

which is, however, omitted there for brevity.

$$H=H^{(1)}+\frac{1}{2}\sum_{|\kappa|<\kappa_c} P_\kappa^* P_\kappa-\sum_{|\kappa|<\kappa_c} M_\kappa^2 P_\kappa \rho_\kappa\,, \tag{4.1}$$

with the subsidiary condition

$$P_\kappa \psi=0\,, \quad (P_\kappa^*=P_{-\kappa}) \tag{4.2}$$

$H^{(1)}$ is defined by (3.1) and κ_c is the critical wave vector as usual.

If the function ψ satisfies tee subsidiary conduction (4.2) strictly, the eigen values of the new Hamiltonian are the same as those of $H^{(1)}$. Now, consider a canonical transformation $\exp(iS'/\hbar)$ by which H is transformed to

$$e^{-iS'/\hbar} H e^{iS'/\hbar}\,. \tag{4.3}$$

Let S' be given as

$$S'=\sum_{|\kappa|<\kappa_c} (M_\kappa \rho_{-\kappa}+\mathcal{E}_\kappa v_\kappa) Q_\kappa\,, \tag{4.4}$$

where Q_κ is a quantity conjugate to P_κ, i.e., there exists a relation $[Q_\kappa,\ P_\kappa]=i\hbar\delta_{\kappa\kappa'}$, and $Q_\kappa^*=Q_{-\kappa}$. $\mathcal{E}_\kappa$ is a constant chosen so that the following two equations hold:

$$e^{-iS'/\hbar} P_\kappa e^{iS'/\hbar}=P_\kappa+M_\kappa \rho_{-\kappa}+v_\kappa\,, \qquad e^{-iS'/\hbar} P_\kappa^* e^{iS'/\hbar}=P_\kappa^*+M_\kappa \rho_{-\kappa}-v_\kappa\,. \tag{4.5}$$

With use of the random phase approximation, the transformed Hamiltonian is

$$\begin{aligned} e^{-iS'/\hbar} H e^{iS'/\hbar} &=\sum_{k\sigma} E_k n_{k\sigma}+\frac{1}{2}\sum_{|\kappa|<\kappa_c} \{P_\kappa^* P_\kappa+\omega_p^2 Q_\kappa^* Q_\kappa\} \\ &\quad -\frac{1}{2}\sum_{|\kappa|<\kappa_c} v_\kappa v_{-\kappa}+\sum_{|\kappa|<\kappa_c} (U_\kappa-\mathcal{E}_\kappa v_\kappa)\rho_\kappa+\sum_{|\kappa|<\kappa_c} \frac{1}{i\hbar} M_\kappa Q_\kappa \sum_{k\sigma} (E_{k-\kappa}-E_k) c_{k\sigma}^* c_{k-\kappa\sigma} \\ &\quad +\sum_{|\kappa|>\kappa_c} U_\kappa \rho_\kappa+\frac{1}{2}\sum_{|\kappa|>\kappa_c} M_\kappa^2 \rho_\kappa \rho_{-\kappa}\,, \end{aligned} \tag{4.6}$$

where ω_p is the well-known plasma frequency, $\omega_p^2=4\pi ne^2/m^*$. The third term represents the shift of the zero point energy of the system and need not be considered any more*). The fifth term represents the plasma-electron interaction which can be eliminated by another transformation, which however, has no concern with the impurity scattering problem. All the other therms have obvious meanings.

Let U_κ^0 be defined by

$$U_\kappa^0=U_\kappa-\mathcal{E}_\kappa v_\kappa M_\kappa\,, \tag{4.7}$$

then U_κ^0 represents the effective impurity potential to be determined.

The subsidiary condition (4.2) is also transformed to

$$(P_\kappa+M_\kappa \rho_{-\kappa}+\mathcal{E}_\kappa v_\kappa)\psi=0$$

From now on, the procedures are similar to those of the previous section. A transformation $\exp(iS/\hbar)$ is required to eliminate the virtual part of the impurity potential. This time, however, the problem must be divided into tow parts. For $|\kappa|>\kappa_c$, the required transformation is the same as that generated by (3.14) and the same equation (3.16) follows**). Now, two exchange terms cannot be omitted without appropriate reasoning, so that the equation is very hard to solve. In the lack of the exact treatment, it is assumed that the omission is allowed and one can use (3.18) in this case. For $|\kappa|<\kappa_c$, the transformation is just what is defined by (3.14) with $U^0(\boldsymbol{k}-\kappa,\ \boldsymbol{k})$ there replaced by U_κ^0 defined by (4.7). Then the transformed Hamiltonian is

---

*) In the electron-phonon case, the corresponding term reduces the phonon frequency.

**) It must be kept in mind that now in (3.16) all the exchange terms with long wave length M_κ with $|\kappa|<\kappa_c$ are eliminated as a result of the canonical transformation (4.4).

$$e^{-iS/\hbar}e^{-iS'/\hbar}He^{iS'/\hbar}e^{iS/\hbar}=\sum_{k\sigma}E_kn_{k\sigma}+\frac{1}{2}\sum_{|\kappa|<\kappa}(P_\kappa^*P_\kappa+\omega_p^2Q_\kappa^*Q_\kappa)$$

$$+\sum_{|\kappa|<\kappa_c}\frac{1}{i\hbar}M_\kappa Q_\kappa\sum_{k\sigma}(E_{k-k}-E_\kappa)c_{k\sigma}^*c_{k-\kappa\sigma}$$

$$+\sum_{<|\kappa|<\kappa_c>}U_\kappa^0\rho_\kappa+\sum_{<|\kappa|>\kappa_c>}U_\kappa^0\rho_\nu+\frac{1}{2}\sum_{|\kappa|>\kappa_c}M_\kappa^2\rho_\kappa\rho_{-\kappa}+\text{higher order terms.} \qquad (4.9)$$

Again, $\langle|\kappa|<\kappa_c\rangle$ and $\langle|\kappa|>\kappa_c\rangle$ mean to retain in the summation those terms which corresponds to the real processes. U_κ^0 for $|\kappa|>\kappa_c$ has, as assumed above, the expression (3.18), while U_κ^0 for $|\kappa|<\kappa_c$ is still undetermined. The subsidiary condition is transformed further to

$$\left(P_\kappa+M_\kappa\rho_{-\kappa}-\frac{i}{\hbar}[S,\ \rho_{-\kappa}]+\mathcal{E}_\kappa v_\kappa+\text{higher order terms}\right)\psi=0\ ,$$

where

$$-\frac{iS}{\hbar}=\sum_{k\sigma}\sum_{\kappa}\frac{U_{-\kappa}^0}{E_k-E_{k-\kappa}}c_{k-\kappa\sigma}^*\,c_{k\sigma}\ .$$

After calculating the commutator and making the random phase approximation, one obtains

$$\left\{P_\kappa+M_\kappa\rho_{-\kappa}+\mathcal{E}_\kappa v_\kappa+\sum_{k\sigma}\frac{M_\kappa U_\kappa^0}{E_k-E_{k-\kappa}}(n_{k-\kappa\sigma}-n_{k\sigma})+\text{higher order terms}\right\}\psi=0$$

v_κ is chosen in such a way that there exists no coupling between the impurity atom and the plasma through the subsidiary condition. This is achieved if the following equation holds.

$$v_\kappa=\mathcal{E}_\kappa^{-1}\sum_{k\sigma}\frac{M_\kappa U_\kappa^0}{E_k-E_{k-\kappa}}(n_{k-\kappa\sigma}-n_{k\sigma})\ . \qquad (4.10)$$

Then the subsidiary condition in the lowest order approximation is

$$(P_\kappa+M_\kappa\rho_{-\kappa})\psi=0\ , \qquad (4.11)$$

which is the same as that when there is no impurity atom. (4.7) and (4.10) give

$$\frac{U_\kappa^0-U_\kappa}{M_\kappa}=\mathcal{E}_\kappa^2\sum_{k\sigma}\frac{M_\kappa U_\kappa^0}{E_k-E_{k-\kappa}}(n_{k-\kappa\sigma}-n_{k\sigma})$$

and from $\mathcal{E}_\kappa^2=1$ one obtains finally

$$U_\kappa^0=\frac{U_\kappa^0}{1-M_\kappa^2\sum_{k\sigma}(n_{k-\kappa\sigma}-n_{k\sigma})/(E_{k-\kappa}-E_k)}\ , \qquad (4.12)$$

which is the same as (3.18). Thus the e-e interaction is for the most part eliminated to make the plasma. Non the less its screening effect is essentially the same as in the Nakajima's method. As is desired, there exists on coupling between the impurity atom and the plasma through the subsidiary condition, so it seems that the effective impurity potential derived will not depend so much on the extent to which the wave function satisfies this condition.

§ 5. The Effective Potential in Metals

In this section, a detailed investigation of the effective impurity potential (3.18) is made for the case where the conduction electrons are degenerate.

Let I_κ be defined as

$$I_\kappa=-\sum_{k\sigma}\frac{n_{k-\kappa\sigma}-n_{k\sigma}}{E_{k-\kappa}-E_k}\ . \qquad (5.1)$$

In the limit of small κ, or for nearly forward scattering, I_κ can easily be calculated:

$$I_\kappa=-\sum_{k\sigma}\frac{f_{k-\kappa}-f_k}{E_{k-\kappa}-E_k}$$
$$\doteqdot-\sum_{k\sigma}\frac{\partial f}{\partial E_k}$$
$$\doteqdot n(\zeta)\ , \tag{5.2}$$

where f_k is the Fermi distribution which is substituted into $n_{k\sigma}$ in (5.1), and $n(\zeta)$ is the state density including the spin state at the Fermi level*.

Then from Eqs. (3.18), (5.2) and (3.6), one obtains the self-consistent impurity potential

$$U_\kappa{}^0=\frac{-4\pi Ze^2}{\kappa^2+q^2}\ , \tag{5.3}$$

where q is the screening constant given by (2.4). Thus in the limit of the forward scattering, or, as will be pointed out later, if the polarization of the screening electrons is ignored, one is led to exactly the same result as that of the simplest T.F. method. It is obvious that the effect of this polarization is larger for the larger κ or for the smaller impact parameter. This comes out from the exact calculation of I_κ, which can be carried out in the free electron approximation and in perfectly degenerate case. The final result is

$$I_\kappa=n(\zeta)G\left(\frac{\kappa}{2k_0}\right)\ , \tag{5.4}$$

where

$$G(x)=\frac{1}{2}\left[1+\frac{1}{2x}(1-x)\log\left|\frac{1+x}{1-x}\right|\right]\ ,$$
$$\kappa=|\kappa| \tag{5.5}$$

and k_0 is the absolute value of the Fermi wave vector. The effective potential is then

$$U_\kappa{}^0=\frac{-4\pi Ze^2}{\kappa^2+q^2G(\kappa/2k_0)}\ . \tag{5.6}$$

The expression of the potential in ordinary space, or the Fourier transformation of (5.6) cannot be obtained analytically, but it approaches, for small r, to the bare coulomb type more rapidly than (2.3) does.

The function $G(x)$ has the following expansion formulae:

$$G(x)=1-\frac{x^2}{1.3}-\frac{x^4}{3.5}-\cdots\quad\text{for } x<1, \tag{5.7a}$$

$$G(x)=\frac{x^{-2}}{1.3}+\frac{x^{-4}}{3.5}+\cdots\quad\text{for } x>1. \tag{5.7b}$$

In Fig. 1, $G(x)$ is plotted as a function of x. As one may have anticipated, the screening parameter $G(x)$ is a monotonically decreasing function of the argument x. Namely, the effect of the screening diminishes as the impact parameter decreases. For the straight backward scattering ($x=1$), the screening parameter is exactly one half of the semi-classical value (2.4)**.

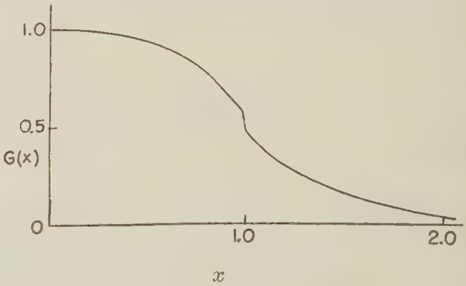

Fig. 1. $G(x)$ as a function of x.

All the quantitative result obtained so far have been based on the free electron approximation and effects of the band structure has been ignored, so one is not in a position to derive any conclusion about the interband effect. It is likely, however, that when the impurity potential induces the interband transition or similar effects, the matrix elements to be used, for example, for the calculation of the transition probability will not be those originated from the classical potential (2.3), but will be rather those obtained from the bare coulomb potential.

It is easily shown that the effect of temperature is to modify the screening parameter by a factor of order of kT/ζ, where k is the Boltzmann constant and T is the absolute temperature, and hence is quite negligible in ordinary metals at ordinary temperature.

§ 6. The Effective Potential in Semi-Conductors

In this section, a detailed investigation of the effective potential (3.18) is made in the case where the screening electrons obey the Boltzmann statistics. U_κ and $M_\kappa{}^2$ in (3.18) is redefined by

---

* For such κ's, (5.1) is not strictly valid (cf. § 3).

** Strictly speaking, the value of κ for which $x=1$ holds lies in the region where (4.12) cannot be used off-hand, because in this region exchange effect cannot be omitted without further justification.

$$U_\kappa = -4\pi Ze^2/\kappa^2\mathcal{E}\ ,$$
$$M_\kappa{}^2 = 4\pi e^2/\kappa^2\mathcal{E}\ , \tag{6.1}$$

where $\mathcal{E}$ is the static dielectric constant of the material.

Now, the Boltzmann distribution

$$f_k = \frac{e^{-\beta E_k}}{Z}$$

with

$$\beta = 1/kT \tag{6.2}$$

is substituted into $n_{k\sigma}$ in (5.1)*). Z is a function of T though the equation

$$\sum_{k\sigma} f_k = n\ , \tag{6.3}$$

where n is the number of the conduction electrons in the crystal.

In the following two limiting cases, I_κ can be expanded into power series:

Case A; $kT \gg \hbar^2\kappa^2/2m^* = E_\kappa$,

$$I_\kappa = \frac{n}{kT}\left[1 - \frac{1}{6}\left(\frac{E_\kappa}{kT}\right) + \frac{1}{6}\left(\frac{E_\kappa}{kT}\right)^2 - \cdots\right]. \tag{6.5a}$$

Case B; $kT \ll E_\kappa$,

$$I_\kappa = \frac{n}{kT}\left[\left(\frac{kT}{E_\kappa}\right) + 2\left(\frac{kT}{E_\kappa}\right)^2 + 12\left(\frac{kT}{E_\kappa}\right)^2 + \cdots\right]. \tag{6.4b}$$

In deriving Eqs. (6.4a) and (6.4b), the relation (6.3) was used. (6.4a) is valid for nearly forward scattering, and (6.4b) for large angle scattering of those electrons whose energy is much larger than the thermal average value. If only the first term of the series (6.4a) is retained, the effective potential has the simplest form

$$U_\kappa{}^0 = \frac{-4\pi Ze^2}{\kappa^2 + q_D{}^2}\ , \tag{6.5}$$

where

$$q_D{}^2 = \frac{4\pi ne^2}{kT} \tag{6.6}$$

is the screening constant. (6.5) is nothing but the Debye-Hückel potential and $q_D{}^{-1}$ is the Debye length. Thus again in the limit of the forward scattering in which the polarization effect is negligible, the result agrees with that of the simplest T.F. method.

The exact calculation of I_κ leads

$$I_\kappa = -\sum_{k\sigma} \frac{n_{k-\kappa\sigma} - n_{k\sigma}}{E_{k-\kappa} - E_k}$$
$$= \sum_{k\sigma} n_{k\sigma}\left(\frac{1}{E_{k-\kappa} - E_k} - \frac{1}{E_k - E_{k+\kappa}}\right)$$
$$\frac{m^*}{\lambda Z\pi^2\hbar^2\kappa}\int_0^\infty dt\cdot xe^{-\lambda\kappa^2}\log\left|\frac{x+\xi}{x-\xi}\right|\ , \tag{6.7}$$

where

$$\xi^2 = \frac{\lambda\kappa^2}{4} = \frac{E_\kappa}{4kT} \tag{6.8}$$

and

$$\lambda = \frac{\hbar^2}{2m^*kT}\ .$$

With use of the relation

$$\sum_{k\sigma} \frac{e^{-\lambda\kappa^2}}{Z} = \frac{1}{4\pi^{3/2}Z\lambda^{3/2}} = n\ , \tag{6.9}$$

one obtains

$$I_\kappa = \frac{n}{kT}F(\xi) \tag{6.10}$$

where

$$F(\xi) = \frac{1}{\sqrt{\pi}}\cdot\frac{1}{\xi}\int_0^\infty dx\cdot xe^{-\kappa^2}\log\left|\frac{x+\xi}{x-\xi}\right|. \tag{6.11}$$

The effective impurity potential is

$$U_\kappa{}^0 = \frac{-4\pi Ze^2}{\kappa^2 + q_D{}^2F(\xi)}\ . \tag{6.12}$$

The function $F(\xi)$, or the screening parameter, is evaluated numerically and is plotted against ξ in Fig. 2.

The variation of $F(\xi)$ with respect to κ is understandable by the argument given in § 5. Its variation with respect to the temperature is in the reverse. This will be due to the fact that at high temperatures, the electrons (or holes) are hard to heap up around the

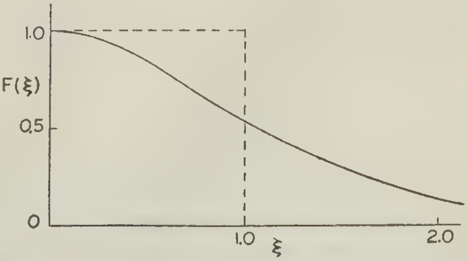

Fig. 2. $F(\xi)$ as a function of ξ. In calculating the electric resistance in § 7, $F(\xi)$ is replaced by the dashed line.

---

*) It will be very hard to comprehend what sort of approximation it is to take the ensemble average over the electron distribution in the denominator of (3.18). The same question is applicable to the case of metals except when the conduction electrons are perfectly degenerate.

impurity atom owing to the temperature agitation.

It is expected that the temperature and the carrier concentration dependence of the electric resistance will differ from those in which the Debye-Hückel potential (6.5) is used. This difference, however, may hardly be checked by experiment, because other factors may have much stronger temperature and concentration dependence. A detailed examination will be made in the next section.

§ 7. The Effect of the New Potential on the Electric Conductivity

The relaxation time τ_k of the electric current j_k is[9]

$$\frac{1}{\tau_k}=\frac{\pi Nc}{\hbar}\sum_{k'}|\langle \boldsymbol{k}|U|\boldsymbol{k}'\rangle|^2(1-\cos\theta)\delta(E_k-E_{k'}), \tag{7.1}$$

where c is the atomic concentration of the impurity atom, N is the number of the lattice points in the crystal, θ is the scattering angle and U is the impurity potential which is given by (5.6) for metals and (6.12) for semi-conductors. In the following, τ_k is calculated for each case separately.

Case I: *Degenerate Case.*

Substitution of (5.6) into (7.1) gives after the integration of angular variables

$$\frac{1}{\tau_k}=\frac{\pi(Ze^2)^2m^*Nc}{\hbar^3k^3}\boldsymbol{I}(\alpha)\ , \tag{7.2}$$

where

$$\boldsymbol{I}(\alpha)=2\int_0^1\frac{x^3}{\{x^2+\alpha^2G(x)\}^2}dx \tag{7.3a}$$

and

$$\alpha=q/2k\ ,$$
$$k=|\boldsymbol{k}|\ . \tag{7.3b}$$

The electric conductivity σ is

$$\sigma=\frac{ne^2}{m^*}\tau_{k_0}$$
$$=\frac{\nu\hbar^3k_0^3}{\pi cm^*(Ze)^2\boldsymbol{I}(\alpha_0)}\ , \tag{7.4}$$

where ν is the number of the free electron per atom, k_0 is the Fermi wave-length and $\alpha^0=q/2k_0$. The integration (7.3a) cannot be carried out analytically, but if only first two terms in the expansion (5.7a) are retained it can be done to give

$$\boldsymbol{I}(\alpha_0)=\frac{1}{(1-\alpha_0/3)^2}$$
$$\times\left[\log\left(1+\frac{1-(\alpha_0^2/3)}{\alpha_0^2}\right)+\frac{1}{1+(\alpha_0^2)/(1-\alpha_0^2/3)}\right]. \tag{7.5}$$

If only the first term of (5.5a) is retained, one obtains the well-known formula of the residual resistance in which (7.5) is replaced by

$$\boldsymbol{I}'(\alpha_0)=\log\left(1+\frac{1}{\alpha_0^2}\right)-\frac{1}{1+\alpha_0^2}\ . \tag{7.6}$$

For a numerical example, let us consider metallic copper for which $\alpha_0\sim0.8$ and $I(\alpha_0)/I'(\alpha_0)\sim1.2$\*), so that the residual resistance is raised by about this factor, as can be expected qualitatively.

Case II. *Non-Degenerate Case*

Substitution of (6.2) into (7.4) and the integration over the angular variables give

$$\frac{1}{\tau_k}=\frac{\pi(Ze^2)^2m^*Nc}{\varepsilon^2\hbar^3k^3}2\int_0^{\sqrt{\eta}}\frac{x^3}{\{x^2+\gamma^2F(x)\}^2}dx, \tag{7.7}$$

where

$$F(x)=\frac{1}{\sqrt{\pi}}\cdot\frac{1}{x}\int_0^\infty dy\cdot ye^{-y^2}\log\left|\frac{y+x}{y-x}\right|,$$
$$\gamma^2=\frac{\pi ne^2\hbar^2}{(kT)^22m^*\varepsilon^2} \tag{7.8}$$
$$\eta=\frac{E_\kappa}{kT}\ .$$

The electric conductivity is given by

$$\sigma=\beta\sum_{k\sigma}j_{kx}^2\frac{e^{-\beta E_k}}{Z}\tau_{\boldsymbol{k}}\ , \tag{7.9}$$

where j_{kx} is the x-component of the electric current. Substituting (7.7) into (7.9) and carrying out the integration over $\boldsymbol{k}$, one obtains

$$\sigma=\frac{2^{5/2}\varepsilon^2\nu(kT)^{3/2}}{3m^{*1/2}\pi^{3/2}(Ze)^2}\int_0^\infty \alpha\eta\cdot\eta^3e^{-\eta}\frac{1}{J_\gamma(\sqrt{\eta})}\ , \tag{7.10}$$

where

$$J_\gamma(\sqrt{\eta})=2\int_0^{\sqrt{\eta}}\frac{x^2}{\{x^2+\gamma^2F(x)\}^2}dx\ . \tag{7.11}$$

The integrand of (7.13) with $J_\gamma(\sqrt{\eta})$ removed has a sharp maximum at $\eta=3$, while $J_\gamma(\sqrt{\eta})$ is a slowly varying function, so the integration can be performed approximately by putting $J_\gamma(\sqrt{\eta})$ constant $J_\gamma(\sqrt{3})$. This means that the electrons which have the largest contrubution to the conductivity are those whose energy is twice the average kinetic energy.

---

*) Taken from ref. 8).

After this one obtains

$$\sigma=\frac{2^{7/2}\mathcal{E}^2\nu(kT)^{3/2}}{m^{*1/2}\pi^{3/2}(Ze)^2 J_\gamma(\sqrt{3})}\,. \tag{7.12}$$

Now, three cases are considered: These are Conwell-Weisskopf's, Brooks-Herring's and the present case which are treated separately.

[I] Conwell-Weisskopf's Formula.

Conwell and Weisskopf used the bare coulomb potential as the scattering potential. This corresponds to the case $\gamma=0$ in (7.11). In this case, the integration (7.10) diverges. They avoided this by introducing a lower limit in the integration over x, which, from the classical dynamics, is written

$$x=2k\sqrt{\frac{\eta}{1+(2\mathcal{E}kTd\eta^2/Ze^2)^2}}\,,$$

where d is the average distance between the impurity atoms. This yields

$$J_0(\sqrt{3})=\log\left(1+\left(\frac{6\mathcal{E}kTd}{Ze^2}\right)^2\right). \tag{7.13}$$

(7.13) and (7.12) give the Conwell-Weisskpf's formula[10].

[II] Brooks-Herring's formula.

Brooks and Herring[11] used for U in (7.1) the Debye-Hückel potential (6.5). This corresponds to the case $F(\xi)=1$ in (7.7). In this case $J_\gamma(\sqrt{3})$ is easily calculated and is given by

$$J_\gamma(\sqrt{3})=\log\left(1+\frac{3}{\gamma^2}\right)-\frac{1}{1+3/\gamma^2}\,. \tag{7.14}$$

(7.14) and (7.12) give the Brooks-Herring's formula.

[III] The Present Case.

The analytical integration of (7.10) is hopeless, so the potential is simplified by putting

$$F(x)=1 \text{ for } 0<x<1,$$
$$=0 \text{ for } x>1.$$

This corresponds to replacing the screening parameter $F(x)$ plotted in Fig. 2 by a simple step function plotted there also by a dashed line. Then the integration is elementarily carried out and the result is

$$J_\gamma(\sqrt{3}=\log\left(3+\frac{3}{\gamma^2}\right)-\frac{1}{1+1/\gamma^2}\,. \tag{7.15}$$

For the typical values of parameters such as m^*, $\mathcal{E}$ and for the simple case $n=N$, the function $J_\gamma(\sqrt{3})$ is numerically calculated for each case and plotted against n for constant T (Fig. 3) and against T for constant n (Fig. 4).

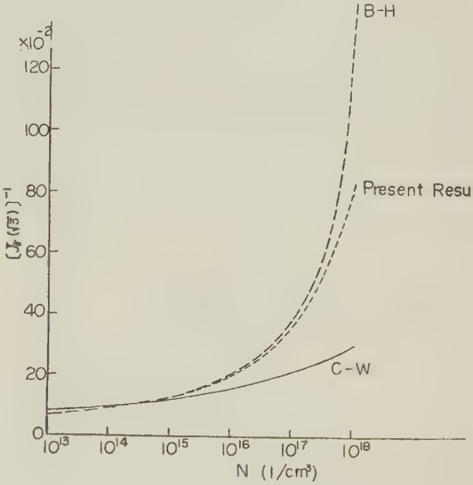

Fig. 3. $[J_\gamma(\sqrt{3})]^{-1}$ as a function of N. Values; $\varepsilon=16.1$, $T=80$, $Z=1$ and $m^*=m/4$ are chosen. Without common factors, the electron mobility is proportional to $[J_\gamma(\sqrt{3})]^{-1}$.

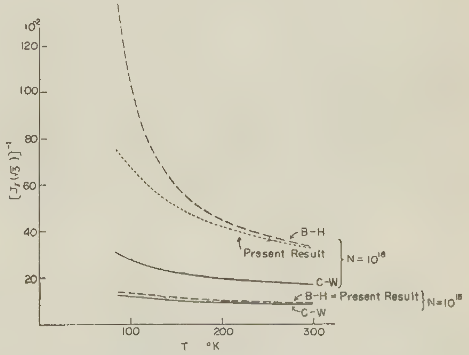

Fig. 4. $[J_\gamma(\sqrt{3})]^{-1}$ as a function of T. Values; $\varepsilon=16.1$, $Z=1$ and $m^*=m/4$ are chosen.

According to Fig. 3, the present potential yields the electron mobility in the lower concentration region nearly equal to what B–H's case yields. In the lowest concentration region, both results nearly coincide with C–W's case. As the carrier concentration increases, however, these three begin to deviate from one another and the new result lies between the older two. The interpretation is as follows: At the lower concentration there are few screening electrons, so that the impurity potential is nearly coulombic and its effect is rather over the long range. Consequently, the fraction which nearly forward scattering processes possess in the total cross section is overwhelmingly large and hence the polarization effect is negligible. As the concentration increases, the screening becomes much more effective and the effect of the impurity atom is limited in the short range. The large angle scattering then tends to possess a larger fraction in the total cross section and at the same time the reduction of the screening parameter tends to be effective on the phenomenon. The last is the reason why the present potential yields the result which lies between the older two. The screening effect was under-estimated by Conwell and Weisskopf, while over-estimated by Brooks and Herring.

Fig. 4 indicates similar features. These features may be suggested as a possible effect which is conspicuous for large γ.

§ 8. Summary and Discussions

The method of Thomas-Fermi was used to show that the requirement of the self-consistency was extended to include a certain correlation effect between the conduction electrons. The effective potential derived was shown to contain the result of the simplest T.F. method in the limit of the forward scattering. Actually, the screening parameter depends on the way of the scattering in such a way that it decreases as a impact parameter decreases. This is due to the polarization of the screening electrons by the colliding electron.

The method of Bardeen and Pines, applied to the problem of the impurity potential, was shown to yield entirely the same results as the T.F. method within the scope of this paper.

The effect of the new potential on the electric resistance was shown to be rather little in the lowest order of approximation. In case of metals, it is raised slightly from the value known so far. In case of semi-conductors, it was concluded that the truth lies between the two assumptions adopted hitherto.

All the problem was treated in the free electron approximation except that the effective mass was used. It seems at first sight that the procedures can directly be extended to the cases in which the band structure of the material is included. However, it is not obvious whether such an extension is realistic or not, and this question cannot be answered unless the problem is reconstructed in a more fundamental formalism in which the ion core field, the impurity potential and the field due to the conduction electrons are treated all in equal importance.

In calculating the electric resistance in § 7, the assumption was tacitly made that the transformation which led to the effective potential had no influence on the electric current operators. This assumption has an intimate relation with the discussion given in § 3 on the convergence of the expansion (3.9), and cannot be examined before the method of treating the non-adiabatic motion of the screening electrons is established.

Apart from that, two approximations were made. One is the random phase approximation made in solving Eq. (3.12). This approximation may at first sight have been justified, for the results agreed with those of the T.F. method. One may also think that the random phase approximation is quivalent to the procedure of taking the ensemble average in the statistical treatment as the T.F. method. However, a little reflexion shows that this is not the case, because what were omitted as a result of this approximation are very complicated interaction terms which cannot be treated by the T.F. method. It will be very cumbersome to justify this approximation more clearly, but such an attempt is desirable.

Another approximation, or rather the assumption is that the exchange terms play no essential role in determining the self-consistent potential. This assumption was made in § 3 without any reasoning. In § 4, the introduction of the collective coordinates eliminates the long range part of the exchange interaction, but there still remains the short range part which cannot be ignored without further justification. It is required to treat the exchange terms more properly.

Thus to the extent of this paper, the dynamical method is equivalent to the T.F. method, and cannot be claimed to have made much progress in determining the effective interaction. Still it is more general than the T.F. method in exhibiting the assumptions and approximations on which the T.F. method is established, and in finding out the problems which future theory must solve and the T.F. method could never do.

Though the dynamical method is not yet so well established, it is systematic within its limit of validity, and there are some problems to which the method can be applied. One of them is the screening of magnetic interaction by conduction electrons, which will be discussed in a forthcoming paper.

Acknowledgment

The author wishes to thank Profs. R. Kubo and Y. Uemura and members of their laboratories for much stimulating discussion, especially Dr. H. Hasegawa for his continual encouragement throughout this work.

Appendix

The screening of the Coulomb interaction in metals by the Nakajima's method

In this appendix, it is shown that in metals the screening of the coulomb interaction between the conduction electrons is derived by the method of § 3. The procedure is similar to that used by Bohm and Pines in their earlier investigations on this subject, but the result differs in the fact that the correlation is more properly treated and the effective potential, if derived correctly, depends on the way of the interaction.

The Hamiltonian of the system is

$$H_0=\sum_{k\sigma} E_k n_{k\sigma}+\frac{1}{2}\sum_{\kappa} M_\kappa{}^2\rho_\kappa\rho_{-\kappa}\,. \tag{A.1}$$

Let the first term be H_0 and the second H_I.

Again a transformation is made

$$e^{-iS/\hbar}He^{iS/\hbar}=H-\frac{i}{\hbar}[S,\ H]-\frac{1}{2\hbar^2}[S[S,\ H]]+\cdots\,. \tag{A.2}$$

It is required that S satisfies the equation

$$H_I{}^0-\frac{i}{\hbar}[S,\ H_0]=0\,. \tag{A.3}$$

$H_I{}^0$ is the undetermined interaction which is expressed in a form

$$H_I{}^0=\frac{1}{2}\sum_{k\sigma}\sum_{k'\sigma'}\sum_{k} M^0(\boldsymbol{k},\ \boldsymbol{k}',\ \kappa)c_{k-\kappa\sigma}{}^*c_{k\sigma}c_{k'\sigma'}{}^*c_{k'-\kappa\sigma'}\,.$$

$M^0(\boldsymbol{k},\ \boldsymbol{k}',\ \kappa)$ is to be determined by another equation

$$-\frac{i}{\hbar}[S,\ H_I{}^0]+H_I-H_I{}^0=0\,. \tag{A.4}$$

The solution of (A.3) is

$$-\frac{i}{\hbar}S=\sum_{k\sigma}\sum_{k'\sigma'}\sum_{\kappa}\frac{M^0(\boldsymbol{k},\ \boldsymbol{k}',\ \kappa)}{E_{k-\kappa}-E_k+E_{k'}-E_{k'-\kappa}}c_{k-\kappa\sigma}{}^*c_{k\sigma}c_{k'\sigma'}{}^*c_{k'-\kappa\sigma}\,. \tag{A.5}$$

With use of this, (A.4) is explicity written down and after the random phase approximation is made and exchange terms are dropped out, one obtains the equation

$$M_\kappa{}^2\sum_{k'\sigma'}\Big\{\{M^0(\boldsymbol{k}',\ \boldsymbol{k}_2,\ \kappa)\frac{n_{k'\sigma'}-n_{k'-\kappa\sigma'}}{E_{k_1-\kappa}-E_{k_1}+E_{k'}-E_{k'-\kappa}}$$
$$+M^0(\boldsymbol{k}_1,\ \boldsymbol{k}',\ \kappa)\frac{n_{k'\sigma'}-n_{k'-\kappa\sigma'}}{E_{k_2-\kappa}-E_{k_2}+E_{k'}-E_{k'-\kappa}}\Big\}+M_\kappa{}^2-M^0(\boldsymbol{k}_1,\ \boldsymbol{k}_2,\ \kappa)=0\,. \tag{A.6}$$

Even this equation is difficult to solve. So the problem is simplified by taking only those scattering processes in which two electrons collide with each other, each electron conserving its energy throughout the process. In this case, single parameter κ suffices to specify the effective potential M^0. (A.6) is then much simplified to

$$2M_\kappa^2\sum_{k'\sigma'}\frac{n_{k'\sigma'}-n_{k'-\kappa\sigma}}{E_{k'}-E_{k'-\kappa}}M_\kappa^0+M_\kappa^2-M_\kappa^0=0\ ,$$

whence

$$M_\kappa^0=\frac{M_\kappa^2}{1-2M_\kappa^2\sum(n_{k\sigma}-n_{k-\kappa\sigma})/(E_k-E_{k-\kappa})}\ . \tag{A.7}$$

For small κ,

$$M_\kappa^0=\frac{4\pi e^2}{\kappa^2+2q^2}\ , \tag{A.8}$$

where q is the screening constant defined by (2.5). The simplifying assumptions used for the derivation of (A.7) seems to hold actually to some extent on account of the high degeneracy of the conduction electrons as well as of the Pauli principle. The trouble with the exchange terms may arise from the treatment in which the coulomb and the exchange effects are equally important. The introduction of the correlation hole prior to the treatment of the exchange may reduce the latter effect. This will be the central principle of Bohm and Pine's theory. As for the mathematical regior of the method, anything convincing cannot be said without studying the effects of higher order terms and of the subsidiary condition.

References

1) L. Nordheim: Ann. Physik **9** (1931) 607.
2) A. Sommerfeld and H. Bethe: Handbuch der Phys. XXIV, 2.
3) J. Bardeen: Phys. Rev. **52** (1937) 688.
4) H. Frohlich: Proc. Roy. Soc. **A, 215** (1952) 291.
5) S. Nakajima: Proc. of the International Conference of Theoretical Phys. Kyoto and Tokyo (1954).
6) J. Bardeen and D. Pines: Phys. Rev. **99** (1955) 1140.
7) D. Bohm and D. Pines: Phys. Rev. **82** (1951) 635; **85** (1952) 338; **92** (1953) 609.
8) J. Friedel: Advances in Phys. **3** (1954) 446.
9) For instance, A. H. Wilson: *The Theory of Metals* (Camb. Univ. Press, 1953) 266.
10) E. M. Conwell and V. F. Weisskopf: Phys. Rev. **77** (1950) 388.
11) See § 3 in the paper of P. P. Debye and E. M. Conwell: Phys. Rev. **93** (1954) 693.

JOURNAL OF THE PHYSICAL SOCIETY OF JAPAN, Vol. 14, No. 9, SEPTEMBER, 1959

Properties of Semiconductive Barium Titanates

By Osamu SABURI

Technical Laboratory, Murata Manufacturing Co.

(Received April 23, 1959)

The resistivity of barium titanate which is usually of the order of $10^9 \sim 10^{12}$ ohm-cm, may be remarkably reduced with suitable control in valency. The valency-controlled barium titanate, whose resistivity is of the order of $10 \sim 10^4$ ohm-cm at room temperature, shows anomalous positive character in the temperature dependency of the resistivity. For example, the resistivity of barium titanate containing 0.1 mol. percent of cerium abruptly changes by 10^4 between 120°C and 150°C.

Some semiconductive properties and their relations to the crystal transition and the composition of the materials are reviewed, for the valency-controlled barium titanates, and assumptions are proposed for the role of additives on the reduction of the resistivity of the barium titanates.

§ 1. Introduction

The anomaly in resistivity-temperature character of barium titanate was first reported by H. A. Sauer and S. S. Flaschen as positive temperature coefficient of resistance thermistor materials1). They described positive resistivity-temperature characters and their voltage dependencies for some valency-controlled barium titanates. Similar study was done by G. G. Harman for barium titanate containing samarium2).

This paper first attempts to show what kind of additives may be effective upon the reduction of the resistivity of barium titanates.

Sauer et al. already reported that those cations whose valencies are higher than the host ions are only effective substituents for producing semiconductive barium titanates. However, should any substitution occur in ionic crystal, we might generally expect that an impurity level in the energy band would be produced and hence bring any influence on conduction properties. From this point of view, several cations were picked up as substituents in our experiment, which were supposed to be close to Ba^{+2} or Ti^{+4} in their sizes and have higher or lower valency than Ba^{+2} or Ti^{+4}.

Assumptions for the mechanism of the conductivity in the barium titanates may be available from those experimental results.

The effects of quantities on the resistivity and crystal structure for those additives which is effective upon reducing the resistivity, the effects of the deviation from the stoichiometry for some valency-controlled barium titanates will be also explained.

Our another attempt is to show the relation between crystal transition and positive temperature character of resistivity of the valency-controlled barium titanates, with the data obtained for the barium titanates and barium-strontium titanates containing proper additives.

Furthermore, some dielectric properties and semiconductive properties of titled materials, such as frequency spectra of resistivity and dielectric constant, rectification phenomena, thermo-e.m.f., Hall e.m.f. will be shown with the effects of different electrode materials.

The barium titanates of low resistivity will be referred as semiconductive barium titanates in the following descriptions.

§ 2. Preparation of Samples and Methods of Measurements

The methods of preparing samples were mainly the same as those for ceramics, except that specially purified raw materials were used.

As the base material, we used barium-titanyl-oxalate which had been precipitated from barium chloride and titanium tetra-chloride dropped into oxalic acid3), where the purity of each raw material was of the order of 99.99%.

The additive cations were basically introduced in the forms of oxalates, so far as they were available. In case the oxalate of the cation to be introduced was water soluble or not available, oxide or chloride of the cation was used.

The base materials and the additives were throughly mixed with a pot-mill of polyethylene, with adequate amount of barium carbonate or titanium dioxide to compensate the deviation from the stoichiometry caused by the additives.

The mixed materials were fired in alumina crucibles at about 1000°C. for 1 hr.. After firing, the materials usually turned white (occasionally very slightly colored) and, formed very brittle lumps.

The lumps were crushed and pressed into discs of 20 mm in diameter and about 2 mm in thickness, under the hydraulic pressure of 600 kg/cm², unless otherwise mentioned.

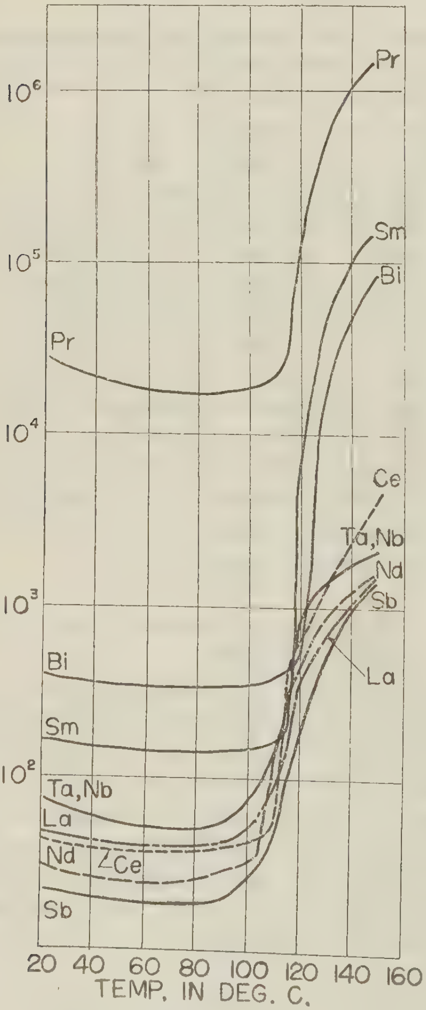

Fig. 1. Resistivity-temperature characters of semiconductive barium titanates containing various additives.

Those discs were fired at 1350°C~1400°C for 2 hrs. in an electric furnace with carborundum heating elements, where high alumina saggers and zirconia sand were used, and the atmosphere was not specially controlled.

Resistivity was determined by a direct measurement of the current flowing through the sample under impressed voltage of 0.01~0.1 V/mm. Provided that indium amalgam electrodes were used, the resistivity measured by the above mentioned method coincided with the value measured by 4-probe method.

For the measurements of dielectric properties, an impedance bridge and a Q-meter were used.

Hall voltages were measured with the apparatus of the sensitivity of 1 μV, which had been reported by J. J. Donoghue et al.⁴⁾.

Lattice constants were estimated with a recording X-ray diffractometer with $K\alpha_1$ of copper target.

§ 3. Experimental Results

1. *The effects of the kinds of the additives*

Each additives of 0.3 molecular percent of the mother material was introduced for studying the effects of the kinds of the additives.

Among various kinds of additives that were surveyed, Bi, Ce, La, Nb, Nd, Pr, Sb, Sm and Ta were effective upon the reduction of the resistivity of the barium titanate and those samples containing one of the above

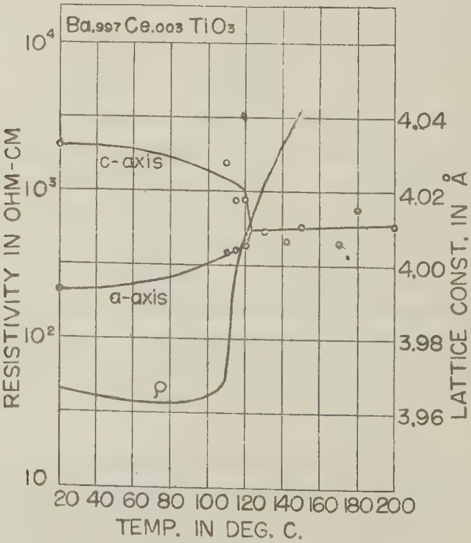

Fig. 2. Correspondence of the anomaly in the resistivity-temperature character to the crystal transition.

mentioned additives showed anomalous positive temperature character of resistivity as illustrated in Fig. 1. One example of the correspondencies of the anomalies in the resistivity-temperature characters with the transitions in crystal structures is shown in Fig. 2 for the barium titanate containing 0.3 mol. % of Ce.

Table I. Ceramic and electric properties of barium titanates containing various additives.

Properties of introduced element			Properties of the specimen including the element				
Element	Valencies	Ionic radii	Color	Shrinkage	Lattice const. at 25°C		Resistivity at 25°C
					a-axis	c-axis	
—	—	Å	—	%	Å	Å	ohm-cm
Ag	+1 +2	1.26 —	light gray	84.0	3.9944	4.0204	3.1×10^{9}
Bi	+5 +3	0.74 1.20	blue	85.5	3.9952	4.0374	5.8×10^{2}
Ce	+3 +4	1.40 —	blue	80.0	3.9936	4.0272	4.2×10
Co	+2 +3	0.78 0.65	violet	85.5	3.9812	4.0120	5.5×10^{8}
Ga	+3	0.62	ivory	82.6	3.9936	4.0280	7.0×10^{8}
La	+3	1.16	blue	82.0	3.9936	4.0315	4.5×10
Mn	+7 +6 +4 +3 +2	0.46 — — — 0.83	brown	86.2	3.9920	4.0280	1.1×10^{8}
Mo	+6 +4 +3	0.62 — —	grayish violet	82.6	3.9944	4.0096	5.0×10^{8}
Nb	+5 +3	0.70 —	blue	84.7	3.9936	4.0280	8.0×10
Nd	+3	1.10	light blue	86.2	3.9952	4.0280	2.8×10
Pr	+3 +4	1.12 —	blue	80.6	3.9944	4.0220	3.5×10^{4}
Sb	+5 +3	0.62 0.90	blue	82.0	3.9944	4.0106	2.2×10
Sm	+3 +2	0.97 —	grayish blue	80.0	3.9952	4.0196	2.1×10^{2}
Ta	+5	0.68	blue	83.4	3.9968	4.0220	8.0×10
Th	+4	0.95	yellow	87.7	3.9952	4.0112	3.0×10^{9}
V	+5 +4 +3 +2	0.59 — — 0.72	light yellow	85.5	3.9944	4.0122	4.0×10^{9}
W	+6 +4 +3	— — —	light yellow	80.6	3.9952	4.0162	4.1×10^{9}
Zn	+2	0.74	light yellow	81.3	3.9920	4.0196	3.7×10^{10}

On the other hand, for the barium titanates containing one of Ag, Co, Ga, Mo, Mn, V, W and Zn, resistivity was not appreciably reduced and the anomaly in the resistivity-temperature character as caused by Bi, Ce or others could never be observed.

Those specimens whose resistivities were remarkably reduced were characterized with bluish color. Color, lattice constant and resistivity at room temperature are shown in Table I, for every specimen mentioned here.

2. *The effects of the quantity of the additives*

The effects of the quantity of the additives were studied for the barium titanates containing La or Ce, which had turned out to be effective for reducing the resistivity.

The result shown in Fig. 3 tells us that the barium titanates containing La or Ce of less than 0.05 mol. %, and those containing La or Ce of more than 0.5 mol. % show comparatively higher resistivity. The anomalous positive temperature character of resistivity as shown in Fig. 1, was not apparent for those specimens of high resistivity.

Fig. 3 also tells us that the tetragonal lattice of barium titanate tends to cubic at room temperature with increasing quantity of La or Ce.

The variation of the positive temperature character of resistivity with the variation of the content of La or Ce is shown in Fig. 4. From this result, we may suppose that the optimum quantity of the additives would be about 0.3 mol. % for obtaining lowest resistivity, and that the optimum one would be about 0.1 mol. % for obtaining highest positive temperature coefficient of resistivity.

3. *The effects of the deviation from the stoichiometry for the barium titanates*

It has been known that the properties of barium titanate are greatly affected by the deviation from the stoichiometry, that is the deviation from the unity of the molecular ratio of Ba:Ti. The effects of the deviation were checked for the semiconductive barium titanates.

Experimental results are shown in Fig. 5, for the barium titanates containing 0.3 mol. % of La or 0.1 mol. % of Ce with excess Ba or

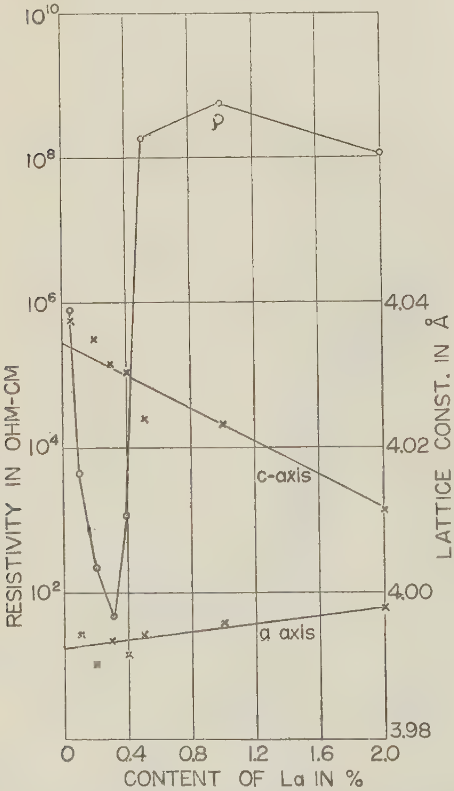

Fig. 3 (a). Dependencies of resistivity and lattice constants on the content of La.

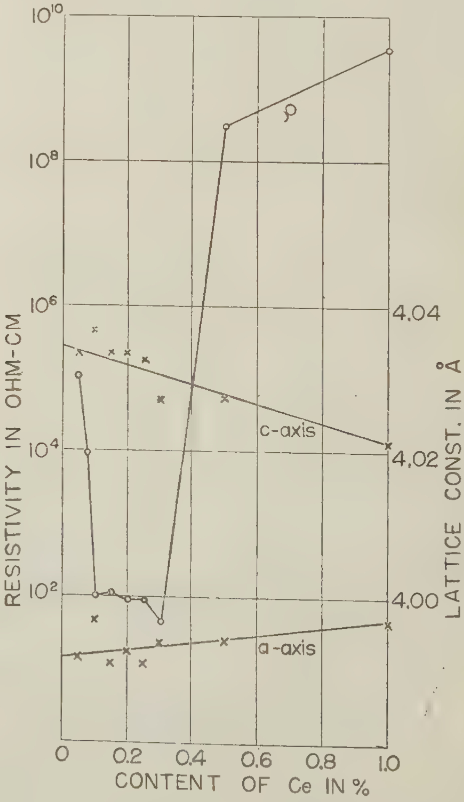

Fig. 3 (b). Dependencies of resistivity and lattice constants on the content of Ce.

Ti. With the results shown in Fig. 5, we may conclude that the deviation from the stoichiometry has not much influence upon the resistivity-temperature character.

4. *Properties of the barium-strontium titanate with Ce*

As is well known, increasing quantity of strontium causes decreasing Curie temperature in barium-strontium titanate system. Should the anomaly of resistivity in the semiconductive barium titanate happen with the the transition in crystal structure, one might expect that the temperature where the resistivity anomaly happens will shift with the variation of the content of strontium in semiconductive barium-strontium titanate system.

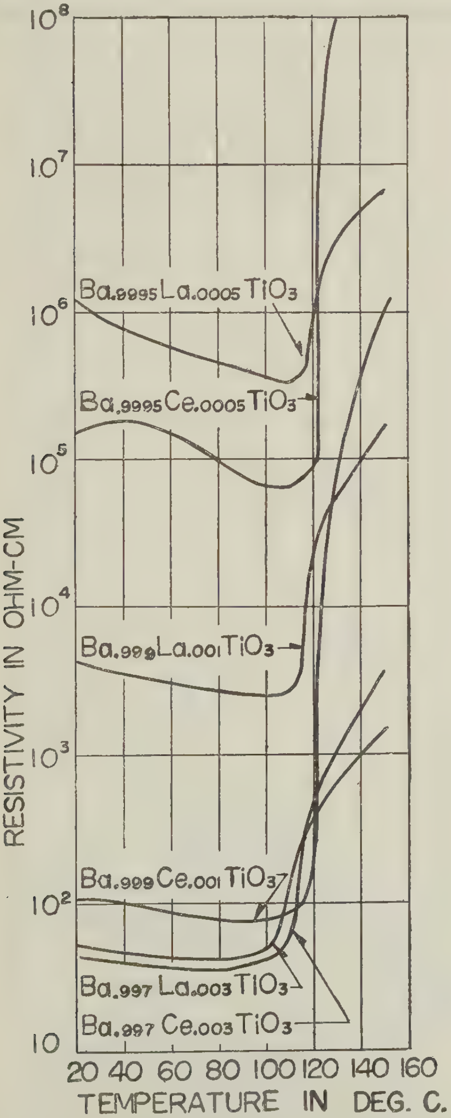

Fig. 4. Dependencies of resistivity-temperature characters on the content of La or Ce.

Fig. 6 illustrates a series of resistivity-temperature characters for the specimens with different content of strontium, and shifting of crystal transition point with the content of strontium.

The expected correspondence of the anomaly in resistivity with the crystal transition is observed in Fig. 6.

5. *Properties of reduced barium titanates*

Even no additions are introduced, the resistivity of barium titanate can be remarkably reduced with suitable reduction (making deficits of oxygen atoms), that is, with heating in vacuum or hydrogen atmosphere.

Pure barium titanate fired in air is usually yellow and has considerably high resistivity, however, its color turns bluish and its resistivity is lowered after the reduction treatment.

If the reduction is not so heavy, the treated barium titanate shows an anomalous positive temperature character of resistivity. But, if

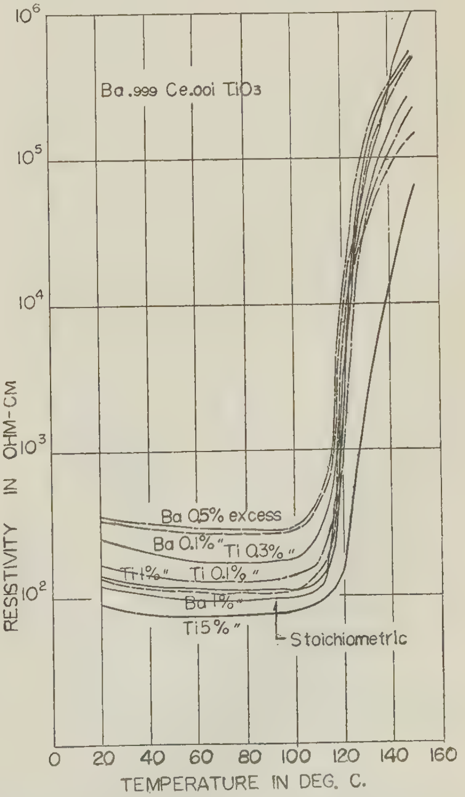

Fig. 5 (a). Dependencies of resistivity-temperature characters on the deviations from stoichiometry.

the reduction becomes much heavier, the positive character becomes poor, or can even no more be observed.

Such behavior of barium titanate is illustrated in Fig. 7. The specimens were reduced in hydrogen atmosphere at the conditions written in the figure.

6. *Properties of valency-controlled single crystals.*

The properties of barium titanates mentioned above are all concerned with the ceramics, that is the barium titanates in polycrystal states.

One might wonder what behavior could be observed for single crystals. To answer this question, some measurements were done with valency-controlled barium titanates in singles crystal states.

Specimens were single crystals of butterfly type (about 15 mm at longest sides) which had been grown from barium titanate melted in potassium fluoride. Method of producing single crystals was the one reported by Remeika⁵⁾, except that iron was not introduced but barium titanate powder containing 0.3 mol. % of La, Sb, Nd or Ce was used as raw material. Though we can not expect that the same amounts of additives as in the raw materials would be introduced into single crystals, we can expect that a certain amount of each additive was introduced into the crystals, inferring from their color (dark greyish green for the ones containing La, Sb or Nd, dark yellow for the ones containing Ce).

The resistivity of these single crystals is considerably high; typical temperature characters for them are shown in Fig. 8, where no similar anomaly in resistivity as reported for polycrystals is observed.

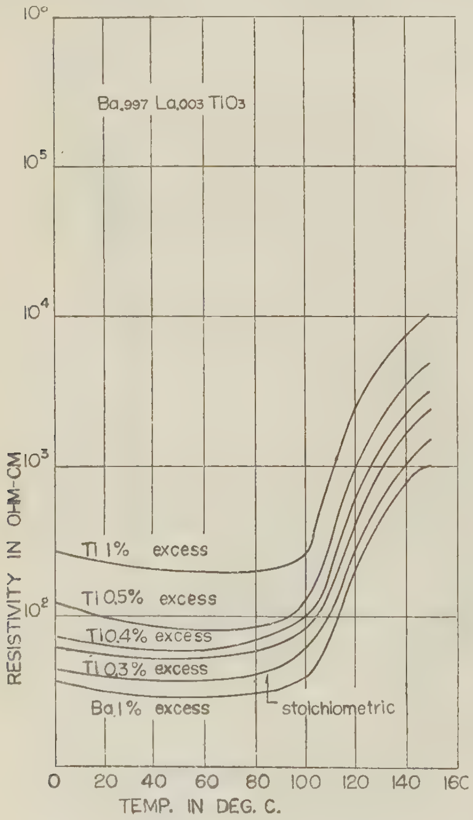

Fig. 5(b). Dependencies of resistivity-temperature characters on the deviations from stoichiometry.

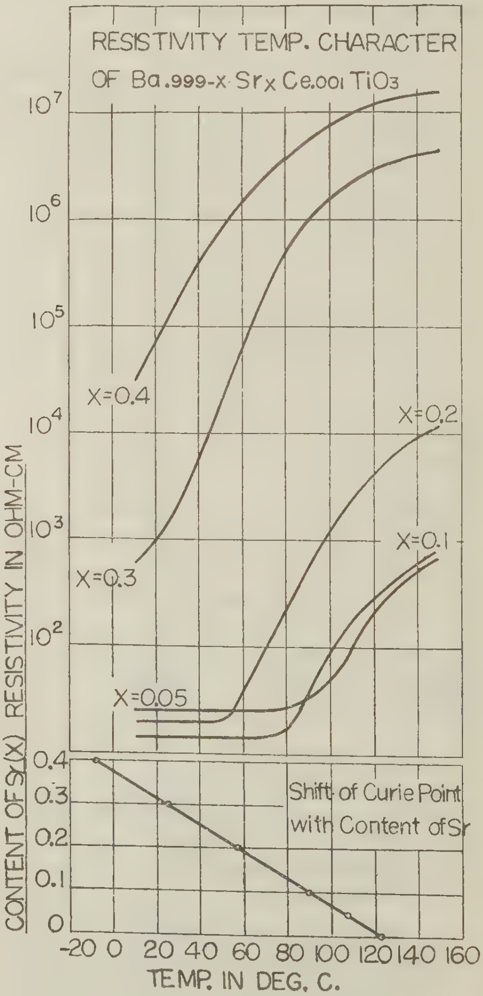

Fig. 6. Variation of resistivity-temperature curve and shift of Curie point with content of Sr in Ba–Sr titanate system.

7. *The resistivity-temperature characters in the extended temperature region*

Typical resistivity-temperature characters of semiconductive barium titanates in the extended temperature region are shown in Fig. 9, where the measurements were done between −70°C and +400°C.

Until the temperature gets t_1, the resistivity decreases with increasing temperature as usually shown in common semiconductors. The resistivity abruptly increases at the temperature just above t_1, and its rate of change amounts as much as 10^4. However, when the temperature exceeds t_2, the resistivity begins again to fall with increasing temperature, where logarithm of resistivity is proportional to the inverse absolute temperature.

The temperature t_1 depends upon the composition of the barium titanates, as it corresponds to the crystal anomaly as shown in Fig. 2 and Fig. 6. Whereas, the temperature t_2 is not so much affected by the composition but is equally about 200°C for every specimen. The activation energies gotten from the inclinations of log. resistivity *vs.* 1/absolute temperature curve are about 0.03 to 0.15 eV for temperature region below t_1, and are about 0.8 to 1.46 eV for temperature region above

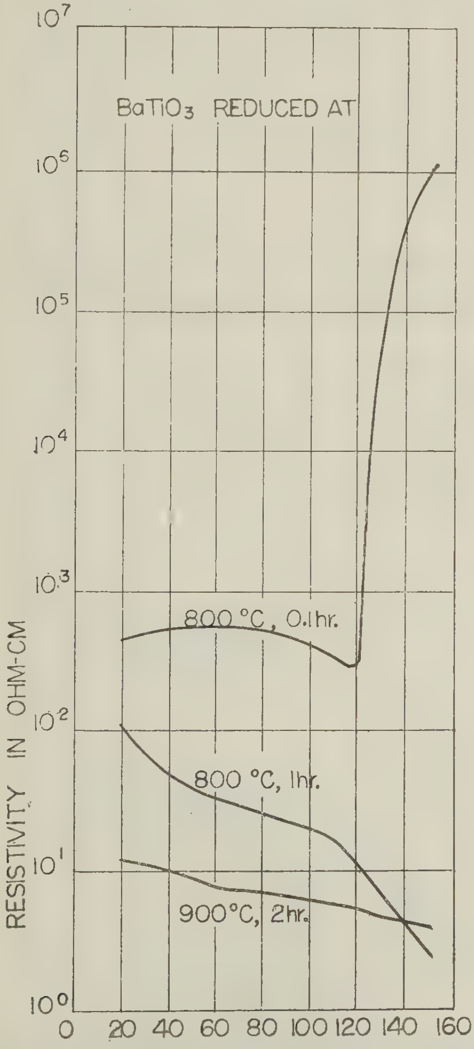

Fig. 7. Resistivity-temperature characters of reduced barium titanates.

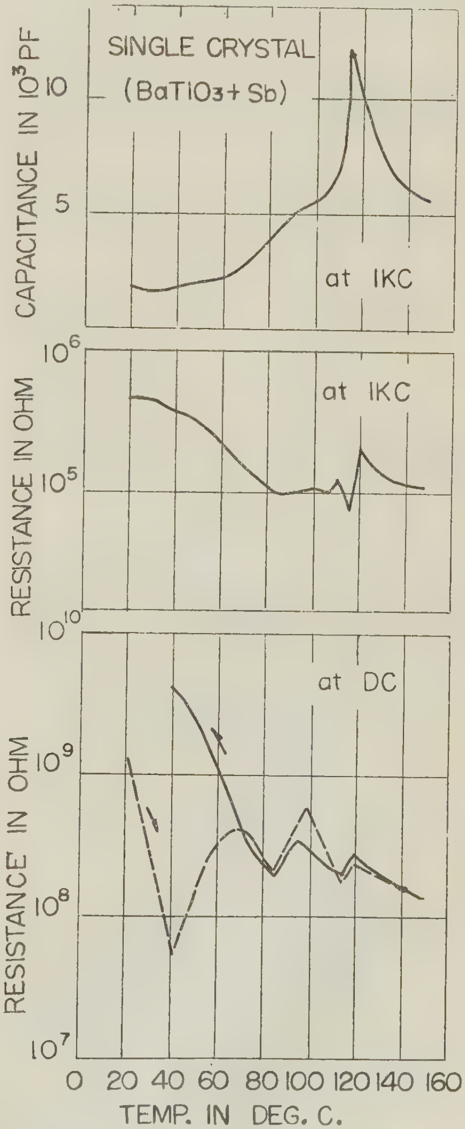

Fig. 8. Temperature characters of resistance at DC, capacitance and parallel resistance of a single crystal of valency-controlled barium titanate with Sb.

t_2. The temperature coefficients of the resistivity in the temperature region between t_1 and t_2 are about 8 to 60%/°C, as calculated with the equation:

Temperature coefficient:

$$\alpha=(1/0.434\Delta t)\log R_1/R_2\,.$$

8. *The voltage dependency of the resistivity and the effects of the electrode materials on the contact resistance*

In this study, the measurements of resistance, unless otherwise mentioned, consisted of the direct measurements of current through the specimens under a certain impressed voltage (2 probe method).

The comparison of the results of 2 probe method with those of 4 probe method and the voltage dependency of the resistivity are illustrated in Fig. 10, when ohmic electrodes of indium-amalgam were used, and the arrangement for 4-probe method was as shown

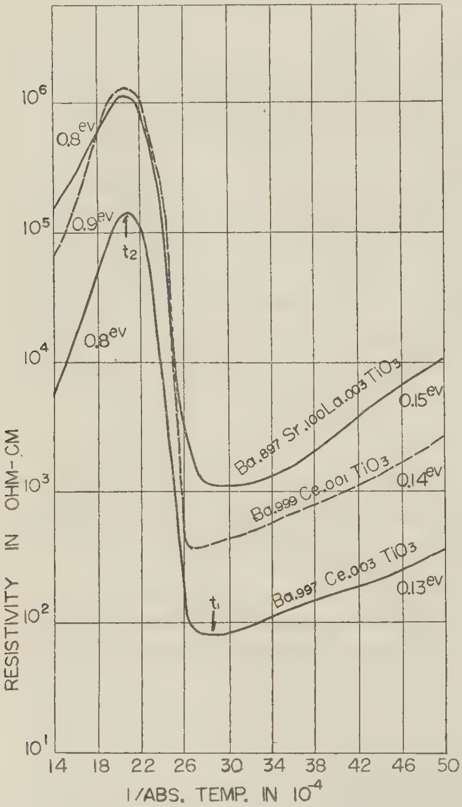

Fig. 9. Resistivity-temperature characters in extended temperature region.

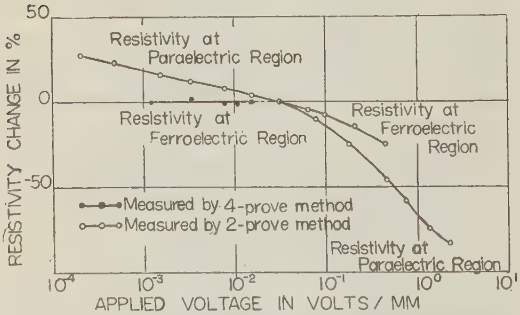

Fig. 10. Voltage dependendies of resistivity in ferroelectric and paraelectric regions.

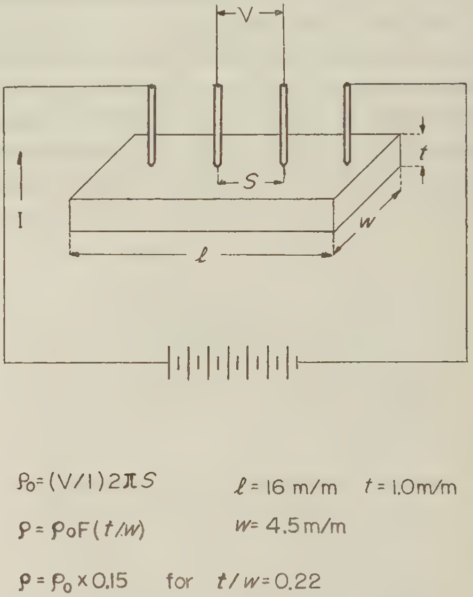

Fig. 11. Arrangement for the 4-pobe method of measurement of resistivity.

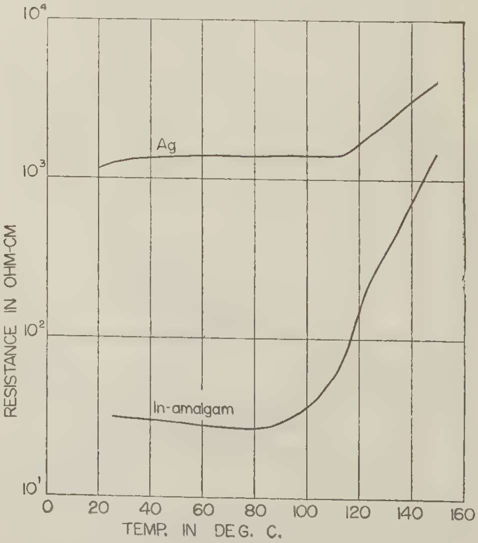

Fig. 12. Apparent resistance-temperature characters shown in the specimen with silver electrodes and in the specimen with indium-amalgam electrodes.

in Fig. 11.

Fig. 10 tells us that for certain voltages (0.01~0.1 volt/mm) the value measured with 2-probe method coincide with those measured with 4-probe method fairly well, and that the resistivity is more voltage sensitive in paraelectric region than in ferroelectric region.

All measurements with resistivity reported in this paper were done at the impressed voltage of 0.01~0.1 volt/mm, and with indium-amalgam electrodes.

Some materials show higher contact resistance than indium-amalgam, as shown in Fig. 12, which result was obtained for fired-silver electrodes.

9. *Frequency spectra of resistivity and dielectric constant for the semiconductive barium titanates*

In this section, the resistivity (ρ) and dielectric constant (ε) and their frequency depend-

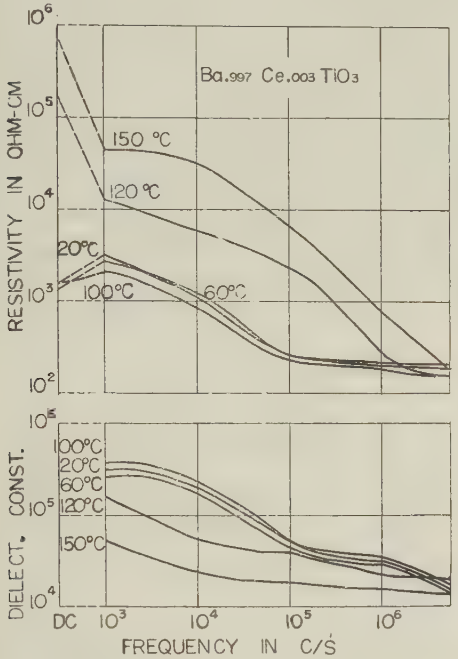

Fig. 13. Frequency character of resistivity and dielectric constant for the semiconductive barium titanate with 0.3 mol. % of Ce.

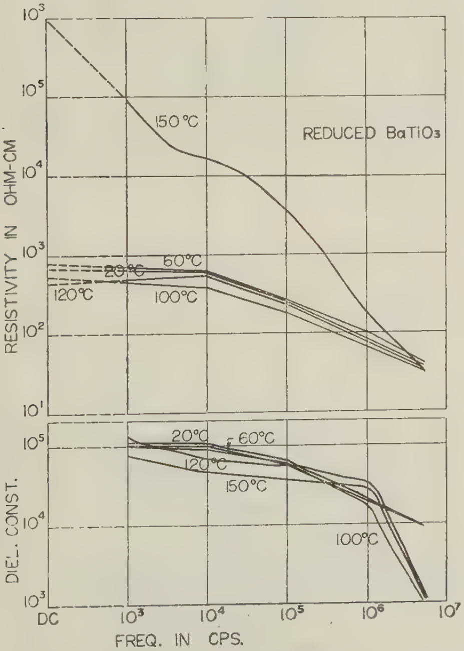

Fig. 14. Frequency character of resistivity and dielectric constant for the reduced semiconductive barium titanate.

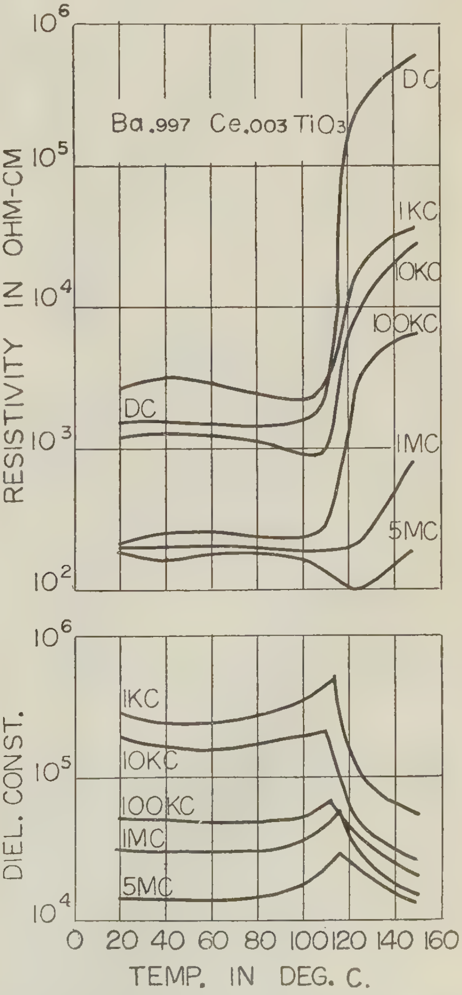

Fig. 15. Temperature character of resistivity and dielectric constant for the semiconductive barium titanate with 0.3 mol. % of Ce.

encies will be explained for typical semiconductive barium titanates with ohmic electrodes, ρ and ε are calculated from the measured parallel resistance and parallel capacitance.

Fig. 13 shows the frequency spectra of ρ and ε for barium titanate containing 0.1 mol. % of Ce, and Fig. 14 shows those for weakly reduced barium titanate.

Fig. 13 and Fig. 14 are rearranged in Fig. 15 and Fig. 16 respectively, with the frequencies as the parameter. The temperature dependencies of ρ and ε with the frequencies as the parameter for $Ba_{.999}Ce_{.001}TiO_3$ and $Ba_{.897}Sr_{.100}La_{.003}TiO_3$ are respectively shown in Fig. 17 and Fig. 18. A dispersion is observed at lower frequency region for every sample, and the positive temperature character decreases with increasing frequency.

10. *Thermo-e.m.f. for the semiconductive barium titanates*

The thermo-e.m.f.s for some representative semiconductive barium titanates were measured as total thermo-e.m.f.s against copper, with cold junction maintained at 15°C and hot junction elevated up to 415°C. Experimental results are as shown in Fig. 19, the e.m.f. per degree $(d\theta/dT)$ appears constant in each specimen for the referred whole tem-

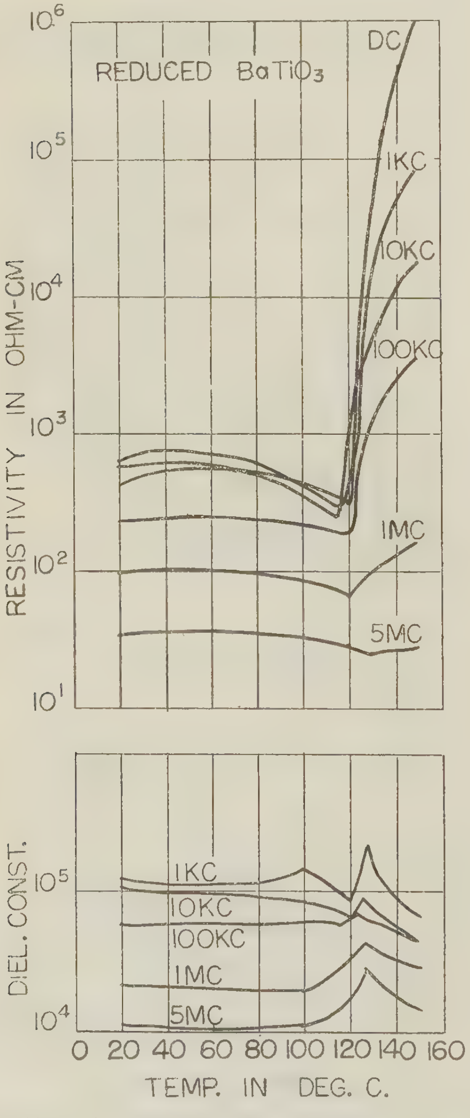

Fig. 16. Temperature character of resistivity and dielectric constant for the reduced semiconductive barium titanate.

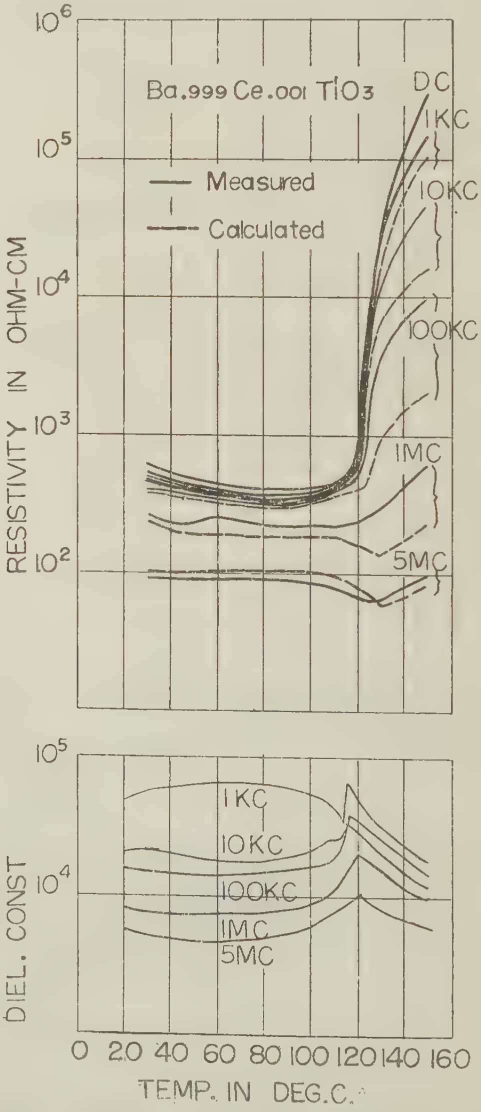

Fig. 17. Temperature character of resistivity and dielectric constant for the semiconductive barium titanate with 0.1 mol % of Ce.

perature region including Curie point. The value of $d\theta/dT$ is about 690 to 860μV/°C which depends upon the material. The sign of the generated e.m.f. indicates that those materials are N-type semiconductors.

11. *Rectifying phenomena in the semiconductive barium titanates*

With the semiconductive barium titanate with ohmic electrode on one surface and non-ohmic electrode on the other, a certain rectifying phenomenon may be observed. Fig. 20 shows an example of this phenomenon when fired silver and indium-amalgam electrodes were used, where the maximum ratio of forward to backward current is about 600. Semiconductive barium titanates are proved to be N-type also from the direction of easy flow at the rectifying contact.

12. *Hall effects in the semiconductive barium titanates*

In spite of the endeavor to detect a small e.m.f. using sensitive apparatus, no accurate value of Hall constant has been obtained for the semiconductive barium titanates, as the

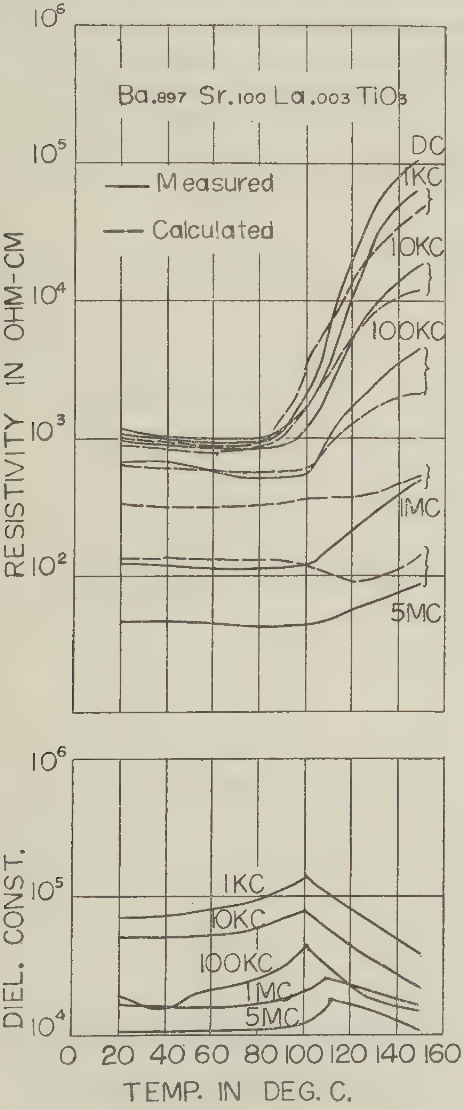

Fig. 18. Temperature characters of resistivity and dielectric constant for the semiconductive barium-strontium titanate.

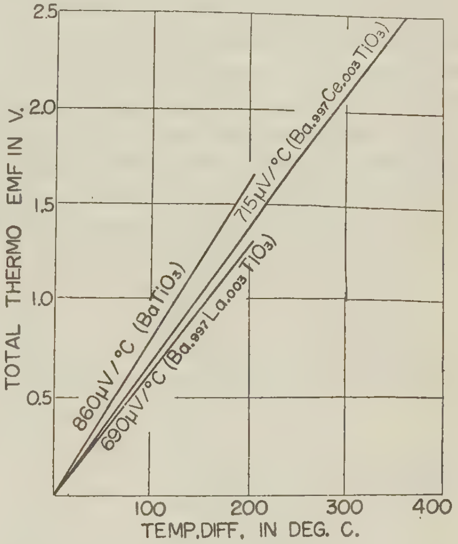

Fig. 19. Thermo e.m.f. in semiconductive barium titanates.

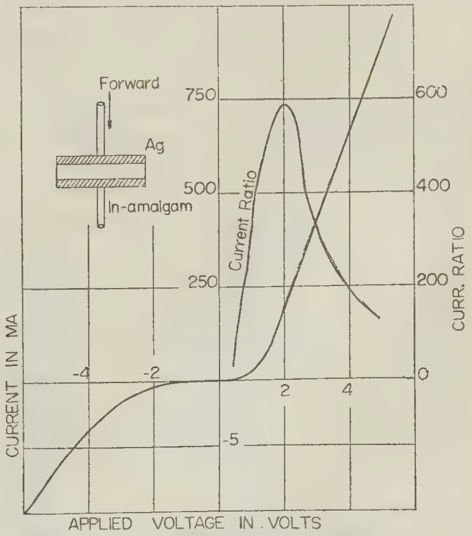

Fig. 20. Rectifying character of semiconductive barium titanates.

generated e.m.f. is very small and interfered with considerably strong noise. However, the order of magnitude of the Hall constant value is estimated at about 10^{-2} cm^3/coulomb, at room temperature, and the sign of Hall e.m.f. indicates that those materials are N-type.

13. *Behaviors of the semiconductive barium titanates with silver electrodes*

As mentioned in section 7, some electrode materials put on barium titanates show high contact resistance. Here, some characters of barium titanates with silver electrodes fired on both surfaces of them will be briefly surveyed, though these characters should not be considered to be proper to the barium titanates.

The resistance shown with silver electrodes greatly depends upon the applied voltage as illustrated in Fig. 21.

The apparent capacity shown with this specimen considerably depends upon frequency, as illustrated in Fig. 22. Fig. 23 and Fig. 24 respectively illustrate examples of the effects of d.c. biasing voltage and those of impressed a.c. voltage upon the apparent capacity and dissipation factor for the specimen with silver electrodes.

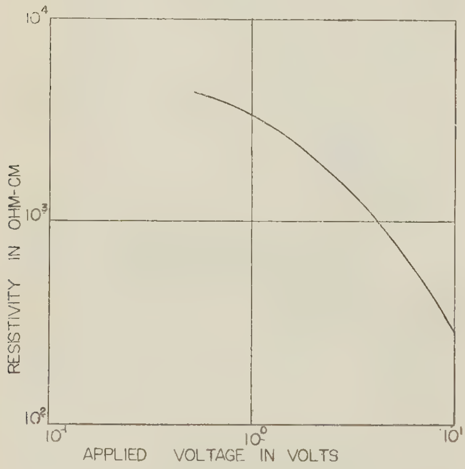

Fig. 21. Voltage dependency of contact resistance for semiconductive barium titanate with silver electrodes.

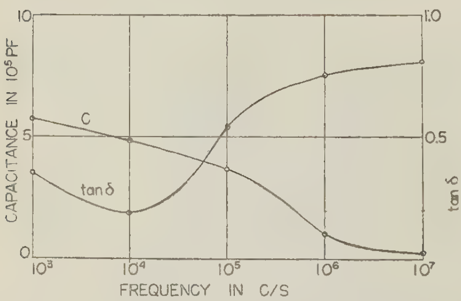

Fig. 22. Frequency characters of capacitance and tan δ shown by the semiconductive barium titanate with silver electrodes.

§ 4. Discussions

1. *Mechanism of generation of the conductivity in the barium titanates*

Fig. 25 shows the proposed substitutions of various cations for Ba^{+2} or Ti^{+4}. For example, we choose Ag^{+1}, Sb^{+3}, La^{+3}, Ce^{+3}, Pr^{+3}, Bi^{+3} and Th^{+4} as the substituents for Ba^{+2}. Cations written above Ba^{+2} or Ti^{+4} are those which have smaller valencies than the host ions, and cations written below Ba^{+2} or Ti^{+4} are those which have larger valencies than

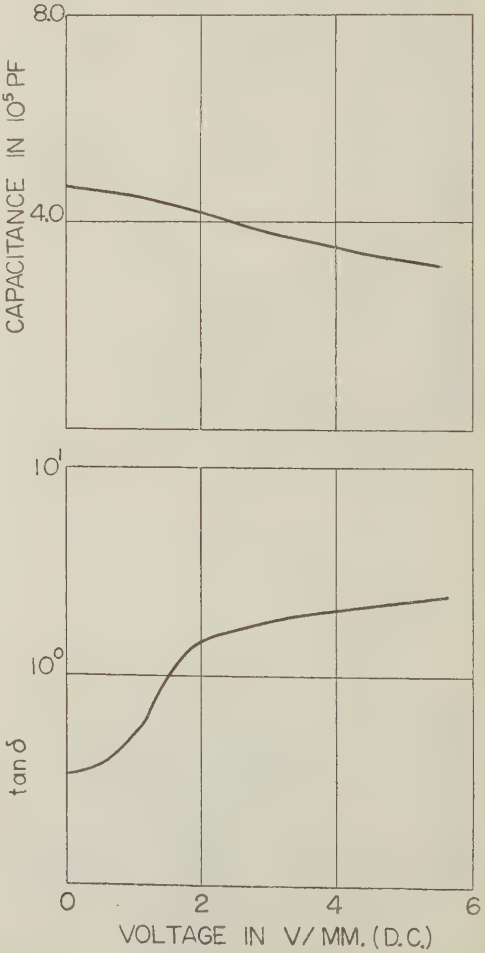

Fig. 23. D.C. bias voltage effects on capacitance and tan δ for the semiconductive barium titanate with silver electrodes.

the host ions. The cations surrounded by the bold squares are the ones that have appeared to be effective for reducing the resistivity of barium titanates in our experiment.

Referring to Fig. 25, we may conclude that the effective cations for reducing the resistivity should have larger valencies than the host ions. Th^{+4}, V^{+5}, Mo^{+6}, W^{+6} and Mn^{+6} seem to oppose this conclusion. However, Mn, V, Mo and W have more than two valency states, and we might assume that they were introduced into Ti site with the valencies of not more than four. Furthermore, Th^{+4} ion which was expected to occupy the Ba site might actually entered into Ti site.

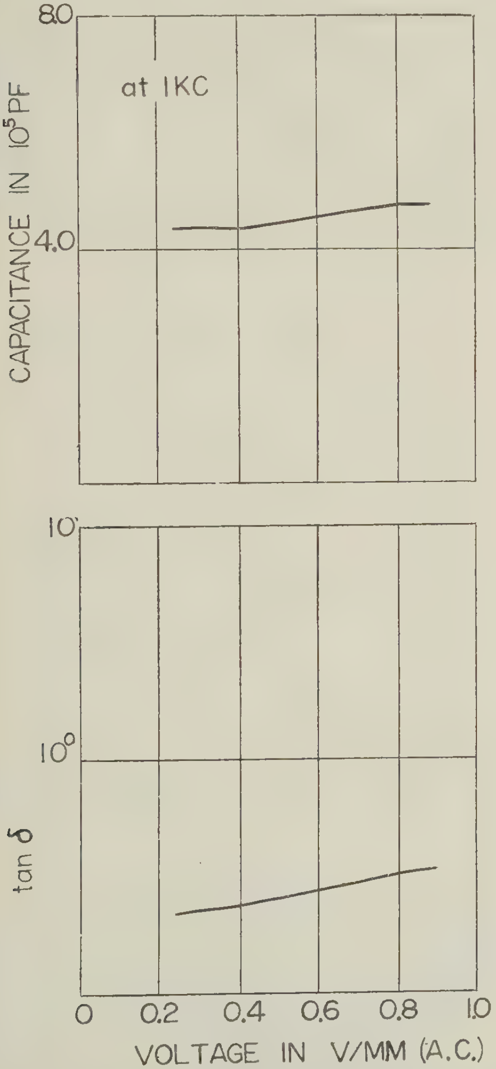

Fig. 24. A.C. applied voltage effects on capacitance and tan δ for the semiconductive barium titanate with silver electrodes.

Of course, these mechanisms are only of assumption, and should be validated with the determination of the valency states of the introduced cations.

The bluish colors of semiconductive barium titanates suggest the existences of Ti^{+3} ions, as they are popular in reduced TiO_2 crystals.

Should these assumptions be true, we may suppose the following process of substitution,

$$Ba^{+2}Ti^{+4}O_3^{-2}+xLa=Ba_{1-x}^{+2}La_x^{+3}Ti_{1-x}^{+4}Ti_x^{+3}O_3^{-2}$$

$$Ba^{+2}Ti^{+4}O_3^{-2}+xTa=Ba^{+2}Ti_{1-2x}^{+4}Ti_x^{+3}Ta_x^{+5}O_3^{-2},$$

and in case of reduction without any additives,

$$Ba^{+2}Ti^{+4}O_3^{-2}-xO=Ba^{+2}Ti_{1-2x}^{+4}Ti_{2x}^{+3}O_{3-x}^{-2}.$$

And we may suppose that the conductivity is caused by the electron exchange between Ti^{+4} and Ti^{+3}. The fact that the semiconductive barium titanates are N-type seems to support the above mechanism of producing available electrons.

Experimental results shown in Fig. 2 and Fig. 6 tell us that the anomalous positive temperature character of resistivity corresponds to the crystal transition, as the resistivity-temperature characters are always raised just below the Curie points.

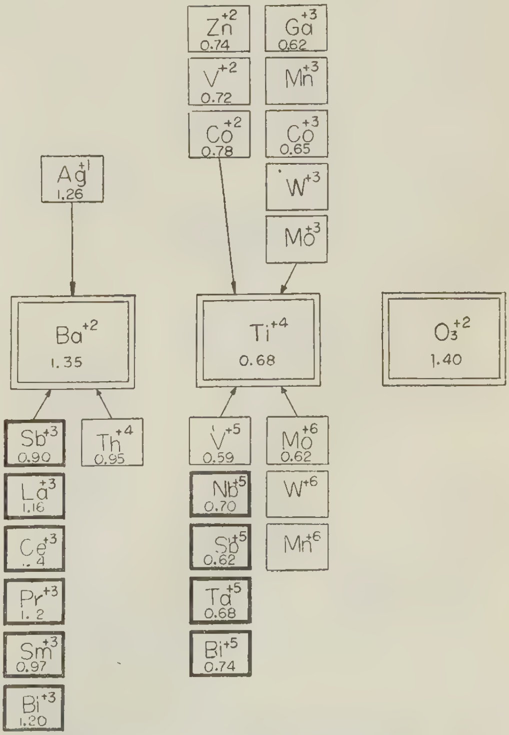

Fig. 25. Intended substitutions for Ba and Ti ions.

Though we may predict the anomalous temperature character of resistivity produced with a certain cooperation of the conduction and the crystal transition, detailed mechanism of the cooperation has not been clarified.

2. *Semiconductive properties of the barium titanates*

The semiconductive barium titanates are identified as N-type from the experimental results for thermo-e.m.f., rectification, and also from those for Hall voltage.

The activation energy below the temperature t_1 as low as 0.03 eV to 0.15 eV denotes the existance of high donor level.

It seems somewhat queer that the thermo-e.m.f.: $d\theta/dT$ is independent of temperature in the temperature region including the Curie point; the depth of the Fermi level: ΔE_f is about 0.24 eV to 0.28 eV as calculated from the value of $d\theta/dT$ with the relation:

$$\frac{d\theta}{dT} = \pm\left[\frac{\Delta E_f}{eT} + \frac{2k}{e}\right],$$

where T is assumed to be 273°K.

3. *Frequency spectra of ρ and ε for the semiconductive barium titanates*

Here we discuss the frequency spectra of ρ and ε shown by the barium titanates with indium-amalgam electrodes, that is, the character regarded as proper to the semiconductive materials. As shown in Fig. 15, Fig. 16, Fig. 17 and Fig. 18, the resistivity-temperature character in the neighbor of the Curie point is steepest at d.c., and is apt to become less steep with increasing frequency. However, this phenomenon should be considered as caused by our method of measuring parallel resistance and parallel capacitance. Generally, we may denote the equivalent circuit of these conductive specimen with the network shown by Fig. 26, where R_0 denotes the leakage resistance that corresponds to the actual conductance as shown at d.c., C_p denotes the apparent capacity, R_p denotes purely alternative losses in concerning with C_p. These R_0, C_p and R_p are of course functions of temperature and frequency.

Now, roughly assuming that the dielectric tangent, $\tan\delta = 1/\omega C_p R_p$, is constant and in-

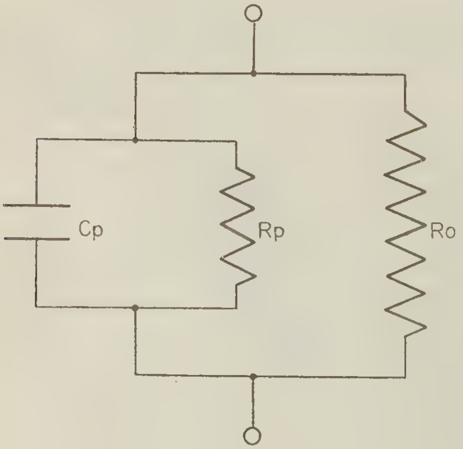

Fig. 26. Equivalent circuit for semiconductive barium titanates with ohmic contacts.

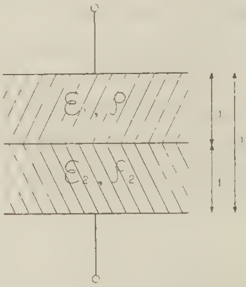

Fig. 27. Double layers.

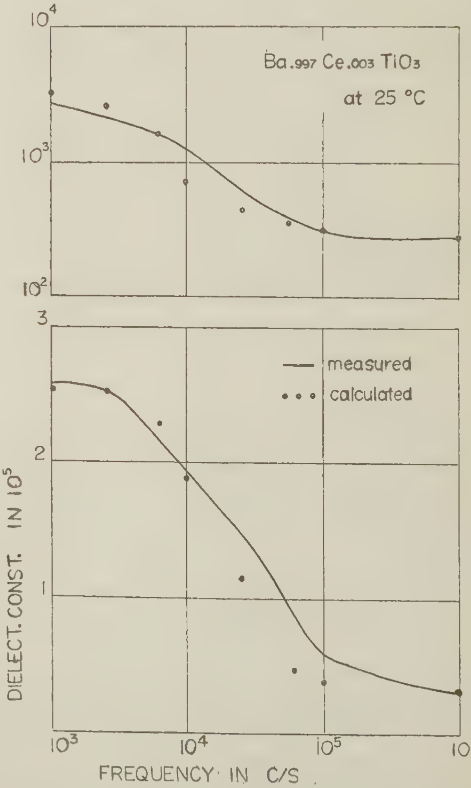

Fig. 28. Comparison of measured value and calculated value for the dispersions in resistivity and dielectric constant.

dependent of the frequency, we may calculate the resistivity-temperature character at each frequency from the assumed value of $\tan\delta$ and the resistivity-temperature character at d.c. The calculated results are shown in Fig. 17 and Fig. 18 as dotted lines, and fairly good coincidence of them with the measured values suggest us that the resistivity-temperature character observed at d.c. would be maintained still at 5 Mc.

Some of the dielectric dispersions shown in Fig. 13 and Fig. 14 may be explained as that caused with interfacial polarization, though not all of them can be done. Here we imagine double layers as shown in Fig. 27, for the measured character of Fig. 28 which is abstracted from Fig. 13. Assuming d_1/d_2 is equal to unity, we may have the calculated values shown in Fig. 28 by dots, with values: $\mathcal{E}_1=2.5\times10^4$, $\rho_1=2.75\times10^4$ ohm-cm, $\mathcal{E}_2=4.3\times10^5$ and $\rho_2=2.5\times10^3$ ohm-cm. The coincidence of calculated and measured value suggests the validity of this explanation for this case.

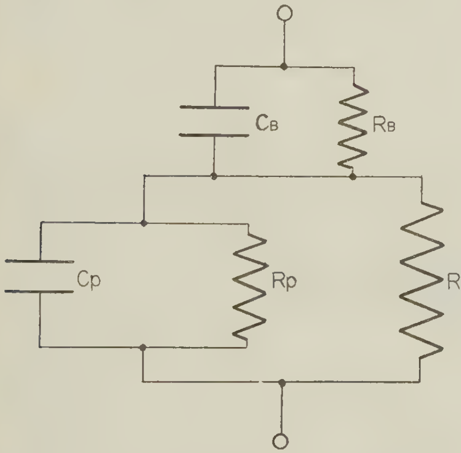

Fig. 29. Equivalent circuit for semiconductive barium titanates with non-ohmic contacts.

4. *Barrier layers*

From various results as shown in Fig. 21, Fig. 22, Fig. 23 and Fig. 24, we may reasonably suppose the existence of barrier layer at the contacts of silver and semiconductor for the specimen with silver electrodes, in which case the equivalent circuit should be written as Fig. 29. Barrier capacitance amounts about $4.4\times10^{-1}\mu$F/cm^2 and barrier conductance is about 1×10^{-3} mho/cm^2.

5. *Various effects on producing semiconductive barium titanates*

Each additive has its own optimum quantity for producing semiconductive barium titanate of minimum resistivity, as shown in Fig. 3. Close care should be paid for weighing the raw materials, as the optimum quantities are critical. The reason why the excess amounts of additives tend to make the barium titanate an insulator is a problem still to be studied.

On the other hand, the deviation from the stoichiometry is not critical as known from Fig. 5. Additional experiment informed us that the forming pressure of green body is also not critical as shown in Fig. 30, which was obtained for $Ba_{.999}Ce_{.001}TiO_3$.

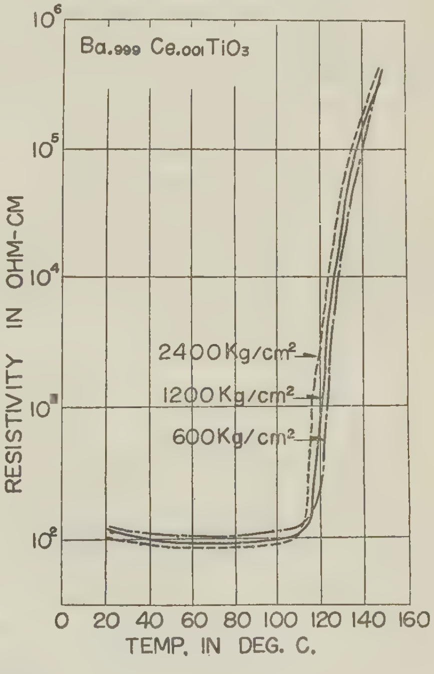

Fig. 30. Effect of forming pressure on resistivity-temperature character.

§5. Conclusion

The conductivity of semiconductive barium titanates is supposed to be produced by the control of valency of Ti^{+4} ions, generating Ti^{+3} ions which present available electrons.

The mechanism for the generation of the anomalous positive temperature character is still not clear, however, it is obvious that the anomaly in resistivity is just caused with the transition in the crystal.

The similar anomaly in resistivity would be predicted in other crystals which have any crystal transition and of which constituent ions possess more than two valency states.

Lead titanate, lead zirconate, barium zirconate titanate are the examples of these expected crystals, though we have not yet obtained successful results for them.

Those barium titanates with positive temperature character of resistivity are not only of interest from the stand point of solid state physics but also important for practical applications.

Thermally sensitive resistor which was hitherto characterized with negative temperature coefficient is now available with great positive temperature coefficient. Thermally non-sensitive resistor may also be available, utilizing suitable compositions and temperature region. Besides, applications for arrester, regulator, barrier capacitor, non-destructive rectifier are also predicted.

Acknowledgement

The investigation has been begun with valuable suggestion of Dr. Kiyoshi Abe, Professor Emeritus of Kyoto University.

The writer wishes to express his gratitude to Dr. K. Abe and Dr. Tetsuro Tanaka, Professor of Kyoto University, for the incessant direction and encouraging advices.

He also wishes to thank Mr. Akira Kawabata and Mr. Toshio Iguchi, members of Institute for Chemical Research, Kyoto University, Mr. Kikuo Wakino, Juichiro Ozawa, chief researchers of Murata Technical Laboratory, for their helpful suggestions and cooperation.

He is much indebted to Mr. Takami Tanaka, Mr. Toshihiro Iwatsuki, Researchers in Murata Tech. Lab. in their interests and endeavors in measurements and preparations of specimens.

References

1) H. A. Sauer and S. S. Flaschen: *Proceedings 1956 Electronic Components Symposium* (1956) 41.
2) George G. Harman: Phys. Rev. **106** (1957) 1358.
3) W. S. Clabaugh, E. M. Swiggard and R. Gilchrist: J. Res. Nat. Bur. Stand. **56** (1956) 289,
4) J. J. Donoghue and W. P. Eatherly: Rev. Sci. Instr. **22** (1951) 513.
5) J. P. Remeika: J. Amer. Chem. Soc. **76** (1954) 940.

JOURNAL OF THE PHYSICAL SOCIETY OF JAPAN, Vol. 14, No. 9, SEPTEMBER, 1959

On the Theory of Thermoelectricity

By Jan TAUC

Institute of Technical Physics, Czechoslovak
Academy of Sciences, Praha, Czechoslovakia

(Received April 24, 1959)

The meaning of the inner electrical field inside a two band semiconductor the gap of which depends on temperature is discussed in connection with the theory of the thermoelectromotive force in such semiconductors.

In a recent paper Haga1) discusses the theory of the thermoelectromotive force in a two band semiconductor. In this note, I wish to communicate a few remarks on some questions mentioned in his paper.

The definition of an electric field in a two band semiconductor the gap of which is not constant is ambiguous in a similar sense as e. g. the electrochemical potential $-e\varphi+\mu$ cannot be in all cases decomposed into an electrical part $-e\varphi$ and chemical part μ; this problem is discussed in textbooks on thermodynamics (cf. e. g.2)). In a semiconductor, the decomposition is possible as we can calculate the chemical potential μ from the concentrations of electrons using the Fermi-

Dirac statistics. If the gap ε_g is not constant, one has to consider three parts of the potential acting on the electron which one cannot, without an appropriate theory, determine separately.

However, it is always possible to write the current density equations in the form:

$$i_x^{(k)} = \frac{\sigma^{(k)}}{e}\left(eE_x + T\frac{d(\mu_a/T)}{dx} + Q_a^{*(k)}\frac{1}{T}\frac{dT}{dx}\right) \quad (1)$$

This form can be justified by general considerations of the thermodynamics of irreversibe processes (see 3)). Here E_x denotes the electric field, μ_a is the chemical potential measured as illustrated in Fig. 1, $Q_a{}^{*(k)}$ are heats of transfer of electrons ($k=1$) or holes ($k=2$); the index a means that the quantities are measured from an arbitrary zero energy level. The second term in Eq. (1) may be considered in a certain sense as an "inner" force which together with the third term gives rise to the electric field, the integral of which can be measured as the thermo-electromotive force.

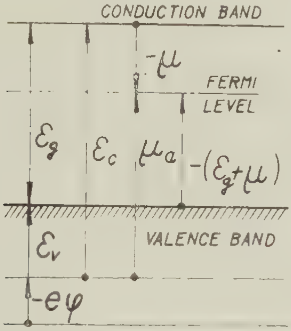

Fig. 1. Energy levels.

The chemical potential can be written as the sum $\mu_a = \varepsilon_c + \mu = \varepsilon_v + \varepsilon_g + \mu$ (μ has the same meaning as in ref. 1)). The heat of transfer can be written $Q_a{}^{*(1)} = \varepsilon_c + Q^{*(1)}$, $Q_a{}^{*(2)} = \varepsilon_v - Q^{*(2)}$, where $Q^{*(1)}$, $Q^{*(2)}$ are the kinetic energies of transfer of electrons and holes which are given by the equations:

$$Q^{*(k)} = \frac{K_2^{(k)}}{K_1^{(k)}} \quad (2)$$

(for K_1, K_2 see ref. 1)).

We put these expressions into Eq. (1), set $i_x{}^{(1)} + i_x{}^{(2)} = 0$ and calculate E_x. Integrating E_x along x quite similarly as was done in Ref. [1] we obtain the same formula for Q as Eqs. (22) and (24) in this reference or in a paper by the author⁴⁾. This is of course obvious as the use of the electrochemical potential is equivalent to the use of the electrical potential; both differ by the chemical potential which is the same in the points x_0, x_3 (see Fig. 1 of ref. 1)). The first term in Eq. (4) of ref. 1) is certainly equal to zero; μ is only the function of the composition and temperature of the semiconductor which must be the same in both points; there may be some doubt about the justification of the integration per partes but it is evident that we can suppose e. g. the contacts to be constructed so that μ is a continuous and differentiable function of x across them.

The final formula for the thermoelectric power is the same whether ε_g depends on T or not. The reason for this is that the generation of the thermoelectric power is connected with the flow of entropy as was first pointed out by Ehrenfest⁵⁾. In fact, we can write Eq. (1) in the form

$$i_x{}^{(k)} = \frac{\sigma^{(k)}}{e}\left(eE_x + \frac{d\mu_a}{dx} + S^{*(k)}\frac{dT}{dx}\right) \quad (3)$$

where $S^{*(k)} = (Q_a{}^{*(k)} - \mu_a)/T$ are the entropies of transfer. It is seen from this definition, that $S^{*(k)}$ are independent of the zero energy level and of ε_c, ε_v. Using $S^{*(k)}$ we can write the expression for the absolute thermoelectromotive power Q of a two band semiconductor in the form:

$$Q = -\frac{1}{e}\left[\frac{\sigma^{(1)}}{\sigma^{(1)}+\sigma^{(2)}} S^{*(1)} + \frac{\sigma^{(2)}}{\sigma^{(1)}+\sigma^{(2)}} S^{*(2)}\right] \quad (4)$$

The use of the internal electric field inside a two band semiconductor proved valuable also in the theory of photovoltaic effects⁶⁾ even if ε_g was not constant (cf. e. g. the case of ε_g varied by external pressure, the so called photopiezoelectric effect described in ref. 7)).

References

1) E. Haga: J. Phys. Soc. Japan **14** (1959) 35.
2) E. A. Guggenheim: *Thermodynamics* (North-Holland Publ., Amsterdam, 1950) chap. 10.
3) S. R. De Groot: *Thermodynamics of Irreversible Processes* (North-Holland Publ., Amsterdam, 1952).
4) J. Tauc: Phys. Rev. **95** (1954) 1394.
5) P. Ehrenfest and A. Rutgers: Proc. Kon. Acad. Amsterdam **32** (1929) 698.
6) J. Tauc: Rev. Mod. Phys. **29** (1957) 308.
7) J. Tauc and M. Závětová: Czechoslovak. J. Phys. **9** (1959). (in the press)

JOURNAL OF THE PHYSICAL SOCIETY OF JAPAN, Vol. 14, No. 9, SEPTEMBER, 1959

Theory of Thermoelectric Power of Ionic Crystals, III

By Eijiro HAGA

Department of Physics, Faculty of Science, Niigata University

(Received April 23, 1959; revised manuscript received July 23, 1959)

When temperature gradient is given in a specimen of AgCl doped with CuCl, its thermoelectric power changes with time owing to the thermal diffusion of copper ions, and then reaches its steady value. If the temperature gradient is removed after such a steady state is attained, the electronmotive force continues to exist for a while, but it decreases with time according as the copper ions diffuse again to the previous homogeneous distribution. The expressions for such processes are derived under proper assumptions. The time constant for them is estimated with use of the conductivity data of Ebert and Teltow. The information on the heat of transport of Cu^+ will be obtained if experiments on such processes are carried out.

§ 1. Introduction

On the mechanism of thermal diffusion of ions or atoms in solids the theoretical study has not been well developed.[1] Here we want to point out that we obtain an information about the heat of transport characterizing the behaviour of ions in thermal diffusion from the knowledge of the thermoelectromotive force. Recently, the theories of the thermoelectromotive force of $AgCl(Br)+CdCl_2(Br_2)$[2,3] and $NaCl+CdCl_2$[4] have been proposed and the former has been compared with the experiments.[5,6] When temperature gradient is set up in those crystals, the complexes (Cd^{++}-vacancy pairs) will diffuse in the crystal, and accordingly the free vacancies will be denoted from the complexes or conversely they will combine with the cadmium ions to form complexes. As a result of these processes, the concentration gradient of free vacancies and so the electric field, E, changes with time. The thermoelectric power is, however, independent of time as mentioned in (I)[3], since it does not depend on the concentration gradient of charge carriers. This time independence is due to the fact that the complexes are neutral and so do not contribute to the electric conduction.

In the case of $(AgCl+CuCl)$ specimens which will be considered in the present paper, the interstitial copper ions are supposed to diffuse instead of neutral complexes in the cases mentioned previously. Therefore, when temperature gradient is set up in the specimen, the thermoelectromotive force changes with time and reaches the steady value. In such a steady state, the concentration of copper ions varies along the specimen and its distribution can be expressed in terms of the value of the heat of transport of copper ions and other parameters. When the temperature gradient is removed after such the steady state is attained, the interstitial copper ions diffuse again and accordingly the residual electromotive force decays with time. From the analysis of such processes, the information on the heat of transport of the interstitial copper ions can be obtained. Besides, we shall analyse the conductivity data of Ebert and Teltow[7], and estimate, from such an analysis, the value of the time constant, τ, for the above processes.

§ 2. Thermoelectric Power

The electrical current densities of Ag^+ interstitials, vacancies and Cu^+ interstitials, j_i, j_v and j_{cu}, are given, respectively, by

$$j_i=\frac{\sigma_i}{e}\left(eE-\frac{kT}{c_i}\frac{\partial c_i}{\partial x}-\frac{Q_i^*}{T}\frac{\partial T}{\partial x}\right), \tag{1}$$

$$j_v=\frac{\sigma_v}{e}\left(eE+\frac{kT}{c_v}\frac{\partial c_v}{\partial x}+\frac{Q_v^*}{T}\frac{\partial T}{\partial x}\right), \tag{2}$$

$$j_{cu}=\frac{\sigma_{cu}}{e}\left(eE-\frac{kT}{c_{cu}}\frac{\partial c_{cu}}{\partial x}-\frac{Q_{cu}^*}{T}\frac{\partial T}{\partial x}\right), \tag{3}$$

where σ_i, c_i and Q_i^* are the partial conductivity, the mol fraction and the heat of transport of the Ag^+ interstitial, respectively, and σ_v, c_v, Q_v^*, σ_{cu}, c_{cu} and Q_{cu}^* are defined similarly. We shall assume that the charge neutrality and the local equilibrium expressed by

$$c_i + c_{cu} = c_v \,, \tag{4}$$

$$c_i c_v = N_0'/N_0 \cdot \exp(-\mu_F/kT) \tag{5}$$

are valid approximately, where N_0 and N_0' are the concentrations of the normal and interstitial sites of Ag^+, respectively, and μ_F is the Gibbs free energy of forming a pair of Frenkel defects. Then the concentration gradients of the Ag^+ interstitials and vacancies can be expressed in terms of that of the Cu^+ interstitials.

The thermoelectric power, Q, with the silver electrodes is obtained from the gradient of electrochemical potential of a silver ion as done in (I). Making use of Eqs. (1)~(5) we obtain

$$\begin{aligned} eQ = & -\frac{2kTt_{cu}c_v}{c_{cu}(c_i+c_v)} \cdot \frac{(c_{cu})_{x=L}-(c_{cu})_{x=0}}{\Delta T} - k\ln c_v + \alpha \\ & -\frac{1}{T}\left[t_i(h_F+Q_i^*+Q_v^*) + t_{cu}(Q_v^*+Q_{cu}^*) - Q_v^* + \frac{c_i t_{cu} h_F}{c_i+c_v} \right], \end{aligned} \tag{6}$$

where ΔT is the temperature difference between the ends of the specimen of the length L, and t_i and t_{cu} are the transport numbers of the Ag^+—and Cu^+—interstitials, respectively, and α is the notation used in (I).

Now, we calculate $(c_{cu})_{x=L}-(c_{cu})_{x=0}$ in Eq. (6) as a function of time t. Let us consider only the case that L is so long that the time constant, τ, is much longer than the time required to set up ΔT in the specimen. When ΔT is set up in the specimen at $t=0$, the local equilibrium will be established at the same time, and accordingly there will be more Cu^+ interstitials in the higher temperature side than in the lower one. Then, copper ions diffuse in the electric field which is determined by the condition that the total electric current vanishes. Hence, in the side where c_{cu} is increasing owing to the diffusion, the Cu^+ interstitials drop into the Ag^+ vacancies and, in the other side, they are donated from copper ions on the lattice sites so that the local equilibrium is approached. In response to such the current of copper ions, the Ag^+ interstitial concentration decreases or increases owing to the combination with vacancies or the inverse process. Such a combination or a generation contributes to the change of the concentrations of Cu^+ interstitials, Ag^+ interstitials and vacancies with time. On the other hand, the variation of the total concentration of copper ions, y, is only due to the x dependence of the current of Cu^+ interstitials:

$$\frac{\partial y}{\partial t} = -\frac{\partial (j_{cu}/eN_0)}{\partial x} \,. \tag{7}$$

Substituting the electric field E obtained from the condition $j_i + j_v + j_{cu} = 0$ to Eq. (3), we have

$$j_{cu} = -D_{cu}\left(\frac{\partial c_{cu}}{\partial x} + S\frac{\partial T}{\partial x}\right), \tag{8}$$

where

$$D_{cu} = \frac{2kT\sigma c_v t_{cu}(1-t_{cu})}{e c_{cu}(c_i+c_v)} \,, \tag{9}$$

$$S = \frac{c_{cu}(c_i+c_v)}{2kT^2 c_v}\left[\frac{c_i h_F}{c_i+c_v} - \frac{t_i}{1-t_{cu}}(h_F+Q_i^*+Q_v^*) + (Q_v^*+Q_{cu}^*)\right]. \tag{10}$$

Here σ is the total conductivity of the specimen. The mass action law between copper ions and silver vacancies

$$y = c_{cu}(1+c_v K) \,, \tag{11}$$

where K is the equilibrium constant, is assumed to be valid approximately. Then the left-hand side of Eq. (7) is expressed in terms of $\partial c_{cu}/\partial t$ from Eqs. (4), (5) and (11):

$$\frac{\partial y}{\partial t}=\frac{2c_v y/c_{cu}-c_{cu}}{c_i+c_v}\frac{\partial c_{cu}}{\partial t}\,. \tag{12}$$

In differentiating Eq. (8) with respect to x, the terms coming from the differentiation of D_{cu} and S are of the order of $(\partial T/\partial x)^2$, since the derivatives of c_i, c_v and c_{cu} with respect to x are obviously of the order of $\partial T/\partial x$. Hence, considering the terms in Eq. (7) up to the order of $\partial T/\partial x$, we have

$$\frac{\partial c_{cu}}{\partial t}=D\frac{\partial^2 c_{cu}}{\partial x^2}\,, \tag{13}$$

where

$$D=\frac{c_i+c_v}{2c_v y/c_{cu}-c_{cu}}\frac{D_{cu}}{eN_0}\,. \tag{14}$$

The boundary condition of the diffusion equation (13) is given by[8]

$$(j_{cu})_{x=0}=(j_{cu})_{x=L}=0\,, \tag{15}$$

which is rewritten as

$$\left(\frac{\partial c_{cu}}{\partial x}\right)_{x=0}=\left(\frac{\partial c_{cu}}{\partial x}\right)_{x=L}=-S\frac{\partial T}{\partial x} \tag{16}$$

from Eq. (8). The initial condition is given by

$$(c_{cu})_{t=0}=c_{cu}{}^0+\left(x-\frac{L}{2}\right)\left(\frac{\partial c_{cu}}{\partial T}\right)_{t=0}\frac{\partial T}{\partial x}\,, \tag{17}$$

where $c_{cu}{}^0$ is independent of x. Eq. (13) has been solved under the similar boundary and initial conditions to Eqs. (16) and (17) by Yokota.[9] We find easily the following solution:

$$\begin{aligned}c_{cu}=&\,c_{cu}{}^0-\left(x-\frac{L}{2}\right)S\frac{\partial T}{\partial x}\\&-\frac{4L}{\pi^2}\left[S+\left(\frac{\partial c_{cu}}{\partial T}\right)_{t=0}\right]\sum_{m=0}^{\infty}\frac{\cos\left[(2m+1)\pi x/L\right]\exp\left[-(2m+1)^2t/\tau\right]}{(2m+1)^2}\frac{\partial T}{\partial x}\,,\end{aligned} \tag{18}$$

where

$$\tau=L^2/\pi^2 D\,. \tag{19}$$

From Eq. (18) the difference of c_{cu} between the ends of the specimen is given by

$$\frac{(c_{cu})_{x=L}-(c_{cu})_{x=0}}{\Delta T}=-S+\left[S+\left(\frac{\partial c_{cu}}{\partial T}\right)_{t=0}\right]F\left(\frac{t}{\tau}\right)\,, \tag{20}$$

where

$$F(x)=\frac{8}{\pi^2}\sum_{m=0}^{\infty}\frac{\exp\{-(2m+1)^2x\}}{(2m+1)^2}\,. \tag{21}$$

The value of $F(x)$ is shown in Fig. 1, where the value of $\exp(-x)$ is also shown for comparison.

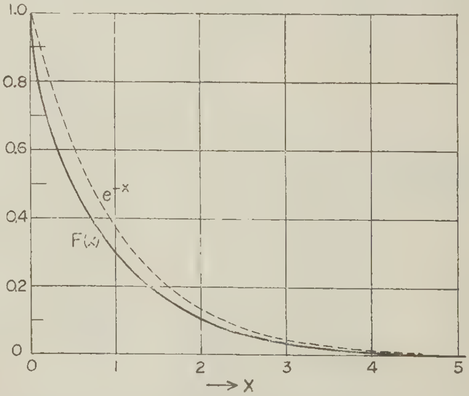

Fig. 1. The full line shows $F(x)$ vs x and the dashed line shows $\exp(-x)$ drawn for comparison.

From Eqs. (6) and (20) we obtain the expression for the thermoelectric power:

$$\begin{aligned}eQ=&-\frac{1}{T}\frac{t_i}{1-t_{cu}}(h_F+Q_i{}^*+Q_v{}^*)+\frac{Q_v{}^*}{T}-k\ln c_v+\alpha\\&-\frac{t_{cu}}{T}\left[\frac{c_i h_F}{c_i+c_v}+\frac{2kT^2c_v}{c_{cu}(c_i+c_v)}\left(\frac{\partial c_{cu}}{\partial T}\right)_{t=0}-\frac{t_i}{1-t_{cu}}(h_F+Q_i{}^*+Q_v{}^*)+(Q_v{}^*+Q_{cu})\right]F\left(\frac{t}{\tau}\right)\,.\end{aligned} \tag{22}$$

The value of $h_F+Q_i^*+Q_v^*$ is found by measuring the steady value of Q. Furthermore, we find the value of $Q_v^*+Q_{cu}^*$ by measuring the variation of Q with time. If the quantity of CuCl mixed is small, the difference between the initial and steady values of Q is small, since the terms of Q depending on time include the factor t_{cu}. Therefore, we have to mix a proper amount of CuCl in order to find the value of $Q_v^*+Q_{cu}^*$ from the easy measurements.

§ 3. Residual Electromotive Force

In the steady state in the presence of temperature difference between the ends of the specimen, $\varDelta T$, the concentration distribution of Cu^+ depends on Q_{cu}^* as mentioned above. Hence, when the temperature difference is removed, the information on Q_{cu}^* is obtained from the residual electromotive force, $\varDelta V$. Let us consider it in the present section. When $\varDelta T$ is removed at time $t=0$, the system will immediately attain the local equilibrium corresponding to the Cu^+ amount at each place. The potential difference between the ends of the specimen, $\varDelta V$, is given by the difference of the electrochemical potential of a silver ion:

$$e\varDelta V=\int_0^L\left(-eE+\frac{kT}{c_i}\frac{\partial c_i}{\partial x}\right)dx=-\frac{2kTt_{cu}c_v}{c_{cu}(c_i+c_v)}[(c_{cu})_{x=L}-(c_{cu})_{x=0}]\ . \tag{23}$$

The partial differential equation (13) and the boundary condition (16) with $\partial T/\partial x=0$ are valid at the present case also, while the initial condition is different. The latter is easily obtained as follows. Differentiating Eq. (11) with respect to x and making use of Eqs. (4), (5) and (18), we have, in the steady state,

$$\frac{\partial y}{\partial x}=\left[-\frac{2c_vy/c_{cu}-c_{cu}}{c_i+c_v}S+\frac{c_i(y-c_{cu})}{c_i+c_v}\frac{h_F}{kT^2}+c_vc_{cu}\frac{dK}{\partial x}\right]\frac{\partial T}{\partial x}\ . \tag{24}$$

In the moment when $\varDelta T$ is removed, we have

$$\frac{\partial y}{\partial x}=\frac{2c_vy/c_{cu}-c_{vu}}{c_i+c_v}\frac{\partial c_{cu}}{\partial x}\ . \tag{25}$$

We can equate Eq. (25) to Eq. (24), since the value of y does not change at the instant of elimination of $\varDelta T$. Thus we obtain the initial condition:

$$\left(\frac{\partial c_{cu}}{\partial x}\right)_{t=0}=\left[-S+\frac{c_i(y-c_{cu})}{2c_vy/c_{cu}-c_{cu}}\frac{h_F}{kT^2}+\frac{c_vc_{cu}(c_i+c_v)}{2c_vy/c_{cu}-c_{cu}}\frac{dK}{dT}\right]\frac{dT}{\partial x}\ . \tag{26}$$

Now Eq. (13) is solved as

$$\frac{(c_{cu})_{x=L}-(c_{cu})_{x=0}}{L}=\left(\frac{\partial c_{cu}}{\partial x}\right)_{t=0}F\left(\frac{t}{\tau}\right) \tag{27}$$

with $(\partial c_{cu}/\partial x)_{t=0}$ given by Eq. (26). From Eqs. (23), (26) and (27), we obtain the expression for $\varDelta V$:

$$\frac{e\varDelta V}{\varDelta T}=\frac{t_{cu}}{T}\left[\frac{c_ih_F-2kT^2c_v^2dK/dT}{2c_vy/c_{cu}-c_{cu}}-\frac{t_i}{1-t_{cu}}(h_F+Q_i^*+Q_v^*)+(Q_v^*+Q_{cu}^*)\right]F\left(\frac{t}{\tau}\right)\ . \tag{28}$$

Here it should be remarked that the right-hand side is equal to the factor in Eq. (22) depending on time, as easily seen from Eq. (24) with $\partial c_{cu}/\partial x$ in place of $-S\partial T/\partial x$, since y is independent of x in the moment when $\varDelta T$ is set up. Thus we find the value of $Q_v^*+Q_{cu}^*$ by measuring $\varDelta V$.

§ 4. Estimation of Time Constant

Ebert and Teltow has measured the electrical conductivity of AgCl doped with CuCl of several concentrations.[7] The ratio of the electrical conductivity of an impure specimen to that of the pure specimen, z, is written as, from Eqs. (4) and (5).

$$z=\frac{\xi(1+\phi')+1/\xi\cdot(\phi-\phi')}{1+\phi}, \qquad \xi=\frac{c_v}{x_0}, \tag{29}$$

where ϕ and ϕ' are the ratios of the mobilities of the Ag$^+$—and the Cu$^+$— interstitial to that of the Ag$^+$ vacancy, respectively, and x_0 is the concentration of the Frenkel defect in the pure AgCl. From the minimum value of z drawn against y, the value of ϕ' is found by making use of the values of ϕ found from the conductivity data of AgCl doped with CdCl$_2$. Such values of ϕ' are shown in Fig. 2.

Eq. (11) is rewritten, in terms of ξ, as

$$\frac{y}{x_0(\xi-1/\xi)}=1+x_0K\cdot\xi\,. \tag{30}$$

Therefore, when the left-hand side of Eq. (30) is plotted against ξ at a fixed temperature, the plots are expected to be on a straight line passing (0, 1). From the gradient of this line the equilibrium constant K is to be obtained. Fig. 3 shows such a plot at 275°C, where the value of x_0 found for AgCl doped with CdCl$_2$ is used. Fig. 2 shows also the value of K obtained in such a way, which is represented as

$$K=\exp\left[\frac{0.94}{kT(ev)}-8.4\right]. \tag{31}$$

The values of c_i, c_v and c_{cu} are obtained by making use of the value of ξ obtained from the measured value of z and Eqs. (4) and (5).

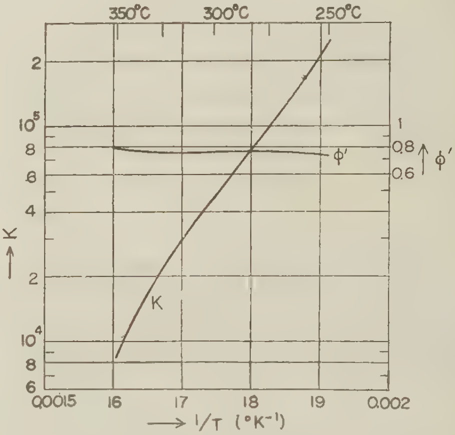

Fig. 2. The equilibrium constant, K, and the mobility ratio of the Cu$^+$ interstitial to the Ag$^+$ vacancy, ϕ', drawn against $1/T$ (°K^{-1}).

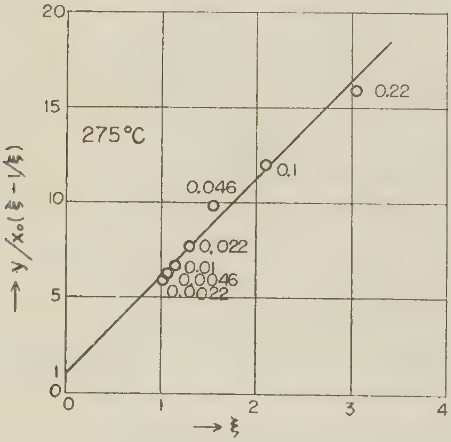

Fig. 3. $y/x_0(\xi-1/\xi)$ *vs* ξ at 275°C. The values in the figure show those of y in Mol-%.

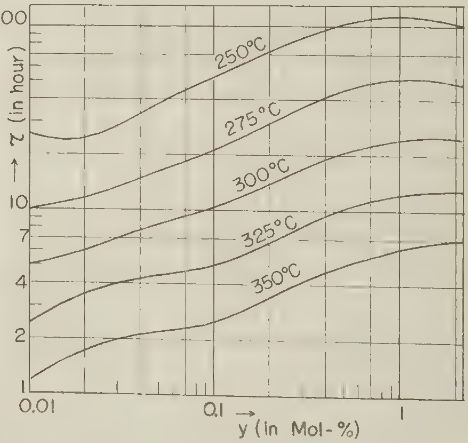

Fig. 4. The time constant, τ, in hour *vs* y in Mol-% for L=1 cm.

Also, the values of t_i and t_{cu} are obtained from

$$t_i=\frac{\phi}{z\xi(1+\phi)}, \qquad t_{cu}=\frac{\phi'}{z(1+\phi)}\left(\xi-\frac{1}{\xi}\right). \tag{32}$$

Thus, the time constant, τ, is estimated as shown in Fig. 4 L=1 cm.

The author wishes to express his sincere thanks to Mr. Yokota, Mr. Miyatani and Mr. Endo for their kind advices and discussions. The present work was supported by the research grant of the Ministry of Education.

References

1) K. Wirtz: Phys. Z. **44** (1943) 221.
2) R. E. Howard and A. B. Lidiard: Phil. Mag. **2** (1957) 1462.
3) E. Haga: J. Phys. Soc. Japan **13** (1953) 1090.
4) E. Haga: J. Phys. Soc. Japan **14** (1959) 992.
5) R. E. Christy, E. Fukushima and H. T. Li: J. Chem. Phys. **30** (1959) 136.
6) Y. Suzuki, S. Endo and E. Haga: J. Phys. Soc. Japan **14** (1959) 729.
7) I. Ebert and J. Teltow: Ann. Physik. (6) **5** (1955) 268.
8) G. Jaffe: Ann. Physik. **6** (1933) 217, 249; Phys. Rev. **85** (1952) 354.
9) I. Yokota: J. Phys. Soc. Japan **8** (1953) 595.

JOURNAL OF THE PHYSICAL SOCIETY OF JAPAN, Vol. 14, No. 9, SEPTEMBER, 1959

On the Crystal Growth of Cadmium Sulphide

By Sumiaki IBUKI

Research Laboratory, Mitsubishi Elec. Mfg. Co.,
Amagasaki, Japan

(Received December 1, 1958)

The crystal growth of CdS has been investigated in detail mainly by the method of sublimation and recrystallization in the flow of nitrogen gas, with special reference to the process of growth and the forms of grown crystals, and the conditions have been searched for under which various kinds of crystal forms such as needle, lamina, plate, rod, block, twin and whisker forms are grown. To this end, the degree of vaporization in sublimating region, the temperature and saturated vapor pressure in growing region, the thermal decomposition, the origination of growth as well as the effect of dislocation upon crystal growth have been investigated. Further, the degree of perfection and luminescence of grown crystals have also been observed.

§ 1. Introduction

In the course of investigating physical properties of cadmium sulphide (CdS) and its industrial applications, it is essential to establish the growing formula of CdS single crystals. Thus, in the present study, the author has observed in detail the crystal growth of CdS, paying special attention to the process of growth and the forms of grown crystals, and has searched for the conditions under which various kinds of crystal forms are grown.

For preparing CdS single crystals, three different methods have been used. Thus, the author at first adopted the so-called Frerichs's method[1], and next used the method of sublimation of CdS powder in the flow of inert gas[2] and finally studied the method of recrystallization of crystalline powder in a sealed quartz vessel[3]. The first method is rather complicated on account of too many variables, and the second is, on the contrary, comparatively favorable for controlling the growth of single crystals, while the last one is fitted to obtaining relatively thick and big crystals.

In the present paper are presented some results obtained mainly by the second method, together with discussions on some interesting facts observed.

§ 2. Method of Sublimation in the Flow of Nitrogen Gas

Molten CdS is obtainable only at high temperature and at high pressures[4], and the solid CdS generally begins to sublime as the temperature rises. To prepare single crystals starting from CdS powder, therefore, we must at first vaporize CdS powder by sublimation and then crystallize by condensing the vapor. The author has performed this process by sublimating polycrystalline powder of CdS in the flow of nitrogen gas and then leading the vapor into lower temperature zone where CdS deposits and crystallizes[2)].

The experimental apparatus used is shown schematically in Fig. 1. The crystal growth was performed in a combustion tube made of quartz. To begin with, the electric furnace was heated up and, at the same time, the flow of nitrogen gas was led through the tube. After the temperature at the center of the tube has been raised up to about 1,050°C～1,150°C, a quartz boat containing CdS powder was inserted into the center of the combustion tube, and then a quartz pipe (i.e. cooler), which was cooled by the flow of nitrogen gas, was inserted from the exit side.

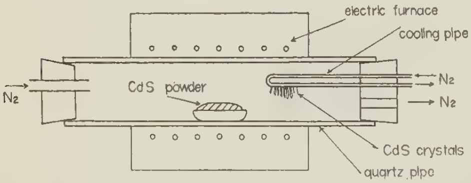

Fig. 1. Crystal growing apparatus.

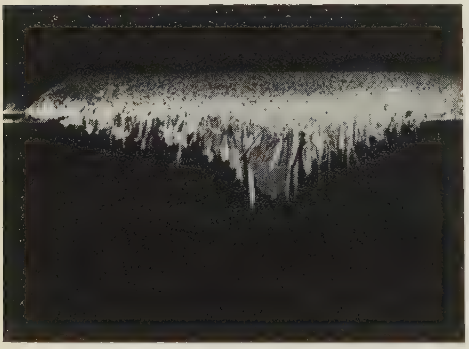

Fig. 2. Grown crystals on the cooler.

With the rise of the temperature of the boat, CdS began gradually to sublime. The vapor was carried by the flow of nitrogen gas towards the exit and the crystal growth of CdS started on the surface of the cooler whose temperature was between 800°C and 1,000°C. After a few hours single crystals grew up to dimensions as large as 10～20 mm in length and 2～10 mm in width. It was observed that crystals were grown also on the surface of the tube wall at about the same time. The heating of the furnace was stopped when CdS powder in the boat was sublimed thoroughly, but the flow of nitrogen gas was continued until the temperature of the furnace became as low as 400°C. Fig. 2 shows single crystals grown on the surface of the cooler which was drawn out from the combustion tube when its temperature was lowered to room temperature. It is to be noted that in performing these processes the purification of CdS powder and the cleaning of nitrogen gas as well as of the combustion tube have been made thoroughly.

§ 3. Factors affecting the Crystal Growth by the Method of Sublimation

We shall next discuss several factors affecting the crystal growth by the method of sublimation. Most important ones are the sublimation temperature of CdS powder, the velocity of flow of nitrogen gas, the temperature of region where crystals are grown and the vapor pressure of CdS, etc.

(1) *Sublimation temperature of CdS powder*

The pressure of nitrogen gas surrounding the subliming CdS is nearly equal to atmospheric pressure. In order to supply the vapor necessary for sustaining the crystal growth, therefore, the minimum temperature of the region of sublimation should be as high as 1,050°C. The forms of crystals grown at this temperature are usually needles or laminas. By raising the temperature, the vapor pressure of CdS increases and crystals of plate- and rod-shapes are liable to growup. But, in these circumstances, both the vaporization of impurities and the degree of thermal decomposition increase.

(2) *Sublimation speed and saturated vapor pressure of CdS*

As mentioned already, CdS powder was sublimed in a quartz boat whose area is about 7 cm^2. The sublimation speed in case when the velocity of flow of nitrogen gas is very small is as shown in Table I, but in practice the sublimation speed depends upon the grain size, weight and surface area of the powder as well as upon the rate of flow of nitrogen gas. Moreover, the vapor pressure in subliming region and the rate of supply of vapor are determined by the sublimation speed and the rate of flow of nitrogen gas. For instance, needle-shape crystals are likely to grow up in case when the rate of flow of nitrogen gas is increased, and by increasing the weight of powder, rod-shape crystals are more likely to grow up. If, we use helium in place of nitrogen gas, there is a tendency that needle-shape crystals grow up more easily.

The second factors affecting growing crystals are the temperature of growing region, the saturated vapor pressure corresponding to the said temperature and the degree of supersaturation of CdS. The author has therefore attempted to calculate the saturated vapor pressure of CdS. In Table I and Fig. 3 are shown those values for higher temperatures which were calculated from the weight of sublimed CdS, the volume of flow of nitrogen gas and the maximum temperature of growing region. On the other hand, the so-called method of molecular effusion was adopted to compute the values for lower temperatures. Thus, as shown in Fig. 4, CdS held in a quartz container whose upper cover has a small hole of diameter of 0.06 mm was kept in the quartz tube and then the tube was evacuated. The tube was then inserted into an electric furnace kept at a definite temperature so as to sublimate CdS, and after having kept the tube at a constant temperature for a long time, CdS was rapidly cooled and the loss of weight of CdS was measured.

Table I. Sublimation speed in flowing nitrogen gas and saturated vapor pressure.

Temperature °C	Sublimation speed g/hr	Saturated vapor pressure mmHg
900		4
950		9
1,000		20
1,050	0.4–0.6	40
1,075	0.8–1.1	
1,100	1.3–1.6	78
1,125	1.8–2.2	
1,150	2.7–3.3	

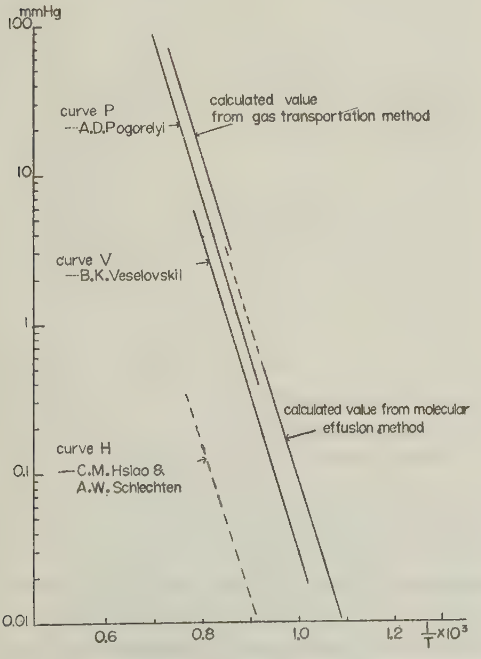

Fig. 3. Saturated vapor pressure of Cd S.

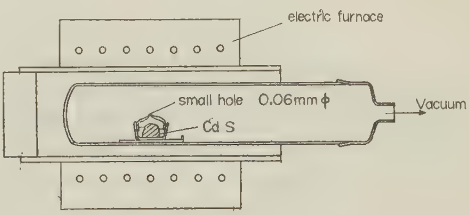

Fig. 4. Apparatus for measuring of vapor pressure.

Table II. Sublimation speed in vacuum and saturated vapor pressure.

Temperature T(°C)	Sublimated Weight G(mg)	Measured time τ(hr)	Sublimation speed (g/hr)	Saturated vapor pressure p(mmHg)
650	1.2	48	2.50×10^{-5}	0.0122
700	0.9	8	1.13×10^{-4}	0.0571
750	2.3	8	2.88×10^{-4}	0.150
800	3.0	3	1.00×10^{-3}	0.526
900	10.4	2	5.20×10^{-3}	2.90

In performing the present experiment, special attention was paid to the following points: (1) as specimens sufficiently pure CdS crystals were used which had been prepared by sublimation and recrystallization in a quartz tube; (2) the degree of vacuum of the tube was kept superior to 10^{-5} mmHg; and (3) the time duration of keeping the electric furnance at a definite temperature was made sufficiently long, so that the periods necessary for heating and cooling of CdS could be neglected.

The results obtained are shown in Table II, and by using the data the saturated vapor pressure of CdS can be calculated as follows.

Now, according to Knudsen, the saturated vapor pressure P is given by

$$P=\frac{WG}{\sqrt{\rho\tau}}\,, \qquad (1)$$

where ρ is the density of CdS vapor, G is the weight of CdS spouted from the small outlet (being of 0.06 mm in diameter) during the period τ, and W is the flowing resistivity of the outlet which is connected with the area A of the outlet by the relation:

$$W=\frac{\sqrt{2\pi}}{A}\,. \qquad (2)$$

If we regard CdS vapor as an ideal gas, its density ρ is given by

$$\rho=\frac{M}{RT}\,, \qquad (3)$$

where M is the molecular weight of CdS, T is its temperature and R is the gas constant.

Thus, combining (1), (2) and (3), we have

$$P=\sqrt{\frac{2\pi RT}{M}}\cdot\frac{1}{A}\cdot\frac{G}{\tau}\,. \qquad (4)$$

The values of P as calculated by this equation are given in the fifth column of Table II and are shown graphically in Fig. 3. In Fig. 3 are also shown for comparison the data obtained by A. D. Pogorelyi[5] (curve P), C. M. Hsiao and A. W. Schlechten[6] (curve H), and B. K. Veselovskii[7] (curve V). It will be seen that the present author's data are somewhat larger than the others'.

An empirical formula for P fitting our data is found to be

$$\log_{10}P=9.36-\frac{10.39\times10^3}{T}\,. \qquad (5)$$

(3) *Thermal decomposition of CdS*

The thermal decomposition of sublimed vapor surrounding heated CdS must not be looked over in the discussion of the sublimation of CdS. Since, in our measurement, the stoichiometric ratio of Cd : S remained unchanged before and after the sublimation, it may be supposed that CdS sublimed as molecules. However, we are obliged to consider that there are some possibilities of causing the thermal decomposition of CdS vapor in accordance with Pogorelyi's report[5] and with the fact that a little deposits of Cd metals are sometimes observed on lower temperature parts of the cooler during the process of crystal growth.

Thus, we shall now calculate the degree of thermal decomposition of CdS, which is expressed by

$$\mathrm{CdS\ (solid)}\rightarrow\mathrm{Cd\ (gas)}+\tfrac{1}{2}\mathrm{S_2\ (gas)}\,. \qquad (6)$$

If, in this case, K_p denotes the equilibrium constant of reaction, the equilibrium pressures for gaseous Cd and S_2, denoted by $P_{\mathrm{Cd\ (gas)}}$ and $P_{\mathrm{S_2\ (gas)}}$ respectively, are given by the equation:

$$K_p=P_{\mathrm{Cd\ (gas)}}\cdot P^{1/2}_{\mathrm{S_2\ (gas)}}\,. \qquad (7)$$

The constant K_p can also be expressed in terms of the difference of free energy ΔF_T before and after the occurrence of the chemical transformation as follows:

$$\Delta F_T=-RT\log K_p\,, \qquad (8)$$

while, ΔF_T itself can be calculated by the equation:

$$\Delta F_T=-T\int_0^T\frac{\Delta H_T}{T^2}dT+iT\,, \qquad (9)$$

where i is a constant relating to the difference of entropy and ΔH_T is the difference of heats of formation and is expressed in terms of the difference of specific heats at constant pressure ΔC_p as:

$$\Delta H_T=\Delta H_0+\int_0^T\Delta C_p dT\,, \qquad (10)$$

where ΔH_0 is the difference of heats of formation at absolute zero temperature.

Thus, by (8), (9) and (10), the constant K_p can be obtained as a function of temperature by substituting following numerical values[8]:

$$\left\{\begin{array}{lll} C_p(\mathrm{CdS})=12.9+0.90\times10^{-3}T & & (\mathrm{cal/mol}),\\ C_p(\mathrm{Cd})\ =\ 5.0 & & (\mathrm{cal/g\text{-}atom}),\\ C_p(\mathrm{S_2})\ =\ 6.5+0.001T & & (\mathrm{cal/mol});\end{array}\right.$$

$$\left\{\begin{array}{lll} \Delta H_{298}(\mathrm{CdS})=-34{,}500 & & (\mathrm{cal/mol}),\\ \Delta H_{298}(\mathrm{Cd})\ =\ 26{,}970 & & (\mathrm{cal/g\text{-}atom}),\\ \Delta H_{298}(\mathrm{S_2})\ =\ 29{,}690 & & (\mathrm{cal/mol});\end{array}\right.$$

$$\left\{\begin{array}{lll} \Delta F_{298}(\mathrm{CdS})=-33{,}600 & & (\mathrm{cal/mol}),\\ \Delta F_{298}(\mathrm{Cd})\ =\ 18{,}690 & & (\mathrm{cal/g\text{-}atom}),\\ \Delta F_{298}(\mathrm{S_2})\ =\ 18{,}280 & & (\mathrm{cal/mol}).\end{array}\right.$$

If, then, we take into account that the value of $P_{\mathrm{Cd\ (gas)}}$ is twice as large as that of $P_{\mathrm{S_2\ (gas)}}$, these equilibrium vapor pressures can be calculated as function of temperature. The results are shown in Table III.

Comparing the author's numerical values given in the table with calculated data by S. Shionoya[9] on the equilibrium vapor pressures of gaseous Zn and S_2 from thermally decomposed ZnS, it is found that they are consivered to be appropriate, because the vapor pressure of S_2 from CdS at 1,000°C is about twenty times as large as that from ZnS and is nearly one-third of saturated vapor pressure of CdS.

Since, however, it is desirable that the vapor pressures of gaseous Cd and S_2 are as small as possible, it is necessary to prevent further progress of thermal decomposition by the use of pure nitrogen free from water-vapor or oxygen.

Table III. Equilibrium vapor pressure of gaseous Cd and S_2 from thermally decomposed CdS

Temperature °C	$P_{S_2 (g)}$ mmHg	$P_{Cd (g)}$ mmHg
600	8.49×10^{-4}	1.70×10^{-3}
700	1.53×10^{-2}	3.06×10^{-2}
800	1.59×10^{-1}	3.17×10^{-1}
900	1.09	2.18
1,000	5.47	10.9
1,100	21.4	41.8
1,200	69.3	139
1,300	191	382

(4) *Discussion on saturated vapor pressure*

Calculating the vapor pressure by the use of Eq. (4), it was found that the saturated vapor pressure of CdS in the temperature range as measured by the author varies from 0.01 mmHg up to 4 mmHg. In comparison with the data for the effusion of mercury the flow of vapor through the small hole of the vessel may be regarded as molecular so far as the vapor pressure is less than 0.5 mmHg, because the dimension of the hole is as small as 0.06 mm in diameter. Further, since there exists no transition point in the above-mentioned temperature range, the vapor pressure higher than 0.5 mmHg may still be estimated by Eq. (4), notwithstanding that the flow is no more molecular.

The values of vapor pressure as calculated by the gas transportation method are also plotted against the temperature in Fig. 3. It will readily be seen that they are slightly larger than those calculated by Eq. (4), but inclinations of these two curves, as well as those of curves P, V and H, are all the same, indicating that the value obtained by the author for the energy necessary for sublimation is nearly equal to those obtained by Hsiao⁶⁾ and Veselovskii⁷⁾. Also, the author's values are several times as large as the equilibrium vapor pressures of thermally decomposed CdS.

From these considerations it can be said that the author's values for saturated vapor pressure are appropriate, though, as mentioned already, they are somewhat larger than Pogorelyi's⁵⁾ and Veselovskii's values⁷⁾, but it seems that Hsiao's values⁶⁾ are too small.

§ 4. Aspects of Crystal Growth

In this section, aspects of crystal growth by sublimation method will be described in some detail.

(1) *General view*

As soon as the boat containing CdS powder was inserted into the center of the combustion tube and the cooler was set from the exit side, the sublimation of CdS immediately began to occur, and its vapor was carried downstream by the flow of nitrogen gas and was condensed on the cooler. At the beginning, grains of relatively large size were deposited at the place of higher temperature, while at the place of lower temperature smaller grains were deposited. With the progress of sublimation and the increase of vapor pressure, however, these grains grew

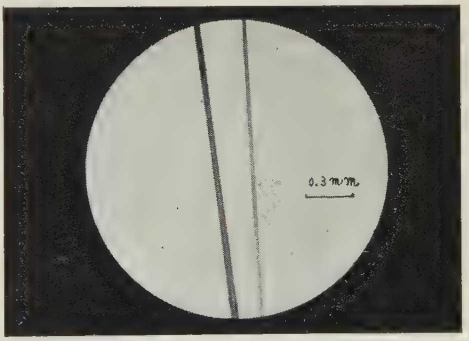

Fig. 5. Needle-shape crystals.

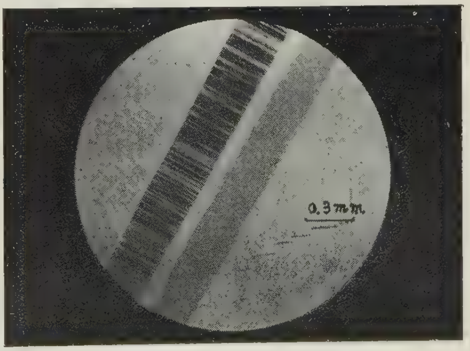

Fig. 6. Laminar crystals.

up and needle-shape crystals as shown in Fig. 5 broke out from nuclei sprouted on the grains. In the case of higher vapor pressure, laminar crystals as shown in Fig. 6 were apt to grow up. Since, in the present experiments, the vapor pressure became still higher, fine needle-shaped and laminar crystals did not grow up. In regions of higher temperatures plate-shape crystals as shown in Fig. 7 were grown up in conformity with the degree of supersaturation, and the dimensions of plates increased to as large as 25×25×1 mm when kept under appropriate conditions. In regions of still higher temperatures, rod-shape crystals as shown in Fig. 8 were grown up slowly.

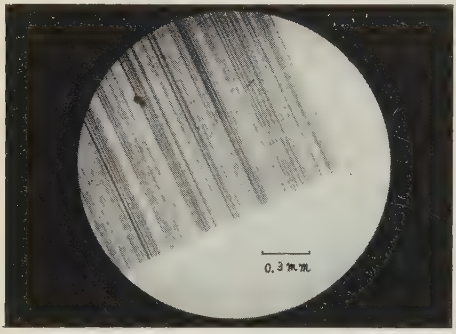

Fig. 7. Plate-shape crystal.

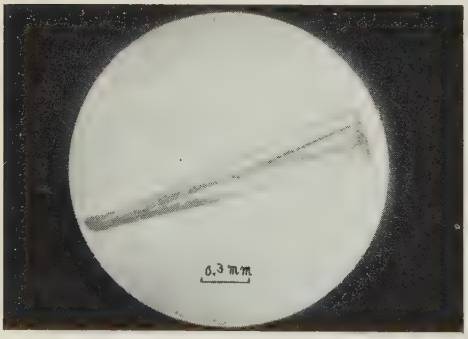

Fig. 8. Rod-shape crystal.

Fig. 2 shows the appearance of the cooler drawn out of the tube when the present experiments were finished. It is found that rodshape crystals, and plate- and clear needle-shape ones are likely to grow up in the regions of 950°C∼1,050°C and 880°C∼960°C respectively, while grown crystals have a tendency to take the forms of complicated needles, laminae and dendrites in the region of 800°C∼850°C and sometimes fine whiskers in the lower region of 650°C∼780°C. Further, orange grains of crystals and yellow powder are found in the regions of 880°C∼750°C and 750°C∼500°C respectively and sometimes a small amount of metallic Cd is obtained in the lower temperature region.

(2) *Growth of needle-shape crystals*

It has been reported by Sears[10] that the screw dislocations may be nuclei of needle-shape crystalls, and in reality these dislocations were observed to lie scattered on the crystalline grains. It was observed, however, that these crystals began to grow abruptly from granular crystals with growing directions parallel to the gradient of vapor density, just at the moment when the sectional areas at the tips of granular crystals became as to fit the degree of supersaturation of the vapor. Under adequate conditions the growing speed of needles was very large, taking sometimes the value of 1 cm/min in case when the diameter of needles were several tens microns.

(3) *Growth of laminar crystals*

It was observed that girdle-shaped or laminar crystals were originated at the side faces of needles, as shown in Fig. 9. Clear crystals free from striations were grown up at the start, but, with the increase of vapor pressure, striations and protuberances appeared on the flat surfaces of the crystals and

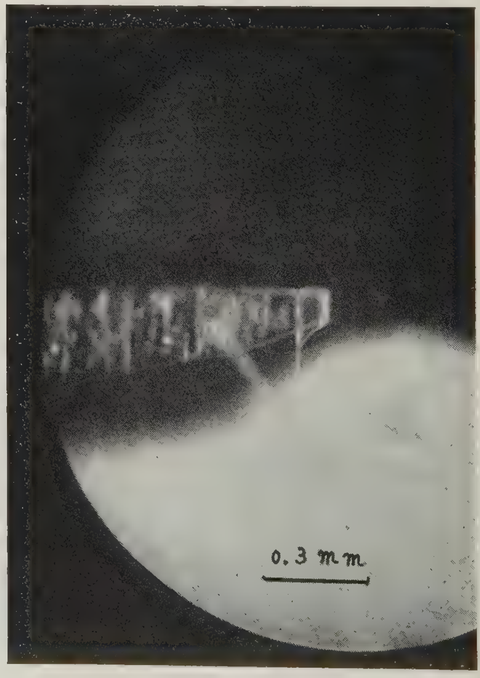

Fig. 9. Growth of laminar crystal,

then changed to be twinlike, because the temperature of growing region was as low as 800°C∼850°C. In conformity with the increase of supersaturation, crystals became of stalactic or granular forms. Under some conditions crystals of the form of thin plate adhered to them.

In short, clear laminar crystals cannot be obtained in the region of 800°C∼850°C as long as the vapor pressure fluctuates or increases. But, if we keep the vapor pressure at a constant value, we can obtain large laminar crystals. In fact, the author was able to produce by Frerichs's method a laminar crystal of as large as about 100×5 ×0.2 mm.

The flat plane of the laminar crystal corresponds to the $(11\bar{2}0)$ plane of the hexagonal type and its growing direction is in most cases perpendicular to the c-axis. In some crystals, however, their growing directions are oblique to the c-axis, and moreover, in some of them the spiral growth is observed.

(4) *Growth of plate-shape crystals*

Plate-shape crystals originated in the region of 880°C∼980°C were grown up continually as long as suitable conditions were kept throughout the process. At first, crystals grew along the direction perpendicular to the c-axis in the $(11\bar{2}0)$ plane, but, as the vapor pressure was increased, the growth in that direction was stopped and the widths of the crystals were increased due to the growth parallel to the c-axis.

If, during the process, there occurred fluctuations in the vapor pressure or mixing of impurities, crystals of various forms were grown up as shown in Figs. 10, 11, 12 and 13. Fig. 10 shows 'islands' due to the

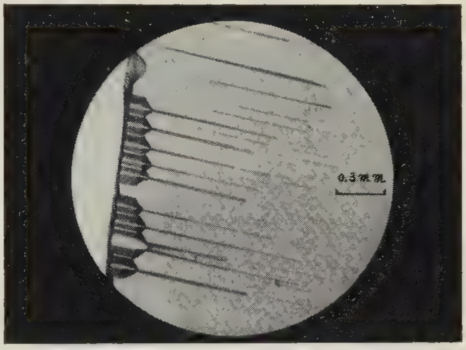

Fig. 10. Growth of 'Island'.

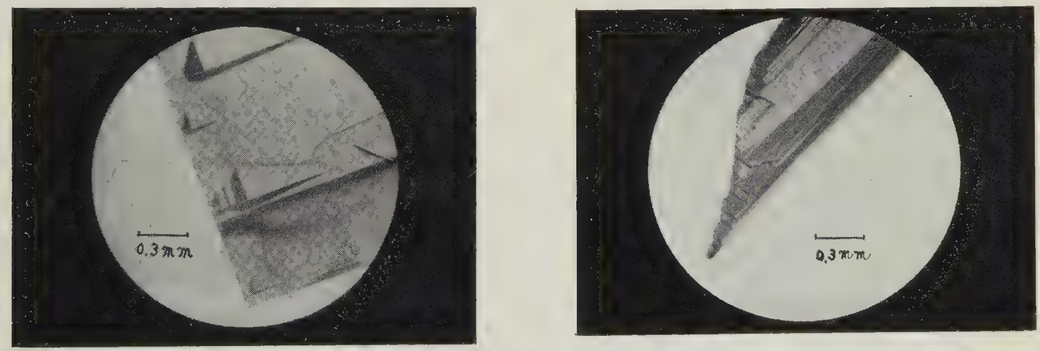

Fig. 11. Growth end.

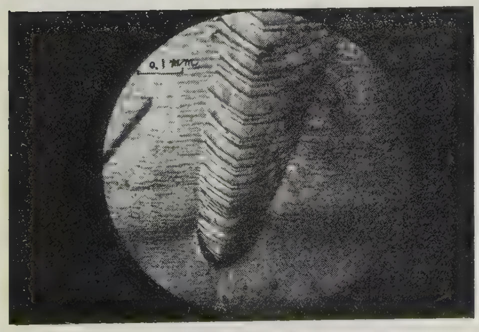

Fig. 12. Variation of growth speed by dislocation.

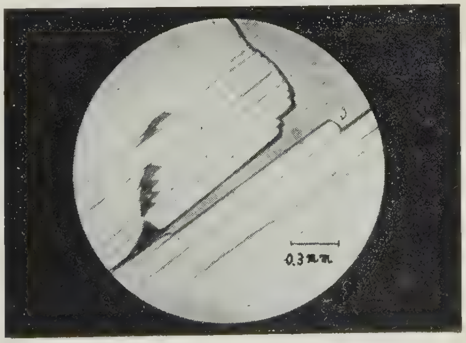

Fig. 13. Growth of needle-shape crystals.

occurrence of dislocations and Fig. 11 shows crystals having remarkable irregularities at their growing edges, while Fig. 12 gives a crystal whose growing speed was altered by dislocation lines. Further, Fig. 14 shows needles grown up from the edge of a plate-shape crystal as well as two-dimensional crystals grown up again from these needles.

Striations on the surfaces of crystals as shown in Fig. 7 are also due to such fluctuations in the vapor pressure.

In case when there was any difference in the vapor pressure along the direction of $[1\bar{1}00]$ axis, there was grown up a crystal as shown in Fig. 14 whose edge makes a certain angle with the c-axis.

Thus, it may be concluded that in order to obtain the normal crystal growth it is essential to keep the vapor pressure constant. In fact, by keeping the vapor pressure constant for several hours we were able to obtain sometimes large single crystals of plateshape as large as 20×20×1 mm.

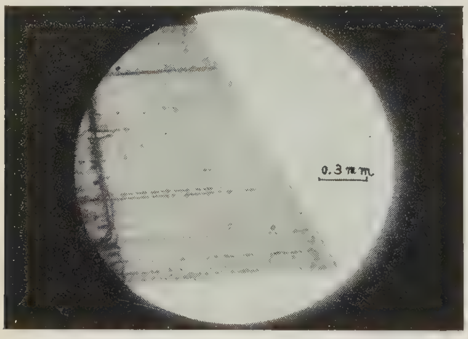

Fig. 14. Growth end and c-axis.

(5) *Growth of rod-shape crystals*

As mentioned already, rod-shape crystals were grown up in the temperature region of 950°C~1,050°C.

In general, needle-shape crystals grown up in the lower temperature region have uniform sectional areas and extend in the direction of the c-axis, having in most cases hexagonal pyramids as their tips. In the case of rod-shape crystals grown up in the higher temperature region, on the contrary, their sectional areas increase along the direction of crystal growth as shown in Fig. 8, suggesting that rod-shape crystals are composed of needle-shape crystals whose growing directions are somewhat inclined to the c-axis. In some cases, tips of the crystals are flat, concave or hollow-ringed (cf. Fig. 15).

The growing process of rod-shape crystals is not quite clear, however. Judging from the fact that the sectional areas increase rather rapidly along the direction of crystal growth, it is not likely to consider above mentioned shape to be due to mosaic structure. It is also impossible to consider these rods to be twins or random assemblies of many crystals.

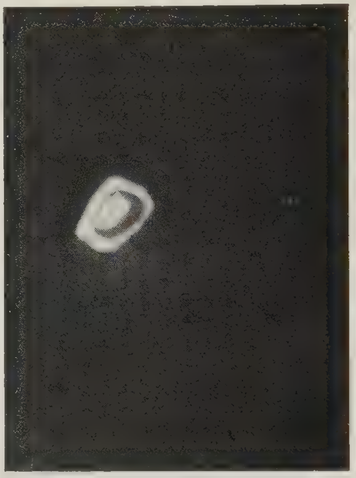

Fig. 15. Top of rod-shape crystal.

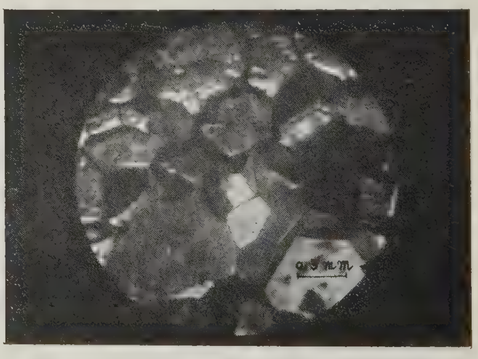

Fig. 16. Block crystals.

(6) *Growth of block crystals*

In the region whose temperature was higher than 1,100°C, block crystals as shown in Fig. 16 were grown up frequently*. These crystals were formed massively, because the growing speed along the c-axis was slow and was nearly equal to those in other directions. The directions of the c-axes of various block crystals are disordered.

---

* Similar block crystals are frequently observed in the case of crystal growth at high temperature in a sealed quartz vessel.

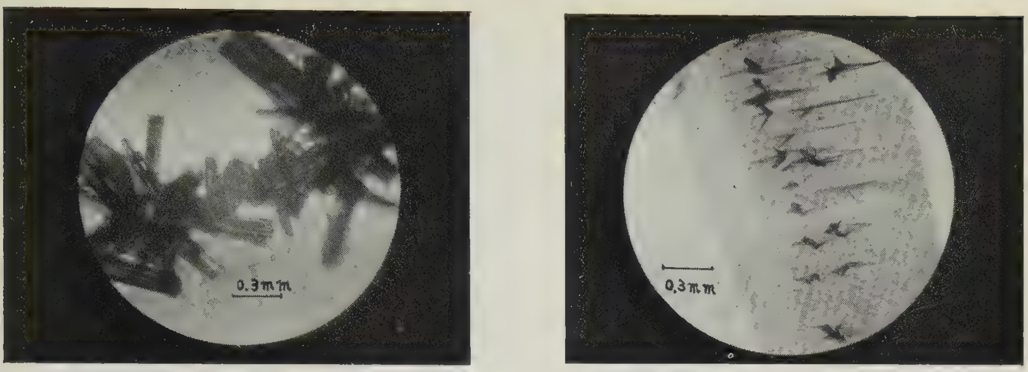

Fig. 17. Crystals grown at low temperature region.

It is to be added here that the growth of block crystals by the method in the flow of nitrogen gas is seriously affected by impurities.

(7) *Growth of network crystals*

In case when the flow velocity of nitrogen gas was very large, it was frequently observed that network or slender fibre crystals were grown up at low temperature region of 650°C～780°C. Since, in this case, the vapor was cooled down rapidly, crystals of small size and complex form were grown up. Curious forms as shown in Fig. 17 were observed rarely, and sometimes slender and long whiskers as shown in Fig. 30 with diameters of several microns were observed.

(8) *Growth of twin crystals*

Twin crystals were frequently grown up when the flow velocity of nitrogen gas was fairly large and the pipe was cooled down sufficiently. It was frequently observed that in some of these twins the twin plane is perpendicular to the surface in which the two wings are lying, and in this case there are two kinds of twins: in one kind the angle between the c-axis and the twin plane is 28.5°

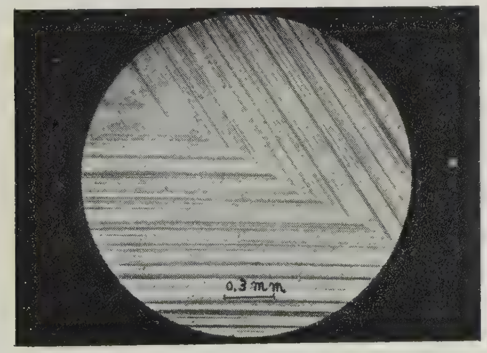

Fig. 18. 28.5° twin.

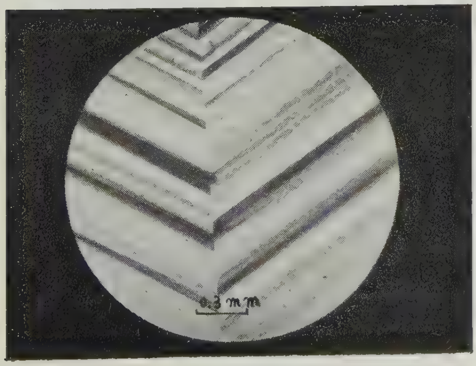

Fig. 19. 58° twin.

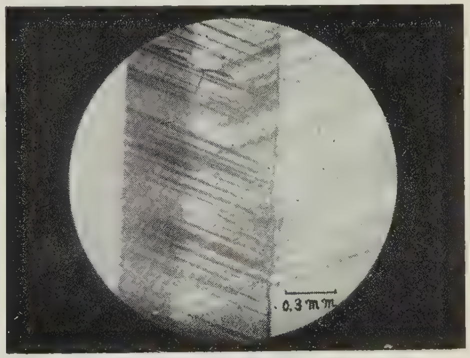

Fig. 20. 73° twin.

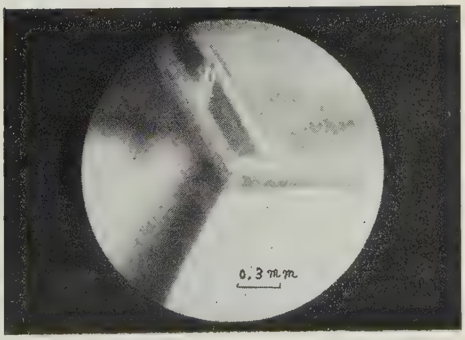

Fig. 21. Repeated twin.

as shown in Fig. 18, while in the other the said angle is 58° as shown in Fig. 19. Moreover, we observed some twins in which the two crystals make an angle of 120° with each other and the angle between the line of intersection of these two crystals and the c-axis is 73° or 69.5° as shown in Fig. 20. Also, the repeated twins having three wings separated mutually by an angle of 120° as shown in Fig. 21 were rarely observed.

The growth of these twin crystals may perhaps be due to several kinds of causes, namely (1) the branching of needle-shape crystals under favorable vapor pressure, (2) the branching of plate-shape crystals in the course of crystal growth as shown in Fig. 22, and (3) the irregularities broken out on the surfaces of plate-shape crystals.

§ 5. Observations on the Grown Crystals

(1) *Inspections by X-rays*

It was found out by X-ray observations that a typical plate-shape crystal as shown in Fig. 7 is a single crystal of hexagonal type with lattice constants a=4.136 Å and c=6.714 Å and its surface corresponds with the (1120)-surface. Striations on the surface of this crystal are parallel to the c-axis.

Fig. 23 shows the Laue photograph of a plate-shape crystal and Fig. 24 gives the rotational diffraction photograph of a needle-shape crystal as obtained by rotating it

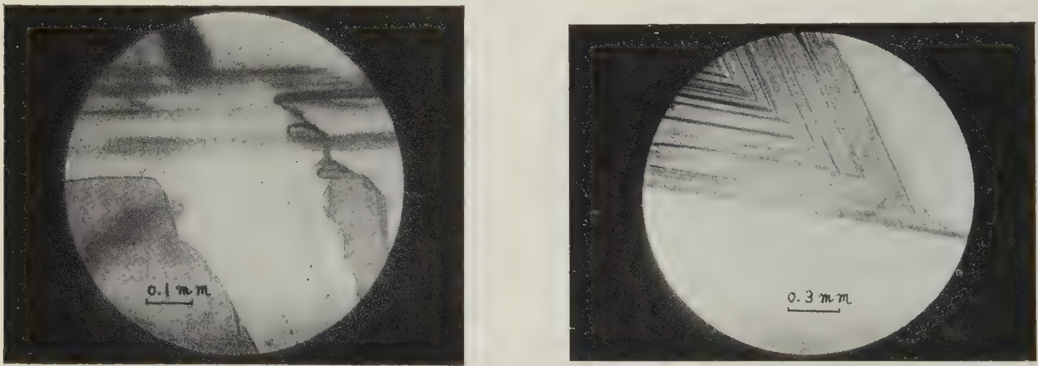

Fig. 22. Growth of twin.

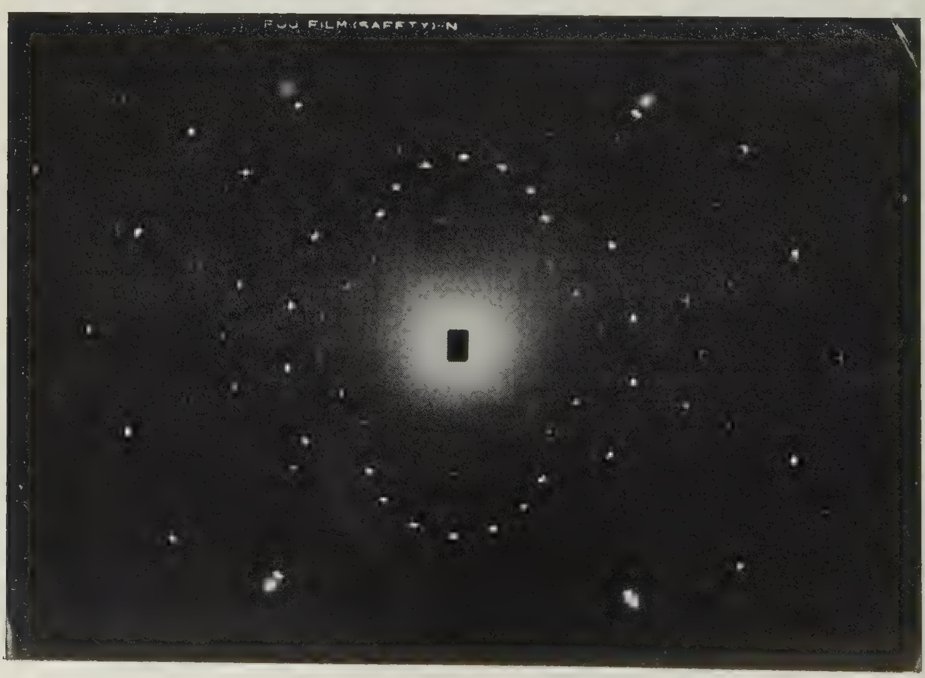

Fig. 23. X-ray Laue photograph.

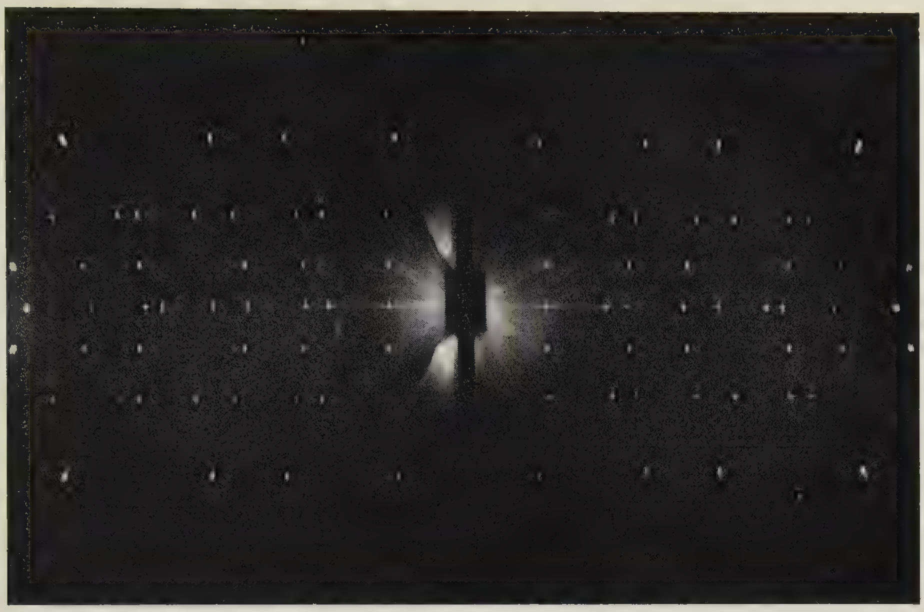

Fig. 24. X-ray rotation photograph.

around its c-axis. No strain nor any disorder is found in these photographs except diffused dispersions which are supposed to be due to lattice vibrations.

Observation of Debye photographs of rod-shape and block crystals shows that they are also of hexagonal type.

(2) *Inspections by electron-rays*

A transmission photograph of electron-rays through a very thin plate-shape crystal with thickness of about 300 Å is given in Fig. 25.

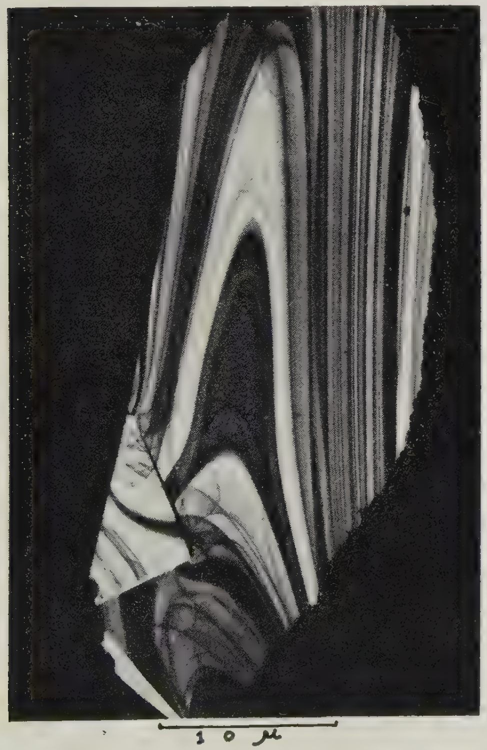

Fig. 25. Transmission photograph by electron-rays.

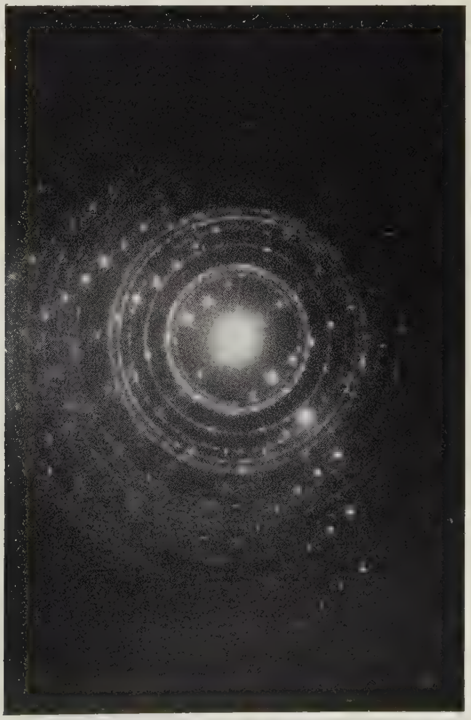

Fig. 26. Electron diffraction photograph (Rings are referred to ZnO).

In this figure are observed interference stripes of equal thickness, which indicate that the crystal structure is clear even in extremely thin parts.

Fig. 26 gives the electron diffraction photograph of the crystal where microscopic picture is shown in Fig. 25. From Fig. 26 it is found that the surface of the thin plate corresponds to the (1120)-surface and that this diffraction pattern can be interpreted by taking $a=4.136$ Å and $c=6.714$ Å.

(3) *Results of spectroscopic analysis of the specimens*

In Table IV are shown the results of spectroscopic analysis on the degree of impurities contained both in the crystalline powder as used in the present experiment and in the grown crystals. It can be generally said that detected quantities of impurities of impurities are somewhat more in such crystals that were grown up in lower and higher temperature regions.

Table IV. Spectrochemical analysis results of impurity contained in CdS.

	Powder %	Crystal %
Si	0.01 —0.001	0.01 --0.001
Fe	0.001—0.0001	0.001—0.0001
Al	0.0001	0.0001
Mg	0.001	0.001—0.0001
Ca	0.001	0.001—0.0001
Ag	0.001–0.0001	0.001—0.0001
Cu	0.001—0.0001	0.001—0.0001

(4) *Visual and optical observations*

By visual inspections of single crystals it is noticed, first of all, that there are striations on their surfaces which, as mentioned before, were caused by the variation of grown velocitiy. Some of the striations start on the way of crystal growth or form the "islands" as shown in Fig. 10. The starting-points of these striations and islands can be connected by a straight line which seems to be concerned with the line of dislocation. In Fig. 12 it is observed that the growing speed is changed due to the dislocation appeared in the central part of the picture. Further, it is supposed that in case when needle-shape crystals were grown up from plate-shape ones, as shown in Fig. 13, the dislocations exposed on the side faces of the latter play an important role.

Next, it was found that due to the difference of growing speeds along the $[1\bar{1}00]$ axis and the c-axis, the edge of grown crystal makes a certain angle with the c-axis as shown in Fig. 14. Values of the said angle hitherto observed were 10°, 23.5°, 28.5°, 35°, 38.5°, 41°, 47°, 53°, 55°, 58°, 65°, 69.5°, 73°, 79.5° and 90°, and among them most frequently

Table V. Angle between c-axis and growth ends.

6C	10°5′	19°35′	28°5′	35°25′	41°39′	46°51′	calculated
	10°	—	28-29°	35°	41-41.5°	47°	measured
5C	12°3′	23°7′	32°38′	40°29′	46°51′	52°1′	calculated
	—	23.5°	—	41-41.5°	47°	52.5°	measured
4C	14°56′	28°5′	38°40′	46°51′	53°8′	58°0	calculated
	—	28-29°	38.5-39°	47°	52.5°	58°	measured
3C	19°35′	35°25′	46°51′	54°54′	60°39′	64°53′	calculated
	—	35°	47°	54-55°	—	65-66°	measured
2C	28°5′	46°51′	58°0′	64°53′	69°27′	72°39′	calculated
	28-29°	47°	58°	65-66°	69-70°	72-73°	measured
1C	46°51′	64°53′	72°39′	76°49′	79°23′	81°7′	calculated
	47°	65-66°	72-73°	76-77°	79-80°	81.5°	measured
-	$\sqrt{3}a$	$2\sqrt{3}a$	$3\sqrt{3}a$	$4\sqrt{3}a$	$5\sqrt{3}a$	$6\sqrt{3}a$	

observed values were 47°, 58°, 69.5°, 73°, 79.5° and 90°. By taking into account that crystal grows by steps of unit cell, these angles can be calculated by the use of lattice constants ***a*** and ***c***. Both the measured and calculated values are given in Table V.

The atomic arrangements of twins whose two wings lie in a plane as shown in Fig. 18 and 19 are represented in Figs. 27 and 28. In case of twins in which the angle between the line of intersection of two crystals and the c-axis is 73° or 69.5°, considerable amounts of atomic displacements from normal site should be necessary for stable atomic arrangements even if we restrict our considerations to the line of intersection of two crystals, so that the two planes should intersect with each other by an appropriate and definite angle, giving rise to produce vacancies on the line of intersection which have possibilities of trapping impurities.

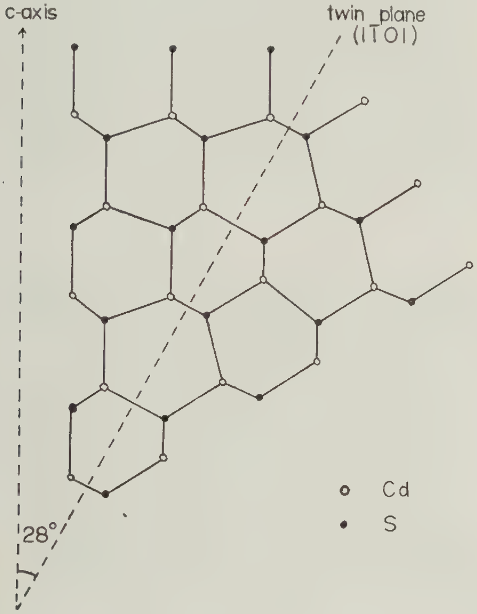

Fig. 27. Atomic arrangement of 28° twin, projected to (11$\bar{2}$0) plane.

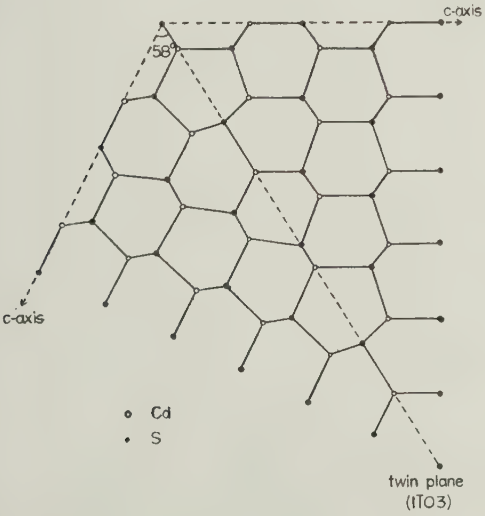

Fig. 28. Atomic arrangement of 58° twin, projected to (11$\bar{2}$0) plane.

Crystals as shown in Fig. 7 are quite uniform even when they are inspected by polarized light. However, any irregularities of crystals and variations in their thickness as well as twin boundaries can be detected by polarized light. The maximum transmission of polarized light through a crystal is obtained when the plane of polarized light is parallel to the c-axis.

As an addendum, a visible transmission curve through a plate-shape crystal with size of 10×10×0.33 mm is shown in Fig. 29.

(5) *Perfect crystals*

Many 'whiskers' were observed among needle-shape crystals grown up in low temperature region, and some of them were of nearly perfect crystal structure and were

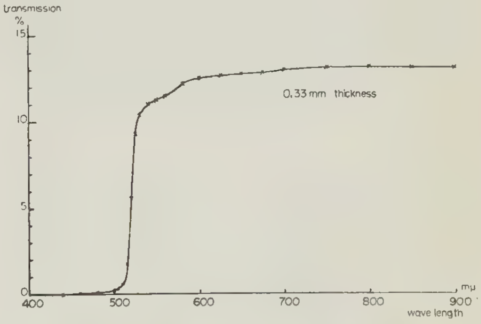

Fig. 29. Spectral transmission curve.

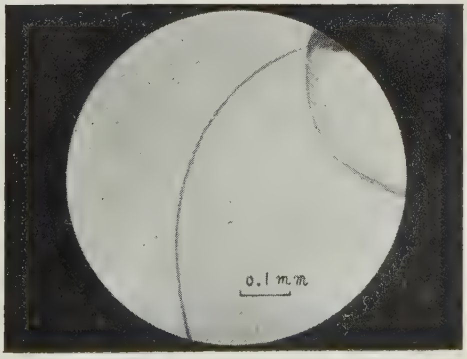

Fig. 30. Elastically bended needle crystal.

easily bent elastically in the form of a circular arc. A typical one is shown in Fig. 30. If, in this case, we denote the radius of cross-section of a whisker and its radius of curvature by r and R respectively, the magnitude of extension e of the whisker is given by the formula:

$$e=r/R\,. \tag{11}$$

If we take $r=15.5\mu$ and $R=1.4\,\text{mm}$ this formula gives $e=1.1\times10^{-2}$. This value seems to be adequate as compared with the corresponding values 1.5×10^{-2} and 1.1×10^{-2} for Cu[11] and Zn[12] respectively.

(6) *Luminescence*

Red luminescence was emitted when CdS crystals containing very small amount of silver or copper were irradiated by 3650 Å ultraviolet rays. In this case, however, luminescence was not always emitted uniformly from the whole parts of crystals but strongly emitted locally from the boundaries or irregularities of crystals as shown in Figs. 31 and 32. On the other hand, it might be possible that luminescence is unusually strong at the edge of a crystal because of its high refractive index, even though the whole part of the crystal radiates uniform luminescence. In reality, crystals containing more amount of silver or copper radiate from their whole parts, but even in those cases luminescence is rather strong at irregularities of crystals. In another case, luminescence is not always strong in all irregular parts of crystals as shown in Fig. 32, and in some cases there can be seen fairly different intensities along the boundaries.

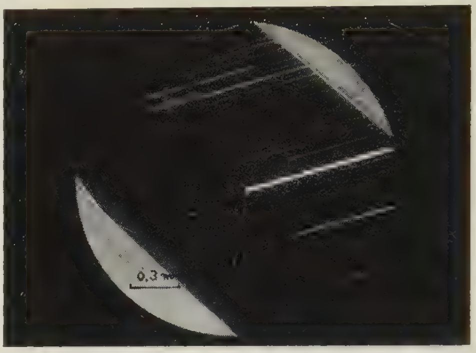

Fig. 31. Luminescence (White lines are red luminescent by 3650Å UV light.).

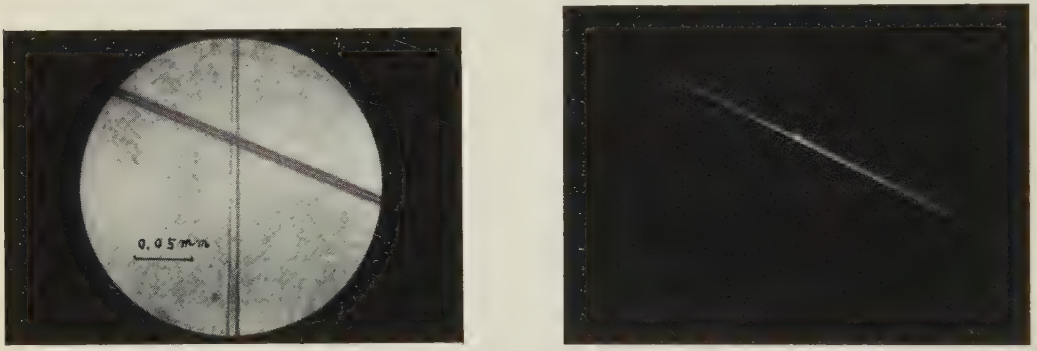

Fig. 32. Transmission (left) and luminescence (right).

In short, it may be concluded that luminescence is strong at specific irregularities or boundaries, and this phenomenon can be utilized as one useful means to search for irregularities of crystals. Moreover, the aspects of luminescence change according to the heattreatment of crystals and this phenomenon is also a notable fact, because it seems to be related with the movement of impurities, irregularities or dislocations.

There was no luminescence from the axis of intersection of 28.5° or 58° twins, but strong radiation was observed from the axis of intersection of 69.5° or 73° twins. The latter phenomenon seems to be related with the fact that impurities are likely to be captured by vacancies which are produced in the process of crystal growth.

§ 6. Summary and Conclusion

In the present paper, the author has discussed the process of growth of CdS single crystals by the method of sublimation and recrystallization in the flow of nitrogen gas and inspected grown crystals in detail. The results obtained may be summarized in the following lines.

In order to obtain any required crystal shape it is quite essential to keep the vapor pressure continuously at a definite value. Values of the vapor pressure suitable for the growth of specific kinds of crystal seapes are as follows: 8∼35 mmHg for the growth of rod-shape crystals; 2∼13 mmHg for plate-shape crystals; 0.4∼3 mmHg for thick needles of about one-tenth mm in diameter and 0.005 ∼0.05 mmHg for fine needles of scores of microns in diameter.

In the course of observations on growing crystals, the author has paid special attention to the following two points: one point is to ascertain the origins of crystal growth and the other is to search for dislocations which were easily found out, since the CdS crystals were thin and transparent, and, at the same time, to study the effect of those dislocations upon the crystal growth.

For instance, it has been recognized that needle-shape crystals were grown up from screw dislocations, while whiskers were grown up from irregularities of the cooler in the highest temperature region where the CdS vapor was condensed. As to the growth of laminar crystals from the side-faces of needle-shape ones as shown in Fig. 9, it has been supposed that at first a needle-shape crystal grows up in the form of spiral and then a laminar crystal begins to grow up form the growing tip of the spiral just at the moment when the tip has become in such a direction along which the vapor-density gradient is appropriate. It has also been observed that dislocations have serious influences upon the growth of needle-shape crystals from grains or from plate-shape crystals, the occurrence of striations on plate-shape crystals, the variation of growing velocities, the origination of twins, luminescence and so on.

In general, CdS single crystals are yellow in color, transparent and thin, and are also chemically stable in air, so that they are quite suitable for investigating optically the process of crystal growth and internal irregularities. They are also very suitable for studying the profound characteristics of CdS peculiar to semiconductors, such as visualization of dislocations, the relation to luminescence, the appearance of penetrated impurities as well as properties of perfect crystals. In a future paper, the author intends to carry out investigations on these matters by making use of various forms of clear and large single crystals obtained in the present experiment.

Acknowledgement

In conclusion, the author wishes to express his sincere thanks to Professors Y. Uchida and K. Tanaka of Kyoto University, Professor R. Kiriyama of Osaka University, Assistant Professor S. Shionoya of Yokohama University and Dr. H. Yamashita in our laboratory for their kind guidance. The author's thanks are also due to Mr. Seto of Kyoto University, Mr. S. Maruyama of Osaka Women's College and members in our laboratory for their instructive suggestions and cooperations.

References

1) S. Ibuki: Mitsubishi Denki **30** (1956) 136 (in Japanese).
2) S. Ibuki and K. Awazu: J. Phys. Soc. Japan **11** (1956) 1297.
3) H. Yamashita and S. Ibuki: J. Phys. Soc. Japan **13** (1958) 226.
4) E. Tiede and A. Schleede: Ber. Deut. Chem. Ges. **53** (1920) 1717.
5) A. D. Pogorelyi: J. Phys. Chem. **22** (1948) 731 (in Russian).
6) C. M. Hsiao and A. W. Schlechten: J. Metal **4** (1952) 65.
7) B. K. Veselovskii: J. Appl. Chem. **15** (1942) 422 (in Russian).
8) *Selected Values of Chem. Thermodyn. Prop.*, M.B.S. (1952). *Intern. Crit. Table*, National Research Council (1928).
9) S. Shionoya and K. Kikuchi: Nippon Kagaku Kaishi **77** (1956) 291 (in Japanese).
10) S. S. Brenner and G. W. Sears: Acta Met. **4** (1956) 268.
11) S. S. Brenner: Acta Met. **4** (1956) 62.
12) P. V. Coleman and G. W. Sears: Acta Met. **5** (1957) 131.

JOURNAL OF THE PHYSICAL SOCIETY OF JAPAN, Vol. 14, No. 9, SEPTEMBER, 1959

Induced Conductivity of CdS by β- and γ-rays

By Sumiaki IBUKI

Research Laboratory, Mitsubishi Elec. Mfg. Co., Amagasaki, Japan

(Received December 1, 1958)

Properties of CdS crystals were investigated under irradiation by β-rays from 10 *mc* of Sr^{90} or from the accelerator of Van de Graaff type and γ-rays from 1 *c* of Cs^{137} or from 200 *c* of Co^{60}. The ohmic contact of electrodes and the crystal uniformity were first inspected, and some properties concerning the induced conductivity of CdS crystals by β- and γ-rays were discussed in comparison with those observed when the crystals were irradiated by visible light. It has been concluded that the sample crystals grown by the author's method are uniform and that they have low trap density and high sensitivity for β- or γ-rays. It was also shown that the elementary phenomena of the induced conductivity in the case of β- or γ-ray irradiation were quite similar to those in the case of visible-light irradiation, and that the number of electrons excited into the conduction band by a β-particle was about one hundred times larger than that by a γ-particle of 1.3~1.5 Mev.

§ 1. Introduction

It has been well known that the CdS single crystal is a high sensitive photoconductor and its electric resistivity is decreased by irradiation of X-, γ-, β- and α-rays[1)-4)]. By making use of the above property of the crystal, some trials have been made[5)] to use the crystal as the detector of γ-rays.

The author successfully obtained large single crystals of CdS as reported in the previous papers[6)]. In the present paper will be reported several properties of these crystals induced by irradiation of β- and γ-rays as well as visible light and some interesting results particularly about the elementary process of photoconductivity and the efficiency of irradiation for β- or γ-rays.

§ 2. Samples and Electric Contacts

Samples used in the present experiment were plate-shape crystals which were cloven parallel to the c-axis of the CdS single crystal. In order to examine the electrode contacts, voltage *versus* current (V-I) charac-

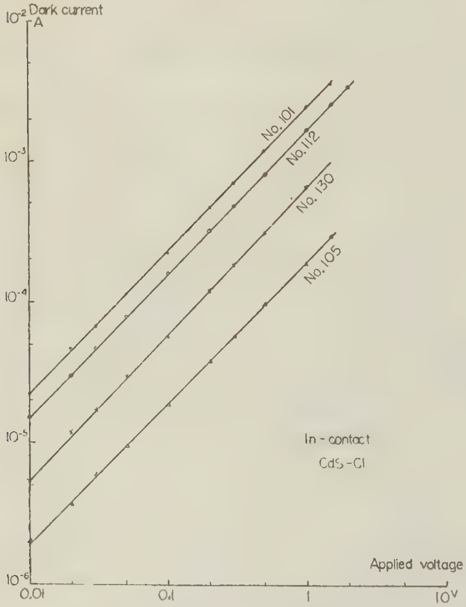

Fig. 1. Voltage dependence of dark current.

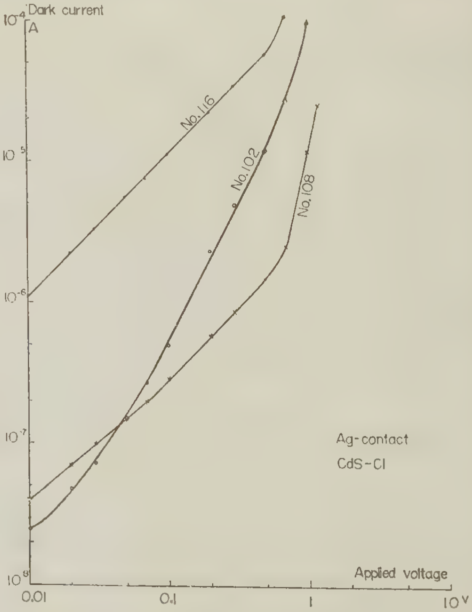

Fig. 2. Voltage dependence of dark current.

teristics at low applied voltage were measured for the electrodes of several kinds of materials, namely, In, Ag-paste, evaporated Ag and Acquadag. The results are shown in Figs. 1∼4. Among these materials evaporated In was most favorable to the electrode as already reported⁷⁾; the so-called barrier effect at the contact parts was not observed and the V-I curve was a straight line down to low voltage region as shown in Figs. 1 and 3. Moreover, $1/f$ noise caused by electrode contact was very little in the case of In electrode in comparison with the cases of other materials.

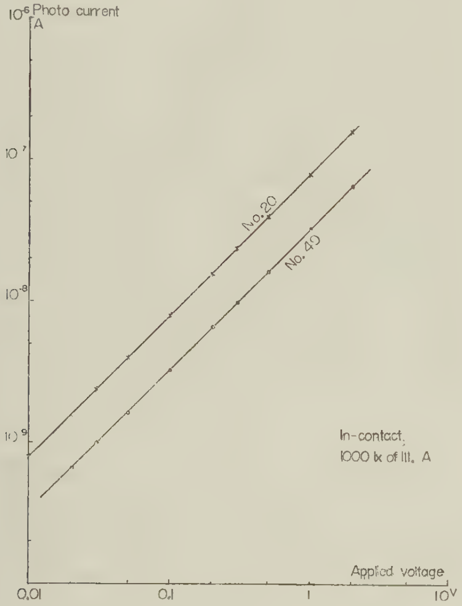

Fig. 3. Voltage dependence of photocurrent.

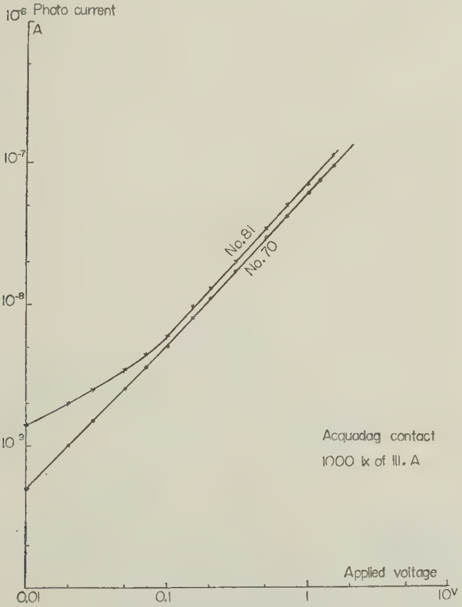

Fig. 4. Voltage dependence of photocurrent.

The uniformity of sample crystals was examined by the following experiments. First, a sample crystal was uniformly illuminated on its whole surface area by light flux and a shutter was inserted so as to cut the light flux as shown in the inset in Fig. 5. Then

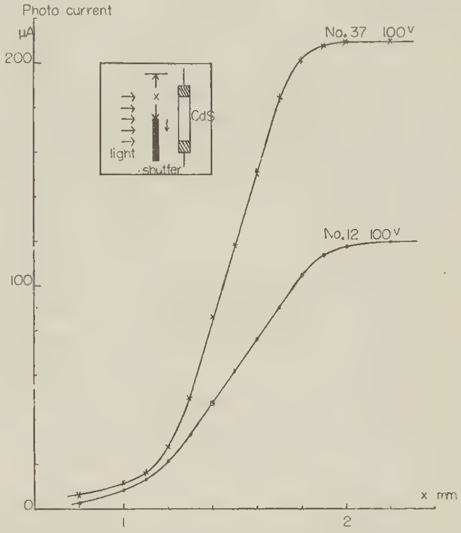

Fig. 5. Uniform characteristics of crystals.

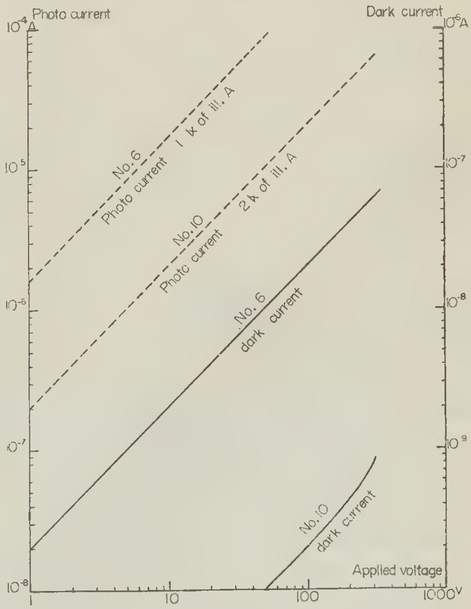

Fig. 6. Voltage dependence of dark and photocurrent.

the relation between the irradiated area and the photocurrent induced in the crystal was measured by moving the shutter from the one electrode side towards the other side. The curve showing this relationship is shown in Fig. 5. It has been reported[8),9)] that uniform ZnS and CdS crystals are hardly obtainable and curves similar to that in Fig. 5 fluctuate. But CdS crystals produced by the author are exceedingly uniform and hence the potential gradient is equal everywhere in the whole crystal, as can be seen from Fig. 5.

§ 3. Some Properties of Photoconductivity

Some properties of the CdS crystal irradiated by visible light was previously investigated in order to compare them with the effects induced by irradiation of β- and γ-rays.

V-I curves of the dark current and the photocurrent excited by the light from illuminant A are shown in Fig. 6. The photocurrent increases linearly with applied voltage up to high voltage region, but the dark current seems to be influenced by space charge in high voltage region.

Photocurrent characteristic *versus* light intensity is given in Fig. 7. The photocurrent increases almost linearly with light intensity in lower intensity region, but its increasing rate approaches a half power of light intensity in higher intensity region. As will be discussed in § 5, a knick point appears on the curve in Fig. 7 for the light intensity, at which the density of excited free photoelectrons becomes equal to that of traps.

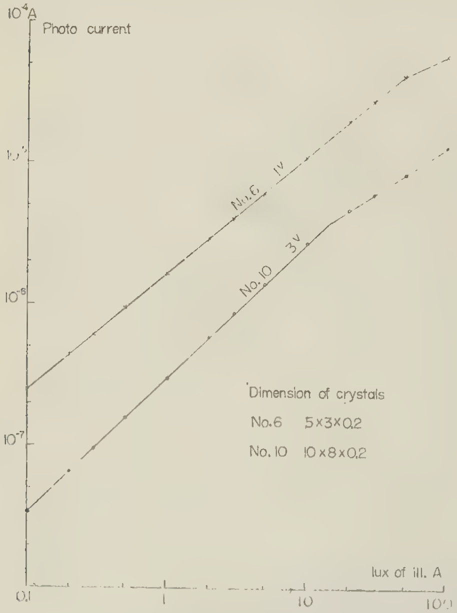

Fig. 7. Photocurrent-irradiation characteristics.

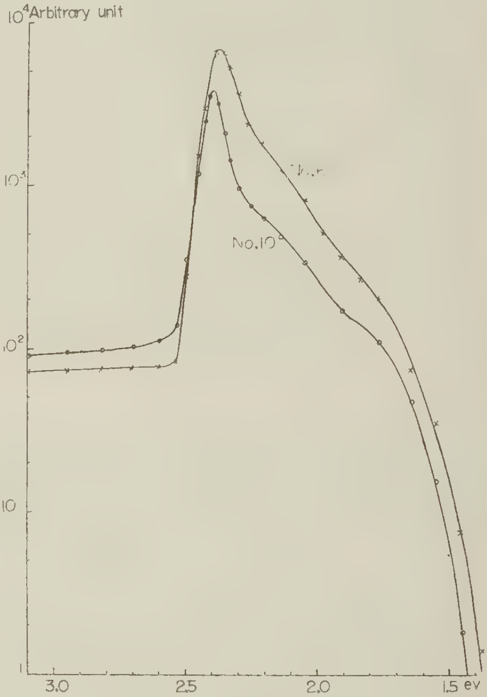

Fig. 8. Spectral sensitivity.

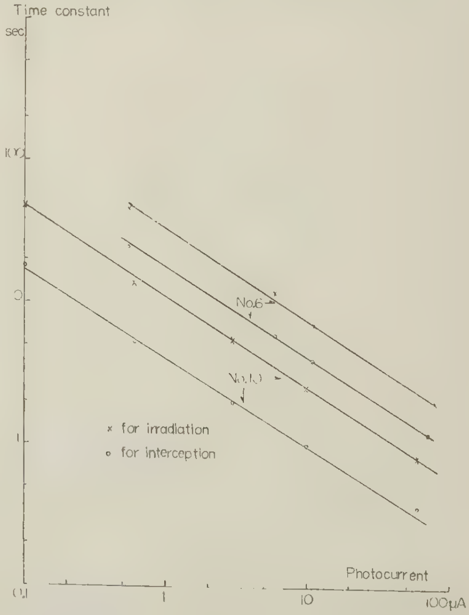

Fig. 9. Time constant-photocurrent characteristics (50 V).

The spectral sensitivity of photoconductivity in the visible region is given in Fig. 8. In this figure there are found one strong peak at absorption edge and several small humps at longer wavelength side, whose positions agree well with those of the optical absorption peaks.

The time constant was measured when the crystal put in dark was exposed to the visible light or when the irradiating light was shut off. The results are shown in Fig. 9, by taking photocurrent as the abscissa in order to compare below them with those for β- and γ-rays. It will be seen from this figure that the time constant decreases with increasing photocurrent and its magnitude at the instant of irradiation is larger than that at the instant of shut-off. Besides these facts, we have also observed that the time constant seems to decrease to some extent when the applied voltage is raised, and that high sensitive crystals show larger time constant, while low sensitive crystals smaller one.

§ 4. Properties for β- and γ-rays

Some properties of CdS crystals were investigated for β- and γ-rays irradiation. The voltage dependence of the current excited by β-rays from 10 *mc* of Sr^{90} is shown in Fig. 10. It will be seen that the conductivity of the crystal changes from $1\times10^{-8}\Omega^{-1}\,cm^{-1}$ to $1\times10^{-4}\Omega^{-1}\,cm^{-1}$ by the irradiation at a distance of 5 cm from the β-ray source. The crystals prepared by the author have far higher sensitivity than those used by Hollander5), their conductivity being $5\times10^{-5}\Omega^{-1}\,cm^{-1}$ by the irradiation of β-rays at a distance of 5 mm apart from 5 *mc* source. In the author's experiments the number of electrons, which knocked the area of 5×3 mm of the crystal, is calculated to be 1.8×10^5 per second and then the current induced in the crystal is 60 μA, namely 3.8×10^{14} electrons per second under the applied electric field of 500 V/cm. It is estimated, therefore, that the amplification of 2.1×10^9 is performed in the CdS crystal.

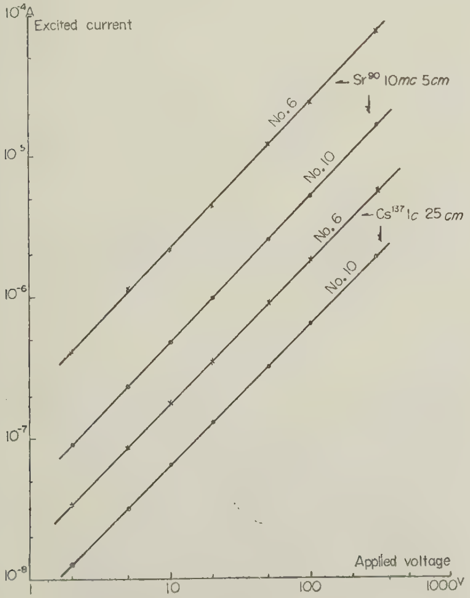

Fig. 10. Voltage dependence of excited current by radio isotope.

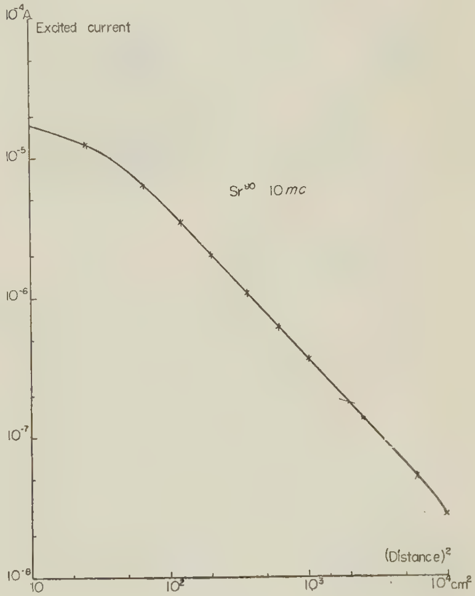

Fig. 11. Distance dependence of excited current (50 V, No. 6).

The excited current characteristic plotted against the distance from the β-ray source to the CdS crystal is given in Fig. 11. The current range in this figure covers just the range in which the linear relationship holds between the photocurrent and the light intensity. Near the β-ray source the induced current does not increase inversely proportional to the square of the distance, because the source has a disk shape of 30 mm in diameter and 5 mm in thickness. On the contrary, the current shows a tendency to fall off rather rapidly at large distances from the source because of the effect of the absorption of β-rays by air. In the intermediate range, however, the current increases just inversely proportional to the square of the distance.

The absorption of β-rays from Sr^{90} by various aluminium plates was measured. The geometry of experimental arrangements and the results obtained are given in Fig. 12. It will be seen that remarkable absorption occurs in the case of aluminium plates of thickness of 0.1~0.3 mm, and this fact can be explained by the absorption of low energy β-rays generated by the back scattering due to the source and its holder. Taking the point A on the absorption curve as the base-point, the half-thickness for 2.2 Mev β-rays from Sr^{90} becomes 0.6 mm for aluminium, namely 162 mg/cm². This value is nearly equal to 150 mg/cm² which is calculated from the well-known formula:

$$a=0.046E^{3/2}\ (\mathrm{gr/cm^2})\,, \qquad (1)$$

where a is the half-thickness and E the maximum energy. The intensity of β-rays transmitted through the substance of d cm in thickness is given by

$$I=I_0 \exp(-Kd)\,, \qquad (2)$$

where K is the absorption constant in cm^{-1} and I the intensity of the incident rays. The absorption curve approximately fits the above equation between the points B and C in Fig. 12, but it deviates from this equation in the part between the points D and E corresponding to large thickness of aluminium plate. This deviation can be explained by the effects of Bremsstrahlung X-rays. Considering the point F in this figure as the practical range R mg/cm of β-rays from Sr^{90}, R becomes 1080 mg/cm², which corresponds to about 4 mm in thickness. This value agrees fairly well with the value of 1060 mg/cm² calculated from the equation[10]:

$$R=0.542E-0.133\ (\mathrm{mg/cm^2})\,. \qquad (3)$$

Even when the geometry of experimental arrangements was changed, the shape of absorption curve was changed only slightly and the half-thickness and the practical range remained nearly constant. Thus the absorption of β-rays by aluminium plate can be measured with satisfactory precision and reproducibility by the use of CdS crystals.

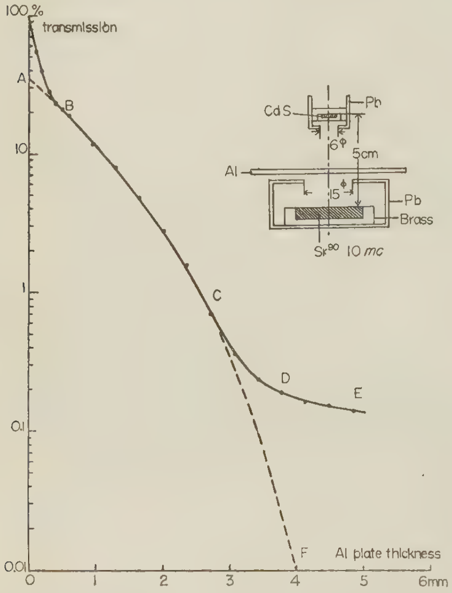

Fig. 12. Absorption of β-rays from Sr^{90} by Al plate.

Time constant was measured when the CdS crystal was irradiated by β-rays from Sr^{90} or when it was screened off from them, and it was found, as expected from the results in the case of visible light, that the time constant at the instant of irradiation-on was

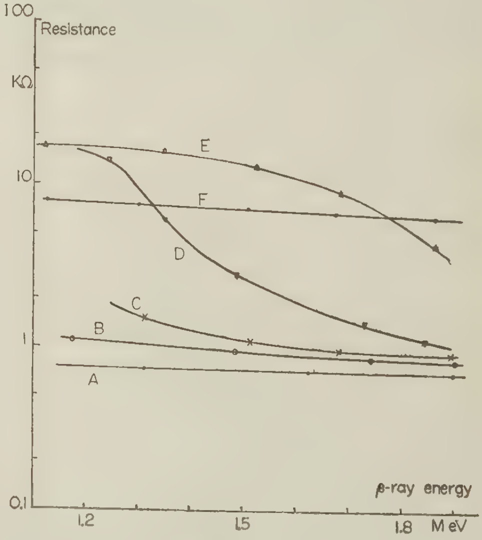

Fig. 13. β-rays irradiation characteristics from Van de Graaff generator (No. 1).
A irradiating current 0.1 μA
B 0.025 μA
C 0.025 μA+1 mm thickness Al plate
D 0.025 μA+2 mm thickness Al plate
E 0.025 μA+3 mm thickness Al plate
F 0.0015 μA

somewhat longer than that at the instant of screening-off, and that the magnitudes of both these time constants were nearly equal to those for visible light respectively in case when the conductivity of the crystal for β-ray irradiation was the same as that for visible light irradiation.

In Figs. 13 and 14 are shown the results of measurements on the resistance and the energy characteristics for exciting particle of the CdS crystal when it is irradiated by β-rays from the accelerator of Van de Graaff type manufactured in our laboratory. In Fig. 13 the conductivity of the crystal seems to increase slightly with the increase of the energy of exciting β-rays, but taking the focusing effects of β-rays into account, it may be considered that the conductivity is almost flat in the range from 1 to 2 Mev. In Fig. 14, which shows the conductivity *versus* exciting β-ray intensity, the conductivity becomes to be proportional to a half power of exciting intensity at the exciting current of 2.4×10^{-11} A, namely the number of irradiating electrons of 1.1×10^{9} electrons/cm³ sec, and then it tends to saturate at 7.5×10^{-9} A, namely 3.1×10^{11} electrons/cm³ sec. For irradiation of β-rays from Van de Graaff the *V-I* characteristic of the CdS crystal was also linear in low voltage range, but the resistivity of the crystal was decreased by the high density irradiation of β-rays because the temperature of the crystal was raised. The time constant was less than one second in the whole intensity range of exciting current in Fig. 14.

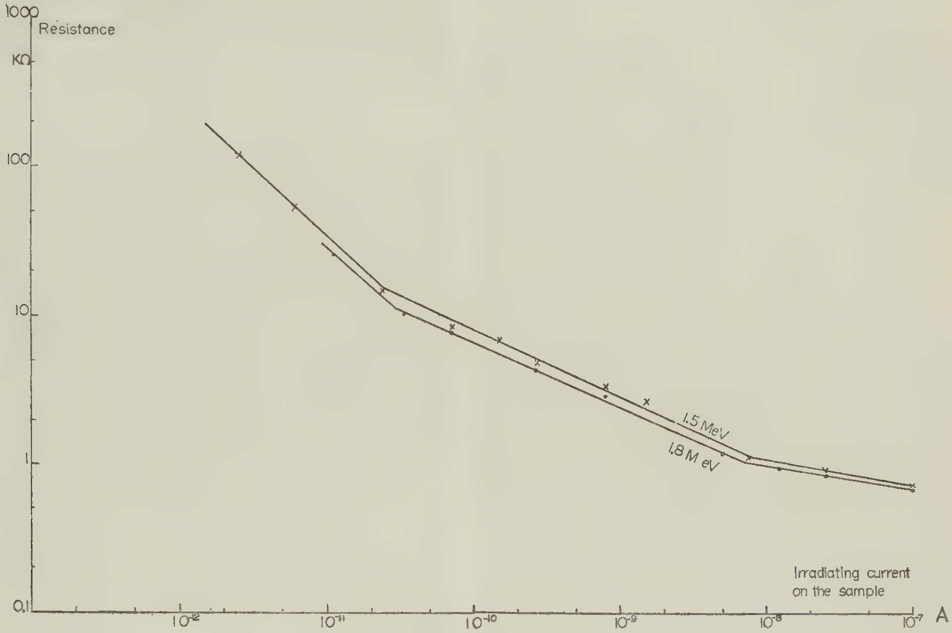

Fig. 14. β-rays irradiation characteristics from Van de Graaff generator (No. 1).

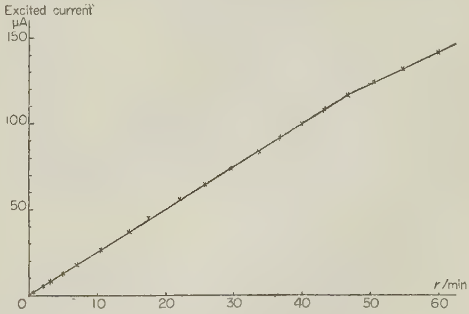

Fig. 15. Co⁶⁰ irradiation characteristics (No. 10, 90 V).

Some experimental results in the case of γ-ray irradiation are given below. Fig. 15 shows the intensity dependence of excited current for irradiation of γ-rays from 200 *c* of Co⁶⁰. The current increases proportionally to the irradiating intensity from 10 to 2800 *r*/hr, but a knick appears at 2,850 *r*/hr, where the electric resistance of the CdS crystal is 750 kΩ. This value agrees well with that of the resistance at the knick of the photocurrent curve in Fig. 4.

The experiments were also carried out for the irradiation of γ-rays from 1 *c* of Cs^{137}. The *V-I* characteristic of the CdS crystal was linear as in the case of β-ray irradiation. The relation between the excited current and the irradiated intensity was linear in the range from 0.4 to 40 *r*/hr, when the crystal was exposed at various distances from the γ-ray source. In the experiments of the sample No. 6 the number of γ-particles, which knocked the area of 5×3 mm of the crystal at 25 cm apart from 1 *c* of Cs^{137}, were calculated to be 7.1×10^5 particles/sec, and then the electron current excited by these γ-particles was 5μA, namely 3×10^{13} electrons/sec under the electric field of 500 V/cm. It is concluded, therefore, that the amplification of 4.4×10^7 is performed in the CdS crystal and the degree of amplification is about fiftieth of that for β-ray irradiation. From the above facts it may be concluded that the electron current excited by γ-rays is generally less and hence the time constant is larger than those for β-rays when the number of irradiating particles is the same for both γ- and β-rays excitations. The time constants in the case of irradiating-on and -off of γ-rays were approximately the same as those in the case of β-ray irradiation so long as the conductivity of the crystal had the same value on irradiation. It is interesting, however, that under the irradiation of γ-rays of 0.4~40 *r*/hr from Cs^{137} the induced current turned to zero as soon as the applied voltage was cut off and it did not returned to the former value without the time lag of a few second after the voltage was re-applied.

§ 5. Discussions

Let us consider first the elementary process of the photo-conductivity of CdS crystals. Writing $Q\,\text{cm}^{-3}\,\text{sec}^{-1}$ for the number of electrons excited by light into conduction band and $M\,\text{cm}^{-3}$ for the density of traps, then the time rate of change in the density n of photoelectrons in conduction band is given by

$$dn/dt=Q-Bn(n+M)\,, \qquad (4)$$

provided that photoelectrons have the same recombination coefficient B for both hole and trap, and that the number of thermally excited electrons is very small. At the stationary state $dn/dt=0$ and then

$$Q=Bn(n+M)\,. \qquad (5)$$

For low light intensity $n\ll M$ and Eq. (5) becomes

$$n=Q/BM\,. \qquad (6)$$

In this case photoelectrons mainly recombine with traps and the photocurrent, which is proportional to n, will increase linearly with the increase of exciting light intensity. On the other hand, for intense light $n\gg M$ and Eq. (5) leads to

$$n^2=Q/B\,. \qquad (7)$$

Then the recombination of photoelectrons occurs only with holes because the traps are filled and the photocurrent will be proportional to a half power of light intensity. Thus the curve of photocurrent *versus* light intensity will show a knick point at the light intensity satisfying the condition $n=M$. These behaviors of photocurrent are seen in both curves in Fig. 7 and the knick appears at the point corresponding to the photocurrent of 40μA and the illumination of 50 lux under the applied voltage of 1 V for the sample No. 6 or to 4μA and 14 lux under 3 V for the sample No. 10.

In general the photocurrent in a sample is expressed by

$$I=e\tau\mu\, Vn'/L^2\,, \qquad (8)$$

where V is the applied voltage, L the distance between electrodes, and e, τ and μ are the charge, the life time and the mobility of photoelectron respectively. Here n', the number of photoelectrons, is related to the density by $n=n'/$(sample volume). By using the values of quantities in Eq. (8) measured at the knick point in Fig. 7, the density of traps M can be calculated because $n\simeq M$ at this point: that is, we have $M\simeq2.6\times10^{15}\,\text{cm}^{-3}$ for the sample No. 6, whose dimension is $5\times3\times0.2$ mm, by using $I=40\mu$A, $L=0.5$ cm, $V=1$ V and $\tau=80$ m sec and $M\simeq1.4\times10^{14}\,\text{cm}^{-3}$ for the sample No. 10, whose dimension is $10\times8\times0.2$ mm, since $I=4\mu$A, $L=1$ cm, $V=3$ V and $\tau=50$ m sec, where the value of μ is taken as $100\,\text{cm}^2$/volt. sec.

Furthermore, by making use of the above values of $n(\simeq M)$ and τ at the knick point, the magnitude of the capture cross section s of a hole for a photoelectron can be obtained from the equation:

$$\tau=1/vsn\,, \qquad (9)$$

where v is the thermal velocity of photoelectron; that is, taking $v=10^7$ cm/sec at room temperature, $s \cong 5\times10^{-22}$ for the sample No. 6 and $s \cong 2\times10^{-20}$ for the sample No. 10.

Next the sensitivity of CdS crystals for β- and γ-rays will be discussed. Writing F for the number of exciting particles and η for the efficiency by these particles to produce the conducting electrons, then from Eq. (8)

$$\eta=\frac{I}{e.F}\cdot\frac{L^2}{\tau\mu V}\,, \tag{10}$$

because $n'=F\eta$. From this equation it is possible to compare the efficiency for β-rays from Sr^{90} with that for γ-rays from Cs^{137} or from Co^{60}. From Figs. 10 and 11 the sample No. 6 has the exciting current of 2μA under the applied voltage of 100 V for β-ray irradiation at a distance of 20 cm from 10 *mc* of Sr^{90} and for γ-ray irradiation at a distance of 25 cm from 1 *c* of Cs^{137} respectively. Therefore, taking the number of particles which knocked the sample in each case, the following ratio can be calculated from Eq. (10), namely:

$$\eta_{Sr^{90}}/\eta_{Cs^{137}}=65,\ \text{for No. 6}\,, \tag{11}$$

because the valves of time constant are the same under the same excited current for β- or γ-rays irradiation. For the sample No. 10 the following valves can be obtained in the same way:

$$\left.\begin{array}{l}\eta_{Sr^{90}}/\eta_{Cs^{137}}=42,\ \text{for No. 10}\,,\\ \eta_{Sr^{90}}/\eta_{Co^{60}}=30,\ \text{for No. 10}\,.\end{array}\right\} \tag{12}$$

From the above values in Eqs. (11) and (12) it may be concluded that the efficiency of exciting the electrons by β-rays of Sr^{90} is about fifty times larger than that by γ-rays of Cs^{137}. Here it should be noted that the ratio of efficiency is calculated in the linear range of excited current *versus* irradiation intensity.

Further, by making use of Eq. (10), it will be tried to obtain the absolute values of η for both β- and γ-particles having the same energy. The electric resistance of the sample No. 1 has the value of 15 KΩ for the irradiation of 2.2×10^{-11} A of 1.5 Mev β-rays from the accelerator of Van de Graaff type, as shown in Fig. 14. Substituting $V=15$ V, $I=$ 1 mA, $L=0.5$ cm, $\tau=50$ m sec and $\mu=100$ cm²/volt. sec into Eq. (10), the value of η becomes

$$\eta=1.5\times10^5 \text{ for a β-particle of 1.5 Mev.} \tag{13}$$

In the experiments of the γ-irradiation from 200 *c* of Co^{60} the sample No. 10 shows the excited electron current of 120μA and the life time of 50 m sec under the applied voltage of 90 V for the exciting intensity of 47.5 *r*/min, as shown in Fig. 15. Substituting these values and $\mu=100$ cm²/volt. sec into Eq. (10), the value of η is given by

$$\eta=3.2\times10^3 \text{ for a γ-particle of 1.3 Mev.} \tag{14}$$

These results show that about 10^2 times of conducting electrons are more produced in the above grade crystals by a single β-particle than a single γ-particle, both being nearly of the same energy of 1.3∼1.5 Mev. Here it should be noted that the calculation has been carried out by using the experimental values near the knick points in Figs. 14 and 15.

The lower limit for detecting β-and γ-rays depends on the dark resistance of CdS crystals; for example, it is possible for the sample No. 6 to detect such a small number of β-particles as 5×10^2 particles/cm² sec at the position apart 2 m from 10 *mc* of Sr^{90}. But in this case the sample crystal shows a large time constant of about 3 minutes.

Lastly let us discuss how the energy of exciting β- or γ-rays is consumd in CdS crystals. It may be considered that some parts of the energy are used for the excitation of electrons and some parts for the generation of lattice imperfections. For the heavy irradiation of β-rays from Van de Graaff generator the following phenomena were observed: the increase of dark current, the decrease of photocurrent and the change in the characteristic of photocurrent *versus* irradiating intensity after irradiation. These facts clearly indicate the production of lattice imperfections, but it cannot be decided how much of incident energy is dissipated to the generation of imperfections or to the excitation of electrons, because the ratio of the number of produced lattice imperfections to that of excited electrons has not been defined in this report. However, the following consideration may be allowed for rough estimation of energy dissipation; the energy for one electron excitation is estimated to be about 2 ev from the measurements of the spectral sensitivity of photoconduction, and the energy for the generation of one lattice imperfection seems to be 6∼10 ev because the energy of sublimation is about 2.1 ev for CdS crystals11). On the other hand, for the irradiation of 1.5

Mev β-rays from Van de Graaff generator the absorbed energy is roughly estimated as 900 Kev per single β-particle, because the specific gravity of CdS is 4.82 and hence the CdS crystal of 0.2 mm in thickness absorbs 60% of incident energy. Of this absorbed energy, the energy of about 300 Kev may be dissipated to electron excitation because $\eta=1.5\times10^5$ and the energy for exciting one electron is 2 ev, and the great part of remaining energy of about 600 Kev to the generation of lattice imperfections. Thus the lattice imperfections of about 10^4 may be produced by a single β-particle because of their generation energy of 6～10 ev.

§ 6. Summary

The ohmic contact of evaporated In and the uniformity of CdS crystals produced by the author have been verified in § 2. The behaviors of photoconductivity described in § 3 have been explained by the elementary process as discussed in § 5 and it has been shown that the CdS crystals have low trap density and high sensitivity. The properties of CdS crystals induced by β- and γ-rays irradiation, which are given in § 4, are similar to those induced by visible light and the behaviors of exciting current can also be comprehended by the same process of conductivity as for the photoconduction. But it has been confirmed in § 5 that the exciting efficiencies for β- and γ-rays are very much larger than that for visible light; the efficiencies for β-and γ-rays of 1.3～1.5 Mev have been calculated to be about 10^5 and 10^3 respectively.

Acknowledgement

The author would like to express his sincere thanks to Professor Y. Uchida for continual encouragements and valuable discussions. He is also very much indebted to Dr. H. Yamashita, Mr. G. Imamura, Mr. S. Ogura, and Mr. K. Miyashita in our laboratory for their kind advices and discussions.

References

1) E. Schnürer: Ann. Physik. **15** (1954) 15. C. H. Bachman *et al*: Amer. J. Roentgenol. and Radium Ther. **73** (1955) 98.
2) G. Frohnkeyer *et al*: Z. Phys. **137** (1954) 117.
3) T. Takaki and T. Suzuki: Acta Cryst. **8** (1955) 441.
4) W. Kolb: Ann Physik. **14** (1954) 397.
5) L. E. Hollander: Nucleonics **14** (1956) 68.
6) S. Ibuki and K. Awazu: J. Phys. Soc. Japan **11** (1956) 1297. H. Yamashita and S. Ibuki: J. Phys. Soc. Japan **13** (1958) 226.
7) R. W. Smith: Phys. Rev., **97** (1955) 1525.
8) A. Lempicki: J. Opt. Soc. Amer. **46** (1956) 611.
9) S. H. Liebson: J. Electrochem. Soc. **102** (1955) 529.
10) L. E. Glendenin: Nucleonics **2** (1948) 12.
11) S. Ibuki: J. Phys. Soc. Japan **14** (1959) 1181. F. Seitz and J. S. Koehler: *Peaceful Uses of Atomic Energy, Geneva Conference*, **7** (1956) 615.

JOURNAL OF THE PHYSICAL SOCIETY OF JAPAN, Vol. 14, No. 9, SEPTEMBER, 1959

Accurate Determination of Hydrogen Positions in NH_4Cl by Electron Diffraction

By Shigeya KUWABARA

Department of Physics, Faculty of Science, Hiroshima University, Hiroshima, Japan

(Received February 9, 1959)

The hydrogen position in NH_4Cl was determined by the difference Fourier syntheses from the electron diffraction Debye-Scherrer ring intensity data at a room temperature and a low temperature (−40°C). The primary extinction effect for strong reflections such as (110) plane was corrected from the variation of their intensities by changing the accelerating voltages between 20 and 60 kv. By the use of the least square method, the temperature factors were determined from higher order reflections whose atomic scattering factors are not affected by ionization.

The difference Fourier syntheses showed the coordinate (xxx) of the hydrogen atoms to be $x=0.153$ for both the room temperature and the low temperature phases, when the atomic scattering factors for ionized atoms $N^{-0.45}$, $Cl^{-0.81}$ and $H^{+0.315}$ were taken. Only the room temperature phase showed the rotatory vibration of the hydrogen atoms. The result of our experiment was compared with those of X-ray, neutron and other electron diffraction data.

§ 1. Introduction

The crystal structure determination by electron diffraction was performed at first by Laschkarew and Usyskin[1] on ammonium chloride in 1933 and, since then, this method has been extensively developed mainly by Pinsker *et al.*[2] and Cowley[3]. Though the electron diffraction method in crystal structure determination has not so well established yet as the *X*-ray diffraction and neutron diffraction methods, it possesses some merits compared with the latter two. While the *X*-ray diffraction method gives the electron distribution and the neutron diffraction gives the position of neuclei, the electron diffraction method can bring us a direct information of the potential distribution in crystals and is more sensitive to the existence of light neuclei, especially of hydrogen, than the *X*-ray method as is clear from Fig. 1[4], in which the atomic scattering factors for *X*-rays f (Fig. 1a) and for electrons E (Fig. 1b) of N, Cl and H atoms are shown; E is given by

$$E=(me^2/2h^2)(Z-f)/\sin^2\theta/\lambda^2) , \qquad (1)$$

where Z is the atomic number and m, e, h, λ and θ have their usual meaning. Further, the electron diffraction method is sensitive to the displacement of electron cloud in atoms. For instance, if an atom is ionized positively the scattering factor E increases in the region of small $\sin\theta/\lambda$ values. In general, the atomic scattering factors for electrons become respectively larger or smaller for lower scattering angles when the atoms are ionized positively or negatively. In the latter case, in particular, the atomic scattering factors may become zero or even negative. The comparison of the distribution maps obtained by *X*-ray diffraction, neutron diffraction and electron diffraction methods will be, therefore, fruitful for detecting the distortion of electron cloud from a spherical electron distribution of atoms in crystals caused by, say, the atomic bonding.

The serious defect of the electron diffraction method is due to the complicated dynamical diffraction effect, in particular the effect of primary extinction[5,6]. However, this effect can be corrected or at least partly removed by changing the wave length of electrons[7], or the grain size of samples[6], or by the use of intensity statistics[8].

The crystal structure of ammonium chloride is well known, and the position of hydrogen atoms in it was determined for both the room temperature and the low temperature phases by *X*-ray[8] and neutron diffraction[10,11] methods and for the room temperature phase by the electron diffraction method[1,12]. However, the results concerning the hydrogen position in these works are not in agreement with each other. In the present study, the structure analysis of ammonium chloride was performed by the electron diffraction method with an accurate intensity measurement, and the result was compared with those of other workers. The structure of the low temperature phase of ammonium chloride was also studied for comparison with that of the room temperature phase.

§ 2. Experimental Procedures

To avoid the effect of the moisture of the atmosphere, specimens were prepared by evaporating ammonium chloride in the electron diffraction camera onto thin collodion films which were put on the surface of fine meshes used for electronmicroscopy. After evaporation, twelve photographs with different exposure times were taken for each specimen. The diffraction patterns were examined carefully by tilting the specimen films about 50–70° so as to detect a preferred orientation if any: a slight texture with the (111) plane parallel to the specimen films was observed when the thickness of the evaporated films was thin (*cf.* Fig. 2), while no preferred orientation was observed for the thick films.

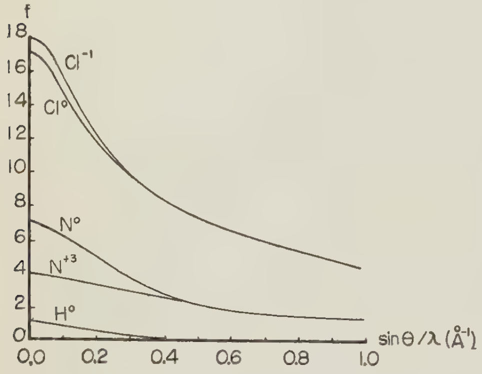

Fig. 1 (a). Atomic scattering factors for X-rays. The values of Cl^{-1}, and N^0 were given by Berguhuis et al., and Cl^0, N^{+3} and H^0 by James and Brindley[4].

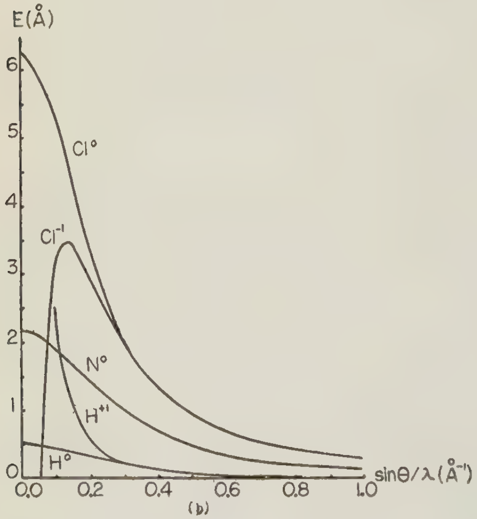

Fig. 1 (b). Atomic scattering factors for electrons. The value of Cl^{-1} was calculated by (1) from the data of Berguhuis et al., N^0 and H^0 were given by Ibers, and Cl^0 and H^{+1} by Vainstein[4].

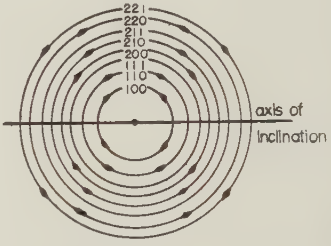

(a)

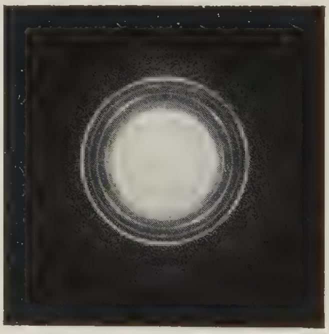

(b)

Fig. 2. Schematical diagram (a) and the real pattern (b) of NH_4Cl when the specimen film which has the texture with (111) plane parallel to it is inclined to the electron beam with 70° (the angle between the film normal and the beam).

Films of the thicknesses about 300–400° A gave the best diffraction patterns free from texture and strong background. The accelerating voltage was changed from 20 to 60 kv.

A special low temperature specimen holder was used to study the low temperature phase ammonium chloride, the construction of which was the same as that described by Honjo *et al.*[13] Dry ice or liquid air was used as the cooling reagent. Most of the experiment at low temperature were performed at −40°C, The Karle and Karle method[14] was used to measure the integrated intensities of stronger reflections. The microphotometer used was *Rigakudenki MP*-1 type. Special precautions were taken to avoid the so-called Schwarzschild-Villiger effect, and the battery of 200 *AH* was used as a light source to minimize the fluctuation of the galvanometer deviation. The *Fuji Process Hard* photographic plates were used and they were developed by diluted solutions (1 : 1) of *D*-72 developer at 20±1°C for 2 min. The photographic density-intensity curves were linear up to $D=0.7$ for the higher accelerating voltages (60 kv), and 0.5 for lower voltages (20 kv). Usually D values less than 0.8∼1.0 were used for the intensity measurement.

After subtracting the smooth backgrounds from the total intensity curves, the integrated intensities of the Debye-Scherrer rings were measured from the microphotometer traces. In this case, however, the effect of the collodion films could be neglected because of the large thickness of the specimen films. As is shown in Fig. 5, the peaks of stronger reflections are seen clearly though those of weaker reflections are obscure for the lower exposure time microphotometer traces. However, for the higher exposure time relatively weaker reflections such as (222) and (420) could be seen clearly in the traces (each top corner of Fig. 5). Six microphotometer traces were measured for each photographic plate, and each of the traces with different exposure times was patched together to give the total integrated intensities. For very weak reflections such as (400) and (421), however, visual method was applied because the peaks of reflected intensities are obscured by the emulsion grain of the photographic plates.

§ 3. Experimental Results

The room temperature phase of ammonium chloride exists in the temperature range between −30.5°C and 180.3°C. The lattice constant is $a=3.866°\text{A}$. According to the neutron diffraction data[10] the space group is given by O_h^1-Pm3m and the hydrogen atoms occupy with the same probability each of the sets of tetrahedra around the nitrogen atom, which are shown by the dark small circles and the opened small circles, respectively, in Fig. 3, and the hydrogen atoms show the rotatory vibrations. Below the temperature −30.5°C appears the low temperature phase, of which the lattice constant is almost the same as that of the room temperature phase, however, the space group is given by $T_d^1-P\bar{4}3m$ and the hydrogen atoms can occupy only one of the sets of the tetrahera with no rotatory vibration[11].

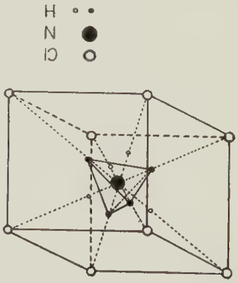

Fig. 3. Structure of NH₄Cl. Dark small circles show one configuration and opened small circles another configuration.

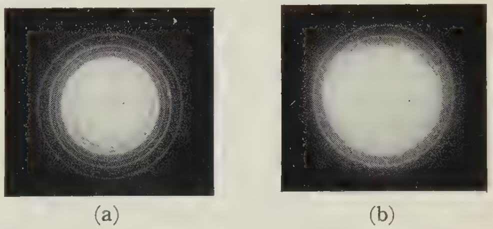

Fig. 4. Debye-Scherrer rings of room temperature phase (a) and low temperature phase (−40°) (b) of NH₄Cl.

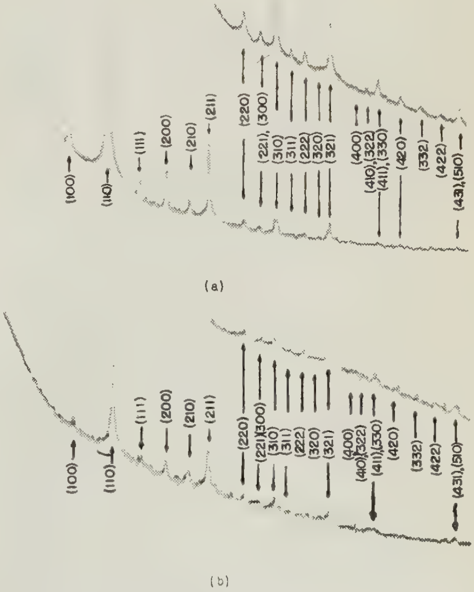

Fig. 5. Microphotometer traces. (a) Room temperature phase. (b) Low temperature phase.

Table I. Intensity ratios of room temperature phase NH$_4$Cl. The values of Stasova and Vainstein[12)] and Laschkarew and Usyskin[1)] (25-30 kv) are listed for comparison.**

hkl	Present experiment	Stasova and Vainstein	Laschkarew and Usyskin	*hkl*	Present experiment	Stasova and Vainstein
100	139±4	489	336	422	(5)	5.9
110	3820±70*	3065	1793	430, 500	(0.5)	—
111	125±3	159	125	431, 510	15±1	16
200	236±4	286	250	511, 333	(0.5)	1.2
210	149±4	130	136	520, 432	(2)	2.4
211	470±8	469	417	521	(7)	4.2
220	74±1	54	97	440	(1.0)	—
221, 300	23±1	32	28	522, 441	(0.5)	—
310	100	82	114	530, 433	(4)	2.4
311	14±1	14	—	600, 442	(1.5)	1.2
222	23±1	30	—	611, 532	(4)	2.3
320	4±0.3	4.6	—	620	(0.7)	—
321	101±2	99	108	443, 621, 540	(0.5)	—
400	(4)	2	—	541	(1.3)	—
410, 322	6±0.3	5.4	—	622	(0.5)	—
411, 330	21±1	20	—	631	(1.2)	—
331	(0.5)	1.9	—	550, 710, 543	(1.3)	—
420	11±1	12	—	633, 552, 721	(1.0)	—
421	(3)	4.7	—	642	(0.5)	—
332	8.8±0.8	8.4	—			

** The mean errors of the measurement are given in this table for all the microphotometered intensities. Those for the visual estimation are about fifteen percent. The systematic errors are difficult to estimate. However, if these errors are taken into account, the total errors of the intensity measurement will become larger than those given in this table.

a) ***Room temperature phase.*** An example of the Debye-Scherrer rings for the room temperature phase of NH$_4$Cl without preferred orientation is shown in Fig. 4a. Examples of the microphotometer traces are shown in Fig. 5a. In Table I the measured intensities are tabulated, where the values except the one marked by asterisk are the averages obtained from all the experiments. The values with brackets show the results obtained visually. The value with asterisk was obtained by correcting the primary extinction effect which will be described later. The values obtained by Stasova and Vainstein[12)] and Laschkarew and Usyskin[1)] are listed together for comparison. Their values were normalized so as to result in general fits with our values, where the (100) and (110) reflections were omitted because of the larger discrepancies from our results. The discrepancy for the (100) reflection seems to be due to the difference in the estimation of the background which is considerably steep in the region of small sin θ/λ values*. Excepting these two reflection, their results coincide generally well with that of the present experiment.

(i) *Correction of primary extinction effect.* The large discrepancy in the intensity of the (110) reflection between the results of Stasova and Vainstein and Laschkarew and Usyskin in Table I suggests that the intensity of this strong reflection is considerably affected by the primary extinction effect. This effect was corrected in the present experiment by the extrapolation method[7)]. Fig. 6a shows an example of the results of this procedure for the room temperature phase. It is evident that the (110) reflection is accompanied by a large primary extinction effect, while this effect is negligible for the other reflections. The value corrected by this method is given in Table I with asterisk.

---

* A sector camera of Tokyo Institute of Technology was used to examine the (100) intensity obtained from the present experiment. However, the results was the same within the experimental error.

(ii) *Direct Fourier synthesis.* As the first step of the analysis, the potential distribution along a body diagonal was obtained by the three dimensional Fourier synthesis from the observed intensity values. The signs of the structure factors were determined by assuming the centrosymmetrical structure of the room temperature phase as quoted before. For the evaluation of the structure factors of component reflections in the multiple rings as in the case of (221) and (300), *etc.* the coordinate of hydrogen atoms $x=0.154$ obtained from the neutron diffraction data[10,11] was used, the effect of the temperature factors being neglected. The result of this Fourier synthesis is shown in Fig. 7, giving the coordinate $x=0.15-0.17$. However, since the peak of the hydrogen atom in the figure is quite broad, and moreover, the effect of the temperature factor was not taken into account, the reliable value of the hydrogen coordinate may not be obtained by the direct Fourier synthesis as above.

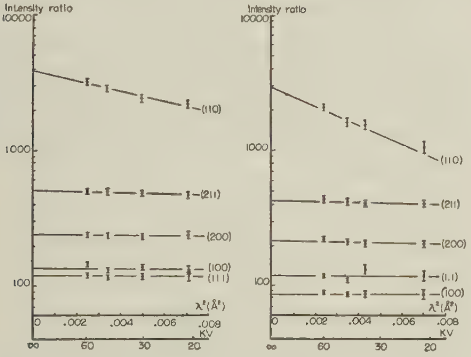

(a) (b)

Fig. 6. Calibration of the primary extinction effect. (a) Room temperature phase. (b) Low temperature phase (−40°C).

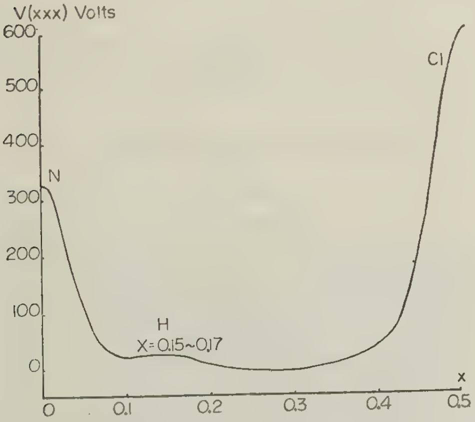

Fig. 7. Potential distribution along a body diagonal direction.

(iii) *Evaluation of the temperature factors.* The knowledge of the temperature factors is very important for determining the exact position of the hydrogen atoms. In order to know the general behavior of the thermal vibration of the component atoms in the crystal, the difference Fourier synthesis was performed by assuming the neutron diffraction data[10] $B=B_N=B_{Cl}=B_H=2.0Å^2$ for the temperature factors and $x=0.154$ for the hydrogen coordinate. The latter is needed for the sake of the intensity evaluation of multiple rings. The normalization of the observed structure factors was performed by the condition[15]

$$\sum|S_{hkl,obs}|=\sum|S_{hkl,cal}|,$$

where $S_{hkl,obs}$ and $S_{hkl,cal}$ are the observed and calculated structure factors. The summations were carried out for all the reflections observed. The three dimensional difference Fourier synthesis along a body diagonal is shown in Fig. 8a, where the peak of the hydrogen atom is seen clearly at the coordination $x=0.155$. However, infavorable peaks and valleys are found at and near the positions of N and Cl atoms. When the temperature factor B is taken $1.1Å^2$ [12], the difference synthesis gives $x=0.148$, and valleys are found at the positions of N and Cl atoms, as is shown in Fig. 8b.

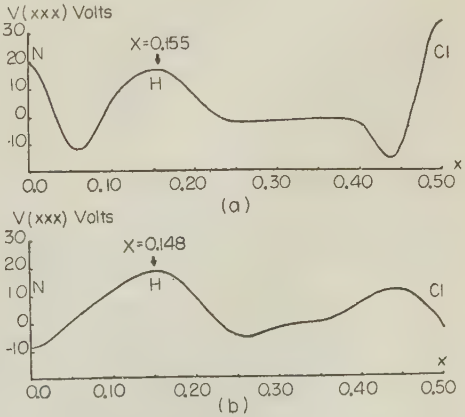

Fig. 8. Three dimensional difference Fourier syntheses of room temperature NH_4Cl along a body diagonal with $B=2.0$ (a) and $B=1.1$ Å² (b).

The above two examples show that the position of the hydrogen atom is affected strongly by the temperature factors. Fig. 9 shows this effect schematically.

The calculated structure factors showed the best agreement with the observed values for $B=1.3 Å^2$. The two dimensional difference Fourier synthesis was performed by the use of this B value in order to confirm the existence of an anisotropic thermal vibration of the hydrogen atom as was revealed by the neutron diffraction study[10]. The result is shown in Fig. 10, where the rotatory vibration of the hydrogen atom is recognized clearly. The half angle of the rotatory vibration was estimated to be $\alpha=12°$, which coincides with the value obtained by neutron diffraction.

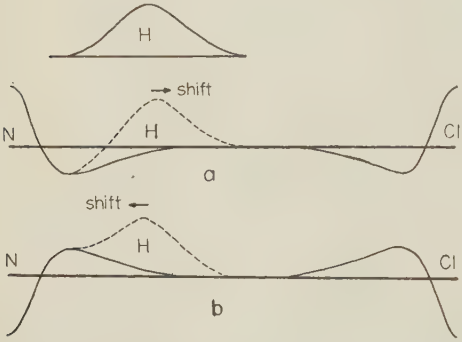

Fig. 9. Schematical representation of the effect of temperature factor to the hydrogen position in the difference Fourier syntheses.
a) The case when B factor is too large.
b) The case when B factor is too small.

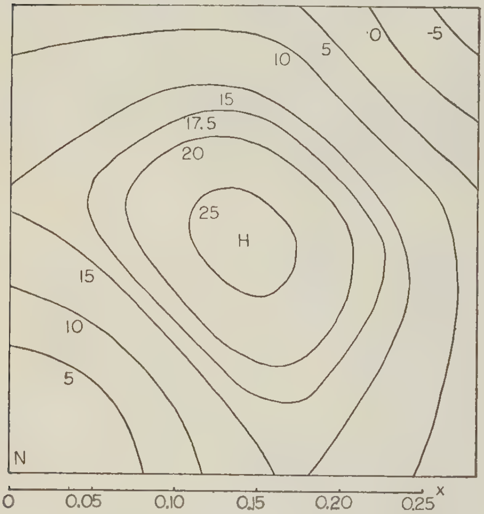

Fig. 10. Two dimensional difference Fourier synthesis of room temperature phase NH_4Cl along (001) axis with $B=1.3 Å^2$ and the parameter $x=0.154$, the anomalous thermal vibration due to the hydrogen atoms being neglected in getting each structure factor from the observed multiple reflections. The contour lines are shown in *Volts·*Å unit.

The temperature factor for each atom can be determined more accurately by the following procedures. Let B_N', B_{Cl}' and B_H' be the true temperature factors, and B_N, B_{Cl} and B_H the calculated temperature factors. Then the calculated and the observed structure factors can be given by

$$\begin{aligned} S_{hkl,cal}=&E_N \exp(-B_N \sin^2\theta/\lambda^2) \\ &+(-1)^{h+k+l}E_{Cl}\exp(-B_{Cl}\sin^2\theta/\lambda^2) \\ &+\tfrac{1}{2}E_H\exp(-B_H\sin^2\theta/\lambda^2)\sum[\quad], \end{aligned} \tag{3}$$

and

$$\begin{aligned} KS_{hkl,obs}=&E_N \exp(-B_N' \sin^2\theta/\lambda^2) \\ &+(-1)^{n+k+l}E_{Cl}\exp(B_{Cl}'\sin^2\theta/\lambda^2) \\ &+\tfrac{1}{2}E_H\exp(-B_H'\sin^2\theta/\lambda^2)\sum[\quad], \end{aligned} \tag{4}$$

where K is the scaling factor, and the notation $\sum[\quad]$ in the last terms in (3) and (4) represents the contribution of the hydrogen atoms accompanied with rotatory oscillation[10] and is given by

$$\begin{aligned} \sum[\quad]=&\sum[J_0(2\pi\sqrt{W}\sin\alpha) \\ &\times\cos\{2\pi\cos\alpha(hx+ky+lz)\}], \end{aligned}$$

and

$$w=(hy-kx)^2+(lx-hz)^2+(kz-ly)^2 .$$

J_0 is the *zero*th order Bessel function, and x, y, z are the coordinate of the eight statistical position of the hydrogen atoms in the assumed structure. From (3) and (4) we obtain approximately

$$\begin{aligned} S_{hkl,cal}-&KS_{hkl,obs} \\ =&E_N\Delta B_N\sin^2\theta/\lambda^2+(-1)^{h+k+l}E_{Cl}\Delta B_{Cl}\sin^2\theta/\lambda^2 \\ &+\tfrac{1}{2}E_H\Delta B_H\sin^2\theta/\lambda^2\sum[\quad], \end{aligned} \tag{5}$$

where

$$\Delta B_N=B_N'-B_N,\ \Delta B_{Cl}=B_{Cl}'-B_{Cl}$$

and

$$\Delta B_H=B_H'-B_H .$$

These unknown values of K, ΔB_N, ΔB_{Cl} and ΔB_H can be determined by the least square method. The calculation was carried out for all the observed reflections except those of lower orders, (100)-(300), for which the effect of ionization of atoms may be appreciable. The temperature factors thus obtained deviated considerably from the initial value

$B=1.3\text{Å}^2$. The final results are

$$B_N=1.33,\quad B_{Cl}=1.22 \text{ and } B_H=2.38\text{Å}^2 \qquad (6)$$

for $x=0.154$ and $\alpha=12°$. It is not essentially important to assume these x and α values at least for the determination of the temperature factors of N and Cl.

Fig. 11 shows the two dimensional difference Fourier synthesis using the above factors. Three dimensional synthesis is shown in Fig. 12 by the full line. The coordinate of the hydrogen atom revealed by this figure is $x=0.152$.

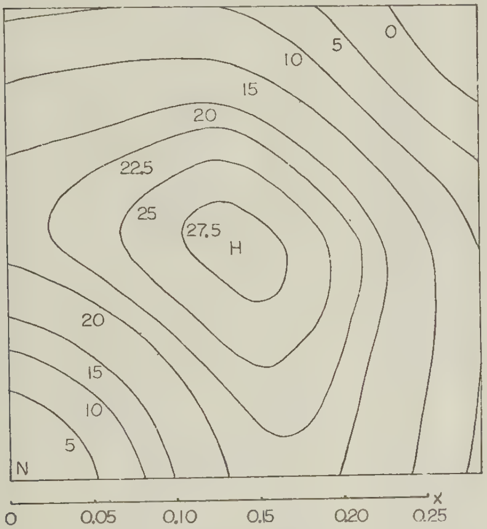

Fig. 11. Two dimensional difference Fourier synthesis of room temperature phase NH_4Cl along (001) axis with $B_H=2.38$, $B_N=1.33$, $B_{Cl}=1.22\text{Å}^2$ $\alpha=12°$ and $x=0.154$. The contour lines are shown in *Volts·*Å unit.

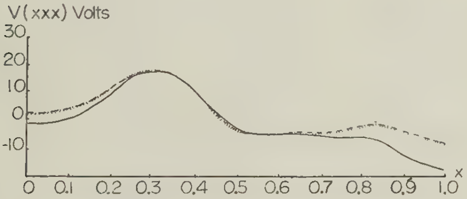

Fig. 12. Three dimensional difference Fourier syntheses of room temperature phase NH_4Cl along the body diagonal with $B_N=1.33$, $B_{Cl}=1.22$, $B_H=2.38$ Å^2 and $\alpha=12°$. Full line shows the case calculated from the neutral atoms with $x=0.154$, and the chain line the case of $N^{-0.46}$, $Cl^{-0.81}$ and $H^{+0.315}$ with $x=0.153$, for both of which the unobserved structure factors were not included in the syntheses. If they are taken into account, the result is given by the dotted line for the latter case.

(iv) *Ionization effect.* As is shown in Fig. 12, there is a deep valley at the position of Cl atom, and moreover, the discrepancy between the observed and calculated structure factors for lower order reflections is considerable (*cf.* Table III). These facts seems to show that the atomic scattering factors for the neutral atoms used in the present calculation are not adequate as the result of the ionization of atoms in the crystal. This effect may change the position of hydrogen atoms considerably.

As is shown in Fig. 1a, the change of the atomic scattering factors for *X*-rays by ionization effect takes place only in the region of small value of $\sin\theta/\lambda$, and the deviation of the values for ionized atoms from those for neutral atoms may be approximated to be linear to the $\sin\theta/\lambda$ in the range of $\sin\theta/\lambda=0-0.4\text{Å}^{-1}$. By multiplying $\sin^2\theta/\lambda^2$ to (1), we get the following expressions:

$$E'=E\sin^2\theta/\lambda^2=(me^2/2h^2)(Z-f) \qquad (7)$$

or

$$\Delta E'=-(me^2/2h^2)\Delta f\,. \qquad (8)$$

Since $\Delta E'$ is proportional to the change of atomic scattering factor for *X*-rays Δf, $\Delta E'$ may be also linear to $\sin\theta/\lambda$ in the range of $\sin\theta/\lambda=0-0.4\text{Å}^{-1}$. Then we can put

$$\begin{aligned}\Delta E_N'&=C_N\Delta(\sin\theta/\lambda)\\ \Delta E_{Cl}'&=C_{Cl}\Delta(\sin\theta/\lambda) \qquad (9)\\ \Delta_H'&=C_H\Delta(\sin\theta/\lambda)\,,\end{aligned}$$

where $\Delta(\sin\theta/\lambda)=0.4-\sin\theta/\lambda$, and C_N, C_{Cl} and C_H are the parameters to be determined. From (3) and the above expressions, we get

$$\begin{aligned}&\sin^2\theta/\lambda^2(S_{hkl,obs}-S_{hkl,cal})\\ &\quad=C_N\Delta(\sin\theta/\lambda)\exp(-B_N\sin^2\theta/\lambda^2)\\ &\qquad+(-1)^{h+k+l}C_{Cl}\Delta(\sin\theta/\lambda)\exp(-B_{Cl}\sin^2\theta/\lambda^2)\\ &\qquad+\tfrac{1}{2}C_H\Delta(\sin\theta/\lambda)\exp(-B_H\sin^2\theta/\lambda^2)\sum[\quad]\,. \qquad (10)\end{aligned}$$

C_N, C_{Cl} and C_H can be determined for a given value of x by the least square method with the condition of the neutrality of total charges in the crystal

$$C_N+C_{Cl}+4C_H=0\,. \qquad (11)$$

When the values of C_N, C_{Cl} and C_H are known, the extrapolated values of Δf to the zero scattering angle give the charge of each atom.

In Table II the calculated values of the formal charges of the atoms for the several x values are tabulated. Because of the rela-

Table II. Variation of formal charges with the coordinate x.

x	N	Cl	H
0.146	−0.55	−0.85	0.35
0.152	−0.46	−0.82	0.32
0.153	−0.45	−0.81	0.31_5
0.154	−0.44	−0.80	0.31
0.155	−0.40	−0.80	0.30
0.156	−0.39	−0.79	0.29_5
0.157	−0.37	−0.79	0.29
0.158	−0.34	−0.78	0.28
0.159	−0.30	−0.78	0.27
0.160	−0.27	−0.77	0.26
0.161	−0.24	−0.76	0.25
0.162	−0.20	−0.76	0.24
0.163	−0.17	−0.75	0.23
0.164	−0.14	−0.74	0.22
0.170	+0.11	−0.63	0.13

tively small contribution of the hydrogen atoms for the large $\sin\theta/\lambda$ region, the temperature factors (6) may remain unchanged by ionization of the atoms. Then, the x value may be determined by the condition of the minimum reliability factor of the structure factors. The best agreement between the observed and the calculated structure factors was found for $x=0.153$ and charges of the atoms $N^{-0.45}$, $Cl^{-0.81}$ and $H^{+0.315}$. Table III shows the comparison of the observed and calculated values of the structure factors. The calculated structure factors for neutral atoms are also given in this table to show the large discrepancy in the region of small $\sin\theta/\lambda$ values. The structure factors corresponding to the unobserved reflections, the intensities of which would be considerable if they could be observed, are given by bars, and the ones corresponding to the reflections, the intensities of which would be very weak or practically zero even if they could be observed, are given by 0.00's. When the reflections which were not observed in the experiment are excluded the reliability factors become 0.08 and 0.10 for the ionized atoms $N^{-0.45}$, $Cl^{-0.81}$ and $H^{+0.315}$, and for the neutral atoms, respectively, however, when the calculated structure factors of the unobserved reflections corresponding to the very weak intensities, even if they could be observed, are taken into account the reliability factors become 0.10 and 0.12, respectively.

Table III. The observed and calculated structure factors for room temperature phase NH_4Cl with $x=0.153$.

hkl	S_{obs}	S_{cal}		*hkl*	S_{obs}	S_{cal}
		Neutral	$N^{-0.45}$ $Cl^{-0.81}$ $H^{+0.315}$			
100	−1.05	−2.06	−1.07	441	−0.13	−0.14
110	5.51	5.44	5.12	530	0.38	0.36
111	−1.50	−1.45	−1.33	433	0.36	0.34
200	2.74	3.13	2.95	531	—	−0.14
210	−1.22	−1.15	−1.14	600	0.31	0.33
211	2.37	2.35	2.28	442	0.29	0.31
220	1.54	1.93	1.91	610	—	−0.11
221	−0.50	−0.54	−0.54	611	0.32	0.30
300	−0.80	−0.85	−0.85	532	0.31	0.29
310	1.41	1.43		620	0.24	0.27
311	−0.55	−0.54		443	−0.10	−0.11
222	1.29	1.33		621	−0.10	−0.11
320	−0.32	−0.33		540	−0.10	−0.11
321	1.18	1.15		541	0.23	0.24
400	0.71	0.85		533	0.00	−0.09
410	−0.34	−0.35		622	0.21	0.23
322	−0.29	−0.30		542	—	−0.09
411	0.68	0.81		630	—	−0.11
330	0.77	0.92		631	0.21	0.21
331	−0.14	−0.21		444	—	0.19
420	0.66	0.76		632	—	−0.08
421	−0.25	−0.23		700	0.00	−0.07
332	0.62	0.64		550	0.19	0.18
422	0.49	0.57		710	0.19	0.18
430	−0.13	−0.15		543	0.19	0.18
500	−0.17	−0.19		711	0.00	−0.07
431	0.51	0.54		551	0.00	−0.08
510	0.50	0.53		640	—	0.16
511	−0.13	−0.17		641	—	−0.08
333	−0.18	−0.23		720	0.00	−0.08
520	−0.18	−0.16		633	0.17	0.16
432	−0.20	−0.18		552	0.17	0.16
521	0.46	0.43		721	0.16	0.15
440	0.35	0.39		642	0.12	0.14
522	−0.13	−0.14				

The chain line of Fig. 12 shows the three dimensional difference Fourier synthesis for this ionized atoms, the unobserved structure factors being neglected in the calculation. The peak value of the hydrogen atom estimated in this figure gives $x=0.152$.

(v) *Final result.* Through all the procedures of Fourier syntheses mentioned above the contribution of the unobserved reflections has not been taken into account. When all of these values are calculated and the difference Fourier synthesis is extended up to the range of $\sin\theta/\lambda=1.05\,\text{Å}^{-1}$(*hkl*=554), we obtain the curve as dotted in Fig. 12. The coordinate x estimated from this figure gives 0.153. As there is no shift in the coordinate, this result is satisfactory.

The standard deviations of the potential and the coordinate of the hydrogen atom can be estimated by the following expressions which are analogous to those of *X*-rays[16)].

$$\sigma(V)=(h^2/2\pi\,\mathrm{mea}^3)\{\sum(|S_{hkl,obs}|-|S_{hkl,cal}|)^2\}^{1/2}\,, \tag{12}$$

$$\sigma(x)=(h^2/\mathrm{mea}^4)\frac{\{\sum h^2(|S_{hkl,obs}|-|S_{hkl,cal}|)^2\}^{1/2}}{\partial^2 V/\partial x^2}\,. \tag{13}$$

The results thus obtained are $\sigma(V)=2$ volts and $\sigma(x)=0.003$ when the $S_{hkl,obs}$ and $S_{hkl,cal}$ corresponding to the observed reflections are used in the calculation. Even when the S_{hkl}'s corresponding not only to the observed reflections but also to the ones which would be very weak even if they could be observed are taken into account, these standard deviations were almost the same.

b*) *Low temperature phase. Examples of Dabye-Scherrer rings and the microphotometer traces for the low temperature phase are shown in Figs. 4b and 5b, respectively. In Table IV the result of the intensity measurement is given, all the values of which were averaged from the experiment at −40°C. The value with asterisk was given by correcting the primary extinction effect. Fig. 6b shows an example of the result of such a correction for low temperature phase.

Table IV. Intensity ratios of low temperature phase (−40°C) NH_4Cl.*

hkl	Intensity	*hkl*	Intensity
100	86±1	431, 510	29±2
110	2900±90*	511, 333	(1)
111	111±3	520, 432	(3)
200	228±6	521	12±1
210	124±6	440	(2)
211	496±11	522, 441	(1)
220	117±4	530, 433	(8)
221, 300	25±2	531	(1)
310	100	600, 442	(4)
311	17±2	610	(0.5)
222	28±2	611, 532	(8)
320	(5)	620	(2)
321	96±1	443, 621, 540	(1.5)
400	(6)	541	(4)
410, 322	(10)	622	(1.5)
411, 330	42±2	631	(3)
331	(1.5)	550, 710, 543	(4)
420	22±1	640	(1)
421	(4)	633, 552, 721	(3)
332	15±1	642	(3)
422	11±1	732, 651	(5)
430, 500	(0.7)	741, 811, 554	(4)

* See the foot-note of Table I.

The temperature factors were calculated by almost the same method as is described in (*iii*) of ***a***). In the present case, however, the structure factors have imaginary parts[11)], so only the real parts of the structure factors were used to determine the temperature factors assuming the coordinate of the hydrogen atoms $x=0.154$*. The results are given by

$$B_N=0.48,\ B_{Cl}=0.41 \text{ and } B_H=2.48\,\text{Å}^2. \tag{14}$$

In the calculation, the structure factors of lower order reflections were omitted by the same reason as was mentioned in ***a***).

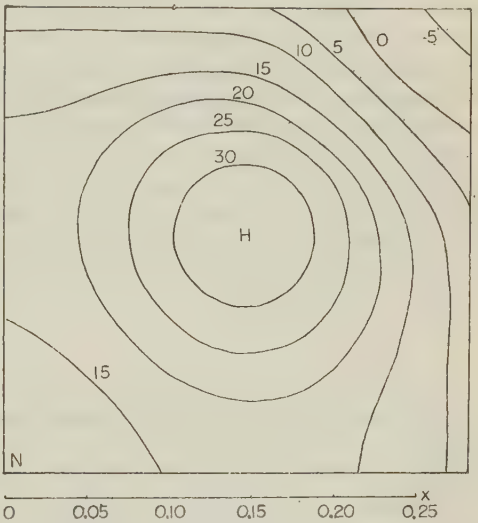

Fig. 13. Two dimensional difference Fourier synthesis of low temperature phase NH_4Cl (−40°C) along (001) axis with $B_H=2.48$, $B_N=0.48$, $B_{Cl}=0.41\,\text{Å}^2$ and $x=0.154$. The contour lines are shown in *Volts*·Å unit.

Fig. 13 shows the result of the two dimensional difference Fourier synthesis calculated for the neutral atoms, where the shape of the potential near the center of the hydrogen atom is not distorted as in Fig. 11 for the room temperature phase. In Fig. 14, the three dimensional difference synthesis is given along the direction of the body diagonal of

---

* The real parts of the observed structure factors are given by

$$S^{\text{real}}_{\text{obs}}=|S_{\text{obs}}|\frac{S^{\text{real}}_{\text{cal}}}{|S_{\text{cal}}|}\,.$$

the crystal for the neutral atoms. The coordinate thus determined was $x=0.152$, which is the same as the case of room temperature phase. It is shown that there is a deep valley at the position of Cl atom, too.

Ionization effect was calculated in the same way as before, but in this case only the real parts of the structure factors were used. The changes of the formal charges of the atoms with the change of the coordinate x are the same as Table II.

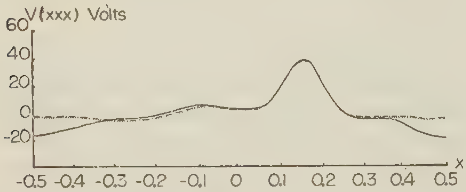

Fig. 14. Three dimensional difference Fourier syntheses of low temperature phase NH_4Cl (−40°C) along the body diagonal with $B_N=0.48$, $B_{Cl}=0.41$, $B_H=2.48$ Å^2. Full line shows the case calculated from neutral atoms with $x=0.154$, and the chain line the case of $N^{-0.45}$, $Cl^{-0.81}$ and $H^{+0.315}$ with $x=0.153$, for both of which the unobserved structure factors were not included in the syntheses. If they are taken into account, the result is given by the dotted line for the latter case.

The best agreement between the observed and the calculated structure factors was found when the coordinate was $x=0.153$, which is the same as in the case of the room temperature phase. In Fig. 14, the chain line shows the difference synthesis, where only the observed reflections were used in the calculation, and the dotted line the synthesis, where all of the structure factors which were not observed in the experiment were added in the calculation up to the region to $\sin\theta/\lambda=1.05$ Å^{-1}. These syntheses were carried out for the ionized atoms $N^{-0.45}$, $Cl^{-0.81}$, and $H^{+0.315}$ corresponding to $x=0.153$. The estimated values of the coordinate were 0.152 and 0.153, respectively. The latter case is satisfactory because of no shift in the coordinate.

Table V shows the observed and the calculated structure factors of these ionized atoms and of the neutral atoms. The reliability factors were 0.08 and 0.11 for the ionized and neutral atoms, respectively, when the contribution of the unobserved structure factors, which correspond to the very weak reflections even if they could be observed in the experiment, are taken into account, and 0.05 and 0.08 when only the observed reflections are used. The standard deviations of potential and coordinate were the same as in the case of room temperature phase for both the cases where the unobserved structure factors were neglected and taken into account.

Table V. The observed and calculated structure factors for low temperature phase NH_4Cl with $x=0.153$.

hkl	$\lvert S_{obs}\rvert$	$\lvert S_{cal}\rvert$		hkl	$\lvert S_{obs}\rvert$	$\lvert S_{cal}\rvert$
		Neutral	$N^{-0.45}$ $Cl^{-0.81}$ $H^{+0.315}$			
100	0.91	2.17	1.13	532	0.49	0.50
110	5.26	5.55	5.25	620	0.44	0.47
111	1.54	1.58	1.53	443	0.20	0.19
200	3.18	3.29	3.06	621	0.19	0.18
210	1.22	1.23	1.22	540	0.19	0.18
211	2.67	2.68	2.53	541	0.45	0.44
220	2.11	2.24	2.18	533	0.00	0.17
221	0.59	0.67	0.64	622	0.39	0.42
300	0.88	1.01	0.98	542	—	0.16
310	1.55	1.64		630	—	0.18
311	0.67	0.62		631	0.41	0.39
222	1.55	1.56		444	—	0.37
320	0.39	0.37		632	—	0.15
321	1.27	1.38		700	0.00	0.14
400	0.96	1.06		550	0.37	0.36
410	0.48	0.44		710	0.37	0.36
322	0.42	0.39		543	0.37	0.36
411	1.04	1.03		711	0.00	0.14
330	1.21	1.20		551	0.00	0.14
331	0.26	0.27		640	0.35	0.33
420	1.05	0.99		641	—	0.14
421	0.32	0.30		720	0.00	0.14
332	0.89	0.84		633	0.31	0.33
422	0.79	0.79		552	0.31	0.33
430	0.17	0.22		721	0.31	0.33
500	0.21	0.26		642	0.32	0.31
431	0.78	0.77		722	0.00	0.13
510	0.76	0.75		544	0.00	0.13
511	0.21	0.26		730	—	0.30
333	0.26	0.32		731	—	0.13
520	0.26	0.24		553	0.00	0.13
432	0.27	0.26		650	0.00	0.12
521	0.65	0.64		643	—	0.12
400	0.55	0.62		732	0.30	0.28
522	0.20	0.22		651	0.30	0.28
441	0.19	0.21		800	0.00	0.27
530	0.58	0.55		810	0.00	0.12
433	0.56	0.53		740	0.00	0.12
531	0.20	0.21		652	—	0.12
600	0.55	0.55		741	0.27	0.25
442	0.51	0.51		811	0.28	0.27
610	0.21	0.18		554	0.28	0.27
611	0.49	0.50				

§ 5. Discussion

a) Characters of the Fourier maps. As is shown in Figs. 11 and 13, the difference of the potential shape of the hydrogen atom is not spurious but gives the fundamental difference of the behavior of the hydrogen atoms in the crystal: the distortion of the hydrogen potential for the room temperature phase shows distinctly the existence of the rotatory vibration of the hydrogen atoms and there is no such a distortion for the low temperature phase. The peak height of the hydrogen atom for the room temperature phase is about half of that of the low temperature phase (Figs. 12 and 14). This will confirm the consistency of the models assumed in the calculation of Fourier syntheses.

b) *Ionization effect.* It is interesting that the value of the coordinate of the hydrogen atom and the ionization effect are the same for both room temperature and low temperature phases. It should be emphasized that the formal charges in the crystal are not integers but the fractional numbers: this crystal can be recognized as partly ionic and partly covalent. Such a conclusion was also obtained from the electron diffraction data of Li_2O[17]. Thus the electron diffraction method is very useful to detect the ionization effect of the crystals.

As is shown from the dotted lines in Figs. 12 and 14, the backgrounds are not perfectly flat nor zero. This may be due to the fact that we used the atomic scattering factors for the isolated atoms modified by the method mentioned in § 3***a***) (*iv*). Such a method is an approximation and moreover the true atomic scattering factors in the crystal may be different from those of the isolated atoms. Then the more detailed discussion can not be given until we will get the accurate knowledge of the scattering factors in the crystals.

c) *Comparison with the other experiments.* In Table VI the results of the other experiments are listed for comparison. Temperature factors obtained by neutron diffraction coincide with those of X-ray diffraction for the room temperature phase. However, they are larger than those of the present experiment, though the intensity ratios of our experiment coincide generally well with those of Stasova and Vainstein for the room temperature phase. Such a discrepancy could not be explained.

Though the coordinate of the hydrogen atoms obtained by X-ray is very small, our results coincide with those of neutron diffrac-

Table VI.

Method	Workers	Temperature	x (N-H distance)	Temperature factors			
				B_N	B_{Cl}	B_H	(Å^{-2})
Neutrons	Levy and Peterson[10]	r. t.	0.154±0.003 (1.03±0.02Å)	2.0	2.0	2.5	($\alpha=12°$)
	Goldschmidt and Hurst[11]	liq. air	0.154±0.003 (1.03±0.02Å)	0.44	0.17	3.1	
X-rays	Watanabe and Yamada[9]	r. t.	0.140±0.004 (0.94±0.03Å)	2.0	1.9	—	
		−60°C	0.140±0.004 (0.94±0.03Å)	1.8	1.3	—	
Electrons	Laschkarew and Usyskin[1]	r. t.	0.142±0.010 (0.95±0.07Å)	—	—	—	
	Stasova and Vainstein[12]	r. t.	0.146±0.006 (0.98±0.04Å)	$1\leq B<2$			
	Present author	r. t.	0.153±0.003 (1.02±0.02Å)	1.33	1.22	2.38	($\alpha=12°$)
		−40°C	0.153±0.003 (1.02±0.02Å)	0.48	0.41	2.48	

tion. Assuming the results of X-rays and neutron diffraction are both correct, the potential distribution of the 1*s* electron[9] and the nucleus[10] of the hydrogen atom can be given as in Fig. 15. As shown in (1), the contribution of electron is quite opposite to that of nucleus, so the potential due to the 1*s* electron is negative. The quantity which is given by electron diffraction synthesis is the resultant potential. As is seen in this figure, the shift of the peak value is so small ($\Delta x=0.001$) that the position of the peak of the resultant potential is almost the same as that of the nucleus. Thus the value $x=0.153$ of our experiment coincides with the resultant peak within the experimental error.

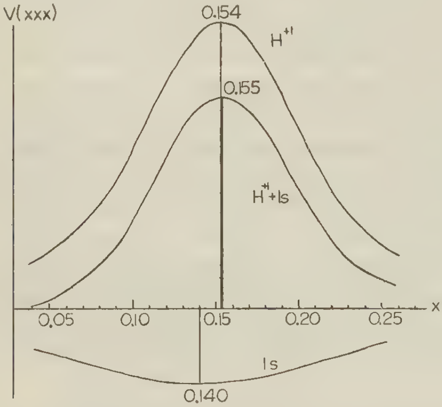

Fig. 15. Potential of nucleus and 1*s* electron of hydrogen atom.

The intensity ratios of the experiment of Stasova and Vainstein are almost the same as those in the present experiment except the (100) and (110) reflections. However, the coordinate of the hydrogen atom is much smaller than ours. If they determined the position of hydrogen atom by paying much attention for the factors which were mentioned in § 3*a*), the same value would result as in the present experiment.

d) *The effect of complex scattering factors.* So far we did not consider the effect of the phase shift due to the complex atomic scattering factors[18,19,20]. However, since in our experiment the accelerating voltage was high (60kv max.) and the atoms are light, the effect of the phase shift on the intensities, if any, is only ~5 percent for the reflections of higher scattering angles, being less than the error of the intensity measurement, ~15 percent, in such a region.

Acknowledgement

Finally the author wishes to express his hearty thanks to Prof. S. Miyake for his kind suggestion of this experiment and discussion. He is also indebted to Prof. T. Watanabe, Prof. G. Honjo and Dr. J. M. Cowley for their kind advice and discussions. His thanks are also due to Prof. H. Tazaki for his interest and encouragement through the experiment, Mr. Y. Yamada for his discussion and Mr. N. Kitamura for the allowance for using the sector camera in some part of the experiment.

References

1) W. G. Lasckarew and I. D. Usyskin: Z. Phys. **85** (1933) 618.
2) Communications au III Cong. Inter. Crys. (1954), *Paris*.
3) J. M. Cowley: Acta Cryst. **6** (1953) 522; **9** (1956) 391.
4) J. Berguhuis, LJ. M. Haanappel, M. Poters, B. O. Loopstra, C. H. MacGillavry and A. L. Veenendaal: Acta Cryst. **8** (1955) 478. J. A. Ibers: Acta Cryst. **11** (1958) 178. B. K. Vainstein: J. Exp. Theor. Phys. USSR **25** (1953) 157. W. H. Bragg, M. von Laue and C. Hermann: *International Tables for the Determination of Crystal Structures* (G. Bell and Sons, Ltd., London, 1939).
5) S. Lennander: Ark. Fys. **8** (1954) 551.
6) S. Kuwabara: J. Phys. Soc. Japan **10** (1955) 416; **12** (1957) 637.
7) G. Honjo and N. Kitamura: Acta Cryst. **10** (1957) 533.
8) S. Nagakura: Acta Cryst. **10** (1957) 601; J. Phys. Soc. Japan **13** (1958) 1005.
9) T. Watanabe and Y. Yamada: *unpublished*.
10) H. Levy and S. W. Peterson: Phys. Rev. **86** (1952) 766; J. Amer. Chem. Soc. **75** (1953) 1536.
11) G. H. Goldschmidt and D. G. Hurst: Phys. Rev. **83** (1951) 88; **86** (1952) 797.
12) M. M. Stasova and B. K. Vainstein: Trudy Inst. Krist. Akad. Nauk **12** (1956) 18.
13) G. Honjo, N. Kitamura and K. Mihama: J. Phys. Soc. Japan **11** (1956) 527.
14) J. Karle and I. I. Karle: J. Chem. Phys. **18** (1950) 957.
15) B. K. Vainstein: J. Phys. Chem. USSR **29** (1955) 327.
16) D. W. J. Kruickshank: Acta Cryst. **2** (1949) 65.
17) V. K. Vainstein and V. F. Dvoryankin: Krist. Akad. Nauk **1** (1956) 626.
18) R. Glauber and V. Schomaker: Phys. Rev. **89** (1953) 667.
19) J. A. Hoerni and J. A. Ibers: Phys. Rev. **91** (1953) 1182.
20) J. A. Ibers and J. A. Hoerni: Acta Cryst. **7** (1954) 405.

JOURNAL OF THE PHYSICAL SOCIETY OF JAPAN, Vol. 14, No. 9, SEPTEMBER, 1959

The Magnetic Investigation of Mn^{++}, Co^{++}, Ni^{++}, Cu^{++} Ammine and Anhydrate Salts

By Kiyoshi KIDO and Takashi WATANABE

Department of Physics, Faculty of Science,
Tokyo Metropolitan University, Tokyo, Japan

(Received August 29, 1958)

The object of this paper is to investigate how the magnetic interaction and the crystalline field depend on the number of coordinations in the complex salts. As the results of our measurements, it is found that the magnetic susceptibilities of $Mn(NH_3)_6Cl_2$, $Mn(NH_3)_2Cl_2$, $Mn(NH_3)Cl_2$, $MnCl_2$, $Co(NH_3)_6Cl_2$, $Co(NH_3)_2Cl_2$, $Co(NH_3)Cl_2$, $CoCl_2$; $Ni(NH_3)_6Cl_2$, $Ni(NH_3)_2Cl_2$, $Ni(NH_3)Cl_2$, $NiCl_2$; $Cu(NH_3)_4SO_4 \cdot H_2O$, $Cu(NH_3)_2SO_4$, $CuSO_4$ follow well the Curie-Weiss law in the temperature range from 90°K to 600°K. Any appreciable deviation from the Curie-Weiss law has not been observed, and it seems that the Curie constant C and the Weiss temperature θ in the equation $\chi_m = C/T+\theta$ generally increase as the coordination number proceeds lower.

§ 1. Introduction

$Mn(NH_3)_6Cl_2$, $Co(NH_3)_6Cl_2$, $Ni(NH_3)_6Cl_2$ and their diammine and monoammine salts are stable, and their physical and chemical properties were investigated by Biltz¹⁾. When heated in vacuum, the hexammine salts convert successively into di- and monoammine salts at fixed temperatures. The transformation points are given in Table I and Fig. 3.

The values of the susceptibility of anhydrated chloride of iron group given by Starr, Bitter and Kaufmann²⁾, and Bizett, Tisäi and Terrier³⁾ are in very close agreement with our results above 90°K, while the values for $Cu(NH_3)_4SO_4 \cdot H_2O$ by Volger⁴⁾ are partially different from ours. For $CuSO_4$ anhydrate the measurement was carried out by de Haas and Gorter⁵⁾ and Borovik-Romanov, Karasik and Kleines⁶⁾.

The crystal structures of $Mn(NH_3)_6Cl_2$, $Co(NH_3)_6Cl_2$, $Ni(NH_3)_6Cl_2$,⁷⁾ $MnCl_2$, $CoCl_2$, $NiCl_2$,⁸⁾ $Cu(NH_3)_4SO_4 \cdot H_2O$⁹⁾ and $CuSO_4$¹⁰⁾ are readily known, yet the structures of the salts with intermediate coordinations are not certain.

§ 2. Apparatus used and Preparation of Samples

The method used for measuring the susceptibility at various temperatures is one of the Weiss-Föx principle that has been constantly used by one of the authors¹¹⁾. In the present measurement, the whole moving part was enclosed by a glass tube and was kept in vacuum or in dry air as shown schematically in Fig. 1.

For the measurement at high temperature a heating chamber made of quartz as shown in Fig. 2 (a) was attached to the above-mentioned glass tube and a platinum wire of 0.5 mm in diameter was antimagnetically wound around the quartz tube for heating the chamber. For the measurement at low temperature a chamber made of copper block was attached and the lower part of the chamber was dipped dry ice or liquid nitrogen as required as shown in Fig. 2 (b). The magnet

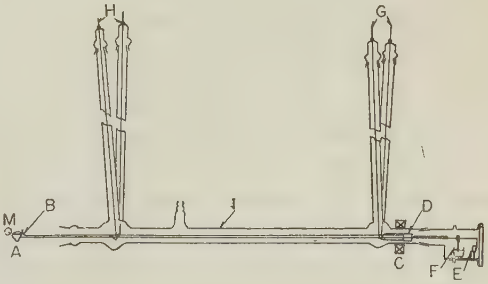

Fig. 1. Schematic picture of the apparatus of susceptibility measurement.
A sample holder, B thermocouple,
C and D compensating coil,
E mirror, F oil damper,
G lead of compensating coil,
H lead of thermocouple,
I glass tube,
M pole center of electromagnet.

used is of the Weiss-II type and a magnetic field of about 6000 oersted is obtained in the air gap between pole pieces at a distance of 3.2 cm apart.

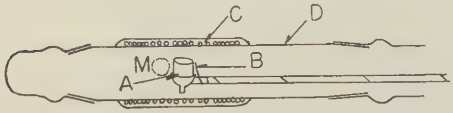

Fig. 2 (a). Schematic picture of heating oven.
A sample and holder, B thermocouple,
C heater of *Pt* wire, D quartz tube,
M pole center of electromagnet.

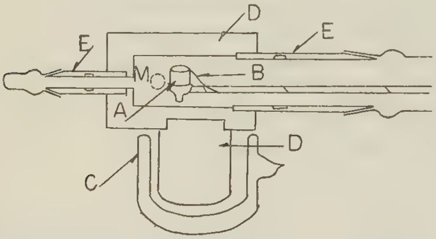

Fig. 2 (b). Schematic picture of cryoelement.
C De'war vessel, D copper block,
E blass tube.

As standards the following compounds were used:

H_2O $\chi_g=-0.720\times10^{-6}$,
$Fe(NH_4)$alum $\chi_g=30.4\times10^{-6}$ (at 290°K) and
$CuSO^4\cdot5H_2O$ $\chi_g=5.97\times10^{-6}$ (〃)

χ_g being the gram susceptibility, and for the diamagnetic correction the following values of molecular susceptibility were used:

H_2O $\chi_m=-13.0\times10^{-6}$,
SO_4^- $\chi_m=-39.0\times10^{-6}$,
NH_3 $\chi_m=-14.5\times10^{-6}$,
Cl^- $\chi_m=-22.1\times10^{-6}$.

A copper-constantan thermoelement of 0.06 mm in diameter calibrated by the melting points of Cd, Zn and Sn metals, sublimation point of dry ice and boiling point of liquid nitrogen was attached to the sample vessel as shown in Figs. 2 (a) and (b). A correction for the temperature difference between the thermocouple and the sample was done by comparing the temperature of the thermocouple with the temperature deduced from the χ_g value of $Fe(NH_2)$-alum in the range from 90°K to 300°K. This result was reproduced within an accuracy of ±1.5°K in the ranges 90°K∼110°K and 200°K∼300°K. The error in observation of magnetic susceptibility χ_g lay within ±0.5%.

Preparation of samples.

$Mn(NH_3)_6Cl_2$, $Co(NH_3)_6Cl_2$:—The recrystallized salts of $MnCl_2\cdot4H_2O$ and $CoCl_2\cdot6H_2O$ were dehydrate, being kept at 200°C for 4 hours. The anhydrated salts thus obtained were shutt off from air, and were held in ammonia gas flowing slowly until these salts converted into white powder of $Mn(NH_3)_6Cl_2$ and pink powder of $Co(NH_3)_6Cl_2$. To avoid decomposition, these salts were kept in ammonia gas atmosphere.

$Ni(NH_3)_6Cl_2$:—By dissolving 25 grams of recrystallized $NiCl_2\cdot6H_2O$ in 200 cc of water and adding conc. NH_3 aqueous solution to this solution until a green precipitation disappears, clear deep purple solution was obtained. Next 100 cc of saturated NH_4Cl aqueous solution being added, sparking blue micro crystals precipitated in the solution. In this condition it was left for 24 hours, and then filtered. The mico crystals were washed by a mixture of saturated NH_4Cl solution and NH_3 aqueous solution, and they were held in a desicator containing water free CaO during a few days.

$Cu(NH_3)_6SO_4\cdot H_2O$:—Conc. NH_3 aqueous solution of excess more than 4 equivalent being added in the saturated $CuSO_4\cdot5H_2O$ solution, the solution changed to dark blue solution of copper tetrammine sulfate. Alcohol being added very slowly to the solution thus obtained, micro crystals of $Cu(NH_3)_4SO_4\cdot H_2O$ precipitated in the solution. In this condition it was left for 24 hours and then filtered. The precipitation was washed by alcohol and left in water free CaO desicator during a few days.

Extra pure grade reagents of $MnCl_2\cdot4H_2O$, $CoCl_2\cdot6H_2O$, $NiCl_2\cdot6H_2O$ and $CuSO_4\cdot5H_2O$ prepared by Kanto Chemical Co. were recrystallized and used for the test.

$Mn(NH_3)_2Cl_2$, $Mn(NH_3)Cl_2$, $Co(NH_3)_2Cl_2$, $Co(NH_3)Cl_2$, $Ni(NH_3)_2Cl_2$, $Ni(NH_3)Cl_2$ and $Cu(NH_3)_2SO_4$ were obtained by thermal decomposition of hexammine chlorides of Mn^{++}, Co^{++}, Ni^{++} and copper tetrammine monohydrate sulfate in vacuum.

The decomposing temperature of hexammine, diammine and monoammine given by Biltz[1)] are shown in the following Table I. In Table I, the results obtained by the present authors are also included in the second column,

Table I.

	$6NH_3$		$2NH_3$		NH_3	
	Biltz	Present authors	Biltz	Present authors	Biltz	Present authors
$MnCl_2$	318°K	290°K	463°K	440°K	546°K	500°K
$CoCl_2$	362	340	510	480	574	520
$NiCl_2$	398	380	519	500	583	540

	$4NH_3H_2O$	$2NH_3$
	Present authors	Present authors
$CuSO_4$	290°K	260°K

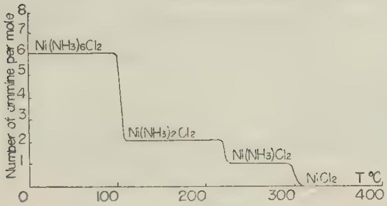

Fig. 3. Diagram of equilibrium temperature range in various coordination Ni^{++} salts.

and the decomposition temperatures of nickel ammine chloride complexes obtained by the authors are shown in in Fig. 3.

The color of each intermediate coordination compound is as follows.

$Mn(NH_3)_2Cl_2$	white
$Mn(NH_3)Cl_2$	whitely pink
$Co(NH_3)_2Cl_2$	violet
$Co(NH_3)Cl_2$	blue
$Ni(NH_3)_2Cl_2$	green
$Ni(NH_3)Cl_2$	yellow green
$Cu(NH_3)_2SO_4$	cobalt.

Anhydrated manganous, cobaltous and nickel chloride were obtained by dehydration at 200°C for 4 hours, and anhydrated copper sulfate at 260°C for 4 hours in vacuum.

§ 3. Results of the Observation

The magnetic susceptibilities of paramagnetic salts above mentioned obey the Curie-Weiss law,

$$\chi_m=\frac{C}{T+\theta}\,, \tag{1}$$

where χ_m is the molar susceptibility. Introducing the observed value of χ_m in the above relation (1), we get the value of C and θ. Magnetic moment p (Bohr magneton unit) is given as

$$p=\frac{1}{\beta}\sqrt{\frac{3kC}{N}}=2.839\sqrt{C}\,, \tag{2}$$

where k, β and N are the Boltzmann factor, the Bohr magneton and the Avogadro number respectively.

(1) $Mn(NH_3)_6Cl_2$, $Mn(NH_3)_2Cl_2$, $Mn(NH_3)Cl_2$, $MnCl_2$ (Table II and Fig. 4)

(2) $Co(NH_3)_6Cl_2$, $Co(NH_3)_2Cl_2$, $Co(NH_3)Cl_2$, $CoCl_2$ (Table III and Fig. 5)

(3) $Ni(NH_3)_6Cl_2$, $Ni(NH_3)_2Cl_2$, $Ni(NH_3)Cl_2$, $NiCl_2$ (Table IV and Fig. 6)

(4) $Cu(NH_3)_4SO_4\cdot H_2O$, $Cu(NH_3)_2SO_4$, $CuSO_4$ (Table V and Fig. 7)

Table II.

	C	p	θ
$Mn(NH_3)_6Cl_2$	4.35	5.92±0.03	0°C±2°
$Mn(NH_3)_2Cl_2$	4.21	5.84 〃	1°C 〃
$Mn(NH_3)Cl_2$	4.08	5.74 〃	3°C 〃
$MnCl_2$	3.83	5.64 〃	4°C 〃

Table III.

	C	p	θ
$Co(NH_3)_6Cl_2$	2.95	4.88±0.03	17°C±2°
$Co(NH_3)_2Cl_2$	3.10	5.00 〃	−8 〃
$Co(NH_3)Cl_2$	3.26	5.10 〃	−14 〃
$CoCl_2$	3.30	5.16 〃	−28 〃

Table IV.

	C	p	θ
$Ni(NH_3)_2Cl_1$	1.25	3.18±0.03	6°C±2°
$Ni(NH_3)_2Cl_2$	1.27	3.20 〃	−38 〃
$Ni(NH_3)Cl_2$	1.36	3.24 〃	−46 〃
$NiCl_2$	1.34	3.28 〃	−67 〃

Table V.

	C	p	θ
$Cu(NH_3)_4SO_4\cdot H_2O$	0.393	1.78±0.03	4°C±2°
$Cu(NH_3)_2SO_4$	0.457	1.92 〃	22 〃
$CuSO_4$	0.514	2.10 〃	67 〃

§ 4. Discussion of the Results

In the hexammine complex salts $Mn(NH_3)_6\cdot Cl_2$, $Co(NH_3)_6Cl_2$, and $Ni(NH_3)_6Cl_2$, the octahedral complex ions of $M(NH_3)_6^{+2}$-type and the

Cl^- ions form anti-calcium difluoride type structure (anti-CaF_2) as shown in Fig. 8, and each divalent metal ion at the center is surrounded by the octahedron of six ammonia molecules. And this octahedral complex ion is surrounded by eight Cl^- ions (cubic symmetry) and the Cl^- ion by four complex ions (tetragonal symmetry). Since each ion is completely equivalent in the coordination in space, if the symmetry character of these hexammine chloride salts keeps complete O_h symmetry it is suggested that these salts are dominated by cubic field and anisotropy does not appear. On this assumption, the distances between nearest Cl–Cl and metal-metal ions can be calculated by use of the X-ray data[7] of the powdered salt, and the results are given in Table VI. The observed value of θ, however, is not small except for $Mn(NH_3)_6Cl_2$. It may be considered that the effect of lower part of crystalline field or spin orbital coupling without exchange interaction cannot be neglected, and then small displacement of the Cl^- ion and NH_3 molecule may happen.

The crystal structures of diammine and monoammine salts are not yet certain. Diammine complex salts may belong either to the planar four coordination of $CuCl_2 \cdot 2H_2O$ type, to the tetragonal coordination of $Zn(NH_3)_2Cl_2$

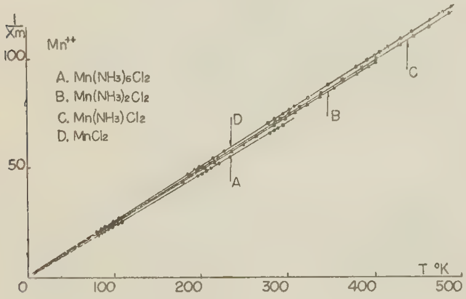

Fig. 4. Reciprocal molar susceptibility versus temperature (°K) for Mn^{++}-complex and chloride anhydrate salts.

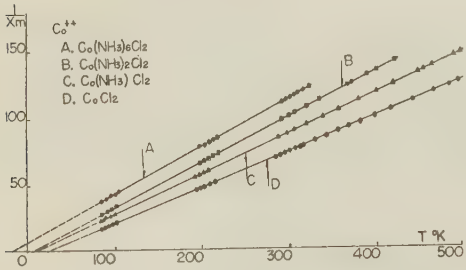

Fig. 5. Reciprocal molar susceptibility versus temperature (°K) for Co^{++}-complex and chloride anhydrate salts

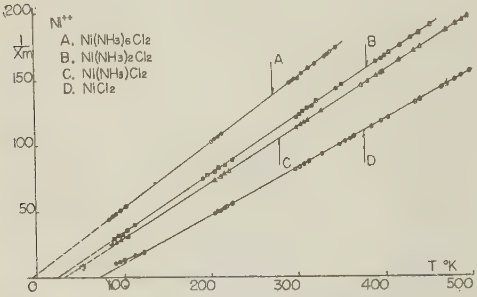

Fig. 6. Reciprocal molar susceptibility versus temperature (°K) for Ni^{++}-complex and chloride anhydrate salts.

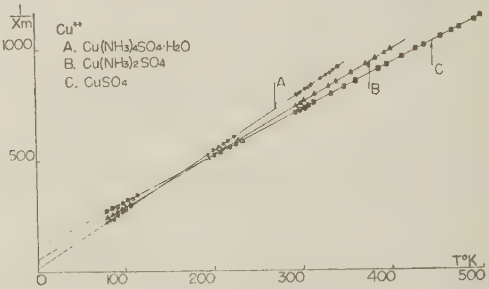

Fig. 7. Reciprocal molar susceptibility versus temperature (°K) for Cu^{++}-complex and sulfate anhydrate salts.

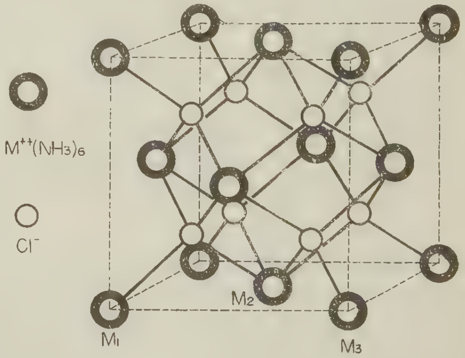

Fig. 8. Crystal structure of $M(NH_3)_6Cl_2$.

Table VI.

	a_0*	Cl–Cl	M–Cl	M_1–M_2**	M_1–M_3**
$Mn(NH_3)_6Cl_2$	1.198Å	5.099Å	4.41Å	7.20Å	10.198Å
$Co(NH_3)_6Cl_2$	10.10	5.05	4.37	7.12	10.10
$Ni(NH_3)_6Cl_2$	10.064	5.032	4.35	7.11	10.064

* a_0 is the lattice constant of cubic unit cell.
** M_1, M_2 and M_3 are shown in Fig. 8.

type or to the chain like polynuclear complex salt of $Cd(NH_3)_2Cl_2$ type. Anhydrated chloride salts $MnCl_2$, $CoCl_2$ and $NiCl_2$ form layer crystal structure D_{3d} of $CdCl_2$ type[8].

The symmetry of $Cu(NH_3)_4SO_4\cdot H_2O$ structure is orthorhombic bipyramidal and its crystal structure is shown in Fig. 9 as the cross-sectional view in the *b–c* plane which was determined by Mazzi[9] and Zemann[9]; unit cell constants are $a=7.07$, $b=12.12$, $c=10.66kx$ ($\pm 1\%$). This salt contains four copper ions in unit cell, differing from $CuSO_4\cdot 5H_2O$. The structure of the copper sulfate pentahydrate is of monoclinic symmetry and has two copper ions in unit cell. And $Cu(NH_3)_4SO_4\cdot H_2O$ has a chain of $-H_2O-Cu-H_2O-Cu-$ along the *c*-axis (Fig. 9).

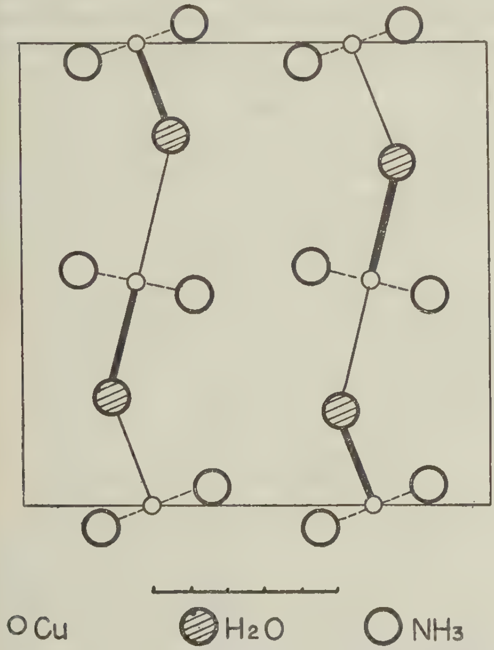

Fig. 9. Projection of the unit cell of $Cu(NH_3)_4SO_4\cdot H_2O$ on its (100) plane. After F. Mazzi.

The crystal structure of $Cu(NH_3)_2SO_4$ is unknown. The structure of the copper sulfate anhydrate $CuSO_4$ has been determined by Hammel[10] and has nearly rhombic symmetry and contains four copper ions in unit cell.

The origin of the Weiss temperature θ is due mainly to the influence of the anisotropic crystalline field and the exchange interaction. So if the splitting caused by crystalline field is small, the Weiss temperature θ can be expressed by the following relation after Van Vleck,

$$\theta=\frac{\Sigma_n W(n)}{k\Sigma_n{}^1}-\frac{\Sigma_n\Sigma_{n'}W(n)|M(nn')|^2}{k\Sigma_n\Sigma_{n'}|(nn')|^2}. \qquad (3)$$

Let us consider the spectroscopic energy $W(n)$ of the energy level of one ion, where n stands for a combination of quantum numbers. $M(n,n')$ are the matrix elements of magnetic moment of the ion in the direction of magnetic field. The index in the summation sign indicates that in the summation over the different levels n' the original level n is excluded. It may be shown, however, that this becomes zero in isotropic substances, as does also its average value in any powder. Therefore an anisotropic effect in powder, if any, may be faint from the above hypothesis.

A relation between the Weiss temperature and the exchange interaction energy J is given by the expression;

$$\theta=\frac{2zJS(S+1)}{3K}, \qquad (4)$$

where z is the number of ions at the nearest neighbour sites, J the energy of exchange interaction, and S the spin quantum number.

In the case of powdered sample a part of the exchange interaction is isotropic. Therefore, neglecting the Weiss constant due to anisotropy we estimate isotropic exchange interaction alone. We also neglect the Weiss constant due to magnetic dipole interaction as it may be of order of magnitude smaller than $10^{-2}\,cm^{-1}$.

i) Mn^{++}, $3d^5\,{}^6S_{5/2}$.

In this case, since the orbital level is singlet, the level is not splitted by a crystalline field and hence an anisotropy caused by the crystalline field does not remain. Thus θ in (3) becomes zero, and therefore the Weiss temperature θ is supposed to be equal to the isotropic exchange interaction. In the manganous salts which were measured by the present authors, the Weiss temperature is very small in magnitude compared with other salts. They may probably be normal paramagnetic salts at very low temperature. Especially in the manganous hexammine chloride $Mn(NH_3)_6Cl_2$, the value of θ is too small for estimating the Weiss temperature in the temperature range of the present experiment. In the case of $MnCl_2$ as shown in Table II, θ equals 4°C, so the exchange energy can be estimated as

$J=0.15\ \mathrm{cm}^{-1}$. Moreover, it seems reasonable that the g-value for the manganous hexammine chloride has been estimated to be 2.00 from the experimental results of molar susceptibility. The g-values for the diammine and the monoammine and the anhydrate salts are smaller than the g-value of the hexammine salt. These g-values are tabulated in Table VII.

Table VII.

	g
$Mn(NH_3)_6Cl_2$	2.00 ± 0.03
$Mn(NH_3)_2Cl_2$	1.98 〃
$Mn(NH_3)Cl_2$	1.97 〃
$MuCl_2$	1.96 〃

Table VIII.

	g
$Co(NH_3)_6Cl_2$	2.46 ± 0.03
$Co(NH_3)_2Cl_2$	2.51 〃
$Co(NH_3)Cl_2$	2.63 〃
$CoCl_2$	2.67 〃

ii) Co^{++}, $3d^7\ {}^4F_{5/2}$.

In the cobaltous salts, the value of θ for $Co(NH_3)_6Cl_2$ is positive, differing from the others as seen in Table III, so this salt is expected to show an antiferromagnetic behaviour at very low temperature.

In Table VIII, the g-values of cobaltous salts are given which are all quite apart from 2.00. It seems that the effect of spin-orbit coupling[12] and anisotropic field cannot be neglected from these results. A more detailed discussion on the present problem may be reserved to the future because of lack of experimental results on the susceptibility measurement of the single crystal and on the paramagnetic reasonance of these salts. The exchange energy can be evaluated by a relation (4), and we get, $J=0.8\ \mathrm{cm}^{-1}$ for $Co(NH_3)_6Cl_2$, and $J=2.0\ \mathrm{cm}^{-1}$ for $CoCl_2$.

iii) Ni^{++}, $3d^8\ {}^3F_4$.

In nickel hexammine chloride, we get $\theta=6.5°K$. In Date's experiment, the paramagnetic resonance line at liquid helium temperature could not be observed for the single crystal of this salt[13].

The g-value for this salt is in fair agreement with those of the other dilute nickel salts such as nickel ammonium Tutton.

In the diammine and the monoammine salt, the $\chi-T$ relation deviates slightly from the Curie-Weiss law at about 90°K and θ is negative and it may show a metamagnetic behaviour at low temperature. In Table IX, the g-values evaluated from the observed molar susceptibility of powdered nickel salts are shown. The exchange energies obtained from (4) are $J=0.7\ \mathrm{cm}^{-1}$ for $Ni(NH_3)_6Cl_2$ and $J=10\ \mathrm{cm}^{-1}$ for $NiCl_2$.

iv) Cu^{++}, $3d^9\ {}^2D_{5/2}$.

The crystal structure of copper tetrammine sulfate monohydrate $Cu(NH_3)_4SO_4\cdot H_2O$ is different from that of the copper sulfate pentahydrate as shown in Fig. 9. According to the experiments of paramagnetic resonance, the g-value of $Cu(NH_3)_4SO_4\cdot H_2O$ is rather smaller than that of the $CuSO_4\cdot 5H_2O$[14),15),16)]

Table IX.

	g
$Ni(NH_3)_6Cl_2$	2.24 ± 0.03
$Ni(NH_3)_2Cl_2$	2.26 〃
$Ni(NH_3)Cl_2$	2.28 〃
$NiCl_2$	2.32 〃

Table X.

	g
$Cu(NH_3)_4SO_4\cdot H_2O$	2.0 ± 0.03
$Cu(NH_3)_2SO_4$	2.22 〃
$CuSO_4$	2.43 〃

As shown in Table X the g-value of cupric tetramine sulfate monohydrate is nearly equal to that obtained by paramagnetic resonance. Date has found in his experiment that the absorption line of the paramagnetic resonance shows an extremely large broadening at the temperature below 20.4°K. The exchange energy of this salt is estimated of $J=0.9\ \mathrm{cm}^{-1}$.

Since the orbital ground level of Cu^{++} ion is singlet in tetragonal crystalline field and there is no effect caused by a crystalline field, the exchange energy may be considered as purely isotropic. The Weiss temperature θ of the copper tetrammine sulfate monohydrate is obtained as $\theta=4°C$ which is fairly different from 15°C as given by Volger.

For the salts of copper diammine sulfate and copper sulfate anhydrate, the Weiss temperatures are all positive and larger than that of copper tetrammine sulfate monohydrate and the g-values are larger also (Tables V and X). In the above calculation of exchange energy, the number of nearest neighbour ions z was taken as 6 and 4 in the hexammine salt and anhydrated salt respectively.

§ 5. Conclusion

According to the fact mentioned above we may conclude as follows:

1) For the salts with the same kind of positive ions, the value of θ decreases as the coordination number increases.

The above results can be explained by the consideration that in the hexammine salts or other ammine salts the crystalline field becomes more symmetrical than in the anhydrated salts, and since the distance between metal ions is longer than that of anhydrated salts for ammine ligands, the exchange interaction decreases as the coordination number increases. In the case of hexammine complex their crystal structures are more symmetrical than the other salts, but θ is not small except for Mn^{++}. It may show that the splitting of ground level due to lower symmetry or exchange interactions is so complicated that it cannot simply be explained.

2) The Weiss temperature θ increases in magnitude as

$$Mn^{++} < Co^{++} < Ni^{++} .$$

This behaviour can be found in all salts of any coordination in the present experiment except for $Co(NH_3)_6Cl_2$.

3) As for the g-values, Co^{++} has the largest value (2.46–2.67), while for Mn^{++} and Cu^{++} they are nearly 2.00 except anhydrated salts.

In the Co^{++}, the lowest level is triplet, with fourfold spin degeneracy, which will split into a number of doublets by the combined effect of the spin-orbit coupling and a tetragonal or trigonal field as shown in Fig. 10. Regarding the large anisotropy on the g-value found in the experiment of paramagnetic resonance, the effect of spin-orbit coupling may be seen of more importance than that of tetragonal or trigonal field[12)].

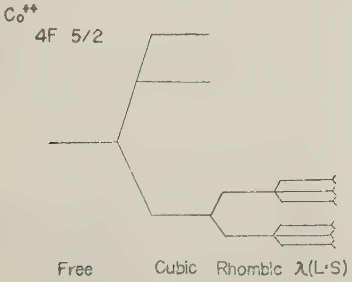

Fig. 10. Schematic energy level of Co^{++} ion in crystalline electric field,

The present experiment was carried out in the temperature range from 90°K to 600°K. All salts show normal paramagnetic behaviour in the above temperature range. Furthermore, in the experiment at lower temperatures, magnetic properties of these paramagnetic salts are expected to present more interesting phenomena and the problem is reserved for a future investigation.

Acknowledgement

The present authors wish to express their sincere thanks to Assist. Prof. Kanomata of our university who has helped us in constructing an apparatus and to Dr. Oyagi of Tokyo University of Education and to Mr. Takamoto of Gakushuin University for their kind advice in purifying the samples.

Our thanks are also due to Dr. Haseda of Tohoku University for his kind advice shown by him in performing the observation at low temperature and to Mrs. Nose who helped us in the present experiment.

The liquid nitrogen used in the experiment was kindly supplied by Dr. Monna of Nippon Oxygen Co.

References

1) W. Biltz: *Einführung in die Chemie der Komplex-Verbindungs* (R. Weinland, Leipzig 1924) 492.
2) C. Starr, F. Bitter and A. R. Kaufmann: Phys. Rev. **58** (1940) 977.
3) H. Bizzet, B. Tisäi and C. Terrier: Compt. rend. **243** (1956) 1295.
4) J. Volger: Thesis (Leiden, 1946), also given in C. J. Gorter: *Paramagnetic Relaxation* (Leiden, 1947).
5) W. J. de Haas and C. J. Gorter: Leiden Communication 215a (1931).
6) A. S. Borovik-Romanov, V. R. Karasik and N. M. Kleines: J. Exp. Theor. Phys. USSR **31** (1956) 18.
7) R. W. G. Wyckoff: *Crystal Structure*, vol. **2** (Interscience Publ., New York, 1951) 34.

8) R. W. G. Wyckoff: *Crystal Structure*, vol. **1** (Interscience Publ., N. Y., 1951) 23.
9) F. Mazzi: Acta Cryst. **8** (1955) 137. J. Zemman: Experimentia **4** (1949) 2.
10) F. Hammel: Ann. chim. **11** (1939) 247.
11) K. Kido: Sci. Rep. Tohoku Univ. **21** (1932) 149.
12) M. Pryce: Nature **164** (1949) 116.
13) M. Date: private communication.
14) H. Abe and K. Ono: J. Phys. Soc. Japan **11** (1956) 949.
15) K. Okamura and M. Date: Phys. Rev. **84** (1954) 314.
16) H. J. Gerrizen: Thesis (Leiden, 1955) 84.

Journal of the Physical Society of Japan Vol. 14, No. 9, September, 1959

Effect of the Basic Strength of Attached Groups on Light Absorption Spectra, IV. Proton Dissociations of Some Aromatic Molecules in Their Excited State

By Reikiti Itoh

Kobayasi Institute of Physical Research, Kokubunji, Tokyo

(Received March 27, 1959)

A general standard of the classification is given for the acid-base character of some aromatic molecules with special reference to the change of the character after and before the first excitation. The criterion is $\Delta q \gtreqless 0$, Δq being the change in the π-electron density of the special member of the attached group after and before the excitation. This corresponds to $pK_{a_1} \lesseqgtr pK_{a_2}$ where pK_{a_1} and pK_{a_2} are the proton dissociation constants in the ground and the excited state respectively. Examples are the case of acridon cation which gives $\Delta q=0.099$ corresponding to $pK_{a_2}-pK_{a_1}=2.48$ (observed value 2.6) and the case of 3-oxyacridine which gives $\Delta q=-0.18$ corresponding to $pK_{a_2}-pK_{a_1}=-4.52$ (observed value, if any, -5.27). Though the cases of naphthylamine and naphthol were treated in the previous paper III, some corrections about the term values and the discussion of the paper III are given in the present paper.

§ 1. Introduction

Recently, several authors have treated the excited state of some aromatic molecules based on the spectroscopic experiments. Among those authors, Förster¹⁾, Weller,²⁾ Koizumi and Mataga³⁾ have discussed about the derivatives of naphthalene; α- and β-naphthol, and α- and β-naphthylamine etc. Afterwards, Perkampus,⁴⁾ Weller⁵⁾ and Kokubun⁶⁾ have discussed about the excited state of the nitrogen hetero cycles; acridine, phenazine and their oxyderivatives. Molecules in the former group have smaller pK values after the first excitation; while those in the latter group have larger pK value after the excitation except 3-oxyacridine. All these are the results deduced by analyzing spectroscopic data on the light absorption or fluorescent emission. However, no theoretical explanation of these experiments on the basis of the molecular orbital treatment have appeared so far. The aim of the present paper is to give an explanation of the proton dissociation in the excited state of these molecules based on the semi-empirical molecular orbital method.

In the previous papers I⁷⁾ and II⁸⁾, the induction effect on the light absorption spectra in the alkylamino group was discussed on the ground of

$$\alpha_j-\alpha_i=k(pK_{b_i}-pK_{b_j}), \qquad (1)$$

where α_i is the coulomb integral of the ith group.* If we use the acidic strength of the group, the equation may be written in the form,

---

* There are several alkylamino groups such as, in the order of decreasing $|\alpha|$ value, NH_2, $NHCH_3$, NHC_2H_5, $N(CH_3)_2$, $NCH_3C_2H_5$ and $N(C_2H_5)_2$ etc.

$$\alpha_j-\alpha_i=k(pK_{aj}-pK_{ai}),$$

because the sum of pK_a and pK_b should be constant in the same molecule. The constant k was determined so that the equation (1) led to the observed light absorption spectra of triphenylmethane dyes and various aniline derivatives.

In the paper III⁹⁾, the author offered the treatment of the dissociation of naphthalene derivatives, naphthylamine and naphthol in their excited state on the basis of the molecular orbital treatment, where he assumed the same relation in the whole molecule because of the occurrence of the proton dissociation in the attached group. There were used 2 and 1 to the case of the excited and the ground state of the molecule in place of j and i respectively, i.e.

$$\alpha_2-\alpha_1=k(pK_{a_2}-pK_{a_1}). \qquad (2)$$

As indicated in the papers I and III, the Pariser-Parr approach in the S.C.F. treatment gives the coulomb integral of the atom r of molecule in the form,

$$\alpha_r=I_r+(q/2)(E_r-I_r), \qquad (3)$$

where I_r and E_r are the ionization potential and the electron affinity of the atom r in its valence state respectively and q is the π-electron density of the atom. Then the equation (2) is given by

$$\alpha_2-\alpha_1=(q_e-q_g)(E_r-I_r)/2, \qquad (4)$$

where q_e and q_g are the π-electron densities of the atom r in the excited and the ground state respectively. Combining the equation (2) with (4), we obtain the equation.

$$(q_e-q_g)(E_r-I_r)/2=k(pK_{a_2}-pK_{a_1}). \qquad (5)$$

Since the factor E_r-I_r of the left hand side of the equation is positive, the difference Δq of the π-electron density in the two states determines the sign of the right hand side of the equation. In other words, acids or bases can be classified into the following groups;

a) $\Delta q>0,\ pK_{a_2}>pK_{a_1}$
b) $\Delta q=0,\ pK_{a_2}=pK_{a_1}$
c) $\Delta q<0,\ pK_{a_2}<pK_{a_1}$.

Since pK_{a_2} is the acidic strength in the excited state, a) is the case in which the base becomes more basic after the first excitation; acridine, acridon and phenazine are known as examples of this case. In the case b), there occurs no change in the acid-base character by the first excitation; pyridine base is an example of this case. While c) is the case where the acid becomes more acidic after the excitation; examples are naphthylamines and naphthols with α- and β-substitution and were treated in the previous paper III. 3-Oxyacridine also belongs to this group.

In the present paper, it is intended to apply the equation (5) to the proton dissociation of some aromatic molecules belonging to the group a) and c).

§2. Proton Dissociation of Naphthyl Amine and Naphthol in Their Excited States

Though the basic concept appeared in the previous paper III is correct, there need some corrections on the data and discussion of the paper. As illustrated briefly in the paper, the concept of the proton dissociation is based on the result of the induction effect between σ- and π-electrons of the atom attaching the proton in the molecule. Therefore it will be convenient for us to discuss the effect rather in details about which the same situation has appeared in the hydrogen bond effect on the near ultraviolet absorption spectra of some aromatic molecules.¹⁰⁾ For example, let us consider a system composed from a molecule, a substituted group and a polar solvent. We know in some cases¹¹⁾ that substitution of the aromatic molecule B by an electron donating group AH causes the shift of the absorption spectra to the longer wave length, the origin of which is attributed to the stabilization of the energy levels of the electron partaking in the light absorption by B owing to the migration of the π-electron of AH. The formation of the hydrogen bond with the solvent molecule increases the distance between the atom A and the hydrogen atom H by about 0.03 A. Then the σ-electron sharing in the AH bond is more strongly localized to the atom A than without the hydrogen bond, which causes interaction between σ- and π-electron through the induction and drives the π-electrons of AH (nonbonding electrons) to the parent molecule B much more than without it. The stabilization energy ΔU due to the electron migration is given by the calculation based on the method of the electron migration theory¹¹⁾ used in the previous papers II and III. It is naturally expected that the interaction between AH and B depends upon the position of the substitution, e. g. α- and β-position of the naphthalene molecule. We should therefore use different constants of the induction for different positions. Fortunately one can evaluate the constants from one another using the data observed in the hydrogen bond effect in the following manner. For the system under consideration, four kinds of ΔU can be chosen; ΔU_e, ΔU_g, ΔU_{oe} and ΔU_{og}. The first two of these correspond to the case of hydrogen bond formation and the second two correspond to the case where no hydrogen bond is formed. The shift of the absorption spectra due to the hydrogen bond formation is given by

$$\Delta\tilde{\nu}_H=[(\Delta U_e-\Delta U_g)-(\Delta U_{oe}-\Delta U_{og})]/hc, \qquad (6)$$

where suffixes e and g indicate the excited and the ground state of B respectively. Integrals appeared in the terms ΔU's are indicated by the suffix o when there is no hydrogen bond formation. Among those, the resonance integrals and the coulomb integrals in the previous paper III are connected with each other by the relations

$$\rho_k-\rho_{ok}=\gamma_k=\gamma, \quad \chi-\chi_o=\alpha ,$$

and the energy levels for the vacant orbitals of B are connected by

$$\omega_k-\omega_{ok}=\beta_k=\beta ,$$

where $\alpha>0$, $\beta>0$ and $\gamma>0$ are assumed because of the increase of the electron donating character of AH due to the above induction. After the neglect of the terms higher than those of the second order, $\dfrac{\alpha-\beta}{\chi_o-\omega_{o1}}\ll 1$ and $\dfrac{\gamma-T\alpha}{\rho_{o1}-T\chi}\ll 1$, we obtain

$$\Delta\tilde{\nu}_H=\frac{\alpha-\beta}{\chi_o-\omega_{o2}}\left(\frac{\mu_{o,\,\mathrm{mig}}}{2\mathrm{x}e}\tilde{\nu}_o-\Delta\tilde{\nu}_o\right), \qquad (7)$$

where use has been made of the relations* $\chi_o<\omega_{o1}<\omega_{o2}<0$, and

$$\mathrm{hc}\,\tilde{\nu}_o=\omega_{o2}-\omega_{o1},\ \mathrm{hc}\,\Delta\tilde{\nu}_o=\Delta U_{oe}-\Delta U_{og} ,$$

$$\mu_{o,\,\mathrm{mig}}=2\mathrm{xe}\ \text{ and }\ \mathrm{x}=\int\psi_{o1}\,\psi_{o1}\,d\tau.$$

From these equations and (7), the relations $\tilde{\nu}_o>0$, $\Delta\tilde{\nu}_o<0$ and $\Delta\tilde{\nu}_{\mathrm{H}}<0$ are deduced, if the attached group has the electron donating character only. The quantity $\mu_{\mathrm{o,mig}}$ expresses the contribution of the migrating electron to the dipole moment and is estimated by the relation,

$$\mu_{o,\,\mathrm{mig}}=\mu_{\mathrm{obs}}-\mu_{\mathrm{AH}}+\mu_{\mathrm{CA}} , \qquad (8)$$

if we assume the validity of the bond additivity of the dipole moment. x denotes the length from the center of the gravity of the π-electron system of B to AH. The equation (7) was examined for the cases of aniline, phenol and *p*-aminoazobenzen by the author who gave

	aniline	phenol	p-aminoazobenzene	
$\Delta\nu_{\mathrm{H}}$	–646	–277	–1197	cm^{-1}
$\Delta\nu_{\mathrm{H,\,obs}}$	–610	–240	–1107	

respectively, assuming the value $\alpha-\beta=1.01$ eV for the first two cases and 1.75 eV for the last. The data necessary for some cases were given in the previous paper.[10)]

The deduction of the constant k_o in the previous paper III by the first order perturbation is not correct. Among the quantities in the equation (7), ν_o, ω_{o2}, x, e and χ_o can be assumed to be common for aniline and phenol and for α- and β-naphthol respectively.** Since the factor α–β can be assumed not to differ in the former because of the iso-electronic character of the π-electrons in the attached groups, the origin of the difference in the shift $\Delta\tilde{\nu}_H$ can be ascribed to the difference in $\mu_{\mathrm{o,o,mig}}$ and in $\Delta\tilde{\nu}_o$ for the former substances. On the other hand, there is no remarkable difference in $\mu_{\mathrm{o,mig}}$ and in $\Delta\tilde{\nu}_o$ for the latter (See Table I). The difference in the shift for these are, therefore, likely to come from the factor α–β. Since the values of $\mu_{\mathrm{o,mig}}$ are nearly equal for the former, the comparison of the shifts $\Delta\tilde{\nu}_H$'s in the paper III cannot give the difference in the constant of the induction for the latter, which may probably be given by the shifts in the latter. The value β in the equation (7) is considered to be much smaller in the latter than in the former because the π-electron system is much larger in naphthalene than in benzene. Then for the comparison of k values of two naphthols we may consider only α value which is the difference in the coulomb integral of AH due to the formation of the hydrogen bond with the solvent. Now we can estimate the constant k for β-naphthol by the following assumption that the same magnitude m of the localization of the σ-election in the attached group caused by the hydrogen bond formation corresponds to the same difference of pK value for both naphthols in the proton dissociation. Since the two quantities for α- and β-naphthol are represented by

---

* For the details of the deduction of the equation (7), see the previous paper[10)] by the author. T is the overlap integral between the π-orbitals of B and AH, ψ_{0_i} and ξ.

** Exactly speaking, χ_o's are different for $\mathrm{NH_2}$ and OH group.

$$\alpha_\alpha = k_\alpha \cdot m \quad \text{and} \quad \alpha_\beta = k_\beta \cdot m$$

respectively, the ratio of $\varDelta\tilde{\nu}_{\mathrm{H}}$ for each naphthol gives

$$k_\alpha \cdot 293 / k_\beta \cdot 403 = 140/410 \sim 280/590,$$

where use has been made of the data shown in the Tables I and II. If we choose $k_\alpha = 0.4375$ eV taking the mean value of those determined in the previous papers I and II, k_β is determined as 0.670～0.932 eV. Following the same procedure as in the paper III by taking the above values of k_α and k_β and the data of ionizations* into calculation, we obtain the resultant pK differences after and before the first excitation. These are listed in Table V. If the situation of the hydrogen bond effect for the two naphthylamines is the same as for the two naphthols, it would be necessary to use two different constant k_α and k_β for these two naphthylamines. Since data of the hydrogen bond effect suitable for this purpose are not available, the same value k is used for both of the two naphthylamines in the present calculation.

Table I. Data for two naphthols

	$\mu_{o,\mathrm{mig}}$	μ_{obs}	$\varDelta\nu_0$	$\varDelta\nu_{\mathrm{H,obs}}$
α–naphhtol	0.76D	1.43D[13]	–1050	–140,–280
β–naphthol	0.86	1.53	–1660cm^{-1}	–410,–590[12]cm^{-1}

As to the two values of $\varDelta\nu_{H,\mathrm{obs}}$, proton acceptor of the former and the latter is ethylether and triethylamine respectively. $\mu_{o,\mathrm{mig}}$'s were calculated by the equation (8) using $\mu_{\mathrm{CO}}=0.86$ D and $\mu_{\mathrm{OH}}=1.53$ D.[14]

Table II. Data for naphthalene

ω_{01}	ω_{02}	x	ν_0
–8.10 eV[15]	4.10 eV	2×1.39 A	32200 cm^{-1} [16]

Values of x are assumed to be the same for two naphthols and ω_{02} was estimated from ω_{01} and ν_0.

§3. Proton Dissociations of Acridon Cation and 3-Oxyacridine in Their Excited States

In this section, we shall discuss the molecules or ions belonging to the group a) or c).

i) *Acridon cation.*

Recently Kokubun[6] has reported about the acid-base character of acridon base. Based on the absorption and the fluorescent spectra observed by him, he pointed out that the acridon becomes stronger base after the first excitation. Without refering to the activity coefficient of the ion, he estimated $pK_{a_2}=1.26$ and $\varDelta pK_a=2.6$ from the frequency difference between the first absorption maxima by acridon and by its cation ; $\varDelta\tilde{\nu}=1200\,\mathrm{cm}^{-1}$.

Now let us examine the character of the excited acridon cation by the equation (5) on the basis of the molecular orbital treatment. The molecule of the acridon cation has the symmetry corresponding to the point group C_{2v}. If we choose the 15 π-orbitals as the bases of the representation, the characters for the operations of this group are as follows ;

Operation : R	E	C_2	σ_v	$\sigma_{v'}$
$\Gamma(C_{2v})$	15	–3	–15	3.

With the help of the character table of the irreducible representations, we get

$$\Gamma(\mathrm{C}_{2v}) = 9\mathrm{B}_2 + 4\mathrm{A}_2 + 2\mathrm{A}_2.^{**}$$

The orbitals belonging to each species are expressed as

$$\begin{aligned}\psi_{\alpha_2} = {} & c_1\phi_9 + c_2(\phi_{12}+\phi_{13}) + c_3(\phi_{11}+\phi_{14}) + c_4\phi_{10} \\ & + c_5(\phi_1+\phi_8) + c_6(\phi_7+\phi_2) + c_7(\phi_6+\phi_5) \\ & + c_8(\phi_5+\phi_4) + c_9\phi_{15}\,,\\ \psi_{\alpha_2} = {} & c_1(\phi_{13}-\phi_{12}) + c_2(\phi_{14}+\phi_1-\phi_{11}-\phi_8) \\ & + c_3(\phi_4+\phi_2-\phi_5-\phi_7) + c_4(\phi_3-\phi_6)\end{aligned}$$

and

$$\psi'_{\alpha_2} = c_1(\phi_1-\phi_8+\phi_{11}-\phi_{14}) + c_2(\phi_4-\phi_5+\phi_7-\phi_2),$$

---

* Ionization data used here, were taken from the works by Mulliken,[17] Dewar and Paoloni[18] which are

I_2: N^+ (sp^3, V_4) to N^{++} (sp^2, V_3) –28.76 eV,
I_1: N (sp^4, V_3) to N^+ (sp^3, V_4) –12.24 eV
for the ammonium like N atom and
I_2: O^+ (s^2p^3, V_3) to O^{++} (s^2p^2, V_0) –36.68 eV,
I_1: O (s^2p^4, V_2) to O^+ (s^2p^3, V_3) –14.73 eV
for the O atom in the hydroxy group respectively.

** The A_2 molecular orbitals, $\psi_{\alpha_2}=c_1(\phi_{13}-\phi_{12})+c_2(\phi_1-\phi_8)+c_3(\phi_{14}-\phi_{11})+c_4(\phi_4-\phi_5)+c_5(\phi_2-\phi_7)+c_6(\phi_3-\phi_6)$, can be approximated by two $\varPsi_{\alpha_2}$'s, because we see $c_2=\pm c_3$ and $c_4=\pm c_5$ (the double signs are to be read in the same order).

where ϕ_i is the $2p\pi$ orbitals of the ith atom (Fig. 1). The distribution of the π-electrons in the cation is determined by using the following approximations;

a) All the coulomb integrals of the carbon atoms except those for $i=9$, 15 12 and 13 are assumed to have the same value, i.e. $\alpha_i=\alpha$.

b) $\alpha_9=\alpha+3\beta$ is assumed for the protonated hetero nitrogen atom 9. This is slightly larger than $\alpha+2.4\,\beta$ deduced by Mataga.[19]

c) $\alpha_{15}=\alpha+1.4\,\beta$ is assumed for the oxygen atom 15 in OH.

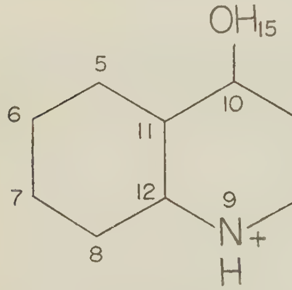

Fig. 1. Molecular figure of acridon cation.

d) $\alpha_{12}=\alpha_{13}=\alpha+0.5\beta$ is assumed because of the π-electron attraction by the protonated hetero nitrogen atom. Mataga gave a slightly smaller value $\alpha+0.4\,\beta$.

e) The resonance integrals between two adjacent atoms are assumed to have the same value β.

Solving the secular equations by using these approximations, we obtain the energy levels and the normalized coefficients of the atomic π-orbitals in each molecular orbital, a part of which is given in Table III. The first excited state is predicted to be obtained by promoting an electron in the highest occupied orbital ψ_{b_2} to the one with the same species. The transition from the ground state to it ($\psi_{b_2}\rightarrow\psi_{b_2}$) is shown to be an allowed one by the group theory and corresponds to the energy difference between $x=-0.891527$ and $x=0.256320$, where $x=(\alpha-\epsilon)/\beta$ with $\beta=-23000\,\text{cm}^{-1}$[20] and the energy ϵ of the molecular orbital. The dipole moment responsible for this transition has the direction pointing from the 9th to the 15th atom in Fig. 1, which coincides with that obtained by the spectral analysis. The first absorption spectrum of acridon cation is thus calculated as $26400\,\text{cm}^{-1}$. If we take account of the solvent effect which lowers the absorption energy by ca $1000\sim2000\,\text{cm}^{-1}$[21] even in the case of the non-polar solvent, the agreement of the above value with the observed one $23800\,\text{cm}^{-1}$ is quite satisfactory. For the oxygen atom of the OH group, the change Δq in the π-electron density due to the excitation is given by

$$\Delta q=\Delta c_9^2=0.099.$$

Then we obtain

$$\Delta pK_r=\frac{1}{2}\Delta q\frac{I_1-I_2}{k}=2.48\,,$$

which is in agreement with the value 2.6 deduced from the spectroscopic data by Kokubun.

Table III. c_i^2 values for the B_2 molecular orbitals ψ_{b_2}.

i	$x=-0.891527$	i	$x=0.256320$
1	0.091841	1	0.030955
2	0.102073*	2	0.082059*
3	0.007215*	3	0.009365
4	0.003533*	4	0.310345
5	0.117786*	5	0.003143*
6	0.000274	6	0.090498
7	0.126203	7	0.000443*
8	0.091929	8	0.087280*
9	0.013664	9	0.113125*

The coefficients c_i's corresponding to the c_i^2 values with asterisks should be taken negative.

ii) *3-Oxyacridine.*

Perkampus and Rössel[4] have reported that 3-oxyacridine shown in Fig. 2 increases its pK value after the first excitation and $\Delta pK=3.0$. We shall examine this by the equation (5). As denoted in the case of acridon cation, the oxygen atom should increase the π-electron density when it has a larger pK value after the first excitation (see Eq. (5)). As easily seen in Fig. 2, 3-oxyacridine has no symmetry axis in the molecular plane and we have to solve the secular equations of degree 15. The computing machine, E. T. L. Mark II, was used in the course of the calculations.

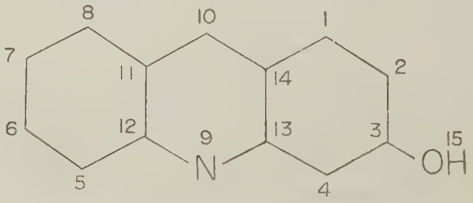

Fig. 2. Molecular figure of 3-oxyacridine

Table IV. c_i^2 values for the molecular orbitals of 3-oxyacridine.

$x=-0.75988$		$x=0.35772$	
i		i	
1	0.00152	1	0.09558*
2	0.18045	2	0.05735
3	0.08055	3	0.04995
4	0.05479	4	0.03697*
5	0.04087*	5	0.06905*
6	0.07872*	6	0.06875
7	0.00012*	7	0.02855
8	0.07408	8	0.10410*
9	0.00652	9	0.14175
10	0.05456*	10	0.26009
11	0.04746	11	0.00287*
12	0.01611	12	0.02829*
13	0.01123*	13	0.02394*
14	0.15644*	14	0.01661*
15	0.19658*	15	0.01617*

The coefficients c^i's corresponding to the c_1^2 values with asterisks should be taken negative.

The same approximations as used in the above was adopted except that $\alpha_9=\alpha+0.5\beta$ for the coulomb integral of the ring nitrogen atom, and $\alpha_{12}=\alpha_{13}=\alpha$ for those of the carbon atoms neighboring nearest to the ring nitrogen. A part of the energy levels and the normalized atomic orbital coefficients of each molecular orbital are given in Table IV. Those values are correct within the fourth decimal for the highest occupied level in the first excited state with $x=0.35772$. Those for the orbitalwith $x=-0.75988$, (the one in the ground state) are worse than those of the former in accuracy, though they give the π-electron density precisely enough in our approximation. The first absorption is obtained at 25300 cm^{-1} agreeing with the observation 24000 cm^{-1} within the limit of error caused by the solvent effect. The change in the π-electron density on the oxygen atom due to the first excitation is given by

$$\Delta q=\Delta c^2{}_{15}=-0.18,$$

and after using the equation (5), we have

$$\Delta pK_a=-4.52,$$

which indicates that 3-oxyacridine becomes more stronger acid after the first excitation contrary to the result by Perkampus and Rössel. Though we did not calculate about 3-oxyacridinium cation, the change in the π-electron density on the ring nitrogen atom due to the excitation, which is given from Table IV by

$$\Delta q=\Delta c_9{}^2=0.14\ ,$$

may be used to estimate the change in the basicity of the ring nitrogen due to the first excitation. From the comparison of two Δq's, it can be said that OH group becomes more acidic while the ring nitrogen becomes more basic in the first excited state respectively.

Therefore the first step of the proton dissociation of 3-oxyacridinium cation treated by Perkampus and Rössel will occur at OH group rather than at ring nitrogen atom as indicated by Weller.[5] Thus it is likely that the red shift of the first absorption maxima of 3-oxyacridine occurred in acidic region of pH, from 4200 A to 4600 A, corresponds to the dissociation of the proton of OH group and the blue shift of the absorption maxima, from 4600 A to 4300 A, occurred in alkaline region of pH corresponds to that of the ring nitrogen atom.

This conclusion can be in accordance with the result deduced from the consideration about the chemical kinetics by the author[22] who gave the equation,

$$hc(\tilde{\nu}_{\text{acid}}-\tilde{\nu}_{\text{alkali}})=-2.303RT\,(pK_{a_2}-pK_{a_1}), \qquad (9)$$

where $\tilde{\nu}_{\text{acid}}$ and $\tilde{\nu}_{\text{alkali}}$ are the absorption wave numbers of the ion or molecule in acidic and basic form respectively. Then our predicted value $\Delta pK_a=-4.52$ for 3-oxyacridine should be compared with that deducing from the first step of the dissociation of 3-oxyacridinium cation treated by Perkampus and Rössel, i.e., $\Delta pK=-5.27$. The situation is different in the case of acridon cation where, from Table III, Δq on the ring nitrogen atom is obtained as $\Delta q=-0.06$ denoting that though the first step of the proton dissociation occurs at OH group as indicated by Kokubun,[6] the basicity of the ring nitrogen atom is weakened slightly by the first excitation. In this connection, it is easily seen that the blue shift (from 23200 cm^{-1} to 24500 cm^{-1}) in the first step[6] corresponding to the dissociation of the proton of OH group and the red shift (from 24500 cm^{-1} to 23000 cm^{-1}) in the second step corresponding to that of the ring nitrogen are in agreement with the result of the equation (9) respectively.

§ 4. Results and Discussions

We set out the final results in Table V, where the first group is of the molecules belonging to c) group and the second one is of those belonging to a) group defined in §1. We see from Table V that the general agreement of the calculated values with those deduced from the spectroscopic data is good.

Table V. Results and comparison with spectroscopic data.

	α-naphthylamine	β-naphthylamine	α-naphthol	β-naphthol	3-oxyacridine
Δq	–0.41	–0.21	–0.19	–0.09	–0.18
$\Delta\alpha$	3.387	1.735	2.082	0.986	1.976 eV
ΔpK_{calc}	–7.74	–3.89	-4.77	–(1.11∼1.54)	-4.52
ΔpK_{obs}	—	–6[a]	–6.87[b] –5.62[c]	–6.67[b] –6 [a]	–5.27[d]

	acridon cation
Δq	0.099
$\Delta\alpha$	–1.087 eV
pK_{calc}	2.48
pK_{obs}	2.60[e]

a) Th. Förster, reference 1).
b) A. Weller, reference 2).
c) R. Itoh, reference 22).
d) H.H. Perkampus and Th. Rössel, reference 4).
e) H. Kokubun, reference 6).

$\Delta\alpha$ is the change in the coulomb integral of the attached group due to the first excitation.

In the first group we used two k values according to the different positions of the substitution in two naphthols, the ratio of these values were estimated by using the equation (7) which expresses the absorption shift due to the hydrogen bond formation.* The equation is correct under the assumption $\frac{\alpha-\beta}{\chi_0-\omega_{01}} \ll 1$. Though this assumption is valid in the case where the parent molecule is benzene, it is not so good in the case where the parent molecule is naphthalene because of the smallness of the term $\chi_0-\omega_{01}$ as easily seen from the data shown in Table II and $\chi_0=-9.8$ eV (for NH_3) and –10.8 eV (for OH). Also it is noted that $\Delta\tilde{\nu}_{H}$ involves the term $\mu_{o,\text{mig}}$ and $\Delta\tilde{\nu}_0$ which are not equal for two naphthols, and the agreement is poor.

Among the hetero nitrogen cycles, acridine and phenazine are the typical bases which increase their basicity after the first excitation. Since these molecules have no attached groups, our treatment based on the effect of basic strength of the attached groups on light absorption spectra can not be applied to these molecules. However, if we determine by some way the constant of the induction on the ring nitrogen atom, equation (5) may be applied to those molecules where the constant k will have considerably small value. From the comparison of the predicted value with spectroscopic analysis, we conclude that the change in the acid-base character of the whole molecule or ion after and before the excitation can be estimated by the difference in the π-electron density of the special atom in the attached group after the first excitation.

The author wishes to thank to Prof. I. Oshida for his helpful discussion at the Institute and to Dr. Y. Komamiya and Mr. H. Toda for their services in driving the computing machine, E.T.L. Mark II, at the Electrotechnical Laboratory.

This work was supported by the Scientific Research Fund granted by the Ministry of Education.

---

* Observed pK_a values 9.37 and 9.49 for α- and β-naphthol indicate that α-naphthol is slightly more acidic than β-naphthol. This leads us to expect that the hydrogen bond is stronger for the former than the latter to the same polar solvent. But the observed values for $\Delta\tilde{\nu}_H$ indicate that $\Delta\tilde{\nu}_H$ is larger for β-naphthol than for α-naphthol in L_B band, while this is reverse for L_A band (in Platt's notation). Inspite of the pK_a observation prefering to $\Delta\tilde{\nu}_H$ of L_A band, we take that of L_B in the present case because of the first excited state. This may be a main reason of the disagreement in the case of β-naphthol. From the view point of the polarization direction, it is better to use $\Delta\tilde{\nu}_H$ of L_A for the comparison of two naphthols because the theoretical first absorption in naphthalene corresponds to the L_A band in polarization.

References

1) Th. Förster: Z. Elektrochem. **54** (1950) 42, 531.
2) A. Weller: Z. Elektrochem. **56** (1952) 662.
3) M. Koizumi and N. Mataga: Nature **175** (1955) 731.
4) H.H. Perkampus and Th. Rössel: Z. Elektrochem. **60** (1956) 1102.
5) A. Weller: Z. Elektrochem. **61** (1957) 956.
6) H. Kokubun: Z. Elektrochem. **62** (1958) 599.
7) R. Itoh: J. Phys. Soc. Japan **12** (2957) 644.
8) R. Itoh: J. Phys. Soc. Japan **12** (1957) 809.
9) R. Itoh: J. Phys. Soc. Japan **13** (1958) 389.
10) R. Miyasaka (Itoh): Busseiron-Kenkyu no. 62 (1053) 94. For references about the hydrogen bond effect, see previous paper III.
11) A. L. Sklar: J. Chem. Phys. **7** (1939) 984, K.F. Herzfeld: Chem. Rev. **41** (1947) 739.

12) S. Nagakura and M. Gouterman: J. Chem. Phys. **26** (1957) 881.
13) Landolt-Börnstein, *Tabellen*, dritter Ergänzungsband, Eg II, 74, p. 141.
14) P. Smyth: J. Amer. Chem. Soc. **60** (1938) 183.
15) K. Watanabe: J. Chem. Phys. **26** (1957) 542.
16) Landolt-Börnstein, *Tabellen*, Bd. 1, Teil 3, Molekeln III, p. 290.
17) R. S. Mulliken: J. Chem. Phys. **2** (1934) 782.
18) M.J.S. Dewar and L. Paoloni: Trans. Faraday Soc. **53** (1957) 261.
19) S. Tsuno and N. Mataga: Busseiron-Kenkyu **2**, no. 3 (1958) 665.
20) H.B. Klevens and J.R. Platt: J. Chem. Phys. **17** (1949) 470.
21) Y. Ooshika: J. Phys. Soc. Japan **9** (1954) 594.
22) R. Itoh: J. Phys. Soc. Japan **12** (1957) 829.

JOURNAL OF THE PHYSICAL SOCIETY OF JAPAN Vol. 14, No. 9, SEPTEMBER, 1959

Spin-Spin Interaction in the Paramagnetic Salts

By Kō SUGIHARA

Physical Institute, Nagoya University, Nagoya

(Received April 30, 1959)

The spin-spin interaction via phonon exchange is proposed as a new mechanism of the so-called exchange interaction between the electron spins of the paramagnetic ions in crystal which has been overlooked hitherto. The interaction Hamiltonian derived by Van Vleck to account for the spin-lattice relaxation phenomenon is used for the numerical estimate. It is shown that the interaction through phonon exchange may have the same order of magnitude as the dipolar coupling in some of the paramagnetic salts.

This interaction is temperature independent and at large distances falls off as inverse cube power of the inter-atomic distance. In nickel Tutton salts, the magnitude of the interaction is about 10^{-3}cm^{-1} at the distance 12A which is comparable to that of the dipolar interaction.

§1. Introduction

Experimentally the exchange interaction in the paramagnetic salts can be estimated by the magnetic specific heat measurements.1) The exchange contribution to the specific heat can be found by subtraction of the single ion contribution which is estimated by using the magnetically diluted samples and the dipolar contribution.

However it is not conclusive that the exchange contribution comes only from the isotropic exchange interaction since the interaction H appears in the form $Tr(H^2)$. Further, informations on the exchange interaction are obtained from the line width of the magnetic resonance2) and the susceptibility measurement.3)

As magnetic ions in the paramagnetic salts are separated fairly well from each other by a distance of the order 6 or 7A, direct exchange may be negligibly small and the superexchange via the intervening nonmagnetic ions4) may be effective especially in the concentrated salts. But the origin of this indirect coupling still remains in an indistinct situation.

The exchange interaction between a pair of neighboring magnetic ions varies considerable from one salt to another and the fact that there appears to be particulary strong interaction between paramagnetic neighbors in the cyanides of 3*d* group and the complexes of the 4*d* and 5*d* groups*) suggests that the mechanism of exchange coupling between two magnetic ions involves the diamagnetic ions lying between them.5) In this paper we shall propose an interaction resulting from a phonon exchange between the magnetic ions. Important properties of the interaction are the long range character and the temperature-independence. In some salts, e.g. nickel Tutton salts the order of magnitude of the coupling is comparable to that of the dipolar coupling.

---

*) For these salts strong crystal field or covalent bonding exists.

§ 2. Level Splittings in Crystal Field

Here we shall consider the nickel Tutton salts as an easily calculable example. Nickel Tutton salts are monoclinic crystals and there are two Ni^{2+} in the unit cell. Each divalent cation is surrounded by a distorted octahedron (nearly regular octahedron) of six water molecules and each magnetic complex $Ni^{2+}(H_2O)_6$ has differently oriented principal axis. Griffiths and Owen[6] has investigated a number of nickel Tutton salts in the paramagnetic resonance experiments. The orbital level ^3F in a cubic field splits as shown in Fig. 1. Triply degenerate levels Γ_4 and Γ_5 are lifted by a tetragonal and rhombic field and the spin triplet in the ground state Γ_2 splits into three singlets W_1, W_2 and W_3.

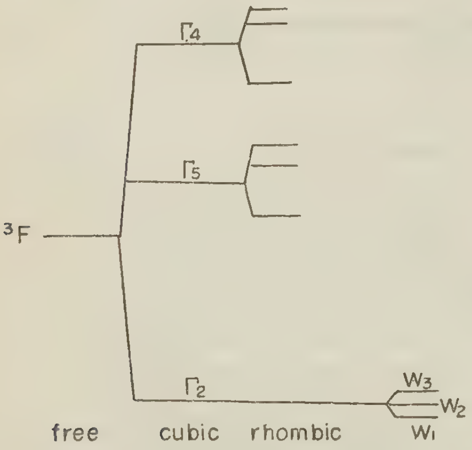

Fig. 1. Level splitting of Ni^{2+}

It is easily shown that

$$\Delta_{52} : \Delta_{45} = 5 : 4 , \tag{2.1}$$

where Δ_{52} and Δ_{45} are the energy gaps between $\Gamma_5-\Gamma_2$ and $\Gamma_4-\Gamma_5$ respectively. By combining the resonance data with the susceptibility measurements they obtain the spin–orbit coupling constant λ as about $-250\,\mathrm{cm}^{-1}$ which is 25% smaller than the free ion value and $g=2.25$ for all salts. From these data $\Delta_{52}=8000\,\mathrm{cm}^{-1}$ and $\Delta_{45}=6400\,\mathrm{cm}^{-1}$ are obtained. From the measurements of the optical absorption and g–value Owen[7] concludes $\lambda=-270\,\mathrm{cm}^{-1}$ and $\Delta_{52}=8400\,\mathrm{cm}^{-1}$ which are consistent with the resonance data.

Recently Low[8] investigated the paramagnetic and optical spectra of Ni–doped MgO crystal and obtained similar results.

§ 3. Spin–Spin Interaction through Phonon Exchange

Our eventual purpose in this work is to calculate the spin–dependent self–energy resulting from emission and absorption of one phonon between two magnetic ions i and j. We shall first define the Hamiltonian of the total system in the form

$$\mathscr{H} = H_O + H_L + \sum_j (H_{S.O}{}^{(j)} + H_{O.L}{}^{(j)}), \tag{3.1}$$

where H_O is the Stark energy of the orbit which will be assumed to be due to the point dipoles of the surrounding six water molecules and H_L is the energy of lattice vibrations. These two terms form the unperturbed Hamiltonian and the perturbation terms $H_{S.O}{}^{(j)}$ and $H_{O.L}{}^{(j)}$ denote the spin-orbit coupling and the distorted part of the crystalline field due to the lattice vibration of the j–th magnetic ion respectively. $H_{O.L}{}^{(j)}$ is the interaction introduced by Van Vleck[9] in his theory of the paramagnetic relaxation.

Here, we shall consider the process in which i–spin emitts (or absorbs) one phonon and j–spin absorbs (or emitts) it. According to the various combinations of $H_{S.O}$ and $H_{O.L}$ in the perturbational calculation, many processes will appear and the effective term among them has the following type

$$\begin{aligned}\mathscr{H}'_{ij} = \sum_{k,\nu} \sum_{p,q=i,j} \sum_{\delta=\pm1} &< N_{K\nu} | H_{S.L}{}^{(P)} | N_{K\nu}-\delta > \\ &< N_{K\nu}-\delta | H_{S.L}{}^{(q)} | N_{K\nu} > \\ &\times (\delta \hbar \omega_{K\nu})^{-1} ,\end{aligned} \tag{3.2}$$

where $N_{K\nu}$ is the phonon number with wave vector $\boldsymbol{K}$ and polarization ν. $H_{S.L}{}^{(i)}$ is the Hamiltonian of i–th ion inducing the spin–lattice relaxation and can be written as

$$\begin{aligned} H_{S.L}{}^{(i)} = \sum_{t.t'} \{ &< \Gamma_2 | H_{S.O}{}^{(i)} | \Gamma_{5t'} > \\ &< \Gamma_{5t'} | H_{S.O}{}^{(i)} | \Gamma_{4t} > < \Gamma_{4t} | H_{O.L}{}^{(i)} | \Gamma_2 > \\ &+ < \Gamma_2 | H_{O.L}{}^{(i)} | \Gamma_{4t} > < \Gamma_{4t} | H_{S.O}{}^{(i)} | \Gamma_{5t'} > \\ &< \Gamma_{5t'} | H_{S.O}{}^{(i)} | \Gamma_2 > \} (\Delta_{52} \Delta_{42})^{-1} \\ &+ < \Gamma_2 | H_{S.O}{}^{(i)} | \Gamma_{5t} > < \Gamma_{5t} | H_{O.L}{}^{(i)} | \Gamma_{5t'} > \\ &< \Gamma_{5t'} | H_{S.O}{}^{(i)} | \Gamma_2 > (\Delta_{52})^{-2} ,\end{aligned} \tag{3.3}$$

where Γ_{4t} and Γ_{5t} are the states which belong to Γ_4 and Γ_5 respectively. Since Ni^{++} and Cr^{+++} belong to the same orbital configuration and the difference of $3d$-electron numbers is five, so we can use the same expression for $H_{S.L}$*) as that for the chrome alum given by Van Vleck.10) Then

$$H_{S.L}=\mathcal{E}_1[Q_3(2S_z^2-S_x^2-S_y^2)$$
$$+\sqrt{3}\,Q_2(S_y^2-S_x^2)]$$
$$+\mathcal{E}_2[Q_4(S_xS_y+S_yS_x)+(S_zS_x+S_xS_z)$$
$$+Q_6(S_yS_z+S_zS_x)]\,, \tag{3.4}$$

with

$$\mathcal{E}_1=175\sqrt{3}\,\lambda^2\rho_2/(99\varDelta_{52}^2)\,,$$
$$\mathcal{E}_2=4\lambda^2[\rho_1+5\rho_2/33]/\varDelta_{52}^2+8\lambda \tag{3.5}$$
$$[\rho_1-5\rho_2/44]/(\varDelta_{52}\,\varDelta_{42})\,,$$
$$\rho_1=12e\mu<r^2>/7a^5\,,$$
$$\rho_2=-66e\mu<r^4>/7a^7\,. \tag{3.6}$$

Now the vibrations of a complex $M\cdot(H_2O)_6$ (M: magnetic ion) are specified by a set of normal coordinates Q_k which has been discussed in detail by Van Vleck.9)

$<r^2>$ and $<r^4>$ denote the mean square and fourth power radius of the $3d$-electron respectively, a the distance between the magnetic ion and any one of the water molecules and μ the dipole moment of a water molecule. Any other process than (3.2) are negligibly small since the ratio to (3.2) is the order $\hbar\omega_{K\nu}/\varDelta\ll1$. Hereafter, we shall restrict our calculation only to the term involving $\mathcal{E}_1$ which is the same order as $\mathcal{E}_2$. Displacement of a water molecules from the equilibrium position is expanded in Debye waves as follows

$$\xi(r)=\sqrt{\frac{\hbar}{2NM}}\sum_{K.\nu}\mathbf{e}_{K.\nu}(\omega_{K\nu})^{-1/2}(a_{K\nu}\exp(i\boldsymbol{Kr}).$$
$$+a_{K\nu}^*\exp(-i\boldsymbol{Kr})). \tag{3.7}$$

Since (3.7) is the expression commonly used, it may need no explanation. Using (3.7), we can express Q_2 and Q_3 as

$$Q_2^{(j)}=i\sqrt{\frac{\hbar}{2NM}}\sum_{K.\nu}(\omega_{K\nu})^{-1/2}(a_{K\nu}\exp(i\boldsymbol{Kr}_j)$$
$$-a_{K\nu}^*\exp(-i\boldsymbol{Kr}_j))$$
$$\times(e_{K\nu}^{(x)}\sin(\boldsymbol{KX})-e_{K\nu}^{(y)}\sin(\boldsymbol{KY}))\,,$$
$$Q_3^{(j)}=i\sqrt{\frac{\hbar}{6NM}}\sum_{K.\nu}(\omega_{K\nu})^{-1/2}(a_{K\nu}\exp(i\boldsymbol{Kr}_j)$$
$$-a_{K\nu}^*\exp(-i\boldsymbol{Kr}_j))$$
$$\times(e_{K\nu}^{(x)}\sin(\boldsymbol{KX})+e_{K\nu}^{(y)}\sin(\boldsymbol{KY}) \tag{3.8}$$
$$-2e_{K\nu}^{(z)}\sin(\boldsymbol{KZ}))\,,$$

where $\mathbf{r}_j$ is the coordinate of j-th magnetic ion and $X=(a,o,o)$, $\mathbf{Y}=(o,a,o)$, $\boldsymbol{Z}=(o,o,a)$. By inserting (3.4) and (3.8) into (3.2), it is easily shown that phonon number $N_{K\nu}$ cancels out, so that interaction turns out to be temperature independent. The effective spin Hamiltonian (3.2) becomes

$$\mathscr{H}'_{ij}=-\mathcal{E}_1^2\frac{V}{(2\pi)^3}\frac{1}{3NM}\sum_{\nu}v_\nu^{-2}\iiint\cos(\boldsymbol{K},\boldsymbol{r}_i-\boldsymbol{r}_j)$$
$$[F_{K\nu}(2S_{zi}^2-S_{xi}^2-S_{yi}^2)+3G_{K\nu}(S_{yi}-S_{xi}^2)]$$
$$[F_{K\nu}(2S_{zj}^2-S_{xj}^2-S_{yj}^2)+3G_{K\nu}(S_{yj}^2-S_{xj}^2)]$$
$$dKd\Omega_K\,, \tag{3.9}$$

where v_ν is the sound velocity for the polarization ν and

$$F_{K\nu}=e_{K\nu}^{(x)}\sin(\boldsymbol{KX})+e_{K\nu}^{(y)}\sin(\boldsymbol{KY})$$
$$-e_{K\nu}^{(z)}\sin(\boldsymbol{KZ})\,, \tag{3.10}$$
$$G_{K\nu}=e_{K\nu}^{(x)}\sin(\boldsymbol{KX})-e_{K\nu}^{(y)}\sin(\boldsymbol{KY})\,.$$

For simplicity, we have picked up the interaction between the equivalent ions and omitted the term between the inequivalent ones which can be easily written down.

It is very complicated to evaluate the integral (3.9) in general case, so we shall confine our consideration to the following special case :

$\boldsymbol{r}_i-\boldsymbol{r}_j=\boldsymbol{R}\|Z$ -axis, $R\gg a$ and $K_oR\gg1$ (K_o : cut off wave vector). Thus we obtain

$$\mathscr{H}'_{ij}=A\,(S_{yi}^2-S_{xi}^2)\,(S_{yj}^2-S_{xj}^2)+O(a^4/R^5), \tag{3.11}$$

$$A=-\frac{90}{\pi R^3v^2W}\left(\frac{\lambda^2}{\varDelta_{52}}\right)^2. \tag{3.12}$$

The coefficient A is the lowest order term ($\sim a^2/R^3$) in the expansion of a/R. In writing down (3.12), we have used the relation $\varDelta_{52}=25e\mu<r^4>/3a^6$ which is valid for the point dipole model. v is the effective common velocity for v_ν and W the density.

Using our simplified assumption, it is easily shown that the cross term such as $F_{K\nu}\,G_{K\nu}$ disappears rigorously and term containing $F_{K\nu}^2$ is negligibly small since the ratio to the term containing $G_{K\nu}^2$ is $\sim a^2/R^2$. In general cases, these terms may appear in the same order of magnitudes as that of $G_{K\nu}^2$. To evaluate (3.12) numerically, we use the following values of the constants

$$\lambda=-250\,\text{cm}^{-1}\,,\quad \varDelta_{52}=8000\text{cm}^{-1}\,,\quad W=2\,,$$
$$v=2.3\times10^5\text{cm/sec},^{**)}\quad R=12\text{Å} \tag{3.13}$$

---

*) For brevity, we shall omit the suffix specifying magnetic ion.

**) There are no available specific heat data of Tutton salts, so we take the value of v used Van Vleck for alums.

$R=12$Å[†] is the distance between a pair of equivalent magnetic ions satisfying the conditions $R \gg a$ and $K_0R \gg 1$ ($K_0=1.9\times10^8\mathrm{cm}^{-1}$). The value of A computed from (3.12) with the aid of (3.13) is

$$A=-1.5\times10^{-3}\mathrm{cm}^{-1}, \qquad (3.14)$$

and now it is remarkable that (3.14) is the same order as the dipolar coupling. It is easily shown that the oscillating terms proportional to $\cos(K_0R)/K_0R^2$ or $\sin(K_0R)/K_0R^2$ which are neglected in (3.11) are unimportant even if R is the distance between the nearest neighbor pair[*].

Our calculation is based on the two assumptions: i) the magnetic ion is purely ionic and ii) the water molecule can be regarded as point dipole. However the experimental observations that λ in salts is reduced considerably as compared with free ion value suggest our assumptions are oversimplified.

Nevertheless the final conclusion will not be altered drastically even if we treat the problem in more detail taking account of the charge transfer between the magnetic ion and the ligand.

§ 4. Conclusion

The discussion of the preceding section may be summarized in the following conclusions. In some paramagnetic salts, the spin—spin interaction via phonon exchange has a comparable order of magnitude to that of the dipolar coupling. This interaction falls off as inverse cube power of distance at the large distances and temperature-independent. In the diluted salts this interaction will be more important than the indirect coupling suggested by Kramers. Up to the present, informations on the mechanism of the spin coupling in the paramagnetic salts are quite incomplete, so it may be desirable to clarify the mechanisms from both experimental and theoretical investigations.

References

1) B. Bleaney and K. W. H. Stevens: Rep. Progr. Phys. **16** (1953) 276. A. H. Cooke: Progress in Low Temperature Physics **1** (1955) 224. R. J. Benzie, A. H. Cooke and S. Whitley: Proc. Roy. Soc. **A, 232** (1955) 277. T. Nakamura and N. Uryu: J. Phys. Soc. Japan **11** (1956) 760.
2) D. M. H. Bagguley and J.H.E. Griffiths: Proc. Roy. Soc. **A, 201** (1950) 366. K. Yosida: Progr. Theor. Phys. **5** (1950) 1047. B. Bleaney and K.D. Bowers: Proc. Roy. Soc. **A, 214** (1952) 451. H. Kumagai, H. Abe and J. Shimada: J. Phys. Soc. Japan **7** (1952) 385. B. Bleaney and D. J. E. Ingram: Proc. Phys. Soc. London **A, 65** (1952) 953. J.M. Baker and B. Bleaney: Conférence de Physique des Basses Températures, Paris (1955). F. R. McKim and W.P. Wolf: Proc. Phys. Soc. London **B, 69** (1956) 1231.
3) B. C. Guha: Proc. Roy. Soc. **A, 206** (1951) 353.
4) H. A. Kramers: Physica **I** (1934) 182. P. W. Anderson: Phys. Rev. **79** (1950) 350.
5) K. D. Bowers and J. Owen: Rep. Progr. Phys. **18** (1955) 304. J.H.E. Griffiths, J. Owen, J.G. Park and M.F. Partridge: Phys. Rev. **108** (1957) 1345.
6) J.H.E. Griffiths and J. Owen: Proc. Roy. Soc. **A, 213** (1952) 459.
7) J. Owen: Proc. Roy. Soc. **A, 227** (1955) 183.
8) W. Low: Phys. Rev. **109** (1958) 247.
9) J. H. Van Vleck: J. Chem. Phys. **7** (1939) 72.
10) J. H. Van Vleck: Phys. Rev. **57** (1940) 426.

[†] There are equivalent pairs at the distances 6.1Å, 9Å and 9.5Å.

[*] When $R=6.1$Å, $K_0R=12\gg1$ and $a/R\fallingdotseq1/3<1$.

JOURNAL OF THE PHYSICAL SOCIETY OF JAPAN Vol. 14, No. 9, SEPTEMBER, 1959

Measurement of Plasma Temperature and Electron Density

By Kiyoshi MURAKAWA and Shizuyo MIZUNO-HASHIMOTO

Aeronautical Research Institute, University of Tokyo, Komaba-machi Meguro-ku, Tokyo

(Received May 18, 1959)

This investigation aims at measuring the temperature of the plasma obtained by passing condensed discharge through a Geisler tube containing neon. The wave-length of Ne I $\lambda 5852$ emitted from condensed discharge was compared with that of the same line emitted from arc discharge, the comparison being made with a Fabry-Perot etalon. Red shift of the line by spark discharge was detected. From the amount of the shift the half-value width contributed by the ionic field and electrons was calculated by Lindholm's formula. Subtracting this (vectorially) from the observed half-value width, the width contributed by the Doppler effect alone was obtained, and then the plasma temperature was calculated. From the line profiles of $H\gamma$ and Ne I $\lambda 4715$ Holtsmark's so-called normal field strength F_n was obtained, and therefore the electron density could be deduced. In our present example the mean plasma temperature was $T=6\times 10^3$ K, and the mean electron density $N=1\times 10^{10}$ per cm.^{3}

§ 1. Introduction

For some time we are interested in measuring the temperature and the electron density in a plasma obtained by passing discharge through neon. As a first step toward this object condensed discharge through a Geisler tube was studied, because this is the easiest arrangement for spectroscopic determination of the above-mentioned quantities. A preliminary description of the result obtained was published1) in Japanese in 1958. Since then somewhat stronger spark discharge has been employed and somewhat higher temperature has been obtained.

Dynamic characteristics of the plasma in discharges through neon and argon was measured previously by Olsen and Huxford.2) The plasma seems to have been generated in a bulb similar to that of the present work, so their results will be referred to frequently in the present paper. Temperature of discharge in hydrogen (constant current) was measured by several investigators.3) In the case of hydrogen contribution of the ionic field and electrons to the width of spectral line is large compared with that of the Doppler effect, but in the case of neon, if adequate lines are selected, the latter effect is expected to be larger than the former, and can be used in calculating the plasma temperature. The primary purpose of the present investigation is to examine experimentally to what extent this expectation is satisfied.

§ 2. Experimental Arrangement

The plasma source was a discharge through a Geisler tube which was made of pyrex glass and whose capillary portion was about 3 mm in inner diameter. Neon of about 5 mm Hg pressure was filled in the tube. The electric circuit is shown schematically in Fig. 1. In order to get condensed discharge, a condenser with a capacity of $0.02\mu F$ was used and the current passed through a spark gap and the Geisler tube. This type of discharge will be denoted as spark discharge. In order to compare with this an ordinary a.c. discharge, discharge was passed by

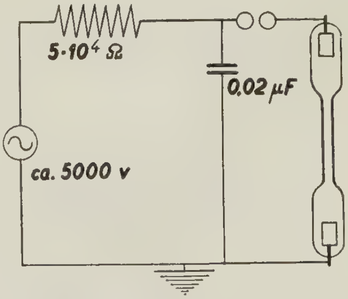

Fig. 1. Schematic diagram of the circuit for the condensed discharge in Geisler tube containing neon.

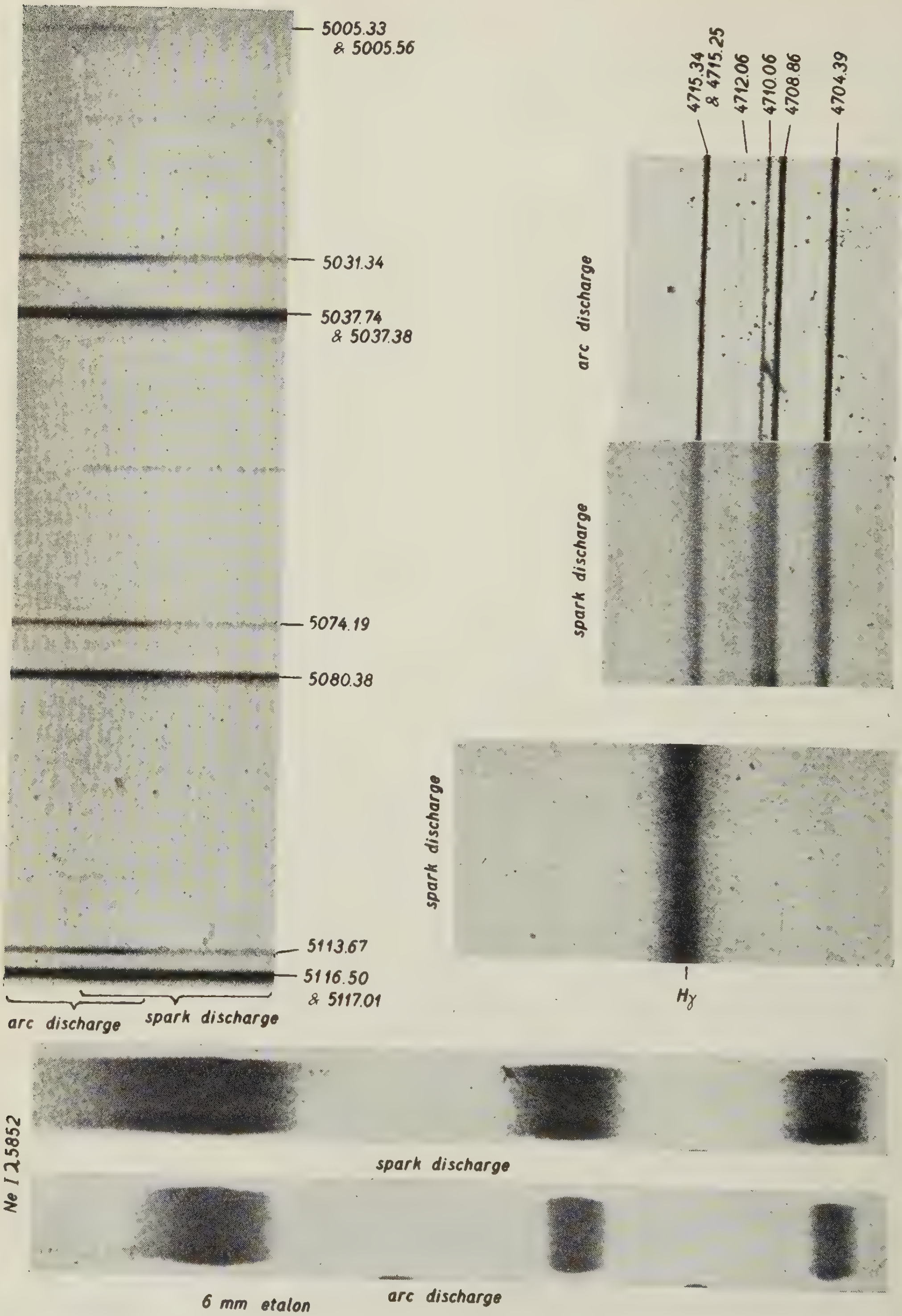

Fig. 2. Enlargement of some spectrograms. The four upper spectrograms were taken with a two-prism spectrograph. The two lower pictures were taken with a Fabry-Perot etalon.

displacing the condenser and the spark gap and lowering the output voltage of the transformer. This type of discharge will be called arc discharge.

For the purpose of spectroscopic observation, the light emitted from the capillary portion was viewed "side off". The spectrum was photographed by means of a two-prism spectrograph equipped with a camera-lens having 1.5 m focal length. When the displacement of a spectral line due to spark discharge had to be measured, a silvered or multi-layer coated etalon was employed. In order to get intensity marks, a step-filter having 30 steps with $\Delta D=0.15$ was used. Some of the spectrograms are reproduced in Fig. 2.

§ 3. Plasma Temperature

In order to determine the plasma temperature by means of Doppler effect, the line Ne I λ5852 was selected. First the interference pattern of λ5852 emitting from arc discharge was photographed and then, without touching the Geisler tube and the Fabry-Pérot etalon, that of λ5852 emitting from spark discharge was photographed. See Figs. 2 and 3. This method enables us to determine precisely the displacement of the line when the discharge condition is varied, and was adopted long ago by Ross and one of the authors.4) From the microphotometer trace of the interference patterns, the intensity distribution (line profile) was obtained, as shown in Fig. 4. In the analysis, it was assumed that natural neon consists of 10 parts of Ne^{20} and 1 part of Ne^{22} and that in Ne I λ5852 the Ne^{22}-component lies to the violet side of the Ne^{20}-component by the amount $\Delta\nu=0.072\ \mathrm{cm}^{-1}$ (according to Nagaoka and Mishima5)). In the following only the Ne^{20}-component (after making the correction due to Ne^{22}) is considered. Assuming that in arc discharge the line Ne I λ5852 undergoes no influence of the ionic field nor of the electrons, it was found that the spark discharge displaces the line to the red by the amount $\Delta\nu_{\parallel s}=-0.027\ \mathrm{cm}^{-1}$. It was also found that the half-value width of the line emitting from the spark discharge is $\Delta\nu_{h}=0.230\ \mathrm{cm}^{-1}$, in which the width due to the Fabry-Perot etalon is eliminated.

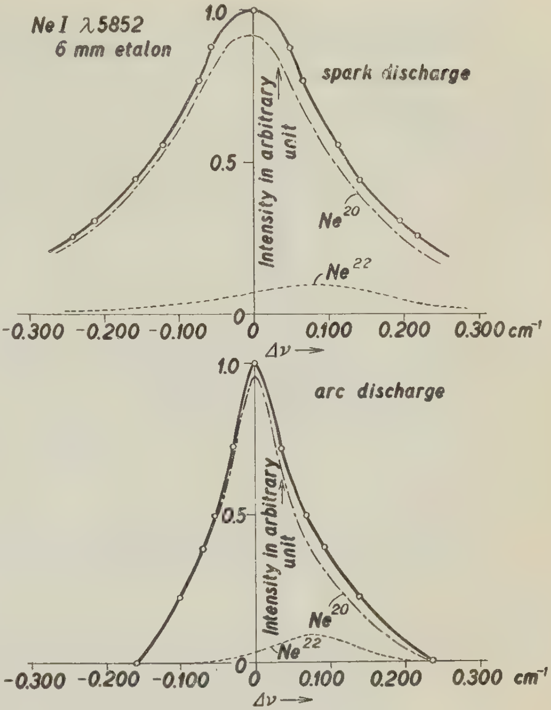

Fig. 4. Intensity distribution (profile) of the line Ne I λ5852 obtained with a 6 mm etalon.

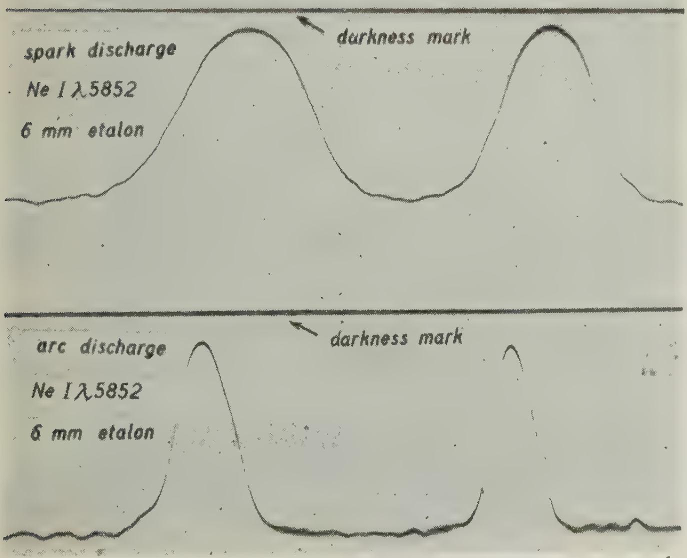

Fig. 3. Microphotometer trace of the interference patterns of the Fabry-Perot etalon (reduced about 1/3 from the original)

Ne I λ5852 was classified by Paschen as $1.5\,s_2-2\,p_1$. The initial level is $[2p\,3p]_0$, and the final level $[2p\,3s]_1$, in which $2p^5$ is abbreviated as $2p$. In the previous work¹⁾ it was shown that in Ne I the mixing of $2p\,3s$ and $2p\,3d$ is negligible, and that the Stark effect of λ5852 (in uniform electric field) is given by

$$\Delta\nu=-\gamma F^2\,,$$

$$\gamma=4.00\times10^{-12}\,,$$

in which F (electric field strength) is measured in volt/cm and $\Delta\nu$ in cm^{-1}, and it is assumed that F is adequately small. The value of γ was calculated by the method of Foster.⁷⁾

In the case of spark discharge the fluctuation of the ionic field and the collision damping by electrons give rise to broadening and displacement of spectral line.⁸⁾ In the case of a spectral line which exhibits quadratic Stark effect, Lindholm⁹⁾ showed that

$$\Delta\nu_h=0.0450\gamma^{\frac{2}{3}}v^{\frac{1}{3}}N/c\,,$$

$$\Delta\nu_{\rm dis}=0.0387\gamma^{\frac{2}{3}}v^{\frac{1}{3}}N/c\,,$$

in which γ is the Stark effect constant N the electron density (per cm³), and c is the velocity of light. The mean velocity of electron is denoted by v and is connected with the temperature by the relation

$$\frac{1}{2}m\,v^2=\frac{3}{2}k\,T.$$

From the formulas given by Lindholm, we get

$$\frac{\Delta\nu_h}{\Delta\nu_{\rm dis}}=\frac{0.0450}{0.0387}=1.16$$

In our case we got $\Delta\nu_{\rm dis}=-0.027$ cm^{-1}. Using the above-mentioned relation, we get $\Delta\nu_h=0.031$ cm^{-1}. This is the width contributed by the ion and electron alone and does not include the contribution of the Doppler effect.

The line profile $U(\Delta\nu)$ contributed by the ionic field alone can be calculated, using the probability function $W(F)$ introduced by Holtsmark.¹⁰⁾ The numerical calculation of $W(F)$ was published by Pannekoek and Verwey.¹¹⁾ Using their numerical values, the form of $U(\Delta\nu)$ was calculated, as shown in Fig. 5.

The line profile due to the electron alone can be assumed to be of dispersion type⁸⁾ and can be written as

$$I_{\rm el}=\frac{c}{(\Delta\nu-k)^2+\Delta\nu_h^2/4}\,.$$

The line profile contributed by the ionic field and the electron (neglecting the Doppler effect) can be expressed (as a first approximation) as

$$I(\Delta\nu)\,d\nu=d\nu\int_{-\infty}^{\infty}\frac{cU(x)\,dx}{(\Delta\nu-k-x)^2+\Delta\nu_h^2/4.}$$

On the other hand Doppler effect alone should give rise to a line profile of a gaussian type. The combination of the above-mentioned expression and gaussian distribution is much complicated and there is no simple way of deducing the Doppler width from the observed width.¹²⁾ We have therefore assumed that the Doppler width is the mean of the linear difference width and the square difference width, and obtained the Doppler half-value width $\Delta\nu_D=0.213$ cm^{-1}. It is connected with the absolute temperature T, the mass number M, and the wave.number ν (cm^{-1}) by the relation

$$\Delta\nu_{\rm D}=7.2\times10^{-7}\,\nu\sqrt{T/M}.$$

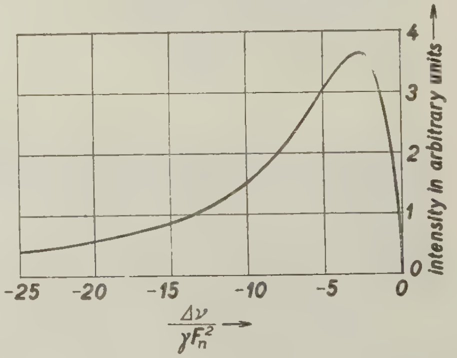

Fig. 5. Line profile of Ne I λ5852 calculated by means of Holtsmark's method and neglecting the influence of the electron and the Doppler effect.

Putting $\nu=17083$ cm^{-1}, $\Delta\nu_D=0.213$ cm^{-1}, $M=20$ in the formula, we get $T=6.0\times10^3$ K.

We shall see later that the value of F_n (Holtsmark's so-called normal field strength) is 1.7×10^4 volt/cm. Putting this value in Fig. 5 we see that the ionic field alone contributes 0.009 cm^{-1} to the half-value width and -0.003 cm^{-1} to the shift. It can be seen that in spark discharge the electron effect in Ne I λ5852 is larger than the ionic field effect in both half-value width and red shift.

§ 4. Electron Density in a Plasma

The electron density N can be deduced from the normal field strength F_n via the relation

$$F_n = 2.61\, N^{2/3} e\ ,$$

where e is the electron charge.

F_n can be determined from the profile of a line showing a linear Stark effect. Ne I λ4715 was selected for this purpose (the assumption of a linear effect is sufficient for our purpose, although this line suffers a quadratic effect in a small electric field). The hydrogen line can also be utilized, as was done by Olsen and Huxford.[2)] The Geisler tube used contained a trace of hydrogen, but no strong hydrogen line was obtained in the case of arc discharge. In the case of spark discharge, however, hydrogen lines (especially Hα, Hβ and Hγ) came out strongly. Microphotometer traces of the lines Ne I λ4715—4704 and the line Hγ are reproduced in Fig. 6.

From the microphotometer trace the line profile of Hγ was obtained, as shown in Fig. 7. It must be remarked that on the central part of Hγ two lines of Ne II are superposed. Using the theoretical profile curve for Hγ published by Olsen and Huxford, the value of F_n was determined so that the wing of the observed profile of Hγ would coincide with the wing of the theoretical profile (Holtsmark's classical theory applies only to the wing of the profile where the influence of the electron plays a minor role), and $F_n = 1.8 \times 10^4$ volt/cm was obtained.

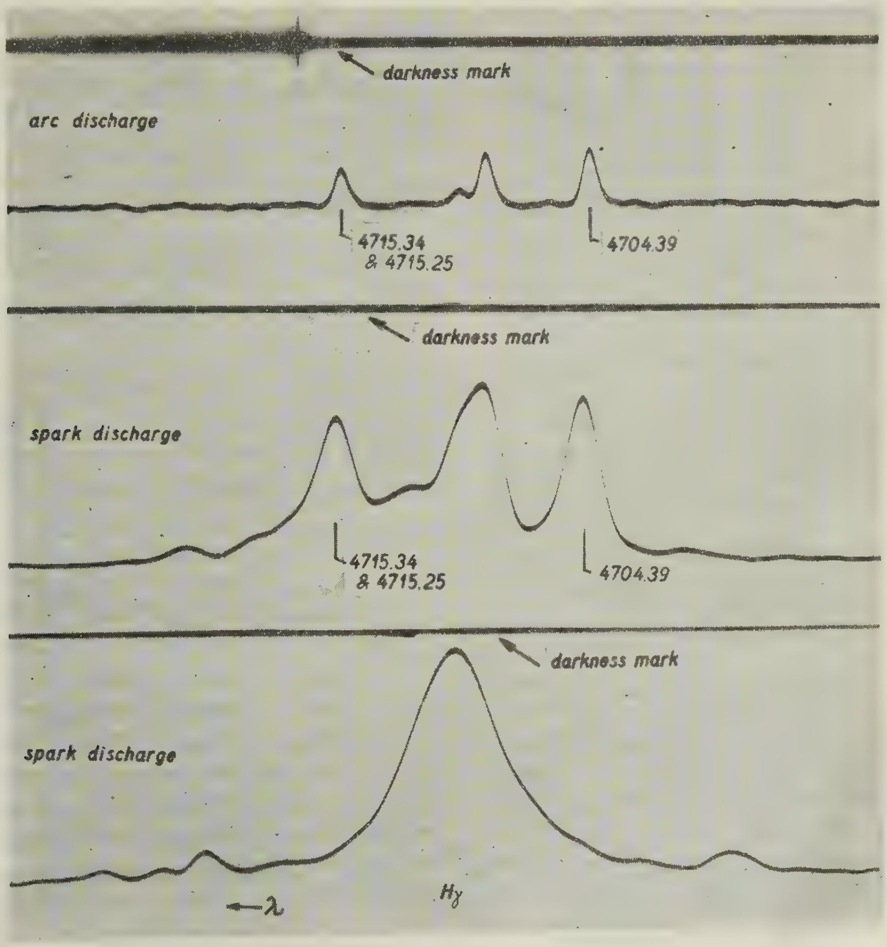

Fig. 6. Microphotometer trace of the lines Ne I λ4715-4704 and the line Hγ (reduced about 1/3 from the original).

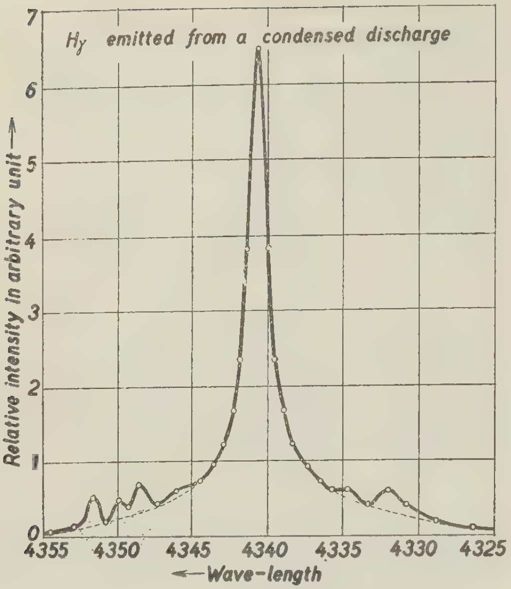

Fig. 7. Line profile or Hγ.

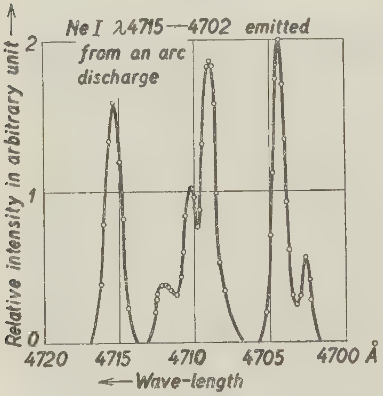

Fig. 8. Intensity distribution of the lines Ne I λ4715-4704 emitted from arc discharge.

The case of Ne I λ4715 is much more complicated, as shown in Figs. 8 and 9. The line λ4715 (in zero electric field) consists of a strong and a weak component, but Foster and Rowles[13] showed that in a sufficiently strong field they fuse together (Paschen-Back effect analog). The Stark effect for the line λ4715 is shown schematically in Fig. 10. The profile for λ4715 was calculated using the data published by Foster and Rowles and the method of Holtsmark. In Fig. 10 (and in Fig. 11) m_l of the optical electron is denoted as m_l for brevity. The experimental profile for λ4715 is such that the wing on the red side alone can be utilized, because the wing on the violet side is strongly disturbed by the wings of other lines. The wing on the red side of λ4715 is contributed mainly by (p_9)—$2p\,6d\,(d_4')$. The relative intensities of the components due to the transition) (p_9)—$2p\,6q$ were calculated by the method of Foster[7] in a rough way and the theoretical curve was calculated (Fig. 11), but the accuracy of calculation is such that it is sufficient for concluding that the

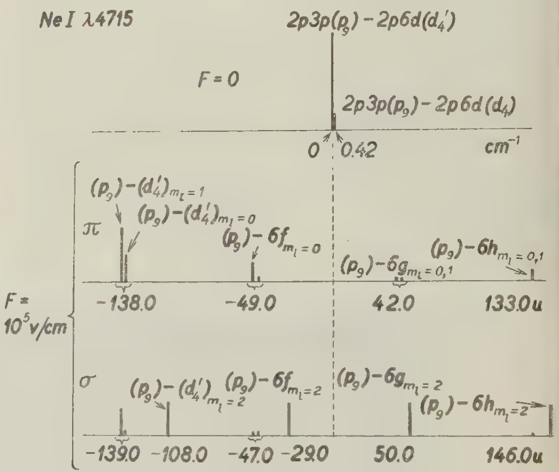

Fig. 10. Stark effect of the lines Ne I λ4715. The positions of the splitted components were taken from the article of Foster and Rowles. The relative intensities were calculated roughly by the authors. It was assumed that the lower level is not displaced by the electric field.

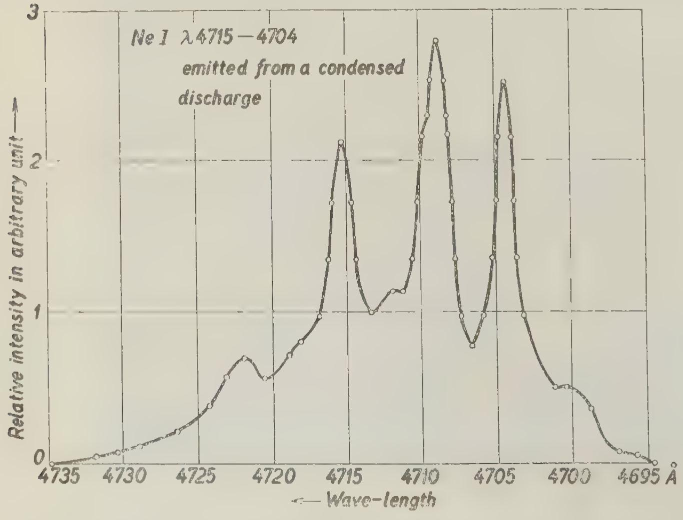

Fig. 9. Intensity distribution of the lines Ne I λ4715-4704 emitted from spark discharge.

effect of the transition $(p_9)-2p\,6f$ on the solid curve of Fig. 11 is negligible. It was found that the wing of λ4715 on the red side can be accounted for by putting $F_n=1.5\times10^4$ volt/cm. Since the conclusion from Hγ seems to have a somewhat better accuracy, the mean of F_n is taken to be $F_n=1.7\times10^4$ volt/cm. Putting this value in the above-mentioned formula, we get the electron density $N=1\times10^{16}$ (per cm³).

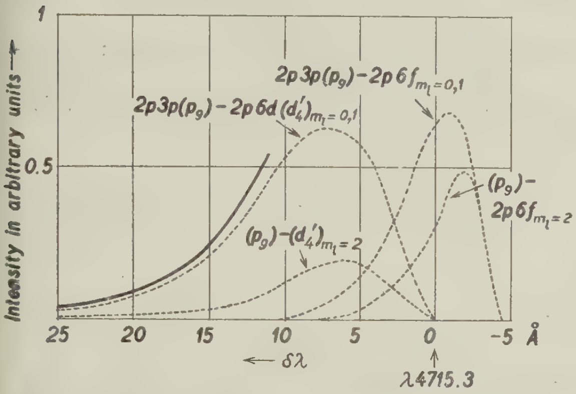

Fig. 11. Intensity distribution of the components $(p_9)-(d_4')$ and $(p_9)-6f$ of λ4715, calculated by Holtsmark method, neglecting the electron effect. It is assumed that $F_n=15$ kv/cm. The resultant intensity distribution that is useful for comparing with the experimental profile of the wing on the red side is shown by a solid curve. Paschen's notation for spectral term is in parentheses.

In the case of Ne I λ5037.7 $(2p\,3p-2p\,5d)$, the line profile for the spark discharge is degraded to the red (see Fig. 2), owing to the lack of $p-h$ component. The value of F_n deduced from this line is in agreement with the above-mentioned value of F_n, but in this case the accuracy is not so good.

§ 5. Physical Meaning of the Results Obtained

Since the current in the plasma varied with time, the physical meaning of the results obtained is somewhat more complicated than in the case of constant discharge current. The current and the potential were measured with a Tekronix c.r.o. and the wave forms are shown in Fig. 12. The main trend is similar to that of Olsen and Huxford,[2] so that it can be expected that also the time variation of the intensity of individual spectral line is similar. This was found indeed to be the case. The c.r.o. traces of the photomultiplier currents are reproduced in Fig. 13, but they are not new as compared with those published by Olsen and Huxford.[2]

Olsen and Huxford showed that although the discharge current reaches its maximum in a few μ sec and vanishes within 10 μ sec, the ion concentration keeps its approximately flat value for over 30 μ sec. We may therefore expect that once a high temperature is attained in the spark discharge, this will not decrease so rapidly as the discharge current.

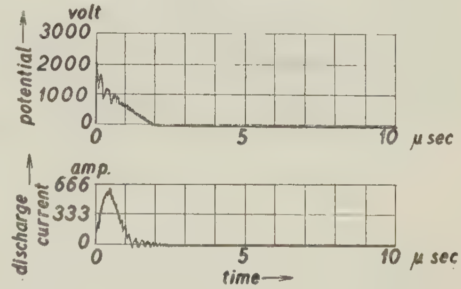

Fig. 12. Cathode-ray oscilloscope traces of the potential and the discharge current.

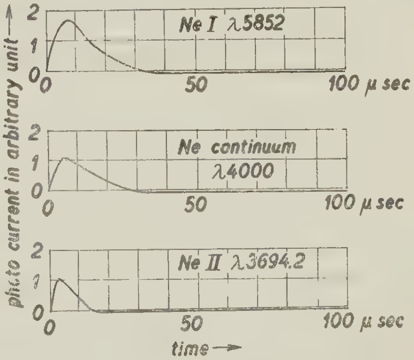

Fig. 13. Cathode-ray oscilloscope traces of the photo currents for individual spectral lines.

The line profiles of Ne I λ5852 and λ4715 and Hγ that were deduced in the present investigation are mean profiles, in which the mean is taken over the time, the intensity of the respective line at each instant being the weight. If we keep in mind the above-mentioned conclusion of Olsen and Huxford, we may assume that the mean plasma temperature deduced from the profile of Ne λ5852 (in the present work) would not be much lower than the maximum temperature.

Measurement of plasma temperature and

electron density will be continued, and it is hoped that by modifying the experimental set-up it would be possible to get a higher temperature than that reported here.

References

1) K. Murakawa and S. Mizuno: Bull. Aeron. Res. Inst. Univ. Tokyo, **1** (1958) 153.
2) H. N. Olsen and W. S. Huxford: Phys. Rev. **87** (1952) 922.
3) G. Jurgens: Z. Phys. **134** (1952) 21.
   H. Griem: Z. Phys. **137** (1954) 280.
   P. J. Dickerman: J. Appl. Phys. **29** (1958) 598. *Conference on Extremely High Temperature*, ed. by H. Fischer and L. C. Mansur, (John Wiley and Sons, N.Y. 1958) 77.
4) J. S. Ross and K. Murakawa: Phys. Rev. **85** (1952) 559.
5) H. Nagaoka and T. Mishima: Sci. Papers Inst. Phys. Chem. Res. Tokyo **13** (1930) 293.
6) F. Paschen: Ann. Physik [4] **60** (1919) 405.
7) J. S. Foster: Proc. Roy. Soc. **A, 117** (1927) 137.
8) See, for example, the review article of R. G. Breene: Rev. Modern Phys. **29** (1957) 94.
9) E. Lindholm: Dissertation Uppsala Univ. (1942).
10) J. Holtsmark: Phys. Z. **20** (1919) 162.
    P. Debye: Phys. Z. **20** (1919) 160.
11) A. Pannekoek and S. Verwey: Proc. Acad. Amsterdam **38** (1935) 479.
12) H. C. v. d. Hulst and J.J.M. Reesinck: Astrophys. J. **106** (1947) 121.
13) J. S. Foster and W. Rowles: Proc. Roy. Soc. **A, 123** (1929) 80.

Errata

Crystal Structure of 2-Amino Azulene

By Yoshito TAKAKI, Yoshio SASADA and Isamu NITTA

J. Phys. Soc. Japan **14** (1959) 771

Page	Column	Line		Should be read
772	left	5	$(kh0)$'s	$(hk0)$'s
773	Fig. 3	near the middle of the lowest line	11 0 3	11 0 1

Rheological Equation of Voigtian Material

By Wataru SEGAWA

J. Phy. Soc. Japan **14** (1959) 1102

Page	Column	Line		Should be read
1104	left	11	$\partial A/\partial I_3{}^*=1$	$\partial A/\partial I_3{}^*=0$
1104	left	24	$g'^{\lambda\mu}\dfrac{\partial A}{\partial I_1}$	$g'^{\lambda\mu}\dfrac{\partial A}{\partial I_1}+$
1104	right	6	anisotropy	inherent anisotropy
1106	right	7	anisotropy	inherent anisotropy

Short Notes

This section is intended to secure prompt publication of important discoveries in physics. The reports should not exceed 800 words in length. A figure of size 7 cm × 7 cm will be counted as 150 words.

J. Phys. Soc. Japan **14** (1959) 1243

A Quantitative Study of the *M* Centre in KCl

By Tetsuhiko Tomiki
The Department of Physics,
The Faculty of Science,
Tohoku University, Sendai, Japan

(Received July 13, 1959)

As reported in the preceding short note1), two experimental results are obtained:

$$\Delta N_F/\Delta(f_M\cdot N_M)=2\ , \qquad (1)$$

$$2\eta_M=\eta_F=0.56,\ \text{above } 130°\text{C} \qquad (2)$$

where N_F and N_M are the concentration of the F and M centres, respectively, and are defined as follows:

$$N_F=1.31\cdot10^{16}H_F\cdot K_{F,\max}\ , \qquad (3)$$

$$f_MN_M=1.06\cdot10^{16}H_M\cdot K_{M,\max}\ . \qquad (4)$$

η is the quantum yield in the photochemical reaction $M+(\text{photon})_M\rightarrow F$, and defined by the next equations:

$$\left.\begin{aligned}\eta_M&=\partial(f_M\cdot N_M)/\partial q_M\ , &(5)\\ \eta_F&=\partial N_F/\partial q_M\ , &(6)\end{aligned}\right\}\ \text{for } q_M=0$$

where, q_M denotes the quanta absorbed in the M band. The result (2) shows that the M centre carries one electron at most. However, it is rather difficult to accept the relation $\eta_F=0.56$ without restriction, because the M centre decomposes thermally into the F centre above 130°C. Furthermore, the relation (1) indicates that f_M should be equal to 1.5, if the optical dipole-moment of the M centre is directed along the ⟨110⟩ of the host crystal, as is in the Seitz model.2) This is quite contradicted to the relation (2).

However, it is shown that the paradox is removed when the hypothesis by van Doorn3), the 2nd absorption band of the M centre hidden in the F band, is admitted. Then, the optically detected change ΔN_F should be multiplied with overlapping factor $\boldsymbol{p}$ in order to obtain the net variation of the number of F centre. $\boldsymbol{p}$ is obtainable under the requirement that the net quantum yield η_F^* should be unity:

$$\eta_F^*\equiv\partial(\boldsymbol{p}N_F)/\partial q_M=1.0\ . \qquad (7)$$

By using Eqs. (2) and (6), we have:

$$\boldsymbol{p}=1.8\ . \qquad (8)$$

If the oscillator strength of the 1st and 2nd bands of the M centre is denoted as f_{M1} and f_{M2}, respectively, then, the following equations are derived under the assumption that the dipole-moment of the M centre is directed to the ⟨110⟩:

$$\Delta(\boldsymbol{p}N_F)/\Delta(f_{M1}\cdot2N_0)=2\boldsymbol{p}\ ,$$

$$\Delta(\boldsymbol{p}N_F)=\Delta(6N_0)\ ,$$

where N_0 is the density of the M centre per cc whose dipole-moment is parallel to one of the ⟨110⟩. Thus,

$$f_{M1}=0.83\ ,\quad f_{M2}\cong1-f_{M1}=0.17\ . \qquad (9)$$

By using these constants we can estimate the net quantum yield η_M^* of the M centre above 130°C. From Eqs. (2) and (5) we have:

$$\eta_M=\partial(f_MN_M)/\partial q_M=\partial(2f_{M1}\cdot N_0)/\partial q_M\ ,$$

hence,

$$\begin{aligned}\eta_M^*&\equiv\partial(6N_0)/\partial q_M=3\eta_M/f_{M1}\\ &=3\times0.28/0.83=1.0\ . \qquad (10)\end{aligned}$$

Thus, the postulation (7) that requires $\eta_F^*=1.0$ leads to the conclusion that the quantum yield of the M centre η_M^* should also be equal to unity and, furthermore, $f_{M1}=0.83<1$. According to Eq. (10), it is possible to recalculate the quantum yield η_M^* using η_M. Then, η_M^* is expressed as follows:

$$\eta_M^*=1/\{1+1.40\cdot10^{-7}\exp(0.50/kT)\}\quad \text{for } kT \text{ in ev.} \qquad (11)$$

The obtained values, $A/B_0$4)$=1.40\cdot10^{-7}$ and $E=0.50$ ev, are also considered to be plausible. The simple calculation shows that the half width of the 2nd band of the M centre is the order of 0.08 ev at room temperature, if we assume that the absorption maximum is located at the peak of the F band. This result seems to be in concordance with the experimental fact that the half width of the F band is unaltered even when the "pure" M band exists on the red side of the F band1). The fact that the F band shows dichroism when it was illuminated with {110} polarized light in this band might reasonably be ascribed to the 2nd band of the M centre.

The author is very grateful to Prof. M. Ueta for his kind interest, and to Mr. Osaka for his discussions.

References

1) T. Tomiki: J. Phys. Soc. Japan **14** (1959) 1114.
2) F. Seitz: Rev. Mod. Phys. **18** (1946) 384.
3) C. Z. van Doorn: Philips Res. Rep. **12** (1957) 384.
4) N. F. Mott and R. W. Gurney: *Electronic Processes in Ionic Crystals* (Oxford, 1946) 135.

J. PHYS. SOC. JAPAN **14** (1955) 1244

Antiferromagnetic Resonance in $CoCl_2 \cdot 6H_2O$

By Muneyuki DATE*

The Research Institute for Iron,
Steel and Other Metals,
Tōhoku University, Sendai

(Received June 4, 1959)

We observed the antiferromagnetic resonance of $CoCl_2 \cdot 6H_2O$ in the frequency range 9.5 to 38 GC/sec at liquid helium temperatures. The antiferromagnetic properties of the hydrated cobaltous chloride have been reported first by Haseda and Kanda¹⁾ from the measurements of the powder susceptibility. Recently, X-ray analysis of the crystal structure²⁾, specific heat³⁾, susceptibility of the single crystal,⁴⁾ and proton magnetic resonance of this salt⁵⁾ were investigated and it became clear that the easy direction is parallel to the c-axis.

Up to present, paramagnetic resonance experiments of this compound were attempted by Gerritsen (80° and 20°K)⁶⁾ and by the present author (4.2°K at 9 GC/sec),⁷⁾ but no resonance was observed and it has been considered that this may be due to the short spin lattice relaxation time of the Co^{++} ion. Recently we attempted to detect the paramagnetic resonance of this salt at 35 GC/sec region at 4.2°K and observed very broad absorption lines. T_1 is estimated to be about 4×10^{-12} sec at $T=4.2$°K and the principal g-values to be $g_a'=2.9$, $g_b=5.0$ and $g_c=4.0$, where the a'-axis inclines to the direction of the a-axis by about 32° because of the monoclinic structure ($\beta=122°12'$). It is interesting to note the results of the susceptibility measurements by Haseda.⁴⁾ He obtained $g\,'=2.7$, $g_b=4.9$ and $g_c=4.9$. Appreciable difference is seen in g_c. The cause of discrepancy may be considered as follows. From the results of our experiments, considerable amount of the antiferromagnetic state (short range order) seems to survive even near 4°K and this produces the shift of paramagnetic resonance line because the antiferromagnetic and paramagnetic resonance lines are not much separated in this direction. Pure antiferromagnetic resonance was observed below 2.1°K. Between 2.1°K and 4.2°K, very broad and unmeasurable lines exist. We observed the frequency, the angular and temperature dependences of the antiferromagnetic resonance lines. One of the experimental results is shown in Fig. 1. The critical frequency is measured as 34630 ± 50 MC/sec below which the resonance line describes a circle in the b-c plane just as in the a-b plane of $CuCl_2 \cdot 2H_2O$ at 9 GC/sec⁸⁾ and above which the resonance can be observed all directions in b-c plane. The critical field resonance is also seen. From this results, $c_2/c_1 \sim 2$ can be obtained by Nagamiya-Yosida theory⁹⁾ ¹⁰⁾ of antiferromagnetic resonance for the case of orthorhombic symmetry. The critical field is 7.2 kilo-oersted at 1.5°K. It must be noted, however, that the experimental results show slight but systematic deviations from Nagamiya-Yosida theory. The line width was also measured. Generaly speaking, the width is large compared with that of $CuCl_2 \cdot 2H_2O$. At 1.5°K, the narrowest one is of 100 Oe and the broadest one is of 2000 Oe. Detailed results and discussions will be published later.

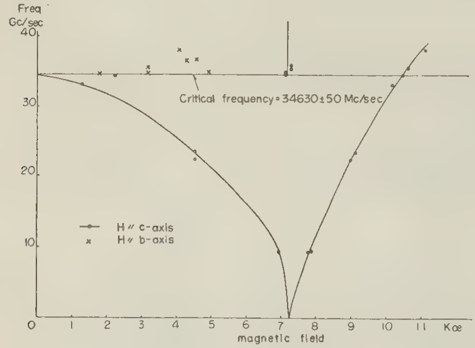

Fig. 1. Frequency-field diagram of antiferromagnetic resonance in $CoCl_2 \cdot 6H_2O$ at 1.5°K. Magnetic field is parallel to c-(easy) axis and b-axis.

Finally, the present author wishes to express his cordial thanks to Prof. Fukuroi for his continual encouragement during the course of present experiments. He is also indepted to Drs. Sugawara and Haseda for useful discussions on the present problem.

References

1) T. Haseda and E. Kanda: J. Phys. Soc. Japan **12** (1957) 1051.
2) J. Mizuno, K. Ukei and T. Sugawara: J. Phys. Soc. Japan **14** (1959) 383.
3) S. A. Friedberg: unpublished.
4) T. Haseda: to be published in this journal.
5) T. Sugawara: short note in this issue.
6) H. J. Gerritsen: Thesis (Leiden, 1955) 88.
7) M. Date: presented at the Meeting of the Phys. Soc. Japan (1955).
8) For example, J. Ubbink: Thesis (Leiden, 1953).
9) T. Nagamiya: Progr. Theor. Phys. **6** (1951) 342, 350; **11** (1954) 309.
10) K. Yosida: Progr. Theor. Phys. **6** (1951) 691; **7** (1952) 25, 425. See also T. Nagamiya, K. Yosida and R. Kubo: Advances in Physics **4** (1955) 1.

---

[*] Now at the Department of Physics, Facaulty of Science, Ôsaka Univ., Ôsaka.

J. PHYS. SOC. JAPAN **14** (1959) 1245

Crystalline Field Splitting in Ferrous Fluosilicate

By Taiichiro OHTSUKA

Research Institute for Iron,
Steel and Other Metals,
Tohoku University

(Received June 17, 1959)

When a large initial splitting of the spin state makes paramagnetic resonance unobservable, the splitting may be determined to a limited extent by measuring the susceptibility of single crystals at low temperatures. A rather large splitting of the lowest spin levels of $Fe^{2+}(^5D_4)$ in ferrous Tutton salt has been determined by this method.[1] Similar measurements have now been made on ferrous fluosilicate.

The isomorphous series of this crystal are known to have trigonal symmetry. The trigonal axis (c-axis) of the crystal coincides with the magnetic axis of the complex. Measurements were made parallel and perpendicular to the c-axis by the A. C. Hartsohn bridge method. The results are shown in Fig. 1.

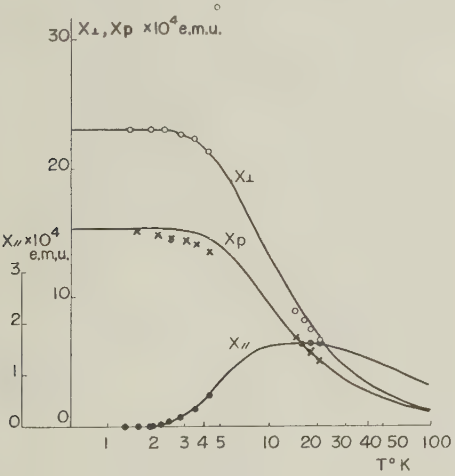

Fig. 1. $\chi_{//}$ (susceptibility parallel to c-axis) is plotted on an enlarged scale. χ_p is for a powder specimen. Solid lines are curves calculated using the values listed in Table I.

Table I.

	D	$g_{//}$	$g_\perp$
$FeSiF_6\cdot 6H_2O$	$-10.4\,cm^{-1}$	2.00	2.14
$Fe(SO_4)_2\cdot(NH_4)_2\cdot 6H_2O$*	$+14\,cm^{-1}$	2.32	2.06

* The ground spin doublet is split by an amount $6.4\,cm^{-1}$.

The pertinent parameters have been derived using the spin Hamiltonian $\mathscr{H}=-DS_z^2+g\beta\boldsymbol{H}\cdot\boldsymbol{S}$ with $S=2$. An expression for the susceptibilities for the case of axial symmetry may be readily derived and these have been used to fit the experimental results. The results may be expressed fairly well with a level scheme in which a spin singlet ($M=0$) lies lowest. The parameters derived are listed in Table I where the corresponding values for the ferrous Tutton salt have been listed for comparison. It is interesting to note that the sign of D and the anisotropy of g are opposite for the two salts. A similar change of sign seems to exist in the corresponding manganous salts.[2]

There is doubt as to the validity of the spin Hamiltonian for the Fe^{2+} case because the cubic field gives an orbital triplet lowest.[3] Our experiments are confined to low temperatures, however, and thus reflect only the splitting between the two lowest levels. The parameter D derived from our experiment corresponds to this splitting. It is probably incorrect to describe the scheme and the spacing of the excited levels with this D and the spin Hamiltonian. Measurements must be extended to higher temperatures in order to determine the details of the excited levels but the analysis will become progressively difficult because the splittings are then expected to become smaller than kT and one will get only an averaged out effect. There are reasons (the comparatively narrow line width of Mn^{2+} ions added as impurities)[1] to suspect that the excited spin doublets are split by rhombic distortion. Baker and Bleaney[4] report resonance at 20°K when the r.f. and external fields are directed along the c-axis. This could be due to transitions between the excited levels admixed by the rhombic field. If so the intensity should decrease when the temperature is lowered below about 14°K.

Proton resonance of the ligand water molecules have also been observed. With the external field perpendicular to the c-axis, 8 lines are observed with an overall splitting of 1 Mc/sec at 4.2°K. The splitting decreases and becomes very small as the field is rotated towards the direction parallel to the c-axis. This fact and the temperature dependence of the splittings are in close correspondence with the susceptibility results.

Acknowledgements are due to Prof. E. Kanda for his constant encouragement and to Assist. Profs. T. Haseda and T. Sugawara for various discussions.

References

1) T. Ohtsuka, H. Abe and E. Kanda: Sci. Rep. RITU, Tohoku Univ. **9** (1957) 476.
2) B. Bleaney and D. J. E. Ingram: Proc. Roy. Soc. **A, 201** (1950) 366.
3) A. Abragam and M. H. L. Pryce: Proc. Roy. Soc. **A, 205** (1951) 135.
4) Quoted by B. Bleaney and K. W. H. Stevens: Rep. Progr. Phys. **16** (1953) 108.

J. PHYS. SOC. JAPAN **14** (1959) 1246

Semiconducting Properties of Bi-Sb Alloys

By Seiichi TANUMA

The Research Institute for Iron,
Steel and Other Metals,
Tohoku University, Sendai

(Received June 24, 1959)

Bi and Sb crystallize with the same lattice structure, and the alloys between them become also solid solutions with the similar lattice structure in all composition.[1] It has been found that this alloy system, in spite of the crystallographic simpleness, shows anomalous electrical properties which can be explained by an assumption that the alloys of intermediate composition become intrinsic semiconductors. The resistivity, the Hall effect and the magneto-resistance of polycrystalline specimens which were prepared from zone refined constituent metals were measured in the temperature range from 4.2°K to 300°K. The plots of logarithmic resistivity versus reciprocal temperature are shown in Fig. 1. The similar plot for the Hall coefficient is also exemplified with the specimen #6 in the same figure. The sign of Hall coefficients was negative in all the present specimens. The concentration-dependence of both the resistivities and the Hall coefficients at 4.2°K and 200°K are shown in Fig. 2 (a) and (b). As shown in Fig. 1, the resistivity curves of the alloys containing Sb more than 4 atomic per cent seem to be non-metallic, or rather semiconductive. Fig. 2 proves that the alloys of intermediate compositions have high resistivities with the peak at around 10∼20 atomic per cent of Sb which is probably due to the depletion of carriers in them. The author regards that the positive gradients of the curves in Fig. 1 are due to the intrinsic semiconductivity. Then the maximum gradient in each alloy multiplied by twice the Boltzmann constant, $2k$, are plotted in Fig. 2 (c). This quantity may be regarded as a measure of the width of the forbidden energy band, even in the present case where the carriers are degenerate. Fig. 2 (c) suggests that the semiconductive range of the alloys spreads from 4 to about 50 atomic per cent of Sb. The increase of resistivity with the temperature rise which appears at high temperatures and which does not arise in the typical semiconductor, may be explained by the following assumption; the temperature variation of the carrier mobilities varies with temperature as T^{-p} with $p \gtrsim 2.5$ at higher temperatures instead of with $p=1\sim1.5$ which is in the case of the typical phonon scattering. This assumption is also supported by the temperature variation of the magneto-resistance observed. The occurrence of the semiconductive properties in this alloy system can be explained by examining the electronic structure of the Bi type crystal calculated by Mase.[2] The whole data and the detailed discussions will shortly be published.

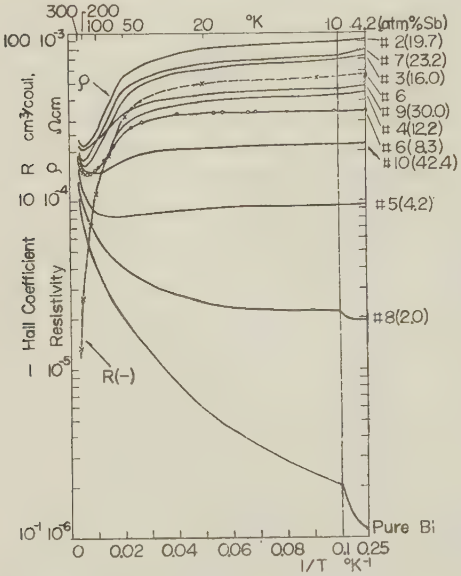

Fig 1. The logarithm of the resistivities and the Hall coefficient *versus* the reciprocal temperature.

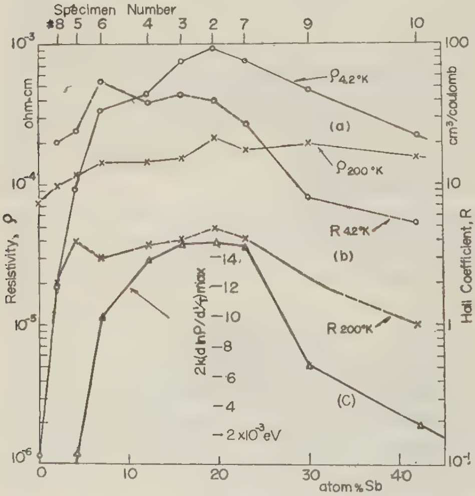

Fig. 2. The constitution dependencies of the resistivities (a), the Hall coefficients at 250 oersted (b), and $2k(\mathrm{d}\ln\rho/\mathrm{d}\,1/T)_{\max}$ (c).

The author wishes to express his sincere thanks to Prof. T. Fukuroi for his encouragements and to Mr. S. Mase of University of Nagoya for his stimulating discussions. A part of this study owes to the Research Fund from the Ministry of Education.

References

1) M. Hansen: *Constitution of Binary Alloys* (McGraw-Hill, 1958) 332.
2) S. Mase: J. Phys. Soc. Japan **13** (1958) 434; **14** (1959) 585.

J. PHYS. SOC. JAPAN **14** (1959) 1247

Curie Point in Thin Ni Films Determined by Electrical Method

By Kaizo KUWAHARA

Department of Physics, Faculty of Science, Hiroshima University

(Received July 13, 1959)

It is well known1)2) that the Curie point in thin films of ferromagnetics differs from that in bulk specimens. On the other hand, it is also well known3) that the electrical resistance of ferromagnetics shows an anomaly at the Curie point. Therefore, the electrical method has a possibility to determine the Curie point, and a few experiments along this line have been reported.4)5)

The present work is also based on the same idea as above. In this case, however, the reliability in the determination of Curie point would be much higher than the above experiments, because the decrease in resistance with applied magnetic field, which distinctly occurs near the Curie point, was utilized together with the resistance anomaly.

The experiment has been carried out with Ni films evaporated on slide glasses for microscope. To avoid oxidation, mechanical scratches and other troubles*, SiO_2 was coated upon the film surface. After over 10 hours of annealing at 420°C in vacuum, when the resistance of specimens ceased to drop, the resistance R and the longitudinal magnetoresistance $\Delta R/R$ (at 500 oe) were measured at various temperatures by means of potentiometer. In Fig. 1 an example is shown in the specimen of 576A. The kink in R and the minimum in $\Delta R/R$ occur at the same temperature, which gives the Curie point. In the case of such extremely thin films as 50A or below, there is no such appreciable kink in R as in thicker ones. It is not troublesome, however, to determine the Curie point, by referring to the minimum in $\Delta R/R$ in this case.

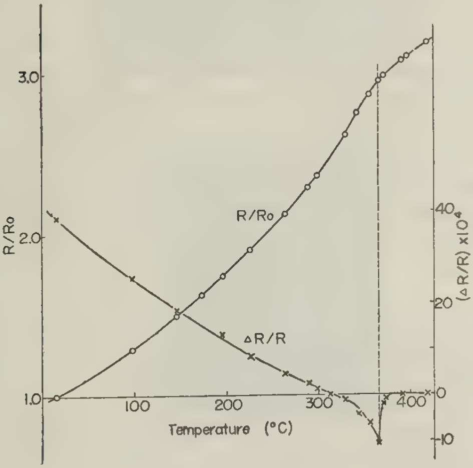

Fig. 1. Temperature dependence of R/R_0 and $\Delta R/R$, in the specimen of 576 A. R_0 is the resistance at 16°C. The minimum of $\Delta R/R$ coincides with the kink of R in temperature.

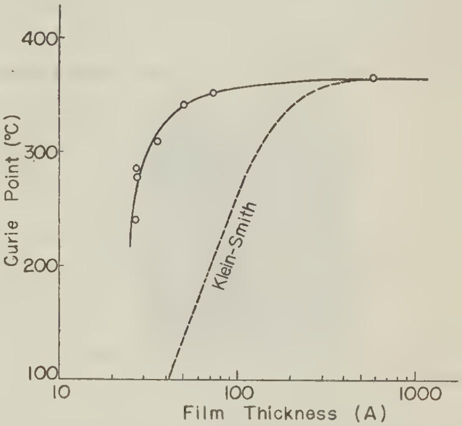

Fig. 2. Variation of Curie point with film thickness. The circles and the solid curve are obtained in this experiment. The dotted curve is derived by Klein and Smith theoretically.

The Curie point determined is plotted against film thickness in Fig. 2. As seen in this figure, the Curie point seems to fall effectively with the decrease in film thickness below 100A. Although this result coincides in tendency with the theory of Klein-Smith1) and the previous experiments,2)4)5) the details are considerably different from them, which might be a problem to be studied in the theory of spontaneous magnetization.

References

1) J. Klein and S. Smith: Phys. Rev. **18** (1951) 378.
2) E. C. Crittenden and R. W. Hoffman: Rev. Mod. Phys. **25** (1953) 310.
3) See, for instance, R. M. Bozorth: *Ferromagnetism* (D. Van Nostrand, New York, 1951) 762.
4) G. Goureaux and A. Colombani: Compt. rend. **246** (1958) 741.
5) W. Hellenthal: Z. Naturforsch. **13a** (1958) 566.

---

* For instance, when the uncoated films of 100 A or below are annealed, their resistance rises abnormally and irreversibly to a value 300 times or more as large as that before annealing and exhibits a semiconductor type variation with temperature.

J. Phys. Soc. Japan **14** (1959) 1248

Proton Resonance in the Antiferromagnetic State of $NiCl_2 \cdot 6H_2O$ and $CoCl_2 \cdot 6H_2O$

By Tadashi SUGAWARA

The Research Institute for Iron, Steel and Other Metals, Tohoku University, Sendai

(Received June 4, 1959)

In the previous short note on the proton resonance of nickel salts the author and Kim[1] reported that the resonance line in the paramagnetic $NiCl_2 6H_2O$ disappeared suddenly at about 8°K. However, it was found later that below 6°K the resonance consisted of a number of weak lines situated nearly symmetrically about the central frequency. The same behavior was observed also in $CoCl_2 \cdot 6H_2O$, which is isomorphous with $NiCl_2 \cdot 6H_2O$, at temperatures below 2.3°K.

As an example, the angular dependence of the low field spectrum in the *ac*-plane of $CoCl_2 \cdot 6H_2O$ at 2.08°K is shown in Fig. 1. Fig. 2 is a plot of the shift of a line in the spectrum as a function of temperature. The experimental points can be represented by a Brillouin function as shown in the Figure. These results are characteristics of the proton resonance in the antiferromagnetic state of a hydrated salt.[2] By extrapolating the curve in Fig. 2 to the ground line the Neél temperature was determined as 2.35 ± 0.05°K. The spectrum shown in Fig. 1 suggests that there are four inequivalent protons in a unit cell, of which two are located near the Co^{2+} ion and the other two are far from the ion. This proton arrangement seems to be consistent with the crystal structure reported by Mizuno *et al.*[3] From a preliminary analysis, based on the crystal structure, of the spectrum, it was found that the Co-spin is ordered parallel to the *c*-axis in agreement with the results of the susceptibility measurement[4] and the electron spin resonance.[5]

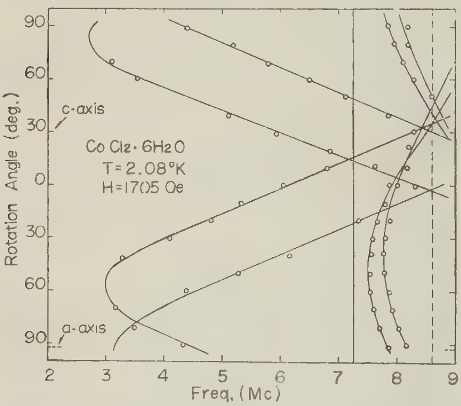

Fig. 1. Low frequency branch of the rotation spectrum in the *ac*-plane of $CoCl_2 \cdot 6H_2O$ at 2.08°K. The whole spectrum is nearly symmetrical about 8.6 MC. The resonance frequency for the undisplaced proton is 7.26 MC. There are some weak lines, not shown in the figure, of unknown origin.

The spectrum in $NiCl_2 \cdot 6H_2O$ was similar to that in $CoCl_2 \cdot 6H_2O$ except for the slightly different angular dependence and the smaller shift. In Fig. 2 is shown the temperature dependence of the shift of a line in this salt corresponding to that in $CoCl_2 \cdot 6H_2O$. By the same procedure described above the Neél temperature was determined as 5.8 ± 0.1°K. The observed spectrum can be explained qualitatively by assuming that the Ni-spin is ordered in the direction perpendicular to the *c*-axis. This fact seems not to be inconsistent with the result of the susceptibility measurement.[4]

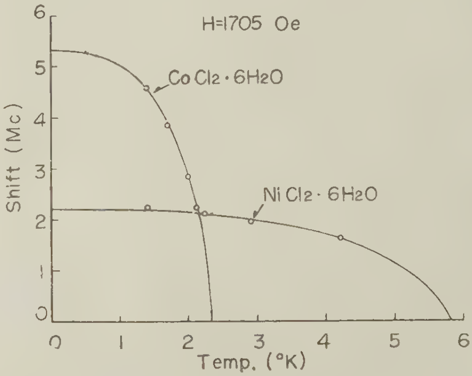

Fig. 2. Temperature dependence of the shift of a proton line. The external field is in the *ac*-plane and is nearly perpendicular to the *a*-axis.

The author wishes to thank Dr. Haseda for supplying good single crystals used in this work and also for communicating his unpublished magnetic data.

References

1) P. H. Kim and T. Sugawara: J. Phys. Soc. Japan **13** (1958) 968.
2) N. J. Poulis and G. E. G. Hardeman: Physica **18** (1952) 201.
3) J. Mizuno, K. Ukei and T. Sugawara: J. Phys. Soc. Japan **14** (1959) 383.
4) T. Haseda: to be published.
5) M. Date: short note in this issue.

J. PHYS. SOC. JAPAN **14** (1959) 1249~1250

X-ray Observations of the Surfaces of Plastically Deformed LiF Crystals with the Berg-Barret Method

By Mitsuru YOSHIMATSU
Research Laboratory, Rigaku Denki Co., Ltd.
2627, Kichijoji, Musashino, Tokyo
and Kazutake KOHRA
Institute of Physics, College of General Education,
University of Tokyo, Komaba, Meguro, Tokyo

(Received July 11, 1959)

It has been recently shown that the Berg-Barret Method[1] of X-ray diffraction can reveal not only substructures of plastically deformed metals[2] but also individual dislocation lines.[3] With this method we observed the surfaces of LiF single crystals* plastically deformed by cleaving, thermal quenching and mechanical bending, by utilizing the (200) or (400) reflexion with CuKα.

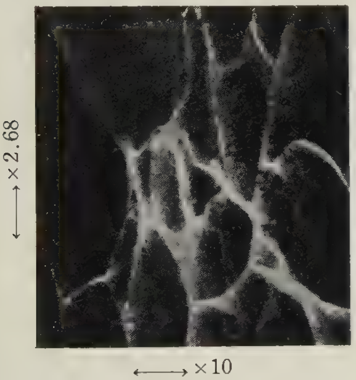

Fig. 1. Subgrain boundaries.

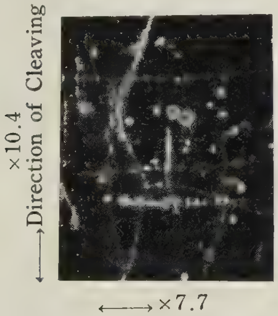

Fig. 2. Arrays of spots.

(i) The (200) reflexion photographs from cleaved surfaces vary highly sensitively with specimens, depending probably on the original properties of the crystal as well as the condition of cleaving. Few remarkable features are here described.

The lines corresponding to subgrain boundaries show almost always asymmetrical behaviour in intensity, being sharply defined at one side, while diffuse at another side (Fig. 1). In the optical micrographs of etched surface, surface[4], the grain boundary consists of the array of etch pits without any indication of asymmetry.

Arrays of spots are sometimes observed in X-ray photographs (Fig. 2). By comparison with the optical etch pit photographs, it is confirmed that each of individual spots corresponds to a dislocation cluster, which was called "Rosett" by Gilman and Johnston.[5]

Sometimes lines are observed running nearly parallel or perpendicular to the direction of cleaving (Fig. 3), which seem to correspond to the crack fronts and step lines, respectively.

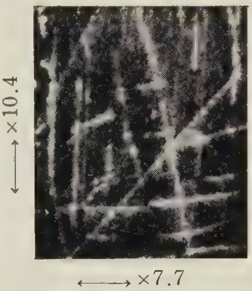

Fig. 3. Crack Fronts and Step Lines.

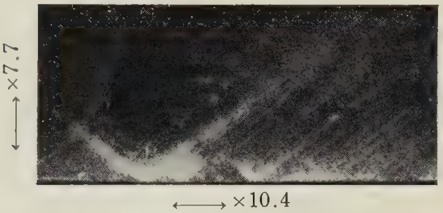

Fig. 4. Photograph of a bent crystal.

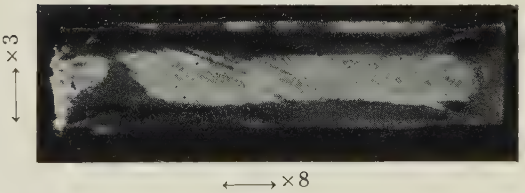

Fig. 5. Photograph of a quenched crystal.

(ii) Some crystals were bent with the radius of curvature 200 mm at room temperature and then annealed at 500°C for three hours. The (400) reflexion photograph from the side face is shown in Fig. 4. The slip lines appear densely in the vicinity of the point where the tools for bending contact the surface. Similar photographs were obtained also from the specimen not heat-treated, but the slip lines were not so distinct.

(iii) The (200) reflexion photographs of the crystal which was quenched from 400°C into water were taken. The features of the photographs were very different with specimens. One example is shown in Fig. 5. As a general tendency, the central part and the neighbourhood of the edge are intense, where slip lines run in the (110) direction.

---

* The crystals were purchased from Harshaw Chem. Co..

The authors should like to represent their sincere thanks to Prof. E. Fukushima and Prof. M. Sakamoto, Mr. K. Kobayashi and Mr. T. Arai for their valuable advices and discussions and to Mr. H. Nimura for his kind preparation of some etched surfaces.

References

1) W. F. Berg: Naturwiss. **19** (1931) 391. C. S. Barret: Trans. Amer. Inst. Mech. Engrs. **161** (1945) 15.
2) For instance, M. Yamamoto, S. Hayami and Z. Nishiyama: Memoirs. Inst. Sci. Ind. Res. **13** (1956) 11. Z. Nishiyama and S. Hayami: ibid. **14** (1958) 129.
3) J. B. Newkirk: J. Appl. Phys. **29** (1958) 995; Phys. Rev. **110** (1958) 1465.*
4) J. J. Gilman and W. G. Johnston: *Dislocation and Mechanical Properties of Crystals* (John Wiley, New York, 1957) 116.
5) refer to 4).

---

* (Note in proof.) The following paper has been recently published; J. B. Newkirk: Trans. Amer. Inst. Mech. Engrs. **215** (1959) 483.

J. PHYS. SOC. JAPAN **14** (1959) 1250~1251

X-ray Observation of the Strain Field in Germanium Single Crystals with the Use of the Anomalous Transmission

By Zensho ISHII

Electrotechnical Laboratory, Nagatacho, Tokyo

and Kazutake KOHRA

Institute of Physics, College of General Education, University of Tokyo, Komaba, Meguro, Tokyo

(Received July 9, 1959)

The transmitted intensity of X-rays increases anomalously when the incident X-rays satisfy the Bragg-Laue condition on a net plane in a nearly perfect crystal with sufficient thickness. This phenomenon, being highly sensitive to the perfectness of the crystals, was applied for observing individual dislocation lines by Borrmann et al with the divergent beam method and, later, by Barth et al with the parallel beam method. With the latter method wider area of the crystal can be observed than with the former method.

With the parallel beam we observed the change of the X-ray transmission caused by the strain field in germanium single crystals when the (2$\bar{2}$0) reflexion takes place with CuK. The crystals were about 1 mm thick and the surface was parallel to the (111) plane.

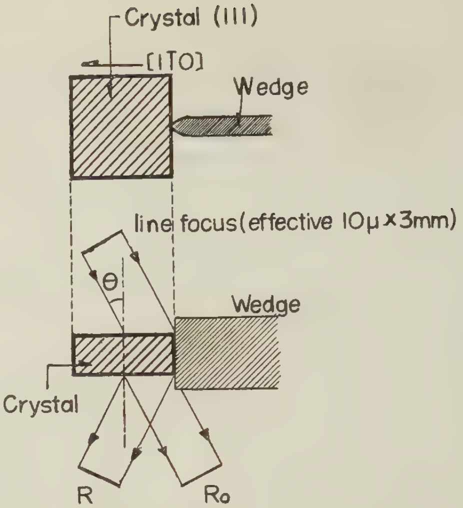

Fig. 1. Schematic diagram of the method to press the crystal.

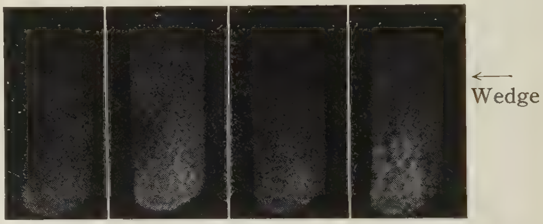

f=0, 40, 200, 320 gw

Fig. 2. Transmission photographs (R) of the pressed crystal.

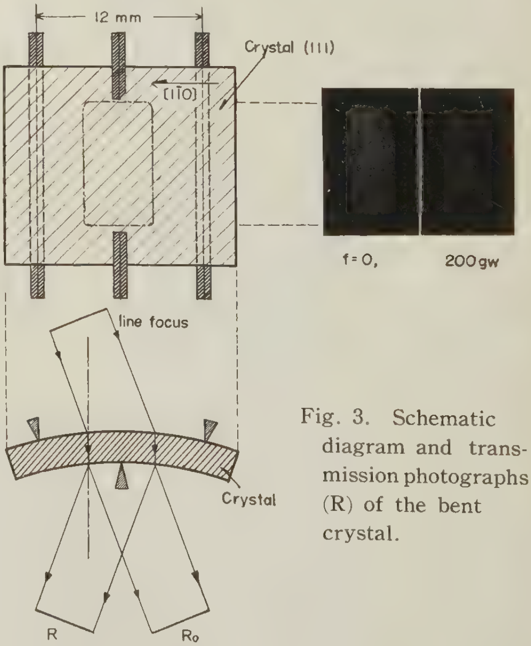

Fig. 3. Schematic diagram and transmission photographs (R) of the bent crystal.

(i) As shown in Fig. 1, the side face (1$\bar{1}$0) of the crystal was pressed with a wedge. The load was changed in the sequence of 0, 40, 200 and 320 g weight and then in the reversal sequence. A few examples of photographs are shown in Fig. 2.

It is seen that the transmission intensity is nearly zero in the vicinity of the wedge. This region is caused by the decrease of anomalous transmission owing to the imperfectness induced in the crystal structure, resulting from the strain field. The heavier is the load, the more extended is the region where the transmission is nearly zero. When the load was taken away, the pattern recovered the initial one.

(ii) A similar effect was observed when a crystal was bent. The photographs are shown in Fig. 3, where the load of 200 g weight was applied. The transmission decreases over the whole region and especially in the vicinity of the wedge.

The present method would be useful for studying the strain field in a nearly perfect crystal.

We should like to express our sincere thanks to Professor E. Fukushima and to Dr. M. Hatoyama for their kind interests and helpful discussions.

References

1) G. Borrmann, W. Hartwig and H. Irmler: Z. Naturforsch. **13a** (1958) 423.
2) H. Barth and R. Hosemann: Z. Naturforsch. **13a** (1958) 792. This method was used independently by us; Z. Ishii and K. Kohra: Annual Meeting of Phys. Soc. Japan (Tokyo), 17th. October, 1958.

Note in proof:

Recently the following paper has appeared, in which the transmitted intensity is quantitatively measured for germanium crystals deformed with the condition corresponding to the one of (ii) in the present note: L. P. Hunter: J. Appl. Phys. **30** (1959) 874.

J. Phys. Soc. Japan **14** (1959) 1251

Alpha Excitation Functions of Iron-54

By Shigeo Tanaka, Michiaki Furukawa,
Masuo Yagi, Shiro Iwata and Hiroshi Amano
Institute for Nuclear Study, University of Tokyo, Tanashi, Tokyo

(Received June 20, 1959)

Excitation functions of the reactions, $Fe^{54}(\alpha, n)Ni^{57}$, $Fe^{54}(\alpha, p)Co^{57}$, $Fe^{54}(\alpha, 2n)Ni^{56}$, and $Fe^{54}(\alpha, pn)Co^{56}$ were measured by the activation method. Bombardments were made with monoenergetic beams of 32 MeV alpha-particles from the 63-inch INS (Tokyo) cyclotron. Energy dependence of the cross sections was measured by the stacked-foil technique in which thin iron foils (8μ thick and of natural isotopic abundance) were interspaced with aluminum absorbers. After bombardments cobalt, nickel and iron were chemically separated. The Co^{56} was counted with an NaI scintillation counter so biased as to cut gamma rays below 1 MeV. The absolute yield was calculated by comparing the samples with those of the calibrated Co^{56} standard. The absolute yield of Co^{57} was obtained by counting the photopeaks from 0.13 MeV gamma rays in a well type NaI scintillation counter, Compton tails from Co^{56} and Co^{58} being subtracted. The nickel fractions were allowed to decay to produce Co^{57} and Co^{56}, and nearly the same counting procedures were applied. Necessary corrections were made to all the counting data. Nuclear data used in this calculations of the absolute cross sections were obtained from "Table of Isotopes" of Seaborg et al.

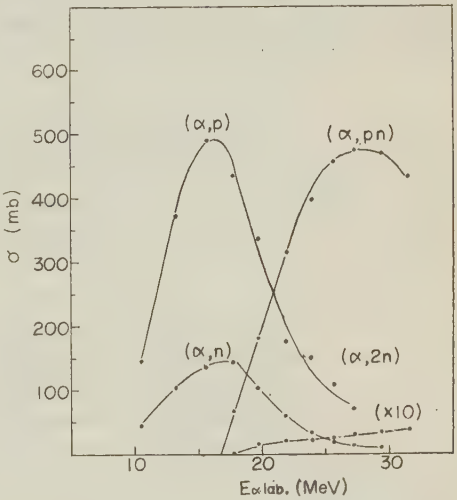

Fig. 1. Alpha excitation functions of Fe^{54}.

These results are shown in Fig. 1. $\sigma(\alpha, p)$ was generally a few times larger than $\sigma(\alpha, n)$. $\sigma(\alpha, pn)$ was larger than $\sigma(\alpha, 2n)$ by a factor of 10^2. Owing to the poor knowledge of decay scheme on Ni^{56}, the latter result is somewhat ambiguous. The results are at present analyzed on the basis of the statistical theory of nuclear reaction. The full reports on the alpha excitation functions including other types of reaction are to be published elsewhere in near future.

J. Phys. Soc. Japan **14** (1959) 1252~1253

A Mechanism for Producing Extrusions and Intrusions during Fatigue

By Ryutaro Nagai
Department of Physics, Tokyo Gakugei University

(Received May 11, 1959)

Forsyth[1] and others[2][3] have observed small extrusions and intrusions on the surface of fatigued metals and ionic crystals e.g. aluminium 4% copper and silver chloride. Cottrell and Hull[2] have suggested that they are the result of slip on two intersecting slip planes and Mott[4] has suggested a mechanism in which a dislocation, which has a component of its Burgers vector normal to the surface, moves round a closed circuit by cross slip. The mechanism of Cottrell and Hull does not seem to explain the co-existence of the extrusion with the intrusion along a slip band, and the mechanism of Mott is not so far, it seems, applicable to intrusion.

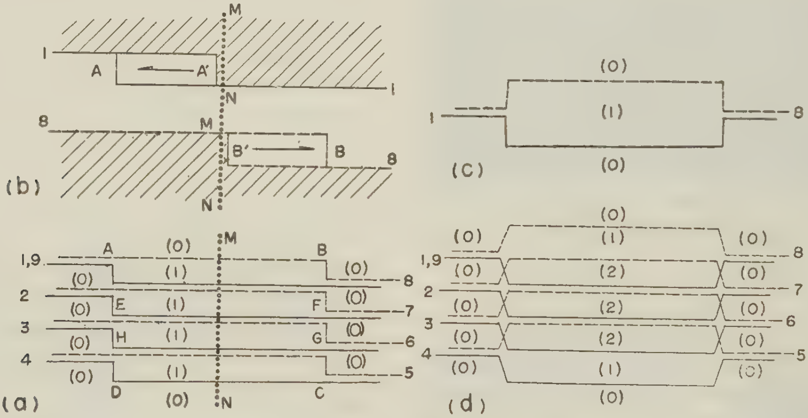

Fig. 1. (a) (c) (d): Slip lines produced on the surface. (Exchange of —— for ---- leads to exchange of extrusion for intrusion. —— Rising vertically to the surface, above this line. ---- Rising, below this line. $\overset{\text{——}}{\text{----}}$ Cancels each other. (0), (1), (2), ..., (−1), ... Height or depth vertical to the surface.) (b): Displacement of the jogs along the edge dislocation lines, in case of an excess of atoms. (Oblique lines indicate the extra plane of atoms.)

I would like to suggest another mechanism by which such extrusions and intrusions could occur, and by which the effect of a stress is not entirely cancelled by the reversed stress. Let a stress be applied to a crystal activating a Frank-Read source which with every rotation causes the new loop to expand on the adjacent parallel slip plane e.g. case (iii) of H. Suzuki[5], which may be a rare case, in which, the source is composed of elements of a hexagonal network, and the two pole dislocations are of the screw components of the opposite sign. Now let each edge dislocation 1, 2, 3, 4 with no jogs cut through a screw dislocation MN, so producing a jog in itself at MN. When the dislocations 1, 2, 3, 4 intersect the surface, they will produce the slip lines 1, 2, 3, 4 on the surface, each of which contains a step. If the stress is now reversed, the source will produce dislocations 5, 6, 7, 8 of the opposite sign which will also produce the slip lines 5, 6, 7, 8 each of which contains a step. The slip planes of 5 will coincide with the slip planes of 4. If, however, that jog is displaced along the dislocation line with respect to the first jog, Fig. 1(a) an extrusion ABCD will be formed after many cycles in case of an excess of atoms, and an intrusion in case of an excess of vacancies. In Fig. 1, the solid (dashed) line indicates the positive (negative) edge dislocation in the crystal and the positive (negative) slip line on the surface, at the same time. A probable reason why the first jog at MN should be displaced to A, E, H, D and to C, G, F, B along the pure edge dislocation line while the latter glides through the crystal towards the surface, can be seen if we consider Fig. 1(b). The jog A′ is produced first and the jog B′ on the reversed stress along the line of intersection with the screw dislocation MN. If these jogs pass through a region with an excess of atoms, such as interstitial atoms in metals (which have been worked or are being worked) or atoms in supersaturated alloys, the jog A′ moves to A, and B′ to B[6] (almost without the help of diffusion) and the result is an extrusion. If the region contained an excess of vacancies, they would move in the opposite direction with the result of an intrusion. At higher temperatures, the extrusion and the intrusion will become more complicated and irregular, because, if an edge dislocation passes through a region having an excess of atoms or vacancies, a row (or rows) of them may be added to the extra plane and grows. The row is also equivalent to the edge dislocation line between two jogs,[7] as shown in Fig. 1(c) (d) in case of an excess of atoms. In this case, the primary extrusion can be left on the reversed stress, even if the segments of the positive loops have not entirely got out of the crystal.

In order to explain the observed thickness of an extrusion of the alloy, $\sim 0.1\mu$, it would require 4×10^2 loops to be generated from the source per half cycle, and at least 3.5×10^3 cycles would be necessary so that the length of the extrusion may be 1μ, in case of Fig. 1(a).

A mechanism for growing a void which involves the interaction of a Frank-Read source with two screw dislocations of opposite sign will be published elsewhere.[7]

Another mechanism would be found if the straight slip lines without steps (jogs) e.g. 1, 2, 3→5, 6, 7→1, 2, 3→5, 6, 7, ··· appeared in turn, but it seems weak at present.

References

1) P. J. E. Forsyth: Nature **171** (1953) 172; Proc. Roy. Soc. **A, 242** (1957) 198.
2) A. H. Cottrell and D. Hull: Proc. Roy. Soc. **A, 242** (1957) 211.
3) D. F. Gibbons et al.: private communication; Extrusions in ultrasonic experiments of tin and zinc, (1958).
4) N. F. Mott: Proc. Roy. Soc. **A, 242** (1957) 1; Acta Met. **6** (1958) 195.
5) H. Suzuki: J. Phys. Soc. Japan **9** (1954) 531.
6) W. T. Read: *Dislocations in Crystals* (McGraw-Hill, 1953) 48, 85.
7) R. Nagai: Met. Phys. (Kinzoku Buturi) **5** (1959) 29.

J. PHYS. SOC. JAPAN **14** (1959) 1253～1254

Time Decrease of Permeability in Silicon-Iron

By Kunirô TSUSHIMA, Mitsuru ASANUMA
and Syôhei MIYAHARA

Department of Physics, Faculty of Science,
Hokkaido University, Sapporo, Japan

(Received June 29, 1959)

Snoek[1] showed that the existence of interstitial solutions of carbon and nitrogen is the cause of time decrease of initial permeability of iron and other body centered cubic ferromagnetic metals and alloys.

He assumed the decrease with respect to time should be represented as

$$r_t=r_0+r_a(1-e^{-t/\tau}),\quad \tau=\tau_0 e^{Q/RT} \qquad (1)$$

Here r_t : reluctivity at time t.

r_0, r_a: constant with respect to time.

Rathenau *et al.*[2] found for iron that by modifying (1) only one activation mechanism of elementary jumps of nitrogen atoms is involved in a restricted region where

$$g\left(\equiv\frac{r_t-r_0}{r_\infty-r_0}\right)=0\sim0.9\ ,$$

We performed similar experiment for 4% Si-Fe. Specimens were annealed in purified hydrogen at 850°C for a week to remove carbon and nitrogen as possible as we could.

Then the initial permeability μ was measured on a toroid, composed of 10 rings (2.5 cm external, 1.5 cm internal diameter, 0.02 cm thickness) of polycrystalline 4% Si-Fe. By determining selfinductance using alternating current bridge (1 Kc/sec), μ was measured with the measuring field of 1×10^{-4} oe.

Time decrease at each temperature is shown in Fig. 1. Assuming the relation (1), we plott $\ln t$ versus $1/T$ for some values of the parameter g, which is shown in Fig. 2. Up to g=0.3, straight line relationship is found and the slopes give the value of activation energy

$$Q=0.80\pm0.04\ \text{ev.}$$

Above value is in agreement with other data[3] of activation energy of diffusion of carbon in α-iron. For g larger than 0.3, this analysis cannot be applied.

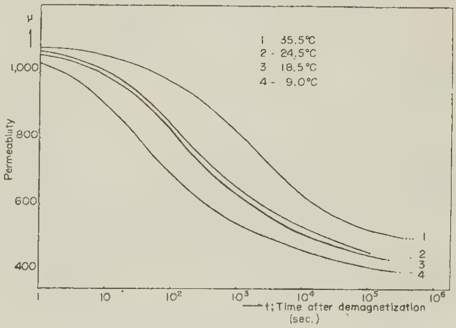

Fig. 1. Time decrease of μ in 4% Si-Fe after demagnetization at various temperatures.

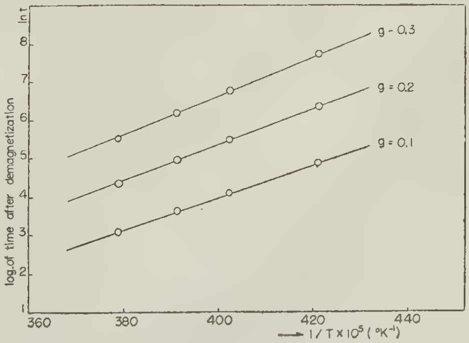

Fig. 2. Log. of time (sec.) *versus* inverse absolute temperature for g=0.1～0.3.

References

1) J. I. Snoek: Physica **6** (1939) 161, 591.
2) A. J. Bosman, P. E. Brommer, H. J. Van Daal and G. W. Rathenau: Physica **23** (1957) 989.
3) Y. Tomono: J. Phys. Soc. Japan **7** (1952) 174. E. S. Anolick and J. Singer: J. Appl. Phys. Suppl. **30** (1959) 193 S. L. J. Dijkstra: Philips Res. Rep. **2** (1947) 357. C. A. Wert and C. Zener: Phys. Rev. **76** (1949) 1169. P. Brissoneau: J. Phys. Chem. Solids **7** (1958) 22.

J. PHYS. SOC. JAPAN **14** (1959) 1254

Changes of Coercivities by Heat Treatment and Cold-Rolling in Cu-Co Alloy

By Masayoshi SATŌ and Tadayasu MITUI

Department of Physics, Faculty of Science, Hokkaido University, Sapporo, Japan

(Received June 25, 1959)

Magnetic properties on the Cu-Co alloys containing a few percent cobalt have been studied by many investigators[1~6]. Sucksmith *et al*[1,2] have measured changes of coercivities induced by heat treatment and cold-drawing. We also carried out the same study, but, as shown in followings, the results were remarkably different from his.

We studied the alloy containing ca. 2 wt % Co to clarify how the size, shape and the orientation of the precipitates affect magnetic properties. For this purpose the coercive force H_c and the reverse field H_r which is the field required to reduce the remanence to zero against the aging time at various temperatures were measured; the results are shown in Fig. 1. Though it is difficult to explain the great peak appeared in the curves for 600°C aging earlier than other peak, it might be due to eventual imperfections in the matrix.

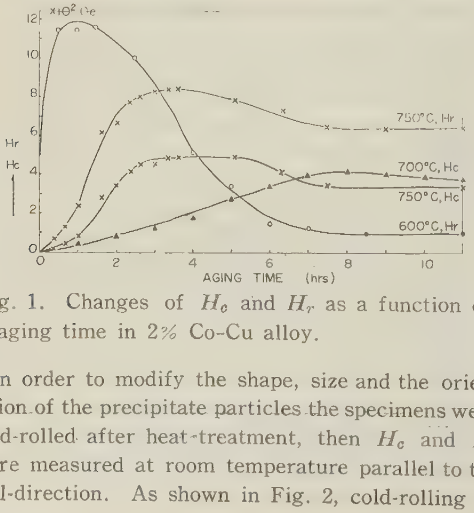

Fig. 1. Changes of H_c and H_r as a function of aging time in 2% Co-Cu alloy.

In order to modify the shape, size and the orientation of the precipitate particles the specimens were cold-rolled after heat-treatment, then H_c and H_r were measured at room temperature parallel to the roll-direction. As shown in Fig. 2, cold-rolling up to 70~80% reduction effects an increase of coercive force, further reduction causes coercive force to decrease. The value of H_r shows a similar behavior except for the earlier stage of reduction as shown in Fig. 3.

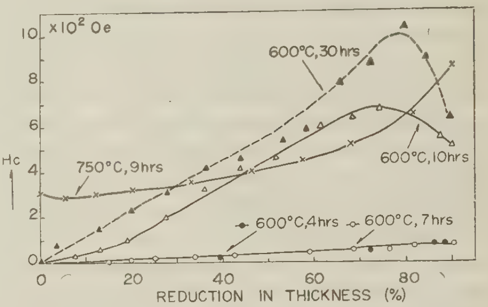

Fig. 2. Changes of H_c as a function of the roll reduction in thickness in 2% Co-Cu alloy.

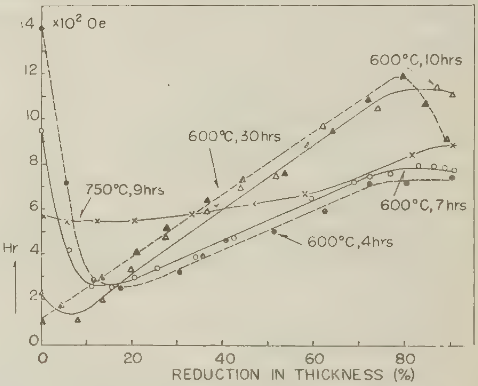

Fig. 3. Changes of H_r as a function of the roll reduction in thickness in 2% Co-Cu alloy.

The changes of H_c and H_r are not so simple to be explained by homogeneous deformation of the particles. Those might be explained in terms of shape effect taking not only the elongation of the particles but also the superparamagnetism induced by cutting-off into account. Moreover, the cutting-off effect was also found in the measurement of the magnetic anisotropy by one of the authors[7].

The detailed report will be published in this Journal.

References

1) G. Bate, D. Schofield and W. Sucksmith: Phil. Mag. **46** (1955) 621.
2) B. W. Lothian, A. C. Robinson and W. Sucksmith: Phil. Mag. **3** (1958) 999.
3) P. L. Weil: J. phys. rad. **20** (1958) 282.
4) J. J. Becker: Conference of Magnetism and Magnetic Materials, Boston. (1957) 288.
5) J. J. Becker: J. Appl. Phys. **29** (1958) 317.
6) T. Mitui: J. Phys. Soc. Japan **13** (1958) 549.
7) T. Mitui: Read at the March, 1959 Meeting of the Phys. Soc. Japan.

JOURNAL OF THE PHYSICAL SOCIETY OF JAPAN, Vol. 14, No. 10, OCTOBER, 1959

Scattering of Protons by Silicon and Sulphur

By Yukiyasu ODA*, Minoru TAKEDA, Chuin HU and Shōhei KATO
Department of Physics, Osaka University, Osaka

(Received March 20, 1959)

The angular distributions of protons in elastic and inelastic scattering by Si and S have been studied, changing the bombarding energy from 4.95 Mev to 5.45 Mev with the interval of 100 Kev. The angular distributions of proton groups from the reaction $Si^{28}(p, p')Si^{28*}$ ($Q=-1.78$ Mev) are nearly symmetric about 90° for any bombarding energy and the total cross-section changes appreciably with the incident energy. On the other hand, the results for the reaction $S^{32}(p, p')S^{32*}$ ($Q=-2.24$ Mev) show large variation with the energy in both angular distribution and total cross-section. The energy dependence of the angular distribution of elastically scattered protons by silicon is found to be more remarkable than that by sulphur in the energy region studied.

§ 1. Introduction

Many experiments have been carried out on the elastic and inelastic scattering of protons on light even-even nuclei for various bombarding energies. In our laboratory, the angular distribution of inelastically scattered protons for the first excited states of Ne^{20},[1),2)] Mg^{24} [3)] and Si^{28} [4)] has been studied recently changing the energy of the proton beam from the 44-inches Osaka University Cyclotron. These results obtained in the energy region from 4.8 to 5.5 Mev show a remarkable energy dependences of differential cross section and angular distribution. In cases of these target nuclei, some resonance phenomena were found. Thus it is generally supposed that the inelastic scattering of protons proceeds mainly through the compound nucleus formation. On the other hand, in the elastic scatterings in neon, the angular distribution of protons changes rapidly with energies, supporting the existences of some resonance levels.

In the present study, the measurements of the angular distribution of protons elastically scattered from silicon and sulphur, and that of inelastically scattered proton groups corresponding to the first excited levels of Si^{28} and S^{32} have been performed in the energy region from 4.95 to 5.45 Mev. In order to facilitate the simultaneous measurement of angular distributions of the proton groups scattered elastically and inelastically by respective nucleus, we selected SiH_4 and SH_2 gases as targets.

§ 2. Methods and Results

The gas targets of SiH_4 and SH_2 were used for the purpose mentioned in § 1. SH_4 was produced by the reaction[5)]

$$SiCl_4+AlLiH_4=SiH_4+AlCl_3+LiCl$$

distillating by isopentan bath. SH_2 gas purified by distillating the commercial gas of 99% purity through the liquid air, has been used. These gases were filled usually at a pressure of 180 mmHg in the target cell.

We used NaI(Tl) scintillation counter as a detector, and pulse heights were analysed by the 20 channel pulse height analyser. The counter, scattering chamber and associated equipments were similar to those described in detail in the previous report[2)]. The definitions of scattering angles were made to the accuracy of about ±0.1° and the angular resolutions were ±1° in the range of laboratory scattering angles from 20° to 164°30′. The incident proton energies were reduced by aluminium absorbers in step of 100 kev.

The typical pulse height spectra of scat-

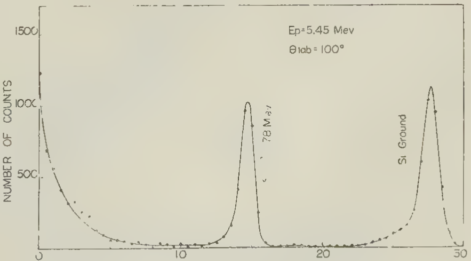

Fig. 1. The pulse height spectrum for protons scattered from silicon at the scattering angle of 100° with the incident energy of5.45 Mev.

---

* Now at Physics Department, Tokyo Institute of Technology, Oh-okayama, Tokyo.

tered protons by silicon at 100° and that by sulphur at 164°30′ in the laboratory system at the incident energy of 5.45 Mev are shown in Figs. 1 and 2, respectively. In the case of silicon, the inelastically scattered protons leaving Si^{29} (natural isotope abundance 4.68%) in the first excited state, were observed with low intensities and separated well from those of Si^{28}. Thus the inelastically scattered protons from Si^{29} would not disturb the measurement of the angular distributions of protons corresponding to the level of 1.78 Mev of Si^{28}. In the case of sulphur, the number of protons elastically scattered from nitrogen and oxygen (present as the contaminants) was small compared with that from sulphur, and their intensity was about 2% of that of protons elastically scattered from sulphur. The protons which excited the first level of S^{34} (the isotope abundance 4.22%) were not separated from these corresponding to the level of 2.24 Mev of S^{32}. The errors in the determinations of the differential cross sections for the inelastic scattering of protons by S^{32} would, however, be small since the isotope abundance of S^{34} is very low.

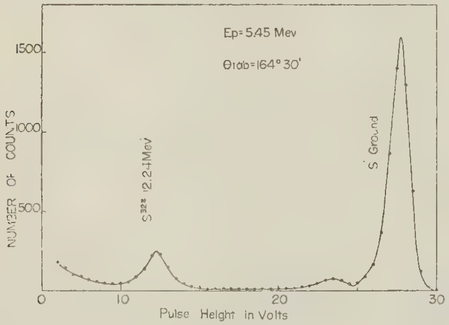

Fig. 2. The pulse height spectrum for protons scattered from sulphur at the scattering angle of 164°30′ with the incident energy of 5.45 Mev.

The angular distributions of elastically scattered protons by silicon and sulphur at various bombarding energies are illustrated in Figs. 3 and 4. Although the atomic numbers of target nuclei are now somewhat greater than that of neon studied in previous work, the curves in these figures show rather remarkable variations with the incident energy as in the case of neon. The resonance like anomaly found in the case of elastic scattering by silicon corresponds especially well to that found for the inelastic scattering. The discussions for these relations will be given later.

The observed angular distributions of the scattered protons which leave the nuclei Si^{28}

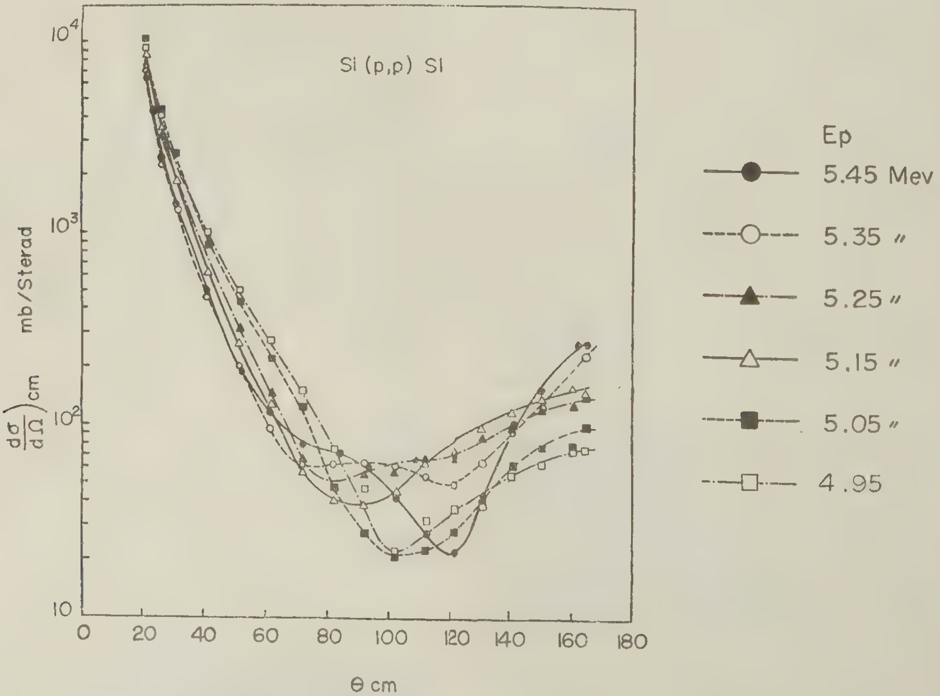

Fig. 3. The angular distributions of protons elastically scattered from silicon.

in their 1.78 Mev levels, and S^{32} in the 2.24 Mev level are shown in Figs. 5 and 6, respectively.

The angular distributions of inelastically scattered protons by Si^{28} show nearly symmetric about 90° for any bombarding energy. A resonance like anomaly is found at the energy of 5.45 Mev in the case of Si^{28}. These results agree with those obtained by Yamabe, et al.[4] in our laboratory in general features, except that our absolute values of cross sections are usually smaller than their values by about 10%. Both results are compatible in the position of the anomaly, the shapes of the angular distributions at corresponding energies and the feature of variation of cross sections with energy. It is possible that the discrepancy between these results might have been risen from the difference in bombarding energies, because the only little variation of the incident energy produce generally appreciable change in absolute cross section near the resonance.

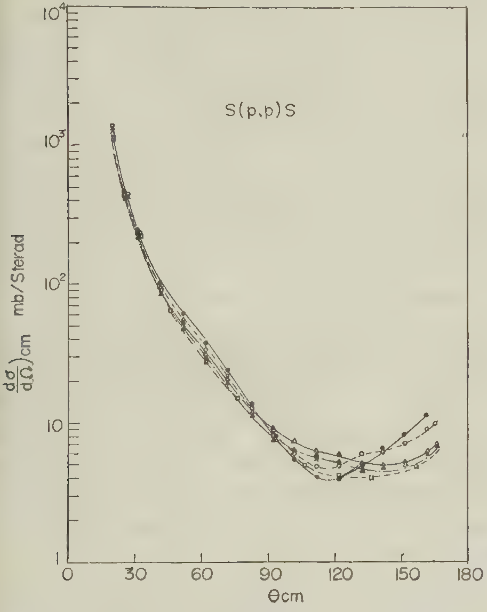

Fig. 4. The angular distributions of protons elastically scattered from sulphur. The curve indications of corresponding energies are given in Fig. 3.

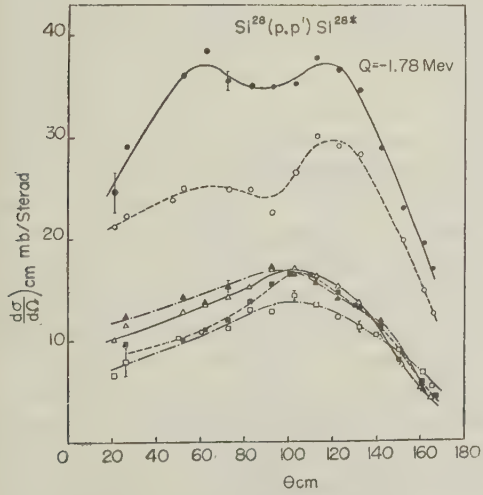

Fig. 5. The angular distributions of protons inelastically scattered from Si^{28}($Q = -1.78$ Mev). The curve indications of corresponding energies are given in Fig. 3.

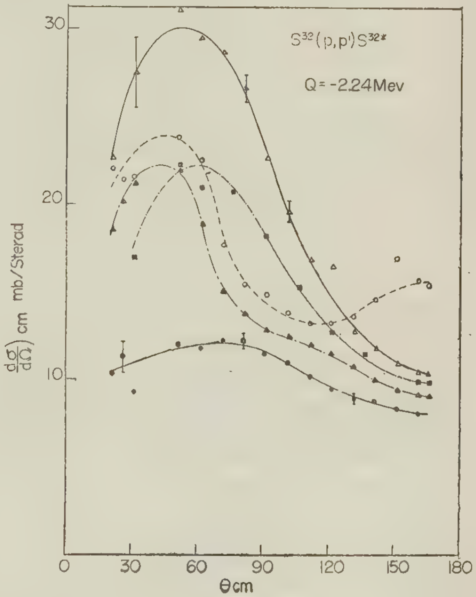

Fig. 6. The angular distributions of protons inelastically scattered from S^{32}($Q = -2.24$ Mev). The curve indications of corresponding energies are given in Fig. 3.

The angular distributions of inelastically scattered protons from S^{32}, on the other hand, show relatively larger asymmetry about 90° than those of neon and silicon, and are sensitive to the incident energy in the region from 4.95 to 5.45 Mev. The lack of the data of differential cross sections for the inelastic scattering in each nucleus at 40° in the laboratory system arises from the fact that the both proton groups from the H(p, p)H scattering and the inelastic scattering overlap with each other. The differential proton-proton scattering cross sections were measured at 40°, 50° and 60° in the center of mass system simultaneously with the inelastic scattering cross sections and are used to normalize the absolute values for elastic and inelastic scattering cross sections of these nuclei. In the case of inelastic scatterings, the main uncertainty in the final values of the cross sections is due to the subtraction of the background. The relative error of cross sections is generally about 5% for elastic and inelastic scattering and about 10% for forward angles for inelastic scattering. For the absolute cross sections, the over all errors do not exceed ±10%.

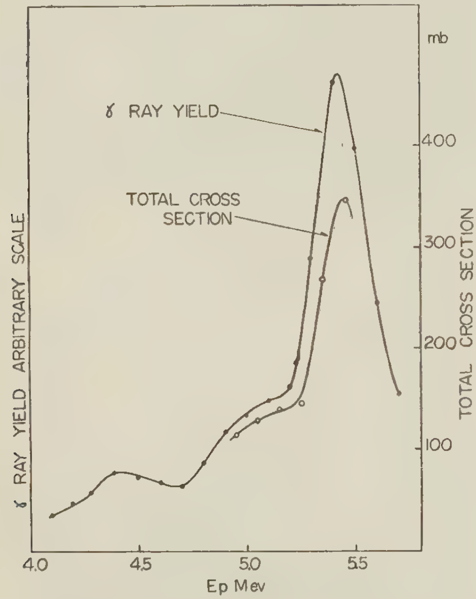

Fig. 7. The energy dependence of total cross sections and relative γ-ray yield for the reaction $Si^{28}(p, p')\ Si^{28*}(Q=-1.78$ Mev).

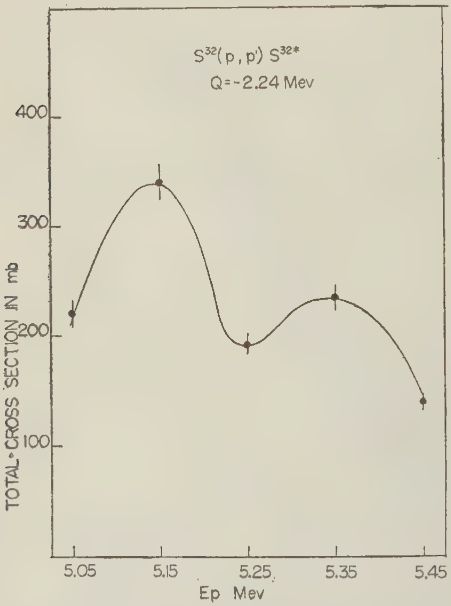

Fig. 8. The energy dependence of total cross sections for the reaction $S^{32}(p, p')\ S^{31*}(Q=-2.24$ Mev).

The energy dependences of total cross sections for inelastic scatterings from Si^{28} and S^{32} are shown in Figs. 7 and 8. Okada et al. in our laboratory have measured the excitation curves of gamma radiations resulting from the inelastic scatterings at 90° with respect to the proton beam[6),7)]. Resonances were found at 2.9, 3.5, 4.4, 5.0 and 5.4 Mev for silicon and at 4.8, 5.1, 5.3 and 5.6 Mev for sulphur. Their result is also illustrated in Fig. 7.

§ 3. Discussion

As have been stated, the observed angular distributions of inelastically scattered protons show large variations for small changes in bombarding energy. It would therefore be difficult to consider that the excitations are induced only through one of the direct processes which would not be so sensitive to the incident energy.

As will be stated below, however, it is easy to consider that the observed reactions are performed mainly through the formation of compound nucleus and its subsequent decay. Let both the continuum and statistical assumptions about the compound nucleus be violated in the experimental condition, then only a small number of compound nucleus levels concern with the reactions and the angular distributions would be expected to show a marked energy dependence. In our case, both assumptions would not be valid, since the compound nucleus P^{29} and Cl^{33} have relatively low excitation energies of ∼8 and 7 Mev respectively. On the basis of the experimental results obtained at lower energies[8)], the mean level spacing which is expected to hold in these energy regions seems to be about 200 kev and is probably larger than the beem energy spread. Therefore the angular distributions of the scattered protons resulting from the excitation of the particular level in compound nucleus would be expected to change their shape with proton energies. Now, the results for inelastic scattering represented in Figs. 5 and 6 and also those for elastic scattering shown in Figs. 3 and 4 show fairly marked variations with bombarding energy and suggest that the compound nucleus formations play predominant roles. For the case of silicon, C. Hu and others have observed further the angular distributions of the inelastically scattered protons at higher incident energies of 8.0, 11.0 and 14.0 Mev[9]. The inelastic angular distributions by silicon were also studied at 7.97, 8.55, 8.96, 9.28 and 9.45 Mev by Greenless et al.[10] and at 12.0 Mev by Conzett[11]. Fused quartz (SiO_2) was used as a target for these experiments. These distributions also change their shapes rapidly with proton energies. All these features seem thus to support that our reactions proceed mainly through the compound nucleus formations. The departures from 90° symmetry in the angular distributions would be caused by the interferences of the outgoing waves with different parities, although some parts of the asymmetry might be caused by the direct interaction process.

Here we discuss our present results in details. From the observed angular distribution of 1.78 Mev gamma rays from Si^{28} at the resonance energy of 5.4 Mev, Okada et al. assigned the spin and parity of the compound nucleus level of P^{29} at the excitation energy of 7.9 Mev as $5/2(+)$. Our experimental results seem also to support this assignment. First, the total cross section illustrated in Fig. 7 is about 400 mb at 5.4 Mev resonance. The magnitude is nearly in the limit of the maximum cross section $3\pi/k^2$ which is allowed by the theory assuming the reaction through single level. Next, we can reproduce the shape of the angular distributions at 5.45 Mev well postulating that the reaction proceeds through the compound nuclear state which has the assignment as above and decays to the final system of the channel spins $S'=3/2(l'=2)$ and $5/2(l'=0, 2)$ being mixed adequately. Here l' is the orbital angular momentum of outgoing protons.

The total cross sections for the inelastic scattering by S^{32} illustrated in Fig. 8 show that there are at least two resonances, one near 5.15 Mev and the other near 5.35 Mev, both of which have the width of about 100 kev. We suppose that the compound nucleus formation plays main role also in this case. We do not discuss here, however, the details of the possibilities for the theoretical interpretation of our experimental results of inelastic scattering, because other experimental knowledges about the nature of the compound states are not enough.

In order to investigate the results for the elastic scattering, we rearranged the data shown in Figs. 3 and 4 into the form of excitation curves at various scattering angles. Although we cannot find out any peculiar feature in the curves for sulphur thus obtained, we can find two anomalies in the case of silicon. Namely we find the one at 5.05 Mev, which is especially evident at angles $\theta \geq 100°$. It is worth while to note that in Fig. 7 one can observe an inelastic scattering anomaly at this point of energy. We can find another elastic scattering anomaly near 5.4 Mev only at the backward scattering angles $\theta \simeq 160°$. Although we observe an extremely sharp resonance behavior of inelastic scattering at this point of energy, we can find corresponding elastic scattering anomaly at only extremely backward angles.

These facts show somewhat complicated features of the conditions of the experiment studied with a beam of medium resolution as in our case. It seems that, beside the peculiar resonance levels recognized well in our experiments, there may be a certain number of levels which do not show marked resonance behaviors. Thus, except at the special resonance points of energy, our results would contain the contributions from those unresolved levels which are overlapping or neighboring to each other. These features will probably affect the variation of scattering phenomena with the change of incident energy, and further will stand for the relatively small asymmetries about 90° found in the results for the angular distribution of inelastically scattered protons.

Acknowledgements

The authors wish to thank Professor T. Wakatsuki for his interest in this work. They are indebted to the crew of the Osaka University Cyclotron for their supports throughout the experiments. They also acknowledge the guidance of Professor H. Kuroya for the production of silane.

References

1) M. Kondo and T. Yamazaki: J. Phys. Soc.

Japan **13** (1958) 771.
2) Y. Oda, M. Takeda, C. Hu and S. Kato: J. Phys. Soc. Japan **14** (1959) 387.
3) S. Yamabe: J. Phys. Soc. Japan **13** (1958) 237.
4) S. Yamabe, M. Kondo, T. Yamazaki and A. Toi: J. Phys. Soc. Japan **13** (1958) 777.
5) A. E. Finholt, A. C. Bond, Jr., K. E. Wilzbach and H. I. Schlesinger: J. Amer. Chem. Soc. **69** (1947) 2692.
6) E. Okada, I. Miura, T. Wakatsuki and Y. Hirao: J. Phys. Soc. Japan **13** (1958) 541.
7) E. Okada, I. Miura, T. Wakatsuki and Y. Hirao: to be published.
8) H. O. Cohn, J. K. Bair, J. D. Kington and H. B. Willard: Phys. Rev. **99** (1955) 644.
9) C. Hu, K. Kikuchi, S. Kobayashi, K. Matsuda, Y. Nagahara, Y. Oda, N. Takano, M. Takeda and T. Yamazaki: to be published.
10) G. W. Greenless, L. G. Kuo, J. Lowe and M. Petrauic: Proc. Phys. Soc. London **71** (1958) 347.
11) H. E. Conzett: Phys. Rev. **105** (1957) 1329.

JOURNAL OF THE PHYSICAL SOCIETY OF JAPAN, Vol. 14, No. 10, OCTOBER, 1959

Angular Distributions of Protons from the Reaction $^{12}C(\alpha, p)^{15}N$

By Itaru NONAKA, Hisashi YAMAGUCHI, Takashi MIKUMO, Iwao UMEDA*, Tatsuo TABATA* and Saburo HITAKA**

Institute for Nuclear Study, University of Tokyo,
Tanashi-Machi, Kitatama-Gun, Tokyo

(Received June 19, 1959)

Angular distributions of protons corresponding to the ground state transition from the reaction $^{12}C(\alpha, p)^{15}N$ have been measured at twelve energies of alpha particles between 25 and 39 MeV. Each angular distribution shows pronounced diffraction-like patterns, but there exists apparently a systematic shift in the shape and magnitude of angular distributions as the energy changes. At lower energies a sharp rise in the backward angles is observed, while at higher energies it is not observed.

Angular distributions of protons corresponding to some excited state transitions have also been measured at 34.6 MeV.

§ 1. Introduction

Recently, angular distributions of the proton group (P_0) corresponding to the ground state transition of the reaction $^{12}C(\alpha, p)^{15}N$ have been measured by R. Sherr and M. Rickey(1) at alpha particle energies of 30.5 MeV and 40.5 MeV, by C. E. Hunting and N. S. Wall(2) at 30.5 MeV, and by S. Yamabe, M. Kondo and T. Yamazaki(3) at 22.0 MeV. S. T. Butler(4) explained the result of C. E. Hunting and N. S. Wall as a typical evidence of direct interaction mechanism. This model, essentially like that of N. Austern, S. T. Butler and H. McManus(5), predicts that the differential cross section in the reaction $X(\alpha, p)Y$ is

$$d\sigma/d\omega \propto [\sum_l j_l(QR)]^2 F(\theta) ,$$

where $l\hbar$ is the orbital angular momentum transferred to the nucleus, Q the momentum transferred to the nucleus, R the nuclear radius, and $j_l(QR)$ is the spherical Bessel function of order l. Selection rules concerning the allowed l's are

$$|\boldsymbol{J}_X+\boldsymbol{J}_Y+\boldsymbol{i}|_{\min} \leq l \leq J_X+J_Y+i$$

where $\boldsymbol{J}_X, \boldsymbol{J}_Y, \boldsymbol{i}$ are, respectively, the spins of the target nucleus, of the residual nucleus and of the emitted proton.

All these angular distributions show sharp diffraction-like patterns, but they are quite different in shape at different energies.

---

* Kyoto University.

** Kyushu University.

In order to study the reaction mechanism we have made the measurements of angular distributions of this reaction at alpha particle energies between 25.0 and 38.6 MeV. We have also made measurements of angular distributions of proton groups P_{12}, P_3 and P_{456} corresponding to the transitions leaving the residual ^{15}N nucleus at 5.28- and 5.31 MeV (P_{12}), 6.33 MeV (P_3), and 7.16-, 7.31- and 7.58 MeV (P_{456}) at $E_\alpha=34.6$ MeV.

§ 2. Experimental Procedure

At the Institute for Nuclear Study, University of Tokyo (I.N.S.J.), a 160 cm cyclotron[6] is now available for research. This cyclotron can be used in two ways, either as a fixed frequency (F–F) cyclotron or as a frequency modulated (F–M) cyclotron, by changing the oscillator-dee system. Moreover, when used as a F–F cyclotron one of the main advantages of this cyclotron is that it is of variable energy type; one can obtain beams of protons between 8 and 14 MeV, of deuterons between 13 and 21 MeV, and of alpha particles between 27 and 43 MeV. This machine is thus particularly suited for the investigations of the change of angular distributions as functions of bombarding energies.

Fig. 1 is a schematic diagram of the experimental arrangement. The general experimental methods are already described by K. Kikuchi, S. Kobayashi and K. Matsuda[7].

The alpha particle beam produced by the cyclotron was brought into a scattering chamber of 100 cm in diameter, after passing through a pair of quadrupole magnets and a sector-type focussing magnet, and through a concrete shield. The beam was collected in Faraday cup after passing through the target located at the centre of this chamber.

A system of beam collimating slits 5 mm in diameter, was inserted in front of the scattering chamber, and the intensity of the beam at the Faraday cup was about 0.1 μA. The beam energy spread was estimated to be within about 0.5% at the target.

For the experiments at $E_\alpha<27$ MeV, aluminium absorbers were inserted before the beam collimator. At $E_\alpha=25$ MeV the beam intensity was one order of magnitude less than that without absorbers.

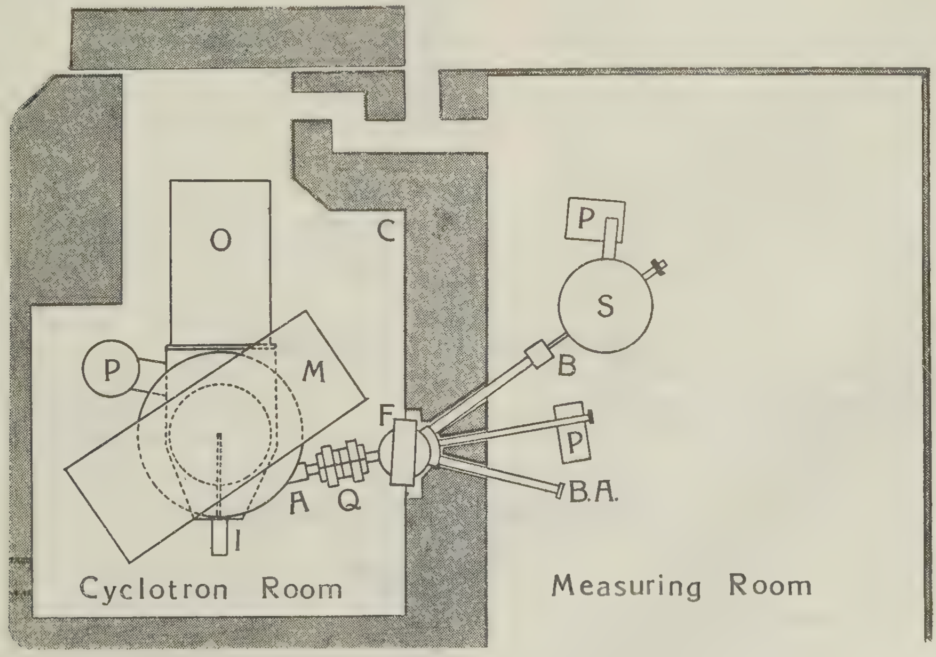

Fig. 1. Cyclotron and scattering chamber system.

M: Main magnet
O: Oscillator system
F: Focussing magnet
S: Scattering chamber
P: Pumps
Q: Quadrupole magnets
C: Concrete shield
B: Foil changer

(i) *Experiments at* $E_\alpha = 34.6$ MeV

At first (in spring, 1958) we measured the spectra and angular distributions of protons from this reaction at $E_\alpha = 34.6$ MeV as a "Test Experiment" of our cyclotron. At that time the protons emerging from the target were detected by a telescope of a proportional counter and a NaI(Tl)-scintillation counter set on the turn table in the scattering chamber. By inserting aluminium absorbers of suitable thickness between the target and the proportional counter, we could make all the outgoing alpha particles stop in the absorbers, while protons lost little energy.

The proportional counter contained about 30 cmHg of Argon-CO_2 mixture (5% CO_2). This counter was used to suppress the gamma-ray background especially in the backward angles. In front of the proportional counter a brass circular aperture of 8 mm in diameter was inserted to define the solid angle accepted by the counter system (order of 10^{-4} steradians).

After passing through the proportional counter, protons stopped in the NaI(Tl) crystal of 5 mm thick followed by a RCA 6342 photomultiplier. The energy resolution was about 3% (full width at half maximum). Signal pulses were sent, through a cathode-follower, to the counting room about 50 meters apart from the measuring room where the scattering chamber was set. And after being amplified by a linear amplifier they were fed into a 10-channel pulse height analyzer. This analyzer was gated by the pulses from the proportional counter, biased adequately in to separate protons from gamma-ray background.

We took the data with and without the proportional counter and found that as long as the ground state group (P_0) was concerned, it was sufficient to make the measurements without the proportional counter even at the largest angle (165°) by choosing the crystal as thin as possible.

As the target, we used a polystyrene film of 10 microns in nominal thickness* (measured thickness 2.94–3.11 mg/cm²). But, because of the large cross sections of $\alpha - p$ scattering, a great number of recoil protons produced by

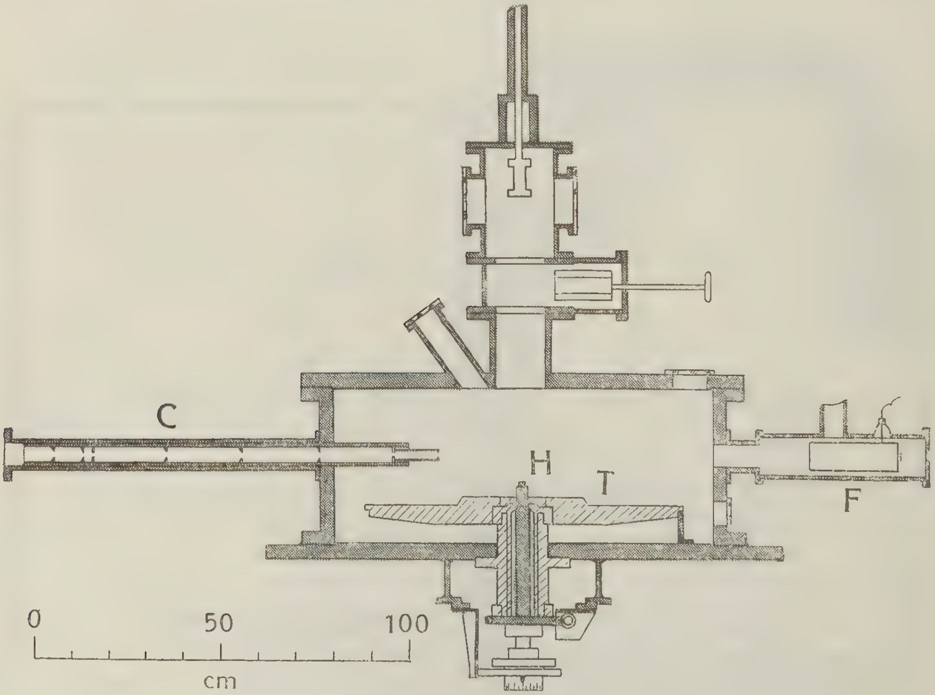

Fig. 2. Cross sectional view of the scattering chamber.

C: Collimation system
T: Turn table
H: Target holding system
F: Faraday cup

---

* Purchased from Matsushita Denko Co. Ltd., Kobe.

the hydrogen atoms contained in the target masked the proton groups from the reaction $^{12}C(\alpha, p)^{15}N$ at forward angles. And there often happened pile-up of pulses in the amplifier and we were unable to measure the complete angular distributions even for the ground state group (P_0).

For the above reason, we used a soot target at small angles. About 0.5 mg/cm² of soots of benzene on a gold foil of 1 micron thick was used. But because of the difficulties in preparing homogeneous soot target, it was used only for measurements of relative values on differential cross sections.

(ii) *Experiments at other energies*

The main purpose of our present experiments was to investigate the change of angular distributions of the ground state proton group (P_0) with the alpha particle energy. For this aim, it was of interest to make measurements at extremely small and large angles, so we made use of small photomultipliers Du Mont 6467. Two NaI(Tl) scintillation counters making an angle of 180° from each other were placed on the turn table in the scattering chamber. The dimensions of the "forward" crystal were 2 cm×2 cm×0.5 cm, and those of the "backward" crystal were 2 cm×2 cm ×0.3 cm. The energy resolution (full width at half maximum) was about 5%. We chose the above photomultipliers at the sacrifice of the resolution, because of their small dimensions.

Thus we could take data at two angles at the same time ranging from 11° to 169°. Electronic circuits were essentially the same as in (i), except that 20-channel pulse height analysers were used in place of a 10-channel analyser.

The angle between the beam and the target was 45°, and the "forward" counter observed the "transmitted" particles and the "backward" counter the "reflected" ones. The schematic arrangement in the scattering chamber is shown in Fig. 2. The absolute values of the differential cross sections measured at 90° by both counters agreed very well in almost all the cases.

The beam current was measured by the Faraday cup and a beam current integrator, and furthermore monitored by a CsI(Tl) scintillation counter located at one of the side windows of the scattering chamber making an angle of 30° from the beam direction.

For the reason described in (i), we were obliged to prepare self supporting carbon targets by the following method[8]; we coated a glass plate by vinyl acetate dissolved in cyclohexanone*. After the evaporation of the solvent, we sprayed colloidal carbon onto this film. Carbon dispersion in water, "Hitasol" AF-1**, was particularly suitable for this purpose as it contained much less elements other than carbon (99.8% carbon) compared with ordinary carbon dispersion. We diluted this dispersion with water and sprayed it under a pressure of about 5 kg/cm².

After the sprayed carbon was dryed, the glass plate was immersed in a bath of cyclohexanone. As the vinyl acetate dissolved in cyclohexanone, a film of carbon peeled off from the glass plate and we scooped it on a target frame. After washing the carbon film in fresh cyclohexanone and drying it, we decomposed volatile substances, such as organic compounds and ammonia remained in colloidal carbon, by heating it over 500°C in vacuum.

By this method we could obtain a very homogeneous carbon foil of 2.37 mg/cm² which was used in the present experiments. With this carbon target we yet observed recoil protons in the forward angles, but its number was far smaller than in the case of polystyrene target and there were no such troubles as described in (i).

The errors indicated in the figures of angular distributions (Figs. 7) include those from two sources, the one being the errors in the estimation of background subtraction and the other the statistical one.

As the ground state proton group was far apart from the first and second excited state group, the background subtraction was generally easy and clear-cut except for extreme forward and backward angles where it happened more or less ambiguities in determing the background level under the peak. A smooth curve, generally a straight line, was drawn through the minima or through the extrapolated background level on both sides of the peak. But the errors from this source were estimated to be between 1 to 3% at most and were far smaller than those from the statistical source.

---

* Other organic solutions like polystyrene in benzene or collodion in amyl acetate were also suitable.

** Purchased from Hitachi Chemical Industry Co. Ltd.

As the cross sections of (α, p) reactions are generally small it was difficult to reduce the statistical errors, and they lay between 3 to 10%.

The estimated errors in the determination of mean target thickness were about 1%, arising chiefly from the measurements of target areas for both polystyrene and carbon foil targets. The errors estimated in the beam current integration were about 1%, and in the detector solid angles were 1%. Considering the inhomogeneities which may exist in the target, the absolute values of the differential cross sections indicated in the coordinates may have errors of about 20%.

§ 3. Results and Discussions

(i) *Experiments at* $E_\alpha=34.6$ MeV

Figs. 3 and 4 show typical histograms taken at $\Theta_{\rm lab}=50°$ and $\Theta_{\rm lab}=40°$ at $E_\alpha=34.6$ MeV (Lab.) with a polystyrene target. At extreme forward angles ($\Theta_{\rm lab}\leqq 40°$) a very strong proton group corresponding to recoil protons from

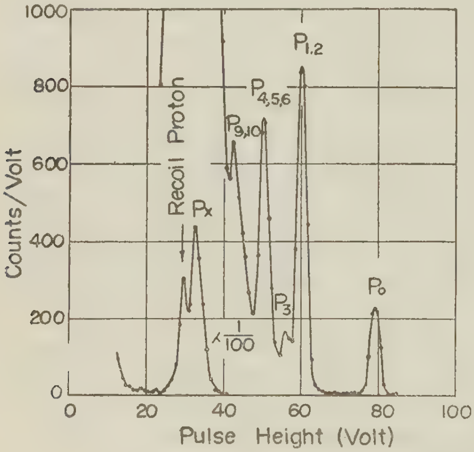

Fig. 3. Histogram of protons from a polystyre target. $E_\alpha=34.6$ MeV $\Theta_{\rm lab}=50°$.

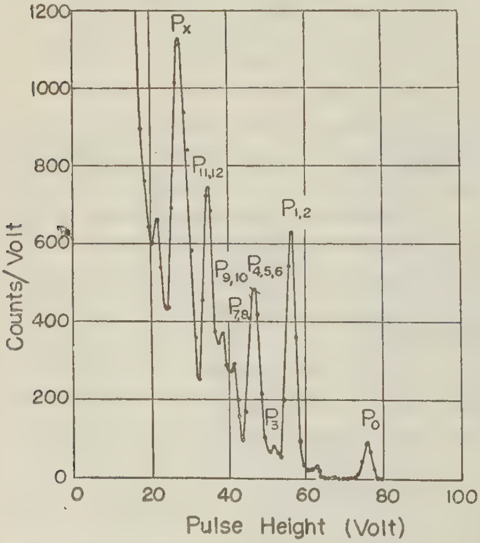

Fig. 4. Histogram of protons from a polystyrene target. $E_\alpha=34.6$ MeV $\Theta_{\rm lab}=40°$.

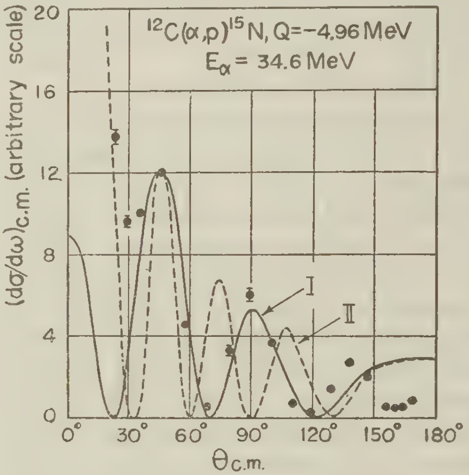

Fig. 5. Angular distribution of ground state proton group (P_0) at $E_\alpha=34.6$ MeV. Calculated angular distributions are also shown for comparison.

I: $R=3.67\times10^{-13}$ cm
II: $R=5.58\times10^{-13}$ cm

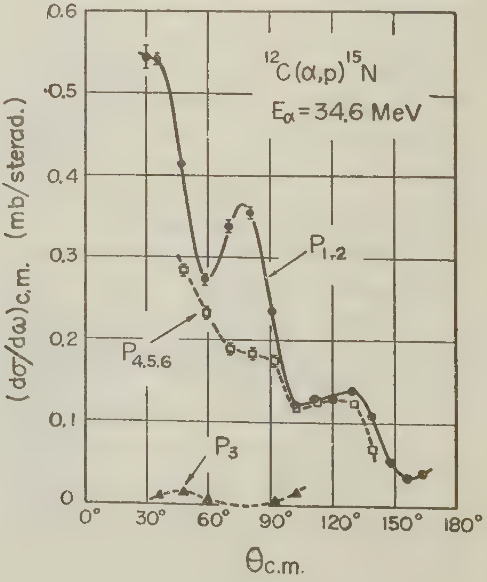

Fig. 6. Angular distribution of P_{12}, P_3, P_{456} groups at $E_\alpha=34.6$ MeV.

the $(CH)_n$ target masked the excited state groups P_{12}, P_3 and P_{456}.

The soot target with Au backing used for small angles might have poor homogeneity, so the data were taken only to obtain relative cross sections and weve normalized to the data taken at same angles with polystyrene target. At small angles, even with this soot target the recoil protons due to the water vapour adsorbed at the surface of target prevented the measurements of proton groups corresponding to higher excitations. Moreover, the P_3 group was so weak compared with either P_{12} or P_{456} groups, that it was quite difficult to obtain a complete angular distributions of this P_3 group. Fig. 5 shows the angular distribution of P_0 group and Fig. 6 shows those of P_{12}, P_3 and P_{456} groups at $E_\alpha=34.6$ MeV.

(ii) *Experiments at other energies*

As the groups corresponding to higher excitations were difficult to be investigated in the circumstances stated above, we decided to investigate the change of angular distributions of ground state group P_0 as functions of bombarding energies using the self supporting carbon target mentioned in § **2.** (ii).

We collected the angular distributions obtained at twelve bombarding energies in Fig. 7. The three dimensional view of $d\sigma/d\omega$ as functions of E and θ is shown in Fig. 8. Figs. 7, 8 include the results at $E_\alpha=34.6$ MeV

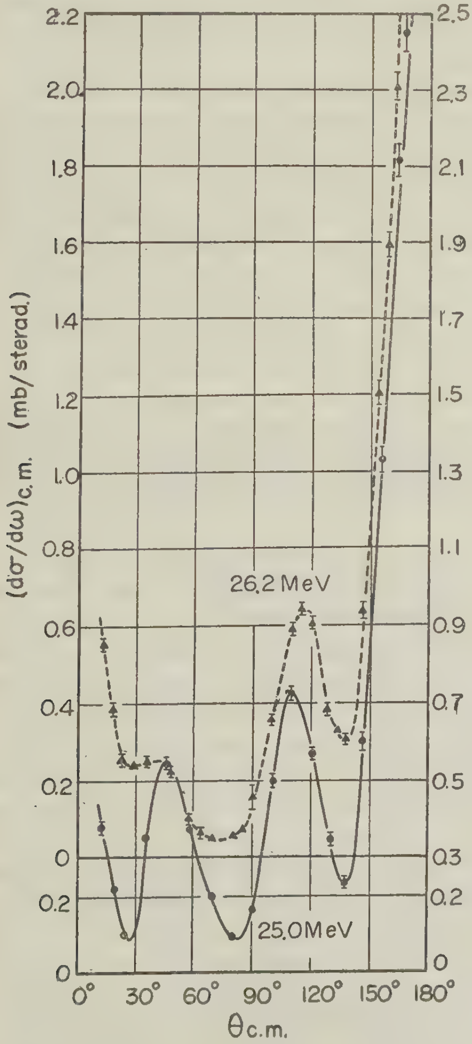

Fig. 7a. Change of angular distributions of ground state proton group P_0 between 25 and 26 MeV.

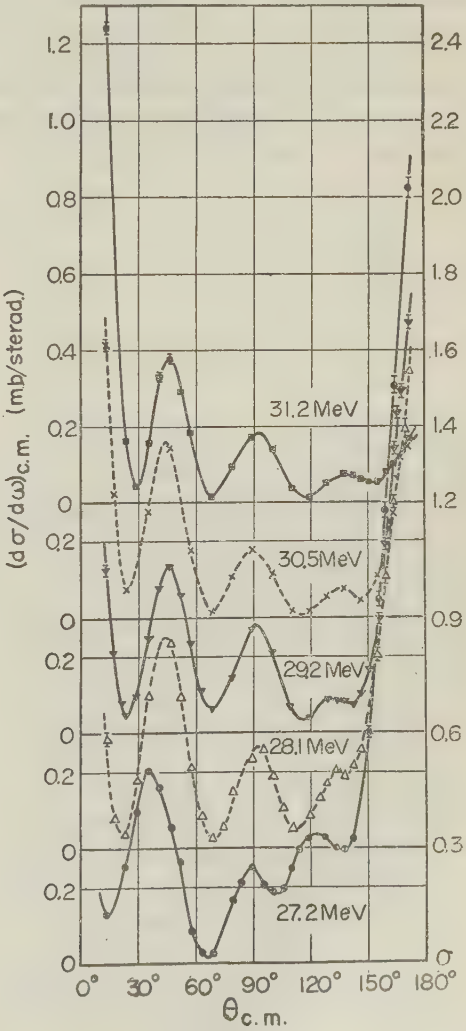

Fig. 7b. Change of angular distribution of ground state proton group P_0 between 27 and 31 MeV.

with polystyrene and soot targets. They are consistent with the results obtained with the carbon target, though the absolute values of the former are a little less. Present results are in reasonable agreement with those of R. Sherr and M. Rickey[1)] and of C. E. Hunting and N. S. Wall[2)] at neighbouring energies.

There are several remarkable features is the shape and magnitude of angular distributions.

(1) In the energy region between 25 and 26 MeV (Fig. 7a), angular distributions have two peaks and three valleys and there appear remarkable rises in the backward angles. These data were obtained, as mentioned above, by reducing the energies of alpha particles by introducing absorbers, and unfortunately we were unable to obtain beams of enough intensity with energies below 25 MeV. The preliminary results obtained by Osaka University group[3)] at $E_\alpha=22$ MeV hold qualitatively the features of those at 25 MeV; at 22 MeV the second peak approaches to the first one and the former becomes smaller than the latter.

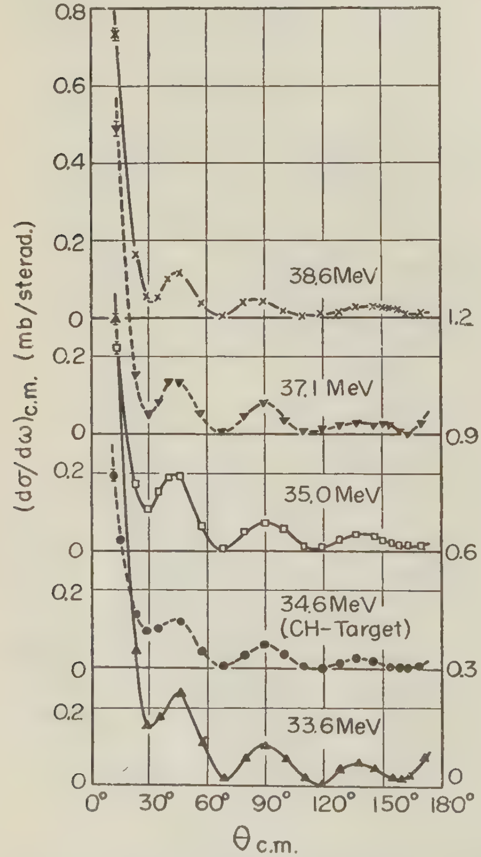

Fig. 7c. Change of angular distribution of ground state proton group P_0 between 33 and 39 MeV.

(2) In the energy region between 27 and 31 MeV (Fig. 7b), there appear three peaks and four valleys and their positions and magnitudes change systematically with energies. Particularly, the greater the beam energy becomes, the less the rise in the backward angles and the greater the rise in the forward angles.

(3) In the energy region between 33 and 39 MeV (Fig. 7c), there appears little rise of cross sections in the backward angles. The shapes of all these angular distributions resemble one another, the positions of peaks and valleys differ little, and the cross sections become smaller as the beam energies become higher.

(4) In Fig. 9, the differential cross sections at fixed laboratory angles are shown as functions of alpha particle energies. They show some resonance-like peaks and valleys, but this fact is considered to come from the changes of angular distributions with alpha particle energies and not necessarily from compound nucleus formation. In Fig. 10, the total cross section of P_0 group, σ_t, integrated from the angular distributions is shown as a function of alpha particle energies. The relative errors are estimated to be not greater than 10%, and it is sure that σ_t shows only a monotonously decreasing function of energies.

Detailed analyses have not yet been done, but we might conclude at least that any simple model of nuclear reaction is not sufficient to explain all our results. Concerning only to the angular region $\theta_{c.m.}<130°$, one might say that the reaction proceeds by either knock-on or stripping mechanism, as was described by S. T. Butler[4)]. But calculations by this model cannot fit the data very well at $E_\alpha=34.6$ MeV as is shown in Fig. 5, calculated values of $[j_1(QR)]^2$ for two nuclear radii $R=5.58\times10^{-13}$ cm and 3.67×10^{-13} cm normalized to the experimental value at the first maximum. Each first minimum calculated is too deep to fit the observed data. The second minimum and the second maximum are rather better fitted by $R=3.67\times10^{-13}$ cm than by $R=5.58\times10^{-13}$ cm, But the former value is too small as compared with the value gene-

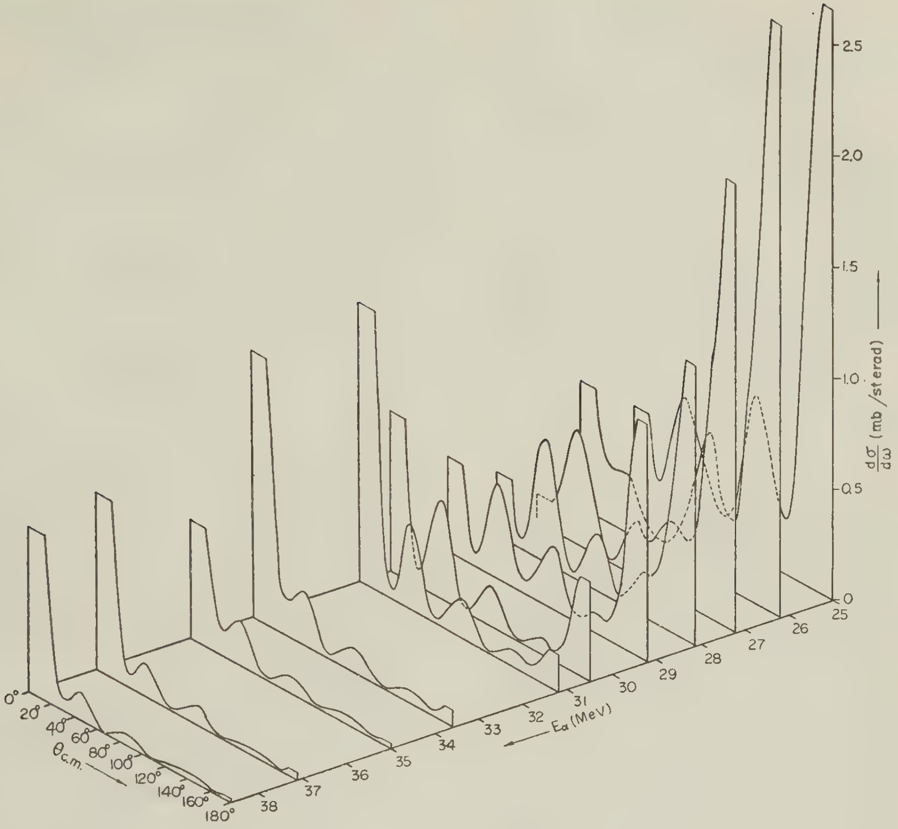

Fig. 8. $(d\sigma/d\omega)_{\mathrm{c.m.}}$ as functions of E_α and $\theta_{\mathrm{c.m.}}$

rally allowed in other experiments. One cannot fit the calculated values at all to the data in the backward region neither at E_α= 34.6 MeV nor at E_α=30.5 MeV.

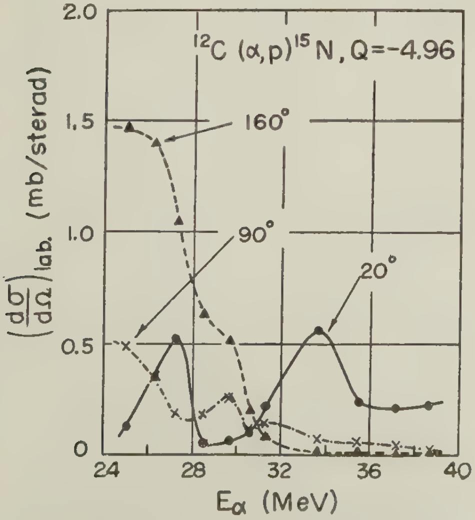

Fig. 9. Differential cross sections as functions of alpha particle energies at $\Theta_{\mathrm{lab}}=20°$ 90° and 160°.

The extraordinary rises of cross sections at large angles at alpha particle energies between 25 and 31 MeV might remind us some sort of heavy particle stripping suggested by G. E. Owen and L. Madansky[9]. But this model alone might not explain all the angular distributions. It may be that our results are ex-

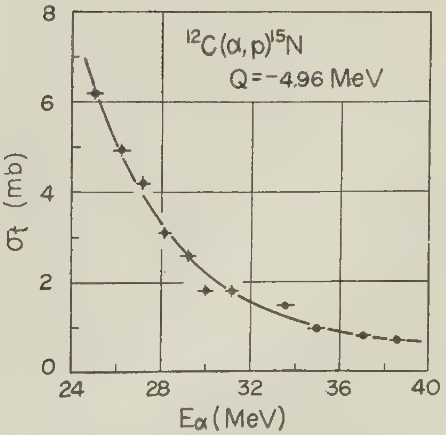

Fig. 10. Total cross section σ_t as a function of alpha particle energies.

plained by mixing the knock-on, stripping, heavy particle stripping and perhaps compound nucleus formation. Tne method of analyses used by G. F. Pieper and N. P. Heydenburg[10] for the reaction $^{19}F(\alpha, p)^{22}Ne$ at $E_\alpha = 6$ MeV may be helpful, and also the idea of semiclassical treatment of direct reactions by S. T. Butler et al.[11] may be useful.

At any rate, it is dangerous to ascribe the reaction mechanism to any model from an angular distribution obtained at a single energy and with a particular target. The accumulated data obtained here might be helpful to deduce something about the mechanism of the reaction $^{12}C(\alpha, p)^{15}N$.

Acknowledgement

The authors are very greatful to the devoted help by the cyclotron crew of I.N.S.; Messrs. T. Karasawa, A. Suzuki, H. Ogawa, T. Yamada, H. Adachi and Y. Miyazawa. The authors have also a distinct pleasure to thank the members of the Institute for their illuminating discussions.

The experiment at $E_\alpha = 34.6$ MeV was done as one of the " Test Experiments " of I.N.S. cyclotron and parts of the work were done by the temporal vising physicists from other universities; Drs. N. Ryu (Hiroshima University), Y. Nakano (Hokkaido Gakugei University) and Messrs. K. Takeshita (Kyushu University), T. Ishimatsu (Kyushu University), Y. Nakashima (University of Tokyo), and Ching Lin Wang (Kyoto University) and Miss. S. Mizuno (University of Tokyo).

The authors thank also Dr. N. S. Wall of M.I.T., Dr. M. Rickey of the University of Washington and the Osaka University group for sending us their preliminary data and for their helpful discussions. They express their cordial thanks to Prof. S. Kikuchi, Director of the Institute for his encouragement throughout these works.

References

1) R. Sherr and M. Rickey: Bull. Amer. Phys. Soc. Ser. II, **2** (1957) 29; Ann. Progr. Rep. Washington Univ. (1957).
2) C. E. Hunting and N. S. Wall: Bull. Amer. Phys. Soc. Ser. II, **2** (1957) 181; private communication.
3) S. Yamabe, M. Kondo and T. Yamazaki: private communication.
4) S. T. Butler: Phys. Rev. **106** (1957) 272.
5) N. Austern, S. T. Butler and H. McManus: Phys. Rev. **92** (1953) 350.
6) Construction of I. N. S. cyclotron will be reported in this journal in near future.
7) K. Kikuchi, S. Kobayashi and K. Matsuda: J. Phys. Soc. Japan **14** (1959) 121.
8) T. Mikumo: to be published.
9) G. E. Owen and L. Madansky: Phys. Rev. **99** (1955) 1608(L); **105** (1957) 1766.
10) G. E. Pieper and N. P. Heydenburg: Phys. Rev. **111** (1958) 264.
11) S. T. Butler, N. Austern and C. Pearson: Phys. Rev. **112** (1958) 1227.

JOURNAL OF THE PHYSICAL SOCIETY OF JAPAN Vol. 14, No. 10, OCTOBER, 1959

Excitation Functions for (*p*, *n*) Reactions with Titanium, Vanadium, Chromium, Iron and Nickel up to Ep=14 MeV

By Shigeo TANAKA and Michiaki FURUKAWA

Institute for Nuclear Study, University of Tokyo, Tanashi, Tokyo

(Received June 20, 1959)

The absolute (p, n) cross sections on Ti^{47}, Ti^{48}, V^{51}, Cr^{52}, Fe^{56}, Fe^{57}, Ni^{61} and Ni^{64} were measured by the activation method at proton energies up to 14 MeV. The experimental results were compared with the predictions based on statistical model in terms of $\sigma(p, n)/\sigma_{total}$, and it was shown that the predictions based on this simple model are not necessarily in disagreement with the experiments.

§ 1. Introduction

The (p, n) cross sections were extensively measured by the Zurich group for the energies from the threshold of the (p, n) reaction to 6.7 MeV[1,2,3,4] According to Shapiro's calculation[5], agreement of the experimental values with the statistical theory was good for most nuclei so far as energy dependence was concerned. But the agreement was not always close and the assumption of a large variety of nuclear radii was necessary even for the nuclei of the same atomic number. Recently, Howe[6] extended the results of the Zurich group with copper and zinc into the energy region above the Coulomb barrier and confirmed that this variation, as far as compound model was assumed, is identified with the variation of the relative probability that the compound nucleus decays by neutron emission. He also suggested, as an alternative explanation, a picture of nuclear reactions in which a large fraction of events consist of direct proton-nucleon collisions at these low energies.

During the last several years, a growing number of experiments have thrown doubt on the validity of some of the assumptions and models on which the statistical theory of nuclear reaction is based[7,8,9]. However, it is obvious that quantitatively in this energy region the direct interactions are always relatively less important in comparison with the more probable statistical reaction[10,11,12].

Since few data[10,13] are available on the (p, n) cross section above 6.7 MeV, the excitation function measurements at higher energy region would give light on a more conclusive test for the validity of the statistical model of nuclear reaction.

§ 2. Experiments

The measurements of excitation functions were made for the (p, n) reactions of nuclides Ti^{47}, Ti^{48}, V^{51}, Cr^{52}, Fe^{56}, Fe^{57}, Ni^{61} and Ni^{64} for the proton energies up to about 14 MeV, above the thresholds of the competing reactions, (p, pn), $(p, 2n)$, etc. The target foils of natural isotopic abundance were activated with monoenergetic proton beams from 63-inch INS (Tokyo) cyclotron. All the bombardments were performed with extremely monochromatized external beams which were focussed by the quadrapole magnet and collimated successively by the narrow carbon slits only enough to obtain currents not less than about 0.5μA. The titanium, the iron and the nickel targets were rolled metal foils about 2 to 5 mg/cm² thick. The chromium targets were prepared by electrodeposition from bichromate solution onto thin copper plate, followed by dissolution of copper backing with nitric acid. The vanadium targets were prepared by spattering slurries of vanadium pentoxide in clear lacquer onto thin aluminum foils of known thickness. The 3 cm × 3 cm foils were used for the cyclotron bombardment when the section of the beam was about 0.5 cm². The foils were large enough to intercept all the protons including the scattered protons. The beam was collected by a Faraday cup. The signal from the cup was led to a 100% feedback type beam current integrator.

When it was difficult to distinguish the activity due to a (p, n) reaction from the interfering activities by means of a counting technique, chemical separation was performed.

For each target nucleus two kinds of cross section were measured: absolute (p, n) cross section measured with about 10 MeV protons which gave no second particle emission and relative cross section over the whole range of energies up to 14 MeV.

The absolute values of the cross sections were calculated from the formula $\sigma=\frac{A_0}{\lambda}\frac{1}{N}\frac{S}{A_t}$, where A_0/λ is the number of reaction product in the foil with A_t nuclei per area S by N protons. A_t/S was calculated from the measured weight and area of the foil, A_0/λ from the decay constant λ and the measured disintegration rate corrected for decay and N from the charge collected by the Faraday cup.

Table I lists the half-life and the probability of β^+ and β^- emission for the (p, n) reaction product used in the cross section calculation. These were obtained from the compilation of Seaborg et el[14]. and from the newer nuclear data in literature.

Energy dependence of the cross sections was measured by using the stacked-foil technique in which several target foils were interspaced with aluminum absorbers. In the most case of the bombardments, initial proton energies of 10 and 14 MeV were used. The energies of protons just entering and leaving each target foil were determined by calculating the energy loss in each foil in the stack. The energy loss in the aluminum absorber was calculated from the range-energy curve of Aron et al., and the dE/dx value in the other target foils was calculated in each case from the stopping power formula of Bethe et al[16]. The calculation leads to error onlv through the use of estimated mean excitation potential, I, in the stopping power formula and it can be shown that the error will be small over the range of proton energies used in this experiment for a variety of I.

The counting procedures were as follows.

Titanium targets: The disintegration rate of 16d-V^{48} was determined by a gamma-gamma coincidence counting after short-lived interfering activities had decayed. The relative yields of V^{48} were obtained by counting with an NaI scintillation counter set to count gamma rays above 0.6 MeV. Analysis of decay curves of 0.51 MeV gamma rays from positron annihilation gave the V^{47}/V^{48} ratios after subtraction of Compton tails from more energetic gamma rays. The yields of 31 m-V^{47} were given by applying these V^{47}/V^{48} ratios to the absolute yields of V^{48}.

Vanadium targets: Relative yields of 28d-Cr^{51} were given by counting with an NaI scintillation counter. To obtain the absolute yield of Cr^{51}, a source in a small volume was prepared from one of the targets and counted with an NaI scintillation counter in a defined geometry. The disintegration rate of Cr^{51} was thus determined by counting the photopeak from 0.32 MeV gamma ray.

Chromium targets: The Mn^{52m}/Mn^{52} ratios were given by analyzing decay curves of 1.45 MeV gamma ray from 21 m-Mn^{52m} and 5.7d-Mn^{52}. The disintegration rate of Mn^{52} was obtained by a gamma-gamma coincidence after short-lived activities had decayed. The relative yields of Mn^{52} were obtained by counting gamma rays above 0.6 MeV with an NaI scintillation counter.

Iron targets: After chemical separation, the cobalt fraction was made to a constant volume and a small portion was taken onto

Table I.

Reaction	Abundance in target	Half-life of product	Probability of β^+ and β^- emission
$Ti^{47}(p, n)V^{47}$	7.28%	31 m	97%
$Ti^{48}(p, n)V^{48}$	73.9	16.2 d	57
$V^{51}(p, n)Cr^{51}$	99.8	27.8 d	9*(0.32 MeV γ)
$Cr^{52}(p, n)Mn^{52m}$	83.8	21 m	99
$Cr^{52}(p, n)Mn^{52}$	83.8	5.7 d	33
$Fe^{56}(p, n)Co^{56}$	91.7	77 d	20
$Fe^{57}(p, n)Co^{57}$	2.19	270 d	100*(0.13 MeV γ)
$Ni^{61}(p, n)Cu^{61}$	1.19	3.3 h	66
$Ni^{64}(p, n)Cu^{64}$	1.08	12.8 h	57

* Relative intensity of gamma radiation.

a gold-spattered polyvinyl acetate film 50γ/cm^2 thick. After the source was dried in air, it was counted with a 4π methane proportional counter. The correction for the absorption loss in the foil was made. The relative yields of Co^{56} were obtained by counting with an NaI scintillation counter set to count gamma rays above 0.6 MeV. The absolute yields of Co^{57} were given by counting photo-peaks of the 0.13 MeV gamma rays in a well type NaI scintillation counter after subtraction of Compton tails from more energetic gamma rays.

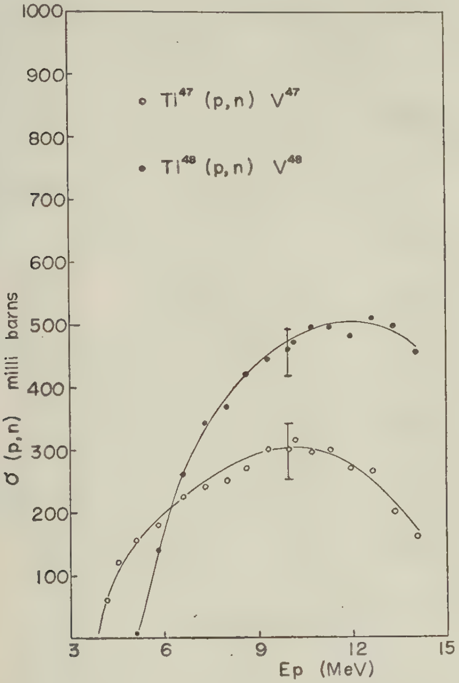

Fig. 1. The excitation functions for the reactions Ti^{47} (p, n)V^{47} and Ti^{48}(p, n)V^{48}.

Nickel targets: All the targets were chemically separated by means of anion exchange resin. Known portions of the copper fractions were evaporated to driness in counting dishes. These samples were counted with an end-window type Geiger Müller counter. The decay was followed for about 100 hours. Analysis of curves gave the Cu^{61}/Cu^{64} ratios after corrections for backscattering and absorption by air and the counter window. The disintegration rate of 12.8h-Cu^{64} was determined in the 4π beta proportional counter. The absolute yields of Cu^{61} were obtained from these Cu^{61}/Cu^{64} ratios and the disintegration rate of Cu^{64}.

§ 3. Results and Discussion

The absolute cross sections of the reactions studied are plotted as a function of the proton energy in Figures 1 to 5.

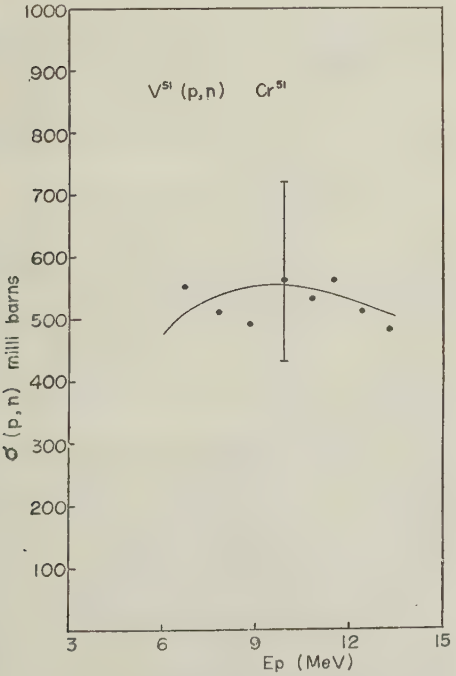

Fig. 2. The excitation function for the reaction V^{51}(p, n)Cr^{51}.

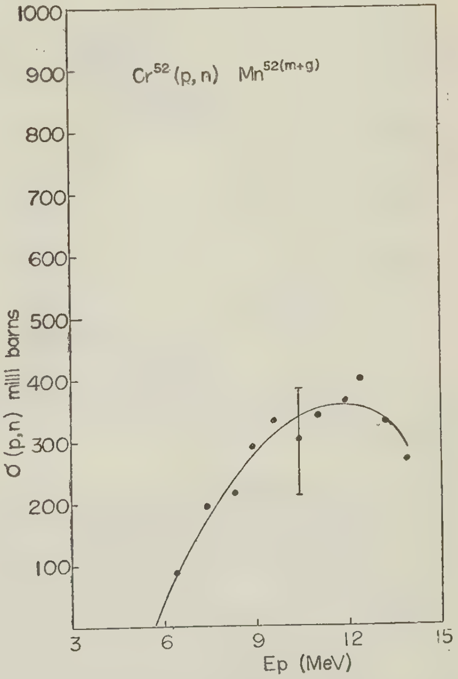

Fig. 3. The excitation function for the reaction Cr^{52}(p, n)Mn$^{52(m+g)}$.

The estimated standard error in the absolute cross sections, not including the uncertainty in the nuclear data, is shown in each figure. The curve in Figure 3 is the sum of σ_m and σ_g.

If the results of a measurement of the (p, n) cross section were analyzed in the light of the statistical theory assuming that the (p, n) cross section is the same as the total reaction cross section at this energy region, agreement with theory would be fairly good so far as energy dependence is concerned. Such an analysis, however, requires a large variation of assumed nuclear radii even from one isotope to another in a single element to fit the magnitude of cross section[5,6]. It appears as if the same could be said for the present results.

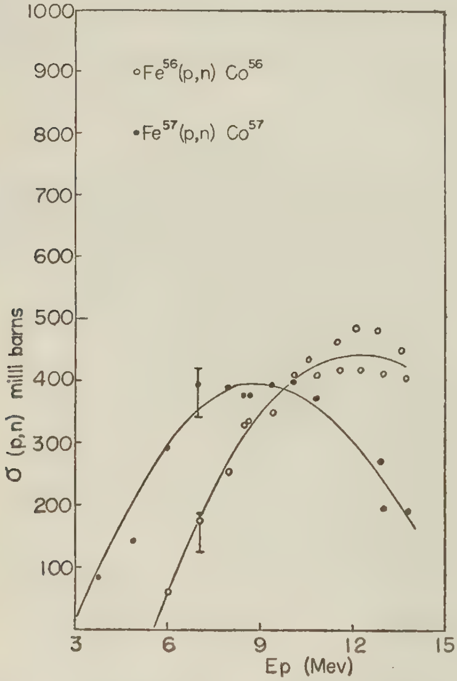

Fig. 4. The excitation functions for the reactions $Fe^{56}(p, n)Co^{56}$ and $Fe^{57}(p, n)Co^{57}$.

As far as the statistical model is assumed to be applicable, this discrepancy may be mainly due to the assumption which neglects the proton emission. When the proton binding energy of the compound nucleus is less than the neutron binding energy by a sufficient margin, it is obvious that the proton emission is not always negligible. This is especially the case when the fact is taken into account that the level densities in the two different residual nuclei may not be the same for the same exitation energy.

On this point of view, the full calculations about the emission probabilities of all the probable modes of decay of a compound nucleus were made as follows:

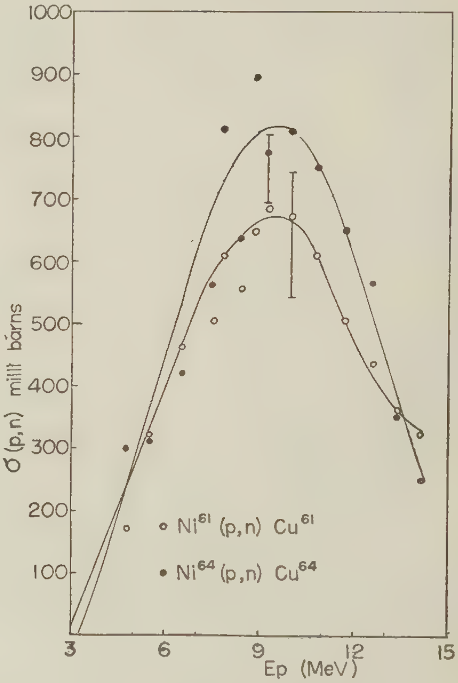

Fig. 5. The excitation functions for the reactions $Ni^{61}(p, n)Cu^{61}$ and $Ni^{64}(p, n)Cu^{64}$.

(a) The energy distribution of the emitted particle b is given by

$$N_b(\mathcal{E})\, d\mathcal{E} = \text{const. } \mathcal{E}\sigma_c(\mathcal{E})\omega(E)\, d\mathcal{E}\ .$$

Here $\mathcal{E}$ is the channel energy and E the excitation energy of the residual nucleus corresponding to the channel energy $\mathcal{E}$. Then $E = E_0 - Q_{cb} - \mathcal{E}$, where E_0 is the excitation energy of the compound nucleus and Q_{cb} is the binding energy of the particle b to the compound nucleus.

(b) σ_c is the capture cross section of evaporated particle on the residual nucleus and the values of σ_c were taken from Shapiro's calculation[5] for charged particles and $\sigma_c = \pi R^2$ for neutrons. (where the nuclear radii R is $r_0 \times A^{1/3}$) Here, the nuclear potential was conventionally assumed to be a square well, and the barrier was assumed to be independent of the excitation energy.

(c) The level density ω of the residual nucleus is based on a Fermi degenerate gas model and is given by $\omega(E)=c\exp[2(aE)^{1/2}]$, in which a and c are constants. It was assumed that a is the same for all residual nuclei studied, and the value of a chosen was 2, which is in agreement with many measurements of excitation functions with α-particles and with high-energy neutrons[17]. The dependence of the level density on the odd-even effect was taken into account on the basis of the work of Brown and Muirhead[18]

$$\omega_{0-0}/12 \sim \omega_{0-e}/5 \sim \omega_{e-e}/1 \ .$$

(d) Above the separation energy of a secondary proton emission γ-ray de-excitation may be considered more intensive than the proton emission until the excitation energy is 1~2 MeV above the separation energy owing to the Coulomb barrier. But unfortunately, the proper method for calculating γ-ray de-excitation is uncertain. In this paper, γ-ray de-excitation was allowed for by shifting the

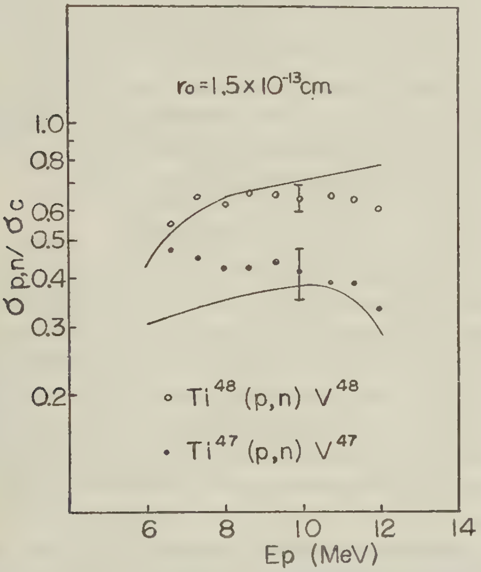

Fig. 6. The comparison of calculated and experimental values $\sigma(p, n)/\sigma_c$ for Ti^{47} and Ti^{48}.

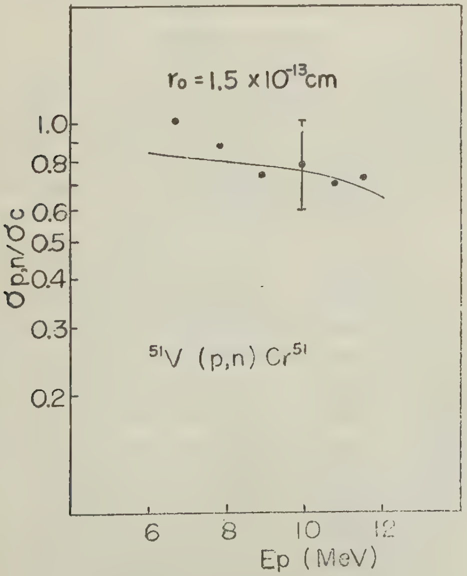

Fig. 7. The comparison of calculated and experimental values $\sigma(p, n)/\sigma_c$ for V^{51}.

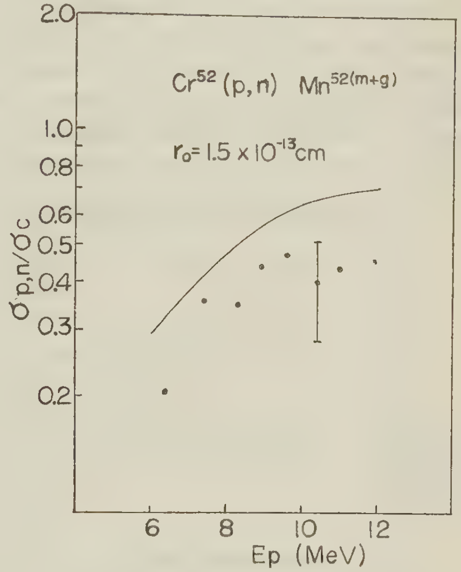

Fig. 8. The comparison of calculated and experimental values $\sigma(p, n)/\sigma_c$ for Cr^{52}.

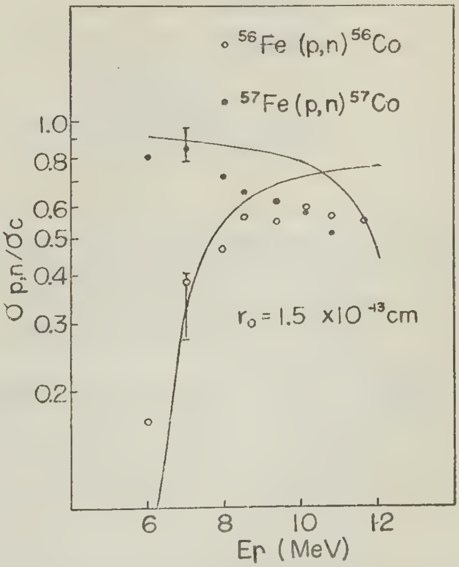

Fig. 9. The comparison of calculated and experimental values $\sigma(p, n)/\sigma_c$ for Fe^{56} and Fe^{57}.

threshold for the secondary proton emission 2 MeV upward.

(e) The emission probability calculations are very sensitive to the values of the binding energies of various particles. These values were obtained from the compilation of Way et al[19]. and they agree with those from recent mass measurements.

The experimental and theoretical values are compared through the values of $\sigma(p, n)/\sigma_c$. The solid curves in Figures 6 to 10 represent the calculated values of this quantity. The experimental points in Figures 6 to 10 are obtained from the observed (p, n) cross sections and the calculated total reaction cross section σ_c. The total reaction cross secton σ_c depends sensitively on the parameter r_0.

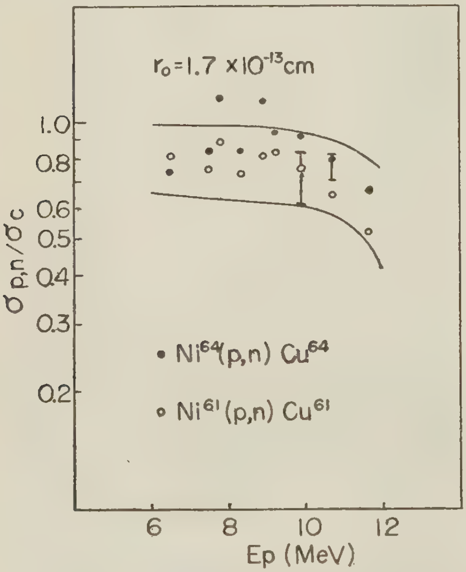

Fig. 10. The comparison of calculated and experimental values $\sigma(p, n)/\sigma_c$ for Ni^{61} and Ni^{64}.

Unfortunately, the same value of r_0 could not be taken consistently for all comparisons. The value $r_0=1.5\times10^{-13}$ cm was taken for all targets except for nickel, and 1.7×10^{-13} cm had to be chosen for nickel to fit the large (p, n) cross section.

It appears that the discrepancies between experimental and theoretical values do not exceed a factor of 1.5. This agreement, in view of the strong dependence of the calculations on some of the assumptions enumerated above, can not be claimed to be very meaningful. But the prediction of the statistical theory is not necessarily in disagreement with experiments. It may be profitable that, to discuss the validity of statistical theory, a review of some of the assumptions embodied in the present calculation is taken into account. The assumption of a square well potential in (b) may not be proper. It has been pointed out by K. Kikuchi[20] that the use of an exponential diffuse potential is more preferable to calculate the evaporation process. Besides, the assumption in (b) that the nuclear barrier is independent of excitation energy may not be valid. An increase in penetration with excitation would increase the emission of low-energy charged-particles. Indeed, it has been shown by Fulmer and Goodman[21] that the (p, α) cross sections agree with the assumption of a lowered Coulomb barrier for the excited compound nucleus.

Acknowledgements

This work was done with the aid of the visiting researchers from other universities: Drs. K. Otozai, S. Kume, S. Fukushima, S. Iwata (Osaka University), T. Shiokawa, M. Yagi (Shizuoka University) and Y. Kusaka (Konan University), to whom authors' thanks are due. Authors' thanks are also due to Drs. K. Kikuchi and T. Mikumo for their valuable discussion, and to Prof. I. Nonaka and the other staff of low energy division for their encouragement. We are also grateful to the cyclotron crew for their cyclotron operation.

References

1) J. P. Blaser, F. Boehm, P. Marmier and D. C. Peaslee: Helv. Phys. Acta. **24** (1951) 3.
2) J. P. Blaser, F. Boehm, P. Marmier and P. Scherrer: Helv. Phys. Acta **24** (1951) 441.
3) J. P. Blaser, P. Marmier, F. Boehm and P. Scherrer: Helv. Phys. Acta **24** (1951) 465.
4) F. Boehm, P. Marmier and P. Preiswerk: Helv. Phys. Acta **25** (1952) 599.
5) M. M. Shapiro: Phys. Rev. **90** (1953) 171.
6) H. A. Howe: Phys. Rev. **109** (1958) 2083.
7) R. M. Eisberg and G. Igo: Phys. Rev. **93** (1954) 425.
8) B. L. Cohen: Phys. Rev. **98** (1955) 49.
9) B. L. Cohen and A. G. Rubin: Phys. Rev. **113** (1959) 579.
10) S. N. Ghoshal: Phys. Rev. **80** (1950) 939.
11) P. C. Gugelot: Phys. Rev. **81** (1951) 51.
12) S. Hayakawa, M. Kawai and K. Kikuchi: Progr. Theor. Phys. **13** (1955) 415.
13) H. G. Blosser and T. H. Handley: Phys. Rev.

100 (1955) 1340.
14) D. Strominger, J. M. Hollander and G. T. Seaborg: Rev. Mod. Phys. **30** (1958) 585.
15) W. A. Aron, B. G. Hoffman and F. C. Williams: U. S. Atomic Energy Commission Report AECU-663 (1949).
16) M. S. Livingston and H. A. Bethe: Rev. Mod. Phys. **9** (1937) 245.
17) G. Igo and H. E. Wegner: Phys. Rev. **102** (1956) 1364.
18) G. Brown and H. Muirhead: Phil. Mag. **2** (1957) 473.
19) K. Way, R. W. King, C. L. McGinnis and R. van Lieshout: *Nuclear Level Schemes*, A=40∼A=92. U. S. Atomic Energy Commission Report TID-5300 (1955).
20) K. Kikuchi: Progr. Theor. Phys. **17** (1957) 643.
21) C. B. Fulmer and C. D. Goodman: Bull. Amer. Phys. Soc. Ser **II**, **4** (1959) 9.

JOURNAL OF THE PHYSICAL SOCIETY OF JAPAN, Vol. 14, No. 10, OCTOBER, 1959

The Field Dependence of the Mobility of Electrons in *n*-Germanium

By Hisanao SATO
Department of Physics, University of Nagoya

(Received May 6, 1959)

The mobility of electrons in *n-Ge* at an arbitrary field strength is calculated by assuming the distribution function $f(\boldsymbol{p})$ in the form

$$f(\boldsymbol{p})=A\exp\left(-\frac{|\boldsymbol{p}+\boldsymbol{p}_0|^2}{2mkT}\right),$$

where T is the electron temperature and $\boldsymbol{p}_0$ represents the uniform displacement of the electron distribution in the direction of the electric field. Two parameters T and $\boldsymbol{p}_0$ are determined by the same way as Fröhlich and Paranjape did. Interaction constants between electrons and acoustical- and optical-modes of vibration are determined from the temperature dependence of the zero-field mobility. At room temperatures it is found that the electron temperature is determined almost by optical-mode scattering at low fields, but that the energy loss of electrons due to acoustical-mode scattering cannot be neglected at very high fields. Consequently the current density versus electric field relation becomes much different from Shockley's predictions. It seems that the agreement with the experimental results becomes more satisfactory.

§ 1. Introduction

The temperature dependence of the lattice-scattering mobility in *n*-type germanium was found to be $T^{-1.66}$[1]. This result is different from the theoretical prediction $T^{-1.5}$ which is derived by assuming that electrons are scattered by acoustical phonons[2]. Harrison[3] attributed this discrepancy to the scattering of electrons by optical phonons. He estimated the relative importance of acoustical-mode and optical-mode scattering by expanding the matrix elements for scattering in powers of the electron wave number and studying the first non-vanishing terms. He concluded that in *n*-type germanium the matrix elements for scattering by optical modes are large compared to those for scattering by acoustical modes. Although the amplitude of optical modes are small, their contribution to the mobility must become comparable to that of acoustical modes at about 300°K (we assume a characteristic temperature of optical phonons is equal to it).

It has been reported that at high electric field the current deviates from Ohm's law and become proportional to the square root of the field strength[4]. Shockley[5] analyzed this current versus field relation theoretically, assuming that steady-state conditions are realized by the processes in which electrons lose their momentum and energy to acoustical vibrations. It has been remarked that his theory is not in agreement with experiments quantitatively. Yamashita and Watanabe[6] solved the Boltzmann equation by assuming the distribution function in the from

$$f(\boldsymbol{p})=f_0(p)+\mathrm{P}_1(\cos\theta)f_1(p)\,, \qquad (1)$$

where $\mathrm{P}_n(\cos\theta)$ is the Legendre polynomials of degree n, the polar axis being chosen in the direction of the electric field. But the quantitative discrepancy between theory and experiment was not explained.

Sodha and Agrawal[7] calculated the low field mobility, taking optical modes into consideration. At low fields we can write the mobility μ in the form

$$\mu=\mu_0(1-\nu F^2)\,, \qquad (2)$$

where μ_0 is the zero-field mobility and F the field strength. If we consider the scattering by acoustical modes only, the theoretical magnitude of ν becomes about a hundred times as large as the experimental value. Sodha and Agrawal concluded that their calculation could not remove this discrepancy. Yamashita[8] evaluated ν also, taking account of the scattering by both acoustical and optical modes and solving the Boltzmann equation on the assumption (1). He showed that theoretical ν was in agreement with the experimental one very nicely.

At high fields the average energy of electrons increases and the mobility decreases since relaxation times are approximately inversely proportional to the velocity of electrons. Under steady-state conditions, the distribution function of electrons is so determined that the rates of gain and loss of energy (or momentum) balance each other. If we consider the scattering by acoustical modes only, electrons become hot even in a weak field because the energy loss of electrons by the emission of acoustical phonons is small. On the contrary, the energy of optical phonons emitted by electrons is so large that the optical modes play an essential role in determing the energy exchange between electrons and lattice vibrations except at very low temperatures.

The purpose of this paper is to remove the discrepancy between Shockley's theory and experiments in the hot electron problem and to study the scattering mechanism of electrons by lattice vibrations in n-type germanium. To solve the Boltzmann equation we assume the distribution function in the form

$$f(\boldsymbol{p})=A\exp\left(-\frac{|\boldsymbol{p}+\boldsymbol{p}_0|^2}{2mkT}\right), \qquad (3)$$

supposing that the exchange of energy and momentum between electrons is so fast that they are in internal equilibrium. In (3) T is the temperature of electrons and $\boldsymbol{p}_0/m$ is their drift velocity. Estimating the contribution of optical modes to the mobility from the experimental zero-field mobility μ_0, we calculate the low field mobility, (2), and the mobility of hot electrons. In § 3 it is shown that the rate of the energy loss of electrons is determined almost by the optical-mode scattering at room temperatures. But at very high fields (§ 5), where the average energy of electrons become high, it appears that one cannot neglect the acoustical-mode scattering since high energy electrons can emitt a high energy phonon.

§ 2. The Boltzmann Equation

When a static electric field F is in the z direction, the Boltzmann equation is

$$eF\frac{\partial f}{\partial p_z}+\left(\frac{\partial f}{\partial t}\right)_L+\left(\frac{\partial f}{\partial t}\right)_e=0\,, \qquad (4)$$

where $(\partial f/\partial t)_L$ and $(\partial f/\partial t)_e$ are the rate of change of f due to collisions with phonons and between electrons, respectively. We assume that the energy of electrons E is a parabolic function of momentum p; $E=p^2/2m$, m being the effective mass.

Now we shall write the explicit from of $(\partial f/\partial t)_L$. According to Harrison[3], the matrix element of the perturbing potential H' is of first order in powers of the phonon wave number $(q/\hbar)$ for scattering by acoustical modes, whereas for scattering by optical modes the zero order term remains nonvanishing. Thus we have

$$|H'|^2=\frac{C^2q^2}{2N_0M\hbar\omega_q}\begin{Bmatrix}n_q\\ n_q+1\end{Bmatrix} \qquad (5)$$

for acoustical-mode scattering, and

$$|H'|^2=\frac{C'^2q_L^2}{2N_0M\hbar\omega}\begin{Bmatrix}n_0\\ n_0+1\end{Bmatrix} \qquad (6)$$

for optical-mode scattering, where $q_L/\hbar$ is equal to inverse atomic distance. C and C' are constants of the same order of magnitude.

As usual, the energy of an optical phonon, $\hbar\omega$, is assumed to be constant, while for an acoustical phonon

$$\hbar\omega_q = sq\ , \tag{7}$$

where s is the sound velocity. Then we have for acoustical-mode and optical-mode scattering respectively

$$\left(\frac{\partial f}{\partial t}\right)_{ac} = \frac{2\pi B_a}{\hbar q_L} \sum_{\boldsymbol{q}} q n_q [\{f(\boldsymbol{p}+\boldsymbol{q})e^x - f(\boldsymbol{p})\}\delta(E_{\boldsymbol{p}+\boldsymbol{q}} - E_{\boldsymbol{p}} - \hbar\omega_q)$$

$$+\{f(\boldsymbol{p}-\boldsymbol{q}) - f(\boldsymbol{p})e^x\}\delta(E_{\boldsymbol{p}-\boldsymbol{q}} - E_{\boldsymbol{p}} + \hbar\omega_q)]\ , \tag{8}$$

$$\left(\frac{\partial f}{\partial t}\right)_{op} = \frac{2\pi B_0}{\hbar} n_0 \sum_{\boldsymbol{q}} [\{f(\boldsymbol{p}+\boldsymbol{q})e^u - f(\boldsymbol{p})\}\delta(E_{\boldsymbol{p}+\boldsymbol{q}} - E_{\boldsymbol{p}} - \hbar\omega)$$

$$+\Delta(E)\{f(\boldsymbol{p}-\boldsymbol{q}) - f(\boldsymbol{p})e^u\}\delta(E_{\boldsymbol{p}-\boldsymbol{q}} - E_{\boldsymbol{p}} + \hbar\omega)]\ , \tag{9}$$

where for simplicity we have used following notations:

$$(B_a/q_L) = (C^2/2N_0Ms),\quad B_0 = (C'^2 q_L^2/2N_0M\hbar\omega),\quad x = (sq/kT_0),\quad u = (\hbar\omega/kT_0),$$

$$n_q = (e^x - 1)^{-1},\quad n_0 = (e^u - 1)^{-1},\quad \Delta(E) = 1 \quad \text{for } E \geq \hbar\omega$$

$$0 \quad \text{for } E < \hbar\omega\ .$$

T_0 is the lattice temperature.

In n-type germanium, similarly to other semiconductors, the energy of most electrons satisfies

$$E \ll q_D^2/8m \tag{10}$$

even in hot electron states, where $q_D/\hbar$ is the Debye cut off wave number. Accordingly the energy of acoustical phonons interacting with electrons is small enough to apply classical statistics;

$$n_q = \frac{kT_0}{sq}\ . \tag{11}$$

§ 3. The Low-Field Mobility

We assume (3) and expand it in powers of $\boldsymbol{p}_0$, which has only z-component in an isotropic case:

$$f = f_0 + f_1 + f_2 + f_3\ , \tag{12}$$

where

$$f_0 = A\exp\left(-\frac{E}{kT}\right),\qquad f_1 = -\frac{p_0 p_z}{mkT} f_0\ ,$$

$$f_2 = \left(\frac{p_0^2}{2mkT}\right)\left(\frac{p_z^2}{mkT} - 1\right) f_0\ ,\qquad f_3 = \frac{p_0^3 p_z}{2(mkT)^2} f_0 - \left(\frac{p_0 p_z}{mkT}\right)^3 f_0\ .$$

A is determined by $\sum f = \sum f_0 = N$, where N is the number of conduction electrons. We need to consider terms f_2 and f_3 to calculate ν in (2), since p_0 is proportional to F in lowest order and p_0^3 to F^3

Following Fröhlich and Paranjape[7] we shall determine T and p_0 by the conditions that in stationary states the rate of gain of energy and momentum furnished by the field is equal to the rate of dissipation to the lattice vibrations. Multiplying the Boltzmann equation (4) by p_z or E and summing over the momentum space, we obtain

$$NeF = \sum_{\boldsymbol{p}} p_z \left(\frac{\partial f}{\partial t}\right)_L, \tag{13}$$

$$Fj = -\sum_{\boldsymbol{p}} E \left(\frac{\partial f}{\partial t}\right)_L, \tag{14}$$

since both energy and momentum are conserved in the case of the electron-electron collisions;

$$\sum_p p_z\left(\frac{\partial f}{\partial t}\right)_e = \sum_q E\left(\frac{\partial f}{\partial t}\right)_e = 0\,. \tag{15}$$

In (14) j is the current density and from (3)

$$j = -\frac{e}{m}\sum_q p_z f = \frac{Nep_0}{m}. \tag{16}$$

i) the calculation of collision terms

To calculate (13) and (14) we substitute (12) into $(\partial f/\partial t)_L$. Then it may be written as the expansion in powers of p_0;

$$\left(\frac{\partial f}{\partial t}\right)_L = \left(\frac{\partial f}{\partial t}\right)_L^0 + \left(\frac{\partial f}{\partial t}\right)_L^1 + \left(\frac{\partial f}{\partial t}\right)_L^2 + \left(\frac{\partial f}{\partial t}\right)_L^3. \tag{17}$$

Details of the calculation of these terms are given in Appendix.

By expanding the right-hand side of (A10) and (A17), in powers of the temperature difference and retaining first order terms, we obtain

$$\left(\frac{\partial f}{\partial t}\right)_{ac}^0 = \Gamma\left(\frac{4ms^2}{kT_0}\right)\gamma E^{1/2}\left(1-\frac{E}{2kT_0}\right)f_0(T_0)\,, \tag{18}$$

$$\left(\frac{\partial f}{\partial t}\right)_{op}^0 = \Gamma a n_0 \gamma u^2(\sqrt{E+\hbar\omega} - \Delta(E)e^u\sqrt{E-\hbar\omega})f_0(T_0)\,, \tag{19}$$

where

$$\gamma = (T-T_0)/T_0\,. \tag{20}$$

$$a = (B_0/B_a)(sq_L/2\hbar\omega)\,, \tag{21}$$

and Γ is a constant defined by (A7). $f_0(T_0)$ is the thermal equilibrium distribution;

$$f_0(T_0) = A_0\exp\left(-\frac{E}{kT_0}\right)\,, \tag{22}$$

where A_0 is determined by the number N. an_0 represents the ratio of the effects of optical-mode scattering to that of acoustical-mode scattering.

$(\partial f/\partial t)_L{}^1$ is given by (A13) and (A17), which can be used for hot electrons. In this section $f_1(T)$ may be expanded as follows;

$$f_1(T) = -\frac{p_0p_z}{mkT}f_0(T) = -\frac{p_0p_z}{mkT_0}\left(1-\frac{5}{2}\gamma+\gamma\frac{E}{kT_0}\right)A_0\,e^{-E/kT_0} = f_1(T_0)\left(1-\frac{5}{2}\gamma+\gamma\frac{E}{kT_0}\right). \tag{23}$$

Then we get

$$\left(\frac{\partial f}{\partial t}\right)_L^1 = -\Gamma\{\sqrt{E} + an_0u(\sqrt{E+\hbar\omega}+\Delta(E)e^u\sqrt{E-\hbar\omega})\}f_1(T_0)\left(1-\frac{5}{2}\gamma+\gamma\frac{E}{kT_0}\right). \tag{24}$$

In order to calculate the current correctly to terms of order F^3, we may put $T=T_0$ in f_2 and f_3. Then, as shown in appendix B, we have except for terms proportional to $P_2(\cos\theta)$

$$\left(\frac{\partial f}{\partial t}\right)_{ac}^2 = \left(\frac{p_0^2}{2mkT_0}\right)\Gamma\left(\frac{8ms^2}{kT_0}\right)\cos^2\theta\cdot\sqrt{E}\left(1-\frac{E}{2kT_0}\right)f_0(T_0)\,, \tag{25}$$

$$\left(\frac{\partial f}{\partial t}\right)_{op}^2 = \left(\frac{p_0^2}{2mkT_0}\right)\Gamma an_0(2u^2)\cos^2\theta(\sqrt{E+\hbar\omega} - \Delta(E)e^u\sqrt{E-\hbar\omega})f_0(T_0)\,, \tag{26}$$

$$\left(\frac{\partial f}{\partial t}\right)_L^3=-\Gamma\{\sqrt{E}+an_0u(\sqrt{E+\hbar\omega}+\Delta(E)e^u\sqrt{E-\hbar\omega})\}f_3(T_0)\,. \tag{27}$$

ii) the calculation of p_0

p_0 is determined from (13), the right-hand side of which is a function of the electron temperature T or γ. We have to calculate it correctly to linear terms in γ, since γ is of order F^2. From (24) we obtain

$$\sum_P p_z\left(\frac{\partial f}{\partial t}\right)_L^1=N\left(\frac{p_0}{m}\right)\left(\frac{8m}{3}\right)\left(\frac{kT_0}{\pi}\right)^{1/2}\Gamma\mathrm{G}\left\{1+\gamma\left(\frac{\mathrm{H}}{\mathrm{G}}-\frac{5}{2}\right)\right\}, \tag{28}$$

where

$$\mathrm{G}=1+an_0u(u/2)^2e^{u/2}K_2(u/2)\,, \tag{29}$$

$$\mathrm{H}=3+an_0u(u/2)^2e^{u/2}\{3K_2(u/2)+uK_1(u/2)\}\,, \tag{30}$$

in which K_n is the modified Bessel function of the second kind.[10]

The zero-field mobility μ_0 is given by substituting $\gamma=0$ and $p_0=m\mu_0F$ in (28) which on the other hand, is equal to NeF:

$$\mu_0=e\left[\frac{8m}{3}\left(\frac{kT_0}{\pi}\right)^{1/2}\Gamma\mathrm{G}\right]^{-1}. \tag{31}$$

This is different from the ordinary definition of the mobility obtained by neglecting electron-electron collisions.[11]

From (27), puting $p_0=m\mu_0F$ in $f_3(T_0)$, we have

$$\sum_P p_z\left(\frac{\partial f}{\partial t}\right)_L^3=NeF\left(\frac{\mu_0F}{v_T}\right)^2\left(\frac{2\mathrm{H}}{5\mathrm{G}}-1\right), \tag{32}$$

where $v_T=(2kT_0/m)^{1/2}$ means the thermal velocity of electrons. Substituting (28) and (32) into (13), we obtain finally

$$\frac{p_0}{m}=\mu_0F\left[1-\left(\frac{\mathrm{H}}{\mathrm{G}}-\frac{5}{2}\right)\left\{\gamma+\frac{2}{5}\left(\frac{\mu_0F}{v_T}\right)^2\right\}\right]. \tag{33}$$

iii) the calculation of γ

It follows from (18) and (19) that

$$\sum_P E\left(\frac{\partial f}{\partial t}\right)_L^0=-\gamma Ne(3s^2\mathrm{I}/\mu_0\mathrm{G})\,, \tag{34}$$

and from (25) and (26)

$$\sum_P E\left(\frac{\partial f}{\partial t}\right)_L^2=-Ne(2s^2\mathrm{I}/\mu_0\mathrm{G})(\mu_0F/v_T)^2\,, \tag{35}$$

where

$$\mathrm{I}=1+an_0\left(\frac{v_T}{s}\right)^2\left(\frac{u}{2}\right)^4e^{u/2}K_1(u/2)\,. \tag{36}$$

Then we get from (14), using the approximate relation $Fj=Ne\mu_0F^2$,

$$\gamma=\frac{(\mu_0F)^2\mathrm{G}}{3s^2\mathrm{I}}-\frac{2}{3}\left(\frac{\mu_0F}{v_T}\right)^2. \tag{37}$$

iv) numerical results

The current density j can now be calculated from (16), (33) and (37) as follows:

$$j=\frac{Ne\,p_0}{m}=Ne\mu_0F\left[1-\left(\frac{\mathrm{H}}{\mathrm{G}}-\frac{5}{2}\right)\left\{\frac{(\mu_0F)^2G}{3s^2\mathrm{I}}-\frac{4}{15}\left(\frac{\mu_0F}{v_T}\right)^2\right\}\right]. \tag{38}$$

Provided that the scattering by optical modes is negligible or $a=0$, ν in (2) becomes from (38)

$$\nu=\nu_0=\frac{\mu_0^2}{6s^2}\left(1-\frac{4s^2}{5v_T^2}\right)\simeq\frac{\mu_0^2}{6s^2}\,. \tag{39}$$

In order to estimate the magnitude of a, we make use of the experimental results of the zero-field mobility. By fitting the theoretical μ_0 to the data, it is found that a becomes 0.22. This value seems reasonable from the theoretical point of view.

Choosing $(\hbar\omega/k)=300°\mathrm{K}$, $s=5.4\times10^5$ cm/sec, and $m=m_0/4$[11], m_0 being the free electron mass, we find that the value of I is determined almost by optical modes at ordinary temperatures; $\mathrm{I}\gg1$. This is easily seen from the definition of G and I. In G the term due to optical modes will be of order unity. On the other hand, in I the term caused by the optical-mode scattering has a factor $(v_T/s)^2$, which is of order 10^3. Further due to the small value of a it appears that $s^2(\mathrm{I/G})$ becomes far smaller than v_T^2 and therefore f_2 and f_3 have negligible effects on ν. Thus in our case ν can be written as

$$\nu=\left(\frac{\mathrm{H}}{\mathrm{G}}-\frac{5}{2}\right)\frac{\mathrm{G}}{3s^2\mathrm{I}}\mu_0^2\,. \tag{40}$$

From the fact that I is determined by optical modes, it follows that electrons exchange their energy mainly with optical modes. This is in agreement with Yamashita's result.[8]

Table I. The variation of ν/ν_0 with temperature and a.

	ν/ν_0	
T°K	$a=0.2$	$a=0.3$
100	0.060	0.049
200	0.055	0.035
300	0.059	0.047

Table I gives the variation of ν/ν_0 with temperature and a, where we take $m=m_0/4$, ignoring the anisotropy of the energy band and the intervalley effects. Since I is nearly proportional to m^{-1}, ν/ν_0 is nearly proportional to m.

§4. Field Independent Drift Velocity due to Optical-mode Scattering

The drift velocity becomes constant and independent of the electric field under the conditions that the average energy of electrons is much larger than the energy of optical phonons, but still so small that the acoustical-mode scattering can be ignored as regards the energy exchange between electrons and lattice vibrations.

We assume the electron distribution centered about $\boldsymbol{p}=\boldsymbol{p}_0$ in momentum space:

$$f=f_0(|\boldsymbol{p}+\boldsymbol{p}_0|)=f_0+f_1=f_0(E)+\frac{p_0p_z}{m}\frac{\partial f_0}{\partial E}\,, \tag{41}$$

neglecting higher order terms since the average energy of electrons becomes large at high fields. We need not assume a paticular functional from of f_0 in this section.

Substituting f_0 into (8) we obtain

$$\left(\frac{\partial f}{\partial t}\right)^0_{ac}=\Gamma\left(\frac{4ms^2}{kT_0}\right)\sqrt{E}\left\{\left(f_0+kT_0\frac{\partial f_0}{\partial E}\right)+\frac{E}{2}\left(\frac{\partial f_0}{\partial E}+kT_0\frac{\partial^2 f_0}{\partial E^2}\right)\right\}, \tag{42}$$

which was given by Yamashita and Watanabe[6]. Substituting f_0 into (9) and expanding $f_0\,(E\pm\hbar\omega)$, we have

$$\left(\frac{\partial f}{\partial t}\right)^0_{op}=\Gamma au\hbar\omega\left(\frac{f_0}{\sqrt{E}}+\sqrt{E}\frac{\partial f_0}{\partial E}\right). \tag{43}$$

For $E\gg\hbar\omega$, it follows from (A13) and (A19) that

$$\left(\frac{\partial f}{\partial t}\right)^1_L=-\Gamma\{1+au(1+2n_0)\}\sqrt{E}\,f_1\,, \tag{44}$$

from which the condition (13) becomes

$$\sum_p p_z\left(\frac{\partial f}{\partial t}\right)_L=\frac{4}{3}p_0\Gamma\{1+au(1+2n_0)\}N\langle E^{1/2}\rangle=NeF\,, \tag{45}$$

where

$$N\langle E^{1/2}\rangle = \sum E^{1/2} f_0 \,.$$

Next, from (42) and (43), we compute the rate of the energy loss as follows:

$$-\sum_p E\left(\frac{\partial f}{\partial t}\right)_L = N\Gamma\left[au\hbar\omega\langle E^{1/2}\rangle + \left(\frac{2ms^2}{kT_0}\right)\{\langle E^{3/2}\rangle - 2kT_0\langle E^{1/2}\rangle\}\right]. \tag{46}$$

(46) suggests that the rate of the energy loss is determined only by optical modes, provided that the average energy satisfies

$$\langle E\rangle \ll au\hbar\omega\left(\frac{kT_0}{2ms^2}\right) = a\hbar\omega\left(\frac{\hbar\omega}{2ms^2}\right). \tag{47}$$

Using the values of constants obtained in § 3, (47) becomes

$$\langle E\rangle \ll 70\hbar\omega \tag{47'}$$

which is compatible with the assumption $E \gg \hbar\omega$.

Neglecting the terms corresponding to the acoustical-mode scattering in (46), we have

$$-\sum E\left(\frac{\partial f}{\partial t}\right)_L = N\Gamma au\hbar\omega\langle E^{1/2}\rangle = NFe(p_0/m)\,. \tag{48}$$

Eliminating $\langle E^{1/2}\rangle$ from (45) and (48), we obtain the drift velocity p_0/m as

$$\frac{p_0}{m} = \left(\frac{\hbar\omega}{m}\right)^{1/2}\left[\frac{4}{3}\{(au)^{-1}+1+2n_0\}\right]^{-1/2}. \tag{49}$$

The calculated drift velocity, shown in Table II, is somewhat smaller than Ryder's data.

Table II. Field independent drift velocity for $(\hbar\omega/k)=300°\text{K}$, $m=m_0/4$, $a=0.22$.

T°K	p_0/m (cm/sec)
300	4.5×10^6
200	5.6×10^6
100	7.3×10^6

§ 5. The Mobility of Hot Electrons

(47′) shows that electrons lose their energy mainly through the interactions with optical modes, unless the electron temperature becomes about $2\cdot10^4$°K. If it is accepted as true, the current is not proportional to $F^{1/2}$ at any field strength in n-type germanium, since this dependence is a consequence of taking account of the acoustical-mode scattering only.

As it has been seen in § 3 that the contributions of f_2 and f_3 are quite small to the determination of the field dependent mobility even in a weak field, here

$$f = f_0 + f_1\,, \qquad f_0 = A\exp(-E/kT)\,, \qquad f_1 = -\frac{p_0 p_z}{mkT} f_0\,. \tag{50}$$

Then the following equations are easily obtained; from (A10) and (A17)

$$-\sum_p E\left(\frac{\partial f}{\partial t}\right)_L = N\Gamma\left(\frac{8m}{3}\right)\left(\frac{kT}{\pi}\right)^{1/2}(3s^2)\mathrm{I}(\alpha) = F\cdot j\,, \tag{51}$$

where

$$\mathrm{I}(\alpha) = \frac{1-\alpha}{\alpha} + an_0\left(\frac{v_T}{s}\right)^2\frac{\alpha u^3}{16}(e^{u(1-\alpha)}-1)e^{\alpha u/2}K_1(\alpha u/2)\,, \tag{52}$$

and from (A14) and (A16)

$$\sum_p p_z\left(\frac{\partial f}{\partial t}\right)_L = \left(\frac{p_0}{m}\right)N\Gamma\left(\frac{8m}{3}\right)\left(\frac{kT}{\pi}\right)^{1/2}\mathrm{G}(\alpha) = NeF\,, \tag{53}$$

where

$$\mathrm{G}(\alpha) = 1 + an_0\left(\frac{u}{2}\right)\left(\frac{\alpha u}{2}\right)^2\{(e^{u(1-\alpha)}+1)K_2(\alpha u/2) + (e^{u(1-\alpha)}-1)K_1(\alpha u/2)\}\,, \tag{54}$$

and $\alpha=(T_0/T)$. From (51), (53) and (31) we get the drift velocity as a function of the electron temperature,

$$\frac{p_0}{m}=\mu_0 F\sqrt{\alpha}\,[\mathrm{G}(1)/\mathrm{G}(\alpha)]\,, \tag{55}$$

and the electron temperature as a function of the electric field,

$$(\mu_0 F)^2=\frac{3s^2\mathrm{I}(\alpha)\mathrm{G}(\alpha)}{\alpha[\mathrm{G}(1)]^2}. \tag{56}$$

We have calculated the drift velocity numerically in Fig. 1 from (55) and (56), taking the values of constants; $\mu_0=3800\,\mathrm{cm}^2/\mathrm{volt\ sec}$ at $T_0=300°\mathrm{K}$, $a=0.22$, and $m=m_0/4$, neglecting the anisotropy of the band and the intervalley effects as in § 3. The theoretical curve in Fig. 1 is in fairly agreement with Ryder's data at 298°K (circles). Concerning this calculations, we should remark that the contributions of the acoustical mode to $\mathrm{I}(\alpha)$ are not negligiblly small for $\alpha\lesssim 0.1$, or $T\gtrsim 3000°\mathrm{K}$. Consequently the drift velocity does not become flat, but increases gradually. For instance, $p_0/m=5.4\times10^6$ cm at $F=4.7\times10^3$ volts/cm and 5.6×10^6 cm at 7.8×10^3 volts/cm, which are considerably larger than that obtained in § 4.

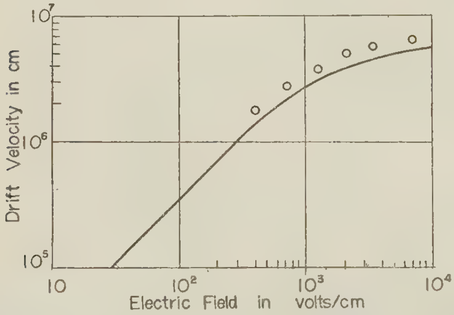

Fig. 1. Drift velocity as a function of electric field at 300°K in n-Ge. Circles are taken from Ryder's paper.

§ 6. Concluding Remarks

We have calculated the mobility of electrons by the method of Fröhlich and Paranjape. If we suppose that the electron-electron collisions are effective enough, it seems resonable to determine T and p_0 in (3) from the conditions (13) and (14) that the rates of change of momentum and energy summed over all electrons balance. The reason why the results of Sodha and Agrawal are so different from ours is not clear. But it is certain that the rate of the energy loss of electrons is determined by the collisions with optical modes at low fields. The conclusion is derived from the value of I in § 3, and since $\mathrm{I}\gg 1$, ν/ν_0 becomes very small compared to unity.

In cases where the electron density is so low that the interactions between them may be neglected, the assumption (3) is in general not good. Although the zero-field mobility given by (31) is not correct in that case, it can be interpreted as the first approximation of the variation method, if we write as usual

$$f=f_0+p_z c(E)\frac{\partial f_0}{\partial E},$$

and

$$c(E)=\sum_{r=0}^{\infty} c_r E^r$$

where f_0 is the thermal equilibrium distribution[12]. We shall discuss the application of the variation principle to the mobility at an arbitrary field strength in the following paper where the relations between the method of this paper and Yamashita's one will become clear.

Lastly, we note the effect of f_2 and f_3 in (12) on the low field mobility. In n-type germanium we concluded that they play no role because of the smallness of a. From (38) ν can be written as

$$\nu=\frac{\mathrm{G}}{3s^2\mathrm{I}}\left(\frac{\mathrm{H}}{\mathrm{G}}-\frac{5}{2}\right)\mu_0^2(1-\xi)\,,$$

where $\xi=(4\mathrm{I}/5\mathrm{G})(s/v_T)^2$ indicates the term due to f_2 and f_3. At the temperatures for which $u\leq 1$, ξ is very small compared to unity for all values of the parameter a. However, it may not always be negligibly small at low temperatures; for example, $\xi\simeq 0.14$ for $a=1$ and $u=3$.

The author would like to express his thanks to Prof. K. Ariyama and Dr. S. Nakajima for reading and commenting on this paper.

Appendix A

We expand $f(\boldsymbol{p}\pm\boldsymbol{q})$ in powers of p_0 similar to (12). Then by energy conservation the zeroth order term can be written as

$$f_0(\boldsymbol{p}\pm\boldsymbol{q})=f_0(p)e^{\mp\alpha x} \tag{A1}$$

for acoustical-mode scattering, and

$$f_0(\boldsymbol{p}\pm\boldsymbol{q})=f_0(p)e^{\mp\alpha u} \tag{A2}$$

for optical-mode scattering, where $\alpha = T_0/T$. For f_1, f_2, and f_3 we must put $p_z \pm q_z$ in place of p_z;

$$f_1(\boldsymbol{p}\pm\boldsymbol{q}) = -\frac{p_0(p_z\pm q_z)}{mkT} f_0(\boldsymbol{p}\pm\boldsymbol{q}) \,, \tag{A3}$$

$$f_2(\boldsymbol{p}\pm\boldsymbol{q}) = \left(\frac{p_0^2}{2mkT}\right)\left(\frac{(p_z\pm q_z)^2}{mkT} - 1\right) f_0(\boldsymbol{p}\pm\boldsymbol{q}) \,, \tag{A4}$$

$$f_3(\boldsymbol{p}\pm\boldsymbol{q}) = \left[\frac{p_0^3(p_z\pm q_z)}{2(mkT)^2} - \frac{1}{6}\left(\frac{p_0(p_z\pm q_z)}{mkT}\right)^3\right] f_0(\boldsymbol{p}\pm\boldsymbol{q}) \,. \tag{A5}$$

Substituting (11) and (A1), or (A3), into (8), we get

$$\left(\frac{\partial f}{\partial t}\right)^0_{ac} = \left(\frac{2\pi B_a}{\hbar}\right)\left(\frac{kT_0}{sq_L}\right) \sum_{\boldsymbol{q}} [\{e^{x(1-\alpha)}-1\}\delta_+ + \{e^{\alpha x}-e^x\}\delta_-] f_0(p) \,, \tag{A6}$$

$$\left(\frac{\partial f}{\partial t}\right)^1_{ac} = -\frac{p_0 f_0(p)}{mkT}\left(\frac{2\pi B_a}{\hbar}\right)\left(\frac{kT_0}{sq_L}\right) \sum_{\boldsymbol{q}} [\{(p_z+q_z)e^{x(1-\alpha)}-p_z\}\delta_+ + \{(p_z-q_z)e^{\alpha x}-p_z e^x\}\delta_-] \,, \tag{A7}$$

where sufficis + and − mean the terms corresponding to the emission and to the absorption of phonons, respectively. The integrals in the $\boldsymbol{q}$ space are carried out by introducing polar coordinates q, β, ψ, the polar axis being in the direction of p:

$$\sum_{\boldsymbol{q}} \to \frac{V}{(2\pi)^3\hbar^3}\iiint q^2 dq d\cos\beta d\psi \,.$$

Integration over β can be used to eliminate the δ-functions.

From (10) and the energy conservation, we have

$$\cos\beta_\pm = \frac{1}{2p}(\mp q + 2ms) \,, \tag{A8}$$

$$0 \le q \le 2p \pm 2ms \,. \tag{A9}$$

Since $x \ll 1$ and $\alpha \le 1$, we can expand $e^{x(1-\alpha)}$, $e^{\alpha x}$, and e^x, and then (A6) becomes

$$\begin{aligned}\left(\frac{\partial f}{\partial t}\right)^0_{ac} &= \left(\frac{2\pi B_a}{\hbar}\right)\left(\frac{kT_0}{sq_L}\right)\frac{Vmf_0(p)}{(2\pi)^2\hbar^3 p}\left[(1-\alpha)\left\{\int_0^{2p+2ms} xq\,dq - \int_0^{2p-2ms} xq\,dq\right\} - \alpha(1-\alpha)\int_0^{2p} x^2 q dq\right] \\ &= \Gamma\left(\frac{4ms^2}{kT_0}\right)(1-\alpha)\sqrt{E}\left(1-\frac{E}{2kT}\right) f_0(p) \,,\end{aligned} \tag{A10}$$

where

$$\Gamma = \left(\frac{2\pi B_a}{\hbar}\right)\left(\frac{kT_0}{sq_L}\right)\frac{V(4m)(2m)^{1/2}}{(2\pi)^2\hbar^3} \,. \tag{A11}$$

Making use of the relation

$$\int_0^{2\pi}(q_z)_\pm d\psi = \int_0^{2\pi} q\{\cos\theta\cos\beta_\pm + \sin\theta\sin\beta_\pm\cos\psi\}d\psi = 2\pi q\cos\theta\cos\beta_\pm \,, \tag{A12}$$

we obtain from (A7)

$$\left(\frac{\partial f}{\partial t}\right)^1_{ac} = -\frac{p_0 f_0(p)}{mkT}\left(\frac{2\pi B_a}{\hbar}\right)\left(\frac{kT_0}{sq_L}\right)\sum_{\boldsymbol{q}} [q_z\delta_+ - q_z\delta_-] = -\Gamma\sqrt{E}\, f_1(\boldsymbol{p}) \,. \tag{A13}$$

For optical-scattering, the energy conservation leads to

$$\cos\beta_\pm = \frac{1}{2pq}(q_0^2 \mp q^2) \,, \tag{A14}$$

$$\mp p \pm \sqrt{p^2 \pm q_0^2} \leq q \leq p + \sqrt{p^2 \pm q_0^2}\,, \tag{A15}$$

where

$$q_0^2/2m = \hbar\omega\,. \tag{A16}$$

From (9)

$$\begin{aligned}\left(\frac{\partial f}{\partial t}\right)_{op}^{0} &= \left(\frac{2\pi B_0}{\hbar}\right) n_0 f_0(p)\Big[(e^{u(1-\alpha)}-1)\sum_{q}\delta_{+} + \Delta(E)(e^{\alpha u}-e^{u})\sum_{q}\delta_{-}\Big]\\ &= \Gamma a n_0 u\Big[(e^{u(1-\alpha)}-1)\sqrt{E+\hbar\omega} + \Delta(E)(e^{\alpha u}-e^{u})\sqrt{E-\hbar\omega}\Big] f_0(p)\,,\end{aligned} \tag{A17}$$

where

$$a = (B_0/B_a)(sq_L/2\hbar\omega)\,.$$

We can easily verify the following relation from (A12), (A14) and (A15)

$$\sum_{q}(p_z \pm q_z)\delta_{\pm} = 0\,. \tag{A18}$$

Then it follows that

$$\begin{aligned}\left(\frac{\partial f}{\partial t}\right)_{op}^{1} &= \left(-\frac{p_0 f_0(p)}{mkT}\right)\left(\frac{2\pi B_0 n_0}{\hbar}\right)\sum_{q}\Big[\{(p_z+q_z)e^{u(1-\alpha)}-p_z\}\delta_{+} + \Delta(E)\{(p_z-q_z)e^{\alpha u}-p_z e^{u}\}\delta_{-}\Big]\\ &= -\Gamma a n_0 u\left(\sqrt{E+\hbar\omega} + \Delta(E)e^{u}\sqrt{E-\hbar\omega}\right) f_1(p)\,.\end{aligned} \tag{A19}$$

Appendix B

To calculate the current to terms of order F^3, we can put $T=T_0$ in f_2 and f_3. Substituting $f_2(T_0)$ into (8) and (9), we have

$$\left(\frac{\partial f}{\partial t}\right)_{ac}^{2} = \frac{p_0^2 f_0(T_0)}{2(mkT_0)^2}\left(\frac{2\pi B_a}{\hbar}\right)\left(\frac{kT_0}{sq}\right)\sum_{q}\Big[\{(p_z+q_z)^2-p_z^2\}\delta_{+} + \{(p_z-q_z)^2-p_z^2\}e^{x}\delta_{-}\Big]\,, \tag{B1}$$

$$\left(\frac{\partial f}{\partial t}\right)_{op}^{2} = \frac{p_0^2 f_0(T_0)}{2(mkT_0)^2}\left(\frac{2\pi B_0}{\hbar}\right) n_0 \sum_{q}\Big[\{(p_z+q_z)^2-p_z^2\}\delta_{+} + \Delta(E)\{(p_z-q_z)^2-p_z^2\}e^{u}\delta_{-}\Big]\,. \tag{B2}$$

The integration over ψ gives

$$\begin{aligned}\frac{1}{2\pi}\int_0^{2\pi}(\pm 2p_z q_z + q_z^2)_{\pm}\,d\psi &= \pm 2pq\cos^2\theta\cos\beta_{\pm} + q^2\left(\cos^2\theta\cos^2\beta_{\pm} + \frac{1}{2}\sin^2\theta\sin^2\beta_{\pm}\right)\\ &= \frac{1}{2}q^2\left[\cos^2\theta\left(3\cos^2\beta_{\pm} \pm \frac{4p}{q}\cos\beta_{\pm} - 1\right) + (1-\cos^2\beta_{\pm})\right],\end{aligned}$$

which becomes for acoustical-mode scattering from (A8)

$$\frac{1}{2}q^2(1-\cos^2\beta_{\pm})(1-3\cos^2\theta) \pm 2msq\cos^2\theta\,, \tag{B3}$$

and for optical-mode scattering from (A14)

$$\frac{1}{2}q^2(1-\cos^2\beta_{\pm})(1-3\cos^2\theta) \pm q_0^2\cos^2\theta\,. \tag{B4}$$

Terms proportional to $(1-3\cos^2\theta)$ play no role in our calculations since their contributions to (13) and (14) are vanishing. Therefore we take only the last terms of (B3) and (B4), which come from the change of the energy of electrons by collisions. Then

$$\begin{aligned}\left(\frac{\partial f}{\partial t}\right)_{ac}^{2} &= \frac{p_0^2 f_0(T_0)}{2(mkT_0)^2}\left(\frac{2\pi B_a}{\hbar}\right)\left(\frac{kT_0}{sq_L}\right)\sum_{q}\Big[2ms\cos^2\theta\, q\{\delta_{+}-\delta_{-}\} - 2ms\cos^2\theta\, qx\delta_{-}\Big]\\ &= \left(\frac{p_0^2}{2mkT_0}\right)\Gamma\left(\frac{8ms^2}{kT_0}\right)\cos^2\theta\sqrt{E}\left(1-\frac{E}{2kT_0}\right) f_0(T_0)\,.\end{aligned} \tag{B5}$$

$$\left(\frac{\partial f}{\theta t}\right)_{op}^{2}=\frac{p_0^2 f_0(T_0)}{2(mkT_0)^2}\left(\frac{2\pi B_0}{\hbar}\right)n_0 q_0^2\cos^2\theta\sum_{\boldsymbol{q}}[\delta_+-\Delta(E)e^u\delta_-]$$

$$=\left(\frac{p_0^2}{2mkT_0}\right)\Gamma a n_0(2u^2)\cos^2\theta(\sqrt{E+\hbar\omega}-\Delta(E)e^u\sqrt{E-\hbar\omega})f_0(T_0)\,. \tag{B6}$$

To compute $(\partial f/\partial t)_L{}^3$ we put $T=T_0$ in $f_3(\boldsymbol{p})$ and $f_3(\boldsymbol{p}\pm\boldsymbol{q})$. Now we can show

$$\sum_{\boldsymbol{q}}(p_z\pm q_z)^3\delta_\pm=0\,, \tag{B7}$$

which is exact for optical-mode scattering, and for acoustical-mode scattering it holds approximately by the neglect of $2ms$ in (A8) and (A9). Accordingly we obtain in the same way as $(\partial f/\partial t)_L{}^1$

$$\left(\frac{\partial f}{\partial t}\right)_{L}^{3}=-\Gamma\{\sqrt{E}+a n_0 u(\sqrt{E+\hbar\omega}+\Delta(E)e^u\sqrt{E-\hbar\omega})\}f_3(T_0)\,, \tag{B8}$$

where

$$f_3(T_0)=\frac{p_0^3 p_z}{2(mkT_0)^2}f_0(T_0)-\frac{1}{6}\left(\frac{p_0 p_z}{mkT_0}\right)^3 f_0(T_0)\,. \tag{B9}$$

References

1) F. J. Morin: Phys. Rev. **93** (1954) 62.
2) F. Seitz: Phys. Rev. **73** (1948) 549.
3) W. A. Harrison: Phys. Rev. **104** (1956) 766.
4) E. J. Ryder: Phys. Rev. **90** (1957) 766.
5) W. Shockley: Bell Syst. Tech. J. **30** (1951) 990.
6) J. Yamashita and M. Watanabe: Progr. Theor. Phys. **12** (1954) 443.
7) M. S. Sodha and D. B. Agrawal: Canad. J. Phys. **36** (1958) 707.
8) J. Yamashita: Phys. Rev. **111** (1958) 1529.
9) H. Frohlich and B. V. Paranjape: Proc. Phys. Soc. London **B**, **69** (1956) 21.
10) A. Gray and G. B. Mathews: *A Treatise on Bessel Functions and their Applications to Physics* (MacMillan & Co. London, 1922).
11) P. P. Debye and E. M. Conwell: Phys. Rev. **93** (1954) 693.
12) A. H. Wilson: *The Theory of Metals.* (Cambridge at the University Press, 1953).

JOURNAL OF THE PHYSICAL SOCIETY OF JAPAN, Vol. 14, No. 10, OCTOBER, 1959

A Few Quarternary Systems of Perovskite Type $A^{2+}B^{4+}O_3$ Solid Solutions

By Takuro IKEDA

Kobayasi Institute of Physical Research, Kokubunji, Tokyo

(Received May 6, 1959)

The properties of the quarternary systems (Sr–Pb)(Ti–Zr)O_3 and (Ba–Pb)(Ti–Sn)O_3 are studied. The shift of transition points with composition is measured by the temperature variation of the dielectric constant of the ceramic sample, and the phase diagrams at room temperature are determined with help of X-ray measurement.

The phase diagram of (Sr–Pb)(Ti–Zr)O_3 includes two ferroelectric phases F_α (rhombohedral) and F_β (tetragonal), two antiferroelectric ones A_α (pseudotetragonal) and A_β (tetragonal) and a paraelectric one P. A_β occupies larger area than expected. The diagram of (Ba–Pb)(Ti–Sn)O_3 resembles that of (Ba–Pb)(Ti–Zr)O_3 previously reported by the author and consists of F_1, F_2 (the same as the low temperature phases in $BaTiO_3$), F_α, F_β and P, although the immiscible region is found in the composition containing smaller amounts of Ba and Ti.

Roth early classified graphically the perovskite ABO_3 compounds on the basis of electronic polarizability of A ion and ionic radius of B ion. The present author advances this line experimentally by taking up a factor of A ion and one of B ion, using many data already published as well as the present results. The arrangement of A ions nearly agrees with that in terms of the electronic polarizability. Concerning the disposition of B ions, however, the ordering of Ti–Zr–Hf–Sn is adopted, and in addition, Sn and Hf ions are arranged near Zr ion. This diagram may be rather successfully applied to the classification of perovskite $A^{2+}B^{4+}O_3$ solid solutions.

Furthermore, the possibilities for dielectric and piezoelectric use of the ceramic materials belonging to these systems are examined. Larger dielectric constants are found with certain compositions in (Ba–Pb)(Ti–Sn)O_3, but a striking improvement for PZT ceramics may be rather questionable in both systems.

§ 1. Introduction

In order to find the origin of ferroelectricity and antiferroelectricity of the perovskite type $A^{2+}B^{4+}O_3$ compounds, many reports have already been published concerning the families with various A^{2+} ions and B^{4+} ions. Of all, several earlier studies performed by the workers in our country have brought many informations on their properties; for instance, (Pb–Ba)TiO_3 by Shirane *et al*[1], Pb(Ti–Zr)O_3 by Sawaguchi[2], (Pb–Ba)ZrO_3 and (Pb–Sr)ZrO_3 by Shirane *et al*[3][4], and (Pb–Sr)TiO_3 by Nomura and Sawada[5], etc. As shown by the effect of addition of Pb^{2+} ion, the ionic radius was not found to be only a factor, but the polarizability had to be considered. Taking account of such circumstances, some studies have been attempted to classify these $A^{2+}B^{4+}O_3$ compounds by certain appropriate factors. Wood[6] classified various perovskite type crystals graphically in terms of ionic radii of A and B ions, and found the unsatisfactory positions of some ions, e.g. Sn^{4+} aud Ce^{4+}. Roth[7] extended more elaborate studies, and the electronic polarizability of A ion was taken up as a factor in addition to the ionic radii of A and B ions. One of his results is shown in Fig. 1, where the ordinate indicates the electronic polarizability of A^{2+} ion and the abscissa the ionic radius of B^{4+} ion. In that case, the position of Sn^{4+} ion is not still adequate, mainly because of the immiscibility of PbO and SnO_2. In order to advance these attempts, rather more studies on the systems (A–A′)(B–B′)O_3 will be desired. The previous work of the author on the system (Ba–Pb) (Ti–Zr)O_3 gave a datum along these lines. In the present paper, some effects of Sr^{2+} and Sn^{4+} ions are examined. Such classification in terms of a factor of A^{2+} ion and one of B^{4+} ion will be experimentally devised here, and may be expected to give further informations on the roles of A^{2+} and B^{4+} ions.

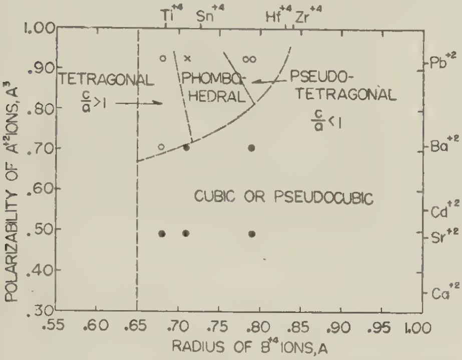

Fig. 1. Classification of $A^{2+}B^{4+}O_3$ compounds (Roth)

Concerning the effects of Sr^{2+} and Sn^{4+} ions, several binary systems have been studied. Substituting Pb of $PbTiO_3$ by Sr, the Curie point falls monotonously with concentration and the tetragonal F_β phase changes to the paraelectric phase, as shown by Nomura and Sawada.[5] The antiferroelectricity of (Pb–Sr)ZrO_3 system was examined in detail by Shirane *et al*[3]; two antiferroelectric phases, A_α and A_β, are seen, where A_α belongs to the orthorhombic crystal class, the same as that of $PbZrO_3$ (pseudotetragonal with the axial ratio smaller than one) and A_β the tetragonal one. In the system Pb(Ti–Zr)O_3, a ferroelectric F_α phase (rhombohedral) appears together with F_β and A_α, and the boundary between F_α and F_β is hardly removed with varying temperature, as shown by the elegant studies of Sawaguchi.[2] The properties of Pb(Ti–Sn)O_3 and Ba(Ti–Sn)O_3 systems have been studied by several authors. Jaffe *et al*[9] reported the phase diagram of Pb(Ti–Sn)O_3 including F_β and other ferroelectric phase, and the dissociation region of the specimens containing more than 75 mole percent of Sn. The crystal form of the latter phase was not exactly known and was only described as pseudocubic. The effect of substituting Ti of $BaTiO_3$ partly by Sn has been known; namely, it is similar to that of Zr ion, but the shift of the transition points is faster than in the case of Zr.[10] The dielectric properties of (Pb–Ba)SnO_3 were reported,[11] but the phase relations were not clearly studied, except the ferroelectricity of (Pb70–Ba30)SnO_3 at −120°C.

Some ceramics of $BaTiO_3$ and its families are important for industrial purposes. The ceramics of $BaTiO_3$ containing more or less amounts of $PbTiO_3$ or $CaTiO_3$ have been fairly used for the electromechanical transducers. Many improvements of their qualities have been attempted. Jaffe *et al*) reported the excellent properties of Pb(Ti–Zr)O_3 ceramics of compositions near the boundary between F_α and F_β (PZT). It was shown by the present author[8] that some ceramics belonging to the system (Ba–Pb) (Ti–Zr)O_3 offer better materials in a few points. For obtaining better dielectric materials, on the other hand, much efforts has always been made. For instance, Coffeen[12] studied some influences of adding $PbSnO_3$, $Bi_2(SnO_3)_3$ (less than 50%) and others to $BaTiO_3$. A few studies on the quarternary systems by the author may be believed to provide several improvements along these lines.

§ 2. (Sr-Pb)(Ti-Zr)O_3

(a) *Preparation of samples*

$SrCO_3$, PbO, TiO_2 and ZrO_2 were mixed in proper mole ratio, calcined and sintered. TiO_2 used here is especially produced from $TiCl_4$ and has purity of 99.57%. $SrCO_3$ and ZrO_2 are of reagent grade, and PbO of c. p. grade. The volatilization of PbO was prevented as well as possible by firing in PbO atmosphere, and the inner parts of the specimen were used for electric and x-ray measurements. They were not chemically analyzed after firing, but their positions in the phase diagram are indicated by the mixing composition. The Curie point of each sample prepared twice or more agrees within a few degrees at worst.

(b) *Dielectric constant versus temperature*

The dielectric constant of small square plates with various compositions was measured at 550 Kc by the tuning method, with increasing temperature above room temperature. Most of the curves show peaks, which correspond to Curie points. Some of them containing less amount of Ti have humps below Curie points. These occur at other transition points. With varying composition, any shifts of these points are examined and shown as various sections in Fig. 2.

In comparison with other data on the binary systems, A_α phase is determined, which is believed to have the same structure as that of $PbZrO_3$.

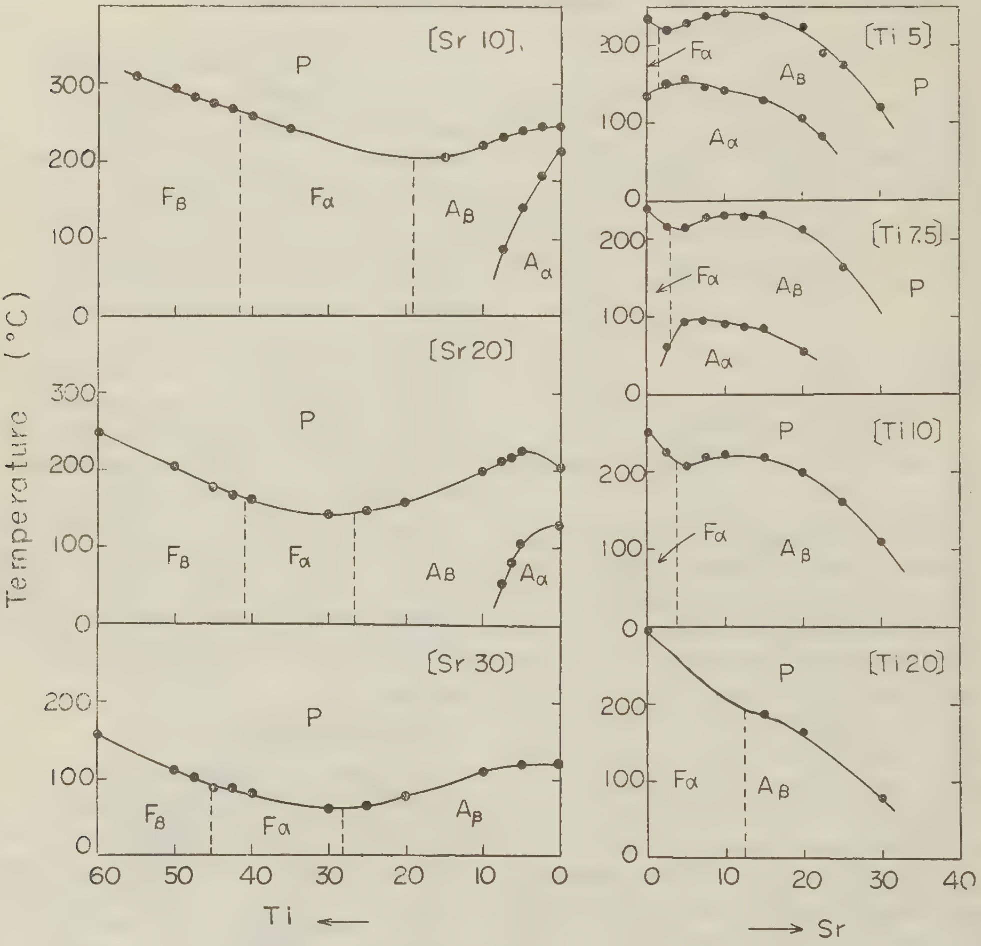

Fig. 2. Transition point in (Sr–Pb) (Ti–Zr)O_3

(c) *Dielectric hysteresis and thermal expansion*

F_α and F_β phases appearing in $Pb(Ti\text{–}Zr)O_3$ system could not be located in above experiment. In order to know how A_β phase spreads over and where the boundary between A_β and F_α is situated, dielectric hysterese are at first observed at 50 c/s by the Sawyer-Tower method.

Some specimens show clear ferroelectric hysterese, and others only straight lines. In those with intermediate composition, however, are observed narrow ferroelectric-like hysterese or double-hysteresis-like (stranguiated) patterns, and it is not possible to decide to which phase they belong.

In the case of the thermal expansion experiment in $Pb(Ti\text{–}Zr)O_3$[13] and $(Pb\text{–}Sr)ZrO_3$[3] systems, it has been shown that an abnormal contraction occurs at transition point from a ferroelectric to a paraelectric phase and a rapid expansion from an antiferroelectric to another phase. Providing that these facts hold also in the present case, the thermal expansion measurements are to give further means of the determination.

Some results on the observations of dielectric hysterese and the thermal expansion measurements are listed in Table I; where E: expansion, C: contraction (at the transition point with increasing temperature), F: ferroelectric hysteresis, D: double hysteresis, N: narrow hysteresis and L: straight line. In addition, the crystal structures are examined by the X-ray powder method, as described in the next section, and are indicated as well; R shows the rhombohedral class, and T the pseudotetragonal with the axial ratio c/a smaller than one.

Table I.

Composition Ti	Sr	Crystal From	Thermal Expansion	Dielectric Hysteresis	Phase Change
5	2.5		E E	N	$A_\alpha \to A_\beta \to P$
	5		E E	N	
	15			L	
	20	T			
	30			L	$A_\beta \to P$
7.5	2.5	T	E C	F-like	$A_\alpha \to F_\alpha \to P$
	5		E E	N	$A_\alpha \to A_\beta \to P$
	15			L	
	20	T			
10	2.9	R	C	F	$F_\alpha \to P$
	5		E	F-like	$A_\beta \to P$
	10	T	E	N	
	15			L	
	20	T		L	
15	5	R	C	F	$F_\alpha \to P$
	10	T	E	F-like	$A_\beta \to P$
	15			L	
20	15	T		F-like	$A_\beta \to P$
	20	T	E	D	
	30			L	
25	20	T	E	F-like	$A_\beta \to P$
	30			L	
30	20	R		F	$F_\alpha \to P$
	30	R		F	

With varying temperature, the boundary between A_β and F_α phases may probably be rather vertical to the composition axis, for any hump corresponding to the transition between these phases is not found so far as the present specimens are concerned. Thus determined are the phase changes of the samples and the boundaries between F_α and A_β phases, as indicated in Table I. and by dotted lines in Fig. 2.

The determination of the phases by the results of the thermal expansion agrees with those of the x-ray measurement. The samples, being considered to belong to A_β and lie near the border to F_α, show apparent ferroelectric-like hysterese. As for the reason, the following possibilities may be considered; one is that the samples become ferroelectric under the high electric field and remain in the same state in more or less time after removal of the field, and another that they are mostly antiferroelectric in one direction and slightly ferroelectric in other directions. But further examinations will be desired, especially by using single crystals.

(d) *X-ray measurement*

The lattice parameters of the powdered specimens are measured by the diffractometer, using CuKα radiation. The samples on the Ti rich side near $PbTiO_3$ must belong to F_β after Nomura *et al.*[5] With increasing Zr concentration, the tetragonality decreases and F_α phase appears at the composition containing about 45% of Ti. Fig. 3 shows the results in (Sr20–Pb80) $(Ti\text{–}Zr)O_3$ composition. The tetragonality disappears between 42.5 and 40% of Ti, and the rhombohedrality in F_α phase occurs discontinuously. These circumstances are similar to those in the case of $Pb(Ti\text{–}Zr)O_3$ system. The boundaries between F_α and F_β are thus determined in each section of various Sr concentration, and indicated in Fig. 2, where these boundaries are considered to be nearly parallel to the

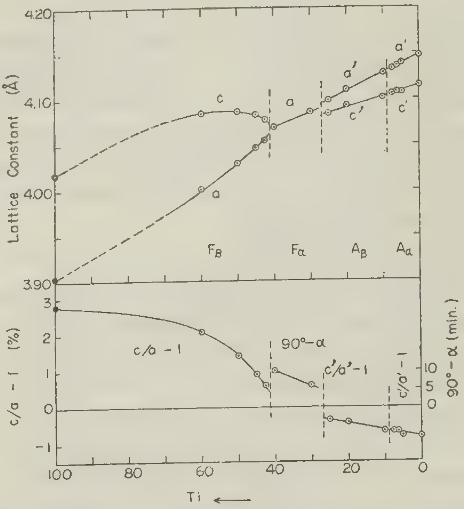

Fig. 3. Lattice parameter of (Sr20–Pb80) $(Ti\text{–}Zr)O_3$ (● after Nomura *et al*)

temperature axis for the same reason as in the earlier works.

In A_β phase, the structure is tetragonal and the axial ratio of the pseudo cell is smaller than one. This fact is also used for the determination of the border of A_β phase, as described above. The phase denoted by A_α is believed to belong to the same crystal class as that of $PbZrO_3$—orthorhombic—and most of the lines can be given indices, by assuming a pseudotetragonal cell. In Fig. 3, the parameters in A_α are thus indicated.

(e) *Phase diagram at room temperature*

Using above results, the phase diagram of this system is easily determined at room temperature and shown in Fig. 4. The location of the boundary between F_α and F_β resembles to the case of (Ba–Pb)(Ti–Zr)O_3 system, except that it is somewhat inflated towards F_α side here. A_β phase, which appears as intermediate phase in (Pb–Sr)ZrO_3 and in Pb(Ti–Zr)O_3 containing less than 3% of Ti, occupies a considerably large region in the present diagram.

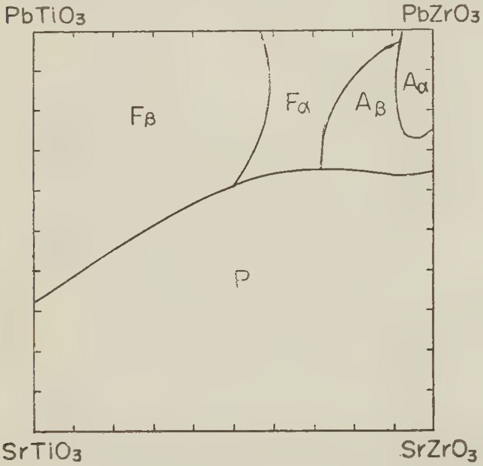

Fig. 4. Phase diagram of (Sr–Pb) (Ti–Zr)O_3

(f) *Dielectric and piezoelectric ceramics*

An outline of the distribution of the dielectric constant at room temperature of the ceramics can be seen even by poorly sintered specimens (porosity: 25–32%), and is shown in Fig. 5(a). Generally speaking, Curie point falls and the dielectric constant increases with increasing Sr concentration, and moreover, its variation with temperature becomes smaller. The ceramics near the boundary between F_α and F_β phases have larger dielectric constants.

The radial electromechanical coupling coefficient k_r of the disc-shape ceramics, prepoled under the field of 30 KV/cm and aged at 95°C in two days (someone at room temperature), is measured and the distribution is shown by a few contour lines in Fig. 5(b). These data are taken with the relatively porous ceramics, and therefore larger value will be expected with carefully sintered ones. The staffs of the Clevite Research Center have made continuous efforts for obtaining piezoelectric ceramics, and recently reported the effects of adding Sr or Ca to PZT ceramics.$^{14)}$ They fired the dense specimens and reported the value of k_r reaching 50% at a certain composition of the same system.

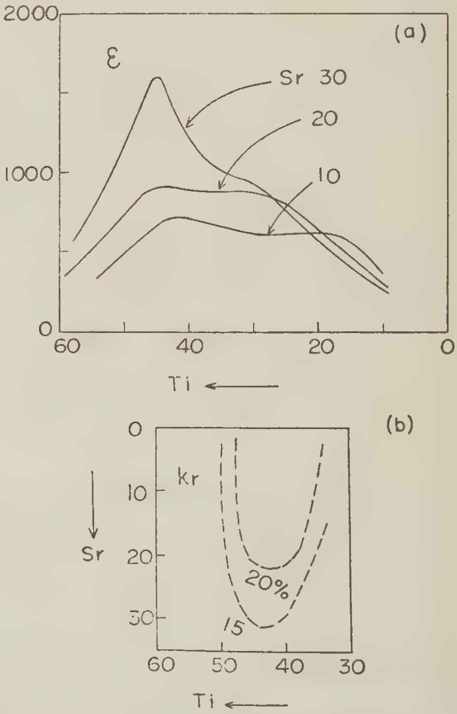

Fig. 5. (a) Dielectric constant ε and (b) radial electromechanical coupling coefficient k_r at room temperature in (Sr–Pb)(Ti–Zr)O_3

§ 3. (Ba-Pb)(Ti-Sn)O_3

(a) *Preparation of samples*

The technique for preparing the samples was the same as that in the former system. $BaCO_3$ and SnO_2 of reagent grade were used. The firing temperature had to be usually lower, and it was difficult to obtain dense ceramics. Hence the dielectric and piezoelectric measurements were performed by rather poorly sintered specimens.

(b) *Dielectric constant versus temperature*

The curves of the dielectric constant *vs.* temperature of the specimens containing less than 90% of Ba show only peaks above room temperature, which correspond to Curie points. In those with smaller concentration of Pb and Sn in the vicinity of $BaTiO_3$, a few humps are shown in the curves, which are known to correspond to the other transition points by observing the shifts of these points with varying composition. In Fig. 6, the transition points as well as Curie points are plotted against compositions. The samples containing smaller amount of Ti are insoluble in the present preparation. F_1 and F_2 in the figure are believed to be the same phases in the case of $BaTiO_3$ at lower temperature, which are both ferroelectric and belong to the rhombohedral and orthorhombic crystal classes respectively. The boundary between F_α and F_β is determined by the X-ray measurement described in the following.

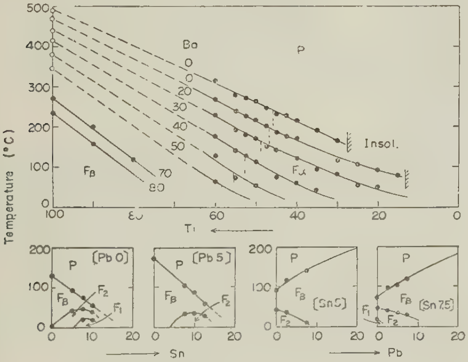

Fig. 6. Transition point in (Ba–Pb) (Ti–Sn)O_3

(c) *X-ray measurement of the sample containing less than 50% of Ba*

The x-ray measurement by the diffractometer, using CuKα radiation, reveals the boundary between F_α and F_β. Some of the results are shown in Fig. 7. The tetragonality in F_β phase on the Ti rich side decreases towards the Sn side and F_α phase appears.

The phase denoted here by F_α was not determined in the system Pb(Ti–Sn)O_3 (0% of Br in the present case) by Jaffe *et al*,[9] who reported only the pseudocubic structure. The back side reflections ($h^2+k^2+l^2=16$, 20, 22, 24 and 26) are examined and the patterns are explained by the rhombohedral class ($\alpha \lesssim 90°$), as described in the previous paper.[4][8] The deviation from 90° decreases with increasing Sn and Ba contents, as seen in the figure.

The boundaries between F_α and F_β in Fig. 7 is thus determined on each Ba content section. Although any shifts of them with temperature are not examined, they may be considered to be nearly parallel to the temperature axis for the same reason as before.

(d) *Phase diagram at room temperature*

The phase diagram of this system is thus obtained at room temperature, and shown in Fig. 8. This resembles that of (Ba–Pb) (Ti–Zr)O_3 system, except the immiscibility near PbO:SnO_2 and the slight shifts of the phase boundaries towards the Ti side. Although the samples containing smaller amounts of Ti and Ba are insoluble, the role of Sn^{4+} ion is infered; that is, Sn ion may be considered to have a little stronger effect than Zr ion for advancing an antiferroelectric tendency.

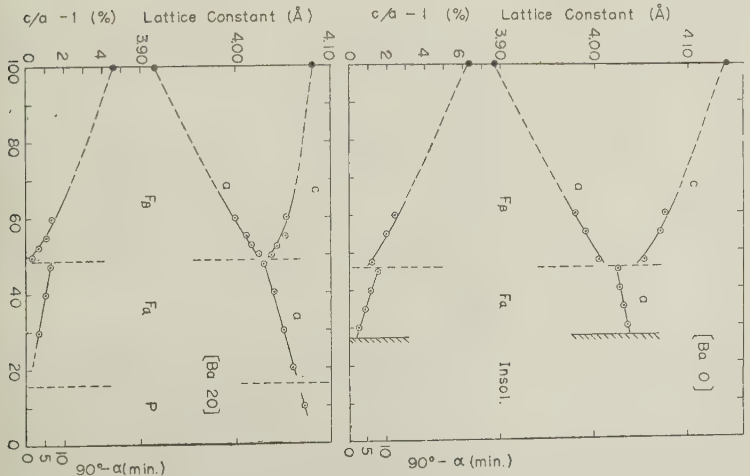

Fig. 7. Lattice parameter in (Ba–Pb) (Ti–Sn)O_3 (● after Shirane *et al*)

(e) *Dielectric and piezoelectric ceramics*

In this experiment, the dense ceramics were not fired and the data for the dielectric and piezoelectric materials are obtained by the poorly sintered specimens (porosity: 21–29%). Fig. 9 shows the outline of them. The higher dielectric constant is found in the samples with composition of Ba~30% and Ti~25–40%.

The electromechanical coupling coefficients shows maximum near the boundary between F_α and F_β, but the value may not be so large as expected, even taking account of their porosity.

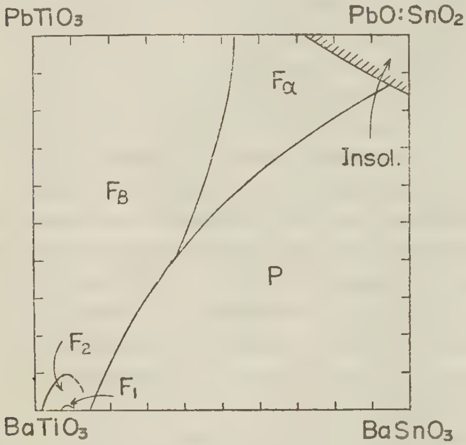

Fig. 8. Phase diagram of (Ba–Pb) (Ti–Sn)O_3

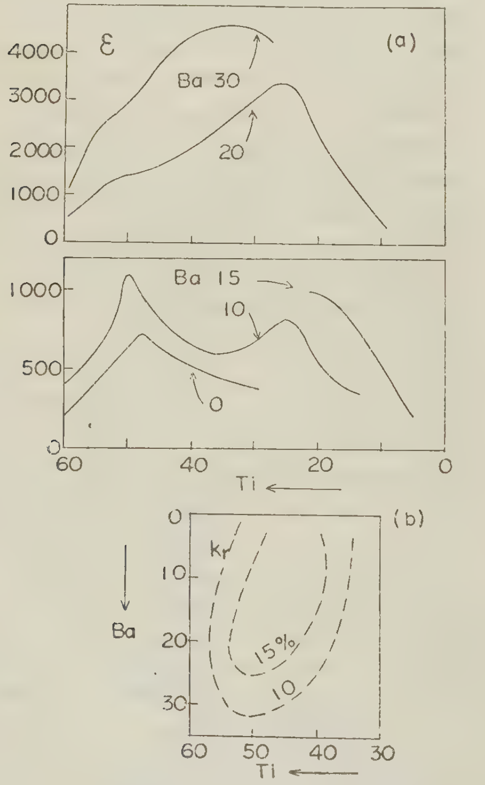

Fig. 9. (a) Dielectric constant ε and (b) electromechanical coupling coefficient k_r in (Ba-Pb) (Ti-Sn)O_3

§ 4. Classification of Perovskite $A^{2+}B^{4+}O_3$ Solid Solutions

Roth7) early reported the classification of ABO_3 type compounds, and one of his results is shown in Fig. 1. In order to advance along his line, let us remember many earlier reports on the phase relations of perovskite $A^{2+}B^{4+}O_3$ solid solutions, including the data by the present author. Fig. 10 shows most of the phase diagrams already published; they are after the following authors:

(Pb–Ba)TiO_3	Shirane and Suzuki1),
(Pb–Sr)TiO_3	Nomura and Sawada5)
(Pb–Ca)TiO_3	Ikeda15),
(Ba–Sr)TiO_3	Gränicher und Jakits15),
(Ba–Ca)TiO_3	Ikeda15; Berlincourt and Kulcsar17),
(Sr–Ca)TiO_3	McQuarrie18),
(Pb–Ba)ZrO_3	Shirane3),
(Pb–Sr)ZrO_3	Shirane2),
Pb(Ti–Zr)O_3	Sawaguchi2),
Pb(Ti–Sn)O_3	Jaffe, Roth and Marzullo9),
Pb(Ti–Hf)O_3	Jaffe *et al*9),
$PbHfO_3$	Shirane and Pepinsky19),
Pb(Zr–Sn)O_3	Takeda20),
Ba(Ti–Zr)O_3	Kell and Hellicar21),
Ba(Ti–Sn)O_3	Novosil'tsev and Khodakov10),
Pb(Ti-Zr–Sn)O	Jaffe *et al*9)
(Pb–Ba–Ca)TiO_3	McQuarrie22); Ikeda15),
(Ba–Sr–Ca)TiO_3	McQuarrie13),
(Ba–Ca) (Ti–Zr)O_3	McQuarrie and Behnke23),
(Pb–Ba) (Ti–Zr)O_3	Ikeda9),
(Pb–Sr) (Ti–Zr)O_3	present paper,
(Pb–Ba) (Ti–Sn)O_3	present paper.

In order to derive them from one diagram, the one giving by Roth in Fig. 1 is not always sufficient; especially, some positions of B^{4+} ions must be shifted.

The present author will propose to classify these solid solutions experimentally by one factor of A^{2+} ion and that of B^{4+} ion. Fig. 11 shows his attempt at room temperature, where the coordinates are arbitrary. The temperature axis is taken vertically to the paper.

The arrangement of A^{2+} ions agrees well with that in Fig. 1, and the electronic polarizability of A ion may play an important role.

As shown by the data on the system Pb(Zr–Sn)O_3 after Takeda20) and on $PbHfO_3$ after Shirane *et al*,19) the ordering of B ions is considered as Zr–Hf–Sn. So far as the

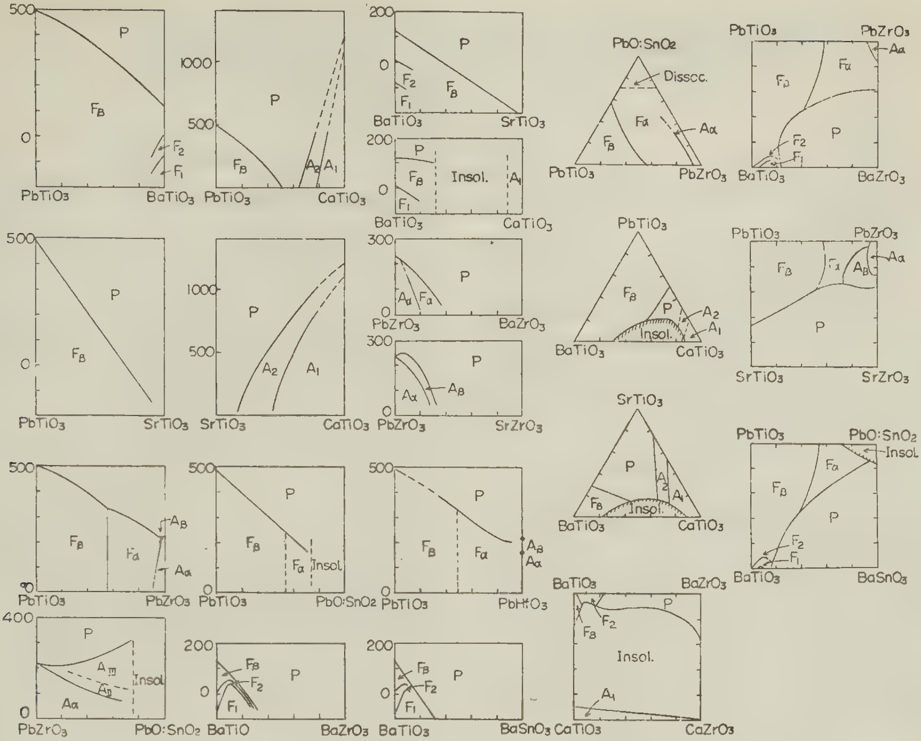

Fig. 10. Phase diagrams of $A^{2+}B^{4+}O_3$ solid solutions

neighbourhood of $PbZrO_3$ is concerned, Sn and Hf ions had to be arranged to the left side of Zr ion. The positions along the abscissa in the present figure are determined by taking account of the shift of Curie point by adding Sn and Zr to $BaTiO_3$ and the position of the boundary between F_α and F_β, shown in several diagrams in Fig. 10.

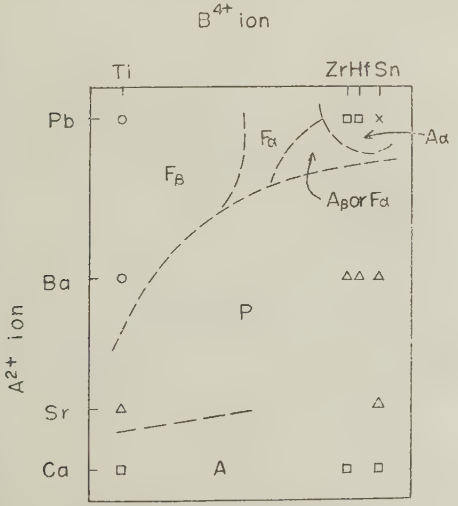

Fig. 11. Classification of perovskite $A^{2+}B^{4+}O_3$ compounds (○ ferroelectric, □ antiferroelectric, △ paraelectric, × insoluble)

The phase F_1 and F_2 in the vicinity of $BaTiO_3$ are seen only in the (Ba–A′)(Ti–B′)O_3 type diagram, and they are not pictured in the figure.

The factor important for producing ferroelectricity has been believed to be the ionic polarizability of B^{+} ion. In the perovskite type compounds, a correction for the Lorentz field is significant at the atomic position of B ion in the unit cell and the polarizability of B ion necessary for occurrance of ferroelectricity is smaller than above; which was shown by Slater[24] in the case of $BaTiO_3$, although he treated a second order transition. It was concluded by his computation that the polarization assigned to Ti ion is 37% of the total polarization in $BaTiO_3$, of which 31% is the ionic contribution. Although the values of electronic polarizabilities of Sn and Hf ions are unknown to the author and so it cannot be discussed by which the arrangement of B ions is determined, the role of the electronic polarizability may not be ignored.

The present attempt of classifying the compounds by a factor of A ion and that of B ion is impossible, of course, to explain the detailed circumstances. None the less, it may be said that this agrees rather well with the various facts.

§ 5. Conclusion

The following results are obtained from above experiments:

(1) The phase changes in the quarternary system (Sr–Pb)(Ti–Zr)O_3 and (Ba–Pb)(Ti–Sn)O_3 are examined and the phase diagrams at room temperature are determined. The effects of Sr and Sn ions are discussed. An enlarged area of A_β phase in the former system may be of interest.

(2) By using the data early published as well as the present results, an experimental classification or perovskite $A^{2+}B^{4+}O_3$ compounds is attempted. This may be applied to classify ABO_3 type solid solutions rather with success, including the distribution of their transition points. The arrangement of A ions agrees well with the ordering by the factor of electronic polarizability. That of B ions is not so simple, but the positions of Sn and Hf ions differ remarkably from Roth's intention, where the ionic radius of B ion was taken into account.

(3) The possibilities for industrial use of the ceramics in these systems are considered, but the more excellent piezoelectric materials may not be felt to meet our expectation. The dielectric ceramics possessing considerably larger dielectric constant are found somewhere in (Ba–Pb) (Ti–Sn)O_3 system.

The author is very grateful to Prof. O. Nomoto, Dr. M. Marutake and Mr. A Takeda, the research members of the Kobayasi Institute of Physical Research, for their helpful discussions. He also wishes to thank to Dr. S. Nomura of the Tokyo Inst. Techn. for giving an information on (Pb–Ba)SnO_3, to Dr. H. Hagihara and Mr. H. Yamashita in the institute for affording facilities for X-ray measurement, and to Mr. T. Ichikawa and Mr. Y. Yasui for their help to the preparation of the samples and dielectric measurement. The present studies were supported by the scientific expenditure of the Ministry of Education.

References

1) G. Shirane and K. Suzuki: J. Phys. Soc. Japan **6** (1951) 274.
2) E. Sawaguchi: J. Phys. Soc. Japan **8** (1953) 615.
3) G. Shirane: Phys. Rev. **86** (1952) 219.
4) G. Shirane and S. Hoshino: Acta Cryst. **7** (1954) 203.
5) S. Nomura and S. Sawada: J. Phys. Soc. Japan **10** (1955) 108.
6) E. A. Wood: Acta Cryst. **4** (1951) 353.
7) R. S. Roth: J. Res. Nat. Bur. Stand. **58** (1957) 75.
8) T. Ikeda: J. Phys. Soc. Japan **14** (1959) 168.
9) B. Jaffe, R. S. Roth and S. Marzullo: J. Res. Nat. Bur. Stand. **55** (1955) 239.
10) N. S. Novosil'tsev and A. L. Khodakov: Soviet Physics Technical Physics (1955) 306. (Translated into English).
11) D. A. N. CCCP **97** (1954) 237.
12) W. W. Coffeen: J. Amer. Ceram. Soc. **37** (1954) 480.
13) G. Shirane and A. Takeda: J. Phys. Soc. Japan **7** (1952) 5.
14) F. Kulcsar: J. Amer. Ceram. Soc. **42** (1959) 49.
15) T. Ikeda: J. Phys. Soc. Japan **13** (1958) 335.
16) H. Gränicher and O. Jakits: Nuovo Cimento **11** Suppl. (1954) 480.
17) D. A. Berlincourt and F. Kulcsar: J. Acoust. Soc. Amer. **24** (1952) 709.
18) M. McQuarrie: J. Amer. Ceram. Soc. **38** (1955) 444.
19) G. Shirane and R. Pepinsky: Phys. Rev. **91** (1953) 812.
20) A. Takeda: Bull. Kobayasi Inst. Phys. Res. **6** (1956) 142 (in Japanese).
21) R. C. Kell and N. J. Hellicar: Acustica **6** (1956) 235.
22) M. McQuarrie: J. Amer. Ceram. Soc. **40** (1957) 35.
23) M. McQuarrie and F. W. Behnke: J. Amer. Ceram. Soc. **37** (1954) 539.
24) J. C. Slater: Phys. Rev. **78** (1950) 748.

JOURNAL OF THE PHYSICAL SOCIETY OF JAPAN, Vol. 14, No. 10, OCTOBER, 1959

Doping Influences on Activator Diffusion in Oxide-coated Cathode Nickel

By Hiroyuki MIZUNO

Matsushita Electronics Corporation, Takatsuki

(Received May 26, 1959)

The influences of doping on the minute activator diffusion in oxide-coated cathode nickel were measured by a method similar to Swalin and Martin's[1] and the following conclusions were derived; (1) the influences of doping on the activator diffusion in oxide-coated cathode nickel are significant, (2) as the Mn, Fe, or Si content in oxide-coated cathode nickel increases, the diffusion coefficient of Mg in base nickel decreases monotonously, and (3) as the Mg content in oxide-coated cathode nickel increases, the diffusion coefficient of Mn increases monotonously.

§ 1. Introduction

In recent years a number of investigations have been reported which have extended the understanding of the behaviours of oxide-coated cathode. Although there are still a few different opinions, it is now generally accepted that the impurity semiconductor picture seems to interpret the behaviours of oxide-coated cathode fairly well; that is, the impurities responsible for thermionic emission of oxide-coated cathode are free Ba atoms developed in oxide-coating by chemical reduction, thermal decomposition, and electrolysis during the so-called activation process. The chemical reduction by reducing agents (activators) contained in base nickel is, therefore, an important mechanism for the development of such impurities. It is, in general, supposed that the activators in base nickel diffuse out to the boundary between oxide-coating and base nickel, and there react with the BaO coating to yield Ba atoms. On the basis of thermochemistry, one of the most prominent studies on this topic is the theory by Rittner[2]. He proposed the following conclusions from the analysis of the factors limiting the yield of impurity centers (free Ba atoms) of oxide-coated cathode: the reaction mechanism most favourable for generating free Ba in oxide-coated cathode may be the one in which the rate of reducing reaction is limited by the rate of activator diffusion in base nickel. Accordingly, the rate of activator diffusion is one of the most important subjects in the investigations of oxide-coated cathode. At present, dilute nickel alloys containing reducing agents are used as base metal of oxide-coated cathode. However, examining carefully a number of studies on the influences of base nickel on cathode emission and comparing them with each other, one is struck by the mutual contradictions among them. It may be attributed to the fact that even minute quantities of reducing agents in base nickel play a profound rôle. It does not suffice to make studies on the effects of a relatively large, controlled quantity of a main activator added to base nickel; even when we use nickel alloy containing the same amount of a main activator, qualitatively different results may often be obtained. In other words, the effects of doping on the agency of the other activators contained simultaneously in the base nickel should be taken into consideration.

From the facts described above, it is reasonable to suppose in the first place that one has to do essentially with the interaction effects of activators on the diffusion rates of the other activators simultaneously present in base nickel. Swalin and Martin[1] have measured the diffusion rates of Mn, Al, Ti, and W in nickel at temperature range between 1100°C and 1300°C. They carried out, however, the experiments without being aware of the mutual interactions of activators in base nickel and therefore it seems to us that their results do not immediately determine the diffusion rates of activators in base nickel.

Grube and Jedele[3] were the first to find out that the diffusion rate of Cu in pure nickel is about three times larger than that in nickel containing 0.5% Mn at 1000°C. This fact suggests that the diffusion rate of activator in base nickel of oxide-coated cathode should also be influenced by the other doping elements. Thus, a question arises as to the interaction influences of diffusions of activators in base nickel. It is very important to know what kind of influences the doping impurities on the activator diffusion in base nickel have. If the influences can be determined, it will become possible to explain some of the obscure behaviours of oxide-coated cathode. The author has previously reported the outline of these influences observed by a rather simple experimental method⁴⁾. In this paper a method similar to Swalin and Martin's¹⁾ has been introduced to observe exactly the interactions of doping, the results of which we have already reported partly⁵⁾ and the experimental proofs illustrating the interaction influence have been presented.

In section 2 the experimental method is described and in section 3 the results obtained from the experiments are given, while in section 4 these results are discussed. The results of the experiments indicate that the effect of doping influences on activator diffusion in base nickel is very significant to interpret the complex behaviours of oxide-coated cathode.

§ 2. Experimental Method

2.1 *Materials*

The alloys used in the experiments were prepared by vacuum melting to provide strict control on the quality of each alloy specimen. The results of the spectral analysis of these specimens are shown in Tables I and II. These tables also indicate that the influence of one activator (marked as "controlled") on the diffusion of another activator (marked with star *) is observed on each classified specimen; for example, the influence of Mn activator on the diffusion of Mg activator in base nickel is measured on the specimens shown as "*A*" in Tables I and II. In Table III there are shown the total contents of oxygen, hydrogen and nitrogen gases contained in one specimen sampled out at random from each classification, which were determined by *N.R.C.* vacuum melting gas analyser.

Table I. Components in Ni alloy. (weight. p.c.t.)

Element / Classification	Co	Cu	Fe	Mn	C	Mg	Si	S	Al
A	0.01	T_r	T_r	controlled	T_r	0.10*	T_r	T_r	T_r
B	0.01	T_r	controlled	T_r	T_r	0.10*	T_r	T_r	T_r
C	0.01	T_r	T_r	T_r	T_r	0.10*	controlled	T_r	T_r
D	0.01	T_r	T_r	0.10*	T_r	controlled	T_r	T_r	T_r

T_r: Less than 0.002.

Table II. Components in electrolytic Ni. (weight. p.c.t.)
(Only containing controlled one impurity)

Element / Classification	Co	Cu	Fe	Mn	C	Mg	Si	S	Al
A	0.01	T_r	T_r	controlled	T_r	T_r	T_r	T_r	T_r
B	0.01	T_r	controlled	T_r	T_r	T_r	T_r	T_r	T_r
C	0.01	T_r	T_r	T_r	T_r	T_r	controlled	T_r	T_r
D	0.01	T_r	T_r	T_r	T_r	controlled	T_r	T_r	T_r

T_r: Less than 0.002.

Table III. Content of gas included in Ni. (weight. p.c.t.)

Gas / Classification	$O_2 \times 10^{-3}$	$H_2 \times 10^{-5}$	$N_2 \times 10^{-4}$
A	0.84	8.0	0.75
B	0.79	9.0	0.56
C	0.83	8.5	0.62
D	0.80	9.0	0.61

2.2 *Experimental technique*

The strips of nickel alloy were made from the specimens in Tables I and II through successive processes of roll and annealing until about 3 mm thickness was obtained and then the strips were cut into the form of a disk of 2 cm diameter. These disks were polished carefully to remove contaminations from their surfaces with several kind of grinders and at last completely finished with emery papers. Thereafter the surfaces were cleaned with nitric acid and rinsed with acetone. When finished, grains of 0.3∼1.0 mm diameter were observed on the disk surface. The disk with the components as shown in Table I was inserted between the two disks belonging to the corresponding row of Table II. These two side disks contain the same amount of controlled solute as the center disk except the element with star mark. After inserting 10 micron tungsten wires as marker at the diffusion interfaces, the three disks were pressed by the oil press machine of 3000 kg/cm² and then welded together closely in the form of the diffusion couple. Details of the couple are shown in Fig. 1. The two interfaces of the couple were hardly discerned without the tungsten markers.

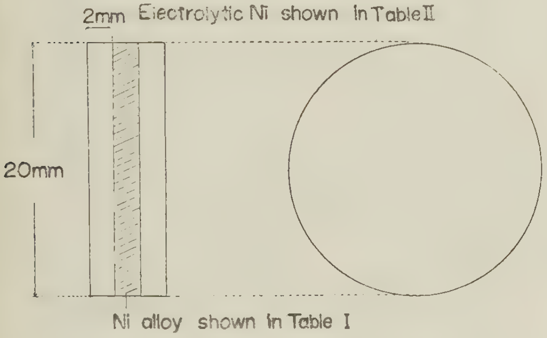

Fig. 1. Design of test couple.

The diffusion couple was put into a silica tube in close contact with a thermo-couple, which was placed in a furnace having an entirely constant temperature distribution. The silica tube was evacuated to 5×10^{-7} mm Hg throughout the experiments. The temperature of the furnace was regulated by an automatic regulator and monitored by a recorder within a tolerance of 0.5% throughout the works. After annealing for long enough to attain a considerable penetration depth of activator, the surfaces of the couple were polished and etched with concentrated nitric acid so that the tungsten markers embedded at the interfaces were readily observed. The couple was cut carefully about 20∼50 micron thickness by the lathe with its axis perpendicular to the interface, the distance from the interface being measured by both micrometer with direct reading to 1 micron and cathetometer. Each cut on both sides weighed from 50 to 80 mg and was parallel within the accuracy of 5 micron. The concentration of the activators in these cuts were measured by spectral analysis within a probable error of 7%.

§ 3. Results

3.1 *Calculation of diffusion coefficient*

Fick's equation of diffusion can be applied to our case, assuming that diffusion coefficient D is constant because of the low solute diffusion in base nickel. Taking x axis perpendicular to the interface and $x=0$ at the interface, the following solution can be easily derived for concentration C at distance x from the interface and annealing time $t>0$;

$$\frac{2(C-C_0)}{C_m-C_0}=1-\mathrm{erf}\,(y)\,, \qquad (1)$$

where $x/2\sqrt{Dt}$, C_m, and C_0 are the uniform concentrations of the activator in the middle and end disks at $t=0$ respectively. As was already shown in Table II, C_0 is always equal to zero in our experiments and so Eq. (1) becomes;

$$C=\frac{C_m}{2}\{1-\mathrm{erf}\,(y)\}\,. \qquad (1')$$

In order to calculate the diffusion coefficient from Eq. (1′), first of all, the impurity content in each cut is plotted as the function of the penetration depth x. The penetration curves of the star marked activator in base nickels containing various contents of the other element were plotted after annealing of 100 hours at 1000°C; for example, the curves for Mg in the base nickels doped with various concentrations of Mn are shown in Fig. 2. On the other hand, in Eq. (1′) it is possible to determine y for the various values of C referring to the table of the integrated error function⁶⁾. Since the relation of C to x is given in the penetration curve, y can be easily determined as a function of penetration depth x. Fig. 3 shows the y as a function of x for Mg in the base nickels doped with various concentrations of Mn. Thus, it is possible to determine exactly the diffusion coefficient D of the activator from the probable line of y

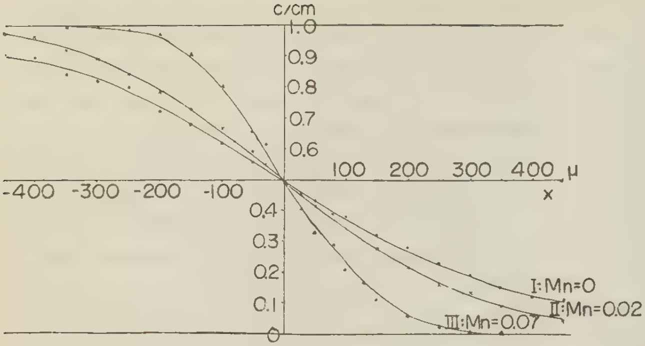

Fig. 2. Mg distribution for various concentrations of Mn. (1000°C, 100 hours)

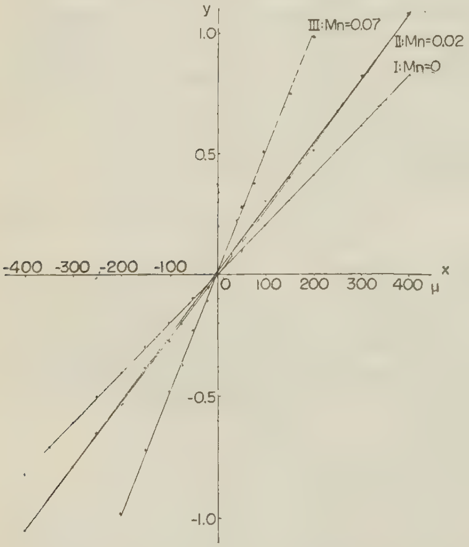

Fig. 3. y versus x plot of activator Mg for various concentrations of Mn. (1000°C, 100 hours)

versus x. The slope of the line of Fig. 3 gives $1/2\sqrt{Dt}$, since $y=x/2\sqrt{Dt}$. Thus the diffusion coefficient of one activator in base nickel of oxide cathode can be obtained in the presence of another element of various concentrations. In Figs. 2 and 3 the curves I, II, and III correspond to the cases for Mn contents of 0, 0.02, and 0.07 weight % respectively. Finally the diffusion coefficient of one activator can be obtained as a function of concentration of another activator.

3.2 *Results of experiments*

The influence of concentration of one activator on the diffusion of another for annealing of 100 hours at 1000°C are shown in Figs. 4, 5, 6, and 7 for various doping cases. Fig. 4 shows the influence of Mn concentration on Mg diffusion in base nickel, Fig. 5 that of Fe concentration on Mg diffusion, and similarly Figs. 6 and 7 that of Si on Mg diffusion and that of Mg on Mn diffusion respectively. The plots on these curves for a given concentration exhibit a considerably good agreement to each other within an experimental error. From these results one can readily understand that the diffusion rate of low solute activator in base nickel is significantly influenced by the simultaneous presence of other activator. Generally speaking, it may be concluded that

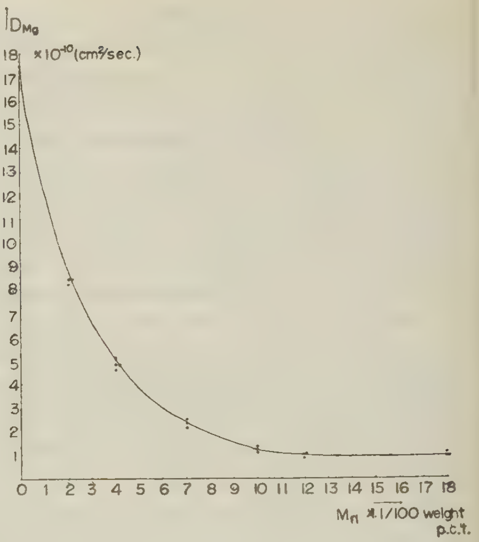

Fig. 4. Diffusion coefficient of Mg for various Mn concentrations. (1000°C, 100 hours)

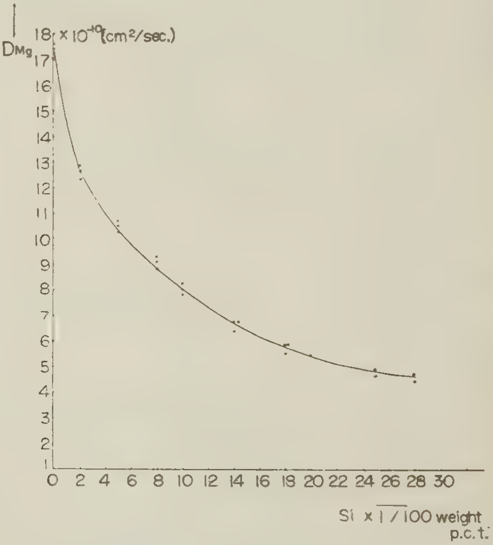

Fig. 5. Diffusion coefficient of Mg for various Fe concentrations. (1000°C, 100 hours)

the diffusion rate of solute Mg of low concentration in base nickel decreases by the addition of another element such as Mn, Fe, or Si into it, whereas that of Mn increases by the addition of Mg.

A large percentage of the errors in our experiments may come from spectral analysis of elements in a minute sample of cut. Particularly for the analysis of Mg the error was most serious because of the difficulties of analysis. Therefore, corrections were carried out by repeating the analysis for the whole amount of each sample. Probable error of analysis was estimated as about 7% even in this case. In order to eliminate the errors as possible as we can, we have carried out these spectral analysis carefully on every pair of cuts which are equidistant from the interfaces and the results have agreed with each other.

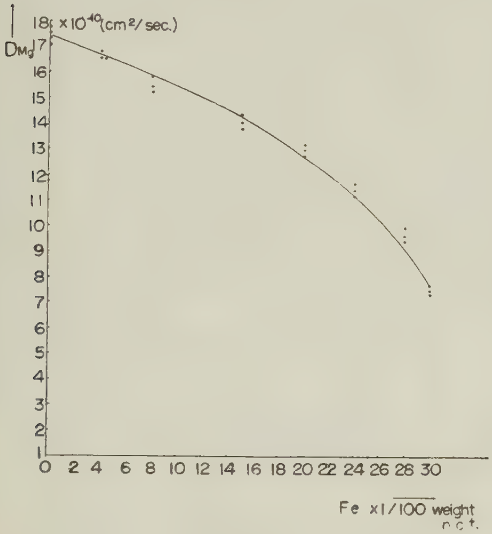

Fig. 6. Diffusion coefficient of Mg for various Si concentrations. (1000°C, 100 hours)

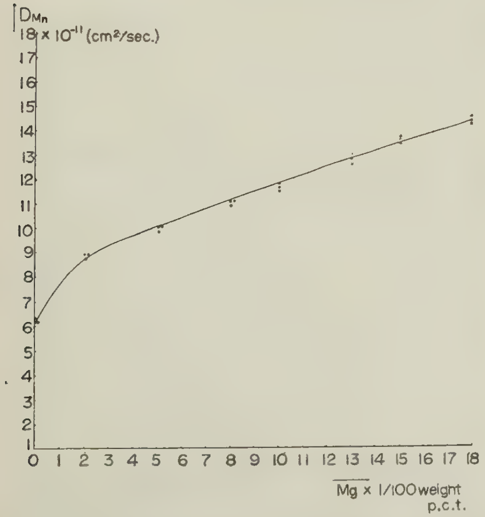

Fig. 7. Diffusion coefficient of Mn for various Mg concentrations. (1000°C, 100 hours)

There are some other factors by which experimental errors may be introduced. They are cutting operation, temperature variation during annealing, and difference of structure defects in samples, etc. The error in thickness of cuts was within the accuracy of 5 micron for each sample. The annealing temperature was automatically controlled and recorded within the fluctuation of ±0.5%, the fluctuation of the temperature being ±5° from the center value of 1000°C. It may be supposed that the defects of the structure of testing nickel give considerable influences on the activator diffusion and therefore much attention was paid to the process of manufacturing of nickel ingot by using a vacuum melting method. The entire surface of each ingot was scraped off in order to take off the shrinkage cavity. Even if a single pore was detected in the disks by microscope, the entire ingot was rejected. By such a careful selection of the ingots the author could get such a consistency as shown in Figs. 4, 5, 6 and 7.

§ 4. Discussions

So far it has been supposed that the diffusion of the reducing agent in base nickel of oxide-coated cathode depends only upon the concentration gradient of itself, and therefore that the rate of activation should be determined only by the amount (density) of reducing agent in base nickel. The mechanism of activation of oxide-coated cathode by reducing agents of low concentration in base nickel is, however, by no means such a simple one. Indeed, there are some experiments to suggest the supposition that the rate of activation due to the reducing agents is not only determined by the relatively large amount of the main reducing agent but also by the minute quantities of solute elements of low concentration. The influences of the latter have been so far neglected. Poehler7) has found that base nickel containing 0.38% Mg or 4.0% Al makes cathode less active than pure nickel. This is contradictory to the results by Benjamin8) with base nickel containing 0.07% Mg and to those by Bound and Briggs with 0.05–0.10% Al–Ni alloy. Rittner[2] has suggested a possibility to explain such contradictions on the basis of the formation of interface layer, that is, the interface layer produced by main activator has a significant influence on the emission afforded by the small quantity of "real activators," which are probably contained in base nickel in addition to the former. He has further proposed a simple explanation of the harmfulness of Mn element in base nickel for emission[7],[8], provided that the interface layer formed by Mn contains no barium. After his opinion, the presence of the reducing element in base nickel, which yields an interface compound containing no barium, may be harmful to emission because the interface layer is not only a barrier separating the real activators from BaO coating but also makes a sink for the activators and free Ba atoms.

According to our opinion, however, the contradictory results of the experiments above mentioned should be explained on the basis of doping influences on activator diffusion in base nickel. Comparing Fig. 4 with Figs. 5 and 6, one can readily see that the deleterious influences of Mn on Mg diffusion are most significant. Therefore, Mn may be most harmful for emission of cathode even at very initial stage of cathode life where the interface may not be grown up so much as it could influence the behaviours of oxide-coated cathode. As shown in Fig. 5, the influence of Fe element on Mg diffusion is also deleterious though not so significant as that of Mn. Thus, it may be safely concluded that the lowering of cathode emission by the poor reducing metals, Mn and Fe, is caused by their suppressive actions for Mg diffusion. Moreover, the above experimental results seem to suggest that Fe is not so harmful as Mn for the emission of oxide cathode. On the other hand, the cathode having considerable amount of Si element in base nickel shows a relatively high emission in spite of its deleterious influence on Mg diffusion (see Fig. 6). This is probably due to the high reducing agency of Si. In this case the degree of activation at the initial stage of life may be considered to depend mainly on the following three conditions; (1) total amount of Si and Mg simultaneously present in base nickel. (2) diffusion rate of Mg decreased by Si concentration. (3) diffusion rate of Si presumably increased by Mg concentration.

As was shown by Fisher[10], the diffusion along grain boundaries can mask the volume diffusion at low temperature. Hoffman and Turnbull[11] have pointed out that the self-diffusion in polycrystalline silver takes place more rapidly than that in single crystal silver at low temperature region. At a higher temperature region, however, the rates of both diffusions approach to each other and become nearly equal. The difference at low temperature is essentially associated with the grain boundary diffusion along the internal interfaces of polycrystal. According to Fisher's calculations, the logarithm of the specific density should vary linearly with penetration depth x in the case of grain boundary diffusion at low temperature, whereas that does linearly with x^2 in the homogeneous volume diffusion at higher temperature. The logarithm of the specific density of activator Mg was plotted against the square of penetration depth x^2 in Fig. 8 as a typical example. From this figure it seems reasonable to conclude that in our experimental temperature range the diffusion coefficient is not significantly different from that of volume diffusion.

Recently, very interesting explanations on our experimental results[5] have been presented by van Zanten[12]. He suggested that the de-

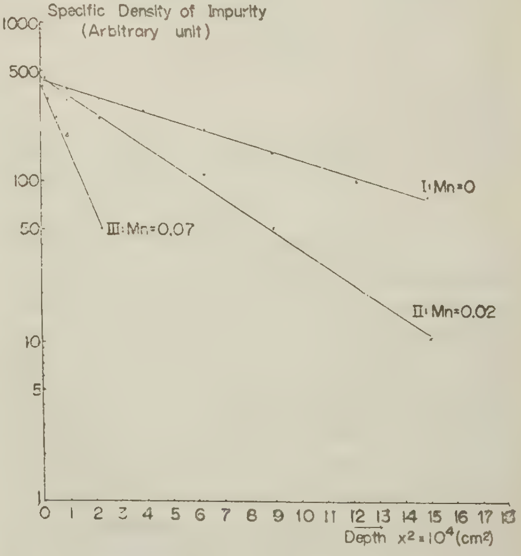

Fig. 8. Penetration curves of Mg for various Mn concentrations. (1000°C, 100 hours)

creases of diffusion coefficient of Mg, when nickel contains Mn, might be due to the reduction of MnO by Mg and that the discrepancy between the diffusion coefficients of Mg obtained by Swalin and those obtained by us or by the group in Philips laboratory might be explained by the concept of "Freies und Gebundenes Magnesium". This may be one possible interpretation for the mechanism of doping interactions, but the exact explanation is still left for future works.

§ 5. Conclusion

We have carried out some experiments concerning the doping influences on activator diffusion in base nickel of oxide-coated cateode and it has become clear that Mn, Fe, and Si decrease the diffusion rate of Mg in base nickel whereas Mg increases that of Mn. From these results it is concluded that the rate of diffusion of activator is determined mainly by the influences of doping elements rather than by its density in base nickel. We have proposed some explanations on the contradictory results of cathode emission so far published by means of doping influences on activator diffusion.

Acknowledgement

The writer wishes to express his sincere thanks to Professor Y. Uchida for his continual guidance and encouragement, and to Dr. K. Fukuda for his kind discussions and advices.

References

1) R. A. Swalin and A. Martin: Trans. Amer. Inst. Mining Met. Engrs. **205** (1956) 567.
2) E. S. Rittner: Philips Res. Rep. **8** (1953) 184.
3) G. Grube and A. Jedele: Z. Elektrochem. **38** (1932) 799.
4) H. Mizuno and T. Masuda: Ōyōbutsuri **27** (1958) 78 (in Japanese). H. Mizuno: ibid **27** (1958) 319 (in Japanese). H. Mizuno: J. Phys. Soc. Japan **12** (1957) 1315.
5) H. Mizuno: J. Appl. Phys. **29** (1958) 1265.
6) W. Jost: *Diffusion in Solid, Liquid and Gases* (Academic Press, New York, 1952).
7) H. A. Poehler: Proc. Inst. Radio Engrs. **40** (1952) 190.
8) M. Benjamin: Phil. Mag. **20** (1935) 1.
9) A. M. Bound and T. H. Briggs: Inst. Radio Engrs. **39** (1951) 788.
10) J. C. Fisher: J. Appl. Phys. **22** (1951) 74.
11) R. E. Hoffman and D. Turnbull: J. Appl. Phys. **22** (1951) 634.
12) P. G. van Zanten: Vortrag Diskussionstagung "Technologie der Vakuumröhren" der Nachrichten-technischen Gesellschaft in V.D.E. am 20 und 21 November, 1958.

JOURNAL OF THE PHYSICAL SOCIETY OF JAPAN, Vol. 14, No. 10 OCTOBER, 1959

Electrical Properties of N-Type InSb in High Electric Field at 77°K.

By Yasuo KANAI

Electrical Communication Laboratory, Musashinoshi, Tokyo

(Received June 2, 1959)

The current-voltage character and Hall coefficient of n-type InSb with different electron density were measured in a pulsive high electric field, at 77°K. In a high electric field, impact ionization from full band to conduction band occurred and the resistivity and Hall coefficient of n-type InSb decreased rapidly with increasing electric field. In the same region of electric field, Hall mobility decreased and drift velocity reached a maximum value and then decreased. In the curve of the electron density *versus* μE^2, the rate of energy gain from electric field, there existed a critical value of μE^2 where the electron density increased infinitely. This critical value of μE^2 increased with decreasing electron mobility at low field, and, in one sample, also increased with decreasing strength of the transverse magnetic field.

§ 1. Introduction

In a high electric field free carriers in solid obtain sufficient energy from electric field and their distribution function deviates significantly from the form in thermal equilibrium state. In this situation, free carriers are called to be hot and the Ohm's law ceases to be valid. Recently the hot carrier phenomena in semiconductors have been investigated experimentally and theoretically.[1]

As is well known, for a conducting carrier with mobility μ, the rate of energy gain from electric field E is μE^2. Hence one may expect that the hot carrier phenomena in a semiconductor in which the conducting carrier has large mobility will occur at rather low electric field. As such semiconductor with large mobility we chose n-type InSb, because the electron in InSb has the largest mobility in all of semiconductors. In this report our experimental results on the electrical properties of n-type InSb in a pulsive high electric field at 77°K are described.

§ 2. Experimental Procedures

2–1 *Preparation of the samples*

First of all, ingots of InSb were purified by zone refining method. After purification, single crystals of InSb were grown by the zone leveling method. In some cases large single crystals grew naturally in the course of zone refining. In these cases we cut single crystals directly from the ingots.

Next, specimens of n-type InSb were cut from these single crystals in the form approximately $0.2 \times 0.2 \times 1.0$ cm^3 and the resistivity and Hall coefficient of these specimens were measured at 77°K. Furthermore, to check the uniformity of the specimen, Hall coefficients R(A) and R(B) at two positions A and B near the ends of the specimen were also measured at the same temperature, and the quantity $\Delta R/R = R(A) \sim R(B)/R(A)+R(B)$ was used as a measure of the uniformity of the specimen. (See Fig. 1).

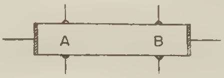

Fig. 1. To check the uniformity of the InSb specimen, Hall coefficients at two positions A and B were measured at 77°K.

All values of electrical properties, i.e., resistivity, Hall coefficient, Hall mobility, electron density, uniformity and degenerate temperature of our specimens are listed in Table I. In calculating the degenerate temperature, we used $m^* = 0.013$m as the value for effective mass, and assumed a standard parabolic form for the conduction band in InSb. The non-parabolic character of the conduction band in this material[2] will reduce the degenerate temperature to lower values for the specimens with high electron density.

After the measurements of the specimens,

Table I. Electrical properties of our samples

Sample No.	Resistivity ρ in ohm-cm	Hall coefficient* R in cm^3/Coul.	Electron density* $n=1/R\cdot e$ in no./cm^3	Hall mobility* $\mu=R/\rho$ in cm^2/V. sec	Uniformity* $\Delta R/R$ in per cent	Degenerate temperature T_D in °K
1	7.55×10^{-2}	1.58×10^{4}	3.95×10^{14}	2.09×10^{5}	12	17.5
2	4.80×10^{-2}	1.06×10^{4}	5.88×10^{14}	2.21×10^{5}	9.1	22.6
3	2.32×10^{-2}	4.26×10^{3}	1.46×10^{15}	1.84×10^{5}	8.3	41.5
4	1.46×10^{-2}	1.20×10^{3}	5.20×10^{15}	0.82×10^{5}	—	96.9
5	9.16×10^{-3}	1.16×10^{3}	5.38×10^{15}	1.27×10^{5}	5.2	99.0
6	5.70×10^{-3}	4.97×10^{2}	1.26×10^{16}	0.87×10^{5}	—	179

* All of these values were measured at 77°K in a low electric field.

samples of approximately 0.05×0.05 0.5 cm^3 were prepared for the measurements in high electric field. Current leads and the probes for measurements of resistivity and Hall coefficient were attached to the samples by soldered contacts. It is said usually that there exist some barrier layer between semiconductor and metal electrode, but fortunately it was found that this undesirable effect was negligiblly small in the case of n-type InSb. Hence in some cases the resistivity was measured not by the probes but by the current leads of the samples (See Fig. 2). These two methods of measurement gave the same values always.

2–2 *Apparatus for measurements*

To avoide the heating effect, pulsive electric field was applied to the samples. The pulse-generator consisted of hydrogen-filled. thyratron and delayed circuit. The output impedance was about 2 ohm and the maximum output voltage was approximately ±300 V. The pulse width was about 2 micro sec., and the repetition rate was 1–700 c/s.

The schematic representation of the measuring circuit is shown in Fig. 2. When the sample impedance was smaller than 2 ohm, matching resistance was omitted. As shown in Fig. 2, the voltage, current and Hall voltage of the samples were measured by the syncroscope at the positions of switch, A or A′, B and C respectively. In the course of measurements, the sample was immersed directly in liquid nitrogen.

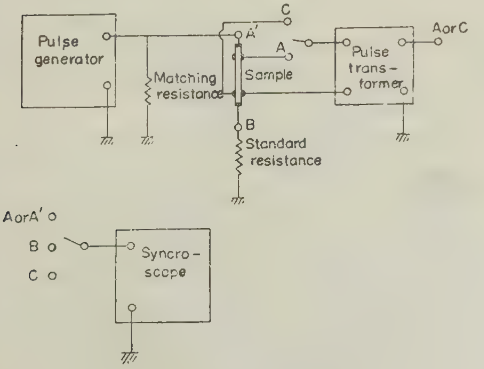

Fig. 2. Schematic representation of the measuring circuit.

§ 3. Results and Discussion

3–1 *Current-voltage character and Hall coefficient of n-type InSb crystals with different electron density*

Fig. 3 shows the current-voltage characters

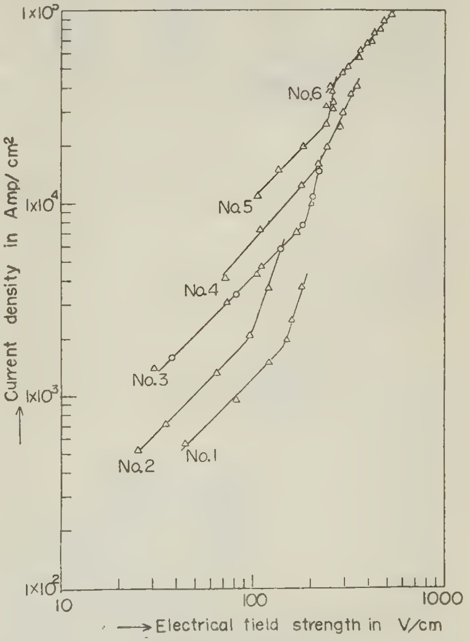

Fig. 3. Current-voltage character of n-type InSb at 77°K. The symbols ○ △ show the values obtained by changing the polarity of electric field.

of various samples with different electron density in the absence of magnetic field. The current-voltage character in a magnetic field and Hall coefficient of these samples are also shown in Figs. 4 and 5. In these figures, it is cleary shown that, in a low electric field the current density was proportional to the electric field and the Ohm's law was valid, but in a high electric field, except the case for sample No. 6, the current density increased more rapidly with increasing electric field, and in the same region Hall coefficient decreased. Namely, in a high electric field the number of conduction electron increased very rapidly with increasing electric field.

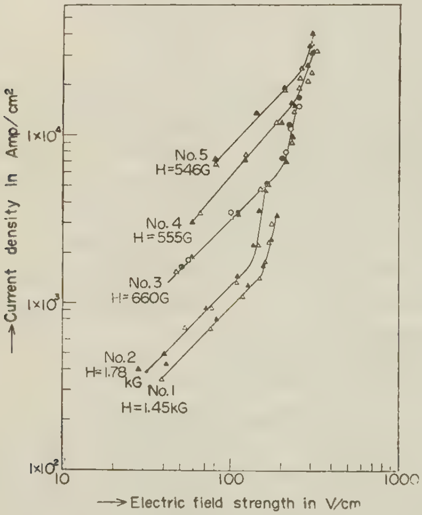

Fig. 4. Current-voltage character of n-type InSb in a transverse magnetic field at 77°K. The symbols ○ △ ● ▲ shows the values obtained by changing the polarity of electric and magnetic field.

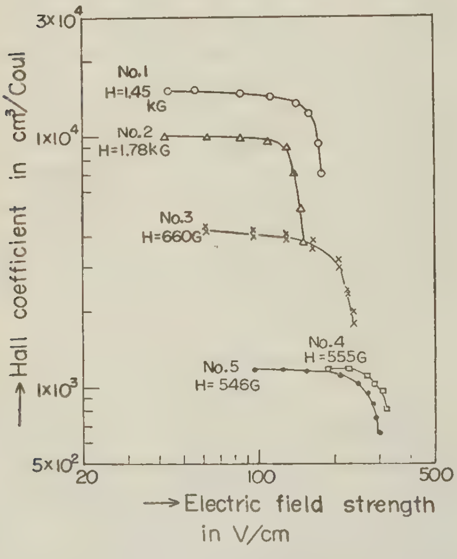

Fig. 5. Hall coefficient *versus* electric field strength curves of n-type InSb at 77°K.

As is well known, the donor impurities in n-type InSb are completely ionized at 77°K, hence the increase of the electron density in a high electric field may be caused by the ionization process from full band to conduction band. Two different mechanism of ionization processes, i.e. the field ionization process and impact ionization process, may be considered in our case. But the fact that the critical value of electric field where the current density begins to increase rapidly with increasing electric field varies from sample to sample will reject the possibility of the field ionization process as the cause of the rapid increase of electron density in n-type InSb in a high electric field. Hence we may believe that the increase of the electron density in high electric field is due to the impact ionization from full band to conduction band by the energetic electrons.3)4)

To analyse our experimental data presented above, there are some difficulties. One of these difficulties is the fact that the current-voltage character depends on the magnetic field strength (See 3–2), and another difficulty is the lack of the expression for the Hall coefficient in a high electric field. As mentioned in §1, in a high electric field, the distribution function deviates significantly from the form of thermal equilibrium state, then the expression for the Hall coefficient will become very complicated. For simplicity, however, we *assume* that the usual expression $R=1/ne$ is also valid in a high electric field. Then we may obtain, as usual, the Hall mobility by the formula $\mu=R/\rho$ and drift velocity by $v_d=\mu E$.

Resistivity, Hall mobility and drift velocity versus electric field strength curves for our samples are shown in Figs. 6–8. Some interesting features are found in Figs. 5–8. Namely, except the cases for samples Nos. 4 and 5, the Hall mobility begins to decrease with the onset of decrease of Hall coefficient, and, with increasing electric field, the drift velocity reaches the maximum value and then decreased.

Fig. 9 shows the electron density versus rate of energy gain curves for various samples of n-type InSb with different electron concentrations. In this figure we may find that at certain critical values of μE^2, the electron density increases infinitely, i.e. electrical breakdown occurs. Furthermore, this critical values of μE^2 increase with decreasing electron mobility at low electric field.

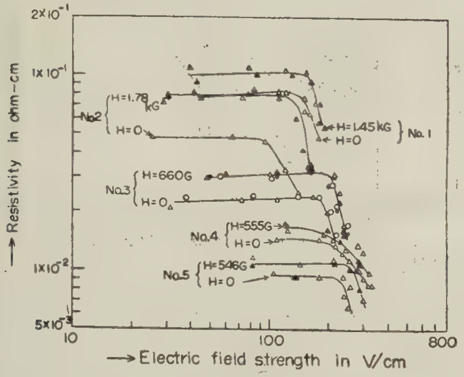

Fig. 6. Resistivity with and without transverse magnetic field *versus* electric field strength curves for n-type InSb at 77°K. The symbols ○ △ ● ▲ show the values obtained by changing the polarity of electric and magnetic field.

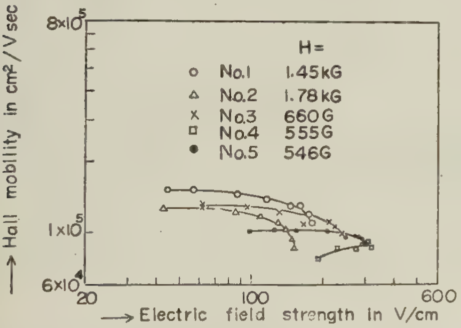

Fig. 7. Hall mobility *versus* electric field strength curves for n-type InSb at 77°K.

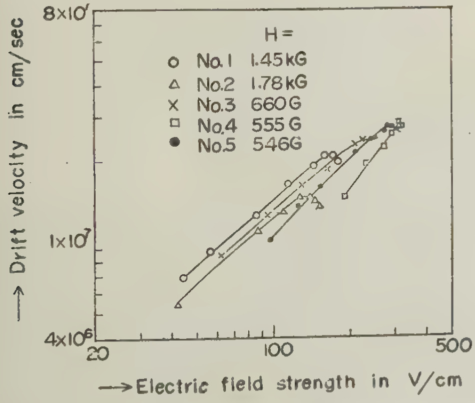

Fig. 8. Drift velocity *versus* electric field strength curves for n-type InSb at 77°K.

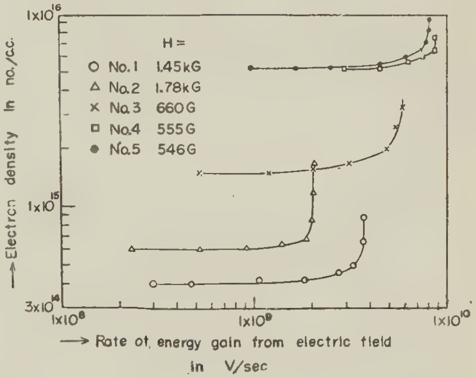

Fig. 9. Electron density *versus* rate of energy gain curves for n-type InSb at 77°K.

3–2 *Effect of the strength or direction of transverse magnetic field.*

Figs. 10–15 show the effects of the strength of transverse magnetic field upon the current-voltage character etc. of a n-type InSb sample No. 1. As one can see in these figures the increase of magnetic field strength results in the decrease of conductivity, Hall mobility, drift velocity and critical values of μE^2. In Fig. 16 the dependence of critical values of μE^2 upon the magnetic field strength is shown.

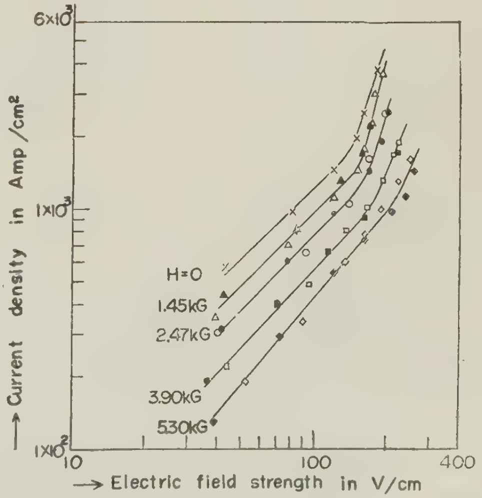

Fig. 10. Current-voltage character of n-type InSb sample No. 1 in various strength of transverse magnetic field at 77°K.

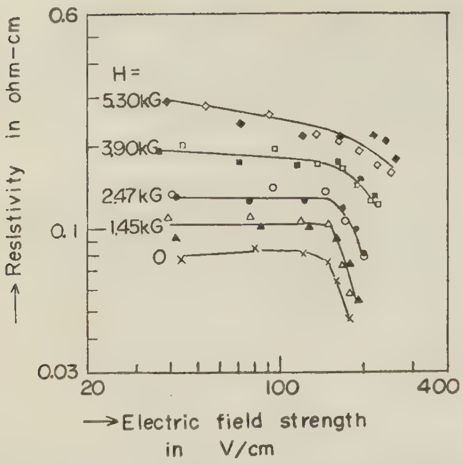

Fig. 11. Resistivity *versus* electric field strength curves of n-type InSb sample No. 1 with and without transverse magnetic field at 77°K.

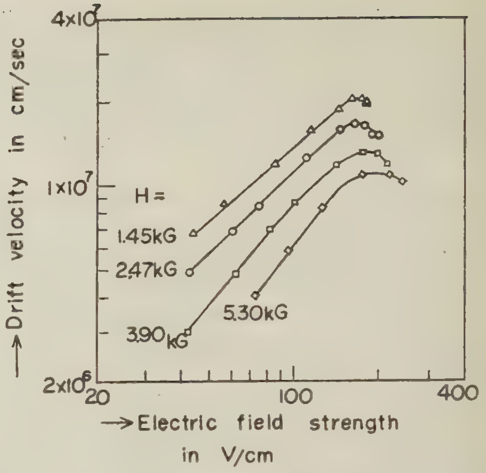

Fig. 14. Drift velocity *versus* electric field strength curves for n-type InSb sample No. 1 at 77°K.

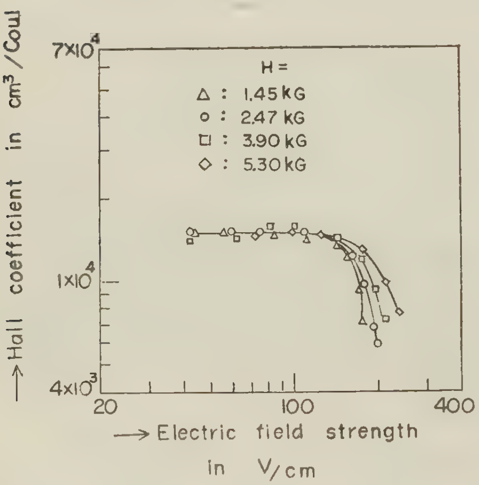

Fig. 12. Hall coefficient *versus* electric field strength curves for n-type InSb sample No. 1 at 77°K.

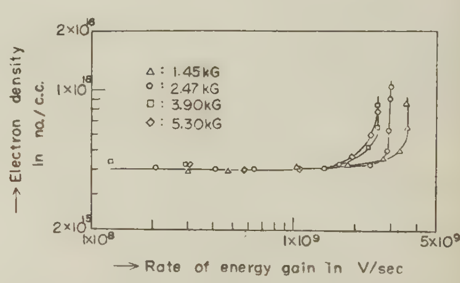

Fig. 15. Electron density *versus* rate of energy gain curves for n-type InSb sample No. 1 at 77°K.

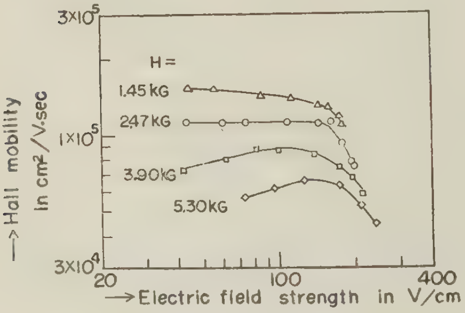

Fig. 13. Hall mobility *versus* electric field strength curves for n-type InSb sample No. 1 at 77°K.

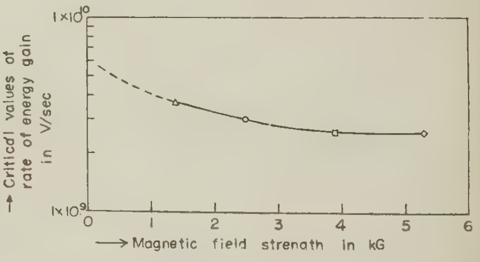

Fig. 16. Critical values of rate of energy gain *versus* magnetic field strength curves for n-type InSb sample No. 1 at 77°K.

Fig. 17 shows the current-voltage character of a sample No. 4 when the current flow was in the [110] direction of crystal axis and the transverse magnetic field was applied in the direction of [001] or [$1\bar{1}0$] or [$1\bar{1}1$]. This result shows that the current-voltage character of n-type InSb is isotropic in the transverse magnetic field which was applied to the various directions of crystal axis.

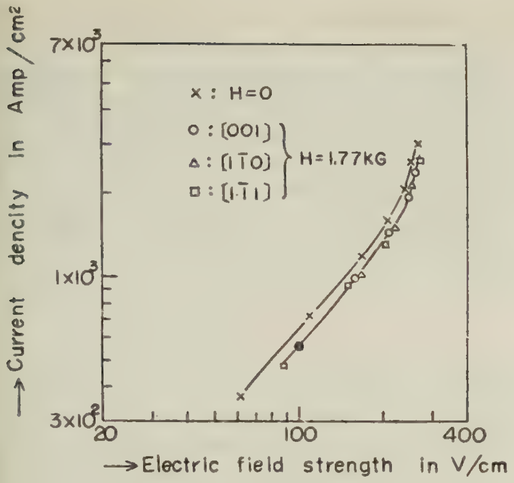

Fig. 17. Current-voltage character of n-type InSb sample No. 4 at 77°K. Current flow was in [110] direction and transverse magnetic field was applied in the direction [001] or [1$\bar{1}$0] or [1$\bar{1}\bar{1}$].

§ 4. Conclusion and Acknowledgement

Several years ago Shockley[5)] calculated the current-voltage character of semiconductor with spherical energy surface in a high electric field, assuming that the acoustic phonon scattering was the main process of energy loss in the material. His results showed that the critical field strength E_c, where the deviation from Ohm's law caused by the reduction of mobility of conduction carrier set in, was given approximately by the formula,

$$\mu_0 E_c \equiv v_{dc} = 1.5\ v_s$$

where μ_0 : low field mobility

v_s : sound velocity in the crystal

His calculation was used to analyse the experimental data of germanium and silicon obtained by Ryder.[6)]

If one applys Shockley's calculation to n-type InSb, one may expect that the deviation from Ohm's law begins at rather low electric field (~10 V/cm),[4)] because of the large electron mobility in InSb. Our experimental results mentioned above didn't show any deviation from Ohm's law near the expected region of electric field. Hence we can believe that the main process of energy loss of electron in InSb in a low electric field is not the acoustic phonon scattering but probably the optical phonon scattering.

In a higher electric field the resistivity and Hall coefficient of n-type InSb rapidly decreased with increasing electric field, and this behaviour was believed to be caused by the onset of impact ionization from full band to conduction band. In these region the mobility also decreased and drift velocity reached a maximum value and then decreased with increasing electric field. As one can see in Fig. 9, we can define the critical values of μE^2 for electrical breakdown where the number of conduction electron increased infinitely. This critical value of μE^2 increased with decreasing electron mobility at low field, and in one sample, also increased with decreasing the strength of the transverse magnetic field.

A few years ago Fröhlich and Paranjape[7)] proposed the mechanism of collective breakdown, and recently Stratton[8)] discussed the pre-breakdown behaviour of polar semiconductor upon the same mechanism. Their results showed that there existed a critical value of the rate of energy gain. Following the Stratton's calculation we can obtain 8.9×10^9 V/sec as the critical value of μE^2 for InSb at 77°K and this value is in good agreement with the experimental value; 6×10^9 V/sec (See Fig. 9). But there are some discrepancies between the Stratton's calculation and our experimental results. For instance his calculation showed the gradual increase of drift velocity with increasing electric field, but in our experiment the drift velocity reached a maximum value and then decreased. Taking into account the fact that there is a critical value of $\mu E^2 (\equiv E v_d)$, however, the decrease of drift velocity with increasing electric field is quite natural.

In a sample with lower mobility at weak electric field, there exist more imperfections than in a sample with higher mobility. So the excess energy gain corresponding to the energy loss due to the imperfections will be necessary to cause the breakdown. This is the reason why the critical value of the rate of energy gain is higher in a sample with lower mobility than in a sample with higher mobility. But the reason why the critical value of μE^2 decreases with increasing strength of transverse magnetic field is not yet understood.

The author wants to express his thanks to Dr. T. Niimi for his kind guidances and to

Messrs. R. Nii and N. Watanabe for their valuable helps.

References

1) For the review of hot carrier phenomena in semiconductors, see; S. H. Koenig: J. Phys. Chem. Solids **8** (1959) 227.
2) E. O. Kane: J. Phys. Chem. Solids **1** (1957) 247.
3) M. Glicksman and M. C. Steele: Phys. Rev. **110** (1958) 1204. M. C. Steele and M. Glicksman: J. Phys. Chem. Solids **8** (1959) 242.
4) Y. Kanai: J. Phys. Soc. Japan **13** (1958) 967.
5) W. Shockley: Bell Syst. Tech. J. **30** (1951) 990.
6) E. J. Ryder: Phys. Rev. **90** (1953) 766.
7) H. F. Fröhlich and B. V. Paranjape: Proc. Phys. Soc. London **B, 69** (1958) 21.
8) R. Stratton: Proc. Roy. Soc. A, **246** (1959) 406.

JOURNAL OF THE PHYSICAL SOCIETY OF JAPAN, Vol. 14, No. 10, OCTOBER, 1959

Study on Vacuum Deposition of Metals, II. On the Change with Aging Time in Thickness and Resistivity of Vacuum Deposited Gold Film

By Yoshibumi FUJIKI

Institute of Physics, Kyoto Prefectural Medical College.

(Received June 6, 1959)

Changes with aging time in electrical resistivity and thickness of vacuum deposited gold film were measured on the same specimen. Kiessig's X-ray interference method was employed for the measurement of film thickness. It was observed that film thickness decreased in exactly the same manner as the resistivity. The proportionality constant between resistivity change and fractional-volume change was about 2.5×10^{-4} ohm·cm which agreed well with the quenching experiment of gold in bulk by Bauerle and Koehler, and this suggests that the resistivity change in vacuum deposited gold film at room temperature is predominantly due to a vacancy mechanism just as the case of quenched material in bulk.

§1. Introduction

In a previous work¹⁾ the writer observed that Au–Pb alloys were formed when Au and Pb vapours were deposited successively in vacuum. But no alloy formation was observed when Pb vapour was deposited on Au deposit which was annealed at room temperature for about a week in vacuum. The writer supposed that this would be due to the annealing of defects, especially vacancies, which were stored in Au film by the deposition.

The electrical resistivity of vacuum deposited film is usually higher than that of bulk material and a part of this excess resistivity can undergo irreversible change upon annealing. Story and Hoffman²⁾ investigated the stress annealing in vacuum deposited copper film and found the parallelism between stress relaxation and resistivity decrease by annealing near room temperatures, and they attributed these phenomena to the disappearance of vacancies with aging.

On the other hand, it is established³⁾⁴⁾ that the quenching of bulk material from high temperature gives rise to the freezing-in of vacancies, and by the annealing after quenching the decrease in resistivity and the volume contraction occur as the result of disappearance of vacancies. Bauerle and Kohler⁴⁾ found that there exists a proportionality between the resistivity change and the fractional-volume change for gold. The annealing temperature was near room temperature.

If the writer's supposition and Story and

Hoffman's suggestion about vacuum deposited film described above were correct, the volume contraction of film and the resistivity decrease with annealing would be observed corresponding to the quenching experiment of bulk specimens. The writer intended to verify this and carried out the simultaneous measurements of thickness and electrical resistivity on a same specimen of vacuum deposited gold film.

§ 2. Experimental Procedure

The evaporation apparatus and procedures were similar to those described in the previous work.[1)] Specimen used was 99.99% Au. The pressure at deposition was near 2×10^{-5} mmHg. Substrate distances were in the range of 6~10 cm. Substrates were standard soft glass microscope slides cut to the size 50mm×3.5mm. These were cleansed with usual procedures. Platinum electrodes, to which the gold film was made electrically contact, were fixed by baking on both ends of each substrate and copper ribbon leads were soldered to electrodes. Electrical resistance was measured by a Wheatstone bridge.

The measurement of film thickness was performed by the X-ray interference method due to Kiessig.[5)] The apparatus used is shown schematically in Fig. 1. The specimen holder, to which a long lever was attached, was supported by a knife edge and the end of the lever was hung from the arm of balance. The other end of the arm was connected to the oscillating lever which was driven with constant angular velocity by the rotation of a heart cum, thus resulting in the oscillation of specimen for a range of small angle around the critical angle of total reflection. The distance between the specimen and the photographic film was 33.3 cm. X-rays used was Cu K_α radiation with nickel filter. To save the exposure time, crystal monochrometer was not used. Voltage applied to X-ray tube was 40 kV and tube current was about 40 mA and the exposure time required for each photograph was 30~40 minutes. To make the measurement accurate, two films were loaded in a cassette simultaneously. All measurements were carried out in air and at room temperature, and the film thickness was measured in every one to three hours just after the deposition.

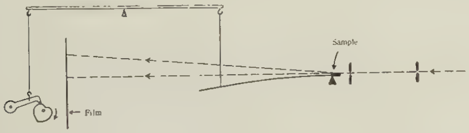

Fig. 1. Schematic diagram of the apparatus for X-ray interference with thin film.

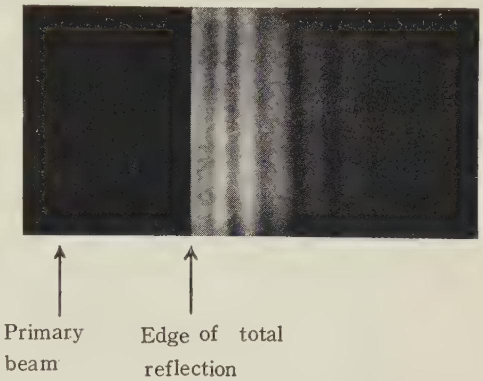

Fig. 2. An example of interference fringes.

One of the photographs of interference fringes obtained is shown in Fig. 2. The condition of interference is given by the following equations:

$$
\begin{aligned}
(2m+1)\lambda/2 &= 2d\sqrt{\alpha^2-2\eta} \quad \text{for maxima,}\\
m\lambda &= 2d\sqrt{\alpha^2-2\eta} \quad \text{for minima,}\\
&\qquad (m=0,1,2,\cdots) \qquad (1)
\end{aligned}
$$

where λ is the wavelength of X-rays, α the glancing angle, η the difference between unity and refractive index, and d the film thickness. Then, using any two interference maxima, d and η are given by the following equations:

$$d=\frac{\lambda}{2}\sqrt{\frac{(m_i+1/2)^2-(m_j+1/2)^2}{\alpha_i^2-\alpha_j^2}}, \qquad (2)$$

$$\eta=\frac{1}{2}\cdot\frac{\alpha_i^2(m_j+1/2)^2-\alpha_j^2(m_i+1/2)^2}{(m_j+1/2)^2-(m_i+1/2)^2}. \qquad (3)$$

There still remains some uncertainty for the determination of the order of interference. Riedmiller[6)] and others used the trial and error method. To eliminate the ambiguity the writer employed the following method.

First, an arbitrary order n $(0, 1, 2, \cdots)$ is given to the observed interference maxima. Then the true order of interference m_i corresponding to the n_ith maximum would be

$$m_i=m'+n_i\,,$$

where m' is a constant which must be determined. Putting this relation in Eq. (2), we obtain

$$(2m'+1+n_i+n_j)\frac{\lambda^2}{4d^2}=\frac{\alpha_i^2-\alpha_j^2}{n_i-n_j}\,. \qquad (4)$$

Plotting values of $\dfrac{\alpha_i^2-\alpha_j^2}{n_i-n_j}$ against n_i+n_j, we shall obtain a straight line. The abscissa of the point where this straight line cuts the x-axis will give the value of $-(2m'+1)$, and m' is thus determined. One of the examples is shown in Fig. 3. (This procedure was also useful for the check of the accuracy of measurements.)

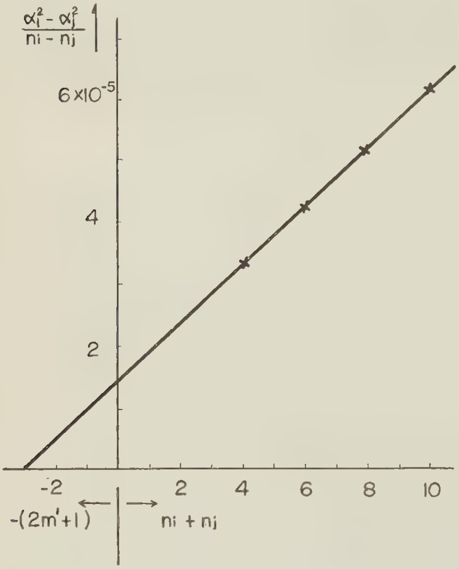

Fig. 3. Graphical determination of the order of the interference maxima.

The accuracy of the thickness measurement seemed to be affected more or less by the quality of photograph. Though the mean error of determined value of film thickness with each photograph was less than 0.5%, the resultant d values plotted against aging time showed somewhat larger fluctuations (*cf*. Fig. 4). This tendency was larger for thicker films because of the greater absorption of X-rays by the specimen (*cf*. Fig. 5). The mean error of η became somewhat larger than that of d as can be seen from Eqs. (2) and (3). The range of error for each photograph was 0.3~2%, but the results plotted against aging time showed comparatively large fluctuations (*cf*. Fig. 6).

§ 3. Results and Discussions

Results obtained are shown in Figs. 4 and 5. Specimen thickness decreased in exactly the same manner as the electrical resistivity at all stages of the annealing process. Proportionality factor between the resistivity change and the fractional-thickness change was about 2.5×10^{-4} ohm cm. The black circles superimposed in Figs. 4 and 5 show d values calculated from resistivity change using the proportionality factor of 2.5×10^{-4} ohm cm. It seems to suggest that vacancies migrate to the surface of the specimen, thus resulting in the decrease in thickness and the resistivity.

The theoretical estimation[7] shows that the resistivity increase per atom per cent of vacancies is about 1.5 micro-ohm cm for gold. It is also estimated[8] that the increase in volume per vacancy is 0.4~0.6 times the atomic volume. In the present case it may be justifiable to suppose that vacancies migrate predominantly to the surface of specimen and consequently the change of thickness is equivalent to the volume change. Taking the resistivity increase as 1.5 micro-ohm cm per atom per cent (Jongenburger's value[7]) and the increase in volume per vacancy as 0.6 times the atomic volume, we obtain the proportionality constant between resistivity and fractional-volume change as 2.5×10^{-4} ohm cm which is the value obtained from the present work. By the quenching experiment of gold wire by Bauerle and Koehler,[4] the proportionality constant between resistivity and fractional-volume change was about 3×10^{-4} ohm cm. Compared this with the present result the agreement of the order of the proportionality factor is fairly well. It is concluded from these results that the resistivity change observed in the vacuum deposited film at room temperature is due to the vacancy mechanism just like the case of quenched material in bulk.

The vacancy concentration obtained by the present work is $5\sim6\times10^{-2}$. This value is extraordinarily high compared with the quenching experiment of bulk specimen. (Equilibrium concentration of vacancies[9] at 1000°C is of the order of 5×10^{-4}.) But Story and Hoffman[2] also found the high concentration of vacancies of the same order as that in the present work in their experiment on vacuum deposited copper film. The mechanism of freezing-in of the vacancies by deposition would presumably be different from the case of quenching of bulk specimen.

The decay curves in Figs. 4 and 5 show some sudden breaks. The cause of these

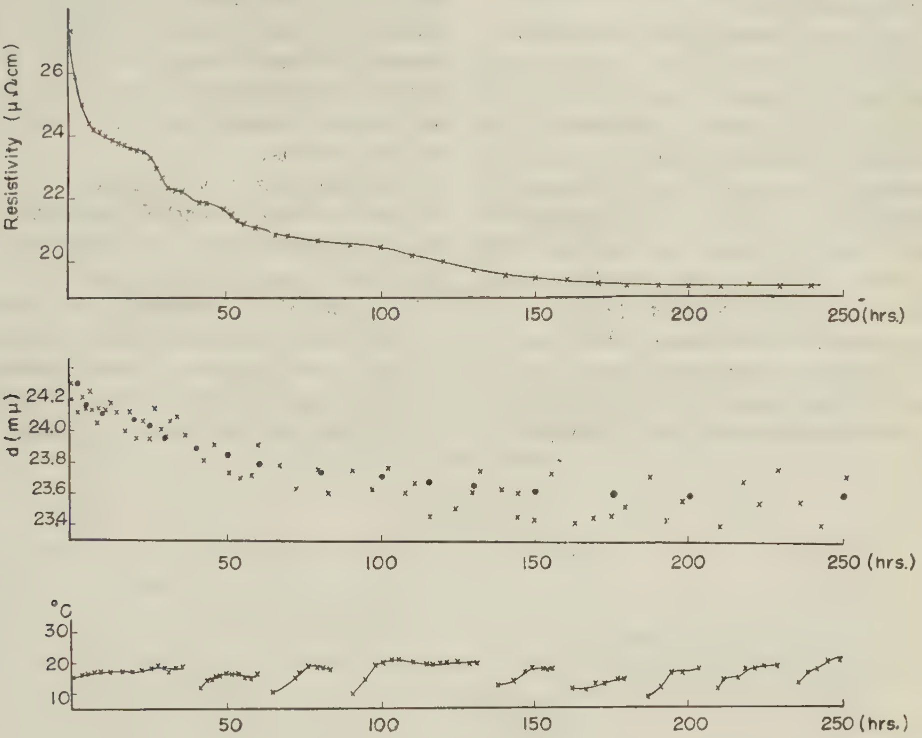

Fig. 4. Resistivity and film thickness change with aging time.

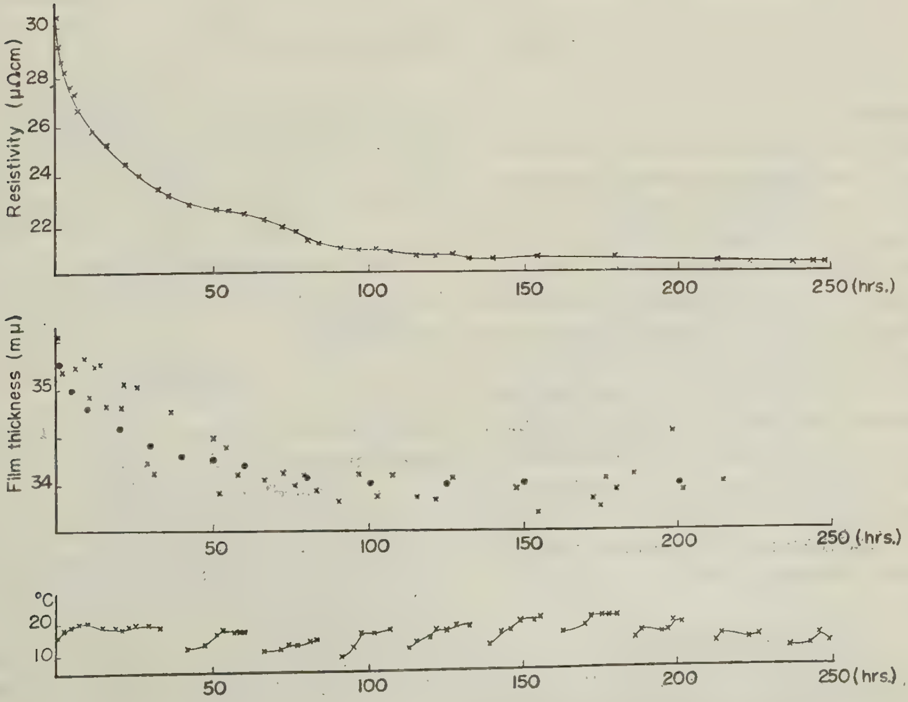

Fig. 5. Resistivity and film thickness change with aging time.

breaks is not clear, but it is not adequate to discuss here the matter, because the annealing temperature was not constant throughout the present experiment.

There are some anxieties for the contamination of film by foreign gas atoms which would strike the film and stick to it by the deposition.[10] This would be checked by the comparison of η values of films with that of bulk specimen, because η of an element is proportional to its density. Unfortunately the writer could not know the correct value of η for gold in bulk. These impurity atoms would affect upon the slope of decay curve, but this is not discussed here. But so long as the amounts of resistivity change and the fractional-volume change are concerned, the effect of the impurity atoms may be neglected in the present work, because the contribution of interstitial atoms to the resistivity change is large compared with that of vacancies, and the proportionality constant between resistivity and fractional-volume change should be much larger than the value obtained in the present work if the resistivity and volume change were attributed to these impurity atoms.

The change of η with aging time is shown in Fig. 6. (Figs. 4 and 6 were obtained by the same specimen). Fluctuations of the observed values of η are comparatively large and the detail of change is not clear. But the tendency of the increase of η, and consequently the increase of density with aging time corresponding to the volume contraction of film may be seen from the figure.

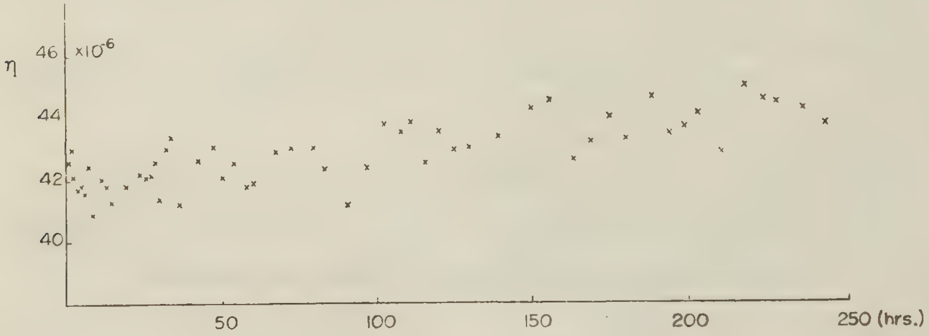

Fig. 6. Change of η with annealing time.

§ 4. Summary

The resistivity change and the decrease in thickness of vacuum deposited gold film with aging were measured simultaneously on the same specimen. It was observed that the specimen thickness decreased in exactly the same manner as the specimen resistance. The proportionality constant between resistivity change and fractional-volume change was 2.5×10^{-4} ohm cm which agreed well with that obtained by the quenching experiment of gold wire by Bauerle and Koehler. It is concluded from the result that the resistivity annealing in vacuum deposited gold film is mainly due to vacancy mechanism just as in the case of quenched material in bulk.

Acknowledgements

The writer wishes to express his sincere thanks to Professor K. Tanaka of Kyōto University for his kind advice and the encouragement throughout the present investigation. The writer's thanks are also due to Professor J. Takamura of Kyōto University for his valuable advice and discussions. Further, he is grateful to Messrs. T. Yoshida and R. Suganuma in our Institute for their assistance.

References

1) Y. Fujiki: J. Phys. Soc. Japan **14** (1959) 913.
2) H. S. Story and R. W. Hoffman: Proc. Phys. Soc. London **B, 70** (1957) 950.
3) F. J. Bradshaw and S. Pearson: Phil. Mag. **1** (1956) 812; **2** (1957) 379. J. Takamura: Kinzoku-Butsuri **2** (1956) 112 (in Japanese).
4) J. E. Bauerle and J. S. Koehler: Phys. Rev. **107** (1957) 1493.
5) H. Kiessig: Ann. Physik [5] **10** (1931) 769.
6) R. Riedmiller: Ann. Physik [5] **20** (1934) 377.

7) P. Jongenburger: Appl. Sci. Research **B 3** (1953) 273. F. Abelès: Compt. rend. **237** (1953) 796.
8) J. D. Eshelby: J. Appl. Phys. **25** (1954) 255. P. Jongenburger: Phys. Rev. **106** (1957) 66. L. Tewordt: Phys. Rev. **109** (1958) 61.
9) J. S. Koehler, F. Seitz and J. E. Bauerle: Phys. Rev. **107** (1957) 1499.
10) O. S. Heavens: *Optical Properties of Thin Solid Films* (Academic Press, New York, 1955) 8.

JOURNAL OF THE PHYSICAL SOCIETY OF JAPAN, Vol. 14, No. 10, OCTOBER, 1959

Elastic Stiffness Constants of Cadmium Sulfide

By Taizō MASUMI
Institute of Physical and Chemical Research,
31, Kamifujimae-Cho, Bunkyo-Ku, Tokyo, Japan
and Toshio TANAKA
Department of Applied Physics, University of Tokyo,
Tokyo, Japan

(Received June 20, 1959)

The elastic stiffness constants $\|c_{ij}\|$ of wurtzite type cadmium sulfide single crystals have been determined on several specimens in the form of cube at room temperature by the ultrasonic pulse echo method at 5.0 and 10 Mc/sec. The results are as follows: $c_{11}=0.778$; $c_{12}=0.447$; $c_{33}=0.881$; $c_{44}=0.147$; $c_{36}=0.159$: in units of 10^{12} dynes per cm^2 by using the value of density $\rho=4.83$ g/cm^3.

§ 1. Introduction

Elastic stiffness constants of a crystal usually inform us of the nature of the binding between constituent atoms in the crystal. We have attempted to examine the elastic properties of large cadmium sulfide single crystals in cube-form as a fundamental study of physical quantities of the crystal.

§ 2. Experimental Procedures

Gobrecht and Bartschat[1][2] have examined the elastic and piezoelectric properties of wurtzite type cadmium sulfide crystals. But, in their experiments, some of the constants have been left undetermined, since they have used flaky crystals with preferred crystal orientations. The samples used in our experiment are the specimens cleaved and machined out of wurtzite type cadmium sulfide ingots[3] produced by the Eagle-Picher Company, whose resistivity ranges from 10^5 to 10^8 ohm·cm in dark at room temperature. The crystal directions are determined with the help of X-rays and the sizes of the specimens are, for example, of the order of 7.54 mm × 7.56 mm × 10.16 mm for the directions of $[01\bar{1}0]$, $[2\bar{1}\bar{1}0]$, and $[0001]$, respectively. Flatness of surfaces prepared with No. 800 carborundum is satisfactory and the crystals are etched in dilute hydrochloric acid.

For the measurement of elastic constants of the crystal, the usual ultrasonic pulse echo method[1] was adopted, because of its convenience and adaptability to a wide range of experimental conditions. In our experiment, an ultrasonic wave in pulse generated by a quartz transducer, whose frequency is 5.0 or 10.0 Mc/sec and pulse width 0.5 μsec, has been chosen. Neither the corresponding wavelength is longer than the sample dimensions, nor the transmitted and reflected waves would interfere with each other in the crystal. Both the longitudinal and transverse shear waves have been used. The elapsed time between initiation and receipt of the pulse is measured in the pattern displayed on a Tektronix 535 type oscilloscope as shown in Photo. 1. Sound velocity v is obtained by

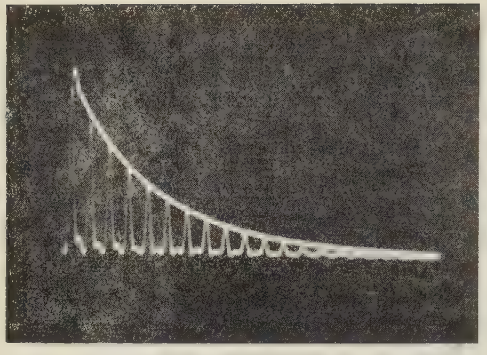

Photo. 1. A displayed pattern of pulse echoes reflected from the rear surface back to the tranceducer.

dividing the round trip distance d by the elapsed time T averaged over several echoes.

§ 3. Results

Sound velocities v's determine the elastic stiffness tensor $\|c_{ij}\|$ of hexagonal crystal[5)]

$$\|c_{ij}\| = \begin{Vmatrix} c_{11} & c_{12} & c_{13} & 0 & 0 & 0 \\ c_{12} & c_{11} & c_{13} & 0 & 0 & 0 \\ c_{13} & c_{13} & c_{33} & 0 & 0 & 0 \\ 0 & 0 & 0 & c_{44} & 0 & 0 \\ 0 & 0 & 0 & 0 & c_{44} & 0 \\ 0 & 0 & 0 & 0 & 0 & c_{66} \end{Vmatrix}$$

$$c_{66} = (c_{11} - c_{12})/2$$

through the following relations,

$$v_1 = \sqrt{c_{11}/\rho} \qquad \text{(longitudinal wave)}$$

$$\left.\begin{aligned} v_2 &= \sqrt{c_{66}/\rho} \\ v_3 &= \sqrt{c_{44}/\rho} \end{aligned}\right\} \qquad \begin{aligned} &\text{for } \sigma = (\sigma_1, \sigma_2, o) \\ &\text{(transverse waves)} \end{aligned}$$

$$v_1 = v_2 = \sqrt{c_{44}/\rho} \qquad \text{(transverse waves)} \quad \text{for } \sigma = (o_1\, o_1\, \sigma_3)$$

$$v_3 = \sqrt{c_{33}/\rho} \qquad \text{(longitudinal wave)}$$

$$v_{1,3}{}^2 = \frac{1}{2\rho}\Big\{(c_{11}+c_{44})\sin^2\theta + (c_{44}+c_{33})\cos^2\theta \pm \sqrt{(c_{11}-c_{44})^2 \sin^4\theta + (c_{44}-c_{33})^2\cos^4\theta + 2\sin^2\theta\cos^2\theta(c_{11}c_{44}+c_{33}c_{44}-2c_{33}c_{11} + 2c_{13}{}^2 + 4c_{13}c_{44})}\Big\}$$

$$\text{for } \sigma = (\sigma\sin\theta, o, \sigma\cos\theta)$$

$$v_2{}^2 = \frac{1}{\rho}(c_{66}\sin^2\theta + c_{44}\cos^2\theta)\,,$$

where the suffixes i, j are specified from the selected combinations of the stress and strain directions and σ denotes the phonon wave vector with respect to the [0001] direction.

The experimental results of $\|c_{ij}\|$ for wurtzite type cadmium sulfide are shown in Table I except c_{13}, where we have used the value of $\rho = 4.83\text{g/cm}^3$ as the density and c_{12} was determined from the subsidiary relation for the expression $\|c_{ij}\|$.

Table I. Experimental values of elastic stiffness constants of wurtzite type cadmium sulfide at room temperature by the ultrasonic pulse echo method in 5 Mc/sec region.

Elastic stiffness constants $\|c_{ij}\|$	Propagation direction σ	Displacement direction u Type of wave	Round trip distance d(mm)	Elapsed time T (μsec)	Sound velocity v (m/sec)	Values of c_{ij} $\times 10^{12}$ (dyne/cm²)
c_{11}	$[01\bar{1}0]$	$[01\bar{1}0]$ Longitudinal	7.56	3.766	4,013	0.778
	$[2\bar{1}\bar{1}0]$	$[2\bar{1}\bar{1}0]$ long.	7.54	3.756	4,013	0.778
c_{12}	$c_{12} = c_{11} - 2c_{66}$					0.447
c_{33}	[0001]	[0001] long.	10.16	4.76	4,270	0.881
c_{44}	$[01\bar{1}0]$	[0001] Transverse	7.54	8.63	1,750	0.147
	[0001]	$[01\bar{1}0]$ trans.	10.16	11.6	1,750	0.147
c_{66}	$c_{66} = (c_{11} - c_{12})/2$					
	$[01\bar{1}0]$	$[2\bar{1}\bar{1}0]$ trans.	7.54	8.31	1,810	0.159
	$[2\bar{1}\bar{1}0]$	$[01\bar{1}0]$ trans.	7.56	8.36	1,810	0.159

Probable errors are less than 1% for c_{11} and c_{33}. In the measurements for transverse waves, the accuracy is rather worse, though plausible agreements are found between the different directions of propagation. Here, we shall not enter into discussions in detail on these values, because the value of c_{13} has been left undetermined yet.

§4. Acknowledgements

The authors wish to express their sincere thanks to Professor Y. Suge and Professor T. Inui for their encouragements and to Dr. A. Hikata and Dr. M. Tsutsumi of Government Mechanical Laboratory for their kind arrangements for our experiments. Sincere gratitudes are also due to Dr. M. Kobayashi for his kind discussions.

References

1) H. Gobrecht and A. Bartschat: Z. Phys. Bd. **152** (1958) S. 417.
2) H. Gobrecht and A. Bartschat: Z. Phys. Bd. **153** (1959) S. 529.
3) W. E. Medcalf and R. H. Fahrig: J. Electrochem. Soc. **105** (1958) 719.
4) H. Huntington: Phys. Rev. **72** (1947) 321. H. J. McSkimin: J. Appl. Phys. **24** (1953) 988. H. J. McSkimin and W. L. Bond: Phys. Rev. **105** (1957) 116.
5) M. Born and K. Huang: *Dynamical Theory of Crystal Lattices.* (Oxford, 1954).

JOURNAL OF THE PHYSICAL SOCIETY OF JAPAN, Vol. 14, No. 10, OCTOBER, 1959

Deformation Twinning of Tin Single Crystals under Impact Loading

By Ken-ichiro ISHII

Chikusa Branch, Nagoya Institute of Technology, Nagoya

(Received January 30, 1959)

The impact test has been carried out on the mechanical twinning of 99.98% pure tin crystals, the time of stressing being 10^{-3} sec. The twinning occurred with a sharp yield process, when the [001] axis was nearly perpendicular (±15°) to the specimen axis. The upper yield stress scattered from 0.7 to 2.5 kg/mm², while the lower yield stress and also the stress for the further thickening of the generated twin lamella were from 0.1 to 0.2 kg/mm².

Twinning occurred where large local stress was expected. The critical shear stress law approximately holds for the upper yield stress after indentation, the stress being 0.8 ± 0.1 kg/mm².

Two explanations for the upper yield stress for twinning appear possible. In the first place, it may be the stress required to initiate the twin with the aid of the local stresses, and in the second place, it may be the stress required for the growth of the nucleated twin lamella across the crystal. It is likely that the growth of the twin nuclei is controlled by the critical shear stress law, and that the growth is suppressed by the appearence of slip.

§ 1. Introduction

In some metals such as tin and iron, it is known that twins are readily formed under impact loading. Chalmers¹⁾ found that the twin in tin crystals will be formed under impact loading, if the stress is applied perpendicular to the [001] axis. It is generally known that the yielding of mild steel occurs at stresses higher than the static yield point if the time of loading is small. For example, Clark and his co-workers²⁾ studied extensively the delayed yield phenomenon of low carbon steel. The delay time was also found in β-brass³⁾⁴⁾ and in zinc⁴⁾ single crystals. It may be expected that the delay time phenomenon would also exist in tin crystals, which might favour twinning under impact loading. A number of reviews⁵⁾⁶⁾⁷⁾⁸⁾ have been published on the general aspects of twinning, to which the readers are referred. In this paper, many literatures, especially those of Russian workers, are quoted from these reviews. The following sections describe the results of the impact test with special reference to the orientation dependence, the location of twins, and the effect of indentation. With these results, the origin of the yield process of twinning is discussed

§ 2. Experimental Procedure

The tin crystals were grown from commercial pure tin in the shape of a cylinder 4 mm in diameter and about 20 mm in length cut undistorted. The specimens were of 99.98 wt per cent purity. The orientation was so arranged that the [103] twinning direction and the [001] direction or the slip direction, will lie in a plane with the cylinder axis. As shown in Fig. 1, the angle λ between the [103] direction and the cylinder axis, were changed from 0° to 60°, and so the angle between the [001] axis and the specimen axis, from 30° to 90°, to observe the orientation dependence of twinning.

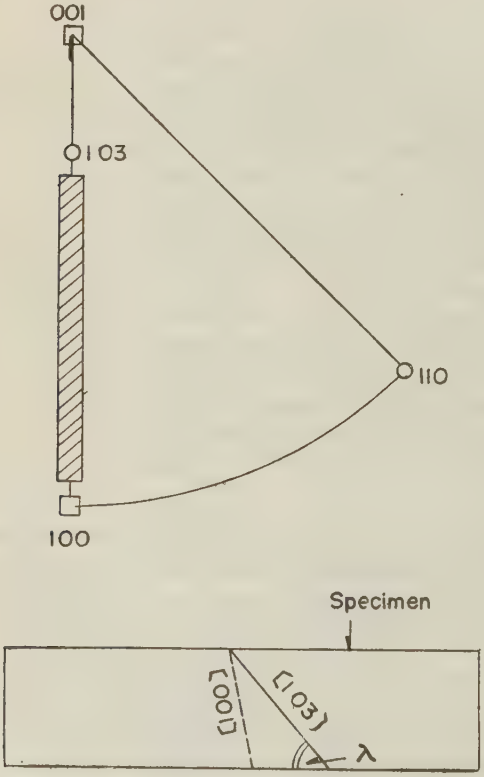

Fig. 1. Orientation of the specimens used.

A small impact tester, which is illustrated in Fig. 2 was used. The specimen was fixed to a massive iron block, about 50 kg, and was struck with a striker pendulum, 28 cm long and about 100 gm. After a high temperature anneal (at 200°C), the specimen was soldered on an end to a brass protecter against the striker and on the other end to a brass base attatched to the holder on the iron block, so that the impact load may be applied uniformly.

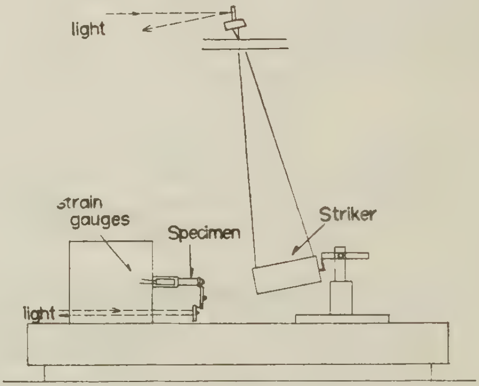

Fig. 2. Apparatus.

The impact load was measured with strain gauges pasted on the holder, or alternatively, the amplitude of repulsion of the striker after impact was used after calibration with these gauges. The period of an impact, from the begining to the end, was about 10^{-3} sec. The contraction of the specimen after impact was measured with a set of mechanical and optical levers, to the accuracy of 10^{-4} cm.

As was done in the earlier experiments[3)4)], the specimen was subjected to increasing amount of impact loads. When the specimen was struck at a small velocity, the collision between the striker and the specimen was elastic, and by increasing the velocity step by step, a velocity was reached where the plastic deformation either with slip or twinning began. In this way, the critical stress was taken as the highest stress obtained before the onset of plastic deformation.

§ 3. Results

(I) *The yield process of twinning*

When the impact test was made with a number of specimens in which the angle λ was about 50°, i.e., the [001] axis was nearly perpendicular to the cylinder axis, no appreciable slip was observed, but a sharp yield process of twinning occurred. An example is shown in Fig. 3. The upper yield stress, as shown in Fig. 6, scattered from sample to sample ranging from 0.7 to 2.5 kg/mm², while the lower yield stress ranged from 0.1 to 0.2 kg/mm². The parallel sided twin lamella appeared with the yielding. The stress for further thickening was measured by further applying a number of impacts. As is shown in Fig. 3, and 4, the stress for thickening is of the same order of magnitude as the lower yield stress, usually accompanied with a small variation.

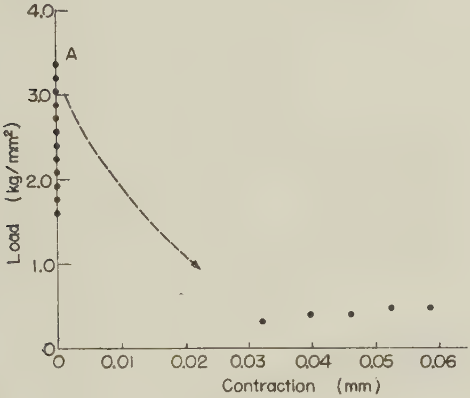

Fig. 3. Load vs. contraction by repeated impact for a specimen in which $\lambda=43°$. The velocity of impact was increased successively until the yield of twinning occurred at Point *A*. After the yield the velocity was kept constant, to observe the stress for the thickening.

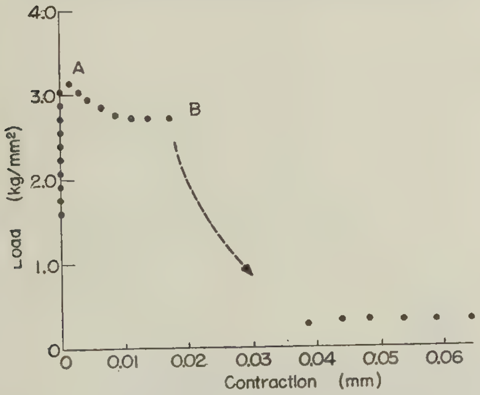

Fig. 4. Load vs. contraction by repeated impact, for a specimen in which $\lambda=38°$. The yield of slip first occurred at Point *A*, followed by several slips. Twinning occurred at Point *B*. The velocity of impact was increased successively until it caused the yield by slip, kept constant during the process of slip, and then at a smaller velocity during the process of thickening of the twin.

(II) *Orientation dependence*

With the specimens in which the angle λ is less than about 40°, and thus the resolved shear stress on the slip plane is large for a given load, the slip first occurred sometimes. The critical shear stress for slip was about 0.9 kg/mm², of the same order of magnitude as the minimum of the observed upper yield stress for twinning. When the slip first occurred, it continued to take place if a number of impact was further applied, and as shown in Fig. 4, twinning eventually occurred. The amount of the preceding slip scattered considerably, and in some specimens the yield process of twinning did not occur until a severe distortion took place. An example is shown in Fig. 5. The condition for the occurrence of twinning after slip is left unknown. The specimens used for the measurements shown in Fig. 4 and 5 were cut from one and the same long single crystal, and were subjected to the impact tests in the same way, but the result was different in that twinning occurred in the one and slip alone in the other.

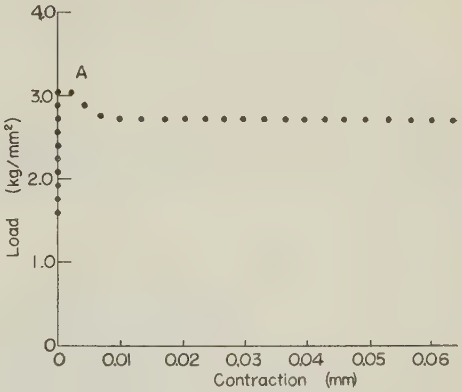

Fig. 5. Load vs. contraction by repeated impact for a specimen in which $\lambda=38°$. Here the velocity of impact was increased successively until the yield of slip occurred at Point *A*, and then kept constant. The yield process of twinning did not occur, but the slip continued extensively.

In Fig. 6, the critical loads observed are shown. As will be seen, the critical shear stress law does not hold for the twinning, while it roughly does for slip.

The result that slip alone occurred when

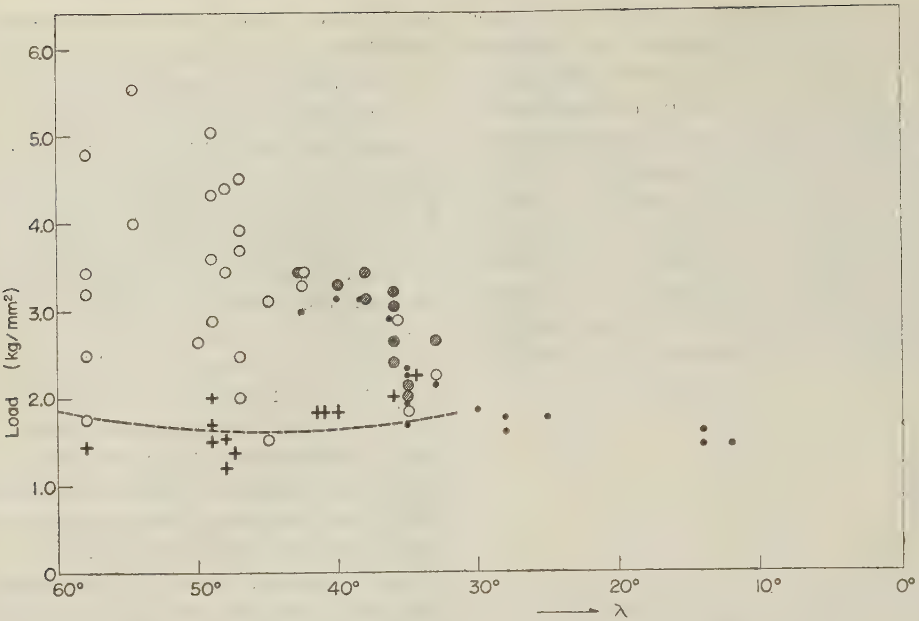

Fig. 6. Critical load vs. orientation, either for slip or twinning.

○: twinning without prior slip.
●: slip.
▨: slip, for which twinning occurred later.
+: twinning without prior slip at the indentation.
---: the average of the upper yield stresses after indentation.

the angle λ was less than 30° may be attributed only to the fact that the minimum stress for twinning was not attained with the applied load.

(III) *Location of twins*

(a) Ordinary cases

It has been observed with about sixty specimens that the twin lamellae ran through an end of the specimen in the ordinary cases irrespective of whether the yielding occurred without slip or after slip under impact loading. An example is shown in Fig. 7a. Some exceptional cases are described below.

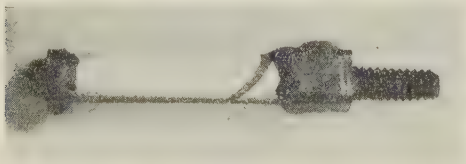

a

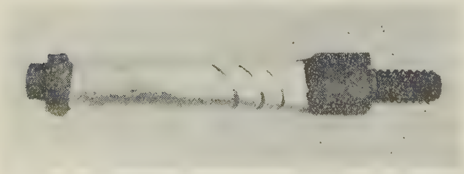

b

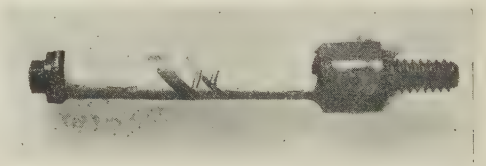

c

Fig. 7. Location of twins.
(a) The twin lamella running through an end of the specimen as observed in the ordinary cases.
(b) The twin lamellae running through the grain boundaries. The sample was prestrained with steady loading about 1% in contraction.
(c) The twin lamellae generated at the indentations.

(b) Effect of grain boundary

Sometimes, a small grain of different orientation happend to remain in the finished specimen. Twinning seldom occurred through the grain boundary when the impact test was made with such specimens. However, often they were formed through the boundary, if the prior slip was made with steady loading before the impact test. An example is shown in Fig. 7b. (Twinning did not occur with steady loading alone.)

(IV) *Effect of indentation*

Bell and Cahn⁹⁾ observed that if a small indentation was made in the zinc crystal while it was under a sufficiently high stress (about 2 kg/mm², resolved), a burst of twinning resulted. However, if the indentation was made first and load applied after, the small twins so produced would not grow but generally remained unchanged when the specimen broke.

After these experiments mentioned above, the impact test was made on tin crystals *after* giving an indentation with a knife edge. The results did not necessarily coincide with those obtained in zinc crystals, but, as shown in Fig. 7(c), the twin appeared through the indentation. The yielding in this case also occurred as in the ordinary impact test. The upper yield stresses are shown in Fig. 6. As is shown in the figure, the upper yield stress after indentation seems to be relatively lower and has less scatter than in the ordinary cases. It may be said that the critical shear stress law approximately holds for the upper yield stress after indentation, the stress being 0.8±0.1 km/mm².

§ 4. Discussions

Garber¹⁰⁾ studied the process of twinning in calcite and sodium nitrate crystals. He found that, a small wedge or lens shaped twin lamella suddenly appeared at a certain load, grew longer and thicker as the load was increased, shortened and finally disappeared when the load was relaxed. He found further that when the load was large enough, the small twin suddenly spreaded across the whole section of the crystal, becoming parallel sided, and a smaller stress then caused the twin to thicken. As quoted in the preceding section, Bell and Cahn⁹⁾ obtained a good evidence that a high local stress is required to initiate a mechanical twinning in zinc crystals. It is now generally believed that a high local stress is required for the nucleation of twinning, in most substances if not universal.

(a) *Nucleation caused by local stresses*

In tin crystals also this seems to be the case: The twins will have nucleated in ordinary cases with the aid of the local stresses at an end of the specimen, where the twins are observed to run (§ 3. III (a)). The twin observed at grain boundary as described in § 3 III (b) will suggest that they bave been formed with the aid of the local stresses by slip.

(b) *Origin of the upper yield stresses*

Two origins of the upper yield stress appear possible. In the first place, it may be the stress for the nucleation of twins with the aid of the local stresses in the crystal, i.e., at an end, at the concentrated stress by slip, or at the indentation. The wide scatter in the observed upper yield stresses would be attributed to the possible wide scatter in the local stresses.

The second possible interpretation is that it is not the stress for the nucleation, but is the stress for the nucleated twins to grow. When the local stress is large enough, nucleation will occur at a low external stress, and so the stress for the further growth will appear as the upper yield stress. A possible example for this would be the yielding at the indentation. It is not clear whether the twins were always nucleated during the indentation itself or during the impact given after the indentation, but they might be readily nucleated there during the impact, even if they had not been nucleated directly by the indentation. In either case, the observed upper yield stress after indentation will be the stress required for the growth of these twin nuclei.

The critical shear stress law for twinning has been proposed by several workers¹¹⁾¹²⁾¹³⁾¹⁴⁾¹⁵⁾. Hall¹³⁾ suggested that the law might hold for the growth of the twin nuclei. The result of the present experiment that the law approximately holds for the upper yield stress after indentation, may be explained that the growth of the nuclei is controlled by the law.

(c) *Resistance to the growth*

The variation of the upper yield stress may be associated with the resistive stresses against the growth of twins, when the observed yield stress is the stress required for the growth. Garber¹⁰⁾ found that an elastic twin sometimes remained stable. He attributed this to distortion of the lattice by slip. Williams¹⁶⁾ confirmed that a small cleavage crack immobilized a twin which had behaved elastically until it reached there. This idea is supported⁷⁾ by the obsevation that 'stopped' elastic twins are common in calsite crystals at high temperatures and in metals in which slip occurs readily.

J. J. Cox and his co-workers¹⁷⁾ found in iron crystals that the prior slip prevented or inhibited the twinning at low temperatures. One way to explain this is that the growth of the wedge shaped twin is prevented by the imperfections produced by slip.

In the case of twinning in tin crystals under impact load, the restraint by the solder at an end of the crystal or the distortions produced by the indentation may have suppressed the growth. As was described in §3 (II), the slip sometimes occurred extensively, even when the applied load seemed sufficient for the twinning. An explanation would be that the twins would have been nucleated immediately after the slip occurred even if the yield process did not occur, and then the growth was prevented by slip. Further examinations are required to establish the experiment.

§5. Conclusion

The impact test has been carried out on 99.98% pure tin crystals, the time of stressing being 10^{-3} sec. The orientation was so arranged that the [001] and the [103] direction lie in a plane with the specimen axis. The angle λ between the [103] direction and the specimen axis was varied from 0° to 60°, to observe the orientation dependence.

1. Twinning occurred with a sharp yield process when the [001] axis was nearly perpendicular to the specimen axis, i.e., the angle λ being between 45° and 60°. The upper yield stress scattered from sample to sample ranging from 0.7 to 2.5 kg/mm², while the lower yield stress and also the stress for further thickening of the generated twin lamella ranged from 0.1 to 0.2 kg/mm².

2. Slip occurred exclusively, when the angle λ was less than 30°. The critical shear stress for slip was about 0.9 kg/mm² under the impact loading, and so the minimum stress for twinning was not attained in these orientations. With the intermediate orientations, the result scattered among slip, twinning, or twinning after slip.

3. The twin lamellae usually ran through an end of the specimen. It sometimes ran through the grain boundary, if there were any, when the specimen was prestrained with steady loading.

4. If an indentation was made before impact, twinning occurred there accompanied again with the yield process. The upper yield stress after indentation is controlled approximately by the critical shear stress law, the stress being 0.8±0.1 kg/mm².

5. The observations on the location of twins will suggested that they have been nucleated with the aid of the local stresses, as was observed earlier in zinc crystals.

6. Two origins for the upper yield stress appear possible. In the first place, it may be the stress for the nucleation of twin lamella with the aid of the local stresses in the crystal, and in the second place, it may be the stress for the growth of the generated twin lamella across the crystal, when the local stress is large enough. The result that the critical shear stress law holds for the upper yield stress after indentation may be interpreted that it holds for growth of twin nuclei. It is likely that the growth of twin lamellae is often suppressed by slip.

Acknowledgement

The writer wishes to express his thanks to professor K. Tanaka and to Professor Y. Matsunaga for much help and encouragement, to Assistant Professor T. Fukutomi, and S. Maruyama, and to Dr. H. Kihō for many useful discussions, and to many others for their kind assistance.

References

1) B. Chalmers: Proc. Phys. Soc. London **47** (1935) 733.
2) D. S. Clark and D. S. Wood: Proc. Amer. Soc. Test. Mat. **49** (1949) 717. D. S. Wood and D. S. Clark: Trans. Amer. Soc. Met. **43** (1951) 571. D. S. Wood and D. S. Clark: Trans. Amer. Soc. Met. **44** (1952) 726. T. Vreeland Jr., D. S. Wood and D. S. Clark: Trans. Amer. Soc. Met. **45** (1953) 620. J. H. Hendrickson, D. S. Wood and D. S. Clark: Trans. Amer. Soc. Met. **48** (1956) 540.
3) I. R. Kramer and R. Maddin: Trans. Amer. Inst. Min. (Metall.) Engrs. **194** (1952) 197.
4) T. S. Liu, I. R. Kramer and M. A. Steinberg: Acta Met. **4** (1956) 364.
5) C. S. Barrett: *Structure of Metals.* (McGraw-Hill, New York, 1952).
6) R. Clark and G. B. Claig: *Progress in Metal*

Physics **3** (Pergamon Press, London, 1952) 115.
7) R. W. Cahn: Advances in Phys. **3** (1954) 363.
8) E. O. Hall: *Twinning and Diffusionless Transformations in Metals* (Butterworths Sci. Publ., London, 1954).
9) R. L. Bell and R. W. Chan: Acta Met. **1** (1953) 752.
10) R. I. Garber: C. R. Acad. Sci. U.S.S.R. **21** (1938) 229; J. Phys. U.S.S.R. **2** (1940) 313, 319; **3** (1941) 179; Zh. Eksp. Teor. Fiz. **16** (1946) 923; J. Phys. U.S.S.R. **17** (1947) 5; Zh. Exsp. Teor Fiz. **17** (1947) 63; Dokl. Akad. Nauk U.S.S.R. **57** (1947) 555.
11) N. N. Davidenkov, A. F. Kolesnikov and K. N. Federov: J. Exp. Teor. Phys. U.S.S.R. **3** (1933) 350.
12) N. Thompson and D. J. Millard: Phil. Mag. **43** (1952) 421.
13) E. O. Hall: Phil. Mag. **43** (1952) 70, 121.
14) H. Suzuki and C. S. Barrett: Acta Met. **6** (1958) 156.
15) C. J. Maiden and J. D. Campbell: Phil. Mag. **3** (1958) 872.
16) Williams: In Cahn's review, 7), p. 426.
17) J. J. Cox, O. T. Horn, and R. F. Mehl: Trans. Amer. Soc.Met. (1957) 118.

JOURNAL OF THE PHYSICAL SOCIETY OF JAPAN, Vol. 14, No. 10, OCTOBER, 1959

Monitoring X-ray Tube Output with Ionization Chamber

By Kenzo TANAKA, Jun-ichi CHIKAWA and Tadashi YAMANAKA

Department of Physics, Faculty of Science, Kyoto University

(Received May 26, 1959)

The intensity of X-ray beam can be stabilized by using an ionization chamber as a monitor which is placed between an X-ray tube and a specimen. Namely, the filament current of the X-ray tube is controlled so as to keep the output potential of the ionization chamber constant. The ionization chamber was designed in consideration of the response for wavelengths and the statistical fluctuation of the output voltage. Thus, high stability of a demountable X-ray tube as well as of a sealed-off one was obtained without rigorous regulation of tube voltage. If an X-ray tube is operated at 40 kVp and tnbe voltage is stabilized within ±1%, the fluctuation of intensity can be limited to ±0.1%. Then, the fluctuation of intensity in a broad diffraction line of a polycrystalline specimen which was measured for five hours could not be distinguished from the statistical fluctuation. But the fluctuation of intensity in a diffraction line of a single crystal was ±0.2% for the sealed-off tube and ±0.5% for the demountable one.

§ 1. Introduction

Stability is one of the most important factors that must be considered in intensity measurements with X-ray diffractometer. If the accuracy of the measurements is to be raised, high stability of the X-ray tube is required. Many methods of stabilization and monitoring have already been reported. In monitoring of the X-ray tube output, a second counter[1)] or an ionization chamber[2)] was used in order to register a constant fraction of the tube output. The comparison of different ways of the monitoring with a second counter was discussed by Gillam and Cole[3)], but the accuracy and limitation in monitoring with an ionization chamber have not yet been tested quantitatively. From the point of view to secure the most accurate intensity measurements in the least time, we have adopted monitoring with the ionization chamber[4)].

In this method*, the current for heating X-ray tube filament is controlled so as to keep constant the output potential of the ionization chamber which is placed between the X-ray tube and a specimen. Consequently, the intensity of incident beam irradiating the specimen can be kept constant. And the increase of statistical fluctuation caused by monitoring with the ionization chamber is negligible, because the number of quanta detected per second is very large. Hence the measurements can be performed rapidly. This is an advantage of the method. On the other hand, it is thought to be a disadvantage that the ionization chamber detects not only the characteristic radiation, but also a part of the continuous radiation. However, it was found that this disadvantage was not too important in practical aspect, provided that the ionization chamber was designed so as to possess higher response for the wavelength of the characteristic radiation. In the present paper are described how to design an ionization chamber and the accuracy achieved in this way.

---

* Strictly speaking, this method should be called a stabilizer using an ionization chamber as a monitor.

§ 2. Apparatus

An outline and the principle of the apparatus are shown in Fig. 1. The X-ray beam passes through the ionization chamber which is placed between the X-ray tube and the specimen. The output potential of the ionization chamber is amplified by a D.C. amplifier, and then applied to the grids of tubes V_5, which control the impedance of transformer T_4 connected in series with heating transformer T_3. Thus, the power of heating the filament of the X-ray tube is controlled by the output potential of the ionization chamber.

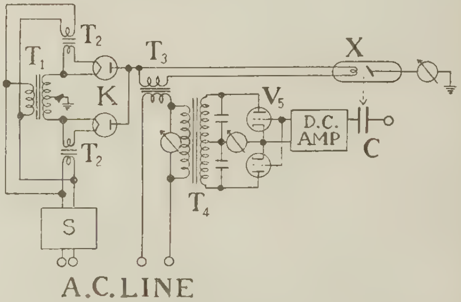

Fig. 1. Principle of the method. T_1: high tension transformer, T_2: filament transformer for kenotron, T_3: filament transformer for X-ray tube, T_4: transformer, K: kenotron, S: ferro resonance type automatic voltage regulator whose stability is ±1%, X: X-ray tube, C: plates of ionization chamber.

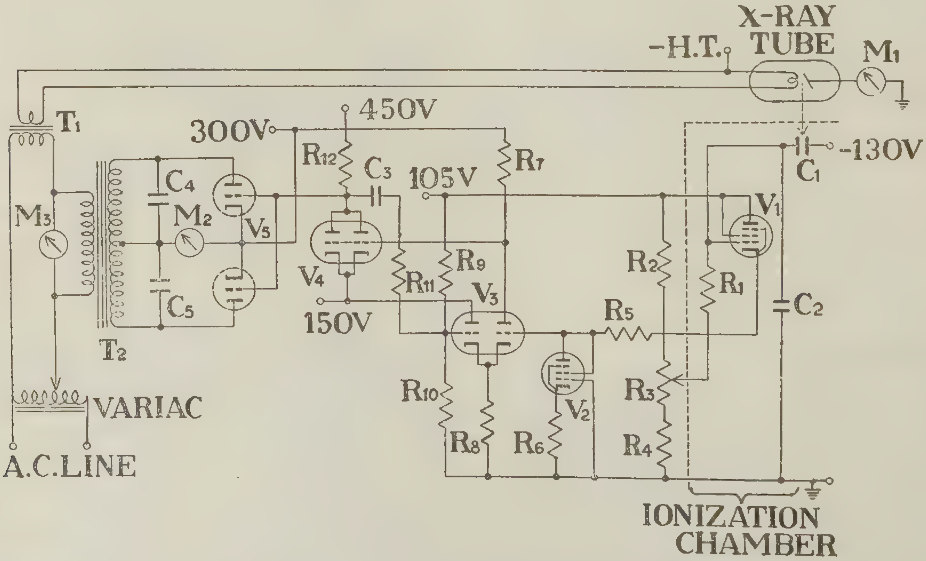

Fig. 2. Circuit diagram of the ionization chamber amplifier. R_1: 1000 M; R_2: 39 K; R_3: 10 K; R_4: 50 K; R_5, R_6: 2 K; R_7: 600 K; R_8: 110 K; R_9, R_{10}: 30 K; R_{12}: 500 K; C_1: plates of the ionization chamber; C_2: 100 $\mu\mu$F; C_4, C_5: 0.25μF; R_{11}, C_3: selected to be suitable for X-ray tube: in our case 2 M and 0.1 μF respectively; V_1, V_2: 6AK5; V_3, V_4: 12AX7; V_5: 6AS7; T_1: filament transformer; T_2: 4:1 transformer; M_1, M_2: mA. meters for X-ray tube current and load tube current; M_3: voltmeter.

The D.C. amplifier is shown in Fig. 2. C_1 is the capacitance between the plates of the ionization chamber. The ionization current produces a potential difference across a resistance R_1. It is amplified by the preamplifier which is composed of tubes V_1 and V_2. These tubes cancel the effect by the variation of their filament voltage so that the change in intensity of X-ray beam is hardly observed, even if the filament voltage varies between 4 and 4.5 volts. The main amplifier is composed of tubes V_3 and V_4 in an ordinary way. In order to prevent the over-all circuit from breaking into the oscillation, the feedback loop between V_3 and V_4 is used. C_3 and R_{11} in the loop are suitably chosen for the X-ray tube used.

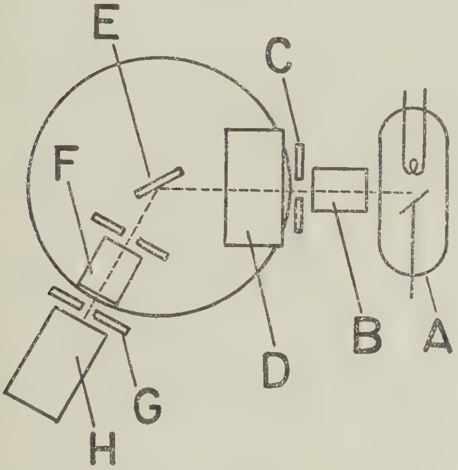

Fig. 3. Position of the ionization chamber. A: X-ray tube; B, F: soller slits; C: divergence slit; D: ionization chamber; E: specimen; G: receiving slit; H: scintillation counter.

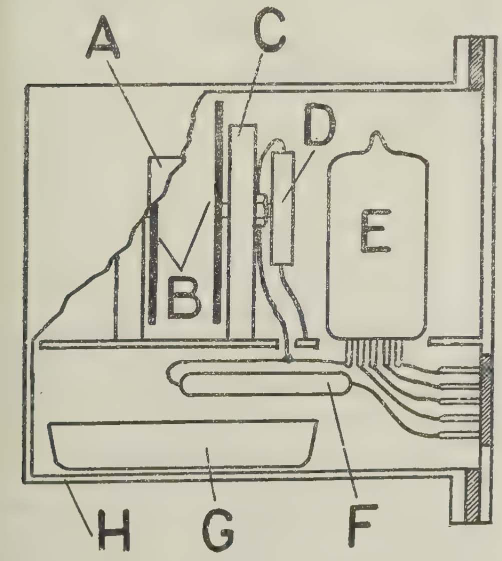

Fig. 4. The ionization chamber. A: Mylar window; B: plates; C: polystyrene rod; D: 100$\mu\mu$F condenser; E: pre-amplifier; F: 1000 M resistor; G: drier; H: air-tight brass box.

The position of the ionization chamber is shown in Fig. 3. The chamber is placed between the divergence slit and the specimen, in order to keep the intensity of incident beam irradiating the specimen constant.

Fig. 4 shows the inside of the ionization chamber. The plates are made of copper and are of 25 mm × 45 mm in dimension. The plates are supported by polystyrene rods parallel to each other with a separation of 14 mm. The size of plates and the distance between the plates were not critical in operation by the use of the amplifier in Fig. 2. Tube V_1, resistor R_1, capacitor C_2 shown in Fig. 2 and plates are mounted in a brass box which is air-tight and serves as an electrical shield. The entrance and exit windows were covered with thin Mylar. The chamber was filled with air of one atmospheric pressure.

§ 3. Fluctuation of Output Voltage of Ionization Chamber

The charges produced by the X-ray quanta in the ionization chamber are collected on its plates whose capacitance is C_1. Then the time constant of this circuit is CR_1, where $C=C_1+C_2$. When CR_1 is too large, the over-all circuit may break into oscillation. In order to prevent this oscillation, the gain of the amplifier for high frequencies must be reduced by choosing suitable C_3 and R_{11} in the feedback-loop between tubes V_3 and V_4 in Fig. 2. Therefore, it is desirable that the value of CR_1 is small. On the other hand, a large value of CR_1 is required to make the statistical fluctuation of the output voltage small. Then, the value of C was so determined that the statistical fluctuation for the minimum intensity of the range used usually was adequately small.

The number of quanta absorbed per second in the ionization chamber can be estimated from the potential developed across the resistance R_1. When the chamber is filled with air, a quantum detected by the chamber will produce a pulse of about 250 unit electronic charges[5)], because a very large portion of the radiation detected with the chamber is CuKα and CuKβ, as will be shown later. If n quanta be absorbed in the chamber per second, the potential of V volts developed across the resistance R_1 is approximately given be

$$V=250neR_1\ .$$

Since the fluctuation of the charge of a pulse produced by a quantum of CuKα radiation is small, the fractional fluctuation of output voltage V is approximately

$$\frac{\delta V}{V}=\frac{1}{(2nCR_1)^{1/2}}=\left(\frac{250e}{2CV}\right)^{1/2}\approx\frac{4.5\times10^{-9}}{(CV)^{1/2}}\ ,$$

where C and V are expressed in fared and volt respectively, and δV is the standard deviation of V, provided that the X-ray source is kept constant. When one wishes to maintain the fluctuation of intensity of the X-ray source below the order of 0.1%, it is desirable that the statistical fluctuation of output voltage of the ionization chamber is of the order of 0.01%, namely:

$$\frac{\delta V}{V}\approx\frac{4.5\times10^{-9}}{(CV)^{1/2}}\sim10^{-4}\ .$$

When the horizontal divergence of the incident beam was limited to 0.5° by the slit and the X-ray tube was operated at 4 mA, 40 kVp full-wave rectification in our apparatus, the output voltage of the ionization chamber was about 1 volt. Therefore, we chose 100 $\mu\mu$F for C_2. When the output voltage of the chamber is larger than 1 volt, we have

$$\frac{\delta V}{V}<4.5\times10^{-4}\ .$$

Thus the above requirement is satisfied. Of course, the increase of the standard deviation by monitoring would be negligible, when the number of photons detected by the counter is taken for a fixed time-interval.

§ 4. Response of Ionization Chamber for Wavelength

We shall here discuss the response of the ionization chamber in case when a Cu-target X-ray tube is used. As the total number of X-ray photons detected with the ionization chamber is kept constant in the present method, the intensity of CuKα varies with the spectrum of the beam from the X-ray tube. Since the spectrum of the beam depends upon the X-ray tube voltage, it is necessary to regulate it. However, the fluctuation of the X-ray tube voltage is allowed to a certain extent, if the ionization chamber has such a response for wavelengths that the intensity of continuous radiation detected by the ionization chamber is small in comparison with

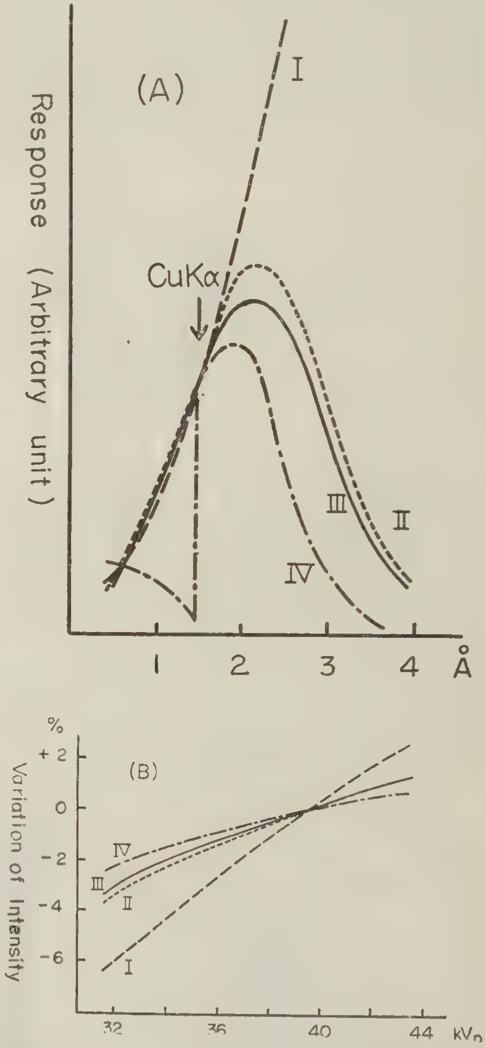

Fig. 5. (A): The response of the ionization chamber calculated from the absorption of air and transmission of the windows of the tube and the chamber, provided that the chamber was filled with air of one atmospheric pressure and that the absorption of Mylar window of the chamber was neglected. The response were normalized for CuKα (1.54 Å).
(B): X-ray tube voltage *versus* intensity of the diffracted beam with X-ray tube stabilized by using the ionization chamber as a monitor. The scintillation counter with a pulse height analyzer was used in intensity measurements. The curves in (A) and (B) were obtained in the cases shown in Table I.

that of characteristic radiation.

In practice, the response of the ionization chamber filled with air for shorter wavelengths than that of CuKα is low, since the length of the plates in the direction of incident beam, which is limited by the space on a goniometer, is about 3 cm. The response for longer wavelengths is reduced by making the window of the X-ray tube thicker or by inserting an Al foil between the chamber and the X-ray tube. Fig. 5 (A) shows the response calculated from the absorption by air and the transmissions of the window of the tube and of the foil inserted, when the length of the plates is 2.5 cm. The curves in this figure were obtained in the cases as shown in Table I. Fig. 5 (B) shows the curves of X-ray tube voltage *versus* intensity of (110) peak of polyethylene specimen in the cases listed in Table I with the X-ray tube stabilized by using the ionization chamber as a monitor. The intensities were measured by a scintillation counter with a pulse height analyzer and a 20μ Ni filter, excepting curve IV for which a 10μ Ni filter was used. The same results were also obtained when the intensities were measured with the balanced filters. It is seen from Fig. 5 that the slope of the curves of X-ray tube voltage *versus* intensity of diffracted beam becomes smaller, as the ratio of the intensity of CuKα to that of the continuous radiation detected by the ionization chamber is increased by inserting a suitable foil or by using an appropriate foil as the window of X-ray tube.

Table I. Description of the curves in Fig. 5.

Curve in Fig. 5	Window of X-ray tube	Inserted foil between tube and chamber
I	Be (0.125 mm)	None
II	Be (0.125 mm) +Mica (0.013 mm)[7]	None
III	Be (0.125 mm)	Al (18μ)
IV	Be (0.125 mm)	Ni (10μ)

In a usual apparatus, the tube current and the tube voltage are regulated, and if high stability of them is obtained by the use of a sealed-off tube, good stability of the X-ray beam will be achieved, as will be seen later. But it is difficult to regulate the tube voltage strictly. In the stabilizer described here, the strict regulation will not necessarily be required. If the X-ray tube is operated at 40 kVp and the tube voltage is stabilized within ±1%, the fluctuation of intensity can be limited to ±0.1%, as can be seen from Fig. 5 (B). The use of line voltage regulator may be sufficient to obtain the stability stated above, though it cannot keep the peak voltage constant.

§ 5. Results

In order to check the ability of the chamber for stabilizing the intensity of diffracted beam, the counter arm of the diffractometer was set at the angle of the (110) peak of a polyethylene specimen and the number of counts detected in a fixed time interval of 16$\frac{2}{3}$ sec was recorded 20 times in every half an hour. The mean, $\bar{n}$, of 20 readings and the variance S^2 about the mean were calculated. These results for the demountable X-ray tube and for the sealed-off X-ray tube are respectively shown on the left-hand sides of Table II. In using the demountable tube with the window of 0.125 mm Be foil, an 18 μAl foil was placed between the X-ray tube and the ionization chamber, as described in § 4. Since the window of the sealed-off X-ray tube was Be 0.12 mm+Mica 0.013 mm, no material was placed between the tube and the chamber. In both cases, the primary voltage of a high tension transformer was stabilized by a ferro resonance type voltage

Table II.

	Experimental data for demountable tube				Experimental data for sealed-off tube			
	With ionization chamber		With current stabilizer		With ionization chamber		With current stabilizer	
	$\bar{n}$	S^2	$\bar{n}$	S^2	$\bar{n}$	S^2	$\bar{n}$	S^2
	20112	23471	20732	15906	20147	16508	21266	23947
	20079	16991	20298	360446	20160	22066	21319	14788
	20135	11484	20350	237645	20089	13079	21389	31719
	20077	21944	20760	174808	20152	27768	21449	9741
	20112	13800	21028	13707	20146	8049	21401	24727
	20073	14661	21130	32952	20189	20233	21363	10351
	20066	11945	21099	15603	20197	17053	21307	23308
	20152	16854	21128	19364	20120	33439	21338	10734
	20127	14421	21283	30655	20134	13080		
	20126	14798	20982	37828	20162	14272		
mean	20106	16037	20930	96610	20166	18555	21353	18664

where $\bar{n}$=mean of 20 readings,
S^2=observed variance about $\bar{n}$.

regulator, whose stability was ±1%, as shown in Fig. 1. Both these X-ray tubes were operated at 40 kVp full-wave rectification. On the right-hand sides of Table II are shown the results obtained by using a tube current stabilizer in place of the stabilizer using the ionization chamber as a monitor.

The stability of the demountable tube is proved by the stabilizer using an ionization chamber as a monitor, so that the fluctuation of intensity cannot be distinguished from statistical fluctuation, because its standard deviation is expected to be $(\bar{n})^{1/2}$, when the increase of variance by monitoring can be neglected. When the demountable tube was used with the current stabilizer, the variance S^2 about the mean was very large, and high stability could not be obtained.

For the sealed-off X-ray tube, the difference between the current stabilizer and the stabilizer using the ionization chamber as a monitor cannot be clearly recognized because of the disturbance caused by the statistical fluctuation. Although the larger fluctuation of $\bar{n}$ in the use of the former stabilizer was found, it might be due to the fact that the tube current was regulated only within ±0.3% by this stabilizer.

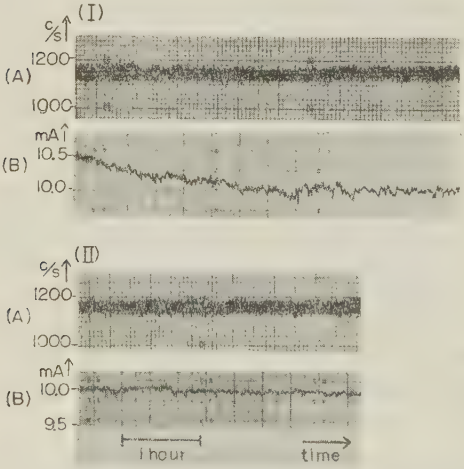

Fig. 6. (I). (A): The intensity of diffracted beam recorded by counting-rate meter; (B): The tube current of demountable X-ray tube recorded continuously at the same time, when the X-ray tube was stabilized by using the ionization chamber as a monitor. Both (A) and (B) were recorded with the time constant of 4 sec.

(II). The results obtained for the sealed-off X-ray tube under the same condition as (I).

When the X-ray tube output was stabilized by monitoring the ionization chamber, the diffracted X-ray intensity was also recorded by the counting-rate meter and the fluctuation of X-ray tube current was recorded at the same time. The results for the demountable tube are shown in Fig. 6 (I) and for the sealed-off tube in Fig. 6 (II). The tube current in the demountable tube was reduced from 10.5 mA to 9.8 mA during the first two hours, and then became roughly stationary for the rest, but its fluctuation was still larger than that of the sealed-off tube. This seems to come from the vacuum condition of the tube. On the other hand, the tube current in the sealed-off tube was nearly constant. This fact means that considerably good stability can be obtained by a current stabilizer for a sealed-off X-ray tube.

As described in § 2, the increase of variances due to using the ionization chamber as a monitor could not be found in these experimental results, as shown in Table II, because the variances S^2 are nearly equal to the theoretical values, namely to $\bar{n}$ for unmonitoring system. (The variances calculated from 20 readings were a little smaller than those expected theoretically. This tendency was also seen in the measurement of a single crystal used as a specimen and cannot be understood theoretically.) These results were obtained under the condition that the output voltage of the ionization chamber was about 1.5 volts. It is an advantage of this method that measurements can be carried out for a shorter time, since the increase of variances by monitoring is negligible.

When an NaCl single crystal was used instead of polyethylene as a specimen, the slow variation in the intensity of the (200) reflection was observed. (In this case, a receiving slit of 1′ was used, and the intensity was attenuated by an Al foil placed in front of the detector, so that the output voltage of the ionization chamber was 1.5 volts.) The result is shown in Table III. It took ten minutes to obtain 20 readings. The variances S^2 calculated from the 20 readings were the same as those in the case of polyethylene specimen, so that these variances S^2 are not given in Table III. This fact shows that the fluctuation in a short time does not occur. However, the variances were calcu-

Table III.

For demountable tube $\bar{n}$	For sealed-off tube $\bar{n}$
20277	19821
20342	19872
20261	19818
20147	19888
20161	19940
20132	19924
20162	19908
20308	19888
20125	19944
20062	19865
mean 20198	mean 19885

where $\bar{n}$ is the mean of the 20 readings.

lated from ten values of $\bar{n}$ which were obtained in every 30 minutes. They were 7672 for the demountable tube and 1771 for the sealed-off tube respectively. The variance in the same condition as before is theoretically expected to be $\bar{n}/20$. The fluctuation except for the statistical seems to be equal to the root of difference between the observed and the theoretical values, so that, the fractional fluctuation would be 0.41% for the demountable tube and 0.14% for the sealed-off tube, respectively. These fluctuations seem to be caused by some disturbance such as the wandering of focal spot on the target.

Acknowledgements

We wish to express our sincere thanks to Mr. Y. Hujihara, Mr. K. Katayama and Mr. H. Suita for their interests and discussions. We further appreciate the valuable and kind assistance of Mr. M. Shiojiri in carrying out the present experiment.

References

1) U. W. Arndt, W. A. Coates and D. P. Riley: Proc. Phys. Soc. London **B**, **66** (1953) 1009.
2) C. M. Hargreaves, E. Prince and W. A. Wooster, J. Sci. Instr. **29** (1952) 82.
3) E. Gillam and D. G. Cole: J. Sci. Instr. **30** (1953) 429.
4) C. K. Jones: Rev. Sci. Instr. **24** (1953) 380.
5) L. H. Gray: Proc. Cambr. Phil. Soc. **40** (1944) 72.
6) L. I. Schiff and R. D. Evans: Rev. Sci. Instr. **7** (1936) 456.
7) J. Taylor and W. Parrish: Rev. Sci. Instr. **26** (1955) 367.

JOURNAL OF THE PHYSICAL SOCIETY OF JAPAN Vol. 14, No. 10, OCTOBER, 1959

A New Fine Focus X-ray Tube

By Yoshihiro KAMIYA

Physical Institute, Nagoya University, Nagoya, Japan

(Received June 4, 1959)

A fine focus X-ray tube of the new type was constructed. The electron gun has double wehnelt cylinders. The size of the X-ray source was measured by means of an X-ray pinhole camera. The size of the source becomes very small for the positive value of the bias voltage on the inner cylinder with which the image of the filament is formed on the anode. The finest X-ray source obtained is 40μ in half width and 400μ in length. The peak specific loading is about 8×10^5W/cm^2 at the filament temperature 1,700°K which assures long life of the filament.

§ 1. Introduction

The recent development of crystal physics demands intense X-ray sources. For this purpose the rotating anode tubes were introduced making the specific loading 5–10 times that of the stationary anode$^{1-2)}$. The high specific loading is also accomplished by reducing the size of the X-ray source to about $50\,\mu$. Such a small source can be obtained by the magnetic focus or by the electronstatic focus. Many investigators used the former$^{3)}$. However, the latter is more convenient for its simple construction and easy operation.

Ehrenberg and Spear⁴⁾ studied the electrostatic system and obtained the fine circular focus about 35 $\mu\phi$ in half width with the total current 0.5 mA and the specific loading 1.1×10^6 W/cm². They used the electron gun of telefocal type provided with a guard cylinder which is at the potential of the filament. Gay et al.²⁾ used the rotating anode and obtained the rectangular focus, the width of which can be varied from 2 mm to 50 μ. Tomita⁵⁾ studied fine rectangular focus and attained the half width 40 μ. Hosemann⁶⁾ developed the positive bias method, while all of the above authors applied negative bias to Wehnelt cylinder. He obtained relatively large focus about 130 μ in half width having clean cut edge.

Fine focus X-ray tubes with high loading are also required in the field of medical radiography, particularly in enlargement radiography as developed by Takahashi et al.⁷⁾ and others⁸⁾. The fine focus is required for high resolution of radiograph and the high specific loading for short exposure time, which indespensable for living objects because of the inevitable movements.

In order to construct X-ray tubes adequate for medical radiography and also for crystal physics, we investigated the electron gun with double Wehnelt cylinders. We studied in detail the focusing characteristics of the gun and obtained rectangular focus of half width 40 μ and length 400 μ. The specific loading was about 5.0×10^5 W/cm² at relatively-low temperature of the filament.

§ 2. Experiment

A demountable X-ray tube with rotating copper anode was used in the present experiment. Although the effect of rotation is small for fine focus, we adopted the rotating anode for safety at large focus. The electron gun consists of a spiral filament, an inner Wehnelt cylinder and an outer Wehnelt cylinder (Fig. 1). The former cylinder has a rectangular aperture 8 mm×3 mm and the latter has a circular hole 10 mmϕ. The spiral filament is thoriated tungsten wire of 0.1 mmϕ. The outer diameter of the spiral is 1 mm and the length 3 mm. The filament was set parallel to the aperture of the inner cylinder. To avoid the misalignment caused by thermal deformation, the filament was heated in air before setting it in the cylinder. Parameter h, which indicates the position of the filament (Fig. 1), was measured by means of a micrometer screw of pitch 0.67 mm. Distance l and L (Fig. 1), the length of the gun and the gun-anode distance, can be varied without breaking the vacuum and are measured by the indicator outside the vacuum. The axis of the gun was set vertically and the whole gun assembly can be rotated about the axis.

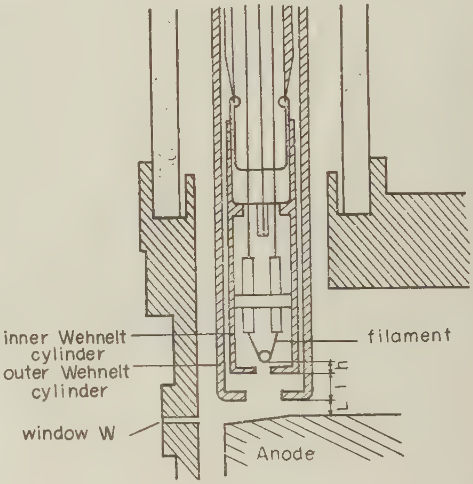

Fig. 1. Schematic drawing of the electron gun.

Bias voltages V_i and V_0 are applied to the inner and the outer Wehnelt cylinder, respectively. They were varied between ±800 V and were supplied from dry cells. Full wave rectified high tension of 30 kV was used without a filtering condensor. Most experiments were carried out at the heating current of the filament 4 A which corresponds to the filament temperature about 1,700°K, as measured by an optical pyrometer. The central ray of the X-ray beam leaves the target at an angle 6° (0.1 rad) and emerges horizontally from window W of the tube. Thus the apparent length of the X-ray source is demagnified by one tenth.

Pinhole cameras were used to study the shape of X-ray source. The magnifications of cameras were 5 and 10, and the diameter of the pinhole was 8 $\mu\phi$. A pinhole of 15 $\mu\phi$ was first bored on a lead plate by a steel pin which was pointed carefully by an oil stone and examined by a microscope. Then,

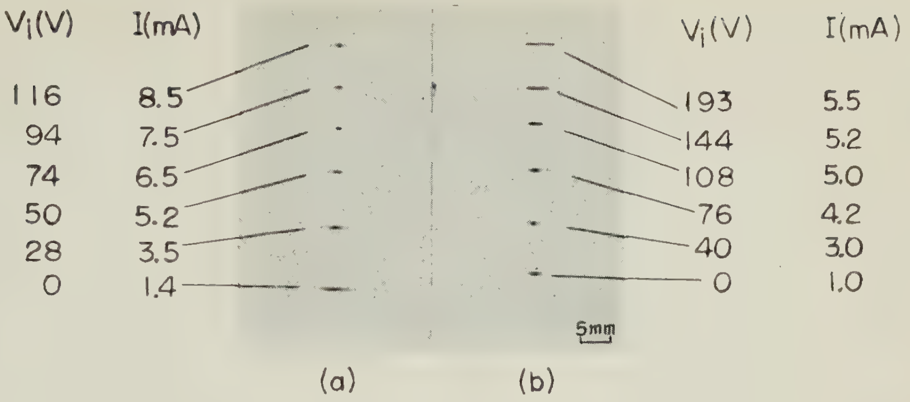

Fig. 2. Sets of pinhole images. Mag. ×10

Geometrical parameters
a) $h=0.54$ mm, $1=11.0$ mm, $L_w=10.0$ mm, $V_0=-130$ V
b) $h=0.54$ mm, $1=11.0$ mm, $L_w=4.0$ mm, $V_0=-680$ V

the plate was hammered on a glass plate until the hole became $8\,\mu\phi$ which was adequate for our purpose.

Many sets of pinhole images were photographed to study the effect of various parameters on the shape of the X-ray source. In every set, V_i was varied keeping all other parameters constant. The image recording was made on Fuji X-ray film with the exposure about 150 mA. Sec. Two examples of the set are reproduced in Fig. 2. In this figure the horizontal and the vertical direction correspond respectively to the width and the length of the rectangular X-ray source, the length being demagnified one tenth due to the geometrical condition mentioned before.

For the detailed study of the intensity distribution along the width of the source, we adopted a steel slit instead of the pinhole, the gap of the slit being about $10\,\mu$. We used Fuji Process Plate in this case because it has low fog-density and small grain size. By microphotometory we obtained the intensity distribution and then determined width w (1/2) at $I/I_0=0.5$ and that w(1/10) at $I/I_0=0.1$, where I_0 is the intensity at the center. In the microphotometory we used short exposure so that the intensity is proportional to the darkness.

In the enlargement radiography, we used the resolution of test-charts as a conventional specification of X-ray source. A test-chart consists of three tungsten fibers of equal diameter, set parallel to each other with gaps nearly equal to the diameter. The diameter used was 13, 17, 20, 25 etc. μ. We took projection micrographs of test-charts at direct magnification about 4, setting the fiber horizontally and vertically. The resolution was indicated by the minimum resolvable

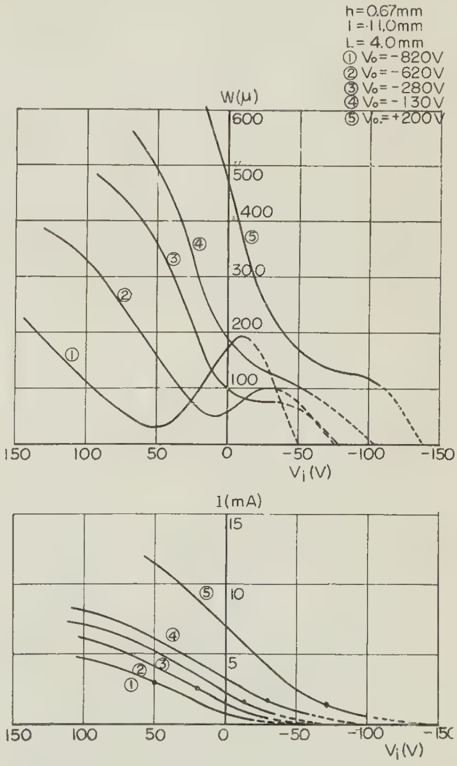

Fig. 3. Width w and current I as the function of V_i.

diameter of the fiber.

§ 3. Results

Effect of bias voltages. Pinhole image in Fig. 2 means that the width of the source varies with V_i, while the length remains almost constant. This variation is caused by change of strength of the cylindrical lens which is formed by the rectangular aperture of the inner Wehnelt cylinder. We estimated the width w from the size of the image. Fig. 3a gives a typical example of the variation of w with V_i, taking V_0 as a parameter. Width w decreases with decreasing V_i and reaches a minimum (Curves 1 and 2 in Fig. 3a, see also Figs. 4 and 5). The minimum is interpreted as the image of the filament (Sec. 4). Width w and voltage V_i at the minimum are denoted by w_m and V_{im}, respectively. The increase of the width with the further decrease of the bias voltage is due to defocusing of the image. Near the *cut-off* the width decreases again due to the action of emission area limiting (Sec. 4). A plateau appears instead of the minimum, when the image is formed near the *cut-off* (Curves 3,4 and 5 in Fig. 3a).

As voltage V_0 is lowered, voltage V_{im} becomes higher and width w_m becomes smaller. This tendency was observed independent of the geometrical parameters (Figs. 4 and 5) and is interpreted in Sec. 4. Variation of beam current I with voltage V_i is given in Fig. 3b. On each curve in Fig. 3b, voltage V_{im} is marked by a circle. The current at V_{im}, which is denoted by I_m, is almost independent of V_0. This tendency was also observed for other geometrical parameters.

Effect of geometrical parameters. For usual triode X-ray tubes, the adjustment of *h*, the parameter indicating the position of the filament, is critical in obtaining fine focus. If parameter *h* is not adequate, a required fine focus cannot be obtained at any value of bias voltages. In our tube, however, it is not critical because at a fixed valued of *h* we can make width w_m small enough by applying adequate V_0 (Fig. 4). The effect of bias voltage V_i becomes more remarkable

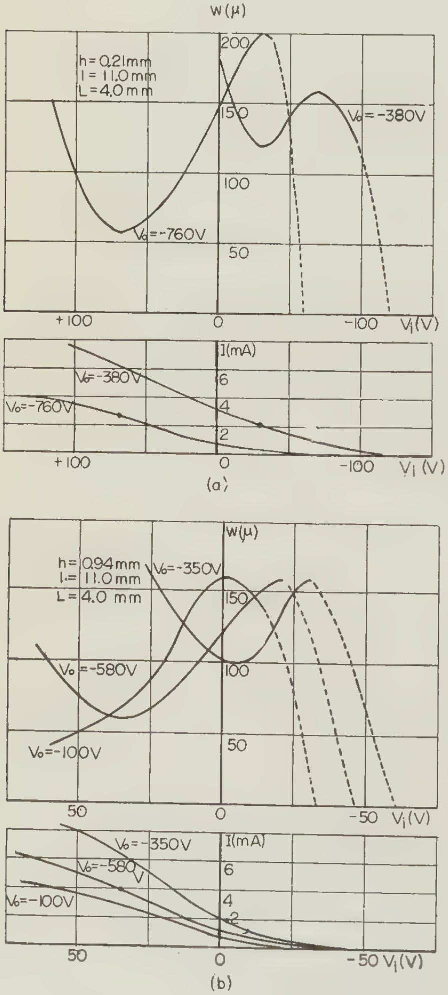

Fig. 4. Effect of *h* on gun characteristics.

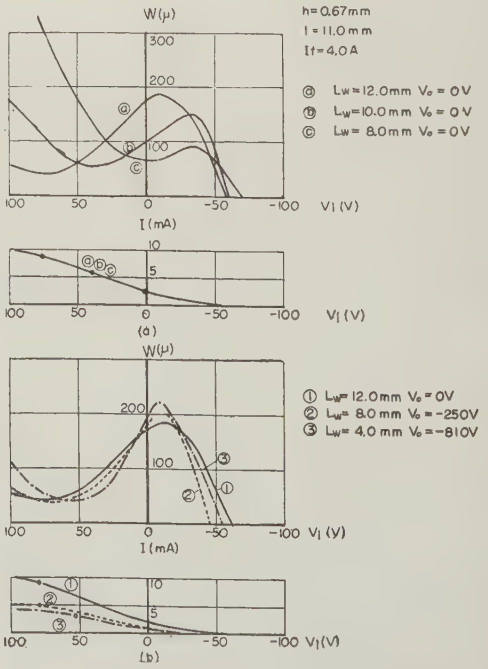

Fig. 5. Effect of *L* on gun characteristics.

for larger h. Therefore, the scale of the abscissa in Fig. 4a is taken twice that of Fig. 4b.

The diagram showing the relation between w and V_i depends on the value of L (Fig. 5a). We found that the dependency can be almost completely canceled by the proper change of V_0 (Fig. 5b). However, this cancellation is only on the w-V_i diagram and the total beam current available at the minimum spot I_m varies with L (Fig. 5b). Thus by increasing L, it is possible to increase the total beam current without accompanying any remarkable change in w-V_i diagram. This relation is important in the practical design of the tubes.

The length of rectangular focus varies with l, the parameter indicating the length of for the gun, while it remains almost constant the variation of the other parameters. Utilising this effect, we obtained proper ratio 10:1 of the length to the width of the rectangular focus.

Finest focus obtained in the present experiment. Rectangular focus of order 400 μ×40 μ was obtained at various combinations of the parameters (Figs. 3, 4 and 5). Typical examples are $L=10$ mm, $l=13$ mm, $h=0.34$ mm, $V_0=-68$ V, $V_i=120$ V and $L=12$ mm, $l=11$ mm, $h=0.54$ mm, $V_0=0$ V, $V_i=80$ V. At these combinations, total current of about 10 mA is available at the filament temperature 1,700°K. So far as we tried, the width less than 40 μ was not obtained.

According to Oosterkamp's formula,⁹⁾ the surface temperature of the stationary anode turns out to be 800°C for specific loading 7×10^5W/cm². In the present experiment, the specific loading less than 3×10^5W/cm² caused no damage on the anode, while that more than 6×10^5W/cm² produced faint trace on the rotating anode surface after several hours. Total current of 10 mA corresponds approximately to specific loading 8×10^5W/cm² which causes damage on the anode.

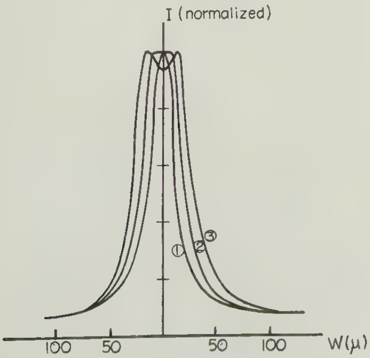

Fig. 6. Intensity distributions on an anode.

Intensity distribution along the width and resolution of the test-chart. The analysis of slit photographs reveals the exact intensity distribution along the width (Fig. 6). For the finest focus, the half width is 35 μ and width at one tenth intensity is 140 μ. The width of the finest focus measured by the pinhole image is 40 μ. Thus the half width is nearly equal to the width obtained from pinhole image.

Test-chart of 13 μ was resolved by the finest focus in the present experiment (Fig. 7). The chart of 13 μ would not be resolved if the source were homogenous and 30 μ wide¹⁰⁾ or it had Gaussian distribution of the intensity with the half width 30 μ. The resolution of 13 μ in the present experiment may imply that the intensity distribution in our source has a very sharp peak.

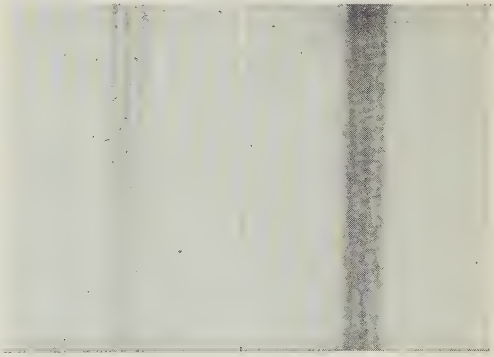
(a) (b)

Fig. 7. Projection X-ray micrographs of test-chart 13μ.

(a) and (b) represent respectively the resolutions corresponding to the width and the length of X-ray source.

Grid current. Since a positive voltage is usually applied to the inner Wehnelt cylinder in the present tube, a part of the electrons from the filament flows to the inner cylinder, causing a considerable grid current. The grid current varies with the cylinder voltage as shown in Fig. 8. For the normal operation the grid current is about 20 mA and its power is about 2 W. This caused no trouble in the present experiment.

§ 4. Mechanism of focusing

So far the fine focus was usually obtained by negative biased triode systems. The triode system is equivalent to an immersion lens[11]. For the fine focus X-ray tubes, it is advantageous to make the demagnified image of the filament on the anode.[4] Besides the focusing action, this type of the immersion lens has the action of limiting the emission area of a filament and, at the extreme case, the electron beam is "*cut-off*". Thus the proper combination of focusing action and the action of the emission area limiting may produce a very fine spot on the anode. When, however, this type of the gun is used near the *cut-off* to make the emission area very small, the focusing action of the lens is too strong to form the image on the anode. Therefore, the spot on the anode cannot be very small. Moreover, the space charge formation which limits the emission area reduces the current density at the surface of the filament. Thus a high filament temperature is required to obtain a sufficient beam current. This makes the life of the filament short.

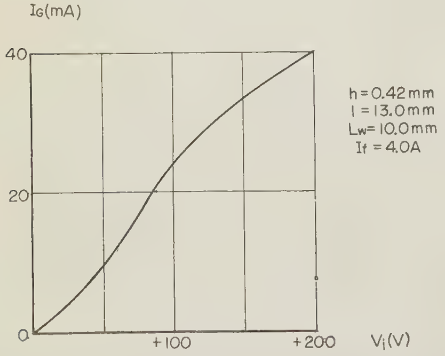

Fig. 8. Grid current I_g an the function of V_i.

When a positive potential is applied to Wehnelt cylinder, a part of the electrons flows to the cylinder (Fig. 9). As a result the area of the filament which can emit electrons outsides the cylinder is limited. The control of the emission area by the bias voltage is not so easy as that for the negative bias. The field before the filament is stronger than that of the negative bias. Thus a large current density is available on the filament surface at low temperature. The positive bias is adequate also to produce a fine focus because it gives high demagnification factor.

The magnification factor M for a unipotential lens is given by $M=f/a-f$, where f is the focal length and a the distance between lens and object. In order to decrease the magnification factor, large a and small f are desireable. The same argument is valid for the immersion systems. In the system of Ehrenberg and Spear, the magnification factor is 1/3. For the negative bias system a short focal length is obtained by heavy bias. When, however, the heavy bias is applied, the principal plane of the lens comes near the filament making a small. The short focal length does not always improve the magnification factor. It is difficult to obtain a magnification factor better than that of Ehrenberg and Spear. For the positive bias,

Table I.

w(1/2)	w(1/10)	w(1/100)	I (mA)	W (Watt)	W/cm²	T$_f$(°K)	
0.13 mm	0.3 mm	0.60 mm	13	650	6.9×10^4	?	Hosemann
0.15	0.33	0.61	13	650	6.6×10^4	?	
0.05	?	?	?	?	?	?	Gay et al.
0.05	0.08	?	0.5	25	?	?	Ehreberg et al.
0.03	0.12	?	0.5	25	1.1×10^6	?	
0.035	0.14	?	2	60	1.6×10^5	1,300°K	Present tube
0.063	0.22	?	2.5	75	1.8		
0.080	0.27	?	3.0	90	1.4		

w(1/2) : width at $I/I_0=1/2$
w(1/10) : width at $I/I_0=1/10$
w(1/100): width at $I/I_0=1/100$
I : total beam current
W : total power
W/cm²: specific loading
T$_f$: temp. of filament

on the other hand, the principal plane lies far from the filament making a large. By combining the focusing action of the outer cylinder and the action of positive bias of the inner cylinder, it is possible to obtain a higher demagnification factor than that of the usual negative biased gun.

§ 5. Discussions

Comparison with other fine focus tubes. Fine focus tubes given in references are listed in Table I. The tube of Ehrenberg and Spear gives small half width and low background. However, it is used only at fine focus. In the tube of Gay et al. the width of the rectangular focus can be varied. Since, however, they obtained the fine focus near the *cut-off*, the total current may be small even at high temperatures of the filament. On the other hand, we obtained the fine focus at the image of the filament. Thus the available total current is much larger than that near the *cut-off*. This means long life of the filament which is particularly important for sealed-off tubes for medical radiography. To make the focus very small, we applied the positive bias to the inner cylinder. In this respect our tube is similar to that of Hosemann.

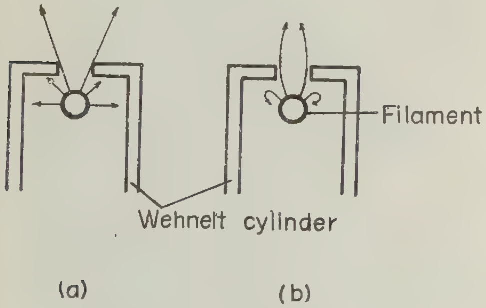

Fig. 9. Illustration of effect of emission area limiting.
a) positive bias
b) negative bias

One of the advantage of the negative bias is the stable performance with the auto-bias method. An auto-bias method is also possible for the positive bias. Our cathode system is a little complicated because it has two Wehnelt cylinders. However, it does not necessarily required two bias voltages. By adopting a proper geometry, we can short-circuit one of the cylinders to the filament or two cylinders to each other.

Further possibility of the fine focus tubes. For the fine focus tube with high loading, the combined action of focusing and emission area limiting is used. It is noteworthy that Ando et al.[12] reported the oxide-cored cathode which emits the electrons from area of the order 30 $\mu\phi$. If such a cathode is used for obtaining a fine focus, the action of the emission area limiting is not required. They showed that the immersion lens can produce sharp image of the cathode. This indicates that the aberrations of the immersion lens is not very large. Thus it may be possible to obtain the focus much finer than 40 μ by the electro-static systems.

Acknowledgement

The author expresses his deep appreciation to Prof. Ryozi Uyeda for his suggestion and valuable discussions and thanks to Prof. S. Takahashi for his encouragement throughout the work. Thanks are due to Prof. Y. Kainuma for furnishing the X-ray tube and to Messrs. T. Hichiri, T. Tsuji and Y. Goto for help in the experiment.

References

1) A. Taylor: J. Sci. Instrum. **26** (1949) 225.
2) P. Gay, P. B. Hirsch, J. S. Thorp and J. N. Kellar: Proc. Phys. Soc. London **B, 64** (1951) 374.
3) S. Goldsztaub: Acta Cryst. **9** (1956) 118.
4) W. Ehrenberg and W. E. Spear: Proc. Phys. Soc. London **B 64** (1951) 67.
5) T. Tomita: Sci. Rep. Saitama Univ. **2a** (1955) 49.
6) R. Hosemann: Zeit. angew. Phys. **7** (1955) 532.
7) S. Takahashi and K. Komiyama: Nippon Acta Radio. **14** (1954) 220 (in Japanese). S. Takahashi and M. Yoshida: Acta Radiol. **48** (1957) 280.
8) K. Aderhold and L. Seifert: Fortschr. Röntgenstr. **81** (1954) 181.
9) W. J. Oosterkamp: Philips Res. Rep. **3** (1948) 303.
10) V. E. Cosslett and W. C. Nixon: J. Appl. Phys. **24** (1953) 616.
11) O. Klemperer: *Electron Optics*, Cambridge University Press (1953) chap. 9.
12) K. Ando, O. Kamigaito. Y. Kamiya, T. Takahashi and R. Uyeda: J. Phys. Soc. Japan **14** (1959) 180.

JOURNAL OF THE PHYSICAL SOCIETY OF JAPAN, Vol. 14, No. 10, OCTOBER, 1959

Electron Microscopic Observation of the Superlattice in Serpentine*

By Yoshihiro KAMIYA, Minoru NONOYAMA and Ryozi UYEDA

Physical Institute, Nagoya University, Nagoya, Japan

(Received June 3, 1959)

The superlattice of spacing about 90 Å in Yu Yen Stone, a variety of serpentine, was studied by electron microscopy (Brindley et al: Acta Cryst. **11** (1958) 99). About 500 electron micrographs showing fringes corresponding to the superlattice were taken, many of which were through-focus series. The intensity profile of fringes varies with the amount of defocus and it also varies from specimen to specimen even at the exact focus. These phenomena are explained qualitatively by theories of image formation. "Extra" terminating half-lines and stepped structures of fringes were studied and it was concluded that the former represent real dislocations in the crystal but the latter are ghosts. The spacing of the superlattice was found not to be constant and this material is not therefore adequate for magnification calibration of electron microscopes (Uyeda et al: J. Phys. Soc. Japan **13** (1958) 461).

§ 1. Introduction

After Menter's[1)] epoch-making experiment with phthalocyanines, several kinds of crystal lattices were observed directly by electron microscopy[2)–6)]. Among them, Brindley et al.[6)] found the fringe system corresponding to the supperlattice in a variety of serpentine mineral, called Yu Yen Stone. Since the spacing of the superlattice is appropriate, *ca.* 90Å, one of the present authors[7)] used it for the magnification calibration of electron microscopes. In the course of the work, various interesting phenomena were observed concerning the intensity profile of the fringe system and imperfections of the superlattice. The present work was carried out to study these phenomena in more detail.

We took about 500 electron micrographs of the superlattice, many of which were through-focus series. We found that the intensity profile of a fringe system changes with the amount of defocus. A more important result is that the intensity profile is not the same for all specimens, even when the micrographs are taken at the exact focus. We interpret these results by theories of image formation. Dislocations and stepped structures of fringes were also studied by through-focus series. We conclude that the former represent real dislocations but the latter, ghosts. The magnification calibration of electron microscopes by the superlattice in Yu Yen Stone is not reliable because the superlattice spacing is not constant.

§ 2. Experimental

Two kinds of samples were used in the present experiment. The first is a variety of antigorite called 'Yu Yen Stone' from Manchuria (U.S. National Museum, No. 94356) and the second, picrolite from Quebec.** Both belong to the serpentine class of minerals. According to Zussman and Brindley[8)], the former has a superlattice of spacing about 90Å and the latter about 40Å. Most of the experiment was carried out with Yu Yen Stone and picrolite was studied only to confirm that it produces fringe systems with spacing about 40Å.

To prepare specimens for electron microscopy, tiny pieces of sample were first ground in an agate mortar, then water was poured into the mortar. Thus finely ground crystallites floated on the surface of the water. A specimen grid with thin carbon film was put on the surface, then removed and dried. In this way the crystallites were attached to the carbon film.

The specimens thus prepared were examined in the electron microscope (JEM5-G, Japan

---

* A preliminary report of this paper was read before the Fourth International Conference on Electron Microscopy, Berlin, September, 1958.

** Specimen furnished by Prof. G. W. Brindley.

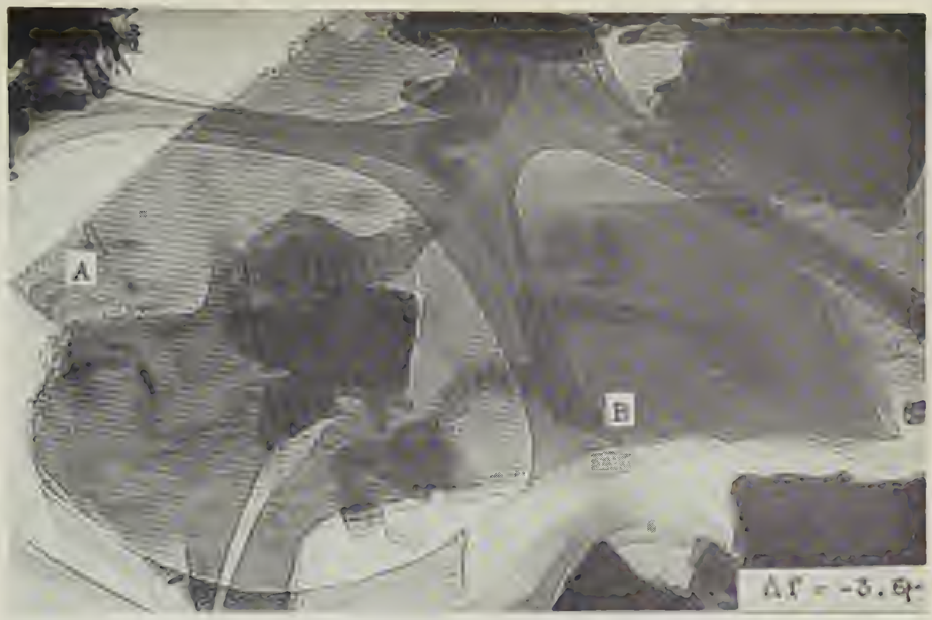

Fig. 1. Regular fringes. ×80,000
In Part B moiré patterns of superlattice is appearing.

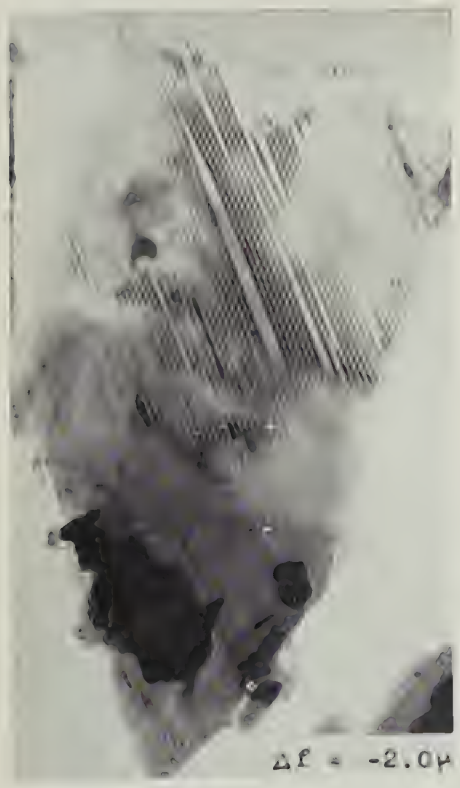

Fig. 2. Irregular spacing. ×80,000

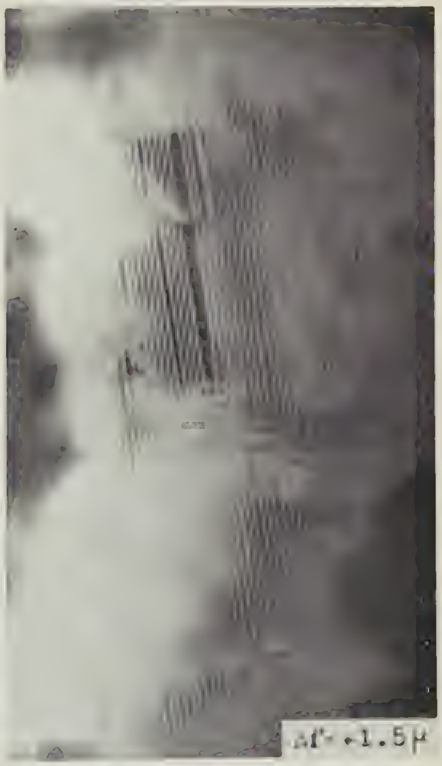

Fig. 3. Irregular spacing. ×80,000

Electron Optics Lab. Co.) operated at accelerating voltages 80 or 100 kv and at a magnification of about ×30,000. Most of the crystallites appeared dark on the screen and did not show fringes. Only those which appeared relatively bright showed fringes. Micrographs were usually taken at ×30,000 with an exposure time of about 10 seconds.

The amount of defocus was estimated from the breadth of Fresnel fringes along the boundary of crystals or supporting film. Crystals were not always flat and they did not always lie in the same plane as that of the supporting film. Moreover, slight astigmatism was sometimes recognized on micrographs. Therefore the estimated values of

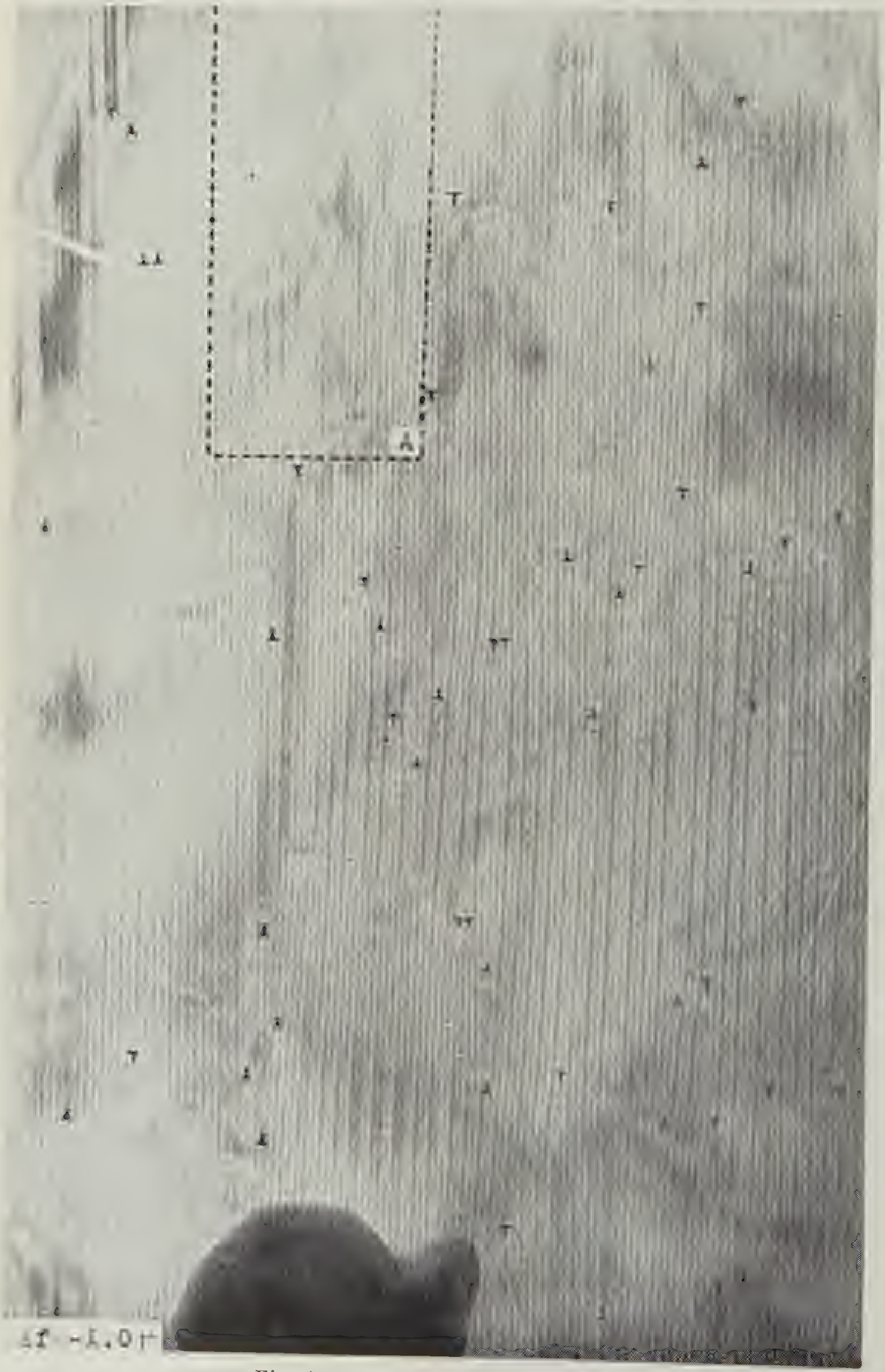

Fig. 4. Dislocations. ×220,000
In Part A fringes are distorted and diffuse.

defocus are not accurate.

§ 3. Explanation of Electron Micrographs

(a) *Regular fringes.* Fringe systems corresponding to the superlattice were observed on most of the micrographs. However, systems containing more than 20 regular fringes were rare. Fig. 1 was taken at considerable

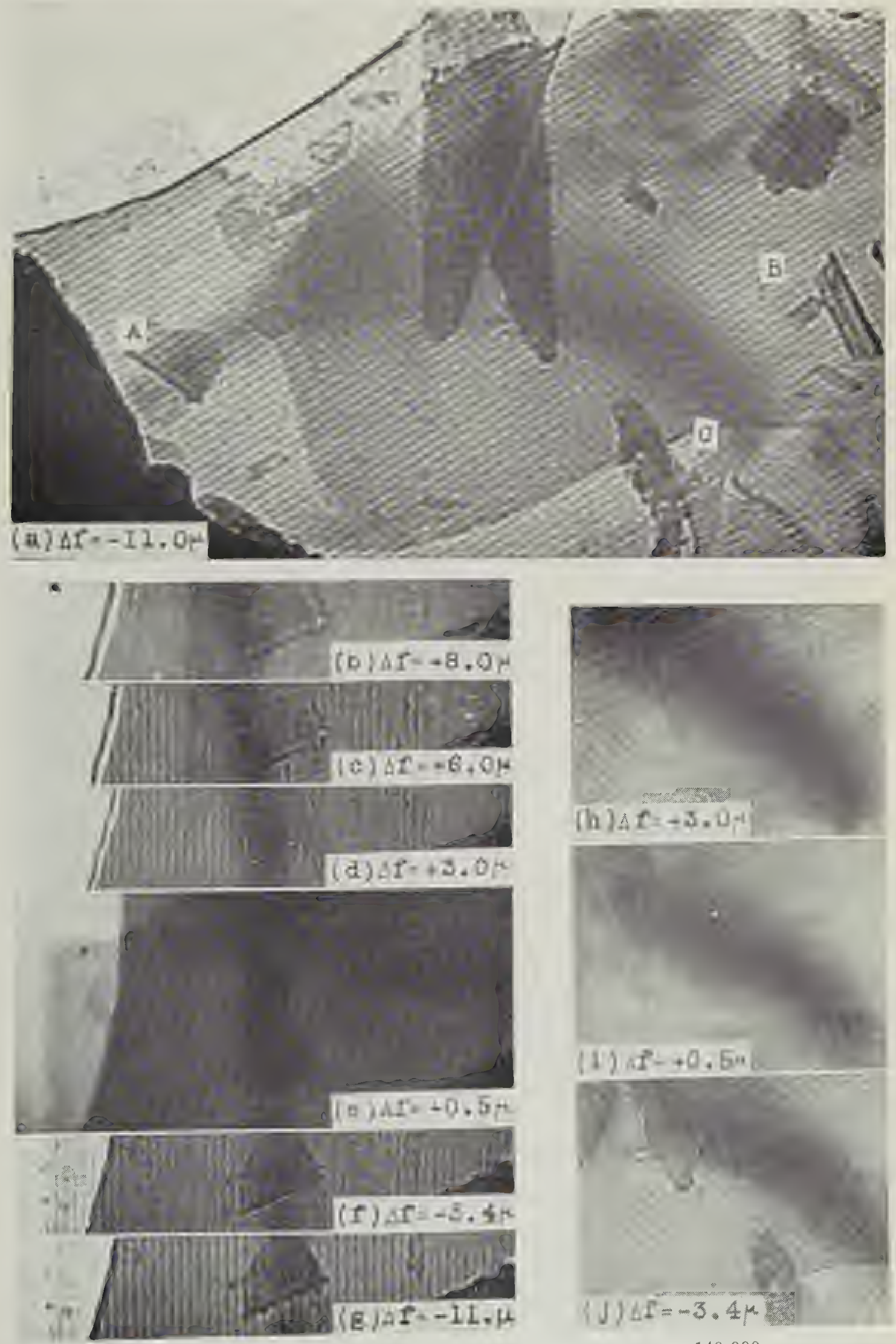

Fig. 5. Through-focus series of regular fringes. ×140,000
(b)–(g): through-focus series of Part A of (a)
(h)–(j): through-focus series of Part C of (a)

defocus. In Part A of the figure, the black and white parts of the fringes appear to have the same width. In the present paper such fringes are referred to as normal. Fig. 5 and 6 give examples of through-focus series of regular fringes.

In Fig. 5 the fringes look almost normal except near the exact focus. However, detailed observation reveals that the intensity profile of the fringe system is not always the same: At Part A of Fig. 5a the fringes are normal (N), at Part B the white lines are sharp (SW), at Part C the white lines are sharp and the black lines split into two (SWp), in Figs. 5d and f the black lines are sharp (SB) and in Figs. 5h and j the black lines are sharp and a weak line appears between two successive lines (SBi). It is most

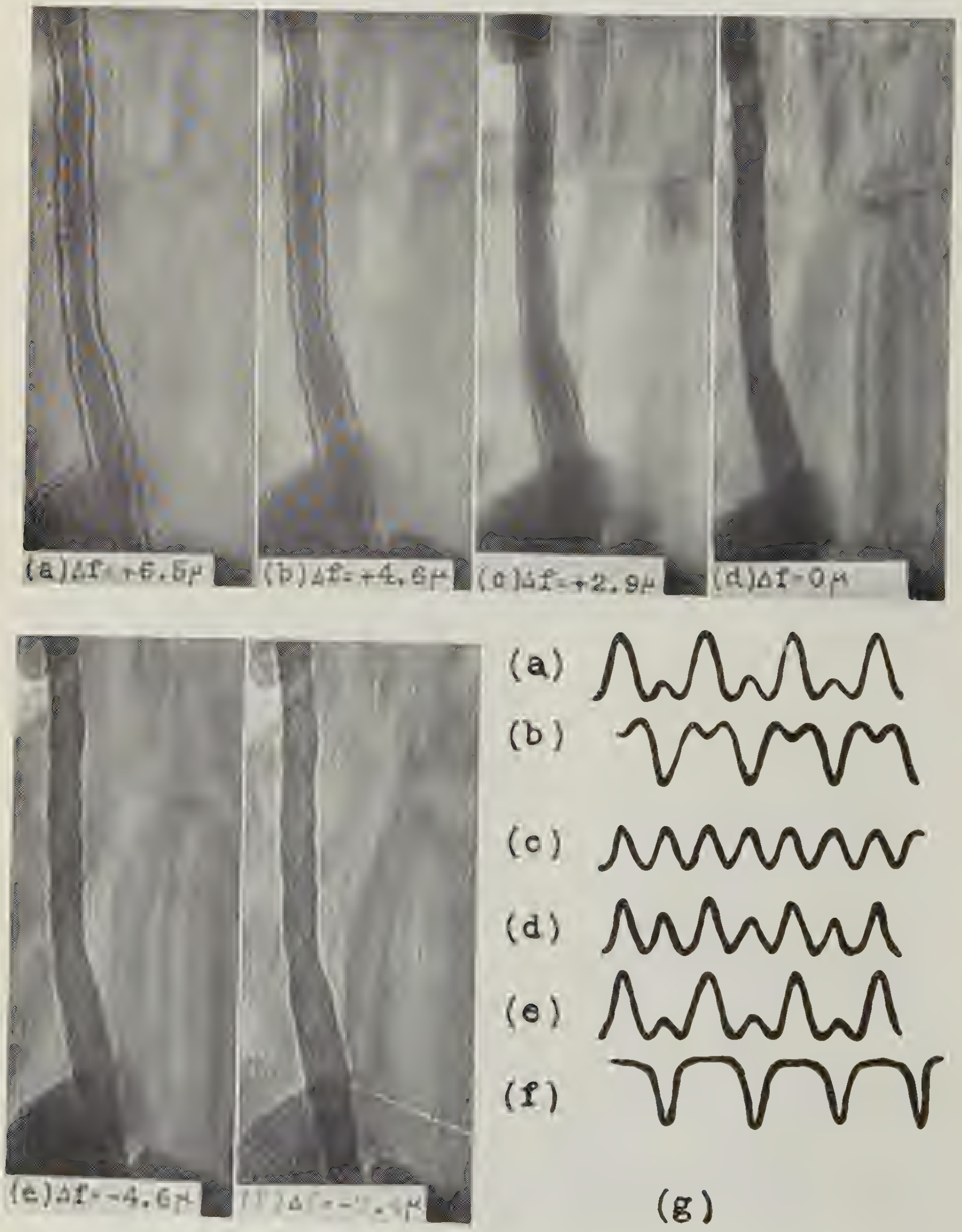

Fig. 6. Through-focus series of regular fringes. ×140,000
(a)-(f): through-focus series.
(g) : schematic illustration of intensity profile.

striking that in Fig. 5e which was taken near the exact focus, the spacing of fringes is one-half that of the normal fringes (H).

In Fig. 6 no normal fringes appear and the variation of the intensity profile is more remarkable than in Fig. 5. Typical intensity profiles are illustrated in the figure. It is noteworthy that the profiles of Figs. 6a and b are similar respectively to those of e and f. The difference of defocus between a and e is about 10μ and that between b and f, 11μ.

The variation of intensity profiles was studied for 14 through-focus series and the results are summarized in Fig. 14. In Fig.

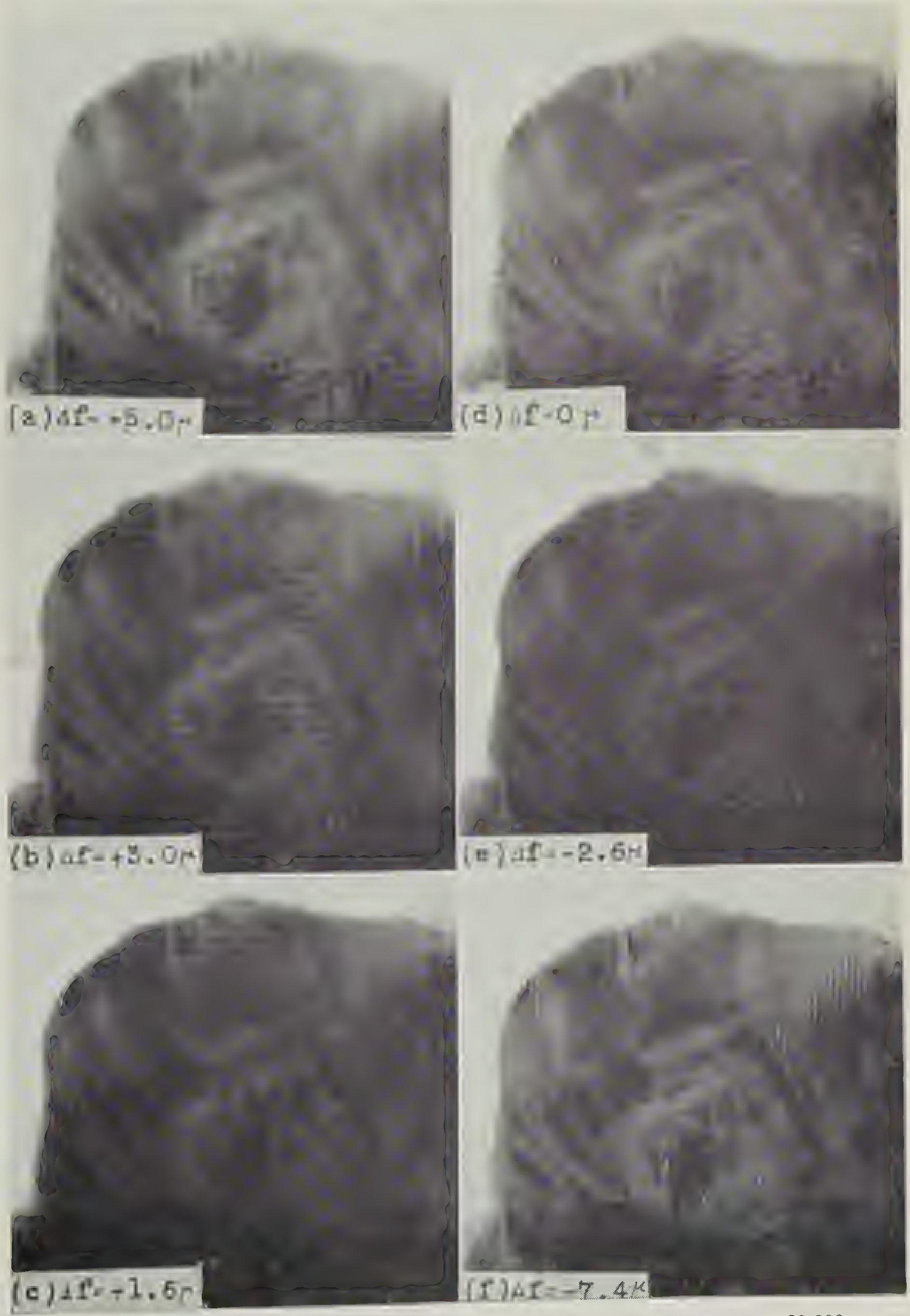

Fig. 7. Through-focus series of fringes disturbed by dark bands. ×80,000

14 we find that:

(1) Intensity profiles vary with the amount of defocus. Normal fringes appear usually in out-of-focus images. Near the exact focus, the contrast of fringes is usually low and the spacing of fringes is often halved. The amount of defocus where normal fringes appear is usually about 5–10μ.

(2) Result (1) gives only the general trend and there are deviations from (1). The manner of variation of the intensity profile is different from specimen to specimen (Fig. 5 and Fig. 6) and at exact focus is not always the same. In an extreme case, normal fringes of good contrast appear at the exact focus (Fig. 7).

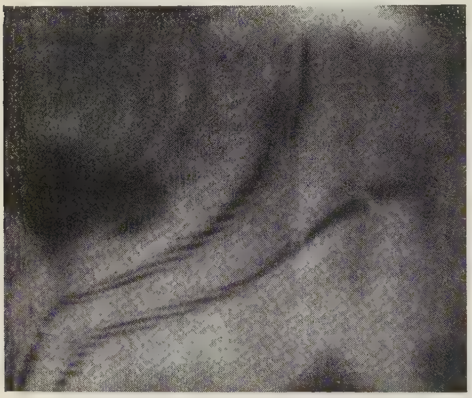

Fig. 8. Extinction contours split up by moiré effect. ×64,000.

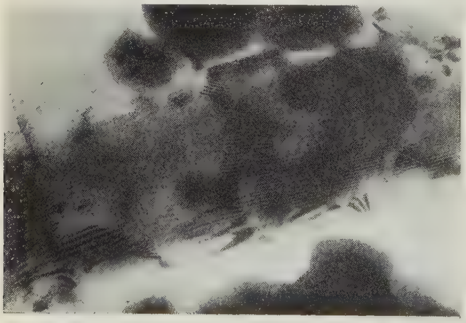

Fig. 9. Moiré pattern. ×60,000

(a) *Irregularities.* Irregularities of fringes may be divided into (a) irregular spacings, (b) dislocations and (c) dark bands sometimes with stepped structures. Figs. 2 and 3 give remarkable examples of irregular spacings. The spacing of the fringes is different from specimen to specimen. We measured the spacing on more that 20 plates, the measured values lying between 80 and 120Å. This in itself does not necessarily imply a variation in spacing, since the magnification of the electron microscope is not very reliable. However, we often found that the spacing is different in different regions of the same plate, for example 92, 97 and 103Å. This proves that the variation of spacing is real. Fig. 12 shows the fringes with the smallest spacing ever observed for Yu Yen Stone (38Å.). This value seems to be true because fringes with spacing 107Å were simultaneously observed on the same plate. Picrolite also produces good fringes (Fig. 13) although as with Yu Yen Stone the spacing may not be constant. In Fig. 13 the smallest spacing is 44Å and the largest 55Å.

In Fig. 4 a number of dislocations are seen. Fig. 11 shows a set of through-focus micrographs of a dislocation.

Dark bands were observed on almost every micrograph. Even in Fig. 5a, showing one of the most regular arrays of fringes, a dark band appears. Fringes in Fig. 6 are also disturbed by dark bands, particularly Figs. 6d, e and f. In these figures the dark bands moved during observation as already described by Uyeda et al⁽⁷⁾. Most of the dark bands move to some extent during observation. On dark bands the intensity profile of fringes is different from that of the other part (Figs. 5a, h, j,; Fig. 10a). The through-focus study in Fig. 10 shows that a stepped structure observed at a certain focus (Fig. 10b) changes gradually to straight fringes (Fig. 10j). Fig. 8 gives another example of dark bands. This suggests that the dark bands are a type of extinction contour.

§ 4. Interpretation and Discussion

(a) *Intensity profile*

Cowley & Moodie⁽⁹⁾ developed the theory of Fourier images of periodic structures and confirmed their results by light optical experiments. According to them, the image of a two-dimensional grating varies with the defocus and when the light source is very far from the grating, as in electron microscopes, the same image is repeated for a defocus

$$\Delta f_0 = d^2/\lambda\,, \tag{1}$$

where d is the spacing of the grating and λ, the wavelength.

The spacing of fringes of phthalocyanine and other crystals as observed by Menter and others[1)-4)] are too small to study the variation of images with defocus. Komoda[10)] reproduced in his paper a series of three through-focus micrographs of Cu-phthalocyanine. The fringes of about 12Å spacing were observed at $\Delta f=-0.2\mu$ and -1.0μ while no fringes were seen at $\Delta f=-0.5\mu$. He interpreted this result in terms of the theory of Fourier images. However, further experiments may be desirable to confirm the result because the experiment is very difficult.

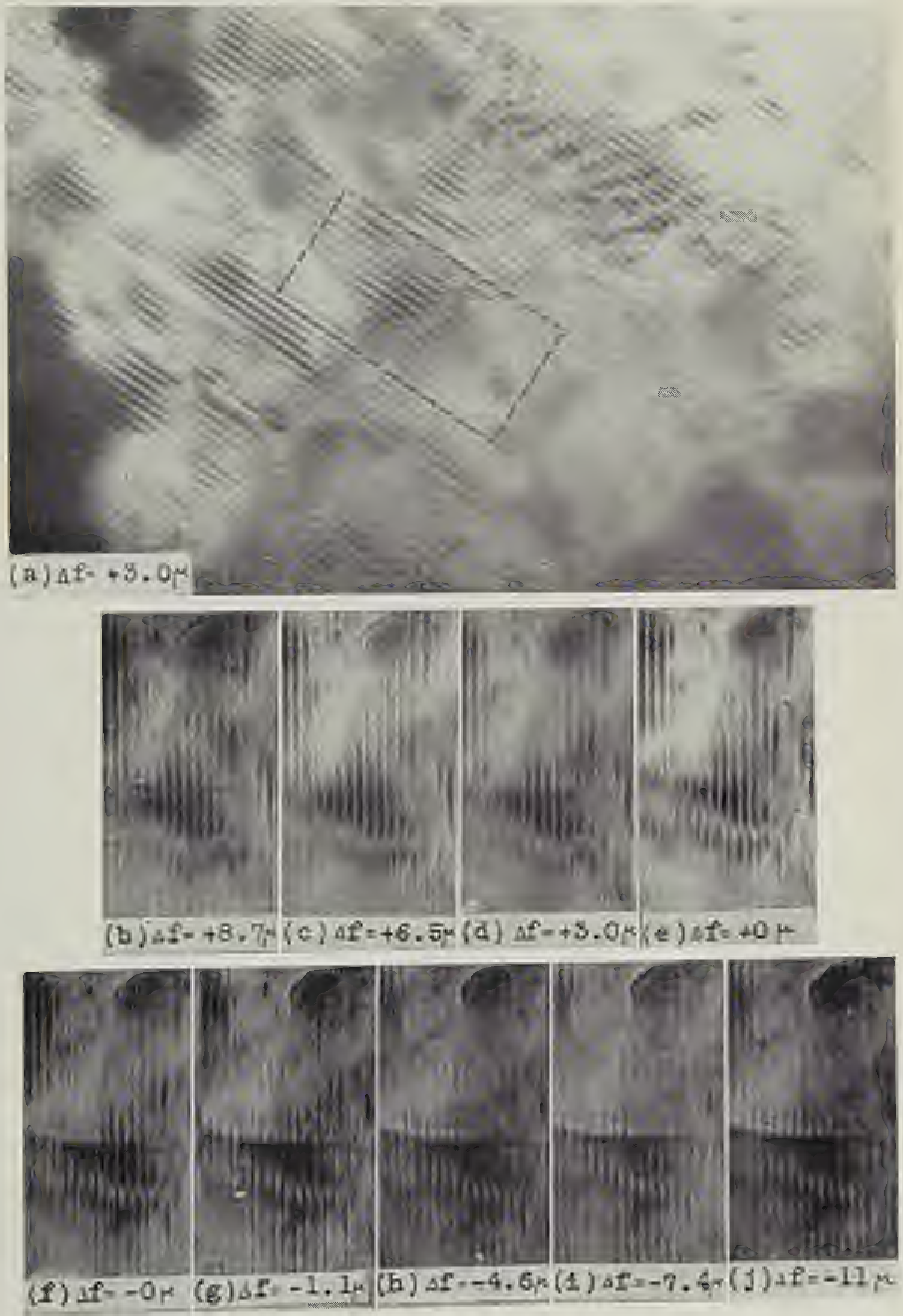

Fig. 10. Through-focus series of stepped structure. × 130,000

Labaw & Wyckoff[5] studied the fringes from indanthrene scarlet which have spacings of about 20Å. They found that the intensity profile of the fringes appeared sometimes normal, sometimes sharp black etc. similar to those denoted by N, SBi, SW and SWp in the present paper. Labaw & Wyckoff considered that the profile is determined not only by the amount of defocus but also by the crystal thickness and orientation. However, they did not carry out systematic experiments, probably because the spacing was still to small.

Lenz & Scheffels[11] discussed through-focus micrographs of a periodic structure of spacing about 100Å in biological sections. They found that the contrast is low at the exact focus and becomes high out-of-focus. They also found that at a certain defocus a weak intermediate line appears between two successive strong

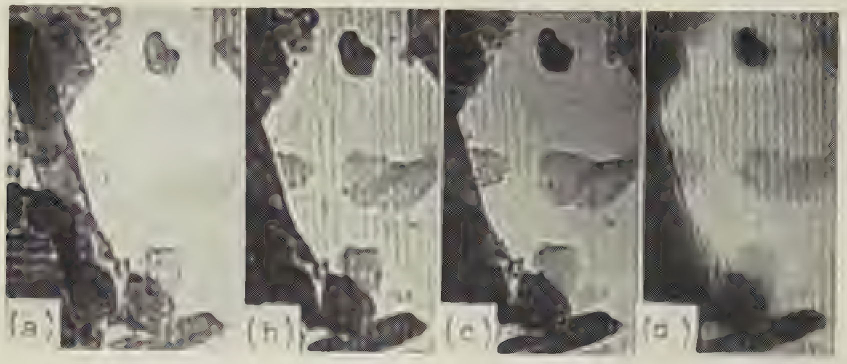

$\Delta f=-7.4\mu$ $\Delta f=-5.5\mu$ $\Delta f=-3.7\mu$ $\Delta f=+3.4\mu$

Fig. 11. Through-focus series of edge dislocation. ×110,000

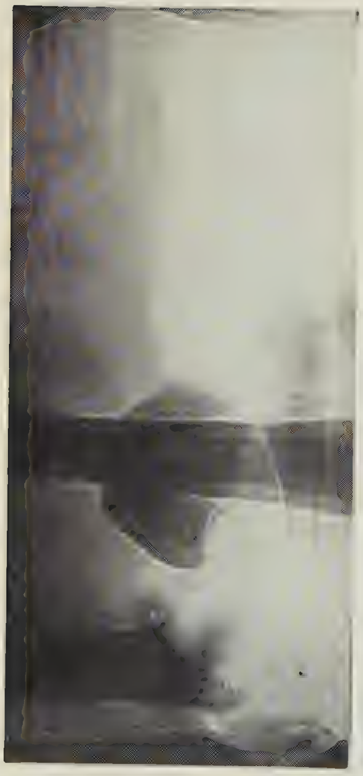

Fig. 12. Fringes of Yu Yen Stone with smallest spacing. ×210,000

Fig. 13. Fringes of picrolite. ×210,000

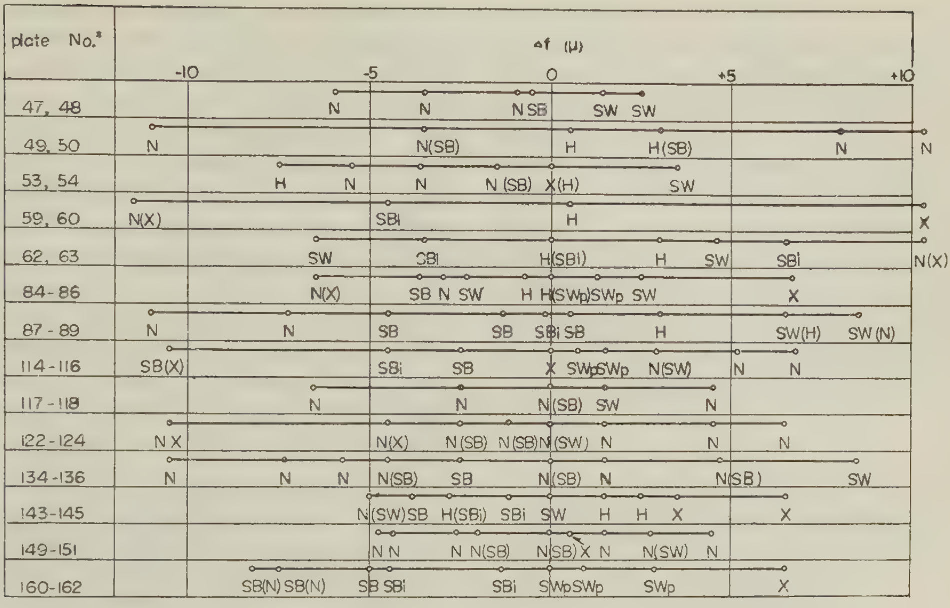

* One plate contains three pictures

Fig. 14. Variation of intensity profile with defocus Δf.
N: Normal; H: Half spacing; SB: Sharp black; SW: Sharp while; SBi: Sharp black with intermediate weak lines; SWp: Sharp while with paired black lines; X: Fringes seem diffused.

lines. They studied theoretically the defocused image of a phase grating and concluded that the highest contrast is obtained at defocus of $d^2/2\lambda$. This means that the highest contrast appears midway between two invisible images, because a phase grating is invisible at the exact focus and it is again invisible at defocus d^2/λ, according to Eq. (1).

Result (1) of Sec. 3 (a) may be essentially the same phenomenon as that studied by Cowley & Moodie[8)] and others[11)]. The phenomenon may be outlined as follows. When a plane wave falls on a thin crystal, many orders of diffracted waves are simultaneously reflected by the superlattice net-planes. The interference of the 0th order wave and the 1st order wave produces a set of interference fringes below the crystal (Fig. 15a). The interference between the 0th and 1st order and that between the 0th and the -1st order produce two sets of interference fringes (Fig. 15b). What we observe under an electron microscope is a section of the interference fringes on the object plane which is conjugate to the image plane. Since the angle between two sets of interference fringes is $2\theta=\lambda/d$, it is easily understood in Fig. 15b that the same image is repeated with a defocus of $2d^2/\lambda$. When, however, the shift of the image by $d/2$ is overlooked, the repeat period is d^2/λ which is Δf_0 as already given in Eq. (1). The contrast of the image is the highest when plane XX is focused and it vanishes when X′X′ is focused (Fig. 15b). Since the crystal is not very absorbing, it is nearly a phase grating and thus the plane equivalent to X′X′ lies near the crystal, resulting in low contrast at the exact focus. The distance between XX and X′X′ is $d^2/2\lambda$. In the present experiment $d=90\text{Å}$, $\lambda=0.04\text{Å}$ and thus $d^2/2\lambda=10\mu$. This is in agreement with the experimental value 5–10μ given in result (1).

In the present experiment, several orders of reflections are simultaneously excited, as is confirmed by selected area diffraction. Therefore, not only the 1st and the −1st order waves, higher order waves also take part in the formation of interference fringes. The observed variation of intensity profile with defocus may be qualitatively interpreted as arising from the multiple interference of several diffracted waves. We do not here go into the detailed analysis of the observed intensity profiles. The theory of multiple interference, which corresponds to the automatic Fourier synthesis[5)], will be published elsewhere.

It is usually believed that an in-focus image is the most exact image. If this is correct, result (2) means that the superlattice structure of Yu Yen Stone is not always the same. This may partly be correct. However, it is hardly believable that fringes of so high a contrast as those in Fig. 7 are the most exact image, because, as was already pointed out by Brindley et al.,[6] the atoms of Yu Yen Sione are Si, Mg- and O and they are distributed more or less uniformly across the large unit cell of the structure.

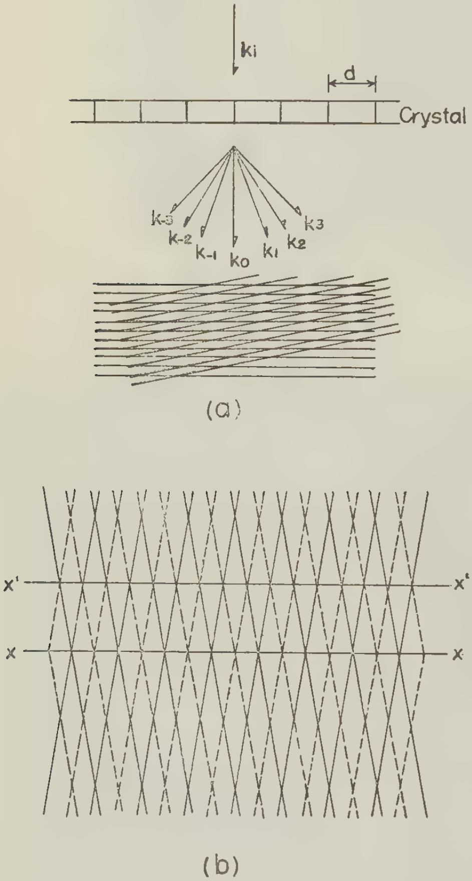

(a)

(b)

Fig. 15. Schematic illustration of interference fringes.

High contrast fringes can appear, according to the dynamical theory of diffraction[12], even when a crystal is composed only of light atoms. However, for the appearance of high contrast fringes, the crystal must be as thick as

$$D_0 = \lambda E / 2V_h\,, \qquad (1)$$

where E is the accelerating voltage of electrons and V_h, Fourier coefficient of periodic potential in the crystal. In the present experiments, accurate values of V_h are not known. However, the values given in Table I may be a reasonable estimate for low orders of h. For the superlattice, the estimated value of D_0 is surely much larger than the thickness of the crystal which may be between 500 and 1,500Å. This proves that the observed high contrast is not caused by the simple dynamical effect which is related only to the superlattice. It may be explained when the dynamical effect related to the fundamental lattice is taken into account (Sec. 4c).

Table I.

	V_h	$\lambda E/2V_h$
Fundamental lattice	1–10 volt	200–2,000 Å
Superlattice	0.01–0.1 volt	2–20μ

It is noteworthy that for phthalocyanine the thickness of specimens is comparable to D_0 in Eq. (2), and thus a high contrast may appear even at exact focus. It is also noteworthy that, in biological specimens, there is no complicated problem of superlattice and fundamental lattice. However, atomic arrangement in short range is irregular even when the specimen has a periodic structure. The irregularity produces the incoherent scattering[13], most of which is stopped by the objective aperture, resulting in a contrast even at the exact focus. (In both crystalline and biological specimens, the effect of inelastic scattering must be taken into account in the detailed theory of image formation.)

(b) *Dislocations*

Hashimoto[14] pointed out that a dislocation appearing on an electron micrograph does not necessarily indicate a real dislocation in the crystal lattice. When a crystal is covered by an uneven layer of contamination, the fringes corresponding to the crystal lattice periodicity are severely distorted in out-of-focus images, sometimes including ghost dislocations. According to our result, a dislocation which appeared distinctly on one micrograph appeared on all micrographs independent of the degree of defocus. This proves that the observed dislocations are not ghosts. Sometimes, however, the fringes are not distinct around dislocations. For example, in Part A of Fig. 4, it is not clear whether the observed distortion represents a real distortion of the lattice or is an artefact caused by contamination.

(c) *Irregular spacings*

Uyeda et al⁷⁾ pointed out that the fringes of Yu Yen Stone usually appeared undistorted and were adequate for the magnification calibration of electron microscopes. On the other hand, Zussman and Brindley⁸⁾ reported that the superlattice spacing of Yu Yen Stone is distributed between *ca.* 85–110Å. Prof. Brindley¹⁵⁾ pointed out to one of the present authors (R.U.) that Yu Yen Stone is not an adequate material for the calibration and if it is used for this purpose, a supplementary calibration TlCl test as described by Uyeda et al. is indispensable. In the present experiment Prof. Brindley's opinion is proved to be correct.

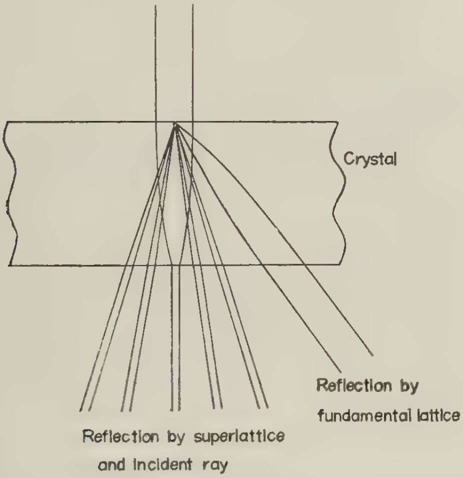
Crystal
Reflection by fundamental lattice
Reflection by superlattice and incident ray

Fig. 16. Illustration of the extinction of the primary wave.

Hashimoto¹⁶⁾ pointed out that when a crystal is curved the spacing in the image appears different from that in the crystal. However, it is not reasonable to attribute the variation of spacing observed in the present experiment to this effect. Hashimoto's theory is essentially based upon Niehrs' theory which is valid only for thick crystal. In the present experiment crystals are thin, satisfying condition (3) and (4) so far as the superlattice is concerned.

(d) *Dark bands*

Uyeda et al⁷⁾ already described dark bands observed on electron micrographs of Yu Yen Stone and interpreted them as moiré patterns. On the other hand, Cowley¹⁶⁾ assumed that dark bands were extinction contours and gave an explanation for stepped structures. According to him, the incident wave on a dark band is reflected by a net plane of the fundamental lattice. The reflected wave is stopped by the objective aperture of the electron microscope and does not take part in the formation of image. The amplitude of the primary wave, however, is modified according to Pendellösung, because the thickness of the specimens is comparable to D_0 for the fundamental lattice. Since the superlattice reflections are weak, we can assume that they are produced from the modified incident beam. Therefore, at a certain thickness of the crystal, the amplitude of the primary wave can become comparable with those of weak superlattice reflection (Fig. 16). The phase relation between the incident and reflected waves are also modified and high contrast is possible even at the exact focus.

This effect can appear in a variety of ways according to crystal thickness and orientation. Thus, it can explain qualitatively the anomalously high contrast of fringes and the local variation of the intensity profile, including stepped structures. Sometimes, this effect takes place not only on limited bands but also over a wide area; for example, the dark areas with high contrast in Figs. 2 and 3 are probably due to this effect. As is shown by selected area diffraction, a few of the fundamental lattice reflections are usually strong almost everywhere. Therefore, it may be reasonable to consider that the contrast is enhanced more or less everywhere by this effect.

Cowley's theory seems to be essentially correct. However, dark bands observed for Yu Yen Stone are always short while extinction contours should be endless. Therefore this difficulty must be elucidated before Cowley's theory is fully substantiated.

Yu Yen Stone often shows moiré patterns (Fig. 9), indicating that two crystal sheets are overlapping with a small relative rotation. The moiré patterns are produced by low order net planes of the fundamental lattice. When crystals are thick, moiré patterns appear only on extinction contours¹⁸⁾. In Fig. 8 extinction contours split up into short bands as a result of the moiré effect. It is reasonable to interpret the short dark banbs observed for Yu Yen Stone as arising from the moiré effect.

If this interpretation is correct, a sheet of Yu Yen Stone is almost always overlapping another and thus moiré patterns of the superlattice should also appear. In Fig. 8 the angle of rotation is estimated to be of the order of 1/100 rad or more and the spacing of the superlattice moiré is expected to be 0.9μ or less. However, such moirés were very seldom observed (but see Part B of Fig. 1). If we assume that one of the overlapping sheets has the superlattice and the other has no superlattice, we can explain the fact that the moiré patterns of the fundamental lattice always appear but those of the superlattice do not appear. Another possibility is that one of the two sheets is so thin that it does not show fringes of the superlattice. It is not yet confirmed that either of the assumption is really the case.

§ 5. Acknowledgement

The authors offer their sincere thanks to Professor G. W. Brindley of The Pennsylvania State University and Dr. George Switzer of The United States National Museum for furnishing the serpentine samples used in this experiment. The authors also wish to express their thanks to Dr. J. Zussman for helpful discussions, to Dr. J. M. Cowley for sending us the manuscript of his paper before the publication and to Dr. J. W. Menter for valuable advices in preparing this paper.

References

1) J. W. Menter: Proc. Roy. Soc. **A, 236** (1956) 119.
2) J. W. Menter: Proc. Stockholm Conf. Electron Microscopy (1956) 88.
3) R. Neider: Proc. Stockholm Conf. Electron Microscopy (1956) 93.
4) G. A. Bassett and J. W. Menter: Phil. Mag. **2** (1957) 1482.
5) L. W. Labaw and R. G. W. Wyckoff: Proc. Nat. Acad. Sci. **43** (1957) 1032.
6) G. W. Brindley, J. J. Comer, R. Uyeda and J. Zussman: Acta Cryst. **11** (1958) 99.
7) R. Uyeda, T. Masuda, H. Tochigi, K. Ito and H. Yotsumoto: J. Phys. Soc. Japan **13** (1958) 461.
8) J. Zussman and G. W. Brindley: American Mineralogist **42** (1957) 133.
9) J. M. Cowley and A. F. Moodie: Proc. Phys. Soc. London **120** (1957) 486, 497, 505.
10) T. Komoda: Electron-Microscopy **6** (1958) 137 (in Japanese).
11) F. Lenz and W. Scheffels: Z. Naturforschung **13a** (1958) 226.
12) H. Niehrs: Z. Phys. **138** (1954) 138.
13) R. Uyeda: J. Phys. Soc. Japan **10** (1955) 256.
14) H. Hashimoto: J. Phys. Soc. Japan **13** (1958) 764.
15) G. W. Brindley: private communication (1958)
16) H. Hashimoto: Read before the annual meeting of Soc. Electron-Microscopy, Japan (1958).
17) J. M. Cowley: Acta Cryst. **12** (1959) 367.
18) H. Hashimoto: J. Phys. Soc. Japan **13** (1958) 534.

JOURNAL OF THE PHYSICAL SOCIETY OF JAPAN, Vol. 14, No. 10, OCTOBER, 1959

Transition from Dynamical to Kinematical Intensities of Electron Diffraction by Crystals

By Shizuo MIYAKE

Institute for Solid State Physics, University of Tokyo, Komaba, Tokyo

(Received June 25, 1959)

The transition from dynamical to kinematical intensities of electron diffraction from crystals with the change of wave-length of electrons and crystal thickness is theoretically discussed. It is pointed out that the usual treatment of the dynamical theory by the two-wave approximation fails to apply in the range of very short wave-length and small crystal thickness, even with the correction of the dynamical Fourier potential, so that the advent of some convenient treatments taking account of many reflected waves is of essential necessity for consideration of the transition of reflected intensities. It is pointed out, at the same time, that the application of the pseudo-kinematical theory using the complex atomic scattering amplitude calculated on isolated atoms is not permissible in the case of electron diffraction by crystals even for their thinnest limit.

§ 1. Introduction

The crystal structure determination by electron diffraction method has recently been remarkably developed mainly by the efforts of Soviet school[1),2)] and considerable successes have been reported by them and other researchers on many examples of crystals. There remain, however, a number of difficulties to overcome to meet the increasing demand for higher accuracy and wider applications of this method. Some of them are technical difficulties such as those lying in the choice and the preparation of suitable samples and in the measurement of diffracted intensities.

The other difficulties, being of more theoretical nature, arises from the circumstance that the relation between the structure amplitude and the observed value of reflected intensity is generally not simple due to the strong interactions of electrons with crystals. In this respect, the consideration on the transition from dynamical to kinematical intensities of electron diffraction by crystals, with the change of wave-length of electrons and crystal thickness, is fundamentally important for the theoretical basis of the electron diffraction method in crystal structure determination. The present paper is devoted to the study of this kind of problem in spite of the same problem having been disscussed already in a number of papers and text-books,[1),3)] because the previous treatments contain unsatisfactory points to be criticized as is pointed out later.

For understanding of the considerations in what follows, some of well known relations in the dynamical theory of electron diffraction are briefly quoted below.[4),5),1)]

The solution of Schrödinger equation for electrons in the periodic potential field $V(\vec{r})$ within a crystal is given by the Bloch wave function

$$\Psi_B=\sum_g \psi_g \exp 2\pi i(\vec{k}_0+\vec{g})\cdot\vec{r} \qquad (1)$$

where $\vec{g}$ denotes the reciprocal lattice point vector, and $\vec{k}_0$ the wave vector of the primary wave in the crystal. The amplitudes ψ_g of component plane waves in (1) satisfy the relations

$$(\kappa^2-k_g{}^2)\psi_g+\frac{2me}{h^2}\sum_{g'\neq g} V_{g-g'}\psi_{g'}=0 \qquad (2)$$

where V_g is the Fourier component of $V(\vec{r})$, and

$$\kappa^2=(V_0+E)\frac{2me}{h^2}=\frac{1}{\lambda^2} \qquad (3)$$

E being the total energy of electron, and κ and λ, the mean wave number and wave-length of electron within the crystal, respectively. The simultaneous equations (2) are called the fundamental equations in the dynamical theory.

The number of the component waves ψ_g, and accordingly that of the simultaneous equations (2) is infinite in general. This number is usually reduced to a few by retaining only the strong component waves related to the reciprocal lattice points lying most closely to the Ewald sphere. The lattice planes corresponding to these points are regarded as satisfying more or less nearly the Bragg conditions concerned. When Bragg condition is nearly satisfied only by a lattice plane $h(h_1h_2h_3)$, (2) is reduced to the fundamental equations of the two-wave approximation,

$$\begin{aligned}(\kappa^2-k_0{}^2)\psi_0+\frac{2me}{h^2}V_{-h}\psi_h=0\\ \frac{2me}{h^2}V_h\psi_0+(\kappa^2-k_h{}^2)\psi_h=0\end{aligned}\qquad(4)$$

By applying these equations to a crystal plate of the thickness H, the integrated intensity of transmitted reflexion J is calculated as

$$J\propto|V_h|\qquad \lambda H\to\infty \qquad (5a)$$

$$J\propto|V_h|^2\qquad \lambda H\to 0 \qquad (5b)$$

The relation (5b) indicates that the intensity of reflexion tends to the kinematical value in the limit of small crystal thickness and short wave-length of electrons. This behaviour has usually been received as providing the theoretical basis of the electron diffraction method in crystal structure determination.

§ 2. Invariant Property of the Fundamental Equations

In the treatment of the avove two-wave approximation, the primary extinction effect caused by the dynamical interaction between the primary wave and the h-reflexion is taken into account. However, the influence of other reflexions is generally not negligible in the case of electron diffractio.n In particular, it is important to allow for the interactions among reflexions corresponding to the reciprocal lattice points lying on the lattice point row passing through both the reciprocal space origin and the lattice point $\vec{h}(h_1h_2h_3)$, since the points on this row are necessarily located closely to the Ewald sphere. Hoerni[6)] called the interactions due to this circumstance the systematic interactions, as it may be appreciable in any reflecting condition. When another lattice plane $h'(h_1'h_2'h_3')$ nearly satisfies the Bragg condition additionally, the reciprocal lattice points on the net plane containing the points $\vec{h}$ and $\vec{h'}$ and the reciprocal space origin are crowded near the Ewald sphere. Hoerni called the dynamical interactions which take place under such a condition the accidental interactions, as it arises under special conditions in which the incident electron beam is nearly parallel to some of zone axes of the crystal.

For further considerations, it is to be noted of an invariant property, possessed by the fundamental equations (2) with respect to the change of wave-length, under the conditions that:

(a) κ is quite large compared with the reciprocal lattice periods,

(b) interactions among reflexions other than the systematic and accidental intractions are negligible.

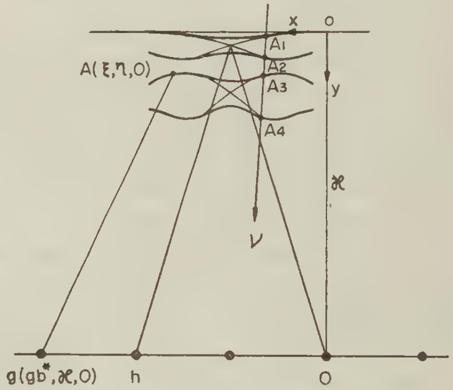

Fig. 1.

For simplicity, we concern with the case in which only the systematic interactions are important. Fig. 1 shows schematically a section of reciprocal space by a plane containing the reciprocal lattice point row concerned. We take the coordinate origin o at the distance κ from the reciprocal space origin O on the line which passes through O perpendicularly to the lattice point row. When this line is chosen as the y-axis and the x- and z-axes are chosen parallel to the lattice point row and perpendicular to the plane of the figure, respectively, the coordinates of an arbitrary lattice point $\vec{g}(g, 0, 0)$ on the row is given by $(gb_1{}^*, \kappa, 0)$, and those of a wave point A on the dispersion surface by $(\xi, \eta, 0)$, where $b_1{}^*$ is the reciprocal lattice period along the point row. Since by the conditions (a) and (b) we have $\kappa \gg b_1^*$ and $\kappa \gg \xi$, we obtain by neglecting higher order quantities the relation

$$\kappa^2 - k_g^2 = 2\kappa\eta - C_g(\xi) \,, \qquad (6)$$

where

$$C_g(\xi) = (gb_1^* - \xi)^2 \,. \qquad (6a)$$

Thus, the equations (2) are written as

$$(x - C_g(\xi))\psi_g + \frac{2me}{h^2} \sum_{g' \neq g} V_{g-g'}\psi_{g'} = 0 \qquad (7)$$

where

$$x = 2\kappa\eta \qquad (8)$$

Since the eigenvalues of x are independent of κ, the ratios of the eigenvectors $\psi_0 : \psi_1 : \psi_2 : \cdots$ are also independent of κ. In other words, the solution of (2) does not depend on the wave-length of electrons under the assumed conditions. The same is valid for the case when the accidental interactions are predominant.

In relation with the above conclusion, it may be worthy to add here a remark to the experimental method developed by Honjo and Kitamura,[7)8)] who showed that the intensity measurement of reflexions with varying wavelengths of electrons, and its extrapolation to the short wave-length limit, give an effective method for obtaining the kinematical values of the intensities of reflexion from a crystal of finite thickness, in accordance with the relation (5b). There might, however, arise the following objection concerning their method: since the curvature of the Ewald sphere becomes reduced with the decreasing wave-length, the number of reciprocal lattice points locating simultaneously in the neighbourhood of the Ewald sphere increases under the conditions of systematic as well as of accidental interactions, so that the dynamical interactions among reflexions might not be reduced by decreasing the wave-length. However, from the invariant property of the fundamental equation as shown above, it is clear that the complexity due to the dynamical interactions among reflexions is never aggravated by the reason of decreasing the wavelength of electrons.

§ 3. Conflicting Results of Different Theories

As mentioned before, the relation (5b) is derived by the two-wave approximation not taking account of the dynamical interactions among reflexions except the primary extinction effect. It appears to be probable that the influence of neglected weak reflexions may be approximately corrected by taking account of the so-called dynamical Fourier potential introduced by Bethe[1)]. By the use of the dynamical potential, however, we are confronted with a confusing result for the reflected intensity in the limit $\lambda H \to 0$, as revealed in what follows.

The reduced fundamental equations of the two-wave approximation corrected for the dynamical Fourier potential are obtained by replacing V_0 in (3) by $V_0 + \varDelta V_0$, or by $V_0 + \varDelta V_0'$, and V_h and V_{-h} in (2) by $V_h + \varDelta V_h$ and $V_{-h} + \varDelta V_{-h}$, respectively, where the dynamical potential terms $\varDelta V_0$ etc. are given by

$$\varDelta V_0 = -\frac{2me}{h^2} \sum_{\substack{g\neq 0\\ g\neq h}} \frac{V_g V_{-g}}{\kappa^2 - k_g^2} \,,$$

$$\varDelta V_0' = -\frac{2me}{h^2} \sum_{\substack{g\neq 0\\ g\neq h}} \frac{V_{g-h} V_{-g+h}}{\kappa^2 - k_g^2}$$

$$\varDelta V_h = \varDelta V_{-h}^* = -\frac{2me}{h^2} \sum_{\substack{g\neq 0\\ g\neq h}} \frac{V_g V_{h-g}}{\kappa^2 - k_g^2} \qquad (9)$$

When this kind of theory is applied to the crystal plate with the thickness H, the integrated intensity J of a transmitted reflexion turns out to be

$$J \propto |V_h + \varDelta V_h| \,, \qquad \lambda H \to \infty \qquad (10a)$$

$$J \propto |V_h + \varDelta V_h|^2 \,, \qquad \lambda H \to 0 \qquad (10b)$$

Since $\kappa^2 - k_g^2$ in (9) is the quantity which is not depending on κ as has been proved for the systematic and accidental interactions, $\varDelta V_h$ is independent of the wave-length of electrons. Furthermore, $\varDelta V_h$ is independent of the thickness of the crystal. Therefore, the integrated intensity of reflexion in the limit $\lambda H \to 0$ as expressed by (10b) never coincides with the result (5b). As the magnitude of $\varDelta V_h$ can be appreciable for low order reflexions from most of crystals, the discrepancy is not trivial so that it amounts to necessitating us a serious reconsideration as to how we should derive the kinematical values of reflected intensities from the observation.

On the other hand, Schoemaker and Glauber,[9)] Cowley,[10)] and Hoerni[6)] anticipated that the reflected intensity from a crystal will tend, in the limit of sufficiently small thickness of the crystal ($H \to 0$), to the pseudo-kinematical value calculated from the crystal structure factor using the complex atomic scattering amplitude, which was introduced by Schoemaker and Glauber[9][10] in order to explain the anomalous values of the atomic distances in molecules containing heavey elements derived from electron diffraction by gases. However, the intensity thus calculated agrees in general with neither (5b) nor (10b).

§ 4. Failure of the Two-wave Approximation in the Limit $\lambda H \to 0$

We have now the three kinds of conflicting results for the reflected intensity in the limit $\lambda H \to 0$ by different approaches, of which the former two are based on the two-wave approximation, one being taking account of the primary extinction effect only, and the other the influence of weak reflexions also. In order to reach *a* unified result, we point out, first of all, the fact that the treatments of two-wave approximation of either forms are not permissible in the consideration of the reflected intensity in the limit $\lambda H \to 0$, when the dynamical effects other than that due to the primary extinction are remarkable as is usually the case in electron diffraction.

The wave field of electron in the crystal, being subjected to the boundary condition with respect to the given incident beam, is expressed by a superposition of the Bloch functions

$$\Psi = \sum_i \alpha^{(i)} \Psi_B^{(i)} \tag{11}$$

where i is the index of the wave points and $\alpha^{(i)}$ the weighting amplitude. The wave points are determined as the intersecting points of the dispersion surface in reciprocal space with the straight line ν running in the direction perpendicular to the crystal surface through the end point of the vector $-\vec{K}_0$ drawn from the reciprocal space origin, where $\vec{K}_0$ is the wave vector of the incident electron wave. We designate the wave points determined in this way by $\cdots A_1, A_2, A_2 \cdots$, according to the increasing value of the η-coordinate of them (Fig. 1). The intensity of the reflexion $g(g_1g_2g_3)$ transmitting the crystal plate is given by

$$I_g = \sum_i \sum_j u_g^{(i)} u_g^{(j)*} \exp \pi i (x^{(j)} - x^{(i)}) \lambda H, \tag{12}$$

$$x^{(i)} = 2\kappa \eta^{(i)} \tag{13}$$

where

$$u_g^{(i)} = \alpha^{(i)} \psi_g^{(i)} . \tag{14}$$

$u_g^{(i)}$,s satisfy the relations due to the boundary condition

$$\sum_i u_g^{(i)} = \begin{cases} 1, & g=0 \\ 0, & g \neq 0 \end{cases} \tag{15}$$

where the amplitude of the incident wave is assumed to be unity.

For thick crystals, the reflected intensity averaged over H is given, from (12) and (15), by

$$\bar{I}_g = \sum_i | u_g^{(i)} |^2 = - \sum_{i \neq j} \sum u_g^{(i)} u_g^{(j)*} \tag{16}$$

When the Bragg condition is nearly satisfied with respect to the lattice plane $h(h_1h_2h_3)$, the straight line ν intersects with the part of the dispersion surface near the intersection of the spheres of radius κ drawn around the reciprocal space origin O and the lattice point h; the position of the wave points A_1 and A_2 are located there. Under the assumed condition, only the amplitudes $u_h^{(1)}$ and $u_h^{(2)}$ may be predominant in (16) for the h-reflexion. Disregarding the second order of other small amplitudes, we obtain the averaged intensity

$$\bar{I}_h = | u_h^{(1)} |^2 + | u_h^{(2)} |^2 = - (u_h^{(1)} u_h^{(2)*} + u_h^{(1)*} u_h^{(2)}) \tag{17}$$

This procedure corresponds to the two-wave approximation, by which the results (5a, b) and (10a, b) have been obtained.

When the value of λH is small, on the other hand, the intensity for the h-reflexion is written by using (12) and (15) in the following expansion form

$$I_h = - \sum_{i \neq j} \sum u_h^{(i)} u_h^{(j)} \left\{ \left[(x^{(i)} - x^{(j)}) \frac{\pi \lambda H}{2} \right]^2 + \cdots \right\} \tag{18}$$

where, for simplicity, the crystal is assumed to be centrosymmetrical so that $u_h^{(i)}$ are real quantities.[12] In (18) the contributions of the amplitudes $u_h^{(i)} (i \neq 1, 2)$ are not necessarily negligible as in (16) even when they are small compared with $u_h^{(1)}$ and $u_h^{(2)}$, since the magnitudes of the terms in (18) depend not only on those of $u_h^{(i)}$ but also on the positions of the wave points concerned. The conflicting results of the two-wave approximations is a natural consequence of the inappropriate application of them to the range of small λH, disregarding the wave points other then A_1 and A_2.

§ 5. Discussions

It may be clear from the above consideration that, for the argument of the reflected intensity in the limit $\lambda H \rightarrow 0$, it is of essential necessity to develop a more elaborated theory taking account of many weak reflexions. Very recently, Fujimoto13) has succeeded in formulating the dynamical theory by the method of scattering matrix,* extending the theory of Niehrs and Wagner14), and studied the dependence of the intensities of transmitted reflexions on the change of wave-length of electrons and crystal thickness in detail. By his theory, which takes account of the interactions among reflexions other than the primary extinction effect also, it was shown that the integrated intensity of reflexion tends to the kinematical value in the limit $\lambda H \rightarrow 0$. The similar conclusion was independently obtained by Fujiwara15), who developed a theory which is a more complete formulation of the theory of a new approach to the dynamical theory given by Cowley and Moodie16). He has taken account of the interactions of different reflexions by the iteration of the Born approximation for the wave field *within* the crystal, starting from the field due to the first order Born approximation formerly derived by Artmann17).

By the theories of Fujimoto and Fujiwara, we can conclusively believe that the relation (5b) holds even under complicated interactions among reflexions, although the validity of (5b) is fortunate so long as it is derived from (4) neglecting the interactions to be taken into account.

It can be at the same time concluded from their theories that the intensity of reflexion in the limit $H \rightarrow 0$ does not tend to the pseudo-kinematical value. The reason for the failure of the pseudo-kinematical theory even for the thinnest crystals may be physically understood as follows. The complex atom scattering factor used in the pseudo-kinematical theory is calculated by the knowledge of the distorted wave field in an isolated atom, whereas the wave field in atoms composing the crystal is entirely different from that in the isolated atom as the result of the superposition of scattered waves from a large number of atoms. In order to reproduce the distorted wave field in an isolated atom, infinite number of plane waves of continuously varying directions of propagation are needed, while the wave field in the crystal is expressed by the superposition of plane waves with discrete directions of propagation even for the thin limit of the crystal. In other words, it is not enough to reduce the thickness of the crystal plate in order to attain the isolated-atom limit. This limit will be reached by reducing the surface area of the plate also. The application of the complex atom scattering amplitude obtained for isolated atoms to thin crystals may give, therefore, nothing but a misleading conclusion.

So far as the above consideration is concerned, the reduction of λ and of H result in the same kinematical limiting value for the intensity of reflexion. However, the additional complex term to the Fourier potential due to the inelastic scattering, as was formulated in the theory of Yoshioka18), will vanish only by reducing the value of λ. Therefore, the simultaneous reduction of the wave-length of electrons and the crystal thickness may be most advantageous for the work of crystal structure determination by the electron diffraction method.

As pointed out in the present paper, the two-wave approximation corrected for the dynamical Fourier potential is not permissible for the calculation of the intensity of reflexion when λH is quite small. However, this approximation may not be meaningless so far as it is applied to argue qualitatively the reflected intensity from thick crystals, or the refractive index for electrons within the crystal, although the numerical accuracy of the correction terms (9) seems to be doubtful in general.

References

1) Z. G. Pinsker: *Electron Diffraction* (English translation by Spink and Feigl, London, Butterworth, 1953).
2) B. K. Vainstein: *Structural Electron Diffraction* (Acad. Sci. U.S.S.R., Moscow, 1956) (in Russian).
3) M. Blackman: Proc. Roy. Soc. A, **173** (1939) 68.
4) H. A. Bethe: Ann. Physik **87** (1928) 55. G. P.
5) Thomson and W. Cochrane: *Theory and Practice of Electron Diffraction* (Macmillan,

---

* The similar formulation has been very recently given by Dr. H. Niehrs independently. (Private communication from Dr. Niehrs)

London, 1939).
6) J. Hoerni: Phys. Rev. **102** (1956) 1534.
7) G. Honjo and N. Kitamura: Acta Cryst. **10** (1957) 533.
8) S. Kuwabara: J. Phys. Soc. Japan **14** (1959) 1205.
9) V. Schoemaker and R. Glauber: Nature **170** (1952) 290.
10) J. M. Cowley: Acta Cryst. **9** (1956) 391.
11) R. Glauber and V. Schoemaker: Phys. Rev. **89** (1953) 667.
12) S. Miyake and R. Uyeda: Acta Cryst. **8** (1955) 335.
13) F. Fujimoto: J. Phys. Soc. Japan **14** (1959) (To be published).
14) H. Niehrs and E. H. Wagner: Z. Phys. **143** (1955) 285.
15) K. Fujiwara: J. Phys. Soc. Japan **14** (1959) (To be published).
16) J. M. Cowley and A. F. Moodie: Acta Cryst. **10** (1957) 609.
17) K. Artmann: quoted by H. Raether in Handb. Phys. **32** (Springer, Berlin, Göttingen and Heidelberg, 1957) 475.
18) H. Yoshioka: J. Phys. Soc. Japan **12** (1957) 618.

JOURNAL OF THE PHYSICAL SOCIETY OF JAPAN, Vol. 14, No. 10, OCTOBER, 1959

Neutron Diffraction Study of Antiferromagnetic $MnTiO_3$ and $NiTiO_3$*

By Gen SHIRANE,
Westinghouse Research Laboratory, Pittsburgh, Pennsylvania
S. J. PICKART
Naval Ordnance Laboratory, White Oak, Silver Spring, Maryland and Brookhaven National Laboratory, Upton, New York
and Yoshikazu ISHIKAWA
Institute for Solid State Physics, University of Tokyo, Tokyo, Japan

(Received May 28, 1959)

$MnTiO_3$ and $NiTiO_3$ have a rhombohedral crystal structure similar to $FeTiO_3$ in which layers of Fe and Ti atoms alternate along the rhombohedral axis with oxygen layers between them. A powder neutron diffraction study shows that $MnTiO_3$ has a magnetic structure with the Mn^{2+} spins antiparallel within each layer. On the other hand, $NiTiO_3$ has the same magnetic structure as $FeTiO_3$, in which the spins are parallel within each layer and adjacent layers are antiparallel. The spins are directed along the [111] direction in $MnTiO_3$ and perpendicular to it in $NiTiO_3$. In addition to the magnetic study, the nuclear intensities indicate that the Ni and Ti in $NiTiO_3$ are only 88 per cent ordered.

§ 1. Introduction

Extensive studies have been carried out within the past few years on the magnetic properties of ilmenite-type compounds. Ilmenite ($FeTiO_3$) has a rhombohedral lattice[1] very closely related to the corundum structure of hematite (α-Fe_2O_3). Several solid solution systems between these two types of compounds are known, the most thoroughly studied among them being the ilmenite-hematite system.[2,3,4] The antiferromagnetic spin structures of both the end members of this system were determined by neutron diffraction analysis.[5,6] An interesting feature of the solid solutions is the appearance in some of the ilmenite-rich compositions of a strong spontaneous magnetization, which was shown to be due to an ordering of Fe and Ti in the α-Fe_2O_3 spin arrangement.[6)]

---

* This work was carried out in part at Brookhaven National Laboratory under the auspices of the U.S. Atomic Energy Commission and the National Security Agency.

Ishikawa and Akimoto[7)] have reported recently on the magnetic properties of other compounds isomorphous with ilmenite, such as $MnTiO_3$, $CoTiO_3$, and $NiTiO_3$, as well as their solid solutions with α-Fe_2O_3. The magnetic behavior of the systems containing $CoTiO_3$ and $NiTiO_3$ was found to be quite similar to that of the $FeTiO_3$ series. The $MnTiO_3$ system, however, showed no appreciable spontaneous moment at any composition, a result suggesting that pure $MnTiO_3$ has a different spin structure from pure $FeTiO_3$ and $NiTiO_3$.

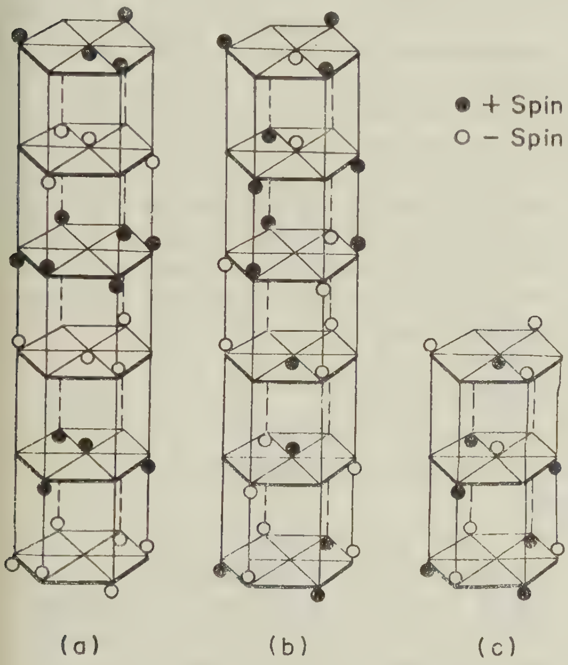

Fig. 1. Three possible magnetic structures for ilmenite-type compounds. The structures are idealized and the Ti layer (the B layer) is omitted. Model (a) is observed in $FeTiO_3$ and $NiTiO_3$ and Model (c) in $MnTiO_3$.

The three possible spin arrangements for ilmenite are illustrated in Fig. 1, in which a hexagonal unit cell containing only the magnetic atoms has been adopted. The layers of magnetic atoms, which may be designated the A layers, are separated by O–B–O layers, where O represents an oxygen layer and B a Ti layer. When α-Fe_2O_3 is added to this ilmenite structure, the magnetic atoms enter the B layers and those on the A layers will result in different structures depending upon the spin configuration of the end member, $MeTiO_3$, where Me represents magnetic atom.

$FeTiO_3$ was found to have the structure shown in Fig. 1(a). in which the arrangement within each layer is ferromagnetic. The addition of Fe on the B layers in this case destroys the ferromagnetic ordering on the A layers, as shown by the neutron diffraction study. The ferrimagnetic ordering based upon the hematite spin lattice develops when the concentration of α-Fe_2O_3 reaches a critical value of about 15 per cent.

Models (b) and (c) have the common feature that the spins in the A layers are antiparallel. In the light of a molecular field calculation[7)] showing that the moments on the B layer are parallel in (b), the observed moment should increase linearly with increasing concentration of α-Fe_2O_3. On the other hand, model (c) results in antiparallel spins on the B layer, and on this basis model (c) was predicted for $MnTiO_3$.

The present paper describes a neutron diffraction study of $MnTiO_3$ and $NiTiO_3$. Besides the magnetic structure there is additional interest, for the case of $NiTiO_3$, in the degree of order of Ni and Ti. Because the two metal positions in the lattice are almost equivalent, some disorder might be expected. Neutron diffraction offers a particular advantage over x-ray diffraction in fixing the degree of order, since the scattering amplitude of Ti (-0.38×10^{-12}cm) and Ni ($+1.03\times10^{-12}$cm) have opposite signs. The same is not true for $MnTiO_3$ because of the manganese scattering amplitude (-0.36×10^{-12}cm).

Approximately 30 grams of $NiTiO_3$ and $MnTiO_3$ powder were prepared for the neutron diffraction study. $NiTiO_3$ was fired according to the method described previously.[8)] A mixture of NiO and TiO_2 was heated in air at 1350°C for three hours, then cooled in the furnace at a rate of approximately 300°C/hr. This compound is quite stable in air and exhibits high electrical resistivity. A chemical analysis of the sample gave the stoichiometric ratio within experimental limits. $MnTiO_3$ was obtained by the reaction of $Mn_3O_4+3TiO_2$ in a vacuum furnace with 10^{-4}mm Hg pressure. The sample was kept at 1300°C for 24 hours and cooled in the furnace to room temperature, the total cooling time being 5-6 hours. Chemical analysis revealed a slight deficiency in Mn content (about 2 per cent). However, an X-ray powder picture did not show any trace of impurities, and the lattice constants are identical with a sample[7] having a Néel temperature of 41°K and an effective moment corresponding to Mn^{2+}. In the present calculation for $MnTiO_3$, the stoichiometric ratio was used with the assumption of divalent manganese. The possible implication of non-stoichiometry will be discussed later.

§ 2. Crystal Structures

Although a hexagonal unit cell is used in Fig. 1 for the magnetic models, the crystal structure can be described more conveniently by using a rhombohedral cell containing two molecular units. The atomic positions are given by the following five parameters for the space group $R\bar{3}$:

2 Me at $\pm(u_1, u_1, u_1)$ Me=Fe, Mn or Ni
2 Ti at $\pm(u_2, u_2, u_2)$
6 O at $\pm(x, y, z)$

If Me and Ti are incompletely ordered, as in the case of $FeTiO_3$, the ordering parameter S must be treated as an additional parameter. Since the magnetic atoms Me constitute the A layers of Fig. 1, S is the fraction of Me at $\pm(u_1, u_1, u_1)$, which ranges from unity for complete order to one half for complete disorder. These six parameters determine the X-ray intensities as well as that part of neutron intensities due to nuclear scattering.

When a magnetic order develops, the total neutron intensity can be written as (see Bacon[9].)

$$I_{hkl}=K(F^2_{\text{nucl}}+q^2F^2_{\text{mag}})$$

where q is determined by the direction of the spins with respect to the scattering vector. The magnetic structure factor, F_{mag}, depends only on the magnetic stoms and is therefore a function of u_1 and S, as well as p, the magnetic scattering amplitude. It should be noted that

$$p=0.269\,\mu f$$

where f, the form factor, is not a well established quantity. The effective magnetic moment μ depends upon the degree of quenching of orbital moment and must be determined experimentally together with the form factor.

The main purpose of the present study, the determination of the magnetic structure, requires the accurate determination of only two parameters from the nuclear scattering peaks, u_1 and S. The oxygen parameters are nevertheless quite important, not only to determine the scale factor K (which in turn decides the magnitude of the magnetic moment for each model considered), but also to calculate the proper metal-oxygen distances. For these reasons a careful analysis of the nuclear diffraction data was carried out. Since only about twenty reflections are available to determine six parameters, the two metal parameters were first fixed by X-ray measurements, and then the remaining four parameters, x, y, z and S, adjusted to obtain the best agreement with the neutron data.

The crystal structures of $MnTiO_3$, $NiTiO_3$, and $FeTiO_3$, were studied by Posnjak and Barth.[1,10] They established the structure of $FeTiO_3$ by using single crystals as well as powder specimens; powder intensities alone were used for $NiTiO_3$. The parameters determined were:

$$u_1(\text{Fe})=0.358 \quad u_2(\text{Ti})=\frac{1}{2}-u_1\,,$$
$$u_1(\text{Ni})=0.353$$

with the same oxygen parameters in each case

$$x=0.555 \quad y=-0.055 \quad z=0.250\,.$$

Though no intensity calculations were performed explicitly for $MnTiO_3$, parameters similar to those of $FeTiO_3$ were expected because of the close resemblance of the powder intensities in these two compounds.

X-ray powder intensities of $NiTiO_3$ and $MnTiO_3$ were taken with a Norelco diffractometer using Cu Kα radiation. The first 13 lines up to (211) were used to determine the metal parameters, by assuming the oxygen parameters given by Posnjak and Barth. The best values are:

$$u_1(\text{Ni})=0.353\pm0.002 \quad u_1(\text{Mn})=0.357\pm0.002$$

is good agreement with the reported values. The assumption $u_2=1/2-u_1$ made in these calculations is borne out by the agreement between calculated and observed values.

Powder neutron data were obtained at room temperature and 4.2°K (Figs. 2 and 3). Samples were placed in a cylindrical aluminium container of 3/8 inch diameter; the intensities were measured at angular intervals of 0.1° in 2θ, the counting time (approximately 10 minutes) being determined by a monitor. The nuclear intensities at the two temperatures agree with each other quite satisfactorily for both compounds. The observed intensities were compared with computed ones after applying appropriate normalization and angular factors; the small correction due to the temperature factor was neglected in the calculation. With the use of the two metal parameters given by the X-ray data, the three oxygen parameters and the ordering parameter S were adjusted to fit the data.

The intensities calculated for $NiTiO_3$ with the reported oxygen parameters did not give satisfactory agreement, especially for (111), (100), and (210), if $S=1$. Reflection with $h+k+l=2n+1$ have a structure factor proportional to (b_1-b_2), were b_1 is the effective scattering amplitude at (u_1, u_1, u_1). On the other hand, reflections with $h+k+l=2n$ are

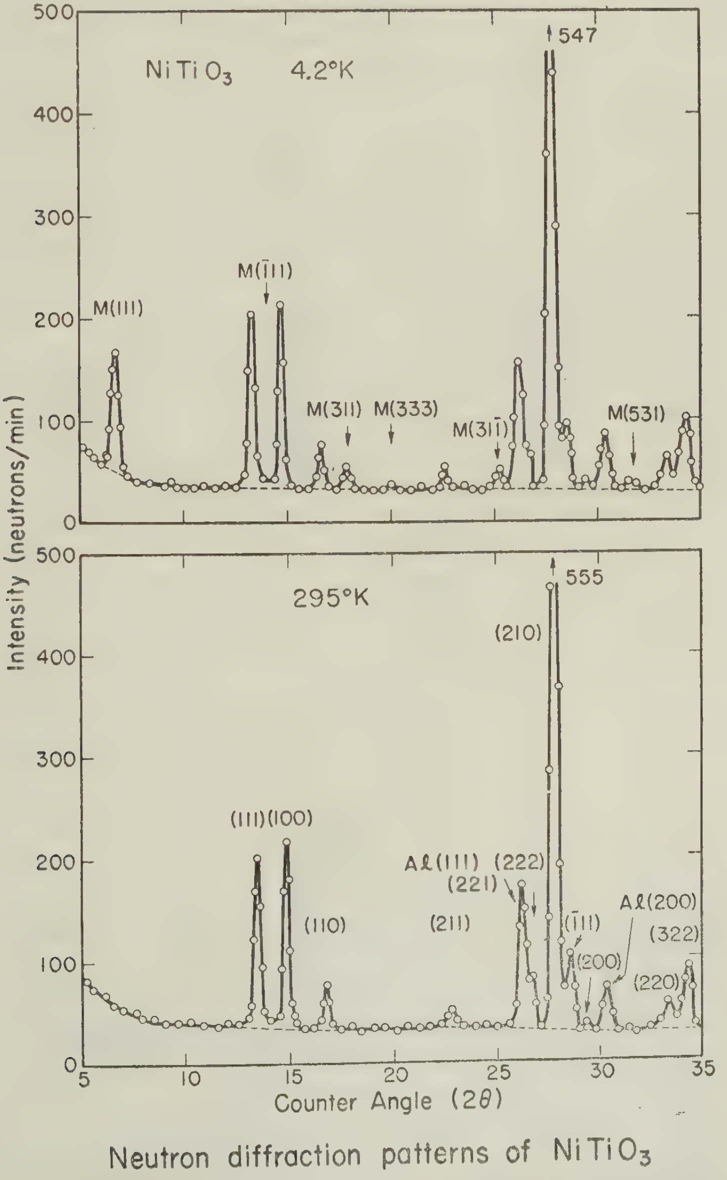

Fig. 2. Neutron diffraction patterns of $NiTiO_3$ taken above and below the Néel point. The wave length $\lambda=1.064$A.

proportional to (b_1+b_2) and are independent of the distribution of Ni and Ti on the different sites. The agreement was considerably improved by adjusting S from 1 to 0.92. Still better agreement was obtained by refining the oxygen parameters and then readjusting the ordering parameter. The best values of the parameters are:

$$x=0.555 \quad y=-0.045 \quad z=0.235 \quad S=0.94\,.$$

Agreement with the (210) peak could be obtained only by use of the S parameter. The oxygen parameters are very close to the improved values found for $FeTiO_3$.[6] One may note that the oxygen parameters reported previously satisfy the requirements of the higher symmetry **R**$\bar{3}$C of α-Fe_2O_3, that is, $y=1/2-x$ and $z=1/4$, though these are not necessary for **R**$\bar{3}$. The new oxygen parameters give more reasonable metal-oxygen bond distances, as shown in Table I. The agreement between calculated and observed intensities is presented in Table II (a).

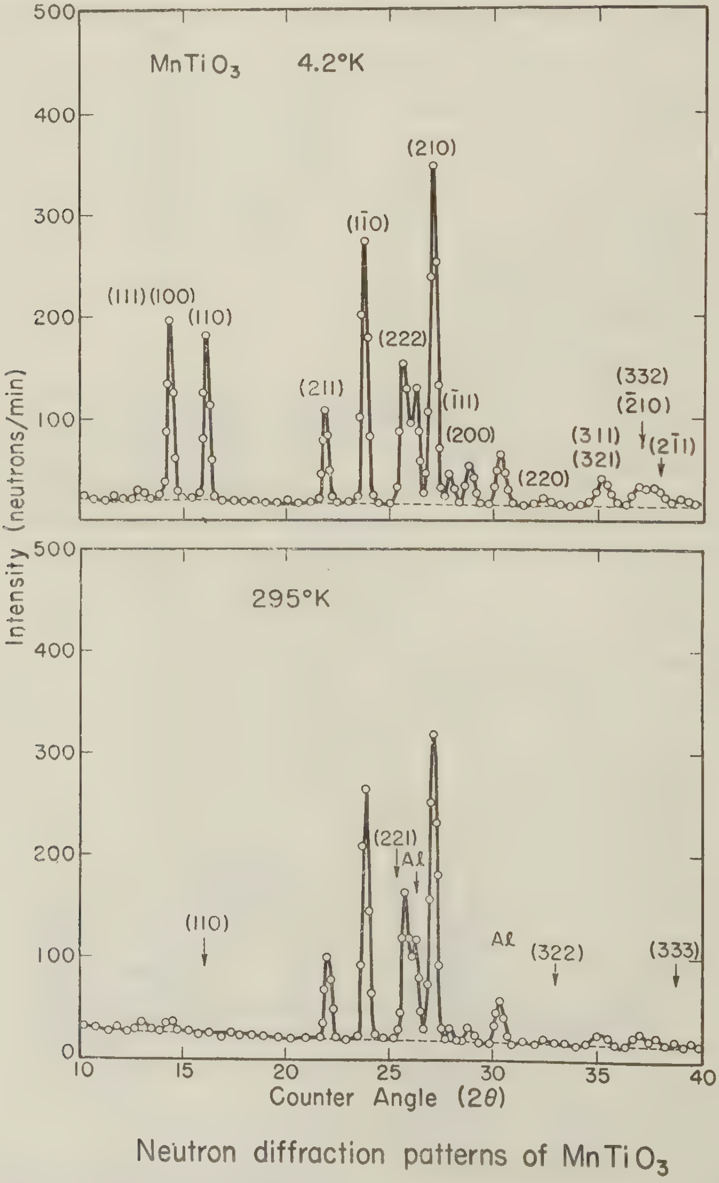

Fig. 3. Neutron diffraction patterns of $MnTiO_3$ taken above and below the Néel point. The wave length $\lambda=1.055$A.

Table I. Structural parameters of $MnTiO_3$ and $NiTiO_3$. The data on $FeTiO_3$ and α-Fe_2O_3 are shown for comparison. The lattice constants are taken from a paper by Ishikawa and Akimoto[7] and the origin is chosen according to Barth and Posnjak.[1]

	$MnTiO_3$	$FeTiO_3$	$NiTiO_3$	α-Fe_2O_3
a	5.610 A	5.538 A	5.437 A	5.424 A
α	54°30′	54°41′	55°07′	55°17′
u_1 (Me)	0.357	0.358	0.353	0.355
x	0.560	0.555	0.555	0.550
y	−0.050	−0.040	−0.045	−0.050
z	0.220	0.235	0.235	0.250
Me-O	2.26, 2.10 A	2.15, 2.03 A	2.14, 2.03 A	2.09, 1.98 A
Ti-O	2.12, 1.86 A	2.14, 1.92 A	2.06, 1.92 A	
r_{Me}	0.91 A	0.83 A	0.78 A	0.67 A
Order S		0.95	0.94	
Spin Direction	[111]	[111]	in (111)	in (111) >260°K [111] <260°K

Table II (a). Calculated and observed nuclear intensities for $NiTiO_3$.

$S=0.94$ $x=0.555$ $y=-0.045$ $z=0.235$

hkl	I_{cal}	I_{obs}	
		295°K	4.2°K
(111)	315	327	334
(100)	295	321	311
(110)	75	72	82
(211)	29	31	31
$(1\bar{1}0)$	7	< 5	< 5
(210)	1260	1240	1255
$(\bar{1}11)$	152	166	140
(200)	5	13	13
(220)	105	96	90
(322)	205	215	230
(311) (321)	379	380	408
$(\bar{2}10)$	166	150	165
(332) $(2\bar{1}\bar{1})$	25	20	25
(333)	44	39	37
(310) $(\bar{2}11)$ (331)	555	529	560
(320) (300) $(22\bar{1})$	231	234	232
(422)	1	<10	<10
(433) (432)	353	343	332
(421)	229	234	232

Table II (b). Magnetic intensities of $NiTiO_3$ at 4.2°K.

Calculated intensities are obtained by assuming $S=0.94$, $\mu_{eff}=2.25\mu_B$, the spin direction in (111) and the form factor of Ni metal. The scale factor was determined by the nuclear intensities shown in Table II (a). (hkl) indices are based on the double rhombohedral cell.

hkl	I_{cal}	I_{obs}
(111)	287	277
$(\bar{1}11)$	18	~15
(311)	41	39
(333)	18	<15
(331)	0	7
$(31\bar{1})$	44	44
(531)	22	25
(553) (511)	2	< 7
(555)	2	<10
$(51\bar{1})$	6	<10
(755) (733)	9	~10

$MnTiO_3$ requires somewhat different oxygen parameters than $NiTiO_3$:

$$x=0.560 \quad y=-0.050 \quad z=0.220$$

This is expected because of the difference in the ionic radii of Mn and Ni. As for the ordering of Mn and Ti, no information can be obtained because of the similarity of b_{Mn} (−0.36) and b_{Ti} (−0.38); moreover, it is even difficult to assign Mn to the position $u=0.357$ instead of $u=0.143$. The final assignment of Mn to u_1 gives more consistent interatomic distances and is also slightly favored by the intensity calculations (see Table III). It may be added that the oxygen parameters of this compound could be determined more accurately than in $NiTiO_3$ because of the insensitivity of the diffraction data to the ordering parameter S.

§ 3. Magnetic Structure

The neutron diffraction patterns obtained below the Néel temperature show several changes in the intensities (see Figs. 2 and 3). The new lines in $NiTiO_3$ require the doubling of the rhombohedral unit cell as was the case in $FeTiO_3$; on the other hand, the "magnetic" unit cell of $MnTiO_3$ is identical with the "chemical" unit cell.

All of the observed magnetic lines of $NiTiO_3$, when indexed with the double cell, have h, k, and l all odd. This implies that only the hexagonal **c** axis is doubled but not the **a**, satisfying the condition for models (a) and (b). Model (b) cannot satisfy the strong magnetic (111) reflection with any possible spin direction. The observed intensities can be explained satisfactorily by assuming model (a) and a spin direction lying in the (111) plane, as shown in Table II (b). The specific direction within this plane cannot be defined by powder data alone. Assuming this spin structure, the magnetic moment obtained was 2.25 μ_B, in good agreement with susceptibility measurements[7)], and suggesting a contribution from unquenched orbital moment. The form factor falls off much more slowly than that of Mn^{2+} [11)] and Fe^{3+} [12)], and is closest to that of Ni metal as determined by the polarized neutron technique[13)]. It should be noted, however, that because of the limited accuracy of the magnetic intensities at higher angles, the conclusion should be taken with some reserve. In the calculations an ordering parameter $S=0.94$ was used and it was assumed that the remaining Ni on B layers are not magnetically ordered. If their spins form an ordered arrangement such as (a) or (b) within the B layers, they will contribute to the calculated values of the magnetic intensities, but this correction is small.

The magnetic intensities of $MnTiO_3$ can be explained by assuming model (c) and a spin direction along [111]. If we assume $S=1$, the observed intensities require a moment of 4.55 μ_B, which is 91 per cent of the Mn^{2+} moment. This value was determined mainly by the intensities of (100) and (110). With this effective moment and the Mn^{2+} form factor[11)], quite satisfactory agreement was obtained between observed and calculated values, as shown in Table III.

Table III. Calculated and observed integrated intensities for $MnTiO_3$.

Effective moment, $\mu_{eff}=4.55\mu_B$ Spin direction along [111]

hkl	I_{obs} 295°K	I_{cal} Nucl.	 Mag.	 Total	I_{obs} 4.2°K
$(\bar{1}11)$	6	5	0	5	7
(100)	4	3	152	155	162
(110)	< 2	0	155	155	149
(211)	80	79	5	84	82
$(1\bar{1}0)$	238	250	0	250	244
(221)	<15	0	13	13	<18
(222)	139	134	9	143	153
(210)	321	319	10	329	341
$(\bar{1}11)$	10	8	20	28	31
(200)	23	20	25	45	52
(220)	9	8	2	10	10
(322)	< 4	1	0	1	< 4
(311) (321)	31	27	15	42	46
$(\bar{2}10)$ (332)	27	20	10	30	35
$(2\bar{1}1)$	14	12	12	24	24
(333)	5	5	0	5	5
(310) (331)	46	41	1	42	46
$(\bar{2}11)$	18	19	0	19	19
(320)	16	17	4	21	20
(300) $(22\bar{1})$	< 8	2	1	3	<10
(422)	22	26	1	27	20
(433) (432)	116	122	1	123	113

It is of course possible that the ordering of Mn and Ti is incomplete, as in $FeTiO_3$ and $NiTiO_3$. If we attribute the decrease of the moment from the spin-only value to disorder, S must be 0.91. Though this is not unreasonable compared with the value 0.94 for $NiTiO_3$ and 0.95 for $FeTiO_3$[6)], one might expect a larger activation energy of disorder for $MnTiO_3$, because of the larger difference between Mn-O and Ti-O distances. Moreover, there are several other possible causes for the smaller effective moment. Chemical analysis indicated a slight excess of Ti over Mn, and this departure from stoichiometry is in the correct direction to explain the low observed value. The existence of some manganese in the trivalent state cannot be excluded. In this respect, we may note that the effective Mn moment obtained by the susceptibility measurements[7)] is slightly (2 per cent) smaller than the expected value for Mn^{2+}. Thus the observed effect may be a combination of these factors with disorder playing a major part, and it is not possible, at present, to separate them unambiguously.

§ 4. Discussion

The results of the present neutron diffraction study are in good agreement with the previous magnetic measurements. In particular, the magnetic structure of $MnTiO_3$ proved to be the model predicted by the magnetic measurements on the $MnTiO_3$–α-Fe_2O_3 system. Another important result is the observation of incomplete order of Ni and Ti in $NiTiO_3$. Though direct evidence could not be obtained in the case of $MnTiO_3$, the estimated magnetic moment seems to indicate some disorder in this compound. From these results one might conclude that this is a general characteristic of ilmenite compounds. It would be an interesting problem to investigate the dependence of this disorder on the heat treatment of the specimen and its effect on the magnetic properties.

Superexchange interactions in rhombohedral sesquioxides have been discussed by Li14) and Iida15). There are three important Me-O-Me configurations, two of which, Γ_a and Γ_b, involve metal atoms on different layers and are expected to be stronger than the third one, Γ_c, which is the interaction within the same layer. If, however, the ordering of Me and Ti in $MeTiO_3$ is perfect, and all Ti atoms are in the tetravalent state, the antiferromagnetic order must be propagated three-dimensionally through two layers of oxygen by Me-O-O-Me interactions. As pointed out by Kramers16), such interactions would normally be expected to be much weaker than the singleanion superexchanges.

When the order is incomplete, some magnetic atoms enter on the B layers, and their role cannot be deduced from the neutron diffraction data. However, indirect evidence was obtained in the study of the $FeTiO_3$-α-Fe_2O_3 system6), where the addition of α-Fe_2O_3 decreases the antiferromagnetic Néel temperature of $FeTiO_3$. This was interpreted as a destruction of the ferromagnetic coupling within the A layers by a strong antiferromagnetic coupling between the A and B layers. This indicates that at least trivalent magnetic atoms on the B layers are not taking part in the three-dimensional propagation of the $FeTiO_3$-type magnetic order. This conclusion should also apply to $NiTiO_3$, which has essentially the same magnetic structure as $FeTiO_3$ except for the spin direction. Nevertheless, a further study of the $NiTiO_3$–α-Fe_2O_3 system is desirable to provide additional evidence.

$MnTiO_3$ has an antiferromagnetic arrangement within each A layer. A molecular field calculation7) has shown that the moments introduced on the B layer are arranged antiparallel to each other. In this case strong interactions Γ_a and Γ_b do not disturb the ordering on the A layers, implying that the addition of α-Fe_2O_3 should not change the magnetic structure. Experimental confirmation of this point has yet to be carried out.

If pure $MnTiO_3$ is partially disordered it is possible that Γ_a and Γ_b, as well as a long range Me-O-O-Me interaction, may play a role in the propagation of order between the layers. At present we cannot separate these two effects. It may be worthwhile pointing out that there are two kinds of configuration:

$$\mathrm{Mn}\overset{p}{-}\mathrm{O}-\mathrm{O}\overset{q}{-}\mathrm{Mn} \quad \text{positive}$$

$$\mathrm{Mn}\overset{q}{-}\mathrm{O}-\mathrm{O}\overset{q}{-}\mathrm{Mn} \quad \text{negative}$$

where p and q are bond distances corresponding to 2.10A and 2.26A respectively.14) This situation is analogous to the case of Cr_2O_3 where the interaction is through only one oxygen.

§ 5. Acknowledgments

The authors are very grateful to Drs. R. Nathans and W. J. Takei for stimulating discussions.

References

1) T. F. W. Barth and E. Posnjak: Z. Krist. **88** (1934) 265.
2) T. Nagata and S. Akimoto: Geofisica Pura e Applic. Milano **34** (1956) 36.
3) Y. Ishikawa and S. Akimoto: J. Phys. Soc. Japan **12** (1957) 1083.
4) R. M. Bozorth, D. E. Walsh and A. J. Williams: Phys. Rev. **108** (1957) 157.
5) C. G. Shull, W. A. Strauser and E. O. Wollan: Phys. Rev. **83** (1951) 33.
6) G. Shirane, S. J. Pickart, R. Nathans and Y. Ishikawa: J. Phys. Chem. Solids **10** (1959) 35.
7) Y. Ishikawa and S. Akimoto: J. Phys. Soc. Japan **13** (1958) 1110, 1298.
8) Y. Ishikawa and S. Sawada: J. Phys. Soc.

Japan **11** (1956) 496.
9) G. E. Bacon: *Neutron Diffraction* (Oxford, 1955) 151.
10) E. Posnjak and T. F. W. Barth: Z. Krist **88** (1934) 271.
11) L. M. Corliss, N. Elliott and J. M. Hastings: Phys. Rev. **104** (1956) 924.
12) L. M. Corliss, J. M. Hastings and F. G. Brockman: Phys. Rev. **90** (1953) 1013.
13) R. Nathans, C. G. Shull, G. Shirane and A. Andresen: J. Phys. Chem. Solids (in press).
14) Y. Y. Li: Phys. Rev. **102** (1956) 1015.
15) A. Iida: J. Phys. Soc. Japan **11** (1956) 1300.
16) H. A. Kramers: Physica **1** (1934) 182.

JOURNAL OF THE PHYSICAL SOCIETY OF JAPAN, Vol. 14, No. 10, OCTOBER, 1959

On Galvanomagnetic Effects in P-Type Crystals of PbTe

By Kisaburo SHOGENJI

Hitachi Central Research Laboratoty, Kokubunji, Tokyo

(Received June 5, 1959)

This paper describes measurements of the magnetoresistance and of the planar Hall effect of p-type PbTe crystals; it also describes an interpretation of the electronic band structure of the crystal. The measurements were made at 90°K as a function of the magnetic field strength and of the angle between the magnetic field and the current through the specimen. The coefficients relating to the galvanomagnetic effects were determined from the experimental data. Using these coefficients the electronic band structure of the crystal is shown to be $\{111\}$ energy spheroids, presumably prolate with a mass ratio of 0.3.

§ 1. Introduction

Several investigations on the electrical properties of PbTe crystals have been made by us recently[1][2]. It is also desirable to know the electronic band structure of PbTe in order to get more systematic information about its electrical properties. Therefore measurements of magnetoresistance and of planar Hall effect of p-type PbTe were made; also its band structure was interpreted by analyzing the experimental data.

Many investigations have been made on magnetoresistance effect of semiconductors, for example: a theoretical one by Seitz[3], experimental ones on germanium by Esterman-Forner[4] and by Pearson-Suhl[5], on Silicon by Pearson-Herring[6], and many others[7]. However it seems to us that investigations on the magnetoresistance of semi-conducting intermetallic compounds are fewer and less detailed than those made on germanium and Silicon. Research has been reported on InSb by Frederikse-Hosler[8], and on Bi_2Te_3 by Drabble *et al*[9]. For a group of PbS, PbSe and PbTe semiconductors, investigations have been made by Putley[10], Hirahara-Murakami[11], Irie[12] and Algaier[13]. Also the planar Hall effect has been investigated theoretically and experimentally by goldberg-Davis[14], and has been measured on PbSe crystals by Hirahara-Murakami[11]. Theoretical investigations on the relationship between magnetoresistance and band structure of semiconductors have been made by Abeles-Meiboom[15], Shibuya[16] and Herring[17].

In this paper measurements of magnetoresistance and planar Hall effect are reported. Before these experiments are described, a phenomenological description of magnetoresistance and planar Hall effect will be made, in section 2, as a function of the magnetude and the direction of the applied magnetic field and of the applied electric current through the specimen. This description has the form of a mathematical series of ascending powers of the magnetic field. The terms up to the fourth power of the field are calculated, since the experimental results, which will be given in this paper, show us the necessity of at least the fourth power into consideration. In section 3 several expressions relating the constants of the galvanomagnetic effects to the band structure will be deduced by means of Shibuya's theory[16]. The experimental results will be analyzed according to Shibuya's theory in the following section.

The experiments will be described in section 4. The specimens used have their long axes in the [100] and the [110] directions respectively. The measurements of the magnetoresistance and of the planar Hall effect were made as a function of the magnitude and of the direction of the applied magnetic field. The constants of the galvanomagnetic effects were determined by the dependence of these effects upon the field, and these constants were used in the determination of the band structure of the crystal.

§ 2. Phenomenological Description of the Galvanomagnetic Effects.

PbTe crystals have the NaCl type lattice structure with the symmetry O_h. Seitz[3] deduced a phenomenological formula for the magnetoresistance of a cubic crystal. Also Mason *et al*[18]. calculated expression for the magnetoresistance and Hall effect up to the fifth power of H for a crystal with the symmetry O_h. In this paper phenomenological expressions for the magnetoresistance and for the planar Hall effect are deduced, and the expressions are transformed into forms suitable for comparison with the experimental results. These calculations were made using Mason's results[18].

An early paper by Seitz[3][5] gave the following expressions for the magnetoresistance of a semiconductor.

$$\mathbf{I}=\sigma_0\mathbf{E}+\alpha(\mathbf{E}\times\mathbf{H})+\beta\mathbf{E}H^2+\gamma\mathbf{H}(\mathbf{E}\cdot\mathbf{H})+\delta T\mathbf{E}\ , \tag{2–1}$$

$$\mathbf{E}=\rho_0[\mathbf{I}+a(\mathbf{I}\times\mathbf{H})+b\mathbf{I}H^2+c\mathbf{H}(\mathbf{I}\cdot\mathbf{H})+dT\mathbf{I}]\ , \tag{2–2}$$

where **I** is the current density, **E** and **H** are the electric and magnetic fields ; σ_0 and ρ_0 are ordinary conductivity and ordinary resistivity; T is a diagonal tensor with elements $H_1{}^2$, $H_2{}^2$ and $H_3{}^2$; α and a are constants relating to the Hall effect ; β, γ, δ, b, c and d are constants of the magnetoresistance. A later report by Mason *et al*[18]. contained an expression for the magnetoresistance and the Hall effect as a function of the electric current and of the magnetic field which extended to the fifth power of the magnetic field. The expression is

$$\begin{aligned}E_i=&[\rho_{ij}+\pi_{ijkl}H_kH_l+\zeta_{ijklmn}H_kH_lH_mH_n+\cdots]I_j\\&+\varepsilon_{ijk}[R_{km}H_m+\kappa_{kmno}H_mH_nH_o+\lambda_{kmnopq}H_mH_nH_oH_pH_q+\cdots]I_j\ ,\end{aligned} \tag{2–3}$$

where $i, j, k, \cdots$ are suffixes expressing directions ; ρ_{ij} is the resistivity ; π_{ijkl} and ζ_{ijklmn} are coefficients relating to the magnetoresistance ; κ_{kmno} and λ_{kmnonq} are coefficients relating to the Hall effect, and R_{km} is the Hall coefficients at low field ; ε_{ijk} is as follows :

$$\varepsilon_{ijk}\begin{cases}=\ \ 1 & \text{for}\quad i, j, k\quad \text{is}\quad (1, 2, 3), (2, 3, 1), (3, 1, 2)\\ =-1 & \text{for}\qquad\qquad\qquad (2, 1, 3), (1, 3, 2), (3, 2, 1)\ .\end{cases}$$

Hereafter the following abbreviations will be used for the pairs of suffixes in conformity with the notations used in Mason's paper[18] :

$$11\rightarrow1,\ 22\rightarrow2,\ 33\rightarrow3,\ 23=32\rightarrow4,\ 13=31\rightarrow5,\ 12=21\rightarrow6\ .$$

The independent coefficients of Eq. (2–3) for O_h can be shown as follows[18] :

$$\begin{aligned}\rho_{ij}&\rightarrow\rho_0\\R_{ij}&\rightarrow R\\\pi_{ijkl}&\rightarrow\pi_{11},\ \pi_{12},\ \pi_{66}\\\kappa_{ijkl}&\rightarrow\kappa_{11},\ \kappa_{12}\\\zeta_{ijklmn}&\rightarrow\delta_{111},\ \zeta_{112},\ \zeta_{122},\ \zeta_{123},\ \zeta_{441},\ \zeta_{442}\\\lambda_{ijklmn}&\rightarrow\lambda_{111},\ \lambda_{112},\ \lambda_{123}\ .\end{aligned}$$

Therefore Eq. (2–3) becomes

$$\begin{aligned}E_1=&\rho_0 I_1+\pi_{11}I_1H_1{}^2+\pi_{12}I_1(H_2{}^2+H_3{}^2)+2\pi_{66}H_1(I_2H_2+I_3H_3)\\&+\zeta_{111}I_1H_1{}^4+6\zeta_{112}I_1H_1{}^2(H_2{}^2+H_3{}^2)+\delta_{122}I_1(H_2{}^4+H_3{}^4)+6\zeta_{123}I_1H_2{}^2H_3{}^2\\&+12\zeta_{441}H_1H_2H_3(I_2H_3+I_3H_2)+4\zeta_{442}H_1[I_3H_3(H_1{}^2+H_3{}^2)+I_2H_2(H_1{}^2H_2{}^2)\\&+(R+3\kappa_{12}H^2+5\lambda_{112}H^4)(I_2H_3-I_3H_2)+(\gamma_{11}-3\gamma_{12})(I_2H_3{}^3-I_3H_2{}^3)\\&+(\lambda_{111}-5\lambda_{112})(I_2H_3{}^5-I_3H_2{}^5)+(30\lambda_{123}-10\lambda_{112})[I_2H_3H_1{}^2H_2{}^2-I_3H_2H_1{}^2H_3{}^2]+\cdots\,.\end{aligned}\tag{2–4}$$

Similar equations can be derived for E_2 and E_3. The voltage appearing in any direction across the specimen can be calculated for simple geometry for any possible combination of directions of the electric current and the magnetic field.

When an electric current flows in the [100] direction and a magnetic field is in the $x-y$ plane, namely ; the magnetic field rotates about an axis in the z-direction, we obtain

$$\begin{aligned}E^{100}_{100}\langle 001\rangle = I\,[&\rho_0+(\pi_{11}\cos^2\theta+\pi_{12}\sin^2\theta)H^2\\&+(\zeta_{111}\cos^4\theta+6\zeta_{112}\cos^2\theta\sin^2\theta+\zeta_{122}\sin^2\theta)H^4]\,,\end{aligned}\tag{A–1}$$

where θ is the angle between I and H. The superscript expresses the direction of the voltage, the subscript the direction of the current, and $\langle 001\rangle$ expresses the direction of the rotational axis of the field. In a similar way, when the magnetic field lies in the $y-z$ plane we obtain

$$E^{100}_{100}\langle 100\rangle=I[\rho_0+\pi_{12}H^2+\{\zeta_{122}(\cos^4\theta'+\sin^4\theta')+6\zeta_{123}\cos^2\theta'\sin^2\theta'\}H^4]\,.\tag{A–2}$$

In this case the angle between I and H is always 90°, and θ' is the angle between the H and the z-direction. When the current flows in the [110] direction, the electric field appearing in the same direction for various rotational axes of the magnetic field is given by

$$\begin{aligned}E^{001}_{001}\langle 001\rangle=I\Bigg[&\rho_0+\Bigg\{\frac{\pi_{11}+\pi_{12}}{2}+\pi_{66}(\cos^2\theta-\sin^2\theta)\\&+\Bigg\{\frac{\zeta_{111}+\zeta_{122}}{4}(1+4\sin^2\theta\cos^2\theta)\\&+\frac{3}{2}\zeta_{112}(\cos^2\theta-\sin^2\theta)+2\zeta_{442}(\cos^2\theta-\sin^2\theta)\Bigg\}H^4\Bigg]\,.\end{aligned}\tag{B–1}$$

$$\begin{aligned}E^{110}_{110}\langle 1\bar{1}0\rangle=I\Bigg[&\rho_0+\Bigg\{\frac{\pi_{11}}{2}\cos^2\theta+\pi_{12}\left(\frac{\cos^2\theta}{2}+\sin^2\theta\right)+\pi_{66}\cos^2\theta\Bigg\}H^2\\&+\Bigg\{\frac{\zeta_{111}}{4}\cos^4\theta+3\zeta_{112}\cos^2\theta\left(\frac{\cos^2\theta}{2}+\sin^2\theta\right)+\zeta_{122}\left(\frac{\cos^4\theta}{4}+\sin^4\theta\right)\\&+3(\zeta_{123}+2\zeta_{441})\cos^2\theta\sin^2\theta+2\zeta_{442}\cos^4\theta\Bigg\}H^4\Bigg]\,,\end{aligned}\tag{B–4}$$

$$\begin{aligned}E^{110}_{110}\langle 110\rangle=I\Bigg[&\rho_0+\Bigg\{\frac{\pi_{11}}{2}\cos^2\theta'+\pi_{12}\left(\frac{\cos^2\theta'}{2}+\sin^2\theta'\right)-\pi_{66}\cos^2\theta'\Bigg\}H^2\\&+\Bigg\{\frac{\zeta_{111}}{4}\cos^4\theta'+\zeta_{112}\cos^2\theta'\left(\frac{\cos^2\theta'}{2}+\sin^2\theta\right)+\zeta_{122}\left(\frac{\cos^4\theta'}{4}+\sin^4\theta'\right)\\&+3(\zeta_{123}-2\zeta_{441})\cos^2\theta'\sin^2\theta'-2\zeta_{442}\cos^4\theta'\Bigg\}H^4\Bigg]\,.\end{aligned}\tag{B–5}$$

In Eq. (B–5) θ' express the angle between H and the $[1\bar{1}0]$ direction.

When the current flows in the [100] direction and the magnetic field rotates in the $x-y$ plane, the electric field that appears in the [010] direction is a measure of the planar Hall effect. Thus

$$E^{010}_{100}\langle 001\rangle=I(\pi_{66}H^2+2\zeta_{442}H^4)\sin 2\theta\,.\tag{Ap–1}$$

Similarly

$$E^{1\bar{1}0}_{110}\langle 001\rangle=\frac{1}{2}\{(\pi_{11}-\pi_{12})H^2+(\zeta_{111}-\zeta_{112})H^4\}\sin 2\theta\ . \qquad \text{(Bp—1)}$$

Table I gives the directions of the current, of the voltage and of the axis of rotation in the above equations.

The potential gradient which appears through the specimen for special directions of the applied field and current can be calculated from the above equations as follows:

$$E^{100}_{100}[100]=I[\rho_0+\pi_{11}H^2+\zeta_{111}H^4]\ , \qquad \text{(i)}$$

$$E^{100}_{100}[001]=I[\rho_0+\pi_{12}H^2+\zeta_{122}H^4]\ , \qquad \text{(ii)}$$

$$E^{110}_{110}[110]=I\left[\rho_0+\frac{\pi_{11}+\pi_{12}+2\pi_{66}}{2}H^2+\frac{\zeta_{111}+6\zeta_{112}+\zeta_{122}+8\zeta_{442}}{4}H^4\right], \qquad \text{(iii)}$$

$$E^{110}_{110}[1\bar{1}0]=I\left[\rho_0+\frac{\pi_{11}+\pi_{12}-2\pi_{66}}{2}H^2+\frac{\zeta_{111}+6\zeta_{112}+\zeta_{122}-8\zeta_{442}}{4}H^4\right], \qquad \text{(iv)}$$

$$E^{110}_{110}[001]=I[\rho_0+\pi_{12}H^2+\zeta_{122}H^4]\ , \qquad \text{(v)}$$

$$E^{110}_{110}[\theta=45°]=I\left[\rho_0+\frac{\pi_{11}+3\pi_{12}+2\pi_{66}}{4}H^2\right.$$
$$\left.+\frac{\zeta_{111}+18\zeta_{112}+5\zeta_{122}+12\zeta_{123}+24\zeta_{441}+8\zeta_{442}}{16}H^4\right]^{*}, \qquad \text{(vi)}$$

$$E^{010}_{100}[110]=I[\pi_{66}H^2+2\zeta_{442}H^4]\ , \qquad \text{(vii)}$$

$$E^{1\bar{1}0}_{110}[010]=I\left[\frac{\pi_{11}-\pi_{12}}{2}H^2+\frac{\zeta_{111}-\zeta_{112}}{2}H^4\right]. \qquad \text{(viii)}$$

Table I. Specifications of the curves in Figs. 2~5 and corresponding equations.

Curve	Direction of **I**	Direction of **E**	Axis of rotation
A-1	[100]	[100]	[001]
A-2	[100]	[100]	[100]
B-1	[110]	[110]	[001]
B-4	[110]	[110]	[1̄10]
B-5	[110]	[110]	[110]
Ap-1	[100]	[010]	[001]
Bp-1	[110]	[11̄0]	[001]

Table II. Specifications of the curves in Figs. 6 and 7 and corresponding equations.

Curve	Direction of **I**	Direction of **E**	Direction of **H**	Angle between **I** and **H**	Corresponding curve in Table I
(i)	[100]	[100]	[100]	0°	A-1
(ii)	[100]	[100]	[001]	90°	A-1 A-2
(iii)	[110]	[110]	[110]	0°	B-1 B-4
(iv)	[110]	[110]	[11̄0]	90°	B-1 B-5
(v)	[110]	[110]	[001]	90°	B-4 B-5
(vi)	[110]	[110]		45°	B-4
(vii)	[100]	[010]	[110]	45°	Ap-1
(viii)	[110]	[11̄0]	[010]	45°	Bp-1

The superscripts indicate the direction of the potential gradient, the subscripts the direction of the current, and [110] or [010] indicates the direction of the magnetic field. Equations (vii) and (viii) give the planar Hall voltage, while the other equations give the magnetoresistance.

Table II shows the directions of the current, of the potential gradient and of the magnetic field; θ is the angle between the current and the magnetic field. The last column gives the curves of Table I which contain as a special case the condition listed in the corresponding row of Table II.

§ 3. Theoretical Considerations

Shibuya[16)] calculated magnetoresistance effect of semiconductors in which the electrons or the holes obeyed Maxwell statistics and interacted with the accoustical mode of the lattice vibration. In his paper the electronic energy is assumed to be expressed as families of spheroidal surfaces in $\boldsymbol{k}$-space. The calculations were made for the following three cases: the spheroids have six {100} axes as symmetrical axes (case **a**), twelve {110} axes (case **b**), and eight {111} axes (case **c**). One of the most important results of his calculations is that there exist the following relations between the coefficients of the magnetoresistance in connection with the electronic band structure of the crystals.

---

* Eq. (vi) is the special case for $\theta=45°$ in Eq. (B-4).

$$\begin{aligned} \beta+\gamma+\delta=0 &\text{ and } \delta>0 \text{ for (case } \mathbf{a}) , \\ \beta+\gamma-\delta=0 &\text{ and } \delta<0 \text{ for (case } \mathbf{b}) , \\ \beta+\gamma=0 &\text{ and } \delta<0 \text{ for (case } \mathbf{c}) , \\ \delta=0 &\text{ for spherical energy surface.} \end{aligned} \tag{3-1}$$

We may obtain information on the band structure from magnetoresistance experiments by using Eq. (3–1). But Eq. (3–1) only is not enough to decide whether the spheroids are prolate or oblate. Here we deduce several formulas from Shibuya's theory in order to obtain additional information about the band structure from our experiments.

First we calculate the conductivity tensor for various directions of the magnetic field. The tensor form becomes the same as for the above three cases, although the expressions for the tensor elements are different from one another.

When **H** is in the [100] direction, the conductivity tensor is

$$L=\begin{vmatrix} L_1 & 0 & 0 \\ 0 & L_2 & L_3 \\ 0 & -L_3 & L_2 \end{vmatrix} . \tag{3-2}$$

The resistivity is expressed in terms of the elements of tensor (3–2) as follows:

$$\rho_{11}=1/L_1 , \tag{3-3}$$

$$\rho_{\perp}=L_2/(L_2^2+L_3^2) , \tag{3-4}$$

where ρ_{11} is the resistivity when the current is parallel to the magnetic field, and $\rho_{\perp}$ is the resistivity when the current is perpendicular to the magnetic field. In this case $\rho_{\perp}$ is expressed by Eq. (3–4) for any direction of the current is perpendicular to the field. When **H** is in the [110] direction.

$$L=\begin{vmatrix} L_1 & L_3 & -L^4 \\ L_3 & L_1 & L_4 \\ L_4 & -L_4 & L_2 \end{vmatrix} , \tag{3-5}$$

$$\rho_{11}=1/(L_1+L_3) . \tag{3-6}$$

When **H** is in the [1$\bar{1}$0] direction, the conductivity tensor is expressed with the same elements L_i's as tensor (3–5) by

$$L=\begin{vmatrix} L_1 & -L_3 & L_4 \\ -L_3 & L_1 & L_4 \\ -L_4 & -L_4 & L_2 \end{vmatrix} . \tag{3-7}$$

When the current flows in the [110] direction and **H** is in the [1$\bar{1}$0] direction the resistivity becomes, tensor elements (3–7) being used,

$$\rho_{\perp}=L_2/\{L_2(L_1-L_3)+2L_4^2\} . \tag{3-8}$$

The planar Hall effect is a phenomenon in which a voltage appears across the specimen in a plane fixed by the current and the magnetic field and is perpendicular to the current. The planar Hall voltage has its maximum value at $\theta=45°$. Therefore the maximum planar Hall voltage for a [100] specimen is obtained when the following conditions are satisfied: the direction of **I** is [100], the direction of **H** is [110] and the direction of **E** is [010]. Thus, using the elements of conductivity tensor (3–5), E is expressed as

$$E=\frac{I(L_4^2-L_2L_3)}{(L_1+L_3)\{2L_4^2+L_2(L_1-L_3)\}} . \tag{3-9}$$

For a [110] specimen, the maximum value of the planar Hall voltage appers when the direction of **I** is [110], the direction of **H** is [100], and the direction of **E** is [1$\bar{1}$0]. Using the elements of Eq. (3–2)

$$\begin{aligned} E&=\frac{I}{2}\left\{\frac{1}{L_1}-\frac{L_2}{(L_2^2+L_3^2)}\right\} \\ &=\frac{I}{2}(\rho_{11}-\rho_{\perp}) . \end{aligned} \tag{3-10}$$

Thus the resistivity and the planar Hall voltage are expressed in terms of the conductivity tensor.

Next we give explicit forms of some of the above formulas for the resistivity. The expressions are different from one another for the three cases so that some information on the band structure can be obtained by comparing the results of calculations with experimental results. Shibuya[16] expressed his calculated result by a closed formula. Eq. (3–1) was obtained by the expansion of the closed formula in a series of ascending powers of **H** and examination of the coefficients of H^2. We shall mention here the terms proportional to H^4 as we did in section 2. Expansition of Shibuya's formula into an ascending power series of **H** up to the fourth power, which has been performed below is not mathematically precise. Nevertheless we have performed the expansion and compared the calculated results with the experimental results with the expectation that we would be able to obtain some information on the band structure, for example, the shape of the spheroids.

Eq. (3-3) is expanded as an ascending power series of **H** and this series is compared with Eq. (i). Thus we obtain relations between the constants of magnetoresistance and the parameter which is related to the band structure. For the three cases mentioned above the relations obtained are

$$\rho_0=3/NeA(r+2) \qquad \text{for all three cases,} \tag{3–11}$$

$$\pi_{11}=0 \quad \text{and} \quad \zeta_{111}=0 \qquad \text{for (case } \mathbf{a}\text{),} \tag{3–12}$$

$$\left.\begin{aligned} \pi_{11}&=\frac{(r-1)^2B^2}{2(r+2)}\rho_0 \\ \xi_{111}&=\frac{(r-1)^2(r+1)B^4\rho_0}{4(r+2)}Ei\left(-\frac{r+1}{2}B^2H^2\right) \end{aligned}\right\} \qquad \text{for (case } \mathbf{b}\text{),} \tag{3–13}$$

$$\left.\begin{aligned} \pi_{11}&=\frac{2(r-1)^2B^2}{3(r+2)}\rho_0 \\ \zeta_{111}&=\frac{2(r-1)^2(2r+1)B^4\rho_0}{9(r+2)}Ei\left(-\frac{2r+1}{3}B^2H^2\right) \end{aligned}\right\} \qquad \text{for (case } \mathbf{c}\text{),} \tag{3–14}$$

where $r=m_2/m_1$ is the ratio of the mass perpendicular to the rotational axis of the energy spheroid to that parallel to it, N being the carrier density. A and B are given in Shibuya's paper[16]; A being generalized mobility. $Ei(-X)$, the exponential integral, by itself becomes infinite at $X=0$, but Eq. (i) combined with coefficients (3–13) or (3–14) converges at $H=0$ because of the factor H^4. Strictly speaking, expressions (3–13) and (3–14) are not to be considered as the coefficients of the power series corresponding to Eq. (i), as they contain a function Ei of H. For the present purpose, however, we use such expressions as Eqs. (3–13) and (3–14), and comment upon this point will be made later.

Similarly comparison between Eqs. (3–6) and (iii) is made. At first Eq. (iii) is rewritten as follows:

$$\rho=\rho_0+\Pi H^2+ZH_2\,. \tag{3–15}$$

Then

$$\rho_0=3/NeA(r+2) \qquad \text{for all cases,}$$

$$\left.\begin{aligned} \Pi&=\frac{(r-1)^2}{2(r+2)}B^2\rho_0 \\ Z&=\frac{(r+1)(r-1)^2B^4\rho_0}{4(r+2)}Ei\left(-\frac{r+1}{2}B^2H^2\right) \end{aligned}\right\} \qquad \text{for (case } \mathbf{a}\text{),} \tag{3–16}$$

$$\left.\begin{aligned} \Pi&=\frac{3(r-1)^2}{8(r+2)}B^2\rho_0 \\ Z&=\frac{3(3r+1)(r-1)^2\beta^4\rho_0}{32(r+2)}Ei\left(-\frac{3r+1}{4}B^2H^2\right) \end{aligned}\right\} \qquad \text{for (case } \mathbf{b}\text{),} \tag{3–17}$$

$$\left.\begin{aligned} \Pi&=\frac{(r-1)^2}{3(r+2)}B^2\rho_0 \\ Z&=\frac{(r-1)^2B^4\rho_0}{9}Ei\left(-\frac{r+2}{3}\beta^2H^2\right) \end{aligned}\right\} \qquad \text{for (case } \mathbf{c}\text{).} \tag{3–18}$$

§ 4. Experiments

Procedures. The specimen used were of synthetic *p*-type. The method of crystal growing was the same as that described in a previous paper[1]. Two parallelepiped specimens about 3 × 2 × 1 mm^3 were cut from a single crystal. The directions of the long axes were [100] and [110]. Current leads and resistivity probes were attached to the specimen in the manner previously described[1]. Magnetoresistance and planar Hall effect were measured by the usual *dc* method using these two specimens. The current during the measurements was 50 *mA* and 100 *mA*; at these currents the voltage to be measured was verified to be proportional to the current. The magnetic field extended up to 10300 gauss produced by an electromagnet of 9 *A* exciting current. The polepiece of the magnet was 200 *mm* in diameter, the gap between polepieces 38 *mm*. All measurements were made at 90°K using a Dewar vessel and liquid air. When the measurements were made, the specimen was rotated about an axis which was perpendicular to the magnetic field, and the strength of the magnetic field was varied.

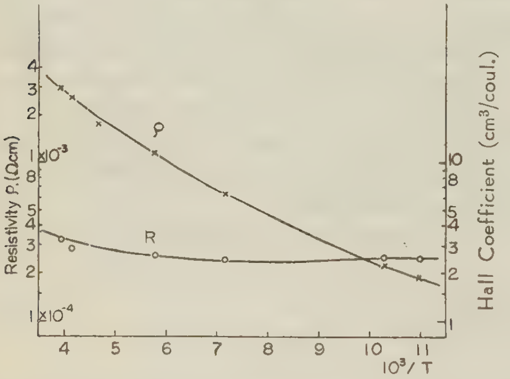

Fig. 1. Temperature dependence of resistivity and low field Hall coefficient.

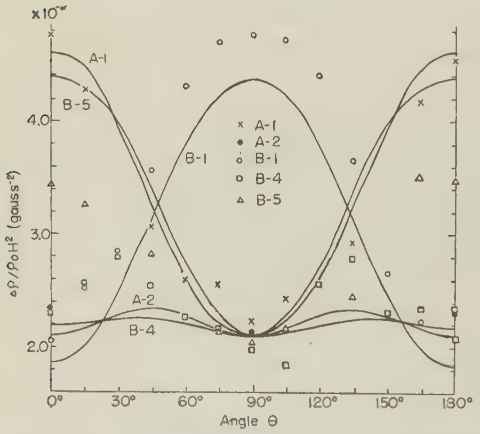

Fig. 2. Angular dependence of magnetoresistance at 5500 gauss.

Results. Fig. 1 shows the resistivity and the low field Hall coefficient of the crystal as a function of $1/T$, T being the absolute temperature. Their temperature variations are normal for PbTe crystals[1]. The resistivity is $1.93 \times 10^{-4} \Omega cm$ and the Hall coefficient is $+2.48\ cm^3/coul.$ at 90°K.

In Figs. 2 and 3 magnetoresistance is shown as a function of the angle between the current and the magnetic field. The ordinate is $\Delta\rho/\rho_0 H^2 = \{\rho(H) - \rho(H=0)\}/\rho(H=0)H^2$, and the abscissa is the angle between **I** and **H**, except curves A-2 and B-5 for which the angle between **I** and **H** is always 90° and θ in the figures represents the angle between the mag-

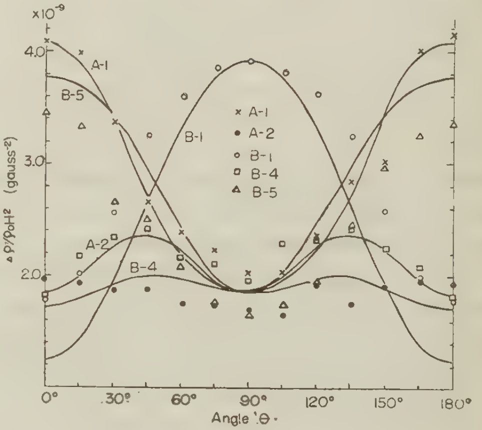

Fig. 3. Angular dependence of magnetoresistance at 8000 gauss.

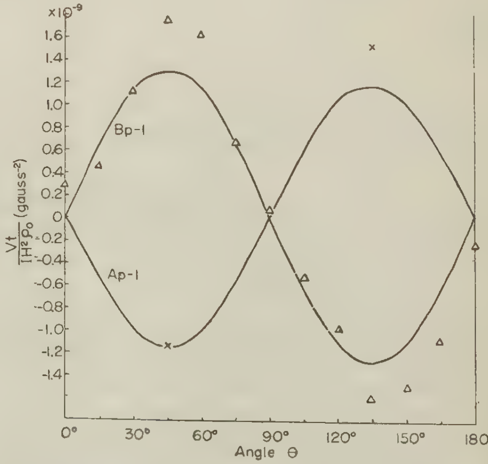

Fig. 4. Angular dependence of planar Hall effect at 5500 gauss. The dimension of the ordinate is the same as that of Figs. 2 and 3. The ordinate represents $Vt/IH^2\rho_0$, where V is the measured voltage, t the thickness of the specimen, I the current through the specimen.

netic field and the [010] and the [110] directions respectively. The field strength is 5500 gauss in Fig. 2 and 8000 gauss in Fig. 3. The nomenclature used for the curves corresponds to that of Table I. From these figures it is seen that the angular variation of magnetoresistance does not necessarily follow the $A+B\sin^2\theta$ law predicted by low field theory[3]. The curves shown in the figures are those obtained by calculation, which will be described later.

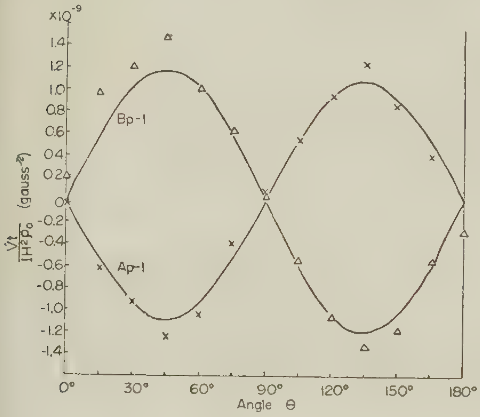

Fig. 5. Angular dependence of planer Hall effect at 8000 gauss.

Figs. 4 and 5 show the planar Hall effect as a function of the angle θ for magnetic field of 5500 gauss and 8000 respectively. The dimension of the ordinate is chosen to be the same as that in Figs. 2 and 3 for the sake of convenience of comparison. The angular variation seems to follows, within experimental accuracy, the $\sin 2\theta$ law as described by the theory[14].

Magnetic field dependence of magnetoresistance and planar Hall effect is shown in Fig. 6, log. $\Delta\rho/\rho_0$ *vs.* log H being plotted. Variation of magnetoresistance and planar Hall effect with respect to the magnetic field is smaller than that given by the H^2 low. The straight lines shown in the figures are so drawn that they fit the experimental points. The exponents n's of the lines with respect to **H** are listed in Table III.

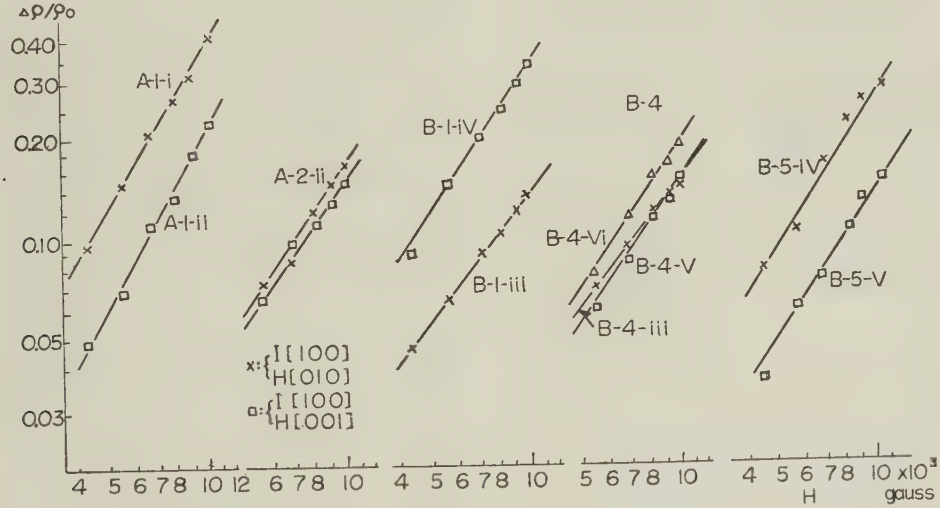

Fig. 6. (a) Field dependence of magnetoresistance, $\Delta\rho/\rho_0$ as a function of H.

The angular variation shown in Figs. 2 and 3 does not necessarily satisfy the $A+B\sin^2\theta$ low. This fact suggests that terms of higher powers of **H**, namely; terms proportional to H^4, have appreciable effect on the results. And the results shown in Fig. 6 also support the view that the experiments deviate from the law. When we plot $\Delta\rho/\rho_0 H^2$ vs. H^2, we can see whether the magnitude of the magnetoresistance is proportional to H^2 or not. If the plots are horizontal straight lines, the field dependence is expressed as H^2 rigorously. If they are inclined straight lines, the field dependence is expressed by $\Delta\rho/\rho_0=(\Pi H^2+ZH)^4/\rho_0$, and Π and Z are determined from the point of intersection with the ordinate axis and from the slope respectively. The results are shown in Fig. 7. It is seen from the figure that the experimental points are fairly well approximated by inclined straight lines. The coefficients determined from these lines are indicated in Table III. The agreement is satisfactorily good between coefficients which are evaluated from different curves but correspond to the same conditions, e.g. A-1-ii and A-2-ii. By combining these values and Eqs. (i)~(iv) we can determine consistently the constants of galvanomagnetic effects, which are indicated in Table IV.

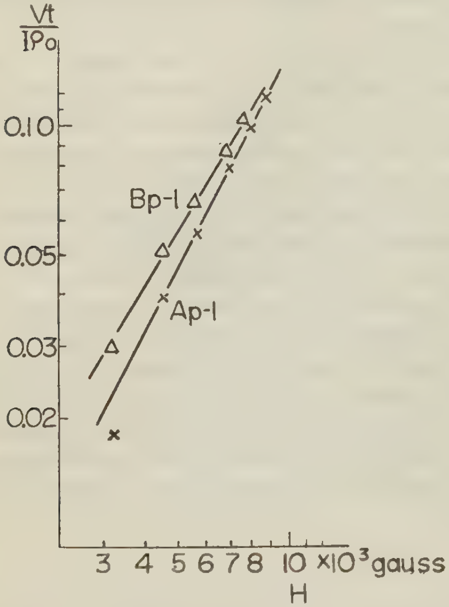

Fig. 6. (b) Field dependence of planar Hall effect. The dimension of the ordinate is the same as that of Fig. 6 (a).

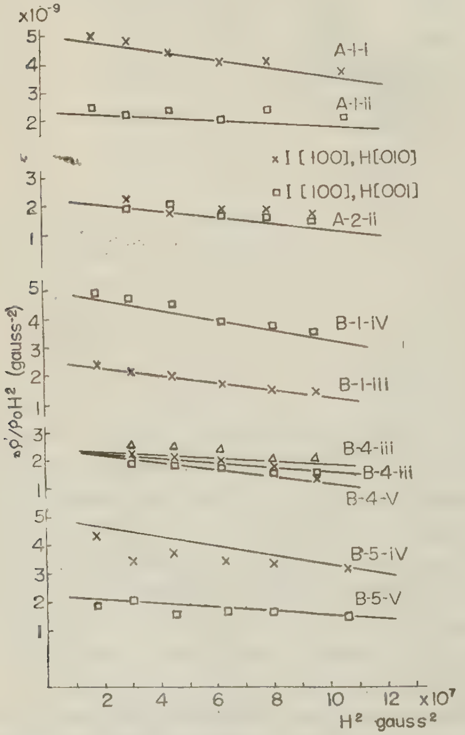

Fig. 7 (a). Field dependence of magnetoresistance. $\Delta\rho/\rho_0 H^2$ as a function of H^2.

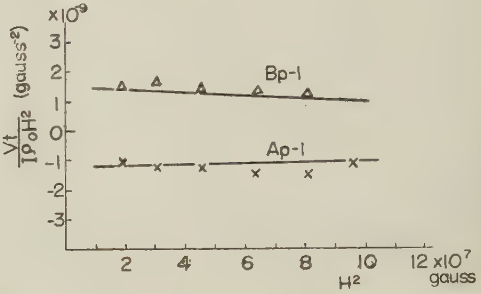

Fig. 7 (b). Field dependence of planar Hall effect. The dimension of the ordinate is the same as that of Fig. 7 (a).

Table III. Experimental values and theoretical formulas expressing the dependence of the galvanomagnetic effects upon the magnetic field.

Curve	π/ρ_0		Z/ρ_0	Exponen n of H^n
	Experimental value $\times 10^9$ (gauss^{-2})	Theoretical expression	Experimental value $\times 10^{18}$ (gauss^{-4})	Experimental value
A-1-i	5.2	$b+c+d$	−16	1.6
A-1-ii	2.6	b	− 6	1.8
A-2-ii	2.3		− 7	1.4
B-1-iii	2.6	$b+c+(d/2)$	−13	1.3
B-4-iii	2.2		− 8	1.3
B-1-iv	5.3	$b+(d/2)$	−18	1.5
B-5-iv	4.3		−12	1.5
B-4-v	2.3	b	− 8	1.3
B-5-v	2.2		− 8	1.5
B-4-vi	2.8	$b+(c/2)+(d/4)$	− 8	1.4
Ap-1-vii	2.5	$c/2$	− 1	1.8
Bp-1-viii	3.6	$(c+d)/2$	− 2	1.6

The straight lines shown in Fig. 7 are calculated by using Eqs. (i)~(viii) and the constants indicated in table IV. It must be noted that the constants listed in Table III are not used in the calculation of these lines. The solid curves of Figs. 2~5 are also obtained by calculating Eqs. (A-1), (A-2),⋯ and (Bp-1) with the constants shown in Table IV. It is known, from these figures, that the constants obtained from the field dependence of galvanomagnetic effects can also

Table IV. Values of the coefficient of galvanomagnetic effects.

a	-1.3×10^{-4} gauss^{-1}	α	6.6×10^{-1} Ω^{-1}cm^{-1} gauss^{-1}
b	2.3×10^{-9} gauss^{-2}	β	-9.7×10^{-5} Ω^{-1}cm^{-1} gauss^{-2}
c	-2.5×10^{-9} 〃	γ	9.8×10^{-5} 〃
d	5.3×10^{-9} 〃	δ	-2.8×10^{-5} 〃
π_{11}/ρ_0	5.2×10^{-9} 〃	ζ_{111}/ρ_0	-16×10^{-18} gauss^{-4}
		ζ_{112}/ρ_0	-7×10^{-18} 〃
π_{12}/ρ_0	2.3×10^{-9} 〃	ζ_{122}/ρ_0	-7×10^{-18} 〃
		ζ_{123}/ρ_0	3×10^{-18} 〃
π_{66}/ρ_0	-1.2×10^{-9} 〃	ζ_{441}/ρ_0	$\sim0.7\times18^{-18}$ 〃
		ζ^{442}/ρ_0	1×10^{-18} 〃

represent their angular dependence tolerably well. From the consistency shown in Table III and Figs. 2∼7, we think that these constants are reliable enough to be worthy of qualitative or partially quantitative discussions.

§ 5. Analysis

The constants of the galvanomagnetic effects derived in the preceding section can be considered to represent the characteristic values of the crystal as described before. Thus their values are used here in order to discuss the electronic band structure of the crystal. The fact that the longitudinal magnetoresistance, in general, is not zero but has a larger value shows that the band is far from that given by the simple spherical energy surface model.

The coefficients of H^2 are examined first. The relations between the coefficients expressed by Eq. (3–1) become, using Table IV, as follows:

$$\beta+\gamma+\delta=-2.7\times10^{-5}\,,$$
$$\beta+\gamma-\delta=+2.9\times10^{-5}\,,$$
$$\beta+\gamma=+1\times10^{-6}$$

and $\delta<0$. Therefore this crystal corresponds to (case **c**), *i.e.*; the band structure is approximated by energy spheroids having {111} axes as symmetrical axes. The mass ratio r is obtained by solving

$$\frac{\beta}{\delta}=\frac{(r+2)(2r+1)}{2(r-1)^2}\,. \tag{5–1}$$

The solution is: $r=3.5$ or $r=0.3$. The carrier density N is calculated by Eqs. (34), (35) and (23) of Shibuya's paper:

$$N=\begin{cases}2.36\times10^{18} & \text{for } r=3.5\\ 2.70\times10^{18} & \text{for } r=0.3\end{cases} \tag{5–2}$$

Moreover using $\sigma_0=NeA(r+2)/3$ and Eq. (7) of Shibuya's paper, we obtain

$$B=\begin{cases}9.9\times10^{-5} & \text{for } r=3.5\\ 2.1\times10^{-4} & \text{for } r=0.3\end{cases} \tag{5–3}$$

By combining the equations given in Table I of Shibuya's paper, we can also calculate the value of B. The value thus obtained is nearly equal to the value given by (5–3).

Saturation values of magnetoresistance are required in order to determine which value of r should be used. Unfortunately we could not produce a field strong enough to obtain saturation values. Therefore only a few comments will be given on the choice of values for r's by referring to the coefficients of H^4 determined in section 4. We have calculated the coefficients of H^4 by Eqs. (3–14) and (3–18) as shown in Table III. The coefficients obtained however are not constant but contain a factor Ei$(-X)$ whose argument includes the magnetic field. Unfortunately this factor varies by a fairly large amount within the range of magnetic fields used. Nevertheless, we compare the experimental values with the calculated ones. The coefficients of the fourth power of **H** must always be negative, because the equations, from which the coefficients are calculated, include the factor Ei$(-X)$ whose value is always negative. This requirement is, of course, realized in our experiments as shown in the figures and tables.

Let us examine the ratio of ζ_{111} to Z, referring to Eqs. (3–14) and (3–18) neglecting the slight difference between the arguments of the two equations. This ratio becomes 2.9 for $r=3.5$; or 1.4 for $r=0.3$, while corresponding value obtained experimentally is seen to be 1.5 from Table IV and Eqs. (i), (iii), (3–15) and (3–18). Therefore $r=0.3$, *i.e.*, prolate, seems more reasonable, although we must not jump to conclusions. The ratio of coefficients π_{11}/Π becomes, referring to Eqs. (3–12), (3–13), (3–14), (3–16), (3–17) and (3–18), as follows: 0 for (case **a**); 4/3 for (case **b**); 2 for (case **c**); these values being true regardless of the value of r. The corresponding experimental value is 2.0 which is deduced using Eqs. (i), (iii), (3–15) and Table IV. This value supports our conclusion that the crystal belongs to (case **c**).

§ 6. Discussions of the Results

The results of the calculation and analysis of this paper must be carefully examined. First of all a comment will be made on Eqs. (3–14) and (3–18). These equations are not considered simply to represent the coefficients of the fourth power of **H**. But it is believed that these equations have some relation to the coefficients, for example, proportional relation. On the basis of the assumption that expressions (3–14) and (3–18) are proportional to the coefficients, we have derived $r=0.3$ in the preceding section.

On the other hand Allgaier[13)] has recently published magnetoresistance data for PbS, PbSe and PbTe, and given a consideration on their band structure. Especially for PbTe he has obtained a definite conclusion and pointed out that his data and conclusion agree pretty well with our data and conclusion, which had been published previously in this journal.[19)] He has obtained $r=0.25\sim0.17$ by analyzing his data by means of Gold-Roth theory.[20)] His conclusion coincides with ours in that PbTe is to be represented by the {111} model and that the energy spheroids are prolate. Moreover his value of r is not much different from the value given in this paper.

Next it must be examined whether the assumptions on the basis of which Shibuya's calculation[16)] is made hold for these experiments or not. One of the questions is whether the holes of the crystal are degenerate or non-degenerate at the temperature of the measurements. The effective mass of the hole was given as $0.94\,m$ in our previous paper.[1)] Then the degenerate temperate of this crystal is calculated in the usual manner to be obout 80°K. The effective mass given in the previous paper is, however, the inertial mass; and the '*density-of-states*' mass is four times as large as the inertial mass if the crystal is expressed by the {111} eight-valley model. Therefore the degenerate temperature becomes lower by a factor of four. The holes in the crystal at the temperature of the measurements are not degenerate and Shibuya's theory can be applied to the crystal from this point of view.

The relaxation time for scattering used in Shibuya's calculation is inversely proportional to the square root of the carrier energy, which corresponds to the acoustical mode of lattice vibration. PbTe crystal is, however, thought to be an ionic or partial ionic crystal and, as pointed out in our previous paper,[1)] it is possible that the carriers are scattered mainly by the optical mode of lattice vibration. The relaxation time corresponding to the optical mode is independent of the carrier energy. One may doubt whether Shibuya's theory can be applied to this crystal.

The calculated expressions for the galvanomagnetic effects generally consist of the product of two factors, one of which is a function of the dependence of the relaxation time on the energy and also a function of the applied statistics, while the other is a function only of the shape of the energy band.[6)15)16)17)] Therefore relations (3–1) still represent the characteristics of the band structure and the discussion of section 5 dealing with ratios of magnetoresistance coefficients is also adequate when the relaxation time is different from that used by Shibuya.[16)] Thus it is concluded that the main parts of our analyzed results need not be corrected if the optical mode of lattice vibration is the main source of scattering, and even if the holes are degenerate.

In finishing this paper we will sum up the results as follows: *i*) Phenomenological expressions for galvanomagnetic effects are derived as a function of the magnetic field. The expressions are power series of **H** which have been calculated up to the fourth power. *ii*) Expanding Shibuya's formula the coefficients of the above power series are calculated as a function of parameters which represent the shape of the band structure. *iii*) Magnetoresistance and planar Hall effect of p-type PbTe are measured as a function of the field strength and of the angle θ. *iv*) The constants for the galvanomagnetic effects are determined from the measurements as a function of the field strength. The constants determined are coefficients of H^2 and H^4, and they corresponds reasonably well with the values measured as a function of θ. *v*) Using the constants relating to H^2, the band structure is shown to be represented by {111} energy spheroids. *vi*) Using the constants relating to H^4, it is speculated that the spheroids may be prolate with the mass ratio of 0.3. *vii*) The above conclusions agree reasonably well with those ef Allgaier. *viii*) The applicability of Shibuya's theory to this crystal is examined and verified.

The writer wishes to express his sincere thanks to Professor Y. Sakaki, at whose laboratory in Nagoya University the main parts of this work were done, for his kind guidance and encouragement. He is very grateful to Professor A. Okazaki and Professor K. Ariyama, who gave kind and critical review of the original manuscript. He is indebted to Dr. S. Uchiyama, who helped him by preparing the experiments for this research, by making measurements during the preliminary phases of the work, and by his suggestion and discussion.

References

1) K. Shogenji and S. Uchiyama: J. Phys. Soc. Japan **12** (1957) 252. S. Uchiyama and K. Shogenji: ibid. 431.
2) Y. Sakaki, K. Shogenji, Y. Un-no, S. Uchiyama and Y. Sugiyama: Mem. Fac. Eng. Nagoya Univ. **7** (1955) 72. K. Shogenji, S. Uchiyama and Y. Un-no: ibid. **8** (1956) 110. S. Uchiyama and K. Shogenji: E.T.J. Japan **4** (1958) 50.
3) F. Seitz: Phys. Rev. **79** (1950) 372.
4) F. Esterman and A. Foner: Phys. Rev. **79** (1950) 365.
5) G. L. Pearson and H. Suhl: Phys. Rev. **83** (1951) 768.
6) G. L. Pearson and C. Herring: Physica **20** (1954) 975.
7) B. Lax: Rev. Mod. Phys. **30** (1958) 122.
8) H. P. R. Frederikse and W. R. Hosler: Phys. Rev. **108** (1957) 1136, 1146.
9) J. R. Drabble, R. D. Groves and R. Wolfe: Proc. Phys. Soc. London **71** (1958) 430. J. R. Drabble: *ibid.* **72** (1958) 380.
10) E. H. Putley: Proc. Phys. Soc. London **B**, **68** (1955) 22.
11) E. Hirahara and M. Murakami: Bull. Fac. Eng. Hiroshima Univ. **4** (1955) 259.
12) T. Irie: J. Phys. Soc. Japan **11** (1956) 840.
13) R. S. Allgaier: Phys. Rev. **112** (1958) 828.
14) C. Goldberg and R. E. Davis: Phys. Rev. **94** 1121.
15) S. Meiboom and B. Abeles: Phys. Rev. **93** (1959) 1121. B. Abeles and S. Meiboom: ibid. **95** (1954) 31.
16) M. Shibuya: J. Phys. Soc. Japan **9** (1954) 134; Phys. Rev. **95** (1954) 1385.
17) C. Herring: Bell Syst. Tech. J. **34** (1955) 237.
18) W. P. Mason, W. H. Hewitt and R. F. Wick: J. Appl. Phys. **24** (1953) 166.
19) K. Shogenji and S. Uchiyama: J. Phys. Soc. Japan **12** (1957) 1477.
20) L. Gold and L. M. Roth: Phys. Rev. **107** (1957) 358.

JOURNAL OF THE PHYSICAL SOCIETY OF JAPAN, Vol. 14, No. 10, OCTOBER, 1959

Magnetic Susceptibility of Liquid Alloys of Copper with Cobalt, Iron, Manganese, and Chromium

By Yasuaki NAKAGAWA*

Department of Physics, Faculty of Science, University of Tokyo

(Received June 6, 1959)

A systematic investigation has been made on the magnetic susceptibility of a series of transition metals dissolved in molten copper at temperatures up to 1600°C. These molten metals are miscible in all proportions except for the Cu-Cr system.

The susceptibilities of the Cu–Co and Cu–Fe alloys follow the Curie-Weiss law. The Curie constant is roughly proportional to the concentration of Co or Fe. The paramagnetic Curie temperature for the Cu-Co system rises monotonously with the concentration of Co, while that for the Cu-Fe system shows a maximum at an intermediate composition. In the Cu-Mn and Cu-Cr systems, only the Cu-rich alloys show the Curie-Weiss paramagnetism, while the alloys containing more than 50% Mn or more than 5% Cr show rather temperature-independent paramagnetism.

§ 1. Introduction

The magnetic properties of dilute alloys of transition metals in noble metals have fully been studied by many investigators. The more enriched alloys, however, have been ignored in most cases, because the solid solubility is in general restricted. A systematic investigation on the variation of the magnetic properties with the composition of the alloys is possible in the liquid state, since these metals are miscible in almost all proportions. As reported previously by the present author,[1][2] the magnetic properties of the transition metals and alloys in the liquid state are not essentially different from those in the solid state. Accordingly, the magnetic properties in the solid state can be inferred to a certain extent from the measurements in the liquid state. In 1941 Weil[3] measured the magnetic susceptibilities of various transition metals dissolved in molten non-magnetic metals. Since his measurements were carried out below 1400°C, only the alloys having lower liquidus temperatures were studied.

The present work has been made at higher temperatures up to 1600°C. Specimens investigated are of the alloys of 3*d*-transition metals, such as Co, Fe, Mn and Cr, with a noble metal, Cu. The temperature dependence of the susceptibility can well be determined, because the liquidus temperatures for these alloys are fairly below 1600°C, except for the Cu-Cr alloys.

§ 2. Experimental Method

The measurements of magnetic susceptibility were made by Faraday's method using Sucksmith's ring balance. A silicon-carbide resistance furnace was used for the measurements at high temperatures, as described in our previous paper.[1] Each alloy specimen, weighing about 400 mg, was prepared by using this apparatus. The procedure was as follows: the two component metals of the alloy were contained together in a small alumina crucible fixed to the balance, and were heated by the furnace under a purified argon atmosphere. After the specimen had completely been melted and homogenized, its susceptibility was measured at various temperatures during successive cooling and heating cycles. The temperature was controlled step by step, the average cooling or heating rate being about 5°C/min.

During the first melting process, the magnetic susceptibility was measured to confirm the complete melting and mixing of the metals. Among the metals investigated, only chromium has the melting point higher than 1600°C. Because diffusion of the atoms in the liquid state is very rapid, the homogeneous liquid alloys could be formed in ten or twenty minutes at 1600°C, except for the Cu-Cr alloys. In the latter case, dissolution of solid chromium in molten copper is so sluggish that it took over an hour for the Cu-Cr specimens to reach thermal equilibrium.

---

* Present address: Department of Physics and Chemistry, Gakushuin University, Mejiro, Tokyo.

Temperatures were measured by Pt-PtRh thermocouple situated close to the specimen, calibrated *in situ* at the four transition temperatures of pure iron: ferromagnetic Curie point (770°C), α-γ transformation point on heating (910°C), γ-δ transformation point (1400°C), and melting point (1535°C); at these temperatures the magnetic susceptibility showed abrupt changes. The transition temperatures mentioned above are mainly based on a recent work of Pattison and Willows[4], being somewhat different from those described in our previous paper[1].

The metals used for the specimens were of very high purity. Electrolytic copper, cobalt, iron and manganese were used after being melted in a high vacuum induction furnace. The principal impurities determined by chemical analysis were carbon and silicon, the concentrations of which were as follows: C—0.006% in Cu, 0.008% in Co, 0.008% in Fe, and 0.010% in Mn; Si—0.001% in Cu, 0.060% in Co, 0.004% in Fe, and 0.010% in Mn. Chromium was spectroscopically pure obtained from Johnson, Matthey & Co.; the 'electrolytic flakes deoxidized' were used without the vacuum melting treatment. The compositions of the alloy specimens were not determined by chemical analysis but calculated from the mixing ratios. In this paper the compositions are hereafter expressed by atomic percent.

§ 3. Experimental Results

Cu-Co and Cu-Fe. Phase diagrams for the Cu-Co and Cu-Fe systems are similar to each other, showing very restricted solid solubility and nearly flat liquidus curve in the intermediate composition range.[5]

The susceptibility vs. temperature curves obtained for these alloys are shown in Fig. 1 and Fig. 2. Both Cu-Co and Cu-Fe alloys exhibit extensive supercooling of the liquid phase. The susceptibility curve measured during cooling is smooth at the liquidus temperature, T_L, and shows a large dis-

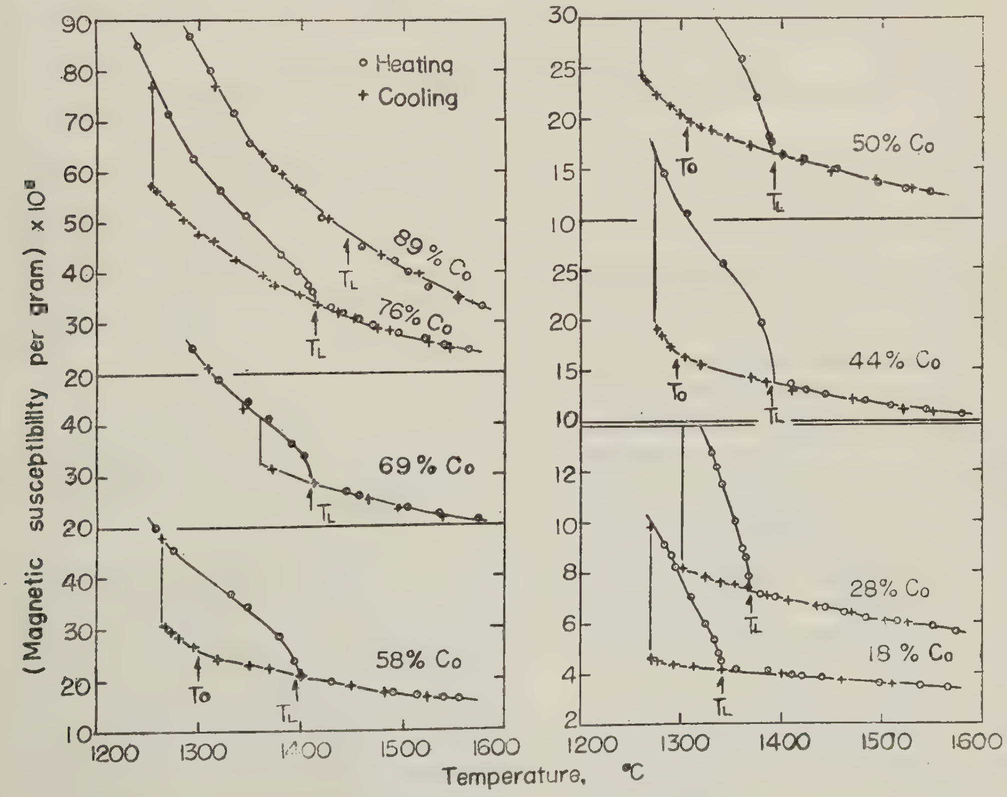

Fig. 1. Susceptibility curves for Cu-Co alloys.
T_L is the liquidus temperature; T_0 is the limit of liquid immiscibility.

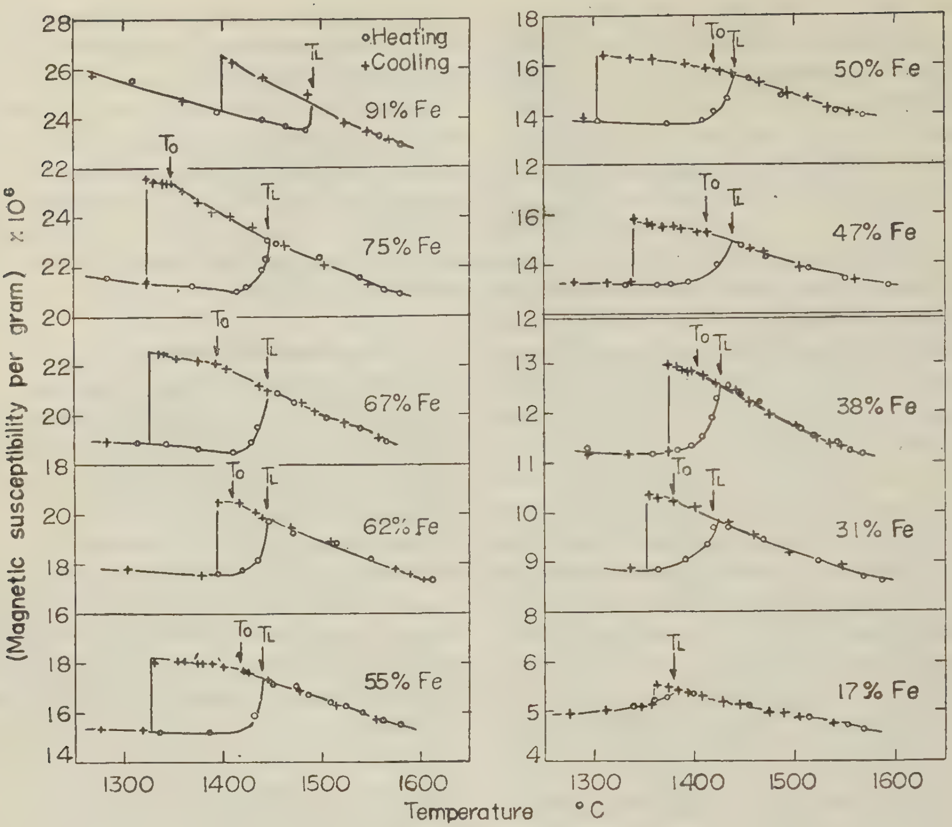

Fig. 2. Susceptibility curves for Cu-Fe alloys.
T_L is the liquidus temperature; T_0 is the limit of liquid immiscibility.

continuity at the temperature about 100°C below T_L, where the solid phase is precipitated abruptly from the supercooled liquid solution. The precipitation of the solid phase causes an increase in susceptibility for the Cu-Co alloys wheras a decrease for the Cu-Fe alloys.

It is found in some cases that the susceptibility curve exhibits anomalous behaviour in the supercooled region; the curve has an angular point at a certain temperature denoted as T_0 in the figures. At this temperature the supercooled liquid solution breaks up into two liquid phases. This is confirmed by the microscopic examination of the quenched specimens. A detailed report on this subject has already been published elsewhere.[6]

Cu-Mn. Copper and manganese form a continuous series of solid solutions having a face-centred cubic structure. The liquidus temperatures reported by many investigators agree fairly well, while there are remarkable discrepancies for the solidus temperatures of the manganese-rich alloys.*

The results of the susceptibility measurements are shown in Fig. 3. The susceptibility shows a maximum at the liquidus temperature, T_L. Below T_L, the susceptibility measured during cooling deviates appreciably from that measured during heating, although the supercooling of the liquid phase in these alloys is not extensive. The deviation is mainly due to the segregation which takes place upon solidification. The segregation is confirmed by the microscopic examination of the quenched specimens. By annealing at

---

* According to Hansen[5], the most reliable solidus curve for the Cu-Mn system is that obtained by Dean *et al.*[7], which is based on incipient melting studies by means of micrographic investigation. Also the present author has studied the solidus curve by the similar method. The results will be published elsewhere. It is to be noted here that the solidus curve determined by the present author is in disagreement with that obtained by Dean *et al.*, being rather close to an earlier work of Grube *et al.*[8]

850°C for several hours, the segregated specimens are not completely homogenized, and so the susceptibility curves below T_L, shown in Fig. 3, do not represent the values for the equilibrium state. At temperatures above T_L, the susceptibility curves are well reproducible, because of rapid diffusion in the liquid state. For the manganese-rich alloys, the susceptibility in the liquid state is nearly independent of both temperature and the composition of the alloys.

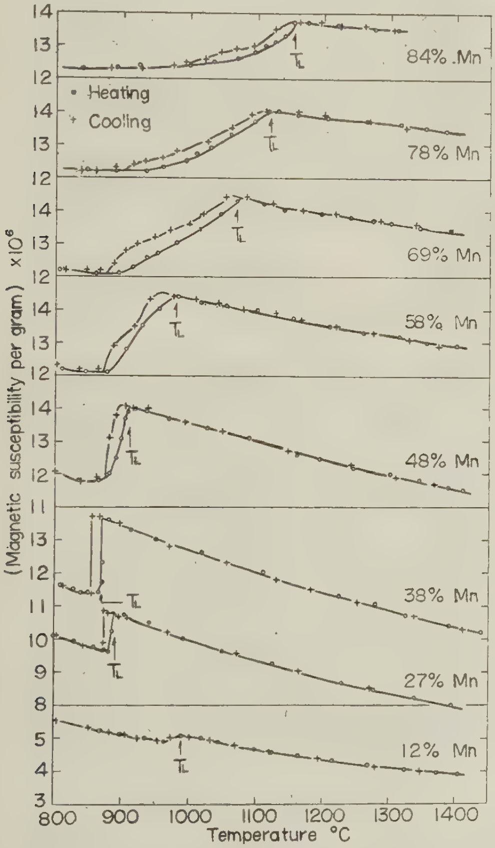

Fig. 3. Susceptibility curves for Cu-Mn alloys. T_L is the liquidus temperature.

Cu-Cr. Since the solubility of chromium in molten copper is fairly restricted, only the copper-rich alloys are investigated. The susceptibility curves obtained for these alloys and for pure copper are shown in Fig. 4. It is confirmed by the microscopic examination of the quenched specimen that an angular point on the susceptibility curve corresponds certainly to the liquidus temperature, T_L. According to Hansen,[5] there have been no reliable data on the liquidus curve for the Cu-Cr system. The liquidus curve obtained in the present work is shown in Fig. 5, together with that determined by Siedschlag[9] using fairly impure chromium. The liquid immiscibility is not found in the range up to 15% Cr.

The susceptibility curves for various Cu-Cr alloys show discontinuity at the same temperature, T_E, which must be a eutectic temperature of this system. The susceptibility shows a gradual change between T_L and T_E. Contrary to the Cu-Mn system, the temperature hysteresis is not found in this system. This is certainly due to the fact that the solid phases precipitated are of almost pure chromium and copper. The susceptibilities of these solid phases can be

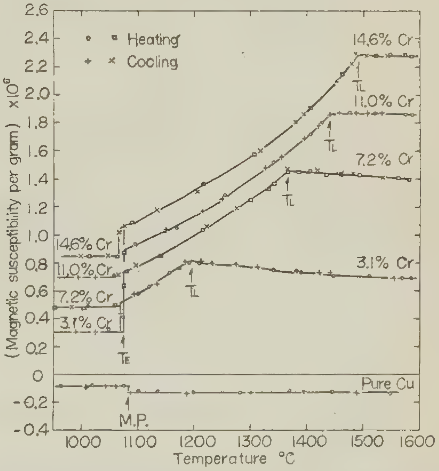

Fig. 4. Susceptibility curves for Cu-Cr alloys and pure Cu.
T_L is the liquidus temperature; T_E is the eutectic temperature.

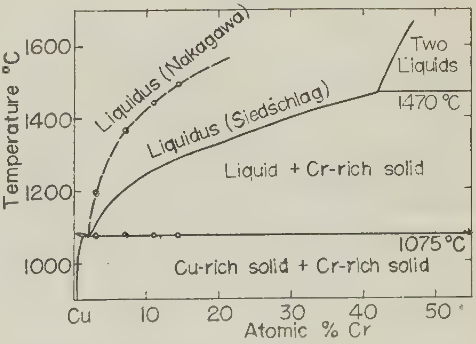

Fig. 5. Phase diagram for Cu-Cr system.
–– o ––: Liquidus curve obtained by the present work. Other lines are due to Hansen's book[5].

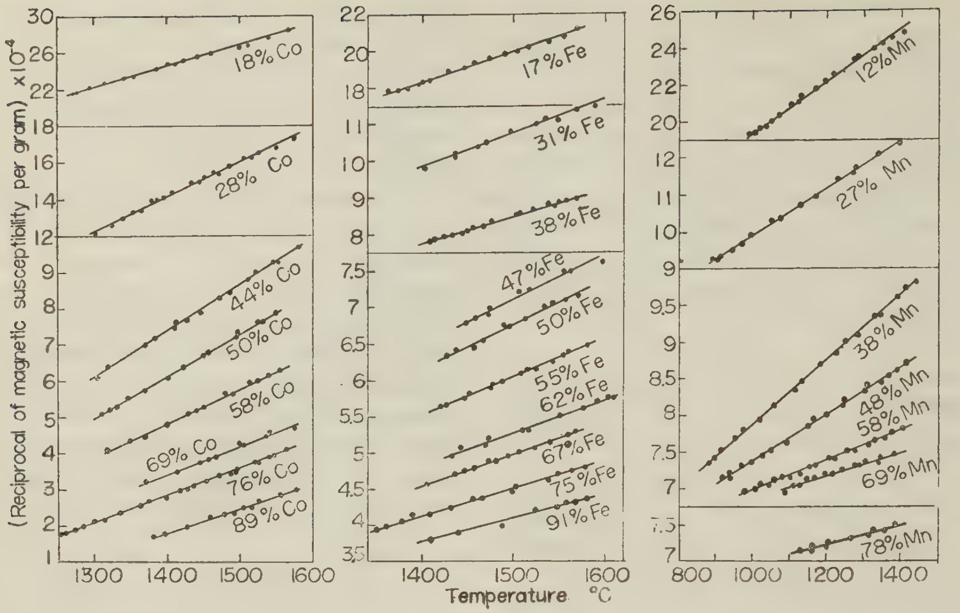

(a) Cu–Co alloys (b) Cu-Fe alloys (c) Cu-Mn alloys

Fig. 6. Curie-Weiss dependence of susceptibility on temperature. The values of susceptibility are corrected for diamagnetism of copper.

estimated from the data shown in Fig. 4; the susceptibility per gram of chromium-rich phase is 5.8×10^{-6}, being independent of temperature, and that of copper-rich phase is 0.15×10^{-6} at 1050°C, its temperature dependence being not determined.

§ 4. Analysis of the Results on Homogeneous Liquid Alloys

It is shown that the magnetic susceptibilities of these alloys above the liquidus temperatures follow in general the Curie-Weiss law:

$$\chi=C/(T-\theta)\,, \tag{1}$$

where χ is the susceptibility per gram and T the temperature. The two parameters, C and θ, are the Curie constant per gram and the paramagnetic Curie temperature, respectively. As shown in Fig. 6, the reciprocal of susceptibility plotted against temperature lies on a straight line, from which C and θ are determined. For the Cu-Co and Cu-Fe alloys, the susceptibility in the supercooled liquid state also fits Eq. (1), as far as the separation into two liquid phases does not occur.

It is expected that the Curie-Weiss paramagnetism of these alloys is only due to the atoms of transition elements. Therefore, the measured values of susceptibility are corrected by taking into account the diamagnetic contribution of copper. The susceptibility per gram of molten copper is -0.13×10^{-6}, being independent of temperature, as shown in Fig. 4. For the alloys containing more than 30% transition metals, this correction becomes ineffective. The diamagnetic contribution of the closed-shell electrons of the transition elements is completely ignored. In Fig. 7 (a) the Curie constants per mole, C_M, are plotted against the atomic concentration of the transition metals. C_M is related to C in Eq. (1) as

$$C_M=C[xM_A+(1-x)M_B]\,, \tag{2}$$

where M_A and M_B are the atomic weights of A and B, and x is the atomic concentration of A. Fig. 7 (b) shows the values of θ in absolute temperature unit.

The Curie-Weiss law is derived from a theory based on the Heitler-London model.* According to the theory, C_M is given as

$$C_M=\frac{xN\mu^2}{3k}4S(S+1)\,, \tag{3}$$

---

* The Curie-Weiss law can also be derived from Stoner's collective electron theory. However, a detailed analysis based on this theory requires a knowledge about the ferromagnetic state at low temperatures, which is lacking in the present case.

provided that the atoms of the transition elements have the resultant spin S, and the copper atoms have no magnetic moment. In Eq. (3), x is the atomic concentration of the transition element, N is Avogadro's number, k is Boltzmann's constant, and μ is the Bohr magneton. The theoretical curves for C_M are also shown in Fig. 7 (a) for various values of S. The experimental curves of C_M for the Cu-Co and Cu-Fe systems do not show marked deviations from the theoretical curves for $S=1$ and $S=3/2$, respectively.* The electronic configurations of cobalt and iron are thus considered to be $(3d)^8(4s)^1$ and $(3d)^7(4s)^1$, respectively. If the concentrations of cobalt and iron are sufficiently low, the measured values of C_M approach the theoretical values for $S=3/2$ and $S=2$, respectively, corresponding to the electronic configurations $(3d)^7(4s)^2$ and $(3d)^6(4s)^2$.

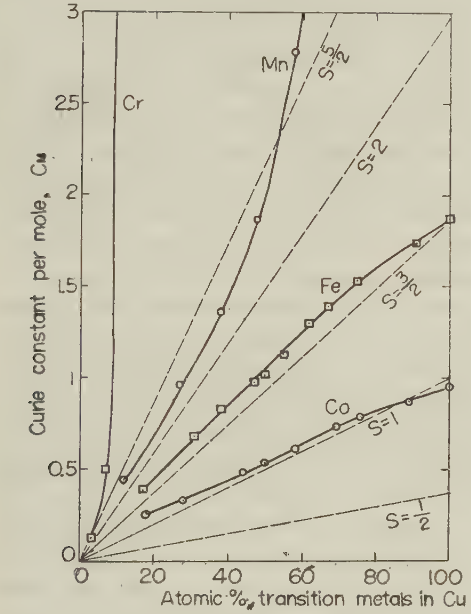

(a) Curie constant

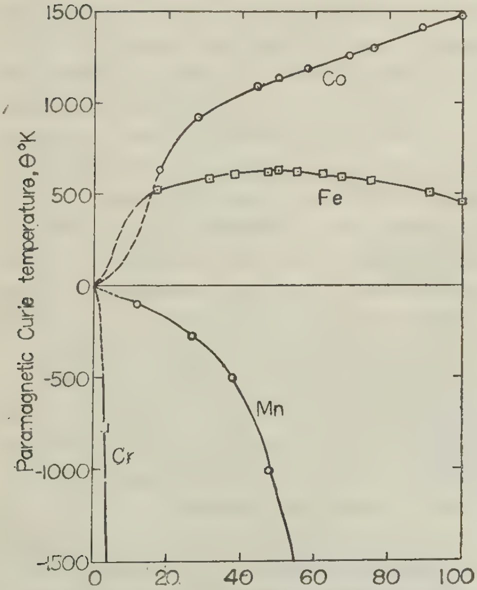

(b) Paramagnetic Curie temperature

Fig. 7. Curie constant and paramagnetic Curie temperature vs. composition of alloys.

The values of θ are always positive in both Cu-Co and Cu-Fe alloys. The θ vs. composition curve for the Cu-Fe system has a flat maximum at an intermediate composition, while that for the Cu-Co system rises monotonously with the concentration of cobalt.

The results on the copper-rich alloys of Cu-Mn are similar to those on the Cu-Co and Cu-Fe alloys. In the range up to 50% Mn, the C_M vs. composition curve lies between the two theoretical curves for $S=2$ and $S=5/2$. The electronic configuration of the manganese atoms in these alloys is thus considered to be $(3d)^6(4s)^1$ or $(3d)^5(4s)^2$. For the alloys containing more than 50% Mn, C_M becomes extremely large, and θ tends to negative infinity. The Curie-Weiss law has no physical significance in this case, since the susceptibility is nearly independent of temperature.

In the Cu-Cr system, even the copper-rich alloys show the temperature-independent paramagnetism. The Curie-Weiss law is applicable only to the most dilute alloy, in which the electronic configuration of the chromium atoms is probably $(3d)^5(4s)^1$.

§ 5. Discussion

As mentioned above, the electronic configurations of the atoms of the transition elements are determined from the temperature dependence of the susceptibilities. The configurations of cobalt and iron determined here are quite consistent with those determined from the data on Ni-Fe, Ni-Co and

---

* The values of C_M and θ for pure iron and cobalt are calculated from the data reported in our previous paper[1]. The data are slightly modified by taking into account the alteration of the standard temperatures, upon which the calibration of thermocouple was based. (see §2)

Co-Fe alloys.[1][2]

The magnetic interactions between the atoms of the transition elements are estimated from the values of θ, being ferromagnetic in the Cu-Co and Cu-Fe systems whereas antiferromagnetic in the Cu-Mn and Cu-Cr systems. However, the dependence of θ on the concentration of the alloys cannot be explained by any simple theory. In the Cu-Co and Cu-Fe systems, if only a direct exchange interaction between the cobalt or iron atoms is effective, θ should decrease very rapidly with addition of copper to cobalt or iron. The effect of short-range ordering may to some extent account for the discrepancy between the above theory and the experimental fact. As reported elsewhere,[6] both the Cu-Co and Cu-Fe systems have the pronounced tendency towards liquid immiscibility. Thus the number of pairs of cobalt or iron atoms are laraer than that for the perfectly random distribution of the atoms, and consequently the magnetic interaction becomes stronger. However, the maximum in θ vs. composition curve for the Cu-Fe system cannot be accounted for by this effect. It is likely that there exist other kinds of magnetic interaction, for example, a superexchange interaction through the non-magnetic copper atoms.

Previously, Weil[3] has measured the susceptibilities of cobalt and iron dissolved in molten gold and antimony. The results on Au-Co and Au-Fe are very similar to those on Cu-Co and Cu-Fe investigated here, while the results on Sb-Co and Sb-Fe are fairly different. Weil has also measured the susceptibilities of liquid Cu-Mn alloys in the range up to 68% Mn. The results are in good agreement with the present results. With respect to chromium, Weil has studied only Sb-Cr alloys.

The susceptibilities of these alloys in the solid state have been studied by many investigators. For the Cu-Co and Cu-Fe systems, only the very dilute alloys have been investigated.[10][11][12] A continuous series of solid solution in the Cu-Mn system has been studied by Myers[13]. The results are similar to those obtained for the liquid state, but the Curie-Weiss law is applicable only to the alloys containing less than 25% Mn in the solid state, while it is applicable up to 50% Mn in the liquid state. For the Cu-Cr system, there has been only a room temperature measurement of the susceptibility of the quenched specimen[14].

Manganese and chromium show the Curie-Weiss paramagnetism in the dilute alloys whereas the temperature-independent paramagnetism in the enriched alloys. Although the temperature-independent paramagnetism is usually explained by the band theory of metals, the Heitler-London theory is also applicable to it. If the antiferromagnetic interaction between the atoms of transition elements becomes extremely large, it may depend very sensitively on the interatomic distance, as expected from the Bethe-Slater curve. In this case even a small change in interatomic distance due to thermal expansion can produce an appreciable change in magnetic interaction. As reported in detail in our previous paper,[2] this effect results in an apparent large value of the Curie constant. The temperature-independent paramagnetism corresponds to the case where the apparent Curie constant becomes infinitely large.

It is shown by the experimental results that the Cu-Cr alloys show the temperature-independent paramagnetism even in rather dilute alloys, while the Cu-Mn alloys show the ordinary Curie-Weiss paramagnetism even in fairly enriched alloys. These results are accounted for by the following two facts. Firstly, the antiferromagnetic interaction may be stronger in chromium than in manganese, since the diameter of $3d$-shell is larger. Secondly, as can be expected from the phase diagrams, the short-range ordering in the Cu-Cr alloys may increase the number of pairs of the same kinds of atoms, while that in the Cu-Mn alloys may decrease it; thus the antiferromagnetic interaction is enlarged in Cu-Cr, while it is reduced in Cu-Mn.

In conclusion, the author emphasizes that the magnetic properties of a series of transition metals vary continuously with the atomic number, at least in the liquid state. Cobalt and iron behave very similarly, though the former is more ferromagnetic. Manganese is less antiferromagnetic than chromium. These results are consistent with the Bethe-Slater curve. The atomic magnetic moments of these transition metals in the liquid state vary systematically with the atomic number, and the electronic configurations are close to $(3d)^n(4s)^1$. In the solid state, there may be a discontinuous change in electronic configuration between high-d and low-d elements, namely Ni and Co on the one hand and Fe, Mn and Cr on the other hand, which has been suggested by Lomer and Marshall15) on the basis of recent X-ray measurement by Weiss and DeMarco16). However, it is possible to suppose that the discontinuous change in d-electron density observed by X-ray is only due to the difference in crystal structure. It should be mentioned here that the magnetic properties of the liquid phase are similar to those of the face-centred cubic phase, as described in our previous paper1).

Acknowledgments

The author wishes to express his sincere gratitude to Professor S. Kaya for his encouragement and interest in the present work. The author is also indebted to Dr. Y. Tomono, Dr. S. Iida, and Dr. H. Sekizawa for their helpful discussions.

References

1) Y. Nakagawa: J. Phys. Soc. Japan **11** (1956) 855.
2) Y. Nakagawa: J. Phys. Soc. Japan **12** (1957) 700.
3) L. Weil: Thèse, Univ. Strasbourg (1941)
4) J. R. Pattison and P. W. Willows: J. Iron Steel Inst. **183** (1956) 390.
5) M. Hansen: *Constitution of Binary Alloys* (McGraw-Hill, 1958).
6) Y. Nakagawa: Acta Met. **6** (1958) 704.
7) R. S. Dean, J. R. Long, T. R. Graham, E. V. Potter and E. T. Hayes: Trans. Amer. Soc. Met. **34** (1945) 443.
8) G. Grube, E. Oestreicher and O. Winkler: Z. Elektrochem. **45** (1939) 776.
9) E. Siedschlag: Z. anorg. Chem. **131** (1923) 173.
10) A. Hildebrand: Ann. Physik **30** (1937) 593.
11) F. Bitter, A. R. Kaufmann, C. Starr and S. T. Pan: Phys. Rev. **60** (1941) 134.
12) F. T. Hedgcock: Phys. Rev. **104** (1956) 1564.
13) H. P. Myers: Canad. J. Phys. **34** (1956) 527.
14) A. Knapwost and H. Zeiger: Naturwiss. **42** (1955) 296.
15) W. M. Lomer and W. Marshall: Phil. Mag. **3** (1958) 185.
16) R. J. Weiss and J. J. DeMarco: Rev. Mod. Phys. **30** (1958) 59.

JOURNAL OF THE PHYSICAL SOCIETY OF JAPAN, Vol. 14, No. 10, OCTOBER, 1959

On the Viscosity of Irradiated Polymers, II

By Mitio INOKUTI and Kanji KATSUURA

Department of Applied Physics, Faculty of Engineering,
University of Tokyo, Tokyo, Japan

(Received July 1, 1959)

The intrinsic viscosity of a polymeric substance crosslinked as well as degraded by irradiation with high-energy radiations is discussed for various types of initial molecular size distributions. The intrinsic viscosity as a function of radiation dose is shown to behave in a great variety of ways depending on the relative importance of crosslinking and degradation, and in particular, on the shape of the initial distribution. The effect of endlinking instead of crosslinking is also examined.

§1. Introduction

The intrinsic viscosity of a polymeric substance exposed to high-energy radiations is one of the most important quantities in the study of the effects of radiation on polymers. Gradual accumulation of reliable experimental data in recent years1) seems to require a careful theoretical analysis of the intrinsic viscosity of an irradiated polymeric substance.

In a previous paper2) (hereafter referred to as I), one of the authors (M.I.) examined the quantity for various types of initial molecular size distributions according to a formalism recently developed by Saito[3)–5)] and concluded that there exists a remarkable relationship between the initial distribution and the radiation-induced change of the intrinsic viscosity. The discussions in I are, however, confined to the coefficient $A_1(\lambda, \alpha)$ in the expansion of the intrinsic viscosity $\eta(R)$ at radiation dose R

$$\eta(R)/\eta(0)=1+A_1(\lambda, \alpha)R+A_2(\lambda, \alpha)R^2+\cdots, \tag{1}$$

where α stands for the viscosity exponent in Staudinger's law ($1/2\leq\alpha<1$) and λ for the ratio of the probability $\dot{r}$ of degradation per monomer unit per unit radiation dose to the probability $\dot{c}$ of crosslinking per monomer unit per unit radiation dose.

It is now the main purpose of the present paper to extend the discussions in I to the coefficient $A_2(\lambda, \alpha)$ in (1), so as to clarify more delicate and subtle features of the relationship between the initial distribution and the change of the intrinsic viscosity. Further we will examine the intrinsic viscosity of a polymeric substance into which endlinking instead of crosslinking is introduced by irradiation. Then the relationship in which we are interested exhibits a tendency qualitatively similar to the case of crosslinking, although the correlation is more pronounced in comparison with the latter case.

Another purpose is to give a detailed numerical analysis of $A_1(\lambda, \alpha)$ for a type of initial distribution, which is not only flexible in the sense that it covers a great variety with variation of a parameter involved but also experimentally interesting in the sense that it can approximately represent an actual distribution in an ordinary sample of polymers.

§ 2. General Formulation

As in I, we define the molecular size distribution $m(p, R)dp$ of a polymeric system as the fraction of polymers whose degree of polymerization lies between p and $p+dp$ when the system has been irradiated up to radiation dose R. The constancy of the total number of monomers imposes a normalization condition upon $m(p, R)$, namely,

$$\int_0^\infty pm(p, R)dp=1\ . \tag{2}$$

By the procedure described in I, we calculate $m(p, R)$ as a power series in R and we gave there the result up to the first order. The next term which is of the second order can be similarly obtained, although the calculation is rather complicated. Thus we have

$$\begin{aligned} m(p, R)&=e^{-(\lambda+2)pt}\{m(p, 0)+\psi_1(p)t \\ &\quad+\psi_2(p)t^2+O(t^3)\} \\ &=m(p, 0)+\{\psi_1(p)-(\lambda+2)pm(p, 0\}t \\ &\quad+\{\psi_2(p)-(\lambda+2)p\psi_1(p) \\ &\quad+\tfrac{1}{2}(\lambda+2)^2p^2m(p, 0)\}t^2+O(t^3)\ , \end{aligned} \tag{3}$$

where $t=\dot{c}R$, $\lambda=\dot{r}/\dot{c}$, and $m(p, 0)$ stands for the initial distribution and $\psi_1(p)$ and $\psi_2(p)$ are defined as follows:

$$\psi_1(p)=2\lambda F(p)+\int_0^p dll(p-l)m(l, 0)m(p-l, 0)\ , \tag{4}$$

$$\begin{aligned} \psi_2(p)=\lambda^2\int_p^\infty dlF(l) &\\ +4\lambda\int_0^p dll(p-l)F(l)m(p-l, 0) &\\ +\int_0^\infty dll(p-l)m(p-l, 0) &\\ \times\int_0^l dkk(l-k)m(k, 0)m(l-k, 0)\ , & \end{aligned} \tag{5}$$

where

$$F(p)=\int_p^\infty m(l, 0)dl\ . \tag{6}$$

According to the Staudinger's law the intrinsic viscosity $\eta(R)$ at dose R is

$$\eta(R)/\eta(0)=f_{\alpha+1}(R)/f_{\alpha+1}(0)\ , \tag{7}$$

where we have used the following notation:

$$f_\beta(R)=\int_0^\infty m(p, R)p^\beta dp\ . \tag{8}$$

Now we substitute (3) into the right-hand side of (7), rearrange the terms and compare the result with (1) to arrive at the following expressions for $A_1(\lambda, \alpha)$ and $A_2(\lambda, \alpha)$, the former of which has already been given in I. Namely,

$$\begin{aligned} A_1(\lambda, \alpha)&=-\left(\frac{\dot{c}\,\alpha}{\alpha+2}\right)\frac{f_{\alpha+2}(0)}{f_{\alpha+1}(0)}\{\lambda-\lambda_0(\alpha)\} \\ &=\left(\frac{\dot{r}\,\alpha}{\alpha+2}\right)\frac{f_{\alpha+2}(0)}{f_{\alpha+1}(0)}\left\{\frac{\lambda_0(\alpha)}{\lambda}-1\right\}\ , \end{aligned} \tag{9}$$

$$\lambda_0(\alpha)=\left(\frac{\alpha+2}{\alpha}\right)\left\{\frac{I(\alpha)}{f_{\alpha+2}(0)}-2\right\}\ , \tag{10}$$

and

$$A_2(\lambda,\alpha)=\frac{\dot{c}^2 f_{\alpha+3}(0)}{f_{\alpha+1}(0)}\{P(\alpha)\lambda^2-2Q(\alpha)\lambda+R(\alpha)\}\,, \tag{11}$$

$$P(\alpha)=\frac{\alpha(\alpha+1)}{2(\alpha+2)(\alpha+3)}\,, \tag{12}$$

$$Q(\alpha)=\frac{I(\alpha+1)-4J_1}{2f_{\alpha+3}(0)}-\frac{\alpha+1}{\alpha+3}\,, \tag{13}$$

$$R(\alpha)=2+\frac{J_2-2I(\alpha+1)}{f_{\alpha+3}(0)}\,, \tag{14}$$

where $I(\beta)$, J_1 and J_2 are repeated integrals defined as follows:

$$I(\beta)=\int_0^\infty dp p^{\beta+1}\int_0^p dl l(p-l)m(l,0)m(p-l,0)$$
$$(\beta=\alpha \text{ or } \alpha+1)\,, \tag{15}$$

$$J_1=\int_0^\infty dp p^{\alpha+1}\int_0^p dl l(p-l)F(l)m(p-l,0)\,, \tag{16}$$

$$J_2=\int_0^\infty dp p^{\alpha+1}\int_0^p dl l(p-l)m(p-l,0)$$
$$\times\int_0^l dk k(l-k)m(k,0)m(l-k,0)\,. \tag{17}$$

It should be noted that by interchanging orders of integrations we can rewrite the integrals in the following way:

$$I(\beta)=\int_0^\infty dl l m(l,0)\int_0^\infty dp(p+l)^{\alpha+1}p m(p,0)\,, \tag{18}$$

$$J_1=\frac{1}{(\alpha+2)(\alpha+3)}\Big\{(\alpha+2)I(\alpha+1)+f_{\alpha+4}(0)f_0(0)$$
$$-\int_0^\infty dp p^2 m(p,0)\int_0^\infty dk(p+k)^{\alpha+2}m(k,0)\Big\}\,, \tag{19}$$

$$J_2=\int_0^\infty dk k m(k,0)\int_0^\infty dl l(l+k)m(l,0)$$
$$\times\int_0^\infty dp p(p+l+k)^{\alpha+1}m(p,0)\,. \tag{20}$$

Now we will evaluate $A_2(\lambda,\alpha)$ for some types of initial molecular size distributions and discuss the result together with those obtained in I, so that we may clarify the relationship between the initial distribution and the radiation-induced change of the intrinsic viscosity more closely than in I. For this purpose it will be helpful to quote a theorem that gelation is possible if and only if $\lambda<4$ irrespective of the initial distribution.[2),3)]

§ 3. Application to Some Types of Initial Molecular Size Distributions

1) *Poisson distribution*

When the initial distribution is Poisson-like, namely,

$$m(p,0)=u^{-2}\exp(-p/u)\,, \tag{21}$$

where u is the initial number-average degree of polymerization, we have by (8), (15), (16) and (17)

$$f_\beta(0)=u^{\beta-1}\Gamma(\beta+1)\,,$$
$$I(\beta)=u^{\beta+1}\Gamma(\beta+5)/6\,,$$
$$J_1\ =u^{\alpha+2}\Gamma(\alpha+5)/6\,,$$
$$J_2\ =u^{\alpha+2}\Gamma(\alpha+8)/180\,.$$

Then we obtain $A_1(\lambda,\alpha)$ and $A_2(\lambda,\alpha)$ by (9)-(14), namely,

$$A_1(\lambda,\alpha)=-\dot{c}u\alpha\{\lambda-\lambda_0(\alpha)\}\,, \tag{22}$$

$$\lambda_0(\alpha)\ =(\alpha+2)(\alpha+7)/6\,, \tag{23}$$

$$A_2(\lambda,\alpha)=\frac{(\dot{c}u)^2\alpha(\alpha+1)}{2}\Big\{\lambda^2-\frac{(\alpha+2)(\alpha+7)}{3}\lambda$$
$$+\frac{(\alpha+2)(\alpha+3)(\alpha+7)(\alpha+14)}{90}\Big\}$$
$$=\frac{(\dot{c}u)^2\alpha(\alpha+1)}{2}\Big[\Big\{\lambda-\frac{(\alpha+2)(\alpha+7)}{6}\Big\}^2$$
$$+\frac{(1-\alpha)(\alpha+2)(\alpha+7)(3\alpha+14)}{180}\Big]\,. \tag{24}$$

It is worth noting that $A_2(\lambda,\alpha)$ is positive definite for any λ for $1/2\leq\alpha<1$, while $A_1(\lambda,\alpha)$ may be either positive or negative. This situation seems to be characteristic of a sufficiently broad initial distribution. For, as will be shown later, it is in a striking contrast with the case where the initial distribution is uniform or nearly uniform.

Consequently, we can distinguish the behavior of the intrinsic viscosity as a function

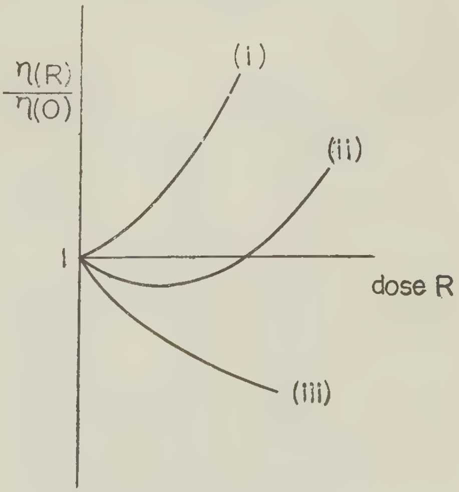

Fig. 1. Schematic representation of the behavior of the intrinsic viscosity when the initial distribution is Poisson-like.

of dose in the following way.

(i) $\lambda_0(\alpha)>\lambda$

$A_1>0$, $A_2>0$, gelation possible.

(ii) $4>\lambda>\lambda_0(\alpha)$

$A_1<0$, $A_2>0$, gelation possible.

(iii) $\lambda>4$

$A_1<0$, $A_2>0$, gelation impossible.

We give a typical viscosity-dose curve for each of the three cases in Fig. 1.

2) *Uniform distribution*

When the initial distribution is uniform and every polymer has degree of polymerization u, namely,

$$m(p,\,0)=u^{-2}\delta(p/u-1)\,, \tag{25}$$

we have

$$f_\beta(0)=u^{\beta-1}\,,$$
$$I(\beta)=(2u)^{\beta+1}\,,$$
$$J_1\;=u^{\alpha+2}\left\{\frac{2^{\alpha+2}(\alpha+1)-1}{(\alpha+2)(\alpha+3)}\right\}\,,$$
$$J_2=2\cdot 3^{\alpha+1}u^{\alpha+2}\,.$$

In the evaluation of these integrals, it is more convenient to make use of (18)-(20) rather than (15)-(17).

Then $A_1(\lambda,\alpha)$ and $A_2(\lambda,\alpha)$ is given as follows.

$$A_1(\lambda,\,\alpha)=-\left(\frac{\dot{c}u\alpha}{\alpha+2}\right)\{\lambda-\lambda_0(\alpha)\}\,, \tag{26}$$

$$\lambda_0(\alpha)=2(\alpha+2)(2^\alpha-1)/\alpha\,, \tag{27}$$

$$A_2(\lambda,\,\alpha)=(\dot{c}u)^2\{P(\alpha)\lambda^2-2Q(\alpha)\lambda+R(\alpha)\}\,, \tag{28}$$

$$Q(\alpha)=\frac{2^{\alpha+1}(\alpha^2+\alpha+2)-(\alpha^2+3\alpha+4)}{(\alpha+2)(\alpha+3)}\,, \tag{29}$$

$$R(\alpha)=2(3^{\alpha+1}+1-2^{\alpha+2})\,. \tag{30}$$

Table I. Values of $\lambda_0(\alpha)$, $\lambda_1(\alpha)$ and $\lambda_2(\alpha)$ for the uniform distribution

α	$\lambda_0(\alpha)$	$\lambda_1(\alpha)$	$\lambda_2(\alpha)$
0.50	4.1422	3.3874	7.4296
0.55	4.3033	3.4380	7.8234
0.60	4.4695	3.4910	8.2300
0.65	4.6409	3.5466	8.6494
0.70	4.8176	3.6050	9.0819
0.75	4.9998	3.6656	9.5286
0.80	5.1877	3.7284	9.9904
0.85	5.3815	3.7933	10.4678
0.90	5.5813	3.8602	10.9613
0.95	5.7874	3.9291	11.4719
1.00	6.0000	4.0000	12.0000

A simple analysis shows that $A_2(\lambda,\alpha)$ has two real, positive zeros with respect to λ, so that we rewrite it as

$$A_2(\lambda,\,\alpha)=(\dot{c}u)^2P(\alpha)\{\lambda-\lambda_1(\alpha)\}\{\lambda-\lambda_2(\alpha)\}\,,$$
$$(\lambda_2(\alpha)>\lambda_1(\alpha))\,. \tag{31}$$

We give numerical values of $\lambda_1(\alpha)$, $\lambda_2(\alpha)$ and $\lambda_0(\alpha)$ in Table I and Fig. 2.

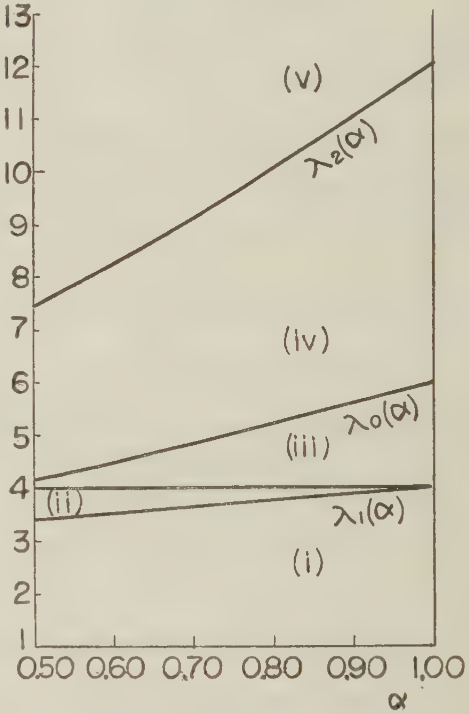

Fig. 2. Values of $\lambda_1(\alpha)$, $\lambda_2(\alpha)$ and $\lambda_0(\alpha)$ plotted against α when the initial distribution is uniform.

According to the values of λ and α, we classify the behavior of the intrinsic viscosity as follows.

(i) $\lambda_1(\alpha)>\lambda$

$A_1>0$, $A_2>0$, gelation possible.

(ii) $4>\lambda>\lambda_1(\alpha)$

$A_1>0$, $A_2<0$, gelation possible.

(iii) $\lambda_0(\alpha)>\lambda>4$

$A_1>0$, $A_2<0$, gelation impossible.

(iv) $\lambda_2(\alpha)>\lambda>\lambda_0(\alpha)$

$A_1<0$, $A_2<0$, gelation impossible.

(v) $\lambda>\lambda_2(\alpha)$

$A_1<0$, $A_2<0$, gelation impossible.

In Fig. 3 we give a typical viscosity-dose curve for each of the domains indicated in Fig. 2.

The possibility of a viscocity-dose curve with a maximum (case (iii)) for a nearly uniform initial distribution has already been predicted in I. In this connection, it is very interesting that Pearson[6] observed such a viscosity-dose curve for poly-(ethylene oxides), whose molecular size distribution were reportedly nearly uniform.

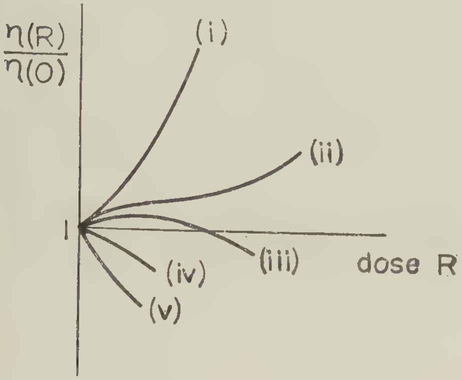

Fig. 3. Schematic representation of the behavior of the intrinsic viscosity when the initial distribution is uniform.

3) *Rectangular distribution*

We will examine the rectangular distribution defined in I, namely,

$$m(p,\,0)=\begin{cases}(2\xi u^2)^{-1} & (1-\xi<p/u<1+\xi)\\ 0 & \text{(otherwise)}\,,\end{cases} \tag{32}$$

where u stands for the number-average degree of polymerization. We regard the dimensionless parameter ξ as small compared with unity; therefore we have now to do with a sharp or nearly uniform initial distribution. In this case we have

$$A_1(\lambda,\,\alpha)=-\left(\frac{\dot{c}u\alpha}{\alpha+2}\right)\left\{1+\frac{\alpha+1}{3}\xi^2+\cdots\right\}\times\{\lambda-\lambda_0(\alpha)\}\,, \tag{33}$$

$$\lambda_0(\alpha)=\left(\frac{\alpha+2}{\alpha}\right)\left\{2(2^\alpha-1)-\frac{2^\alpha\alpha(\alpha+1)}{6}\xi^2+\cdots\right\}, \tag{34}$$

$$A_2(\lambda,\,\alpha)=(\dot{c}u)^2\left\{1+\frac{(2\alpha+3)}{3}\xi^2+\cdots\right\}\times\{P(\alpha)\lambda^2-2Q(\alpha)\lambda+R(\alpha)\}\,, \tag{35}$$

$$Q(\alpha)=\frac{2^{\alpha+1}(\alpha^2+\alpha+2)-(\alpha^2+3\alpha+4)}{(\alpha+2)(\alpha+3)}-\frac{2^{\alpha-1}(\alpha^3+\alpha^2+4\alpha-4)+2}{3(\alpha+2)}\xi^2+\cdots\,, \tag{36}$$

$$R(\alpha)=2(3^{\alpha+1}+1-2^{\alpha+2})-(2/3)(3^\alpha-2^\alpha)(\alpha+1)(\alpha+2)\xi^2+\cdots\,, \tag{37}$$

after laborious calculations.

As far as ξ is sufficiently small, $A_2(\lambda,\,\alpha)$ given by (35) has two positive zeros with respect to λ and it can be written in the form (31). To examine the dependence of the zeros $\lambda_1(\alpha)$ and $\lambda_2(\alpha)$ on ξ, or the broadness of the initial distribution, we have to resort to numerical computation since the expressions (36) and (37) are rather complicated. Then we find that both $\lambda_1(\alpha)$ and $\lambda_2(\alpha)$ decrease with increase of ξ at least for small ξ. It means that the regions $4>\lambda>\lambda_1(\alpha)$ and $\lambda>\lambda_2(\alpha)$ become wider and the region $\lambda_0(\alpha)>\lambda>4$ narrower as the initial distribution attains broadness.

In experiments the initial distribution cannot be exactly uniform, but has some broadness, even if advanced fractionation techniques are employed. A rectangular distribution with small ξ must be rather more realistic in a so-called "fractionated" sample of a polymeric substance. In view of this fact, observation of a viscosity-dose curve with an inflection point (case (ii)) is highly probable for a nearly uniform initial distribution, although, to the best of the authors, knowledge, it has never been reported. On the other hand, a viscosity-dose curve with a maximum (case (iii)) can be observed practically only if α is sufficiently large.

4) *Superposition of two uniform distributions*

In order to confirm the conclusion concerning the rectangular distribution, we consider a superposition of two uniform distributions

$$m(p,\,0)=(2u^2)^{-1}\{\delta(p/u-1-\zeta)+\delta(p/u-1+\zeta)\}\,, \tag{38}$$

where u is the number-average degree of polymerization and ζ will be regarded as small. We calculate $A_1(\lambda,\,\alpha)$ and $A_2(\lambda.\,\alpha)$ as

$$A_1(\lambda,\,\alpha)=-\left(\frac{\dot{c}u\alpha}{\alpha+2}\right)\{1+(\alpha+1)\zeta^2+\cdots\}\times\{\lambda-\lambda_0(\alpha)\}\,, \tag{39}$$

$$\lambda_0(\alpha)=\left(\frac{\alpha+2}{\alpha}\right)\left\{2(2^\alpha-1)-\frac{2^\alpha\alpha(\alpha+1)}{2}\zeta^2+\cdots\right\}, \tag{40}$$

$$A_2(\lambda,\,\alpha)=(\dot{c}u)^2\{1+(2\alpha+3)\zeta^2+\cdots\}\times\{P(\alpha)\lambda^2-2Q(\alpha)\lambda+R(\alpha)\}\,, \tag{41}$$

$$Q(\alpha)=\frac{2^{\alpha+1}(\alpha^2+\alpha+2)-(\alpha^2+3\alpha+4)}{(\alpha+2)(\alpha+3)}-\frac{2^{\alpha-1}(\alpha^3+\alpha^2+4\alpha-4)+2}{(\alpha+2)}\zeta^2+\cdots\,, \tag{42}$$

$$R(\alpha)=2(3^{\alpha+1}+1-2^{\alpha+2})$$
$$-2(3^{\alpha}-2^{\alpha})(\alpha+1)(\alpha+2)\zeta^2+\cdots\ . \qquad (43)$$

Thus we see that the expressions (39)–(43) are very similar to (33)–(37) so that the situation is qualitatively similar to the case where the initial distribution is rectangular.

§ 4. Generalized Poisson Distribution

The initial distributions which we have so far dealt with are either nearly uniform or Poisson-like. Although main features of the relationship between the initial distribution and the viscosity-dose curve have been understood, detailed analysis is necessary for an initial distribution which covers a wide range of a parameter involved. For such a purpose it is convenient to consider the distribution[7]

$$m(p,\ 0)=\frac{b^{b+1}}{u^2\Gamma(b+1)}\left(\frac{p}{u}\right)^{b-1}e^{-bp/u}\ , \qquad (44)$$

where u is the number-average degree of polymerization and $b(\geqq 1)$ is a parameter specifying the shape. We call (44) as the generalized Poisson distribution. It is normalized as (2). The βth moment turns out to be

$$f_\beta(0)=(u/b)^{\beta-1}\Gamma(\beta+b)/\Gamma(1+b)\ , \qquad (45)$$

where $\beta\geqq 0$. The parameter b is connected with the ratio of the weight-average $P_w(0)$ to the number-average $P_n(0)$ degree of polymerization in the following way:

$$P_w(0)/P_n(0)=\{f_2(0)/f_1(0)\}/\{f_1(0)/f_0(0)\}=1+1/b\ . \qquad (46)$$

If $b=1$, (44) reduces to the Poisson distribution; and if $b=\infty$, to the uniform distribution.

When we want to approximate the actual distribution of a polymer sample, we can determine the value of b by the relation (46), since the quantity on the left-hand side of (46) is obtained by measurements of light scattering and the osmotic pressure.

For this initial distribution, $A_1(\lambda,\ \alpha)$ is given as

$$A_1(\lambda,\ \alpha)=-\left(\frac{\dot{c}\,\alpha u}{\alpha+2}\right)\left(1+\frac{\alpha+1}{b}\right)\{\lambda-\lambda_0(\alpha)\}\ , \qquad (47)$$

$$\lambda_0(\alpha)=\left(\frac{\alpha+2}{\alpha}\right)\left\{\frac{\Gamma(2b+3+\alpha)\Gamma(b+1)}{\Gamma(b+2+\alpha)\Gamma(2b+2)}-2\right\}\ , \qquad (48)$$

The results of numerical computation given in Table II and Fig. 4 confirm quantitatively the very conclusion of I that $\lambda_0(\alpha)$ is larger or smaller than 4 according as the initial discribution is narrow or broad. Further these numerical values can be profitably used in analysis of experimental data, as will be reported elsewhere

Table II. Values of $\lambda_0(\alpha)$ for the generalized Poisson distribution.

α \ b	3	4	5	6	8	10	12	14
0.50	3.5658	3.6686	3.7403	3.7932	3.8658	3.9135	3.9471	3.9721
0.52	3.6111	3.7169	3.7908	3.8453	3.9203	3.9695	4.0043	4.0301
0.54	3.6566	3.7656	3.8417	3.8979	3.9753	4.0261	4.0620	4.0887
0.56	3.7025	3.8146	3.8931	3.9510	4.0309	4.0833	4.1204	4.1480
0.58	3.7487	3.8641	3.9449	4.0046	4.0870	4.1411	4.1794	4.2078
0.60	3.7953	3.9140	3.9972	4.0587	4.1436	4.1994	4.2389	4.2684
0.62	3.8422	3.9643	4.0499	4.1133	4.2008	4.2584	4.2992	4.3295
0.64	3.8894	4.0150	4.1031	4.1684	4.2586	4.3180	4.3600	4.3914
0.66	3.9370	4.0661	4.1567	4.2239	4.3169	4.3781	4.4215	4.4539
0.68	3.9850	4.1176	4.2108	4.2800	4.3758	4.4389	4.4837	0.5170
0.70	4.0332	4.1695	4.2654	4.3366	4.4353	4.5003	4.5465	4.5809
0.72	4.0819	4.2218	4.3205	4.3938	4.4953	4.5624	4.6099	4.6454
0.74	4.1308	4.2746	4.3760	4.4514	4.5559	4.6250	4.6740	4.7107
0.76	4.1801	4.3278	4.4320	4.5096	4.6172	4.6883	4.7388	4.7766
0.78	4.2298	4.3814	4.4885	4.5683	4.6790	4.7523	4.8043	4.8432
0.80	4.2798	4.4354	4.5455	4.6275	4.7414	4.8169	4.8705	4.9106
0.82	4.3302	4.4899	4.6030	4.6872	4.8045	4.8821	4.9373	4.9786
0.84	4.3810	4.5448	4.6609	4.7475	4.8681	4.9480	5.0049	5.0474
0.86	4.4321	4.6001	4.7194	4.8084	4.9324	5.0146	5.0732	5.1170
0.88	4.4835	4.6559	4.7784	4.8698	4.9973	5.0819	5.1421	5.1872
0.90	4.5354	4.7121	4.8378	4.9318	5.0628	5.1498	5.2118	5.2583
0.92	4.5875	4.7688	4.8978	4.9943	5.1289	5.2184	5.2823	5.3301
0.64	4.6401	4.8259	4.9583	5.0573	5.1957	5.2878	5.3534	5.4026
0.96	4.6930	4.8835	5.0193	5.1210	5.2632	5.3578	5.4253	5.4760
0.98	4.7463	4.9415	5.0808	5.1852	5.3313	5.4285	5.4980	5.5501

§ 5. Endlinking

Let us consider the change of the intrinsic viscosity of a polymeric substance into which endlinking instead of crosslinking is introduced by irradiation. A treatment quite analogous to the case of crosslinking can be performed by employing Saito's theory.[4)] We will evaluate the coefficient B_1 in the expansion

$$\eta(R)/\eta(0)=1+B_1R+B_2R^2+\cdots\,. \tag{49}$$

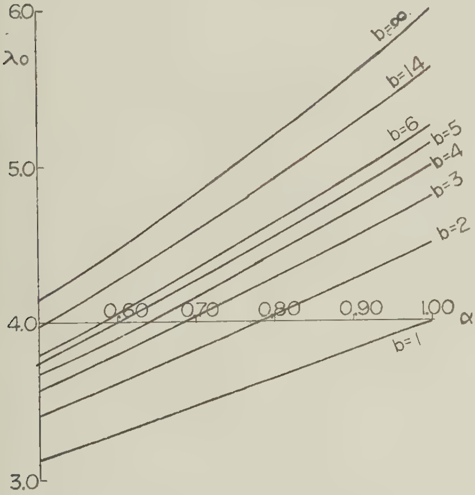

Fig. 4. Value of $\lambda_0(\alpha)$ plotted against α for various values of b.

To discuss the effect of endlinking, we have to classify polymers according to the number of ends involved in a polymer. Thus we define $m_k(p, R)dp$ as the fraction of polymers whose degree of polymerization lies between p and $p+dp$ and whose number of ends is k when the substance has been irradiated up to dose R. By a procedure used in the paper I we calculate $m_k(p, R)$ as a power series in R. Now we regard the polymeric substance initially contains only linear polymers with molecular size distribution $m(p, 0)$ and the number-average degree of polymerization u. Let $\dot{r}$ be the probability of degradation per monomer unit per unit dose and σ the probability of endlinking per degraded monomer, then $m_k(p, R)$ is

$$\begin{aligned} m_k(p, R)=\delta_{k2}m(p, 0)+\dot{r}R[2F(p)\delta_{k2} \\ -\{2\sigma u+(2\sigma+1)p\}\delta_{k2}m(p, 0) \\ +2\sigma u\delta_{k3}G(p)]+O(R^2)\,, \end{aligned} \tag{50}$$

where

$$F(p)=\int_p^\infty dlm(l, 0)\,,$$

$$G(p)=\int_0^p dllm(l, 0)m(p-l, 0)\,,$$

and δ_{kj} is the Kronecker symbol.

Substituting (50) into

$$\frac{\eta(R)}{\eta(0)}=\sum_{k=2}^{\infty}\int_0^\infty dpp^{\alpha+1}m_k(p, R)\Big/\int_0^\infty dpp^{\alpha+1}m(p, 0)\,, \tag{51}$$

and comparing the result with (49), we obtain the following formula for $B_1(\sigma, \alpha)$, namely,

$$B_1(\sigma, \alpha)=\left(\frac{\dot{r}\alpha}{\alpha+2}\right)\frac{f_{\alpha+2}(0)}{f_{\alpha+1}(0)}\{\theta(\alpha)\sigma-1\}\,, \tag{52}$$

where

$$\theta(\alpha)\equiv\frac{2(\alpha+2)}{\alpha}\left\{\frac{uI^*(\alpha)-uf_{\alpha+1}(0)}{f_{\alpha+2}(0)}-1\right\}\,, \tag{53}$$

$$I^*(\alpha)\equiv\int_0^\infty dpp^{\alpha+1}\int_0^p dllm(l, 0)m(p-l, 0)\,, \tag{54}$$

$$f_\beta(0)\equiv\int_0^\infty dpp^\beta m(p, 0)\,. \tag{55}$$

Remembering the fact that gelation occurs as a result of endlinking if and only if $\sigma>1/4$ for any initial molecular size distribution,[4)] we can predict the behavior of $\eta(R)/\eta(0)$ as follows. If $1/\theta(\alpha)>\sigma>1/4$, the viscosity-dose curve has a minimum. On the other hand, if $1/4>\sigma>1/\theta(\alpha)$, the intrinsic viscosity increases in the beginning and reaches a maximum, though it falls off for large dose. As will be shown later, $1/\theta(\alpha)>1/4$ holds when the initial distribution is sufficiently broad; and $1/\theta(\alpha)<1/4$ when it is sufficiently narrow.

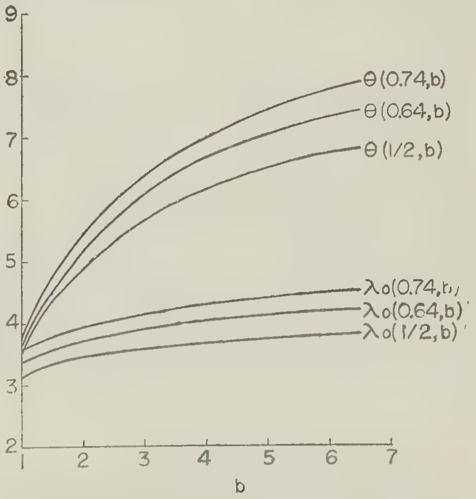

Fig. 5. Dependence of $\lambda_0(\alpha)$ and $\theta(\alpha)$ on b.

Thus we find a parallelism between crosslinking and endlinking, which can be easily visualized when we note the parameter $1/\lambda$ in crosslinking corresponds to the parameter σ in endlinking and compare (52) and (53) with (9) and (10) respectively.

To examine the dependence of $B_1(\sigma, \alpha)$ on the shape of the initial distribution, we carry out calculation of $B_1(\sigma, \alpha)$ when $m(p, 0)$ is the generalized Poisson distribution (44). The result is

$$B_1(\sigma, \alpha)=u\dot{r}\left(1+\frac{\alpha+1}{b}\right)\left(\frac{\alpha}{\alpha+2}\right)\{\theta(\alpha)\sigma-1\}\,, \tag{56}$$

$$\theta(\alpha)=\frac{2(\alpha+2)}{\alpha}\left\{\frac{\Gamma(b+1)\Gamma(2b+\alpha+2)}{\Gamma(2b+1)\Gamma(b+\alpha+2)}-\frac{2b+\alpha+1}{\alpha}\right\}. \tag{57}$$

In Fig. 5 we give $\theta(\alpha)$ and $\lambda_0(\alpha)$ as functions of b for a few values of α. The both curves bear qualitative resemblance to each other, but $\theta(\alpha)$ depends on b, or the shape of the initial distribution, more strongly than $\lambda_0(\alpha)$. This implies that the correlation between the initial distribution and the viscosity-dose curve is more emphasized in endlinking than in crosslinking. It is mathematically a consequence of the difference between $I(\alpha)$ and $I^*(\alpha)$ appearing in $A_1(\lambda, \alpha)$ and $B_1(\sigma, \alpha)$ respectively. (See (15) and (54).)

§ 6. Discussions

We will summarize the results obtained here. Generally the viscosity-dose curve shows a great deal of variety depending on the shape of the initial molecular size distribution.

If the initial distribution is sufficiently sharp, we may expect that the viscosity-dose curve with a maximum or an inflection point should be observed for a proper value of λ. And the curve can be concave either upward or downward near $R=0$. Further it cannot have a minimum. To get a rough idea of the sharpness necessary for such a situation, or for $\lambda_0(\alpha)>4$, we may set $\alpha=1$ in (10), since $\lambda_0(\alpha)$ is an increasing function of α for $1/2\leq\alpha<1$. Thus by simple manipulation, we have

$$\lambda_0(1)=6f_2^{\,2}(0)/f_3(0)\,.$$

Therefore, requiring $\lambda_0(1)>4$, we arrive at the following inequality:

$$P_z(0)/P_w(0)=\{f_3(0)/f_2(0)\}/\{f_2(0)/f_1(0)\}<3/2\,, \tag{58}$$

where $P_z(0)$ and $P_w(0)$ are the z- and the weight-average degree of polymerization at $R=0$. The condition (58) may be understood as a criterion for a " sufficiently sharp " initial distribution.

If the initial distribution is broad, the viscosity-dose curve may have a minimum for a proper value of λ, but never a maximum. The curve is definitely concave upward near $R=0$.

When high-energy radiation causes endlinking instead of crosslinking the situation is qualitatively the same, although the viscosity-dose curve is more sensitive to the shape of the initial distribution.

A few words about an assumption involved in Saito's formalism as well as in our treatment should be needed to avoid misunderstanding. Namely, we assume that crosslinking and degradation should take place under irradiation with constant probabilities $\dot{c}$ and $\dot{r}$, or that reactions leading to crosslinking and degradation should proceed uniformly under irradiation. And it is in the scope of this assumption that we can expect rather complicated behaviors of the intrinsic viscosity depending on the types of initial molecular size distributions. Sometimes we have to do with the case where $\dot{c}$ and $\dot{r}$ depend on time. Such a non-uniform process, as it may be called, is encountered, for instance, when diffusion plays a significant role in the reaction mechanism[8], or when the amount or additives or impurities which react as radical scavengers changes appreciably during irradiation.[9] If necessary, the time dependence of $\dot{c}$ and $\dot{r}$ can be taken into account by a procedure similar to that adopted by Watanabe[8] and Saito[9] in discussions of such non-uniform processes.

We have neglected the effect of branching resulting from crosslinking on the intrinsic viscosity and used the simple Staudinger's law (7) or (51). We believe, however, that our conclusion would not be seriously modified, if we would consider the effect, because our treatment is concerned exclusively with the initial stage of irradiation where the number of branching is presumably very small. In fact, the number of branching is estimated to be order of unity per number-average molecule according to Saito.[4)]

Although Shultz et al[10)] attempted to calculate the intrinsic viscosity of crosslinked polystyrene considering the effect of branching, their result was not satisfactory. According to our view, their calculation involves at least two ambiguities. Firstly, their approximation $\eta(R) \propto P_w^{\alpha}(R)$ is not reasonable, since the molecular size distribution becomes essentially modified by crosslinking, endlinking and degradation. Secondly, the correction due to branching they obtained is appreciable even in the neighborhood of $R=0$, where it is physically expected to be small. In any way, it seems to be very difficult to evaluate the effect of branching.

In conclusion we emphasize that precise measurement of the intrinsic viscosity of an irradiated polymeric substance offers a powerful clue to the determination of the initial molecular size distribution.

Acknowledgements

The authors are very grateful to Professor A. Amemiya of the University of Tokyo and Professor O. Saito of the Chuō University for their discussions and encouragements throughout the work. Further the authors highly appreciate invaluable suggestions and comments of Dr. M. Matsumoto of the Kurashiki Rayon Co., Ltd. Thanks are also due to the members of the Electronic Computer Laboratory of the Faculty of Engineering, University of Tokyo, who kindly gave the authors facilities for numerical calculations by means of the TAC (Tokyo Automatic Computer). The authors are indebted to the Ministry of Education for the Scientific Research Fund.

References

1) F. A. Bovey: *The Effects of Ionizing Radiation on Natural and Synthetic High Polymers*, Polymer Reviews **1**, (Interscience Publ. New York, 1958).
2) M. Inokuti: J. Phys. Soc. Japan **14** (1959) 79.
3) O. Saito: J. Phys. Soc. Japan **13** (1958) 198.
4) O. Saito: J. Phys. Soc. Japan **13** (1958) 1451.
5) O. Saito: J. Phys. Soc. Japan **13** (1958) 1465.
6) R. W. Pearson: *Radioisotopes in Scientific Research* **1**, Proc. 1st UNESCO Int. Conf., Paris, 1957 (Pergamon 1958) 158.
7) M. Matsumoto: private communication.
8) T. Watanabe: J. Phys. Soc. Japan **13** (1958) 1316.
9) O. Saito: J. Phys. Soc. Japan **14** (1959) 798.
10) A. R. Shultz, P. I. Roth and G. B. Rathmann: J. Polymer. Sci. **22** (1956) 495.

JOURNAL OF THE PHYSICAL SOCIETY OF JAPAN, Vol. 14, No. 10, OCTOBER, 1959

Determination of Molecular Weight Distributions of High Polymers by Fractionation

By Hiroshi OKAMOTO

The Electrical Communication Laboratory, Nippon Telegraph and Telephone Public Corporation, Musashino, Japan

(Received July 3, 1959)

There are several impudent assumptions in the determination of molecular weight distributions of high polymers by fractionation. Therefore the reliability of the molecular weight distribution is very problematical. We reconsider the theoretical basis of two fractionation methods, the one is Spencer's method and the other is the successive precipitation method (SPM). Solving simultaneous integral equations, a modified Spencer's method is proposed. Though it necessitates to measure the ratio of the volume of the solution phase to that of the precipitated phase, the results are more accurate than Spencer's method. A modified SPM is also proposed. The results are also compared with the numerical calculation made by other authors and found to be in accord with them.

Molecular weights of high polymers may be established from appropriate physical measurements on dilute solutions, such as light scattering or osmotic method etc. These methods are all absolute, that is, if the experiments were carried out ideally, no error would be introduced in the results.

In the case of determination of molecular weight distributions of high polymers by fractionation, such a situation is not satisfied. Because many impudent assumptions are postulated in the procedure of the fractionation, there must be unavoidable errors in the resultant distribution curves.

Billmeyer and Stockmeyer[1] had studied about Spencer's fractionation method[2] and from many experimental resuls they had rather negative conclusion about this method. Other study [3][4][5][6] about the above mentioned problem were made only by numerical calculations. It seems to be difficult to obtain the general conclusions from them.

Under these circumstances, we try to reconsider the theoretical basis of the two fractionation method, one is Spencer's method and the other is the successive fractionation. Thus we can find a modified method to determine the distribution curves and a fractionation condition to reduce the errors as small as possible.

Recently, Broda, Niwińska, Potowiński[7] discussed the so called summative fractionation method. The auther considers that the first order approximation of their method is nothing but Spencer's method and a further analytical treatment is needed.

CHAPTER I

§ 1.1. Introduction

The procedure of Spencer's method is as follows. A series of polymer solutions is prepared. Each solution is separated into two phases by successive variation of its solvent power. This can be established by successive variation of the content of the non-solvent or of the temperature of each solution. The quantities actually measured are the weight fraction of the precipitated polymer $W(s)$ and the weight-average molecular weight of it $m(s)$. To simplify the problem, Spencer proposed an artificial assumption, namely, that all of the polymer above a certain molecular weight $x(s)$ is in the precipitate and that all bellow $x(s)$ is in the solution phase. Where we use "s" as a parameter which represents the solvent power of the solution, that is, "s" have a one to one correspondence to the non-solvent content or the temperature of the solution.

According to this assumption, if $f(x)$ is the distribution function of the molecular weight,

$$W(s)=\int_{x(s)}^{\infty} f(x)dx \qquad (1.1)$$

$$M(s)=m(s)W(s)=\int_{x(s)}^{\infty} xf(x)dx\ , \qquad (1.2)$$

From Eq. (1.1) and (1.2)

$$\frac{dM}{dw}=x(s) \tag{1.3}$$

The procedure is, then, to plot $m(s)W(s)$ versus $W(s)$ and draw a smooth curve through the points. The curve is differentiated to give the corresponding values of $x(s)$ and $W(s)$. A plot of $1-W(s)$ versus $x(s)$ is the integral distribution curve.

It is an obvious fact, however, that Eq. (1.1) and Eq. (1.2) are not exact. There must be a continuous function $K(s, x)$ which determines the phase separation of the solution.

$$W(s)=\int_0^{\infty}K(s, x)f(x)dx \tag{1.4}$$

$$M(s)=\int_0^{\infty}K(s, x)xf(x)dx \tag{1.5}$$

To treat the problem exactly, solving integral equations (1.4) and (1.5) we must find an unknown function $f(x)$ from the two functions of variable "s", $W(s)$ and $M(s)$ which are able to be obtained from the experiments.

Following the theory of Flory,[8] Sott[9] and Münster,[10] $K(s, x)$ is given by

$$K(s, x)=\frac{1}{1+R(s)\exp\left[-\sigma(s)x\right]} \tag{1.6}$$

Where $R(s)$ is the ratio of the volume of the solution phase to that of the precipitated phase and $\sigma(s)$ is a complicated function of several interaction parameters and the composition of the solution.

For example, for a single solvent solution,

$$\sigma=v\left(1-\frac{1}{r_n}\right)-v'\left(1-\frac{1}{r_n'}\right)+\chi\{(1-v)^2-(1-v')^2\} \tag{1.7}$$

where, v and v' are the volume concentrations of the polymer in the solution and the precipitated phase, r_n and r_n' are the number average molecular weights of each phase and χ is the interaction parameter between the solvent molecule and the polymer segment. Takenaka and his co-workers[11] had already proposed to solve the integral equation (1.4) with Eq. (1.7) by numerical calculation using the electronic computor. Though their method is rigorous, it necessitates the knowledge of many quantities R, v, v', r_n, r_n' and χ. In practice this must be a quite inconvenient task.

We propose to solve the problem as a simultaneous integral equation regarding $f(x)$ and $\sigma(s)$ as two unknown functions, and $W(s)$, $M(s)$ and $R(s)$ as three known functions of s which are able to be obtained from the experiments.

§ 1.2. Mathematical Calculation of the Problem

We write down again the fundamental equation as

$$W(s)=\int_0^{\infty}\frac{1}{1+R(s)\exp\left[-\sigma(s)x\right]}f(x)dx \tag{1.8}$$

$$M(s)=m(s)W(s)=\int_0^{\infty}\frac{1}{1+R(s)\exp\left[-\sigma(s)x\right]}x^{\alpha}f(x)dx \tag{1.9}$$

When $\alpha=1$, $m(s)$ is the weight-average molecular weight, when $\alpha=-1$, $1/m(s)$ is the number average molecular weight and if the distribution curve is plotted against the intrinsic viscocity, α is idential with that encountered in the intrinsic viscocity molecular weight relationship

$$[\eta]=KM^{\alpha}\,.$$

And $m(s)$ is given by

$$m(s)=\frac{1}{K}[\eta]\,.$$

We define $x(s)$ by the following equation,

$$W(s)=\int_{x(s)}^{\infty}f(x)dx \tag{1.10}$$

$\varDelta(s)$ is also defined as,

$$M(s)=\int_{x(s)}^{\infty}x^{\alpha}f(x)dx+\varDelta(s) \tag{1.11}$$

[illegible]

[illegible]

The second term of the right hand side of the Eq. [illegible]

[illegible]

[illegible]

[illegible]

[illegible]

[illegible]

[illegible]

[illegible]

[illegible]

$$[illegible]$$

[illegible]

$$[illegible]$$

[illegible]

$$[illegible]$$

[illegible]

$$[illegible]$$

[illegible]

$$[illegible]$$

[illegible]

$$[illegible]$$

[illegible]

[illegible]

and the shifts diminish as $\log R$ becomes large. We can also recognize that the conditions I and II are nearly satisfied with $f(x)=-1/2(\log 0.996)^3\times 0.996^x x^2$. Matsumoto also calculated for the box type and the two peaks type distributions. For the box type distribution, his calculated curves seemed to lie on the right side of the true curve. We tried similar and more detailed numerical calculation for the box type distribution and found that the calculated curve increases rapidly and moves from the right to the left side of the true curve near the end of the distribution at the higher molecular weight side (Fig. 2).

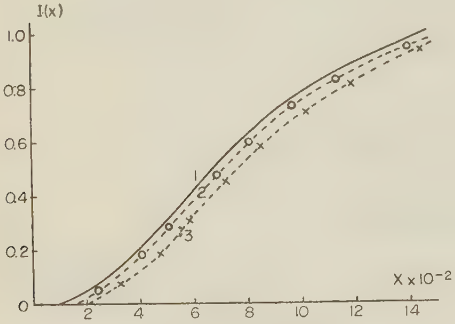

Fig. 1. Comparison of the true integral distribution curve (1) and the curves calculated following Spencer's methods (2) and (3). R is 1000 for the curve (2) and is 500 for the curve (3). $f(x)$ is $-1/2(\log 0.996)^3 0.996^x x^2$. This figure is copied from Matsumoto's work[6].

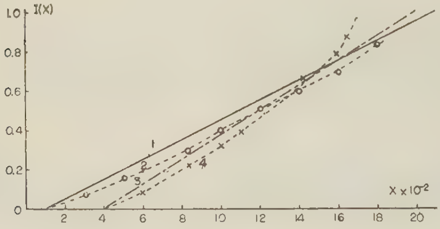

Fig. 2. Comparison of the true integral distribution curves (1) and (3) and the curves calculated following Spencer's methods (2) and (3) for the box type distribution. Curves (1) and (2) are copied from Matsumoto's work[6]. The curve (2) are calculated for the curve (1) under the condition $R=100$, the curve (3) are calculated for the curve (2).

This irregularity arises from the fact that the conditions I and II do not hold in this region. $f(x)$ has two discontinuous points at both ends of the distribution.

From the statistical analysis of their experiments, Billmeyer and Sockmeyer[1] concluded that Spencer's method cannot yield a very detailed description of the molecular weight distribution. They considered three types of the distribution curves, a rectanglar box, a triangle and a parabola.

According to our consideration, all of such distribution curves do not satisfy the conditions I and II, because they all have two or three discontinous points.

The application of Spencer's method is questionable for these cases. This must be one of the important reason of the failure of Spencer's method.

An important question arises, how can we know that $f(x)$ does satisfy the conditions I and II or not. At the start point of the experiment, we know nothing about $f(x)$ and we cannot determine R properly to satisfy the condition II. To answer the question, it must be one of the possible way that we check that the zeroth or the first order approximate function are satisfied by the conditions I and II or not. If they are satisfied, we can almost safely conclude (strictly, not always) that the true distribution curve also satisfies the conditions. If the approximated function does not satisfy the conditions, we can strictly say that the obtained distribution functions never represent the true function. And we are obliged to recommence the fractionation under larger R.

We must add a short remark for the measurement of the average molecular weight. It must be avoided to use Z or higher order average molecular weight. Because for these averages the theory developed in § 1.2 does not hold and we cannot use the final result Eq. (1.25).

CHAPTER II

§ 2.1. Introduction

We have reconsidered the theoretical basis of Spencer's method heretofore and proposed a more reliable method. However, the author considers that the method which is most widely employed now is the successive fractionation method, especially the successive precipitation method (SPM).

There are several impudent assumptions in the usual procedure of the SPM, which is as follows.

The polymer sample of which molecular weight distribution is to be determined is dissolved by an appropriate solvent or solvent mixture. By means of lowering the temperature or adding the precipitant its solvent power is lowered slowly until two phase separation occurs. Then the precipitated phase is taken out of the apparatus. The ratio of the weight of the precipitated polymer to that of the whole polymer W_1 and the average molecular weight of the precipitated polymer m_1 are measured. The supernatant phase remained is again separated into two phases by further lowering the solvent power and W_2 and m_2 are measured, the similar procedures are repeated $n-1$ times. Finally W_n and m_n are also measured for the remaining solution. Usually, the integral molecular weight distribution curve is assumed to be

$$I(m_i)=\sum_{\lambda=0}^{n-\lambda=i+1} W_n{}^{-\lambda}+\frac{1}{2}W_i\,. \tag{2.1}$$

As Schulz[3] had already pointed out, the actual molecular weight distribution of each fraction is considerably overlapped each other. Because this overlapping is apparently neglected in Eq. (2.1), the reliability of the obtained distribution curve is very doubtful. The influence of these neglections upon the results have only been numerically calculated by G. V. Schulz,[3] Matsumoto and Ohyanagi,[6] however, the general conclusion cannot be drawn by the numerical calculation.

The questions, how does this neglection affect the result and how should we perform the experiments to minimize the errors due to this, have not yet been answered.

We try to answer such questions in the following along the similar treatment described in Chapter I.

§ 2.2. Mathematical Calculation of the Problem

There are $n-1$ separation functions for each fractionation step.

$$K_i(x)=\frac{1}{1+R_i\exp[-\sigma_i x]} \tag{2.2}$$

$$i=1,\,2,\,\cdots\,n-1$$

W_i is written as

$$W_i=\int K_i\prod_{\lambda=1}^{i-1}(1-K_\lambda)f dx \tag{2.3}$$

The average molecular weight is measured as the number average or the weight average and in many cases the intrinsic viscocity is used instead of the molecular weight. So that,

$$M_i=m_i W_i=\int K_i\prod_{\lambda=1}^{i-1}(1-K_\lambda)x^\alpha f dx \tag{2.4}$$

The relation between m_i and α is the same as those described in Chapter I.

W_n and M_n are written as

$$W_n=\int\prod_{\lambda=1}^{n-1}\{1-K_\lambda(x)\}f(x)dx \tag{2.5}$$

$$M_n=\int\prod_{\lambda=1}^{n-1}\{1-K_\lambda(x)\}x^\alpha f(x)dx \tag{2.6}$$

And we can find the following relations

$$\sum_{\lambda=0}^{n-\lambda=i+1} W_{n-\lambda}=\int\prod_{\lambda=1}^{i}\{1-K_\lambda(x)\}f(x)dx \tag{2.7}$$

$$\sum_{\lambda=0}^{n-\lambda=i+1} M_{n-\lambda}=\int\prod_{\lambda=1}^{i}\{1-K_\lambda(x)\}x^\alpha f(x)dx \tag{2.8}$$

We defined y_i as the inflection point of K_i and $y_i-\delta y_i$ is defined by the following relation

$$\sum_{\lambda=0}^{n-\lambda=i+1} W_{n-\lambda}=\int_0^{i-\delta i} f(x)dx \tag{2.9}$$

$$\int_{i-\delta i}^{i} f dx = \int_0^i \left\{1-\prod_{\lambda=1}^{i-1}(1-K_\lambda)\right\} f dx + \int_0^i K_i \prod_{\lambda=1}^{i-1}(1-K_\lambda) f dx - \int_i^\infty (1-K_i)\prod_{\lambda=1}^{i-1}(1-K_\lambda) f dx\,. \tag{2.10}$$

Where the intergration limits i and $i-\delta i$ are used in places of y_i and $y_i-\delta y_i$. Using these abbreviations, the following relation is obtained.

$$W_i = \int_{i-\delta i}^{i-1-\delta(i-1)} f(x)dx \tag{2.11}$$

We call the integration range of Eq. (11) $[y_{i-1}-\delta y_{i-1}, y_i-\delta y_i]$ as d_i hereafter.

Next, Δ_i is defined as

$$\Delta_i = M_i - \int_{i-\delta i}^{i-1-\delta(i-1)} x^\alpha f(x)dx \tag{2.12}$$

It is important to notice the following consideration.

If

$$\Delta_i \ll \int_{i-\delta i}^{i-1-\delta(i-1)} x^\alpha f(x)dx\,, \tag{III}$$

then m_i is in the range

$$y_i-\delta y_i \leqq m_i^{1/\alpha} \leqq y_{i-1}-\delta y_{i-1}\,. \tag{2.13}$$

When d_i is so small that $f(x)$ can be seen to be constant in d_i and α is equal to 1, the following relations stand.

$$m_i = \frac{1}{2}(y_{i-1}-\delta y_{i-1}+y_i-\delta y_i) \tag{2.14}$$

$$\int_0^{m_i} f(x)dx = \sum_{\lambda=0}^{n-\lambda=i+1} W_{n-\lambda} + \frac{1}{2}W_i \tag{2.15}$$

Eq. (2.14) is the same as Eq. (2.1). The usual assumptions are found to be adequate in this case. But this is only an ideal case. If the condition III does not hold, however small d_i may be, Eq. (2.13), (2.14) do not stand.

Therefore, there are two important factors in the fractionation, the one is to make d_i as small as possible and the other is to make Δ_i satisfy the condition III. The former corresponds to the analyzability of the fractionation. To clarify these situations, we proceed to calculate Eq. (2.9) and Eq. (2.11). We can prove the following relations by the analogous process which was used to derive Eq. (1.14) from Eq. (1.15)

$$\int_0^i \left\{1-\prod_{\lambda=1}^{i-1}(1-K_\lambda)\right\} f dx \cong \int_0^i K_{i-1} f dx \cong \sum_{n\geqq 0}(-)^n E_{n+1,i}\left(\frac{d^n f}{dx^n}\right)_i \left(\frac{y_{i-1}}{\log R_{i-1}}\right)^{n+1} \tag{2.16}$$

where,

$$E_{n,i} = \sum_{\nu\geqq 0}(-)^\nu \frac{1}{(\nu+1)^n}\left(\frac{1}{R_{i-1}}\right)^{\nu+1} \exp\left[(\nu+1)\sigma_{i-1}y_i\right]$$

and

$$\int_0^i K_i \prod_{\lambda=1}^{i-1}(1-K_\lambda) f dx - \int_i^\infty (1-K_i)\prod_{\lambda-1}^{i-1}(1-K_\lambda) f dx \cong -2\sum_{\nu\geqq 0} C_{2\nu+2}\frac{d^{2\nu+1}}{dx^{2\nu+2}}\left\{\prod_{\lambda=1}^{i-1}(1-K_\lambda) f\right\}_i \left(\frac{y_i}{\log R_i}\right)^{2\nu+2}. \tag{2.17}$$

Then Eq. (2.9) reduces to

$$\int_{i-\delta i}^{i} f dx \simeq \left[E_{1,i}\left(\frac{y_{i-1}}{\log R_{i-1}}\right) - 2C_2\frac{d}{dx}\left\{\prod_{\lambda=1}^{i-1}(1-K_\lambda)\right\}_i \left(\frac{y_i}{\log R_i}\right)^2\right] f(x_i) +$$
$$+\left[-E_{2,i}\left(\frac{y_{i-1}}{\log R_{i-1}}\right)^2 - 2C_2\prod_{\lambda-1}^{i-1}(1-K_\lambda)_i\left(\frac{y_i}{\log R_i}\right)^2\right]\left(\frac{df}{dx}\right)_i + \cdots \tag{2.18}$$

As δy_i is defined for $\sum_{\lambda=0}^{n-\lambda=i+1} W_{n-\lambda}$ so $\delta y_i'$ is defined for $\sum_{\lambda=0}^{n-\lambda=i+1} M_{n-\lambda}$.

$$\int_{i-\delta'i}^{i} x^{\alpha} f dx = \int_{0}^{i} \left\{ 1 - \prod_{\lambda-1}^{i-1} (1-K_{\lambda}) \right\} x^{\alpha} f dx + \int_{0}^{i} K_i \prod_{\lambda=1}^{i-1} (1-K_{\lambda}) x^{\alpha} f dx - \int_{i}^{\infty} (1-K_i) \prod_{\lambda=1}^{i-1} (1-K_{\lambda}) x^{\alpha} f dx \tag{2.19}$$

The right hand side of Eq. (2.19) reduces to

$$\cong \sum_{n \geqq 0} (-)^n E_{n+1,i} \left. \frac{d^n(x^{\alpha} f)}{dx^n} \right)_i \left(\frac{y_{i-1}}{\log R_{i-1}} \right)^{n+1} - 2 \sum_{\nu \geqq 0} C_{2\nu+2} \frac{d^{2\nu+1}}{dx^{2\nu+1}} \left\{ \prod_{\lambda=1}^{i-1} (1-K_{\lambda}) x^{\alpha} f \right\} \left(\frac{y_i}{\log R_i} \right)^{2\nu+2} \tag{2.20}$$

$$\begin{aligned} &\cong y_i^{\alpha} f(y_i) \left[E_{1,i} \frac{y_{i-1}}{\log R_{i-1}} - 2C_2 \frac{d}{dx} \left\{ \prod_{\lambda=1}^{i-1} (1-K_{\lambda}) \right\}_i \left(\frac{y_i}{\log R_i} \right)^2 \right] + y_i^{\alpha} \left. \frac{df}{dx} \right)_i \left[-E_{2,i} \left(\frac{y_{i-1}}{\log R_{i-1}} \right)^2 \right. \\ &\left. -2C_2 \prod_{\lambda=1}^{i-1} (1-K_{\lambda})_i \left(\frac{y_i}{\log R_i} \right)^2 \right] + \alpha y_i^{\alpha-1} f(y_i) \left[-E_{2,i} \left(\frac{y_{i-1}}{\log R_{i-1}} \right)^2 - 2C_2 \prod_{\lambda=1}^{i-1} (1-K_{\lambda})_i \left(\frac{y_i}{\log R_i} \right)^2 \right] + \cdots \end{aligned} \tag{2.21}$$

Comparing this equation with Eq. (2.17)

$$\cong \int_{i-\delta i}^{i} x^{\alpha} f(x) dx - \alpha y_i^{\alpha-1} f(y_i) \left[E_{2,i} \left(\frac{y_{i-1}}{\log R_{i-1}} \right)^2 + 2C_2 \prod_{\lambda=1}^{i-1} (1-K_{\lambda})_i \left(\frac{y_i}{\log R_i} \right)^2 \right] + \cdots \tag{2.22}$$

Thus, from Eq. (2.11) $\varDelta_i$ is approximately equal to

$$\begin{aligned} \varDelta_i \cong \alpha y_{i-1}^{\alpha-1} f(y_{i-1}) &\left[E_{2,i-1} \left(\frac{y_{i-2}}{\log R_{i-2}} \right)^2 + 2C_2 \prod_{\lambda=1}^{i-2} (1-K_{\lambda})_{i-1} \left(\frac{y_{i-1}}{\log R_{i-1}} \right)^2 \right] \\ - \alpha y_i^{\alpha-1} f(y_i) &\left[E_{2,i} \left(\frac{y_{i-1}}{\log R_{i-1}} \right)^2 + 2C_2 \prod_{\lambda=1}^{i-1} (1-K_{\lambda})_i \left(\frac{y_i}{\log R_i} \right)^2 \right] \end{aligned} \tag{2.23}$$

Considering that

$$\int_{i-\delta i}^{i-1-\delta(i-1)} x^{\alpha} f(x) dx = (x'_{i-1} - x_i') \xi_i^{\alpha} f(\xi_i) \tag{2.24}$$

$$x_i' < \xi_i < x'_{i-1} \qquad x_i' = y_i - \delta y_i \qquad x'_{i-1} = y_{i-1} - \delta y_{i-1}$$

To satisfy the condition III, it is sufficient that the following relation is satisfied.

$$\{E_{2,i-1} + 2C_2(1-K_{i-2})_{i-1}\} \frac{\alpha}{\{\log R\}^2} \ll \frac{x'_{i-1} - x_i'}{\eta} \tag{III$'$}$$

$$x_i' < \eta < x'_{i-1} \qquad R_{i-1} \leqq R \leqq R_{i-2}$$

where the approximation

$$\prod_{\lambda=1}^{i-2} (1-K_{\lambda})_{i-1} \cong (1-K_{i-2})_{i-1}$$

is used. The restrictions for $f(x)$ such as I and II in Chap. I should be also satisfied in the above discussions.

§ 2.3. Discussions

Among the two factors which are important in the SPM, the one to make d_i small is closely related to the number of the fractions. Roughly speaking, to make d_i small, the number of the fractions must be increased. But, however small d_i may be, if the conditions III or III′ is not satisfied, the value of m_i goes out of the range d_i and the reliability of the results become problematical. Conversely, however small $\varDelta_i$ may be, if d_i is large, the variation of $f(x)$ is smoothed out and the detailed knowledge of $f(x)$ can not be obtained.

The magnitude of $E_{2,i-1} + 2C_2(1-K_{i-2})_{i-1}$ is not known so far as the values of y_{i-1} and y_{i-2} are not given. They cannot be determined directly from the experiments but the magnitude of $E_{2,i-1} + 2C_2(1-K_{i-2})_{i-1}$ never exceeds $\log 2 + \pi^2/12$ and there will not occur appreciable errors when this factor is replaced by 1 so that

$$\frac{\alpha}{(\log R)^2} \ll \frac{x'_{i-1}-x_i'}{\eta} \qquad \text{III}$$

Though we have not the knowledge of x_i' etc., if the total range of the molecular weight is assumed to be equally divided into n fractions

$$\frac{x'_{i-1}-x_i'}{\eta} < \frac{1}{n-1}$$

so that

$$\frac{\alpha}{(\log R)^2} < \frac{1}{n-1}\ . \qquad \text{IV}$$

This is the most simplified from of the condition III. If we divide the sample into 10 fractions under the condition that R is comparable or greater than several hundreds, the results are probably satisfactory. Such fractionation can comparatively easily be attained without special intention.

Perhaps a more reliable estimation for the value of x_i' may be as follows

$$x_i' = \frac{W_{i+1}m_i^{1/2} + W_i m_{i+1}^{1/2}}{W_{i+1} + W_i}\ . \qquad (2.25)$$

When $\varDelta_i$ is found to be negligible, it may be a better approximation for $f(x)$ to assume it as a linear function of x in the range d_i. In this case

$$W_i = f_i(x'_{i-1}-x_i') + \frac{1}{2}(f_{i-1}-f_i)(x'_{i-1}+x_i') \qquad (2.26)$$

$$M_i = \frac{f_i}{\alpha+1}\left\{(x'_{i-1})^{\alpha+1}-(x_i')^{\alpha+1}\right\} + \frac{f_{i-1}-f_i}{\alpha+2}\,\frac{\{(x'_{i-1})^{\alpha+2}-(x_i')^{\alpha+2}\}}{x'_{i-1}-x_i'}$$

$$i=1, 2, \cdots n-1\ . \qquad (2.27)$$

$$W_n = \frac{1}{2} f_{n-1} x'_{n-1} \qquad (2.28)$$

$$M_n = \frac{1}{\alpha+2} f_{n-1}(x'_{n-1})^{\alpha+1} \qquad (2.29)$$

where

$$f_i = f(x_i') \qquad (2.30)$$

$$f(x) = f_i + (f_{i-1}-f_i)\frac{x-x_i'}{x'_{i-1}-x_i'} \quad x_i' \leqq x \leqq x'_{i-1} \qquad (2.31)$$

We must solve the above simultaneous equation with respect to f_i and x_i'.

Generally speaking, in the region $df/dx>0$, m_i is larger that $1/2(x'_{i-1}+x_i')$ and in the region $df/dx<0$, m_i is smaller than $1/2(x'_{i-1}+x_i')$. So the usual procedure will yield a more sharp distribution curve than the true one, this error will nearly be avoided with the assumption of linear from of $f(x)$.

Though the procedure becomes more complicated, higher order approximation may be possible. We estimate $\varDelta_i$ from Eq. (2.22) with the values of x_i' and $f(x)$ determined from the procedure usual or proposed in Eq. (2.26) to Eq. (2.28). Then, $M_i - \varDelta_i$ is used for the second approximation to $\int_{i'}^{(i-1)'} x^\alpha f(x)dx$.

References

1) E. W. Billmeyer and W. H. Stockmeyer: J. Polymer Sci. **5** (1949) 121.
2) R. S. Spencer: J. Polymer Sci. **4** (1948) 606.
3) G. V. Schulz: Z. phys. Chem. **B, 47** (1940) 155.
4) E. V. Syre: J. Polymer Sci. **10** (1953) 175.
5) M. Matsumoto and Y. Ohyanagi: Kobunshi Kagaku **11** (1954) 7.
6) M. Matsumoto: Kobunshi Kagaku **11** (1954) 182.
7) A. Broda, T. Niwińska and S. Polowiński: J. Polymer Sci. **32** (1958) 343.
8) P. J. Flory: J. Chem. Phys. **12** (1944) 425.
9) R. S. Scott: J. Chem. Phys. **13** (1945) 178.
10) A. Münster: J. Polymer Sci. **5** (1950) 333.
11) H. Takenaka, Y. Ogawa and T. Ikeda: Lecture at the Annual Meeting of the High Polymer Society of Japan (1958).

JOURNAL OF THE PHYSICAL SOCIETY OF JAPAN, Vol. 14, No. 10, OCTOBER, 1959

Magnetohydrostatic Equilibrium for Plasma in a Torus Tube

By Taro KIHARA

Department of Physics, Faculty of Science, University of Tokyo

(Received May 20, 1959)

A solution of the magnetohydrostatic problem of finding the equilibrium configuration of a plasma in a slightly bending torus tube with circular cross section is reported. Both the plasma and the tube wall are assumed to be perfectly conducting. The ratio of the tube radius to the radius of curvature, R, of the tube axis is assumed to be so small that its square is negligible. The method is an application of a perturbed cylindrical coordinate sytsem, in which the line element ds is given by

$$ds^2=(1-\xi R^{-1}r\cos\theta)^2dr^2+(1-\eta R^{-1}r\cos\theta)^2r^2d\theta^2+(1+R^{-1}r\cos\theta)^2dz^2\ ,$$

ξ and η being functions of r satisfying $\xi=d(r\eta)/dr$. A result is the following. If an axially symmetric plasma cylinder with the material pressure monotonically decreasing towards the plasma surface is slightly bent into a torus, then two isobaric surfaces are closer in the more distant part from the torus axis than in the less distant part.

§1. Introduction

There are several magnetohydrodynamic investigations[1)2)] on the equilibrium configuration and its stability of a cylindrical plasma contained in a cylindrical tube. In the present paper is treated the case where the cylinder slightly bends into a torus with circular cross section. Plasma in a torus tube plays an important role in researches on controlled fusion.

Biermann et al.[3)] gave solutions to the problem assuming that the electric currents flow exclusively at the surface of the plasma; their method is exact but is restricted to this particular assumption. In the present paper the problem is solved without this restriction, although the solution is limited to small perturbations. Both the plasma and the tube wall are assumed to be perfectly conducting. The ratio of the tube radius to the radius of curvature of the tube axis is assumed to be so small that its square is negligible.

We consider a plasma in equilibrium, i.e. under the condition

$$\boldsymbol{J}\times\boldsymbol{B}=\mathrm{grad}\,P\ , \qquad (1)$$

which expresses balance between the electromagnetic and mechanical forces. Here $\boldsymbol{B}$ is the magnetic field satisfying $\mathrm{div}\,\boldsymbol{B}=0$; $\boldsymbol{J}$ is the current density, $\boldsymbol{J}=\mu^{-1}\,\mathrm{rot}\,\boldsymbol{B}$ with the constant permeability μ; P is the pressure assumed to be a scalar.

For a cylindrical plasma with axial symmetry an equilibrium configuration is given, in terms of the cylindrical coordinates r, θ, z, by

$$B_r=0\ ,\quad B_\theta=f(r)\ ,\quad B_z=g(r)\ , \qquad (2)$$

where $f(r)$ and $g(r)$ are arbitrary functions of r. The condition (1) is equivalent to

$$\frac{1}{2\mu}\frac{d}{dr}(f^2+g^2)+\frac{1}{\mu}\frac{f^2}{r}=-\frac{dP}{dr}\ . \qquad (3)$$

The cylindrical plasma is in equilibrium when it is surrounded by a cylindrical wall at $r=$constant.

Our aim is to discuss the perturbation to the equilibrium configuration (2) when the cylinder slightly bends into a torus. For this purpose we try to modify the cylindrical coordinates for which the line element ds is given by

$$ds^2=dr^2+r^2d\theta^2+dz^2\ .$$

Let R denote the radius of curvature of the tube axis. One might first expect to use an orthogonal curvilinear coordinates r, θ, z defined by

$$ds^2=dr^2+r^2d\theta^2+(1+R^{-1}r\cos\theta)^2dz^2\ , \qquad (4)$$

with the curved z-axis on the tube axis. Here positive and negative $\cos\theta$ correspond, respectively, the more and the less distant parts from the torus axis. This choice is not very convenient, since the field quantities are complicated in general in this coordinate system. One might then expect to use another orthogonal curvilinear coordinates defined by

$$ds^2=(1-\alpha R^{-1}r\cos\theta)(dr^2+r^2d\theta^2)+(1+R^{-1}r\cos\theta)^2dz^2\,, \tag{5}$$

with constant α. Here use has been made of the assumption that the square of the curvature of the z-axis can be neglected. This system, however, is not yet useful enough; and it will be generalized farther in the following.

§ 2. Solution

We introduce, neglecting the square of the curvature R^{-1}, a "perturbed cylindrical coordinate system" defined by

$$ds^2=\left(1-\frac{\xi}{R}r\cos\theta\right)^2dr^2+\left(1-\frac{\eta}{R}r\cos\theta\right)^2r^2d\theta^2+\left(1+\frac{1}{R}r\cos\theta\right)^2dz^2\,, \tag{6}$$

in which ξ and η are functions of r only. In order that r and θ defined by (6) with constant z indicate orthogonal curvilinear coordinates in a plane, it is necessary that the Gaussian curvature,

$$-\frac{1}{h_1h_2}\left[\frac{\partial}{\partial\theta}\left(\frac{1}{h_2}\frac{\partial h_1}{\partial\theta}\right)+\frac{\partial}{\partial r}\left(\frac{1}{h_1}\frac{\partial h_2}{\partial r}\right)\right],$$

in which

$h_1\equiv 1-R^{-1}\xi r\cos\theta$ and $h_2\equiv(1-R^{-1}\eta r\cos\theta)r$,

vanishes. The condition is calculated to be

$$\xi=\frac{d}{dr}(r\eta)\,. \tag{7}$$

This is also sufficient for (6) to be orthogonal curvilinear coordinate system in a Euclidian space. Equation (6) reduces to (5) when ξ is a constant.

With respect to this coordinate system we can prove, up to the first order of the curvature R^{-1}, the following. The vector $\boldsymbol{B}$ having the components

$$B_r=0\,,\quad B_\theta=\left(1+\frac{\xi-1}{R}r\cos\theta\right)f(r)\,,$$

$$B_z=\left(1-\frac{r}{R}\cos\theta\right)g(r) \tag{8}$$

is source-free,

$$\operatorname{div}\boldsymbol{B}=0\,,$$

and moreover the r-component of its curl vanishes:

$$(\operatorname{rot}\boldsymbol{B})_r=0\,.$$

The θ- and z-components are

$$(\operatorname{rot}\boldsymbol{B})_\theta=-\left(1+\frac{\xi-1}{R}r\cos\theta\right)\frac{dg}{dr}\,,$$

$$(\operatorname{rot}\boldsymbol{B})_z=\frac{1}{r}\frac{d}{dr}(rf)+\frac{1}{R}\cos\theta\left[(2\xi-1)\frac{d}{dr}(rf)+\left(r\frac{d\xi}{dr}-1\right)f\right],$$

where the condition (7) has been used. The current density, $\boldsymbol{J}$, is given by $\mu^{-1}\operatorname{rot}\boldsymbol{B}$.

Now, $\xi(r)$, and hence $\eta(r)$ also, can be determined in such a way that the magnetic field (8) satisfies the equilibrium condition (1). The condition is equivalent to $\operatorname{rot}(\boldsymbol{J}\times\boldsymbol{B})=0$, which is calculated to be

$$\frac{d}{dr}(r^2f^2\xi)=r^2\frac{d}{dr}(f^2+g^2)+3rf^2\,. \tag{9}$$

Hence

$$(\operatorname{rot}\boldsymbol{B})_z=\left(1+\frac{r}{R}\cos\theta\right)\frac{1}{r}\frac{d}{dr}(rf)+\frac{r}{Rf}\cos\theta\frac{d}{dr}g^2\,.$$

The electric current density vanishes where both $d(rf)/dr$ and dg/dr vanish. Integrating (9) we have

$$f^2\xi=\frac{1}{r^2}\int_0^r(f^2-2g^2)rdr+f^2+g^2\,; \tag{9a}$$

The pressure depends on r only and is determined by

$$\frac{1}{2\mu}\frac{d}{dr}(f^2+g^2)+\frac{1}{\mu}\frac{f^2}{r}=-\frac{dP}{dr}\,, \tag{10}$$

which has the same form as (3). Integrating we have

$$P=\text{const.}-\frac{1}{2\mu}(f^2+g^2)-\frac{1}{\mu}\int_0^r\frac{f^2}{r}dr\,, \tag{10a}$$

Thus we have generalized the cylindrical configuration (2) into a toroidal one (8) by use of a curvilinear coordinate system (6) with the conditions (7) and (9). This toroidal plasma is in equilibrium when it is surrounded by a tube wall at $r=$constant.

From (9) and (10) we obtain

$$\frac{d}{dr}(r^2f^2\xi)=-2\mu r^2\frac{dP}{dr}+rf^2\,.$$

Therefore, if the pressure is a monotonically decreasing function of r, ξ is always positive, and, by virtue of (7), η is also positive:

$$\xi>0\,,\quad \eta>0\quad\text{if}\quad dP/dr\leqq 0\quad\text{for all}\quad r\,.$$

For positive ξ we have from (6),

$$(ds\text{ at constant }\theta\text{ and }z)<dr\quad\text{for}\quad\cos\theta>0\,,$$

$(ds$ at constant θ and $z) > dr$ for $\cos\theta < 0$. Since an isobaric surface coincides with a surface of constant r, we can express one of our results as follows. *If an axially symmetric plasma cylinder with the material pressure monotonically decreasing towards the plasma surface is slightly bent into a torus, then two isobaric surfaces are closer in the more distant part from the torus axis than in the less distant part.* It is to be noted that this conclusion is not at all self-evident; if the numerical coefficient of the last term of (9) were less than 2 instead of being 3, then the conclusion would not hold.

§ 3. Example

As an example let us consider the case where

$$f(r)=\begin{cases} r^n & \text{for } r<1 \\ r^{-1} & \text{for } 1<r<r_1\,, \end{cases}$$

$$[g(r)]^2=\begin{cases} g_0^2(1-r^{2n}) & \text{for } r<1 \\ 0 & \text{for } 1<r<r_1\,, \end{cases}$$

$$P=0 \text{ and } \boldsymbol{J}=0 \quad \text{for } 1<r<r_1\,,$$

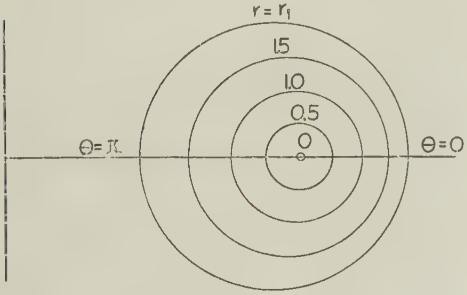

Fig. 1. Lines of constant r in the (r, θ)-plane for $\alpha=1/2$, $r_1=2$, $R=4$.

n and g_0^2 being positive constants. This indicates a plasma of unit radius in a tube of radius r_1 $(r_1 \ll R)$, the averaged B_θ at the plasma surface being taken as unity. Using (10a) we have

$$P=\frac{1}{2\mu}\left(1+\frac{1}{n}-g_0^2\right)(1-r^{2n}) \quad \text{for} \quad r<1\,,$$

from which follows $g_0^2<1+n^{-1}$. The ξ and η are calculated to be

$$\xi=\eta=\alpha \qquad \text{for} \quad r<1\,,$$

$$\xi=\alpha+\ln r, \quad \eta=\xi+r^{-1}-1 \quad \text{for} \quad 1<r<r_1\,,$$

where

$$\alpha=1+\frac{1}{2n+2}-\frac{n}{n+1}g_0^2>\frac{1}{2n+2}\,.$$

In this case the relation (6) for $r<1$ reduces to (5). Lines of constant r in the (r, θ)-plane are such as shown in Fig. 1; these lines are cross sections of isobaric surface fop $r<1$.

In the foregoing we did not consider the stability of the equilibrium, which is influenced only in the second power of the curvature. When the curvature is small at least, the equilibrium configuration discussed in the above example is stable when g_0^2 is sufficiently large and r_1 is sufficiently small.

References

1) R. J. Tayler: Proc. Phys. Soc. London **B, 70** (1957) 1049.
2) T. Kihara: J. Phys. Soc. Japan **13** (1958) 473. See also, S. Kaneko: J. Phys. Soc. Japan **13** (1958) 947.
3) L. Biermann, K. Hain, K. Jörgens and R. Lüst: Z. Naturforsch. **12a** (1957) 826. See also, R. Lüst and A. Schlüter: Z. Naturforsch. **12a** (1957) 850.

JOURNAL OF THE PHYSICAL SOCIETY OF JAPAN, Vol. 14, No. 10, OCTOBER, 1959

F–M Conversion in Additively Colored KCl Crystals

By Masamitsu HIRAI

Department of Physics, The Faculty of Science,
University of Tohoku, Sendai

(Received May 22, 1959)

The photochemical reaction of F→M conversion in an additively colored KCl crystal was investigated as a function of the concentration of F centers, under the condition such as differently colored crystals absorb the equal number of incident photons.

The process of the F band bleaching is separated into two steps of the fast and slow bleaching. During earlier stages of F light irradiation the F band displayed the fast bleaching and its amount in each crystals was equal, and independent on the F center concentration, but the growth rate of the M band was proportional to the square root of the concentration of F center. An absorption band, which may be Petroff's A band, was induced on the red side of the F band, but the appearance of this band was dominant in the crystal lightly colored. These experimental results show that the mechanism of the optical F→M conversion depends on the F center concentration, and that the M center is converted from the F center through certain intermediate states.

In the case of the F centers converted from U centers, the growth of the M band was small as compared with that of additively colored crystals containing only F centers, and the growth of the A band was also negligibly small.

§1. Introduction

The optical bleaching of the F center in additively colored alkali halide crystals have been investigated by many authors and the following phenomena have been well known. When the additively colored KCl crystals were irradiated with F light, the F band bleaches, while the M band appeares on the red side of the F band and succesively, the enhancement of the R_1, R_2, N and K bands is observed. However, Petroff[1] observed that the A and B bands appear very close to the F band at the red and violet sides of it before the other bands grow up. These bands have been explained as follows.

The M band corresponds to the transition in the absorption center which has the symmetry of C_{2v} or D_{2h}, which was determined from the experiments of its dichroic property[2] and fluorecence[3]. As to the R_1 and R_2 bands, Seitz[4] states that they arise from transitions in F_2^+ and F_2 centers respectively, which consist of the two nearest adjacent negative ion vacancies and a traped electron for the former center, or two traped electrons for the latter center[5].

The Göttingen workers believe that A and B bands occupy an important genetic relationship in the formation of the other bands, however, Seitz[6] states that these bands are characteristic of Petroff's specimens rather than of the alkali halides in general, for these bands are not observed in the crystals of other labolatories. However, Harman et al. observed that the absorption on the red side of the F band increses, when the additively colored KCl crystals (Harshaw Chemical Co.) were irradiated with F light at room temperature, and measured at liquid air temperature. Furthermore, Markham and Konitzer[7] reported also on the B band in the additively colored KCl crystals. Then it seems still probable to consider that accompaning with the F light irradiation A and B bands will apear as characteristic of the alkali halide crystals in general. However, up to the present, the intrinsic properties of these bands or the relationship to the other bands are not particularly investigated.

As mentioned above, although many investigations on each band have been made, the information on the process, in which the F band is converted to the other bands are very few. In the present paper, in order to clarify this process the mechanism of F→M conversion was investigated, by observing how the growth of the M band depends on the density of the F centers, and how the A or B bands relate to the F→M conversion and also to the half width of the F band.

Furthermore, the bleaching of the F band in the crystals containing U centers was also investigated. When the additively colored alkali halide crystal is heated in the hydrogen gas, it displays a bell shaped absorption band in the ultra violet region. This band is called U band and arises from the electronic transition in the U center, which is considered to be a negatively charged hydrogen ion occupying halogen ion site substitutionally and its absorption maximum situates at 216 mμ in KCl crystal[8]. When this crystal is irradiated by the U light, U band is bleached and F band appeares again. There is no centers other than F center in this conversion process. On this process, Mott and Gurney[9] explained as follows. The excited level of the U center is metastable as a result of crossing of the crystalline Franck-Conson curves, then if the U center absorbes U light, the hydrogen atom escapes from the U center to the interstitial site in the crystal, leaving an F center. The paramagnetic reresonance[10] showed that these interstitial hydrogen atoms combine to form interstitial hydrogen molecules at room temperature.

When KCl+U→F crystal is irradiated with F light, the F band bleaches and the M, R_1, R_2, and N bands appear on the red side of the F band as in the case of additive coloration, however, the behavior of bleaching or growth of these bands are somewhat different. The mechanisms of F→M conversion in this crystal were also investigated, and compared with the cases of KCl+F crystal. KCl+U→F crystal means KCl+U crystal containing the F centers and the interstital hydrogen molecules, which are produced by U light irradiation. KCl+F and KCl+U crystals mean the crystals containing F or U centers only, respectively.

All measurments were made at room temperature.

§ 2. Experimental Procedures

KCl crystals grown by Kyropoulos method were heated with K metals in the Terex tube at 460°C∼550°C, then these crystals were quenched down to room temperature. Concentration of F centers in these crystals were $2.1\times10^{16}\sim6.9\times10^{17}/\text{cm}^3$ and the M band absorption in these crystals were only a trace. Table I shows the description of specimens, thickness, total number of F centers, density of F centers and growth rate of M band.

Table I. Description of used specimens in the present experiment.

Sample (No.)	Thickness d (mm)	Number of F centers [a]	Density of F centers (cm^{-3})	Growth rates of M band
1	0.17	1.17×10^{16}	6.9×10^{17}	0.47
2	0.28	1.08×10^{16}	3.9×10^{17}	0.29
3	0.84	1.04×10^{16}	1.3×10^{17}	0.18
4	1.57	1.23×10^{16}	7.9×10^{16}	0.13
5	4.22	0.91×10^{16}	2.1×10^{16}	0.07

[a]: The number of the F centers obtained by equation (2), which gives the number of the F centers contained in the specimen whose volume $d\times1\times1\,\text{cm}^{-3}$.

In order to compare the bleaching of the F band or the growth of the M band in several crystals colored additively with different concentration, the total number of F center in crystals must be made equal for each specimen. By cleaving the lightly colored crystals into thick slices, and cleaving the heavily colored crystals into thin slices, the total number of F centers in each specmen was made equal. Because, if the number of F centers in one specimen is larger than that in another one, it will be natural that the bleaching of the F band or the growth of the M band in the former specimen will occur in larger quantity and rapidly. Second column in Table I shows the thickness of each specimen and third column shows the number of F centers contained in such specimens of thickness shown in the second column. Using these specimens, it was investigated how much M centers will be produced from equal number of F centers, and how the growth of the M band depends on the density of F centers, when the crystals were illuminated in this same condition.

Using Smakula's equation[11] the number of F centers was obtained optically, i.e.,

$$n_F f_F = 1.31\times10^{17}\frac{n'}{(n'^2+2)^2}\cdot\alpha_m\cdot W_F \qquad (1)$$

where, n_F is the number of F centers per cubic centimenter, f_F is oscillator strength of the F center, n' and α_m are the refractive index and absorption coefficient at the absorption peak of the F band in the crystals, W_F is the half width of the F band in electron volts. Putting $n'=1.49$, $W_F=0.35$ e.v. and $f_F=0.81$ for KCl crystal, a simplified equation $n_F=1.09\times10^{16}\ (\log_{10} I_0/I)/d$ was used. I/I_0 is the transparency at the absorption peak of the F band, and d is thickness of the specimens in centimeter. Then the equation

$$n_F=1.09\times10^{16}\,(\log_{10} I_0/I)_F \qquad (2)$$

gives the number of F centers in the specimen whose volume is $d\times1\times1$ cm³.

The KCl+U crystals were obtained as follows: KCl crystals obtained from Harshaw Chemical Co. were colored with F centers, then these crystals were heated in the hydrogen gas of about 100 atomospheric pressure at 530°C for two hours. These cryrtals contain about 1×10^{18} U centers per cubic centimeter. This crystal was cleaved to a piece of 1 mm thickness, and was irradiated with ultraviolet light (containing U light) from the hydrogen discharge tube through the quartz window. Thus irradiated KCl+U crystal contains 1.3×10^{17} F centers per cubic centimeter, which were converted from U centers. The coloration of F centers converted with this method was not uniform, so that the number of F center is the average value.

F light irradiations were made with the monochromatic light of which wavelength and band width are 560 mμ and 40 mμ respectively. Number of the incident photons were measured by a thermopile as 5.2×10^{14} photons per cm² per sec. on the surface of specimen. Absorption measurements were made between the region from 400 mμ to 1000 mμ.

§ 3. Experimental Results

Fig. 1 shows a sequence of absorption measurements at successive stages of F light irradiation for the KCl+F crystal. This specimen was cleaved from the same colored block as the specimen of No. 5 represented in Table I and its thickness is 2.23 mm.

Curve (a) shows the absorption specta before the specimen is irradiated. In this curve, the half width of the F band is 0.35 e.v., and the M band adsorption is only a trace. Curve (b) shows the state attained after two minutes' irradiation. In spite of the considerable bleaching of the F band, the growth of the M band is very little, but instead of the small growth of the M band the absorption on the red side of the F band (may be A band) has increased and half width of the F band has also increased up to 0.41 e.v.. Curve (c) shows the state after 20 minutes' irradiation, in spite of a little bleaching of the F band during states from (b) to (c), the M band has grown rapidly. While the A band has decreased and the half width of the F band has also decreased down to 0.39 e.v.. Curve (e) shows the final state after 140 minutes' irradiation. The R_1, R_2 and N bands appeared and the peak of the F band shifted to the violet. During the irradiation the K band showed a monotonic increase.

The growth rate of the M band, the bleaching rate of the F band, the change of its half width and the change of the A band etc. depend on the density of F centers.

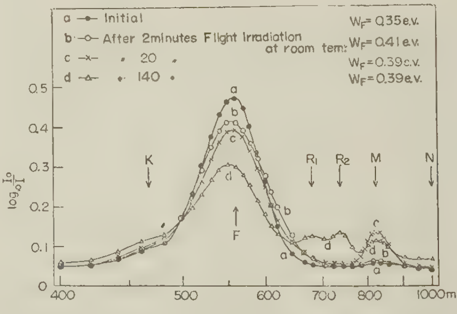

Fig. 1. A sequence of absorption measurements at succesive stages of F light irradiation for KCl+F crystals at room temperature.

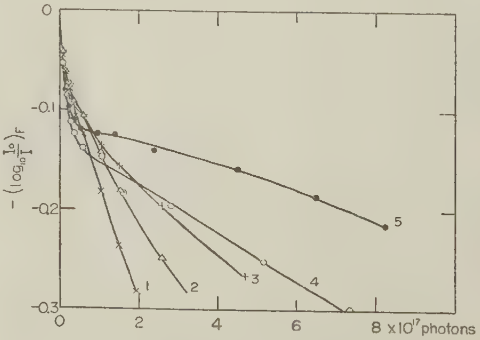

Fig. 2. Bleaching curves of the F band in KCl crystals colored additively with various concentration of F centers.

A. *Bleaching of the F band and Growth of the M band*

Fig. 2 shows the optical bleaching curves of the F bands in the specimens tabulated in Table I, as a function of absorbed F light quanta. $-(\log_{10} I_0/I)_F$ means the decrease of optical density at the absorption peak ($560\,\mathrm{m}\mu$) of the F band.

During earlier stages of irradiation, the F band bleaches by equal amount independently on the density of F centers (fast bleaching), but during later stages of prolonged irradiation, the F band in heavily colored specimens bleachs more rapidly, than that of lightly colored one (slow bleaching).

Fig. 3-A shows the growth curves of the M band, which are measured simultaneously with the measurements of the F band bleaching. $(\log_{10} I_0/I)_M$ represents the increment of optical density at the M band peak ($820\,\mathrm{m}\mu$). These curves show that the growth of the M band depends on the density of the F centers colored additively. In heavily colored specimens the growth rate of the M band is larger than that of lightly colored one, and the optical density at the peak of the M band in the former crystals reaches more rapidly to the maximum value than that in the latter crystal.

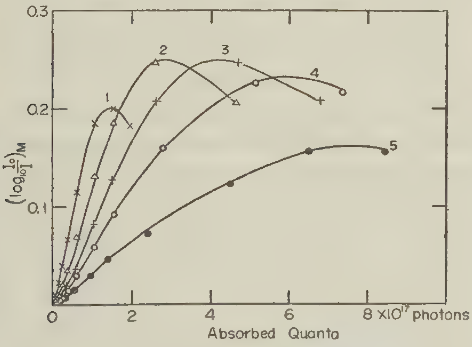

Fig. 3-A. Grow curves of the M band.

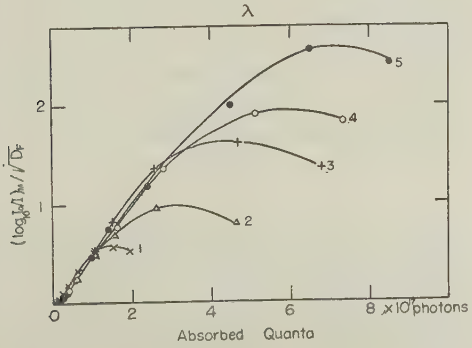

Fig. 3-B. Normalized grow curves of the M band.

The number of the F centers contained in each specimen were nearly equal, and all specimens were irradiated under the same condition, then it was expected that the bleaching of the F band and the growth of the M band will be the same in all specimens. However, Figs. 2 and 3-A show that F→M conversion take place more easily in heavily colored crystals. The fifth column in Table I shows the growth rates of M band, which are expresed as the tangent at the origin of the curves in Fig. 3-A. Comparing the F center concentration of each specimen shown in Table I, it will be cleared that the growth rate of the M band is proportional to the square root of the F center concentration. (See Fig. 3-B)

Figs. 4-A and 4-B show the bleaching

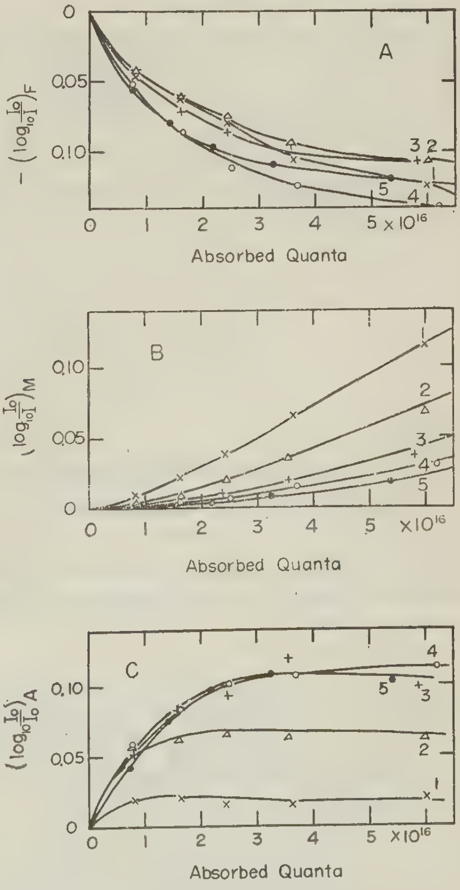

Fig. 4-A. Bleaching curves of the F band.
4-B. Grow curves of the M band.
4-C. Grow curves of the A band.

curves of the F band and the grow curves of the M band during about three minutes' irradiation. These figures suggest that in lightly colored crystals the F band may be converved to another absorption band rather than the M band. Relating with the variation of half width of the F band, this band will be examined in the next section.

B. *Relation between the A band and half width of the F band*

Curve (b) in Fig. 1 was the absorption spectrum at the state after two minutes' irradiation in the specimen of No. 5, of which growth of M band is small. As compared with curve (a) in this figure, it is clear that the absorption on the red side of the F band has increased and that the position of the half height in the red side (ε_r) of the F band has also shifted to the red. Then it is supposed that an absorption band overlaps on the red side of the F band.

Curve (c) in Fig. 5 shows this overlapping absorption band, which was analysed as follows. Curve (b) in Fig. 5 is identical with curve (b) in Fig. 1, and half width of the F band (in this curve) is 0.41 e.v.. Curve (a) is a reduced F band which are obtained as follows, and half width is 0.35 e.v.. The absorption intensity at the F peak of curve (a) in Fig. 1 was reduced to that at the F peak of curve (b) in Fig. 5, and next, the absorption intensities at other wave lengths of curve (a) in Fig. 1 were reduced to curve (a) in Fig. 5 with the ratio of two F-peaks. Shadowed area between curves (a) and (b) in Fig. 5 is the amount of absorption due to the band overlapping on the red side of the F band. Plotting the differences of the absorption curves (a) and (b) at each wave length, curve (c) was analysed. $\bar{A}$ shown in Fig. 5 represents the height of the absorption band, of which peak situates at 620 mμ (2.0 e.v.) and half width is 0.20 e.v. at room temperature. While the peak of Petroff's A band situates at 600 mμ (2.1 e.v.) at liquid air temperature, therefore it is supposed that the absorption band (c) shown in Fig. 5 is identical to Petroff's A band.

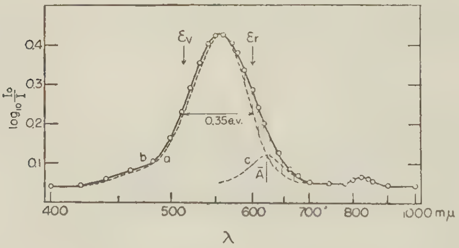

Fig. 5. Analysis of the A band, which is represented by curve (c) corresponding to the shadowed area.

Figs. 6–A and 6–B show the variation of $\bar{A}$ and ε_r in each specimen as a funclion of absorbed F light quanta. $\Delta\varepsilon_r$ is the shift of half height-position in the red side of the F band (ε_r). These figures show that the behavior of ε_r has a parallel rolation with $\bar{A}$, and that the A band in lightly colored crystals grows more largely and it bleaches gradually during prolonged irradiation.

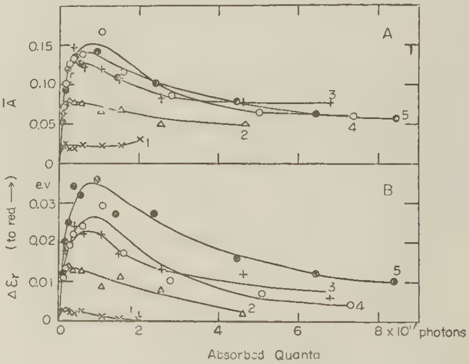

Fig. 6–A. Variation of the absorption intensities at the A band peak. $(\log_{10} I_0/I)_A$ reperesents the absorption intensity of the A band, i.e. $\bar{A}$ shown in Fig. 5.

Fig. 6–B. Shifts of the half height-position in the red side of the F band.

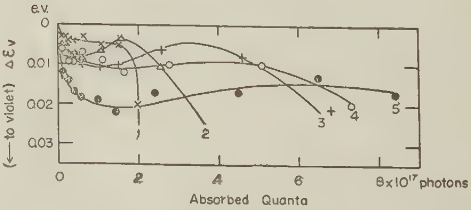

Fig. 7. Shifts of the half height-position in the violet side of the F band. (ε_v).

Fig. 7, shows the shift of the half height position in the violet side of the F band (ε_r). From the figure, it is proper to suppose that an absorption band overlaps on the violet side of the F band.

C. *Bleaching of the F band in KCl+U→F crystal.*

Fig. 8 shows a sequence of absorption spectra at successive stages of F light irradiation for KCl+U→F crystal. This specimen contains 1.3×10^{17} F centers per cubic centimeter, which are converted from U centers, and the density of F centers in this crystal corresponds to that of KCl+F specimen of No. 3. Curve (a) in Fig. 8 shows the absorption spectrum at initial state before the specimen is irradiated. Curves (b), (c) and (d) show the states after 1.5, 7 and 33 minutes' irradiation, respectively. Curve (e) shows the change when the specimen was kept in dark for about 20 hours at room temperature after the measurement of curve (d).

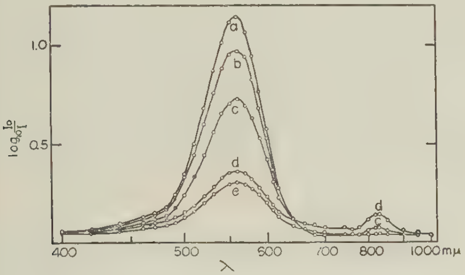

Fig. 8. A sequence of absorption spectra at successive stages of F light irradiation for KCl+U→F crystal.

This series of absorption spectra differ from that in Fig. 1 of additive coloration. Firstly, the M band grows slowly and slightly, secondly, the increment of the A band and the shift of ε_r are small, thirdly, in spite of considerable bleaching of the F band the growth of the M, R and N bands are very small, fourthly, the K band does not appear, and finally, when the specimen was kept in dark at room temperature after getting the state corresponding to curve (d) in Fig. 8, not only the R_1, R_2 and M bands are unstable but also the F band bleaches a little simultaneously. The last result agrees with the results reported previously[12].

§ 4. Discussion

A. *F→M Conversion in KCl+F Crystals.*

Oscillator strengths of the A and M centers were determined as follows: As shown in Fig. 7 ε_v shifts to the violet side, so that it is probable to consider that a certain absorption band, which may be Petroff's B band, overlaps on the violet side of the F band. Then it was assumed that at the end of t_i minutes' F light irradiation, the bleached F centers may be converted to the M, A or B centers as follows:

$$-n_F(t_i)=n_M(t_i)+n_A(t_i)+n_B(t_i) \tag{3}$$

where, $-n_F(t_i)$ is the number of optically bleached F centers, and $n_M(t_i)$, $n_A(t_i)$ or $n_B(t_i)$ are the number of the M, A or B center converted from F centers. Assuming that the number of the M and A centers may be expressed by Smakula's formula, $n_M(t_i)$ and $n_A(t_i)$ are expressed as follows;

$$n_M(t_i)=2.54\times10^{16}\frac{\alpha_M(t_i)W_M}{f_M} \quad \text{(for M center)} \tag{4}$$

$$n_A(t_i)=2.52\times10^{16}\frac{\alpha_A(t_i)W_A}{f_A} \quad \text{(for A center)} \tag{4'}$$

where, $\alpha_M(t_i)=(\log_{10} I_0/I)_M(t_i)$ and $\alpha_A(t_i)=(\log_{10} I_0/I)_A(t_i)$ and they represent the increment of optical density at the M and A band peaks, W_M and W_A are half widths of the M and A bands in electron volts, f_M and f_A are the oscillator strengths of the M and A centers, respectively. Then using equation (2) for $n_F(t_i)$, equation (3) is expressed as follows:

$$-1.09\times10^{16}\cdot\alpha_F(t_i) =2.54\times10^{16}\frac{\alpha_M(t_i)W_M}{f_M} +2.52\times10^{16}\frac{\alpha_A(t_i)W_A}{f_A}+n_B(t_i)$$

where $\alpha_F(t_i)=(\log_{10} I_0/I)_F(t_i)$ and it represents the decrease of optical density at the F band peak. Putting $W_M=0.13$ e.v. and $W_A=0.20$ e.v. (which are determined from the present absorption measurement on each band), and substituting the observed values of $\alpha_F(t_i)$,

Table II. Oscillator strengths of the A and M bands.

Sample (No.)	f_M	f_A
1	0.23	0.78
2	0.24	0.83
3	0.28	0.77
4	0.29	0.59
5	0.34	0.69
average	0.28±0.02	0.73±0.04

$\alpha_M(t_i)$ and $\alpha_A(t_i)$ into the above equation, the oscillator strengths f_A and f_M were obtained as tabulated in Table II. Average values of them were determined as 0.73 ± 0.04 and 0.28 ± 0.02, respectively. In the above calculation it was assumed that n_B for each specimen are unknown constants because the ε_v, of which shift may be proportional to the number of B centers, are nearly constant at earlier successive stages of irradiation, as compared with the changes of the F, A or M bands. Furthermore, the change of the K or R bands were not taken into consideration in the above calculation, because they were also negligibly small as compared with the change of the F, A or M bands up to the end of three minutes' irradiation.

In equation (4) and (4′), putting $f_M=0.28$ and $f_A=0.73$, we can determine the number of M and A centers converted from F centers. Namely,

$$n_M(t_i)=1.18\times10^{16}\cdot\alpha_M(t_i) \qquad \text{(for M center)}$$
$$n_A(t_i)=0.69\times10^{16}\cdot\alpha_A(t_i) \qquad \text{(for A center)}$$

Fig. 9B shows the summation of $n_M(t_i)$ and $n_A(t_i)$ at successive stages of irradiation, and shows that $n_M(t_i)+n_A(t_i)$ for all specimens are nearly equal, independently of F center concentration. Fig. 9A shows the number of bleached F centers in each specimen, and shows that the number of bleached F center is nearly equal to the summation of $n_M(t_i)$ and $n_A(t_i)$ for all specimens. Then, from these results one may suppose as follows; the fast bleaching of F band is independent on the concentration of F centers, and although the ionized electrons from F centers may be almost captured as the A or M centers, in the heavily colored crystals they are captured as M centers, whereas in lightly colored crystals they are captured as A centers. Thus the M center increases proportionally to the square root of F center concentration.

As mentioned previously in this section, it is probable to consider that a part of the ionized electrons from F centers are captured as the B centers. Because, there is slight difference between the summation of A and M centers and the number of bleached F centers, that is, this difference will be due to the B centers. However, it is difficult to determine the half width or the oscillator strength of the B center quantitatively, then at the present one can not state quantitatively on the B center.

As shown in Fig. 6, in stead of small growth of M band in lightly colored crystals the A band grew largely and it bleached gradually during prolonged irradiation. This results suggest that the F center will be converted to M center through the intermediate states, which are represented by A or B centers. However, the models of these intermediate states are not clear.

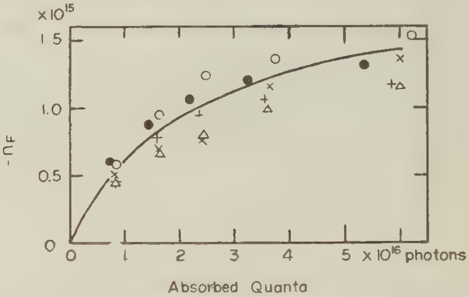

Fig. 9-A. The number of the bleached F cecters at the end of t_i minutes' F light irradiation for each specimen.

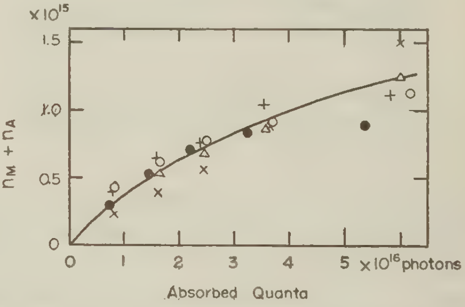

Fig. 9-B. The summation of the number of the A and M center optically converted from F centers at the end of t_i minutes' F light irradiation for each specimen.

Although a cause for the dependence on F center concentration of the slow bleaching of F band will be tentatively explained as follows; in heavily colored crystals a number of the vacancies, which act as the electron trapping center, has been introduced automatically into the crystals, because these crystals were quenched down very quickly from higher temperature to room temperature, then in the heavily colored crystals the ionized electrons from F center will be captured by these traps more than in the lightly colored crystals. But more detailed experiments are needed to conclude this.

B. *F→M Conversion in KCl+U→F Crystals.*

As shown in Fig. 6 for the bleaching of F band in KCl+U→F crystal the increment of the A band and the shift of ε_r are very small as compared with the case of KCl+F crystal. Furthermore, the growth of the M band was also small. Then in the case of this crystal, it is supposed that the behavior of the optically ionized electrons from F centers differ from that of KCl+F crystal. It is probable to consider as follows; as mentioned in the section of introduction, in this crystal considerable amount of hydrogen molecules present at the interstitial sites, so that the electrons from F centers will be captured by these hydrogen molecules before they are captured as M centers or as intermediate states (A or B centers). Therefore it may be a reason for the small growth of A, B or M bands. A process, which the electrons will be captured by hydrogen molecules, are explained as follows:

$$F+H_2 \rightarrow V_- + e + H_2 \rightarrow V_- + H^- + H \rightarrow U + H$$
$$F + H \rightarrow U$$

where, F, V_-, e, H^-, H and H_2 mean the F center, negative ion vacancy, electron, hydrogen ion, hydrogen atom and hydrogen molecule, respectively.

As shown in Fig. 9, the decrease of the K band in KCl+U→F crystal is contrast with the increase of the K band in KCl+F crystal, then these facts will be a clue to research the K band.

§ 5. Conclusion

Seitz stated that the A and B bands are not the characteristic of alkali halide crystals. However, from the present experimental results, it seems proper to conclude that the A and B bands appear as the characteristic of alkali halide crystals attending upon photochemical reaction of F→M conversion in additively colored crystals, and relate with the formation of other bands.

When the F centers, of which total number are equal in all specimens but the density are different, are bleached by the F light, it was observed that the M centers increase proportionally to the square root of the F center concentration. However, this result has not been explained by the present experiment only.

Acknowledgements

The writer wishes to express his sincere thanks to Prof. M. Ueta for his continued guidance and encouragements throughout this work.

He appreciates the kind assistance of Mr. H. Watanabe.

References

1) S. Petroff: Z. Phys. **127** (1950) 443.
2) M. Ueta: J. Phys. Soc. Japan **7** (1952) 107.
3) J. Lambe and W. D. Compton: Phys. Rev. **106** (1957) 684.
4) F. Seitz: Rev. Mod. Phys. **18** (1946) 384.
5) R. Herman, M. C. Wallis and R. F. Wallis: Phys. Rev. **103** (1956) 87. W. D. Compton and C. C. Klick: Phys. Rev. **112** (1958) 1620.
6) F. Seitz: Rev. Mod. Phys. **26** (1954) 7.
7) J. D. Konitzer and J. J. Markham: Phys. Rev. **107** (1957) 685.
8) F. Seitz: Rev. Mod. Phys. **26** (1954) 90.
9) N. F. Mott and R. W. Gurney: *Electronic Processes in Ionic Crystals*, 2nd ed. (Oxford, 1948) chap. 4.
10) C. J. Delbecq, B. Smaller and P. H. Yuster: Phys. Rev. **104** (1956) 599.
11) A. Smakula: Z. Phys. **59** (1930) 603.
12) M. Ueta and M. Hirai: J. Phys. Chem. Solids **2** (1957) 83.

JOURNAL OF THE PHYSICAL SOCIETY OF JAPAN, Vol. 14, No. 10, OCTOBER, 1959

Optical Studies on Thallium-activated Alkali-iodide Crystals

By Yoichi UCHIDA and Riso KATO

Department of Physics, Kyoto University

(Received May 23, 1959)

Absorption and emission spectra of KI–Tl and NaI–Tl phosphors have been investigated at both room and liquid air temperatures. In order to perform optical measurements on NaI-Tl, special caution was given to prevent the crystal surface from being clouded by moisture. In the absorption spectra of NaI–Tl, new bands due to the presence of thallium were found. Their maximum absorption coefficients seemed to vary with the square of the thallium concentrations. The similar fact has already been found by Yuster and Delbecq in their investigation on KI–Tl. In emission, both KI and NaI crystals containing high concentrations of thallium showed a subsidiary band overlapping the short wavelength tail of the hitherto observed main band. The relations between these absorption and emission bands were investigated and discussions were given in terms of an extended model proposed by Seitz.

§ 1. Introduction

Based upon the various experimental works[1] available at that time, a theoretical explanation of the properties of thallium-activated alkalihalide phosphors was first given by Seitz[2]. He postulated that the absorptions and emissions observed in the phosphors are due to transitions in thallous ions which occupy the normal positive ion sites. The observed bands were interpreted in terms of the states of thallous ion perturbed by the crystalline interactions. Utilizing this approach and with the idea of the simplified configuration coordinates Williams[3] computed with fairly good agreement the positions of the absorption band, called *A* by Seitz, and of the associated emission band in KCl-Tl. Then a series of systematic works[4] performed by Johnson, Williams and their coworkers succeeded fairly well in the interpretation of the absorption and emission spectra, their temperature dependence and recently of the problem on the oscillator strength[5],[6] of absorption bands. In their quantitative treatments of the problem, however, the single isolated thallium center was mainly considered. Yuster and Delbecq[7] studied the absorption spectra of KI-Tl phosphors containing various concentrations of thallium. They found several new bands at high Tl concentration and assumed that these bands arose when two thallous ions occupy the neighbouring sites. The symmetry surrounding a thallous ion having another one as a nearest neighbour is no longer cubic but is reduced to D_{2h} symmetry. This symmetry permits nine absorption bands which may vary with the square of the concentration of thallium.

The present work was undertaken for the purpose of investigating the effects of the paired thallous ions on both absorption and emmission spectra in KI-Tl and NaI-Tl crystals containing high concentrations of thallium. In some of the absorption bands of NaI-Tl crystal it was found that their absorption coefficients vary with the square of the thallium concentrations, the fact having been already reported by Yuster and Delbecq on KI-Tl crystals. In emission, both KI-Tl and NaI-Tl crystals with high Tl concentrations showed a new emission band when they were excited by the light of the absorption on the long wavelength side of the *A* band. The relation between these absorption and emission were discussed in terms of an extended model used by Seitz.

§ 2. Experimental Procedure

Single crystals of KI-Tl and NaI-Tl were grown by the Kyropoulos method in our laboratory. Concentrations of thallium in the crystals of KI-Tl were measured spectroscopically and found to be nearly 10 per cent of those added to each melt. The NaI-Tl crystal is so hygroscopic that its surface was readily clouded by moisture in air. To keep the surface clear for the optical measurement the following processes were devised. The crystal of NaI-Tl was cleaved in a dry room and put into a small quartz cell (Fig. 1b), and the cell was connected to a pump system. The crystal was slowly warmed until its surface became clear. The cell was then evacuated and sealed off. If the cell is evacuated without warming, the surface of the crystal suddenly turns white and opaque. After these procedures the cell containing the NaI-Tl crystal was utilized for the measurement. Absorption spectra were measured using a Beckman Model D. U. Spectrophotometer and also a Shimazu Q. B.-50 type Spectrophotometer. A conventional cryostat was employed for the measurements at liquid air temperature. A Fuess Medium Dispersion Quartz Spectrograph in conjunction with a mercury lamp was adapted for a monochromator in order to produce monochromatic lights exciting the phosphors. The emission spectra were photographed by a Hilger small quartz spectrograph in the direction normal to the exciting light as shown schematically in Fig. 1a.

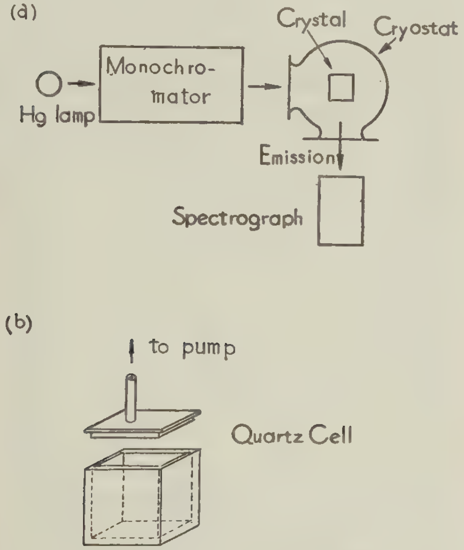

Fig. 1. Experimental arrangements for measuring the emission spectra, (a): block diagram of the apparatus; (b): the quartz cell used for the optical measurements on NaI-Tl.

§ 3. Results

a) *Absorption Spectra*

In KI-Tl, Yuster and Delbecq found the eight absorption bands with peaks at 224, 233, 244, 250, 252, 282, 290 and 293 mμ by cooling the crystals down to liquid helium temperature as shown schematically in Fig. 12. In the present work the three crystals having thallium added to each melt at the varying concentration of 0.05, 0.5 and 5 mole per cent respectively were studied. Their absorption spectra at liquid air temperature are shown in Fig. 2. In these spectra the peaks are not resolved more sharply at this temperature than at liquid helium temperature, as observed by Yuster and Delbecq[7], because the bands

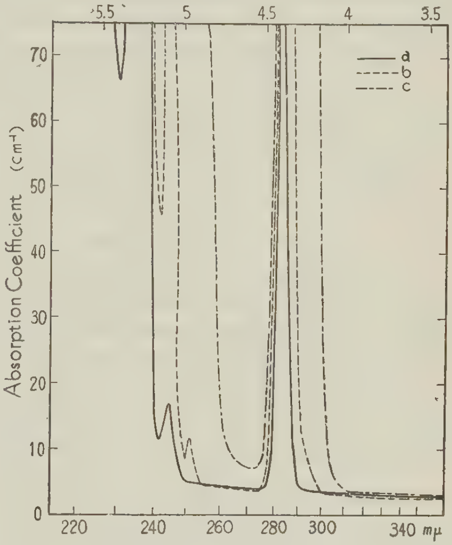

Fig. 2. Absorption spectra of KI-Tl crystals at liquid air temperature. The concentration of thallium added to the melt, a: 0.05 mole per cent; b: 0.5 mole per cent; c: 5 mole per cent.

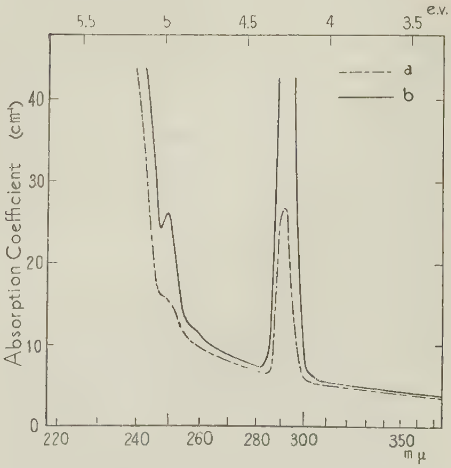

Fig. 3. Absorption spectra of NaI-Tl crystals at liquid air temperature. The concentration of thallium added to the melt, a: 0.005 mole per cent; b: 0.05 mole per cent.

become broader as temperature and concentration of thallium increase. Neverthless the band which covers the range from 280 to 300 mμ at our highest concentration of thallium may be concluded to consist of two bands: the single band at 282 mμ and the composite band at 290∼293 mμ as interpreted from the results of Yuster and Delbecq.

Similar results were obtained on the absorption spectra of NaI-Tl phosphors. The seven crystals of NaI-Tl having the concentration of thallium added to the melt of 0.005, 0.05, 0.2, 0.5, 2, 3 and 5 mole per cent respectively were studied. The absorption spectra at liquid air temperature of the NaI-Tl crystals containing lower concentrations of thallium are shown in Fig. 3. The band around 236 mμ is not sharply separated from the long wavelength tail of the fundamental absorption band of NaI. The absorption band at 250 mμ is fairly well resolved from the 244 mμ band in the case of 0.05 mole per cent of thallium content. The absorption spectra due to higher concentrations of thallium are shown in Fig. 4. At these concentrations two shoulders began to appear; the one at about 260 mμ superimposed on the long wavelength tail of the 250 mμ band, and the other at 305 mμ on the tail of a strong absorption at 290 mμ. The absorption spectra at still higher thallium concentrations are shown in Fig. 5. At these high thallium concentrations the peak heights of the bands at 236, 250 and 290 mμ were too high to be measured with our instruments, and thus the maximum absorption coefficient of the 250 mμ band was estimated in the region of low thallium concentrations ranging from 0.005 to 0.2 mole per cent, while that of the 305 mμ band was estimated up to the highest concentration. Although the resolution of the peaks was not complete, as stated above, the estimation was carried out by substracting

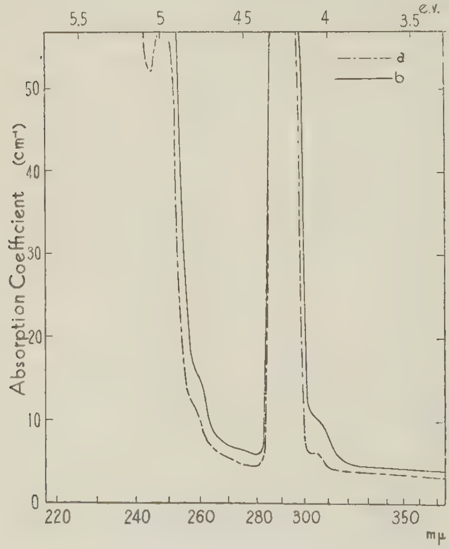

Fig. 4. Absorption spectra of NaI-Tl crystals at liquid air temperature. The concentration of thallium added to the melt, a: 0.2 mole per cent; 2 mole per cent.

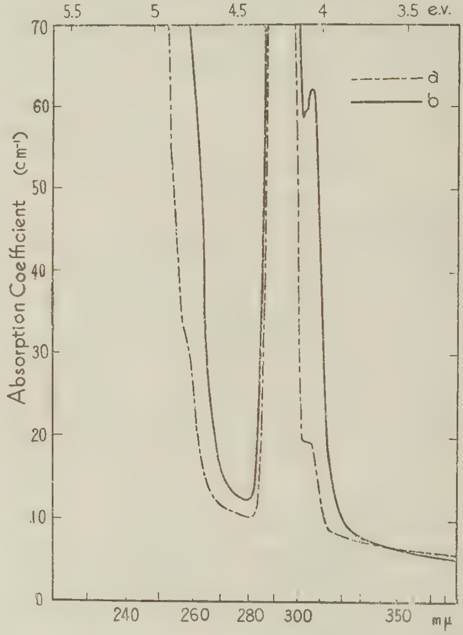

Fig. 5. Absorption spectra of NaI-Tl crystals at liquid air temperature. The concentration of thallium added to the melt, a: 3 mole per cent; b: 5 mole per cent.

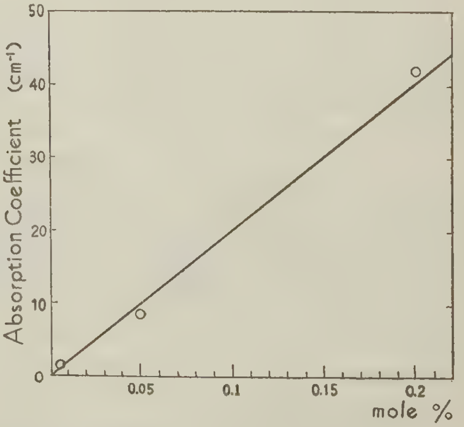

Fig. 6. Variation of maximum absorption coefficient, at liquid air temperature, as a function of thallium concentration for the band at 250 mμ.

the background from the measured absorption.

Figs. 6 and 7 show the variation of the maximum absorption coefficient of the band at 250 mμ and 305 mμ respectively at liquid air temperature as a function of thallium concentration. It is seen that the maximum absorption coefficient of the band at 250 mμ obviously varies linearly with the concentration of thallium, while that of the band at 305 mμ varies in some other fashion, most likely with the square of the concentration of thallium. The shoulder at 260 mμ appears to be proportional in height to the band at 305 mμ with the varied concentrations of thallium as seen in Fig. 4. So the band at 260 mμ should also be considered to vary with the square of the concentration of thallum. The results we obtained above on NaI-Tl remind us of the results obtained on KI-Tl by Yuster and Delbecq.

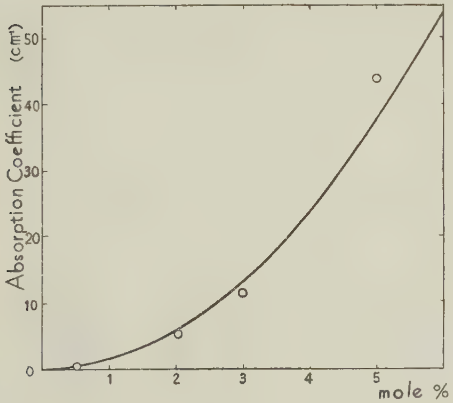

Fig. 7. Variation of maximum absorption coefficient, at liquid air temperature, as a function of thallium concentration for the band at 305 mμ.

b) *Emission Spectra*

Before presenting our results on KI-Tl, it seems convenient to refer to the results obtained by von Meyern1) and Yuster and Delbecq7). It has been described that the luminescence spectrum of KI-Tl, when excited by ultra-violet light, consists of a single band with its maximum at about 415 mμ. In the present investigation, however, a new band has appeared under some circumstances to be described below at about 332 mμ overlapping the short wavelength tail of the 415 mμ (Fig. 8a). In Fig. 8 the densitometer curves of typical emission spectra of KI-Tl phosphors are shown with their peak heights suitably normalized. The curve of type (a) was obtained at room temperature for the crystal containing the highest concentration of thallium when excited by the light at 296 or 302 mμ of a mercury lamp. Two peaks were observed at 332 and 415 mμ. But when the same crystal was excited by 280 mμ of mercury at room temperature, the curve of type (b) consisting of a single band (415 mμ) was obtained. Finally the curve of type (c) was given when excited by 253 mμ; here the shorter wavelength emission (332 mμ) appeared weak compared with the case when the crystal was excited by 296 or 302 mμ. The emission spectrum of type (b) was also given when the crystal with the lowest thallium concentration was excited by the light of any absorption band. However, it should be remarked that, when excited at liquid air temperature by any light, the emission spectrum always consisted of a single band of type (b) with the peak shifting slightly toward the longer wavelength side and the bandwidth becoming narrower.

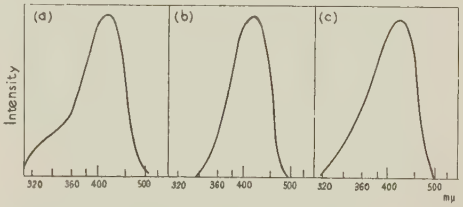

Fig. 8. Densitometer curves of emission spectra of KI-Tl crystals at room temperature. The concentration of thallium added to the melt is 5 mole per cent. (a): the spectrum excited by 296 mμ or 302 mμ; (b): by 280 mμ; (c): by 253 mμ light of mercury lamp.

Curve (c) also shows the emission spectrum of the crystals containing lower concentrations of thallium when excited by the light of any absorption band.

In the case of NaI-Tl, similar phenomena were observed except for the excitation at liquid air temperature. The emission spectra of NaI-Tl at room temperature are shown in Fig. 9. The concentration of thallium added to the melt was 2 mole per cent. The curve (a) is for the emission spectrum excited by 302 or 312 mμ of mercury, (b) by 289 mμ and (c) by 253 mμ of mercury. As is noticed in the figure, the curves (a) and (c) are composite, but (b) is single.

At liquid air temperature the same crystal, when excited by 302 mμ, gave rise to the emission spectrum which consisted of two bands at about 330 mμ and 425 mμ respectively, as shown in Fig. 10 (a). While by 289 mμ, a single band at 425 mμ was resulted as shown in Fig. 10 (b).

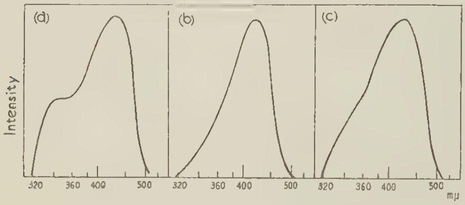

Fig. 9. Densitometor curves of emission spectra of NaI-Tl crystals at room temperature. The concentration of thallium added to the melt is 2 mole per cent. (a): the spectrum excited by 302 or 312 mμ; (b): by 289 mμ; (c): by 253 mμ.

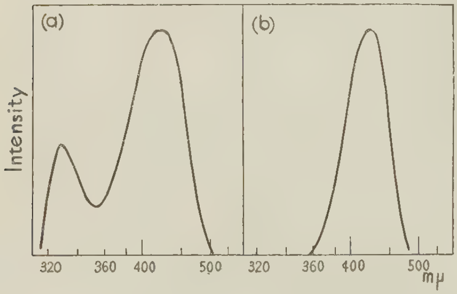

Fig. 10. Densitometer curves of emission spectra of the same crystal used in Fig. 9, but at liquid air temperature. (a): the spectrum excited by 302 or 312 mμ; (b): by 289 mμ.

By presuming an equivalent mechanism on the emission of type (a) the shorter wavelength bands were compared for KI-Tl and NaI-Tl crystals and it was found that the band remains still appreciable at lower concentration of thallium for NaI in comparison with that in KI. The intensity ratio of the two emissions, $I_{\text{short}}/I_{\text{long}}$, is slightly larger for NaI-Tl than KI-Tl, although it increased with concentration of thallium. The remarkable difference between the emission spectrum of NaI-Tl and that of KI-Tl is in that the short wavelength band of NaI-Tl does not vanish at liquid air temperature when excited by the light of absorption band at 305 mμ, while in the case of KI-Tl, it vanishes at liquid air temperature when excited by the light of corresponding absorption bands at 290∼293 mμ even at the highest concentration of thallium.

§ 4. Discussion

The observed absorption bands of NaI-Tl phosphors may be interpreted by the analogy with those[7)] of KI-Tl, considering the two types of the thallium center: the single thallous ion and the paired thallous ions in the crystal. The fact that the peak height of the absorption band at 250 mμ in NaI-Tl seems to vary linearly with the thallium concentration indicates that the absorption is caused by the single isolated thallous ions in the crystal. The shorter wavelength band at about 236 mμ was not sufficiently resolved from the background and the peak was not definitely confirmed. But the origins of this absorption and of the 290 mμ band might be ascribed to the single thallium center, since they were observed even at a low thallium concentration. Thus, considering the intensities of these three absorption bands respectively, they can be assigned to the transitions between the states of single thallous ions in the crystal as follows;

(1) the band at 290 mμ is associated with the transition ${}^1S_0 \to {}^3P_1$,

(2) the band at 250 mμ is ascribed to the transition ${}^1S_0 \to {}^3P_2$,

(3) the band at about 236 mμ may be due to the transition ${}^1S_0 \to {}^1P_1$.

Here, according to Seitz, the transition corresponding to the absorption at 250 mμ is considered to be allowed on account of the perturbation due to the littice vibration.

The bands at 305 and 260 mμ, which are observed at fairly high thallium concentrations, appear to vary with the square of the thallium concentration and, therefore, they are considered to be ascribed to the paired thallium center. Then considering the energies associated with these absorption, the band at 305 mμ is assumed to be ascribed to the transition corresponding to ${}^1S_0 \to {}^3P_1$ and the band at 260 mμ to ${}^1S_0 \to {}^3P_2$ both in the thallous ion perturbed by the neighbouring thallous ion. Some other absorptions which vary with the square of the thallium concentration, may be allowed from the symmetry consideration, but they would not be observed, being concealed under much stronger absorptions due to the single thallous ions.

The fact that the shorter wavelength emission bands (332 mμ for KI-Tl and 330 mμ for NaI-Tl) which are observed at fairly high thallium concentrations are preferentially excited by the light of absorption bands at 290～293 mμ for KI-Tl and 305 mμ for NaI-Tl, shows that these emission bands are associated with the paired thallous ions.

In the case of KI-Tl, the shorter wavelength emission band vanishes at liquid air temperature, although absorption at 290～293 mμ are appreciable. From this fact, the transition giving rise to the shorter wavelength emission is assumed to follow some thermal activation process. Assuming the contribution of the state $^3P_0$ of thallous ion which may become emitting when two toallous ions occupy the neighbouring sites in the crystal, a possible explanation of this emission process is given in Fig. 11.

(1) Through the excitation by the light of 290～293 mμ absorptions, the paired thallium centers in KI-Tl arrive at the perturbed state $(^3P_1)$ which corresponds to the $^3P_1$ state of the single thallous ion, the perturbed state in the paired center being denoted by the corresponding state of the single ion bracketted in ( ). The $(^3P_1)$ state of the paired thallium center is assumed to be connected to the underlying state $(^3P_0)$ of the same center perturbed but corresponding to the $^3P_0$ state of the single thallous ion through a potential barrier.

(2) Going over this potential barrier by

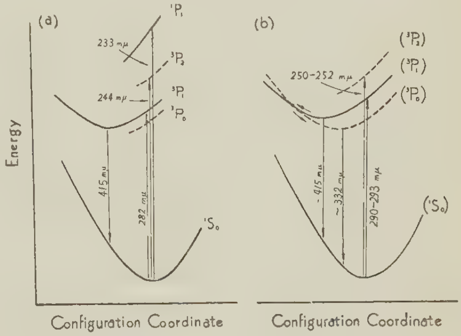

Fig. 11. Configuration coordinate curves of the luminescent centers in KI-Tl; (a) for the single thallium center and (b) for the paired thallium center.

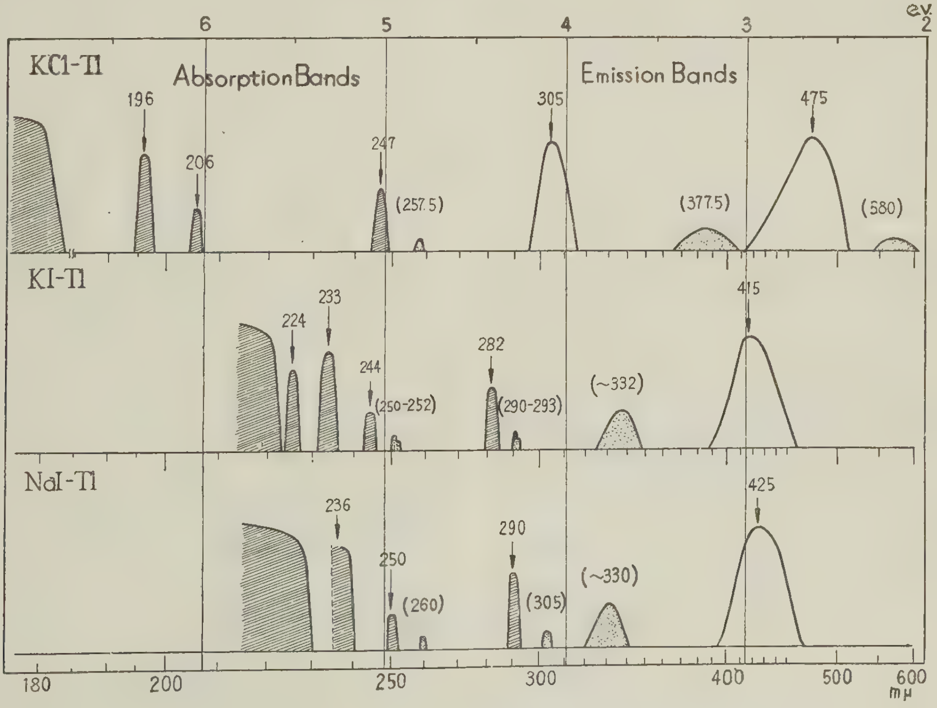

Fig. 12. Diagram schematically summarizing the distribution of absorption and emission bands in KCl-Tl, KI-Tl and NaI-Tl crystals respectively. Shaded bands are absorptions appearing at low concentrations of thallium, while dotted bands show absorptions or emissions at high concentrations. Blank bands are emissions at low concentrations of thallium.

thermal activation, the systems arrive at the minimum point of the ($^3P_0$) state.

(3) Then the systems return to the ground state ($^1S_0$) emitting the light of shorter wavelength band at 332 mμ.

In the paired thallium center, the state ($^3P_1$) also can make transition to the ground state. But the associated emission with this transition is assumed to be concealed under the main band at 415 mμ. Through the excitation by 290～293 mμ, the single thallium centers are also excited to the $^3P_1$ state by absorbing the light at the tail of strong absorption band at 282 mμ and gives rise to the main emission at 415 mμ. Only the single thallium centers are excited by 282 mμ and therefore a single emission band at 415 mμ is observed (Fig. 8b). At liquid air temperature, the paired thallium centers can be excited through the excitation by 290～293 mμ, but the process of going over the potential barrier is considered to be suppressed, so the only single emission band (415 mμ) is observed (Fig. 8b). Thus Fig. 11 shows schematically the configuration coordinate curves for the single and paired thallium centers in KI-T1 and illustrates the observed transitions which give rise to the two emission bands.

In the case of NaI-T1 phosphors, a similar interpretation is possible if one assumes that the potential barrier which connects the two states in the paired thallium center is rather low and can be passed over even at liquid air temperature. Anotner interpretation may be possible without assuming the contribution of the state $^3P_0$ which might become emitting in the paired thallium center. The transition from the state ($^3P_1$) to the ground state in paired thallium center may directly give rise to the shorter wavelength emission at about 330 mμ. But in the latter speculation the analogous relation to the KI-T1 is no longer maintained.

Concerning the emission when excited to much higher states by the lights of B or C absorption bands, so called by Seitz, or further by the light of the fundamental absorption band, both crystals showed more complicated phenomenon. Namely, the contributions of host sensitized luminescence seems to exist partly. About these emission processes the more detailed investigation is now in progress.

Fig. 12 illustrates schematically all the absorption and emission bands in KC1-T1, KI-T1 and NaI-T1 hitherto known including the results obtained in the present investigation.

Acknowledgments

The authors would like to acknowledge the contributions of Miss Toshiko Nakagawa, who grew several of the crystals and assisted in the spectral measurements. This research was supported in part by a grant-in-aid for promoting scientific researches sponsored by the Ministry of Education.

References

1) R. Hilsch: Z. Phys. **44** (1927) 860. R. Hilsch and R. W. Pohl: Z. Phys. **48** (1928) 384. W. Koch: Z. Phys. **57** (1929) 638. M. Forro: Z. Phys. **56** (1929) 534; **58** (1930) 613. W. von Meyeren: Z. Phys. **61** (1930) 321. W. Bunger: Z. Phys. **66** (1930) 311. W. Bunger and W. Flechsig: Z. Phys. **69** (1932) 673.
2) F. Seitz: J. Chem. Phys. **6** (1938) 163.
3) F. E. Williams: J. Chem. Phys. **19** (1951) 457.
4) F. E. Williams: Phys. Rev. **82** (1951) 281. F. E. Williams and M. Hebb: Phys. Rev. **84** (1951) 1181. P. D. Johnson and F. E. Williams: J. Chem. Phys. **20** (1952) 124; **21** (1953) 125. F. E. Williams: J. Phys. Chem. **57** (1953) 780. P. D. Johnson: J. Chem. Phys. **22** (1954) 1143 L.
5) R. S. Knox and D. L. Dexter: Phys. Rev. **104** (1956) 1245.
6) F. E. Williams, B. Segall and P. D. Johnson: Phys. Rev. **108** (1957) 46.
7) P. H. Yuster and C. J. Delbecq: J. Chem. Phys. **21** (1953) 892.

JOURNAL OF THE PHYSICAL SOCIETY OF JAPAN, Vol. 14, No. 10, OCTOBER, 1959

On the Preferential Bleaching of the M Band in KCl Crystal with Polarized Light

By Takehiko ISHII, Tetsuhiko TOMIKI
and Masayasu UETA

*Department of Physics, The Faculty of Science,
University of Tohoku, Sendai*

(Received June 24, 1959)

The temperature dependence of the dichroic properties of the M center in KCl crystal was investigated. At the temperatures above 60°C, the thermal reorientation of the M center in the *ground* state occurs. The measured value of the activation energy for it was 1.0 eV. It was suggested that vacancy clusters may trap free electrons to form new M centers in the course of the bleaching of the M band and this process may be responsible for the temperature dependence of dichroism of the M band.

§ 1. Introduction

When the additively colored alkali halide crystal is irradiated with light in the F band at room temperature, various absorption bands appear on the long wavelength side of the F band¹⁾. Except the A band observed by Petroff²⁾, the M band is the first one which is developed by F bleaching. The M band has been of interest for this reason and studied by many authors. However, the phenomena associated with the M center are so complex that the models³⁾ proposed so far are not conclusive. The R band composed of two bands, R_1 and R_2, is the second to appear in the course of F bleaching.

The behavior of the R band is so closely related to those of F and M bands. Therefore, it will be necessary to know the interrelation between these bands for the investigation of the M center. In KCl crystals, M, R_1 and R_2 bands appear at 820 mμ, 670 mμ, and 730 mμ, respectively at room temperature.

The preferential bleaching of the M band⁴⁾ and the luminescence of the M center⁵⁾ stimulated with polarized light have given some insights on the symmetry properties of the center. The investigations already carried out seem to show that the dipole matrix element of the center is oriented along the face diagonal of the crystal.

Previously, the behavior of the preferential bleaching of the M band in KCl has been reported⁶⁾ when the temperature of the specimen was altered. The main results seem to suggest two facts: (1) When the crystal containing M center is irradiated with light in its absorption band, which is polarized along the direction of the face diagonal, the number of the centers of which dipole matrix elements are normal to it increases; (2) the thermal reorientation of the M center may occur in the ground state. The experiments reported here were carried out to examine these affairs in detail, and it was suggested that one part of electrons ionized from M centers during light bleaching might be trapped by vacancy clusters to form new M centers. Furthermore, the value of 1.0 ev was obtained as the activation energy for the thermal reorientation of the M centers. Some investigations on the dichroism of other bands have been also described.

§ 2. Experimental Procedures

Hitachi Model EPBU spectrophotometer was employed for measurements of optical absorption. The polarizer was of a type of the Rochon prism made of calcite. It was placed just behind the exit slit of the monochromator as shown in Fig. 1 which indicates the optical arrangement. The condenser lens and cryostat windows made of glass did not affect the polarization state of light. To obtain high temperature, oil or water in the cryostat was heated by a nichrome coil inserted in it. Low temperature was obtained by either ice and rocksalt, dryice and methyl alcohol or liquid air. The measurement of temperature was made with copper-constantan thermocouple dipped into the copper block on which the specimen was mounted. The obtained constancy of temperature was within the order of 1°C.

KCl single crystals used in this experiment were grown from the melt by Kyropoulos method. Additive coloration was performed by heating the crystal with potassium metal at about 500°C, and successively quenching to room temperature. The concentration of the F centers in the sample was of the order of 2 or $4\times10^{17}\,\mathrm{cm}^{-3}$. In order to eliminate the reflection loss from the surface, the pure KCl crystal-plate was used as the reference for the measurement of optical absorption.

The M band was developed by illumination with F-absorption light at 560 mμ having a band pass of 80 or 40 mμ. Here the light fell normally upon the (100) surface and was polarized along the [100] direction of the specimen. The development and the bleaching of the M band were carried out with the same optical arrangement as that employed in the absorption measurements. In Fig. 2, the development of the M band by F bleaching was shown against the time of exposure to F light. Except some special cases, the developmedt of the M band was discontinued when its height reached the position of (a) in Fig. 2, because with further illumination, the R band is enhanced.

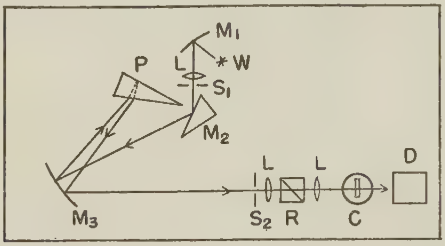

Fig. 1. Optical system for the absorption measurement.
W: tungsten lamp; $S_{1,2}$: slits; L: lens; $M_{1,2,3}$: mirrors; P: prism; R: Rochon prism; C: cryostat; D: detector.

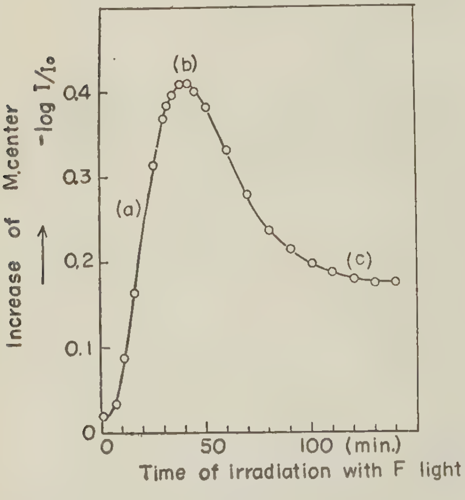

Fig. 2. The development of the M band by F-bleaching.

§ 3. Experimental Results

3.1 *Some observations of the dichroism of the F, M and R bands*

When the M band is preferentially bleached by exposure to M light polarized in the [011] direction, at room temperature, dichroism appears in the F and R bands as well as in the M band. However, it becomes quite difficult to induce dichroism by this procedure at −30°C. The preferential bleaching of the F band also induces dichroism in the F, M and R bands. These phenomena have already been reported and the assumption that the second absorption band of the M center overlaps on F absorption band has been proposed by van Doorn and Haven³⁾.

It was observed when the sample containing F, M and R centers was irradiated for about 4 hours at room temperature with R_2 light ($\lambda=730\,\mathrm{m}\mu$, band pass$\sim$30 m$\mu$, photon intensity$\sim2.4\times10^{14}\,\mathrm{cm}^{-2}\mathrm{sec}^{-1}$) polarized in the [011] direction, weak dichroism also appeared in the F, M and R bands. This fact may hardly be explained only by the model which requests the another absorption band of the M center overlapping with the F band, and it will be necessary to assume the existence of close coupling of R centers with F and M centers.

When dichroism was induced in the F and M bands by irradiating the specimen with M light polarized in the [011] direction, $\delta^{\mathrm{M}}>0$ and $\delta^{\mathrm{F}}<0$ were obtained, where δ^{M} and δ^{F} are defined by the following notation:

$$\delta^{\times}=\mathrm{A}^{\times}_{[0\bar{1}1]}-\mathrm{A}_{[011]}$$

here, × indicates the absorption band such as the F, M or R band and $\mathrm{A}^{\times}_{[ijk]}$ shows the logarithm of the inverse transmission at the peak of the × band measured with light polarized in the [*ijk*] direction.

The sample was illuminated with F light

polarized in the [011] direction after dichroism had been induced in the F, M and R bands by exposure to [011]-polarized M light. Then, the R and M bands developed as shown in Fig. 3. We can clearly see that δ^F, δ^M and δ^R reverse their signs simultaneously in the course of this F bleaching.

The reversal of the sign, however, did not occur when F bleaching was carried out in this turn with F light polarized along the [0$\bar{1}$1] direction, after the dichroism had been induced with [011]-polarized M light. Since the free electrons ionized by F light have not history, the fact that δ's reverse their signs or not depending on the state of polarization of light used in this F bleaching, seems to suggest the existence of some couplings between these centers.

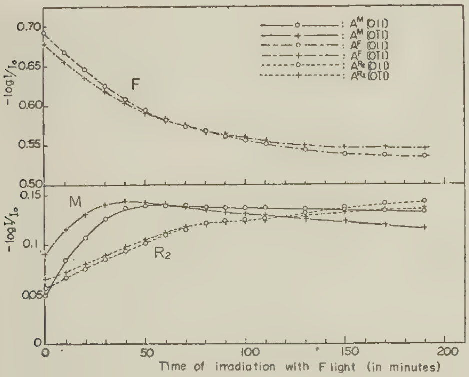

Fig. 3. Changes of the dichroism of F, M and R bands by the exposure to [011]-polarized F light. Dichroism had been initially induced in each band by illumination with [011]-polarized M light.

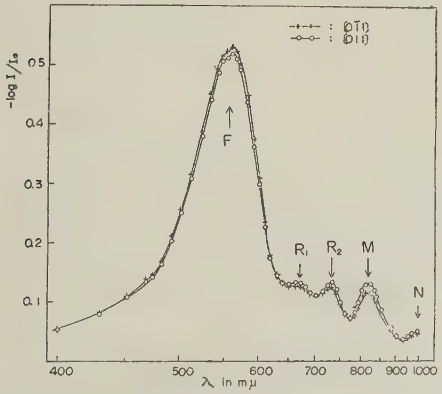

Fig. 4. The absorption spectrum showing a shoulder peak in the F band. The specimen were irradiated for 200 minutes with [011] polarized light of 560 mμ with a band pass of 8 mμ at room temperautre.

The prolonged irradiation with polarized F light induced a shoulder peak at the shorter wavelength side of the F band. Fig. 4 shows the absorption spectrum after 200 minutes' illumination at room temperature with light polarized in the [011] direction whose wavelength was 560 mμ and band pass was about 8 mμ.

This shoulder peak did not appear in the similar experiment at liquid air temperature, nor resolved when the specimen was quenched to that temperature after the peak had been induced at room temperature. This may be due to the shift of F absorption band to shorter wavelength side. The peak did not appear in the case of the irradiation with 560 mμ light polarized in the [011] direction with a broad band pass, say, of about 40 mμ. The origin of this shoulder peak is not clear.

3.2 *The temperature dependence of the preferential bleaching of the M band.*

Figs. 5(a)–(g) show the preferential bleaching of the M bands at various temperatures with [011] polarized light at the peak of the M band with a band pass of 40 mμ. The M

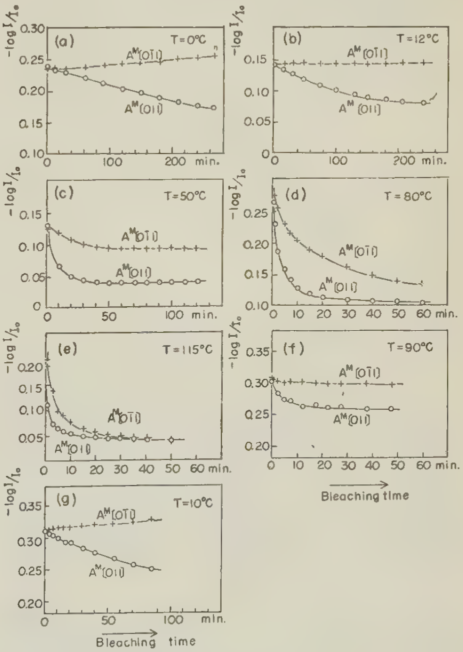

Fig. 5. Preferential bleaching of the M band with [011]-polarized M light at (a) 0°C, (b) 12°C, (c) 50°C, (d) 80°C, (e) 115°C, (f) 10°C, (g) 90°C. The M bands were developed at 12°C in samples (a)—(e), at 35°C in sample (f) and at 90°C in sample (g).

band was developed at 12°C in Figs. 6 (a)–(e), at 35°C in (f) and at 90°C in (g), respectively. In Fig. 5 (g), $A^{M}_{[0\bar{1}1]}$ remains almost constant, but in the similar experiment with other samples it decreased, although the amounts of decrease were not large.

F bleaching at 90°C makes a broad band enhance on the long wavelength side of the F band and it overlaps with the M band completely. This broad band is unstable thermally, and decreases slightly in the dark and then reaches a stationary state. The measurements were made after keeping the specimen in the dark for an hour or so until the broad band became stable both thermally and optically. Therefore, the change in absorption in Fig. 5 (g) can be considered to be due to M centers. From the measurements shown in Fig. 5 (a)–(g), the following results are derived: $A^{M}_{[0\bar{1}1]}$ increases with irradiation time if the M bleaching with polarized light is carried out at the temperature lower than that at which the M centers were created. On the other hand, $A^{M}_{[0\bar{1}1]}$ decreases remarkably if the preferential bleaching is made at the temperature higher than that at which the M centers were produced. If the M center has the dipole matrix element oriented along the face diagonal, the fact that $A^{M}_{[0\bar{1}1]}$ does not decrease in some cases may suggest the number of the M centers which contribute to $A^{M}_{[0\bar{1}1]}$ and have not dipole matrix elements in the $[0\bar{1}1]$ direction increases by irradiation with [011]-polarized M light. In Fig. 6 (d), both $A^{M}_{[011]}$ and $A^{M}_{[0\bar{1}1]}$ decrease rapidly at the initial stage of preferential bleaching, but the former becomes constant in the subsequent bleaching, whereas the latter continues to decrease. In Fig. 5 (e), the dichroism in the M band vanishes in the course of the preferential bleaching. These facts may imply the thermal reorientation of the M center in its ground state. The decrease in $A^{M}_{[0\bar{1}1]}$ in the region where $A^{M}_{[011]}$ is nearly constant may be attributed to the thermal reorientation of M centers, and the optical ionization of the correrponding increment may keep the resultant constancy of $A^{M}_{[011]}$. The thermal reorientation process will be described in the next section.

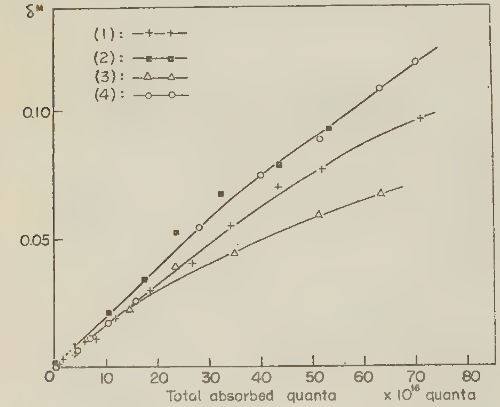

Fig. 6. δ^{M} plotted against total absorbed quanta in the preferential bleaching of the M band at 10°C. The M band was developed at 10°C until its height reached the position (a), (b) and (c) in Fig. 2, in the samples (1), (2) and (3), respectively. In the sample (4), the concentration of M centers is much higher.

The preferential bleaching of the M band at various temperatures is suitably described in terms of the quantum yield for inducing dichroism in the M band. We define the quantum yield as

$$\eta=(\partial\Delta/\partial q_{a})_{t=0}\ ,$$

here, q is the total absorbed quanta, Δ is the product of δ^{M} and the half width of the M band, and $t=0$ indicates the time at which the irradiation of M light starts. η corresponds to the difference between the relative number of the M centers with dipole matrix elements in the [011] direction and that in the $[0\bar{1}1]$ direction, induced per absorbed photon. As shown in Fig. 6, the experimental values of η were the same for the four specimens at 10°C. In the specimen of No. 1 M developing had been made until its height had arrived at the position (a) in Fig. 2, in No. 2 at (b) and in No. 3 at (c), respectively, and in No. 4 the concentration of the M centers was much larger. This means that the value of η is independent both of the number of M centers and the stage of M developing. Thus, it is possible to define η as a quantity characteristic of the M center only.

Fig. 7 shows the curve of $\log\eta$ versus reciprocal kT. The curve (a) corresponds to the case where the M band was bleached preferentially at the temperature at which the M band had been created. The curve (b) corresponds to the case where the M band was generated at 12°C. The curve (a) has a kink point which appears between 30°C and 20°C. It is interesting to note that a kink point appears also between 30°C and 20°C in the curve which shows a relation between log R and inverse kT[7], where R is the ratio of the number of M centers to that of F centers at the moment when the height of the M band reached its maximum in the process of F bleaching.

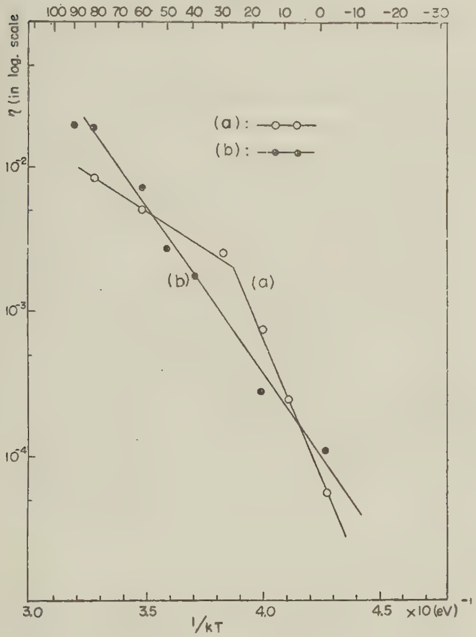

Fig. 7. log η plotted against $1/kT$.
For curve (a): the bleaching of the M band was carried out at the same temperature as that at which the band was developed.
For curve (b): the M band was developed at 12°C in all specimens and bleached at various temperatures.

3.3 *The thermal reorientation of the M center*

The thermal reorientation of the M center suggested in §3.2 was confirmed by the variations in $A^{M}_{[011]}$ and $A^{M}_{[0\bar{1}1]}$ when the sample was kept in the dark after dichroism had been induced in the M band at high temperature. Since photons were completely avoided, the changes in $A^{M}_{[011]}$ and $A^{M}_{[0\bar{1}1]}$ were attributed to the reorientation of the dipole matrix elements of M centers in the ground state caused by the ionic motions. Fig. 8 shows the curve of $A^{M}_{[011]}$, $A^{M}_{[0\bar{1}1]}$ and log δ^{M} versus the time of keeping in the dark at 87°C after dichroism was induced in the M band with [011]-polarized M light at the same temperature. The decrease in $A^{M}_{[0\bar{1}1]}$ was smaller than the increase in $A^{M}_{[011]}$. Under

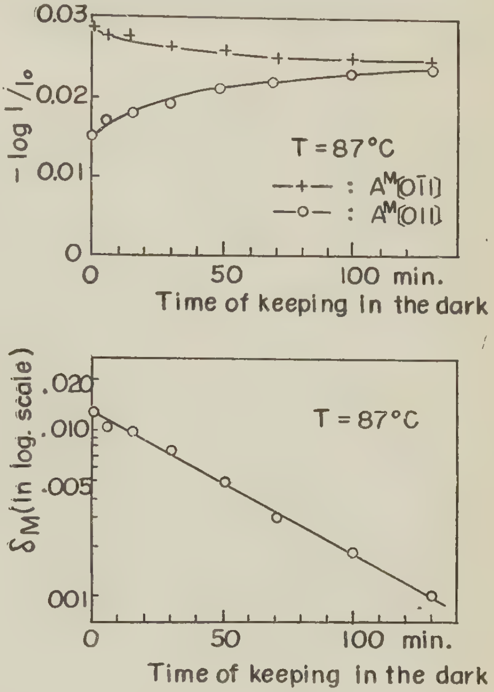

Fig. 8. Changes in $A^{M}{}_{[011]}$, $A^{M}{}_{[0\bar{1}1]}$ and log δ^{M} when the samples were kept in the dark at 87°C.

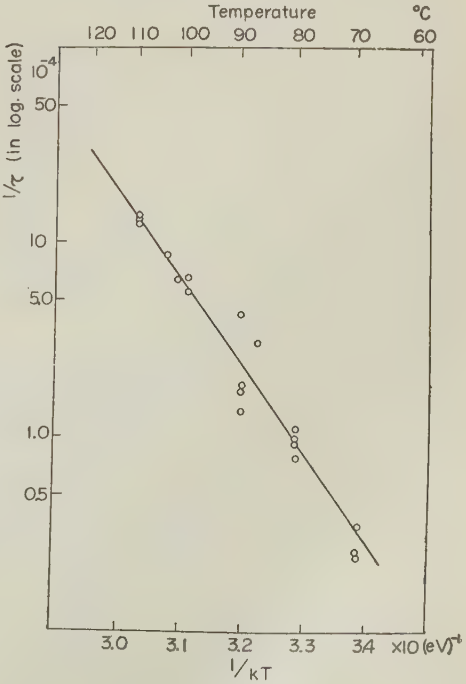

Fig. 9. $1/\tau$ plotted against $1/kT$.

the assumption that the dipole matrix elements of M centers are oriented along the face diagonals and their thermal reorientation occurrs with the same probability $1/\tau\,\mathrm{sec}^{-1}$ for the possible six orientations, it is calculated that δ^{M} varies as

$$\delta^{M}=\mathrm{const.}\times\exp(-6/5\cdot t/\tau)\ .$$

This is consistent with the result shown in Fig. 8. From Fig. 8 $1/\tau$ at 87°C is obtained. From the same measurements at various temperatures, the curve which shows the relation of $\log(1/\tau)$ against $1/kT$ was obtained as shown in Fig. 9. The measured values of τ differed slightly according to the thermal treatment of the sample. The data shown in Fig. 9 were obtained with the specimens cleaved at room temperature, and warmed slowly up to the temperature at which the measurment was done. As is well known, $1/\tau$ varies as $1/\tau=B_0\exp(-W/kT)$ and this relation is satisfied in Fig. 9. The gradient of the curve gives the activation energy W, for the reorientation of the M center in the ground state. We obtained the following values from the figure:

$$W=1.0\,\mathrm{ev},\quad B_0=3.5\cdot10^{10}\,\mathrm{sec}^{-1}.$$

§ 4. Discussion and Conclusions

An assumption to explain the dischroism exhibited by the F band is that the another absorption band of the M center is hidden under the F band. The fact that the preferential bleaching of the R band induces dichroism in both the F and the M bands may hardly be explained by such a simple assumption as described above. The dichroism in the F band seems to come partly from some interactions such as distortion of the crystalline field around the color center through the coexistence of F, M and R centers. The reversal of the sign of dichroism caused by irradiation with polarized F light described in § 3.1. may indicate the existence of such interactions. In respect to this point, it should be noted that when the crystal containing F, M and R centers is illuminated with light in the F absorption band, the emission of the R center and the M center is enhanced⁵⁾.

Now, let us consider the temperature dependence of the variations in $A^{M}_{[0\bar{1}1]}$, in the preferential bleaching with [011]-polarized M light. We assume here that the dipole matrix element of the M center is oriented along the face diagonal of the crystal. In § 3.2, it is described that the number of the M centers whose dipole matrix elements lie in the [0$\bar{1}$1] direction increases in some cases by irradiation with [011] polarized M light. The reason for this is as follows: In these cases, $A^{M}_{[0\bar{1}1]}$ does not decrease in spite of the fact that the number of the M centers which contribute to $A^{M}_{[0\bar{1}1]}$ and have the dipole matrix elements in the directions other than [0$\bar{1}$1] should be decreased by irradiation with [011]-polarized M light. It may be considered that there are two possibilities to cause the increase of the number of M centers of which dipole matrix elements are normal to the polarization direction of bleaching light, a) reorientation of the M centers in the excited state as a result of ionic motions, b) electron trapping by vacancy clusters to form new M centers. As described in § 3.2, the preferential bleaching of the M band was strongly dependent on the thermal history of the specimens in respect to the M center formation, and, moreover, the density of vacancy cluster may be influenced by the thermal history, too. Therefore, the electron trapping process will be predominant among two possibilities.

Another contribution to $A^{M}_{[0\bar{1}1]}$ in the preferential bleaching with [011]-polarized M light is the thermal reorientation of M centers in the ground state. This occurs at high temperature and decrease the number of the M center with dipole matrix elements in the [0$\bar{1}$1]. Thus, the temperature dependence of the preferential bleaching of the M band may be understood as the competing process of (a), (b) and (c) given below:

(a) Electron trapping of the vacancy clusters to form M centers,
(b) Ioninzation of M centers,
(c) Thermal reorientation of M centers in the ground state.

The processes (b) and (c) are predominant at high temperature and not so frequent to occur at lower temperature, in consistence with the observations.

References

1) F. Seitz: Rev. Mod. Phys. **26** (1954) 7.
2) St. Petroff: Z. Phys. **27** (1950) 443.
3) F. Seitz: ref. 1. C. Z. van Doorn and Y. Haven:

Phys. Rev. **100** (1955) 753. C. Z. van Doorn: Philips Res. Rept. **12** (1957) 309.
4) M. Ueta: J. Phys. Soc. Japan **7** (1952) 107. H. Kanzaki: Phys. Rev. **110** (1958) 1063.
5) C. Z. van Doorn: ref. 3. J. Lambe and W. D. Compton: Phys. Rev. **106** (1957) 684. G. Kuwabara and A. Misu: J. Phys. Soc. Japan **13** (1958) 1038.
6) T. Ishii, T. Tomiki and M. Ueta: J. Phys. Soc. Japan **13** (1958) 1411.
7) T. Tomiki: J. Phys. Soc. Japan (to be published).

JOURNAL OF THE PHYSICAL SOCIETY OF JAPAN, Vol. 14, No. 10, OCTOBER, 1959

Flow of a Visco-Elastic Liquid near a Stagnation Point

By S. K. SHARMA

Department of Mathematics,
Indian Institute of Technology, Kharagpur

(Received April 28, 1959)

The problem of viscous flow near a stagnation point has been exactly solved by Froessling.[1]

In this paper equations of motion for the flow of a visco-elastic liquid near a stagnation point, occurring when a stream of such a liquid impinges on a wall at right angles to it and flows away radially in all directions, have been set up and solved by the Karman-Pohlhausen method. The effect of elasticity is found to depend upon a non-dimensional parameter $\tau^*=\tau a$ (where τ is the flow parameter or the relaxation time constant and a is a constant of dimensions T^{-1} depending on the velocity in potential flow). Behaviour for small values of this parameter has been studied. It is observed that the boundary layer thickness and the shearing at the wall increase with an increase in τ^*, while the normal stress at the wall is independent of both elasticity and viscosity. The stream lines get closer to the wall with an increase in the parameter.

§ 1. Introduction

A number of approaches have been tried to investigate the rheological behaviour of the so-called Visco-elastic fluids, i.e. fluids which when sheared demonstrate elastic properties besides viscous ones. Oldroyd, Strawbridge and Toms[2] have shown that the behaviour of dilute (ca. 3 percent) solution of highly polymerized methyl methacrylate in an organic liquid in a simple shearing motion can be represented approximately, at sufficiently small rates of shear, by the stress-strain law proposed by Jeffreys[3]

$$S^i{}_j+\tau\dot{S}^i{}_j=2\mu(d^i{}_j+\lambda\dot{d}^i{}_j)\,, \qquad (1.1)$$

where $S^i{}_j$ is the deviatoric stress tensor, τ and λ are the relaxation and retardation time constants respectively of the fluid, and μ is the coefficient of viscosity as in Newtonian flow, $d^i{}_j$ is the rate of deformation tensor and dot denotes the rate of change.

In this paper we have discussed the problem of flow of a visco-elastic liquid near a stagnation point when only relaxation phenomenon of the liquid is considered and the stress strain law is taken in the form

$$S^i{}_j+\tau\tilde{S}^i{}_j=2\mu\, d^i{}_j\,, \qquad (1.2)$$

where $\tilde{S}^i{}_j$ denotes the rate of stress and is equal to the expression[4]

$$\frac{\partial}{\partial t}S^i{}_j+S^i{}_{j,k}\,v^k-S^i{}_k\,v^j{}_{,k}-S^k{}_j\,v^i{}_{,k}+S^i{}_j\,v^k{}_{,k}.$$

Some interesting results are obtained.

§ 2. Equations of Motion

The stress-strain relations given by (1.2), when transformed into cylindrical system of coordinates, take the form

$$t^{r}_{r}+\tau\left[\frac{\partial t^{r}_{r}}{\partial t}+u\frac{\partial t^{r}_{r}}{\partial r}+\frac{v}{r}\frac{\partial t^{r}_{r}}{\partial \theta}+w\frac{\partial t^{r}_{r}}{\partial z}-2\left(t^{r}_{r}\frac{\partial u}{\partial r}+\frac{t^{r}_{\theta}}{r}\frac{\partial u}{\partial \theta}+t^{r}_{z}\frac{\partial u}{\partial z}\right)\right]=2\mu\frac{\partial u}{\partial r}, \tag{2.1}$$

$$t^{r}_{\theta}+\tau\left[\frac{\partial t^{r}_{\theta}}{\partial t}+u\frac{\partial t^{r}_{\theta}}{\partial r}+\frac{v}{r}\frac{\partial t^{r}_{\theta}}{\partial \theta}+w\frac{\partial t^{r}_{\theta}}{\partial z}-t^{r}_{r}\left(\frac{\partial v}{\partial r}-\frac{v}{r}\right)-t^{r}_{\theta}\left(\frac{\partial u}{\partial r}+\frac{1}{r}\frac{\partial v}{\partial \theta}+\frac{u}{r}\right)-t^{r}_{z}\frac{\partial v}{\partial z}-\frac{t^{\theta}_{\theta}}{r}\frac{\partial u}{\partial \theta}-t^{\theta}_{z}\frac{\partial u}{\partial z}\right]=\mu\left(\frac{1}{r}\frac{\partial u}{\partial \theta}+\frac{\partial v}{\partial r}-\frac{v}{r}\right), \tag{2.2}$$

$$t^{r}_{z}+\tau\left[\frac{\partial t^{r}_{z}}{\partial t}+u\frac{\partial t^{r}_{z}}{\partial r}+\frac{v}{r}\frac{\partial t^{r}_{z}}{\partial \theta}+w\frac{\partial t^{r}_{z}}{\partial z}-t^{r}_{r}\frac{\partial w}{\partial r}-t^{z}_{z}\frac{\partial u}{\partial z}-\frac{t^{r}_{\theta}}{r}\frac{\partial w}{\partial \theta}-t^{r}_{z}\left(\frac{\partial w}{\partial z}+\frac{\partial u}{\partial r}\right)-\frac{t^{z}_{\theta}}{r}\frac{\partial u}{\partial \theta}\right]=\mu\left(\frac{\partial w}{\partial r}+\frac{\partial u}{\partial z}\right), \tag{2.3}$$

$$t^{\theta}_{\theta}+\tau\left[\frac{\partial t^{\theta}_{\theta}}{\partial t}+u\frac{\partial t^{\theta}_{\theta}}{\partial r}+\frac{v}{r}\frac{\partial t^{\theta}_{\theta}}{\partial \theta}+w\frac{\partial t^{\theta}_{\theta}}{\partial z}-2t^{r}_{\theta}\left(\frac{\partial v}{\partial r}-\frac{v}{r}\right)-2t^{\theta}_{\theta}\left(\frac{1}{r}\frac{\partial v}{\partial \theta}+\frac{u}{r}\right)-2t^{\theta}_{z}\frac{\partial v}{\partial z}\right]=2\mu\left(\frac{1}{r}\frac{\partial v}{\partial \theta}+\frac{u}{r}\right), \tag{2.4}$$

$$t^{\theta}_{z}+\tau\left[\frac{\partial t^{\theta}_{z}}{\partial t}+u\frac{\partial t^{\theta}_{z}}{\partial r}+\frac{v}{r}\frac{\partial t^{\theta}_{z}}{\partial \theta}+w\frac{\partial t^{\theta}_{z}}{\partial z}-t^{r}_{\theta}\frac{\partial w}{\partial r}-\frac{t^{\theta}_{\theta}}{r}\frac{\partial w}{\partial \theta}-t^{z}_{z}\frac{\partial v}{\partial z}-t^{\theta}_{z}\left(\frac{\partial w}{\partial z}+\frac{1}{r}\frac{\partial v}{\partial \theta}+\frac{u}{r}\right)-t^{r}_{z}\left(\frac{\partial v}{\partial r}-\frac{v}{r}\right)\right]=\mu\left(\frac{\partial v}{\partial z}+\frac{1}{r}\frac{\partial w}{\partial \theta}\right), \tag{2.5}$$

$$t^{z}_{z}+\tau\left[\frac{\partial t^{z}_{z}}{\partial t}+u\frac{\partial t^{z}_{z}}{\partial r}+\frac{v}{r}\frac{\partial t^{z}_{z}}{\partial \theta}+w\frac{\partial t^{z}_{z}}{\partial z}-2\left(t^{z}_{z}\frac{\partial w}{\partial z}+t^{r}_{z}\frac{\partial w}{\partial r}+\frac{t^{\theta}_{z}}{r}\frac{\partial w}{\partial \theta}\right)\right]=2\mu\frac{\partial w}{\partial z}. \tag{2.6}$$

Momentum equations are

$$\rho\left[\frac{\partial u}{\partial t}+u\frac{\partial u}{\partial r}+\frac{v}{r}\frac{\partial u}{\partial \theta}+w\frac{\partial u}{\partial z}-\frac{v^2}{r}\right]=-\frac{\partial p}{\partial r}+\frac{\partial t^{r}_{r}}{\partial r}+\frac{1}{r}\frac{\partial t^{r}_{\theta}}{\partial \theta}+\frac{\partial t^{r}_{z}}{\partial z}+\frac{t^{r}_{r}-t^{\theta}_{\theta}}{r}, \tag{2.7}$$

$$\rho\left[\frac{\partial v}{\partial t}+u\frac{\partial v}{\partial r}+\frac{v}{r}\frac{\partial v}{\partial \theta}+w\frac{\partial v}{\partial z}+\frac{uv}{r}\right]=-\frac{1}{r}\frac{\partial p}{\partial \theta}+\frac{\partial t^{r}_{\theta}}{\partial r}+\frac{1}{r}\frac{\partial t^{\theta}_{\theta}}{\partial \theta}+\frac{\partial t^{\theta}_{z}}{\partial z}+\frac{2t^{r}_{\theta}}{r}, \tag{2.8}$$

$$\rho\left[\frac{\partial w}{\partial t}+u\frac{\partial w}{\partial r}+\frac{v}{r}\frac{\partial w}{\partial \theta}+w\frac{\partial w}{\partial z}\right]=-\frac{\partial p}{\partial z}+\frac{\partial t^{r}_{z}}{\partial r}+\frac{1}{r}\frac{\partial t^{\theta}_{z}}{\partial \theta}+\frac{\partial t^{z}_{z}}{\partial z}+\frac{t^{r}_{z}}{r}, \tag{2.9}$$

and the equation of continuity is

$$\frac{\partial u}{\partial r}+\frac{u}{r}+\frac{1}{r}\frac{\partial v}{\partial \theta}+\frac{\partial w}{\partial z}=0. \tag{2.10}$$

§ 3. Solution of Equations

The flow under consideration is along the negative z-axis and is caused when a stream of visco-elastic liquid impinges perpendicularly on a wall $z=0$, and flows away radially in all directions. The stagnation point is at the origin.

Taking U and W to be the velocities in frictionless case, we have

$$U=ar,\quad W=-2az.$$

If stagnation pressure is denoted by p_0, the pressure in the ideal flow is given by

$$p-p_0=\frac{\rho}{2}(U^2+W^2)=\frac{\rho}{2}a^2(r^2+4z^2).$$

The frictionless case suggests that the velocity field in the boundary layer region may be taken to be

$$u=rf'(z),\quad w=-2f(z). \tag{3.1}$$

Substituting from (3.1) into equations (2.1) to (2.6), we get

$$t^{r}_{r}+\tau\left[rf'\frac{\partial t^{r}_{r}}{\partial r}-2f\frac{\partial t^{r}_{r}}{\partial z}-2(f't^{r}_{r}+rf''t^{r}_{z})\right]=2\mu f', \tag{3.2}$$

$$t^{r}_{\theta}+\tau\left[rf'\frac{\partial t^{r}_{z}}{\partial r}-2f'\,t^{r}_{\theta}-rf''\,t^{\theta}_{z}\right]=0, \tag{3.3}$$

$$t^{r}_{z}+\tau\left[rf'\frac{\partial t^{r}_{z}}{\partial r}-2f\frac{\partial t^{r}_{z}}{\partial z}-rf''\,t^{z}_{z}+f'\,t^{r}_{z}\right]=\mu rf'', \tag{3.4}$$

$$t^{\theta}_{\theta}+\tau\left[rf'\frac{\partial t^{\theta}_{\theta}}{\partial r}-2f\frac{\partial t^{\theta}_{\theta}}{\partial z}-2f'\,t^{\theta}_{\theta}\right]=2\mu f', \tag{3.5}$$

$$t^{\theta}_{z}+\tau\left[rf'\frac{\partial t^{\theta}_{z}}{\partial r}-2f\frac{\partial t^{\theta}_{z}}{\partial \theta}+f'\,t^{\theta}_{z}\right]=0, \tag{3.6}$$

$$t^{z}_{z}+\tau\left[rf'\frac{\partial t^{z}_{z}}{\partial r}-2f\frac{\partial t^{z}_{z}}{\partial z}+4f'\,t^{z}_{z}\right]=-4\mu f'. \tag{3.7}$$

From equations (3.1) to (3.7) the values of the deviatoric stresses correct to the orders of $(\mu\tau)$ and $(\tau)^2$ are found to be

$$\left.\begin{aligned}
t^r{}_r&=2\mu[f'+\tau(2ff''+2f'^2+r^2f''^2)],\\
t^r{}_\theta&=0,\\
t^r{}_z&=\mu r[f''-\tau(6f'f''-2ff''')],\\
t^\theta{}_\theta&=2\mu[f'+2\tau(ff''+f'^2)],\\
t^\theta{}_z&=0,\\
t^z{}_z&=-4\mu[f'+2\tau(ff''-2f'^2)].
\end{aligned}\right\}\tag{3.8}$$

On substitution of these values the momentum equations (2.8) and (2.9) take the form

$$-\frac{1}{\rho}\frac{\partial p}{\partial r}=r[f'^2-2ff''-\nu f''' +\nu\tau(4f'f'''-2ff^{\mathrm{IV}})],\tag{3.9}$$

and

$$-\frac{1}{\rho}\frac{\partial p}{\partial z}=4ff'+2\nu f''+6\nu\tau(ff'''-3f'f''),\tag{3.10}$$

where a prime denotes differentiation with respect to z.

Applying the condition of integrability to equations (3.9) and (3.10) we get

$$\frac{\partial}{\partial z}[f'^2-2ff''-\nu f''+\nu\tau(4f'f'''-2ff^{\mathrm{IV}})]=0,\tag{3.11}$$

which on integration gives

$$2ff''-f'^2+\nu f''-\nu\tau(4f'f'''-2ff^{\mathrm{IV}})=c,\tag{3.12}$$

where c is an integration constant.

Boundary conditions are

$$f'(\delta^*)=a,\ f''(\delta^*)=0,$$

and

$$f'''(\delta^*)=\tau[4f'''(\delta^*)a-2f(\delta^*)f^{\mathrm{IV}}(\delta^*)],\tag{3.13}$$

where δ^* is the boundary layer thickness. Equation (3.12), on application of boundary condition (3.13), gives

$$c=-a^2.\tag{3.14}$$

From equation (3.9) and (3.12), we get

$$\frac{1}{\rho}\frac{\partial p}{\partial r}=cr$$

or

$$p=-\frac{a^2\rho}{2}(r^2+4F(z)),\tag{3.15}$$

where $F(z)$ is to be determined from equation (3.10).

Equation (3.12) can be rewritten as

$$(2ff''-f'^2+\nu f''')-\nu\tau(4f'f'''-2ff^{\mathrm{IV}})+a^2=0.\tag{3.12.1}$$

The boundary conditions are

$$\left.\begin{aligned}f=f'&=0\\ F&=0\end{aligned}\right\}\ \text{at}\ z=0,$$
$$f'=a\qquad \text{at}\ z=\delta^*.$$

The constants a^2 and ν can be removed from equation (3.12.1) by a similarity transformation

$$\eta=\sqrt{\frac{a}{\nu}}\frac{z}{\delta},\quad f(z)=\sqrt{a\nu}\ \phi(\eta,\delta),\tag{3.16}$$

where

$$\delta=\sqrt{\frac{a}{\nu}}\delta^*.$$

Effecting the transformation (3.16), equation (3.12.1) takes the form

$$\delta(2\delta\phi\phi''-\delta\phi'^2+\phi'''+\delta^3) -\tau^*(4\phi'\phi'''-2\phi\phi^{\mathrm{IV}})=0,\tag{3.12.2}$$

where primes denote differentiation with respect to η and $\tau^*=\tau a$ is a non-dimensional parameter.

Equation (3.12.2) shows that the elasticity effect depends on a non-dimensional parameter τ^*, $\tau^*=0$ giving the non-elastic viscous case.

Boundary condition in terms of ϕ are

$$\begin{aligned}&\phi(0)=0=\phi'(0),\\ &\phi'(1)=\delta,\ \phi''(1)=0,\ \phi'''(0)=-\delta^3.\end{aligned}\tag{3.17}$$

Proceeding now to solve equation (3.12.2) by Karman-Pohlhausen method, we assume a quartic profile

$$\phi(\eta)=a_0+a_1\eta+a_2\eta^2+a_3\eta^3+a_4\eta^4.\tag{3.18}$$

Applying the boundary conditions (3.17), we get

$$\phi(\eta)=\frac{\delta^3+6\delta}{8}\eta^2-\frac{\delta^3}{6}\eta^3-\frac{2\delta-\delta^3}{16}\eta^4.\tag{3.18.1}$$

Integrating equation (3.12.2) with respect to η between the limits 0 to 1, we have

$$\delta\left[2\delta(\phi\phi')^1{}_0-3\delta\int_0^1\phi'^2d\eta+(\phi'')^1{}_0+\delta^3\right] -\tau^*\left[6\int_0^1\phi'\phi'''d\eta-2(\phi\phi''')^1{}_0\right]=0.\tag{3.12.3}$$

Substituting the value of ϕ from (3.18.1) and putting $\delta^2=x$, equation (3.12.3) reduces to

$$3x^4+(44+119\tau^*)x^3-(912+1344\tau^*)x^2 +(2520+5796\tau^*)=0.\tag{3.12.4}$$

Equation (3.12.4) gives either $x=0$, which is not possible, or

$$3x^3+(44+119\tau^*)x^2-(912+1344\tau^*)x$$
$$+(2520+5796\tau^*)=0\,. \qquad (3.12.5)$$

When the non-dimensional parameter $\tau^*=0$, which gives the effect of elasticity as taken to be zero, (3.12.5) reduces to the corresponding equation in the non-elastic viscous case, viz.

$$3x^3+44x^2-912x+2520=0\,. \qquad (3.12.6)$$

This equation has two positive and one negative roots. Negative root is, however, not admissible as δ can not be imaginary. Out of the two positive roots 3.491151 and 8.894263, the latter is to be discarded as it gives rise to an absurdity in that it renders $\dfrac{u}{U}>1$ within the boundary layer.

The velocity profile corresponding to $\delta^2=3.491151$ is found to agree closely with that given by Froessling.

The roots of the equation (3.12.5) nearest to 3.491151 corresponding to different values of τ^* are given by the table below. The values of $\phi''(0)$ have also been tabulated.

Table I.

τ^*	δ^2	δ	$\phi''(0)$
0.000	3.491151	1.86846	4.43346
0.001	3.496308	1.86984	4.43914
0.002	3.501464	1.87122	4.44485
0.004	3.511764	1.87397	4.45619
0.006	3.523059	1.87699	4.46867
0.008	3.532347	1.87945	4.47889
0.010	3.542617	1.88218	4.49023
0.020	3.592688	1.89543	4.54557

The table shows that the boundary layer thickness as well as $\phi''(0)$ increase with an increase in τ^*.

Integrating equation (3.10), we get

$$a^2F=f^2+\nu f'+3\nu\tau\,(ff''-2f'^2)+D\,, \qquad (3.10.1)$$

where D is a constant of integration.

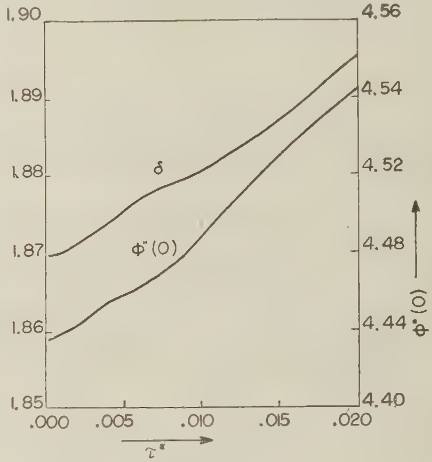

Fig. 1.

Applying the boundary conditions, $D=0$; or we get

$$a^2F=f^2+\nu f'+3\nu\tau\,(ff''-2f'^2). \qquad (3.10.2)$$

From (3.10.2) and (3.15), we get

$$p=-\frac{a^2\rho}{2}\left[r^2+\frac{4}{a^2}\{f^2+\nu f'\right.$$
$$\left.+3\nu\tau(ff''-2f'^2)\}\right]. \qquad (3.13)$$

The deviatoric normal stress component is

$$t^z_z=-4\mu\{f'+2\tau\,(ff''-2f'^2)\}\,. \qquad (3.14)$$

The value of the normal stress component at the wall, therefore, is

Table II.

η	$\tau^*=0.00$		$\tau^*=0.01$		$\tau^*=0.02$	
	ϕ	r	ϕ	r	ϕ	r
0.0	0.00000	∞	0.00000	∞	0.00000	∞
0.1	0.02110	6.8843	0.02136	6.8422	0.02162	6.8010
0.2	0.08026	3.5298	0.08120	3.5091	0.08213	3.4894
0.3	0.17158	2.4141	0.17353	2.4006	0.17544	2.3875
0.4	0.28958	1.8582	0.29274	1.8482	0.29583	1.8386
0.5	0.42921	1.5264	0.43371	1.5185	0.43811	1.5108
0.6	0.58582	1.3065	0.59172	1.3000	0.59750	1.2937
0.7	0.74517	1.1584	0.86093	1.0772	0.86996	1.0721
0.8	0.93248	1.0356	0.94222	1.0302	0.95076	1.0256
0.9	1.11735	0.9460	1.11423	0.9474	1.12360	0.9434
1.0	1.30381	0.8758	1.31528	0.8719	1.32650	0.8683

$$(T^z_z)_{z=0}=(t^z_z)_{z=0}-(p)_{z=0}$$
$$=\frac{\rho}{2}a^2r^2\,, \qquad (3.15)$$

which is independent of μ as well as τ.

The shearing at the wall is

$$(T^r_z)_{z=0}=(t^r_z)_{z=0}$$
$$=\mu r f''(0)$$
$$=\frac{\mu a^{3/2}}{\sqrt{\nu}}r\phi''(0)\,, \qquad (3.16)$$

which shows that shearing stress at the wall increases with τ^*.

Equation of stream line is

$$r^2\phi(\eta)=\text{constant}\,. \qquad (3.17)$$

Taking the constant to be unity, the stream lines have their equation as

$$r^2\phi(\eta)=1.$$

Table II gives the values of $\phi(\eta)$ and r for different values of η and τ^*. This table suggests that elasticity brings flow nearer to the wall. The pattern of flow is, however, the same as in Newtonian liquid.

§ 4. Conclusion

The results of this theoretical investigation may be summed up as follows:

1) The elastic effect in case of a single relaxation time visco-elastic model depends upon a non-dimensional parameter, an increase in the parameter causing an increase in the boundary layer thickness and also the shearing at the wall.

2) Normal stress at the wall is independent of elasticity as well as viscosity.

8) Stream lines get closer to the wall with an increase in the parameter.

The author is indebted to Prof. B. R. Seth for his guidance throughout this investigation.

References

1) H. Schlichting: *Boundary Layer Theory* (Pergamon Press Ltd., London, 1955).

2) J. G. Oldroyd, D. J. Strawbridge and B.A.Toms: Proc. Phys. Soc. London **B, 64** (1951) 44.

3) H. Jeffreys: *The Earth*, 2nd ed. (Camb. Univ. Press, 1929) 265.

4) C. Truesdell: J. Rat. Mech. Anal. **4** (1955) 83.

JOURNAL OF THE PHYSICAL SOCIETY OF JAPAN Vol. 14, No. 10, OCTOBER, 1959

The Flow of a Viscous Fluid past a Triangular Cylinder

By Mitutosi KAWAGUTI

Aeronautical Research Institute, University of Tokyo

(Received May 25, 1959)

The flow of a viscous fluid past an equilateral triangular cylinder has been studied using Imai's method of treating Oseen's approximation. The expression for the velocity in the flow field near the triangular cylinder is obtained correct to the order of R^2, and those for the frictional, pressure and total drag to the order of R. The drag of the triangular cylinder at high Reynolds numbers is estimated by use of Imai's new theory of drag and is compared with Asaka and Ôshima's experimental results.

§ 1. Introduction

It is well known that the steady two-dimensional flow of an incompressible viscous fluid past a fixed cylindrical obstacle at a small Reynolds number can be successfully dealt with on the basis of the Oseen approximation. However, investigations have hitherto been restricted to the cases of cylinders with rather simple cross-sectional shapes, such as circular and elliptic cylinders and a flat plate.

A few years ago, I. Imai put forward a

new method of solving Oseen's equations for arbitrary cylindrical obstacles,[4] which enables us to obtain the velocity distribution in the flow region near the cylinder and the lift and drag acting upon it in the form of power series in the Reynolds number R. Using this method, M. Hasegawa studied the flow past a thin symmetrical Joukowski aerofoil.[3]

In this paper, the flow past an equilateral triangular cylinder will be studied by use of Imai's method. The expression for the velocity in the region near the triangular cylinder is obtained correct to the order of R^2, the lowest order term being $O(1)$, and the expressions for the pressure, frictional and total drag to the order of R, the lowest order terms being $O(R^{-1})$. In §7, the drag at high Reynolds numbers are estimated according to Imai's new theory[4] by using our theoretical results at low Reynolds numbers, and compared with Asaka and Ôshima's experimental results at high Reynolds number.[1]

In the course of our study, it was found that the total drag remains invariant, within the accuracy of our approximation, when the cylinder is rotated by an angle π, whereas the pressure and frictional drags change their values in the second approximation i.e., $O(1)$. These results have been found to be valid for the cases of more general cross-sectional shapes. The discussion concerning this fact will be given in an accompanying paper.[8]

§2. Oseen's Equations of Motion and the Boundary Conditions.*

Oseen's approximate equations for the two-dimensional steady motion of an incompressible viscous fluid can be written as

$$U\frac{\partial u}{\partial x}+\frac{1}{\rho}\frac{\partial p}{\partial x}-\nu\Delta u=0\,, \tag{2.1}$$

$$U\frac{\partial v}{\partial x}+\frac{1}{\rho}\frac{\partial p}{\partial y}-\nu\Delta v=0\,, \tag{2.2}$$

where U is the velocity of uniform flow parallel to the x-axis, $\Delta=\partial^2/\partial x^2+\partial^2/\partial y^2$, (u, v) are the component velocities, p is the pressure, ρ the density, and ν the kinematic viscocity. The equation of continuity is satisfied by taking a stream function Ψ such that

$$u=\frac{\partial \Psi}{\partial y}\,,\quad v=-\frac{\partial \Psi}{\partial x}\,. \tag{2.3}$$

Eliminating p from (2.1) and (2.2), we have

$$\Delta\omega-2k\frac{\partial\omega}{\partial x}=0\,, \tag{2.4}$$

where ω is the vorticity defined as

$$\omega=\frac{\partial v}{\partial x}-\frac{\partial u}{\partial y}=-\Delta\Psi\,, \tag{2.5}$$

and $2k=U/\nu$.

Introducing complex variables

$$z=x+iy\,,\qquad \bar{z}=x-iy\,, \tag{2.6}$$

$$W=u-iv\,, \tag{2.7}$$

we obtain from (2.3)

$$W=2i\frac{\partial\Psi}{\partial z}\,, \tag{2.8}$$

and hence, by (2.5)

$$\frac{\partial W}{\partial \bar{z}}=2i\frac{\partial^2\Psi}{\partial z\partial\bar{z}}=\tfrac{1}{2}i\Delta\Psi=-\tfrac{1}{2}i\omega\,. \tag{2.9}$$

For the boundary conditions, we have

(a) $W\to U$, as $|z|\to\infty$, (2.10)

(b) $W\equiv 0$, on the surface of the cylinder, (2.11)

(c) ω and W are one-valued throughout the field of flow. (2.12)

§3. The General Expressions for ω and W

As is well known, the most general solution of (2.4) can be expressed as

$$\omega=\Re\sum_{n=0}^{\infty}C_n e^{kx}K_n(kr)e^{ni\theta}\,, \tag{3.1}$$

where (r, θ) are polar coordinates, K_n is the modified Bessel function and C_n's are complex constants. Here n must be integers and C_n should satisfy the relation

$$\Re\sum_{n=0}^{\infty}C_n=0\,, \tag{3.2}$$

in order that ω and W should be one-valued throughout the field of flow outside the cylinder (cf. (2.12)).

Substituting from (3.1) into (2.9) and integrating, we can find the general expression for W as

$$W=\frac{i}{2k}e^{kx}\Big\{A_1K_0(kr)+\sum_{n=1}^{\infty}(A_{n+1}e^{ni\theta}-\overline{A}^{n}e^{-ni\theta})K_n(kr)\Big\}+\frac{df}{dz}\,, \tag{3.3}$$

where

---

* As for the detail of this method, reference should be made to Imai's original paper.[4]

$$A_n=\sum_{i=n}^{\infty} C_i \qquad (n=1,2,\cdots), \tag{3.4}$$

and $f(z)$ is an arbitrary analytic function of z.

The arbitrary constants A_n as well as the analytic function $f(z)$ are to be determined from the appropriate boundary conditions.

§ 4. Transformation Function from Equilateral Triangle to Unit Circle

In this paper, we consider two cases of flow past an equilateral triangular cylinder:

a) the case where the forward stagnation point coincides with one of the vertices of the triangle (Fig. 1a),

and

b) the case where the forward stagnation point coincides with the middle point of a side of the triangle (Fig. 1b).

We shall refer to them as the case (a) and (b) respectively. It is to be noted that the case (b) will be obtained from the case (a) by rotating the cylinder by an angle π about an axis perpendicular to the plane of flow.

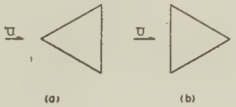

Fig. 1.

The transformation function from the equilateral triangle in the z-plane onto the unit circle in the Z-plane is given by

$$z=A\int_{-1}^{Z}(1+\varepsilon Z^{-3})^{2/3}dZ+B, \tag{4.1}$$

where A and B are constants which may be determined from the magnitude and the position of the triangle, and ε is 1 or -1 for the case (a) or (b) respectively.

Expanding the integrand of (4.1) in descending powers of Z and integrating, we have

$$z=Z-\tfrac{1}{3}\varepsilon Z^{-2}+\tfrac{1}{45}Z^{-5}-\tfrac{1}{162}\varepsilon Z^{-8}+\tfrac{7}{2673}Z^{-11}+\cdots, \tag{4.2}$$

where the constants have been determined by the conditions that centres of the triangle and the unit circle are the origins of the z- and Z-planes and that the coefficient of Z in (4.2) is unity. Thus the length of one side of the triangle becomes 2.371, but it does not mean any loss of generality of our solution.

Most of our calculation was performed by using very simple transformation function:

$$z=Z-\tfrac{1}{3}\varepsilon Z^{-2}, \tag{4.3}$$

but for the sake of checking, we have calculated the first approximation for the total drag by using more exact one:

$$z=Z-\tfrac{1}{3}\varepsilon Z^{-2}+\tfrac{1}{45}Z^{-5}-\tfrac{1}{162}\varepsilon Z^{-8}+\tfrac{7}{2673}Z^{-11}. \tag{4.4}$$

As is shown later, the transformation function (4.3) is sufficiently accurate for our purpose.

§ 5. Determination of A_n

For the convenience of our calculation, we make use of a function $g(z)$ defined as

$$\begin{aligned} g(z)=&\tfrac{1}{32}k^3A^1\{z^2\ln z-\tfrac{1}{2}z^2-(2S+1)z^2\}\\ &+\tfrac{1}{8}k^2\bar{A}_1z(\ln z-1)-\tfrac{1}{4}k\bar{A}_2\ln z\\ &+\tfrac{1}{4}k\sum_{n=3}^{\infty}(n-3)!\,\bar{A}_n(\tfrac{1}{2}kz)^{2-n}, \end{aligned} \tag{5.1}$$

where

$$S=\ln(2/k)-\gamma, \tag{5.2}$$

$\gamma=0.57721\cdots$ being Euler's constant.

In view of the form of W, it will be natural to suppose that A_n is in general $O(k^n)$, so that we put

$$\bar{A}_n=k_n(a_{n0}+ka_{n1}+k^2a_{n2}+\cdots), \tag{5.3a}$$

$$g(z)=k^3\{g_0(z)+kg_1(z)+k^2g_2(z)+\cdots\}, \tag{5.3b}$$

$$f(z)=k^{-1}\{f_0(z)+kf_1(z)+k^2f_2(z)+\cdots\}. \tag{5.3c}$$

Inserting (5.3) into (3.3), and expanding Bessel functions in increasing powers of k and equating to zero coefficients of powers of k in order to satisfy the boundary condition (2.11), we have a series of equations:

$$f_0'(z)=4ig_0''(z), \tag{5.4}$$

$$f_1'(z)=\tfrac{1}{2}(z+\bar{z})f_0'(z)+4ig_1''(z)+2i\bar{g}_0'(\bar{z}), \tag{5.5}$$

$$\begin{aligned} f_2'(z)=&\tfrac{1}{2}(z+\bar{z})f_1'(z)-\tfrac{1}{8}(z+\bar{z})^2f_0'(z)\\ &+i\{4g_2''(z)+2\bar{g}_1'(\bar{z})+\bar{z}g_0'(z)\}, \end{aligned} \tag{5.6}$$

$$\begin{aligned} f_3'(z)=&\tfrac{1}{2}(z+\bar{z})f_2'(z)-\tfrac{1}{8}(z+\bar{z})^2f_1'(z)\\ &+\tfrac{1}{48}(z+\bar{z})^3f_0'(z)+i\{4g_3''(z)+2\bar{g}_2'(\bar{z})\\ &+\bar{z}g_1'(z)+\tfrac{1}{2}z\bar{g}_0(\bar{z})-\tfrac{1}{8}\bar{a}_{20}z(\ln z-2S-1)\}, \end{aligned} \tag{5.7*}$$

on the profile.

---

* In Reference (4), there were misprints: the terms $(1/16)(z+\bar{z})^3f_0'(z)$ in Eqs. (5.6) and (8.4) should be read as $(1/48)(z+\bar{z})^3f_0'(z)$.

Using the transformation function (4.3), we can map the region outside the triangle onto the region outside a unit circle ($Z\bar{Z}=1$) in the Z-plane. Thus we can consider the equations (5.4)–(5.7) on the unit circle in the Z-plane.

On the other hand, it is known from Imai's investigation[5] that the exact solution of the Navier-Stokes equations for the viscous flow past an arbitrary cylinder has in general the asymptotic expression

$$f(z)=Uz+\frac{m+i\Gamma}{2\pi}\ln z-i\frac{k^{1/2}m^2}{4\pi^{1/2}U}\frac{1}{z^{1/2}}+O\left(\frac{1}{z}\right), \tag{5.8}$$

and that the drag and lift of the cylinder are given by

$$X=\rho Um, \qquad Y=\rho U\Gamma. \tag{5.9}$$

It may be noted that the third term on the right-hand side of (5.8) does not appear in the Oseen approximation.

§ 5.1 The First Approximation

In view of the above considerations, we can determine the first approximations: a_{10}, a_{20}, $f_0'(z)$, and $g_0'(z)$, from (5.4) and (5.5), as:

$$a_{10}=-\frac{18iU}{4+9S}, \tag{5.10}$$

$$a_{20}/a_{10}=\varepsilon/6, \tag{5.11}$$

$$f_0'(z)/a_{10}=\frac{i}{2}\frac{Z(3Z+\varepsilon)}{(3Z^3+2\varepsilon)}, \tag{5.12}$$

$$g_0'(z)/a_{10}=\tfrac{1}{8}\ln Z-\tfrac{1}{24}(\varepsilon/Z). \tag{5.13}$$

Using the more exact transformation function (4.4), we have

$$a_{10}=-\frac{2iU}{0.4357+S}. \tag{5.14}$$

for the value of a_{10}, instead of (5.10).

§ 5.2 The Second Approximations

We can determine the second approximations from (5.6) as

$$a_{11}/a_{10}=-(1/6)\varepsilon, \tag{5.15}$$

$$a_{21}/a_{10}=-(11+36S)/72, \tag{5.16}$$

$$\begin{aligned} f_1'(z)/a_{10}=&\frac{i}{18}(4+9S)+\frac{i}{48}\frac{\varepsilon}{Z}\\ &-\frac{i}{144}\frac{\{9\varepsilon Z^2-(66-216S)Z+32\varepsilon\}}{(3Z^3+2\varepsilon)}, \end{aligned} \tag{5.17}$$

$$\begin{aligned} g_1'(z)/a_{10}=&-\frac{1}{16}\left(Z-\frac{\varepsilon}{3Z^2}\right)(\ln Z-2S-1)\\ &-\frac{1}{48}\varepsilon\ln Z+\frac{11+36S}{288}\frac{1}{Z}\\ &+\frac{19}{864}\frac{\varepsilon}{Z^2}-\frac{1}{288}\frac{1}{Z^3}. \end{aligned} \tag{5.18}$$

---

§ 5.3 The Third Approximations

$$a_{12}/a_{10}=-\frac{1597-2187S}{1944(4+9S)}, \tag{5.19}$$

$$a_{22}/a_{10}=-\frac{109-829S-972S^2}{1296(4+9S)}\varepsilon, \tag{5.20}$$

$$\begin{aligned} f_2'(z)/a_{10}=&-\frac{i}{288}\frac{19-36S}{Z}+\frac{17}{1296}\frac{i\varepsilon}{Z^2}-\frac{i}{864Z^3}\\ &-i\frac{(3518+8019S+26244S^2)Z^2+(3870+4854S)\varepsilon Z-(3076+6057S-1944S^2)}{2592(4+9S)(3Z^3+2\varepsilon)}, \end{aligned} \tag{5.21}$$

$$\begin{aligned} g_2'(z)/a_{10}=&\frac{\varepsilon}{288}\left(3Z-\frac{\varepsilon}{Z^2}\right)(\ln Z-2S-1)-\frac{1597-2187S}{15552(4+9S)}\ln Z\\ &+\frac{109-829S-972S^2}{5184(4+9S)}\frac{\varepsilon}{Z}-\frac{407+1080S}{31104}\frac{1}{Z^2}-\frac{\varepsilon}{1728Z^3}-\frac{17+27S}{7776Z^4}-\frac{\varepsilon}{5184Z^5}. \end{aligned} \tag{5.22}$$

§ 6. Velocity and Drag

The complex velocity can be determined by (cf. ref. 4)

$$W=e^{kx}\sum_{n=0}^{\infty}k^n\{F_{n+1}(z)-G_n(z,\bar{z})\}, \tag{6.1}$$

where

$$F_n(z)=f_n'(z)-4ig_n''(z) \qquad (n=1, 2), \tag{6.2a}$$

$$F_3(z)=f_3'(z)-4ig_3''(z)+(i/8)\bar{a}_{20}z(\ln z-2S-1)\,, \tag{6.2b}$$

and

$$G_0(z)=\tfrac{1}{2}(z+\bar{z})f_0'(z)+2i\bar{g}_0'(\bar{z})\,, \tag{6.3a}$$

$$G_1(z)=\tfrac{1}{2}(z+\bar{z})f_1'(z)-\tfrac{1}{8}(z+\bar{z})^2f_0'(z)+2i\bar{g}_1'(\bar{z})+i\bar{z}g_0'(z)\,, \tag{6.3b}$$

$$\begin{aligned}G_2(z)=&\tfrac{1}{2}(z+\bar{z})f_2'(z)-\tfrac{1}{8}(z+\bar{z})^2f_1'(z)+\tfrac{1}{48}(z+\bar{z})^3f_0'(z)\\&+2i\bar{g}_2'(\bar{z})+i\bar{z}g_1'(z)+\tfrac{1}{2}iz\bar{g}_0(\bar{z})\,.\end{aligned} \tag{6.3c}$$

The total drag can be computed from (5.12), (5.17), and (5.21) using the above-mentioned relations (5.8) and (5.9):

$$D=\frac{18\pi U^2\rho}{k(4+9S)}\left\{1-k^2\frac{2785+4374S+8748S^2}{1944(4+9S)}+O(k^3)\right\}. \tag{6.4}$$

If we choose the length of a side of the triangle L as the characteristic length, and define the Reynolds number as $R=LU/\nu$, we have a formula for the total drag coefficient:

$$C_D=\frac{D}{\frac{1}{2}\rho U^2L}\frac{72\pi}{R(4+9S)}\left\{1-\left(\frac{R}{2L_0}\right)^2\frac{2785+4374S+8748S^2}{1944(4+9S)}+O(R^3)\right\}, \tag{6.5}$$

where

$$L_0=2.371\,, \tag{6.6}$$

$$S=1.672-\ln R\,. \tag{6.7}$$

The frictional drag D_f can be calculated by use of the formula:

$$D_f=-\eta\oint\left(\frac{\partial V_s}{\partial n}\right)\sin\alpha ds\,, \tag{6.8}$$

where the integration must be carried out over the entire surface, and (s, n) are the curvilinear orthogonal coordinates, $n=0$ corresponding to the surface, and where the positive directions of s and n are chosen as shown in Fig. 2, V_s is the component of the velocity in the positive direction of s, η the viscocity, and α is the angle between n and x-axis (cf. Fig. 2).

Performing the integration in (6.8), we have the frictional drag coefficient as

$$\begin{aligned}C_{Df}=&\frac{72\pi}{R(4+9S)}\\&\times\left[0.3889+\frac{\varepsilon R}{2L_0}(-0.1019+0.3333S)\right.\\&+\left(\frac{R}{2L_0}\right)^2\left\{0.0236-0.2500S-\frac{0.5139}{4+9S}\right\}\\&\left.+O(R^3)\right].\end{aligned} \tag{6.9}$$

The pressure drag coefficient can be easily obtained as the difference of the total and the frictional drag.

The drag coefficients thus obtained are given in Fig. 3, where the first approximation to the total drag coefficient obtained by using the transformation function (4.4) is also given to show the sufficient accuracy of the very simple transformation (4.3).

It is to be noted that the total drag for the cases (a) and (b) are the same to the

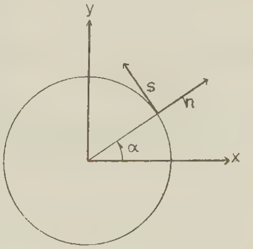

Fig. 2.

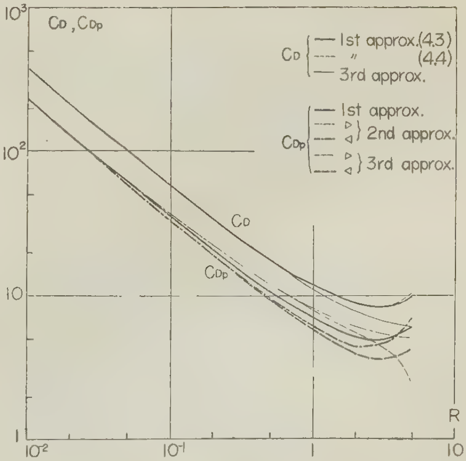

Fig. 3.

order of our approximation $O(R)$, although the pressure and frictional drags separately are not the same for the two cases to the order $O(1)$. This fact seems to be true also for cylinders of more general shape. Such a discussion will be given in an accompanying paper.[8)]

In view of the behaviour of the curves in Fig. 3, we may take

(i) $R \leq 5$ for C_D,

(ii) $R \leq 2$ for C_{Df},

as the Reynolds number ranges for which the formulae (6.5) and (6.9) are valid.

It is also to be noted that the ratio of the frictional drag to the total drag C_{Df}/C_D is not constant but a function of Reynolds number, although the ratios are known to be constant for the cases of circular and elliptic cylinders.[11),12)] (cf. Fig. 4).

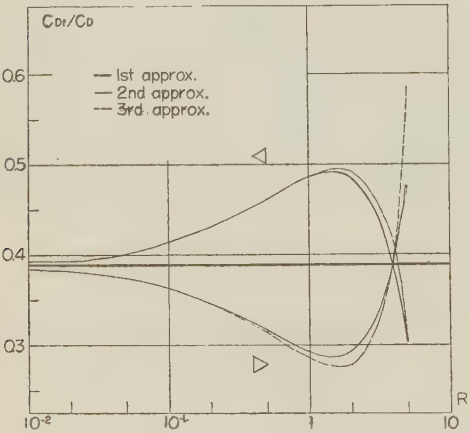

Fig. 4.

§ 7. Imai's New Theory of Drag

Recently I. Imai has proposed a new theory for the drag of a two-dimensional obstacle in a laminar flow,[6)] according to which the total drag coefficient at an arbitrary (but not so small) Reynolds number R is give by

$$C_D^{1/2} = C_{D\infty}^{1/2} + \beta R^{-1/2}, \tag{7.1}$$

where $C_{D\infty}$ is the limiting value of C_D for the same obstacle when $R \to \infty$, which may be calculated on the basis of Kirchhoff's free streamline theory, and β is a constant which depends on the shape of the obstacle.

In the case of a circular cylinder, Imai has shown that (7.1) is sufficiently accurate even for a rather low Reynolds number ($R=4$), using Brodetsky's results by the free streamline theory,[2)] the author's[7)] and A. Thom's[10)] numerical results, and Tomotika and Aoi's results[11)] by Oseen's approximation.

As for the case of a triangular cylinder, we know the results by the free streamline theory (case (a) corresponding to the flow past a flat plate, and case (b) to the flow past a bent lamina),[9)] although we have no numerical solution in an intermediate Reynolds number range. Thus, using our results by Oseen's approximation at Reynolds number of 3, we have the formulae:

$$\text{case (a)} \quad C_D^{1/2} = 0.699 + 3.279 R^{-1/2}, \tag{7.2}$$

$$\text{case (b)} \quad C_D^{1/2} = 0.938 + 2.865 R^{-1/2}. \tag{7.3}$$

Imai also proposed a formula[6)] for the drag of a two-dimensional obstacle in a turbulent flow, according to which the pressure drag coefficient is given by

$$C_{Dp}^{1/2} = C_{D\infty} + \beta^* R^{*-1/2}, \tag{7.4}$$

where R^* is the so-called effective Reynolds number for which Imai suggested the value of 30~50, and β^* is another constant.

If we determine the value of β^* from the value of the pressure drag coefficient at Reynolds numbr of 2, we have

$$\text{case (a):} \quad C_{Dp}^{1/2} = 0.699 + 1.998 R^{*-1/2}, \tag{7.5}$$

$$\text{case (b):} \quad C_{Dp}^{1/2} = 0.938 + 2.380 R^{*-1/2}, \tag{7.6}$$

for the pressure drag of the triangular cylinder.

On the other hand, Asaka and Ôshima[1)] studied experimentally the flow past a triangular cylinder at Reynolds number of $3\sim5\times10^4$, and obtained the values of the pressure drag coefficients: $C_{Dp}=1.34$ for case (a), and $C_{Dp}=1.773$ for case (b). Using these values, we can determine the effective Reynolds numbers R^* as: $R^*=16.4$ for case (a), and $R^*=26.3$ for case (b). The effective Reynolds number thus obtained are rather low compared with those for a circular cylinder. It seems that the discrepancy may be mainly due to the fact that we were compelled to use the results at very low Reynolds number ($R=2$), in order to determine the value of β^*.

§ 8. Conclusion

In this paper, the flow of a viscous fluid past an equilateral triangular cylinder has been studied using Imai's method of treating Oseen's approximation. The expression for the velocity in the flow field near the triangular cylinder was obtained correct to the order of R^2, and those for the frictional pressure and total drag to the order of R. The drag of the triangular cylinder at high Reynolds numbers was estimated by use of Imai's new theory of drag and was compared with Asaka and Ôshima's experimental, results. In the course of the study, it has been found that there exists a very simple relation between the flow past a triangular cylinder and that past the cylinder which can be obtained by rotating the original one by an angle π, such that total drag is not changed by the rotation within the order of our approximation.

Acknowledgements

In conclusion, I wish to express my hearty gratitude to Professor Isao Imai for his discussions and kind inspection of the manuscript, and to Professor Saburô Asaka who kindly showed me unpublished data.

References

1) S. Asaka and K. Ôshima: Natural Sci. Rep. Ochanomizu Univ. **7** (1956) 10.
2) S. Brodetsky: Proc. Roy. Soc. A, **102** (1923) 542.
3) M. Hasegawa: Trans. Soc. Mech. Engrs. Japan **19** (1953) 21 (in Japanese).
4) I. Imai: Proc. Roy. Soc. A, **224** (1954) 141.
5) I. Imai: Proc. Roy. Soc. A, **208** (1951) 21.
6) I. Imai: Univ. of Maryland, Inst. Fluid Dyn. and Appl. Math., Tech. Note BN–104 (1957).
7) M. Kawaguti: J. Phys. Soc. Japan **8** (1953) 747.
8) M. Kawaguti: J. Phys. Soc. Japan **14** (1959) 000.
9) H. Lamb: *Hydrodynamics*, 6th ed, (Cambr. Univ. Press, 1932) 104.
10) A. Thom: Proc. Roy. Soc. A, **141** (1933) 651.
11) S. Tomotika and T. Aoi: Quart. J. Mech. Appl. Math. **3** (1950) 140.
12) S. Tomotika and T. Aoi: Quart. J. Mech. Appl. Math. **6** (1953) 290.

JOURNAL OF THE PHYSICAL SOCIETY OF JAPAN Vol. 14, No. 10, OCTOBER, 1959

Reversal Flow Theorem concerning Oseen's Approximation

By Mitutosi KAWAGUTI

Aeronautical Research Institute, University of Tokyo

(Received May 25, 1959)

We sought for the simple relations which exist between the two-dimensional flow of a viscous fluid past a cylindrical obstacle and the flow past the same obstacle rotated by an angle π about its axis, within the accuracy of Oseen's approximation. It is shown that the forces acting upon the cylinder do not change by the rotation of the cylinder, as far as the terms of order $O(R^{-1})$ are concerned. Further, for the special cases of symmetrical obstacles which experience no lift, it is shown that the total drags for the original and the rotated bodies coincide with each other within the accuracy of $O(R)$.

§ 1. Introduction

In a preceding paper, the author studied the flow past an equilateral triangular cylinder by Oseen's approximation.[1] In the course of the study, it was found that there exists a very simple relation between the flow past a triangular cylinder and that past a cylinder which can be obtained by rotating the original one by an angle π about its axis.

It occurred to the author that there may hold some simple relations between a flow past an obstacle and the flow past the same obstacle rotated by an angle π for the cases of cylinders of more general shape.

In this paper, we shall seek for such relations within the accuracy of Oseen's approximation.

§ 2. First Approximation

Since we shall use the same method and procedure as in the preceding paper,[1] we shall omit the detail of procedure and only show the results. We shall refer to the preceding paper as I.

We shall assume that the analytic function which transforms the profile of the cylindrical obstacle in the z-plane onto the unit circle in the Z-plane is given by

$$z=c_0Z+c_1Z^{-1}+\varepsilon c_2Z^{-2}+\cdots+\varepsilon^{n-1}c_nZ^{-n} \quad (2.1)$$

where ε is 1 for the original profile, and -1 for the rotated profile. In general, c_n may be complex numbers, but we may assume $|c_0|=1$ without loss of generality.

Proceeding as in I, we have a series of n equations for $a_{10}, a_{20}\cdots, a_{n0}$:

$$\left.\begin{array}{l} -U-\frac{i}{2}\bar{a}_{10}S+ia_{10}P+\cdots+i\varepsilon^{n-1}a_{n0}P=0 \\ \varepsilon a_{10}P+\cdots+\varepsilon^{n-1}a_{n-1,0}P+\bar{a}_{20}P=0 \\ \cdot\quad\cdot\quad\cdot\quad\cdot\quad\cdot\quad\cdot\quad\cdot \\ \varepsilon^{n-1}a_{10}P+\varepsilon^{n-1}a_{10}P+\cdots+a_{n0}=0 \end{array}\right\} \quad (2.2)$$

where U is the undisturbed velocity, a_{ij} is the coefficient of k^{i+j} in the expression of $\bar{A}_i$ (I. 5.3 a), and P stands for a certain function of c_i's independent of ε.

Eq. (2.2) can be regarded as a system of simultaneous equations for the unknown (a_{10}, $\varepsilon a_{20}, \cdots, \varepsilon^{n-1}a_{n0}$) whose coefficients are independent of ε. Therefore, $a_{10}, \varepsilon a_{20}, \cdots, \varepsilon^{n-1}a_{n0}$ are the same for the cases $\varepsilon=+1$ (original body) and $\varepsilon=-1$ (rotated body).

§ 3. The Second and Third Approximations

We shall now proceed to the higher approximations. In order to simplify the problem, let us assume that $c_0, \cdots, c_n$ in the transformation function (2.1) are real, so that the flow with which we are concerned is restricted to the flow past an obstacle that has symmetry about the x-axis. In this case, all the values of a_{ij} become purely imaginary.

Proceeding in the same way as in the first approximation, we can easily show that

(i) for the second approximation, εa_{11}, $\varepsilon^2 a_{21}, \cdots, \varepsilon^n a_{n1}$ have the same values for the original and the rotated cases.

(ii) for the third approximation, $a_{12}, \varepsilon a_{22}, \cdots, \varepsilon^{n-1}a_{n2}$, have the same values for the both cases.

Further we can guess from the process of our study that, in general, for the m-th approximation, the values of $\varepsilon^{m+1}a_{1\,m-1}, \cdots, \varepsilon^{m+n}a_{n,m-1}$ are the same for the both cases.

§ 4. The Drag and Lift

The drag and lift of a cylindrical obstacle submerged in a flow of a viscous fluid can be determined from the coefficient of $1/z$ in $f'(z)$ (cf. (I. 5.8), (I. 5.9)).

Now the first approximation of $f'(z)$ can be expressed as

$$f_0'(z)=\frac{i}{2}\frac{a_{10}}{z}+O\left(\frac{1}{z^2}\right) \quad (4.1)$$

Therefore, considering the results of § 2, we can say that, in the first approximation, the values of the drag and lift are the same for the original and the rotated bodies.

As a corollary of the theorem mentioned above, it can easily be shown that there acts no lift upon the cylinder whose cross-sectional shape has a symmetry about a line perpendicular to the direction of the undisturbed flow, as far as the first approximation in Oseen's approximate theory is concerned.

As for the higher approximations, we have restricted ourselves to the case of flow past an obstacle that has symmetry about the x-axis. Therefore, we are only concerned with the drag. Now we have

$$f_1'(z)=U+\frac{\varepsilon}{z}Q_1+\frac{i}{2}\frac{a_{11}}{z}+O(z^{-2}) \quad (4.2)$$

$$f_2'(z)=\frac{1}{z}Q_2+\frac{i}{2}\frac{a_{12}}{z}+O(z^{-2}) \quad (4.3)$$

where Q_1 and Q_2 are functions of c_i's and U independent of ε. Hence, we can conclude that if we expand the total drag as

$$C_D=C_{D1}+C_{D2}+C_{D3}+\cdots \quad (4.4)$$

where C_{D1}, C_{D2} and C_{D3} are the terms of order R^{-1}, R^0 and R^1 respectively, the values of C_{D1} and C_{D3} are the same for the original and the rotated bodies, while the values of C_{D2} are of the same magnitude but of opposite sign.

§ 5. The Value of C_{D2}

Further, if we can show that $C_{D2}=0$, the total drags for the original and the rotated bodies coincide with each other within the accuracy of $O(R)$. Although the author could not succeed in the general demonstration of the fact that $C_{D2}=0$, it can be shown that in a fairly general case where the transformation function is given by

$$z=Z+c_1Z^{-1}+c_2Z^{-2}+c_3Z^{-3}+c_4Z^{-4} \quad (c_i\text{: real}) \tag{5.1}$$

the value of C_{D2} is identically zero.

It seems to the author that the values of C_{D2} may be zero in more general cases. Even if it were not the case, the value of C_{D2} would be fairly small, since the terms in $Z^{-n}(n\geq 5)$ in the transformation function behave as $\cos n\theta$ and $\sin n\theta$ on the surface of the cylinder, and they could have little effect upon the symmetry of the profile about the line perpendicular to the direction of the undisturbed flow.

Further, it may be noted that even when $C_{D2}=0$, the second approximations of the pressure and the frictional drag do not vanish, as was shown for the triangular cylinder in the preceding paper.

§ 6. Conclusion.

In this paper, we sought for the simple relations which exist between a flow past an obstacle and the flow past the same obstacle rotated by an angle π. It was shown that the forces acting upon the cylinder do not change by the rotation of the cylinder, as far as the terms of order $O(R^{-1})$ are concerned. Further, for the special cases of symmetrical obstacles which experience no lift, it was shown that the total drags for the original and the rotated bodies coincide with each other within the accuracy of the third approximation to Oseen's approximate equation, i.e. $O(R)$.

In conclusion, I wish to express my hearty gratitude to Professor Isao Imai for his discussions and kind inspection of the manuscript.

Reference

1) M. Kawaguti: J. Phys. Soc. Japan **14** (1959) 1425.

Journal of the Physical Society of Japan, Vol. 14, No. 10, October, 1959

Two-dimensional Stokes Flow of an Electrically Conducting Fluid in a Uniform Magnetic Field

By Hirowo YOSINOBU
Junior College of Engineering, University of Osaka Prefecture
and Tsunehiko KAKUTANI
Department of Physics, Faculty of Science, Kyoto University

(Received June 29, 1959)

This paper deals with the two-dimensional flow of a viscous, incompressible and electrically conducting fluid past a cylinder in a uniform magnetic field, using Stokes approximation. Detailed calculation is carried out for the flow past a circular cylinder in two cases: one in a parallel magnetic field and the other in a transverse magnetic field. The expansion formulae for the drag per unit span of the cylinder are obtained in terms of the Hartmann number in each case.

§ 1. Introduction

Magnetohydrodynamics is a new field in physics which has been developed in connexion with geo- and astrophysics and aero-space sciences. In particular, it seems to become more attractive to physicists lately in connexion with the problems of nuclear fusion. Many problems in magnetohydrodynamics have been so far investigated for their own importance and interest in each field. However, it may also be one of the effective ways of developing this new field to investigate how the well-established classical hydrodynamic problems may be modified under the new magneto-hydrodynamic circumstances. Indeed, since Hartmann's pioneering work, not a few works have been carried out along this line.

Recently, Chester[1] has investigated the effect of magnetic field upon the Stokes flow past a sphere. In the present paper, applying his ideas to the two-dimensional Stokes flow, we deal with the flow of a viscous and electrically conducting fluid past a circular cylinder in two cases: one in a uniform magnetic field parallel to the main stream and the other in a transverse uniform magnetic field. It is well known that the Stokes approximation cannot give an appropriate solution for the two-dimensional flow past a cylinder under the ordinary hydrodynamical circumstances, unless the flow field is bounded. In the present case where the fluid is electrically conducting and flows in the uniform magnetic field, however, appropriate solutions can be obtained. In the first case, where the uniform magnetic field is parallel to the main stream, the solution indicates that rotational flow field with appreciable vortices and induced electric currents is confined in two parabolic regions in front and in rear of the cylinder and that outside these regions the vorticity falls off exponentially and the flow is almost uniform. Similar parabolic regions are also formed on both sides of the cylinder in the second case, where the uniform magnetic field is transverse to the main stream. This fact enables us to obtain appropriate solutions in the present case, while in the classical Stokes flow no acceptable solution can be obtained except trivial one implying the fluid everywhere at rest, since the rotational field extends over the whole region.

The expansion formulae for the drag per unit span of the cylinder are also obtained in power series of Hartmann number. Numerical results show that the drag is always greater in the transverse magnetic field than in the parallel magnetic field, as is intuitively expected.

§ 2. Fundamental Equations and Stokes Approximation

We consider a steady flow of a viscous, incompressible and electrically conducting fluid past a circular cylinder with radius a in the presence of a uniform magnetic field. As the fluid is electrically conducting, electric current is induced, when the flow goes across the line of magnetic induction. This induced current, coupled with the magnetic field, yields a body force acting on the fluid, viz. Lorentz force. The interaction between the magnetic field and the motion of the fluid having to be taken into account, we must solve the hydrodynamic equations and the electromagnetic equations simultaneously.

The fundamental equations governing the motion of the fluid are the equation of continuity:

$$\operatorname{div} V=0\,, \tag{2.1}$$

and the modified Navier-Stokes equation:

$$\rho(V\cdot\operatorname{grad})V=-\operatorname{grad}P+\rho\nu\Delta V+q\boldsymbol{E}+\boldsymbol{J}\times\boldsymbol{B}. \tag{2.2}$$

Electromagnetic field is subject to the Maxwell equations:

$$\operatorname{curl}\boldsymbol{H}=\boldsymbol{J}\,, \tag{2.3}$$

$$\operatorname{div}\boldsymbol{B}=0\,, \tag{2.4}$$

$$\operatorname{curl}\boldsymbol{E}=0\,, \tag{2.5}$$

$$\operatorname{div}\boldsymbol{D}=q\,. \tag{2.6}$$

In the above six equations, we have used the usual notations for quantities of the field and adopted the rationalized M. K. S. system. The derivatives of the field quantities with respect to time do not appear, since we consider the steady state only. As a complementary relation to these equations, Ohm's law is assumed:

$$\boldsymbol{J}=\sigma(\boldsymbol{E}+V\times\boldsymbol{B})+qV\,, \tag{2.7}$$

where σ is the electric conductivity of the fluid. We also assume the fluid to be homogeneous and isotropic, so that the following two relations connect the magnetic induction $\boldsymbol{B}$ with the magnetic field $\boldsymbol{H}$ and the electric displacement $\boldsymbol{D}$ with the electric field $\boldsymbol{E}$ respectively:

$$\boldsymbol{B}=\mu\boldsymbol{H}\,, \tag{2.8}$$

$$\boldsymbol{D}=\varepsilon\boldsymbol{E}\,, \tag{2.9}$$

where the constants μ and ε are the magnetic permeability and the dielectric constant of the fluid respectively. Equations (2.1)∼(2.9) are the fundamental equations to be solved for the present problem.

We choose the origin of coordinates at the centre of a cross section of the cylinder and take the x_1-axis parallel to the direction of the undisturbed magnetic field, the x_3-axis along the axis of the cylinder and the x_2-axis perpendicular to both the x_1-and x_3-axes. The undisturbed flow is supposed to be parallel to the x_1-axis in the first case and to the x_2-axis in the second case.

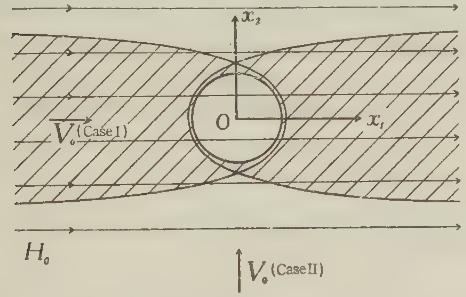

Fig. 1. Sketch of the field.

First, we neglect the terms involving excess charge q in (2.2) and (2.7) as in usual magnetohydrodynamic problems. We then assume two-dimensionality of the problem: namely 1) all the quantities in (2.1)~(2.9) are independent of x_3, so that all the derivatives of these quantities in x_3 disappear in the above equations, and 2) the fluid velocity V and the magnetic field $\boldsymbol{H}$ lie in the x_1 x_2-plane. In consequence of these assumptions, curl $\boldsymbol{H}$ in (2.3), and hence $\boldsymbol{J}$ too, becomes parallel to the x_3-axis. Also, owing to the assumption 2), $\boldsymbol{V}\times\boldsymbol{B}$ in (2.7) becomes parallel to the x_3-axis. Hence, we may conclude from (2.7) that $\boldsymbol{E}$ has only the x_3-component, E_3. Thus, solving Eq. (2.5), we obtain

$$E_3=E_0\,(\text{const})\,. \tag{2.10}$$

Since there is no electric current at infinity, the constant E_0 must be zero in the first case, because $\boldsymbol{V}$ and $\boldsymbol{B}$ at infinity are parallel to each other. Similarly, in the second case where $\boldsymbol{V}$ and $\boldsymbol{B}$ at infinity are perpendicular to each other, so that $\boldsymbol{V}\times\boldsymbol{B}$ is equal to $-V_0\mu H_0\boldsymbol{k}$, the constant E_0 must be equal to $V_0\mu H_0$, where V_0 and H_0 are the undisturbed velocity and magnetic field at infinity and $\boldsymbol{k}$ is one of the fundamental unit vectors $(\boldsymbol{i}, \boldsymbol{j}, \boldsymbol{k})$ referring to the coordinate system. Hence, we have, in the first case,

$$\boldsymbol{J}=\sigma\mu(\boldsymbol{V}\times\boldsymbol{H})\,, \tag{2.11}$$

and in the second case,

$$\boldsymbol{J}=\sigma\mu(V_0H_0\boldsymbol{k}+\boldsymbol{V}\times\boldsymbol{H})\,. \tag{2.12}$$

Substituting (2.11) and (2.12) into (2.2) and (2.3), and introducing non-dimensional variables $\boldsymbol{v}=\boldsymbol{V}/V_0$, $\boldsymbol{h}=\boldsymbol{H}/H_0$, $p=a/(\rho\nu V_0)\cdot P$ and $(x, y, z)=(x_1/a, x_2/a, x_3/a)$, we have, in the first case,

$$R(\boldsymbol{v}\cdot\nabla)\boldsymbol{v}=-\nabla p+\nabla^2\boldsymbol{v}+M^2(\boldsymbol{v}\times\boldsymbol{h})\times\boldsymbol{h}\,, \tag{2.13}$$

$$R_m(\boldsymbol{v}\times\boldsymbol{h})=\nabla\times\boldsymbol{h}\,, \tag{2.14}$$

and in the second case,

$$R(\boldsymbol{v}\cdot\nabla)\boldsymbol{v}=-\nabla p+\nabla^2\boldsymbol{v}+M^2(\boldsymbol{k}+\boldsymbol{v}\times\boldsymbol{h})\times\boldsymbol{h}\,, \tag{2.15}$$

$$R_m(\boldsymbol{k}+\boldsymbol{v}\times\boldsymbol{h})=\nabla\times\boldsymbol{h}\,, \tag{2.16}$$

where $R=aV_0/\nu$ is the Reynolds number, $R_m=aV_0\sigma\mu$ the magnetic Reynolds number, $M=(\sigma/\rho\nu)^{1/2}a\mu H_0=(SRR_m)^{1/2}$ the Hartmann number, ($S=\mu H_0^2/\rho V_0^2$ being the pressure number), and ∇ stands for $\boldsymbol{i}(\partial/\partial x)+\boldsymbol{j}(\partial/\partial y)$.

We now assume R_m to be small and apply the Stokes approximation to Eqs. (2.14) and (2.16). Then, neglecting the left-hand sides of (2.14) and (2.16), we have, in both cases,

$$\nabla\times\boldsymbol{h}=0\,. \tag{2.17}$$

Assuming that the permeabilities of the fluid and the cylinder are effectively equal, and bearing in mind that the magnetic field is uniform and parallel to the x_1-axis at infinity, we obtain as the solution of (2.4) and (2.17),

$$\boldsymbol{h}=\boldsymbol{i}\,, \tag{2.18}$$

so that to the Stokes approximation the magnetic field is everywhere uniform and parallel to the x_1-axis. Inserting (2.18) into (2.13) and (2.15), and assuming R to be small, we have, to the Stokes approximation,

$$-\nabla p+\nabla^2\boldsymbol{v}+M^2(\boldsymbol{v}\times\boldsymbol{i})\times\boldsymbol{i}=0\,, \tag{2.19}$$

and

$$-\nabla p+\nabla^2\boldsymbol{v}+M^2(\boldsymbol{k}+\boldsymbol{v}\times\boldsymbol{i})\times\boldsymbol{i}=0\,, \tag{2.20}$$

where the terms of Lorentz force have been retained, since M^2 is considered to be finite in spite of the vanishing R and R_m by taking S to be infinite.

We now introduce the non-dimensional perturbed velocities $\boldsymbol{v}'=\boldsymbol{v}-\boldsymbol{i}$ in the first case in (2.19) and $\boldsymbol{v}'=\boldsymbol{v}-\boldsymbol{j}$ in the second case in (2.20). Then these equations can be written down in a single identical form:

$$-\nabla p+\nabla^2\boldsymbol{v}'+M^2(\boldsymbol{v}'\times\boldsymbol{i})\times\boldsymbol{i}=0\,. \tag{2.21}$$

The triple vector product in this equation is expanded as

$$\begin{aligned}(\boldsymbol{v}'\times\boldsymbol{i})\times\boldsymbol{i}&=(\boldsymbol{i}\cdot\boldsymbol{v}')\boldsymbol{i}-(\boldsymbol{i}\cdot\boldsymbol{i})\boldsymbol{v}'\\&=u\boldsymbol{i}-\boldsymbol{v}'\\&=-v\boldsymbol{j}\,,\end{aligned} \tag{2.22}$$

where u and v are the x-and y-components of $\boldsymbol{v}'$, respectively. Thus, we have finally the following equation:

$$-\nabla p+\nabla^2\boldsymbol{v}'-M^2 v\boldsymbol{j}=0\,, \tag{2.23}$$

which should be solved in combination with the equation of continuity for $\boldsymbol{v}'$:

$$\nabla\cdot\boldsymbol{v}'=0\,. \tag{2.24}$$

§ 3. General Solutions and their Properties

We shall now proceed to solve the above simultaneous equations (2.23) and (2.24). Eliminating p from (2.23), we have

$$\nabla^2\omega-M^2\frac{\partial v}{\partial x}=0\,, \tag{3.1}$$

where $\omega=\partial v/\partial x-\partial u/\partial y$ is the vorticity. Eq. (2.24) shows that the perturbed velocity field has a stream function ψ such that

$$\left.\begin{aligned} u&=-\frac{\partial\psi}{\partial y}\,,\\ v&=\frac{\partial\psi}{\partial x}\,,\end{aligned}\right\} \tag{3.2}$$

and

$$\omega=\nabla^2\psi\,. \tag{3.3}$$

Substituting (3.2) and (3.3) into (3.1), we obtain the equation for ψ as

$$\left(\nabla^4-M^2\frac{\partial^2}{\partial x^2}\right)\psi=0\,. \tag{3.4}$$

In general, the solution of this equation can be expressed in the form:

$$\psi=\psi_1+\psi_2\,, \tag{3.5}$$

where ψ_1 and ψ_2 are solutions of equations

$$\left(\nabla^2-M\frac{\partial}{\partial x}\right)\psi_1=0\,, \tag{3.6}$$

and

$$\left(\nabla^2+M\frac{\partial}{\partial x}\right)\psi_2=0\,, \tag{3.7}$$

respectively. An equation similar to (3.6) and (3.7) is already familiar to us in the classical Oseen flow. Putting $\psi_1=e^{\frac{1}{2}Mx}f_1$ and $\psi_2=e^{-\frac{1}{2}Mx}f_2$ in (3.6) and (3.7) respectively, we have a single identical equation for f_1 and f_2 as:

$$\left\{\nabla^2-\left(\frac{M}{2}\right)^2\right\}(f_1,\,f_2)=0\,. \tag{3.8}$$

The fundamental solutions for (3.8) are expressed as

$$(f_1,\,f_2)=\left.\begin{matrix}I_n(kr)\\K_n(kr)\end{matrix}\right\}\times\left\{\begin{matrix}\sin n\theta\\ \cos n\theta\,,\end{matrix}\right. \tag{3.9}$$

where

$$k=\frac{1}{2}M,\ \ x=r\cos\theta,\ \ \ y=r\sin\theta, \tag{3.10}$$

and I_n, K_n denote the modified Bessel functions. The function $I_n(kr)$ is known to become infinite exponentially, when kr is large. On the other hand, the function $K_n(kr)$ becomes exponentially small when kr is large. Thus, bearing in mind that the perturbed velocity must vanish at infinity, the appropriate general solution for (3.4) is given by

$$\begin{aligned}\psi&=\psi_1+\psi_2\\ &=A_0e^{kx}K_0(kr)+B_0\int_0^\theta kr[K_1(kr)+K_0(kr)\cos\chi]e^{kr\cos\chi}d\chi\\ &\quad+2e^{kx}\sum_{n=1}^{\infty}K_n(kr)(A_n\cos n\theta+B_n\sin n\theta)\\ &\quad+C_0e^{-kx}K_0(kr)+D_0\int_0^\theta kr[K_1(kr)-K_0(kr)\cos\chi]e^{-kr\cos\chi}d\chi\\ &\quad+2e^{-kx}\sum_{n=1}^{\infty}K_n(kr)(C_n\cos n\theta+D_n\sin n\theta)\,,\end{aligned} \tag{3.11}$$

where A_n's, B_n's, C_n's and D_n's are arbitrary constants. As was shown by Filon[2)] in the classical Oseen flow, the term multiplied by B_0 in (3.11), which is a fundamental solution of (3.6), contains non-periodic term in θ and may be expanded as

$$\int_0^\theta kr[K_1(kr)+K_0(kr)\cos\chi]e^{kr\cos\chi}d\chi=\theta+\text{periodic terms in }\theta\,. \tag{3.12}$$

In the classical Oseen flow, this many-valuedness should be cancelled out by adding another many-valued fundamental solution θ, since the stream function must be one-valued. Similarly, in the present problem, we must add another many-valued function, the term multiplied by D_0 in (3.11), which is a fundamental solution of (3.7) and is expanded as

$$\int_0^\theta kr[K_1(kr)-K_0(kr)\cos\chi]e^{-kr\cos\chi}d\chi=\theta+\text{periodic terms in }\theta\,. \tag{3.13}$$

Necessity of one-valuedness of the stream function ψ imposes the following condition on the arbitrary constants B_0 and D_0:

$$B_0+D_0=0\ . \tag{3.14}$$

Thus, we have obtained the general solution for Eqs. (2.23) and (2.24).

The radial component u_r and the circumferential component u_θ of the perturbed velocity are derived from the stream function, as follows:

$$\begin{aligned} u_r &= -\frac{1}{r}\frac{\partial\psi}{\partial\theta} \\ &= ke^{kx}\Big[(B_1-B_0)K_1(kr)+\sum_{n=1}^{\infty}\cos n\theta\{(B_{n+1}-B_n)K_{n+1}(kr)+(B_n-B_{n-1})K_{n-1}(kr)\} \\ &\qquad -\sum_{n=1}^{\infty}\sin n\theta\{(A_{n+1}-A_n)K_{n+1}(kr)+(A_n-A_{n-1})K_{n-1}(kr)\}\Big] \\ &\qquad -ke^{-kx}\Big[(D_1+D_0)K_1(kr)+\sum_{n=1}^{\infty}\cos n\theta\{(D_{n+1}+D_n)K_{n+1}(kr)-(D_n+D_{n-1})K_{n-1}(kr)\} \\ &\qquad -\sum_{n=1}^{\infty}\sin n\theta\{(C_{n+1}+C_n)K_{n+1}(kr)-(C_n+C_{n-1})K_{n-1}(kr)\}\Big]\ , \end{aligned} \tag{3.15}$$

$$\begin{aligned} u_\theta &= \frac{\partial\psi}{\partial r} \\ &= ke^{kx}\Big[(A_1-A_0)K_1(kr)+\sum_{n=1}^{\infty}\cos n\theta\{(A_{n+1}-A_n)K_{n+1}(kr)-(A_n-A_{n-1})K_{n-1}(kr)\} \\ &\qquad +\sum_{n=1}^{\infty}\sin n\theta\{(B_{n+1}-B_n)K_{n+1}(kr)-(B_n-B_{n-1})K_{n-1}(kr)\}\Big] \\ &\qquad -ke^{-kx}\Big[(C_1+C_0)K_1(kr)+\sum_{n=1}^{\infty}\cos n\theta\{(C_{n+1}+C_n)K_{n+1}(kr)+(C_n+C_{n-1})K_{n-1}(kr)\} \\ &\qquad +\sum_{n=1}^{\infty}\sin n\theta\{(D_{n+1}+D_n)K_{n+1}(kr)+(D_n+D_{n-1})K_{n-1}(kr)\}\Big]\ . \end{aligned} \tag{3.16}$$

This solution has some remarkable properties. Since, for large values of kr, the modified Bessel function $K_n(kr)$ has the asymptotic expression:

$$K_n(kr)\sim\left(\frac{\pi}{2kr}\right)^{\frac{1}{2}}e^{-kr}\ , \tag{3.17}$$

all terms involving e^{kx} on the right-hand sides of Eqs. (3.15) and (3.16) are of the order of

$$(kr)^{-\frac{1}{2}}\,e^{-kr(1-\cos\theta)}\ . \tag{3.18}$$

Hence, they become exponentially small, as r tends to ∞, except in the region

$$kr(1-\cos\theta)=2kr\sin^2\frac{1}{2}\theta=O(1)\ , \tag{3.19}$$

so that

$$\theta=O((kr)^{-\frac{1}{2}})\ . \tag{3.20}$$

For large values of r they are sensible only in the vaguely parabolic region open in the direction of the positive x-axis. (cf. Fig. 1). Similarly, all terms involving e^{-kx} in (3.15) and (3.16) are of the order of

$$(kr)^{-\frac{1}{2}}e^{-kr(1+\cos\theta)}\ . \tag{3.21}$$

Hence, they are also sensible only in the vaguely parabolic region open in the direction of the negative x-axis (also cf. Fig. 1). In like manner, it is easily found that the vorticity is also sensible only in these parabolic regions, outside which the flow is nearly irrotational and uniform. The structures of these parabolic regions are similar to that of the wake formed behind a cylinder in the classical Oseen flow, but their mechanisms of formation are different from each other. Roughly speaking, in the classical Oseen flow, the vortices produced at the surface of the cylinder are diffused by viscosity of the fluid and swept away by the main stream. Thus, the vortices are mostly confined in the parabolic region behind the cylinder. As $R\to 0$, the fluid flows very slowly and can hardly sweep away the vortices. So, they are diffused equally in all directions and are distributed over the whole region. The vorticity falls off only as r^{-1}, as r becomes large. This is the reason why we cannot have an appropriate solution in the classical Stokes flow. In the present case where the magnetic field is present, however, the disturbances in velocity caused by the cylinder are transmitted as the so-called Alfvén wave along the lines of magnetic induction. The vortices are, therefore, not only diffused by viscosity but also transmitted along the lines of magnetic induction, though they are hardly swept away by the main stream since $R=0$. Hence, two parabolic rotational regions are formed along the lines of magnetic induction independently of the direction of the main stream, as shown above. This fact enables us to have appropriate solutions in the present case.

§ 4. Boundary Conditions

We shall now proceed to determine the arbitrary constants A_n's, B_n's, C_n's and D_n's in the general solution (3.11) by the boundary conditions.

Since the conditions at infinity have already been satisfied by the general solutions (3.15) and (3.16), we have only to consider the conditions at the surface of the cylinder. However, before applying the conditions to the general solutions, we consider some symmetrical properties of the flow in order to simplify the following calculations.

In the first case where the magnetic field is parallel to the undisturbed velocity, ψ must be an odd function of y, since the components of the perturbed velocity $u(=-\partial\psi/\partial y)$ and $v(=\partial\psi/\partial x)$ must be even and odd functions of y, respectively. This implies that

$$A_n=0 \quad \text{and} \quad C_n=0 \,. \tag{4.1}$$

Further considerations of symmetry with respect to the y-axis also imply that

$$D_n=(-1)^{n+1}B_n \,. \tag{4.2}$$

Then, the radial and the circumferential components of the perturbed velocity (3.15) and (3.16) are rewritten as

$$u_r=k\Big[(e^{kx}-e^{-kx})(B_1-B_0)K_1(kr)$$
$$+\sum_{n=1}^{\infty}\cos n\theta\{e^{kx}+(-1)^{n+1}e^{-kx}\}\{(B_{n+1}-B_n)K_{n+1}(kr)+(B_n-B_{n-1})K_{n-1}(kr)\}\Big] \,, \tag{4.3}$$

and

$$u_\theta=k\Big[\sum_{n=1}^{\infty}\sin n\theta\{e^{kx}+(-1)^{n+1}e^{-kx}\}\{(B_{n+1}-B_n)K_{n+1}(kr)-(B_n-B_{n-1})K_{n-1}(kr)\}\Big] \,, \tag{4.4}$$

respectively.

In the second case where the magnetic field is perpendicular to the undisturbed velocity, the similar considerations of symmetries with respect to the x- and the y-axes also imply that

$$B_n=0 \,, \qquad D_n=0 \,, \tag{4.5}$$

and

$$C_n=(-1)^{n+1}A_n \,, \tag{4.6}$$

respectively. Thus, the components of the perturbed velocity given in (3.15) and (3.16) are reduced to

$$u_r=-k\Big[\sum_{n=1}^{\infty}\sin n\theta\{e^{kx}+(-1)^{n+1}e^{-kx}\}\{(A_{n+1}-A_n)K_{n+1}(kr)+(A_n-A_{n-1})K_{n-1}(kr)\}\Big] \,, \tag{4.7}$$

and

$$u_\theta=k\Big[(e^{kx}-e^{-kx})(A_1-A_0)K_1(kr)$$
$$+\sum_{n=1}^{\infty}\cos n\theta\{e^{kx}+(-1)^{n+1}e^{-kx}\}\{(A_{n+1}-A_n)K_{n+1}(kr)-(A_n-A_{n-1})K_{n-1}(kr)\}\Big] \,, \tag{4.8}$$

respectively.

We now apply the boundary conditions at the surface of the cylinder to (4.3), (4.4) and (4.7), (4.8) in order to determine the constants B_n's and A_n's. The conditions to be satisfied by the perturbed velocity are, in the first case,

$$\boldsymbol{v}'=-\boldsymbol{i}\ , \quad \text{i. e.} \quad \left.\begin{aligned} u_r&=-\cos\theta \\ u_\theta&=\sin\theta \end{aligned}\right\} \text{ at } r=1\ , \tag{4.9}$$

and, in the second case,

$$\boldsymbol{v}'=-\boldsymbol{j}\ , \quad \text{i. e.} \quad \left.\begin{aligned} u_r&=-\sin\theta \\ u_\theta&=-\cos\theta \end{aligned}\right\} \text{ at } r=1\ . \tag{4.10}$$

We shall begin with the first case. Substituting (4.9) into (4.3) and (4.4), and making use of Fourier expansions:

$$\{e^{k\cos\theta}+(-1)^{n+1}e^{-k\cos\theta}\}\cos n\theta=\sum_{m=0}^{\infty}F_{n,m}(k)\cos m\theta\ , \tag{4.11}$$

$$\{e^{k\cos\theta}+(-1)^{n+1}e^{-k\cos\theta}\}\sin n\theta=\sum_{m=1}^{\infty}G_{n,m}(k)\sin m\theta\ , \tag{4.12}$$

we have

$$\begin{aligned} -\cos\theta=k\sum_{m=0}^{\infty}\cos m\theta\Big[&F_{0,m}(k)(B_1-B_0) \\ &+\sum_{n=1}^{\infty}F_{n,m}(k)\{K_{n+1}(k)(B_{n+1}-B_n)+K_{n-1}(k)(B_n-B_{n-1})\}\Big]\ , \end{aligned} \tag{4.13}$$

$$\sin\theta=k\sum_{m=1}^{\infty}\sin m\theta\left[\sum_{n=1}^{\infty}G_{n,m}(k)\{K_{n+1}(k)(B_{n+1}-B_n)-K_{n-1}(k)(B_n-B_{n-1})\}\right]. \tag{4.14}$$

Equating the coefficients of $\cos m\theta$ and $\sin m\theta$ on both sides of these equations, we obtain the following set of equations:

$$0=F_{0,0}(k)K_1(k)(B_1-B_0)+\sum_{n=1}^{\infty}F_{n,0}(k)\{K_{n+1}(k)(B_{n+1}-B_n)+K_{n-1}(k)(B_n-B_{n-1})\}\ , \tag{4.15}$$

$$-\frac{1}{k}=F_{0,1}(k)K_1(k)(B_1-B_0)+\sum_{n=1}^{\infty}F_{n,1}(k)\{K_{n+1}(k)(B_{n+1}-B_n)+K_{n-1}(k)(B_n-B_{n-1})\}\ , \tag{4.16}$$

$$0=F_{0,m}(k)K_1(k)(B_1-B_0)+\sum_{n=1}^{\infty}F_{n,m}(k)\{K_{n+1}(k)(B_{n+1}-B_n)+K_{n-1}(k)(B_n-B_{n-1})\}\ , \quad (m=2,\ 3,\ 4,\ \cdots) \tag{4.17}$$

$$\frac{1}{k}=\sum_{n=1}^{\infty}G_{n,1}(k)\{K_{n+1}(k)(B_{n+1}-B_n)-K_{n-1}(k)(B_n-B_{n-1})\}\ , \tag{4.18}$$

$$0=\sum_{n=1}^{\infty}G_{n,m}(k)\{K_{n+1}(k)(B_{n+1}-B_n)-K_{n-1}(k)(B_n-B_{n-1})\}\ . \quad (m=2,\ 3,\ 4,\ \cdots) \tag{4.19}$$

Since $F_{n,0}(k)$, $F_{n,m}(k)$ and $G_{n,m}(k)$ are expressed as*

$$F_{n,0}(k)=\frac{1}{2\pi}\int_{-\pi}^{\pi}\{e^{k\cos\theta}+(-1)^{n+1}e^{-k\cos\theta}\}\cos n\theta\,d\theta=0\ , \tag{4.20}$$

$$\begin{aligned} F_{n,m}(k)&=\frac{1}{\pi}\int_{-\pi}^{\pi}\{e^{k\cos\theta}+(-1)^{n+1}e^{-k\cos\theta}\}\cos n\theta\cos m\theta\,d\theta \\ &=\begin{cases} 0\ , & (m\text{: even}) \\ 2\{I_{n-m}(k)+I_{n+m}(k)\}\ , & (m\text{: odd}) \end{cases} \end{aligned} \tag{4.21}$$

$$\begin{aligned} G_{n,m}(k)&=\frac{1}{\pi}\int_{-\pi}^{\pi}\{e^{k\cos\theta}+(-1)^{n+1}e^{-k\cos\theta}\}\sin n\theta\sin m\theta\,d\theta \\ &=\begin{cases} 0\ , & (m\text{: even}) \\ 2\{I_{n-m}(k)-I_{n+m}(k)\}\ , & (m\text{: odd}) \end{cases} \end{aligned} \tag{4.22}$$

---

* Here we make use of the fact that when s is any positive integer, the modified Bessel function $I_s(x)$ can be expressed as:

$$I_s(x)=\frac{1}{2\pi}\int_{-\pi}^{\pi}e^{x\cos\theta}\cos s\theta\,d\theta\ ^{3)}\ .$$

it is easily found that all terms in Eqs. (4.15), (4.17) and (4.19) for even m should vanish. Then, Eqs. (4.16)∼(4.19) for odd m will serve as a system of linear algebraic equations for determining the B_n's. In order to facilitate later calculations, we shall now transform this system into more convenient form. Subtracting (4.16) from (4.18) and (4.17) from (4.19) for odd m, and making use of (4.21) and (4.22), we have, after some rearrangements,

$$\beta_{0,2s+1}B_0+\sum_{n=1}^{\infty}\beta_{n,2s+1}B_n=\begin{cases}\dfrac{1}{2k}, & (s=0)\\ 0, & (s=1,\ 2,\ 3,\ \cdots)\end{cases} \tag{4.23}$$

where

$$\beta_{0,2s+1}=I_{2s+1}(k)K_1(k)+I_{2s}(k)K_0(k)\ , \qquad (s=0,\ 1,\ 2,\ \cdots) \tag{4.24}$$

$$\beta_{n,2s+1}=I_{n+2s+1}(k)K_{n+1}(k)-I_{n+2s}(k)K_n(k)+I_{n-2s}(k)K_n(k)-I_{n-2s-1}(k)K_{n-1}(k)\ . \qquad \begin{pmatrix}s=0,\ 1,\ 2,\ \cdots\\ n=1,\ 2,\ 3,\ \cdots\end{pmatrix} \tag{4.25}$$

Similarly, adding (4.16) to (4.18) and (4.17) to (4.19) for odd m, we have

$$\beta'_{0,2s+1}B_0+\sum_{n=1}^{\infty}\beta'_{n,2s+1}B_n=0\ , \qquad (s=0,\ 1,\ 2,\ \cdots) \tag{4.26}$$

where

$$\beta'_{0,2s+1}=I_{2s+1}(k)K_1(k)+I_{2s+2}(k)K_0(k)\ , \qquad (s=0,\ 1,\ 2,\ \cdots) \tag{4.27}$$

$$\beta'_{n,2s+1}=I_{n+2s+2}(k)K_n(k)-I_{n+2s+1}(k)K_{n-1}(k)+I_{n-2s-1}(k)K_{n+1}(k)-I_{n-2s-2}(k)K_n(k)\ . \qquad \begin{pmatrix}s=0,\ 1,\ 2,\ \cdots\\ n=1,\ 2,\ 3,\ \cdots\end{pmatrix} \tag{4.28}$$

Thus, the B_n's can be determined by solving this system of simultaneous linear algebraic equations (4.23) and (4.26).

Next, we shall proceed to the second case. Substituting (4.10) into (4.7) and (4.8), and carrying out calculations similar to those in the first case, we get a system of simultaneous linear algebraic equations for determining the A_n's:

$$\alpha_{0,2s+1}A_0+\sum_{n=1}^{\infty}\alpha_{n,2s+1}A_n=\begin{cases}\dfrac{1}{2k}, & (s=0)\\ 0, & (s=1,\ 2,\ 3,\ \cdots)\end{cases} \tag{4.29}$$

$$\alpha'_{0,2s+1}A_0+\sum_{n=1}^{\infty}\alpha'_{n,2s+1}A_n=0\ , \qquad (s=0,\ 1,\ 2,\ \cdots) \tag{4.30}$$

where

$$\alpha_{0,2s+1}=I_{2s+1}(k)K_1(k)-I_{2s}(k)K_0(k)\ , \qquad (s=0,\ 1,\ 2,\ \cdots) \tag{4.31}$$

$$\alpha_{n,2s+1}=I_{n+2s+1}(k)K_{n+1}(k)-I_{n+2s}(k)K_n(k)-I_{n-2s}(k)K_n(k)+I_{n-2s-1}(k)K_{n-1}(k)\ , \qquad \begin{pmatrix}s=0,\ 1,\ 2,\ \cdots\\ n=1,\ 2,\ 3,\ \cdots\end{pmatrix} \tag{4.32}$$

$$\alpha'_{0,2s+1}=I_{2s+1}(k)K_1(k)-I_{2s+2}(k)K_0(k)\ , \qquad (s=0,\ 1,\ 2,\ \cdots) \tag{4.33}$$

$$\alpha'_{n,2s+1}=I_{n+2s+1}(k)K_{n-1}(k)-I_{n+2s+2}(k)K_n(k)-I_{n-2s-2}(k)K_n(k)+I_{n-2s-1}(k)K_{n+1}(k)\ . \qquad \begin{pmatrix}s=0,\ 1,\ 2,\ \cdots\\ n=1,\ 2,\ 3,\ \cdots\end{pmatrix} \tag{4.34}$$

§ 5. Forces on the Cylinder

Next, we shall calculate the force experienced by the cylinder. The first contribution to this force comes from the viscous stress exerted by the surrounding fluid on the surface of the cylinder, while the second comes from Maxwell's magnetic stress acting on the surface of the cylinder. Let X_1 and X_2 be the components of the force parallel to the x_1-

and x_2-axes acting on the unit axial length of the cylinder. Then we have

$$X_1=\int_C P_{n1}dC+\int_C T_{n1}dC\ , \tag{5.1}$$

and

$$X_2=\int_C P_{n2}dC+\int_C T_{n2}dC\ , \tag{5.2}$$

where dC is the line-element of the contour C of the cylinder and integrations are taken round the contour. P_{n1}, P_{n2} and T_{n1}, T_{n2} are the x_1, x_2-components of the viscous stress and Maxwell's stress acting on the surface of the cylinder, respectively and they are expressed as

$$P_{n1}=\left(-P+2\rho\nu\frac{\partial V_1}{\partial x_1}\right)l+\rho\nu\left(\frac{\partial V_2}{\partial x_1}+\frac{\partial V_1}{\partial x_2}\right)m\ , \tag{5.3}$$

$$P_{n2}=\rho\nu\left(\frac{\partial V_2}{\partial x_1}+\frac{\partial V_1}{\partial x_2}\right)l+\left(-P+2\rho\nu\frac{\partial V_2}{\partial x_2}\right)m\ , \tag{5.4}$$

$$T_{n1}=\mu\left(H_1^2-\frac{1}{2}H^2\right)l+\mu H_1H_2m\ , \tag{5.5}$$

$$T_{n2}=\mu H_1H_2l+\mu\left(H_2^2-\frac{1}{2}H^2\right)m\ , \tag{5.6}$$

where V_1, V_2 and H_1, H_2 are the x_1, x_2-components of the velocity $\boldsymbol{V}$ and the magnetic field $\boldsymbol{H}$ respectively, H the magnitude of $\boldsymbol{H}$ and l, m the direction-cosines of the outward normal to the contour of the cylinder.

Inserting (5.3) and (5.4) into the first integrals in (5.1) and (5.2), we have, after some calculations,

$$\int_C P_{n1}dC=\rho\nu V_0\int_s(-pl-\omega m)ds\ , \tag{5.7}$$

$$\int_C P_{n2}dC=\rho\nu V_0\int_s(\omega l-pm)ds\ , \tag{5.8}$$

where the non-dimensional variables introduced in § 2 have been used and the integrations $\int_s ds$ are now taken round the contour s in the non-dimensional xy-plane corresponding to the contour of the cylinder C in the x_1x_2-plane. Making use of (2.23), (3.2), (3.3), (3.6) and (3.7), we can express the pressure p and the vorticity ω in terms of ψ_1 and ψ_2 as

$$p=-M\frac{\partial}{\partial y}(\psi_1-\psi_2)\ , \tag{5.9}$$

and

$$\omega=M\frac{\partial}{\partial x}(\psi_1-\psi_2)\ , \tag{5.10}$$

respectively. Substitution of (5.9) and (5.10) into (5.7) and (5.8) yields

$$\int_C P_{n1}dC=\rho\nu V_0M\int_s\left\{-\frac{\partial}{\partial x}(\psi_1-\psi_2)m+\frac{\partial}{\partial y}(\psi_1-\psi_2)l\right\}ds=\rho\nu V_0M\int_s\frac{\partial}{\partial s}(\psi_1-\psi_2)ds\ , \tag{5.11}$$

$$\int_C P_{n2}dC=\rho\nu V_0M\int_s\left\{\frac{\partial}{\partial x}(\psi_1-\psi_2)l+\frac{\partial}{\partial y}(\psi_1-\psi_2)m\right\}ds=\rho\nu V_0M\int_s\frac{\partial}{\partial n}(\psi_1-\psi_2)ds\ , \tag{5.12}$$

where $\partial/\partial s$ and $\partial/\partial n$ denote the partial differentiations along the circumferential curve s and the outward normal n to s, respectively. The second integrals in (5.1) and (5.2) are both zero, since $H_1=H_0$ (const) and $H_2=0$, to the present approximation. In order to obtain finite values of the integrals, higher approximation for $\boldsymbol{H}$ should be considered. On the other hand, however, they can be calculated when the electric current and the magnetic field inside the cylinder are given, since they must be transformed into volume integrals of the corresponding components of Lorentz force acting on the cylinder, as

$$\int_C T_{n1} dC = \mu \iint_S (J_2 H_3 - J_3 H_2) dS \,, \tag{5.13}$$

$$\int_C T_{n2} dC = \mu \iint_S (J_3 H_1 - J_1 H_3) dS \,, \tag{5.14}$$

where J_1, J_2 and J_3 are the x_1, x_2 and x_3-components of the current density $\boldsymbol{J}$ and the integrations $\iint_S dS$ should be taken over the cross-sectional area of the cylinder. Since $H_1 = H_0$ and $H_2 = H_3 = 0$ to the present approximation, the integral on the right-hand side of (5.13) is zero and (5.14) is reduced to

$$\int_C T_{n2} dC = \mu \iint_S J_3 H_0 dS \,. \tag{5.15}$$

Consideration of the symmetry of the flow in the present problem yields $X_2 = 0$ in the first case and $X_1 = 0$ in the second case. Hence, no lift appears in both cases.

The drag D^{I} in the first case is then expressed as

$$D^{\mathrm{I}} = \rho \nu V_0 M \int_s \frac{\partial}{\partial s} (\psi_1 - \psi_2) ds \,. \tag{5.16}$$

The only contributions to the above integral will arise from multivalued solutions in ψ_1 and ψ_2. Considering (3.11), (3.12), (3.13) and (3.14), we can readily evaluate the integral, obtaining

$$D^{\mathrm{I}} = 4\pi \rho \nu V_0 M B_0 \,. \tag{5.17}$$

The drag D^{II} in the second case is expressed as

$$D^{\mathrm{II}} = \rho \nu V_0 M \int_s \frac{\partial}{\partial n} (\psi_1 - \psi_2) ds + \mu \iint_S J_3 H_0 dS \,. \tag{5.18}$$

Bearing the boundary condition (4.10) in mind, the above first integral is transformed into a simpler form as:

$$\begin{aligned} \int_s \frac{\partial}{\partial n} (\psi_1 - \psi_2) ds &= \int_s \left\{ -\frac{\partial}{\partial n} (\psi_1 + \psi_2) + 2 \frac{\partial \psi_1}{\partial n} \right\} ds = \int_0^{2\pi} (-u_\theta)_{r=1} d\theta + 2 \int_0^{2\pi} \left(\frac{\partial \psi_1}{\partial r} \right)_{r=1} d\theta \\ &= 2 \int_0^{2\pi} \left(\frac{\partial \psi_1}{\partial r} \right)_{r=1} d\theta \,. \end{aligned} \tag{5.19}$$

Making use of the relation given in the footnote in §4, this can be evaluated, giving

$$2 \int_0^{2\pi} \left(\frac{\partial \psi_1}{\partial r} \right)_{r=1} d\theta = 4\pi k \{ A_0 (I_1 K_0 - I_0 K_1) + \sum_{n=1}^{\infty} A_n (I_{n+1} K_n - I_n K_{n-1} - I_n K_{n+1} + I_{n-1} K_n) \,, \tag{5.20}$$

where the argument $k = M/2$ of the functions I_n and K_n is omitted for brevity.

Next, we shall calculate the second integral in (5.18). Since, as was shown in §2, there exists the constant electric field $E_3 = \mu V_0 H_0$ in the second case, constant current density $J_3 = \sigma^* \mu V_0 H_0$ must appear inside the cylinder, where σ^* is the electric conductivity of the cylinder. Then, we can easily evaluate the integral, obtaining

$$\mu \iint_S J_3 H_0 dS = \pi a^2 \sigma^* \mu^2 V_0 H_0^2 = \rho \nu V_0 \pi \left(\frac{\sigma^*}{\sigma} \right) M^2 \,. \tag{5.21}$$

Substituting (5.20) and (5.21) into (5.18), we have

$$\begin{aligned} D^{\mathrm{II}} = 4\pi \rho \nu V_0 \Big[& \frac{1}{2} M^2 \{ A_0 (I_1 K_0 - I_0 K_1) \} \\ & + \sum_{n=1}^{\infty} A_n (I_{n+1} K_n - I_n K_{n-1} - I_n K_{n+1} + I_{n-1} K_n) + \frac{1}{4} \left(\frac{\sigma^*}{\sigma} \right) M^2 \Big] \,. \end{aligned} \tag{5.22}$$

Thus, we have obtained the expressions for the drag (5.17) in the first case and (5.22) in the second case, respectively. We have now only to calculate B_0 by (4.23) and (4.26), and the A_n's by (4.29) and (4.30), respectively. For small values of M, B_0 and the A_n's are obtained to the order of M as follows:

$$B_0=\frac{2}{M(2\Omega+1)}\left\{1-\frac{4\Omega+1}{2\Omega+1}\left(\frac{M}{4}\right)^2+O(M^4)\right\}, \tag{5.23}$$

$$A_0=-\frac{2}{M(2\Omega-1)}\left\{1-\frac{8\Omega+1}{2\Omega-1}\left(\frac{M}{4}\right)^2+O(M^4)\right\}, \tag{5.24}$$

$$A_1=\frac{2}{M(2\Omega-1)}\left\{\left(\frac{M}{4}\right)^2+O(M^4)\right\}, \tag{5.25}$$

where $\Omega=-\{\gamma+\ln(M/4)\}$, $\gamma=0.57721\cdots$ being Euler's constant. The drag coefficients $C_{D^{\mathrm{I}}}=D^{\mathrm{I}}/\rho\nu V_0$ and $C_{D^{\mathrm{II}}}=D^{\mathrm{II}}/\rho\nu V_0$ are given to the order of M^2 by

$$C_{D^{\mathrm{I}}}=\frac{8\pi}{2\Omega+1}\left\{1-\frac{4\Omega+1}{2\Omega+1}\left(\frac{M}{4}\right)^2+O(M^4)\right\}, \tag{5.26}$$

and

$$C_{D^{\mathrm{II}}}=\frac{8\pi}{2\Omega-1}\left\{1-\frac{8\Omega^2+4\Omega+1-2(2\Omega-1)^2(\sigma^*/\sigma)}{2\Omega-1}\left(\frac{M}{4}\right)^2+O(M^4)\right\}, \tag{5.27}$$

respectively.

Table I. Drag coefficients *versus* Hartmann numbers

M	$C_{D^{\mathrm{I}}}$	$C_{D^{\mathrm{II}}}(\sigma^*/\sigma=0)$	$C_{D^{\mathrm{II}}}(\sigma^*/\sigma=1/2)$	$C_{D^{\mathrm{II}}}(\sigma^*/\sigma=1)$	$C_{D^{\mathrm{II}}}(\sigma^*/\sigma=2)$
0	0	0	0	0	0
0.001	1.53	1.74	1.74	1.74	1.74
0.005	1.90	2.24	2.24	2.24	2.24
0.01	2.12	2.56	2.56	2.56	2.56
0.05	2.92	3.79	3.79	3.80	3.81
0.1	3.48	4.76	4.78	4.79	4.82
0.5	6.10	—	—	—	—
1.0	8.63	—	—	—	—

Numerical values of $C_{D^{\mathrm{I}}}$ and $C_{D^{\mathrm{II}}}$ for various values of M and σ^*/σ have been computed by (5.26) and (5.27), respectively. They are tabulated in Table I and are shown graphically in Fig. 2. It will be seen that the drag is always greater in the second case than in the first case for the same values of M.

§ 6. Conclusion

We have considered the flow of a viscous and electrically conducting fluid past a circular cylinder in a uniform magnetic field. Analysis has been carried out in the limiting case where both the Reynolds number R and the magnetic Reynolds number R_m vanish, while the pressure number S is infinite so that the Hartmann number M is finite. It is worth noticing that appropriate solutions can be obtained for the two-dimensional flow past a circular cylinder in the present case in spite of $R=0$, for

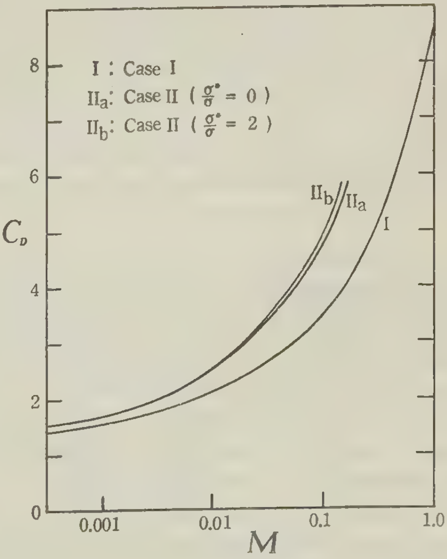

Fig. 2. Drag coefficients *versus* Hartmann number.

which no reasonable solution can be obtained in the classical case.

It will be expected that the present analysis can be generalized for the flow passing across a uniform magnetic field obliquely. Inspecting the linearized equations for the present problem, (2.23) and (2.24), and the boundary conditions at the surface of the cylinder, (4.9) and (4.10), an appropriate linear combination of the present solutions in the first and the second cases will yield the solution for such flow.

For a flow at finite Reynolds and magnetic Reynolds numbers, with finite pressure number, a new method of solution should be devised, which will be discussed in another paper to be published in a near future.

Acknowledgement

In conclusion, the writers wish to express their cordial thanks to Professor S. Tomotika for his continual guidance and encouragement, and especially for his kind inspection of the manuscript.

References

1) W. Chester: J. Fluid Mech. **3** (1957) 304.
2) L. N. G. Filon: Proc. Roy. Soc. **A**, **113** (1927) 7.
3) G. N. Watson: *Theory of Bessel Functions*, 2nd ed. (Cambridge, 1948) 181.

JOURNAL OF THE PHYSICAL SOCIETY OF JAPAN, Vol. 14, No. 10, OCTOBER, 1959

Statistical Aspects of Fracture in Concrete, I.

An Analysis of Flexural Failure of Portland Cement Mortar from the Standpoint of Stochastic Theory

By Motoo HORI

Central Research Laboratory, Onoda Cement Co., Ltd., Tokyo, Japan

(Received June 5, 1959)

An application of the theory of stochastic processes to the static fracture of non-homogeneous brittle materials such as portland cement concrete is presented. A large number of flexural failure tests on standard mortar specimens made in accordance with JIS have been performed under constant loads as well as under uniformly increasing loads, and the results are analyzed statistically from the standpoint of stochastic theory. It is concluded that the scatter observed in the breaking time or the static strength of concrete appears to be a result of inherent characteristics of the material itself associated with a Markoff process as a kind of rate process.

§ 1. Introduction

It is well known that the results of mechanical strength tests on solid materials generally show a remarkable scatter even under assumably identical conditions. Recent studies indicate that most of the observed scatter cannot necessarily be attributed to the impropriety of testing techniques or the inhomogeneity of test specimens, but must rather be considered as due to inherent characteristics of the material itself. In fact, it appears that the phenomenon of rupture in solids may be usually interpreted as a kind of Markoff process from the standpoint of stochastic theory. The theory of stochastic processes was first applied to the brittle fracture of glass by M. Hirata[1),2)], and then extended to various types of failure of polycrystalline metals and polymeric substances by T. Yokobori[3)] and B. D. Coleman[4)] respectively. This theory accounts not only for the structure sensitivity of mechanical breakdown, but also for its time dependence, in contrast to the classical extreme-value theories based on the weakest-link concept[5].

In non-homogeneous brittle materials, such as portland cement concrete, however, the stochastic-process model for fracture has not yet been applied, since the essential fluctuations associated with a Markoff process cannot easily be distinguished from the statistical variations caused by the macroscopic heterogeneity of test pieces. In order to verify the applicability of the stochastic theory to the static fracture of concrete, therefore, a large number of flexural failure tests on the standard mortar specimens as specified in JIS R 5201–1956 have been carried out under a series of sustained loads, as well as under loads increasing at a uniform rate used in the conventional strength test.

§ 2. Test Specimens

Test specimens were prepared in accordance with the Japanese Industrial Standard on "the Physical Testing Method of Cement" (JIS R 5201–1956) with some modifications as below. Extreme care was taken to reduce the apparent dispersion of test results due to non-uniformity of the specimens as much as possible.

(i) *Materials used.* Cement: Ordinary portland cement (Onoda Cement Co., Ltd.). Aggregate: Standard sand from Toyoura district.

(ii) *Mix proportion.* Water-cement ratio by weight 0.55. Cement-sand ratio by weight 1 : 2. Flow 195 mm.

(iii) *Type of specimens.* Prisms with the dimensions of 40×40×160 mm.

(iv) *Number of specimens.* At least about 100 specimens from three batches of mortar.

(v) *Mixing.* By means of a concrete mixer.

(vi) *Molding.* Two layers of mortar in molds, each layer compacted with 15 strokes by a tamping rod.

(vii) *Capping and demolding.* 8 and 24 hours after molding.

(viii) *Curing.* 24 hours in moist air, and subsequently, 27 days in lime-saturated water.

(ix) *Temperature and humidity.* Temperature: 20±1°C. Relative humidity: Not less than 80 and 90 per cent in the testing room and the moist air, respectively.

§ 3. Testing Procedure and Equipments

As preliminary experiments for checking the homogeneity of the specimens prepared, structure-insensitive mechanical properties, such as density and modulus of elasticity, were measured prior to rupture tests. Bulk density was determined within ±0.5 per cent by weighing. Dynamic modulus of elasticity was determined by using the so-called sonic resonance tests, namely, by measuring the fundumental flexural resonant frequency with a frequency monitor accurate to ±2 per cent, in accordance with "the Tentative Method of Test for Fundumental Transverse, Longitudinal, and Torsional Frequencies of Concrete Specimens" (ASTM C 215–58 T).

The flexural failure tests were carried out carefully by means of a bending strength tester of Michaelis double lever type as described in JIS R 5201–1956, which applied the load at the center point of a 10-cm span. In the conventional static strength measurements, the loading was adjusted strictly to the specified rate of 5 kg per second, corresponding to the increase in extreme-fiber stress of 1.17 kg/cm² per second. In the sustained loading experiments, the load was applied as quickly as possible without producing vibra-

Table I. Number of the specimens tested.

Loading condition	Bulk density	Dynamic modulus of elasticity	Static flexural strength	Breaking time under constant load
I (1.17 kg/cm²/sec)	116	116	116	0
II 60.0 kg/cm²	97	97	20	77
III 62.0 kg/cm²	116	116	18	98
IV 66.1 kg/cm²	116	116	16	100
V 67.5 kg/cm²	97	97	12	85
VI 71.5 kg/cm²	113	32	18	95
VII 75.7 kg/cm²	111	111	18	93
Total	766	685	218	548

tion, and then the time required for fracture under the constant load was measured with a stop-watch.

Seven series of flexure tests were conducted under different loading conditions, using more than some 100 specimens for each series. In the first series, the conventional flexural strength was measured at the specified rate of loading on a total of 116 test specimens. In each of other six series, however, most of the specimens were tested under the constant load, except about 10 to 20 specimens randomly selected for the conventional strength measurements. These series of sustained loading experiments were performed at the extreme-fiber stresses of 60.0, 62.0, 66.1, 67.5, 71.5 and 75.7 kg/cm² respectively. (See Table I.)

§ 4. Results of Preliminary Tests

The results of preliminary tests on the bulk density and the dynamic modulus of elasticity are presented in Table II, which gives the coefficient of variation within the limits of instrumental error. It is shown, therefore, that all the specimens tested may be regarded as practically uniform, so far as the structure-insensitive properties are concerned.

Table II. Results of preliminary tests.

	Bulk density	Dynamic modulus of elasticity
Number of specimens	766	685
Mean	2.16 g/cm³	2.79×10^5 kg/cm²
Standard deviation	6.8×10^{-3} g/cm³	5.3×10^3 kg/cm²
Coefficient of variation	0.32%	1.9%

The test results for the static flexural strength are summarized in Table III. The analysis of variance confirms that the variation in the average strengths for different series is not significant at the confidence level of 95 per cent, and consequently, that all the samples can be considered as having been drawn at random from a normal population. In fact, the frequency distribution of the flexural strength as a whole is approximately normal, as may be seen from the histogram in Fig. 1. The coefficient of variation is estimated at about 5.3 per cent, much greater than for the density or the modulus of elasticity, but rather small considering the structure sensitivity of the fracture process.

Table III. Test results for the static flexural strength.

Series	Number of test specimens	Average strength (kg/cm²)	Standard deviation (kg/cm²)	Coefficient of variation (%)
I	116	71.7	3.9	5.4
II	20	70.7	3.5	5.0
III	18	69.9	3.3	4.8
IV	16	69.6	4.5	6.5
V	12	71.2	2.7	3.8
VI	18	71.5	3.5	4.9
VII	18	72.1	3.6	5.0
Total	218	71.3	3.8	5.3

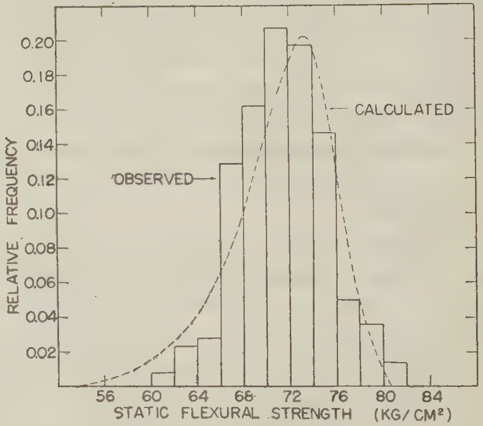

Fig. 1. Frequency histogram of the static flexural strength.

Table IV. Comparative data for the strongest and the weakest specimens.

	Specimen	Flexural strength (kg/cm²)	Bulk density (g/cm³)	Dynamic modulus of elasticity (10^5kg/cm²)
Strongest	S—I	80.9	2.16	2.81
	S—II	80.5	2.15	2.73
	S—III	80.3	2.15	2.79
	Mean	80.6	2.15	2.78
Weakest	W—III	62.1	2.17	2.84
	W—II	61.8	2.16	2.77
	W—I	60.5	2.15	2.79
	Mean	61.5	2.16	2.80

Furthermore, the regression analysis indicates that none of the correlations of the static strength with the density and the modulus of elasticity are significant at the confidence level of 95 per cent. As shown in Table IV, for example, no significant difference can be detected even between the structure-insensitive quantities measured on the strongest and the weakest specimens. This fact may also be taken as an indirect evidence that the homogeneity of the specimens used was quite satisfactory.

§ 5. Results of Sustained Loading Tests

It should be noticed that all the specimens tested under a constant load will not break at the same time, but there will be a characteristic distribution of breaking times. The results of sustained loading experiments actually show that the scatter of the delayed time for fracture under constant loads is much wider than that of the static strength, and that the frequency distribution is too positively skewed to be considered as normal.

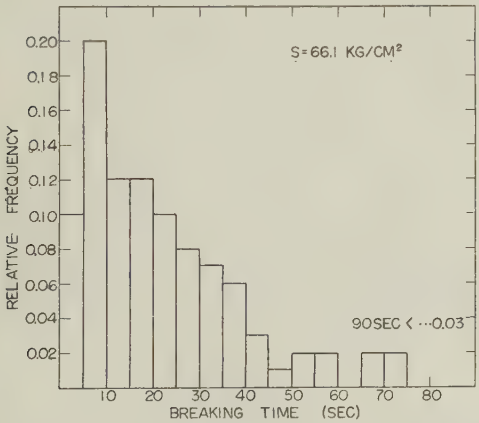

Fig. 2. Typical frequency histogram of the breaking time under a constant load.

As a typical example, the frequency histogram for the breaking times at the extreme-fiber stress of 66.1 kg/cm² is illustrated in Fig. 2. The distribution curves of breaking times under various constant loads are about the same in general trend, although the average time or the most probable time decreases rapidly with increasing load.

§ 6. Application of the Stochastic-Process Theory

The problems on the initiation of fracture appear to be explained in terms of a Markoff process. Let us take this approach in the present case, adopting the instant of load application as the origin of time t. If the transition probability of fracture, $\mu(t)dt$, is defined as the probability that a specimen known to be unbroken at a time t will break in the next time interval dt, then

$$\mu(t)dt = = -\frac{dP(t)}{P(t)} = -d\{\log P(t)\}\ , \qquad (1)$$

where $P(t)$ denotes the probability that the fracture has not yet occurred at time t, that is, the cumulative distribution function of survival. On integrating Eq. (1), we obtain

$$P(t) = \exp\left\{-\int_0^t \mu(t)dt\right\}\ . \qquad (2)$$

The probability density function of the breaking time can be written as

$$q(t) = -\frac{dP(t)}{dt} = \mu(t)\exp\left\{-\int_0^t \mu(t)dt\right\}\ . \qquad (3)$$

Hence, the mode t_m, the mean $\bar{t}$, and the variance σ_t^2 are given by

$$\left.\frac{d\mu(t)}{dt}\right|_{t=tm} = \mu^2(t_m)\ , \qquad (4)$$

$$\bar{t} = \int_0^\infty tq(t)dt = \int_0^\infty P(t)dt\ , \qquad (5)$$

$$\sigma_t^2 = \int_0^\infty t^2q(t)dt - \left\{\int_0^\infty tq(t)dt\right\}^2\ . \qquad (6)$$

In actual failure tests, the probability functions defined above may be directly determined from the observed histogram of breaking times. We shall now consider an ensemble of the specimens used in each experiment, and denote the number of specimens that survive without breaking to time t by $n(t)$. If the initial size of the ensemble N is very large, $n(t)$ will be related to $P(t)$ by

$$P(t) = \frac{1}{N}n(t)\ , \qquad (7)$$

with fluctuations that become negligible as N approaches infinity. On the other hand, if we consider a finite set of test specimens, the probability $P_n(t)$ that at a given time t there are n unbroken specimens left in our sample is obviously

$$P_n(t) = \frac{N!}{n!\,(N-n)!}P^n(t)\{1-P(t)\}^{N-n}\ . \qquad (8)$$

The average number of survivors at a given time is therefore

$$\bar{n}(t)=\sum_{n=N}^{0} nP_n(t)=NP(t) \,, \tag{9}$$

with a variance

$$\sigma_n{}^2(t)=\sum_{n=N}^{0}(n-\bar{n})^2P_n(t)=NP(t)\{1-P(t)\} \,. \tag{10}$$

These equations confirm that if one replace $n(t)$ by its average value $\bar{n}(t)$ Eq. (7) is vaild even for finite N, and that the coefficient of variation in $n(t)$ goes to zero with increasing N as $N^{-1/2}$.

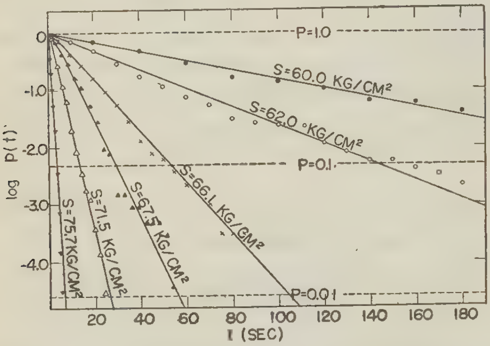

Fig. 3. Time dependence of the cumulative distribution function of survival.

When $P(t)$ is calculated in this way from the actual results of our sustained loading tests, the semi-logarithmic plot of $P(t)$ *versus* t for each stress may be represented fairly well by a straight line except some initial deviations, as shown in Fig. 3. The negative tangent of this line gives the transition probability density $\mu(t)$, which is thus found to be almost constant under a sustained load. Putting $\mu(t)=m$, Eqs. (2) and (3) reduce to

$$P(t)=\exp(-mt) \,, \tag{11}$$

$$q(t)=m\exp(-mt) \,, \tag{12}$$

which express a monotonously decreasing distribution with the mean of $1/m$. The initial discrepancy between the ideal distribution (12) and the observed histogram as in Fig. 2 indicates that the time lag required for $\mu(t)$ to reach its final value m is not strictly negligible. Supposing that $\mu(t)$ approaches m with a retardation time of τ, and putting $\mu(t)=m(1-e^{-t/\tau})$, one gets

$$P(t)=\exp[-m\{t-\tau(1-e^{-t/\tau})]\} \,, \tag{13}$$

$$q(t)=m(1-e^{-t/\tau})\exp[-m\{t-\tau(1-e^{-t/\tau})\}] \,. \tag{14}$$

From these considerations, it follows that the theory of stochastic processes can at least approximately be applied to the static failure of such heterogeneous materials as protland cement mortar. Since the static fracture of concrete accompanies necessarily somewhat plastic deformations in contrast with the purely brittle fracture of glass, however, the apparent time dependence of the transition probability density should be considered especially in the initial stage. It is accordingly suggested that the rupture phenomenon of inhomogeneous concrete may not be accurately described as a single process, but rather as two successive events of the formation and growth of critical cracks. If the transition probability densities of these two processes are assumed to be maintained constant in time and denoted by m_1 and m_2, the whole fracture process will be determined by

$$P(t)=\frac{1}{m_2-m_1}\{m_2\exp(-m_1t)-m_1\exp(-m_2t)\} \,, \tag{15}$$

$$q(t)=\frac{m_1m_2}{m_2-m_1}\{\exp(-m_1t)-\exp(-m_2t)\} \,, \tag{16}$$

which are in qualitative agreement with the observed distribution.

§ 7. Relationship of the Transition Probability to Loading Conditions

As illustrated in Fig. 3, it appears that the transition probability for fracture is in general closely related to the applied load. The final value of the transition probability density m is plotted against the applied extreme-fiber stress S in Fig. 4, which shows a roughly linear relationship of $\log m$ to S or $\log S$. Consequently, following two types of empirical formulae are obtained.

$$m=A\exp(\alpha S) \,, \tag{17a}$$

$$m=BS^{\beta} \,. \tag{17b}$$

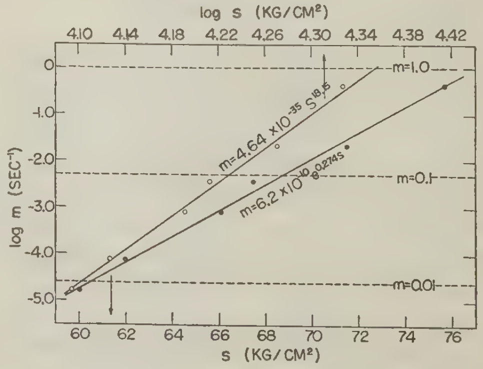

Fig. 4. Transition probability density for fracture plotted against applied extreme-fiber stress.

Here A, α, B, and β are parameters independent of S and in the present case $A=6.2\times10^{-10}$ (sec^{-1}), $\alpha=0.274$ (cm^2/kg), $B=4.64\times10^{-35}$[(cm^2/kg)$^\beta$/sec], and $\beta=18.15$. These two equations produce practically equivalent results over a considerable range of m. The first type can be directly predicted from a simplified theory of absolute reaction rates and has been approximately verified by recent experiments on various materials[1),3),6),7),8)]. The second type has the advantage that it leads to differential equations that are easier to handle than those derived from the first type.

Since the stress distribution within a real specimen is neither macroscopically nor microscopically uniform, the transition probability density of fracture must be defined in any volume element of the material. The weakest-link hypothesis permits us to derive a general superposition principle for calculating the transition probability for the whole volume of the specimen under consideration. This hypothesis states that the probability, $P(t)$, that a specimen composed of N elements has not yet broken at time t is equal to the probability that any element of the specimen has not yet broken at time t, that is to say,

$$P(t)=\prod_{n=1}^{N} P_n(t)\ , \tag{18}$$

where $P_n(t)$ is the probability that the n-th element has a lifetime greater than t. Insertion of Eq. (18) into Eq. (1) thus yields a superposition formula relating to transition probabilities as follows.

$$\mu(t)=\sum_{n=1}^{N} \mu_n(t)\ . \tag{18$'$}$$

Accordingly, the overall transition probability for the specimen under distributed stresses will be written in the integral form

$$\mu(t)\cong m=\iiint_V \rho(S)dV\ , \tag{19}$$

where V represents the loaded volume of the specimen. In analogy to Eq. (17b), for example,

$$m=\frac{B'}{V}\iiint_V S^\beta dV\ , \tag{19$'$}$$

where B' is a constant regardless of S. Equation (19) gives a mathematical expression of the so-called size effect of strength, implying that the breaking probability increases as the specimen volume increases.

As an example, we shall compare the breaking probabilities in tension and bending tests. While a macroscopically uniform distribution of uniaxial tensile stresses is realized in tension tests, a linear distribution of tensile and compressive stresses is induced by a bending moment in flexure tests. The transition probability for rupture under the uniform tensile stress $S=S_0$, m_t, is given by

$$m_t=\frac{B'}{V}\iiint_V S^\beta dV=B'S_0{}^\beta\ . \tag{20}$$

On the other hand, for a rectangular beam with a breadth of $2b$, a height of $2h$, and a span length of $2l$ subjected to pure bending, it is readily seen that the stress variation across a cross section becomes $S=S_0(x/h)$, where S_0 is the maximum tensile stress on the extreme fiber and x is the distance from the neutral axis. Substitution of this stress function into Eq. (19$'$) yields

$$\begin{aligned} m_b&=\frac{B'}{8bhl}\cdot 2b\cdot 2l\cdot S_0{}^\beta\int_0^h \frac{x^\beta}{h^\beta}dx\\ &=\frac{B'S_0{}^\beta}{2(\beta+1)}\ . \end{aligned} \tag{21}$$

Hence,

$$\frac{m_b}{m_t}=\frac{B_b}{B_t}=\frac{\bar{t}_t}{\bar{t}_b}=\frac{1}{2(\beta+1)}\ . \tag{22}$$

In the case of $\beta=18.15$, $\bar{t}_b/\bar{t}_t=38.3$. It has long been recognized that the breaking time or the fracture strength is much greater in bending than in tension.

In addition, Eqs. (17) suggest that the phenomenon of stress relaxation in viscoelastic substances also results in the time-dependent behavior of the transition probability discussed in the preceding section. Let us now for simplicity use a three-element Maxwell model, consisting of an elastic spring of modulus E_1 linked in parallel with a Maxwell unit, in which another spring of modulus E_2 is connected in series with a Newtonian dashpot of viscosity η. Then, the stress acting on the pure-spring element E_1 under a total load S_0 varies with time according to

$$S=S_0\left\{1-a\exp\left(-\frac{t}{\tau}\right)\right\}\ , \tag{23}$$

where $a=E_2/(E_1+E_2)$ and $\tau=\eta(E_1+E_2)/(E_1\cdot E_2)$. By substituting Eq. (23) into Eq. (17b) and taking $m_0=BS_0{}^\beta$, we get

$$m = BS^{\beta} = m_0\left\{1 - a\exp\left(-\frac{t}{\tau}\right)\right\}^{\beta}, \qquad (24)$$

which is found to give a frequency distribution of breaking times qualitatively similar to Eq. (14). It is natural to expect that the time constant of breaking probability is of the same order of magnitude as that of viscoelasticity.

§ 8. Considerations as a Rate Process

The rupture phenomenon usually seems to be understood as a kind of rate process associated with the nucleation or the propagation of critical cracks from a microscopic point of view[3),8),9),10),11)]. The theory of absolute reaction rates as developed originally by H. Eyring[12)] leads to

$$I = \frac{ZkT}{h}\exp\left\{-\frac{F(S)}{kT}\right\}, \qquad (25)$$

for the rate of a stress-dependent rate process, which corresponds to the transition probability density introduced above, $\mu(t)$, for the breaking process. Here Z is the number of atoms available for the reaction, $F(S)$ is the free energy of activation, T is the absolute temperature, k is Boltzmann's constant, and h is Planck's constant. Replacing $F(S)$ by a Taylor's expansion about $S=0$ and neglecting all terms after the second, or assuming $F(S) = F_0 - \alpha' S$, we can write

$$I = \frac{ZkT}{h}e^{-F_0/kT}\exp\left(\frac{\alpha'}{kT}S\right). \qquad (25')$$

It thus turns out that the theoretical rate equation gives as a first approximation an apparently identical expression with the empirical formula (17a). Without taking account of the effects of stress-concentrating flaws and stress relaxation, however, the experimental values of the activation free energy obtained from Eq. (17a) are not necessarily consistent with its molecular interpretation[8)].

The theory of rate processes provides a reasonable explanation for the marked dependence of the breaking time on temperature and humidity. The rate equation (25) points out that the rate of fracture should increase rapidly with increasing temperature, provided that the free energy of activation does not depend significantly upon temperature. On the contrary, the effects of moisture adsorption are generally thought to reduce the activation free energy for fracture[2),6)], so that the breaking probability would become small at high temperature because of the evaporation of adsorbed water. As a consequence, the fracture strength of glass reaches a minimum at a temperature of about 200°C[2),13),14)]. In the case of concrete containing a considerable amount of water, it might be expected that the breaking time would vary in a more complicated manner with the temperature and humidity of surrounding medium. In practice, experimental observations have shown that the flexural strength of concrete has a relatively high value in dry atmosphere or at low temperature.

§ 9. Statistical Interpretation of the Static Strength

In this section, the conventional static strength in a constant rate of loading experiment will be analyzed from the standpoint of the theory of stochastic processes. Denoting the rate of loading as v, we have

$$\mu[S(t), t] \cong m[S(t)] = m(vt), \qquad (26)$$

where the time dependence of the transition probability under a constant load is neglected. Therefore, Eqs. (2) and (3) reduce to

$$P'(S) = \exp\left\{-\frac{1}{v}\int_0^S m(S)dS\right\}, \qquad (27)$$

$$q'(S) = \frac{1}{v}m(S)\exp\left\{-\frac{1}{v}\int_0^S m(S)dS\right\}. \qquad (28)$$

The mode S_m, the mean $\bar{S}$, and the variance $\sigma_S{}^2$ are given by

$$v\frac{dm(S)}{dS}\bigg|_{S=S_m} = m^2(S_m), \qquad (29)$$

$$\bar{S} = \int_0^\infty Sq'(S)dS = \int_0^\infty P'(S)dS, \qquad (30)$$

$$\sigma_S{}^2 = \int_0^\infty S^2 q'(S)dS - \left\{\int_0^\infty Sq'(S)dS\right\}^2. \qquad (31)$$

These equations can be used to predict the results of a static strength measurement from a knowledge of the functional form of $m(S)$ obtained by the dead loading experiment. According to Eq. (17a),

$$P'(S) = \exp\left\{-\frac{A}{\alpha v}(e^{\alpha S} - 1)\right\}, \qquad (27a)$$

$$q'(S) = \frac{A}{v}\exp\left\{\alpha S - \frac{A}{\alpha v}(e^{\alpha S} - 1)\right\}, \qquad (28a)$$

$$S_m = \frac{1}{\alpha}\log\left(\frac{\alpha v}{A}\right), \qquad (29a)$$

$$\bar{S}=\frac{1}{\alpha}e^{A/\alpha v}\int_{A/\alpha v}^{\infty}e^{-x}\frac{dx}{x}=\frac{1}{\alpha}\left\{\log\left(\frac{\alpha v}{A}\right)+\int_{A/\alpha v}^{\infty}\log x\cdot e^{-x}dx\right\}, \tag{30a}$$

$$\sigma_S{}^2=\frac{1}{\alpha^2}e^{A/\alpha v}\left[\int_{A/\alpha v}^{\infty}(\log x)^2e^{-x}dx-e^{A/\alpha v}\left\{\int_{A/\alpha v}^{\infty}\log x\cdot e^{-x}dx\right\}^2\right]. \tag{31a}$$

For large values of $\alpha v/A$, Eqs. (30a) and (31a) become nearly

$$\bar{S}\cong\frac{1}{\alpha}\left\{\log\left(\frac{\alpha v}{A}\right)-\gamma\right\}, \tag{30a$'$}$$

$$\sigma_S{}^2\cong\frac{\pi^2}{6\alpha^2}. \tag{31a$'$}$$

Here γ is Euler's constant $(0.5772\cdots)$. According to Eq. (17b),

$$P'(S)=\exp\left\{-\frac{BS^{\beta+1}}{(\beta+1)v}\right\}, \tag{27b}$$

$$q'(S)=\frac{BS^{\beta}}{v}\exp\left\{-\frac{BS^{\beta+1}}{(\beta+1)v}\right\}, \tag{28b}$$

$$S_m=\left(\frac{\beta v}{B}\right)^{1/(\beta+1)}, \tag{29b}$$

$$\bar{S}=\Gamma\left(\frac{\beta+2}{\beta+1}\right)\left\{\frac{(\beta+1)v}{B}\right\}^{1/(\beta+1)}, \tag{30b}$$

$$\sigma_S{}^2=\left\{\Gamma\left(\frac{\beta+3}{\beta+1}\right)-\Gamma^2\left(\frac{\beta+2}{\beta+1}\right)\right\}\left\{\frac{(\beta+1)v}{B}\right\}^{2/(\beta+1)}, \tag{31b}$$

where Γ denotes the gamma function.

The numerical values of two parameters in Eq. (17a), $A=6.2\times10^{-10}$ (see^{-1}) and $\alpha=0.274$ (cm^2/kg), which were determined from the results of dead-loading flexure tests, were inserted into Eq. (28a) to obtain the theoretical distribution curve of the static flexural strength at the specified rate of loading $v=1.17$ (kg/cm^2/sec), shown in Fig. 1. Inspection of Fig. 1 indicates that the agreement between theory and experiment for the strength distribution is fairly good. As a matter of fact, the average value $\bar{S}=71.1$ (kg/cm^2) and the standard deviation $\sigma_S=4.7$ (kg/cm^2) for the predicted distribution are in satisfactory agreement with those for the observed histogram. (See Table III.). Although the negative skewness of the theoretical curve, $k=-1.14$, seems inconsistent with approximate normality of the experimental distribution, this discrepancy is probably due to the initial time dependence of the transition probability density $\mu(t)$. Consequently, it follows that most of the statistical variations in the results of static strength tests on concrete may be regarded as essential fluctuations associated with a stochastic process.

It is worth while to note that the dynamic theory of stochastic processes is equivalent to the static theory of extreme-value statistics based upon the weakest-link concept, as far as the static behavior of strength is concerned. It is evident that the distribution function of the static strength (27) is compatible with the weakest-link hypothesis (18) regardless of the functional form of $\mu(t)$ or $m(S)$. In addition, Eqs. (27a) and (27b) are identical in form to the first (exponential-type) and the third (Weibull-type) asymptotic distributions for the smallest values in extreme-value statistics respectively[15]. This implies that all the conclusions that J. Tucker[16] derived previously by applying W. Weibull's theory[17] to concrete must also be drawn from the standpoint of the present theory.

The stochastic-process theory permits a successful interpretation of the dependence of the observed strength on testing speed, sample size, stress distribution, temperature, humidity, and other influencing factors. For example, there exists considerable experimental evidence[18] to Eq. (29a) showing that the strength of concrete increases logarithmically with the rate of loading. Weibull's formula[17] in regard to the size effect of strength, $S_m\propto V^{-1/(\beta+1)}$, can be obtained immediately by noting that the parameter B in Eq. (29b) is proportional to the volume of the specimen V. For the ratio of the flexural strength S_{mb} to the tensile strength S_{mt}, Eqs. (29b) and (22) yield $S_{mb}/S_{mt}=(B_t/B_b)^{1/(\beta+1)}=(2\beta+2)^{1/(\beta+1)}$. The numerical value of $S_{mb}/S_{mt}=1.21$ for $\beta=18.15$ turns out to be somewhat too small compared with the experimental data[19], probably because this treatment ignores the presence of plastic deformations in concrete. The effects of temperature and humidity on the static strength of concrete will be discussed quantitatively in a future publication.

§ 10. Conclusions

The results of flexural failure tests on the standard mortar specimens prepared in accordance with JIS 5201-1956 have been analyzed statistically from the standpoint of the stochastic theory. It is concluded that the scatter observed in the delayed time for fracture or the static fracture strength of portland cement mortar appears to be a result of inherent characteristics of the material itself associated with a Markoff process as a kind of rate process. The theory of stochastic processes is therefore believed to be at least approximately applicable to the static failure of such inhomogeneous materials as concrete. More detailed investigations on the statistical aspects of rupture in concrete are now in progress and will be presented in the succeeding papers of this series.

In conclusion, the author expresses his sincere thanks to Prof. M. Hirata, University of Tokyo, for his suggestions and encouragement during the course of this work.

References

1) M. Hirata: Bull. Math. Stat. **3** (1949) 57 (in Japanese).
2) N. Terao: J. Phys. Soc. Japan **7** (1952) 627; **8** (1953) 545, 550.
3) T. Yokobori et al: J. Phys. Soc. Japan **6** (1951) 78, 81; **7** (1952) 44, 48, 122; **8** (1953) 104, 265; **10** (1955) 368; **13** (1958) 305.
4) B. D. Coleman et al: J. Appl. Phys. **27** (1956) 862; **28** (1957) 1058, 1065; **29** (1958) 968, 1091.
5) See, for example, B. Epstein: J. Appl. Phys. **19** (1948) 140.
6) T. C. Baker and F. W. Preston: J. Appl. Phys. **17** (1946) 170, 179.
7) W. F. Busse, E. T. Lessig, D. L. Loughborough and L. Larrick: J. Appl. Phys. **13** (1942) 715.
8) F. Bueche: J. Appl. Phys. **26** (1955) 1133; **28** (1957) 784; **29** (1958) 1231.
9) F. B. Hodgdon, D. A. Stuart and F. E. Bjorklund: J. Appl. Phys. **21** (1950) 1156.
10) J. C. Fisher: J. Appl. Phys. **19** (1948) 1062.
11) B. D. Coleman: J. Polymer Sci. **20** (1956) 447.
12) See, for example, S. Glasstone, K. J. Laidler and H. Eyring: *The Theory of Rate Processes* (McGraw-Hill, New York, 1941).
13) B. Vonnegut and J. L. Glathart: J. Appl. Phys. **17** (1946) 1082.
14) R. J. Charles: J. Appl. Phys. **29** (1958) 1549, 1554, 1657.
15) See, for example, E. J. Gumbel: *Statistical Theory of Extreme Values and Some Practical Applications*, N.B.S. Appl. Math. Ser. no. 33 (1954).
16) J. Tucker: Proc. Amer. Soc. Test. Mat. **41** (1941) 1072; **45** (1945) 952, 976.
17) W. Weibull: Ing. Vetenskaps Akad. Handl. no. 151 (1939); no. 153 (1939).
18) P. G. Jones and F. E. Richart: Proc. Amer. Soc. Test. Mat. **36 II** (1936) 380.
19) H. F. Gonnerman and E. C. Schuman: Proc. Amer. Soc. Test. Mat. **28 II** (1928) 527.

Short Notes

This section is intended to secure prompt publication of important discoveries in physics. The reports should not exceed 800 words in length. A figure of size 7 cm × 7 cm will be counted as 150 words.

J. PHYS. SOC. JAPAN **14** (1959) 1453

Energy Loss of Electrons passing through a Graphite Single Crystal at Different Incident Angles*

By Hiroshi WATANABE
Hitachi Central Research Laboratory
Kokubunji, Tokyo, Japan

(Received August 1, 1959)

When fast electrons pass through a thin solid foil, they excite plasma oscillation and lose the energy characteristic to the material of the foil. Ichikawa[1)] found theoretically that the characteristic energy loss value for graphite single crystal depends upon the incident angle of the fast electrons, and he pointed out that the experimental values at different incident angles give us information about the resonance energy parameters of graphite. Using the electron velocity analyzer of Möllenstedt type[2),3)], we measured the characteristic loss values for graphite at incident angles 0° and 45°.

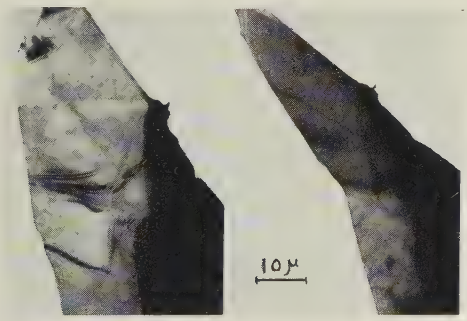

(a) (b)

Fig. 1. Electron micrographs of a single crystal foil (a) the incident beam is parallel to c-axis, i.e. $\Theta=0°$, (b) $\Theta=45°$.

Fig. 1a and 1b give electron micrographs of a thin foil of graphite prepared by stripping. The angle Θ between the incident electron beam and c-axis of the crystal is 0° in Fig. 1a and 45° in Fig. 1b. The energy of electrons which have passed through the central portion (ca. $2\,\mu\times10\,\mu$) of the foil was analyzed. The result is given in Table I, which shows that the loss value *does not* depend upon the incident angle Θ.

Table I. The energy loss value of 25 kev electrons at incident angles of 0° and 45°.

Θ	energy loss value	number of measurement
0°	6.8±0.2 ev	9
45°	6.8±0.2 ev	13

The plasma frequency of π-electrons in graphite is given by Ichikawa[1)] as

$$\omega_p{}^2=\frac{4\pi ne^2}{m}[1-m/m(\Theta)^*] \qquad (1)$$

where

$$1/m(\Theta)=\frac{1}{2\hbar^2}\left[\sin^2\Theta+\frac{1}{2}\cdot\frac{\gamma_1}{\gamma_0}\cdot\left(\frac{c}{a}\right)^2\cdot\cos^2\Theta\right]a^2\gamma_0 \qquad (2)$$

and γ_0, γ_1 are the resonance energy between the nearest neighbors in a lattice layer and that between the nearest neighbors in the successive two layers, respectively. When $\Theta=0°$ in Eq. (2), ω_p depends only upon γ_1. Thus the γ_1 is estimated to be 0.33 ev from the energy loss value at $\Theta=0°$, being consistent with currently evaluated value of 0.2–0.5 ev[4),5)]. From the present result that the loss value does not depend upon the incident angle, γ_0 is estimated to be about 1.6 ev. Hove[4)] obtained 1.63 ev from a calculation of the magnetic susceptibility, and Noziére[6)] 2 ev from the cyclotron resonance and infra-red data. Our result 1.6 ev is in a good agreement with these values.

References

1) Y. Ichikawa: Phys. Rev. **109** (1958) 653.
2) G. Möllenstedt: Optik **5** (1949) 499.
3) H. Watanabe: J. Phys. Soc. Japan **10** (1955) 321.
4) J. Hove: Phys. Rev. **100** (1956) 645.
5) T. Komatsu and T. Nagamiya: J. Phys. Soc. Japan **6** (1951) 438.
6) P. Noziére: Phys. Rev. **109** (1958) 1515.

---

* Read at the 1958 Gatlinburg Conference on Penetration of Charged Particles in Matter.

J. PHYS. SOC. JAPAN **14** (1959) 1454

Nuclear Magnetic Resonance of Na^{23} in Sodium Chloride Crystals

By Eizo OTSUKA, Yudo OSHIO, Toyohide KOBAYASHI
and Hazimu KAWAMURA

Department of Applied Physics, Osaka City University, Osaka

(Received August 20, 1959)

The nuclear resonance line width of Na^{23} in a NaCl crystal usually observed is rather broader than the one calculated by the Van Vleck formula[1] for the dipolar broadening. The extra line width has been thought to arise from the satellites broadened an account of the internal strains through quadrupole interaction[2]. If this is true, the more perfect is the crystal, the narrower will be the line width. With this end in view, we have grown two single crystals of NaCl, which could seemingly avoid the fatal multiplication of dislocations. Moreover, the starting materials for the crystals were those obtained through careful precrystallization.

The observed second moments of the resonance lines of Na^{23} in these crystals are very small as expected. The data obtained from the measurements for the lower half of the crystal A in Fig. 1 are listed in Table I for two directions of the external magnetic field. For comparison we have also listed the calculated values for dipolar interaction, together with the observed ones for an ordinary NaCl crystal which was used in a former experiment[3] as a standard specimen as well as for a ten percent deformed crystal. The best crystal gives the values equal to the theoretical dipolar widths within the experimental errors. The deformed crystal also yields small values; however, this is caused by the run-away of the satellites as proved by the intensity measurement. The ordinary crystal lies in an intermediate situation and the rather large difference between the values of the second moments for the two directions would be attributed to the anisotropy due to crystal dislocations similar to that discussed in a previous paper[4]. From simple analyses[3)-6)] it is roughly estimated that the dislocation densities for the best, ordinary and deformed crystals are $c<10^7$, $c=3\sim4\times10^8$ and $10^9<c<10^{10}\,\mathrm{cm}^{-2}$, respectively.

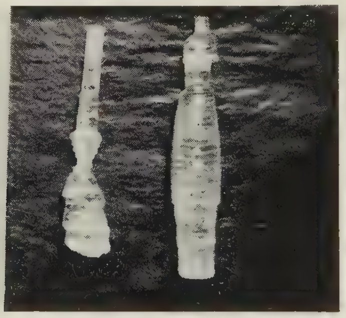

Fig. 1. The two single crystals of NaCl referred to from left to right as A and B in the text. The scale is shown for comparison.

Table I. Second moments in gauss^2.

Crystal	$H_0//[100]$	$H_0//[110]$
A	0.54 ± 0.04	0.54 ± 0.02
Ordinary crystal	1.24 ± 0.07	1.00 ± 0.04
Deformed crystal	0.53 ± 0.04	0.54 ± 0.03
Theoretical	0.555	0.550

Table II. T_1 by pulse-method at room temperature.

Crystal	T_1 in sec.
A	16.0
B	15.4
Ordinary crystal	12.5
Mixed crystal[3] (0.81 NaCl. 0.19 NaBr)	12.4

We have been interested also in the spin-lattice relaxation time of various kinds of NaCl crystals. Using a cross-coil system, we have measured T_1's for a couple of crystals by the consecutive 90° pulse method[7]. The results are shown in Table II. It should be understood that the experimental error is of the order of ten percent. The order of length of T_1, however, is consistent with a preliminary saturation experiment.

In conclusion, the extra-width of the nuclear resonance line of Na^{23} in NaCl is due to lattice imperfections as expected and the spin-lattice relaxation time is sample-dependent. It is not yet certain whether one should account for the difference of T_1 as arising from different purities or other types of imperfections such as dislocations.

References

1) J. H. Van Vleck: Phys. Rev. **74** (1948) 1168.
2) R. V. Pound: Phys. Rev. **79** (1950) 685.
3) H. Kawamura, E. Otsuka and K. Ishiwatari: J. Phys. Soc. Japan **11** (1956) 1064.
4) E. Otsuka: J. Phys. Soc. Japan **13** (1958) 1155.
5) E. Otsuka and H. Kawamura: J. Phys. Soc. Japan **12** (1957) 1071.
6) G. D. Watkins: Thesis, Harvard University 1952.
7) E. L. Hahn: Phys. Rev. **80** (1950) 580.

J. PHYS. SOC. JAPAN **14** (1959) 1455

Piezoelectric Effect in a Rectifying Contact of Semiconductor

By Tetsuro TANAKA and Hiroyoshi KAWAMURA
Institute for Chemical Research, Kyoto University, Kyoto

(Received August 1, 1959)

There is a space charge layer in a rectifying contact of metal rectifier or *p–n* junction, which brings the potential gradient in the layer. As the thickness of the space charge layer and accordingly the quantity of total space charge vary with the applied voltage, the barrier acts as a capacitor and the capacitance is the same as for a parallel plate capacitor. As the inter-electrode spacing of this capacitor is in equilibrium with the applied voltage, this construction is apparently similar to that of a condenser-microphone, and when mechanical force is applied to this capacitor, electromotive force appears between the two electrodes.

A barium titanate ceramic disc was attached on the non-rectifying side of selenium rectifier as shown in Fig. 1(a) for applying a vibrating force on the contact. The metal bodies on both sides serve to give a uniform vibrating force to the barrier. The output voltage at no biasing state may be related to the diffusion potential V_d, and the output voltage under the biasing voltage V may be related to (V_d+V). Curve (a) in Fig. 2 is a plot of $\log(V_d+V)$ *vs.* output voltage V_{op}.

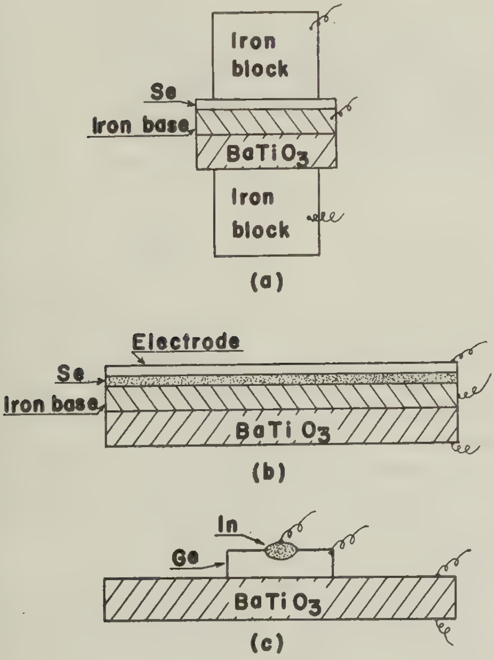

Fig. 1. Schematic diagram of specimens.

In this case, the vibrating force acts in the direction perpendicular to the barrier surface. It is seen that V_{op} is proportional to $(V_d+V)^{1/3}$. The value of V_d derived from the relation between V and barrier capacitance C was about 0.7 volts. In another experiment, specimen as shown in Fig. 1(b) was used. In this case the vibrating force was applied in the direction parallel to the barrier surface. From the results shown in Fig. 2 (b), V_{op} is approximately proportional to $(V_d+V)^{1/2}$ for this specimen. The value of V_d was also 0.7 volts.

A germanium *p–n* junction was attached on a barium titanate ceramic disc as shown in Fig. 1(c), and vibrating force was applied in the direction parallel to the barrier surface. The observed relation between V_{op} and (V_d+V) is shown in Fig. 2(c), where V_d is also 0.7 volts. In this case V_{op} is proportional to (V_d+V).

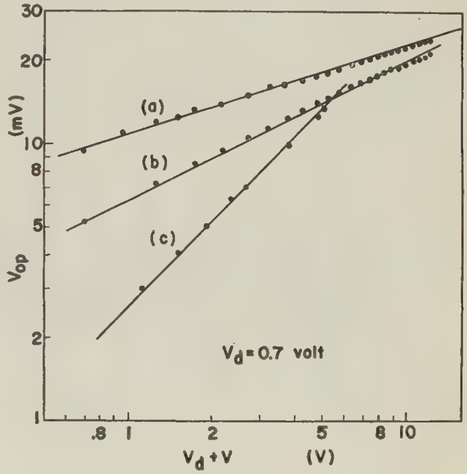

Fig. 2. Characteristic curves of V_{op} *vs.* (V_d+V).

By simple consideration, it may be derived that V_{op} should be proportional to (V_d+V) no matter if the barrier thickness is proportional to $(V_d+V)^{1/2}$ or $(V_d+V)^{1/3}$. The experimental results, however, are different from that are expected from the theory. It has not been clarified whether the discrepancy between theory and experiment came from the incompleteness in theory or from the imperfectness of measuring procedure. But the fact that there exists a remarkable piezoelectric effect in a rectifying contact, and that the output voltage increases with the biasing voltage is very interesting from the standpoint of practical use. More detailed studies will be reported in a near future.

J. PHYS. SOC. JAPAN **14** (1959) 1456

On the Superstructure of the Ordered Alloy Au_3Zn[R]

By Hiroshi IWASAKI

The Research Institute for Iron, Steel and Other Metals, Tôhoku University, Sendai

(Received July 15, 1959)

In the binary system Au–Zn, it is known that the solid solution with a stoichiometric composition Au_3Zn forms the superlattice with long period below 420°C. It is specified as Au_3Zn[H] and is thought to have a Ag_3Mg-type anti-phase domain structure[1]. However, the superlattice is stable only in temperature range 420°C∼270°C and transforms without atomic diffusion into the room-temperature phase Au_3Zn[R] with very complicated structure. Recently, Wilkens and Schubert[2] have studied the structure of this phase using the X-ray powder method and proposed a modified Au_3Zn[H] structure with an orthorhombic unit cell of lattice constants, $a=5.574$ kX, $b=5.583$ kX and $c=16.616$ kX.

The present author also studied the structures of Au_3Zn[R] and Au_3Zn[H] by the single crystal oscillation method, and came to conclude a different structure for Au_3Zn[R]. This structure, specified as $Au_3Zn[R_1]$, has a tetragonal symmetry with a unit cell of lattice constants, $a=5.575\pm0.004$ kX and $c=33.34\pm0.07$ kX*, in which 48 gold atoms and 16 zinc atoms are included. From the clear extinction rule of the observed diffraction spots, the space group was uniquely determined as $D_{4h}^{20}-I4_1/acd$. The atomic positions as shown in Table I were determined by comparing the calculated intensities with the observed ones.

Table I

Kind of atom	Position	x	y	z
Au	16(f)	0.194	0.194	0.250
Au	16(e)	0.250	0.250	0.125
Au	16(d)	0	0	0.059 ± 0.001
Zn	16(d)	0	0	0.181 ± 0.001

The arrangement of atoms is sketched in Fig. 1, in which for the sake of convenience each atom is placed on the lattice point of Au_3Zn[H]. The real structure of $Au_3Zn[R_1]$ is to be obtained by shifting many of the atoms along the direction of arrows.

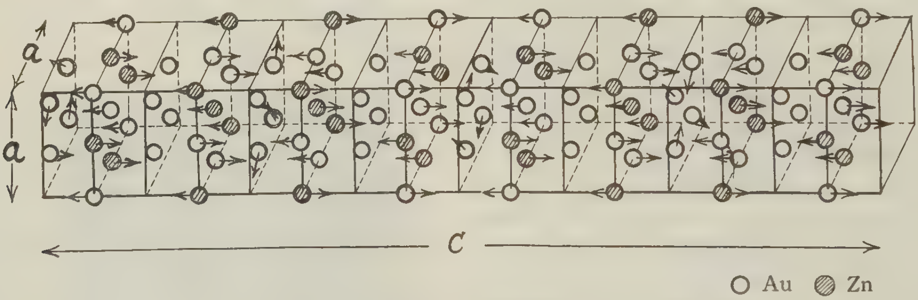

Fig. 1. The arrangement of atoms of $Au_3Zn[R_1]$.

It appears that $Au_3Zn[R_1]$ is a thermodynamically stable phase and is formed at a composition slightly poorer in zinc than stoichiometric Au_3Zn. At a composition richer in zinc than stoichiometric Au_3Zn the formation of the orthorhombic structure with a- and b-axis nearly equal to a-axis of and with c-axis half as long as c-axis of $Au_3Zn[R_1]$ has been found also by the present work, which corresponds to the structure proposed by German workers for Au_3Zn[R]. The present author specifies this structure as $Au_3Zn[R_2]$. There is a close relationship between the structures of $Au_3Zn[R_1]$ and $Au_3Zn[R_2]$. The former may correspond to an anti-phase domain structure of the latter with the period of out-of-step $M=1$, one unit cell of $Au_3Zn[R_2]$ and its shifted cell with a shifting vector, $(\boldsymbol{a}+\boldsymbol{b})/2$, being alternately stacked in the $\boldsymbol{c}$-direction, where $\boldsymbol{a}$, $\boldsymbol{b}$ and $\boldsymbol{c}$ refer to the unit lattice vectors of $Au_3Zn[R_2]$. However, the stacking does not appear to be strictly regularly repeated, as it can be seen on oscillation photographs of $Au_3Zn[R_1]$ that diffraction spots with indexes $h+k=$odd are broadened in the stacking direction.

A full report will later be published.

The author wishes to express his sincere gratitude to Prof. S. Ogawa for his kind guidance. He is also indebted to Dr. M. Hirabayashi for his valuable suggestion.

References

1) K. Schubert, B. Kiefer, M. Wilkens and R. Haufler: Z. Metallkde **46** (1955) 692.
2) M. Wilkens and K. Schubert: Z. Metallkde **49** (1958) 633.

---

* Referring to the face-centered cubic disordered unit cell, $a\sim\sqrt{2}a_f$ and $c\sim8a_f$.

J. PHYS. SOC. JAPAN **14** (1959) 1457~1458

Fine Structure in the $N^{14}(\gamma, n)N^{13}$ Activation Curve

By Naoshi MUTSURO, Yuji OHNUKI,
Kazuo SATO, Kosuke KAGEYAMA
and Motoharu KIMURA

Department of Physics, Tohoku
University Sendai, Japan

(Received August 1, 1959)

Photoneutron reactions of N^{14} have been measured by several authors for ten1)-3) years, and they observed some gross resonances besides the "giant resonance" in the energy region of 11~17 MeV.

Fujii4) tried to explain these gross resonances by extra-particle excitation mode. He assumed that N^{14} consists of C^{12}-core and two nucleus moving independently each other around it, and he obtained $E_r=13.5$ Mev, $\Gamma=0.9$ Mev as a gross resonance.

In order to check the existence of above gross resonance, $N^{14}(\gamma, n)N^{13}$ activation curve was measured in the energy region of 10~17 MeV.

The activation curve was taken by the Tohoku University 25 Mev betatron bremsstrahlung γ rays. Basic experiment consists of irradiation of a number of samples at various betatron energies every 70 Kev or 140 Kev step, and activation curve was taken by residual activity measurement. NaN_3 powder covered by aluminum thin foil (2.5 cmϕ $\times$0.5 cm in shape) were used as N^{14} samples, they were irradiated at 25 cm from the betatron target one after another.

In order to detect 10.1 min β^+ activity from N^{13}, NaN_3 sample was irradiated in the γ ray beam for 10 min and after waiting for 1 min to cool off the 6.6 sec aluminum activity to negligibly small compared to N^{13} activity, counts were taken for 9 min by scintillation counter set to annihilation peak. γ ray dose of each run was measured by Victoreen Radocon chamber, which is located at the centre of Lucite 11.7 cm cube, which was situated at 1.5 m from betatron target.

Number of counts for each run was normalized by unit dose. Activation curve is shown in the figure, in which the ordinate is in arbitrary scale, and the abscissa represents the integrator setting calibrated by threshold energy of the reaction $Cu^{63}(\gamma, n)Cu^{62}$ and $C^{12}(\gamma, n)C^{11}$ correct within ± 0.05 Mev.

The threshold energy of $N^{14}(\gamma, n)N^{13}$ reaction was obtained as 11.49 ± 0.05 Mev. A number of breaks are seen in the activation curve which are summarized also in the table. The 1-st column is the energies at each break, 2nd one is the corresponding energies of each levels of N^{14} as cited from Ajzenberg and Lauritzen table5). The breaks above 13.87 Mev are supposed as newly observed levels.

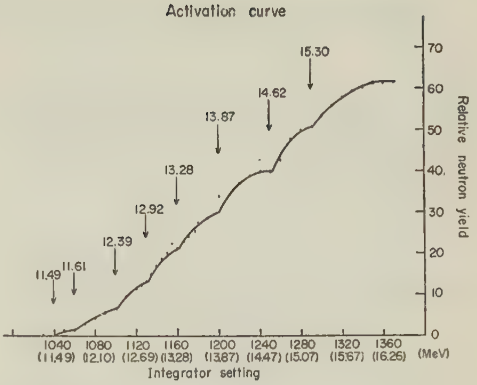

Above 15.3 Mev, perhaps a few breaks would exist, but we could not confirm yet, further investigation being aimed.

Because the energy interval of each activation point was such a broad one as 70 Kev or 150 Kev, other breaks may exist besides ones which were observed in this experiment. Even if other breaks existed, their intensity would be weak, perhaps less than 10% of the intensity of the detected breaks. From above results, we think that the resonance of single particle mode which Fujii3) predicted, may not exist, and that the gross resonance which has been seen in previous works may correspond the group of comparatively sharp resonances observed by us.

Table. Summary of observed "Breaks".

energy at each "breaks" in activation curve	corresponding level energy of N^{14}
11.49±0.05 Mev	11.49 Mev
11.61 〃	11.65
12.39 〃	12.42
12.92 〃	12.92
13.28 〃	13.24
13.87 〃	
14.62 〃	
15.80 〃	

As the spin of the ground state of N^{14} is 1^+, it is supposed that the levels corresponding to these breaks have odd parity, and possible spins for them are 2, 1 or 0. If the 12.42 Mev (4^-) level really corresponds to our 12.39 Mev break, there remains some questions to be studied.

We are now proceeding more precise experiment, and also planning the experiment to find out another breaks in the higher energy region.

Authors are indebted Mr. M. Mishina, Mr. A. Ono and Mr. T. Inoue for operating the betatron.

References

1) J. G. V. Taylor, L. B. Robinson and R. N. H. Haslam: Canad. J. Phys. **32** (1954) 238.

2) J. R. Atkinson: Proceeding of the 1954 Glasgow Conference on Nuclear and Meson Physics (1955) 151.
3) R. W. Parson: private communication.
4) S. Fujii: Progr. Theor. Phys. **21** (1959) 511.
5) F. Ajzenberg and T. Lauritzen: Rev. Mod. Phys. **27** (1955) 73.

J. PHYS. SOC. JAPAN **14** (1959) 1458~1459

Rotational Transitions in Hydrogen and Deuterium

By Kazuo TAKAYANAGI

Department of Physics, Saitama University, Urawa

(Received July 30, 1959)

In a previous paper[1] the rotational excitation by collision in hydrogen gas was studied and the probability for the jump $l=0\to l=2$ was calculated, assuming an intermolecular potential of the Morse type. Using the same potential, calculation has been extended recently to the transitions 1→3, 2→4 in hydrogen and the corresponding transitions in deuterium[2]. The effective cross sections at T°K are of the form

$$Q(T)=\pi R_c^2F(T)=\pi R_c^2\beta^2(F(T)/\beta^2)\ .$$

R_c is a collision diameter introduced in the course of simplifying procedure. A reasonable choice of R_c is given by the closest distance of approach in the classical head-on collision with the mean velocity. β is a parameter indicating the relative importance of the non-spherical part of the potential. In the reference 1, $\beta=0.075$ was adopted. Results obtained in the reference 2 are summarized in Table I.

These values of F/β^2 make it possible to calculate the ultrasonic dispersion curves for these gases. The method of calculation is similar to the one used by Rhodes[3]. For hydrogen, the contribution from the fifth and the higher rotational levels were neglected. For deuterium, $F(3\to5)/\beta^2=3.75\times10^{-3}$ was assumed somewhat arbitrarily and the sixth and the higher levels were neglected. The ideal gas formula for the sound velocity was used without correction.

Table I. Values of F/β^2.

Rotational transition	H_2			D_2		
	100°K	200°K	300°K	100°K	200°K	300°K
0→2	2.7×10^{-3}	5.9×10^{-2}	2.0×10^{-1}	9.0×10^{-2}	5.4×10^{-1}	1.13
1→3	1.7×10^{-5}	2.6×10^{-3}	1.7×10^{-2}	4.0×10^{-3}	6.8×10^{-2}	2.1×10^{-1}
2→4	1.7×10^{-7}	1.6×10^{-4}	2.0×10^{-3}	2.5×10^{-4}	1.16×10^{-2}	5.4×10^{-2}

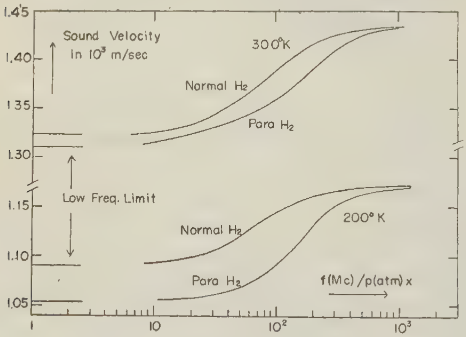

Fig. 1.

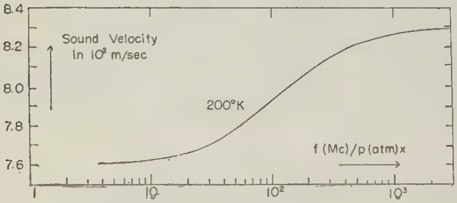

Fig. 2.

Fig. 1 shows the resulting curves for hydrogen at 200°K and 300°K. We have left the product $[R_c(\text{in Å})]^2\beta^2\equiv x$ undetermined. In the present cases, R_c is of the order of 4Å, so that it is expected that $x\simeq0.1$. Fig. 2 shows the dispersion curve for normal deuterium at 200°K. To calculate the corresponding curve at 300°K, we need the excitation probabilities among the higher levels. It is seen from the figures that the hydrogen and deuterium show the dispersion in almost the same frequency region. That this is actually the case

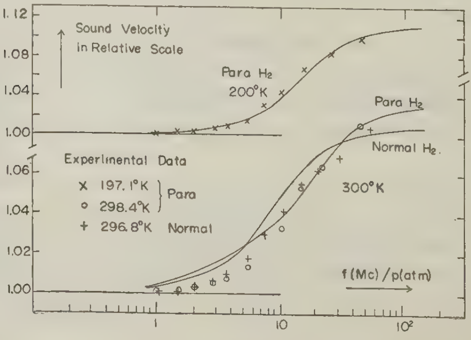

Fig. 3.

has been found experimentally[4]. In Fig. 3, comparisons are made between the experimental[3] and the theoretical curves for hydrogen. Following the reference 3, the relative velocities are plotted instead of their absolute values. $x=0.1$ was adopted since it gives a good fit at 200°K. The disagreement between the theory and the experiment at 300°K for the lower frequencies will probably be due to the presence of the other type of reactions such as

$$H_2(l=4)+H_2(l=0)\rightarrow H_2(l=2)+H_2(l=2)\ .$$

References

1) K. Takayanagi: Proc. Phys. Soc. London **A**, **70** (1957) 348.
2) K. Takayanagi: Sci. Repts. Saitama Univ. **A**, **3**, no. 2 (1959) in press.
3) J. E. Rhodes, Jr.: Phys. Rev. **70** (1946) 932.
4) E. Stewart and J. L. Stewart: J. Acoust. Soc. Amer. **24** (1952) 194.

J. PHYS. SOC. JAPAN **14** (1959) 1459~1460

Magnetic Anisotropy of Evaporated Films Formed in Magnetic Field

By Minoru TAKAHASHI, Denjiro WATANABE,
Tetsuzo SASAGAWA, Hideo SAITO
and Shiro OGAWA

The Research Institute for Iron, Steel and Other Metals, Tohoku University, Sendai

(Received July 31, 1959)

It has been reported[1] that thin films of some ferro-magnetic metals exhibit a distinct uniaxial anisotropy in the film plane when they are formed in magnetic field or are heat-treated in magnetic field after evaporation, but any quantitative observation of the anisotropy has never been done. The present authors succeeded in measuring quantitatively the anisotropy of evaporated films of Fe, Co, Ni and Ni–Fe, formed in magnetic field, by a highly sensitive torquemeter which was newly designed (sensitivity $\approx 5\times10^{-3}$ dyn-cm). As a substrate on which films were evaporated a quartz plate 13 mm in diameter was used. The plate surface was finely finished so as to be optically flat. Metals were evaporated from a small tungsten coil onto the substrate 5 cm distant from it. The substrate temperature was maintained at room temperature or at 300°C. The applied magnetic field ranged from 250 to 1500 Oe. The evaporation chamber was beforehand sufficiently degassed and the degree of vacuum was about 10^{-5} mm Hg when the evaporation was carried out. The specimen was horizontally held in vacuum in the torquemeter, in which a Helmholtz coil was used as a field source. The intensity of the magnetic field was

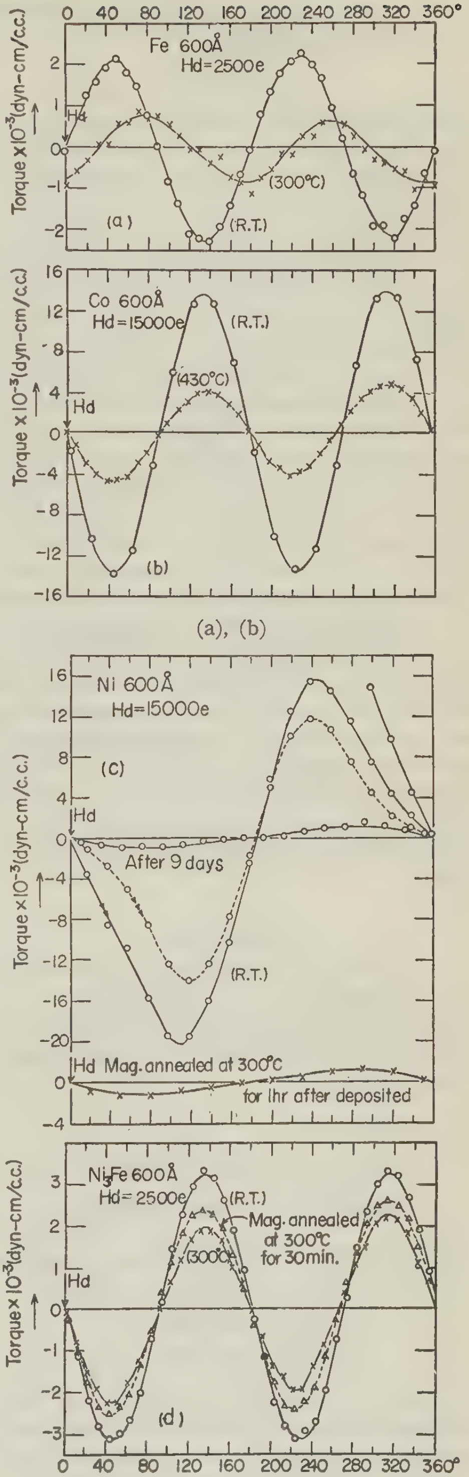

(a), (b)

(c), (d)

Fig. 1. Torque curves for Fe, Co, Ni and Fe-Ni evaporated in magnetic field. θ is the angle between the evaporating field axis and the direction of the measuring field.

Table I. Values of anisotropy constant for evaporated films of Fe, Ni, Co and Fe–Ni.

Anisotropy const. / Temp. of substrate	K_u(Fe) (erg/cc)	K_u(Co) (erg/cc)	K_1(Ni) (erg/cc)	K_u(Ni_3Fe) (erg/cc)
Room temp.	2.2×10^3	13.8×10^3	$\sim1.0\times10^3$	3.2×10^3
300°C	0.8×10^3	4.4×10^3*	$\sim1.0\times10^3$	2.1×10^3 (2.5×10^3)**

* The substrate temperature was 430°C.

** After formed at 300°C and then successively annealed magnetically for 30 min.

414 Oe.

Some examples of torque curves are shown in Fig. 1. Here, H_a is the field strength applied during the film formation and the arrow shows the field direction. In all cases except Ni the curves can almost be approximated by $-K_u \sin 2\theta$. The uniaxial anisotropy constants calculated from these curves are given in Table I. It is remarkable that the less anisotropy is shown when the substrate has been held at the higher temperature and that in the case of Fe films the direction of H_a becomes nearly the direction of difficult magnetization rather than that of easy magnetisation. It is also worth while reporting that the torque value of nickel formed at room temperature is very changeable with lapse of time after the formation and that not uniaxial but unidirectional anisotropy is shown by the torque curve which has attained the stationary state.

The detailed report will be published in the near future.

References

1) M. S. Blois: J. Appl. Phys. **26** (1955) 975. H. J. Williams and R. C. Sherwood: J. Appl. Phys. **28** (1957) 548. N. V. Kotel'nikov: Dokl. Nauk. SSSR. **113** (1957) 97 (Phys. Abst. **60** (1957) 732).

J. Phys. Soc. Japan **14** (1959) 1460~1461

A 4^+–0^+ Cross-Over Transition

By Haruhiko MORINAGA and Kasuke TAKAHASHI
Department of Physics, Tohoku University, Sendai

(Received August 24, 1959)

Low-lying 4^+ states in even-even nuclei decay to the ground states by cascade, in most cases, through underlying 2^+ states. So far, no direct transition to the ground state has been established[1]. Such transitions are of interest especially in connection with the collective behaviors of the nuclear matter, as in the cases of electric quadrupole and octupole transitions[2]. Unfortunately, such electric hexadecapole cross-over transitions are expected to occur with extremely small branchings (an order of 10^{-7} or so).

We have detected one of such transitions in the decay of Ni^{60} (Fig. 1). In order to detect the 4^+–0^+ cross-over transitions of the 2.505-Mev in the presence of the well-known 1.172-Mev and 1.333-Mev gamma-rays of intensities 10^7 stronger than the former, we looked for the photoneutrons released from heavy water by the 2.505-Mev gamma-rays, using a dysprosium neutron detector.

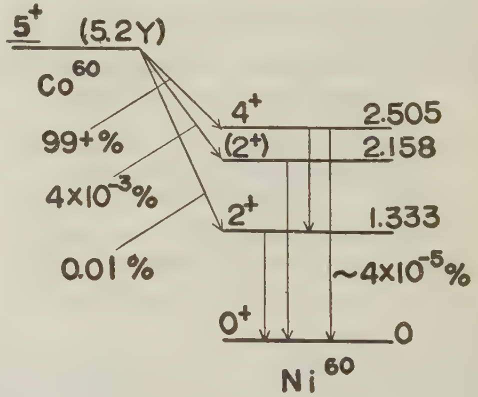

Fig. 1. Decay scheme of Co^{60}.

One gram sample of dysprosium oxide was taped on the surface of a cylindrical glass vessel containing 900 millilitre heavy water and irradiated in the 10,000 curie Co^{60} source at Japan Atomic Energy Research Institute. After 15 hour irradiation the characteristic 2.32-hour activity was produced in the dysprosium sample. In order to avoid a cumbersome calculation, the same detector assembly was irradiated with a Na^{24} source and the dysprosium activities produced were compared. After correcting for the difference in the geometries in two measurements and the energies of the released photoneutrons, we found that the branching ratio of the direct ground state transition from the 4^+ state to the cascade transition was 4×10^{-7}, if the former activation was assumed to be entirely due to the 2.505-Mev gamma-rays. Actually it is difficult to expect any high energy gamma-rays of other sources in the Co^{60} source with an intensity of an order of millicuries than this cross-over transition. So, we may conclude that the activity is produced by the 2.505-Mev cross-over transitions. The measured branching, however, may be subject to an error because of the rough estimate used in the correction, but the order will not be altered by more elaborate calculations.

Using the Weisskopf single particle estimate for both 4^+–2^+ and 4^+–0^+ transitions, one obtains a theoretical branching ratio of 1.3×10^{-7}. The measured value is very close to this value in the order of magnitude.

This work was done at Japan Atomic Energy Research Institute. We are grateful to Dr. A. Danno, Dr. E. Takekoshi, and Dr. K. Yoshihara for their help during the course of this experiment. The heavy water was loaned from Reactor Development Section of the Institute. This work was partly supported by the Ministry of Education.

References

1) R. G. Fluharty and M. Deutsch: Phys. Rev. **78** (1949) 182(A). The authors report a high energy gamma-ray in Sc^{46} which may be of this type, but the evidence that this corresponds to the 4^+–0^+ cross-over is scarce. Often in the type of even-even nucleus like Ti^{46}, to which Sc^{46} decays, the second 2^+ state appears below the 4^+ level which may give rise to such a gamma-ray.

2) S. Suekane and Y. Yamaguchi: Progr. Theor. Phys. **17** (1957) 449.

Errata

Fine Structure in the Giant Resonance for Cu^{63} and Ag^{107} (γ, n) Reactions

By Teruo NAKAMURA, Kiyoji FUKUNAGA, Kunio TAKAMATSU,
Minoru YATA and Shinjiro YASUMI
J. Phys. Soc. Japan **14** (1959) 1117

Page	Column	Line	Wrong	Corrected
1117	right	4 from the bottom	4×10^{-17} sec from $\Gamma\gamma=16.7$ ev	6.2×10^{-20} sec from $\Gamma=10.7$ kev
1117	right	2 from the bottom	5×10^{-9} cm	8×10^{-12} cm

PROGRESS OF THEORETICAL PHYSICS

CONTENTS

Progress of Theoretical Physics Vol. 21, No. 1, January 1959

On the Unstable States in Quantum Field Theory .... Tetsuo GOTŌ.. 1
A Note on the Nuclear Reactions in Stars .... S. NAKAMURA, T. OHMURA and M. TAKETANI.. 18
A Nucleonic Cascade Theory and an Analysis of Extensive Air Showers .... H. FUKUDA, N. OGITA and A. UEDA.. 29
Octupole Type Deformation of Nuclear Surface .... Shōta SUEKANE.. 74
Interpretation of the Optical Model in Nuclear Reactions .... S. HAYAKAWA, T. SASAKAWA, K. TOMITA, M. YASUNO and M. YOKOTA.. 85
Radiative $K-\mu$ Decay and Quantum Electrodynamics at Small Distances .... Kichiro HIIDA.. 98
Exciton and Plasmon in Insulating Crystals .... Chiuji HORIE..113
On the Validity of Dispersion Relations in Perturbation Theory .... Noboru NAKANISHI..135
Low Energy Kaon-Nucleon Reactions .... A. KOMATSUZAWA, R. SUGANO and Y. NOGAMI..151
Collective Motion and Particle Excitation in Many Fermion System .... Shuji TAKAGI..174
Properties of Nuclear Forces indicated by $d(\gamma, p)n$ .... Shih-Hui HSIEH..185

Letters to the Editor:

Q-Value Dependence of Decay Probability ......K. FUJII and K. IWATA..207
A Possible Symmetry in Sakata's Composite Model ....S. OGAWA..209
Natures of Nuclear Forces indicated by the Photodisintegration of the Deuteron, IV ....S. H. HSIEH..211
A Note on the Theories of Metals and of Pressure Ionization ...... S. K. TRIKHA..212
Drift and Hall Mobilities of Electrons in Nondegenerate Impure n-Semiconductors ....M. S. SODHA and P. C. EASTMAN..214
A Note on the Physical State of Unstable Particles ......N. NAKANISHI..216
On the Geometrical Structure of Benzene-Iodine Complex ......S. AONO..217

Price $ 1.25 per copy
$ 15.00 per year (postage inclusive)
Annual dues for foreign members (individual subscribers)
$ 12.00 (postage inclusive)
〃 for foreign members of the Physical Society of Japan
$ 10.00 (postage inclusive)

Application for members, subscriptions and orders for back numbers should be sent, directly or through book-dealers, to

The Publication Office
in
Yukawa Hall, Kyoto University, Kyoto, Japan

. . . .

ANNOUNCEMENT

REVISED Price List of Back Numbers (for subscribers abroad)

*Vols. 1–4	$ 6.40 each
*Vols. 5 & 6	$13.00 each (single copy: $2.50)
*Vols. 7 and succeeding ones	$ 8.00 each (single copy: $1.50)

Back number prices are effective for volumes other than last four (4) volumes (the current volume inclusive).

Thus, volumes 1 through 16 will be regarded as back numbers while volume 20 is being published.

The revised prices will be effective on and after August 1, 1958.

. . . .

JOURNAL OF THE PHYSICAL SOCIETY OF JAPAN, Vol. 14, No. 11, NOVEMBER, 1959

Elastic Scattering of Protons by Helium between 9.2 MeV and 14.5 MeV

By Junpei SANADA

Institute for Nuclear Study, University of Tokyo,
Tanashi-Machi, Tokyo

(Received July 1, 1959)

The Scattering of protons by helium has been investigated from 9.2 MeV to 14.5 MeV with the INSJ variable-energy 160 cm cyclotron. The full angular distribution curves were taken at 12.04 MeV and 14.32 MeV. Both curves have a minimum at 115° and show the evidence of Coulomb-nuclear interference, though very small, at near 18° in the center-of-mass system. Tentative phase shift analysis has been made. It was found that the D-wave phase shifts are closely related with the shape of angular distribution at forward angles and they are small but cannot be neglected. Excitation curves between 9.2 MeV and 14.5 MeV were also taken at four angles of 25°31′, 49°21′, 90°0′ and 168°41′ in the center-of-mass system. $k^2\sigma(\theta)$ *versus* energy curves increase gradually with proton energy. They display no new state in Li^6 except the $\frac{1}{2}^-$ first excited state. The differential cross sections at energies near 9.5 MeV have served to resolve the confliction between the values hitherto obtained.

§1. Introduction

Helium plus one nucleon system is the first 1P shell nucleus. Its level structure is very interesting from viewpoints of the nature of nuclear forces and the excitation of alpha-particle core. Already many experiments¹⁾ on the elastic scattering of nucleons by helium have been performed and reveal through analyses²⁾ in terms of phase shifts that the virtual ground state and the first excited state of He^5 and Li^5 form the inverted doublet of $P_{3/2}$ and $P_{1/2}$. The $P_{3/2}$ state are confirmed also from another basis, *e.g.* from $He^4(d, p)He^5$ reaction³⁾. But the nature of $P_{1/2}$ state is more obscure than that of $P_{3/2}$ state. One of the purpose of the present work is to obtain further information about the behavior of $P_{1/2}$-wave phase shift.

On one hand, Brockman⁴⁾ observed the angular distribution at 17.45 MeV and showed the possibility of the existence of the $D_{5/2}$ state below this energy. He investigated successively the differential cross sections at 12 energies between 11.4 MeV and 18 MeV. He found that the contribution of the D-waves remains small. It is the worthwhile to check these apparently conflicting results by obtaining the fine excitation curves and full angular distributions with better angular resolution. If the existence of $D_{5/2}$ state be true, the differential cross sections should change more than ten percent as a peak or like the dispersion curve with bombarding energy.

We will now refer to the related theories. While the $P_{3/2}$ and $P_{1/2}$ phase shifts with large inverted splitting are accounted theoretically by using the spin-orbit force⁵⁾ which has been introduced rather phenomenologically, the attempts to find the splitting due to tensor force have also been made⁶⁾, especially due to the large tensor force⁷⁾ included in the two body potential which is lead by the meson theory of nuclear forces. If the spin-orbit force is valid, the D-wave phase shifts should be also inverted. However, if the tensor force is valid, the D-wave phase shifts should become normal⁷⁾. Then even if one cannot find the resonance concerning $D_{5/2}$ state, informations whether D-wave phase shifts are inverted or normal are very useful for the knowledge of the nature of nuclear forces.

The further interesting fact is the existence of $J=3^+/2$ state at an excitation energy of 16.80 MeV which is well known from the $He^3(d, p)He^4$ reaction⁹⁾. The deuteron reduced width of this state is very larger than that for proton and the state is a good single particle state of He^3+d, which arises presumably from a complex configuration such as excitation of alpha-particle core. It seems likely that a state with $J=1^+/2$ might lie near in energy to $J=3^+/2$ state[10]. The fine excitation curves will give informations about this problem.

§ 2. Experimental Method

A. General considerations

External proton beam from the INSJ 160 cm variable-energy cyclotron was lead through vacuum pipes to the 100 cm scattering chamber in the next room and focused by a combination of a pair of quadrupole magnets and a sector magnet. The details of apparatus above described will be soon given in a report[11] of this journal. The diagram of the experimental arrangement is shown in Fig. 1. Well colimated beam passed through a small gas target chamber, which was located at the center of the scattering chamber, and was collected by a Faraday cup. The beam current integrator was 100 percent feedback type deviced by Higinbotham and Rankowitz.[12] The gas target chamber was filled with thank helium, the purity of which was 99.6 mole percent. Protons scattered by helium entered the detecting system. Scintillation counters, consisting of cesium iodide crystal combined with a 6342 photo-multiplier tube, were set up on the turn table in the scattering chamber as shown in Fig. 1. Pulses from the counter were amplified with a Jordan and Bell type amplifier[13] and analysed with a Johnstone type twenty channel pulse height analyser.[14]

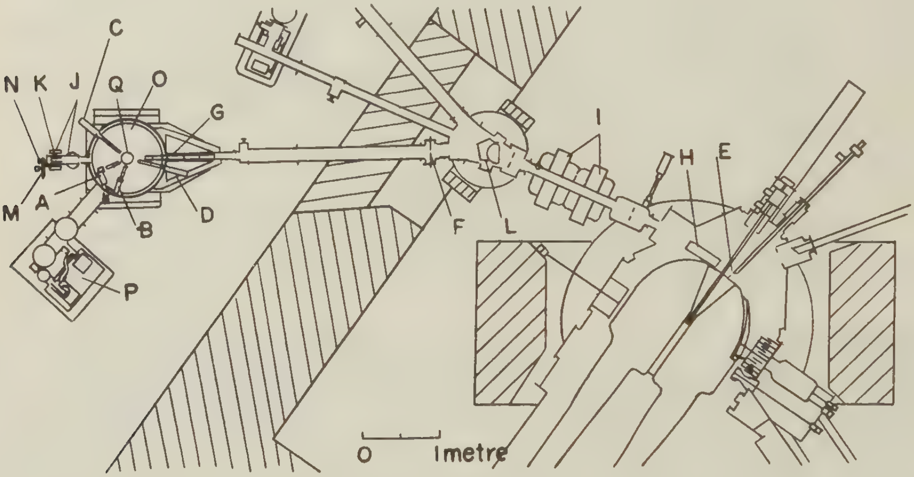

Fig. 1. The experimental arrangement. *A*: Detector I. *B*: Detector II. *C*: Detector III. *D*: Detector IV. *E*: Collimating slit. *F*: First defining slit. *G*: Second defining slit. *H*: Magnetic channel. *I*: Quadrupole magnets. *J*: Magnets for sweeping secondary electrons. *K*: Faraday cup. *L*: Sector magnet. *M*: Foil wheel. *N*: Ionization chamber. *O*: Scattering chamber. *Q*: Small gas target chamber.

Some details of the instrumentation which is characteristic of the present work are given in the paragraphs below.

B. Collimator

Most of unused part of external beam was stopped by a collimating slit, which was installed on the end of the current probe in the vacuum tank of cyclotron and was 2 mm in width. Two slits were inserted before and after a pair of quadrupole magnets to stop further diverging beam. The first defining slight was 7 mm in width and the second defining hole was 3.5 mm in diameter. Each was separated by 3.9 m. Thus the angular divergence of the beam was less than 0.1°. Three antiscattering baffles were inserted between the defining slits. Another two antiscattering baffles were added beyond the second defining hole to limit the spray of protons to a cone of half angle 0.6°. All these diaphragms were made of graphite to reduce the scattering and the neutron background.

C. Small gas target chamber

Because there were many sources of impurity vapor, such as concentric cables and other electronic components, in the scattering chamber, we decided to use a separated small gas target chamber. In earlier stage we attempted to use a chamber of 8 cm diameter with Mylar window developed by Corelli, Livingston and Seidlitz.[16] We found however two defects. Mylar became apt to break by a slight shock after traverse of protons of about 300 microcoulombs, because of high current density. The second was high background at the forward angles mainly due to the double scattering of incident protons by Mylar. The final form of the gas target chamber is shown in Fig. 2. A Mylar foil of 25 micron thick is cemented to a thin stainless steel plate and is made exchangeable easily. Moreover, the positions of beam entrance and exit on Mylar foil were changed by turning the target chamber step by step without breaking the vacuum of the scattering chamber. The diameter of the target chamber is increased to 15 cm. The background was reduced by a factor of four. The Mylar window is 1.6 cm high and extended to 290° of arc. The wall of the target chamber is made of brass of 1 cm thick. It bears one atmospheric pressure with slight deformation, though there is no intermediate supporting rod at the opening.

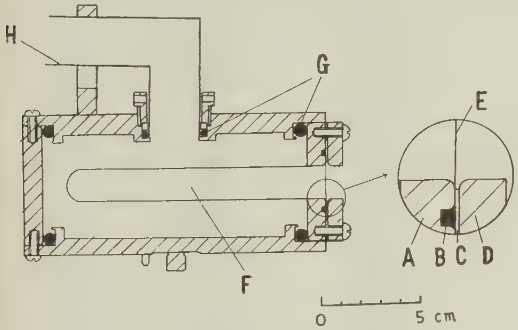

Fig. 2. Small gas target chamber. *A*: Side wall made of brass. *B*: Square gasket. *C*: Thin stainless steel plate. *D*: Semicircular ring. *E*: Mylar. *F*: Window. *G*: O-ring. *H*: Copper pipe to pumps, gas inlet and manometer.

D. Detector system

We used four detectors. When the measurements of angular distribution were made, the two detectors on the turn table were used as main detectors and the detector on the side wall of the scattering chamber set at an angle of 40° in the laboratory system was used as a monitor. When the excitation curves were taken, four detectors were used simultaneously. Dimensions of analysing slits are summarized in Table I. Good angular resolution was borne in mind particularly for the forward angles to obtain the fine structure of the angular distribution. The thicknesses of cesium iodide crystals were selected as thin as possible according to the range of protons to be detected. The gamma-ray and neutron background was negligible.

E. Procedure

After outgassing and flushing with helium, the target chamber was filled with the target gas to a pressure of 30 cm Hg. The pressure was measured with a mercury manometer which was read with a precision cathetometer. The temperature of target gas was measured with an alcohol thermometer, which was calibrated against the Dr. Siebert and Kühn's

Table I. Analysing slit dimensions. Values listed are in millimeters.

	For angular distribution		For excitation curve			
	Detector I.	Detector II.	Detector I.	Detector II.	Detector III.	Detector IV.
Width of front slit	2.023	5.007	2.973	5.007	4.005	4.015
Width of rear slit	2.014	4.996	3.105	4.996		
Height of rear slit	6.008	7.661	6.135	7.661	Circular 10.027 in diameter	Circular 8.005 in diameter
Center to rear slit	304.2	262.3	303.1	258.4	518.1	507.6
Distance between slits	200.1	143.1	201.1	143.1	340.6	343.3

standard thermometer. Relative value of the energy of protons was obtained from the frequency of proton resonance in the magnetic field of the sector magnet. At three values of energy, both ends and the middle of the energy range used, the energy of protons was measured by the combination of aluminium absorbers and a shallow ionization chamber. Using the range energy relation obtained by Bichsel, Mozley and Aron,[16] the relation between the frequency of proton resonance in the sector magnet and the absolute value of beam energy was decided.

In the measurement of differential cross sections, the sequence of angle in the angular distribution or of beam energy in the excitation curve was taken at random. At several angles or beam energies, the differential cross sections were measured twice or thrice at time appreciably separated each other.

§ 3. Results

Table II and Table III indicate the results of the angular distribution at 14.32 MeV and

Table II. Experimental and calculated cross sections at 14.32 MeV.

	Experimental values		Calculated values	
			$\delta_0 = -77°42'$ $\delta_1^- = 50°\ 0'$ $\delta_1^+ = 92°36'$	$\delta_0 = -75°34'$ $\delta_1^- = 63°39'$ $\delta_1^+ = 102°\ 5'$ $\delta_2^- = 6°57'$ $\delta_2^+ = 9°\ 3'$ $\delta_3^- = 1°19'$ $\delta_3^+ = 2°10'$
θ c.m.	σ c.m. (mb/sterad)	Estimated error %	σ c.m. (mb/sterad)	σ c.m. (mb/sterad)
9°47′	670.9	4.0	724.3	661.1
11° 2′	516.9	3.3	517.8	483.8
12°17′	418.5	2.5	409.3	394.8
13°31′	368.5	2.4	349.8	349.2
14°46′	339.5	1.9	314.9	324.3
16° 1′	317.9	1.7	293.3	310.3
17°16′	287.7	1.6	279.9	302.2
18°31′	296.7	1.2	272.1	297.0
19°46′	290.7	1.5	264.4	293.3
21° 0′	284.9	1.2	258.9	289.5
22°15′	276.7	1.2	255.3	287.3
23°29′	268.5	1.2	252.0	284.4
24°44′	265.5	1.2	249.8	281.2
25°58′	258.5	1.2	245.5	277.8
28°27′	251.7	1.2	239.0	270.1
30°54′	248.6	1.2	232.1	261.3
37° 3′	225.8	0.9	213.0	235.8
43° 9′	201.9	1.2	191.3	207.6
49° 9′	171.7	1.1	168.4	179.1
55° 7′	152.3	1.4	145.0	151.4
60°59′	124.2	1.4	122.6	125.7
66°47′	103.2	1.5	100.3	102.3
72°43′	81.42	0.9	79.54	80.68
78°19′	60.80	1.1	61.95	62.79
83°48′	47.50	1.2	46.90	47.62
89°13′	34.50	1.0	34.55	35.17
94°30′	24.32	1.3	24.90	25.37
99°39′	17.45	1.2	17.88	18.13
104°43′	13.41	1.3	13.30	13.29
109°37′	10.35	1.4	10.95	10.65
114°29′	9.98	1.7	10.51	9.96
119°11′	11.16	1.4	11.75	10.96
123°47′	13.51	1.6	14.31	12.63
128°18′	16.93	1.4	17.89	16.80
132°42′	20.79	1.4	22.21	20.90
136°59′	26.62	1.3	27.02	25.83
141°12′	31.82	1.2	32.06	30.87
145°20′	36.30	1.2	37.19	35.85
149°23′	41.35	1.1	42.12	40.96
153°22′	45.64	1.1	46.80	45.67

Table III. Experimental and calculated cross sections at 12.04 MeV.

	Experimental values		Calculated values	
			$\delta_0 = -71^\circ 12'$ $\delta_1^- = 51^\circ 54'$ $\delta_1^+ = 99^\circ 48'$	$\delta_0 = -68^\circ 47'$ $\delta_1^- = 63^\circ 46'$ $\delta_1^+ = 105^\circ 43'$ $\delta_2^- = 5^\circ 15'$ $\delta_2^+ = 6^\circ 41'$ $\delta_3^- = 55'$ $\delta_3^+ = 1^\circ 27'$
θ c.m.	σ c.m. (mb/sterad)	Estimated error %	σ c.m. (mb/sterad)	σ c.m. (mb/stread)
9°45′	988	3.7	1075	992
12°15′	561.0	2.6	582.8	547.8
14°45′	420.0	1.7	424.4	414.3
17°16′	357.3	1.2	361.0	364.7
18°30′	353.9	1.2	343.6	351.7
19°45′	330.1	1.2	330.8	342.2
21° 0′	320.4	1.2	321.1	335.0
23°29′	301.1	1.1	306.5	323.6
25°58′	294.1	1.1	295.7	314.1
28°26′	285.9	1.1	285.0	303.7
30°54′	270.0	1.1	275.2	293.5
37° 2′	248.2	0.9	250.3	265.7
43° 8′	223.4	1.1	223.9	235.7
64°42′	127.1	1.3	126.7	129.4
67° 0′	114.9	1.2	117.0	119.2
69°18′	104.2	1.2	107.6	109.3
71°34′	96.13	1.1	98.57	100.0
72°42′	91.88	1.1	94.22	95.54
73°50′	87.62	1.1	89.97	91.17
74°57′	83.74	1.3	85.83	86.97
77°11′	76.66	1.1	77.87	78.74
79°24′	69.89	1.1	70.38	71.07
81°30′	61.78	1.1	63.70	64.24
83°48′	54.87	1.1	56.83	57.21
89°11′	41.06	1.0	42.66	42.50
94°28′	30.66	1.2	31.57	31.31
99°38′	21.81	1.3	23.46	22.90
114°27′	13.58	1.7	14.70	13.58
119°10′	15.01	1.4	15.95	14.81
128°16′	21.80	1.5	22.68	21.77
136°58′	32.24	1.3	32.99	32.60
145°19′	43.64	1.3	44.00	44.33
153°21′	54.68	1.2	54.75	55.77

and 12.04 MeV respectively. Table IV indicates the results of the excitation curves. The differential cross sections, which were measured twice or thrice, agreed within the experimental error. This served as the check of the stability of the instruments. The weighted means of these values are listed in the tables. The scattering angles and the differential cross sections in Tables II and III were transformed from the laboratory system into the center of mass system by means of a Lorentz transformation. The difference between this and the nonrelativistic transformation was at most 0.6 percent. In the case of the excitation curves the transformation was performed nonrelativistically, because the measurements were made without the monitor and the accuracy of differential cross sections is not so high. Their individual value suffered already the occrsional occurrence of a few percent fluctuation of the integrated current.

§ 4. Corrections and Errors

The errors in the third column in Tables II and III were estimated as follows. Errors due to counting statistics were ranging from 0.3 to 1.5 percent. Uncertainties in the geometry of analysing slits were less than 0.2 percent. Geometrical correction was applied using the relation developed by Critchfield.17) Error in measurement of gas density was 0.2 percent, including the uncertainty in the correction of the amount of impurity. Though

Table IV. Experimental results of excitation curves.

Proton energy in Lab. system (MeV)	$\sigma(\theta$ c.m.) in mb/sterad at			
	θ c.m. $=25°31'$	49°21′	90°0′	168°41′
14.52	256	173	32.7	58.9
14.38	251	169	32.5	57.5
14.02	253	179	33.3	59.3
13.97	262	178	33.5	60.9
13.82	266	185	34.8	64.4
13.55	264	185	35.0	62.4
13.50	268	182	34.7	61.2
13.34	255	179	33.2	60.3
13.21	275	189	35.7	65.0
13.07	268	188	36.4	64.7
12.97	284	192	36.4	65.3
12.87	299	200	39.1	68.7
12.83	277	199	36.8	65.0
12.65	298	205	38.6	67.0
12.37	289	201	38.3	67.5
12.23	293	201	38.7	67.7
12.21	299	207	39.9	69.4
12.13	294	202	38.3	67.7
12.04	292	206	40.7	69.6
11.81	304	210	40.2	70.1
11.61	309	206	40.5	71.5
11.57	320	226	41.9	76.3
11.36	313	211	41.5	73.7
11.22	314	211	42.9	73.6
11.15	320	217	42.7	74.8
11.09	322	217	43.5	74.3
10.93	325	214	43.8	75.5
10.86	320	217	44.3	75.4
10.67	334	224	45.3	77.2
10.40	361	226	46.8	79.1
10.27	350	229	47.2	80.2
10.09	353	235	48.3	82.1
9.67	364	244	50.3	84.6
9.63	368	244	51.1	84.3
9.55	368	240	50.5	84.9
9.33	373	243	53.6	85.6
9.27	376	253	52.2	88.8
9.24	379	247	52.3	88.5

the amount of impurity was small, its contribution as background to the proton pulses at forward angles was not negligible. We observed well separated proton pulses due to heavier nuclei in the target gas at above 40° in the laboratory system. Assuming that they were nitrogen and oxygen, we estimated the amount of background pulses due to impurity at forward angles by making use of the results on the elastic scattering of protons from these nuclei.[18] This procedure was supported experimentally by the measurements of the proton-proton scattering,[19] which were made with the same instruments as those of the present work and showed separated proton pulses due to heavier nuclei until 15° in the laboratory system. At the extreme forward angles the Coulomb scattering was assumed. Thus estimated background amounted to 6 percent of whole proton pulses at 8° in the laboratory system and decreases with increasing angle. Uncertainty in this background subtraction was supposed to be a half of the estimated background, though it might be rather over estimation, because of safety.

At the forward angles some protons scattered from the structures in the scattering chamber entered the detector as mentioned in paragraph C of section 2. This background was measured by evacuating the gas target chamber.

Error in the alignment of instruments to the incident beam was 0.001 radian. This produced uncertainty of 2 percent in differential cross section at 8° in the laboratory system. The uncertainty decreased rapidly with increasing angle. The scattering angle was determined by reading the precise graduations on the periphery of the turn table. Its uncertainty is 0.01 degrees. Error in determination of the total number of incident protons was 0.8 percent.

Quadratic combination of the errors described above was in general less than 2 percent except at forward angles.

Counting statistics in the case of excitation curves was ranging from 0.4 to 1.7 percent.

The uncertainties of the mean energy of the proton beam in the scattering volume were less than 0,4 percent. The energy spread of the incident beam was 0.5 percent.

§ 5. Discussions

It is worthwhile to compare the results of the present work with the experimental and theoretical results so far obtained.

In proton-helium scattering, orbital angular momentum is no longer a constant of motion in virtue of spin-orbit interaction and waves of different total angular momentum are scattered differently. Thus, the cross section is expressed in terms of S phase shift δ_0, $P_{1/2}$ phase shift δ_1^-, $P_{3/2}$ phase shift δ_1^+, $D_{3/2}$ phase shift δ_2^-, $D_{5/2}$ phase shift δ_2^+, and so on. We attempted at first to fit the angular distribution at 14.32 MeV with S- and P-waves only. The present analysis is not thorough, but tentatively accomplished by trial and error, not by the iteration with regular step. We started with the values of phase shifts obtained by interpolation between the results at 9.48 MeV[20] and at 17.45 MeV.[21] A set of $\delta_0=-77°42'$, $\delta_1^-=50°0'$ and $\delta_1^+=92.36'$ gives the agreement with the experimental angular distribution, except the region of Coulomb-nuclear interference. The calculated values of differential cross section are listed in the fourth column of Table III. They are also shown in Fig. 3 together with experimental values. The values of phase shifts are compatible with those obtained by Brockman.[1] However, it was difficult to fit in the experimental results with S- and P-waves only.

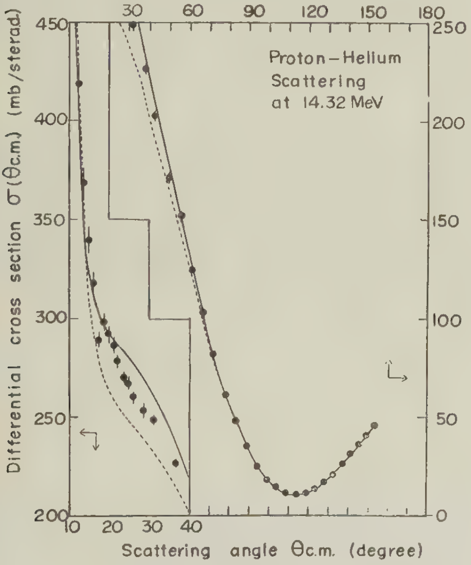

Fig. 3. Angular distribution at 14.32 MeV. The dashed curve indicates the calculated cross sections with *S*- and *P*-waves only (forth column of Table II). The solid curve indicates the calculated cross sections with phase shifts obtained by Gammel and Thaler[22] (fifth column of Table II).

Gammel and Thaler[22] have made an analysis in terms of an optical model potential interaction between the proton and alpha-particle. The purpose of their work was to predict the polarization of protons than the angular distribution. But it is interesting to use the phase shifts calculated by them in the angular distribution, as an example containing larger D phase shifts. The values of phase shifts were taken from Table III of reference 22. The results are listed in the fifth column of Table III and shown in Fig. 3. The fit is better than that with S- and P-waves only, but some over compensations are seen.

The calculations were made also to the angular distribution at 12.04 MeV. The results are shown in Table III and in Fig. 4. Almost the same discussions as above can be applied to this case. As to the case with S- and P-waves only, however, appreciably smaller values of phase shifts than those obtained by Brockman[1] were needed to fit particularly the forward angular distribution, and the agreement between the experimental and calculated values becomes very good. Consequently the decrease of $P_{1/2}$ and $P_{3/2}$ phase shifts might be more rapid from 9.5 MeV to 12 MeV than acceded so far.

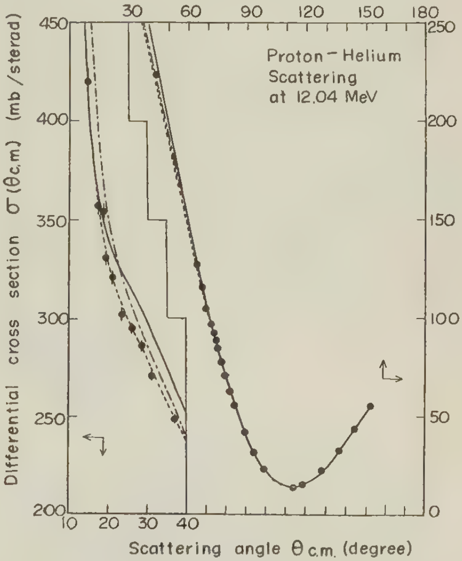

Fig. 4. Angular distribution at 12.04 MeV. The dashed curve indicates the calculated cross sections with *S*- and *P*-waves only (forth column of Table III). The solid curve indicates the calculated cross sections with phase shifts obtained by Gammel and Thaler[22] (fifth column of Table III). The dash-dotted curve indicates the calculated cross sections with $\delta_0=-66°54'$, $\delta_1^-=60°6'$ and $\delta_1^+=108°42'$, which were obtained by Brockman (see Table III of reference 1).

The excitation curves are shown in Fig. 5 in the form of $k^2\sigma(\theta\,\text{c.m.})$ versus proton energy together with other experimental results,(1, 20, 21, 24, 25, 26) k being the wave number of incident proton. The $k^2\sigma$ curves increase monotonously with increasing energy from 7.5 MeV to above 10 MeV and then decrease slightly to 17.45 MeV, except at 25°31′. The very broad resonance of $P_{1/2}$-wave is included in this energy range and recently Miller and

Phillips[23] have analysed the results hitherto obtained in terms of the dispersion theory of Wigner and Eisenbud. They have decided level parameters. $(E_{res})_{lab}$ for $P_{1/2}$ state has become 10.8 MeV.

We add a comparison between the values of differential cross section at energies near 9.5 MeV, because several results have been conflicting each other. The results by Cork and Hartsough at 9.73 MeV[25] and by Williams and Rasmussen at 9.76 MeV[26] agree well with the present work. The agreement of Putnam's results[20] at 9.48 MeV is also good except at 25°31′. Low values of the results at 9.55 MeV by Freemantle et al.[24] are seen in a forward hemisphere.

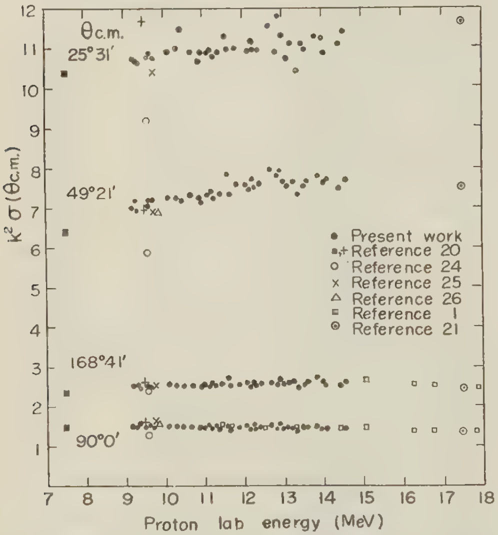

Fig. 5. Excitation curves. The results are shown together with cross sections obtained so far.

§ 6. Conclusions

D-wave phase shifts are closely related with the shape of angular distribution at forward angles and they are small but cannot be neglected in the present energy range. The experiments on the full angular distribution at higher energy such as 20 MeV are desirable for the behavior of D-wave phase shifts.

There is no resonance of $5^+/2$ or $1^+/2$ state between 9.2 MeV and 14.5 MeV. The excitation curves together with angular distributions will serve to a precise analysis for $P_{1/2}$ state.

Thorough phase shift analysis will be accomplished after obtaining the results of the polarization in proton-helium scattering in the present energy range, on which we are now making measurements.

Acknowledgement

The author is particularly indebted to Professor S. Kikuchi for his guidance and encouragement throughout the course of this work; Professors S. Suwa and I. Hayashi, and Messrs. K. Nisimura and K. Fukunaga for their active participation in obtaining the data. Gratitude is due to the operating crew of the cyclotron, particularly Messrs. T. Karasawa, A. Suzuki and H. Ogawa.

References

1) The scattering of protons by helium was reviewed by K. W. Brockman: Phys. Rev. **108** (1957) 1000. The scattering of neutrons by helium was reviewed by J. D. Seagrave: Phys Rev. **92** (1953) 1222. See also K. B. Mather and P. Swan: *Nuclear Scattering* (Camb. Univ. Press, 1958).
2) C. L. Critchfield and D. C. Dodder: Phys. Rev. **76** (1949) 602. D. C. Dodder and J. L. Gammel: Phys. Rev. **88** (1952) 520. R. K. Adair: Phys. Rev. **86** (1952) 155.
3) E. K. Warburton and J. N. Mc Gruer: Phys Rev. **105** (1957) 639.
4) K. W. Brockman: Phys. Rev. **102** (1956) 391.
5) S. Sack, L. C. Biedenharn and G. Breit: Phys. Rev. **93** (1954) 321. S. Hochberg, H. S. W. Massey, H. H. Robertson and L. Underhill: Proc. Phys. Soc. London **A**, **68** (1955) 746.
6) A. Sugie, P. E. Hodgson and H. H. Robertson: Proc. Phys. Soc. London **A**, **70** (1957) 1. T. Terasawa: Progr. Theor. Phys. **22** (1959) 150.
7) S. Nagata, T. Sasakawa T. Sawada and R. Tamagaki: Progr. Theor. Phys. **22** (1959) 274.
8) Supplement of Progr. Theor. Phys. **3** (1956).
9) T. W. Bonner, J. P. Conner and A. B. Lillie: Phys. Rev. **88** (1952) 473. W. E. Burcham: *Handbuch der Physik*, Bd. XL, 1, (Springer-Verlag, 1957).
10) A. Galonsky and C. H. Johnson: Phys. Rev. **104** (1956) 421.
11) S. Kikuchi et al.: J. Phys. Soc. Japan (to be published).
12) W. A. Higinbotham and S. Rankowitz: Rev. Sci. Instr. **22** (1951) 688.
13) W. H. Jordan and P. R. Bell: Rev. Sci. Instr. **18** (1947) 703.
14) C. W. Johnstone: Nucleonics **11**, no. 1 (1953) 36.
15) J. C. Corelli, M. Livingston and L. Seidlitz: Rev. Sci. Instr. **28** (1957) 471.

16) H. Bichsel, R. F. Mozley and W. A. Aron: Phys. Rev. **105** (1957) 1788.
17) D. O. Caldwell and J. R. Richardson: UCLA-22, 1954 (unpublished). C. L. Critchfield and D. C. Dodder: Phys. Rev. **75** (1949) 419.
18) W. E. Burcham, W. M. Gibson and A. Hossaian: Phys. Rev. **92** (1953) 1266. R. G. Freemantle, D. J. Prowse and J. Rotblat: Phys. Rev. **96** (1954) 1268. B. B. Kinsey and T. Stone: Phys. Rev. **103** (1956) 975.
19) S. Kikuchi, J. Sanada, S. Suwa, I. Hayashi, K. Nisimura and K. Fukunaga: J. Phys. Soc. Japan (to be published).
20) T. M. Putnam, J. E. Brolley, Jr. and L. Rosen: Phys. Rev. **104** (1956) 1303.
21) K. W. Brockman: Phys. Rev. **102** (1956) 391.
22) J. L. Gammel and R. M. Thaler: Phys. Rev. **109** (1958) 2041.
23) P. D. Miller and G. C. Phillips: Phys. Rev. **112** (1958) 2043.
24) R. G. Freemantle, T. Grotdal, W. M. Gibson, R. Mc Keague, D. J. Prowse and J. Rotblat: Phil. Mag. **45** (1954) 1090.
25) B. Cork and W. Hartsough: Phys. Rev. **96** (1954) 1267.
26) J. H. Williams and S. W. Rasmussen: Phys. Rev. **98** (1955) 56.

JOURNAL OF THE PHYSICAL SOCIETY OF JAPAN Vol. 14, No. 11, NOVEMBER, 1959

A Large Multiplate Cloud Chamber for Cosmic Ray Observation

By Saburo MIYAKE, Kensaku HINOTANI, Itsuo KATSUMATA
and Tatsunosuke KANEKO

Osaka City University, Osaka, Japan

(Received July 27, 1959)

A large multiplate cloud chamber has been constructed for the observation of the extensive air showers by extremely high energy cosmic radiations. Its dimensions of sensitive volume are 200 cm wide, 130 cm high and 90 cm deep. It contains 21 sheets of lead plate of 1 cm thick, so that the total thickness of the absorber corresponds to about 48 radiation length or about three times of nuclear interaction mean free path. The design and operational character are reported in this paper.

§ 1. Introduction

The main purpose of the use of a large multiplate cloud chamber in the present case is to study high energy events by cosmic ray particles, especially, to observe directly the central region of extensive air showers. The frequency of such events is very small but each event has proper characteristic. The structure of events seems to be so complicated that other equipments, for example, G.M. counters or ionization chambers etc. except the cloud chamber are not useful to clarify the true structure. A multiplate cloud chamber is very useful in the stage of qualitative measurements but the dimensions of the chambers so far used are too small for this purpose. Since it is believed that the core region which supplies the energy to extensive shower region has the spread of about 1–2 m, and this region contains high energy nucleons, mesons and numerous electrons and γ rays; it is thought to be favourable that the dimension of the chamber is about 2 m to study the structure of the core region and the amount of the material in the chamber which acts as an absorber or target of high energy event is enough to observe various components separately.

The multiplate cloud chamber reported here has been constructed in 1958 and it is now being used at cosmic ray observatory of Tokyo University on Mt. Norikura.

§ 2. Design and Construction

Cloud chamber

Fig. 1 shows the crossectional sketch of the cloud chamber. It is made of steel and the inside surface of the chamber is plated with nickel. The total sensitive volume is about 3 m^3 although the dead space for photograph was decreased. The glass plates of front and both sides are tempered glass (" Temperite " Asahi Glass Co.) of 1.2 cm thickness. The chamber was over pressure type and glass plates were reinforced by out side steel frames as they do not obstruct the illumination and the photographing. The width was planned to enlarge as much as possible and the limit was at 200 cm due to restriction for manufacturing of the front glass. The height of the chamber was determined as 130 cm to be possible to contain about twenty sheets of lead absorber of about 1 or 2 cm thick. The depth was determined as 90 cm from restriction of the depth of a focus in photographic system and the illuminated depth of 65 cm was taken by photograph. The lead plates were enclosed by steel sheet of 0.25 cm thick and steel frame to strengthen for the bending and their surface was coated by nickel to prevent rust and was polished for good reflection of light. A cleaning electric field was given to the lead plates alternately.

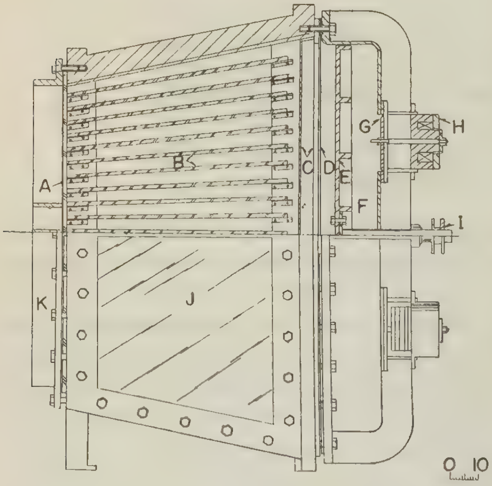

Fig. 1. Cross sectional sketch of the cloud chamber, showing *A*, the front glass; *B*, lead plates; *C*, velvet attached perforated plate; *D*, rubber diaphragm for expansion; *E*, stopper of rubber diaphragm controlling the expansion rate; *F*, back chamber space; *G*, exhaust valve for expansion; *H*, electromagnet for exhaust valve; *I*, rod with a toothed wheel of chain controlling the position of the stopper; *J*, the side glass; *K*, frame for front glass.

The chamber was tested at 1 atm. and used at 0.5 atm. over the atmospheric pressure. In operation, the bending by inner pressure is about 1 cm at the centre of the front glass plate.

Expansion mechanism

A rubber diaphragm which is pressed against a perforated plate with a large number of 6 mm holes is moved to its stopper by reducing the pressure of the back chamber. Six exhaust valves were installed in the back chamber as shown in Fig. 2 and they are operated by electromagnet. The expansion of the chamber is made by opening the exhaust valves simultaneously. When an expansion is made, the back chamber is compressed by opening a electromagnetic valve to an external tank containing compressed air of about 4 atm. The chamber is fully expanded after about 10 milliseconds, from the trigger pulse, and recompressed in about one min. After an ex-

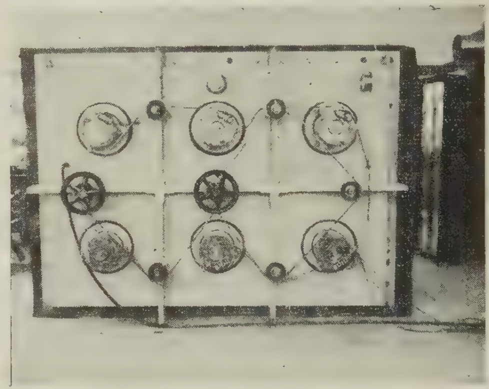

Fig. 2. Back view of the cloud chamber showing the six exhaust valves and seven rods for control of the stopper. Upper small valve is slow expansion valve.

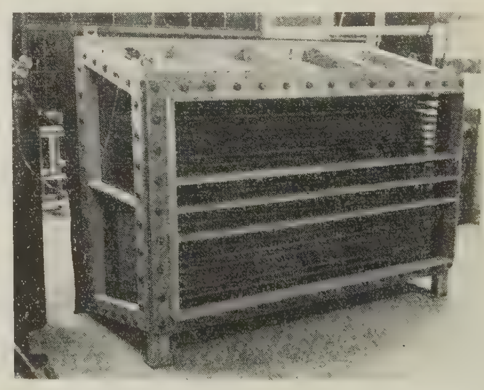

Fig. 3. Photograph of the cloud chamber.

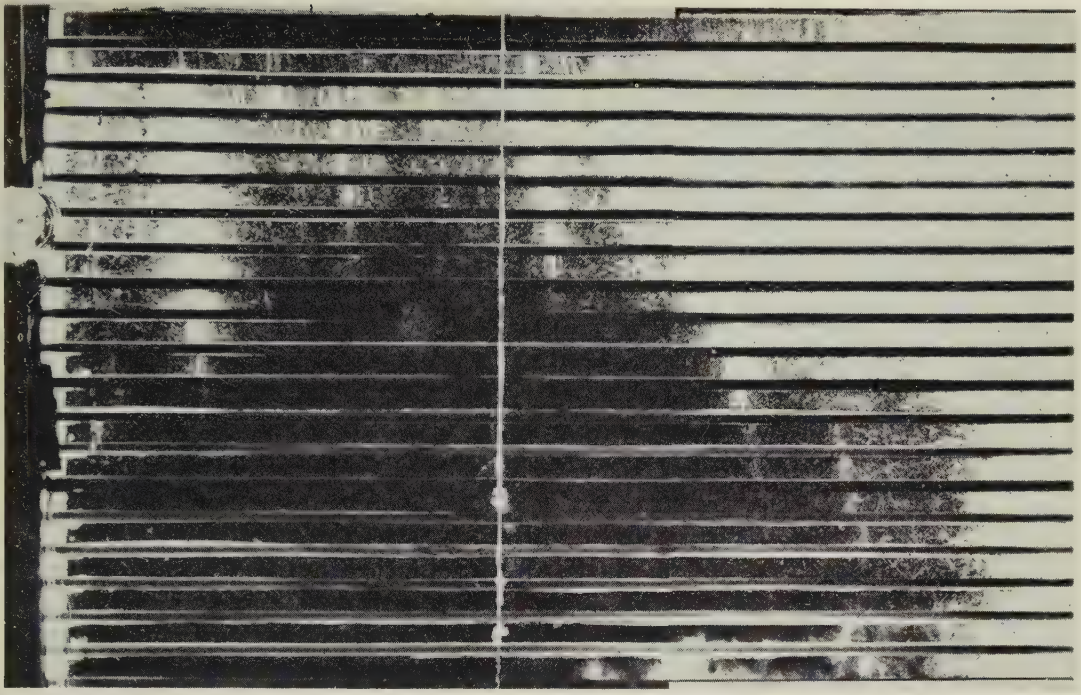

Fig. 4(a). Cinemascopic picture of an extensive air shower core. The shower size is estimated as 3×10^6 particles from the data of scintillation counters and the position of the shower core is 1 m on the right from the centre, namely, in this picture, the core falls on the right hand edge of this picture. From the number of tracks in the top space, the lateral distribution of charged particles in the vicinity of the shower core is obviously seen and energy flow distribution is also seen from the depth that the electron cascade has diminished.

pansion, slow expansions are repeated four times by using of slow expansion valve to clear out fog nuclei. The dead time of the chamber after an expansion is about 15 min.

Illumination

The chamber is illuminated from both sides by three flash tubes respectively. Light from the flash tube is reflected by parabolic mirror and illuminates the chamber through the solar slit. The flash tube is a xenon discharge tube which is made of fused quartz tube and hard glass sheath. The electric power source of flash tube is supplied from a condenser bank charged up to 10 kv for each tube.

Photography

Photographs were stereoscopically taken by three cameras. Two 35 mm cameras were mounted at a distance of 330 cm from the centre of the chamber as stereoangle was 17°. A 60×90 mm camera was mounted at front of the chamber at same distance. Photographs were taken at an aperture value of 8 to 11. The cameras are operated automatically by electromagnetic relay and motor.

Control circuits

The control circuit is composed of gate circuits, time sequence circuits, delayed pulse generators and operational circuits for expansion valve, cameras, sweeping electric field, flash tubes slow expansion valves and compression valves. And long delay circuit for the dead time interval of the chamber is composed of univibrator and scaler circuit and it makes also to operate a slow valve repeatedly.

Safety precausions

The cloud chamber is filled with 0.5 atmospheric over pressure argon gas. In a case of a diaphragm failure, the compressed air flows into the cloud chamber, and so the compressed air may results the destruction of the chamber. To avoid such accident, prevention has been made to get the compressed air out of the chamber instantaneouslly by opening the exhaust valves.

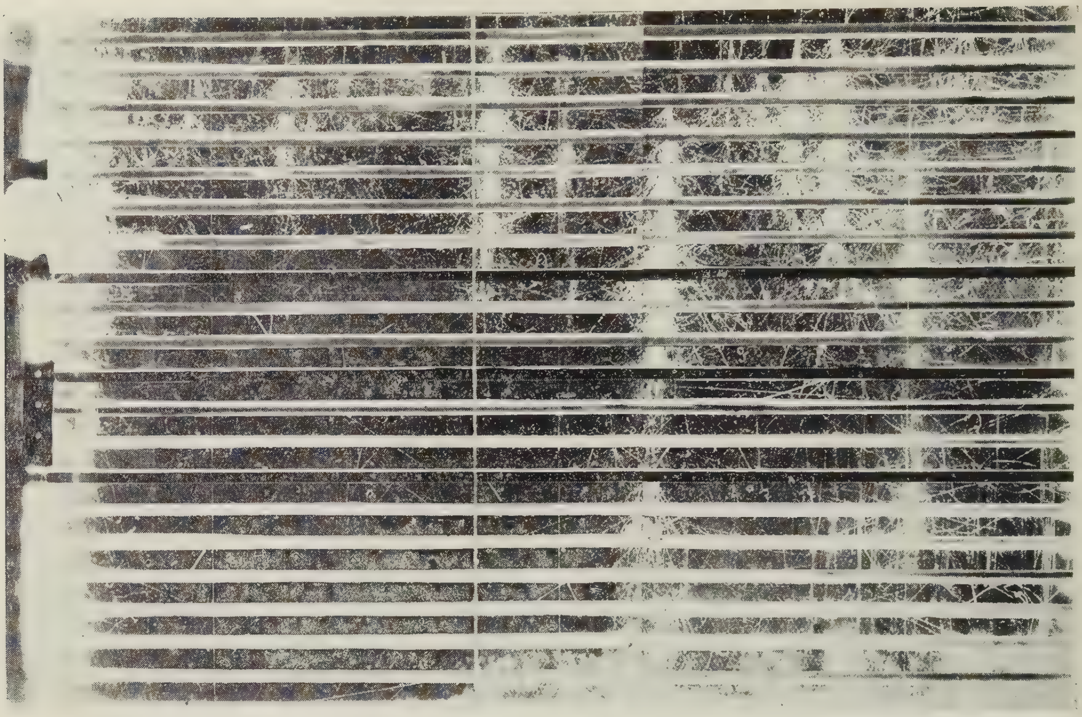

Fig. 4(b). This picture also shows the central region of extensive air shower. The shower size is estimated as 8×10^5 particles and the position of the shower core is about 1 m from the centre of the chamber. The age of the air shower seems to be young and hard showers by high energy nucleon components are seen in lower part of the chamber.

Chamber operations

The cloud chamber has been operated with ten plastic scintillators to study extensive air showers. Figures 4 a and b show typical photographs of the central region of the extensive air shower.

JOURNAL OF THE PHYSICAL SOCIETY OF JAPAN Vol. 14, No. 11, NOVEMBER, 1959

On the Theory of Brownian Motion and Spin Relaxation*

By Takeyasu KOTERA and Morikazu TODA

Department of Physics,
Faculty of Science, Tokyo University of Education,
Tokyo, Japan

(Received August 3, 1959)

The Brownian motion of a harmonic oscillator is treated quantum-mechanically and the same method is applied to the relaxation of a spin. The method is quite general and applicable to a system displaced from the equilibrium state by an arbitrary amount initially. The oscillator or the spin is interacting with a thermostat composed of a great number of harmonic oscillators. The equation of motion is solved in operator form taking average as to the thermostat to the second order of the interaction parameter. The Langevin equation, the Kramers-Chandrasekhar equation for a harmonic oscillator and the Bloch equation for a static field are derived.

§ 1. Introduction

The problem of Brownian motion has been investigated by many authors and formulated in many equivalent forms. It can be said, however, that the problem is recovering its fundamental importance since it is intimately connected to the fundamental theory of the statistical mechanics, that is, to the statistical mechanics of the irreversible processes. While the latter is concerned with large systems in which irreversible processes take place, the former focuses attention on small systems which behave purely mechanically under the influence of the environments.

The essential feature of the problem of the Brownian motion is to ask the motion of a small system under the influence of random, fluctuating disturbances. The motion of a colloidal particle in a gas or in a liquid is the best known example.

Since the classical works of Einstein and of Smoluchowsky the problem of Brownian motion is usually treated by the theory of stochastic processes. Useful concepts in this field, such as friction constant, fluctuating force, and relaxation time, common relations, e.g. Einstein relation, and important equations, Smoluchowski-Chapman equation and Langevin equation, are established in early days. Kramers[1)] generalized the idea of random flights and derived the so-called Kramers equation, which was extensively studied by Chandrasekhar.[2)] In the theory of stochastic processes, the equation which characterizes the dynamical system is the Langevin equation; by its aid estimation of the moments required in reducing the Smoluchowski-Chapman equation into Fokker-Planck type of differential equation is made possible.

From the microscopic point of view, however, the current way of analysis[2)] is not perfect in the sense that one has to introduce some hypothesis on macroscopic and unknown parameters such as the friction constant and the correlation constant of the fluctuating force. The relation between these two constants is usually determined by fitting the asymptotic behavior of the system under a certain condition to that of the equilibrium state. And the assumption of splitting the force into two parts is only justified by the results obtained afterwards. On the other hand, if one applies the general theory of the statistical mechanics of the irreversible processes from the beginning to the special system under consideration one will be led to a more consistent theory.

In previous papers[3),4)] one of the authors developed a method of treating Brownian motion which enables us to give the Kramers equation and the Langevin equation their dynamical ground: In a paper[3)] it was shown that the Liouville equation in quantum-mechanical form for the density matrix can be transformed into a operator equation which goes over to the classical Kramers-Chandrasekhar equation by the Wigner transformation, and that the Langevin equation can be derived therefrom. In the other paper it was shown, in classical mechanics, that the Langevin equation can be derived directly from the Newton's equation of motion and that the friction constant, random force and the relation between them are derived naturally in the course of calculation.

---

* Parts of the paper are based on a thesis submitted by Dr. Kotera in partial fulfillment of the requirements for a D. S. degree in Physics, Tokyo University of Education, 1959.

The purpose of this paper is to examine from purely microscopic point of view, starting from the Heisenberg's equation of motion, the validity of the current results, such as the Langevin equation for Brownian motion. To get through the analysis completely the interaction between the system and the thermostat is assumed. The problem is thus reduced to very special cases, without loosing, however, the essential point of the problem.

The point is that the irreversible behavior and the state of thermal equilibrium to approach are derived from the Heisenberg equation without any *ad hoc* assumption except that the thermostat is always in equilibrium.

The system, which we shall consider, consists of many oscillators interacting one another. We shall divide those into two parts: one oscillator whose motion we shall observe and the other oscillators which shall play as a whole the role of a thermostat. To treat this system we shall investigate the equation of motion of operators in Heisenberg representation.

We shall separate from each of these operators an operator with bar. Instead of considering the interaction within the thermostat explicitly we shall put some conditions (cf. Eq. (29)) on the barred operators of the thermostat assuming that the thermostat is always in the thermal equilibrium state.

The separation of an operator can be made in such a way that the time rate of change of the barred operator is of second order with respect to the interaction parameter. The rest of the operator is the part depending on other oscillators to the first order of the interaction parameter.

To get the relaxation equation for the density matrix in the $x-p$ representation we shall transfer from the Heisenberg representation to the Schroedinger representation. But we may treat the density matrix from the start (cf. Appendix B and the reference 3). When we make the classical distribution function from the density matrix using Wigner's method we get the Kramers-Chandrasekhar equation.

In the same manner we shall derive the Bloch equation[5] for a spin in a static magnetic field. The spin, whose magnitude is $\frac{1}{2}$, is then assumed to be coupled with a thermostat composed of a great number of harmonic oscillators.

§ 2. The Basic Equation for the System

We consider a system of many harmonic oscillators interacting one another. Then the hamiltonian is

$$\mathscr{H}=H_0+\lambda V\,, \tag{1a}$$

where

$$H_0=\sum_i H_i\,,\qquad H_i=\hbar\omega_i(a_i{}^*a_i+\tfrac{1}{2})\,. \tag{1b}$$

Suffix i labels the i-th oscillator. a_i and $a_i{}^*$ are related to the coordinate x_i and the momentum p_i of the i-th oscillator by the relations

$$\left.\begin{aligned} x_i&=\sqrt{\frac{\hbar}{2\omega_i m_i}}\,(a_i+a_i{}^*)\,,\\ p_i&=-i\sqrt{\frac{\hbar m_i\omega_i}{2}}\,(a_i-a_i{}^*)\,. \end{aligned}\right\} \tag{2}$$

We shall consider the Brownian motion of a specified oscillator, say, the i-th oscillator and take the other oscillators $j, k, \cdots (\neq i)$ as forming a thermostat. We shall use this specification throughout and call the i-th oscillator the central oscillator whose Brownian motion is to be noticed. Suffix i is used for the central oscillator only and suffixes j, k, are used always for oscillators in the thermostat.

Farther we assume that the leading terms of the interaction between the oscillators including the central one to be quadratic with respect to the displacements of the oscillators. Thus

$$\lambda V=\lambda\sum_j{}' c_{ij}x_ix_j+\lambda\sum_{j<k}{}' c_{jk}x_jx_k\,. \tag{3}$$

The first term on the right hand side of this equation represents the interaction of the central oscillator with the thermostat and the second term is responsible for the interaction within the thermostat. More generally we may add a term $V'(x_j, x_k, \cdots)$ to the right hand side of Eq. (3) assuming that V' depends on the coordinates of the thermostat only and that V' is of higher order in λ, the coupling constant: $V'=O(\lambda^2)$.[†] This term consists of unharmonic interaction within the thermostat and seems necessary to garantee the state of thermal equilibrium for the thermostat. However, as will be seen below, so long as we are concerned with the Brownian motion of the central oscillator, introduction of this extra-term gives no essential modification in the following calculation. We shall therefore omit this term for a while.

The equation of motion for the operator a_i runs

$$\dot{a}_i=-i\omega_i a_i+if_i/\sqrt{2\omega_i m_i}\,, \tag{4}$$

with

$$f_i=-\lambda\sum_j{}' c_{ij}/\sqrt{2\omega_j m_j}\cdot(a_j+a_j^*)\,. \tag{5}$$

A similar equation holds for a_i^*. Making use of the canonical transformation

$$\left.\begin{aligned} A_i&=e^{-(i/\hbar)H_0t}a_i\,e^{(i/\hbar)H_0t}=e^{i\omega_i t}a_i\,,\\ A_i^*&=e^{-(i/\hbar)H_0t}a_i^*\,e^{(i/\hbar)H_0t}=e^{-i\omega_i t}a_i^*\,, \end{aligned}\right\} \tag{6}$$

we rewrite Eq. (4) and its conjugate equation in the form

$$\left.\begin{aligned} \dot{A}_i&=if_i\,e^{i\omega_i t}/\sqrt{2\omega_i m_i}\,,\\ \dot{A}_i^*&=-if_i\,e^{-i\omega_i t}/\sqrt{2\omega_i m_i}\,. \end{aligned}\right\} \tag{7}$$

We shall introduce the interaction adiabatically from the infinite past ($t=-\infty$). This can be done by the replacement

$$\lambda\rightarrow\lambda\,e^{st}$$

and by taking the limit $s\rightarrow+0$.

Using Eqs. (5) and (6) we rewrite Eqs. (7) as

$$\left.\begin{aligned} \dot{A}_i&=\frac{-i\lambda}{\sqrt{2\omega_i m_i}}\sum_j{}'\frac{c_{ij}}{\sqrt{2\omega_j m_j}}(e^{-i\omega_j t}A_j+e^{i\omega_j t}A_j^*)e^{st+i\omega_i t}\,,\\ \dot{A}_i^*&=\frac{i\lambda}{\sqrt{2\omega_i m_i}}\sum_j{}'\frac{c_{ij}}{\sqrt{2\omega_j m_j}}(e^{-i\omega_j t}A_j+e^{i\omega_j t}A_j^*)e^{st-i\omega_i t}\,. \end{aligned}\right\} \tag{8}$$

These are the equations of motion for the central oscillator. We have analogous equations for the oscillator j of the thermostat. For instance for A_j,

$$\begin{aligned} \dot{A}_j=&\frac{-i\lambda}{\sqrt{2\omega_j m_j}}\frac{c_{ji}}{\sqrt{2\omega_i m_i}}(e^{-i\omega_i t}A_i+e^{i\omega_i t}A_i^*)e^{st+i\omega_j t}\\ &-\frac{i\lambda}{\sqrt{2\omega_j m_j}}\sum_k{}''\frac{c_{jk}}{\sqrt{2\omega_k m_k}}(e^{-i\omega_k t}A_k+e^{i\omega_k t}A_k^*)e^{st+i\omega_j t}\,, \end{aligned} \tag{9}$$

where the sum in the second term is taken over the thermostat oscillators k excluding j. If we add the extra-term V' mentioned before, we have an extra-term on the right hand side of Eq. (9). This is the only effect of V'.

If there were no interaction, $\lambda=0$, operators A_i, A_j, etc would be constant in time. We deal with the case where the coupling constant λ is sufficiently small, and want to solve the problem up to the second order in λ. As in the previous paper[3)] we divide the operators A and A^* into two parts. For instance

$$\begin{aligned} A_j=\overline{A}_j&-\frac{i\lambda}{\sqrt{2\omega_j m_j}}\frac{c_{ji}}{\sqrt{2\omega_i m_i}}\left(\overline{A}_i\int_{-\infty}^t e^{st+i(\omega_j-\omega_i)t}\,dt+\overline{A}_i^*\int_{-\infty}^t e^{st+i(\omega_j+\omega_i)t}\,dt\right)\\ &-\frac{i\lambda}{\sqrt{2\omega_j m_j}}\sum_k{}''\frac{c_{jk}}{\sqrt{2\omega_k m_k}}\left(\overline{A}_k\int_{-\infty}^t e^{st+i(\omega_j-\omega_k)t}\,dt+\overline{A}_k^*\int_{-\infty}^t e^{st+i(\omega_j+\omega_k)t}\,dt\right). \end{aligned} \tag{10}$$

Or

$$\begin{aligned} A_j=\overline{A}_j&-\frac{i\lambda}{\sqrt{2\omega_j m_j}}\frac{c_{ji}}{\sqrt{2\omega_i m_i}}\left(\overline{A}_i\frac{e^{st+i(\omega_j-\omega_i)t}}{s+i(\omega_j-\omega_i)}+\overline{A}_i^*\frac{e^{st+i(\omega_j+\omega_i)t}}{s+i(\omega_j+\omega_i)}\right)\\ &-\frac{i\lambda}{\sqrt{2\omega_j m_j}}\sum_k{}''\frac{c_{jk}}{\sqrt{2\omega_k m_k}}\left(\overline{A}_k\frac{e^{st+i(\omega_j-\omega_i)t}}{s+i(\omega_j-\omega_k)}+\overline{A}_k^*\frac{e^{st+i(\omega_j+\omega_k)t}}{s+i(\omega_j+\omega_k)}\right). \end{aligned} \tag{11}$$

We have the conjugate equation for A_j^*.

Similarly we have

[†] This restriction can be omitted (cf. § 6).

$$A_i=\overline{A}_i-\frac{i\lambda}{\sqrt{2\omega_i m_i}}\sum_j{}'\frac{c_{ij}}{\sqrt{2\omega_j m_j}}\left(\overline{A}_j\frac{e^{si+i(\omega_i-\omega_j)t}}{s+i(\omega_i-\omega_j)}+\overline{A}_j{}^*\frac{e^{st+i(\omega_i+\omega_j)t}}{s+i(\omega_i+\omega_j)}\right), \tag{12}$$

and the conjugate equation for $A_i{}^*$.

We note the fact that A_i, A_j, etc fluctuate: their time derivatives are first order in λ. The time rate of change of $\overline{A}_i$, $\overline{A}_j$, etc are much smaller because it is second order in λ. This can be shown easily from Eqs. (9), (10) and their conjugate equations.

Farther we can verify that

$$[\overline{A}_j, \overline{A}_i]=\mathrm{O}(\lambda^2)\,, \qquad [\overline{A}_j{}^*, \overline{A}_i{}^*]=\mathrm{O}(\lambda^2)\,, \qquad [\overline{A}_j, \overline{A}_i{}^*]=\delta_{ji}+\mathrm{O}(\lambda^2)\,. \tag{13}$$

These relations will be used later on. We have to note also that terms like $[\overline{A}_j, \overline{A}_i{}^*]$ or $[A_j{}^*, \overline{A}_i]$ for $j\neq i$ are of first order in λ.

In order to withdraw the interaction between the oscillators of the thermostat, in deriving the equation of motion of the central oscillator i, we shall take the average (of functions of the operators $\overline{A}_j$ and $\overline{A}_j{}^*$) as to the thermostat which is always in the state of thermal equilibrium. Especially we shall assume that the average $\langle\overline{A}_j\rangle$ of $\overline{A}_j$ $(j\neq i)$ or $\langle\overline{A}_j{}^*\rangle$ of $\overline{A}_j{}^*$ vanishes. So, in deriving the time derivative of the operators of the i-th oscillator we may put

$$c_{jk}=0 \qquad \text{for} \qquad j, k\neq i\,. \tag{14}$$

Using Eq. (11) and its conjugate equation we get from Eq. (8)

$$\begin{aligned}\dot{A}_i=&-\frac{i\lambda}{\sqrt{2\omega_i m_i}}\sum_j{}'\frac{c_{ij}}{\sqrt{2\omega_j m_j}}(\overline{A}_j e^{-i\omega_j t}+\overline{A}_j{}^* e^{i\omega_j t})\,e^{st+i\omega_i t}\\ &-\frac{\lambda^2e^{2st}}{2\omega_i m_i}\sum_j{}'\frac{c_{ij}{}^2}{2\omega_j m_j}\left(\overline{A}_i\left[\frac{1}{s+i(\omega_j-\omega_i)}-\frac{1}{s-i(\omega_j+\omega_i)}\right]\right.\\ &\left.\qquad+\overline{A}_i{}^* e^{2i\omega_i t}\left[\frac{1}{s+i(\omega_j+\omega_i)}-\frac{1}{s-i(\omega_j-\omega_i)}\right]\right),\end{aligned} \tag{15}$$

and its conjugate equation. Taking the limit $s\to+0$, we make use of the relation

$$\lim_{s\to+0}\left(\frac{1}{s+ix}\right)=\pi\delta(x)-i\,\mathrm{P}\left(\frac{1}{x}\right).$$

Then Eq. (15) may be rewritten as follows:

$$\begin{aligned}\dot{A}_i=&-\frac{i\lambda}{\sqrt{2\omega_i m_i}}\sum_j{}'\frac{c_{ij}}{\sqrt{2\omega_j m_j}}(\overline{A}_j e^{-i\omega_j t}+\overline{A}_j{}^* e^{i\omega_j t})\,e^{i\omega_i t}\\ &-\frac{\lambda^2}{2\omega_i m_i}\sum_j{}'\frac{c_{ij}{}^2}{2\omega_j m_j}\left(\overline{A}_j\left[\pi\delta(\omega_j-\omega_i)-i\,\mathrm{P}\left(\frac{2\omega_j}{\omega_j{}^2-\omega_i{}^2}\right)\right]\right.\\ &\left.\qquad+\overline{A}_i{}^* e^{2i\omega_i t}\left[-\pi\delta(\omega_j-\omega_i)-i\,\mathrm{P}\left(\frac{2\omega_j}{\omega_j{}^2-\omega_i{}^2}\right)\right]\right).\end{aligned} \tag{16}$$

Similarly the conjugate equation is obtained for $A_i{}^*$.

§ 3. Langevin Equation

Differentiating Eq. (6) with respect to time, we have

$$\left.\begin{aligned}\dot{a}_i&=-i\omega_i a_i+e^{-i\omega_i t}\dot{A}_i\,,\\ \dot{a}_i{}^*&=i\omega_i a_i{}^*+e^{i\omega_i t}\dot{A}_i{}^*\,.\end{aligned}\right\} \tag{17}$$

By the aid of Eq. (16), we may rewrite the above equations, to the second order in λ, as (in the second order terms of λ in Eq. (16), $\overline{A}_i$ or $\overline{A}_i{}^*$ may be replaced by A_i or $A_i{}^*$)

$$\dot{a}_i=-i\omega_i a_i-i\lambda\sqrt{\frac{1}{2\omega_i m_i}}\sum_j{}'\frac{c_{ij}}{\sqrt{2\omega_j m_j}}(\bar{A}_j e^{-i\omega_j t}+\bar{A}_j^* e^{i\omega_j t})$$
$$-\frac{\lambda^2}{2\omega_i m_i}\sum_j{}'\frac{c_{ij}^2}{2\omega_j m_j}\left(a_i\left[\pi\delta(\omega_j-\omega_i)-i\,\mathrm{P}\left(\frac{2\omega_j}{\omega_j^2-\omega_i^2}\right)\right]\right.$$
$$\left.+a_i^*\left[-\pi\delta(\omega_j-\omega_i)-i\,\mathrm{P}\left(\frac{2\omega_j}{\omega_j^2-\omega_i^2}\right)\right]\right)\,, \tag{18}$$

and the conjugate equation for a_i^*. Considering the relation (2) and disregarding the principal value terms (for these represent the reaction by the thermostat oscillators on the central oscillator resulting only a shift of frequency or a level-shift), we find

$$p_i=m_i\dot{x}_i\,, \tag{19a}$$

$$\dot{p}_i+\zeta p_i+\omega_i^2 m_i x_i=-\lambda\sum_j{}' c_{ij}\sqrt{\frac{\hbar}{2\omega_j m_j}}(\bar{A}_j e^{-i\omega_j t}+\bar{A}_j^* e^{i\omega_j t})\,, \tag{19b}$$

where

$$\zeta=\frac{\pi\lambda^2\bar{c}^2 g}{2\omega_i^2 m_i m_j} \tag{19c}$$

and g is the density of the thermostat oscillators at $\omega_j=\omega_i$ and $\bar{c}^2$ is the average of c_{ij}^2 over the thermostat oscillators at $\omega_j=\omega_i$.

From Eqs. (19a) and (19b) we have

$$\ddot{x}_i+\zeta\dot{x}_i+\omega_i^2 x_i=-\frac{\lambda}{m_i}\sum_j{}' c_{ij}\sqrt{\frac{\hbar}{2\omega_j m_j}}(\bar{A}_j e^{-i\omega_j t}+\bar{A}_j^* e^{i\omega_j t})\,. \tag{20}$$

This corresponds to the classical Langevin equation. The right hand side of Eq. (20) represents the fluctuating random force, which, as we shall see later, supplies thermal energy to the oscillator (fluctuation-dissipation theorem). We take the ensemble average as to the thermostat oscillators noticing that the average values of $\bar{A}_j$ and $\bar{A}_j^*$ on the right hand side of Eq. (20) vanish (cf. Eq. (29)). We get

$$\langle\ddot{x}_i\rangle+\zeta\langle\dot{x}_i\rangle+\omega_i^2\langle x_i\rangle=0\,. \tag{21}$$

This corresponds to the equation for a classical damped-oscillator.

§ 4. The Relaxation Equation

First, we observe the variation of an arbitrary operator F which we consider as a polynomial of a_i and a_i^*, where we can generally fix that operators a_i's appear always to the right of operators a_i^*'s, that is;

$$F=\sum_{\nu,\nu'}F_{\nu,\nu'}a_i^{*\nu}a_i^{\nu'}\,. \tag{22}$$

So, we have to consider the variation of the form $a_i^{*\nu}a_i^{\nu'}$. Because of Eq. (6), we have

$$\frac{d}{dt}(a_i^{*\nu}a_i^{\nu'})=i\omega_i(\nu-\nu')a_i^{*\nu}a_i^{\nu'}+e^{i\omega_i(\nu-\nu')t}\frac{d}{dt}(A_i^{*\nu}A_i^{\nu'})\,. \tag{23}$$

Here we calculate the time derivative of the operator which appears in the last term of the above equation. As

$$\frac{d}{dt}(A_i^{*\nu}A_i^{\nu'})=A_i^{*\nu}\left(\frac{d}{dt}A_i^{\nu'}\right)+\left(\frac{d}{dt}A_i^{*\nu}\right)A_i^{\nu'}\,, \tag{24}$$

we have then terms like $A_i^{*\nu}A_i\cdots\dot{A}_iA_i\cdots$. Using Eqs. (12), (16) and their conjugate equations, we take the limit $s\to+0$, and disregard the principal-value parts (as in § 3, they contribute to a level-shift only) as before. But we must be careful about the commutation relation (13) and non-commutativity of A_i and $\overline{A}_i$ etc. After some calculation, neglecting terms higher than the third, we get finally

$$\begin{aligned}\frac{d}{dt}(A_i^{*\nu}A_i^{\nu'})=&-\frac{\lambda^2}{2}\left(\frac{1}{2\omega_i m_i}\right)\sum_j{}'\left(\frac{c_{ij}^2}{2\omega_j m_j}\right)\pi\delta(\omega_i-\omega_j)(\overline{A}_j\overline{A}_j^*+\overline{A}_j^*\overline{A}_j)\\&\times\left(\nu'(\nu'-1)e^{2i\omega_i t}A_i^{*\nu}A_i^{\nu'-2}+\nu(\nu-1)e^{-2i\omega_i t}A_i^{*\nu-2}A_i^{\nu'}\right)\\&+2\lambda^2\left(\frac{1}{2\omega_i m_i}\right)\sum_j{}'\left(\frac{c_{ij}^2}{2\omega_j m_j}\right)\pi\delta(\omega_i-\omega_j)\overline{A}_j^*\overline{A}_j\nu\nu' A_i^{*\nu-1}A_i^{\nu'-1}\\&-\lambda^2\left(\frac{1}{2\omega_i m_i}\right)\sum_j{}'\left(\frac{c_{ij}^2}{2\omega_j m_j}\right)\pi\delta(\omega_i-\omega_j)(\nu'+\nu)A_i^{*\nu}A_i^{\nu'}\\&+\lambda^2\left(\frac{1}{2\omega_i m_i}\right)\sum_j{}'\left(\frac{c_{ij}^2}{2\omega_j m_j}\right)\pi\delta(\omega_i-\omega_j)\\&\times\left\{e^{2i\omega_i t}\left(\nu' A_i^{*\nu+1}A_i^{\nu'-1}+\frac{\nu'(\nu'-1)}{2}A_i^{*\nu}A_i^{\nu'-2}\right)\right.\\&\left.+e^{-2i\omega_i t}\left(\nu A_i^{*\nu-1}A_i^{\nu'+1}+\frac{\nu(\nu-1)}{2}A_i^{*\nu-2}A_i^{\nu'}\right)\right\}\\&+\lambda(\text{terms linear as to }\overline{A}_j\text{ and }\overline{A}_j^*)\,.\end{aligned}\tag{25}$$

We can omit the last terms first order in λ, as they are linear with respect to $\overline{A}_j$ and $\overline{A}_j^*$ of the thermostat and vanish after taking average as to the thermostat: we are not interested in these terms (cf. §2 and Eq. (29)). In virtue of Eqs. (25) and (6), Eq. (23) may be written as

$$\begin{aligned}\frac{d}{dt}(a_i^{*\nu}a_i^{\nu'})=&\,i\omega_i(\nu-\nu')a_i^{*\nu}a_i^{\nu'}\\&-\frac{\lambda^2}{2}\left(\frac{1}{2\omega_i m_i}\right)\sum{}'\left(\frac{c_{ij}^2}{2\omega_j m_j}\right)\pi\delta(\omega_i-\omega_j)(\overline{A}_j\overline{A}_j^*+\overline{A}_j^*\overline{A}_j)\\&\times(\nu'(\nu'-1)a_i^{*\nu}a_i^{\nu'-2}+\nu(\nu-1)a_i^{*\nu-2}a_0^{\nu'})\\&+2\lambda^2\left(\frac{1}{2\omega_i m_i}\right)\sum_j{}'\left(\frac{c_{ij}^2}{2\omega_j m_j}\right)\pi\delta(\omega_i-\omega_j)\overline{A}_j^*\overline{A}_j\nu\nu' a_i^{*\nu-1}a_i^{\nu'-1}\\&-\lambda^2\left(\frac{1}{2\omega_i m_i}\right)\sum_j{}'\left(\frac{c_{ij}^2}{2\omega_j m_j}\right)\pi\delta(\omega_i-\omega_j)(\nu'+\nu)a_i^{*\nu}a_i^{\nu'}\\&+\lambda^2\left(\frac{1}{2\omega_i m_i}\right)\sum_j{}'\left(\frac{c_{ij}^2}{2\omega_j m_j}\right)\pi\delta(\omega_i-\omega_j)\left(\nu' a_i^{*\nu+1}a_i^{\nu'-1}\right.\\&\left.+\nu a_i^{*\nu-1}a_i^{\nu+1}+\frac{\nu'(\nu'-1)}{2}a_i^{*\nu}a_i^{\nu'-2}+\frac{\nu(\nu-1)}{2}a_i^{*\nu-2}a_i^{\nu'}\right)\,.\end{aligned}\tag{26}$$

Considering the following commutation relations,

$$\left.\begin{aligned}&[a_i^*,\,a_i^{*\nu}a_i^{\nu'}]=-\nu' a_i^{*\nu}a_i^{\nu'-1}\,,\\&[a_i\,,\,a_i^{*\nu}a_i^{\nu'}]=\nu a_i^{*\nu-1}a_i^{\nu'}\,,\end{aligned}\right\}\tag{27}$$

we have from Eqs. (22) and (26)

$$\begin{aligned}\frac{d}{dt}F=&\,i\omega_i\{a_i^*[a_i,F]+[a_i^*,F]a_i\}\\&-\frac{\lambda^2}{2}\left(\frac{1}{2\omega_i m_i}\right)\sum_j{}'\left(\frac{c_{ij}^2}{2\omega_j m_j}\right)\pi\delta(\omega_i-\omega_j)(\overline{A}_j\overline{A}_j^*+\overline{A}_j^*\overline{A}_j)\\&\times([a_i^*,[a_i^*,F]]+[a_i,[a_i,F]])\end{aligned}$$

$$
\begin{aligned}
&-2\lambda^2\left(\frac{1}{2\omega_i m_i}\right)\sum_j{}'\left(\frac{c_{ij}^2}{2\omega_j m_j}\right)\pi\delta(\omega_i-\omega_j)\overline{A}_j{}^*\overline{A}_j[a_i{}^*,[a_i,F]]\\
&-\lambda^2\left(\frac{1}{2\omega_i m_i}\right)\sum_j{}'\left(\frac{c_{ij}^2}{2\omega_j m_j}\right)\pi\delta(\omega_i-\omega_j)(-[a_i{}^*,F]a_i+a_i{}^*[a_i,F])\\
&+\lambda^2\left(\frac{1}{2\omega_i m_i}\right)\sum_j{}'\left(\frac{c_{ij}^2}{2\omega_j m_j}\right)\pi\delta(\omega_i-\omega_j)\Big(-a_i{}^*[a_i{}^*,F]+[a_i,F]a_i\\
&+\frac{1}{2}[a_i{}^*[a_i{}^*,F]]+\frac{1}{2}[a_i[a_i,F]]\Big)\,.
\end{aligned}
\tag{28}
$$

As we have said in § 2, we take the average as to the thermostat;

$$
\left.
\begin{aligned}
&\langle(\overline{A}_j{}^*\overline{A}_j+\overline{A}_j\overline{A}_j{}^*)\rangle=2\langle N_j(\omega_j)\rangle+1\,,\\
&\langle\overline{A}_j{}^*\overline{A}_j\rangle=\langle N_j(\omega_j)\rangle\,,\\
&\langle\overline{A}_j\rangle=\langle\overline{A}_j{}^*\rangle=0\,,
\end{aligned}
\right\}
\tag{29}
$$

where N_j is the quantum number of the j-th oscillator of thermostat. The above two of Eqs. (29) are consistent because of Eqs. (13).

From Eq. (28), taking the average as to the thermostat oscillators and considering Eq. (29), we get the following equation written for the matrix elements:

$$
\begin{aligned}
\left(\frac{d}{dt}F\right)_{n,n'}=&\,i\omega_i(n-n')F_{n,n'}\\
&-\pi\lambda^2\left(\frac{1}{2\omega_i m_i}\right)\left(\frac{\bar{c}^2 g}{2\omega_i m_j}\right)\Big\{\left(\langle N_j(\omega_i)\rangle+\frac{1}{2}\right)\Big(\sqrt{n(n-1)}\,F_{n-2,n'}\\
&-2\sqrt{n(n'+1)}\,F_{n-1,n'+1}+\sqrt{(n'+1)(n'+2)}\,F_{n,n'+2}+\sqrt{n'(n'-1)}\,F_{n,n'-2}\\
&-2\sqrt{(n+1)n'}\,F_{n+1,n'-1}+\sqrt{(n+1)(n+2)}\,F_{n+2,n'}\Big)\\
&+2\langle N_j(\omega_i)\rangle\Big((n+n'+1)F_{n,n'}-\sqrt{nn'}\,F_{n-1,n'-1}\\
&-\sqrt{(n+1)(n'+1)}\,F_{n+1,n'+1}\Big)\\
&+(n+n')F_{n,n'}-2\sqrt{nn'}\,F_{n-1,n'-1}+\frac{1}{2}\sqrt{n(n-1)}\,F_{n-2,n'}\\
&+\frac{1}{2}\sqrt{n'(n'-1)}\,F_{n,n'-2}-\frac{1}{2}\sqrt{(n'+1)(n'+2)}\,F_{n,n'+2}\\
&-\frac{1}{2}\sqrt{(n+1)(n+2)}\,F_{n+2,n'}\Big\}\,,
\end{aligned}
\tag{30}
$$

where n means the n-th excitation of the i-th (central) oscillator and $F_{n,n'}$ means the n, n' element of the operator F.

Now, this Eq. (30) for the operator F in Heisenberg representation will be translated to the equation for the density matrix σ in Schroedinger representation. This can be done by noting that $\langle F\rangle=\mathrm{trace}\,(F\sigma)$, or by the following rules.

$$
\begin{aligned}
&F_{n',n}\rightarrow\sigma_{n,n'}\,,\\
&(n'-n)F_{n',n}\rightarrow(n'-n)\sigma_{n,n'}\,,\\
&\sqrt{n'(n'-1)}\,F_{n'-2,n}\rightarrow\sqrt{(n'+1)(n'+2)}\,\sigma_{n,n'+2}\,,
\end{aligned}
$$

etc.

where $\sigma_{n,n'}$ means the n, n' element of the density matrix σ of the i-th (central) oscillator. Then we have the following equation;

$$
\begin{aligned}
\frac{d}{dt}\sigma_{n,n'}=&-i\omega_i(n-n')\sigma_{n,n'}\\
&-\pi\left(\frac{\lambda^2\bar{c}^2g}{4\omega_i^2m_im_j}\right)\Big\{\left(\langle N_j(\omega_i)\rangle+\frac{1}{2}\right)\Big(\sqrt{(n'+1)(n'+2)}\,\sigma_{n,n'+2}\\
&-2\sqrt{n(n'+1)}\,\sigma_{n-1,n'+1}+\sqrt{n(n-1)}\,\sigma_{n-2,n'}+\sqrt{(n+1)(n+2)}\,\sigma_{n+2,n'}\\
&-2\sqrt{(n+1)n'}\,\sigma_{n+1,n'-1}+\sqrt{n'(n'-1)}\,\sigma_{n,n'-2}\Big)\\
&+2\langle N_j(\omega_i)\rangle\Big((n+n'+1)\sigma_{n,n'}-\sqrt{(n+1)(n'+1)}\,\sigma_{n+1,n'+1}-\sqrt{nn'}\,\sigma_{n-1,n'-1}\Big)\\
&+(n+n')\sigma_{n,n'}-2\sqrt{(n+1)(n'+1)}\,\sigma_{n+1,n'+1}+\frac{1}{2}\sqrt{(n'+1)(n'+2)}\,\sigma_{n,n'+2}\\
&+\frac{1}{2}\sqrt{(n+1)(n+2)}\,\sigma_{n+2,n'}-\frac{1}{2}\sqrt{n(n-1)}\,\sigma_{n-2,n'}\\
&-\frac{1}{2}\sqrt{n'(n'-1)}\,\sigma_{n,n'-2}\Big\}\,. \qquad (31)
\end{aligned}
$$

The average of the quantum number $N_j(\omega_i)$ of the thermostat oscillator j whose frequency is equal to ω_i, is given by the well-known formula

$$\langle N_j(\omega_i)\rangle=\frac{1}{e^{\theta}-1}\,, \qquad (32)$$

when the temperature of the thermostat is T, where

$$\theta=\frac{\hbar\omega_i}{kT}\,, \qquad (33)$$

then, Eq. (31) may be written as follows;

$$
\begin{aligned}
\frac{d}{dt}\sigma_{n,n'}=&-i\omega_i(n-n')\sigma_{n,n'}\\
&-\frac{\kappa}{2}\{\sqrt{(n'+1)(n'+2)}\,\sigma_{n,n'+2}+\sqrt{(n+1)(n+2)}\,\sigma_{n+2,n'}\\
&+e^{-\theta}(\sqrt{n(n-1)}\,\sigma_{n-2,n'}+\sqrt{n'(n'-1)}\,\sigma_{n,n'-2})\\
&-(1+e^{-\theta})(\sqrt{n(n'+1)}\,\sigma_{n-1,n'+1}+\sqrt{(n+1)n'}\,\sigma_{n+1,n'-1})\\
&+[n+n'+e^{-\theta}(n+n'+2)]\sigma_{n,n'}-2\sqrt{(n+1)(n'+1)}\,\sigma_{n+1,n'+1}\\
&-2e^{-\theta}\sqrt{nn'}\,\sigma_{n-1,n'-1}\} \qquad (34)
\end{aligned}
$$

where

$$
\begin{aligned}
\kappa&=\left(\frac{\lambda^2\bar{c}^2\pi g}{2\omega_i^2m_im_j}\right)(1-e^{-\theta})^{-1}\\
&=\zeta(1-e^{-\theta})^{-1}\,. \qquad (35)
\end{aligned}
$$

Here, ζ is the same as defined by Eq. (19c).

Eq. (34) is the generalization of the relaxation equation which Montroll and Shuler[6] derived. As they treated the diagonal terms only, the terms corresponding to $\sigma_{n,n'+2}$, $\sigma_{n+2,n'}$, $\sigma_{n-2,n'}$, $\sigma_{n,n'-2}$, $\sigma_{n-1,n'+1}$ and $\sigma_{n+1,n'-1}$ did not appear in their equation. From the equation of their type, the Kramers-Chandrasekhar equation can not be derived in its complete form.

§ 5. Kramers Chandrasekhar Equation

Using the density matrix element $\sigma_{n,n'}$, we can write the density matrix ρ in the q-representation as

$$\rho(q_1, q_2; t)=\sum_{n,n'} \sigma_{n,n'}(t)\rho_{n,n'}(q_1, q_2) , \tag{36}$$

where

$$\rho_{n,n'}(q_1, q_2)=\sqrt{\frac{\alpha}{2^n n! \sqrt{\pi}}}\sqrt{\frac{\alpha}{2^{n'} n'! \sqrt{\pi}}} H_n(\alpha q_1)H_{n'}(\alpha q_2) \exp\left(-\frac{\alpha^2}{2}(q_1^2+q_2^2)\right) . \tag{37}$$

Here $H_n(\alpha q_1)$ is the Hermite polynomial of order n and q_1 or q_2 is the coordinate of the i-th (central) oscillator, and

$$\alpha=\sqrt{\frac{m_i\omega_i}{\hbar}} . \tag{38}$$

If we use the n-representation, then

$$\rho_{n,n'}=|n\rangle\langle n'| ,$$

where $|n\rangle$ (or $\langle n|$) is the ket (or bra) vector of n-th excitation. Because

$$a_i|n\rangle\langle n'|=\sqrt{n}\, |n-1\rangle\langle n'| , \qquad a_i^*|n\rangle\langle n'|=\sqrt{n+1}\, |n+1\rangle\langle n'| ,$$

and

$$a_i=\frac{1}{\sqrt{2}}\left(\alpha q_1+\frac{1}{\alpha}\frac{\partial}{\partial q_1}\right), \qquad a_i^*=\left(\alpha q_1-\frac{1}{\alpha}\frac{\partial}{\partial q_1}\right) ,$$

we have the following relations;

$$\left.\begin{aligned}\sqrt{n}\, \rho_{n-1,n'} &=\frac{1}{\sqrt{2}}\left(\alpha q_1+\frac{1}{\alpha}\frac{\partial}{\partial q_1}\right)\rho_{n,n'} ,\\ \sqrt{n+1}\, \rho_{n+1,n'} &=\frac{1}{\sqrt{2}}\left(\alpha q_1-\frac{1}{\alpha}\frac{\partial}{\partial q_1}\right)\rho_{n,n'} .\end{aligned}\right\} \tag{39}$$

On the other hand, from Eqs. (36) and (34) we have

$$\begin{aligned}\frac{\partial}{\partial t}\rho(q_1, q_2; t)=&\sum_{n,n'}\left(\frac{d}{dt}\sigma_{n,n'}(t)\right)\rho_{n,n'}(q_1, q_2)\\ =&-i\omega_i\sum_{n\,n'}(n-n')\sigma_{n,n'}\rho_{n,n'}\\ &-\frac{\kappa}{2}\sum_{n\,n'}\{\sqrt{(n'+1)(n'+2)}\,\sigma_{n,n'+2}+\sqrt{(n+1)(n+2)}\,\sigma_{n+2,n'}\\ &+e^{-\theta}(\sqrt{n(n-1)}\,\sigma_{n-2,n'}+\sqrt{n'(n'-1)}\,\sigma_{n,n'-2})\\ &-(1+e^{-\theta})(\sqrt{n(n'+1)}\,\sigma_{n-1,n'+1}+\sqrt{(n+1)n'}\,\sigma_{n+1,n'-1})\\ &+[n+n'+e^{-\theta}(n+n'+2)]\sigma_{n,n'}\\ &-2\sqrt{(n+1)(n'+1)}\,\sigma_{n+1,n'+1}-2e^{-\theta}\sqrt{nn'}\,\sigma_{n-1,n'-1}\}\rho_{n,n'}\\ =&-i\omega_i\sum_{n,n'}(n-n')\rho_{n,n'}\sigma_{n,n'}\\ &-\frac{\kappa}{2}\sum_{n\,n'}\{\sqrt{n'(n'-1)}\,\rho_{n,n'-2}+\sqrt{n(n-1)}\,\rho_{n-2,n'}\\ &+e^{-\theta}(\sqrt{(n+1)(n+2)}\,\rho_{n+2,n'}+\sqrt{(n'+1)(n'+2)}\,\rho_{n,n'+2})\\ &-(1+e^{-\theta})(\sqrt{(n+1)n'}\,\rho_{n+1,n'-1}+\sqrt{n(n'+1)}\,\rho_{n-1,n'+1})\\ &+[n+n'+e^{-\theta}(n+n'+2)]\rho_{n,n'}-2\sqrt{nn'}\,\rho_{n-1,n'-1}\\ &-2e^{-\theta}\sqrt{(n+1)(n'+1)}\,\rho_{n+1,n'+1}\}\sigma_{n,n'} .\end{aligned} \tag{40}$$

Making use of the relation (39) and noting Eq. (38) we have from Eqs. (40) and (36)

$$\frac{\partial}{\partial t}\rho(q_1, q_2; t)=-\frac{i}{\hbar}\left[-\frac{\hbar^2}{2m}\left(\frac{\partial^2}{\partial q_1^2}-\frac{\partial^2}{\partial q_2^2}\right)+\frac{m\omega^2}{2}(q_1^2-q_2^2)\right]\rho(q_1, q_2; t)$$

$$-\frac{\kappa}{2}(1+e^{-\theta})\left[\frac{m\omega}{\hbar}(q_1-q_2)^2\right]\rho(q_1,q_2;t)$$
$$+\frac{\kappa}{2}(1-e^{-\theta})\left[(q_1-q_2)\left(\frac{\partial}{\partial q_2}-\frac{\partial}{\partial q_1}\right)\right]\rho(q_1,q_2;t)\,. \tag{41}$$

This is to be compared to the equation which Zwazig[7)] derived from the relaxation equation of Montroll and Shuler.[6)]

To make the classical distribution function expressed in terms of position r and momentum p from the density matrix, we make use of the Wigner's distribution function; that is

$$f(r,p;t)=\frac{1}{\pi\hbar}\int_{-\infty}^{\infty} e^{i2py/\hbar}\,dy\rho(r,y;t)\,, \tag{42}$$

where

$$q_1=r-y\,,\qquad q_2=r+y\,. \tag{43}$$

From the transformation (43), the following relations are derived easily;

$$\left.\begin{aligned}&-\left(\frac{\partial^2}{\partial q_1^2}-\frac{\partial^2}{\partial q_2^2}\right)=\frac{\partial^2}{\partial r\partial y}\,,\qquad q_1^2-q_2^2=-4ry\,,\\&(q_1-q_2)^2=4y^2\,,\qquad (q_1-q_2)\left(\frac{\partial}{\partial q_2}-\frac{\partial}{\partial q_1}\right)=-2y\frac{\partial}{\partial y}\,,\end{aligned}\right\} \tag{44}$$

Integrating partially, and bearing Eq. (42) in mind, from (44) we have

$$\left.\begin{aligned}i\frac{p}{\hbar}\frac{\partial f}{\partial r}&=\frac{1}{\pi\hbar}\int_{-\infty}^{\infty} e^{i2py/\hbar}\,dy\left\{\frac{1}{2}\left(\frac{\partial^2}{\partial q_1^2}-\frac{\partial^2}{\partial q_2^2}\right)\right\}\rho\,,\\ i\hbar r\frac{\partial f}{\partial p}&=\frac{1}{\pi\hbar}\int_{-\infty}^{\infty} e^{i2py/\hbar}\,dy\left\{\frac{1}{2}(q_1^2-q_2^2)\right\}\rho\,,\\ -\hbar^2\frac{\partial^2}{\partial p^2}f&=\frac{1}{\pi\hbar}\int_{-\infty}^{\infty} e^{i2py/\hbar}\,dy(q_1-q_2)^2\rho\,,\\ 2\frac{\partial}{\partial p}(pf)&=\frac{1}{\pi\hbar}\int_{-\infty}^{\infty} e^{i2py/\hbar}\,dy(q_1-q_2)\left(\frac{\partial}{\partial q_2}-\frac{\partial}{\partial q_1}\right)\rho\,.\end{aligned}\right\} \tag{45}$$

By multiplying $e^{i2py/\hbar}/\pi\hbar$ to Eq. (41) and integrating over y, and using Eq. (45) we have the following equation;

$$\frac{\partial}{\partial t}f+\frac{p}{m}\frac{\partial}{\partial r}-m\omega^2 r\frac{\partial}{\partial p}f=\frac{\kappa}{2}(1+e^{-\theta})m\omega\hbar\frac{\partial^2}{\partial p^2}f+\kappa(1-e^{-\theta})\frac{\partial}{\partial p}(pf)\,, \tag{46}$$

Here, we write

$$\hbar\omega\theta^*=2\tanh(\theta/2)\,. \tag{47}$$

As easily seen, at high temperatures

$$\theta^*\approx\frac{1}{kT}\,. \tag{48}$$

Bearing in mind that $\kappa(1-e^{-\theta})=\zeta$ (cf. Eqs. (19c) and (35)), we obtain finally

$$\frac{\partial}{\partial t}f+\frac{p}{m}\frac{\partial}{\partial r}f-m\omega^2 r\frac{\partial}{\partial p}f=\zeta\frac{\partial}{\partial p}\left\{(pf)+\frac{m}{\theta^*}\frac{\partial}{\partial p}f\right\}\,. \tag{49}$$

This is Kramers-Chandrasekhar equation. Here we notice that our ζ is twice the Zwanzig's[7)]. As there were extra or rather missing terms in his calculation, his ζ had to be a half of ours.

§ 6. Spin Relaxation

In this section we shall be concerned with the relaxation phenomena of a spin $\frac{1}{2}$ under a constant magnetic field. As before, we consider the thermostat composed of a infinite number of harmonic oscillators. The interaction between the spin and the thermostat oscillators will be assumed simply to be

$$\lambda V = \sum \lambda_j (Q_{jx} s_x + Q_{jy} s_y + \varepsilon_j Q_{jz} s_z) \tag{50}$$

where $\vec{Q}_j = (Q_{jx}, Q_{jy}, Q_{jz})$ stands for the coordinate of the j-th oscillator in the thermostat, $\boldsymbol{s} = (s_x, s_y, s_z)$ the spin coordinate and ε_j is a numerical constant introduced in order to ascertain slight generality.

Such a problem is included in the general treatment by F. Bloch[5]. According to his result the relaxation equation is

$$d\boldsymbol{M}/dt = \gamma \boldsymbol{M} \times \boldsymbol{H} - \boldsymbol{i} M_x / T_2 - \boldsymbol{j} M_y / T_2 - \boldsymbol{k}(M_z - M_0)/T_1 \,, \tag{51}$$

where M_x, M_y and M_z are the components of magnetization $\boldsymbol{M}$, $\boldsymbol{i}$, $\boldsymbol{j}$ and $\boldsymbol{k}$ the unit vectors along x, y and z axises. $\gamma = 2\mu / s\hbar$ as usual. The external field is along the z-axis and M_0 is the equilibrium magnetization. If the interaction is the form given by Eq. (50), the theory of Bloch indicates that

$$\left.\begin{aligned} \frac{1}{T_1} &= 2\Phi'_{11}(1+e^{-\kappa}) \,, \\ \frac{1}{T_2} &= \frac{1}{2T_1} + \Phi^0_{11} \,, \end{aligned}\right\} \tag{52}$$

with $\kappa = \hbar\omega_0 / kT = \gamma \mathrm{H}_0 / kT$. We have $(Q^{\pm} = Q_x \pm iQ_y)$

$$\left.\begin{aligned} \Phi'_{11} &= \frac{\pi}{4\hbar^2} \sum_{E'} P(E')(E'|\lambda_j Q_j^{\pm}|E'+\hbar\omega_0)(E'+\hbar\omega_0|\lambda_j Q_j^{\pm}|E') \,, \\ \Phi^0_{11} &= \frac{\pi}{4\hbar^2} \sum_{E'} P(E')(E'|\lambda_j \varepsilon_j Q_{jz}|E')(E'|\lambda_j \varepsilon_j Q_{jz}|E') = 0 \,, \end{aligned}\right\} \tag{53}$$

where $P(E')$ is the probability that the thermostat has the energy $E' = \sum (n_j + \frac{1}{2})\hbar\omega_j$. As only the oscillator with frequency $\omega_j = \omega_0$ has the matrix elements

$$(n|Q_j^{\pm}|n+1) = (n+1|Q_j^{\pm}|n) = \sqrt{n+1}\sqrt{\frac{\hbar}{2m_j\omega_j}} \,, \tag{54}$$

we are lead to

$$\frac{1}{2T_1} = \frac{1}{T_2} = \pi \frac{1+e^{-\kappa}}{1-e^{-\kappa}} \sum_j \frac{\lambda_j^2}{4m_j\omega_j\hbar} \delta(\omega_j - \omega_0) \,. \tag{55}$$

This is the consequence of Bloch applied to the present case.

Now we shall use the method of the foregoing sections to this problem. The total hamiltonian is

$$\mathscr{H} = 2\mu\, \mathrm{H}_0 \cdot s_z + \sum_j \left(\frac{\vec{P}_j^2}{2m_j} + \frac{1}{2} m_j \omega_j^2 \vec{Q}_j^2 \right) + \lambda V + V' \tag{56}$$

where V' stands for the interaction within the thermostat. If we write

$$\left.\begin{aligned} s^{\pm} &= s_x \pm i s_y \,, \\ Q_j^{\pm} &= Q_{jx} \pm i Q_{jy} \,, \end{aligned}\right\} \tag{57}$$

the equations of motion for the spin become

$$\left.\begin{aligned}
\dot{s}^{+}&=i\omega_0 s^{+}+\frac{i}{\hbar}\sum\lambda_j(-Q_j{}^{+}s_z+\varepsilon_j Q_{jz}s^{+})\,,\\
\dot{s}^{-}&=-i\omega_0 s^{-}+\frac{i}{\hbar}\sum\lambda_j(Q_j{}^{-}s_z-\varepsilon_j Q_{jz}s^{-})\,,\\
\dot{s}_z&=\frac{i}{\hbar}\sum\lambda_j\frac{1}{2}(-Q_j{}^{-}s^{+}+Q_j{}^{+}s^{-})\,.
\end{aligned}\right\}\tag{58}$$

Next, we define

$$\left.\begin{aligned}
&S^{\pm}=e^{\pm i\omega_0 t}s^{\pm}\,, && S_z=s_z\,,\\
&A_j{}^{\pm}=e^{i\omega_j t}(a_{jx}\pm ia_{jy})\,, && A_{jz}=a_{jz}e^{i\omega_j t}\,,\\
&A_j{}^{*\pm}=e^{-i\omega_j t}(a_{jx}{}^{*}\pm ia_{jy}{}^{*})\,, && A_{jz}{}^{*}=a_{jz}{}^{*}e^{-i\omega_j t}\,,
\end{aligned}\right\}\tag{59}$$

where

$$\left.\begin{aligned}
\vec{a}_j&=\sqrt{\frac{m_j\omega_j}{2\hbar}}(\vec{Q}_j+i\vec{P}_j/m_j\omega_j)\,,\\
\vec{a}_j{}^{*}&=\sqrt{\frac{m_j\omega_j}{2\hbar}}(\vec{Q}_j-i\vec{P}_j/m_j\omega_j)\,.
\end{aligned}\right\}\tag{60}$$

Commutation relations are

$$\left.\begin{aligned}
&[A_j{}^{+},A_k{}^{-}]=[A_j{}^{*+},A_k{}^{*-}]=[A_j{}^{+},A_k{}^{*+}]=[A_j{}^{-},A_k{}^{*-}]=0\,,\\
&[A_j{}^{+},A_k{}^{*-}]=[A_j{}^{-},A_k{}^{*+}]=2\delta_{jk}\,,\\
&[A_{jz},A_{kz}{}^{*}]=\delta_{jk}\,.
\end{aligned}\right\}\tag{61}$$

With these transformations we get the following set of equations for the spin

$$\left.\begin{aligned}
\dot{S}^{+}&=\frac{i}{\hbar}\sum\lambda_j\sqrt{\frac{\hbar}{2m_j\omega_j}}\{-(e^{-i\omega_j t}A_j{}^{+}+e^{i\omega_j t}A_j{}^{*+})S_z e^{-i\omega_0 t}\\
&\qquad\qquad+\varepsilon_j(e^{-i\omega_j t}A_{jz}+e^{i\omega_j t}A_{jz}{}^{*})S^{+}\}\,,\\
\dot{S}^{-}&=\frac{i}{\hbar}\sum\lambda_j\sqrt{\frac{\hbar}{2m_j\omega_j}}\{(e^{-i\omega_j t}A_j{}^{-}+e^{i\omega_j t}A_j{}^{*-})S_z e^{i\omega_0 t}\\
&\qquad\qquad-\varepsilon_j(e^{-i\omega_j t}A_{jz}+e^{i\omega_j t}A_{jz}{}^{*})S^{-}\}\,,\\
\dot{S}_z&=\frac{i}{\hbar}\sum\lambda_j\sqrt{\frac{\hbar}{2m_j\omega_j}}\{-\tfrac{1}{2}(e^{-i\omega_j t}A_j{}^{-}+e^{i\omega_j t}A_j{}^{*-})S^{+}e^{i\omega_0 t}\\
&\qquad\qquad+\tfrac{1}{2}(e^{-i\omega_j t}A_j{}^{+}+e^{i\omega_j t}A_j{}^{*+})S^{-}e^{-i\omega_0 t}\}\,.
\end{aligned}\right\}\tag{62}$$

An analogous set of equations holds for the thermostat oscillators. That is

$$\left.\begin{aligned}
\dot{A}_j{}^{+}&=-\frac{i\lambda_j}{\sqrt{2m_j\omega_j\hbar}}S^{+}e^{i(\omega_0+\omega_j)t}+\dot{A}_j{}^{+\prime}\,,\\
\dot{A}_j{}^{-}&=-\frac{i\lambda_j}{\sqrt{2m_j\omega_j\hbar}}S^{-}e^{i(-\omega_0+\omega_j)t}+\dot{A}_j{}^{-\prime}\,,\\
\dot{A}_{jz}&=-\frac{i\lambda_j}{\sqrt{2m_j\omega_j\hbar}}S_z e^{i\omega_j t}+\dot{A}_{jz}{}'\,,\\
&\text{etc.}
\end{aligned}\right\}\tag{63}$$

The terms $\dot{A}_j{}'$ etc. are those due to the interaction within the thermostat. The operators with bar are to be introduced by, for instance,

$$\left.\begin{aligned}
S^+ &= \bar{S}^+ + \frac{i}{\hbar}\sum \lambda_j \sqrt{\frac{\hbar}{2m_j\omega_j}}\Big\{ -\Big(\bar{A}_j^+\int^t e^{-i(\omega_j+\omega_0)t}\,dt + \bar{A}_j^{*+}\int^t e^{i(\omega_j-\omega_0)t}\,dt\Big)\bar{S}_z \\
&\quad + \varepsilon_j\Big(\bar{A}_{jz}\int^t e^{-i\omega_j t}\,dt + \bar{A}_{jz}^*\int^t e^{i\omega_j t}\,dt\Big)\bar{S}^+\Big\}, \\
S_z &= \bar{S}_z + \frac{i}{\hbar}\sum \lambda_j \sqrt{\frac{\hbar}{2m_j\omega_j}}\Big\{ -\frac{1}{2}\Big(\bar{A}_j^-\int^t e^{-i(\omega_j-\omega_0)t}\,dt + \bar{A}_j^{*-}\int^t e^{i(\omega_j+\omega_0)t}\,dt\Big)\bar{S}^+ \\
&\quad + \frac{1}{2}\Big(\bar{A}_j^+\int^t e^{-i(\omega_j+\omega_0)t}\,dt + \bar{A}_j^{*+}\int^t e^{i(\omega_j-\omega_0)t}\,dt\Big)\bar{S}^-\Big\}, \\
A_j^+ &= \bar{A}_j^+ - \frac{i\lambda_j}{\sqrt{2m_j\omega_j\hbar}}\bar{S}^+\int^t e^{i(\omega_0+\omega_j)t}\,dt + A_j^{+\prime}, \\
&\text{etc.}
\end{aligned}\right\} \tag{64}$$

where, as before, A_j' etc. are the terms due to the interaction within the thermostat. These terms may be omitted for the equation of motion of the spin. Instead, we put the equilibrium properties on the barred operators of the thermostat oscillators: For example, the averaged quantities like $\langle\bar{A}_j\rangle$ are to vanish. We insert the above expressions in the right hand side of Eqs. (62) and take the average. After rather lengthy calculation we get finally

$$\left.\begin{aligned}
\frac{d}{dt}\langle S^+\rangle &= -\sum\frac{\pi\lambda_j^2}{4m_j\omega_j\hbar}\{\langle\bar{A}_j^{*+}\bar{A}_j^-\rangle\delta(\omega_j-\omega_0)\langle S^+\rangle + \delta(\omega_j-\omega_0)\langle S^+\rangle\}, \\
\frac{d}{dt}\langle S^-\rangle &= -\sum\frac{\pi\lambda_j^2}{4m_j\omega_j\hbar}\{\langle\bar{A}_j^-\bar{A}_j^{*+}\rangle\delta(\omega_j-\omega_0)\langle S^-\rangle - \delta(\omega_j-\omega_0)\langle S^-\rangle\}, \\
\frac{d}{dt}\langle S_z\rangle &= -\sum\frac{\pi\lambda_j^2}{4m_j\omega_j\hbar}\{\langle\bar{A}_j^-\bar{A}_j^{*+} + \bar{A}_j^{*+}\bar{A}_j^-\rangle\delta(\omega_j-\omega_0)\langle S_z\rangle + \delta(\omega_j-\omega_0)\}.
\end{aligned}\right\} \tag{65}$$

The average is, however, as is seen easily,

$$\begin{aligned}
&\frac{1}{2}\langle\bar{A}_j^{*+}\bar{A}_j^- + \bar{A}_j^-\bar{A}_j^{*+}\rangle = \langle\bar{A}_j^{*+}\bar{A}_j^-\rangle + 1 = \langle\bar{A}_j^-\bar{A}_j^{*+}\rangle - 1 \\
&= \frac{1}{\hbar\omega_j}\left\{\left\langle\frac{P_{jx}^2}{2m_j} + m_j\omega_j^2Q_{jx}^2\right\rangle + \left\langle\frac{P_{jy}^2}{2m_j} + m_j\omega_j^2Q_{jy}^2\right\rangle\right\} = \frac{2\langle E_j\rangle}{\hbar\omega_j} = \frac{1+e^{-\hbar\omega_j/kT}}{1-e^{-\hbar\omega_j/kT}}.
\end{aligned} \tag{66}$$

Therefore the relaxation equation takes the form

$$\frac{d}{dt}\langle \boldsymbol{S}\rangle = -\frac{1+e^{-\kappa}}{1-e^{-\kappa}}\sum\frac{\lambda_j^2\pi\delta(\omega_j-\omega_0)}{4\omega_j m_j\hbar}(\boldsymbol{i}\langle S_x\rangle + \boldsymbol{j}\langle S_y\rangle + 2\boldsymbol{k}(\langle S_z\rangle - \langle S_z\rangle_0)) \tag{67}$$

where

$$S^{\pm} = S_x \pm iS_y\,, \qquad \langle S_z\rangle_0 = \frac{1}{2}\left(\frac{e^{-\kappa/2}-e^{\kappa/2}}{e^{-\kappa/2}+e^{\kappa/2}}\right). \tag{68}$$

Thus the Bloch equation is justified.

Before closing this section it seems worth noting the following: We may place the $\bar{S}$-operators to the left of $\bar{A}$-operators in Eqs. (64). If we do so, Eqs. (65) are to be changed accordingly. But the relaxation equation is not changed as can be seen easily.

Appendix A.

As a special case of Eq. (26) in § 4, we can derive the equation governing the change of energy of the i-th (central) oscillator[8]. In Eq. (26) we put $\nu=\nu'=1$. Then we have the following equation;

$$\begin{aligned}
\frac{d}{dt}(a_i^*a_i) &= \lambda^2 2\pi\left(\frac{1}{2\omega_i m_i}\right)\sum_j{}'\left(\frac{c_{ij}^2}{2\omega_j m_j}\right)\delta(\omega_i-\omega_j)\bar{A}_j^*\bar{A}_j \\
&\quad - \lambda^2\pi\left(\frac{1}{2\omega_i m_i}\right)\sum_j{}'\left(\frac{c_{ij}^2}{2\omega_j m_j}\right)\delta(\omega_i-\omega_j)[2a_i^*a_i - a_i^{*2} - a_i^2].
\end{aligned} \tag{A.1}$$

Here we take the average with respect to the thermostat oscillators, on which we put the same properties as before (cf. Eqs. (29)). Then we have

$$\frac{d}{dt}(a_i^* a_i) = \frac{\lambda^2 \bar{c}^2 \pi g}{2\omega_i^2 m_i m_j} \left\{ \langle N_j(\omega_i) \rangle - \frac{1}{2}(2a_i^* a_i - a_i^{*2} - a_i^2) \right.$$

$$= \zeta \left\{ \langle N_j(\omega_i) \rangle + \frac{1}{2} - \frac{1}{2}(a_i^* a_i + a_i a_i^* - a_i^{*2} - a_i^2) \right\}, \tag{A.2}$$

(cf. Eq. (19c)). Because the energy of the i-th (central) oscillator E_i can be expressed as

$$E_i = \hbar\omega_i \left(a_i^* a_i + \frac{1}{2} \right), \tag{A.3}$$

and its time derivative is

$$\frac{d}{dt} E_i = \hbar\omega_i \frac{d}{dt}(a_i^* a_i), \tag{A.4}$$

we have, from Eq. (A.2), the following equation;

$$\frac{d}{dt} E_i = \zeta \left\{ \hbar\omega_i \left(\langle N_j(\omega_i) \rangle + \frac{1}{2} \right) - \frac{\hbar\omega_i}{2}(a_i^* a_i + a_i a_i^* - a_i^{*2} - a_i^2) \right\}. \tag{A.5}$$

According to the relation (2), we can write

$$\frac{\hbar\omega_i}{2}(a_i^* a_i + a_i a_i^* - a_i^{*2} - a_i^2) = \frac{p_i^2}{m}. \tag{A.6}$$

So, Eq. (A.5) may be written as

$$\frac{d}{dt} E_i = \zeta \left\{ \hbar\omega_i \left(\langle N_j(\omega_i) \rangle + \frac{1}{2} \right) - \frac{p_i^2}{m} \right\}. \tag{A.7}$$

This must be compared with the equation

$$\frac{d}{dt} E_i = \zeta \left\{ \hbar\omega_i \left(\langle N_j(\omega_i) \rangle + \frac{1}{2} \right) - E_i \right\}, \tag{A.8}$$

which can be derived from the Montroll-Shuler's relaxation equation[6].

We rather think that Eq. (A.7), which can be derived also from the Kramers-Chandrasekhar equation, is more reasonable one than Eq. (A.8). The Eq. (A.8) is too sooth to describe the process in which the system approaches to equilibrium.

Appendix B.

We can show that Eq. (34) is equivalent to the following operator equation derived previously by one of the authors[3] for the density matrix σ:

$$\frac{\partial \sigma}{\partial t} = \frac{1}{i\hbar}(H_0 \sigma - \sigma H_0) + \zeta \left\{ \left(\langle N_j(\omega_i) \rangle + \frac{1}{2} \right) \hbar\omega_i m_i \frac{\partial^2 \sigma}{\partial p^2} + \frac{\partial}{\partial p} \left(\frac{p\sigma + \sigma p}{2} \right) \right\}. \tag{B.1}$$

To verify this equivalence, we have only to note the following;

$$\{x(x\sigma - \sigma x) - (x\sigma - \sigma x)x\}_{n,n'} = \{x^2\sigma - 2x\sigma x + \sigma x^2\}_{n,n'}$$

$$= \frac{\hbar}{2m_i\omega_i} \{(n+1)\sigma_{n,n'} + \sqrt{(n+1)(n+2)}\,\sigma_{n+2,n'} + n\sigma_{n,n'} + \sqrt{n(n-1)}\,\sigma_{n-2,n'}$$

$$-2\sqrt{(n+1)(n'+1)}\,\sigma_{n+1,n'+1} - 2\sqrt{(n+1)n'}\,\sigma_{n+1,n'-1} - 2\sqrt{n(n'+1)}\,\sigma_{n-1,n'+1}$$

$$-2\sqrt{nn'}\,\sigma_{n-1,n'-1} + \sqrt{(n'+1)(n'+2)}\,\sigma_{n,n'+2} + (n'+1)\sigma_{n,n'}$$

$$+\sqrt{(n'-1)n'}\,\sigma_{n,n'-2} + n'\sigma_{n,n'}\},$$

and

$$
\begin{aligned}
\{x(p\sigma+\sigma p)-(p\sigma+\sigma p)x\}_{n,n'} &= \{xp\sigma+x\sigma p-p\sigma x-\sigma p x\}_{n,n'}\\
&= \frac{i\hbar}{2}\{(n+1)\sigma_{n,n'}-\sqrt{(n+1)(n+2)}\,\sigma_{n+2,n'}-n\sigma_{n,n'}+\sqrt{n(n-1)}\,\sigma_{n-2,n'}\\
&\quad +2\sqrt{(n+1)(n'+1)}\,\sigma_{n+1,n'+1}-2\sqrt{nn'}\,\sigma_{n-1,n'-1}\\
&\quad -\sqrt{(n'+1)(n'+2)}\,\sigma_{n,n'+2}+(n'+1)\sigma_{n,n'}+\sqrt{(n'-1)n'}\,\sigma_{n,n'-2}-n'\sigma_{n,n'}\}\,. \qquad \text{(B.3)}
\end{aligned}
$$

Further we have (cf. Eqs. (32) and (33))

$$\frac{1+e^{-\theta}}{2(1-e^{-\theta})}=\frac{1}{e^{\theta}-1}+\frac{1}{2}=\left(\langle N_j(\omega_i)\rangle+\frac{1}{2}\right), \qquad \text{(B.4)}$$

and in general

$$\frac{\partial}{\partial p}G=\frac{1}{i\hbar}(xG-Gx)\,. \qquad \text{(B.5)}$$

By repeated use of the last equation, we get from Eq. (34) the operator equation (B.1).

Appendix C.

If we regard p, x as classical variables instead of operators, we can derive the Kramers-Chandrasekhar equation by the method as follows.

Let

$$\left.\begin{aligned}\bar{a}_j&=\bar{A}_j\,e^{-i\omega_j t}\,,\\ \bar{a}_j{}^*&=\bar{A}_j{}^*\,e^{i\omega_j t}\,,\end{aligned}\right\} \qquad \text{(C.1)}$$

and

$$\left.\begin{aligned}\bar{p}_j&=-i\sqrt{\omega_j m_j\hbar/2}\,(\bar{a}_j-\bar{a}_j{}^*)\,,\\ \bar{x}_j&=\sqrt{\hbar/2\omega_j m_j}\,(\bar{a}_j+\bar{a}_j{}^*)\,,\end{aligned}\right\} \qquad \text{(C.2)}$$

then, Eq. (19) may be written as

$$\left.\begin{aligned}\dot{x}_i&=p_i/m_i\,,\\ \dot{p}_i&=-\omega_i^2 m_i x-\zeta p_i-\lambda\sum_j c_{ij}\bar{x}_j\,.\end{aligned}\right\} \qquad \text{(C.3)}$$

Further from Eqs. (6), (12) and its conjugate equation we have

$$\left.\begin{aligned}p_i&=\bar{p}_i-\frac{\pi\lambda}{2}\sum_j{}'\,c_{ij}\,\delta(\omega_i-\omega_j)\bar{x}_j\,,\\ x_i&=\bar{x}_i-\frac{\pi\lambda}{2\omega_i m_j}\sum_j{}'\,c_{ij}\,\delta(\omega_i-\omega_j)\,\bar{p}_j\,,\end{aligned}\right\} \qquad \text{(C.4)}$$

where $\bar{p}_i$ and $\bar{x}_i$ have analogous meaning as $\bar{p}_j$ and $\bar{x}_j$ defined by the relations (C.1) and (C.2). And we must notice that $\bar{p}_j$ and $\bar{x}_j$ in Eqs. (C.4) are those of the thermostat oscillators whose angular frequency are equal to ω_i.

Here we regard Eqs. (C.3) and (C.4) as the equations for the classical variables. This is reasonable, for we may consider a, a^*, A and A^* as the classical variables transformed from the classical variables p and x. In this interpretation, the following translations are needed

$$\left.\begin{aligned}[a,G]&\to\frac{\partial}{\partial a^*}G\,,\\ [a^*,G]&\to-\frac{\partial}{\partial a}G\,,\end{aligned}\right\} \qquad \text{(C.5)}$$

where G is an arbitrary function of a and a^*.

Now, we introduce an arbitrary function $F(p_i, x_i)$ of classical variables p_i and x_i. Using the classical Eq. (C.3) we get

$$\begin{aligned}\frac{d}{dt}F&=\dot{p}_i\frac{\partial}{\partial p_i}F+\dot{x}_i\frac{\partial}{\partial x_i}F\\&=-\omega_i^2m_ix_i\frac{\partial}{\partial p_i}F+\frac{p_i}{m_i}\frac{\partial}{\partial x_i}F\\&\quad-\zeta p_i\frac{\partial}{\partial p_i}F-\lambda\sum_j{}'c_{ij}\bar{x}_j\frac{\partial}{\partial p_i}F\,.\end{aligned}\tag{C.6}$$

Here we assume that

$$\left.\begin{aligned}\langle\bar{x}_j^2\rangle&=\frac{kT}{m_j\omega_j^2}\,,\\\langle\bar{x}_j\bar{p}_j\rangle&=0\,,\end{aligned}\right\}\tag{C.7}$$

where $\langle\ \rangle$ means the average taken over the thermostat oscillators. These assumptions correspond to those of (29). Then using Eq. (C.4) and considering that the difference between p_i and $\bar{p}_i$ is the order of λ, we have to the second order in λ

$$\left\langle-\lambda\sum_j{}'c_{ij}x_j\frac{\partial}{\partial p_i}F\right\rangle=\zeta m_ikT\frac{\partial^2}{\partial p_i^2}F\,.\tag{C.8}$$

Taking the average of Eq. (C.6) over the thermostat oscillators, from Eq. (C.8) we have

$$\frac{d}{dt}F=-\omega_i^2m_ix_i\frac{\partial}{\partial p_i}F+\frac{p_i}{m_i}\frac{\partial}{\partial x_i}F-\zeta p_i\frac{\partial}{\partial p_i}F-\zeta m_ikT\frac{\partial^2}{\partial p_i^2}F\,.\tag{C.9}$$

Let $f(p_i, x_i; t)$ be the distribution function of i-th (central) oscillator, then the following relation must be satisfied;

$$\int\left(\frac{d}{dt}F\right)f\,dp_i\,dx_i=\int F\frac{\partial}{\partial t}f\,dp_i\,dx_i\,.\tag{C.10}$$

Using Eqs. (C.9) and (C.10), we get

$$\begin{aligned}\int F\frac{\partial}{\partial t}f\,dp_i\,dx_i&=\int\left(-\omega_i^2m_ix_i\frac{\partial}{\partial p_i}F+\frac{p_i}{m_i}\frac{\partial}{\partial x_i}F-\zeta p_i\frac{\partial}{\partial p_i}F+\zeta m_ikT\frac{\partial^2}{\partial p_i^2}F\right)f\,dp_i\,dx_i\\&=\int F\left(\omega_i^2m_ix_i\frac{\partial}{\partial p_i}f-\frac{p_i}{m_i}\frac{\partial}{\partial x_i}f+\zeta\frac{\partial}{\partial p_i}(p_if)+\zeta m_ikT\frac{\partial^2}{\partial p_i^2}f\right)dp_i\,dx_i\,,\end{aligned}\tag{C.11}$$

where to get the last line we have used the partial integration.

To satisfy Eq. (C.11) for an arbitrary function F, the distribution function f must satisfy the following equation

$$\frac{\partial}{\partial t}f-\omega_i^2m_ix_i\frac{\partial}{\partial p_i}f+\frac{p_i}{m_i}\frac{\partial}{\partial x_i}f=\zeta\frac{\partial}{\partial x_i}\left(p_if+m_ikT\frac{\partial}{\partial p_i}f\right)\,.\tag{C.12}$$

This is the classical Kramers-Chandrasekhar equation which we have wanted to derive.

References

1) H. A. Kramers: Physica **7** (1940) 284.
2) S. Chandrasekhar: Rev. Mod. Phys. **15** (1943) 1.
3) M. Toda: J. Phys. Soc. Japan **13** (1958) 1266.
4) M. Toda: J. Phys. Soc. Japan **14** (1959) 722.
5) R. K. Wangsness and F. Bloch: Phys. Rev. **89** (1953) 728. F. Bloch: ibid **102** (1956) 104; **105** (1957) 1206.
6) E. W. Montroll and K. E. Shuler: J. Chem. Phys. **26** (1957) 454.
7) R. W. Zwanzig: J. Chem. Phys. **28** (1958) 365.
8) M. Toda and T. Kotera: Busseiron-Kenkyu II **4** (1958) 448 (in Japanese).

JOURNAL OF THE PHYSICAL SOCIETY OF JAPAN Vol. 14, No. 11, NOVEMBER, 1959

Electrical Properties of Alkali Antimonides

By Shunji IMAMURA

Technical Research Laboratories, Japan Broadcasting Corporation,
361, Kinuta-machi, Setagaya-ku, Tokyo, Japan

(Received June 5, 1959)

Systematic studies of the preparation procedures and the electrical characteristics of the alkali antimonides, such as sodium, potassium, rubidium and cesium antimonides, were carried out. It has been found that these antimonides can be classified into two groups, i.e., a group which transits from p-type to n-type with successive activation, e.g. sodium and potassium antimonides, and a group which keeps constantly p-type, e.g. cesium antimonide. Rubidium antimonide was recognized to be an intermediate compound lying between these two groups. Supply of excess alkali metal, deposition of additional antimony and superficial oxidation gave remarkable effects on the dark and photoconductivity and the photoemission, but these effects proceeded in opposite derections in these two groups. With decreasing temperature, the mobility of n-type compound decreased, whereas that of p-type one increased. A picture of impurity states in these compounds was proposed in order to interprete the above mentioned phenomena, taking the ionic radius of alkali atom and the crystal structure into consideration.

§ 1. Introduction

Alkali antimonides are intermetallic compound composed of alkali metal and antimony as represented by M_3Sb. Among them, cesium antimonide (Cs–Sb) is a well known photocathode material with high efficiency in visible spectral region. Many investigations on the mechanism of photoemission have been concentrated on this material.[1] Cs–Sb has usually not stoichiometic composition and is a p-type semiconductor confirmed by the measurements of Hall effect[2] and thermoelectromotive force.[3] Other alkali antimonides, such as Rb–Sb, K–Sb and Na–Sb, have been scarcely studied so far because of their low efficiency of the emission for visible light. However, it is worthwhile to investigate systematically these all alkali antimonides, not only Cs–Sb, in order to obtain more information about their emission mechanism.

In 1953, Suhrmann and Kangro[4] reported that K_3Sb was an n-type semiconductor. This fact seems to be strange compared with the p-type conduction in Cs–Sb. In 1958, we showed[5] that Rb–Sb, K–Sb and Na–Sb were n-type semiconductors and that the dark and photoconductivity and the photoemission behaved in opposite manner to Cs–Sb when a small amount of antimony or oxygen was introduced on these materials. Recently, Sommer[6] independently reported almost similar results. The main purpose of the present paper is to elucidate these remarkable phenomena in alkali antimonides.

§ 2. Preparation of Samples and Experimental Method

As is usual for the experimental study of photo-cathode, great care must be taken to avoid impurities and contaminations. We used Sb of the purity of 99.999% containing As as main impurity and alkali chromate of the highest purity commercially available as alkali metal source.

Fig. 1(a) shows the experimental tube for the measurements of conductivity, photoconductivity, photoemission and optical transmission. For the measurement of Hall effect the another tube shown in Fig. 1(b) was employed, whose electrodes were made of nonmagnetic materials.

After evacuation and degassing, Sb was deposited onto the aquadag electrode provided on the inner wall of the glass tube. In order to obtain the electric characteristics in bulk and to separate the internal from the external photoelectric effect, much thicker layer than that in usual photo-tubes was adopted. The thickness of Sb layer, ranged from 1000 Å to 2000 Å, was monitored by the optical transmission which was previously calibrated by multiple interference method. The alkali metal was distilled by heating the mixture of the alkali chromate and the reducing agents such as powdered Al, Si and W. At temperatures between 150° and 180°C, the alkali antimonides were prepared by the reaction of the alkali metal vapor with Sb layer.

In Cs–Sb, the thickness of the final layer is about 8.1 times larger than that of the initially deposited Sb layer.[7] In other alkali antimonides, an expansion of the same order may be expected.

During the formation processes, the resistance, the photoemission current, the photoconduction current and the sign of thermo-electromotive force were measured.

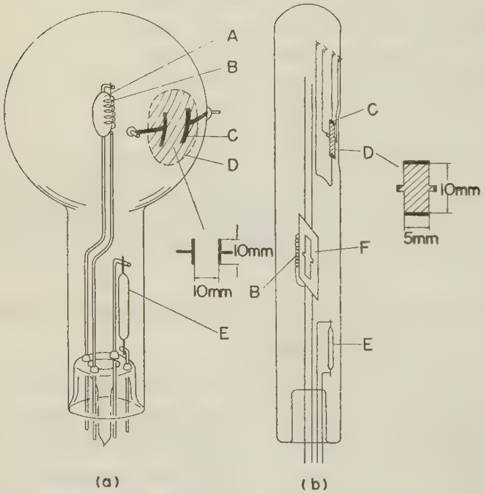

(a) (b)

Fig. 1. Schematic pictures of the experimental tubes. (a) Tube for the measurements of dark and photoconductivity, photoemission and optical transmission. (b) Tube for measurement of Hall effect. *A*: Anode. *B*: Sb evaporator. *C*: Aquadag electrode. *D*: Alkali antimonide sample. *E*: Alkali metal source. *F*: Movable mask for Sb deposition.

§ 3. Experimental Results

3.1. Behaviors in the course of preparation

Fig. 2 shows schematically the behaviors of the dark resistance at 170°C, the photoemission current at 20°C and the photoconduction current at 20°C in the course of preparation. In abscissa, " M ", " Sb " and " O_2 " denote an alkali metal reaction with Sb layer, an additional small amount deposition of Sb and a superficial oxidation at oxygen pressure about 10^{-4} mm Hg respectively. The abscissa shows also the sign of majority carrier determined by thermo-electromotive force.

Dark resistance:

In Cs–Sb (Fig. 2a), if Cs supply proceeded, the resistance increases rapidly and then reaches a maximum value, at this stage the color of the layer is transparent yellow. If Cs is supplied furthermore, the resistance decreases and then slowly increases, the color becoming deep red. The resistance decreases considerably by the process " Sb " or " O_2 ". Fig. 2b shows the behaviors of K–Sb as a representative of Rb–Sb, K–Sb and Na–Sb. After the maximum resistance is established, the resistance decreases relatively rapidly and the color changes abruptly from red to violet, though this color change is insufficient in some samples of Rb–Sb and is not apparent in Na–Sb. This state corresponds to the nearly degenerated one, which will be described later. In contrast with Cs–Sb, the resistance increases by " Sb " or ', O_2 ".

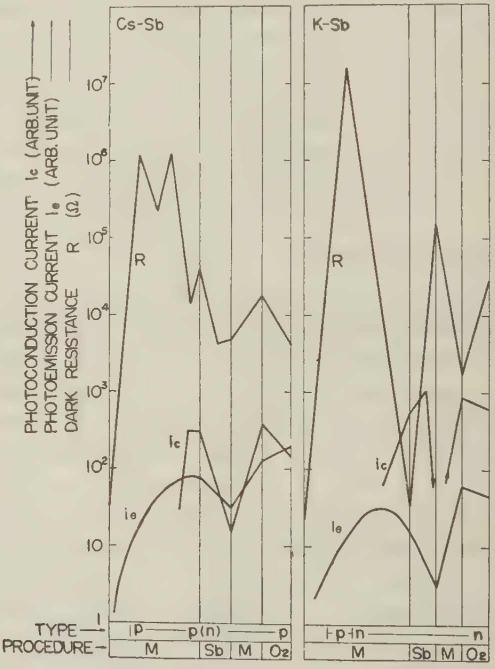

(a) (b)

Fig. 2. Schematic representation of the behaviors in the course of preparation. (a) Cesium antimonide. (b) Potassium antimonide.

Photoconduction:

Photoconduction current could not be measured until the resistance bigins to decrease through the maximum value and becomes appreciable with over alkali supply. In the K–Sb group, enhancement of the photoconductivity is brought by additional deposition of Sb after the resistance decreased fairly, in contrast with the case of Cs–Sb. "O_2" suppresses the photoconductivity and increases noise current in all antimonides.

Photoemission:

The photoemission increases with increasing resistance during alkali metal supply. If alkali metal supply is continued further, after the resistance peak is established the emission decreases slowly in Cs–Sb and rapidly in other antimonides. "Sb" causes also the emission decrease in all antimonides. "O_2" causes the emission increase in Cs–Sb, i.e., the so-called "oxygen sensitization" occurs, whereas in other antimonides this treatment causes the emission decrease, though some samples, especially Rb–Sb, show the opposite behavior. The absolute luminous sensitivity was 40–60 μA/lm for Cs–Sb, 10–20 μA/lm for Rb–Sb, 5–10 μA/lm for K–Sb and <1 μA/lm for Na–Sb.

Thermo-electromotive force:

The sign of the thermo-electromotive force was observed during the preparation. In Cs–Sb, the sign is always negative, indicating that positive charge carriers are predominant. If plenty of Cs is occasionally introduced, some samples change to n-type. However, this state is not stable, but returns to p-type with subsequent heat treatment. This phenomenon is considered to be surface conduction and seems to be the same as observed by several investigators.[8] In K–Sb and Na–Sb the transition from p-type to n-type takes place just after, or in some cases even before, the peak resistance is attained. In Rb–Sb, this transition occurs rather later than former two, and some samples keep p-type conduction and do not degenerate.

3.2 Electrical properties

Temperature dependence of conductivity:

Temperature dependence of the conductivity was measured over the range from 500° to 77°K, at several stages during preparation. In Cs–Sb, the slope in log conductivity versus $1/T$ plot decreases with Cs supply from ca. 0.4 eV at initial stage to ca. 0.15 eV at final stage. Wallis[9] has collected in his paper many different values of activation energy of Cs–Sb ranged from 0.4 to 0.025 eV, which were reported by many investigators. Such dispersion seems to be proper characteristics expectable from inhomogeneity of this compound. The curve of largest slope serves the value of the zero interception of the intrinsic order ($10^3-10^4\ \Omega^{-1}\,\mathrm{cm}^{-1}$), and so it is considered ideally to give the minimum energy difference between the conduction band and the filled band.

Fig. 3 shows a typical one in K–Sb as a representative of all n-type compounds. The slope decreases with alkali metal supply. The largest slope is considered similarly to give the intrinsic gap, and the mean value for many samples is listed in Table I with the values for other compounds. A remarkable

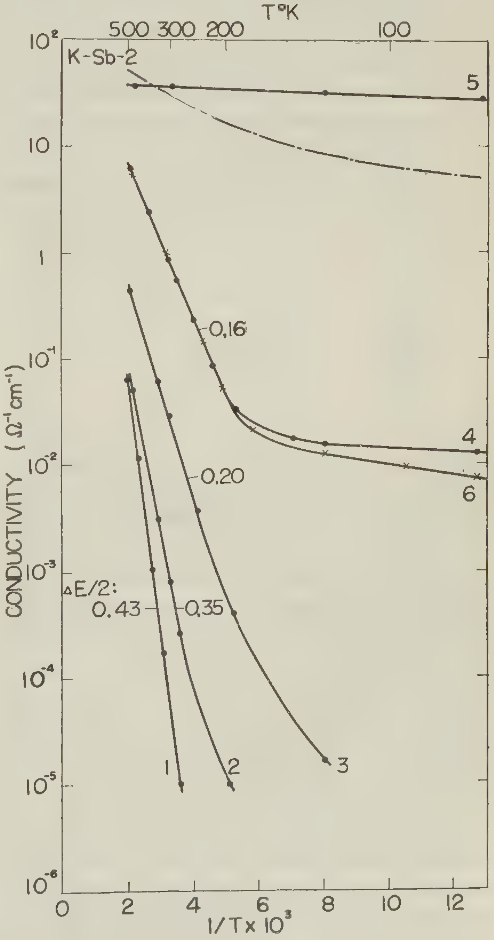

Fig. 3. Conductivity vs. $1/T$ for K–Sb. Numbers denote the preparation stages. Chain curve shows a degeneration limit.

Table I. Maximum value of electric activation energy.

	Cs–Sb	Rb–Sb	K–Sb	Na–Sb
Max. activation energy $\varDelta E/2$ (eV)	0.4	0.5	0.5	0.6

difference from Cs–Sb is the flat part at low temperatures (curve 4). At the final stage of activation, temperature dependence almost disappears (curve 5). This state gives the large value of carrier concentration of the order of $10^{18}\,\mathrm{cm}^{-3}$ by using the value of mobility $\mu=10\,\mathrm{cm}^2\,\mathrm{v}^{-1}\,\mathrm{sec}^{-1}$ as given later, and satisfies a condition for degeneration (chain curve) calculated from the equation:

$$T=\left(\frac{h^2}{2mk}\right)\left(\frac{3n}{8\pi}\right)^{2/3}.$$

Hence, supply of excess alkali atom to Rb–Sb, K–Sb and Na–Sb makes finally a degenerated state. The color of the layer is red in the state 4 and is violet in the state 5. According to the detailed measurement of optical transmission spectra, however, actual layer is not so homogeneous that even at earlier stage of activation (e.g. curve 4) the degenerated state is partially produced. The flat part of curve 4 is presumably due to this partial semi-metallic conduction. Curve 6 is obtained by "Sb" and shows that the degeneration has been removed.

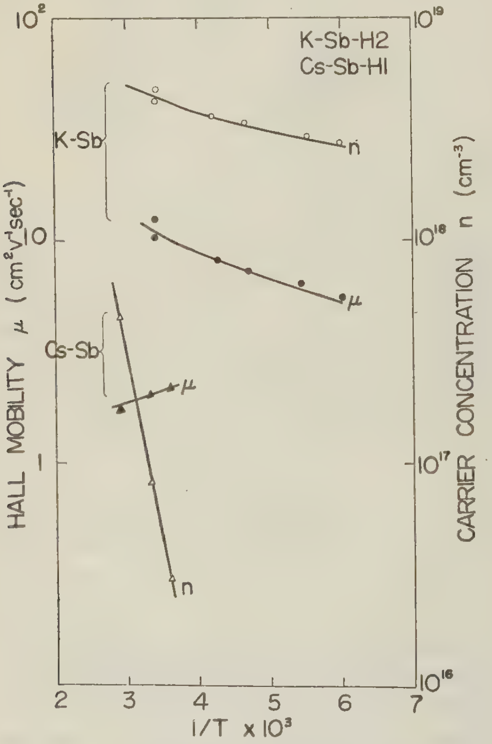

Fig. 4. Hall mobility and carrier concentration vs. $1/T$.

Hall effect:

The sign of the majority carriers observed in this measurement coincided with that in the thermo-electromotive force measurement. As is shown in Fig. 4, Hall mobility of Cs–Sb increases with decreasing temperature, in agreement with Sakata's observation.[2] As a contrast, the mobility of the nearly degenerated K–Sb, as a representative of all n-type compounds, decreases with decreasing temperature. This may be taken as an indication of the presence of impurity scattering due to large impurity concentration in n-type compound. The mobility of Cs–Sb is, in general, smaller than that of other n-type antimonides by about one order of magnitude, though the values are dispersing.

§ 4. Impurity Model for Alkali Antimonides and Discussion

Before discussing the impurity state in these antimonides, we must consider chemical impurities in host material. Since Sb is the common component in these compounds, impurities contained in Sb will not be a cause for the opposite behaviors in two groups. Alkali metal vaporization is performed by a fractional distillation process, and so the alkali metal vapor is considered to be fairly pure. However, in the procedure of reaction of Sb with the alkali metal vapor of lower vapor pressure, such as Na, impurities of higher vapor pressure, such as Cs, should be avoided, because it forms quickly undesired compound. Existence of such alkali metal as Cs gives definite effect on the photoemission because of its high efficiency. But this effect was not observed in the present experiment. Consequently, chemical impurities may be left out of consideration. In practice, deposited Sb layer does not form regular lattice, and the reaction with alkali metal is essentially a solid phase reaction. Then, many imperfections must exist in these compounds. Microscopic density of Cs_3Sb calculated from X-ray's data is $4.42\,\mathrm{g\,cm}^{-3}$, while macroscopic density calculated from optically determined thickness is $1.54\,\mathrm{g\,cm}^{-3}$. This discrepancy may be taken as a support of above suggestion. Lattice defect, stacking fault, dislocation and grain boundary must effect on the electrical properties. On the other hand, there are such definite experimental results as Cs–Sb is a *p*-type semiconductor and contains excess Cs atoms.[10,11] Although it is difficult to determine the origin of the acceptors, it is one reasonable way to identify the Cs atom, which occupied Sb site substitutionally, as acceptors, as was pointed out by Jack and Wachtel.[10] In other alkali antimonides, the same interpretation may be adopted on the *p*-type conduction at initial stage in activation process. When alkali atoms are introduced in large quantity, these excess atoms, this time, occupy the interstitial positions in the lattice if possible and act as donors. Ionic radii of K and Na are so small that it is possible to enter the interstitial position, and, therefore, if donor concentration N_D becomes larger than acceptor concentration N_A, a transition from *p*- to *n*-type may be observed. In Cs–Sb, however, it is difficult to occupy the interstitial position because of the large ionic radius of Cs, so that *n*-type conduction does not appear, except surface conduction of *n*-type. Rb is considered to have the limit radius for this possibility. It has been reported so far that Cs_3Sb has a cubic lattice[10] and K_3Sb and Na_3Sb have a hexagonal structure,[12] provided that the preparation methods have been different from those used in photo-cathodes. Table II shows microscopic densities calculated from X-ray's data assuming that each compound is able to crystalize in two different structures, because the transition between these may be possible. Parentheses denote the interpolated values. Remarkable result is that the density of *n*-type sample is smaller in hexagonal form than that in cubic one and that of *p*-type sample is small in cubic form. Crystal form of small density is able to involve larger amount of interstitial atoms than that of larger density. In K–Sb, for instance, interstitial K atom is more stable in hexagonal crystal than in cubic one.

Table II. Densities of alkali antimonides calculated from X-ray's data,[10),12)] assuming that crystal structure of each compound is either cubic or hexagonal. Parentheses denote interpolated values.

Compound	ionic radius of alkali ion (Å)	lattice const.		density (g cm^{-3})
		a(Å)	c(Å)	
β-Li_3Sb : cub.	0.78	5.56		5.47
α-Li_3Sb : hex.	0.78	4.70	8.31	2.98
Na_3Sb : cub.	0.98	(6.9)		(3.81)
Na_3Sb : hex.	0.98	5.35	9.49	3.43
K_3Sb : cub.	1.33	(8.2)		(2.85)
K_3Sb : hex.	1.33	6.02	10.69	2.36
Rb_3Sb : cub.	1.48	(8.9)		(3.54)
Rb_3Sb : hex.	1.48	(6.1)	(11.0)	(3.54)
Cs_3Sb : cub.	1.70	9.18		4.42
Cs_3Sb : hex.	1.70	(6.2)	(11.2)	(4.63)

The interpretation of decrease of activation energy with alkali metal supply and the estimation of the donor concentration at degenerated state are made as follows: If N_D increases successively, the distance between donor impurities decreases and the wave functions of the impurities overlap. Though the levels will distribute at random in the forbidden band, the model proposed by Conwell[13] may be applied in this problem. That is to say, the vanishing of the activation energy should occure at $r_s=2\kappa a_H^*$, where r_s is given by $4/3\times\pi r_s^3=1/N_D$, κ is a suitable dielectric constant and a_H^* is the radius of the first Bohr orbit for a carrier of effective mass m^*. The value of κ of Cs–Sb may be estimated to be slightly larger than the optical dielectric constant $\kappa_0=4$, obtained from the refractive index,[9] as $\kappa=6$, by taking some ionic natures of this compound into consideration. Nearly equal value of κ is expected for the other compounds, too. Assuming $m^*=0.3\,\mathrm{m}$, r_s

$=2\kappa a_H{}^*=2.1\times10^{-7}$ cm, hence $N_D=2.7\times10^{19}$ cm^{-3}. This value is fairly in agreement with the free carrier concentration at the degenerated state, though somewhat larger. This large value of N_D must give some effects on the crystal lattice more or less. A variation of crystal structure, presumably from cubic to hexagonal or from amorphous to hexagonal one, accompanying the color change and abrupt increase of N_D may possibly occur in this condition.

In n-type sample, "Sb" and "O_2" decrease the interstitial and substitutional atoms composing some compounds with these elements, and consequently the conductivity decreases, though still $N_D>N_A$ holds. In n-type sample, N_D decreases in the similar way, and thereupon the conductivity increases.

The detailed discussions of the photoemission and the photoconduction will be presented in the subsequent paper.

At last, we must state a remark on the intrinsic electrical nature of the alkali antimonides. The Brillouin zone of Cs–Sb of cubic structure is just filled with electrons at the stoichiometric composition Cs_3Sb[10] so that the property of intrinsic semiconductor will be expected. But, it is somewhat questionable to assume that the hexagonal alkali antimonide with stoichiometric composition is an intrinsic semiconductor as it is the case for cubic structure, because the zone of such structure may be not completely filled with electrons.

§ 5. Conclusions

From the systematic studis of the preparation procedures and the electrical properties, a picture of donor and acceptor states in each alkali antimonide consistent with the experimental results has been presented taking the ionic radius of alkali atom and the crystal structure into consideration. The present viewpoint should be further correlated to the explanation of photoelectric phenomena, as will be described in the subsequent paper. Photoelectrical study will infer whether the present model has a more general validity or not.

References

1) For examples, A. H. Sommer: Proc. Phys. Soc. London **55** (1943) 145. H. Miyazawa: J. Phys. Soc. Japan **8** (1953) 169. L. Apker, E. Taft and J. Dickey: J. Opt. Soc. Amer. **43** (1953) 78.
2) V. P. Zhuze, I. V. Mochan and S. M. Ryvkin: Zhur. Tekh. Fiz. **18** (1948) 1494. See Chem. Abstr. **46** (1952) 4303. T. Sakata: J. Phys. Soc. Japan **8** (1953) 793: ibid. **9** (1954) 1030.
3) T. Sakata: J. Phys. Soc. Japan **8** (1953) 125.
4) R. Suhrmann and Cl. Kangro: Naturwiss. **40** (1953) 137.
5) S. Imamura: presented at the Meeting of the Physical Society of Japan, March 1958 (Manuscript **1**, p. 188).
6) A. H. Sommer: J. Appl. Phys. **29** (1958) 1568.
7) S. Munesue: private communication.
8) S. Yu. Luk'yanov and I. S. Mazover: J. Exp. Theor. Phys. (U. S. S. R.) **9** (1939) 1459. See Chem. Abstr. **36** (1942) 6407. P. G. Borzyak: Zhur. Tekh. Fiz. **20** (1950) 923. See Chem. Abstr. **45** (1951) 437.
9) G. Wallis: Ann. Physik **17** (1956) 401.
10) K. H. Jack and M. M. Wachtel: Proc. Roy. Soc. **A**, **349** (1957) 46.
11) N. S. Khlebnikov: Zhur. Tekh. Fiz. **17** (1947) 333. See Chem. Abstr. **42** (1948) 816.
12) G. Brauer and E. Zintil: Z. Phys. **37B** (1937) 323.
13) E. M. Conwell: Phys. Rev. **103** (1956) 51.

JOURNAL OF THE PHYSICAL SOCIETY OF JAPAN Vol. 14, No. 11, NOVEMBER, 1959

Photoelectrical Properties of Alkali Antimonides

By Shunji IMAMURA

Technical Research Laboratories, Japan Broadcasting Corporation, 361, Kinuta-machi, Setagaya-ku, Tokyo, Japan

(Received June 5, 1959)

Photoemission, photoconduction and optical absorption of sodium, potassium, rubidium and cesium antimonides were studied at several stages in the course of preparation. In the former three, supply of excess alkali atoms caused the decrease in optical absorption and photoemission at the photon energies higher than the absorption edge, whereas in the last one these phenomena were not remarkable. Photoconduction characteristics were interpreted by assuming two impurity states (donor and acceptor) in each antimonide. At last, two kinds of energy band structures in k-space were proposed on the basis of the crystal structures (cubic and hexagonal), using the energy values obtained from measurements.

§ 1. Introduction

Many studies have been concentrated on the photoemission[1] and the optical absorption[2] of Cs-Sb. Photoemission of this compound is usually attributed to a volume effect, because of the large optical absorption coefficient and the high quantum efficiency in the spectral region within which the photo-electrons are available. But only a few measurements were carried out on photoconductivity[2], despite of great importance for the understanding of the optical excitation process in this compound.

In addition, very few studies on the photoemission were made on the other antimonides of alkali metals[4], such as Rb-Sb, K-Sb and Na-Sb. Recently, the photoelectric characteristics of these compounds were reported by Spicer[5] in cooperation with Sommer. Entirely independently of these investigators, we made detailed studies on photoelectrical properties, including the spectral distribution of the photoemission and photoconduction[6].

In the preceding paper[7], we have discussed the physical nature of the impurity states in these alkali antimonides. Present paper has two purpose. The first is to examine the correlation of the impurity with the optical properties, such as photoconduction, photoemission and optical absorption, and the second is to give a suitable energy band model for these alkali antimonides.

§ 2. Experimental Method

In the preparation of samples, special care was taken on the layer thickness. Since these materials are photo-emitter, the measurement of the photoconduction is disturbed by the emitted photo-electrons which skim toward the positive electrode. For this reason, so far the photoconduction measurement has not been carried out in the spectral region within which the photoemission is available. To avoid this difficulty, the comparatively thick layers, from 1.0μ to 2.0μ, were employed. When incident light falls on glass side surface as illustrated in Fig. 1, almost light is absorbed in the layer, because of the large optical absorption coefficient, and the transmitted light is very weak at the vicinity of vacuum side surface. Thus, the photoconductivity can be measured over extended spectral range without interference due to externally emitted photo-electrons. For the measurement of the photoemission the light was projected from vacuum side. We have shown in the preceding paper that activation and additional treatment give considerable change on the electrical characteristics. Therefore, the optical and photoelectrical measurements were made at several stages in these processes. The light from tungsten lamp was chopped at the frequency of 180 cp and the photo-current was measured using a high sensitivity tuned amplifier. Such method was especially required

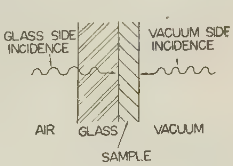

Fig. 1. Direction of light incidence.

for the measurement of photoconductivity, because the photo-current was quite only a fraction of the dark current. The glass prism double monochromator was employed for the spectral measurement. In order to measure the photoconductivity decay, sample was illuminated with pulsed light from argon discharge tube, whose pulse width is shorter than 1μ sec, and the photo-current was observed with a cathode-ray oscilloscope.

§ 3. Experimental Results and Discussion

3.1 Optical absorption

Samples with different thickness were prepared for the measurement of transmittance. The difference of the logarithms of transmission for different thickness is proportional to the absorption coefficient. Although satisfactory method to determine the absorption edge has not been developed yet so far, the edge can be approximately given by extrapolation of the above mentioned transmission difference curve, even if exact value of layer thickness is unknown. Fig. 2 shows the transmission spectra and the transmission difference curves for typical samples. The magnitude of absorption coefficient in higher photon energy region is estimated to be of the order of 10^5 cm^{-1}. The absorption in lower photon energy

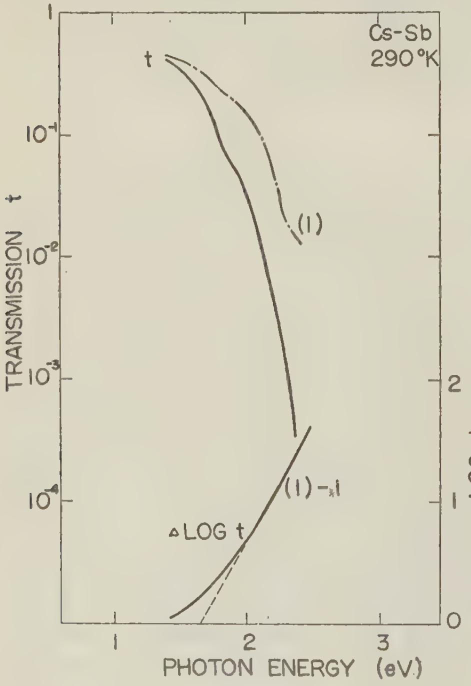

Fig. 2(a).

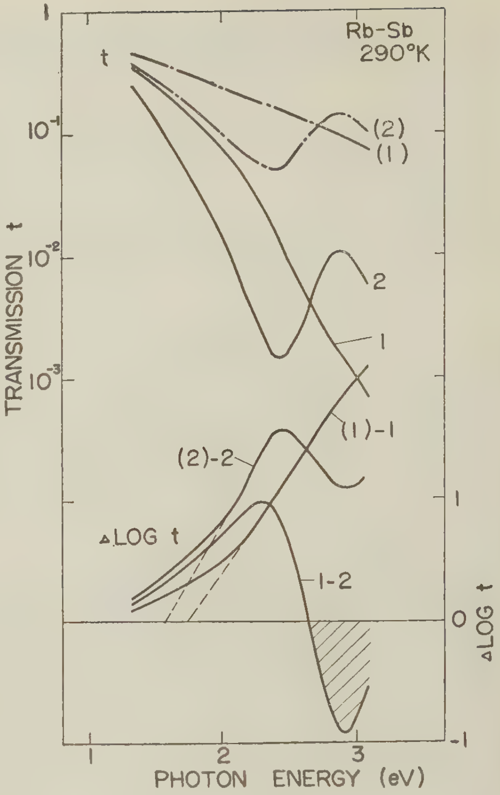

Fig. 2(b).

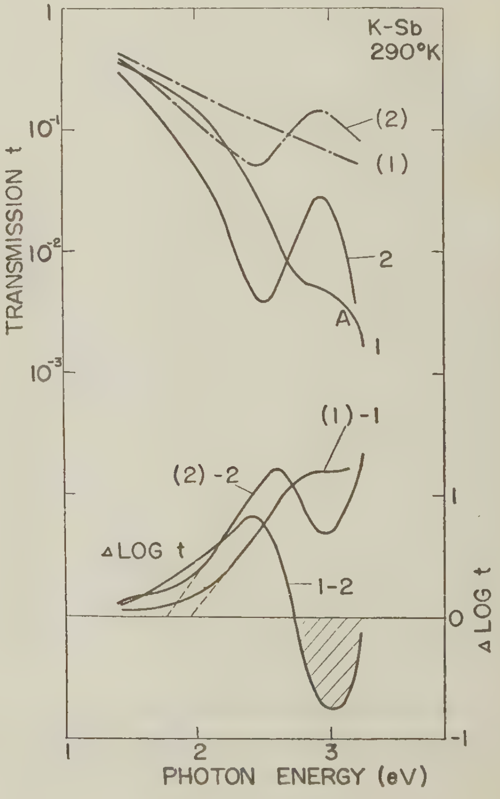

Fig. 2(c).

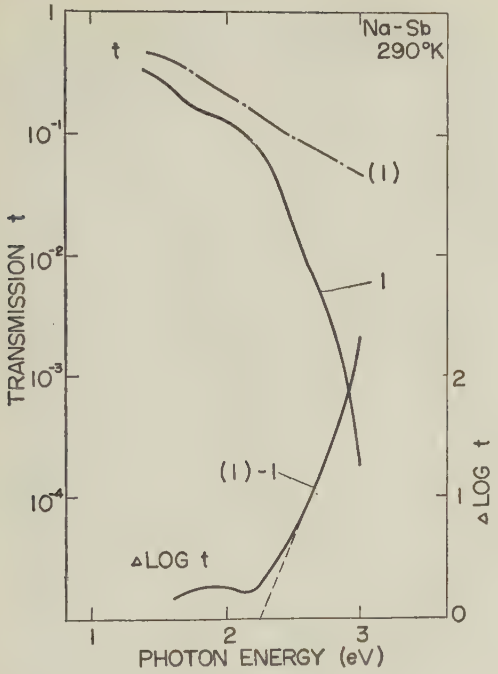

Fig. 2(d).

Fig. 2. Optical transmission spectra for the layers with different thickness, at 290°K. Thickness of initially deposited Sb layer is 100 to 120Å for chain curve and 150 to 170Å for solid curve. Degree of activation by alkali metal supply increases from 1 to 2. (a): Cs-Sb, (b): Rb-Sb, (c): K-Sb and (d): Na-Sb.

region cannot be considered to be intrinsic one.

During activation process, remarkable phenomena appeared in K-Sb and Rb-Sb. In Fig. 2 (c), for example, curves 1 and (1) represent the transmission in the state of high electric resistivity, curves 2 and (2) associate with the electrically degenerated state developed by addition of K atom to the states 1 and (1), and curves (1)–1 and (2)–2 give the difference of the transmission in these two states. As seen from curve 1–2, the absorption decreases remarkably in the higher photon energy region (hatched area), making a trough of absorption curve, and increases in the lower photon energy region, with alkali metal supply. In appearance, there were the color change from red to violet and an appreciable crystal growth, at this moment. Small hamp A of curve 1 suggests a partial proceeding of the color change at the initial stage of activation. These phenomena occure also in Rb-Sb (Fig. 2b), except some samples which retained high resistivity even though a large quantity of alkali atom was introduced. Consequently, abrupt color change and abrupt resistivity decrease occur at the same time. These phenomena were not distinct in Na-Sb and never occured in Cs-Sb. Since the absorption decrease takes place at the photon energies higher than the absorption edge, this is, at least, not caused by the excess alkali atoms, but considered to be due to a change in the energy band structure.

3.2 Photoemission

Fig. 3 shows the spectral quantum yields of photoemission. Degree of activation increases in suffixed numerical order. Since the absorption coefficient and the quantum yields are fairly large in this spectral region, the emission of all alkali antimonidies should be due to a volume effect. Then, the minimum energy for the transition from filled band to

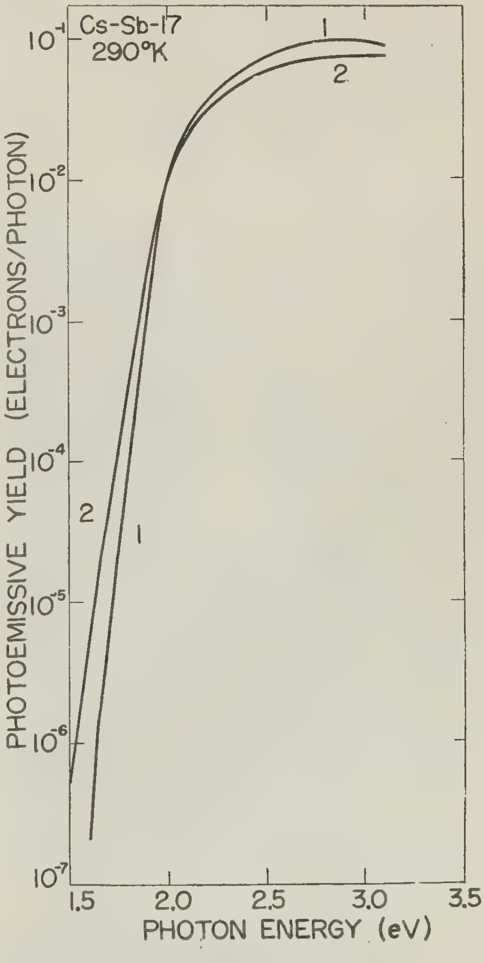

Fig. 3(a).

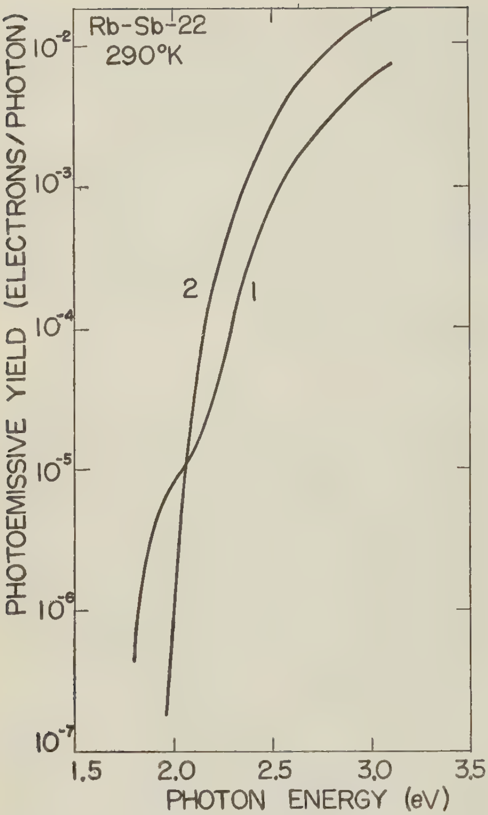

Fig. 3(b).

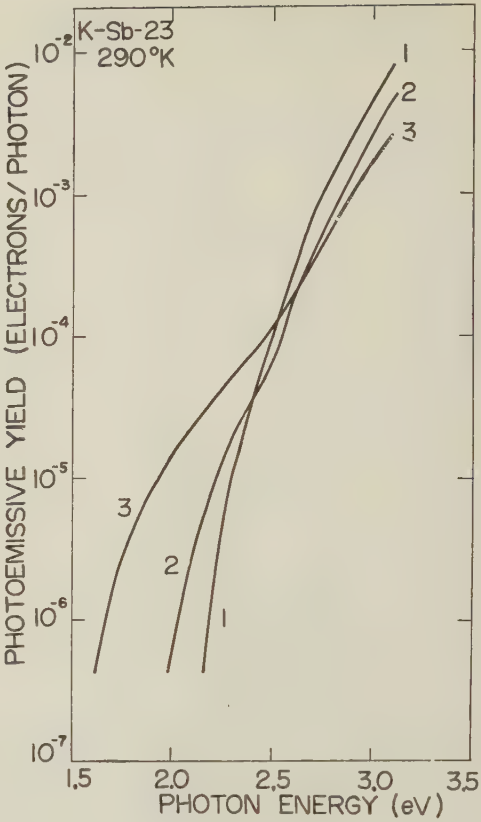

Fig. 3(c).

vacuum level can be approximately determined from the photoemission threshold energy. When a large quantity of alkali atom is introduced, the spectral yields increase at lower photon energy and decrease at higher photon energy. The increase is supposed to be due to the excitation of excess alkali atoms, which exist predominantly at the surface. However, the decrease of yields is considered to be more important and is attributed to the impurity scattering of the electrons excited by volume effect. The luminous sensitivity decreases also by excess alkali metal supply. In addition, it was observed that these changes are more remarkable in n-type Rb-Sb, K-Sb and Na-Sb, which are n-type compounds. It seems likely to deduce that n-type alkali antimonides are able to admit a large quantity of excess alkali atom than that p-type Cs-Sb does.

3.3 Photoconduction

Spectral response:

The measurement of the spectral distribution of photoconductivity was difficult, because magnitude of the photo-current was very small and unstable, and the noise current was large. Fig. 4 shows typical spectral response curves. No distinct change is found at the energy of absorption edge or the photoemission threshold. But, the value of the threshold of photoconductivity is fairly in agreement with the twice of the largest activation energy of electric conduction. Distinct change cannot be observed at the energy corresponding to the above mentioned absorption trough in K-Sb and Rb-Sb. If a small amount of Sb is deposited on the surface of these n-type alkali antimonides or infra-red light is overlapped, the response quenches especially in higher photon energy region as shown in Fig. 4d.

Temperature dependence:

Measurement of the temperature dependence of photoconductivity was carried out at the several stages in the course of preparation. Curve 1 in Fig. 5 was obtained at electrically degenerated state, which was developed by excess alkali atom supply and had low resistivity. The response is very low at room

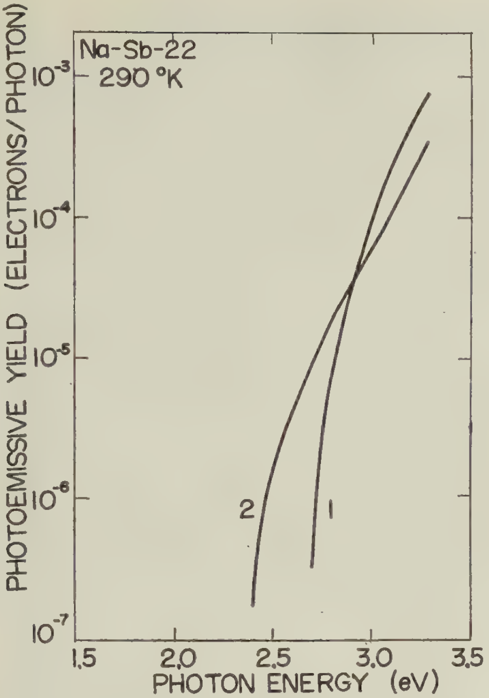

Fig. 3(d).

Fig. 3. Spectral distribution of photoemissive yield. Degree of alkali metal supply increases in suffixed numerical order. (a): Cs-Sb, (b): Rb-Sb, (c): K-Sb and (d): Na-Sb.

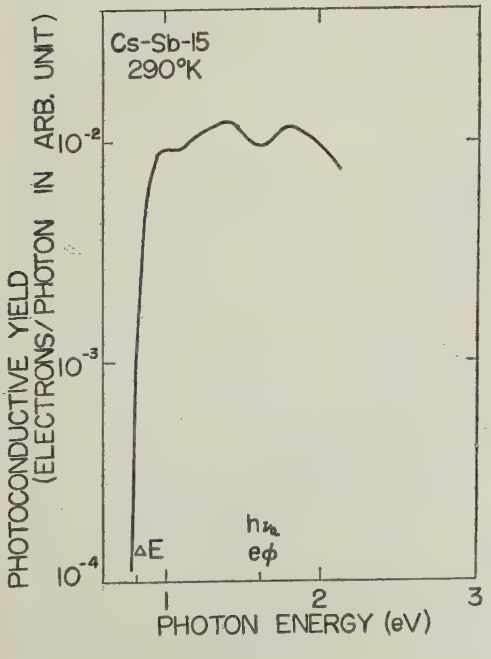

Fig. 4(a).

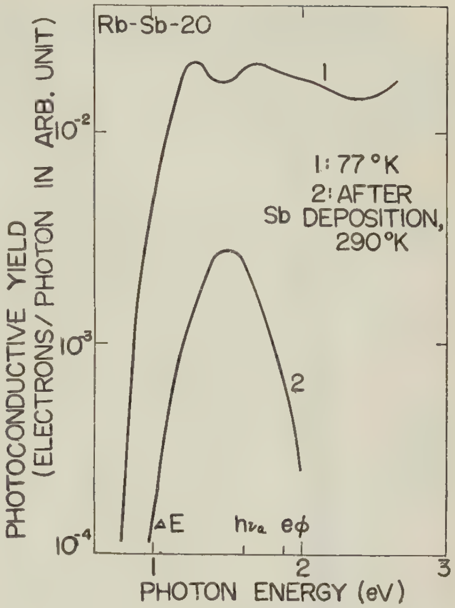

Fig. 4(b).

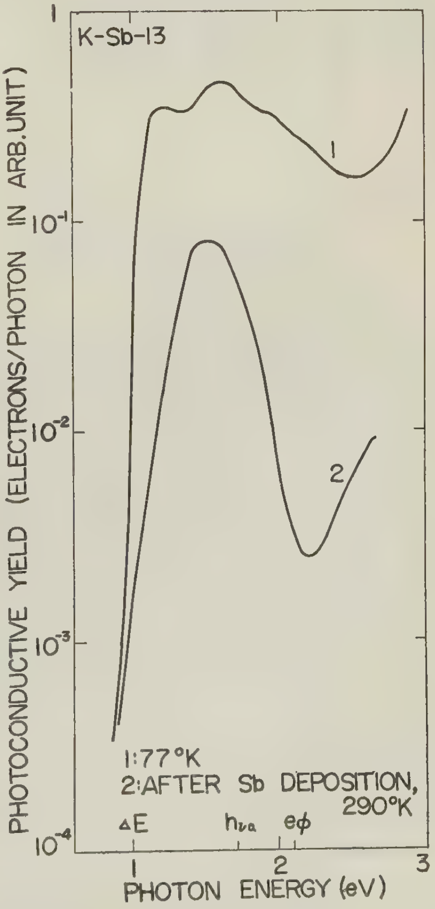

Fig. 4(c).

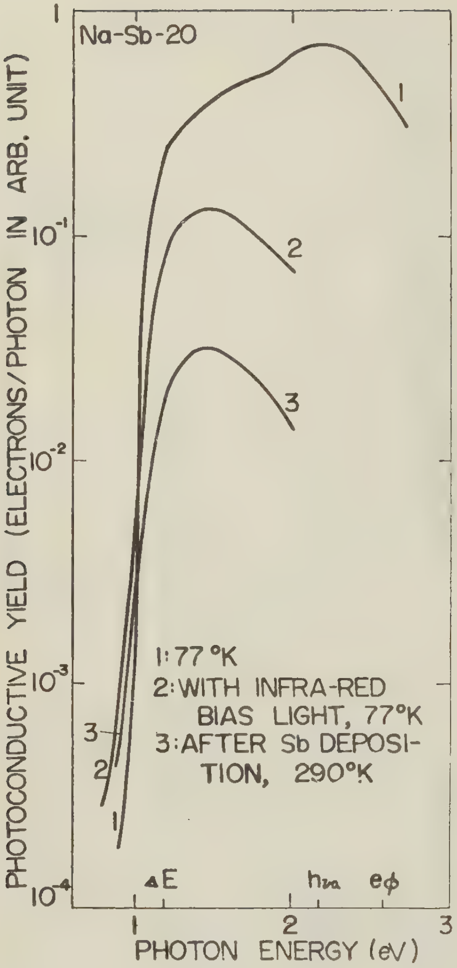

Fig. 4(d).

Fig. 4. Spectral distribution of photoconductivity. (a): Cs-Sb, (b); Rb-Sb, (c): K-Sb and (d): Na-Sb. $h\nu_a$, $e\phi$ and ΔE indicate absorption edge, phoemission threshold and twice of maximum activation energy of conductivity respectively.

temperature, but increases rapidly with decreasing temperature. When a small amount of Sb is deposited, the sensitivity increases at room temperature and decreases at low temperatures (curves 2 and 3) in comparison to curve 1. The sensitivity of Cs-Sb is usually lower than those of other compounds by many factors, as shown in Fig. 5 (curve A).

Decay time:

Photoconductivity decay could not be expressed by a simple exponential curve. However, the time constant obtained from the fast decay at initial period is considered to give a measure of the life-time of the excess carriers. In a strongly n-type K-Sb sample the time constant was 300μ sec at 77°K and was 1.4μ sec at 290°K. This temperature dependence of time constant is in agreement with the tendency in the temperature dependence of photoconductivity. In the sample quoted above, the time constant decreased remarkably when infra-red light was overlapped, indicating that the trapped carriers (in this case, holes) were released on this occasion.

Light spot scanning measurement:

The area between electrodes was scanned by the thin light beam of 0.5 mm thick. It was found that the distribution of local photoconductivity was non-uniform and changed with time, in most samples of high resistivity. The rate of change depends on applied voltage and does not depend on illumination intensity, and finally a stationary state is established requiring several minutes or more. In n-type

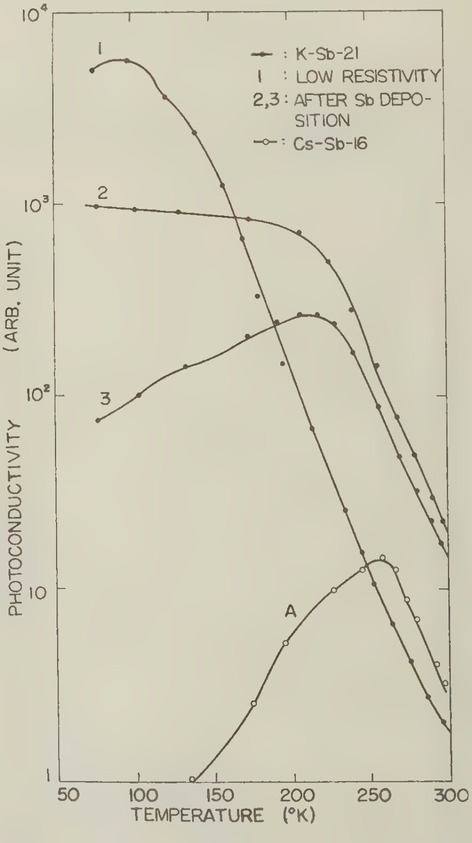

Fig. 5. Temperature dependence of photoconductivity. Curves 1, 2 and 3: for K-Sb, of which curve 1 was obtained at degenerated state and other curves were obtained by Sb deposition in suffixed numerical order. Curve A: Cs-Sb.

sample, the local photo-response in the stationary state is highest in the vicinity of the positive electrode, as shown in Fig. 6. These results indicate that the photo-sensitive point in high resistive n-type compound corresponds to a negatively charged center. Since during this change the color of layer was invariant, it could not be to relate to an electrolytic process[8].

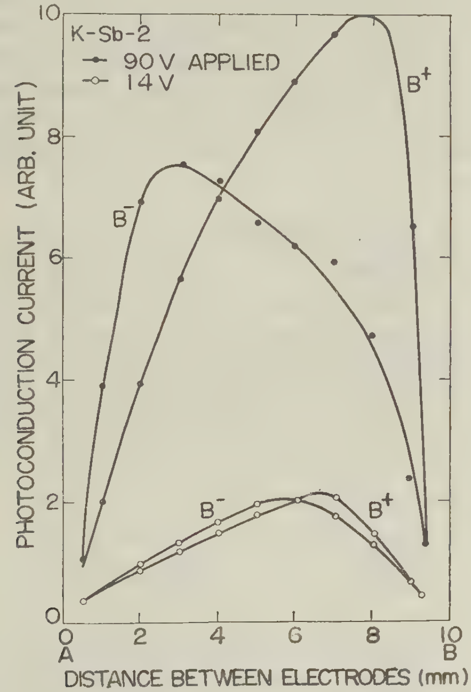

Fig. 6. Distribution of local photoconductivity in stationary state. B^+ and B^- denote the polarity of applied vollage at B side electrode.

Mechanism of photoconduction:

The donors and the acceptors are considered to be interstitial and substitutional alkali atoms respectively, as described in the preceding paper. In n-type compound, the donor concentration N_D is larger than the acceptor concentration N_A, and then the acceptors have been compensated negatively with donor electrons. If electron-hole pairs are produced by optical excitation of the filled band electrons as described in the next section, some of free holes are trapped by the negatively charged acceptors. As a result,

$$\Delta n = \Delta p_f + \Delta p_t\,, \tag{1}$$

when Δn, Δp_f and Δp_t are concentration of excess free electrons, free holes and trapped holes respectively (Fig. 7). The photo-sensitivity is related to the concentration and the life-time of free carriers. If the concentration and the life-time of the trapped holes are large, the corresponding excess free electrons are able to contribute to photoconduction.

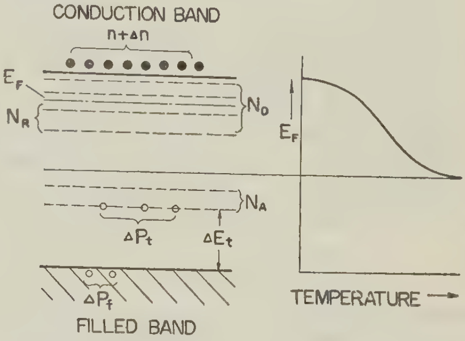

Fig. 7. Model of impurity states for illuminated *n* type compound.

Now, we consider the life-time. After the removal of optical excitation, the decay rate of hole and the time constant are given by

$$-\frac{d\Delta p_t}{dt} = q_t v n \Delta p_t + \Delta p_t \nu \exp\left(-\frac{\Delta E_t}{kT}\right)$$

$$\equiv \left(\frac{1}{\tau_t}\right)_1 \Delta p_t + \left(\frac{1}{\tau_t}\right)_2 \Delta p_t\,, \tag{2}$$

and

$$-\frac{d\Delta p_f}{dt} = q_f v N_R \Delta p_f$$

$$\equiv \left(\frac{1}{\tau_f}\right)\Delta p_f\,, \tag{3}$$

where q_t is the capture cross-section of acceptor for a free electron when occupied by a hole, v is the thermal velocity of free electron, n is the free electron concentration, ν is attempt-to-escape-frequency, ΔE_t is the energy difference between filled band and acceptor levels occupied by a hole, q_f is the recombination cross section of free electron and free hole through recombination center and N_R is the concentration of recombination centers. Eq. (2) represents the rates with which trapped hole density decreases by capture of free electrons and by thermal process. Eq. (3) represents the recombination rate of free carriers. Consequently, the life-time of excess carriers is controlled by three components;

$$\frac{1}{\tau} = \left(\frac{1}{\tau_t}\right)_1 + \left(\frac{1}{\tau_t}\right)_2 + \left(\frac{1}{\tau_f}\right).$$

Now, we assume that the donors below the Fermi level E_F act as the recombination centers. In the strongly n-type sample, temperature dependence of life-time is determined by the second term, because N_R is large and E_F, in this case, is temperature independent. Therefore, the sharp increase in photoconductivity with decreasing temperature (Curve 1 in Fig. 5) is understood. When a small amount of Sb is doposited, it combines with impurity alkali atom, and the sample becomes normally n-type. The decrease of impurity concentration implies the decrease of n, N_R and Δp_t. Then, the quenching of photoresponse is mainly due to the decrease of Δp_t, despite of increased life-time due to the decrease of n and N_R. In normally n-type sample, E_F shifts toward the middle of the forbidden gap with temperature rise. Therefore the density of the donors below E_F, which act as recombination centers, decreases with temperature rise, enhancing the photoresponse: temperature dependence is determined by the third term. At higher temperatures, the photoresponse decreases again with temperature rise, according to the first and the second terms. Thus, the fact, that the Sb deposition causes the enhancement of photoresponse at room temperature and makes the response peak at intermediate temperatures (Curve 3 in Fig. 5), may be understood.

The reverse may hold principally in p-type Cs-Sb. But, in this case, donor concentration is so small that the number of trapped electrons is smaller than that of trapped holes in n-type sample, though the acceptor concentration may be of the same order in both cases. Hence, the efficiency of photoconductivity in p-type sample is lower than that in n-type sample.

§ 4. Energy Band Structures in Alkali Antimonides

The energy values obtained from the different measurements are summarized in Table I, though they are not unique or highly accurate. The optical absorption edge coincides nearly with the photoemission threshold, indicating that the electron affinity should be small. The photoconduction threshold coincides nearely with the largest value of the electric conduction activation energy and does not coincide with the absorption edge. If the photoconductivity originates from impurity atoms, the photoemission is to be expected at the threshold energy of photoconductivity because of the small value of electron affinity, and the distinct absorption must be observed at this energy because of the large impurity concentration. But, these were not the cases. Hence, we postulate that the threshold energy of photoconductivity and the intrinsic dark conductivity is of an indirect transition between filled and conduction bands. The optical indirect transition is, of course, of small probability and produces the photoelectrons mostly in deep layer, so that appreciable photoconductivity and no photoemission should be observed. At the photon energies corresponding to direct transition, the both photo-electric effects should be observed though the photoconductivity may be quenched by surface recombination.

Table I. Excitation energies for different phenomena.

	Absorption edge $h\nu_a$ (eV)	Photoemission threshold $e\phi$ (eV)	Photoconduction threshold $h\nu_c$ (eV)	Max. activation energy for elec. cond. $\Delta E/2$ (eV)
Cs-Sb	1.6	1.6	0.9	0.4
Rb-Sb	1.8−1.6	1.9	0.9	0.5
K-Sb	1.9−1.7	2.1	1.0	0.5
Na-Sb	2.2	2.6	1.0	0.6

In these materials, filled band and conduction band are simply considered to be p-band associated with antimony and s-band associated with alkali atom respectively. So far it has been reported that K-Sb and Na-Sb take a hexagonal structure[9] and that Cs-Sb takes a cubic structure[10]. Since p-band of hexagonal structure splits into two bands, at least $\mathbf{k}=0$, whereas that of cubic structure does not split, at least $\mathbf{k}=0$[11], aforementioned absorption through may be attributed to the p-band splitting. Therefore the abrupt change of absorption spectra attendant upon increasing activation must correspond to the change from cubic to hexagonal structure or from amorphous to hexagonal one. In Cs-Sb, p-band splitting is absent and then the anomalous absorption change cannot be expected. Although the structure of Rb-Sb has not been investigated, the author supposes that this compound has two kinds of crystal structure (cubic and hexagonal).

Putting all accounts together, the energy band sheme can be tentatively given as illustrated in Fig. 8.

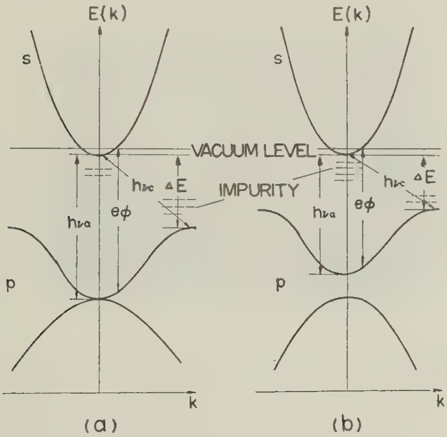

Fig. 8. Model of energies as a function of **k**. (a) for cubic and (b) for hexagonal structures of alkali antimonides.

§ 5. Conclusions

Optical absorption, photoemission and photoconduction of alkali antimonides were studied systematically during the preparation, as it was the case of the measurement of the electrical characteristics. Taking the ionic radius of alkali atom into consideration the preceding paper established a model which allowed to interprete the electric properties. The model was also feasible to interprete some of the photoelectrical properties. In addition, this paper proposed two kinds of energy band structure in **k**-space, depending on crystal structures. Abrupt changes in the spectral absorption and the electric conductivity during activation process were interpreted by considering the transition between these crystal structures.

In conclusion, the author wishes to express his appreciation to Dr. Hiroji Mitsuhashi, Dr. Jiro Yamashita and Dr. Ken'ichi Takeya for many helpful discussions and suggestions, to Mr. Mutsumu Kinoshita for experimental assistance, and to Dr, Akira Yamashita and Dr. Kohichi Miyaji for continuous encouragements.

References

1) For examples, P. Görlich: Z. Phys. **101** (1936) 335. A. H. Sommer: Proc. Phys. Soc. London **55** (1943) 145. H. Miyazawa: J: Phys. Soc. Japan **8** (1953) 169. L. Apker, E. Taft and J. Dickey: J. Opt. Soc. Amer. **43** (1953) 78.
2) J. A. Burton: Phys. Rev. **72** (1947) 231. See also V. K. Zworykin and E. G. Ramberg: *Photoelectricity* (John Wiley & Sons, New York, 1949) 59. G. Wallis: Ann. Physik **17** (1956) 401.
3) P. G. Borzyak: Zhur. Tekh. Fiz. **20** (1950) 923. See Chem. Abstr. **45** (1951) 437. S. Pakswer and W. O. Reed: J. Appl. Phys. **22** (1951) 987.
4) P. Görlich: Phil. Mag. **25** (1938) 256. V. Schwetzoff and S. Robin: Compt rend. **233** (1951) 518: ibid. **234** (1952) 316. W. J. Harper and W. J. Choyke: Rev. Sci. Instr. **27** (1956) 966.
5) W. E. Spicer: Phys. Rev. **112** (1958) 114.
6) S. Imamura: Presented at the Meeting of the Physical Society of Japan, March 1958 (Manuscript **1**, p. 188).
7) S. Imamura: J. Phys. Soc. Japan **14** (1959) 1491.
8) H. Miyazawa and S. Fukuhara: J. Phys. Soc. Japan **7** (1952) 645.
9) G. Brauer and E. Zintl: Z. Phys. **37B** (1937) 323.
10) K. H. Jack and M. M. Wachtel: Proc. Roy. Soc. **A**, **239** (1957) 46.
11) H. Bethe: Ann. Physik **3** (1929) 133.

JOURNAL OF THE PHYSICAL SOCIETY OF JAPAN, Vol. 14, No. 11, NOVEMBER, 1959

Quenching Effect in KCl Crystals

By Masayoshi SAKAMOTO

Department of Physic, Tokyo College of Science
Tokyo, Japan

(Received June 5, 1959)

Effects of thermal quenching on KCl crystals were studied in both clear and colored specimens. These were subjected to two types of quenching, down- and up-quenching. The etching method was carried out to examine generated dislocations and the photoelastic method was used to see the distribution of the residual stresses.

The results of the experiments are as follows: (1) Generated dislocations, distributing from the crystal surface toward the interior, were perceived. (2) They ranged over a lunar area along the edges in the cross section of the specimen. (3) The range, in which the residual stresses exist, has also the same lunar form along the edges. Therefore, the residual stresses are considered as resulting from the thermal generation of slips. These experimental facts can be explained on the basis of thermal stresses.

§ 1. Introduction

In the research processes on colored alkali halide crystals, specimens are often subjected to thermal quenching. Therefore, it is interesting as well as necessary to study and and expound what kinds of effect thermal quenching will have in alkali halide crystals. As a typical sample, KCl was chosen among many alkali halides. This report deals with the experimental results obtained mainly by the etching method and partly by the photoelastic method with respect to the quenching effects on both clear and colored KCl crystals.

§ 2. Experimental Procedure

(i) Clear specimens were prepared through cleavage from the ingots produced by Kyropoulos method. Colored crystals were obtained through the usual additive coloring method. The density of color center was usually within $10^{16}\sim10^{17}$. Colored specimens were also prepared through cleavage from these crystals. The mean size of the specimens in both clear and colored specimens was $5\times5\times3$ mm^3.

(ii) Two types of quenching were performed. The one is the down-quenching, cooling down from high temperature (up to 500°C) to room temperature and the other the up-quenching, recovering from low temperature (liquid air temperature) to room temperature. In the case of down-quenching, two methods were used. The one, denoted A, was to cool the specimen through heat conduction on a metal plate after withdrawing from the crucible. The other, denoted B, was to air-cool the specimen within the crucible with a fan. These two methods were also used similarly but conversely in the case of up-quenching. The one, denoted B′, was to recover the temperature of the specimen keeping it within the container. The other, denoted C, was to recover its temperature by placing it in aceton just after withdrawing from the container.

(iii) In order to examine the generated dislocations and slip lines, the same etching method as in our previous reports[1,2] was applied. The increase in density of generated dislocations were visually observed by comparing the etch pattern within the same surface region of the specimen before and after subjecting them to thermal quenching.

(iv) The photoelectric method was also used in order to see the distribution of residual stresses within specimens. For this purpose, the polarization apparatus, attached to the Olympus universal type metal microscope, was employed.

§ 3. Experimental Results

(i) *Etch patterns of the generated dislocations*

An etch pattern on the (001) plane of the clear specimen, quenched down from 500°C to room temperature by B method, is shown in Fig. 1(b) and compared with the one on the same region before quenching, Fig. 1(a).

The etch pits are seen to be aligned in ⟨100⟩ direction, showing that they correspond to screw type dislocation.[3)]

An etch pattern in the colored specimen, quenched down from 500°C to room temperature by A method, is shown in Fig. 2(b) and

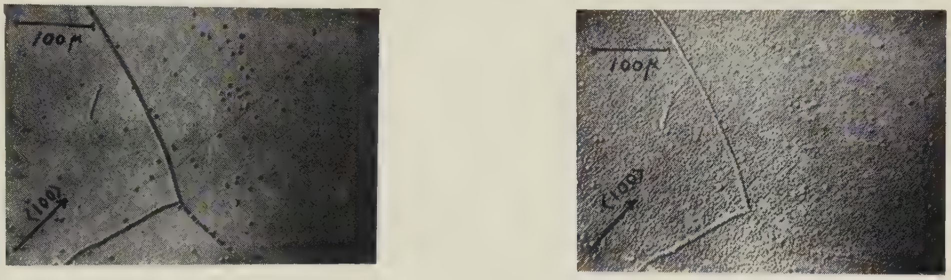

a b

Fig. 1. An example of etched (001) plane of a "down-quenched" clear specimen (×150), (a) before quenching and (b) after quenching.

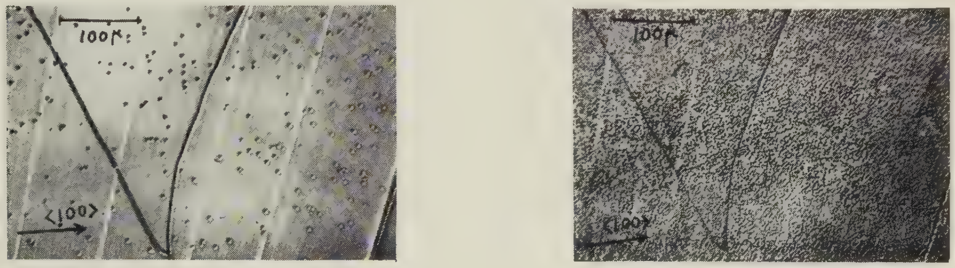

a b

Fig. 2. An example of etched (001) plane of a "down-quenched" colored specimen (×150), (a) before quenching and (b) after quenching.

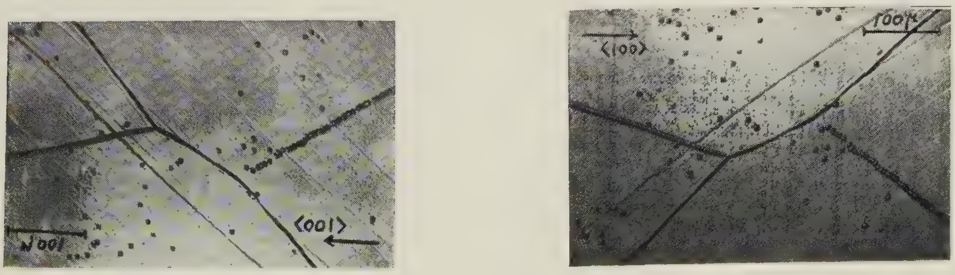

a b

Fig. 3. An example of etched (001) plane of an "up-quenched" clear specimen (×150), (a) before quenching and (b) after quenching.

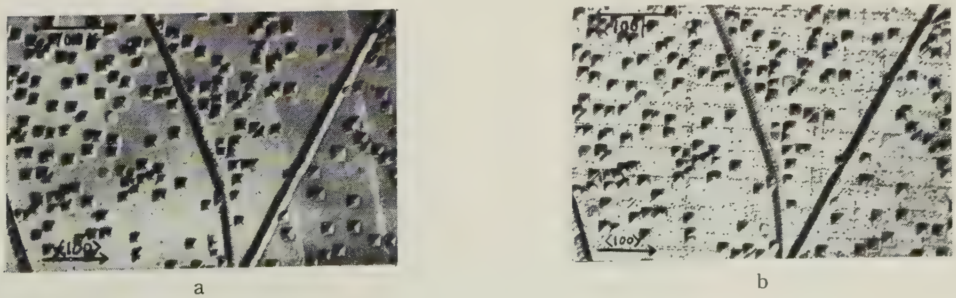

a b

Fig. 4. An example of etched (001) plane of an "up-quenched" colored specimen (×150), (a) before quenching and (b) after quenching.

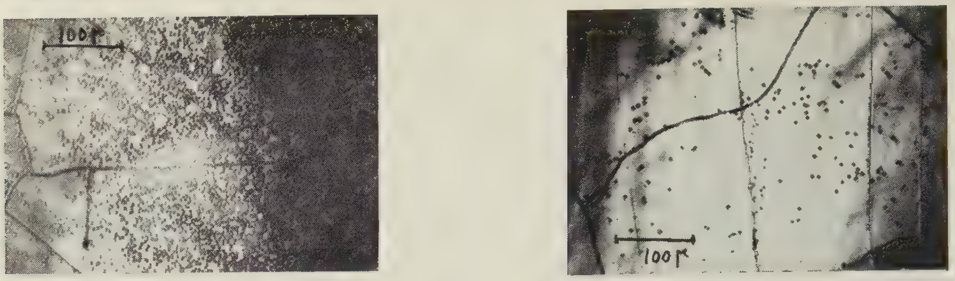

a b

Fig. 5. An etch pattern of a cleaved plane 800 μ in distance below and parallel to the top surface of the specimen (× 150), (a) edge part and (b) central part.

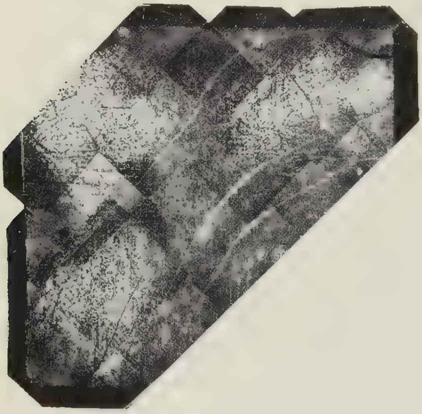

(a)

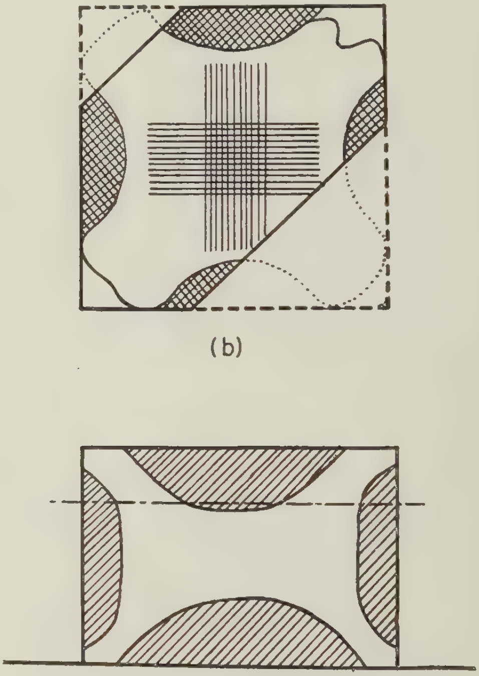

(b)

(c)

Fig. 6. A panoramic view of an etch pattern of a cleaved cross section in a "down-quenched" specimen; (a) a panoramic view, (b) a schematic diagram of (a) and (c) its horizontal perspective.

compared with that of the same region before quenching, Fig. 2(a). The alignment of etch pits is not so remarkable in the colored specimen as in the clear one.

In Fig. 3(b), an etch pattern of the (001) plane in the clear specimen, up-quenched from −183°C to room temperature by C method, is shown and compared with the one of the same region, Fig. 3(a), before quenching. It may be clearly seen that the etch pits are arranged in ⟨100⟩ type direction and consist of screw type dislocations.

Fig. 4(a) and (b) show the similar case in the colored specimen.

The distribution of the generated dislocations within specimens has been studied by etching of the cross section cleaved parallel to the surface of the specimen. The distribution of the generated dislocations on a cleaved plane parallel to and 800 μ in depth from the top surface of the specimen, down-quenched from 500°C to room temperature by A method, is shown in Fig. 5(a). It is seen that the generated dislocations are distributed over a range of 300 μ in distance from the edge of the specimen. Fig. 5(b) shows a central part of the same cleaved surface. The estimated density is almost equal to that before quenching showing that there was no appreciable plastic deformation in this region.

Inspecting several pictures indicated above, it may well be said that the thermal stresses by quenching make many slips from the surface toward the interior of the specimens

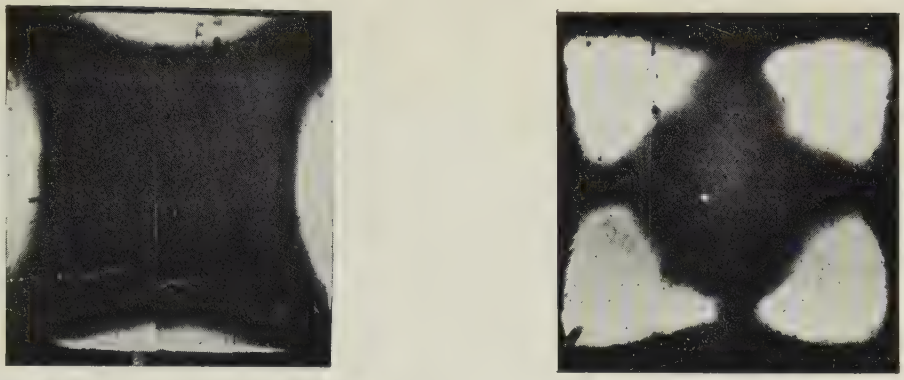
a b

Fig. 7. Photoelastic patterns of the "down-quenched" specimen in Fig. 6. Directions of the crossed nicols are (a) 45° or 135° against the edges of the square and (b) parallel to the latters.

and so the generated dislocations are related to these slips.

(ii) *Form the slipped area*

A panoramic view of the etched plane, cleaved parallel to the top surface of the clear specimen, is shown in Fig. (6)a. This specimen was down-quenched from 400°C by B method. In order to save time and effort, part of the square plane was not photographed as it in no way deters the experiment. Fig. 6(b) is its graphic diagram, in which the area of the generated dislocations has a lunar form along the edge of the square and there was no generation in the range between those areas. Slip lines, widely observed in the central part, are presumably originating from the top surface, as seen in Fig. 6(c).

(iii) *Photoelastic patterns*

Photoelastic patterns of the same specimen as the one in Fig. 6 are shown in Fig. 7. Fig. 7(a) is in case when the orthogonally crossed nicols make 45°C angle against $\langle 100 \rangle$ type directions and Fig. 7(b) in case they are parallel or at right angle to the same directions. It is considered that both pictures evince a distribution of the residual stresses resulting from the plastic deformation in the specimen. It should be noted that the lunar region, seen in Fig. 7(a), coincides with the same one, seen in Fig. 6(a). This fact strongly suggests that the residual stresses must have resulted from the plastic deformation by

Table on Densities of the Generated Dislocations.

	Starting temperature in °C	Estimated quenching rate in °C/min	Quenching method	Generated dislocation density in cm^{-3}	
				Clear crystal*	Colored crystal**
Down-quenching	180	(150)	A	~ 0	~ 0
	270	(250)	A	~ 0	~ 0
	400	(350)	A	4.6×10^5	0.6×10^5
	500	(150)	B	1.0×10^6	4.6×10^5
	500	(450)	A	$>10^9$	2.7×10^6
Up-quenching	-77	(10)	B′	~ 0	~ 0
	-77	(700)	C	0.8×10^5	0.8×10^5
	-183	(15)	B′	~ 0	~ 0
	-183	(1600)	C	5.5×10^5	4.4×10^5

*,** Mean density of the background dislocations before quenching is $2 \sim 4 \times 10^4$ cm^{-2} in the clear specimen and $4 \sim 9 \times 10^4$ cm^{-2} in the colored one.

thermal quenching.

(iv) *Mean density of the generated dislocations*

Mean densities of the generated dislocations are shown in the following table. The quenching rates are estimated to show the order of magnitude. Densities are mean values of several results taken upon the same specimen, respectively.

(a) The primary characteristics, noted from the above table, is that no dislocations will be generated when the starting temperatures are low in the same quenching method. This fact may suggest that no slips will occur until thermal stresses reach critical value.

(b) Secondly, densities of the generated dislocations in the colored specimen are less than that in the clear specimen under the same quenching process.

(c) Thirdly, densities of the generated dislocations increase with the rate of quenching under the same starting temperature. This fact may be explained, as will be discussed later, from the character of the density which is proportional to the temperature gradient perpendicular to the crystal surface.

§ 4. Discussions

(i) *Interpretation of the photoelastic patterns*

Transmitted intensity of an incident monochromatic light is generally proportional to the factor, $(\sin\delta/2)\times(\sin 2\phi)$.[4] Here, δ is a phase difference between the two double-refracted beams which have two axes of principal stress on the specimen in the directions of vibrating plane and ϕ is an angle which the directions of the principal stress make against the polarizer's plane. The directions of the principal axes of the residual stresses are distributed as Fig. 8, from the symmetrical quality of the specimen (square). Speaking characteristically, three main parts can be discerned in Fig. 8: (a) part which is the periphery of the square along the edge, (b) part including the diagonal of the square and (c) part which is central in the square. In (a) part, ϕ will be 45° and therefore transmitted light will be maximum when the directions of the orthogonally crossed nicols make 45° to 135° against x axis. In (b) part, ϕ will be 45° and transmitted light will be maximum similarly when the directions of the orthogonally crossed nicols are parallel or at right angles to x axis. On the other hand, (c) part is dark in both Fig. 7(a) and (b). This fact may suggest that δ becomes very small, because δ is proportional to $\sigma_x\sim\sigma_y$ and also these two are almost equal in this region.

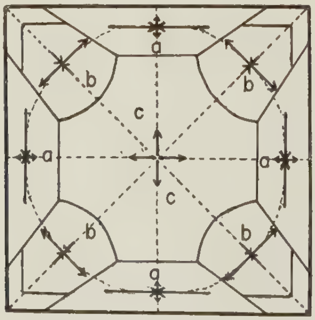

Fig. 8. A simple schematic diagram showing the directions of principal axes of the residual stress.

(ii) *Interpretation of the form of slipped area*

It is considered from the facts observed in § 3. (i), (ii) that the slips are generated from the surfaces toward the interior of the specimen by thermal stress. Therefore, let us delve into the problem of why the slipped area has a lunar form along the edge of the square (its cross section). At first, for simplicity's sake, assuming that the temperature variation along the axis perpendicular to the cross section is small, a two dimensional equation of the thermal stress may be considered as follows,[5] when the coordinates are taken as in Fig. 9,

$$\left.\begin{aligned}\frac{\partial\sigma_x}{\partial x}+\frac{\partial\tau_{xy}}{\partial y}-\frac{\alpha E}{1-2\nu}\frac{\partial T}{\partial x}=0\\ \frac{\partial\tau_{xy}}{\partial x}+\frac{\partial\sigma_y}{\partial y}-\frac{\alpha E}{1-2\nu}\frac{\partial T}{\partial y}=0\end{aligned}\right\} \qquad (1)$$

Here, σ_x, σ_y are normal components of stress parallel to x, y axis; τ_{xy}, α, E and ν are shearing stress, thermal expansion coefficient, elastic constant and Poisson's ratio, respectively. These equations can not be solved exactly. It is believed, however, that σ_y is proportional to the temperature distribution from the experimental situations.

Therefore, it is assumed that

$$\sigma_y=\frac{\alpha E}{1-2\nu}T. \qquad (2)$$

In the vicinity of the free end along x axis $\sigma_x \cong 0$ and also $|\partial\sigma_x/\partial x| \ll |\partial\sigma_y/\partial x|$,[6] so that it may suffice to discuss mainly σ_y's variation.

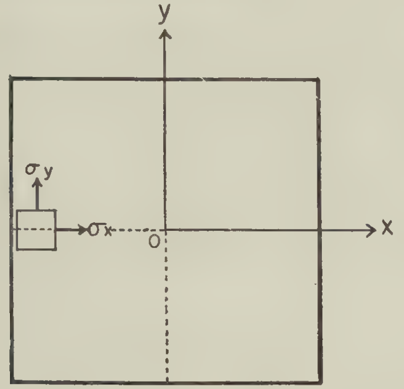

Fig. 9. Determination of the coordinate axes.

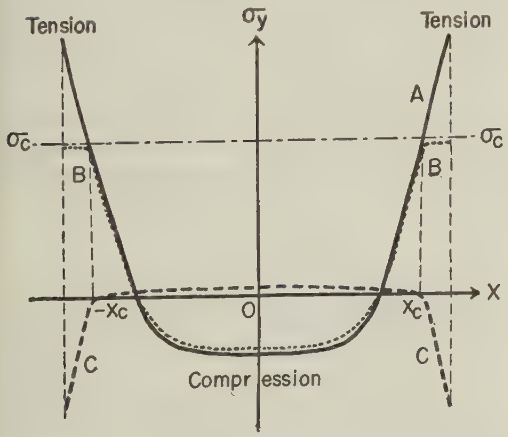

Fig. 10. σ_y's distribution along x-axis and its variation.

Considering σ_y's distribution just before the moment of slip generation qualitatively, it must extend along the substantial curve (A) as shown in Fig. 10. Denoting the critical stress value as σ_c and its position on x axis as x_c, yielding will occur in the whole part of $\sigma_y > \sigma_c$ and then the curve must move to the dotted line (B) in Fig. 10 in order to reach a new equilibrium. Now, in the region $|x| > x_c$, denoting σ_y's gradient just before the yielding as $(\partial\sigma_y/\sigma x)_{\text{bef.}}$, just after that as $(\partial\sigma_y/\partial x)_{\text{af.}}$, and the effective stress distribution due to the generated dislocations as $(\partial\sigma_y/\partial x)_{\text{disl.}}$, then

$$\left(\frac{\partial\sigma_y}{\partial x}\right)_{\text{af.}} = \left(\frac{\partial\sigma_y}{\partial x}\right)_{\text{bef.}} - \left(\frac{\partial\sigma_y}{\partial x}\right)_{\text{disl.}} . \tag{3}$$

Since the transposition of the curve is negligibly small, it can be said that $(\partial\sigma_y/\partial x)_{\text{af.}} \cong 0$ in this region.

As for the last term of equation (3), according to Read,[7]

$$\left(\frac{\partial\sigma_y}{\partial x}\right)_{\text{disl.}} = \frac{2G}{1-\nu} b_y N , \tag{4}$$

where G, b_y and N are shearing modulus, y component of Burgers vector and the density of pure edge-type dislocations, respectively. Therefore, in this region, it is

$$\left(\frac{\partial\sigma_y}{\partial x}\right)_{\text{bef.}} \simeq \frac{2G}{1-\nu} b_y N . \tag{5}$$

Substituting (2) into (5) in this region, then

$$N \cong \frac{\alpha}{(1-2\nu)b_y}\left(\frac{\partial T}{\partial x}\right) . \tag{6}$$

Next, to find the appropriate solution for the boundary conditions of this problem,[8] thus

$$T = \text{const.} \times [\sum_l f(p_l,\ t) \cos p_l x] \cdot [\sum_m g(q_m,\ t) \cos q_m y]$$

then,

$$\frac{\partial T}{\partial x} = \text{const.} \times [\sum_l f^*(p_l,\ t) \sin p_l x] \cdot [\sum_m g(q_m,\ t) \cos q_m y] . \tag{7}$$

Substituting (7) into (6), it will be easily understood that N's distribution approaches a lunar form along the edge of the square.

(iii) *Numerical evaluation of the generated dislocation density*

It is presumed that the quantitative reliability of equation (6), considering its introduction, is relatively poor. However, substituting the following experimental values

$$\alpha = 3 \times 10^{-5}\ [\text{deg}^{-1}]$$
$$b_y = 6 \times 10^{-8}\ [\text{cm}]$$
$$1-2\nu = 0.75$$

into (6),

$$N = 6.7 \times 10^2 \times \left(\frac{\partial T}{\partial x}\right) .$$

Considering $(\partial T/\partial x) \sim 10^3$, then N becomes $\sim 10^6$, which is not very far off from the results of the experiments.

(iv) *Results of the table*

(a) The fact that there was no generation of dislocations in the case of low starting temperature under the same quenching method may be understood when we note that σ_y did not reach σ_c in Fig. 10. But this is true only when the methods are indentical. Effects of the different quenching rates will be discussed later.

(b) The true reason why the generated dislocation densidity of the colored speciments is less than that of the clear ones is yet unknown. Perhaps, the difference in $(\partial T/\partial x)$ between the two types of specimens, resulting from the difference, in thermal conductivity, may not be the causative factor.

(c) Among three quenching methods, comparing A with B and C with B', the results show that the faster the quenching rate, the higher the density of the generated dislocations.

This fact may well be explained if we consider that a fast quenching rate gives rise to a large temperature gradient. It may be notable, however, that in one example of upquenching (−77°C, method) cited in the table, a plastic deformation occurred despite the fact that the difference between the starting and final temperatures was not so large. The reason may be that a large $(\partial T/\partial x)$ before the core is warmed brings $\sigma_y > \sigma_c$ in the peripheral part.

(v) *Quenching process of the specimen*

The fact that a lunar form of the photoelastic pattern (Fig. 7) coincides with that of the slipped area in the cross section (square) of the specimen (Fig. 6) forces us to believe that the residual stress results from the plastic deformation. This suggests that σ_y's distribution should extend along C-curve, shown as broken lines in Fig. 10, because of a new equilibrium in elastic conditions, when the temperature recovers to room temperature. That is, the peripheral part changes from tension field to compression one while, on the other hand, the core part from compression field to weak tension one. This explanation is consistent with the recent findings of Kear and Pratt,[9] qualitatively. A quantitative measurement of the residual stresses is hoped for, as their distribution correspond almost to $(\partial \sigma_y/\partial x)_{\text{disl.}}$.

§ 5. Conclusions

When KCl crystals were quenched thermally, both clear and colored specimens showed the following characteristics resulting mainly from thermal stresses.

(i) New dislocations, distributed from the crystal surface into the interior, were generated. They were considered closely allied to double slips of ⟨110⟩/(110) type.

(ii) The range of generated slips had a lunar form along the edge in the cross section of the specimen.

(iii) The photoelastic pattern also showed the same lunar pattern along the edge of the cross section and so the range of the residual stresses coincided with the one of the generated slips.

(iv) Qualitatively estimating, the concentration of generated dislocations is proportional to the temperature gradient perpendicular to the crystal surfaces.

Acknowledgement

The author wishes to express his thanks to Dr. T. Suzuki, Dr. H. Kanzaki of the Institute for Solid State Physics, University of Tokyo and Prof. A. Ookawa of Gakushuin University, for giving him valuable discussions and suggestions in this work.

He is much indebted to Dr. M. Nishida for his kind aid and also to Mr. K. Takahashi and Miss H. Muramoto for their constant assistance.

References

1) M. Sakamoto and S. Kokayashi: J. Phys. Soc. Japan **13** (1958) 800.
2) M. Sakamoto and S. Kobayashi: J. Phys. Soc. Japan **13** (1958) 1231.
3) J. J. Gilman and W. G. Johnston: *Dislocations and Mechanical Properties of Crystals* (John Wiley, 1957) 116.
4) S. Timoshenko: *Theory of Elasticity* (Maple Press Co., 1951) chap. 5, p. 131.
5) S. Timoshenko: ibid., chap. 14, p. 421.
6) Dr. M. Nishida's private communication.
7) W. T. Read: Acta Met. **5** (1957) 83.
8) H. S. Carslaw: *Mathematical Theory of the Conduction of Heat in Solids* (McMillan and Co., 1921) 110.
9) B. H. Kear and P. L. Pratt: Acta Met. **6** (1958) 457.

JOURNAL OF THE PHYSICAL SOCIETY OF JAPAN, Vol. 14, No. 11, NOVEMBER, 1959

Application of Higher Order Born Approximation to Multiple Elastic Scattering of Electrons by Crystals

By Kunio FUJIWARA

The Institute for Solid State Physics,
Tokyo University, Tokyo, Japan

(Received June 30, 1959)

The calculation of Artmann (quoted in Raether's article in Hand. Phys. **32** 475) for the wave function of electrons in a crystal due to the first order Born approximation was extended to higher order approximations by iterated integrations. As the result, Cowley and Moodie's formula (Acta Cryst. **10** (1957) 609) for the multiple elastic scattering of electrons by crystal was reobtained in an improved form. The convergency of the higher order terms was illustrated by the numerical calculations on two simple examples. An elementary application was also made to the moiré patterns in electronmicrographs.

§1. Introduction

An essential feature which distinguishes the diffraction of electrons by crystals from those of X-ray and neutrons consists in the fact that numerous reflexions are excited simultaneously in a crystal owing to the strong interaction of electrons with crystals and the relative smallness of wave length of electrons. Under the ordinary experimental condition, these reflexions are in strong interactions to each other through the complicated multiple scattering processes. The kinematical theory of electron diffraction which is based on the first order Born approximation, describes the all waves excited by single scattering processes, but nothing about the interactions among them. Though, on the other hand, Bethe's dynamical theory[1] takes into account the interactions in the most general way, it is highly tedious to apply it to the cases where reflexions more than two or three are strongly excited. This makes almost impossible the quantitative comparison of the theoretical results with experimental data.

In 1957, an important diffraction theory was set up by Cowley and Moodie[2] on the basis of the theory of physical optics. They divided a crystal into a number of thin layers and calculated the wave field in a layer from that in the just prior to it by Huygens' principle. Thus, they succeeded in drawing out the vivid picture of multiple scattering processes, assuming that the scattering angles are small so that the wave fronts can be regarded as paraboloids. It is expected that their theory may solve many problems to which Bethe's theory is not applicable.

It is conceived that a quantum mechanical approach to their theory may be feasible by applying higher order Born approximation. To do this, the wave function of electron within a crystal must first be derived in the stage of the first order Born approximation. This had been done by Artmann[3]. In the present work, the extention of Born approximation is accomplished by starting from Artmann's calculation, and, as the results, Cowley and Moodie's formula is reobtained. The essential restriction in Cowley and Moodie's theory for the scattering angles is no longer necessary here. Though the mathematical proof hasn't yet been given on the convergency of wave function for general cases, the results of numerical calculations on simple examples shown in §6 give an instructive suggestion about it. The intensity in the short wave length limit and an approximate formula of scattering by finite crystals and an elementary application to moiré patterns have also been discussed in §§5 and 7, respectively.

§2. Method of Higher Order Born Approximation

In the beginning, the method of higher order Born approximation is outlined. As is well known, the wave equation for electrons scattered by a potential field $V(r)$ is given by

$$(\nabla^2+K^{0 2})\Psi(r)=-(2me/\hbar^2)V(r)\Psi(r)\,, \quad (2.1)$$

where K^0 represents the wave vector of the initial wave. The solution of Eq. (2.1) can be written in the form of integral equation

$$\Psi(\boldsymbol{r})=\psi^{(0)}(\boldsymbol{r})-(2me/\hbar^2)\int G_{K^0}(\boldsymbol{r},\boldsymbol{r}_i)V(\boldsymbol{r}_i)\Psi(\boldsymbol{r}_i)\,d\boldsymbol{r}_i\,, \tag{2.2}$$

where $\psi^{(0)}(\boldsymbol{r})$ is a solution of the homogeneous equation corresponding to Eq. (2.1) and $G_{K^0}(\boldsymbol{r},\boldsymbol{r}_i)$ is Green function.

Substituting the right hand side of (2.2) into the integrand in itself, we obtain

$$\begin{aligned}\Psi(\boldsymbol{r})=\psi^{(0)}(\boldsymbol{r})&-(2me/\hbar^2)\int G_{K^0}(\boldsymbol{r},\boldsymbol{r}_i)V(\boldsymbol{r}_i)\psi^{(0)}(\boldsymbol{r}_i)\,d\boldsymbol{r}_i\\&+(-2me/\hbar^2)^2\int G_{K^0}(\boldsymbol{r},\boldsymbol{r}_i)V(\boldsymbol{r}_i)\int G_{K^0}(\boldsymbol{r}_i,\boldsymbol{r}_j)V(\boldsymbol{r}_j)\Psi(\boldsymbol{r}_j)\,d\boldsymbol{r}_i\,d\boldsymbol{r}_j\,.\end{aligned} \tag{2.3}$$

In the first order Born approximation, the last term of Eq. (2.3) is neglected as a small quantity, while the second term, which we denote as $\psi^{(1)}(\boldsymbol{r})$, is interpreted as describing the wave field generated by single scattering. If Eq. (2.3) retaining the last integral term is substituted further into the same integral, we may improve Born approximation. After iterating similar substitutions, we shall finally obtain

$$\Psi(\boldsymbol{r})=\psi^{(0)}(\boldsymbol{r})+\psi^{(1)}(\boldsymbol{r})+\psi^{(2)}(\boldsymbol{r})+\cdots+\psi^{(m)}(\boldsymbol{r})+\cdots\,, \tag{2.4}$$

where $\psi^{(m)}(\boldsymbol{r})$ is given by

$$\psi^{(m)}(\boldsymbol{r})=-(2me/\hbar^2)\int G_{K^0}(\boldsymbol{r},\boldsymbol{r}_i)V(\boldsymbol{r}_i)\psi^{(m-1)}(\boldsymbol{r}_i)\,d\boldsymbol{r}_i\,. \tag{2.4a}$$

$\psi^{(m)}(\boldsymbol{r})$ may be interpreted as the amplitude of the wave field generated by the m-ple scattering. If

$$|\psi^{(n)}(\boldsymbol{r})|\ll|\psi^{(n-1)}(\boldsymbol{r})|\,, \tag{2.5}$$

the series (2.4) may be terminated at $\psi^{(n)}(\boldsymbol{r})$. In this case we have the solution of the n-th order Born approximation.

§ 3. Evaluation of $\psi^{(1)}(\boldsymbol{r})$

As is clear from Eq. (2.4a), all $\psi^{(m)}(\boldsymbol{r})$'s may be derived, once the form of $\psi^{(1)}(\boldsymbol{r})$ within the crystal is known. As mentioned before, $\psi^{(1)}(\boldsymbol{r})$ was already calculated by Artmann[3]. However, his calculation, the detail of which has not been published, was performed assuming that only the waves scattered in forward directions are appreciable. In what follows, his result is amended by allowing for the backward scattering as well as the forward scattering, although his approximation will be adopted again in the later discussions.

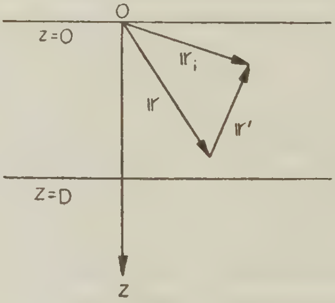

Fig. 1.

Let us assume the crystal be an infinite plate with thickness D, and choose the z-axis normal to the surface as shown in Fig. 1. Then

$$V(\boldsymbol{r})=\sum_h v_h\exp(2\pi i\boldsymbol{h}\boldsymbol{r})\qquad\text{for}\quad 0\leq z\leq D\,. \tag{3.1}$$

If a beam of electrons enters the crystal through the surface $z=0$ with wave number K^i, the wave equation in the crystal can be written as

$$(\nabla^2+K^{0^2})\Psi(\boldsymbol{r})=-(2me/\hbar^2)\cdot(\sum_h{}' v_h e^{2\pi i\boldsymbol{h}\boldsymbol{r}})\Psi(\boldsymbol{r})\,, \tag{3.2}$$

where

$$K^{0^2}=K^{i^2}+(2me/\hbar^2)\cdot v_0 \tag{3.3}$$

and the prime on $\sum$ indicates the absence of the term $\boldsymbol{h}=0$. We ask the solution of Eq. (3.2) under the following boundary conditions:

1) The amplitudes of the scattered waves whose wave vectors have positive z-components should be zero at the surface $z=0$.

2) The amplitudes of the waves whose wave vectors have negative z-components should be zero at the surface $z=D$.

The unperturbed wave function is taken as

$$\psi^{(0)}(\boldsymbol{r})=A_0\exp(i\boldsymbol{K}^0\boldsymbol{r})\ , \tag{3.4}$$

where $\boldsymbol{K}^0$ denotes the wave vector of the initial wave in the crystal. Evidently, the above conditions cannot take into account the refraction of the waves at the boundaries. Though for the rigorous treatment, therefore, we should take the incident wave in vacuum instead of (3.4) as the unperturbed state, we shall avoid it here on account of slow convergency of the series in the required calculation.

Using the Fourier integral form of the Green function

$$G_{K^0}(\boldsymbol{r},\boldsymbol{r}_i)=\frac{-1}{(2\pi)^3}\int\frac{\exp[-i\boldsymbol{k}(\boldsymbol{r}_i-\boldsymbol{r})]}{\boldsymbol{k}^2-\boldsymbol{K}^{0^2}}\,d\boldsymbol{k}\ , \tag{3.5}$$

we obtain for $\psi^{(1)}(\boldsymbol{r})$

$$\psi^{(1)}(\boldsymbol{r})=A_0\left(\frac{2me}{\hbar^2}\right)\sum_{\boldsymbol{h}}{}' v_h\iint\frac{\exp[-i\boldsymbol{k}(\boldsymbol{r}_i-\boldsymbol{r})]}{(2\pi)^3(\boldsymbol{k}^2-\boldsymbol{K}^{0^2})}\exp[i(\boldsymbol{K}^0+2\pi\boldsymbol{h})\boldsymbol{r}_i]\,d\boldsymbol{k}\,d\boldsymbol{r}_i\ . \tag{3.6}$$

Putting $\boldsymbol{r}_i-\boldsymbol{r}\equiv\boldsymbol{r}'$, we have

$$\psi^{(1)}(\boldsymbol{r})=A_0(2me/\hbar^2)\sum_{\boldsymbol{h}}{}' v_h\exp[i(\boldsymbol{K}^0+2\pi\boldsymbol{h})\boldsymbol{r}]\cdot I(\boldsymbol{h})\ , \tag{3.7}$$

where

$$I(\boldsymbol{h})=\frac{1}{(2\pi)^3}\iint\frac{\exp[i(\boldsymbol{K}^0+2\pi\boldsymbol{h}-\boldsymbol{k})\boldsymbol{r}']}{\boldsymbol{k}^2-\boldsymbol{K}^{0^2}}\,d\boldsymbol{r}'d\boldsymbol{k}\ . \tag{3.8}$$

$I(\boldsymbol{h})$ can be calculated in the following way:

$$\begin{aligned}I(\boldsymbol{h})=&\frac{1}{(2\pi)^3}\int\frac{d\boldsymbol{k}}{\boldsymbol{k}^2-\boldsymbol{K}^{0^2}}\int_{-\infty}^{\infty}\exp[i(K_x{}^0+2\pi h_x-k_x)x']\,dx'\int_{-\infty}^{\infty}\exp[i(K_y{}^0+2\pi h_y-k_y)y']\,dy'\\&\times\left[\int_{-z}^{0}\exp[i(K_z{}^0+2\pi h_z-k_z)z']\,dz'+\int_{0}^{D-z}\exp[i(K_z{}^0+2\pi h_z-k_z)z']\,dz'\right].\end{aligned} \tag{3.9}$$

The integrals over x' and y' are reduced to $2\pi\cdot\delta(K_x{}^0+2\pi h_x-k_x)$ and $2\pi\cdot\delta(K_y{}^0+2\pi h_y-k_y)$, respectively, and those over z' are also easy to carry out. After performing the integrations over k_x and k_y, we obtain

$$\begin{aligned}I(\boldsymbol{h})=&\frac{1}{2\pi i}\int_{-\infty}^{\infty}\frac{1}{[(K_x{}^0+2\pi h_x)^2+(K_y{}^0+2\pi h_y)^2+k_z{}^2]-(K_x{}^{0^2}+K_y{}^{0^2}+K_z{}^{0^2})}\\&\times\left[\frac{1-\exp[-i(K_z{}^0+2\pi h_z-k_z)z]}{K_z{}^0+2\pi h_z-k_z}+\frac{\exp[i(K_z{}^0+2\pi h_z-k_z)(D-z)]-1}{K_z{}^0+2\pi h_z-k_z}\right]dk_z\ .\end{aligned}$$

When the wave vectors $\boldsymbol{K}^h(K_x{}^h, K_y{}^h, K_z{}^h)$ and ${}^h\boldsymbol{K}({}^hK_x, {}^hK_y, {}^hK_z)$ are introduced as shown in Fig. 2, $I(\boldsymbol{h})$ is reduced to

$$\begin{aligned}I(\boldsymbol{h})=&\frac{1}{2\pi i}\int_{-\infty}^{\infty}\frac{1-\exp[-i(K_z{}^0+2\pi h_z-k_z)z]}{(k_z{}^2-K_z{}^{h^2})(K_z{}^0+2\pi h_z-k_z)}\,dk_z\\&+\frac{1}{2\pi i}\int_{-\infty}^{\infty}\frac{\exp[i(K_z{}^0+2\pi h_z-k_z)(D-z)]-1}{(k_z{}^2-{}^hK_z{}^2)(K_z{}^0+2\pi h_z-k_z)}\,dk_z\ ,\end{aligned} \tag{3.10}$$

where use has been made of the relations

$$K_x{}^0+2\pi h_x=K_x{}^h={}^hK_x\ ,$$
$$K_y{}^0+2\pi h_y=K_y{}^h={}^hK_y$$

and

$$K_x{}^{0^2}+K_y{}^{0^2}+K_z{}^{0^2}=K_x{}^{h2}+K_y{}^{h2}+K_z{}^{h2}={}^hK_x{}^2+{}^hK_y{}^2+{}^hK_z{}^2\ .$$

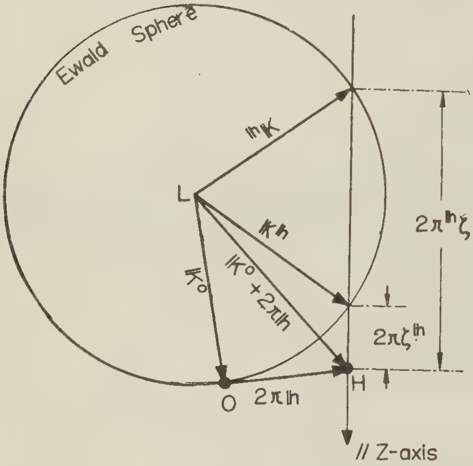

Fig. 2.

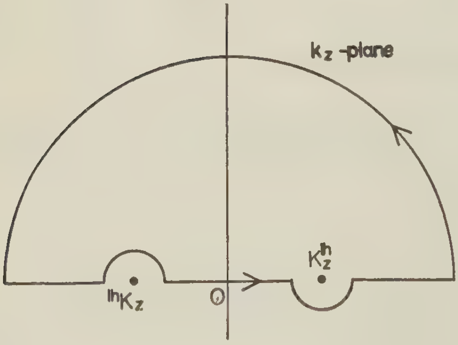

(a) Contour C_1.

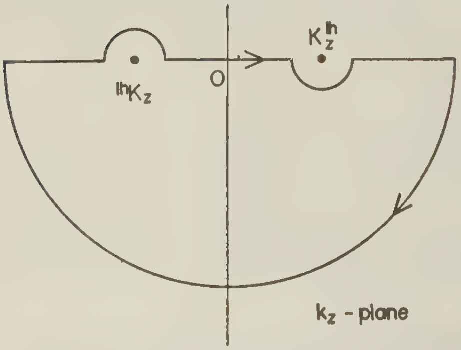

(b) Contour C_2.

Fig. 3. Contours for the evaluation of the integrals in Eq. (3.10).

The integrals in (3.10) may be evaluated by contour integrals on the complex k_z-plane, since the integrands have simple poles at $k_z=\pm K_z{}^h=\mp{}^hK_z$. The contour C_1 for the first integral and C_2 for the second should be chosen as shown in Fig. 3 in accordance with the boundary conditions mentioned above.* Using the theorem of residues and defining the excitation errors, ζ^h and ${}^h\zeta$, as (Cf. Fig. 2)

$$-2\pi\zeta^h=K_z{}^0+2\pi h_z-K_z{}^h \qquad (3.11a)$$
$$-2\pi\,{}^h\zeta=K_z{}^0+2\pi h_z-{}^hK_z\ , \qquad (3.11b)$$

we have

$$I(\boldsymbol{h})=\frac{1}{4\pi K_z{}^h}\left[\exp(2\pi i\zeta^h z)\cdot\left(\frac{\exp(-2\pi i\zeta^h z)-1}{-\zeta^h}\right)\right.$$
$$+\exp(2\pi i\,{}^h\zeta\cdot z)$$
$$\left.\cdot\left(\frac{\exp(-2\pi i\,{}^h\zeta D)-\exp(-2\pi i\,{}^h\zeta z)}{-{}^h\zeta}\right)\right]. \qquad (3.12)$$

Allowing for the relations

$$\boldsymbol{K}^h\boldsymbol{r}=(\boldsymbol{K}^0+2\pi\boldsymbol{h})\boldsymbol{r}+2\pi\zeta^h\cdot z$$
$${}^h\boldsymbol{K}\boldsymbol{r}=(\boldsymbol{K}^0+2\pi\boldsymbol{h})\boldsymbol{r}+2\pi\,{}^h\zeta\cdot z\ ,$$

we obtain

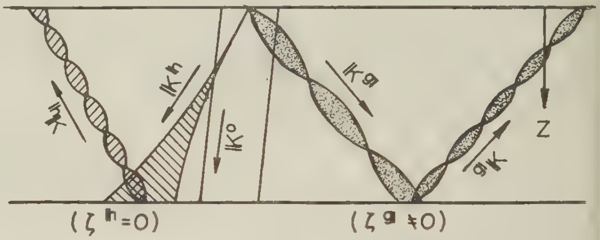

Fig. 4. Illustration of the Intensities of the waves given by Eq. (3.13).

---

* The validity of the adoption of these contours can easily be verified by the more detailed treatment which introduces the Green function in the form

$$G_{K^0}(\boldsymbol{r},\boldsymbol{r}_i)=-\int\frac{d\boldsymbol{k}}{(2\pi)^3}\left[\frac{\mathrm{P}}{\boldsymbol{k}^2-K^{0^2}}\right.$$
$$\left.+\lambda(\boldsymbol{k})\cdot\delta(\boldsymbol{k}^2-K^{0^2})\right]\exp[i\boldsymbol{k}(\boldsymbol{r}-\boldsymbol{r}_i)]\ ,$$

where $\lambda(\boldsymbol{k})$ is the factor which should be determined to satisfy the boundary conditions.

$$\psi^{(1)}(\boldsymbol{r})=A_0\left(\frac{me}{2\pi\hbar^2}\right)\sum_{h}{}'\frac{v_{\boldsymbol{h}}}{K_z{}^{\boldsymbol{h}}}\left[\exp(i\boldsymbol{K}^{\boldsymbol{h}}\boldsymbol{r})\cdot\left(\frac{\exp(-2\pi i\zeta^{\boldsymbol{h}}z)-1}{-\zeta^{\boldsymbol{h}}}\right)\right.$$
$$\left.+\exp(i\,{}^{\boldsymbol{h}}\boldsymbol{K}\boldsymbol{r})\cdot\left(\frac{\exp(-2\pi i\,{}^{\boldsymbol{h}}\zeta D)-\exp(-2\pi i\,{}^{\boldsymbol{h}}\zeta z)}{-{}^{\boldsymbol{h}}\zeta}\right)\right]. \tag{3.13}$$

The first term in (3.13), which came from the first integral over z' in (3.9), is that previously derived by Artmann[3)] taking account of the forward scattering only. The second term which was newly added corresponds to the backward reflection. The intensities of the waves calculated by Eq. (3.13) vary with z in the manners as illustrated in Fig. 4.

§ 4. Calculation of $\psi^{(n)}(\boldsymbol{r})$

It should be noticed that $\psi^{(1)}(\boldsymbol{r})$, which has been derived from the plane wave $\psi^{(0)}(\boldsymbol{r})$, is a superposition of plane waves owing to the fact that $V(\boldsymbol{r})$ can be written in the form of Fourier series. Such a result suggests that all $\psi^{(m)}(\boldsymbol{r})$'s may be evaluated from Eq. (2.4a) in similar way as the derivation of $\psi^{(1)}(\boldsymbol{r})$ from $\psi^{(0)}(\boldsymbol{r})$. Thus, it is expected, in principle, that the complicated multiple scattering phenomena can be dealt with for any reflecting condition. However, in Bragg case, where we have strong reflected waves propagating in the directions more or less nearly parallel to the surface under the usual experimental conditions, the convergency of $\psi^{(m)}(\boldsymbol{r})$ is expected to be so slow with increasing m that the application of the present method cannot be practicable. We, therefore, will hereafter restrict ourselves to Laue case, where most of strong reflections transmit the crystal. We further assume that only the waves scattered in forward directions are appreciable. This assumption which has been adopted by Bethe[1)], Artmann[3)] and Cowley and Moodie[2)], seems to be reasonable provided that the glancing angle of the incidence is not extremely small.

We, first of all, calculate the function $\psi^{(2)}(\boldsymbol{r})$ from $\psi^{(1)}(\boldsymbol{r})$. Substituting the first term of (3.13) and (3.5) into (2.4a) for $m=2$, we obtain

$$\psi^{(2)}(\boldsymbol{r})=4\pi A_0\left(\frac{me}{2\pi\hbar^2}\right)^2\sum_{h}{}'\sum_{g}{}'\frac{v_{\boldsymbol{h}-\boldsymbol{g}}\cdot v_{\boldsymbol{g}}}{K_z{}^{\boldsymbol{g}}}\iint\frac{\exp[-i\boldsymbol{k}(\boldsymbol{r}_i-\boldsymbol{r})]}{(2\pi)^3(\boldsymbol{k}^2-\boldsymbol{K}^{0^2})}$$
$$\times\exp[i\{\boldsymbol{K}^{\boldsymbol{g}}+2\pi(\boldsymbol{h}-\boldsymbol{g})\}\boldsymbol{r}_i]\cdot\left(\frac{\exp(-2\pi i\zeta^{\boldsymbol{g}}z_i)-1}{-\zeta^{\boldsymbol{g}}}\right)d\boldsymbol{k}\,d\boldsymbol{r}_i\,.$$

Taking account of

$$\boldsymbol{K}^{\boldsymbol{g}}\boldsymbol{r}_i+2\pi(\boldsymbol{h}-\boldsymbol{g})\boldsymbol{r}_i-2\pi\zeta^{\boldsymbol{g}}z_i=[(\boldsymbol{K}^0+2\pi\boldsymbol{g})\boldsymbol{r}_i+2\pi\zeta^{\boldsymbol{g}}z_i]+2\pi(\boldsymbol{h}-\boldsymbol{g})\boldsymbol{r}_i-2\pi\zeta^{\boldsymbol{g}}z_i$$
$$=(\boldsymbol{K}^0+2\pi\boldsymbol{h})\boldsymbol{r}_i\,,$$

we have

$$\psi^{(2)}(\boldsymbol{r})=4\pi A_0\left(\frac{me}{2\pi\hbar^2}\right)^2\sum_{h}{}'\sum_{g}{}'\frac{v_{\boldsymbol{h}-\boldsymbol{g}}\cdot v_{\boldsymbol{g}}}{K_z{}^{\boldsymbol{g}}\cdot\zeta^{\boldsymbol{g}}}$$
$$\times\left[\exp[i\{\boldsymbol{K}^{\boldsymbol{g}}+2\pi(\boldsymbol{h}-\boldsymbol{g})\}\boldsymbol{r}]\iint\frac{\exp[i\{\boldsymbol{K}^{\boldsymbol{g}}+2\pi(\boldsymbol{h}-\boldsymbol{g})-\boldsymbol{k}\}\boldsymbol{r}']}{(2\pi)^3(\boldsymbol{k}^2-\boldsymbol{K}^{0^2})}\,d\boldsymbol{k}\,d\boldsymbol{r}'\right.$$
$$\left.-\exp[i(\boldsymbol{K}^0+2\pi\boldsymbol{h})\boldsymbol{r}]\iint\frac{\exp[i(\boldsymbol{K}^0+2\pi\boldsymbol{h}-\boldsymbol{k})\boldsymbol{r}']}{(2\pi)^3(\boldsymbol{k}^2-\boldsymbol{K}^{0^2})}\,d\boldsymbol{k}\,d\boldsymbol{r}'\right]. \tag{4.1}$$

The second integral in (4.1) is nothing but (3.8), and the first integral may also be reduced to the same integral, if $\boldsymbol{K}^{\boldsymbol{g}}-2\pi\boldsymbol{g}$ in the exponent is replaced by $\boldsymbol{K}^0$. Then, consulting the first term of (3.12), we obtain

$$\psi^{(2)}(\boldsymbol{r})=A_0\left(\frac{me}{2\pi\hbar^2}\right)^2\sum_{h}{}'\sum_{g}{}'\frac{v_{\boldsymbol{h}-\boldsymbol{g}}\cdot v_{\boldsymbol{g}}}{K_z{}^{\boldsymbol{h}}\cdot K_z{}^{\boldsymbol{g}}}\exp(i\boldsymbol{K}^{\boldsymbol{h}}\boldsymbol{r})$$
$$\times\left[\frac{\exp[2\pi i(\zeta^{\boldsymbol{g}}-\zeta^{\boldsymbol{h}})z]-1}{\zeta^{\boldsymbol{g}}(\zeta^{\boldsymbol{g}}-\zeta^{\boldsymbol{h}})}+\frac{\exp(-2\pi i\zeta^{\boldsymbol{h}}z)-1}{\zeta^{\boldsymbol{h}}\cdot\zeta^{\boldsymbol{g}}}\right]. \tag{4.2}$$

For the simple evaluation of $\psi^{(3)}(\boldsymbol{r})$, we rearrange the terms in the square bracket in (4.2) as

$$\exp(i\boldsymbol{K}^h\boldsymbol{r})\left[\frac{\exp[2\pi i(\zeta^g-\zeta^h)z]-1}{\zeta^g(\zeta^g-\zeta^h)}+\frac{\exp(-2\pi i\zeta^h z)-1}{\zeta^h\cdot\zeta^g}\right]$$
$$=\left[\frac{\exp[i\{\boldsymbol{K}^g+2\pi(\boldsymbol{h}-\boldsymbol{g})\}\boldsymbol{r}]}{\zeta^g(\zeta^g-\zeta^h)}+\frac{\exp(i\boldsymbol{K}^h\boldsymbol{r})}{\zeta^h(\zeta^h-\zeta^g)}+\frac{\exp[i(\boldsymbol{K}^0+2\pi\boldsymbol{h})\boldsymbol{r}]}{\zeta^h\cdot\zeta^g}\right]. \tag{4.3}$$

Substituting (4.2) with (4.3) into (2.4a) for $m=3$ and rewriting $\boldsymbol{g}$ and $\boldsymbol{h}$ as $\boldsymbol{g}_1$ and $\boldsymbol{g}_1+\boldsymbol{g}_2$ respectively, we have

$$\psi^{(3)}(\boldsymbol{r})=4\pi A_0\left(\frac{me}{2\pi\hbar^2}\right)^3\sum_{\boldsymbol{h}}{}'\sum_{g_2}{}'\sum_{g_1}{}'\frac{v_{\boldsymbol{h}-(g_1+g_2)}\cdot v_{g_2}\cdot v_{g_1}}{K_z{}^{g_1+g_2}\cdot K_z{}^{g_1}}\iint\frac{\exp[-i\boldsymbol{k}(\boldsymbol{r}_i-\boldsymbol{r})]}{(2\pi)^3(\boldsymbol{k}^2-\boldsymbol{K}^{0^2})}$$
$$\times\exp[2\pi i\{\boldsymbol{h}-(\boldsymbol{g}_1+\boldsymbol{g}_2)\}\boldsymbol{r}]\left[\frac{\exp[i(\boldsymbol{K}^{g_1}+2\pi\boldsymbol{g}_2)\boldsymbol{r}_i]}{\zeta^{g_1}(\zeta^{g_1}-\zeta^{g_1+g_2})}\right.$$
$$\left.+\frac{\exp(i\boldsymbol{K}^{g_1+g_2}\boldsymbol{r}_i)}{\zeta^{g_1+g_2}(\zeta^{g_1+g_2}-\zeta^{g_1})}+\frac{\exp[i\{\boldsymbol{K}^0+2\pi(\boldsymbol{g}_1+\boldsymbol{g}_2)\}\boldsymbol{r}_i]}{\zeta^{g_1+g_2}\cdot\zeta^{g_1}}\right]d\boldsymbol{r}_i\,d\boldsymbol{k}\,. \tag{4.4}$$

Since the integrals contained in (4.4) have the forms similar to that in (3.8), we obtain

$$\psi^{(3)}(\boldsymbol{r})=A_0\left(\frac{me}{2\pi\hbar^2}\right)^3\sum_{\boldsymbol{h}}{}'\sum_{g_2}{}'\sum_{g_1}{}'\frac{v_{\boldsymbol{h}-(g_1+g_2)}\cdot v_{g_2}\cdot v_{g_1}}{K_z{}^h\cdot K_z{}^{g_1+g_2}\cdot K_z{}^{g_1}}\cdot\exp(i\boldsymbol{K}^h\boldsymbol{r})\left[\frac{\exp[2\pi i(\zeta^{g_1}-\zeta^h)z]-1}{\zeta^{g_1}(\zeta^{g_1}-\zeta^{g_1+g_2})(\zeta^{g_1}-\zeta^h)}\right.$$
$$\left.+\frac{\exp[2\pi i(\zeta^{g_1+g_2}-\zeta^h)z]-1}{\zeta^{g_1+g_2}(\zeta^{g_1+g_2}-\zeta^{g_1})(\zeta^{g_1+g_2}-\zeta^h)}-\frac{\exp(-2\pi i\zeta^h z)-1}{\zeta^h\cdot\zeta^{g_1+g_2}\cdot\zeta^{g_1}}\right]. \tag{4.5}$$

For the evaluation of $\psi^{(4)}(\boldsymbol{r})$ from $\psi^{(3)}(\boldsymbol{r})$, it is again advantageous to rearrange the terms in the square bracket in (4.5) as

$$\exp(-i\boldsymbol{K}^h\boldsymbol{r})\cdot\left[\frac{\exp[i\{\boldsymbol{K}^{g_1}+2\pi(\boldsymbol{h}-\boldsymbol{g}_1)\}\boldsymbol{r}]}{\zeta^{g_1}(\zeta^{g_1}-\zeta^{g_1+g_2})(\zeta^{g_1}-\zeta^h)}+\frac{\exp[i\{\boldsymbol{K}^{g_1+g_2}+2\pi(\boldsymbol{h}-\boldsymbol{g}_1-\boldsymbol{g}_2)\}\boldsymbol{r}]}{\zeta^{g_1+g_2}(\zeta^{g_1+g_2}-\zeta^{g_1})(\zeta^{g_1+g_2}-\zeta^h)}\right.$$
$$\left.+\frac{\exp(i\boldsymbol{K}^h\boldsymbol{r})}{\zeta^h(\zeta^h-\zeta^{g_1})(\zeta^h-\zeta^{g_1+g_2})}-\frac{\exp[i(\boldsymbol{K}^0+2\pi\boldsymbol{h})\boldsymbol{r}]}{\zeta^h\cdot\zeta^{g_1+g_2}\cdot\zeta^{g_1}}\right]. \tag{4.6}$$

Without the rearrangement we have six integrals to evaluate and the expression for $\psi^{(4)}(\boldsymbol{r})$ becomes much lengthy, while the number of integrals can be reduced to four when (4.6) is taken into account. The calculations of higher $\psi^{(n)}(\boldsymbol{r})$ are also much simplified by making the similar rearrangements of calculated terms. Thus, we have a general expression for $\psi^{(n)}(\boldsymbol{r})$:

$$\psi^{(n)}(\boldsymbol{r})=A_0\left(\frac{me}{2\pi\hbar^2}\right)^n\sum_{\boldsymbol{h}}{}'\sum_{g_{n-1}}{}'\sum_{g_{n-2}}{}'\cdots\sum_{g_2}{}'\sum_{g_1}{}'$$
$$\times\frac{v_{\boldsymbol{h}-(g_1+g_2+\cdots+g_{n-1})}\cdot v_{g_{n-1}}\cdot v_{g_{n-2}}\cdot\;\cdots\;\cdot v_{g_2}\cdot v_{g_1}}{K_z{}^h\cdot K_z{}^{g_1+\cdots+g_{n-1}}\cdot K_z{}^{g_1+\cdots+g_{n-2}}\cdot\;\cdots\;\cdot K_z{}^{g_1+g_2}\cdot K_z{}^{g_1}}$$
$$\times\exp(i\boldsymbol{K}^h\boldsymbol{r})\cdot Z_n(\zeta_1,\zeta_2,\cdots,\zeta_{n-1},\zeta^h;z)\,, \tag{4.7}$$

where

$$Z_n(\zeta_1,\zeta_2,\cdots,\zeta_{n-1},\zeta^h;z)$$
$$=\sum_{m=1}^{n-1}\frac{\exp[2\pi i(\zeta_m-\zeta^h)z]-1}{\zeta_m(\zeta_m-\zeta^h)\prod\limits_{\substack{k=1\\k\neq m}}^{n-1}(\zeta_m-\zeta_k)}+(-1)^n\frac{\exp(-2\pi i\zeta^h z)-1}{\zeta^h\cdot\prod\limits_{k=1}^{n-1}\zeta_k}\,. \tag{4.8}$$

In (4.8), ζ_m is the abbreviated notation of $\zeta^{g_1+g_2+\cdots+g_m}$ and means the excitation error of the reciprocal lattice point corresponding to the vector $2\pi(\boldsymbol{g}_1+\boldsymbol{g}_2+\cdots+\boldsymbol{g}_m)$, as shown in Fig. 5.

The formula (4.7) with (4.8) is essentially similar to that previously derived by Cowley and

Moodie[2]. Particularly, the factor $Z_n(\zeta_1, \zeta_2, \cdots, \zeta_{n-1}, \zeta^h; z)$ given by (4.8) coincides exactly with the result of their calculations. However, the essential assumption in their theory that all scattering angles should be small is no longer necessary here, so long as only the forward scattering is appreciable. Under the same condition, (4.7) is applicable also to the cases of oblique incidence without any revision, since K_z's are adopted instead of K's. The formula (4.7) as well as Cowley and Moodie's gives the pictorial image of the n-ple scattering process in which the incident wave $\boldsymbol{K}^0$ turns to $\boldsymbol{K}^h$ through the $n-1$ intermediate states characterised by $\boldsymbol{K}^{g_1}, \boldsymbol{K}^{g_1+g_2}, \cdots, \boldsymbol{K}^{g_1+\cdots+g_{n-1}}$.

The expansion of $Z_n(\zeta_1, \zeta_2, \cdots, \zeta_{n-1}, \zeta^h; z)$ into power series of ζ's gives another useful expression for Z_n:

$$
\begin{aligned}
&Z_n(\zeta_1, \zeta_2, \cdots, \zeta_{n-1}, \zeta^h; z) \\
&=\sum_{k=n}^{\infty} \frac{(2\pi i z)^k}{k!} \sum_{m_1=0}^{k-n} (-1)^{m_1} \cdot \binom{k-1}{m_1} \cdot \sum_{m_2=0}^{k-n-m_1} \; \sum_{m_3=0}^{k-n-(m_1+m_2)} \cdots \sum_{m_{n-1}=0}^{k-n-(m_1+\cdots+m_{n-2})} \\
&\quad \times [(\zeta^h)^{m_1} \cdot (\zeta_{n-1})^{m_2} \cdot (\zeta_{n-2})^{m_3} \cdots (\zeta_3)^{m_{n-2}} \cdot (\zeta_2)^{m_{n-1}} \cdot (\zeta_1)^{k-n-(m_1+\cdots+m_{n-1})}] \, .
\end{aligned}
\tag{4.9}
$$

If all ζ's are zero, (4.9) is reduced to

$$Z_n = (2\pi i z)^n / n! \, . \tag{4.10}$$

Other special forms of Z_n are given in Appendix.

§ 5. Intensities in the Short Wave Length Limit

Miyake[4] has recently pointed out that the well-known treatment of the two-wave approximation of dynamical theory is not legitimate for calculating the intensities of reflexion in the short wave length or small crystal size limit. In this connection, it may be significant to study the behavior of the intensity of reflexion in the limit $K \to \infty$ with the present theory, assuming that the relativistic effects could be taken into account by the mass correction in wave length.

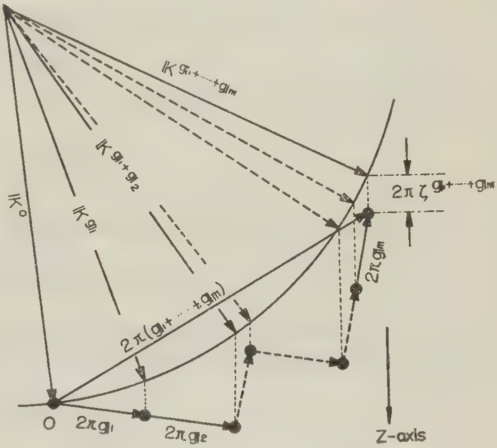

Fig. 5. Illustration of $\boldsymbol{K}^{g_1+\cdots+g_m}$ and $\zeta^{g_1+\cdots+g_m}$.

The expression (4.9) shows that Z_n approaches to the constant value $(2\pi i z)^n/n!$ as $K \to \infty$, since all ζ's, in which we are interested, tend to $O(1/K)$. Then, from (4.7), we obtain

$$\phi^{(n)}(\boldsymbol{r}) \to O(1/K^n) \qquad \text{as} \quad K \to \infty \, .$$

It can be concluded, therefore, that

$$\Psi(\boldsymbol{r}) - \phi^{(0)}(\boldsymbol{r}) \to A_0 \left(\frac{ime}{\hbar^2} \right) \cdot z \cdot \sum_h{}' \frac{v_h}{K_z^h} \cdot \exp(i\boldsymbol{K}^h \boldsymbol{r}) \qquad \text{as} \quad K \to \infty \, .$$

In other words, the intensity of reflexion in the short wave length limit is equal to the exact excitation value of kinematical intensity. It appears that this result is the same as that due to the usual method of two-wave approximation (Pinsker, Blackman). However, it should be noticed that the simultaneous occurence of many reflexions in a crystal is taken into account here. Thus, the present result amounts to a more general theoretical confirmation than before to the experimental method developed by Honjo and Kitamura[5] for obtaining the kinematical value of reflected intensity by varying the wave length of electrons.

§ 6. Convergence Test of Wave Function for Simple Examples

Concerning the method of higher order Born approximation, a question may arise as to whether the wave functions derived successively from low order approximations do converge or not. Though no conclusive answer has yet been obtained to this question, two simple examples quoted below may be instructive to show how the wave functions converge and to suggest the convergency in more general cases.

(a) *Free electron model* (v_0*-scattering*)

Now we consider that a beam of electron enters the hypothetical crystal whose potential field is

$$V(r)=\begin{cases} v_0 & \text{for} \quad 0\leq z\leq D \\ 0 & \text{otherwise.}\end{cases} \tag{6.1}$$

For further simplification, the direction of the incident beam is assumed to be normal to the surface. Neglecting the reflection at the surfaces of crystal, we may write immediately the wave function in the form

$$\Psi(\boldsymbol{r})=\begin{cases} \exp(i\boldsymbol{K}^i\boldsymbol{r}) & \text{in vacuum} \\ \exp(i\boldsymbol{K}^0\boldsymbol{r}) & \text{in crystal ,}\end{cases} \tag{6.2}$$

where the wave number vector $\boldsymbol{K}^0$ in crystal is defined as

$$\boldsymbol{K}^{02}=\boldsymbol{K}^{i2}+(2me/\hbar^2)\cdot v_0 \,. \tag{6.3}$$

When K^i is large enough we have

$$K^0\simeq K^i+\frac{mev_0}{\hbar^2K^i} \,,$$

so that the wave function in the crystal is approximately given by

$$\Psi(\boldsymbol{r})\simeq\exp(i\boldsymbol{K}^i\boldsymbol{r})\cdot\exp[i(mev_0/\hbar^2K^i)z] \,. \tag{6.4}$$

We show below that the power series obtained by the application of the higher order Born approximation also gives the same result. Adopting $\exp(i\boldsymbol{K}^i\boldsymbol{r})$ as $\psi^{(0)}(\boldsymbol{r})$, we obtain from (4.7)

$$\psi^{(n)}(\boldsymbol{r})=\frac{(imev_0z/\hbar^2K^i)^n}{n!}\cdot\exp(i\boldsymbol{K}^i\boldsymbol{r}) \,.$$

Here use has been made of (4.10), since all ζ's in Z_n should be equal to ζ^0 (the excitation error of the origin of reciprocal space) and apparently $\zeta^0=0$. It is easily shown that

$$\begin{aligned}\sum_{n=0}^{\infty}\psi^{(n)}(\boldsymbol{r})&=\exp(i\boldsymbol{K}^i\boldsymbol{r})\cdot\left(1+i\alpha z-\frac{\alpha^2}{2}z^2-i\,\frac{\alpha^3}{6}z^3+\cdots\right)\\ &=\exp(i\boldsymbol{K}^i\boldsymbol{r})\cdot\exp(i\alpha z) \,,\end{aligned} \tag{6.5}$$

where

$$\alpha=mev_0/\hbar^2K^i \,.$$

In Fig. 6, $|\psi^{(n)}(\boldsymbol{r})|$ is plotted against n for two cases. The open circles in the figure correspond to the case where $v_0=10$ volts, $\lambda=0.048$ Å and $z=50$ Å, and the full circles to the case where $v_0=20$ volts, $\lambda=0.048$ Å and $z=200$ Å. The former shows the monotonous decrease of $|\psi^{(n)}(\boldsymbol{r})|$ with increasing n. In the latter case, on the other hand, $|\psi^{(n)}(\boldsymbol{r})|$ increases until n reaches 3, and then turns to decrease with increasing n. It should be noticed that the wave function converges ultimately despite that a tendency of divergence was observed for the first two or three terms.

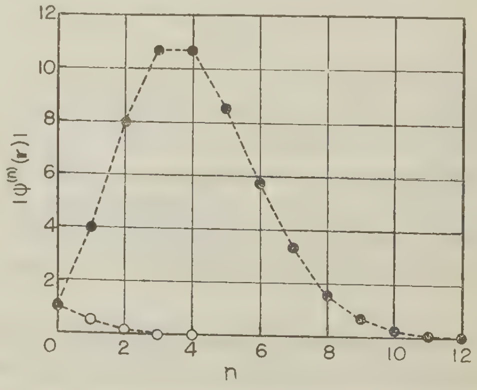

Fig. 6. $|\psi^{(n)}(\ )|$ versus n curves for v_0-scattering

(b) *The pendulum solution of Bethe*

It has been proved by Cowley and Moodie that their theory gives Bethe's pendulum solution[1] when the same condition of the two-wave approximation as in the usual dynamical theory is assumed. Their result is most easily confirmed for the condition of the exact excitation of the reflexion $\boldsymbol{h}$. Using (4,7) and (4.10) and taking into account only the interactions between waves $\boldsymbol{o}$ and $\boldsymbol{h}$, we may write the amplitude of the reflected wave $\boldsymbol{h}$ as follows:

$$\psi_h = A_0\left(\frac{me}{2\pi\hbar^2}\right)\frac{v_h}{K_z^h}(2\pi iz) + A_0\left(\frac{me}{2\pi\hbar^2}\right)^3 \frac{v_h v_{-h} v_h}{K_z^h K_z^0 K_z^h}\cdot\frac{(2\pi iz)^3}{3!}$$
$$+ A_0\left(\frac{me}{2\pi\hbar^2}\right)^5 \frac{v_h v_{-h} v_h v_{-h} v_h}{K_z^h K_z^0 K_z^h K_z^0 K_z^h}\cdot\frac{(2\pi iz)^5}{5!} + \cdots .$$

Assuming $v_h = v_{-h}$ and $K_z^0 = K_z^h$ and putting $mev_h/\hbar^2 K_z^0 = \alpha$, we have

$$\psi_h \propto \alpha\cdot z - \frac{(\alpha z)^3}{3!} + \frac{(\alpha z)^5}{5!} - \cdots = \sin(\alpha z) .$$

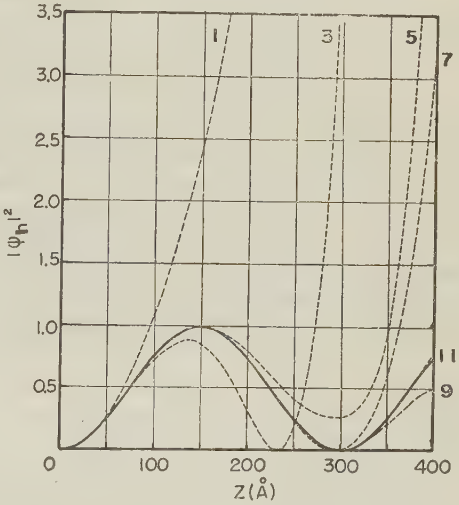

Fig. 7. A numerical calculation on the pendulum solution of Bethe. $v_h = 10$ volts and $\lambda = 0.0502$ Å (56 KeV) are adopted. The solid curve represents the pendulum solution. The dotted curve with index n shows the result in n-th order Born approximation. For the 200 KeV-electron, values of z should be doubled.

This is nothing but the pendulum solution. Fig. 7 shows a result of numerical calculation for $v_h = 10$ volts and $\lambda = 0.0502$ Å (56 KeV). In the figure, the solid curve represents Bethe's pendulum solution $\sin^2(\alpha z)$, and the dotted curves with index n show the intensities of reflection $\boldsymbol{h}$ of the n-th order Born approximations, respectively. We see here how the range where Born approximation is valid is extended with increasing n.

§ 7. Extensions of the Present Theory

In this paragraph we treat the diffraction by finite crystals and overlapping crystals as the extended applications of the present theory.

(a) *Approximate asymptotic form of the wave scattered by a finite crystal*

In the derivation of $\psi^{(1)}(r)$ in § 3, we had a great advantage that the integrals over x' and y' in (3.9) are reduced to δ-functions because of the assumption of infinite plate crystal. It seems to be difficult to treat rigorously the scattering from a finite crystal by the present theory, since such an advantage is no longer available now. Therefore, we shall content ourselves with deriving the following approximate result.

We consider a crystal of parallelepiped with the side lengths L_1, L_2 and L_3 as shown in Fig. 8 (a). The asymptotic form of wave function at a point r far away from the crystal is given by

$$\Psi(r) \sim \psi^{(0)}(r) + \frac{me}{2\pi\hbar^2}\cdot\frac{\exp(iK^0 r)}{r}\iiint\limits_{crystal}\exp[-iK^0(r\cdot r_i)/r]\cdot V(r_i)\Psi(r_i)\,dr_i . \tag{7.1}$$

Strictly speaking, the wave number in vacuum K^i must be taken instead of the wave number in crystal K^0. However, for simplicity of calculation, we adopt K^0 and omit the zero term from $V(r)$. If L_1 and L_2 are large compared with L_3 and the direction of the incident beam is nearly perpendicular to the xy-plane, we may neglect the edge effect and substitute (4.7) for the infinite crystal into $\Psi(\boldsymbol{r}_i)$ in the integrand of (7.1) as the approximation. Then, we shall have the wave function in the form of spherical wave:

$$\Psi(\boldsymbol{r})\sim\phi^{(0)}(\boldsymbol{r})+\phi^{(1)}(\boldsymbol{r})+\phi^{(2)}(\boldsymbol{r})+\cdots+\phi^{(n)}(\boldsymbol{r})+\cdots, \tag{7.2}$$

where

$$\begin{aligned}\phi^{(n)}(\boldsymbol{r})=&A_0\left(\frac{me}{2\pi\hbar^2}\right)^n\cdot\frac{\exp(iK^0r)}{2\pi ir}\\&\times\sum_{\boldsymbol{h}}{}'\sum_{\boldsymbol{g}_{n-1}}{}'\cdots\sum_{\boldsymbol{g}_2}{}'\sum_{\boldsymbol{g}_1}{}'\frac{v_{\boldsymbol{h}-(\boldsymbol{g}_1+\cdots+\boldsymbol{g}_{n-1})}\cdot v_{\boldsymbol{g}_{n-1}}\cdot\cdots\cdot v_{\boldsymbol{g}_2}v_{\boldsymbol{g}_1}}{K_z^{\boldsymbol{g}_1+\cdots+\boldsymbol{g}_{n-1}}\cdot\cdots\cdot K_z^{\boldsymbol{g}_1+\boldsymbol{g}_2}\cdot K_z^{\boldsymbol{g}_1}}\\&\times[\sin(\pi\eta_x^{\boldsymbol{h}}L_1)/\pi\eta_x^{\boldsymbol{h}}]\cdot[\sin(\pi\eta_y^{\boldsymbol{h}}L_2)/\pi\eta_y^{\boldsymbol{h}}]\\&\times\left[\sum_{m=1}^{n-1}\frac{\exp[2\pi i(\zeta_m-\eta_z^{\boldsymbol{h}})L_3]-1}{\zeta_m(\zeta_m-\eta_z^{\boldsymbol{h}})\prod\limits_{\substack{k=1\\k\neq m}}^{n-1}(\zeta_m-\zeta_k)}+(-1)^n\frac{\exp(-2\pi i\eta_z^{\boldsymbol{h}}L_3)-1}{\eta_z^{\boldsymbol{h}}\prod\limits_{k=1}^{n-1}\zeta_k}\right].\end{aligned} \tag{7.3}$$

$\eta^{\boldsymbol{h}}$ in (7.3) is the excitation error vector defined as

$$2\pi\eta^{\boldsymbol{h}}=\frac{K^0\boldsymbol{r}}{r}-(\boldsymbol{K}^0+2\pi\boldsymbol{h})$$

and is illustrated in Fig. 8(b). It is clear that the formula (7.3), which contains Laue functions, gives diffraction spots of finite sizes. As to the Fraunhofer diffraction of electrons by a finite crystal, a more detailed theory which takes into account the refraction phenomena at the surfaces of crystal has been developped by Kato[6] by using the two-wave approximation. The formula (7.3) may be regarded as the rough extension of his formula to the cases containing many reflexions.

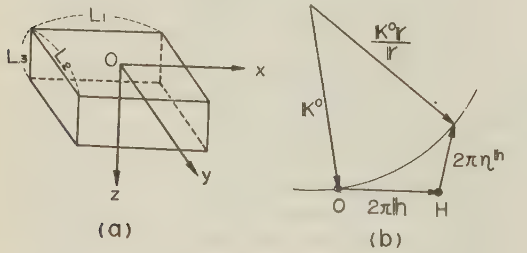

Fig. 8(a). Illustration of a finite crystal. (b) Definition of the excitation error vector $2\pi\eta^{\boldsymbol{h}}$.

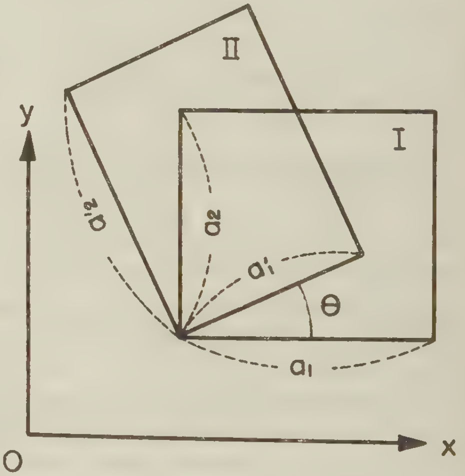

Fig. 9. An arrangement of the unit cells of overlapping crystals.

(b) *Elementary application to Moiré patterns*

Let us consider the overlapping crystals, the potential field within which is given by

$$V(\boldsymbol{r})=\begin{cases}\sum\limits_{\boldsymbol{h}}v_{\boldsymbol{h}}\exp(2\pi i\boldsymbol{hr}) & \text{for}\quad 0\leq z\leq D\\ \sum\limits_{\boldsymbol{h}'}v_{\boldsymbol{h}'}\exp(2\pi i\boldsymbol{h}'\boldsymbol{r}) & \text{for}\quad D\leq z\leq D+D'\\ 0 & \text{otherwise.}\end{cases} \tag{7.4}$$

In the case when the both crystals have orthorhombic cells, whose fundamental vectors are $\boldsymbol{a}_1$, $\boldsymbol{a}_2$, $\boldsymbol{a}_3$ and $\boldsymbol{a}_1'$, $\boldsymbol{a}_2'$, $\boldsymbol{a}_3'$, respectively, and $\boldsymbol{a}_1$, $\boldsymbol{a}_2$, $\boldsymbol{a}_1'$ and $\boldsymbol{a}_2'$ lie in the xy-plane (parallel to the surface) as shown in Fig. 9 (7.4) can be written by using Miller's indices (l, m, n) and (l', m', n') as follows:

$$V(\boldsymbol{r})\begin{cases}\sum V_{lmn}\cdot\exp\left[2\pi i\left(\dfrac{l}{a_1}x+\dfrac{m}{a_2}y+\dfrac{n}{a_3}z\right)\right] & \text{for}\quad 0\leq z\leq D\\ \sum V_{l'm'n'}\cdot\exp\left[2\pi i\left\{\left(\dfrac{l'}{a_1'}\cos\theta-\dfrac{m'}{a_2'}\sin\theta\right)x+\left(\dfrac{l'}{a_1'}\sin\theta+\dfrac{m'}{a_2'}\cos\theta\right)y+\dfrac{n'}{a_3'}z\right\}\right] & \\ & \text{for}\quad D\leq z\leq D+D'\,.\end{cases}\tag{7.5}$$

The amplitude of the waves scattered by these crystals may easily be calculated by following the same procedure as before. Using (2.4a) for $m=1$ and (7.4), we obtain

$$\phi^{(1)}(\boldsymbol{r})=\begin{cases}-A_0\left(\dfrac{me}{2\pi\hbar^2}\right)\sum\limits_{g}\dfrac{v_g}{K_z^g}\left[\dfrac{\exp(-2\pi i\zeta^g z)-1}{\zeta^g}\right]\exp(i\boldsymbol{K}^g\boldsymbol{r}) & \text{for}\quad 0\leq z\leq D\\ -A_0\left(\dfrac{me}{2\pi\hbar^2}\right)\cdot\left[\sum\limits_{g}\dfrac{v_g}{K_z^g}\left\{\dfrac{\exp(-2\pi i\zeta^g D)-1}{\zeta^g}\right\}\exp(i\boldsymbol{K}^g\boldsymbol{r})\right. & \\ \qquad\left.+\sum\limits_{g'}\dfrac{v_{g'}}{K_z^{g'}}\left\{\dfrac{\exp(-2\pi i\zeta^{g'}z)-\exp(-2\pi i\zeta^{g'}D)}{\zeta^{g'}}\right\}\exp(i\boldsymbol{K}^{g'}\boldsymbol{r})\right] & \\ & \text{for}\quad D\leq z\leq D+D'\,.\end{cases}\tag{7.6}$$

The first term of $\phi^{(1)}(\boldsymbol{r})$ for $D\leq z\leq D+D'$ describes the waves which came into the second crystal after having been scattered once in the first crystal. By substituting (7.6) into (2.4a) for $m=2$, this term will produce the following field in the second crystal:

$$\frac{v_{h'}\cdot v_g}{K_z^{g+h'}K_z^g}\left(\frac{\exp(-2\pi i\zeta^g D)-1}{\zeta^g}\right)\cdot\exp(i\boldsymbol{K}^{g+h'}\boldsymbol{r})$$
$$\times\left[\frac{\exp[2\pi i(\zeta^g-\zeta^{g+h'})D]-\exp[2\pi i(\zeta^g-\zeta^{g+h'})z]}{\zeta^g-\zeta^{g+h'}}\right],\tag{7.7}$$

which represents the wave scattered once in each of the crystals. The interference of $\phi^{(0)}(\boldsymbol{r})$ with (7.7) at the exist surface $z=D+D'$ may be expressed simply as

$$A_0\exp[i\{K_x^0x+K_y^0y+K_z^0(D+D')\}]$$
$$\times[1+C\cdot\exp[2\pi i\{(g_x+h_x')x+(g_y+h_y')y\}]]\,,\tag{7.8}$$

and will give the moiré pattern. The factor C, which determines the contrast of the image, can be calculated from (7.7). The spacings of the parallel and rotation moiré patterns are easily given by using (7.5).

The result mentioned above contains nothing new, since Cowley[7)] and other authors have dealt with the theory of moiré patterns up to date. It may be expected, however, that the present theory will prove its true merits, if it is applied to some complicated problems, *e.g.*, those of the moiré patterns produced by more than three waves, the dependence of the contrasts of moiré patterns on the other waves excited simultaneously and so on.

In conclusion the author wishes to express his sincere thanks to Prof. Shizuo Miyake for his kind guidance and encouragement throughout the present work.

Appendix

The expressions for $Z_n(\zeta_1,\cdots,\zeta_{n-1},\zeta^h;\,z)$ in the cases, where (4.8) is no longer available, are given below for $n\leq3$. It should be noticed that the formula (4.8) is symmetric as to ζ's except ζ^h.

[I]. If only ζ^h is zero, $Z_n(\zeta_1,\cdots,\zeta^h;\,z)$ should be written as

$$Z_n=\sum_{m=1}^{n-1}\frac{\exp(2\pi i\zeta_m z)-1}{\zeta_m^2\prod\limits_{\substack{k=1\\k\neq m}}^{n-1}(\zeta_m-\zeta_k)}+(-1)^n\frac{(-2\pi iz)}{\prod\limits_{k=1}^{n-1}\zeta_k}\,.$$

[II]. $Z_2(\zeta_1, \zeta^h; z)$

(1) $\zeta_1=0$

$$Z_2=[1-(2\pi iz\zeta^h+1)\cdot\exp(-2\pi i\zeta^h z)]/(\zeta^h)^2 \,.$$

(2) $\zeta_1=\zeta^h$

$$Z_2=[2\pi iz\cdot\zeta^h+\exp(-2\pi i\zeta^h z)-1]/(\zeta^h)^2 \,.$$

[III]. $Z_3(\zeta_1, \zeta_2, \zeta^h; z)$

(1) $\zeta_1=0$

$$Z_3=\frac{\exp[2\pi i(\zeta_2-\zeta^h)z]-1}{\zeta_2^2(\zeta_2-\zeta^h)}+\frac{2\pi iz\cdot\exp(-2\pi i\zeta^h z)}{\zeta_2\zeta^h}+\frac{(\zeta_2+\zeta^h)\cdot[\exp(-2\pi i\zeta^h z)-1]}{(\zeta_2\zeta^h)^2} \,.$$

(2) $\zeta_1=\zeta_2$

$$Z_3=\frac{(\zeta^h-2\zeta_1)[\exp[2\pi i(\zeta_1-\zeta^h)z]-1]}{\zeta_1^2(\zeta_1-\zeta^h)^2}+\frac{2\pi iz\cdot\exp[2\pi i(\zeta_1-\zeta^h)z]}{\zeta_1(\zeta_1-\zeta^h)}-\frac{\exp(-2\pi i\zeta^h z)-1}{\zeta_1^2\zeta^h} \,.$$

(3) $\zeta_1=\zeta^h$

$$Z_3=\frac{2\pi iz}{\zeta^h(\zeta^h-\zeta_2)}+\frac{\exp[2\pi i(\zeta_2-\zeta^h)z]-1}{\zeta_2(\zeta_2-\zeta^h)^2}-\frac{\exp(-2\pi i\zeta^h z)-1}{\zeta_2(\zeta^h)^2} \,.$$

(4) $\zeta_1=\zeta_2=0$

$$Z_3=\frac{-1}{(\zeta^h)^3}\left[\exp(-2\pi i\zeta^h z)\left\{\frac{1}{2}(2\pi iz)^2(\zeta^h)^2+2\pi iz\zeta^h+1\right\}-1\right].$$

(5) $\zeta_1=\zeta^h=0$

$$Z_3=\frac{-1}{\zeta_2^3}\left[\frac{1}{2}(2\pi iz)^2\zeta_2^2+(2\pi iz)\zeta_2-\exp(2\pi i\zeta_2 z)+1\right].$$

(6) $\zeta_1=\zeta_2,\ \zeta^h=0$

$$Z_3=\frac{1}{\zeta_1^3}[\exp(2\pi i\zeta_1 z)\cdot(2\pi iz\zeta_1-2)+2\pi iz\cdot\zeta_1+2] \,.$$

(7) $\zeta_1=\zeta^h,\ \zeta_2=0$

$$Z_3=\frac{1}{(\zeta^h)^3}[2\pi iz\zeta^h\{\exp(-2\pi i\zeta^h z)+1\}+2\{\exp(-2\pi i\zeta^h z)-1\}] \,.$$

(8) $\zeta_1=\zeta_2=\zeta^h$

$$Z_3=\frac{1}{(\zeta^h)^3}\left[\frac{1}{2}(2\pi iz)^2(\zeta^h)^2-(2\pi iz)\zeta^h-\exp(-2\pi i\zeta^h z)+1\right].$$

To the numerical evaluation of the relatively high order terms, the use of (4.9) seems to be convenient, if we terminate the summation over k at a sufficient large number N.

References

1) H. A. Bethe: Ann. Physik **87** (1928) 55.
2) J. M. Cowley and A. F. Moodie: Acta Cryst. **10** (1957) 609; Proc. Phys. Soc. London **71** (1958) 533; Acta Cryst. **12** (1959) 353, 360.
3) K. Artmann: Cf. H. Raether: Hand. Phys. **32** (Springer-Verlag; Berlin, Goettingen and Heiderberg, 1957) 475.
4) S. Miyake: J. Phys. Soc. Japan **14** (1959) 1347
5) G. Honjo and N. Kitamura: Acta Cryst. **10** (1957) 533.
6) N. Kato: J. Phys. Soc. Japan **7** (1952) 406.
7) J. M. Cowley: Acta Cryst. **12** (1959) 367.

JOURNAL OF THE PHYSICAL SOCIETY OF JAPAN, Vol. 14, No. 11, NOVEMBER, 1959

A Theoretical Treatment of the Excess Energies of Binary Metallic Solutions

By Mitsuo SHIMOJI

Faculty of Science, Hokkaido University, Sapporo

(Received July 4, 1959)

A simplified theoretical treatment of the excess energy of a binary metallic solution, which is based upon a principle of the cellular approximation, is presented. The average size of the atomic polyhedron of a metallic solution, corresponding to the boundary correction of the metallic state, is determined under the condition of a minimum of the total energy of the system. This calculation contains many factors such as the effects of the lowest energy of the valence electrons, the Fermi energy, the interelectronic energy, the ion-core repulsive energy, the van der Waals energy etc. As the purpose of any theory of metallic solutions is to predict the excess quantities from the knowledge of the properties of the pure components, a semi-empirical expression determined only from the quantities of the pure metals is employed in some parts for the estimation of the above factors quantitatively. The present calculation is free from the classical elasticity theory which has been used in the theories of solid solutions, some difficulties having been pointed out. Furthermore, the energetic asymmetry of most metallic solutions can qualitatively or quantitatively be explained by the present treatment.

§ 1. Introduction

In recent years thermodynamic data of metallic solutions have extensively been reviewed by Lumsden¹⁾, Wagner²⁾ and Kubaschewski et al³⁾. However, the quantitative theoretical works on these experimental results have been rather limited. Statistical thermodynamics of metallic solutions has been discussed by many authors¹⁾,⁴⁾⁻⁹⁾, but the statistical theory is not sufficient to predict the excess properties of the metallic solutions except when each component has the same electronegativity. A satisfactory treatment of the calculation of the excess functions of metallic solutions needs a quantum mechanical consideration. Of course it is very difficult to obtain an exact solution of Schroedinger's equation for any metallic solution as well as for any pure metal. Thus a simplified model is necessary to enable one to treat the problem easily. As is well known the cellular method developed by Wigner and Seitz¹⁰⁾ is very useful to estimate the cohesive energy, the lattice constant and the compressibility of simple pure metals, as reviewed in Seitz's¹¹⁾ and Mott-Jones'¹²⁾ text books and others¹³⁾⁻¹⁵⁾.

Quantum mechanical calculations of the excess energies of the dilute metallic solutions have been made by Huang¹⁶⁾ for Au–Ag alloys and by Arafa¹⁷⁾ for Cu–Ag and Ag–Au. For the systems of the finite concentrations and of multivalent metals, Varley¹⁸⁾ has made progress in calculating the excess energy and obtained a reasonable order of magnitude of the energy etc., though the calculation of the strain energy has been based on the classical elasticity theory. This elastic model, which has been used by many investigators, has the difficulties to obey a vague idea of atomic sizes and other concepts, pointed out by Oriani⁵⁾,¹⁹⁾. Then it is desirable for an atomic theory of metallic solutions to be free from the elastic model. Friedel²⁰⁾ has investigated the screening effects in the alloys from the point of view of a modification of the Thomas-Fermi method. It is to be noted that Friedel's theory gives no effect for a system, where both components have the same valency, and no absolute value of the excess energy, though it does give the curvature of the heat of solution determined by the sign of the excess valency, etc.

The aim of this paper is to devise a simple procedure for calculation of the excess energy of the concentrated metallic solutions from the view point of the cellular method without using the classical elasticity theory in order to predict the thermodynamic properties of metallic solutions in terms of properties of pure components.

§ 2. Average Size of Atomic Sphere

In the quantum mechanical calculation of the cohesive energy of pure metals there are three important factors. The first is the boundary correction associated with the change of the state from the free atomic state to its crystalline one. In other words, the boundary correction gives the lowest energy of electrons in the metal relative to the energy of valence electrons in the free atom. The second is the kinetic energy of the conduction electrons or Fermi energy. The third is the interelectronic energy composed of Coulomb, exchange, correlation energy etc. This last factor is very small in total compared with the other two factors. Thus the effects of the boundary correction and of Fermi energy determine the cohesive forces of metals to first approximation. Furthermore, the effects of ionic (exchange) repulsion emphasized by Fuchs[21] and the van der Waals force stressed by Friedel[22] can not be neglected in such a metal as the noble metals. The cohesive forces of both pure metals and metallic solutions may be explained qualitatively, or quantitatively to some extent, if the above effects are adequately calculated.

In a theory concerning metallic solutions it is not always necessary to calculate the "total" cohesive energy of the solution. The aim of the theory of metallic solutions is to understand the change of cohesive energy due to mixing process. Then it is worth emphasizing that the calculation of the excess energy of a metallic solution could be done by using a semi-empirical result of the pure metals to a certain extent. Such a semi-empirical relation might independently be achieved to a complete calculation of pure metals in the future, though the satisfactory results have not yet been gained except in a few cases such as monovalent metals[15]. A calculation for metallic solutions may be impossible now without some semi-empirical relations of pure components, since the calculated results for pure metals are rarely obtained now except for simple systems.

The atomic polyhedron in the cellular approximation can be replaced by a sphere of the same volume.[10]–[12] Thus the energy of a pure metal has been calculated as a function of the size of the atomic sphere mentioned above. The lattice parameter is determined from the point of a minimum of the energy in the relation between the energy and the size of the atomic sphere. This means that the size of an atomic polyhedron corresponds to the minimum of the total energy in any metal. If this principle is extended also to metallic solutions, an average atomic polyhedron should have a size corresponding to the minimum of the total energy of the solution. From this extended principle the size of the atomic sphere, r_m, could be determined. Thus

$$(\partial E(r)/\partial r)_{r_m}=0 \qquad (2.1)$$

is the fundamental equation in the present theory of metallic solutions. $E(r)$ is the total interaction energy of the solution. In a binary system one can put

$$E(r)=x_A E_{AA}(r)+x_B E_{BB}(r)+\varDelta E^* \qquad (2.2)$$

where x_A and x_B are atomic fractions of A and B, E_{AA} and E_{BB} and the interaction energies of the pure states respectively. $\varDelta E^*$ denotes the energy due to the electrochemical effect or electronegativity effect, the effect of the change of van der Waals forces between the unlike atoms, and others.

$$E(r)\approx x_A E_{AA}(r)+x_B E_{BB}(r) \qquad (2.2')$$

determines the average size of the atomic sphere to first approximation, when $\varDelta E^*$ is small. In a later section § 4, a consideration will be given in the case of taking into account the value of $\varDelta E^*$.

A semi-empirical equation of state for each pure component may be employed in solving (2.1) and (2.2). If an exact solution is obtained for any pure metal in the future, this equation will be able to be confirmed theoretically, as explained in the following section. The present principle will hold as it stands for any result of pure metals. According to Slater[23] the semi-empirical equation of state of a pure metal is given by

$$\begin{aligned} E_{ii}(r)+\varDelta I=&-L_i+L_i a_i^2(r_{ii}-r)^2 \\ &+L_i a_i^3(r_{ii}-r)^3+\cdots, \end{aligned} \qquad (2.3)$$

where L_i is the energy of sublimation at 0°K, r_{ii} is the interatomic distance at 0°K and the parameter a_i is connected with the Grüneisen constant, γ_i, by

$$\gamma_i = a_i r_{ii}/2 - 1/3 \,. \tag{2.4}$$

The difference of the energy between the state of the free atom and that of the ionized ion, where the valence electrons are removed to an infinite distance is shown by ΔI. Putting $L_i a_i^2 = l_i$, substituting (2.3) into (2.2′) and solving (2.1) and (2.2′), one obtains from the first order expression of (2.3)

$$r_m^{(1)} = (x_A l_A r_{0A} + x_B l_B r_{0B})/(x_A l_A + x_B l_B) \,, \tag{2.5}$$

where r_{0A} is the radius of the atomic sphere of pure A, easily deduced from the interatomic distance r_{AA}. The term r_{0B} has the corresponding meaning for B. If the crystalline forms of pure metals are different from each other, (2.5) should be slightly modified. From (2.5) Vegard's law is obtained, if $l_A = l_B$.

$$r_m^{(0)} = x_A r_{0A} + x_B r_{0B} \,. \tag{2.6}$$

It should be noted that (2.5) has a corresponding form to Varley's recent calculation[24)], in which the effect of hydrostatic work due to the size factor in liquid alloys has been studied. The present result is, however, based upon such a generalized equation as (2.1); more detailed expression of r_m than (2.5) can be obtained numerically, provided the higher order expression is adopted in (2.3). Interpretation of equation of state, (2.3), will be given in the following section.

§ 3. Excess Energy with Non-Redistribution of Electrons

The first step to calculate the change of the total energy of a metallic solution is to evaluate the lowest energy of electrons at the bottom of the Brillouin zone of the crystal as a function of the radius of the atomic sphere.[11),12)] The size of the atomic sphere has to satisfy the condition of the total energy minimum as described in the foregoing section. In other words the size of the atomic sphere changes, on the average, from r_{0A} and r_{0B} to r_m in accordance with (2.1). Then the lowest energy of valence electrons for the metal A, $\mathcal{E}_{0A}$, may be written as follows:

$$\mathcal{E}_{0A}(r_m) = \mathcal{E}_{0A}(r_{0A}) + (r_m - r_{0A})\left(\frac{\partial \mathcal{E}_{0A}}{\partial r}\right)_{r=r_{0A}} + \frac{(r_m - r_{0A})^2}{2}\left(\frac{\partial^2 \mathcal{E}_{0A}}{\partial r^2}\right)_{r=r_{0A}} + \cdots \,, \tag{3.1}$$

where $\mathcal{E}_{0A}(r_{0A})$ denotes the value for the pure state and $\mathcal{E}_{0A}(r_m)$ for the solution. This may be evaluated in principle by making use of the familiar procedures in the cellular approximation, for example by the Wigner and Seitz method or the quantum defect method, computed from the spectroscopic data of the free atom.

The second step is to calculate the effect of the average Fermi energy. As is well known, this is given by

$$\mathcal{E}_{FA}(r_m) = \frac{3}{5}\,\frac{K Z_A^{2/3}}{r_m^2} \,, \tag{3.2}$$

and

$$K = \frac{h^2}{8m^*}\left(\frac{9}{4\pi^2}\right)^{2/3} , \tag{3.3}$$

where h is Planck's constant, m^* is the effective mass of electrons, Z_A is the valency of A. In a rigorous treatment the effective mass should be employed, but, in a first approximation, the normal mass of the electrons may be used, when an exact solution of the electronic zone structure in alloys has not been obtained. It is instructive to note the recent development for a non-rigid band model of alloys investigated by Cohen and Heine[25)] as well as Jones' work for a rigid band model[26)]. Future developments for the band structures of metals will be available for improving the present discussion. Furthermore, (3.2) assumes that the electron wave functions have a characteristic of the periodicity of the non-perturbed lattice in spite of the fact that the potential in the metallic solution is no longer periodic owing to the existence of the different kinds of the atoms. Though more rigorous consideration for the electron wave function may be necessary in order to know the correct change of the Fermi energy of the solution, the approximation of the nearly free electrons may be permitted as an approach to the goal as in Varley's paper.[18)]

It is known that the interelectronic energy (Coulomb-, exchange- and correlation energy etc.) is small compared to the effects of the boundary correction and of the Fermi energy.[11)–15)] Then the latter two factors determine mainly the amount of the cohesive energy of metals. In the following discussion for the sake of brevity the effect of the interelectronic energy is not taken into account.

The ionic repulsive energy and the van der Waals energy originating from the field of the ion-core must be influenced by this mixing process, since the change in the radius of the atomic sphere causes variation of the exchange energies and dispersion energies due to a synchronized motion of the bounded electrons of each ion. E^{RV} is defined as the energy due to these effects of the ions.

The energy of pure monovalent metals at 0°K is thus given by[11),12)]

$$E_{AA}(r_{AA})=\mathcal{E}_{0A}(r_{0A})+\mathcal{E}_{FA}(r_{0A})+E_A{}^{RV}=-L_A-I_A\ , \tag{3.4}$$

where I_A is the first ionization potential of A. For the atomic sphere A in solutions one has

$$E_A(r_{mm})=\mathcal{E}_{0A}(r_m)+\mathcal{E}_{FA}(r_m)+E_A{}^{RV}(r_m)=-I_A-L_A+\{l_A(r_{AA}-r_{mm})^2+\cdots\}\ . \tag{3.5}$$

From (3.4) and (3.5) one can calculate the change of the interaction energy of the atomic sphere A on mixing, when there are no charge transfer between the unlike atoms and no appreciable change of the van der Waals force constants between them.

$$\begin{aligned}E_A(r_{mm})-E_A(r_{AA})=\mathcal{E}_{0A}(r_m)-\mathcal{E}_{0A}(r_{0A})+\mathcal{E}_{FA}(r_m-)-\mathcal{E}_{FA}(r_{0A})\\ +E_A{}^{RV}(r_m)-E_A{}^{RV}(r_{0A})=\{l_A(r_{AA}-r_{mm})^2+\cdots\}\ .\end{aligned} \tag{3.6}$$

When use is made of (3.2), (3.6) becomes

$$\mathcal{E}_{0A}(r_m)-\mathcal{E}_{0A}(r_{0A})=-\frac{3K}{5}\left(\frac{1}{r_m{}^2}-\frac{1}{r_{0A}{}^2}\right)-\{E_A{}^{RV}(r_m)-E_A{}^{RV}(r_{0A})\}+\{l_A(r_{AA}-r_{mm})^2+\cdots\}. \tag{3.7}$$

In this way one can calculate the effect of the boundary or so in the case of monovalent metals.

The above consideration can be extended to the case of polyvalent metals. Corresponding to (3.5), one has for the Z_A valence

$$E_A(r_{mm})=Z_A[\mathcal{E}_{0A}(r_m)+\mathcal{E}_{FA}(r_m)]+E_A{}^{RV}(r_m)=-\sum_{i=1}^{Z_A}I_i-\Delta Q-L_A+l_A(r_{AA}-r_{mm})^2+\cdots\ , \tag{3.8}$$

where I_i is the i-th ionization potential, ΔQ is the difference of the interelectronic energy between that in the free atom and that in the metal. By extending the method used to derive (3.7), one obtains

$$\begin{aligned}&Z_A[\mathcal{E}_{0A}(r_m)-\mathcal{E}_{0A}(r_{0A})]\\ &\quad=-\frac{3KZ_A{}^{5/3}}{5}\left(\frac{1}{r_m{}^2}-\frac{1}{r_{0A}{}^2}\right)+\{l_A(r_{AA}-r_{mm})^2+\cdots\}-\{E_A{}^{RV}(r_m)-E_A{}^{RV}(r_{0A})\}\ ,\end{aligned} \tag{3.9}$$

corresponding to (3.7).

Thus one can calculate the change of the total interaction energy of a binary metallic solution on mixing without reference to a direct calculation of the lowest energy of the valence electrons by making use of (3.9), when l_A and $E_A{}^{RV}$ are determined from the experimental data of pure metals only. The detailed study of each term in these equations should be developed, though these empirical expressions are enough for the present purpose.

The change of the total energy of binary solutions (excess energy) on mixing is, if there is no charge transfer,

$$\begin{aligned}\Delta E=&\,x_A\{E_A(r_{mm})-E_{AA}(r_{AA})\}+x_B\{E_B(r_{mm})-E_{BB}(r_{BB})\}+\Delta E^{RV}\\ =&\,x_A\{Z_A[\mathcal{E}_{0A}(r_m)+\mathcal{E}_{FA}(r_m)-\mathcal{E}_{0A}(r_{0A})-\mathcal{E}_{FA}(r_{0A})]+E_A{}^{RV}(r_m)-E_A{}^{RV}(r_{0A})\}\\ &+x_B\{Z_B[\mathcal{E}_{0B}(r_m)+\mathcal{E}_{FB}(r_m)-\mathcal{E}_{0B}(r_{0B})-\mathcal{E}_{FB}(r_{0B})]+E_B{}^{RV}(r_m)-E_B{}^{RV}(r_{0B})\}+\Delta E^{RV}\end{aligned} \tag{3.10}$$

where ΔE^{RV} is the correction due to the forces of the ions on mixing. For example the effect associated with the difference between the force constants of the van der Waals energy of the unlike atoms. Making use of (3.8) and (3.9), (3.10) is rewritten as follows.

$$\Delta E = x_A\{l_A(r_{AA}-r_{mm})^2+\cdots\}+x_B\{l_B(r_{BB}-r_{mm})^2+\cdots\}+\Delta E^{RV}\,. \tag{3.11}$$

If r_m is given by (2.5), (3.11) is

$$\Delta E = x_A x_B (r_{AA}-r_{BB})^2/(x_A/l_B+x_B/l_A)+\Delta E^{RV}. \tag{3.12}$$

More detailed expressions than the quadratic equation will be found also by solving the higher order equations in (2.1), (2.3) and (3.10).

The contents of ΔE^{RV} include the deviation of exchange repulsive energy from the expression such as (3.9) and the effect due to the difference of the van der Waals force constants. The former may be evaluated by some method of Born and Mayer type[27] or Fuchs type[21], but the correction based upon these methods may have no detailed formula except for copper. Then only the latter correction is taken into account. It may be very important, especially when there are easily polarizable d-electrons of different degrees in each ion as in noble and transition metals.[30] This effect can be represented by means of the geometric mean rule for the force constants as in the usual non-electrolyte solutions[4]. From London's consideration[7][8], one can write roughly[4]

$$\Delta E^{RV} = x_A x_B c(f_A-f_B)^2/r_m^3 \tag{3.13}$$

where c is the number of the interaction pairs depending upon the crystal structure, f_A and f_B are the force constants appropriately defined respectively. It is readily found that no effect of this type exists if both components have the same value of van der Waals forces.

It is to be noted that ΔE, (3.12), shows always a positive excess energy due to the disparity of atomic radii and the difference of the van der Waals forces. The former corresponds to the terms of the size factor based on the classical elasticity theory, but it has more sound base than in the elastic model because of its derivation from the equation of state to be explained in principle by quantum mechanics. Furthermore one should remember the effect of the van der Waals forces always provides a positive quantity to the excess energy, even if there is no size factor.

It is of interest that there is a possibility of applicability of the geometric mean rule such as (3.13) in Pauling's view, taking into account the effect of d-electrons in a form of the spd hybrid metallic resonance.[29],[30]

§ 4. Excess Energy with Redistribution of Electrons

In this section the effect of the electronic redistribution on mixing is considered. This effect called the electrochemical effect gives always the negative excess energy, corresponding to a tendency to form a stable alloy phase. If one of the components of the metallic solution has a greater attraction for electrons than the other, an increased probability of finding the electrons near the first may be expected. In the extreme case this tendency means an ionic bonding in ionic crystals. As is well known this effect in molecules can be explained by the concept of electronegativity which depends upon the ionization potential as well as upon the electron affinity.[31],[32] This approach may be extended to metallic solutions,[6],[8],[33] but a more improved approach based upon the cellular approximation is employed here.

The main reason why the electrons in metallic solutions accumulate near one of the atoms in comparison with the other may be found in the fact that the ionization potential of the former is greater than that of the latter, and briefly the large electron affinity of the former. The theoretical investigation of the cohesive energy of metallic solutions has been developed so as to evaluate the effect of the charge transfer qualitatively or quantitatively. In the present treatment this effect is estimated by means of a modification of Varley's method. The difference between the present theory and Varley's is in the point that the height of the maximum of the electronic energy is measured at the average atomic size of metallic solutions or at the respective pure atomic sizes, in addition to the fact that the classical elasticity theory was used in Varley's paper.

If the charge n leaves from one cell, A, and distributes itself uniformly over the other cell, B, the latter accepts on the average $x_A n/x_B$ charge. Hence the average energy of the binary metallic solution which corresponds to (2.2) can be expressed by

$$E(r_m)=x_A[Z_A-n]\mathcal{E}_{0A}(r_m)+x_B[Z_B+x_A n/x_B]\mathcal{E}_{0B}(r_m)+x_A E_A{}^{RV}(r_m)+x_B E_B{}^{RV}(r_m)+\Delta E^{RV}$$
$$+\frac{3x_A K Z_A{}^{5/3}}{5r_m{}^2}\left(1-\frac{n}{Z_A}\right)^{5/3}+\frac{3x_B K Z_B{}^{5/3}}{5r_m{}^2}\left(1-\frac{x_A n}{x_B Z_B}\right)^{5/3}. \tag{4.1}$$

Expanding (4.1) to the second power in n, one obtains

$$E(r_m)=x_A\left\{Z_A\mathcal{E}_{0A}(r_m)+\frac{3}{5}\frac{KZ_A{}^{5/3}}{r_m{}^2}\right\}+x_B\left\{Z_B\mathcal{E}_{0B}(r_m)+\frac{3}{5}\frac{KZ_B{}^{5/3}}{r_m{}^2}\right\}$$
$$+x_A E_A{}^{RV}(r_m)+x_B E_B{}^{RV}(r_m)+\Delta E^{RV}$$
$$+n x_A\{\mathcal{E}_{0B}(r_m)+KZ_B{}^{2/3}/r_m{}^2-\mathcal{E}_{0A}(r_m)-KZ_A{}^{2/3}/r_m{}^2\}$$
$$+n^2 x_A/x_B\{x_B K/3Z_A{}^{1/3}r_m{}^2+x_A K/3Z_B{}^{1/3}r_m{}^2\}\,. \tag{4.2}$$

The simplified equation (4.2) holds, when the amount of charge transfer is small compared to the valency of the pure state. In principle n in (4.1) or (4.2) can be determined from the condition

$$\partial E(n)/\partial n=0\,. \tag{4.3}$$

This equation can be easily calculated if (4.2) is used. As a result the excess energy, corresponding to (3.10), is given by

$$\Delta E=[x_A\{l_A(r_{AA}-r_{mm})^2+\cdots\}+x_B\{l_B(r_{BB}-r_{mm})^2+\cdots\}]$$
$$+x_A x_B c(f_A-f_B)^2/r_m{}^3$$
$$-x_A\,x_B\frac{3r_m{}^2\{\mathcal{E}_{0B}(r_m)-\mathcal{E}_{0A}(r_m)+K(Z_B{}^{2/3}-Z_B{}^{2/3})/r_m{}^2\}^2}{4K(x_A/Z_A{}^{1/3}+x_A/Z_B{}^{1/3})}\,, \tag{4.4}$$

where r_m should satisfy the condition of the energy minimum such as (2.1). However, an analytical expression for r_m is not easily obtained in contrast to (2.6) deduced from the condition of non-redistribution for the electronic charge. Then one had better calculate the energy of the system in a given r_m and, from the graphical relation between the size of the atomic cell and the energy, the most probable size of the system can be obtained.

As the first approximation, Vegard's law for the interatomic distance may be useful in view of the fact that the deviation from this law is not appreciable in most alloys. If this approximation is adopted, (4.4) can readily be calculated. Of course a numerical calculation based upon the above described procedure can evaluate the difference of the energy due to the deviation from this simplification. Thus an approximate expression of (4.4) is given by

$$\Delta E/x_A x_B=(x_B l_A+x_A l_B)(r_{BB}-r_{AA})^2+c(f_A-f_B)^2/r_m{}^{(0)3}$$
$$-\frac{3}{4}\frac{r_m{}^{(0)2}\{\mathcal{E}_{0B}(r_m{}^{(0)})-\mathcal{E}_{0A}(r_m{}^{(0)})+K(Z_B{}^{2/3}-Z_A{}^{2/3})/r_m{}^{(0)2}\}^2}{K(x_B/Z_A{}^{1/3}+x_A/Z_B{}^{1/3})}, \tag{4.5}$$

where for $r_m{}^{(0)}$ one is referred to (2.6), i.e. Vegard's law. The first two terms of the right hand side of equations (4.4) or (4.5) corresponds to (3.10) obtained in the foregoing section. The second term means, of course, ΔE^{RV}. However, the last term due to the charge redistribution gives always a negative value for the excess energy and shows a tendency of compound formation i.e. attraction between unlike atoms. In other words, this last term corresponds to the electrochemical effect caused from the difference of the electronegativities of both components. The effect due to the electrostatic effect originating from the above process may be negligibly small except for the superlattice formation.[18]

The compiled values of L_i, $\mathcal{E}_{0i}(r_{0i})$, $KZ_i^{2/3}/r_{0i}^2$, a_i and r_{ii} for some pure metals, which are necessary to evaluate (2.6), (4.4) and (4.5), are given in Table I. Using these values with (2.7) and (3.9), one can calculate the excess energies of solutions on basis of (4.3) or (4.4) except the factor of the van der Waals force, which has to be considered only qualitatively.

Comparisons of the theory with experiment may be made by making use of Kopp-Neumann's law for the specific heat of an alloy, since the deviation from this law is very small in most alloys at high temperatures, where the observed data are often obtained.

Table I. Fundamental constans of pure metals useful in calculation of the excess energies of metallic solutions.

Metal	L_i (eV)	$-\varepsilon_{0i}(r_{0i})$ (eV)	$KZ_i^{2/3}/r_{0i}^2$ (eV)	a_i (Å^{-1})	r_{ii} (Å)
Cu	3.54	15.48	7.10	1.41	2.550
Ag	3.00	13.85	5.52	1.39	2.883
Au	3.93	16.47	5.56	1.58	2.878
Cd	1.16	14.33	7.49	1.93 (1.5)*	3.042
Zn	1.37	16.29	9.57	1.70 (1.5)*	2.748
Hg	0.7	15.38	7.23		3.10
Al	3.30	18.30	11.76	1.21	2.80, 2.85
Ga	2.5	17.94	10.49	(1.4)*	2.7
In	2.56	16.08	8.71	1.38* (1.3)*	3.14
Tl	1.88	16.72	8.26	1.40* (1.3)*	3.42
Sn	3.5	18.71	10.24	1.15* (1.2)*	3.16
Pb	2.04	18.31	9.54	1.37* (1.4)*	3.49

L_i, $\varepsilon_{0i}(r_{0i})$ and $KZ^{2/3}/r_{0i}^2$: taken from Varley's table.
a_i: taken from Slater's table, and* calculated from the Grüneisen constant. The values in parentheses correspond to those in liquid states.
r_{ii}: the Goldshmidt atomic diameter. (c.n. 12)

§ 5. Energetic Asymmetry of Liquid Solutions

The properties of infinitely or moderately dilute mixtures are often of interest in the studies of metallic solutions, since in such solutions the complication due to the presence of the solute may considerably be reduced. The excess heat can be expanded in power series of the atomic fraction of the solute, x_B,

$$\Delta H=\alpha x_B+\beta x_B^2+\gamma x_B^3+\cdots \qquad (5.1)$$

at a dilute concentration. From this one readily obtains the partial molar excess heat of the solute B or the solvent A as follows.

$$\Delta\overline{H}_B=\alpha+2\beta x_B+\cdots\,, \qquad (5.2)$$

$$\Delta\overline{H}_A=-\beta x_B^2\,. \qquad (5.3)$$

The constant α in these equations denotes the partial molar excess heat of the solute in an infinitely dilute solution, as may be seen in (5.2). On the other hand, the constant, β, may determine the curvature of the excess heat at the dilute concentration.

These constants can be evaluated on the basis of the present theory, because the excess heat may nearly be equal to the excess energy in condensed phases. Thus one obtains, for example from the simplified expression (4.5),

$$\begin{aligned}\alpha=&(r_{BB}-r_{AA})^2 l_B+c(f_A-f_B)^2/r_{0A}^3\\&-3\{\mathcal{E}_{0B}(r_{0A})-\mathcal{E}_{0A}(r_{0A})\\&+K(Z_B^{2/3}-Z_A^{2/3})/r^2_{0A}\}^2 r^2_{0A}Z_B^{1/3}/4K\,, \qquad (5.4)\end{aligned}$$

and

$$\begin{aligned}\beta=&(r_{BB}-r_{AA})^2(l_A-2l_B)+c(f_A-f_B)^2 r_{0B}^3/r_{0A}^6\\&-3\{\mathcal{E}_{0B}(r_{0A})-\mathcal{E}_{0A}(r_{0A})\\&+K(Z_B^{2/3}-Z_A^{2/3})/r^2_{0A}\}^2(r^2_{0A}Z_B^{1/3}/4K)\\&\times\{-(Z_B/Z_A)^{1/3}+2(r_{BB}/r_{AA})-1\}\,. \qquad (5.5)\end{aligned}$$

Positive values of α may be obtained from the prominence of the first and the second terms or the effects of the size factor and the van der Waals force, while negative values may indicate the prominent contribution of the electrochemical factor.

If the component A is regarded as the solute, i.e. in the opposite side of (5.1), the constants, α', β' and $\gamma'\cdots$ may be introduced.

$$\Delta H' = \alpha' x_A + \beta' x_A^2 + \gamma' x_A^3 + \cdots . \tag{5.1'}$$

Corresponding to (5.4),

$$\begin{aligned}\alpha' = {} & (r_{BB} - r_{AA})^2 l_A + c(f_A - f_B)^2 / r_{0B}^3 \\ & -3\{\mathcal{E}_{0B}(r_{0B}) - \mathcal{E}_{0A}(r_{0B}) + K(Z_B^{2/3} - Z_A^{2/3})/r_{0B}^2\}^2 r_{0B}^2 Z_A^{1/3}/4K .\end{aligned} \tag{5.4'}$$

Table II. Energetic asymmetry of binary liquid metallic solutions at extremely high dilution.

Systems observed as $2\alpha' \approx \alpha$	Zn–Sn	Zn–In	Zn–Ga	Cd–Pb	Cd–Sn	Cd–Tl	Cd–In
Calculated ratio from (5.7)	1.6	1.4	1.6	1.5	1.9	1.2*	1.7

Systems observed as $\alpha' \approx \alpha$	Cd–Zn	Ga–In	Ga–Sn	In–Pb	Tl–Sn	Pb–Sn	Cd–Ga
Calculated ratio from (5.7)	1.2	0.9	1.0	0.9	1.6*	1.3	1.8*

* In these systems the electrochemical factor must be taken into account in addition to the size factor.

If $r_{AA} = r_{BB}$ and $Z_A = Z_B$, the relation $\alpha = \alpha'$ can readily be found. For $r_{AA} \neq r_{BB}$ and $Z_A = Z_B$ the asymmetric relation $\alpha \neq \alpha'$ is obtained generally, but $\alpha = \alpha'$ may hold for special systems.

Firstly one considers the case of the positive excess energies ($\alpha > 0$. $\alpha' > 0$), such as in the liquid mixture of divalent metals. These systems (Cd–Tl. Cd–Pb, Cd–Sn, Zn–In, Zn–Sn etc.) show, according to Kleppa's observation,[34]

$$2\alpha' \approx \alpha \qquad \text{for } Z_A < Z_B. \tag{5.6}$$

In order to examine the above experimental relation, the following simplification is adopted for convenience, since the size factor predominates at least over the electrochemical factor, as long as $\alpha > 0$. From (5.4) and (5.4')

$$\frac{\alpha}{\alpha'} = \frac{l_B}{l_A} = \frac{L_B a_B^2}{L_A a_B^2} . \tag{5.7}$$

Of course this approximate expression shows only the most effective factor in (5.4) or (5.4'), but may be suitable for a qualitative discussion. As long as l_B and l_A are known, the relation between α and α' may be examined by using (5.7). Calculated values of l_B/l_A are shown in Table II. It is readily found that the ratio of l_B (higher valence) to l_B (divalence) exceeds at least 1.4, but that the ratio of l_B (tetravalence) to l_A (trivalence) shows values below 1.3 except Tl–Sn alloys. In most cases the prediction of (5.7) or (5.7') is in good agreement with the experimental results on the energetic asymmetry of the excess energy. It is thus to be noted that the relation between α and α' is not always only due to the valence electron effects but due to mixed effects of the boundary correction, Fermi energy and so on. It is of interest to note that some systems do not obey the above condition (5.7), as seen in Table II. To these systems a more rigorous condition than (5.7) should be applied.

Secondly similar consideration can be given to the case of the negative excess energy ($\alpha < 0$), as seen in the mixture of noble metals with multivalent metals. For example, the rule of the relative valence effect proposed by Hume-Rothery[35] indicates that the solid solubility of the alloy of monovalent metals with those of higher valence is smaller in the side of those having higher valence than in those of having lower valence. In other words, the excess energy at high dilution has, in the case of noble metals being the solvent, a steep slope against the concentration compared with that in the opposite case. Thus the relative valence effect requires

$$\alpha<\alpha' \text{ or } |\alpha|>|\alpha'| \qquad \text{for } Z_A<Z_B. \tag{5.8}$$

Apparently (5.8) contradicts (5.6). However, this may be explained, since the electrochemical factor predominates over the size factor as long as the excess energy is negative. For example from (5.4) and (5.4′)

$$|\alpha|/|\alpha'|\approx(Z_B/Z_A)^{1/3} \qquad \text{for } r_{0A}\approx r_{0B}. \tag{5.9}$$

For the relative valence effects,[18] (5.9) is in agreement with Varley's result since the present treatment should be coincident in principle with Varley's especially for $r_{0A}\approx r_{0B}$. Thus the discrepancy of experimental data with the relative valence effects may occur owing to (5.7), if the excess energy is positive. However, this rule may be associated with a condition such as (5.9). which holds only for the negative excess energy. Furthermore, it is worth noting that a complete explanation of solid solubility of an alloy requires knowledge of the band structure, which depends on the crystal structure, the excited electronic state of the components and the boundary correction etc., since the transformation of alloy phases is accompanied with touching of Fermi surfaces at the Brillouin zone of the alloy.[12] In liquid alloys this correction may be less important than in solid alloys, because the Brillouin zone in liquid state has not very definite meaning compared with that in solid state.

Thirdlly the relation between α and β in (5.1) and (5.2) is considered as the properties of moderately dilute mixtures. According to the theory of regular solutions,

$$-\beta/\alpha=1 \tag{5.10}$$

is obtained because of random mixing. However, it is found experimentally that in most system, such as solutions of divalent metals with metals of higher valence $|\beta|$ differs considerably from $|\alpha|$, e.g. $-\beta/\alpha\approx2$. These experimental results can not be explained by the quasi-chemical theory even if deviations from randomness are taken into account. This behavior is probably on account of the fact that these systems must be represented by more refined model than the regular solution model, for example Hardy's sub-regular solution model,[36] Oriani and Murphy's approach[37] and others.[38]

The present theory can immediately be applied to the discussion of the ratio of β/α as well as that of α/α'. For brevity the same assumptions used in the foregoing discussion

Table III. Energetic asymmetry of binary liquid metallic solutions at moderate dilution.

Solvent	Solute	Calc. (5.11)	Obs. Relation	Solvent	Solute	Calc. (5.11)	Obs. Relation
Zn	Cd	0.8	*	In	Zn	0.6	*
Zn	Ga	1.4	**	In	Cd	0.3	*
Zn	Sn	1.4	**	In	Tl	0.6	*
Cd	Zn	1.2	*	In	Pb	0.9	*
Cd	Ga	1.5	**	In	Ga	1.1	*
Cd	Tl	1.2	**	Sn	In	0.8	*
Cd	Sn	1.5	**	Sn	Ga	1.0	*
Cd	Pb	1.3	**	Sn	Zn	0.4	*
Cd	In	1.4	**	Sn	Ag	1.2	**
Ga	Zn	0.4	*	Pb	Cd	0.5	*
Ga	In	0.9	*	Pb	Sn	1.2	*
Ga	Sn	1.0	*	Pb	In	1.1	*
Ga	Cd	0.1	*	Pb	Ag	1.3	**
				Pb	Au	1.6	**

* means an observed relation $-\beta/\alpha\approx1$, while ** does $-\beta/\alpha\geq2$. For noble metals the calculated ratio is obtained from solid a_t. It should be noted that the expansion such as (5.11) is inadequate if $|l_B-l_A|\ll l_B$ is not satisfied. Of course the tendency of the prediction is reasonable.

concerning the ratio of α and α' are employed in accordance with $\alpha>0$ and $\alpha<0$. Then

$$-\frac{\beta}{\alpha}=1+\frac{l_B-l_A}{l_B} \quad \text{for } \alpha>0, \tag{5.11}$$

while

$$-\frac{\beta}{\alpha}=1+\frac{Z_A^{1/3}-Z_B^{1/3}}{Z_A^{1/3}} \quad \text{for } \alpha<0 \text{ and } r_{0A}\approx r_{0B}. \tag{5.12}$$

The comparisons (5.11) and (5.12) with experimental results are shown in Table III. The agreement is reasonably good in most systems in spite of the crude approximation. $\beta=-\alpha$ $(\alpha>0)$ could hold, if l_B of the solute B is equal to, or less than l_A of the sovent A. $-\beta/\alpha\approx 2$ $(\alpha>0)$, if l_B is larger than l_A. On the other hand, the valence of the solvent has to be larger than that of the solute, in order to make it hold that $\alpha<0$ and $-\beta/\alpha>1$. If more detailed equations, (5.4) and (5.5), than (5.11) or (5.12) are used, disagreements found in some systems could be removed.

Thus the behaviour of the excess energy of a metallic solution at dilute concentrations can be predicted by using the present theoretical results, (5.4), (5.5), or more simply (5.7), (5.9), (5.11) and (5.12). These equations indicate that the factors due to boundary corrections and Fermi energies etc. of components, being indirectly related to their valences, determine the excess energies of metallic solutions. The influence of the formal valence effect cannot simply be concluded owing to the more fundamental effect mentioned above, as may be seen in the case of the solutions of the divalent metals with metals of higher valence contradictory to the relative valence effect.

§ 6. Application to Solid Solutions

The numerical calculation based on the present equation (4.5) is applied to solid solutions of the monovalent noble metals, since thermodynamic data of these alloys have been well established. In obtaining the calculated values shown in Table IV it is assumed that $\mathcal{E}_0$ and $\mathcal{E}_F$ of monovalent metals in alloys are equal to those in the pure metals respectively, because E^{RV} cannot be calculated accurately. The values are due to neglection of the effect of the van der Waals energy, being, probably reasonable for Au–Cu alloys. However, this omission may not hold in both Ag–Au and Cu–Ag systems because of the presence of the less polarizable d-electrons of Ag. For example, theoretical sublimation energies (upper limit) for monovalent noble metals based on the quantum defect method by Kambe[39] show 59.3 kcal./mole for Cu, 55.8 kcal./mole for Ag and 48.9 kcal/mole for Au, while experimental values 81.2, 68.0 and 92.0 kcal./mole are found respectively. The most important discrepancy of these results is that the minimum sublimation energy occurs experimentally for Ag, while the calculated values decrease from Cu to Ag to Au. One of the reasons for this discrepancy may be due to the van der Waals force of d-electrons, though other factors may, of course, be taken into account. If the energy of the van der Waals forces of d-electrons is much greater in Cu and Au (the order of magnitude is assumed 1 eV for both metals, and the energy of Au slightly greater than that of Cu) than in Ag (for example roughly 0.1 eV), the minimum sublimation energy could be found in Ag. The correction due to the effects of d-electrons seems to be reasonable to improve the calculated results in these solid solutions.

Table IV. Excess heats of noble metal solid solutions at equiatomic fraction (kcal./mole).

System	Present	Varley	Obs.[3]
Au–Cu	0.9	1.6	−0.90
Au–Ag	−5.7	−1.7	−0.95, −1.07
Cu–Ag	4.6	1.3	no solution

A very different approach based on the concept of the existence of resonating covalent bonds in metals proposed by Pauling, has been applied to the calculation of the misfit strain energy of Au–Cu solid alloys by Hultgren.[40] As a feature of the theory of Pauling, the strain energy is reduced by redistribution of electrons, causing the favour of the size factor. This effect could be discussed from the present point of view, if (4.4) is used.

As pointed out in the discussion of the foregoing section, the excess heats of most solutions does not always indicate the symmetric behaviour. In other words, the definition of the regular solutions does not always hold except for a few special systems. Cu-Au alloys, the well known example of superlattices, cannot be explained by the term of the interchange energy independent of the composition being the basic assumption of the regular solution.[41),42)] This fact could be explained by the present theory, if one calculates (4.5). However, $\varepsilon_{0\mathrm{Au}}$ and $\varepsilon_{0\mathrm{Cu}}$ in (4.5) are not obtained accurately, since E^{RV} in (3.7) has not been investigated in detail in this system. Then a somewhat different approach based on Frölich's simple treatment[43)] for alkali metals is extended to a discussion of the energy of the lowest electronic state of this system. According to Frölich's work, the lowest energy of the electrons in simple metals can be expressed in the form

$$\varepsilon_{0i}=-\frac{3e^2}{r_{0i}}+\frac{e^2R_{0i}^2}{r_{0i}^3}, \qquad (6.1)$$

where the first term represents the potential energy, and the second the kinetic energy of the lowest electronic state. The constant R_{0i} in the second term can be estimated from the ionization energy and varies from one metal to another. On the other hand, the first term always gives the same value to monovalent metals, if there is no difference of the atomic sizes. Then one can calculate the electrochemical factor in the solution of the monovalent metals such as Au–Cu alloys from (4.5) and (6.1). Thus the excess energy is

$$\Delta E=x_{\mathrm{Au}}x_{\mathrm{Cu}}\left\{(x_{\mathrm{Au}}l_{\mathrm{Cu}}+x_{\mathrm{Cu}}l_{\mathrm{Au}})(r_{\mathrm{AuAu}}-r_{\mathrm{CuCu}})^2 -\frac{3}{4}\frac{(R_{0\mathrm{Au}}{}^2-R_{0\mathrm{Cu}}{}^2)^2}{Kr_m{}^{(0)4}}\right\}. \qquad (6.2)$$

This equation shows that the electrochemical energy between monovalent metals is inversely proportional to the fourth power of the average atomic sizes. The concentration dependance of the excess energy of Au–Cu alloys may be calculated, if the constants in (6.1) are given. As the present theory gives qualitatively the reasonable value for the excess energy, these constants are provisionally determined so as to satisfy the experimental data at equiatomic fraction. The calculated values at other concentrations are in agreement with experimental ones as seen in Table V. Of course the above method for the determination of constants in (6.1) or (6.2) can be improved, but the direction of the change of the excess energy, that increases with the increases of the concentration of Cu, may hold as it stands, aside from the minor difference of the absolute magnitude.

The metallic solutions of multivalent metals dissolved monovalent metals are of interest to examine for the valence effect on mixing, as seen in the foregoing section. Though the qualitative explanation for the excess energy of liquid solutions may be satisfactory, more detailed calculation for that of solid solutions is given. As the solute, zinc and cadmium are chosen, since the equations of state of these metals have been studied in detail com-

Table V. The concentration dependence of $\Delta H/x_{\mathrm{Cu}}x_{\mathrm{Au}}$ in the Au–Cu solid solutions.

Atomic fraction of Cu	Calculated values (cal.)	Observed values (cal.)[3)]
0.3	−3700	−4100
0.5	−5120 (adjusted)	−5120
0.7	−5700	−6200

Table VI. $\Delta H/x_B$ in some solid solutions (eV).

A	B	Observed at $x_B=0.1$[3)]	Calculated at $x_B\to0.1$[3)]
Cu	Zn	−0.36	−0.58
Ag	Zn	−0.01	−0.21
Ag	Cd	−0.34	−0.51
Au	Cd	−0.41	−3.5

pared with those of other multivalent metals. Typical examples of the calculation in the dilute range of α alloys are presented in Table VI. The order of magnitude of calculated values is in agreement with the observed data.

Thus one can calculate the excess energy of metallic solutions at any concentration as long as each term in (4.4) or (4.5) is known. Most calculated results may qualitatively be reasonable, but quantitative agreement with experimental values will not be obtained without detailed knowledge of $\mathcal{E}_{0i}$, $\mathcal{E}_{Fi}$, E_i^{RV}, and l_i of each pure metal. The present stage of both theoretical and experimental investigations of theses terms of pure metals is not satisfactory except for simple alkali metals. It is necessary to ascertain the properties of pure metal in order to understand those of metallic solutions.

Furthermore, it is a weak point that the present treatment is based upon the free electron approximation as is also the case in Varley's work. To understand the deviation from the free electron approximation is very important in order to understand the change of the excess energy due to the phase transformation of alloys, as expected from works of Jones and Cohen-Heine. The Fermi energy having a central position in the sublimation energy of a metal is very sensitive to the changes of the Brillouin zone structure and the number of the conduction electrons. However, the free electron approximation may be rather suitable in liquid phases, since there is no definite structure of the zone in liquid state except in a physical meaning as an average structure. For solid solutions this approximation should be carefully improved.

Lastly it should be noted that the small corrections for correlations between free electrons considered in Varley's work are disregarded here. Such corrections may, however, yield no appreciable change of the present conclusion, if theoretical results concerning pure metals are taken into account. However, this conclusion may be doubtful in some complex metals.[13)]

§7. Conclusion

i) The semi-empirical equation of state of a pure metals is applicable to the calculation of the excess energy. The interatomic distance giving a minimum of the total energy should correspond to the average size of the atomic cells (polyhedra) in the metallic solutions. In this way, one part of the excess energy, i.e., the size factor can be calculated in any desired degree of approximations beyond the quadratic representation without reference to the classical elasticity theory.

ii) There is a possibility that a positive excess energy is yielded without the negligible size factor, when the difference between the van der Waals forces of both components is strong. This will be the case, as in the mixture of the transition metals with the noble metals, both having polarizable *d*-electrons. The same conclusion may be obtained from the Pauling scheme of the *spd* hybrid resonance.

iii) The effect of charge transfer is obtained in the present treatment from the point of view of taking into account the change of the total energy at the "average size" of the atomic polyhedra of the solution, but in Varley's treatment from that at the respective pure atomic sizes. As a result, for example, the lowest energy of electrons, $\mathcal{E}_0$, in the former theory is kept constant except the effect of charge transfer throughout the whole concentration, but in the present treatment it varies, as seen in (4.4). The present treatment may be suitable for a discussion concerning the dependence of the excess energy upon concentration. Of course both approaches may coincide, if each component has the same atomic sizes.

iv) The order of magnitude of the calculated excess energy may be reasonable in spite of the crude approximation. However, the points to be improved in the future are the change of the Brillouin zone, that of the interelectronic energy, and that of wave functions due to the disturbance of the periodic field etc. The present treatment should be regarded as the first approximation for the excess energy of a metallic solution.

References

1) J. Lumsden: *Thermodynamics of Alloys* (Institute of Metals, London, 1952).
2) C. Wagner: *Thermodynamics of Alloys* (Addison-Wesley, 1952).
3) O. Kubaschewski and J. A. Catterall: *Thermochemical Data of Alloys* (London, 1956).
4) J. H. Hildebrand and R. L. Sott: *Solubility of Non-Electrolytes* (Reinhold, 1952).

5) A. W. Lawson: J. Chem. Phys. **15** (1947) 831.
6) M. Shimoji and K. Niwa: Acta. Met. **5** (1957) 496.
7) A. M. Evseev: J. Phys. Chem U.S.S.R. **31** (1957) 1957.
8) B. W. Mott: Phil. Mag. **48** (1957) 259.
9) M. Shimoji: in Proceedings of International Symposium on Physical Chemistry of Metallic Solutions and Intermetallic Compounds N.P.L. Teddington (1958).
10) E. P. Wigner and F. Seitz: Phys. Rev. **43** (1933) 804; **46** (1934) 509.
11) F. Seitz: *The Modern Theory of Solids* (McGraw-Hill, 1940).
12) N. F. Mott and H. Jones: *The Theory of the Properties of Materials and Alloys* (Oxford, 1936).
13) E. P. Wigner and F. Seitz: *Solid State Physics*, vol. **1** (Academic Press, 1955) 97.
14) F. S. Ham: *Solid State Physics*, vol. **1**, (Academic Press, 1955) 127.
15) H. Brooks: *Theory of Alloy Phases* (Amer. Soc. Met., 1956) 199.
16) K. Huang: Proc. Phys. Soc. London **60** (1948) 161.
17) M. K. I. Arafa: Proc. Phys. Soc. London **B**, **62** (1949) 238.
18) J. H. O. Varley: Phil. Mag. **45** (1954) 887.
19) R. A. Oriani: Acta Met. **4** (1956) 15; J. Phys. Chem. Solids. **2** (1957) 327.
20) J. Friedel: Adv. in Phys. **3** (1954) 446.
21) K. Fuchs: Proc. Roy. Soc. **A**, **151** (1935) 585.
22) J. Friedel: Phil. Mag. **43** (1952) 153.
23) J. C. Slater: *Introduction to Chemical Physics* (McGraw-Hill, 1939).
24) J. H. O. Varley: in Proceedings of International Symposium on Physical Chemistry of Metallic Solutions and Intermetallic Compounds N.P.L. Teddington (1958).
25) M. H. Cohen and V. Heine: Adv. in Phys. **7** (1958) 395.
26) H. Jones: Proc. Roy. Soc. A, **144** (1934) 255.
27) M. Born and J. E. Mayer: Z. Phys. **75** (1932) 1.
28) F. London: Trans. Faraday Soc. **33** (1937) 8.
29) W. Hume-Rothery and G. V. Raynor: *The Structure of Metals and Alloys* (Institute of Metals, London, 1954).
30) L. Pauling and J. Sherman: J. Amer. Chem. Soc. **59** (1937) 1450.
31) L. Pauling: *The Nature of the Chemical Bond* (Cornell Univ. Press, 1942).
32) R. S. Mulliken: J. Chem. Phys. **2** (1934) 782.
33) K. Niwa and M. Shimoji: in Proceedings of International Symposium on Physical Chemistry of Metallic Solutions and Intermetallic Compounds N.P.L. Teddington (1958).
34) O. J. Kleppa: *Liquid Metals and Solidification* (Amer. Soc. Met., 1957).
35) W. Hume-Rothery., Mabott and Channel-Evance: Phil. Trans. **A**, **233** (1934) 1.
36) H. K. Hardy: Acta Met. **1** (1953) 202.
37) R. A. Oriani and W. K. Murphy: J. Phys. Chem. **62** (1958) 199, 327.
38) F. E. Wittig: Z. Elecktrochem. **63** (1959) 327.
39) K. Kambe: Phys. Rev. **99** (1955) 419.
40) R. Hultgren: J. Metals, no. 10 (1957) 1240.
41) L. Guttman: *Solid State Physics* vol. **3** (Academic Press, 1956) 145.
42) M. Shimoji: J. Phys. Soc. Japan **11** (1956) 91.
43) H. Frölich: Proc. Roy. Soc. **A**, **158** (1937) 97.

JOURNAL OF THE PHYSICAL SOCIETY OF JAPAN, Vol. 14, No. 11, NOVEMBER, 1959

Algebraic Method to obtain Irreducible Representations of Space Groups with an Application to White Tin

By Shoichi MASE

Department of General Education, Nagoya University

(Received July 14, 1959)

Algebraic method to construct irreducible representations of space groups is presented by making an example of white tin having screw axes and glide planes in the symmetry operations. In present method it is enough to treat explicitly at most only symmetry elements equal in number to the operations of the point group to which concerned lattice belongs, regardless of the cases with or without spin and also of interior points or the points of the Brillouin zone boundary. This becomes very simplification compared to usual group-theoretical method.

§ 1. Introduction.

In the study of electronic structure of solids, the group theory plays an important role and many results have been published. The pioneering works by Seitz[1)] and Bouckaert-Smoluchowski-Wigner[2)] were extended by Herring[3)] to the case of complex crystals containing screw axes and glide planes in their symmetry operations, and recently the construction of the representations of the so-called double space group in the case with spin was discussed by Elliott.[4)] The theory of the representations of space groups is purely mathematical and it is group-theoretically completed. For practical object to obtain the representations, however, there is far simpler way to perform the calculation. We study the symmetry properties of the Brillouin zone of white tin with use of the theory of hypercomplex number or algebra. Though, as is expressed in later section, we can obtain not a few knowledges for the symmetry properties of white tin from the references on the studies of diamond lattice[3),4),5)], it may be not unuseful to derive partly the same results by different method, since much of 230 space groups contain the screw axes and glide planes in their symmetry operations and the advantage of algebraic method is in the case of such complex crystals.*

Generally a crystal is kept at invariance by rotations, translations proper to the crystal and also their combination. The assembly of all these operations makes a group and we designate this group, the space group, by $\mathfrak{G}$. Following to Seitz's notation the elements of $\mathfrak{G}$ are expressed by

$$\{\varepsilon|\boldsymbol{t}\}\{A|\tau_A\}\in\mathfrak{G}\,.$$

$\{A|\boldsymbol{\tau}_A\}$ means the rotation A about certain fixed point followed by the translation $\boldsymbol{\tau}_A$. $\boldsymbol{t}$ is a linear combination of the basic primitive translation vectors $\boldsymbol{t}_1, \boldsymbol{t}_2$ and $\boldsymbol{t}_3$ of the crystal, i.e.

$$\boldsymbol{t}=l\boldsymbol{t}_1+m\boldsymbol{t}_2+n\boldsymbol{t}_3\,,$$

$$-\frac{N}{2}\leq l,\, m,\, n\,(\text{integer})\leq\frac{N}{2}\,,$$

and τ_A the non-primitive translation vector determined by A. The assembly of N^3 elements composed of only pure translations $\{\varepsilon/\boldsymbol{t}\}$, which is called as the translation group $\mathfrak{T}$, is an invariant subgroup of the space group and the factor group (mod $\mathfrak{T}$) is composed of the elements

$$\mathfrak{T}\{A|\tau_A\},\ \mathfrak{T}\{B|\tau_B\},\ \cdots\ \mathfrak{T}\{X|\tau_X\}\,. \quad (1)$$

The order of this factor group is 48 in grey tin and 16 in white tin. We call N^3 elements $\mathfrak{T}\{A|\boldsymbol{\tau}_A\}$ etc as coset and the element $\{A|\boldsymbol{\tau}_A\}$ etc as coset representative (we abbreviate this as C.R.). The group $\mathfrak{G}(\boldsymbol{k})$ of wave number $\boldsymbol{k}$ is composed of the elements in $\mathfrak{G}/\mathfrak{T}$ satisfing the condition

$$\boldsymbol{ak}=\boldsymbol{k}+\boldsymbol{h}\,(\boldsymbol{h}\text{: reciprocal lattice vector})\,. \quad (2)$$

We denote all these as

$$\mathfrak{T}\{\alpha|\tau_\alpha\},\ \mathfrak{T}\{\beta|\tau_\beta\},\cdots\mathfrak{T}\{\partial|\tau_\delta\}\in\mathfrak{G}(\boldsymbol{k})\,,\quad (3)$$

---

* Dr. C. Herring has kindly called to the author's attention a work by O. V. Kovalev and G. Ya. Lyubarskii: Zh. tekh. Fiz. **28** (1958) 1151, which uses some similar concept. Since, however, its translation could not be in hand during the preparation of this paper, the author wishes to discuss of their results in later opportunity.

and we assume the order of the factor group of $\mathfrak{G}(\boldsymbol{k}) (\mathrm{mod}\, \mathfrak{T})$ to be $c(\boldsymbol{k})$.

In the consideration of the representations of $\mathfrak{G}(\boldsymbol{k})$ on the basis of Bloch functions, it is not always necessary to take account of all elements of $\mathfrak{T}$. (i) At certain $\boldsymbol{k}$, just only C. R. s may make a subgroup of $\mathfrak{G}(\boldsymbol{k})$. (ii) On certain symmetry lines in the Brillouin zone the assembly of the product of C. R. and unity or inverse square root of the representation of some translation $T_x=\{\boldsymbol{\varepsilon}|\boldsymbol{t}_x\}$, whichever is determined by the corresponding C.R., may make a group. (iii) At some symmetry points on the zone boundary we can find a group composed of the combination of C.R.s and the elements $\mathfrak{T}_0\{\boldsymbol{\varepsilon}|o\}, \mathfrak{T}_0\{\boldsymbol{\varepsilon}|\boldsymbol{t}_a\}\cdots\mathfrak{T}_0\{\boldsymbol{\varepsilon}|\boldsymbol{t}_d\}$, where $\mathfrak{T}_0$ is the assembly of the translations such that the elements give the representation as $\exp(-2\pi i\boldsymbol{k}\boldsymbol{t})=1$ and where $\{\boldsymbol{\varepsilon}|o\}, \{\boldsymbol{\varepsilon}|\boldsymbol{t}_a\}\cdots \{\boldsymbol{\varepsilon}|\boldsymbol{t}_d\}$ are pure translations generated by the combination between C. R. s, giving essentially different representations. (iv) On certain symmetry lines on the zone boundary there is the case to need the combination of (ii) and (iii). In order to obtain the representations group-theoretically, it is necessary to find such group in $\mathfrak{G}(\boldsymbol{k})$. Since, however, we know that the representation of an element $\{\boldsymbol{\varepsilon}|\boldsymbol{t}\}$ of $\mathfrak{T}$ on the basis of the Bloch function is $\exp(-2\pi i\boldsymbol{k}\boldsymbol{t})$, we can immediately obtain the representations of $\mathfrak{G}(\boldsymbol{k})$ if we can obtain the representations of C. R. s, and then it is not always necessary to construct such groups. This can be made possible by the use of the theory of algebra.

We designate the assembly of the linear combination of C. R. s of $\mathfrak{G}(\boldsymbol{k})$ with coefficients of complex number as $\mathfrak{A}(\boldsymbol{k})$ in which addition of the elements is defined. The multiplication rule between C. R. s is

$$\{\boldsymbol{\alpha}|\boldsymbol{\tau}_\alpha\}\{\boldsymbol{\beta}|\boldsymbol{\tau}_\beta\}=T_{\alpha\beta}\{\boldsymbol{\gamma}|\boldsymbol{\tau}_\gamma\}\,, \tag{4}$$

where $\{\boldsymbol{\gamma}|\boldsymbol{\tau}_\gamma\}$ is also a C. R. of $\mathfrak{G}(\boldsymbol{k})$ and $T_{\alpha\beta}$ is a pure translation determined by $\boldsymbol{\alpha}$ and $\boldsymbol{\beta}$. Since the representation of $\mathfrak{T}$ is a constant times the diagonal matrix, we treat $T_{\alpha\beta}$ not as matrix but as the combination parameter of complex number when considering representation (the unit matrix is absorbed into the matrix of $\{\boldsymbol{\gamma}|\boldsymbol{\tau}_\gamma\}$). Then $\mathfrak{A}(\boldsymbol{k})$ is an algebra of the order $c(\boldsymbol{k})$ over the field of complex number, i. e. $c(\boldsymbol{k})$ C. R. s of $\mathfrak{G}(\boldsymbol{k})$ are the bases of $\mathfrak{A}(\boldsymbol{k})$. (On the definition of algebra and related terminology, see Appendix A). If $T_{\alpha\beta}=1$ for all $\boldsymbol{\alpha}$ and $\boldsymbol{\beta}$, $\mathfrak{A}(\boldsymbol{k})$ is equal to a group ring. We refer to several theorems of algebra necessary for obtaining irreducible representations (we abbreviate as I. R.):[6]

a) If the unit element $\boldsymbol{e}$ of the centrum $\mathfrak{z}(\boldsymbol{k})$ of $\mathfrak{A}(\boldsymbol{k})$ is expressed as

$$\boldsymbol{e}=\sum_{l=1}^{q}\boldsymbol{e}^{(l)},\ \boldsymbol{e}^{(l)}\boldsymbol{e}^{(m)}=\delta_{lm}\boldsymbol{e}^{(l)}\,,$$

(actually the orthogonal idempotents $\boldsymbol{e}^{(l)}$ can be expressed uniquely by making use of $q(\boldsymbol{k})$ bases of the centrum, when the order of $\mathfrak{z}(\boldsymbol{k})$ being assumed to be $q(\boldsymbol{k})$), $\mathfrak{z}(\boldsymbol{k})$ is expressed by the direct sum of $q(\boldsymbol{k})$ orthogonal ideals

$$\mathfrak{z}(\boldsymbol{k})=\sum_{l=1}^{q}\mathfrak{z}^{(l)}(\boldsymbol{k})\,,\ \mathfrak{z}^{(l)}(\boldsymbol{k})\mathfrak{z}^{(m)}(\boldsymbol{k})=\delta_{lm}\mathfrak{z}^{(l)}(\boldsymbol{k})\,.$$

b) $\mathfrak{A}(\boldsymbol{k})$ satisfing a) is decomposed into $q(\boldsymbol{k})$ orthogonal ideals

$$\mathfrak{A}(\boldsymbol{k})=\sum_{l=1}^{q}\mathfrak{A}\boldsymbol{e}^{(l)}=\sum_{l=1}^{q}\mathfrak{A}\mathfrak{z}^{(l)}=\sum_{l=1}^{q}\mathfrak{A}_l(\boldsymbol{k})\,,$$

$$\mathfrak{A}_l(\boldsymbol{k})\mathfrak{A}_m(\boldsymbol{k})=\delta_{lm}\mathfrak{A}_l(\boldsymbol{k})\,.$$

Therefore

$$\mathfrak{A}(\boldsymbol{k})\boldsymbol{e}^{(l)}=\mathfrak{A}_l(\boldsymbol{k})=\boldsymbol{e}^{(l)}\mathfrak{A}(\boldsymbol{k})$$

and then $\boldsymbol{e}^{(l)}$ is also the orthogonal idempotent of $\mathfrak{A}_l(\boldsymbol{k})$. If the order of simple ideal $\mathfrak{A}_l$ is N_l,

$$c(\boldsymbol{k})=\sum_{l=1}^{q}N_l\,.$$

c) From N_l independent elements of $\mathfrak{A}_l(\boldsymbol{k})$, by proper transformation of the bases we can obtain n_l^2 matrixes, the dimension be n_l, such that

$$\boldsymbol{e}_{ii}^{(l)}\boldsymbol{e}_{ii}^{(l)}=\boldsymbol{e}_{ii}^{(l)},\ \boldsymbol{e}_{ij}^{(l)}\boldsymbol{e}_{mk}^{(l)}=\delta_{jm}\boldsymbol{e}_{ik}^{(l)}\,,$$

(Wedderburn's theorem). Therefore $N_l=n_l^2$.

d) The l-th I. R. of any element of $\mathfrak{A}(\boldsymbol{k})$ can be obtained by taking the basis of any one of n_l left ideals of $\mathfrak{A}_l(\boldsymbol{k})$, $\{\boldsymbol{e}_{1j}^{(l)}, \boldsymbol{e}_{2j}^{(l)},\cdots\boldsymbol{e}_{n_lj}^{(l)}\}$ $j=1\sim n_l$, as the representation module:

$$\{\boldsymbol{\alpha}|\boldsymbol{\tau}_\alpha\}\{\boldsymbol{e}_{1j}^{(l)}, \boldsymbol{e}_{2j}^{(l)},\ \cdots\boldsymbol{e}_{n_lj}^{(l)}\}$$

$$=\{\boldsymbol{e}_{1j}^{(l)}, \boldsymbol{e}_{2j}^{(l)},\ \cdots\boldsymbol{e}_{n_lj}^{(l)}\}\begin{pmatrix} a_{11}^{(l)}\cdots a_{1n_l}^{(l)} \\ \vdots \qquad \vdots \\ a_{n_l1}^{(l)}\cdots a_{n_ln}^{(l)} \end{pmatrix},$$

$$\{\boldsymbol{\alpha}|\boldsymbol{\tau}_\alpha\}\in\mathfrak{A}(\boldsymbol{k})\,.$$

The n_l representations occurred from different j are isomorphic. Then it is enough to take only $j=1$. Though the bases $\boldsymbol{e}_{ij}^{(l)}$ satisfing *c*) are not determined uniquely, the representations by different bases are isomorphic.

This procedure to obtain the representations is essentially the same in both cases with and without spin, except that in the former case the multiplication for the elements operating on spin part must be made by the spin representation of the rotation group. In order to construct the representation, the introduction of independent element $\bar{\boldsymbol{E}}$ corresponding to 2π-rotation is unnecessary in algebraic theory. Then the order of the algebra we must treat is at most 24 (by making use of direct product) even in diamond lattice.

In order to calculate the electronic states, we construct the basis functions belonging to the irreducible representations. This is easily performed by means of the representation module $\{\boldsymbol{e}_{11}^{(l)}, \boldsymbol{e}_{21}^{(l)}, \cdots \boldsymbol{e}_{n_l 1}^{(l)}\}$. For example, if we wish to obtain the tight binding Bloch functions belonging to the representation X_l, we operate $\boldsymbol{e}_{i1}(X_l)$ to the Bloch function of type $u, w, \sigma (u = s, p, d, \cdots; w = s_1, s_2, \cdots s_n,$ n the number of sublattices; $\sigma = \pm$, i.e. two spin states):[7]

$$\psi_i(X_l) = \boldsymbol{e}_{i1}(X_l)\chi_{u,w,\sigma}(\boldsymbol{k}) \quad i = 1 \cdots n_l \, .$$

ψ_i corresponding to different i are mutually orthogonal and we obtain n_l sets of functions, corresponding to n_l fold degeneracy. Of course, it is enough to take up only one set. In other type of approximation, we can do similarly. In this paper, however, we do not try to apply our results in concrete calculation.

§ 2. The Symmetry Operations in White Tin

White tin lattice has the space group $D_{4h}^{19} \frac{4_1}{a} \frac{2}{m} \frac{2}{d}$ symmetry. The lattice is composed of two sublattices and one atom is surrounded by four nearest neighbours (Fig. 1). We choose a four fold rotation reflection axis as z-axis and bisect lines of two binary axes as x- and y-axis. The primitive translations are

$$T_1 = (x+a, y+a, z-c) \, ,$$
$$T_2 = (x+a, y-a, z+c) \, , \qquad (5)$$
$$T_3 = (x-a, y+a, z+c) \, .$$

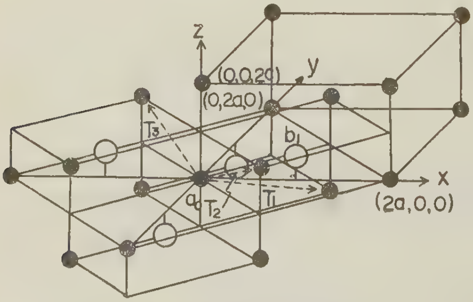

Fig. 1. White tin lattice.

The values of a and c are

$$2a = 5.82 \text{ Å}, \ 2c = 3.18 \text{ Å} \, .$$

C. R. s of $\mathfrak{G}$ are 16 elements as follows:

(i) $\boldsymbol{E}$ is the unit element,

(ii) $\boldsymbol{C}_2$ is the rotation by π about z-axis,

(iii) $\boldsymbol{S}_4^+$ and $\boldsymbol{S}_4^-$ are the rotations by $\pm\pi/2$ about z-axis followed by the reflection at the plane through the origin and perpendicular to the rotation axis,

(iv) $\boldsymbol{U}_{xy}$ and $\boldsymbol{U}_{x\bar{y}}$ are the rotations by π about the bisecting lines between x-, y-axis and x-, $\bar{y}$-axis respectively, i. e. about the binary axes,

(v) $\boldsymbol{M}_x$ and $\boldsymbol{M}_y$ are the mirror planes which contain x-, z-axis and y-, z-axis respectively,

(vi) $\boldsymbol{J}$ is the inversion at the origin followed by the non-primitive translation $\overrightarrow{a_0 b_1} \equiv \tau(a, 0, c/2)$,

(vii) $\boldsymbol{JC}_2$, (viii) $\boldsymbol{JS}_4^+$ and $\boldsymbol{JS}_4^-$, (ix) $\boldsymbol{JU}_{xy}$ and $\boldsymbol{JU}_{x\bar{y}}$, (x) $\boldsymbol{JM}_x$ and $\boldsymbol{JM}_y$.

The operations (i)$\sim$(v) are represented by $\{A|0\}$ and the operations (vi)$\sim$(x) by $\{A|\tau\}$. By $\{A|0\}$ and $\{A|\tau\}$, the atom of a-site is transformed into an atom of a-site and that of b-site respectively. The multiplication of some element $\boldsymbol{P}$ in (i)$\sim$(v) and $\boldsymbol{JQ}$ in (vi)$\sim$(x) is

$$\boldsymbol{P} \cdot \boldsymbol{JQ} = \{\varepsilon | p\tau - \tau\} \boldsymbol{J} \cdot \boldsymbol{PQ} \equiv T(P) \boldsymbol{J} \cdot \boldsymbol{PQ} \, , \quad (6)$$

and also the multiplication of $\boldsymbol{JP}$ and $\boldsymbol{JQ}$ is

$$\boldsymbol{JP} \cdot \boldsymbol{JQ} = \{\varepsilon | -p\tau + \tau\} \boldsymbol{PQ} \equiv T^{-1}(P) \boldsymbol{PQ} \, . \quad (6)'$$

Therefore, if we know only the multiplication rules between $\boldsymbol{P}$ and $\boldsymbol{Q}$ and also $\boldsymbol{P}$ and $\boldsymbol{J}$, we can obtain immediately the multiplication between all other elements by taking account of $T(P)$ and $T^{-1}(P)$. The result is shown in Table I.

By using (5), we can obtain primitive reciprocal lattice vectors

$$b_1 = \left(\frac{1}{2a}, \frac{1}{2a}, 0\right) ,$$
$$b_2 = \left(\frac{1}{2a}, 0, \frac{1}{2c}\right) , \qquad (7)$$
$$b_3 = \left(0, \frac{1}{2a}, \frac{1}{2c}\right) .$$

Table I. The multiplication table for the symmetry elements in ordinary space.

	E	C_2	S_4^+	S_4^-	U_{xy}	$U_{x\bar{y}}$	M_x	M_y	J
E	E	C_2	S_4^+	S_4^-	U_{xy}	$U_{x\bar{y}}$	M_x	M_y	J
C_2	C_2	E	S_4^-	S_4^+	$U_{x\bar{y}}$	U_{xy}	M_y	M_x	$T_1^{-1}T_2^{-1}JC_2$
S_4^+	S_4^+	S_4^-	C_2	E	M_y	M_x	U_{xy}	$U_{x\bar{y}}$	$T_2^{-1}JS_4^+$
S_4^-	S_4^-	S_4^+	E	C_2	M_x	M_y	$U_{x\bar{y}}$	U_{xy}	$T_1^{-1}T_2^{-1}T_3^{-1}JS_4^-$
U_{xy}	U_{xy}	$U_{x\bar{y}}$	M_r	M_y	E	C_2	S_4^+	S_4^-	$T_2^{-1}JU_{xy}$
$U_{x\bar{y}}$	$U_{x\bar{y}}$	U_{xy}	M_y	M_x	C_2	E	S_4^-	S_4^+	$T_1^{-1}T_2^{-1}T_3^{-1}JU_{x\bar{y}}$
M_x	M_x	M_y	$U_{x\bar{y}}$	U_{xy}	S_4^-	S_4^+	E	C_2	JM_x
M_y	M_y	M_x	U_{xy}	$U_{x\bar{y}}$	S_4^+	S_4^-	C_2	E	$T_1^{-1}T_2^{-1}JM_y$

Table II. The coset representatives of $\mathfrak{G}(\boldsymbol{k})$ (i.e. the bases of $\mathfrak{A}(\boldsymbol{k})$) and the representations of primitive translations at symmetry points, lines, and planes.
$p=\exp(-2\pi i k_x a)$, $q=\exp(-2\pi i k_y a)$, and $r=\exp(-2\pi i k_z c)$.

Symbol	Components of $\boldsymbol{k}$			Representations of T			Bases of $\mathfrak{A}(\boldsymbol{k})$
	k_x	k_y	k_z	T_1	T_2	T_3	
Γ	0	0	0	1	1	1	all 16 elements
H	$1/2a$	0	0	-1	-1	-1	all 16 elements
X	$1/4a$	$1/4a$	0	-1	1	1	E, C_2, U_{xy}, $U_{x\bar{y}}$, J, JC_2, JU_{xy}, $JU_{x\bar{y}}$
W	$1/4a$	$1/4a$	$1/4c$	$-i$	$-i$	$-i$	E, C_2, S_4^+, S_4^-, JU_{xy}, $JU_{x\bar{y}}$, JM_x, JM_y
V	0	0	k_z	r^*	r	r	E, C_2, M_x, M_y, JS_4^+, JS_4^-, JU_{xy}, $JU_{x\bar{y}}$
B	$1/2a$	0	k_z	$-r^*$	$-r$	$-r$	E, C_2, M_x, M_y, JS_4^+, JS_4^-, JU_{xy}, $JU_{x\bar{y}}$
Δ	k_x	k_x	0	p^2	1	1	E, U_{xy}, $JU_{x\bar{y}}$, JC_2
Σ	k_x	0	0	p	p	p^*	E, M_x, JM_y, JC_2
Z	$1/4a$	$1/4a$	k_z	$-r^*$	r	r	E, C_2, JU_{xy}, $JU_{x\bar{y}}$
Z'	k_x	$(1/2a)-k_x$	0	-1	$-p^2$	$-p^{*2}$	E, $U_{x\bar{y}}$, JC_2, JU_{xy}
L	$1/4a$	0	$1/4c$	1	-1	1	E, M_x, J, JM_x
Q	$1/4a$	k_y	$1/4c$	q	$-q^*$	q	E, JM_x
P	k_x	0	k_z	pr^*	pr	p^*r	E, M_x
S	k_x	k_y	0	pq	pq^*	p^*q	E, JC_2
R	k_x	k_x	k_z	p^2r^*	r	r	E, $JU_{x\bar{y}}$
T	k_x	$(1/2a)-k_x$	k_z	$-r^*$	$-p^2r$	$-p^{*2}r$	E, JU_{xy}

The general vector $\boldsymbol{h}$ is

$$\boldsymbol{h}=n_1\boldsymbol{b}_1+n_2\boldsymbol{b}_2+n_3\boldsymbol{b}_3\ .$$

Thus we can obtain first Brillouin zone (Fig. 2) surrounded by the planes of the types (100) and (1$\bar{1}$0). In Table II we give the bases of $\mathfrak{A}(\boldsymbol{k})$ and the representations of T_1, T_2 and T_3. Before we close this section, we show the value of $\boldsymbol{k}$ of the points A and C (though these are not special points):

$$A=\left(0,0,\frac{1}{4c}\left(1+\frac{c^2}{a^2}\right)\right),$$

$$C=\left(\frac{1}{2a},0,\frac{1}{4c}\left(1-\frac{c^2}{{}^2a}\right)\right).$$

§ 3. The Representations for Algebras of k-vectors. Case without Spin

Following to the principle outlined in § 1,

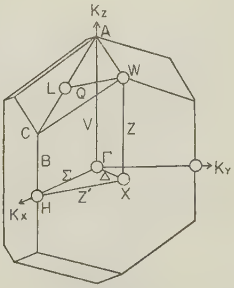

Fig. 2. First Brillouin zone for white tin lattice.

we calculate the representations of algebra $\mathfrak{A}(\boldsymbol{k})$ of wave number $\boldsymbol{k}$. In this section we concern with the spinless case, then the structure of $\mathfrak{A}(\boldsymbol{k})$ can be seen by combining Table I and II.

We begin with the point Γ. In this point every translations give the same representation as the identity. Then $\mathfrak{A}(\Gamma)$ is equivalent to the direct product of subalgebras {(i)∼(v)} and $\{\boldsymbol{E}, \boldsymbol{J}\}$. The algebra $\mathfrak{A}'(\Gamma)$ composed of (i)∼(v) has the centrum, the bases of which being the following elements

$$\boldsymbol{E},\ \boldsymbol{C}_2,\ (\boldsymbol{S}_4{}^+ + \boldsymbol{S}_4{}^-),\ (\boldsymbol{U}_{xy} + \boldsymbol{U}_{x\bar{y}}),\ (\boldsymbol{M}_x + \boldsymbol{M}_y)\ . \tag{8}$$

Then we should have four I. R. of one dimension and one I. R. of two dimensions. The unit elements $\boldsymbol{e}^{(l)}$ of five orthogonal ideals are

$$\begin{aligned}
\boldsymbol{e}^{(1)} &= \frac{1}{8}\{\boldsymbol{E} + \boldsymbol{C}_2 + (\boldsymbol{S}_4{}^+ + \boldsymbol{S}_4{}^-) + (\boldsymbol{U}_{xy} + \boldsymbol{U}_{x\bar{y}}) \\
&\qquad + (\boldsymbol{M}_x + \boldsymbol{M}_y)\}\ , \\
\boldsymbol{e}^{(2)} &= \frac{1}{8}\{\boldsymbol{E} + \boldsymbol{C}_2 + (\boldsymbol{S}_4{}^+ + \boldsymbol{S}_4{}^-) - (\boldsymbol{U}_{xy} + \boldsymbol{U}_{x\bar{y}}) \\
&\qquad - (\boldsymbol{M}_x + \boldsymbol{M}_y)\}\ , \\
\boldsymbol{e}^{(3)} &= \frac{1}{8}\{\boldsymbol{E} + \boldsymbol{C}_2 - (\boldsymbol{S}_4{}^+ + \boldsymbol{S}_4{}^-) + (\boldsymbol{U}_{xy} + \boldsymbol{U}_{x\bar{y}}) \\
&\qquad - (\boldsymbol{M}_x + \boldsymbol{M}_y)\}\ , \\
\boldsymbol{e}^{(4)} &= \frac{1}{8}\{\boldsymbol{E} + \boldsymbol{C}_2 - (\boldsymbol{S}_4{}^+ + \boldsymbol{S}_4{}^-) - (\boldsymbol{U}_{xy} + \boldsymbol{U}_{x\bar{y}}) \\
&\qquad + (\boldsymbol{M}_x + \boldsymbol{M}_y)\}\ , \\
\boldsymbol{e}^{(5)} &= \frac{1}{2}\{\boldsymbol{E} - \boldsymbol{C}_2\}\ ,
\end{aligned} \tag{9}$$

where $\boldsymbol{e}^{(5)}$ gives two dimensional representation. From four independent elements of ideal $\mathfrak{A}'(\Gamma)\boldsymbol{e}^{(5)}$, we construct new bases of the ideal

$$\begin{aligned}
\left.\begin{matrix}\boldsymbol{e}^{(5)}_{11} \\ \boldsymbol{e}^{(5)}_{22}\end{matrix}\right\} &= \frac{1}{4}\{\boldsymbol{E} - \boldsymbol{C}_2 \pm (\boldsymbol{M}_x - \boldsymbol{M}_y)\}\ , \\
\left.\begin{matrix}\boldsymbol{e}^{(5)}_{21} \\ \boldsymbol{e}^{(5)}_{12}\end{matrix}\right\} &= \frac{1}{4}\{\boldsymbol{U}_{xy} - \boldsymbol{U}_{x\bar{y}} \pm (\boldsymbol{S}_4{}^+ - \boldsymbol{S}_4{}^-)\}\ .
\end{aligned} \tag{10}$$

It is easily seen that these equations satisfy the theorem (c) in § 1. The representation of $\mathfrak{A}'(\Gamma)$ is obtained by theorem (d) in § 1. On the other hand algebra $\{\boldsymbol{E}, \boldsymbol{J}\}$ has two idempotents

$$\left.\begin{matrix}\boldsymbol{e}^{(1)} \\ \boldsymbol{e}^{(2)}\end{matrix}\right\} = \frac{1}{2}(\boldsymbol{E} \pm \boldsymbol{J})\ . \tag{11}$$

Final representation is the direct product of two I. R. of subalgebras. This and other important results are listed in the table in next section and Appendix B and C.

The point H has the same C. R. s as the point Γ. The translations, however, give distinct representations. Because of it, the structure of the centrum $\mathfrak{z}(H)$ becomes essentially different from that of $\mathfrak{z}(\Gamma)$. The elements commutative to all elements of $\mathfrak{A}(H)$ are the following four:

$$\boldsymbol{E},\ \boldsymbol{C}_2,\ \boldsymbol{M}_x + \boldsymbol{M}_y,\ \boldsymbol{J}\boldsymbol{M}_x - \boldsymbol{J}\boldsymbol{M}_y\ . \tag{12}$$

Then we obtain four orthogonal idempotents

$$\begin{aligned}
\left.\begin{matrix}\boldsymbol{e}({}^2H_1) \\ \boldsymbol{e}({}^2H_2)\end{matrix}\right\} &= \frac{1}{4}(\boldsymbol{E} + \boldsymbol{C}_2 \pm \boldsymbol{M}_x \pm \boldsymbol{M}_y)\ , \\
\left.\begin{matrix}\boldsymbol{e}({}^2H_3) \\ \boldsymbol{e}({}^2H_4)\end{matrix}\right\} &= \frac{1}{4}(\boldsymbol{E} - \boldsymbol{C}_2 \pm \boldsymbol{J}\boldsymbol{M}_x \mp \boldsymbol{J}\boldsymbol{M}_y)\ .
\end{aligned} \tag{13}$$

All these give two dimensional representations. We can calculate new bases $\boldsymbol{e}_{ij}({}^2H_i)$ from each ideal $\mathfrak{A}(\boldsymbol{k})\boldsymbol{e}({}^2H_i)$, and then I. R.

In other points, lines and planes, the method is the same and we give only the bases of centrums $\mathfrak{z}$, from which we can obtain orthogonal idempotents of each centrum, and and then bases of representations:

$$\begin{aligned}
&\mathfrak{z}(X) : \{\boldsymbol{E},\ \boldsymbol{U}_{xy}\}\ , \\
&\mathfrak{z}(W) : \{\boldsymbol{E},\ (\boldsymbol{S}_4{}^+ + i\boldsymbol{S}_4{}^-)\}\ , \\
&\mathfrak{z}(V) : \{\boldsymbol{E},\ \boldsymbol{C}_2,\ (\boldsymbol{M}_x + \boldsymbol{M}_y),\ (\boldsymbol{J}\boldsymbol{S}_4{}^+ + \boldsymbol{J}\boldsymbol{S}_4{}^-), \\
&\qquad (\boldsymbol{J}\boldsymbol{U}_{xy} + \boldsymbol{J}\boldsymbol{U}_{x\bar{y}})\}\ , \\
&\mathfrak{z}(B) : \{\boldsymbol{E},\ \boldsymbol{C}_2,\ (\boldsymbol{M}_x + \boldsymbol{M}_y),\ (\boldsymbol{J}\boldsymbol{S}_4{}^+ + \boldsymbol{J}\boldsymbol{S}_4{}^-), \\
&\qquad (\boldsymbol{J}\boldsymbol{U}_{xy} + \boldsymbol{J}\boldsymbol{U}_{x\bar{y}})\}\ , \\
&\mathfrak{z}(\varDelta) : \{\boldsymbol{E},\ \boldsymbol{U}_{xy},\ \boldsymbol{J}\boldsymbol{U}_{x\bar{y}},\ \boldsymbol{J}\boldsymbol{C}_2\} \equiv \mathfrak{A}(\varDelta)\ , \\
&\mathfrak{z}(\varSigma) : \{\boldsymbol{E},\ \boldsymbol{M}_x,\ \boldsymbol{J}\boldsymbol{M}_y,\ \boldsymbol{J}\boldsymbol{C}_2\} \equiv \mathfrak{A}(\varSigma)\ , \\
&\mathfrak{z}(Z) : \{\boldsymbol{E}\}\ , \\
&\mathfrak{z}(Z') : \{\boldsymbol{E}\}\ , \\
&\mathfrak{z}(L) : \{\boldsymbol{E},\ \boldsymbol{M}_x,\ \boldsymbol{J},\ \boldsymbol{J}\boldsymbol{M}_x\} \equiv \mathfrak{A}(L)\ , \\
&\mathfrak{z}(Q) : \{\boldsymbol{E},\ \boldsymbol{J}\boldsymbol{M}_x\} \equiv \mathfrak{A}(Q)\ , \\
&\mathfrak{z}(P) : \{\boldsymbol{E},\ \boldsymbol{M}_x\} \equiv \mathfrak{A}(P)\ , \\
&\mathfrak{z}(S) : \{\boldsymbol{E},\ \boldsymbol{J}\boldsymbol{C}_2\} \equiv \mathfrak{A}(S)\ , \\
&\mathfrak{z}(R) : \{\boldsymbol{E},\ \boldsymbol{J}\boldsymbol{U}_{x\bar{y}}\} \equiv \mathfrak{A}(R)\ , \\
&\mathfrak{z}(T) : \{\boldsymbol{E},\ \boldsymbol{J}\boldsymbol{U}_{xy}\} \equiv \mathfrak{A}(T)\ .
\end{aligned} \tag{14}$$

We see the commutation relation of certain elements $\{\boldsymbol{\alpha}|\boldsymbol{\tau}_\alpha\}$ and $\sum_\beta\{\boldsymbol{\beta}|\boldsymbol{\tau}_\beta\}$, where all $\boldsymbol{\tau}_\beta$ is assumed to be the same in the summation, of $\mathfrak{A}(\boldsymbol{k})$ corresponding to interior points of the Brillouin zone.

$$\{\boldsymbol{\alpha}|\boldsymbol{\tau}_\alpha\}\cdot\sum_\beta\{\boldsymbol{\beta}|\boldsymbol{\tau}_\beta\}=\sum_\beta\{\boldsymbol{\varepsilon}|\boldsymbol{\alpha}\boldsymbol{\tau}_\beta+\boldsymbol{\tau}_\alpha-\boldsymbol{\tau}_{\alpha\beta}\}\cdot\{\boldsymbol{\alpha}\boldsymbol{\beta}|\boldsymbol{\tau}_{\alpha\beta}\}\,, \tag{15a}$$

$$\sum_\beta\{\boldsymbol{\beta}|\boldsymbol{\tau}_\beta\}\cdot\{\boldsymbol{\alpha}|\boldsymbol{\tau}_\alpha\}=\sum_\beta\{\boldsymbol{\varepsilon}|\boldsymbol{\beta}\boldsymbol{\tau}_\alpha+\boldsymbol{\tau}_\beta-\boldsymbol{\tau}_{\alpha\beta}\}\{\boldsymbol{\beta}\boldsymbol{\alpha}|\boldsymbol{\tau}_{\alpha\beta}\}\,, \tag{15b}$$

where $\boldsymbol{\tau}_{\alpha\beta}$ is 0 or $\boldsymbol{\tau}$, whichever is determined by the element $\boldsymbol{\alpha}\boldsymbol{\beta}_0$, where $\boldsymbol{\beta}_0$ being any one of the elements in the summation. In other word it is assumed that $\{\boldsymbol{\alpha}\boldsymbol{\beta}|\boldsymbol{\tau}_{\alpha\beta}\}$ and $\{\boldsymbol{\beta}\boldsymbol{\alpha}|\boldsymbol{\tau}_{\alpha\beta}\}$ are the bases of $\mathfrak{A}(\boldsymbol{k})$. Since $\{\boldsymbol{\varepsilon}|\boldsymbol{\alpha}\boldsymbol{\tau}_\beta+\boldsymbol{\tau}_\alpha-\boldsymbol{\tau}_{\alpha\beta}\}$ and $\{\boldsymbol{\varepsilon}|\boldsymbol{\beta}\boldsymbol{\tau}_\alpha+\boldsymbol{\tau}_\beta-\boldsymbol{\tau}_{\alpha\beta}\}$ give the same representation $\exp(-2\pi i\boldsymbol{k}(\boldsymbol{\tau}_\alpha+\boldsymbol{\tau}_\beta-\boldsymbol{\tau}_{\alpha\beta}))$, $\{\boldsymbol{\alpha}|\boldsymbol{\tau}_\alpha\}\cdot\sum_\beta\{\boldsymbol{\beta}|\boldsymbol{\tau}_\beta\}$ and $\sum\{\boldsymbol{\beta}|\boldsymbol{\tau}_\beta\}\cdot\{\boldsymbol{\alpha}|\boldsymbol{\tau}_\alpha\}$ are equivalent, if

$$\boldsymbol{\alpha}\cdot\sum_\beta\boldsymbol{\beta}=\sum_\beta\boldsymbol{\beta}\cdot\boldsymbol{\alpha}\,. \tag{16}$$

This fact means that the structure of $\mathfrak{z}(\boldsymbol{k})$ is determined by only the rotational part. Since $\{\boldsymbol{\alpha}|\boldsymbol{\tau}_\alpha\}=\{\boldsymbol{\varepsilon}|\boldsymbol{\tau}_\alpha\}\{\boldsymbol{\alpha}|o\}$, the representation of any element $\{\boldsymbol{\alpha}|\boldsymbol{\tau}_\alpha\}$ of $\mathfrak{A}(\boldsymbol{k})$ is expressed by the product of the representation of $\{\boldsymbol{\alpha}|o\}$ and $\exp(-2\pi i\boldsymbol{k}\boldsymbol{\tau}_\alpha)$. This fact was derived group-theoretically by Koster[8]. $\sum_\beta\boldsymbol{\beta}$ satisfing (16) is the summation of the elements belonging to some class of the point group. Above result is unchanged even when considering the spin. In the interior points of Brillouin zone, the labour for obtaining the representations is almost the same in group-theoretical and present methods, because the procedure to classify into classes in group theory and that to search for the bases of the centrum in algebraic theory need nearly the same labour. At the points on the Brillouin zone boundary, however, present method is very often superior to group theory, as we can see if we calculate group-theoretically the representation, for example, of the point W.

§ 4. The Representations. Case with Spin

In this section we take account of the spin. Since spin space and ordinary space are distinct, the effect to the spatial part due to symmetry operations is the same as expressed in the previous section. Since the spin part is invariant by the translation, we may consider for the operations on spin part only that of the point group to which the space group belongs. These rotational parts are expressed by the spin representation of the rotation group. For example the rotations by θ about x-, y- and z-axis are expressed by

$$R_x(\theta)=\begin{pmatrix}\cos\dfrac{\theta}{2} & -i\cdot\sin\dfrac{\theta}{2}\\ -i\cdot\sin\dfrac{\theta}{2} & \cos\dfrac{\theta}{2}\end{pmatrix},$$

$$R_y(\theta)=\begin{pmatrix}\cos\dfrac{\theta}{2} & -\sin\dfrac{\theta}{2}\\ \sin\dfrac{\theta}{2} & \cos\dfrac{\theta}{2}\end{pmatrix},$$

$$R_z(\theta)=\begin{pmatrix}\exp\left(-i\,\dfrac{\theta}{2}\right) & 0\\ 0 & \exp\left(i\,\dfrac{\theta}{2}\right)\end{pmatrix}.$$

Improper rotation is expressed by taking the unit matrix for the inversion. The multiplication between spin representations gives clearly the same results as that of usual representations of three dimensional rotation group except that negative sign occurs because of two valuedness of spin representation. The result for the multiplication between C. R. s is shown in Table III.

As was expressed in § 1, we take account of only 16 C. R. s explicitly and do not make usual enlargement of algebra by adding $R(2\pi)$. Therefore the representations occured in this section are essentially different from those in the previous section. The structure of $\mathfrak{A}(\boldsymbol{k})$ can be seen by combining Table II and III. The bases of each centrum of $\mathfrak{A}(\boldsymbol{k})$ are

$$\begin{aligned}
&\mathfrak{z}(\Gamma):\ \{\boldsymbol{E},\,(\boldsymbol{S}_4^{+}+\boldsymbol{S}_4^{-}),\,\boldsymbol{J},\,(\boldsymbol{JS}_4^{+}+\boldsymbol{JS}_4^{-})\}\,,\\
&\mathfrak{z}(H):\ \{\boldsymbol{E}\}\,,\\
&\mathfrak{z}(X):\ \{\boldsymbol{E},\,\boldsymbol{JU}_{xy}\}\,,\\
&\mathfrak{z}(W):\ \{\boldsymbol{E},\,\boldsymbol{C}_2,\,(\boldsymbol{S}_4^{+}+i\boldsymbol{S}_4^{-}),\,(\boldsymbol{JU}_{xy}+i\boldsymbol{JU}_{x\bar{y}})\,,\\
&\qquad\qquad(\boldsymbol{JM}_x+i\boldsymbol{JM}_y)\}\,,\\
&\mathfrak{z}(V):\ \{\boldsymbol{E},\,(\boldsymbol{JS}_4^{+}+\boldsymbol{JS}_4^{-})\}\,,\\
&\mathfrak{z}(B):\ \{\boldsymbol{E},\,(\boldsymbol{JS}_4^{+}+\boldsymbol{JS}_4^{-})\}\,,\\
&\mathfrak{z}(\Delta):\ \{\boldsymbol{E}\}\,,\\
&\mathfrak{z}(\Sigma):\ \{\boldsymbol{E}\}\,,\\
&\mathfrak{z}(Z):\ \{\boldsymbol{E},\,\boldsymbol{C}_2,\,\boldsymbol{JU}_{xy},\,\boldsymbol{JU}_{x\bar{y}}\}\equiv\mathfrak{A}(Z)\,, \qquad\qquad (17)\\
&\mathfrak{z}(Z'):\ \{\boldsymbol{E},\,\boldsymbol{U}_{x\bar{y}},\,\boldsymbol{JU}_{xy},\,\boldsymbol{JC}_2\}\equiv\mathfrak{A}(Z')\,,\\
&\mathfrak{z}(L):\ \{\boldsymbol{E},\,\boldsymbol{M}_x,\,\boldsymbol{J},\,\boldsymbol{JM}_x\}\equiv\mathfrak{A}(L)\,,\\
&\mathfrak{z}(Q):\ \{\boldsymbol{E},\,\boldsymbol{JM}_x\}\equiv\mathfrak{A}(Q)\,,\\
&\mathfrak{z}(P):\ \{\boldsymbol{E},\,\boldsymbol{M}_x\}\equiv\mathfrak{A}(P)\,,\\
&\mathfrak{z}(S):\ \{\boldsymbol{E},\,\boldsymbol{JC}_2\}\equiv\mathfrak{A}(S)\,,\\
&\mathfrak{z}(R):\ \{\boldsymbol{E},\,\boldsymbol{JU}_{x\bar{y}}\}\equiv\mathfrak{A}(R)\,,\\
&\mathfrak{z}(T):\ \{\boldsymbol{E},\,\boldsymbol{JU}_{xy}\}\equiv\mathfrak{A}(T)\,.
\end{aligned}$$

The bases of the representation modules of each $\mathfrak{A}(\boldsymbol{k})$ are given in Appendix C. When $\mathfrak{A}(\boldsymbol{k})$ and $\mathfrak{z}(\boldsymbol{k})$ are isomorphic, all representations are one dimensional. These one dimensional representations, however, are degenerated by time reversal symmetry because of the existence of inversion symmetry in white tin. For a convenience of the inspection and for the relation to Appendixes, we show characters χ in Table IV. The so-called single and double group representations are divided into two parts by a line. In the table the decomposition of the representations due to the addition of spin and the degeneracy due to time reversal symmetry (we abbreviate as T.R.S.) are also shown.

§ 5. Relation between White Tin and Grey Tin

As is well known, tin shows allotropic change in crystal structure. Grey tin is unstable at the temperatures above 18°C. This temperature of the transformation is excep-

Table III. Multiplication table in the case with spin.

	E	C_2	S_4^+	S_4^-	U_{xy}	$U_{x\bar{y}}$	M_x	M_y	J
E	E	C_2	S_4^+	S_4^-	U_{xy}	$U_{x\bar{y}}$	M_x	M_y	J
C_2	C_2	$-E$	S_4^-	$-S_4^+$	$-U_{x\bar{y}}$	U_{xy}	$-M_y$	M_x	$T_1^{-1}T_2^{-1}JC_2$
S_4^+	S_4^+	S_4^-	$-C_2$	E	M_y	$-M_x$	U_{xy}	$U_{x\bar{y}}$	$T_2^{-1}JS_4^+$
S_4^-	S_4^-	$-S_4^+$	E	C_2	M_x	M_y	$-U_{x\bar{y}}$	U_{xy}	$T_1^{-1}T_2^{-1}T_3^{-1}JS_4^-$
U_{xy}	U_{xy}	$U_{x\bar{y}}$	M_x	M_y	$-E$	$-C_2$	$-S_4^+$	$-S_4^-$	$T_2^{-1}JU_{xy}$
$U_{x\bar{y}}$	$U_{x\bar{y}}$	$-U_{xy}$	M_y	$-M_x$	C_2	$-E$	S_4^-	$-S_4^+$	$T_1^{-1}T_2^{-1}T_3^{-1}JU_{x\bar{y}}$
M_x	M_x	M_y	$-U_{x\bar{y}}$	U_{xy}	$-S_4^-$	S_4^+	$-E$	$-C_2$	JM_x
M_y	M_y	$-M_x$	U_{xy}	$U_{x\bar{y}}$	$-S_4^+$	$-S_4^-$	C_2	$-E$	$T_1^{-1}T_2^{-1}JM_y$

Table IV. Characters of the representations for the bases of $\mathfrak{A}(\boldsymbol{k})$ in the cases without and with spin.

a) Γ : Upper sign for Γ_l and lower sign for Γ_l'.

	E	C_2	$S_4^+ S_4^-$	$U_{xy}U_{x\bar{y}}$	M_xM_y	J	JC_2	$JS_4^+JS_4^-$	$JU_{xy}JU_{x\bar{y}}$	JM_xJM_y
Γ_1, Γ_1'	1	1	1	1	1	±1	±1	±1	±1	±1
Γ_2, Γ_2'	1	1	1	−1	−1	±1	±1	±1	∓1	∓1
Γ_3, Γ_3'	1	1	−1	1	−1	±1	±1	∓1	±1	∓1
Γ_4, Γ_4'	1	1	−1	−1	1	±1	±1	∓1	∓1	±1
${}^2\Gamma_5, {}^2\Gamma_5'$	2	−2	0	0	0	±2	∓2	0	0	0
Γ_6, Γ_6'	2	0	$\sqrt{2}$	0	0	±2	0	$\pm\sqrt{2}$	0	0
Γ_7, Γ_7'	2	0	$-\sqrt{2}$	0	0	±2	0	$\mp\sqrt{2}$	0	0

Γ_l	$\Gamma_1(\Gamma_1')$	$\Gamma_2(\Gamma_2')$	$\Gamma_3(\Gamma_3')$	$\Gamma_4(\Gamma_4')$	${}^2\Gamma_5({}^2\Gamma_5')$
$\Gamma_l \times D_{1/2}$	$\Gamma_6(\Gamma_6')$	$\Gamma_6(\Gamma_6')$	$\Gamma_7(\Gamma_7')$	$\Gamma_7(\Gamma_7')$	$\Gamma_6+\Gamma_7(\Gamma_6'+\Gamma_7')$

b) H

	E	C_2	M_x	M_y	JM_x	JM_y	all others
${}^2H_1$	2	2	2	2	0	0	0
${}^2H_2$	2	2	−2	−2	0	0	0
${}^2H_3$	2	−2	0	0	2	−2	0
${}^2H_4$	2	−2	0	0	−2	2	0
${}^4H_5$	4	0	0	0	0	0	0

H_l	${}^2H_l \quad l=1\sim4$
$H_l \times D_{1/2}$	${}^4H_5$

c) X

	E	U_{xy}	JU_{xy}	all others
${}^2X_1$	2	2	0	0
${}^2X_2$	2	−2	0	0
X_3	2	0	$2i$	0
X_4	2	0	$-2i$	0

X_l	${}^2X_l \quad l=1, 2$
$X_l \times D_{1/2}$	X_3+X_4

d) W: $\omega = \exp\{i(\pi/4)\}$.

	E	C_2	S_4^+	S_4^-	JU_{xy}	$JU_{x\bar{y}}$	JM_x	JM_y
$^2W_1$	2	0	$1+i$	$1-i$	0	0	0	0
$^2W_2$	2	0	$-(1+i)$	$-(1-i)$	0	0	0	0
$^1W_3$	1	$-i$	ω	ω^*	ω	ω^*	i	1
$^1W_4$	1	$-i$	$-\omega$	$-\omega^*$	$-\omega$	$-\omega^*$	i	1
$^1W_5$	1	$-i$	ω	ω^*	$-\omega$	$-\omega^*$	$-i$	-1
$^1W_6$	1	$-i$	$-\omega$	$-\omega^*$	ω	ω^*	$-i$	-1
W_7	2	$2i$	0	0	0	0	0	0

W_l	$^2W_1$	$^2W_2$
$W_l \times D_{1/2}$	$(^1W_3 + {}^1W_5) + W_7$	$(^1W_4 + {}^1W_6) + W_7$

$^1W_3$, $^1W_5$ and $^1W_4$, $^1W_6$ are respectively degenerated by T.R.S.

e) V, B : $p = \exp(-\pi i k_z c)$ for $X = V$ and $p = -i \cdot \exp(-\pi i k_z c)$ for B.

	E	C_2	$M_x M_y$	$JS_4^+ JS_4^-$	$JU_{xy} JU_{x\bar{y}}$
X_1	1	1	1	p	p
X_2	1	1	-1	p	$-p$
X_3	1	1	-1	$-p$	p
X_4	1	1	1	$-p$	$-p$
$^2X_5$	2	-2	0	0	0
X_6	2	0	0	$\sqrt{2}\,p$	0
X_7	2	0	0	$-\sqrt{2}\,p$	0

X_l	X_1	X_2	X_3	X_4	$^2X_5$
$X_l \times D_{1/2}$	X_6	X_6	X_7	X_7	$X_6 + X_7$

f) Σ, Δ : $p = \exp(-2\pi i k_x a)$ for $X = \Sigma, \Delta$

Σ	E	M_x	JC_2	JM_y
Δ	E	U_{xy}	JC_2	$JU_{x\bar{y}}$
X_1	1	1	p	p
X_2	1	-1	p	$-p$
X_3	1	-1	$-p$	p
X_4	1	1	$-p$	$-p$
X_5	2	0	0	0

X_l	X_l $l = 1 \sim 4$
$X_l \times D_{1/2}$	X_5

g) Z, Z' : $p = \exp(-\pi i k_z c)$ for $X = Z$ and $p = \exp(-2\pi i k_x a)$ for Z'.

Z	E	C_2	JU_{xy}	$JU_{x\bar{y}}$
Z'	E	$U_{x\bar{y}}$	JC_2	JU_{xy}
$^2X_1$	2	0	0	0
$^1X_2$	1	i	ip	$-p$
$^1X_3$	1	i	$-ip$	p
$^1X_4$	1	$-i$	ip	p
$^1X_5$	1	$-i$	$-ip$	$-p$

X_l	$^2X_1$
$X_l \times D_{1/2}$	$(^1X_2 + {}^1X_3) + (^1X_4 + {}^1X_5)$

$^1X_2$, $^1X_3$ and $^1X_4$, $^1X_5$ are respectively degenerated by T.R.S.

h) L : Upper sign for L_l and lower sign for L_l'.

	E	M_x	J	JM_x
$L_1 L_1'$	1	1	± 1	± 1
$L_2 L_2'$	1	-1	± 1	∓ 1
$^1L_3\, {}^1L_3'$	1	i	± 1	$\pm i$
$^1L_4\, {}^1L_4'$	1	$-i$	± 1	$\mp i$

L_l	L_l	L_l' $l = 1, 2$
$L_l \times D_{1/2}$	$(^1L_3 + {}^1L_4)$	$(^1L_3' + {}^1L_4')$

$^1L_3$, $^1L_4$ and $^1L_3'$, $^1L_4'$ are respectively degenerated by T.R.S.

i) Q, P, S, R, T: $p = 1$ for $X = Q$ and P, $p = \exp(-2\pi i k_x a)$ for S, $p = \exp(-\pi i(2k_x a + k_z c))$ for R and $p = i \cdot \exp(-\pi i(2k_x a + k_z c))$ for T.

Q	E	JM_x
P	E	M_x
S	E	JC_2
R	E	$JU_{x\bar{y}}$
T	E	JU_{xy}
X_1	1	p
X_2	1	$-p$
$^1X_3$	1	ip
$^1X_4$	1	$-ip$

X_l	X_l $l = 1, 2$
$X_l \times D_{1/2}$	$(^1X_3 + {}^1X_4)$

$^1X_3$ and $^1X_4$ are degenerated by T.R.S.

tionally low in monoatomic metals. Since white tin is not so good conductor, while grey tin is a good semiconductor (the energy gap is the order of 0.08 ev), we may expect that the difference of both energy band structures is comparatively small. This clarification, however, need quantitative calculation, which is beyond the scope of present paper. Another interesting point is to see how the energy state changes with slight modification of grey tin to the D_{4h}^{19}-lattice due to pressure or any other effect.

Diamond crystal is obtained from white tin lattice by compressing in the directions of x-, y-axis and stretching in z-direction till the stage $a\rightarrow a'/\sqrt{2}$, $c\rightarrow a'$, $2a'$ being the lattice constant of grey tin. Following to usual description, we rotate x-, and y-axis in Fig. 1 by $-45°$ about z-axis and choose the axes as those in Fig. 3. Brillouin zone of grey tin lattice is shown in Fig. 4. C. R. s of $\mathfrak{G}$ are the following 48 elements:

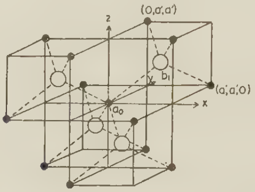

Fig. 3. Diamond lattice.

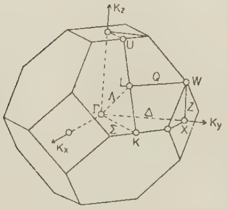

Fig. 4. First Brillouin zone for diamond lattice.

(i) $\boldsymbol{E}$ is the unit element,

(ii) $\boldsymbol{C}_2(x)$, $\boldsymbol{C}_2(y)$ and $\boldsymbol{C}_2(z)$ are the rotations by π about the axis shown in each parenthesis,

(iii) $\boldsymbol{S}_4^{\pm}(x)$, $\boldsymbol{S}_4^{\pm}(y)$ and $\boldsymbol{S}_4^{\pm}(z)$ are the rotations by $\pm(\pi/2)$ about the axis shown in each parenthesis followed by the reflection at the plane perpendicular to the rotation axis and through the origin,

(iv) $\boldsymbol{M}_{xy}$, $\boldsymbol{M}_{x\bar{y}}$, $\boldsymbol{M}_{yz}$, $\boldsymbol{M}_{y\bar{z}}$, $\boldsymbol{M}_{zx}$ and $\boldsymbol{M}_{z\bar{x}}$ are the reflections at the planes through [110] and z-axis, etc.,

(v) $\boldsymbol{D}^{\pm}_{xyz}$, $\boldsymbol{D}^{\pm}_{\bar{x}yz}$, $\boldsymbol{D}^{\pm}_{\bar{x}\bar{y}z}$ and $\boldsymbol{D}^{\pm}_{x\bar{y}z}$ are the rotations by $\pm(2/3)\pi$ about the body diagonals [111], etc.,

(vi) $\boldsymbol{J}$ is the inversion at the origin followed by the non-primitive translation $\boldsymbol{\tau}\equiv\overrightarrow{a_0b_1}$,

(vii) $\boldsymbol{J}\times$ (ii), (viii) $\boldsymbol{J}\times$ (iii), (ix) $\boldsymbol{J}\times$ (iv), (x) $\boldsymbol{J}\times$(v).

The symmetry elements of white tin and grey tin are corresponded as

$$\boldsymbol{E}\rightarrow\boldsymbol{E},\ \boldsymbol{C}_2\rightarrow\boldsymbol{C}_2(z),\ \boldsymbol{S}_4^{\pm}\rightarrow\boldsymbol{S}_4^{\pm}(z),\ \boldsymbol{U}_{xy}\rightarrow\boldsymbol{C}_2(y),$$

$$\boldsymbol{U}_{x\bar{y}}\rightarrow\boldsymbol{C}_2(x),\ \boldsymbol{M}_x\rightarrow\boldsymbol{M}_{xy},\ \boldsymbol{M}_y\rightarrow\boldsymbol{M}_{x\bar{y}},\ \boldsymbol{J}\rightarrow\boldsymbol{J}\ .$$

The shape of the Brillouin zone is classified into two types bordered by the case $a=c$, where Brillouin zone becomes that of body centred cubic. In the range $c/a>1$, the shape is much similar to that in Fig. 4, while in the range $c/a<1$, the shape is essentially the same as in Fig. 2.

The symmetry point W and symmetry lines V, Σ, Z and Q of white tin are isomorphic to the corresponding point and lines of grey tin*. These energy states should be qualitatively the same in both cases. The lines $\varDelta$ and $\varLambda$ with the inclusion of both ends are only symmetry lines to consider in detail. We do not, however, consider of one dimensional representations in O_h^7, since there is no further splitting by lowering of the symmetry from O_h^7 to D_{4h}^{19} because of the existence of the inversion symmetry in both cases. We show schematic diagrams of energy splittings:

O_h^7				D_{4h}^{19}		
A′ (with spin)		A (without spin)		B (without spin)		B′ (with spin)
${}^4\Gamma_8^{\pm}$	$\longleftarrow$	${}^2\Gamma_{12}^{\pm}$	$\longrightarrow$	$\Gamma_1^{\pm}+\Gamma_3^{\pm}$	$\longrightarrow$	$\Gamma_6^{\pm}+\Gamma_7^{\pm}$
$\Gamma_6^{\pm}+{}^4\Gamma_8^{\pm}$	$\longleftarrow$	${}^3\Gamma_{15}^{\pm}$	$\longrightarrow$	$\Gamma_2^{\pm}+{}^2\Gamma_5^{\pm}$	$\longrightarrow$	$\Gamma_6^{\pm}+\Gamma_6^{\pm}+\Gamma_7^{\pm}$
$\Gamma_7^{\pm}+{}^4\Gamma_8^{\pm}$	$\longleftarrow$	${}^3\Gamma_{25}^{\pm}$	$\longrightarrow$	$\Gamma_4^{\pm}+{}^2\Gamma_5^{\pm}$	$\longrightarrow$	$\Gamma_6^{\pm}+\Gamma_7^{\pm}+\Gamma_7^{\pm}$
$\varDelta_6+\varDelta_7$	$\longleftarrow$	${}^2\varDelta_5$	$\longrightarrow$	$\varDelta_2+\varDelta_3$	$\longrightarrow$	$\varDelta_5+\varDelta_5$
${}^4X_5$	$\longleftarrow$	${}^2X_1$, ${}^2X_2$	$\longrightarrow$	${}^2X_1$	$\longrightarrow$	X_3+X_4
${}^4X_5$	$\longleftarrow$	${}^2X_3$, ${}^2X_4$	$\longrightarrow$	${}^2X_2$	$\longrightarrow$	X_3+X_4
$({}^1L_4^{\pm}+{}^1L_5^{\pm})+L_6^{\pm}$	$\longleftarrow$	${}^2L_3^{\pm}$	$\longrightarrow$	$L_1^{\pm}+L_2^{\pm}$	$\longrightarrow$	$({}^1L_3^{\pm}+{}^1L_4^{\pm})+({}^1L_3^{\mp}+{}^1L_4^{\pm})$.

Since the change occurs directly from A′ to B′, there is no essential change at $\varDelta$ and L. But further splitting occurs at Γ and X. The magnitude of the splitting, of course, depends on the degree of the deviation from O_h^7. Herman[9)] suggested that the valence band edge is at the point Γ. Then we are particularly interesting for the splitting of ${}^4\Gamma_8{}^+$. In so small $\boldsymbol{k}$ as perturbational approximation is satisfied, warped surfaces at ${}^4\Gamma_8{}^+$ in grey tin become ellipsoidal after deformation to the D_{4h}^{19}-lattice.

---

* Table VIII by Elliott[4)] does not communicate Herring's corrected result faithfully.

The author wishes to express his gratitude to Dr. Conyers Herring for his support and some advice of present work.

Appendix A. Terminology

We write down briefly the terminology used in text for a convenience to some readers who are unfamiliar with algebra.

(a) Ring

The definition of ring $\mathfrak{R}$ is as follows:

(i) The product $\boldsymbol{\alpha\beta}$ of any elements $\boldsymbol{\alpha}$ and $\boldsymbol{\beta}$ of $\mathfrak{R}$ is determined uniquely as the element of $\mathfrak{R}$.

(ii) The following combination law

$$\boldsymbol{\alpha\beta}\cdot\boldsymbol{\gamma}=\boldsymbol{\alpha}\cdot\boldsymbol{\beta\gamma}$$

is satisfied of the multiplication.

(iii) The assembly $\mathfrak{R}$ is a commutative group as to the addition (this additive Abel group is called a module), i.e. the addition and subtraction of any elements $\boldsymbol{\alpha}$ and $\boldsymbol{\beta}$ of $\mathfrak{R}$ is contained in $\mathfrak{R}$

(iv) On the multiplication and addition, the following distribution laws

$$(\boldsymbol{\alpha}+\boldsymbol{\beta})\boldsymbol{\gamma}=\boldsymbol{\alpha\gamma}+\boldsymbol{\beta\gamma}\ ,\ \boldsymbol{\gamma}(\boldsymbol{\alpha}+\boldsymbol{\beta})=\boldsymbol{\gamma\alpha}+\boldsymbol{\gamma\beta}$$

are satisfied.

(b) Field

If all non-zero elements of a ring constitute a group as to the multiplication, we call such ring the field $\mathfrak{K}$. The assembly of usual complex numbers is a commutative field.

(c) Algebra

We assume $\mathfrak{K}$ to be a commutative field and that any element of $\mathfrak{K}$ is commutative to any element of ring $\mathfrak{A}$. If ring $\mathfrak{A}$ is a module of finite order c, $\mathfrak{A}$ is called algebra of order c over the field $\mathfrak{K}$. Then, with use of c bases $\boldsymbol{a}_i$ of $\mathfrak{A}$, $\mathfrak{A}$ is expressed as

$$\mathfrak{A}=\sum_{i=1}^{c}\boldsymbol{a}_i\mathfrak{K}\ .$$

The multiplication between the bases $\boldsymbol{a}_i$ and $\boldsymbol{a}_j$ is given by

$$\boldsymbol{a}_i\boldsymbol{a}_j=\sum_{k=1}^{c}c_{ij}^{k}\boldsymbol{a}_k\ ,\ c_{ij}^{k}\in\mathfrak{K}\ .$$

c_{ij}^{k} must be, however, determined to satisfy the combination law in (a)(ii).

(d) Ideal

Left ideal $\mathfrak{l}$ and right ideal $\mathfrak{r}$ of algebra $\mathfrak{A}$ are the submodules satisfing the following conditions respectively

$$\mathfrak{A}\mathfrak{l}=\mathfrak{l},\ \mathfrak{r}\mathfrak{A}=\mathfrak{r}\ .$$

The submodule satisfing two conditions at the same time is called ideal.

(e) Centrum

The commutative subalgebra composed of all elements commutative to all elements of algebra $\mathfrak{A}$ is called the centrum $\mathfrak{z}$ of $\mathfrak{A}$.

(f) Idempotent

The idempotent is defined as the element $\boldsymbol{a}$ satisfing the following formula

$$\boldsymbol{aa}=\boldsymbol{a}\neq 0\ .$$

(g) Representation Module

If the module $\mathfrak{M}$ expressed with use of the bases $\boldsymbol{a}_i$ of finite order as

$$\mathfrak{M}=\sum_{i=1}^{c}\boldsymbol{a}_i\mathfrak{K}$$

satisfies the following condition

$$\mathfrak{A}\mathfrak{M}\subseteq\mathfrak{M}\ ,$$

we call $\mathfrak{M}$ the representation module of $\mathfrak{A}$ over $\mathfrak{K}$.

Appendix B. Representation Modules. Case without Spin

a) Γ: $p=1$ for $X=\Gamma$, $p=-1$ for $X=\Gamma'$.

$$\boldsymbol{e}(\Gamma_l)=\frac{1}{16}\sum\chi_{\Gamma_l}^{*}(R)\boldsymbol{R}\ ,\ \Gamma_l=\Gamma_1\cdots\Gamma_4\,;\ \Gamma_1'\cdots\Gamma_4'$$

$$\left.\begin{array}{l}\boldsymbol{e}_{11}({}^2X_5)\\ \boldsymbol{e}_{22}({}^2X_5)\end{array}\right\}=\frac{1}{8}[\boldsymbol{E}-\boldsymbol{C}_2\pm(\boldsymbol{M}_x-\boldsymbol{M}_y)+p\{\boldsymbol{J}-\boldsymbol{JC}_2\pm(\boldsymbol{JM}_x-\boldsymbol{JM}_y)\}]\ ,$$

$$\left.\begin{array}{l}\boldsymbol{e}_{21}({}^2X_5)\\ \boldsymbol{e}_{12}({}^2X_5)\end{array}\right\}=\frac{1}{8}[\boldsymbol{U}_{xy}-\boldsymbol{U}_{x\bar{y}}\pm(\boldsymbol{S}_4{}^+-\boldsymbol{S}_4{}^-)+p\{\boldsymbol{JU}_{xy}-\boldsymbol{JU}_{x\bar{y}}\pm(\boldsymbol{JS}_4{}^+-\boldsymbol{JS}_4{}^-)\}]\ .$$

b) H: $p=1$ for H_1, $p=-1$ for H_2, and $q=1$ for H_3, $q=-1$ for H_4 .

$$\left\{\begin{array}{l}
\left.\begin{array}{l} \boldsymbol{e}_{11}({}^2H_l)\\ \boldsymbol{e}_{22}({}^2H_l)\end{array}\right\}=\frac{1}{8}[\boldsymbol{E}+\boldsymbol{C}_2+p(\boldsymbol{M}_x+\boldsymbol{M}_y)\pm\{\boldsymbol{S}_4^+ +\boldsymbol{S}_4^- +p(\boldsymbol{U}_{xy}+\boldsymbol{U}_{x\bar{y}})\}]\ ,\\
\left.\begin{array}{l} \boldsymbol{e}_{21}({}^2H_l)\\ \boldsymbol{e}_{12}({}^2H_l)\end{array}\right\}=\frac{1}{8}[\boldsymbol{J}+\boldsymbol{JC}_2+p(\boldsymbol{JM}_x+\boldsymbol{JM}_y)\pm\{\boldsymbol{JS}_4^+ +\boldsymbol{JS}_4^- +p(\boldsymbol{JU}_{xy}+\boldsymbol{JU}_{x\bar{y}})\}]\ ,
\end{array}\right.$$

$$\left\{\begin{array}{l}
\left.\begin{array}{l} \boldsymbol{e}_{11}({}^2H_l)\\ \boldsymbol{e}_{22}({}^2H_l)\end{array}\right\}=\frac{1}{8}[\boldsymbol{E}-\boldsymbol{C}_2+q(\boldsymbol{JM}_x-\boldsymbol{JM}_y)\pm\{\boldsymbol{M}_x-\boldsymbol{M}_y+q(\boldsymbol{J}-\boldsymbol{JC}_2)\}]\ ,\\
\left.\begin{array}{l} \boldsymbol{e}_{21}({}^2H_l)\\ \boldsymbol{e}_{12}({}^2H_l)\end{array}\right\}=\frac{1}{8}[\boldsymbol{U}_{xy}-\boldsymbol{U}_{x\bar{y}}-q(\boldsymbol{JS}_4^+-\boldsymbol{JS}_4^-)\pm\{\boldsymbol{S}_4^+-\boldsymbol{S}_4^- -q(\boldsymbol{JU}_{xy}-\boldsymbol{JU}_{x\bar{y}})\}]\ .
\end{array}\right.$$

c) X: $p=1$ for ${}^2X_1$ and $p=-1$ for ${}^2X_2$.

$$\left.\begin{array}{l} \boldsymbol{e}_{11}({}^2X_l)\\ \boldsymbol{e}_{22}({}^2X_l)\end{array}\right\}=\frac{1}{4}\{\boldsymbol{E}+p\boldsymbol{U}_{xy}\pm(\boldsymbol{J}+p\boldsymbol{JU}_{xy})\}\ ,$$

$$\left.\begin{array}{l} \boldsymbol{e}_{21}({}^2X_l)\\ \boldsymbol{e}_{12}({}^2X_l)\end{array}\right\}=\frac{1}{4}\{\boldsymbol{C}_2+p\boldsymbol{U}_{x\bar{y}}\mp(\boldsymbol{JC}_2+p\boldsymbol{JU}_{x\bar{y}})\}\ .$$

d) W: $p=1$ for ${}^2W_1$ and $p=-1$ for ${}^2W_2$.

$$\boldsymbol{e}_{11}({}^2W_l)=\frac{1}{4}\{\boldsymbol{E}+\boldsymbol{C}_2+p(\boldsymbol{S}_4^+ +\boldsymbol{S}_4^-)\}\ ,$$

$$\boldsymbol{e}_{22}({}^2W_l)=\frac{1}{4}\{\boldsymbol{E}-\boldsymbol{C}_2-ip(\boldsymbol{S}_4^+-\boldsymbol{S}_4^-)\}\ ,$$

$$\boldsymbol{e}_{21}({}^2W_l)=\frac{1}{4}\{\boldsymbol{JU}_{xy}+\boldsymbol{JU}_{x\bar{y}}+p(\boldsymbol{JM}_x+\boldsymbol{JM}_y)\}\ ,$$

$$\boldsymbol{e}_{12}({}^2W_l)=\frac{1}{4}\{i(\boldsymbol{JU}_{xy}-\boldsymbol{JU}_{x\bar{y}})+p(\boldsymbol{JM}_x-\boldsymbol{JM}_y)\}\ .$$

e) V, B: $p=\exp(\pi ik_zc)$ for $X=V$ and $p=i\cdot\exp(\pi ik_zc)$ for B.

$$\boldsymbol{e}(X_l)=\frac{1}{8}\sum\chi_{X_l}{}^*(R)\boldsymbol{R}\ ,\quad X=V, B\ ;\ l=1\sim 4\ ,$$

$$\left.\begin{array}{l} \boldsymbol{e}_{11}({}^2X_5)\\ \boldsymbol{e}_{22}({}^2X_5)\end{array}\right\}=\frac{1}{4}\{\boldsymbol{E}-\boldsymbol{C}_2\pm(\boldsymbol{M}_x-\boldsymbol{M}_y)\}\ ,$$

$$\left.\begin{array}{l} \boldsymbol{e}_{21}({}^2X_5)\\ \boldsymbol{e}_{12}({}^2X_5)\end{array}\right\}=\frac{1}{4}p\{\boldsymbol{JU}_{xy}-\boldsymbol{JU}_{x\bar{y}}\pm(\boldsymbol{JS}_4^+-\boldsymbol{JS}_4^-)\}\ .$$

f) Σ, Δ

$$\boldsymbol{e}(X_l)=\frac{1}{4}\sum\chi_{X_l}{}^*(R)\boldsymbol{R}\ ,\quad X=\Sigma, \Delta\ ;\ l=1\sim 4\ .$$

g) Z, Z'

$$\left.\begin{array}{l} \boldsymbol{e}_{11}({}^2Z_1)\\ \boldsymbol{e}_{22}({}^2Z_1)\end{array}\right\}=\frac{1}{2}(\boldsymbol{E}\pm\boldsymbol{C}_2)\ ,$$

$$\left.\begin{array}{l} \boldsymbol{e}_{21}({}^2Z_1)\\ \boldsymbol{e}_{12}({}^2Z_1)\end{array}\right\}=\frac{1}{2}\exp(\pi ik_zc)(\boldsymbol{JU}_{xy}\pm\boldsymbol{JU}_{x\bar{y}})\ .$$

$$\left.\begin{array}{l} \boldsymbol{e}_{11}({}^2Z_1')\\ \boldsymbol{e}_{22}({}^2Z_1')\end{array}\right\}=\frac{1}{2}(\boldsymbol{E}\pm\boldsymbol{U}_{x\bar{y}})\ ,$$

$$\left.\begin{array}{l} \boldsymbol{e}_{21}({}^2Z_1')\\ \boldsymbol{e}_{12}({}^2Z_1')\end{array}\right\}=\frac{1}{2}\exp(2\pi ik_xa)(\boldsymbol{JC}_2-\boldsymbol{JU}_{xy})\ .$$

h) L

$$\boldsymbol{e}(X_l)=\frac{1}{4}\sum\chi_{X_l}{}^*(R)\boldsymbol{R}\ ,\quad X=L, L'\ ;\ l=1, 2.$$

i) Q, P, S, R, T

$$\boldsymbol{e}(X_l)=\frac{1}{2}\sum\chi_{X_l}{}^*(R)\boldsymbol{R},\ \ X=Q, P, S, R, T\,;\ l=1, 2\,.$$

Appendix C. Representation Modules. Case with Spin

a) Γ : $p=1$, $q=1$ for $X_l=\Gamma_6$, $p=-1, q=1$ for Γ_7, $p=1, q=-1$ for $\Gamma_6{}'$ and $p=-1, q=-1$ for $\Gamma_7{}'$.

$$\left.\begin{array}{l}\boldsymbol{e}_{11}(X_l)\\ \boldsymbol{e}_{22}(X_l)\end{array}\right\}=\frac{1}{8}\Big[\boldsymbol{E}\pm i\boldsymbol{C}_2+p\cdot\exp\left(\mp i\ \frac{\pi}{4}\right)\boldsymbol{S}_4{}^++p\cdot\exp\left(\pm i\ \frac{\pi}{4}\right)\boldsymbol{S}_4{}^-+q\,\Big\{\boldsymbol{J}\pm i\boldsymbol{J}\boldsymbol{C}_2$$

$$+p\cdot\exp\left(\mp i\ \frac{\pi}{4}\right)\boldsymbol{J}\boldsymbol{S}_4{}^++p\cdot\exp\left(\pm i\ \frac{\pi}{4}\right)\boldsymbol{J}\boldsymbol{S}_4{}^-\Big\}\Big]\,,$$

$$\left.\begin{array}{l}\boldsymbol{e}_{21}(X_l)\\ \boldsymbol{e}_{12}(X_l)\end{array}\right\}=\frac{1}{8}\Big[\pm\boldsymbol{M}_x+i\boldsymbol{M}_y\pm p\cdot\exp\left(\pm i\ \frac{\pi}{4}\right)\boldsymbol{U}_{xy}\mp p\cdot\exp\left(\mp i\ \frac{\pi}{4}\right)\boldsymbol{U}_{x\bar{y}}$$

$$+q\,\Big\{\pm\boldsymbol{J}\boldsymbol{M}_x+i\boldsymbol{J}\boldsymbol{M}_y\pm p\cdot\exp\left(\pm i\ \frac{\pi}{4}\right)\boldsymbol{J}\boldsymbol{U}_{xy}\mp p\cdot\exp\left(\mp i\ \frac{\pi}{4}\right)\boldsymbol{J}\boldsymbol{U}_{x\bar{y}}\Big\}\Big]\,.$$

b) H

$$\left.\begin{array}{l}\boldsymbol{e}_{11}({}^4H_5)\\ \boldsymbol{e}_{22}({}^4H_5)\end{array}\right\}=\frac{1}{4}\left\{\boldsymbol{E}\pm\frac{\sqrt{2}}{2}\,i(\boldsymbol{M}_x+\boldsymbol{M}_y)+\boldsymbol{J}\pm\frac{\sqrt{2}}{2}\,i(\boldsymbol{J}\boldsymbol{M}_x+\boldsymbol{J}\boldsymbol{M}_y)\right\},$$

$$\left.\begin{array}{l}\boldsymbol{e}_{33}({}^4H_5)\\ \boldsymbol{e}_{44}({}^4H_5)\end{array}\right\}=\frac{1}{4}\left\{\boldsymbol{E}\pm\frac{\sqrt{2}}{2}\,i(\boldsymbol{M}_x+\boldsymbol{M}_y)-\boldsymbol{J}\mp\frac{\sqrt{2}}{2}\,i(\boldsymbol{J}\boldsymbol{M}_x+\boldsymbol{J}\boldsymbol{M}_y)\right\},$$

$$\left.\begin{array}{l}\boldsymbol{e}_{21}({}^4H_5)\\ \boldsymbol{e}_{12}({}^4H_5)\end{array}\right\}=\frac{1}{4}\left\{-i\boldsymbol{C}_2\pm\frac{\sqrt{2}}{2}\,(\boldsymbol{M}_x-\boldsymbol{M}_y)-i\boldsymbol{J}\boldsymbol{C}_2\pm\frac{\sqrt{2}}{2}\,(\boldsymbol{J}\boldsymbol{M}_x-\boldsymbol{J}\boldsymbol{M}_y)\right\},$$

$$\left.\begin{array}{l}\boldsymbol{e}_{31}({}^4H_5)\\ \boldsymbol{e}_{13}({}^4H_5)\end{array}\right\}=\frac{1}{4}\left\{i\boldsymbol{U}_{xy}+\frac{\sqrt{2}}{2}(\boldsymbol{S}_4{}^++\boldsymbol{S}_4{}^-)\mp i\boldsymbol{J}\boldsymbol{U}_{xy}\mp\frac{\sqrt{2}}{2}\,(\boldsymbol{J}\boldsymbol{S}_4{}^++\boldsymbol{J}\boldsymbol{S}_4{}^-)\right\},$$

$$\left.\begin{array}{l}\boldsymbol{e}_{41}({}^4H_5)\\ \boldsymbol{e}_{14}({}^4H_5)\end{array}\right\}=\frac{1}{4}\left\{i\boldsymbol{U}_{x\bar{y}}\pm\frac{\sqrt{2}}{2}(\boldsymbol{S}_4{}^+-\boldsymbol{S}_4{}^-)\mp i\boldsymbol{J}\boldsymbol{U}_{x\bar{y}}-\frac{\sqrt{2}}{2}(\boldsymbol{J}\boldsymbol{S}_4{}^+-\boldsymbol{J}\boldsymbol{S}_4{}^-)\right\}.$$

c) X: $p=1$ for $X_l=X_3$ and $p=-1$ for X_4.

$$\left.\begin{array}{l}\boldsymbol{e}_{11}(X_l)\\ \boldsymbol{e}_{22}(X_l)\end{array}\right\}=\frac{1}{4}\{\boldsymbol{E}-ip\boldsymbol{J}\boldsymbol{U}_{xy}\pm(i\boldsymbol{C}_2+p\boldsymbol{J}\boldsymbol{U}_{x\bar{y}})\}\,,$$

$$\left.\begin{array}{l}\boldsymbol{e}_{21}(X_l)\\ \boldsymbol{e}_{12}(X_l)\end{array}\right\}=\frac{1}{4}\{i\boldsymbol{U}_{x\bar{y}}-p\boldsymbol{J}\boldsymbol{C}_2\pm(\boldsymbol{U}_{xy}+ip\boldsymbol{J})\}\,.$$

d) W

$$\boldsymbol{e}(W_l)=\frac{1}{8}\sum\chi_{W_l}{}^*(R)\boldsymbol{R}\,,\ \ l=3\sim6\,,$$

$$\left.\begin{array}{l}\boldsymbol{e}_{11}(W_7)\\ \boldsymbol{e}_{22}(W_7)\end{array}\right\}=\frac{1}{4}\left\{\boldsymbol{E}-i\boldsymbol{C}_2\mp\exp\left(i\,\frac{\pi}{4}\right)\boldsymbol{S}_4{}^+\mp\exp\left(-i\ \frac{\pi}{4}\right)\boldsymbol{S}_4{}^-\right\},$$

$$\left.\begin{array}{l}\boldsymbol{e}_{21}(W_7)\\ \boldsymbol{e}_{12}(W_7)\end{array}\right\}=\frac{1}{4}\left\{\mp(\boldsymbol{J}\boldsymbol{M}_x-i\boldsymbol{J}\boldsymbol{M}_y)+\exp\left(-i\ \frac{\pi}{4}\right)\boldsymbol{J}\boldsymbol{U}_{xy}-\exp\left(i\,\frac{\pi}{4}\right)\boldsymbol{J}\boldsymbol{U}_{x\bar{y}}\right\}.$$

e) V, B: $p=\pm\exp(\pi ik_zc)$ for $X_l=V_6$ and V_7 respectively, and $p=\pm i\cdot\exp(\pi ik_zc)$ for $X_l=B_6$ and B_7 respectively.

$$\left.\begin{array}{l}\boldsymbol{e}_{11}(X_l)\\ \boldsymbol{e}_{22}(X_l)\end{array}\right\}=\frac{1}{4}\left\{\boldsymbol{E}\pm i\boldsymbol{C}_2+p\cdot\exp\left(\mp i\ \frac{\pi}{4}\right)\boldsymbol{J}\boldsymbol{S}_4{}^++p\cdot\exp\left(\pm i\ \frac{\pi}{4}\right)\boldsymbol{J}\boldsymbol{S}_4{}^-\right\},$$

$$\left.\begin{array}{l}\boldsymbol{e}_{21}(X_l)\\ \boldsymbol{e}_{12}(X_l)\end{array}\right\}=\frac{1}{4}\left\{i\boldsymbol{M}_y\pm\boldsymbol{M}_x\pm p\cdot\exp\left(\pm i\ \frac{\pi}{4}\right)\boldsymbol{J}\boldsymbol{U}_{xy}\mp p\cdot\exp\left(\mp i\ \frac{\pi}{4}\right)\boldsymbol{J}\boldsymbol{U}_{x\bar{y}}\right\}.$$

f) Σ, Δ: $\boldsymbol{M}_x \to \boldsymbol{U}_{xy}$ and $\boldsymbol{J}\boldsymbol{M}_y \to \boldsymbol{J}\boldsymbol{U}_{x\bar{y}}$ for Δ.

$$\left.\begin{matrix} \boldsymbol{e}_{11}(\Sigma_5) \\ \boldsymbol{e}_{22}(\Sigma_5) \end{matrix}\right\} = \frac{1}{2}\{\boldsymbol{E} \pm i \cdot \exp(2\pi i k_x a)\boldsymbol{J}\boldsymbol{C}_2\},$$

$$\left.\begin{matrix} \boldsymbol{e}_{21}(\Sigma_5) \\ \boldsymbol{e}_{12}(\Sigma_5) \end{matrix}\right\} = \frac{1}{2}\{\pm \boldsymbol{M}_x + i \cdot \exp(2\pi i k_x a)\boldsymbol{J}\boldsymbol{M}_y\}.$$

g) Z, Z'

$$\boldsymbol{e}(X_l) = \frac{1}{4}\sum \chi_{X_l}{}^*(R)\boldsymbol{R}, \quad X = Z, Z'; \ l = 2 \sim 5.$$

h) L

$$\boldsymbol{e}(X_l) = \frac{1}{4}\sum \chi_{X_l}{}^*(R)\boldsymbol{R}, \quad X = L, L'; \ l = 3, 4.$$

i) Q, P, S, R, T

$$\boldsymbol{e}(X_l) = \frac{1}{2}\sum \chi_{X_l}{}^*(R)\boldsymbol{R}, \quad X = Q, P, S, R, T; \ l = 3, 4.$$

References

1) F. Seitz: Ann. Math. **37** (1936) 17.
2) L. P. Bouckaert, R. Smoluchowski, and E. Wigner: Phys. Rev. **50** (1936) 58.
3) C. Herring: J. Franklin Inst. **233** (1942) 525.
4) R. J. Elliott: Phys. Rev. **96** (1954) 130.
5) W. Döring and V. Zehler: Ann. Physik **13** (1953) 214.
6) K. Shoda: *Chusho Daisugaku* (*Abstract Algebra*) (1932), in Japanese.
7) W. M. Lomer: Proc. Roy. Soc. **A**, **227** (1955) 330.
8) G. F. Koster: *Solid State Physics* Vol. **5** (Academic Press, 1957).
9) F. Herman: J. Electronics Ser. 1, **1** (1955) 103.

JOURNAL OF THE PHYSICAL SOCIETY OF JAPAN, Vol. 14, No. 11, NOVEMBER, 1959

Effect of External Illumination on Carrier Lifetime in Semiconductors

By Jun'ichi OKADA

Matsuda Research Laboratory, Tokyo Shibaura Electric Co.,
Kawasaki, Japan

(Received July 29, 1959)

The lifetime of excess carriers in a nondegenerate semiconductor which is illuminated with a light in fundamental absorption band and a longer wavelength light is discussed. The recombination equations for many recombination-center levels in the presence of a steady external illumination are formulated. For steady-state case these equations can be solved exactly, but transient solutions are obtained only for specific cases. These results show that both steady-state and transient lifetimes are identical for small densities of recombination centers. This simple lifetime for single recombination-center level case is discussed.

§1. Introduction

Measurements of carrier lifetime in semiconductors are often made under a uniform and constant external illumination in the fundamental absorption band.

Ransom and Rose,[1] for example, have measured the temperature dependence of the lifetime in n-type germanium with various intensities of background illumination, and interpret the results in terms of both the activation energy and the densities of different recombination centers. Furthermore, when trapping effects are present, the measurements of lifetime as determined by the simple recombination centers can be made with the saturation of the traps by a steady illumination in fundamental absorption band.2) The dependence of lifetime on injection level can also be measured by varying the intensity of a steady external illumination.3)

However, no theoretical work has been reported that would explain in detail the effect of external illumination.

Moreover, it is also interesting to investigate the change of lifetime by illuminating with the long wavelength light which is absorbed only by a single recombination center.

In this paper we shall consider the effect of external illumination on carrier lifetime. The recombination equations in the presence of a steady external illumination will be formulated first. Then the steady-state and transient solutions of the equations will be discussed.

§ 2. Recombination Equations in the Presence of External Illumination

As shown in a previous paper,3) the behavior of excess carriers in a nondegenerate semiconductor where the recombination takes place via localized defect levels may be expressed by the equations of the form

$$\left.\begin{aligned}&\frac{d\Delta n}{dt}=L_n-\Sigma_j\Delta R_{nj}=L_n-\Delta R_n\,,\quad \frac{d\Delta p}{dt}L_p-\Sigma_j\Delta R_{pj}=L_p-\Delta R_p\,,\\&\frac{d\Delta N_j^+}{dt}=-\frac{d\Delta N_j^-}{dt}=\Delta R_{pj}-\Delta R_{nj}\pm L_j\qquad (j=1,2,\cdots)\,,\\&\Delta n=\Delta p+\Sigma_j\Delta N_j^+=\Delta p-\Sigma_j\Delta N_j^-,\quad \Delta N_j^+=-\Delta N_j^-\,,\end{aligned}\right\}\tag{2.1}$$

where

$$\left.\begin{aligned}&\Delta R_{nj}=\gamma_{nj}\{N_{j0}^+\Delta n-(n_0+n_j+\Delta n)\Delta N_j^-\}\,,\\&\Delta R_{pj}=\gamma_{pj}\{N_{j0}^-\Delta p-(p_0+p_j+\Delta p)\Delta N_j^+\}\,,\end{aligned}\right\}\tag{2.2}$$

and

$$N_{j0}^-=N_j\frac{n_0}{n_0+n_j}=N_j\frac{p_j}{p_0+p_j}\,,\qquad N_{j0}^+=N_j\frac{n_j}{n_0+n_j}=N_j\frac{p_0}{p_0+p_j}\,.\tag{2.3}$$

Here ΔR_{nj} and ΔR_{pj} are the net rates of capture of excess electrons and holes respectively by j-level, γ_{nj} and γ_{pj} are the rates of capturing an electron and a hole by a single j-center, ΔN_j^- and ΔN_j^+ are the changes of densities N_j^- and N_j^+ of filled and unfilled j-recombination centers respectively (from the electron point of view), N_j is the density of j-recombination centers, Δn and Δp are the changes in the thermal equilibrium densities n_0 and p_0 of free electrons and holes respectively, n_j and p_j are the densities of free electrons and holes when the Fermi level equals to the effective energy E_j of j-level, L_n and L_p are the rates of generation of electrons and holes by external means, and $\pm L_j$ is the rate of excitation of electrons or holes bound in j-level (+ sign for electrons and − sign for holes).

When external illumination is present, we can write

$$L_n=(L_n)^e+L(t)\,,\qquad L_p=(L_p)^e+L(t)\,,\tag{2.4}$$

where $(L_n)^e$ and $(L_p)^e$ are the generations of electrons and holes respectively by external illumination and $L(t)$ is the injection for measuring the carrier lifetime.

For a steady illumination, it is necessary to satisfy the steady-state conditions

$$(L_n)^e=(\Delta R_n)^e\,,\qquad (L_p)^e=(\Delta R_p)^e\,,\qquad \left(\frac{d\Delta N_j^+}{dt}\right)=0\qquad (j=1,2,\cdots)\tag{2.5}$$

where $(\quad)^e$ refers to external illumination.

Furthermore, we must consider following two cases.

Case A. Illumination in fundamental absorption band

In this case, we have

$$(L_n)^e=(L_p)^e=(L)^e \tag{2.6}$$

and

$$(\Delta R_{nj})^e=(\Delta R_{pj})^e \qquad (j=1,\ 2,\ \cdots). \tag{2.7}$$

Case B. Illumination with long wavelength Light

Here we assume that the long wavelength light excites electrons bound in recombination centers at t-level. In this case, we have

$$(L_n)^e=L_t=L_{nt}\,, \qquad (L_p)^e=0\,, \qquad L_j=0 \qquad (j\neq t) \tag{2.8}$$

and

$$\left.\begin{aligned}&(\Delta R_{nj})^e=(\Delta R_{pj})^e \qquad (j\neq t)\,,\\&(\Delta R_{nt})^e=(\Delta R_{pt})^e+L_{nt}\,.\end{aligned}\right\} \tag{2.9}$$

On the other hand, if the quantities such as δR_n, δn, δN_j^+, etc. denote the changes by $L(t)$, Eqs. (2.1) give

$$\left.\begin{aligned}&\frac{d\delta n}{dt}=L-\delta R_n\,, \quad \frac{d\delta p}{dt}=L-\delta R_p\,, \quad \frac{d\delta N_j^+}{dt}=\delta R_{pj}-\delta R_{nj}\,,\\&\delta n=\delta p+\Sigma_j\delta N_j^+\,, \qquad \delta N_j^+=-\delta N_j^-\,.\end{aligned}\right\} \tag{2.10}$$

Supposing that the disturbances by $L(t)$ are small enough that only first-order terms in δn, δp and δN_j^+ ($j=1,\ 2,\ \cdots$) need be considered, we get from Eqs. (2.2)

$$\left.\begin{aligned}&\delta R_{nj}=\gamma_{nj}[\{N_{j0}^{\ +}+(\Delta N_j^+)^e\}\delta n+\{n_0+n_j+(\Delta n)^e\}\delta N_j^+]\,,\\&\delta R_{pj}=\gamma_{pj}[\{N_{j0}^{\ -}-(\Delta N_j^+)^e\}\delta p-\{p_0+p_j+(\Delta p)^e\}\delta N_j^+]\,.\end{aligned}\right\} \tag{2.11}$$

Eqs. (2.10) and (2.11) constitute the fundamental equations which determine the behavior of excess carriers in the presence of a steady external illumination.

§ 3. Steady-State Lifetime

In this section we shall consider the case where the measurements of carrier lifetime is made under steady-state conditions

$$\frac{d\delta n}{dt}=\frac{d\delta p}{dt}=\frac{d\delta N_j^+}{dt}=0\,,$$

or

$$L=\delta R_n=\delta R_p\,, \qquad \delta R_{nj}=\delta R_{pj}\,. \tag{3.1}$$

For this case, the lifetimes of electrons and holes are defined by

$$\tau_n=\frac{\delta n}{\delta R_n}\,, \qquad \tau_p=\frac{\delta p}{\delta R_p}\,. \tag{3.2}$$

Using Eqs. (3.1) and (3.2), and the relations given in the case A or B in Appendix A, the dependence of the steady-state lifetimes on external illumination is given as

$$\left.\begin{aligned}\frac{1}{\tau_n}=&[\Sigma_j\{B_{pj}H_{pj}-\Delta n(\gamma_{nj}H_{pj}B_{pj}/B_j)+\Delta p(\gamma_{nj}H_{nj}B_{pj}/B_j)\}-(\gamma_{nt}B_{pt}L_{nt}/B_t^2)]\\&+\lambda[\Sigma_j\{B_{nj}H_{nj}+\Delta n(\gamma_{pj}H_{pj}B_{nj}/B_j)\\&\quad-\Delta p(\gamma_{pj}H_{nj}B_{nj}/B_j)\}-(\gamma_{pt}B_{nt}L_{nt}/B_t^2)]\,,\\\frac{1}{\tau_p}=&[\Sigma_j\{B_{nj}H_{nj}+\Delta n(\gamma_{pj}H_{pj}B_{pj}/B_j)-\Delta p(\gamma_{pj}H_{nj}B_{nj}/B_j)\}-(\gamma_{pt}B_{nt}L_{nt}/B_t^2)]\\&+\frac{1}{\lambda}[\Sigma_j\{B_{pj}H_{pj}-\Delta n(\gamma_{nj}H_{pj}B_{pj}/B_j)\\&\quad+\Delta p(\gamma_{nj}H_{nj}B_{pj}/B_j)\}+(\gamma_{nt}B_{pt}L_{nt}/B_t^2)]\,,\end{aligned}\right\} \tag{3.3}$$

where

$$\lambda=\frac{(1+H_p)-\Delta n\Sigma_j(\gamma_{nj}H_{pj}/B_j)+\Delta p\Sigma_j(\gamma_{nj}H_{nj}/B_j)+(\gamma_{nt}L_{nt}/B_t^2)}{(1+H_n)+\Delta n\Sigma_j(\gamma_{pj}H_{pj}/B_j)-\Delta p\Sigma_j(\gamma_{pj}H_{nj}/B_j)-(\gamma_{pt}L_{nt}/B_t^2)}\,, \tag{3.4}$$

and

$$\Delta p=\frac{1+H_p}{1+H_n}\Delta n-\frac{1}{1+H_n}\,\frac{L_{nt}}{B_t}\,. \tag{3.5}$$

Here

$$H_n=\Sigma_jH_{nj}=\Sigma_j\frac{\gamma_{pj}N_{j0}^-}{B_j}\,,\qquad H_p=\Sigma_jH_{pj}=\Sigma_j\frac{\gamma_{nj}N_{j0}^+}{B_j}\,, \tag{3.6}$$

and

$$B_j=B_{nj}+B_{pj}=\gamma_{nj}(n_0+n_j+\Delta n)+\gamma_{pj}(p_0+p_j+\Delta p)\,. \tag{3.7}$$

Since there is no fear of confusion, $(\ )^e$ is omitted here and hereafter Δn, Δp, ΔN_j^+, etc. refer only to the changes by steady external illumination. In these expressions the lifetimes for the case A are obtained by setting $L_{nt}=0$ and for the case of the excitation of the holes in t-level by long wavelength light, L_{nt} must be replaced by $-L_{pt}$.

If we make the assumption that all N_j's are small enough compared to any one of the quantities n_0, p_0, n_j, p_j, Eqs. (3.4) and (3.5) reduce

$$\lambda=\frac{1+(\gamma_{nt}L_{nt}/B_t^2)}{1-(\gamma_{pt}L_{pt}/B_t^2)}\,,\qquad \Delta p=\Delta n-\frac{L_{nt}}{B_t}\,. \tag{3.8}$$

(i) *Case A*

Since $L_{nt}=0$, we obtain from Eqs. (3.8)

$$\lambda=1\,,\qquad \Delta p=\Delta n\,. \tag{3.9}$$

Substituting Eqs. (3.9) into Eqs. (3.3), single lifetime is given by

$$\frac{1}{\tau}=\frac{1}{\tau_n}=\frac{1}{\tau_p}=\Sigma_j\frac{\tau_{j0}(1+2\Delta\varphi)+\tau_{j\infty}(\Delta\varphi)^2}{(\tau_{j0}+\tau_{j\infty}\Delta\varphi)^2}\,, \tag{3.10}$$

where

$$\left.\begin{aligned}&\Delta\varphi=\frac{\Delta n}{n_0+p_0}=\frac{\Delta p}{n_0+p_0}\,,\qquad \tau_{j0}=\tau_{nj}\frac{p_0+p_j}{n_0+p_0}+\tau_{pj}\frac{n_0+n_j}{n_0+p_0}\,,\\ &\tau_{j\infty}=\tau_{nj}+\tau_{pj}\,,\qquad \tau_{nj}=\frac{1}{\gamma_{nj}N_j}\,,\qquad \tau_{pj}=\frac{1}{\gamma_{pj}N_j}\,.\end{aligned}\right\} \tag{3.11}$$

(ii) *Case B*

From Eq. (2.9), L_{nt} can be written as

$$\frac{L_{nt}}{B_t}=\frac{\Sigma_jB_{pj}H_{pj}}{B_{nt}}\Delta n+\frac{\Sigma_jB_{nj}H_{nj}}{B_{nt}}\Delta p\,. \tag{3.12}$$

Thus, as long as $\gamma_{nj}N_j$ and $\gamma_{pj}N_j$ are smaller than $\gamma_{nt}(n_0+n_t+\Delta n)$ for all N_j's, $L_{nt}/B_t\ll\Delta n$ or Δp and $L_{nt}/B_t^2\ll1$. In this case we obtain from Eqs. (3.8)

$$\lambda\simeq1\,,\qquad \Delta p\simeq\Delta n\,, \tag{3.13}$$

and Eqs. (3.3) reduce to a single lifetime given by

$$\frac{1}{\tau}=\frac{1}{\tau_n}=\frac{1}{\tau_p}=\Sigma_j\frac{\tau_{j0}(1+2\Delta\varphi)+\tau_{j\infty}(\Delta\varphi)^2}{(\tau_{j0}+\tau_{j\infty}\Delta\varphi)^2}+\frac{\tau_{t0}-\nu_{nt}\tau_{t\infty}}{\tau_{t0}+\tau_{t\infty}\Delta\varphi}\cdot\frac{1+\Delta\varphi}{\nu_{nt}+\Delta\varphi}\cdot\Sigma_j\frac{1}{\tau_{j0}+\tau_{j\infty}\Delta\varphi}\,, \tag{3.14}$$

where

$$\nu_{nt}=\frac{n_0+n_t}{n_0+p_0}\ . \tag{3.15a}$$

For the case where the holes in t-level are excited, ν_{nt} is replaced by

$$\nu_{pt}=\frac{p_0+p_t}{n_0+p_0}\ . \tag{3.15b}$$

§ 4. Transient Lifetime

In this section we shall consider the decay of δn and δp following a sudden interruption of excitation L. However, it is impossible to obtain general analytical solutions of Eqs. (2.10) for many recombination level case. Thus, we shall limit ourselves here to some elementary cases where the solutions can easily be obtained.

4.1. *Single recombination-center level*

Solutions of Eqs. (2.10) for this case have been given by Sandiford[5)] and Wertheim,[6)] and are of the form

$$\delta n=C_n^- \exp(-t/\tau_-)+C_n^+ \exp(-t/\tau_+) \tag{4.1}$$

(see Appendix B)

If the density of recombination centers is sufficiently small, we can neglect shorter time constant since measurements of lifetime yield longer one. For this case, with $\Delta n=\Delta p$, we obtain from Eqs. (B.3) and (B.4) in Appendix B

$$\tau=\frac{(\tau_0+\tau_\infty\Delta\varphi)^2}{\tau_0(1+2\Delta\varphi)+\tau_\infty(\Delta\tau)^2} \qquad \text{for case A,} \tag{4.2}$$

and

$$\tau=\frac{(\tau_0+\tau_\infty\Delta\varphi)^2}{\tau_0(1+2\Delta\varphi)+\tau_\infty(\Delta\varphi)^2+(\tau_0-\nu\tau_\infty)((1+\Delta\varphi)/(\nu+\Delta\varphi))\Delta\varphi} \qquad \text{for case B,} \tag{4.3}$$

where ν is $(n_0+n_1)/(n_0+p_0)$ or $(p_0+p_1)/(n_0+p_0)$ corresponding to the excitation of electrons or holes.

4.2. *Two recombination-center levels*

In this case it is easy to show that the solution of Eqs. (2.10) is of the form

$$\delta n=C_{n1}\exp(-t/\tau_1)+C_{n2}\exp(-t/\tau_2)+C_{n3}\exp(-t/\tau_3)\ , \tag{4.4}$$

and three time constants are given by a equation of the form

$$\left(\frac{1}{\tau}\right)^3-p\left(\frac{1}{\tau}\right)^2+q\left(\frac{1}{\tau}\right)-r=0\ , \tag{4.5}$$

where the expressions for the quantities p, q and r are given in Appendix C.

If the densities N_1 and N_2 of both recombination centers are small enough, the largest time constant is approximately

$$\frac{1}{\tau}=\frac{r}{q}\ . \tag{4.6}$$

With $\Delta n=\Delta p$ the lifetime under external illumination are given from Eq. (4.6) as follows.

(i) *Case A*

$$\frac{1}{\tau}=\frac{\tau_{10}(1+2\Delta\varphi)+\tau_{1\infty}(\Delta\varphi)^2}{(\tau_{10}+\tau_{1\infty}\Delta\varphi)^2}+\frac{\tau_{20}(1+2\Delta\varphi)+\tau_{2\infty}(\Delta\varphi)^2}{(\tau_{20}+\tau_{2\infty}\Delta\varphi)^2}\ . \tag{4.7}$$

(ii) *Case B where electrons or holes in 2-level are excited*

$$\frac{1}{\tau}=\frac{\tau_{10}(1+2\Delta\varphi)+\tau_{1\infty}(\Delta\varphi)^2}{(\tau_{10}+\tau_{1\infty}\Delta\varphi)^2}+\frac{\tau_{20}(1+2\Delta\varphi)+\tau_{2\infty}(\Delta\varphi)^2}{(\tau_{20}+\tau_{2\infty}\Delta\varphi)^2}$$
$$+\frac{\tau_{20}-\nu_2\tau_{2\infty}}{\tau_{20}+\tau_{2\infty}\Delta\varphi}\left[\frac{1}{\tau_{10}+\tau_{1\infty}\Delta\varphi}+\frac{1}{\tau_{20}+\tau_{2\infty}\Delta\varphi}\right]\frac{1+\Delta\varphi}{\nu_2+\Delta\varphi}\Delta\varphi\,. \tag{4.8}$$

where ν_2 is $(n_0+n_2)/(n_0+p_0)$ or $(p_0+p_2)/(n_0+p_0)$ corresponding to the excitation of electrons or holes in 2-level.

Moreover, since other two time constants are of the order of $(1/B_1)+(1/B_2)$ and $1/(B_1+B_2)$, and are associated with smaller amplitudes, it is possible to neglect them in measurements of lifetime.

4.3. *A recombination-center level and A trap level*

We consider here the case of a hole trap level in conjunction with a recombination level.

Let subscripts r and t refer to recombination center and hole trap respectively. We obtain

$$\frac{d\delta n}{dt}=-\delta R_{nr}\,,\qquad \frac{d\delta p}{dt}=-\delta R_{pr}-\delta R_{pt}\,, \tag{4.9a}$$

$$\frac{d\delta N_r^+}{dt}=\delta R_{pr}-\delta R_{nr}\,,\qquad \frac{d\delta N_t^+}{dt}=\delta R_{pt}\,, \tag{4.9b}$$

$$\delta n=\delta p+\delta N_r^+ +\delta N_t^+\,, \tag{4.9c}$$

and the equation determining the time constants has the same form as Eq. (4.5).

In order to investigate the effect of external illumination on carrier lifetime, it is necessary to consider two larger time constants. This is complicated and it is difficult to obtain analytical solutions. Thus we shall be concerned only with the case where the carrier lifetime is measured with the saturation of the trap by constant external illumination in fundamental absorption band. In this case, Eq. (4.9b) gives

$$N_t^-\simeq\Delta N_t^+\,. \tag{4.10}$$

Since ΔN_t^+ is given, from Eq. (A.2) in Appendix A, as

$$\Delta N_t^+=\frac{N_t^-\Delta p}{p_0+p_t+\Delta p}\,, \tag{4.11}$$

Eq. (4.10) is satisfied only when

$$\Delta p\gg p_0+p_t\,. \tag{4.12}$$

Under these conditions, $\delta N_t^+\simeq 0$ and Eqs. (4.9) reduce to the equations for a single recombination center level with external illumination. Thus, if the density of recombination center is small, the lifetime is given by Eq. (4.2) and we have

$$\tau=\frac{(\tau_{r0}+\tau_{r\infty}\Delta\varphi)^2}{\tau_{r0}(1+2\Delta\varphi)+\tau_{r\infty}(\Delta\varphi)^2} \qquad (\Delta\varphi\gg\nu_{pt}), \tag{4.13}$$

where $\nu_{pt}=(p_0+p_t)/(n_0+p_0)$ and for an electron trap ν_{pt} is replaced by $\nu_{nt}=(n_0+n_t)$ (n_0+p_0).

§ 5. Discussion

The results presented above show that both steady-state and transient lifetime are identical for small densities of recombination centers. This identification may be proved more generally by assuming that the change in electron (or hole) occupation of the recombination centers is negligible compared with the free excess carrier concentrations.

For simplicity, we shall discuss here this simple lifetime for single level case.

5.1. *Illumination in fundamental absorption band*

In this case we have the lifetime of the form

$$\tau=\frac{(\tau_0+\tau_\infty\Delta\varphi)^2}{\tau_0(1+2\Delta\varphi)+\tau_\infty(\Delta\varphi)^2}\,, \tag{5.1}$$

and the variation of τ with $\Delta\varphi$ is monotonous between $\tau=\tau_0$ (for $\Delta\varphi=0$) and $\tau=\tau_\infty$ (for $\Delta\varphi\to\infty$). This is also observed experimentally and an example is shown in Fig. 1 for p-type germanium specimen.

In our experiments, carrier lifetimes were measured by photoconductivity decay method described in the previous paper.[3] For external illumination a 24-watt tungsten lamp fed from a d.c. supply was used and $\Delta\varphi$ was changed by varing the intensity of this light. The value of $\Delta\varphi$ was calculated by using the relation

$$\Delta\varphi = M\cdot\frac{V_0 - V_L}{V_L}\,, \tag{5.2}$$

where V_L and V_0 are the voltage across the specimens with and without external illumination, M is given by $b/(1+b)$ for n-type or $1/(1+b)$ for p-type and b is the ratio of the mobilities (μ_n/μ_p). As shown in Fig. 1, if we use proper values of τ_0 and τ_∞, the agreement between the calculated curve and the experimental data is fairly good.

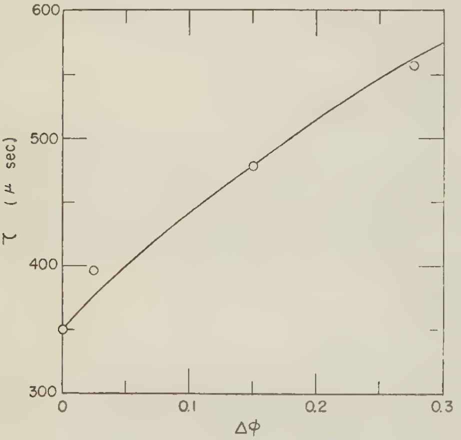

Fig. 1. Lifetime in a p-type germanium sample as a function of excess carrier concentrations injected by the illumination in fundamental absorption band. The open circles represent experimental results. The solid line was calculated from Eq. (5.1) with $\tau_0 = 350\,\mu$ sec and $\tau_\infty = 850\,\mu$ sec.

On the other hand, several authors[3),6),7)] have shown that the lifetime in darkness or without external illumination depends on injection level $\Delta\varphi$ as

$$\tau = \frac{\tau_0 + \tau_\infty \Delta\varphi}{1 + \Delta\varphi}\,. \tag{5.3}$$

Apparently, this expression is simpler than that of Eq. (5.1). Thus, in the case where τ_0 and τ_∞ are determined from the measurements of the dependence of τ on $\Delta\varphi$, it is unfavourable to use the method of varing the intensity of external illumination, even though the injection level $\Delta\varphi$ can be measured exactly.

Furthermore, in Eq. (5.1) τ_0 is a function of temperature and $\Delta\varphi$ may also vary with temperature $(\Delta\varphi \propto (L)^e \cdot \tau(T))$. This implies that the temperature dependence of the lifetime under external illumination is not simple. In other words, even in a single recombination level case, the behavior of the variation of lifetime with temperature can be changed by the application of external illumination. This is contradictory to the interpretation of Ransom and Rose[1)]. Therefore, in order to arrive at the correct interpretation of the process, it is necessary to investigate the variation of lifetime with injection level at various temperatures.

5.2. *Illumination with long wavelength light*

The lifetime for this case is of the form

$$\frac{(\tau_0 + \tau_\infty \Delta\varphi)^2}{\tau_0(1+2\Delta\varphi) + \tau_\infty(\Delta\varphi)^2 + (\tau_0 - \nu\tau_\infty)((1+\Delta\varphi)/(\nu+\Delta\varphi))\Delta\varphi}\,, \tag{5.4}$$

and the variation of τ with $\Delta\varphi$ depends strongly on ν. Especially, if ν is sufficiently small so that $\tau_0 \gg \nu\tau_\infty$, for $\Delta\varphi \ll 1$ we obtain from Eq. (5,4)

$$\tau = \tau_0 \frac{1 + (\Delta\varphi/\nu)}{1 + 2(\Delta\varphi/\nu)}\,, \tag{5.5}$$

and, in contrast with the case discussed in sub-section 5.1, τ decreases with increasing $\Delta\varphi$ even when τ_∞ is larger than τ_0. The dependence of τ on $\Delta\varphi$ is plotted in a qualitative fashion in Fig. 2 for arbitrary values of

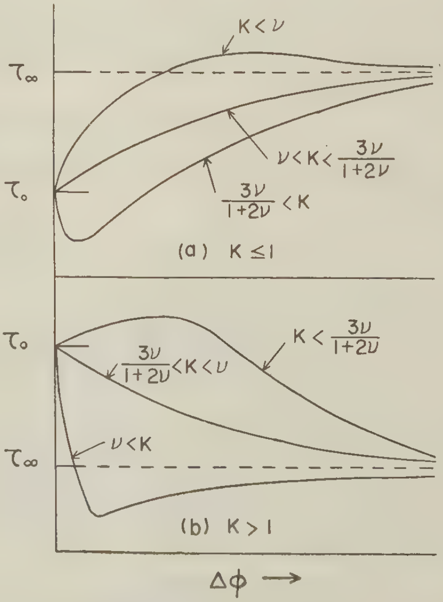

Fig. 2. Dependence of lifetime on excess carrier concentrations injected by the long wavelength light. K is the ratio τ_0/τ_∞.

the parameters τ_0, τ_∞ and ν.

Experimentally, however, in this case it is difficult to obtain a measurable value of $\Delta\varphi$, because the optical absorption due to recombination centers is very small. Thus, in most cases, the effect of the illumination with a long wavelength light may be undetected.

On the other hand, in order to observe this effect, it is necessary to introduce a large amount of recombination centers. In this case, the lifetime decreases considerably and the experimental results must be analyzed by using more general equations such as Eqs. (3.3).

Acknowledgement

The author would like to thank Mr. Katsuhisa Suzuki for making lifetime measurements.

Appendix A

As shown in previous papers,[3),4)] we have from Eqs. from (2.6) to (2.8) the relations between the quantities changed by steady external illumination as follows.

Case A. Illumination in fundamental absorption band

$$\frac{\Delta p}{\Delta n}=\frac{1+H_p}{1+H_n}\,, \tag{A.1}$$

$$\Delta N_j^+=H_{nj}\Delta p-H_{pj}\Delta n\,. \tag{A.2}$$

Case B. Illumination with long wavelength light

$$(1+H_p)\Delta n=(1+H_n)\Delta p+\frac{L_{nt}}{B_{nt}}\,, \tag{A.3}$$

$$\Sigma_j(B_{pj}H_{pj}\Delta n+B_{nj}H_{nj}\Delta p)=\frac{B_{nt}}{B_t}L_{nt}\,, \tag{A.4}$$

and

$$\left.\begin{aligned}\Delta N_j^+&=H_{nj}\Delta p-H_{pj}\Delta n\,,\\ \Delta N_t^+&=H_{nt}\Delta p-H_{pt}\Delta n+\frac{L_{nt}}{B_t}\,.\end{aligned}\right\} \tag{A.5}$$

For the case where the holes in t-level are excited, L_{nt} and $B_{nt}L_{nt}$ must be replaced by $-L_{pt}$ and $B_{pt}L_{pt}$ respectively. Here H_n, H_p and B_j are given by Eqs. (3.6) and (3.7).

Appendix B

As shown by Wertheim,[6)] τ_+ and τ_- in Eq. (4.1) are given by

$$\tau_\pm=\frac{2}{(\alpha_n+\alpha_p)[1\pm(1-y)^{1/2}]}\,, \tag{B.1}$$

where

$$y=4(\alpha_n\alpha_p-\beta_n\beta_p)(\alpha_n-\alpha_p)^{-2}\,, \tag{B.2}$$

and

$$\left.\begin{aligned}\alpha_n&=\gamma_n[(N_0^++\Delta N^+)+(n_0+n_1+\Delta n)]\,,\\ \beta_n&=\gamma_n(n_0+n_1+\Delta n)\,,\\ \alpha_p&=\gamma_p[(N_0^--\Delta N^+)+(p_0+p_1+\Delta p)]\,,\\ \beta_p&=\gamma_p(p_0+p_1+\Delta p)\,.\end{aligned}\right\} \tag{B.3}$$

If the density of recombination centers is sufficiently small so that $N_0^+<(n_0+n_1)$ and $N_0^-<(p_0+p_1)$, these two time constants are expressed as

$$\tau_-=\frac{\alpha_n+\alpha_p}{\alpha_n\alpha_p-\beta_n\beta_p}\,,\qquad \tau_+=\frac{1}{\alpha_n+\alpha_p}\,. \tag{B.4}$$

Appendix C

The coefficients in Eq. (4.5) are given by

$$\left.\begin{aligned}p&=a_{11}+a_{22}+a_{33}\,,\\ q&=a_{11}a_{22}+a_{22}a_{33}+a_{33}a_{11}-a_{12}a_{21}\\ &\quad-a_{23}a_{32}-a_{31}a_{13}\,,\\ r&=a_{11}a_{22}a_{33}+a_{12}a_{23}a_{31}+a_{21}a_{32}a_{13}\\ &\quad-a_{11}a_{23}a_{32}-a_{22}a_{31}a_{13}-a_{33}a_{12}a_{21}\,,\end{aligned}\right\} \tag{C.1}$$

where

$$\left.\begin{aligned}a_{11}&=\gamma_{n1}(N_1^++\Delta N_1^+)+\gamma_{n2}(N_2^++\Delta N_2^+)\\ &\quad+\gamma_{n2}(n_0+n_2+\Delta n)\,,\\ a_{12}&=-\gamma_{n2}(n_0+n_2+\Delta n)\,,\\ a_{13}&=\gamma_{n1}(n_0+n_1+\Delta n)-\gamma_{n2}(n_0+n_2+\Delta n)\,,\\ a_{21}&=-\gamma_{p2}(p_0+p_2+\Delta p)\,,\\ a_{22}&=\gamma_{p1}(N_1^--\Delta N_1^+)+\gamma_{p2}(N_2^--\Delta N_2^+)\\ &\quad+\gamma_{p2}(p_0+p_2+\Delta p)\,,\\ a_{23}&=-\gamma_{p1}(p_0+p_1+\Delta p)\\ &\quad+\gamma_{p2}(p_0+p_2+\Delta p)\,,\\ a_{31}&=\gamma_{n1}(N_1^++\Delta N_1^+)\,,\\ a_{32}&=-\gamma_{p1}(N_1^-+\Delta N_1^+)\,,\\ a_{33}&=\gamma_{n1}(n_0+n_1+\Delta n)+\gamma_{p1}(p_0+p_1+\Delta p)\,.\end{aligned}\right\}$$

References

1) P. Ransom and F. W. G. Rose: J. Electronics **1** (1956) 625.
2) J. A. Hornbeck and J. R. Haynes: Phys. Rev. **97** (1955) 311.
3) J. Okada: J. Phys. Soc. Japan **13** (1958) 793.
4) J. Okada: J. Phys. Soc. Japan **12** (1957) 1338.
5) D. J. Sandiford: Phys. Rev. **105** (1957) 524.
6) G. K. Wertheim: Phys. Rev **109** (1958) 1086.
7) W. Shockley and W. T. Read, Jr.: Phys. Rev. **87** (1952) 835.

JOURNAL OF THE PHYSICAL SOCIETY OF JAPAN, Vol. 14, No. 11, NOVEMBER, 1959

Dynamical Theory of Electron Diffraction in Laue-case*, I. General Theory

By Fuminori FUJIMOTO

Institute of Physics, College of General Education,
University of Tokyo, Komaba, Meguro-ku, Tokyo

(Received July 2, 1959)

A new formulation of the theory of electron diffraction for the Laue-case, based upon the matrix representation of Niehrs and Wagner, is presented by introducing the scattering matrix for an electron elastically scattered by a plate-like crystal. The intensity and also the integrated intensity of reflections for thin crystals are computed. The results obtained here indicate that the intensity does not approach to that of the pseudo-kinematical theory, but to that of the kinematical theory. The theory predicts also the failure of Friedel's law in the case of non centro-symmetric crystals. The formula for the scattered amplitude can be transformed into the form which coincides with the result given by Cowley and Moodie derived on the basis of the Huygens' principle.

§ 1. Introduction

In the dynamical theory of electron diffraction, initiated by Bethe,1) the Schrödinger equation for an electron in the periodic potential of a crystal is solved under appropriate boundary conditions, by assuming the wave function to be the superposition of plane waves. The problem is reduced, in this case, to solve the secular equation of infinite order.2) For the practical calculation, the number of waves is reduced by neglecting all waves other than the incident and a few reflected waves. Such a treatment, however, becomes rapidly difficult with increasing number of waves, and in the usual treatment of the "*two-wave approximation*", only two waves, the incident and a diffracted, are considered. However, the other diffracted waves which are neglected in the two-wave approximation may sometimes take an important role, e.g. in the forbidden reflection such as the 222-reflection from diamond type crystals3),4) and in the failure or Friedel's law.5),6)

In order to take into account the effect of other reflection waves, Bethe1) introduced the so called "*dynamic potential*" instead of v_h, the Fourier component of the periodic potential in crystal. However, this procedure does not only give the exact solution, but it sometimes leads to serious paradox as to the diffracted intensity in the Laue-case for a thin crystal, as pointed out by Miyake.7)

For the sake of more extensive treatment of many reflections, Niehrs and Wagner8) used the matrix representation and derived some useful relations among the waves in the crystal. In the present paper, the scattering matrix,9) which connects the amplitudes of the incident and the diffracted waves, for an infinite, parallel-sided crystal plate in the Laue-case, is obtained by extending their theory. The intensity of diffracted waves and also the integrated intensity of reflection are obtained, without solving the secular equation, by expanding the component of the scattering matrix in the power series of $D/2k$, where D is the thickness of the crystal and k, the wave number of electron in crystal. The intensity obtained by the present method is in accordance with the result of the recent theory of Cowley and Moodie10) which was derived by appling Huygens' principle for the electron diffraction, and Fujiwara's theory11) which was derived by the interation of the Born approximation for the scattered waves within the crystal.

§ 2. Scattering Matrix

The Schrödinger equation for an electron of energy E in a field of the crystal potential $V(\boldsymbol{r})$ has the form:

$$\Delta\Psi+\frac{8\pi^2m}{h^2}\{E-V(\boldsymbol{r})\}\Psi=0\,. \qquad (1)$$

---

* During the preparation of this manuscript, the author was told that H. Niehrs had independently developed a similar theory.

The potential $V(\boldsymbol{r})$ and the wave function can be expanded as

$$\left.\begin{aligned} &-\frac{8\pi^2 m}{h^2}V(\boldsymbol{r})=\sum_h v_h \exp(i\boldsymbol{b}_h\cdot\boldsymbol{r}) ,\\ &\text{and}\\ &\Psi=\sum_h \psi_h \exp(i\boldsymbol{k}_h\cdot\boldsymbol{r}) \quad (\boldsymbol{k}_h=\boldsymbol{k}_0+\boldsymbol{b}_h), \end{aligned}\right\} \qquad (2)$$

where $\boldsymbol{b}_h$ is 2π-times the reciprocal lattice vector and $\boldsymbol{k}_h$ is the wave vector of the $\boldsymbol{h}$-reflection wave. Substituting (2) into (1), we obtain

$$(k^2-k_h^2)\psi_h+\sum_{g\neq h} v_{h-g}\psi_g=0 , \qquad (3)$$

where

$$k^2=\frac{8\pi^2 m}{h^2}(E+v_0) .$$

If we express (3) in matrix representation, we obtain

$$\begin{pmatrix} \cdots\cdots\cdots\cdots\cdots\cdots\cdots\cdots \\ \cdots k^2-k_0^2 \cdots v_{0h} \cdots v_{0g} \cdots \\ \cdots\cdots\cdots\cdots\cdots\cdots\cdots\cdots \\ \cdots v_{h0} \cdots k^2-k_h^2 \cdots v_{hg} \cdots \\ \cdots\cdots\cdots\cdots\cdots\cdots\cdots\cdots \\ \cdots v_{g0} \cdots v_{gh} \cdots k^2-k_g^2 \cdots \\ \cdots\cdots\cdots\cdots\cdots\cdots\cdots\cdots \end{pmatrix} \begin{pmatrix} \vdots \\ \psi_0 \\ \vdots \\ \psi_h \\ \vdots \\ \psi_g \\ \vdots \end{pmatrix} =0, \qquad (4)$$

where

$$v_{lm}=v_{l-m}=v_{ml}^* . \qquad (5)$$

Introducing the "Ampassung" ζ and the "Anregungsfelher" ρ_h (Fig. 1), we have

$$k_h=k-\rho_h-\zeta\cos\theta_h . \qquad (6)$$

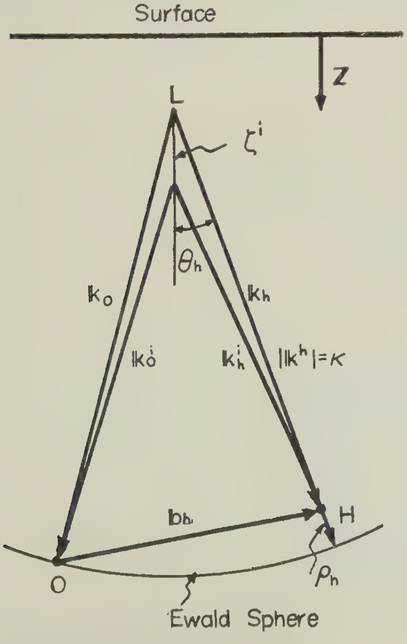

Fig. 1. Construction I.

In the Laue-case, ζ is so small in comparison with k that we may neglect ζ^2 and $\rho\zeta$, and further we can assume $\cos\theta_h=1$. Hence, $(k^2-k_h^2)$ may be written as

$$k^2-k_h^2=2k\zeta+2k\rho_h+\rho_h^2=-x+p_h , \qquad (6)$$

where

$$2k\zeta=-x , \quad \text{and} \quad 2k\rho_h+\rho_h^2=p_h . \qquad (8)$$

If only the reciprocal lattice points are considered which lie on a plane passing through the origin and being nearly perpendicular to the incident direction, p_h depends only on the component of k along that plane but not on the magnitude of k.

Substituting (7) into (4), we obtain

$$\mathrm{M}\phi=x\phi , \qquad (9)$$

where M is an hermitian matrix given by

$$\mathrm{M}=\begin{pmatrix} \cdots\cdots\cdots\cdots\cdots\cdots \\ \cdots p_0 \cdots v_{0h} \cdots v_{0g} \cdots \\ \cdots\cdots\cdots\cdots\cdots\cdots \\ \cdots v_{h0} \cdots p_h \cdots v_{hg} \cdots \\ \cdots\cdots\cdots\cdots\cdots\cdots \\ \cdots v_{g0} \cdots v_{gh} \cdots p_g \cdots \\ \cdots\cdots\cdots\cdots\cdots\cdots \end{pmatrix} . \qquad (10)$$

Matrix M is independent of k, so that, the eigen value x^i and the eigen vector ϕ^i whose components are $\cdots\psi_0^i, \cdots\psi_h^i, \cdots\psi_g^i, \cdots$ are also independent of k.

Assuming that the incident wave is of unit amplitude and ϕ^i is normalized, we can put the amplitude of the $\boldsymbol{h}$-wave belonging to the i-th wave field as

$$u_h^i=\alpha_i\psi_h^i ,$$

where α_i is the coefficient which is determined by the boundary condition at the entrance surface given by

$$\sum_i u_h^i=\sum_i \alpha_i\psi_h^i=\delta_{h0} . \qquad (11)$$

Multiplying the both sides of (11) by ψ_h^{j*} and summing up with the index h, we obtain α_j from the orthogonality of the eigen vector ϕ^i:

$$\alpha_j=\psi_0^{j*} .$$

Then we have

$$u_h^i=\psi_0^{i*}\psi_h^i . \qquad (12)$$

This result was previously given by Niehrs and Wagner.[8)]

The wave function for the $\boldsymbol{h}$-reflection is given by

$$\Psi_h=\sum_i u_h^i \exp(i\boldsymbol{k}_h^i\cdot\boldsymbol{r}) , \qquad (13)$$

where $\boldsymbol{k}_h^i$ is the wave vector of the $\boldsymbol{h}$-reflection of the i-th wave field and may be written in terms of of ζ^i and wave vector $\boldsymbol{k}_h$ corresponding to the wave point L for which $\zeta=0$ (Fig. 1), namely

$$\boldsymbol{k}_h{}^i=\boldsymbol{k}_h-\zeta^i\boldsymbol{z}\ , \tag{14}$$

where $\boldsymbol{z}$ is the unit vector normal to the crystal surface directing inwardly. Substituting (8), (12) and (14) into (13), we get

$$\begin{aligned}\Psi_h&=\sum_i \psi_0{}^{i*}\psi_h{}^i \exp(-i\zeta^i z)\exp(i\boldsymbol{k}_h\cdot\boldsymbol{r})\\&=\sum_i \psi_0{}^{i*}\psi_h{}^i \exp\left(i\frac{z}{2k}x^i\right)\exp(i\boldsymbol{k}_h\cdot\boldsymbol{r})\ .\end{aligned} \tag{15}$$

On the other hand, we obtain the following equation from (9) for one of the eigen values:

$$\mathrm{M}^n\boldsymbol{\psi}^i=(x^i)^n\boldsymbol{\psi}^i\ ,$$

and for the h-component:

$$(x^i)^n\psi_h{}^i=\sum_g \psi_g{}^i(\mathrm{M}^n)_{hg}\ , \tag{16}$$

where $(\mathrm{M}^n)_{hg}$ is the h, g component of the matrix M^n. Multiplying the both sides of (16) by $\psi_0{}^{i*}$ and summing up with i, we get

$$\begin{aligned}\sum_i (x^i)^n\psi_0{}^{i*}\psi_h{}^i&=\sum_i\sum_g \psi_0{}^{i*}\psi_g{}^i(\mathrm{M}^n)_{hg}\\&=\sum_g\Big(\sum_i \psi_0{}^{i*}\psi_g{}^i\Big)(\mathrm{M}^n)_{hg}=(\mathrm{M}^n)_{h0}\ ,\end{aligned} \tag{17}$$

since we have

$$\sum_i \psi_0{}^{i*}\psi_g{}^i=\delta_{g0}$$

by the boundary condition. Using (17), we can rewrite equation (15) as follows:

$$\begin{aligned}\Psi_h&=\sum_i\left[\psi_0{}^{i*}\psi_h{}^i\sum_n\frac{1}{n!}\left(i\frac{z}{2k}x^i\right)^n\right]\exp(i\boldsymbol{k}_h\cdot\boldsymbol{r})\\&=\left[\exp\left(i\frac{z}{2k}\mathrm{M}\right)\right]_{h0}\exp(i\boldsymbol{k}_h\cdot\boldsymbol{r})\ .\end{aligned} \tag{18}$$

This represents that the amplitude of the $\boldsymbol{h}$-reflection wave in the crystal is given by

$$\left[\exp\left(i\frac{z}{2k}\mathrm{M}\right)\right]_{h0}.$$

When we apply (18) for the plate-like crystal with thickness D and assume the amplitude of incident wave is Φ_0, the amplitude φ_h of the diffracted waves at the exit surface is given by

$$\begin{pmatrix}\varphi_0\\ \varphi_1\\ \varphi_2\\ \vdots\end{pmatrix}=\exp\left(i\frac{D}{2k}\mathrm{M}\right)\begin{pmatrix}\Phi_0\\ 0\\ 0\\ \vdots\end{pmatrix},$$

where S is the scattering matrix given by

$$\mathrm{S}=\exp\left(i\frac{D}{2k}\mathrm{M}\right). \tag{19}$$

The wave function of the scattered wave transmitted from the exit surface of the crystal is written as

$$\Psi=\sum_h \Phi_0\mathrm{S}_{h0}\exp[i(\gamma_h-\Gamma_h)D]\exp(i\boldsymbol{K}_h\cdot\boldsymbol{r})\ ,$$

where $\boldsymbol{K}_h$ is the wave vector of the $\boldsymbol{h}$-reflection in vacuum and γ_h and Γ_h are the normal components of $\boldsymbol{k}_h$ and $\boldsymbol{K}_h$ respectively.

In the case where we cannot put $\cos\theta_h=1$, we can also obtain the scattering matrix in a similar way as above. The results are given in Appendix.

§ 3. Intensity

According to (18), the intensity of the $\boldsymbol{h}$-reflection wave is given by

$$I_h=\left|\left[\exp\left(i\frac{D}{2k}\mathrm{M}\right)\right]_{h0}\right|^2,$$

which may be expanded as follows:

$$\begin{aligned}I_h=&\left(\frac{D}{2k}\right)^2|\mathrm{M}_{h0}|^2+\frac{i}{2}\left(\frac{D}{2k}\right)^3[(\mathrm{M}^2)_{h0}\mathrm{M}_{h0}{}^*-\mathrm{M}_{h0}(\mathrm{M}^{*2})_{h0}]\\&-\left(\frac{D}{2k}\right)^4\left[\frac{1}{6}(\mathrm{M}^3)_{h0}\mathrm{M}_{h0}{}^*-\frac{1}{4}(\mathrm{M}^2)_{h0}(\mathrm{M}^{*2})_{h0}+\frac{1}{6}\mathrm{M}_{h0}(\mathrm{M}^{*3})_{h0}\right]+\cdots\ ,\end{aligned} \tag{20}$$

where M* is the conjugate matrix of M. The first term of (20) is

$$\left(\frac{D}{2k}\right)^2|\mathrm{M}_{h0}|^2=\left(\frac{D}{2k}\right)^2|v_h|^2\ . \tag{21}$$

The 2nd term is

$$\begin{aligned}
&\frac{i}{2}\left(\frac{D}{2k}\right)^3[(\mathrm{M}^2)_{h0}\mathrm{M}_{h0}{}^*-\mathrm{M}_{h0}(\mathrm{M}^{*2})_{h0}]\\
&=\frac{i}{2}\left(\frac{D}{2k}\right)^3[\{\sum_g{}'v_{h-g}v_g+v_h(p_0+p_h)\}v_h{}^*-v_h\{\sum_g{}'v_{h-g}{}^*v_g{}^*+v_h{}^*(p_0+p_h)\}]\\
&=\frac{i}{2}\left(\frac{D}{2k}\right)^3[v_h{}^*\sum_g{}'v_{h-g}v_g-v_h\sum_g{}'v_{h-g}{}^*v_h{}^*]\\
&=\left(\frac{D}{2k}\right)^3\mathfrak{I}(v_h\sum_g{}'v_{-g}v_{g-h})\ ,
\end{aligned}\tag{22}$$

where the symbol $\mathfrak{I}$ indicates the imaginary part and the prime after the symbol $\sum$ indicates the absence of zero and h terms. The 3rd term is

$$\begin{aligned}
&\left(\frac{D}{2k}\right)^4\left[\frac{1}{4}|(\mathrm{M}^2)_{h0}|^2-\frac{1}{3}\mathfrak{R}\{(\mathrm{M}^3)_{h0}\mathrm{M}_{h0}{}^*\}\right]\\
&=\left(\frac{D}{2k}\right)^4\Bigg[\frac{1}{4}|\sum_g{}'v_{h-g}v_g|^2+\frac{1}{2}(p_0+p_h)\mathfrak{R}\{v_{-h}\sum_g{}'v_{h-g}v_g\}+\frac{1}{4}|v_h|^2(p_0+p_h)^2\\
&\quad-\frac{1}{3}\mathfrak{R}\Bigg\{v_{-h}\{v_h{}^3+v_h(p_0{}^2+p_0p_h+p_h{}^2)+v_h\sum_g{}'|v_g|^2+v_h\sum_g{}'|v_{h-g}|^2\\
&\quad+(p_0+p_h)\sum_g{}'v_{h-g}v_g+\sum_{\substack{g,l\\ g\neq l}}{}'v_{h-g}v_{g-l}v_l+\sum_g{}'p_gv_{h-g}v_g\}\Bigg\}\Bigg]\,.
\end{aligned}\tag{23}$$

where the symbol $\mathfrak{R}$ indicates the real part.

The higher order terms are much more complicated. If the crystal is sufficiently thin and the accerelating voltage sufficiently high, the higher terms can be neglected.

§ 4. Comparison of the Present Theory with the Kinematical Theory

When D is small or k is large we may neglect higher order terms in (20), and obtain

$$I_h=\left(\frac{D}{2k}\right)^2|v_h|^2\,. \tag{24}$$

This indicates that for thin crystals, (i) the intensity given by the dynamical theory coincides with that of kinematical theory, even if we take into account many reflections, and (ii) the intensity is independent of the incident direction, since (24) does not include any factor dependent upon the incident direction. This means, in terms of the Ewald construction, that the reciprocal lattice points are elongated in the direction normal to the crystal surface, just as in the kinematical theory for very thin crystals, and this circumstance may explain the appearance of the cross grating pattern. It must be noted here, however, that the critical thickness of the crystal within which (24) holds varies with the incident direction. As we shall see in the next paper, (24) is applicable up to a certain value of the thickness of crystal. This thickness is largest at the Bragg position and decreases as the direction of the incident beam deviates from the Bragg position. A rough estimation shows that this critical thickness at the Bragg position is about 15A for the 111-reflection from Au.

When $D/2k$ is large, the value of the third term including p_h, which depends on the incident beam, becomes appreciable, and by this contribution the intensity falls rapidly for increasing value of p_h. Thus the characteristic of the two-dimensional pattern becomes gradually lost with increasing $D/2k$.

§ 5. Relation between the Scattering Matrix and the Two-wave Approximation

It is of interest to study the relation between the treatments by the scattering matrix and that by the two-wave approximation. Select the terms related only with the indices 0 and h from each of the terms in the expansion series of the matrix component S_{h0}. Then we can see that the sum of these terms coincides with the h, 0 component of the scattering matrix S_B for two-wave approximation, which is expressed by

$$S_B=\exp\left(i\frac{D}{2k}M_B\right),$$

where

$$M_B=\begin{pmatrix} p_0 & v_{-h} \\ v_h & p_h \end{pmatrix}.$$

The amplitude of **h**-reflection, φ_h, can be written as

$$\varphi_h=\varphi_h{}^B+\varphi_h{}',$$

where $\varphi_h{}^B$ is the amplitude calculated exactly by the two-wave approximation as

$$\varphi_h{}^B=\frac{2v_h i}{\sqrt{(p_0-p_h)^2+4v_h{}^2}}\cdot\sin\left(\frac{1}{2}\sqrt{(p_0-p_h)^2+4v_h{}^2}\,\frac{z}{2k}\right)\cdot\exp\left(i\frac{z}{2k}\,\frac{p_0+p_h}{2}\right),$$

and $\varphi_h{}'$ is the sum of terms which involve 0, h and other indices and represents the contribution due to the interaction of 0-and h-waves with other waves.

§ 6. Failure of Friedel's Law

The experimental observation of the failure of Friedel's law was reported on zincblend by Miyake and Uyeda[5] and the theoretical explanation by Kohra,[6] who considered the simultanious reflection of 331 and 33$\bar{1}$ in the Bragg case.

The second term in (20) vanishes for centro-symmetric crystals, but not for non-centro-symmetric crystals. In the latter case, the intensity of **h**- and $\bar{\boldsymbol{h}}$-reflection becomes

$$\left.\begin{aligned} I_h&=\left(\frac{D}{2k}\right)^2|v_h|^2+\left(\frac{D}{2k}\right)^3\Im\Big(v_h{\sum_g}'v_{-g}v_{g-h}\Big)+\cdots \\ &\text{and} \\ I_{-h}&=\left(\frac{D}{2k}\right)^2|v_h|^2-\left(\frac{D}{2k}\right)^3\Im\Big(v_h{\sum_g}'v_{-g}v_{g-h}\Big)+\cdots, \end{aligned}\right\} \qquad (25)$$

This indicates the failure of Friedel's law in the Laue-case. The difference between I_h and I_{-h} appears in the third power of $D/2k$ and this term is independent of the incident direction. In general, this difference appears in each odd power term which vanishes for centro-symmetric crystals.

As we see from (25), the asymmetry of the intensity arises from the interaction of weak waves, without any strong simultanious reflection. This may also be valid in the Bragg-case.

§ 7. Integrated Intensity

For experimental verification of the theory, it is necessary to calculate the intengrated intensity of the reflection. The integrated intensity for the Laue-case was given by Blackman[12] on the basis of the two-wave approximation. But his result may not be applicable when the interaction with other waves are strong. Let us now consider the integrated intensity of the **h**-reflection by the present formulation. When the crystal is slightly out of the Bragg position, the intensity of reflection becomes weak and the influence of the interactions due to weak waves becomes relatively important. In particular, the so called "*systematic interactions*", the interactions between the reflections corresponding to the reciprocal lattice points lying on the lattice row passing through the origin and the reciprocal lattice point H is important[4]. In the following we consider only the "systematic interactions", and further assume that $\overline{OH}$ is parallel to the surface and that every Fourier coefficient of the potential is real.

When $D/2k$ is small, (24) is valid at the Bragg position. Outside the Bragg position, however, we should take into account the higher order terms, and we have

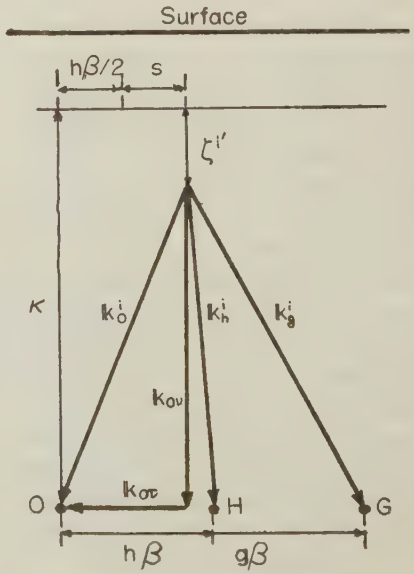

Fig. 2. Construction II.

$$I_h=\left(\frac{D}{2k}\right)^2 v_h{}^2-\frac{1}{12}\left(\frac{D}{2k}\right)^4[v_h{}^2\{4(v_h{}^2+2\sum_g{}' v_g{}^2)+(p_0-p_h)^2\}$$
$$-3(\sum_g{}' v_{h-g}v_g)^2-2(p_0+p_h)v_h\sum_g{}' v_{h-g}v_g+4v_h\sum_{\substack{g,l\\ g\neq l}}{}' v_{h-g}v_{g-l}v_l+4v_h\sum_g{}' p_g v_{h-g}v_g]+\cdots. \tag{26}$$

Introducing the new parameters ζ' for ζ, and s as are shown in Fig. 2, we have

$$k_{0\nu}+\zeta'=k\,, \qquad k_{0\tau}=\frac{h}{2}\beta+s\,,$$

where τ and ν indicate the tangential and normal components with respect to the surface, respectively, and $\beta=2\pi/d$. Thus, we have

$$p_0=-\left(\frac{h}{2}\beta+s\right)^2, \qquad p_h=-\left(\frac{h}{2}\beta-s\right)^2, \qquad \text{and} \qquad p_g=-\left(g\beta-\frac{h}{2}\beta-s\right)^2. \tag{27}$$

Substituting (27) into (26) and neglecting the higher order terms, we have

$$I_h=\left(\frac{D}{2k}\right)^2 v_h{}^2-\frac{1}{12}\left(\frac{D}{2k}\right)^4[4v_h{}^2(v_h{}^2+2\sum_g{}' v_g{}^2)-3(\sum_g{}' v_{h-g}v_g)^2$$
$$+4v_h\sum_{\substack{g,l\\ g\neq l}}{}' v_{h-g}v_{g-l}v_l-4v_h\sum_g{}' v_{h-g}v_g(g^2-hg)\beta^2]-\frac{1}{3}\left(\frac{D}{4k}\right)^4 v_h{}^2(h\beta s)^2\,. \tag{28}$$

The integrated intensity can be expressed as

$$J_h=\int_{-\infty}^{+\infty} I_h d\alpha=\frac{1}{k}\int_{-\infty}^{+\infty} I_h ds\,.$$

If we take into account all the terms in I_h, I_h is positive for any value of s. But if we take only the first two terms in (26), I_h becomes negative for the value of s beyond the certain value s_0, for which I_h given by (28) is zero. As the value of I_h near the Bragg position is important in the integration, we approximately get

$$J_h=\frac{1}{k}\int_{-s_0}^{s_0} I_h ds=\frac{4}{3k}\Bigg[\left(\frac{D^2}{2k}\right)v_h{}^2-\frac{1}{12}\left(\frac{D}{2k}\right)^4\{4v_h{}^2(v_h{}^2+2\sum_g{}' v_g{}^2)-3(\sum_g{}' v_{h-g}v_g)^2+4v_h\sum_{\substack{g,l\\ g\neq l}}{}' v_{h-g}v_{g-l}v_l$$
$$-4v_h\sum_g{}' v_{h-g}v_g(g^2-hg)\beta^2\}\Bigg]^{3/2}\left\{\frac{1}{3}\left(\frac{D}{2k}\right)^2 v_h{}^2(h\beta)^2\right\}^{-1/2}.$$

When v_h is neither zero nor very small, J_h can be rewritten as

$$J_h=\frac{2\sqrt{3}}{3}\frac{D}{2k^3}\frac{v_h{}^2}{\theta_0}\Bigg[1-\frac{1}{2}\left(\frac{D}{2k}\right)^2\Bigg\{v_h{}^2+2\sum_g{}' v_g{}^2-\frac{3}{4}\left(\sum_g{}'\frac{v_{h-g}v_g}{v_h}\right)^2$$
$$+\frac{1}{v_h}(\sum_{\substack{g,l\\ g\neq l}}{}' v_{h-g}v_{g-l}v_l-\sum_g{}' v_{h-g}v_g(g^2-hg)\beta^2)\Bigg\}\Bigg], \tag{29}$$

where $\theta_0=h\beta/2k$ is the Bragg angle. For small value of $D/2k$, the second terms in the bracket of (29) can be neglected and we have

$$J_h=1.15\frac{D}{2k^3}\frac{v_h{}^2}{\theta_0}\,. \tag{30}$$

The integrated intensity is proportional to the square of v_h in accordance with the characteristic of the kinematical theory, and (30) coincide with the corresponding formula of Blackman except for the numerical factor 1.15. The appearance of this factor may be due to the neglect of higher terms, for if we make a similar approximation in Blackman's formulation, we have the same factor.

When v_h is zero, the integrated intensity can be calculated by taking into account the higher order terms. This will be discussed, in the next paper, for the case of the 222-reflection for the crystal of diamond type for which $v_{222}=0$.

§ 8. Another Method of Calculation of the Scattering Matrix

In the preceding sections we studied the power expansion of the amplitude of diffracted waves with respect to $D/2k$. In this section, we consider the expansion with respect to the Fourier coefficient v's.

The matrix element $(\mathrm{M}^n)_{h0}$ is given by the sum of terms of the n-th order product of v's and p's. Select from the sum the terms including the m-th order product of v's, say v_{h-g_1}, $v_{g_1-g_2}$, $\cdots$, $v_{g_{m-1}}$, then the sum of these terms makes the $n-m$-th order homogeneous and symmetric polynomial with respect to p's. This polynominal can be written in the form

$$v_{h-g_1}v_{g_1-g_2}\cdots v_{g_{m-1}}\left[\frac{p_0^n}{(p_0-p_h)(p_0-p_{g_1})\cdots(p_0-p_{g_{m-1}})}+\frac{p_h^n}{(p_h-p_0)(p_h-p_{g_1})\cdots(p_h-p_{g_{m-1}})}\right.$$
$$\left.+\sum_{i=1}^{m-1}\frac{p_{g_i}^n}{(p_{g_i}-p_0)(p_{g_i}-p_h)(p_{g_i}-p_{g_1})\cdots(p_{g_i}-p_{g_{i-1}})(p_{g_i}-p_{g_{i+1}})\cdots(p_{g_i}-p_{g_{m-1}})}\right]. \tag{31}$$

The term (31) is not contained in $(\mathrm{M}^n)_{h0}$ for which $n<m$. Since, however, the braket in (31) vanishes for $0\leqq n<m$, we can add these zero terms to the terms including m-th order product of v in the expansion of S_{h0}. We have thus

$$\sum_{n=0}^{\infty}\sum_{g_1g_2\cdots g_{m-1}}\frac{1}{n!}\left(i\frac{z}{2k}\right)^n v_{h-g_1}v_{g_1-g_2}\cdots v_{g_{m-1}}$$
$$\times\left[\frac{p_0^n}{(p_0-p_h)(p_0-p_{g_1})\cdots(p_0-p_{g_{m-1}})}+\frac{p_h^n}{(p_h-p_0)(p_h-p_{g_1})\cdots(p_h-p_{g_{m-1}})}\right.$$
$$\left.+\sum_{i=1}^{m-1}\frac{p_{g_i}^n}{(p_{g_i}-p_0)(p_{g_i}-p_h)(p_{g_i}-p_{g_1})\cdots(p_{g_i}-p_{g_{i-1}})(p_{g_i}-p_{g_{i+1}})\cdots(p_{g_i}-p_{g_{m-1}})}\right]$$
$$=\sum_{g_1g_2\cdots g_{m-1}}v_{h-g_1}v_{g_1-g_2}\cdots v_{g_{m-1}}$$
$$\times\left[\frac{\exp(i\cdot z/2k\cdot p_0)}{(p_0-p_h)(p_0-p_{g_1})\cdots(p_0-p_{g_{m-1}})}+\frac{\exp(i\cdot z/2k\cdot p_h)}{(p_h-p_0)(p_h-p_{g_1})\cdots(p_h-p_{g_{m-1}})}\right.$$
$$\left.+\sum_{i=1}^{m-1}\frac{\exp(i\cdot z/2k\cdot p_{g_i})}{(p_{g_i}-p_0)(p_{g_i}-p_h)(p_{g_i}-p_{g_1})\cdots(p_{g_i}-p_{g_{i-1}})(p_{g_i}-p_{g_{i+1}})\cdots(p_{g_i}-p_{g_{m-1}})}\right], \tag{32}$$

where the symbol $\sum\limits_{g_1g_2\cdots g_{m-1}}$ indicates the sum for all the possible permutations of $m-1$ values of g under the condition $h-g_1$, g_1-g_2, $\cdots$, $g_{m-1}\neq 0$. If we put $p_0=0$, and $p_g=2k\rho_g$ neglecting ρ_g^2 in (8), we have for (31)

$$\frac{v_{h-g_1}v_{g_1-g_2}\cdots v_{g_{m-1}}}{(2k)^{m-1}}\left[\frac{(2k\rho_h)^{n-1}}{(\rho_h-\rho_{g_1})(\rho_h-\rho_{g_2})\cdots(\rho_h-\rho_{g_{m-1}})}\right.$$
$$\left.+\sum_{i=1}^{m-1}\frac{(2k\rho_{g_i})^{n-1}}{(\rho_{g_i}-\rho_h)(\rho_{g_i}-\rho_{g_1})\cdots(\rho_{g_i}-\rho_{g_{i-1}})(\rho_{g_i}-\rho_{g_{i+1}})\cdots(\rho_{g_i}-\rho_{g_{m-1}})}\right]. \tag{31$'$}$$

Therefore, we have for (32)

$$\sum_{g_1g_2\cdots g_{m-1}}\frac{v_{h-g_1}v_{g_1-g_2}\cdots v_{g_{m-1}}}{(2k)^m}\left[\frac{\exp(iz\rho_h)-1}{\rho_h(\rho_h-\rho_{g_1})(\rho_h-\rho_{g_2})\cdots(\rho_h-\rho_{g_{m-1}})}\right.$$
$$\left.+\sum_{i=1}^{m-1}\frac{\exp(iz\rho_{g_i})-1}{\rho_{g_i}(\rho_{g_i}-\rho_h)(\rho_{g_i}-\rho_{g_1})\cdots(\rho_{g_i}-\rho_{g_{i-1}})(\rho_{g_i}-\rho_{g_{i+1}})\cdots(\rho_{g_i}-\rho_{g_{m-1}})}\right]. \tag{32$'$}$$

And (18) can be written as follows:

$$\Psi_h=\sum_{m=1}^{\infty}\sum_{g_1g_2\cdots g_{m-1}}\frac{v_{h-g_1}v_{g_1-g_2}\cdots v_{g_{m-1}}}{(2k)^m}\left[\frac{\exp(iz\rho_h)-1}{\rho_h(\rho_h-\rho_{g_1})\cdots(\rho_h-\rho_{g_{m-1}})}\right.$$
$$\left.+\sum_{i=1}^{m-1}\frac{\exp(iz\rho_{g_i})-1}{\rho_{g_i}(\rho_{g_i}-\rho_h)(\rho_{g_i}-\rho_{g_1})\cdots(\rho_{g_i}-\rho_{g_{i-1}})(\rho_{g_i}-\rho_{g_{i+1}})\cdots(\rho_{g_i}-\rho_{g_{m-1}})}\right]$$
$$\times\exp(i\boldsymbol{k}_h\cdot\boldsymbol{r})$$
$$=\sum_{m=1}^{\infty}\sum_{g_1g_2\cdots g_{m-1}}\exp(-i\rho_hz)\frac{v_{h-g_1}v_{g_1-g_2}\cdots v_{g_{m-1}}}{(2k)^m}\left[\frac{\exp(iz\rho_h)-1}{\rho_h(\rho_h-\rho_{g_1})\cdots(\rho_h-\rho_{g_{m-1}})}\right.$$
$$\left.+\sum_{i=1}^{m-1}\frac{\exp(iz\rho_{g_i})}{\rho_{g_i}(\rho_{g_i}-\rho_h)(\rho_{g_i}-\rho_{g_1})\cdots(\rho_{g_i}-\rho_{g_{i-1}})(\rho_{g_i}-\rho_{g_{i+1}})\cdots(\rho_{g_i}-\rho_{g_{m-1}})}\right]$$
$$\times\exp(i\boldsymbol{k}^h\cdot\boldsymbol{r})\,, \tag{33}$$

since $k_h=k^h-\rho_h$, where $\boldsymbol{k}^h$ is the vector in the direction of $\boldsymbol{k}_h$ and $|\boldsymbol{k}^h|=k$ (see Fig. 1). (33) coincides with the result given by Cowley and Moodie,10) which was obtained by the iteration of Huygens' principle.

If we take into account the direction cosine of the wave vector of each wave with respect to the surface normal, which we have assumed to the equal to unity, we get the result coinciding with that of Fujiwara's theory11) which was deduced by the iteration of Born approximation (see Appendix).

§ 9. Discussions

i) Bethe's second approximation

It is usually believed that the intensity of reflection at the Bragg position in the Laue-case for small D or large k, approaches to that due to the kinematical theory. This conclusion was derived from the two-wave approximation of Bethe. However, as Miyake7) has recently pointed out, Bethe's result for the small limit of $D/2k$ does not coincide with that of the kinematical theory if we use, instead of v_h, the dynamic potential V_{12} given by

$$V_{12}=v_h-\sum_g{}'\frac{v_{h-g}v_h}{k^2-k_g^2}\,.$$

Let us use g and g' for the upper index i in $u_h{}^i$ corresponding to the couple of branches of dispersion surface passing through the vicinity of the section of the two spheres of radius k, having the reciprocal lattice points G and H–G as centres (see Fig. 3). Then, we can say that the dynamic potential was introduced by taking into account only the weak waves $u_g{}^h$ and $u_g{}^{h'}$ ($g\neq 0$, h), whose amplitudes are approximately given by

$$u_g{}^{h,h'}=-\frac{u_0{}^{h,h'}v_g+u_h{}^{h,h'}v_{g-h}}{k^2-k_g{}^2}\,.$$

Since this relation may be accurate except for small $k^2-k_g{}^2$, the geometry of dispersion surface (h and h') may be corrected fairly well by taking into account the effect of the weak waves $u_g{}^h$ etc.

On the other hand, in the present theory, by which formally the same intensity limit is obtained as that of the two-wave approximation, namely, that of the kinematical theory, for small D and λ, the weaks $\boldsymbol{h}$-

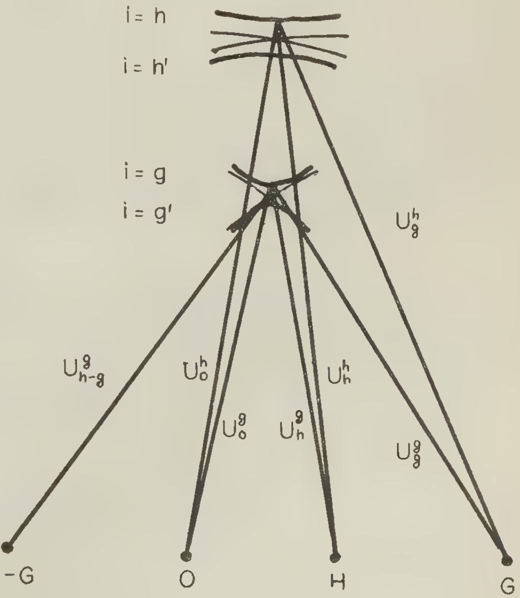

Fig. 3. The relation between amplitude and wave field.

waves u_h^g, $u_h^{g'}$ etc. are taken into account besides the u_g^h etc. The effect of the waves u_h^g, $u_h^{g'}$ etc. may be important especially for the limit of small $D/2k$. The failure of the use of the dynamic potential in calculating the intensity of reflection in thin limit is due to the neglect of the waves u_h^g, $u_h^{g'}$ etc.

ii) Pseudo-kinematical theory

When the molecule is composed of heavy and light atoms, the diffraction intensity is affected by the phase shift, as was studied by Glauber and Schomaker,$^{13)}$ and Hoerni and Ibers.$^{14)}$ Horni extended this study to the crystal by simply replacing the ordinary atomic structure factor in the kinematical formula of reflected intensity by the complex atomic structure factor. He graphycally showed that in the limit of small D and λ the intensity due to the dynamical theory taking account of the multiple scattering approaches to that of the pseudo-kinematical theory. However, it is actually difficult to confirm the agreement between the former two theory by his graph, especially for small D and λ.

On the other hand, our theory, which starts from the dynamical theory taking account of many reflections, indicates the fact that the intensity of reflection by the dynamical theory approaches to that of the kinematical theory rather than that of the pseudo-kinematical theory. This result is in a sharp contradiction to the result of Hoerni.

Hoerni calculated the intensity of 111- and $\bar{1}\bar{1}\bar{1}$-reflections at the Bragg position from cadmium sulphide, which has the polar axis [111], by the pseudo-kinematical and also by the dynamical theories, and showed the failure of Friedel's law. The intensities given by the pseudo-kinematical theory are

$$\left.\begin{aligned} &I_{111}=1.22\times10^{-4}\,D^2 \\ \text{and}\qquad &I_{\bar{1}\bar{1}\bar{1}}=0.925\times10^{-4}\,D^2\,. \end{aligned}\right\} \tag{34}$$

This result differs again from the conclusion of the present theory. The intensity given by (34), which shows the failure of Friedel's law, is proportional to D^2, whereas in our result (25) the difference between I_{111} and $I_{\bar{1}\bar{1}\bar{1}}$ appears first in the $(D/2k)^3$ term.

In the dynamical theory, the effect of multiple scattering, and so the effect of phase shift, are automatically taken into account. The difference between the results of these theories may arise from the fact that, in the dynamical theory, only the discrete set of waves whose wave vectors are related by the reciprocal lattice vectors are considered in the crystal, whereas in the pseudo-kinematical theory, continuous set of waves are considered in an atom, as was emphasised by Miyake.$^{7)}$

iii) The intensity formula (20) expressed by the power series in $D/2k$ is practically applicable for small D or λ. When D or λ is large, we cannot simply apply the present method, since in this case it is appropriate to consider the intensity averaged over D which is given by

$$\overline{I_h}=\sum_i |u_h^i|^2=\sum_i |\psi_0^{i*}\psi_h^i|^2\,.$$

In order to obtain ψ_0^i and ψ_h^i, it is necessary to solve the secular equation.

The author would like to thank Prof. S. Takagi for his guidance throughout this work, and Prof. K. Kohra for his helpful discussions. This work was partly supported by a research grant of the Ministry of Education.

Appendix

If we consider the direction cosine of each beam with respect to the surface normal which is almost equal to 1 in the Laue-case, we get the following equation instead of (7)

$$k^2-k_h^2=2k\zeta\cos\theta_h+p_h=-x\cos\theta_h+p_h\,,$$

and (9) becomes

$$\mathrm{M}\phi=x\mathrm{Q}^2\phi\,, \tag{35}$$

as was shown by Niehrs and Wagner. Here the matrix Q is the diagonal matrix whose elements are

$$\mathrm{Q}_{hg}=\delta_{hg}\sqrt{\cos\theta_h}\,.$$

We can rewrite (35) as follows:

$$Q^{-1}MQ^{-1}\cdot Q\phi = xQ\phi\ . \tag{36}$$

$Q^{-1}MQ^{-1}$ is an hermitian, whose eigen vector is $Q\phi$. If $Q\phi$ is normalized, the amplitude $u_h{}^i$ is given by

$$\begin{aligned} u_h{}^i &= \psi_0{}^{i*}\psi_h{}^i \cos\theta_0 \\ &= \sqrt{\cos\theta_0}\,\psi_0{}^{i*}\sqrt{\cos\theta_h}\,\psi_{hi}\sqrt{\frac{\cos\theta_0}{\cos\theta_h}}\ . \end{aligned} \tag{37}$$

We can derive the wave function of the **h**-reflection wave by the same way as we get (18), namely

$$\Psi_h = \left[\exp\left(i\frac{z}{2k}Q^{-1}MQ^{-1}\right)\right]_{h0}\sqrt{\frac{\cos\theta_0}{\cos\theta_h}} \times \exp(i\boldsymbol{k}_h\cdot\boldsymbol{r})\ . \tag{38}$$

Then, the scattering matrix is given by

$$\begin{aligned} S &= Q^{-1}\exp\left(i\frac{z}{2k}Q^{-1}MQ^{-1}\right)Q \\ &= \exp\left(i\frac{z}{2k}Q^{-2}M\right), \end{aligned}$$

and we have

$$[(Q^{-2}M)^n]_{h0} = \sum_{g_1g_2\cdots g_{n-1}} \frac{v_{hg_1}v_{g_1g_2}\cdots v_{g_{n-1}0}}{\cos\theta_h\cos\theta_{g_1}\cdots\cos\theta_{g_{n-1}}}\ ,$$

since

$$(Q^{-2}M)_{hg} = \frac{v_{hg}}{\cos\theta_h}\ , \qquad (v_{hh}=p_h)$$

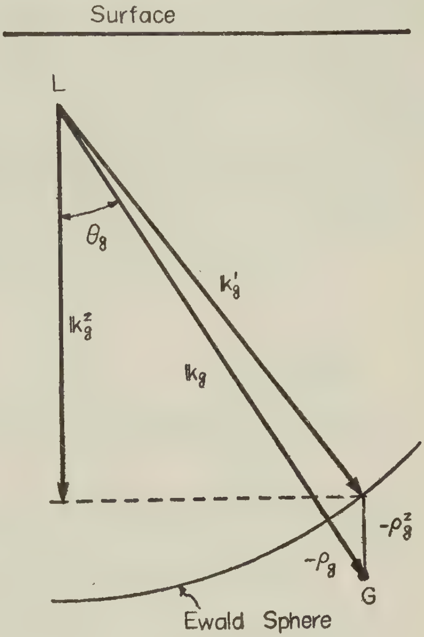

Fig. 4.

If we use the symbol $\rho_h{}^z$, $\boldsymbol{k}_h{}^z$, $\boldsymbol{k}_h{}'$ defined in Fig. 4, (38) is rewritten as follows:

$$\begin{aligned} \Psi_h = &\sum_{m=1}^{\infty}\sum_{g_1g_2\cdots g_{m-1}} \exp(-i\rho_h{}^z z)\,\frac{v_{h-g_1}v_{g_1-g_2}\cdots v_{g_{m-1}}}{(2k)^m\cos\theta_h\cos\theta_{g_1}\cdots\cos\theta_{g_{m-1}}} \\ &\times\left[\frac{\exp(iz\rho_h{}^z)-1}{\rho_h{}^z(\rho_h{}^z-\rho_{g_1}{}^z)\cdots(\rho_h{}^z-\rho^z_{g_{m-1}})}\right. \\ &\left.+\sum_{i=1}^{m-1}\frac{\exp(iz\rho_{g_i}{}^z)-1}{\rho_{g_i}{}^z(\rho_{g_i}{}^z-\rho_h{}^z)(\rho_{g_i}{}^z-\rho_{g_1}{}^z)\cdots(\rho_{g_i}{}^z-\rho^z_{g_{i-1}})(\rho_{g_i}{}^z-\rho^z_{g_{i+1}})\cdots(\rho_{g_i}{}^z-\rho^z_{g_{m-1}})}\right] \\ &\times\exp(i\boldsymbol{k}_h{}'\cdot\boldsymbol{r}) \\ = &\sum_{m=1}^{\infty}\sum_{g_1g_2\cdots g_{m-1}} \exp(-i\rho_h{}^z z)\,\frac{v_{h-g_1}v_{g_1-g_2}\cdots v_{g_{m-1}}}{2^m k_h{}^z k_{g_1}{}^z\cdots k^z_{g_{m-1}}}\left[\frac{\exp(iz\rho_h{}^z)-1}{\rho_h{}^z(\rho_h{}^z-\rho_{g_1}{}^z)\cdots(\rho_h{}^z-\rho^z_{g_{m-1}})}\right. \\ &\left.+\sum_{i=1}^{m-1}\frac{\exp(iz\rho_{g_i}{}^z)-1}{\rho_{g_i}{}^z(\rho_{g_i}{}^z-\rho_h{}^z)(\rho_{g_i}{}^z-\rho_{g_1}{}^z)\cdots(\rho_{g_i}{}^z-\rho^z_{g_{i-1}})(\rho_{g_i}{}^z-\rho^z_{g_{i+1}})\cdots(\rho_{g_i}{}^z-\rho^z_{g_{m-1}})}\right] \\ &\times\exp(i\boldsymbol{k}_h{}'\cdot\boldsymbol{r})\ . \end{aligned} \tag{39}$$

(39) agrees with the result given by Fujiwara.11) The first term in (39) is

$$\Psi_h{}^1 = \frac{v_h}{2k_h{}^z}\,\frac{1-\exp(-i\rho_h{}^z z)}{\rho_h{}^z}\exp(i\boldsymbol{k}_h{}'\cdot\boldsymbol{r})\ .$$

This formula was obtained by Raether.15)

References

1) H. Bethe: Ann. Physik **87** (1928) 55.
2) E. Lamla: Ann. Physik **32** (1938) 178, 226. E. Fues and E. H. Wagner: Z. Naturforsch. **6** (1951) 1.
3) R. D. Heidenreich: Phys. Rev. **77** (1950) 271.
4) J. A. Hoerni: Phys. Rev. **102** (1956) 1534.
5) S. Miyake and R. Uyeda: Acta Cryst. **3** (1950) 314.
6) K. Kohra: J. Phys. Soc. Japan **9** (1954) 690.
7) S. Miyake: J. Phys. Soc. Japan **14** (1959) 1347.
8) H. Niehrs and E. H. Wagner: Z. Phys. **143** (1955) 285.
9) See, for example, M. Lax: Rev. Mod. Phys. **23** (1951) 287.
10) J. M. Cowley and A. F. Moodie: Acta Cryst. **10** (1957) 609.
11) K. Fujiwara: J. Phys. Soc. Japan **14** (1959) 1513.
12) M. Blackman: Proc. Roy. Soc. **A, 173** (1939) 68.
13) R. Glauber and V. Schomaker: Phys. Rev. **89** (1953) 667.
14) J. A. Hoerni and J. A. Ibers: Phys. Rev. **91** (1953) 1182.
15) H. Raether: *Elektroneninterferenzen*, Handb. d. Physik XXXII (Springer, Berlin, 1959) 475.

JOURNAL OF THE PHYSICAL SOCIETY OF JAPAN Vol. 14, No. 11 NOVEMBER, 1959

On the Magnetic Anisotropy of a Pyrrhotite Crystal*

By Itsuo MIKAMI, Tokutaro HIRONE, Hiroshi WATANABE
Seijiro MAEDA, Kengo ADACHI
The Research Institute for Iron, Steel and Other Metals, Tohoku University, Sendai
and
Motohiko YAMADA**
Faculty of Liberal Arts and Science, Yamagata University, Yamagata

(Received November 12, 1958, Revised manuscript received August 10, 1959)

Measurement of the magnetic anisotropy energy of a single crystal of natural pyrrhotite in c-plane was made by means of the torque method at room temperature up to a magnetic field of 20000 oe and at low temperature in a constant field. It was found that the easy axis lay along $[2\bar{1}0]$ direction above -80°C which, however, changed to [100] direction below that temperature. The torque curves in c-plane were composed of two- and six-fold symmetric parts. It was also found that in the range of strong magnetic fields the six-fold symmetric part at room temperature decreased with the inverse square of the applied field; such a field dependence is explained assuming a triad structure for the single crystal of pyrrhotite. A remark is also given on the origin of the two-fold symmetric torque.

§ 1. Introduction

The experiment by Weiss and others[1)2)] on a single crystal of natural pyrrhotite revealed that this crystal was paramagnetic along [001] direction while it was ferromagnetic in (001) plane. In (001) plane they found a magnetic anisotropy of two-fold symmetry superposed on that of six-fold. They regarded the two-fold part as essential. On the other hand Kaya and Miyahara[3)] obtained a result which showed a complete six-fold symmetry and concluded that the six-fold symmetric part was essential. However, the magnetic field used by these authors was not so strong that sufficient knowledge on the magnetic anisotropy of this crystal was not obtained. The present authors have measured the magnetic anisotropy of a single crystal of natural pyrrhotite from the same source as those used by Kaya and Miyahara up to a field of about 20000 oe. In this paper the results of the measurement are shown together with some remarks on the origin of the field dependence of the torque curve.

---

* A part of this investigation is based upon the dissertation (Master Course (1956), Tohoku University) presented by Itsuo Mikami, now at the Hitachi Central Research Laboratory, Tokyo.

** Now at the Research Institute for Iron, Steel and Other Metals, Tohoku University, Sendai.

§ 2. The Method of Measurement and the Specimen

For the measurement of the magnetic anisotropy constant a vacuum torque-meter was used. The temperature was measured by a copper-constantan thermo-junction attached to the specimen and the induced thermo-e.m.f. was led to a potentiometer by means of fine spiral wires of the same material which did not introduce any detectable mechanical influence in the performance of the torque-meter.

A circular disk of about 8.5 mm in diameter and 0.5 mm in thickness was cut from a crystal of natural pyrrhotite. The deviation in diameter was about 0.5 mm. The torque due to the anisotropy of the demagnetizing energy expected from such deviation is less than 1% of the torque due to the crystalline anisotropy energy, so that the effect of the shape is negligible in our case. It was also shown from the Laue spots taken at the center of the disk that the normal of the basal plane of the disk deviated 5° from [001] direction and its projection on (001) basal plane lay along [100] direction. It was also found that mosaic spread was about 1°.

§ 3. The Experimental Results

(1) Torque measurements at room temperature

First the magnetic field was applied in the basal plane and the resulting torque is shown in Figs. 1 and 2, in which the ordinate represents the torque per unit volume and φ_0 indicates the angle from [$2\bar{1}0$] axis. In Fig. 1 the torque curves at several field strengths from 800 up to 7500 oe are shown and in Fig. 2. those from 9800 to 19150 oe. Each curve can be understood by the superposition of those with six-fold and two-fold symmetry. The six-fold symmetric parts are shown in Fig. 3. These six-fold symmetric torque curves pass through zero at $\varphi_0=0$. It should be noted that throughout the measurement the stable position of the specimen was not found in the vicinity of $\varphi_0=\pm 30°$ or [100] direction, showing that [$2\bar{1}0$] axis is the direction of easy magnetization at room temperature. The field dependence of the six-fold symmetric torque at $\varphi_0=15°$ is shown in Fig. 4. As is shown, the magnitude of torque increases at first, reaches its maximum at about 6000 oe, and then decreases to zero as

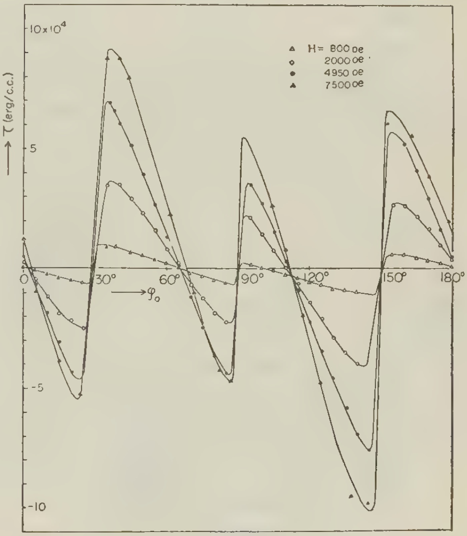

Fig. 1. Torque curves in c-plane at room temperature, field strength (H) from 800 to 7500 oe.

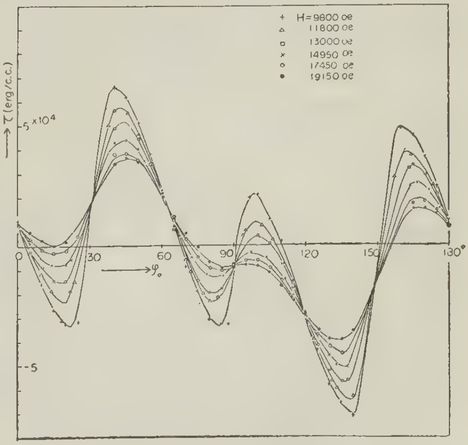

Fig. 2. Torque curves in c-plane at room temperature, field strength from 9800 to 19150 oe.

H increases further. The shape of the torque curve becomes sinusoidal at strong field.

When the six-fold symmetric part is substracted from the observed torque values there remains a two-fold symmetric torque, as shown in Fig. 5.1. In the high field range the curves are smooth and nearly sinusoidal but in the low field range they show steps at $\varphi_0=90°$ and $180°$. The relation between the amplitude of the two-fold symmetric torque and field strength is shown in Fig. 5.2. The amplitude seems to reach a saturated value of about 3×10^4 ergs per unit volume at about 10000 oe.

(2) Torque measurements at low temperatures

The temperature variation of the torque was measured below the room temperature by keeping the field strength constant at 12900 oe. In Fig. 6 the measured torque values at different temperatures are shown. The torque amplitude decreases at first with lowering temperatures. It seemes at $-80°C$ the direction of the easy magnetization changes from [2$\bar{1}$0] to [100].

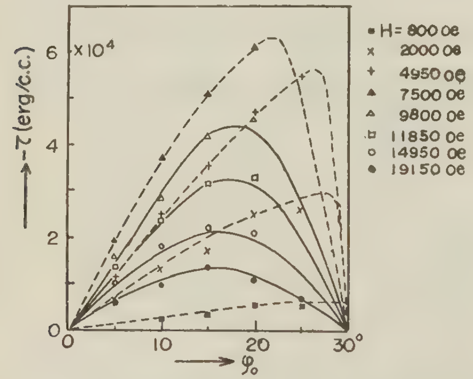

Fig. 3. Six-fold symmetric torque curves in c-plane separated from observed torque curves (Figs. 1 and 2). Solid lines are theoretical curves calculated by Eq. (2) and dotted lines connect the experimental values.

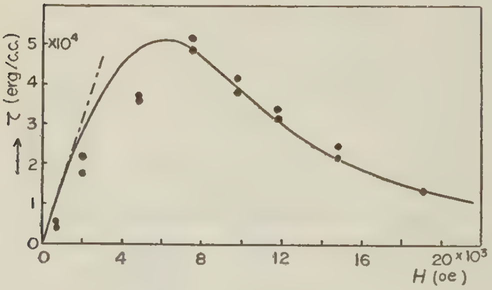

Fig. 4. Relation between six-fold symmetric torque at $\varphi_0=15°$ and magnetic field strength.
· ; experimental value.
———; theoretical curve.
-·-·-·-; 2/3 HI_s cos 15°.

§ 4. Interpretation of the Experimental Results

As has been analyzed above, it is convenient for the following discussion to separate the experimental results into two, namely the six-fold symmetric anisotropy and the two-

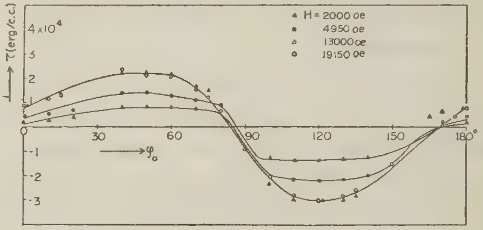

Fig. 5.1. Two-fold symmetric torque curves in c-plane which are separated numerically from observed torque curves (cf. Fig. 1 and Fig. 2).

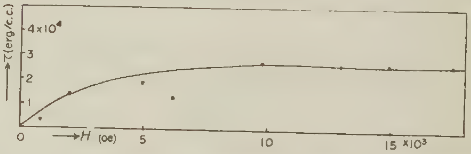

Fig. 5.2. Relation between two-fold symmetric torque amplitude and magnetic field strength.

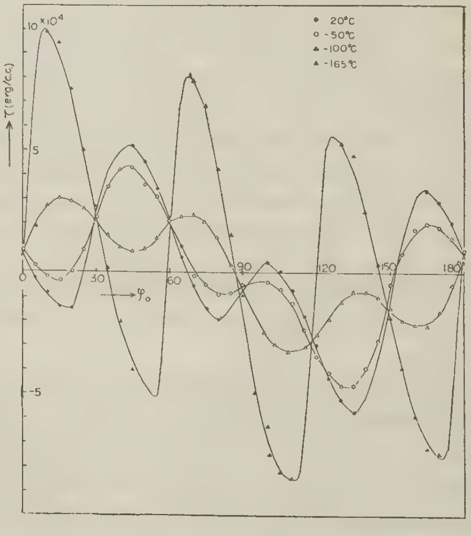

Fig. 6. Variation of torque curve with lowering temperature. A constant field, $H=12900$ oe is applied in measurements and φ_0 is the angle from [2$\bar{1}$0] direction.

fold one. At first the six-fold part is discussed. In a normal ferromagnetic crystal the torque amplitude increases monotonously with the strength of the applied magnetic field until saturation is reached. However, in the present case the torque amplitude with the six-fold symmetry decreased in high fields. Such an unusual magnetic behavior of the pyrrhotite crystal can be explained by assuming a twin-like structure in this crystal.

According to Bertant[4] the crystal lattice of pyrrhotite belongs to the pseudo-orthorhombic (monoclinic) system. An actual crystal of pyrrhotite is thought to be an aggreagate of three kinds of small crystal domains with such orthorhombic symmetry; each domain has common c-axis but the orientations of *a*- and *b*- axis distribute among the three directions which make an angle of $2\pi/3$ with one another respectively. Such an assembly of crystallites or domains behaves, as a whole, like a pseudo-hexagonal crystal. Since the c-axis of each crystal domain is the axis of the two-fold symmetry, the magnetic anisotropy in c-plane of the whole crystal is to be produced by the superposition of those of the individual crystal domains with two-fold symmetry. Based on the model here proposed, it is shown that the field dependence of the apparent six-fold anisotropy can be reproduced theoretically together with its change with the magnetic field.

When K_1, I_s, and H denote the postulated two-fold symmetric magnetic anisotropy constant within c-plane, the saturation magenetization of each domain, and intensity of the external magnetic field respectively, the energy of each domain per unit volume, E_k $(k=1, 2, 3)$, is given by

$$E_k=-K_1\cos^2\left(\alpha_k-\frac{2}{3}k\pi\right)-HI_s\cos(\alpha_k-\varphi_0)\,, \tag{1}$$

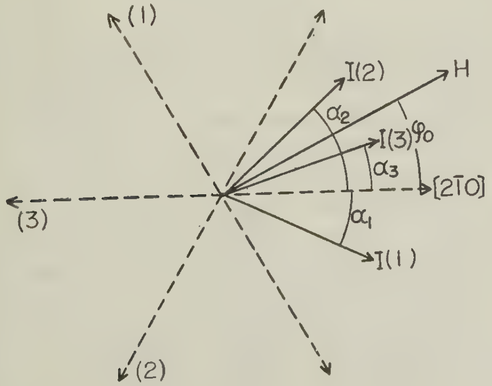

Fig. 7. Schematic diagram of three domains in c-plane.
(K) ←-→; anisotropy axis of domain k.
$I(K)$ ⟵; magnetization vector of domain k.

where α_k and φ_0 are, as shown in Fig. 7, the orientation of the magnetization of domain k and the direction of the external field. By assuming that the total volume of each kind of domain is equal, following results can be obtained.

(1) When the magnetic field is sufficiently small, then the torque per unit volume τ is given by

$$\tau(\varphi_0)=\frac{2}{3}HI_s\sin\varphi_0\left(-\frac{\pi}{6}\leq\varphi^0\leq\frac{\pi}{6}\right).$$

The torque amplitude will be proportional to the field H. Torque curves at 800 oe and also probably at 2000 oe presented in Fig. 3 are described qualitatively by this equation.

(2) In a strong field the directions of magnetizations in each crystal domains fall in the field direction $(\alpha=\varphi_0)$, then the total energy of the system is shown to be independent of φ_0, resulting the negligibly small torque.

(3) In the intermediate field range $HI_s>K_1$, the torque is shown to be expressed by the following type of equation.

$$\tau(\varphi_0)=-\frac{3}{2}K_1\eta^2(1-2\eta^2)\sin 6\varphi_0 +10K_1\eta^5\sin 12\varphi_0 \tag{2}$$

with

$$\eta=K_1/HI_s\,.$$

As seen from it the torque changes as $\sin 6\varphi_0$ and with the increase of the field strength the torque amplitude approaches zero in proportion to H^{-2}. When H approaches a value K_1/I_s, the term proportional to $\sin 12\varphi_0$ in Eq. (3) becomes effective, and the departure from simple sinusoidal curve of $\sin 6\varphi_0$ becomes appreciable. The theoretical curve shown in Figs. 3 and 4 were obtained by choosing the best value of K_1 and by putting 80 gauss for the saturation magnetization I_s after Lotgering[5]. The value of K_1 thus determined is 2.83×10^5 ergs per c.c. at room temperature.

Now for the two-fold symmetric part of the torque in c-plane three possible origins could be enumerated:

(1) The total volume of each kind of

micro-crystal domain ($k=1, 2, 3$) mentioned above is slightly different from one another. In this case a small uniaxial anisotropy remains in c-plane.

(2) Basal plane of the specimen used in our experiment slightly inclines to the crystallographic c-plane.

(3) Some imperfections such as ferromagnetic precipitates exist in this natural single crystal.

As the normal of the basal plane of our specimen deviated by 5° from [001] direction and its projection on (001) plane lay along [100] direction, the case (2) will be probable*.

§ 5. Origin of the magnetic anisotropy

It was previously shown by Bertaut that the crystal lattice of pyrrhotite is built by alternate stacking of the net planes of iron ions with and without vacant sites. Considering the measured value of the saturation magnetization, it is more probable that ferric ions are in the planes which contain vacant sites[7]. In order to get the two-fold symmetric anisotropy in c-plane, it might be possible to consider some type of ordering of vacant sites and iron ions in these net planes. An atomic arrangenent is proposed in Fig. 8. In the c-planes including vacancies, there appear linear arrays of iron atoms with and without vacancies in alternate succession. It is assumed here that the ions in the arrays including vacancy are trivalent. The anisotropy energy in c-plane which is caused mainly from Fe^{2+} ions is estimated to be the order of 10^6 ergs per unit volume[8]. This is somewhat greater than that obtained by the present experiment, namely, 2.83×10^5 ergs per unit volume. This difference in the value of K_1, however, will be lowered by assuming that both the ferrous and ferric ions are not arranged perfectly in order. Of course it should be assumed that the direction of such parallel linear array in each crystal domain is in either of the three equivalent directions $[2\bar{1}0]$, [120] and $[2\bar{1}0]$. Reversal of the sign K_1 (the change of apparent six-fold symmetric anisotropy axis from the $[2\bar{1}0]$ to [100] direction) at −80°C may be due to the change of the energy levels of ferrous ion induced by the temperature change of the axial ratio c/a.

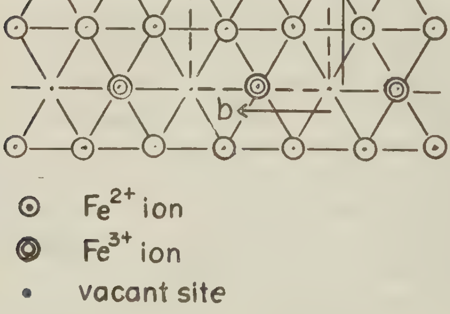

Fig. 8. Proposed ionic ordering in the vacancy including c-plane. Dotted line shows basal plane of the unit cell.

The present authors wish to express their hearty thanks to Prof. N. Tsuya, who kindly arranged for them the specimen of pyrrhotite and gave valuable suggestion for the present investigation. They also wish to express their sincere thanks to Prof. S. Chikazumi of Gakushuin Univ. and Prof. M. Yamamoto of Tohoku Univ. for their kind and valuable suggestions to the interpretation of torque curves. The present work was supported in part by the Grand-in-Aid of Scientific Researches of the Ministry of Education.

References

1) P. Weiss: J. phys. radium **4** (1904) 459.
2) P. Weiss and H. Kuntz: Arch. Sci. **20** (1905) 621.
3) S. Kaya and S. Miyahara: Sci. Rep. Tohoku Univ. **27** (1938) 450.
4) F. Bertaut: Acta Cryst. **6** (1953) 557.
5) F. K. Lotgering: Philips Res. Rep. **11** (1956) 190.
6) M. Yamamoto, T. Iwata and M. Kobayashi: private communication.
7) K. Yosida: Progr. Theor. Phys. **6** (1951) 356.
8) K. Adachi and I. Mikami: unpublished work (1957).

---

* It is to be mentioned for (3) that Yamamoto, Iwata and Kobayashi[6] found precipitate-like domain patterns in c-plane of the same specimen.

JOURNAL OF THE PHYSICAL SOCIETY OF JAPAN, Vol. 14, No. 11, NOVEMBER, 1959

Effects of Ionizing Radiations on Synthetic Polymer Solutions

By Shintaro SUGAI

Physics Department, Faculty of Science, Hokkaido University
Sapporo, Hokkaido

(Received May 6, 1959)

Aqueous solutions, containing disolved oxygen, of sodium salt of carboxy-methyl cellulose and of polyacrylic acid and so on were irradiated with γ-rays from Co^{60} or with 90 KV X-rays, and the degeneration of molecules in the solutions brought about under various conditions was studied by viscometric, ultracentrifugal, and electrical measurements.

Ideal indirect kinetics of main chain fractures through activated water has been recognized in all the cases from highly concentrated solutions to fairly diluted ones. In the case of extremely diluted solutions, however, free-radical recombination seems to make the reaction inefficient.

From a simple consideration of these fact, a certain information as to the molecular extension and form in the solution has been derived.

Inclusion of salts and alcohols in the solution protects effectively the degeneration due to irradiation, which can be explained satisfactorily likewise on the assumption of "*indirect effect*".

The molecular contraction and change of molecular form caused by the inclusion of salts have been estimated.

The irradiation effect on dilute solutions of non-electrolyte polymers was also investigated. The efficiency of chain fractures comes out not much smaller than in the case of polyelectrolyte molecules in the same concentration range. Here the rate of fracture seems to indicate again the "*indirect effect*".

It may therefore be concluded that electrical charges on polyelectrolyte molecules, in a certain range, are not essential for degradation and their extension is not much different from that of non-electrolyte molecules.

It has been observed that, in the case of concentrated polyelectrolyte solutions containing oxygen, irradiation does not give rise to formation of gel, although micro-gel may be formed.

§ 1. Introduction

Recently, many investigators observed the the effect of irradiation on various solid polymers, and it has been concluded that polymers can be divided into two groups from view-point of radiation chemistry: in one of them degradation of molecules is the main reaction, and in the other crosslinking between molecules is the most important effect²⁾.

However, in the case of copolymers or in more complicated cases, where some low molecular substances are included in the solid polymers, circumstances turn out considerably complex²⁾.

In the case of polymer solution, which is one of the typical many-component systems, similar complications may well be expected to arise.

It is probably for this reason that there have hitherto been comparatively few researches concerning the effect of ionizing radiation on polymer solutions, especially on synthetic ones, notwithstanding that such researches have acquired importance in the branch of radiation biology³⁾ as well as of polymer science.

Some authors have found that synthetic polymer solutions are very sensitive to ionizing radiations compared with solid polymers, especially in the case of dilute aqueous solution containing oxygen⁴⁾.

Explanation which have been given to such a tendency is based on the idea of the so-called "*indirect effect of radiation on solution*⁵⁾."

If the reaction occurring in the solution due to irradiation be indirect, the total dose R necessary to producea certain amount of degeneration should be related, under simple circumstance, to the concentration c of the solution by

$$R/c = constant \quad (\equiv k). \qquad (1)$$

Alexander and Fox confirmed the validity of this relation by measuring the viscosity change of dilute aqueous solution of polymethacrylic acid partly neutralized with sodium hydroxide[6]. For verifying Eq. (1), poly-electrolyte aqueous solutions of polymer prove most useful, since the physical and chemical properties can be measured over an extended range of concentration than in the case of non-electrolyte polymer solutions.

Alexander and Charlesby observed, on the other hand, that the main reaction due to irradiation occuring in dilute aqueous solutions of polymer is always a chain scission[7], and that, while in a number of cases of concentrated non-electrolyte aqueous solutions gel formation takes place[8], no gel formation ensures in concentrated polyelectrolyte aqueous solutions.

Further, according to many authors, the rate of reaction in the irradiated dilute aqueous solution of polymer depends not only on the concentration of the polymer and quantity of oxygen but also largely on the molecular extension[9] The dependency upon the molecular extension serves as an indication of the indirect effect of radiation on the solution.

As for the irradiation effect on non-aqueous polymer solutions, there have been but few researches. One of the authors[10] has noted the direct effect of γ-rays upon polystyrene (*PS*)-carbon tetrachloride (CCl_4) solution, while another has called attention to the indirect effect for the same system[11].

In this case it is, as pointed out above, not easy to check the validity of Eq. (1) exactly. Therefore use cannot be made of Eq. (1) for determining whether the effect is direct or indirect. According to the existing data, the effect in non-electrolyte solutions is comparatively small, which is likely to be considered as indicating the direct effect.

However, in consideration of the circumstances that the range of concentration where the measurement can be made is comparatively high and that the molecular extension in non-electrolyte solution may be small compared with that in polyelectrolyte one, small yield of reaction will not necessarily lead to the conclusion of direct effect.

Also it must be noted that when polyelectrolyte aqueous solution completely free from oxygen is irradiated, scission yield is comparatively small.

In the present work, the irradiation effects of γ- and *X*-rays on polyelectrolyte aqueous solutions were studied over a concentration range from extreme dilution to high concentration, by making use of viscometric, ultracentrifugal, and electrical measurements. Special attension was paid to the relation between reaction rate and molecular extension.

The difference in irradiation effect between polyelectrolyte and non-electrolyte solutions was also examined.

§ 2. Experimental Procedures

Polyelectrolytes used in this study were sodium salts of carboxy-methyl cellulose (*Na-CMC*), and of polyacrylic acid (*Na-PA*), and copolymer (*CP*) of poly-(potassium methacrylate) and polymethyl methacrylate (ratio 3 : 1).

Average degree of polymerization (*DP*) and that of etherification of *Na-CMC* were respectively 560 (calculated from the intrinsic viscocity[12]) and 0.685. However, according to the ultracentrifugal patterns of highly concentrated aqueous solutions, *Na-CMC* was found to consist of two groups, characteristics of which are indicated in Table I.

Table I. Characteristics of *Na-CMC* used in this study.

1 Degree of Etherification 0.685
Degree of Polymerization 560
Max. Value of η_{sp}/c of Aqueous Solution 1.0×10^4 *cc/gr* ($c = 4.5 \times 10^{-5}$ *gr/cc*)
2 Ultracentrifugal Coefficient (Aqueous Solution including 1 *Mol NaCl*)

c	s_1	s_2	f_1
gr/cc	*sved*	*sved*	%
2.4×10^{-3}	2.0	7.9	66.7
6.7×10^{-4}	2.5		100

s_1, s_2 : ultracentrifugal coefficients of two groups
f_1 : fraction of the first group

DP of *Na-PA* (calculated from the intrinsic viscosity[13]) was about 1.0×10^4.

The data concerning the properties of *CP* is very meager, only its behaviour in aqueout solution including 1 *Mol* of potassium chloride is known to resemble that of non-electrolyte.

The samples were purified by the ordinary method, the specific conductivity of the water used being $1.0\times10^{-6}\,\Omega^{-1}cm^{-1}$.

The viscosity was measured with Ostwald-type viscometer at 25°*C* and the electric conductivity was determined by supplying 1000 *c/s A.C.* with impedance bridge and cathode-ray oscilloscope.

Ultracentrifugal patterns were obtained by the use of Spinco *E* Centrifugal *M*achine at 56000 *r/m*.

As γ-ray source, 42 *Curies* of Co^{60} in charge of Department of Radiology and 20 *milli-Curies* of Co^{60} (needle type) were used. The latter was intended for the irradiation at extremely low dose-rate.

As X-ray source served a 90 *KV* X-ray tube with no filter.

The solution containing oxygen was sealed in a glass vessel, the volume ralio between the solution and air in the vessel being kept constant throughout the experiment. It is to be noted that no stabilizers were introduced in the solutions, because even a small quantity of foreign substance in the solution may effectively protects the solution from degeneration. Exact measurement of degeneration due to irradiation was achieved by comparison with the natural degeneration of non-irradiated solution, which had been stocked under the same condition.

Non-electrolyte polymers subjected to irradiation were polyvinyl alcohol (*PVA*), polyvinyl chloride (*PVC*) and polystyrene (*PS*). *DP* of these polymers determined by measuring the intrinsic viscosity came out respectively 2260, 750 and 2400. Aqueous or non-aqueous solutions of these samples containing oxygen were irradiated under the same conditions as described above.

§ 3. Experimental Results

A) *Degradation of molecule in dilute aqueous solution of polyelectrolyte.*

Relative changes in specific viscosity η_{sp} of the dilute aqueous solution of various polyelectrolytes caused by γ-ray and *X*-ray irradiations are shown in Table II, which shows that viscosity of all dilute solutions studied in this case decreases markedly under any dose-rate of irradiation and that the higher the concentration of solution, the smaller is the effect of irradiation.

These results are qualitatively in accord with those hitherto reported and seem to suggest the indirect effect of the ionizing radiation on polyelectrolyte aqueous solutions.

Table II. Relative decrease in specific viscosity $-\Delta\eta_{sp}$ of dilute aqueous solutions of various polyelectrolytes (γ-rays).

polyelectrolyte	c	dose-rate	dose	$-\Delta\eta_{sp}$
	gr/cc	*r/min*	*r*	%
Na-CMC	6.7×10^{-4}	85	420	6.7
	2.4×10^{-4}	〃	〃	9.0
	2.4×10^{-5}	〃	〃	18.3
	2.5×10^{-6}	17	〃	37.0
	1.2×10^{-4}	5.6×10^{-2}	〃	30.0
Na-PA	2.5×10^{-4}	8.5	340	6.1
	6.0×10^{-5}	〃	〃	32.1
CP	8.0×10^{-4}	〃	〃	3.4
	1.9×10^{-4}	〃	〃	19.2
	3.2×10^{-5}	〃	〃	77.6
Na-CMC	1.2×10^{-5}	200*	550	21.2

* X-ray irradiation

Table III. The relation between dose *R* required for producing $\Delta\eta_{sp}=10\%$ and concentration of solution c under γ-ray irradiation.

polyelectrolyte	*viscometer*	c	*dose-rate*	R	R/c
		gr/cc	*r/min*	*r*	*r·cc/gr*
Na-CMC	I	2.0×10^{-3}	220	7500	3.7×10^{6}
		6.7×10^{-4}	190	610	0.9×10^{6}
		5.6×10^{-4}	85	800	1.4×10^{6}
		2.4×10^{-4}	170	320	1.3×10^{6}
		6.7×10^{-5}	〃	200	2.9×10^{6}
		〃	190	90	1.4×10^{6}
		〃	85	110	1.7×10^{6}
	II	1.7 〃 10^{-4}	33	150	0.9×10^{6}
		〃	9	125	0.8×10^{6}
		2.3×10^{-5}	85	110	1.7×10^{6}
		7.5×10^{-6}	33	130	2.0×10^{7}
		〃	9	120	〃
		2.3×10^{-6}	85	320	1.4×10^{8}
	III	9.7×10^{-4}	12	700	0.8×10^{6}
		2.5×10^{-4}	〃	250	1.0×10^{6}
		2.5×10^{-5}	〃	120	5.0×10^{6}
Na-PA	II	2.5×10^{-4}	8.5	400	1.6×10^{6}
		6.0×10^{-5}	〃	80	1.3×10^{6}
		9.6×10^{-6}	〃	10	1.0×10^{6}
CP	II	3.2×10^{-5}	〃	55	1.4×10^{6}
		1.9×10^{-4}	〃	200	1.1×10^{6}
		8.0×10^{-4}	〃	930	1.2×10^{6}

In order to examine quantitatively the indirect effect through the activated water, inquiry must be made as to whether relation (1) holds good or not. Theoretically speaking, relation (1) for viscosity change holds strictly only within a narrow range of concentration, since free radical recombination may be not strictly taken into consideration[14].

Actually however, as shown in Table III, which gives the degeneration of three polyelectrolytes at various concentrations, Eq. (1) is satisfied over a considerably wide range of concentration. Thus from Table III the following conclusions may be drawn:

1) The ideal type of indirect effect on viscosity change is realized in polyelectrolyte solution, notwithstanding the complicated circumstances described above, except at extremely dilute concentration.
2) Degeneration does not depend on dose-rate over a wide range. Therefore a dosemeter can be made by the use of these solutions, especially for low dose.
3) There appears a marked inefficiency of radiation in causing degeneration in extremely dilute solutions. (Probably, it arises from recombination of free radicals.)

Table IV. Change of intrinsic viscosity and scission yield of chain in *Na-CMC* aqueous solution due to γ-irradiation (does-rate 220 *r/min*).

c	*dose*	$[\eta]_{irr}/[\eta]_{no}$	*N*	*G*
gr/cc	*r*			
2.0×10^{-3}	2200	0.97	0.031	0.27
6.7×10^{-4}	4300	0.75	0.333	0.41
〃	1700	0.92	0.086	
2.4×10^{-4}	850	0.85	0.176	0.47
6.7×10^{-5}	210	0.88	0.136	0.51
〃	420	0.71	0.408	
〃	850	0.56	0.785	

N: number of scission per original molecule.

Table V. Change of ultracentrifugal figures of *Na-CMC* aqueous solution including 1 *Mol* NaCl* due to γ-ray irradiation (dose-rate 170 *r/min*).

c	*dose*	s_1	s_2	f_1
gr/cc	*r*	*seved*	*seved*	*%*
2.4×10^{-3}	0	2.0	7.9	66.7
〃	6.8×10^4	1.8	6.5	70.5
6.7×10^{-4}	0	2.5		100.0
〃	4.3×10^3	2.1		〃

* NaCl was introduced in the solutions after irradiation.

Now, to ascertain the main-chain fractures of polymer molecules and to calculate the rate of reaction, the intrinsic viscosity changes must be examined. In Table IV are given the intrinsic viscosity of irradiated *Na-CMC* queous solution and the efficiency of main-chain fractures *G*-values were calculated on the assumption of random fracture[15], which is justified by the observation on the change of ultracentrifugal patterns, as shown in Table V. One sees that the greater the molecular weight, the faster is the reaction, that is, that the fracture of main-chain takes place at random.

G-values in Table IV are considerably smaller than those reported in the case of degradation of polymethacrylic acid. This may

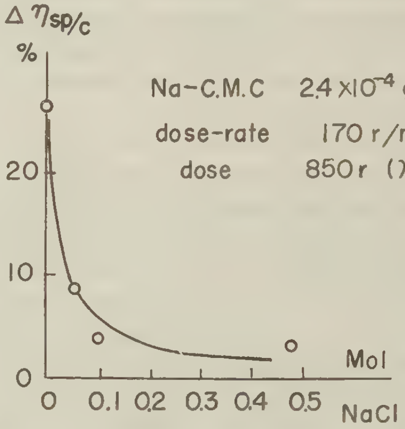

Fig. 1. Change of degeneration of irradiated *Na-CMC* aqueous solutions due to salt inclusion.

Table VI. Change of fracture efficiency under γ-ray irradiation due to salt inclusion (does-rate 170 *r/min*, dose 850 *r*).

c (*Na-CMC*)	quantity of NaCl	$[\eta]_{irr}/[\eta]_{no}$	*N*	*G*
gr/cc	*Mol*			
2.4×10^{-4}	0	85.0	0.176	0.47
〃	0.05	90.1	0.110	0.29
〃	0.48	92.5	0.081	0.22

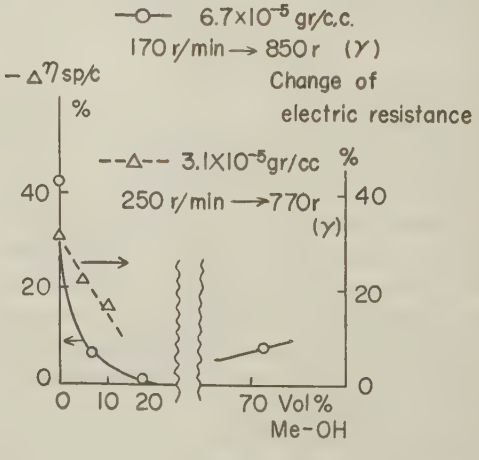

Fig. 2. Protection effects of methyl alcohol in irradiated *Na–CMC* aqueous solutions.

probably be accounted for by assuming that *Na-CMC* molecules are much smaller than those of polymethacrylic acid.

Table IV indicates another interesting fact that G is not constant but gradually increases as the concentration of the solution decreases, while Eq. (1) is satisfied in the same range of concentration. Discussion will be given later.

The general dependency of molecular degradation due to irradiation on molecular extension can be seen from Fig. 1, which shows data on the change in viscosity of *Na-CMC* aqueous solutions including various quantities of sodium chloride, and also from Table VI, which gives G-values for these solutions. Evidently, the salt acts as effective protector against degradation of molecules in polyelectrolyte aqueous solution.

Fig. 2 indicates another type of protection, which arises from the existence of alcohol in the solution. The protective power is here considerably great. It is true, the inclusion of alcohol in aqueous solutions of polyelectrolytes is very likely to change the molecular extension[16], but it will be noted later that protection in this case cannot completely be explained only be molecular contraction.

Finally, it is to be remarked that there exists an after effect of degeneration in *Na-CMC* aqueous solution subjected to irradiation of high dose, whereas aqueous solutions of the other two polyelectrolytes did not show any indication of after effect. Alexander and Charlesby also did not observe any after effect in the irradiated synthetic polymer solutions.

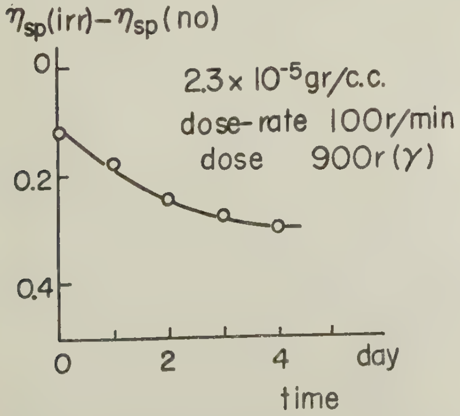

Fig. 3. After-effect of *Na–CMC* aqueous solution.

In view of the fact that solid cellulose exhibits a larger after-effect[17], the tendency as seen in Fig. 3 may probably be regarded as characteristic of *Na-CMC* molecules.

B) Effect of γ-rays on the electric conductivity of dilute aqueout solution of polyelectrolyte.

Various results mentioned in *A*) indicate the molecular degradation in the irradiated dilute aqueous solutions of polyelectrolyte. Now comes up the question: what kind of effect is brought about by the ionizing radiaon the electric properties of polyelectrolytes?

There have been few investigations with reference to this point, although some workers seem to have confirmed the effect of irradiation upon the electrical properties of low molecular solutions[18].

It is known that the electric conductivity of polyelectrolyte aqueous solution has no definite dependency on molecular weight[19]. Some authors, however, have shown that, if between the two solutions, in which the same sort of molecules are disolved with the same concentration, there is a great difference in molecular weight of the disolved molecules, they will have different conductivities[20].

Now, from Fig. 4 which shows the change

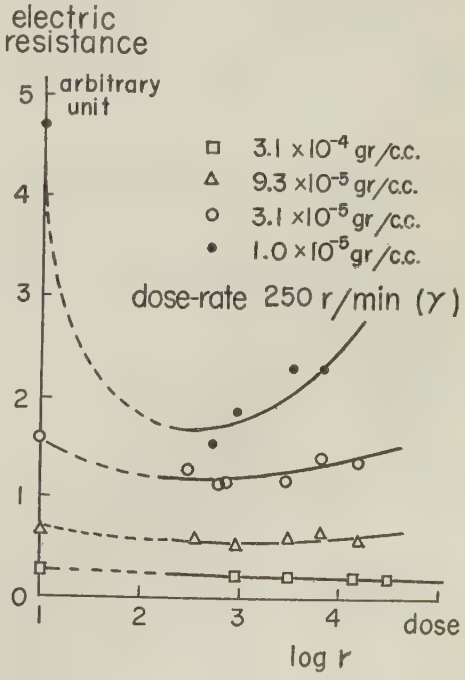

Fig. 4. Change of electric-resistance of *Na–CMC* aqueous solution due to irradiation.

in electric conductivity of irradiated solutions for 1000 *c/s A.C.*, it is mainfest that, while at higher concentrations the change in conductivity is much smaller than that in viscosity, it increases as the concentration is lowered. This suggest that in dilute solution the marked degradation of molecules is brought about so far as to cauge an appreciable change in conductivity.

If the dependency of the change in conductivity on the concentration of solution be such that it satisfies Eq. (1), it would definitely indicate the indirect effect. Actually, however, the dependency proved to be so complex that Eq. (1) could not be checked in this case.

What is interesting to be noticed in Fig. 4 is the fact that the change in conductivity of irradiated solution versus radiation dose has a maximum.

That this does not mean gel-formation in strongly irradiated solution is evident, since the curve of viscosity change turns out monotonous, as shown in Fig. 5. In order to make further inquiry into this phenomenon, the temperature dependency of the conductivity of irradiated solution was investigated. The results are illustrated in Fig. 6, which shows that the conductivity of irradiated solution is certainly greater than that of non-irradiated one at low temperatures, while the situation is revesed at higher temperatures. The reverse temperature is 30°*C* in this case.

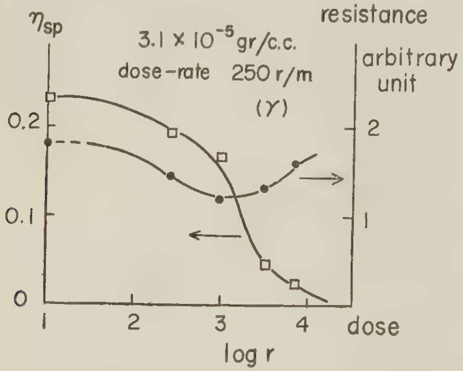

Fig. 5. Comparison of electric-resistance change of *Na-CMC* solution with viscosity change.

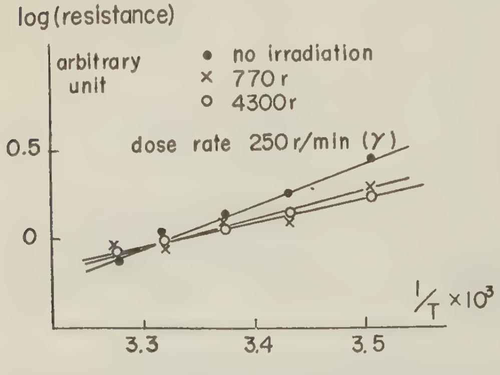

Fig. 6. Temperature dependency of electric resistance of irradiated *Na-CMC* aqueous solutions.

Thus, it must be remembered that the change in conductivity of the irradiated polyelectrolyte solution depends on temperature, that is, that if temperature, at which measurement was carried out, were different, the curve in Fig. 4 have come out entirely different.

In this connection it is to be noticed that methyl alconol acts as protecting agency against the change in conductivity and that, the after effect mainfests itself in some cases, as in the case of viscosity change.*

C) *Concentrated aqueous solutions of polyelectrolyte.*

As shown in Table V, ultracentrifugal measurement indicated the molecular degradation in highly concentrated *Na-CMC* aqueous solutions.

Table VII gives the change in viscosity of some concentrated solutions of *Na-CMC* and *CP*. Even in the case where the concentration is so high that all the molecules may be considered to be in contact with each other, the viscosity of the solution shows a decrease but no increase, at least when oxygen is present in the solutions, the fact which implies that no gel formation takes place.

But, what is to be noticed, it was observed that in some cases the ultracentrifugal velocity of the irradiated concentrated aqueous solutions of *CP* increased appreciably at the initial stage of irradiation, as shown also in Table VII.

Thus the possibility of intermolecular linkage can not completely be neglected. Be that as it may, macro-gel as revealed in the irradiated concentrated aqueous solutions of *PVA* was not observed in this case.

The question remains for solution whether the electric charges on polymers stand in any causal relation to this difference.

The fact that *Na-CMC* in solid state is far more insensitive to irradiation that in solution implies that the degradation in the solution must be caused by a reaction through the activated solvent molecules.

---

* Preliminary results are shown in Busseiron Kenkyu 2nd ed. **4** (1959) 735.

Table VII. Degeneration of concentrated solutions of *Na-CMC* and *CP* and of solid *Na-CMC* due to γ-ray irradiation.

1. *Na-CMC*

c	dose-rate	dose	$-\Delta\eta_{sp}/c$
gr/cc	*r/min*	*r*	*%*
6.7×10^{-3}\*	600	1.0×10^{3}	0
〃 *	〃	2.5×10^{3}	0.5
〃 *	〃	1.8×10^{4}	8.2
solid **	300	3.0×10^{3}	0

* Measurements were made by diluting the solutions to 6.7×10^{-4} *gr/cc*.

** Measurement was made by making the dilute solution ($c=6.7\times10^{-5}$ *gr/cc*) after irradiation.

2. *CP*

c	dose-rate	dose	$-\Delta\eta_{sp}/c$	s_{25}***
gr/cc	*r/min*	*r*	*%*	*sved*
9.0×10^{-3}	0	0		4.04
〃	35	2000	2.2*	4.47
4.5×10^{-3}	0	0		5.99
〃	10	700	4.8**	6.74
〃	〃	1600	19.5**	6.22
〃	〃	7200	48.0**	5.01

* Measurement was made by use of salt free solution.

** Viscosity measurements was made by use of 1 *Mol KCl* solutions. Salt was introduced in the solutions after irradiation.

*** Ultracentrifugal coefficient (temperature 25°*C*) of 1 *Mol KCl* aqueous solutions (salt was introduced after irradiation.)

D) Non-electrolyte polymer solutions

It may be of interest to examine the mechanism of degeneration in polyelectrolyte aqueous solutions by comparison with that in non-electrolyte polymer solutions, aqueous or non-aqueous, in which molecular extension may be widely different from that in electrolyte solutions[21].

The effect on non-electrolyte solutions of various polymers is shown in Table VIII, where R/c is calculated for dose R necessary to produce 10% relative change in specific viscosity.

The degeneration in dilute aqueous solution of *PVA* is probably due to the action of activated waters as in the case of polyelectrolyte aqueous solutions, efficiency of degeneration being, as can be seen from Table VIII, comparable to that in the case of electrolyte. The value of about 0.5 recently reported[22] for the *G*-value of chain scission in *PVA* aqueous solution is not less than that in the case of *Na-CMC* aqueous solution in the present study.

For non-aqueous solutions, concentration dependency of the change in viscosity or the relation between the sort of the solvent and the degeneration seems to indicate likewise the indirect reaction of radiation.

That degeneration in *PS*-benzene solution is relatively small harmonizes with the known fact that benzene is a very stable solvent against irradiation.

Table VIII. Degeneration of non-electrolyte polymer solution due to γ-ray irradiation.

1. Change of specific viscosity and relation between R ($-\Delta\eta_{sp}=10\%$) and c.

polymer-solvent	c	*dose-rate*	*dose*	$-\Delta\eta_{sp}/c$	R	R/c
	gr/cc	*r/min*	*r*		*r*	*r·cc/gr*
PVA—water	4.0×10^{-3}	210	1500	0		
〃	1.0×10^{-3}	〃	1500	6.0	4.0×10^{3}	4.0×10^{6}\*
〃	〃	〃	3500	9.4		
PVC—nitro-benzene	3.7×10^{-3}	80	2800	2.4	1.2×10^{4}	3.2×10^{6}
〃	1.2×10^{-3}	〃	〃	4.5	6.0×10^{3}	5.0×10^{6}
PS—benzene	2.7×10^{-3}	〃	4800	2.5	2.4×10^{4}	8.0×10^{6}
PS—CCl₄	3.4×10^{-3}	50	11000	13.7	4.8×10^{3}	1.0×10^{6}

* Viscometer type II.
Other data were obtained by using viscometer type I.

2. Scission yields *G* for non-electrolyte polymers containing oxygen.

polymer	*solvent*	*G*	*reference*
PVA	*water*	0.3～0.5	22
PS	CH_3Cl	1.6	11
〃	CCl_4	0.75	〃
〃	*benzene*	0.18	*present study*

And also, it is to be remarked that scission yields in the non-electrolyte solutions are not always smaller than those in polyelectrolyte solutions, which indicates that electric charges are not essential for degradation of polyelectrolyte molecules *at least in the concentration range above* $1.0\times10^{-3}\,gr/cc$. In other words, the effective molecular extension of polyelectrolyte molecule may not be very different from that of non-electrolyte molecule in above described range. However, in the case of diluted solutions ($<1.0\times10^{-3}\,gr/cc$), to which measurement is not yet accessible, considerable difference of molecular extension and G-value of chain scission might be expected.

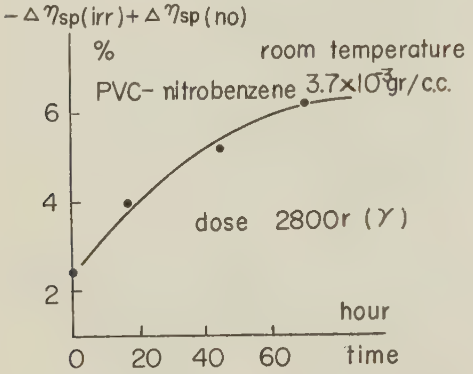

Fig. 7. After-effect in the case of non-electrolyte polymer solution.

It should be noted that, as shown in Fig. VII, marked after effect of irradiation is recognized in non-aqueous solutions. Durup obtained similar results for PS-CCl_4 solutions. If this after effect is taken into account in the calculation of scission yields, their values will come out considerably great; therefore except in the case where the solvent is extremely stable, it is not at all correct to say that the non-electrolyte and non-aqueous solutions of polymers are insensitive to radiation.

§ 4. Qualitative Discussions

The general scheme of the reaction induced by irradiation in the solution may be represented by[23])

$$\text{solvent} \xrightarrow{\gamma} \text{free radical } r \qquad (2)$$

$$r+S \longrightarrow S_i \qquad (3)$$

$$r+S_i \longrightarrow S_i \qquad (4)$$

$$r+P \longrightarrow \text{inactive radical} \qquad (5$$

$$r+r \longrightarrow \text{stable product} \qquad (6$$

where S means a solute molecule, S_i any reaction product, and P a protector such as alcohol. It being possible to know the rate constant of reaction in each case and S and P in the solution, the production rate of S_i can be calculated.

Now, free radicals produced in aqueous solutions are H· and ·OH, and therefore stable products in the reaction (6) may be considered to be H_2 and H_2O. However, if oxygen in the solution, comparatively stable radical HO_2· and recombination product H_2O_2 are produced.

These oxidative agents are more effective in causing the polymer molecule in the solution to degenerate than H· or ·OH radical because of their longer life. Mean free path of H· or ·OH radical may be considerably smaller than molecular extension[24]).

A) Molecular extension and degeneration efficiency.

Reaction (6) makes the degeneration less probable; the more so, if the space including no polymer molecule becomes larger. Therefore, by determining the dependency of fracture efficiency on concentration of the solution, some information concerning the molecular extension may be obtained.

Strictly speaking, estimation of the molecular extension would require a close study on the mean free path of degradative agent. But it may not be unreasonable to assume that in the case of *Na-CMC* aqueous solution the free space begins to appear at the concentration of $5.0\times10^{-5}\,gr/cc$, since the inefficiency of viscosity change becomes remarkable below this critical concentration, as shown in Table III. Moreover, from the fact that the curve of η_{sp}/c versus c of *Na-CMC* solution has a large maximum approximately at this critical concentration, it may be inferred that the molecules attain considerably large extension, free space becoming remarkable, as the concentration is further lowered.

Simple calculation based on the assumption of spherical molecule, which will be justified later, gives the value of about 1500 A for the molecular diameter at this critical region.

The insensitivity of *Na-PA* solutions becomes appreciable at the concentration as low as $1.0\times10^{-5}\,gr/cc$. This is probably due to the larger molecular weight of *Na-PA* than of *Na-CMC*.

B) Molecular form of polyelectrolyte molecules in the solution.

As is well known, the molecular form of high polymer in the solution is implicated in the constant α given by the equation

$$\eta_{sp}/c = AM^{\alpha}\ , \qquad (7)$$

where A is a constant and M is the molecular weight of the polymer. α takes the value 2 in the case of rod-like polymer, while 1 and 1/2 respectively for random coil and rigid sphere25).

Now, applying the results of irradiation fractures shown in Table III and IV, one can obtain the values of α. As the relative viscosity change of the irradiated solution depends on the irradiation dose r, it follows from Eq. (7) that

$$\begin{aligned} -1/(\eta_{sp}/c)\cdot d(\eta_{sp}/c)/dr &= -\alpha/M\cdot dM/dr \\ &= -\alpha/M_0\cdot dM/dr\ , \qquad (8) \end{aligned}$$

which holds for the initial stage of reaction, M_0 being the initial molecular weight.

On the other hand, viscosity change of the irradiated solution is proportional to the dose r at the initial stage of reaction, so that dose R necessary for producing 10% relative change in viscosity is given by

$$1/10R = 1/(\eta_{sp}/c)\cdot d(\eta_{sp}/c)/dr\ . \qquad (9)$$

Eqs. (8), (9) and (1) yield

$$1/10kc = \alpha/M_0\cdot dM/dr = 1/10R\ . \qquad (10)$$

The value of k in Eq. (10) depends on the average shear rate used in viscosity measurements. Thus Eq. (10) may be used for the securing at least qualitative information concerning α-values.

From Table IX, where variations of α-values are given, it may well be inferred that *Na-CMC* molecule takes a rod-like shape at higher concentrations, while as the concentration is lowered it gradually increases in size, developing into a shape of random-coil type, and as a consequence the scission yield increases owing to the dimension of free radical recombination.

Table IX. Values of α concerning Na-CMC molecules in dilute aqueous solutions.

c	k (*average*)	R	dN/dr	α^*	α^{**}
gr/cc	$r\cdot cc/gr$	r	r		
6.7×10^{-5}	1.0×10^{7}	150	8.0×10^{-4}	1.8	1.3
2.4×10^{-4}	〃	320	2.1×10^{-4}	2.0	1.8
6.7×10^{-4}	〃	610	6.4×10^{-5}	2.3	2.5
2.0×10^{-3}	〃		1.4×10^{-5}	3.5	

* calculation by aid of k and dN/dr

** 〃 of R and dM/dr

R and N are given in Tables III and IV.

Variation of α-values due to inclusion of salt in the solution can also be calculated by using Eq. (10), in which k is not constant any more.

Table X. Variation of α-values due to inclusion of sodium chloride in *Na-CMC* aqueous solutions ($c = 2.4\times10^{-4} gr/cc$).

Salt	R	$-1/P_0\cdot dP/dr$	α
Mol	r	$/r$	
0	320	1.8×10^{-4}	1.8
0.05	990	1.2×10^{-4}	0.84
0.48	1510	8.8×10^{-5}	0.75

P: degree of polymerization.

The results are shown in Table X, which indicates that a small quantity of salt changes the molecular form effectively and leads to the formation of rigid sphere. These consequences are consistent with the results obtained by other method26).

B) Protection effect of alcohols

According to some authors, the end-to-end distance h of a polyelectrolyte molecule in the solution, of which the solvent has dielectric constant ε, is given by[27]

$$h^2 = (Z^2e^2h_0^2/3\varepsilon kT)D\ , \qquad (11)$$

where h_0 is the end-to-end distance of the same molecule having no charge, and D is a constant. From this equation it follows that

$$-1/h^2\cdot dh^2/d\varepsilon = 1/\varepsilon\ . \qquad (12)$$

Therefore the relative change of h is at most 10% under the condition described in Fig. 2, and so the effective protection of alcohols seems not to be wholly due to the change in molecular extension.

Protective powers calculated by the ordinary method for *Na-CMC* aqueous solutions are as listed in Table XI, in which the values are compared with other data obtained in the case of irradiated protein solution28).

D) Electric conductivity and irradiation.

It was already shown in § **3** *B*) that an interesting electrical degeneration is brought about by the irradiation in an extremely diluted *Na-CMC* aqueous solution. But, inasmuch as there is no satisfactory theory

Table XI. Protective powers of alcohols in *Na-CMC* aqueous solutions.

polymer	*c*	*protector*	*concentration*	*protective power*
	gr/cc		*vol%*	
Na-CMC	6.7×10^{-5}	*Me-OH*	6.5	0.0087
〃	〃	〃	17.0	0.047
〃	1.0×10^{-4}	*Et-OH*	0.2	0.13
〃	〃	〃	4.0	0.032
〃	〃	〃	10.0	0.079
carboxy-peptidase		*thiourea*		4.7
〃		*glucase*		0.79
〃		*urea*		0.00075

available with respect to the electrical phenomena of polyelectrolyte solutions, the introduction of any assumption will be too bold to explain the observed facts. Therefore only a brief note shall be added here.

The electric conductivity of a polyelectrolyte aqueous solution in low frequency *A.C.* can be expressed by[29]

$$\kappa = ne(u_1+u_2)\,, \tag{13}$$

where n is the number density of free ions having charge e, u_1 their mobility, and u_2 the mobility of a single ion on polymer chain.

n and u_2 depend on temperature, concentration of solution and molecular weight, but u_1 seems to be independent of the molecular weight of the polymer.

If the effect of irradiation be simply to cause depolymerization of molecule, change in conductivity $\Delta\kappa$ comes out, by Eq. (13), to be

$$\Delta\kappa/\kappa = \Delta n/n + \Delta u_2/(u_1+u_2)\,. \tag{14}$$

Thus, at least in the case of dilute aqueous solution of *Na-CMC* at *ca.* 30°*C*, the following important relation can be obtained:

$$\Delta n \cdot \Delta u_2 < 0\,. \tag{15}$$

Acknowledgements

The author expresses his thank to Prof. J. Furuichi for continuous guidance and valuable discussions, and also to Mr. M. Ishikawa for helpful assistances.

References

1) *For example*, A. Charlesby: Proc. Roy. Soc. A, **215** (1952) 187. P. Alexander and A. Charlesby: Proc. Roy. Soc. A, **223** (1954) 392. C. D. Bopp and O. Sisman: Nucleonics **13** (1955) 28, 51.
2) P. Alexander and A. Charlesby: Nature **173** (1954) 578. A. Charlesby: Proc. Roy. Soc. A, **230** (1955) 136.
3) D. E. Lea: *Action of Radiations on Living Cells* (Camb. Univ. Press, London, 1944). P. Alexander: *Atomic Radiation aud Lif* (Penguin Books Ltd., London, 1957).
4) T. Svedberg and S. Brohult: Nature **143** (1939) 938.
5) General Survey: Disc. Faraday. Soc. **12** (1952)
6) P. Alexander and M. Fox: Nature **170** (1952) 1022. Trans. Faraday. Soc. **50** (1954) 605.
7) P. Alexander and A. Charlesby: J. Poly. Sci. **23** (1956) 356.
8) J. Berkovitch, A. Charlesby and V. Desreux: J. Poly. Sci. **25** (1957) 490. A. Danno: J. Phys. Soc. Japan **13** (1958) 722.
9) See 6).
10) P. Y. Feng: Nucleonics **16** (1958) 114.
11) J. Durup: J. Poly. Sci. **30** (1958) 533.
12) T. Kagawa and M. Fukuda: J. Chem. Soc. Japan, Ind. Section, **54** (1951) 97.
13) A. Takahashi and T. Kagawa: J. Chem. Soc. Japan, Ind. Section, **60** (1957) 1059.
14) F. A. Bovey: *The Effects of Ionizing Radiation on Natural and Synthetic Polymers* (Int. Pub., New York, 1958) 220.
15) E. W. Montroll and R. Simha: J. Chem. Phys. **8** (1940) 721.
16) R. MacFarlane, Jr. and R. M. Fuoss: J. Poly. Sci. **23** (1957) 403.
17) R. E. Gregg and Z. I. Kertesz: Science **124** (1956) 893.
18) A. Hilsenrod: J. Chem. Phys. **24** (1956) 917.
19) W. Kern: Z. Phys. Chem. **A**, **181** (1938) 249.
20) R. M. Fuoss and D. Edelson: J. Poly. Sci. **6** (1951) 523.
21) A. Katchalasky: J. Poly. Sci. **12** (1954) 172.
22) A. Matsumoto: Nuclear Engineering **4** no. 7 (1958) 27. (in Japanese)
23) See 14).
24) See 3).
25) A. Katchalsky and H. Eisenberg: J. Poly. Sci. **6** (1951) 145.
26) A. Katchalsky, O. Kunzle and W. Kuhn: J. Poly. Sci. **5** (1950) 283.
27) *Flow Properties of Disperse System*, ed. by J. J. Hermans (North-Holland, Amsterdam, 1953) 220.
28) W. M. Dale and J. V. Davis: Brit. J. Cancer **3** (1949) 31.
29) R. M. Fuoss: J. Poly. Sci. **12** (1954) 185.

JOURNAL OF THE PHYSICAL SOCIETY OF JAPAN Vol. 14, No. 11, NOVEMBER, 1959

Ferromagnetic Crystalline Anisotropy of Fe-Mn-Ferrite System

By Zenya FUNATOGAWA, Nahonori MIYATA and Seiji USAMI
Department of Physics, Yokohama National University, Yokohama

(Received May 9, 1959)

Ferromagnetic resonance absorption of microwave (9300 Mc/s) in synthetic single crystals of $Mn_xFe_{3-x}O_4$ $(0.2 \leqq x \leqq 1.15)$ has been investigated to study their magnetic crystalline anisotropy, g-factor and line width. The pronounced valley in the curve, magnetic crystalline anisotropy $(-K_1/M)$ *vs.* composition (x), was observed in the temperature region between 90°K and 300°K. $-K_1/M$ was a minimum in the region $0.6 < x < 0.7$ and changed its sign. g-value and line width decreased with x more rapidly in the region $x < 0.6$ than $x > 0.6$. It seems difficult to explain these experimental results on the view point of one-ion-model which proved successful in many other ferrites.

§ 1. Introduction

Both experimental[1] and theoretical[2] investigations have been reported recently on the magnetic crystalline anisotropy of ferrites, which is one of the most fundamental properties of ferromagnetic substances. It is now expected that the study may be systematically extended to wider dimension, the solid solution of simple ferrites, because the research previously obtained seems to be limited to simple ferrites prepared from the different raw materials and by the different methods of crystallization.

The research on Fe_3O_4-$MnFe_2O_4$ system is reported here. There are two things interesting in this system; (1) the research on the magnetite side connected with the pronounced variation of the anisotropy constant with temperature[3] just above the electronic order-disorder transformation, the relation between them being not clear today, (2) the dependence of anisotropy on the composition of the solid solution of simple ferrites, neglecting the phenomenon mentioned in (1). The content of this paper is limited to the problem of (2). The study on (1) will be reported later. The data of magnetite used here are quoted from Bickford's paper[3].

§ 2. Specimens

The Bridgman method was used to get large crystals, which was not necessary for the microwave absorption experiment but useful to study the magnetostriction or the electric resistance etc. of the same materials.

Fe_2O_3 and $MnCO_3$ were used for the raw materials, the impurity content of which was analysed spectroscopically and given in Table I. According to the colorimetric and gravimetric analysis, cobalt, which exerted a harmful influence upon the study of the anisotropy, was less than 0.04 wt.% in both compounds. The ferrite powder was made by the usual ceramic technique; perfect mixing, prefiring at 1200°C and dry crushing with the steel ball mill. Large crystals, 1 cm in diameter and 5 cm in length, were grown in the air by the same way as J. Smiltens[4] with a higher speed, 2.8 cm/h, and cooled slowly in CO_2 gas atmosphere.

Table I. Spectroscopic analysis of raw materials.

Raw material Element	Fe_2O_3	$MnCO_3$
Fe	7+	trace
Mn	5+	7+
Si	6+	trace
Mg	5+	6+
Pb	trace	trace
Sn	trace	trace
Ni	3+	3+
Al	4+	
Mo	2+	
V	trace	
Cu	6+	3+
Zn	trace	trace
Ti	3+	
Co	3+	3+
Ca	4+	6+
Cr	4+	
Ag		trace

According to M. W. Shafer's paper[5] it was concluded that specimens prepared by the process mentioned above were excess or deficient in oxygen compared with the stoichiometric composition in the region of magnetite side or Mn-ferrite side, respectively. In our case, the shift of the transition temperature[6] indicated that magnetite obtained had the composition $Fe_{2.99}V_{0.01}O_4$ where V was vacancy. On the other hand, by the chemical analysis of a specimen, $Mn_{1.15}Fe_{1.85}O_{4+\varepsilon}$, ε was ±0.1 and it was not clear whether it was deficient in oxygen or not. Besides, the same analysis of three different parts of the crystal along the direction of the crystal growth (bottom, middle and top) showed no segregation of Fe and Mn within ±2%.

Specimens, cut from the bottom of the crystals, were completed in the shape of sphere, about 0.5 mm in diameter, by polishing by the method evolved by W. L. Bond[7] and etching in HCl solution to take away the surface layer. The X-ray analysis showed that they had the single spinel structure over the whole region as expected and their lattice constants depended linearly on the Mn concentration within the experimental error, ±0.07% (Fig. 1). Their compositions are:

(1) x=0.2, 0.4, 0.6, 0.75, 0.85, 0.97, 1.03, 1.15, for the measurement at room temperature.

(2) x=0.6, 0.85, for the measurement of the temperature dependency between 90°K and 300°K and x=0.4, 1.15, for that between 90°K and 500°K.

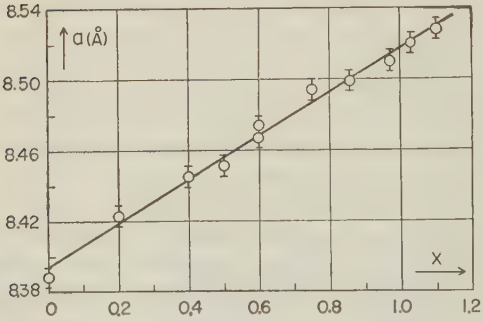

Fig. 1. Lattice constant a *vs.* composition x of $Mn_xFe_{3-x}O_4$.

§ 3. Experimental Procedures

(a) *Microwave techniques*

The apparatus was constructed according to the general scheme of the ferromagnetic resonance experiment. As specimens of Mn-rich side showed the large absorption and the narrow line width, the direct method of observing the minimum point of Q of the cavity was available. But for those of Fe-rich (magnetite) side the field modulation system was needed because the line width was broad and absorption intensities became smaller. ΔH was measured by the field modulation method: it was the distance from peak to peak in the differential curve of the absorption line shape. The microwave frequency was about 9300 Mc/s and its precise value was determined each time by the heterodyne frequency meter. For the measurement of the applied magnetic field we used the proton resonance apparatus[8] and also referred to the D. P. P. H. paramagnetic resonance.

(b) *Method of analysis*

Spherical specimens were set by the X-ray diffraction photographic method so as to rotate about a [110]-axis within ±1°. They were mounted with the dental cement to hold them rigidly at a high temperature. Magnetic anisotropy constant, g-value and line width were analysed by the usual way from the measurement of the static magnetic field where the ferromagnetic resonance absorption was observed in the specimen at the various crystallographic orientations in a (110)-plane. The 2nd term in the expression of the magnetic crystalline anisotropy energy, K_2, was neglected here. This abbreviation scarcely affected an error on the results, as indicated by the analysis.

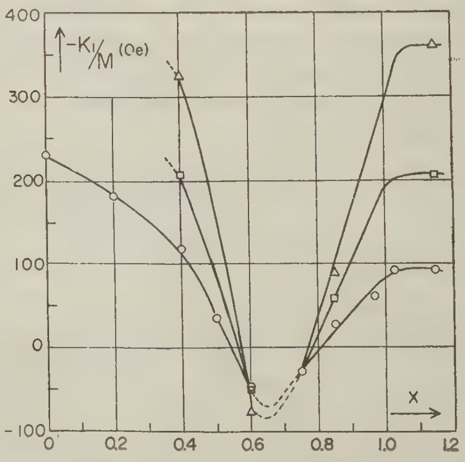

Fig. 2. Magnetic crystalline anisotropy $-K_1/M$ *vs.* composition x with a parameter of temperature; ○: 290°K, □: 190°K, △: 90°K.

§ 4. Experimental Results

Ferromagnetic crystalline anisotropy ($-K_1/M$) is plotted against composition (x) in Fig. 2 with the parameter of temperature and Fig. 3 shows its temperature dependency of each specimen. The pronounced valley is observed in the curve in Fig. 2. $-K_1/M$ is a minimum in the region $0.6<x<0.7$ and changes its sign.

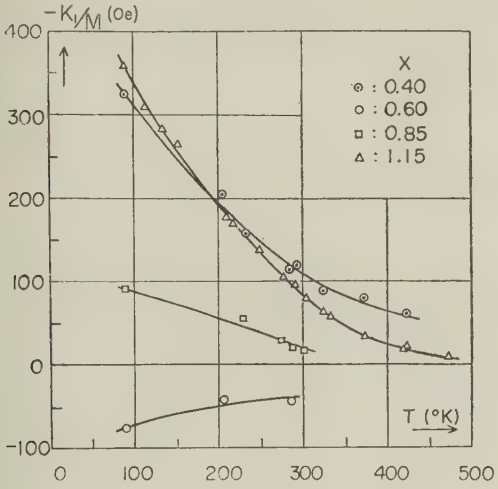

Fig. 3. Magnetic crystalline anisotropy $-K_1/M$ *vs.* temperature T of each specimen.

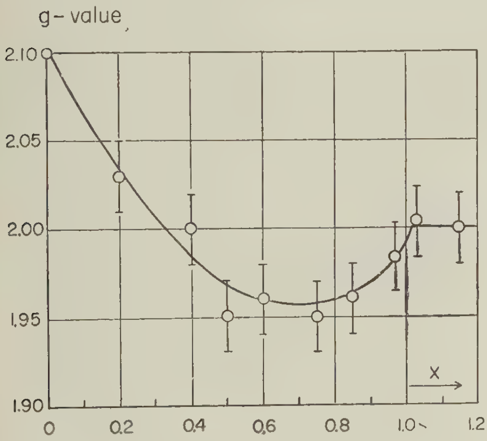

Fig. 4. g-value *vs.* composition x at room temperature.

g-value *vs.* composition at room temperature is shown in Fig. 4. g-value is 2.00 ± 0.02 in Mn excess Mn-ferrite and slightly less than 2.00 in the region $0.5\leq x\leq0.97$ independent of temperature. For $x=0.2$ and 0.4, though special, the g-value is appreciablly large, about 2.2, at liquid oxygen temperature and followed by the considerably narrow line width.

The tendency of the line width variation with the content x is gradual in the region $0.6\leq x\leq1.15$. But after passing through $x=0.6$ to the magnetite, it shows a considerable change and ΔH becomes broad rapidly (Fig. 5). Here the line width ΔH means the average value of them for three principal directions, ⟨100⟩, ⟨110⟩, ⟨111⟩.

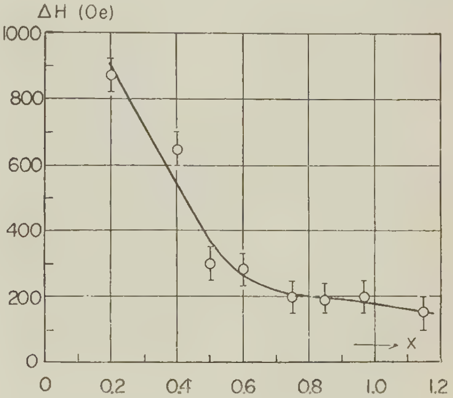

Fig. 5. Line width ΔH *vs.* composition x at room temperature.

§ 5. Discussions

(a) *Comparison with the results previously obtained*

The anisotropy constant of Mn-ferrite and its dependence on temperature have been reported by many authors[9]. Results described in § 4 are in good agreement with these.

Recently R. F. Penoyer and M. W. Shafer reported on the anisotropy of the same ferrite system as ours at the 4th Conference of Magnetism and Magnetic Materials (Nov. 1958). The details are still unknown to us. But so far as we have heard, they used the torque method, static one, contrary to our microwave, dynamic, method, and obtained the consistent results with ours, in spite of the difference of the experimental technique. g-value of Mn-ferrite is in good agreement with other authors' but ΔH is rather large.

(b) *Consideration of experimental results*

(1) Ferromagnetic anisotropy constant, $-K_1/M$

The dependence on temperature of each specimen seems to be in good agreement with the theory of Yoshida and Tachiki[2].

The curve $-K_1/M$ *vs.* x is very curious. As mentioned in § 2, this ferrite system has the simple spinel phase. Then, from the view point of the one-ion-model, K_1/M is expected to depend linearly on the composition x, as in the case of Mg-ferrite[10], if Mn^{2+} is substituted linearly for Fe^{2+}, through the medium of Fe^{3+} at the A-site, from magnetite, inverse spinel[11], to Mn-ferrite, nearly normal spinel[12].

But according to the analysis of the electric resistance of this ferrite system, it was concluded by authors[13] that by the substitution for Fe^{2+} in magnetite by Mn^{2+} the latter occupied B-sites until the concentration where the normal type spinel was stable. Now if we assume that the boundary of the inverse and partly normal type distribution of Mn-ions takes place at $x \approx 0.6$, the relation of $-K_1$ *vs.* x at 0°K, neglecting the transformation of magnetite at a low temperature, is expected to be the solid line shown in Fig. 6. The reason is as follows.

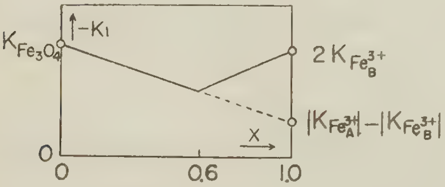

Fig. 6. Schematic expression of $-K_1$ *vs.* x.

$K_{Fe^{3+}_A}>0$, $K_{Fe^{3+}_B}<0$ by Folen and Rado's experiment on Mg-ferrite[14] (each term represents the contribution of Fe^{3+} ion at A and B-site, respectively, to the anisotropy constant) and

$K_{Ni^{2+}_B}\sim 0$, $K_{Mn^{2+}}\sim 0$ by the theoretical consideration by Yoshida and Tachiki[2].

When Mn^{2+} ions are substituted at B-sites for Fe^{2+} over all concentration, the anisotropy constant K_1 goes linearly from the value of magnetite to that of Ni-ferrite. As the latter is inverse type spinel, its anisotropy is given by $|K_{Fe^{3+}_A}|-|K_{Fe^{3+}_B}|$. Mn-ferrite of the perfect normal type has the anisotropy of $2K_{Fe^{3+}_B}$. Then, if the assumption about the distribution of Mn-ions, mentioned above, is correct, a minimum should appear in the curve $-K_1$ *vs.* x at $x \approx 0.6$.

But these considerations do not explain the experimental fact of the positive value of K_1, because the anisotropy constant of Ni-ferrite is negative,[15],[16] K_1/M being -400 Oe at 4°K. Also it should be mentioned that the experimental values of K_1/M of Mn-ferrite at 4°K, previously obtained by many authors[8], are dispersed in the range from -433 Oe to -1250 Oe. The reason is not clear today but may be attributed to the difference of the source of the specimens.

A. H. Eschenfelder[17] showed that the higher valency of Mn-ion than +2 should be considered in the region $x \gtrsim 0.7$ to explain the magnetization of this ferrite system. But the positive value of K_1 is not attributed to this fact.

(2) *g*-value

The observed g-value is expressed theoretically by the equation[18]

$$g=\sum_i g_i<S_{zi}>_{av}/\sum_i<S_{zi}>_{av} ,$$

where g_i is the g-value and $<S_{zi}>_{av}$ is the quantum statistical average value of z-component of the spin, respectively, of i-th ion. Now both Fe^{3+} and Mn^{2+} are in ^6S state and only Fe^{2+} ions, which are always at the B-sites, help to make g different from 2.00. Then g should vary nearly linearly with x in the region $0 \leqq x \leqq 1$, independent of Mn-ion distribution. The experiment shows that the situation is not like this.

According to T. Okamura[19] and D. W. Healy et al[16], the internal field, the physical meaning of which is not clear now, should be considered for the explanation of the frequency dependency of g-value of ferrites. One should

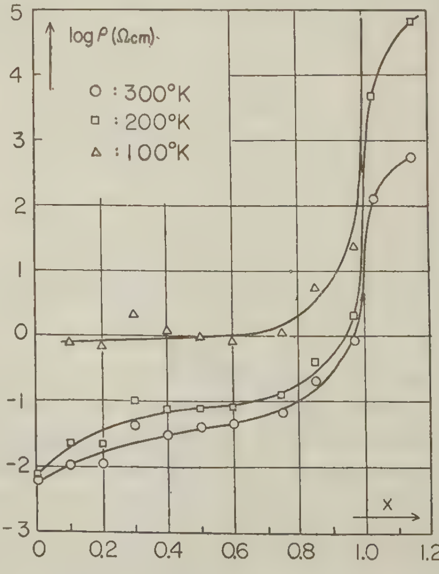

Fig. 7. Specific electric resistance *vs.* composition x at various temperature.

take care of this fact for the analysis of *g*-value.

Low electric resistance of specimens should also be taken into account, because the skin effect may affect the absolute value of *g*-factor. But Figs. 4 and 7 show no intimate relation between them.

(3) Resonance line width, ΔH

The origin of ΔH is not clearly understood today. Values of it in Fig. 5 should be treated with the caution to the skin effect which changes the absorption line shape and the absolute value of ΔH.

(c) *Conclusion*

As we have seen above, it seems that the experimental results are too complicated to be explained from the stand point of the one-ion model. Also, it should be noticed that the quantitative knowledge about the ion distribution on lattice points, for instance by the neutron diffraction experiment, is expected to give us the important information to analyse the physical properties of Fe-Mn ferrite system.

The research on other ferrite systems, now proceeded in our laboratory, will make clear the origin of phenomena described here.

Acknowledgement

The authors are indebted to Dr. H. Kitagawa of the Hitachi Central Laboratory and to Mr. T. Karasawa and other members of Tokyo Denki Kagaku Kogyo Co.. They also wish to thank Mr. Y. Gondo in our laboratory for his valuable discussions. This work was partly supported by the Scientific Research Expenditure of the Ministry of Education.

References

1) R. M. Bozorth, E. F. Tilden and A. J. Williams: Phys. Rev. **99** (1955) 1788. C. M. van der Burgt: Philips Res. Rep. **12** (1957) 97.
2) K. Yoshida and M. Tachiki: Progr. Theor. Phys. **17** (1957) 331. W. P. Wolf: Phys. Rev. **108** (1957) 1152.
3) L. R. Bickford, Jr.: Phys. Rev. **78** (1950) 449.
4) J. Smiltens: J. Chem. Phys. **20** (1952) 990.
5) M. W. Shafer: I. B. M. Jour. (July 1958) 193.
6) E. J. W. Verwey and P. W. Haayman: Physica **8** (1941) 979.
7) W. L. Bond: Rev. Sci. Instr. **22** (1951) 344.
8) H. W. Knoebel and E. L. Hahn: Rev. Sci. Instr. **22** (1951) 904.
9) J. F. Dillon, Jr., S. Geschwind and V. Jaccarino: Phys. Rev. **100** (1955) 750. P. E. Tannenwald: Phys. Rev. **100** (1955) 1713. R. L. White and I. H. Solt: Phys. Rev. **104** (1956) 56. A. Nakamura: Denki-shikenjo-iho **22** (1958) 499 (in Japanese). U. Enz: Physica **24** (1958) 609. J. F. Dillon, Jr. and H. E. Earl, Jr.: J. Appl. Phys. **30** (1959) 202.
10) G. T. Rado, V. J. Folen and W. H. Emerson: Progr. I. E. E. **B**, **104** Suppl. 5 (1957) 198.
11) C. G. Shull, E. O. Wollan and W. C. Koehler: Phys. Rev. **84** (1951) 912.
12) J. M. Hastings and L. M. Corliss: Phys. Rev. **104** (1956) 328.
13) Z. Funatogawa, N. Miyata and S. Usami: J. Phys. Soc. Japan **14** (1959) 854.
14) V. J. Folen and G. T. Rado: J. Appl. Phys. **29** (1958) 438.
15) W. A. Yager, J, K. Galt and F. R. Merrit: Phys. Rev. **99** (1955) 1203.
16) D. W. Healy and R. A. Johnson: Phys. Rev. **104** (1956) 634.
17) A. H. Eschenfelder: J. Appl. Phys. **29** (1958) 378.
18) N. Tsuya: Progr. Theor. Phys. **7** (1952) 263. R. K. Wangsness: Phys. Rev. **86** (1952) 146.
19) T. Okamura: Sci. Rep. R. I. T. U. **6A** (1954) 89.

JOURNAL OF THE PHYSICAL SOCIETY OF JAPAN Vol. 14, No. 11, NOVEMBER, 1959

Temperature Dependence of the Magnetostriction Constants in Iron and Silicon Iron

By Eiji TATSUMOTO and Tetsuhiko OKAMOTO

Department of Physics, Faculty of Science, Hiroshima University, Hiroshima

(Received June 15, 1959)

The magnetostriction constants λ_{100} and λ_{111} of Fe, 1.08 and 3.83% Si-Fe have been measured by using single crystals at temperatures below Curie point down to liquid air temperature with two newly designed apparatuses.

In iron, λ_{100} has a minimum around 400°K, while λ_{111} monotonously decreases in numeral with increasing temperature. Addition of silicon to iron has a tendency to make the minimum in λ_{100} disappear and to decrease λ_{111} numerically at any temperature, retaining the similar monotonous variation with temperature.

Several existing theories have been applied to account for the experimental results, but no theory appears to be successful in interpreting them.

§ 1. Introduction

Practically, the anisotropic magnetostriction phenomena are characterized by the two magnetostriction constants λ_{100} and λ_{111}.

From a theoretical standpoint, it would be of much importance to observe the influence of temperature and alloying element on the magnetostriction constants, since temperature and composition of alloy are the most important factors affecting the interaction responsible for the magnetostriction. No satisfactory observation of magnetostriction constants has been done except for that of iron done by Takaki[1)] and that of 3.5% Si-Fe by Shturkin[2)], because of great experimental difficulties. The purpose of the present work is to perform such observation on iron, 1.08% Si-Fe and 3.83% Si-Fe, by using a new technique which has the same performance as the strain gauge technique.

Since Goldman[3)] successfully utilized the strain gauge technique for measuring the magnetostriction constants λ_{100} and λ_{111}, the technique has been widely used, but mostly at room temperature. This technique is especially excellent in the respect that small samples can be used. However, we can use paper strain gauges neither at temperatures much higher than room temperature, because of their burning, nor at much lower temperatures on account of uncertainty of the gauge factors which are defined as the ratio of the resistance change to the strain. In the present experiment, instead of the paper strain gauge a straight gauge wire that composes the main part of the paper strain gauges has been used, in order to make the observation possible at any temperature. The principle of this new technique is very simple as follows. A specimen maintained at any temperature is connected with a thin and long quartz rod and a straight strain gauge wire kept at room temperature in order and in series. Thus, the distortion of the specimen can be directly converted to that of the gauge wire, so that the strain of the specimen at the temperature can be computed from the strain of the gauge wire, provided the gauge factor is known at room temperature. The gauge factor can easily be obtained by measuring the known strain of the specimen.

As to the observation of λ_{100} and λ_{111}, it is, in general, experimentally difficult to obtain the reliable λ_{100}, because of the uncertainty of the domain configuration at a reference state. The difficulty has already been overcome by the authors by making use of the (001)−[100] single crystal strips[*)] and by producing technically a simple and definite domain structure in the specimen at the reference state[4)]. On the other hand, λ_{111} can be measured without any experimental dif-

---

[*] For example, the notation (001)−[100] signifies that the crystal plane (001) and the crystal axis [100] coincide with the surface plane and the longitudinal direction of the specimen, respectively.

ficulty with the [111] single crystal rods or strips on account of the symmetrical orientations of the domains referred to the [111] direction at the ordirary demagnetized state. In the present experiment the $(1\bar{1}0)-[111]$ single crystal strips have been used.

§ 2. Specimens

The specimens are the $(001)-[100]$ and $(1\bar{1}0)-[111]$ single crystal strips of iron, 1.08% Si-Fe and 3.83% Si-Fe, the sizes of which are 0.3∼0.5 mm in thickness, 3∼5 mm in width and 50 mm in length. They are all produced by Fujiwara's method[5]. Before making use of them for the measurement, all the specimens are annealed at the temperatures, 850°C 1000°C, lower than the allotropic transformation temperature for 3∼5 hours in a vacuum furnace.

§ 3. Measurement of λ_{100} and λ_{111}

As is well known, in the ferromagnetic metals and alloys of the cubic structure, the magnetostriction of a single magnetic domain occurring from an imaginary nonferromagnetic state is represented practically by the phenomenological equation[6]

$$\begin{aligned}\frac{dl}{l_0}=\lambda_0+\frac{3}{2}\lambda_{100}(\alpha_1^2\beta_1^2+\alpha_2^2\beta_2^2+\alpha_3^2\beta_3^2)\\+3\lambda_{111}(\alpha_1\alpha_2\beta_1\beta_2+\alpha_2\alpha_3\beta_2\beta_3\\+\alpha_3\alpha_1\beta_3\beta_1)+\cdots ,\end{aligned} \tag{1}$$

where λ_{100} and λ_{111} are the magnetostriction constants which are characteristic of the material and which vary with temperature; l_0 is the length along the measuring direction and λ_0 the isotropic strain occurring from the imaginary nonferromagnetic state; α's and β's are the direction cosines of the intrinsic magnetization vector and measuring orientation, respectively, referred to the cubic axes. The magnetostriction constants λ_{100} and λ_{111}, as long as the domain configuration is known completely at a definite reference state, are successfully obtained by measuring the so-called saturation magnetostriction from a reference state demagnetized adequately.

In the first place, the $(001)-[100]$ specimens are used for measuring λ_{100}. As the reference state, we use the one having the simple and definite domain structure shown schematically in Fig. 1[7]. This domain structure is easily produced by utilizing the circular field induced by a comparatively weak direct current through the specimen, since the field in the specimen is nearly parallel to the easy magnetization axis $\langle 100\rangle$ as is illustrated in the same figure. In this reference state, we have λ_0 from Eq. (1) as the magnetostriction in the [100] direction, $(dl/l_0)_{\perp[100]}$. In the state where the magnetization is saturated in the [100] direction, we also have $\lambda_0+(3/2)\lambda_{100}$ as the magnetostriction in the same direction, $(dl/l_0)_{//[100]}$. Then, we get $(3/2)\lambda_{100}$ as the difference between two states. Now, we may consider that the difference is almost equal to the so-called saturation magnetostriction in the [100] direction observed in this case, $(dl/l)_{[100]\mathrm{sat.}}$, because of negligibly small differences among the dimensions of the three states (the imaginary nonferromagnetic, the reference and the saturation magnetization state); that is,

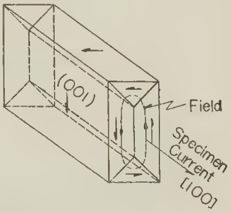

Fig. 1. Domain structure of the (001)−[100] single crystal strip in the presence of a sufficiently large direct current.

$$\left(\frac{dl}{l}\right)_{[100]\mathrm{sat.}}\simeq\frac{3}{2}\lambda_{100}\ . \tag{2}$$

The current sufficient to produce the domain structure as shown in Fig. 1 is obtained by measuring the saturation magnetostriction as a function of the current. As an example, a run of the measurements made on the iron specimen at room temperature is given in Fig. 2, where the circles show the saturation magnetostriction measured when demagnetized by a gradually decreasing alternating field in the presence of a current (method (a)); the crosses show those measured when the reverse process was operated (method (b)). The necessary and sufficient current is taken obviously above the current which begins to have the constant saturation magnetostriction. In the present experiment, the method (a) has always been adopted, since smaller current can be used than with the method (b).

In the next place, the $(1\bar{1}0)-[111]$ specimens are used for measuring λ_{111}. In this case we may take the ordinary demagnetized state as the reference state. In this reference state we have $\lambda_0+(1/2)\lambda_{100}$ as the magnetostriction in [111] direction, $(dl/l_0)_{<100>[111]}$, since all domains are symmetrical about the [111] direction. In the state where the magnetization is saturated in the [111] direction, we have $\lambda_0+(1/2)\lambda_{00}+\lambda_{111}$ as the magnetostriction in the same direction, $(dl/l_0)_{//[111]}$. Then, the difference between the two states is λ_{111}. Thus, for the same reason as in the case of λ_{100}, we obtain

$$\left(\frac{dl}{l}\right)_{[111]\text{sat.}} \simeq \lambda_{111} \ . \tag{3}$$

where $(dl/l)_{//[111]}$ is the so-called saturation magnetostriction in the [111] direction observable in this case. It is noted, however, that the [111] single crystal rods or strips can be employed as well.

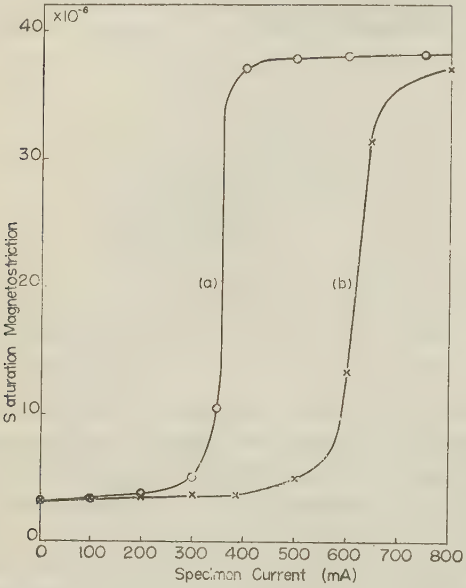

Fig. 2. Difference in longitudinal saturation magnetostriction *vs.* specimen current for the (001)–[100] iron specimen at room temperature; the circles correspond to measurements made on the specimen demagnetized in the presence of a specimen current; the crosses correspond to measurements made on the specimen in the presence of a specimen current after the demagnetization with no specimen current.

§ 4. Apparatus for Low Temperatures

For the measurement at temperatures below room temperature, the apparatus is diagrammatically shown in Fig. 3. The magnetizing coil is inclined by about 10° referred to the vertical line, so that the specimen and the quartz pipe may contact well with the top surface of the specimen base made by micata. The magnetizing coil constant $(4\pi n)$ is 450 and the field is uniform within 2% in a region 100 mm long around the central part. To each end of the specimen, a small copper plate is soldered. Its bottom is fixed with a small screw to the sample base, and its top is sharpened and inserted tightly into the bottom of the quartz pipe, which is 1.5 mm in inner-diameter, 2.5 mm in outer-diameter and 260 mm in length. To the top of the quartz pipe, the bottom end of the straight gauge wire of 0.025 mm in diameter and 60 mm in length is fixed by wax and the other top end is connected with a silk thread, the other free end of which is weighted with a load of 10 gr, through a pulley so as to stretch the gauge wire elastically.

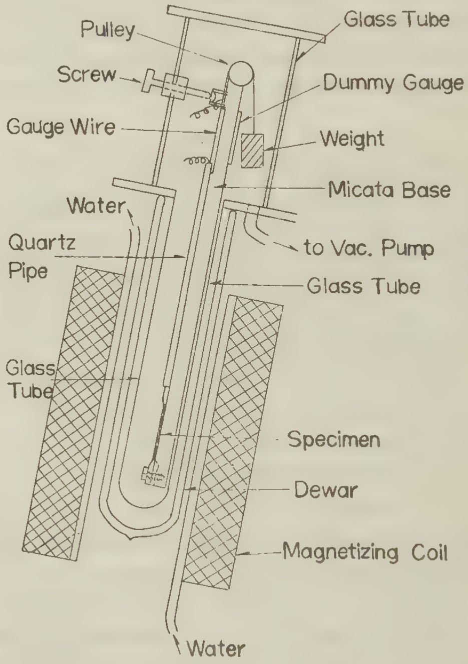

Fig. 3. Apparatus for measuring magnetostriction at low temperatures.

Such a combination is set in a container which is constructed with two glass tubes which are different in size. Inside of the container vacuum can be maintained. The top end of the gauge wire can be fixed with a small screw out of the container, when the specimen is settled down to a certain temperature. Then, the linear distortion of the specimen is directly converted, via the quartz pipe, to that of the gauge wire as the reverse linear distortion, and this is observed as the corresponding strain by measuring the resistance change with D. C. Wheatstone bridge circuit, the dummy gauges of which are made by the same kind of the wires. Accordingly, we can calculate the strain of specimen from the strain of gauge wire thus measured. In this case, we obviously need to know the gauge factor of the gauge wire. This method will be described in the following section.

§ 5. Temperature Dependence of the Gauge Factor of Paper Strain Gauges

At present, it seems that there is no measurement on the gauge factor of paper strain gauges at low temperatures, except that by Day and Sevand[8] who used the ordinary technique measuring the constant bending of a beam on which the gauges are cemented. In the present work, the measurement was made as an auxiliary project as follows.

As mentioned previously, in order to accomplish the measurement of λ_{100} or λ_{111}, we need to know the gauge factor of the strain gauge wire set in the apparatus at room temperature. The gauge factor can be computed by comparing a certain strain of the specimen, which is measured by the paper strain gauges cemented on its both surface planes, with the same strain which is measured by the strain gauge wire. In practice, it is convenient to measure $(3/2)\lambda_{100}$ of the $(001)-[100]$ specimens or λ_{111} of the $(1\bar{1}0)-[111]$ specimens as a standard strain. Thus, we can measure contrariwise the gauge factor of the paper strain gauges at any temperature by the same method, as long as the paper strain gauges stick tightly on the specimen. As glues, Duco cement and the similar kind of cements have been tried, and they were all ascertained to be available for any temperature down to the liquid air temperature. However, no confirmation has been made whether they are still available even when immersed directly in such as liquid air.

In the present experiment, the paper strain gauges, type S_{121}, made by Shinkoh communication Industry Co., Ltd. were used and their gauge factor was measured at temperatures below room temperature down to liquid air temperature. In Fig. 4 this is plotted with one of the results obtained by Day and Sevand[8]. The gauge factor of type S_{121} decreases slightly and the decreasing rate increases with decreasing temperature. This temperature dependence is distinctly different from that due to Day and Sevand. Therefore, we may conclusively say that the temperature variation depends on materials of the wire.

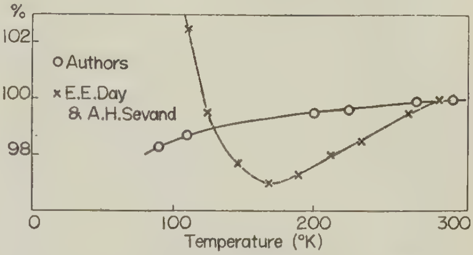

Fig. 4. Temperature dependence of the gauge factor below room temperature. The ordinate shows the gauge factor in percentage referred to that at room temperature.

Now, we can use the paper strain gauges for measurements of such strain as magnetostriction at various low temperatures, at least down to liquid air. In the measurement of magnetostriction, however, we should not disregard their own magnetoresistance, since it is, in general, fairly large in high fields as well as at low temperatures. In the present experiment, it was scarcely observed even in liquid air temperature, because the measurement was made in a comparatively weak field less than 900 oersteds in every case.

§ 5. Apparatus for High Temperatures

For the measurement at temperatures above room temperature, the apparatus for low temperatures was somewhat reformed as is diagrammatically shown in Fig. 5. The same magnetizing coil is horizontally set, inside which a noninductive electric furnace is

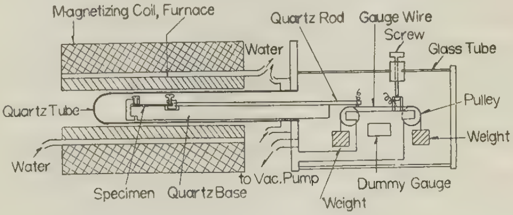

Fig. 5. Apparatus for measuring magnetostriction at high temperatures.

inserted. The sample base and the vacuum container are changed to the ones of quartz. The left end of the specimen is fastened by a small molybdenum fixer having a screw to the quartz base, and the specimen and the quartz rod of 2 mm in diameter and 380 mm in length are connected in series with a small molybdenum joint having two screws. The straight strain gauge wire of 40 mm long is fixed with wax to the quartz rod and stretched elastically from both sides by weighting two equal loads of 10 gr each as shown in the figure, so that no tension acts on the specimen. All the other parts are not reformed further.

In this equipment at elevated temperatures the molybdenum joint comes often loose as its thermal expansion is larger than that of quartz. To fix tightly together, therefore, a small copper wedge is inserted between them, as its thermal expansion is larger than that of molybdenum. Thus, all fixing goes well in the ascending process in temperature, but in the reverse process they become often slack. We may suppose then that the slackness results from the plastic deformation either of the specimen, or of the molybdenum fixer or of the copper wedge happening at elevated temperatures. However, this fact can be disregarded because we can safely operate the equipment in the ascending process in temperature. Furthermore, the pressure of the molybdenum fixers acting on the specimen would presumably change the domain structure around there, but even if it happens, it also matters little for the measurements of the magnetostriction constants, because in the case of λ_{111} it has no relation with the measurement and in the case of λ_{100} the domain structure at the reference state is newly produced, as was described previously, by using the current.

§ 6. Influences of Temperature and Addition of Silicon on λ_{100} and λ_{111}

Figs. 6 and 7 show the magnetostriction constants λ_{100} and λ_{111} which have been measured at temperatures above liquid air temperature up to the Curie point.

In iron, an essential feature of the temperature dependences of λ_{100} and λ_{111} may be regarded as the minimum appearing around 400°K in λ_{100}, since the minimum has a tendency to disappear with the increase of amount of silicon as is seen in Fig. 6 and was not found in 3.5% Si-Fe on which Shturkin made the measurement at higher temperatures than 0°C[2]. This minimum was found for the first time by Takaki who made the measurement on iron single crystal rods at temperatures above room temperature[1]. For all the temperatures at which he measured λ_{100}, however, the values which he obtained are slightly smaller than those obtained in the present experiment. This is, presumably, attributable to the ambiguous domain configuration at the remanent which he preferred as the reference state. In the λ_{100} *vs.* temperature curve, there appear two maxima as seen in Fig. 6; the one appearing at the low temperature was first found in the present measurement, though this is presumably not very essential but only resulted from an appearance of the minimum just mentioned above at the high temperature side. The other one appearing at the high temperature evidently results from rapid decreasing of the intrinsic magnetization near the Curie point.

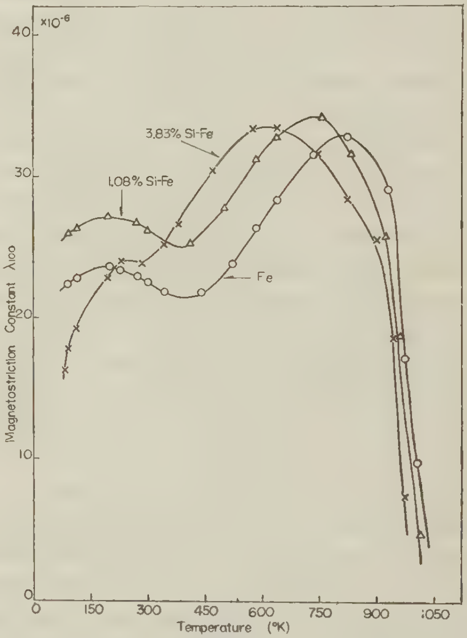

Fig. 6. Temperature dependence of the magnetostriction constant λ_{100}.

By addition of small amount of silicon to iron, the feature of the temperature dependence of λ_{100} is fairly altered, while that of λ_{111} is not changed at all as is seen in Figs. 6 and 7; that is, in the case of λ_{100} the minimum appearing around 400°K has a tendency to disappear, so that even the order in magnitude of the values of λ_{100} for Fe, 1.08% Si-Fe and 3.83% Si-Fe changes at different temperatures, while in the case of λ_{111} the monotonous variation with temperature is preserved so that only the numerical value decreases with increasing temperature. In Fig. 8, the values of λ_{100} and λ_{111} at room temperature are plotted as functions of the amount of silicon. These values also have already been obtained by the authors by means of paper strain gauges[4)]. In this figure, in addition, are plotted the values at room temperature which were obtained by Carr and Smoluchowski[9)] and also are plotted those values at absolute zero which were estimated by extrapolating the λ_{100} or λ_{111} *vs.* temperature curve obtained in the present experiment down to absolute zero temperature. In the case of λ_{100}, however, the estimated values, particularly for 1.08% Si-Fe, do not seem quite accurate, because λ_{100} may possibly happen to decrease rapidly near the liquid air temperature like that of 3.83% Si-Fe. For estimating the values more accurately by extrapolation, it is presumably necessary to measure λ_{100} at temperatures lower than liquid air temperature. In the case of λ_{111}, however, the estimated values may be quite reliable. As is inferred from Fig. 8, both λ_{100} and λ_{111} undoubtedly change their sign inversely at a certain amount of silicon, but it should be noted that the amount is fairly altered with temperature.

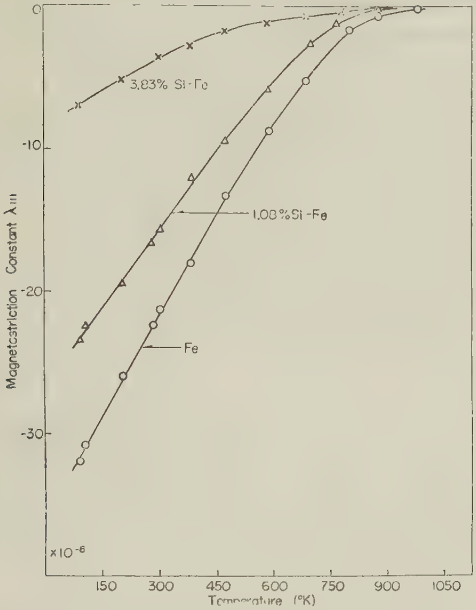

Fig. 7. Temperature dependence of the magnetostriction constant λ_{111}.

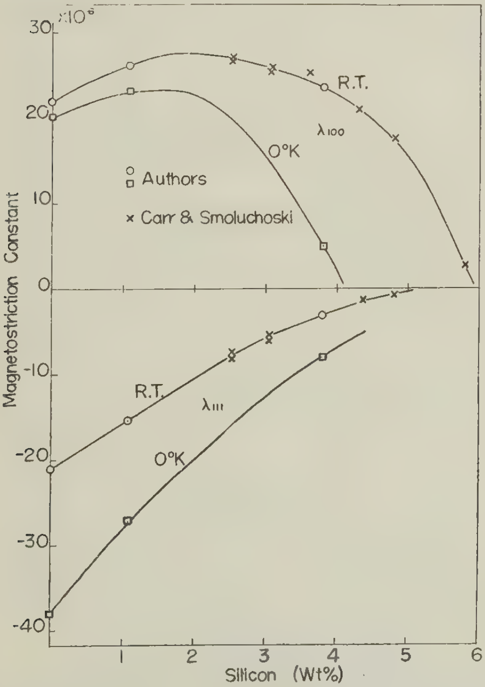

Fig. 8. Dependence of λ_{100} and λ_{111} on the amount of silicon in weight percentage in iron. The values at absolute zero were obtained by extrapolating the λ_{100} and λ_{111} *vs.* temperature curves in Figs. 6 and 7 down to absolute zero.

The formal origin of magnetostriction may be attributable to the interaction between intrinsic magnetization and crystal strain, as has been pointed out by Kittel[10)]. Consequently, the magnetostriction equation can be derived from the interaction energy, i.e. magnetoelastic energy[6)] For a body-centered cubic crystal

$$\begin{aligned} dl/l = {} & h_1(\alpha_1{}^2\beta_1{}^2+\alpha_2{}^2\beta_2{}^2+\alpha_3{}^2\beta_3{}^2-1/3) \\ & +2h_1(\alpha_1\alpha_2\beta_1\beta_2+\alpha_2\alpha_3\beta_2\beta_3+\alpha_3\alpha_1\beta_3\beta_1) \\ & +h_4(\alpha_1{}^4\beta_1{}^2+\alpha_2{}^4\beta_2{}^2+\alpha_3{}^4\beta_3{}^2+2s/3-1/3) \\ & +2h_5(\alpha_1\alpha_2\alpha_3{}^2\beta_1\beta_2+\alpha_2\alpha_3\alpha_1{}^2\beta_2\beta_3 \\ & +\alpha_3\alpha_1\alpha_2{}^2\beta_3\beta_1)+h_3s\,. \end{aligned} \tag{4}$$

with

$$h_1=\frac{B_1}{c_{11}-c_{12}}\,, \qquad h_2=-\frac{B_2}{c_{44}}\,,$$

$$h_4=-\frac{B_4}{c_{11}-c_{12}}\,, \qquad h_5=\frac{B_5}{c_{44}}$$

and

$$s=\alpha_1^2\alpha_2^2+\alpha_2^2\alpha_3^2+\alpha_3^2\alpha_1^2\ ,$$

where h_1, h_2, h_3, h_4 and h_5 are the magnetostriction constants; B_1, B_2, B_4, and B_5 are the magnetoelastic coupling constants as named by Kittel; c_{11}, c_{12} and c_{44} are the elastic moduli. Formally, the first two terms result from quasi dipole-dipole interaction and the other terms from quasi quadrapole-quadrapole interaction. Eq. (1) just corresponds to the first two terms in which h_1 and h_2 can be rewritten as (3/2) λ_{100} and (3/2) λ_{111} respectively. If the practical magnetostriction phenomena are represented more effectively by Eq. (4) than Eq. (1), the observed $(dl/l)_{[100]\text{sat.}}$ and $(dl/l)_{[111]\text{sat.}}$, as previously denoted, are not $(3/2)\lambda_{100}$ and λ_{111}, but h_1+h_4 and $(2/3)h_2+(2/9)h_5$, respectively; $(1/3)h_3$ is omitted, in this case, because of numerical smallness in comparison with the others.

On the other hand, the magnetostriction was formerly calculated classically as atomic dipole-dipole interaction by Akulov(11) and Becker(12), and recently by Néel(13) with somewhat advanced idea. In the case of Becker's calculation, the magnetostriction constants are

$$\left.\begin{aligned}\lambda_{100}&=\frac{2SI_s^2}{c_{11}-c_{12}}\\ \text{and}\qquad&\\ \lambda_{111}&=\frac{4SI_s^2}{3c_{44}}\end{aligned}\right\}\qquad(5)$$

for a body-centered lattice. Here I_s is the intrinsic magnetization, and S a constant depending on the geometry of the crystal lattice, 0.4. Accordingly, as the temperature rises, both λ_{100} and λ_{111} monotonously decrease in proportion to I_s^2. In the case of λ_{100} this is quite different from the results obtained in the present experiment as is shown in Fig. 6. It is presumed that, further addition of quadrapole-quadrapole interaction may improve the discrepancy; in other words, h_4 or h_5 is likely to be responsible for it. Such a presumption has been attempted by S. Taniguchi* but the non monotonous variation of λ_{100} with temperature has not been explained successfully.

The greater part of the observed magnetostriction may be suspected to have its origin in the spin-orbit interaction, as was treated by Van Vleck concerning the crystalline anisotropy. By taking account of both the spin-spin and the spin-orbit interactions, Vonsovski has obtained an interesting result which was quoted by Lee in his article(15). According to this result, the departure from the law of the temperature dependence of magnetostriction proportional to I_s^2 is regarded as due to the effect of spin-orbit interaction. This result does not seem to be incompatible with the temperature dependences of $(dl/l)_{[100]\text{sat.}}$ and $(dl/l)_{[111]\text{sat.}}$ obtained in the present work; but further detailed considerations will not be given here, because unfortunately the authors are not accessible to Vonsovski's original paper.

In conclusion, the magnetostriction constants λ_{100} and λ_{111} vary only if the responsible interaction alters. However, any existing theory does not seem to be successful in interpreting the results obtained in the present experiment.

The authors are indebted to Mr. H. Kimura and Mr. Y. Uchida for the loan of their 3.8% Si-Fe specimens. The present work was partly supported by the Science Research Grant from the Ministry of Education.

References

1) H. Takaki: Z. Phys. **105** (1937) 92.
2) D. A. Shturkin: Bull. Acad. Sci. U. S. S. R. **9** (1947) 661.
3) T. E. Goldman: Phys. Rev. **75** (1949) 140.
4) E. Tatsumoto, T. Okamoto, A. Nishimura and A. Fukai: J. Sci. Hiroshima Univ. **A**, **22** (1958) 123.
5) T. Fujiwara and E. Tatsumoto: J. Sci Hiroshima Univ. **A**, **13** (1940) 235.
6) R. Becker and W. Döring: *Ferromagnetismus* (Springer, Berlin, 1939) 275.
7) E. Tatsumoto: Phys. Rev. **109** (1958) 658.
8) E. E. Day and A. H. Sevand: Proc. Soc. Exp. Stress Anal. **8** (1950) 133.
9) W. J. Carr and R. Smoluchowski: Phys. Rev. **83** (1951) 1236.
10) C. Kittel: Rev. Mod. Phys. **21** (1949) 541.
11) N. S. Akulov: Z. Phys. **52** (1928) 389.
12) R. Becker: Z. Phys. **62** (1930) 253.
13) L. Néel: J. phys. radium **15** (1954) 225.
14) J. H. Van Vleck: Phys. Rev. **52** (1937) 1178.
15) E. W. Lee: Rep. Progr. Phys. **18** (1955) 184.

---

* Lecturered at the meeting of the Physical Society of Japan, Nov. 1956, but not yet published.

JOURNAL OF THE PHYSICAL SOCIETY OF JAPAN Vol. 14, No. 11, NOVEMBER, 1959

Magnetic Hyperfine Spectrum of H_2CO by a Maser

By Hiroshi TAKUMA, Tadao SHIMIZU and Koichi SHIMODA

Department of Physics, Faculty of Science,
University of Tokyo, Tokyo

(Received July 4, 1959)

The magnetic hyperfine structure in $J=3$, $K_{-1}=1$, $\Delta J=0$ transition of formaldehyde at 29 Gc/sec was studied by a beam type maser spectrometer. The hyperfine components corresponding to $\Delta F=0$ transitions were observed with good signal-to-noise ratio. The splittings are measured as 23.0 kc/sec and 10.4 kc/sec which are compared with theory. As well as the $\boldsymbol{I}\cdot\boldsymbol{J}$ coupling, spin-spin interaction term $\boldsymbol{I}_1\cdot\boldsymbol{I}_2$ between the two protons is fairly large and cannot be neglected. Coupling constants were determined as $\mu_N{}^2 g_H{}^2 r^{-3}=19.9$ kc/sec and $\sum_g \langle J_g{}^2\rangle(A_{1g}+A_{2g})=54.6$ kc/sec.

§ 1. Introduction

A beam type maser spectrometer was successfully applied to observe the magnetic hyperfine structure of ammonia. However, the application of the technique to other molecules is strongly limited by the focuser action for the molecules. The Q branch transition of formaldehyde shows probably the next strongest emission spectrum to ammonia in the centimeter wave range, because the molecule has small moment of inertia, large dipole moment, and very slight asymmetry to allow closely spaced pairs of levels (K-type doubling). Thus the calculated intensity is very close to get self-sustained oscillation under a typical condition. The microwave absorption spectra of formaldehyde, formaldehyde $-d_1$ and $-d_2$ have been studied[1] in our laboratory as well as their Zeeman effects[2]. Then the study of magnetic hyperfine structure of formaldehyde by the beam type maser spectrometer was planned and the result on the $J=3$ $K_{-1}=1$ line is reported in this paper. Work on other lines of formaldehyde will be reported later.

§ 2. Theoretical Treatment

A theory of the magnetic hyperfine structure of this type of molecule was discussed by Okaya[3], and a more general theory of magnetic hyperfine structure of an asymmetric molecule was developed by Posener[4]. A somewhat different theory which is essentially similar to that of Posener has been developed and is given below. This theory is more suitable to the case of a slightly asymmetric molecule in computing the energy levels.

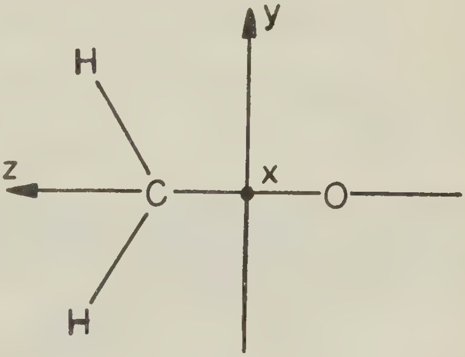

Fig. 1. Molecular axis of H_2CO.

The Hamiltonian of a formaldehyde-type molecule with C_{2v} symmetry in $^1\Sigma$ state based on Pauli approximation can be written as[3-6];

$$\begin{aligned}\boldsymbol{H}=&A(J_z-L_z)^2+B(J_y-L_y)^2+C(J_x-L_x)^2 && (1.0)\\ &+(e\mu_N/c)\sum_{K=1,2}\sum_i r_{Ki}^{-3}(\boldsymbol{r}_i-\boldsymbol{r}_K)\times\{\boldsymbol{v}_i-[1+Z_KM_p/g_KM_K]\boldsymbol{v}_K\}g_K\cdot\boldsymbol{I}_K && (1.1)\\ &-(e\mu_N/c)\sum_{K=1,2}\sum_{K\neq L}Z_Lr_{KL}^{-3}(\boldsymbol{r}_K-\boldsymbol{r}_L)\times\{[1+Z_KM_p/g_KM_K]\boldsymbol{v}_K-\boldsymbol{v}_L\}g_K\cdot\boldsymbol{I}_K && (1.2)\\ &+\mu_N^2r_{HH}^{-3}g_H^2[\boldsymbol{I}_1\cdot\boldsymbol{I}_2-3r_{HH}^{-2}(\boldsymbol{I}_1\cdot\boldsymbol{r}_{HH})(\boldsymbol{I}_2\cdot\boldsymbol{r}_{HH})]\,, && (1.3)\end{aligned}$$

where the notations are the same as in ref. 3) and 6), the capital letter suffix denotes the nucleus, and the small letter the electron. The physical meaning of the term (1.0) in Eq. (1) is the pure rotational energy of nuclear frame, (1.1) represents the energy of the proton spins in the magnetic field produced by electrons in the molecule, (1.2) represents the magnetic energy of protons in the field produced by other nuclear charges, and the last term (1.3) represents the spin-spin interaction energy of two protons in the molecule. For a nearly symmetric prolate top the rotational part of the molecular wave function can be conveniently expanded in a power series of the asymmetric parameter $b(=(C-B)/(2A-B-C)$[7]. The rotational energy can be expressed as;

$$W=A\langle J_z^2\rangle+B\langle J_y^2\rangle+C\langle J_x^2\rangle=\frac{B+C}{2}\,J(J+1)+\left(A-\frac{B+C}{2}\right)w(b)\,, \tag{2.1}$$

where

$$w(b)=K^2+\sum_{n=1}^{\infty}C_nb^n\,. \tag{2.2}$$

The expansion coefficient C_n is tabulated in reference 7). The molecular fixed axis x, y, z are taken for H_2CO as shown in Fig. 1, and $b=-0.0098290$. For the convenience of the later treatment[7,8], $\langle J_x^2\rangle$ etc. are calculated as

$$\left.\begin{aligned}\langle J_z^2\rangle&=\frac{\partial W}{\partial A}=K^2-\sum_{n=1}^{\infty}(n-1)C_nb^n\\ \langle J_y^2\rangle&=\frac{\partial W}{\partial B}=\frac{1}{2}\left\{J(J+1)-K^2-C_1+\sum_{n=1}^{\infty}[(n-1)C_n-(n+1)C_{n+1}]b^n\right\}\\ \langle J_x^2\rangle&=\frac{\partial W}{\partial C}=\frac{1}{2}\left\{J(J+1)-K^2+C_1+\sum_{n=1}^{\infty}[(n-1)G_n+(n+1)C_{n+1}]b^n\right\}.\end{aligned}\right\} \tag{3}$$

The appropriate coupling scheme for the molecule with two identical nuclei with spin I_1 and I_2 should be

$$\bar{I}_1+\bar{I}_2=\bar{I}\,,\qquad \bar{I}+F=J\,,$$

where $\bar{I}_1=-I_1$, $\bar{I}_2=-I_2$ and $\bar{I}=-I$ are used in order to retain proper commutation relations in the molecular fixed system[9]. When the perturbation theory is used to account for the excitation of electronic states due to molecular rotation, the Hamiltonian for the nuclear spin interaction can be written as[3-6];

$$H=\sum_{K=1,2}[A_{Kx}\bar{I}_{Kx}J_x+A_{Ky}\bar{I}_{Ky}J_y+A_{Kz}\bar{I}_{Kz}J_z]+\mu_N^2g_H^2r^{-3}[\boldsymbol{I}_1\cdot\boldsymbol{I}_2r^2-3(\boldsymbol{I}_1\cdot\boldsymbol{r})(\boldsymbol{I}_2\cdot\boldsymbol{r})]r^{-2} \tag{4}$$

where A_{Kx} etc. are constants determined from the electronic states and the molecular structure, $\boldsymbol{r}$ the vector between the two protons, and r the magnitude of $\boldsymbol{r}$.

The energy level shift due to these interactions will be obtained in the first order approximation from the eigenvalue of the matrix

$$\langle I_1I_2IFJ\tau|H|I_1'I_2'I'F'J'\tau'\rangle\,.$$

When the molecule has a C_{2v} symmetry, the nuclear spin part of the eigenfunction is odd or even respectively corresponding to the even or odd symmetry of the rotational part of wave function $|J\tau\rangle$. Therefore, the elements $\langle I|H|I-1\rangle$ will vanish. The total proton spin is $I=1$ for the rotational wave function with odd symmetry, and $I=0$ for even symmetry. Therefore the rotational levels with even symmetry have no magnetic hyperfine splittings, since $I=0$. The magnetic hyperfine structures of transitions between odd rotational levels are considered. The I, J dependent term of the spin-spin interaction between the identical nuclei, $[r^2\boldsymbol{I}_1\cdot\boldsymbol{I}_2-3(\boldsymbol{I}_1\cdot\boldsymbol{r})(\boldsymbol{I}_2\cdot\boldsymbol{r})]r^{-2}$, is shown to be equivalent to[10]

$$\frac{I(I+1)+4I_1(I_1+1)}{(2I-1)(2I+3)(2J-1)(2J+3)}\left[3(\bar{\boldsymbol{I}}\cdot\boldsymbol{J})^2-\frac{3}{2}(\bar{\boldsymbol{I}}\cdot\boldsymbol{J})-\bar{\boldsymbol{I}}^2\cdot\boldsymbol{J}^2\right].$$

On the other hand, J, τ dependent term of the spin-spin interaction is[8]

$$\frac{1}{J(J+1)}\left[\boldsymbol{J}^2-3\sum_g\left(\frac{r_g^2}{r^2}\right)\boldsymbol{J}_g^2\right].$$

Therefore, Eq. (4) is equivalent to the next equation for $I=1$ and $I_1=\frac{1}{2}$*

$$H=\sum_{K=1,2}\sum_{g=x,y,z}A_{Kg}\bar{I}_{Kg}J_g-\frac{3\mu_N^2g_H^2r^{-3}}{2J(J+1)(2J-1)(2J+3)}$$
$$\times\left\{3(\bar{\boldsymbol{I}}\cdot\boldsymbol{J})[2(\bar{\boldsymbol{I}}\cdot\boldsymbol{J})-1]-2\bar{\boldsymbol{I}}^2\boldsymbol{J}^2\right\}\left[\frac{1}{2}J(J+1)-\sum_g\left(\frac{r_g^2}{r^2}\right)J_g^2\right]. \tag{5}$$

Inserting the following relation[11],

$$\bar{I}_{Kg}=\frac{(\bar{\boldsymbol{I}}_K\cdot\bar{\boldsymbol{I}})(\bar{\boldsymbol{I}}\cdot\boldsymbol{J})}{I(I+1)J(J+1)}J_g \tag{6}$$

Eq. (5) is reduced to

$$H=\sum_{K=1,2}\sum_{g=x,y,z}A_{Kg}\frac{(\bar{\boldsymbol{I}}_K\cdot\bar{\boldsymbol{I}})(\bar{\boldsymbol{I}}\cdot\boldsymbol{J})}{2J(J+1)}J_g^2-\frac{3\mu_N^2g_H^2r^{-3}}{2J(J+1)(2J-1)(2J+3)}$$
$$\times\{3(\bar{\boldsymbol{I}}\cdot\boldsymbol{J})[2(\bar{\boldsymbol{I}}\cdot\boldsymbol{J})-1]-2\bar{\boldsymbol{I}}^2\boldsymbol{J}^2\}\left[\sum_g\left(\frac{r_g^2}{r^2}\right)J_g^2-\frac{1}{3}\boldsymbol{J}^2\right]. \tag{7}$$

The matrix element which is diagonal in I, J, τ, is

$$\langle IJ\tau|H|IJ\tau\rangle=\sum_g(A_{1g}+A_{2g})\frac{(\bar{\boldsymbol{I}}\cdot\boldsymbol{J})}{I(I+1)J(J+1)}\langle J_g^2\rangle$$
$$-\frac{(3\mu_N^2g_H^2/r^3)\{3(\bar{\boldsymbol{I}}\cdot\boldsymbol{J})[2(\bar{\boldsymbol{I}}\cdot\boldsymbol{J})-1]-2I(I+1)J(J+1)\}}{2J(J+1)(2J-1)(2J+3)}\left[\sum_g\left(\frac{r_g^2}{r^2}\right)\langle J_g^2\rangle-\frac{1}{3}J(J+1)\right], \tag{8}$$

where $(\bar{\boldsymbol{I}}_K\cdot\bar{\boldsymbol{I}})$ has been replaced by 1 for the state with $I=1$. The first order approximation of the energy level shift W_1 due to magnetic interactions is obtained by putting $2(\bar{\boldsymbol{I}}\cdot\boldsymbol{J})=I(I+1)-F(F+1)+J(J+1)$.

$$\left.\begin{aligned}
W_1&=-\frac{1}{2(J+1)}\sum_g(A_{1g}+A_{2g})\langle J_g^2\rangle+\frac{(3\mu_N^2g_H^2r^{-3})}{2(J+1)(2J+3)}\left[\sum_g\left(\frac{r_g^2}{r^2}\right)\langle J_g^2\rangle-\frac{1}{3}J(J+1)\right],\\
&\qquad\text{for } F=J+1\\
W_1&=\frac{1}{2J(J+1)}\sum_g(A_{1g}+A_{2g})\langle J_g^2\rangle-\frac{(3\mu_N^2g_H^2r^{-3})}{2J(J+1)}\left[\sum_g\left(\frac{r_g^2}{r^2}\right)\langle J_g^2\rangle-\frac{1}{3}J(J+1)\right],\\
&\qquad\text{for } F=J\\
W_1&=\frac{1}{2J}\sum_g(A_{1g}+A_{2g})\langle J_g^2\rangle+\frac{(3\mu_N^2g_H^2r^{-3})}{2J(2J-1)}\left[\sum_g\left(\frac{r_g^2}{r^2}\right)\langle J_g^2\rangle-\frac{1}{3}J(J+1)\right].\\
&\qquad\text{for } F=J-1\,.
\end{aligned}\right\} \tag{4}$$

In the case of Q-branch transitions, $\Delta F=0$ components have appreciable transion probabilities and $\Delta F=\pm1$ transitions are much weaker. The frequency shift $\Delta\nu$ of the hyperfine component of $\Delta J=0$, $\Delta F=0$ transitions, is

$$\Delta\nu_{J+1}=-\sum_g\frac{1}{2(J+1)}(A_{1g}+A_{2g})\Delta\langle J_g^2\rangle+\frac{(3\mu_N^2g_H^2r^{-3})}{2(J+1)(2J+3)}\sum_g\left(\frac{r_g^2}{r^2}\right)\Delta\langle J_g^2\rangle\,,\qquad\text{for } F=J+1$$
$$\Delta\nu_J=\sum_g\frac{1}{2J(J+1)}(A_{1g}+A_{2g})\Delta\langle J_g^2\rangle-\frac{(3\mu_N^2g_H^2r^{-3})}{2J(J+1)}\sum_g\left(\frac{r_g^2}{r^2}\right)\Delta\langle J_g^2\rangle\,,\qquad\text{for } F=J$$
$$\Delta\nu_{J-1}=\sum_g\frac{1}{2J}(A_{1g}+A_{2g})\Delta\langle J_g^2\rangle+\frac{(3\mu_N^2g_H^2r^{-3})}{2J(2J-1)}\sum_g\left(\frac{r_g^2}{r^2}\right)\Delta\langle J_g^2\rangle\,,\qquad\text{for } F=J-1\,,$$

---

* For a more detailed treatment see ref. (4).

where $\Delta\langle J_g^2\rangle$ is the difference of $\langle J_g^2\rangle$ between the two levels involved.

§ 3. Experimental Procedure and the Result

The block diagram of the maser spectrometer is shown in Fig. 2. A one-klystron system with a crystal modulator driven at 45 Mc/sec is used to allow sensitive amplification of the beat frequency from a crystal mixer[12]. The maser tank, beam source and focuser are the same ones as used in the ammonia maser by one of the authors[13].

Preparing of the gaseous formaldehyde has been one of the difficulties encountered, because it polymerizes quite easily even under a low pressure or in the liquid state at a dry ice temperature. Several methods were tried, but no satisfying way was found to supply a constant flow of formaldehyde gas. The simplest and most convenient one was simply to heat the powder of paraformaldehyde.

A cylindrical cavity of TM_{010} mode, 12 cm in length, is rather closely coupled, the loaded Q being about 4000.

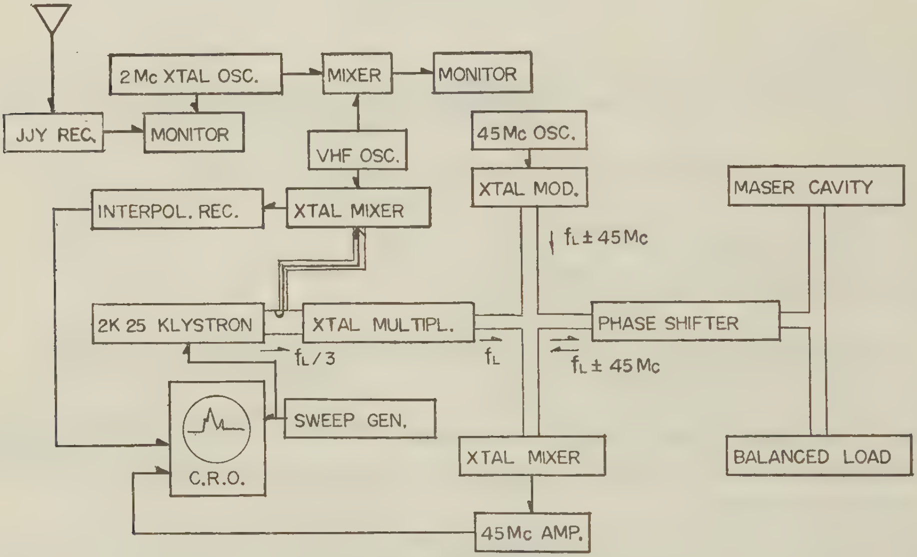

Fig. 2. Block-diagram of the maser spectrometer.

The measured line is the Q-branch transition $3_{12}\rightarrow 3_{13}$, the center frequency of which is about $\nu_0=28{,}974.85$ Mc/sec. The emission spectrum was observed as a triplet, as shown in Fig. 3. At the focuser voltage of 20 kV, the signal-to-noise ratio was about 10, with the effective band-width of 1.5 kc/sec. The line disappeared at the focuser voltage arround 9 kV. The sensitivity of one-klystron system is limited by the difficulty of balancing the signal at two frequencies $\nu_L \pm \nu_{if}$, where ν_L and ν_{if} are respectively the frequency of the

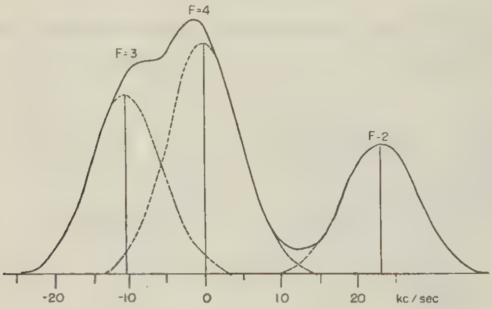

Fig. 3. Calculated hyperfine pattern ($\Delta F=0$) of the $3_{12}\rightarrow 3_{13}$ line of H_2CO.

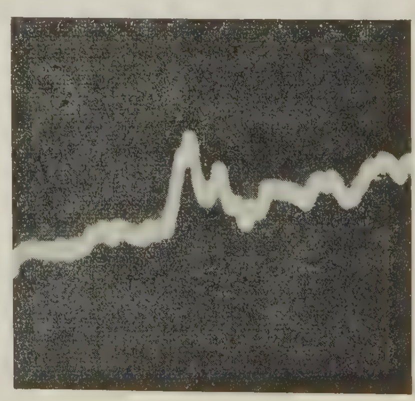

Fig. 4. An oscilloscope pattern of the $3_{12}\rightarrow 3_{13}$ line of H_2CO.

local oscillator and the amplifier. The two-klystron system without crystal modulator should improve the signal-to-noise ratio. However, the frequency fluctuation is found to increase even by using automatic frequency control, when the frequence noise of the two klystrons are not sufficiently small. Signal-to-noise ratio was large enough to observe the hyperfine pattern with the present system. Since the intensity of the $\Delta F=0$ component is approximately proportional to $2F+1$, the triplet is easily assigned as shown in Fig. 4. The splittings $\Delta\nu_2-\Delta\nu_4$, $\Delta\nu_4-\Delta\nu_3$ and the half-width $\Delta\nu$ are determined.

$$\Delta\nu_2-\Delta\nu_4=23.0\pm1.5 \text{ kc/sec}$$

$$\Delta\nu_4-\Delta\nu_3=10.4\pm0.7 \text{ kc/sec}$$

$$\Delta\nu= 5.8\pm0.4 \text{ kc/sec}$$

§ 4. Discussion

The splittings of hyperfine components are obtained from Eq. (11) as

$$\Delta\nu_{J+1}=-\frac{\Delta X}{2(J+1)}+\frac{\Delta Y}{2(J+1)(J+3)}; \quad \text{for } F=J+1$$

$$\Delta\nu_J=\frac{\Delta X}{2J(J+1)}+\frac{\Delta Y}{2J(J+1)}; \quad \text{for } F=J$$

$$\Delta\nu_{J-1}=\frac{\Delta X}{2J}-\frac{\Delta Y}{2J(2J-1)}; \quad \text{for } F=J-1\,,$$

where $\Delta X=\sum_g (A_{1g}+A_{2g})\Delta\langle J_g^2\rangle$, and $\Delta Y=3\mu_N^2 g_H^2 r^{-3}\sum_g (r_g^2/r^2)\Delta\langle J_g^2\rangle$. From the experimental values of hyperfine splittings two constants are obtained as

$$(\Delta X)_{\text{exp.}}=54.6 \text{ kc/sec}\,, \quad (\Delta Y)_{\text{exp.}}=358 \text{ kc/sec}$$

From Eq. (3), neglecting the first order terms of b, we obtain $\langle J_y^2\rangle=\frac{1}{2}J(J+1)-K^2-C_1$, and $\Delta\langle J_y^2\rangle=-\Delta(C_1/2)=J(J+1)/2=6$. Therefore, for $r_x=r_z=0$, and $r_y=r$, the expression can be written as $\Delta Y=18\mu_N^2 g_H^2 r^{-3}$. The observed value of ΔY gives

$$(\mu_N^2 g_H^2 r^{-3})_{\text{exp.}}=19.9\pm1.3 \text{ kc/sec}\,.$$

On the other hand, H–H distance in H_2CO has been known as[1] $r=1.87\text{A}$. Thus the calculated value is

$$(\mu_N^2 g_H^2 r^{-3})_{\text{calc.}}=18.2 \text{ kc/sec}\,.$$

The calculated value of $\mu_N^2 g_H^2 r^{-3}$ is in fairly good agreement with the experimental value. Another constant, ΔX, cannot be calculated because of the lack of knowledge concerning the electronic states of the molecule. Taking the same approximation as in the calculation of ΔY, it may be written as

$$\Delta X=\frac{J(J+1)}{2}(\beta-\alpha)\,,$$

where $\alpha=A_{1x}+A_{2x}$ and $\beta=A_{1y}+A_{2y}$. The experimental value is

$$\beta-\alpha=9.1\pm0.6 \text{ kc/sec}\,.$$

Recently Thaddeus et. al. has observed the magnetic hyperfine structure in the transition, $2_{11}\rightarrow2_{12}$, as*

$$\Delta\nu_1-\Delta\nu_3=22.35\pm0.4 \text{ kc/sec}$$

$$\Delta\nu_3-\Delta\nu_2=12.59\pm0.2 \text{ kc/sec}\,.$$

According to the analysis given above, the constants are obtained as

$$(\mu_N^2 g_H^2 r^{-3})_{\text{exp.}}=20.2 \text{ kc/sec}$$

$$\beta-\alpha= 9.2 \text{ kc/sec}\,.$$

These are in good agreement with our results on the $3_{12}\rightarrow3_{13}$ transition, thus confirming the theory given above.

In conclusion the authors would like to thank Mr. T. Oka for his helpful suggestions and discussions. Thanks are also due to Dr. A. Okaya and Mr. P. Thaddeus for the information of their experiments.

References

1) H. Hirakawa, A. Miyahara and K. Shimoda: J. Phys. Soc. Japan **11** (1956) 334. H. Hirakawa, T. Oka and K. Shimoda: J. Phys. Soc. Japan **11** (1956) 1207. T. Oka: to be published.
2) K. Kondo, H. Hirakawa, A. Miyahara, T. Oka and K. Shimoda: to be published.
3) A. Okaya: J. Phys. Soc. Japan **11** (1956) 249.
4) D. W. Posener: Austral. J. Phys. **11** (1958) 1.
5) G. R. Gunther-Mohr, C. H. Townes and J. H. Van Vleck: Phys. Rev. **94** (1954) 1191.
6) J. P. Gordon: Phys. Rev. **99** (1955) 1253.
7) C. H. Townes and A. L. Schawlow: *Microwave Spectroscopy* (McGraw-Hill, 1955).
8) J. K. Bragg and S. Golden: Phys. Rev. **75** (1949) 735.
9) J. H. Van Vleck: Rev. Mod. Phys. **23** (1951) 213.
10) J. M. B. Kellogg, I. I. Rabi, N. F. Ramsey, and J. R. Zacharias: Phys. Rev. **57** (1940) 677.
11) E. U. Condon and G. H. Shortley: *The Theory of Atomic Spectra* (Cambridge, 1953).
12) K. Shimoda and T. C. Wang: Rev. Sci. Instr. **26** (1955) 1148.
13) K. Shimoda: J. Phys. Soc. Japan **13** (1958) 939.

---

* private communication.

JOURNAL OF THE PHYSICAL SOCIETY OF JAPAN, Vol. 14, No. 11, NOVEMBER, 1959

Electrical Polarizabilities of Rare Gas Atoms by the Hartree-Fock Wave Functions

By Shobu KANEKO

Department of Physics, Faculty of Science,
University of Tokyo

(Received July 4, 1959)

The perturbation method is applied to the Hartree-Fock equation to calculate the dipole polarizabilities, the results being a coupled set of integro-differential equations. This theory is applied to helium and makes clear the accuracy of the Sternheimer approximation. The calculated value of the polarizability by this theory is about ten per cent smaller than the value obtained by the Sternheimer approximation. For neon and argon calculations are made by use of the Sternheimer approximation. All the calculated values of the polarizabilities are compared with the values obtained by other authors and the experimental values. The calculated value for helium agrees quite well with the experimental one and for neon and argon the calculated values are about 1.5 times the experimental ones.

§ 1. Introduction

The intermolecular potential of gases has been investigated semiempirically by the theory of the equations of state and transport coefficients[1]. The long range parts of this intermolecular potential, even if they may be a many body force's potential, have close relation to the dipole polarizability[2]; hence the quantum mechanical calculation of it for various molecules has been desired. The calculations of the polarizability have been made by use of the variational method by many authors, i.e. by Kirkwood[3], Buckingham[4], Bravin[5], Pople and Schofield[6], and Wikner and Das[7]. The calculations have been made also by use of the numerical method by Sternheimer[8,9], Sundbom[10] and very recently by Dalgarno and Parkinson[11].

In this article we derive, using the perturbation method, an equation by use of which the polarizability can be calculated within the limits of the Hartree-Fock approximation; and we get a coupled set of integro-differential equations satisfied by the radial parts of the perturbed wave functions under the assumption on them (see (17′) in § 3) which is consistent with the Hartree approximation, for example in case of helium. For helium, as it is the simplest case, the rigorous equation is solved self-consistently to see the accuracy of the Sternheimer approximation (see § 4). But for neon and argon the calculations are so laborious that we treat the problems by the Sternheimer approximation; we will make calculation more exactly in future.

In solving differential equations for the perturbation of the wave functions, the present author used the Parametron Computor PC–1 at the University of Tokyo.

§ 2. Polarizability in a Uniform Electric Field

In the following we consider an atom or ion with q electrons and a nucleus of the charge number N. The normal state of the atomic system is assumed to be in the configuration of the complete shell. The Hamiltonian of the system in the applied electric field $\boldsymbol{E}$, is written as

$$\mathscr{H}=\sum_{i=1}^{q}\left[-\frac{1}{2}\nabla_i^2-\frac{N}{r_i}+(\boldsymbol{E}\cdot\boldsymbol{r}_i)\right]+\sum_{ij}{}'\frac{1}{r_{ij}}\,, \tag{1}$$

in which $\boldsymbol{r}_i$ is the position vector of the i-th electron referred to the nucleus and r_{ij} the distance between the i-th and the j-th electrons; the prime in $\sum_{ij}'$ means that the sum is over all pairs $(j\neq i)$, each pair being counted once; ∇_i^2 is the Laplacian operator for the i-th electron. Hereafter Hartree's atomic units are used throughout in this article.

In the Hartree-Fock method the normalized wave function Ψ of the system is written in the form of Slater determinant as

$$\Psi=\frac{1}{\sqrt{q!}}\begin{vmatrix}\psi_1(\boldsymbol{r}_1)\eta_1(\zeta_1) & \psi_1(\boldsymbol{r}_2)\eta_1(\zeta_2)\cdots\cdots & \psi_1(\boldsymbol{r}_q)\eta_1(\zeta_q)\\ \psi_2(\boldsymbol{r}_1)\eta_2(\zeta_1) & \psi_2(\boldsymbol{r}_2)\eta_2(\zeta_2)\cdots\cdots & \psi_2(\boldsymbol{r}_q)\eta_2(\zeta_q)\\ \vdots & \vdots & \vdots\\ \psi_q(\boldsymbol{r}_1)\eta_q(\zeta_1) & \psi_q(\boldsymbol{r}_2)\eta_q(\zeta_2)\cdots\cdots & \psi_q(\boldsymbol{r}_q)\eta_q(\zeta_q)\end{vmatrix}, \tag{2}$$

where $\psi_i(\boldsymbol{r}_j)$ and $\eta_i(\zeta_j)$ are respectively the orthonormal one-electron orbital wave function and spin function, and ζ_j is the spin coordinate of the j-th electron. The best one-electron wave functions $\psi_i(\boldsymbol{r})$ are determined by the well-known Hartree-Fock equations:

$$\left[-\frac{1}{2}\nabla_1^2-\frac{N}{r_1}+\sum_j\int\frac{|\psi_j(\boldsymbol{r}_2)|^2}{r_{12}}d\boldsymbol{r}_2+(\boldsymbol{E}\cdot\boldsymbol{r}_1)-\mathcal{E}_i\right]\psi_i(\boldsymbol{r}_1)-\sum_{j//}\int\frac{\psi_j^*(\boldsymbol{r}_2)\psi_i(\boldsymbol{r}_2)}{r_{12}}d\boldsymbol{r}_2\psi_j(\boldsymbol{r}_1)=0\ , \tag{3}$$

in which the wave functions were assumed to be transformed so as to diagonalize the energy parameter matrix[12]), and $\mathcal{E}_i$ are its diagonal elements; the summations $\sum_j$ and $\sum_{j//}$ are respectively extended over all occupied states and over all states with parallel spin to the i state including the i state itself; the asterisk means the complex conjugate.

We choose the z-axis parallel to the applied electric field, that is $\boldsymbol{E}=(0,0,E)$, and use the spherical polar coordinate in the following.

Assuming the term Ez_1 to be small compared with the others, we use the perturbation method. The wave functions $\psi_i(\boldsymbol{r})$ and the energy parameters $\mathcal{E}_i$ are expanded with respect to E:

$$\left.\begin{aligned}\psi_i(\boldsymbol{r})&=\psi_i^{(0)}(\boldsymbol{r})+\psi_i^{(1)}(\boldsymbol{r})+O(E^2)\ ,\\ \mathcal{E}_i&=\ \mathcal{E}_i^{(0)}\ +\ \mathcal{E}_i^{(1)}\ +O(E^2)\ .\end{aligned}\right\} \tag{4}$$

Here $\psi_i^{(0)}(\boldsymbol{r})$ and $\mathcal{E}_i^{(0)}$ are the unperturbed wave functions and the energy parameters respectively; $\psi_i^{(1)}(\boldsymbol{r})$ and $\mathcal{E}_i^{(1)}$ are the first order perturbed wave functions and the energy parameters respectively which are of the order of E.

Substituting the expansions (4) into the equations (3), we obtain

$$\left[-\frac{1}{2}\nabla_1^2-\frac{N}{r_1}+\sum_j\int\frac{|\psi_j^{(0)}(\boldsymbol{r}_2)|^2}{r_{12}}d\boldsymbol{r}_2-\mathcal{E}_i^{(0)}\right]\psi_i^{(0)}(\boldsymbol{r}_1)-\sum_{j//}\int\frac{\psi_j^{(0)*}(\boldsymbol{r}_2)\,\psi_i^{(0)}(\boldsymbol{r}_2)}{r_{12}}d\boldsymbol{r}_2\psi_j^{(0)}(\boldsymbol{r}_1)=0 \tag{5}$$

from the zero-th order terms with respect to E, and

$$\begin{aligned}&\left[-\frac{1}{2}\nabla_1^2-\frac{N}{r_1}+\sum_j\int\frac{|\psi_j^{(0)}(\boldsymbol{r}_2)|^2}{r_{12}}d\boldsymbol{r}_2-\mathcal{E}_i^{(0)}\right]\psi_i^{(1)}(\boldsymbol{r}_1)\\ &\quad+\left[\sum_j\int\frac{\psi_j^{(1)*}(\boldsymbol{r}_2)\psi_j^{(0)}(\boldsymbol{r}_2)+\psi_j^{(0)*}(\boldsymbol{r}_2)\psi_j^{(1)}(\boldsymbol{r}_2)}{r_{12}}d\boldsymbol{r}_2+Ez_1-\mathcal{E}_i^{(1)}\right]\psi_i^{(0)}(\boldsymbol{r}_1)\\ &\quad-\sum_{j//}\int\frac{\psi_j^{(0)*}(\boldsymbol{r}_2)\psi_i^{(0)}(\boldsymbol{r}_2)}{r_{12}}d\boldsymbol{r}_2\psi_j^{(1)}(\boldsymbol{r}_1)\\ &\quad-\sum_{j//}\int\frac{\psi_j^{(1)*}(\boldsymbol{r}_2)\psi_i^{(0)}(\boldsymbol{r}_2)+\psi_j^{(0)*}(\boldsymbol{r}_2)\psi_j^{(1)}(\boldsymbol{r}_2)}{r_{12}}d\boldsymbol{r}_2\psi_j^{(0)}(\boldsymbol{r}_1)=0\end{aligned} \tag{6}$$

from the first order terms. The conditions of orthonormality on $\psi_i(\boldsymbol{r})$ become

$$\int\psi_j^*(\boldsymbol{r})\psi_i(\boldsymbol{r})\,d\boldsymbol{r}=\int\psi_j^{(0)*}(\boldsymbol{r})\psi_i^{(1)}(\boldsymbol{r})d\boldsymbol{r}+\int\psi_j^{(1)*}(\boldsymbol{r})\psi_i^{(0)}(\boldsymbol{r})\,d\boldsymbol{r}+O(E^2)=0\ . \tag{7}$$

The zero-th order equations (5) are the normal Hartree-Fock equation in the absence of the perturbing electric field and its solutions are usually written in the central field type

$$\psi_i^{(0)}(\boldsymbol{r})=\frac{P_0(n_il_i:r)}{r}Y_{l_im_i}(\vartheta,\varphi)\ . \tag{8}$$

Here n_i, l_i and m_i are respectively the principal, azimuthal and magnetic quantum numbers of the i state; $P_0(nl\colon r)$ is the radial wave function and $Y_{lm}(\vartheta, \varphi)$ is the spherical harmonics of the l-th order. They are normalized according to

$$\left.\begin{aligned}&\int_0^\infty P_0(nl\colon r)P_0(n'l\colon r)\,dr=\delta_{n,n'}\,,\\&\int_0^\pi\int_0^{2\pi} Y^*_{l,m}(\vartheta,\varphi)Y_{l'm'}(\vartheta,\varphi)\sin\vartheta\,d\vartheta\,d\varphi=\delta_{l,l'}\cdot\delta_{m,m'}\,.\end{aligned}\right\}\tag{9}$$

The equations (6) determine the perturbed wave functions $\psi_i^{(1)}(r)$ under the suitable boundary conditions and are investigated in detail in the next section.

According to the expansion of $\psi_i(r)$, the wave function Ψ of the system is also expanded in the form

$$\begin{aligned}\Psi&=\Psi^{(0)}+\ \Psi^{(1)}\ +O(E^2)\\&=\Psi^{(0)}+\sum_{i=1}^{q}\Psi_i^{(1)}+O(E^2)\,,\end{aligned}\tag{10}$$

where

$$\Psi^{(0)}=\frac{1}{\sqrt{q!}}\begin{vmatrix}\psi_1^{(0)}(r_1)\eta_1(\zeta_1) & \psi_1^{(0)}(r_2)\eta_1(\zeta_2)\cdots\cdots\cdots & \psi_1^{(0)}(r_q)\eta_1(\zeta_q)\\ \vdots & \vdots & \vdots\\ \psi_q^{(0)}(r_1)\eta_q(\zeta_1) & \psi_q^{(0)}(r_2)\eta_q(\zeta_2)\cdots\cdots\cdots & \psi_q^{(0)}(r_q)\eta_q(\zeta_q)\end{vmatrix}$$

and

$$\Psi_i^{(1)}=\frac{1}{\sqrt{q!}}\begin{vmatrix}\psi_1^{(0)}(r_1)\eta_1(\zeta_1) & \psi_1^{(0)}(r_2)\eta_1(\zeta_2)\cdots\cdots\cdots & \psi_1^{(1)}(r_q)\eta_1(\zeta_q)\\ \vdots & \vdots & \vdots\\ \psi_i^{(1)}(r_1)\eta_i(\zeta_1) & \psi_i^{(1)}(r_2)\eta_i(\zeta_2)\cdots\cdots\cdots & \psi_i^{(1)}(r_q)\eta_i(\zeta_q)\\ \vdots & \vdots & \vdots\\ \psi_q^{(0)}(r_1)\eta_q(\zeta_1) & \psi_q^{(0)}(r_2)\eta_q(\zeta_2)\cdots\cdots\cdots & \psi_q^{(0)}(r_q)\eta_q(\zeta_q)\end{vmatrix}\,.\tag{11}$$

Then the perturbation of the charge distribution of the system is given by

$$\Psi^*\Psi-\Psi^{(0)*}\Psi^{(0)}=2\,\mathrm{Re}\,(\Psi^{(0)*}\Psi^{(1)})+O(E^2)\,,\tag{12}$$

in which Re stands for the real part. Hence the induced dipole moment P_{ind} of the system is expressed in the form

$$P_{\mathrm{ind}}=-2\sum_{k=1}^{q}\sum_{i=1}^{q}\int\mathrm{Re}\,(\Psi^{(0)*}\Psi_i^{(1)})z_k\,dr_1\cdots dr_q\,,\tag{13}$$

and the polarizability α is given by

$$\alpha=\frac{P_{\mathrm{ind}}}{E}=-\frac{2}{E}\sum_{k=1}^{q}\sum_{i=1}^{q}\int\mathrm{Re}\,(\Psi^{(0)*}\Psi_i^{(1)})z_k\,dr_1\cdots dr_q\,.\tag{14}$$

By use of (7) and (11) this is expressed in terms of the one-electron function as

$$\alpha=-\frac{1}{E}\sum_i\int\mathrm{Re}\,(\psi_i^{(0)*}z\psi_i^{(1)})\,dr\,.\tag{15}$$

We make use of the expansion for the spherical harmonics[13)]

$$\cos\vartheta\,Y_{lm}(\vartheta,\varphi)=\sum_{l'}\sqrt{\frac{2l+1}{2l'+1}}(10l0|1ll'0)(10lm|1ll'm)Y_{l'm}(\vartheta,\varphi)\tag{16}$$

in which $(l_1m_1l_2m_2|l_1l_2lm)$ is the Clebsch-Gordan coefficient, and expand $\psi_i^{(1)}(r)$ in terms of spherical harmonics $Y_{lm}(\vartheta,\varphi)$ as

$$\psi_i^{(1)}(\mathbf{r})=\sum_{l_i'm_i'}C(l_i\to l_i':m_i')\frac{P_1(n_il_i\to l_i':r)}{r}Y_{l_i'm_i'}(\vartheta,\varphi)\,. \tag{17}$$

Substituting these expressions into the equation (15) we see that only the terms proportional to $Y_{l_i+1m_i}(\vartheta,\varphi)$ and $Y_{l_i-1m_i}(\vartheta,\varphi)$ contribute to the polarizability α. Then if we choose the coefficients $C(l_i\to l_i':m_i)$ for $l_i'=l_i+1$ and $l_i'=l_i-1$ as

$$C(l_i\to l_i':m_i)=-E\sqrt{\frac{2l_i+1}{2l_i'+1}}(10l_i0|1l_il_i'0)(10l_im_i|1l_il_i'm_i)\,, \tag{18}$$

the polarizability is given by

$$\alpha=\sum_{n_il_im_i\zeta_il_i'}2\left(\frac{2l_i+1}{2l_i'+1}\right)(10l_i0|1l_il_i'0)^2(10l_im_i|1l_il_i'm_i)^2I(n_il_i\to l_i')\,,$$

where we have used the notation

$$I(nl\to l')=\int_0^\infty P_0(nl:r)P_1(nl\to l':r)r\,dr\,. \tag{19}$$

Using the values of the Clebsch-Gordan coefficients (see for example Condon and Shortley[14)]) and performing the summation over m_i, we finally obtain

$$\begin{aligned}\alpha&=\frac{4}{3}\sum_{nl}[(l+1)I(nl\to l+1)+lI(nl\to l-1)]\\&=\sum_n\frac{4}{3}I(ns\to p)+\sum_n\left[\frac{4}{3}I(np\to s)+\frac{8}{3}I(np\to d)\right]\\&\quad+\cdots\cdots\cdots\,.\end{aligned} \tag{20}$$

Here the sums extend over the occupied shells; this form of expression was first derived by Sternheimer[8)] from the one-electron point of view.

§ 3. Perturbed Hartree-Fock Equation

In this section we consider the first order equations (6) in detail and use an assumption on the symmetry of the perturbed wave functions $\psi_i^{(1)}(\mathbf{r})$:

$$\begin{aligned}\psi_i^{(1)}(\mathbf{r})=&C(l_i\to l_i+1:m_i)\frac{P_1(n_il_i\to l_i+1:r)}{r}Y_{l_i+1m_i}(\vartheta,\varphi)\\&+C(l_i\to l_i-1:m_i)\frac{P_1(n_il_i\to l_i-1:r)}{r}Y_{l_i-1m_i}(\vartheta,\varphi)\,.\end{aligned} \tag{17'}$$

Without this assumption the equations for $P_1(n_il_i\to l_i':r)$ are all coupled with each other through the third and fourth terms of the equations (6). Here we note that the equations obtained under the assumption (17′) are exact within the limits of Hartree approximation, because the couplings arise from the perturbations of the exchange interactions between electrons.

As usual it is convenient to use the expansion of $1/r_{12}$ in terms of r_1, r_2 and $\cos\vartheta_{12}$, namely

$$\frac{1}{r_{12}}=\sum_k U_k(r_1,r_2)Y_k(\vartheta_{12})\sqrt{\frac{4\pi}{2k+1}}\,, \tag{21}$$

in which

$$U_k(r_1,r_2)=\begin{cases}r_1^k/r_2^{k+1} & \text{for}\quad r_1<r_2\\ r_2^k/r_1^{k+1} & \text{for}\quad r_1>r_2\,.\end{cases} \tag{22}$$

$Y_k(\vartheta)$ is the abbreviation of $Y_{k0}(\vartheta, \varphi)$ and ϑ_{12} is the angle between r_1 and r_2, i.e.

$$\cos\vartheta_{12}=\cos\vartheta_1\cos\vartheta_2+\sin\vartheta_1\sin\vartheta_2\cos(\varphi_1-\varphi_2)\ .$$

Now let us consider the first terms of the equations (6). The Coulomb interaction terms composed of the unperturbed wave functions are written, by substituting (8) and using (21), as

$$\sum_j\int\frac{|\phi_j^{(0)}(\boldsymbol{r}_2)|^2}{r_{12}}\,d\boldsymbol{r}_2=\sum_{n_jl_j}2(2l_j+1)\int_0^\infty P_0(n_jl_j:r)^2U_0(r_1, r_2)dr_2\ ,$$

where we have used the property of the spherical harmonics[13]:

$$\sum_{m_j}Y^*_{l_jm_j}(\vartheta, \varphi)Y_{l_jm_j}(\vartheta, \varphi)=\frac{2l_j+1}{4\pi}\ .$$

Hence the first terms of the equations (6) become

$$\left[-\frac{1}{2}\nabla_1{}^2-\frac{N}{r_1}+\sum_j\int\frac{|\phi_j^{(0)}(\boldsymbol{r}_2)|^2}{r_{12}}\,d\boldsymbol{r}_2-\varepsilon_i^{(0)}\right]\phi_i^{(1)}(\boldsymbol{r}_1)$$
$$=\sum_{l_i'}C(l_i\to l_i':m_i)\frac{Y_{l_i'm_i}(\vartheta_1, \varphi_1)}{r_1}\left[-\frac{1}{2}\frac{d^2}{dr_1{}^2}-\frac{Y(r_1)}{r_1}+\frac{l_i'(l_i'+1)}{2r_1{}^2}-\varepsilon^{(0)}_{n_il_i}\right]P_1(n_il_i\to l_i':r_1)\ . \tag{23}$$

Here the summation extends over $l_i'=l_i+1$ and $l_i'=l_i-1$; the function $Y(r)$ is defined by

$$Y(r)=N-\sum_{nl}2(2l+1)Y_0^{(0)}(nl, nl:\ r)\ , \tag{24}$$

in which

$$Y_k^{(0)}(nl, n'l':\ r)\equiv r\int_0^\infty U_k(r, s)P_0(nl:\ s)P_0(n'l':\ s)\,ds\ . \tag{25}$$

From the expression (23) we see that the angular dependence of the first terms of the equations (6) is only through the spherical harmonics $Y_{l_i+1,m_i}(\vartheta, \varphi)$ and $Y_{l_i-1,m_i}(\vartheta, \varphi)$. Hence it is sufficient for our purpose to consider only terms having the same angular dependence in the equations (6). We use this fact in the following calculation.

We next consider the contributions from the second terms separately. If we use the equations (8), (17) and (21) again, the first term may be expressed in the form

$$\sum_j\int\frac{\phi_j^{(1)*}(\boldsymbol{r}_2)\phi_j^{(0)}(\boldsymbol{r}_2)+\phi_j^{(0)*}(\boldsymbol{r}_2)\phi_j^{(1)}(\boldsymbol{r}_2)}{r_{12}}\,d\boldsymbol{r}_2\phi_i(\boldsymbol{r}_1)=4\,\mathrm{Re}\sum_{n_jl_jm_j}\sum_{kl_j'}C(l_j\to l_j':m_j)\frac{P_0(n_jl_j:r_1)}{r_1}$$
$$\cdot\int_0^\infty P_0(n_jl_j:\ r_2)P_1(n_jl_j\to l_j':\ r_2)U_k(r_1, r_2)\,dr_2\sqrt{\frac{4\pi}{2k+1}}\,Y_{l_im_i}(\vartheta_1, \varphi_1)$$
$$\cdot\int_0^\pi\int_0^{2\pi}Y^*_{l_jm_j}(\vartheta_2, \varphi_2)Y_{l_j'm_j}(\vartheta_2, \varphi_2)Y_k(\vartheta_{12})\sin\vartheta_2\,d\vartheta_2\,d\varphi_2\ . \tag{26}$$

Owing to the addition theorem of the spherical harmonics[13],

$$Y_k(0)Y_k(\vartheta_{12})=\sum_{m_k}Y^*_{k,m_k}(\vartheta_2, \varphi_2)Y_{k,m_k}(\vartheta_1, \varphi_1)\ , \tag{27}$$

the integral on angular variables appeared in (26) is reduced to

$$Y_{l_im_i}(\vartheta_1, \varphi_1)\int_0^\pi\int_0^{2\pi}Y^*_{l_jm_j}(\vartheta_2, \varphi_2)Y_{l_j'm_j}(\vartheta_2, \varphi_2)Y_k(\vartheta_{12})\sin\vartheta_2\,d\vartheta_2\,d\varphi_2$$
$$=\frac{Y_{l_im_i}(\vartheta_1, \varphi_1)Y_{k,0}(\vartheta_1, \varphi_1)}{Y_k(0)}\int_0^\pi\int_0^{2\pi}Y^*_{l_jm_j}(\vartheta_2, \varphi_2)Y_{l_j'm_j}(\vartheta_2, \varphi_2)Y_{k,0}(\vartheta_2, \varphi_2)\sin\vartheta_2\,d\vartheta_2\,d\varphi_2$$
$$=\frac{Y_{10}(\vartheta_1, \varphi_1)Y_{l_im_i}(\vartheta_1, \varphi_1)}{Y_1(0)}\sqrt{\frac{3(2l_j+1)}{4\pi(2l_j'+1)}}(10l_j0|1l_jl_j'0)(10l_jm_j|1l_jl_j'm_j)\ ,$$

where the equation (16) has been used. Performing the summation over m_j we get the result in the form

$$\sum_j \int \frac{\psi_j^{(1)*}(r_2)\psi_j^{(0)}(r_2)+\psi_j^{(0)*}(r_2)\psi_j^{(1)}(r_2)}{r_{12}}\, dr_2 \psi_i^{(0)}(r_1)=4 \sum_{n_j l_j l_j'} C(l_j\to l_j':m_j)\frac{Y_{l_i' m_i}(\vartheta_1, \varphi_1)}{r_1}$$
$$\cdot P_0(n_j l_j:r_1)\left[\frac{l_j+1}{3}\frac{Y_1^{(1)}(n_j l_j, n_j l_j\to l_j+1:r_1)}{r_1}+\frac{l_j}{3}\frac{Y_1^{(1)}(n_j l_j, n_j l_j\to l_j-1:r_1)}{r_1}\right] \tag{28}$$

where the function $Y_k^{(1)}(n_1l_1, n_2l_2\to l_2': r)$ is defined by

$$Y_k^{(1)}(n_1l_1, n_2l_2\to l_2': r)\equiv r\int_0^\infty U_k(r, s)P_0(n_1l_1: s)P_1(n_2l_2\to l_2': s)\, ds\ . \tag{29}$$

The contribution from the term $Ez_1\psi_i^{(0)}(r_1)$ is easily found to be

$$Ez_1\psi_i^{(0)}(r_1)=-r_1P_0(n_il_i: r)\sum_{l_i'} C(l_i\to l_i': m_i)Y_{l_i' m_i}(\vartheta_1, \varphi_1)\ , \tag{30}$$

and there is no contribution from the term $\mathcal{E}_i^{(1)}\psi_i^{(0)}(r)$ because it has the angular dependence of $Y_{l_i m_i}(\vartheta_1, \varphi_1)$.

Next we consider the contributions from the third terms of the equation (6). As in the case treated above these terms become, by use of equations (8), (17) and (21),

$$\sum_{j//} \int \frac{\psi_j^{(0)*}(r_2)\psi_i^{(0)}(r_2)}{r_{12}}\, dr_2\psi_j^{(1)}(r_1)=\sum_{n_j l_j m_j}\sum_{k l_j'} C(l_j\to l_j': m_j)\frac{P_1(n_jl_j\to l_j': r_1)}{r_1}\, Y_{l_j' m_j}(\vartheta_1, \varphi_1)$$
$$\cdot \int_0^\infty P_0(n_jl_j: r_2)P_0(n_il_i: r_2)U_k(r_1, r_2)\, dr_2$$
$$\cdot \sqrt{\frac{4\pi}{2k+1}}\int_0^\pi\int_0^{2\pi} Y^*_{l_j m_j}(\vartheta_2, \varphi_2)Y_{l_i m_i}(\vartheta_2, \varphi_2)Y_k(\vartheta_{12})\sin\vartheta_2\, d\vartheta_2\, d\varphi_2\ . \tag{31}$$

By use of the addition theorem and the expression for the product of two spherical harmonics[15],

$$Y_{l_1 m_1}(\vartheta, \varphi)Y_{l_2 m_2}(\vartheta, \varphi)=\sum_l \sqrt{\frac{(2l_1+1)(2l_2+1)}{4\pi(2l+1)}}(l_10l_20|l_1l_2l0)(l_1m_1l_2m_2|l_2l_2lm)Y_{lm}(\vartheta, \varphi)\ , \tag{32}$$

the integral on the angular variables of the equation (31) is reduced to

$$\sum_{m_j} C(l_j\to l_j': m_j)\sqrt{\frac{4\pi}{2k+1}}\, Y_{l_j' m_j}(\vartheta_1, \varphi_1)\int_0^\pi\int_0^{2\pi} Y^*_{l_j m_j}(\vartheta_2, \varphi_2)Y_{l_i m_i}(\vartheta_2, \varphi_2)Y_k(\vartheta_{12})\sin\vartheta_2\, d\vartheta_2\, d\varphi_2$$
$$=\frac{4\pi}{2k+1}\sqrt{\frac{(2l_i+1)(2k+1)}{4\pi(2l_j+1)}}\sum_{m_j m_k}(-1)^{m_k}C(l_j\to l_j': m_j)(l_i0k0|l_ikl_j0)(l_im_ik-m_k|l_ikl_jm_j)$$
$$\cdot Y_{km_k}(\vartheta_1, \varphi_1)Y_{l_j' m_j}(\vartheta_1, \varphi_1)\ . \tag{33}$$

Here again using the formula (32) and choosing the term proportional to $Y_{l_i' m_i}(\vartheta_1, \varphi_1)$, we can substitute the product $Y_{km_k}(\vartheta_1, \varphi_1)\ Y_{l_j' m_j}(\vartheta_1, \varphi_1)$ by

$$\sqrt{\frac{(2k+1)(2l_j'+1)}{4\pi(2l_i'+1)}}(k0l_j'0|kl_j'l_i'0)(km_kl_j'm_j|kl_j'l_i'm)Y_{l_i' m_i}(\vartheta_1, \varphi_1)\ .$$

Then the right-hand side of the equation (33) is transformed into

$$\sqrt{\frac{(2l_i+1)(2l_j'+1)}{(2l_i'+1)(2l_j+1)}}(l_i0k0|l_ikl_j0)(k0l_j'0|kl_j'l_i'0)(10l_j0|1l_jl_j'0)Y_{l_i' m_i}(\vartheta_1, \varphi_1)$$
$$\cdot\sum_{m_j m_k}(-1)^{m_k}(l_im_ik-m_k|l_ikl_jm_j)(10l_jm_j|1l_jl_j'm_j)(km_kl_j'm_j|kl_j'l_i'm_i)\ .$$

Here from the property of the Clebsch-Gordan coefficient $(l_im_ik-m_k|l_ikl_jm_j)$[15], we get the relation $m_i = m_j + m_k$. Then the summations over m_j and m_k are not independent but they reduce to a summation over one variable only, say m_k, if we consider m_i to be given. This sum can be represented by the Racah coefficient. Namely, by use of the symmetry relations of the Clebsch-Gordan coefficient[15)]

$$\begin{aligned}(l_1m_1l_2m_2|l_1l_2l_3m_3) &= (-1)^{l_1+l_2-l_3}(l_2m_2l_1m_1|l_2l_1l_3m_3)\\ &= (-1)^{l_1+l_2-l_3}(l_1-m_1l_2-m_2|l_1l_2l_3-m_3)\\ &= (-1)^{l_1-m_1}\sqrt{\frac{2l_3+1}{2l_2+1}}\,(l_1m_1l_3-m_3|l_1l_3l_2-m_2)\\ &= (-1)^{l_2+m_2}\sqrt{\frac{2l_3+1}{2l_1+1}}\,(l_3-m_3l_2m_2|l_3l_2l_1-m_1)\,,\end{aligned} \tag{34}$$

and a property of the Racah coefficient $W(abcd\colon ef)$,[15)]

$$\begin{aligned}&\sum_{\beta}(a\alpha b\beta|abe\alpha+\beta)(e\alpha+\beta d\gamma-\alpha-\beta|edc\gamma)(b\beta d\gamma-\alpha-\beta|bdf\gamma-\alpha)\\ &\qquad =\sqrt{(2e+1)(2f+1)}\,(a\alpha f\gamma-\alpha|afc\gamma)W(abcd\colon ef)\,,\end{aligned} \tag{35}$$

we can reduce the summation appeared in the equation (33) to

$$(-1)^k\sqrt{(2l_j+1)(2l_j'+1)}\,(10l_im_i|1l_il_i'm_i)W(l_ik1l_j'\colon l_jl_i')\,.$$

Hence finally we obtain the result as follows

$$\begin{aligned}\sum_{j//}\int\frac{\phi_j^{(0)*}(r_2)\phi_i^{(0)}(r_2)}{r_{12}}\,dr_2\phi_j^{(1)}(r_1) &= -E\sum_{n_jl_j}\sum_{kl_j'}(-1)^k\sqrt{(2l_j+1)(2l_j'+1)}\sqrt{\frac{2l_i+1}{2l_i'+1}}\\ &\quad\cdot(l_i0k0|l_ikl_j0)(k0l_j'0|kl_j'l_i'0)(10l_j0|1l_jl_j'0)(10l_im_i|1l_il_i'm_i)\\ &\quad\cdot W(l_ik1l_j'\colon l_jl_i')\frac{P_1(n_jl_j\to l_j'\colon r_1)}{r_1}Y_{l_i'm_i}(\vartheta_1,\varphi_1)\frac{Y_k^{(0)}(n_il_i,\,n_jl_j\colon r_1)}{r_1}\,.\end{aligned} \tag{36}$$

The Racah coefficients are calculated and tabulated by Biedenharn et al.[16)] and Obi et al.[16)]

The contributions from the other terms may be calculated analogously, so only the results are given here:

$$\begin{aligned}\sum_{j//}\int\frac{\phi_j^{(1)*}(r_2)\phi_i^{(0)}(r_2)}{r_{12}}\,dr_2\phi_j^{(0)}(r_1) &= -E\sum_{n_jl_j}\sum_{kl_j'}(-1)^{k+1}(2l_j+1)\sqrt{\frac{2l_i+1}{2l_i'+1}}\,(l_i0k0|l_ikl_j'0)\\ &\quad\cdot(k0l_j0|kl_jl_i'0)(10l_j0|1l_jl_j'0)(10l_im_i|1l_il_i'm_i)W(l_ik1l_j\colon l_j'l_i')\\ &\quad\cdot\frac{P_0(n_jl_j\colon r_1)}{r_1}Y_{l_i'm_i}(\vartheta_1,\varphi_1)\frac{Y_k^{(1)}(n_il_i,\,n_jl_j\to l_j'\colon r_1)}{r_1}\,,\end{aligned} \tag{37}$$

$$\begin{aligned}\sum_{j//}\int\frac{\phi_j^{(0)}(r_2)\phi_i^{(1)}(r_2)}{r_{12}}\,dr_2\phi_j^{(0)}(r_1) &= \sum_{n_jl_j}\sum_{kl_i'}\left(\frac{2l_j+1}{2l_i'+1}\right)(l_j0k0|l_jkl_i'0)^2\\ &\quad\cdot C(l_i\to l_i'\colon m_i)\frac{P_0(n_jl_j\colon r_1)}{r_1}Y_{l_i'm_i}(\vartheta_1,\varphi_1)\frac{Y_k^{(1)}(n_jl_j,\,n_il_i\to l_i'\colon r_1)}{r_1}\,.\end{aligned} \tag{38}$$

Then using the results obtained above we finally get the equations satisfied by $P_1(n_il_i\to l_i'\colon r)$ as follows

$$\begin{aligned}&\left[-\frac{1}{2}\frac{d^2}{dr^2}-\frac{Y(r)}{r}+\frac{(l_i+1)(l_i+2)}{2r^2}-\varepsilon^{(0)}_{n_il_i}\right]P_1(n_il_i\to l_i+1\colon r)=rP_0(n_il_i\colon r)\\ &\qquad -\frac{4}{3}\frac{P_0(n_il_i\colon r)}{r}\sum_{n_jl_j}\Big[(l_j+1)Y_1^{(1)}(n_jl_j,\,n_jl_j\to l_j+1\colon r)+l_jY_1^{(1)}(n_jl_j,\,n_jl_j\to l_j-1\colon r)\Big]\\ &\qquad +\frac{1}{(10l_i0|1l_il_i+10)}\sum_{n_jl_jkl_j'}(-1)^k\sqrt{2l_j+1}\,(10l_j0|1l_jl_j'0)\left[\sqrt{2l_j'+1}\,(l_i0k0|l_ikl_j0)\right.\end{aligned}$$

$$
\begin{aligned}
&\cdot (k0l_j'0|kl_j'l_i+10)\,W(l_ik1l_j':\,l_jl_i+1)\,\frac{P_1(n_jl_j\to l_j':r)}{r}\,Y_k^{(0)}(n_il_i,\,n_jl_j:r)\\
&-\sqrt{2l_j+1}\,(l_i0k0|l_ikl_j'0)(k0l_j0|kl_jl_i+10)\,W(l_ik1l_j:l_j'l_i+1)\\
&\cdot\frac{P_0(n_jl_j:r)}{r}\,Y_k^{(1)}(n_il_i,\,n_jl_j\to l_j':r)\Big]+\frac{1}{2l_i+3}\sum_{n_jl_jk}(2l_j+1)\\
&\cdot (l_j0k0|l_jkl_i+10)^2\,\frac{P_0(n_jl_j:r)}{r}\,Y_k^{(1)}(n_jl_j,\,n_il_i\to l_i+1:r)\,, \qquad (39)
\end{aligned}
$$

and

$$
\begin{aligned}
\Big[-\frac{1}{2}\frac{d^2}{dr^2}-\frac{Y(r)}{r}+\frac{(l_i-1)l_i}{2r^2}-\varepsilon^{(0)}_{n_il_i}\Big]&P_1(n_il_i\to l_i-1:r)=rP_0(n_il_i:r)\\
&-\frac{4}{3}\frac{P_0(n_il_i:r)}{r}\sum_{n_jl_j}\Big[(l_j+1)Y_1^{(1)}(n_jl_j,\,n_jl_j\to l_j+1:\,r)+l_jY_1^{(1)}(n_jl_j,\,n_jl_j\to l_j-1:r)\Big]\\
&+\frac{1}{(10l_i0\,|\,1l_il_i-10)}\sum_{n_jl_jkl_j'}(-1)^k\sqrt{2l_j+1}\,(10l_j0|1l_jl_j'0)\Big[\sqrt{2l_j'+1}\,(l_i0k0|l_ikl_j0)\\
&\cdot (k0l_j'0|kl_j'l_i-10)\,W(l_ik1l_j':\,l_jl_i-1)\,\frac{P_1(n_jl_j\to l_j':r)}{r}\,Y_k^{(0)}(n_il_i,\,n_jl_j:\,r)\\
&-\sqrt{2l_j+1}\,(l_i0k0|l_ikl_j'0)(k0l_j0|kl_jl_i-10)\,W(l_ik1l_j:l_j'l_i-1)\\
&\cdot\frac{P_0(n_jl_j:r)}{r}\,Y_k^{(1)}(n_il_i,\,n_jl_j\to l_j':r)\Big]+\frac{1}{2l_i-1}\sum_{n_jl_jk}(2l_j+1)\\
&\cdot (l_j0k0|l_jkl_i-10)^2\,\frac{P_0(n_jl_j:r)}{r}\,Y_k^{(1)}(n_jl_j,\,n_il_i\to l_i-1:r)\,. \qquad (40)
\end{aligned}
$$

The boundary conditions for $P_1(nl\to l':\,r)$ are

$$
P_1(nl\to l':\,r)=\begin{cases} 0 & \text{for}\quad r=0\\ \text{const. }\exp-\sqrt{|\varepsilon^{(0)}_{nl}|}\,r & \text{for}\quad r\to\infty\,,\end{cases} \qquad (41)
$$

which come from the demand on the wave function. These equations are coupled with each other and can be solved self-consistently by the method of successive approximation, but in this article we solve them only for helium.

§ 4. Sternheimer Approximation

Starting from a one-electron point of view, Sternheimer[8] obtained, instead of (6), the following equation for $\phi_i^{(1)}(\boldsymbol{r})$

$$
\begin{aligned}
\Big[-\frac{1}{2}\nabla_1^2-\frac{N}{r_1}+\sum_j\int\frac{|\phi_j^{(0)}(\boldsymbol{r}_2)|^2}{r_{12}}\,d\boldsymbol{r}_2-\sum_{j\parallel}\int\frac{\phi_j^{(0)*}(\boldsymbol{r}_2)\,\phi_i^{(0)}(\boldsymbol{r}_2)}{r_{12}}\,d\boldsymbol{r}_2\,\frac{\phi_j^{(0)}(\boldsymbol{r}_1)}{\phi_i^{(0)}(\boldsymbol{r}_1)}-\varepsilon_i^{(0)}\Big]&\phi_i^{(1)}(\boldsymbol{r}_1)\\
=-Ez_1\phi_i^{(0)}(\boldsymbol{r}_1)\,.&\qquad (42)
\end{aligned}
$$

This equation can be written by use of (8), (17) and (21) in the form

$$
\Big[-\frac{1}{2}\frac{d^2}{dr^2}+\frac{l'(l'+1)}{2r^2}+\{V^{(0)}_{nl}(r)-\varepsilon^{(0)}_{nl}\}\Big]P_1(nl\to l':r)=rP_0(nl:r)\,, \qquad (43)
$$

which corresponds to (39) and (40). Here $V^{(0)}_{nl}(r)$ is the potential energy appeared in the equation (42).

Comparing the equation (42) with the rigorous equations (6), we see that Sternheimer neglected the influence on the perturbation of $\phi_i(\boldsymbol{r})$ from the perturbations of the other orbitals.

In practical calculation, however, the set of equations (39) and (40) is not so easy to treat as the Sternheimer's equation; for the former is a coupled set of integro-differential equations whereas the latter is an uncoupled set of ordinary differential equations. We adopt

Sternheimer's approximation in this article except for helium, for which we shall solve the exact equation (39) self-consistently in order to estimate the accuracy of the Sternheimer approximation.

§ 5. Method of Calculation

Next we describe our method of solving the differential equation (43). The unperturbed radial wave functions $P_0(nl:r)$ are solutions of the Hartree-Fock equation

$$\left[-\frac{1}{2}\frac{d^2}{dr^2}+\frac{l(l+1)}{2r^2}+\{V_{nl}^{(0)}(r)-\varepsilon_{nl}^{(0)}\}\right]P_0(nl:r)=0\ , \tag{5'}$$

and are tabulated for each atom[17),18),22),19)] but the potentials $V_{nl}^{(0)}(r)$ are not given for neon and argon. So we use the method given by Sternheimer[8)], which we shall modify slightly for convenience.

We define a function $U_{nl}(r)$ as follows

$$U_{nl}(r)=\frac{l(l+1)}{r^2}+2\{V_{nl}^{(0)}(r)-\varepsilon_{nl}^{(0)}\}\ , \tag{44}$$

and approximate the second derivative of $P_0(nl:r)$ with respect to r by the second difference according to Lagrange's three-point method of interpolation, that is by

$$\frac{2}{\delta_{n-1}(\delta_{n-1}+\delta_n)}\left[\frac{\delta_{n-1}}{\delta_n}P_0(nl:r_{n+1})-\left(1+\frac{\delta_{n-1}}{\delta_n}\right)P_0(nl:r_n)+P_0(nl:r_{n-1})\right],$$

in which $\delta_n=r_{n+1}-r_n$. Then $U_{nl}(r)$ is given by the equation (5′) as follows:

$$U_{nl}(r_n)=\frac{2}{P_0(nl:r_n)\delta_{n-1}(\delta_{n-1}+\delta_n)}\left[\frac{\delta_{n-1}}{\delta_n}P_0(nl:r_{n+1})-\left(1+\frac{\delta_{n-1}}{\delta_n}\right)P_0(nl:r_n)+P_0(nl:r_{n-1})\right]. \tag{45}$$

The differential equation (43) can be written by use of the function $U_{nl}(r)$ in the form

$$\frac{d^2}{dr^2}P_1(nl\to l':r)=U'_{nl}(r)P_1(nl\to l':r)-I_{nl}(r)\ ,$$

where

$$U'_{nl}(r)=U_{nl}(r)+[l'(l'+1)-l(l+1)]/r^2\ ,$$

$$I_{nl}(r)=2rP_0(nl:r)\ .$$

Replacing again the second derivative with respect to r by the Lagrange approximation, we obtain

$$\begin{aligned}P_1(nl\to l':r_{n+1})=P_1(nl\to l':r_n)&+\frac{\delta_n}{\delta_{n-1}}[P_1(nl\to l':r_n)-P_1(nl\to l':r_{n-1})]\\&+\frac{\delta_n(\delta_{n-1}+\delta_n)}{2}[U'_{nl}(r_n)P_1(nl\to l':r_n)-I_{nl}(r_n)]\ .\end{aligned} \tag{46}$$

We use this formula for the outward integration of the equation (43) starting from the neighbourhood of $r=0$. The correspoding formula for the inward integration is

$$\begin{aligned}P_1(nl\to l':r_{n-1})=P_1(nl\to l':r_n)&+\frac{\delta_{n-1}}{\delta_n}[P_1(nl\to l':r_n)-P_1(nl\to l':r_{n+1})]\\&+\frac{\delta_{n-1}(\delta_{n-1}+\delta_n)}{2}[U'_{nl}(r_n)P_1(nl\to l':r_n)-I_{nl}(r_n)]\ .\end{aligned} \tag{47}$$

For excitations $ns\to p$ and $np\to s$ except for $1s\to p$, the equation (43) is integrated outward with starting values obtained in the following. For small r the equation (43) becomes[20)]

$$\left[-\frac{d^2}{dr^2}-\frac{2N}{r}+\frac{l'(l'+1)}{r^2}+2\{v_{nl}^{(0)}-\mathcal{E}_{nl}^{(0)}\}+\mathrm{O}(r^2)\right]P_1(nl\to l':r)=2Ar^{l+2}+\mathrm{O}(r^{l+3})\,,$$

where $v_{nl}^{(0)}$ and A are constants. The right-hand side of this equation can be neglected as compared with the left-hand side in the neighbourhood of $r=0$. Then this equation is the same as the equation for $P_0(nl':r)$ except for the constant term $2\{v_{nl}^{(0)}-\mathcal{E}_{nl}^{(0)}\}$. But this constant term is negligible compared with $l'(l'+1)/r^2$ and $2N/r$ in the neighbourhood of $r=0$. Hence $P_1(nl\to l':r)$ is approximately proportional to $P_0(nl':r)$ for small r; and the proportional constant is to be determined by the boundary condition (41). In practice we start integration of the equation (43) by use of the equation (46) from two points near $r=0.05$.

For the excitation $1s\to p$, the integration is started from the origin and the gradient of the solution at that point is determined so as to satisfy the boundary condition (41).

For the excitation $np\to d$ singularity at the origin is strong compared with the above-mentioned case; hence we use the inward integration of the equation (43) starting from a large radius R. Let the equation (43) be written for simplicity as

$$\left.\begin{aligned}&\frac{d^2}{dr^2}P_1(nl\to l':r)=F(r)P_1(nl\to l':r)\,,\\&F(r)=U'_{nl}(r)-\frac{I_{nl}(r)}{P_1(nl\to l':r)}\,.\end{aligned}\right\}\tag{48}$$

Then $F(r)$ is certainly positive and not too rapidly varying in the neighbourhood of $r=R$; at large distances from the nucleus it is nearly a constant and is given by $-2\mathcal{E}_{nl}^{(0)}$. So we can assume that $F(r)$ is constant for $r>R$. Then an approximate solution of the equation (48) satisfying the boundary condition is given by

$$\begin{aligned}P_1(nl\to l':r)&\sim P_1(nl\to l':R)\exp\left[-\int_R^r\sqrt{F(r)}\,dr\right]\\&\sim P_1(nl\to l':R)\exp\left[-\sqrt{F(R)}(r-R)\right].\end{aligned}\tag{49}$$

In practical calculation, if $P_1(nl\to l':R)$ is assumed, $F(R)$ is calculated from the equation (48) and $P_1(nl\to l':R+\delta)$ is obtained from the equation (49). Then the numerical integration can be performed by use of the integration formula (47). The correct value of $P_1(np\to d:R)$ is determined so as to satisfy the boundary condition at the origin.

Since for helium the potential field $V_{1s}^{(0)}(r)$ effective for an electron is published, we can solve the equation (43) for 1s state by the Störmer-Levy method(27). Thus we can estimate the accuracy of our method explained above. Thereby starting values near $r=0$ can be assumed to be proportional to the unperturbed wave function $P_0(2p:r)$ and the proportional constant is to be determined from the boundary condition (41).

Also for helium, we solve the rigorous equation self-consistently to estimate the accuracy of the Sternheimer approximation. In this case the equation (39) becomes

$$\begin{aligned}&\left[-\frac{1}{2}\frac{d^2}{dr^2}-\frac{2}{r}+\frac{Y_0^{(0)}(1s,1s:r)}{r}+\frac{1}{r^2}-\mathcal{E}_{1s}^{(0)}\right]P_1(1s\to p:r)\\&\qquad=rP_0(1s:r)-\frac{2}{3}P_0(1s:r)\frac{Y_1^{(1)}(1s,1s\to p:r)}{r}\,.\end{aligned}\tag{50}$$

The second term of the right-hand side of this equation represents the perturbation of the Coulomb interaction energy due to the applied electric field. This is an integro-differential equation which is solved self-consistently by the successive approximation method. First $Y_1^{(1)}(1s,1s\to p:r)$ is estimated by use of $P_1(1s\to p:r)$ which has been obtained by the Sternheimer approximation, and next the equation (50) is solved by the method explained above. Then, using the solution $P_1(1s\to p:r)$ so obtained, we calculate

$Y_1^{(1)}(1s, 1s\to p:r)$ again and compare it with the former one. This procedure is to be carried out until the self-consistency is obtained.

§ 6. Results and Discussions

By the method described above the functions $P_1(nl\to l':r)$ in the Sternheimer approximation are calculated for each orbital of the atoms. In the course of numerical calculation the Parametron Computor PC-1 has been employed to solve the equations (43).

Table I. Calculated values of the polarizability α in the Sternheimer approximation and contributions to it from various shells. All values are in units A^3.

Atom	He	Ne	Ar
$1s\to p$	0.220	0.0002	0.00002
$2s\to p$		0.226	0.011
$2p\to s$		0.024	−0.012
$2p\to d$		0.365	0.006
$3s\to p$			0.829
$3p\to s$			−0.486
$3p\to d$			2.056
Total	0.220	0.615	2.404

Table II. Values of the polarizability α calculated by various methods and experimental ones. All values are in units A^3.

Atom	He	Ne	Ar
Kaneko (S)[a]	0.2205	0.615	2.40
Kaneko (S.L)[b]	0.2200	—	
Kaneko[c]	0.196	—	
Sternheimer[d]	0.224	—	
Dalgarno[e]	—	0.38	
Variational method	0.218[f]		2.03[g]
		0.736[b]	2.909[h]
Statistical model[i]	—	2.01	2.88
Experimental	0.207[j]	0.398[k]	1.63[k]

a) Values calculated by the Sternheimer approximation.
b) Value calculated by the Störmer-Levy method.
c) The most rigorous value within the Hartree-Fock approximation.
d) See reference 9).
e) See reference 11).
f) Value calculated by Wikner and Das see reference 7).
g) Value calculated by Pople and Schofield see reference 6).
h) Values calculated by Bravin see reference 5).
i) Values calculated by Gombás see reference 26).
j) See reference 23).
k) These values are taken from reference 24).

After the perturbations $P_1(nl\to l':r)$ have been obtained, the integrals $I(nl\to l')$ are evaluated, and the polarizability α is calculated from the equation (20). The results of the calculation are presented in Table I. Contribution of the outermost shell to the polarizability α is predominant, as already mentioned by Pauling[21], Buckingham[4] and Sternheimer[8]. For neon values of the present author are obtained by use of the unperturbed wave functions found by Brown[18], who takes account of the exchange interaction only between $2p$ electrons; his wave functions are more loosely bounded than the exact solutions of Hartree-Fock equation. Owing to this charactor of the unperturbed wave function, our value of the polarizability is expected larger than the value obtained by the more rigorous unperturbed functions. After the calculations are over, we find a new solution of Hartree-Fock equation for neon obtained by Worsley[22] and the calculation of the polarizability by Dalgarno and Parkinson[11] who used an analytic wave function adjusted so as to approximate the Worsley's function. Their values are cited in Table II, agreement with the experimental value being very good compared with ours. By comparison between the two values for neon, we see that the accuracy of the calculated value of the polarizability depends sensitively on the accuracy of the unperturbed wave function used.

For comparison's sake, the experimental values[23],[24] and the values calculated by different methods from ours are shown in Table II. For helium, a calculation was made by Sternheimer[9] with use of Löwdin's[25] analytical function which was an approximation to Hartree's wave function; and as an example of the variational method to this problem the value calculated by Wikner and Das[7] is quoted. For neon and argon the calculations were made by use of the variational method by Bravin[5] and Pople and Schofield[6], and by use of the statistical model of atoms by Gombás[26].

For helium a calculated value of the polarizability obtained by the Störmer-Levy method[27] for the perturbed wave function is also shown in Table II as Kaneko (S.L). The agreement between calculated values by both methods is very good, so we can suppose the error resulted from using the integration formulae (46) and (47) to be at most few per cent for neon and argon, even if we consider the fact that they have wave functions with nodes in contrast to helium which has only nodeless 1*s* wave function.

Also for helium the calculated value of the polarizability obtained by use of the solution of the equation (50) is shown in Table II as Kaneko. This is the most rigorous theoretical value of the polarizability for helium within the limits of Hartree-Fock approximation. From this result we see that the rigorous theory gives the polarizability about ten per cent smaller. Hence we may deduce from this result that if we take account of the influence due to the perturbation of the interelectronic potential energy the Sternheimer approximation will be improved considerably. We are new planning to solve the integrodifferential equations (39) and (40) for neon and argon.

In conclusion the author wishes to express his sincere thanks to Prof. T. Kihara for his continual guidance and for his kindness in reading the original manuscript, and to Prof. M. Kotani for many suggestions and guidances. Thanks are also due to Prof. H. Takahasi and members of his laboratory for helps in programming and operating the Parametron Computor PC–1.

Note added in proof. The polarizability for helium has just been calculated in a similar way by A. Dalgarno: Proc. Roy. Soc. **A, 251** (1959) 282.

References

1) J. O. Hirschfelder, C. F. Curtiss and R. B. Bird: *Molecular Theory of Gases and Liquids* (Wiley, 1954).
2) About the two body force see reference 1). About the three body force see Y. Midzuno and T. Kihara: J. Phys. Soc. Japan **11** (1956) 1045.
3) J. G. Kirkwood: Phys. Z. **33** (1932) 57.
4) R. A. Buckingham: Proc. Roy. Soc. **A, 160** (1935) 94.
5) A. V. Bravin: JETP (U.S.S.R.) **27** (1954) 384.
6) J. A. Pople and P. Schofield: Phil. Mag. **2** (1957) 591.
7) E. G. Wikner and T. P. Das: Phys. Rev. **107** (1957) 497.
8) R. M. Sternheimer: Phys. Rev. **96** (1954) 951.
9) R. M. Sternheimer: Phys. Rev. **107** (1957) 1565.
10) M. Sandbom: Arkiv Fysik **13** (1958) 539.
11) A. Dalgarno and D. Parkinson: Proc. Roy. Soc. **A, 250** (1959) 422.
12) D. R. Hartree: Proc. Roy. Soc. **A, 150** (1935) 9.
13) See, for example, H. A. Bethe and E. E. Salpeter: *Handbuch der Physik* vol. **35** (Springer, 1957).
14) E. U. Condon and G. H. Shortley: *The Theory of Atomic Spectra* (Cambridge, 1935).
15) A. R. Edmonds: *Angular Momentum in Quantum Mechanics* (Princeton Univ. Press, 1957).
16) L. C. Biedenharn: Tables of Racah Coefficients. ORNL no. 1098 (1952). A. Simon, J. H. van der Sluis and L. C. Biedenharn: Tables of the Racah Coefficients, ORNL no. 1679 (1954). S. Obi, T. Ishidzu, H. Horie, S. Yanagawa, Y. Tanabe and M. Sato: Tables of the Racah Coefficients Part I. Ann. Tokyo Astr. Obs. **3** (1953) 89; Part II. Ann. Tokyo Astr. Obs. **4** (1954) 1. M. Sato: Progr. Theor. Phys. **13** (1955) 405.
17) For He; W. S. Wilson and R. B. Londsay: Phys. Rev. **47** (1935) 681.
18) For Ne; F. W. Brown: Phys. Rev. **44** (1933) 214.
19) For Ar; D. R. Hartree and W. Hartree: Proc. Roy. Soc. **A, 166** (1938) 450.
20) See, for example, D. R. Hartree: *The Calculation of Atomic Structure* (Wiley, 1957).
21) L. Pauling: Proc. Roy. Soc. **A, 114** (1927) 181.
22) B. H. Worsley: Canad. J. Phys. **36** (1958) 289.
23) L. Essen: Proc. Phys. Soc. London **B, 66** (1953) 189.
24) Landolt Börnstein: *Zahlenwerte und Funktionen aus Physik, Chemie, Astronomie, Geophysik und Technik* vol. **1**, Part 1, *Atome und Ionen* (Springer, 1950).
25) P. O. Löwdin: Phys. Rev. **90** (1953) 120.
26) P. Gombás: *Handbuch der Physik* vol. **36**, (Springer, 1956).
27) See, for example, W. E. Milne: *Numerical Solution of Differential Equations* (Wiley, 1953).

JOURNAL OF THE PHYSICAL SOCIETY OF JAPAN Vol. 14, No. 11, NOVEMBER, 1959

Luminescence Processes in the KCl:Tl Phosphor in a Multidimensional Configuration Space

By Hiroshi KAMIMURA and Satoru SUGANO

Department of Physics, Faculty of Science, University of Tokyo
Tokyo, Japan

(Received July 3, 1959)

In order to explain the 3050Å and 4750Å emissions of KCl:Tl phosphor which are raised by excitation in any of the absorption bands, a multidimensional configuration coordinate model is introduced. This is achieved by taking into account the Jahn-Teller effect for the excited states of the thallium ion. The Jahn-Teller effect is treated by means of an intermediate coupling scheme within the *6s6p* configuration, because the mixing of the ^3P and ^1P states by the spin-orbit interaction is essential to understand the optical properties. It is shown that introduction of a tetragonal distortion of the emission center is able to explain the luminescence processes of this phosphor both semi-quantitatively and qualitatively: Under the tetragonal and trigonal distortions, both the crossing of the pure spin singlet ^1P and triplet ^3P curves and the appearance of two minima in the $^3P_1$ energy curves are expected. The former accounts for the non-radiative transition from the $^1P_1$ state to the $^3P_1$ state and the latter does for the two emission bands. The two types of distortions are equally able to give semi-quantitative agreement of the relative strengths of the absorption and emission bands with experiments, but only the tetragonal distortion explains the polarization of the 3050Å emission observed.

Finally Johnson and Williams' model is criticized.

§ 1. Introduction

Alkali halide thallium phosphors have been widely investigated by many authors, because they are physically simplest among luminescent materials. Among them, KCl : Tl has been most fully examined. In a potassium chloride crystal, a thallium introduces two clearly resolved absorption bands peaking at 1960Å and 2490Å with subsidiary one at 2060Å and two emission bands with peaks at 3050Å and 4750Å. Excitation in any of the three absorption bands results in emission in both two emission bands.[1)]

Seitz[2)] has suggested that the $^1P_1$, $^3P_2$ and $^3P_1$ excited states of the Tl$^+$ ions, suitably modified in the crystal, are responsible for the 1960Å, 2060Å and 2490Å absorption bands respectively. More recently Williams[3)] has calculated energies of the $^1S_0$ ground state and the $^3P_1$ excited state by using the properties of the free ion. The energies are given as a function of the distance Δa between the thallium ion and the neighboring chlorine ion in the one-dimensional configuration coordinate. For the $^1P_1$ state Johnson and Williams[1)] have derived a similar curve from the experimental data. The curve thus derived intersects with the $^3P_1$ curve near the minimum in order that the emission by excitation in any of the $^3P_1$ and $^1P_1$ bands may take place.

If the similar treatment to Williams' is also applied to the $^1P_1$ curve, however, it would not intersect with the $^3P_1$ curve but be nearly parallel to it. The reason is that his treatment does not involve the spin effects explicitly. In facts, using the same mathematical calculation as Williams', Knox and Dexter[4)] have found that the $^1P_1$ curve simply displaces upward by about three electron volts from the $^3P_1$ curve. Thus, insofar as spin effects may be neglected, the one-dimensional configuration coordinate model will not be suitable for explaining the experimental facts.

The purpose of the present investigation is to propose an alternative way to explain the experimental facts by considering the Jahn-Teller effect of the excited states of the thallium ion. In doing so, it is necessary to introduce multidimensional configuration coordinate curves for these states. The excited states with the *6s6p* configuration in cubic crystals have orbital degeneracies. Therefore, they undergo the Jahn-Teller effect to remove the degeneracies. Öpik and Pryce[5] have already considered such a Jahn-Teller effect only for the ^3P state. In the thallium ion, however, the departure from Russell-Saunders coupling is considerable and the mixing of the ^3P and ^1P states by spin-orbit interactions is essential to understand the optical spectrum. Therefore, we deal here with the Jahn-Teller effect of the excited states by means of an intermediate coupling scheme.

§ 2. The Secular Matrix for the Excited State (6s6p)

We take the following Hamiltonian for the excited states with the *6s6p* electron configuration :

$$\mathscr{H}=\sum_{i=1,2}\left\{-\frac{\hbar^2}{2m}\Delta_i+v(r_i)+V_{crys}(r_i)+\zeta_i l_i\cdot s_i\right\}+\frac{e^2}{r_{12}}+W+V, \qquad (2.1)$$

where $v(r_i)$ is the potential energy due to core electrons and thallium nucleus, $V_{crys}(r_i)$ that of the cubic crystal field* to which *6s* and *6p* electrons are exposed, $l_i\cdot s_i$ the spin-orbit interaction, W the term of the Jahn-Teller effect and V the quasi-elastic potential energy. In our treatment, V_{crys} is considered to include all the effects computed by Williams.

If we restrict our attention to the thallium ion and its six neighboring chlorine ions, even vibrations of the system are A_{1g}, E_g and T_{2g} whose normal coordinates are expressed by (Q_1), (Q_2, Q_3) and (Q_4, Q_5, Q_6) respectively. They are given in Fig. 1. Then, W and V are expanded in terms of these normal coordinates as follows :

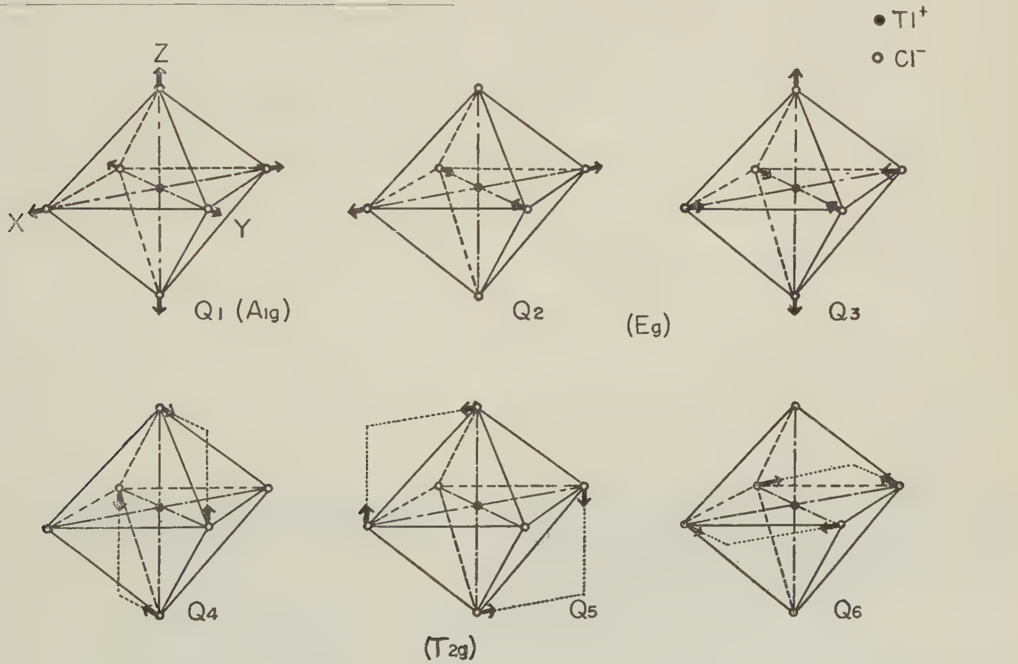

Fig. 1.

$$W=V_1Q_1+V_2Q_2+V_3Q_3+V_4Q_4+V_5Q_5+V_6Q_6,$$
$$V=1/2\cdot\alpha Q_1^2+1/2\cdot\beta(Q_2^2+Q_3^2)+1/2\cdot\gamma(Q_4^2+Q_5^2+Q_6^2), \qquad (2.2)$$

where V_i's $(i=1,\ldots,6)$ represent the coupling between the electrons and nuclear displacements. Since the term of Q_1 in W appears equally in all the diagonal elements of the secular matrix for $\mathscr{H}$, it will be included in V_{crys} as $V_{crys}(r, Q_1)$, which has already been calculated by Williams.

The excited states with the *6s6p* configuration consist of three triplet states $^3P_0$, $^3P_1$ and $^3P_2$ and one singlet state $^1P_1$. Let $|LSJM>$

---

* The cubic crystal field can be expanded in terms of *Cubic Harmonics*. *s* and *p* electrons feel only the first term, the spherically symmetric one.

Table I. The matrix elements of the Hamiltonian (2.1). The diagonal

SJ	$^3P_2$					
M	2	1	0	−1	−2	1
	$_3+\sqrt{\frac{3}{2}}AQ_3$	$-\frac{1}{2}B(Q_5-iQ_4)$	$\frac{\sqrt{3}}{2}AQ_2+\frac{i}{\sqrt{6}}BQ_6$	0	0	$-\frac{1}{2}B(Q_5-iQ_4)$
		$E_3-\frac{\sqrt{3}}{2\sqrt{2}}AQ_3$	$-\frac{1}{2\sqrt{6}}B(Q_5-iQ_4)$	$\frac{3}{2\sqrt{2}}AQ_2+\frac{i}{2}BQ_6$	0	$-\frac{3\sqrt{3}}{2\sqrt{2}}AQ_3$
			$E_3-\sqrt{\frac{3}{2}}AQ_3$	$\frac{1}{2\sqrt{6}}(Q_5-iQ_4)$	$\frac{\sqrt{3}}{2}AQ_2+\frac{i}{\sqrt{6}}BQ_6$	$\frac{\sqrt{3}}{2\sqrt{2}}B(Q_5+iQ_4)$
				$E_3-\frac{3}{2\sqrt{2}}AQ_3$	$\frac{1}{2}B(Q_5-iQ_4)$	$-\frac{3}{2\sqrt{2}}AQ_2+\frac{i}{2}BQ_6$
					$E_3+\sqrt{\frac{3}{2}}AQ_3$	0
						$E_2-\frac{\sqrt{3}}{2\sqrt{2}}AQ_3$

be the eigenvectors of these states. Then in terms of these eigenvectors the secular matrix for $\mathscr{H}$ is given as Table I shows, where we have omitted the common terms

$$\sum_{i=1,2} V_{crys}(r_i,\ Q_1)+V \tag{2.3}$$

in the diagonal elements to save space.

In the table, the constants A and B are defined in terms of eigenvectors $|1,m>$ of the single p-electron as follows,

$$A=-1/\sqrt{6}\cdot<1,0\,|\,v_3\,|\,1,0>\ ,$$
$$B=\sqrt{3}/2\cdot<1,0\,|\,v'_6\,|\,1,0>\ , \tag{2.4}$$

v_3 and v'_6 being the single electron part of V_3 and V'_6 respectively. In the expression of B, the quantization axis is referred to the trigonal axis of the crystal and $V'_6=1/\sqrt{3}\cdot(V_4+V_5+V_6)$. E's are given by

$$E_1=F_0-G_1-\zeta_p\ ,$$
$$E_2=F_0-G_1-1/2\cdot\zeta_p\ ,$$
$$E_3=F_0-G_1+1/2\cdot\zeta_p\ , \tag{2.5}$$
$$E_4=F_0+G_1\ ,$$

F_0 and G_1 being Slater integrals, ζ_p a constant of the spin-orbit coupling for a 6p-electron. It should be remarked that these constants are considered not to be those of a free thallium ion but of a thallium ion in the crystal. Therefore, as we shall see later, they are determined empirically in our theory.

elements of the term $V_{crys}(r_i,Q_1)+V$ are omitted to save space.

$^3P_1$		$^3P_0$	$^1P_1$		
0	-1	0	1	0	-1
$\frac{3}{2}AQ_2+\frac{i}{\sqrt{2}}BQ_6$	0	$\sqrt{\frac{3}{2}}AQ_2+\frac{i}{\sqrt{3}}BQ_6$	0	0	0
$\frac{1}{2\sqrt{2}}B(Q_5-iQ_4)$	$\frac{3}{2\sqrt{2}}AQ_2+\frac{i}{2}BQ_6$	$\frac{1}{\sqrt{3}}B(Q_5-iQ_4)$	0	0	0
0	$\frac{\sqrt{3}}{2\sqrt{2}}B(Q_5-iQ_4)$	$\sqrt{3}\,AQ_3$	0	0	0
$\frac{1}{2\sqrt{2}}B(Q_5+iQ_4)$	$\frac{3}{2}\sqrt{\frac{3}{2}}AQ_3$	$-\frac{1}{\sqrt{3}}B(Q_5+iQ_4)$	0	0	0
$-\frac{3}{2}AQ_2+\frac{i}{2}BQ_6$	$-\frac{1}{2}B(Q_5+iQ_4)$	$\sqrt{\frac{3}{2}}AQ_2-\frac{i}{\sqrt{3}}BQ_6$	0	0	0
$\frac{1}{2\sqrt{2}}B(Q_5-iQ_4)$	$-\frac{3}{2\sqrt{2}}AQ_2-\frac{i}{2}BQ_6$	0	$\frac{1}{\sqrt{2}}\zeta_p$	0	0
$E_2+\sqrt{\frac{3}{2}}AQ_3$	$-\frac{1}{2\sqrt{2}}B(Q_5-iQ_4)$	0	0	$\frac{1}{\sqrt{2}}\zeta_p$	0
	$E_2-\frac{\sqrt{3}}{2\sqrt{2}}AQ_3$	0	0	0	$\frac{1}{\sqrt{2}}\zeta_p$
		E_1	0	0	0
			$E_4+\sqrt{\frac{3}{2}}AQ_3$	$-\frac{1}{\sqrt{2}}B(Q_5-iQ_4)$	$\frac{3}{\sqrt{2}}AQ_2+iBQ_6$
				$E_4-\sqrt{6}\,AQ_3$	$\frac{1}{\sqrt{2}}B(Q_5-iQ_4)$
					$E_4+\sqrt{\frac{3}{2}}AQ_3$

§ 3. Multidimensional Configuration Coordinate Energy Surface

The secular matrix of (2.1) has 12 dimensions and so it is difficult to solve it generally. In this paper, however, we confine ourselves to the cases of special distortions, that is, tetragonal and trigonal distortions of the octahedron $Tl^+(Cl^-)_6$. For these cases the matrix can be solved rather easily. Such a treatment seems to be justified by Öpik and Pryce's proof[5] that the energy of the stationary point of a lower symmetry always lies between those of the tetragonal and trigonal stationary points for the *P*-state.

For tetragonal distortions, we can put $Q_2=Q_4=Q_5=Q_6=0$. Then the matrix is reduced to two 3-dimensional, two 2-dimensional and two 1-dimensional matrices. From these, arise four non-degenerate and four doubly degenerate energy levels.

The results of trigonal distortions turn out to be equivalent to those of tetragonal distortions if one replaces A with $-\sqrt{2}/3\cdot B$, Q_3 with $Q'_6=1/\sqrt{3}\cdot(Q_4+Q_5+Q_6)$, β with γ and takes the trigonal axis as the quantization axis. It is, therefore, sufficient for us to discuss only the case of the tetragonal distortion.

In order to solve the secular matrices and illustrate the multidimensional configuration coordinate energy surfaces of the excited states, it becomes necessary to know the values of the parameters G_1 and ζ_p. Since the orbital functions of the *6s* and *6p* electrons are considered to be significantly affected by the surrounding ions, values of the parameters G_1 and ζ_p are determined so as to get the best fit of relative positions of the $^1P_1$, $^3P_2$ and $^3P_1$ crystal states to the observed three absorption peaks (1960Å, 2060Å and 2490Å) instead of using values of a free thallium ion. They are given in Table II.

Table II. The values of G_1, ζ_P, λ and R_{Abs} determined by various methods

	Free ion (Hartree)	Free ion (Matched with exp.)	Williams et al.	Ours.	Obs.
G_1	1.70_5 eV	1.04_6	-0.10_5	0.20_4	
ζ_P	0.64_0 eV	1.01_5	1.02	0.76_5	
λ	(1.00)	0.87_2	0.87	(1.00)	
R_{abs}	184	27.8	2	3.9	5

Then, using these values of G_1 and ζ_p, we can obtain configuration coordinate curves without quasi-elastic terms for the excited states in a sub-space (Q_1-space) by taking $X=\sqrt{6}/2\cdot AQ_3$ as abscissa. These curves are illustrated in Fig. 2. This figure is considered to represent a section of the multidimensional configuration space passing through a fixed Q_1-point* and being perpendicular to the ordinary one-dimensional configuration coordinate space (Q_1-space). In Fig. 2, only the relative energies among the excited states are given and those to the ground state are out of our consideration. Each energy curve is designated by the notation $\mathcal{E}_i{}^M$ according to the quantum number *SLJM* associated with it at $Q_3=0$. The superscript *M* is a good quantum number even at $Q_3\neq 0$ and the subscript *i* is arranged in such a way that $i=1$, 2, 3, and 4 correspond to $^1P_1$, $^3P_2$, $^3P_1$ and $^3P_0$ respectively. The dashed lines associated with $\mathcal{E}_1{}^{\pm1}$, $\mathcal{E}_1{}^0$, $\mathcal{E}_3{}^{\pm1}$ and $\mathcal{E}_3{}^0$ states show the energy levels of the corresponding states obtained by neglecting the non-diagonal elements of the secular matrix. They are important to discuss non-radiative transitions from the $^1P_1$ curve to the $^3P_1$ curve as seen later.

As pointed out in the first section, $V_{crys}(r, Q_1)$ is considered to cause parallel shifts of the excited states, if it is independent of the spin associated with these states and if all the states are constructed from the same *s*- and *p*- crystal orbitals. Therefore, as far as we deal with the relative energies among the excited states as treated here, it is not necessary to calculate $V_{crys}(r, Q_1)$.**

When one attempts to complete the configuration coordinate curves by adding the quasi-elastic term $V=\beta/3A^2\cdot X^2$ to the curves

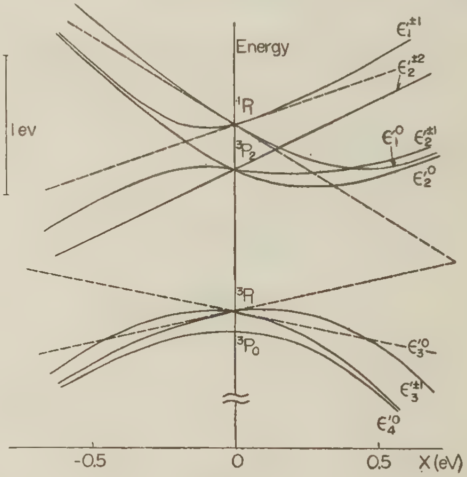

Fig. 2.

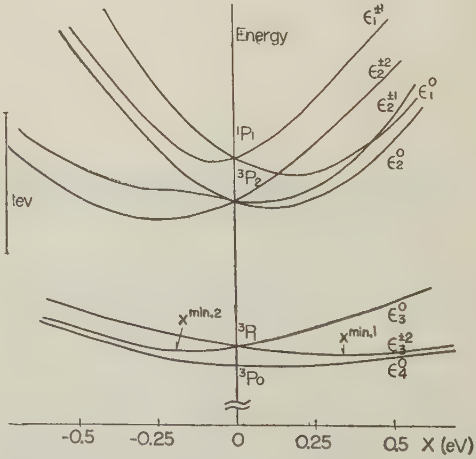

Fig. 3.

---

* When we use the configuration coordinate curves in the Q_3-space for the comparison with experiments, a fixed Q_1-point should be considered as the stationary point in the Q_1-space.

** Of course, $V_{crys}(r, Q_1)$ has a different form for each of the *P* excited and *S* ground states. Therefore, in case that the relative energies of the excited states to the ground state should be dealt with, it will become necessary to know $V_{crys}(r, Q_1)$ together with F_0, as was done by Williams.[3)] of Fig. 2, it becomes necessary to know the value of β/A^2. This parameter is determined empirically by the method which will be described in the next section. The curves thus completed are given in Fig. 3. In this figure, we can see that the $^3P_1$ state has two minima, $X^{\min,1}$ and $X^{\min,2}$, at the positive and negative sides of X respectively.

§4. Comparison with Experiments

(4.1) *Assignments of the emission bands*

The energy levels expressed by dashed lines of Fig. 2 repulse each other at the crossing region and curve into $\mathcal{E}_1{}^M$ and $\mathcal{E}_3{}^M$, because there exist non-diagonal elements between the states corresponding to these lines. The electronic wavefunctions, therefore, depend strongly upon Q_3 in the neighborhood of the crossing. This fact will be responsible for non-radiative transitions between the $\mathcal{E}_1{}^M$ and $\mathcal{E}_3{}^M$ states.[6] Hence, we may reasonably suppose that the luminescent center relaxes to the respective minima of the energy levels $\mathcal{E}_3{}^{\pm 1}$ and $\mathcal{E}_3{}^0$ after being excited in any of the 1960Å and 2490Å absorption bands. Since the energy levels $\mathcal{E}_3{}^{\pm 1}$ and $\mathcal{E}_3{}^0$ contain the $^1P_1$ character by virtue of the spin-orbit interaction, emissions are allowed from both $\mathcal{E}_3{}^{\pm 1}$ and $\mathcal{E}_3{}^0$ levels. Moreover, we can see that, since the absolute value of $X^{\min,1}$ is larger than that of $X^{\min,2}$ (see Fig. 3), the emission from the minimum $X^{\min,2}$ of the $\mathcal{E}_3{}^0$ excited level will locate at the shorter wavelength side than the other when we assume the parabolic dependence of the ground state upon Q_3. This feature is considered to be general because it is valid for any reasonable values of the parameters assumed. Hence, we assign the 3050Å and 4750Å emissions to the transitions from the stationary points $X^{\min,2}$ and $X^{\min,1}$ respectively.

(4.2) *Quantitative comparison*

In order to justify the values of the parameters ζ_p and G_1 determined in the previous section (Table II), the ratio of the oscillator strength of the 1960Å absorption to that of the 2490Å absorption, R_{abs}, is calculated by using these values. Such a ratio has been calculated in various ways by several authors. Knox and Dexter[4] computed this ratio by using Hartree's wavefunction of the gaseous Tl$^+$ ion, and they found that the result was considerably larger than the experimental one. This clearly means that the wavefunctions are significantly deformed in the crystal. More recently, the ratio was calculated by Williams et al[7] by using for ζ_p the free ion value and for G_1 the value determined to fit the relative positions of the $^1P_1$ and $^3P_1$ crystal states to those of the observed absorption peaks 1960Å and 2490Å. The reason they mentioned was that, though the wavefunctions were modified in the crystal from those of the gaseous state, the change would not be significant in the vicinity of the thallium nucleus where the value of ζ_p had to be almost determined. This, however, seems to be unreasonable, because the wavefunctions in the vicinity of the nucleus will also be affected by the change in the normalization constants of the wavefunctions caused by a deformation of the tails of the wavefunctions. All these calculated values of the ratio are collected in Table II together with those of the parameters ζ_p and G_1 used. The ratio we have obtained shows the best agreement with the experimental one.

The ratio of the transition probabilities of the two emissions* is given by expanding the wavefunctions at $X^{\min,1}$ and $X^{\min,2}$ in terms of ψ_1, ψ_2 and ψ_3, eigenfunctions of the $^1P_1$, $^3P_2$ and $^3P_1$ states respectively, as follows,

$$\begin{aligned}\phi_3{}^{\pm 1} &= a_3{}^{\pm 1}(X^{\min,1})\ \psi_1 + b_3{}^{\pm 1}(X^{\min,1})\psi_2 \\ &\quad + c_3{}^{\pm 1}(X^{\min,1})\ \psi_3, \qquad (4.1)\\ \phi_3{}^0 &= a_3{}^0(X^{\min,2})\ \psi_1 + c_3{}^0(X^{\min,2})\ \psi_3\ ,\end{aligned}$$

and by inserting $a_3{}^0$ and $a_3{}^{\pm 1}$ into the following expression,

$$S_{\text{emiss}} = \frac{a_3{}^0\,(X^{\min,2})^2\ \nu_{3050}{}^3}{2a_3{}^{\pm 1}\,(X^{\min,1})^2\ \nu_{4750}{}^3}\ , \qquad (4.2)$$

ν_{3050} and ν_{4750} being the frequencies of the 3050Å and 4750Å emissions respectively.

Determination of the stationary points $X^{\min,1}$ and $X^{\min,2}$ is achieved by adjusting the single parameter β/A^2 so as to make the energy difference of the two excited levels at $X^{\min,1}$ and $X^{\min,2}$ to be 0.02 eV, which has been experimentally obtained from the temperature dependence of the ratio of the two emission strengths.

At these stationary points, the expansion coefficients in (4.1) are computed as

---

* These emissions are considered as spontaneous emissions.

$$a_3^{\pm 1}(X^{\mathrm{min},1})=0.27_5 \qquad a_3^{0}(X^{\mathrm{min},2})=-0.41_6$$
$$b_3^{\pm 1}(X^{\mathrm{min},1})=-0.39_4 \qquad c_3^{0}(X^{\mathrm{min},2})=0.90_9$$
$$c_3^{\pm 1}(X^{\mathrm{min},1})=-0.87_7$$

which give

	(calc.)	(obs.)
S	= 4.3	6.

The quantitative feature that the 3050Å emission is stronger than the 4750Å one is thus explained.

The values of $Q_3^{\mathrm{min},1}$ and $Q_3^{\mathrm{min},2}$ which correspond to $X^{\mathrm{min},1}$ and $X^{\mathrm{min},2}$ respectively are obtained by seeking separately the values of β and A in β/A^2. The vibrational frequency of the excited state responsible for the emission has been given as $\nu_e=4.6\times 10^{12}$ c/s from the observed band widths of the 3050Å emission band both at low and high temperatures.[8] If we assume the ν_e to belong to the E_g mode of vibrations, the force constant β is given by the formula, $\beta=(2\pi)^2 \nu_e^2 M$, M being the mass of the single Cl^+ ion as far as we deal with the $Tl^+(Cl^-)_6$ octahedron. Then, using the empirical values of ν_e and β/A^2, we find β to be 0.86 and $|A|$ to be 0.37, where a.u. and eV are used for the units of length and energy respectively. From the X^{min} and $|A|$ thus determined, $|Q_3^{\mathrm{min},1}|$ and $|Q_3^{\mathrm{min},2}|$ are given as follows

$$|Q_3^{\mathrm{min},1}|=0.77\ \text{a.u.} \qquad |Q_3^{\mathrm{min},2}|=0.35\ \text{a.u.}\ .$$

These values are of the order of magnitudes of vibrational amplitudes and considered reasonable.

Let us turn to the case of the trigonal distortion. In this case, we assume the empirically determined ν_e to be the frequency of the T_{2g} vibration. Then, γ is connected to the ν_e by the formula, $\gamma=(2\pi)^2\ \nu^2 M/4$, which gives γ as $\gamma=\beta/4$. Bearing in mind the fact that the previously given discussion on the assignment and relative intensities of the emission bands is valid also in the case of the trigonal distortion if we assume the relations $X=-1/\sqrt{3}\cdot BQ_6'$, $V=3\gamma/2B^2\cdot X^2$ and $3\gamma/2B^2=\beta/3A^2$, the value of $|B|$ is derived as $|B|=3/2\sqrt{2}\cdot|A|=0.39$. Then we find the relation $|Q_6'|=\sqrt{2}\,|Q_3|$.

Theoretical estimate of the values of A and B is feasible, if one restricts himself to the $Tl^+(Cl^-)_6$ octahedron and adopt a point-charge model, in which the effective charges of the central positive ion and the surrounding negative ion are assumed to be +1 and −1 respectively. Then A and B are given in the a.u. by the following formulae.

$$A=-\sqrt{2}/10R^2\cdot(6\overline{r^2}/R^2-25\overline{r^4}/R^4),$$
$$B=3/5R^2\cdot(2\overline{r^2}/R^2-5\overline{r^4}/R^4)\quad, \tag{4.3}$$

where $\overline{r^2}$ and $\overline{r^4}$ denote respectively the mean square and mean fourth power radius of the *6p* orbit.

In order to estimate A and B numerically, we evaluate $\overline{r^2}$ and $\overline{r^4}$ by using the numerical Hartree's *6p* function of the excited gaseous Tl^+ ion.[9] R is the distance between the Tl^+ and Cl^- ions and assumed here to be the lattice constant of the pure KCl crystal. Then, from the numerical values, $R^2=35.16$ a.u., $\overline{r^2}/R^2=0.442$ and $\overline{r^4}/R^4=0.313$, we get the following values for A and B in the unit previously used for the empirical values of A and B.

	A	B
Calc.	0.56	−0.32
Emp.	±0.37	±0.39

These values show fair agreement with those determined empirically. Since the model adopted here is a crude one, we cannot decide at this stage any preference between the tetragonal and trigonal distortions.

(4.3) *Polarization of the emission*

Recently Klick and Compton[10] have found that at liquid helium temperature the 3050Å emission shows polarization by excitation with the polarized light of the 2490Å absorption band. According to their result, the emission shows most remarkable polarization when the electric vector of the exciting light is oriented along the cubic axis of the KCl crystal and it is polarized in such a way that the emission is most intense when the electric vector of the emitting light is parallel to that of the exciting light. The polarization disappears at liquid nitrogen temperature.

Such an experimental fact may be accounted for by our model as follows. Let us take the (001) axis of the KCl crystal as the z-axis and suppose that the exciting light is polarized along this axis. In our model, the tetragonal distortion has three equivalent sets of distortions corresponding to the tetragonal axis being along the x-, y-, or z-axis of the crystal. Let d-A be a name of the distortion where the tetragonal axis being along the z-axis, and d-B, d-C names of the distortions where it is along the x- and y-axes respectively. The excitation polarized in the z-axis causes the transition to the $\mathcal{E}_3{}^0$ level for the d-A distortion and transitions to the $\mathcal{E}_3{}^{\pm 1}$ level both for the d-B and d-C. Since the transition from the stationary point $X^{\mathrm{min},2}$ of the $\mathcal{E}_3{}^0$ level has been ascribed to the 3050Å emission, such an excitation will stimulate the 3050Å emission polarized in the z-axis. At the same time, it will stimulate the 4750Å emission which is polarized to some degree but not so perfectly as the 3050Å emission is. The reason is that, since the $\mathcal{E}_3{}^{\pm 1}$ level is degenerate in our model, the z-polarized excitation will stimulate the 4750Å emission whose electric vector lies in the yz- and xz-planes for the d-B and d-C distortions respectively. Therefore, if one observes the emission light propagating along the x-axis, the former is seen depolarized and the latter polarized in the z-axis.

The polarization of the 3050Å emission thus derived from our model is qualitatively accordant with the experimental one, if the tetragonal distortion of the emission center is assumed. It is evident that the trigonal distortion is unable to account for the observed polarization. However, there remain some questions for the 4750Å emission, because Klick and Compton have reported that the 4750Å emission is depolarized even at liquid helium temperature while our model gives a slight polarization in the z-axis.

Throughout the above-mentioned discussion, the effects of lattice vibrations have been out of our consideration. It is obvious that lattice vibrations act so as to depolarize the emission, because slightly split components of the levels mix with each other by the effect of lattice vibrations so as to smear out the anisotropy associated with each component. This means breakdown of an adiabatic approximation.

At present, however, we are unable to answer the question why the emission of the KCl:Tl phosphor is not perfectly depolarized by the effect of lattice vibrations, but we should like to mention the following facts: The energy of a vibration qnantum in the excited states is estimated as about 150 cm^{-1} from the frequency ν_e already mentioned, and the energy minima of the $\mathcal{E}_3{}^0$ and $\mathcal{E}_3{}^{\pm 1}$ levels are lower than the energy at $Q_3=0$ by about 400 cm^{-1} and 240 cm^{-1} respectively.

Therefore, we are able to define one or two vibrational levels associated with the electronic states corresponding to the stationary points.

§ 5. Concluding Discussions

As far as one sticks to the important experimental fact that both the 3050Å and 4750Å emissions are stimulated by excitation in any of the absorption bands, it becomes necessary to set up two minima on the low lying ${}^3P_1$ curve or its "progeny" before it intersects with the ground state energy curve, and to let the emission center excited by the 1960Å absorption light relax to the ${}^3P_1$ progeny with high efficiency.

In Johnson and Williams' model, such a requirement is fulfilled by depressing the ${}^1P_1$ curve across the ${}^3P_1$ curve. In our model, the two minima of the ${}^3P_1$ curve are naturally derived by considering the splitting of this level by the action of the Jahn-Teller effect. Furthermore, the crossing of the ${}^1P_1$ and ${}^3P_1$ curves, though it does not really occur because of the repulsion due to spin-orbit interactions, is caused by such situation that the dependence of the M component of the ${}^1P_1$ state upon Q_3, apart from the non-diagonal elements of the secular matrix and the quasi-elastic term, is equal to that of the corresponding M component of the ${}^3P_1$ state multiplied by minus two. This situation was illustrated in Fig. 2 by dashed lines. The crossing of the two states is important for the emission center in the excited ${}^1P_1$ state to relax to the ${}^3P_1$ state with high efficiency.

As pointed out in the first section of this paper, insofar as one may neglect dependence of the effects of the surroundings on the spin associated with the excited states of the thallium ion, the ${}^3P_1$ and ${}^1P_1$ curves will be nearly parallel. Then it is clear that Johnson and Williams' model is not suitable for this problem. We cannot, however, exclude the possibility that the surroundings would cause the effects on the thallium ion depending strongly upon its spin. Such effect might be interpreted as follows: Let us consider the excited states in which an electron is transferred from one of the neighboring chlorine ions to the thallium ion and makes a homopolar cevalent binding between the thallium and chlorine atoms. There are six equivalent such excited states corresponding to the six equivalent chlorine ions. Then, taking into account a resonance among these states, we obtain the $^1A_{1g}$, $^1T_{1u}$ and ^1E_g states as the group theory shows. If the $^1T_{1u}$ state thus obtained has energy comparable* to that of the ^1P state of the Tl^+ ion, configuration mixing can be interpreted as the effects of the surroundings on the thallium ion depending strongly upon its spin.

The above-mentioned discussion seems to show that a definite preference of one model over another should be given in a more advanced stage where detailed calculations of the $^1P_1$ state as a function of the Q_1 configuration coordinate have been performed. At the present stage, however, our model would be more interesting than Johnson-Williams' because of the theoretical fact that the Jahn-Teller effect has always to act on degenerate levels and of the experimental fact that the 3050Å emission is polarized at liquid helium temperature as expected from our model.

It would also be interesting to point out Patterson and Klick's finding that the treatment of one-dimensional configuration coordinate curves cannot account for all the absorption and emission data in a self-consistent way. That is, the ratio of the frequencies of vibrations in the excited and ground states can be empirically determined in two ways; one is from an analysis of the temperature variation of the emission and absorption band widths, and the other is from the ratio of the low temperature band widths of the absorption and emission bands. They have found that such two ways give different results. Then they discussed that this self-inconsistency might be related to such approximation as the use of a one-dimensional configuration coordinate model. This self-inconsistency might be avoided by the use of a multidimensional configuration coordinate model like ours.

Finally we should like to notice that no attempt has been made in this paper to explain concentration dependence of the relative intensities of the 3050Å and 4750Å emission bands and the slight difference of their excitation spectra. These effects might be interpreted to be due to interactions between thallium ions. In any way, it seems impossible to interpret these effects, especially the former, by using any models which treat only the single thallium ion.

Note added in proof

Recently Williams and Johnson (Phys. Rev. **113** (1959) 97) have reported a newly revised model. They assume the following empirical relation, for the energy curves of the pure spin states in a configuration coordinate space.

$$E=\eta_1(q-q_0)^2+\eta_2^2(q-q_0)^3+E_0\ ,$$

q being a configuration coordinate. Then, the parameters q_0, E_0, η_1 and η_2 are suitably adjusted after including the spin-orbit interaction so as to give the energy configuration coordinate diagram which explains reasonably many experimental informations. The essential point of this will be in that the energy curves of the pure spin singlet and triplet states intersect with each other. In this sense, the revised model is not different from their earlier one, but entirely different from ours. Therefore, the discussion given in the last section of our paper can also be applied to the revised model.

Acknowledgements

The authors should like to express their sincere thanks to Prof. M. Kotani, Prof. Y. Uemura and Prof. G. Kuwabara for their encouragements and valuable criticism given to this work.

References

1) P. D. Johnson and F. E. Williams: J. Chem. Phys. **20** (1952) 124.

---

* In pure crystals, the energy required for an electron to be transfered from a chlorine ion to a neighboring potassium ion is considered to correspond approximately to the energy of the first exciton peak, 7.6 eV. If the potassium ion is substituted by a thallium impurity, the required energy will change by the amount of the difference between the first ionization energies of potassium and thallium atoms as far as lattice distortions induced by the substitution are neglected. By using values 4.3 eV and 6.1 eV for the ionization energies of potassium and thallium atoms respectively, the energy required for KCl:Tl is given as 5.8 eV. Though this does not include the energies of resonance and spin-pairing, it is comparable to the energies of the absorption bands of KCl:Tl.

2) F. Seitz: J. Chem. Phys. **6** (1938) 150.
3) F. E. Williams: J. Chem. Phys. **19** (1951) 457.
4) R. S. Knox and D. L. Dexter: Phys. Rev. **104** (1957) 1245.
5) U. Öpik anp M.H.L. Pryce: Proc. Roy. Soc. A, **233** (1957) 425.
6) K. Huang and A. B. Rhys: Proc. Roy. Soc. A, **204** (1950) 406.
R. Kubo and Y. Toyozawa: Progr. Theor. Phys. **13** (1955) 160.
7) F. E. Williams, B. Segall and P. D. Johnson: Phys. Rev. **108** (1957) 46.
8) D. A. Patterson and C. C. Klick: Phys. Rev. **105** (1957) 401.
9) A. S. Douglas, D. R. Hartree and W. A. Runciman: Proc. Camb. Phil. Soc. **51** (1955) 486.
10) C. C. Klick and W. D. Compton: J. Phys. Chem. Solids **7** (1958) 170.

JOURNAL OF THE PHYSICAL SOCIETY OF JAPAN Vol. 14, No. 11, NOVEMBER, 1959

Photoconductivity and Luminescence of the F and M Centers in Potassium Chloride

By Goro KUWABARA, Akira MISU, Toshimitsu WATANABE, and Yoshio NISHIYAMA

Department of Physics, Faculty of Science, University of Tokyo

(Received July 3, 1959)

The photoconductivity and luminescence of additively colored KCl crystals by excitation with light in the F band were measured at room temperature as a function of the M center concentration. With the growth of the M band, the photocurrent decreased, while the emission intensity increased. This result would suggest that for a crystal containing M centers the photoconductivity due to the F center and the luminescence due to the M center are the competing processes in the excited state of F centers.

§ 1. Introduction

The potassium chloride crystal containing only F centers luminesces by excitation with light in the F band at low temperatures below about −50°C[1,2]. The emission intensity, increasing rapidly with the decrease of temperature, attains a saturation value at about −180°C, and in some cases its quantum efficiency attains as high as 0.9.[3]

On the other hand, this crystal shows photoconductivity above −180°C by irradiation with the F light, and the photocurrent increases with the rise of temperature.[4] These two phenomena, i.e. the photoconductivity and luminescence of the F center are interpreted as the competing processes with each other in the excited state of the F center.

When a crystal contains only the F band, nearly all of the excited F centers are considered to be ionized at room temperature. This may be confirmed by the analysis of temperature dependence of luminescence and photoconductivity or by the quantum efficiency for the conversion of F to F'.[5]

However, if the M band is grown in a crystal by irradiating with the strong F light, the crystal becomes luminescent even at room temperature by excitation with the F light.

This luminescence, which has a peak at about 1.06 μ is partially polarized perpendicularly to the polarization of the exciting F light and is considered to be due to the M center. Its quantum efficiency, increasing with the increase of M center concentration, attains about 30 percent of the efficiency of the F emission observed at low temperatures for the same crystal containing only F centers.[2]

The mechanism, by which the energy absorbed by the F center is emitted as the luminescence of the M center has not been fully understood as yet. For this problem it may be useful to investigate the relation between the luminescence and photoconductivity.

When the M band is grown in the crystal, it is expected that the ionization probability of an excited F center decreases at room temperature, because the considerable amount of the absorbed energy by the F center is reemitted as the luminescence as described above.

Therefore, the photocurrent which here means the product of quantum efficiency η and Scubweg w for unit electric field strength, should also decrease.

However, contrary to this expectation, Barth[6] has recently reported that the photocurrent induced by the F light at room temperature is entirely independent of the amount of M centers. In his paper no comment has been given on the luminescence. But if his crystal containing M centers was also luminescent at room temperature by excitation with light in the F band, his result might be explained as follows. At least at room temperature the absorbed energy by the F center is transfered to the M center *via* conduction electrons, or with the growth of the M band the Schubweg increases so that the photocurrent remains constant. If the former is the case, the polarization of the M luminescence is unlikely to occur.

In order to clarify this point, we measured simultaneously the photocurrent and emission intensity at room temperature by the excitation with the F light as a function of M center concentration.

§2. Experimental Procedures

The experimental arrangement is shown in Fig. 1.

A capacitor was charged with the photocurrent due to electrons released by a flash of light (duration is −0.02 sec) and its potential rise was determined by a D.C. amplifier with an electrometer tube. The minimum detectable charge was ca. 2×10^{-14} coul.

In order to avoid the current flowing over the surface of a crystal, the so-called blocking electrode arrangement was adopted, i. e. a specimen was mounted between two Nesa electrodes so that it did not touch the electrodes. To minimize the effect of space charge, the amount of illuminating light was reduced as far as possible and further, between successive measurements the applied voltage was reduced to zero and the crystal was irradiated with light until the photocurrent in the reverse direction, which flows by the space charge potential, entirely disappeared. With these precautions, the results were fairly reproducible, and the photocurrent was quite linear both to the number of the absorbed quanta and the applied voltage.

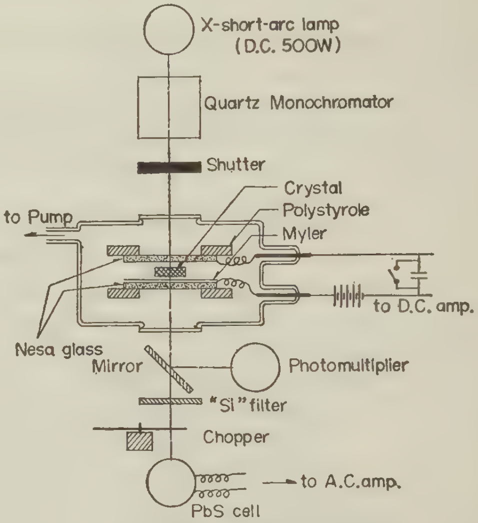

Fig. 1. Experimental arrangement

For the irradiation, the light from Xenon arc lamp passed through a quartz double monochromator was used, and the luminescence passed through an infrared transmitting filter (a slice of a Si crystal) was measured with a PbS cell. In the case of photoconductivity measurement, the slit width of the monochromator was 6 mμ in wave length.

The potassium chloride crystal was additively colored and quenched in liquid air to remove the bands other than the F. In order to create photoelectrons as uniformly as possible throughout a crystal, the initial number of the F center was controlled to be of the order of 3×10^{-16} cm^{-3}, and the thickness of specimens was about 1 mm.

§3. Results and Discussions

An example of absorption and spectral photoconductivity curves for the same crystal with and without the M band were shown in Fig. 2 (a) and (b).

From these curves, it may be safe to conclude that the photoelectrons measured in our experiment were liberated from F or M centers.

In this case the ratio of the photoconductivity (ηw) due to M centers to that due to F centers was calculated as 1/13. This value scattered considerably from specimens to specimens, but the mean value was 1/10. This result agrees with that obtained by Barth. The Schubweg w may be the same for electrons from F and M centers in the same crystal, so this value can be taken as the ratio of quantum efficiencies at room temperature.

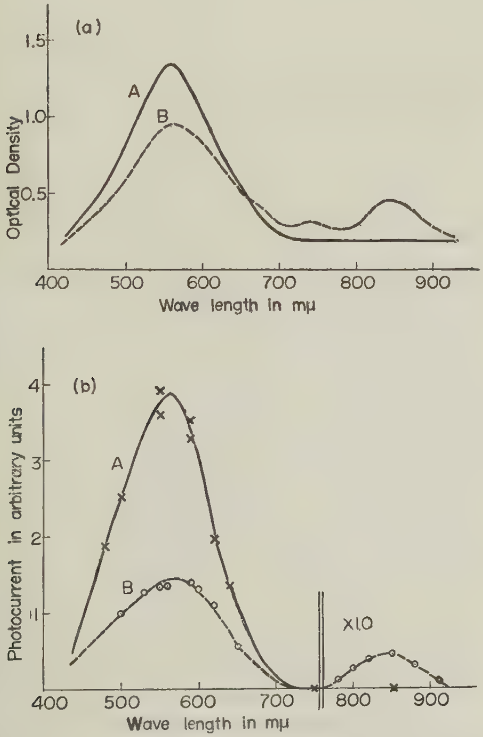

Fig. 2. Absorptions (a) and spectral resposes of photoconductivity (b) for an additively colored KCl crystal

In Fig. 3, the photoconductivity and emission intensity at room temperature for light in the F band were plotted against the M center concentration. This shows that when the M band grows up the photoconductivity due to F centers decreases to 1/3～1/5 of that for the same crystal containing only F centers.

Of course, we cannot solely ascribe the decrease of photoconductivity to the decrease of quantum efficiency η, because the possibility of variation of Schubweg w is not excluded. However, our result clearly contradicts with that obtained by Barth and is in conformity with the fact that a part of the absorbed energy in F centers is emitted as luminescence due to M centers.

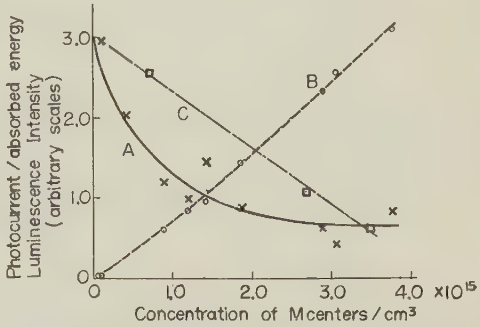

Fig. 3. Photocurrent (A) and luminescence intensity (B) at room temperature for light in the F band *vs* concentration of M centers. (C) is the intensity of luminescence due to the F center at low temperature.

The decrease of the photoconductivity seemed to be more rapid than the increase of the luminescence, which varied almost linearly with the concentration of M centers. This might be due to the decrease of Schubweg.

As to the mechanism of the luminescence of M centers, two explanations have been proposed, i.e. overlapping of the second M band with the F band, or transfer of energy from F to M centers by some interactions between them.

In order to get a clue for this problem, the efficiency of the F emission at low temperatures (−170°) was measured for one crystal and was shown in Fig. 3. It decreased with the growth of the M band, even though we take into account the amount of the F light absorbed in the second M band hidden under the F. This preliminary experiment might support the latter explanation, because according to the former the efficiency of the F emission is expected to be constant irrespectively of the presence of M centers. In this case, however, because of the low thermal ionization probability of excited M centers, the contribution of these centers to the photoconductivity by the F light may be negligible.

References

1) K. H. Becker and H. Pick: Nachr. Akad. Wiss. Göttingen (1956) 167. Th. P. J. Botden, C. Z. van Doorn and Y. Haven: Philips Res. Rep. **9** (1954) 469, **11** (1956) 479, **12** (1957) 309. J. Lambe and W. D. Compton: Phys. Rev. **106** (1957) 684.
2) G. Kuwabara and A. Misu: J. Phys. Soc. Japan **13** (1958) 1038
3) C. Z. van Doorn: Philips Res. Rep. **13** (1958) 296
4) G. Glaser: Nachr. wiss. Göttingen **3** (1937) 31
5) R. W. Pohl: Proc. Phys. Soc. London **49** (1937) sup. 1.
6) N. Barth: Z. Phys. **149** (1957) 370

JOURNAL OF THE PHYSICAL SOCIETY OF JAPAN Vol. 14, No. 11 NOVEMBER, 1959

Multiplet Structure and Hyperfine Structure of the Spectrum of Mercury

By Kiyoshi MURAKAWA

Aeronautical Research Institute, University of Tokyo, Komaba-machi, Meguro-ku, Tokyo

(Received July 11, 1959)

Analysis of the spectrum of Hg I resulted in locating the level $5d^9 6s^2 6p$ $^1F_3$ in the range 4392—4139 cm^{-1} measured from the ionization limit or 79792—80045 cm^{-1} measured from the normal state. The compositions of some levels of the configurations $5d^9 6s^2 6p$ and $5d^{10} 6s 6p$ were calculated.

The hfs of some lines of the mercury spectrum was measured, using enriched isotope as well as natural mercury. The quadrupole moment of Hg^{201} that was deduced from the hfs of $5d^9 6s^2 6p$ $^1D_2$ is 0.43 barn (1 barn$=10^{-24}$ cm^2), the shielding correction being neglected. If the correction is introduced, this becomes somewhat smaller, but is still in reasonable agreement with the value 0.4_2 barn that was published previously by the author. The agreement seems to indicate that the wave functions for the configuration $5d^9 6s^2 6p$ given in the present work are accurate enough for calculating the quadrupole moment. It is concluded that $Q(\mathrm{Hg}^{201})=0.4_2$ barn, the shielding correction being included.

I. Multiplet Structure of the Spectrum of Hg I.

§ 1. Configuration $5d^9 6s^2 6p$

In the year 1935 the author[1)] published a list of the wave-lengths of the spectrum of Hg I in the red and infra-red region (this work will be referred to as MS 1), and found the level $5d^9 6s^2 6p$ $^1D_2=5507.4$ cm^{-1} (measured from the ionization limit of Hg I). In the second paper[2)] (to be referred to as MS 2) further study of the spectrum of Hg I was made, and the level $5d^9 6s^2 6p$ $^3F_4=7238.5$ was found. In the third paper[3)] (to be referred to as MS 3) the level $5d^9 6s^2 6p$ $^3D_3=11064.9$ was found. The level $5d^9 6s^2 6p$ $^1F_3$ was very difficult to detect and the supposition was made that this level would lie near the ionization limit [$^1F_3 \sim 0$(?)]. It is to be noted that the above mentioned symbols for the levels of Hg I are only conventional ones and have no definite physical meaning. From the point of view of their Stark-effect investigations, Ishida and Hiyama[4)] discussed the levels found in MS1 and MS2 and came to the conclusion that their findings are in agreement with the existence of the above-mentioned levels. The paper MS3 was overlooked by Ishida and Hiyama, and concerning the level $5d^9 6s^2 6p$ $^3D_3$ no paper other than MS3 was published until recently Lichten[5)] found that this level is metastable.

The purpose of the present chapter is to discuss about the level $5d^9 6s^2 6p$ $^1F_3$ whose

Table I. Term-values and effective quantum numbers

m		5	6	7	8	9	10	11	12	13
m	$^3F_3$	6944.7	4439.1	3079.5	2259.8	1728.9	1364.3	1104.0	912.2	766.1
	n^*	3.9749	4.9720	5.9694	6.9685	7.9670	8.968	9.971	10.971	11.969
m	$^1F_3$	6942.6	4438.8	3077.6	2258.8	1728.8	1363.7	1103.7	910.7	765.4
	n^*	3.9757	4.9721	5.9713	6.9702	7.9674	8.971	9.971	10.977	11.974
m $^3F_3-$ m $^1F_3$		2.1	0.3	1.9	1.0	0.1	0.6	0.3	1.5	0.7

position has still remained in doubt.

In order to discuss the perturbation in $6smf$ $^3F_3$ and $^1F_3$, the term values and the effective quantum numbers are given in Table I. They were taken, without any change, from MS3, but this time the difference of m^2F_3 and m^1F_3 is also given. As was mentioned in MS3, no perturbation can be noticed (within the limit of experimental error) near the end of the series. The irregularities in $m^3F_3-m^1F_3$ for $m\geqq 9$ that are noticed in Table I lie outside the limit of experimental error and have no physical meaning. On the other hand irregularities in $m^3F_3-m^1F_3$ for $m=6$ and 7 are undoubtedly meaningful. We may assume that the level d^9s^2p $^1F_3$ lies near and somewhat higher than $6f^1F_3$. This assumption is also in agreement with the solution of the energy matrix for $J=3$ of the configuration $5d^96s^26p$. The combination $6d^1D_2-d^9s^2p$ $^1F_3$ can be expected to appear in the wave-length region somewhat shorter than λ11885. A search was made for unclassified lines in this region on the plates which were the basis of MS2, but they were too weak to be measured. The wave-lengths of the lines in question were therefore taken from articles of other authors,[6,7] and are listed in Table II. At present it is impossible to decide which of them really corresponds to $6d^1D_2-d^9s^2p$ $^1F_3$, so that we have to be satisfied with the rather vague answer that the level d^9s^2p $^1F_3$ lies between 4392 and 4139 cm^{-1} measured from the ionization limit of Hg I, that is, between 79792 and 80045 cm^{-1} measured from the normal state of Hg I.

Table II. Weak unclassified lines shorter than λ11885

I	λ (Å)	ν (cm^{-1})	$6\,^1D_2-\nu$
0d*	11712*	8536	4392
1d*	11599*	8619	4232
0**	11476**	8712	4139

* λ and I according to Masaki and Morita[6]

** λ and I according to Wiedmann and Schmidt[7]

§ 2. Wave Function of $5d^96s^26p$ and $5d^{10}6s6p$

In the section §6 we shall be interested in calculating the quadrupole moment (Q) of Hg^{201}. For that purpose we need the compositions of the wave functions of the levels belonging to the configurations $5d^96s^26p$ and $5d^{10}6s6p$. In Hg I these two configurations overlap and must not be considered separately. The energy matrix published by Hume and Crawford[8] in the analysis of Pb III will be adopted in the present work. The same notations as theirs will be used here, except that we write ζ instead of their a.

The levels of the configuration $5d^96s^26p$ (Hg I) can be assumed to be of jj-coupling in a rough approximation. All the levels of this configuration converging to $d^9s^2{}^2D_{5/2}$ (Hg II) have been detected, but very few converging to d^9s^2 $^2D_{3/2}$ (Hg II) are known at present.[9] It is therefore impossible to get accurate parameter values, but we shall see in §6 that in spite of this difficulty wave functions accurate enough for calculating the value of Q can be obtained.

Fitting the observed levels to the energy matrix, the value of $\zeta(6p)$ was found to be 4300 for the configuration $6s6p$, and 3700 for the configuration $5d^96s^26p$. $F_2=550$ and $\zeta(5d)=6000$ were found for the latter.

Apparently we have

$$^3F_4'(d^9p)=K_1\ {}^3F_4(d^9p)+K_2\ {}^3F_4(sf)\ ,$$

$$K_1=0.979_3,\ K_2=-0.202_1,\ C=215.6\ ,$$

in which $^3F_4'(d^9p)$ means the wave function of the level which we designate as $d^9s^2p^3F_4$

for brevity.

The wave function of the levels with $J=3$ can then be calculated. For example, we get

$$ {}^3D_3'(d^9p)=K_1\,{}^3D_3(d^9p)+K_2\,{}^3F_3(d^9p)+ K_3{}^1F_3(d^9p)+K_4\,{}^3F_3(sf)+K_5\,{}^1F_3(sf)\ , $$

$$ K_1=0.325_1,\ K_2=0.732_9,\ K_3=-0.595_5,\ K_4=-0.038_4,\ K_5=0.031_2. \qquad (1) $$

From this we calculate $g_J({}^3D_3')$ to be 1.08_0. This is to be compared with the value $g_J({}^3D_3')=1.0871\pm0.0005$ observed by Lichten and McDermott.[10] The agreement can be considered good.

The level $d^9p\ {}^1D_2$ is perturbed somewhat by $d^{10}s\ mp{}^3P_2$ (see MS1), but if we neglect the perturbation, we get the wave function

$$ {}^1D_2'(d^9p)=K_1{}^3P_2(d^9p)+K_2\,{}^3D_2(d^9p)+K_3\,{}^1D_2(d^9p) +K_4\,{}^3F_2(d^9p)\ , $$

$$ K_1=0.435_8,\ K_2=-0.509_3,\ K_3=0.619_1,\ K_4=-0.333_7. \qquad (2) $$

Table III. g-factors of $6s6p$ levels of Hg I

Level	g (calculated)	g (observed)	reference
${}^3P_2$	1.500	1.5016 ± 0.0004	10
${}^3P_1$	1.476	1.479	13
${}^1P_1$	1.012	1.019	13

The wave functions for the levels of $6s6p$ were the most difficult to calculate, owing to the presence of the perturbation. In determining the composition, the g-values published by Nagaoka and Mishima[11] and Green and Loring[12] were also used. [The g-values (see Table III) are listed in the review article by Moore[13]]. The value of $g({}^3P_2)$ was most accurately measured by Lichten and McDermott.[10]

In the author's previous calculation for the interaction constant B for ${}^3P$, Langer's formula for the series-perturbation was used. In the mean time this method has turned out to give a value of B that is not accurate enough for our purpose, so extrapolation from Pb III and Tl II has been used. We get in this way $B=2500$. Then the wave function for $sp{}^3P_2$ is given by

$$ P_2'(sp)=K_1{}^3P_2(sp)+K_2{}^3P_2(d^9p)\ , \qquad K_1=0.996,\quad K_2=-0.088. \qquad (3) $$

From the observed value of $g({}^3P_2)$ we see that neither ${}^3D_2(d^9p)$ nor ${}^3F_2(d^9p)$ is appreciably mixed with ${}^3P_2(sp)$, so this was considered in constructing (3).

In determining the composition of ${}^3P_1'(sp)$, the uncertainty regarding the value of B is partly eliminated by taking the observed value[13] of $g({}^3P_1)$ into consideration. In this way we get

$$ {}^3P_1'(sp)=K_1\,{}^3P_1(sp)+K_2\,{}^1P_1(sp)+K_3\,{}^3P_1(d^9p) +K_4\,{}^1P_1(d^9p)+K_5\,{}^3D_1(d^9p)\ , $$

$$ K_1=0.906_8,\ K_2=-0.307_2,\ K_3=0.264_0,\ K_4=0.116_9,\ K_5\approx0. \qquad (4) $$

The composition of ${}^1P_1(sp)$ published previously was

$$ {}^1P_1(6s6p)=K_1\,{}^3P_1(6s6p)+K_2\,{}^1P_1(6s6p) +K_3\,{}^1P_1(6s7p)+K_4\,{}^1P_1(d^9p), $$

$$ K_1=-0.158,\ K_2=0.883,\ K_3=0.286,\ K_4=0.336. \qquad (5) $$

It is somewhat unsatisfactory that the coefficient of ${}^3P_1(d^9p)$ vanishes, and this would probably explain why the calculated g is slightly smaller than the observed g, even if allowance is made for the electrodynamic correction.

It is to be remarked that all the wave functions that are given here neglect the mixing of $5s5d^{10}6s^26p$, and therefore they predict values of magnetic hyperfine structure splittings with rather unsatisfactory accuracy, so they can be used only for calculating Q.

II. Hyperfine Structure of the Spectrum of Mercury.

§ 3. Experimental Arrangement

In a previous paper by Suwa and the author[14] (to be referred to as HF1) the regularity in the hyperfine structure (hfs) of the spectra of Hg I and Hg II was studied. In a later year the author had the chance of utilizing an enriched isotope "196" (see Table IV), which was suited for studying the components due to the isotopes 204 as well as 196. The result of the measurement of the

Table IV. Isotopic constitution (%) of the samples of mercury

Sample label	Isotope						
	196	198	199	200	201	202	204
196	1.46	7.48	9.03	13.15	7.87	25.24	35.78
Natural	0.15	10.1	17.0	23.3	13.2	29.6	6.7

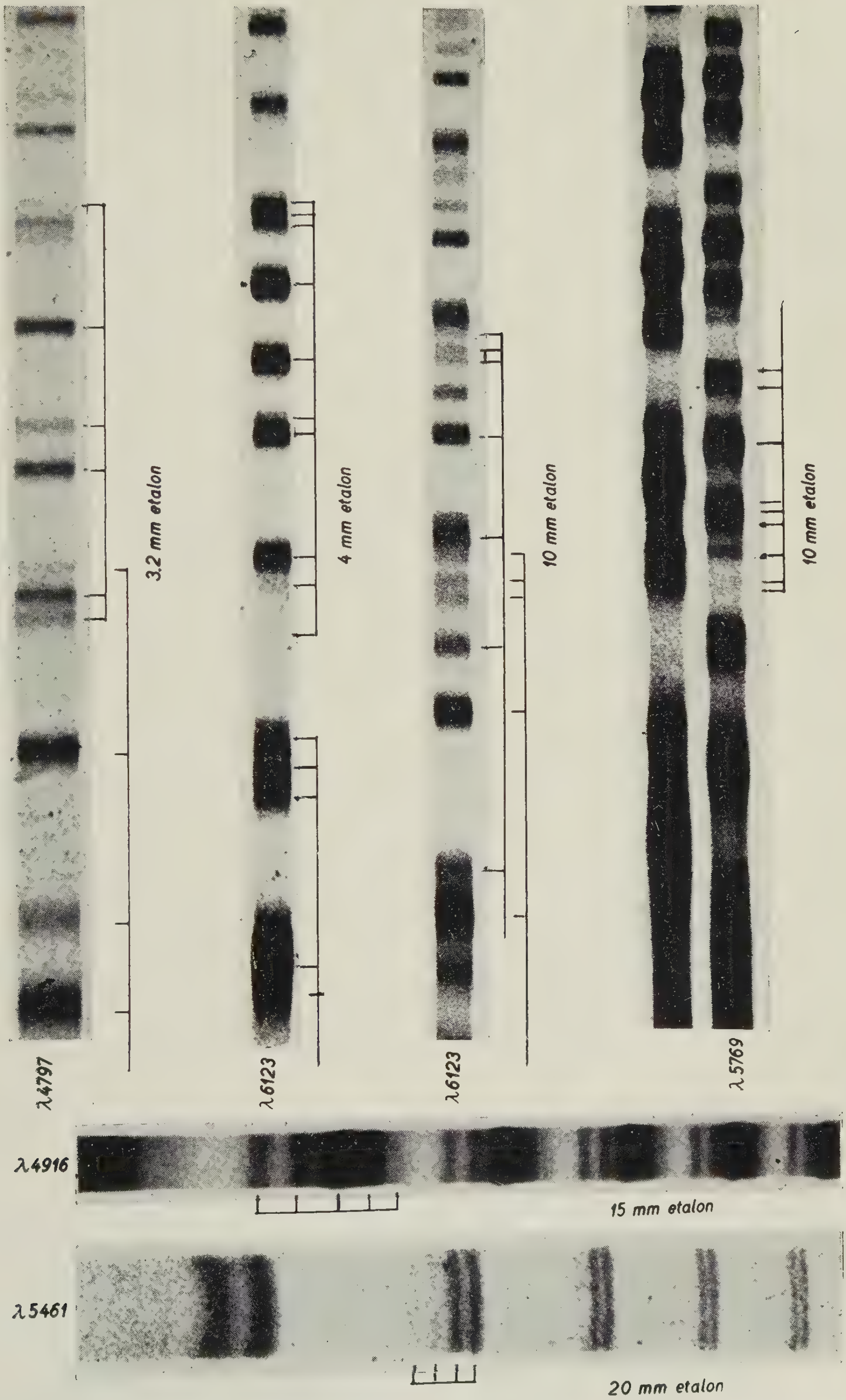

Fig. 1. Enlargement of interference patterns in the spectrum of mercury. The picture of λ5461 in this figure was taken using the enriched isotope 196. The others were taken using natural mercury.

hfs of Hg II λ6150, Hg I λ5461 and λ6123 and Hg III λ4797 was published[15] (this paper will be referred to as HF2). It was found that the hfs of Hg III λ4797 is especially suited for studying the isotope shift, although this line could not be excited by the discharge using the enriched isotope. Taking the configuration mixing into account, the value of $Q(\mathrm{Hg}^{201})$ was calculated to be 0.45 ± 0.04 barn ($1\ \mathrm{barn} = 10^{-24}\ \mathrm{cm}^2$)[16] (this paper will be referred to as HF3). In a subsequent paper[17] (to be referred to as HF4) the shielding correction was treated somewhat more rigorously, and $Q(\mathrm{Hg}^{201}) = 0.4_2 \pm 0.04$ barn was deduced.

The object of the present paper is to describe in somewhat more detail the results which were obtained by improving the light source since the publication of HF1.

In the experimental investigations that were performed in Tokyo, natural mercury only was used. A liquid air cooled hollow cathode discharge tube was used for exciting the lines of Hg I, and a high frequency electrodeless discharge tube similar to that of Lacroute[18] was employed for exciting the lines of Hg III, Hg II and also Hg I λ6123. In order to resolve the hfs, a (silvered or multi-layer dielectric coated) Fabry-Pérot etalon was employed, but in some cases a Lummer plate had to be crossed in order to avoid overlapping of orders.

In the investigations that were performed in Wisconsin, enriched isotope "196" as well as natural mercury were used, a liquid air cooled discharge tube having an iron hollow cathode being employed. The discharge current was extremely small, so only lines due to Hg I and the line Hg II λ6150 could be excited.

Interference patterns of some lines of mercury are reproduced in Fig. 1.

§ 4. Hyperfine Structure of Hg III λ4797.

The interpretation of the hfs of Hg III λ4797 was given by Mrozowski[19] and the classification was given by Foster.[20] Foster[21] also measured the hfs of this line, but the resolution attained by him was not so satisfactory.

The complete resolution was achieved and published in HF2, and the hfs together with the ratio of the distances of the neighboring isotopes is given in Fig. 2; see also Fig. 1. The respective components due to 199 and 201 do not split practically, so the measured positions of 199 and 201 represent their centers of gravity respectively. Since the isotope shift in λ4797 is large, the ratio given in Fig. 2 might be regarded as the most accurate one available since the publication of HF2. Blaise, Chabbal and Jacquinot[22] deduced the ratio from the hfs of Hg I λ15295 ($7s\,{}^3S_1 - d^9s^2p\,{}^3P_2$). In this line the distance 200—202 is given as $0.1431\ \mathrm{cm}^{-1}$, which is to be compared with the corresponding distance $0.6043\ \mathrm{cm}^{-1}$ of λ4797 given in Fig. 2.

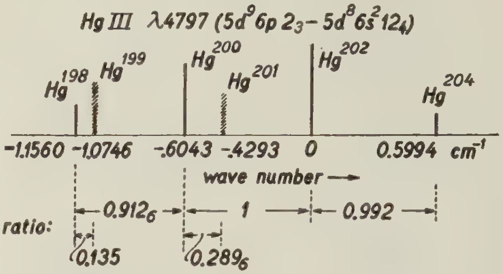

Fig. 2. Hfs of Hg III λ4797. The accuracy of measurement is $\pm 0.0012\ \mathrm{cm}^{-1}$.

§ 5. Hyperfine Structure of Hg I.

In the previous work HF1, the splitting of $6p\,{}^1P_1$ of Hg^{199} deduced from the hfs of different lines was somewhat inconsistent; and the splitting $0{,}175\ \mathrm{cm}^{-1}$ was tentatively adopted, the final decision pending on future detailed study. In the mean time the inconsistency was found to be due to the shift of some hfs components of Hg^{199}, the amount of shift depending on the strength of the discharge current and the construction of the hollow cathode. The discharge current was therefore made as small as possible, and it was found that the above-mentioned splitting is $-0.179_9\mathrm{cm}^{-1}$ (see HF3).

The distance $F = 1/2 - 3/2$ (Hg^{201}) was measured in two lines and the result is

λ5769 ($6^1P_1 - 6^3D_2$), $a-b$ (Fig. 3, HF1): $0.042_6\mathrm{cm}^{-1}$

λ5790 ($6^1P_1 - 6^1D_2$), $g-h$ (Fig. 2, HF1): 0.043_0

mean: $0.042_8\mathrm{cm}^{-1}$.

These values allow us to interpret the hfs of λ4916 accurately; see Fig. 3. The calculated position is in parentheses. The centers of gravity of 199- and 201-components were at first calculated. Then the positions of the even isotopes were calculated, using the ratio given in Fig. 2. The isotope shift predicted in this way is in reasonable agreement with the observation made by McClung and Holmes.[23]

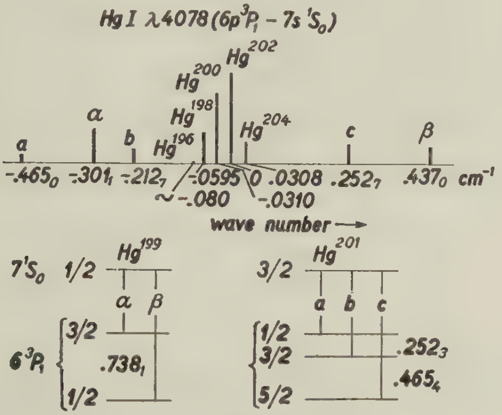

Fig. 3. Hfs of Hg I λ4916.

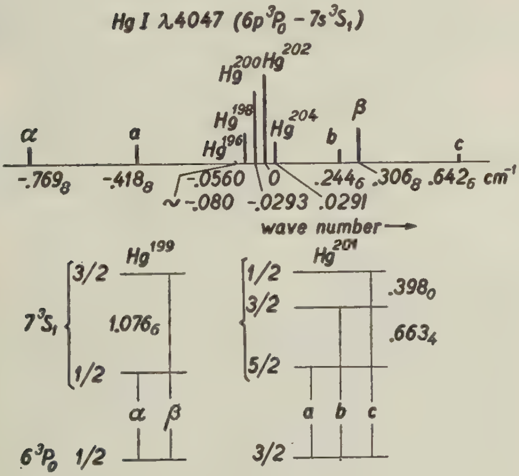

Fig. 4. Hfs of Hg I λ4047.

The hfs of λ4047 ($6p\ ^3P_0-7s^3S_1$) was studied with the utmost care. It was found that the shift (accompanied by intensity modification) of the hfs components caused by an inadequate discharge condition was most conspicuous for Hg^{199} ($I=1/2$), but not negligible for Hg^{201} ($I=3/2$). Within the limit of experimental error no shift of the same cause was detected for the components arising from the even isotopes. The hfs measured in the present work is shown schematically in Fig. 4. It is almost identical with the result given in HF1, but the present one is slightly more accurate, and also indicates the position of Hg^{196}, although this could not be measured so accurately.

The hfs of λ4078 ($6p\ ^3P_1-7s^1S_0$) is shown in Fig. 5. The hfs splittings of the odd isotopes for the lower level $6p\ ^3P_1$ can be deduced as shown in the figure; within the limit of experimental error, they are in agreement with those published by Blaise and Chantrel[24] and by Sagalyn, Melissinos and Bitter.[25]

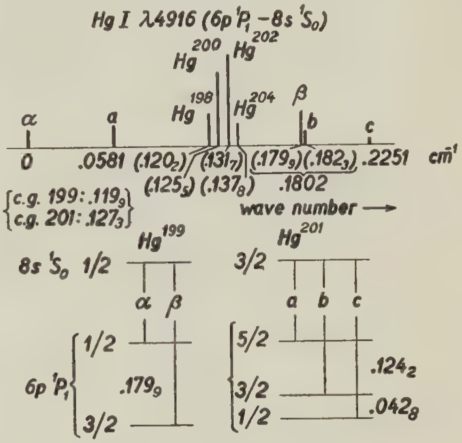

Fig. 5. Hfs of Hg I λ4078.

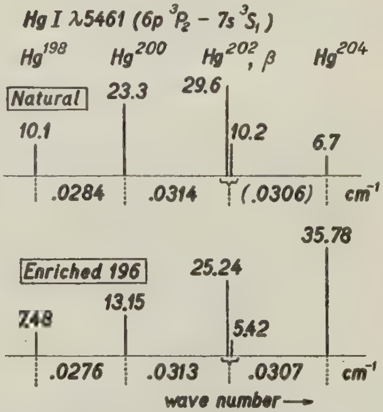

Fig. 6. Result of measurement of the central components of λ5461.

The determination of the hfs of λ5461 ($6p\ ^3P_2-7s^3S_1$) was very time-consuming. The main difficulty arises from the fact that the Hg^{202}-line has superposed on it a partial component of Hg^{199} that is called β in Fig. 6. Not only the intensity but also the position of β is changed by the discharge condition. In order to eliminate this uncertainty a very weak excitation just sufficient to start the discharge was employed. The abstract of the final solution was published in HF2. The position of β was predicted by measuring the hfs splitting of 199 in the line $\lambda 3654$ ($6\,^3P_2-6^3D_2$) accurately. It was found that β should be $0.001_1\ \text{cm}^{-1}$ distant from 202 on the violet side. This finding makes it possible to determine the position of 202 accurately. The result of measurement of the positions of the even isotope components is shown schematically in Fig. 6.

The hfs of 6^3P_2 of the odd isotopes has been measured very accurately (with a magnetic resonance method) by Lichten and his coworkers.[26] Assuming that the velocity of light is

$$c=(2.997923\pm 0.000008)\times 10^{10}\ \text{cm/sec},$$

their findings can be summarized as

$$\Delta\nu\ (\text{Hg}^{199},\ ^3P_2,\ F=5/2-F=3/2)$$
$$=22666.559\pm 0.005\ \text{Mc.}$$
$$=0.7560755\ \text{cm}^{-1},$$
$$\Delta\nu\ (\text{Hg}^{201},\ ^3P_2,\ F=7/2-F=5/2)$$
$$=11382.629\pm 0.001\ \text{Mc.}$$
$$=0.3796839\ \text{cm}^{-1},$$
$$\Delta\nu\ (\text{Hg}^{201},\ ^3P_2,\ F=5/2-F=3/2)$$
$$=8629.522\pm 0.001\ \text{Mc.}$$
$$=0.2878501\ \text{cm}^{-1},$$
$$\Delta\nu\ (\text{Hg}^{201},\ ^3P_2,\ F=3/2-F=1/2)$$
$$=5377.492\pm 0.002\ \text{Mc.}$$
$$=0.1793740\ \text{cm}^{-1}.$$

These values combined with the hfs of $\lambda 4047$ make it possible to calculate the positions of the hfs components of the odd isotopes in $\lambda 5461$. This is presented in Fig. 7 in which only the even isotopes and the components α, g, f, h and γ were measured. Other components were calculated. In Fig. 7 the hfs splittings of the lower level are given only four decimal places, (although the original data given by Lichten et al have far larger accuracy), because the accuracy attained by the technique of present day spectroscopy rarely surpasses this.

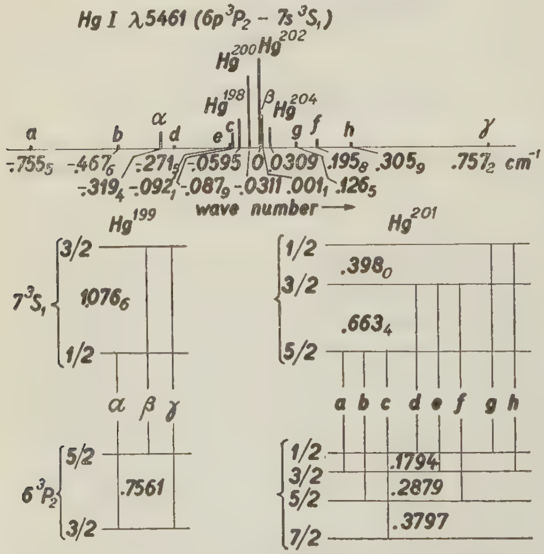

Fig. 7. Hfs of Hg I $\lambda 5461$ constructed.

Finally the hfs of $\lambda 6123$ is shown in Fig. 8, which is, it is hoped, superior to Fig. 6 of HF1. This was achieved by use of high-frequency electrodeless discharge through mercury vapor of very low pressure, the increased intensity and the narrow line breadth being favorable for hfs work. The 198-component has superposed on it a partial component of 201, if the resolution is not high enough. It was therefore decided to employ a 20 mm etalon crossed by a Lummer plate, but this naturally reduced the intensity very much. With this arrangement only the components 198, 200, 202 and β could be photographed. The distance 198–200 is now 0.1941 instead of $0.1886\ \text{cm}^{-1}$ published in HF2.

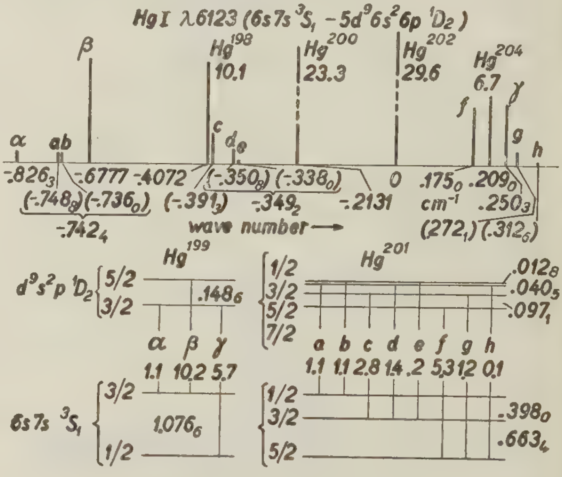

Fig. 8. Hfs of Hg $\lambda 6123$.

The ratio of isotopic shifts of the spectrum of mercury calculated by use of data given in the present work is listed in Table V, in which the results of other authors[27, 38] are quoted for comparison.* The ratio can be considered to be constant for every line observed.

---

* The positions of the odd isotopes in Hg III $\lambda 4797$ published by the author in HF2 seems to have been overlooked by Blaise.[28]

Table V. Ratio of isotopic shifts in the spectrum of mercury

Line	Isotope						
	196	198		200		202	204
Hg III λ4797			0.912_6	:	1	:	0.992
Hg I λ6123			0.910_9	:	1	:	0.98_1
Hg I λ5461			0.913	:	1	:	0.994
Hg I λ4078	0.6_6	:	0.91_9	:	1	:	0.994
Hg I λ4047	0.8_2	:	0.91_1	:	1	:	0.993
weighted mean	0.7_4	:	0.912_6	:	1	:	0.992
Bitter et al[27]	0.79	:	0.91	:	1	:	1.0
Blaise[28]	0.7	:	0.90	:	1	:	1.0

Line	Isotope				
	199—200	:	200—201	:	200−202
Hg III λ4797	0.778_3	:	0.289_6	:	1
Hg I λ4078	0.77_7	:	0.29_3	:	1
Hg I λ4047	0.77_8	:	0.29_0	:	1
adopted ratio	0.778_3	:	0.289_6	:	1
Bitter et al[27]	0.795	:	—	:	1
Blaise[28]	0.79	:	0.29	:	1

Table VI. Quadrupole coupling constant of Hg^{201}

Level	A (cm^{-1})	B ($10^{-3}cm^{-1}$)	B' ($10^{-3}cm^{-1}$)	Q' (barn)
$6p\ {}^3P_2$	−0.111812*	13.322*	0.27754*	0.46
$6p\ {}^3P_1$	−0.1816	− 8.98	−1.122	0.46
$6p\ {}^1P_1$	0.0443	10.58	1.32_2	0.42
$d^9s^2p\ {}^1D_2$	−0.0220	−23.0	−0.48	0.43

* Calculated using the data published by Lichten and his coworkers.[26]

§ 6. Quadrupole Moment of Hg^{201}

The quadrupole coupling constant $B(Hg^{201})$ of each of the levels 6^3P_2, 6^3P_1, 6^1P_1 and $d^9s^2p\ {}^1D_2$ is given in Table VI. The constant B given in this table is defined by the formula of Casimir:[29]

$$\nu=\nu_0+\frac{A}{2}K+B\left[\frac{\frac{3}{8}K(K+1)-\frac{1}{2}I(I+1)J(J+1)}{I(2I-1)J(2J-1)}\right],$$

$$K=F(F+1)-I(I+1)-J(J+1).$$

The quadrupole coupling constant which is convenient for treating experimental data and was used by the author in previous publications will be denoted by B' in the present paper. Since B' is given by

$$\nu=W_0+\frac{A}{2}K+B'\,K(K+1)\ ,$$

we have the relation

$$B=B'\,\frac{8}{3}\,I(2I-1)\,J(2J-1)\,.$$

Use of B instead of B' has the merit that it does not include I and J explicitly.

The quadrupole moment is given by

$$Q=-\frac{B\ 0.7455}{\sum\frac{\zeta<3\cos^2\theta-1>_{Av}}{Z^*H(1+\varDelta)}}\ , \qquad (6)$$

in which B is measured in units of $10^{-3}cm^{-1}$, and Q in units of barn $(=10^{-24}cm^2)$. $\sum$ means that the expression should be summed with respect to $p, d, f, \cdots$ electrons. H is the relativity correction,[29] and $\varDelta$ is the shielding correction (radial plus angular corrections) introduced by Sternheimer.[30] Sternheimer's $1/(1-R)$ is our $1+\varDelta$. Z^* is the effective charge (in the case of Hg I $Z^*(6p)=80-5=75$, $Z^*(5d)=80-20=60$). We shall put $\omega=3\cos^2\theta-1$ for brevity. The relativity correction factors for $<r^{-3}>$ in the case of Hg I are $R'=1.29$, $S=1.56$, $R_2'=1.065$, $R_2''=1.228$, $S_2=1.065$.

The data published by Lichten et al[26] indicate that Hg^{201} may have a magnetic octupole moment, but since at present it is not possible to calculate accurately the hfs perturbation of 6^1P_1, 6^3P_1 and 6^3P_0 on 6^3P_2, no attempt was made to calculate the octupole coupling constant C from their data.

The method of calculation of Q from 6^3P_2 was published in HF2. Using the new wave function (3), we get $Q'=0.46$ barn, where Q' means that the shielding correction is neglected. This value is equal to the one given in HF2.

For the level ${}^3P_1$, we have the formulas:
For sp configuration

$$({}^3P_1|\omega/r^3|{}^3P_1)=\frac{1}{15}(-R'+4S)<r_p{}^{-3}>,$$

$$({}^1P_1|\omega/r^3|{}^1P_1)=-\frac{2}{15}(R'+2S)<r_p{}^{-3}>, \qquad (7)$$

$$({}^3P_1|\omega/r^3|{}^1P_1)=\frac{\sqrt{2}}{15}(R'-S)<r_p{}^{-3}>.$$

For pd configuration (for the configuration d^9p we need only reverse the sign for the d-part)

$$({}^3P_1|\omega/r^3|{}^3P_1) = \frac{1}{250}(-12R_2'+13R_2''+24S_2)<r_d^{-3}> + \frac{1}{150}(11R'-8S)<r_p^{-3}>\ ,$$

$$({}^1P_1|\omega/r^3|{}^1P_1) = -\frac{1}{125}(12R_2'+7R_2''+6S_2)<r_d^{-3}> - \frac{1}{75}(R'+2S)<r_p^{-3}>\ , \tag{8}$$

$$({}^3P_1|\omega/r^3|{}^1P_1) = \frac{3\sqrt{2}}{250}4R_2'-R_2''-(3S_2)<r_d^{-3}> + \frac{\sqrt{2}}{30}(R'-S)<r_p^{-3}>\ .$$

Putting values of R', S, R_2', R_2'', S_2 and ζ_p and ζ_d in the formulas (7), (8) and (4), and then together with the value of $B({}^3P_1)$ in (6), we get $Q'=0.46$ barn which agrees completely with Q' obtained from 6^3P_2.

Blaise and Chantrel[24] and Sagalyn et al[25] deduced from 6^3P_1 a value of Q' higher than 0.5. But this value seems to be inaccurate, owing to the use of inadequate wave function.

The value of Q' obtained from $6p\,{}^1P_1$ was published in HF2, and is listed in Table VI.

In order to treat $d^9s^2p\ {}^1D_2$, we need the following formulas for the configuration pd:

$$({}^3P_2|\omega/r^3|{}^3P_2) = \frac{1}{125}(-36R_2'-R_2''+12S_2)<r_d^{-3}> + \frac{1}{25}(3R'-4S)<r_p^{-3}>\ ,$$

$$({}^3D_2|\omega/r^3|{}^3D_2) = -\frac{1}{525}(92R_2'+7R_2''-24S_2)<r_d^{-3}> + \frac{1}{45}(R'+8S)<r_p^{-3}>\ ,$$

$$({}^1D_2|\omega/r^3|{}^1D_2) = -\frac{2}{175}(12R_2'+7R_2''+6S_2)<r_d^{-3}> + \frac{2}{15}(R'+2S)<r_p^{-3}>\ ,$$

$$({}^3F_2|\omega/r^3|{}^3F_2) = -\frac{16}{18375}(23R_2'+343R_2''+84S_2)<r_d^{-3}> - \frac{4}{525}(7R'+29S)<r_p^{-3}>\ ,$$

$$({}^3P_2|\omega/r^3|{}^3D_2) = -\frac{1}{175\sqrt{15}}(108R_2'-7R_2''+74S_2)<r_d^{-3}> - \frac{1}{5\sqrt{15}}(R'+2S)<r_p^{-3}>\ , \tag{9}$$

$$({}^3P_2|\omega/r^3|{}^3F_2) = -\frac{4}{875\sqrt{21}}(36R_2'-49R_2''+38S_2)<r_d^{-3}> - \frac{4}{25\sqrt{21}}(R'+2S)<r_p^{-3}>\ ,$$

$$({}^3D_2|\omega/r^3|{}^3F_2) = -\frac{4}{525\sqrt{35}}(44R_2'+49R_2''+57S_2)<r_d^{-3}> + \frac{4}{45\sqrt{35}}(R'+17S)<r_p^{-3}>\ ,$$

$$({}^3P_2|\omega/r^3|{}^1D_2) = -\frac{2}{175\sqrt{10}}(12R_2'+7R_2''-19S_2)<r_d^{-3}> - \frac{2}{5\sqrt{10}}(R'-S)<r_p^{-3}>\ ,$$

$$({}^3D_2|\omega/r^3|{}^1D_2) = \frac{2}{25\sqrt{6}}(-4R_2'+R_2''+3S_2)<r_d^{-3}> + \frac{2}{15\sqrt{6}}(R'-S)<r_p^{-3}>\ ,$$

$$({}^3F_2|\omega/r^3|{}^1D_2) = -\frac{8}{175\sqrt{210}}(16R_2'-49R_2''+33S_2)<r_d^{-3}> + \frac{8}{15\sqrt{210}}(R'-S)<r_p^{-3}>\ .$$

By use of the formulas (2), (9), (6) combined with the constant B (Table VI), we get $Q'=0.43$ barn.

The shielding correction factor Δ is not known accurately in the case of Hg I. But for $6s6p$ of heavy elements it is most likely (HF4) that $\Delta=-0.1$. If this is assumed, we get $Q(\mathrm{Hg}^{201})=0.4_2$ barn from the levels ${}^3P_2$ and ${}^3P_1$.

Concerning the configuration d^9s^2p, the value of Δ is unknown. Δ_p would be probably -0.1, and Δ_d would be negative. If this is assumed, we get a value of Q somewhat smaller than 0.43 barn. In view of the above-mentioned uncertainty, the agreement with 0.4_2 barn may be considered to be not poor. We may assume therefore that the wave function for $d^9s^2p\ {}^1D_2$ given by (2) is essentially adequate for calculating Q.

As a summary we may conclude that

$$Q(\mathrm{Hg}^{201})=0.4_2 \text{ barn.}$$

This is in agreement with the result of

Pound and Wertheim[32] who obtained $Q(\mathrm{Hg}^{201}) = 0.46\ (+0.28,\ -0.11)$ barn.

The kindness of Dr. Lichten in showing me the results of his experiments prior to publication is greatly appreciated.

References

1) K. Murakawa: Proc. Phys.-Math. Soc. Japan **17** (1935) 14.
2) K. Murakawa: Proc. Phys.-Math. Soc. Japan **18** (1936) 345.
3) K. Murakawa: Z. Physik **108** (1938) 168.
4) Y. Ishida and S. Hiyama: Sci. Papers Inst. Phys. Chem. Res. Tokyo **37** (1940) 227.
5) W. Lichten: Phys. Rev. **109** (1958) 1191.
6) O. Masaki and T. Morita: J. Sci. Hiroshima Univ. **7** (1937) 305.
7) G. Wiedmann and W. Schmidt: Z. Phys. **106** (1937) 273.
8) J. N. P. Hume and M. F. Crawford: Phys. Rev. **84** (1951) 486.
9) H. Beutler: Z. Phys. **86** (1933) 710.
10) W. Lichten and M. McDermott: Bull. Amer. Phys. Soc. **3** (1958) 371; private communication.
11) H. Nagaoka and T. Mishima: Proc. Imp. Acad. Japan **2** (1926) 383.
12) J. B. Green and R. A. Loring: Phys. Rev. **46** (1934) 888.
13) C. E. Moore: *Atomic Energy Levels*, vol. **3**, Circ. Nat. Bur. Stand. (1958) 467.
14) K. Murakawa and S. Suwa: J. Phys. Soc. Japan **5** (1950) 429.
15) K. Murakawa: Phys. Rev. **93** (1954) 1232.
16) K. Murakawa: Phys. Rev. **98** (1955) 1285.
17) K. Murakawa: Phys. Rev. **110** (1958) 393.
18) P. Lacroute: Ann. Physique **3** (1935) 5.
19) S. Mrozowski: Phys. Rev. **57** (1940) 207.
20) E. W. Foster: Proc. Roy. Soc. **A, 200** (1950) 429.
21) E. W. Foster: Proc. Roy. Soc. **A, 208** (1951) 367.
22) J. Blaise, R. Chabbal and P. Jacquinot: J. phys. radium **15** (1954) 749.
23) F. McClung and J. R. Holmes: Phys. Rev. **100** (1955) 1792.
24) J. Blaise and H. Chantrel: J. phys. radium **18** (1957) 193.
25) P. L. Sagalyn, A. C. Melissinos and F. Bitter: Phys. Rev. **109** (1953) 375.
26) W. Faust, M. McDermott and W. Lichten: Bull. Amer. Phys. Soc. **3** (1958) 371.
27) F. Bitter, S. P. Davis, B. Richter and J. E. R. Young: Phys. Rev. **96** (1954) 1531.
28) J. Blaise: Thesis, Univ. Paris (1958).
29) H. Casimir: Verhandel. Teylers Tweede Genootschap, Haarlem **11** (1936).
30) R. M. Sternheimer: Phys. Rev. **95** (1954) 736; **105** (1957) 158.
31) R. V. Pound and G. K. Wertheim: Phys. Rev. **102** (1956) 396.

Short Notes

This section is intended to secure prompt publication of important discoveries in physics. The reports should not exceed 800 words in length. A figure of size 7 cm × 7 cm will be counted as 150 words.

J. PHYS. SOC. JAPAN **14** (1959) 1634

Infrared Absorption of α-$Ag_2Te_xS_{1-x}$

By Shin-ya MIYATANI
Department of Physics, Faculty of Science, Niigata University

(Received August 31, 1959)

The α–β transition temperature of $Ag_2Te_xS_{1-x}$ i.e. the mixture of Ag_2Te and Ag_2S which is prepared by melting $(Ag_2Te)_x$ and $(Ag_2S)_{1-x}$ sealed in a fused silica tube, is lowered by mixing so that it is below room temperature for the mixing ratio x between 0.2 and 0.8. Since the ionic conductivity due to mobile Ag ions is large in the α phase (e.g. 0.16 $\Omega^{-1}cm^{-1}$ at 15°C for $x=0.7$)[1], Ag ions and the same number of electrons can be easily supplied to or removed from the specimen of such a mixing ratio at room temperature by sending a proper current accross the galvanic cell Ag|AgI+5%AgCl| specimen|Pt, which has the e.m.f. E related to the reduced Fermi energy η as given by $\eta=\eta_s-eE/kT$ where η_s is η in Ag-saturated state[1]. Further this mixture is so soft that it can be easily rolled or pressed to thin foil (up to several microns) thin enough to get large interference effect at the transmission of infrared ray. From the distance of interference fringes[2] in the transmission curve recorded against wave number $1/\lambda$, we obtain the value of the refractive index n and accordingly the reflectivity as 4.0 and (3/5)[2], respectively, (the extinction coefficient $\ll n$) and then we obtain the value of the absorption coefficient α. Thus the curves of α vs $1/\lambda$ are obtainable for various electrical conductivities σ_e or Fermi energies of one specimen, keeping it on the specimen-holder of spectrograph (Hilger's double beam). Fig. 1 shows an example of such measurements for $x=0.7$ where (a) shows σ_e vs eE/kT or η and (b) α vs $1/\lambda$ corresponding to (a), where the value of η_s is estimated by comparing the σ_e vs eE/kT plots with theoretical curve $F_{1/2}$ (Fermi function of order 1/2) vs η, assuming the relaxation time τ is energy-independent. (a) shows also $R\sigma_e$ (mobility), making use of which we obtain m_e (effective mass of electron)$=0.08\,m$ and $\tau=6.6\times10^{-14}$ sec.

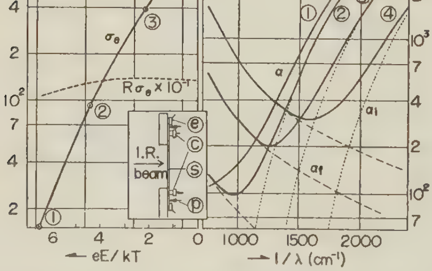

Fig. 1. (a) $\sigma_e(\Omega^{-1}cm^{-1})$ and $R\sigma_e(cm^2s^{-1}v^{-1})\times10^{-1}$ vs eE/kT or η for $x=0.7$ at 20°C, where R is Hall coefficient. (b) α (cm^{-1}) vs $1/\lambda$ or $h\nu/kT$ at 20°C. The broken line is α_f extrapolated under the assumption of α_f proportional to λ^2 and the dotted line is $\alpha-\alpha_f$ that is α_i. The arrangement of the specimen (s), Ag|AgI+5% AgCl (c), probe for measuring σ_e (p), and Pt electrode (e) is also shown schematically. This result is confirmed by changing the thickness of specimen as 9.2, 17, 26, and 40 μ.

The absorption is now, as seen in Fig. 1 (b), attributed to two effects; the free electron absorption α_f dominant in the small $1/\lambda$ region and the intrinsic absorption $\alpha_i=\alpha-\alpha_f$ dominant in the large $1/\lambda$ region. As for the former, Drude-Zener's formula[2,3] holds well, yielding the value of τ as 5.4×10^{-14} sec (compare with 6.6×10^{-14} sec). As for the latter, the change of α_i due to the degeneracy is to be given by Eq. (5.4) in the reference (2). Plotting $\log(\alpha_{i0}(\nu)/\alpha_i(\nu)-1)$ against η, taking $h\nu/kT$ as parameter, we see that this equation is in fact valid, where α_{i0} is defined as α_i in non-degenerate state and so taken as equal to α_i for the curve No. 1. We obtain thus $m_h/(m_e+m_h)=0.6$ and $E_G/kT=6.4$ (E_G is the energy gap.). Next, α_{i0}, that is, α_i for the curve No. 1 seems to be accounted for by the plane wave approximation, i.e. Eq. (2.15) in the reference (2), yielding the values of $m_em_h/(m_e+m_h)$ and E_G/kT as $0.44m$ and 6.4 respectively. Similar absorption curves are also obtained for other mixing ratios, showing the increase of E_G with decreasing x.

Finally, the electrical properties of this system (e.g. the relation between E and the concentration of excess Ag, the η-dependence of $R\sigma_e$ and Nernst coefficient etc.) indicate that the simplifying assumptions such as the standard form of conduction band and the energy-independence of τ are not exactly valid, necessitating the reinvestigation of the absorption curve, which is left to the future.

References

1) S. Miyatani: J. Phys. Soc. Japan **10** (1955) 786; **13** (1958) 341; **14** (1959) 996.
2) H. Y. Fan: Rep. Progr. Phys. **19** (1956) 107.
3) F. Seitz: *The Modern Theory of Solids* (McGraw-Hill Book Co., New York, 1940) 638.

J. PHYS. SOC. JAPAN **14** (1959) 1635

The Aging of Permeability in Manganese-Zinc Ferrite

By Syôhei MIYAHARA and Tokio YAMADAYA
Department of Physics, Hokkaido University.

(Received August 27, 1959)

Though the presence of continued decrease of the effective permeability after sintering has been well known in Mn–Zn ferrites, its origin has not yet been made clear. As Mn–Zn ferrite is not stable in air at lower temperatures, it is made usually by rapid cooling, therefore it is to be expected that in Mn–Zn ferrite certain irreversible changes such as oxidation, precipitation, etc, might progress further at room temperature. On the other hand, it is also possible that it is due to disaccomodation, since there are some evidences for the presence of disaccomodation in some ferrites[1-4].

In order to make clear whether the decrease of permeability after sintering arises from irreversible structural change or from disaccomodation, we performed the following experiment.

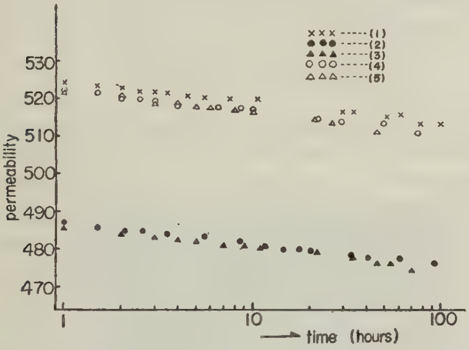

Fig. 1. Changes of Permeability with time at room temperature after sintering. All measurements in this figure were made for the same specimen.

(1) Permeability changes after sintering without any disturbance.

(2) Permeability changes after A. C. demagnetization following the measurements (1).

(3) Permeability changes after A. C. demagnetization following the measurements (2).

(4) Permeability changes after thermal demagnetization following the measurements (3).

(5) Permeability changes after thermal demagnetization following the measurements (4).

Ring specimens were made by the usual ceramic techniques from $MnCo_3$, ZnO and Fe_2O_3.

The final sintering was made in Air at 1300°C and cooled rapidly. Nominal composition of the pecimens was $(Mn_{0.5}\ Zn_{0.5})\ O\cdot Fe_2O_3$.

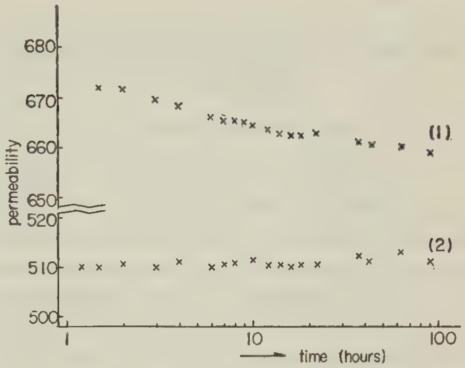

Fig. 2. Comparison of the permeability changes of two equal specimens number different measuring conditions.

(1) Permeability changes after sintering.

(2) Permeability changes after sintering. In this case A. C. demagnetization is applied in every measurement at one minute before the measuement.

All measurements were carried out by using an A. C. Bridge at 1 kc/sec with measuring field of less than one millioersted. Demagnetization was done either by A.C field of 50 c/sec with maximum field of about 10 oersteds, or by heating up the specimen to 100°C and cooling slowly. Results are shwn in Fig. 1 and Fig. 2.

From Fig. 1, it can be concluded that the time decrease of permeability after sintering is reproduced again by applying a thermal demagnetization to the same specimen.

It is also shown in Fig. 1 that the curves after thermal demagnetization are very similar to those after A. C. demagnetization. The continued decrease of permeability after sintering is not found if we demagnetize the specimen at every measurement as shown in Fig. 2.

From these results we may conclude that the decrease of permeability after sintering (the so called natural aging) does not arise from irreversible structural change, but from disaccomodation.

Referencers

1) J. L. Snoek: *New developments in ferromagnetic materials* (Elsevier Publ., New York, 1949) 54.
2) U. Enz: Physica. **24** (1958) 609.
3) K. OHTA: Bull. Kobayasi Inst. Phys. Res. **8** (1958) 17.
4) Y. Shichijo and H. Sato: *Ferrite* (1959) 48 (in Japanese).

J. Phys. Soc. Japan **14** (1959) 1636

Diffusion of Nickel in Single Crystals of Copper

By Akira Ikushima

Department of Physics, University of Tokyo

(Received September 19, 1959)

In order to investigate the behaviour of iron-group transition elements as an impurity in noble metals, several experiments of tracer diffusion have been performed[1-4]. In this note, the diffusion data of nickel in single crystals of 99.99% pure copper is reported.

As the experimental techniques used in this work were nearly the same as the one described in detail in Mackliet's paper[1], the details will not be mentioned here.

The penetration plots are shown in Fig. 1, and the diffusion coefficients calculated from these plots are given in Table I.

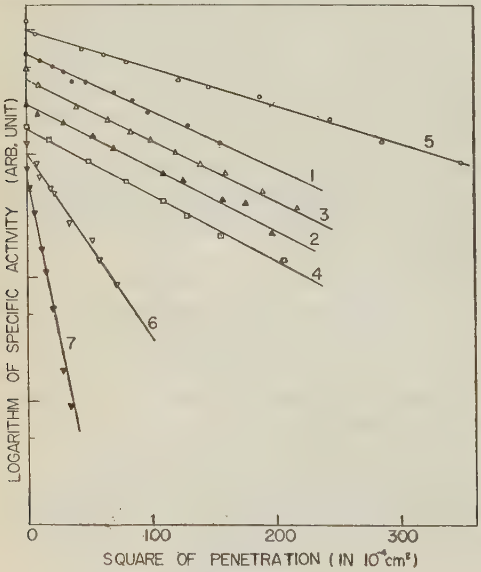

Fig. 1. Penetration plots.

Table I. Diffusion of Ni^{63} in Copper

No.	Temperature (°C)	Diffusion Time (sec.)	Diffusion Coefficient. (cm²/sec.)
1	1061	1.19×10^{4}	2.00×10^{-9}
2	1031	1.83×10^{4}	1.17×10^{-9}
3	973	6.67×10^{4}	4.04×10^{-10}
4	906	1.78×10^{5}	1.15×10^{-10}
5	852	1.02×10^{6}	3.47×10^{-11}
6	758	2.17×10^{6}	3.36×10^{-12}
7	695	4.01×10^{6}	5.45×10^{-13}

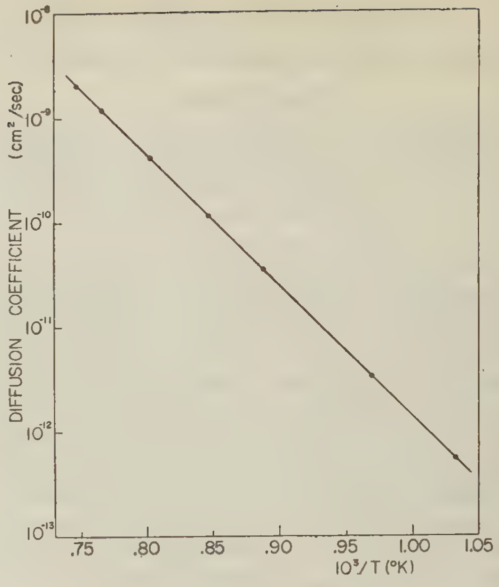

Fig. 2. Plot of $\log D$ *vs* $1/T$.

The plot of the diffusion coefficients *vs* temperature is shown in Fig. 2. Under the assumption that the diffusion coefficient can be described by $D=D_0\exp(-Q/RT)$, these data are fitted to the formula by the least square calculation with

$$\log_{10}D_0=0.58\pm0.02$$

$$(\text{i.e. } D_0=3.8\pm0.2\,\text{cm}^2/\text{sec.})\ ,$$

$$Q=56.8\pm0.1\,\text{kcal/mole}\ .$$

D_0 and Q of the present results are in good agreement with the earlier data reported by Mackliet[1]. If Lazrrus' formura of Q[5] with the screened coulomb potential around the impurity atom calculated by Alfred an March[6] is used, the present result of Q indicates that the excess valence of the nickel atom as an impurity in copper is about minus one with respect to copper. This suggests that the electronic structure of the nickel atom in this case would be $(3d)^{10}(4s)^0$. This is also consistent with other data.[7-9]

The author wishes to thank Professor Y. Tomono for help and advice during the course of the study.

This work is partly supported by the Scientific Expenditure from the Ministry of Education.

References

1) C. A. Mackliet: Phys. Rev. **109** (1958) 1964.
2) Y. Tomono and A. Ikushima: J. Phys. Soc. Japan **13** (1958) 762.
3) A. Ikushima: J. Phys. Soc. Japan **14** (1959) 111.
4) M. Sakamoto: J. Phys. Soc. Japan **13** (1958) 845.
5) D. Lazarus: Phys. Rev. **93** (1954) 973.
6) L. C. R. Alfred and N. H. March: Phys. Rev. **103** (1956) 877.
7) T. Sugawara: J. Phys. Soc. Japan **14** (1959) 643.
8) A. R. Kaufmann and C. Starr: Phys. Rev. **63** (1943) 445.
9) E. W. Pugh, B. R. Coles, A. Arrott and J. E. Goldman: Phys. Rev. **105** (1957) 814.

J. PHYS. SOC. JAPAN **14** (1959) 1637~1638

Microwave Investigation of Plasma in Shock Tube*

By Mikio TAKEYAMA, Shiro Hamamura
and Toshiatsu ODA

*Department of Physics, Faculty of Science,
Hiroshima University, Hiroshima*

(Received September 9, 1959)

A microwave investigation was carried out on the plasma produced in shock tube as shown in Fig. 1. The shock tube used consisted of an X band microwave rectangular guide section whose one end was connected with one of the side arms of a magic Tee. The higher pressure chamber of the shock tube, 60 cm in length, was filled with hydrogen gas of about 8 atm. and the lower, 100 cm long, with argon gas of 10 mmHg. The diaphragm used in the tube was of cellophane 0.04 mm thick.

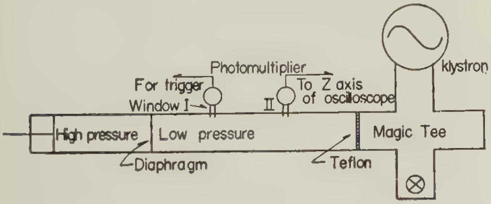

Fig. 1. Schematics of shock microwave tube.

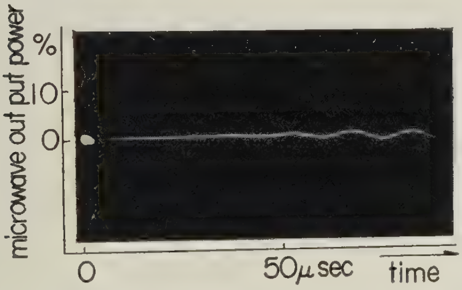

Fig. 2. Oscilloscope trace of microwave signal reflected from shock wave of low temperature.

When the electron density of the plasma produced is relatively small, the microwave reflection due to the complex dielectric constant of the plasma is slight, but when the density is so large that the plasma frequency exceeds the microwave frequency and the plasma works as a metal disk, the microwave is almost totally reflected, provided that the width of plasma is comparable with the guide wave length of the microwave.

In the present experiment, the magic Tee was initially balanced. Since the microwave exists as standing wave in the shock tube, it is reflected every time shock front travels one half wave length. The frequency of the reflected microwave signal can be a measure of the shock velocity. The photomultiplier tubes I and II are set at the window on one side of the tube. The tube I is used for triggering an ocilloscope and the tube II to provide a marker for the optical measurement of the shock velocity. The gain of the D. C. amplifier of the oscilloscope was adjusted to be so low as to be insensible to the dielectric reflection and the shock sonic noises by hydrogen gas.

The experimental results obtained by the microwave of wave length 3.4 cm are shown in Fig. 2 and Fig. 3. The zero point on the time axis in Fig. 2 indicates the time when the shock front passes at the window I. As is seen in this figure, the intensity of the reflection gradually increases with time. It shows a gradual increase of the ionization of argon gas behind the shock front, and the shock wave velocity (1.7 mm/μ sec.) derived from the frequency of the reflected signal agreed with the value by optical measurement (1.8 mm/μ sec.).

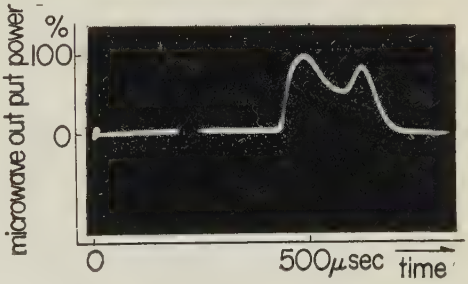

Fig. 3. Typical oscilloscope trace of microwave signal totally reflected from hot plasma.

It has been confirmed from the position of marker in Fig. 3 that the total reflection of the microwave begins with the shock front reaching the end of the tube. It seems to be plausible that the plasma frequency is lower than the microwave frequency before the shock front reaches the end of the tube, while the former becomes higher than the latter after the shock front is reflected from the end, since the temperature of the reflected shock wave is expected to be more than twice as high as that of the incident one, from the theoretical consideration,[1,2] and the electron density in the reflected plasma to be higher than that in the incident one. The duration of the total reflection of microwave was about 200 μ sec.

The two peaks appearing in the photograph of of Fig. 3, which were reproducible in every observation, have not yet been analysed in detail, but it seem that this phenomenon is caused by the interaction between the reflected shock front and the contact discontinuity.

---

* in part read before the meeting on plasma physics of Phys. Soc. of Japan April 1, 1959.

The authors gratefully acknowledge valuable comments with Dr. Robert G. Jahn of the California Institute of Technology. We also thank Prof. I. Takahashi of Kyoto University and Prof. H. Takeyama for their encouragement and useful suggestions.

References

1) E. L. Resler et al: J. Appl. Phys. **23** (1952) 1390.
2) H. Petschek and S. Byron: Ann. Physics **1** (1957) 270.

J. PHYS. SOC. JAPAN **14** (1959) 1638

Etch-Figure in CdS Single Crystals

By Makoto KIKUCHI and Sigeru IIZIMA
Electrotechnical Laboratory, Tokyo, Japan

(Received September 16, 1959)

Recently, several works have been reported on the growth of large solid single crystals of CdS[1]. We have succeeded in making large CdS single crystals by Reynolds-Czyzak method[2]. Powder of luminescent grade cadmium sulphide was sealed in vacuum in fused quartz ampoule, which was then heated at 1225°C for 100 hrs.

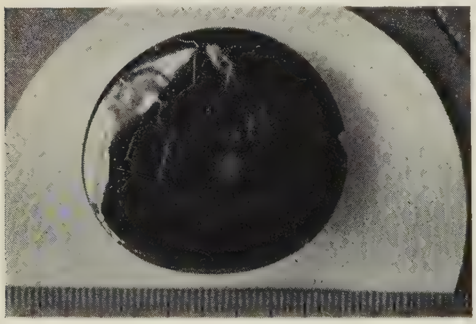

Fig. 1. Single crystals of cadmium sulphide. (Scale; 1 mm per division.)

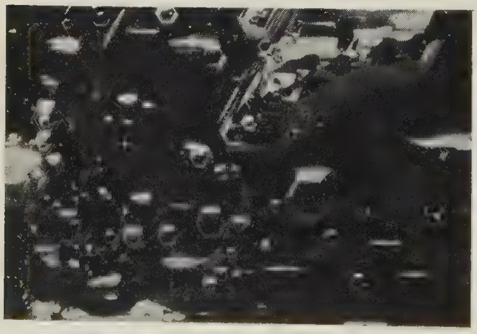

Fig. 2. Photomicrograph of etched surface of (1000).

As is shown in the photograph of Fig. 1, the disk obtained by this method consists of large single crytals bounded by grain boundaries. Some of these cystals have direction of growth parallel to the *c* axis. This has been confirmed by etching the crystals in conc. HCl. Photomicrograph of the etched surface of (1000) plane which contacted with the wall of the ampoule is shown in Fig. 2.

It has been found out that the method oridinarily used for determining the crystal orientation of germanium single crystals etched with superoxol etchant[3] was quite useful also for CdS crystals when the surfaces were subjected to proper etching. The light-figure pattern of the surface etched with conc. HCl is illustrated in Fig. 3. As is shown, sixfold symmetry is clearly revealed.

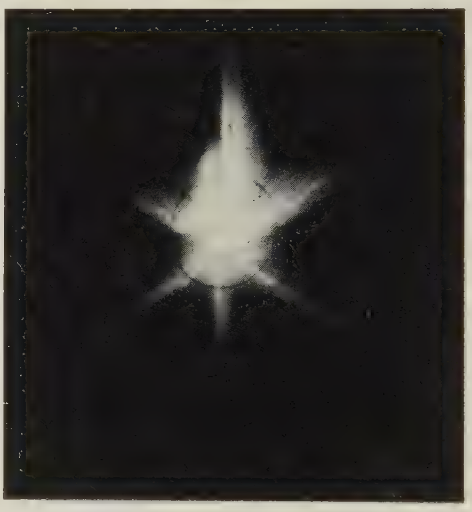

Fig. 3. Light-figure pattern of etched (1000) surface.

The experimental details of growing flaky, prismatic, or solid CdS crystals by controlling temperature, firing time, volume of CdS powder etc. will be presented in the near future with their electrical and optical properties.

References

1) S. J. Czyzak and W. M. Baker: J. Chem. Phys. **29** (1958) 1375. D. R. Boyd and Y. T. Sihvonen: J. Appl. Phys. **30** (1959) 176.
2) D. C. Reynolds and S. J. Czyzak: J. Appl. Phys. **23** (1952) 932.
3) M. Kikuchi: Bull. Electrotech Lab. **19** (1955) 58 (in Japanese).

J. Phys. Soc. Japan **14** (1959) 1639~1640

Note on the Effect of Oxygen Molecules Contained in Solid Hydrogen on the Rate of Ortho-para Conversion

By Kazuko Motizuki and Takeo Nagamiya
Department of Physics, Osaka University

(Received August 17, 1959)

A few years ago we made a theoretical study of the ortho-para conversion in solid H_2 and solid D_2 and the results were published in J. Phys. Soc. Japan **11** (1956) 93, **11** (1956) 654 and **12** (1957) 163 (quoted as I, II and III).

In these papers the effect of oxygen molecules dissolved in solid hydrogen was closely examined, beside the natural convesion process due to the interaction between hydrogen molecules. The oxygen molecule in its ground state has a spin of magnitude one and the corresponding magnetic moment has two Bohr magnetons. Therefore, due to the dipole-dipole interaction between the oxygen molecule and the nuclear spin moments of the ortho-H_2 molecules or the para-D_2 molecules, the ortho or para molecules convert into para or ortho molecules, respectively. In our previous papers, we assumed that the direction of the oxygen spin does not change during the ortho-para conversion process. However, it is also possible that the spin of the oxygen molecule can change its direction, since the anisotropy energy for this spin is expected to be much smaller than the rotational level difference between ortho and para states.

The interaction Hamiltonian between the oxygen molecule and the ortho hydrogen molecule is the same as H_{rs} of Eq. (2.6) of I, i.e., the interaction between the proton spin moments of one hydrogen molecule and the magnetic moment due to rotation of the other hydrogen molecule, except that the rotational magnetic moment of the oxygen molecule. Thus, taking the change of spin direction of the oxygen molecule into account, the transition probability in the case of H_2 can be calculated by Eq. (B. 6) of I, W_i (2) being given by Eq. (B. 11), provided that the common factor $\mu_p{}^4[4+(\mu_R/\mu_p)^2]$ of the coefficients C_i is now replaced by $\mu_p{}^2\mu_{0_2}^2$. The term 4 in the square blaket of the former has come from the proton-proton dipolar interaction. Similar replacement has be done in the case of D_2 (Eq. (3.3) of III). Furthermore, the nomalization factor $9\times 9=81$ of Eq. (A. 5) of I and Eq. (3.4) of III is to be replaced by $9\times 3=27$.

Therefore the conversion rate obtained previously should be modified as follows. The constant of the rate of conversion for H_2 and that for D_2 at a distance R from the oxygen molecule become

$$k_{oxy}(H_2)=644\times(R_0/R)^{12} \text{ per hour}$$

$$k_{oxy}(D_2)=68.6\times(R_0/R)^{12} \text{ per hour}$$

respectively, insteated of Eq. (4.2) of I and Eq. (4.2) of III (the previous numerical factors were 250 and 35.9, respectively). Therefore we find now that the distance, at which the conversion rate due to an oxygen molecule and the conversion rate due to the mutual interaction of hydrogen molecules become equal to each other, is $R=2.95R_0$ and $3.74R_0$,

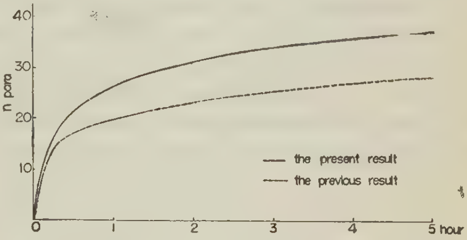

Fig. 1. Number of para-molecules produced around an oxygen molecule as a function of time, for 75% initial ortho-concentration.

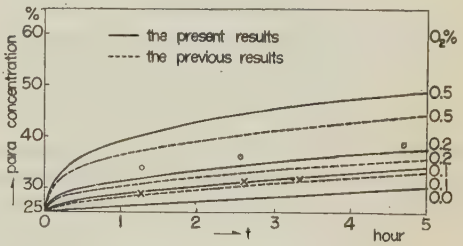

Fig. 2. Increase of the average concentration of para-molecules as a function of time for various values of the molar oxygen concentration and 75% initial ortho-concentration. ⊙ and × represent experimental values obtained at Tōhoku University.

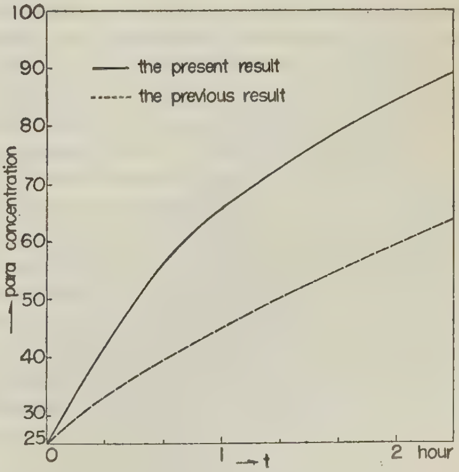

Fig. 3. The average concentration of para-molecules in normal hydrogen as a function of time for a molar oxygen concentration of $\alpha=0.01\%$.

respectively (instead of the previous vulues $2.70R_0$ and $3.54R_0$). In paper I, we have calculated the number of para-H_2 molecules produced around an oxygen molecule and the increase in average concentration of the para-H_2 molecules as function of time (Fig. 1 and Fig. 2 of I) for the case where there is no self-diffusion. In paper II, we have given the increase in para concentration for the case where there is a rapid self-diffusion (Fig. 1). These results have to be modified as in Figs. 1, 2 and 3 of this paper. We give the results only for the case of 75% ortho-hydrogen.

The writers are indebted to Professor K. Husimi for calling our attention to the possibility of the directional change of the oxygen spin moment.

J. PHYS. SOC. JAPAN **14** (1959) 1640

Localized Electron Model and Thermoelectric Power

By Mikio TSUJI

General Education Department, Kyusyu University, Otsubo-machi, Fukuoka

(Received August 20, 1959)

From his analysis of the results of the measurements of the electrical conductivities and the thermoelectric powers of α–Fe_2O_3 and NiO, Morin[1] has derived a conclusion that the mobilities of the carriers of the crystals have a strong temperature dependency which should be described in terms of activation energies for the transport of the carriers. A mechanism of the jumping of the carriers between adjacent ions with an activation energies has been presented by Yamashita and Kurosawa[2] based on a model of localized electron which is tightly bound to an ionic lattice. Now, Morin has analysed his data by using a formula of the thermoelectric power of usual semiconductor theory neglecting the terms due to the kinetic energy of carriers. In the present note, we shall derive a formula of the thermoelectric power of a crystal in which carriers are tightly bound to ions and the jumping of a carrier from an ion to another need an activation energy, and show that Morin's analysis is not satisfactorily consistent. For simplicity, we use the terms 'electron' and 'hole'. For example, in α–Fe_2O_3, 'electron' means Fe^{2+} ion and 'hole' means Fe^{4+} ion. If there are an electric field E_x and a temperature gradient $\partial T/\partial x$ along x-axis in crystal, the current densities due to the electrons j_e and hole, j_h are given by

$$\left.\begin{aligned} j_e&=-eD_e\left(-\frac{\partial n_e}{\partial x}-\frac{en_e}{kT}E_x-\frac{Q_e{}^*n_e}{kT^2}\frac{\partial T}{\partial x}\right),\\ j_h&=eD_h\left(-\frac{\partial n_h}{\partial x}+\frac{en_h}{kT}E_x-\frac{Q_h{}^*n_h}{kT^2}\frac{\partial T}{\partial x}\right),\end{aligned}\right\}\qquad(1)$$

respectively, where D_e and D_h are the diffusion coefficients of the electrons and holes, and n_e and n_h are the carrier densities. $Q_e{}^*$ and $Q_h{}^*$ are given by

$$Q_e{}^*=-k\frac{d\ln W_e}{d(1/T)},\qquad Q_h{}^*=-k\frac{d\ln W_h}{d(1/T)},\qquad(2)$$

where W_e and W_h are the probabilities of the jamping of an electron and a hole from an ion site to adjacent one per unit time and, if we put the lattice constant as a, there are following relations,

$$D_e=a^2W_e,\qquad D_h=a^2W_h\qquad(3)$$

If we neglect a possible temperature dependences of $Q_e{}^*$ and $Q_h{}^*$, we have

$$\left.\begin{aligned} W_e&=\text{const}\times\exp(-Q_e{}^*/kT),\\ W_h&=\text{const}\times\exp(-Q_h{}^*/kT).\end{aligned}\right\}\qquad(4)$$

The carrier densities are given by the Boltzmann distribution,

$$\left.\begin{aligned} n_e&=N\exp\{-(E_1-\zeta)/kT\},\\ n_h&=N\exp\{-(\zeta-E_2)/kT\},\end{aligned}\right\}\qquad(5)$$

where E_1 is the energy of Fe^{2+} ion, E_2 the energy of Fe^{3+} ion, and ζ the chemical potential. Putting (5) into (1), and using the condition $j_e+j_h=0$, we obtain the absolute thermoelectric power S as follows,

$$S=\frac{1}{eT}\frac{\sigma_h(Q_h{}^*+\zeta-E_2)-\sigma_e(Q_e{}^*+E-\zeta)}{\sigma_e+\sigma_h},\qquad(6)$$

where σ_e σ_h are given by

$$\left.\begin{aligned} \sigma_e&=e^2D_en_e/kT=e\mu_en_e,\\ \sigma_h&=e^2D_hn_h/kT=e\mu_hn_h,\end{aligned}\right\}\qquad(7)$$

μ_e and μ_h being the mobilities. The total conductivity is

$$\sigma=\sigma_e+\sigma_h.\qquad(8)$$

Using (3), (4) and (7), we have

$$\frac{\sigma_e}{\sigma_h}=\frac{\mu_e{}^0}{\mu_h{}^0}\exp\left\{\frac{(Q_h{}^*+\zeta-E_2)-(Q_e{}^*+E_1-\zeta)}{kT}\right\},\qquad(9)$$

where $\mu_e{}^0$ and $\mu_h{}^0$ are temperature-independent factors of the mobilities. Comparing our formulas (6) and (9) with Morin's formulas, we see that Morin's $\zeta-E_2$ and $E_1-\zeta$ should be replaced by $\zeta-E_2+Q_h{}^*$ and $E_1-\zeta+Q_e{}^*$ respectively. Thus the values of n_e, n_h, μ_e and μ_h computed by Morin are, in actuality, $n_e\exp(-Q^*/kT)$, $n_h\exp(-Q_h{}^*/kT)$, $\mu_e\exp(Q_e{}^*/kT)=\mu_e{}^0/T$ and $\mu_h\exp(Q_h{}^*/kT)=\mu_h{}^0/T$ respectively. Therefore the 'mobilities' computed by Morin should not have strong temperature dependency of activation energy type. Thus, if our model is accepted, the analysis of Morin may become to be unsatisfactory.

References

1) F. J. Morin: Phys. Rev. **93** (1954) 1195, 1199; Bell Syst. Tech. J. **37** (1958) 1047.

2) J. Yamasita and T. Kurosawa: J. Phys. Chem. Solids **5** (1958) 34.

J. PHYS. SOC. JAPAN **14** (1959) 1641~1642

Effect of Re-crystallization on the Temperature Dependence of Photocurrent of Silver Chloride Crystals

By Noriaki ITOH
Department of Electrical Engineering, College of Engineering, Osaka University
and Tokuo SUITA
Department of Nuclear Engineering, College of Engineering, Osaka University

(Received September 4, 1959)

As previously reported, the photocurrent-temperature curve of silver chloride crystals has a sharp maximum at about −80°C[1]. It was also shown that this abrupt change of photocurrent was due to the change of life time of electrons and at the maximum point the life time was estimated to be 5×10^{-6} sec by calculating the Schubweg of electrons from voltage-photocurrent curve. In the decreasing part of photocurrent with increasing temperature, the logarithm of the photocurrent was found to be a linear function of the reciprocal of temperature in Kelvin, and the extrapolation of the curve showed that the life time at room temperature was lower than 10^{-8} sec.

It was also reported by F. C. Brown[2], by J. W. Mitchell[3], by P. Süptitz[4] and by R. S. Van Heyningen and F. C. Brown[5], that the photocurrent of silver chloride crystals depended on the atmosphere in which the crystals were grown. They showed that the specimens made in vacuum or in nitrogen atmosphere has short life time ($< 10^{-8}$ sec) at room temperature, whereas the specimens made in air has longer life time (10^{-6} sec) at room temperature.

These results were unexpected for us, because the crystals used in our measurement were grown in air by the Kyropoulos method. The difference between the methods of crystal preparation of F. C. Brown and J. W. Mitchell and our methods was that we get specimens after recrystallizing raw precipitate of AgCl several times, although they get specimens through only one crystallization from well purified precipitate.

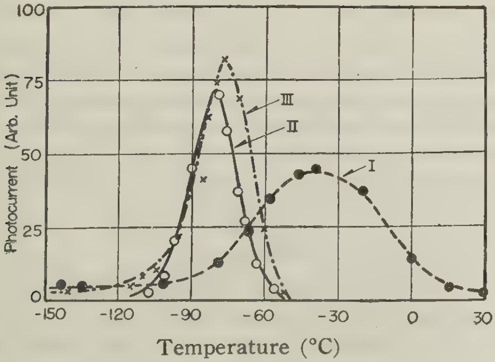

Fig. 1.

In order to clarify whether recrystallization in air shortened the life time of electrons in our specimens at room temperature, we measured the temperature dependence of photocurrent of specimen grown just from precipitate in air, spcimens recrystallized three times in air and also specimens grown in vacuum from precipitate. (Each specimens will be refered to as I, II, and III respectively.) The specimen III was grown by Kyropoulos method in a specially made vacuum cell of 10^{-3} mmHg, into which the cooling pipe was inserted through vacuum seal glass piston. The measuring apparatus was just the same as that reported previously[1].

The results are shown in Fig. 1. The typical peak of photocurrent which had been observed in recrystallized specimens disappeared in specimen I. It should be noted that in the specimen III grown in vacuum from precipitate, photocurrent has the same peak as in specimen II. The life time of specimen I at room temperature is shown to be larger than that of specimen II or III. Recrystallization in air may remove some impurities which make the life time at room temperature higher. The darkenability of specimens I, II and III were also measured and it was found that the specimen I has one third darkenability as the secimen II and III, which is consistent with Brown and Wainfan's results[6].

Qualitative spectrographic analysis of sample I and II was also tried in order to find the difference in impurity content. Some traces of Fe, Ca, Cu, Mg, Mn, Na and Si was detected and it was found that the line of Ca, Cr and Cu in sample II was clearly diminished.

Considering from the facts that the crystal made in vacuum seems to have the same metallic impurity and the effect of metallic impurity on photocurrent is quite different, (see the paper to be published), the disappearance of the peak of photocurrent temperature curve of sample It seems to be due to the effect of oxygen or moisture, which seems to be removed by recrystallization.

The facts that the photocurrent of specimen I do not decrease abruptly from the maximum as the temperature increases and its photographic sensitivity at room temperature is lower seems to be explained if we consider that the oxygen is attached to the sensitivity centers and make them inefficient as suggested by F. Seitz and F. C. Brown[7]. Further experiments on the effect of metallic impurities are now in progress.

We wish to thank to Dr. E. Mizuki and other staffs of Fuji Photofilm Company for supplying silver chloride raw materials and for their valuable discussions. We also thank to Mr. H. Kawaguchi

of Japan Atomic Energy Research Institute for the spectrographic analysis of silver chloride crystals.

References

1) N. Itoh and T. Suita: *Photographic Sensitvity*, ed. by S. Fujisawa, vol. **2** (Maruzen, Tokyo, 1958) 41. J. Phys. Soc. Japan **14** (1959) 894.
2) F. C. Brown: J. Phys. Chem. Solids **4** (1958) 206.
3) J. W. Mitchell: Phil. Mag. **2** (1957) 1276.
4) P. Süptitz: Z. Phys. **153** (1958) 184.
5) R. S. Van Heyningen and F. C. Brown: Phys. Rev. **111** (1958) 462.
6) F. C. Brown and N. Wainfan: Phys. Rev. **105** (1957) 93.
7) F. C. Brown and F. Seitz: *Photographic Sensitivity*, ed. by S. Fujisawa, vol. **2** (Maruzen, Tokyo, 1958) 11.

J. Phys. Soc. Japan **14** (1959) 1642

Possible Evidence for the Light Induced Plasticity in Germanium

By Makoto Kikuchi
Electrotechnical Laboratory, Tokyo, Japan
and
Mitsuyoshi Saito
Institute of Science and Technology, Waseda University, Tokyo, Japan

(Received August 28, 1959)

It has been reported previously that the surface hardness of germanium illuminated with infrared or ultraviolet light, is much less than that in darkness[1]). Recently, it turned out that when a germanium specimen was bent and fractured under strong illumination, much higher densities of etch pits were revealed on the surface than on the surface of the specimens fractured in darkness[2]).

Here is reported an experimental result which seems to serve as an evidence for the light induced plasticity. Germanium rod specimens were cut from zone-levelled single crystals in the size of 3.2×1.8 ×20 mm. The resistivity of n-type sample ranged from 15 to 17 ohm-cm. The sample was arranged as shown in Fig. 1 and subjected to heavy wedge at the middle point. A razor blade was used as the wedge and the weight of roughly 2 kilogram was applied. An infrared drier lamp was used as the light source, since it had already been found that light of wevelength between 2.0 and 4.0 microns was responsible for the effect being observed.

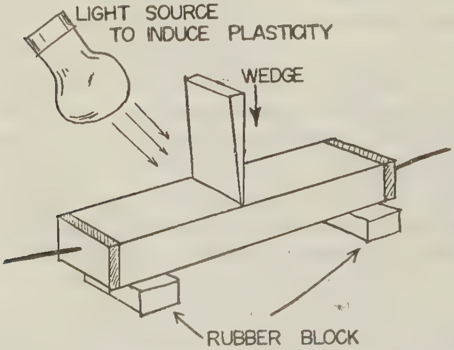

Fig. 1. The arrangement of the sample for room temperature bending under illumination.

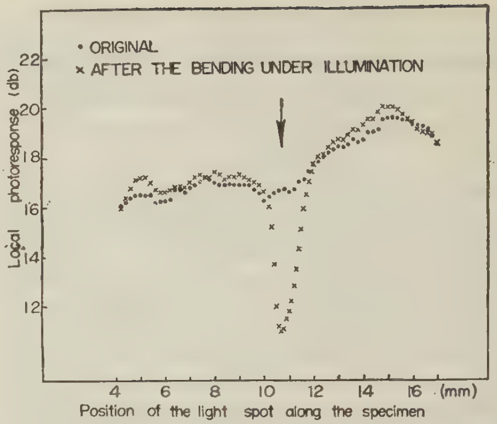

Fig. 2. Photoresponse observed by scanning a small light spot along on the rod specimen. The light is chopped at 225 cps.

The effect of bending under the illumination at room temperature was observed through the change of local photoresponse, snce it is the replica of the change of minority carrier lifetime. Typical result is shown in Fig. 2, where the distribution of photoresponse before and after 1.5 hours' bending are compared. As is shown, the photoresponse is remarkably reduced at the middle of the specimen, where the wedge was pressed.

The temperature rise of the sample caused by the illumination was prevented by applying alcohol on the specimen, so it could be estimated that the temperature did not exceed 90°C. Therefore, it may be concluded that the observed effect is not caused by the thermally induced plastic flow.

The local reduction of the photoresponse shown in Fig. 2 can be explained as the decrease of the hole lifetime caused by the locally produced dislocations and lattice irregularities. In fact, some change was caused by the above mentioned treatment in the surface recombination velocity, but this did not result in such characteristic valley in the curves shown in Fig. 2.

Detailed experimental procedures and results will be presented in the near future.

References

1) G. C. Kuczynski et al: Phys. Rev. **108** (1957) 946.
2) G. C. Kuczynski et al: J. Appl. Phys. **30** (1959) 267.

J. PHYS. SOC. JAPAN **14** (1959) 1643~1644

The Kinetics of Radical Reactions in γ-Irradiated Polyvinyl Chloride

By Kenzi HUKUDA, Jiro ISHII
and Zenêmon MIDUNO

Department of Physics, Faculty of Science, Kyusyu University, Hukuoka, Japan

(Received September 1, 1959)*

The rates of production and extinction of radicals in the γ-irradiated polyvinyl chloride have been investigated by means of the electron spin magnetic resonances at 3 cm wavelength. The pure powder of polyvinyl chloride without any plasticizer was pressed to the form of discs of 2–3 mm thickness and 11 mm diameter under the pressure of about 2000 kg/cm² and the temperature of about 120°C. These discs were irradiated with the medical γ-source of cobalt-60 and the dose rates were measured by the ferrous-ferric dosimetry. The samples were irradiated and preserved in glass tubes in which the atomospheric pressure was about 10^{-3}mmHg and placed in the air only during the ESR measurements. The two hyperfine lines ($m_I = \pm 1/2$) of divalent manganese diluted in MgO crystals served both as g-markers and as intensity standards of the electron spin resonances.

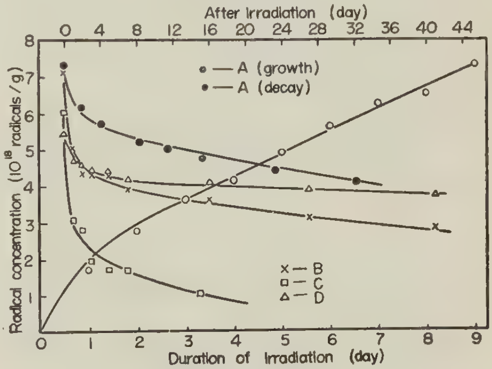

Fig. 1. Time dependences of radical concentrations during and after irradiations of γ-ray. The lines are drawn with the equations (1) and (2).

Table I.

Sample	λ_1 $\left(\frac{1}{\text{day}}\right)$	λ_2 $\left(\frac{\text{g}}{\text{radicals. day}}\right)$	v_{10} $\left(\frac{\text{radicals}}{\text{g}}\right)$	v_{20} $\left(\frac{\text{radicals}}{\text{g}}\right)$
A	0.010	0.62×10^{-18}	5.6×10^{18}	1.7×10^{18}
B	0.010	0.62×10^{-18}	4.0×10^{18}	3.1×10^{18}
C	0.060	1.0×10^{-18}	2.3×10^{18}	3.7×10^{18}
D	0.002	0.50×10^{-18}	4.0×10^{18}	1.4×10^{18}

Fig. 1 shows the measured concentrations of radicals produced in the sample A during the irradiation and also shows the decrease of radical concentrations in the samples A, B, C and D after irradiations. The sample A was irradiated at the dose rate of about 3×10^5 roentgen/day and the temperature of 30°C and after the irradiation it was preserved at the same temperature. The samples B, C and D were all irradiated at 15°C and then preserved at 30 °C, 51°C and 15°C respectively. The dose rate for the sample B was about 7×10^5 r/day and the samples C and D were irradiated at lower dose rate while they were not measured. These results cannot be explained by the ordinary nth order reaction equations such as

$$\frac{dv}{dt}=a-\lambda v^n$$

for radical growth and

$$\frac{dv}{dt}=-\lambda v^n$$

for radical decay, where v, a and λ are the radical concentration, the radical production rate and the radical reaction constant respectively. For instance, if we assume the above equations, the values of n must be about 7 and 3 respectively for radical decays of the samples A and B at the same tempeture of 30°C and for the radical growth of the sample A it must be smaller than unity. Accordingly we assume the existence of two groups of radicals with different reaction mechanisms one of which is of first-order and the other is of second-order and also assume that there is no interaction between the two groups. Then during the irradiation the representation for v becomes,

$$v=\frac{a_1}{\lambda_1}(1-e^{-\lambda_1 t})+\sqrt{\frac{a_2}{\lambda_2}}\tanh(\sqrt{a_2\lambda_2}\,t) \qquad (1)$$

after the irradiation,

$$v=v_{10}e^{-\lambda_1 t}+\frac{v_{20}}{1+v_{20}\lambda_2 t} \qquad (2)$$

---

* The original manuscript was first received two and half months ago, but unfortunately was misplaced in the office of Kyusyu Branch of the Society. At our request, the authors kindly undertook to resubmit the manuscript. We wish to express our deep regret for the dely in the publication of this note. (Editorial Committee)

where v_{10} and v_{20} are the radical concentrations of the two groups when the irradiation is ceased. The curves of Fig. 1 are drawn by the above equations with the numerical values of Table I for λ_1, λ_2, v_{10} and v_{20} and with 0.65×10^{18} radicals. g^{-1}. day^{-1} and 1.8×10^{18} radicals. g^{-1}. day^{-1} for a_1 and a_2 of the sample A.

From these results the activation energies for λ_1 and λ_2 are estimated to be 18 kcal/mol and 4 kcal/mol respectively and the ratio of the numbers of radicals which belong to the two groups must vary with the temperature. Above interpretation is of course not unique one, but it seems to be plausible that there are more than two groups with different reaction mechanisms. The assumption of the two groups, however, has been indicated to give considerably good approximation to the measured variations of the radical concentrations.

The authors wish to express their thanks to Prof. M. Takayanagi, Mr. Y. Ishida and Mr. T. Aramaki for their helpful advice and discussions.

J. Phys. Soc. Japan **14** (1959) 1644~1645

Measurement of Galvanomagnetic Tensors of Bismuth Single Crystals at Low Temperatures

By Shoichi Mase

Department of General Education, Nagoya University

and Sei-ichi Tanuma

Research Institute for Iron, Steel and Other Metals, Tôhoku University

(Received August 31, 1959)

The galvanomagnetic effects of bismuth single crystals at low temperatures have been extensively studied. Recent report for the longitudinal effect by Babiskin[1] has particularly attracted our attention. His experimental result seems not to be in accordance with the approximate theory of galvanomagnetic effect in a strong magnetic field such as $\omega\tau>1$, which predicts that the field dependent part of the longitudinal resistivity tensor is only a small correction due to the quantum effect, so far as the intensity of the magnetic field being within the quantum limit.

The authors measured the tensors of three single crystals with different orientations at 4.2°K and in the magnetic field up to about 10,000 Oersted. A large single crystal from which above three samples were cut out was grown using repeatedly zone-refined sample from Tanadac bismuth having five nine purity. We chose one of the binary axes and the trigonal axis as x- and z-axis respectively. Symmetric and antisymmetric tensors, $\rho^s_{ik}(\boldsymbol{H})$ and $\rho^a_{ik}(\boldsymbol{H})$, are defined as

$$E_i=\sum_k\rho^s_{ik}(H)J_k+\sum_{k(\neq i)}\rho^a_{ik}(\boldsymbol{H})J_k\,,$$

$$\rho^{s,a}_{ik}(\boldsymbol{H})=\rho^{s,a}_{ki}(-\boldsymbol{H})\,.$$

Figs. 1–2 are the representative results of our

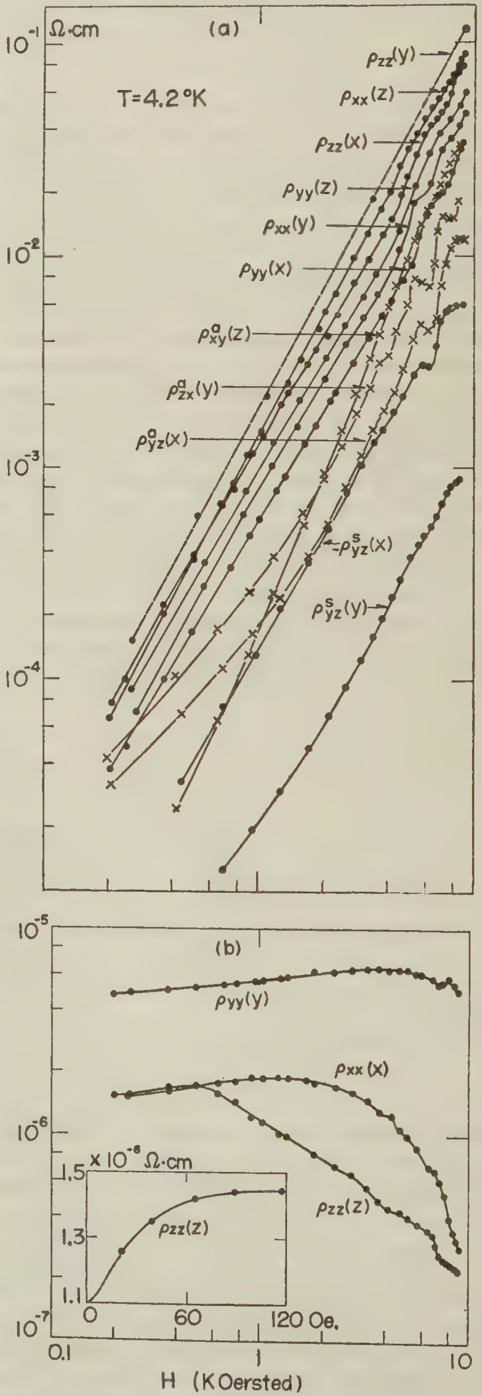

Fig. 1. Symmetric and antisymmetric tensors *versus* H curves.

measurements. Some curves in Figs. 1–2 are qualitatively in accordance with those by the several authors[2]. As one can see clearly from Fig. 2, the longitudinal tensors are conspicuously smaller than the transverse tensors and very slight misalignment of relative direction of the magnetic field or the potential probes and the sample can cause a drastic increase in the magnitude of the longitudinal tensor with the magnetic field due to the transverse component. The negative magneto-resistance shown in Fig. 1 (b) may be due to physical imperfections such as slip boundaries or due to other undesirable effects[3]. Unfortunately there was an evidence that some part of the anisotropy of the tensors shown in Fig. 1 (a) is attributed to the same causes. (It is, however, very difficult in bismuth with very long mean free path to get rid of such spurious effect). The magnitude of each longitudinal tensor in presence of the lowest field (except one run for $\rho_{zz}(z)$) is considerably larger than the respective value in zero field ($\rho^0_{xx}=1.12\times10^{-6}\,\Omega\text{cm}$, $\rho^0_{yy}=1.48\times10^{-6}\,\Omega\text{cm}$ and $\rho^0_{zz}=1.10\times10^{-6}\,\Omega\text{cm}$). This is due to the fact that at 4.2°K the condition $\omega\tau>1$ is necessary satisfied even in presence of the lowest field and the solution is in saturation region of usual solution of the Boltzmann equation (applicable to the case $\omega\tau<1$). It is illustrated in second run for $\rho_{zz}(z)$ (the inset in Fig. 1 (b)). The detail will be published elsewhere.

The authors express their sincere thanks to Prof. K. Ariyama and Prof. T. Fukuroi for their kind encouragements and discussions.

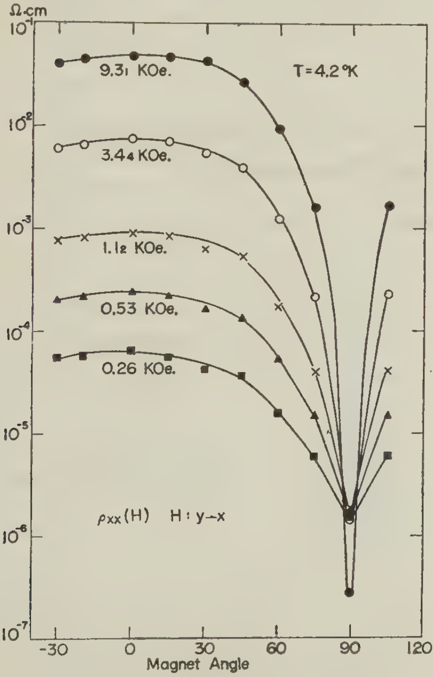

Fig. 2. Symmetric tensor ρ_{zz}(H) *versus* magnet angle.

References

1) J. Babiskin: Phys. Rev. **107** (1957) 981.
2) P. B. Alers and R. T. Webber: Phys. Rev. **91** (1953) 1060. J. M. Reynolds, H. W. Hemstreet, T. E. Leinhardt and D. D. Triantos: Phys. Rev. **96** (1954) 1203. T. Okada: private communication through Busseiron Kenkyu **3** (1958) 313. (in Japanese)
3) N. E. Alekseevskii, N. B. Brandt and T. I. Kostina: Soviet Physics JETP **7** (1958) 924.

J. PHYS. SOC. JAPAN **14** (1959) 1645

A Note on the Drag of a Screen at Low Reynolds Number

By P. G. MORGAN
Department of Engineering, University of Manchester, England

(Received September 21, 1959)

The work recently reported by Sawada[1] on the drag of a lattice of parallel circular cylinders at low Reynolds numbers shows considerable ingenuity in the manufacture of the lattice. This method of carrying out tests has been used previously, and a criticism is given below.

The overall size of the lattice is 6 cm. × 6 cm. while the cross section of the tower itself is 50 cm. × 50 cm., If we consider the lattice to be stationary and the air moving past it, some air flows through the lattice while the remainder flows around it; the proportions depend upon the resistance of the lattice, and the calculations for a wire gauze screen have been given by Taylor and Davies[2]. Experiments carried out by the author on wire gauzes falling through glycerine, in order to examine the flow resistance at low Reynolds numbers, show that there is a marked difference in the drag of a given wire gauze screen, depending upon the ratio

$$\frac{\text{area of screen}}{\text{area of the duct through which the screen moves}}$$

For wire gauze screens of small open area ratio i.e. high solidity, the differences in resistance are some 20%.

Considerable difficulty has been experienced in our work in keeping the plane of the screen horizontal in free fall experiments; this has been overcome for the screens of higher resistance by fitting a light framework, similar to that shown by Sawada, and measuring the force required to pull the screen upwards with a constant velocity.

References

1) T. Sawada: J. Phys. Soc. Japan **14** (1959) 837.
2) G. I. Taylor and R. M. Davies: A.R.C.R. & M. 2237 (1944).

Errata

Study on Vacuum Deposition of Metals, II. On the Change with Aging Time in Thickness and Resistivity of Vacuum Deposited Gold Film

By Yoshibumi FUJIKI

J. Phys. Soc. Japan **14** (1959) 1308～1313

1) In Fig. 2, the arrows should be shifted to the right about 1.5 mm.
2) P. 1309, left column, line 16, should be read: 2×10^{-5} mmHg.

X-ray Observations of the Surfaces of Plastically Deformed LiF Crystals with the Berg-Barret Method

By Mitsuru YOSHIMATSU and Kazutake KOHRA

J. Phys. Soc. Japan **14** (1959) 1249–1250

Page	Column	Line	Wrong	Corrected
1249	left	4	Berg-Barret	Berg-Barrett
1249	left	12	Berg-Barret	Berg-Barrett
1249	right	3	surface, surface[4],	surface[4],
1250	left	13	Barret	Barrett

X-ray Observation of the Strain Field in Germanium Single Crystals with the Use of the Anomalous Transmission

By Zensho ISHII and Kazutake KOHRA

J. Phys. Soc. Japan **14** (1959) 1250–1251

Page	Column	Line	Wrong	Corrected
1250	left	10 from the bottom	Borrmann *et al*	Borrmann *et al*[1]
1250	left	9 from the bottom	Barth *et al*	Barth *et al*[2]
1250	left	2 from the bottom	CuK	CuKα
1250	right	Fig. 2		Fig. 2 should be seen upside-down.

CONTENTS

SUPPLEMENT, Progress of Theoretical Physics **No. 9 1959**

Introduction .... H. YUKAWA
Some Considerations on a Nonlinear Field Theory .... H. KITA
Theory of Invariant Variation and the Generalized Canonical Dynamics...... R. UTIYAMA
Coordinate Systems in General Relativity and Geometrical Representation for Physical Quantities .... M. IKEDA and Y. MIYACHI
On Wave Propagation in Non-linear Fields .... T. TANIUCHI

SUPPLEMENT, Progress of Theoretical Physics **No. 10 1959**

Thermodynamics Basis of Relaxation Spectrometry .... K. OKANO
Phenomenological Theory of Non-linear Viscoelasticity.................... M. YAMAMOTO
Molecular Theory of Relavation Phenomena in Polymers.... O. NAKADA & Y. CHIKAHISA
General Theory of Relaxations in the Polymer Chain .... A. MIYAKE
On the Mechanical Relaxation Time Spectra of Crystalline Polymers .... K. NAGAMATSU
Viscoelastic Properties of Network Structure .... S. HAYASHI
The Viscoelastic Behavior of Concentrated Polymer Solutions .... T. KOTAKA, M. KURATO and S. ONOGI
Dielectric Relaxation in High Polymers .... T. TANAKA and Y. ISHIDA
A Short Review of Discussions on the Glass Transition, Second-order Transition, and Relaxation Phenomena in High Polymers .... A. NISHIOKA
Effects of Distribution of Correlation Times upon T_1 and T_2 in Nuclear Magnetic Resonance .... A. ODAJIMA
Relaxation Phenomena and Molecular Motion in Solid State of High Polymers..S. NOHARA
The Apparent Second-order Transition of High Polymers with Special Emphasis on its Manifestation in the Mechanical Properties .... T. HIDESHIMA
Transition Phenomena in High Polymers .... R. CHUJO
Features and Interpretation of Sorption Processes in Polymer-vapor Systems .... H. FUJITA, A. KISHIMOTO and H. ODANI
Transport Phenomena in Polymer Membranes .... Y. KOBATAKE

Price: per copy (postage inclusive) overseas.... $1.00
inland...... ¥ 300.

Subscribe to: The Publication Office, Supplement, Progress of Theoretical Physics, Yukawa Hall, Kyoto University
Kyoto, Japan

PROGRESS OF THEORETICAL PHYSICS

CONTENTS

Progress of Theoretical Physics Vol. 21, No. 2, February 1959

On a New Approach to Cosmology ....H. NARIAI and Y. UENO..219
On the Analogy between Strong Interaction and Electromagnetic Interaction
....Yasunori FUJII..232
Quantum Field Theory in terms of Euclidean Parameters ......Tadao NAKANO..241
Radial Dependence of Imaginary Part of Nuclear Optical Potential..........
....K. HARADA and N. ODA..260
Nuclear Moments of Inertia........................T. MIYAZIMA and Y. WADA..269
On the Representations of Field Quantities. II..................Hitoshi WAKITA..299
The Evolution of Massive Stars. I......S. SAKASHITA, Y. ŌNO and C. HAYASHI..315
Neutrino and Gravity ....Satio HAYAKAWA..324
On the Method of "Auxiliary Variables" ....Kazuo HIROIKE..327
Gauge Invariance and the Meissner Effect..N. FUKUDA, Y. WADA and S. OTAKE..343
Letters to the Editor:
On the Geometrical Structure of Benzene-Ionide Complex ......S. AONO..354
On the Possibility of Helium Burning in Gians Stars in a Globular Cluster ....H. YAMAZAKI, S. SAKASHITA and Y. ŌNO..355
On the Gauge-Invariant Meissner Effect ....S. NAKAJIMA..357
On Critical Magnetic Fields of Superconductors ....S. NAKAJIMA..358
Contents of Journ. Phys. Soc. of Japan, Vol. 13, No. 12 360

Price $ 1.25 per copy
$ 15.00 per year (postage inclusive)
Annual dues for foreign members (individual subscribers)
$ 12.00 (postage inclusive)
" for foreign members of the Physical Society of Japan
$ 10.00 (postage inclusive)

Application for members, subscriptions and orders for back numbers should be sent, directly or through book-dealers, to
The Publication Office
in
Yukawa Hall, Kyoto University, Kyoto, Japan

. . . .

ANNOUNCEMENT

REVISED Price List of Back Numbers (for subscribers abroad)

*Vols. 1–4	$ 6.40 each
*Vols. 5 & 6	$13.00 each (single copy: $2.50)
*Vols. 7 and succeeding ones	$ 8.00 each (single copy: $1.50)

Back number prices are effective for volumes other than last four (4) volumes (the current volume inclusive).

Thus, volumes 1 through 16 will be regarded as back numbers while volume 20 is being published.

The revised prices will be effective on and after August 1, 1958.

. . . .

JOURNAL OF THE PHYSICAL SOCIETY OF JAPAN, Vol. 14, No. 12, DECEMBER, 1959

Photoneutron Cross Sections for Ag^{107}, Mo^{92} and Zr^{90}

By Naoshi MUTSURO, Yuji OHNUKI, Kazuo SATO
and Motoharu KIMURA

Department of Physics, Tohoku University Sendai, Japan

(Received August 1, 1959)

Photoneutron cross sections and the yield curves were taken by the residual activity method for Ag^{107}, Mo^{92} and Zr^{90}. Threshold energy were obtained as 9.35±0.1 MeV, 9.15±0.1 MeV, 12.38±0.1 MeV and 12.3 ±0.1 Mev for $Ag^{107,109}$, Mo^{92} and Zr^{90} respectively. The energy for the maximum cross section was obtained as 14.5 MeV for Ag^{107}, 16.5 MeV for Mo^{92} and 17 MeV for Zr^{90}. The giant resonance widths were measured about 5.3 MeV, 2.7 MeV and 2.9 MeV respectively. Intrinsic quadrupole moment determined from above data was $(1.9\pm0.7)\times10^{-24}\,\mathrm{cm}^2$ for Ag^{107}.

§ 1. Introduction

The measurement of photoneutron cross section curves have been made by many authors for ten years, and the systematics of (γ, n) reactions were framed by a few authors[1),2)]. On the other hand, the widths of giant resonance show large fluctuation from nucleus to nucleus, and general tendency of the fluctuation was as follows; resonance widths for colsed shell nuclei are appreciably narrower than those of nuclei situated between closed shells.

O kamoto[3)] and Danos[4)] explained those tendency by the nuclear deformation, which is the extension of the hydrodynamical model for the nuclear photoeffect which leads to two giant resonance energies associated with each axis of a deformed nuclei.

Recently Fuller[5)] et al. obtained the cross section curves for Ta^{181}, Tb^{159}, and other elements by good energy resolution experiment, and showed that the giant resonance for Ta^{181} and Tb^{159} was clearly split into two peaks, but Carver[6)] et al. did not observe such splitting for Ta^{181} and also in our laboratory we did not obtain such splitting[7)]. It is the object of our present works to check the above effect for the medium weight nuclei, and we measured the cross section curves for Mo^{92} and Zr^{90} which are closed shell nuclei and for Ag^{107}, which is situated between two closed shells of $N=50$ and $N=82$.

§ 2. Experimental Procedure

The activation curves of photoneutron yield were taken by the Tohoku University 25 MeV betatron bremsstrahlung γ rays. The energy calibration of betatron was made by the use of threshold energy of the reaction $Cu^{63}(\gamma, n)Cu^{62}$, $Fe^{54}(\gamma, n)Fe^{53}$ and $C^{12}(\gamma, n)C^{11}$ and its energy are 10.8 MeV[8)], 13.8 MeV[9)] and 18.7 MeV[10)] respectively. The energy calibration curve is presented in Fig. 1.

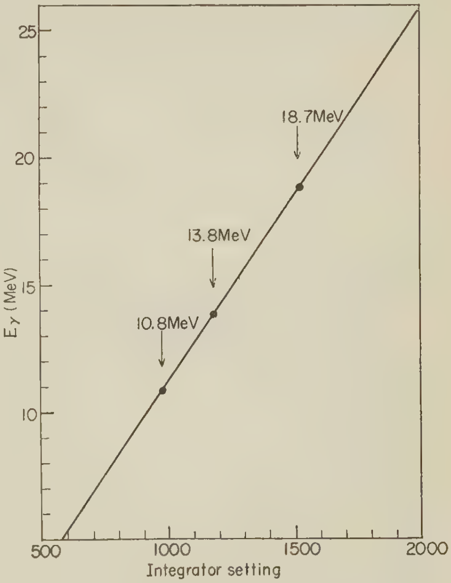

Fig. 1. Energy calibration curve.

During this work, we checked betatron energy frequently by the above threshold energy, and we found that the energy of the betatron were constant within ±10 KeV.

The basic experiment consists of irradiation of a number of samples at various betatron energy, and the yield curves were taken by residual activity measurements.

In the case of $Ag^{107}(\gamma, n)Ag^{106}$ reaction, by using natural silver, two different kinds of activity were formed, one of which is from $Ag^{109}(\gamma, n)Ag^{108}$ and another from $Ag^{107}(\gamma, n)Ag^{106}$ reaction, half-lives of Ag^{108} and Ag^{106} being 2.4 min. and 24 min. respectively.

In order to detect 24 min. β^+ activity from Ag^{106}, Ag sample was irradiated in the γ ray beam for 20 min. and after waiting for 20 min. to cool off the 2.4 min. activity to 1/500, counts were taken for 10 min. by G–M or scintillation counter set to the annihilation peak.

The Ag sample were 3 cm×3 cm×0.15 cm in shape and irradiated at 1.5 m from the betatron target one after another. In the case of Mo^{92}, natural Mo which is shaped 3 cm×3 cm and 0.2 mm thick was irradiated for 15 min. at the same position of the case of Ag^{107}, and after waiting for 2 min. counted for 10 min. by scintillation counter set to the annihilation peak. Counting efficiency of scintillation counter was regularly checked by counting rate of Na^{22}, which was placed at the standard position with respect to the scintillation crystal, the variation of counting efficiency was constant within statistical error during these works. In the case of Zr^{90}, natural Zr shaped 2 cm×2 cm and 0.3 cm thick was irradiated for 2 min. at the same position and after waiting for 2 min. measured for 2 min. by scintillation counter. In order to detect isomeric state of Zr^{89}, the 0.588 MeV γ ray, the half-life of which is 4.4 min., was measured by scintillation counter set to this energy.

During above irradiation, care was taken to hold the dose rate from betatron constant, because average photon flux incident on the

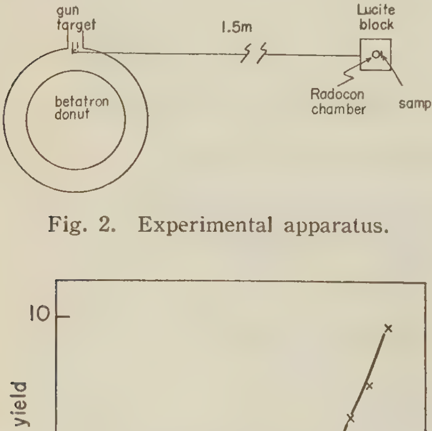

Fig. 2. Experimental apparatus.

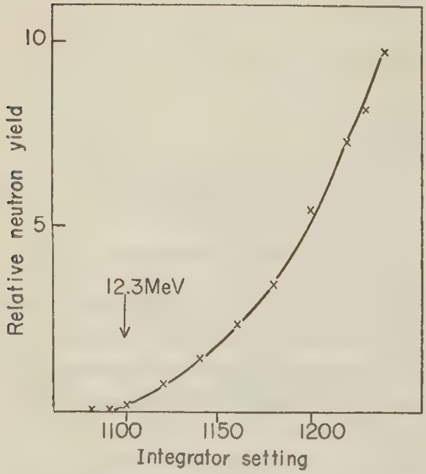

Fig. 3–1. Activation curve near threshold for $Zr^{90}(\gamma, n)Zr^{89*}$.

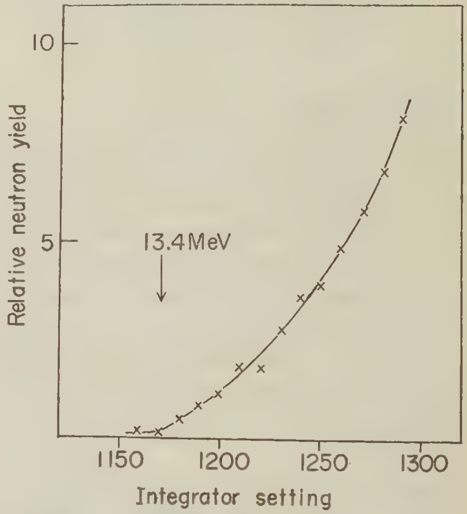

Fig. 3–2. Activation curve near threshold for $Mo^{92}(\gamma, n)Mo^{91}$.

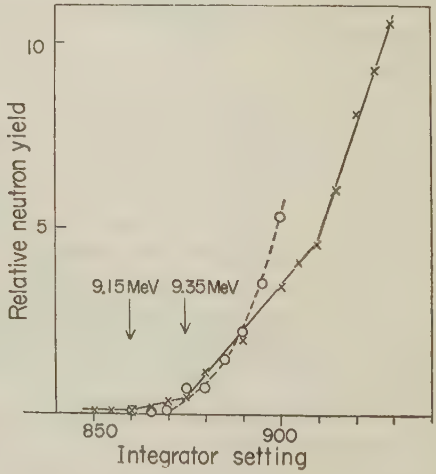

Fig. 3–3. Activation curve near threshold for $Ag(\gamma, n)$.

× measured by G-M counter.

○ measured by scintillation counter setting to 0.51 MeV.

Table I. Summary of threshold measurement.

Reaction	Present data (Mev)	Previous data (Mev)	Q (Mev)	Reference
$Zr^{90}(\gamma n)Zr^{89m}$	12.3±0.1	12.3 12.1±0.1	10.99	11) 12)
$Mo^{92}(\gamma n)Mo^{91}$	13.4±0.1		12.38	
$Ag^{107}(\gamma n)Ag^{106}$	9.35±0.1	9.588 9.43±0.05	9.03	13) 14)
$Ag^{109}(\gamma n)Ag^{108}$	9.15±0.1	9.14±0.05	9.12	14)

sample in a given irradiation dose of Q is Q/t_R, where t_R is the irradiation time, and recorded number of counts were corrected to unit dose rate and to saturation activity by multiplying each reading by $t_R/1-\exp(-\lambda t_R)$.

γ ray dose was measured by means of Victoreen Radocon chamber, which is located at the center of Lucite of 11.7 cm cube. All the samples were irradiated just behind the Radocon chamber. The over all apparatus for each irradiation was presented in Fig. 2.

§ 3. Experimental Results and Discussion

Fig. 3 represents activation curves near threshold of each element. The threshold energy of each element is shown in Table I, the 1st column is reactions, the 2nd contains the threshold energy measured in present work, 3rd those by previous[8),11)-13)] data and 4th represents Q-values calculated from mass data.

In the case of Ag and Zr^{90}, the present data are in agreement with previous ones within experimental error. Threshold energy of Mo^{92} has not been observed previously. There were large deviations in energy calculated from mass data in the case of Mo^{92} and Zr^{90}, this is the general tendency in the case of closed shell nuclei. The activation curves were represented in Fig. 4. Absolute neutron yields were normalized by $Cu^{63}(\gamma, n)Cu^{62}$ yields which was measured by Saskatchewan group[14)] in absolute scale. $Zr^{90}(\gamma, n)Zr^{89*}$ neutron yield

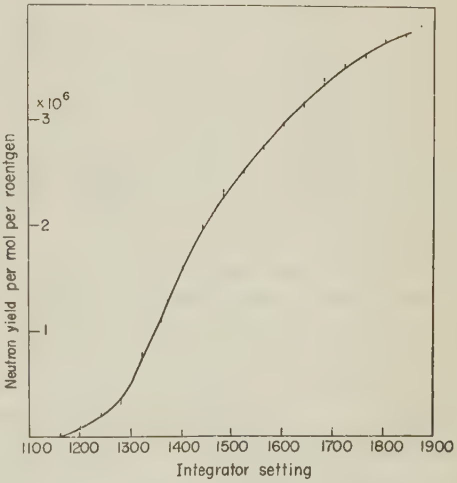

Fig. 4-2. Activation curve for $Mo^{92}(\gamma, n)Mo^{91}$.

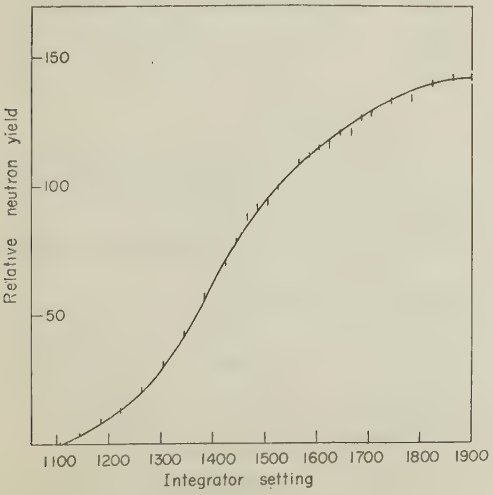

Fig. 4-1. Activation curve for $Zr^{90}(\gamma, n)Zr^{89m}$.

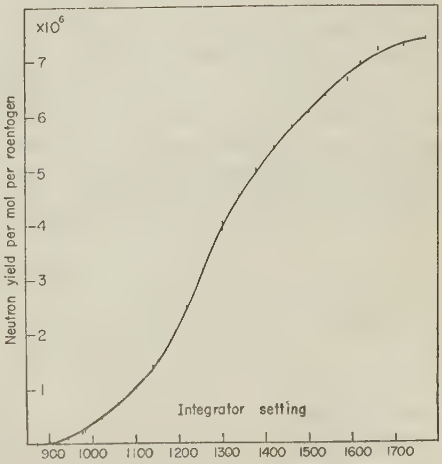

Fig. 4-3. Activation curve for $Ag^{107}(\gamma, n)Ag^{106}$.

represents the relative value. The cross section curves were deduced from activation curves of Fig. 4 by means of photon difference method[14].

Cross section curves of each element are shown in Fig. 5.

As the shape of cross section curve depends sensitively upon a little variations of activation curve, we made three activation curves independently from each successive activation points. These three curves then yield then three cross section curves. The three γ ray resonance energies and the widths at half-maximum thus obtained fall within ±0.5 MeV and ±0.3 MeV respectively. In the case of neutron closed shell nuclei Zr^{90} and Mo^{92}, giant resonance widths show about 2~3 MeV, and $E_{\max}$ about 16.5 MeV for both. Above 18 MeV, cross sections are almost constant to 23 MeV and its value is comparatively large as seen in Fig. 5. This scheme may be explained by the comparatively large contribution of direct process to total cross section in this energy region. In order to check above effect more precisely, it is desirable to measure angular distribution of neutrons from $Y^{90}(\gamma, n)$ reaction in this energy region.

Maximum cross section was measured as 190 mb in $Mo^{92}(\gamma, n)Mo^{91}$ reaction. In the case of Ag^{107}, the width of giant resonance was about 5.3 MeV which was factor of 2 larger than for Zr^{90} and Mo^{92}. $E_{\max}$ of Ag^{107} was about 14.0 MeV, and the cross section is measured as 240 mb at this energy. A small peak was found near threshold in contrast to Mo^{92} case, which is supposed to be $E2$ absorption by the surface oscillation.

All the data concerning the cross sections for each element are represented in Table II, in which the 5th column shows the calculated values of sum rule. In the case of Mo^{92}, the measured σ_{int} deviates largely from the sum rule. But in this case, (γ, p) cross section was anormally large[15] in these mass number region, and if we add this to (γ, n) cross section, integrated cross section will agree fairly good to the sum rule. In the case of Ag^{107},

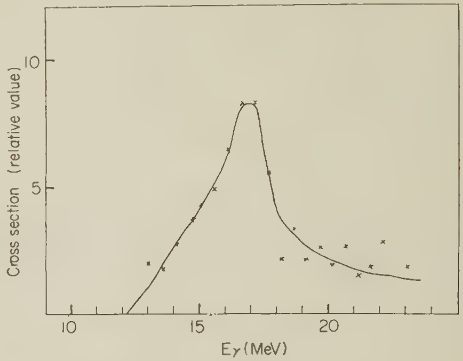

Fig. 5–1. Cross section curve for $Zr^{90}(\gamma, n)Zr^{89*}$.

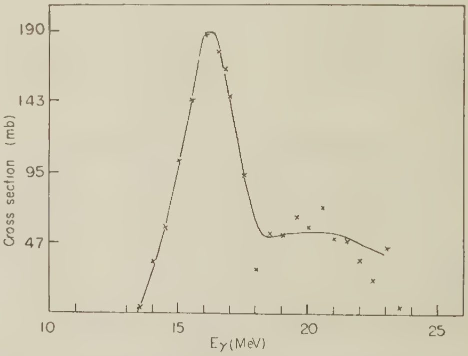

Fig. 5–2. Cross section curve for $Mo^{92}(\gamma, n)Mo^{91}$.

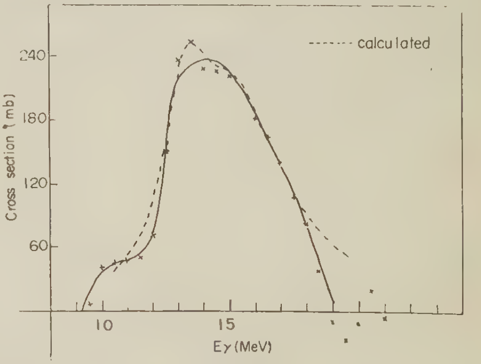

Fig. 5–3. Cross section curve for $Ag^{107}(\gamma, n)Ag^{106}$.

Table II. Summary of cross section measurement.

Reaction	$E_{\max}$ (MeV)	$\sigma_{\max}$ (mb)	Γ (MeV)	σ_{int}	* $\int_0^\infty \sigma dE$
$Zr^{90}(\gamma n)Zr^{89m}$	16.8		2.9		
$Mo^{92}(\gamma n)Mo^{91}$	16.0	190	2.7	1.48 MeV–b	1.92
$Ag^{107}(\gamma n)Ag^{106}$	14.0	240	5.3	2.48 MeV–b	2.21

* We assume $x=0.5$.

present data agree with the sum rule.

The giant resonance of Ag^{107} has large width compared to Mo^{92} and Zr^{90} case. Let us assume that, as Danos[4] has predicted, this giant resonance is split into two resonances which can not be resolved on account of their broadness, and that each resonance shape is of Lorentz type. Then we can express the (γ, n) cross section in the following way as Fuller[5] et al. have done.

$$\sigma(\gamma, n)=\frac{\sigma_a}{1+[(E^2-E_a{}^2)/E\Gamma_a]^2}+\frac{\sigma_b}{1+[(E^2-E_b{}^2)/E\Gamma_b]^2} \tag{1}$$

where E_a, E_b represent two resonance energy. Γ_a, Γ_b are full widths of two resonances lines at half maxima. σ_a and σ_b were adjusted by observed maximum cross section value, and the most suitable values of E_a, E_b, Γ_a and Γ_b which give the best fit to observed cross section curve are given by

$$\left.\begin{array}{ll} E_a=13.3\,\text{MeV} & \Gamma_a=2\,\text{MeV} \\ E_b=15.3\,\text{MeV} & \Gamma_b=4.5\,\text{MeV} \end{array}\right\} \tag{2}$$

$\Gamma_a=2.0$ MeV, $\Gamma_b=4.5$ MeV seems reasonable if we compare with those of Mo^{92} and Zr^{90}. The cross section curve by above parameters was shown by the dotted line in Fig. 6. According to the calculation of Danos, who treated a nucleus as spheroidal shape, the ratio of two resonance energy was represented by

$$E_a/E_b=0.911a/b-0.089 \tag{3}$$

where b and a are the length of minor and major axis of spheroid.

Substituting $E_a=13.3$ MeV, $E_b=15.3$MeV into eq. (3), we get:

$$a/b=1.164\,. \tag{4}$$

On the other hand the intrinsic quadrupole-moment is given by:

$$Q_0=\frac{2}{5}Zr_0{}^2A^{2/3}\left[\left(\frac{a}{b}\right)^2-1\right]\Big/\left[\frac{a}{b}\right]^{2/3} \tag{5}$$

substituting (4) into (5) and taking $r_0=1.20\times10^{-13}$ cm we get

$$Q_0=(1.9\pm0.7)\times10^{-24}\,\text{cm}^2 \tag{6}$$

This result agrees very well to the value, $Q_0=1.7$ or $1.9\times10^{-24}\,\text{cm}^2$ which was obtained from the Coulomb excitation experiment[16].

Thus we suppose that in the case of Ag^{107}, the giant resonance is perhaps split into two resonances, but we cannot resolve by their broadness.

Acknowledgement

The authors are indebted to Professor M. Miwa and Dr. K. Okamoto for valuable discussion. They are also ought to say thanks Mr. K. Kageyama and Mr. T. Inoue for operating the betatron.

References

1) R. Nathans and J. Halpern: Phys. Rev. **93** (1954) 437.
2) R. Nathans and P. J. Yergin: Phys. Rev. **98** (1955) 1296.
3) K. Okamoto: Phys. Rev. **110** (1958) 143.
4) M. Danos: Nuclear Phys. **5** (1958) 23.
5) E. G. Fuller and M. S. Weiss: Phys. Rev. **11** (1958) 560.
6) J. H. Carver and W. Turchinetz: Proc. Phys. Soc. London **73** (1959) 69.
7) N. Mutsuro and M. Kimura: (to be published).
8) Warren L. Bendel et al: Phys. Rev. **111** (1958) 1297.
9) L. Katz, H. E. Johns et al: Phys. Rev. **82** (1951) 271.
10) L. Katz and R. N. Haslam et al: Phys. Rev. **95** (1954) 464.
11) Fox. R. E.: Phys. Rev. **95** (1954) 613A.
12) W. E. Ogle and L. J. Brown: Phys. Rev. **78** (1950) 63.
13) R. Basile: Ann. Phys. **2** (1957) 267.
14) L. Katz and A. D. W. Cameron: Canad. Phys. **29** (1951) 518.
15) W. A. Butler and G. M. Almy: Phys. Rev. **91** (1953) 58. E. V. Weinstock and J. Halpern: Phys. Rev. **94** (1954) 1651.
16) N. P. Heydenberg and G. M. Temmer: Phys. Rev. **95** (1954) 861.

JOURNAL OF THE PHYSICAL SOCIETY OF JAPAN, Vol. 14, No. 12, DECEMBER, 1959

Search for the "Anomalous" Scattering of Mu-Mesons (On the Apparatus using a Delayed Coincidence Method)

By Takashi KITAMURA

Institute of Polytechnics, Osaka City University, Osaka

(Received May 22, 1959)

As a result of the discussion about the experimental results on the anomalous scattering of mu-mesons so-far obtained, we came to the conclusion that their apparatuses have two principal deficiency in reaching a definite information: uncertainties in determining the identity and momenta of mu-mesons.

Hence, we have a plan to complete the experiment by using an arrangement of Wilson cloud chamber and G. M. counters which is capable of selecting only mu-mesons, their momenta being determined with a thick absorber within a narrow range of $\left(1^{+0.15}_{-0.20}\right)$ GeV/C and a delayed coincidence method to separate mu-mesons from the other particles. In this paper, moreover, we estimated the possibility to trigger this arrangement with other particles than mu-mesons and found the contribution to be quite negligible.

§ 1. Introduction

It has been believed[1] that mu-meson behaves in many respects as an heavy electron whose mass is about 207 times larger than that of the electron; its interaction with matter is caused mainly through the electromagnetic field in addition to a very weak Fermi type interaction. In the first stage, the idea that the spin of mu-meson should be half-integer was presumed from experimental informations in which the conclusion rested on the assumed identification of the light neutral particles in $\pi-\mu$ decay, μ^--capture and $\mu-e$ decay with the neutrino of β-decay. The analysis of cosmic ray bursts experiment also showed[2] that the spin of mu-meson was smaller than or equal to unity. However, a number of experiments about the scattering of cosmic ray mu-mesons have shown strange results[4)-10)]. This so-called "anomalous" scattering deviates from the scattering distribution predicted by electromagnetic interactions alone. The experimental aspects of the anomalous scattering so far obtained are tabulated in Table. Among these experiments about the mu-meson scattering, all but one performed by Amaldi *et al.*[3] clamied to have observed the anomalous scattering for various momentum regions.

On the other hand, while these researches for the anomalous scattering were being performed, the similarity of the mu-meson to the electron has become almost conclusive by the Columbia experiment[11] that the spin of the mu-meson is half integer and its g-factor is 2.0064 ± 0.0048. Accordingly, we can consider that the mu-meson is the normal Dirac particles as far as its static properties are concerned. In high energy mu-mesons, however, there may occur some anomalies in its dynamic properties which could be revealed at high energies. Moreover, the smallness of the Compton wave length of the high energy mu-meson might faciliate to examine the deviation (if any) of the electromagnetic interaction at small distances from the conventional one. Therefore, the experiment to determine whether the anomalous scattering is real or false, is very significant for the dynamic properties of the mu-meson. As far as possible in avoiding ambiguities which were apparent in the previous observations, we have completed the measurement on the scattering distribution of mu-mesons by using a delayed coincidence method.

The purpose of this paper is to discuss the utility of the experimental arrangement using a delayed coincidence method. We shall critically discuss in § **2** on various theories given up to date which attempted the interpretation on a presence of the anomalous scattering and also in § **3** on the experimental results of mu-meson scattering obtained so-far. On the basis of these discussions we shall show the

Table Recent experiments on the mu-meson scattering.

Reference	method*	scattering material	momentum region	minimum angle for anomalous scattering	cross section for anomalous scattering cm²/nucleon	number of triggering particles
Amaldi and Fidecaro (1950)	counter-hodoscope (sea-level)	6 cm of iron	$200<E<320$ MeV $320<E$ MeV E: energy	20 degrees 20 degrees	0.8×10^{-28} 0.04×10^{-28}	249,168 204,914
Whittemore and Shutt (1952)	method III (sea-level)	5 cm of lead	$0.3\leq E\leq 3.1$ GeV	Result consistents with distribution expected from Moliére's scattering theory for point charge nucleus.		~7000
George, Redding and Trent (1953)	method I (60 m.w.e. underground)	2 cm of lead	$200>E$ MeV	15 degrees	2×10^{-28}	1071 (0 cm lead below chamber) 1625 (5 cm lead below chamber)
			$200<E$ MeV		$<\sim10^{-29}$	1490 (10 cm lead below chamber)
Kannangara and Shrikantia (1953)	nuclear emulsion (60 m.w.e. underground)	Silver, bromine etc.	$100<p\beta$ 600 MeV/c P: momentum $C\beta$: velocity	7 degrees	15×10^{-28}	
Leontic and Wolfendale (1954)	method I (under 1 meter of lead at sea-level)	2 cm of lead	$250<p$ MeV/c	10 degrees	1.5×10^{-28}	625 photographs
McDiarmid (1954) (1955)	method II (26 m.w.e. underground)	2 cm of lead	250 MeV/c$<p\beta<$1.5 GeV/c 600 MeV/c$<p\beta<$3 GeV/c	Result consistents with distribution expected from Moliére's scattering theory for point charge nucleus.		3016 traversals 17972 traversals
		2.54 cm of iron	600 MeV/c$<p\beta<$3 GeV/c			18420 traversals
Lloyd and Wolfendale (1955)	method III (sea-level)	50.9 g/cm² lead	600 MeV/c$<p\beta<$3 GeV/c $2<p\beta<15$ GeV/c			1678 2581
		54.7 g/cm² iron	600 MeV/c$<p\beta<$3 GeV/c $2<p\beta<15$ GeV/c			1705 2608
Lloyd, Rössle and Wolfendale (1957)	method III (sea-level)	1 cm of lead	$5<P<100$ GeV/c			272

* Method I, II and III are various methods of momentum determination: method I means "not measured but inferred from spectrum", method II "estimated from observed scattering" and method III "magnetic curvature".

reason why the delayed-coincidence-apparatus is superior to the previous. Finally, in § 4 and 5, we shall discuss on possibilities that the other particles beside mu-meson might trigger the apparatus.

§ 2. Various Theories Concerning the Anomalous Scattering of Mu-meson

Various attempts have been made in order to explain the observed results showing the anomalous scattering. Firstly, different authors[12),13)] calculated the elastic and the inelastic scattering of mu-meson by nucleus to the first order of Born's approximation using a single particle nuclear model. It was found that these theoretical results are too small to explain the observed distributions at large angles. Secondly, a direction to interpret it in terms of non-Coulomb interactions between fast mu-meson and nucleon was taken as a matter of course[14)]. This attempt, however, was excluded by further observations that the cross section for the anomalous scattering should be proportional to the square of the mass number of material used[8),9)]. Davidson[15)] suggested that the giant nuclear dipole resonance could be responsible for the large angle scattering. Although such a phenomenon was certainly found[16)], the observed cross section was too small to interpret that of the anomalous scattering. Also this event would be caused only by low energy mu-mesons because an existence of the giant resonance is at only γ-rays near 20 MeV, so that Davidson's suggestion couldn't account for the anomalous scattering of high energy mu-mesons which has been observed after publishing of this interpretation. Afterwards, Gatto[17)] studied an influence of correlations between the constituent nucleons on the scattering of mu-meson by a nucleus. Tidman[18)] and Fowler[19)] individually evaluated an influence of the anomalous magnetic moment of mu-meson on the large angle scattering. However, both influences also were too small. It has recently been suggested by Fowler[20)] that the large angle scattering may possibly be interpreted by a mechanism which essentially is the elastic counterpart of the star production by mu-mesons utilizing the result calculated by phase shift analysis about high energy electron scattering of Yennie *et al.*[21)] The reason for the apparent success of this theory is essentially due to the fact that he assumed a large inelastic cross section, that is, 4 mb per lead nucleus for incident mu-mesons having energies greater than 1 GeV to transfer an energy larger than 150 MeV to a nucleus. George and Evans[22)], however, have shown that the observed cross section for 1_p stars and showers by mu-mesons at various depths underground is average $(4.6\pm0.5)\times10^{-30}$ cm^2 /nucleon and the cross section for 0_p stars are only 1/4 of its value. Moreover, it has been suggested by the author and Oda[23)] that a part of the former and greater part of the latter might possibly be attributed to secondary pi-mesons produced by mu-mesons. This suggestion is supported by the latest McDiarmid's experiment[24)] about nuclear disintegrations of mu-mesons. Therefore, the value of 4 mb for the inelastic cross section is too large to be acceptable. Fowler also argued that the cross section of producing stars and showers rises fairly rapidly in energies above 10 GeV and it may become larger than 4 mb. On the contrary, the study of underground hard showers in our laboratory[25)] has shown that secondary high energy pi-mesons produced by mu-mesons increase the apparent cross section for mu-mesons-producing-showers, so that the genuine inelastic cross section for high energy mu-meson showers should be smaller than the observed value. Thus, we have had, up to present, no theory possible to interpret the anomalous scattering of mu-meson.

§ 3. Discussion on the Anomalous Scattering Results to Date

We shall now proceed to examine in detail each of the typical anomalous scattering results shown in Table.

George *et al.*[5)] asserted existence of the anomalous scattering of mu-meson near 200 MeV from their observation with a circular cloud chamber at a depth of 60 meters of water-equivalent (m.w.e.) underground. Generally, Coulomb scattering distribution of mu-meson which should be used for determining the magnitude of anomalous scattering degrees, is very sensitive to the intensity of low energy mu-mesons at that depth. Wolfendale *et at.*[9)], Nishida *et al.*[26)] and the author[27)] independently concluded that the results could not be accepted as evidence of the existence of the anomalous scattering of mu-meson because of an uncertainty in the knowledge of the spectrum of low energy particles traversing the cloud chamber. McDiarmid[8] also concluded that experimental results for mu-mesons of energies of a few hundred MeV were suffered from a difficulty at the experimental arrangement to distinguish between Moliére's (point charged model)[28] and Cooper and Rainwater's (extended charged model)[29] distributions because of very large angles of the mu-mesons scattered. Moreover, the bearing of secondary pi-mesons originated from hard showers of mu-mesons, discribed in the preceding, can have the most influence upon the information about the anomalous scattering at this energy region. In this way, when the anomalous scattering of low energy mu-mesons becomes more and more questionable, the conclusive disproof was obtained by means of a measurement on the pair production of mu-mesons by high energy γ-rays which was performed in 1956 by Masek *et al.*[30] The observed yield was compatible with the theoretical cross section which had been derived by modifying the conventional formula for the pair production of fermions by photons in a Coulomb field for the effect of a finite nuclear size. The energy transferred to nucleus in this measuremeut was between 40 MeV and 200 MeV. Thus, it was definitely concluded that there is little or no anomalies of mu-mesons below the corresponding energy.

In the experiment of McDiarmid[8], a multiplate cloud chamber was used at a depth of 26 m.w.e. underground. The meson momenta were estimated through multiple scattering measurements in six two cm thick lead plates and divided into three groups: group I (150 MeV/C $<p\beta<$ 1000 MeV/C), group II (300 MeV/C $<p\beta<$ 2200 MeV/C) and group III (600 MeV/C $<p\beta<$ 5 GeV/C). He asserted scattering, interpreted as anomalous, was found in Group III. The present author has investigated what energies of mu-meson affected much on the conclusion in this measurement. By using the Cooper and Rainwater theory, $f(p\theta)$, and momentum spectrum of McDiarmid's group III, $S(p)$, the calculated curves of $f(p\theta)\cdot S(p)dp$ at various values of scattering angle θ have been calculated. Those curves are drawn in Fig. 1. From the figure it is clear that the scattering distribution at large angles (larger than 5 degrees) is completely determined by an intensity of mesons in the 0.6~1.5 GeV/C region. This fact indicates that an evaluation of the intensity of mu-mesons having momenta near the threshold in the apparatus used has a great influence on the value of Coulomb scattering distribution and, as a result of it, on the conclusion led by such a measurement.

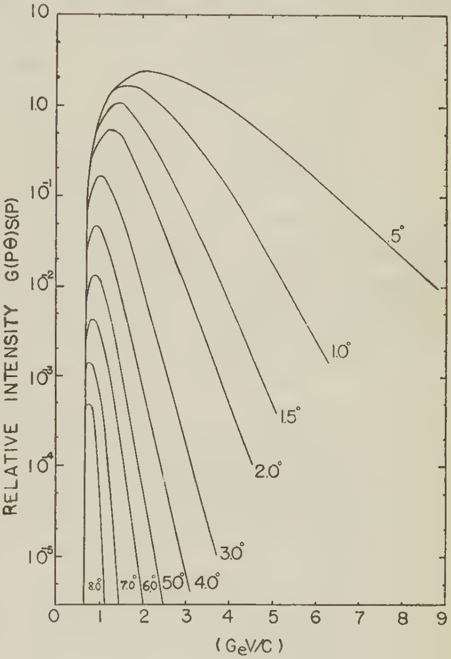

Fig. 1. Function $f(p\theta)\,S(p)\,dp$ at McDiarmid's experiment.

Nevertheless, McDiarmid's experimental result would have a great measuring error in determining momenta of the mesons because of using of the method of multiple scattering measurement as discussed in Olbert's paper[31] which first presented the method. In this connection, the comparison of McDiarmid's experimental points with our Coulomb scattering distribution calculated by the above-described $\int_{\theta_0}^{\infty} d\theta \int_{p_0}^{\infty} f(p\theta)\cdot S(p)dp$, represented no anomalous scattering that quite agreed with a conclusion independently obtained by Nishida *et al.*[26] from their analysis of McDiarmid's result. This fact may be considered that the experimental method of McDiarmid is very hard on giving the definite conclusion. Thereupon, we cannot but agree that McDiarmid's evidence is not conclusive.

In the following, we shall refer to the experiments which bear on the scattering of higher energy mu-mesons, using a magnetic cloud chamber. A main problem associated with this method is in an accurancy of the momentum determinations. In the magnetic cloud chamber, it is usual to measure the residual-value-curvature, ΔC, of tracks of high speed in case of no magnetic field. Corresponding to this curvature there is a "maximum detectable momentum". According to the data given in Wilson's book[32], however, occasional tracks may have large unexpected apparent curvatures; a distortion which produces a curvature of nearly $1.2\,\mathrm{m}^{-1}$ can occur in one of 40 tracks in a cloud chamber which has measured value of $0.16\,\mathrm{m}^{-1}$ for ΔC. In a measurement of the momentum spectrum of mu-mesons in a chamber for which $\Delta C = 0.2\,\mathrm{m}^{-1}$, we found that one track in 50 had a curvature of nearly $1.5\,\mathrm{m}^{-1}$ and among them some distorted tracks were almost completely expressed with only a parabola equation that absolutely cannot be separated from their true curvature values[34]. Experiments in which very rare events are measured, show clear that this sort of distortions can be misleading and for this reason we feel that magnetic cloud chamber measurements of mu-meson scattering must be regarded with caution.

There is further the question of small admixture of protons in the mu-meson "beam". There is some evidence that the elasticity of high energy proton-proton collisions may have[35] a value near 0.7 and the recent data of accelerator shows[36] an unexpected large value of elasticity in collisions of proton-proton near 2 or 3 GeV, so that the absorption mean free path of protons in the atmosphere would be larger than the 200–300 g/cm² previously assumed. This has the effect of increasing

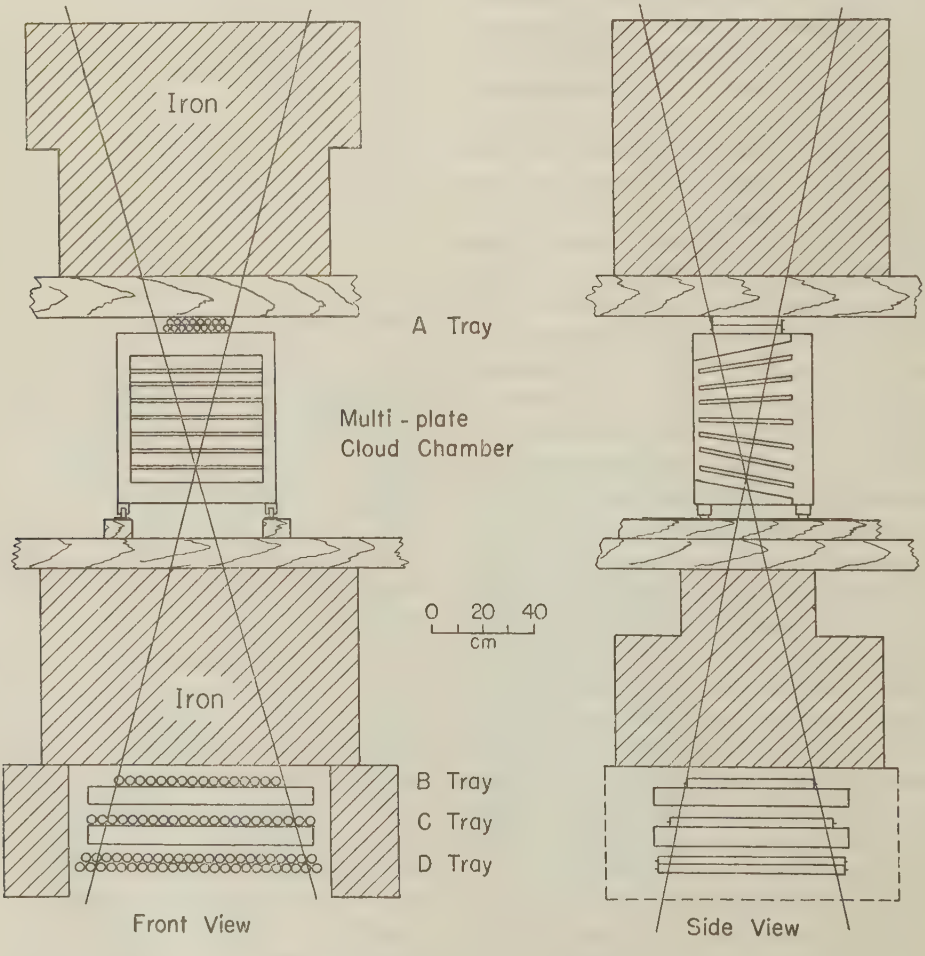

Fig. 2. Arrangement of apparatus.

the proton intensity. A suitable choice of the longer absorption mean free path may bear the proton contamination which is responsible for the anomalous scattering observed by Lloyd *et al.*[9]

Thus, it is hard to draw a very definite conclusion of existense of the anomalous scattering for mu-mesons from the measurements up to date. At the present that its existence in low energy mu-mesons has been excluded by the mu-pairs experiment, it is accordingly the most importance to measure the scattering distribution of moderate energy mu-mesons. Our present experiment was planned with the method capable of selecting only mu-mesons, their momenta being determined with a thick absorber and a delayed coincidence method within a narrow range of $\left(1^{+0.15}_{-0.2}\right)$ GeV/C.

§ 4. Experimental Arrangement

The arrangement is illustrated in Fig. 2. An upper absorber consists of iron block having a density of 7.0 g/cm^3 (its error ±4.5 %) and total thickness of 1.0 metre. It is expected that incident nuclear-active particles from the atmosphere decrease considerably under the iron absorber but incident mu-mesons do not. A cloud chamber has an effective volume $47\times35\times50$ cm^3 and contains seven one cm lead plates. The thickness 75 cm of iron absorber below the chamber serves to define a residual range of particles passing through this absorber corresponded to a momentum of 1 GeV/C. Iron was used for an economical reason because it is almost equal to lead from view point of capability of absorbing nuclear-active particle. After traversing the iron, the mesons stopped and decayed in either of two 8 cm thick carbon slabs. Two rather than just one carbon slab were used to increase the detection efficiency. The triggering method of the present apparatus is $AB-D+(B \text{ or } C \text{ or } D)_{\text{delay}}$. After passing through trays A and B (i.e. through the chamber), such mu-mesons as come to rest in the carbon slab and decay into electron are possible to trigger this arrangement. In the triggering method, the anti-coincidence of D tray with AB coincidence pulses was used for excluding a chance delayed-coincidence between ABD prompt coincidence pulses and pulses in single discharge of tray B, C or D. Each counter in tray B, as well as in trays C and D were hodoscoped for the prompt pulse. Whenever a delayed coincidence occurred, neon bulbs were photographed together with the triggered cloud chamber. In this way the track in the cloud chamber could be checked for their alignment with the struck counters.

§ 5. Other Particles Contributions Beside Mu-meson

It is conceivable that the present apparatus may be triggered by other particles than mu-mesons. We shall evaluate those phenomena using Olbert's production spectrum[37] which is an over-all energy spectrum of secondary pi-mesons produced by nucleon-air nucleus collisions. Difference between the energy distributions of secondary particles in nucleons-iron and air nucleus collisions is represented by (mass number)$^{1/3}$ law. Henceforth, we shall call the above iron absorber as absorber A and the lower iron absorber as absorber B. Let x g/cm^2 and y g/cm^2 represent each one of upward measured distances from each bottom surface of those absorbers A and B, respectively.

[I] Delayed coincidence triggering

A) *Incident nucleons*

We shall treat only vertical incident particles because inclined incident ones are much fewer. By doing this these calculations will be able to be simplified. The possibility that the present apparatus may be triggered by $\pi-\mu-e$ decay event in the process discussed below, is caused by the fact that a lifetime of 10^{-8} sec in $\pi-\mu$ process is quite negligible for the time of 10^{-6} sec in $\mu-e$ process.

a) A pi-meson, having been produced in a penetrating shower in the upper absorber A, traverses the chamber and the absorber B and comes to rest in the carbon and decays to a electron through the $\pi-\mu-e$ process.

The frequency may be expressed in the following form,

$$\int_0^{700(\mathrm{Fe})} \exp\left\{-\frac{1030(\mathrm{air})}{\lambda_{\mathrm{abs}}(\mathrm{air})}\right\} \exp\left\{-\frac{700(\mathrm{Fe})-x(\mathrm{Fe})}{\lambda_{\mathrm{abs}}(\mathrm{Fe})}\right\} G(x(\mathrm{Fe})+79(\mathrm{pb})+525(\mathrm{Fe});\ 1030(\mathrm{air}))$$
$$\times \exp\left\{-\frac{x(\mathrm{Fe})525(\mathrm{Fe})}{\lambda_{\mathrm{col}}(\mathrm{Fe})}\right\} \exp\left\{-\frac{79(\mathrm{pb})}{\lambda_{\mathrm{col}}(\mathrm{pb})}\right\} \exp\left\{-\frac{\mu}{p\tau}(x(\mathrm{Fe})+525(\mathrm{Fe})+79(\mathrm{pb}))\right\} dx \quad [\mathrm{cm}^2\,\mathrm{sec}^{-1}\,\mathrm{sr}^{-1}]\,.$$

All lengths are measured in units of g/cm². (air) symbol refers to thickness of air, (Fe) to thickness of iron and so on. p attributes to a momentum of a secondary pi-meson, μ to its rest energy and τ to its mean lifetime. The first term in the integrand represents a feature of the nucleonic component decreasing as an approximately exponential function with an absorption mean free path in air, $\lambda_{\mathrm{abs}}(\mathrm{air})$, from the top of atmosphere to sea-level (1030 g/cm² air). Function $\exp\left(-\frac{1030}{\lambda_{\mathrm{abs}}}\right)\cdot G$ (range; 1030) bases on the Olbert's assumption that meson-producing component is absorbed exponentially throughout the atmosphere with an effective absorption mean free path. The second term shows the probability that the incident nucleons being absorbed with the absorption mean free path λ in absorber A may survive to a producing point x g/cm². The third term is a value of Olbert's production spectrum at a range $(x(\mathrm{Fe})+525(\mathrm{Fe})+79(\mathrm{pb}))$ g/cm², namely, an intensity of pi-mesons having the residual range which corresponds to total thickness of remaining layers in absorber A, absorber B and lead plates in the chamber. These pi-mesons come to rest just within the carbon layer. So this intensity must be given by a integrated value over a thickness of the carbon layer. The fourth and fifth terms show the probability that these pi-mesons having the above range do not interact with matter during passing the passage of their range. We should use a collision mean free path instead of an absorption mean free path in those terms because the pi-mesons would lose almost all of their energy on account of their low energy even in nuclear interactions within the layers which are to be passed. The sixth term expresses the survival probability of pi-mesons that the pi-mesons don't decay to mu-mesons in performing their passing range.

By comparing a calculated numerical result of the above equation and an intensity of mu-mesons having 1 GeV/C to be measured under absorber A, $(3\times10^{-6})\times$(thickness of carbon layer) $[\mathrm{cm}^{-2}\,\mathrm{sec}^{-1}\,\mathrm{sr}^{-1}]$[38], we can get an order of the contribution in this case. The ratio, using the values of $\lambda_{\mathrm{abs}}(\mathrm{Air})=125$ g/cm² air, $\lambda_{\mathrm{abs}}(\mathrm{Fe})=200$ g/cm² iron, $\lambda_{\mathrm{col}}(\mathrm{Fe})=130$ g/cm² iron and $\lambda_{\mathrm{col}}(\mathrm{pb})=160$ g/cm² lead, was calculated to be 5.0×10^{-7}.

b) A pi-meson, produced as in *a*) above, decays from within the lower absorber, the mu-meson travelling on to decay in the carbon.

With a similar treatment in case *a*) this intensity will be express as follows.

$$\int_0^{700(\mathrm{Fe})} \exp\left(-\frac{1030(\mathrm{air})}{\lambda_{\mathrm{abs}}(\mathrm{air})}\right) \exp\left(-\frac{700(\mathrm{Fe})-x(\mathrm{Fe})}{\lambda_{\mathrm{abs}}(\mathrm{Fe})}\right) \int_0^{525(\mathrm{Fe})} G(x(\mathrm{Fe})+79(\mathrm{pb})+(525-y)(y))$$
$$\times \exp\left(-\frac{x(\mathrm{Fe})}{\lambda_{\mathrm{col}}(\mathrm{Fe})}\right) \exp\left(-\frac{79(\mathrm{pb})}{\lambda_{\mathrm{col}}(\mathrm{pb})}\right) \left\{1-\exp\left(-\frac{\mu}{p\tau}y(\mathrm{Fe})\right)\right\} dxdy \quad [\mathrm{cm}^{-2}\,\mathrm{sec}^{-1}\,\mathrm{sr}^{-1}]\,.$$

The last term represents the probability that incident pi-mesons decay into mu-mesons through $\pi-\mu$ process within the absorber B. The remaining terms have the same physical meanings as adopted in *a*). In using the same mean free path values, we obtained 1.5×10^{-6} as a ratio of this calculated result to the intensity of the mu-mesons.

c) A proton incident from the atmosphere, traverses the upper iron absorber A to produce a pi-meson which goes on to decay in the carbon.

This intensity will be

$$\frac{1}{2}\int_0^{525(\mathrm{Fe})} \exp\left(-\frac{1030(\mathrm{air})}{\lambda_{\mathrm{abs}}(\mathrm{air})}\right) \exp\left(-\frac{700(\mathrm{Fe})}{\lambda_{\mathrm{abs}}(\mathrm{Fe})}\right) \exp\left(-\frac{79(\mathrm{pb})}{\lambda_{\mathrm{col}}(\mathrm{pb})}\right) G(y(\mathrm{Fe}))$$
$$\times \exp\left(-\frac{525(\mathrm{Fe})-y(\mathrm{Fe})}{\lambda_{\mathrm{abs}}(\mathrm{Fe})}\right) \exp\left(-\frac{y(\mathrm{Fe})}{\lambda_{\mathrm{col}}}\right) \exp\left(-\frac{\mu}{p\tau}y(\mathrm{Fe})\right) dy \quad [\mathrm{cm}^{-2}\,\mathrm{sec}^{-1}\,\mathrm{sr}^{-1}]\,.$$

The factor outside the integral is due to the view that only proton flux in nucleonic component is favourable to this case. We may use collision mean free path at the third term because an occurance of any interactions of the incident particles within lead plates in a chamber will be able to be noticed with the chamber photographs.

The ratio between this calculated result and the mu-mesons intensity was found to be 4.0×10^{-6}.

d) A proton incident from the atmosphere traverses the upper iron absorber and cloud chamber as in *c*) above, and produces a π meson which decays within the lower absorber, the mu-meson traveling on to decay in the carbon.

An intensity of this event was estimated with a similar treatment and the ratio to the mu-meson was 1.0×10^{-6}.

In order to distinguish the Cooper and Rainwater theory for finite nucleus from the Moliére theory for point nucleus, it is necessary to get data of about 5000 traversals as estimated from these differential scattering probability. The data would be got with about 1000 particles of mu-mesons scattered in five plates in middle of the chamber as their scattering phenomena in the top and bottom plates might be rejected because of the distortions of those tracks there. Therefore, thinking of the number of mu-mesons to be measured, the present result that a total intensity of the above-described events caused by nucleons and pi-mesons have been led to a rate of 7.0×10^{-6} per the mu-meson intensity, suggests that their contributions to the apparatus would be quite negligible for the mu-mesons even if actual mean free path values for absorption and collision were longer than those values adopted in the above calculations. Also, bearing in mind that almost all of the above-discussed events producing pi-mesons just capable of triggering the present apparatus are accompanied with the other secondary particles of energies which have a possibility of passing across *D* tray, we can say it is nearly impossible to trigger the apparatus for these events by virture of an action of anti-coincidence of *D* tray. In practice, on our measuring results of about 1000 particles by means of this equipment, we have observed none of such cloud chamber photographs which had other coinciding secondary particles than mu-mesons triggering the apparatus (hard showers in absorber A), or had a triggering mu-meson and a lightening of many neon bulbs in a hodoscope *B*-tray (hard showers in absorber *B*). This fact seems to give support to the view that our above conclusion on the events caused by nucleons gives correct evaluations.

B) *Incident pi-mesons*

From the preceding results, the similar events arised from incident pi-mesons from the atmosphere instead of incident nucleons are known to be quite ignored because the pi-meson intensity at sea-level is assumed to be only few percent of the nucleon's one.

C) *Incident mu-mesons*

a) Nuclear showers of mesons

Although it is much less likely, a pi-meson having been produced in a nuclear shower of mu-mesons in the absorber *A*, may possibly produce a triggering of the apparatus. So long as we use the semi-classical procedure of Williams and Weizsäcker[39] as a cross-section for production of pi-mesons by fast mu-mesons, a ratio of the intensity of the pi-mesons to that of the mu-meson triggering the apparatus was no more than a degree of 2.0×10^{-5}. In addition, most of the event is impossible to trigger the apparatus by virture of the action of anti-coincidence in *D* tray because of the narrowness of angles between the pi-mesons produced and the parent mu-mesons.

b) Nuclear disintegration initiated by mu-mesons

This is a low energy star produced by mu-mesons which may be very nearly regarded as an elastic process. If the recoiling nucleons have not enough energy to penetrate a thickness of one cm of lead plates in the cloud chamber, such a event seems to be a scattering phenomenon.

An angle of scatter of an incident mu-meson of energy E_μ in this event is given from the conservation of energy and momentum by approximate elastic process treatment. This expression is as follows;

$$\theta = \sqrt{\frac{2m_pC^2E_p}{E_\mu{}^2 - E_\mu E_p}}$$

where m_pC^2 is a rest mass energy of proton and E_p is an energy of recoiling nucleons.

On the other hand, the cross section for a production of the event with energy E_p released by a fast mu-meson of energy E_μ has been expressed by the Williams and Weizsäcker expression[39),

$$\sigma(E_\mu, E_p)=\left(\frac{2\alpha\sigma_{h\nu}}{\pi}\right)\frac{dE_p}{E_p}\ln\left(\frac{E_\mu}{E_p}\right)$$

where α is a fine structure constant and $\sigma_{h\nu}$ is the cross-section for the production of stars by photons. Now, we can put a value of 1 GeV in E_μ of this expression because energies of measured mu-mesons have been taken as the value. The angular distribution of mu-mesons scattered with this event is obtained from the above two equations. As shown in Fig. 3, the differential scattering probability near 7 degrees was evaluated to be of the order of 10^{-6} per degree which was very smaller compared to the Cooper and Rainwater theory.

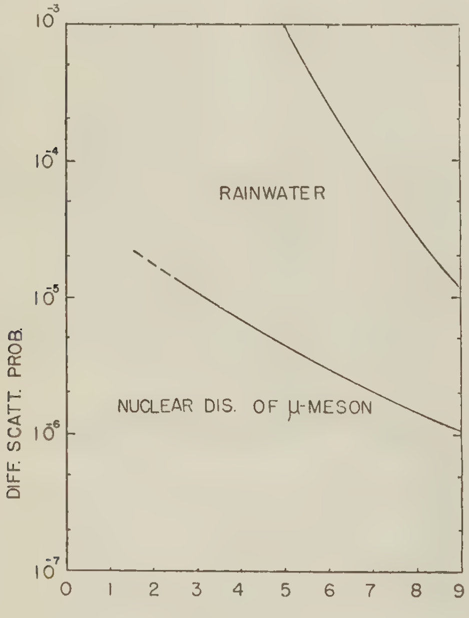

Fig. 3. Contribution of nuclear disintegrations of mu-meson.

[II] Prompt coincidence triggering

In order to clarify a significance of delayed coincidence method, it is better we make also an observation with a prompt coincidence method *ABD* which selects all of particles penetrating through the absorber and the apparatus. When using this method, it is also possible that the counter system may be triggered by a nucleonic component. From Mylori and Wilson's data[40), a ratio between intensities at sea-level of protons having larger than 1 GeV/C and of mu-mesons of the same momentum is assumed to be of 10^{-3} order. Taking an assumption that the proton flux attenuates with an absorption mean free path of 200–300 g/cm² of iron in penetrating absorbers *A* and *B*, the ratio between proton and mu-meson flux to trigger the prompt coincidence-arrangement may decrease to a value smaller than 10^{-4}. Taking into account an existence of an elasticity in nucleon-nucleus collisions, however, we cannot assert that this value is so small as the contribution of these proton does not disturb the observation with the prompt coincidence.

By using the above-discussed apparatus, we have observed the scattering distributions of mu-mesons having momenta of $\left(1^{+0.15}_{-0.20}\right)$ GeV/C determined with the delayed coincidence and having larger momenta than 1 GeV/C with the prompt coincidence. From the observations, we excluded the possibility that the anomalous scattering of mu-meson is in existence at the moderate energies[41).

Acknowledgements

The author is indebted to Professor Y. Watase and Dr. S. Fukui (Osaka University) for many stimulating discussion and valuable suggestions. It is a pleasure to acknowledge the invaluable contributions made by Messers. H. Nishimura and M. Teranaka who assisted in the numerical calculations, equipment setup and experimental runs throughout the course of this work.

References

1) For example, R. E. Marshak: "*Meson Physics*" (McGraw-Hill Book Company), Inc. New York, (1952), chap 6.
2) R. F. Christy and S. Kusaka: Phys. Rev. **59** (1941) 414.
3) E. Amaldi and G. Fidecaro: Nuovo Cim. **7** (1950), 535.
4) W. L. Whittemore and R. P. Shutt: Phys. Rev. **88** (1952) 1312.
5) E. P. George, J. L. Redding and P. T. Trent: Proc. Phys. Soc. **A**, **66** (1953) 533.
6) M. L. T. Kannangara and G. S. Shrikantia: Phil. Mag. **44** (1953) 1049.
7) B. Leontic and A. W. Wolfendale: Phil. Mag. **44** (1954) 1101.

8) B. McDiarmid: Phil. Mag. **45** (1954) 933; **46** (1955) 177.

9) J. L. Lloyd and A. W. Wolfendale: Proc. Phys. Soc. **A, 68** (1955) 1045.

10) J. L. Lloyd, E. Rössle and A. W. Wolfendale: Proc. Phys. Soc. **A, 70** (1957) 421.

11) R. L. Gawrin, L. M. Lederman and M. Weinrich: Phys. Rev. **105** (1957) 1415; T. Coffin, R. L. Garwin, L. M. Lederman, S. Penman and A. M. Sachs: Phys. Rev. **106** (1957) 1108.

12) E. Amaldi, G. Fidecaro and F. Marian: Nuovo Cim. **7** (1952) 533.

13) R. Gatto: Nuovo Cim. **10** (1953) 1559.

13) For example, G. N. Fowler: Proc. Phys. Soc. **A, 68** (1955) 482.

15) J. P. Davidson: Nuovo Cim. **11** (1954) 205.

16) S. Kaneko, T. Kubozoe, M. Okazaki and M. Takahata: Jour. Phys. Soc. Japan **10** (1955) 600.

17) R. Gatto: Nuovo Cim. **12** (1955) 669.

18) D. A. Tidman: Proc. Phys. Soc. **A, 67** (1954) 559.

19) G. N. Fowler: Nuclear Physics **1** (1956) 119.

20) G. N. Fowler: Nuclear Physics **3** (1957) 121.

21) D. R. Yennie, D. G. Ravenhall and R. N. Wilson: Phys. Rev. **95** (1954) 500.

22) E. P. George and J. Evans: Proc. Hhys. Soc. **A, 68** (1955) 825.

23) T. Kitamura and M. Oda: Prog. Theor. Phys. **16** (1956) 252.

24) B. McDiarmid: Phys. Rev. **109** (1958) 1792.

25) S. Higashi, T. Oshio, H. Shibata, K. Watanabe and Y. Watase: in press.

26) Nishida, Oghita and Takaghi: Soryushiron Kenkyu (Japanese) **9** (1955) 411.

27) T. Kitamura, Soryushiron Kenkyu (Japanese) **10** (1956) 477.

28) G. Moliére: Z. Naturforsh **29** (1947) 133; **39** (1948) 78,

29) L. N. Cooper and J. Rainwater: Phys. Rev. **97** (1955) 492.

30) G. E. Masek and W. K. H. Panofsky: Phys. Rev. **101** (1956) 1094; G. E. Masek, A. J. Lazarus and W. K. H. Panofsky: Phys. Rev. **103** (1956) 374.

31) S. Olbert: Phys. Rev. **87** (1952) 319; M. Annis, H. S. Bridge and S. Olbert: Phys. Rev. **89** (1953) 1216.

32) J. G. Wilson: "The principle of Cloud-Chamber Technique" (Cambridge) University Press, London, 1951, chap 6.

33) S. Fukui, T. Kitamura and S. Ozaki: Journal of the Institute of Polytechnics, Osaka City University **5** (1954) 11.

34) N. A. Dobrotin, G. T. Zacepin, S. T. Nikolsky and G. B. Hristiansen, Sup Nuovo Cim, III 635 (1956); "*Proceeding Oxford Conference on Extensive Air Showers*" April, 1956.

35) For example and W. A. Wallenmeyer: Phys. Rev. **105** (1957) 1058.

36) S. Olbert: Phys. Rev. **96** (1955) 1400.

37) B. Rossi: Rev. Mod. Phys. **20** (1948) 537.

38) J. G. Wilson: "*Progress in Cosmic Ray Physics*" North-Holland Publishing Company, Amsterdam, Vol. I, chap 7.

39) M. G. Mylori and J. G. Wilson: Proc. Phys. Soc. **A, 67** (1954) 404.

40) S. Fukui, T. Kitamura and Y. Watase: Phys. Rev. **113** (1959) 315.

JOURNAL OF THE PHYSICAL SOCIETY OF JAPAN, Vol. 14, No. 12, DECEMBER, 1959

Temperature Dependence of Surface Voltage of Silver Bromide

By Sanemi SONOIKE and Hisawo WAKABAYASI
Faculty of Engineering, Chuo University, Tokyo

(Received July 27, 1959)

The temperature dependence of surface voltage of silver bromide crystals has been studied. The change in the surface voltage is due to the change in the ionic space charge voltage between silver metal and silver bromide. Near and on free surface, silver ions and electrons move, and their surface levels change under the condition that their change cancels the voltage change due to the ionic space charge of this side. The curve of surface voltage vs temperature consists of two straight lines, one of which refers to the impurity region, the other refers to the intrinsic region. The more Cd the sample contains, the higher temperature the knee point moves to. The formation energy of Frenkel defect and other quantities were obtained.

§ 1. Introduction

One of us has observed the electron diffraction patterns of silver bromide monocrystal surfaces in the temperature region from room temperature to about 300°C, and found that when the specimens were illuminated by the light from the heater of the furnace, in which they were set, metallic silver precipitated on their surfaces,[1] the amount of which was larger in the impurity region than in the intrinsic region.

If the difference of surface structure between two regions was characteristic to silver bromide, we would be able to observe the surface change in dark with silver bromide. So we intend to find the temperature dependence of the surface voltage of silver bromide monocrystal in dark, which contains known amounts of impurities. In our experiments, cadmium was used as the impurity.

§ 2. Apparatus

Specimens were made from melt in the air, cut by Ti-saw, and lapped and etched by HBr. After these treatments, they were rinsed for about twenty minutes. One side of a silver bromide monocrystal is free, and the other side is coated by silver metal, which were developed by usual development process. The samples are 1 mm thick.

The arrangement around the sample is shown in Fig. 1. The free surface was placed against the reed of a vibrating reed electrometer, which is made of semi-transparent glass coated with platinum. The coated surface of the sample is in contact with a platinum plate, which is the other electrode of the electrometer and is grounded. The sample can be heated by the heater placed under the platinum plate, and is insulated from it by mica plates. The heater is made of platinum. By controlling the heater current the sample can be heated at any arbitrary temperature between room temperature and the melting point of silver bromide. The temperature of the crystal was measured by a copper-constantan thermocouple, which is welded on a silver plate placed on the platinum plate.

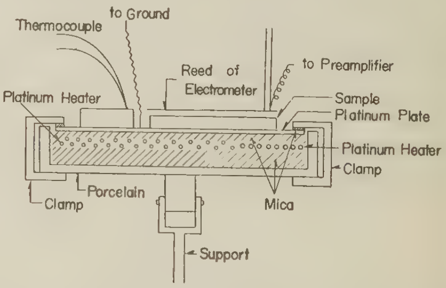

Fig. 1. Schematic arrangement of crystal, electrodes and heater.

The above parts are placed in a bell jar together with the preamplifier, and the system was evacuated to 10^{-4} mm Hg. The bell jar is shielded from electric disturbance and also screened from light. The block diagram of the apparatus is shown in Fig. 2.

For the experiment in the lower temperature region, the platinum heater was replaced by a copper rod, the end of which was immersed in liquid oxygen. By heat conduction of the rod, the temperature of the sample could be made to fall to about 130°C below zero. By immersing the rod in glycerine bath with heater, the sample could be heated to 120°C. But this apparatus was used only for the preliminary test in the lower temperature region.

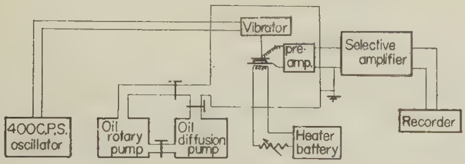

Fig. 2. Block diagram of complete apparatus.

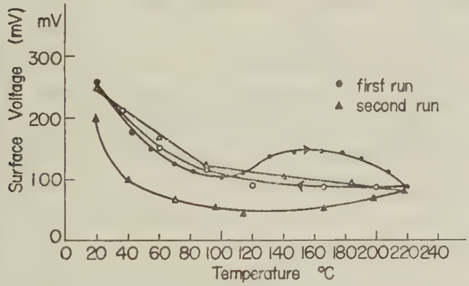

Fig. 3. The temperature dependence of the surface voltage of a silver bromide crystal. After heating the crystal, it cooled along the same path.

§ 3. Experimental Results

In the preliminary test, the upper electrode of the electrometer was contaminated at higher temperatures by evaporated material from the crystal surface and the temperature region was restricted to be below 220°C.

The change of the surface voltage of silver bromide containing 0.01 Mol.–% of cadmium bromide is shown in Fig. 3. In the first run, its surface voltage decreased until the temperature of the crystal was elevated to about 100°C, and increased thereafter. It remained nearly constant in the temperature region from 140°C to 180°C. In higher temperature region, it again decreased. After keeping the crystal at about 220°C for an hour, we gradually cooled it. Then its surface voltage changed along another path, and increased a little down to about 100°C. Below 100°C, the surface voltage increased more steeply, and below 80°C took nearly the same path as in heating. So in the curve of surface voltage versus temperature, we found a knee point near 100°C. The elevation of surface voltage in the first run was not observed in the case of silver chloride samples. Silver bromide is soluble in hydrobromic acid, and silver chloride is not soluble in hydrochloric acid. Each acid was used in the last stage of etching. We might suppose that the elevation was due to the evaporation of bromine. The behavior in the first run may show the character of etching.

In the second run, we could not find the increase of surface voltage between 100°C and 140°C. In heating, the voltage change followed different paths from run to run, but nearly the same path was taken in cooling. So the latter path was used to calculate various figures for the crystal.

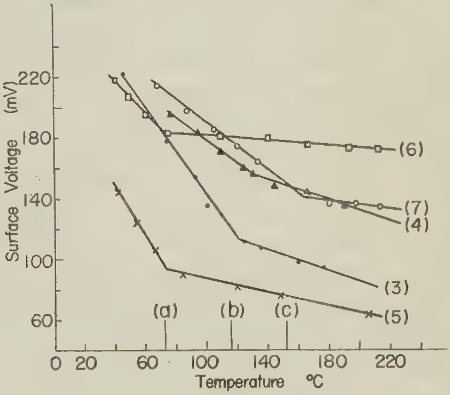

Fig. 4. The temperature dependence of the surface voltage of silver bromide crystals. The associated number indicates the corresponding one in the paper. (a) is the calculated knee point temperature for crystal 5 and 6, (b) is that for crystal 3 and 4, and (c) is that for crystal 7.

The experimental results are shown in Fig. 4. Each voltage was measured after the crystal was kept half an hour at each temperature. Crystal 3 and 4 contain 0.01 Mol.–% of cadmium bromide, and crystal 7 contains 0.05 Mol.–% of cadmium bromide. Crystal 5 and 6 contained no intended impurities, but they were estimated to contain 0.001 Mol.–% of divalent cation impurities, according to the results of our experiment and the ionic conductivity experiment. The amount of the impurity ingredient—cadmium bromide—was weighed before doping. We did not analyse chemically the amounts of impurities solved in the silver bromide crystals.

From Fig. 4, the curve of surface voltage versus temperature may be represented by two straight lines. One is in the temperature region from room temperature to the knee point temperature, which corresponds to surface voltage change in the impurity region and the other is in the higher temperature region than the knee point, which corresponds to surface voltage change in the intrinsic region.

It is easily seen that the more impurities the crystal contains, the higher temperature the knee point moves to. We could expect that in the intrinsic region, all lines would overlap one another because the behavior in this region must be independent of the amounts of impurities. But it is not our case. It is hard to measure the absolute surface voltage, and we cannot expect their overlappings, but their parallelism among them. Besides, they were frequently not parallel, as will be accounted by our interpretation in the next paragraph.

The behavior of surface voltage of silver bromide crystal in the temperature region from room temperature to 140°C below zero is utterly different by the pre-treatment. After heating the sample from room temperature and keeping it at 120°C, its temperature was made to fall. Below room temperature, surface voltage versus temperature curve continued to follow the line determined by the experiments at higher temperatures. At temperatures from −20°C to −40°C, the curve becomes flatter. But by illuminating the crystal with light shorter than 400 mμ the path again followed the extrapolated line, though its gradient was less steep below 0°C. In the temperature region from −100°C to −120°C, there appeared no change of surface voltage.

When we cooled the crystal from room temperature without heating it, the surface voltage of silver bromide increased with a gentler slope than after heating it, and it changed a little from −50°C to −120°C. The surface voltage versus temperature curve obtained for crystal 4 is shown in Fig. 5. Whether the sample at low temperature attains to thermal equilibrium in our observation time is doubtful.

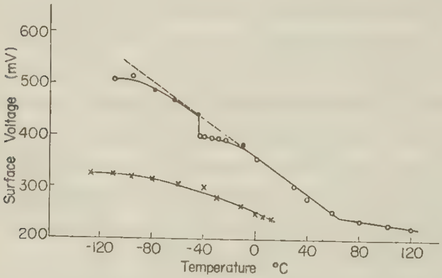

Fig. 5. The temperature dependence of the surface voltage of silver bromide crystal 4 in the temperature region from room temperature to 120°C below zero.

§ 4. Interpretation

In order to interprete these curves in Fig. 4, we shall propose the following mechanism. According to Lehovec,[2] there is an ionic space charge layer between the surface and the bulk in an ionic crystal. In our case, the one surface is coated by silver metal. The work required for taking away a silver ion from silver metal to infinity is $-E$ ev. (E is negative.) Silver bromide is of Frenkel defect type, and a silver ion occupies a normal lattice site or an interstitial site. By $-W$ ev, we represent the work required for taking away a silver ion from an interstitiai site of silver bromide to infinity, and $-U$ ev stands for the work required for taking away a silver ion from a normal lattice site to infinity. E, U, and W are not equal. When silver bromide is in contact with silver metal, silver ions move and an ionic space charge layer will be established. We measure voltage in silver bromide, taking the voltage of silver metal for zero. The voltage in the crystal is denoted by V. The schematic diagram of E, U, W and V with other quantities which will appear later, is shown in Fig. 6.

The number per unit volume of silver ions at interstitial sites of the crystal $-n_{Ag\cdot^{+}}-$ and that of silver vacancies $-n_{Ag\square^{-}}-$ will be determined by E, U, W and V. From the

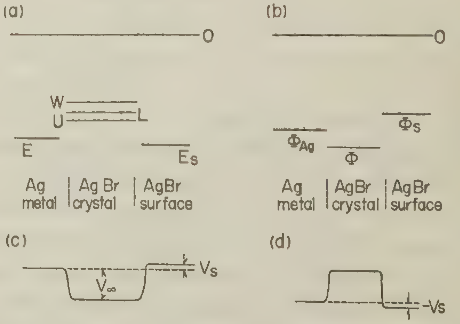

Fig. 6. Energy level diagram for silver ion and electron (a) Energy levels for silver ion (b) Energy level for electron (c) Potential for silver ion (d) Potential for electron.

equilibrium equation, we have the following equations

$$n_{Ag\cdot^{+}}=N_1\exp\{-(W-E+eV)/kT\} \qquad (1)$$

$$n_{Ag\square^{-}}=N_2\exp\{-(E-U-eV)/kT\} \qquad (2)$$

where we denote the number of interstitial sites available to a silver ion per unit volume by N_1, and the number of normal silver ion lattice sites per unit volume by N_2. N_1/N_2 is 2 in this case. k is Boltzmann constant, e is the charge of proton and T is the temperature of the crystal in absolute unit.

In the interior of the silver bromide monocrystal, the charge must be neutral, where voltage V is constant and its value is denoted by V_∞. The charge neutrality in the interior will be established with cadmium impurity, which increases silver ion vacancies. Then we have

$$n_{Ag\square^{-}}=n_{Ag\cdot^{+}}+cN_2 \qquad (3)$$

where cN_2 is the number of Cd^{++} at lattice sites in place of silver ions per unit volume and c is Mol.-% of cadmium ions dissolved in the crystal. From the equations (1), (2) and (3), we obtain

$$\left.\begin{aligned} eV_\infty &= E-U+kT\ln\left\{\frac{c}{2}+\sqrt{\left(\frac{c}{2}\right)^2+\frac{N_1}{N_2}\exp-\frac{W-U}{kT}}\right\} \\ &= E-L \end{aligned}\right\} \qquad (4)$$

$-L$ ev is the work required for taking away a silver ion from the interior of silver bromide crystal to infinity. If we could measure V_∞, V_∞ versus temperature curve would have a knee point, where

$$c^2=\frac{N_1}{N_2}\exp\left(-\frac{W-U}{kT}\right) \qquad (5)$$

It is not this voltage, but surface voltage that we can measure.

On the free surface of the crystal, we may make the following assumptions. There is the surface level of silver ions on the free surface, which corresponds to the work required for taking away a silver ion from the surface to infinity. We denote it by $-E_s$ ev. So we obtain the equation on the free surface similar to the equation (4). It is

$$\left.\begin{aligned} e(V_\infty-V_s) &= E_s-U+kT\ln\left\{\frac{c}{2}+\sqrt{\left(\frac{c}{2}\right)^2+\frac{N_1}{N_2}\exp-\frac{W-U}{kT}}\right\} \\ eV_s &= E-E_s \end{aligned}\right\} \qquad (6)$$

where V_s is the surface voltage of the crystal referred to the silver metal.

The dependence of surface voltage of the crystal on temperature will be determined by E_s because E is almost independent of temperature. In order to explain our results, we must suppose that E_s varies in a wide range and its change shows a knee point at some temperature. It is unreasonable to suppose that E_s changes abruptly at some temperature which is different according to the amount of cadmium impurities in the bulk.

It was shown in the former experiment that surface state of silver bromide crystal changed as its temperature rose and metallic silver precipitated on its surface. It may be natural to conjecture that electrons could contribute to the surface change on the free surface. On the other surface, silver ions only move in the boundary between silver and silver bromide, for silver bromide is an ionic crystal and the diffusion of electron may be neglected in our observation times. On the free surface both silver ions and electrons may contribute to equilibrium and there may be some factors that hinder the contribution of electrons. They may be removed by such procedure as illuminating the surface with shorter waves than 400 mμ. We denote the work required for taking away an electron in silver bromide crystal to infinity by $-\phi$ eV, and that from its surface by $-\phi_s$ eV.

The voltage induced by electrons for equilibrium between free surface and silver bromide crystal is $(\phi_s-\phi)/e$, and that by silver ions is $(L-E_s)/e$. There does exist only one voltage, so that they must be equal. We have

$$L-E_s=\phi_s-\phi \qquad (7)$$

The equation (7) would not always be consistent, if E_s, ϕ_s, and ϕ were all nearly constant. There was change of surface state. It would be preferable that E_s could change. Then the equation will become consistent. We have

$$\begin{aligned} eV_s &= E-E_s \\ &= eV_\infty+\phi_s-\phi \end{aligned}$$

The dependence of V_s on temperature is entirely determined by V_∞, if $\phi_s-\phi$ is constant. We can measure V_s, and it is equivalent to measuring V_∞ which is the voltage established by the ionic space charge layer near the silver coated surface. Then the curve of surface voltage versus temperature may have a knee point which can be controlled by the amounts of cadmium. In the above argument, the number of electrons which move to and from the free surface is supposed to be small and not to affect the charge neutrality condition.

In the intrinsic region, where the contribution of the impurities is negligible, we have the equation for V_s as follows

$$eV_s=E-\frac{U+W}{2}+\frac{kT}{2}\ln\frac{N_1}{N_2}+\phi_s-\phi \qquad (8)$$

The curve of surface voltage versus temperature seems to be a line with the same slope for all crystals because the factors except $\phi_s-\phi$ are determined by the bulk characters and $\phi_s-\phi$ is assumed to be constant. In reality, there are some discrepancies from one crystal to another. So we assume that $\phi_s-\phi$ is not constant and has a term proportional to change of E_s. That is:

$$\phi_s-\phi=(\phi_s-\phi)_1-\alpha kT\ln\left\{\frac{c}{2}+\sqrt{\left(\frac{c}{2}\right)^2+\frac{N_1}{N_2}\exp-\frac{W-U}{kT}}\right\} \qquad (9)$$

$$eV_s=eV_\infty+(\phi_s-\phi)_1-\alpha kT\ln\left\{\frac{c}{2}+\sqrt{\left(\frac{c}{2}\right)^2+\frac{N_1}{N_2}\exp-\frac{W-U}{kT}}\right\} \qquad (10)$$

where $(\phi_s-\phi)_1$ is the term of $\phi_s-\phi$ which is independent of E_s, and α is a constant, which has different values from sample to sample. α is determined mainly by surface condition of the sample. We attribute the difference of the slope between the samples to α.

Neglecting the dependence of $W-U$ on temperature, we get a value as a knee point temperature, which is higher than the observed one. We must consider the dependence of each level on temperature, and may assume that the dependence of each level on temperature is linear. We have

$$E=E_0-kT\ln A_1 \qquad (11a)$$

$$(\phi_s-\phi)_1=(\phi_s-\phi)_{10}-kT\ln A_2 \qquad (11b)$$

$$W=W_0-kT\ln B_1 \qquad (11c)$$

$$U=U_0-kT\ln B_2 \qquad (11d)$$

where each character with suffix 0 represents respectively the energy level at 0°K of the energy level denoted by each character.

The expression for eV_s is:

$$\begin{aligned} eV_s=E_0-U_0+(\phi_s-\phi)_{10}-kT\ln\frac{A_1A_2}{B_2} \\ +(1-\alpha)kT\ln\left\{\frac{c}{2}+\sqrt{\left(\frac{c}{2}\right)^2+\frac{N_2B_2}{N_1B_1}\exp-\frac{W_0-U_0}{kT}}\right\} \end{aligned} \qquad (12)$$

In the impurity region, we have:

$$eV_{s1}=E_0-U_0+(\phi_s-\phi)_{10}-kT\ln\frac{A_1A_2}{B_2c^{1-\alpha}} \qquad (13)$$

where V_{s1} is the surface voltage in the impurity region, and the term $\exp-(W_0-U_0)/kT$ is neglected.

In the intrinsic region, we have

$$eV_{s2}=E_0-\frac{U_0+W_0}{2}+(\phi_s-\phi)_{10}+\frac{\alpha}{2}(W_0-U_0)$$
$$-kT\ln\frac{A_1A_2}{B_2}\left(\frac{N_2B_2}{N_1B_1}\right)^{(1-\alpha)/2} \qquad (14)$$

where V_{s2} is the surface voltage of silver bromide in the intrinsic region, and the concentration of impurity is neglected in the logarithm term.

The dependence of surface voltage on temperature in each region is represented by a straight line. Extrapolating these lines to 0°K, we obtain:

$$eV_{s1}-eV_{s2}=\frac{W_0-U_0}{2}\times(1-\alpha) \qquad (15)$$

The value of $V_{s1}-V_{s2}$ at 0°K is determined experimentally, while W_0-V_0 obtained by Teltow[4] is 1.27 eV. The value of α which we obtained are shown in Table I.

Table I.

Sample Number	Molar Percent of Impurity	$2\times(eV_{s1}-eV_{s2})$	α	N_1B_1/N_2B_2	Knee Point Temperature expe.	Knee Point Temperature calc.
3	$1.\times10^{-4}$	1.00 eV	0.21	3.9×10^8	392°K	393°K
4	1.	0.36_5	0.71	0.7	400	393
5	0.1	1.02	0.20	4.2	344	342
6	0.1	0.76	0.40	4.2	344	342
7	5.	0.62	0.51	0.7	442	440

The difference of the slopes of two lines in the two region is

$$\varDelta G=k\ln\left(\frac{N_1B_1}{N_2B_2c^2}\right)^{(1-\alpha)/2} \qquad (16)$$

$\varDelta G$ is calculated from the experimental data. We can find N_1B_1/N_2B_2 which must be nearly constant, for it involves only the intrinsic factors of silver bromide crystal not affected by its surface state. α is sensitive to surface condition and its value are different from sample to sample. If the experimentally determined value of N_1B_1/N_2B_2 are nearly constant, we may conclude that our assumptions are reasonable.

We have the following table.

We can easily see that N_1B_1/N_2B_2 is constant for the samples which were cut from the crystal containing the same amounts of impurities. Furthermore, the discrepancy between the samples is little except for crystal 7. Crystal 7 seemed to be strained in being lapped.

The knee point temperatures were calculated by using the values of the impurity concentration c and N_1B_1/N_2B_2 obtained from Fig. 7. There is also good agreement between their experimental and calculated values.

Under the condition that B_1/B_2 is 0.65×10^8, the formation energy of Frenkel defect E_F is dependent on temperature as follows:

$$E_F=W-U=W_0-U_0-kT\ln\frac{B_1}{B_2}$$
$$=1.27-1.6\times10^{-3}T \qquad (19)$$

The equation (19) shows that B_1/B_2 is larger than one. Rough evaluation of B_1 and B_2 can be made as follows. In the equation (12), there are two terms involving the temperature T. If we plot the curve of the term involving the impurity concentration c, the curve has a minimum near the knee point temperature, while the curve obtained experimentally has a slightly negative slope in the high temperature side of the knee point. If, as a very rough approximation, the sum of two terms dependent on temperature is assumed to be zero in the intrinsic region of silver bromide crystal, and if it is further assumed that α is zero, then we have

$$A_1A_2/B_2=(N_1B_1/N_2B_2)^{1/2}$$

whence, substituting $N_1B_1/N_2B_2=1.3\times10^8$,

$$A_1A_2/B_2\fallingdotseq10^4$$

The value of A_1 for silver is nearly equal to one. We assume that A_2 might vary from 1 to 10^{-3}. Then B_2 must vary inside the region from 10^{-2} to 10^{-7}. From the above relation, B_1 must vary from 10^6 to 10. As the temperature rises higher, it becomes easier to take away a silver ion from a normal lattice site, and the work required to take away a silver ion from an interstitial site increases. The level of U elevates, and that of W drops, as the temperature of the silver bromide crystal rises. The difference between the lattice site and the interstitial site tends to disappear by thermal motion of the lattice.

The knee point temperature T_k is determined by the equation (5),

$$c^2=\frac{N_1B_1}{N_2B_2}\exp\{-(W_0-U_0)/kT\} \qquad (5)$$

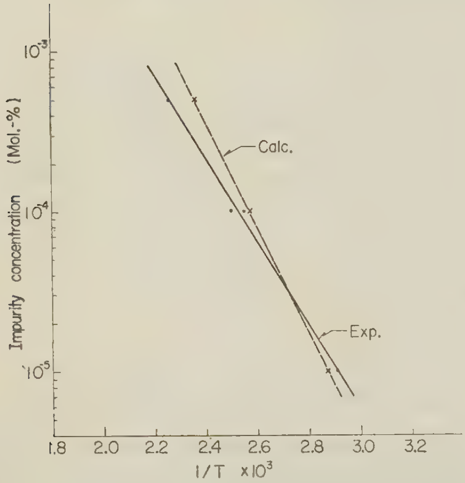

Fig. 7. The curve of the logarithm of the impurity concentration versus the reciprocal of the absolute temperature. From the slope of the line, we have $E_F{}^0=1.03$ eV and $N_1B_1/N_2B_2 = 1.3\times10^8$.

The curve of $\ln c$ versus the reciprocal of the absolute temperature is a straight line. The experimental result is shown in Fig. 7. The dotted line is the calculated one under the condition that $E_F{}^0$ is Teltow's 1.27 eV, and N_1B_1/N_2B_2 is 3×10^8. The formation energy of Frenkel defect, $E_F{}^0$, can be determined from the slope of the line. The value 1.03 eV is obtained, and the value 1.3×10^8 is obtained for N_1B_1/N_2B_2.

The value of α differs from sample to sample, though the samples are cut from the same crystal. But the knee point temperatures of the samples supposed to contain the same amount of cadmium coincide with each other. Therefore, $E_F{}^0$ is experimentally determined without trouble over α. The discrepancy between 1.27 eV and 1.03 eV may be removed by improvement. Improvement may be obtained by the following ways:

1) more accurate measurement of the temperature of the samples
2) better and uniform treatment of surfaces
3) exact knowledge about the amounts of impurities

Lidiard[5] calculated that the association of silver vacancies and cation impurities is virtually complete at room temperature. Surface voltage of silver bromide would not change at temperatures near and below 0°C because the impurities do not contribute to its change. We found its change at further lower temperatures. Whether the flatness of the surface voltage change below room temperature is caused by complex pairs, or by the absorption on the surface cannot decided in the present stage. But it seems that silver ions may move hardly below -100°C, and complex pairs which decrease the concentration of effectively dissoluble cadmium may contribute to the change of surface voltage. This problem might be solved by the experiments in the wider range of temperature from liquid oxygen temperature to 220°C. The result will appear later.

Acknowledgements

The authors wish to thank Dr. T. Ninomiya for numerous helpful conversations throughout the course of this work. The authors are also grateful to Professor H. Takahasi for helpful suggestions and criticism to the manuscript. Sincere appreciation is extended to Mr. K. Akimoto and Mr. S. Oyama for their encouragement. To Mr. H. Motoi, the authors wish to their sincere gratitude for his continual efficient and untiring assistance. The present investigation has been partly supported by the Special Research Grant from Chuo University.

References

1) S. Sonoike: J. Appl. Phys. Japan **22** (1953) 19.
2) K. Lehovec: J. Chem. Phys. **21** (1953) 1123.
3) S. Sonoike: J. Appl. Phys. Japan **25** (1956) 115.
4) I. Ebert and J. Teltow: Ann. Phys. **15** (1955) 268.
5) A. B. Lidiard: *Handbuch der Physik* **20** (Springer, 1957) 309.

JOURNAL OF THE PHYSICAL SOCIETY OF JAPAN, Vol. 14, No. 12, DECEMBER, 1959

Study on Precipitation Phenomena during Aging of Aluminium-Silver Alloy in Thin Evaporated Films*

By Yasushige FUKANO** and Shiro OGAWA
The Research Institute for Iron, Steel and Other Metals
Tohoku University, Sendai

(Received April 14, 1959)

Precipitation phenomena during aging have been observed on aluminium-20 wt. per cent silver alloy in thin evaporated films by electron micryscopy and electron diffraction. A super-saturated solid solution has successfully been obtained in thin films by a new quenching method. In a preprecipitation stage aggregates composed of random clusters have been found in electron micrographs, no appreciable diffraction effect having been perceived. In a true precipitation stage precipitates have been found in electron micrographs to change from a needle-like to a three dimensional shape with increasing aging, the axial ratio obtained from diffraction patterns changing from 1.63_3 to 1.59 passing 1.61_2. It is a merit of the present study that a hexagonal precipitate with the ideal axial ratio has been detected in the course of aging. Except this point, the results obtained confirm generally those reported by X-ray studies. So called "equal-thickness interference fringes" have been found in images of precipitates aged at 250°C.

§ 1. Introduction

The precipitation process of age-hardened alloys such as aluminium-copper, aluminium-silver etc. will be elucidated in more detail, if both morphology and crystal structures of precipitates are examined on one and the same specimen without using replicas. For this purpose the direct observation on thin films by means of electron microscopy together with electron diffraction is most adequate[1]. Evidence for structural transitions in alloys will directly be obtained by this method, and therefore various changes of physical and mechanical properties of alloys accompanying aging will fully be explained.

In order to realize the direct observation of aging two types of specimen preparation are available, that is to say, one is thin-sectioning of bulk alloys by electropolishing or chemical etching and the other is vacuum evaporation. The latter method was adopted in the present experiment because of its easiness and simplicity. This method has been tried by some investigators[2)-5)] but without success, for they could not get a supersaturated solid solution, by quenching of thin films, from which the observation on the aging process should be started. In the present study a quenching unit for evaporated alloy films was prepared with a new idea. This apparatus enabled us to quench thin films successfully, and the direct observation on the aging process of aluminium-20 wt. per cent silver alloy could be carried out by electron microscopy and electron diffraction. The description of the quenching unit and the quenching method and of results obtained will be given in § 2 and § 3, respectively.

§ 2. Experimental Method

1. *Quenching unit*

The most necessary condition for quenching of thin films is to keep the cooling speed at least in the same order of magnitude as that of water quenching of bulk material. Moreover, the following must be avoided.

(1) Formation of oxides or other compounds.
(2) Contamination by organic compounds such as grease.
(3) Breakdown of films.

It seems to be the best way, therefore, that alloy films are quenched without being exposed to air, immediately after the solution treatment has been done in vacuum or in inert gas. Bulk materials are usually quenched by putting directly into liquid refrigerant, say, cold water, but it is clear that this method is inadequate to thin films. Winkelmann tried quenching of films by sudden fall of a heated specimen onto a cooled metal plate in vacuum. According to him, thermal radiation from the specimen suddenly placed in surroundings of low temperature might quickly decrease the specimen temperature. But, at the same time, a considerable quantity of heat must be given to the film by a film supporter the cooling speed of which is far smaller than that of the former because of its large heat capacity. Thus, the cooling speed of the film is thought to be maintained almost in the same order of magnitude as that of the supporter. This point is considered as a main source from which he could not get a supersaturated solid solution.

---

* A short note concerning the present work has been published in Acta Cryst. **9** (1956) 971.

** Now at Department of General Education, Nagoya University.

If a film heated in vacuum can quickly be contacted with some inert gas of large accommodation coefficient, a considerably large cooling speed must be obtained without formation of any harmful compound. Under such an idea a quenching unit as shown in Fig. 1 was prepared. It permitted the most effective heat exchange between films and inert gas and enabled the specimen temperature to be instantaneously decreased below room temperature. The unit consists of a heating chamber, *A*, a nozzle part, *B*, from *c* in which gas is jetted into the heating chamber, and a cooling chamber *C*, in which the cooling of a specimen film as well as well as of inert gas is completed. *A* is made of a transparent quartz tube 8 mm in diameter and 0.7 mm in wall thickness on which a heating coil of nickrom wire, *a*, is tightly wound. The specimen is placed at the central part of the quartz tube without being put in any container. The specimen temperature can be measured by a thermocouple of Pt-PtRh, *b*. But, as the high accuracy of temperature measurement was not necessary for quenching, the thermocouple was removed on the actual procedure, in order that it might not interfere with a jet of gas, and the quenching temperature was then estimated by the coil current. The cooling tube, *e*, in *C* is made of hard glass 10 mm in diameter and 0.5 mm in wall thickness and is beforehand cooled by liquid nitrogen contained in a Dewar's vessel *d*. In *e* is contained a helical winding of thin platinum or silver wire to promote heat exchange between inert gas and the specimen. *g* in *B* is a gas reservoir into which gas is filled to 2 atmospheric pressure through a valve, *h*, before quenching. Carbon dioxide gas was selected as an innert gas suitable for the present experiment, owing to its large accommodation coefficient. The dissociation of this gas does not thermally proceed below 2000°C, that is to say, the reaction $2CO_2 \rightleftarrows 2CO+O_2$ does not actually take place. The dissociated volume is about 2 per cent at 2000°C. The specimen film was heated above 500°C for $1\sim2$ hours in vacuum of 10^{-5} mmHg to obtain a homogeneous solid solution and then was quenching.

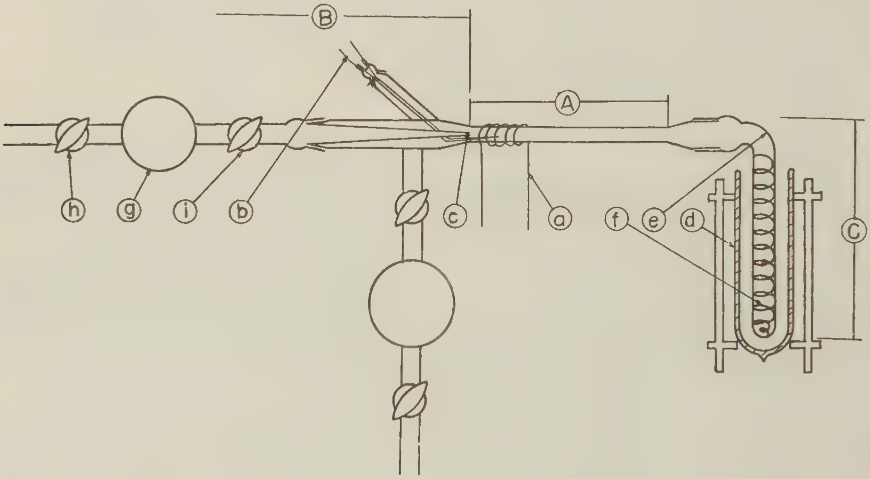

Fig. 1. Schematic diagram of the quenching unit.

2. *Quenching method and heat treatment for aging*

The quenching procedure is carried out in the following order:

(1) The valve, *i*, is opened and the gas is jetted into *A* through *c*.
(2) Cold water is poured onto *A*.
(3) The electric current through *a* is switched off.

These three operations must be done almost simultaneously. The object of the operation (2) is firstly to prevent carbon dioxide gas from temperature increase due to heat exchange with the inside wall of *A* and secondly to avoid blowing-off of *C* due to thermal expansion of the gas filled in *A*. The specimen film is instantaneously blown away by the jetted gas and is fallen down onto the bottom of *e*. At the same time, as soon as the gas reaches the cooling tube, it transforms instantaneously to dry ice by giving heat to *f* and *e*. The process may be analysed in the following way; the gas jetted from the nozzle forms a narrow stream, without filling *A*, and brings the film away to the cooling chamber, carrying it on the tip of its stream. In this moment the tip may get little heat from the inside of *A* because of a sufficiently short length of the heating coil. In order that the above procedure may completely be finished, the distance between the nozzle tip and the film, and the size of the heating coil may have to be finely adjusted. The breakdown of some films is unavoidable owing to the abrupt transport, but about two-thirds of the total number of the tried films could be subjected to the successive aging experiments without being broken down. This comparatively little damage may depend upon a flying manner of a film, that is to say, this is apt to blown away with its surface parallel to the flying direction. After the quenching was finished, the unit was again highly evacuated, dry ice formed being gradually sublimated, and then the film was exposed to air. The time actually required from the finish of the quenching till the observation by electron diffraction or electron microscopy is estimated at least 2 hours.

Heat-treatments for aging were done in high vacuum as follows;

(1) When the heating temperature was below 200°C, films were placed at the bottom of *e* which was immersed into hot water or an oil bath.
(2) When the temperature is above 200°C, they were placed at *A*.

3. *Preparation of specimens*

Specimens used in the present study were single-crystalline evaporated films of aluminium-20 wt. per cent silver. The two component metals were simultaneously evaporated onto cleavage surfaces of rocksalt, which were maintained at about 450°C after having been heated up to 500°C, from two wires of aluminium and silver laid in a small tungsten filament 0.2 mm in diameter. Evaporated quantities were so adjusted that the desired composition and the desired thickness, 800 ~1000Å, might be obtained. Both of the composition and the thickness were, however, considerably different from the expected values because of uncertain evaporated quantity of aluminium. This metal is soluble in tungsten and hence some quantity of it always remains unevaporated. To obtain a composition as close to the desired one as possible, a planned quantity of aluminium was somewhat increased by experience. Uncertainty of the distance between the filament and the substrates, caused by a not negligible extent of the evaporation sourse, may also give rise to some error in the composition and the thickness. Films evaporated onto pieces of rocksalt were freed from the substrates by immersion into distilled water and mounted on nickel plates 3 mm in diameter and less than 0.1 mm in thickness with small holes 0.1~0.3 mm in diameter, covered by thin collodion films. Films prepared in this way were well orientated, their surfaces being parallel with (001) plane. Electron micrographs showed, however, clear subgrains having probably twisted boundaries with the axis of rotation lying in the film plane, as suggested by diffraction spots without arcing and visible over a wide angular extent.

4. *Temperature rise in films by irradiation of electron beam*

Specimen films were examined first by electron diffraction and then by electron microscopy after quenching and after every aging. The electron microscope was made by Hitachi Company (HU-7), the operating voltage being 50 KV, and electron micrographs were taken on photographic plates at a magnification of 10,000×. This microscope, however, did not permit to take diffraction patterns at the same specimen position as that in case of microscopy, and hence diffraction experiments had to be done in an independent diffraction camera. Owing to a large film thickness, microscopic images on the fluorescent screen were often too dark to be observed in detail unless the irradiation was more intensified than usual. This increased intensity, however, gave rise to true precipitation in a super-saturated solid solution during observation. The precipitates much resembled those formed in an early stage of 165°C aging, but further progress of the precipitation did not occur even after observation for about one hour. The acceleration of precipitation by irradiation could naturally be avoided by decreasing the intensity at the cost of readiness of observation. When a specimen was subjected to the repeated quenches and the prolonged observation in the electron microscope, the increase of its contamination made the electron image darker and the minute observation more difficult. Nevertheless, the images with marked contrast in themselves in true precipitation stages suffered scarcely serious interference.

5. *Determination of the axial ratio of hexagonal precipitates*

The axial ratio, c/a, of hexagonal precipitates was determined from diffraction spots $(0\bar{1}11)$, $(0\bar{1}12)$ and $(10\bar{1}3)$, which were caused by lattice planes nearly perpendicular to the film plane, as follows:

$$\left(\frac{c}{a}\right)^2=\frac{l_1^2A-l_2^2}{4/3\cdot(1-A)},$$

where,

$$A=\frac{d_{h_1k_1i_1l_1}}{d_{h_2k_2i_2l_2}}=\left(\frac{R_2}{R_1}\right)^2 \qquad (1)$$

where R_1 or R_2 is a distance between (000) spot and $(h_1k_1l_1)$ or $(h_2k_2l_2)$ spot on the diffraction pattern. The accuracy of measurements of R_2 and R_1 was somewhat decreased due to radial elongation of the hexagonal spots, but the change in the axial ratio with aging could be determined at an error of about ±0.01. When hexagonal spots $(10\bar{1}0)$ $(10\bar{1}1)$ were fortunately observed by tilting the specimen to the electron beam, the following equation was used:

$$\left(\frac{c}{a}\right)^2=\frac{1}{4/3\cdot(A-1)},$$

where

$$A=\left(\frac{d_{10\bar{1}0}}{d_{10\bar{1}1}}\right)^2=\left(\frac{R_{10\bar{1}0}}{R_{10\bar{1}1}}\right)^2 \qquad (2)$$

Mean values of results from the above two methods were used as the axial ratio of precipitates. Individual values of c and a were not determined.

§ 3. Experimental results

Six specimens were examined by electron microscopy and electron diffraction throughout various aging stages after quenching, and the results obtained are classified into the following two; (1) low temperature aging in which true precipitation does not yet take place and (2) high temperature aging in which true precipitation already proceeds. It was done in the first place to examine whether the quenching caused a supersaturated solid solution or not, and the first aging state was detected by this procedure. In the second aging state shape, size, distribution and the axial ratio of precipitates of hexagonal phase were studied, depending on aging temperature.

1. *Low temperature aging*

Photos. 1 and 2 show a typical electron micrograph and a typical diffraction pattern, respectively, taken from a specimen aged at room temperature for two hours after quenching. In the former, complex aggregates composed of minute dark spots are seen, e.g., in *A* or *B*. These aggregates always exist in specimens aged at temperature below 100°C and are believed to consist of small clusters of silver atoms. This point will be discussed in § 4. The electron diffraction patterns seem to be scarcely influenced by the presence of aggregates. Sharp diffraction spots due to the face-centered single phase are accompanied by no appreciable extra scattering, except a comparatively strong background scattering which is markedly reduced in high temperature aging. A small elastic strain of the matrix lattice due to the occurrence of small clusters may be responsible for this phenomenon. Although shape and size of individual clusters forming an aggregate could not definitely be determined in the present observation, it may roughly be said from random shapes and

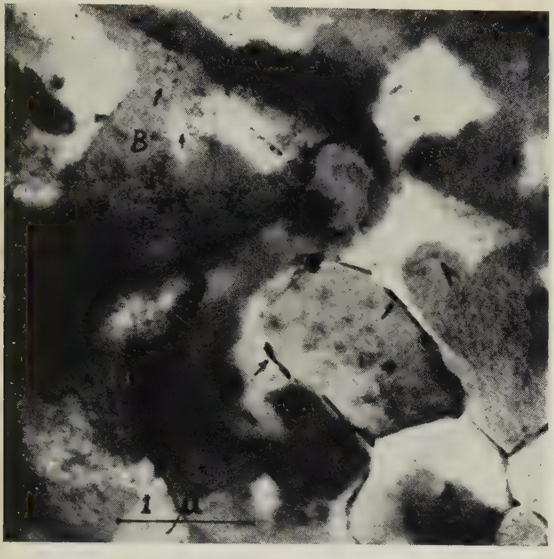

Photo. 1. Electron micrograph taken from a specimen aged at room temperature for two hours after quenching.

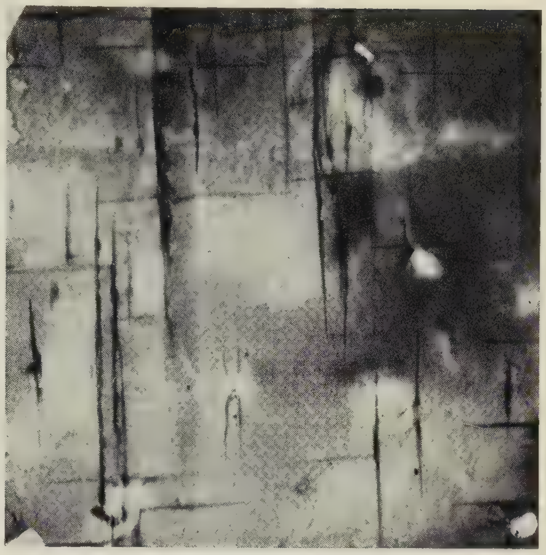

Photo. 3. Electron micrograph taken from a specimen aged at 165°C for 20 minutes after quenching.

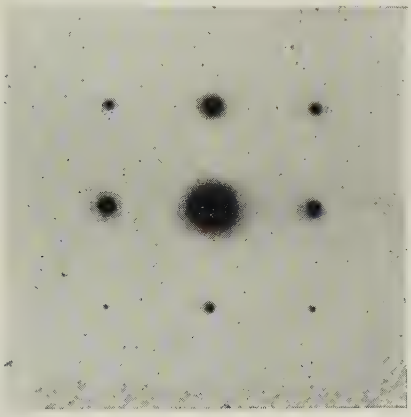

Photo. 2. Electron diffraction pattern corresponding to Photo. 1.

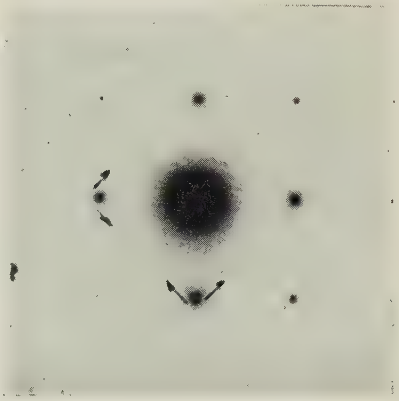

Photo. 4. Electron diffraction pattern corresponding to Photo. 3. The arrows indicate the streaks emerging from diffraction spots.

random sizes of aggregates that each individual cluster is not precipitated on any definite lattice plane and that its shape resembles a sphere, say, about 100Å in diameter.

2. *High temperature aging*

(i) Aging below 200°C

True precipitation was confirmed neither to occur at room temperature aging even after one month nor to occur at 100°C aging even after two hours, but it was found to begin at 165°C after 20 minutes. Needle-like or narrow wedge-like precipitates were grown along [110] and $[1\bar{1}0]$ directions lying in the film plane, (001), originating chiefly from sub-grain boundaries or from lattice imperfections such as small holes inside sub-grains, as shown in Photo. 3. These precipitates began to appear with increasing aging time also at places where there were no apparent imperfection inside sub-grains. Electron diffraction patterns corresponding to this precipitation stage exhibited streaks emerging from diffraction spots of the face-centered cubic matrix, as shown in Photo. 4. The streaks appear to be extended along [110] and $[1\bar{1}0]$ directions in the projection to (001) reciprocal plane. On these streaks diffraction spots due to the hexagonal lattice appeared by further aging at higher temperatures and increased their intensity with aging. This fact seems

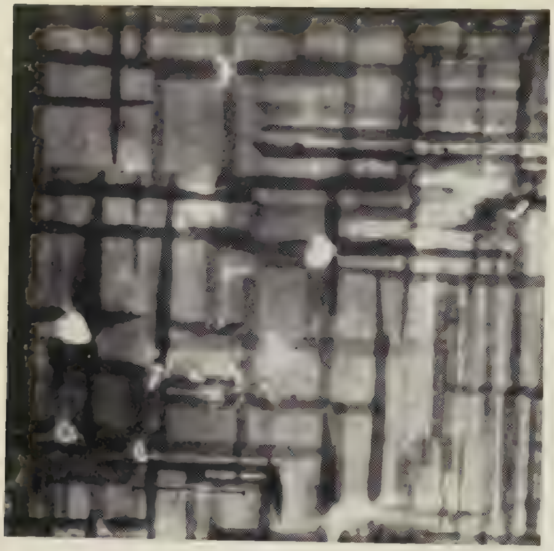

Photo. 5. Electron micrograph taken from a specimen aged at 200°C for 2 hours. This micrograph reproduces the same field as that in Photo. 3, showing the growth of precipitates.

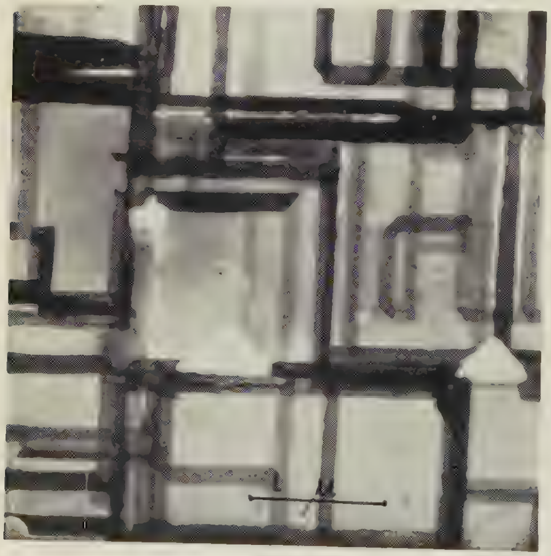

Photo. 6. Electron micrograph taken from a specimen aged at 250°C for 10 hours. Fine parallel striations are seen inside images of some precipitates.

to suggest that the streaks are extended actually along ⟨111⟩ directions in reciprocal space. That is to say, lamellae causing the streaks may be parallel with {111} planes. For the visibleness of ⟨111⟩ streaks on diffraction patterns of normal incidence the rotation of crystallites forming sub-grains and the bending of films may be responsible.

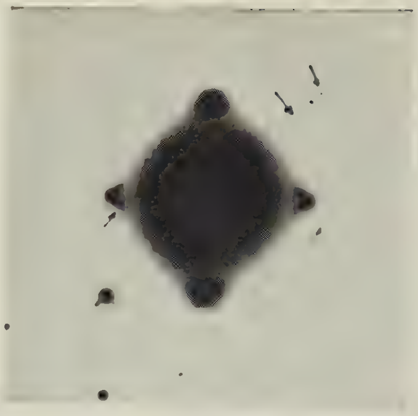

Photo. 7. Electron diffraction pattern corresponding to Photo. 6. The arrows indicate the diffraction spots due to the hexagonal phase.

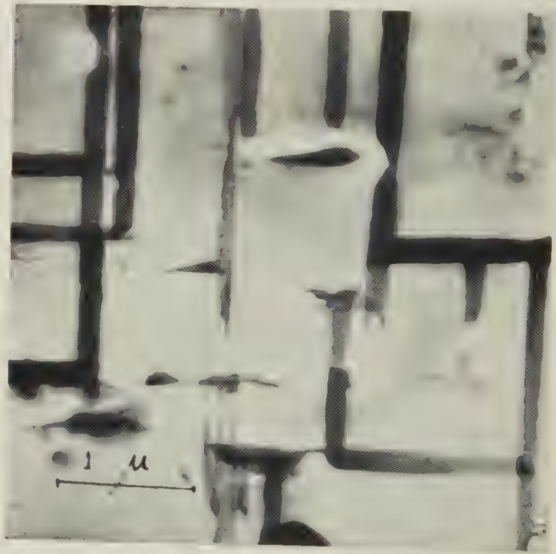

Photo. 8. Electron micrograph taken from a specimen aged at 400°C for 3 hours.

The following view will be held about the earliest stage of precipitation: The needle-like or narrow wedge-like precipitates are very thin lamellae which are formed coherently on the matrix {111} planes and grown preferentially along [110] or $[1\bar{1}0]$ direction. Their thickness may be estimated from the length of the streaks to be at most a few atomic layers, but their width on the {111} planes may be 100Å in the order of magnitude. This view is supported also by the fact that the above precipitates are further developed to plate-like precipitates with their planes parallel to the matrix {111} planes, as shown in Photo 5.

(ii) Aging above 200°C

The thin and narrow precipitates bellow 200°C gradually grow up with aging above 200°C to three-dimensional plates bounded by two {111} planes of the matrix and two film surfaces. Photo. 5, 6, 7 and 8 show electron micrographs and a diffraction pattern in this precipitation stage. The distribution density of precipitates attains maximum after aging at 200°C for 2∼4 hours and decreases with further increase of aging temperature and time. The orientation relationship between precipitates and the matrix can be determined from diffraction pattterns as follows:

$$(111)_{\mathrm{matrix}}//(0001)_{\mathrm{hexagonal}}\ ,$$
$$[110]_{\mathrm{matrix}}//[11\bar{2}0]_{\mathrm{hexagonal}}\ .$$

The thickness of the precipitates along their c axis reaches maximum after 250°C aging. The precipitates exhibit a fairly good habit below this temperature, but above 300°C they begin to dissolve again into the matrix, which causes both ends of their rod to be deformed to a V shape and, at the same time, causes their thickness to be diminished. Behavior of diffraction spots from hexagonal precipitates with increasing temperature just corresponds to the changes of electron micrographs; that is to say, their intensity reaches maximum after 200°C aging and their sharpness increases until 250°C aging. Above the latter temperature the intensity of the diffraction spots from hexagonal precipitates is decreased in spite of the unchanged sharpness of the spots. It is remarkable that the axial ratio of the precipitates changes with aging from 1.63_3 to 1.59. The axial ratio of an ideally close-packed hexagonal lattice, 1.633, was found in the precipitates formed after aging at 200°C for 4 hours (Photo. 5). The measured value was $1.63_3 \pm 0.007$. It decreases to $1.61_2 \pm 0.005$ by 250°C aging and this value exactly corresponds to γ' phase. On further aging above 300°C the axial ratio changes to 1.59 ± 0.01 which nearly coincides with that of γ phase, 1.588.

§ 4. Discussion and Conclusion

It is the essential point of the present paper to confirm to what extent the direct observation throughout the whole aging process can be effectively carried out by electron microscopy and electron diffraction in an aluminium-silver alloy, using thin alloy films quenched by the method described in § 2. There have been many X-ray studies on the aging process of aluminium-silver alloys. According to them, the process can be classified into preprecipitation and true precipitation which are responsible, respectively, for low temperature age-hardening and high temperature age-hardening. The results of the present study will be discussed in the light of these X-ray studies, as follows.

As-quenched or low temperature aged (below 100°C) specimens do not exhibit in their electron micrographs any sign of true precipitation except at some of sub-grain boundaries where something looking like precipitates is seen, as indicated by the arrows in Photo. 1. There are only aggregates consisting of random distribution of minute dark spots inside sub-grains. It was impossible due to a low resolving power of the present electron microscope and due to a considerable thickness of the films to obtain a distinct information about individual shape and size of dark spots. According to Guinier *et al*6) and Gerold7), the formation of silver-rich spherical small clusters was concluded by X-ray small angle scattering in low temperature aging of super-saturated solid solution of aluminium-silver. Gerold10) showed only clusters with a radius more than 50Å to be responsible for low temperature age-hardening. According to him, a scattering angle, $2\theta_{\max}$, corresponding to maximum intensity of small angle scattering for spherical clusters with a radius of gyration, R, is proportional to $\lambda/2\pi R$. Owing to a very short wave-length of fast electron used in diffraction experiments, however, it is not too much to say that detecting small clusters by small angle scattering around the diffraction spot of Oth order, that is, around the direct spot is made impossible by a high halation in electron diffraction. The effect from clusters may be observed in general also around any diffraction spot of hth order, if they are coherent with the matrix lattice. There is actually seen tolerable diffuse scattering, but a similar one is visible also in diffraction pattern of single-crystalline evaporated films of pure metal. Therefore, true diffuse scattering caused by clusters cannot be distinguishable, being masked by the above scattering, even if it exists. If a culster were a stringlet or a platelet of minute size with its axis or plane of growth parallel to a special lattice plane of the matrix, a diffraction effect suggested by Geisler and Hill⁸⁾—a plane or a rod passing through a reciprocal lattice point—would emerge from diffraction spots including the direct spot. Any diffraction pattern, however, does not exhibit even a sign of the effect. That is to say, clusters may be spherical. The present electron-microscopic observations suggests that their radius is about 100Å.

The locally dense distribution of clusters is thought of as caused by annihilation of silver-laden dislocations inside sub-grains⁹⁾ and by condensation of silver atoms along dislocation loops due to migration of lattice vacancies. The arrows in *B* in Photo. 1 indicate the condensation of silver clusters along single dislocation loops. The existence of something looking like large precipitates along sub-grain boundaries in Photo. 1 resembles the fact found by Heidenreich⁹⁾ in lead-silver alloys. He tried to explain this phenomenon by mass transport of solute atoms by dislocations into grain boundaries. In the present evaporated films sub-grains may be considered to be more loosely connected with one another than in bulk crystals, and this may lead to quick growth of precipitates along sub-grain boundaries under strain-free condition. The thinner the films, the stronger this tendency will become. The fact²⁾,³⁾,⁵⁾ that evaporated films less than 500Å thick with patch-like structure gave always diffraction spots due to hexagonal precipitates in their diffraction patterns even immediately after quenching might be caused partly by the enhanced preferential precipitation at their loosely connected sub-grain boundaries, although the marked precipitation owes its origin largely to an incomplete quenching. A trial to examine whether diffraction spots arising from precipitates appeared immediately after the quenching by the present method or not was done in case of thinner films less than 500Å thick, but did not succeed, as they were all broken owing to the thinness. Generally speaking, the inside of sub-grains will remain super-saturated under an adequate quenching, if the sub-grain size is sufficiently large. On the other hand, a greater part of solute atoms will be diffused out into sub-grain boundaries and a depletion of the atoms inside sub-grains will form two phases in equilibrium with precipitates at boundaries, if the sub-grain size is considerably small and a quenching is inadequate.

X-ray studies on true precipitation, especially on its early stage, was fully done by Köster *et al*¹⁰⁾. Hardy and Heal¹¹⁾ tried to express the development of true precipitation in terms of the following process, chiefly based on the results of Köster *et al*:

Stacking faults in the matrix
  → lamellae of γ' phase
  → three dimensional γ' phase → γ phase

The present results obtained on thin films above 165°C can be expressed in the following way:

Stacking faults in the matrix
  → needle-like or narrow wedge-like γ'' precipitates → lamellae of γ'' precipitates
  → three dimensional γ'' precipitates
  → γ' phase → γ phase

The precipitates denoted by γ'' mean those having the axial ratio of 1.633 characteristic of an ideal hexagonal close-packed lattice.

The face-centred cubic lattice of the matrix is thought of as a sequence of (111) plane,⋯⋯ ABCABCABC⋯⋯. Solute atoms may be diffused into stacking faults such as⋯ABCAC-ABC⋯ formed in the lattice, and thus extremely thin embryos of precipitates are formed, the ideal axial ratio, 1.633, being held. Among possible growing directions of embryos lying on (111) plane, $[\bar{1}10]$, $[\bar{1}01]$ and $[01\bar{1}]$ directions on this plane may be most favorable, because the best coherency can be obtained on the plane and the atomic registry is easiest to be held along the closest-packed directions, ⟨110⟩. The work necessary to add solute atoms to ends of growing embryos is least along these directions. The occurrence of strain field at embryo's ends favors atoms to be diffused here, and the longitudinal growth is still more accelerated, which leads to a needle-like or narrow wedge-like shape.

The axial ratio, 1.633, still persists until the beginning of three-dimensional growth. Thus, γ'' precipitates behave below 200°C as if they were most stable. However, they may be unable to increase so much their thickness that the axial ratio, 1.633, may be recognized by X-rays. This will make the difference between the X-ray results and the present results on the precipitation process, with that it is scarcely possible to distinguish between γ' lamellae and γ'' lamellae only from the streak on a diffraction pattern. Any precipitate with the ideal axial ratio has not so far been reported by X-ray studies. On the other hand, such a precipitate with the ideal axial ratio or with an axial ratio close to it has been found by Götsche⁵⁾ and Watanabe⁴⁾ in evaporated films by means of electron diffraction. It was detected from the beginning in the formation of their evaporated films, but not in the course of precipitation from a super-saturated solid solution. Its detection in thin films, however, may reasonably be understood just in the light of the present study.

As shown in Photo. 6, fine striations were sometimes seen inside images of precipitates. Such striations are often originated from stacking faults formed in face-centred cubic lattices,¹²⁾ as a result of dynamical interaction of electrons with faulted lattices, but the precipitation stage in which the present striations appeared was a considerably developed one, as seen from the diffraction pattern and the micrograph, and hence it is improbable that stacking faults caused them to occur. The striations are believed to be so-called "equal-thickness interference fringe" produced by dynamical interaction of electrons with the crystal lattice in a wedge-shaped part formed by precipitation, as often found in an image of a crystal with a regular habit such as magnesium oxide.¹³⁾⁻¹⁵⁾ Fig. 2 explains how the fringe can be produced by the intensity variation of electron beam along the incident direction in the wedge-shaped part of the precipitate lattice, A, if the responsible Bragg reflection occurs here. The fringe can be caused, however, also by the dynamical interference in the wedge-shaped part of the matrix lattice, B, in the same way, if the responsible Bragg reflection occurs here. The calculation shows that the spacing of the observed fringe may be obtained by either of the two explanations, and therefore, it can not be determined at present which lattice is responsible for the observed fringe. This point will be answered in a future report.

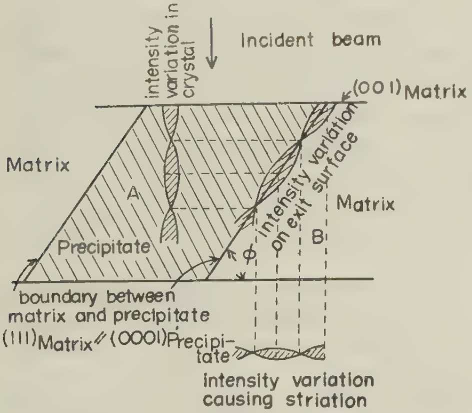
intensity variation in crystal
Incident beam
(001)Matrix
Matrix
A
intensity variation on exit surface
Matrix
Precipitate
φ
B
boundary between matrix and precipitate
(111)Matrix // (0001)Precipitate
intensity variation causing striation

Fig. 2. The intensity variation of electron beam along the incident direction in a wedge-shaped part of the precipitate. The figure represents a cross section parallel to (110) of the matrix.

The present investigation has partly been supported by the fund of the Ministry of Education in Aid of Scientific Researches.

References

1) R. Castaing: Rev. Metall. **52** (1955) 669.
2) A. Winkelmann: Z. angew. Phys. **7** (1955) 7.
3) A. Winkelmann: Z. Metallkunde **47** (1956) 621.
4) D. Watanabe: J. Phys. Soc. Japan **11** (1956) 1072.
5) H. Göttsche: Z. Phys. **134** (1953) 504.
6) A. Guinier: J. Phys. Radium **8** (1942) (3) 124. A. Guinier: Z. Metallkunde **43** (1952) 217. C. B. Walker and A. Guinier: Comt. Rend. **234** (1952) 2379., Acta. Met. **1** (1953) 568.
7) V. Gerold: Z. Metallkunde **46** (1955) 623.
8) A. H. Geisler and J. K. Hill: Acta Cryst. **1** (1948) 238.
9) R. D. Heidenreich: Acta. Met. **3** (1955) 79.
10) R. Glocker, W. Köster, J. Scherb and G. Ziejler: Z. Metallkunde **43** (1952) 208.
11) H. K. Hardy and T. J. Heal: Progr. Met. Physics **5** (1954) 143.
12) M. J. Whelan and P. B. Hirsch: Phil. Mag. **2** (1957) 1121, 1303.
13) R. D. Heidenreich: Phys. Rev. **62** (1942) 291.
14) E. Kinder: Naturwiss. **31** (1943) 149.
15) T. Hibi, K. Kambe and G. Honjo: J. Phys. Soc. Japan **10** (1955) 35.

JOURNAL OF THE PHYSICAL SOCIETY OF JAPAN Vol. 14, No. 12, DECEMBER, 1959

Dielectric Properties of Mixed Crystals of Barium-Strontium Titanate

By Shunkichi KISAKA, Seiji IKEGAMI and Hiromu SASAKI

Radio Department, Matsushita Electric Industrial Co., Ltd. Kadoma, Osaka

(Received April 15, 1959)

Mixed crystals of (Ba-Sr)TiO_3 containing up to about 10 mole per cent of Sr were grown in the same triangular plate shape as $BaTiO_3$ single crystals, and dielectric measurements were performed thereon. Up to 2.25 mole per cent Sr, the dielectric constant *vs* temperature (ε-T) curve near the cubic-tetragonal transition temperature maintains the same form as that of pure $BaTiO_3$, the peak value rising with increasing Sr content. Above 5.64 mole per cent Sr, however, the ε-T curve has a rounded peak and the peak value drops remarkably. The temperature of maximum dielectric constant decreases with increasing Sr content at a constant rate of 2.9°C per mole per cent in spite of this change. The Curie-Weiss temperature also drops with increasing Sr content at nearly the same rate, the difference between these two temperatures being held at about 20°C. The Curie constant also seems to decrease slightly with increasing Sr content. A comparison between the effect of replacing Ba with Sr and the effect of hydrostatic pressure on the transition temperature and the lattice constant suggests that the transition temperature depends mainly on the lattice constant of the tetragonal c-axis.

§ 1. Introduction

Many investigations[1)–6)] concerning the ceramics of (Ba-Sr)TiO_3 solid solution have been made in order to improve the dielectric and the piezoelectric properties of $BaTiO_3$ ceramics, or for other purposes. On the other hand, Remeika's method[7)] for growing $BaTiO_3$ single crystals in which potassium fluoride (KF) is used as a solvent and by which good plate-like crystals are obtained, has extensively and rapidly advanced the fundamental studies on $BaTiO_3$. In the course of our studies on ferroelectric crystals, preparations of mixed crystals with varying strontium (Sr) content from zero up to 10 mole per cent have been tried out by Remeika's method. As a result, the mixed crystals containing Sr of about 10 mole per cent were still found to be able to grow in the same triangular plate shape as does the pure $BaTiO_3$. Reports on the crystal containing Sr of more than 10 mole per cent can be found indeed, but these are all on the "chunky" crystals, and there seems to have been no known case that plate-like crystals have been grown at 10 mole per cent Sr.

In this paper, the results of the dielectric measurements on our single crystals are reported, and compared with those on ceramics of (Ba-Sr)TiO_3 solid solution. The effect of substitution of Sr for barium (Ba) on the transition character is also compared with the influence of hydrostatic pressure on that of $BaTiO_3$ single crystal.

§ 2. Preparation of Crystals

Crystals have been grown by Remeika's method from the solution of 30 grams of mixture in a desired ratio of each powder of $BaTiO_3$ and $SrTiO_3$ in the solvent of 70 grams of KF[8)], using the compositions of solute and solvent as shown in Table I. When the Sr content in solute is increased above 8 mole per cent, crystals having the shape of trian-

Table I. Composition of solute and solvent used for growing (Ba-Sr)TiO_3 mixed crystals.

Number	Solvent KF (g)	Solute		Sr content in solute (mole %)
		$BaTiO_2$ (g)	$SrTiO_3$ (g)	
BS–1	70	30.00	0.00	0.00
BS–2	70	29.53	0.47	1.98
BS–3	70	29.05	0.95	3.99
BS–4	70	28.57	1.43	5.99
BS–5	70	28.08	1.92	8.00
BS–6	70	27.59	2.41	9.99

gular plates (plate-like crystals) tend to decrease in number, but even in the case of BS–6 (Table I), which contains 10 mole per cent Sr, plate-like crystals having one side of more than 10 mm length could still be grown in pairs. So-called "chunky" crystals also grew at the same time. Chemical and X-ray analyses have been performed on both forms of crystals, but only the plate-like crystals have been used in the measurement of the dielectric properties.

Table II. Sr content in plate-like and chunky crystals determined by chemical analyses.

Number	Sr content in solute (mole %)	Sr content in crystal	
		plate-like (mole %)	chunky (mole %)
BS–1	0.00	0.00	0.00
BS–2	1.98	1.40	2.39
BS–3	3.99	2.25	3.05
BS–4	5.99	5.64	5.66
BS–5	8.00	9.06	17.65
BS–6	9.99	9.45	12.51

Table III. Lattice constants of mixed crystal of (Ba-Sr)TiO$_3$ at room temperature by X-ray analyses.

Number	Lattice constant of crystal (Å)			
	plate-like		chunky	
	a-axis	c-axis	a-axis	c-axis
BS–1	3.9960	4.0318	3.9962	4.0342
BS–2	3.9951	4.0292	3.9934	4.0306
BS–3	3.9939	4.0283	3.9930	4.0255
BS–4	3.9933	4.0249	3.9931	4.0249
BS–5	3.9902	4.0223	3.9893	4.0217
BS–6	3.9914	4.0203	3.9912	4.0231

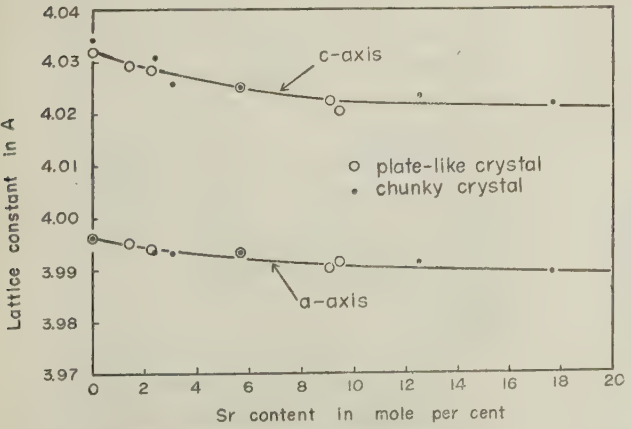

Fig. 1. The variation of lattice constant against Sr content.

§ 3. Chemical and X-ray Analyses

Molar percentage of Sr contained in crystals grown, according to the results of chemical analyses, are shown in Table II. Content of Sr in plate-like crystals is in general smaller than that in the original solute. But in chunky crystals, much more Sr was sometimes found therein than in the solute. Therefore, Sr content in the crystal could not be estimated from that in the solute. On the other hand, content of undesirable elements was found to be very little (less than 0.1 per cent in total), and the spectroscopic analyses, too, showed only faint traces of these impurities.

Moreover, lattice constants of plate-like and chunky crystals were measured by X-ray spectrometer at room temperature (30±2°C). These results are shown in Table III.

Fig. 1 shows the lattice constants of the tetragonal axes of these crystals plotted against Sr content obtained by chemical analyses. Both lattice constants decrease at the same rate with increasing Sr content. This figure will be used to obtain a relation between the Curie temperature and the lattice constant.

§ 4. Dielectric Properties

Only plate-like crystals have been used in measurements of the dielectric properties, since our chunky crystals had small sizes and irregular shapes. Measurements were performed mainly on the dielectric constant-temperature characteristics near the cubic-tetragonal transition temperature. From these measurements, the transition temperature, thermal hysteresis, and discontinuity were obtained as function of Sr content, and the Curie-Weiss temperature and the Curie constant were obtained either graphically or by calculations. Three to five crystals were selected from each group for these measurements.

(1) Method of Measurement of the Dielectric Constant-Temperature Characteristics.

Silver electrodes with guard rings

were evaporated on each crystal in vacuum. Diameter of the guarded electrode is 1.5 to 1.9 mm, the inner diameter of the guard electrode 2.2 to 2.8 mm, and the outer diameter of the guard electrode and the diameter of unguarded electrode are about 4.5 mm. Thickness of crystals is 0.065 to 0.44 mm. Fig. 2 shows the block diagram of the circuit for measuring the electric capacity-temperature characteristics. As shown there, the temperature of the crystal was measured by an iron-constantan thermocouple attached to the guard electrode, its output being fed to the X-axis input terminals of the X-Y recorder. A D.C. voltage proportional to the electric capacity of the specimen was fed to the Y-axis input terminals of the recorder. Thus the dielectric constant-temperature characteristics were automatically recorded by changing slowly the temperature of the specimens.

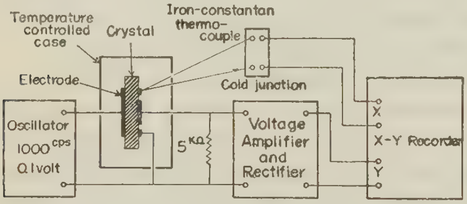
Temperature controlled case
Crystal
Iron-constantan thermo-couple
Electrode
Cold junction
Oscillator
1000 cps
0.1 volt
5 KΩ
Voltage Amplifier and Rectifier
X
X-Y Recorder
Y

Fig. 2. A block diagram of the circuit for measurement of the electric capacity-temperature characteristics.

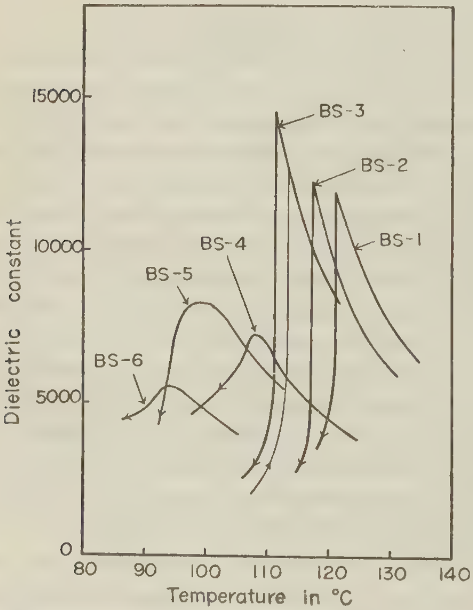

Fig. 3. Representative dielectric constant-temperature characteristic curve.

(2) Results of Measurements and Calculations.

In Fig. 3 is shown the most representative among the dielectric constant-temperature curves of the crystals of each group near the transition temperature. These curves actually show thermal hysteresis at the transition temperature (shown in the curve of BS-3 as an example), and the differences between the temperature of maximum dielectric contant in rising temperature and that in falling temperature are 2 to 4°C. Curves in Fig. 3 show only for decreasing temperature, except for BS-3 which shows both heating and cooling curves.

As is seen in Fig. 3, the characteristic curves for the specimens of BS-2 and BS-3 have similar shapes to that of BS-1 (pure $BaTiO_3$), that is, these curves drop discontinuously at the transition temperature, and the maximum value of the dielectric constant increases with increasing Sr content. But in the specimens BS-4, BS-5 and BS-6, containing more Sr, the discontinuity at the transition temperature disappears and the maximum value also drops, showing an obvious difference from the former. Therefore, it may be said that there is a limit in Sr content below which the transition character of crystal is very little influenced by the substitution of Sr for Ba, but above which it is considerably done. So far as our

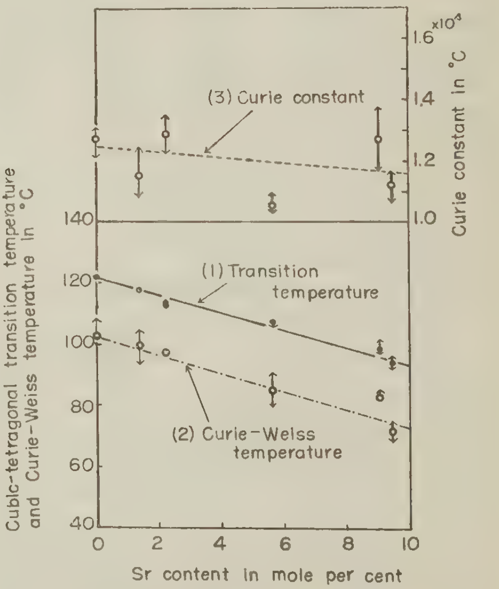

Fig. 4. Variations of the transition temperature, the Curie-Weiss temperature, and the Curie constant with increasing Sr content.

crystals are concerned, this limiting point must lie within 2.25 to 5.64 mole per cent. In the previous reports on ceramics or single crystals of (Ba-Sr)TiO_3 solid solution, this transition from discontinuous to rounded curve have been little noticed because of large rate of change of Sr content in preparation of specimens.

The transition temperature, defined as the temperature of maximum dielectric constant for decreasing temperature, decreases linearly with increasing Sr content, as shown in the curve (1) in Fig. 4. The arrows accompanying each point show the range of the measured values. The rate is estimated as 2.9°C per mole per cent within the range examined.

The average values of the Curie-Weiss temperature and the Curie constant, obtained from the reciprocal dielectric constant *vs.* temperature curve, are shown, respectively, in curves (2) and (3) of Fig. 4. The Curie-Weiss temperature also decreases with increasing Sr content, but in the range of our measurements, the difference between the transition and the Curie-Weiss temperature remained nearly constant independent of Sr content.

The Curie constant also seems to decrease slightly with increasing Sr content, but the values measured show a wide range of variation even among crystals of the same group, so that no definite conclusion can be drawn.

§ 5. Discussion

From the change of the shape of the dielectric constant-temperature curve and the shift of the transition temperature with Sr content mentioned above, it will be concluded that:

(a) Up to about 10 mole per cent Sr, essential character of the transition in the dielectric properties is scarcely influenced.

(b) The substitution of Ba by Sr take place in the form of a homogeneous solid solution up to 2.25 mole per cent.

(c) For Sr content of above 5.64 mole per cent, the crystal is supposed to be in the state of inhomogeneous solid solution, although no localization of constituents could be detected by our X-ray analyses, and because of this inhomogeneity, the dielectric behavior is averaged over a whole crystal, and consequently the dielectric constant-temperature curve has a rounded peak.

In our case, the transition from the homogeneous to the inhomogeneous solid solution occurred somewhere between 2.25 and 5.64 mole per cent Sr. However, it may be possible for this transition to shift to more Sr content by changing some of the conditions in the preparation of crystal.

The shift of the cubic-tetragonal transition temperature in ceramics containing Sr more than 10 mole per cent has been reported by many workers with, however, widely varying results, for instance, S. Sawada *et al*[1]. gave 2.9, D. F. Rushman *et al.*[2] 3.0, W. Jackson *et al.*[3] 3.9, and W. B. Westphal[4] 1.8°C per mole per cent.

The measurements on chunky crystals gave a decrease of Curie temperature of about 3.4[9] and 2.0[10] °C per mole per cent. In general, composition of crystal is different from that of solute, so that it is probable that these results on chunky crystals need to be corrected for Sr content. Though our measurements on the plate-like crystals are not of wide range, it is plausible that the rate of the shift of the transition temperature in (Br-Sr)TiO_3 system is 2.9°C per mole per cent.

Merz[11] observed the influence of hydrostatic pressure upon the transition temperature in $BaTiO_3$ single crystal and compared it with the effect of (Ba-Sr)TiO_3 solid solution. Namely, on the basis of the fact that the application of hydrostatic pressure and the replacement of Ba by Sr in $BaTiO_3$ had likewise the effects of both decreasing the lattice constant and lowering the transition temperature, he calculated the change of the transition temperature with lattice constant for each case, and obtained 3.3×10^3°C Å^{-1} from hydrostatic pressure and of 2.8×10^3°C Å^{-1} from ceramics of solid solution, in quite a good agreement with each other in spite of its simple treatment.

Let us now make similar calculations from a slightly different aspect. Using the results on our crystals (Fig. 1 and 4), the changes of the transition temperature are evaluated against the rates of decrease of:

(a) lattice constant a

(b) lattice constant c

(c) volume a^2c

Similar evaluations are made for the result of hydrostatic pressure, using the elastic compliances s^E of $BaTiO_3$ single crystal by Berlincourt *et al.*[12]. The results are shown in Table IV. As shown therein, both results show good agreement only for the rate of change with respect to the c-axis. This would possibly suggest that the transition temperature depends mainly upon the lattice constant c, but not upon a.

Table IV. Rate of decrease of the transition temperature with change of the lattice constant. a, c and v indicate the lenght of a- and c-axis and the volume of a unit cell respectively, and θ is the transition temperature.

	Rate (°C)	
	substitution by Sr	hydrostatic pressure
$\Delta\theta/(\Delta a/a)$	2.06×10^4	12.45×10^4
$\Delta\theta/(\Delta c/c)$	1.19 〃	1.10 〃
$\Delta\theta/(\Delta v/v)$	0.55 〃	0.93 〃

Merz also reported a slight increase of the peak value of the dielectric constant by hydrostatic pressure, which is similar to our results for $(Ba\text{-}Sr)TiO_3$ mixed crystals with Sr content of up to 2.25 mole per cent. This is a further confirmation of the analogy between the effect of hydrostatic pressure and that of Sr content.

The difference between the transition and the Curie-Weiss temperture, obtained from measurements on many crystals ranging from pure specimens of $BaTiO_3$ to the specimens containing about 10 mole per cent Sr is 20°C. The values obtained by Drougard *et al.*[13] and other workers are about 10°C, only a half of ours. Reason for this discrepancy is not clear.

The Curie constant of pure $BaTiO_3$ single crystal (BS–1 in our case) is 1.27×10^4°C (C.G.S.) in average, in fairly good agreement with that by Merz[14] (1.35×10^4) and by Drougard *et al.*[13] (1.38×10^4°C). It decreases slightly with increasing Sr content, but confirmation of this tendency should await further study, perhaps after growing the plate-like crystals containing more Sr if at all possible.

§ 5. Summary

(1) Mixed crystals of $(Ba\text{-}Sr)TiO_3$ containing Sr up to about 10 mole per cent have been grown in the same triangular shape as the crystal of $BaTiO_3$.

(2) Thermal hysteresis is generally 2 to 4°C.

(3) Below 2.25 mole per cent of Sr, the dielectric constant-temperature curve holds the same shape as that of pure $BaTiO_3$ near the cubic-tetragonal trasition, having a discontinuity, and the maximum of the dielectric constant increases with increasing Sr content. Above 5.64 mole per cent of Sr, the peak is rounded and the maximum value drops remarkably.

(4) The transition temperature decreases linearly at a rate of 2.9°C per mole per cent with increasing Sr content, in spite of the change of shape of the characteristic curve.

(5) The Curie-Weiss temperature also drops at nearly the same rate as the transition temperature, and the difference between these two temperatures is about 20°C.

(6) The Curie constant seems to decrease slightly with increasing Sr content.

(7) The transition temperature depends mainly on tetragonal c-axis.

Acknowledgement

The authors wish to express their sincere thanks to Dr. T. Suita, Dr. R. Kiriyama, and especially Dr. K. Yosida of Osaka University for their valuable suggestions. They are also indebted to Mr. C. Okazaki, Mr. S. Mori and Mr. F. Kanamaru in this Laboratory for their X-ray analyses, and to Mr. M. Itaya and Mr. N. Masaki for their help in the experiments.

References

1) S. Sawada and S. Nomura: Report Inst. Sci. Technol. Univ. Tokyo **4** (1950) 217.
2) D. F. Rushman and M. A. Strivens: Trans. Faraday Soc. **42** (1946) A 231.
3) W. Jackson and W. Reddish: Nature **156** (1945) 717.
4) W. B. Westphal: Progress Report 18, Lab. Ins. Res., M. I. T., (1955) 22.
5) N. S. Novosil'tsev *et al.*: Zhur. Tekh. Fiz. **26** (1956) 310.
6) M. Mcquarrie: J. Amer. Cer. Soc. **38** (1955) 444.
7) J. P. Remeika: J. Amer. Chem. Soc. **76** (1954) 940.
8) S. Kisaka, S. Ikegami and H. Sasaki: Read at the Symposium on the Synthetic Minerals in Nagoya on 6th, Nov. 1958.
9) A. L. Khodakov *et al.*: Dokl. Akad. Nauk.

S. S. S. R. **108** (1956) 825.
10) T. Sakudo. Read at the Meeting (Dielectric Division) of the Physical Society of Japan, March 1958.
11) W. J. Merz: Phys. Rev. **78** (1950) 52.
12) D. Berlincourt and H. Jaffe: Phys. Rev. **111** (1958) 143.
13) M. E. Drougard and D. R. Young: Phys. Rev. **95** (1954) 1152.
14) W. J. Merz: Phys. Rev. **91** (1953) 513.

JOURNAL OF THE PHYSICAL SOCIETY OF JAPAN Vol. 14, No. 12, DECEMBER, 1959

Exciton Structures in Alkali Halides

By Yukio OSAKA

Physical Institute, Tohoku University, Sendai

(Received July 20, 1959)

Exciton structures in alkali-halides are analyzed according to the p^5d configurations based on the "transfer" model for exciton. The ratio of intensity of the absorption peak which is estimated from the p^5d configuration are calculated for some values of parameters. Qualitative comparison with the experimental facts are also given.

§ 1. Introduction

Recentry, the complicated structures of exciton in alkali-halides are found by the experiment on the optical absorption at lower temperatures. We shall investigate this structure from the view of atomic spectroscopy. Peterson(1) analyzed the ratio of intensity between the peaks corresponding to the doublet splitting. He used the atomic data of rare gas which is of isoelectronic configuration with the atoms constituting the crystal concerned. Recent experiments have revealed the many absorption peaks which do not correspond to the doublet splitting. Overhauser(2) calculated the number of absorption peaks which is predicted from the "transfer" model for the exciton. When we analyze the experimentally observed structure of exciton absorption, we need the number of absorption peaks and the ratio of intensity among these peaks which are estimated theoretically. We shall investigate the absorption peaks which do not correspond to the doublet splitting, by introducing the higher p^5d configuration. Although our treatment is carried out using the method of atomic spectroscopy, our analysis is based on the "transfer" model for the exciton.

§ 2. Exciton Structure

As mentioned above, experiments have shown that there appear the absorption peaks which have a splitting nearly equal to the doublet splitting in halogen atom and whose intensities are nearly equal. This experimental fact suggests that in exciton states which have an effect on the optical absorption, the spin-orbit interaction of a hole is larger than the exchange interaction between a hole and an electron. Peterson(1) estimated the ratio of the intensities of the lines corresponding to this splitting, by using the data of atomic spectra in rare gas. This treatment is implicitly based on the assumption that the optical absorption of an exciton is the atomic excitation in halogen ions. We shall assume that the spin orbit interaction of the hole is larger than the exchange interaction between the hole and the electron and investigate the absorption peaks which do not corresponds to the doublet splitting.

We introduce the higher p^5d configuration which is allowed in the optical transition from the ground state p^6. In cubic crystals, d orbits split in $d\varepsilon$ level and $d\gamma$ level. This splitting is large when crystalline electric field is large in case of the atomic d level in solids. In case of an exciton, another effect determine predominantly the splitting between $d\varepsilon$ and $d\gamma$. This effect occurs in the "transfer" model for an exciton. If the energy of empty

p orbit on the alkali-ion is much higher than that of empty s orbit, the electron on the halide-ion transfers only to s orbit on the alkali-ion. In such a case, the L.C.A.O. wave function constructed only from the transferred s orbit includes the wave function having the $d\gamma$ character in the crystals of NaCl-type structure and $d\varepsilon$ in the crystal of CsCl-type structure, as Overhauser[2)] showed. Therefore, the main factor determining the splitting between $d\varepsilon$ and $d\gamma$ is the difference of energy between s-orbit and p-orbit on the alkali-ion. The effect of crystalline fields for the electron is smaller in the "transferred" model for an exciton, because the largest contribution to the crystalline field arises from the next-nearest ions and the crystalline field is cubic. But the approximation which takes into account the s-orbit only as Overhauser did does not seems to hold in the alkali-halide crystal. In the first approximation, the wave function of the electron in the exciton states is similar to that of the trapped electron in case of the F-center. The experimental and theoretical investigations[3)] for the F-center showed that the ground-state wave function of the F-center is constituted by the s-orbit and p-orbit in nearly equal proportion. It seems to be reasonable that similar situation exists in the exciton states. Therefore, we assume that the energy of $d\varepsilon$ level and $d\gamma$ level are nearly equal, that is, we can use the approximately degenerate d level. But, this "d level" mainly makes up the electron transferred orbit rather than the orbit of intra-atomic excitation. Therefore, the following treatment is based on the "transferred" model for the exciton. On the "excitation" model for the exciton, we cannot neglect the effect of the crystalline electric field even approximately.

The ground state S_0 has the p^6 configuration. According to the selection rule, the pure states to which the optical transition is allowed are ${}^1P_1(p^5s)$ and ${}^1P_1(p^5d)$, leaving the higher configurations out of account.

At first, we neglect the exchange interaction between the electron and the hole and consider, in addition to the Coulomb interaction between them, only the spin orbit interaction of the hole. Diagonal energy for the electrostatic energy is given in the following.

$$\left.\begin{aligned} &{}^1P_1(p^5s)\,,\quad {}^3P_1(p^5s)=-F_0 \\ &{}^1P_1(p^5d)\,,\quad {}^3P_1(p^5d)=-F_0'-7F_2'+\varDelta \\ &\qquad\qquad\quad\; {}^3D_1(p^5d)=-F_0'+7F_2'+\varDelta\,, \end{aligned}\right\} \quad (1)$$

where $\varDelta$ denotes the difference of energy between s-function and d-function for the electron and F_0, F_0' and F_2' are derived from the following F^0, $F^{0\prime}$, $F^{2\prime}$ in the same way as T.A.S.[8)], they are all positive quantities. Where

$$F^0=\iint P_s^2(r_1)Q_p^2(r_2)\alpha^0(r_1r_2)\,d\tau_1\,d\tau_2$$

$$F^{0\prime}=\iint P_d^2(r_1)Q_p^2(r_2)\alpha^0(r_1r_2)\,d\tau_1\,d\tau_2$$

$$F^{2\prime}=\iint P_d^2(r_1)Q_p^2(r_2)\alpha^2(r_1r_2)\,d\tau_1\,d\tau_2\,.$$

$P(r_1)$ denotes the radial part of the wave function multiplied by radius for the electron and $Q(r_2)$ denotes the one for the hole. $\alpha^k(r_1r_2)$ is given by

$$\alpha^k(r_1r_2)=\begin{cases} r_1^k/r_2^{k+1} & r_1<r_2 \\ r_2^k/r_1^{k+1} & r_2>r_1 \end{cases}$$

and

$$F_2'=F^{2\prime}/35\,.$$

From these value, we get the following matrix of energy for the five atomic terms.

$$\left.\begin{array}{cccccc} & {}^1P_1(p^5s) & {}^3P_1(p^{53}) & {}^1P_1(p^5d) & {}^3P_1(p^5d) & {}^3D_1(p^5d) \\ {}^1P_1(p^5s) & -F_02 & 2\sqrt{2}\,\lambda & A & 0 & 0 \\ {}^3P_1(p^5s) & 2\sqrt{2}\,\lambda & -F_0+2\lambda & 0 & A & 0 \\ {}^1P_1(p^5d) & A & 0 & \varDelta-F_0'-7F_2' & \sqrt{2}\,\lambda & \sqrt{6}\,\lambda \\ {}^3P_1(p^5d) & 0 & A & \sqrt{2}\,\lambda & \varDelta-F_0'-7F_2'-\lambda & \sqrt{3}\,\lambda \\ {}^3D_1(p^5d) & 0 & 0 & \sqrt{6}\,\lambda & \sqrt{3}\,\lambda & \varDelta-F_0'+7F_2'+\lambda\,. \end{array}\right\} \quad (2)$$

λ is the constant determined by the spin orbit coupling. If we consider the (p^5s) configuration, the doublet splitting ξ is related to λ by

$$\lambda=\xi/6\,.$$

A is the nondiagonal coulomb interaction between ${}^{1,3}P_1(sp^5)$ and ${}^{1,3}P_1(dp^5)$. This term has been calculated making use of the formula given by Racah[4]. The non-vanishing term is the term including the following $F^{1''}$ because of symmetry.

$$F^{1''}=\iint P_s(r_1)P_d(r_1)\alpha^1(r_1r_2)Q_p{}^2(r_2)\,d\tau_1\,d\tau_2\,.$$

But the multiplicative factor for $F_1{}^{1''}$ is shown to be zero, using the formula of Racah[4]. Then, matrix (2) is reduced into two parts. The part for the (p^5d) configuration is

$$\Delta-F_0'-7F_2'+\begin{pmatrix} 0 & \sqrt{2}\lambda & \sqrt{6}\lambda \\ \sqrt{2}\lambda & -\lambda & \sqrt{3}\lambda \\ \sqrt{6}\lambda & \sqrt{3}\lambda & \lambda+14F_2' \end{pmatrix}. \tag{3}$$

The part for the (p^5s) configuration is

$$-F_0+\begin{pmatrix} 0 & 2\sqrt{2}\lambda \\ 2\sqrt{2}\lambda & 2\lambda \end{pmatrix}. \tag{4}$$

We shall calculate the energy and the wave function given by the matrix (3). In order to solve matrix (3), we transform it by the orthogonal transformation matrix T.

$$T=\begin{pmatrix} 1/\sqrt{3} & 1/\sqrt{6} & -1/\sqrt{2} \\ 1/\sqrt{3} & -\sqrt{2/3} & 0 \\ 1/\sqrt{3} & 1/\sqrt{6} & 1/\sqrt{2} \end{pmatrix}.$$

Then, matrix (3) transforms into the following matrix.

$$\lambda\begin{pmatrix} -2+\dfrac{\alpha}{2} & 0 & -\dfrac{\alpha}{2} \\ 0 & -2 & 0 \\ -\dfrac{\alpha}{2} & 0 & 4+\dfrac{\alpha}{2} \end{pmatrix}.$$

where

$$\alpha\equiv 14F_2'/\lambda\,.$$

From this matrix, we obtain the eigenvalue and the eigenfunction of (3) as follows.

eigenvalue	eigenfunction	
-2λ,	$\dfrac{1}{\sqrt{3}}{}^1P_1-\sqrt{\dfrac{2}{3}}{}^3P_1$,	(5a)
$\lambda\dfrac{(2+\alpha)+\sqrt{\alpha^2+36}}{2}$,	$\cos\theta\left(\dfrac{1}{\sqrt{3}}{}^1P_1+\dfrac{1}{\sqrt{6}}{}^3P_1-\dfrac{1}{\sqrt{2}}{}^3D_1\right)$ $-\sin\theta\left(\dfrac{1}{\sqrt{3}}{}^1P_1+\dfrac{1}{\sqrt{6}}{}^3P_1+\dfrac{1}{\sqrt{2}}{}^3D_1\right)$,	(5b)
$\lambda\dfrac{(2+\alpha)-\sqrt{\alpha^2+36}}{2}$,	$\sin\theta\left(\dfrac{1}{\sqrt{3}}{}^1P_1+\dfrac{1}{\sqrt{6}}{}^3P_1-\dfrac{1}{\sqrt{2}}{}^3D_1\right)$ $+\cos\theta\left(\dfrac{1}{\sqrt{3}}{}^1P_1+\dfrac{1}{\sqrt{6}}{}^3P_1+\dfrac{1}{\sqrt{2}}{}^3D_1\right)$,	(5c)

where

$$\mathrm{coo}\,\theta=\sqrt{\frac{1}{2}+\frac{3}{\sqrt{\alpha^2+36}}}\,,\qquad \sin\theta=\sqrt{\frac{1}{2}-\frac{3}{\sqrt{\alpha^2+36}}}\,, \tag{6}$$

Since the ground state is the $S_0(p^6)$ configuration, the ratio of intensity arising from the transitions to the above levels is given by

$$1:(\cos\theta-\sin\theta)^2:(\cos\theta+\sin\theta)^2\,. \qquad (7)$$

The difference of energy among these levels and the ratio of intensity are calculated for some values of α. In Fig. 1, we plot this result. The line due to the transition to the level which is mainly constructed by the $^3D_1$ term is omitted, because the intensity of this level must be very weak. Since we do not know the difference between the average energy of the p^5s configuration and that of the p^5d configuration, we slide Fig. 1 as compared with the observed doublet splitting and compare this expected ratio of intensity and the positions of the lines with the observed peaks which do not correspond to the doublet splitting. Martienssen's[6] experiment for CsI and Teegarden's[7] experiment for KI are qualitatively similar to the case $\alpha \gtrsim 10$ and the case $\alpha \lesssim 5$, respectively. But the expected ratio of intensity is larger than the experimental value in case of KI.

Next, we shall take into account the effect of exchange interaction between the electron and the hole. The energy of p^5d configuration including the exchange interaction is given by Condon-Shortley[8]. This result is as follows;

$$^3D_1=-F_0'+7F_2'$$
$$^3P_1=-F_0'-7F_2'$$
$$^1P_1=-F_0'-7F_2'+20G_1'$$

G_1' is the energy of exchange corresponding to F_1'. From this we obtain the matrix of energy for the p^5d configuration as follows:

$$\Delta-F_0'-7F_2'+\lambda\begin{pmatrix} \gamma & \sqrt{2} & \sqrt{6} \\ \sqrt{2} & -1 & \sqrt{3} \\ \sqrt{6} & \sqrt{3} & 1+\alpha \end{pmatrix},$$

where

$$\gamma\equiv 20G_1'/\lambda\,.$$

Transforming this matrix by the above orthogonal transformation matrix T, we get

$$\lambda\begin{array}{c} \begin{array}{ccc} \quad {}^3P_1 \quad & \quad {}^3D_1 \quad & \quad {}^1P_1 \quad \end{array} \\ \begin{pmatrix} -2+\frac{1}{3}(\alpha+\gamma) & -\frac{\alpha}{2}+\frac{\gamma}{3} & \frac{\gamma}{3} \\ -\frac{\alpha}{2}+\frac{\gamma}{3} & 4+\frac{\alpha}{2}+\frac{\gamma}{3} & \frac{\gamma}{3} \\ \frac{\gamma}{3} & \frac{\gamma}{3} & -2+\frac{\gamma}{3} \end{pmatrix} \end{array}. \qquad (9)$$

For $\gamma \ll \alpha$, we can omit the nondiagonal term $\gamma/3$ in the first approximation.

The parts of the matrix for the $^3P_1$ and $^3D_1$ configuration is written

$$\begin{pmatrix} -2+\frac{\alpha}{3}+\frac{\gamma}{3} & -\frac{\alpha}{2}+\frac{\gamma}{3} \\ -\frac{\alpha}{2}+\frac{\gamma}{3} & 4+\frac{\alpha}{2}+\frac{\gamma}{3} \end{pmatrix}$$
$$=\frac{\gamma}{3}+\begin{pmatrix} -2+\frac{\alpha}{2} & -\frac{\alpha}{2}+\frac{\gamma}{3} \\ -\frac{\alpha}{2}+\frac{\gamma}{3} & 4+\frac{\alpha}{2} \end{pmatrix}.$$

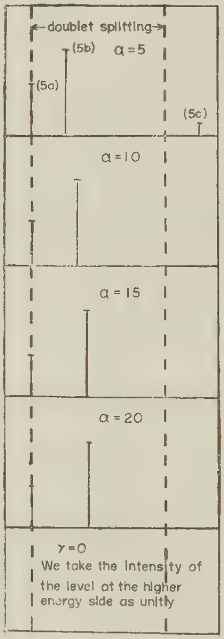

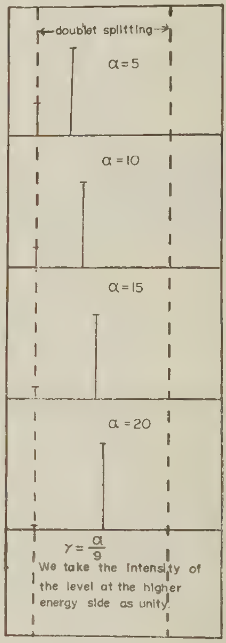

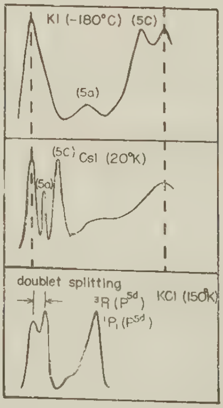

Fig. 1. Case of omitting the exchange interaction.

Fig. 2. Exciton absorption.

Fig. 3. Case of taking into account the exchange interaction.

Since the difference of the energy between the $^3P_1$ level and $^3D_1$ level is large, we omit $\gamma/3$ in the nondiagonal part of the above matrix. Then, we take as the unperturbed states the state of which the energy is determined by the matrix

$$\frac{\gamma}{3}+\begin{pmatrix} -2+\frac{\alpha}{2} & -\frac{\alpha}{2} \\ -\frac{\alpha}{2} & 4+\frac{\alpha}{2} \end{pmatrix} \quad \text{and} \quad -2+\frac{\gamma}{3}\,.$$

If the effect of the nondiagonal term $\gamma/3$ is taken into account as the perturbation between those states, we obtain the following results. The energy difference of the peaks which were shown in Fig. 1, is now modified to

$$\lambda\left(\frac{(2+\alpha)-\sqrt{\alpha^2+36}}{2}+2+\frac{2\gamma}{3}B\right),$$

where

$$B\equiv\gamma/3\bigg/\frac{(2+\alpha)-\sqrt{\alpha^2+36}}{2}+2\,.$$

The ratio of intensities of these peaks is

$$(1-B(\cos\theta+\sin\theta))^2 : ((\cos\theta+\sin\theta)+A)^2\,.$$

The results are shown in Fig. 3, where the parameter γ is set to the value $\alpha/9$.

The fact that the ratio of the intensity of the peaks decreases than in the case where the exchange interaction is omitted, is qualitatively similar to the experimental result of KI. Therefore, we can assign the peaks in KI and CsI to the perks due to the p^5d configuration as is shown in Fig. 2.

§ 3. Discussions

According to the experiment by Teegarden[7], the main feature of the absorption spectrum on KI and NaI is nearly similar. The exciton structures in Hartman's[9] experiment for NaCl and KCl are sketched in Fig. 2. The discussion in the preceeding section suggests that the experiment for NaCl and KCl may be the case $14F_2'\gg\xi\gg 20G_1'$. When $\alpha=14F_2'/\lambda$ is large, the doublet splitting in the p^5d configuration is at most half of that in the p^5s configuration. Therefore, the peak in the higher energy side seems to be the doublet splitting corresponding to the p^5d configuration, whose splitting is too small to be observed at present. From this speculation and the discussion in the preceeding section, it is expected that the parameters F_2', G_1' and ξ have the following relations in each crystals.

In KI (and similar iodide)

$$14F_2'\sim\frac{15}{6}\xi\,,\qquad 20G_1'\sim\frac{14F_2'}{9}\,.$$

In CsI

$$14F_2'\sim\frac{5}{6}\xi\,,\qquad 20G_1'\ll\frac{14F_2'}{9}\,.$$

In NaCl (and KCl)

$$14F_2'\gg\xi\gg G_1'\,.$$

we shall compare these relations with the atomic data of rare gas which has the isoelectronic configuration to the halide ions of the crystal. The intra-atomic excitation of the $2p^53d$ configuration in NeI has the following values according to T.A.S.[8].

F_2'	G_1'	$\xi/1.5$	$\xi/1.5$ (ionic)
15.50	2.98	530.11	521 (unite cm^{-1})

(ionic) denotes the doublet splitting of neon in the ionic configuration. This quantity corresponds to the doublet splitting in the neutral halide of the exciton. The ration F_2'/ξ for the exciton, which is predicted by our analysis, is larger than that of the data in neon. Since the transferred orbit in the alkali-ion has a smaller energy than the intra-atomic excitation in the halogen ion, this fact is understood. The larger values of F_2'/ξ for the exciton are understood. The tendency that F_2' decreases when the energy becomes larger, is confirmed experimentally by the fact that, in Neon I, the values of F_2' are 15.50, 6.60, 3.62 (cm^{-1}), respectively, in case of the excitation p^53d, p^54d, p^55d.

Experimentally, the intensities of the components of the doublet in the exciton which corresponds to that of the neutral halogen atom are nearly equal. These lines are due to the p^5s cofiguration. In case of the atomic spectrum of rare gas, the intensities in KrI are nearly equal. In this case, $G_1\sim 0.150\xi$. where G_1 is the quantity in the p^5s configuration corresponding to G_1' in the p^5d configuration. Therefore, this ratio between G_1 and ξ in the p^5s configuration seems to be reasonable in the p^5s configuration of an exciton. Taking the above estimated value of G_1', the ration $G_1'/G_1\sim 0.10$ in case of KI. In Neon I, in the p^53d configuration $G_1'/\xi\sim 0.4\times10^{-2}$ and in the p^53s configuration $G_1/\xi\sim 2$. From these values $G_1'/G_1\sim 0.2\times10^{-2}$.

Therefore, the value G_1'/G_1 in the exciton of KI is larger than that of the atomic excitation in rare gas. Taking a view-point of the "transfer" model the wave functions in the $p^5 3s$ configuration and in the $p^5 3d$ configuration are not radically different as in the case of the intra-atomic excitation. Then, the large value G_1'/G_1 in the exciton can be understood on the "transfer" model for the exciton.

In our analysis, the difference of the absorption curve in KI and CsI is attributed to that of the magnitude of F_2'/ξ. This difference of F_2'/ξ may be due to that of the transferred orbit or the crystal structure.

Finally, we discuss the approximation neglecting the crystalline electric field for the transferred orbit, which comes from the next-nearest neighbour and the more distant neighbour. According to Bethe[10], the energy difference between $d\varepsilon$ orbit and $d\gamma$ orbit is given by

$$E(d\gamma)-E(d\varepsilon)=\frac{10}{21}D\langle r^4\rangle_{\text{av}}$$

where $\langle r^4\rangle_{\text{av}}$ denotes the average by the transferred orbit and

$$D=-(7e/8)\sum_j{}'(l_j/R_j^9)(5Z_j^4-R_j^4)$$

and l_j, R_j and Z_j are the charge, the distance from the origin and the Z-coordinate of the j-th ion, respectively. If the summation over the nearest neighbours and the more distant neighbours of D is expressed by D' and that over the next-nearest neighbour and the more distant neighbours is expressed by D'', we obtain

$$D'=-3.580e^2/a^5\ ,\quad D''=-0.080e^2/a^5$$

for the crystal of NaCl-type,

$$D'=+9.323e^2/a^5\ ,\quad D''=+2.936e^2/a^5$$

for the crystal of CsCl-type,

where a is the lattice constant.

In our model, D'' determines the effect of the crystalline electric field. From the above value of D'' we can neglect this effect for the crystal of NaCl type, because the overestimation in which we put $a^4=\langle r^4\rangle$ yields about-0.02 e.V., for the $E(d\varepsilon)-E(d\gamma)$, using the typical value of a. However, since the value D'' for the crystal of CsCl type is comparable with D', it seems that the crystalline electric field may have some effect on the absorption curve in CsI even on the "transferred" model for the exciton.

The author wish to express his cordinal thanks to his colleagues of the Physical Institute. Tôhoku University, for stimulating discussions. The present work was partially financed by the Scientific Research Fund of the Ministry of Education.

References

1) R. Peterson: Phys. Chem. of Solids. **1** (1957) 284.
2) A. W. Overhauser: Phys. Rev. **101** (1956) 1702.
3) Kip, Kittel, Levy and Portis: Phys. Rev. **89** (1953) 315. T. Kojima: Jour. of Phys. Soc. of Japan. **12** (1957) 908.
4) G. Racah: Phys. Rev. **61** (1942) 186.
5) Johnson, Phys. Rev. **38** (1931) 1628.
6) W. Martienssen: Phys. Chem. of Solids. **2** (1957) 1.
7) K. J. Teegarden: Phys. Rev. **108** (1957) 660.
8) E. U. Condon and G. H. Shortley: The Theory of Atomic spectra (Cambridge University Press) (1935)
9) P. L. Hartman et al: Phys. Rev. **105** (1957) 123.
10) H. Bethe: ann, d, Physik **3** (1929) 137.

JOURNAL OF THE PHYSICAL SOCIETY OF JAPAN Vol. 14, No. 12, DECEMBER, 1959

Acoustoelectric Effect in Metals

By Nobuo MIKOSHIBA

Electrotechnical Laboratory, Nagatacho, Tokyo

(Received July 27, 1959)

A classical Boltzmann theory is given of the acoustoelectric effect in monovalent metals, using Pippard's approach to the ultrasonic absorption by conduction electrons. Weinreich's phenomenological relation between the acoustoelectric effect and the ultrasonic absorption holds in all frequency ranges for both longitudinal and transverse ultrasonic waves. For longitudinal waves in the intermediate and high frequency ranges, the result is essentially identical with that derived from the quantum-mechanical calculation. The order of magnitude of the acoustoelectric effect in the low frequency range is smaller than Parmenter's result but larger than that obtained by Weinreich-Holstein's approach. A phenomenological theory is developed of the acoustoelectric effect due to electron transfer mechanism in polyvalent metals, the method of which can be applied also to many-valley semiconductors.

§ 1. Introduction

The theories of the acoustoelectric effect in metals have been developed by Parmenter[1] (hereafter denoted by P1), Van den Beukel[2] and the present author[3] in the *intermediate* and *high* frequency ranges, and by Parmenter[4] (hereafter denoted by P2), Weinreich[5] and Holstein[6] in the *low* frequency range. In the previous paper, we discussed that P1 seems deficient for several reasons and Van den Beukel's method may be applicable to real metals. In a recent paper, however, Weinreich et al.[7] have asserted that Van den Beukel's method cannot be correct because it neglects the effect of the space charge caused by ultrasonic waves. On the other hand, P2 and Weinreich-Holstein's approach lead to mutually conflicting results in the low frequency range.

The main object of this paper is to give a reasonable method for the calculation of the acoustoelectric effect in monovalent metals and to discuss Weinreich et al.'s assertion, P2 and Weinreich-Holstein's approach. We shall use the classical Boltzmann equation developed by Pippard[8] and Steinberg[9], of the ultrasonic absorption by conduction electrons, in which the effects of the space charge and the internal electric field are correctly taken into account. The important informations obtained in our theory are as follows:

1) Weinreich's phenomenological relation[10] between the acoustoelectric effect and the ultrasonic absorption holds in *all* frequency ranges for both longitudinal and transverse ultrasonic waves. Then the present author's argument[3] in the previous paper must be revised, which states that the other relation may exist in the low frequency range.

2) For longitudinal waves in the intermediate and high frequency ranges, the result is essentially identical with that derived from the quantum-mechanical calculation (Van den Beukel's method). Then we can conclude that Van den Beukel's method is suitable for the intermediate and high frequency ranges, and involves implicitly the effect of the space charge in the electron-phonon coupling constant.

3) For longitudinal waves in the low frequency range, the obtained result is smaller than that of P2 but larger than that obtained by Weinreich-Holstein's approach.

In § 2, we shall give a brief review of Pippard's theory in some modified form for later uses. In § 3 we shall calculate the acoustoelectric effect in monovalent metals. Comments on P2 and Weinreich-Holstein's approach are given in § 4.

In § 5, a phenomenological theory is developed of the acoustoelectric effect and the ultrasonic absorption due to electron transfer mechanism in polyvalent metals. This theory is also applicable to many-valley semiconductors in the low frequency range. In fact, this theory leads to Weinreich's formula[7] for n-Ge.

§ 2. Ultrasonic Absorption by Conduction Electrons

The Boltzmann equation of conduction electrons under the influence of acoustic waves[9] is given by

$$\frac{\partial f}{\partial t}+(\boldsymbol{v}\cdot\nabla)f+\frac{e}{m}(\boldsymbol{\varepsilon}\cdot\nabla_v)f=-\frac{f-f_0(|\boldsymbol{v}-\boldsymbol{u}|)}{\tau}\,, \qquad (2.1)$$

where $\boldsymbol{v}$ and $\boldsymbol{u}$ are the velocity of an electron and of lattice ions respectively, $\boldsymbol{\varepsilon}$ the internal electric field, τ the relaxation time and $f_0(|\boldsymbol{v}-\boldsymbol{u}|)$ the local equilibrium distribution function. The solution of (2.1) is approximated by

$$f=f_0(|\boldsymbol{v}-\boldsymbol{u}|)-\Psi(\boldsymbol{v})\cdot\partial f_0/\partial v\,, \qquad (2.2)$$

where $\Psi(\boldsymbol{v})$ has the physical meaning of the drift velocity, relative to the local equilibrium, of the electron with the velocity $\boldsymbol{v}$ (hereafter called electron $\boldsymbol{v}$) caused by acoustic waves. Unknown quantities $\boldsymbol{\varepsilon}$, n (nonequilibrium number density of electrons) and j (local current density) are determined by 1) the current expression by f, 2) Maxwell's equation and 3) the equation of continuity.

The absorption coefficient of acoustic waves is written as

$$A=2W/\rho V|u|^2\,, \qquad (2.3)$$

where ρ is the density of metals, V the sound velocity and W the absorbed energy by electrons per unit time and volume. W is given by the expression

$$W=\frac{1}{2}\,\mathrm{Re}\left[\sum_v\frac{E(v)}{\tau(v)}\cdot f'^*(v)\right] \qquad (2.4)$$

where $E(\boldsymbol{v})$ is the excess energy of the electron $\boldsymbol{v}$ from the local equilibrium value and $f'(\boldsymbol{v})$ is the deviation of f from the local equilibrium distribution. It is easily seen that

$$E(\boldsymbol{v})=m\boldsymbol{v}\Psi(\boldsymbol{v})\,,\quad f'(\boldsymbol{v})=-\Psi(\boldsymbol{v})\cdot\partial f_0/\partial v\,. \qquad (2.5)$$

In this connection, we can see that the electron $\boldsymbol{v}$ exerts the force

$$X'(\boldsymbol{v})=-m\boldsymbol{v}\Psi(\boldsymbol{v})/V\tau(\boldsymbol{v}) \qquad (2.6)$$

on acoustic waves, because the acoustic energy density $\frac{1}{2}\rho|u|^2$ suffers the energy loss $m\boldsymbol{v}\Psi(\boldsymbol{v})$ from the electron $\boldsymbol{v}$ in a distance $V\tau(\boldsymbol{v})$.

Inserting (2.4) and (2.5) into (2.3), we get Pippard's formula

$$A=\frac{3Nm}{4\pi\tau\rho V|u|^2}\int_0^\pi\int_0^{2\pi}|\Psi(\boldsymbol{v}_0)|^2\sin\theta d\theta d\phi\,, \qquad (2.7)$$

where we used the identity

$$\sum_v=\frac{2m^3}{h^3}\int v^2dv\sin\theta d\theta d\phi\,,$$

and N and $\boldsymbol{v}_0$ are the equilibrium number density and the Fermi velocity of electrons respectively.

§ 3. Acoustoelectric Effect in Monovalent Metals

The acoustoelectric effect F is defined as the *dc* electric field caused by acoustic waves under the open circuit condition. This definition is equivalent to that eF is the average *dc* force on electrons exerted by acoustic waves[7]. If we denote $X(\boldsymbol{v})$ as the force exerted by acoustic waves on the electron $\boldsymbol{v}$, we get

$$eF=\frac{1}{2N}\,\mathrm{Re}\,[\sum_v X(\boldsymbol{v})\cdot f'^*(\boldsymbol{v})]\,. \qquad (3.1)$$

From (2.6) we see

$$X(\boldsymbol{v})=-X'(\boldsymbol{v})=m\boldsymbol{v}\Psi(\boldsymbol{v})/V\tau(\boldsymbol{v})\,, \qquad (3.2)$$

using the principle of reaction. Then the formula

$$F=\frac{3m\gamma}{4\pi\tau\rho eV^2|u|^2}\int_0^\pi\int_0^{2\pi}|\Psi(\boldsymbol{v}_0)|^2\sin\theta d\theta d\phi \qquad (3.3)$$

is obtained, where $\gamma=\frac{1}{2}\rho|u|^2V$ is the acoustic energy flow density. Comparing (3.3) with (2.7), Weinreich's phenomenological relation

$$A=(NeV/\gamma)F \qquad (3.4)$$

is proved in general.

Making use of the calculation of A by Pippard, we get the following expressions in various cases:

1) Longitudinal Waves:

$$F=\frac{4mv_0{}^2\tau\omega^2}{15\rho eV^4}\cdot\gamma \quad \text{(low frequency range)}\,, \qquad (3.5)$$

$$F=\frac{\pi mv_0\omega}{6\rho eV^3}\cdot\gamma \quad \text{(intermediate and high frequency range)}\,. \qquad (3.6)$$

2) Transverse Waves:

$$F=\frac{mv_0{}^2\tau\omega^2}{5\rho eV^4}\cdot\gamma \quad \text{(low frequency range)}\,, \qquad (3.7)$$

$$F=\frac{4mv_0\omega}{3\pi\rho eV^3}\cdot\gamma \quad \text{(intermediate frequency range)}\,, \qquad (3.8)$$

$$F=\frac{m}{\rho eV^2\tau}\cdot\gamma \quad \text{(high frequency range)}\,, \qquad (3.9)$$

where ω is the angular frequency of waves.

The formula (3.6) is essentially the same as that derived from the quantum-mechanical calculation[2),3)], since the electron-phonon coupling constant has the order of magnitude of the Fermi energy. This fact implies that Van den Beukel's method involves the effect of the internal electric field in the electron-phonon coupling constant[11)].

It will be worth while to estimate whether the effect in metals can be detected experimentally at present. Since the maximum available frequency[12)] of ultrasonic waves may be $\nu=2.5\times10^9$ cyc/sec, we take, as an example, the purest sample of Cu at low temperatures; $\omega=1.6\times10^{10}$, $v_0=1.6\times10^8$ cm/sec, $\rho=9$ g/cm³, $V=5\times10^5$ cm/sec. Then, from (3.6) for longitudinal waves.

$$F\simeq10^{-8}\gamma\ ,$$

taking the units of F and γ as volt/cm and watt/cm² respectively. Therefore the experimental check may be expected in future.

As will be seen in the next section, we should remark that the formula (3.9) for *transverse* waves in the *high* frequency range is identical with Parmenter's result (4.3) for *longitudinal* waves in the *low* frequency range.

§ 4. Weinreich's and Parmenter's Approaches

Several years ago, Weinreich[5)] and Holstein[6)] calculated the acoustoelectric effect by *longitudinal* waves in the *low* frequency range in simple semiconductors, and got very small effect not detectable in experiments. In a recent paper[7)] (see § 5), Weinreich et al. have derived a correct formula in many-valley semiconductors, but have asserted, on the basis of the previous calculation[5),6)] that in metals the effect may be extremely small in virtue of the Coulomb repulsion between electrons. In fact, the straightforward application[4),6)] of Weinreich-Holstein's method to metals gives the small effect

$$F_1\simeq16\pi^4\left(\frac{\lambda_{FT}}{\lambda}\right)^4\cdot\frac{m}{\rho e\tau V^2}\cdot\gamma \tag{4.1}$$

with

$$\lambda_{FT}\equiv mv_0^2/12\pi Ne^2\ . \tag{4.2}$$

Here λ is the wave length of acoustic waves and λ_{FT} is the quantum analog to the Debye length in Fermi-Thomas model.

In a recent paper, Parmenter[4)] has revised Weinreich-Holstein's approach and got the formula

$$F_2\simeq(m/\rho e\tau V^2)\cdot\gamma \tag{4.3}$$

in both simple semiconductors and metals. In our method, this formula is obtained by setting

$$X_2=mu/\tau \tag{4.4}$$

instead of the force X in (3.2). The ratios of the formula F in (3.5) with F_1 and F_2 are

$$F/F_1=\frac{1}{60\pi^4}\left(\frac{\lambda}{\lambda_{FT}}\right)^4\cdot(ql)^2\ \text{ and }\ F/F_2=\frac{4}{15}(ql)^2\ , \tag{4.5}$$

under the condition of the same acoustic energy flow density, where q is the wave vector of waves and l is the mean free path of electrons. From the facts that $ql<1$ and $(\lambda/\lambda_{FT})^4\gg1$ in the low frequency range, we get the inequality $F_1<F<F_2$.

The physical reason of extremely small effect by Weinreich-Holstein's approach may lie on the neglect of the induced motion of lattice ions or charged impurities, as has been pointed out by Parmenter[4)]. On the other hand, Parmenter's method involves this effect; however, he has overestimated the force exerted by waves on electrons. The force X_2 in (4.4) implies that conduction electrons get the drift velocity u from acoustic waves in the time interval τ. But as will be seen from (2.2), the electrons with the drift velocity u are in local equilibrium and cannot affect the acoustic vibration, or inversely speaking they are exerted no force by waves. In fact, the drift velocity relative to u (i.e. relative to $f_0(|\boldsymbol{v}-\boldsymbol{u}|)$) contributes to Λ and F.

§ 5. Acoustoelectric Effect in Polyvalent Metals

According to Leigh's theory[13)] of the elastic stiffness constants of Al, the constant for the shear stress, c $(=c_{44})$, is written as $c=c_0-c_t$. Here c_0 is the component due to the stress-induced changes of the electrostatic energy, the exchange energy between ion cores and so forth; c_t is the component due to electron tranfer mechanism by the electrons which lie on near the centers of the hexagonal faces of the boundary of the Brillouin zone. The shear stress changes the potential energy of the electrons near the centers of the hexagonal faces antisymmetrically. Then the electrons with higher energy transfer to the lower energy positions in momentum space. This situation is analogous to that of many-valley semiconductors such as n-Ge.

For transverse ultrasonic waves, we consider the relaxation of the component of the elastic energy due to electron transfer mechanism and put

$$c=c_0-c_t/(1+i\omega\tau)\ . \tag{5.1}$$

This procedure is similar with Morse[14] and Kittel's[15] approaches to the ultrasonic absorption in metals. Solving the equation $\rho\cdot(\partial^2 s_x/\partial t^2)=c\cdot(\partial^2 s_x/\partial y^2)$ (s_x is the displacement of lattice ions), we get

$$\Lambda=\frac{c_t}{\rho V^3}\cdot\frac{\omega^2\tau}{1+(\omega\tau)^2}\ , \tag{5.2}$$

where the small dispersion of the sound velocity is neglected.

The acoustoelectric effect due to electron transfer mechanism can be calculated as follows. We take the idea analogous to the deformation potential[16] in semiconductors, i.e. the potential energy of the electrons near the hexagonal faces is simply put as $U=\Xi\cdot(\partial s_x/\partial y)$. Then the force exerted by waves is given by

$$X=-\Xi\cdot\left(\frac{\partial^2 s_x}{\partial y^2}\right)=-i\frac{q^2\Xi}{\omega}u\ . \tag{5.3}$$

Next, the fluctuation of the electron concentration in local equilibrium is determined by the definition of c_t, i.e.,

$$n_{\text{eq}}=-c_t\cdot(\partial s_x/\partial y)^2/U=\frac{c_t}{\Xi V}\cdot u\ . \tag{5.4}$$

Thus, solving the equation of the relaxation, $\partial n/\partial t=-(1/\tau)(n-n_{\text{eq}})$, we get

$$n=\frac{(c_t/V\Xi)}{1+(\omega\tau)^2}\cdot u-\frac{i\omega\tau(c_t/V\Xi)}{1+(\omega\tau)^2}\cdot u\ . \tag{5.5}$$

From (5.3) and (5.5) we obtain the formula

$$F=\frac{1}{2Ne}\cdot\text{Re}\,(n^*X)=\frac{c_t}{\rho NeV^4}\cdot\frac{\omega^2\tau}{1+(\omega\tau)^2}\cdot\gamma\ , \tag{5.6}$$

where N is the total number density of the electrons contributing to electron transfer mechanism.

The results (5.2) and (5.6) satisfy Weinreich's relation (3.4). It should be remarked that the theory developed in this section is only applicable to the low frequency range, because we isolate considerations to a small portion of materials in comparison with λ. For Al, we can take[13]

$$c_0=16.2\times10^{11}\ \text{dynes/cm}^2\ ,$$
$$c_t=13.1\times10^{11}\ \text{dynes/cm}^2$$

at very low temperatures. Then Λ and F due to electron transfer mechanism are of the same order as those derived from the free electron model, (3.7).

We can apply (5.2) and (5.6) to n-Ge. For transverse waves ($s_x\propto\exp(i\omega t-iqy)$), the deformation potentials of the valleys are expressed as $U=\pm(\Xi_u/3)\cdot(\partial s_x/\partial y)$, where Ξ_u is the deformation potential constant for uniaxial shear. Then, from (5.4) and $N+n_{\text{eq}}\propto\exp(-U/kT)$ we get easily

$$c_t=\frac{1}{9}\cdot\frac{N\Xi_u^2}{kT}\ . \tag{5.7}$$

Inserting (5.7) into (5.6), we obtain Weinreich's formula for n-Ge:

$$\left.\begin{aligned}\Lambda&=\frac{N\Xi_u^2}{9\rho V^3kT}\cdot\frac{\omega^2\tau}{1+(\omega\tau)^2}\ ,\\ F&=\frac{\Xi_u^2}{9\rho eV^4kT}\cdot\frac{\omega^2\tau}{1+(\omega\tau)^2}\cdot\gamma\ .\end{aligned}\right\} \tag{5.8}$$

§ 6. Remarks

In the Boltzmann theory developed in § 3, the effects of the space charge and the induced motion of ions could be explicitly taken into account. But these effects are implicitly involved in the phenomenological theory ((5.3), (5.4) and (5.5)), where we assumed that electrons followed nearly perfectly to the ionic displacement and then the appreciable electric potential was not produced. Such assumption in metals can be verified from the following consideration. If the formula in § 5 are applied to free electron model and the use is permissible of Morse's calculation[14] of the change of the electronic elastic energy caused by ultrasonic waves, we can get

$$\left.\begin{aligned}c_t&=\frac{4}{15}Nmv_0^2\quad\text{(longitudinal waves)}\\ &=\frac{1}{5}Nmv_0^2\quad\text{(transverse waves)}\ .\end{aligned}\right\} \tag{6.1}$$

Inserting (6.1) into (5.6), the same formulae as (3.5) and (3.7) are obtained, which were derived from the explicit consideration of the effects of the space charge and the induced motion of ions.

In semiconductors, however, such assumption has never been verified. Although Weinreich et al.[7] showed that the phenomenological theory similar to that in § 5 may be applicable to many-valley semiconductors like *n*-Ge, there are some questions whether the theory are applicable to semiconductors with degenerate energy surfaces like *p*-Ge. If we apply tentatively the formula in § 5 to *p*-Ge, we can get the acoustoelectric effect of the same order of magnitude as that in *n*-Ge, when the carrier concentrations are of the same order. This is because that 1) the piezoresistance[17) for the shear stress and 2) the change of the absorption peaks by the shear stress in cyclotron resonance[18) are of the same order in both *n* and *p*-Ge. Therefore, it is expected in future to study applicability of the theory in § 5 to simple and degenerate semiconductors.

Acknowledgements

The author should express his thanks to G. M. Hatoyama and M. Shibuya for their encouragements. He also is indebted to W. Sasaki for valuable discussions.

Note added in proof.

After this manuscript had been submitted to the editor we have read the paper by E. I. Blount [Phys. Rev. **114** (1959) 418], in which essentially the same results as this manuscript were derived from somewhat different approach.

References

1) R. H. Parmenter: Phys. Rev. **89** (1953) 990.
2) A. Van den Beukel: Appl. Sci. Research **B, 5** (1956) 459.
3) N. Mikoshiba: J. Phys. Soc. Japan **14** (1959) 22.
4) R. H. Parmenter: Phys. Rev. **113** (1959) 102.
5) G. Weinreich: Phys. Rev. **104** (1956) 321.
6) T. Holstein: Westinghouse Research Memo 60–94698–3–M15 (unpublished).
7) G. Weinreich, T. M. Sanders and H. G. White: Phys. Rev. **114** (1959) 33.
8) A. B. Pippard: Phil. Mag. **46** (1955) 1104.
9) M. S. Steinberg: Phys. Rev. **111** (1958) 425.
10) G. Weinreich: Phys. Rev. **107** (1957) 317.
11) J. Bardeen and D. Pines: Phys. Rev. **99** (1955) 1140.
12) H. E. Bömmel and K. Dransfeld: Phys. Rev. Letters **1** (1958) 234.
13) R. S. Leigh: Phil. Mag. **42** (1951) 139.
14) R. W. Morse: Phys. Rev. **97** (1955) 1716.
15) C. Kittel: Acta Metallurgica **3** (1955) 295.
16) J. Bardeen and W. Shockley: Phys. Rev. **80** (1950) 72.
17) C. S. Smith: Phys. Rev. **94** (1954) 42.
18) A. C. Rose-Innes: Proc. Phys. Soc. **72** (1958) 514.

Journal of the Physical Society of Japan, Vol. 14, No. 12, December 1959

The X-ray Non-diagram Lines $K\beta'$ of Some Compounds of the Iron Group

By Kenjiro Tsutsumi

Department of Physics, Faculty of Science, Osaka University

(Received August 1, 1959)

The wavelength values and relative intensities of the X-ray non-diagram lines $K\alpha_{3,4}$ of metallic iron and $K\beta'$ of Cr_2O_3, $Cr_2(SO_4)_3 \cdot nH_2O$, MnO_2, $MnSO_4 \cdot 4H_2O$, Fe_2O_3 and $Fe(NH_4)_2(SO_4)_2 \cdot 6H_2O$ were measured by the fluorescent X-ray method using twe different characteristic X-rays. The $K\alpha_{3,4}$ lines did not appear when an iron atom was excited by Ni K rays but were clearly observed when excited by Cu K rays. This was expected from the origin of the $K\alpha_{3,4}$ lines that is supposed to arise from a KL–LL transition. In the case of the $K\beta'$ line no difference was found regardless of whether it was excited by photons of energy lower or higher than $K(Z)+L(Z+1)$ which is necessary to remove simultaneously a K and an L electrons of an atom (Z). Therefore, the author may conclude that the $K\beta'$ line is due not to the double but to the single ionization process and that it can be derived from the difference of the exchange interactions of the states having different total spins ($S+1/2$) and ($S-1/2$), where S is the total spin of the incomplete $3d$ shell and 1/2 is that of the incomplete $3p$ shell in the final state. The energy separations of the $K\beta_1$ and $K\beta'$ lines calculated from the above-mentioned exchange energies nearly agree with those observed in the experiments.

§ 1. Introduction

The X-ray non-diagram line $K\beta'$, or so-called satellite line of the $K\beta_1$ line, has been investigated by many authors[1)-11)], because it has interesting characters different from other non-diagram lines. Such characters may be summarized as follows: (1) the $K\beta'$ line appears on the long wavelength side of the $K\beta_1$ line (parent line), (2) its intensity is large in comparison with other non-diagram lines, and (3) it is distinctly separated from the $K\beta_1$ line only when the substance is a chemical compound having a high magnetic susceptibility. In all the previous investigations only the wavelengths of the $K\beta'$ lines were measured, but the measurements of their intensities were not made. Generally, in the investigations of the X-ray emission spectra -especially of the X-ray emission spectra emitted from compounds- the fluorescent X-ray method has been used, because the substances under investigation have a tendency to decompose or to react chemically with the material of an anticathode by the bombardment of cathode rays. Most of the previous investigations[2)3)8)9)] of the $K\beta'$ lines were carried out by this fluorescence method, but, because the substances under investigation were held on the cathode part in the X-ray tube, they might change chemically by various causes, for instance, temperature rise of their surfaces and reduced pressure in the X-ray tube. In the present experiment this trouble could be avoided by placing the substances outside of the X-ray tube.

On the origin of the $K\beta'$ line many theories have been proposed, and, in order to test the validity of these various theories, measurements of the excitation potentials[13)] of the satellites and their intensities are required. In the present paper these measurements are carried out and a discussion is given of the origin of the $K\beta'$ line.

§ 2. Experiment

Fluorescent X-ray spectra of the non-diagram lines $K\alpha_{3,4}$ from metallic iron and $K\beta'$ from $Cr_2(SO_4)_3 \cdot nH_2O$, Cr_2O_3, MnO_2, $MnSO_4 \cdot 4H_2O$, $Fe(NH_4)_2(SO_4)_2 \cdot 6H_2O$ and Fe_2O_3 were taken with a bent crystal focusing spectrograph of the Johann type by means of the fluorescence method. The diameter of the focal circle was 20 cm and the second order reflection from the (110) plane of a quartz crystal was used. The substances under investigation which emitted the fluorescent spectra were placed on the Rowland circle.

The dispersion on a photographic plate is 7.55 x.u./mm in the region of Fe $K\alpha$, 6.48 x.u./mm in the region of Cr $K\beta$, 7.76 x.u./mm in the region of Mn $K\beta$ and 8.57 x.u./mm in the region of Fe $K\beta$. For the production of the fluorescent spectra, two anticathodes, copper and nickel, were used in the case of iron compounds, nickel and cobalt in the case of the compounds of manganese, and cobalt and iron in the case of the compounds of chromium. Two kinds of fluorescent spectra of each substance were obtained by using the above-mentioned two different anticathodes. The experiment on the $K\alpha_{3,4}$ lines of iron was carried out to confirm the intensity difference which is expected when an iron atom is excited by the radiations from two different anticathodes. From this experiment it can be concluded, as shown in § 4. (i), that the influence of general radiation on the present fluorescent spectra is negligible. The load of X-ray tube was about 40 kV peak and 15 mA, and the time of exposure was varied from 50 to 60 hours in the case of the $K\beta'$ spectra and 150 hours in the case of the $K\alpha_{3,4}$ spectra. All the spectrograms were photographed on Fuji A-1 plates. For the measurements of ralative intensities the auto-calibration single exposure method was chosen with the aid of various thicknesses of aluminum foils.

§ 3. Experimental Results

All of the experimental results are summarized in Table I and II, which give the results on the $K\alpha_{3,4}$ lines and the $K\beta'$ line respectively. In these tables the second column shows the materials which emit the non-diagram lines under investigation. The fourth column shows the anticathodes of the X-ray tube. The fifth column gives the wavelength values of the $K\alpha_1$ line measured by Parratt[18] and the $K\beta_1$ lines measured by Yoshida[8] (Cr_2O_3, $MnSO_4$, MnO_2 and Fe_2O_3) and by Tanaka and Okuno[9] ($Cr_2(SO_4)_3$ and $Fe(SO_4)_2\cdot(NH_4)_2$). The sixth and seventh columns give the $\Delta\lambda$ and Δev of satellites measured from the parent lines respectively.

Table I. The results on the $K\alpha_{3,4}$ lines of iron excited by Cu K and Ni K rays.

element	material		exciter (anti cathode)	α_1	$\Delta\lambda$	Δev	α_3			intensity ratio $\alpha_{3,4}/\alpha_1$
				x.u.	x.u.	ev	x.u.			
Fe (26)	metallic iron		Cu	1932.06	8.15	26.95	1923.91			0.0085
			Ni	1932.06	—	—	—			0.0024

Table II. The results on the $K\beta'$ lines excited by two different characteristic X-rays.

element	material	valency	anti-cathode of exciter	β_1	$\Delta\lambda$	Δev	β'	half max. full width of β'	peak intensity ratio β'/β_1	intensity ratio β'/β_1
				x.u.	x.u.	ev	x.u.	ev		
Cr (24)	$Cr_2(SO_4)_3\cdot nH_2O$	III	Co	2080.6	5.03	14.29	2085.63	16.1	0.18	0.38
			Fe	2080.6	5.11	14.53	2085.71	16.5	0.18	0.37
	Cr_2O_3	III	Co	2080.6	5.03	14.29	2085.63	13.3	0.33	0.49
			Fe	2080.6	5.03	14.29	2085.63	14.2	0.32	0.47
Mn (25)	$MnSO_4$-$4H_2O$	II	Ni	1906.2	4.63	15.70	1910.83	11.5	0.55	0.62
			Co	1906.2	4.63	15.70	1910.83	11.8	0.55	0.61
	MnO_2	IV	Ni	1906.2	4.05	13.72	1910.25	11.8	0.25	0.33
			Co	1906.2	4.05	13.72	1910.25	11.8	0.25	0.35
Fe (26)	$Fe(NH_4)_2\cdot(SO_4)_2\cdot 6H_2O$	II	Cu	1753.0	3.64	14.59	1756.64	9.9	0.31	0.25
			Ni	1753.0	3.64	14.59	1756.64	9.9	0.31	0.25
	Fe_2O_3	III	Cu	1753.0	3.54	14.19	1756.54	10.3	0.32	0.33
			Ni	1753·0	3.54	14.19	1756.54	11.1	0.32	0.33

The wavelength values of the satellites are shown in column eight, and the column nine gives the full widths of half maxima, and the column ten and eleven give the relative intensities of the peak and the area of the satellites to the parent lines respectively.

The wavelength values of these satellites agree well with the previous experimental results[8)9)18)]. Photo. 1 and Photo. 2 are the reproductions of these spectra, and Photo. 3 and Photo. 4 show the microphotometer records. Fig. 1 and Fig. 2 show the intensity curves derived in the usual manner from the photometer records. The intensity curves

Photo. 1. *Kα* spectra of iron on about 2.73/1 of original size.

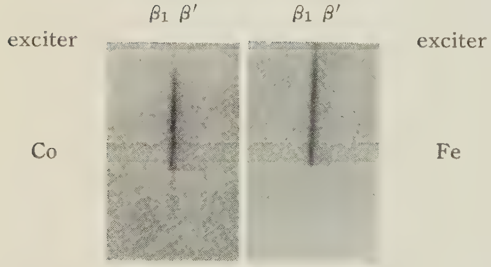

Cr_2O_3

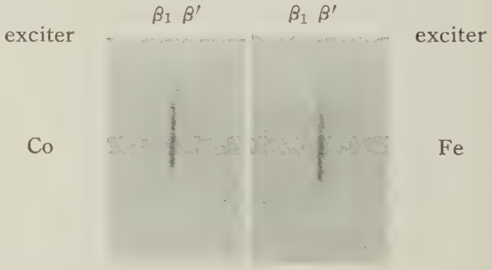

$Cr_2(SO_4)_3 \cdot nH_2O$

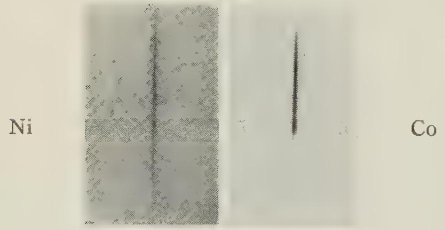

MnO_2

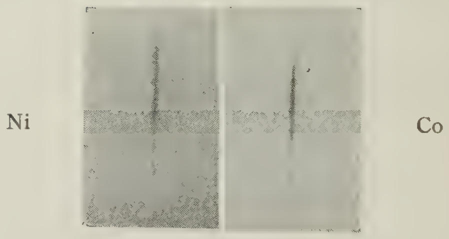

$MnSO_4 \cdot 4H_2O$

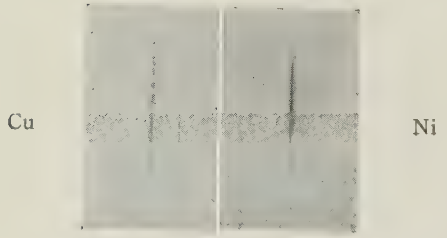

Fe_2O_3

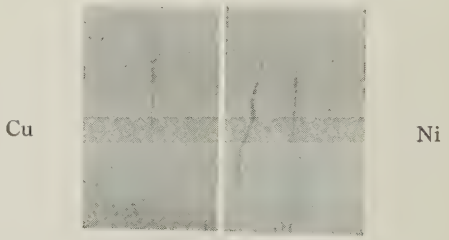

$Fe(NH_4)_2(SO_4)_2 \cdot 6H_2O$

Photo. 2. *Kβ*₁ and *Kβ'* spectra on about 2.73/1 of original size.

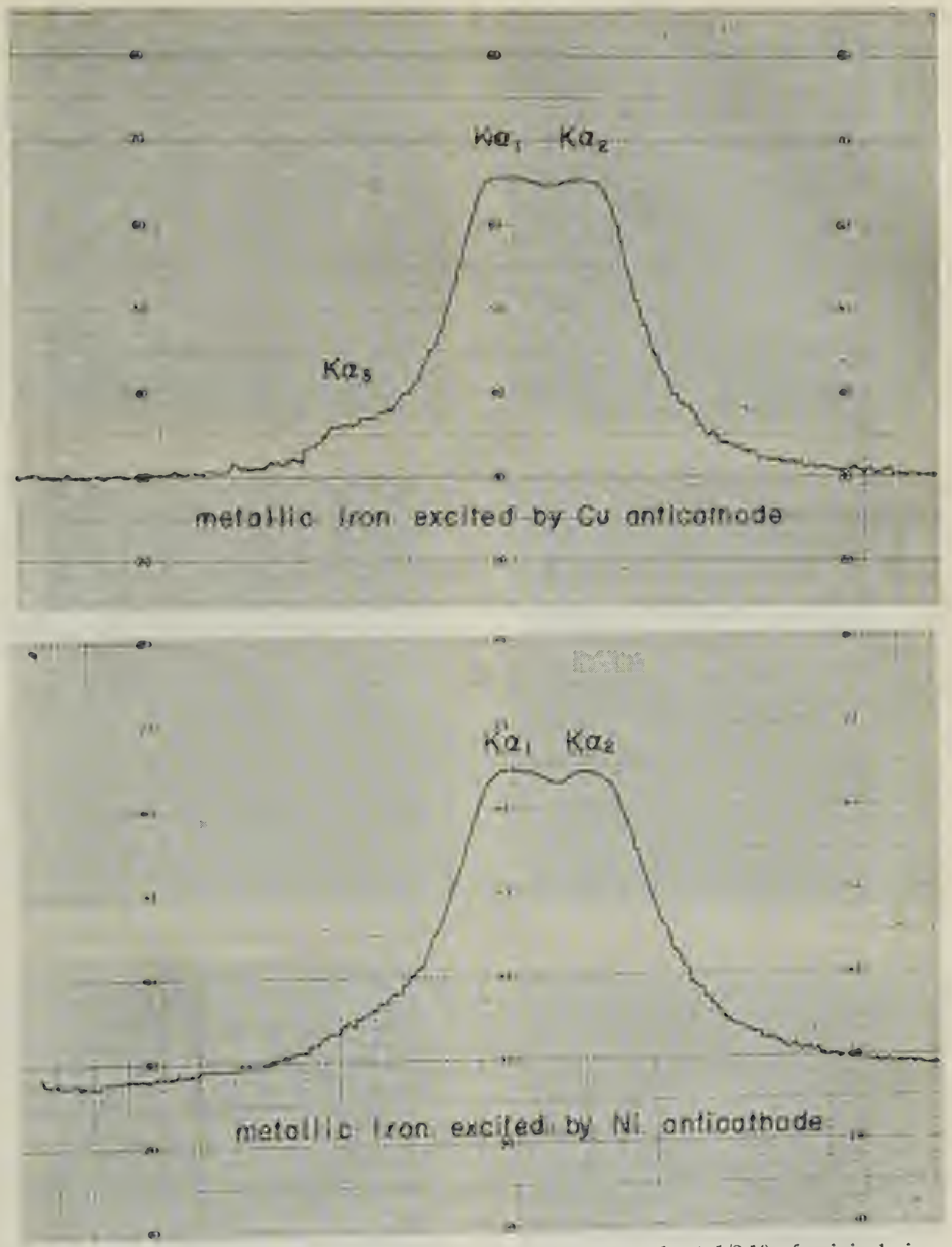

Photo. 3. Photometer records of the $K\alpha$ spectra of iron on about 1/2.10 of original size.

were smoothed and separated into two components of the parent lines and the non-diagram lines, by assuming that the parent line is symmetrical with respect to the position.

§ 4. Discussion and Conclusion

i) $K\alpha_{3,4}$: The origin of the non-diagram lines $K\alpha_{3,4}$ proposed by Druyvesteyn[13] and supported by Parratt[12] and by Sawada[14] is as follows: the $K_{3,4}$ lines are supposed to arise from a KL–LL transition where KL refers to an atomic state in which one K electron and one L electron are missing. The probability[13][15][16][17] of two (or more) electrons being ejected from an atom by successive impacts of electrons or photons (when an atom is excited by X-rays) is much too low to account for the observed satellite intensities, therefore the multiple-ionization process would

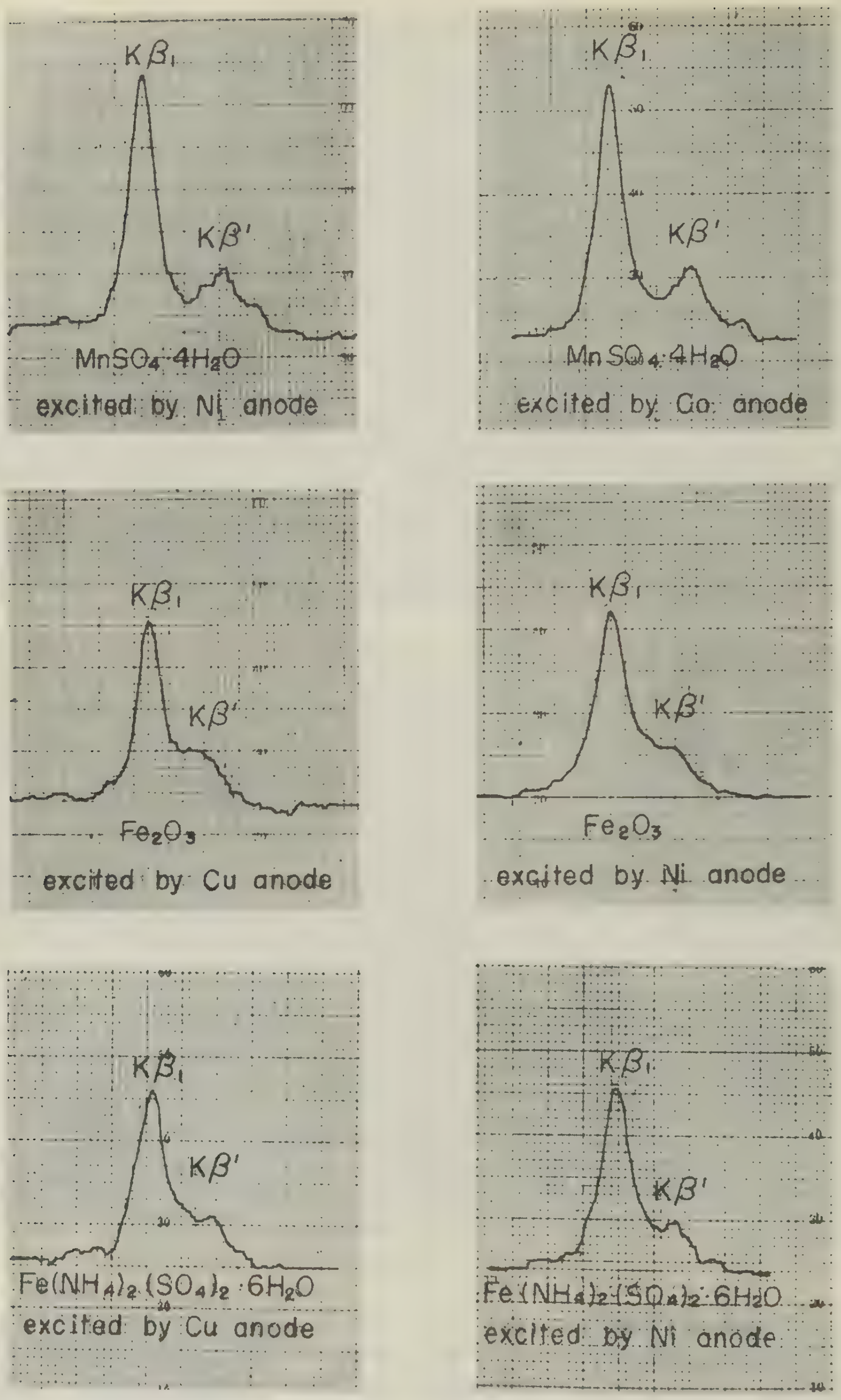

Photo. 4. Photometer records of the $K\beta_1$ and $K\beta'$ spectra on about 1/2.10 of original size.

have to take place by a single impact. Then, the energy of photons necessary to excite the $K\alpha_{3,4}$ satellite lines is approximately equivalent to the total energy required to remove a K electron of an atom of atomic number Z plus the energy required to remove an L electron of an atom $(Z+1)$, since, owing to the vacancy in the inner K shell, the outer L electron can be considered to move in the field of an atom $(Z+1)$. In the fourth column

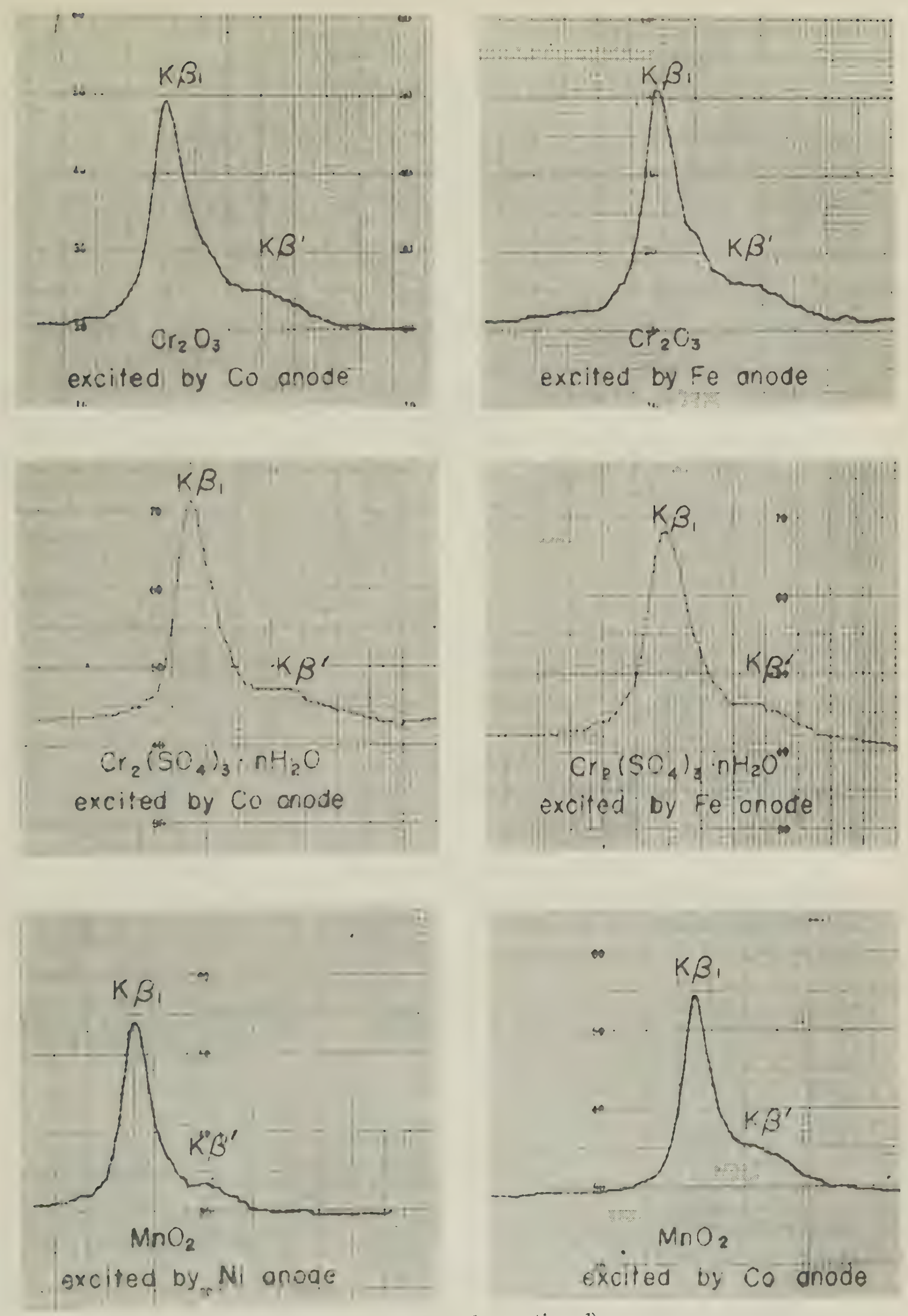

Photo. 4. (to be continued)

of Table III, the excitation potentials of iron $K(26)$ which is necessary to remove only one K electron, $K(26)+L(27)$ which is required to remove simultaneously the K and L electrons of an iron atom, the energy of Cu$K\alpha_1$ rays and the energy of Ni $K\alpha_1$ rays are given in ev respectively. As seen from this table, Cu $K\alpha$ rays excite simultaneously a K and an L electrons of an iron atom, and therefore the Fe $K\alpha_{1,2}$ and $K\alpha_{3,4}$ lines are emitted, but Ni $K\alpha$

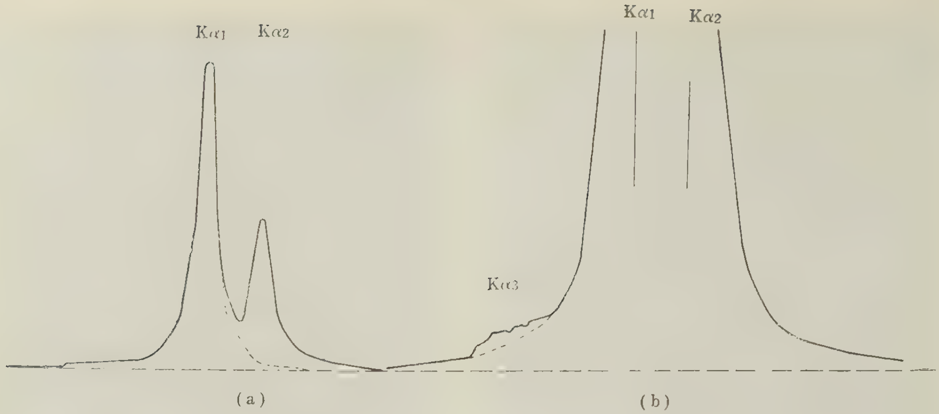

Metallic iron excited by Cu anticathode

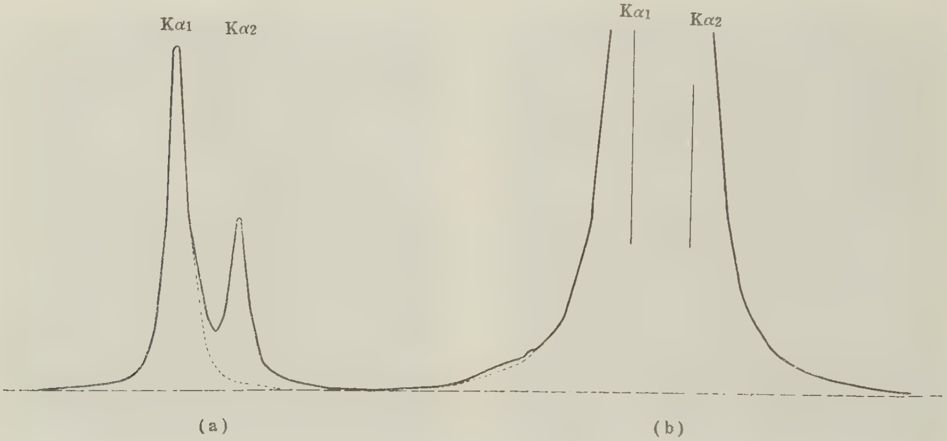

Metallic iron excited by Ni anticathode

Fig. 1. Intensity curves of the $K\alpha$ spectra of iron. The curves (b) are drawn to an intensity scale 7.73 times the scale used in the curves (a).

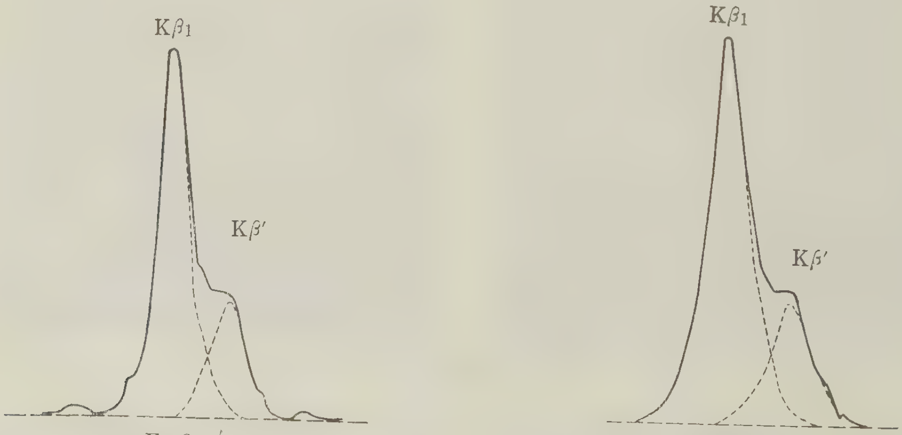

Fe_2O_3
excited by Cu anode

Fe_2O_3
excited by Ni anode

Fig. 2. Intensity curves of the $K\beta_1$ and $K\beta'$ spectra.

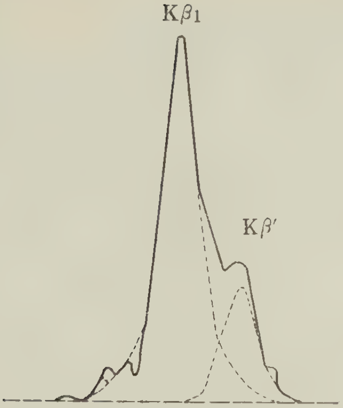

$Fe(NH_4)_2(SO_4)_2 \cdot 6H_2O$

excited by Cu anode

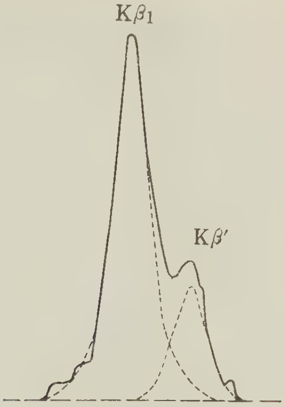

$Fe(NH_4)_2(SO_4)_2 \cdot 6H_2O$

excited by Ni anode

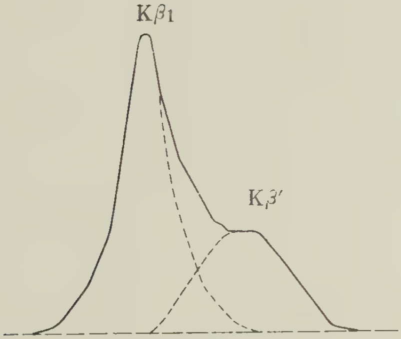

Cr_2O_3

excited by Co anode

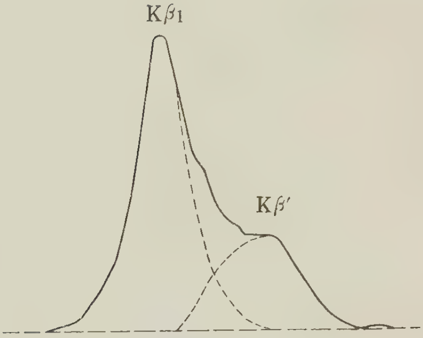

Cr_2O_3

excited by Fe anode

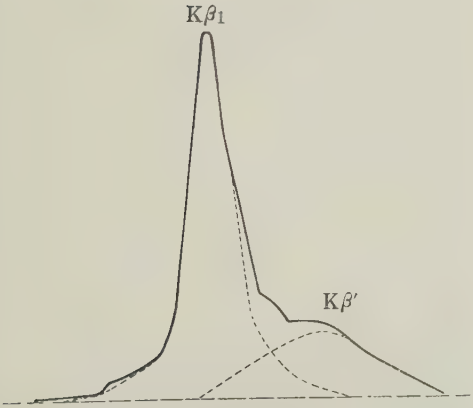

$Cr_2(SO_4)_3 \cdot nH_2O$

excited by Co anode

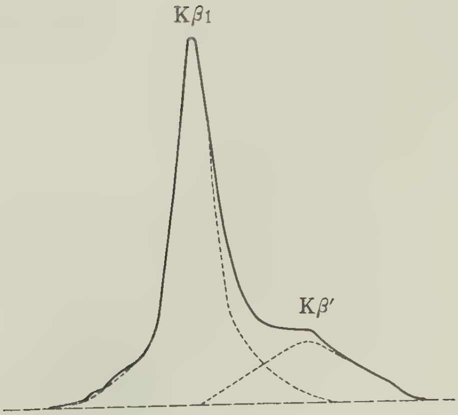

$Cr_2(SO_4)_3 \cdot nH_2O$

excited by Fe anode

Fig. 2. (to be continued.)

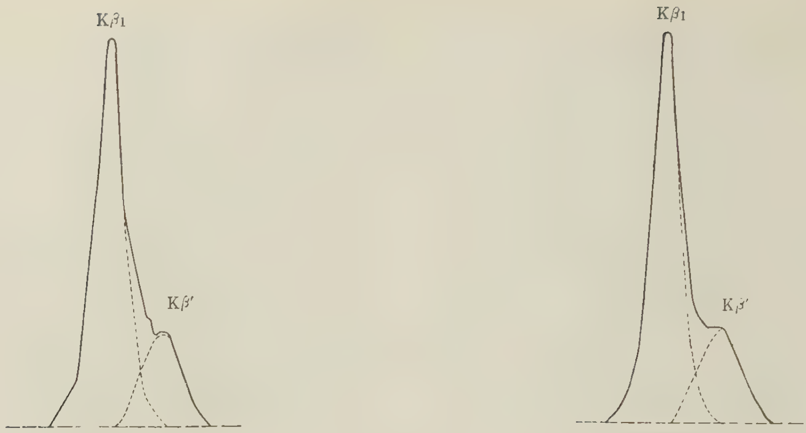

MnO2 excited by Ni anode

MnO2 excited by Co anode

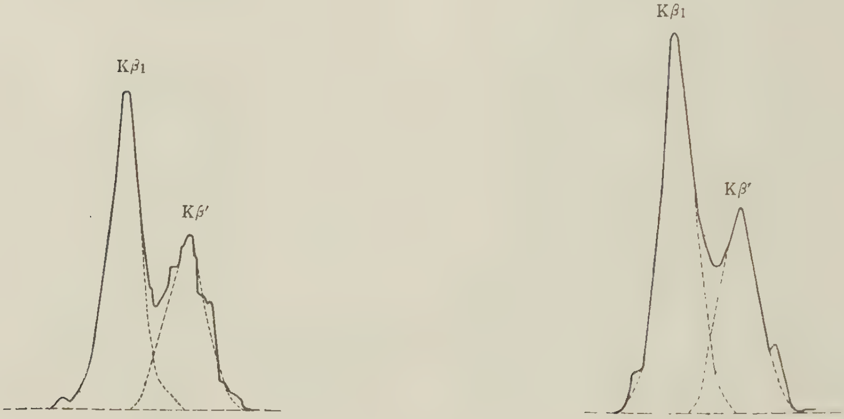

$MnSO_4 \cdot 4H_2O$ excited by Ni anode

$MnSO_4 \cdot 4H_2O$ excited by Co anode

Fig. 2. (to be continued.)

rays excite only a K electron, thus giving rise to only the Fe $K\alpha_{1,2}$ lines. This fact can be clearly seen in Table I, Photo. 1, Photo. 3 and Fig. 1. In the case of excitation with Ni K rays, however, weak $K\alpha_{3,4}$ lines are observed, and this is probably due to the presence of Ni $K\beta$ and general radiations. It is difficult to estimate the influence of general radiation on the present fluorescent spectra because the effect of general radiation is not easily determined theoretically or experimentally. However, this experimental result on the $K\alpha_{3,4}$ lines of iron shows that the contribution of general radiation to the production of the present fluorescent spectra is negligibly small. It can be considered that this is also the case with the experiments on $K\beta'$ lines. The intensity ratio of the $K\alpha_{3,4}$ to $K\alpha_1$ lines observed by Parratt[18] is a little larger than the present result. It may be considered to

Table III. The K ionization potential $K(Z)$ of an atom (Z), the KL ionization potential $K(Z)+L(Z+1)$ of an atom (Z) and the energy of characteristic X-rays used for excitation.

element	Cr	Mn	Fe
Z	24	25	26
			in ev
$K(Z)$	5973	6526	7094
$L(Z+1)$	654	720	796
$K(Z)+L(Z+1)$	6627	7246	7890
energies of characteristic X-rays used for excitation	Fe $K\alpha_1$ 6386 Co $K\alpha_1$ 6912	Co $K\alpha_1$ 6912 Ni $K\alpha_1$ 7458	Ni $K\alpha_1$ 7458 Cu $K\alpha_1$ 8028

be due to the difference of the excitation method.

ii) $K\beta'$: On the origin of the $K\beta'$ line, following explanations have been proposed by various investigators:

(1) N. Seljakow and A. Krasnikow[1)] interpreted the $K\beta'$ and $K\beta_1$ lines to be a relativity doublet. But its $\Delta\lambda$ does not coincide with the value calculated from the frequency difference of the M_{II} and M_{III} levels.

(2) D. Coster and M. J. Druyvesteyn[2)] considered the $K\beta'$ line to arise from the higher multiplicity due to the influence of the incomplete $M_{IV,V}$ shells on the $M_{II,III}$ levels; and so this line is a component of the $K\beta_1$ line. This theory was supported by S. Yoshida[8)].

(3) G. Ortner[3)] assumed new M' levels in the iron group and explained that the $K\beta'$ line was due to the transition from the M' level.

(4) G. B. Deodhar[6)] adopted the Richtmyer double jump theory and explained the $K\beta'$ line as due to a transition

$$KL_{III} \longrightarrow L_{III}M_I ,$$

but the wavelengths calculated from this theory seem to be rather large.

(5) M. Sawada[7)] also explained the $K\beta'$ line from the double jump theory as

$$KL_{II,III} \longrightarrow L_IM_{IV,V} .$$

The wavelengths calculated from this theory coincide fairly good with the experimental results.

(6) M. A. Blochin[10)] assumed that a part of energy quantum of the $K\beta_1$ line was absorbed by a $3d$ electron and this electron was excited to a conduction level.

(7) L. G. Parratt[11)] is attempting to explain from the exciton theory.

According to the Sawada or the Deodhar theory, it is necessary to eject simultaneously one K and one L electrons in order to emit the $K\beta'$ line, and the energy of X-ray photon necessary to excite the $K\beta'$ line is approximately equivalent to the total energy required to remove a K electron of an atom (Z) and an L electron of an atom $(Z+1)$. Table III shows the excitation potential $K(Z)$ required to remove a K electron of an atom (Z), the energy $K(Z)+L(Z+1)$ required to remove simultaneously a K and an L electrons of the atom (Z) and the energies of $K\alpha_1$ rays of anticathodes used for excitation. As shown in this table, the $K\beta_1$ and $K\beta'$ lines must be both emitted by photons with energy higher than $K(Z)+L(Z+1)$, but the $K\beta'$ line must not be emitted by photons with energy lower than $K(Z)+L(Z+1)$. This situation is the same as in the case of the $K\alpha_{3,4}$ lines.

Contrary to the prediction of their double jump theory, the $K\beta_1$ and $K\beta'$ lines are emitted by photons of energy lower than $K(Z)+L(Z+1)$ as shown in Table II, Photo. 2, Photo. 4 and Fig. 2, and no difference is found between intensity ratios of the $K\beta'$ to $K\beta_1$ lines in both cases of excitation. This shows that the origin of the $K\beta'$ line is not the KL double ionization process but the single ionization process.

iii) Origin of $K\beta'$: We may consider that the $K\beta_1$ and $K\beta'$ lines are emitted by transitions from the states having the total spins equal to $S+1/2$ and $S-1/2$ respectively, where S is the total spin of the incomplete $3d$ shell and $1/2$ is that of the incomplete $3p$ shell in the final state having one vacancy in the $3p$ shell owing to the transition of an electron from the complete $3p$ shell to the $1s$ shell. The total spin of $3d$ shell is 5/2 for both Mn^{++} in $MnSO_4 \cdot 4H_2O$ and Fe^{+++} in Fe_2O_3 and 3/2 for Cr^{+++} in Cr_2O_3. Then the energy difference between the $K\beta_1$ and $K\beta'$ lines corresponds to the difference between the exchange energies[19)20)] for $(S+1/2)$ and for $(S-1/2)$.

The exchange interaction of the state having a total spin $(S+s)$ is given by[19)20)21)]

$$-1/2J(1+4\boldsymbol{S}\cdot\boldsymbol{s}) ,$$

where J is the exchange integral having a usual meaning, S is the total spin vector of $3d$ shell and $\boldsymbol{s}$ is that of $3p$ shell.

Then the magnitude of the energy difference ΔE between the exchange interactions for $S+1/2$ and for $S-1/2$ is given by

$$\Delta E = J[(S+1/2)(S+1/2+1) - (S-1/2)(S-1/2+1)] .$$

The ΔE values are $6J$ for Mn^{++}, Fe^{+++} $(S=5/2)$ and $4J$ for Cr^{+++} $(S=3/2)$. The author calculated the J values of $MnSO_4 \cdot 4H_2O$ and Fe_2O_3 in which the five $3d$ electrons occupy each one of $3d$ orbitals and that of Cr_2O_3 in which the three $3d$ electrons belong to each one of d_ε orbitals. Their values are given in Table IV. In this calculation the hydrogen-like wavefunctions[22)] of the $3p$ and $3d$ electrons were used. The effective nuclear charges $(Z-\sigma)$ were determined by Slater's rules[23)] and are also given in Table IV. Two

Table IV. The effective nuclear charges and the calculated J values.

material	Z	Z-σ_{3p}	Z-σ_{3d}	J	Z-σ_{mean}*	J*
Cr	24	12.75	5.3	1.023	9.025	1.622
Mn	25	13.75	5.6	1.02	9.675	1.74
Fe	26	14.75	6.6	1.62	10.675	1.92

$$\sigma_{\text{mean}}{}^{*}=\frac{\sigma_{3p}+\sigma_{3d}}{2}$$

Table V. The calculated and observed energy differences and relative intensities of the $K\beta'$ and $K\beta_1$ lines.

material	energy difference			relative intensity	
	calculated		observed	calculated	observed
	from J	from J*			
		ev	ev		
Cr_2O_3	4.09	6.49	14.29	0.6	0.5
$MnSO_4\cdot 4H_2O$	6.12	10.44	15.70	0.71	0.62
Fe_2O_3	9.72	11.52	14.19	0.71	0.33

alternative J values were calculated for each material, in one of them the effective nuclear charges $Z-\sigma_{3p}$ and $Z-\sigma_{3d}$ were used for the $3p$ and $3d$ wavefunctions and in the other the same nuclear charge $Z-\sigma_{\text{mean}}$ was used for both $3p$ and $3d$ wavefunctions.

As shown in Table V, the values of the energy difference ΔE obtained from the above calculations nearly agree with the energy separations of the $K\beta_1$ and $K\beta'$ lines observed in the above experiments.

The relative intensities of the $K\beta'$ and $K\beta_1$ lines are estimated from the ratio of the multiplicity of each state, that is, $2(S-1/2)+1$: $2(S+1/2)+1$. For Mn^{++} and Fe^{+++} these become 5:7 and for Cr^{+++} 3:5. These values are slightly larger than the observed ones.

The reasons for discrepancies between the calculated and observed values of the energy difference and of the relative intensities may be supposed as follows: (1) the wavefunctions used for $3p$ and $3d$ orbitals are rather approximate (2) the screening constants are not determined precisely, and (3) the influences of neighboring atoms are not taken into consideration. Further it is supposed that some other origins proposed by various authors[1)-11)] may partially contribute to the emission of the $K\beta'$ line.

Thus it may be concluded that the $K\beta'$ line is due not to the double but to the single ionization process and is derived from the difference of the exchange interactions of the states having different total spins $(S+1/2)$ and $(S-1/2)$ where S is the total spin of the incomplete $3d$ shell and 1/2 is that of the incomplete $3p$ shell in the final state.

The author expresses his sincere thanks to Professor M. Sawada, Professor T. Nagamiya, Assistant Professor K. Yoshida and Assistant Professor K. Sakurai for their variable advices and to the members of their laboratories for their kind assistances. His thanks are also due to Professor T. Watanabe, Professor R. Nathans and Assistant Professor T. Horie for criticizing this manuscript.

References

1) N. Seljakow and A. Krasnikow: Zs. f. Phys. **33** (1925) 601; Nature **117** (1926) 554.
2) D. Coster and M. J. Druyvesteyn: Zs. f. Phys. **40** (1927) 765.
3) G. Ortner: Wien Sitzungsber. (IIa) **135** (1925) 71; **136** (1927) 369.
4) S. Eriksson: Zs. f. Phys. **48** (1928) 360.
5) Dolejsek and H. Felcakova: Nature **123** (1929) 412.
6) G. B. Deodhar: Roy. Soc. Proc. (A) **131** (1931) 476.
7) M. Sawada: Mem. Coll. Sci. Kyoto Imp. Univ. (A) **15** (1932) 43.
8) S. Yoshida: Sci. Pap. Ins. Phys. Chem. Res. **20** (1933) 298.
9) S. Tanaka and G. Okuno: Jap. Journ. Phys. **9** (1934) 75; **10** (1935) 1; **10** (1935) 45; Proc. Phys.-Math. Soc. Japan **17** (1935) 540; **18** (1936) 306.
10) M. A. Blochin: "*Physik der Röntgen Strahlen*" Veb-Verlag Technik, Berlin (1957) p. 343.
11) L. G. Parratt: in press.
12) L. G. Parratt: Phys. Rev. **49** (1936) 132.
13) M. J. Druyvesteyn: Zs. f. Phys. **43** (1927) 707.
14) M. Sawada: Jap. Journ. Phys. **11** (1936) 1; Proc. Phys-Math. Soc. Japan **26** (1944) 9; **26** (1944) 47.
15) D. Coster: Phil. Mag. **44** (1922) 546.
16) S. Rosseland: Phil. Mag. **45** (1923) 65.
17) R. D. Richtmyer: Phys. Rev. **49** (1936) 1.
18) L. G. Parratt: Phys. Rev. **50** (1936) 1.
19) W. Heisenberg: Zs. f. Phys. **38** (1926) 411.
20) P. A. M. Dirac: "The Principles of Quantum Mechanics" Oxford. Univ. Press, London (1930).
21) H. Nakano: Proc. Theor. Phys. **9** (1953) 403.
22) E. U. Condon and G. H. Shortley: "The Theory of Atomic Spectra", Cambridge Univ, Press, London (1957) p. 117.
23) J. C, Slater; Phys. Rev, **36** (1930) 57,

JOURNAL OF THE PHYSICAL SOCIETY OF JAPAN, Vol. 14, No. 12, DECEMBER, 1959

X-ray Study on Molecular Rotation in Tetragonal Ammonium Nitrate

By Yasuhiro SHINNAKA
Faculty of Literature and Science, Yamaguchi University

(Received August 6, 1959)

Hindered rotation of nitrate groups in the tetragonal ammonium nitrate was studied by using X-ray diffuse scattering. The first, second, third and fourth order diffuse scatterings of plate-like shape perpendicular to the C^*-direction in the reciprocal lattice were observed. These diffuse scatterings were analyzed referring to the crystal structure as determined previously by using Laue-Bragg scattering. It was found that the correlation among rotating nitrate groups is strong in the C-direction, while it is weak in the direction perpendicular to it and its type is different from that to be expected from the lower temperature modification.

§ 1. Introduction

It is known that ammonium nitrate has five modifications.[1] In the previous papers[2),3)] the author treated the rotation of nitrate groups in the cubic and tetragonal modifications of ammonium nitrate. With regard to the cubic modification[2)] (125.2°C∼169°C), it was found from the study on the X-ray diffuse scattering that the nitrate groups are rotating with one another under considerable correlation. But owing to the complexity of correlation, the observed diffuse scattering could not be discussed by taking full correlation into consideration. With regard to the tetragonal modification[3)] (84.2°C∼125.2°C), the hindered rotation of the nitrate groups was considered from the study on the Laue-Bragg scattering, but the study on the diffuse scattering due to the rotation of nitrate groups was not carried out yet.

In the present paper, the diffuse scattering in the tetragonal modification will be studied and the correlation among the hindered rotating nitrate groups will be discussed. In the tetragonal modification the strength of correlation in the direction of the C-axis will be different from that in the direction perpendicular to the C-axis and so the diffuse scattering will have a characteristic form. Further, on account of the comparatively simple mechanism of rotation in this modification the interpretation of diffuse scattering can be made somewhat satisfactorily. Therefore the present study may also be of interest in giving us additional informations about the diffuse scatterings due to molecular rotation in crystal and further may be useful to deepen the understanding of the diffuse scattering in cubic ammonium nitrate.

§ 2. Observation of Diffuse Scattering

The single crystal was obtained by using the single crystal transformation [orthorhombic modification (32.3°C ∼ −18°C) $\xleftrightarrow[\sim 50^{\circ}\mathrm{C}]{\text{metastable transition}}$ tetragonal modification] as was done in the previous study.[3)] Since the needle axis of the crystal is the A-axis, Laue photographs were taken with the A-axis vertical at about 5° intervals over the whole rotational range by using filtered Cu radiation on cylindrical films (camera radius = 50.7 mm) at about 100°C. In each photograph several diffuse lines were observed in addition to the Laue spots and the ordinary thermal diffuse scatterings as shown in Photo. 1. The broadenings of these diffuse lines are very narrow and their intensities are strong in contrast to those in cubic ammonium nitrate.

The intensity distribution of diffuse scattering in reciprocal lattice was obtained by the usual geometrical method. But the familiar diffuse scatterings due to ordinary thermal vibration observed in neighbouring regions of reciprocal-lattice points were omitted, because they had no particular correlation with the diffuse scattering in question. The obtained distribution in reciprocal space has a plate-like shape: diffuse-scattering densities are distributed in each thin flat volume which has its flat faces normal to the C^*-direction and contains just reciprocal-lattice points (001),

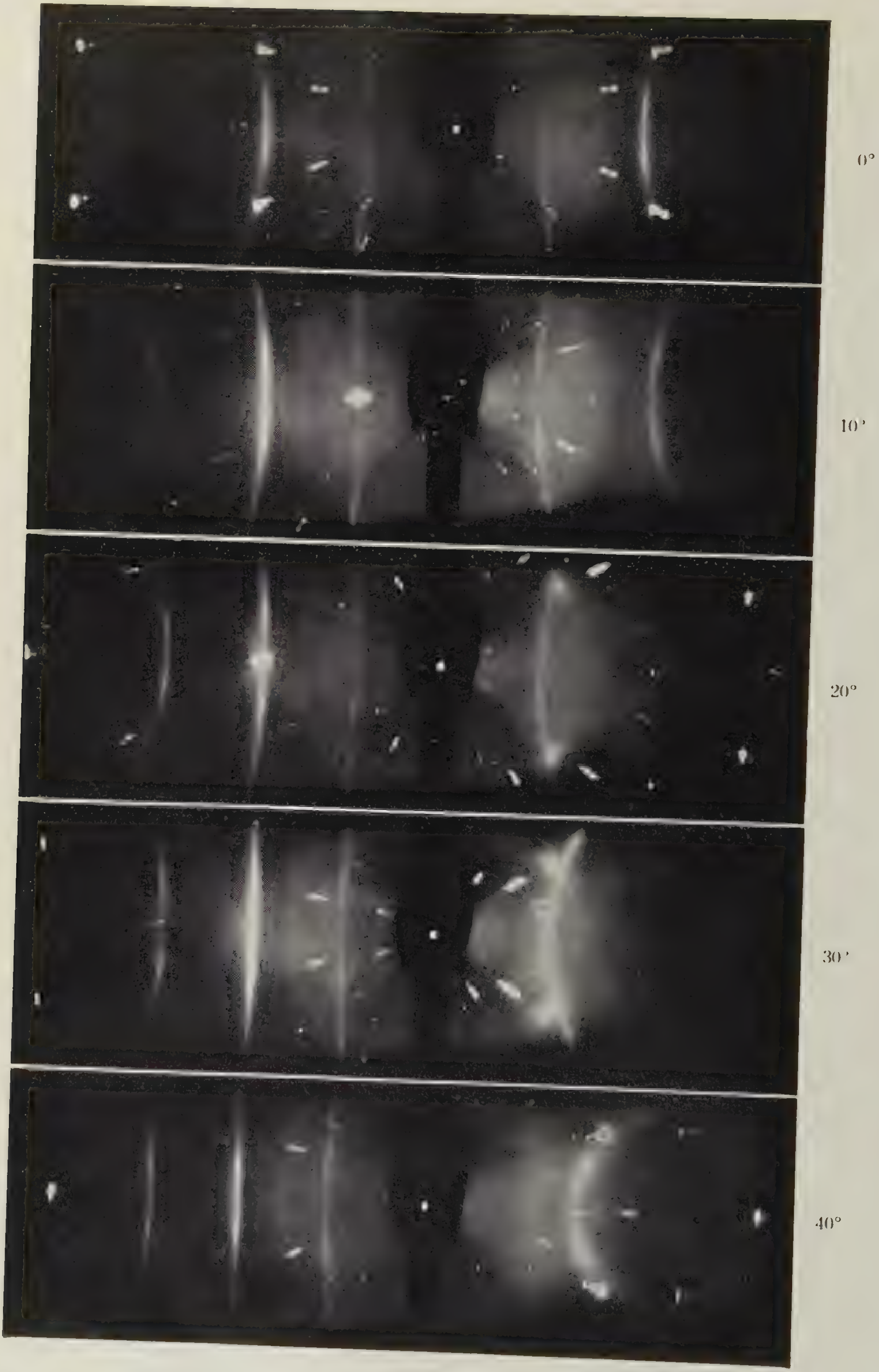

Photo. 1 (A)

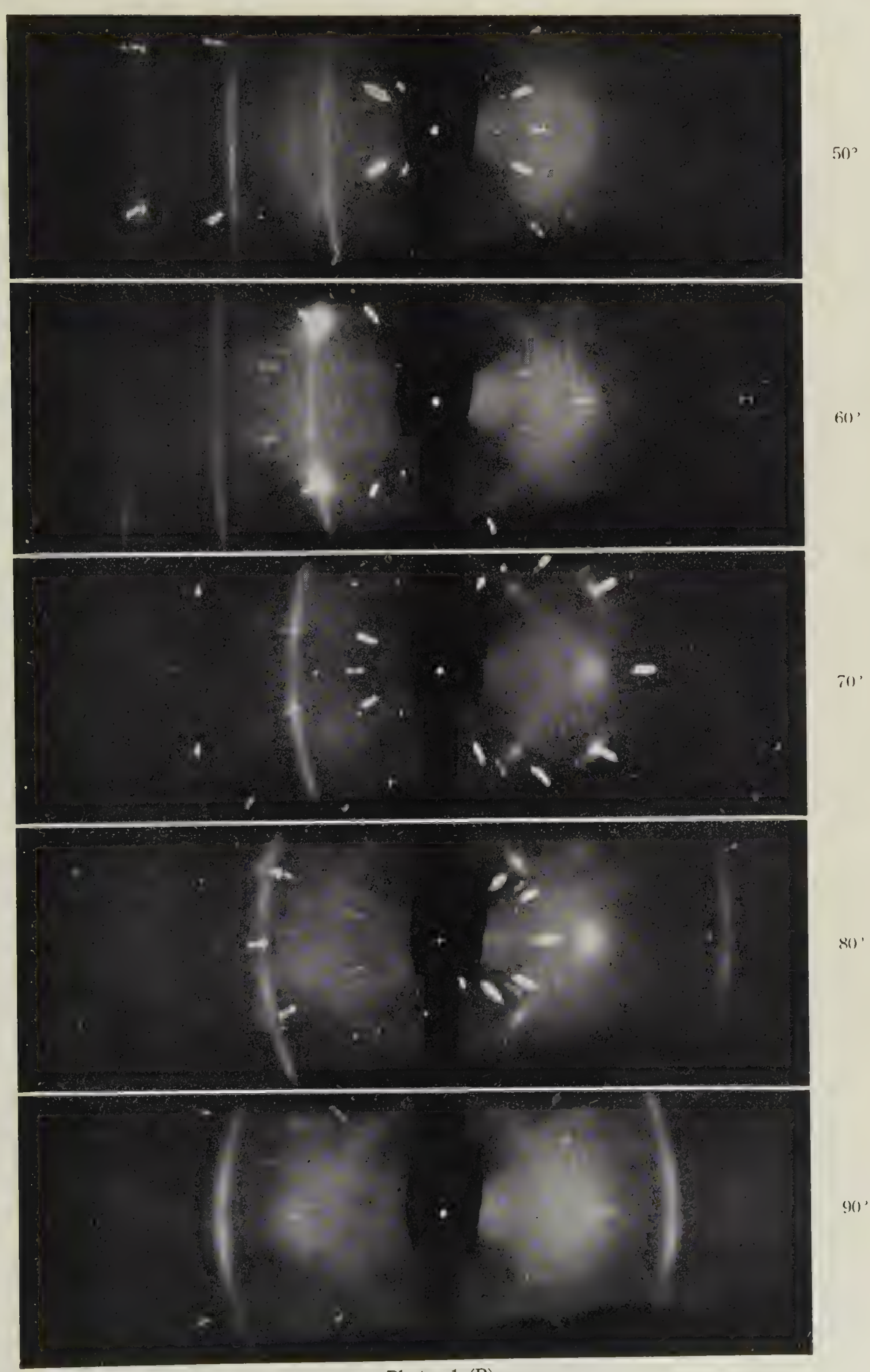

Photo. 1 (B)

Photo. 1. Series of Laue patterns for tetragonal ammonium nitrate in which nitrate groups are hindered rotation. Orientation of crystal given by angle between [010] and direct beam with [100] vertical. Filtered Cu radiation and cylindrical film.

(002) and (003) respectively. This general feature is shown in Fig. 1. Hereafter these plate-like diffuse scatterings will be called the first, second and third order diffuse scatterings respectively. The fourth order was also observed in several photographs, but the zeroth order was not observed.

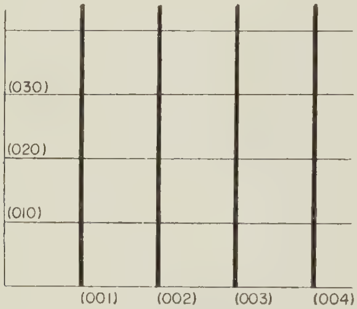

Fig. 1. Schematic reciprocal-lattice representation of observed diffuse scattering showing the general feature of plate-like of the first, second, third and fourth order diffuse scatterings.

The intensity distributions in the first, second and third order diffuse scatterings are shown respectively in Figs. 2(a), 2(b) and 2(c), where the numbers (10, 9, ···, 1, 0) indicate the measure of visual contrast, but they have no exact quantitative meanings. It is to be noticed that these distributions have close relation with the reciprocal lattice; the intensities about the reciprocal-lattice points are weak, while the intensities about centers of each square formed on the reciprocal net are strong.

For the purpose of determining the broadening of each order diffuse scattering in the C^*-direction, photographs were also taken by X-ray impinged on a small part of the crystal in order to avoid the error to be caused by the malorientation of subcrystalline units in the metastable transition. Thus the broadening of the second order diffuse scattering was determined by using the photograph taken under the condition that the sphere of reflec-

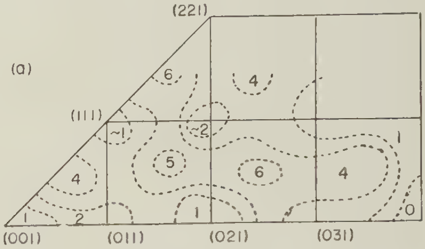

Fig. 2 (a)

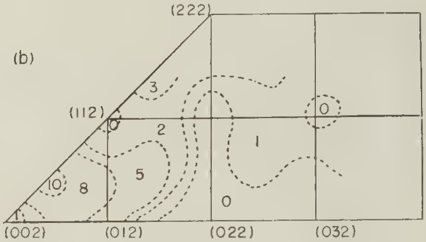

Fig. 2 (b)

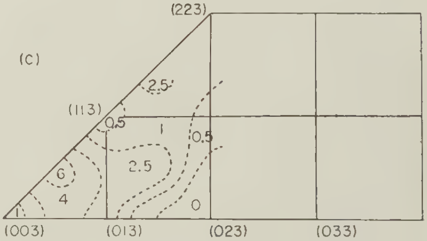

Fig. 2 (c)

Fig. 2. Reciprocal nets showing the intensity distributions in (a) the first, (b) the second and (c) the third order diffuse scatterings.

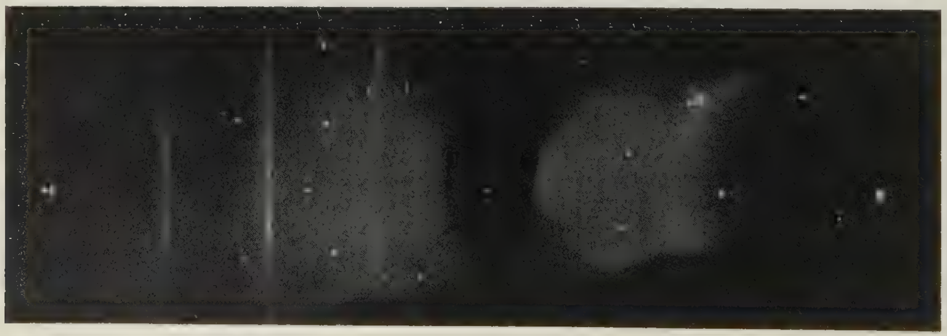

Photo. 2. Taken by X-ray impinged on a small part of the crystal under the condition that the sphere of reflection intersects the plate-like second order diffuse scattering at right angles with [100] vertical. Filtered Cu radiation and cylindrical film.

tion intersects the plate-like second order diffuse scattering at right angles (see Photo. 2). Its half-peak breadth was given as 1°34′ in terms of the scattering angle by using microphotometer. Then, subtracting the half-peak breadth 13′ of Laue spots in the original orthorhombic modification from the value 1°34′, the value 1°21′ was determined approximately as the half-peak breadth of the second order diffuse scattering.

§ 3. Interpretation of Diffuse Scattering

From the plate-like feature of the observed diffuse scatterings, it is assumed that there seems to exist anisotropy of the randomness in the arrangement of the nitrate groups: nitrate groups will take a rather orderly arrangement in the **C**-direction, while a rather random arrangement in the direction perpendicular to it. It is possible to introduce such anisotropy into the tetragonal ammonium nitrate.

According to the previous study[3], atomic positions in the tetragonal unit ($A=5.74$Å, $C=4.95$Å) are approximately as follows:

$2\mathrm{NH_4}$: 0, 0, 0; 1/2, 1/2, 0

two orientations of nitrate

$2\mathrm{NO_3}$ one nitrate group

$$\begin{array}{ll} \mathrm{N} & \frac{1}{2},\ 0,\ u \\ \mathrm{O(1)} & \frac{1}{2},\ 0,\ v \\ \mathrm{O(2)} & \frac{1}{2}+x,\ x,\ w \\ & \frac{1}{2}-x,\ \bar{x},\ w \end{array} \left.\vphantom{\begin{array}{l}1\\1\\1\\1\end{array}}\right\} \text{or} \left\{\begin{array}{l} \frac{1}{2},\ 0,\ \bar{u} \\ \frac{1}{2},\ 0,\ \bar{v} \\ \frac{1}{2}+x,\ x,\ \bar{w} \\ \frac{1}{2}-x,\ \bar{x},\ \bar{w} \end{array}\right.$$

another nitrate group

$$\begin{array}{ll} \mathrm{N} & 0,\ \frac{1}{2},\ u \\ \mathrm{O(1)} & 0,\ \frac{1}{2},\ v \\ \mathrm{O(2)} & \bar{x},\ \frac{1}{2}+x,\ w \\ & x,\ \frac{1}{2}-x,\ w \end{array} \left.\vphantom{\begin{array}{l}1\\1\\1\\1\end{array}}\right\} \text{or} \left\{\begin{array}{l} 0,\ \frac{1}{2},\ \bar{u} \\ 0,\ \frac{1}{2},\ \bar{v} \\ \bar{x},\ \frac{1}{2}+x,\ \bar{w} \\ x,\ \frac{1}{2}-x,\ \bar{w} \end{array}\right. \qquad (1)$$

with $x=0.12$, $u=0.53$, $v=0.75$ and $w=0.42$ (see Fig. 3). The rotation of the nitrate group is required not to be free, but is almost bound in two orientations (in opposite directions). In that structure it may be successfully allowed to approximate the dynamical hindered rotation by the randomness of orientations.

As to the mutual orientations of neighbouring nitrate groups in the *C*-direction, three cases as shown in Fig. 4 are considered to be possible. But among these cases, that the case (3) occurs is clearly improbable judging from the aspect of interatomic distances and the case (2) is to occur in the same frequency with the case (3), for they are in a geometrical relation where they are to occur only alternately along the **C**-direction. From

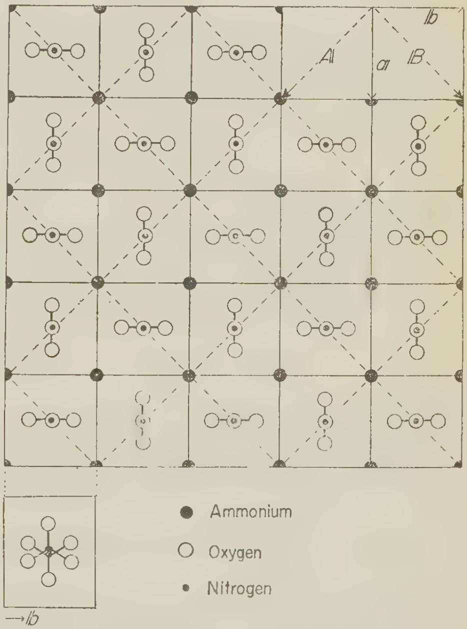

Fig. 3. The structure of tetragonal ammonium nitrate projected on (001). Full line represents the unimolecular pseudocell (**a**, **b**, **c**) and broken line the true unit (**A**, **B**, **C**=**c**).

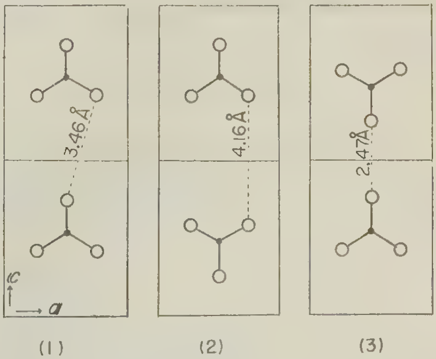

Fig. 4. All sorts of mutual orientations of neighbouring nitrate groups in the **C**-dicrection.

the above consideration it seems that the case (1) will occur more often than the cases (2) and (3). And neighbouring nitrate groups in the direction perpendiculr to the C-direction will be able to take the states such as shown in Fig. 5. In this case it is expected that these states will occur almost to the same degree.

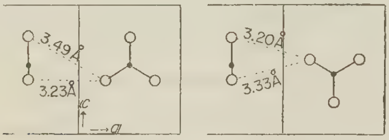

(1) (2)

Fig. 5. All sorts of mutual orientations of neighbouring nitrate groups in the **a**-direction (**a** being the axis of unimolecular pseudocell).

i) *Calculation of intensity distribution*

In the above-mentioned model the crystal is composed of four kinds of unimolecular pseudocells. Suppose that the structure factors of these pseudocells are F_1^+, F_1^-, F_2^+ and F_2^- respectively as follows:

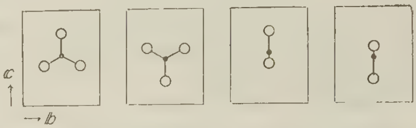

$F_1(+)$ $F_1(-)$ $F_2(+)$ $F_2(-)$

Then the structure amplitude (Y) of the whole crystal due to some instantaneous configuration of nitrate groups and the intensity (I) of the coherent X-ray scattering are respectively given by

$$Y=\sum_n \exp(2\pi i\boldsymbol{h}\cdot\boldsymbol{R}_n)F_1^n+\sum_n \exp(2\pi i\boldsymbol{h}\cdot\boldsymbol{R}_n+\boldsymbol{a})F_2^n\ , \tag{2}$$

$$\begin{aligned}I&=I_e\langle YY^*\rangle\\&=I_e[\sum_n\sum_{n'}\exp(2\pi i\boldsymbol{h}\cdot\boldsymbol{R}_n-\boldsymbol{R}_{n'})\langle F_1^n(F_1^{n'})^*\rangle+\sum_n\sum_{n'}\exp(2\pi i\boldsymbol{h}\cdot\boldsymbol{R}_n-\boldsymbol{R}_{n'})\langle F_2^n(F_2^{n'})^*\rangle\\&\quad+\sum_n\sum_{n'}\exp(2\pi i\boldsymbol{h}\cdot\boldsymbol{R}_n-\boldsymbol{R}_{n'}-\boldsymbol{a})\langle F_1^n(F_2^{n'})^*\rangle+\sum_n\sum_{n'}\exp(2\pi i\boldsymbol{h}\cdot\boldsymbol{R}_n-\boldsymbol{R}_{n'}+\boldsymbol{a})\langle F_2^n(F_1^{n'})^*\rangle]\ ,\end{aligned} \tag{3}$$

where

I_e: the Thomson factor,
$\boldsymbol{R}_n$: position vector of the nth true lattice point,
$\boldsymbol{h}$: $\boldsymbol{h}=\boldsymbol{k}-\boldsymbol{k}_0$ ($\boldsymbol{k}_0$: the wave vector of incident beam, $\boldsymbol{k}$: the wave vector of scattered beam),
F_1^n; F_2^n: the structure factor (F_1^+ or F_1^-; F_2^+ or F_2^-) of the pseudocell pointed by $\boldsymbol{R}_n$; $\boldsymbol{R}_n+\boldsymbol{a}$,
$\langle\ \rangle$: the averages of the product of the F's of two pseudocells separated by $\boldsymbol{R}_n-\boldsymbol{R}_{n'}\equiv\boldsymbol{R}_{nn'}$, $\boldsymbol{R}_{nn'}-\boldsymbol{a}$ and $\boldsymbol{R}_{nn'}+\boldsymbol{a}$ respectively,
$\sum_n\sum_{n'}$: summation is taken over all the lattice points.

In calculating each average value ($\langle\ \rangle$) the probability $P(\boldsymbol{t})$ of finding out that two nitrate groups separated by a constant vector $\boldsymbol{t}$ have the same orientation (++ or −−), was introduced. Suppose that the values of $P(\boldsymbol{t})$ for fundamental vectors $\boldsymbol{C}$, $\boldsymbol{a}$, $\boldsymbol{b}$, $\boldsymbol{A}$ and $\boldsymbol{B}$ are placed as follows:

$$P(\boldsymbol{C})=P(-\boldsymbol{C})=1-\alpha,\qquad P(\boldsymbol{a})=P(-\boldsymbol{a})=P(\boldsymbol{b})=P(-\boldsymbol{b})=1-\beta\ ,$$

$$P(\boldsymbol{A})=P(-\boldsymbol{A})=P(\boldsymbol{B})=P(-\boldsymbol{B})=1-\gamma\ .$$

Now since $\alpha\sim0$, $\beta\sim1/2$ and $\gamma\sim1/2$ are expected from the observed diffuse scattering, the values of $P(\boldsymbol{t})$ for the other vectors may be put approximately as follows:

$$\begin{aligned}&P(n_3\boldsymbol{C})=\{1+(1-2\alpha)^{|n_3|}\}/2\equiv q(n_3)\ ,\\&P(\pm\boldsymbol{a}+n_3\boldsymbol{C})=P(\pm\boldsymbol{b}+n_3\boldsymbol{C})=(1-\beta)q(n_3)+\beta\{1-q(n_3)\}\ ,\\&P(\pm\boldsymbol{A}+n_3\boldsymbol{C})=P(\pm\boldsymbol{B}+n_3\boldsymbol{C})=(1-\gamma)q(n_3)+\gamma\{1-q(n_3)\}\ ,\\&P(n_1\boldsymbol{a}+n_2\boldsymbol{b}+n_3\boldsymbol{C})=1/2\quad(\text{if } |n_1\boldsymbol{a}+n_2\boldsymbol{b}|>|\boldsymbol{A}|)\ ,\end{aligned} \tag{4}$$

where n_1, n_2 and n_3 are any integers, positive, negative, or zero.

By using these values, if we go to the limit of an infinite crystal, the first term in the formula (3) is given by

$$\begin{aligned}
&\sum_n \sum_{n'} \exp(2\pi i \boldsymbol{h}\cdot \boldsymbol{R}_n - \boldsymbol{R}_{n'}) \langle F_1{}^n (F_1{}^{n'})^* \rangle \\
&\quad = \sum_{\substack{n \quad n' \\ (\boldsymbol{R}_{nn'} = n_3 \boldsymbol{C})}} \sum \exp(2\pi i \boldsymbol{h}\cdot \boldsymbol{R}_n - \boldsymbol{R}_{n'}) [|\overline{F_1}|^2 + (1-2\alpha)^{|n_3|} (\overline{|F_1|^2} - |\overline{F_1}|^2)] \\
&\qquad + \sum_{\substack{n \quad n' \\ (\boldsymbol{R}_{nn'} = \pm \boldsymbol{A} + n_3 \boldsymbol{C},\ \pm \boldsymbol{B} + n_3 \boldsymbol{C})}} \sum \exp(2\pi i \boldsymbol{h}\cdot \boldsymbol{R}_n - \boldsymbol{R}_{n'}) [|\overline{F_1}|^2 + (1-2\gamma)(1-2\alpha)^{|n_3|} (\overline{|F_1|^2} - |\overline{F_1}|^2)] \\
&\qquad + \sum_{\substack{n \quad n' \\ (\boldsymbol{R}_{nn'} = \text{the other values})}} \sum \exp(2\pi i \boldsymbol{h}\cdot \boldsymbol{R}_n - \boldsymbol{R}_{n'}) |\overline{F_1}|^2 \\
&\quad = |\overline{F_1}|^2 \sum_n \sum_{n'} \exp(2\pi i \boldsymbol{h}\cdot \boldsymbol{R}_n - \boldsymbol{R}_{n'}) \\
&\qquad + N[(\overline{|F_1|^2} - |\overline{F_1}|^2) + 2(\cos 2\pi \boldsymbol{h}\cdot \boldsymbol{A} + \cos 2\pi \boldsymbol{h}\cdot \boldsymbol{B})(1-2\gamma)(\overline{|F_1|^2} - |\overline{F_1}|^2)] \\
&\qquad \times [1 + (1-2\alpha) 2 \cos(2\pi \boldsymbol{h}\cdot \boldsymbol{C}) + (1-2\alpha)^2 2 \cos(4\pi \boldsymbol{h}\cdot \boldsymbol{C}) + \cdots]\ , \qquad (5)
\end{aligned}$$

where

$$\overline{F_1} = (1/2)(F_1{}^+ + F_1{}^-), \qquad \overline{|F_1|^2} = (1/2)(|F_1{}^+|^2 + |F_1{}^-|^2),$$

N is the total number of lattice points and $\sum\limits_{\substack{n \quad n' \\ (\boldsymbol{R}_{nn'} = n_3 \boldsymbol{C})}} \sum$ denotes the double summation taken over the lattice points which satisfy the relation $\boldsymbol{R}_n - \boldsymbol{R}_{n'} \equiv \boldsymbol{R}_{nn'} = n_3 \boldsymbol{C}$ and so on.

In the formula (5) the function[4]:

$$J(\boldsymbol{h}\cdot \boldsymbol{C}) \equiv [1 + (1-2\alpha) 2 \cos(2\pi \boldsymbol{h}\cdot \boldsymbol{C}) + (1-2\alpha)^2 2 \cos(4\pi \boldsymbol{h}\cdot \boldsymbol{C}) + \cdots]\ , \qquad (6)$$

is a periodic function of $\boldsymbol{h}\cdot \boldsymbol{C} = l + w$ (l: integer; w: $-1 \sim 1$). If the values of $J(\boldsymbol{h}\cdot \boldsymbol{C})$ near $\boldsymbol{h}\cdot \boldsymbol{C} = 0$ can be obtained, it will serve the present purpose. This series could be summed up strictly, but for the present purpose it suffices to approximate the sum by an integral:

$$J(w) \fallingdotseq 2 \int_0^\infty (1-2\alpha)^m \cos(2\pi w m)\, dm \fallingdotseq \frac{\alpha}{\alpha^2 + \pi^2 w^2}\ , \qquad (7)$$

where in executing the integration the approximation $[-\log(1-2\alpha) \fallingdotseq 2\alpha]$ has been used.

After treating the other terms in the formula (3) in the same way, the formula (3) becomes finally

$$I = I_1 + I_2\ , \qquad (8)$$

with

$$I_1 = I_e |\overline{F_1} + \exp(2\pi i \boldsymbol{h}\cdot \boldsymbol{a}) \overline{F_2}|^2 \sum_n \sum_{n'} \exp(2\pi i \boldsymbol{h}\cdot \boldsymbol{R}_n - \boldsymbol{R}_{n'})\ , \qquad (9)$$

$$\begin{aligned}
I_2 = I_e N [&(\overline{|F_1|^2} + \overline{|F_2|^2} - |\overline{F_1}|^2 - |\overline{F_2}|^2)\{1 + 2(1-2\gamma)(\cos 2\pi \boldsymbol{h}\cdot \boldsymbol{A} + \cos 2\pi \boldsymbol{h}\cdot \boldsymbol{B})\} \\
&+ \left\{ \frac{1}{2} (F_1{}^+ (F_2{}^+)^* + F_1{}^- (F_2{}^-)^* + F_2{}^+ (F_1{}^+)^* + F_2{}^- (F_1{}^-)^*) - \overline{F_1} (\overline{F_2})^* - \overline{F_2} (\overline{F_1})^* \right\} \\
&\times \{2(1-2\beta)(\cos 2\pi \boldsymbol{h}\cdot \boldsymbol{a} + \cos 2\pi \boldsymbol{h}\cdot \boldsymbol{b})\}]\, J(\boldsymbol{h}\cdot \boldsymbol{C})\ , \qquad (10)
\end{aligned}$$

where I_1 represents the Laue-Bragg scattering discussed in the previous papers[3] and I_2 represents the diffuse scattering. It is clear that I_2 has a suitable form for explaining the general feature of the observed diffuse scattering.

ii) *Determination of α*

The curve of $J(w)$ as a function of w is shown in Fig. 6. Its half-peak breadth is $w = 2\alpha/\pi$, while the observed one was approximately 1°15′. Hence α was determined approximately to be 0.11.

iii) *Determination of β and γ*

In calculating the intensity distributions in the reciprocal-lattice planes ($\boldsymbol{h}\cdot\boldsymbol{C}=1, 2, 3$), I_eN was replaced by $K(1+\cos^2 2\theta)/2$ and further it was assumed that atomic scattering factors f_N and f_O are the same as those determined for NaNO$_3$ by P. E. Tahvonen[5] and that both of their temperature factor (e^{-M}) are given by $\exp(-1.5\sin^2\theta)$, where K is a constant for a given crystal and 2θ is the angle of scattering.

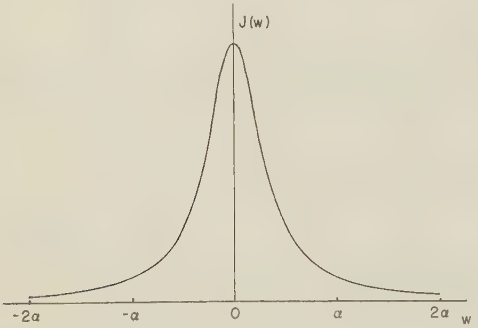

Fig. 6. Variation of $\frac{\alpha}{\alpha^2+\pi^2w^2}$ as a function of w.

The calculated distributions for $\beta=\gamma=1/2$ by using the atomic positions shown in (1) are shown in Figs. 7(a), 7(b) and 7(c). These distributions are clearly different from the observed ones (Figs. 2(a), 2(b) and 2(c)), but it is to be noticed that the regions having strong intensity correspond to the observed ones except for the reduction of the intensity about the reciprocal-lattice points as noticed in observed diffuse scatterings. In order to obtain such reduction, it is required to give the more weight to the factor $(1-2\gamma)$ $(\cos 2\pi\boldsymbol{h}\cdot\boldsymbol{A}+\cos 2\pi\boldsymbol{h}\cdot\boldsymbol{B})$ than to the factor $(1-2\beta)$ $(\cos 2\pi\boldsymbol{h}\cdot\boldsymbol{a}+\cos 2\pi\boldsymbol{h}\cdot\boldsymbol{b})$ in the formula (10). The calculated distributions for $\beta=0.58$, $\gamma=0.49$ and for $\beta=0.5$, $\gamma=0.58$ are shown respectively in Figs. 8(a), 8(b), 8(c) and 9(a), 9(b), 9(c). These distributions as shown in Fig. 9 are in fairly good agreement with the observed ones, but they are still somewhat different from the observed ones quantitatively. This discrepancy may be diminished by taking the more detailed $\boldsymbol{P}(\boldsymbol{t})$ into consideration and further by using more detailed atomic positions.

Moreover, a few words should be added on the zeroth order diffuse scattering. The calculated distribution of it vanishes on account of non-irregularity in the assumed atomic positions projected on the C-face. This facts

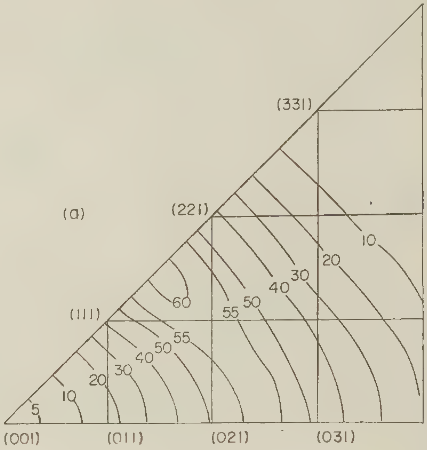

Fig. 7 (a)

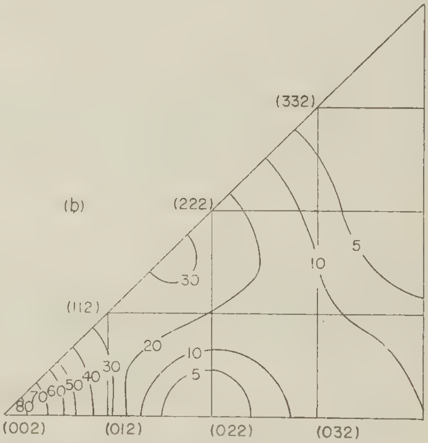

Fig. 7 (b)

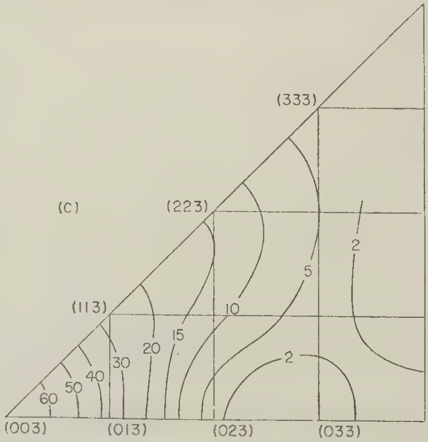

Fig. 7 (c)

Fig. 7. Intensity contours of (a) the first, (b) the second and (c) the third order diffuse scatterings calculated for $\beta=\gamma=1/2$.

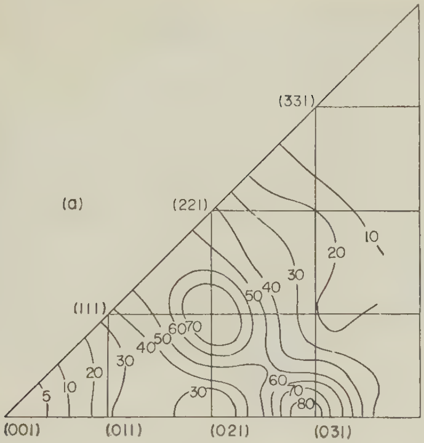

Fig. 8 (a)

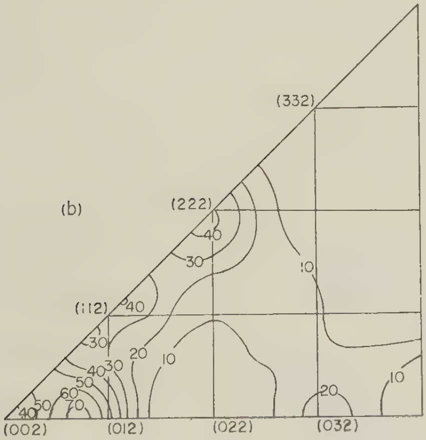

Fig. 8 (b)

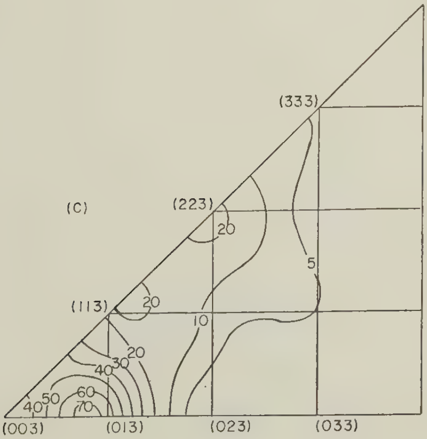

Fig. 8 (c)

Fig. 8. Intensity contours of (a) the first, (b) the second and (c) the third order diffuse scatterings calculated for $\beta=0.58$, $\gamma=0.49$.

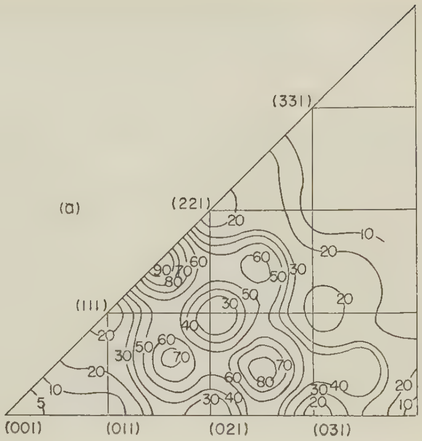

Fig. 9 (a)

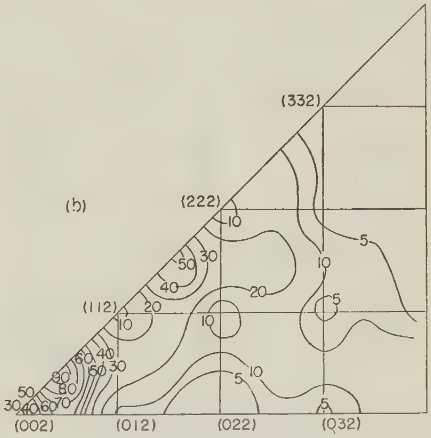

Fig. 9 (b)

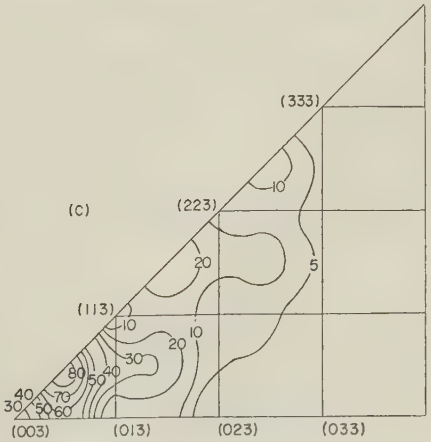

Fig. 9 (c)

Fig. 9. Intensity contours of (a) the first, (b) the second and (c) the third order diffuse scatterings calculated for $\beta=0.5$, $\gamma=0.58$.

coincides with the fact that the zeroth order could not be observed in the present study.

§ 4. Discussion

According to the above results it is considered that the randomness of the nitrate groups in the tetragonal modification will be specified by $\alpha\sim0.11$, $\beta\sim0.5$ and $\gamma\sim0.58$. These values show that the first neighbouring nitrate groups on the *C*-face take the orientations almost independently, but, on the other hand, the second neighbouring nitrate groups are likely to the rather different orientation with one another. Such a behaviour of the nitrate groups is different from that to be expected from the orthorhombic modification (32.3°C∼−18°C).

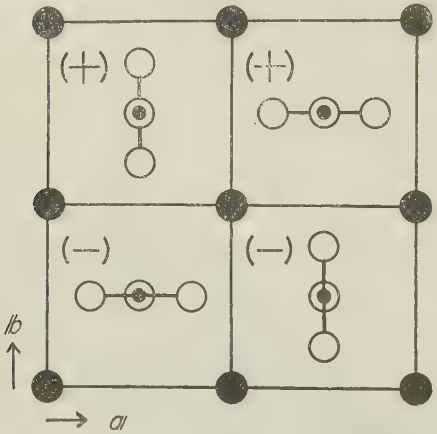

Fig. 10. One of the four equivalent configurations of the nitrate group for $\beta=1/2$, $\gamma=1$.

This fact may be explained by assuming that the weakness of hydrogen bonds are in favour of such a configuration as shown in Fig. 10. As to such configurations specified formally by $\beta=1/2$, $\gamma=1$, four equivalent configurations are to be considered. If the nitrate groups are in favour of taking such configurations locally, the values similar to the observed ones for β, γ will be obtained.

Acknowledgements

The author expresses his cordial thanks to Prof. K. Tanaka of Kyoto University for his kind guidance and discussion throughout the course of this research. He also wishes to thank Messrs. K. Nakamura and Y. Honda for their assistance. A part of this work was supported by the Scientific Research Expenditure of the Ministry of Education.

References

1) F. C. Kracek, E. Posnjak and S. B. Hendricks: J. Amer. Chem. Soc. **54** (1932) 2766.
2) Y. Shinnaka: J. Phys. Soc. Japan **14** (1959) 1073.
3) Y. Shinnaka: J. Phys. Soc. Japan **11** (1956) 393.
4) A. J. C. Wilson: *X-ray Optics*, (Methuen and Co. Ltd., London, 1949).
5) P. E. Tahvonen: Ann. Acad. Sci. Fenn. **AI** (1947) 42.

JOURNAL OF THE PHYSICAL SOCIETY OF JAPAN, Vol. 14, No. 12, DECEMBER, 1959

Proton Magnetic Relaxation in Solutions of a Manganous Salt

By Hide YOSHIOKA and Tetsuo FUJITA
Physics Institute, Nagoya University, Nagoya

(Received July 29, 1959)

The spin-lattice relaxation time T_1 and the spin phase-memory time T_2 of protons in methanol solutions containing manganous ions have been studied by use of the coherent-pulse technique. The relaxation curves were resolved into two components, *i.e.*, a short-time component corresponding to hydroxyl group protons and a long-time component corresponding to methyl group protons. The T_1/T_2 ratio for methyl group protons is considerably larger than unity. This indicates a finite density of unpaired electrons on the methyl group protons of alcohol ligands around a manganous ion. Similar studies are reported for a mixture of methanol and water containing manganous ions.

§ 1. Introduction

The spin-lattice relaxation time T_1 and the spin phase-memory time T_2 of protons in aqueous solutions of paramagnetic salts have been studied by several workers$^{1),2),3)}$. The proton spins in these solutions are relaxed mainly by magnetic interactions between protons and paramagnetic ions. The dipole-dipole interaction between protons can be ignored, because the relaxation time in pure water is of the order of several seconds, and is much longer than that in paramagnetic solutions. Theoretically, it is expected that T_1 is nearly equal to T_2 when the correlation time of the interaction modulated by Brownian motions is very short compared with the Larmor period$^{1)}$. This equality was found experimentally for aqueous solutions of Fe^{+2} and other paramagnetic ions$^{2)}$. However, several solutions containing Mn^{+2} or Cr^{+3} were found to show T_1/T_2 that is considerably larger than unity$^{3)}$. Bloembergen ascribed the abnormally large T_1/T_2 to the existence of a spin exchange interaction between a paramagnetic ion and protons in the hydration shell of the ion$^{4)}$. According to his theory, the anomalous ratio of T_1/T_2 is closely related to (*a*) the covalent bonding between paramagnetic ions and neighboring solvent molecules and also to (*b*) a long electron spin relaxation time. Therefore, it is interesting to study the behavior of T_1 and T_2 using solvents other than water. In this paper, we report the result of experiments using methanol as a solvent.

§ 2. Apparatus and Procedures

The relaxation times were measured by means of the coherent-pulse technique$^{5)}$. A block diagram of an apparatus employed is shown in Fig. 1. The apparatus consists of a magnet, a pulser, a transmitter, an induction head, a receiver, a synchroscope, and a signal integrator.

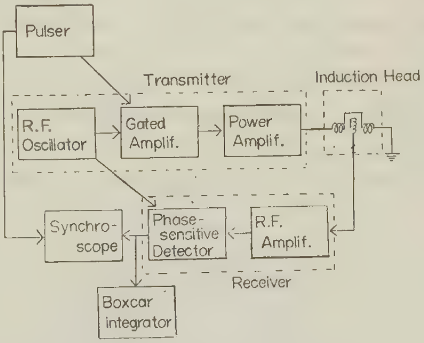

Fig. 1. Block Diagram of the apparatus.

Magnet.—A static magnetic field of 3850 oersteds was obtained from a permanent magnet having a pole face of 14 cm in diameter and a gap width of 4 cm. The field inhomogeneity over the sample of 0.5 cc in volume was about 0.1 oersteds, giving a decay time of the order of 0.5 milliseconds to the free precession.

Transmitter.—A continuously operating rf oscillator was followed by a gated amplifier, which was cut off except when a negative *dc* pulse is applied from the pulser to the cathode of the amplifier tube. The phase-coherent rf pulse, thus obtained, was further amplified and fed to a push-pull power amplifier which was operated in C-class. The output was taken from the tank circuit of the power amplifier by means of an adjustable link coil. One side of this link was grounded through an impedance-matching variable capacitor, while the other side was connected with a transmitting coil placed inside the induction head.

Induction head.—The head was designed in a similar manner as Weaver's[6]. The Helmholz-type transmitting coil had a diameter of 25 mm and a total winding of 12 turns. The receiving coil was wound around the sample in the middle of the transmitting coil and at a right angle to the latter coil. The flux linkage between the transmitting coil and the receiving coil could be made very small by shifting slightly half of the transmitting coil in the direction perpendicular to its axis by means of a micrometer screw. The maximum rf rotating field, H_1, obtained was about 6 oersteds.

Receiver.—The nuclear induction signals from the receiving coil were amplified in four stages of broad-band amplifiers. The over-all gain of the amplifiers was *ca.* 70 *db* and the band pass was *ca.* 0.6 Mc. The amplified rf signals were detected by a diode after superposing a rf carrier from the rf source of the transmitter. This phase-sensitive device made possible the linear detection of the weak signals, and gave a better signal to noise ratio and the sign of the free decay and echoes.

Synchroscope and signal integrator.—The output of the detector of the receiver was displayed on a synchroscope and also fed into the "boxcar integrator". The latter was an electronic measuring circuit which was set up modifying Holcomb and Norberg's design[7]. The experimental results obtained by use of this circuit have been proved to be much accurate compared with those by the photographic recording of signals on a synchroscope.

Pulser.—The pulser gated the transmitter by means of a *dc* negative pulse. A block diagram of the pulser is shown in Fig. 2. Th procedure of producing gate pulses is illustrated in Fig. 3, where the output pulse o each stage is shown on a common time axis The obtained gate pulses had rectangula shapes with the width ranging from 3μsec t 100μsec. The interval between the two gat pulses was equal to an integral multiple o the period of the audio-oscillator, and coul be varied step by step when the delay tim of the second delay circuit was changed b means of a volume control. The measuremen of the time interval was very easy and accurate.

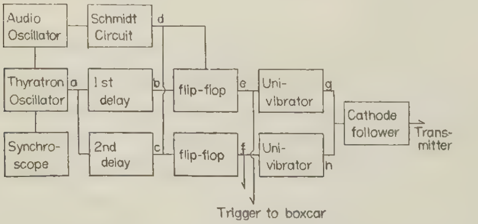

Fig. 2. Block diagram of the pulser. The letter at the output of each stage corresponds to that in Fig. 3.

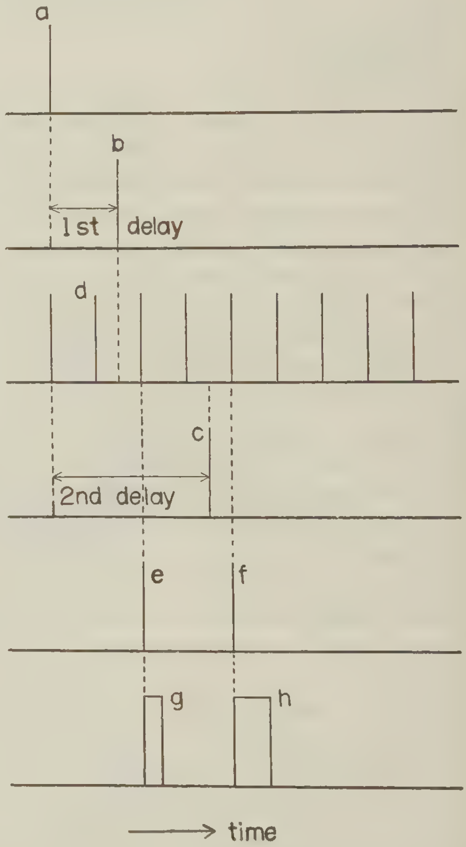

Fig. 3. Illustration of the procedure of making gate pulses. The letter on each pulse corresponds to that in Fig. 2.

The phase-sensitive detection produced a beat between the carrier frequency and the Larmor frequency of induction signals, when the field was off resonance. However, even when the rf carrier was not fed to the phase-sensitive detector, a similar beat was observed when the adjustment of the induction head was not adequate. This beat was caused by the leakage of the carrier through the power amplifier and could readily be made very small compared with amplitudes of the free decay and echo by finely adjusting the micrometer screw of the induction head. This adjustment assured normal operation of the receiver. The remaining small beat caused no trouble when the phase-sensitive detection was performed. The free decay following the rf pulse was obscured by the ringing of the transmitter as well as by the saturation of the initial stage of the receiver. This "dead time" could be reduced by the afore mentioned adjustment to less than 20μ sec.

The spin phase-memory time was measured by the 90°–180° pulse method. According to the Bloch equation[8)], the amplitude E of the echo following a 90–180° pulse sequence is given by

$$E=E_0 \exp(-2\tau/T_2) \qquad (1)$$

where τ is the time interval between the pulses. Thus, T_2 is determined from the slope of a straight line in a semilogarithmic plot.

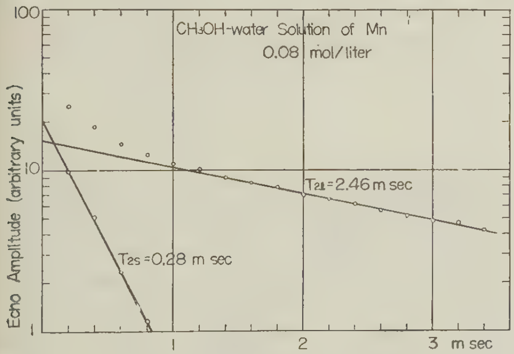

Fig. 4. A spin phase-memory curve for a methanol-water solution of $MnCl_2$.

For methanol solutions and methanol-water solutions, however, $\log E$ *versus* 2τ plot did not give a straight line. An example is shown in Fig. 4, where the curve is resolved in the usual manner and yields two components. Similar decomposition was possible for all solutions. Therefore, we have

$$E=E_{0s}\exp(-2\tau/T_{2s})+E_{0l}\exp(-2\tau/T_{2l}) , \qquad (2)$$

where the two spin phase-memory times, T_{2s} and T_{2l}, are determined from the slopes of the component lines, and the amplitudes, E_{0s} and E_{0l}, are obtained from the extrapolation of the component lines to $2\tau=0$.

The spin-lattice relaxation times were measured by use of the 180°–90° pulse sequence[9)]. In this experiment, the amplitude F of free decay following the second pulse was measured as a function of pulse intervals τ. For a single relaxation time, we have

$$F=F_0\{1-2\exp(-\tau/T_1)\} . \qquad (3)$$

From the null time τ_n for F equal to zero, we have $T_1=\tau_n/\log 2$. In methanol solutions and methanol-water solutions, however, (3) is not valid, but F can be analyzed as

$$F=F_{0s}\{1-2\exp(-\tau/T_{1s})\} \\ +F_{0l}\{1-2\exp(-\tau/T_{1l})\} ,$$

or

$$F_{0s}+F_{0l}-F=2F_{0s}\exp(-\tau/T_{1s}) \\ +2F_{0l}\exp(-\tau/T_{1l}) , \qquad (4)$$

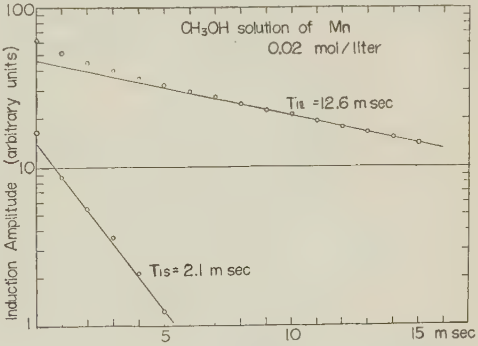

Fig. 5. A spin-lattice relaxation curve for a methanol solution of $MnCl_2 \cdot 4H_2O$.

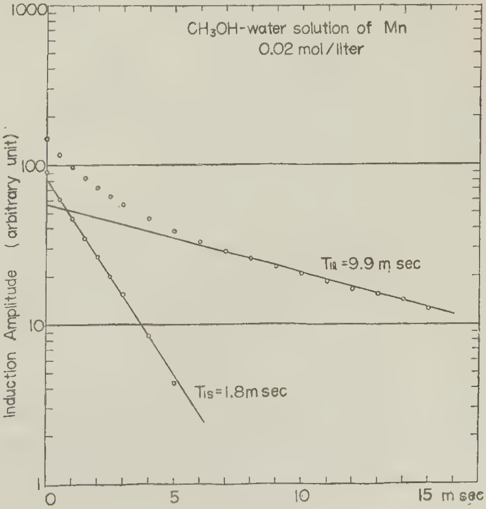

Fig. 6. A spin-lattice relaxation curve for a methanol-water solution of $MnCl_2$.

where $F_{0s}+F_{0l}$ is the value of F for $\tau=\infty$ and was obtained experimentally from the amplitude of the free decay following a 90° pulse in the absence of the 180° pulse. Thus, the relaxation times, T_{1s} and T_{1l}, and the amplitudes, F_{0s} and F_{0l}, can be obtained from a $\log(F_{0s}+F_{0l}-F)$ *versus* τ plot (Fig. 5 and Fig. 6). In this case, the null time is given by

$$F_{0s}+F_{0l}=2F_{0s}\exp(-\tau_n/T_{1s}) +2F_{0l}\exp(-\tau_n/T_{1l}) \ . \qquad (5)$$

When the first term at the right hand side can be ignored, we have

$$T_{1l}=\tau_n/\log\{2F_{0l}/(F_{0s}+F_{0l})\} \ . \qquad (6)$$

§ 3. Result

The values of T_1 and T_2 for aqueous solutions of $MnCl_2\cdot 4H_2O$ are shown as functions of ion concentrations in Fig. 7. They are in good agreement with those reported by Morgan et al.[3] The relaxation curves for methanol solutions of $MnCl_2\cdot 4H_2O$ show the existence of two components as descrined above. In addition, T_{1l} obtained from the null time by the use of (6) taking $F_{0l}/F_{0s}=3$ is in good agreement with that obtained from the semilogarithmic plot. These results indicate that the two kinds of protons, *i.e.*, protons of a hydroxyl group and of a methyl group, are subject to different local field environments. Also, the relaxation curves for methanol-water solutions of $MnCl_2\cdot 4H_2O$ have two components. The mixture solutions have three kinds of protons, *i.e.*, those of a water molecule, of a hydroxyl group and of a methyl group. How ever, chemical exchange of protons betwee a hydroxyl group and a water molecule take place presumably in a much shorter time tha the relaxation time. Accordingly, the tw kinds of protons have the same relaxatio time, giving one component of the relaxatio curves. The other component is due to th methyl group protons. A similar observatio has been reported by Morgan et al.[10] Th ratios, E_{0l}/E_{0s} and F_{0l}/F_{0s} are compared wit those of the numbers of protons in differen groups in Table I.

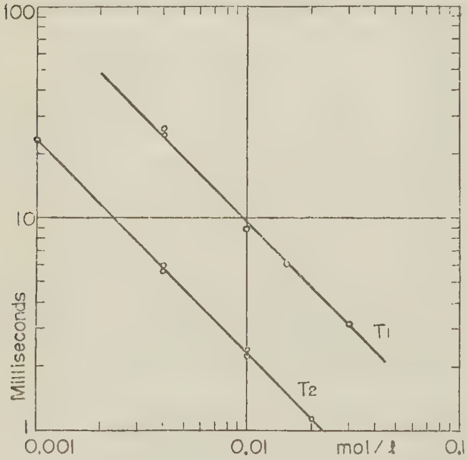

Fig. 7. Relaxation times as functions of ion concentration for aqueous solution of $MnCl_2$.

Table I.

	E_{0l}/E_{0s} (average)	F_{0l}/F_{0s} (average)	H_{CH}/H_{OH} (calc)
methanol	2.6	2.8	3.0
methanol-water	0.75	0.71	0.56

H_{CH} is the number of methyl group protons in the solution, H_{OH} is the number of protons belonging to either hydroxyl groups or water molecules.

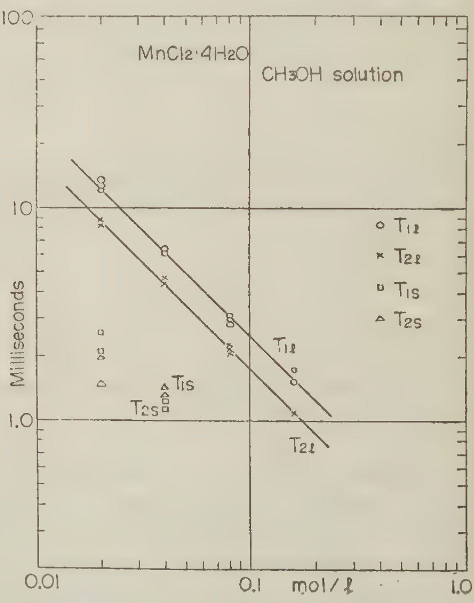

Fig. 8. Relaxation times as functions of ion concentration for methanol solution.

Relaxation times in the methanol solutions and the methanol-water solutions are plotted as functions of ion concentrations in Fig. 8 and Fig. 9. The volume ratio of methanol and water in the latter solution was 1:1. Commercial samples graded as "special pure"

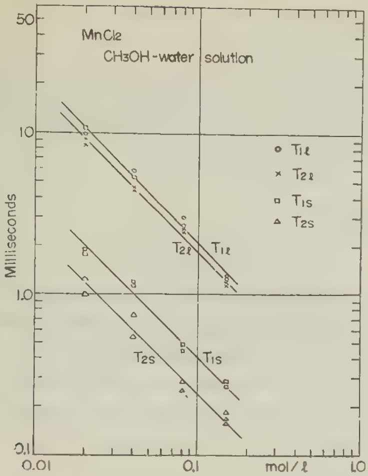

Fig. 9. Relaxation times as functions of ion concentration for methanol-water solution.

were used in this experiment at 10°–15°C.

§ 4. Discussion

The solubility of Mn salt in water and methanol is fairly high. It is known that manganous ions chemically combine with solvent molecules to form complex ions in these solutions. In aqueous solutions, the complex ion is assumed to be $\mathrm{Mn(H_2O)_6^{+2}}$ which has an octahedral symmetry as in Mn Tutton salt crystals. The rate of chemical exchange between the protons in a complex and those in the bulk solvent is considered to be very fast compared with the proton relaxation times, since only single T_1 and T_2 are obtained for each chemical group and these are inversely proportional to the concentration of manganous ions.

The relaxation of protons by the dipole-dipole interaction with manganous ions takes place mainly during the time when the protons stay as members of complex ions. If we neglect the relaxation process taking place while the protons are in the bulk solvent, the relaxation time is given by

$$\left(\frac{1}{T_1}\right)_{\mathrm{dip}}=\frac{2}{15}\frac{\hbar^2\gamma_I{}^2\gamma_s{}^2S(S+1)}{a^6}\left\{\frac{\tau_c}{1+(\omega_I-\omega_s)^2\tau_c{}^2}+\frac{3\tau_c}{1+\omega_I{}^2\tau_c{}^2}+\frac{6\tau_c}{1+(\omega_I+\omega_s)^2\tau_c{}^2}\right\}\frac{zn}{N}\,, \tag{7}$$

$$\begin{aligned}\left(\frac{1}{T_2}\right)_{\mathrm{dip}}=\frac{1}{15}\frac{\hbar^2\gamma_I{}^2\gamma_s{}^2S(S+1)}{a^6}\Bigg\{&4\tau_c+\frac{\tau_c}{1+(\omega_I-\omega_s)^2\tau_c{}^2}+\frac{3\tau_c}{1+\omega_I{}^2\tau_c{}^2}+\frac{6\tau_c}{1+\omega_s{}^2\tau_c{}^2}\\&+\frac{6\tau_c}{1+(\omega_I+\omega_s)^2\tau_c{}^2}\Bigg\}\frac{nz}{N}\,,\end{aligned} \tag{8}$$

where a is the distance between a proton and the manganous ion in the complex; γ_I and γ_s are the gyromagnetic ratios of a proton and a manganous ion respectively; S is the total electron spin of the manganous ion; ω_I and ω_s are Larmor frequencies of a proton and a manganous ion; N and n are the numbers of sovent molecules and manganous ions per unit volume; z is the coordination number of manganous ion; τ_c is the correlation time which is of the order of $4\pi\eta r_0{}^3/3kT$ according to the BPP theory, where η denotes viscosity and r_0 the radius of the complex ion. The order of magnitude of τ_c is 10^{-11} sec with the present solutions. This order was also confirmed by the analysis of the line-width data of electron spin resonance of manganous ions in alcohol-water solutions[11]. Therefore we have $\omega_I\tau_c\ll 1$, and from (7) and (8)

$$\left(\frac{T_1}{T_2}\right)_{\mathrm{dip}}\doteqdot\frac{10+3.5\omega_s{}^2\tau_c{}^2}{10+3\omega_s{}^2\tau_c{}^2}\,.$$

Thus,

$$1<\left(\frac{T_1}{T_2}\right)_{\mathrm{dip}}<1.16\,. \tag{9}$$

This inequality will not be altered if we take into account the relaxation process neglected above, because the interaction between the proton in the bulk solvent and the manganous ions contributes to the relaxation only when the manganous ions sufficiently near the proton so that the correlation time τ_c' satisfies $\omega_I\tau_c'\ll 1$.

Thus, T_1/T_2 larger than 1.16 indicates the existence of other relaxation mechanism. This mechanism is due to the Fermi contact interaction

$$\sum a_i(\boldsymbol{I}\cdot\boldsymbol{S}_i)=\sum_i \frac{16\pi\gamma\hbar\beta}{3}|\psi_i(0)|^2(\boldsymbol{I}\cdot\boldsymbol{s}_i) \tag{10}$$

where $\boldsymbol{s}_i$ is the spin of the i-th magnetic electron and $|\psi_i(0)|^2$ is the probability density of the electron at the resonating nucleus, and β is the Bohr magneton. Since the ground state of the complex is determined by Hund's rule, (10) can be transformed into

$$A(\boldsymbol{I}\cdot\boldsymbol{S})=\left(\frac{1}{n}\sum a_i\right)(\boldsymbol{I}\cdot\boldsymbol{S}) \tag{11}$$

where n is the number of magnetic electrons in a manganous ion. Expression (11) is the spin exchange interaction which was first suggested by Bloembergen[4]. Since this interaction is unaffected by the rotation of the complex, its correlation time is identical with the hydration time or with the relaxation time of the electron spin, whichever is the shorter. Since the large difference between T_1 and T_2 is only observed for ions having long electron spin relaxation times, the correlation time seems to be identical with the latter. Then the expressions for the nuclear relaxation times are given by

$$\left(\frac{1}{T_1}\right)_{\text{ex}}=\frac{2}{3}S(S+1)\hbar^{-2}A^2\tau_s\{1+(\omega_I-\omega_s)^2\tau_s^2\}^{-1}\frac{zn}{N}\ , \tag{12}$$

$$\left(\frac{1}{T_2}\right)_{\text{ex}}=\frac{1}{3}S(S+1)\hbar^{-2}A^2[\tau_s+\tau_s\{1+(\omega_I-\omega_s)^2\tau_s^2\}^{-1}]\frac{zn}{N} \tag{13}$$

where τ_s is the electron spin relaxation time.

The observed T_1 and T_2 are given by

$$\frac{1}{T_1}=\left(\frac{1}{T_1}\right)_{\text{dip}}+\left(\frac{1}{T_1}\right)_{\text{ex}} \tag{14}$$

$$\frac{1}{T_2}=\left(\frac{1}{T_2}\right)_{\text{dip}}+\left(\frac{1}{T_2}\right)_{\text{ex}}\ . \tag{15}$$

$(1/T_1)_{\text{ex}}$ in (14) can be disregarded, since $\omega_s^2\tau_s^2\gg1$ for the present solutions. Then if we assume according to (9)

$$\left(\frac{T_1}{T_2}\right)_{\text{dip}}=1.1 \tag{16}$$

we have

$$\left(\frac{1}{T_2}\right)_{\text{ex}}=\frac{1}{T_2}-\frac{1.1}{T_1} \tag{17}$$

which will be used to estimate the value of A in the following.

Aqueous solution.—From the data on the aqueous solution of MnCl_2 of 0.026 mol/liter concentration, we have $T_1=3.6$ msec and $T_2=1.0$ msec. Then, using (17) and (13) taking $S=5/2$, $z=6$ and $\tau_s=3\times10^{-9}$ sec,[11] we have $A/h=1.0\times10^6\ \text{sec}^{-1}$. This value is larger than that given by Bloembergen. His value seems less accurate than ours since it largely depends upon the estimation of the distance between the manganous ion and the proton of the ligand.

Methanol solution.—The value of T_1 for methyl group protons is *ca.* 5.2 times that for hydroxyl group protons. (Fig. 8). This result indicates that the distance between the manganous ion and the hydroxyl group proton in a ligand molecule is shorter than that between the manganous ion and the metyl group proton. Since T_1 is proportional to the sixth power of the distance, the ratio of the two distances is 1.3. This ratio is resonable if we suppose a geometrical configuration of a manganous ion and a methanol molecule as shown in Fig. 11.

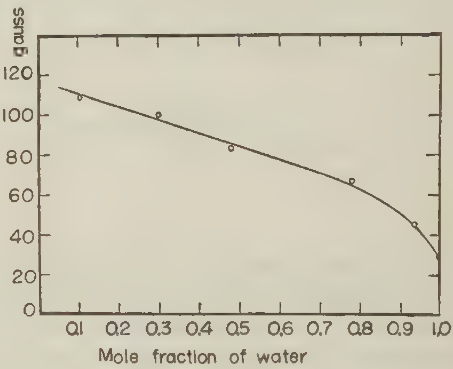

Fig. 10. Line width of hyperfine line of a manganous ion in alcohol-methanol mixture of 0.2 mol MnCl_2 according to McGarvey.[11]

The observed ratio of T_{1s}/T_{2s} for hydroxyl group protons has an experimental error too large to permit any conclusion. However, T_{1l}/T_{2l} for methyl group protons is *ca.* 1.43

from Fig. 8. This ratio indicates the existence of the spin exchange interaction. The value of the electron spin relaxation time, which is necessary to calculate the value of A from (13), has not been reported for methanol solutions. However, we assume that τ_s for the methanol solution is 1/3 times that for the aqueous solution, taking into account the fact that the line width for the alcohol solution is about 3 times that for the aqueous solution[11] (Fig. 10). Then, assuming $z=6$, we have $A/h=2.1\times10^5$ sec^{-1} for methyl group protons.

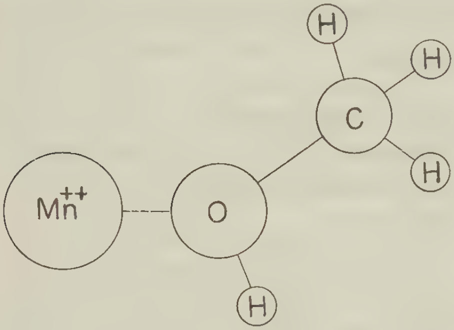

Fig. 11. A model for the geometrical configuration of a manganous ion and a methanol molecule in a complex.

Since A is proportional to the density of unpaired electrons at the resonating nucleus, the existence of the exchange interaction is rather striking. However, this existence was also confirmed by the chemical shift observed by Phillips et al.[12] The $A(\boldsymbol{IS})$ interaction gives a paramagnetic shift quite similar to the Knight shift in metals. The shift is given by

$$\varDelta H=-\frac{1}{\gamma\hbar}A\langle S_z\rangle\frac{nz}{N} \tag{18}$$

where $\langle S_z\rangle$ is the thermal-equilibrium value of S_z, namely

$$\langle S_z\rangle=2\beta S(S+1)H/(3kT)\ . \tag{19}$$

Thus, when $A/h\sim2\times10^5$ sec^{-1}, we have $\varDelta H/H\sim1.7\times10^{-5}$ for 1 mol/liter solution. Phillips et al. observed the shifts of this order for methyl group protons in propyl alcohol and butyl alcohol solutions of $CoCl_2$. They also reported the existence of a similar shift for methanol solutions of $MnCl_2$ although the data have not been published. The spin exchange interaction between methyl group protons and manganous ions gives a proof for the delocalization of magnetic electrons of a manganous ion giving a finite probability of staying on the ligand molecule. Isotropic hyperfine splitting due to a similar interaction with methyl group protons has been observed in the electron spin resonance of methyl-substituted semiquinones.[13),14)]

Methanol-water solution.—The distance of closest approach of the two species of protons to a manganous ion have a ratio of 1.3 as estimated from the observed ratio of $T_{1l}/T_{1s}=5.2$. The exchange interaction constant A for the short-time component becomes 8×10^5 sec^{-1} from the observed ratio $T_{1s}/T_{2s}=1.67$ if it is assumed that $\tau_s\sim1\times10^{-9}$ sec. For the long-time component, T_{1l}/T_{2l} is nearly equal to 1.1. Therefore, the effect of the spin exchange interaction is almost unobservable in contrast to the case of pure methanol solutions. The reason for this result is open to questions, but the result seems to indicate that the weak covalent bonds between manganous ions and methanol molecules are broken by the action of water molecules.

Acknowledgment

The authors wish to thank Prof. R. Uyeda for his support of this research, and to thank Prof. S. Kubo for reading the manuscript. The authors also thank Mr. T. Ohta for his aid in constructing some of the apparatus. One of the authors (H.Y.) thanks to Prof. J. Itoh of Osaka University who introduced him into the field of the nuclear magnetic resonance. This study was partially financed by the Scientific Research Fund of the Ministry of Education.

References

1) N. Bloembergen, E. M. Purcell and R. V. Pound: Phys. Rev. **73** (1948) 679.
2) I. Solomon: Phys. Rev. **99** (1955) 559.
3) J. A. Zimmerman: J. Chem. Phys. **22** (1954) 950. G. Laukien and J. Schlütter: Z. f. Phys. **146** (1956) 113. L. O. Morgan, A. W. Nolle, R. L. Hull and J. Murphy: J. Chem. Phys. **25** (1956) 206. A. W. Nolle and L. O. Morgan: J. Chem. Phys. **26** (1957) 642.
4) N. Bloembergen: J. Chem. Phys. **27** (1957) 572, 595.
5) E. L. Hahn: Phys. Rev. **80** (1950) 580. I. Solomon: Phys. Rev. **110** (1958) 61.
6) H. E. Weaver: Phys. Rev. **89** (1953) 923.
7) D. F. Holcomb and R. E. Norberg: Phys. Rev. **98** (1955) 1074.
8) F. Bloch: Phys. Rev. **70** (1946) 460.
9) H. Y. Carr and E. M. Purcell: Phys. Rev.

94 (1954) 630.

10) L. O. Morgan, J. Murphy and A. W. Nolle: J. Chem. Phys. **24** (1956) 906.

11) B. R. McGarvey: J. Phys. Chem. **61** (1957) 1232.

12) W. D. Phillips, C. E. Looney and C. K. Ikeda: J. Chem. Phys. **27** (1957) 1435.

13) B. Venkataraman and G. K. Fraenkel: J. Chem. Phys. **23** (1955) 588.

14) R. Bersohn: J. Chem. Phys. **24** (1956) 1066.

JOURNAL OF THE PHYSICAL SOCIETY OF JAPAN, Vol. 14, No. 12, DECEMBER, 1959

Paramagnetic Susceptibility of Single Crystals of Some Nickel Salts

By Taiichiro HASEDA, Hanako KOBAYASHI
and Muneyuki DATE

The Research Institute for Iron, Steel and Other Metals,
Tôhoku University, Sendai, Japan

(Received July 13, 1959)

Paramagnetic susceptibility of single crystals of NiK Tutton salt and $NiCl_2 \cdot 6H_2O$ were measured in the temperature range between 1.40°K and 20.4°K. The anisotropic susceptibilities found in NiK Tutton salt are in very good agreement with the calculated values using the splitting parameters which are determined by paramagnetic resonance experiment. In $NiCl_2 \cdot 6H_2O$, the antiferromagnetic transition was found at about 6°K. The easy axis is along the axis perpendicular to crystalline *c* axis in *ac* plane.

§ 1. Introduction

In the previous paper, T. Haseda and M. Date reported the paramagnetic susceptibilities of some of the nickel salts in powdered samples and made theoretical consideration on characteristics of susceptibilities of Ni^{+2} ions. It was, in the first place, found out that the susceptibility *vs* temperature curve was expected to be flat at the lowest temperature in all samples. The susceptibilities of $Ni^{+2}(3d^8)$ ion in the rhombic crystalline field were calculated in the wide temperature range. The calculated susceptibilities on each axis were expected to be strongly anisotropic in the lowest temperature range. The value of susceptibility in one of the axis is larger than the value expected from the Curie law, and the value of one of the other axis has the maximum value at some temperature. The measured susceptibilities in powdered samples are, of course the average of these values. The calculated average of the susceptibilities showed the tendency to be flat in the lowest temperature range. The comparison of the calculated value with the experimental ones was made in the powdered sample of $NiNH_4$ Tutton Salt. Though the good agreement was obtained, it will be more definite when some experiments on single crystals are carried on and the expected strong anisotropy is observed.

In this paper, the measurements are made on single crystals of NiK Tutton salt and the results are discussed on the bases of the theory developed in the previous paper.

One of the other noticeable results in the former investigation, was the large Weiss constant 7°K and the flat behaviour below considerably high temperatures (10°K) found in $NiCl_2 \cdot 6H_2O$. Though the explanation of the latter behaviour was intended under the above mentioned consideration assuming the strongly deformed crystalline field, the large Weiss constant was not examined.

One of the present authors (T.H.) and E. Kanda have found an antiferromagnetic behaviour in $CoCl_2 \cdot 6H_2O$ below 3.0°K[2]. The X-ray investigation of $NiCl_2 \cdot 6H_2O$ is now in progress by J. Mizuno and it has been found that the crystal structure is quite isomorphous to $CoCl_2 \cdot 6H_2O$[3]. Considering from the large Weiss constant of $NiCl_2 \cdot 6H_2O$ and its isomorphism to $CoCl_2 \cdot 6H_2O$ it will be expected that $NiCl_2 \cdot 6H_2O$ is also antiferromagnetic below about 10°K. The measurements on single crystals of $NiCl_2 \cdot 6H_2O$ are intended and the antiferromagnetic nature is revealed in this salt.

§ 2. The Susceptibility of Single Crystals of NiK Tutton Salt

Measurements were made using the a.c. bridge method in the temperature range between 20°K and 1.3°K. The results are listed in Table I and shown in Fig. 1 where K_1, K_2 and K_3 are magnetic principal axes determined by paramagnetic resonance experiment[4),5)]. Considerable anisotropy are found out as expected in the previous paper. However, as is known, in NiK Tutton salt crystal, there are two kinds of Ni^{+2} ions in unit cell. The relation among magnetic principal axes and axes of two kinds of octahedron which is formed by six water molecules around each Ni^{+2} ion in unit cell, is shown in Fig. 2 (a) and (b). The susceptibilities of single Ni^{+2} ion in a rhombic field (in slightly deformed octahedron) are given as

Table I. Molar susceptibility of single crystals of NiK Tutton salt.

T°K	K_1-axis	K_2-axis	K_3-axis
20.4	0.0611	0.0534	0.0531
17.6	0.0720	0.0602	0.0593
16.1	0.0795	0.0665	0.0664
14.9	0.0870	0.0744	0.0737
4.20	0.353	0.204	0.209
3.49	0.435	0.239	0.236
2.91	0.524	0.259	0.260
2.49	0.616	0.278	0.282
1.91	0.813	0.276	0.312
1.48	1.02	0.331	0.335

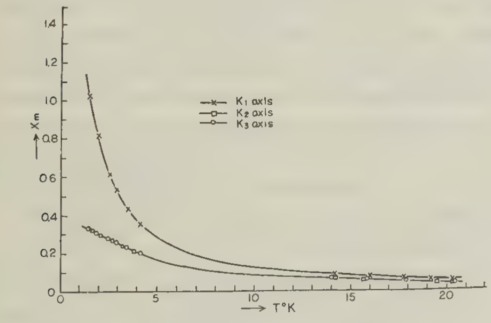

Fig. 1. Paramagnetic susceptibility of NiK Tutton salt.

$$\chi_x = \frac{2Ng^2\beta^2}{\frac{D+E}{2}} \frac{\sinh \frac{D+E}{2kT}}{\exp-\left(\frac{3E-D}{2kT}\right)+2\cosh\frac{D+E}{2kT}},$$

$$\chi_y = \frac{2Ng^2\beta^2}{\frac{D-E}{2}} \frac{\sinh \frac{D-E}{2kT}}{\exp-\left(\frac{3E+D}{2kT}\right)+2\cosh\frac{D-E}{2kT}},$$

$$\chi_z = \frac{2Ng^2\beta^2}{E} \frac{\sinh \frac{E}{kT}}{\exp\left(\frac{D}{kT}\right)+2\cosh\frac{E}{kT}}.$$

Here, x, y and z are the axes of a rhombic field. D and E are the splitting parameters appeared in the spin Hamltonian. The measured susceptibilities along each principal axis are the average value of two kind Ni^{+2} ions in units cell. It is easy to calculate the susceptibility on each principal axis in terms of χ_x, χ_y and χ_z, taking account for the situation shown in Fig. 2. Calculated values of χ_x, χ_y, χ_z and χ_{k_1}, χ_{k_2} and χ_{k_3} are shown in Fig. 3 for NiK Tutton salt. The values of constant used, are as follow,

$$D=-3.50\ \mathrm{cm}^{-1}\,,\quad E=-0.55\ \mathrm{cm}^{-1}\,,$$
$$g=2.25\,,\quad \theta=11^\circ\,,\quad \varphi=-12.5^\circ\,.$$

The ageement between the calculated and

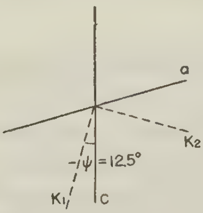

Fig. 2 (a)

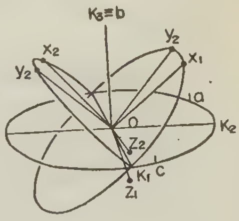

Fig. 2 (b)

(a) Susceptibility axes K_1, K_2 in ac plane of NiK Tutton salt. K_3 is parallel to b-axis and perpendicular to the plane of the figure.

(b) Relative directions of the axes in NiK Tutton salt. (a, b, c)=crystallograyhic axes, $(K_1K_2K_3)$= susceptibility axes, (x, y, Z)=axes of rhombic crystalline field. Z_1Z_2 lie in K_1K_3 plane. $\angle K_1OZ_1=\theta=11°$.

experimental values is very good showing the correctness of the above analysis. If the values given by Griffiths and Owen[5] are used, the results do not alter by the amount up to a few percent.

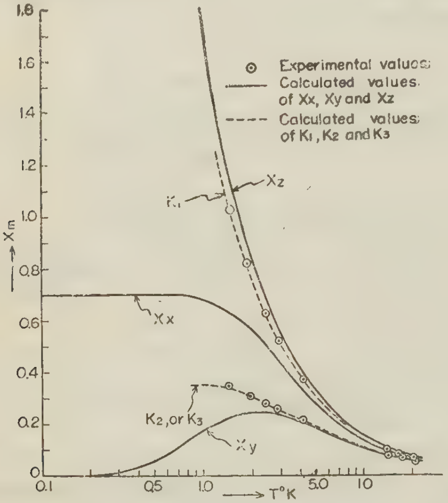

Fig. 3. Calculated susceptibility of NiK Tutton salt.

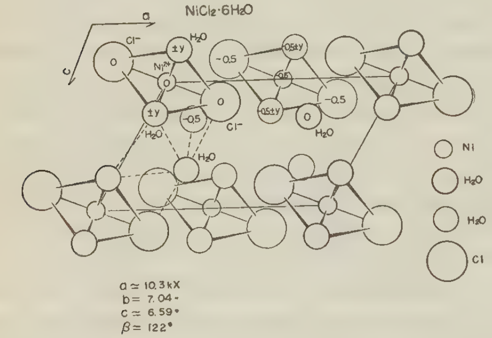

Fig. 4. A rough sketch of crystal structure of $NiCl_2 \cdot 6H_2O$.

§ 3. The Susceptibility of Single Crystals of $NiCl_2 \cdot 6H_2O$

As was mentioned in § 1, the crystal structure of this salt is quite isomorphous to $CoCl_2 \cdot 6H_2O$. Each Ni^{+2} ion is surrounded by four water molecules in a plane and by two chlorine ions along the axis perpendicular to the square of water molecules. Though the detail of the crystal analysis is not yet determined, the rough sketch of the crystal structure is shown in Fig. 4[6]. The measurements of the susceptibility on single crystal of this salt are made by a.c. bridge method, and results are shown in Fig. 5. Measurements are made along the crystalline b and c axis, and the axis perpendicular to c axis in the ac plane ($c\perp$).

As is apparent from Fig. 5, $NiCl_2 \cdot 6H_2O$ is antiferromagnetic below 6.2°K. The Weiss constant Θ of this salt determined in the sample is 10°K[1]*. T_N/Θ is about 0.6. The axis of easy magnetization is along $c\perp$ axis. It will be worthwhile to note that the easy axis in antiferromagnetic state of $CoCl_2 \cdot 6H_2O$ is along $c_{//}$ axis[7], though the detail of spin structure in these salts, is not clear now.

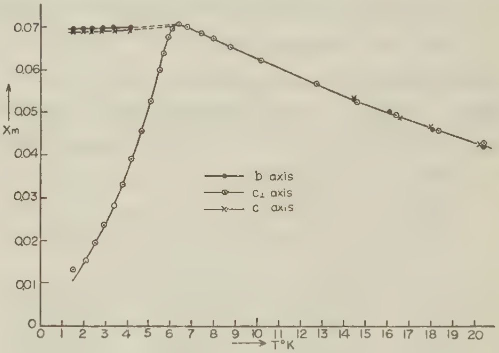

Fig. 5. Molar susceptibility of $NiCl_2 \cdot 6H_2O$.

Special interest may be on the nature of antiferromagnetism in the salt of Ni^{+2} ions concerning with the spin quenching in paramagnetic state of this salt.

As is seen in NiK Tutton salt, the susceptibility becomes anisotropic showing spin quenching of this ion. If, in $NiCl_2 \cdot 6H_2O$, the susceptibility is also anisotropic in paramagnetic range (above 6°K), the transition to antiferromagnetic state will occur in somewhat different manner from the usual cases.

In the present measurement, the anisotropy has not been observed in paramagnetic region within the experimental error which is about ±1.5%. The finer experiment is required and now being intended.

Recently, T. Sugawara have detected the proton resonance in $NiCl_2 \cdot 6H_2O$ and $CoCl_2 \cdot 6H_2O$ below their Néel point[9]. And one of the present authors (M.D.) have succeeded to measure the antiferromagnetic resonance in $CoCl_2 \cdot 6H_2O$ below 2.1°K[10].

Detailed discussion on antiferromagnetic state in $NiCl_2 \cdot 6H_2O$ and $CoCl_2 \cdot 6H_2O$ will be made in the following paper.

---

* In the paper of ref. (1), Weiss constant was determined to be 7°K. However, it is more suitable to decide it as 10°K.

The authors wish to express their sincere thanks to Mr. J. Mizuno for permission to quote the results of crystal analysis of $NiCl_2 \cdot 6H_2O$ before the publication. The authors indebted deeply to Mr. Takashi Satō for preparing the single crystals used in this investigation.

References

1) T. Haseda and M. Date: J. Phys. Soc. Japan **13** (1958) 175.
2) T. Haseda and E. Kanda: J. Phys. Soc. Japan **12** (1957) 1051.
3) J. Mizuno, K. Ukei and T. Sugawara: J. Phys. Soc. Japan **14** (1959) 383.
4) M. Date: Sci. Rep. RITT, **A**, **6** (1954) 390.
5) J. H. E. Griffiths and J. Owen: Proc. Phys. Soc. **A**, **64** (1951) 583; Proc. Roy. Soc. **A**, **213** (1952) 459.
6) J. Mizuno: Private communication.
7) T. Haseda: will be published soon.
8) P. Groth: Chemishe Kristallographie, 1 Teil (Wilhelm Engelmann, Leipzig, 1906).
9) T. Sugawara: J. Phys. Soc. Japan **14** (1959) 1248.
10) M. Date: J. Phys. Soc. Japan **14** (1959) 1244.

JOURNAL OF THE PHYSICAL SOCIETY OF JAPAN, Vol. 14, No. 12, DECEMBER, 1959

Relative Intensities of Zeeman Components in Nuclear Quadrupole Resonance Spectrum

By Masaharu TOYAMA

Department of Chemistry, Faculty of Science
University of Tokyo, Tokyo

(Received August 17, 1959)

The transition probabilities for the Zeeman components in nuclear quadrupole resonance spectrum were formulated in the case of arbitrary field gradient. Interesting behaviours were revealed especially for a nucleus of half-integral spin. When a magnetic field is applied in a direction perpendicular to the principal z-axis in the case of nonaxial field gradient due to the surrounding charges, the inner pair of the Zeeman components is produced by the x-component of the rf field and the outer pair by the y-component. The dependence of the intensities on the Zeeman field is in general not symmetric with respect to the principal axes of the field gradient.

§1. Introduction

Since the Zeeman effect of nuclear quadrupole resonance was first treated by Krüger[1] in the case of axially symmetric field, a large number of studies[2]–[4] have been made on the splitting of energy levels, but few on the intensities of the Zeeman components. The intensities in the nonaxial case have only partially been treated by Dean,[3] Cohen,[4] and others.[5],[6] Such a circumstance depends upon the fact that the calculation of the intensities is fairly complicated compared with that of the energy levels and upon the presupmtion that it would not have any possibility to give useful informations in spite of its complicated nature. For axially symmetric case, the intensity of the outer pair of Zeeman components due to the transitions of $|m|=1/2 \rightleftarrows 3/2$ has been proved to have a maximum value and to be equal to that of the inner pair when the Zeeman field is applied in the direction perpendicular to the principal z-axis of the field gradient. It decreases gradually and finally vanishes as the direction of the Zeeman field approaches to that of the z-axis. It was revealed, however, in the Zeeman experiment on the Cl^{35} resonance in cyanuryl chloride[7] ($\eta_{av}=0.24$) that the intensity in the nonaxial case fairly deviated from the above rule, and in addition it could not be explained by any extension of the axially symmetric case. When the direction of the applied field was not close to the principal xy-plain, the observed intensities obeyed approximately the rule, but in the vicinity of the xy-plane the intensity of the outer pair decreased abruptly, contrary to the expectation from the rule.

Similar phenomenon has been observed even in the case of axially symmetric field ($\eta=0$) by Ting, Manring, and Williams.[8] The third order Zeeman effect for the Cl^{35} resonance line in $NaClO_3$ was observed by applying strong field in the direction perpendicular to the principal z-axis. The resonance line was split into four lines as in the nonaxial case, of which the inner pair was vanishing below the noise level. This intensity relation was interpreted by the dependence of the transition to the direction of the rf field. Similar interpretation is expected to be possible in the nonaxial case.

Dean[3] discussed qualitatively the transition moments in the nine cases when the Zeeman field parallel to the axis x, y, and z, combined with the rf field parallel to the axis x, y, and z. His discussion is, however, not enough to explain the above phenomenon, in particular, the abrupt change in the intensity in the vicinity of the xy-plain. Cohen's calculation[4] was attempted in a special case of the nuclei with spins 5/2, 7/2, and 9/2, in which the rf field was applied parallel to the x-axis. It can not be applied to the resonance of Cl^{35} whose spin is 3/2.

§ 2. Calculation

The electric field gradient $\{q_{ij}\}$ produced at a nucleus by surrounding charges has in general an asymmetry described by an asymmetry parameter

$$\eta=(q_{xx}-q_{yy})/q_{zz}\ , \quad (|q_{xx}|\leq|q_{yy}|\leq|q_{zz}|) \quad (1)$$

where q_{xx}, q_{yy}, and q_{zz} denote the principal components of the field gradient: under this definition η always takes a non-negative number from zero to unity. The nuclear quadrupole interacts with this electric field gradient under the influence of a static magnetic field. The Hamiltonian which defines the system is then expressed as follows:

$$\mathcal{H}_0=\mathcal{H}_Q+\mathcal{H}_M\ ,$$

where

$$\mathcal{H}_Q=-A[(3I_z^2-I^2)+\eta(I_x^2-I_y^2)]\ ,$$

$$\mathcal{H}_M=-\gamma I\cdot H=-\gamma[H_xI_x+H_yI_y+H_zI_z]\ , \quad (2$$

$$A=\frac{eQq_{zz}}{4I(2I-1)}\ ,$$

and eQ denotes the scalar nuclear quadrupole moment, γ the nuclear gyromagnetic ratio, H_x, H_y, and H_z the components of H along the principal axes of the field gradient, and I the nuclear spin operator with the quantum number $I>1/2$ and with the components I_x, I_y, and I_z.

If the eigenvectors $|m\rangle$'s of I_z are taken as the bases, non-vanishing matrix elements for the spin operators are given by[9]

$$\langle m|I_z|m\rangle=m\ ,$$

and

$$\langle m|I_\pm|m\mp1\rangle=[(I\pm m)(I\mp m+1)]^{1/2}, \quad (3)$$

$$(m=I,\ I-1,\cdots,-I)$$

where $I_\pm=I_x\pm iI_y$. The eigenvectors of $\mathcal{H}_0$ are then represented by linear combinations of the basic vectors, from which the energy levels and the intensities are calculated.

Now in the case of half-integral spins two pure quadrupole states $\pm mQ$ are degenerate in the absence of a magnetic field, where mQ designates an eigenstate of $\mathcal{H}_Q$ which should be reduced to the states m for $\eta=0$. This degeneracy is removed by a Zeeman field so that an absorption line due to the transition $|mQ|=m'Q\rightleftarrows m''Q$ (m', $m''>0$) splits into two pairs, $\pm m'M\rightleftarrows\pm m''M$ and $\pm m'M\rightleftarrows\pm m''M$, as shown in Fig. 1, where mM designates an eigenstate of $\mathcal{H}_0$ similarly to mQ. Non-

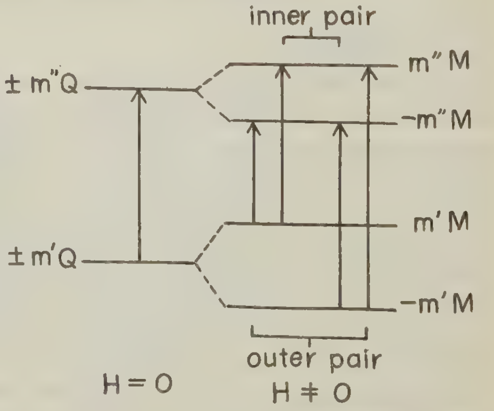

Fig. 1. Zeeman splitting of the nuclear quadrupole energy levels.

vanishing elements of $\mathscr{H}^0$ are expressed in the representation by $|m>$'s as follows:

$$\langle m|\mathscr{H}_Q|m\rangle=-A[3m^2-I(I+1)]\ ,$$

and

$$\langle m\pm1|\mathscr{H}_Q|m\mp1\rangle=-\eta A f^{1/2}(I,\ m)\ , \qquad (4)$$

where

$$f(I,\ m)=\frac{1}{4}(I^2-m^2)[(I+1)^2-m^2]\ . \qquad (5)$$

The eigenvectors of $\mathscr{H}_Q$ are, therefore, given by

$$|mQ>=\sum_{\mu}|m+2\mu><m+2\mu|mQ>$$
$$(|m+2\mu|\leq I)\ . \qquad (6)$$

The coefficients $\langle m+2\mu|mQ\rangle$'s are calculated by use of Eqs. (4) as shown later. It is noted here that

$$\langle m'|mQ\rangle=\langle -m'|-mQ\rangle\ , \qquad (6)'$$

which is derived for half-integral spins from the quadratic property of the original Hamiltonian. (In the later treatment m, m', and other quantum numbers are taken as positive numbers, except when special signs are referred to them).

For the calculation of the intensity parameters described below, it is necessary to have the transition moments between pure quadrupole states. They are classified into two types by the condition $\Delta|m|$ even or odd. Non-vanishing terms of them are derived from Eqs. (6) and (6)′ as follows:

Type I $(\Delta|m|=\text{odd})$

$$\langle\pm(m+2n+1)Q|\boldsymbol{I}_x|\pm mQ\rangle=I_{x,m,m+2n+1}\ ,$$

$$\langle\pm(m+2n+1)Q|\boldsymbol{I}_y|\pm mQ\rangle=\pm\frac{1}{i}I_{y,m,m+2n+1}\ ,$$

$$\langle\mp(m+2n+1)Q|\boldsymbol{I}_z|\pm mQ\rangle=\pm I_{z,m,m+2n+1}\ ,$$

Type II $(\Delta|m|=\text{even})$

$$\langle\mp(m+2n)Q|\boldsymbol{I}_x|\pm mQ\rangle=I_{x,m,m+2n}\ ,$$

$$\langle\mp(m+2n)Q|\boldsymbol{I}_y|\pm mQ\rangle=\pm\frac{1}{i}I_{y,m,m+2n}\ ,$$

$$\langle\pm(m+2n)Q|\boldsymbol{I}_z|\pm mQ\rangle=\pm I_{z,m,m+2n}\ . \qquad (7)$$

For the approximation to the first order of $\boldsymbol{H}$ it is necessary to have the matrix elements of $\mathscr{H}_M$ between each pair of degenerate pure quadrupole states $\pm mQ$. They are derived from Eqs. (2) and (7) to be

$$\langle\pm mQ|\mathscr{H}_M|\pm mQ\rangle=\mp\gamma I_{z,m,m}H_z\ ,$$

and

$$\langle\pm mQ|\mathscr{H}_M|\mp mQ\rangle=-\gamma[I_{x,m,m}H_x\pm iI_{y,m,m}H_y] \qquad (8)$$

The eigenvalues of $\mathscr{H}_0$ are then given to the first order in $\boldsymbol{H}$ by

$$E(\pm mM)=E_Q(\pm m)-\gamma E_M(\pm m)\ , \qquad (9)$$

where $E_Q(\pm m)$'s are the unperturbed quadrupole energies and $E_M(\pm m)$'s the energy shifts of the split levels in the unit of γ:

$$E_M(\pm m)=\pm[I^2_{x,m,m}H_x^2+I^2_{y,m,m}H_y^2+I^2_{z,m,m}H_z^2]^{1/2} \qquad (9)'$$

From Eqs. (8) and (9) the eigenvectors of $\mathscr{H}_0$ in the zeroth order in $\boldsymbol{H}$ are given by

$$|mM>=a_m|mQ>+b_m|-mQ>\ ,$$

and

$$|-mM>=-b_m^*|mQ>+a_m^*|-mQ>\ , \qquad (10)$$

where the coefficients a_m and b_m are given by the following relations:

$$\frac{I_{x,m,m}H_x}{E_M(m)}=a_mb_m^*+a_m^*b_m\ ,$$

$$\frac{I_{y,m,m}H_y}{E_M(m)}=a_mb_m^*-a_m^*b_m\ ,$$

$$\frac{I_{z,m,m}H_z}{E_M(m)}=a_ma_m^*-b_mb_m^*\ ,$$

and

$$a_m a_m^* + b_m b_m^* = 1 \tag{11}$$

In ordinary nuclear spin resonance the transition between two eigenstates E' and E'' $(E'' > E')$ is produced by a magnetic interaction of the nuclear magnetic moment with the rf field $2\boldsymbol{H}_r \cos 2\pi\nu t$. The total Hamiltonian has to include the interaction term given by

$$\mathscr{H}_1 = -2\gamma \boldsymbol{I}\cdot \boldsymbol{H}_r \cos 2\pi\nu t\ .$$

The transition probability is then expressed to the second order of approximation as follows:[10]

$$w(E',\ E'') = \hbar^{-2} T^2(E',\ E'') g(\nu)\ , \tag{12}$$

where $g(\nu)$ is the distribution function of frequencies and $T^2(E',\ E'')$ may be called a square transition moment, which is obtained from Eq. (2)′ as follows:

$$T^2(E',\ E'') = |\langle E''|\gamma \boldsymbol{I}\cdot \boldsymbol{H}_r|E'\rangle|^2 = \gamma^2 \sum_{i,\,j} H_{ri} H_{rj} J_{ij}(E',\ E'')\ , \qquad (i,\ j = x,\ y,\ \text{and}\ z) \tag{13}$$

where

$$J_{ij}(E',\ E'') = \frac{1}{2}[\langle E''|\boldsymbol{I}_i|E'\rangle\langle E'|\boldsymbol{I}_j|E''\rangle + \langle E''|\boldsymbol{I}_j|E'\rangle\langle E'|\boldsymbol{I}_i|E''\rangle] \tag{13$'$}$$

and H_{rx}, H_{ry}, and H_{rz} are the components of the rf field along the principal axes of the field gradient. The distribution $g(\nu)$ is originated from spin-spin interactions, thermal motions of lattice, and inhomogeneity of the external applied field $\boldsymbol{H}$.

Under unsaturation condition,[11] the peak intensity at a resonance frequency $\nu = (E'' - E')/h$ in the absorption spectrum is proportional to

$$P(E',\ E'') = \frac{4\pi N \nu^2}{(2I+1)\Delta\nu \cdot kT} \cdot T^2(E',\ E'')\ , \tag{14}$$

provided that $|E_{\max} - E_{\min}| \ll kT$, where $\Delta\nu$ is the half-value width of the absorption line described by $g(\nu)$, T the absolute temperature, k Boltzmann constant, and N the total number of the resonating nuclei.

In this article let us confine ourselves to the discussion of the case of strong quadrupole coupling and weak magnetic field. Thus the energy levels may be calculated to the first order of $\boldsymbol{H}$ as shown above, but the transition probabilities are enough to be calculated in the zeroth order in $\boldsymbol{H}$, since the accuracy in the measurement of the intensity is far lower than that of the frequency.

In the case of half-integral spins two transitions belonging to the same pair, that is, $\pm m'M \rightleftarrows \pm m''M$ or $\pm m'M \rightleftarrows \mp m''M$, occur with equal probabilities. As the contribution of the splitting of the energy levels to ν^2 in Eq. (14) may be neglected in the zeroth order of approximation in $\boldsymbol{H}$, the relative intensity of these two pairs is given by

$$P_r(m',\ m'') = \frac{T^2(-)}{T^2(+) + T^2(-)} \tag{15}$$

where the plus sign denotes the inner pair $\pm m'M \rightleftarrows \pm m''M$ and the minus sign the outer pair $\pm m'M \rightleftarrows \mp m''M$.

The next problem is to formulate the intensity parameters:

$$J_{ij}(\pm) = J_{ij}(m'M,\ \pm m''M) = J_{ij}(-m'M,\ \mp m''M)\ . \qquad (i,\ j = x,\ y,\ \text{and}\ z) \tag{16}$$

They are obtained from the eigenvectors of $\mathscr{H}_0$ given by Eq. (10) and the transition moments between pure quadrupole states (Eq. (7)) as follows:

Type I $(m''=m'+2n+1)$

$$J_{xx}(\pm)=\frac{1}{2}I^{2}_{x,m',m''}[1\pm F_{m',m''}\{I_{x,m',m'}I_{x,m'',m''}H_x^2+I_{y,m',m'}I_{y,m'',m''}H_y^2+I_{z,m',m'}I_{z,m'',m''}H_z^2\}]\ ,$$

$$J_{yy}(\pm)=\frac{1}{2}I^{2}_{y,m',m''}[1\pm F_{m',m''}\{-I_{x,m',m'}I_{x,m''m''}H_x^2-I_{y,m',m'}I_{y,m'',m''}H_y^2+I_{z,m',m'}I_{z,m'',m''}H_z^2\}]\ ,$$

$$J_{zz}(\pm)=\frac{1}{2}I^{2}_{z,m',m''}[1\pm F_{m',m''}\{-I_{x,m',m'}I_{x,m''m''}H_x^2+I_{y,m',m'}I_{y,m'',m''}H_y^2-I_{zm',m'}I_{z,m'',m''}H_z^2\}]\ ,$$

$$J_{yz}(\pm)=\pm\frac{1}{2}I_{y,m',m''}I_{z,m',m''}[-I_{y,m',m'}I_{z,m'',m''}-I_{z,m',m'}I_{y,m'',m''}]F_{m',m''}H_yH_z\ ,$$

$$J_{zx}(\pm)=\pm\frac{1}{2}I_{z,m',m''}I_{x,m',m''}[I_{z,m'm'}I_{x,m'',m''}-I_{x,m',m'}I_{z,m'',m''}]F_{m',m''}H_zH_x\ ,$$

$$J_{xy}(\pm)=\pm\frac{1}{2}I_{x,m',m''}I_{y,m',m''}[-I_{x,m',m'}I_{y,m'',m'''}+I_{y,m',m'}I_{x,m'',m''}]F_{m',m''}H_xH_y\ . \tag{17}$$

Type II $(m''=m'+2n)$

$$J_{xx}(\pm)=\frac{1}{2}I^{2}_{x,m',m''}[1\pm F_{m',m''}\{I_{x,m',m'}I_{x,m'',m''}H_x^2-I_{y,m',m'}I_{y,m'',m''}H_y^2-I_{z,m',m'}I_{z,m'',m''}H_z^2\}],$$

$$J_{yy}(\pm)=\frac{1}{2}I^{2}_{y,m',m''}[1\pm F_{m',m''}\{-I_{x,m',m'}I_{x,m'',m''}H_x^2+I_{y,m',m'}I_{y,m'',m''}H_y^2-I_{z,m',m'}I_{z,m'',m''}H_z^2\}]\ ,$$

$$J_{zz}(\pm)=\frac{1}{2}I^{2}_{z,m',m''}[1\pm F_{m',m''}\{-I_{x,m',m'}I_{x,m'',m''}H_x^2-I_{y,m',m'}I_{y,m'',m''}H_y^2+I_{z,m',m'}I_{z,m'',m''}H_z^2\}]\ ,$$

$$J_{yz}(\pm)=\pm\frac{1}{2}I_{y,m',m''}I_{z,m',m''}[I_{y,m',m'}I_{z,m'',m''}+I_{z,m',m'}I_{y,m'',m''}]F_{m',m''}H_yH_z\ ,$$

$$J_{zx}(\pm)=\pm\frac{1}{2}I_{z,m',m''}I_{x,m',m''}[I_{z,m',m'}I_{x,m'',m''}+I_{x,m',m'}I_{z,m'',m''}]F_{m',m''}H_zH_x\ ,$$

$$J_{xy}(\pm)=\pm\frac{1}{2}I_{x,m',m''}I_{y,m'.m''}[I_{x,m',m'}I_{y,m'',m''}+I_{y,m',m'}I_{x,m'',m''}]F_{m',m''}H_xH_y\ . \tag{18}$$

Here we put for brevity

$$F_{m',m''}=1/E_M(m')E_M(m'')\ . \tag{19}$$

In equation (17) and (18), $I_{i,m',m''}$ $(m'\neq m'')$ may be regarded as a parameter describing the dependence of the transitions $|mM|=m'M\rightleftarrows m''M$ upon the i-component ($i=x$, y, or z) of the rf field and $I_{i,m,m}$, as the parameter concerning with the orientation of the Zeeman field.

The ordinary spectrum arises from the transitions $\Delta|m|=1$ which belong to the type I. The intensity of this spectrum is expressed by the intensity parameters $J_{ij}(mM, \pm(m+1)M)$ which depend on such pure quadrupole transition moments as $I_{i,m,m}$, and $I_{i,m,m+1}$. Other transitions $\Delta|m|\neq 1$, so-called forbidden transitions, belonging to both types should occur in the case of nonaxial field gradient, but their intensities are ordinarily so weak that they can hardly be detected except for large asymmetry, because they are at most of the second order of magnitude in η.

A. Second order approximation in η

A perturbation method of the second order in η leads to the determination of the coefficients in Eq. (6) as follows,

$$\langle m|mQ\rangle=1-\frac{1}{288}\eta^2\left[\frac{f(I,\ m+1)}{(m+1)^2}+\frac{f(I,\ m-1)}{(m-1)^2}\right]$$

$$\langle m\pm2|mQ\rangle=\mp\eta\frac{f^{1/2}(I,\ m\pm1)}{12(m\pm1)}$$

$$\langle m\pm4|mQ\rangle=\eta^2\frac{f^{1/2}(I,\ m\pm1)f^{1/2}(I,\ m\pm3)}{288(m\pm1)(m\pm2)}\ . \tag{20}$$

Thus the transition moments between pure quadrupole states for allowed transitions ar obtained as follows:

$$\left.\begin{matrix} I_{x,1/2,1/2} \\ I_{y,1/2,1/2} \end{matrix}\right\} = \pm\frac{1}{2}\left(I+\frac{1}{2}\right)-\frac{\eta}{12}\left(I-\frac{1}{2}\right)\left(I+\frac{1}{2}\right)\left(I+\frac{3}{2}\right)$$

$$\mp\frac{\eta^2}{648}\left(I-\frac{1}{2}\right)\left(I+\frac{1}{2}\right)\left(I+\frac{3}{2}\right)\left(I^2+I+\frac{21}{4}\right),$$

$$\left.\begin{matrix} I_{x,3/2,3/2} \\ I_{y,3/2,3/2} \end{matrix}\right\} = \frac{\eta}{12}\left(\pm1+\frac{\eta}{3}\right)\left(I-\frac{1}{2}\right)\left(I+\frac{1}{2}\right)\left(I+\frac{3}{2}\right),$$

$$\left.\begin{matrix} I_{x,5/2,5/2} \\ I_{y,5/2,5/2} \end{matrix}\right\} = \pm\frac{\eta^2}{648}\left(I-\frac{3}{2}\right)\left(I-\frac{1}{2}\right)\left(I+\frac{1}{2}\right)\left(I+\frac{3}{2}\right)\left(I+\frac{5}{2}\right),$$

$$\left.\begin{matrix} I_{x,m,m} \\ I_{y,m,m} \end{matrix}\right\} \leqq O(\eta^3), \qquad \left(m \geqq \frac{7}{2}\right)$$

$$I_{z,m,m} = m + \frac{\eta^2}{72}\left[\frac{f(I,\ m+1)}{(m+1)^2} - \frac{f(I,\ m-1)}{(m-1)^2}\right]; \tag{21}$$

$$\left.\begin{matrix} I_{x,m,m+1} \\ I_{y,m,m+1} \end{matrix}\right\} = \frac{1}{2}\,[(I-m)(I+m+1)]^{1/2}\left[1 \pm \frac{\eta}{24}\cdot\frac{I(I+1)+3m(m+1)}{m(m+1)}\right.$$

$$\left. + \frac{\eta^2}{288}\left\{\frac{(m-2)f(I,\ m-1)}{m(m-1)^2} + \frac{(m+3)f(I,\ m+2)}{(m+1)(m+2)^2} - \frac{f(I,\ m)}{m^2} - \frac{f(I,\ m+1)}{(m+1)^2}\right\}\right],$$

$$I_{z,1/2,3/2} = \frac{\eta}{6}\left(I-\frac{1}{2}\right)^{1/2}\left(I+\frac{1}{2}\right)\left(I+\frac{3}{2}\right)^{1/2},$$

$$I_{z,3/2,5/2} = \frac{\eta^2}{108}\left(I-\frac{3}{2}\right)^{1/2}\left(I-\frac{1}{2}\right)\left(I+\frac{1}{2}\right)\left(I+\frac{3}{2}\right)\left(I+\frac{5}{2}\right)^{1/2},$$

$$I_{z,m,m+1} \leqq O(\eta^3) \qquad \left(m \geqq \frac{5}{2}\right). \tag{21$'$}$$

In these equations I_x components take the upper of the double signs, and I_y the lower ones. It is to be noted that when the asymmetry parameter η is sufficiently small compared with unity and the nuclear spin I is not large, $I_{y,m,m}$ components are negative, while other transition moments are all positive.

The dependence of the relative intensity on the rf field and on the Zeeman field is calculated from Eqs. (15), (17), (21), and (21)′. In particular, when the Zeeman field is applied parallel to each principal axis, the intensity parameters for the allowed transitions $|m| = m \rightleftarrows$

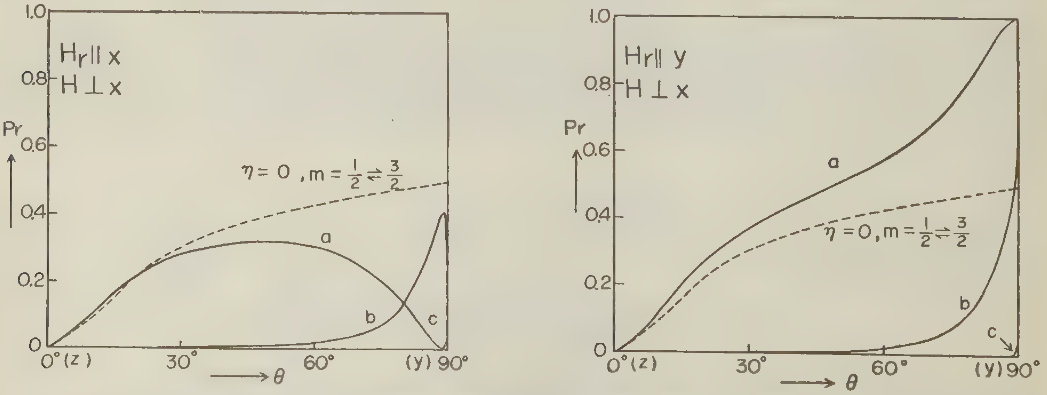

Fig. 2. Relative intensities of the Zeeman components in the case of $I=7/2$ and $\eta=0.05$, where a, b, and c denote three allowed transitions $|m|=1/2\rightleftarrows3/2$, $3/2\rightleftarrows5/2$, and $5/2\rightleftarrows7/2$, respectively, and θ the direction of the static magnetic field measured from the principal z-axis.

$m+1$ are reduced as follows:

$$\begin{aligned}
&\boldsymbol{H}\|x; \quad J_{xx}(+)=I^2_{x,m,m+1}, \quad && J_{yy}(-)=I^2_{y,m,m+1}, \quad && J_{zz}(-)=I^2_{z,m,m+1},\\
&\boldsymbol{H}\|y; \quad J_{xx}(+)=I^2_{x,m,m+1}, && J_{yy}(-)=I^2_{y,m,m+1}, && J_{zz}(+)=I^2_{z,m,m+1},\\
&\boldsymbol{H}\|z; \quad J_{xx}(+)=I^2_{x,m,m+1}, && J_{yy}(+)=I^2_{y,m,m+1}, && J_{zz}(-)=I^2_{z,m,m+1},
\end{aligned} \tag{22}$$

whereas other parameters all vanish. In Fig. 2 the relative intensities are plotted against the orientation of the Zeeman field for the allowed transitions $|m|=1/2 \rightleftarrows 3/2$, $3/2 \rightleftarrows 5/2$, and $5/2 \rightleftarrows 7/2$ in the case of $I=7/2$ and $\eta=0.05$.

B. Exact Treatment for $I=3/2$

For the nuclei with $I=3/2$ only one absorption due to the allowed transition $|m|=1/2 \rightleftarrows 3/2$ is observed in the absence of a magnetic field. The pure quadrupole Hamiltonian $\mathscr{H}_Q$ can be solved analytically in this case as made by Dean,[3)] and the intensities of the Zeeman components are also calculated exactly in terms of η. The results are as follows:

Transition moments between pure quadrupole states:

$$\begin{aligned}
&I_{x,1/2,1/2}=\frac{1}{2\rho}(\rho+1-\eta), && I_{x,3/2,3/2}=\frac{1}{2\rho}(\rho-1+\eta), && I_{x,1/2,3/2}=\frac{\sqrt{3}}{2\rho}\left(1+\frac{1}{3}\eta\right),\\
&I_{y,1/2,1/2}=-\frac{1}{2\rho}(\rho+1+\eta), && I_{y,3/2,3/2}=-\frac{1}{2\rho}(\rho-1-\eta), && I_{y,1/2,3/2}=\frac{\sqrt{3}}{2\rho}\left(1-\frac{1}{3}\eta\right),\\
&I_{z,1/2,1/2}=\frac{1}{2\rho}(2-\rho), && I_{z,3/2,3/2}=\frac{1}{2\rho}(2+\rho), && I_{z,1/2,3/2}=\frac{\eta}{\sqrt{3}\,\rho},
\end{aligned} \tag{23}$$

where

$$\rho=\left(1+\frac{1}{3}\eta^2\right)^{1/2}.$$

Energy levels:

$$\begin{aligned}
&E_Q\left(\pm\frac{3}{2}\right)=-E_Q\left(\pm\frac{1}{2}\right)=3A\rho,\\
&E_M\left(\pm\frac{1}{2}\right)=\pm\frac{1}{2\rho}\left[(\rho+1-\eta)^2H_x^2+(\rho+1+\eta)^2H_y^2+(2-\rho)^2H_z^2\right]^{1/2},\\
&E_M\left(\pm\frac{3}{2}\right)=\pm\frac{1}{2\rho}\left[(\rho-1+\eta)^2H_x^2+(\rho-1-\eta)^2H_y^2+(2+\rho)^2H_z^2\right]^{1/2},
\end{aligned} \tag{24}$$

Intensity parameters for $m=1/2 \rightleftarrows 3/2$:

$$\begin{aligned}
&J_{xx}(\pm)=\frac{3}{8\rho^2}\left(1+\frac{1}{3}\eta\right)^2\left[1\pm\rho^{-2}F_{1/2,3/2}\left\{\frac{3}{4}\left(1-\frac{1}{9}\eta^2\right)H_z^2+\frac{\eta}{2}\left[\left(1-\frac{1}{3}\eta\right)H_x^2+\left(1+\frac{1}{3}\eta\right)H_y^2\right]\right\}\right],\\
&J_{yy}(\pm)=\frac{3}{8\rho^2}\left(1-\frac{1}{3}\eta\right)^2\left[1\pm\rho^{-2}F_{1/2,3/2}\left\{\frac{3}{4}\left(1-\frac{1}{9}\eta^2\right)H_z^2-\frac{\eta}{2}\left[\left(1-\frac{1}{3}\eta\right)H_x^2+\left(1+\frac{1}{3}\eta\right)H_y^2\right]\right\}\right],\\
&J_{zz}(\pm)=\frac{\eta^2}{6\rho^2}\left[1\mp\rho^{-2}F_{1/2,3/2}\left\{\frac{3}{4}\left(1-\frac{1}{9}\eta^2\right)H_z^2+\frac{\eta}{2}\left[\left(1-\frac{1}{3}\eta\right)H_x^2-\left(1+\frac{1}{3}\eta\right)H_y^2\right]\right\}\right],\\
&J_{yz}(\pm)=\pm\frac{3\eta}{8\rho^4}\left(1-\frac{1}{9}\eta^2\right)\left(1+\frac{1}{3}\eta\right)F_{1/2,3/2}H_yH_z,\\
&J_{zx}(\pm)=\mp\frac{3\eta}{8\rho^4}\left(1-\frac{1}{9}\eta^2\right)\left(1-\frac{1}{3}\eta\right)F_{1/2,3/2}H_zH_x,\\
&J_{xy}(\pm)=\mp\frac{3\eta}{4\rho^4}\left(1-\frac{1}{9}\eta^2\right)F_{1/2\,3/2}H_xH_y
\end{aligned} \tag{25}$$

In the above equations $F_{1/2,3/2}$ is given by Eqs. (19) and (24).

These equations hold for $I=3/2$ over the whole range of the asymmetry parameter. In Fig. the relative intensities are plotted against the orientation of the Zeeman field for variou asymmetry parameters from zero to unity in the case of rf field parallel to each principa axis of the field gradient. Fig. 4 illustrates the angular dependence for $\eta=0.4$ in the cas that rf field is applied in various directions deviated from the principal axes.

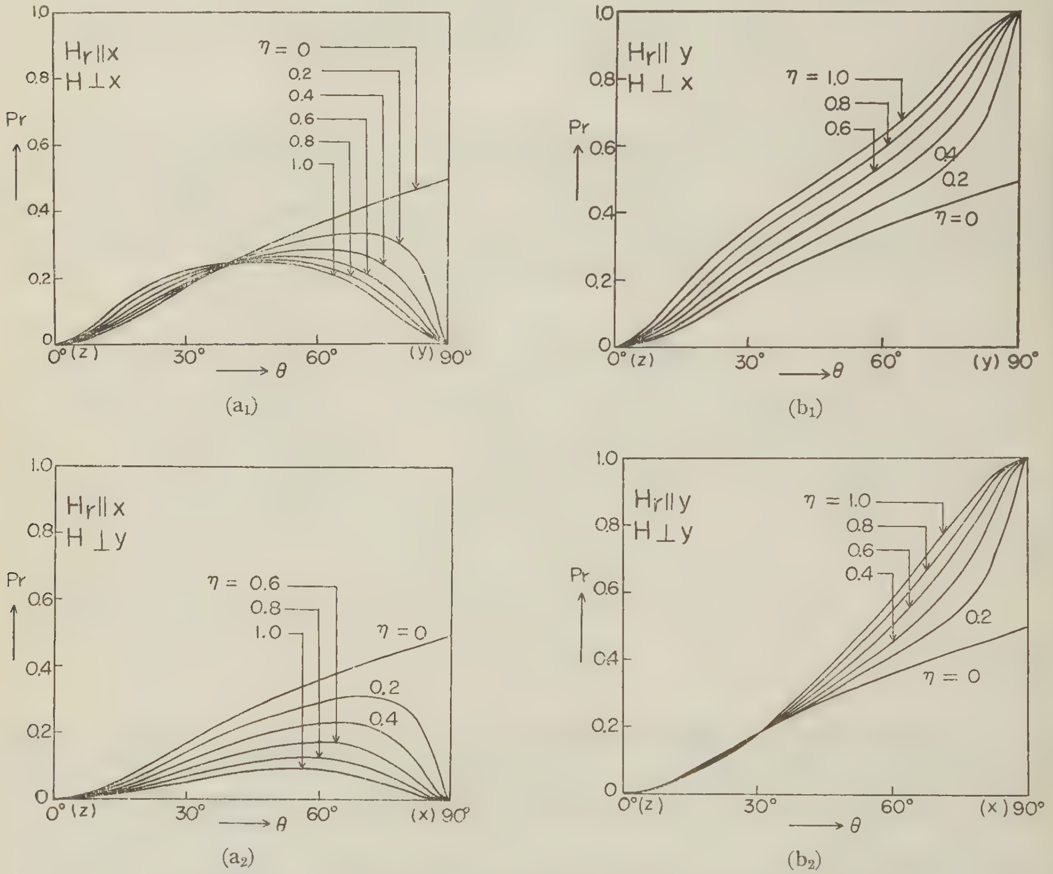

Fig. 3. Relative intensities of the Zeeman components in the case of $I=3/2$, where θ denotes the direction of the static magnetic field.

§ 3. Discussion

From Eqs. (21)′ and (23) (or Eq. (25)), the allowed transitions are concluded to be mainly produced by the x- and y- components of the rf field, of which the x-component contributes more strongly to the intensities. The contribution of the z-component is only in the second order of η^2 even to the transitions $|m|=1/2 \rightleftarrows 3/2$, and to other transitions it is so small for small asymmetry that it may be neglected.

The dependence of the relative intensity on the Zeeman field appears strongly in the transitions $|m|=1/2 \rightleftarrows 3/2$, as shown in Fig. 2; in this case the outer pair of the Zeeman components is observed with considerable intensity. In other transitions, however, the outer pair is so weak for small asymmetry that we can hardly detect but the inner pair, except when the magnetic field is applied in the vicinity of the xy-plane. This fact can be explained in terms of mixing of the degenerate pure quadrupole states $\pm mQ$ (see Eq. (10)); that is, the outer pair of transitions is produced by their mixing, which is complete for the states $|m|=1/2$ with the x- and y-components of the Zeeman field, but for other states $|m|\geqq 3/2$ in the first or higher order of magnitude in η.

Finally let us consider the lowest transitions

$|m|=1/2 \rightleftarrows 3/2$. In the case of small asymmetry the rule for $\eta=0$ holds approximately when the direction of the Zeeman field is not close to the principal xy-plane. Thus, for the Zeeman field parallel to the principal z-axis, the outer pair is so weak in intensity that only the inner pair may be detected, because the inner pair of transitions is produced by the x- and y-components of the rf field, while the outer pair is produced by the z-component (see Eq. (22)). As the direction of the Zeeman field deviates from the z-axis, the intensity of the outer pair increases gradually, whereas the inner pair decreases. The agreement with the rule is remarkable especially in the case of the Zeeman field perpendicular to the rf field (compare Figs. 3(a_1) and (b_2) with (a_2) and (b_1)).

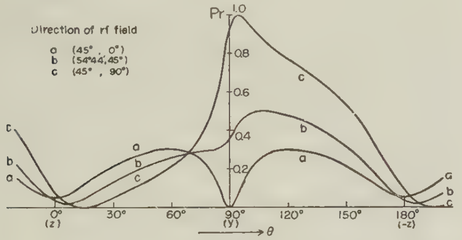

(a) H ⊥ x.

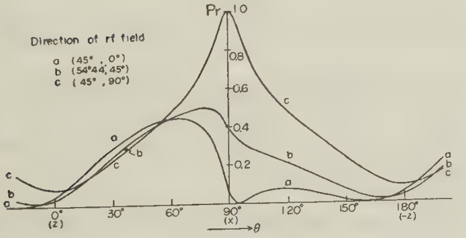

(b) H ⊥ y

Fig. 4. Contribution of the cross terms of intensity parameters to the relative intensities of the Zeeman components in the case of $I=3/2$ and $\eta=0.4$, where θ denotes the direction of the static magnetic field.

The deviation from the rule is, however, expected in the case of the Zeeman field perpendicular to the z-axis. In this case the inner pair is produced by the x-component of the rf field while the outer pair by the y-component (see Eq. (22)). Hence, as the direction of the Zeeman field approaches to the xy-plane, the relative intensity P_r will be observed to decrease abruptly to zero or to increase to unity, according to the rf field parallel to the x-axis or to the y-axis, respectively, as illustrated in Figs. 2 and 3. The intensities $P_\perp(\pm)$ of both pairs for the Zeeman field perpendicular to the z-axis are then expressed to the first order of accuracy in η as follows:

$$P_\perp(+)=KI^2_{x,m,m+1}\sin^2\theta_r\cos^2\varphi_r\ ,$$
$$P_\perp(-)=KI^2_{y,m,m+1}\sin^2\theta_r\sin^2\varphi_r\ . \qquad (26)$$

where K is a constant factor common between both pairs and $(\theta_r,\ \varphi_r)$ is the polar coordinate of the rf field with the pole on the z-axis and with the initial line of φ_r on the x-axis. Even in this case, therefore, it is possible that both pairs are observed with equal intensities as expected from the rule for $\eta=0$; it is fulfilled with the rf field applied in the intermediate direction between the x- and the y-axis.

The above relation explains well the anomaly in the intensities observed in cyanuryl chloride[7] described in the introduction. At the same time it will make us possible to determine the location of the principal x- and y-axes. It has been fairly difficult by other methods, for instance, by the method of no-splitting locus,[12] because the eccentricity of the locus is very small (in the first order in η). It is recommended to apply the intensity relation after a rough estimation by other methods easy to handle. Actual application has proved to give a good result for the Cl^{35}-resonance in 1, 3, 5-trichlorobenzene.[13]

Here we must remind that the above relations hold only when the asymmetry parameter η is small and the spin I is not large; otherwise the situation may be reversed between both pairs, since $I_{i,m,m'}$'s may change their signs for large asymmetry and for large spins, and, in addition, the z-component of the rf field may contribute to the transitions to the order comparable with other components.

In Fig. 3 there is shown the dependence of the relative intensity on the asymmetry parameter for $I=3/2$. The fractional importance of the x-component of the rf field decreases for the outer pair of transitions with the increase in the asymmetry parameter, while that of the y-component increases. Since the signs of the transition moments in Eq. (23) are invariant for arbitrary asymmetry parameters, the situation is never reversed between both pairs in the case of $I=3/2$, but the z-component of the rf field is expected to contribute considerablly to the transitions in the case of large asymmetry. Its contribution is entirely opposite to those of the x- and y-components as is easily seen from Eq. (25); it makes the outer pair of transitions stronger.

The contribution of the cross terms of intensity parameters is at most in the first order of magnitude in η. For large asymmetry, however, they are important for the relative intensity when the direction of the rf field deviates from the principal axes. The dependence of the intensity on the Zeeman field is no more symmetric with respect to the principal axes of the field gradient, as illustrated in Figs. 4(a) and 4(b). The direction of the Zeeman field in which the relative intensity is maximum or minimum is deviated away from the directions of the principal axes.

§ 4. Integral Spins

In the case of integral spins a static magnetic field produces only shifts of the energy levels, since the degeneracy which appears between two pure quadrupole states $\pm mQ$ for half-integral spins has already been removed by an asymmetry of the field gradient. In addition there are only a few kinds of stable nuclei with integral spins and with considerable natural abundances;[14] Li ($I=1$), B^{10} ($I=3$), and N^{14} ($I=1$). The general formulation, then, seems to be not so important as in the case of half-integral spins.

The process to lead the final formulae is quite analogous to that used in the Stark effect of rotational levels.[15] The result for $I=1$ which is most frequently used will be summarized; here are three energy levels designated by $0M$, and $\pm 1M$, so that three transitions should occur corresponding to $0M \rightleftarrows \pm 1M$ and $1M \rightleftarrows -1M$;

Energy levels;

$$E(0M)=2A\ ,$$

$$E(\pm 1M)=-A\left[1\pm\left(\eta^2+\frac{\gamma^2 H_z^2}{A^2}\right)^{1/2}\right],$$

where

$$A=\frac{1}{4}eQq_{zz}\ . \tag{27}$$

Non-vanishing intensity parameters;* for $0M \rightleftarrows \pm 1M$

$$J_{xx}=\frac{1}{2}\left[1\pm\left(1+\frac{\gamma^2 H_z^2}{\eta^2 A^2}\right)^{-1/2}\right]$$

$$J_{yy}=\frac{1}{2}\left[1\mp\left(1+\frac{\gamma^2 H_z^2}{\eta^2 A^2}\right)^{-1/2}\right], \tag{28}$$

for $+1M \rightleftarrows -1M$

$$J_{zz}=\left(1+\frac{\gamma^2 H_z^2}{\eta^2 A^2}\right)^{-1}. \tag{28$'$}$$

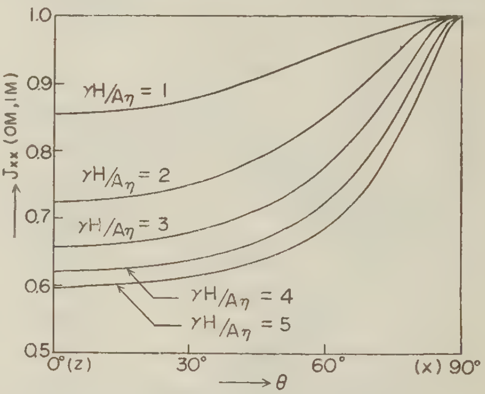

Fig. 5. Dependence of the intensity parameter J_{xx} ($0M$, $1M$) for $I=1$ on the direction of the static magnetic field (θ) and on the parameter $\gamma H/A\eta$.

In Fig. 5 the intensity parameter $J_{xx}(0M, 1M)$ is plotted against the orientation of the Zeeman field to the z-axis. The change in the intensity is symmetric with respect to the principal axes, and depends only on the z-component of the Zeeman field. Its contribution is, however, of much importance only when the asymmtery parameter is comparable with the perturbation by the Zeeman field; otherwise the intensity is almost independent of the Zeeman field. For $|\gamma H| \gg |A\eta|$, the transitions $0M \rightleftarrows \pm 1M$ are produced with equal probabilities by the x- and y-components of the rf field. For $|\gamma H| \ll |A\eta|$, however, the transition $0M \rightleftarrows 1M$ is produced by the x-component while the transition $0M \rightleftarrows -1M$ by the y-component. In the latter case one should consider rather the contribution of ν^2 in Eq. (6), because the asymmetry parameter contributes in the first order to the splitting of energy levels $m=\pm 1$. The transition $1M \rightleftarrows -1M$ is produced by the z-component, but it will hardly be observed in the case of $|\gamma H| \gg |A\eta|$ for two reasons: (1) the transition probability is very small; and (2) the absorption spectrum exists at the region of extremely low frequency.

---

* The results are in good agreement with those by Casabella and Bray, J. Chem. Phys. **28**, 1182 (1958), but their formulae include the Zeeman field only implicitly so that the present ones will be more applicable to actual purposes.

§ 5. Conclusion

For half-integral spins the following properties are derived:

(1) For small asymmetry the rule for $\eta=0$ holds approximately in the case when the direction of the Zeeman field is not so close to the principal xy-plane.

(2) The deviation from the rule is remarkable when the direction of the Zeeman field approaches to the xy-plane: the inner pair of transitions is produced by the x-component of the rf field and the outer pair by the y-component. The critical behaviour in this region suggests a method of precise determination of the principal axes.

(3) The contribution of the product intensity parameters can not be neglected except for very small asymmetry ($\eta \geqq 0.1$); it is of much importance when the rf field deviates from the directions of principal axes, and makes the change in the intensity asymmetric with respect to the principal axes.

For integral spins the intensity is affected by the magnitude of a factor $|\gamma H/\eta A|$, and its dependence on the Zeeman field would be observed only for $|\gamma H/\eta A| \cong 1$ in the case of $I=1$.

In conclusion the author wishes to express his appreciation to Professor Y. Morino under whose guidance this research was developed.

APPENDIX

Corrected Bersohn's Formulae for Zeeman Energies

R. Bersohn[2)] has proposed the formulae for the first order Zeeman effect of nuclear quadrupole energy levels for half-integral spins to the second order of accuracy in η. His formulae, however, should be corrected in the coefficients of η^2-terms as pointed out in the preceeding paper.[7)] The corrected formulae are derived from Eqs. (9)′ and (21) as follows:

$$\begin{aligned}E_M\left(\pm\frac{1}{2}\right)=\pm\Bigg[&\frac{1}{4}H_z^2+\frac{1}{4}(H_x^2+H_y^2)\left(I+\frac{1}{2}\right)^2\\&-\frac{1}{12}\eta(H_x^2-H_y^2)\left(I-\frac{1}{2}\right)\left(I+\frac{1}{2}\right)^2\left(I+\frac{3}{2}\right)\\&-\frac{1}{81}\eta^2H_z^2\left(I-\frac{1}{2}\right)\left(I+\frac{3}{2}\right)\left(I^2+I+\frac{3}{4}\right)\\&+\eta^2(H_x^2-H_y^2)\Bigg\{\frac{1}{144}\left(I-\frac{1}{2}\right)^2\left(I+\frac{1}{2}\right)^2\left(I+\frac{3}{2}\right)^2\\&-\frac{1}{648}\left(I-\frac{1}{2}\right)\left(I+\frac{1}{2}\right)^2\left(I+\frac{3}{2}\right)\left(I^2+I+\frac{21}{4}\right)\Bigg\}\Bigg]^{1/2},\end{aligned}$$

$$\begin{aligned}E_M\left(\pm\frac{3}{2}\right)=\pm\Bigg[&\frac{9}{4}H_z^2\\&+\frac{1}{24}\eta^2H_z^2\left\{\frac{1}{25}\left(I-\frac{5}{2}\right)\left(I-\frac{3}{2}\right)\left(I+\frac{5}{2}\right)\left(I+\frac{7}{2}\right)-\left(I-\frac{1}{2}\right)\left(I+\frac{1}{2}\right)^2\left(I+\frac{3}{2}\right)\right\}\\&+\frac{1}{144}\eta^2(H_x^2+H_y^2)\left(I-\frac{1}{2}\right)^2\left(I+\frac{1}{2}\right)^2\left(I+\frac{3}{2}\right)^2\\&+\frac{1}{216}\eta^3(H_x^2-H_y^2)\left(I-\frac{1}{2}\right)^2\left(I+\frac{1}{2}\right)^2\left(I+\frac{3}{2}\right)^2\Bigg]^{1/2},\end{aligned}$$

$$\begin{aligned}E_M\left(\pm\frac{5}{2}\right)=\pm\Bigg[&\frac{25}{4}H_z^2\\&+\frac{5}{72}\eta^2H_z^2\Bigg\{\frac{1}{49}\left(I-\frac{7}{2}\right)\left(I-\frac{5}{2}\right)\left(I+\frac{7}{2}\right)\left(I+\frac{9}{2}\right)\end{aligned}$$

$$-\frac{1}{9}\left(I-\frac{3}{2}\right)\left(I-\frac{1}{2}\right)\left(I+\frac{3}{2}\right)\left(I+\frac{5}{2}\right)\Big\}$$

$$+\frac{1}{419,904}\eta^4(H_x^2+H_y^2)\left(I-\frac{3}{2}\right)^2\left(I-\frac{1}{2}\right)^2\left(I+\frac{1}{2}\right)^2\left(I+\frac{3}{2}\right)^2\left(I+\frac{5}{2}\right)^2\Big]^{1/2},$$

and

$$E_M(\pm m)=\pm\left|mH_z+\frac{1}{72}\eta^2H_z\left\{\frac{f(I,\ m+1)}{(m+1)^2}-\frac{f(I,\ m-1)}{(m-1)^2}\right\}\right|\qquad\left(m\geqq\frac{7}{2}\right),\tag{29}$$

where the energies are measured in the unit of $-\gamma$. In his formulae Bersohon has omitted the terms of η^3 and η^4 in the states $|m|=3/2$ and 5/2, which come from the second order corrections to the pure quadrupole eigenvectors. However, it seems reasonable to keep these terms as in the above equations, because they contribute to the energies in the second order in η in the special case where the Zeeman field is applied in the direction perpendicular to the z-axis.

References

1) H. Krüger: Z. Physik **130**, (1951) 371.
2) R. Bersohn: J. Chem. Phys. **20** (1952) 1505.
3) C. Dean: Phys. Rev. **96** (1954) 1053.
4) M. H. Cohen: Phys. Rev. **96** (1954) 1278.
5) G. Lamarche and G. M. Volkoff: Can. J. Phys. **31** (1950) 1010.
6) M. Bloom, L. B. Robinson, and G. M. Volkoff: Can. J. Phys. **36** (1958) 1286.
7) Y. Morino, T. Chiba, T. Shimozawa, and M. Toyama: J. Phys. Soc. Japan **13** (1958) 869.
8) Ting, Manring, and Williams, Phys: Rev. **96** (1954) 408.
9) E. Feenberg and G. E. Pake: "*Notes on the Quantum Theory of Angular Momentum*" Addison-Wesley, Cambridge (1953) p. 25.
10) P. A. M. Dirac: "*The Principles of Quantum Mechanics*". London, Oxford (1935) p. 172ff.
11) F. Bloch: Phys. Rev. **70** (1946) 460.
12) H. C. Meal: J. Chem. Phys. **24** (1956) 1101.
13) To be published.
14) G. E. Pake: "*Nuclear Magnetic Resonance*" in Solid State Physics, Vol. 2, Academic Press (1956) p. 3.
15) C. H. Townes and A. L. Shawlow: "*Microwave Spectroscopy*", McGraw-Hill, (1955) p. 248ff.

JOURNAL OF THE PHYSICAL SOCIETY OF JAPAN Vol. 14, No. 12, DECEMBER, 1959

Spectroscopic Investigation of Hydrogen Plasma Produced by an Impulsive Discharge

By Manabu YAMAMOTO
Hitachi Central Research Laboratory, Kokubunji, Tokyo, Japan

(Received June 23, 1959)

Time variation of the radiation intensity was observed during an impulsive discharge through hydrogen gas. Oscillogram traces of the intensity of the Balmer lines and continuum are shown, and the temperature dependence of the spectral intensity is discussed. Temperature of the plasma at various phases of the discharge current is deduced from the time variation of the radiation intensity, from spectral energy distribution of the Balmer continuum, and from electrical conductivity. It is shown that the agreement between theory and experiment is fairly good for ionization and kinetic temperatures, but poor for the excitation temperature. The H_β line tends to vanish more rapidly than theoretically predicted.

§ 1. Introduction

During an impulsive discharge through a gas, the spectrum of radiation emitted from the plasma is observed to vary with the time. For example, lines of the neutral atom are expected to vanish at such phases of the discharge current when the plasma attains very high temperature, while the intensity of continuous radiation increases with increasing temperature, since the latter is emitted during encounters of ions and electrons. The continuous radiation itself extends to the shorter wavelengths with increasing temperature.

The spectroscopic investigations described here were carried out in order to determine the temperature of plasma at various phases of the discharge current, using methods which are based in principle on the spectral characteristics as mentioned above.

§ 2. Discharge Apparatus

The discharge apparatus that was used in shown in Fig. 1. It consists of a fused silica torus of 10 cm mean diameter and 0.9 cm tube radius. It is linked by an oriented iron core, $5\times5\,\text{cm}^2$ in cross section and 80 cm in length. Four turn primary windings wound around the core are connected to the 5 μF capacitor bank through an air gap, which is triggered automatically when the capacitor is charged up to 10 kV. The discharge tube was baked before filling with hydrogen gas of 1 mmHg pressure. The gas is preionized by a 2 Mc high frequency discharge.

The discharge current is measured with a Rogowski coil combined with an R–C integrator. The oscilloscope is synchronized to the pulse put out from the saturable reactor inserted in the primary winding. The current and voltage waveforms are shown in Fig. 2. The discharge lasts for 100 μsec. The peak value of current and corresponding voltage per turn are ca. 10 kA and 1 kV, respectively.

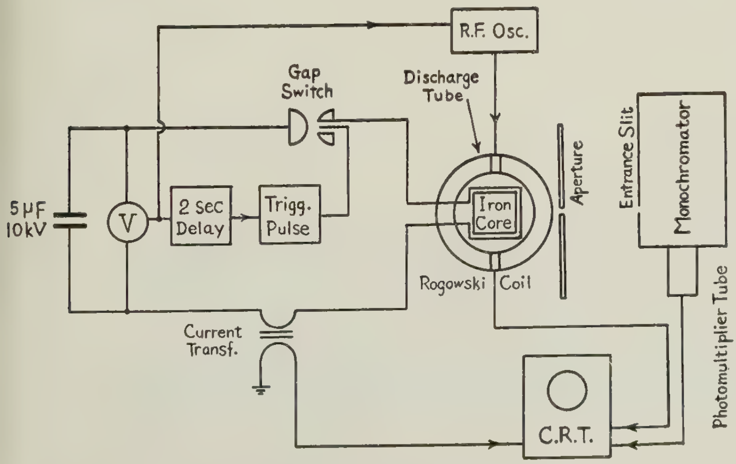

Fig. 1. Schematic diagram of the apparatus.

§ 3. Optical System

In order to study the time

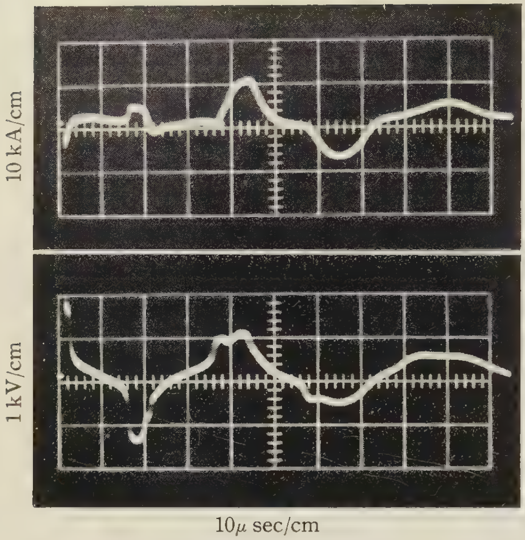

Fig. 2. Current (above) and voltage per turn (below) waveforms.

variation of spectral intensity, light beam emitted from the center of plasma is projected onto the entrance slit of a monochromator, which can select any region between λλ10,000 and 2,000 Å with any desired wavelength interval. The monochromatic light is received by a photomultiplier tube of $S-13$ spectral response (having a fused silica bulb and an Sb–Cs photocathode). To calibrate the relative response of the whole optical system, the radiation emitted from the center of the plasma in a 160 W xenon short arc lamp was chosen as a standard, the intensity distribution of which has been shown to be

$$J(\nu)d\nu=\text{const}\times\exp(-h\nu/kT)d\nu \qquad (1)$$

with $T=7{,}400$°K[1]. The overall response of the optical system for the fixed width of the monochromator slits is shown in Fig. 3.

§ 4. Spectrograms

Before studying the time variation of the spectral intensity, spectra were taken in the usual way (see Fig. 4). Stark effect broadening of the Balmer lines is noticed, the breadth increasing with increasing quantum number of the line (compare with the spectrogram of high frequency discharge of weak excitation). The lines arising from the higher levels form an apparent continuum near the series limit, beyond which extends the true continuum into the ultra-violet region. Since the continuous radiation is due to free-free (Bremsung) or free-bound (recombination) transitions of electrons, the highly excited atoms

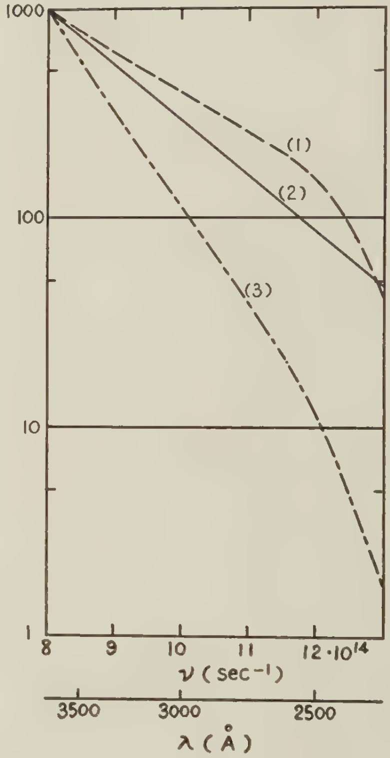

Fig. 3. Calibration of the optical system for the spectral sensitivity. (1) Relative spectral response, (2) exp($-h\nu/kT$) with $T=7{,}400$°K and (3) xenon lamp measured.

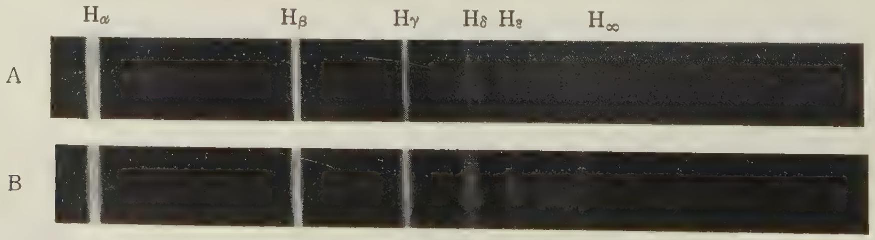

Fig. 4. Spectrograms of the hydrogen discharge. A. High frequency discharge of weak excitation. B. Capacitor discharge. Continuum emitted by the high frequency discharge is due to molecular hydrogen.

may also be regarded as virtually ionized. Hence the ionization potential of an atom placed in the field of neighbouring ions is somewhat lowered. The amount of decrease is, after Unsöld[2],

$$\Delta V_i = 7.0 \times 10^{-7} n_i^{1/3} \text{ (volt)}\,, \tag{2}$$

where n_i is the ion density.

To obtain the ion density n_i, Inglis-Teller's formula is used:

$$\log N = 23.46 - 7.5 \log n_m\,, \tag{3}$$

where n_m is the quantum number of the highest line which lies in the neighbourhood of the continuum but still observed as a separate line. N, the density of perturbers, is given by

$$N \begin{cases} = n_i + n_e & \text{for } T < 10^5/n_m \\ = n_i = n_e & \text{for } T > 10^5/n_m \end{cases} \tag{4}$$

where T is the temperature of plasma. In our case $n_m = 7$ (H_ε), hence $n_e = (5\sim10) \times 10^{16}$ /cm³, which corresponds to 70∼100% ionization of the gas. From Eq. (2),

$$\Delta V_i = 0.3 \text{ (volt)}\,, \tag{5}$$

that is, the ionization potential of hydrogen atom is lowered to 13.3 volt.

These values obtained here are now inserted into Saha's equation

$$\frac{n_e n_i}{n_H} = \frac{2U_i}{U_H} \frac{(2\pi mkT)^{3/2}}{h^3} \times \exp\left[-\frac{e}{kT}(V_i - \Delta V_i)\right], \tag{6}$$

from which the temperature of plasma is deduced. In this expression U_i is the partition function of the ion, and m is the mass of electron. k, h and e are well known physical constants. U_H, the partition function of the hydrogen atom, is

$$U_H = \sum_n g_n \exp(-eV_n/kT)\,, \tag{7}$$

where the sum was taken over $n \leqq 7$. Inserting numerical values obtained above, it is seen that the temperature should exceed 14,000°K for over 70% ionization. As the present calculation is based on the spectrogram taken in the usual manner (time integrated exposure), the plasma must have attained still higher temperature. This is discussed in the following sections.

§ 5. Time Variation of the Intensity of Continuous Radiation

Fig. 5 shows oscillogram traces of the intensity of continuous radiation. It should be noted that the intensity variation accurately follows the variation of current, irrespective of the selected wavelength. A slight but important difference is found, however, between waveforms for the different wavelength. Intensity variation of the shorter wavelength radiation is characterized by a sharp peak at the intensity maximum and a rapid decrease toward the minimum. On the other hand, the variation of the intensity of the longer wavelength radiation is relatively flattened, and a slight, parasitic decrease is observed at the top of intensity (see the waveform of λ3473Å, $t = 45$ μsec; time is measured from the point when the oscillogram trace starts.) This indicates that the continuous radiation extends to the shorter wavelength

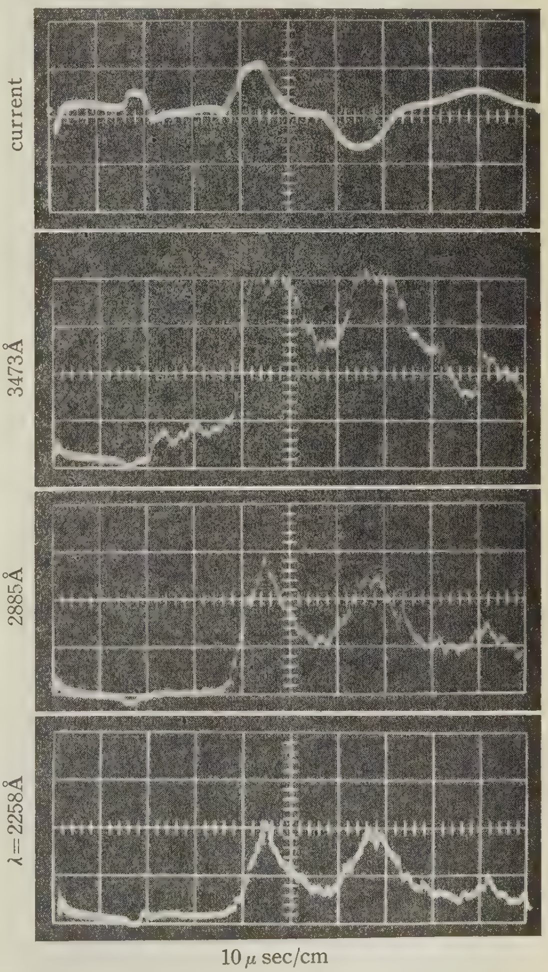

Fig. 5. Time variation of the intensity of continuous radiation. The slit width corresponds to $\Delta\lambda = 5$Å.

at the time of the maximum of current, than it does at the minimum.

From these observed characteristics of the waveforms of the radiation intensity the temperature of plasma was deduced in the following ways. The intensity of continuous radiation is[3)]

$$J_\nu(T)\,d\nu=\frac{32\pi^2e^6}{3\sqrt{3}\,c^3(2\pi m)^{3/2}}\frac{n_in_e}{(kT)^{1/2}}e^{u_1-u}$$

$$\times\left(1+2u_1\sum_{u_2}^{u_4}\frac{1}{n^3}e^{u_n-u_5}\right)d\nu\,, \qquad (8)$$

where $u=h\nu/kT$, $u_1=eV_i/kT$, $u_n=h\nu_n/kT$ and $h\nu_n$ is the energy of the level n measured from the level $n=\infty$.

A. *Temperature Dependence of $J_\nu(T)$*

Fig. 6 shows variation of the intensity of continuous radiation with temperature. The rapid increase of intensity in the temperature range up to 18,000°K is due to increasing ionization, while the gradual decrease beyond that is ascribed to the factor $T^{-3/2}$. Contribution of the intensity of Bremsstrahlung, which depends on $T^{-1/2}$, to the total intensity is less than 12% for $T<20,000$°K. From the slight decrease of intensity observed at the peak of intensity of λ3473Å, it is reasonable to assume that the temperature has reached 20,000°K at $t=45\,\mu$sec. If this temperature is assumed also for the peak intensity of other wavelengths, each of the oscillogram traces gives the temperature of plasma as a function of time. In Table I is shown the value deduced in this way.

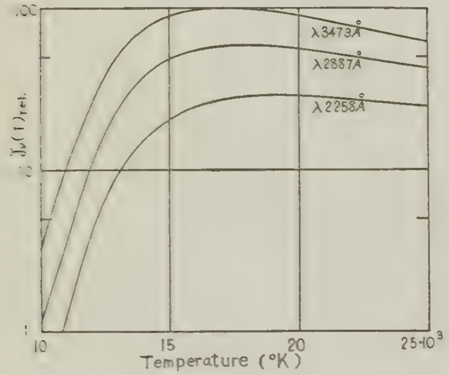

Fig. 6. Intensity of continuous radiation at various wavelengths as a function of temperature.

Table I. Temperature deduced from the time variation of the intensity of continuous radiation.

Time (μ sec)	Temperature (°K)		
	λ3473 Å	λ2887 Å	λ2258 Å
45	20,000	20,000	20,000
50	16,000	14,000	14,000
53	14,000	13,000	13,000
55	14,000	13,000	13,000
60	14,000	14,000	13,000
65	18,000	18,000	17,000
68	19,000	19,000	19,000
70	16,000	15,000	16,000

B. *Frequency Dependence of $J_\nu(T)$*

From Eq. (8)

$$\frac{d\ln J_\nu(T)}{d\nu}=-\frac{h}{kT}\,, \qquad (9)$$

that is, the temperature can be deduced from the relative intensity distribution of the con-

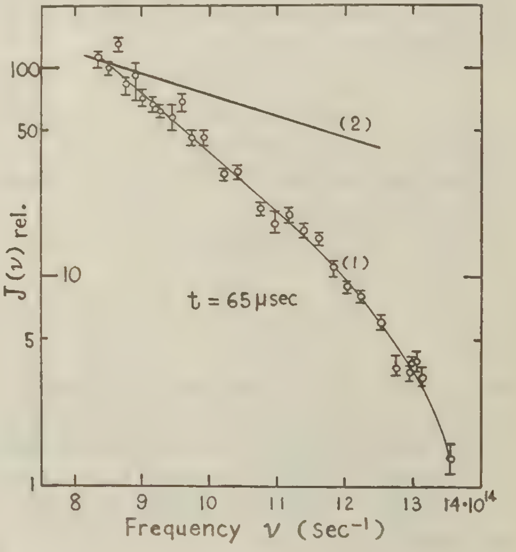

Fig. 7. Intensity distribution of the continuous radiation at t=65 μ sec. (1) Measured points. (2) Corrected for the spectral response of the optical system.

Table II. Temperature deduced from intensity distribution of the Balmer continuum.

Time (μ sec)	Temperature (°K)
44	20,000
50	14,000
53	13,000
65	19,000
70	14,000

tinuous radiation. Fig. 7 shows an example of intensity distribution measured at $t=65$ μsec. The error flags represent ranges of the distribution of data obtained from three successive discharges under the same condition. The temperature measured in this way is shown in Table II.

§ 6. Time Variation of the Line Intensity

Fig. 8 shows time variation of the H_β intensity observed during the discharge. Note that the maximum of intensity does not coincide with that of current, as was the case for the most part of the continuum. Instead, a minimum of the intensity is seen to correspond to the maximum of the current. This is explained by the fact that the line is emitted by neutral atoms that remain still unionized. The intensity of H_β line is given by

$$J_{H_\beta}(T) \propto n_H(T)\exp(-eV_4/kT)\,. \tag{10}$$

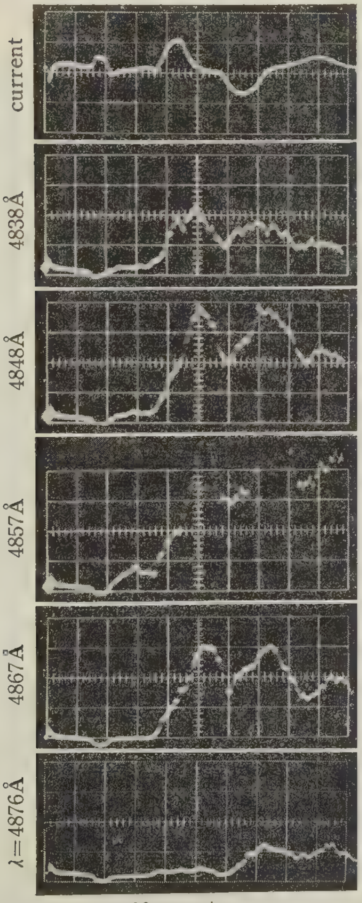

10 μ sec/cm

Fig. 8. Time variation of the intensity of the H_β line. $\Delta\lambda=4$Å

$J_{(H_\beta)}(T)$ is shown in Fig. 9. It has a maximum at $T=16{,}000$°K, and decreases with further increase of the temperature. We assume, therefore, that the temperature of plasma is 16,000°K at the instant when the H_β intensity attains its maximum ($t=53$ μsec in our case). Temperatures at other phases of the discharge current can be deduced from the decrease of the intensity relative to this maximum (see Table III).

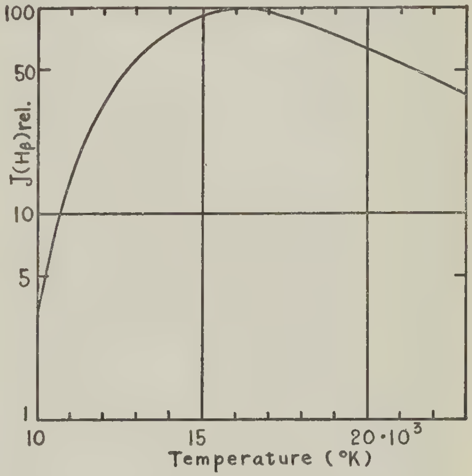

Fig. 9. Variation of the intensity of the H_β line with temperature.

Table III. Temperature deduced from the time variation of the H_β intensity.

Time (μ sec)	Temperature (°K)
45	21,000
50	18,000
53	16,000
60	21,000
64	20,000
66	20,000
70	18,000

Fig. 10 shows the intensity variation of other Balmer lines. It can be noticed that, towards the shorter wavelength, the waveform approximates that of the continuum. The H_ε line, which lies adjacent to the pseudo-continuum, has a waveform similar to that of the intensity of λ3473Å.

Fig. 11 shows the time variation of the intensity of the line 0 II λ2303Å. The oxygen is contained in the plasma as an impurity. The intensity of 0 II lines rises steeply in the temperature range up to 30,000°K[4),5)], so that it follows very closely the variation of current.

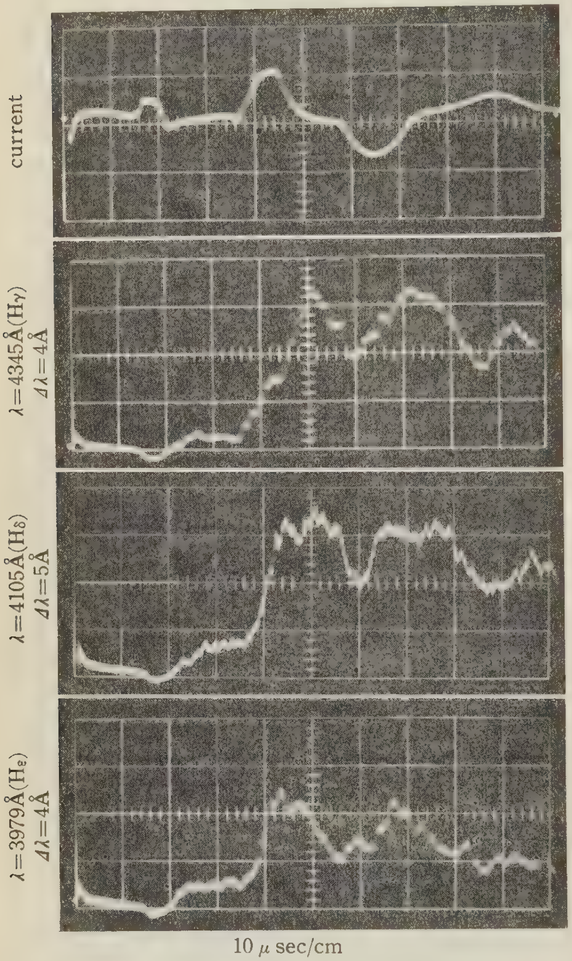

Fig. 10. Time variation of the intensity of the Balmer lines.

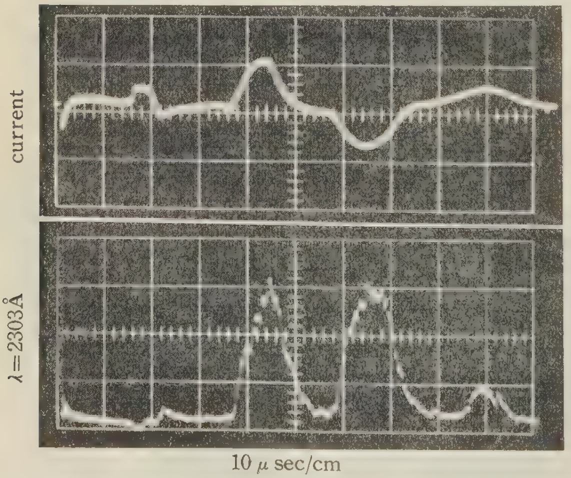

Fig. 11. Time variation of the intensity of the line OII λ 2303 Å.

§ 7. Electrical Conductivity

Electrical conductivity of the plasma was calculated from the observed value of discharge current and electric field, assuming a uniform distribution of the current over the cross section of the tube. Magnetic contractions do not take place in this experiment; the magnetic pressure is still less than the material pressure. The electrical conductivity is not high enough for a sheet current to be assumed.

The value of electrical conductivity calculated in this way is inserted into the conductivity expression

$$\sigma=e^2n_e(3mkT)^{-1/2}(n_HQ_H+n_iQ_i)^{-1}\ , \qquad (11)$$

where

$$Q_H=130\times10^{-16}\ \text{cm}^2$$
$$\text{(cross section of atoms)} \qquad (12)$$

and

$$Q_i=e^4(kT)^{-2}\ln\,[kT/(e^2n_i^{1/3})]$$
$$\text{(cross section of ions)} \qquad (13)$$

after Maecker, Peters and Schenk[5),6)]. The temperature deduced from Eq. (11) is shown in Table IV.

Table IV. Temperature deduced from electrical conductivity.

Time (μ sec)	Conductivity (Ω^{-1} cm^{-1})	Temperature (°K)
42	140	21,000
45	140	21,000
47	140	21,000
49	84	15,000
55	75	15,000
60	97	16,000
64	120	19,000
67	130	20,000
70	90	16,000

§ 8. Discussions

So far a Maxwell-Boltzmann distribution has been assumed both for electrons and excited neutral atoms. If this is valid, the "temperature" may still be different for different processes considered. The intensity of continuous radiation depends below 20,000°K mainly upon n_en_i, and hence the temperature deduced from the temperature dependence of the intensity of continuous radiation (§ 5. A) gives the value associated with the ionization process (ionization temperature). On the other hand, the frequency dependence of the intensity of continuous radiation is related to the kinetic temperature of electrons. It can also be deduced from the electrical conductivity. Finally the intensity of the H_β line depends below 16,000°K on the excitation temperature, and the decrease beyond that is due to the competition between excitation and ionization.

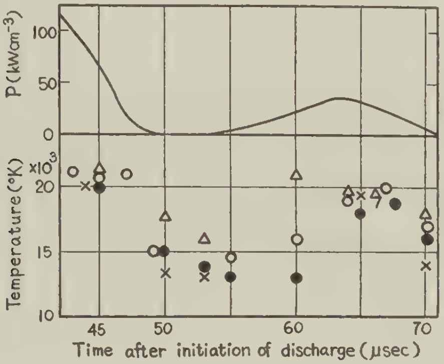

Fig. 12. Temperature deduced from temperature dependence (●) and frequency dependence (×) of the intensity of continuous radiation, from temperature dependence of the H_β intensity (△) and from electrical conductivity (○). Input power density P is also shown.

Now in Fig. 12 the temperatures hitherto obtained by various methods are summarized. It is seen that the agreement is fairly good between ionization and kinetic temperatures. But the excitation temperature shows relatively poor agreement with either one of other temperatures. In particular, a large discrepancy is noticed between excitation and other temperatures at $t=60\ \mu$sec. This is due to the decrease of the H_β intensity, which is unusually larger than theoretically predicted (see Fig. 8). There is further evidence that the equilibrium state cannot be assumed for the excitation process, especially in the early stages of the discharge. From the waveform of the discharge current, it is expected that the H_β intensity has its first peak at around $t=40\ \mu$sec, just prior to the first maximum of current. The intensity of H_β line actually shows a monotonous increase toward the maximum which is first attained after the current peak. In the early stages of the discharge the ionization of the gas is rapidly going on, and the condition seems to be unfavorable for the equilibrium to be established. This may have something to do with the observed fact that the intensity of continuous radiation shows occasionally poor reproducibility at its first peak (see Fig. 13).

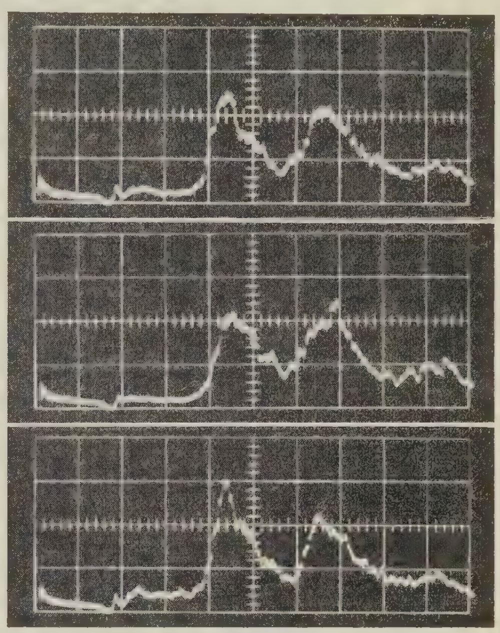

Fig. 13. Oscilloscope traces of the intensity of continuous radiation (λ=2278Å) taken during three successive discharges under the same condition.

The ion temperature has not directly been determined in this experiment. However, it can be shown that the ion temperature is not far below the electron temperature. The energy obtained by an electron in the mean free path λ is

$$\Delta\mathcal{E}=e\lambda E\,, \tag{14}$$

where E is the electric field in the plasma. In our case $\lambda<10^{-3}$ cm, $E<30$ volt/cm and $\Delta\mathcal{E}<3\times10^{-2}$ eV. This is less than 1% of the electron kinetic energy. If this energy were to be dissipated only through the elastic collision against ions, the ion temperature would be 3% lower than the electron temperature7).

The author wishes to express his sincere thanks to Prof. K. Yamamoto for his valuable discussions. He is indebted to Dr. J. Nakamura who has directed the research. He is grateful to Mr. M. Yanaka for his assistance in the experiment.

References

1) H. Maecker und Th. Peters: Z. Phys. **139** (1954) 448.
2) W. Finkelnburg und Th. Peters: Handb. d. Phys. XXVIII (1957) 125.
3) W. Finkelnburg und Th. Peters: ibid. 121; G. Jürgens: Z. Phys. **134** (1952) 21; A. Unsöld: Ann. Phys. **33** (1938) 606.
4) W. Lochte-Holtgreven: Reports on Progress in Physics XXI (1958) 327.
5) H. Maecker, Th. Peters und H. Schenk: Z. Phys. **140** (1955) 119.
6) L. Spitzer, Jr.: Phys. Rev. **80** (1950) 230.
7) W. Finkelnburg und H. Maecker: Handb. d Phys. XXII (1956) 307.
8) S. Yu. Lukyanov and V. I. Sinitsin: *Second United Nations International Conference on the Peaceful Uses of Atomic Energy* (1958) A/CONF. 15/ P/2226.

JOURNAL OF THE PHYSICAL SOCIETY OF JAPAN, Vol. 14, No. 12, DECEMBER, 1959

Anodic Oscillation in Glow Discharge

(I) Simple Correspondences of the Internal Phenomena to the Oscillation

By Kazuyuki OGAWA

Matsuda Research Laboratory, Tokyo Shibaura Electric Co., Kawasaki

(Received July 3, 1959)

Preliminary experiments on the anodic oscillation in glow discharge having no positive column are carried on, and they yield the following results. (1) Whenever the oscillation exists a faint small glow ball appears at a small part of the anode. When only one glow ball appears, one series of wave consists of the only kind of wave-form. On the contrary, in case of two balls two distinct wave-forms appear, and they are smoothly connected when the ratio of the period of each wave-form is integer. (2) It is easy to make the glow ball appear, when the anode has very small surface area compared with that of the cathode. (3) The oscillating zone is located only in the glow ball. (4) The degree of modulation of light intensity variation of the glow ball is 100%. The light intensity pulse builds up at the point where the current is minimum, and it reaches to peak preceding the maximum of the current wave. When two glow balls exist they alternately flush, and one of them corresponds to one of current wave and the other to another one.

The results are discussed in comparison with a hypothesis hitherto accepted, and they lead to a conclusion in which the conventional theory seems to be not always applicable to quantitative treatment of the oscillatory phenomena.

§ 1. Introduction

The fluctuation of tube voltage or that of circuit current in low pressure gaseous discharge is generally divided into two groups. One is noise, which is characterized by irregularity in the phase and amplitude and by being extended over the wide frequency band. The other is oscillation, which has fine coherency and exists within a limited range of frequency. Of course, above classification is made by the external appearances of the fluctuation, not by the cause of it, that is, one observer may receive the phenomena as oscillation what the other receives as noise when the individual occurrences are instable or superimposed irregularly on each other.

Many investigators worked at the field of oscillation, especially related to *striation*, and they found that many types of oscillation related rather to the anode side such as the Faraday dark space[1], the positive column[2], and narrow region around anode[3] than to the cathode side such as the negative glow, the Crookes dark space or the cathode fall and cathode itself. However, the exact relationship between the oscillation and the state of the anode side has yet never been clear. Presumably, the principal cause of this situation may be sought in the complexity of the phenomena. In 1940 Druyvesteyn and Penning[4] suggested the posibility of presence of oscillation when a red sphere appeared at the anode in Ne discharge having no positive column, although the details of the phenomena are remained still unknown. Repeating their experiment, author discovered that the specially designed cold-cathode glow discharge tube generated the anodic oscillation in very simple features as described following sections. The oscillations studied here were found in the frequency band 1 to 15 kc per second and in peak-to-peak amplitude about 7 to 16 volt.

§ 2. Experiments, Results and Discussion

The test tube was kept in discharge by well known electrical device, which consisted of a low impedance power source and a noninductive series resistance (its value was choiced at 40 kΩ, for the oscillation was stable at high resistance). To vary the tube current, the primary a.c. voltage of the power source was regulated by means of an autotransformer. The oscillation* was observed by a cathode-ray oscilloscope (pass band: d.c. to 30 Mc), and when necessity arised, the static valtage-current characteristics of the gap was also observed by both balance-type vacuum-tube voltmeter and ordinary milliammeter. In any case, the total input capacitance and resistance of the measuring system were respectively less than about 20 pf and 5 MΩ. Spectroscopically pure Ne, Ar, and Hg-contaminated Ar were tested at the pressure range 1 to 50 mmHg; these gases were equally capable of generating oscillations. The essential parts of the relationship between the oscillation and the anodic phenomena were not affected by any sorts of gases. Some caution taken in preparing the test tube has been described in the former paper[5].

***Experiment 1**: Studies on electrode configuration and visual observations*

The tests were carried on under the conditions where ordinary glow discharge was maintained; the tube current and gas pressure were required to be relatively small value in order that the contracted or arc discharge might not start. In this category, the tube, which consisted of cylindrical cathode and concentric wire anode or of disk cathode and needle anode perpendicular to the cathode plane, easily generated the oscillations. Hereafter, the former type of the test tube will be called " A " type and the latter " B " type. The oscilliation was found above a defined value of the average tube current, as well as of the gas pressure, which depended upon the construction of the test tube (see Fig. 1). In case of parallel plane electrodes the oscillation did not occur except the case having positive column.

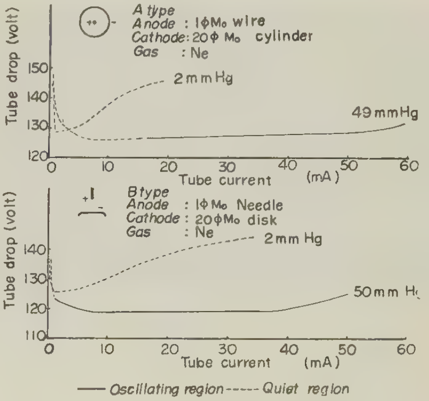

Fig. 1. Typical V-I characteristics and oscillating regions.

When oscillation existed, the faint glow ball attached to a small part of the anode. In such situation the other luminous portion in the discharge space was the negative glow only, as illustrated in Fig. 2. If the appropriate uniform magnetic field was applied along the direction perpendicular to the anode wire in B-type tube, the glow ball was blown out and at the same time the oscillation vanished. Similary, when the polarity of the voltage source was reversed and therefore the glow ball was absent from the beginning, the oscillation did not start. The

---

* In the present paper, unless otherwise appointed, the " oscillation " means voltage fluctuation between anode and cathode.

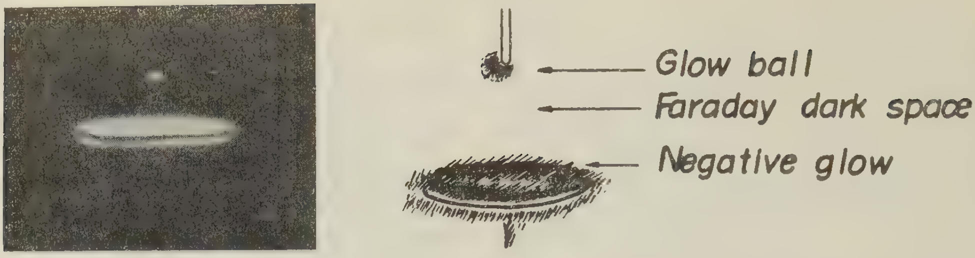

Fig. 2. Outside view of oscillating discharge. Ar 16 mmHg. B-type tube.

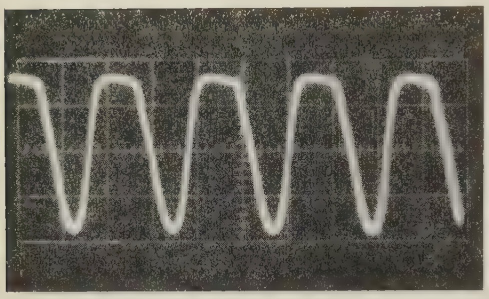

(a) A case which has only one glow ball. Current: 3 mA.

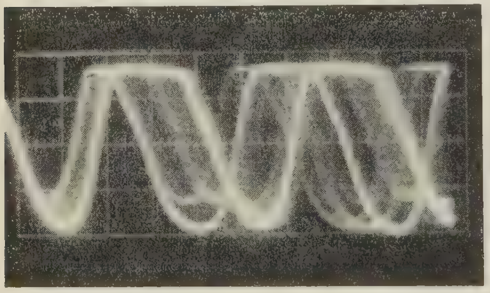

(b) A new glow ball has begun to appear near the old one. Pay attention to the advent of new wave-form having slightly small amplitude. Current: 6.4 mA.

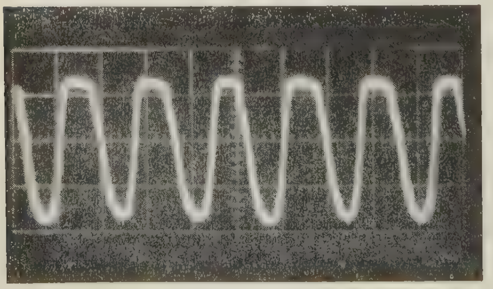

(c) Two balls have been completed, and a smoothly connected wave including two distinct types of wave-form has been established. One type of the wave-form, a slightly sharp one, is three times as long in period as the other. Current: 9.4 mA.

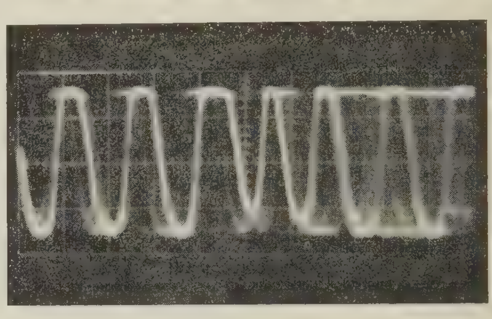

(d) Ratio of the period is changing. Current: 11.4 mA.

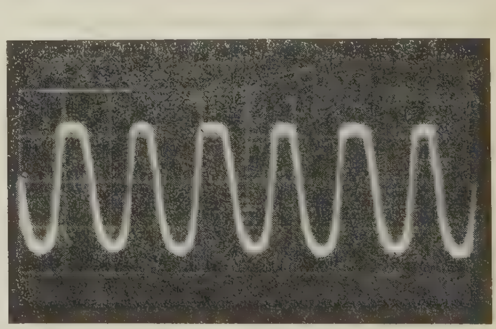

(e) Change in the period has been completed. Current: 15 mA.

Fig. 3. An example of voltage oscillation which varies with the average tube current. Ne 50 mmHg. B-type tube. Only in case (b) each major division of the time scale is 20μsec; in all of the others, is 50μsec.

point where the glow ball would attache could not be expected in A-type tube, but in B-type tube the glow ball was always fastened to the tip of the anode and consequently the oscillation was very stable. It is based upon such a knowledge that *oscillatron* reported in the former paper5) has the form of B type.

The appearance of the voltage oscillation was influenced by the number of glow ball. When there existed only one glow ball, a series of wave consisted of the only kind of wave-form. On the contray, in case of two balls two distinct wave-forms appeared, and they were smoothly connected when the ratio of the period of each wave-form was integer. Often the change of this ratio caused by changing the tube current was an irreversible process and therefore, in that circumstance, the curve of frequency vs tube current, as illustrated in the former paper⁵⁾, drew a hysteresis loop. Fig. 3 shows an example of oscillation* which changes in the way above mentioned.

Now consider the Langmuir probe. When the electron current to the probe reaches a critical value, the probe surface is surrounded by the electron sheath and its potential becomes positive against the plasma. The critical current I is expressed by the relation,

$$I=F\cdot j_r\ .$$

Hence, F is the surface area of the probe and J_r is random electron current density in the plasma. The smaller F becomes, the more I decreases, provided that j_r is fixed. Analogously, the positive anode fall may develop more easily when the anode has small surface area compared with that of the cathode; the electrons are accelerated towards the anode by the anode fall and they excite or ionize the gas atom. Thus, it is possible to conclude that the oscillation is tightly related to the positive anode drop. Similar results are reported by Cobine, Gallagher⁶⁾ and Pupp⁷⁾.

***Experiment 2**: Direct detection of oscillating zone by means of a movable probe*

The location of oscillating zone was directely detected by means of a movable probe. Fig. 4 shows the construction of an experimental tube; the probe is made of 0.1 mm-dia. and 45 mm-length tungsten wire and is driven along a arch from the cathode to the anode side or *vice versa* by simple device utilizing a glass stopcock.

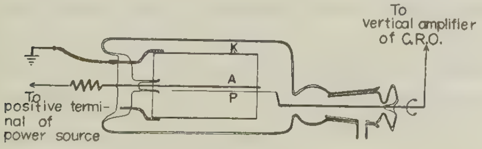
To vertical amplifier of C.R.O.
K
A
P
To positive terminal of power source

Fig. 4. Construction of test tube with a movable probe. K: Cathode. A: Anode. P: Mavable probe.

When the probe was immersed into a glow ball, marked oscillation whose frequency was identically equall to that of the interelectrode oscillation was caught between the probe and the cathode, while the Faraday dark space was quite quiet. The probe, which is connected to an input of a cathode-ray oscillscope through a small condenser, will float on the discharge space at wall potential. Hence, the signal from the probe is to correspond to the fluctuation of wall potential which indicates something to be related to the fluctuation of plasma parameters such as electron or ion temperature and space potential, although it is difficult to measure these factors separately. In the actual case there should exist some disturbances caused by the parts of the discharge space besides the glow ball, for the stretch of the glow ball was much smaller than the length of the probe. Therefore the potential of the probe may be determined to be somewhat smaller than that strictly determined by the glow ball only.

***Experiment 3**: Observation of light intensity oscillation of the glow ball*

The light intensity oscillation of the glow ball in B-type tube was observed in relation to the current (or voltage) oscillation. Fig. 5 shows the experimental arrangement. The rays from the glow ball were brought to focus upon the pinhole P by the aid of converging lens L, lest the light originated from other positions should fall on the photomultiplier tube MS-9S. Phase relation between the

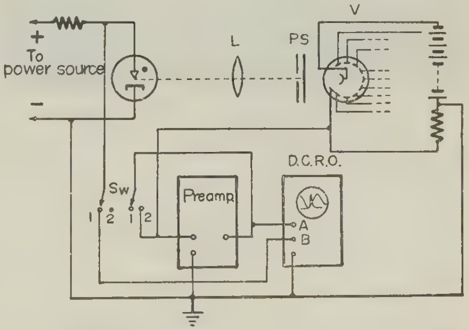

Fig. 5. Experimental arrangement for observation of light intensity variation of the glow ball. L: Converging lens, P: Pinhole, S: Shutter, Sw: Circuit-changing Switch, V: Photomuliplier tube MS-9S, Preamp.: Preamplifier, D.C.R.O.: Dual-trace cathode-ray oscilloscope utilizing electronic switch.

---

* Nearly sinusoidal wave-form has been shown in reference 5.

current oscillation and the light intensity variation was observed by two-channel oscilloscope utilizing an electronic switch. It was previously checked that the current wave-form agreed closely with the inverted voltage wave-form, if a noninductive resistor was used as a current-limiter. According to this proof, the voltage oscillation inverted by the amplifier of the oscilloscope was observed as a current oscillation. The total output of the phototube was observed by the oscilloscope operated at d.c. sense; this measurement was achieved by taking off both of the preamplifier and channel B from the testing circuit by the switch Sw. Then the degree of modulation of the light intensity variation was found to be 100%.

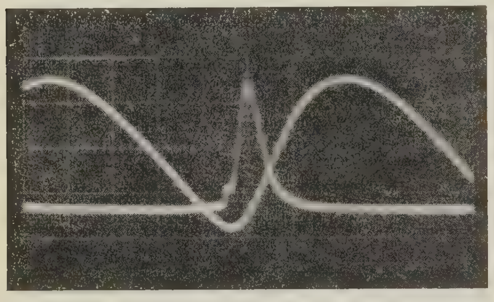

(a) Detail. Each major division of the time scale is 50μ sec.

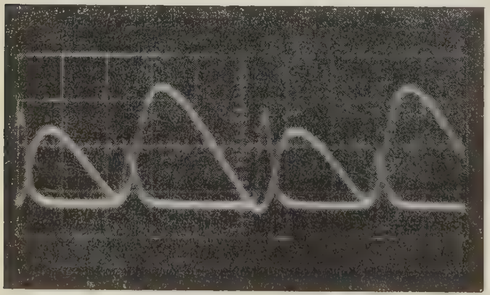

(b) Entire correspondence, when two glow balls exist. Each major division of the time scale is 200μ sec.

Fig. 6. Phase relation between current oscillation and light intensity variation which is shown as sharp pulse. Ne 50 mmHg, B-type tube, Current 14 mA.

From Fig. 6 (a) it will be seen that the current minimum coincides with the build-up point of the optical pulse, and that the rise time of the current pulse is longer than that of the optical pulse by the amount of two to five times. These relations were always unchanged during the change of the average tube current. The diameter of the image of the glow ball was about a half as large as the diameter of the pinhole, and the glow ball was at rest on one point. So, the intensity variation obtained by the phototube may not be ascribable to spacial fluctuation of the glow ball. This fact indicates that the origin of the oscillation exists in the discharge space. Because, if an oscillator exists in the outer circuit and simply modulates the discharge, the light intensity peak is to coincide with the current peak. When two glow balls existed they alternately flushed, and one of them corresponded to one of current wave and the other to another one. Fig. 6 (b) shows such a case.

Another important features of the results relate to a hypothesis which has been hitherto used to explain the mechanism of the anodic oscillation. This hypothesis was firstly proposed by Pupp[7)] in 1933 and recently developed by Yoshimoto[3)] et al. in order to explain the anodic oscillation in arc discharge like commercial fluorescent lamp. It consists of two principal parts:

(1) The ionization in the anode fall occurs suddenly when the potential drop across the anode fall reaches a critical value.

(2) The excess ions generated by sudden ionization reduce the electron space-charge and then anode fall decreases. The difference of anode potential is absorbed by both positive column and series resistance in the outer circuit. The excess ions may be lost by diffusion, and anode fall reappears; thus the anodic oscillation has been interpreted as the alternation of above two processes.

If this conception is valid in the present case, the rise time of the current pulse is to be almost equall to that of the optical pulse, while the experimental facts were not so. It has to be recognized that the oscillation is accompanied by alternative ionization in the anode region, however, the conventional simple theory seems to be not always applicable to quantitative treatment of the oscillatory phenomena.

§ 3. Conclusions

Experiments 1 and 2 showed the reason why the anodic oscillation in the glow discharge is so called, and also showed the desirable experimental conditions for promoting next investigations. From the experiment 3 (opitical data), it became cleare that the conventional theory could not qualitatively interpret the phenomena.

Author wishes to express his cordial thanks to Prof. K. Honda and Dr. H. Tamagawa in Tokyo University for their invaluable advices. Thanks are also due to Prof. I. Takahashi of Kyoto University for his interest and encouragement.

References

1) G. W. Fox; Phys. Rev. **35** (1930) 1066, Phys. Rev. **37** (1931) 815. N. L. Oleson and A. W. Cooper: Phys. Rev. **105** (1957) 1411.
2) L. A. Pardue and J. S. Webb: Phys. Rev. **32** (1928) 946. T. Donahue and G. H. Dieke: Phys. Rev. **81** (1951) 248. N. R. Labrum and E. K. Bigg: Proc. Phys. Soc. **65B** (1952) 356.
3) H. Yosimoto: J. Phys. Soc. Japan **8** (1953) 59, 69.
4) M. J. Druyvesteyn and F. M. Penning: Rev. Mod. Phys. **12** (1940) 172.
5) K. Ogawa: J. Phys. Soc. Japan **14** (1959) 385.
6) J. D. Cobine and C. J. Gallagher: Phys. Rev. **70** (1946) 113.
7) W. Pupp: Phys. Z. **34** (1933) 756.

JOURNAL OF THE PHYSICAL SOCIETY OF JAPAN Vol. 14, No. 12, DECEMBER, 1959

Ion-Electron Relaxation of Plasmas in a Strong Magnetic Field. I

By Taro KIHARA
Department of Physics, Faculty of Science, University of Tokyo

(Received August 12, 1959)

Relaxation between ion and electron temperatures, T_1 and T_2, of dilute fully ionized gases in a magnetic field is discussed. The mean gyration radius, r_g, is assumed to be much smaller than the Debye length, l_D. The rate of relaxation, R, defined by

$$d(T_2-T_1)/dt=-(T_2-T_1)R$$

is calculated to be

$$R=(n_1+n_2)(4m_2/3m_1)(2\pi kT_2/m_2)^{1/2}(Ze^2/kT_2)^2[\ln(l_D/r_g)]^2$$

for

$$r_g\sim Ze^2/kT_2\,.$$

§1. Introduction

Relaxation phenomena in a magnetic field are worth investigating both from academic point of view and in connection with the problem of controlled nuclear fusion. Since the mass ratio of an ion to an electron is far from unity, energy transfer between ion and electron is much smaller than that between ions or between electrons. Hence the ion temperature T_1 and the electron temperature T_2 are often different even when the velocity distributions are both uniform and Maxwellian. The aim of this paper is to derive an expression for the rate of relaxation between ion and electron temperatures in a fully ionized gas composed of one type of positive ion and electrons. Both the gas and the magnetic field are assumed to be uniform in space.

In a previous paper by the same author[1] a corresponding expression in the absence of the magnetic field has been given. The result is

$$\frac{d}{dt}(T_2-T_1)=-(T_2-T_1)R \tag{1.1}$$

with the time t and the rate of relaxation

$$R=\frac{8}{3}(n_1+n_2)\frac{m_2}{m_1}\left(\frac{2\pi kT_2}{m_2}\right)^{1/2}\left(\frac{Ze^2}{kT_2}\right)^2\ln\frac{3kT_2}{4Ze^2\kappa_{12}}\,, \tag{1.2}$$

Here m_1, Ze, and n_1 are the mass, charge, and number density of the ion respectively; m_2, $-e$, n_2 are those of the electron ($Zn_1=n_2$,

$Z^2 \ll m_1/m_2$); k is the Boltzmann constant; κ_{12} is a shielding constant in the effective potential

$$-\frac{Ze^2}{r}\exp(-\kappa_{12}r) \tag{1.3}$$

between an ion and an electron, and it is not far from the Debye shielding constant. The "3/4" in the argument of the logarithm is in reality an irrational number close to 3/4.

The expression (1.2) is exact as a weak-interaction asymptote for $kT_2/Ze^2\kappa_{12} \gg 1$ so far as the effective potential (1.3) is assumed. When the plasma is so hot and dilute that $\ln(kT_2/Ze^2\kappa_{12})$ is much larger than unity, the formula (1.2) is approximated by

$$R=\frac{8}{3}(n_1+n_2)\frac{m_2}{m_1}\left(\frac{2\pi kT_2}{m_2}\right)^{1/2}\left(\frac{Ze^2}{kT_2}\right)^2\ln\frac{kT_2 l_D}{Ze^2}\,, \tag{1.4}$$

where l_D is the Debye length, the inverse of the Debye shielding constant. This expression is independent of the "model constant" κ_{12}. The condition of this approximation is that $[\ln(kT_2 l_D/Ze^2)]^{-1}$ can be neglected in comparison with unity or that a numerical factor of the order of unity can be neglected in the argument of the logarithm.

In the present article this kind of approximation will be used throughout: any logarithm in the following is assumed to be much larger than unity.

The method of deriving (1.2) by use of (1.3) can hardly be applied to plasmas in a magnetic field. Another formulation is given in § 2, by use of which the same result as (1.4) is obtained in § 3. The present method is applied in § 4 to plasmas in a strong magnetic field. Magnetic fields of intermediate strength will be treated in Part II.

§ 2. General Theory of the Ion-Electron Relaxation

The particle velocities of the ion and electron will be denoted by $\boldsymbol{c}_1$ and $\boldsymbol{c}_2$, respectively, with $|\boldsymbol{c}_1| \equiv c_1$ and $|\boldsymbol{c}_2| \equiv c_2$. Since the average value of $m_1 c_1^2/3$ is kT_1, the time rate of change of kT_1 is given by the average value of the time rate of change of $m_1 c_1^2/3$:

$$\left.\begin{aligned}&\frac{d}{dt}kT_1=\frac{1}{3}m_1\nu\langle|\boldsymbol{c}_1+\Delta\boldsymbol{c}_1|^2-c_1^2\rangle_{\mathrm{Av}}\\ &\text{or}\\ &\frac{d}{dt}kT_1=\frac{1}{3}m_1\nu\langle(2\boldsymbol{c}_1+\Delta\boldsymbol{c}_1)\cdot\Delta\boldsymbol{c}_1\rangle_{\mathrm{Av}}\,.\end{aligned}\right\} \tag{2.1}$$

Here $\Delta\boldsymbol{c}_1$ indicates the increment in ion velocity due to encounter with an electron; $\langle\ \rangle_{\mathrm{Av}}$ means the average with respect to the ion velocity and the velocity of the encountering electron and the impact parameter; ν is the number of encounters per unit time.

When the ion temperature T_1 is much smaller than the electron temperature T_2, the average value of $\boldsymbol{c}_1\cdot\Delta\boldsymbol{c}_1$ can be neglected in comparison with the average value of $|\Delta\boldsymbol{c}_1|^2$; hence

$$\frac{d}{dt}kT_1=\frac{1}{3}m_1\nu\langle|\Delta\boldsymbol{c}_1|^2\rangle_{\mathrm{Av}} \qquad \text{for} \quad T_1 \ll T_2\,. \tag{2.2}$$

This is essentially diffusion due to the Brownian motion in the velocity space[2)].

The relation (2.2) can be generalized to

$$\frac{d}{dt}kT_1=\frac{1}{3}m_1\nu\langle|\Delta\boldsymbol{c}_1|^2\rangle_{\mathrm{Av}}\frac{T_2-T_1}{T_2}\,, \tag{2.3}$$

which holds not only for T_1 much smaller than T_2 but also for T_1 not far from T_2 (i.e. for $m_2T_1 \ll m_1T_2$). A proof is the following. Since $m_1 \gg m_2$ the quantity $|\Delta\boldsymbol{c}_1|^2$ averaged with respect to the velocity of the encountering electron and the impact parameter is independent of $\boldsymbol{c}_1$; but $\Delta\boldsymbol{c}_1$ so averaged depends linearly upon $\boldsymbol{c}_1$ (or is proportional to $\boldsymbol{c}_1$ if the magnetic field is absent). Hence, for constant electron temperature, $\langle|\Delta\boldsymbol{c}_1|^2\rangle_{\mathrm{Av}}$ is independent of T_1, and $\langle\boldsymbol{c}_1\cdot\Delta\boldsymbol{c}_1\rangle_{\mathrm{Av}}$ is proportional to T_1. Taking account of the fact that

$$\langle(2\boldsymbol{c}_1+\Delta\boldsymbol{c}_1)\cdot\Delta\boldsymbol{c}_1\rangle_{\mathrm{Av}}$$

vanishes for $T_1=T_2$, we finally obtain

$$2\langle\boldsymbol{c}_1\cdot\Delta\boldsymbol{c}_1\rangle_{\mathrm{Av}}=-(T_1/T_2)\langle|\Delta\boldsymbol{c}_1|^2\rangle_{\mathrm{Av}}\,,$$

by virtue of which (2.3) follows from (2.1). Here we have tacitly neglected the dependence of the shielding constant on the ion temperature. In fact, the shielding constant enters only in the argument of logarithm, and hence the dependence can be neglected.

By used of the relationship

$$\frac{d}{dt}(n_1T_1+n_2T_2)=0\,,$$

the rate of relaxation R defined by (1.1) is calculated to be

$$R=\frac{1}{3}(n_1+n_2)m_1\frac{\nu}{kT_2n_2}\langle|\Delta\boldsymbol{c}_1|^2\rangle_{\mathrm{Av}}\,. \tag{2.4}$$

§ 3. Case of No Magnetic Field

Since an ion does not greatly move during an encounter with an electron, a perturbation method can be used for the calculation of Δc_1. Let, in the absence of magnetic field, the unperturbed position of an ion and the unperturbed trajectory of an encountering electron be

$$(x_1, y_1, z_1)=(0, 0, 0)\ ,$$
$$(x_2, y_2, z_2)=(b, 0, c_2t)\ ,$$

respectively, where b is the impact parameter, t the time.

For a hot dilute plasma we need only to consider weak interactions,

$$Ze^2/b<\frac{1}{2}m_2c_2^2\ ,$$

for which

$$|\Delta \boldsymbol{c}_1|=\Delta c_{1x}=\frac{Ze^2}{m_1}\int_{-\infty}^{\infty}\frac{b}{(b^2+c_2^2t^2)^{3/2}}\,dt=\frac{2Ze^2}{m_1bc_2}\ . \tag{3.1}$$

When the impact parameter b is sufficiently smaller than the limit of weak interaction, $2Ze^2/m_2c_2^2$, the increment in ion velocity is much smaller than the right-hand side of (3.1) and can be neglected in the present degree of approximation.

The average value of $|\Delta \boldsymbol{c}_1|^2$ is given by

$$\frac{\nu}{n_2}\langle|\Delta \boldsymbol{c}_1|^2\rangle_{\rm Av}=\int_{b_0}^{l_D}db\int_0^{\infty}dc_2|\Delta \boldsymbol{c}_1|^2\left(\frac{m_2}{2\pi kT_2}\right)^{3/2}\exp\left(-\frac{m_2c_2^2}{2kT_2}\right)c_24\pi c_2^22\pi b$$
$$=8\left(\frac{2\pi m_2}{kT_2}\right)^{1/2}\left(\frac{Ze^2}{m_1}\right)^2\ln\frac{l_D}{b_0}\ .$$

Here l_D is the Debye length and b_0 is the average limit of weak interaction, $b_0\sim Ze^2/kT_2$. The rate of relaxation, therefore, is given by

$$R=\frac{8}{3}(n_1+n_2)\frac{m_2}{m_1}\left(\frac{2\pi kT_2}{m_1}\right)^{1/2}\left(\frac{Ze^2}{kT_2}\right)^2\ln\frac{kT_2l_D}{Ze^2}\ , \tag{3.2}$$

which agrees with (1.4).

§4. Case of Strong Magnetic Field

Presence of a magnetic field does not influence the result of the preceding section so far as the condition $l_D\ll r_g$ is satisfied. Here r_g is the mean gyration radius of the electrons defined by

$$r_g\equiv\frac{1}{\omega_2}\left(\frac{2kT_2}{m_2}\right)^{1/2}\ ,$$

ω_2 being the cyclotron frequency of electrons. In this section we consider the opposite case of strong magnetic field:

$$Ze^2/kT_2\sim r_g\ll l_D\ .$$

With z-axis in the direction of the magnetic field the unperturbed position of an ion and the unperturbed trajectory of an encountering electron can be chosen as

$$(x_1, y_1, z_1)=(0, 0, 0)\ ,$$
$$(x_2, y_2, z_2)=(b, 0, c_{2z}t)\ ,$$

where c_{2z} is the component of the electron velocity parallel to the magnetic field.

For a hot dilute plasma we need only to consider the range $r_g<b<|c_{2z}|/\omega_p$; in this range we have, like (3.1),

$$|\Delta \boldsymbol{c}_1|=\frac{2Ze^2}{m_1b|c_{2z}|}\ . \tag{4.1}$$

When the time of interaction, $b/|c_{2z}|$, is sufficiently larger than the period of plasma oscillation,

$2\pi/\omega_p$, or when the impact parameter b is sufficiently smaller than the gyration radius r_g the increment $|\Delta \boldsymbol{c}_1|$ in ion velocity is much smaller than the right-hand side of (4.1) and ca be neglected in the present calculation.

Then

$$(\nu/n_2)\langle|\Delta \boldsymbol{c}_1|^2\rangle_{\mathrm{Av}}=2\int_{r_g}^{l_D} db\int_{b\omega_p}^{\infty} dc_{2z}|\Delta \boldsymbol{c}_1|^2\left(\frac{m_2}{2\pi kT_2}\right)^{1/2}\exp\left(-\frac{m_2c_{2z}^2}{2kT_2}\right)c_{2z}2\pi b$$

$$=8\pi\left(\frac{m_2}{2\pi kT_2}\right)^{1/2}\left(\frac{Ze^2}{m_1}\right)^2\int_{r_g}^{l_D} db\int_{\lambda_0}^{\infty} d\lambda\frac{\exp(-\lambda)}{\lambda b}\ .$$

Here

$$\lambda_0\equiv\frac{m_2\omega_p^2b^2}{2kT_2}\sim\left(\frac{b}{l_D}\right)^2,$$

which is much smaller than unity in the dominant part of the integration domain of b. Hence the integral is replaced by

$$\int_{r_g}^{l_D}\left(\ln\frac{1}{\gamma\lambda_0}\right)\frac{db}{b}=\ln\frac{l_D}{\gamma r_g}\cdot\ln\frac{l_D}{r_g}\ .$$

Here $\ln\gamma=0.577$ is Euler's constant, which can be neglected in our approximation. The ra of relaxation for $r_g\sim Ze^2/kT_2$ is, therefore, given by

$$R=\frac{4}{3}(n_1+n_2)\frac{m_2}{m_1}\left(\frac{2\pi kT_2}{m_2}\right)^{1/2}\left(\frac{Ze^2}{kT_2}\right)^2\left(\ln\frac{l_D}{r_g}\right)^2. \tag{4.2}$$

References

1) T. Kihara: J. Phys. Soc. Japan **14** (1959) 402.

2) For example, S. Chandrasekhar: Revs. Modern Phys. **15** (1943) 1.

JOURNAL OF THE PHYSICAL SOCIETY OF JAPAN Vol. 14, No. 12, DECEMBER, 1959

Optical Studies on the Effect of Electric Fields on the Transitions of Barium Titanate

By Kazuo KAWABE*

Faculty of Science, Osaka University

(Received June 23, 1959)

The effect of electric fields on the three transition points of barium titanate was studied experimentally by observing the shift of the curve of the thermal transition of transparency with varying biasing fields. Transparent electrodes, thin films of stannic oxide, were used in order to observe the intensity of light transmitted through crystals to which electric fields were applied. The Curie point is raised up to a critical temperature of 132°C, the required strength of the field being 9 kv/cm, and above this point the transition of the first order no longer takes place. From this fact, the coefficient of P_z^4 in the Devonshire expression of the free-energy function is obtained, which supports the value measured by Drougard. The observed shifts of the Curie point and the 5°C transition point are in good agreement with the values calculated by using the Devonshire function of the sixth order. At the −80°C transition, the experimental value is explained by adding the terms of eighth and tenth powers of polarization to the usual Devonshire function.

The relationship between the polarization of a crystal and the intensity of the transmitted light is pointed out in the case when the crystal is placed between crossed Nichols.

Remarks are also given of the effects which the coating of electrodes has upon the shape of the curve of the thermal transition of transparency at the −80°C transition.

§ 1. Introduction

As is well known, the phase transitions of barium titanate occur at three temperatures in the vicinities of 120°C, 5°C, and −80°C. Above 120°C, the crystal has cubic symmetry, being paraelectric. In the temperature range between 120°C and 5°C, the crystal is spontaneously polarized along a ⟨100⟩ direction, accompanied with tetragonal symmetry. Between 5°C and −80°C, the crystal symmetry is orthorhombic, and the direction of the spontaneous polarization transfers to a pseudo-cubic ⟨110⟩ direction, a face diagonal of the former cubic cell. At −80°C, a further transition to rhombohedral symmetry** spontaneously polarized along a body diagonal (original ⟨111⟩ direction) takes place. If an electrostatic field is applied to this crystal, certain changes in the transition temperatures are expected admittedly to take place.

In fact, it has been found that the Curie point at 120°C is raised linearly by increasing strength of applied electric field by Kaenzig and Maikoff[2] who measured the dielectric constants with biasing fields, and also by Merz[3] who observed the double hysteresis loops. Their results are in good agreement with the value computed from the Clausius-Clapeyron relation[4],[5]. The effect of the biasing field on the transition temperature at 5°C was also estimated by Huibregtse and Young[6] by observing the triple hysteresis loops, but the agreement of their result with the Clausius-Clapeyron relation was not so good.

The present paper aims at studying the effect of the biasing field on the three transition temperatures by means of an optical method, and at treating the effect thermodynamically on the basis of Devonshire's phenomenological theory; such a treatment will give some information about the free-energy function of barium titanate.

When a BaTiO$_3$ single crystal is placed between crossed Nichols, the intensity of light transmitted through the analyzer changes abruptly at the Curie point near 120°C. The transparency of the single crystal of barium titanate for visible light also exhibits marked jumps at the two lower transition points[7),8)]. These optical phenomena have been named in terms of the *thermal transition of transparency* (as an abbreviation of this terminology, TTT is to be used throughout this paper) and are closely related to the polarization and the domain structure of a crystal. Accordingly, it is expected that the application of an electric field would have an appreciable effect upon the transparency of the crystal. Thus the TTT in dependence on the strength of the applied field may be used as a new method to observe the effect of the biasing field on the transition points.*

---

* Now at Mikage College, Kobe University, Kobe.

** Recently Jona and Pepinsky[1] suggested that the symmetry below −80°C would be monoclinic or triclinic rather than rhombohedral.

Experimentals

§ 2. Preparation of Specimens and Electrodes

A mixture of 1:1:4 molar ratio of TiO_2, $BaCO_3$, and Na_2CO_3 (flux) was heated up to about 1200°C in a nickel crucible in a reductive coal-gas atmosphere in order to avoid the oxidation of the crucible[8),9)]. After cooling and crystallization, thin plate-like tetragonal crystals were obtained that had a Curie temperature of about 118°C. Several crystals prepared by the Remeika method[10)] were also used, but the experimental data given by the crystals from both sources made no great difference.

The electrodes must be transparent or at least be translucent when an electric field is applied in the direction at a certain angle to the incident beam of light. It has been known that the thin film of SnO_2 is semiconductive and transparent for visible light. Various methods of coating materials such as glass, rock salt, or fused silica with this film have been reported[11)–13)], especially the coated glass being well-known under the name of *NESA*, and the author could evaporate this film directly on the crystal surface of barium titanate. Stannic chloride solution which was dissolved into hydrochloric acid of *ca.* 6 normals and diluted by *ca.* 50% ethyl alcohol was sprayed onto the crystal in the furnace kept at about 600°C[13)]. Large drops in the sprayed fog made the resultant film opaque. It gave a good result to spray the solution from the bottom of the furnace so as to make only fine drops reach the crystal surface on the ascending air current in the furnace[12)]. The electrical resistance of the film was about several hundred ohms per cm² at room temperature.

§ 3. Effect of Electrostatic Field on TTT

A plate of a $BaTiO_3$ single crystal was placed between crossed Nichols, and the crysta surface was inclined at a certain angle to the direction of the incident beam of light (Fig 1). The crystal was so oriented that the direction of a component P_0 of the polarization was inclined at 45° to the principal planes of the Nichols. Since the direction of an applied field makes a certain angle with the direction of the incident beam, the analyzer transmits the light due to the birefringence which is caused by the component P_0 of the polarization in the direction at right angles to the incident beam. The intensity of the transmitted light is changed as a function of the polarization when the crystal structure transforms from cubic to tetragonal. Accordingly, the cubic-to-tetragonal transition** can be studied by observing this phenomenon.

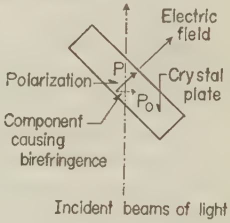

Fig. 1. Setting of the crystal.

At the two lower transition points, namely the tetragonal-to-orthorhombic and orthorhombic-to-rhombohedral transition points, the transparency of barium titanate for visible light exhibits remarkable jumps. For example, the change of the transparency at the 5°C transition is shown in Fig. 2 (a). Applying an electrostatic field to this crystal, the hysteresis loop of transparency as shown in Fig. 2 (a) shifts towards lower temperatures. Therefore, if the specimen is kept at a temperature below and near 5°C and is put under the influence of an electrostatic field, the transparency increases abruptly at the time when the applied field reaches a certain strength (Fig. 2 (b)). The rate of the change of the transition temperatures as a function of the applied field, $\Delta T_t/\Delta E$, can be obtained either by measuring these critical fields or by observing the shift itself of the TTT-curve.

---

* An optical method of studying the movement of domain walls in Rochelle salt crystal has recently been reported by Abe[21)]. He has shown that the optical method is very useful to study the characteristics of wall motion at very low frequencies.

** In the strict sense of the word, this is not the transition between cubic and tetragonal phases, but the transition between cubic- and induced-tetragonal-phases. In this paper, the term cubic-to-tetragonal transition is also used for this transition.

The experimental arrangement used for this transparency measurement has already been described in detail in the previous paper[8]. The crystal was uniformly illuminated by a continuous source and the enlarged image of the crystal was formed by a microscope on a diaphram just in front of a multiplier phototube, the photocurrent of which was magnified by a dc amplifier. The temperature of the specimen was controlled by an electric heater and liquid nitrogen in a modified Dewer flask.

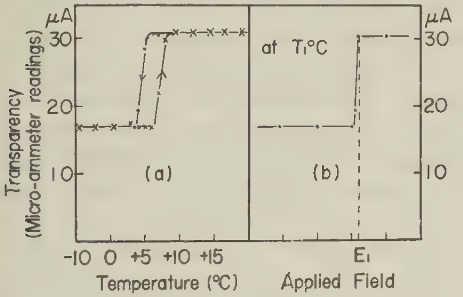

Fig. 2. (a) Thermal transition of transparency near 5°C. (b) Transparency *vs* applied field near and below 5°C.

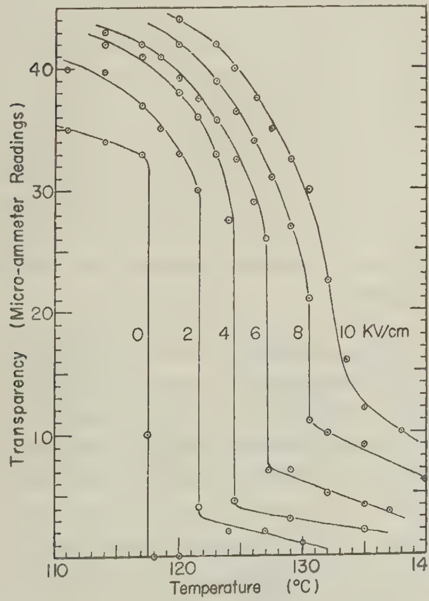

Fig. 3. Temperature-dependence of the optical transmission with various applied fields near 120°C. The numbers near the curves represent the strengths of the applied fields.

§ 4. Experimental Results

a) *Curie point*

The temperature-dependence of the optical transmission at the tetragonal-to-cubic transition with varying biasing fields is shown in Fig. 3. The transition temperature rises with increasing strength of the applied electric field, and the plot of the field strength against transition temperature shows a linear relation as is seen in Fig. 4. The results of electrical measurements are also plotted in the same figure with the intention of comparing. These electrical data were obtained from gold-electroded crystals by measuring the separation of the double hysteresis loops at 60 cps at

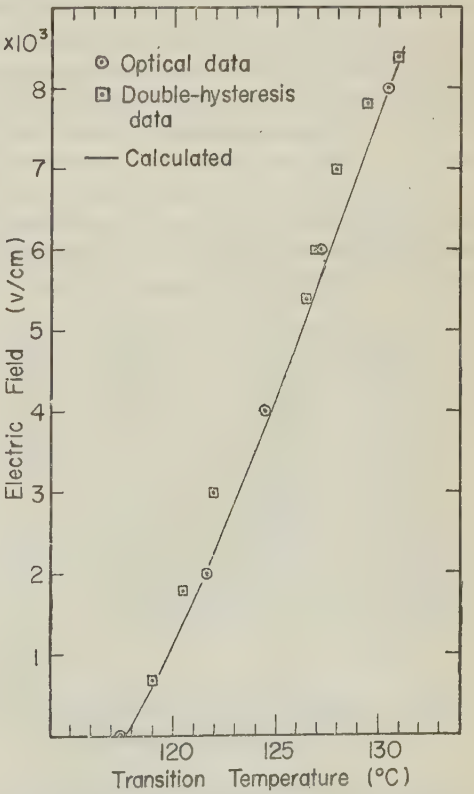

Fig. 4. Transition temperature as a function of the applied field near 120°C.

various temperatures near 120°C. This electrical method gave poorer experimental accuracy than the optical method did. The circuit used for this hysteresis test was that invented by Diamant, Drenck and Pepinsky[20]. Both data are in good agreement, giving the rate of the shift of the Curie point, or strictly speaking, of the transition point, as

$$\Delta T_t/\Delta E = (1.6 \pm 0.1) \times 10^{-3}\ \mathrm{deg/volt\ cm^{-1}}\ ,$$

which is in good agreement with the value measured by Kaenzig and Maikoff (1.2×10^{-3} deg/volt cm^{-1})[1] and with that measured by Merz (1.4×10^{-3} deg/volt cm^{-1}).

As the strength of the applied field increases, the induced polarization in the cubic state increases, and at last the magnitude of the polarization in the cubic state becomes equal to that in the tetragonal state, the transition being no longer of the first order. This critical temperature is about 132°C, and the strength of the corresponding critical field is about 9 kv/cm.

b) *Transition points near 5°C and −80°C*

The transparency of a specimen kept at T_1°C somewhat below 5°C changes as a function of the applied field as is shown in Fig. 2 (b). The critical field required to induce a sudden change of the transparency increases gradually with decreasing temperature of the crystal. If this temperature T_1 is defined as the transition point in the presence of an electric field E_1, the plots of the strength of the critical field against transition temperature become straight lines. several examples of them being shown in Fig. 5. The value of $\Delta T_t/\Delta E$ can be estimated from the inclination of such a straight line. After repeated measurements, the following value is obtained as the average value:

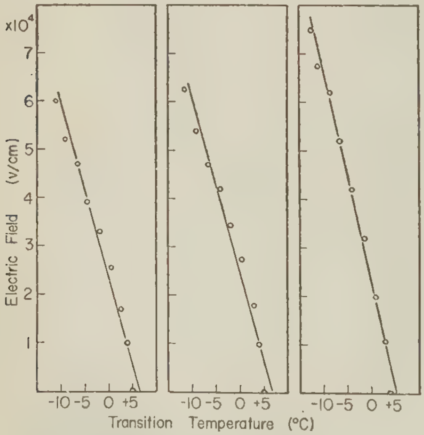

Fig. 5. Examples of the shift of the transition temperature caused by applying electric fields near 5°C.

$$\Delta T_t/\Delta E = (-2.6 \pm 0.2) \times 10^{-4}\ \mathrm{deg/volt\ cm^{-1}}\ ,$$

for the 5°C transition, which is in good agreement with the value obtained by Huibregtse and Young[6], that is -2.8×10^{-4} deg/volt cm^{-1}, from the observation on their triple hysteresis loop.

At the −80°C transition, similar curves to that shown in Fig. 5 were obtained through the similar procedure, but in this case the transition of transparency with field was poorly defined, and the experimental accurary was not so good in this way. At this lowest transition point, the observation on the shift itself of the hysteresis loop of transparency gave better results on the effect of the biasing field. As the field strength increases, the hysteresis loop, and consequently the transition point, shifts towards lower temperatures.

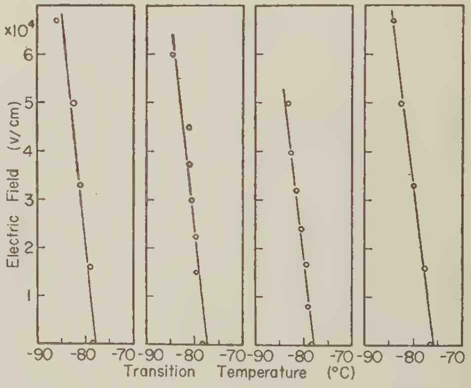

Fig. 6. Examples of the shift of the transition temperature caused by applying electric fields near −80°C.

From this shift the value of $\Delta T_t/\Delta E$ can readily be estimated. It is seen in Fig. 6 that a linear relation holds again between the transition temperature and the strength of the applied field, and the following value is obtained:

$$\Delta T_t/\Delta E = (-1.2 \pm 0.2) \times 10^{-4}\ \mathrm{deg/volt\ cm^{-1}}\ ,$$

for the −80°C transition.

§ 5. Remarks on the TTT-curve near −80°C in the Presence of an Electric Field

It has been shown in the previous report[7] that the TTT at the −80°C transition is characterized by the decrease in the transparency in the lowest phase as shown in Fig. 7 (a). But in the study on the effect of biasing fields for coated crystals, an increase in the transparency took place in the rhombohedral phase (Fig. 7 (b)).

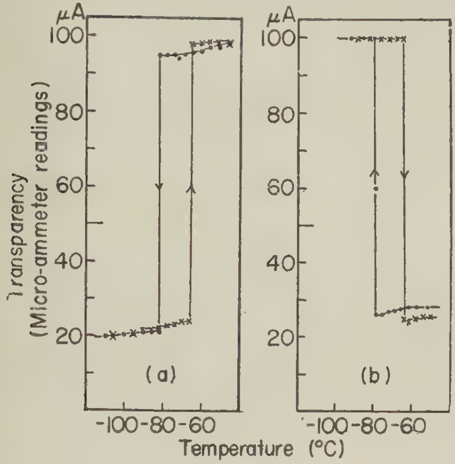

Fig. 7. Thermal transition of transparency near −80°C (a) without and (b) with electrodes.

The following test would give some information about this contradiction. A specimen which had displayed the TTT-curve as shown in Fig. 7 (a) (normal form) in its unelectroded condition was coated over one surface with the transparent electrode and was put under the TTT-test without applying any external electric field, and then both sides were coated and the same procedure was repeated.

In the case of thin crystals (for instance, 14μ in thickness), the normal TTT was made to disappear on account of the coating over one of the plate surfaces, and the coating over both surfaces reversed the form of the TTT (Fig. 7 (b)), that is, transparency increased in the lowest phase. On the contrary, in the case of a relatively thick srystal (for instance, 50μ in thickness) no remarkable electrode-effect presented itself, but after alternate applications and removals of strong electrostatic fields, and only then, the reversed form of the TTT could call the attention.

It has been observed that the displacements of the domain walls in Rochelle-salt crystals caused by thermal motions occur much more freely when they are immersed in an electrolytic solution than when their surfaces are dry, because the surface charge and thus the restoring force cannot develop in the electrolytic solution⁵⁾. If a situation which is to a certain extent similar to the case of Rochelle salt should be expected to take place in the case of coating $BaTiO_3$ crystals with semiconductive films, the transparent electrodes would make domain walls more easily movable in times of the phase change, especially in thin crystals which contain small stress, and consequently, there would appear different domain habits, and hence different transparency, from those without electrodes.

Discussions

§ 6. Comparison with Clausius-Clapeyron Relation

Suppose the transitions of barium titanate to be of the first order, then the well-known relation of Clausius-Clapeyron,

$$\Delta T_t/\Delta E = -\Delta P_z/\Delta S\,, \qquad (1)$$

holds for the rate of the change of the transition temperature with an external electric field, where ΔP_z represents the discontinuous jump of the component of the spontaneous polarization in the direction of the field, and ΔS is the change in the entropy at the transition. For the Curie point, as was mentioned above, this relation holds good.

At the 5°C transition, if the experimental values of ΔP_z measured by Wieder¹⁴⁾ or Huibregtse⁶⁾, and the average value of ΔS measured by several investigators⁵⁾ are used, then the Clausius-Clapeyron relation gives the value of $\Delta T_t/\Delta E$ equal to about -8×10^{-4} deg/volt cm^{-1}, which is not in so good agreement with the present experimental result. At the −80°C transition, the value computed from the Clausius-Clapeyron equation is far from agreeing with the present experimental result, and so the author cannot but consider that such a simple estimation as taking no account of the dependence of ΔP_z and ΔS upon temperature and field will no longer be within the limits of a good approximation at these lower transition points.

§ 7. Phenomenological Calculation Based on the Devonshire Function

a) *Curie point*

In computing the value of $\Delta T_t/\Delta E$ from the Clausius-Clapeyron equation at the Curie point, the experimental data without field were chosen for the numerical values of ΔP_z and ΔS. But in reality, when an electric field is applied to this crystal, the polarization in the cubic phase is no longer zero but varies with the field strength, and hence ΔP_z is not constant but a function of temperature and field strength. In fact, according to the experimental result shown in Fig. 3, ΔP_z vanishes when the transition point is elevated up to about 132°C. Hence it appears likely that ΔS also varies with temperature and field strength in order that the Clausius-Clapeyron relation may holds good.

According to the thermodynamical relation, the entropy S, related to the polarization P, is given as a derivative of the Gibbs free energy $\mathfrak{A}$ by the following formula,

$$S=-(\partial\mathfrak{A}/\partial T)_{P,X}\ , \qquad (2)$$

where T and X represent temperature and stress, respectively. According to Devonshire[4], the Gibbs function per unit volume of a stress-free crystal is expressed in terms of even powers of polarization as follows:

$$\begin{aligned}\mathfrak{A}&=\mathfrak{A}_0+AP^2+BP^4+CP^6\\ &=\mathfrak{A}_0+A_0(T-T_0)P^2+BP^4+CP^6\ , \qquad (3)\end{aligned}$$

where $\mathfrak{A}_0$ is the free energy of the crystal for zero polarization. In Eq. (3) it is assumed that only A is dependent on temperature[3]. Then S is given by $S=-A_0P^2$, and $\Delta T_t/\Delta E$ becomes a function of the polarization only, that is,

$$\Delta T_t/\Delta E=-(P_c-P_t)/(S_c-S_t)=1/[A_0(P_t+P_c)]\ , \qquad (4)$$

where the quantity to which t or c is suffixed refers to the tetragonal or cubic state, respectively. If the numerical values of P_t and P_c at various temperatures are known, the corresponding values of $\Delta T_t/\Delta E$ can be computed from (4).

One way to obtain the values of P_t and P_c is to make use of the optical data shown in Fig. 3. When a double-refractive crystal plate is placed between crossed Nichols, and when the direction of the polarization of the crystal is inclined at 45° to the principal planes of the Nichols, then the intensity of the light of wavelength λ (in air) which has passed through the analyzer, $I(\lambda)$, is given by[15]

$$I(\lambda)=I_0(\lambda)\sin^2(\delta/2)\ , \qquad (5)$$

where $I_0(\lambda)$ is the intensity of the incident light, and δ is the retardation after the light has passed through the crystal of thickness d. The definition of δ is given by the following relationship:

$$\delta=2\pi(d/\lambda)\cdot\Delta n\ , \qquad (6)$$

where Δn is the birefringence of the crystal. Since the light source used for this experiment is a continuous one excluding shorter wavelengths than the absorption edge of barium titanate (about 3800Å[16]), Δn is considered to be approximately independent on wavelength. Then the observed intensity, I_{obs}, is roughly estimated as

$$\begin{aligned}I_{\text{obs}}&=\sum_{\lambda} I(\lambda)\approx I_0\int_0^\infty \sin^2(\pi\cdot\Delta n\cdot d/\lambda)\,d\lambda\\ &=I_0(\pi^2/2)d\cdot\Delta n\ , \qquad (7)\end{aligned}$$

where $I_0(\lambda)$ is assumed to be approximately constant. On the other hand, it has been known that there exists a proportional relationship between Δn and the square of the spontaneous polarization of $BaTiO_3$,[17] *i.e.*, $\Delta n\propto P_s^2$. Therefore, the following expression may be assumed;

$$I_{\text{obs}}\propto P^2\ . \qquad (8)$$

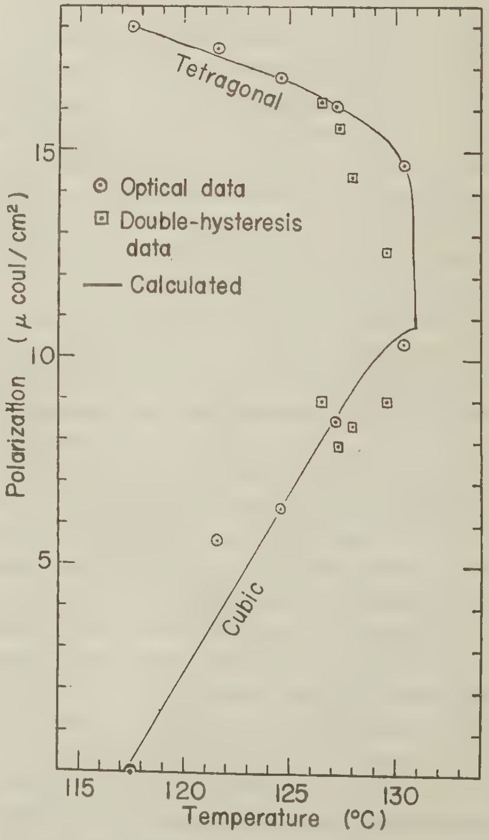

Fig. 8. Polarizations in cubic and tetragonal phases.

From this relation, the values of P_c and P_t at the transition temperatures can readily be estimated by multiplying a proportional constant to the square roots of the observed optical transmissions which are obtained from the data shown in Fig. 3. The values obtained in such a way are plotted in Fig. 8, where the values estimated from double-hysteresis data are also plotted with a view to comparing.

The other way of obtaining the values of polarizations is a calculation based on the Devonshire theory. From thermodynamic considerations, it can be shown that the applied field E is given by $\partial\mathfrak{A}/\partial P=E$,[3),4)] so that

$$E=2A_0(T-T_0)P+4BP^3+6CP^5\ , \qquad (9)$$

the plot of which gives the values of P_t and P_c, if the numerical values of the coefficients are known. These values has been given by Merz[3)], but Drougard *et al.*[18)] have obtained the different value of B showing a dependence on temperature.

To determine this B-value, the present experimental data are of use. It has been mentioned above that the transition temperature is elevated by an electric field up to a critical temperature Θ, where $P_t=P_c$, and the transition of the first order no longer takes place. In other words, the double hysteresis loop vanishes at this temperature, *i.e.*, the two points given by $dE/dP=0$ coincide with each other, that is, the quadratic equation concerning P^2 given by $dE/dP=0$ has the equal roots. For simplicity, B is assemed to be constant in the vicinity of 120°C. Putting the discriminant to be zero, the expression

$$B^2=\frac{5}{3}CA_0(\Theta-T_0) \qquad (10)$$

is obtained, in which $A_0=3.7\times10^{-5}$ cgs[3)] and $C=3.8\times10^{-23}$ cgs[3)]. From the present experiment (Fig. 3), it can readily be found that $\Theta=132$°C and $T_0=107.5$°C. The value of B computed by using these values is -2.39×10^{-13} cgs, which is in good agreement with the mean value of Drougard's data between 120°C and 130°C, that is, about -2.35×10^{-13} cgs[18)]. The propriety of these coefficients is supported by the fact that the valley of the thermodynamic potential surface near 120°C, which is drawn by making use of these coefficients (Fig. 9), coincides approximately with the observed data of the spontaneous polarization.

The values of P_c and P_t can be obtained by the plot of the polarization against the electric field, which is calculated in this way. Such values are plotted in Fig. 8 by the solid line, the agreement with the experimental values being very good. The values of $\Delta T_t/\Delta E$ thus obtained for various temperatures are shown by a solid line in Fig. 4, which is sufficient to explain the experimental results.

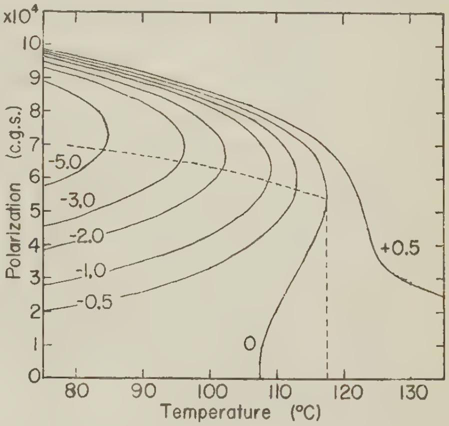

Fig. 9. Chart of the thermodynamic potential surface near the Curie point. The numbers near the contours are in cal/mol. The dotted line gives the experimental temperature dependence of the spontaneous polarization.

b) *Two lower transition points*

At a temperature near 5°C, the crystal transforms from tetragonal to orthorhombic phase, and there appears the x-component in addition to the z-component of the polarization because of the transformation of the direction of polarization from an edge to a face diagonal of the pseudo-cubic cell. The Devonshire function per unit volume is then expressed as follows:

$$\begin{aligned}\mathfrak{A}=\mathfrak{A}_0&+A(P_x^2+P_z^2)+B(P_x^4+P_z^4)\\&+C(P_x^6+P_z^6)+DP_x^2P_z^2\\&+G(P_x^2P_z^4+P_x^4P_z^2)\ , \qquad (11)\end{aligned}$$

the last cross term of the sixth order being added by Huibregtse and Young[6)] in order to obtain a satisfactory explanation of their observation on the 5°C transition. The electric field as a function of polarization is given by

$$\begin{aligned}E_z=2AP_z&+4BP_z^3+6CP_z^5+2DP_x^2P_z\\&+G(2P_x^4P_z+4P_x^2P_z^3)\ . \qquad (12)\end{aligned}$$

To plot E_z against P_z, P_x in Eq. (12) must be eliminated by an additional condition due to the fact that the electric field is applied only in the z-direction, that is, $E_x=0$, or

$$A+2BP_x^2+3CP_x^4+DP_z^2+G(2P_x^2P_z^2+P_z^4)=0\,. \qquad (13)$$

The numerical values of the coefficients have been given by Huibregtse and Young[6], and also by Drougard and Huibregtse[19]. The values of A and B are in accord with those measured by Merz[3] and by Drougard[18], respectively, and the other coefficients take the following values at 0°C: $C=12.2\times10^{-23}$[6] or 9×10^{-23}[19], $D=4\times10^{-13}$, $G=6\times10^{-23}$[6] in cgs units. On the other hand, Merz[3] reported the value of C in the neighbourhood of 120°C as 3.8×10^{-23}. This is the reason why the author considers the coefficient C also to be dependent on temperature. If a straight line is assumed for C as a function of temperature, which passed through the two points (120°C, 3.8×10^{-23} cgs) and (0°C, 11×10^{-23} cgs), then the following expression is obtained for the temperature dependence of C:

$$C=-6\times10^{-25}(T-T_2)\,,\quad T_2=183^\circ\mathrm{C}\,. \qquad (14)$$

In the vicinity of 5°C the effect of the term of CP_z^6 upon the free energy is too large to neglect the temperature dependence of this coefficient. According to Huibregtse and Young, it may also be assumed that D and G are constant. The values of the coefficients used in this calculation are listed as follows:

$$\left.\begin{aligned} &A=3.7\times10^{-5}(T-T_0)\,, \quad T_0=107.5^\circ\mathrm{C}\,.\\ &B=4.5\times10^{-15}(T-T_1)\,, \quad T_1=175^\circ\mathrm{C}\,.\\ &C=-6\times10^{-25}(T-T_2)\,, \quad T_2=183^\circ\mathrm{C}\,.\\ &D=4\times10^{-13}\,.\\ &G=6\times10^{-23}\,. \qquad \text{(in cgs units)} \end{aligned}\right\} \quad (15)$$

The plots of P_z *vs* E_z given by Eq. (12) together with those for tetragonal state are shown in Fig. 10, the temperature of the crystal being a parameter. According to the Devonshire picture, P_z varies with field along the P_z *vs* E_z curve in regions where $\partial P_z/\partial E_z$ (susceptibility) is positive. At the point where the susceptibility is infinite, P_z instantly jumps to a point where the susceptibility is again positive, which is the fundamental idea of Huibregtse on his triple hysteresis loop[6]. Accordingly, the point where $\partial P_z/\partial E_z$ becomes infinite should be considered as the transition point from orthorhombic to tetragonal in the existence of an electric field. These points are readily obtained from the curves shown in Fig. 10, and if these critical fields (at which $\partial P_z/\partial E_z\to\infty$) are plotted against the corresponding transition temperatures, the curve

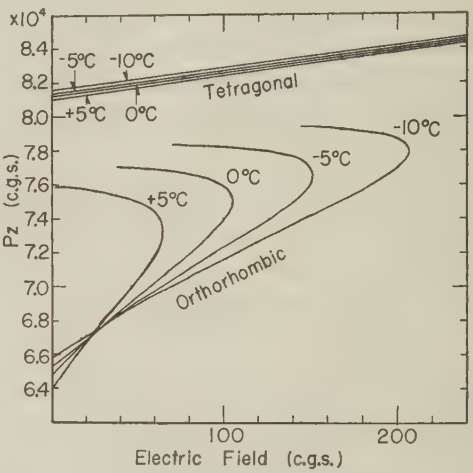

Fig. 10. The z-component of the polarization (P_z) *versus* electric field near 5°C. The numbers near the curves represent the temperature of the crystal.

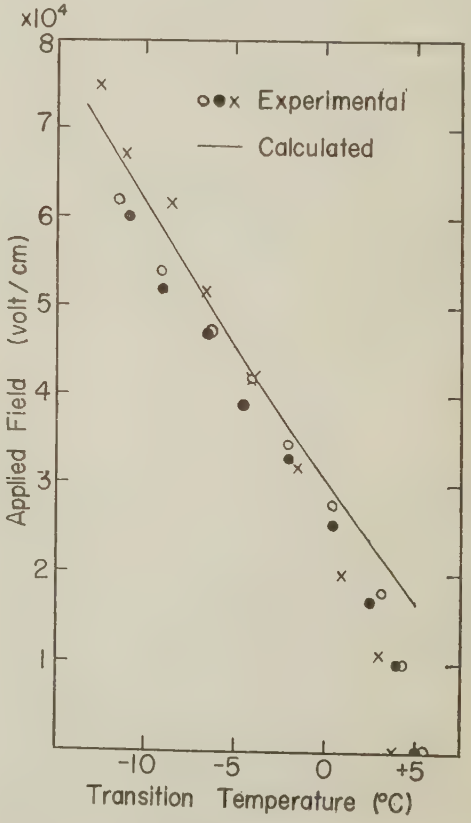

Fig. 11. Shift of the transition temperature near 5°C caused by electric fields.

drawn with solid line in Fig. 11 is obtained, which explains the experimental results satisfactorily. It will also be seen in Fig. 10 that this transition is of the first order, at least in the region of the field strengths in which the present experiment was carried out. It appears likely that the discrepancy with the Clausius-Clapeyron relation would be caused by the neglect of the effect of strong electric field on ΔP_z and ΔS.

When the crystal is cooled down to about −80°C, another transition takes place. It is stated recently that the crystal symmetry of this lowest phase would be monoclinic or triclinic[1], but the author assumes here the symmetry to be rhombohedral according to the conventional interpretation. Then the spontaneous polarization takes the direction in a body diagonal of the former cube cell, and the terms due to another component, P_y, must be added to the expression (11) of the free energy, that is,

$$\begin{aligned}\mathfrak{A}=\mathfrak{A}_0&+A(P_x^2+P_y^2+P_z^2)\\&+B(P_x^4+P_y^4+P_z^4)+C(P_x^6+P_y^6+P_z^6)\\&+D(P_x^2P_y^2+P_y^2P_z^2+P_z^2P_x^2)\\&+G(P_x^4P_y^2+P_y^4P_x^2+P_y^4P_z^2\\&+P_z^4P_y^2+P_z^4P_x^2+P_x^4P_z^2)\,. \qquad (16)\end{aligned}$$

If there exists an electric field only in the z-direction, the x- and y-direction are equivalent concerning the electric field, and therefore, it is possible to take $P_x=P_y$. The following relationship between P_z and E_z is readily derived from (16):

$$\begin{aligned}E_z=2AP_z+4BP_z^3+6CP_z^5&+4DP_zP_x^2\\&+8GP_z^3P_x^2+4GP_zP_x^4\,. \qquad (17)\end{aligned}$$

Similarly to the case of the orthorhombic phase, P_x is eliminated by using an additional condition owing to the fact that there exists no electric field in the x- and y-directions, *i.e.*, $E_x=E_y=0$, or

$$\begin{aligned}A+2BP_x^2+3CP_x^4&+D(P_x^2+P_z^2)\\&+G(3P_x^4+2P_x^2P_z^2+P_z^4)=0\,. \qquad (18)\end{aligned}$$

Eqs. (17) and (18) give the similar plot of P_z *vs* E_z to that in the orthorhombic case.

In determining the numerical values of the coefficients in the vicinity of −80°C, however, it is not assured that the temperature dependence of A, B, and C, and the numerical values of D and G, which are listed in (15), hold good as they are. Assuming that the above-cited temperature dependence of A is also correct at these low temperatures, the other four coefficients will be determined by the simultaneous equations expressing the following four relations: (i) at the transition point, the free energies of the orthorhombic and rhombohedral states have the same value, (ii) the value of P_z given by $E_z=0$ in the orthorhombic state at the transition point is equal to the z-component of the spontaneous polarization at that temperature, (iii) the corresponding statement holds also for the rhombohedral state, and (iv) $\partial P_z/\partial E_z$ is equal to the susceptibility. But the solutions of these simultaneous equations are sharply varying functions of the square of the ratio of the z-component of the spontaneous polarization in the orthorhombic state to that in the rhombohedral state, $P_z^2(\text{ortho})/P_z^2(\text{rhombo})$, presenting little reliability in determining the coefficients in this way.

Another assumption that the relations (15) hold approximately leads to very much larger critical fields than the experimental values. Since the electric field used for the present experiment is static, the switching behavior which is said to govern the ac coercive field[3] may possibly be left out of consideration.

It might be assumed that, since the polarization and the coefficients become large at these low temperatures, the terms of higher orders than sixth would be taken into consideration. If so, in an approximation, the terms

$$\alpha(P_x^8+P_y^8+P_z^8)+\beta(P_x^{10}+P_y^{10}+P_z^{10}) \qquad (19)$$

might be added to the expressions (11) and (16) of the free energies in the orthorhombic and rhombohedral states, respectively, at these low temperatures. These terms are assumed to be small at much higher temperatures than this lowest transition point. The coefficients α and β can be determined by the conditions that the free energies of the orthorhombic- and rhombohedral-states have the same value at the transition point and that the values of P_z giving the minima of the free energies are equal to the z-components of the spontaneous polarizations of the orthorhombic and rhombohedral states at the transition temperature. At that time it is assumed that the other coefficients are given by (15). Then the values $\alpha=-15\times10^{-33}$ and $\beta=10\times10^{-43}$ cgs units are obtained, giving the plots of P_z *vs* E_z as shown in Fig. 12. Similarly to the orthorhombic case, it is assumed that the polarization jumps instantly from the rhombohedral- to orthorhombic-state at the point where $\partial P_z/\partial E_z$ becomes infinite, then this point can be considered as a transition point in the existence of an electric field. These critical fields are plotted against the transition temperatures, then the curve drawn with solid line in Fig. 13 is obtained, which explains the experimental results approximately.

In this lowest phase, the crystal symmetry has not yet been decided finally, and moreover a crystal is divided into fine domains. Therefore, it may not be possible to discuss much on the basis of such a simple calculation of a single-domain crystal as mentioned above, but at least as an experimental formula, the expression of the free energy with the additional terms (19) to (16) holds approximately in the case of the lowest phase.

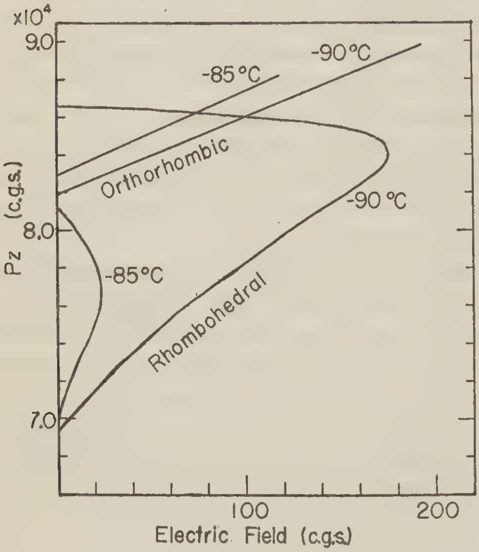

Fig. 12. The z-component of the polarization (P_z) *versus* electric field near −80°C. The numbers near the curves represent the temperatures of the crystal.

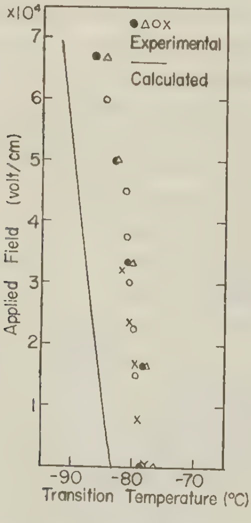

Fig. 13. Shift of the transition temperature near −80°C caused by electric fields.

Summary

(1) Up to this time, electrical measurements have been used for the methods of determining the transition points of barium titanate or of observing the effect of biasing fields on them. Electrical methods require very good specimens. For example, except for crystals with very high purity, the double hysteresis loops can hardly be observed but very curious and asymmetric loops are traced on the oscilloscope. On the other hand, any crystal can be used for the optical test utilizing the shift of the thermal transition of transparency. The only requirement is that the crystal under test is not opaque. The experimental accuracy of this method in the case of the study on the effect of biasing fields was better than that of the electrical method. What with these reasons and what with the comparative simplicity in the experimental procedure, this optical test will be of use as a new method.

(2) When a polarized plate such as a cryslal of barium titanate is placed between crossed Nichols, the plate being so oriented that the direction of the component of the polarization at right angles to the incident beam is inclined at 45° to the principal planes of the Nichols (see Fig. 1), the intensity of the continuous light transmitted through the analyzer is approximately proportional to the birefringence and hence, in the case of barium titanate, to the square of the polarization of this plate.

(3) The Curie point near 120°C is raised by an applied electric field at a rate of 1.6×10^{-3} deg/volt cm^{-1}, which is in good agreement with those measured by other investigators, and at a critical temperature of 132°C, the magnitudes of the polarizations of cubic- and tetragonal- (strictly speaking, induced-tetragonal-) phases become equal, the corresponding critical strength of the field being about 9 kv/cm. Above this critical point any tran-

sition of the first order no longer takes place. From this fact the expansion coefficient B of the free-energy function is estimated as -2.39×10^{-13} cgs units, which supports the value measured by Drougard *et al*. rather than that measured by Merz. The thermodynamic potential surface which is drawn by using this coefficient explains satisfactorily the observed temperature dependence of the spontaneous polarization.

(4) For the Curie point, the relationship

$$\Delta T_t/\Delta E=1/[A_0(P_t+P_c)]$$

is more convenient than the usual Clausius-Clapeyron relation, because the former does not contain the entropy change, ΔS, which varies also with an external electric field. Therefore, this equation yields a profit to leave the entropy change out of consideration, and $\Delta T_t/\Delta E$ can be obtained by measuring or calculating the polarization only.

(5) At the 5°C transition $\Delta T_t/\Delta E=-2.6\times10^{-4}$ deg/volt cm^{-1}, which is in good agreement with the value measured by Huibregtse and Young. The expansion coefficients A, B, and C of the free-energy function are all assumed to be dependent on temperature. For C, a linear relation, $C=-6\times10^{-25}(T-T_2)$, $T_2=183$°C, is assumed. The plots of P_z *vs* E_z based on the Devonshire function gives values of $\Delta T_t/\Delta E$ which give a satisfactory explanation of the experimental results.

(6) At the -80°C transition $\Delta T_t/\Delta E=-1.2\times10^{-4}$ deg/volt cm^{-1}. The terms of eighth and tenth powers of polarization is added to the free-energy function in order to obtain a better fit. The values of the coefficients α and β of the terms of eighth and tenth power, respectively, are obtained as $\alpha=-15\times10^{-33}$, $\beta=10\times10^{-43}$ in cgs units at the lowest transition point. The Clausius-Clapeyron relation does not give satisfactory explanation of the observations on the two lower transitions, probably because of the neglect of the effects of strong fields upon the polarization and entropy.

Acknowledgements

The most part of this work was performed when the author was at Osaka University under the guidance of Professor T. Horie, to whom he expresses his sincere gratitude. He wishes to express his thanks to Professors S. Sawada and S. Nomura of Tokyo Institute of Technology for their suggestive discussions and also for their guidance in the cource of preparation of crystals. He is indebted much to Mr. T. Iwai in Osaka University and to Dr. E. J. Huibregtse in IBM Laboratory for useful suggestions and valuable comments. He wishes also to thank Professors T. Kanda, Y. Masuda and M. Shimizu of Kobe University for their encouragement and for placing apparatus at his disposal.

References

1) F. Jona and R. Pepinsky: Phys. Rev. **105** (1957) 861.
2) W. Kaenzig and N. Maikoff: Helv. Phys. Acta **24** (1951) 343.
3) W. J. Merz: Phys. Rev. **95** (1954) 690.
4) A. F. Devonshire: Adv. in Phys. **3** (1954) 85.
5) G. Shirane, F. Jona and R. Pepinsky: Proc. IRE **43** (1955) 1738.
6) E. J. Huibregtse and D. R. Young: Phys. Rev. **103** (1956) 1705.
7) T. Horie, K. Kawabe, M. Tachiki and S. Sawada: J. Phys. Soc. Japan **10** (1955) 541.
8) T. Horie, K. Kawabe and T. Iwai: Ann. Rept. Fac. Sci. Osaka Univ. **4** (1956) 45.
9) K. Kawabe and S. Sawada: J. Phys. Soc. Japan **12** (1957) 218.
10) J. P. Remeika: J. Amer. Chem. Soc. **76** (1954) 940.
11) R. E. Aitchison: Australian J. App. Sci. **5** (1954) 10.
12) K. Ishiguro, T. Sasaki, T. Arai and I. Imai: J. Phys. Soc. Japan **13** (1958) 296.
13) S. Namba: J. App. Phys. Japan **25** (1956) 258. (in Japanese)
14) W. Wieder: Phys. Rev. **99** (1955) 1161.
15) F. Pockels: *Lehrbuch der Kristalloptik*, 1906, p. 213.
16) T. Horie, K. Kawabe and S. Sawada: J. Phys. Soc. Japan **9** (1954) 823.
17) W. J. Merz: Phys. Rev. **76** (1949) 1221.
18) M. E. Drougard, R. Landauer and D. R. Young: Phys. Rev. **98** (1955) 1010.
19) M. E. Drougard and E. J. Huibregtse: IBM Journ. Res. Develop. **1** (1957) 318.
20) H. Diamant, K. Drenck and R. Pepinsky: Rev. Sci. Instr. **28** (1957) 30.
21) R. Abe: J. Phys. Soc. Japan **13** (1958) 244.

JOURNAL OF THE PHYSICAL SOCIETY OF JAPAN Vol. 14, No. 12, DECEMBER, 1959

Decay Properties of ZnS(Ag) Phosphors

By Tsunesaburo ASADA, Masayoshi MASUDA,
Masayuki OKUMURA and Juzo OKUMA

*Department of Physics, Faculty of Science,
University of Osaka*

(Received August 28, 1959)

The fact that a phosphor exhibits different decay times for different kinds of exciting radiation has recently been reported. This is expected to be found also in ZnS(Ag) phosphor which is often applied in photonuclear experiment. Detailed measurements of such decay properties has been carried out in the present work. It came out clear that the phosphor has two types of decay mode for a kind of radiation, one being exponential and another hyperbolic with time, and that the phosphor has different decay constants in the exponential form decay for different kinds of radiation. The decay constants were obtained to be 100 $m\mu$sec and 10 $m\mu$sec for the α-particle and γ-ray excitation, respectively. Thus, contrary to a previous work by Koontz et al.[10], an apparent difference was observed for these two kinds of excitation. Furthermore, it was observed that in the case of γ-ray excitation the decay is mainly exponential and in the case of α-particle excitation mainly hyperbolic. The difference of decay modes and the difference of the decay constants make it possible to discriminate protons or α-particles from the strong γ-ray background.

§ 1. Introduction

ZnS(Ag) phosphor is generally used in detecting heavy charged particles such as protons or α-particles in the strong γ-ray background. To measure the angular distribution in photonuclear reaction, a sufficient discrimination of the heavy particles from γ-rays is necessary. Several authors[1)-6)] have shown that the ZnS(Ag) phosphor is useful for this purpose because of its large pulse height ratio of light emission for heavy charged particles to that for γ-rays. In order to refine the techniques of photo-nuclear experiments, however, more complete discrimination of protons or neutrons in the γ-ray background is required. In our experiment of photo-nuclear reaction with a betatron using an accurate collimator and a heavy shield, the average γ-ray dose at the proton or neutron counter is very low but the pulsed γ-rays from this machine have a very high instantaneous intensity. Photons accumulated in the very short period of this pulse produce a large light pulse in the scintillation counter. This pile-up effect in scintillation pulses is one of the predominant troubles under this experimental condition and it imposes severe limitation on the kind of the target element to be measured and sometimes leads to poor experimental results.

A fast decay component of ZnS(Ag) phosphor was reported in earlier works[7)-11)] in addition to the well-known long term decay of 10^{-5} sec[12),13)]. So we first made an attempt to eliminate the pile-up effect of the γ-rays by constrncting a very fast counting system, so as to pick up only the fast decay component of the ZnS phosphors. The results proved to be unsuccessful, contrary to our expectation. A precise examination of the characteristic of ZnS phosphors from the point of view of its decay properties was therefore undertaken. The results of such experiment will be reported in the present paper. Our principal conclusion is as follows.

The fast decay component of ZnS phosphors is for the most part attributed to γ-rays and the long term decay principally to heavy charged particles.

The ZnS phosphor has long been considered as having a large ratio of the pulse height for heavy particles to that for γ-rays. This may be due to the fact that the fast decay component, which is sensitive to γ-rays, has been cut off by the use of the linear amplifier whose rise time was considerably long.

§ 2. ZnS Phosphors

The decay properties of phosphors can broadly be divided into two classes. The first is such that the decay takes place in accordance with the equation

$$I = I_0 \exp(-t/T_p) \qquad (1)$$

where I_0 is the initial intensity, I the intensity at time t and T_p the decay constant. Generally, T_p is smaller than 10^{-6} sec. In the second class, the decay takes place in accordance with the equation

$$I = I_0/(1+at)^n \qquad (2)$$

where a and n are constants.

The first decay type is called monomolecular, the luminescence taking place by a simple excitation of the active center with subsequent optical emission from it. The activation energy is stored in the center between excitation and emission. The thallium activated alkali halides belong to this type.

Most of the luminescent materials which are valued for their long decay characteristics obey a decay equation of second type, which is similar to the rate equation for a bimolecular chemical reaction. Several of such materials exhibit photoconductivity when being excited with ultraviolet light. Therefore it may be concluded that atoms become ionized during the excitation and that the luminescent radiation is emitted during recombination of the free electrons and the ionized centers.

The fact that the fast counting system failed as mentioned in § 1, led us to presume that ZnS phosphors when excited by heavy charged particles, such as protons or α-particles, would follow the power law decay scheme while they would follow the exponential decay scheme when excited by electrons or γ-rays.

§ 3. Measurements

In order to measure the value of T_p in Eq. (1), the following experiments were carried out. The block diagram of the detecting system is shown in Fig. 1. The pulse shape produced by a photomultiplier the receiving the luminescence from the ZnS was determined as a function of the resistance at the output of the photomultiplier tube. Two systems of amplifiers, fast and slow, are used in the experiment. The fast system consists of a Tektronix 517A oscilloscope preceded by Spencer Kennedy distributed amplifiers, model 202D and 214B. The slow system consists of a DuMont 301 oscilloscope and a Model 100 linear amplifier. The photomultiplier tube has 14 stages of electron multiplication and it was used in the fast system because of its large multiplication factor. The source of radiation used is either Po–α or Co^{60} of 3 curies, or both together. The ZnS(Ag) powder, type No. P4B1, was offered by Dai Nihon Toryo Co. The powder was deposited on the surface of a glass plate, which was mounted on a photomultiplier tube and covered by a semi-spherical light reflector. The output pulse of the photomultiplier tube provides information on how the luminescence is emitted as a function of time. If the luminescence decays exponentially, one should be able to obtain the time constant of decay by making the resistance smaller and smaller and taking the limit of zero resistance. The measured decay time against the resistance is shown in Fig. 2. In this case, ZnS was excited by α-particles. The observed decay time did not decrease below 100 mμsec when the resistance

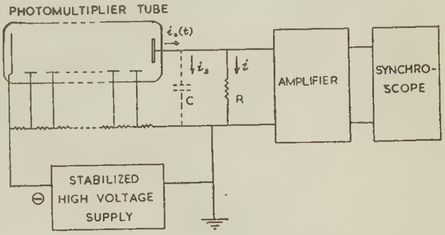

Fig. 1. Block diagram of the detecting system.

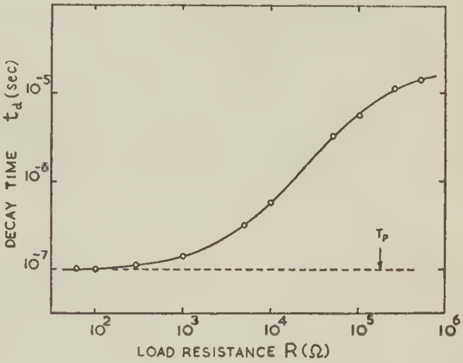

Fig. 2. Curve of the decay time of the observed pulse against the load resistance. T_p is the principal decay constant in the exponential decay.

was varied to below 300 ohms. Under γ-ray excitation, on the other hand, we obtained a principal decay time constant of 10 mμsec and no appreciably shorter decay time.

The rise time of pulses as a function of resistance is shown in Fig. 3. In order to analyse this figure, two types of decay form, exponential and power laws, were adopted for the differential equation of the RC network shown in Fig. 1. R is the load resistance and C is the stray capacitance of collector of photomultiplier tube. Referring to Fig. 1, we obtain the following equation

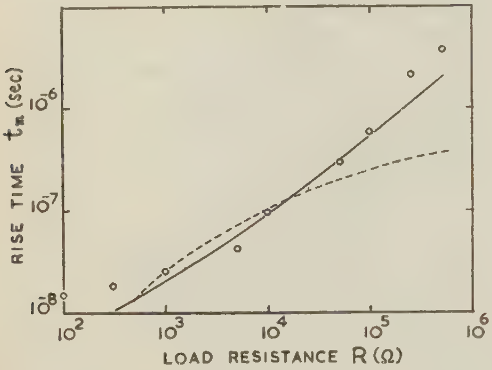

Fig. 3. Curve of the rise time of the observed pulse against the load resistance. Circular points are measured values. Solid and broken lines are calculated by assuming hyperbolic and exponential light decay, respectively.

$$i+i_2=i_0 \exp(-t/T_p) ,$$

if the exponential decay form is assumed. On the other hand, the current across the stray capacitance is expressed by

$$\frac{i_2}{C}=R\frac{di}{dt} .$$

Therefore the following two differential equations are obtained, respectively, for the two assumed types of decay.

(1) Decay form is of exponential type:

$$R\frac{di}{dt}+\frac{i}{C}=\frac{1}{C}\, i_0 \exp\left(-\frac{t}{T_p}\right) \tag{3}$$

where i is the current through R and $i_0 \exp(-t/T_p)$ is the charge flow per unit time from the electron collector to the RC network.

(2) Decay form is of power law type:

$$R\frac{di}{dt}+\frac{i}{C}=\frac{1}{C}\,\frac{i_0}{(1+at)^n} . \tag{4}$$

The solution of Eq. (3) is given by

$$i=\frac{i_0 T_p}{T_p-RC}\left\{\exp\left(-\frac{t}{T_p}\right)-\exp\left(-\frac{t}{RC}\right)\right\} . \tag{5}$$

In the case of $RC \ll T_p$,

$$i=i_0 \exp(-t/T_p) ,$$

and the observed decay should be due only to the decay of the luminescence. The pulse height in this case becomes very small. Assuming the rise time of the pulse, t_m, to be the time interval from zero to maximum amplitude, we obtain this value by differentiating Eq. (5) and putting it equal to zero,

$$t_m=\frac{RCT_p}{RC-T_p}\ln\frac{RC}{T_p} . \tag{6}$$

Namely, t_m is to be nearly proportional to $\ln R$ and a nearly straight line relationship has to exist between t_m and R in the semi-log plot if $T_p/RC \ll 1$. However, it was found difficult to explain our experimental results, assuming this value of t_m. So the assumption of another decay form is preferable. The solution of Eq. (4) is as follows if we assume $n=1$ (this assumption is not too far from the fact reported by Bailey and Prescott[11]).

$$i=\frac{i_0}{RC}\exp\left(-\frac{t}{RC}\right)\int_0^t \frac{\exp(t/RC)}{1+at}\,dt \tag{7}$$

We have not been able to deduce the value of t_m by differentiating Eq. (7). Numerical integration was therefore carried out. The result is shown in Fig. 3, where $n=1$, $a=2.1 \times 10^7$ and $C=10^{-11}$ farad. A fair agreement exists between the measured and calculated results except for a minor disagreement in the region of small R, which might be explained as introduced by the rise time of the detecting system, 7 mμsec. Judging from Fig. 3, we may conclude that the decay type of ZnS(Ag) phosphors excited by α-particles exhibits, as a whole, the power law decay and not the exponential decay except for the fast decay component of 100 mμsec.

§ 4. Discrimination of Heavy Charged Particles from γ-rays

The principal purpose of this experiment is to detect protons or neutrons in the strong γ-ray background produced by the betatron. The effect mentioned in § 3 gives the possibility of obtaining the considerable discrimination of protons or neutrons from γ-rays. In order to ascertain the validity of the picture of decay previously mentioned that protons and neutrons contribute much more to the decay form of power low than γ-rays do, we have carried out the following experiment whose results are shown in Fig. 4. This shows the pulse height curves under several conditions. The curves (a) and (b) were obtained by the slow and fast system, respectively. In this case, Co^{60} of 3 curies and Po–α were put in front of ZnS scintillator at the distance of 20 cm and 5 cm respectively.

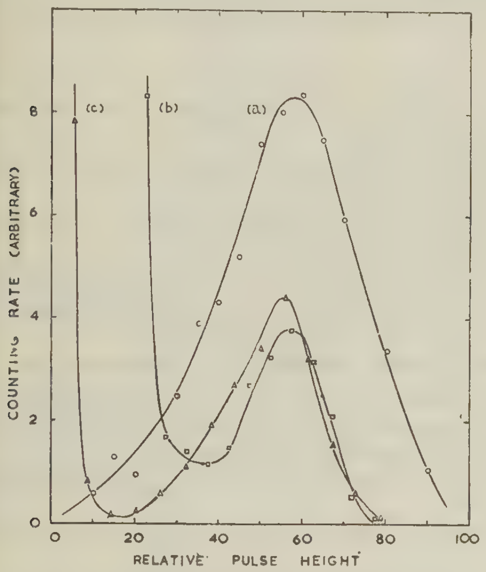

Fig. 4. Pulse height distribution curves. (a) using the slow system. (b) using the fast system. (c) using the fast system in which a condenser was coupled to the load resistance.

Comparing the slow and fast system, it was found that the former gave a better discrimination of α-particles from γ-rays, while the latter gave a good sensitivity to γ-rays. Another curve (c) shows the results of pulse height distribution when in the fast system a condenser was coupled to the load resistance of the collector of the photomultiplier tube. This curve was not useful, contrary to expectation, to eliminate the fast decay component of ZnS phosphors. This may be due to the current saturation in the photomultiplier tube or the high out-put impedance of high voltage power source, or some other reasons which we have not yet understood. A more detailed examination has to be performed to obtain the complete discrimination of heavy charged particles from γ-rays.

In order to check the discrimination properties between protons and γ-rays, experiment of photo-nuclear reaction (γ, p) is preferable. The arrangement of instrument for this purpose is shown in Fig. 5. A 24-Mev betatron was used. The thickness of ZnS powder layer deposited on a glass plate is 20 mg/cm². The proton counter was mounted at angles of 90° to X-ray direction. The pulse height distributions are shown in Fig. 6. In this case, protons were produced by the reaction of Ni(γ, p)Co. From this figure it is seen that slow amplifier system exhibits the proton peak in its pulse height distribution curve but the fast amplifier system shows the pile-up effect of γ-rays only. It was expected that the fast system was better to pick up photo-protons in the strong γ-ray background because of its possibility of eliminating the pile-up effect. However, this expectation failed. Judging from the present experiment

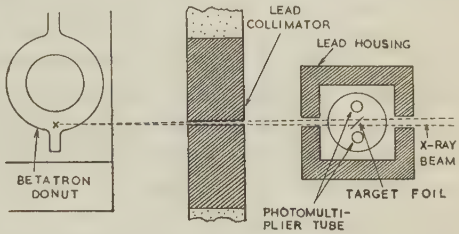

Fig. 5. Arrangement of the apparatus of photonuclear experiments.

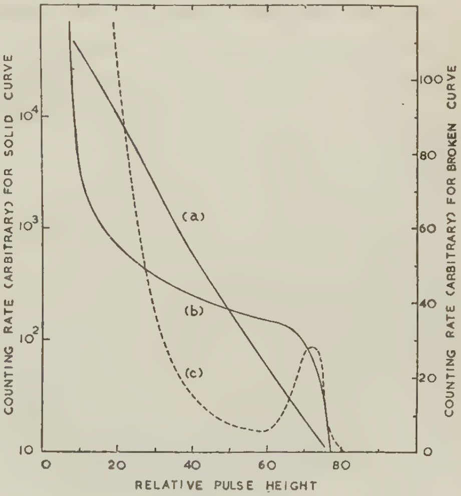

Fig. 6. Curves of pulse height distribution in (γ, p) reaction. (a) by the fast amp. system. (b) by the slow amp. system. Broken curve is obtained by differentiating the curve (b).

and the decay properties of ZnS, it is believed that a more precise examination of the electronics of the detection system would make it possible to obtain a complete discrimination of protons from γ-rays.

§ 5. Summary

First of all, we assumed that ZnS(Ag) phosphors have two types of decay, one is exponential and another hyperbolic. The former has a shorter decay constant, 10^{-7}–10^{-9} sec, and is caused almost by the single excitation by γ-rays and β-rays. The latter has a longer term decay component and is the principal decay mode of ZnS which always exists in addition to the exponential decay. The general mechanism of bimolecular decay is mentioned in § 2. More detailed explanation of the mechanism of this type of decay has been reported in reference 14. According to this, the competition between electron concentration of free electrons in conduction band and concentration of impurities decides the type of decay. The bimolecular decay takes place by the electron concentration when it wins in this competition. Such an assumption of the decay mechanism is consistent with the results of our experiment in which the bimolecular decay is caused by the heavy excitation by protons or α-particles.

The decay times in the exponential form were measured under excitation by α-particles and γ-rays. 100 mμsec and 10 mμsec were obtained as decay constant, respectively. The former agrees with that of Emmerich[9] and Hornyak[8] who reported also a value of 100 mμsec. Decay times of 0.13 and 0.34 μsec under 2.6 Mev neutron excitation have been reported[11]. But a shorter decay time has been also reported by Koontz, Keepin and Ashley[10] under α-particle excitation. The effect of neutron excitation on phosphors, decay properties could be regarded as similar to that of α-particle excitation.

For γ-ray excitation, a very short decay time of 8.5 ± 2.5 mμsec was reported by Bailey and Prescott[11]. Our results give the same information with this.

Contrary to a previous literature which reports the same decay time for γ-ray and α-particle excitation, an apparent difference was observed in our experiment. This effect was not explained by our decay picture.

References

1) A. K. Mann and J. Halpern: Phys. Rev. **82** (1951) 733.
2) A. K. Mann and J. Halpern: Phys. Rev. **87** (1952) 146.
3) E. V. Weinstock and J. Halpern: Phys. Rev. **94** (1954) 1651.
4) S. A. E. Johanson: Phys. Rev. **97** (1955) 434.
5) B. P. Fabricand, B. A. Allison and J. Halpern: Phys. Rev. **103** (1956) 1755.
6) T. Asada, M. Masuda, M. Okumura and J. Okuma: Journ. Phys. Soc. Japan **13** (1958) 1.
7) V. I. Broser, H. Kallmann und C. Reuber: Z. Naturforsch., **5a** (1950) 79.
8) W. S. Emmerich: Rev. Sci. Inst. **25** (1954) 69.
9) W. F. Hornyak: Rev. Sci. Inst. **23** (1952) 264.
10) P. G. Koontz, G. R. Keepin and J. E. Ashley: Rev. Sci. Inst. **26** (1955) 352.
11) G. M. Bailey and J. R. Prescott: Austr. Journ. Phys. **2** (1958) 135.
12) J. Birks: *Scintillation Counters*, Pergamon Press, London (1954) p. 50.
13) S. C. Curran: *Luminescence and the Scintillation Counter Butterworths*, London (1953) p. 131.
14) V. I. Broser and C. Reuber: Z. Naturforsch. **9** (1954) 689.

JOURNAL OF THE PHYSICAL SOCIETY OF JAPAN, Vol. 14, No. 12, DECEMBER, 1959

An Improvement of the WKB Method in the Presence of Turning Points and the Asymptotic Solutions of a Class of Hill Equations

By Haruo MORIGUCHI

Department of Physics, Shizuoka University, Shizuoka

(Received July 31, 1959)

A method of successive approximation, which is essentially a modified form of the WKB method, is developed to express, for large values of parameter h, the asymptotic solutions of a linear second order differential equation

$$\frac{d^2y}{dx^2}-(\lambda+h^2f(x))y=0\ ,$$

in the region where the zeros of the coefficient of y are present. Several simple cases are treated as elementary examples. It is shown that a class of Hill equations is included in the category to which our method is applicable, and that their uniformly valid asymptotic solutions can be expressed in terms of Mathieu functions. The locally valid expressions are also given by means of the above method.

Introduction and Summary

It is well-known that the WKB method originated by Jeffreys, Wentzel, Kramers and Brillouin is one of very powerful methods of approximation for a class of linear second order differential equations of the form

$$\frac{d^2y}{dx^2}+h^2g(x)y=0\ .$$

This method gives the asymptotic forms of the solutions of the given equation for large values of h, and its numerical results are comparatively accurate in spite of the simplicity of expressions, if the coefficient $g(x)$ does not vanish. But when the zeros of $g(x)$ appear in the region considered, we must use more complicated asymptotic solutions or the connection formulas which give the relations between the solutions in two regions seperated by a zero of $g(x)$.

The methods for expressing the asymptotic solutions about the turning points, i.e. the zeros of $g(x)$, have been developed by several authors in the cases in which there appear, for example, a simple turning point, a second order turning point, a pair of simple turning points etc.. (The order of the zero of $g(x)$ is called the order of the turning point.)

On the other hand, the connection formulas have also been well investigated and applied to many examples. It has been pointed out that it is convenient to consider the independent variable in the complex plane for the deduction of the connection formulas and for the study of some kinds of eigenvalue problems.

Thus many problems in mathematics and mathematical physics, e.g. the asymptotic behaviour of special functions, wave motions, energy eigenvalues of quantum mechanical systems, scattering of particles, tunnel effects, compressible flows etc. have been solved successfully by means of the WKB method.

In spite of these facts, however, some problems are left to be investigated in pure and applied mathematics. One of them is to extend the method to the cases in which more complicated turning points appear.

In this paper we shall first remark that the methods ever developed to obtain the asymptotic solutions about turning points can be unified, so to speak, into a principle, which gives a set of transformations of variables for deriving simple approximate equations. These transformations are nothing but slightly modified forms of the usual WKB transformations, and they make it possible to select large terms in the given differential equation without any change of the important characters of the equation. By means of the transformed equation we can find the asymptotic solutions uniformly valid in certain region, where the turning points may appear. This procedure is applicable also to the cases never treated before; for example, the uniformly valid asymptotic solutions of a class of Hill equations can be obtained in terms of Mathieu functions. Further by the repeated use of these transformations we can proceed to the approximations of any order required.

For higher order approximations a more conventional method is also possible, in wnich the usual formal series expansion method is adopted and the connection formulas are derived. This conventional method seems to be sufficient for many of the practical problems.

We shall divide this paper in two parts. In Part I we state the fundamental idea and discuss some elementary examples. Further a note on the conventional method is added with special reference to the second order turning point. And in Part II a class of Hill equations is considered on the basis of the modified WKB transformations and the asymptotic solutions uniformly valid are expressed in terms of Mathieu functions. A few comments are also added with respect to the solutions locally valid.

It should be mentioned that, although this paper is concerned with only the real region of independent variable and the coefficient of the differential equation is supposed to be regular in the region considered, it is easy to see that the restrictions are not always necessary. Further for the purpose of clarifying the method, all the mathematical arguments on the asymptotic nature of the results are omitted and many of conditions to be satisfied are not expressed explicitly. But it would not injure the applicability of our method.

Our results can be summarized as follows. We consider a class of differential equations of the form

$$\frac{d^2y}{dx^2}-(\lambda+h^2f(x))y=0\ ,$$

where $f(x)$ is a regular function of x, h is a large parameter and λ is a constant small compared with h^2. Introducing a set of transformations of variables

$$\tau=\tau(t)=\int^x\sqrt{f(x)}\,dx\ ,\qquad y=\psi^{-1/4}y_1\ ,\qquad \psi=f/(d\tau/dt)^2\ ,$$

we have

$$\frac{d^2y_1}{dt^2}-\left(\frac{\lambda}{\psi}+h^2\left(\frac{d\tau}{dt}\right)^2+Q\right)y_1=0\ ,$$

where

$$Q=\psi^{-1/4}\frac{d^2\psi^{1/4}}{dt^2}=-\psi^{-3/4}\frac{d^2\psi^{-1/4}}{dx^2}\ .$$

By means of suitable choice of the functional form $\tau=\tau(t)$, we can obtain an approximate equation which gives the asymptotic solutions of the first equation. And the repeated use of similar transformations accompanied with suitable translation of independent variable (which we shall call the turning point correction) leads to the higher order approximations. To the equation once transformed, the method of formal series expansion is also applicable.

The examples of the transformations are given as follows.

i) *A simple turning point at* $x=0$:

$$\lambda=0\ ,\qquad f(x)=ax+bx^2+cx^3+\cdots\ .$$

$\tau(t)$ to be used is

$$\tau(t)=\frac{2}{3}t^{3/2}=\int_0^x\sqrt{f(x)}\,dx$$

and y_1 can be approximated by Airy functions.

ii) *A second order turning point at* $x=0$:

$$|\lambda|\ll h^2\ ,\qquad f(x)=ax^2+bx^3+cx^4+\cdots\ .$$

$\tau(t)$ to be used is

$$\tau(t)=t^2/4=\int_0^x \sqrt{f(x)}\,dx\,,$$

and y_1 can be approximated by Weber functions.

iii) *A pair of simple turning points at $x=\xi$ and $x=\eta$:*

$$\lambda=0\,,\qquad f(x)=(x-\xi)(x-\eta)g(x)\,,\qquad g(x)\neq 0$$

$\tau(t)$ to be used is

$$\tau(t)=\frac{2I}{\pi}\int_{-1}^t \sqrt{t^2-1}\,dt=\int_\xi^x \sqrt{f(x)}\,dx\,,$$

where

$$I=\int_\xi^\eta \sqrt{f(x)}\,dx\,,$$

and y_1 can be approximated by Weber functions. The famous formula for the eigenvalue problem with vanishing boundary conditions at infinity and the transparency of potential wall can be refined in this way.

iv) *Hill equations with simple turning points*:

$$\lambda=0\,,\qquad f(x+2\pi)=f(x)\,,$$
$$f(\xi+2n\pi)=f(\eta+2n\pi)=0\,,\qquad f'(\xi+2n\pi)\neq 0\,,\qquad f'(\eta+2n\pi)\neq 0\,,$$
$$-\pi<\xi<\eta<\pi\,,\qquad n=0,\ \pm 1,\ \pm 2,\ \cdots\,.$$

$\tau(t)$ to be used is

$$\tau(t)=I\int_\alpha^t \sqrt{\sin 2t-q}\,dt/K=\int_\xi^x \sqrt{f(x)}\,dx\,.$$

where

$$I=\int_\xi^\eta \sqrt{f(x)}\,dx\,,\qquad K=\int_\alpha^\beta \sqrt{\sin 2t-q}\,dt\,,$$

α and β are the zeros of $\sin 2t-q$ $(0<\alpha<\beta<\pi)$, and q as well as α and β should be determined by

$$\int_\beta^{\alpha+\pi} \sqrt{\sin 2t-q}\,dt/K=\int_b^{a+2\pi} \sqrt{f(x)}\,dx/I;$$

and y_1 can be approximated by Mathieu functions.

iv) *Hill equations witn second order turning points:*

$$|\lambda|\ll h^2\,,\qquad f(x+2\pi)=f(x)\,,\qquad f(x+2n\pi)=ax^2+bx^3+\cdots\qquad (a\neq 0)\,.$$

$\tau(t)$ to be used is

$$\tau(t)=I\sin^2\frac{t}{2}=\int_0^x \sqrt{f(x)}\,dx$$

where

$$I=\int_0^{2\pi} \sqrt{f(x)}\,dx$$

and y_1 can be approximated by Mathieu functions.

In all the above expressions the branches of multivalued functions should be taken in suitable manner.

Part I An Improvement of the WKB Method about Turning Points

§ 1. An Introductory Remark on the Modified WKB Transformations

Our problem is to investigate the method for obtaining the asymptotic solutions of a class of differential equations of the form

$$\frac{d^2y}{dx^2}-(\lambda+h^2f(x))y=0, \tag{1.1}$$

where λ is a constant of $O(h^k)$ $(k<2)$, $f(x)$ is a regular function of x and h is a large parameter.

As is well-known, in a region where the coefficient $\lambda+h^2f(x)$ does not vanish, the asymptotic solutions of (I.1) for $h\to\infty$ are given by means of the following procedure.

Let us introduce a set of transformations of variables

$$\tau=\int^x P(x)dx, \qquad y=P^{-1/2}y_1 \tag{1.2}$$

where

$$P=(f(x)+\lambda/h^2)^{1/2} \tag{1.3}$$

Then (1.1) transforms into

$$\frac{d^2y_1}{d\tau^2}-(h^2+Q(\tau))y_1=0, \tag{1.4}$$

where

$$Q(\tau)=P^{-1/2}\frac{d^2}{d\tau^2}P^{1/2}=-P^{-3/2}\frac{d^2}{dx^2}P^{-1/2}.$$

Therefore, neglecting $Q=O(1)$, we have the first approximate solutions

$$y_1\sim\exp(\pm h\tau),$$

hence

$$y\sim P^{-1/2}\exp(\pm h\tau). \tag{1.5}$$

Again introducing similar transformations for (1.4)

$$\tau_1=\int^\tau P_1 d\tau, \qquad y_1=P_1^{-1/2}y_2, \tag{1.6}$$

where

$$P_1=(1+Q/h^2)^{1/2}=1+O(h^{-2}),$$

we have

$$\frac{d^2y_2}{d\tau_1^2}-(h^2+Q_1(\tau_1))y_2=0. \tag{1.7}$$

where

$$Q_1=P_1^{-1/2}\frac{d^2}{d\tau_1^2}P_1^{1/2}=-P_1^{-3/2}\frac{d^2}{d\tau^2}P_1^{-1/2}=O(h^{-2}).$$

Thus we have the second approximate solutions

$$\left.\begin{aligned} y &\sim P^{-1/2}P_1^{-1/2}\exp\left(\pm h\int(1+Q/h^2)^{1/2}d\tau\right) \\ &\sim P^{-1/2}(1-Q/4h^2)\exp\left\{\pm\left(h\tau+\frac{1}{2h}\int Q d\tau\right)\right\}\cdot(1+O(h^{-3})) \end{aligned}\right\} \tag{1.8}$$

or making use of the expansion

$$P=(f(x)+\lambda/h^2)^{1/2}=\{f(x)\}^{1/2}+\lambda/2h^2\{f(x)\}^{1/2}+O(\lambda^2h^{-4}) ,$$

we have

$$y\sim f^{-1/4}(1-\lambda/4h^2f-Q'/4h^2)\exp\left\{\pm\left(h\tau'+\lambda\int f^{-1}d\tau'/2h+\int Q'd\tau'/2h\right)\right\} , \tag{1.9}$$

where

$$\tau'=\int f^{1/2}dx , \qquad Q'=f^{-1/4}\frac{d^2}{d\tau'^2}f^{1/4} .$$

In this way we can proceed to the approximate solutions of any order required by the repeated use of similar procedure, and clearly these solutions give the asymptotic forms of the exact solutions.

These procedures, however, are not applicable in the region containing turning points, namely the zeros of $P(x)$, which transform into the singular points of the transformed equation. (If $\lambda \ll h$, the zeros of $P(x)$ are close to those of $f(x)$. Therefore the zeros of $f(x)$ will be called the turning points, when the distinction is not so important, the order of the turning point being the order of the corresponding zero.)

To avoid this difficulty and to proceed to higher order approximations, several methods have been developed since Jeffreys, Wentzel, Kramers and Brillouin, especially in the case of isolated simple or second order turning point. Some authors have adopted the idea that the leading singular terms in the transformed equation shauld be taken into account. And other authors have employed the alternative forms of the transformed equation, which is equivalent to (1.4) and contains no singular points. The latter seems to have more possibility of extension.

Now let us remember that the singularity of the transformed equation has its origin in the singularity of the transformation of the independent variable (1.2). This fact suggests us a set of transformations of the form

$$\tau=\tau(t)=\int\sqrt{f(x)}\,dx , \qquad y=\{\psi(t)\}^{-1/4}y_1 \tag{1.10}$$

and the use of independent variable t instead of τ. In fact, putting

$$\psi(t)=f\Big/\left(\frac{d\tau}{dt}\right)^2 \tag{1.11}$$

and substituting (1.9) and (1.10) into (1.1), we have the transformed equation

$$\frac{d^2y_1}{dt^2}-\left(\frac{\lambda}{\psi}+h^2\left(\frac{d\tau}{dt}\right)^2+Q\right)y_1=0 , \tag{1.12}$$

where

$$Q=\psi^{-1/4}\frac{d^2\psi^{1/4}}{dt^2}=-\psi^{-3/4}\frac{d^2\psi^{1/4}}{dx^2} . \tag{1.13}$$

It is the main point of this paper to use (1.12) as the starting point. If $(d\tau/dt)^2$ and f have common zeros of the same order, then the transformed equation has no singularity there. Therefore in the region where $d\tau/dt \neq 0$, the transformed equation can be approximated by

$$\frac{d^2y_1}{dt^2} - h^2\left(\frac{d\tau}{dt}\right)^2 y_1 = 0 \tag{1.14}$$

and in the neighbourhood of a zero of $d\tau/dt$, say $t=\alpha$, we can replace λ/ψ and Q by their values at $t=\alpha$. Thus we have an approximate equation

$$\frac{d^2y_1}{dt^2} - \left(\frac{\lambda}{\psi(\alpha)} + Q(\alpha) + h^2\left(\frac{d\tau}{dt}\right)^2\right) y_1 = 0 \tag{1.15}$$

in the region containing $t=\alpha$ and no other zeros of $d\tau/dt$. Further when a suitable choice of the functional form $\tau=\tau(t)$ is done, the approximate equation reduces to a well investigated differential equation. Of course the addition of first few terms of Taylor expansion of λ/ψ and Q is desirable, it possible. In many examples such a choice is possible and the repeated use of the similar procedure leads to the higher order approximations.

The following three sections of this part will be devoted to rather simple examples, in which the character of our modification of the WKB transformations can be illustrated, and in Part II a class of Hill equations will be treated by means of our transformations.

Beyond the examples treated here, several cases, for example, a fixed singular point, a fixed singular point accompanied with a simple turning point etc. can be reduced to well-known differential equations. The latter leads to a refinement of the WKB phase shift formula[11]. Further if only the first approximations or formal series solutions are wanted, our transformations are applicable to many other equations.

In some cases it will be convenient to take $h^2f(x)$ in the place of $f(x)$ in (1.9).

§ 2. A Simple Turning Points and Imai's Formulas

The asymptotic solutions of a differential equation with a simple turning point have been investigated by many authors and it may be regarded as a classical example. (See, e.g. references 2, 12, 13, 14, 21.) We shall begin with this case.

Let us consider

$$\frac{d^2y}{dx^2} + h^2 f(x) y = 0\,, \tag{2.1}$$

where $f(x)$ is a regular function of x and has only one simple zero, say $x=0$, in the region considered and can be expanded as

$$f(x) = ax + bx^2 + cx^3 + \cdots\,. \qquad (a>0)\,. \tag{2.2}$$

In this case the regularity of the differential equation is conserved, if we adopt a set of transformations

$$\tau(t) = \frac{2}{3}t^{3/2} = \int_0^x \sqrt{f(x)}\,dx\,, \qquad y = \psi^{-1/4}y_1\,, \qquad \psi = f/t\,, \tag{2.3}$$

where the branches of $\sqrt{f}$ and $t^{3/2}$ should be taken so that the correspondence between x and t is one-to-one and the regions $x>0$ and $x<0$ transforms into $t>0$ and $t<0$ respectively. Then ψ is a nonvanishing positive function and (2.1) transforms into

$$\frac{d^2y_1}{dt^2} + (h^2t - Q(t))y_1 = 0\,, \tag{2.4}$$

where

$$Q = \psi^{-1/4}\frac{d^2\psi^{1/4}}{dt^2} = -\psi^{-3/4}\frac{d^2\psi^{-1/4}}{dx^2}\,, \tag{2.5}$$

$\psi^{1/4}$ being understood to designate the positive value.

In (2.4) only the first term of the coefficient is of $O(h^2)$, while in (2.1) all terms were of $O(h^2)$. Therefore we have an approximate equation

$$\frac{d^2y_1}{dt^2}+h^2ty_1=0\ ,$$

and its solutions are given by Airy functions:

$$y_1=t^{1/2}Z_{1/3}\left(\frac{2}{3}ht^{3/2}\right)$$

where $Z_{1/3}$ is the Bessel function of order one third. The asymptotic expansion for the large values of $ht^{3/2}$ give the usual WKB solution (1.4):

$$y_1\sim\text{const.}\ t^{-1/4}\exp\left(\pm i\frac{2}{3}ht^{3/2}\right)\cdot(1+O(h^{-1})) \tag{2.6}$$

$Q(t)$ in (2.4), however, contains the terms of constant and of first degree in t. For proceeding to higher order approximations it is convenient to rewrite (2.4) in the same form as the first equation (2.1). To do so, let us put

$$x_1=t-\delta \tag{2.7}$$

where δ is the zero of $h^2t-Q(t)$:

$$h^2\delta-Q(\delta)=0 \tag{2.8}$$

Then (2.4) can be written as

$$\frac{d^2y_1}{dx_1^2}+h^2(a_1x_1+R_1(x_1))y_1=0 \tag{2.9}$$

where a_1 is given by

$$h^2a_1=h^2-Q'(\delta) \tag{2.10}$$

and $R_1(x_1)$ is a function of x_1, which can be expanded as

$$R_1(x_1)=\frac{1}{h^2}(b_1x_1^2+c_1x_1^3+\cdots) \tag{2.11}$$

where

$$b_1=-\frac{1}{2}Q''(\delta)\ ,\qquad c_1=-\frac{1}{3!}Q'''(\delta)\ ,\ \cdots \tag{2.12}$$

(2.9) is of exactly the same form as (2.1), and by means of the transformations similar to (2.3) we can proceed to the second approximations. The rewriting of independent variable (or the translation of lower limit of integration in the transformation of variable) is simple but it is an important procedure, which we shall call the turning point correction. The choice of the coefficient a_1 instead of 1 is not so essential, but it gives some convenience.

The second transformations are given as

$$\tau_1(t_1)=\frac{2}{3}t_1^{3/2}=\int^{x_1}\sqrt{f_1(x_1)}dx_1\ ,\qquad y_1=\psi_1^{-1/4}y_2\ ,\qquad \psi_1=f_1/t_1 \tag{2.13}$$

where

$$f_1(x_1)=a_1x_1+R_1(x_1)$$

And the transformed equation is

$$\frac{d^2y_2}{dt_1^2}+(h^2t_1-Q_1(t_1))y_2=0\ , \tag{2.14}$$

where

$$Q_1(t_1)=\psi_1^{-1/4}\frac{d^2\psi_1^{1/4}}{dt^2}=-\psi_1^{-3/4}\ \frac{d^2\psi^{-1/4}}{dx_1^2}\ .$$

It should be noted that $R_1(x_1)/x_1$ is bounded even at $x_1=0$, and we have

$$\left.\begin{aligned}&\tau_1=\int_0^{x_1}(a_1x_1)^{1/2}\left(1+\frac{R_1(x_1)}{a_1x_1}\right)^{1/2}dx_1=\frac{2}{3}a_1^{1/2}x_1^{1/2}+\int_0^{x_1}\frac{R_1(x_1)}{(a_1x_1)^{1/2}}dx_1+O(h^{-4})\ ,\\&t_1=a_1^{1/3}x_1+O(h^{-2})\ ,\qquad f_1=a_1^{2/3}t_1+O(h^{-2})\ ,\end{aligned}\right\} \tag{2.15}$$

hence

$$\psi_1=a_1^{2/3}+O(h^{-2})\ .$$

Therefore Q_1 is $O(h^{-2})$, and a small quantity of higher order than Q in (2.4). In this way we can proceed to the approximations of any order by means of the repeated use of the turning point correction and the modified WKB transformations. It is to be noted that the turning point correction permits the expansions of the type of (2.15) in the higher order approximations. The approximate solution of each order is expressed in the form of (2.6) (with different argument). The asymptotic nature of the solution given in this way is easily varified. Further, according to Lagrange's theorem (Appendix II) δ defined by (2.8) can be expanded as

$$\delta=\frac{1}{h^2}Q(0)+\frac{1}{h^4}Q(0)Q'(0)+\cdots\ ,$$

and for a_1 we have

$$a_1=1-\frac{1}{h^2}Q'(0)-\frac{1}{h^4}Q''(0)Q(0)-\cdots\ .$$

For small values of t or x, we have, from (2.3) and (2.2),

$$\begin{aligned}\frac{2}{3}t^{3/2}=\frac{2}{3}a^{1/2}x^{3/2}+\frac{1}{5}a^{-1/2}bx^{5/2}+\frac{1}{7}\left(a^{-1/2}c-\frac{1}{4}a^{-3/2}b^2\right)x^{7/2}\\+\frac{1}{9}\left(da^{-1/2}-\frac{1}{2}a^{-3/2}bc+\frac{1}{8}a^{-5/2}b^3\right)x^{9/2}+\cdots\ ,\end{aligned}$$

which gives

$$Q(t)=\lambda'+a't+b't^2+c't^3+\cdots\ ,$$

where

$$\lambda'=-\frac{3}{7}\left(\frac{3}{5}\ \frac{b^2}{a^2}-\frac{c}{a}\right)a^{-1/3}\ ,\qquad a'=\left(\frac{4}{3}\ \frac{d}{a^2}-\frac{28}{15}\ \frac{bc}{a^3}+\frac{56}{75}\ \frac{b^3}{a^4}\right)\ ,\ \cdots$$

Therefore

$$\delta=\frac{\lambda'}{h^2}+O(h^{-4})\ ,\quad a_1=1-\frac{a'}{h^2}-O(h^{-4})\ .$$

In a similar way we have

$$b_1 = -b' - O(h^{-2})$$

and

$$\frac{2}{3} t_1{}^{3/2} = \frac{2}{3} a_1{}^{1/2} x_1{}^{3/2} + \frac{1}{5} \frac{b_1}{a_1{}^{1/2}} \frac{x_1{}^{5/2}}{h^2} + O(h^{-4})$$

Substituting these expressions into the approximate solution of (2.9)

$$y_1 = x_1{}^{1/2} Z_{1/3}\left(\frac{2}{3} a_1{}^{1/2} x_1{}^{3/2}\right),$$

we have

$$y \sim f^{-1/4} \tau^{1/6} \xi^{1/2} Z_{1/3}\left(\frac{2}{3} \kappa^{1/2} \xi^{3/2}\right),$$

where

$$\kappa = 1 - \frac{a'}{h^2}, \qquad \xi = \left(\frac{3}{2}\tau\right)^{2/3} - \frac{\lambda'}{h^2}.$$

This is the first step of the refined WKB solutions due to Imai[5)] and has been applied to the electronic theory of metals by Kuhn[11)]. From the approximate solution of (2.14)

$$y_2 = t_1{}^{1/2} Z_{1/3}\left(\frac{2}{3} h t_1{}^{3/2}\right),$$

we have

$$y \sim f^{-1/4} \tau^{1/6} f_1{}^{-1/4} t_1{}^{3/4} Z_{1/3}\left(\frac{2}{3} h t_1{}^{3/2}\right).$$

This formula corresponds to the second step of Imai's solution[6)], which has been applied to several problems in mathematical physics by himself[7),8)].

§ 3. A Turning Point of Second Order

In this section we shall consider a differential equation

$$\frac{d^2y}{dx^2} - (\lambda + h^2 f(x)) y = 0, \tag{3.1}$$

where λ is a constant of $O(h^k)$ $(k<2)$ and $f(x)$ is a regular function of x that has a zero of second order at $x=0$ and hence can be expanded as

$$f(x) = ax^2 + bx^3 + cx^4 + \cdots \qquad (a \neq 0). \tag{3.2}$$

This case has been treated, for example, by McKelvey[16)] in somewhat different manner. Our procedure leads to the essentially same results as his except that he has used the representations in terms of Whittaker's function.

Let us introduce a set of transformations

$$\tau(t) = \frac{t^2}{4} = \int_0^x \sqrt{f(x)}\, dx, \qquad y = \phi^{-1/4} y_1, \qquad \phi = \frac{4f}{t^2}, \tag{3.3}$$

where the suitable choice of the branches should be done for the one-to-one correspondence between x and t as in the preceding section. Then we have the transformed equation

$$\frac{d^2 y_1}{dt^2} - \left(\frac{\lambda}{\phi(t)} + \frac{h^2}{4} t^2 + Q(t)\right) y_1 = 0, \tag{3.4}$$

where

$$Q=\psi^{-1/4}\frac{d^2\psi^{1/4}}{dt^2}=-\psi^{-3/4}\frac{d^2\psi^{-1/4}}{dx^2}\ .$$

Here ψ is a nonvanishing positive function and of $O(1)$. Therefore we have the first approximate equation

$$\frac{d^2y_1}{dt^2}-\left(\frac{\lambda}{\psi(0)}+Q(0)+\frac{h^2}{4}t^2\right)y_1=0\ , \tag{3.5}$$

the solutions of which are given by the Weber functions, namely

$$y_1=W_\nu(h^{1/2}t)\ , \tag{3.6}$$

where W_ν is the Weber function of order ν:

$$W_\nu(z)=cD_\nu(z)+dD_\nu(-z)$$

or

$$W_\nu(z)=cD_\nu(z)+d\mathscr{D}_\nu(z)\ ,$$

c and d being arbitrary constants and

$$\nu+\frac{1}{2}=\left(-\frac{\lambda}{h\psi(0)}-\frac{1}{h}Q(0)\right).$$

(See Appendix I)
The asymptotic form of $W_\nu(h^{1/2}t)$ is expressed as

$$W_\nu\sim\text{const.}\ e^{\pm\frac{h}{4}t^2}\,t^{\mp\left(\nu+\frac{1}{2}\right)-\frac{1}{2}}\ ,$$

and we have

$$y\sim\text{const.}\ f^{-1/4}e^{\pm\frac{h}{4}t^2}\,t^{\mp\frac{1}{h}\left(\frac{\lambda}{\psi(0)}+Q(0)\right)}\ . \tag{3.7}$$

On the other hand the usual WKB method gives

$$\begin{aligned} y&\sim\text{const.}\ f^{-1/4}\exp\left(\pm\int\sqrt{h^2f(x)+\lambda}\,dx\right)\\ &\sim\text{const.}\ f^{-1/4}\exp\left(\pm h\int\sqrt{f}\,dx\pm\frac{\lambda}{2h}\int\frac{1}{\sqrt{f}}dx\right). \end{aligned} \tag{3.8}$$

The leading terms of (3.7) and (3.8) are in accord with each other.

For obtaining more refined solutions, we should use the turning point corrections in the first place, as in the case of a simple turning point. The lack of the procedure corresponding to this turning point correction is the reason why the earlier methods due to Goldstein[4], Langer[12] etc. could not give the solutions suitable for practical applications except in the case in which λ is extremely small. Introducing a new variable x_1 given by

$$x_1=t-\delta\ , \tag{3.9}$$

where δ is the value of t for which the coefficient of y_1 in (3.5) takes the extremum value, we can rewrite (3.6) as

$$\frac{d^2y_1}{dx_1{}^2}-(\lambda_1+h^2f_1(x_1))y_1=0\ , \tag{3.10}$$

where

$$f_1(x_1)=a_1x_1^2+R_1(x_1)\ ,$$
$$R_1(x_1)=b_1x_1^3+c_1x_1^4+\cdots\ ,$$
$$\lambda_1=\frac{\lambda}{\psi(\delta)}+Q(\delta)+\frac{h^2}{4}\delta^2\ ,$$
$$a_1=\frac{1}{4}+\frac{\lambda}{2h^2}\left(\frac{d^2}{dt^2}\frac{1}{\psi(t)}\right)_{t=\delta}+\frac{1}{2h^2}Q''(\delta)\ ,$$
$$b_1=\frac{\lambda}{6h^2}\left(\frac{d^3}{dt^3}\frac{1}{\psi(t)}\right)_{t=\delta}+\frac{1}{6h^2}Q'''(\delta)\ ,$$
$$\cdots\cdots\cdots$$

and δ is given by

$$-\lambda\frac{\psi'(\delta)}{\psi^2(\delta)}+Q'(\delta)+\frac{h^2}{2}\delta=0\ .$$

or by means of Lagrange's theorem (see Appendix II)

$$\delta=\frac{2\lambda}{h^2}\frac{\psi'(0)}{\psi(0)}-\frac{2}{h^2}Q'(0)-\cdots\ .$$

(3.10) is of the same form as (3.1), but $R_1(x_1)$ is a quantity of $O(\lambda)$ or $O(1)$. (In what follows, we shall use the notation $O(\lambda)$ in the meaning of $O(1)$, if $\lambda=O(h^k)$ $(k<0)$). As well as in the preceding case, the rewriting of a_1 is not essential, but it gives a comparatively accurate solutions near the turning point.

Repeating the transformations similar to (3.3) after the turning point correction, we can obtain the higher approximations. In fact, putting

$$\tau_1(t_1)=\frac{t_1^2}{4}=\int_0^{x_1}\sqrt{f_1(x_1)}\,dx_1\ ,\qquad y_1=\psi_1^{-1/4}y_2\ ,\qquad \psi_1=4f_1/t_1^2 \tag{3.11}$$

in (3.10), we have

$$\frac{d^2y_2}{dt_1^2}-\left(\frac{\lambda_1}{\psi_1(t_1)}+\frac{h^2}{4}t_1^2+Q_1(t_1)\right)y_1=0\ , \tag{3.12}$$

where

$$Q_1(t_1)=\psi_1^{-1/4}\frac{d^2\psi_1^{1/4}}{dt_1^2}\ .$$

Here we should remember the fact that $R_1(x_1)/x_1^2$ is bounded everywhere and τ_1 can be expanded as

$$\tau_1(t_1)=\int_0^{x_1}\sqrt{a_1x_1^2}\,dx_1+\frac{1}{2}\int_0^{x_1}\frac{R_1(x_1)}{\sqrt{a_1x_1^2}}dx_1+\cdots\ .$$

Therefore

$$\psi_1=2a_1^{1/2}+O(\lambda/h^2)\ ,\qquad Q_1=O(\lambda/h^2)$$

and

$$\lambda_1/\psi_1=\lambda_1/2a_1^{1/2}+O(\lambda^2/h^2)\ .$$

Introducing x_2 given by

$$x_2=t_1-\delta_1\ ,$$

we have

$$\frac{d^2y_2}{dx_2^2}-(\lambda_2+h^2 f_2(x_2))y_2=0\ , \tag{3.13}$$

where

$$f_2(x_2)=a_2x_2^2+R_2(x_2)\ ,$$

and

$$R_2(x_2)/x_2^2=O(\lambda^2/h^4)\ .$$

is a quantity smaller than R_1. In this way we can proceed to the higher approximations of any order.

§ 4. A Pair of Simple Turning Points

When λ in the equation (3.1) becomes large and the zeros of $\lambda+h^2f(x)$ are not so close to those of $f(x)$, the method in the preceding section is not suitable. The existing method in such cases is to treat the turning points separately and then to match the two solutions with each other in the region between the turning points. However there exists a set of transformations which leads to a uniformly valid approximations in the whole region. It should be mentioned that Miller and Good[8] and Langer[15] have published these transformations previously, although they have not shown the possibility of higher approximations.

Now let us consider a differential equation

$$\frac{d^2y}{dx^2}-h^2f(x)y=0\ , \tag{4.1}$$

where $f(x)$ has two simple zeros at $x=\xi$ and $x=\eta$ $(\xi<\eta)$, and λ should be interpreted to be included in $f(x)$. Further we suppose, for simplicity, that

$$f(x)>0 \quad \text{for} \quad x<\xi \text{ and } x>\eta\ , \qquad f(x)<0 \quad \text{for} \quad \xi<x<\eta\ . \tag{4.2}$$

The case in which the sign of $f(x)$ is inverted can be treated in a similar manner.

The transformations available for this equation are

$$\tau(t)=\frac{2Ii}{\pi}\int_{-1}^{t}\sqrt{1-t^2}\,dt=\int_{\xi}^{x}\sqrt{f(x)}\,dx\ , \qquad y=\psi^{-1/4}y_1\ , \qquad \psi=-f/(1-t^2)\ , \tag{4.3}$$

where

$$I=\int_{\xi}^{\eta}\sqrt{|f(x)|}\,dx\ , \tag{4.4}$$

and the branches of the square roots should be chosen so that t is a regular function of x and the regions where $f(x)>0$ and $f(x)<0$ transform into $t^2>1$ and $t^2<1$ respectively. Then the transformed equation is

$$\frac{d^2y_1}{dt^2}+\left\{\frac{4h^2I^2}{\pi^2}(1-t^2)-Q(t)\right\}y_1=0\ , \tag{4.5}$$

where

$$Q(t)=\psi^{-1/4}\frac{d^2\psi^{1/4}}{dt^2}=O(1)\ . \tag{4.6}$$

Therefore the first approximate solutions are given by

$$y_1=W_\nu\left(2\sqrt{\frac{hI}{\pi}}\,t\right), \tag{4.7}$$

where W_ν is the Weber function of order ν and

$$\nu+\frac{1}{2}=\frac{Ih}{\pi}\,. \tag{4.8}$$

The asymptotic expressions of (4.7) for $\sqrt{h}\,t\to\infty$ and $\nu\to\infty$ give the same leading terms as the usual WKB solutions. In Langer's paper[15] more detailed discussions are presented on the relations between the solution of the present form and of the usual WKB form in the separated regions, each of which contains one turning point respectively.

Further the eigenvalues for the vanishing boundary conditions at infinity are given by those of (4.7):

$$\nu=\frac{Ih}{\pi}-\frac{1}{2}=n=0,\ 1,\ 2,\ \cdots\,,$$

that is

$$h\int_\xi^\eta\sqrt{|f(x)|}\,dx=\left(n+\frac{1}{2}\right)\pi\,, \tag{4.9}$$

which is the well-known formula in the usual WKB method. Thus we have the approximate eigenvalues as well as the uniformly approximate eigenfunctions, in contrast to the usual WKB method. The normalization constant is given by

$$\int_{-\infty}^{\infty}|y|^2dx=\frac{2I}{\pi}\int_{-\infty}^{\infty}\frac{t^2-1}{f}y_1^2dt\,. \tag{4.10}$$

The second and higher approximations can also be obtained by the turning point correction and the transformations similar to (4.3). Let us introduce t_1 and y_2 by the transformations

$$\frac{2}{\pi}\int_{-1}^{t_1}\sqrt{1-t_1^2}\,dt_1=\frac{1}{Ii}\int_{\xi_1}^{t}\sqrt{f_1(t)}\,dt\,,\qquad y_1=\phi_1^{-1/4}y_2\,,\qquad \phi_1=-f/(1-t_1^2) \tag{4.11}$$

where

$$-f_1(t)=\frac{4I^2}{\pi^2}(1-t^2)-\frac{1}{h^2}Q(t)\,, \tag{4.12}$$

$$I_1=\int_{\xi_1}^{\eta_1}\sqrt{|f_1(t)|}\,dt\,, \tag{4.13}$$

and ξ_1 and η_1 are the zeros of $f_1(t)$ which tend to -1 and 1 respectively for $h\to\infty$. If we rewrite (4.12) as

$$f_1(t)=\frac{4I^2}{\pi^2}(t-\xi_1)(t-\eta_1)+R_1(t)\,, \tag{4.14}$$

where $R_1(t)$ is a regular function of $O(h^{-2})$ and

$$R_1(\eta_1)=R_1(\xi_1)=0\,,$$

then we have

$$i\int_{\xi_1}^{t}\sqrt{f_1(t)}\,dt=\frac{2I}{\pi}\int_{\xi_1}^{t}\sqrt{(t-\xi_1)(\eta_1-t)}\,dt+O(h^{-2})\,. \tag{4.15}$$

Therefore the second transformed equation can be approximated by Weber's equation more precisely than the first. If we choose a suitable coefficient of $(t-\eta_1)(t-\xi_1)$ in $f_1(t)$, then the first approximate solutions could be refined in the neighbourhood of, at least, one of the turning points as in § 2, although we cannot say it is a very important procedure.

The corrected turning points ξ_1 and η_1 are given as

$$\xi_1=-1+\frac{\pi^2}{8I^2h^2}Q(-1)+\cdots, \quad \eta_1=1-\frac{\pi^2}{8I^2h^2}Q(1)+\cdots, \tag{4.16}$$

by means of Lagrange's theorem (Appendix II).

It will be easily seen that these procedures lead to a refinement of the formula (4.9). This is an alternative approach to the refinement of the WKB quantum condition and the results are essentially equivalent to Dunham's formula[3]. For example, the second approximation is given by

$$\frac{2Ih}{\pi}\int_{\xi_1}^{\eta_1}\left(1-t^2-\frac{\pi^2}{4I^2h^2}Q(t)\right)^{1/2}dt=\left(n+\frac{1}{2}\right)\pi, \tag{4.17}$$

or

$$Ih-\frac{\pi^2}{4Ih}\{Q(1)+Q(-1)\}-\frac{\pi}{4Ih}\int_{-1}^{1}\frac{h^2R_1(t)}{\sqrt{1-t^2}}dt+O(h^{-3})=\left(n+\frac{1}{2}\right)\pi. \tag{4.18}$$

If the sign of $f(x)$ is inverted, a similar procedure leads to a refinement of the penetration probability in tunnel effect[9] as well as the method in § 3.

§ 5. A Conventional Method for Derivation of Connection Formulas

The method of uniform approximation developed in the preceding sections can be applied to any order required, but in practical problems we need to calculate some complicated integrals in the higher order approximations. Therefore it is desirable to find connection formulas for the usual WKB solutions valid in the region without turning points and the approximate solutions valid in the neighbourhood of the turning points. In fact, especially for the problems in an infinite region the utility of the connection formulas or similar procedures have been proved in many examples. One of the results of this kind is the famous quantum condition for an oscillator, and it can be derived without any knowledge of the explicit forms of the solutions in the neighbourhood of the turning points.

In this section we shall add a crude sketch of such a conventional method to deduce the connection formulas. The fundamental line of thought is not new and it was adopted by early authors who have contributed to the WKB method.

Let us consider a differential equation

$$\frac{d^2y}{dx^2}-h^2f(x)y=0, \tag{5.1}$$

where we suppose, for simplicity, that $f(x)$ has at most two zeros in the region considered and can be expanded as

$$f(x)=a_0+a_2x^2+a_3x^3+\cdots \tag{5.2}$$

If we start from the equation once transformed by the modified WKB transformations, we could obtain more accurate results. And this is also a reason why we take up the rather classical idea after the explanation of the possibility of uniform approximations. But here we suppose that $a_2, a_3, \cdots$ are the quantities of $O(1)$, since the *method* may not be altered by the order of magnitude of the coefficient.

Putting

$$x^2=\tau^2/2ha_2^{1/2} \tag{5.3}$$

in (5.1), we have

$$\frac{d^2y}{d\tau^2}+f_1(\tau)y=0, \tag{5.4}$$

where

$$f_1(\tau)=\nu+\frac{1}{2}-\frac{\tau^2}{4}-\frac{b_3}{h^{1/2}}\tau^3-\frac{b_3}{h}\tau^4-\cdots, \qquad b_n=(2a_2^{1/2})^{-n/2-1}a_n, \qquad \nu+\frac{1}{2}=-(2a_2^{1/2})^{-1}a_0. \tag{5.5}$$

If $\tau^2 \ll h$, we can treat the terms of the third and higher degrees of τ as the perturbation for the Weber equation

$$\frac{d^2Y_0}{d\tau^2}+\left(\nu+\frac{1}{2}-\frac{\tau^2}{4}\right)Y_0=0. \tag{5.6}$$

and the approximate solutions of (5.4) is given by the formal series expansion as

$$y=Y=Y_0+h^{-1/2}Y_1+hY_2+\cdots. \tag{5.7}$$

On the other hand if $\tau^2 \gg \tau_n^2$, where τ_n $(n=1, 2)$ are the zeros of $f_1(\tau)$, the usual WKB approximations are valid and the solution can be written as

$$y \sim f_1^{-1/4}\exp\left[\pm\left\{t+\frac{1}{2}\int Q\,dt\right\}-\frac{Q}{4}\right], \tag{5.8}$$

where

$$t=\int^{\tau}\sqrt{f_1(\tau)}\,d\tau=h\int^{x}\sqrt{f(x)}\,dx, \tag{5.9}$$

$$Q=f_1^{-1/4}\frac{d^2f_1^{1/4}}{dt^2}=-f_1^{-3/4}\frac{d^2f_1^{-1/4}}{d\tau^2}=-\frac{1}{h}f^{-3/4}\frac{d^2f^{-1/4}}{dx^2}. \tag{5.10}$$

Now, in the region where the both conditions $\tau^2 \ll h$ and $\tau^2 \gg \tau_n^2$ hold, (5.6) and (5.7) must be compatible, and we can substitute (5.2) into (5.8) and (5.9). Therefore comparing them with each other we can find the connection formulas. For representing the WKB solution in the form of the inverse power series of $h^{1/2}$ we may use the expansion

$$\left.\begin{aligned}&\sqrt{|f_1(\tau)|}=\left(\frac{\tau^2}{4}-\frac{\tau_n^2}{4}\right)^{1/2}\left\{1+\frac{4}{h^{1/2}}\frac{g_1(\tau)-g_1(\tau_n)}{\tau^2-\tau_n^2}\right\}^{1/2}=\left(\frac{\tau^2}{4}-\frac{\tau_n^2}{4}\right)^{1/2}\left\{1+\frac{2}{h^{1/2}}\frac{g_1(\tau)-g_1(\tau_n)}{\tau^2-\tau_n^2}+\cdots\right\}\\&h^{-1/2}g_1(\tau)=-f_1(\tau)-\frac{\tau^2}{4}+\nu+\frac{1}{2},\end{aligned}\right\}, \tag{5.11}$$

where τ_n is a zero of $f_1(\tau)$, and expressed as

$$\tau_{\substack{1\\2}}=\pm\left[(4\nu+2)^{1/2}-\frac{2}{h^{1/2}}(4\nu+2)^{-1/2}g_1(\pm(4\nu+2)^{1/2})+\cdots\right] \tag{5.12}$$

by means of Lagrange's theorem (Appendix II). Other formulas necessary to treat the Weber functions are enumerated in Appendix I.

Similar procedure can be applied to the equations of other forms, if the first approximate solutions have been known.

Clearly when the higher order approximations by the method in §3 or §4 are already known, the perturbation procedure is unnecessary and, even if the connection formulas are wanted, the simple procedure adopted, for example, by Kramers and Ittman[10] or present author[19] will be sufficient.

Part II The Asymptotic Solutions of a Class of Hill Equations

§6. The Uniform Asymptotic Representation in Terms of Mathieu Functions I

The second part of this paper is concerned with the uniform and local asymptotic representations for the solutions of a class of Hill equations. The study of Hill equations has been one of the subjects of the WKB method since the early stage of this method, but their uniformly valid asymptotic representations have not yet been given in any closed form.

In this and in the next section we shall show that the asymptotic solutions of a class o Hill equations can be represented uniformly in terms of Mathieu functions, when the equations possess only one simple turning point of second order or only one pair of simple turning points in each period of the coefficient.

The fundamental line of thought is the same as in § 3 and § 4. In the first place let us consider a Hill equation with second order turning points

$$\frac{d^2y}{dx^2}-(\lambda\pm h^2 f(x))y=0\,,\qquad \lambda=O(h^k)\quad (k<2)\,, \tag{6.1}$$

where, we suppose, $f(x)$ is a regular periodic function of x with period 2π and it is positive except for the zeros of second order at $x=2n\pi$ $(n=0,\pm1,\pm2,\cdots)$. Now let us introduce a set of transformations

$$\sin^2\frac{t}{2}=\frac{1}{I}\int_0^x\sqrt{f(x)}\,dx\,,\qquad y=\psi^{-1/4}y_1\,,\qquad \psi=f/\sin^2 t\,, \tag{6.2}$$

where

$$I=\int_0^{2\pi}\sqrt{f(x)}\,dx\,. \tag{6.3}$$

If we take the branch of $\sqrt{f(x)}$ as

$$\left.\begin{array}{lll}\sqrt{f(x)}>0 & \text{for} & 4n\pi<x<(4n+2)\pi\,,\\ \sqrt{f(x)}<0 & \text{for} & (4n-2)\pi<x<4n\pi\,,\\ & n=(0,\pm1,\pm2,\cdots)\,, & \end{array}\right\} \tag{6.4}$$

then the correspondence between x and t is one-to-one for all values of x, and ψ is a non-vanishing regular periodic function of t with period π. By means of (6.2), (6.1) transforms into

$$\frac{d^2y_1}{dt^2}-\left(\frac{\lambda I^2}{\psi}\pm I^2h^2\sin^2 t+Q\right)y_1=0\,, \tag{6.5}$$

where

$$Q=\psi^{-1/4}\frac{d^2\psi^{1/4}}{dt^2}\,.$$

(6.5) is again a Hill equation with regular coefficients and the leading terms are in accord with Mathieu equation. For large values of h, only the term $I^2h^2\sin^2 t$ is dominant except in the neighbourhood of $t=n\pi$, where the other terms can be replaced by the values at $t=n\pi$.

For obtaining more refined solutions we should introduce the turning point correction. Let us put

$$x_1=t-\delta\,. \tag{6.6}$$

Here δ is the value of t, for which the bracketed coefficient of y_1 in (6.5) takes the extremum value. Then we can rewrite the coefficient of (6.5) as

$$\lambda'\pm a_1^2\sin^2 x_1+R_1(x_1)=\lambda'\pm h^2 f_1(x_1)\,, \tag{6.7}$$

where

$$\lambda'=\frac{\lambda I^2}{\psi^2(\delta)}\pm I^2h^2\sin^2\delta+Q(\delta)\,, \tag{6.8}$$

$$a_1^2=I^2h^2\cos 2\delta\pm\frac{1}{2}\lambda I^2\left(\frac{d^2}{dt^2}\frac{1}{\psi(t)}\right)_{t=\delta}\pm\frac{1}{2}Q''(\delta)\,, \tag{6.9}$$

and δ is given by

$$\pm I^2h^2 \sin 2\delta - \lambda I^2 \frac{\psi'(\delta)}{\psi^2(\delta)} + Q'(\delta) = 0 \qquad \text{or} \qquad \delta = \pm \frac{\lambda}{2h^2} \frac{\psi'(0)}{\psi^2(0)} + \cdots . \tag{6.10}$$

As is easily seen, $R_1(x_1)$ is a regular periodic function with the zeros of third order at $x_1 = n\pi$ ($n = 0, \pm 1, \pm 2, \cdots$). As well as in § 3, the rewriting of the coefficient of $\sin^2 x_1$ is not always necessary for proceeding to the higher order approximations, but it gives more accurate solutions in the neighbourhood of the turning points. Now neglecting $R_1(x_1)$ which is small everywhere, we have approximate solutions of (6.5) in terms of Mathieu functions

$$y_1 \sim M(\lambda', \pm a_1^2; x_1) , \tag{6.11}$$

where $M(b, q; x)$ is the general solution of

$$\frac{d^2M}{dx^2} - (b + q \sin^2 x)M = 0 . \tag{6.12}$$

Introducing the transformations similar to (6.2) again, we can proceed to the second approximations. In fact, putting

$$\sin^2 \frac{t_1}{2} = \frac{1}{I_1} \int_0^{x_1} \sqrt{f_1(x_1)}\, dx_1 , \qquad y_1 = \psi_1^{-1/4} y_2 , \qquad \psi_1 = f_1/\sin^2 t_1 , \tag{6.13}$$

where

$$I_1 = \int_0^{\pi} \sqrt{f_1(x_1)}\, dx_1 ,$$

we have

$$\frac{d^2y_2}{dt_1^2} - \left\{ \frac{\lambda' I_1^2}{\psi_1} \pm I^2h^2 \sin^2 t_1 + Q_1(t_1) \right\} y_2 = 0 , \tag{6.14}$$

where

$$Q_1 = \psi_1^{-1/4} \frac{d^2 \psi_1^{1/4}}{dt^2} .$$

(6.14) is again of the same form a (6.5), but Q_1 and $1/\psi_1(t_1) - 1/\psi_1(0)$ are of smaller order than the corresponding terms in (6.5), as may be varified by the consideration similar to that in § 3.

In this way we can proceed to higher order approximations by means of the repetition of similar transformations. The eigenvalues for the periodic boundary conditions are also found from the corresponding eigenvalues of Mathieu equations. Lagrange's theorem is useful also for this purpose.

§ 7. The Uniform Asymptotic Representation in Terms of Mathieu Functions II

In this section we consider a Hill equation with two simple turning points in each period of the coefficient.

When λ in (6.1) is large, it is convenient to employ the method corresponding to that in § 4. Let us write the equation to be considered as

$$\frac{d^2y}{dx^2} - h^2 f(x) y = 0 , \tag{7.1}$$

where $f(x)$ is a regular periodic function with period 2π and has two simple zero in each period:

$$\left.\begin{array}{ll} f(x+2\pi)=f(x)\,, & f(\xi+2n\pi)=f(\eta+2n\pi)=0\,, \\ f'(\xi+2n\pi)\neq 0\,, & f'(\eta+2n\pi)\neq 0\,, \\ 0<\xi<\eta<2\pi\,. & (n=0,\ >1,\ >2,\ \cdots) \end{array}\right\} \quad (7.2)$$

Further we suppose that

$$f(x)>0 \quad \text{ror} \quad \xi<x<\eta\,, \quad \text{and} \quad f(x)<0 \quad \text{for } \eta<x<\xi+2\pi\,. \quad (7.3)$$

Now let us introduce a set of transformations of variables

$$\frac{1}{K}\int_{\alpha}^{t}\sqrt{\sin 2t-q}\,dt=\frac{1}{I}\int_{\xi}^{x}\sqrt{f(x)}\,dx\,, \qquad y=\psi^{-1/4}y_1\,, \qquad \psi=f/(\sin 2t-q)\,, \quad (7.4)$$

where

$$I=\int_{\xi}^{\eta}\sqrt{f(x)}\,dx\,, \qquad K=\int_{\alpha}^{\beta}\sqrt{\sin 2t-q}\,dt\,, \quad (7.5)$$

α, β and q should be determined by the following relations

$$\left.\begin{array}{l} \sin 2\alpha-q=0\,, \qquad \sin 2\beta-q=0\,, \qquad 0<\alpha<\beta<\alpha\,, \\ \dfrac{\int_{\beta}^{\alpha+\pi}\sqrt{q-\sin 2t}\,dt}{\int_{\alpha}^{\beta}\sqrt{q-\sin 2t}\,dt}=\dfrac{\int_{\eta}^{\xi+2\pi}\sqrt{f(x)}\,dx}{\int_{\xi}^{\eta}\sqrt{f(x)}\,dx\,,} \end{array}\right\} \quad (7.6)$$

and the branches of the square roots should be taken in such a way that the correspondence between x and t is regular and one-to-one.

Then we have the transformed equation

$$\frac{d^2y_1}{dt^2}-\left\{\frac{h^2I^2}{K^2}(\sin 2t-q)+Q(t)\right\}y_1=0\,, \quad (7.7)$$

where

$$Q(t)=\psi^{-1/4}\frac{d^2\psi^{1/4}}{dt^2}\,. \quad (7.8)$$

(7.7) is again a Hill equation and can be approximated by Mathieu equation, since ψ is a nonvanishing periodic function.

We can derive more refined solutions, if we rewrite (7.7) as

$$\frac{d^2y_1}{dt^2}-h^2(\lambda+a\sin 2t+R(t))y_1=0\,. \quad (7.9)$$

Here λ and a are given by

$$\lambda+a\sin 2\alpha_1=R(\alpha_1)=0\,, \qquad \lambda+a\sin 2\beta_1=R(\beta_1)=0\,, \quad (7.10)$$

where α_1 and β_1 are the zeros of

$$f_1(t)=\frac{I^2}{K^2}(\sin 2t-q)+\frac{1}{h^2}Q(t)\,, \quad (7.11)$$

which tend to α and β respectively for $h\to\infty$. Further if we adopt a suitable coefficient a which makes $R'(\alpha_1)$ or $R'(\beta_1)$ be zero, the approximation could be more accurate near $t=\alpha_1$ or β_1. But we cannot say it is a very important procedure.

The higher approximations can be given by means of the iteration of similar procedures, making use of $f_1(t)$ in (7.7) instead of $f(x)$ in (7.1). The increasing of the accuracy of approximation can be verified by a consideration similar to those in the previous examples.

Thus it has been shown that a class of Hill equations can be solved asymptotically by means of Mathieu functions to any order wanted.

In conclusion it will be interesting to remember that Kramers and Ittmann[10] have employed Mehler's approximation formulas

$$\frac{1}{\pi}\int_{-1}^{1}\frac{f(x)}{\sqrt{1-x^2}}dx\sim\frac{1}{3}\left\{f(0)+f\left(\frac{\sqrt{3}}{2}\right)+f\left(-\frac{\sqrt{3}}{2}\right)\right\},$$

$$\frac{1}{\pi}\int_{0}^{1}f(x)\sqrt{\frac{1-x}{x}}dx\sim 0.262f(0.0495)+0.192f(0.389)+0.046f(0.812),$$

for evaluation of elliptic or hyperelliptic integrals which often appear in the WKB method.

§ 8. Supplementary Notes on the Local Approximate Expressions

The approximate solutions of Hill equations which is valid locally, that is, valid only over a single period, have been investigated by many authors since Jeffreys applied his method to Mathieu equations. Especially for Mathieu equations many useful formulas have been derived; without them the practical utility of the methods in the preceding two sections would be diminished. But the uniformity of existing asymptotic expressions seems to be incomplete even over a single period of the coefficient. Therefore it will be worthwhile to remember that the method given in § 3 or § 4 is applicable to derive the approximate solutions valid uniformly over one period of the coefficient.

We shall begin with some classical facts. Let us consider a Hill equation

$$\frac{d^2y}{dx^2}-(\lambda+h^2f(x))y=0, \tag{8.1}$$

where $f(x)$ is a regular periodic sunction of period ω. According to Floquet's theory, for a set of linearly independent solutions $u_1(x)$ and $u_2(x)$ of (8.1) there exists a constant matrix

$$A=\begin{pmatrix}a_{11} & a_{12}\\ a_{21} & a_{22}\end{pmatrix}, \tag{8.2}$$

for which

$$\begin{pmatrix}u_1(x+\omega)\\ u_2(x+\omega)\end{pmatrix}=\begin{pmatrix}a_{11} & a_{12}\\ a_{21} & a_{22}\end{pmatrix}\begin{pmatrix}u_1(x)\\ u_2(x)\end{pmatrix}. \tag{8.3}$$

The eigenvalues ν_1, ν_2 and the trace $\operatorname{tr} A$ of matrix A are independent of the selection of $u_1(x)$ and $u_2(x)$. Floquet's indices μ_1 and μ_2 are related to ν_1 and ν_2 by

$$e^{\omega\mu_1}=\nu_1, \qquad e^{\omega\mu_2}=\nu_2,$$

and Floquet's solutions are expressed as

$$e^{\mu_1 x}v_1(x), \qquad e^{\mu_2 x}v_2(x),$$

where v_1 and v_2 are periodic functions with period ω. If $|\operatorname{tr} A|>2$, then the solutions of (8.1) are unstable; if $|\operatorname{tr} A|<2$, then they are stable; and if $\operatorname{tr} A=2$ or -2, then there exists a periodic solution with period ω or 2ω respectively. Thus if we know the solutions over a single period of $f(x)$, say $0\leqq x\leqq\omega$, we can continue the solutions to any region by means of (8.3). In what follows we assume for simplicity $0\leqq f(x)\leqq 1$. Now the usual WKB solutions are given as follows:

In the region where $\lambda+h^2f(x)>0$, we have

$$y\sim\frac{1}{\sqrt[4]{\lambda+h^2f(x)}}\exp\left(\pm\int\sqrt{\lambda+h^2f(x)}\,dx\right), \tag{8.4}$$

and in the region where $\lambda+h^2f(x)<0$, we have

$$y\sim\frac{1}{\sqrt[4]{|\lambda+h^2f(x)|}}\exp\left(\pm i\int\sqrt{|\lambda+h^2f(x)|}\,dx\right). \tag{8.5}$$

By means of these approximate solutions as well as the connection formulas, we have the following results.

For $\lambda\geqslant0$,

$$\operatorname{tr}A=2\cosh\int_0^\omega\sqrt{\lambda+h^2f(x)}\,dx>2 \tag{8.6}$$

and all the solutions are unstable.

For $\lambda\leqslant-h^2$,

$$\operatorname{tr}A=2\cos\int_0^\omega\sqrt{|\lambda+h^2f(x)|}\,dx\,, \tag{8.7}$$

hence

$$|\operatorname{tr}A|\leq2\,,$$

and all the solutions are stable (this result shows that the WKB approximation cannot represent the narrow unstable regions for $\lambda\leqslant-h^2$).

And for $-h^2\leqslant\lambda\leqslant0$,

$$\operatorname{tr}A=\cos\int_\xi^\eta\sqrt{|\lambda+h^2f(x)|}\,dx\left\{2\exp\left(\int_\eta^{\xi+\omega}\sqrt{\lambda+h^2f(x)}\,dx\right)+\frac{1}{2}\exp\left(-\int_\eta^{\xi+\omega}\sqrt{\lambda+h^2f(x)}\,dx\right)\right\}, \tag{8.8}$$

where ξ and η are the adjacent zeros of $\lambda+h^2f(x)$ and we have assumed that $\lambda+h^2f(x)<0$ for $\xi<x<\eta$. For the large values of h (we have assumed so) the bracketed factor in (8.8) is large and the stable regions are restricted in the narrow ranges near $\lambda=\lambda_n$, where λ_n is given by

$$\int_\xi^\eta\sqrt{|\lambda_n+h^2f(x)|}\,dx=\left(n+\frac{1}{2}\right)\pi \qquad n=0,\,1,\,2,\,\cdots \tag{8.9}$$

(8.9) gives the asymptotic forms of the stable regions and the eigenvalues for which there exist periodic solutions with period ω. The breadth of the stable regions are asymptotically given from the gradient of λ-tr A curve at $\lambda=\lambda_n$.

When λ is close to 0 or $-h^2$, we cannot get correct informations by such a simple method and we have to apply the method in § 3.

Here we shall confine ourselves to Mathieu equation

$$\frac{d^2y}{dx^2}-(\lambda+h^2\sin^2x)y=0\,, \tag{8.10}$$

where $\lambda\leqslant h^2$. When λ is close to zero, the modified WKB transformations introduced in § 3 are

$$\frac{t^2}{4}=\int_0^x\sin x\,dx=1-\cos x\,,\qquad y=\phi^{-1/4}y_1\,,\qquad \phi=\frac{4\sin^2x}{t^2}=2-\frac{1}{4}t^2\,, \tag{8.11}$$

and the transformed equation is

$$\frac{d^2y_1}{dt^2}-\left\{\frac{\lambda}{2}\left(1-\frac{t^2}{8}\right)^{-1}+\frac{h^2}{4}t^2+Q(t)\right\}y_1=0\,. \tag{8.12}$$

where

$$Q(t)=\phi^{-1/4}\frac{d^2\phi^{1/4}}{dt^2}=-\frac{1}{16}\left(1-\frac{t^2}{8}\right)^{-1}-\frac{3}{256}t^2\left(1-\frac{t^2}{8}\right)^{-2}, \tag{8.13}$$

or after the turning point correction we have

$$\frac{d^2y_1}{dt^2}+\left\{\mu-\frac{k^2}{4}t^2+\frac{\mu}{64}\frac{t^4}{1-t^2/8}+\frac{3}{1024}t^4\frac{1+t^2/16}{(1-t^2/8)^2}\right\}y_1=0\,, \tag{8.14}$$

where

$$\mu=-\frac{1}{2}\lambda+\frac{1}{16}\,,\qquad k^2=h^2+\frac{1}{4}\lambda-\frac{5}{64}\,. \tag{8.15}$$

(8.14) corresponds to (3.10).

The region to be considered can be taken as

$$-\frac{\pi}{2}\leqq x\leqq\frac{\pi}{2}\,,$$

which corresponds to

$$-2\leqq t\leqq 2\,,$$

and in this region ϕ is bounded from zero.

The first approximate solution of (8.14) is given by

$$y_1\sim W_\nu(\sqrt{k}\,t)\,, \tag{8.16}$$

where

$$\nu+\frac{1}{2}=\frac{\mu}{k}\,.$$

The corresponding approximate value of tr A is

$$\mathrm{tr}\,A\sim-\sqrt{\frac{2}{\pi}}\,\Gamma(-\nu)\{D_\nu(2\sqrt{k})D_\nu'(2\sqrt{k})+D_\nu(-2\sqrt{k})D_\nu'(-2\sqrt{k})\}\,, \tag{8.17}$$

which is the formula filling up the gap between (8.6) and (8.8). Making use of the modified WKB transformations again for (8.14), we can proceed to higher approximations. The conventional method in § 5 is also applicable to (8.14) and the expressions given by Sips[22)] can be derived in the neighbourhood of the turning points.

When $\lambda\sim-h^2$, we can treat

$$\frac{d^2y}{dx^2}+(\lambda+h^2\sin^2 x)y=0\,, \tag{8.18}$$

instead of (8.10). Thus, putting

$$\frac{t^2}{4}=1-\cos x\,,\qquad y=\phi^{-1/4}y_1\,,\qquad \phi=2-\frac{t^2}{4}\,, \tag{8.19}$$

we have approximate solutions

$$\left.\begin{aligned}&y_1\sim W_{\nu'}(\sqrt{k'}\,t)\,,\qquad \nu'+\frac{1}{2}=\frac{\mu'}{k'}\,,\qquad \mu'=\frac{\lambda}{2}+\frac{1}{16}\,,\qquad k'^2=-h^2-\frac{1}{4}\lambda-\frac{5}{64}\,,\\ &\text{and}\\ &\mathrm{tr}\,A\sim-\sqrt{\frac{2}{\pi}}\,\Gamma(-\nu')\{D_{\nu'}(2\sqrt{k'})D_{\nu'}'(2\sqrt{k'})+D_{\nu'}(-2\sqrt{k'})D_{\nu'}'(-2\sqrt{k'})\}\,,\end{aligned}\right\} \tag{8.20}$$

which fills up the gap between (8.7) and (8.8).

Further if $-h^2 \ll \lambda \ll 0$ in (8.10) or (8.18), we can apply the method in § 4 instead of th usual WKB method which does not give any solution over one period in a closed form. Le us write the equation

$$\frac{d^2y}{dx^2} - h^2 F(x) y = 0 \, , \tag*{(8.21}$$

where

$$F(x) = \sin^2 x + \frac{\lambda}{h^2} = \sin^2 x - \lambda' \, .$$

Then, according to § 4, we have

$$y - \sqrt[4]{\frac{1-t^2}{\lambda' - \sin^2 x}} \, W_\nu \left(2 \sqrt{\frac{Ih}{\pi}} t \right) , \tag*{(8.22}$$

where

$$\nu + \frac{1}{2} = \frac{Ih}{\pi} \, , \qquad I = 2 \int_0^{x_0} \sqrt{\lambda' - \sin^2 x} \, dx \, , \qquad (x_0 = \sin^{-1} \lambda'^{1/2})$$

and

$$\frac{2}{\pi} \int_0^t \sqrt{1-t^2} \, dt = \frac{1}{I} \int_0^x \sqrt{\lambda' - \sin^2 x} \, dx \, .$$

In this way we can find the approximate solutions of Mathieu or other Hill equations with the turning points of the same character. And the repeated use of similar procedures leads to the higher order approximations without any other special techniques except the turning point correction.

Appendix I Formulas Related to Weber Functions

Some formulas related to Weber functions are enumerated here. They are useful for the treatment of the approximate solutions discussed in the text. When a divergent integral appears in the formula, it should be interpreted as the principal value or finite part, that is, when $f(x)$ is given as

$$f(x) = f_0(x) + \frac{c_{-1}}{x} + \frac{c_{-2}}{x^2} + \cdots + \frac{c_{-n}}{x^n} \, ,$$

where $f_0(x)$ is regular at $x=0$, then $\int_0^x f(x) dx$ means

$$\int_0^x f(x) dx = \int_0^x f_0(x) dx + c_{-1} \log x - \frac{c_{-2}}{x} - \cdots - \frac{1}{n-1} \frac{c_{-n}}{x^{n-1}} \, ,$$

and for $a<0$, $\int_a^x f(x) dx$ means

$$\int_a^x f(x) dx = \int_a^x f_0(x) dx + c_{-1} \log \left| \frac{x}{a} \right| - c_{-2} \left(\frac{1}{x} - \frac{1}{a} \right) - \cdots - \frac{c_{-n}}{n-1} \left(\frac{1}{x^{n-1}} - \frac{1}{a^{n-1}} \right) .$$

Further the notation $pf \frac{f(0)}{g(0)}$ means $\lim_{x \to 0} \frac{f(x)}{g(x)}$ if the limit exists, and zero if $g(0)=0$ and $f(0) \neq 0$.

1) *Definition and funpamental expressions*

$D_\nu(x)$ and $\mathscr{D}_\nu(x)$ are the linearly independent solutions of Weber's equation

$$\frac{d^2y}{dx^2} + \left(\nu + \frac{1}{2} - \frac{x^2}{4} \right) y = 0 \, . \tag{I.1}$$

We have the following formulas

$$D_\nu(x)=2^{\nu/2+1/4}x^{-1/2}W_{\nu/2+1/4,\,-1/4}\left(\frac{x^2}{2}\right), \tag{I.2}$$

$$D_\nu(x)\sim\begin{cases} e^{-x^2/4}x^\nu\left\{1-\dfrac{\nu(\nu-1)}{2x^2}+\dfrac{\nu(\nu-1)(\nu-2)(\nu-3)}{2\cdot4\cdot x^4}+\cdots\right\} & (x\to+\infty)\\ \cos\nu\pi e^{-x^2/4}|x|^\nu\left\{1-\dfrac{\nu(\nu-1)}{2x^2}+\dfrac{\nu(\nu-1)(\nu-2)(\nu-3)}{2\cdot4\cdot x^4}+\cdots\right\} & \\ \quad+\dfrac{\sqrt{2\pi}}{\Gamma(-\nu)}e^{x^2/4}|x|^{-\nu-1}\left\{1+\dfrac{(\nu+1)(\nu+2)}{2x^2}+\cdots\right\}, & (x\to-\infty)\end{cases} \tag{I.3}$$

$$D_\nu(0)=\Gamma\left(\frac{1}{2}\right)2^{\nu/2}\Big/\Gamma\left(\frac{1-\nu}{2}\right),\qquad D_\nu'(0)=\Gamma\left(-\frac{1}{2}\right)2^{(\nu-1)/2}\Big/\Gamma\left(-\frac{\nu}{2}\right), \tag{I.4}$$

$$\mathscr{D}_\nu(x)\sim e^{x^2/4}x^{-\nu-1}\left\{1+\frac{(\nu+1)(\nu+2)}{2x^2}+\cdots\right\}, \tag{I.5}$$

$$\mathscr{D}_\nu(0)=-\frac{\sin^2(\nu\pi/2)}{D_\nu'(0)},\qquad \mathscr{D}_\nu'(0)=\frac{\cos^2(\nu\pi/2)}{D_\nu(0)}, \tag{I.6}$$

$$\mathscr{D}_\nu'(x)D_\nu(x)-D_\nu'(x)\mathscr{D}_\nu(x)=1,$$

$$D_\nu(x)=\mathscr{D}_\nu(x)\int_x^\infty\frac{dx}{\{\mathscr{D}_\nu(x)\}^2},\qquad \mathscr{D}_n(x)=D_n(x)\int_0^x\frac{dx}{\{D_n(x)\}^2}\qquad(n=0,\,1,\,2\cdots), \tag{I.8}$$

The simplest special cases are the following functions:

$$D_0(x)=e^{-x^2/4},\qquad \mathscr{D}_0(x)=e^{-x^2/4}\int_0^x e^{x^2/2}dx,$$

$$D_{-1}(x)=e^{x^2/4}\int_0^x e^{-x^2/2}dx,\qquad \mathscr{D}_{-1}(x)=e^{x^2/4}.$$

If ν is not equal to a positive integer or zero, $D_\nu(x)$ and $D_\nu(-x)$ are linearly independent solutions of (I.1). Therefore we need not $\mathscr{D}_\nu(x)$ except the cases in which $\nu=n=0,\,1,\,2,\,\cdots$. In the asymptotic expansion for $x\to-\infty$ the exponentially decreasing part is meaningful only in the cases in which ν is sufficiently close to an integer.

2) *Recurrence formulas*

The following forms of recurrence relations are convenient for integration or other operations.

$$D_1D_\nu=D_0D_{\nu+1}+\nu D_0D_{\nu-1}=2D_0D_\nu'+2\nu D_0D_{\nu-1}, \tag{I.9}$$

$$2D_\nu'=D_{\nu+1}-\nu D_{\nu-1}, \tag{I.10}$$

$$\frac{d}{dx}(D_0D_\nu)=-D_0D_{\nu+1},\qquad D_0D_\nu=\int_x^\infty D_0D_{\nu+1}dx, \tag{I.11}$$

$$\frac{d}{dx}\left(\frac{D_\nu}{D_0}\right)=\nu\frac{D_{\nu-1}}{D_0}, \tag{I.12}$$

$$\frac{d}{dx}\left(\frac{1}{D_\nu D_\mu}\right)=\frac{D_{\nu+1}D_\mu-\mu D_\nu D_{\mu-1}}{D_\mu^2D_\nu^2}, \tag{I.13}$$

$$D_\mu^2\frac{d}{dx}\left(\frac{D_\nu}{D_\mu}\right)=\nu D_\mu D_{\nu-1}-\mu D_\nu D_{\mu-1}=D_\nu D_{\mu+1}-\nu D_\mu D_{\nu+1}, \tag{I.14}$$

$$\frac{d}{dx}(D_\nu D_\mu)=-D_{\nu+1}D_\mu+\mu D_\nu D_{\mu-1}=-D_{\mu+1}D_\nu+D_\mu D_{\nu-1}, \tag{I.15}$$

$$D_\nu D_{\mu+1}=D_\mu(D_{\nu+1}+\nu D_{\nu-1})-\mu D_{\mu-1}D_\nu, \tag{I.16}$$

$$D_m D_\mu = D_0 \sum_{k=0}^{m} k! \binom{m}{k}\binom{\nu}{k} D_{\nu+m-2k} \qquad (m=\text{integer}) , \tag{I.17}$$

$$x^n D_0 = D_n + \frac{n(n-1)}{2} D_{n-2} + \frac{n(n-1)(n-2)(n-3)}{2\cdot 4} D_{n-4} + \cdots$$
$$+\begin{cases} \dfrac{n!}{(n/2)!\,2^{n/2}} D_0 & (n=\text{even}) \\[2ex] \dfrac{n!}{\{(n-1)/2\}!\,2^{(n-1)/2}} & (n=\text{odd}) \end{cases} \tag{I.18}$$

$$D_1 \mathscr{D}_n = D_0 \mathscr{D}_{n-1} + (n+1) D_0 \mathscr{D}_{n+1} , \tag{I.19}$$

$$2\mathscr{D}_n' = -(n+1)\mathscr{D}_{n+1} + \mathscr{D}_{n-1} , \tag{I.20}$$

$$\frac{d}{dx}(D_0 \mathscr{D}_n) = -(n+1) D_0 \mathscr{D}_{n+1} , \tag{I.21}$$

$$\frac{d}{dx}\left(\frac{\mathscr{D}_n}{D_0}\right) = \frac{\mathscr{D}_{n-1}}{D_0} \qquad (n=\text{integer}) . \tag{I.22}$$

3) *Related functions*

$D_\nu^{(k)}(x)$ and $\mathscr{D}_\nu^{(h)}(x)$ are the particular solutions of inhomogeneous equation

$$\frac{d^2y}{dx^2} + \left(\nu + \frac{1}{2} - \frac{x^2}{4}\right) y = -D_\nu^{(k-1)}(x) , \qquad (D_\nu^{(0)}(x) = D_\nu(x)) \tag{I.23}$$

and

$$\frac{d^2y}{dx^2} + \left(\nu + \frac{1}{2} - \frac{x^2}{4}\right) y = -\mathscr{D}_\nu^{(k-1)}(x) , \qquad (\mathscr{D}_\nu^{(0)}(x) = \mathscr{D}_\nu(x)) \tag{I.24}$$

respectively. We have

$$D_\nu^{(k)}(x) = \frac{1}{k!}\,\frac{\partial^k}{\partial \nu^k} D_\nu(x) , \tag{I.25}$$

$$\mathscr{D}_\nu^{(k)}(x) = \frac{1}{k!}\,\frac{\partial^k}{\partial \nu^k} \mathscr{D}_\nu(x) , \tag{I.26}$$

$$D_1 D_\nu^{(k)} = \{D_{\nu+1}^{(k)} + \nu D_{\nu-1}^{(k)} + D_{\nu-1}^{(k-1)}\} D_0 , \tag{I.27}$$

$$D_\nu^{(k)}(x) = D_\nu(x) \int_0^\infty \frac{dx_1}{\{D_\nu(x_1)\}^2} \int_{x_1}^\infty D_\nu(x_2) D_\nu^{(k-1)}(x_2)\, dx_2 . \tag{I.28}$$

4) *Integral formulas*

$$(\nu-\mu)\int_x^\infty D_\nu D_\mu\, dx = D_\mu D_\nu' - D_\nu' D_\mu , \tag{I.39}$$

$$(\nu-\mu)\int_0^x \frac{dx_1}{\{D_\nu(x_1)\}^2} \int_{x_1}^\infty D_\nu(x_2) D_\mu(x_2)\, dx_2 = -\frac{D_\mu(x)}{D_\nu(x)} + pf\,\frac{D_\mu(0)}{D_\nu(0)} , \tag{I.30}$$

$$\begin{aligned} I_\nu(x) &= \int_x^\infty \{D_\nu(x)\}^2 dx = D_\nu(x) D_{\nu-1}(x) + \nu I_{\nu-1}(x) \\ &= \{D_\nu(x)\}^2 \frac{\partial}{\partial \nu}\left\{\frac{D_\nu'(x)}{D_\nu(x)}\right\} = \{D_\nu(x)\}^2 \frac{d}{dx}\left\{\frac{D_\nu^{(1)}(x)}{D_\nu(x)}\right\} , \end{aligned} \tag{I.31}$$

$$\left.\begin{aligned} I_n(0) &= \sqrt{\frac{\pi}{2}}\, n! , \\ I_\nu(0) &= \frac{\Gamma(1+\nu)}{2^{3/2}\pi^{1/2}}\left\{2\pi + \sin \pi\nu \left(\psi\left(1+\frac{1}{2}\nu\right) - \psi\left(\frac{1}{2}+\frac{1}{2}\nu\right)\right)\right\} . \end{aligned}\right\} \tag{I.32}$$

5) *Zeros and extrema*

$D_\nu(x)$ has no zero in $x>2\left(\nu+\frac{1}{2}\right)^{1/2}$ if ν is real.

When $n<\nu<n+1$, where $n=0, 1, 2, \cdots$, then $D_\nu(x)$ has n zeros and at most only one of them lies in $x<-2\left(\nu+\frac{1}{2}\right)^{1/2}$. If $\nu<0$, $D_\nu(x)$ has no zero.

The zeros of D_ν and $\mathscr{D}_\nu$ are simple and distributed alternatively.

If ν is larger than and sufficiently close to $n=0, 1, 2, \cdots$, then D_ν has a large negative zero, which is asymptotically expressed as

$$|x_0|\sim 2k+(2n+1)\log k+\frac{(2n+1)}{k}\log k+\cdots , \tag{I.33}$$

where

$$k=-\log(2^{-n/2}\pi^{-1/2}n!\,\nu'), , \qquad \nu'=\nu-n ,$$

If ν is smaller than and sufficiently close to $n=0, 1, 2, \cdots$, then $|D_\nu|$ takes minimum value at $x=x_m$, where x_m is asymptotically expressed as

$$-x_m=|x_m|\sim 2k'+(2n+1)\log k'+\frac{(2n+1)}{k'}\log k'+\cdots , \tag{I.34}$$

where

$$k'=-\log(2^{-n/2}\pi^{-1/2}n!\,\nu') , \qquad \nu'=n-\nu .$$

Appendix II Inversion of Transcendental Functions

For calculation of various quantities appearing in the turning point correction and for approximate determination of eigenvalues, we need inversion of transcendental functions and substitution of a transcendental function into another. For this purpose the theorem due to Lagrange* is very useful. According to it, if

$$\zeta=a+\varepsilon\varphi(\zeta) , \tag{II.1}$$

then under a suitable condition we have

$$f(\zeta)=f(a)+\sum_{n=1}^{\infty}\frac{\varepsilon^n}{n!}\frac{d^{n-1}}{da^{n-1}}[f'(a)\{\varphi(a)\}^n] . \tag{II.2}$$

As a special case of this theorem we see that if

$$w=\varphi_0(z)-\varepsilon\varphi_1(z) \tag{II.3}$$

and

$$\varphi_0(z_0)=w , \qquad \varphi_0'(z_0)\neq 0 , \tag{II.4}$$

then we have

$$z=z_0(w)+\varepsilon\frac{\varphi_1(z_0)}{\varphi_0'(z_0)}+\frac{\varepsilon^2}{2!}\frac{1}{\varphi_0'(z_0)}\frac{d}{dz_0}\left(\frac{\varphi_1^2(z_0)}{\varphi_0'(z_0)}\right)+\frac{\varepsilon^3}{3!}\left(\frac{1}{\varphi_0'(z_0)}\frac{d}{dz_0}\right)^2\left(\frac{\varphi_1^3(z_0)}{\varphi_0'(z_0)}\right)+\cdots . \tag{II.5}$$

For example, let us consider

$$h^2\delta-Q(\delta)=0 \tag{II.6}$$

or

---

* E. T. Whittaker and C. N. Watson: *A Course of Modern Analysis* (Cambridge, 1927) 132.

$$\delta-\varepsilon Q(\delta)=0\ , \qquad (\varepsilon=h^{-2})\ , \tag{II.7}$$

which appeared in (2.8) in the text. In this case we can put

$$w=0\ , \qquad \varphi_0(\delta)=\delta\ , \qquad \varphi_1(\delta)=Q(\delta)$$

in (II.3) and we have

$$\delta=0+\varepsilon\frac{Q(0)}{1}+\frac{\varepsilon^2}{2}\left(\frac{dQ^2(\delta)}{d\delta}\right)_{\delta=0}+\frac{\varepsilon^3}{3!}\left(\frac{d^2Q^3(\delta)}{d\delta^2}\right)_{\delta=0}+\cdots\ . \tag{II.8}$$

References

1) G. Breit: *Handbuch der Physik* Vol. **41**, Part 1 (Springer, 1959) 257.
2) T. M. Cherry: Trans. Amer. Math. Soc. **68** (1959) 224.
3) J. L. Dunham: Phys. Rev. **41** (1932) 713.
4) S. Goldstein: Proc. London Math. Soc. **28** (1928) 81.
5) I. Imai: Phys. Rev. **74** (1948) 113.
6) I. Imai: Phys. Rev. **80** (1950) 1112.
7) I. Imai: IRE Trans. AP-4, no. 3 (1956) 233.
8) I. Imai: Quart. Appl. Math. **16** (1958) 33.
9) B. Jeffreys: Proc. Cambr. Phil. Soc. **38** (1942) 401.
10) H. A. Kramers and G. P. Ittmann: Z. Phys. **58** (1929) 217.
11) T. S. Kuhn: Phys. Rev. **79** (1950) 515.
12) R. E. Langer: Trans. Amer. Math. Soc. **33** (1931) 23.
13) R. E. Langer: Phys. Rev. **51** (1937) 669.
14) R. E. Langer: Trans. Amer. Math. Soc. **67** (1949) 461.
15) R. E. Langer: Trans. Amer. Math. Soc. **90** (1959) 113.
16) R. W. McKelvey: Trans. Amer. Math. Soc. **79** (1955) 103.
17) N. W. McLachlan: *Theory and Application of Mathieu Functions* (Oxford, 1947) 228, 231 and references given there.
18) S. C. Miller and R. H. Good: Phys. Rev. **91** (1953) 174.
19) H. Moriguchi: J. Phys. Soc. Japan **14** (1959) 968.
20) N. F. Mott and H. S. W. Massey: *The Theory of Atomic Collisions* (Oxford, 1949) 126, 209.
21) J. Olver: Phil. Trans. Roy. Soc. **A**, **247** (1954) 307.
22) R. Sips: Trans: Amer. Math. Soc. **66** (1949) 93; **90** (1959) 340.

JOURNAL OF THE PHYSICAL SOCIETY OF JAPAN, Vol. 14, No. 12, DECEMBER 1959

Further Investigation on the Transition of Two-Dimensional Separated Layer at Subsonic Speeds

By Hiroshi SATO

Aeronautical Research Institute, University of Tokyo

(Received August 3, 1959)

Experiments have been made on the artificially excited transition of two-dimensional separated layer at subsonic speeds. The response characteristics of laminar layer to the sinusoidal external disturbances are found to be in good agreement with theoretical calculations based on the Orr-Sommerfeld equation. The effect of excitation becomes maximum when the frequency of external excitation coincides with that of naturally excited sinusoidal velocity fluctuation in the laminar layer. No remarkable abrupt turbulent bursts are found in the transition region. The wave-form of velocity fluctuation changes gradually from sinusoidal to irregular patterns.

§ 1. Introduction

On the natural transition of two-dimensional separated layer, experimental investigations were carried out and reported by the present author in 1956[1]. In the transition region were found sinusoidal velocity fluctuations which were apparently caused by the dynamical instability of extremely small disturbances in the laminar layer. The non-dimensional frequency of the fluctuation lied inside the theoretical unstable zone. The author predicted that the sinusoidal fluctuation might correspond to the one which received maximum amplification in the linearized theory. At that time, however, it was not possible to confirm this prediction since theoretical and experimental results were still wanted.

Since then, in the theoretical phase, Lessen and Fox[2] extended Lessen's earlier work on the neutral disturbances in the separated layer[3] to the unstable cases assuming infinite Reynolds number. The wave speed and amplification rate of small disturbances of various wave numbers were determined by numerical calculations.

The present experimental program has been started in order to make more detailed comparisons with these theoretical results. The laminar separated layer is excited by sound from outside. The wave speed and amplification rate of excited velocity fluctuation are measured. Some features in the mechanism of transition are also clarified.

The author appreciates discussions and advices given by the Turbulence Research Group in Japan which has been conducted by Professor Itiro Tani. Acknowledgement is extended to Messrs. Y. Onda and S. Kyoya who were helpful in carrying out the experimental program.

This work was financially assisted by a grant-in-Aid for Fundamental Scientific Research from the Ministry of Education.

§ 2. Experimental Arrangement

Experiments have been carried out in a 20 cm by 60 cm low-turbulence wind-tunnel at Aeronautical Research Institute (which superseded Institute of Science and Technology in 1957). Most of the experimental arrangement and technique used in the present work have been described in reference 1.

The separated layer is created by the separation of laminar boundary layer along a flat plate from a 90-degrees rear-edge. Details of test-section are shown in Fig. 1. The

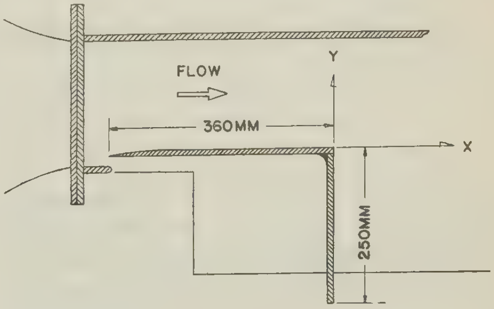

Fig. 1. Dimensions of plate used for excited transition of separated layer. (This plate corresponds to "Plate III" in reference 1).

main-stream velocity could be changed from 3 to 30 m/s. However, the general features of transition process have been found not to be influenced by the Reynolds number in the above wind-speed range if each quantity is properly non-dimensionalized. Therefore, most of the detailed measurements have been made at one wind-speed, 10 m/s. The longitudinal turbulence level of main-stream at the speed is 0.08 percent. Measurements of mean and fluctuating velocities have been made by hot-wire anemometers. The over-all frequency response of electronic equipment for the hot-wire is flat from 20 cps up to 20,000 cps. The spectral component of velocity fluctuation is observed by using a narrow-band RC-type band-pass filter. The output from amplifier is recorded by taking pictures of screen of a dual-beam cathode-ray oscilloscope.

The artificial excitation is realized by the sound from a 10-watt loudspeaker placed facing the test-section. The survey of sound field by a small microphone has proved that the intensity of sound is uniform in the test-section. No noticeable reasonance effect has been found in the frequency range from 30 to 800 cps. The background noise level determined by a standard noise-meter was 62 decibels* at the main-stream velocity, 10 m/s and the maximum intensity of sound from loudspeaker was around 100 decibels at the test-section.

The two-dimensionality of flow in the transition region was confirmed by the mean-velocity survey.

The over-all accuracy of measurement is estimated to be around 5 percent in most cases. In some special measurements, however, the accuracy might be poorer mainly because of the difficulties in reproducing the flow field. For example, the frequency of sinusoidal fluctuation varies around ±5 percent by some unknown causes. Since the origin of so-called natural transition is untraceable, some scatter of experimental data is unavoidable. There are many experimental conditions which might be responsible for the poor reproducibility of flow, such as room temperature, back-ground noise, slight vibrations, etc.

§ 3. Experimental Results

The results obtained in the previous experiment on the natural transition[1] are summarized as follows:

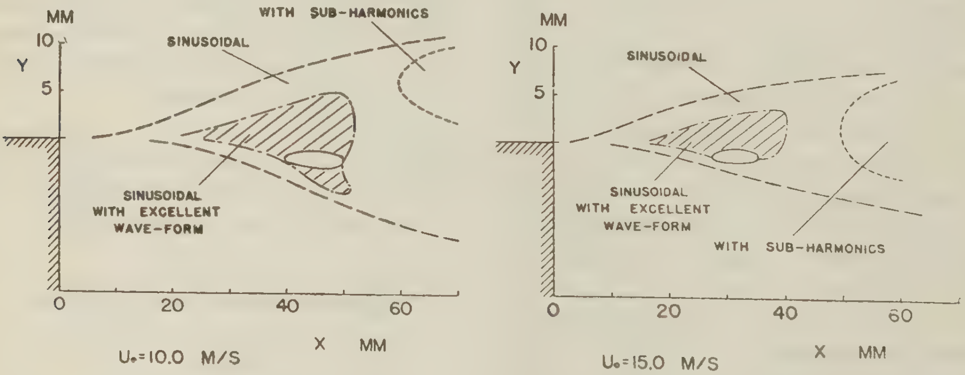

Fig. 2. Map of patterns of velocity fluctuations. U_0: main-stream velocity.

The boundary layer on the flat plate before separation is laminar and has the well-known Blasius-type velocity distribution. After the separation, the layer remains laminar in some distance and then appears the velocity fluctuation of a regular sinusoidal wave-form. The frequency of fluctuation is roughly proportional to 3/2 power of mainstream velocity. The fluctuation increases the amplitude and develops into turbulence further downstream. Fig. 2 gives a crude idea on the extent of region where the sinusoidal fluctuation is found. Inside a shaded region the wave-form is sinusoidal. Inside a small region enclosed by a full line, the amplitude of fluctuation is very small and the wave-form is not sinusoidal. There is also a region where the fundamental sinusoidal fluctuation is accompanied by a sub-harmonic component. No remarkable turbulent burst has been found in the transition region of separated layer. A detailed discussion on the above-mentioned nature of velocity fluctuation is given in the following sections.

---

* Decibel is the standard scale of sound intensity. 0 decibel $=2\times10^{-4}$ dyne/cm^2.

The increase of thickness of separated layer is gradual as far as the layer remains laminar

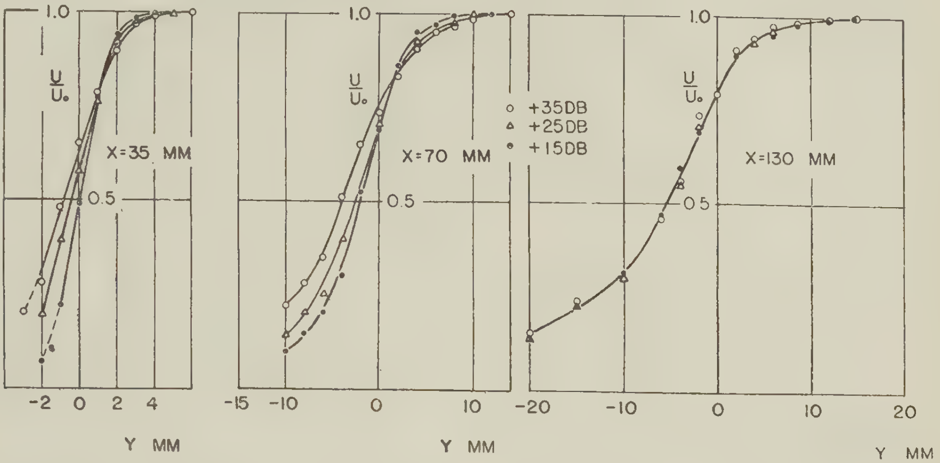

Fig. 3. Fffect of excitation on mean-velocity distribution. Main-stream velocity 10.0 m/s. Frequency of excitation 240 cps.

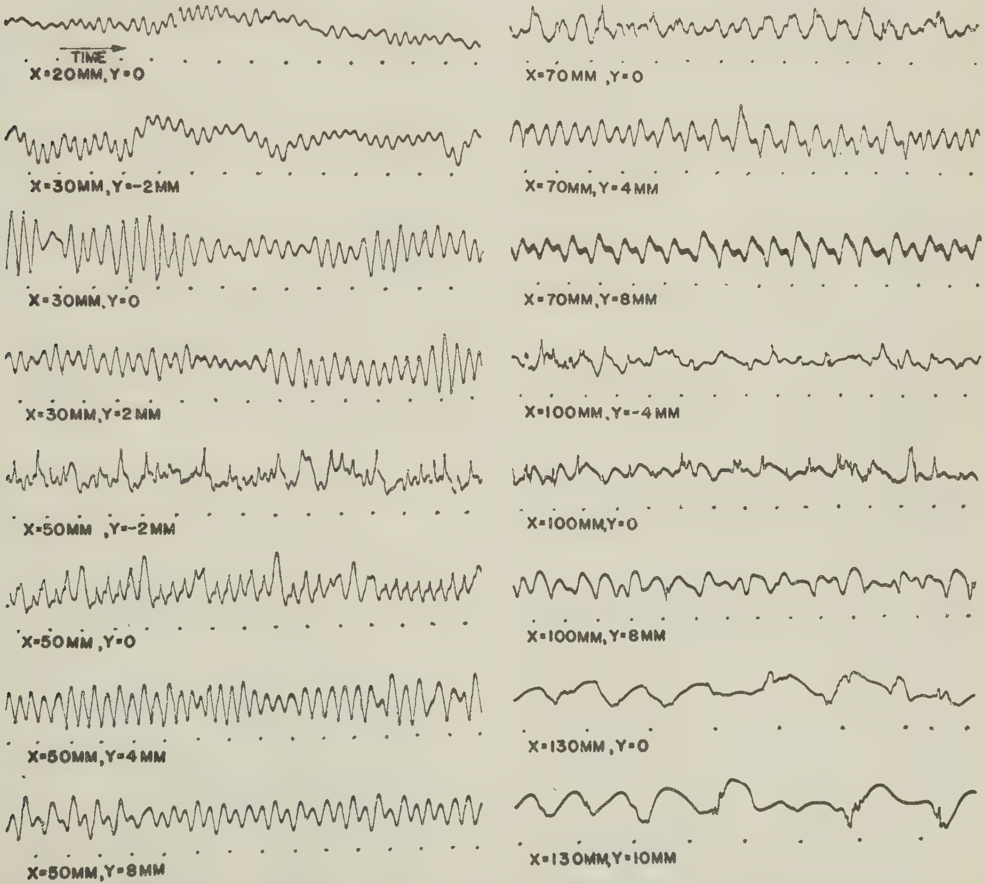

Fig. 4. Development of u-fluctuation in natural transition. Main-stream velocity 10.0 m/s. Time mark between dots 0.01 sec.

and becomes remarkable when the velocity fluctuation appears in the layer.

The effect of excitation on the transition depends strongly on the intensity and frequency of incoming sound. Generally speaking, the effect becomes noticeable as the intensity of sound is increased and is most pronounced when the frequency of sound coincides with that of above-mentioned naturally-excited sinusoidal velocity flucutuation. When these two frequencies are far different, the effect of excitation is hardly observed.

3.1 *Mean-velocity distributions*

The artificial excitation does not change so much the general feature of mean-velocity distribution. Fig. 3 shows an example. The frequency of exciting sound is 240 cps which is the frequency of naturally-excited fluctuation. The parameter for three curves is the intensity of incoming sound. For example, +35 DB means that the total sound level at the test-section is 35 decibels above the background sound noise. The origin of co-ordinate is the separation point and X- and Y-axis are parallel and perpendicular to the main-stream, respectively. The broadening of layer due to excitation is evident at two stations, $X=35$ mm and $X=70$ mm. This broadening might be caused by the high-intensity velocity fluctuations induced by sound. At $X=130$ mm, the effect of excitation is hardly detected. Stations $X=35$ mm and $X=70$ mm lie inside the region of sinusoidal fluctuations as shown in Fig. 2. On the other hand, the layer is turbulent at $X=130$ mm. Fig. 3 suggests that at $X=130$ mm, some sort of energy equilibrium has been reached and this equilibrium is universal regardless to the process of transition.

3.2 *Wave-forms of velocity fluctuations*

Fig. 4 shows patterns of u-fluctuations at

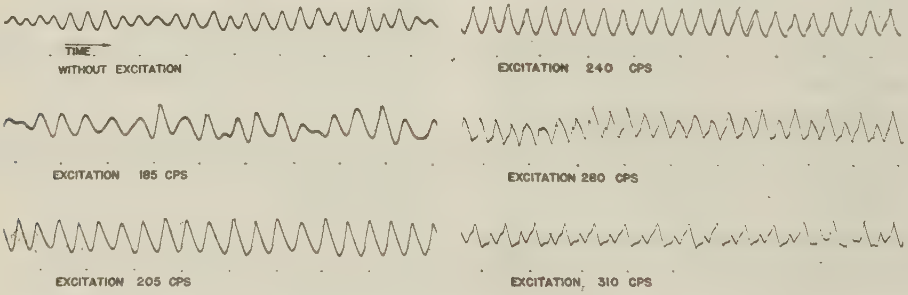

Fig. 5. Fffect of excitation on patterns of u-fluctuation. Main-stream velocity 10.0 m/s. X=35 mm, Y=1 mm.

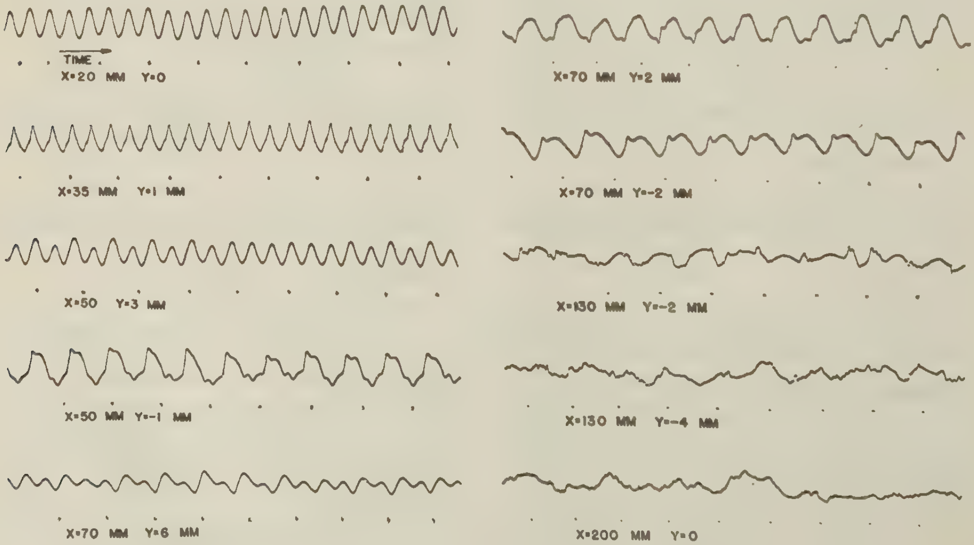

Fig. 6. Development of u-fluctuation with excitation 250 cps. Main-stream velocity 10.0 m/s.

various points in the layer without excitations. At $X=30$ mm and 50 mm, regular sinusoidal wave-forms are observed. At $X=70$ mm, the fluctuation of half frequency prevails at $Y=4$ mm and 8 mm. The turbulent pattern appears at $X=100$ mm. The intermittent burst is not so noticeable as found in the boundary layer along a solid wall.

The effect of excitation on the wave-form is illustrated in Fig. 5. The frequency of natural fluctuation is 240 cps. The effect of excitation is obvious for all cases. It should be remarked here that the output from hot-wire anemometer due to the sound itself is very small and negligible comparing with signals due to induced velocity fluctuations. With excitation frequency from 185 to 280 cps, the frequency of induced fluctuation coincides with that of incoming sound but with 310 cps, the sub-harmonic (155 cps) fluctuation is also induced.

Patterns of excited u-fluctuation at various positions are reproduced as Fig. 6 in a wide range of X and Y. The frequency of exciting sound is set equal to that of natural fluctuation—250 cps in this case. At $X=20$ mm, $Y=0$, the wave-form is purely sinusoidal. At $X=35$ mm, $Y=1$ mm, some distortion is observed. At $X=50$ mm, $Y=-1$ mm, the sub-harmonic component of half frequency and the harmonic component of doubled frequency are evidently shown. In three traces at $X=70$ mm, the predominant frequency is 125 cps. At $X=130$ mm and 200 mm, no particular frequency is observed any more. The intermittent burst is hardly pointed out in any trace. The variation of wave-form is gradual.

3.3 *Distribution of velocity fluctuations*

The effect of excitation on the intensity of velocity fluctuation is shown in Fig. 7. As the intensity of sound is increased, the value of $\sqrt{\overline{u^2}}/U_0$ increases uniformly at various Y-positions and its distribution remains nearly similar. When excited with a sound of +35 decibels, the intensity of fluctuation becomes 4 times the initial value. This fact suggests that the intensity of velocity fluctuation in the so-called natural transition region is influenced very much by the experimental arrangement, especially by the intensity and spectrum of sound noise at the test-section. Schubauer and Skramstad have already pointed out that the transition point in the boundary layer on a solid wall can be moved at will by varying the frequency and intensity of exciting sound[4)].

The extraordinary large value of $\sqrt{\overline{u^2}}/U_0$ at $Y=-2$ mm, for the excitation by the sound of +35 decibels is due to the particular amplitude distribution of certain spectral component. This point is made clear in the following section.

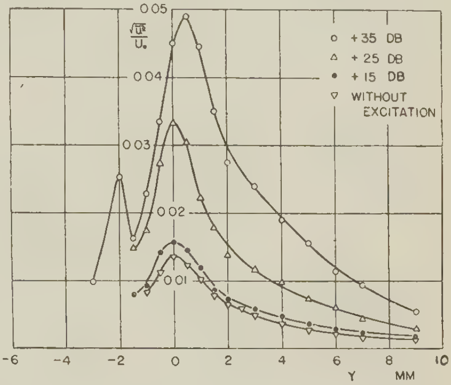

Fig. 7. Effect of excitation on velocity fluctuations. Main-stream velocity 10.0 m/s. X=30 mm. Excitation frequency 240 cps.

3.4 *Spectral components of velocity fluctuations*

Details of velocity fluctuation are revealed by the observation of spectral components. For instance, the energy spectrum such as shown in Fig. 8 is a quantitative representation of wave-form of fluctuation shown in Fig. 4. Although the definition of energy spectrum is somewhat ambiguous when a predominant frequency exists in the fluctuation, the energy spectrum in Fig. 8 is based on the usual way of definition, namely, $\overline{u}_f{}^2$ is the mean value of energy per cycle per second. This treatment might be justified by the fact that in the case of natural transition, the wave-form of fluctuation is not purely sinusoidal and the spectrum around the predominant frequency has some distribution. The scale for $\overline{u}_f{}^2$ in the figure is taken arbitrary, while relative values at three different stations are expressed correctly. At $X=35$ mm, $Y=1$ mm, there exist a high peak at 240 cps and another peak at about 500 cps. The latter apparently corresponds to the harmonic component. At $X=70$ mm, $Y=1$ mm, two peaks are clearly observed, one at 240 cps and the other at 120 cps corresponding to the sub-harmonic component. At X=130 mm, Y=0, no particular peaks are present.

It is now obvious that three spectral components are significant. They are fundamental, sub-harmonic and second-harmonic components. We are now to investigate the distribution of these components in X- and Y-direction. Fig. 9 shows some results obtained by measuring spectral components at various X-sections with the tuning frequency of band-pass filter fixed. The frequency of exciting sound is kept at 242 cps which is the frequency of naturally-excited fluctuation. The level of excitation is either +15 decibels or +35 decibels. "+0 DB" means that no artificial excitation is applied. The absolute value of root-mean-square, $\sqrt{\bar{u}_f^2}$ is not significant. Only the relative value with the same tuning frequency is to be compared. Generally speaking, with excitation level +15 decibels, the amplitude of spectral component is increased uniformly, keeping the similar distributions with those in the natural transi-

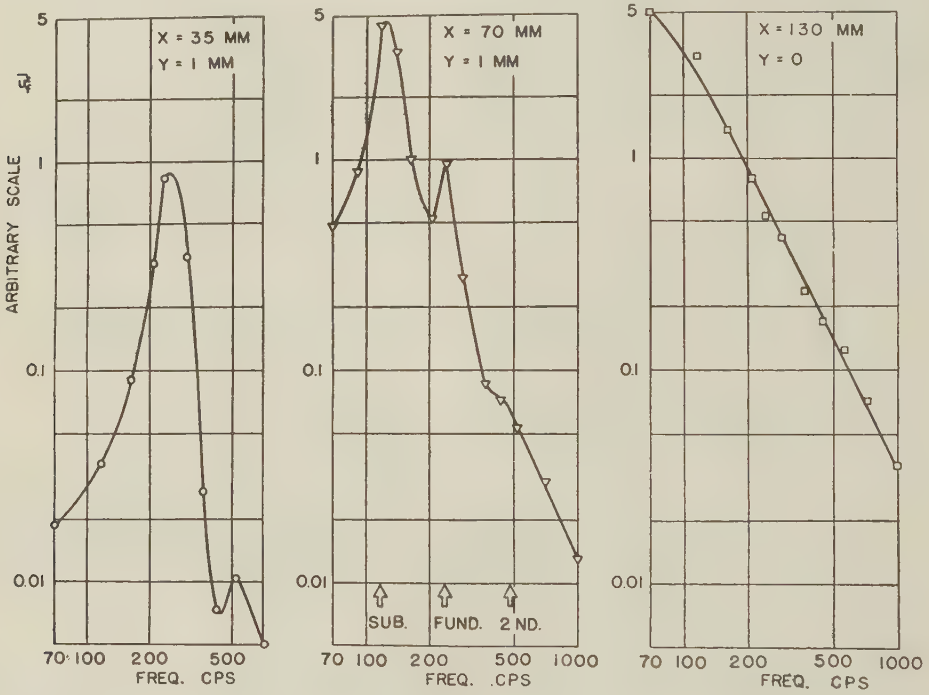

Fig. 8. Energy spectrum of u-fluctuation without artificial excitations. Main-stream velocity 10.0 m/s.

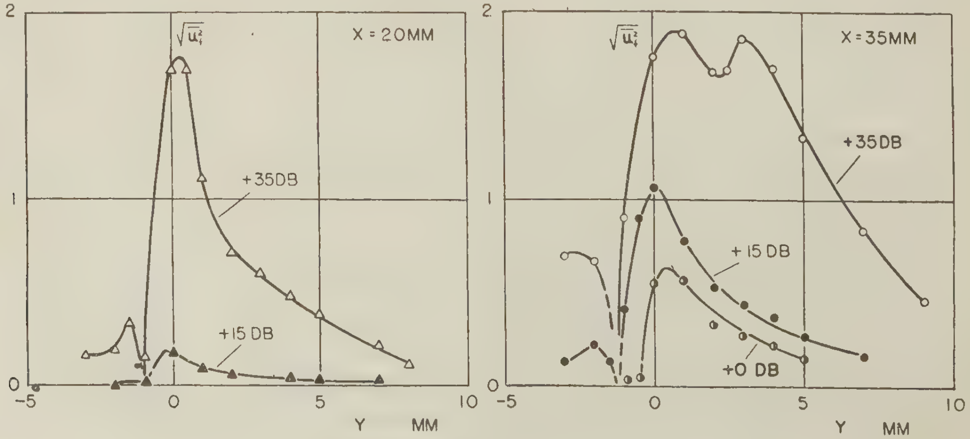

Fig. 9 (A)

tion. At $X=20$ mm, the increase of fundamental component due to excitation is remarkable. The ratio of values of $\sqrt{\overline{u_f}^2}$ with excitation +35 decibels and +0 decibels reaches around 30, while harmonic and subharmonic components are much less affected by the excitation. At $X=35$ mm, components of 121 cps and 484 cps become larger and moreover, distributions have maxima at about $Y=-1$ mm where the fundamental component is nearly zero. Thus it is clear that the wave-form near $Y=-1$ mm suffers from con-

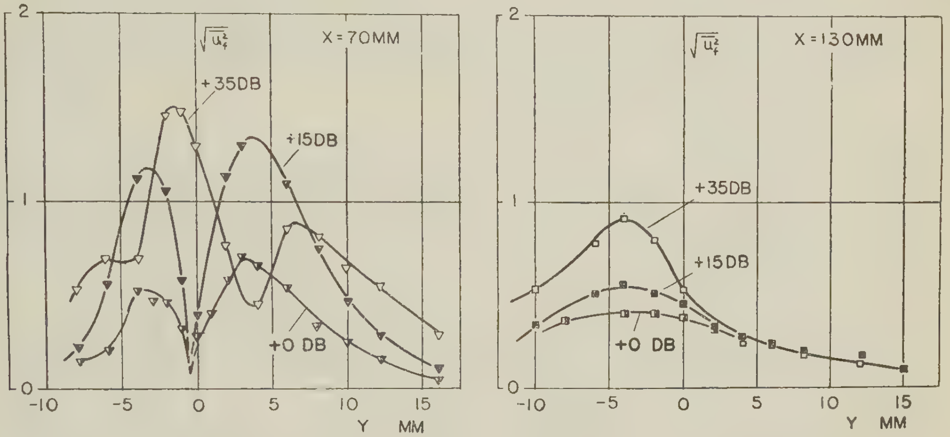

Fig. 9 (A) Distribution of fundamental component (242 cps) with excitation 242 cps.

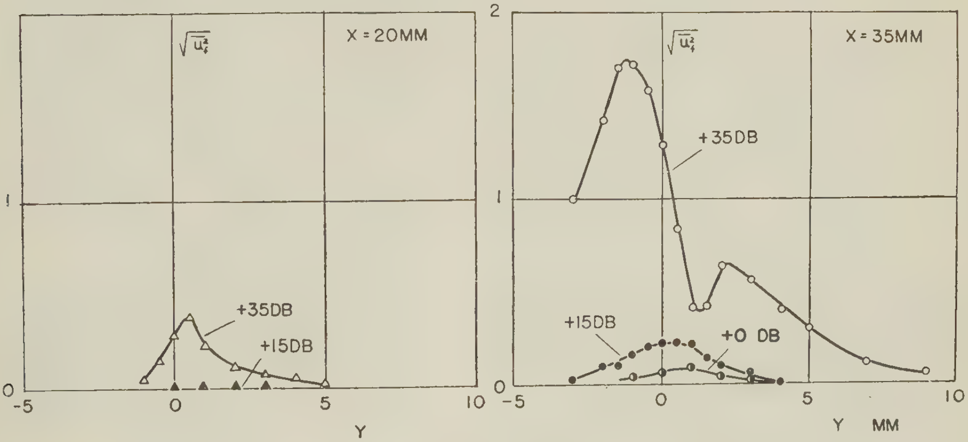

Fig. 9 (B)

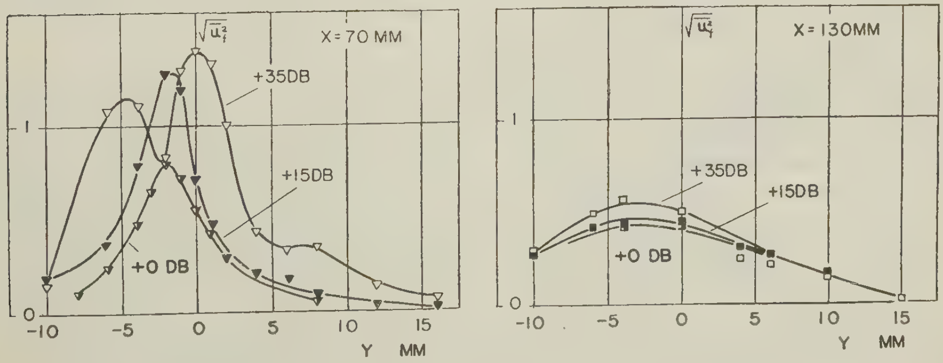

Fig. 9 (B) Distribution of harmonic component (484 cps) with excitation 242 cps.

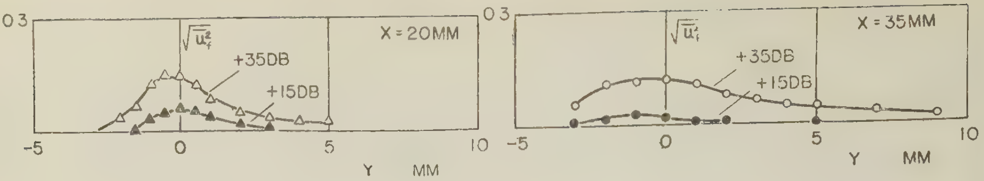

Fig. 9 (C)

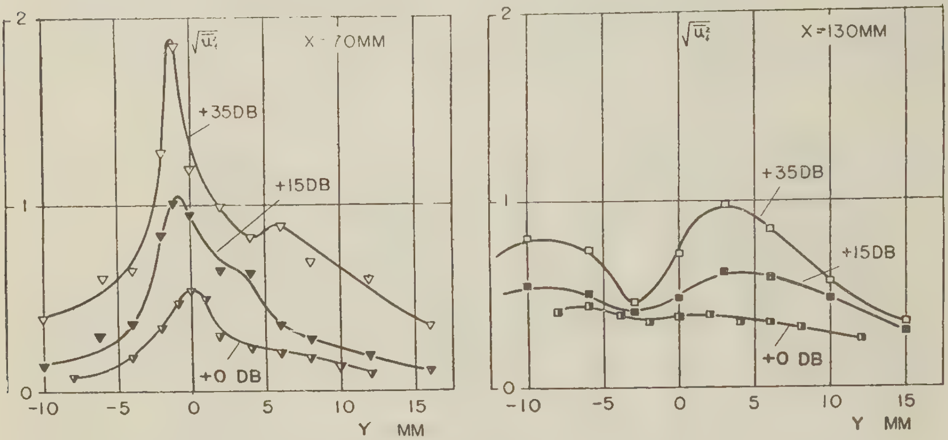

Fig. 9 (C) Distribution of sub-harmonic component (121 cps) with excitation 242 cps.

siderable distortions. This explains the fact that no sinusoidal pattern is observed inside the small region shown in Fig. 2. The somewhat curious distributions of fundamental component at $X=20$ mm and 35 mm are explained in the next section in connection with theoretical results.

At $X=70$ mm, distributions of fundamental and harmonic components are completely altered by the intense excitation. With the excitation level of +35 decibels, the maximum values of fundamental and harmonic components are reached at $X=35$ mm, while the sub-harmonic component has a maximum at $X=70$ mm. It is now apparent that the fundamental and harmonic components have a close relationship with each other. The generation of harmonic component might be the result of remarkable increase of the amplitude of fundamental component. On the other hand, the physical process in the development of sub-harmonic component is not well-known. At $X=130$ mm, the effect of excitation is small. This fact again suggests that the energy equilibrium is almost accomplished there. The layer is, therefore, called as " fully turbulent " at $X=130$ mm and further downstream.

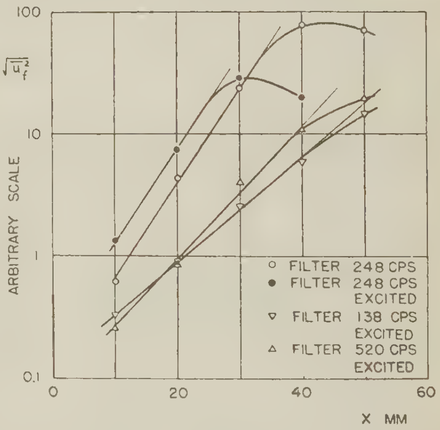

Fig. 10. Growth of spectral components in logarithmic plot. $U_0=10.0$ m/s.

The growth of spectral components in X-direction is shown in Fig. 10 in a more direct way. This is actually a plot of maximum value of $\sqrt{\overline{u_f^2}}$ at each X-section with various excitation frequencies. The tuning frequency of filter is always set equal to the frequency of exciting sound. The general trend of four curves is the same, that is, in a semi-logarithmic plot, $\sqrt{\overline{u_f^2}}$ increases linearly with X when X is not large, then it deviates from being linear, reaches maximum and decreases.

Since it was confirmed experimentally that the distribution of $\sqrt{\bar{u}_f^2}$ in Y-direction is similar at various X-section as far as $\log\sqrt{\bar{u}_f^2}$ is linear to X, the gradients of those straight lines give the rate of exponential growth. It is easily observed that the rate is maximum for the component of frequency of naturally-excited fluctuation—248 cps in this case. The quantitative discussion concerning the rate of growth is given in the following section.

An important subject in the stability theory of laminar flow is the neutral curve which discriminates the unstable zone from the stable zone, for instance, in the wave number-Reynolds number diagram. The frequency of neutral oscillation is to be determined experimentally by the use of present method of artificial excitation. When the amplitude of certain spectral component is not increased by the artificial disturbance of the same frequency, the disturbance is either damped or in neutral equilibrium. Therefore, the limit of amplification of artificial disturbance gives the neutral oscillation. Some results in the laminar separated layer are shown in Fig. 11, in which $\sqrt{\bar{u}_{fe}^2}$ and $\sqrt{\bar{u}_{fn}^2}$ denote root-mean-square values of spectral component of frequency f with and without excitation, respectively. αc_r is the frequency non-dimensionalized by the main-stream velocity U_0 and the momentum thickness θ which is calculated by

$$\theta=\int_{-\infty}^{\infty}\frac{U}{U_0}\left(1-\frac{U}{U_0}\right)\,dy\ .$$

Points for various wind-speeds drop on a single curve. When $\sqrt{\bar{u}_{fe}^2}/\sqrt{\bar{u}_{fn}^2}$ is larger than 1, the external disturbance is amplified and the limiting point on the abcissa at which $\sqrt{\bar{u}_{fe}^2}/\sqrt{\bar{u}_{fn}^2}$ approaches 1, corresponds to the frequency of neutral oscillation. An arrow in the figure indicates the theoretical prediction for the neutral frequency at infinite Reynolds number given by Lessen[3]. The agreement between experimental and theoretical results is good.

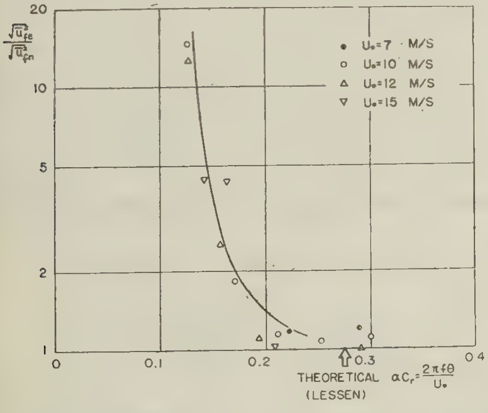

Fig. 11. Determination of the frequency of neutral oscillation.

§ 4. Comparison with Linearized Theory

As a first step of comparing above-mentioned experimental results with linearized theory, the mean-velocity distribution is considered. In the previous report, the measured mean-velocity distribution of laminar speparated layer has been proved to be in good agreement with the theoretical, so-called "similar distribution" when U/U_0 is plotted against Y/θ[1]. The agreement is also good for the present case with artificial excitations.

The existing linearized theory of small disturbance is based on the similar distribution, and the stream function of disturbance Ψ is given by

$$\Psi=\varphi(y)\exp i\alpha(x-ct)$$

where φ is the amplitude function and α is the wave number. c is usually a complex number expressed by $c=c_r+ic_i$. c_r is the wave speed in X-direction and αc_i is the amplification rate with respect to time. x, y and t are non-dimensionalized coordinates by the use of momentum thickness of layer θ as a reference length and main-stream velocity U_0 as a reference velocity. Eigenvalues α, c_r and c_i and eigenfunction $\varphi(y)$ is to be determined by the Orr-Sommerfeld equation under suitable boundary conditions. For the comparison of experimental results with the theory, x- and t-axis is related as $x=c_rt$. Then αc_r is the non-dimensional frequency and $\alpha c_i/c_r$ is the special rate of amplification—amplification rate along X-axis. Since αc_r, c_r and $\alpha c_i/c_r$ are directly deduced from the measurements, these are taken as three eigenvalues. Concerning the amplitude function, $\varphi'(y)$ is compared with the distribution of spectral components of u-fluctuation.

The frequency of sinusoidal fluctuation found in the case of natural transition is plotted in the non-dimensional form in Fig. 12, where $\alpha c_r = 2\pi f\theta / U_0$, θ being the momentum thickness at the section where the fluctuation is found. Whole data are actually taken from the previous experiment[1]. In the figure, Plate I, II and III denote three "boundary-layer plates" with different length as explained in reference 1. The neutral curve in this figure was obtained theoretically by Lessen[3]. It is worth while to note that the theoretical value of αc_r for neutral disturbance changes quite little with respect to Reynolds number within the range of experiment. This fact justifies that the present experimental results obtained at pretty high Reynolds number might be compared with theoretical results calculated for infinite Reynolds number. In the right of figure, the spacial rate of amplification $\alpha c_i / c_r$ obtained by Lessen and Fox for infinite Reynolds number is shown against αc_r. From Fig. 12, we conclude that the naturally-excited sinusoidal fluctuation is theoretically unstable and moreover, it receives maximum amplification among various disturbances in the laminar layer.

The second eigenvalue c_r, the propagation velocity of sinusoidal fluctuation is plotted against αc_r in Fig. 13. Most of the data are obtained with artificial excitations. The pro-

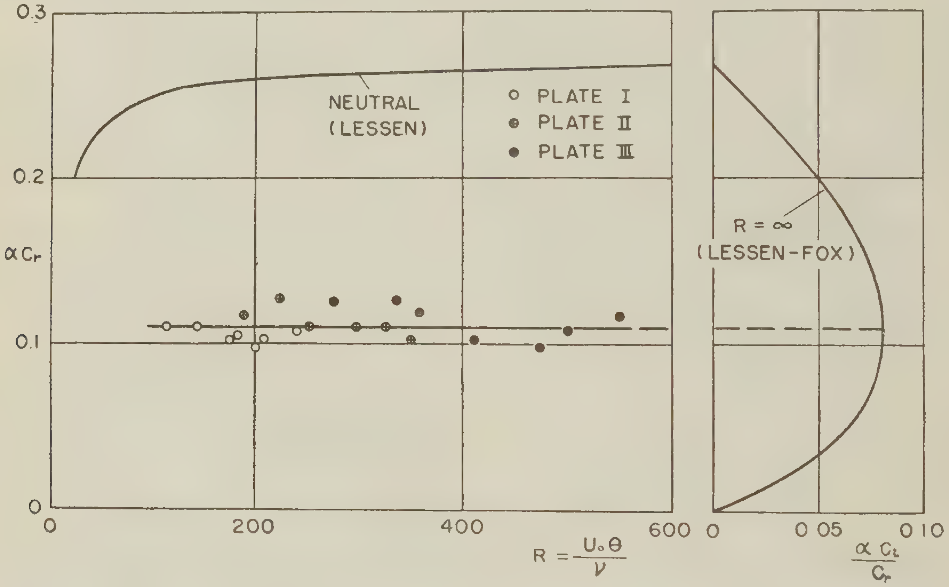

Fig. 12. Comparison of theoretical and experimental results on the frequency of sinusoidal fluctuations.

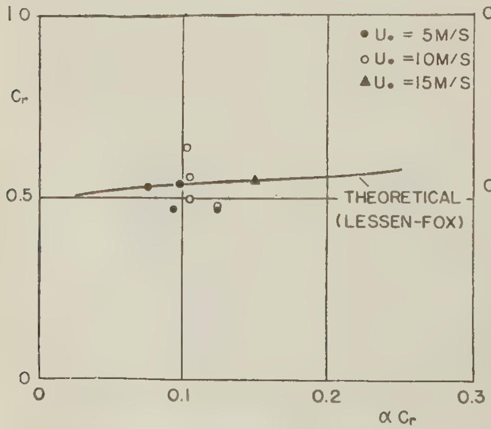

Fig. 13. Propagation velocity of sinusoidal fluctuations.

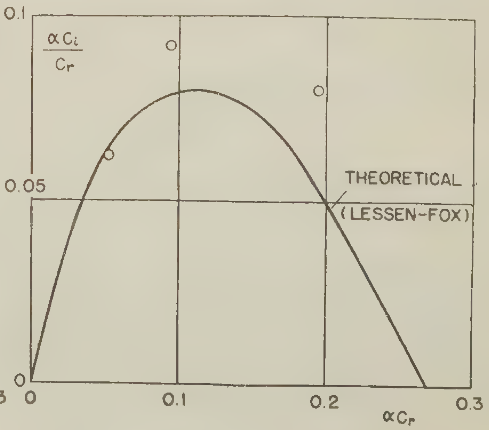

Fig. 14. Spacial rate of amplification of sinusoidal fluctuations.

pagation velocity is determined from the phase lag of signals from two hot-wires placed in the layer apart in X-direction as described in reference 1. The accuracy of determining c_r is affected much by the distortion of wave-form of fluctuation and unfortunately, some distortion was inevitable since sometimes two hot-wires had to be placed with separation of 10 mm in order to obtain a sufficient phase lag. Thus the accuracy of measured value of c_r may be around 15 percent. Considering this situation, the experimental results at three main-stream velocites show a reasonable agreement with theoretical predictions given by Lessen and Fox for infinite Reynolds number.

The comparison of spacial rate of amplification $\alpha c_i/c_r$ is shown in Fig. 14. The rate is calculated by a relation,

$$\sqrt{\overline{u_f^2}}(x_1)\exp \alpha c_i\cdot(t_2-t_1)=\sqrt{\overline{u_f^2}}(x_2)\,.$$

as proposed by Schubauer and Skramstad[4]. Assuming the relation between time and distance as $x_2-x_1=(t_2-t_1)c_r$, the spacial rate of amplification becomes

$$\frac{\alpha c_i}{c_r}=\frac{1}{x_2-x_1}\log\frac{\sqrt{\overline{u_f^2}}(x_2)}{\sqrt{\overline{u_f^2}}(x_1)}\,.$$

It is noticed here that in the present case the excitation by sound is not local but distributed in the whole flow field. However, since the growth rate of fluctuation is very large, the fluctuation directly caused by the sound at sections of measurement is very small compared with the fluctuation resulted by the amplification of excitation given further upstream. Therefore, there is no essential difference between local and distributed excitations in the case of separated layer.

The rate of amplification is calculated from the data shown in Fig. 10 and compared with theoretical results in Fig. 14. The agreement of measurement and theory is satisfactory.

These three quantities, αc_r, c_r and $\alpha c_i/c_r$ make a complete set of eigenvalues in the linearized equation of small disturbance. The wave length of sinusoidal fluctuations in the natural transition calculated from αc_r and c_r is about 30 in θ unit. Considering that the whole thickness of separated layer is about 6θ, the wave length is around 5 times the layer thickness. These numbers may find some practical use.

The distribution of amplitude of sinusoidal fluctuation is shown in Fig. 15. Measurements were made without artificial excitations, tuning the filter with the frequency of natural fluctuation. The root-mean-square values of spectral component at $X=35$ mm and 70 mm are plotted against $y=Y/\theta$ taking maximum value as unity. These experimental distributions are, therefore, those of amplified oscillations and quite unfortunately, the theoretical calculation on the amplitude function for amplified oscillation is not available. Thus the direct comparison is not possible. In the figure, $\varphi'(y)$ for neutral oscillation for infinite Reynolds number is shown. The theoretical distribution becomes zero at about $y=0.4$ and a 180-degrees phase reversal takes place at the point. For the experimental distribution, such a sharp phase reversal is not possible,

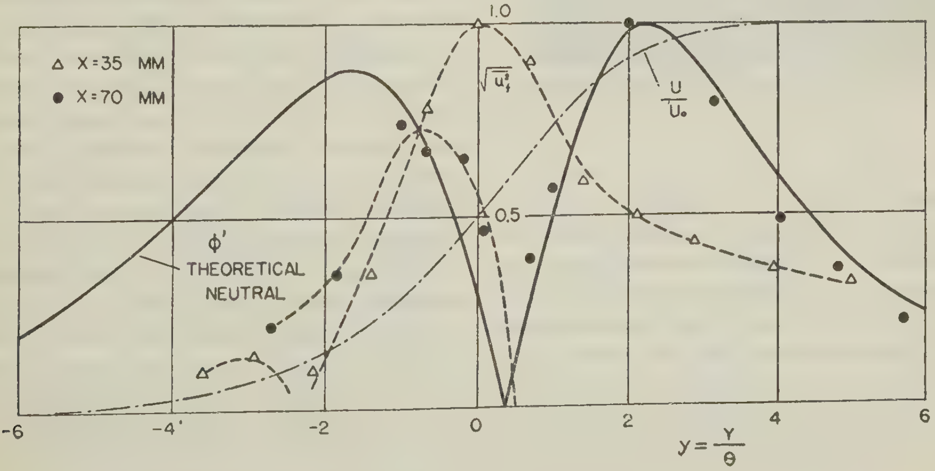

Fig. 15. Amplitude function of sinusoidal velocity fluctuation.

since in the case of amplified oscillation the phase gradually changes in Y-direction. Nevertheless, a large phase shift is observed around $y=-2.3$ for the distribution at $X=35$ mm. Curious distributions as shown in Figs. 7 and 9 (A) at about $Y=-1$ mm are mainly due to this large phase shift in the fundamental component.

Since $\varphi'(y)$ for amplified oscillation can be pretty different from that of neutral oscillation, no concrete conclusion is drawn from Fig. 15. It might be a misunderstanding if one states that at $X=70$ mm the theoretical and experimental distribution is in fair agreement. In fact, at $X=70$ mm, the growth of $\sqrt{\overline{u_f^2}}$ in X-direction is no more exponential. The computation of amplitude function for the amplified oscillation is wanted in order to make more detailed discussion.

A general view of whole flow field was obtained by taking a picture of stream-lines in a water tank. A plate similar to the one used in the wind-tunnel experiment was held fixed in a moving stream. Fine aluminum powder was scattered on the surface of water for the visualization of flow. Fig. 16 shows a single row of vortices in the separated layer.

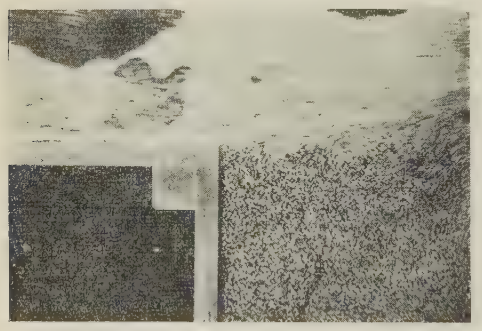

Fig. 16. Picture of stream-line of separated layer taken in a water tank, main-stream velocity, 10 cm/s. Flow from left to right.

Only three vortices are visible since vortex is destroyed further downstream. This kind of configuration of vortices is equivalent to the distribution of amplitude shown in Fig. 15. By a rough estimate, the wave length—distance between two adjacent vortices—is about 35 times of momentum thickness of layer. This number coincides well with that observed in the wind-tunnel by hot-wire anemometers.

§ 5. General Feature of Transition Region

The sinusoidal velocity fluctuation in the separated layer is weak at first and is amplified as the distance downstream is increased. The growth of disturbance is exponential as far as the amplitude remains small. As the fluctuation is amplified more, it gradually changes its wave-form and at the same time, the growth of amplitude becomes more gradual than being exponential. This is clearly illustrated in Fig. 17 in which $(\sqrt{\overline{u^2}}/U_0)_{\max}$ the maximum value of fluctuation level at each X-section is plotted against X. The growth is nearly exponential until $(\sqrt{\overline{u^2}}/U_0)_{\max}$ reaches about 0.03. This linearity limit indicates a point where the non-linear interaction of velocity fluctuations begins. Before the linearity limit is reached, each Fourier component of fluctuation grows independently each other. Beyond this linearity limit, the conventional linearized equation is no more valid and the non-linear interaction should be taken into account. Since the interaction characterizes the turbulent motion, this point where the non-linearity begins, may be appropriately called "transition point". This, however, does not mean that the transition takes place at a point. This definition of transition point seems to be more definite and reasonable than other definitions. In reference 5, it is shown that the same definition is also applicable for the two-dimensional jet as well as the boundary-layer along a flat plate.

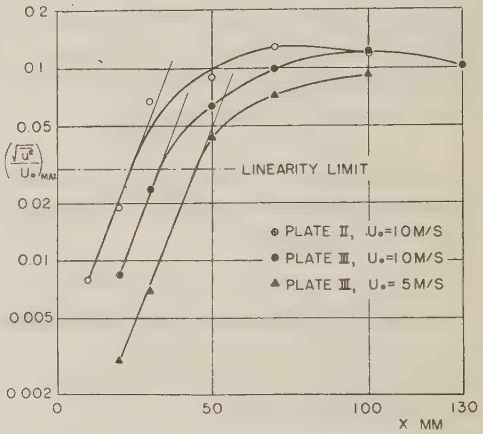

Fig. 17. Logarithmic plot of maximum intensity of velocity fluctuation.

The transition distance determined by the above definition is approximately in agreement with those determined in reference 1 in two ways, one from the growth of thickness of layer and the other from the energy of velocity fluctuation integrated throughout the layer.

Thus the flow field is classified into four regions, namely

(1) Laminar region—There exist no velocity fluctuations.

(2) Linear region—The two-dimensional sinusoidal fluctuation grows exponentially.

(3) Non-linear region—Non-linear interaction and the three-dimensionality of fluctuations are remarkable.

(4) Fully-developed turbulent region—Energy equilibrium is reached.

This classification is applicable for other types of flow which involve transition.

The intermittent burst is not clearly observed in the separated layer. It is true that the amplitude of flucuation does not always remain constant, but the change of amplitude does not necessarily mean the existence of turbulent spot. In fact, the abrupt change of amplitude is not remarkable and the particular pattern of turbulent spot as shown in reference 6 is not observed. As described in reference 5, the intermittent turbulent burst was not observed in the transition region of two-dimensional jet. Considerations given in reference 5 on this point can be applied for the present case.

The effect of artificial excitation in the transition region is summarized as follows:

The transition point shifts upstream as the intensity of excitation is increased. This shift is most remarkable when the frequency of excitation coincides with that of naturally-excited fluctuation. The maximum value of fluctuation in the transition region is apparently increased by artificial excitations. The excitation sometimes changes the distribution of spectral components as shown in Fig. 9. Because of these effects, resulting wave-form of fluctuation in the transition region becomes sometimes very curious as shown in Fig. 6. These all are results of non-linear interaction among spectral components of different wave length as well as components in different directions. Moreover, the dissipation of energy due to viscosity becomes significant when the amplitude of fluctuation becomes large although the viscous effect is negligible for the velocity fluctuation in the linear region. These complicated situations in the non-linear region can not be expressed in a simple formulation, and at present, little is known about the mechanism of non-linear interaction theoretically. In the fully turbulent region, the artificial excitation gives no significant influence.

If we observe from a proper system of coordinates, the sinusoidal fluctuation found in the separated layer is a row of vortices as shown in Fig. 16. At the same time, the vortex street formed behind a cylinder is nothing but the sinusoidal velocity fluctuation if the observation is made by the use of a hot-wire anemometer. Therefore, there are no essential difference between vortex street and sinusoidal fluctuation. Sinusoidal fluctuations already found in the boundary layer along a flat plate⁴⁾ and in the jet⁵⁾ are similar in many points. The fluctuation in the separated layer obviously belongs to the same group. The vortex street formed behind a cylinder is different from these three as mentioned in reference 5.

There are slight distinctions between the boundary layer along a flat plate and the jet in the nature of transition⁵⁾. The separated layer and the jet are much alike and they belong to a same family—the free boundary-layer. A more extensive discussion on the general feature of free boundary-layer is found in reference 7.

§ 6. Conclusion

(1) The sinusoidal velocity fluctuation found in the separated layer corresponds to the disturbance which is unstable and receives maximum amplification in the linearized theory.

(2) Small disturbances superposed on the laminar separated layer grow exponentially as far as their amplitudes remain small. The propagation velocity and the rate of amplification of these disturbances are determined experimentally and they are in good agreement with results of the linearized theory.

(3) The transition point is defined as the limiting point of exponential growth of velocity fluctuation. This point divides the transition region into two parts, linear region and non-

linear region.

(4) The turbulent bursts in the separated layer are much less remarkable than those found in the boundary layer along a flat plate.

References

1) H. Sato: J. Phys. Soc. Japan **11** (1956) 702.
2) M. Lessen and J. A. Fox: 50 *Jahre Grenzschichtforschung* ed. by H. Görtler and W. Tollmien, Vieweg, Braunschweig, (1955) 122.
3) M. Lessen: NACA Rep. 979 (1950).
4) G. B. Schubauer and H. K. Skramstad: NACA Rep. **909** (1948).
5) H. Sato: J. Fluid Mech. (in the press).
6) G. B. Schubauer and P. S. Klebanoff: NACA Rep. 1289 (1956).
7) H. Sato: Rep. Aero. Res. Inst. Univ. Tokyo (in the press).

JOURNAL OF THE PHYSICAL SOCIETY OF JAPAN, Vol. 14, No. 12, DECEMBER, 1959

On a Method of Successive Approximations applied to the Axisymmetric Flows of an Incompressible Perfect Fluid

By Tamedi SIMASAKI and Keishiro NIU

Department of Physics, University of Osaka Prefecture,
Sakai, Osaka

(Received August 18, 1959)

The fundamental equation for the steady axisymmetric flow of an incompressible inviscid fluid is expressed in a complex form as:

$$\frac{\partial F}{\partial \xi}=\frac{F-\bar{F}}{2(\zeta-\bar{\zeta})}.$$

We here replace this by the following approximate equation:

$$F_N=\int\frac{F_{N-1}-\bar{F}_{N-1}}{2(\zeta-\bar{\zeta})}d\bar{\zeta}+g_N(\zeta)\ ,$$

where F_N and F_{N-1} are the Nth and the $(N-1)$th approximations of the complex velocity potential F respectively, and $g_N(\zeta)$ is an appropriate complementary function of ζ. Treatment of this equation is very simple and its validity is ascertained by numerical calculations for the cases of a sphere and prolate spheroid for which exact solutions are already known. In the case of a sphere, approximate solutions converge uniformly to the exact one, while in the case of a prolate spheroid it is seen that the velocity potential on the surface is rather rapidly improved step by step.

§ 1. Introduction

One of the most important problems in hydrodynamics is to know the velocity distribution around a body placed in a uniform flow. For an incompressible perfect fluid it is possible to obtain the velocity distribution around a two-dimensional body with any sectional form by the method of conformal mapping. In the three-dimensional problem, however, even for the flow around an axisymmetric body with very simple sectional form, no general and simple method exists, except for the so-called slender-body theory, the method of sources and sinks, etc.

In 1953 Imai proposed an ingenious simple method by the use of complex variables for treating axisymmetric flows.[1] On the surface of a sphere, the velocity distribution obtained by Imai's method agrees perfectly with the exact one, but in the case of a prolate spheroid agreement becomes worse as the eccentricity increases. Moreover, at a point not on the surface the agreement is not good even in the case of a sphere.

In the present paper, we develop, by extending Imai's method, a general method of successive approximations to derive the velocity distribution of higher order for the whole field of flow around an axisymmetric body with arbitrary shape.

§ 2. Fundamental Equation

We consider the steady flow of an incompressible perfect fluid past an axisymmetric body which is placed in such a manner that its axis of symmetry (taken as the ξ-axis) coincides with the direction of a uniform flow. In this case it is sufficient to consider the matter only in any one of the planes passing through the ξ-axis. In such a plane we take the η-axis perpendicular to the ξ-axis and denote the velocity components along the ξ- and η-axes by u and v respectively. Then, introducing the velocity potential Φ and Stokes' stream function Ψ, we have

$$\left.\begin{aligned} u&=\frac{\partial\Phi}{\partial\xi}=\frac{1}{\eta}\frac{\partial\Psi}{\partial\eta}\,, \\ v&=\frac{\partial\Phi}{\partial\eta}=-\frac{1}{\eta}\frac{\partial\Psi}{\partial\xi}\,, \end{aligned}\right\} \qquad (1)$$

These equations may be rewritten as:

$$\left.\begin{aligned} \frac{\partial\Phi}{\partial\xi}&=\frac{\partial}{\partial\eta}\left(\frac{\Psi}{\eta}\right)+\frac{\Psi}{\eta^2}\,, \\ \frac{\partial\Phi}{\partial\eta}&=-\frac{\partial}{\partial\xi}\left(\frac{\Psi}{\eta}\right). \end{aligned}\right\} \qquad (2)$$

We now introduce conjugate complex variables:

$$\zeta=\xi+i\eta\,,\quad \bar{\zeta}=\xi-i\eta\,, \qquad (3)$$

so that

$$\left.\begin{aligned} \frac{\partial}{\partial\zeta}&=\frac{1}{2}\left(\frac{\partial}{\partial\xi}-i\frac{\partial}{\partial\eta}\right), \\ \frac{\partial}{\partial\bar{\zeta}}&=\frac{1}{2}\left(\frac{\partial}{\partial\xi}+i\frac{\partial}{\partial\eta}\right). \end{aligned}\right\} \qquad (4)$$

Then we have, from (2),

$$\frac{\partial\Phi}{\partial\bar{\zeta}}+i\frac{\partial}{\partial\bar{\zeta}}\left(\frac{\Psi}{\eta}\right)=\frac{\Psi}{2\eta^2}\,, \qquad (5)$$

which may also be written as:

$$\frac{\partial F}{\partial\bar{\zeta}}=\frac{F-\bar{F}}{2(\zeta-\bar{\zeta})}\,, \qquad (6)$$

where

$$F=\Phi+i\frac{\Psi}{\eta}\,, \qquad (7)$$

and $\bar{F}$ is the conjugate function to F. Hereafter we call F the "complex velocity potential".

Eq. (6) is the fundamental equation for our problem to be solved under appropriate boundary conditions.

§ 3. Boundary Conditions and an Equation for Successive Approximations

The function F must satisfy not only the fundamental equation (6) but also appropriate boundary conditions, which are reduced to the following three parts:

(i) The function F must agree with the expression for the uniform flow at infinity;

(ii) The velocity components normal to the axis of symmetry as well as to the surface of the obstacle must be zero;

(iii) Stokes' stream function Ψ along the axis of symmetry as well as on the surface of the obstacle must be zero.

It is to be remarked here that the conditions (ii) and (iii) are of course synonimous to each other theoretically.

It is very difficult to find out intuitively the function F satisfying Eq. (6) subject to the above boundary conditions. In applying the boundary conditions, it will be convenient to transform the ζ-plane to a new z-plane in which the inside of the unit circle corresponds to the sectional area of the body in the ζ-plane. We denote such a transformation function by

$$\zeta=\zeta(z)\,, \qquad (8)$$

which may be obtained by the use of usual methods, such as Imai's one.[2)]

Then, with the new independent variables z and $\bar{z}$, the fundamental equation (6) is expressed by

$$\frac{\partial F}{\partial\bar{z}}=\frac{F-\bar{F}}{2(\zeta-\bar{\zeta})}\frac{d\bar{\zeta}}{d\bar{z}}\,, \qquad (9)$$

which is integrated with respect to $\bar{z}$, giving

$$F=\int\frac{F-\bar{F}}{2(\zeta-\bar{\zeta})}\frac{d\bar{\zeta}}{d\bar{z}}d\bar{z}+g(z)\,, \qquad (10)$$

where $g(z)$ is a complementary function of z alone which should be determined subjected to the boundary conditions (i) and (ii) or (i) and (iii).

Eq. (10) is an integral equation for F and there is no general method to solve it. Accordingly we adopt here a method of successive approximations or a method of iterations as follows. Namely, we replace Eq. (10) by the following equation:

$$F_N=\int\frac{F_{N-1}-\bar{F}_{N-1}}{2(\zeta-\bar{\zeta})}\frac{d\bar{\zeta}}{d\bar{z}}d\bar{z}+g_N(z), \qquad (11)$$

where F_N and F_{N-1} are the Nth and $(N-1)$th approximations of F respectively. Since, however, F_{N-1} is merely an approximation as obtained in the preceding stage of iteration, it is doubtful that the complementary function $g_N(z)$ as determined by using the conditions (i) and (ii) satisfies the remaining condition (iii) as well at the same time, and also it cannot be expected that the condition (ii) is satisfied as well in the case of using the conditions (i) and (iii) for determining the function $g_N(z)$.

Therefore, if we introduce two pairs of expressions for the velocity components along the r- and θ-directions in the ζ-plane as:

$$v_{rN}=\frac{\partial \Phi_N}{\partial r}, \qquad v_{\theta N}=\frac{1}{r}\frac{\partial \Phi_N}{\partial \theta}, \qquad (12)$$

and

$$v'_{rN}=\frac{1}{\eta}\frac{\partial \Psi_N}{r\partial \theta}, \qquad v'_{\theta N}=-\frac{1}{\eta}\frac{\partial \Psi_N}{\partial r}, \qquad (13)$$

v_{rN} will not agree with v'_{rN} and $v_{\theta N}$ will not agree with $v'_{\theta N}$.

But if we choose an appropriate zeroth approximation F_0 as the starting solution and select suitable two conditions out of the three boundary conditions (i), (ii) and (iii), we can improve the convergency of F_N.

In the present paper, we choose (i) and (iii) for the boundary conditions and check the discrepancies between each approximate solution and the exact one. Thus the remaining problem is to choose an appropriate zeroth approximation F_0. The choice of F_0 is, however, rather arbitrary. For example, we can choose as F_0 the complex velocity potential for the uniform flow which should be disturbed by the insertion of an obstacle or the potential for the flow past a sphere with diameter of the same order as the mean diameter of the obstacle concerned. We adopt here the expression for the uniform flow, since it is the simplest one.

In the subsequent sections, we shall build up concrete expressions for the complex velocity potentials and calculate numerical values of the velocity components or the velocity potentials for the cases of a sphere and prolate spheroids with various eccentricities.

§ 4. Case of a Sphere

In this case the transformation function is given by $\zeta(z)=z$. We here consider a uniform flow with unit speed along the positive direction of the x-axis.

When a sphere of unit radius is placed in the uniform flow with its center at the origin of the coordinate system, the velocity potential Φ_0 and Stokes' stream function Ψ_0 for the zeroth approximation are respectively given by

$$\Phi_0=x=\frac{1}{2}(z+\bar{z}), \qquad (14)$$

$$\Psi_0=\frac{1}{2}y^2=-\frac{1}{8}(z-\bar{z})^2, \qquad (15)$$

where

$$z=x+iy \quad \text{and} \quad \bar{z}=x-iy.$$

Then, by (7), the zeroth approximation F_0 for the complex velocity potential becomes

$$F_0=\frac{3}{4}z+\frac{1}{4}\bar{z}. \qquad (16)$$

The first approximation F_1 can be obtained by substituting F_0 in the right-hand side of Eq. (11). Thus we have

$$F_1=\int\frac{z-\bar{z}}{4(z-\bar{z})}d\bar{z}+g_1(z)=\frac{1}{4}\bar{z}+g_1(z). \qquad (17)$$

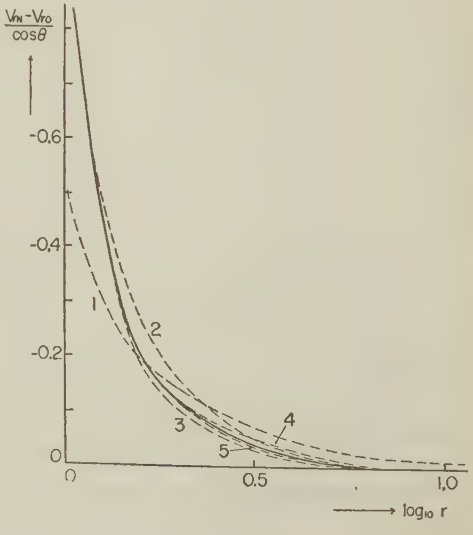

Fig. 1.

The complementary function $g_1(z)$ is easily determined by considering the relation $z\bar{z}=1$ on the surface of the sphere and the boundary conditions (i) and (iii), obtaining

$$g_1(z)=\frac{3}{4}z+\frac{1}{2z}\,. \tag{18}$$

Thus the first approximation F_1 for the complex velocity potential becomes ultimately

$$F_1=\frac{3}{4}z+\frac{1}{4}\bar{z}+\frac{1}{2z}=F_0+\frac{1}{2z}\,. \tag{19}$$

By repeating similar procedures, higher approximate solutions can be obtained step by step. Thus, we have

$$\left.\begin{aligned}
F_2&=F_1-\frac{1}{2^2\cdot 1!\,z}\log(z\bar{z})\,,\\
F_3&=F_2+\frac{1}{2^3\cdot 2!\,z}\log^2(z\bar{z})\,,\\
&\cdots\cdots\cdots\cdots\cdots\cdots\\
F_N&=F_{N-1}+(-1)^{N-1}\frac{1}{2^N\cdot(N-1)!\,z}\log^{N-1}(z\bar{z}),\\
&\cdots\cdots\cdots\cdots\cdots\cdots
\end{aligned}\right\} \tag{20}$$

The last one can easily be verified by mathematical induction.

Figs. 1 and 2 show how the velocity distributions obtained by Eqs. (19) and (20) converge to the exact one. In Fig. 1, $(v_{rN}-v_{r0})/\cos\theta$ is taken as the ordinate, where v_{r0} is the radial velocity component of the uniform flow, and $\log_{10} r$ is chosen as the abscissa, in which r is the distance from the origin. Fig. 2 shows the behaviours of the convergency in the relation $\log_{10} r$ versus $(v_{\theta N}-v_{\theta})/\sin\theta$. The curves of $(v'_{rN}-v_{r0})/2\cos\theta$ and $(v'_{\theta(N+1)}-v_{\theta 0})/\sin\theta$ coincide perfectly with the corresponding curves in Fig. 2 for the same values of N.

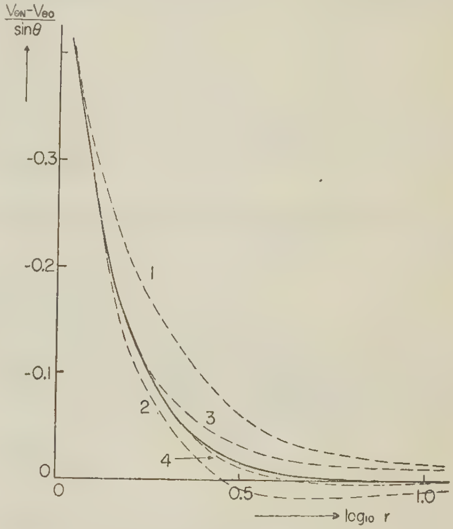

Fig. 2.

The full lines in both figures correspond to the exact solutions. All these figures indicate that our approximate solutions (19) and (20) converge rather rapidly to the exact one, and especially that the curves for the velocity component v_{rN} converge faster than those for v'_{rN} and also the curves for $v_{\theta N}$ converge faster than those for $v'_{\theta N}$. By tending N to infinity, we have, from the expression for the Nth approximate solution F_N given in (20),

$$\begin{aligned}
F_\infty&=\lim_{N\to\infty}\left[\frac{3}{4}z+\frac{1}{4}\bar{z}+\frac{1}{2^1\cdot 0!\,z}\log^0(z\bar{z})-\frac{1}{2^2\cdot 1!\,z}\log^1(z\bar{z})+\cdots\right.\\
&\qquad\left.+(-1)^{N-1}\frac{1}{2^N\cdot(N-1)!\,z}\log^{N-1}(z\bar{z})\right]\\
&=\frac{3}{4}z+\frac{1}{4}\bar{z}+\frac{1}{2z}e^{-(1/2)\log(z\bar{z})}=\frac{3}{4}z+\frac{1}{4}\bar{z}+\frac{1}{2z\sqrt{z\bar{z}}}\,.
\end{aligned} \tag{21}$$

On the other hand, the corresponding exact formulae for the velocity potential and Stokes' stream function are given by Lamb[3] in the forms:

$$\Phi_e=\left(r+\frac{1}{2r^2}\right)\cos\theta\,,\qquad \Psi_e=\frac{1}{2}\left(r^2+\frac{1}{r}\right)\sin\theta\,, \tag{22}$$

from which we obtain, by using the relations $z=re^{i\theta}$ and $\bar{z}=re^{-i\theta}$, the exact expression for the complex velocity potential as:

$$\begin{aligned}
F_e&=\Phi_e+i\frac{\Psi_e}{r\sin\theta}=r\cos\theta+\frac{i}{2}r\sin\theta+\frac{1}{2r^2}(\cos\theta+i\sin\theta)\\
&=\frac{3}{4}z+\frac{1}{4}\bar{z}+\frac{1}{2z\sqrt{z\bar{z}}}\,.
\end{aligned} \tag{23}$$

It will be seen that this expression is in complete agreement with (21).

§ 5. Case of a Prolate Spheroid

An ellipse in the ζ-plane is mapped onto the unit circle in the z-plane by Joukowski's transformation:

$$\zeta=z+\frac{\sigma^2}{z}\,, \tag{24}$$

where σ is connected with the semi-major and semi-minor axes a and b of the ellipse as:

$$a=1+\sigma^2\,, \qquad b=1-\sigma^2\,. \tag{25}$$

In this case, the expression of the complex velocity potential for the uniform flow is given by

$$F_0=\frac{3}{4}\left(z+\frac{\sigma^2}{z}\right)+\frac{1}{4}\left(\bar{z}+\frac{\sigma^2}{\bar{z}}\right). \tag{26}$$

Inserting (26) in the right-hand side of (11) and choosing the complementary function so as to satisfy the boundary conditions (i) and (iii), we get the following first approximate solution for the prolate spheroid:

$$F_1=F_0+\frac{1-\sigma^2}{2z}\,. \tag{27}$$

By similar procedures the second and third approximations can be obtained, and we have

$$\begin{aligned}F_2=F_1+\frac{1-\sigma^2}{4}\Bigg[&\frac{1}{z}+\frac{1+\sigma^2}{\sigma^2 z}\log(1-\sigma^2)+\frac{1}{\bar{z}}-\frac{z}{\sigma^2}\log(z\bar{z})\\&+\left(\frac{z}{\sigma^2}-\frac{1}{z}\right)\log(z\bar{z}-\sigma^2)\Bigg]\,,\end{aligned} \tag{28}$$

$$\begin{aligned}F_3=F_2+\frac{1-\sigma^2}{8}\Bigg[&\left\{\frac{1+\sigma^2}{\sigma^2}\log(1-\sigma^2)+\frac{1+\sigma^2}{\sigma^4}\log^2(1-\sigma^2)+\frac{1-\sigma^2}{\sigma^2}L_2(\sigma^2)\right\}\frac{1}{z}\\&+\frac{1+\sigma^2}{\sigma^2\bar{z}}\log(1-\sigma^2)+\frac{1}{2z}\log^2(z\bar{z})+\left(\frac{1}{z}-\frac{z}{\sigma^2}\right)\{\log(z\bar{z}-\sigma^2)-\log(z\bar{z})\}\log(z\bar{z}-\sigma^2)\\&+\left(\frac{1}{z}+\frac{z}{\sigma^2}\right)L_2\left(\frac{\sigma^2}{z\bar{z}}\right)-\left\{\frac{1}{\sigma^2}(z+\bar{z})+\frac{1+\sigma^2}{\sigma^4}z\log(1-\sigma^2)\right\}\log(z\bar{z})\\&+\left\{\frac{z\bar{z}-\sigma^2}{\sigma^2}\left(\frac{1}{z}+\frac{1}{\bar{z}}\right)+\frac{1+\sigma^2}{\sigma^4}\left(z+\frac{\sigma^2}{z}\right)\log(1-\sigma^2)\right\}\log(z\bar{z}-\sigma^2)\Bigg]\,,\end{aligned} \tag{29}$$

where $L_2(x)$ is Euler's dilogarithm[4)] defined by

$$L_2(x)=\sum_{\gamma=1}^{\infty}\frac{x^\gamma}{\gamma^2}=-\int_0^x\frac{\log(1-y)}{y}dy=\int_0^1\frac{\log y}{y-(1/x)}dy\,. \tag{30}$$

In this case we use the velocity potential itself instead of the velocity in order to see how these solutions converge to the exact one. In this first three stages of approximations, the perturbed velocity potentials ϕ_1, ϕ_2 and ϕ_3 on the surface of the spheroid can be obtained from (27), (28) and (29) respectively. Thus, omitting the term which corresponds to the uniform flow, we have

$$\begin{aligned}\phi_1&=\frac{1-\sigma^2}{2}\cos\theta\,,\\\phi_2&=\frac{1-\sigma^2}{2}\left[2+\frac{1}{\sigma^2}\log(1-\sigma^2)\right]\cos\theta\,,\\\phi_3&=\frac{1-\sigma^2}{2}\left[2+\frac{1}{\sigma^2}\log(1-\sigma^2)+\frac{1}{2\sigma^4}\log^2(1-\sigma^2)+\frac{1}{2\sigma^2}L_2(\sigma^2)\right]\cos\theta\,.\end{aligned} \tag{31}$$

On the other hand, the corresponding exact perturbed velocity potential ϕ_e on the surface of the prolate spheroid is given by Lamb³⁾ in the form:

$$\phi_e = \frac{(1-\sigma^2)^2\{(1+\sigma^2)\log[(1+\sigma)/(1-\sigma)]-2\sigma\}}{2\sigma(1+\sigma^2)-(1-\sigma^2)^2\log[(1+\sigma)/(1-\sigma)]}\cos\theta\ . \tag{32}$$

e	σ^2	ϕ_1/ϕ_e	ϕ_2/ϕ_e	ϕ_3/ϕ_e
0	0	1.0000	1.0000	1.0000
0.1	0.0025	1.0008	0.9994	0.9997
0.2	0.0102	1.0042	0.9991	1.0003
0.3	0.0236	1.0096	0.9975	1.0006
0.4	0.0436	1.0181	0.9953	1.0012
0.5	0.0718	1.0307	0.9918	1.0021
0.6	0.1111	1.0493	0.9863	1.0035
0.7	0.1676	1.0784	0.9770	1.0061
0.8	0.2500	1.1288	0.9587	1.0113
0.9	0.3929	1.2434	0.9075	1.0278
1.0	1.0000	∞	-∞	∞

Table I.

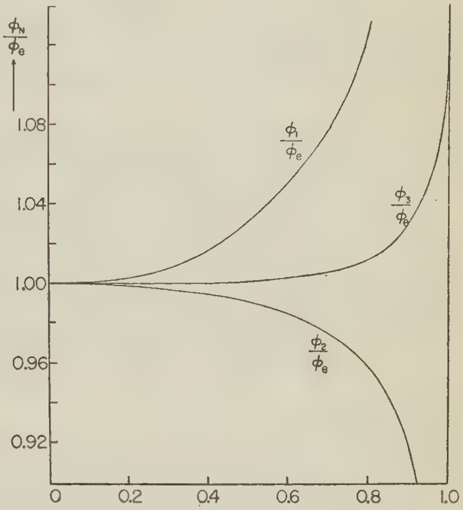

Fig. 3.

Table I and Fig. 3 show how the values of the ratio ϕ_N/ϕ_e ($N=1,\ 2,\ 3$) converge with increasing N for various values of the eccentricity e of the meridian section of the spheroid, where

$$e=\frac{\sqrt{a^2-b^2}}{a}=\frac{2\sigma}{1+\sigma^2}\ . \tag{33}$$

§ 6. Summary

We can see from numerical results obtained in the preceding two paragraphs that the expressions for the axisymmetric flows as given by the iterative use of Eq. (11) together with the boundary conditions (i) and (iii) are improved step by step with the orders of approximation and converge to the exact one in the whole field of flow. Especially in the case of a sphere, the final exact form of the complex velocity potential is obtained straightforwardly, and as for the velocity distribution on the surface, it is obtained exactly in the first stage of approximation. In the case of a prolate spheroid, on the contrary, the velocity potential on the surface is not given exactly in each stage of approximation, but the convergency in the whole field of flow is satisfactorily good.

Thus it may be concluded that the iterative use of Eq. (11) is powerful for dealing with the axisymmetric flow past any obstacle with arbitrary section.

In conclusion, the writers wish to express their cordial thanks to Prof. S. Tomotika for his continual encouragement and also for his kind inspection of the manuscript.

References

1) I. Imai: Tokyo Daigaku Rikogaku-Kenkyusho Hokoku **7** (1953) 183 (in Japanese).
2) I. Imai: Nippon Koku-Gakkaishi **9** (1942) 865 (in Japanese).
3) H. Lamb: *Hydrodynamics* (Cambridge, 1932).
4) W. Gröber und N. Hofreiter: *Integraltafel*, II (Springer, 1950).

Journal of the Physical Society of Japan, Vol. 14, No. 12, December, 1959

The W.K.B. Method for the Differential Equations of the Fourth Order

By Tomoyuki SAITO* and Isao OSHIDA**

**Tokyo University of Agriculture and Technology,*
Koganei, Tokyo
***Kobayasi Institute of Physical Research,*
Kokubunji, Tokyo

(Received August 31, 1959)

Here are studied some types of differential equations of the fourth order, to which the so-called W.K.B. method can be easily extended, and presented some exemplifying solutions up to the first order of approximation. As a physical example, the equation of lateral bending vibration of a not-completely flexible string, whose cross section of finite size is slowly varying along its length, and whose ends are both clamped, is solved. It is also shown that the terms of the first and the third differentation of a linear differential equation of the fourth order can be eliminated by a suitable transformation.

§ 1. Introduction

Not a few linear differential equations of the fourth order are encountered with in physics, which are so important as to require to be solved without diminishing their order, either in order to preserve their physical meaning or to lose no more in the degree of precision of their solutions, although there is the possibility that some of them can be simplified into those of the second order under suitable assumptions.

Although a general method of solving linear differential equations of the fourth order of a general type is not available as yet, many of them appearing in physics happen to take favorable forms or qualities, to our good luck, which make it possible to apply the W. K. B. method.[1]

Generally, a linear differential equation of the fourth order is written in the following form:

$$a(x)y''''+f(x)y'''-y''+g(x)y'-b(x)y=0, \qquad (1)$$

where a, b, f and g are generally functions of the non-dimensionalized independent variable x, and one prime above the unknown function $y(x)$ means one differentiation by x, and so on.

In physics, however, cases are often met with, where f and g are suitably small or sometimes zero, and at the same time a and b are suitably slowly varying functions. The very situation permits our application of the W.K.B. method.

As there are many cases realizing the situation, however, we confine ourselves, here, only to some exemplifying cases.

§ 2. Possibility of Getting Clear of Terms of the First and the Third Differentiation

The original differential equation (1) is written as

$$y''''+A(x)y'''+B(x)y''+C(x)y'+D(x)y=0. \qquad (2)$$

If Eq. (2) could be transformed into one without the terms of the first and the third differentiation, our task of applying the W.K. B. method would be much easier.

By changing both the dependent and independent variables, y and x, to the new ones, u and t, respectively, by the following relations:

$$y\equiv u\cdot\exp\left[-\int\{A+6\zeta)/4\}dx\right],$$

and

$$\frac{dt}{dx}\equiv\exp\left[\int\zeta dx\right],$$

where ζ may be any function of x, satisfying the following non-linear differential equation:

$$\zeta''-3\zeta\zeta'+\zeta^3-(3/5)(A'+A^2/4-2B/3)\zeta$$
$$+(A''-A^3/8+AB/2-C)=0,$$

so the new differential equation concerning $u(t)$ comes out with the intended form.

It is, however, not always possible to find such ζ exactly. Therefore we start with the general form (1). However, the terms of the first and the third differentiation are assumed to be small.

§ 3. W.K.B. Method

By means of putting

$$y \equiv \exp\left[\int \eta(x)\,dx\right],$$

Eq. (1) is transformed into the following equivalent one:

$$a(\eta^4+6\eta^2\eta'+4\eta\eta''+3\eta'^2+\eta''')$$
$$+f(\eta^3+3\eta\eta'+\eta'')-(\eta^2+\eta')+g\eta-b=0. \quad (3)$$

Our conditions are assumed to be such that a, b, f and g are so qualified as to permit the zeroth approximation η_0 on behalf of the true solution of Eq. (3) to be obtained from the following equation:

$$a\eta^4+f\eta^3-\eta^2+g\eta-b=0\,. \quad (4)$$

The first approximation η_1 will be obtained after the necessary order-estimation of the magnitude of the terms in Eq. (3), thus giving the corresponding solution

$$y_1=\exp\left[\int \eta_1 dx\right] \quad (5)$$

as the one with the approximation of the first order.

But the roots of an algebraic equation (4) of the fourth order is not generally expressed in a simple form in terms of its coefficients, and so we confine ourselves, here, to the cases where η_0 is allowed to be obtained from the following equation in the place of Eq. (4):

$$a\eta^4-\eta^2-b=0\,. \quad (6)$$

From Eq. (6) we have

$$\eta^2=(1\pm\sqrt{1+4ab})/2a\,,$$

which turns to the following, according to the value of $|ab|$:

$$\begin{array}{ll} \eta_0{}^2=1/a \text{ or } -b & \text{when } |ab|\ll 1 \\ =\pm\sqrt{b/a} & \text{when } |ab|\gg 1 \\ =(1\pm\sqrt{1+4ab})/2a & \text{when } |ab|\sim O(1)\,. \end{array}$$

These three cases are discussed separately in the following.

Case I: $|ab|\ll 1$

(a) $\eta_0=a^{-1/2}$

For this η_0 to be permitted as the zeroth approximation, the following condition is necessary and sufficient:

$|a'/a^{1/2}|\ll 1$, $|a''|\ll 1$, $|a^{1/2}a'''|\ll 1$, $|f/a^{1/2}|\ll 1$,
$|a^{1/2}g|\ll 1$, besides $|ab|\ll 1$.

There are many variations of cases satisfying the above condition. Among them the following case is examined as typical one.

Example:
When

$$ab\sim a'/a^{1/2}\sim f/a^{1/2}\sim a^{1/2}g\sim O(\epsilon)\,,$$
$$a''\sim O(\epsilon^2)\,, \qquad a^{1/2}a'''\sim O(\epsilon^3)\,,$$

where ϵ means a small quantity compared to unity, then the first approximation (5) is given by

$$y_1=a^{5/4}\exp\left[\int(a^{-1/2}+a^{1/2}b/2-f/2a-g/2)\,dx\right].$$

(b) $\eta_0=(-b)^{1/2}$

The condition for this η_0 to be the zeroth approximation is:

$|b'/b^{3/2}|\ll 1$, $|(b''/b^2)\cdot ab|\ll 1$, $|(b'''/b^{5/2})\cdot ab|\ll 1$,
$|b^{1/2}f|\ll 1$, $|(b''/b^2)\cdot b^{1/2}f|\ll 1$, $|g/b^{1/2}|\ll 1$,

besides

$$|ab|\ll 1\,.$$

Example:
If

$$ab\sim b'/b^{3/2}\sim b^{1/2}f\sim g/b^{1/2}\sim O(\epsilon)\,,$$

and

$$|b''/b^2|\lesssim O(\epsilon)\,, \qquad |b'''/b^{5/2}|\lesssim O(\epsilon)\,,$$

then

$$y_1=b^{-1/4}\exp\left[\int\{(-b)^{1/2}+a(-b)^{3/2}/2-bf/2$$
$$+g/2\}\,dx\right],$$

being correct to the order of ϵ.

It is noted here that the conditions concerning f and g in (a) are different from those in (b), respectively. Under the condition $|ab|\ll 1$, the conditions $|b^{1/2}f|\ll 1$ and $|a^{1/2}g|\ll 1$ follow from the ones $|f/a^{1/2}|\ll 1$ and $|g/b^{1/2}|\ll 1$, respectively.

Therefore, when (a) and (b) are combined to yield the four η_0's, $\pm a^{-1/2}$ and $\pm(-b)^{1/2}$, as the four zeroth-approximation solutions of Eq. (3), simultaneously, the last-mentioned conditions, $|f/a^{1/2}[\ll 1$ and $|g/b^{1/2}|\ll 1$, should replace the preceding ones, $|b^{1/2}f|\ll 1$, and $|a^{1/2}g|\ll 1$ respectively, throughout both (a) and (b).

Case II:

$$|ab|\gg 1\,, \qquad \eta_0=(b/a)^{1/4}\,.$$

If it is assumed that

$$(1/ab)\sim O(\epsilon^4)\,,$$

the condition for which this η_0 is the zeroth approximation is:

$|a'/a^{1/2}|\cdot\epsilon\ll 1$, $|a''|\cdot\epsilon^2\ll 1$, $|a^{1/2}a'''|\cdot\epsilon^3\ll 1$,
$|a^{1/2}(ab)'|\cdot\epsilon^5\ll 1$, $|a(ab)''|\cdot\epsilon^6\ll 1$,

$$|a^{3/2}(ab)'''|\cdot\epsilon^7\ll 1,\ |b'/b^{3/2}|\ll\epsilon,\ |b''/b^2|\ll\epsilon^2,$$
$$|b^{1/2}f|\,\epsilon^3\ll 1,\ |g/b^{1/2}|\cdot\epsilon\ll 1\,.$$

Example 1:

When

$$ab\sim a^{1/2}(ab)'\sim O(\epsilon^{-4}),\ \ a(ab)''\sim O(\epsilon^{-5}),$$
$$a^{3/2}(ab)'''\sim O(\epsilon^{-6}),$$
$$a'/a^{1/2}\sim O(1),\ a''\sim O(\epsilon^{-1}),\ a^{1/2}a'''\sim O(\epsilon^{-2})\,,$$
$$f/a^{1/2}\sim O(1),\ \ a^{1/2}g\sim O(\epsilon^{-2})\,,$$

and

$$b'/b^{3/2}\sim O(\epsilon^2),\ b''/b^2\sim O(\epsilon^3),\ \ b'''/b^{5/2}\sim O(\epsilon^4),$$

then the first approximation is

$$y_1=(a/b)^{3/8}\exp\,[\int(b/a)^{1/4}\{1+a''/2(ab)^{1/2} -a(ab)''/4(ab)^{3/2}+a^{1/2}a'''/8(ab)^{3/4} -a^{3/2}(ab)'''/16(ab)^{7/4}-(f/a^{1/2})/4(ab)^{1/4} -a^{1/2}g/4(ab)^{3/4}\}\,dx]\,,$$

which is correct to the order of ϵ.

Example 2:

The function

$$y=x^5\exp\,[-1/x^2]$$

is an exact solution of the differential equation

$$(x^4/4)y''''-y''-(4/x^8+1/x^4+10/x^2+30)y=0\,.$$

This equation tends to the following one for sufficiently small x:

$$(x^4/4)y''''-y''-(4/x^8)y=0 \tag{7}$$

In this case,

$$a=x^4/4,\qquad b=4/x^8,\qquad f=g=0\,,$$

and for $x\sim O(\epsilon)$,

$$ab\sim O(\epsilon^{-4}),\ a^{1/2}(ab)'\sim O(\epsilon^{-3}),\ a(ab)''\sim O(\epsilon^{-2}),$$
$$a^{3/2}(ab)'''\sim O(\epsilon^{-1}),$$
$$a'/a^{1/2}\sim O(\epsilon),\ a''\sim O(\epsilon^2),\ a^{1/2}a'''\sim O(\epsilon^9),$$
$$b'/b^{3/2}\sim O(\epsilon^3),\ b''/b^2\sim O(\epsilon^6),\ b'''/b^{5/2}\sim O(\epsilon^4).$$

The following formula, being correct to the order of ϵ^2, is obtained for the first approximation solution of Eq. (7):

$$y_1=(a/b)^{3/8}\exp\,[\int(b/a)^{1/4}\{1+1/4(ab)^{1/2}\}dx]$$
$$=\begin{cases} x^5\exp\,[-1/x^2],\qquad x^4\exp\,[1/x^2] \\ \text{and} \\ x^{9/2}\cos\,(1/x^2+\ln x/2),\ x^{9/2}\sin(1/x^2+\ln x/2). \end{cases}$$

Case III:

$$|ab|\sim O(1),\qquad \eta_0=(1\pm\sqrt{1+4ab})/2a.$$

Here the condition for the validity of the zeroth approximation is:

$$|a'/a^{1/2}|\ll 1,\quad |a''|\ll 1,\quad |a^{1/2}a'''|\ll 1,$$
$$|a^{1/2}(ab)'|\ll 1,\quad |a(ab)''|\ll 1,\quad |a^{3/2}(ab)'''|\ll 1,$$
$$|f/a^{1/2}|\ll 1,\quad |a^{1/2}g|\ll 1,\quad \text{besides }|ab|\sim O(1$$

Example:

When

$$|a^{1/2}a'''|\ll|a''|\ll|a'/a^{1/2}|\ll 1,$$
$$|a^{3/2}(ab)'''|\ll|a(ab)''|\ll|a^{1/2}(ab)'|\ll 1,\ |ab|\sim O(1$$

and accordingly

$$|b'''/b^{5/2}|\ll|b''/b^2|\ll|b'/b^{3/2}|\ll 1\,,$$

their magnitudes being of the order of ϵ^3, ϵ and ϵ, respectively, according to their arra from left to right, and moreover

$$f/a^{1/2}\sim a^{1/2}g\sim O(\epsilon),$$

then the first approximation is

$$y_1=\exp\Bigg[\int\Bigg\{\left(\frac{1\pm\sqrt{1+4ab}}{2a}\right)^{1/2}-\frac{1\pm(3/2)\sqrt{1+4ab}}{1\pm\sqrt{1+4ab}}\cdot\frac{(ab)'}{1+4ab}+\left(1\pm\frac{2}{3}\cdot\frac{1}{\sqrt{1+4ab}}\right)\frac{3}{4}\frac{a'}{a} -\left(1\pm\frac{1}{\sqrt{1+4ab}}\right)\frac{f}{4a}-\frac{1}{(\pm\sqrt{1+4ab})}\cdot\frac{g}{2}\Bigg\}dx\Bigg],$$

being correct to the order of ϵ.

Of the signs + and − in front of the root $\sqrt{1+4ab}$, the same ones are to be chosen. For each case of the plus or the minus sign, there are two alternative solutions corresponding to + and − in front of $\{(1\pm\sqrt{1+4ab})/2a\}^{1/2}$.

§ 4. Lateral Bending Vibration of a String Not-Completely Flexible with Finite Cross Section

The lateral bending vibration of a string with finite cross section S, under the tension T, obeys the following differential equation:

$$\rho S\frac{\partial^2 y}{\partial t^2}=\frac{\partial}{\partial s}\left(T\frac{\partial y}{\partial s}\right)-\frac{\partial^2}{\partial s^2}\left(ESk^2\frac{\partial^2 y}{\partial s^2}\right),$$

where ρ is the density, E the Young's modulus of elasticity, ρSk^2 the moment of inertia of the cross section of unit thickness around the line through its center perpendicular to both the string and the displacement y, and s measures the distance along the string.

When the cross section S is constant along the string, together with the other quantities ρ, T, E and k^2, the differential equation is reduced to the one with constant coefficients, and can be solved immediately, giving the following result[2)] for the approximate values of the eigenfrequencies $\omega_n(0)$ of a string of length l, not-completely flexible with its cross section of finite and constant size, and with its ends both clamped:

$$\omega_n(0)\approx(n\pi/l)\sqrt{T/\rho S_0}(1+2\sqrt{ES_0k_0^2/Tl^2}) .$$

S_0 and k_0 mean the constant values of S and k, respectively, and n the order of the eigen-vibrations.

When the constancy of these coefficients breaks down, the situation develops a new phase and we find ourselves at a loss how to meet it.

It their variations upon s are not large, however, we are afforded an opportunity to apply the W.K.B. method.

For a simple illustration, we consider the case where the cross section varies with the distance s, symmetrically on both sides of the middle-point of the string, as follows:

$$S=S_0(1+\alpha x)^2\approx S_0(1+2\alpha x) ,$$
$$k=k_0(1+\alpha x) ,$$
$$|\alpha|\ll 1 , \qquad \text{where } x\equiv s/l .$$

The suffix zero is specified to the values at the middle-point ($x=0$). The other quantities ρ, T and E are assumed to be constant.

As "not-completely flexible" means that the size of the cross section is finite, but small, we assume that

$$\alpha\sim O(\epsilon^{2/3})$$

and

$$S_0/l^2\sim O(\epsilon^{1/3}) , \quad \text{accordingly} \quad k_0/l\sim O(\epsilon^{1/6}) .$$

for instance.

Then it is easily shown that the orders of magnitude of the necessary quantities are as follows:

$$ab\sim a'/a^{1/2}\sim f/a^{1/2}\sim b''/b^2\sim O(\epsilon),$$
$$b'/b^{3/2}\sim O(\epsilon^{1/2}) ,$$
$$a''\sim O(\epsilon^2) , \qquad a^{1/2}a'''\sim O(\epsilon^3), \quad b'''=g=0.$$

This case is classified to Case I.

Omitting the detail of the calculation, the resultant eigenfrequencies are correctly written to the order of $\epsilon^{2/3}$, as follows:

$$\omega_n(\alpha)\approx(n\pi/l)\cdot\sqrt{T/\rho S_0}\cdot(1+2\sqrt{ES_0k_0^2/Tl^2}-\alpha/4),$$

which coincides with $\omega_n(0)$ at the limit of vanishing α, as is expected.

§ 5. Summary

Guided by the principle of the W.K.B. method devised originally for the linear differential equations of the second order, it is considered how to solve those of the fourth order along the same line. The cases are studied, where some special qualifications of the coefficients in the equations permit successful attacks by means of the method.

Some examples are shown with corresponding solutions being correct up to the first order of approximation in each case.

As a simple illustration, the lateral bending vibration of a not-completely flexible string with finite cross section slowly varying along its length, symmetrically on both sides of its middle-point and clamped at both its ends, is discussed.

It is to be said that, in the present paper, rather small portion is surveyed of the vast area where the W.K.B. method would be applicable at least in principle. For instance, in getting η_0 as a starting function of the zeroth approximation, we have had recourse to Eq. (6) instead of Eq. (4), with preference for easiness to trouble. But in order to cover more area for application, the fullest possible use of the latter equation (4) deserves and awaits further consideration.

The authors are indebted to the Ministry of Education for the Scientific Research Fund granted to the Research Group for the Study of Atomic and Molecular Structure.

References

1) H. Jeffreys and B. S. Jeffreys: *Methods of Mathematical Physics*, 2nd ed. (Cambridge University Press, 1950) 522.
T. Kato, H. Hashimoto, Y. Nakata and H. Fujita: *Methods of Solving Differential Equations Approximately* (Iwanami Press, Tokyo, 1958) 172, (in Japanese) etc.
2) C. Tsuboi: *Theory of Vibration* (Kawade Press, Tokyo, 1942) 471. (in Japanese).

Short Notes

This section is intended to secure prompt publication of important discoveries in physics. The reports should not exceed 800 words in length. A figure of size 7 cm × 7 cm will be counted as 150 words.

J. PHYS. SOC. JAPAN **14** (1959) 1820

Antiferromagnetism of $Mn_{3.25}$ Ge

By Kō YASUKŌCHI

Department of Physics, Faculty of Science, University of Tokyo

Tetsuo OHOYAMA

Department of Physics, Faculty of Science, Tokyo Metoropolitan University

Kazuo KANEMATSU

Department of Physics, College of Science and Engineering, Nihon University, Tokyo

(Received October 29, 1959)

It was reported by U. Zwicker et al.[1] that Mn–Ge system contained four intermetallic compounds, Mn_5Ge_3, Mn_5Ge_2, Mn_3Ge_2 and $Mn_{3.25}Ge$, and that the former two were strongly ferromagnetic, while the latter two were presumably weakly ferromagnetic.

In the course of our recent study on the magnetic properties of alloys and compounds of manganese with germanium, an antiferromagnetic behavior was found in a compound $Mn_{3.25}Ge$.

The specimen of this compound was prepared as follows; Powders of electrolytic manganese (99.9%) and germanium (seven-nine purity) were mixed in stoichiometric proportion and sealed in evacuated quartz tube, melted by an electric furnace at 1150°C, and quenched into water at 750°C. The specimen thus obtained was examined with X-ray diffractometer to ascertain its crystal structure. The diffraction lines could be indexed as a hexagonal close packed structure with the lattice constants $a=2.668\pm3$Å, $c=4.309\pm3$Å and $c/a=1.615\pm3$. The temperature dependence of the magnetic susceptibility of this compound was measured by a magnetic balance of torsion type from 90°K up to room temperature under a field of 7.5 kilo.oersteds. The result is shown in Fig. 1. Here the inverse susceptibility is plotted against temperature. This compound has a minimum in the inverse susceptibility-temperature curve and the curve shows that the Curie-Weiss law holds very well at higher temperatures. These behaviors are typical of some antiferromagnetic materials and thus the temperature corresponding to this minimum, 139°K, may be considered as the antiferromagnetic Néel point. The magnetic moment and the asymptotic Curie temperature are $5.47\,\mu_B$ per Mn atom and -266°K respectively.

Recently, Fakidov et al.[2] showed that the Mn_3Ge_2 becomes weakly ferromagnetic and its saturation magnetization disappears at low temperature, and they concluded the parastic ferromagnetism of this compound. Thus we are led to the conclusion that antiferromagnetic exchange coupling may be common in Mn–Ge compounds. The details of our present experiments and the magnetic properties of the other compounds of this system will be published later.

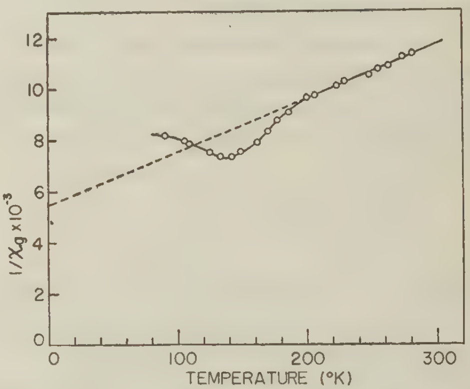

Fig. 1. Inverse susceptibility versus temperature curve of $Mn_{3.25}Ge$.

Finally, the authors wish to experess their hearty thanks to Prof. S. Kaya for his constant encouragement and are also very grateful to Dr. Y. Tomono and Dr. S. Iida who gave them facilities to achieve the work.

References

1) U. Zwicker, E. Jahn and K. Schubert: Z. Metallkde. **40** (1949) 433–436.
2) И. Г. Факидов и Ю. Н. Циовкин: ФММ, **7** (1959) 685–688.

J. Phys. Soc. Japan **14** (1959) 1821

Absorption and Excitation Bands of KCl–Tl in the Extreme Ultraviolet Region

By Goro Kuwabara and Kiyoshi Aoyagi
Department of Physics, Faculty of Science, University of Tokyo

(Received October 16, 1959)

It is well known that KCl–Tl has three absorption and excitation bands characteristic of Tl, lying at 5.04, 5.82, and 6.20 eV, which are usually denoted as A, B, and C band, respectively. But as far as we know, no result on the experiment beyond the C band has been yet published.[1]

On the other hand, the alkali-halide crystals activated with Tl may be expected to luminesce by irradiation with light in the fundamental absorption band, because excitons or free electrons and holes produced by light are supposed to migrate through the crystal and annihilate giving their energy to the lattice or impurity centers. The investigation of this luminescence would afford important informations on the mechanism of energy transport in the crystal. Several experiments[2] along this line have been reported on alkali-iodides. In these crystals, however, the C and exciton bands lie so near to each other that it seems rather difficult to distinguish clearly the effect of the exciton and that of direct excitation of Tl, while KCl, in which both bands are separated as much as 1.3 eV, is suited for this purpose.

The KCl crystals were grown by Kyropoulos method from the melts containing 0.01∼1 mol per cent of Tl. The concentrations of Tl in the crystals were estimated from the absorption intensity in the A band to be of the order of 10^{-2} of those in the melts. The vacuum monochromator constructed in our laboratory is equipped with the concave grating (concave radius 40 cm). The light source is a hydrogen lamp with a hot cathode, and the intensity of the light below 300 mμ was measured by using the fluorescent screen of sodium salicylate. The slit width was about 3 mμ in wave length.

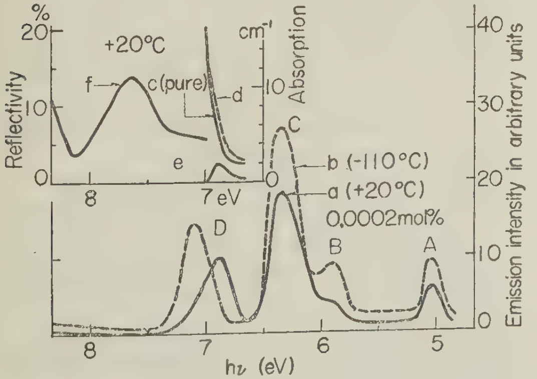

Fig. 1. Excitation spectra of KCl-Tl (0.002 mol percent) at 20°C (a) and −110°C (b). (c) and (d) are the absorption spectra of a pure and a Tl doped KCl. (f) is the reflectivity of a KCl reduced for normal incidence.

The curve (a) and (b) in Fig. 1 are the excitation spectra at 20° and −110°C measured for the normal incidence. Other than the well known three bands, a new excitation band (denoted as D) was found between the exciton (7.6 eV at room temperature cf. Fig. 1 f) and the C band.

When we plot the difference (e) of the absorption curves of a pure (c) and a Tl doped crystal (d) at room temperature, a new absorption band, which coincides precisely with the D band in the excitation spectrum, appears at 6.89 eV. Its absorption intensity is nearly the same order as that of the A band, and varies parallel with those of the A and C bands as the Tl concentration is changed. These results clearly show that the D band is closely related with the Tl center, and not with the exciton absorption in the undisturbed lattice.

The peak of the D band shifts towards higher energy side with the rate of 1.5×10^{-3} eV/deg, as the temperature is decreased, while those of other three bands remain almost at the same positions. This fact might indicate that the D band is associated with the excitation of Cl ions in the nearest neighbours of a Tl center.

In the higher energy side above the D band, the excitation spectrum gradually rises. The reflection loss of about 14 per cent (f) can not account for the low efficiency of excitation at the exciton band. Accordingly we are led to the conclusion that within the temperature and concentration ranges of our experiment the efficiency of luminescence increases monotonously in the tail of the fundamental absorption band, as the energy of an incident photon increases.

At −110°C, however, a considerable amount of emission is observed by light in the exciton band, and its quantum efficiency for the sample containing $10^{17}/\text{cm}^3$ Tl was about 1/18 of that in the C band.

References

1) Prof. Y. Uchida informed us that Dr. Teegarden and his collaborators obtained similar results to those described in this paper.
2) M. Tomura: (unpublished). M. Ueta and T. Ishii: J. Phys. Soc. Japan **14** (1959) 857. K. J. Teegarden: Phys. Rev. **105** (1957) 1222.

J. Phys. Soc. Japan **14** (1959) 1822

Repeated Yielding of Impure Tin Crystals under Successive Impact Loading

By Ken-Ichirō Ishii

Department of Physics, Nagoya Institute of Technology

(Received October 2, 1959)

The dynamic stress-strain curves of metals under impact loading have been studied by Baron1), Maiden and Campbell2), Sakui3), and others. In the present study, the behavior of tin crystals has been examined under successive impact loading. The specimens, 24 mm long and 4.6 mm in diameter, were grown from the melt of 99 per cent tin. The impact test was made with a pair of striker pendulums weighing 180 gm each. After annealing at a high temperature, the specimen was soldered on to one of them and the other was used for loading.

When a number of impacts were applied successively at a moderate velocity of 24 cm/sec., slip took place with a series of discontinuous yields, as shown in Fig. 1a. The stress for slip gradually increased until it reached a saturation value, followed by an abrupt yield. The amount of slip between two consecutive yields was of the order of 0.01 mm. The yielding became less clear at a larger velocity of 28 cm/sec., but a tendency to general yielding was observed4). The elastic collision alone occurred after the initial rapid hardening when the velocity was less than 20 cm/sec. In a purer specimen, grown from the melt of 99.99 per cent tin, slip proceeded smoothly as in Fig. 1b, irrespective of the velocity of impact.

The repeated yielding has been observed from earlier times in mild steels5) when tested at about 200°C. Similar results have been obtained in nickel5), and in α6)- and β-brass5), etc., at moderately elevated temperatures, and in alloys such as duralumin5), β-brass6) and Cu_3Au7) alloy at room temperature. It has been also observed even at 4.2°K; Blewitt8) and his co-workers found it in copper crystals, and Wessel9) in all metals and alloys tested. There may be several mechanisms for the repeated yielding in the above cases. Some of them are quite similar in nature to the present case. They are a) mild steel10) deformed at 200°C with the formation of the Lüders band, and b) copper crystals8) irradiated with neutrons and then deformed at 4.2°K.

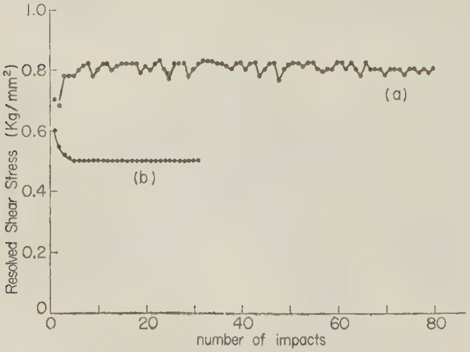

Fig. 1. Stress vs. number of impacts; a) for impure specimen, and b) for purer specimen.

In these three cases, the repeated yielding proceeds from an early stage of the plastic deformation without work-hardening, and at the same time, the yield front propagates successively. It is also noticed that the specimens contain a good amount of imperfections, i.e., solute atoms, impurities, or those produced by the irradiation. So it might be expected that a similar mechanism would be responsible for the results of this kind.

The repeated yielding of mild steels at elevated temperatures is attributed10) to some origin caused by aging and deformation occuring together, and a higher stress is required in order to propagate the front of the Lüders band.

In the case of tin crystals now observed, however, the effect of aging appears to be small. An alternative, or modified, explanation is that the slip is stopped at an obstacle such as segregations in the impure specimens used, which produces the stress concentration in front of the slipped region, and then, the dislocations locked by in the undeformed material will be released. In other words, it would be essentially the same process as the propagation of yield in the lower yield strain of polycrystalline mild steels.11)

References

1) H. G. Baron: J. Iron and Steel Inst. **182** (1956) 354.
2) C. J. Maiden and J. D. Campbell: Phil. Mag. 3, **32** (1958) 872.
3) S. Sakui and T. Mori: J. Appl. Phys. Japan **28** (1959) 309.
4) To be published.
5) For example, T. Sutoki: Sci. Rep. Tohoku Imp. U. **29** (1941) 673.
6) G. W. Ardley and A. H. Cottrell: Proc. Roy. Soc. London, A, **219** (1953) 328.
7) G. W. Ardley: Acta Met. **3** (1955) 525.
8) T. H. Blewitt, J. K. Redman, F. A. Scherrill and R. R. Coltman: Bull. Amer. Phys. Soc. **30** (1955) 32; J. Appl. Phys. **28** (1957) 651.
9) E. T. Wessel: Trans. Amer. Soc. Met. **49** (1957) 149.
10) E. O. Hall: J. Iron and Steel Inst. **170** (1952) 331.
11) A. H. Cottrell: Pittsburgh Conf. on Plastic Def. of Crystals, Carnegie Inst. Tech. and Office of Naval Research, Washington, 1950, p. 60; also his lecture: Trans. Amer. Inst. Min. (Metall.) Engrs. **212** (1958) 192.

J. PHYS. SOC. JAPAN **14** (1959) 1823~1824

The Crystal Structures of $KMnF_3$, $KFeF_3$, $KCoF_3$, $KNiF_3$ and $KCuF_3$

By Atsushi OKAZAKI, Yasutaka SUEMUNE
and Tsutomu FUCHIKAMI*

*Department of Physics, Faculty of Science,
Kyusyu University, Fukuoka, Japan*

(Received August 1, 1959)

The crystal structures of the antiferromagnets KMF_3, where M indicates the $3d$ transition group elements, were examined above and below their Néel temperatures (T_N) by X-ray diffraction using single crystals. The low temperature was attained by a method similar to that of Lonsdale and Smith.[1]

The lattice constants at room temperature were determined from rotation photographs about the [100]. Using high angle reflexions the final value of each lattice constant was determined by graphical extrapolation against $\cos^2\theta$.

At room temperature the structures of $KMnF_3$, $KFeF_3$, $KCoF_3$ and $KNiF_3$ are of the perovskite type and no distortion from cubic symmetry was observed, although Martin, Nyholm and Stephenson[2] have reported that these four compounds were determined as pseudo-cubic by the use of powder sample. On the other hand $KCuF_3$ crystallizes as a modification of the perovskite type, which is tetragonal ($a>c$).

At 78°K (below T_N) $KNiF_3$ and $KCuF_3$ retain their respective symmetry. From the splittings, of high angle reflexions and the relative intensities of their components, $KMnF_3$, $KFeF_3$ and $KCoF_3$ were found to become monoclinic, rhombohedral ($\alpha<90°$) and tetragonal ($a>c$), respectively, where the {400} with Fe$K\alpha$ radiation and the {222} with Cr$K\alpha$ radiation were used mainly.

The results are shown in Table I. The Néel temperatures were determined by Hirakawa and Hashimoto[3] from the magnetic susceptibility measurements.

It is interesting to compare the results of KMF_3 with those of MF_3[4),5)], LaMO_3[6)] and CaMO_3[6)], because in all the cases the dispositions of the magnetic cations relative to the intervening anions are similar. The crystal field splits the $3d$ levels of magnetic cation in an octahedral site into two groups—a set of three degenerate d_ε orbitals and a set of two d_γ orbitals of higher energy. In the case of MF_3 system Hepworth and Jack[4] have accounted for the lower symmetry of MnF_3 than that of the other MF_3 by the fact that the electronic charge distribution of Mn^{3+} ion has the d_γ symmetry. Such a lower symmetry caused by the d_γ symmetry has been discussed about some crystals by Dunitz and Orgel[7] on the basis of Jahn-Teller effect.

The divalent $3d$ ions under consideration have electronic configurations as follows:

	$3d_\varepsilon$			$3d_\gamma$	
Mn^{2+}	↑	↑	↑	↑	↑
Fe^{2+}	↑↓	↑	↑	↑	↑
Co^{2+}	↑↓	↑↓	↑	↑	↑
Ni^{2+}	↑↓	↑↓	↑↓	↑	↑
Cu^{2+}	↑↓	↑↓	↑↓	↑↓	↑

Since LaMO_3 and CaMO_3 systems are also interpreted from the above point of view, in KMF_3 system $KCuF_3$ may be expected to have lower sym-

Table I. Lattice constants and T_N of KMF_3.

	colour	at 298°K symmetry	lattice constants (Å)	at 78°K symmetry	lattice constants (Å)	T_N (°K)
$KMnF_3$	light brown	cubic	$a=4.191\pm0.001$	monoclinic	$(a, b, c)=(4.168, 4.171, 4.185)$* $\beta=89°51'\pm1'$	88
$KFeF_3$	brown	cubic	$a=4.122\pm0.001$	rhombohedral	$a=4.108\pm0.002$ $\alpha=89°51'\pm1'$	121
$KCoF_3$	rosy	cubic	$a=4.069\pm0.001$	tetragonal	$a=4.057\pm0.002$ $c=4.049\pm0.002$	136
$KNiF_3$	yellow-green	cubic	$a=4.015\pm0.001$	cubic	$a=4.002\pm0.002$	280
$KCuF_3$	pale violet	tetragonal	$a=4.140\pm0.001$ $c=3.926\pm0.002$	tetragonal	$a=4.121\pm0.002$ $c=3.913\pm0.002$	243

* For $KMnF_3$ the lower temperature measurements should be done as the present temperature was too near T_N. It could not be determined at present which of the three values in the parentheses corresponds to the letters a, b and c.

---

* On leave of absence from Saga University, Saga, Japan.

metry than the other four compounds above T_N. The expectation should be supported by our result.

Furthermore it may be worth while to compare the results of KMF_3 system with the distortion below T_N of MO system[8].

The experimental and analytical details will be published in the near future.

The single crystals used in this experiment were given by Dr. S. Ogawa of Hokkaido University and Dr. K. Hirakawa and Mr. T. Hashimoto of our laboratory through their courtesy.

References

1) K. Lonsdale and H. Smith: J. Sci. Instrum. **18** (1941) 133.
2) R. L. Martin, R. S. Nyholm and N. C. Stephenson: Chemistry and Industry (1956) 83.
3) K. Hirakawa and T. Hashimoto: to be published.
4) M. A. Hepworth, K. H. Jack, R. D. Peacock and G. J. Westland: Acta Cryst. **10** (1957) 63. M. A. Hepworth and K. H. Jack: Acta Cryst. **10** (1957) 345.
5) E. O. Wollan, H. R. Child, W. C. Koehler and M. K. Wilkinson: Phys. Rev. **112** (1958) 1132.
6) H. L. Yakel, Jr.: Acta Cryst. **8** (1955) 394.
7) J. D. Dunitz and L. E. Orgel: J. Phys. Chem. Solids **3** (1957) 20.
8) W. L. Roth: Phys. Rev. **110** (1958) 1333.

J. PHYS. SOC. JAPAN **14** (1959) 1824

Measuremert of Plasma Temperature and Electron Density

By Kiyoshi MURAKAWA and Shizuyo HASHIMOTO
Aeronautical Research Institute, University of Tokyo, Komaba-machi, Meguro-ku, Tokyo

(Received October 9, 1953)

In a previous article with the same title[1] we described a method of measuring the temperature of a plasma obtained by passing condensed discharge through a Geisler tube containing neon. From the line profiles of $H\gamma$ and NeIλ 4715 the electron density N was deduced in such a way that the wings of the profiles are fitted into the prediction of Holtsmark's theory. This method of determining the electron density was adopted by previous workers[2], but a recent calculation by Griem, Kolb and Shen[3] has shown that the above-mentioned method yields a value of N that is two times as large as the true value. In the case of our light source we get therefore $N=4.8\times10^{15}/\mathrm{cm}^3$ instead of the previous $1\times10^{16}/\mathrm{cm}^3$.

In the work l.c., the wave-length of Ne I λ 5852 emitted from condensed discharge was compared with that of the same line emitted from arc discharge, the latter wave-length being assumed to be free from the influence of the field of ions and electrons. The displacement (expressed in wave-number) of λ 5852 due to the condensed discharge is denoted as $\Delta\nu_{\mathrm{dis}}$. The half-value width due to the broadening effect of the ions and electrons (neglecting the Doppler effect) is denoted as $\Delta\nu_k$. For a line showing a quadratic Stark effect $(\Delta\nu=\gamma F^2)$ such as Ne I λ 5852, Lindholm's formula can be expressed as (the same notations as in l.c. are used)

$$\Delta\nu_k=A\gamma^{2/3}v^{1/3}N/c, \qquad (1)$$

$$\Delta\nu_{\mathrm{dis}}=B\gamma^{2/3}v^{1/3}N/c. \qquad (2)$$

Lindholm obtained $A=0.0450$ and $B=0.0387$.

If we put the values of γ, v, N (for the line Ne I λ 5852) and B in eq. (2), we get $\Delta\nu_{\mathrm{dis}}=0.058\,\mathrm{cm}^{-1}$ which is to be compared with the observed value $\Delta\nu_{\mathrm{dis}}=0.027\,\mathrm{cm}^{-1}$, showing that Lindholm's B is too large. If we determine the value of B by a purely empirical method, we get approximately $B=0.018$. Neon lines other than λ 5852 were examined in the same way as in l.c., and the result was found to yield the same value of B as proposed here.

Retaining the value of A as given by Lindholm, we get $\Delta\nu_k=0.067\,\mathrm{cm}^{-1}$, and therefore the half-value width due to the Doppler broadening effect alone is $\Delta\nu_D=0.192\,\mathrm{cm}^{-1}$. From the value of $\Delta\nu_D$ it follows that the plasma temperature is $T=4.9\times10^3\,\mathrm{K}$ instead of the previous $6.0\times10^3\,\mathrm{K}$. This deduction depends upon Lindholm's theory. In case when the value of A in Lindholm's formula has to be changed, the plasma temperature deduced here would have to be re-calculated accordingly.

Dr. McLane of the Speedway Laboratories (Linde Company) kindly gave us a copy of the article of Griem, Kolb and Shen prior to publication. We thank him heartily for his kindness and for his deep interest in our work.

References

1) K. Murakawa and S. Hashimoto: J. Phys. Soc. Japan **14** (1959) 1235. This article will be referred to as l.c. in the present note.
2) For example G. Jürgens: Z. Physik **134** (1952) 21.
3) H. R. Griem, A. C. Kolb and K. Y. Shen: to be published. See also P. Bogen: Z. Physik **149** (1957) 62, and H. Margenau and M. Lewis: Rev. Modern Phys. **31** (1959) 569.

J. PHYS. SOC. JAPAN **14** (1959) 1825~1826

Stacking Faults in Copper-Nickel Alloys

By Kôichi NAKAJIMA

The Research Institute for Iron, Steel and Other Metals, Tohoku University, Sendai, Japan

(Received October 6, 1959)

It was reported[1] that the density of stacking faults introduced by cold-working in face-centred cubic solid solutions increased with increasing the content of solute atoms, and reached a maximum at the solubility limit of the solution.

The present author examined these phenomena with copper-nickel alloys. The alloys of various compositions were pulverized at room temperature by using a stamp mill and a ball mill. The pulverization was carried out in benzine in order to prevent the samples from oxidation. The X-ray diffraction was taken with a diffractometer " XRD-5 " made by general Electric Co. by using Cu-Kα radiation. The shifts of the (111) and (200) peaks due to cold-working are sharp enough to determine the center of gravity to about ±0.01°. The methods of calculation of the stacking fault probability from the X-ray measurement were reported by some workers[2] and recently Wagner[3] proposed a theory that deformation and twin stacking faults of random distribution in the cold-worked material affect on X-ray diffraction, and showed the following equation:

$$\langle \varDelta(2\theta^\circ)\rangle_{hkl}-\langle \varDelta(2\theta^\circ)\rangle_{h'k'l'}=\mathscr{H}\alpha,$$

where

$$\mathscr{H}=(\langle G\rangle j\tan\theta^\circ)_{hkl}-(\langle G\rangle j\tan\theta^\circ)_{h'k'l'}$$

$\langle \varDelta(2\theta^\circ)\rangle_{hkl}$ shows the observed shift of the (hkl) peak and $G=90\sqrt{3}h_3/\pi^2 i_0^2$. j and $\langle G\rangle$ are the fraction of (hkl) plane and averaged values for the (hkl) reflection, which are affected by stacking faults, respectively. Fig. 1 shows the stacking fault probability calculated by the above equation, from which it will be seen that the stacking fault probability calculated by the above equation, from which it will be seen that the stacking fault probability α increases gradually, and reaches a maximum at 50-50 composition. The effective strain ξ in the matrix was calculated from the line broadening analysis discussed by Williamson and Hall.[4] The density of dislocation ρ calculated from the strain broadening is given by[5]

$$\rho=k\xi^2/Fb^2$$

where k is a constant and F is a strain energy factor. The stacking fault energy γ is obtainable from the following relation by Cottrell:[6]

$$r=\mu a^2/24\pi\gamma\ ,$$

where

$$\alpha=\rho rd$$

r is the width of the extended dislocation. μ and a are the shear modulus and the lattice parameter, respectively. The density of dislocation ρ and the faulting energy γ calculated by these equations are shown in Fig. 2. It will be seen that the faulting energy γ increases rapidly as nickel content increases above 50 per cent nickel.

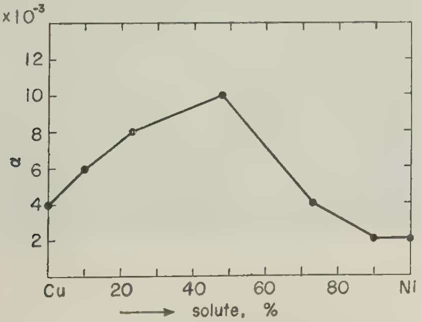

Fig. 1. Stacking fault probability, α.

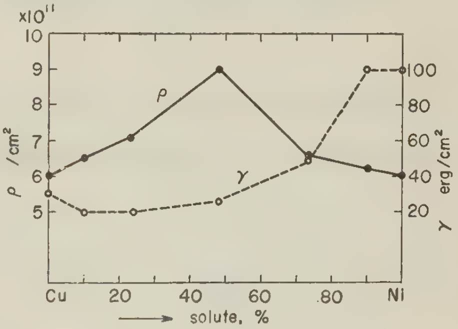

Fig. 2. Density of dislocation, ρ, and stacking fault energy, γ.

The fact that α increases gradually as shown in Fig. 1, and reaches a maximum at 50-50 composition may be interpreted from the point of view that solute atoms concentrate in the faulted layer, and prevent the movement of the stacking fault at room temperature. In fact, Suzuki[7] has pointed out that in a face-centred cubic solid solution the state of thermodynamical equilibrium in the faulted layer will be different from that of the matrix, and will result the concentration of solute atoms in the faulted layer. If this concept is valid, a small angle scattering due to the inhomogenity of the structure should be observed. Weak small angle scattering was actually observed in a specimen of copper-5% aluminium alloy annealed at 100°C after severe cold-rolling. However, the intensity of the double Bragg scattering may not all be negligible compared with some weak scatterings due to the heterogeneity of the structure. Therefore, an alternative explanation of the appearance of the weak small angle scattering may also be possible from the point of view that the scattering is due to double Bragg scattering from slightly misoriented crystals in the annealed sample, and accordingly a more detailed investigation on the small angle scattering is desirable. The full report will be shown before long.

References

1) R. E. Smallman and K. H. Westmacott: Phil. Mag., **2** (1957), 669.
2) M. S. Paterson: J. Appl. Phys., **23** (1952), 805.
3) C. N. J. Wagner: Acta Met., **5** (1957), 427.
4) G. K. Williamson and W. H. Hall: Acta Met., **1** (1953), 22.
5) G. K. Williamson and R. E. Smallman: Phil. Mag., **1** (1956), 34.
6) A. H. Cottell: *Relation of Properties to Micro Structure* (American Society for Metals, 1954), P. 131.
7) H. Suzuki: Sci. Rep. Res. Inst. Tôhoku Univ., **4** (1952), 455.

J. PHYS. SOC. JAPAN **14** (1959) 1826

Frequency Shift in Ammonia Absorption Lines other than (3, 3)

By Kiyokata MATSUURA

Electrotechnical Laboratory, Nagatacho Tokyo

(Received October 3, 1959)

The shift in resonance frequency of ammonia (3, 3) line with pressure has already been reported by us[1], where the shift coefficient, *a*, is given as $(1.8\pm0.1)\times10^{-2}$. The coefficieet *a* is defined in such a way that the apparent center of resonance, ν, is given by $\nu=\nu_0+a\Delta\nu_p$, where $2\Delta\nu_p$ is the width of the line due to pressure broadening.

We have now measured the shift coefficient, *a*, for lines other than (3, 3). Fig. 1 shows the value of *a* for various lines with $J=K$ at 30°C and 100°C. It is seen that *a* decreases with increasing *J* and goes finally to negative values. This would imply that the explanation of the frequency shift would require at least two competing mechanisms.

From the point of view of the accuracy of the atomic clock, it seems noteworthy that the absolute value of *a* is very small for $J=K=5$ or 6. Considering that the intensity of (6, 6) line is comparable with that of (3, 3) line, it seems advisable to use the line (6, 6) in the absorption type atomic clock.

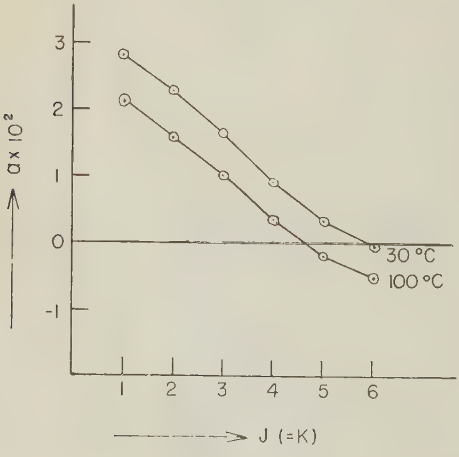

Fig. 1.

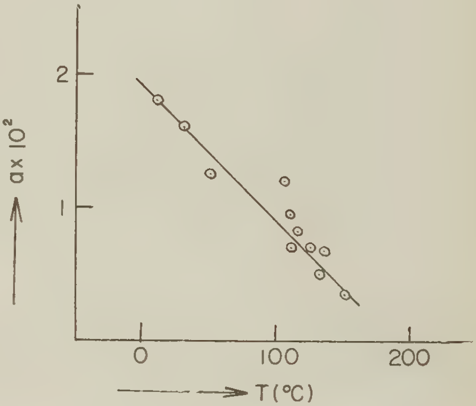

Fig. 2.

Fig. 2 shows the dependence of *a* for (3, 3) line on the temperature of the absorption cell. Other lines show similar temperature dependences. The experiment has been performed, as before, with the absorption-type atomic clock installed at the Laboratory and the absorption cell consists of 30m *K*-band wave guide. The temperature of the cell can be varied from room temperature to 150°C.

Measurements on the shift coefficient for lines with $J\neq K$ are now going on.

Reference

1) K. Matsuura, Y. Sugiura and G. M. Hatoyama: J. Phys. Soc. Japan **12** (1957) 314.

J. PHYS. SOC. JAPAN **14** (1959) 1827

Diffusion of Cu into CdS Single Crystal through Dislocations

By Sumiaki IBUKI and Hirosuke YAMASHITA
Research Laboratory Mitsubishi Electric Mfg. Co., Ltd. Amagasaki, Japan

(Received October 1, 1959)

In case of discussing the diffusion of impurity into crystal, it is not improbable that the diffusion velocity through imperfections, such as vacancies, dislocations, twin boundaries and grain boundaries, is predominently high.[1)]

It is a well-known fact that Cu diffuses very easily into CdS[2)], and also the authors have experienced fairly marked diffusion of Cu at 400 ~500°C. Trying more detailed inspection, we may be able to find some locations where the diffusion of Cu is abnormally remarkable at about as low as 300°C. Moreover, CdS single crystal has some favorable characteristics to observe the above mentioned phenomenon, because as usual the crystal changes its color from transparent yellow to brown acompanied with the inclusion of Cu atoms, and Cu diffusion may be accelerated if Cl atoms are predoped in the crystal.

The authors performed following experiments. Cu and In metals are evaporated on both ends of $(11\bar{2}0)$ surface of CdS: Cl crystal $(10\times1\times0.2\ \mathrm{mm})$ to make narrow bands respectively. After several hours of heat treatment at 300°C in air, we obtained some interesting results. One of microscopic pictures showing the evaporated Cu side is given in photo. 1. Judging from the photo, Cu may be easily sucked thermally into CdS crystal through the tops of dislocations exposed at the surface, and it is expected that when the voltage is applied between each evaporated metals so as to form the positive electrode of Cu, Cu metals may be diffused into CdS only by the electric field.

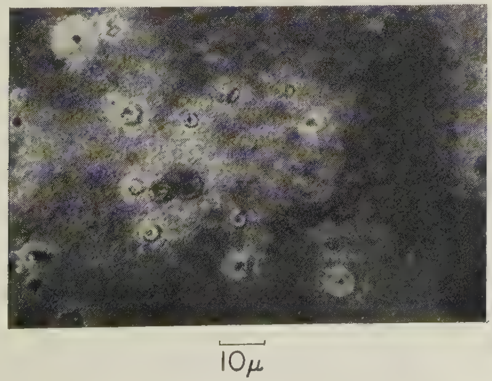

Photo. 1. Cu evaporated layer after 300°C 3 hours' heat treatment.

Several mA of current are flown continually for scores of hours through CdS crystals which have nearly above mentioned sizes and positive electrodes of Cu, then we obtained some distinct results. An example is shown in Photo. 2. It might be concluded from the photo, that the dislocations play more important parts for the electric field diffusion compared with the thermal diffusion. Under certain circumstances, it is found that the evaporated Cu layer covered upon the dislocations disappeared thoroughly, or hemi-circular erosions of Cu layer are observed along the boundary of Cu layer and crystal surface.

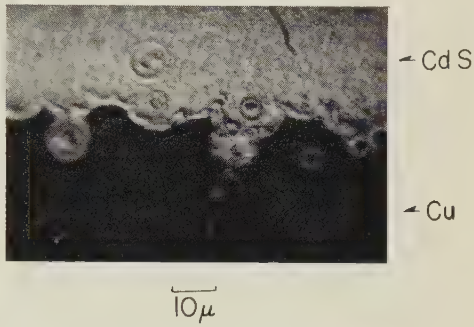

Photo. 2. Boundary between CdS and Cu evaporated layer after 2 mA 60 hr current flow (Resistance 30 Ω)

It is proved clear from those facts that the existence of dislocations influences greatly upon the impurity diffusion into crystal, that is, dislocation may be able to suck strongly impurities at their edges. Detailed reports are to be published later.

References

1) W. C. Dash: J. Appl. Phys. **27** (1956) 1192. J. Roschen and C. G. Thornton: J. Appl. Phys. **29** (1958) 923.
2) K. T. Wilke: Z. Phys. Chem. **205** (1955) 73. R. H. Bube and M. Thomsen: J. Chem. Phys. **23** (1955) 15.

J. Phys. Soc. Japan **14** (1959) 1828

A New Device for measuring Thickness of Evaporated Metal Film by Use of X-ray Interference Fringes

By Yoshibumi Fujiki and Toshiho Yoshida

Institute of Physics, Kyoto Prefectural University of Medicine

(Received October 3, 1959)

W. Hink and W. Petzold[1] improved Kiessig's[2] X-ray interference method using the divergent beam from a micro-focused X-ray source. In their device, the oscillation of a specimen was unnecessary and the exposure time required was reduced to a few per cent of that required in the case of Kiessig's original device. However, their device requires the specially designed micro-focused X-ray source and comparatively large specimen is necessary for obtaining a sufficient number of interference fringes. To avoid these difficulties, we devised a new method.

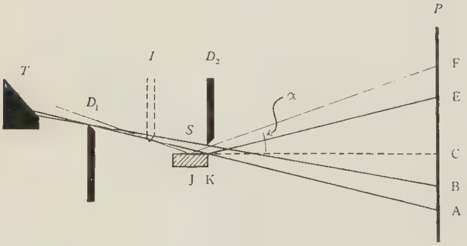

Fig. 1.

In Fig. 1, the beams from a usual line-focused X-ray source T fall on a specimen S with various glancing angles, and the interference fringes are produced on the photographic film P, if the width of the specimen is suitably small and the distance between the specimen and the photographic film is sufficiently large. The beams which would come from the source directly to the photographic film and would mask the interference fringes are screened out by the diaphragms D_1 and D_2. The glancing angle α of the beam corresponding to any interference maximum F will be given by

$$\tan\alpha = \mathrm{CF}/\mathrm{JC} = (\mathrm{AF}-\mathrm{AC})/\mathrm{JC} = (\mathrm{AF}-1/2\cdot\mathrm{AE})/\mathrm{JC}\ ,$$

where J is the mid-point of the specimen, and C the intersection of the extension of specimen surface with the photographic film. Point A is the position where the incident beam, which corresponds to the innermost reflected beam KE, would strike the photographic film directly, where K is the hind edge of the specimen. The uppermost end of the direct incident beam hits the photographic film at B and so the point A is masked. For the purpose of detecting the point A, indicator I is inserted in front of the specimen vertically from the upper side of the apparatus, as shown in Fig. 1. This is made of tungsten wire whose end is sharpened in wedge-shape. The inverted image of this indicator is imposed on the photographic film at the region below A and the errect image above A as is shown in Fig. 2, thus the intersection of these two images determines the point A. Fig. 2 is an example of interference fringes obtained from a gold film evaporated on glass substrate whose width is about 3.5 mm. The distance between the specimen and the photographic film was 40 cm. The wider the specimen width, the broader would become the width of each fringe, but the mean errors of measured values of film thickness d and the unit decrement of refractive index η were not so large for the specimen width mentioned above. Using the interference condition for maxima $(2m+1)\lambda/2=2d\sqrt{\alpha^2-2\eta}$, where m is the order of interference and λ the wavelength, the observed values of d and η were obtained from the photograph shown in Fig. 2 as follows:

$$d=319.6\pm0.8\text{Å},\quad \eta=(43.3\pm0.4)\times10^{-6}.$$

The X-rays used was $Cu\ K_\alpha$ radiation with nickel filter, applied voltage of 30 kV and tube current of 40 mA, and the exposure time required was 3 minutes, which was of the same order as that required in Hink and Petzold's method. This short exposure time makes it possible to pursue the comparatively rapid change of film thickness with aging time.

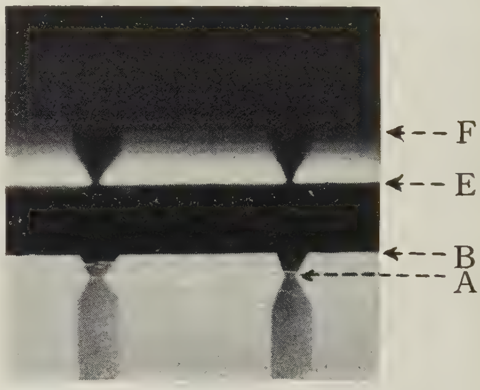

Fig. 2.

The writers are greatful to Professor K. Tanaka of Kyoto University for his valuable suggestions and advice.

References

1) W. Hink and W. Petzold: Z. angew. Phys. **10** (1958) 135.
2) H. Kiessig: Ann. Physik [5] **10** (1931) 769.

J. PHYS. SOC. JAPAN **14** (1959) 1829~1830

Observations of Lattice Defects in Graphite by Moiré Patterns

By Kazuhiko IZUI

Chemistry Division, Japan Atomic Energy Research Institute, Tokai, Ibaraki

(Received October 5, 1959)

Since the first observation of the moiré patterns in graphite crystals,[1] moiré patterns in some other materials have been studied by several workers[2] using the electronmicroscope. The moiré patterns are not only interesting from the electronoptical point of view, but are useful for detecting lattice defects such as dislocations and grainboundaries.[3]

The present note reports some irregularities in moiré patterns in electronmicrographs from graphite, which seem to be caused from lattice defects in the crystal. The specimens used are the spectroscopically pure natural graphite SP-1 and SP-2.

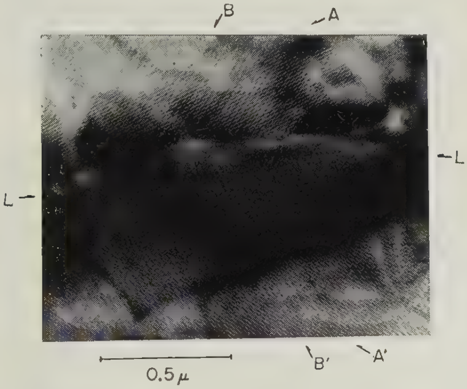

Fig. 1.

In Fig. 1, the moiré lines parallel to the directions A and B, and those parallel to A' and B' are seen respectively in the upper and lower regions bounded by the boundary L. The lines of moiré are produced by the (110), (010), $(2\bar{1}0)$ and $(1\bar{1}0)$ atomic planes of the hexagonal crystal structure, respectively. The angle between A and A' or B and B' is smaller than 60° by about 2×10^{-2} rad. This seems to indicate that within either one of the two overlapping crystals producing moiré, a part bounded by a sub-bundary L is rotated around the c-axis about 10^{-2} rad with respect to the other part. The irregular and obscure lines seen in the back ground seem to be dislocation lines which lie in the basal plane.

In Fig. 2, we can see that the moiré patterns are locally distorted along the curved lines L_1, L_2 and L_3 and the patterns are displaced in parallel by about a half moiré spacing across these lines, while no such displacement except local distortion does occur across the line M. When the incident angle of the electron beam to the specimens was changed, there took place a parallel displacement in the moiré patterns, but the lines L_1, L_2, L_3 and M were not displaced. Further, there took place no change in the contrast of the general back ground. These facts show that the lines L_1, L_2, L_3 and M are neither the extinction contour lines due to curved crystals nor the edges of some other extra overlapping crystals but are due to some lattice defects, such as dislocations. A detailed discussion based on more precise experiments will be published elsewhere in the near future.

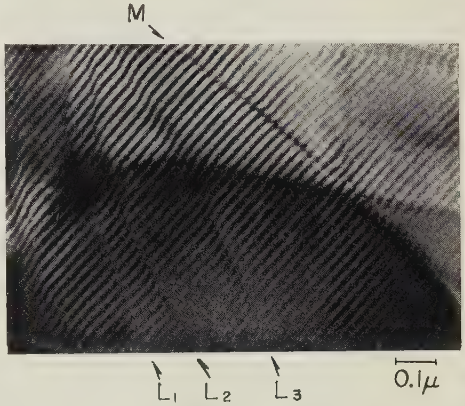

Fig. 2.

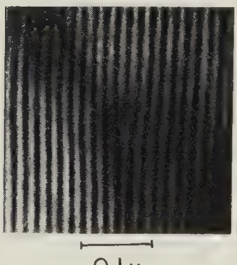

Fig. 3.

The edge dislocation-like patterns as shown in Fig. 3 were sometimes observed. However, in view of the highly anisotropic layer structure of graphite, the dislocation line perpendicular to the basal plane seems to be difficult to exist, and one should be careful to conclude its real existence. This point will be clarified by the future experiments. Recently F. E. Fujita has observed the moiré patterns even in artificial graphite. Experiments are now in progress in co-operation with his group, including the problem of irradiation effects on graphite.

The author wishes to express his sincere thanks to Dr. K. Motojima for his persistent encouragement, and Dr. H. Suzuki and Dr. F. E. Fujita for their valuable guidances and discussions, and to Mr. Ōtsu for his assistance throughout this work.

References

1) T. Mitsuishi, H. Nagasaki and R. Uyeda: Proc. Jap. Acad. **27** (1951) 86.
2) See for review, J. W. Menter: Phil. Mag. Supplement **7** (1958) 299.
3) H. Hashimoto and R. Uyeda: Acta. Cryst. **10** (1957) 143.

J. Phys. Soc. Japan **14** (1959) 1830

Visible Light Emission from Germanium Diffused p–n Junction

By Makoto Kikuchi
Electrotechnical Laboratory, Tokyo, Japan
and
Kenkichi Tachikawa
Research Laboratory, Meiden-sha, Shinagawa, Tokyo, Japan

(Received October 27, 1959)

It is well-known that visible light is emitted from p–n junction in silicon[1] and metal-silicon contact.[2] In both cases, the light is emitted from small spots located near the rectifying region, and the number of these spots increases as the reverse bias voltage is increased.

On the course of study of the visible light emission and the "microplasma" phenomena in silicon junction, it has been one of the key questions for the understanding of fundamental processes underlying those effects, i.e., why visible light had not been observed in germanium p–n junction. The difference in the energy gap for germanium and silicon does not play important role in this discussion, since the visible light corresponds to the region of 1.5 to 3.0 eV, and moreover, the spectral intensity of the light emitted from silicon is observed to extend far beyond the wave length corresponding to the energy gap (1.1 eV), which has been attributed to the *intra-band* transition of high energy electron.[3] If the intraband transition is really the predominant process in the light emission from p–n junction, it might well be expected that germanium junction emits visible light in the same way.

We have concentrated our interest on the differences in the extrinsic properties between germanum and silicon, and pointed out the content of oxygen as one of those factors.

Germanium crystal was melted in *quartz crucible* and kept at 1450°C for about 15 minutes and then single crystal was pulled in <111> direction doped with In. This treatment is to enrich the germanium crystal with oxygen. The crystal was then sliced and n-type layer was made by As diffusion in the thickness of 1−1.5 micron. Small p–n junction area was made by mask-etching as shown in Fig. 1(a). Visible light emission was observed at the periphery of this junction as shown in Fig. 1(b). The colour was a little more reddish than the bright spots observed in the silicon diffused junction. A bright and large white spot was observed neither on the periphery nor on the junction plane. Since the absorption coefficient is greater for germanium than for silicon, the lack of light spots on the junction plane cannot be directly attributed to the lack of event itself.

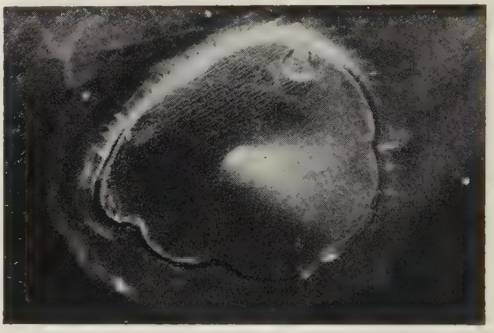

Fig. 1. (a)

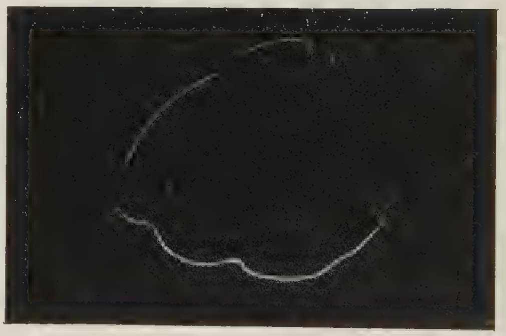

Fig. 1. (b)

Although it is not possible to conclude that the light emission is induced by oxygen only from this experimental result, it may throw light on the understanding of the light emission and microplasma phenomena in semiconductor p–n junction.

References

1) R. Newman: Phys. Rev. **100** (1955), 700. A. G. Chynoweth et al: Phys. Rev. **102** (1956) 369.
2) M. Kikuchi: Journ. Phys. Soc. Japan **14** (1959) 682.
3) A. A. Chynoweth et al: Phys. Rev. **102**, (1956) 369.

J. PHYS. SOC. JAPAN **14** (1959) 1831

Infrared Radiation from Silicon Grown Junction

By Ichizô UCHIDA
Research Laboratory, Nippon Electric Co. Ltd., Tokyo

(Received September 26, 1959)

Since Haynes and Briggs1) succeeded in detecting the recombination radiation of silicon and germanium, several papers2)–7) have been published.

The spectral distribution of silicon recombination radiation has a peak at 1.1 μ at room temperature, the peak being due to the direct transition between the valence and conduction bands. Therefore we can observe the infrared radiation from silicon grown p-n junction in the case of forward current injection by the use of the type 1P25 image tube having Ag–Cs photocathode.

The sample resistivity is 0.08 Ω cm in the p region doped with boron and 2.4 $\Omega\cdot$cm in the n region doped with antimony.

The sample is soldered to a pair of copper-block terminals cooled by means of dry ice and put into a vacuum chamber. The junction temperature is measured by a thermocouple and cooled in the range of from 10°C to -5°C.

The radiation is too weak to be visualized when the current flow through the junction is less than 100 mA, but becomes clearly observable at 300mA. As shown in Fig. 1 the radiation diffuses away from the junction to the n region. This is caused by the fact that the most part of the current carriers consists of positive holes, as can be expected from the relation between the values of resistivity in the p and n regions.

The density of the negative film D_M is measured by means of a micro-photometer and the result is shown in Fig. 2. Fig. 3 shows the experimental results of the relation between the current and the radiation energies measured when a PbS detector is used for a junction current range of from 100 mA to 1 A. By the use of these results we can approximate the linear relation between the maximum density D_M and total radiation energy E. Consequently, the length from the junction to the point where the density is decreased to D_M/e is considered to be comparable to the diffusion length of the radiative carriers. The value is about 300 microns and the life time of holes in the n region is calculated to be 77 μ sec. This value is greater than the life time measured by the photo-conductivity decay method.

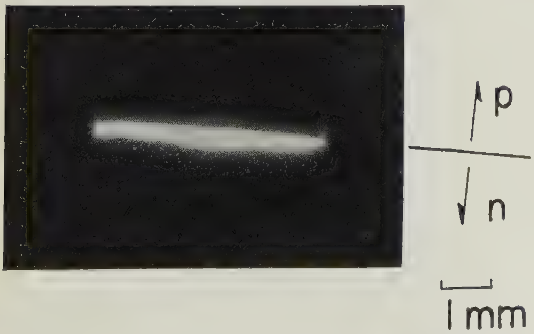

Fig. 1. Infrared radiation from Si grown p-n junction. Sample size is 4.15 $\times 0.74 \times 13.0$ mm.

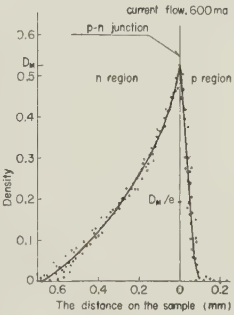

Fig. 2.

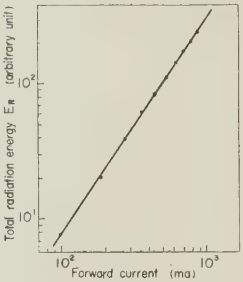

Fig. 3. Total radiation energy from the junction vs. foward current.

According to the injection efficiency calculated from the values of the resistivity, the recombination radiation in the p region must be too weak to be observed, however, the obscure radiation in the p region exists in the Fig. 1. This seems to be due to the scattering light of the internal radiation at the surface of the sample and at the fluorescent screen of the image tube.

The author would like to express his thanks to Dr. Osamu Harashima for his guidance and encouragement. He is also indebted to Mr. Naotaka Sakakibara and Mr. Takeshi Hasegawa for measurement and preparation of the samples.

References

1) J. R. Haynes and H. B. Briges: Phys. Rev. **86** (1952) 647.
2) R. Newman: Phys. Rev. **91** (1953) 1313.
3) W. Von Roosbroeck and W. Shockely: Phys. Rev. **94** (1954) 1558.
4) J. R. Haynes: Phys. Rev. **98** (1955) 1866.
5) J. R. Haynes and W. C. Westphal: Phys. Rev. **101** (1956) 1676.
6) R. Newman: Phys. Rev. **105** (1957) 1715.
7) P. H. Brill and R. F. Schwarz: Phys. Rev. **112** (1958) 330.

J. Phys. Soc. Japan **14** (1959) 1832~1833

An Interpretation of 550 Me Particles

By Masafumi Inoki

Physics Institute, Yamanashi University
Kofu City, Japan

(Received August 31, 1959)

It seems hardly possible that the 550 Me particles observed by Alikhanian et al.[1] should exist in cosmic rays, if one takes into account the fact observed that the several studies[2] recently carried out to check their existence have obtained the results against that. Alikhanian et al. maintained the mass of the particles to be about 550 times the electron mass, on the assumption that each of them had a unit electronic charge, e. However, the assumption was not based on any experimental evidence.

It seems to the author that the failure in detecting the 550 Me particles[2] might possibly be explained, if the particles were assumed to be charged with Ze, Z being a number. To show the idea quantitatively we shall introduce the general equrtions (1), relating the measured momentum, P_z, ionization, I_z, total number of grains in an emulsion, N_z, range, R_z and mass, $\mu(z)$, for a particle charged with Ze, moving at non-relativistic velocities,

$$\begin{aligned}\mu(z)&=Z^{0.55}[1.18P_z^{1.45}R_z^{-0.45}]=Z^{0.55}\mu_{pr}(1)\\ \mu(z)&=Z^{-0.52}[2.04P_zI_z^{0.76}]=Z^{-0.52}\mu_{pi}(1)\\ \mu(z)&=Z^{-2.88}[6.86R_zI_z^{2.44}]=Z^{-2.88}\mu_{ri}(1)\\ \mu(z)&\simeq Z^{-11.8}[bN_z^{3.45}R_z^{-2.45}]=Z^{-11.8}\mu_{rn}(1)\end{aligned} \qquad (1)$$

where $\mu_{pr}(1)$, $\mu_{pi}(1)$, $\mu_{ri}(1)$ and $\mu_{rn}(1)$ represent the simulated masses, which are obtained by assuming that the particle is charged with e, and the indices pr, pi, pi, and rn indicate that the measurement of the mass is done by the methods of momentum-range, momentum-ionization, range-ionization, and range-total grains respectively. The equations (1) were introduced from the semi-experimental curves[3] by means of the following substitution:

$$\begin{aligned}P&=ZP_z\\ I&=(1/Z^2)I_z\\ N&\simeq(1/Z^2)N_z\\ R&=Z^2R_z\end{aligned} \qquad (2)$$

where P, I, N, and R belong to a particle charged with e. It must be noted however that the momentum, P_z, is obtained from the measured radius of curvature, ρ, of the trajectry of a particle in a magnetic field, H, using the ordinary formula, $P_z=300\,H\rho$ MeV/c.

The mass of the 550 Me particles is expressed $\mu_{pr}(1)=550$ by the above notation. So far only the Princeton group has searched for the particles of $\mu_{pr}(1)=550$ with a negative result in its preliminary report.[4] Whereas the Utah,[5] the Columbia,[6] the Milano[7] and the Calcutta[8] groups searched for the particles of $\mu_{ri}(1)=550$, among which only the last one obtained a positive result at sea level.

Alikhanian et al. observed some of the 550 Me particles which were ionizing at about the minimum rate. That fact excludes the possibility of $Z>1$ for the particles. Particles charged with $Z<1$, called subionizers, were searched for by Fitz et al.[9] with a negative result in a small number of cosmic ray particles. The author has tried to find such a value of Z that the particles of $\mu_{pr}(1)=550$ could be found by Alikhanian's study but the particles had a feature to be missed by other's studies to search for the ones of $\mu_{ri}(1)=550$. Thus the author would like to propose that the 550 Me particles are the ones charged with $(Z=1/2)e$. The equations (1) can be solved as follows, if we put $Z=1/2$ and $\mu_{pr}(1)=550$ in them; $\mu(1/2)=370$, $\mu_{pi}(1)=260$, $\mu_{ri}(1)=50$, and $\mu_{rn}(1)\simeq1/10$.

Those mass values seem to explain the failure in the search for the 550 Me particles carried out by the Utah, the Coloumbia and the Milano groups, because a very small number of $\mu_{ri}(1)=50$ and $\mu_{rn}(1)\simeq1/10$ might have been treated as electrons. $\mu_{pi}(1)=260$ would also be difficult to be distinguished from π-mesons in a mass measurement. The result of the Calcutta group is difficult to explain by the above assumption. The author hopes that the reliability of the ionization measurement in the study would be checked again.

The contradiction between the study of Alikhanian and that of the Princeton group might be explained if the counter arrangement to trigger the cloud chambers in the latter had a bias against both a particle ionizing at less than the minimum rate and a slow particle of $R<7$ g/cm² of lead at the top of the counters. The ordinary counters might fail to detect the fast subionizers of $Z=1/2$, which ionize at less than the minimum rate in the region of $R>7$ g/cm² of lead.

There occurs a doubt that the particles of $Z=1/2$, if they really exist, should have been observed so far by emulsion studies. They are supposed to be produced by nuclear collisions, materializations or decay processes, all of which are observable by emulsions. The particles at relativistic velocities, however, have about 1/4 times the minimum ionization rate, which is almost impossible to be distinguished from the background in emulsions. Therefore they can escape from the observation, if the major part of them, at the place where they are produced, have relativistics velocities, corresponding to the kinetic energy larger than about 250 MeV.

In conclusion, the author should like to remark that the 550 Me particles should be carefully checked again in view of what has been described above, because there seems to be some possibility that they are subionizers, if the particles of $\mu_{pr}(1)=550$ proposed by Alikhanian et al. do really be observed without suffering from any experimental error.

References

1) AL. Alikhanian, N. D. Shostakovich, A. T. Dadaian, V. N. Fedorov and B. N. Deriagin: Zh. Eks. Teor. Fiz. **31** (1956) 955.
2) see (4), (5), (6), (7), and (8).
3) D. J. X. Montgomery: *Cosmic Ray Physics* (Princeton Univ. Press, 1949). Bruno Rossi: *High energy Particles* (Prentice-Hall, New York, 1952). J. G. Wilson: *Progress in Cosmic Ray Physics*, vol. 2 (North-Holland Publ., Amsterdum, 1954).
4) Pirové and Hendel: 1958 annual International Conference on High Energy Physics at CERN.
5) J. W. Keuffel, R. L. Call, W. H. Sandman and M. C. Larson: Phys. Lev. Letter **1** (1958) 205.
6) E. Bierman, R. Lea, J. Orear and S. Rosendorff: Phys. Rev. **113** (1959) 710.
7) M. Conversi, E. Fiorini, S. Ratti, C. Rubbia, C. Succi and G. Torelli: Nuovo Cimento, **9** (1958) 740.
8) Nilima Basu and M. S. Sinha: Ind. J. Phys. **32** (1958) 259.
9) H. C. Fitz Jr., William B. Good, James L. Kassner, JR., and Arther E. Ruark: Phys. Rev. **111** (1959) 1406.

J. PHYS. SOC. JAPAN **14** (1959) 1833~1834

Dependence of the Joshi Effect on 'Ageing' under, or and in the Absence of, Continuous Electrical Excitation

By M. VENUGOPALAN

Department of Chemistry, Banaras Hindu University (India).

(Received August 31, 1959)

Comparative studies of the JOSHI effect[1] $\pm\Delta i$, an instantaneous and reversible photovariation of the discharge current i ($+\Delta i$, enhancement and $-\Delta i$, diminution) in halogens under identical conditions of excitation and detection and for constant light intensity and frequency, from the standpoint of the kinetics of the inversion of $+\Delta i$ to $-\Delta i$ and *vice versa* under widely varied conditions of 'ageing' under, or/and in the absence of, discharge (in the former, the discharge tube is kept excited at a fixed potential for a required amount of time and in the latter, *i.e.*, the opposite process, as the system is stood over in the absence of discharge, unexcited in a 'rest period') and temperature showed that $+\Delta i$ is favoured by a temperature rise, but inhibited by a continued exposure to discharge and that in the absence of discharge it is the first to develop, the recovery being facilitated by heating. On the contrary $-\Delta i$ is disfavoured by a temperature rise, but enhanced by a continued exposure to discharge; in the absence of discharge it decreases, this decrease being facilitated by heating. Both the direct and reverse processes are found to be representable by equations of the 'first order' reaction[2].

To explain these time variations in $\pm\Delta i$ due to 'ageing' under, or/and in the absence of, electrical discharge, PRASAD and JATAR[3] suggested that a reversible reaction occurs between the glass and the gas. MOHANTY[4] explained the increase in $-\Delta i$ as due to increased photoemission from the cathode, due to decreased surface work function ϕ, as obtained by 'ageing' under discharge. JOSHI[5] contemplated the formation under discharge of an adsorptionlike photoactive electrode layer consisting of excited particles and ions and characterised by a low work function ϕ as primary to the production of $\pm\Delta i$. The other processes, subsequently leading to $\pm\Delta i$, *viz.*, photoelectron emission from the above layer, their capture or/and their multiplication are practically instantaneous and fully reversible. Evidently the formation of the above layer is the only time dependent process leading to $\pm\Delta i$.

The progressive growth of $-\Delta i$ during 'ageing' under discharge is attributed by RAMANAMOORTHY[6] to the discharge favouring an otherwise slow or practically no formation of the 'electrode layer' contemplated by JOSHI[5] as primary for $\pm\Delta i$. He has suggested[6] that this layer constitutes of (gas) molecules oriented on the 'electrode surface' probably as 'electrical' 'dipoles' possessing characteristic light absorption and low dissociation energy as distinct from those in the gas bluk. Such a discrimination was necessitated since the entire $\pm\Delta i$ could be obtained by irradiating simply the electrodes by wavelengths in and outside the selective absorption of the excited medium[2], its frequencywise variation[2] and also its non-occurrence[2] when the gap alone was illuminated keeping the electrodes screened especially in external sleeve and Geissler tube discharges.

The author[7] has shown that a van der Waals' layer's on a partially chemisorbed electrode surface is the chief seat of $+\Delta i$, whereas a chemisorbed layer on the electrode surface constitutes the chief seat of $-\Delta i$. The time variations in $\pm\Delta i$ due to 'ageing' under discharge has been attributed to a clean up of the van der Waals' layer and development, involving adsorption or/and desorption, of the chemisorbed layer, due to electrical activation caused by, and dependent on the magnitude of, the potential applied to the electrode surface. The constant values of $\pm\Delta i$ obtained at infinite time in the kinetic studies of 'ageing' under, or/and in the absence of, discharge arises out of the establishment of an equilibrium between the gas phase and the absorbed phase. The cessation of discharge is marked by an instantaneous van der Waals' adsorption on a partially chemisorbed surface. It is probable that a surface catalysed reaction[8], at low and ordinary temperatures premitting the stability of a van der Waals' layer, between adsorbed gas particles in these two layers, between adsorbed gas particles in these two layers, takes place. This seems to be improbable at high temperatures when desorption of the chemisorbed layer has set in; but an interaction[9] between two adjacent atoms or radicals in a simple competitively occupied chemisorbed layer is possible. The observed larger time intervals required under 'ageing' in the absence of discharge ('rest period') compared to the shorter periods of 'ageing' under discharge to attain constant values of $\pm \Delta i$ are due to the procesed of adsorption and desorption proceeding at much higher rates than the reaction at the surface.

The electrodes being of dielectric nature, develop active spots on the surface under electrical excitation. A strain caused either by continuation of discharge or a total removal of applied field as under 'rest' or/and any other factor will affect these spots considerably. These centres retains some residual charge after completion of a cycle, conditioned by its previous history, the charge density in various centres, the expansion of active spots and the maintenance of the charge in these spots. This will develop a strain which will be loosened or destrained when allowed to 'rest' or subjected to 'heat' treatment.

Further, RAMANAMOORTHY'S[6] interpretation of the adsorbed layer as consisting of gas molecules oriented on the 'dielectric surface', probably as the 'electrical dipoles seems to be instructive from considerations of the 'time of relaxation of a molecule'[10]. This is the time required for the dipolar molecules to revert to random distribution after the removal of an eletrical field that has caused them to become oriented in a definite direction. The 'theory of dielectric relaxation' as originally proposed by DEBYE[11] possibly explains the larger time required when the electrical field is removed, for the restoration of $\pm \Delta i$, to the original value observed prior to 'ageing' under discharge, compared to the time changes in $\pm \Delta i$ with ageing under discharge. It is also noteworthy, that, as explained above, the strain developed on the dielectric walls under discharge, can be ascribed to the orientation of the dipolar molecules and when allowed to rest, this strain is relaxed due to the oriented molecules reverting to their original distribution.

Grateful thanks of the author are due to Prof. S. S. JOSHI for his valuable suggestions.

References

1) S. S. Joshi: Proc. Indian Sci. Cong., Presidential Address, Chem. Sec. (1943).
2) M. Venugopalan: Ph. D. Thesis, Banaras Hindu Univ. (India), (1956).
3) B. B. Prasad and D. P. Jatar: J. Sci. Res., Banaras Hindu Univ. (India) VI(**1**) (1955–56) 98.
4) S. R. Mohanty: J. Chem. Phys. **21** (1953) 1908.
5) S. S. Joshi: Curr. Sci. (India) **16** (1947) 19.
6) M. V. Ramanamoorthy: Proc. Indian Sci. Cong., Chem. Sec. **A, 23** ((1952).
7) M. Venugopalan: J. Phys. Soc. Japan **13** (1958) 1544.
8) E. K. Rideal: Chemistry & Industry **62** (1943) 335.
9) C. N. Hinshelwood: *Kinetics of Chemical Change* (Oxford Univ. Press, London, 1940); *Cf.* H. S. Taylor: Spier Memorial Lecture, Faraday Society (1951).
10) S. Glasstone, K. J. Laidler and H. Eyring: *The Theory of Rate Processes* (McGraw Hill Book Co., N.Y., 1941).
11) P. W. Debye: *Polar Molecules* (Chem. Catalog. Co., Inc., N.Y., 1929).

Errata

Rheological Equation of Voigtian Material

By Wataru SEGAWA

J. Phys. Soc. Japan **14** (1959) 1102

Page	Column	Line	
1102	right	32	$x^{*k}_{,j}$ should be read $x^{*k}_{,i}$
1104	right	31	"then η_2 and" should be read "then η_1, η_2 and"
1104	right	32, 33	"and η_1 ....Pressure" should be eliminated.

On Galvanomagnetic Effects in P-Type Crystals of PbTe

By Kisaburo SHOGENJI

J. Phys. Soc. Japan **14** (1959) 1360

Page	Column	Line		should be read
1360	left	16	Forner	Foner
1360	right	5	goldberg	Goldberg
1360	right	16	magnetude	magnitude
1361		3 from the bottom	δ_{111}	ζ_{111}
1362		2 (Eq. (2–4))	$\delta_{112}I_1(H_2{}^4+H_3{}^4)$	$\zeta_{112}I_1(H_2{}^4+H_3{}^4)$
1362		3 (Eq. (2–4))	$I_2H_2(H_1{}^2H_2{}^2)$	$I_2H_2(H_1{}^2+H_2{}^2)$
1362		7	for simple geometry	from simple geometry
1362		21 (Eq. (B–1))	$E^{001}_{001}\langle 001\rangle=$	$E^{110}_{110}\langle 001\rangle=$
1362		21 (Eq. (B–1))	$\pi_{66}(\cos^2\theta-\sin^2\theta)$	$\pi_{66}(\cos^2\theta-\sin^2\theta)\}H^2$
1362		7 from the bottom	$+\zeta_{112}\cos^2\theta(\cdots)$	$+3\zeta_{112}\cos^2\theta(\cdots)$
1364	left	7 from the bottom	the current is	the current if the current is
1364	left	5 (Eq. (3–5))	$-L^4$	$-L_4$
1365		12 from the bottom (Eq. (3–5))	$+ZH_2$	$+ZH^4$
1365		6 from the bottom (Eq. (3–17))	β^4	B^4
1365		2 from the bottom	specimen	specimens
1367	right	20	low	law
1367	left	7 from the bottom	low	law
1367	right	7 from the bottom	$(\Pi H^2+ZH)^4/\rho_0$	$(\Pi H^2+ZH^4)/\rho_0$
1369		Table IV	ζ^{442}/ρ_0	ζ_{442}/ρ_0
1369	right	4 (Eq. (5–3))	$2.1\times10_{-4}$	2.1×10^{-4}
1370	left	2 from the bottom	obout	about
1371	left	14	ef	of
1371	right	12 from the bottom	(1959)	(1954)

There are two letters "B–4–iii" indicating the lines of Fig. 7(a), the above of which should be corrected as "B–4–vi".

Theory of Thermoelectric Power of Ionic Crystal, II

By Eijiro HAGA

J. Phys. Soc. Japan **14** (1959) 992

$R\equiv\sqrt{2}\,a$ in the right column line 33 should be read $R\equiv 2a$.

We later discovered mistakes in the computation of Q_c in this paper. We must adopt the following expression as the correct formula of Eq. (15):

$$eQ_c=-\frac{k}{2}\,\frac{T_0}{T}\,\frac{(2\pi\sqrt{2})^{1/2}[(1-p)c_0T_0/T]^{1/2}}{(1+4(\pi\sqrt{2})^{1/2}[(1-p)c_0T_0/T]^{1/2})^2}$$

and Eq. (12) should be omitted. Hence, Table I is revised as follows.

Table I. The value of Q_c in μv/°C in (NaCl$+c_0$ Mol–% CdCl$_2$)

°C \ c_0	0.01	0.1	1
200	−16	−26	−31
300	−14	−23	−26
400	−12	−20	−22
500	−10	−17	−19
600	− 9	−15	−17
700	− 7	−13	−15

Further, the last term in Eq. (20) should be omitted. Instead of Table II in the previous paper, the value of Q_c for AgCl doped with the $CdCl_2$ quantities used in the measurement of thermo-power is estimated as follows.

Toble II. The value of Q_c in $\mu v/°C$ in ($AgCl + c_0$ Mol–% $CdCl_2$)

	250°C				350°C			
c_0 \ R	0	a	2a	3a	0	a	2a	3a
0	+ 40	+ 40	+30	+30	+70	+60	+50	+50
0.022	− 40	− 30	−20	−20	+90	+70	+60	+60
0.068	− 90	− 70	−50	−40	+30	+20	+20	+20
0.20	−170	−100	−70	−50	−80	−50	−30	−20

If we find the values of $h_F + Q_i^* + Q_v^*$ at 250 and 350°C under consideration of Q_c with $R \equiv 2a$, the ones become larger by 10∼20% than previously found (J. Phys. Soc. Japan **14** (1959) 729)

Multiplet Structure and Hyperfine Structure of the Spectrum of Mercury

By Kiyoshi MURAKAWA

J. Phys. Soc. Japan **14** (1959) 1624, 1633

Page 1626, right compartment, lines 9 and 10 should read

$K_1 = 0.972$, $K_2 = -0.197$, $K_3 = -0.090$, $K_4 = 0.091$, $K_5 \approx 0$.

I deeply appreciate the kindness of Dr. Blaise who called my attention to the miscopy.

Page 1629. The figures (only) in Figs. 3 and 5 should be interchanged. The captions are correctly printed.

Statistical Aspects of Fracture in Concrete, I.
An Analysis of Flexural Failure of Portland Cement Mortar from the Standpoint of Stochastic Theory

By Motoo HORI

J. Phys. Soc. Japan **14** (1959) 1444

Page	Column	Line	Now reads in part	Should read
1447	right	Eq. (1)	$\mu(t)dt == -$	$\mu(t)dt = -$
1448	left	4	replace	replaces
		Eq. (13)	$\tau(1-e^{-t/\tau})]\}$,	$\tau(1-e^{-t/\tau})\}]$,
		last	protland	portland
1451	left	18	(see^{-1})	(sec^{-1})

Contents

(Vol. 14)

No. 1

Page

16″ Variable Energy Cyclotron .... Hiroo KUMAGAI, Kazuo ŌNO, Hisao SHÔNO, Izuo HAYASHI, Keiichi KURODA and Minoru IMAIZUMI 1

Note on the Cluster Expansion Theory of Classical Fluids. Watermelon Approximation .... Ryuzo ABE 10

High Electric Field Effects in Germanium $p-n$ Junction .... Jiro YAMAGUCHI and Yoshihiro HAMAKAWA 15

Interaction of Conduction Electrons with Acoustic Phonons .... Nobuo MIKOSHIBA 22

On the Dielectric Losses in Impure Ionic Crystals .... Tosiyuki NINOMIYA 30

On the Theory of Thermoelectricity in Two-Band Semiconductors .... Eijiro HAGA 35

Photo-voltaic Effect in Se-photocells having Artificial Intermediate Layers of CdSe, CdTe, ZnSe and ZnTe .... Hirosi TUBOTA and Hiromichi SUZUKI 38

Lattice Scattering Mobility of Electrons on Cadmium Sulphide .... Hisao MIYAZAWA, Hajime MAEDA and Hiroshi TOMISHIMA 41

Relaxation Time Anisotropy in Cadmium Sulphide Studied with Electrical Resistivity and Magneto-Resistance Effect .... Taizo MASUMI 47

Quantum Theory of Galvanomagnetic Effect I. Basic Considerations .... Ryogo KUBO, Hiroshi HASEGAWA and Natsuki HASHITSUME 56

Excitation of the Molecular Vibration by Collision .... Kazuo TAKAYANAGI 75

On the Viscosity of Irradiated Polymers I. .... Mitio INOKUTI 79

Zerosplitting Cone of Nuclear Quadrupole Spectrum for Spin 5/2 .... Kenji SHIMOMURA and Noriyoshi INOUE 86

Non-Similarity Theory of Decaying Turbulence .... Yutaka SHIGEMITSU 91

SHORT NOTES

Anisotropic Conductivity of CdS Single Crystals .... Shōji TANAKA, Mineo KOBAYASHI and Taizo MASUMI 104

Piezoelectric Properties of Triglycine Sulphate Crystal .... Kazuo HUSHIMI and Keisuke KATAOKA 105

On the Transition Temperature of Copper Ferrite .... Haruyuki OHNISHI, Teruo TERANISHI and Syohei MIYAHARA 106

Grain Boundary Migration and Dimensional Change of Low Carbon Steel .... Minoru OKADA and Toichi WATANABE 107

Electron Spin Resonance of Mn-activated Phosphors .... On MATUMURA 108

Some Ferroelectrical Properties of Triglycine Sulfate .... Hiroo TOYODA, Shigeru WAKU, Hiroyuki SHIBATA and Yoichi TANAKA 109

The Far Infrared Reflectivity of NaCl, KCl and KBr Crystals .... Akiyoshi MITSUISHI, Hiroshi YOSHINAGA and Shigeru FUJITA 110

Diffusion of Manganese in Single Crystals of Copper .... Akira IKUSHIMA 111

The Variation of Superstructure in Iron Selenide Fe_7Se_8 .... Atsushi OKAZAKI 112

Effects of Deuteron Bombardment on CdS Single Crystals .... Shoji TANAKA and Toshio TANAKA 113

Errata

Diffraction of Electromagnetic Waves by Circular Plate and Hole .... Yûkichi NOMURA and Shigetoshi KATSURA 115

Diffusion Processes in Polymers under Irradiation Polyvinyl Alcohol and CCl_4 System .... Tsutomu WATANABE 116

No. 2

Yields and Angular Distributions of Protons from $F^{19}(d\,p)F^{20}$ and $F^{19}(d,p)F^{20}$.... .... Kazuo ŌNO, Junji SHIMADA, Keiichi KURODA, Osamu TANAKA, Hiromichi KAMITSUBO, Atsuko, ITO, Shigeya TANAKA and Minoru IMAIZUMI 117

Elastic and Inelastic Scattering of 14.1-MeV Protons by Medium Weight Nuclei... .... Ken KIKUCHI, Shinsaku KOBAYASHI and Kazuhisa MATSUDA 121

Thermodynamic Foundation of the Theory of Plasma .... Taro KIHARA 128

Hall Effect in Oxide Cathodes .... Tadaichi YABUMOTO 134
Transformation des Reseaux Metalliques sous l'Influence des Elements d'Insertion: Transformation du Nickel sous l'Influence de l'Azote .... Nobuzo TERAO et Aurel BERGHEZAN 139
Stress-Ordering Effect on Thermal Expansion of CuAu Single Crystals .... Makoto HIRABAYASHI 149
Selenium Rectifiers with Artificial Layers of Selenides of Cadmium, Tin, Bismuth and Lead .... Yoshiro MORIGUCHI 152
Studies on (Ba-Pb)(TiZr)O_3 System .... Takuro IKEDA 168
The Electronic Structure of the M Center .... Hiroshi MIMURA and Teturo INUI 175
Oxide-Cored Cathode .... Keiichi ANDO, Osami KAMIGAITO, Yoshihiro KAMIYA, Shigetoshi TAKAHASHI and Ryozi UYEDA 180
Study of Metallic Carbides by Electron Diffraction Part III. Iron Carbides .... Sigemaro NAGAKURA 186
On the Magnetic Properties of Vanadium Sulfide and Selenide .... Ichiro TSUBOKAWA 196
Spectro-Polarization Characteristics of the Sodium Nitrate Polarizer .... Tasaburô YAMAGUTI, Isao MAKINO, Shingo SHINODA and Ippei KUROHA 199
The Steady Flow of Viscous Fluid at Low Reynolds Numbers passing obliquely through a Plane Grid made of Equal Parallel Circular Cylinders .... Kō TAMADA and Hiroomi FUJIKAWA 202
Some Problems on Heat Conduction in Stratiform Bodies .... Václav VODIČKA 216

SHORT NOTES

Nuclear Magnetic Resonance of RbBr .... Junkichi ITOH and Yukio YAMAGATA 225
Anisotropy of Ordinary Hall Effect in Silicon Iron .... Eiji TATSUMOTO and Tetsuhiko OKAMOTO 226
Electrostatic Transformer Type Particle Accelerator using Ceramic $BaTiO_3$—Ferrostac—.. Toshikazu SHIBATA, Atsutomo TOI, Tokuo SUITA ane Shunkichi KISAKA 227
Optical Properties of SiC in Infrared Region .... Masaharu NAMBA 228
Note on the Spin of Excited States of Cadmium 110 .... Mitsuo SAKAI, Haruko OHMURA and Teruo MOMOTA 229
Electronmicroscopic Observations on the KI Single Crystal .... Tetsuhiko TOMIKI 230
Ferrimagnetic Resonance of Polycrystalline Nickel Ferrite-Chromites .... Hiroo YONEMITSU 231
Barrier Temperature at Turnover in Germanium *p-n* Junction .... Jiro YAMAGUCHI and Yoshihiro HAMAKAWA 232
Interaction of Water Vapour with Germanium Real Surface .... Koji KAWASAKI, Kyoichi KANOU and Yoshiyasu SEKITA 233
Size Distribution of Radioactivity of the Natural Radioactive Dust .... Koji KAWASAKI and Keiji KATO 234
Zeeman Study of Nuclear Quadrupole Resonance Spectrum in *p*-Dibromobenzene .... Kenji SHIMOMURA 235

Erratum

On the Ferromagnetic Phase in Manganese-Aluminum System .... Hiroshi KŌNO 237

No. 3

Gamma Rays from the Proton Bombardment of ^{24}Mg, ^{25}Mg and ^{26}Mg .... Iwao MIURA, Tetsuo WAKATSUKI, Yasuo HIRAO and Eiji OKADA 239
Convex-Core Model of Molecules in Crystalline State.. Taro KIHARA and Saburo KOBA 247
Interaction of Exciton with Electron Trapping Centers in Alkali Halide Crystals 1. *F* and *U* Centers in KCl and KBr Crystals .... Masayasu UETA, Masamitu HIRAI and Hiroyuki WATANABE 253
Electrical Resistivity and Superstructure of $CuAu_3$ .... Makoto HIRABAYASHI 262
Electrical Resistivity of Arc-evaporated Carbon Film .... Hiroo TOYODA and Masahisa NAGASIMA 274
Elecrtical Properties of Stannous Selenide .... Sizuo ASANABE 281
A Note on the Theories Underlying the Polarimetric Study of Very Thin Dielectric

Surface Layers ...... Sadao NOMURA and Koreo KINOSHITA 297
Electronmicroscopic Observations of Alkali Halide Crystals ...... Tetsuhiko TOMIKI 304
Nuclear Magnetic Resonance Studies of Water Sorbed on Fibrous Materials ...... Akira ODAJIMA 308
Phenomenological Theory of Visco-elasticity of Three Dimensional Bodies ...... Misazo YAMAMOTO 313
Quantum Theoretical Study on Single, Double and Triple Bonds between Carbon Atoms ...... Sigeru NAGAHARA 331
On the Non-Orthogonality Difficulty in Ferromagnetism ...... Fumihiko TAKANO 348
On Quantitative Measurement of Turbulence by Means of a Constant Resistance Hot-wire Anemometer ...... Nisiki HAYASI 360
The Effect of the Room Shape on the Sound Field in Rooms—Studies on the Measurement of Absorption Coefficient by the Reverberation Chamber Method I— ...... Kozi SATO and Masaru KOYASU 365

SHORT NOTES

Germanium-Silicon Alloy Junctions ...... Yasuo MATSUKURA 374
Electronmicroscopic Observation of the KCl Crystal Containing Potassium Colloid Particles ...... Tadatosi HIBI and Tetsuhiko TOMIKI 375
Etch Patterns on Ferroelectric Triglycine Sulfate ...... Hiroo TOYODA 376
The Proton Magnetic Resonance Absorption of the Trichloroacetic Acid in Solid Phase ...... Masashi YAGI and Masayasu UETA 377
On the Dielectric Loss of Oxidized High-Density Polyethylene ...... Sigeharu OKAMOTO and Keisaku TAKEUCHI 378
Nuclear Quadrupole Resonance Spectra of N^{14} in Urea Crystal ...... Takehiko CHIBA, Masaharu TOYAMA and Yonezo MORINO 379
Electrical Properties of Dilute Alloys of Zinc with Manganese at Low Temperature ...... Yoshio MUTO, Yoshio TAWARA, Yoshio SHIBUYA and Tadao FUKUROI 380
On the Growth Conditions of Germanium ...... Takeo SASAKI 381
Non-Existence of Bound States with Positive Energy ...... Tosio KATO 382
The Crystal Structure of $CoCl_2$-$6H_2O$ ...... Jōji MIZUNO, Kazutoshi UKEI and Tadashi SUGAWARA 383
Change of Surface Recombination Velocity of Germanium by γ-ray Irradiation, using P–N–P Alloy Transistor ...... Kiich KOMATSUBARA 383
Preparation of Anodic Oscillator Tube using Glow Discharge ...... Kazuyuki OGAWA 385
Terminal Zone Cropping and Ultimate Zone Purification ...... Louis GOLD 386

No. 4

Measurement of Bremsstrahlung Spectra with Sodium Iodide Scintillation Crystal ...... Motoharu KIMURA, Naosi MUTSURO, Yuji OHNUKI, Katsufusa SHODA, Masumi SUGAWARA, Tsutomu TOHEI and Haruo YUTA 387
Scattering of Protons by Ne^{20} and Ne^{22} ...... Yukiyasu ODA, Minoru TAKEDA, Chuin HU and Shohei KATO 396
On the Coefficients of Irreversible Processes in a Highly Ionized Gas ...... Taro KIHARA 402
The General Theory of Transport: The Difference between Electric Field and Density Gradient ...... Tadao KASUYA 410
Electrical and Thermal Conductivity of Monovalent Metals; The Influences of Coulomb Interaction ...... Tadao KASUYA and Kazuo YAMADA 416
On the Superstructure of the Orderd Alloy Cu_3 Pd, III. High Temperature Electron Diffraction Study ...... Denjiro WATANABE 436
Electronmicroscopic Observation of the Additively Coloured KCl Crystal ...... Tadatosi HIBI and Tetsuhiko TOMIKI 445
Successive Electronmicroscopic Observation of Coloured and Bleached KCl Crystal ...... Tadatosi HIBI and Keiji YADA 455
Influence of Order-Disorder on Creep of a Superlattice Alloy ...... Taira SUZUKI and Mikio YAMAMOTO 463
Effect of Electron Bombardment on Sodium Chloride ...... Shigetomo YOSHIDA and Toshio IKEDA 473

Configurational Coordinate Curves for Luminescence Center in $Ca_3(PO_4)_2$:Cu ...... Keiji MAEDA 478
Electron Diffraction Study on Polish Layers of Gold, II .... Masao KURIYAMA 487
Nuclear Magnetic Double Resonance Experiment on Two Proton System .... Junkichi ITOH and Riichiro KUSAKA 492
The Electronic Structure of the Protonated Methane CH_5^+ ...... Masatoshi YAMAZAKI 498
Thermo-Remanent Magnetism in the Systems La_2O_3–Fe_2O_3 and Nd_2O_3–Fe_2O_3 .... Hiroshi WATANABE 511
Stabileco de du-dimensia fluo de Szymański .... Hideo TAKAMI 517
The Forces experienced by a Lattice of Elliptic Cylinders in a Uniform Flow at Small Reynolds Numbers .... Sinzi KUWABARA 522
The Forces experienced by Randomly Distributed Parallel Circular Cylinders or Spheres in a Viscous Flow at Small Reynolds Numbers .... Sinzi KUWABARA 527
The Generation of Static Charge on High Polymer .... Shigeyoshi KITTAKA 533

SHORT NOTES

On the Low Lying Levels of Mn^{55}, II .... Sadaaki YANAGAWA 539
Studies on Mercury Fulminato .... Surjit SINGH 540
Low Temperature Thermoelectric Power of Cu-Mn Alloys .... Seiichi TANUMA 541
Simplified Representations on the Firing Characteristics of Vibrational-Ignitor Tubes .... Setsuo OKANISHI and Hitoshi KANAMORI 542
Cyclotron Resonance in Gas Discharge .... Kuniya FUKUDA, Hiroaki MATUMOTO, Yoichi UCHIDA and Hisamitsu YOSHIMURA 543
Effects of γ-Rays on Aqueous Solutions of Synthetic Polymers .... Shintaro SUGAI, Mitsuo ISHIKAWA and Jiro FURUICHI 544
Maximum Principles for Vorticity in Viscous Fluid.... Tosio KATO and Hiroshi FUJITA 545
Interaction of Exciton with R Center in KCl Crystal .... Masayasu UETA and Masamitsu HIRAI 546

Errata

Oxide-Cored Cathode .... Keiichi ANDO, Osami KAMIGAITO, Yoshihiro KAMIYA, Shigetoshi TAKAHASHI and Ryozi UYEDA 547
On Quantitative Measurement of Turbulence by Means of a Constant Resistance Hot-wire Anemometer .... Nisiki HAYASI 547
Preparation of Anodic Oscillator Tube using Glow Discharge........ Kazuyuki OGAWA 547

No. 5

Elastic and Inelastic Scattering of 22 MeV Alpha Particles by Light Elements .... Chuin HU, Shohei KATO, Yukiyasu ODA and Minoru TAKEDA 549
$Be^9(n, 2n)Be^8$ and $B^{11}(n, \alpha)Li^8(\beta)Be^8$ Reactions by 14 MeV Neutrons..Masakatsu SAKISAKA 554
Cell Theory of Classical Liquids. Phase Transition between Gas, Liquid and Solid. Part III. Yvon's Method and its Generalization .... Tohru MORITA 563
Cell Theory of Classical Liquids. Phase Transition between Gas, Liquid and Solid. Part IV. F. C. C. Lattice Gases .... Tohru MORITA 570
Study of Reorientational Motion in Solid State of 1, 2, 3-trichlorobenzene and Hexachlorobenzene by Pure Quadrupole Resonance .... Itaru TATSUZAKI 578
Electronic Structure of Bismuth Type Crystals, II..................... Shoichi MASE 584
Internal Friction of Lead, II .... Yosio HIKI 590
Precipitation Process of Carbon in Alpha-Iron ....Tetsuro SUZUKI and Yuzo TOMONO 597
Electronmicroscopic Observations of the KCl Single Crystal Irradiated with Ultra-Violet Light .... Tetsuhiko TOMIKI and Masayasu UETA 602
On the Diamagnetism of Graphite, I. Energy Levels of π-electrons ....Hisanao SATO 609
The Thermoelectric, Galvanomagnetic and Thermomagnetic Effects of Monovalent Metals, IV. Effect of the Non-equilibrium Distribution of the Phonons.... Mikio TSUJI 618
Theoretical Treatment of the Movement of 180° Domain in $BaTiO_3$ Single Crystal .... Ryuji ABE 633
Nuclear Magnetic Resonance in Dilute Copper Alloys at Low Temperatures, I.

Experimental Aspects .... Tadashi SUGAWARA 643
Theory of Spatially Growing Plasma Waves .... Masao SUMI 653
High Subsonic Flow with Normal Shock Wave at Nearly Critical Mach Number .... Takeo SAKURAI 658
Flash X-Ray Radiography for the Density Measurement in a Hypersonic Air Flow .... Fumio TAMAKI and KIM, Chul-Soo 664
On the New Reverberation Chamber with Nonparallel Walls (Studies on the Measurement of Absorption Coefficient by the Reverberation Chamber Method, II) .... Kozi SATO and Masaru KOYASU 670

SHORT NOTES

A Visualizing Method of Electron Temperature and Plasma Density .... Hajime TAMAGAWA and Junji FUJITA 678
An Abnormal Saturation Behavior in High Resolution Proton Magnetic Resonance Spectra .... Michihiko NAGUMO and Yoshinobu KAKIUCHI 679
Phase Transition in Tungsten Trioxide .... Sigetosi TANISAKI 680
Absorption Spectrum of Copper-Coloured Cuprous Oxide .... Masakazu HAYASHI 681
Visible Light Emission from Metal-Silicon Contact .... Makoto KIKUCHI 682
Nuclear Spin-Spin Coupling between Protons in Vinyl Derivatives .... Tatsuo SHIMIZU, Shin-ichi MATSUOKA, Shuzo HATTORI and Kantaro SENDA 683
Fine Structures of Proton Resonance Spectra of Fluorobenzene Derivatives .... Minoru KIMURA, Shin-ichi MATSUOKA, Shuzo HATTORI and Kantaro SENDA 684
A Metastable Phase in Sn-Mg Alloy Film .... Ryōji SUGANUMA 685
Anomalous Hall Effect due to an *s-d* Interaction in the Dilute Alloys Containg the Transition Elements .... Mikio TSUJI 686
Changes of Ultrasonic Attenuation during Creep of Aluminum .... Akira HIKATA and Masayoshi TUTUMI 687
Size Effects on the Ferrimagnetic Resonance Absorption of Polycrystalline Ferrites and Garnets .... Hiroo YONEMITSU 688
An Application of the FA-Modified TF Model to the Singly Ionized Negative Ion .. .. Shigehiro KOBAYASHI 689
Evaluation of the Nuclear Quadrupole Moment of N^{14} .... Yoshifumi KATO and Osamu NAKAHARA 690

Erratum

A Note on the Theories Underlying the Polarimetric Study of Very Thin Dielectric Surface Layers .... Sadao NOMURA and Koreo KINOSITA 692

No. 6

Absolute Cross Sections of the (γ, n) Reaction for Cu^{63}, Zn^{64} and Ag^{109} .... Teruo NAKAMURA, Kunio TAKAMATSU, Kiyoji FUKUNAGA, Minoru YATA and Shinjiro YASUMI 693
Gamma Rays from Neutron Inelastic Scattering of Magnesium, Aluminum, Iron and Bismuth .... Masanao HOSOE and Shoji SUZUKI 699
Angular Distributions of the Reaction $F^{19}(p, \alpha)O^{16}$ at 8.0–14.2 MeV ...... Hiroshi OGATA 707
Excitation Functions and Angular Distributions of the Reactions $Al^{27}(p, \alpha)Mg^{24}$ at 12.7–14.1 MeV and $Cr^{52}(p, \alpha)V^{49}$ at 9.0–14.2 MeV .... Isao KUMABE, Ching Ling WANG, Maumi KAWASHIMA, Minoru YADA and Hiroshi OGATA 713
On the Brownian Motion of a Classical Oscillator .... Morikazu TODA 722
Thermoelectric Power of AgCl .... Yasumasa SUZUKI, Shigeaki ENDO and Eijiro HAGA 729
Internal Friction of KCl Crystals at Low Temperatures .... Taira SUZUKI, Katsumi SUZUKI and Tomoo KAMIGAKI 731
Defects in Ionic Crystals, II. An Analysis of F and V_1 Centers .. Tatsumi KUROSAWA 741
A Semi-empirical Theory of the Conjugated System, III. Bond Alternation and Electron Fixation .... Yuzuru OOSHIKA 747
Galvano- and Thermomagnetic Effects in α–Ag_2Te .... Shin-ya MIYATANI and Isaaki YOKOTA 750

On the X-Ray Diffuse Scattering by 1-3-5-Triphenylbenzene ...... M. Shehata FARAG 755
Metamagnetism of Methylamine Chrome Alum .... Kazuko MOTIZUKI 759
Crystal Structure of 2-Amino Azulene ...... Yoshito TAKAKI, Yoshio SASADA and Isamu NITTA 771
Study of Segmental Motion in Polymer Solutions by Nuclear Magnetic Resonance ...... Akira ODAJIMA 777
Effects of Gamma Rays on Aqueous Solution of Polyvinyl Alcohol ...... Osamu SAITO 792
Effect of Impurity on Molecular Linking of Irradiated Polymer .... Osamu SAITO 798
A New Type of Antiferromagnetic Structure in the Rutil Type Crystal ...... Akio YOSHIMORI 807
Oscillations in Plasma II ...... Shoji KOJIMA, Kiyoe KATO, Shigeo HAGIWARA and Ri'ichi MATSUZAKI 821
Experimental Studies on the Hypersonic Flow past Plane, Convex and Concave Wedges ...... KIM, Chul-Soo 827
The Drag of Lattice of Many Parallel Circular Cylinders at Low Reynolds Number ...... Takashi SAWADA 837
Downstream Development of the Wakes behind Cylinders .... Sadatoshi TANEDA 843

SHORT NOTES

On the Anomalous Magnetoresistance Effect in n-InSb ...... Wataru SASAKI and Chikako YAMANOUCHI 849
Synthesis of Large CdS and ZnS Crystals ...... Jiro NISHIMURA and Yasaku TANABE 850
Double Proton Magnetic Resonance by a Side Band Method ...... Junkichi ITOH and Siro SATO 851
Avalanche Electroluminescence in CdS Single Crystal ...... Makoto KIKUCHI and Sigeru IIZIMA 852
Ferrimagnetic Resonance Line Width in Polycrystalline Y_3Fe_{5-x}, In_xO_{12} ...... Tomonao MIYADAI, Yuzo SHICHIJO and Ichiro TSUBOKAWA 853
Electric Resistance and Cation Distribution of Fe-Mn Ferrite System ...... Zenya FUNATOGAWA, Nahonori MIYATA and Seiji USAMI 854
Magnetic Annealing Effect in αFe_2O_3 ...... Takao IWATA, Masako IWATA and Mikio YAMAMOTO 855
Quenching Effect of the Photoconductivity Decay in CdS ...... Makoto KIKUCHI and Sigeru IIZIMA 856
Luminescence of KI:TI Induced by Far Ultraviolet Light ...... Masayasu UETA and Takehiko ISHII 857
Distortion of the Octahedral Charge Distribution in Some Cobalt Complexes ...... Tadashi SUGAWARA 858

Errata

Internal Friction of Lead II .... Yosio HIKI 848
The Proton Magnetic Resonance Absorption of the Trichloroacetic Acid in Solid Phase ...... Masashi YAGI and Masayasu UETA 848

No. 7

Elastic and Inelastic Scatterings of Protons from Ti, Cr, Ni, Zn, and O at 8 to 14 MeV ...... Chuin HU, Ken KIKUCHI, Shinsaku KOBAYASHI, Kazuhisa MATSUDA, Yukio NAGAHARA, Yukiyasu ODA, Naoyuki TAKANO, Minoru TAKEDA and Takashi YAMAZAKI 861
$C^{12}(n, n')3\alpha$ Reaction induced by 14.8 MeV Neutrons .... Yoshikazu TSUNEOKA 869
A Jet Shower with Energy of 5×10^{13} eV found in Emulsion Chamber ...... Kiyoshi NISHIKAWA 880
An Experimental Investigation on the Mode of Slip in Face-Centered Cubic Metals ...... Tadami TAOKA, Kō YASUKŌSHI, Ryūkichi HONDA and Isao ŌYAMA 888
Photoconduction and Darkening of AgCl Crystals at Low Temperatures ...... Noriaki ITOH and Tokuo SUITA 894
On the Non-Isothermal Diffusion Theory of Rectifiers .... Tadasi NUMATA 902
Study on Vacuum Deposition of Metals, I. On the Formation of Alloys by Succes-

sive Deposition of Constituent Metal Vapours in Vacuum ..Yoshibumi FUJIKI 913
Effects of Heat Treatment upon the Electrical Properties of Silicon..Yasuo MATUKURA 918
Electronmicroscopic Observation of the Cleavage Plane of KCl Crystal—the Deformation Zone— ....Tetsuhiko TOMIKI 924
β-Ferric Oxyhydroxide and Green Rust ....D. R. DASGUPTA and A. L. MACKAY 932
Anti-Phase Domains in Gold-Copper-Zinc Ordered Alloys Revealed by Electron Microscope ....
..Siro OGAWA, Denjiro WATANABE, Hiroshi WATANABE and Tsutomu KOMODA 936
Proton Magnetic Resonance in Hydrates of Halogen Compounds of Mg, Ca, Sr and Ba..........Syukuro YANO 942
Radiofrequency Spectroscopy Using Three Level Maser Action ......Koichi SHIMODA 954
Stationäre Temperaturverteilung in der Wand vielschichtiger Röhrenleitungen ....
.... Václav VODIČKA 959

SHORT NOTES

Three-Level Maser Detector for Ultramicrowaves ....Koichi SHIMODA 966
Polaron Mobility in Potassium Bromide ......Masami ONUKI and Hajimu KAWAMURA 967
Connection Formulas for WKB Solutions with Two Turning Points..Haruo MORIGUCHI 968
F-centers in LiCl Crystals ...Kiniya FUKUDA, Hiroaki MATSUMOTO and Akizo OKUDA 969
Observation of a Peculiar Type of Domain Structure of Triclinic Tungsten Trioxide
.... Sigetosi TANISAKI 970
Dielectric Property of Triglycine Sulfate Single Crystal at 9000 Mc/s Region ......
..........Atsuo NISHIOKA and Minoru TAKEUCHI 971
NMR Second Moment of a Radical under the Restricted Rotation ....
.... Akira MIYAKE, Richirô CHÛJÔ and Hatsuko ADACHI 972
Ferroelectricity in Potassium Ferrocyanide Trihydrate ....Shigeru WAKU,
Hisao HIRABAYASHI, Hiroo TOYODA, Hiroshi IWASAKI ank Ryoichi KIRIYAMA 973
On the Structure of Green Rust of Iron ....Hide YOSHIOKA 974
Extraordinary Hall Effect in Silicon-Iron Single Crystals ....
.... Eiji TATSUMOTO and Tetsuhiko OKAMOTO 975
Effective Field in the Ordinary Hall Effect in Ferromagnetics ....
.... Eiji TATSUMOTO and Tetsuhiko OKAMOTO 976
An Extended From of Weyl-Laue Theorem and its Application to Surface Problems
.... Akira SUGIYAMA 977
NMR Second Moment of a Radical Rotating in a Periodic Potential ....
.... Akira MIYAKE and Riichiro CHÛJÔ 978
New Cold Cathode Using Magnesium Oxide ....
.... Tetsuji IMAI, Yoshihiko MIZUSHIMA and Yoshitaka IGARASHI 979
Microwave Spectrum of Ethyl Iodide ....Takahiro KASUYA and Takeshi OKA 980

Erratum

On the Viscosity of Irradiated Polymers, I ....Mitio INOKUTI 965

No. 8

Angular Correlation of Gamma Rays from Xe^{126} and Te^{126} ....Mitsuo SAKAI
Hidetsugu IKEGAMI, Toshimitsu YAMAZAKI and Kazusuke SUGIYAMA 983
Decay of I^{124} ....Kazusuke SUGIYAMA,
Hidetsugu IKEGAMI, Toshimitsu YAMAZAKI and Mitsuo SAKAI 986
Theory of Thermoelectric Power of Ionic Crystals, II. ....Eijiro HAGA 992
Ionic Conduction in β-Ag_2Te and β-Ag_2Se ....Shinya MIYATANI 996
Structure of Ferroelectric Domains in Triglycine Sulfate..........
..........Hiroo TOYODA, Shigeru WAKU and Hisao HIRABAYASHI 1003
On the Electronic Structure of the U_2-Center in KCl Crystals, I ....
.... Hiroshi MIMURA and Yasutada UEMURA 1011
Etch Pits Corresponding to Dislocations in Ferroelectric Guanidinium Aluminum Sulfate Hexahydrate ....Terutaro NAKAMURA 1022
Nuclear Quadrupole Resonance of Nitrogin in Amino and Amido Compounds ......
..........Midori MINEMATSU 1030

Thomas-Fermi Model of Positive Ion..........................Shigehiro KOBAYASHI 1039
Higher Order Transitions in Double Resonance ....Ko SUGIHARA 1054
On the Dynamic Mechanical Properties of Polymers at Ultrasonic Frequencies in Relation to their Glass Transition Phenomena .... Yasaku WADA, Hidenori HIROSE, Taro ASANO and Seita FUKUTOMI 1064
X-Ray Study on the Molecular Rotation in Cubic Ammonium Nitrate............. .... Yasuhiro SHINNAKA 1073
On the Anomalous Dispersion of n-Primary Alcohols ....Kenjiro ASAI 1084
Measurement of Ion Sheath Thickness using the Double Probe with Fixed Potential ....Minoru SUGAWARA and Yoshisuke HATTA 1091
Excitation of Oscillations in a Plasma Layer ....Masao SUMI 1093
High Subsonic Flow past a Wedge in a Two-Dimensional Wind Tunnel at its choked State .... Shigeki MORIOKA 1098
Rheological Equation of Voigtian Material ....Wataru SEGAWA 1102
Surface Cracks of Sheet Glass Produced by Sodium Vapor Treatment .... Junn NAKAYAMA 1107

SHORT NOTES

Thermal Stability of the R, N and M Centres and the Oscillator Strength of the M Band of KCL Crystal..................................TetsuhiKo TOMIKI 1114
Antiferromagnetism in $KMnF_3$ ....Shinji OGAWA 1115
Paramagnetic Resonance of Manganese in $KMgF_3$ .... Shinji OGAWA and Yasaburo YOKOZAWA 1116
Fine Structure in the Giant Resonance for Cu^{63} and $Ag^{107}(\alpha, n)$ Reactions......... .... Teruo NAKAMURA, Kiyoji FUKUNAGA, Kunio TAKAMATSU, Minoru YATA and Shinjiro YASUMI 1117
Hot Holes in Tellurium ....Yasuo KANAI 1118
Anomalous Transmission of Electrons in a Film of Molybdenite ....Kazutake KOHRA and Hiroshi WATANABE 1119
On the Magnetic Property of Iron Telluride ....Ichiro TSUBOKAWA and Shoko CHIBA 1120
Thomas-Fermi Model of Compressed Positive Ion...............Shigehiro KOBAYASHI 1121

Errata

An Experimental Investigation on the Mode of Slip in Face-Centered Cubic Metals .... Tadami TAOKA, Kō YASUKŌCHI, Ryūkichi HONDA and Isao OYAMA 1022
Internal Friction of KCl Crystal at Low Temperatures......................... .... Taira SUZUKI, Katsumi SUZUKI and Kazuo KAMIGAMI 1022
On the Non-Isothermal Diffusion Theory of Rectifiers ....Tadasi NUMATA 1022

No. 9

Electroluminescence of ZnS Phosphors Excited by Short Field Pulses .... Shoji TANAKA 1123
Dielectric Susceptibility Tensor of Cadmium Sulfide ....Taizō MASUMI 1140
On the Screening of Impurity Potential by Conduction Electrons...Noboru TAKIMOTO 1142
Properties of Semiconductive Barium Titanates ....Osamu SABURI 1159
On the Theory of Thermoelectricity ....Jan TAUC 1174
Theory of Thermoelectric Power of Ionic Crystals, III...................Eijiro HAGA 1176
On the Crystal Growth of Cadmium Sulphide........................Sumiaki IBUKI 1181
Induced Conductivity of CdS by β- and γ-rays ....Sumiaki IBUKI 1196
Accurate Determination of Hydrogen Positions in NH_4Cl by Electron Diffraction .. .. Shigeya KUWABARA 1205
The Magnetic Investigation of Mn^{++}, Co^{++}, Ni^{++}, Cu^{++} Ammine and Anhydrate Salts.............................Kiyoshi KIDO and Takashi WATANABE 1217
Effect of the Basic Strength of Attached Groups on Light Absorption Spectra, IV. Proton Dissociations of Some Aromatic Molecules in Their Excited State .... Reikiti ITOH 1224
Spin-Spin Interaction in the Paramagnetic Salts ....Kō SUGIHARA 1231
Measurement of Plasma Temperature and Electron Density ....

........................Kiyoshi MURAKAWA and Shizuyo MIZUNO-HASHIMOTO 1235

SHORT NOTES

A Quantitative Study of the M Centre in KCl ....Tetsuhiko TOMIKI 1243

Antiferromagnetic Resonance in $CoCl_2\cdot 6H_2O$ ....Muneyuki DATE 1244

Crystalline Field Splitting in Ferrous Fluosilicate ....Taiichiro OHTSUKA 1245

Semiconducting Properties of Bi-Sb Alloys ....Seiichi TANUMA 1246

Curie Point in Thin Ni Films Determined by Electrical Method....Kaizo KUWAHARA 1247

Proton Resonance in the Antiferromagnetic State of $NiCl_2\cdot 6H_2O$ and $CoCl_2\cdot 6H_2O$ .. .. Tadashi SUGAWARA 1248

X-ray Observations of the Surface of Plastically Deformed LiF Crystals with the Berg-Barret Method ....Mitsuru YOSHIMATSU and Kazutake KOHRA 1249

X-ray Observation of the Strain Field in Germanium Single Crystals with the Use of the Anomalous Transmission..........Zensho ISHII and KAZUTAKE KOHRA 1250

Alpha Excitation Functions of Iron–54..........................Shigeo TANAKA, Michiaki FURUKAWA, Masuo YAGI, Shiro IWATA and Hiroshi AMANO 1251

A Mechanism for Producing Extrusions and Intrusions during Fatigue............ .... Ryutaro NAGAI 1252

Time Decrease of Permeability in Silicon-Iron .... Kunirō TSUSHIMA, Mitsuru ASANUMA and Syôhei MIYAHARA 1253

Changes of Coercivities by Heat Treatment and Cold-Rolling in Cu-Co Alloy...... .... Masayoshi SATŌ and Tadayasu MITUI 1254

Errata

Crystal Structure of 2-Amino Azulene .... Yoshito TAKAKI, Yoshio SASADA and Isamu NITTA 1242

Rheological Equation of Voigtian Material ....Wataru SEGAWA 1242

No. 10

Scattering of Protons by Silicon and Sulphur ....Yukiyasu ODA, Minoru TAKEDA, Chuin HU and Shōhei KATO 1255

Angular Distributions of Protons from the Reaction $^{12}C(\alpha, p)^{15}N$ ....Itaru NONAKA, Hisashi YAMAGUCHI, Takashi MIKUMO, Iwao UMEDA, Tatsuo TABATA and Saburo HITAKA 1260

Excitation Functions for (p, n) Reactions with Titanium, Vanadium, Chromium, Iron and Nickel up to Ep=14 MeV ......Shigeo TANAKA and Michiaki FURUKAWA 1269

The Field Dependence of the Mobility of Electrons in n-Germanium ....Hisanao SATO 1275

A Few Quarternary Systems of Perovskite Type $A^{2+}B^{4+}O_3$ Solutions ..Takuro IKEDA 1286

Doping Influences on Activator Diffusion in Oxide-coated Cathode Nickel......... .... Hiroyuki MIZUNO 1295

Electrical Properties of N-Type InSb in High Electric Field at 77°K....Yasuo KANAI 1302

Study on Vacuum Deposition of Metals, II. On the Change with Aging Time in Thickness and Resistivity of Vacuum Deposited Gold Film..Yoshibumi FUJIKI 1308

Elastic Stiffness Constants of Cadmium Sulfide....Taizō MASUMI and Toshio TANAKA 1313

Deformation Twinning of Tin Single Crystals under Impact Loading..Ken-ichiro ISHII 1315

Monitoring X-ray Tube Output with Ionization Chamber........................ ....Kenzo TANAKA, Jun-ichi CHIKAWA and Tadashi YAMANAKA 1321

A New Fine Focus X-ray Tube.................................Yoshihiro KAMIYA 1327

Electron Microscopic Observation of the Superlattice in Serpentine ....Yoshihiro KAMIYA, Minoru NONOYAMA and Ryozi UYEDA 1334

Transition from Dynamical to Kinematical Intensities of Electron Diffraction by Crystals..Shizuo MIYAKE 1347

Neutron Diffraction Study of Antiferromagnetic $MnTiO_3$ and $NiTiO_3$ .... Gen SHIRANE, S. J. PICKART and Yoshikazu ISHIKAWA 1352

On Galvanomagnetic Effects in *P*-Type Crystals of PbTe.........Kisaburo SHOGENJI 1360

Magnetic Susceptibility of Liquid Alloys of Copper with Cobalt, Iron, Manganese, and Chromium ....Yasuaki NAKAGAWA 1372

On the Viscosity of Irradiated Polymers, II.......Mitio INOKUTI and Kanji KATSUURA 1379

Determination of Molecular Weight Distributions of High Polymers by Fractionation

.... Hiroshi OKAMOTO 1388
Magnetohydrostatic Equilibrium for Plasma in a Torus Tube ....Taro KIHARA 1397
F-M Conversion in Additively Colored KCl Crystals ....Masamitsu HIRAI 1400
Optical Studies on Thallium-activated Alkali-iodide Crystals ....
.... Yoichi UCHIDA and Riso KATO 1408
On the Preferential Bleaching of the M Band in KCl Crystal with Polarized Light
......................Takehiko ISHII, Tetsuhiko TOMIKI and Masayasu UETA 1415
Flow of a Visco-Elastic Liquid near a Stagnation Point ....S. K. SHARMA 1421
The Flow of a Viscous Fluid past a Triangular Cylinder ....Mitutosi KAWAGUTI 1425
Reversal Flow Theorem concerning Oseen's Approximation ......Mitutosi KAWAGUTI 1431
Two-dimensional Stokes Flow of an Electrically Conducting Fluid in a Uniform Magnetic Field ....Hirowo YOSHINOBU and Tsunehiko KAKUTANI 1433
Statistical Aspects of Fracture in Concrete, I. An Analysis of Flexural Failure of Portland Cement Mortar from the Standpoint of Stochastic Theory ......
....Motoo HORI 1444

SHORT NOTES

Energy Loss of Electrons passing through a Graphite Single Crystal at Different Incident Angles ....Hiroshi WATANABE 1453
Nuclear Magnetic Resonance of Na^{23} in Sodium Chloride Crystals ....
.... Eizo OTSUKA, Yudo OSHIO, Toyohide KOBAYASHI and Hajimu KAWAMURA 1454
Piezoelectric Effect in a Rectifying Contact of Semiconductor ....
.... Tetsuro TANAKA and Hiroyoshi KAWAMURA 1455
On the Superstructure of the Ordered Alloy Au_3Zn[R] ....Hiroshi IWASAKI 1456
Fine Structure in the $N^{14}(\gamma, n)N^{13}$ Activation Curve..............Naoshi MUTSURO,
Yuji OHNUKI, Kazuo SATO, Kosuke KAGEYAMA and Motoharu KIMURA 1457
Rotational Transitions in Hydrogen and Deuterium ....Kazuo TAKAYANAGI 1458
Magnetic Anisotropy of Evaporated Films Formed in Magnetic Field ....
....Minoru TAKAHASHI,
Denjiro WATANABE, Tetsuzo SASAGAWA, Hideo SAITO and Shiro OGAWA 1459
A 4^+–0^+ Cross-Over Transition ....Haruhiko MORINAGA and Kasuke TAKAHASHI 1460

Errata

Fine Structure in the Giant Resonance for Cu^{63} and $Ag^{107}(\gamma, n)$ Reactions..........
.... Teruo NAKAMURA,
Kiyoji FUKUNAGA, Kunio TAKAMATSU, Minoru YATA and Shinjiro YASUMI 1461

No. 11

Elastic Scattering of Protons by Helium between 9.2 MeV and 14.5 MeV ....
....Junpei SANADA 1463
A Large Multiplate Cloud Chamber for Cosmic Ray Observation..................
Saburo MIYAKE, Kensaku HINOTANI, Itsuo KATSUMATA and Tatsunosuke KANEKO 1471
On the Theory of Brownian Motion and Spin Relaxation ....
..................................Takeyasu KOTERA and Morikazu TODA 1475
Electrical Properties of Alkali Antimonides..........................Shunji IMAMURA 1491
Photoelectrical Properties of Alkali Antimonides ....Shunji IMAMURA 1497
Quenching Effect in KCl Crystals ....Masayoshi SAKAMOTO 1506
Application of Higher Order Born Approximation to Multiple Elastic Scattering of Electrons by Crystals ....Kunio FUJIWARA 1513
A Theoretical Treatment of the Excess Energies of Binary Metallic Solutions ....
.... Mitsuo SHIMOJI 1525
Algebraic Method to obtain Irreducible Representations of Space Groups with an Application to White Tin.................................Shoichi MASE 1538
Effect of External Illumination on Carrier Lifetime in Semiconductors ....
.... Jun'ichi OKADA 1550
Dynamical Theory of Electron Diffraction in Laue-case, I. General Theory ......
.... Fuminori FUJIMOTO 1558
On the Magnetic Anisotropy of a Pyrrhotite Crystal..........................

.... Itsuo MIKAMI, Tokutaro HIRONE, Hiroshi WATANABE, Seijiro MAEDA, Kengo ADACHI and Motohiko YAMADA 1568

Effects of Ionizing Radiations on Synthetic Polymer Solutions ....Shintaro SUGAI 1573

Ferromagnetic Crystalline Anisotropy of Fe Mn Ferrite System .... Zenya FUNATOGAWA, Nahonori MIYATA and Seiji USAMI 1583

Temperature Dependence of the Magnetostriction Constants in Iron and Silicon Iron.......................... Eiji TATSUMOTO and Tetsuhiko OKAMOTO 1588

Magnetic Hyperfine Spectrum of H_2CO by a Maser .... Hiroshi TAKUMA, Tadao SHIMIZU and Koichi SHIMODA 1595

Electrical Polarizabilities of Rare Gas Atoms by the Hartree-Fock Wave Functions .... Shobu KANEKO 1600

Luminescence Processes in the KCl:Tl Phosphor in a Multidimensional Configuration Space..........................Hiroshi KAMIMURA and Satoru SUGANO 1612

Photoconductivity and Luminescence of the *F* and *M* Centers in Potassium Chloride Goro KUWABARA, Akira MISU, Toshimitsu WATANABE and Yoshio NISHIYAMA 1621

Multiplet Structure and Hyperfine Structure of the Spectrum of Mercury .... Kiyoshi MURAKAWA 1624

SHORT NOTES

Infrared Absorption of α-$Ag_2Te_xS_{1-x}$............................Shin-ya MIYATANI 1634

The Aging of Permeability in Manganese-Zinc Ferrite.......................... .... Syôhei MIYAHARA and Tokio YAMADAYA 1635

Diffusion of Nickel in Single Crystals of Copper ....Akira IKUSHIMA 1636

Microwave Investigation on Plasma in Shock Tube .... Mikio TAKEYAMA, Shiro HAMAMURA and Toshiatsu ODA 1637

Etch-Figure in CdS Single Crystals ....Makoto KIKUCHI and Sigeru IIZIMA 1638

Note on the Effect of Oxygen Molecules Contained in Solid Hydrogen on the Rate of Ortho-para Conversion...........Kazuko MOTIZUKI and Takeo NAGAMIYA 1639

Localized Electron Model and Thermoelectric Power ....Mikio TSUJI 1640

Effect of Re-crystallization on the Temperature Dependence of Photocurrent of Silver Chloride Crystals.....................Noriaki ITOH and Tokuo SUITA 1641

Possible Evidence for the Light Induced Plasticity in Germanium ....Makoto KIKUCHI and Mitsuyoshi SAITO 1642

The Kinetics of Radical Reactions in γ-irradiated Polyvinyl Chloride............. .... Kenzi HUKUDA, Jiro ISHII and Zenemon MIDUNO 1643

Measurement of Galvanomagnetic Tensors of Bismuth Single Crystals at Low Temperatures ....Shoichi MASE and Seiichi TANUMA 1644

A Note on the Drag of a Screen at Low Reynolds Number...........P. G. MORGAN 1645

No. 12

Photoneutron Cross Sections for Ag^{107}, Mo^{92} and Zr^{90} .... Naoshi MUTSURO, Yuji OHNUKI, Kazuo SATO and Motoharu KIMURA 1649

Search for the Anomalous Scattering of Mu-Mesons (On the Apparatus using a Delayed Coincidence Method) ....Takashi KITAMURA 1654

Temperature Dependence of Surface Voltage of Silver Bromide .... Sanemi SONOIKE and Hisawo WAKABAYASHI 1664

Study on Precipitation Phenomena during Aging of Aluminium-Silver Alloy in Thin Evaporated Films ....Yasuchige FUKANO and Shiro OGAWA 1671

Dielectric Properties of Mixed Crystals of Barium-Strontium Titanate .... Shunkichi KISAKA, Seiji IKEGAMI and Hiromu SAKAI 1680

Exciton Structures in Alkali Halides..................................Yukio OSAKA 1685

Acoustoelectric Effect in Metals ....Nobuo MIKOSHIBA 1691

The X-ray Non-Diagram Lines *K* of Some Compounds of the Iron Group........ .... Kenjiro TSUTSUMI 1696

X-ray Study on Molecular Rotation in Tetragonal Ammonium Nitrate .... Yasuhiro SHINNAKA 1707

Proton Magnetic Relaxation in Solutions of a Manganous Salt ....Hide YOSHIOKA and Tetsuo FUJIUA 1717

Paramagnetic Susceptibility of Single Crystals of Some Nickel Salts .... Taiichiro HASEDA, Hanako KOBAYASHI and Muneyuki DATE 1724
Relative Intensities of Zeeman Components in Nuclear Quadrupole Rosonance Spectrum .... Masaharu TOYAMA 1727
Spectroscopic Measurements of the Hydrogen Plasma .... Manabu YAMAMOTO 1739
Anodic Oscillation in Glow Discharge I, Simple Correspondence of the Internal Phenomena to the Oscillation .... Kazuyuki OGAWA 1746
Ion-Electron of Plasmas in a Strong Magnetic Field .... Taro KIHARA 1751
Optical Studies on the Effect of Electric Fields on the Transitions of Barium Titanate .... Kazuo KAWABE 1755
Decay Properties of ZnS(Ag) Phosphors .... Tsunesaburo ASADA, Masayoshi MASUDA, Masayuki OKUMURA and Juzo OKUMA 1766
An Improvement of the WKB Method in the Presence of Turning Points and the Asymptotic Solutions of a Class of Hill Equations .... Haruo MORIGUCHI 1771
Further Investigation on the Transition of Two-dimensional Separated Layer at Subsonic Speeds .... Hiroshi SATO 1797
On a Method of Successive Approximations applied to the Axisymmetric Flows of an Incompressible Perfect Fluid .... Tamedi SIMASAKI and Keishiro NIU 1810
The W. K. B. Method for the Differential Equations of the Fourth Order .... Tomoyoshi SAITO and ISAO OSHIDA 1816

SHORT NOTE

Antiferromagnetism of $Mn_{3.25}Ge$ .... Kō YASUKŌCHI, Tetuo OHOYAMA and Kazuo KANEMATSU 1820
Absorption and Excitation Bands of KCl-Tl in the Extreme Ultraviolet Region .... Goro KUWABARA and Kiyoshi AOYAGI 1821
Repeated Yielding of Impure Tin Crystals under Successive Impact Loading .... Kenichiro ISHII 1822
The Crystal Structures of $KMnF_3$, $KNeF_3$, $KCoF_3$ and $KNiF_3$ .... Atsushi OKAZAKI, Yasutaka SUEMUNE and Tsutomu FUCHIKAMI 1823
Measurement of Plasma Temperature and Electron Density .... Kiyoshi MURAKAWA and Shizuyo HASHIMOTO 1824
Stacking Faults in Copper-Nickel Alloys .... Koichi NAKAJIMA 1825
Frequency Shift in Ammonia Absorption Lines Other than (3,3) .. Kiyokata MATSUURA 1826
Diffusion of Cu into CdS Single Crystal through Dislocations .... Sumiaki IBUKI and Hirosuke YAMASHITA 1827
A New Device for measureing Thickness of Evaporated Metal Film by Use of X-ray Inerference Fringes .... Yoshibumi FUJIKI and Toshiro YOSHIDA 1828
Observations of Lattice Defects in Graphite by Moire Patterns .... Kazuhiko IZUI 1829
Visible Light Emission from Germanium Diffused p-n Junction .... Makoto KIKUCHI and Kenkichi TACHIKAWA 1830
Infrared Radiation from Silicon Grown Junction .... Ichiro UCHIDA 1831
An Interpretation of 550 Me Particles .... Masafumi INOKI 1832
Dependence of the Joshi Effect on "Aging" under, or/and in the Absence of, Continuous Electrical Excitation .... M. Venugopalan 1833

Errata

Pheological Equation of Voigtian Material .... Wataru SEGAWA 1834
On Galvanomagnetic Effects in P-Type Crystals of PbTe .... Kisaburo SHOGENJI 1835
Theory of Thermoelectric Power of Ionic Crystal, II .... Eijiro HAGA 1835
Multiplet Structure and Hyperfine Structure of the Spectrum of Mercury .... Kiyoshi MURAKAWA 1836
Statistical Aspects of Fracture in Concrete, I. An Analysis of Flexural Failure of Portland Cement Mortar from the Standpoint of Stochastic Theory .... Motoo HORI 1836

AUTHOR INDEX TO VOL. 14

ABE Ryuji: Theoretical Treatment of the Movement of 180° Domain in $BaTiO_3$ Single Crystal 633

ABE Ryuzo: Note on the Cluster Expansion Theory of Classical Fluids. Watermelon Approximation 10

ADACHI Hatsuko;

A. MIYAKE, R. CHÛJÔ and ———: NMR Second Moment of a Radical under the Restricted Rotation (S. N.) 972

ADACHI Kongo;

I. MIKAMI, T. HIRONE, H. WATANABE S. MAEDA, ——— and M. YAMADA: On the Magnetic Anisotropy of a Pyrrhotite Crystal 1568

AMANO Hiroshi;

S. TANAKA, M. FURUKAWA, M. YAGI, S. IWATA and ———: Alpha Excitation Functions of Iron–54 (S. N.) 1251

ANDO Keiichi;

———, O. KAMIGAITO, Y. KAMIYA, S. TAKAHASHI and R. UYEDA: Oxide-Cored Cathode 180

AOYAGI Kiyoshi;

G. KUWABARA and ———: Absorption and Excitation Bands of KCl–Tl in the Extrem Ultraviolet Region (S. N.) 1821

ASADA Tsunesaburo;

———, M. MASUDA, M. OKUMURA and J. OKUMA: Decay Properties of ZnS(Ag) Phosphors 1766

ASAI Kenjiro: On the Anomalous Dispersion of n-Primary Alcohols 1084

ASANABE Sizuo: Electrical Properties of Stannous Selenide 281

ASANO Taro;

Y. WADA, H. HIROSE, ——— and S. FUKUTOMI: On the Dynamic Mechanical Properties of Polymers at Ultrasonic Frequencies in Relation to their Glass Transition Phenomena 1064

ASANUMA Mitsuru;

K. TSUSHIMA, ——— and S. MIYAHARA: Time Decrease of Permeability in Silicon-Iron (S. N.) 1253

BERGHEZAN Aurel;

N. TERAO et ———: Transformation des Réseaux Metalliques sous l'Influence des Elements d'Insertion: Transformation du Nickel sous l'Influence de l'Azote 139

CHIBA Shoko;

I. TSUBOKAWA and ———: On the Magnetic Property of Iron Telluride (S. N.) 1120

CHIBA Takehiko;

———, M. TOYAMA and Y. MORINO: Nuclear Quadrupole Resonance Spectra of N^{14} in Urea Crystal (S. N.) 379

CHIKAWA Jun-ichi;

K. TANAKA, ——— and T. YAMANAKA: Monitoring X-ray Tube Output with Ionization Chamber 1321

CHÛJÔ Riichirô;

A. MIYAKE, ——— and H. ADACHI: NMR Second Moment of a Radical under the Restricted Rotation (S. N.) 972

A. MIYAKE and ———: NMR Second Moment of a Radical Rotating in a Periodic Potential (S. N.) 978

DASGUPTA D. R.;

——— and A. L. MACKAY: β-Ferric Oxyhydroxide and Green Rust 932

DATE Muneyuki

———: Antiferromagnetic Resonance in $CoCl_2{\cdot}6H_2O$ (S. N.) 1244

T. HASEDA, H. KOBAYASHI and ———: Paramagnetic Susceptibility of Single Crystals of Some Nickel Salts 1724

ENDO Shigeaki;

Y. SUZUKI, ——— and E. HAGA: Thermoelectric Power of AgCl 729

FARAG, M. Shehata: On the X-Ray Diffuse Scattering by 1–3–5–Triphenylbenzen 755

FUCHIKAMI Tsutomu;
  A. OKAZAKI, Y. SUEMUNE and ———: The Crystal Structures of $KMnF_3$, $KFeF_3$ and KNiF (S. N.) 1823

FUJIKAWA Hiroomi;
  K. TAMADA and ———: The Steady Flow of Viscous Fluid at Low Reynolds Numbers passing obliquely through a Plane Grid made of Equal Parallel Circular Cylinders 202

FUJIKI Yoshibumi;
  ———: Study on Vacuum Deposition of Metals, I. On the Formation of Alloys by Successive Deposition of Constituent Metal Vapours in Vacuum .. 913
  ———: Study on Vacuum Deposition of Metals, II. On the Change with Aging Time in Thickness and Resistivity of Vacuum Deposited Gold Film 1308
  ——— and T. YOSHIDA: A New Device for Measuring Thickness of Evaporated Metal Film by Use of X-ray Interference Fringes (S. N.) 1828

FUJIMOTO Fuminori: Dynamical Theory of Electron Diffraction in Laue-case I, General Theory 1558

FUJITA Hiroshi;
  T. KATO and ———: Maximum Principles for Vorticity in Viscous Fluid (S. N.) 545

FUJITA Junji;
  H. TAMAGAWA and ———: A Visualizing Method of Electron Temperature and Plasma Density (S. N.) 678

FUJITA Shigeru;
  A. MITSUISHI, H. YOSHINAGA and ———: The Far Infrared Reflectivity of NaCl, KCl and KBr Crystals (S. N.) 110

FUJITA Tetsuo;
  H. YOSHIOKA and ———: Proton Magnetic Relaxation in Solutions of a Manganous Salt 1717

FUJIWARA Kunio: Application of Higher Order Born Approximation to Multiple Elastic Scattering of Electrons by Crystals 1513

FUKANO Yasuchige;
  ——— and S. OGAWA: Study on Precipitation Phenomena during Aging of Aluminium-Silver Alley in Thin Evaporated Films 1671

FUKUDA Kuniya;
  ———, H. MATSUMOTO, Y. UCHIDA and H. YOSHIMURA: Cyclotron Resonance in Gas Discharge (S. N.) 543
  ———, H. MATSUMOTO and A. OKUDA: *F*-centers in LiCl Crystals (S. N.) .. 969

FUKUNAGA Kiyoji;
  T. NAKAMURA, K. TAKAMATSU, ———, M. YATA and S. YASUMI: Absolute Cross Sections of the (γ, n) Reaction for Cu^{63}, Zn^{64} and Ag^{109} 693
  T. NAKAMURA, ———, K. TAKAMATSU, M. YATA and S. YASUMI: Fine Structure in the Giant Resonance for Cu^{63} and Ag^{10} (α, n) Reactions (S. N.) 1117

FUKUROI Tadao;
  Y. MUTO, Y. TAWARA, Y. SHIBUYA and ———: Electrical Properties of Dilute Alloys of Zinc with Manganese at Low Temperature (S. N.) 380

FUKUTOMI Seita;
  Y. WADA, H. HIROSE, T. ASANO and ———: On the Dynamic Mechanical Properties of Polymers at Ultrasonic Frequencies in Relation to their Glass Transition Phenomena 1064

FUNATOGAWA Zenya;
  ———, N. MIYATA and S. USAMI: Electric Resistance and Cation Distribution of Fe–Mn Ferrite System (S. N.) 854
  ———, N. MIYATA and S. USAMI: Ferromagnetic Crystalline Anisotropy of Fe–Mn–Ferrite System 1583

FURUICHI Jiro;
  S. SUGAI, M. ISHIKAWA and ———: Effects of γ-Rays on Aqueous Solutions of Synthetic Polymers (S. N.) 544

FURUKAWA Michiaki

S. TANAKA, ———, M. YAGI, S. IWATA and H. AMANO: Alpha Excitation Functions of Iron-54 (S. N.) 1251

S. TANAKA and ———: Excitation Functions for (p, n) Reactions with Titanium, Vanadium, Chromium, Iron and Nickel up to Ep=14 Mev 1269

GOLD Louis: Terminal Zone Cropping and Ultimate Zone Purification 386

HAGA Eijiro;

———: On the Theory of Thermoelectricity in Two-Band Semiconductors .. 35

Y. SUZUKI, S. ENDO and ———: Thermoelectric Power of AgCl 729

———: Theory of Thermoelectric Power of Ionic Crystals, II 992

———: Theory of Thermoelectric Power of Ionic Crystals, III 1176

HAGIWARA Shigeo;

S. KOJIMA, K. KATO, ——— and R. MATSUZAKI: Oscillations in Plasma II .. 821

HAMAKAWA Yoshihiro;

J. YAMAGUCHI and ———: High Electric Field Effects in Germanium p–n Junction 15

J. YAMAGUCHI and ———: Barrier Temperature at Turnover in Germanium p–n Junction 232

HAMAMURA Shiro;

M. TAKEYAMA, ——— and T. ODA: Microwave Investigation on Plasma in Shock Tube (S. N.) 1637

HASEDA, Taiichiro

———, H. KOBAYASHI and M. DATE: Paramagnetic Susceptibility of Single Crystals of Some Nickel Salts 1724

HASEGAWA Hiroshi;

R. KUBO, ——— and N. HASHITSUME: Quantum Theory of Galvanomagnetic Effect I. Basic Considerations 56

HASHIMOTO Shizuyo;

K. MURAKAWA and ———: Measurement of Plasma Temperature and Electron Density 1235

K. MURAKAWA and ———: Measurement of Plasma Temperature and Electron Density (S. N.) 1824

HASHITSUME Natsuki;

R. KUBO, H. HASEGAWA and ———: Quantum Theory of Galvanomagnetic Effect I. Basic Considerations 56

HATTA Yoshisuke;

M. SUGAWARA and ———: Measurement of Ion Sheath Thickness using the Double Probe with Fixed Potential 1091

HATTORI Shuzo;

T. SHIMIZU, S. MATSUOKA, ——— and SENDA: Nuclear Spin-Spin Coupling between Protons in Vinyl Derivatives (S. N.) 683

M. KIMURA, S. MATSUOKA, ——— and K. SENDA: Fine Structures of Proton Resonance Spectra of Fluorobenzene Derivatives (S. N.) 684

HAYASHI Izuo;

H. KUMAGAI, K. ŌNO, H. SHÔNO, ——— K. KURODA and M. IMAIZUMI: 16″ Variable Energy Cyclotron 1

HAYASHI Masakazu: Absorption Spectrum of Copper-Coloured Cuprous Oxide 681

HAYASHI Nisiki: On Quantitative Measurement of Turbulence by Means of a Constant Resistance Hot-wire Anemometer 360

HIBI Tadatosi;

——— and T. TOMIKI: Electronmicroscopic Observation of the Additively Coloured KCl Crystal 445

——— and K. YADA: Successive Electronmicroscopic Observation of Coloured and Bleached KCl Crystal 455

——— and T. TOMIKI: Electronmicroscopic Observation of the KCl Crystal Containing Potassium Colloid Particles (S. N.) 375

HITAKA Akira;

——— and M. TUTUMI: Changes of Ultrasonic Attenuation during Creep of Aluminum (S. N.) 687
HIKI Yosio: Internal Friction of Lead, II 590
HINOTANI Kensaku;
S. MIYAKE, ———, I. KATSUMATA and T. KANEKO: A Large Multiplate Cloud Chamber for Cosmic Ray Observation 1471
HIRABAYASHI Hisao;
S. WAKU, ———, H. TOYODA, H. IWASAKI and R. KIRIYAMA: Ferroelectricity in Potassium Ferrocyanide Trihydrate (S. N.) 973
H. TOYODA, S. WAKU and ———: Structure of Ferroelectric Domains in Triglycine Sulfate 1003
HIRABAYASHI Makoto;
———: Stress-Ordering Effect on Thermal Expansion of CuAu Single Crystals .. 149
———: Electrical Resistivity and Superstructure of CuAu$_3$ 262
HIRAI Masamitsu;
M. UETA, ——— and H. WATANABE: Interaction of Exciton with Electron Trapping Centers in Alkali Halide Crystals 1. *F* and *U* Centers in KCl and KBr Crystals 253
M. UETA and ———: Interaction of Exciton with *R* Center in KCl Crystal .. 546
———: F-M Conversion in Additively Colored KCl Crystals 1400
HIRAO Yasuo;
I. MIURA, T. WAKATSUKI, ——— and E. OKADA Gamma Rays from the Proton Bombardment of ^{24}Mg, ^{25}Mg and ^{26}Mg 239
HIRONE, Tokutaro;
I. MIKAMI, ———, H. WATANABE, S. MAEDA, K. ADACHI and M. YAMADA: On the Magnetic Anisotropy of a Pyrrhotite Crystal 1568
HIROSE Hidenori;
Y. WADA, ———, T. ASANO and S. FUKUTOMI: On the Dynamic Mechanical Properties of Polymers at Ultrasonic Frequencies in Relation to their Glass Transition Phenomena 1064
HITAKA Saburo;
I. NONAKA, H. YAMAGUCHI, T. MIKUMO, I. UMEDA, T. TABATA and ———: Angular Distributions of Protons from the Reaction ^{12}C(α, p)^{15}N 1260
HONDA Ryūkichi;
T. TAOKA, K. YASUKŌCHI, ——— and I. ŌYAMA: An Experimental Investigation on the Mode of Slip in Face-Centered Cubic Metals 888
HORI Motoo: Statistical Aspects of Fracture in Concrete, I. An Analysis of Flexural Failure of Portland Cement Mortar from the Standpoint of Stochastic Theory .. 1444
HOSOE Masanao;
——— and S. SUZUKI: Gamma Rays from Neutron Inelastic Scattering of Magnesium, Aluminum, Iron and Bismuth 699
HU Chuin;
Y. ODA, M. TAKEDA, ——— and S. KATO: Scattering of Protons by Ne^{20} and Ne^{22} 396
———, S. KATO, Y. ODA and M. TAKEDA: Elastic and Inelastic Scattering of 22 MeV Alpha Particles by Light Elements 549
———, K. KIKUCHI, S. KOBAYASHI, K. MATSUDA, Y. NAGAHARA, Y. ODA, N. TAKANO, M. TAKEDA and T. YAMAZAKI: Elastic and Inelastic Scatterings of Protons from Ti, Cr, Ni, Zn, and O at 8 to 14 MeV 861
Y. ODA, M. TAKEDA, ——— and S. KATO: Scattering of Protons by Silicon and Sulphur 1255
HUKUDA Kenzi;
———, J. ISHII and Z. MIDUNO: The Kinetics of Radical Reactions in γ-irradiated Polyvinyl Chloride (S. N.) 1643
HUSHIMI Kazuo;
——— and K. KATAOKA: Piezoelectric Properties of Triglycine Sulphate Crystal (S. N.) 105
IBUKI Sumiaki;

———: On the Crystal Growth of Cadium Sulphide..........................1181
———: Induced Conductivity of CdS by β- and γ-rays 1196
and H. YAMASHITA: Diffusion of Cu into CdS Single Crystal through Dislocations (S. N.) 1827

IGARASHI Yoshitaka;
T. IMAI, Y. MIZUSHIMA and ———: New Cold Cathode Using Magnesium Oxide (S. N.) 979

IIZIMA Shigeru;
M. KIKUCHI and ———: Avalanche Electroluminescence in CdS Single Crystal (S. N.) 852
M. KIKUCHI and ———: Quenching Effect of the Photoconductivity Decay in CdS (S. N.).. 856
M. KIKUCHI and ———: Etch-Figure in CdS Single Crystals (S. N.) 1638

IKEDA Takuro;
———: Studies on (Ba-Pb)(Ti-Zr)O_3 System.................................. 168
———: A Few Quarternary Systems of Perovskite Type $A^{2+}B^{4+}O_3$ Solutions..1286

IKEDA Toshio;
S. YOSHIDA and ———: Effect of Electron Bombardment on Sodium Chloride.. 473

IKEGAMI Hidetsugu:
M. SAKAI, ———, T. YAMAZAKI and K. SUGIYAMA: Angular Correlation of Gamma Rays From Xe^{126} and Te^{126} 983
K. SUGIYAMA, ———, T. YAMAZAKI and M. SAKAI: Decay of I^{124}............ 986

IKEGAMI Seiji;
S. KISAKA, ——— and H. SAKAI: Dielectric Properties of Mixed Crystals of Barium-Strontium Titenate 1680

IKUSHIMA Akira;
———: Diffusion of Manganese in Single Crystals of Copper 111
———: Diffusion of Nickel in Single Crystals of Copper (S. N.) 1636

IMAI Tetsuji;
———, Y. MIZUSHIMA and Y. IGARASHI: New Cold Cathode Using Magnesium Oxide (S. N.) 979

IMAIZUMI Minoru;
K. ŌNO, J. SHIMADA, K. KURODA, O. TANAKA H. KAMITSUBO, A. ITO, S. TANAKA and ———: Yields and Angular Distributions of Protons from $F^{19}(d, p)F^{20}$ and $F^{19}(d, p)F^{20}$ 117
H. KUMAGAI, K. ŌNO, H. SHÔNO, I. HAYASHI, K. KURODA and ———: 16″ Variable Energy Cyclotron 1

IMAMURA Shunji;
———: Electrical Properties of Alkali Antimonides..........................1491
———: Photoelectrical Properties of Alkali Antimonides 1497

INOKI Masafumi: An Interpretation of 550 Me Particles (S. N.).........................1832

ISHII Jiro;
K. HUKUDA, ——— and Z. MIDUNO: The Kinetics of Radical Reactions in γ-irradiated Polyvinyl Chloride (S. N.)..1643

ISHII Ken-ichiro;
———: Deformation Twinning of Tin Single Crystals under Impact Loading..1315
———: Repeated Yielding of Impure Tin Crystals under Successive Impact Loading (S. N.) 1822

ISHII Takehiko;
M. UETA and ———: Luminescence of KI : TI Induced by Far Ultraviolet Light 857
———, T. TOMIKI and M. UETA: On the Preferential Bleaching of the M Band in KCl Crystal with Polarized Light 1415

ISHII Zensho;
——— and K. KOHRA: X-ray Observation of the Strain Field in Germanium Single Crystals with the Use of the Anomalous Transmission (S.N.) 1250

ISHIKAWA Mitsuo;
S. SUGAI, ——— and J. FURUICHI: Effects of γ-Rays on Aqueous Solutions of

Syonthetic Polymers (S. N.) 544

ISHIKAWA Yoshikazu;
- G. SHIRANE, S. J. PICKART and ———: Neutron Diffraction Study of Antiferromagnetic MnTiO$_3$ and NiTiO$_3$ 1352

INOKUTI Mitio;
- ———: On the Viscosity of Irradiated Polymers I 79
- ——— and K. KATSUURA: On the Viscosity of Irradiated Polymers, II 1379

INOUE Noriyoshi;
- K. SHIMOMURA and ———: Zerosplitting Cone of Nuclear Quadrupole Spectrum for Spin 5/2. 86

INUI Teturo;
- H. MIMURA and ———: The Electronic Structure of the M Center 175

ITO Atsuko;
- K. ŌNO, J. SHIMADA, K. KURODA, O. TANAKA, H. KAMITSUBO, ———, S. TANAKA and M. IMAIZUMI: Yields and Angular Distributions of Protons from F^{19}(d, p)F^{20} and F^{19}(d, p)F^{20} 117

ITOH Junkichi;
- ——— and Y. YAMAGATA: Nuclear Magnetic Resonance of RbBr (S. N.) 225
- ——— and R. KUSAKA: Nuclear Magnetic Double Resonance Experiment on Two Proton System 492
- ——— and S. SATO: Double Proton Magnetic Resonance by a Side Band Method (S. N.) 851

ITOH Noriaki;
- ——— and T. SUITA: Photoconduction and Darkening of AgCl Crystals at Low Temperatures 894
- ——— and T. SUITA: Effect of Re-crystallization on the Temperature Dependence of Photocurrent of Silver Chloride Crystals (S. N.) 1641

ITOH Reikiti: Effect of the Basic Strength of Attached Groups on Light Absorption Spectra, IV. Proton Dissociations of Some Aromatic Molecules in Their Excited State 1224

IWASAKI Hiroshi;
- ———: On the Superstructure of the Ordered Au$_3$Zn[R] (S. N.) 1456
- S. WAKU, H. HIRABAYASHI, H. TOYODA, ——— and R. KIRIYAMA: Ferroelectricity in Potassium Ferrocyanide Trihydrate (S. N.) 973

IWATA Masako;
- T. IWATA, ——— and M. YAMAMOTO: Magnetic Annealing Effect in αFe$_2$O$_3$ (S. N.) 855

IWATA Shiro;
- S. TANAKA, M. FURUKAWA, M. YAGI, ——— and H. AMANO: Alpha Excitations Functions of Iron–54 1251

IWATA Takao;
- ———, M. IWATA and M. YAMAMOTO: Magnetic Annealing Effect in αFe$_2$O$_3$ (S.N.) 855

IZUI Kazuhiko: Observations Lattice Defects in Graphite by Moire Patterns (S. N.) .. 1829

KAGEYAMA Kosuke;
- N. MUTSURO, Y. OHNUKI, K. SATO, ——— and M. KIMURA: Fine Structure in the N^{14}(γ,n)N^{13} Activation Curve (S. N.) 1457

KAKIUCHI Yoshinobu;
- M. NAGUMO and ———: An Abnormal Saturation Behavior in High Resolution Proton Magnetic Resonance Spectra (S. N.) 679

KAKUTANI Tsunehiko;
- H. YOSHINOBU and ———: Two-dimensional Stokes Flow of on Electrically Conducting Fluid in a Uniform Magnetic Field 1433

KAMIGAITO Osami;
- K. ANDO, ———, Y. KAMIYA, S. TAKAHASHI and R. UYEDA: Oxide-Cored Cathode 180

KAMIGAKI Tomoo;
- T. SUZUKI, K. SUZUKI and ———: Internal Friction of KCl Crystals at Low Temperatures 731

KAMIMURA Hiroshi;
———— and S. SUGANO: Luminescence Processes in the KCl:Tl Phosphor in a Multidimensional Configuration Space 1612
KAMITSUBO Hiromichi;
K. ÔNO, J. SHIMADA, K. KURODA, O. TANAKA, ————, A. ITO, S. TANAKA and M. IMAIZUMI: Yields and Angular Distributions of Protons from $F^{19}(d, p)F^{20}$ and $F^{19}(d, p)F^{20}$ 117
KAMIYA, Yoshihiro;
K. ANDO, O. KAMIGAITO, ————, S. TAKAHASHI and R. UYEDA: Oxide-Cored Cathode 180
————: A New Fine Focus X-ray Tube 1327
————, M. NONOYAMA and R. UYEDA: Electron Microscopic Observation of the Superlattice in Serpentine 1334
KANAI Yasuo;
————: Hot Holes in Tellurium (S. N.) 1118
————: Electrical Properties of N-Type InSb in High Electric Field at 77°K.. 1302
KANAMORI Hitoshi;
S. OKANISHI and ————: Simplified Representations on the Firing Characteristics of Vibrational-Ignitor Tubes (S. N.) 542
KANEKO Shobu: Electrical Polarizabilities of Rare Gas Atoms by the Hartree-Fock Wave Functions. 1600
KANEKO Tatsunosuke;
S. MIYAKE, K. HINOTANI, I. KATSUMATA and ————: A Large Multiplate Cloud Chamber for Cosmic Ray Observation 1471
KANEMATSU Kazuo;
K. YASUKOCHI, T. OHOYAMA and ————: Antiferromagnetism of $Mn_{3.25}$ Ge (S. N.) 1820
KANOU Kyoichi;
K. KAWASAKI, ————, and Y. SEKITA: Interaction of Water Vapour with Germanium Real Surface (S. N.) 233
KASUYA Tadao;
————: The General Theory of Transport: The Difference between Electric Field and Density Gradient 410
———— and K. YAMADA: Electrical and Thermal Conductivity of Monovalent Metals; The Influences of Coulomb Interaction 416
KASUYA Takahiro;
———— and T. OKA: Microwave Spectrum of Ethyl Iodide (S. N.) 980
KATAOKA Keisuke;
K. HUSHIMI and ————: Piezoelectric Properties of Triglycine Sulphate Crystal (S. N.) 105
KATO Keiji;
K. KAWASAKI and ————: Size Distribution of Radioactivity of the Natural Radioactive Dust (S. N.) 234
KATO Kiyoe;
S. KOJIMA, ————, S. HAGIWARA and R. MATSUZAKI: Oscillations in Plasma II.. 821
KATO Riso;
Y. UCHIDA and ————: Optical Studies on Thallium-activated Alkali-iodide Crystals 1408
KATO Shohei;
Y. ODA, M. TAKEDA, C. HU and ————: Scattering of Protons by Ne^{20} and Ne^{22} 396
C. HU, ————, Y. ODA and M. TAKEDA: Elastic and Inelastic Scattering of 22 MeV Alpha Particles by Light Elements 549
Y. ODA, M. TAKEDA, C. HU and ————: Scattering of Protons by Silicon and Sulphur 1255
KATO Tosio;
————: Non-Existence of Bound States with Positive Energy (S. N.) 382
———— and H. FUJITA: Maximum Principles for Vorticity in Viscous Fluid

(S. N.) 545

KATO Yoshifumi;

——— and O. NAKAHARA: Evaluation of the Nuclear Quadrupole Moment of N^{14} (S. N.) 690

KATSUMATA Itsuo;

S. MIYAKE, K. HINOTANI, ——— and T. KANEKO: A Large Multiplate Cloud Chamber for Cosmic Ray Observation 1471

KATSUURA Kanji;

M. INOKUTI and ———: On the Viscosity of Irradiated Polymers, II 1379

KAWABE Kazuo: Optical studies on the Effect of Electric Fields on the Transitions of Barium Titanate 1755

KAWAGUTI Mitutosi;

———: The Flow of a Viscous Fluid past a Triangular Cylinder 1425

———: Reversal Flow Theorem concerning Oseen's Approximation 1431

KAWAMURA Hajimu;

M. ONUKI and ———: Polaron Mobility in Potassium Bromide (S. N.) 967

E. OTSUKA, Y. OSHIO, T. KOBAYASHI and ———: Nuclear Magnetic Resonance of Na^{23} in Sodium Chloride Crystals (S. N.) 1454

KAWAMURA Hiroyoshi;

T. TANAKA and ———: Piezoelectric Effect in a Rectifying Contact of Semiconductor (S. N.) 1455

KAWASAKI Koji;

———, K. KANOU and Y. SEKITA: Interaction of Water Vapour with Germanium Real Surface (S. N.) 233

——— and K. KATO: Size Distribution of Radioactivity of the Natural Radioactive Dust (S. N.) 234

KAWASHIMA Maumi;

I. KUMABE, C. L. WANG, ———, M. YADA and H. OGATA: Excitation Functions and Angular Distributions of the Reactions Al$^{27}(p, \alpha)$Mg^{24} at 12.7–14.1 MeV and Cr$^{52}(p, \alpha)$V^{49} at 9.0–14.2 MeV 713

KIDO Kiyoshi;

——— and T. WATANABE: The Magnetic Investigation of Mn^{++}, Co^{++}, Ni^{++}, Cu^{++} Ammine and Anhydrate Salts 1217

KIHARA Taro;

Thermodynamic Foundation of the Theory of Plasma 128

———: On the Coefficients of Irreversible Processes in a Highly Ionized Gas.. 402

——— and S. KOBA: Convex-Core Model of Molecules in Crystalline State .. 247

———: Magnetohydrostatic Equilibrium for Plasma in a Torus Tube........1397

———: Ion-Electron of Plasmas in a Strong Magnetic Field..................1751

KIKUCHI Ken;

———, S. KOBAYASHI and K. MATSUDA: Elastic and Inelastic Scattering of 14.1-MeV Protons by Medium Weight Nuclei 121

C. HU, ———, S. KOBAYASHI, K. MATSUDA, Y. NAGAHARA, Y. ODA, N. TAKANO, M. TAKEDA and T. YAMAZAKI: Elastic and Inelestic Scattering of Protons from Ti, Cr, Ni Zn, and O at 8 to 14 MeV 861

KIKUCHI Makoto;

———: Visible Light Emission from Metal-Silicon Contact (S. N.) 682

——— and S. IIZIMA: Avalanche Electroluminescence in CdS Single Crystal (S. N.) 852

——— and S. IIZIMA: Quenching Effect of the Photoconductivity Decay in CdS (S. N.) 856

——— and S. IIZUMA: Etch-Figure in CdS Single Crystals (S. N.) 1638

——— and M. SAITO: Possible Evidence for the Light Induced Plasticity in Germanium (S. N.) 1642

——— and K. TACHIKAWA: Visible Light Emission from Germanium Diffused p-n Junction (S. N.) 1830

KIM, Chul-Soo;

F. TAMAKI and ———: Flash X-ray Radiography for the Density Measure-

ment in a Hypersonic Air Flow 664
———: Experimental Studies on the Hypersonic Flow past Plane, Convex and Concave Wedges 827

KIMURA Minoru;
———, S. MATSUOKA, S. HATTORI and K. SENDA: Fine Structures of Proton Resonance Spectra of Fluorobenzene Derivatives (S. N.) 684

KIMURA Motoharu;
———, N. MUTSURO, Y. OHNUKI, K. SHODA, M. SUGAWARA, T. TOHEI and H. YUTA: Measurement of Bremsstrahlung Spectra with Sodium Iodide Scintillation Crystal 387
N. MUTSURO, Y. OHNUKI, K. SATO, K. KAGEYAMA and ———: Fine Structure in the $N^{14}(\gamma, n)N^{13}$ Activation Curve (S. N.) 1457
N. MUTSURO, Y. OHNUKI, K. SATO and ———: Photoneutron Cross Sections for Ag^{107}, Mo^{92} and Zr^{90} 1649

KINOSHITA Koreo;
S. NOMURA and ———: A Note on the Theories Underlying the Polarimetric Study of Very Thin Dielectric Surface Layers 297

KIRIYAMA Ryoichi;
S. WAKU, H. HIRABAYASHI, H. TOYODA, H. IWASAKI and ———: Ferroelectricity in Potassium Ferrocyanide Trihydrate (S. N.) 973

KISAKA Shunkichi;
T. SHIBATA, A. TOI, T. SUITA and ———: Electrostatic Transformer Type Particle Accelerator using Ceramic $BaTiO_3$—Ferrostac— (S. N.) 227
———, S. IKEGAMI and H. SAKAKI: Dielectric Properties of Mixed Crystals of Barium-Strontium Titanate 1680

KITAMURA Takashi: Search for Anomalous Scattering of Mu-Mesons (on the Apparatus Using a Delayed Coincidence Method) 1654

KITTAKA Shigeyoshi: The Generation of Static Charge on High Polymer 533

KOBA Saburo;
T. KIHARA and ———: Convex-Core Model of Molecules in Crystalline State.. 247

KOBAYASHI Hanako;
T. HASEDA, ——— and M. DATE: Paramagnetic Susceptibility of Single Crystals of Some Nickel Salts 1724

KOBAYASHI Mineo;
S. TANAKA, ——— and T. MASUMI: Anisotropic Conductivity of CdS Single Crystals (S. N.) 104

KOBAYASHI Shigehiro;
———: An Application of the FA-Modified TF Model to the Singly Ionized Negative Ion (S. N.) 689
———: Thomas-Fermi Model of Positive Ion 1039
———: Thomas-Fermi Model of Compressed Positive Ion (S. N.) 1121

KOBAYASHI Shinsaku;
K. KIKUCHI, ——— and K. MATSUDA: Elastic and Inelastic Scattering of 14.1-MeV Protons by Medium Weight Nuclei 121
C. HU, K. KIKUCHI, ———, K. MATSUDA, Y. NAGAHARA, Y. ODA, N. TAKANO, M. TAKEDA and T. YAMAZAKI: Elastic and Inelastic Scatterings of Protons from Ti, Cr, Ni, Zn and O at 8 to 14 MeV 861

KOBAYASHI Toyohide;
E. OTSUKA, Y. OSHIO, ——— and H. KAWAMURA: Nuclear Magnetic Resonance of Na^{23} in Sodium Chloride Crystals (S. N.) 1454

KOHRA Kazutake;
——— and H. WATANABE: Anomalous Transmission of Electrons in a Film of Molybdenite (S. N.) 1119
M. YOSHIMATSU and ———: X-ray Observations of the Surface of Plastically Deformed LiF Crystals with the Berg-Barret Method 1249
Z. ISHII and ———: X-ray Observation of the Strain Field in Germanium Single Crystals with the Use of the Anomalous Transmission (S. N.) 1250

KOJIMA Shoji;

———, K. KATO, S. HAGIWARA and R. MATSUZAKI: Oscillations in Plasma II.. 821
KOMATSUBARA Kiichi: Change of Surface Recombination Velocity of Germanium by γ-ray Irradiation, using P–N–P Alloy Transistor (S. N.)........ 383
KOMODA Tsutomu;
S. OGAWA, D. WATANABE, H. WATANABE and ———: Anti-Phase Domains in Gold-Copper-Zinc Ordered Alloys Revealed by Electron Microscope.......... 936
KOTERA Takeyasu;
——— and M. TODA: On the Theory of Brownian Motion and Spin Relaxation........1475
KOYASU Masaru;
K. SATO and ———: The Effect of the Room Shape on the Sound Field in Rooms—Studies on the Measurement of Absorption Coefficient by the Reverberation Chamber Method I 365
K. SATO and ———: On the New Reverberation Chamber with Nonparallel Walls (Studies on the Measurement of Absorption Coefficient by the Reverberation Chamber Method, II)........ 670
KUBO Ryogo;
———, H. HASEGAWA and N. HASHITSUME: Quantum Theory of Galvanomagnetic Effect I. Basic Considerations........ 56
KUMABE Isao;
———, C. L. WANG, M. KAWASHIMA, M. YADA and H. OGATA: Excitation Functions and Angular Distributions of the Reactions $Al^{27}(p, \alpha)Mg^{24}$ at 12.7–14.1 MeV and $Cr^{52}(p, \alpha)V^{49}$ at 9.0–14.2 MeV 713
KUMAGAI Hiroo;
———, K. ŌNO, H. SHÔNO, I. HAYASHI, K. KURODA and M. IMAIZUMI: 16″ Variable Energy Cyclotron........ 1
KURIYAMA Masao: Electron Diffraction Study on Polish Layers of Gold, II 487
KURODA Keiichi;
K. ÔNO, J. SHIMADA, ———, O. TANAKA, H. KAMITSUBO, A. ITO, S. TANAKA and M. IMAIZUMI: Yields and Angular Distributions of Protons from $F^{19}(d, p)F^{20}$ and $F^{19}(d, p)F^{20}$ 117
KUROHA Ippei;
T. YAMAGUTI, I. MAKINO, S. SHINODA and ———: Spectro-Polarization Characteristics of the Sodium Nitrate Polarizer 199
KUROSAWA Tatsumi: Defects in Ionic Crystals, II. An Analysis of F and V_1 Centers.. 741
KUSAKA Riichiro;
J. ITOH and ———: Nuclear Magnetic Double Resonance Experiment on Two Proton System 492
KUWABARA Goro;
———, A. MISU, T. WATANABE and Y. NISHIYAMA: Photoconductivity and Luminescence of the F and M Centers in Potassium Chloride 1621
——— and K. AOYAGI: Absorption and Excitation Bands of KCl–Tl in the Extrem Ultraviolet Region (S. N.) 1821
KUWABARA Shigeya: Accurate Determination of Hydrogen Positions in NH_4Cl by Electron Diffraction........1205
KUWABARA Sinzi;
———: The Forces experienced by a Lattice of Elliptic Cylinders in a Uniform Flow at Small Reynolds Numbers 522
———: The Forces experienced by Randomly Distributed Parallel Circular Cylinders or Spheres in a Viscous Flow at Small Reynolds Numbers........ 527
KUWAHARA Kaizo: Curie Point in Thin Ni Films Determined by Electrical Method (S. N.) 1247
MACKAY A. L.;
D. R. DASGUPTA and ———: β-Ferric Oxyhydroxide and Green Rust 932
MAEDA Hajime;
H. MIYAZAWA, ——— and H. TOMISHIMA: Lattice Scattering Mobility of Electrons on Cadmium Sulphide........ 41
MAEDA Keiji: Configurational Coordinate Curves for Luminescence Center in $Ca_3(PO_4)_2$:

Cu 478

MAEDA Seijiro;

I. MIKAMI, T. HIRONE, H. WATANABE, ——— K. ADACHI and M. YAMADA: On the Magnetic Anisotropy of a Pyrrhotite Crystal........1568

MAKINO Isao;

T. YAMAGUTI, ——— S. SHINODA and I. KUROHA: Spectro-Polarization Characteristics of the Sodium Nitrate Polarizer 199

MASE Shoichi;

———: Electronic Structure of Bismuth Type Crystals, II 584

———: Algebraic Method to obtain Irreducible Representations of Space Groups with an Application to White Tin 1538

——— and S. TANUMA: Measurement of Galvanomagnetic Tensors of Bismuth Single Crystals at Low Temperatures (S. N.) 1644

MASUDA Masayoshi;

T. ASADA, ———, M. OKUMURA and J. OKUMA: Decay Properties of ZnS(Ag) Phosphors........1766

MASUMI Taizō;

———: Relaxation Time Anisotropy in Cadmium Sulphide Studied with Electrical Resistivity and Magneto-Resistance Effect 47

S. TANAKA, M. KOBAYASHI and ———: Anisotropic Conductivity of CdS Single Crystals (S. N.) 104

———: Dielectric Susceptibility Tensor of Cadmium Sulfide........1140

——— and T. TANAKA: Elastic Stiffness Constants of Cadmium Sulfide......1313

MATSUDA Kazuhisa;

K. KIKUCHI, S. KOBAYASHI and ———: Elastic and Inelastic Scattering of 14.1 MeV Protons by Medium Weight Nuclei........ 121

C. HU, K. KIKUCHI, S. KOBAYASHI, ———, Y. NAGAHARA, Y. ODA, N. TAKANO, M. TAKEDA and T. YAMAZAKI: Elastic and Inelastic Scatterings of Protons from Ti, Cr, Ni, Zn and O at 8 to 14 MeV 861

MATSUOKA Shin-ichi;

T. SHIMIZU, ———, S. HATTORI and K. SENDA: Nuclear Spin-Spin Coupling between Protons in Vinyl Derivatives (S. N.)........ 683

M. KIMURA, ———, S. HATTORI and K. SENDA: Fine Structures of Proton Resonance Spectra of Fluorobenzene Derivatives (S. N.)........ 684

MATSUURA Kiyokata: Frequency Shift in Ammonia Absorption Lines other than (3,3) (S. N.)........1826

MATSUZAKI Ri'ichi;

S. KOJIMA, K. KATO, S. HAGIWARA and ———: Oscillations in Plasma II.... 821

MATSUKURA Yasuo;

———: Germanium-Silicon Alloy Junctions (S. N.)........ 374

———: Effects of Heat Treatment upon the Electrical Properties of Silicon.. 918

MATSUMOTO Hiroaki;

K. FUKUDA, ——— and A. OKUDA: *F*-centers in LiCl Crystals (S. N.)...... 969

K. FUKUDA, ———, Y. UCHIDA and H. YOSHIMURA: Cyclotron Resonance in Gas Discharge (S. N.) 543

MATUMURA On: Electron Spin Resonance of Mn-activated Phosphors (S. N.) 108

MIDUNO Zenemon;

K. HUKUDA, J. ISHII and ———: The Kinetics of Radical Reactions in γ-irradiated Polyvinyl Chloride 1643

MIKAMI Itsuo;

———, T. HIRONE, H. WATANABE, S. MAEDA, K. ADACHI and M. YAMADA: On the Magnetic Anisotropy of a Pyrrhotite Crystal........1568

MIKOSHIBA Nobuo;

———: Interaction of Conduction Electrons with Acoustic Phonons........ 22

———: Acoustoelectric Effect in Metals 1691

MIKUMO, Takashi;

I. NONAKA, H. YAMAGUCHI, ———, I. UMEDA, T. TABATA and S. HITAKA: Angular Distributions of Protons from the Reaction ^{12}C(α, p)^{15}N 1260

MIMURA Hiroshi;
—— and INUI: The Electronic Structure of the U_2-Center in KCl Crystals, I. .1011
MINEMATSU Midori: Nuclear Quadrupole Resonance of Nitrogen in Amino and Amido Compounds 1030
MISU Akira;
G. KUWABARA, —— T. WATANABE and Y. NISHIYAMA: Photoconductivity and Luminescence of the *F* and *M* Centers in Potassium Chloride 1621
MITSUISHI Akiyoshi;
——, H. YOSHINAGA and S. FUJITA: The Far Infrared Reflectivity of NaCl, KCl and KBr Crystals (S. N.) 110
MITUI Tadayasu;
M. SATŌ and ——: Changes of Coercivities by Heat Treatment and Cold-Rolling in Cu-Co Alloy. (S. N.) 1254
MIURA Iwao;
——, T. WAKATSUKI, Y. HIRAO and E. OKADA: Gamma Rays from the Proton Bombardment of ^{24}Mg, ^{25}Mg and ^{26}Mg 239
MIYADAI Tomonao;
——, Y. SHICHIJO and I. TSUBOKAWA: Ferrimagnetic Resonance Line Width in Polycrystalline $Y_3 Fe_{5-x}$, In_xO_{12} (S. N.)........ 853
MIYAHARA Syohei;
H. OHNISHI, T. TERANISHI and ——: On the Transition Temperature of Copper Ferrite (S. N.) 106
K. TSUSHIMA, M. ASANUMA and ——: Time Decrease of Permeability in Silicon-Iron (S. N.)........1253
—— and T. YAMADAYA: The Aging of Permeability in Manganese-Zinc Ferrite (S. N.) 1635
MIYAKE Akira;
——, R. CHÛJÔ and H. ADACHI: NMR Second Moment of a Radical under the Restricted Rotation (S. N.)........ 972
—— and R. CHUJO: NMR Second Moment of a Radical Rotating in a Periodic Potential (S. N.) 978
MIYAKE Saburo;
——, K. HINOTANI, I. KATSUMATA and T. KANEKO: A Large Multiplate Cloud Chamber for Cosmic Ray Observation........1471
MIYAKE Shizuo: Transition from Dynamical to Kinematical Intensities of Electron Diffraction by Crystals 1347
MIYATA Nahonori;
Z. FUNATOGAWA, —— and S. USAMI: Electric Resistance and Cation Distribution of Fe-Mn Ferrite System (S. N.) 854
Z. FUNATOGAWA, —— and S. USAMI: Ferromagnetic Crystalline Anisotropy of Fe–Mn–Ferrite System 1583
MIYATANI Shin-ya;
—— and I. YOKOTA: Galvano- and Thermomagnetic Effects in α–Ag_2Te.... 750
——: Ionic Conduction in β-Ag_2Te ank β-Ag_2Se........ 996
——: Infrared Absorption of α-$Ag_2Te_x S_{1-x}$ (S. N.) 1634
MIYAZAWA Hisao;
——, H. MAEDA and H. TOMISHIMA: Lattice Scattering Mobility of Electrons on Cadmium Sulphide........ 41
MIZUNO Hiroyuki: Doping Influences on Activator Diffusion in Oxide-coated Cathode Nickel 1295
MIZUNO Jōji;
——, K. UKEI and T. SUGAWARA: The Crystal Structure of $CoCl_2{\cdot}6H_2O$ (S. N.). 383
MIZUSHIMA Yoshihiko;
T. IMAI, —— and Y. IGARASHI: New Cold Cathode Using Magnesium Oxide (S. N.) 979
MOMOTA Teruo;
M. SAKAI, H. OHMURA and ——: Note on the Spin of Excited States of

Cadmium 110 (S. N.) 229

MORGAN, P. G.: A Note on the Drag of a Screen at Low Reynolds Number (S. N.) .. 1645

MORIGUCHI Haruo;

———: Connection Formulas for WKB Solutions with Two Turning Points (S. N.) 968

———: An Improvement of the WKB Method in the Presence of Turning Points and the Asymptotic Solutions of a Class of Hill Equations 1771

MORIGUCHI Yoshiro: Selenium Rectifiers with Artificial Layers of Selenides of Cadmium, Tin, Bismuth and Lead 152

MORINAGA Haruhiko:

——— and K. TAKAHASHI: A4^+–0^+ Cross-Over Transition (S. N.) 1460

MORINO Yonezo;

T. CHIBA, M. TOYAMA and ———: Nuclear Quadrupole Resonance Spectra of N^{14} in Urea Crystal (S. N.) 379

MORIOKA Shigeki: High Subsonic Flow past a Wedge in a Two-Dimensional Wind Tunnel at its choked State 1098

MORITA Tohru;

———: Cell Theory of Classical Liquids. Phase Transition between Gas, Liquid and Solid. Part III. Yvon's Method and its Generalization 563

———: Cell Theory of Classical Liquids. Phase Transition between Gas, Liquid and Solid. Part IV. F. C. C. Lattice Gases 570

MOTIZUKI Kazuo;

———: Metamagnetism of Methylamine Chrome Alum 579

——— and T. NAGAMIYA: Note on the Effect of Oxygen Molecules Contained in Solid Hydrogen on the Rate of Ortho-para Conversion (S. N.) 1639

MURAKAWA Kiyoshi;

——— and S. M-HASHIMOTO: Measurement of Plasma Temperature and Electron Density 1235

———: Multiplet Structure and Hyperfine Structure of the Spectrum of Mercury 1624

——— and S. HASHIMOTO: Measurement of Plasma Temperature and Electron Density (S. N.) 1824

MUTO Yoshio;

———, Y. TAWARA, Y. SHIBUYA and T. FUKUROI: Electrical Properties of Dilute Alloys of Zinc with Manganese at Low Temperature (S. N.) 380

MUTSURO Naosi;

M. KIMURA, ———, Y. OHNUKI, K. SHODA, M. SUGAWARA, T. TOHEI and H. YUTA: Measurement of Bremsstrahlung Spectra with Sodium Iodide Scintillation Crystal 387

———, Y. OHNUKI, K. SATO, K. KAGEYAMA and M. KIMURA: Fine Structure in the $N^{14}(\gamma, n)N^{13}$ Activation Curve (S. N.) 1457

———, Y. OHNUKI, K. SATO and M. KIMURA: Photoneutron Cross Sections for Ag^{107}, Mo^{92} and Z^{90} 1649

NAGAHARA Sigeru: Quantum Theoretical Study on Single, Double and Triple Bonds between Carbon Atoms 331

NAGAHARA Yukio;

C. HU, K. KIKUCHI, S. KOBAYASHI, K. MATSUDA, ———, Y. ODA, N. TAKANO. M. TAKEDA and T. YAMAZAKI: Elastic and Inelastic Scatterings of Protons from Ti, Cr, Ni, Zn and O at 8 to 14 MeV 861

NAGAI Ryutaro: A Mechanism for Producing Extrusions and Intrusions during Fatigue (S. N.) 1252

NAGAKURA Sigemaro: Study of Metallic Carbides by Electron Part III. Iron Carbides .. 186

NAGAMIYA Takeo;

K. MOTIZUKI and ———: Note on the Effect of Oxygen Molecules Contained in Solid Hydrogen on the Rate of Ortho-para Conversion (S. N.) 1639

NAGASHIMA Masahisa;

H. TOYODA and ———: Electrical Resistivity of Arc-evaporated Carbon Film .. 274

NAGUMO Michihiko;

——— and Y. KAKIUCHI: An Abnormal Saturation Behavior in High Resolution Proton Magnetic Resonance Spectra (S. N.)........................ 679
NAKAGAWA Yasuaki: Magnetic Susceptibility of Liquid Alloys of Copper with Cobalt, Iron, Manganese, and Chromium........................1372
NAKAHARA Osamu;
Y. KATO and ———: Evaluation of the Nuclear Quadrupole Moment of N^{14} (S. N.) 690
NAKAJIMA Koichi: Stacking Faults in Copper-Nickel Alloys (S. N.)........................1825
NAKAMURA Teruo;
———, K. TAKAMATSU, K. FUKUNAGA, M. YATA and S. YATUMI: Absolute Cross Sections of the (γ, n) Reaction for Cu^{63}, Zn^{64} and Ag^{109}........................ 693
———, K. FUKUNAGA, K. TAKAMATSU, M. YATA and S. YASUMI: Fine Structure in the Giant Resonance for Cu^{63} and $Ag^{107}(\alpha, n)$ Reactions (S. N.)......1117
NAKAMURA Terutaro: Etch Pits Corresponding to Dislocations in Ferroelectric Guanidinium Aluminum Sulfate Hexahydrate 1022
NAKAYAMA Junn: Surface Cracks of Sheet Glass Produced by Sodium Vapor Treatment 1107
NAMBA Masaharu: Optical Properties of SiC in Infrared Region (S. N.)........................228
NINOMIYA Tosiyuki: On the Dielectric Losses impure Ionic Crystals 30
NISHIKAWA Kiyoshi: A Jet Shower with Energy of 5×10^{13} eV found in Emulsion Chamber 880
NISHIMURA Jiro;
——— and Y. TANABE: Synthesis of Large CdS and ZnS Crystals (S. N.).... 850
NISHIOKA Atsuo;
——— and M. TAKEUCHI: Dielectric Property of Triglycine Sulfate Single Crystal at 9000 Mc/s Region (S. N.)........................ 971
NISHIYAMA Yoshio;
G. KUWABARA, A. MISU, T. WATANABE and ———: Photoconductivity and Luminescence of the F and M centers in Potassium Chloride........................1621
NITTA Isamu;
Y. TAKAKI, Y. SASADA and ———: Crystal Structure of 2-Amino Azulene.... 771
NIU Keishiro;
T. SHIMASAKI and ———: On a Method of Successive Approximations applied to the Axisymmetric Flows of an Incompressible Perfect Fluid........................1810
NOMURA Sadao;
——— and K. KINOSHITA: A Note on the Theories Underlying the Polarimetric Study of Very Thin Dielectric Surface Layers........................ 297
NONAKA Itaru;
———, H. YAMAGUCHI, T. MIKUMO, I. UMEDA, T. TABATA and S. HITAKA: Angular Distributions of Protons from the Reaction $^{12}C(\alpha, p)^{15}N$ 1260
NONOYAMA Minoru;
Y. KAMIYA, ——— and Y. UYEDA: Electron Microscopic Observation of the Superlattice in Serpentine 1334
NUMATA Tadasi: On the Non-Isothermal Diffusion Theory of Rectifiers 902
ODA Yukiyasu;
———, M. TAKEDA, C. HU and S. KATO: Scattering of Protons by Ne^{20} and Ne^{22} 396
C. HU, S. KATO, ——— and M. TAKEDA: Elastic and Inelastic Scattering of 22 MeV Alpha Particles by Light Elements........................ 549
C. HU, K. KIKUCHI, S. KOBAYASHI, K. MATSUDA, Y. NAGAHARA, ——— N. TAKANO, M. TAKEDA and T. YAMAZAKI: Elastic and Inelastic Scatterings of Protons from Ti, Cr, Ni, Zn and O at 8 to 14 MeV 861
———, M. TAKEDA, C. HU and S. KATO: Scattering of Protons by Silicon and Sulphur........................1255
ODA Toshiatsu;
M. TAKEYAMA, S. HAMAMURA and ———: Microwave Investigation on Plasma in Shock Tube (S. N.) 1637
ODAJIMA Akira;

———: Nuclear Magnetic Resonance Studies of Water Sorbed on Fibrous Materials 308

———: Study of Segmental Motion in Polymer Solutions by Nuclear Magnetic Resonance 777

OGATA Hiroshi:

———: Angular Distributions of the Reaction $F^{19}(p, \alpha)O^{16}$ at 8.0–14.2 MeV .. 707

I. KUMABE, C. L. WANG, M. KAWASHIMA, M. YADA and ———: Excitation Functions and Angular Distributions of the Reactions $Al^{27}(p, \alpha)Mg^{24}$ at 12.7–14.1 MeV and $Cr^{52}(p, \alpha)V^{49}$ at 9.0–14.2 MeV 713

OGAWA Kazuyuki;

———: Preparation of Anodic Oscillator Tube using Glow Discharge (S. N.).. 385

———: Anodic Oscillation in Glow Discharge, I. Simple Correspondence of the Internal Phenomena to the oscillation 1746

OGAWA Shinji;

———: Antiferromagnetism in $KMnF_3$ (S. N.)..........1115

——— and Y. YOKOZAWA: Paramagnetic Resonance of Magananese in $KMgF_3$ (S. N.) 1116

OGAWA Shiro;

———, D. WATANABE, H. WATANABE, T. KOMODA: Anti-Phase Domains in Gold-Coppe-Zinc Ordered Alloys Revealed by Electron Microscope 936

M. TAKAHASHI, D. WATANABE, T. SASAGAWA, H. SAITO and ———: Magnetic Anisotropy of Evaporated Films Formed in Magnetic Field 1459

Y. FUKANO and ———: Study on Precipitation Phenomena during Aging of Aluminium-Silver Alloy in thin Evaporated Films 1671

OHMURA Haruko;

M. SAKAI, ——— and T. MOMOTA: Note on the Spin of Excited States of Cadmium 110 (S. N.) 229

OHNISHI Haruyuki;

———, T. TERANISHI and S. MIYAHARA: On the Transition Temperature of Copper Ferrite (S. N.) 106

OHNUKI Yuji;

M. KIMURA, N. MUTSURO, ———, K. SHODA, M. SUGAWARA, T. TOHEI and H. YUTA: Measurement of Bremsstrahlung Spectra with Sodium Iodide Scintillation Crystal 387

N. MUTSURO, ———, K. SATO, K. KAGAYAMA and M. KIMURA: Fine Structure in the $N^{14}(\gamma, n)N^{13}$ Activation Curve (S. N.) 1457

N. MUTSURO, ———, K. SATO and M. KIMURA: Photoneutron Cross Sections for Ag^{107}, Mo^{92} and Zr^{90}..........1649

OHOYAMA Tetuo;

K. YASUKOCHI, ——— and K. KANEMATSU: Antiferromagnetism of $Mn_{3.25}Ge$ (S. N.) 1820

OHTSUKA Taiichiro: Crystalline Field Splitting in Ferrous Fluosilicate (S. N.) 1245

OKA Takeshi;

T. KASUYA and ———: Microwave Spectrum of Ethyl Iodide (S. N.) 980

OKADA Eiji;

I. MIURA, T. WAKATSUKI, Y. HIRAO and ———: Gamma Rays from the Proton Bombardment of ^{24}Mg, ^{25}Mg and ^{26}Mg.......... 239

OKADA Jun'ichi: Effect of External Illumination on Carrier Lifetime in Semiconductors..1550

OKADA Minoru;

——— and T. WATANABE: Grain Boundary Migration and Dimensional Change of Low Carbon Stell (S. N.) 107

OKAMOTO Hiroshi: Determination of Molecular Weight Distributions of High Polymers by Fractionation 1388

OKAMOTO Sigeharu;

——— and K. TAKAUCHI: On the Dielectric Loss of Oxidized High-Density Polyethylene (S. N.) 378

OKAMOTO Tetsuhiko;

E. TATSUMOTO and ———: Anisotropy of Ordinary Hall Effect in Silicon Iron

(S. N.) 226
E. TATSUMOTO and ———: Extraordinary Hall Effect in Silicon-Iron Single Crystals (S. N.) 975
E. TATSUMOTO and ———: Effective Field in the Ordinary Hall Effect in Ferromagnetics 976
E. TATSUMOTO and ———: Temperature Dependence of the Magnetostriction Constants in Iron and Silicon Iron 1588

OKANISHI Setsuo;
——— and H. KANAMORI: Simplified Representations on the Firing Characteristics of Vibrational-Ignitor Tubes (S. N.) 542

OKAZAKI Atsushi;
———: The Variation of Superstructure in Iron Selenide Fe_7Se_8 (S. N.) 112
———, Y. SUEMUNE and T. FUCHIKAMI: The Crystal Structures of $KMnF_3$, $KCOF_3$ and $KNiF_3$ (S. N.) 1823

OKUDA Akizo;
K. FUKUDA, H. MATSUMOTO and ———: *F*-centers in LiCl Crystal. (S. N.) .. 969

OKUMA Juzo;
T. ASADA, M. MASUDA, M. OKUMURA and ———: Decay Properties of ZnS (Ag) Phosphors 1766

OKUMURA Masayuki;
T. ASADA, M. MASUDA, ——— and J. OKUMA: Decay Properties of ZnS(Ag) Phosphors 1766

ÔNO Kazuo;
H. KUMAGAI, ———, H. SHÔNO, I. HAYASHI, K. KURODA and M. IMAIZUMI 16″ Variable Energy Cyclotron 1
———, J. SHIMADA, K. KURODA, O. TANAKA, H. KAMITSUBO, A. ITO, S. TANAKA and M. IMAIZUMI: Yields and Angular Distributions of Protons from $F^{19}(d, p)F^{20}$ and $F^{19}(d, p)F^{20}$ 117

ONUKI Masami:
——— and H. KAWAMURA: Polaron Mobility in Potassium Bromide (S. N.) .. 967

OOSHIMA Yuzuru: A Semi-empirical Theory of the Conjugated System, III. Bond Alternation and Electron Fixation 747

OSAKA Yukio: Eciton Structures in alkali Halides 1685

OSHIDA Isao;
T. SAITO and ———: The W. K. B. Method for the Differential Equations of the Fourth Order 1816

OSHIO Yudo;
E. OTSUKA, ———, T. KOBAYASHI and H. KAWAMURA: Nuclear Magnetic Resonance of Na^{23} in Sodium Chloride Crystals (S. N.) 1454

OTSUKA Eizo;
———, Y. OSHIO, T. KOBAYASHI and H. KAWAMURA: Nuclear Magnetic Resonance of Na^{23} in Sodium Chloride Crystals (S. N.) 1454

ŌYAMA Isao;
T. TAOKA, K. YASUKŌCHI, R. HONDA and ———: An Experimental Investigation on the Mode of Slip in Face-Centered Cubic Metals 888

PICKART, S. J.;
G. SHIRANE, ——— and Y. ISHIKAWA: Neutron Diffraction Study of Antiferromagnetic $MnTiO_3$ and $NiTiO_3$ 1352

SABURI Osamu: Properties of Semiconductive Barium Titanates 1159

SAITO Hideo;
M. TAKAHASHI, D. WATANABE, T. SASAGAWA, ——— and S. OGAWA: Magnetic Anisotropy of Evaporated Films Formed in Magnetic Field (S. N.) 1459

SAITO Mitsuyoshi;
M. KIKUCHI and ———: Possible Evidence for the Light Induced Plasticity in Germanium (S. N.) 1642

SAITO Osamu;

———: Effects of Gamma Rays on Aqueous Solution of Polyvinyl Alcohl 792
: Effect of Impurity on Molecular Linking of Irradiated Polymer 798

SAITO Tomoyuki;
——— and I. OSHIDA: The W. K. B. Method for the Differentical Equations of the Fourth Order 1816

SAKAI Mitsuo;
———, H. OHRURA and T. MOMOTA: Note on the Spin of Excited States of Cadium 110 (S. N.).. 229
— , H. IKEGAMI, T. YAMAZAKI and K. SUGIYAMA: Angular Correlation of Gamma Rays from Xe^{126} and Te^{126} 983
K. SUGIYAMA, H. IKEGAMI, T. YAMAZAKI and ———: Decay of I^{124}.......... 986

SAKAMOTO Masayoshi: Quenching Effect in KCl Crystals 1506

SAKISAKA Masakatsu: $Be^9(n, 2n)Be^8$ and $B^{11}(n, \alpha)Li^8(\beta)Be^8$ Reactions by 14 MeV Neutrons 554

SAKURAI Takeo: High Subsonic Flow with Normal Shock Wave at Nearly Critical Mach Number 658

SANADA Junpei: Elastic Scattering of Protons by Helium between 9.2 MeV and 14.5 MeV 1463

SASADA Yoshio;
Y. TAKAKI ——— and I. NITTA: Crystal Structure of 2-Amino Azulene...... 771

SASAGAWA Tetsuzo;
M. TAKAHASHI, D. WATANABE, ———, H. SAITO and S. OGAWA: Magnetic Anisotropy of Evaporated Films Formed in Maghetic Field (S. N.) 1459

SASAKI Hiromu;
S. KISAKA, S. IKEGAMI and ———; Dielectric Properties of Mixed Crystals of Barium-Strontium Titanate 1680

SASAKI Takeo; On the Growth Condictions of Germanium (S. N.) 381

SASAKI Wataru;
—— and C. YAMANOUCHI: On the Anomalous Magnetoresistonce Effect in n–InSb (S. N.) 849

SATO Hiroshi: Further Investigation on the Transition of Two-dimensional separated Layer at Subsonic Speeds 1797

SATO Hisanao;
———On the Dimagnetism of Graphite, I. Energy Levels of π-electrons 609
———: The Field Dependence of the Mobility of Electrons in *n*-Germanium..1275

SATO Kazuo;
N. MITSURO, Y. OHNUKI, ———, K. KAGEYAMA and M. KIMURA: Fine Structure in the $N^{14}(\gamma, n)N^{13}$ Activation Curve (S. N.) 1457
N. MUTSURO, Y. OHNUKI, ———, K. KAGEYAMA and M. KIMURA: Photoneutron Cross Sections for Ag^{107}, Mg^{92} and Jr^{90} 1649

SATO Kozi;
——— and M. KOYASU: The Effect of the Room Shape on the Sound Field in Rooms—Studies on the Measurement of Absorption Coefficient by the Reverberation Chamber Method I— 365
— and M. KOYASU: On the New Reverberation Chamber with Nonparallel Walls (Studies on the Measuament of Absorption Coefficient by the Reverberation Chamber Method, II) 670

SATŌ Masayoshi;
——— and T. MITUI: Changes of Coecivities by Heat Treatment and Cold-Rolling in Cu-Co Alloy (S. N.) 1254

SATO Siro;
J. ITOH and ———: Double Proton Magnetic Resonance by a Side Band Method (S. N.)... 851

SAWADA Takashi: The Drag of Lattice of Many Parallel Circular Cylinders at Low Reynolds Number 837

SEGAWA Wataru: Rheological Equation of Voigtian Material 1102

SEKITA Yoshiyasu;
K. KAWASAKI, K. KANOU and ———: Interaction of Water Vapour with

Germanium Real Surface (S. N.) 233

SENDA Kantaro;
  T. SHIMIZU, S. MATSUOKA, S. HATTORI and ———: Nuclear Spin-Spin Coupling between Protons in Vinyl Derivatives (S. N.) 683
  M. KIMURA, S. MATSUOKA, S. HATTORI and ———: Fine Structures of Proton Resonance Spectra of Fluorobenzene Derivatives (S. N.) 684

SHARMA, S. K.: Flow of a Visco-Elastic Liquid near a Stagnation Point 1421

SHIBATA Hiroyuki;
  H. TOYODA, S. WAKU, ——— and Y. TANAKA: Some Ferroelectrical Properties of Triglycine Sulface (S. N.) 109

SHIBATA, Toshikazu;
  ———, A. TOI, T. SUITA and S. KISAKA: Electrostatic Transformer Type Particle Accelerator using Ceramic $BaTiO_3$—Ferrostac— (S. N.) 227

SHIBUYA Yoshio;
  Y. MUTO, Y. TAWARA, ——— and T. FUKUROI: Electrical Properties of Dilute Alloys of Zinc with Manganese at Low Temperature (S. N.) 380

SHICHIJO Yuzo;
  T. MIYADAI, ——— and I. TSUBOKAWA: Ferrimagnetic Resonance Line Width in Polycrystalline Y_3Fe_{5-x}, In_xO_{12} (S. N.) 853

SHIGEMITSU Yutaka: Non-Similarity Theory of Decaying Turbulence 91

SHIMADA Junji;
  K. ONO, ———, K. KURODA O. TANAKA, H. KAMITSUBO, A. ITO, S. TANAKA and M. IMAIZUMI: Yields and Angular Distributions of Protons from $F^{19}(d, p)F^{20}$ and $F^{19}(d, p)F^{20}$ 117

SHIMIZU Tadao;
  H. TAKUMA, ——— and K. SHIMODA: Magnetic Hyperfine Spectrum of H_2CO by a Maser 1595

SHIMIZU Tatsuo;
  ———, S. MATSUOKA, S. HATTORI and K. SENDA: Nuclear Spin-Spin Coupling between Protons in Vinyl Derivatives (S. N.) 683

SHIMODA Koichi;
  ———: Radiofrequency Spectroscopy Using Three Level Maser Action 954
  ———: Three-Level Maser Detector for Ultramicrowaves (S. N.) 966
  H. TAKUMA, T. SHIMIZU and ———: Magnetic Hyperfine Spectrum of H_2CO by a Maser 1595

SHIMOJI Mitsuo: ATheoretical Treatment of the Excess Energies of Binary Metallic Solutions 1525

SHIMOMURA Kenji;
  ——— and N. INOUE: Zerosplitting Cone of Nuclear Quadrupole Spectrum for Spin 5/2 86
  Zeeman Study of Nuclear Quadrupole Resonance Spectrum in p-Dibromobenzene (S. N.) 235

SHINNAKA Yasuhiro;
  ———: X-Ray Study on Molecular Rotation in Cubic Ammonium Nitrate 1073
  ———: X-Ray Study on Molecular Rotation in Tetragonal Ammonium Nitrate 1707

SHINODA Shingo;
  T. YAMAGUTI, I. MAKINO, ——— and I. KUROHA: Spectro-Polarization Characteristics of the Sodium Nitrate Polarizer 199

SHIRANE Gen;
  ———, S. J. PICKART and Y. ISHIKAWA: Neutron Diffraction Study of Antiferromagnetic $MnTiO_3$ and $NiTiO_3$ 1352

SHODA Katsufusa;
  M. KIMURA, N. MUTSURO, Y. OHNUKI, ———, M. SUGAWARA, T. TOHEI and H. YUTA: Measurement of Bremsstahlung Spectra with Sodium Iodide Scintillation Crystal 387

SHOGENJI Kisaburo: On Galvanomagnetic Effects in P-Type Crystals of PbTe 1360

SHÔNO Hisao;
  H. KUMAGAI, K. ŌNO, ———, I. HAYASHI, K. KURODA and M. IMAIZUMI: 16″ Variable Energy Cyclotron 1
SIMASAKI Tamedi;
  ——— and K. NIU: On a Method of Successive Approximations Applied to the Axisymmetric Flows of an Incompressible Perfect Fluid 1810
SINGH Surjit: Studies on Mercury Fulminato 540
SONOIKE Sanemi: ;
  ——— and H. WAKABAYASHI: Temperature Dependence of Surface Voltage of Silver Bromide 1664
SUEMUNE Yasutaka
  A. OKAZAKI, ———, and T. FUCHIKAMI: The Crystal Structures of $KMnF_3$ $KFeF_3$, $KCoF_3$ and $KNiF_3$ (S. N.) 1823
SUGAI Sintaro;
  ———, M. ISHIKAWA and J. FURUICHI: Effects of γ-Rays on Aqueous Solutions of Synthetic Polymers (S. N.) 544
  ———: Effects of Ionizing Radiations on Synthetic Polymer Solutions 1573
SUGANO Satoru;
  H. KAMIMURA and ———: Luminescence Processes in the KCl : Tl Phosphor in a Multidimensional Configuration Space........1612
SUGANUMA Ryōji: A Metastable Phase in Sn-Mg Alloy Film (S. N.) 685
SUGAWARA Masumi;
  M. KIMURA, N. MUTSURO, Y. ONUKI, K. SHODA, ———, T. TOHEI and H. YUTA: Measurement of Bremsstrahlung Spectra with Sodium Iodide Scientillation Crystal........ 387
SUGAWARA Minoru;
  ——— and Y. HATTA: Measurement of Ion Sheath Thickness using the Double Probe with Fixed Potential 1091
SUGAWARA Tadashi;
  J. MIDUNO, K. UEKI and ———: The Crystal Structure of $CoCl_2 \cdot 6H_2O$ (S. N.).. 383
  ———: Nuclear Magnetic Resonance in Dilute Copper Alloys at Low Temperatures, I. Experimental Aspects 643
  ———: Distorsion of the Octahedral Charge Distribution in Some Cobalt Complexes (S. N.)........ 858
  ———: Proton Resonance in the Antiferromagnetic State of $NiCl_2 \cdot 6H_2O$ and $CoCl_2 \cdot 6H_2O$ (S. N.) 1248
SUGIHARA Ko;
  ———: Higher Order Transitions in Double Resonance........1054
  ———: Spin-spin Iinteraction in the Paramagnetic Salts 1231
SUGIYAMA Akira: An Extended Form of Weyl-Laue Theorem and its Application to Surface Problems (S. N.)........ 977
SUGIYAMA Kazusuke;
  M. SAKAI, H. IKEGAMI, T. YAMAZAKI and ———: Anglar Correlation of Gamma Rays from Xe^{126} and Te^{126} 983
  ———, H. IKEGAMI, T. YAMAZAKI and M. SAKAI: Decay of I^{124}........ 986
SUITA Tokuo;
  T. SHIBATA, A. TOI, ——— and S. KISAKA: Electrostatic Transformer Type Particle Accelerator using Ceramic $BaTiO_3$—Ferrostac— (S. N.) 227
  N. ITOH and ———: Photoconduction and Darkening of AgCl Crystals at Low Temperatures 894
  N. ITOH and ———: Effect of Re-crystalization on the Temperature Dependence of Photocurrent of Silver Chloride Crystals (S. N.) 1641
SUMI Masao;
  ———: Theory of Spatially Growing Plasma Waves 653
  ———: Excitation of Oscillations in a Plasma Layer 1093
SUZUKI Hiromichi;
  H. TUBOTA and ———: Photo-voltaic Effect in Se-photocells having Artificial Intermediate Layers of of CdSe, CdTe, ZnSe and ZnTe 38

SUZUKI Katsumi;
T. SUZUKI ——— and T. KAMIGAKI: Internal Friction of KCl Crystals at Low Temperatures 731
SUZUKI Shoji;
M. HOSOE and ———: Gamma Rays from Neutron Inelastic Scattering of Magnesium, Aluminum, Iron and Bismuth 699
SUZUKI Taira;
——— and M. YAMAMOTO: Influence of Order-Disorder on Creep of a Superlattice Alloy 463
———, K. SUZUKI and T. KAMIGAKI: Interal Friction of KCl Crystals at Low Temperatures 731
SUZUKI Tetsuro;
——— and Y. TOMONO: Precipitation Process of Carbon in Alpha-Iron 597
SUZUKI Yasumasa;
———, S. ENDO and E. HAGA: Thermoelecric Power of AgCl 729
TABATA Tatsuo;
I. NONAKA, H. YAMAGUCHI, T. MIKUMO, I. UMEDA, ——— and S. HITAKA: Angular Distributions of Protons from the Reaction ^{12}C(α, p)^{15}N 1260
TACHIKAWA Kennkichi;
M. KIKUCHI and ———: Visible Light Emission from Germanium Diffused n–p Junction (S. N.) 1830
TAKAHASHI Kasuke;
H. MORINAGA and ———: A 4^+–0^+ Cross-Over Transition (S. N.) 1460
TAKAHASHI Minoru;
———, D. WATANABE, T. SASAGAWA, H. SAITO and S. OGAWA: Magnetic Anisotropy of Evaporated Films Formed in Magnetic Field (S. N.) 1459
TAKAKI Yoshito;
———, Y. SASADA and I. NITTA: Crystal Structure of 2-Amino Azulene 771
TAKAMATSU Kunio;
T. NAKAMURA, ———, K. FUKUNAGA, M. YATA and S. YASUMI: Absolute Cross Sections of the (γ, n) Reaction for Cu^{63}, Zn^{64} and Ag^{109} 693
T. NAKAMURA, K. FUKUNAGA, ———, M. YATA and S. YASUMI: Fine Structure in the Giant Resonance for Cu^{63} and Ag^{107}(α, n) Reactions (S. N.)........1117
TAKAMI Hideo: Stabileco de du-dimensia fluo de Szymański........ 517
TAKANO Fumihiko: On the Non-Orthogonality Difficulty in Ferromagnetism 348
TAKANO Naoyuki;
B. HU, K. KIKUCHI, S. KOBAYASHI, K. MATSUDA, Y. NAGAHARA, Y. ODA, ———, M. TAKEDA and T. YAMAZAKI: Elastic and Inelastic Scatterings of Protons from Ti, Cr, Ni, Zn, and O at 8 to 14 MeV 861
TAKAYANAGI Kazuo;
———: Excitation of the Molecular Vibration by Collision 75
———: Rotational Transitions in Hydrogen and Deuterium (S. N.)........1458
TAKADA Minoru;
Y. ODA, ———, C. HU and S. KATO: Scattering of Protons by Ne^{20} and Ne^{22}.. 396
C. HU, S. KATO, Y. ODA and ———: Elastic and Inelastic Scattering of 22 MeV Alpha Particles by Light Elements........ 549
Y. ODA, ———, C. HU and S. KATO: Scattering of Protons by Silicon and Sulphur........1255
C. HU, K. KIKUCHI, S. KOBAYASHI, K. MATSUDA, Y. NAGAHARA, Y. ODA, N. TAKANO, ——— and T. YAMAZAKI: Elastic and Inelastic Scatterings of Protons from Ti, Cr, Ni, Zn and O at 8 to 14 MeV 861
TAKEUCHI Keisaku;
S. OKAMOTO and ———: On the Dielectric Loss of Oxidized High-Density Polyethylene (S. N.) 378
TAKEUCHI Minoru;
A. NISHIOKA and ———: Dielectric Property of Triglycine Sulfate Single Crystal at 9000 Mc/s Region (S. N.) 971
TAKEYAMA Mikio;

———, S. HAMAMURA and T. ODA: Microwave Investigation of Plasma in Shock Tube (S. N.) 1637
TAKIMOTO Noboru: On the Screening of Impurity Potential by Conduction Electrons..1142
TAKUMA Hiroshi;
———, T. SHIMIZU and K. SHIMODA: Magnetic Hyperfine Spectrum of H_2CO by a Maser 1595
TAMADA Kō;
——— and H. FUJIKAWA: The Steady Flow of Viscous Fluid at Low Reynolds Numbers passing obliquely through a Plane Grid made of Equal Parallel Circular Cylinders 202
TAMAGAWA Hajime;
——— and J. FUJITA: A Visualizing Method of Electron Temperature and Plasma Density (S. N.) 678
TAMAKI Fumio;
——— and KIM, Chul-Soo: Flash X-Ray Radiography for the Density Measurement in a Hypersonic Air Flow 664
TANABE Yasaku;
J. NISHIMURA and ———: Synthesis of Large CdS Crystals (S. N.) 850
TANAKA Kenzo;
———, J. CHIKAWA and T. YAMANAKA: Monitoring X-ray Tube Output with Ionization Chamber 1321
TANAKA Osamu;
K. ÔNO, J. SHIMADA, K. KURODA, ———, H. KAMITSUBO, A. ITO, S. TANAKA and M. IMAIZUMI: Yields and Angular Distributions of Protons from $F^{19}(d, p)F^{20}$ and $F^{19}(d, p)F^{20}$ 117
TANAKA Shigeya;
———, M. FURUKAWA, M. YAGI, S. IWATA and H. AMANO: Alpha Excitation Functions of Iron–54 (S. N.) 1251
——— and M. Furukawa: Excitation Functions for (p, n) Reactions with Titanium, Vanadium, Chromium, Iron and Nickel up to Ep=14 MeV 1269
TANAKA Shigeya;
K. ÔNO, SHIMADA, K. KURODA, O. TANAKA H. KAMITSUBO, A. ITO, ——— and M. IMAIZUMI: Yields and Angular Distributions of Protons From $F^{19}(d, p)F^{20}$ an $F^{19}(d, p)F^{20}$ 117
TANAKA Shōji;
———, M. KOBAYASHI and T. MASUMI: Anisotropic Conductivity of CdS Single Crystals (S. N.) 104
——— and T. TANAKA: Effects of Deuteron Bombardment on CdS Single Crystals (S. N.) 113
———: Elecroluminescence of ZnS Phosphors Excited by Short Field Pulses ..1123
TANAKA Tetsuro;
——— and H. KAWAMURA: Piezoelectric Effect in a Rectifying Contact of Semicondoctor (S. N.) 1455
TANAKA Toshio;
S. TANAKA and ———: Effects of Deuteron Bombardment on CdS Single Crystals (S. N) 113
T. MASUMI and ———: Elastic Stiffness Constants of Cadmiun Sulfide 1313
TANAKA Yoichi;
H. TOYODA, S. WAKU, H. SHIBATA and ———: Some Ferroelectrical Properties of Triglycine Sulfate (S. N.) 109
TANEDA Sadatoshi: Downstream Development of the Wakes behind Cylinders 843
TANISAKI Sigetosi;
———: Phase Transition in Tungsten Trioxide (S. N.) 680
———: Observation of a Peculiar Type of Domain Structure of Triclinic Tungesten Trioxide (S. N.) 970
TANUMA Seiichi;
———: Low Temperature Thermoelectric Power of Cu-Mn Alloys (S. N.) .. 541
———: Semiconducting properties of Bi-Sb Alloys (S. N.) 1246

S. MASE and ———: Measurement of Galvanomagnetic Tensor of Bismuth Single Crystals at Low Temperatures (S. N.) 1644

TAOKA Tadami;
 ———, K. YASUKŌCHI, R. HONDA and ŌYAMA: An Experimental Investigation on the Mode of Slip in Face-Centered Cubic Metals 888

TATSUMOTO Eiji;
 ——— and T. OKAMOTO: Anisotropy of Ordinary Hall Effect in Silicon Iron (S. N.) 226
 ——— and T. OKAMOTO: Extraordinary Hall Effect in Silicon-Iron Single Crystal (S. N.) 975
 ——— and T. OKAMOTO: Effective Field in the Oridinary Hall Effect in Ferromagnetics (S. N.) 976
 ——— and T. OKAMOTO: Temperature Dependence of the Magnetostriction Constants in Iron and Silicon Iron 1588

TATSUZAKI Itaru: Study of Reorientational Motion in Solid State of 1, 2, 3-trichlorobenzene and Hexachlorobenzene by Pure Quadrupole Resonance 578

TAUC Jan: On the Theory of Thermoelectricity 1174

TAWARA Yoshio;
 Y. MUTO, ———, Y. SHICUYA T. FUKUROI: Electrical Properties of Dilute Alloys of Zinc with Manganese at Low Temperature (S. N.) 380

TERANISHI Teruo;
 H. OHNISHI, ——— and S. MIYAHARA: On the Transition Temperature of Copper Ferrite (S. N.) 106

TERAO Nobuzo;
 ——— et A. BERGHEZAN: Transformation des Reseaux Metalliques sous l'Influence des Elements d'Insertion: Transformation du Nickel sous l'Influence de l'Azote 139

TODA Morikazu
 ———: On the Brownian Motion of a Classical Oscillator 722
 T. KOTERA and ———: On the Theory of Brownian Motion and Spin Relaxation .. 1475

TOHEI Tsutomu;
 M. KIMURA, N. MUTSURO, Y. OHNUKI, K. SHODA, M. SUGAWARA, ——— and H. YUTA: Measurement of Bremsstrahlung Spectra with Sodium Iodide Scintillation Crystal 387

TOI, Atsumoto;
 T. SHIBATA, ———, T. SUITA and S. KISAKA: Electrostatic Transformer Type Particle Accelerator using Ceramic BaTiO$_3$—Ferrostatic— (S. N.) 227

TOMIKI Tetsuhiko;
 ———: Electronmicroscopic Observations on the Kl Single Crystals 230
 ———: Electronmicroscopic Observations of Alkali Halide Crystals 304
 T. HIBI and ———: Electronmicroscopic Observation of the KCl Crystal Containing Potassium Colloid Particles (S. N.) 375
 T. HIBI and ———: Electronmicroscopic Observation of the Additively Coloured KCl Crystal 445
 ——— and M. UETA : Electronmicroscopic Observations of the KCl Single Crystal Irradiated with Ultra-Violet Light 602
 ———: Electronmicroscopic Observations of the Cleavage Plane of KCl Crystal—the Deformation Zone— 924
 ———: Thermal Stability of the R, N and M Centres and the Oscillator Strength of M Band of KCl Crystal (S. N.) 1114
 ———: A Ruantitative Study of the M Centre in KCl (S. N.) 1243
 T. ISHII, ——— and M. UETA: On the Preferential Bleaching of the M Band in KCl Crystal with Polarized Light 1415

TOMISHIMA Hiroshi,
 H. MIYAZAWA, H. MAEDA and ———: Lattice Scattering Mobility of Electrons on Cadmium Sulphide 41

TOMONO Yuzo;
 T. SUZUKI and ———: Precipitation Process of Carbon in Alpha-Iron 597

TOYAMA Masaharu;
T. CHIBA, ——— and Y. MORINO: Nuclear Quadrupole Resonance Spectra of N^{14} in Urea Crystal (S. N.)........ 379
———: Relative Intensities of Zeeman Components in Nuclear Quadrupole Resonance Spectrum........1727
TOYODA Hiroo
———, S. WAKU H. SHIBATA and Y. TANAKA: Some Ferroelectrical Properties of Triglycine Sulfate (S. N.)........ 109
——— and M. NAGASHIMA: Electrical Resistivity of Arc-evaporated Carbon Film........ 274
———: Etch Patterns on Ferroelectric Triglycine Sulfate (S. N.)........ 376
———, S. WAKU and H. HIRABAYASHI: Structure of Ferroelectric Domains in Triglycine Sulfate........1003
S. WAKU, H. HIRABAYASHI, ———, H. IWASAK and R. KIRIYAMA: Ferroelectricity in Potassium Ferrocyanide Trihydrate (S. N.)........ 973
TSUBOKAWA Ichiro;
———: On the Magnetic Properties of Vanadium Sulfide and Selenide........ 196
T. MIYADAI, Y. SHICHIJO and ———: Ferrimagnetic Resonance Line Width in Polycrystalline $Y_3\ Fe_{5-x},\ In_xO_{12}$ (S. N.)........ 853
——— and S. CHIBA: On the Magnetic Property of Iron Telluride (S. N.)..1120
TSUJI Mikio;
———: The Thermoelectric, Galvanomagnetic and Thermomagnetic Effects of Monovalent Metals, IV. Effect of the Non-equilibrium Distribution of the Phonons........ 618
———: Anomalous Hall Effect due to an *s-d* Interaction in the Dilule Alloys Containing the Transition Elements (S. N.)........ 686
———: Localized Electron Model and Thermoelectric Power (S. N.)........1640
TSUNEOKA Yoshikazu: $C^{12}(n, n')3\alpha$ Reaction induced by 14.8 MeV Neutrons........ 869
TSUSHIMA Kunirō;
———, M. ASANUMA and S. MIYAHARA: Time Decrease of Permeability in Silicon-Iron (S. N.)........1253
TSUTSUMI Kenjiro: The X-ray Non-Diagram Lines K. of Some Compounds of the Iron Group........1696
TUBOTA Hirosi;
——— and H. SUZUKI: Photo-voltaic Effect in Se-photocells having Artificial Intermediate Layers of CdSe, CdTe, ZnSe and ZnTe........ 38
TUTUMI Masayoshi;
A. HIKATA and ———: Changes of Ultrasonic Attenuation during Creep of Aluminum (S. N.)........ 687
UCHIDA Ichizo: Infrared Radiation from Silicon Grown Junclion (S. N.)........1831
UCHIDA Yoichi;
K. FUKUDA, H. MATSUMOTO, ——— and H. YOSHIMURA: Cyclotron Resonance in Gas Discharge (S. N.)........ 543
——— and R. KATO: Optical Studies on Thallium-activated Alkali-iodide Crystals........1408
UEMURA Yasutada;
H. MIMURA and ———: On the Electronic Structure of the U_2-Center in KCl Crystals, I........1011
UETA Masayasu;
———, M. HIRAI and H. WATANABE: Interaction of Exciton with Electron Trapping Centers in Alkali Halide Crystals 1. *F* and *U* Centers in KCl and KBr Crystals........ 253
M. YAGI and ———: The Proton Magnetic Resonance Absorption of the Trichloroacetic Acid in Solid Phase (S. N.)........ 377
——— and M. HIRAI: Interaction of Exciton with *R* Center in KCl Crystal (S. N.)........ 546
T. TOMIKI and ———: Electronmicroscopic Observations of the KCl Single Crystal Irradiated with Ultra-Violet Light........ 602

——— and T. ISHII: Luminescence of KI:TI Induced by Far Ultraviolet Light (S. N.) 857
T. ISHII, T. TOMIKI and ———: On the Preferential Bleaching of the M Band in KCl Crystal with Polarized Light 1415

UKEI Kazutoshi;
J. MIZUNO, ———, and T. SUGAWARA: The Crystal Structure of $CoCl_2\cdot 6H_2O$ (S. N.) 383

UMEDA Iwao;
I. NONAKA, H. YAMAGUCHI, T. MIKUMO, ———, T. TABATA and S. HITAKA: Angular Distributions of Protons from the Reation $^{12}C(\alpha, p)^{15}N$ 1260

USAMI Seiji;
Z. FUNATOGAWA, N. MIYATA and ———: Electric Resistance and Cation Distribution of Fe–Mn Ferrite System (S. N.) 854
Z. FUNATOGAWA, N. MIYATA and ———: Ferromagnetic Crystalline Anisotropy of Fe–Mn–Ferrite System 1583

UYEDA Ryozi;
K. ANDO, O. KAMIGAITO, Y. KAMIYA, S. TAKAHASHI and ———: Oxide-Cored Cathode 180
Y. KAMIYA, M. NONOYAMA and ———: Electron Microscopic Observation of the Superlattice in Serpentine 1334

VODIČKA Václav;
———: Some Problems on Heat Conduction in Stratiform Bodies 216
———: Stationäre Temperaturverteilung in der Wand vielschichtiger Röhrenleitungen 959

M. VENUGOPALAN: Dependence of the Joshi Effect on "Aging" under, or/and in the Absence of, Continuous Electrical Excitation (S. N.) 1833

WADA Yasaku;
, H. HIROSE, T. ASANO and S. FUKUTOMI: On the Dynamic Mechanical Properties of Polymers at Ultrasonic Frequencies in Relation to their Glass Transition Phenomena 1064

WAKABAYASHI Hisawo;
S. SONOIKE and ———: Temperature Dependence of Surface Voltage of Silver Bromide 1664

WAKATSUKI Tetsuo;
I. MIURA, ———, Y. HIRAO and E. OKADA: Gamma Rays from the Proton Bombardment of ^{24}Mg, ^{25}Mg and ^{26}Mg 239

WAKU Shigeru;
H. TOYODA, ———, H. SHIBATA and Y. TANAKA: Some Ferroelectrical Properties of Triglycine Sulfate (S. N.) 109
H. TOYODA, ——— and H. HIRABAYASHI: Structure of Ferroelectric Domains in Triglycine Sulfate 1003
———, H. HIRABAYASHI, H. TOYODA, H. IWASAKI and R. KIRIYAMA: Ferroelectricity in Potassium Ferrocyanide Trihydrate (S. N.) 973

WANG Ching Ling;
I. KUMABE, ———, M. KAWASHIMA, M. YADA and H. OGATA: Excitation Functions and Angular Distributions of the Reactions $Al^{27}(p, \alpha)Mg^{24}$ at 12.7–14.1 MeV and $Cr^{52}(p, \alpha)V^{49}$ at 9.0–14.2 MeV 713

WATANABE Denjiro;
———: On the Superstructure of the Orderd Alloy Cu_3 Pd, III. High Temperature Electron Diffraction Study 436
S. OGAWA, ———, H. WATANABE and T. KOMODA: Anti-Phase Domains in Gold-Copper-Zinc Ordered Alloys Revealed by Electron Microscope 936
M. TAKAHASHI, ———, T. SASAGAWA, H. SAITO and S. OGAWA: Magnetic Anisotropy of Evaporated Films Formed in Magnetic Field (S. N.) 1459

WATANABE Hiroshi;
———: Thermo-Remanent Magnetism La_2O_3–Fe_2O_3 and Nd_2O_3–Fe_2O_3 511
S. OGAWA, D. WATANABE, ——— and T. KOMODA: Anti-Phase Domains in Gold-Copper-Zinc Ordered Alloys Revealed by Electron Microscope 936

I. MKAMI, T. HJRONE, ———, S. MAEDA, K. ADACHI and M. YAMADA: On the Magnetic Anisotropy of a Pyrrhotite Crystal 1568
WATANABE Hiroshi;
K. KOHRA and ———: Anomalous Transmission of Electrons in a Film of Molybdenite (S. N.) 1119
———: Energy Loss of Electrons passing through a Graphite Single Crystal at Different Incident Angles (S. N.) 1453
WATANABE Hiroyuki;
M. UETA, M. HIRAI and ———: Interaction of Excition with Electron Trapping Centers in Alkali Halide Crystals 1. *F* and *U* Centers in KCl and KBr Crystals 253
WATANABE Takashi;
K. KIDO and ———: The Magnetic Investigation of Mn^{++}, Co^{++}, Cu^{++} Ammine and Anhydrate Salts 1217
WATANABE Toichi;
M. OKADA and ———: Grain Boundary Migration and Dimensional Change of Low Carbon Steel (S. N.) 107
WATANABE Toshimitsu;
G. KUWABARA, A. MISU, ———, Y. NISHIYAMA: Photoconductivity and Luminescence of the *F* and *M* centers in Potassium Chloride 1621
YABUMOTO Tadaichi: Hall Effect in Oxide Cathodes 134
YADA Keiji;
T. HIBI and ———: Successive Electromicroscopic Observation of Coloured and Bleached KCl Crystal 455
YADA Minoru;
I. KUMABE, C. L. WANG, M. KAWASHIMA, ——— and H. OGATA: Excitation Functions and Angular Distributions of the Reactions $Al^{27}(p, \alpha)Mg^{24}$ at 12.7–14.1 MeV and $Cr^{52}(p, \alpha)V^{49}$ at 9.0–14.2 MeV 713
YAGI Masashi;
——— and M. UEDA: The Proton Magnetic Resonance Absorption of the Trichloroacetic Acid in Solid Phase (S. N.) 377
YAGI Masuo;
S. TANAKA, M. FURUKAWA, ———, S. IWATA and H. AMANO: Alpha Excitations of Iron–54 (S. N.) 1251
YAMADA Kazuo;
T. KASUYA and ———: Electrical and Thermal Conductivity of Monovalent Metals; The Influences of Coulomb Interaction 416
YANADA Motohiko;
I. MIKAMI, T. HIRONE, H. WATANABE, S. MAEDA, K. ADACHI and ———: On the Magnetic Anisotropy of a Pyrrhotite Crystal 1568
YAMADAYA Tokio;
S. MIYAHARA and ———: The Aging of Permeability in Manganese-Zinc Ferrite (S. N.) 1635
YAMAGATA Yukio;
J. ITOH and ———: Nuclear Magnetic Resonance of RbBr (S. N.) 225
YAMAGUCHI Hisashi;
I. NONAKA, ———, T. MIKUMO, I. UMEDA, T. TABATA and S. HITAKA: Angular Distributions of Protons from the Reaction $^{12}C(\alpha, p)^{15}N$ 1260
YAMAGUCHI Jiro;
——— and Y. HAMAKAWA: High Electric Field Effects in Germanium *p–n* Junction 15
——— and Y. HAMAKAWA: Barrier Temperature at Turnover in Fermanium *p-n* Junction 232
YAMAGUTI Tasaburô;
———, MAKINO, S. SHINODA and I. KUROHA: Spectro-Polarization Chracteristics of the Sodium Nitrate Polarizer 199
YAMAMOTO Manabu: Spectroscopic Measurements of the Hydrogen Plasma 1739
YAMAMOTO Mikio;

T. SUZUKI and ———: Influence of Order-Disorder on Creep of a Superlattice Alloy 463

T. IWATA, M. IWATA and ———: Magnetic Annealing Effect in αFe_2O_3 (S. N.).. 855

YAMATO Misazo: Phenomenological Theory of Visco-elasticity of Three Dimensional Bodies 313

YAMANAKA Tadashi;

K. TANAKA, J. CHIKAWA and ———: Monitoring X-ray Tube Output with Ionization Chamber 1321

YAMANOUCHI Chikako;

W. SASAKI and ———: On the Anomalous Magnetoresistance Effect in n–InSb (S. N.) 849

YAMASHITA Hirosuke;

S. IBUKI and ———: Diffusion of Cu into CdS Single Crystal through Dislocations (S. N.) 1827

YAMAZAKI Masatoshi: The Electronic Structure of the Protonated Methane CH_5^+ 498

YAMAZAKI Takashi;

C. HU, K. KIKUCHI, S. KOBAYASHI, K. MATSUDA, Y. NAGAHARA, Y. ODA N. TAKANO, M. TAKEDA and ———: Elastic and Inelastic Scatteridgs of Protons from Ti, Cr, Ni, Zn and O at 8 to 14 MeV........861

YAMAZAKI Toshimitsu;

M. SAKAI, H. IKEGAMI, ——— and K. SUGIYAMA: Angular Correlation of Gamma Rays from Xe^{126} and Te^{126}........ 983

K. SUGIYAMA, H. IKEGAMI, ——— and M. SAKAI: Decay of I^{124}........ 986

YANAGAWA Sadaaki: On the Low Lying Levels of Mn^{56}, II (S. N.)........ 539

YANO Syukuro: Proton Magnetic Resonance in Hydrates of Halogen Compounds of Mg, Ca, Sr and Ba........ 942

YASUKŌCHI Kō;

T. TAOKA, ———, R. HONDA and I. ŌYAMA: An Experimental Investigation on the Mode of Slip in Face-Centered Cubic Metals........ 888

———, T. OHOYAMA and K. KANEMATSU: Antiferromagnetism of $Mn_{3.25}$ Ge (S. N.) 1820

YASUMI Shinjiro;

T. NAKAMURA, K. TAKAMATSU, K. FUKUNAGA, M. YATA and ———: Absolute Cross Sections of the (γ, n) Reaction for Cu^{63}, Zn^{64} and Ag^{109} 693

T. MAKAMURA, K. FUKUNAGA, K. TAKAMATSU, M. YATA and ———: Fine Structure in the Giant Resonance for Cu^{63} and $Ag^{107}(\alpha, n)$ Reactions (S. N.)..1117

YATA Minoru;

T. NAKAMURA, K. TAKAMATSU, K. FUKUNAGA, ——— and S. YASUMI: Absolute Cross Sections of the (γ, n) Reaction for Cu^{63}, Zn^{64} and Ag^{109} 693

T. NAKAMURA, K. FUKUNAGA, K. TAKAMATSU, ——— and S. YASUMI: Fine Structure in the Giant Resonance for Cu^{63} and $Ag^{107}(\alpha, n)$ Reactions (S. N.)..1117

YOKOTA Isaaki;

S. MIYATANI and ———: Galvano- and Thermomagnetic Effects in α–Ag_2Te.. 750

YOKOZAWA Yasaburo;

S. OGAWA and ———: Paramagnetic Resonance of Manganese in $KMgF_3$ (S. N.) 1116

YONEMITSU Hiroo;

———: Ferrimagnetic Resonance of Polycrystalline Nickel Ferrite-Chromites (S. N.) 231

———: Size Effects on the Ferrimagnetic Resonance Absorption of Polycrystalline Ferrites and Garnets (S. N.)........ 688

YOSHIDA Shigetomo;

——— and T. IKEDA: Effect of Electron Bombardment on Sodium Chloride.. 473

YOSHIDA Toshiho;

Y. FUJIKI and ———: A New Device for Measuring thickness of Evaporated Metal Film by use of X-ray Interference Fringe (S. N.) 1828

YOSHIMATSU Mitsuru;

——— and K. KOHRA: X-ray Observations of the Surface of Plastically Deformed LiF Crystals with the Berg-Barret Method (S. N.) 1249

YOSHIMORI Akio: A New Type of Antiferromagnetic Structure in the Rutile Type Crystal 807

YOSHIMURA Hisamitsu;
K. FUKUDA, H. MATUMOTO, Y. UCHIDA and ———: Cyclotron Resonance in Gas Discharge (S. N.).. 543

YOSHINAGA Hiroshi;
A. MITSUISHI, ——— and S. FUJITA: The Far Infrared Reflectivity of NaCl, KCl and KBr Crystals (S. N.) 110

YOSHINOBU Hirowo;
——— and T. KAKUTANI: Two-dimensional Stokes Flow of an Electrically Conducting Fluid in a Uniform Magnetic Field 1433

YOSHIOKA Hide;
———: On the Structure of Green Rust of Iron (S. N.) 974
——— and FUJITA: Proton Magnetic Relaxation in Solutions of a Manganous Salt..1717

YUTA Haruo;
M. KIMURA, N. MUTSURO, Y. OHNUKI, K. SHODA, M. SUGAWARA, T. TOHEI and ———: Measurement of Bremsstrahlung with Sodium Iodide Scintillation Crystal 387